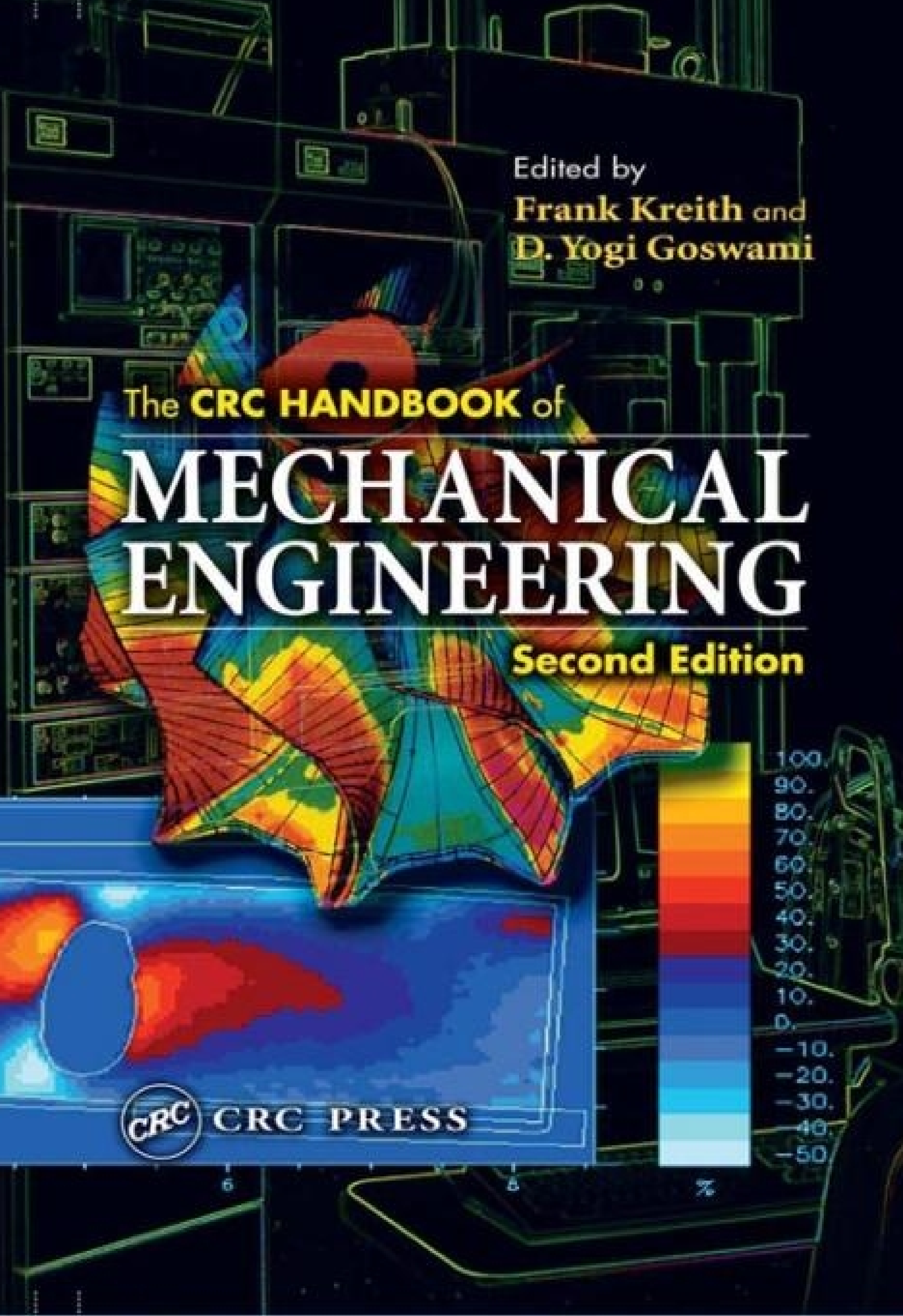

Edited by
Frank Kreith and
D. Yogi Goswami

The CRC HANDBOOK of
MECHANICAL ENGINEERING

Second Edition

CRC PRESS

The CRC HANDBOOK of

MECHANICAL ENGINEERING

SECOND EDITION

The Mechanical Engineering Handbook Series

Series Editor
Frank Kreith
Consulting Engineer

Published Titles

Air Pollution Control Technology Handbook
  Karl B. Schnelle, Jr. and Charles A. Brown
Computational Intelligence in Manufacturing Handbook
  Jun Wang and Andrew Kusiak
Fuel Cell Technology Handbook
  Gregor Hoogers
Handbook of Heating, Ventilation, and Air Conditioning
  Jan F. Kreider
Hazardous and Radioactive Waste Treatment Technologies Handbook
  Chang Ho Oh
Inverse Engineering Handbook
  Keith A. Woodbury
Opto-Mechatronic Systems Handbook: Techniques and Applications
  Hyungsuck Cho
The CRC Handbook of Mechanical Engineering, Second Edition
  Frank Kreith and D. Yogi Goswami
The CRC Handbook of Thermal Engineering
  Frank Kreith
The Handbook of Fluid Dynamics
  Richard W. Johnson
The MEMS Handbook
  Mohamed Gad-el-Hak
Biomedical Technology and Devices Handbook
  James Moore and George Zouridakis

Forthcoming Titles

Multi-Phase Flow Handbook
  Clayton T. Crowe
Shock and Vibration Handbook
  Clarence W. de Silva

The CRC HANDBOOK of

MECHANICAL ENGINEERING

SECOND EDITION

Edited by
Frank Kreith
and
D. Yogi Goswami

CRC PRESS

Boca Raton London New York Washington, D.C.

Library of Congress Cataloging-in-Publication Data

The CRC handbook of mechanical engineering / edited by Frank Kreith, Yogi Goswami. –
2nd ed.
p. cm. — (Mechanical engineering handbook series)
Includes bibliographical references and index.
ISBN 0-8493-0866-6 (alk. paper)
1. Mechanical engineering—Handbooks, manuals, etc. I. Kreith, Frank. II. Goswami, D. Yogi. III. Series.

TJ151.C73 2004
621.3—dc22 2004051970

This book contains information obtained from authentic and highly regarded sources. Reprinted material is quoted with permission, and sources are indicated. A wide variety of references are listed. Reasonable efforts have been made to publish reliable data and information, but the author and the publisher cannot assume responsibility for the validity of all materials or for the consequences of their use.

Neither this book nor any part may be reproduced or transmitted in any form or by any means, electronic or mechanical, including photocopying, microfilming, and recording, or by any information storage or retrieval system, without prior permission in writing from the publisher.

All rights reserved. Authorization to photocopy items for internal or personal use, or the personal or internal use of specific clients, may be granted by CRC Press LLC, provided that $1.50 per page photocopied is paid directly to Copyright Clearance Center, 222 Rosewood Drive, Danvers, MA 01923 USA. The fee code for users of the Transactional Reporting Service is ISBN 0-8493-0866-6/05/$0.00+$1.50. The fee is subject to change without notice. For organizations that have been granted a photocopy license by the CCC, a separate system of payment has been arranged.

The consent of CRC Press LLC does not extend to copying for general distribution, for promotion, for creating new works, or for resale. Specific permission must be obtained in writing from CRC Press LLC for such copying.

Direct all inquiries to CRC Press LLC, 2000 N.W. Corporate Blvd., Boca Raton, Florida 33431.

Trademark Notice: Product or corporate names may be trademarks or registered trademarks, and are used only for identification and explanation, without intent to infringe.

Visit the CRC Press Web site at www.crcpress.com

© 2005 by CRC Press LLC

No claim to original U.S. Government works
International Standard Book Number 0-8493-0866-6
Library of Congress Card Number 2004051970
Printed in the United States of America 1 2 3 4 5 6 7 8 9 0
Printed on acid-free paper

Preface

The purpose of the second edition of the *CRC Handbook of Mechanical Engineering* is to continue providing practicing engineers in industry, government, and academia with up-to-date information on the most important topics of modern mechanical engineering. The book covers traditional topics such as thermodynamics, solid and fluid mechanics, heat and mass transfer, materials, controls, energy conversion, manufacturing and design, robotics, environmental engineering, economics and project management, patent law, and transportation. These topics were covered in the first edition, but they have been updated, new references have been added, and efforts have been made to provide information on computer technology related to the topics at the end of each chapter.

But in the 10 years since the first edition of this handbook was published, changes have taken place in engineering and technology and additional topics that were not treated in the first edition have come to the fore. To bring the new edition up-to-date, chapters on topics such as nanotechnology, MEMS, electronic packaging, global climate change, electric and hybrid vehicles, and bioengineering have been added. Moreover, the editorial supervision for the second edition has been broadened by the addition of Yogi Goswami as co-editor.

In a work of the size of the second edition of this handbook, it is unavoidable that certain errors or omissions may have occurred. Therefore, the editors appreciate the readers calling any of these shortcomings to their attention and every effort will be made to correct them. We also welcome continuous feedback from readers about topics that may have been omitted and should be considered for inclusion in future editions of this work.

The editors would like to thank all the contributors, as well as the CRC staff, especially Helena Redshaw, Jessica Vakili, Cindy Carelli, and Susan Fox, for their assistance in the preparation of this handbook.

Frank Kreith
FKreith@aol.com

D. Yogi Goswami
Goswami@ufl.edu

Editors

Dr. Frank Kreith is Professor Emeritus of Engineering at the University of Colorado, Boulder. From 1998 to 2001 he served as the American Society of Mechanical Engineers [ASME] International Legislative Fellow for Energy and Environment at the National Conference of State Legislatures (NCSL) where he provided assistance on energy, transportation, and environmental protection to legislators in all 50 state governments. Prior to joining NCSL in 1988, Dr. Kreith was the Chief of Thermal Research at the Solar Energy Research Institute (SERI), currently the National Renewable Energy Laboratory. During his tenure at SERI, he participated in the Presidential Domestic Energy Review, served as an advisor to the Governor of Colorado, and was the editor of the *ASME Journal of Solar Energy Engineering*. In 1993, he received the first General Achievement Award from SERI.

From 1951 to 1977, Dr. Kreith taught at the University of California, Lehigh University, and the University of Colorado. He is the author of over 100 peer-reviewed articles and the author of textbooks on heat transfer, solar energy, and transportation. He is the recipient of the Charles Greeley Abbot Award from ASES and the Max Jakob Award from ASME-AIChE. In 1992, he received the Ralph Coats Roe Medal from ASME for providing technical information to legislators about energy conservation and environmental protection, and in 1997 the Washington Award for “unselfish and preeminent service in advancing human progress.” In 1998, Dr. Kreith was awarded the ASME medal for research, publications, and public service.

Dr. Kreith has served as a consultant and advisor all over the world. His assignments include consultancies to Vice Presidents Rockefeller and Gore, the U.S. Department of Energy, NATO, the U.S. Agency for International Development, and the United Nations. He is a registered professional engineer, a Life Fellow of ASME and a Fellow ASES and the American Association for the Advancement of Science [AAAS].

D. Yogi Goswami, Ph.D., P.E., is a professor of mechanical and aerospace engineering and Director of the Solar Energy and Energy Conversion Laboratory at the University of Florida, Gainesville. Dr. Goswami is internationally known for his research in fundamental and applied areas of renewable energy. He has published as an author or editor 7 books, 12 book chapters, 4 conference proceedings, and more than 100 refereed technical papers. He also holds 5 U.S. patents and 1 worldwide patent. In 2001 he received the University of Florida’s award of Research Foundation Professor.

Dr. Goswami is the Editor-in-Chief of *Advances in Solar Energy: An Annual Review of the Developments in Solar Energy,* published by the American Solar Energy Society (ASES). He is also the Editor-in-Chief of the *Solar Energy* journal, published by the International Solar Energy Society (ISES) and a past associate editor of the ASME *Journal of Solar Engineering*. Dr. Goswami has chaired a number of task forces to advise the U.S. Congress and the federal administration on energy policy. He has also made oral presentations on behalf of ISES to the United Nations charrette on world sustainable energy.

Dr. Goswami is a recognized leader in professional scientific and technical societies. He is the President of ISES and a member of the Board of Governors of the ASME International. He has also served as Senior Vice President of ASME-International (2000–2003), President of the International Association for Solar Energy Education (IASEE, 2000–2002), and a member of the Board of Directors of ISES (2000–2002). He has also served as a Vice President for Energy Resources Board of ASME-International (1989–1993), Vice President of IASEE (1998–2000), and a member of the Board of Directors of ASES (1996–2000).

Dr. Goswami is a recipient of the John Yellott Award for Solar Energy from ASME and the Charles Greely Abbott award of the ASES, and more than 20 other awards from engineering and scientific societies. He is a registered professional engineer and a fellow of ASME International and ASES.

Contributor List

Elsayed M. Afify
North Carolina State University
Raleigh, North Carolina

Talyan Altan
Ohio State University
Columbus, Ohio

William F. Ames
Georgia Institute of Technology
Atlanta, Georgia

David C. Anderson
Purdue University
West Lafayette, Indiana

Vincent W. Antonetti
Consultant
Poughkeepsie, NY

Nagaraj K. Arakere
University of Florida
Gainesville, Florida

Anthony F. Armor
Electric Power Research Institute
Palo Alto, California

Roger E. A. Arndt
University of Minnesota
Minneapolis, Minnesota

Barbara Atkinson
Lawrence Berkeley National Laboratory
Berkeley, California

Richard Bajura
West Virginia University
Morgantown, West Virginia

William W. Bathie
Iowa State University
Ames, Iowa

Kenneth J. Bell
Oklahoma State University
Stillwater, Oklahoma

Dale E. Berg
Sandia National Laboratories
Albuquerque, New Mexico

Stanley A. Berger
University of California
Berkeley, California

Arthur K. Bergles
Rensselaer Polytechnic Institute
Troy, New York

Desikan Bharathan
National Renewable Energy Laboratory
Golden, Colorado

Bharat Bhushan
Ohio State University
Columbus, Ohio

Stephen M. Birn
Moog Inc., Aircraft Group
Torrance, California

Kenneth B. Black
University of Massachusetts
Amherst, Massachusetts

Carl J. Bliem (Deceased)
CJB Consulting

Robert F. Boehm
University of Nevada
Las Vegas, Nevada

E. Richard Booser
Consultant
Vero Beach, Florida

Michael L. Brown
Harley-Davidson
Milwaukee, Wisconsin

Matthew Buczek
General Electric R & D Center
Schenectady, New York

George Cain
Georgia Institute of Technology
Atlanta, Georgia

Massimo Capobianchi
Gonzaga University
Spokane, Washington

Van P. Carey
University of California
Berkeley, California

Tien-Chien Chang
Purdue University
West Lafayette, Indiana

John C. Chen
Lehigh University
Bethlehem, Pennsylvania

Liang-Yu Chen
Ohio Aerospace Institute
NASA Glenn Research Center
Cleveland, Ohio

Stuart W. Churchill
University of Pennsylvania
Philadelphia, Pennsylvania

Wendy Clark
National Renewable Energy Laboratory
Golden, Colorado

Robert Clear
Lawrence Berkeley National Laboratory
Berkeley, California

Hugh W. Coleman
University of Alabama
Huntsville, Alabama

H.E. Cook
University of Illinois at Urbana-Champaign
Urbana, Illinois

Nevis E. Cook, Jr.
Colorado School of Mines
Golden, Colorado

Jeff R. Crandall
University of Virginia
Charlottesville, Virginia

Malcolm J. Crocker
Auburn University
Auburn, Alabama

Philip C. Crouse
Philip C. Crouse and Associates
Dallas, Texas

Peter S. Curtiss
Curtiss Engineering
Boulder, Colorado

Mark R. Cutkosky
Stanford University
Stanford, California

Andrea Denver
Lawrence Berkeley National Laboratory
Berkeley, California

Kenneth R. Diller
University of Texas
Austin, Texas

John Fildes
Northwestern University
Evanston, Illinois

John Firor
National Center for Atmospheric Research
Boulder, Colorado

William F. Fischer, III
Lanxide Corporation
Newark, Delaware

John M. Fitzgerald
University of Texas
Fort Worth, Texas

Jean-Pierre Fleurial
California Institute of Technology
Duarte, California

Dan M. Frangopol
University of Colorado
Denver, Colorado

Steven I. Freedman
Gas Research Institute
Deerfield, Illinois

Mohamed Gad-el-Hak
Virginia Commonwealth University
Richmond, Virginia

Sumit Ghosh
Stevens Institute of Technology
Hoboken, New Jersey

Bhuvenesh C. Goswami
Clemson University
Clemson, South Carolina

D. Yogi Goswami
University of Florida
Gainesville, Florida

Hank Grant
University of Oklahoma
Norman, Oklahoma

Victor A. Greenhut
Rutgers University
East Brunswick, New Jersey

Gregory W. Hall
University of Virginia
Charlottesville, Virginia

Ronald R. Hewitt Cohen
Colorado School of Mines
Golden, Colorado

K.G.T. Hollands
University of Waterloo
Waterloo, Ontario, Canada

Trevor D. Howes
University of Connecticut
Storrs, Connecticut

Shou-Heng Huang
Raytheon Appliance Tech Center
Coralville, Iowa

Iqbal Husain
University of Akron
Akron, Ohio

James D. Idol
Rutgers University
Piscataway, New Jersey

Tissa Illangasekare
Colorado School of Mines
Golden, Colorado

Herbert A. Ingley
University of Florida
Gainesville, Florida

Thomas R. Irvine, Jr. (Deceased)
State University of New York, Stony Brook
Stony Brook, New York

B. Johan Ivarsson
University of Virginia
Charlottesville, Virginia

William D. Jackson
HMJ Corporation
Kensington, Maryland

Chand K. Jotshi
AT&TL, Inc.
Gainesville, Florida

Richard L. Kautz
National Institute of Standards & Technology
Boulder, Colorado

Carl J. Kempf
NSK Ltd.
Gunma, Japan

Francis E. Kennedy
Dartmouth College
Hanover, New Hampshire

John Kern
Siemens Power Corporation
Milwaukee, Wisconsin

Jungho Kim
University of Maryland
College Park, Maryland

Nam Ho Kim
University of Florida
Gainesville, Florida

David E. Klett
North Carolina A&T State University
Greensboro, North Carolina

Yoram Koren
University of Michigan
Ann Arbor, Michigan

Steven H. Kosmatka
Portland Cement Institute
Skokie, Oregon

Jan F. Kreider
Kreider & Associates
Boulder, Colorado

Frank Kreith
University of Colorado
Boulder, Colorado

Ajay Kumar
NASA Langley Research Center
Hampton, Virginia

Ashok V. Kumar
University of Florida
Gainesville, Florida

Kam Lau
Automated Precision, Inc.
Rockville, Maryland

Zalman Lavan (Deceased)
Illinois Institute of Technology
Evanston, Illinois

Andrew C. Lee
Purdue University
West Lafayette, Indiana

Kok-Meng Lee
Georgia Institute of Technology
Atlanta, Georgia

Richard L. Lehman
Rutgers University
Piscataway, New Jersey

John Leonard II
Georgia Institute of Technology
Atlanta, Georgia

Frank L. Lewis
University of Texas at Arlington
Arlington, Texas

Alex Lezuo
Siemens Power Generation
Erlangen, Germany

Steven Y. Liang
Georgia Institute of Technology
Atlanta, Georgia

Noam Lior
University of Pennsylvania
Philadelphia, Pennsylvania

Kai Liu
University of Texas
Fort Worth, Texas

Tien-I. Liu
California State University
Sacramento, California

Sergey Edward Lyshevski
Rochester Institute of Technology
Rochester, New York

Marc J. Madou
University of California
Irvine, California

Roop L. Mahajan
University of Colorado
Boulder, Colorado

Ioan Marinescu
Kansas State University
Manahattan, Kansas

Alan T. McDonald
Purdue University
West Lafayette, Indiana

James E. McMahon
Lawrence Berkeley National Laboratory
Berkeley, California

Mehran Mehregany
Case Western Reserve University
Cleveland, Ohio

Michael Merker
American Society of Mechanical Engineers
New York, New York

Michael D. Meyer
Georgia Institute of Technology
Atlanta, Georgia

Anthony F. Mills
University of California
Los Angeles, California

Gregory L. Mines
Idaho National Engineering Laboratory
Idaho Falls, Idaho

Michael F. Modest
The Pennsylvania State University
University Park, Pennsylvania

Robert J. Moffat
Stanford University
Stanford, California

Michael J. Moran
The Ohio State University
Columbus, Ohio

Takeo Nakagawa
Fine Tech Corporation
Tokyo, Japan

Ronald M. Nelson
Iowa State University
Ames, Iowa

Paul Norton
National Renewable Energy Laboratory
Golden, Colorado

Andrew D. Oliver
Sandia National Laboratories
Albuquerque, New Mexico

Ralph P. Overend
National Renewable Energy Laboratory
Golden, Colorado

Roberto Pagano (Deceased)
University of Florida
Gainesville, Florida

Chan S. Park
Auburn University
Auburn, Alabama

John A. Pearce
University of Texas
Austin, Texas

Ira Pence
Georgia Institute of Technology
Atlanta, Georgia

George A. Peters
Peters & Peters
Santa Monica, California

Walter D. Pilkey
University of Virginia
Charlottesville, Virginia

David W. Plummer
Sandia National Laboratories
Albuquerque, New Mexico

John W. Priest
University of Texas
Dallas, Texas

Ari Rabl
Ecole des Mines de Paris
Paris, France

George Raithby
University of Waterloo
Waterloo, Ontario, Canada

Srihari Rajgopal
Case Western Reserve University
Cleveland, Ohio

K.P. Rajurkar
University of Nebraska–Lincoln
Lincoln, Nebraska

Mysore L. Ramalingam
UES, Inc.
Dayton, Ohio

Marshall J. Reed
U.S. Department of Energy
Washington, D.C.

Kitt C. Reinhardt
Air Force Research Laboratory
Kirtland AFB, New Mexico

Rolf D. Reitz
University of Wisconsin
Madison, Wisconsin

Joel L. Renner
Idaho National Engineering Laboratory
Idaho Falls, Idaho

Robert Reuther
U.S. Department of Energy
Morgantown, West Virginia

Alan Ridilla
General Electric R & D Center
Schenectady, New York

Giorgio Rizzoni
The Ohio State University
Columbus, Ohio

Ryan Roloff
Honeywell, Engines, Systems and Services
Tempe, Arizona

Bela I. Sandor
University of Wisconsin
Madison, Wisconsin

Robert E. Schafrik
National Research Council
Washington, D.C.

Paul Schonfeld
University of Maryland
College Park, Maryland

Ramesh K. Shah
Rochester Institute of Technology
Rochester, New York

Thomas E. Shannon
University of Tennessee
Knoxville, Tennessee

Thomas B. Sheridan
Massachusetts Institute of Technology
Cambridge, Massachusetts

Sherif A. Sherif
University of Florida
Gainesville, Florida

Paul W. Shuldiner
University of Massachusetts
Amherst, Massachusetts

Scott Smith
University of North Carolina
Charlotte, North Carolina

W. Glenn Steele, Jr.
Mississippi State University
Mississippi State, Mississippi

G.T. Stevens, Jr.
Univeristy of Texas, Arlington
Arlington, Texas

William B. Stine
California State Polytechnic University
Pasadena, California

Daniel J. Strange
Alfred University
Tucson, Arizona

Nam P. Suh
Massachusetts Institute of Technology
Amherst, Massachusetts

N.V. Suryanarayana
Michigan Technological University
Houghton, Michigan

Larry W. Swanson
GE EER
Irvine, California

Yashitsuga Taketomi
NSK Ltd.
Gunma, Japan

J.M.A. Tanchoco
Purdue University
West Lafayette, Indiana

Donald D. Tippett
University of Alabama in Huntsville
Huntsville, Alabama

Jessica Todd
University of Colorado
Boulder, Colorado

M. Tomizuka
University of California
Berkeley, California

Y.L. Tong
Georgia Institute of Technology
Atlanta, Georgia

James S. Tulenko
University of Florida
Gainesville, Florida

Blake P. Tullis
Utah State University
Logan, Utah

J. Paul Tullis
Tullis Engineering Consultants
Logan, Utah

Jonathan W. Valvano
University of Texas
Austin, Texas

Ian D. Walker
Clemson University
Clemson, South Carolina

Chris Wang
IBM
Tampa, Florida

Shan K. Wang
Consultant
Alhambra, California

W.M.Wang
University of Nebraska–Lincoln
Lincoln, Nebraska

Weiping Wang
General Electric R & D Center
Schenectady, New York

John Webster
University of Connecticut
Storrs, Connecticut

Walter T. Welford (Deceased)
Imperial College of London
London, England

Frank M. White
University of Rhode Island
Narragansett, Rhode Island

Donald F. Wilcock (Deceased)
Tribolock, Inc.

Roland Winston
University of California
Merced, California

C. Channy Wong
Sandia National Laboratory
Albuquerque, New Mexico

Stephen Wood
Florida Institute of Technology
Melbourne, Florida

Lynn L. Wright
Oak Ridge National Laboratory
Oak Ridge, Tennessee

Toskiaki Yamaguchi
NSK Ltd.
Gunma, Japan

Su-Hsia Yang
Purdue University
West Lafayette, Indiana

Darrin J. Young
Case Western Reserve University
Cleveland, Ohio

Thomas H. Young
Merchant & Gould, P.C.
Denver, Colorado

Federica Zangrando
National Renewable Energy Laboratory
Golden, Colorado

Paolo Zannetti
The EnviroComp Institute
Fremont, California

Chen Zhou
Georgia Institute of Technology
Atlanta, Georgia

Hong Zhou
University of California
Irvine, California

Christian A. Zorman
Case Western Reserve University
Cleveland, Ohio

Phillip J. Zulueta
Jet Propulsion Laboratory
Pasadena, California

Table of Contents

Chapter 1 Mechanics of Solids *Bela I. Sandor*

Chapter 2 Engineering Thermodynamics *Michael J. Moran*

Chapter 3 Fluid Mechanics *Frank Kreith*

Chapter 4 Heat and Mass Transfer ***Frank Kreith***

Chapter 5 Electrical Engineering ***Giorgio Rizzoni***

Chapter 14 Robotics *Frank Lewis*

Chapter 15 MEMS Technology *Mohamed Gad-el-Hak*

Chapter 16 Environmental Engineering
Ari Rabl and Jan F. Kreider

Chapter 17 Engineering Economics and Project Management
Chan S. Park and Donald D. Tippett

Chapter 18 Nanotechnology *Sergey Edward Lyshevski*

Chapter 19 Mathematics *William F. Ames and George Cain*

Chapter 20 Patent Law and Miscellaneous Topics *Frank Kreith*

Appendices ***Paul Norton***

1

Mechanics of Solids

Bela I. Sandor
University of Wisconsin–Madison

Ryan Roloff
Honeywell

Stephen M. Birn
Moog Inc., Aircraft Group

Michael L. Brown
Harley-Davidson

1.1 Introduction

Bela I. Sandor

Engineers use the concepts and methods of mechanics of solids in designing and evaluating tools, machines, and structures ranging from wrenches to cars to spacecraft. The required educational background for these includes courses in statics, dynamics, mechanics of materials, and related subjects. For example, knowledge of dynamics of rigid bodies is needed in generalizing the spectrum of service loads on a car, which is essential

---

Professor Sandor wishes to acknowledge the contributions made by Richard C. Duveneck, Ian K. Glasgow, David A. Jahnke, Maan H. Jawad, and Christopher J. Watson.

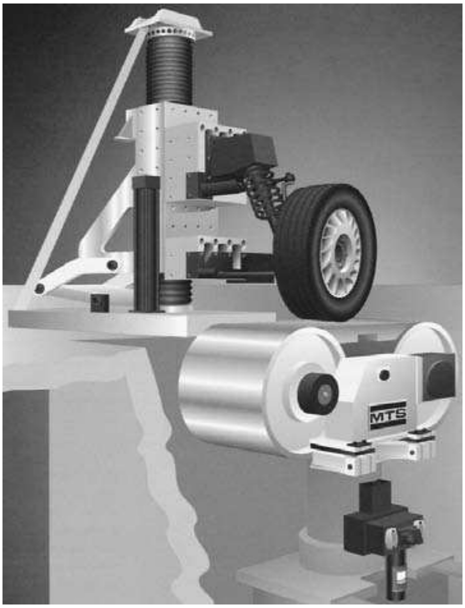

FIGURE 1.1.1 (See Color Figure 1.) Artist's concept of a moving stainless steel roadway to drive the suspension system through a spinning, articulated wheel, simulating three-dimensional motions and forces. (MTS Systems Corp., Minneapolis, MN. With permission.) Notes: Flat-Trac® Roadway Simulator, R&D100 Award-winning system in 1993.

in defining the vehicle's deformations and long-term durability. In regard to structural integrity and durability, the designer should think not only about preventing the catastrophic failures of products, but also of customer satisfaction. For example, a car with gradually loosening bolts (which is difficult to prevent in a corrosive and thermal and mechanical cyclic loading environment) is a poor product because of safety, vibration, and noise problems. Sophisticated methods are available to assure a product's performance and reliability, as exemplified in Figure 1.1.1. A similar but even more realistic test setup is shown in Color Figure 1.[1]

It is common experience among engineers that they need to review some old knowledge or learn something new because what they needed at the moment is not at their fingertips. This chapter may help in such a situation. Within the constraints of a single book on mechanical engineering, it provides overviews of topics with modern perspectives; illustrations of typical applications; modeling to solve problems quantitatively with realistic simplifications; equations and procedures; useful hints and reminders of common errors; trends of relevant material and mechanical system behaviors; and references to additional information.

This chapter is like an emergency toolbox. It includes a coherent assortment of basic tools, such as vector expressions useful for calculating bending stresses caused by a three-dimensional force system on a shaft, and sophisticated methods, such as life prediction of components using fracture mechanics and modern measurement techniques. In many cases much more information should be considered than is covered in this chapter.

1.2 Statics

Bela I. Sandor and Ryan J. Roloff

Vectors. Equilibrium of Particles. Free-Body Diagrams

Two kinds of quantities are used in engineering mechanics. A scalar quantity has only magnitude (mass, time, temperature, etc.). A vector quantity has magnitude and direction (force, velocity, etc.). Vectors are

---

[1] Color figures follow page **1**-104.

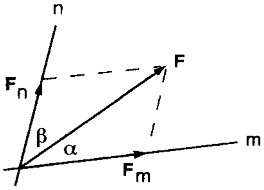

FIGURE 1.2.1 Components $\mathbf{F}_m$ and $\mathbf{F}_n$ of the vector **F**.

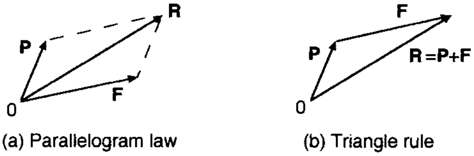

(a) Parallelogram law (b) Triangle rule

FIGURE 1.2.2 Addition of concurrent vectors **F** and **P**.

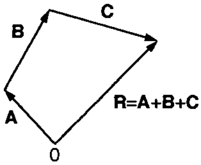

FIGURE 1.2.3 Addition of concurrent vectors **A**, **B**, and **C**.

represented here by arrows and bold-face symbols and are used in analysis according to universally applicable rules that facilitate calculations in a variety of problems. The vector methods are indispensable in three-dimensional mechanics analyses; however, in simple cases, equivalent scalar calculations are sufficient.

Vector Components and Resultants. Parallelogram Law

A given vector **F** may be replaced by two or three other vectors that have the same net effect and representation. This is illustrated for the chosen directions *m* and *n* for the components of **F** in two dimensions (Figure 1.2.1). Conversely, two concurrent vectors **F** and **P** of the same units may be combined to get a resultant **R** (Figure 1.2.2).

Any set of components of a vector **F** must satisfy the *parallelogram law*. According to Figure 1.2.1, the laws of sines and cosines may be useful:

$$\frac{F_n}{\sin\alpha} = \frac{F_m}{\sin\beta} = \frac{F}{\sin\left[180° - (\alpha+\beta)\right]}$$
$$F^2 = F_n^2 + F_m^2 - 2F_nF_m\cos\left[180° - (\alpha+\beta)\right] \tag{1.2.1}$$

Any number of concurrent vectors may be summed, mathematically or graphically, and in any order, using the preceding concepts (see Figure 1.2.3).

Unit Vectors

Mathematical manipulations of vectors are greatly facilitated by the use of unit vectors. A unit vector **n** has a magnitude of unity and a defined direction. The most useful of these are the unit coordinate vectors **i**, **j**, and **k** as shown in Figure 1.2.4. The three-dimensional components and associated quantities of a vector **F** are shown in Figure 1.2.5. The unit vector **n** is collinear with **F**.

The vector **F** is written in terms of its scalar components and the unit coordinate vectors,

$$\mathbf{F} = F_x\mathbf{i} + F_y\mathbf{j} + F_z\mathbf{k} = F\mathbf{n} \tag{1.2.2}$$

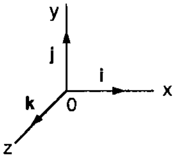

FIGURE 1.2.4 Unit vectors in Cartesian coordinates (the same **i**, **j**, and **k** set applies in a parallel **x′y′z′** system of axes).

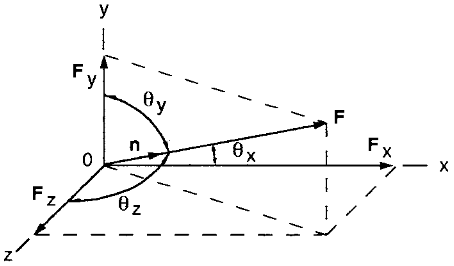

FIGURE 1.2.5 Three-dimensional components of a vector **F**.

where

$$F_x = F\cos\theta_x \quad F_y = F\cos\theta_y \quad F_z = F\cos\theta_z$$

$$F = \sqrt{F_x^2 + F_y^2 + F_z^2}$$

$$n_x = \cos\theta_x \quad n_y = \cos\theta_y \quad n_z = \cos\theta_z$$

$$n_x^2 + n_y^2 + n_z^2 = 1$$

$$\frac{n_x}{F_x} = \frac{n_y}{F_y} = \frac{n_z}{F_z} = \frac{1}{F}$$

The unit vector notation is convenient for the summation of concurrent vectors in terms of scalar or vector components:

Scalar components of the resultant **R**:

$$R_x = \sum F_x \qquad R_y = \sum F_y \qquad R_z = \sum F_z \tag{1.2.3}$$

Vector components:

$$\mathbf{R}_x = \sum \mathbf{F}_x = \sum F_x\mathbf{i} \qquad \mathbf{R}_y = \sum \mathbf{F}_y = \sum F_y\mathbf{j} \qquad \mathbf{R}_z = \sum \mathbf{F}_z = \sum F_z\mathbf{k} \tag{1.2.4}$$

Vector Determination from Scalar Information

A force, for example, may be given in terms of its magnitude *F*, its sense of direction, and its line of action. Such a force can be expressed in vector form using the coordinates of any two points on its line of action. The vector sought is

$$\mathbf{F} = F_x\mathbf{i} + F_y\mathbf{j} + F_z\mathbf{k} = F\mathbf{n}$$

The method is to find **n** on the line of points $A(x_1, y_1, z_1)$ and $B(x_2, y_2, z_2)$:

$$\mathbf{n} = \frac{\text{vector A to B}}{\text{distance A to B}} = \frac{d_x\mathbf{i} + d_y\mathbf{j} + d_z\mathbf{k}}{\sqrt{d_x^2 + d_y^2 + d_z^2}}$$

where $d_x = x_2 - x_1$, $d_y = y_2 - y_1$, $d_z = z_2 - z_1$.

Scalar Product of Two Vectors. Angles and Projections of Vectors

The scalar product, or dot product, of two concurrent vectors **A** and **B** is defined by

$$\mathbf{A} \cdot \mathbf{B} = AB\cos\phi \tag{1.2.5}$$

where **A** and **B** are the magnitudes of the vectors and ϕ is the angle between them. Some useful expressions are

$$\mathbf{A} \cdot \mathbf{B} = \mathbf{B} \cdot \mathbf{A} = A_xB_x + A_yB_y + A_zB_z$$

$$\phi = \arccos\frac{A_xB_x + A_yB_y + A_zB_z}{AB}$$

The projection F' of a vector **F** on an arbitrary line of interest is determined by placing a unit vector **n** on that line of interest, so that

$$F' = \mathbf{F} \cdot \mathbf{n} = F_xn_x + F_yn_y + F_zn_z$$

Equilibrium of a Particle

A particle is in **equilibrium** when the resultant of all forces acting on it is zero. In such cases, the algebraic summation of rectangular scalar components of forces is valid and convenient:

$$\sum F_x = 0 \qquad \sum F_y = 0 \qquad \sum F_z = 0 \tag{1.2.6}$$

Free-Body Diagrams

Unknown forces may be determined readily if a body is in equilibrium and can be modeled as a particle. The method involves **free-body diagrams**, which are simple representations of the actual bodies. The appropriate model is imagined to be isolated from all other bodies, with the significant effects of other bodies shown as force vectors on the free-body diagram.

Example 1

A mast has three guy wires. The initial tension in each wire is planned to be 200 lb. Determine whether this is feasible to hold the mast vertical (Figure 1.2.6).

Solution. The three tensions of known magnitude (200 lb) must be written as vectors.

$$\mathbf{R} = \mathbf{T}_{AB} + \mathbf{T}_{AC} + \mathbf{T}_{AD}$$

$$\mathbf{T}_{AB} = (\text{tension } AB)(\text{unit vector } A \text{ to } B) = 200\text{ lb }\mathbf{n}_{AB} = 200\text{ lb }\frac{\left(d_x\mathbf{i} + d_y\mathbf{j} + d_z\mathbf{k}\right)}{d}$$

$$= \frac{200\text{ lb}}{\sqrt{5^2 + 10^2 + 4^2}}(-5\mathbf{i} - 10\mathbf{j} + 4\mathbf{k})\frac{\text{ft}}{\text{ft}} = -84.2\text{ lb }\mathbf{i} - 168.4\text{ lb }\mathbf{j} + 67.4\text{ lb }\mathbf{k}$$

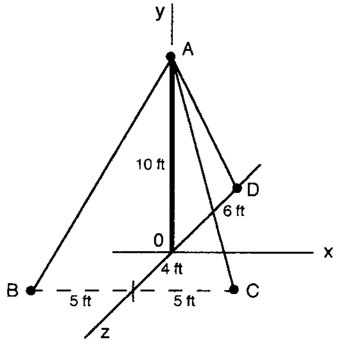

FIGURE 1.2.6 A mast with guy wires.

$$\mathbf{T}_{AC} = \frac{200\text{ lb}}{11.87\text{ ft}}(5\mathbf{i} - 10\mathbf{j} + 4\mathbf{k})\text{ ft} = 84.2\text{ lb }\mathbf{i} + 168.4\text{ lb }\mathbf{j} + 67.4\text{ lb }\mathbf{k}$$

$$\mathbf{T}_{AD} = \frac{200\text{ lb}}{11.66\text{ ft}}(0\mathbf{i} - 10\mathbf{j} + 6\mathbf{k})\text{ ft} = -171.5\text{ lb }\mathbf{j} - 102.9\text{ lb }\mathbf{k}$$

The resultant of the three tensions is

$$\mathbf{R} = \sum F_x\mathbf{i} + \sum F_y\mathbf{j} + \sum F_z\mathbf{k} = (-84.2 + 84.2 + 0)\text{ lb }\mathbf{i} + (-168.4 - 168.4 - 171.5)\text{ lb }\mathbf{j}$$

$$+ (67.4 + 67.4 - 102.9)\text{ lb }\mathbf{k} = 0\text{ lb }\mathbf{i} - 508\text{ lb }\mathbf{j} + 31.9\text{ lb }\mathbf{k}$$

There is a horizontal resultant of 31.9 lb at *A*, so the mast would not remain vertical.

Forces on Rigid Bodies

All solid materials deform when forces are applied to them, but often it is reasonable to model components and structures as rigid bodies, at least in the early part of the analysis. The forces on a rigid body are generally not concurrent at the center of mass of the body, which cannot be modeled as a particle if the force system tends to cause body rotation.

Moment of a Force

The turning effect of a force on a body is called the moment of the force, or torque. The moment M_A of a force **F** about a point *A* is defined as a scalar quantity

$$M_A = Fd \tag{1.2.7}$$

where *d* (the moment arm or lever arm) is the nearest distance from *A* to the line of action of **F**. This nearest distance may be difficult to determine in a three-dimensional scalar analysis; a vector method is needed in that case.

Equivalent Forces

Sometimes the equivalence of two forces must be established for simplifying the solution of a problem. The necessary and sufficient conditions for the equivalence of forces **F** and **F′** are that they have the same magnitude, direction, line of action, and moment on a given rigid body in static equilibrium. Thus,

$$\mathbf{F} = \mathbf{F}' \quad \text{and} \quad M_A = M'_A$$

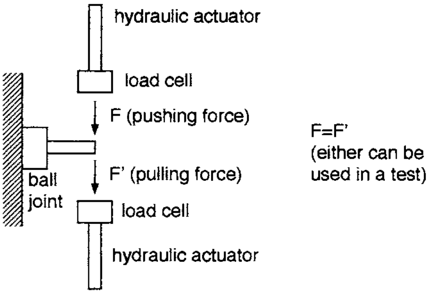

FIGURE 1.2.7 Schematic of testing a ball joint of a car.

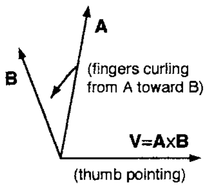

FIGURE 1.2.8 Right-hand rule for vector products.

For example, the ball joint *A* in Figure 1.2.7 experiences the same moment whether the vertical force is pushing or pulling downward on the yoke pin.

Vector Product of Two Vectors

A powerful method of vector mechanics is available for solving complex problems such as the moment of a force in three dimensions. The vector product (or cross product) of two concurrent vectors **A** and **B** is defined as the vector $\mathbf{V} = \mathbf{A} \times \mathbf{B}$ with the following properties:

1. **V** is perpendicular to the plane of vectors **A** and **B**.
2. The sense of **V** is given by the right-hand rule (Figure 1.2.8).
3. The magnitude of **V** is $\mathbf{V} = \mathbf{AB} \sin q$, where q is the angle between **A** and **B**.
4. $\mathbf{A} \times \mathbf{B} \sum \mathbf{B} \times \mathbf{A}$, but $\mathbf{A} \times \mathbf{B} = -(\mathbf{B} \times \mathbf{A})$.
5. For three vectors, $\mathbf{A} \times (\mathbf{B} + \mathbf{C}) = \mathbf{A} \times \mathbf{B} + \mathbf{A} \times \mathbf{C}$.

The vector product is calculated using a determinant,

$$\mathbf{V} = \begin{vmatrix} \mathbf{i} & \mathbf{j} & \mathbf{k} \\ A_x & A_y & A_z \\ B_x & B_y & B_z \end{vmatrix} = A_y B_z \mathbf{i} + A_z B_x \mathbf{j} + A_x B_y \mathbf{k} - A_y B_x \mathbf{k} - A_x B_z \mathbf{j} - A_z B_y \mathbf{i} \tag{1.2.8}$$

Moment of a Force about a Point

The vector product is very useful in determining the moment of a force **F** about an arbitrary point *O*. The vector definition of moment is

$$\mathbf{M}_O = \mathbf{r} \times \mathbf{F} \tag{1.2.9}$$

where **r** is the position vector from point *O* to any point on the line of action of **F**. A double arrow is often used to denote a moment vector in graphics.

The moment $\mathbf{M}_O$ may have three scalar components, M_x, M_y, M_z, which represent the turning effect of the force **F** about the corresponding coordinate axes. In other words, a single force has only one moment about a given point, but this moment may have up to three components with respect to a coordinate system,

$$\mathbf{M}_O = M_x\mathbf{i} + M_y\mathbf{j} + M_z\mathbf{k}$$

Triple Products of Three Vectors

Two kinds of products of three vectors are used in engineering mechanics. The *mixed triple product* (or scalar product) is used in calculating moments. It is the dot product of vector **A** with the vector product of vectors **B** and **C**,

$$\mathbf{A}\cdot(\mathbf{B}\times\mathbf{C}) = \begin{vmatrix} A_x & A_y & A_z \\ B_x & B_y & B_z \\ C_x & C_y & C_z \end{vmatrix} = A_x\left(B_yC_z - B_zC_y\right) + A_y\left(B_zC_x - B_xC_z\right) + A_z\left(B_xC_y - B_yC_x\right) \quad (1.2.10)$$

The *vector triple product* $(\mathbf{A}\times\mathbf{B})\times\mathbf{C} = \mathbf{V}\times\mathbf{C}$ is easily calculated (for use in dynamics), but note that

$$(\mathbf{A}\times\mathbf{B})\times\mathbf{C} \neq \mathbf{A}\times(\mathbf{B}\times\mathbf{C})$$

Moment of a Force about a Line

It is common that a body rotates about an axis. In that case, the moment M_ℓ, of a force F about the axis, say line, ℓ, is usefully expressed as

$$\mathbf{M}_\ell = \mathbf{n}\cdot\mathbf{M}_O = \mathbf{n}\cdot(\mathbf{r}\times\mathbf{F}) = \begin{vmatrix} n_x & n_y & n_z \\ r_x & r_y & r_z \\ F_x & F_y & F_z \end{vmatrix} \quad (1.2.11)$$

where **n** is a unit vector along the line, ℓ, and **r** is a position vector from point O on ℓ, to a point on the line of action of **F**. Note that M_ℓ is the projection of $\mathbf{M}_O$ on line, ℓ.

Special Cases

- The moment about a line ℓ is zero when the line of action of **F** intersects ℓ (the moment arm is zero).
- The moment about a line ℓ is zero when the line of action of **F** is parallel to ℓ (the projection of $\mathbf{M}_O$ on ℓ is zero).

Moment of a Couple

A pair of forces equal in magnitude, parallel in lines of action, and opposite in direction is called a *couple*. The magnitude of the moment of a couple is

$$M = Fd$$

where d is the distance between the lines of action of the forces of magnitude F.

The moment of a couple is a free vector **M** that can be applied anywhere to a rigid body with the same turning effect, as long as the direction and magnitude of **M** are the same. In other words, a couple vector can be moved to any other location on a given rigid body if it remains parallel to its original position (equivalent couples). Sometimes a curled arrow in the plane of the two forces is used to denote a couple, instead of the couple vector **M**, which is perpendicular to the plane of the two forces.

Force-Couple Transformations

Sometimes it is advantageous to transform a force to a force system acting at another point, or vice versa. This method is illustrated in Figure 1.2.9.

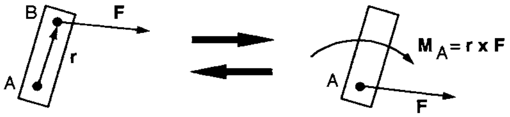

FIGURE 1.2.9 Force-couple transformations.

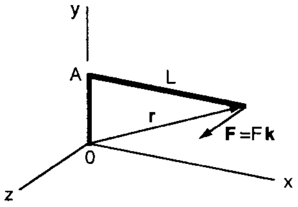

FIGURE 1.2.10 Model of a torque wrench.

1. A force **F** acting at B on a rigid body can be replaced by the same force **F** acting at A and a moment $\mathbf{M}_A = \mathbf{r} \times \mathbf{F}$ about A.
2. A force **F** and moment $\mathbf{M}_A$ acting at A can be replaced by a force **F** acting at B for the same total effect on the rigid body.

Simplification of Force Systems

Any force system on a rigid body can be reduced to an equivalent system of a resultant force **R** and a resultant moment $\mathbf{M}_R$. The **equivalent force-couple system** is formally stated as

$$\mathbf{R} = \sum_{i=1}^{n} \mathbf{F}_i \quad \text{and} \quad \mathbf{M}_R = \sum_{i=1}^{n} \mathbf{M}_i = \sum_{i=1}^{n} \left(\mathbf{r}_i \times \mathbf{F}_i\right) \tag{1.2.12}$$

where $\mathbf{M}_R$ depends on the chosen reference point.

Common Cases

- The resultant force is zero, but there is a resultant moment: $\mathbf{R} = 0$, $\mathbf{M}_R \neq 0$.
- Concurrent forces (all forces act at one point): $\mathbf{R} \neq 0$, $\mathbf{M}_R = 0$.
- Coplanar forces: $\mathbf{R} \neq 0$, $\mathbf{M}_R \neq 0$. $\mathbf{M}_R$ is perpendicular to the plane of the forces.
- Parallel forces: $\mathbf{R} \neq 0$, $\mathbf{M}_R \neq 0$. $\mathbf{M}_R$ is perpendicular to **R**.

Example 2

The torque wrench in Figure 1.2.10 has an arm of constant length L but a variable socket length $d = OA$ because of interchangeable tool sizes. Determine how the moment applied at point O depends on the length d for a constant force **F** from the hand.

Solution. Using $\mathbf{M}_O = \mathbf{r} \times \mathbf{F}$ with $\mathbf{r} = L\mathbf{i} + d\mathbf{j}$ and $\mathbf{F} = F\mathbf{k}$ in Figure 1.2.10,

$$\mathbf{M}_O = (L\mathbf{i} + d\mathbf{j}) \times F\mathbf{k} = Fd\mathbf{i} - FL\mathbf{j}$$

Judgment of the Result

According to a visual analysis, the wrench should turn clockwise, so the **–j** component of the moment is justified. Looking at the wrench from the positive x direction, point A has a tendency to rotate counterclockwise. Thus, the **i** component is correct using the right-hand rule.

Equilibrium of Rigid Bodies

The concept of equilibrium is used for determining unknown forces and moments of forces that act on or within a rigid body or system of rigid bodies. The equations of equilibrium are the most useful equations in the area of statics, and they are also important in dynamics and mechanics of materials. The drawing of appropriate free-body diagrams is essential for the application of these equations.

Conditions of Equilibrium

A rigid body is in static equilibrium when the equivalent force-couple system of the external forces acting on it is zero. In vector notation, this condition is expressed as

$$\begin{aligned} \sum \mathbf{F} &= 0 \\ \sum \mathbf{M}_O &= \sum (\mathbf{r} \times \mathbf{F}) = 0 \end{aligned} \tag{1.2.13}$$

where O is an arbitrary point of reference.

In practice it is often most convenient to write Equation (1.2.13) in terms of rectangular scalar components,

$$\begin{aligned} \sum F_x &= 0 \qquad \sum M_x = 0 \\ \sum F_y &= 0 \qquad \sum M_y = 0 \\ \sum F_z &= 0 \qquad \sum M_z = 0 \end{aligned}$$

Maximum Number of Independent Equations for One Body

1. One-dimensional problem: $\sum F = 0$
2. Two-dimensional problem:

$$\begin{aligned} &\sum F_x = 0 \qquad \sum F_y = 0 \qquad \sum M_A = 0 \\ \text{or} \quad &\sum F_x = 0 \qquad \sum M_A = 0 \qquad \sum M_B = 0 \qquad (x \text{ axis not} \perp \text{AB}) \\ \text{or} \quad &\sum M_A = 0 \qquad \sum M_B = 0 \qquad \sum M_C = 0 \qquad (AB \text{ not } \parallel \text{BC}) \end{aligned}$$

3. Three-dimensional problem:

$$\begin{aligned} &\sum F_x = 0 \qquad \sum F_y = 0 \qquad \sum F_z = 0 \\ &\sum M_x = 0 \qquad \sum M_y = 0 \qquad \sum M_z = 0 \end{aligned}$$

where xyz are orthogonal coordinate axes, and A, B, C are particular points of reference.

Calculation of Unknown Forces and Moments

In solving for unknown forces and moments, always draw the free-body diagram first. Unknown external forces and moments must be shown at the appropriate places of action on the diagram. The directions of unknowns may be assumed arbitrarily, but should be done consistently for systems of rigid bodies. A

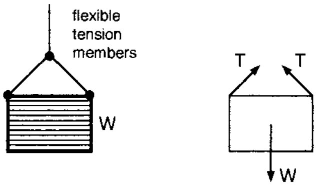

(a) sketch of setup (b) free-body diagram

FIGURE 1.2.11 Example of two-dimensional modeling.

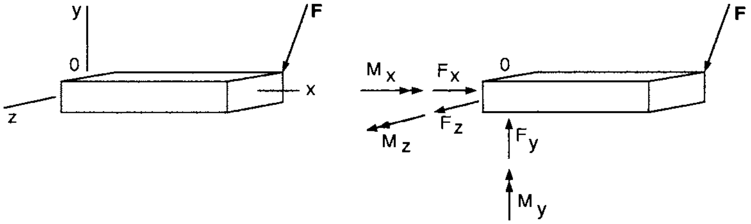

(a) cantilever beam with unsymmetric loading (b) free-body diagram

FIGURE 1.2.12 Example of three-dimensional modeling.

negative answer indicates that the initial assumption of the direction was opposite to the actual direction. Modeling for problem solving is illustrated in Figure 1.2.11 and Figure 1.2.12.

Notes on Three-Dimensional Forces and Supports

Each case should be analyzed carefully. Sometimes a particular force or moment is possible in a device, but it must be neglected for most practical purposes. For example, a very short sleeve bearing cannot support significant moments. A roller bearing may be designed to carry much larger loads perpendicular to the shaft than along the shaft.

Related Free-Body Diagrams

When two or more bodies are in contact, separate free-body diagrams may be drawn for each body. The mutual forces and moments between the bodies are related according to Newton's third law (action and reaction). The directions of unknown forces and moments may be arbitrarily assumed in one diagram, but these initial choices affect the directions of unknowns in all other related diagrams. The numbers of unknowns and of usable equilibrium equations increase with the number of related free-body diagrams.

Schematic Example in Two Dimensions (Figure 1.2.13)

Given: F_1, F_2, F_3, M
Unknowns: P_1, P_2, P_3, and forces and moments at joint A (rigid connection)

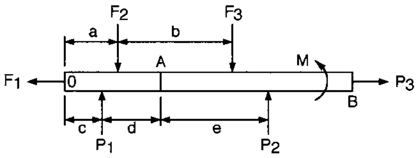

FIGURE 1.2.13 Free-body diagram.

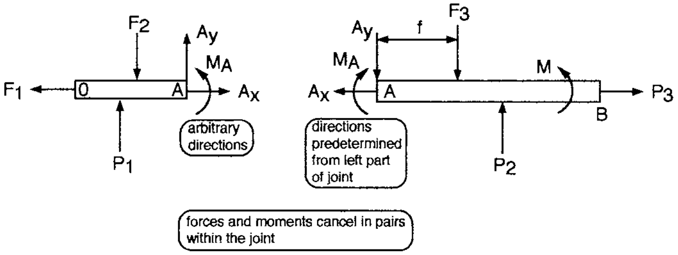

FIGURE 1.2.14 Related free-body diagrams.

Equilibrium Equations

$$\sum F_x = -F_1 + P_3 = 0$$

$$\sum F_y = P_1 + P_2 - F_2 - F_3 = 0$$

$$\sum M_O = P_1 c + P_2(c + d + e) + M - F_2 a - F_3(a + b) = 0$$

Three unknowns (P_1, P_2, P_3) are in three equations.

Related Free-Body Diagrams (Figure 1.2.14)

Dimensions a, b, c, d, and e of Figure 1.2.13 are also valid here.

New Set of Equilibrium Equations

Left part: (OA)

$$\sum F_x = -F_1 + A_x = 0$$

$$\sum F_y = P_1 + A_y - F_2 = 0$$

$$\sum M_O = P_1 c + A_y(c + d) + M_A - F_2 a = 0$$

Right side: (AB)

$$\sum F_x = -A_x + P_3 = 0$$

$$\sum F_y = P_2 - A_y - F_3 = 0$$

$$\sum M_A = -M_A + P_2 e + M - F_3 f = 0$$

Six unknowns (P_1, P_2, P_3, A_x, A_y, M_A) are in six equations. Note that, in the first diagram (Figure 1.2.13), the couple M may be moved anywhere from O to B. M is not shown in the second diagram (O to A) because it is shown in the third diagram (in which it may be moved anywhere from A to B).

Example 3

The arm of a factory robot is modeled as three bars (Figure 1.2.15) with coordinates A: (0.6, –0.3, 0.4) m; B: (1, –0.2, 0) m; and C: (0.9, 0.1, –0.25) m. The weight of the arm is represented by $\mathbf{W}_A = -60$ N$\mathbf{j}$ at A, and $\mathbf{W}_B = -40$ N$\mathbf{j}$ at B. A moment $\mathbf{M}_C = (100\mathbf{i} - 20\mathbf{j} + 50\mathbf{k})$ N · m is applied to the arm at C. Determine the force and moment reactions at O, assuming that all joints are temporarily fixed.

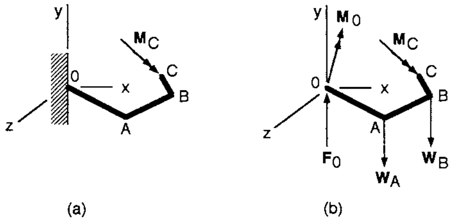

FIGURE 1.2.15 Model of a factory robot.

Solution. The free-body diagram showing the unknown force and moment reactions at O, is drawn in Figure 1.2.15b. From Equation (1.2.13),

$$\sum \mathbf{F} = 0$$

$$\mathbf{F}_O + \mathbf{W}_A + \mathbf{W}_B = 0$$

$$\mathbf{F}_O - 60\ \text{N}\,\mathbf{j} - 40\ \text{N}\,\mathbf{j} = 0$$

$$\mathbf{F}_O = 100\ \text{N}\,\mathbf{j}$$

$$\sum M_O = 0$$

$$\mathbf{M}_O + \mathbf{M}_C + \left(\mathbf{r}_{OA} \times \mathbf{W}_A\right) + \left(\mathbf{r}_{OB} \times \mathbf{W}_B\right) = 0$$

$$\mathbf{M}_O + \left(100\mathbf{i} - 20\mathbf{j} + 50\mathbf{k}\right)\ \text{N}\cdot\text{m} + \left(0.6\mathbf{i} - 0.3\mathbf{j} + 0.4\mathbf{k}\right)\ \text{m} \times \left(-60\ \text{N}\,\mathbf{j}\right) + \left(\mathbf{i} - 0.2\mathbf{j}\right)\ \text{m} \times \left(-40\ \text{N}\,\mathbf{j}\right) = 0$$

$$\mathbf{M}_O + 100\ \text{N}\cdot\text{m}\,\mathbf{i} - 20\ \text{N}\cdot\text{m}\,\mathbf{j} + 50\ \text{N}\cdot\text{m}\,\mathbf{k} - 36\ \text{N}\cdot\text{m}\,\mathbf{k} + 24\ \text{N}\cdot\text{m}\,\mathbf{i} - 40\ \text{N}\cdot\text{m}\,\mathbf{k} = 0$$

$$\mathbf{M}_O = \left(-124\mathbf{i} + 20\mathbf{j} + 26\mathbf{k}\right)\ \text{N}\cdot\text{m}$$

Example 4

A load of 7 kN may be placed anywhere within *A* and *B* in the trailer of negligible weight. Determine the reactions at the wheels at *D*, *E*, and *F*, and the force on the hitch *H* mounted on the car, for the extreme positions *A* and *B* of the load. The mass of the car is 1500 kg, and its weight is acting at *C* (see Figure 1.2.16).

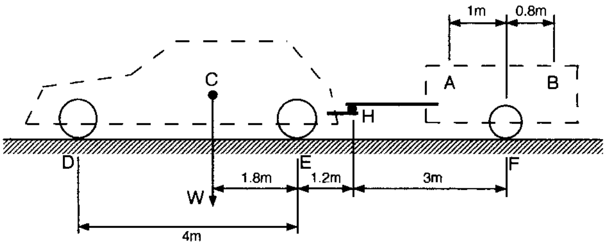

FIGURE 1.2.16 Analysis of a car with trailer.

Solution. The scalar method is best here. Put the load at position A first.

For the trailer alone, with y as the vertical axis:
$\Sigma M_F = 7(1) - H_y(3) = 0,\ H_y = 2.33$ kN
On the car:
$H_y = 2.33$ kN $\downarrow$ Ans.
$\Sigma F_y = 2.33 - 7 + F_y = 0,\ F_y = 4.67$ kN $\uparrow$ Ans.
For the car alone:
$\Sigma M_E = -2.33(1.2) - D_y(4) + 14.72(1.8) = 0$
$D_y = 5.93$ kN $\uparrow$ Ans.
$\Sigma F_y = 5.93 + E_y - 14.72 - 2.33 = 0$
$E_y = 11.12$ kN $\uparrow$ Ans.

Put the load at position B next.

For the trailer alone:
$\Sigma M_F = 0.8(7) - H_y(3) = 0,\ H_y = -1.87$ kN
On the car:
$H_y = 1.87$ kN $\downarrow$ Ans.
$\Sigma F_y = -1.87 - 7 + E_y = 0$
$E_y = 8.87$ kN $\uparrow$ Ans.
For the car alone:
$\Sigma M_E = -(1.87)(1.2) - D_y(4) + 14.72(1.8) = 0$
$D_y = 7.19$ kN $\uparrow$Ans.
$\Sigma F_y = 7.19 + E_y - 14.72 - (-1.87) = 0$
$E_y = 5.66$ kN $\uparrow$ Ans.

Forces and Moments in Beams

Beams are common structural members whose main function is to resist bending. The geometric changes and safety aspects of beams are analyzed by first assuming that they are rigid. The preceding subsections enable one to determine (1) the external (supporting) reactions acting on a statically determinate beam; and (2) the internal forces and moments at any cross section in a beam.

Classification of Supports

Common supports and external reactions for two-dimensional loading of beams are shown in Figure 1.2.17.

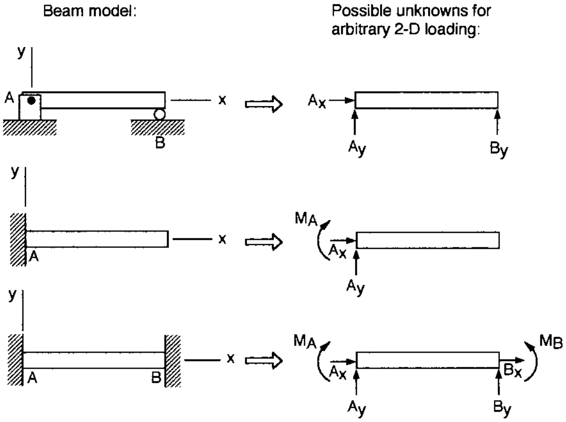

FIGURE 1.2.17 Common beam supports.

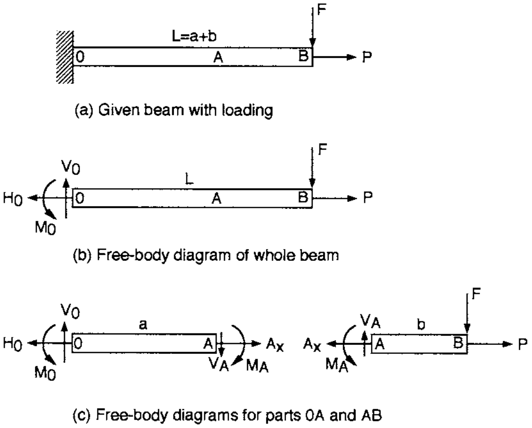

FIGURE 1.2.18 Internal forces and moments in a cantilever beam.

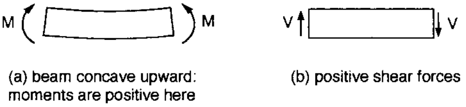

FIGURE 1.2.19 Preferred sign conventions.

Internal Forces and Moments

The internal force and moment reactions in a beam caused by external loading must be determined for evaluating the strength of the beam. If there is no torsion of the beam, three kinds of internal reactions are possible: a horizontal normal force H on a cross section; vertical (transverse) shear force V; and bending moment M. These reactions are calculated from the equilibrium equations applied to the left or right part of the beam from the cross section considered. The process involves free-body diagrams of the beam and a consistently applied system of signs. The modeling is illustrated for a cantilever beam in Figure 1.2.18.

Sign conventions. Consistent sign conventions should be used in any given problem. These can be arbitrarily set up, but the following is slightly advantageous. It makes the signs of the answers to the equilibrium equations correct for the directions of the shear force and bending moment.

A moment that makes a beam concave upward is taken as positive. Thus, a clockwise moment is positive on the left side of a section, and a counterclockwise moment is positive on the right side. A shear force that acts upward on the left side of a section, or downward on the right side, is positive (Figure 1.2.19).

Shear Force and Bending Moment Diagrams

The critical locations in a beam are determined from shear force and bending moment diagrams for the whole length of the beam. The construction of these diagrams is facilitated by following the steps, which are illustrated for a cantilever beam in Figure 1.2.20.

1. Draw the free-body diagram of the whole beam and determine all reactions at the supports.
2. Draw the coordinate axes for the shear force (V) and bending moment (M) diagrams directly below the free-body diagram.
3. Immediately plot those values of V and M that can be determined by inspection (especially when they are zero), observing the sign conventions.
4. Calculate and plot as many additional values of V and M as are necessary for drawing reasonably accurate curves through the plotted points, or do it all by computer.

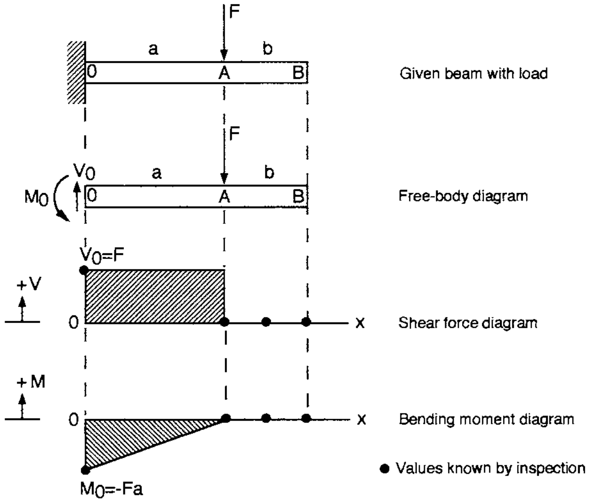

FIGURE 1.2.20 Construction of shear force and bending moment diagrams.

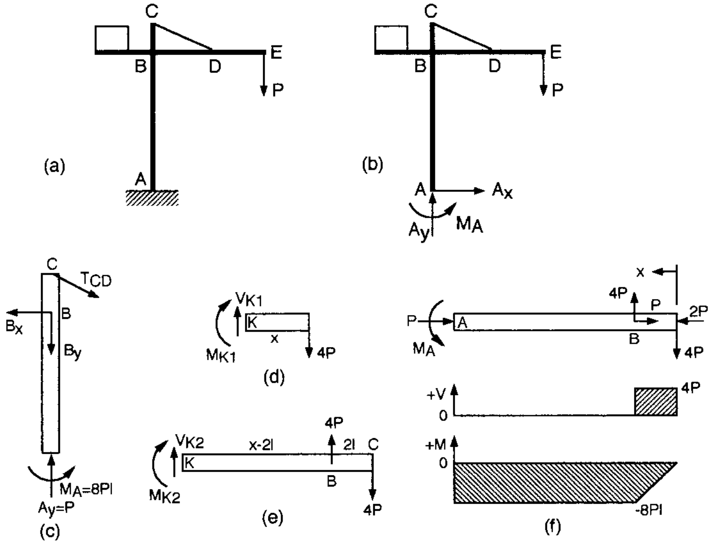

FIGURE 1.2.21 Shear force and bending moment diagrams of a component in a structure.

Example 5

A construction crane is modeled as a rigid bar AC that supports the boom by a pin at B and wire CD. The dimensions are AB = 10ℓ, BC = 2ℓ, BD = DE = 4ℓ. Draw the shear force and bending moment diagrams for bar AC (Figure 1.2.21).

Solution. From the free-body diagram of the entire crane,

$$\sum F_x = 0 \qquad \sum F_y = 0 \qquad \sum M_A = 0$$

$$A_x = 0 \qquad -P + A_y = 0 \qquad -P(8\ell) + M_A = 0$$

$$A_y = P \qquad M_A = 8P\ell$$

Now separate bar AC and determine the forces at B and C.

$$\sum F_x = 0$$

$$-B_x + T_{CD_x} = 0$$

$$\text{(a)}\quad B_x = \frac{2}{\sqrt{5}} T_{CD}$$

$$\sum F_y = 0$$

$$P - B_y - T_{CD_y} = 0$$

$$\text{(b)}\quad B_y = P - \frac{1}{\sqrt{5}} T_{CD}$$

$$\sum M_A = 0$$

$$-\frac{2}{\sqrt{5}} T_{CD}(12\ell) + B_x(10\ell) + M_A = 0$$

$$-\frac{24\ell}{\sqrt{5}} T_{CD} + \frac{20\ell}{\sqrt{5}} T_{CD} = -8P\ell$$

$$\text{(c)}\quad T_{CD} = \frac{8\sqrt{5}}{4} P = 2\sqrt{5}P$$

From (a) and (c), $B_x = 4P$ and $T_{CD_x} = 4P$. From (b) and (c), $B_y = P - 2P = -P$ and $= T_{CD_y} = 2P$.

Draw the free-body diagram of bar *AC* horizontally, with the shear force and bending moment diagram axes below it. Measure *x* from end *C* for convenience and analyze sections $0 \le x \le 2\ell$ and $2\ell \le x \le 12\ell$ (Figure 1.2.21b to 1.2.21f).

1. $0 \le x \le 2\ell$

$$\sum F_y = 0 \qquad\qquad \sum M_K = 0$$

$$-4P + V_{K_1} = 0 \qquad\qquad M_{K_1} + 4P(x) = 0$$

$$V_{K_1} = 4P \qquad\qquad M_{K_1} = -4Px$$

2. $2\ell \le x \le 12\ell$

$$\sum F_y = 0 \qquad\qquad \sum M_K = 0$$

$$4P - 4P + V_{K_2} = 0 \qquad\qquad M_{K_2} - 4P(x - 2\ell) + 4P(x) = 0$$

$$V_{K_2} = 0 \qquad\qquad M_{K_2} = -8P\ell$$

At point *B*, $x = 2\ell$, $M_{K_1} = -4P(2\ell) = -8P\ell = M_{K_2} = MA$. The results for section *AB*, $2\ell \le x \le 12\ell$, show that the combined effect of the forces at *B* and *C* is to produce a couple of magnitude $8P\ell$ on the beam. Thus, the shear force is zero and the moment is constant in this section. These results are plotted on the axes below the free-body diagram of bar *A-B-C*.

Simple Structures and Machines

Equilibrium equations are used to determine forces and moments acting on statically determinate simple structures and machines. A simple structure is composed solely of two-force members. A machine is composed of multiforce members. The method of joints and the method of sections are commonly used in such analysis.

Trusses

Trusses consist of straight, slender members whose ends are connected at joints. Two-dimensional *plane trusses* carry loads acting in their planes and are often connected to form three-dimensional *space trusses*. Two typical trusses are shown in Figure 1.2.22.

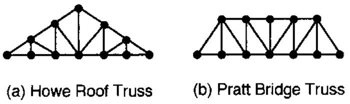
(a) Howe Roof Truss

(b) Pratt Bridge Truss

FIGURE 1.2.22 Schematic examples of trusses.

To simplify the analysis of trusses, assume frictionless pin connections at the joints. Thus, all members are two-force members with forces (and no moments) acting at the joints. Members may be assumed weightless or may have their weights evenly divided to the joints.

Method of Joints

Equilibrium equations based on the entire truss and its joints allow for determination of all internal forces and external reactions at the joints using the following procedure.

1. Determine the support reactions of the truss. This is done using force and moment equilibrium equations and a free-body diagram of the entire truss.
2. Select any arbitrary joint where only one or two unknown forces act. Draw the free-body diagram of the joint assuming unknown forces are tensions (arrows directed away from the joint).
3. Draw free-body diagrams for the other joints to be analyzed, using Newton's third law consistently with respect to the first diagram.
4. Write the equations of equilibrium, $\Sigma F_x = 0$ and $\Sigma F_y = 0$, for the forces acting at the joints and solve them. To simplify calculations, attempt to progress from joint to joint in such a way that each equation contains only one unknown. Positive answers indicate that the assumed directions of unknown forces were correct, and vice versa.

Example 6

Use the method of joints to determine the forces acting at A, B, C, H, and I of the truss in Figure 1.2.23a. The angles are $\alpha = 56.3°$; $\beta = 38.7°$; $\phi = 39.8°$; and $\theta = 36.9°$.

Solution. First the reactions at the supports are determined and are shown in Figure 1.2.23b. A joint at which only two unknown forces act is the best starting point for the solution. Choosing joint A, the solution is progressively developed, always seeking the next joint with only two unknowns. In each

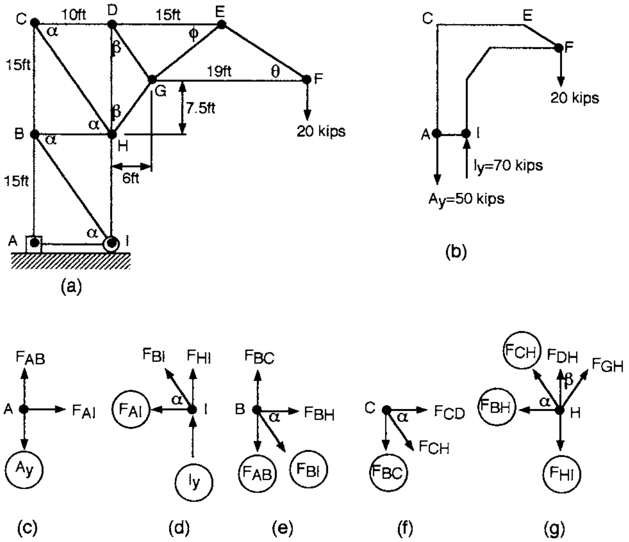

FIGURE 1.2.23 Method of joints in analyzing a truss.

diagram, circles indicate the quantities known from the preceding analysis. Sample calculations show the approach and some of the results.

Joint A:

$$\sum F_x = 0 \qquad \sum F_y = 0$$

$$F_{AI} = 0 \qquad F_{AB} - A_y = 0$$

$$F_{AB} - 50 \text{ kips} = 0$$

$$F_{AB} = 50 \text{ kips (tension)}$$

Joint H:

$$\sum F_x = 0 \qquad \sum F_y = 0$$

$$F_{GH} \sin\beta - F_{CH} \cos\alpha - F_{BH} = 0 \qquad F_{CH} \sin\alpha + F_{DH} + F_{GH} \cos\beta - F_{HI} = 0$$

$$F_{GH}(0.625) + (60.1 \text{ kips})(0.555) - 0 = 0 \qquad -(60.1 \text{ kips})(0.832) + F_{DH} - (53.4 \text{ kips})(0.780) + 70 \text{ kips} = 0$$

$$F_{GH} = -53.4 \text{ kips (compression)} \qquad F_{DH} = 21.7 \text{ kips (tension)}$$

Method of Sections

The method of sections is useful when only a few forces in truss members need to be determined regardless of the size and complexity of the entire truss structure. This method employs any section of the truss as a free body in equilibrium. The chosen section may have any number of joints and members in it, but the number of unknown forces should not exceed three in most cases. Only three equations of equilibrium can be written for each section of a plane truss. The following procedure is recommended:

1. Determine the support reactions if the section used in the analysis includes the joints supported.
2. Section the truss by making an imaginary cut through the members of interest, preferably through only three members in which the forces are unknowns (assume tensions). The cut need not be a straight line. The sectioning is illustrated by lines *l-l*, *m-m*, and *n-n* in Figure 1.2.24.
3. Write equations of equilibrium. Choose a convenient point of reference for moments to simplify calculations such as the point of intersection of the lines of action for two or more of the unknown forces. If two unknown forces are parallel, sum the forces perpendicular to their lines of action.
4. Solve the equations. If necessary, use more than one cut in the vicinity of interest to allow writing more equilibrium equations. Positive answers indicate assumed directions of unknown forces were correct, and vice versa.

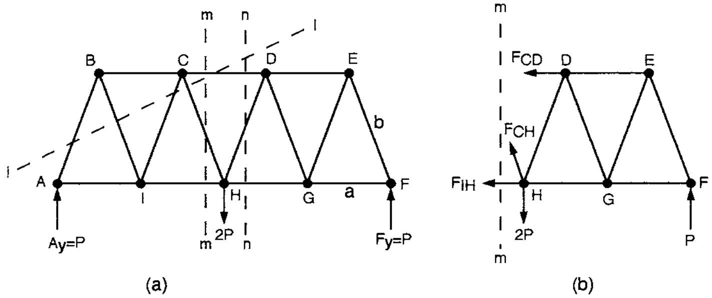

FIGURE 1.2.24 Method of sections in analyzing a truss.

Space Trusses

A space truss can be analyzed with the method of joints or with the method of sections. For each joint, there are three scalar equilibrium equations, $\Sigma F_x = 0$, $\Sigma F_y = 0$, and $\Sigma F_z = 0$. The analysis must begin at a joint at least one force is known and no more than three forces are unknown. The solution must progress to other joints in a similar fashion. Six scalar equilibrium equations are available when the method of sections is used: $\Sigma F_x = 0$; $\Sigma F_y = 0$; $\Sigma F_z = 0$; $\Sigma M_x = 0$; $\Sigma M_y = 0$; and $\Sigma M_z = 0$.

Frames and Machines

Multiforce members (with three or more forces acting on each member) are common in structures. In these cases the forces are not directed along the members, so they are a little more complex to analyze than the two-force members in simple trusses. Multiforce members are used in two kinds of structures. Frames are usually stationary and fully constrained. *Machines* have moving parts, so the forces acting on a member depend on the location and orientation of the member.

The analysis of multiforce members is based on the consistent use of related free-body diagrams. The solution is often facilitated by representing forces by their rectangular components. Scalar equilibrium equations are the most convenient for two-dimensional problems, and vector notation is advantageous in three-dimensional situations.

Often, an applied force acts at a pin joining two or more members, or a support or connection may exist at a joint between two or more members. In these cases, a choice should be made of a single member at the joint on which to assume the external force to be acting. This decision should be stated in the analysis. The following comprehensive procedure is recommended.

Three independent equations of equilibrium are available for each member or combination of members in two-dimensional loading; for example, $\Sigma F_x = 0$, $\Sigma F_y = 0$, $\Sigma M_A = 0$, where A is an arbitrary point of reference.

1. Determine the support reactions if necessary.
2. Determine all two-force members.
3. Draw the free-body diagram of the first member on which the unknown forces act, assuming that the unknown forces are tensions.
4. Draw the free-body diagrams of the other members or groups of members using Newton's third law (action and reaction) consistently with respect to the first diagram. Proceed until the number of equilibrium equations available is no longer exceeded by the total number of unknowns.
5. Write the equilibrium equations for the members or combinations of members and solve them. Positive answers indicate that the assumed directions for unknown forces were correct, and vice versa.

Distributed Forces

The most common distributed forces acting on a body are parallel force systems, such as the force of gravity. These can be represented by one or more concentrated forces to facilitate the required analysis. Several basic cases of distributed forces are presented here. The important topic of stress analysis is covered in mechanics of materials.

Center of Gravity

The center of gravity of a body is the point where the equivalent resultant force caused by gravity is acting. Its coordinates are defined for an arbitrary set of axes as

$$\bar{x} = \frac{\int x\, dW}{W} \qquad \bar{y} = \frac{\int y\, dW}{W} \qquad \bar{z} = \frac{\int z\, dW}{W} \tag{1.2.14}$$

where x, y, z are the coordinates of an element of weight dW, and W is the total weight of the body. In the general case, $dW = \gamma\, dV$, and $W = \int \gamma\, dV$, where γ = specific weight of the material and dV = elemental volume.

Centroids

If γ is a constant, the center of gravity coincides with the centroid, which is a geometrical property of a body. Centroids of lines L, areas A, and volumes V are defined analogously to the coordinates of the center of gravity,

$$\text{Lines:}\quad \bar{x} = \frac{\int x\, dL}{W} \qquad \bar{y} = \frac{\int y\, dL}{L} \qquad \bar{z} = \frac{\int z\, dL}{L} \tag{1.2.15}$$

$$\text{Areas:}\quad \bar{x} = \frac{\int x\, dA}{A} \qquad \bar{y} = \frac{\int y\, dA}{A} \qquad \bar{z} = \frac{\int z\, dA}{A} \tag{1.2.16}$$

$$\text{Volumes:}\quad \bar{x} = \frac{\int x\, dV}{V} \qquad \bar{y} = \frac{\int y\, dV}{V} \qquad \bar{z} = \frac{\int z\, dV}{V} \tag{1.2.17}$$

For example, an area A consists of discrete parts A_1, A_2, A_3, where the centroids x_1, x_2, x_3 of the three parts are located by inspection. The x coordinate of the centroid of the whole area A is $\bar{x}$ obtained from $A\bar{x} = A_1x_1 + A_2x_2 + A_3x_3$.

Surfaces of revolution. The surface areas and volumes of bodies of revolution can be calculated using the concepts of centroids by the theorems of Pappus.

Distributed Loads on Beams

The distributed load on a member may be its own weight and/or some other loading such as from ice or wind. The external and internal reactions to the loading may be determined using the condition of equilibrium.

External reactions. Replace the whole distributed load with a concentrated force equal in magnitude to the area under the load distribution curve and applied at the centroid of that area parallel to the original force system.

Internal reactions. For a beam under a distributed load $w(x)$, where x is distance along the beam, the shear force V and bending moment M are related according to Figure 1.2.25 as

$$w(x) = -\frac{dV}{dx} \qquad V = \frac{dM}{dx} \tag{1.2.18}$$

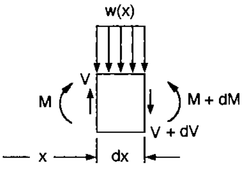

FIGURE 1.2.25 Internal reactions in a beam under distributed loading.

Other useful expressions for any two cross sections A and B of a beam are

$$V_A - V_B = \int_{x_A}^{x_B} w(x)\,dx = \text{area under } w(x)$$

$$M_B - M_A = \int_{x_A}^{x_B} V\,dx = \text{area under shear force diagram} \tag{1.2.19}$$

Example 7

See Figure 1.2.26.

Distributed Loads on Flexible Cables

The basic assumptions of simple analyses of cables are that there is no resistance to bending and that the internal force at any point is tangent to the cable at that point. The loading is denoted by $w(x)$, a continuous but possibly variable load, in terms of force per unit length. The differential equation of a cable is

$$\frac{d^2y}{dx^2} = \frac{w(x)}{T_o} \tag{1.2.20}$$

where T_o = constant = horizontal component of the tension T in the cable.

Two special cases are common:

- *Parabolic cables.* The cable supports a load w that is uniformly distributed horizontally. The shape of the cable is a parabola given by

$$y = \frac{wx^2}{2T_o} \quad (x = 0 \text{ at lowest point}) \tag{1.2.21}$$

  In a symmetric cable, the tension is $T = \sqrt{T_o^2 + w^2x^2}$.
- *Catenary cables.* When the load w is uniformly distributed along the cable, the cable's shape is given by

$$y = \frac{T_o}{w}\left(\cosh\frac{wx}{T_o} - 1\right) \tag{1.2.22}$$

  The tension in the cable is $T = T_o + wy$.

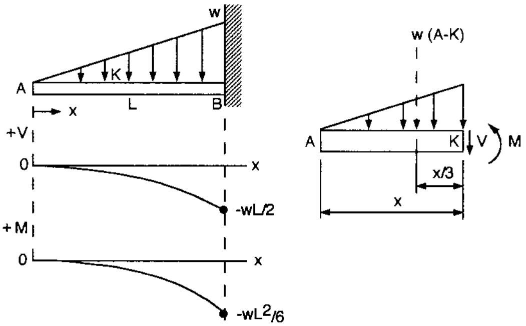

FIGURE 1.2.26 Shear force and bending moment diagrams for a cantilever beam.

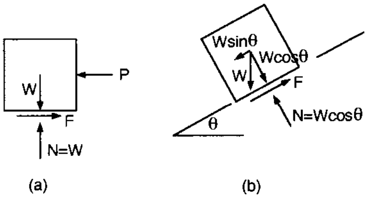

FIGURE 1.2.27 Models showing friction forces.

Friction

A friction force F (or $\mathcal{F}$, in typical other notation) acts between contacting bodies when they slide relative to one another, or when sliding tends to occur. This force is tangential to each body at the point of contact, and its magnitude depends on the normal force N pressing the bodies together and on the material and condition of the contacting surfaces. The material and surface properties are lumped together and represented by the coefficient of friction μ. The friction force opposes the force that tends to cause motion, as illustrated for two simple cases in Figure 1.2.27.

The friction forces F may vary from zero to a maximum value,

$$F_{\max} = \mu N \quad \left(0 \le F \le F_{\max}\right) \tag{1.2.23}$$

depending on the applied force that tends to cause relative motion of the bodies. The coefficient of kinetic friction μ_k (during sliding) is lower than the coefficient of static friction m or μ_s; μ_k depends on the speed of sliding and is not easily quantified.

Angle of Repose

The critical angle θ_c at which motion is impending is the angle of repose, where the friction force is at its maximum for a given block on an incline.

$$\tan\theta_c = \frac{F}{N} = \mu_s \tag{1.2.24}$$

Thus, θ_c is measured to obtain μ_s. Note that, even in the case of static, dry friction, μ_s depends on temperature; humidity; dust and other contaminants; oxide films; surface finish; and chemical reactions. The contact area and the normal force affect μ_s only when significant deformations of one or both bodies occur.

Classifications and Procedures for Solving Friction Problems

The directions of unknown friction forces are often, but not always, determined by inspection. The magnitude of the friction force is obtained from $F_{\max} = \mu_s N$ when it is known that motion is impending. Note that F may be less than $F_{\max}$. The major steps in solving problems of dry friction are organized in three categories as follows:

A. Given: bodies, forces, or coefficients of friction are known. Impending motion is not assured: $F \neq \mu_s N$.
   Procedure: to determine if equilibrium is possible:
   1. Construct the free-body diagram.
   2. Assume that the system is in equilibrium.
   3. Determine the friction and normal forces necessary for equilibrium.
   4. Results: (a) $F < \mu_s N$; the body is at rest; (b) $F > \mu_s N$; motion is occurring, so static equilibrium is not possible. Because there is motion, $F = \mu_k N$. Complete solution requires principles of dynamics.

B. Given: bodies, forces, or coefficients of friction are given. Impending motion is specified. $F = \mu_s N$ is valid.
   Procedure: to determine the unknowns:
   1. Construct the free-body diagram.
   2. Write $F = \mu_s N$ for all surfaces where motion is impending.
   3. Determine μ_s or the required forces from the equation of equilibrium.

C. Given: bodies, forces, and coefficients of friction are known. Impending motion is specified, but the exact motion is not given. The possible motions may be sliding, tipping, or rolling, or relative motion if two or more bodies are involved. Alternatively, the forces or coefficients of friction may need to be determined to produce a particular motion from several possible motions.
   Procedure: to determine the exact motion that may occur, or unknown quantities required:
   1. Construct the free-body diagram.
   2. Assume that motion is impending in one of the two or more possible ways. Repeat this for each possible motion and write the equation of equilibrium.
   3. Compare the results for the possible motions and select the likely event. Determine the required unknowns for any preferred motion.

Wedges and Screws

A wedge may be used to raise or lower a body. Thus, two directions of motion must be considered in each situation, with the friction forces always opposing the impending or actual motion. The self-locking aspect of a wedge may be of interest. The analysis is straightforward, using interrelated free-body diagrams and equilibrium equations.

Screw threads are special applications of the concept of wedges. Square threads are the easiest to model and analyze. The magnitude M of the moment of a couple required to move a square-threaded screw against an axial load P is

$$M = Pr\tan(\alpha + \phi) \tag{1.2.25}$$

where

r = radius of the screw
$\alpha = \tan^{-1}(L/2\pi r) = \tan^{-1}(np/2\pi r)$
L = lead = advancement per revolution
n = multiplicity of threads
p = pitch = distance between similar points on adjacent threads
$\phi = \tan^{-1}\mu$

The relative values of α and ϕ control whether a screw is self-locking; $\phi > \alpha$ is required for a screw to support an axial load without unwinding.

Disk Friction

Flat surfaces in relative rotary motion generate a friction moment M opposing the motion. For a hollow member with radii R_o and R_i, under an axial force P,

$$M = \frac{2}{3}\mu P \frac{R_o^3 - R_i^3}{R_o^2 - R_i^2} \tag{1.2.26}$$

The friction moment tends to decrease (down to about 75% of its original value) as the surfaces wear. Use the appropriate μ_s or μ_k value.

Axle Friction

The friction moment M of a rotating axle in a journal bearing (sliding bearing) is approximated (if μ is low) as

$$M = Pr\mu \tag{1.2.27}$$

where

P = transverse load on the axle
r = radius of the axle

Use the appropriate μ_s or μ_k value.

Rolling Resistance

Rolling wheels and balls have relatively low resistance to motion compared to sliding. This resistance is caused by internal friction of the materials in contact, and it may be difficult to predict or measure.

A coefficient of rolling resistance a is defined with units of length,

$$a \cong \frac{Fr}{P} \tag{1.2.28}$$

where

r = radius of a wheel rolling on a flat surface
F = minimum horizontal force to maintain constant speed of rolling
P = load on wheel

Values of a range upward from a low of about 0.005 mm for hardened steel elements.

Belt Friction

The tensions T_1 and T_2 of a belt, rope, or wire on a pulley or drum are related as

$$T_2 = T_1 e^{\mu\beta} \qquad \left(T_2 > T_1\right) \tag{1.2.29}$$

where β = total angle of belt contact, radians ($\beta = 2\pi n$ for a member wrapped around a drum n times). Use μ_s for impending slipping and μ_k for slipping.

For a V belt of belt angle 2ϕ,

$$T_2 = T_1 e^{\mu\beta/\sin\phi}$$

Work and Potential Energy

Work is a scalar quantity. It is the product of a force and the corresponding displacement. Potential energy is the capacity of a system to do work on another system. These concepts are advantageous in the analysis of equilibrium of complex systems, in dynamics, and in mechanics of materials.

Work of a Force

The work U of a constant force **F** is

$$U = Fs \tag{1.2.30}$$

where s = displacement of a body in the direction of the vector **F**.

For a displacement along an arbitrary path from point 1 to 2, with $d\mathbf{r}$ tangent to the path,

$$U = \int_1^2 \mathbf{F} \cdot d\mathbf{r} = \int_1^2 \left(F_x\, dx + F_y\, dy + F_z\, dz\right)$$

In theory, there is no work when:

- A force is acting on a fixed, rigid body ($dr = 0$, $dU = 0$).
- A force acts perpendicular to the displacement ($\mathbf{F} \cdot d\mathbf{r} = 0$).

Work of a Couple

A couple of magnitude M does work

$$U = M\theta \tag{1.2.31}$$

where θ = angular displacement (radians) in the same plane in which the couple is acting.

In a rotation from angular position α to β,

$$U = \int_{\alpha}^{\beta} \mathbf{M} \cdot d\theta = \int_{\alpha}^{\beta} \left(M_x \; d\theta_x + M_y \; d\theta_y + M_z \; d\theta_z \right)$$

Virtual Work

The concept of virtual work (through imaginary, infinitesimal displacements within the constraints of a system) is useful to analyze the equilibrium of complex systems. The virtual work of a force **F** or moment **M** is expressed as

$$\delta U = \mathbf{F} \cdot \delta \mathbf{r}$$

$$\delta U = \mathbf{M} \cdot \delta \theta$$

There is equilibrium if

$$\delta U = \sum_{i=1}^{m} \mathbf{F}_i \cdot \delta \mathbf{r}_i + \sum_{j=1}^{n} \mathbf{M}_i \cdot \delta \theta_j = 0 \tag{1.2.32}$$

where the subscripts refer to individual forces or couples and the corresponding displacements, ignoring frictional effects.

Mechanical Efficiency of Real Systems

Real mechanical systems operate with frictional losses, so

$$\underset{\text{(output work)}}{\text{input work} = \text{useful work}} + \text{work of friction}$$

The mechanical efficiency η of a machine is

$$\eta = \frac{\text{output work}}{\text{input work}} = \frac{\text{useful work}}{\text{total work required}}$$

$$0 < \eta < 1$$

Gravitational Work and Potential Energy

The potential of a body of weight W to do work because of its relative height h with respect to an arbitrary level is defined as its potential energy. If h is the vertical (y) distance between level 1 and a lower level 2, the work of weight W in descending is

$$U_{12} = \int_{1}^{2} W \, dy = Wh = \text{potential energy of the body at level 1 with respect to level 2}$$

The work of weight W in rising from level 2 to level 1 is

$$U_{21} = \int_2^1 -W\,dy = -Wh = \text{potential energy of the body at level 2 with respect to level 1}$$

Elastic Potential Energy

The potential energy of elastic members is another common form of potential energy in engineering mechanics. For a linearly deforming helical spring, the axial force F and displacement x are related by the spring constant k,

$$F = kx \qquad (\text{similarly, } M = k\theta \text{ for a torsion spring})$$

The work U of a force F on an initially undeformed spring is

$$U = \frac{1}{2}kx^2 \tag{1.2.33}$$

In the general case, deforming the spring from position x_1 to x_2,

$$U = \frac{1}{2}k\left(x_2^2 - x_1^2\right)$$

Notation for Potential Energy

The change in the potential energy V of a system is

$$U = -\Delta V$$

Note that negative work is done by a system while its own potential energy is increased by the action of an external force or moment. The external agent does positive work at the same time because it acts in the same direction as the resulting displacement.

Potential Energy at Equilibrium

For equilibrium of a system,

$$\frac{dV}{dq} = 0$$

where q = an independent coordinate along which displacement is possible.

For a system with n degrees of freedom,

$$\frac{\partial V}{\partial q_i} = 0, \qquad i = 1, 2, \ldots, n$$

Equilibrium is stable if $(d^2V/dq^2) > 0$.
Equilibrium is unstable if $(d^2V/dq^2) < 0$.
Equilibrium is neutral only if all derivatives of V are zero.

In cases of complex configurations, evaluate derivatives of higher order as well.

Moments of Inertia

The topics of inertia are related to the methods of first moments. They are traditionally presented in statics in preparation for application in dynamics or mechanics of materials.

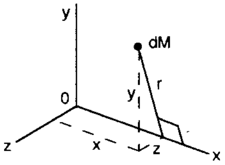

FIGURE 1.2.28 Mass element dM in xyz coordinates.

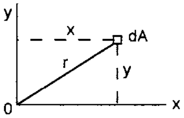

FIGURE 1.2.29 Area A in the xy plane.

Moments of Inertia of a Mass

The moment of inertia dI_x of an elemental mass dM about the x axis (Figure 1.2.28) is defined as

$$dI_x = r^2\ dM = \left(y^2 + z^2\right) dM$$

where r is the nearest distance from dM to the x axis. The moments of inertia of a body about the three coordinate axes are

$$\begin{aligned} I_x &= \int r^2\ dM = \int \left(y^2 + z^2\right) dM \\ I_y &= \int \left(x^2 + z^2\right) dM \\ I_z &= \int \left(x^2 + y^2\right) dM \end{aligned} \qquad (1.2.34)$$

Radius of Gyration. The radius of gyration r_g is defined by $r_g = \sqrt{I_x / M}$, and similarly for any other axis. It is based on the concept of the body of mass M being replaced by a point mass M (same mass) at a distance r_g from a given axis. A thin strip or shell with all mass essentially at a constant distance r_g from the axis of reference is equivalent to a point mass for some analyses.

Moment of Inertia of an Area

The moment of inertia of an elemental area dA about the x axis (Figure 1.2.29) is defined as

$$dI_x = y^2\ dA$$

where y is the nearest distance from dA to the x axis. The moments of inertia (second moments) of the area A about the x and y axes (because A is in the xy plane) are

$$I_x = \int y^2\ dA \qquad I_y = \int x^2\ dA \qquad (1.2.35)$$

The radius of gyration of an area is defined the same way as it is for a mass: $r_g = \sqrt{I_x / A}$, etc.

Polar Moment of Inertia of an Area

The polar moment of inertia is defined with respect to an axis perpendicular to the area considered. In Figure 1.2.29, this may be the z axis. The polar moment of inertia in this case is

$$J_O = \int r^2\ dA = \int \left(x^2 + y^2\right) dA = I_x + I_y \qquad (1.2.36)$$

Parallel-Axis Transformations of Moments of Inertia

It is often convenient first to calculate the moment of inertia about a centroidal axis and then transform this with respect to a parallel axis. The formulas for the transformations are

$$\begin{aligned} I &= I_C + Md^2 && \text{for a mass } M \\ I &= I_C + Ad^2 && \text{for an area } A \\ J_O &= J_C + Ad^2 && \text{for an area } A \end{aligned} \tag{1.2.37}$$

where

I or J_O = moment of inertia of M or A about any line,

I_C or J_C = moment of inertia of M or A about a line through the mass center or centroid and parallel to ℓ

d = nearest distance between the parallel lines

Note that one of the two axes in each equation must be a centroidal axis.

Products of Inertia

The products of inertia for areas and masses and the corresponding parallel-axis formulas are defined in similar patterns. Using notations in accordance with the preceding formulas, products of inertia are

$$\begin{aligned} I_{xy} &= \int xy\,dA \quad \text{for area,} && \text{or} \quad \int xy\,dM \quad \text{for mass} \\ I_{yz} &= \int yz\,dA && \text{or} \quad \int yz\,dM \\ I_{xz} &= \int xz\,dA && \text{or} \quad \int xz\,dM \end{aligned} \tag{1.2.38}$$

Parallel-axis formulas are

$$\begin{aligned} I_{xy} &= I_{x'y'} + A\,d_x d_y \quad \text{for area,} && \text{or} \quad I_{x'y'} + M\,d_x d_y \quad \text{for mass} \\ I_{yz} &= I_{y'z'} + A\,d_y d_z && \text{or} \quad I_{y'z'} + M\,d_y d_z \\ I_{xz} &= I_{x'z'} + A\,d_x d_z && \text{or} \quad I_{x'z'} + M\,d_x d_z \end{aligned} \tag{1.2.39}$$

Note that the moment of inertia is always positive. The product of inertia may be positive, negative, or zero; it is zero if *x* or *y* (or both) is an axis of symmetry of the area. Transformations of known moments and product of inertia to axes that are inclined to the original set of axes are possible but not covered here. These transformations are useful for determining the principal (maximum and minimum) moments of inertia and the principal axes when the area or body has no symmetry. The principal moments of inertia for objects of simple shape are available in many texts.

1.3 Dynamics

Stephen M. Birn and Bela I. Sandor

The two major categories in dynamics are kinematics and kinetics. **Kinematics** involves the time- and geometry-dependent motion of a particle, rigid body, deformable body, or a fluid without considering the forces that cause the motion. It relates position, velocity, acceleration, and time. **Kinetics** combines the concepts of kinematics and the forces that cause the motion.

Kinematics of Particles

Scalar Method

The scalar method of particle kinematics is adequate for one-dimensional analysis. A particle is a body whose dimensions can be neglected (in some analyses, very large bodies are considered particles). The equations described here are easily adapted and applied to two and three dimensions.

Average and Instantaneous Velocity

The average velocity of a particle is the change in distance divided by the change in time. The instantaneous velocity is the particle's velocity at a particular instant.

$$v_{ave} = \frac{\Delta x}{\Delta t} \qquad v_{inst} = \lim_{\Delta t \to 0} \frac{\Delta x}{\Delta t} = \frac{dx}{dt} = \dot{x} \tag{1.3.1}$$

Average and Instantaneous Acceleration

The average acceleration is the change in velocity divided by the change in time. The instantaneous acceleration is the particle's acceleration at a particular instant.

$$a_{ave} = \frac{\Delta v}{\Delta t} \qquad a_{inst} = \lim_{\Delta t \to 0} \frac{\Delta v}{\Delta t} = \frac{dv}{dt} = \dot{v} = \ddot{x} \tag{1.3.2}$$

Displacement, velocity, acceleration, and time are related to one another. For example, if velocity is given as a function of time, the displacement and acceleration can be determined through integration and differentiation, respectively. The following example illustrates this concept.

Example 8

A particle moves with a velocity $v(t) = 3t^2 - 8t$. Determine $x(t)$ and $a(t)$, if $x(0) = 5$.

Solution.

1. Determine $x(t)$ by integration.

$$v = \frac{dx}{dt}$$

$$v\,dt = dx$$

$$\int 3t^2 - 8t\,dt = \int dx$$

$$t^3 - 4t^2 + C = x$$

$$\text{from } x(0) = 5 \qquad C = 5$$

$$x(t) = t^3 - 4t^2 + 5$$

2. Determine $a(t)$ by differentiation.

$$a = \frac{dv}{dt} = \frac{d}{dt}\left(3t^2 - 8t\right)$$

$$a(t) = 6t - 8$$

Four key points can be seen from these graphs (Figure 1.3.1).

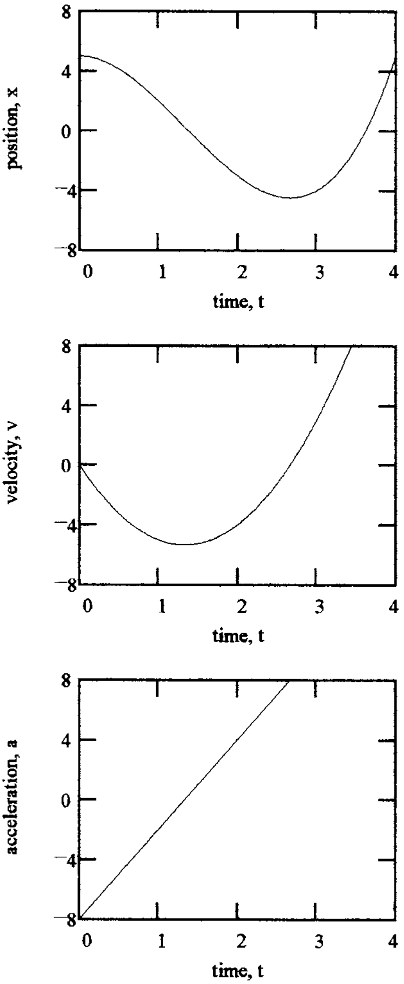

FIGURE 1.3.1 Plots of a particle's kinematics.

1. $v = 0$ at the local maximum or minimum of the x-t curve.
2. $a = 0$ at the local maximum or minimum of the v-t curve.
3. The area under the v-t curve in a specific time interval is equal to the net displacement change in that interval.
4. The area under the a-t curve in a specific time interval is equal to the net velocity change in that interval.

Useful Expressions Based on Acceleration

Equations for nonconstant acceleration are

$$a = \frac{dv}{dt} \Rightarrow \int_{v_0}^{v} dv = \int_{0}^{t} a\,dt \tag{1.3.3}$$

$$v\,dv = a\,dx \Rightarrow \int_{v_0}^{v} v\,dv = \int_{x_0}^{x} a\,dx \tag{1.3.4}$$

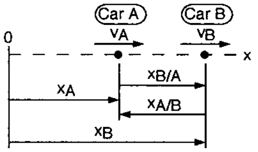

FIGURE 1.3.2 Relative motion of two particles along a straight line.

Equations for constant acceleration (projectile motion; free fall) are

$$v = at + v_0$$
$$v^2 = 2a\left(x - x_0\right) + v_0^2 \tag{1.3.5}$$
$$x = \frac{1}{2}at^2 + v_0 t + x_0$$

These equations are only to be used when the acceleration is known to be a constant. Other expressions are available, depending on how a variable acceleration is given as a function of time, velocity, or displacement.

Scalar Relative Motion Equations

The concept of relative motion can be used to determine the displacement, velocity, and acceleration between two particles that travel along the same line. Equation (1.3.6) provides the mathematical basis for this method. These equations can also be used when analyzing two points on the same body that are not attached rigidly to each other (Figure 1.3.2).

$$x_{B/A} = x_B - x_A$$
$$v_{B/A} = v_B - v_A \tag{1.3.6}$$
$$a_{B/A} = a_B - a_A$$

The notation B/A represents the displacement, velocity, or acceleration of particle B as seen from particle A. Relative motion can be used to analyze many different degrees-of-freedom systems. A degree of freedom of a mechanical system is the number of independent coordinate systems needed to define the position of a particle.

Vector Method

The vector method facilitates the analysis of two- and three-dimensional problems. In general, curvilinear motion occurs and is analyzed using a convenient coordinate system.

Vector Notation in Rectangular (Cartesian) Coordinates

Figure 1.3.3 illustrates the vector method. The mathematical method is based on determining **v** and **a** as functions of the position vector **r**. Note that the time derivatives of unit vectors are zero when the *xyz* coordinate system is fixed. The scalar components $(\dot{x}, \dot{y}, \ddot{x}, \ldots)$ can be determined from the appropriate scalar equations previously presented that only include the quantities relevant to the coordinate direction considered.

$$\mathbf{r} = x\mathbf{i} + y\mathbf{j} + z\mathbf{k}$$
$$\mathbf{v} = \frac{d\mathbf{r}}{dt} = \frac{dx}{dt}\mathbf{i} + \frac{dy}{dt}\mathbf{j} + \frac{dz}{dt}\mathbf{k} = \dot{x}\mathbf{i} + \dot{y}\mathbf{j} + \dot{z}\mathbf{k} \tag{1.3.7}$$
$$\mathbf{a} = \frac{d\mathbf{v}}{dt} = \frac{d^2x}{dt^2}\mathbf{i} + \frac{d^2y}{dt^2}\mathbf{j} + \frac{d^2z}{dt^2}\mathbf{k} = \ddot{x}\mathbf{i} + \ddot{y}\mathbf{j} + \ddot{z}\mathbf{k}$$

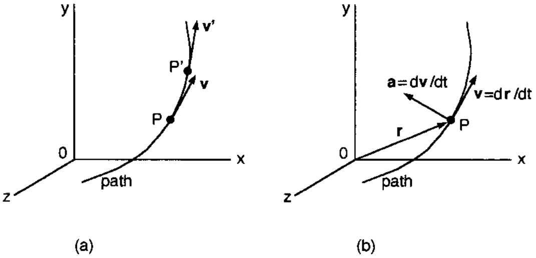

FIGURE 1.3.3 Vector method for a particle.

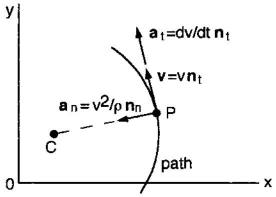

FIGURE 1.3.4 Tangential and normal components. *C* is the center of curvature.

A few key points should be remembered when considering curvilinear motion. First, the instantaneous velocity vector is *always* tangent to the path of the particle. Second, the speed of the particle is the magnitude of the velocity vector. Third, the acceleration vector is not tangent to the path of the particle and not collinear with **v** in curvilinear motion.

Tangential and Normal Components

Tangential and normal components are useful in analyzing velocity and acceleration. Figure 1.3.4 illustrates the method and Equation (1.3.8) comprises the governing equations for it.

$$\begin{gathered} \mathbf{v} = v\mathbf{n}_t \\ \mathbf{a} = a_t\mathbf{n}_t + a_n\mathbf{n}_n \\ a_t = \frac{dv}{dt} \qquad a_n = \frac{v^2}{\rho} \\ \rho = \frac{\left[1+\left(dy/dx\right)^2\right]^{3/2}}{d^2y/dx^2} \\ \rho = r = \text{constant for a circular path} \end{gathered} \tag{1.3.8}$$

The *osculating plane* contains the unit vectors $\mathbf{n}_t$ and $\mathbf{n}_n$, thus defining a plane. When using normal and tangential components, it is common to forget to include the component of normal acceleration, especially if the particle travels at a constant speed along a curved path. For a particle that moves in circular motion,

$$\begin{gathered} v = r\dot{\theta} = r\omega \\ a_t = \frac{dv}{dt} = r\ddot{\theta} = r\alpha \\ a_n = \frac{v^2}{r} = r\dot{\theta}^2 = r\omega^2 \end{gathered} \tag{1.3.9}$$

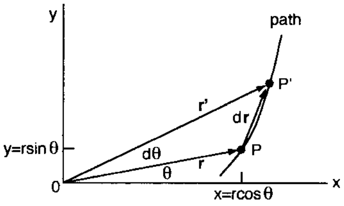

FIGURE 1.3.5 Motion of a particle in polar coordinates.

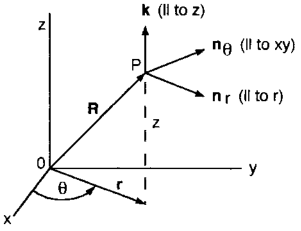

FIGURE 1.3.6 Motion of a particle in cylindrical coordinates.

Motion of a Particle in Polar Coordinates

Sometimes it may be best to analyze particle motion by using polar coordinates as follows (Figure 1.3.5):

$$\mathbf{v} = \dot{r}\mathbf{n}_r + r\dot{\theta}\mathbf{n}_\theta \qquad \text{(always tangent to the path)}$$

$$\frac{d\theta}{dt} = \dot{\theta} = \omega, \ \ \text{rad/s} \tag{1.3.10}$$

$$\mathbf{a} = \left(\ddot{r} - r\dot{\theta}^2\right)\mathbf{n}_r + \left(r\ddot{\theta} + 2\dot{r}\dot{\theta}\right)\mathbf{n}_\theta$$

For a particle that moves in circular motion the equations simplify to

$$\frac{d\dot{\theta}}{dt} = \ddot{\theta} = \dot{\omega} = \alpha, \ \ \text{rad/s}^2$$

$$\mathbf{v} = r\dot{\theta}\mathbf{n}_\theta \tag{1.3.11}$$

$$\mathbf{a} = -r\dot{\theta}^2\mathbf{n}_r + r\ddot{\theta}\mathbf{n}_\theta$$

Motion of a Particle in Cylindrical Coordinates

Cylindrical coordinates provide a means of describing three-dimensional motion as illustrated in Figure 1.3.6.

$$\begin{gathered}\mathbf{v} = \dot{r}\mathbf{n}_r + r\dot{\theta}\mathbf{n}_\theta + \dot{z}\mathbf{k} \\ \mathbf{a} = \left(\ddot{r} - r\dot{\theta}^2\right)\mathbf{n}_r + \left(r\ddot{\theta} + 2\dot{r}\dot{\theta}\right)\mathbf{n}_\theta + \ddot{z}\mathbf{k}\end{gathered} \tag{1.3.12}$$

Motion of a Particle in Spherical Coordinates

Spherical coordinates are useful in a few special cases but are difficult to apply to practical problems. The governing equations for them are available in many texts.

Relative Motion of Particles in Two and Three Dimensions

Figure 1.3.7 shows relative motion in two and three dimensions. This can be used in analyzing the translation of coordinate axes. Note that the unit vectors of the coordinate systems are the same. Subscripts are arbitrary but must be used consistently because $\mathbf{r}_{B/A} = -\mathbf{r}_{A/B}$, etc.

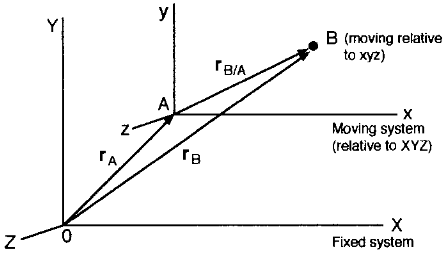

FIGURE 1.3.7 Relative motion using translating coordinates.

$$\begin{aligned} \mathbf{r}_B &= \mathbf{r}_A + \mathbf{r}_{B/A} \\ \mathbf{v}_B &= \mathbf{v}_A + \mathbf{v}_{B/A} \\ \mathbf{a}_B &= \mathbf{a}_A + \mathbf{a}_{B/A} \end{aligned} \tag{1.3.13}$$

Kinetics of Particles

Kinetics combines the methods of kinematics and the forces that cause the motion. Several useful methods of analysis are based on Newton's second law.

Newton's Second Law

The magnitude of the acceleration of a particle is directly proportional to the magnitude of the resultant force acting on it and inversely proportional to its mass. The direction of the acceleration is the same as the direction of the resultant force.

$$\mathbf{F} = m\mathbf{a} \tag{1.3.14}$$

where m is the particle's mass. Three key points should be remembered when applying this equation.

1. **F** is the resultant force.
2. **a** is the acceleration of a single particle (use $\mathbf{a}_C$ for the center of mass for a system of particles).
3. The motion is in a nonaccelerating reference frame.

Equations of Motion

The **equations of motion** for vector and scalar notations in rectangular coordinates are

$$\begin{gathered} \sum \mathbf{F} = m\mathbf{a} \\ \sum F_x = ma_x \qquad \sum F_y = ma_y \qquad \sum F_z = ma_z \end{gathered} \tag{1.3.15}$$

The equations of motion for tangential and normal components are

$$\begin{gathered} \sum F_n = ma_n = m\frac{v^2}{\rho} \\ \sum F_t = ma_t = m\dot{v} = mv\frac{dv}{ds} \end{gathered} \tag{1.3.16}$$

The equations of motion in a polar coordinate system (radial and transverse components) are

$$\begin{aligned} \sum F_r &= ma_r = m\left(\ddot{r} - r\dot{\theta}^2\right) \\ \sum F_\theta &= ma_\theta = m\left(r\ddot{\theta} - 2\dot{r}\dot{\theta}\right) \end{aligned} \tag{1.3.17}$$

Procedure for Solving Problems

1. Draw a free-body diagram of the particle showing all forces. (The free-body diagram will look unbalanced because the particle is not in static equilibrium.)
2. Choose a convenient nonaccelerating reference frame.
3. Apply the appropriate equations of motion for the reference frame chosen to calculate the forces or accelerations applied to the particle.
4. Use kinematics equations to determine velocities and/or displacements if needed.

Work and Energy Methods

Newton's second law is not always the most convenient method for solving a problem. Work and energy methods are useful in problems involving changes in displacement and velocity, if it is not necessary to calculate accelerations.

Work of a Force

The total work of a force **F** in displacing a particle *P* from position 1 to position 2 along any path is

$$U_{12} = \int_1^2 \mathbf{F} \cdot d\mathbf{r} = \int_1^2 \left(F_x\ dx + F_y\ dy + F_z\ dz\right) \tag{1.3.18}$$

Potential and Kinetic Energies

- Gravitational potential energy: $U_{12} = \int_1^2 W\ dy = Wh = V_g$, where W = weight and h = vertical elevation difference
- Elastic potential energy: $U = \int_{x_1}^{x_2} kx\ dx = \frac{1}{2}k(x_2^2 - x_1^2) = V_e$, where k = spring constant
- Kinetic energy of a particle: $T = 1/2mv^2$, where m = mass and v = magnitude of velocity.

Kinetic energy can be related to work by the *principle of work* and *energy*,

$$U_{12} = T_2 - T_1 \tag{1.3.19}$$

where

U_{12} is the work of a force on the particle moving it from position 1 to position 2.
T_1 is the kinetic energy of the particle at position 1 (initial kinetic energy).
T_2 is the kinetic energy of the particle at position 2 (final kinetic energy).

Power

Power is defined as work done in a given time.

$$\text{power} = \frac{dU}{dt} = \frac{\mathbf{F} \cdot d\mathbf{r}}{dt} = \mathbf{F} \cdot \mathbf{v} \tag{1.3.20}$$

where **v** is velocity.

Important units and conversions of power are

$$1\ \mathrm{W} = 1\ \mathrm{J/s} = 1\ \mathrm{N}\cdot\mathrm{m/s}$$

$$1\ \mathrm{hp} = 550\ \mathrm{ft}\cdot\mathrm{lb/s} = 33{,}000\ \mathrm{ft}\cdot\mathrm{lb/min} = 746\ \mathrm{W}$$

$$1\ \mathrm{ft}\cdot\mathrm{lb/s} = 1.356\ \mathrm{J/s} = 1.356\ \mathrm{W}$$

Advantages and Disadvantages of the Energy Method

Using the energy method in engineering problems offers four advantages:

1. Accelerations do not need to be determined.
2. Modifications of problems are easy to make in the analysis.
3. Scalar quantities are summed, even if the path of motion is complex.
4. Forces that do not do work are ignored.

The main disadvantage of the energy method is that quantities of work or energy cannot be used to determine accelerations or forces that do no work. In these instances, Newton's second law must be used.

Conservative Systems and Potential Functions

Sometimes it is useful to assume a conservative system where friction does not oppose the motion of the particle. The work in a conservative system is independent of the path of the particle, and potential energy is defined as

$$\underbrace{U_{12}}_{\substack{\text{work of } \mathbf{F}\\ \text{from 1 to 2}}} = \underbrace{-\Delta V}_{\substack{\text{difference of potential}\\ \text{energies at 1 and 2}}}$$

A special case is one in which the particle moves in a closed path. One trip around the path is called a cycle.

$$U = \oint dU = \oint \mathbf{F}\cdot d\mathbf{r} = \oint \left(F_x\ dx + F_y\ dy + F_z\ dz\right) = 0 \qquad (1.3.21)$$

In advanced analysis, differential changes in the potential energy function (V) are calculated by the use of partial derivatives,

$$\mathbf{F} = F_x\mathbf{i} + F_y\mathbf{j} + F_z\mathbf{k} = -\left(\frac{\partial V}{\partial x}\mathbf{i} + \frac{\partial V}{\partial y}\mathbf{j} + \frac{\partial V}{\partial z}\mathbf{k}\right)$$

Conservation of Mechanical Energy

Conservation of mechanical energy is assumed if kinetic energy (T) and potential energy (V) change back and forth in a conservative system (the dissipation of energy is considered negligible). Equation (1.3.22) formalizes such a situation, in which position 1 is the initial state and position 2 is the final state. The reference (datum) should be chosen to reduce the number of terms in the equation.

$$T_1 + V_1 = T_2 + V_2 \qquad (1.3.22)$$

Linear and Angular Momentum Methods

The concept of linear momentum is useful in engineering when the accelerations of particles are not known but the velocities are. The linear momentum is derived from Newton's second law,

$$\mathbf{G} = m\mathbf{v} \qquad (1.3.23)$$

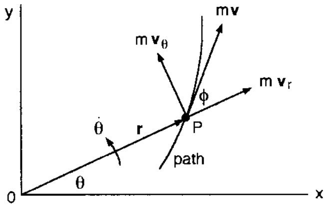

FIGURE 1.3.8 Definition of angular momentum for a particle.

The time rate of change of linear momentum is equal to force. When $m\mathbf{v}$ is constant, the conservation of momentum equation results,

$$\sum \mathbf{F} = \dot{\mathbf{G}} = \frac{d}{dt}(m\mathbf{v})$$

$$\sum \mathbf{F} = 0 \qquad m\mathbf{v} = \text{constant} \qquad (\text{conservation of momentum}) \tag{1.3.24}$$

The method of angular momentum is based on the momentum of a particle about a fixed point, using the vector product in the general case (Figure 1.3.8).

$$\mathbf{H}_O = \mathbf{r} \times m\mathbf{v} \tag{1.3.25}$$

The angular momentum equation can be solved using a scalar method if the motion of the particle remains in a plane,

$$\mathbf{H}_O = mrv\sin\phi = mrv_\theta = mr^2\dot\theta$$

If the particle does not remain in a plane, then the general space motion equations apply. They are derived from the cross product $\mathbf{r} \times m\mathbf{v}$,

$$\begin{gathered} \mathbf{H}_O = H_x\mathbf{i} + H_y\mathbf{j} + H_z\mathbf{k} \\ H_x = m(yv_z - zv_y) \\ H_y = m(zv_x - xv_z) \\ H_z = m(xv_y - yv_x) \end{gathered} \tag{1.3.25a}$$

Time Rate of Change of Angular Momentum

In general, a force acting on a particle changes its angular momentum: *the time rate of change of angular momentum of a particle is equal to the sum of the moments of the forces acting on the particle.*

Vectors: $$\dot{\mathbf{H}}_O = \frac{d}{dt}(\mathbf{r} \times m\mathbf{v}) = \mathbf{r} \times \sum \mathbf{F} = \sum \mathbf{H}_O \tag{1.3.26}$$

Scalars: $$\sum M_x = \dot H_x \qquad \sum M_y = \dot H_y \qquad \sum M_z = \dot H_z$$

$$\sum \mathbf{M}_O = 0 \qquad \mathbf{H}_O = \mathbf{r} \times m\mathbf{v} = \text{constant}$$

$$(\text{conservation of angular momentum}) \tag{1.3.27}$$

A special case is when the sum of the moments about point O is zero. This is the conservation of angular momentum. In this case (motion under a central force), if the distance r increases, the velocity must decrease, and vice versa.

Impulse and Momentum

Impulse and momentum are important in considering the motion of particles in impact. The linear impulse and momentum equation is

$$\underbrace{\int_{t_1}^{t_2} \mathbf{F}\, dt}_{\text{impulse}} = \underbrace{m\mathbf{v}_2}_{\substack{\text{final}\\\text{momentum}}} - \underbrace{m\mathbf{v}_1}_{\substack{\text{initial}\\\text{momentum}}} \tag{1.3.28}$$

Conservation of Total Momentum of Particles

Conservation of total momentum occurs when *the initial momentum of n particles is equal to the final momentum of those same n particles*,

$$\underbrace{\sum_i^n \left(m_i \mathbf{v}_i\right)_1}_{\substack{\text{total initial}\\\text{momentum at time } t_1}} = \underbrace{\sum_i^n \left(m_i \mathbf{v}_i\right)_2}_{\substack{\text{total final}\\\text{momentum at time } t_2}} \tag{1.3.29}$$

When considering the response of two deformable bodies to direct central impact, the coefficient of restitution is used. This coefficient e relates the initial velocities of the particles to the final velocities,

$$e = \frac{v_{Bf} - v_{Af}}{v_A - v_B} = \frac{|\text{relative velocity of separation}|}{|\text{relative velocity of approach}|} \tag{1.3.30}$$

For real materials, $0 < e < 1$. If both bodies are *perfectly elastic*, $e = 1$, and if either body is *perfectly plastic*, $e = 0$.

Kinetics of Systems of Particles

There are three distinct types of systems of particles: discrete particles; continuous particles in fluids; and continuous particles in rigid or deformable bodies. This subsection considers methods for discrete particles that have relevance to the mechanics of solids. Methods involving particles in rigid bodies will be discussed in later sections.

Newton's Second Law Applied to a System of Particles

Newton's second law can be extended to systems of particles,

$$\sum_{i=1}^n \mathbf{F}_i = \sum_{i=1}^n m_i \mathbf{a}_i \tag{1.3.31}$$

Motion of the Center of Mass

The center of mass of a system of particles moves under the action of internal and external forces as if the total mass of the system and all the external forces were at the center of mass. Equation (1.3.32) defines the position, velocity, and acceleration of the center of mass of a system of particles.

$$m\mathbf{r}_C = \sum_{i=1}^n m_i \mathbf{r}_i \qquad m\mathbf{v}_C = \sum_{i=1}^n m_i \mathbf{v}_i \qquad m\mathbf{a}_C = \sum_{i=1}^n m_i \mathbf{a}_i \qquad \sum \mathbf{F} = m\mathbf{a}_C \tag{1.3.32}$$

Work and Energy Methods for a System of Particles

Gravitational Potential Energy. The gravitational potential energy of a system of particles is the sum of the potential energies of the individual particles of the system:

$$V_g = g\sum_{i=1}^{n} m_i y_i = \sum_{i=1}^{n} W_i y_i = mgy_C = Wy_C \tag{1.3.33}$$

where

g = acceleration of gravity
y_C = vertical position of center of mass with respect to a reference level

Kinetic energy. The kinetic energy of a system of particles is the sum of the kinetic energies of the individual particles of the system with respect to a fixed reference frame,

$$T = \frac{1}{2}\sum_{i=1}^{n} m_i v_i^2 \tag{1.3.34}$$

A translating reference frame located at the mass center C of a system of particles can be used advantageously, with

$$T = \underbrace{\frac{1}{2}mv_C^2}_{\substack{\text{motion of total}\\ \text{mass imagined to}\\ \text{be concentrated at C}}} + \underbrace{\frac{1}{2}\sum_{i=1}^{n} m_i v_i'^2}_{\substack{\text{motion of all}\\ \text{particles relative to } C}} \qquad (v' \text{ are with respect to a translating frame}) \tag{1.3.35}$$

Work and Energy

The work and energy equation for a system of particles is similar to the equation stated for a single particle:

$$\begin{gathered}\sum_{i=1}^{n} U_i' = \sum_{i=1}^{n} V_i + \sum_{i=1}^{n} T_i \\ U' = \Delta V + \Delta T\end{gathered} \tag{1.3.36}$$

Momentum Methods for a System of Particles

Moments of Forces on a System of Particles. The moments of external forces on a system of particles about a point O are given by

$$\sum_{i=1}^{n}\left(\mathbf{r}_i \times \mathbf{F}_i\right) = \sum_{i=1}^{n} \mathbf{M}_{i_O} + \sum_{i=1}^{n}\left(\mathbf{r}_i \times m_i \mathbf{a}_i\right) \tag{1.3.37}$$

Linear and Angular Momenta of a System of Particles. The resultant of the external forces on a system of particles equals the time rate of change of linear momentum of that system:

$$\mathbf{G} = \sum_{i=1}^{n} m_i \mathbf{v}_i \qquad \sum \mathbf{F} = \dot{\mathbf{G}} \tag{1.3.38}$$

The angular momentum equation for a system of particles about a fixed point O is

$$\mathbf{H}_O = \sum_{i=1}^{n} \left(\mathbf{r}_i \times m_i \mathbf{a}_i\right)$$

$$\sum \mathbf{M}_O = \dot{\mathbf{H}}_O = \sum_{i=1}^{n} \left(\mathbf{r}_i \times m_i \mathbf{a}_i\right) \tag{1.3.39}$$

This last equation means that *the resultant of the moments of the external forces on a system of particles equals the time rate of change of angular momentum of that system.*

Angular Momentum about the Center of Mass

The preceding equations work well for stationary reference frames, but sometimes a special approach may be useful, noting that *the angular momentum of a system of particles about its center of mass C is the same whether it is observed from a fixed frame at point O or from the centroidal frame, which may be translating but not rotating*. In this case

$$\mathbf{H}_O = \mathbf{H}_C + \mathbf{r}_C \times m\mathbf{v}_C$$

$$\sum \mathbf{M}_O = \dot{\mathbf{H}}_C + \mathbf{r}_C \times m\mathbf{a}_C \tag{1.3.40}$$

Conservation of Momentum

The conservation of momentum equations for a system of particles is analogous to that for a single particle.

$$\left.\begin{aligned} \mathbf{G} &= \text{constant} \\ \mathbf{H}_O &= \text{constant} \\ \mathbf{H}_C &= \text{constant} \end{aligned}\right\} \quad \text{not the same constants in general}$$

Impulse and Momentum of a System of Particles

The linear impulse momentum for a system of particles is

$$\sum_{i=1}^{n} \int_{t_1}^{t_2} \mathbf{F}_i \, dt = \mathbf{G}_2 - \mathbf{G}_1 = m\mathbf{v}_{C_2} - m\mathbf{v}_{C_1} \tag{1.3.41}$$

The angular impulse momentum for a system of particles is

$$\sum_{i=1}^{n} \int_{t_1}^{t_2} \mathbf{M}_{i_O} \, dt = \mathbf{H}_{O_2} - \mathbf{H}_{O_1} \tag{1.3.42}$$

Kinematics of Rigid Bodies

Rigid body kinematics is used when the methods of particle kinematics are inadequate to solve a problem. A rigid body is defined as one in which the particles are rigidly connected. This assumption allows for some similarities to particle kinematics. The two kinds of rigid body motion are translation and rotation. These motions may occur separately or in combination.

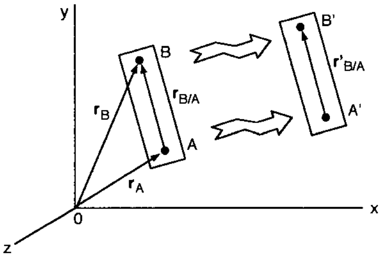

FIGURE 1.3.9 Translational motion of a rigid body.

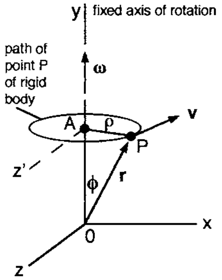

FIGURE 1.3.10 Rigid body rotating about a fixed axis.

Translation

Figure 1.3.9 models the translational motion of a rigid body.

$$\begin{aligned} \mathbf{r}_B &= \mathbf{r}_A + \mathbf{r}_{B/A} \qquad \left(\mathbf{r}_{B/A} = \text{constant}\right) \\ \mathbf{v}_B &= \dot{\mathbf{r}}_B = \dot{\mathbf{r}}_A = \mathbf{v}_A \\ \mathbf{a}_B &= \dot{\mathbf{v}}_B = \dot{\mathbf{v}}_A = \mathbf{a}_A \end{aligned} \tag{1.3.43}$$

These equations represent an important fact: *when a rigid body is in translation, the motion of a single point completely specifies the motion of the whole body.*

Rotation about a Fixed Axis

Figure 1.3.10 models a point P in a rigid body rotating about a fixed axis with an angular velocity ω. The velocity **v** of point P is determined assuming that the magnitude of **r** is constant,

$$\mathbf{v} = \omega \times \mathbf{r} \tag{1.3.44}$$

The acceleration **a** of point P is determined conveniently by using normal and tangential components,

$$\begin{aligned} \mathbf{a}_P &= \underbrace{\alpha \times r}_{\mathbf{a}_t} + \underbrace{\omega \times \left(\omega \times \mathbf{r}\right)}_{\mathbf{a}_n} \\ a_t &= \rho\alpha \qquad a_n = \rho\omega^2 \end{aligned} \tag{1.3.45}$$

Note that *the angular acceleration a and angular velocity w are valid for any line perpendicular to the axis of rotation of the rigid body at a given instant.*

Kinematics Equations for Rigid Bodies Rotating in a Plane

For rotational motion with or without a fixed axis, if displacement is measured by an angle θ,

Angular speed: $$\omega = \frac{d\theta}{dt}$$

Angular acceleration: $$\alpha = \frac{d\omega}{dt} = \omega \frac{d\omega}{d\theta}$$

For a constant angular speed ω,

Angular displacement: $$\theta = \theta_o + \omega t \qquad (\theta = \theta_o \text{ at } t = 0)$$

For a constant angular acceleration α,

$$\omega = \omega_o + \alpha t \qquad (\omega = \omega_o \text{ at } t = 0)$$

$$\theta = \theta_o + \omega_o t + \frac{1}{2}\alpha t^2$$

$$\omega^2 = \omega_o^2 + 2\alpha(\theta - \theta_o)$$

Velocities in General Plane Motion

General plane motion of a rigid body is defined by simultaneous translation and rotation in a plane. Figure 1.3.11 illustrates how the velocity of a point *A* can be determined using Equation (1.3.46), which is based on relative motion of particles.

$$\mathbf{v}_A = \underbrace{\mathbf{v}_B}_{\text{translation}} + \underbrace{\omega \times \mathbf{r}_{A/B}}_{\text{rotation}} \tag{1.3.46}$$

Five important points should be remembered when solving general plane motion problems, including those of interconnected rigid bodies.

1. The angular velocity of a rigid body in plane motion is independent of the reference point.
2. The common point of two or more pin-jointed members must have the same absolute velocity even though the individual members may have different angular velocities.

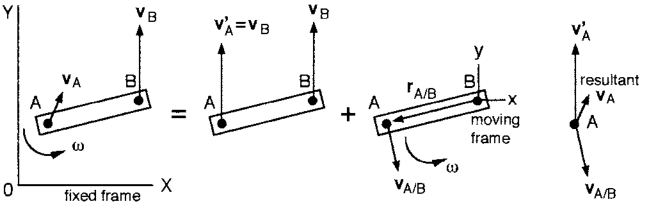

(a) General plane motion
(b) Translation only
(c) Rotation only
(d) Result for point A

FIGURE 1.3.11 Analysis of velocities in general plane motion.

3. The points of contact in members that are in temporary contact may or may not have the same absolute velocity. If sliding occurs between the members, the points in contact have different absolute velocities. The absolute velocities of the contacting particles are always the same if no sliding takes place.
4. If the angular velocity of a member is not known, but some points of the member move along defined paths (i.e., the end points of a piston rod), these paths define the directions of the velocity vectors and are useful in the solution.
5. The geometric center of a wheel rolling on a flat surface moves in rectilinear motion. If no slipping occurs at the point of contact, the linear distance that the center point travels is equal to the portion of the rim circumference that has rolled along the flat surface.

Instantaneous Center of Rotation

The method of *instantaneous center of rotation* is a geometric method of determining the angular velocity when two velocity vectors are known for a given rigid body. Figure 1.3.12 illustrates the method. This procedure can also be used to determine velocities parallel to one of the given velocities, by similar triangles. Velocities $\mathbf{v}_A$ and $\mathbf{v}_B$ are given; thus the body is rotating about point I at that instant. Point I has zero velocity at that instant, but generally has an acceleration. This method does not work for the determination of angular accelerations.

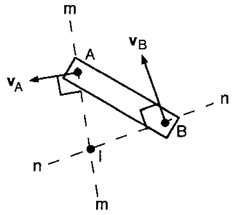

FIGURE 1.3.12 Schematic for instantaneous center of rotation.

Acceleration in General Plane Motion

Figure 1.3.13 illustrates a method of determining accelerations of points of a rigid body. This is similar to (but more difficult than) the procedure of determining velocities.

$$\mathbf{a}_B = \mathbf{a}_A + \alpha \times \mathbf{r}_{B/A} + \omega \times \left(\omega \times \mathbf{r}_{B/A}\right)$$

$$\mathbf{a}_B = \underbrace{\mathbf{a}_A}_{\text{translation}} + \underbrace{\left(\mathbf{a}_{B/A}\right)_t + \left(\mathbf{a}_{B/A}\right)_n}_{\text{rotation}} \tag{1.3.47}$$

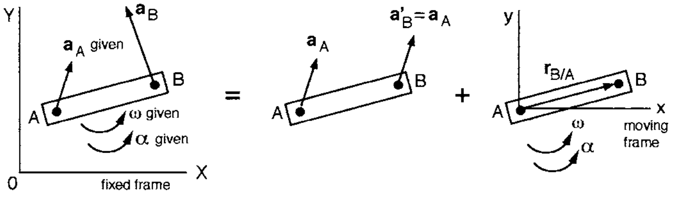

(a) General plane motion

(b) Translation only

(c) Rotation only

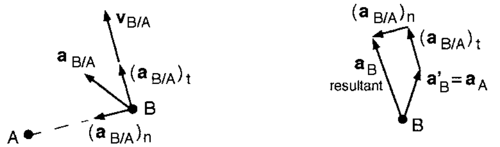

(d) Velocity and acceleration of point B from rotation only

(e) Total acceleration of point B

FIGURE 1.3.13 Accelerations in general plane motion.

Six key points should be considered when solving this kind of a problem.

1. The angular velocity and acceleration of a rigid body in plane motion are independent of the reference point.
2. The common points of pin-jointed members must have the same absolute acceleration even though the individual members may have different angular velocities and angular accelerations.
3. The points of contact in members that are in temporary contact may or may not have the same absolute acceleration. Even when no sliding between the members occurs, only the tangential accelerations of the points in contact are the same; the normal accelerations are frequently different in magnitude and direction.
4. The instantaneous center of zero velocity in general has an acceleration and should *not* be used as a reference point for accelerations unless its acceleration is known and included in the analysis.
5. If the angular acceleration of a member is not known, but some points of the member move along defined paths, the geometric constraints of motion define the directions of normal and tangential acceleration vectors and are useful in the solution.
6. The geometric center of a wheel rolling on a flat surface moves in rectilinear motion. If no slipping occurs at the point of contact, the linear acceleration of the center point is parallel to the flat surface and equal to *ra* for a wheel of radius *r* and angular acceleration α.

General Motion of a Rigid Body

Figure 1.3.14 illustrates the complex general motion (three-dimensional) of a rigid body. It is important to note that here the angular velocity and angular acceleration vectors are not necessarily in the same direction as they are in general plane motion. Equation (1.3.48) gives the velocity and acceleration of a point on the rigid body. These equations are the same as those presented for plane motion.

$$\begin{aligned} \mathbf{v}_B &= \mathbf{v}_A + \omega \times \mathbf{r}_{B/A} \\ \mathbf{a}_B &= \mathbf{a}_A + \alpha \times \mathbf{r}_{B/A} + \omega \times \left(\omega \times \mathbf{r}_{B/A}\right) \\ \mathbf{a}_B &= \mathbf{a}_A + \left(\mathbf{a}_{B/A}\right)_t + \left(\mathbf{a}_{B/A}\right)_n \end{aligned} \tag{1.3.48}$$

The most difficult part of solving a general motion problem is determining the angular acceleration vector. There are three cases for the determination of the angular acceleration:

1. The direction of ω is constant. This is plane motion and $\alpha = \dot{\omega}$ can be used in scalar solutions of problems.
2. The magnitude of ω is constant but its direction changes. An example of this is a wheel that travels at a constant speed on a curved path.
3. The magnitude and direction of ω change. This is *space motion* because all or some points of the rigid body have three-dimensional paths. An example of this is a wheel that accelerates on a curved path.

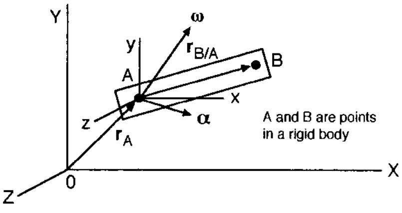

FIGURE 1.3.14 General motion of a rigid body.

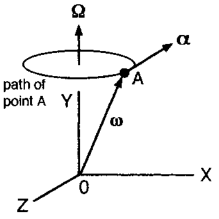

FIGURE 1.3.15 Rigid body fixed at point *O*.

A useful expression can be obtained from the second item and Figure 1.3.15. The rigid body is fixed at point *O* and ω has a constant magnitude. Let ω rotate about the **Y** axis with angular velocity **Ω**. The angular acceleration is determined from Equation (1.3.49).

$$\alpha = \frac{d\omega}{dt} = \Omega \times \omega \tag{1.3.49}$$

For *space motion*, it is essential to combine the results of the first two items, which provide components of α for the change in magnitude and the change in direction. The following example illustrates the procedure.

Example 9

The rotor shaft of an alternator in a car is in the horizontal plane. It rotates at a constant angular speed of 1500 rpm while the car travels at v = 60 ft/sec on a horizontal road of 400 ft radius (Figure 1.3.16). Determine the angular acceleration of the rotor shaft if v increases at the rate of 8 ft/sec^2.

Solution. There are two components of α. One is the change in the direction of the rotor shaft's ω_x, and the other is the change in magnitude from the acceleration of the car.

- Component from the change in direction. Determine ω_c of the car. Use Equation (1.3.49):

$$v = r\omega_c$$

$$\omega_c = 0.15 \text{ rad/sec } \mathbf{k}$$

$$\alpha = \omega_c \times \omega = \begin{vmatrix} \mathbf{i} & \mathbf{j} & \mathbf{k} \\ 0 & 0 & 0.15 \\ 157.1 & 0 & 0 \end{vmatrix} = 23.6\mathbf{j} \text{ rad/sec}^2$$

- Component from the acceleration of the car. Use Equation (1.3.9):

$$\alpha_C r = a_t$$

$$\alpha_C = 0.02\mathbf{k}\,\text{rad/sec}^2$$

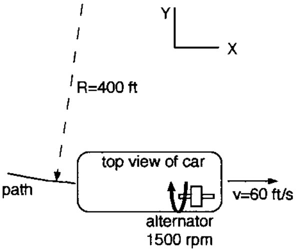

FIGURE 1.3.16 Schematic of shaft's motion.

The angular acceleration of the rotor shaft is

$$\alpha = (23.6\mathbf{j} + 0.02\mathbf{k})\text{rad/sec}^2$$

This problem could also be solved using the method in the next section.

Time Derivative of a Vector Using a Rotating Frame

The basis of determining time derivatives of a vector using a rotating frame is illustrated in Figure 1.3.17.

$$(\mathbf{Q})_{XYZ} = \left(\dot{\mathbf{Q}}\right)_{xyz} + \Omega \times \mathbf{Q}$$

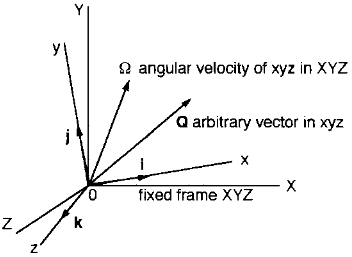

FIGURE 1.3.17 Time derivative of a vector using a rotating reference frame.

Analysis of Velocities and Accelerations Using Rotating and Translating Frames

With the concept of general motion understood, an advantageous method of determining velocities and accelerations is available by the method of rotating reference frames. This method can be used in two cases:

1. For a common origin of *XYZ* and *xyz*, with **r** a position vector to a point *P*,

$$\mathbf{v}_P = \mathbf{v}_{xyz} + \Omega \times \mathbf{r}$$
$$\mathbf{a}_P = \mathbf{a}_{xyz} + \dot{\Omega} \times \mathbf{r} + \Omega \times (\Omega \times \mathbf{r}) + 2\Omega \times \mathbf{v}_{xyz} \tag{1.3.50}$$

2. For the origin *A* of *xyz* translating with respect *XYZ*:

$$\mathbf{v}_P = \mathbf{v}_A + \left(\dot{\mathbf{r}}_{P/A}\right)_{xyz} + \Omega \times \mathbf{r}_{P/A}$$
$$\mathbf{a}_P = \mathbf{a}_A + \mathbf{a}_{xyz} + \dot{\Omega} \times \mathbf{r}_{P/A} + \Omega \times \left(\Omega \times \mathbf{r}_{P/A}\right) + 2\Omega \times \mathbf{v}_{xyz} \tag{1.3.51}$$

where Ω is the angular velocity of the *xyz* frame with respect to *XYZ*. $2\Omega \times \mathbf{v}_{xyz}$ is the Coriolis acceleration.

Kinetics of Rigid Bodies in Plane Motion

Equation of Translational Motion

The fundamental equation for rigid body translation is based on Newton's second law. In Equation (1.3.52), **a** is the acceleration of the center of mass of the rigid body, no matter where the resultant force acts on the body. *The sum of the external forces is equal to the mass of the rigid body times the acceleration of the mass center of the rigid body*, independent of any rotation of the body.

$$\sum \mathbf{F} = m\mathbf{a}_C \tag{1.3.52}$$

Equation of Rotational Motion

Equation (1.3.53) states that *the sum of the external moments on the rigid body is equal to the moment of inertia about an axis times the angular acceleration of the body about that axis*. The angular acceleration α is for the rigid body rotating about an axis. This equation is independent of rigid body translation.

$$\sum \mathbf{M}_C = I_C \alpha \qquad (1.3.53)$$

where $\Sigma \mathbf{M}_C = \dot{\mathbf{H}}_C$, $\mathbf{H}_C = I_C \omega$. An application is illustrated in Color Figure 2.

Applications of Equations of Motion

It is important to use the equations of motion properly. For plane motion, three scalar equations are used to define the motion in a plane:

$$\sum F_x = ma_{C_x} \qquad \sum F_y = ma_{C_y} \qquad \sum M_C = I_C \alpha \qquad (1.3.54)$$

If a rigid body undergoes only translation,

$$\sum F_x = ma_{C_x} \qquad \sum F_y = ma_{C_y} \qquad \sum M_C = 0 \qquad (1.3.55)$$

If the rigid body undergoes pure rotation about the center of mass,

$$\sum F_x = 0 \qquad \sum F_y = 0 \qquad \sum M_C = I_C \alpha \qquad (1.3.56)$$

Rigid body motions are categorized according to the constraints of the motion:

1. *Unconstrained Motion*: Equation (1.3.54) is directly applied, with all three equations independent of one another.
2. *Constrained Motion*: the equations in Equation (1.3.54) are not independent of one another. Generally, a kinematics analysis must be made to determine how the motion is constrained in the plane. Consider two special cases:
   a. Point constraint: the body has a fixed axis.
   b. Line constraint: the body moves along a fixed line or plane.

When considering systems of rigid bodies, it is important to remember that, at most, only three equations of motion are available from each free-body diagram for plane motion to solve for three unknowns. The motion of interconnected bodies must be analyzed using related free-body diagrams.

Rotation about a Fixed Axis not through the Center of Mass

The methods presented previously are essential in analyzing rigid bodies that rotate about a fixed axis, which is common in machines (shafts, wheels, gears, linkages). The mass of the rotating body may be nonuniformly distributed as modeled in Figure 1.3.18. Note that r_C is the nearest distance between the fixed axis O and the mass center C. The figure also defines the normal and tangential coordinate system used in Equation (1.3.57), which comprises the scalar equations of motion using normal and tangential components. The sum of the forces must include all reaction forces on the rigid body at the axis of rotation.

$$\sum F_n = mr_C \omega^2 \qquad \sum F_t = mr_C \alpha \qquad \sum M_O = I_O \alpha \qquad (1.3.57)$$

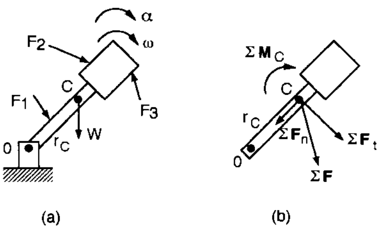

FIGURE 1.3.18 Rotation of a rigid body about a fixed axis.

General Plane Motion

A body that is translating and rotating is in general plane motion. The scalar equations of motion are given by Equation (1.3.54). If an arbitrary axis A is used to find the resultant moment,

$$\sum \mathbf{M}_A = I_A \alpha + \mathbf{r} \times m\mathbf{a}_C \tag{1.3.58}$$

where C is the center of mass. It is a common error to forget to include the cross-product term in the analysis.

General plane motion has two special cases: *rolling* and *sliding*. Figure 1.3.19 shows pure rolling of a wheel without slipping with the center of mass C at the geometric center of the wheel. This is called pure rolling of a balanced wheel. From this figure the scalar equation of motion results,

$$a_{C_x} = r\alpha \qquad \sum \mathbf{M}_A = I_A \alpha \tag{1.3.59}$$

For balanced wheels that slide or do not slide, the following schematic is helpful:

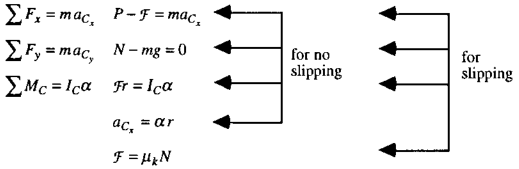
$\sum F_x = ma_{C_x}$ $\quad P - \mathcal{F} = ma_{C_x}$

$\sum F_y = ma_{C_y}$ $\quad N - mg = 0$

$\sum M_C = I_C \alpha$ $\quad \mathcal{F}r = I_C \alpha$

$a_{C_x} = \alpha r$

$\mathcal{F} = \mu_k N$

If slipping is not certain, assume that no slipping has occurred and check whether $\mathcal{F} \le \mu_s N$. If $\mathcal{F} > \mu_s N$ (not possible; there is sliding), start the solution over using $\mathcal{F} = \mu_k N$ but not using $a_{C_x} = r\alpha$, which is not valid here.

For the problem involving unbalanced wheels (the mass center and geometric center do not coincide), Equation (1.3.60) results:

$$\begin{gathered} a_{C_x} \neq r\alpha \qquad a_G = r\alpha \\ \mathbf{a}_C = \mathbf{a}_G + \mathbf{a}_{C/G} = \mathbf{a}_G + \left(\mathbf{a}_{C/G}\right)_n + \left(\mathbf{a}_{C/G}\right)_t \end{gathered} \tag{1.3.60}$$

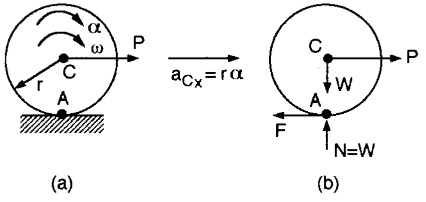

FIGURE 1.3.19 Pure rolling of a wheel.

Energy and Momentum Methods for Rigid Bodies in Plane Motion

Newton's second law in determining kinetics relationships is not always the most efficient, although it always works. When particles are considered, energy and momentum methods are often useful to analyze rigid bodies in plane motion.

Work of a Force on a Rigid Body

The work of a force acting on a rigid body moving from position 1 to 2 is

$$U_{12} = \int_1^2 \mathbf{F} \cdot d\mathbf{r} = \int_1^2 \mathbf{F} \cdot \mathbf{v}\, dt \tag{1.3.61}$$

Work of a Moment

The work of a moment has a similar form, for angular positions θ,

$$U_{12} = \int_{\theta_1}^{\theta_2} \mathbf{M} \cdot d\theta \tag{1.3.62}$$

In the common case in which the moment vector **M** is perpendicular to the plane of motion, $\mathbf{M} \cdot d\theta = M\, d\theta$.

It is important to note those forces that do no work:

- Forces that act at fixed points on the body do not do work. For example, the reaction at a fixed, frictionless pin does no work on the body that rotates about that pin.
- A force that is always perpendicular to the direction of the motion does no work.
- The weight of a body does no work when the body's center of gravity moves in a horizontal plane.
- The friction force $\mathscr{F}$ at a point of contact on a body that rolls without slipping does no work because the point of contact is the instantaneous center of zero velocity.

Kinetic Energy of a Rigid Body

The kinetic energy of a particle only consists of the energy associated with its translational motion. The kinetic energy of a rigid body also includes a term for the rotational energy of the body,

$$T = T_{trans} + T_{rot} = \frac{1}{2} m v_C^2 + \frac{1}{2} I_C \omega^2 \tag{1.3.63}$$

where C is the center of mass of the rigid body.

The kinetic energy of a rigid body rotating about an arbitrary axis at point O is

$$T = \frac{1}{2} I_O \omega^2$$

Principle of Work and Energy

The principle of work and energy for a rigid body is the same as that used for particles with the addition of the rotational energy terms.

$$T_2 = T_1 + U_{12} \tag{1.3.64}$$

where

T_1 = initial kinetic energy of the body
T_2 = final kinetic energy of the body
U_{12} = work of all external forces and moments acting on the body moving from position 1 to 2

This method is advantageous when displacements and velocities are the desired quantities.

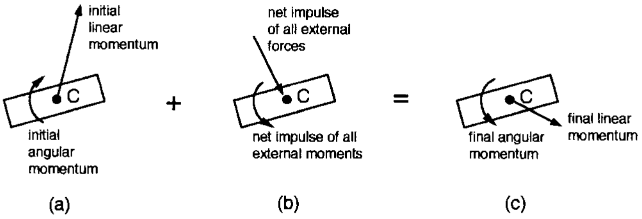

FIGURE 1.3.20 Impulse and momentum for rigid bodies.

Conservation of Energy

The conservation of energy in a conservative rigid body system is

$$T_1 + V_1 = T_2 + V_2 \tag{1.3.65}$$

where

T = kinetic energy
V = total potential energy (gravitational and elastic)

Power

The net power supplied to or required of the system is

$$\text{power} = \dot{T}_{trans} + \dot{T}_{rot} + \dot{V}_g + \dot{V}_e \tag{1.3.66}$$

This can be calculated by taking time derivatives of the kinetic and potential energy terms. Each term is considered positive when it represents the power supplied to the system and negative when power is taken from the system.

Impulse and Momentum of a Rigid Body

Impulse and momentum methods are particularly useful when time and velocities are of interest. Figure 1.3.20 shows how rigid bodies are to be considered for this kind of analysis. Notice that rotational motion of the rigid body must be included in the modeling.

The impulse of the external forces in the given interval is

$$\int_{t_1}^{t_2} \sum \mathbf{F}\, dt = m_{C_2}\left(\mathbf{v}_{C_2} - \mathbf{v}_{C_1}\right) \tag{1.3.67}$$

where

t is time
C is the center of mass
$\Sigma\mathbf{F}$ includes all external forces

The impulse of the external moments in the given interval is

$$\int_{t_1}^{t_2} \sum \mathbf{M}_C\, dt = \mathbf{H}_{C_2} - \mathbf{H}_{C_1} \tag{1.3.68}$$

For plane motion, if $\Sigma\mathbf{M}$ is parallel to w, the scalar expressions are

$$\int_{t_1}^{t_2} \sum M_C \, dt = I_C(\omega_2 - \omega_1)$$

$$\int_{t_1}^{t_2} \sum M_O \, dt = I_O(\omega_2 - \omega_1) \quad \text{for rotation about a fixed point } O \tag{1.3.69}$$

Impulse and Momentum of a System of Rigid Bodies

A system of rigid bodies can be analyzed using one of the two following procedures, illustrated in Figure 1.3.21:

1. Apply the principle of impulse and momentum to each rigid member separately. The mutual forces acting between members must be included in the formulation of the solution.
2. Apply the principle of impulse and momentum to the entire system of bodies, ignoring the mutual forces between members.

Conservation of Momentum

The principle of conservation of linear and angular momentum of particles can be extended to rigid bodies that have no external forces or moments acting on them. The conservation of linear momentum means that the center of mass *C* moves at a constant speed in a constant direction,

$$\sum \mathbf{F} = 0 \Rightarrow \Delta \mathbf{G} = 0$$

$$\mathbf{v}_{C_1} = \mathbf{v}_{C_2} \tag{1.3.70}$$

Likewise, for conservation of angular momentum of rigid bodies,

$$\sum \mathbf{M} = 0 \Rightarrow \Delta \mathbf{H}_C = 0$$

$$I_C \omega_1 = I_C \omega_2 \tag{1.3.71}$$

For a system of rigid bodies, use the same fixed reference point *O* for all parts of the system. Thus, for plane motion,

$$\Delta \mathbf{H}_O = 0 \qquad I_O \omega_1 = I_O \omega_2 \tag{1.3.72}$$

Two important points should be remembered when these equations are used. First, $\Delta \mathbf{H}_C = 0$ does not imply that $\Delta \mathbf{H}_O = 0$, or vice versa. Second, conservation of momentum does not require the simultaneous conservation of angular and linear momenta (for example, there may be an angular impulse while linear momentum is conserved).

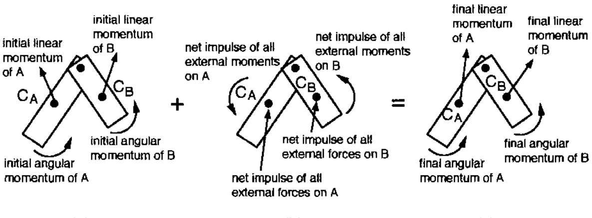

FIGURE 1.3.21 System of rigid bodies.

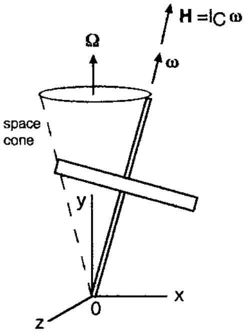

FIGURE 1.3.22 Motion of an inclined, spinning top.

Kinetics of Rigid Bodies in Three Dimensions

The concepts of plane rigid body motion can be extended to the more complicated problems in three dimensions, such as those of gyroscopes and jet engines. This section briefly covers some fundamental topics. Many additional topics and useful methods are included in the technical literature.

Angular Momentum in Three Dimensions

For analyzing three-dimensional angular momentum, three special definitions are used. These can be visualized by considering a spinning top (Figure 1.3.22):

- *Precession* — rotation of the angular velocity vector about the y axis
- *Space Cone* — locus of the absolute positions of the instantaneous axis of rotation
- *Body Cone* — locus of the positions of the instantaneous axis relative to the body; the body cone appears to roll on the space cone (not shown here)

Equation (1.3.73) provides the scalar components of the total angular momentum.

$$\begin{aligned} H_x &= I_x\omega_x - I_{xy}\omega_y - I_{xz}\omega_z \\ H_y &= -I_{xy}\omega_x + I_y\omega_y - I_{yz}\omega_z \\ H_z &= -I_{zx}\omega_x - I_{zy}\omega_y + I_z\omega_z \end{aligned} \tag{1.3.73}$$

Impulse and Momentum of a Rigid Body in Three-Dimensional Motion

The extension of the planar motion equations of impulse and momentum to three dimensions is straightforward:

$$\text{System momenta} = \begin{cases} \text{linear momentum of mass center } (\mathbf{G}) \\ \text{angular momentum about mass center } (\mathbf{H}_C) \end{cases} \tag{1.3.74}$$

where **G** and **H** have different units. The principle of impulse and momentum is applied for the period of time t_1 to t_2,

$$\begin{aligned} \mathbf{G}_2 &= \mathbf{G}_1 + (\text{external linear impulses})\Big|_1^2 \\ \mathbf{H}_{C_2} &= \mathbf{H}_{C_1} + (\text{external angular impulses})\Big|_1^2 \end{aligned} \tag{1.3.75}$$

Kinetic Energy of a Rigid Body in Three-Dimensional Motion

The total kinetic energy of a rigid body in three dimensions is

$$T = \underbrace{\frac{1}{2}mv_C^2}_{\substack{\text{translation}\\ \text{of mass center}}} + \underbrace{\frac{1}{2}\omega \cdot \mathbf{H}_C}_{\substack{\text{rotation about}\\ \text{mass center}}} \tag{1.3.76}$$

For a rigid body that has a fixed point *O*,

$$T = \frac{1}{2}\omega \cdot \mathbf{H}_O \tag{1.3.77}$$

Equations of Motion in Three Dimensions

The equations of motion for a rigid body in three dimensions are extensions of the equations previously stated:

$$\begin{gathered} \sum \mathbf{F} = m\mathbf{a}_C \\ \sum \mathbf{M}_C = \dot{\mathbf{H}}_C = \left(\dot{\mathbf{H}}_C\right)_{xyz} + \Omega \times \mathbf{H}_C \end{gathered} \tag{1.3.78}$$

where

$\mathbf{a}_C$ = acceleration of mass center
$\mathbf{H}_C$ = angular momentum of the body about its mass center
xyz = frame fixed in the body with origin at the mass center
Ω = angular velocity of the *xyz* frame with respect to a fixed *XYZ* frame

Note that an arbitrary fixed point *O* may be used for reference if done consistently.

Euler's Equations of Motion

Euler's equations of motion results from the simplification of allowing the *xyz* axes to coincide with the principal axes of inertia of the body.

$$\begin{aligned} \sum M_x &= I_x\dot{\omega}_x - \left(I_y - I_z\right)\omega_y\omega_z \\ \sum M_y &= I_y\dot{\omega}_y - \left(I_z - I_x\right)\omega_z\omega_x \\ \sum M_z &= I_z\dot{\omega}_z - \left(I_x - I_y\right)\omega_x\omega_y \end{aligned} \tag{1.3.79}$$

where all quantities must be evaluated with respect to the appropriate principal axes.

Solution of Problems in Three-Dimensional Motion

In order to solve a three-dimensional problem, it is necessary to apply the six independent scalar equations:

$$\sum F_x = ma_{C_x} \qquad \sum F_y = ma_{C_y} \qquad \sum F_z = ma_{C_z}$$

$$\sum M_x = \dot{H}_x + \omega_y H_z - \omega_z H_y$$
$$\sum M_y = \dot{H}_y + \omega_z H_x - \omega_x H_z \tag{1.3.80}$$
$$\sum M_z = \dot{H}_z + \omega_x H_y - \omega_y H_x$$

These equations are valid in general. Some common cases are briefly stated:

- *Unconstrained motion.* The six governing equations should be used with *xyz* axes attached at the center of mass of the body.
- *Motion of a body about a fixed point.* The governing equations are valid for a body rotating about a noncentroidal fixed point *O*. The reference axes *xyz* must pass through the fixed point to allow using a set of moment equations that do not involve the unknown reactions at *O*.
- *Motion of a body about a fixed axis.* This is the generalized form of plane motion of an arbitrary rigid body. The analysis of unbalanced wheels and shafts and corresponding bearing reactions falls in this category.

1.4 Vibrations

Bela I. Sandor and Stephen M. Birn

Vibrations in machines and structures should be analyzed and controlled if they have undesirable effects such as noise, unpleasant motions, or fatigue damage with potentially catastrophic consequences. Conversely, vibrations are sometimes employed to useful purposes, such as for compacting materials.

Undamped Free and Forced Vibrations

The simplest vibrating system has motion of one degree of freedom (DOF) described by the coordinate x in Figure 1.4.1. (An analogous approach is used for torsional vibrations, with similar results.) Assuming that the spring has no mass and that no damping occurs in the system, the equation of motion for **free vibration** (motion under internal forces only; $F = 0$) is

$$m\ddot{x} + kx = 0 \qquad \text{or} \qquad \ddot{x} + \omega^2 x = 0 \tag{1.4.1}$$

where $\omega = \sqrt{k/m}$ = natural circular frequency in radians per second.

The displacement x as a function of time t is

$$x = C_1 \sin \omega t + C_2 \cos \omega t \tag{1.4.2}$$

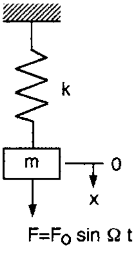

FIGURE 1.4.1 Model of a simple vibrating system.

where C_1 and C_2 are constants depending on the initial conditions of the motion. Alternatively,

$$x = A\sin(\omega t + \phi)$$

where $C_1 = A\cos\phi$, $C_2 = A\sin\phi$, and ϕ is the phase angle, another constant. A complete cycle of the motion occurs in time τ, the *period of simple harmonic motion*,

$$\tau = \frac{2\pi}{\omega} = 2\pi\sqrt{\frac{m}{k}}\ (\text{seconds per cycle})$$

The *frequency* in units of cycles per second (cps) or hertz (Hz) is $f = 1/\tau$.

The simplest case of **forced vibration** is modeled in Figure 1.4.1, with the force F included. Using typical simplifying assumptions as done previously, the equation of motion for a harmonic force of forcing frequency Ω, is

$$m\ddot{x} + kx = F_o\sin\Omega t \tag{1.4.3}$$

The vibrations of a mass m may also be induced by the displacement $d = d_o\sin\Omega t$ of a foundation or another mass M to which m is attached by a spring k. Using the same reference point and axis for x and d, the equation of motion for m is

$$\begin{gathered} m\ddot{x} + k(x - d_o\sin\Omega t) = 0 \\ m\ddot{x} + kx = kd_o\sin\Omega t \end{gathered} \tag{1.4.4}$$

where d_o is the amplitude of vibration of the moving support M, and Ω is its frequency of motion.

The general solution of the forced vibration in the *steady state* (after the initial transient behavior) is

$$\begin{aligned} x &= A\sin\Omega t \\ A &= \frac{F_o}{k - m\Omega^2} = \frac{F_o/k}{1-(\Omega/\omega)^2} \end{aligned} \tag{1.4.5}$$

where Ω is the forcing frequency and w is the natural circular frequency of the system of m and k.

Resonance. The amplitude of the oscillations in forced vibrations depends on the frequency ratio Ω/ω. Without damping or physical constraints, the amplitude would become infinite at $\Omega = \omega$, the condition of **resonance**. Dangerously large amplitudes may occur at resonance and at other frequency ratios near the resonant frequency. A *magnification factor* is defined as

$$MF = \frac{F}{F_o/k} = \frac{A}{d_o} = \frac{1}{1-(\Omega/\omega)^2} \tag{1.4.6}$$

Several special cases of this are noted:

1. Static loading: $\Omega = 0$, or $\Omega \ll \omega$; $MF \simeq 1$.
2. Resonance: $\Omega = \omega$; $MF = 8$.
3. High-frequency excitation: $\Omega \gg \omega$; $MF.\ 0$.
4. Phase relationships: the vibration is in phase for $\Omega < \omega$, and it is 180° *out of phase* for $\Omega > \omega$.

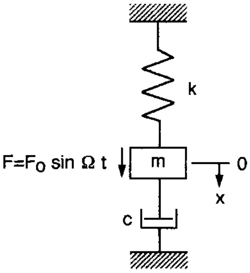

FIGURE 1.4.2 Model of a damped vibrating system.

Damped Free and Forced Vibrations

A vibrating system of one degree of freedom and damping is modeled in Figure 1.4.2. The equation of motion for *damped free vibrations* ($F = 0$) is

$$m\ddot{x} + c\dot{x} + kx = 0 \tag{1.4.7}$$

The displacement x as a function of time t is

$$x = e^{\lambda t} \tag{1.4.8}$$

$$\lambda_{1,2} = \frac{-c}{2m} \pm \sqrt{\left(\frac{c}{2m}\right)^2 - \frac{k}{m}}$$

The value of the coefficient of viscous damping c that makes the radical zero is the *critical damping coefficient* $c_c = 2m\sqrt{k/m} = 2m\omega$. Three special cases of damped free vibrations are noted:

1. Overdamped system: $c > c_c$; the motion is *nonvibratory* or *aperiodic*
2. Critically damped system: $c = c_c$; this motion is also nonvibratory; x decreases at the fastest rate possible without oscillation of the mass
3. Underdamped system: $c < c_c$; the roots $\lambda_{1,2}$ are complex numbers; the displacement is

$$x = Ae^{-(c/2m)t} \sin\left(\omega_d t + \phi\right)$$

where A and ϕ are constants depending on the initial conditions, and the *damped natural frequency* is

$$\omega_d = \omega\sqrt{1 - \left(\frac{c}{c_c}\right)^2}$$

The ratio c/c_c is the *damping factor* ζ. The damping in a system is determined by measuring the rate of decay of free oscillations. This is expressed by the *logarithmic decrement* δ, involving any two successive amplitudes x_i and x_{i+1},

$$\delta = \ln\frac{x_i}{x_{i+1}} = \frac{2\pi\zeta}{\sqrt{1-\zeta^2}} \simeq 2\pi\zeta$$

The simplifying approximation for δ is valid for up to about 20% damping ($\zeta \simeq 0.2$).

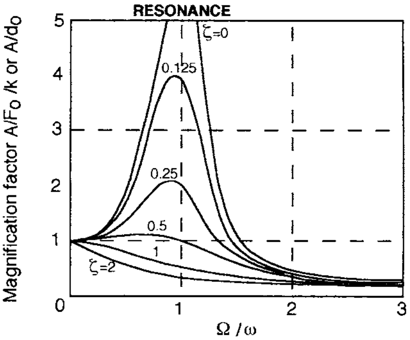

FIGURE 1.4.3 Magnification factor in damped forced vibration.

The *period of the damped vibration* is $\tau_d = 2\pi/\omega_d$. It is a constant, but always larger than the period of the same system without damping. In many real systems the damping is relatively small ($\zeta < 0.2$), where $\tau_d \simeq \tau$ and $\omega_d \simeq \omega$ can be used.

The equation of motion for *damped forced vibrations* (Figure 1.4.2; $F \neq 0$) is

$$m\ddot{x} + c\dot{x} + kx = F_o \sin \Omega t \tag{1.4.9}$$

The solution for steady-state vibration of the system is

$$x = A\sin(\Omega t - \phi) \tag{1.4.10}$$

where the amplitude and phase angle are from

$$A = \frac{F_o}{\sqrt{(c\Omega)^2 + (k - m\Omega^2)^2}}$$

$$\tan\phi = \frac{c\Omega}{k - m\Omega^2}$$

The *magnification factor* for the amplitude of the oscillations is

$$MF = \frac{A}{F_o/k} = \frac{A}{d_o} = \frac{1}{\sqrt{[2\zeta(\Omega/\omega)]^2 + [1 - (\Omega/\omega)^2]^2}} \tag{1.4.11}$$

This quantity is sketched as a function of the frequency ratio Ω/ω for several damping factors in Figure 1.4.3. Note that the amplitude of vibration is reduced at all values of Ω/ω if the coefficient of damping c is increased in a particular system.

Vibration Control

Vibration Isolation

It is often desirable to reduce the forces transmitted, or the noise and motions inside or in the neighborhood of vibrating machines and structures. This can be done to some extent within the constraints of space and additional weight and cost by the use of isolators, such as rubber engine mounts and wheel suspension systems in cars. Many kinds of isolating materials and systems are available commercially.

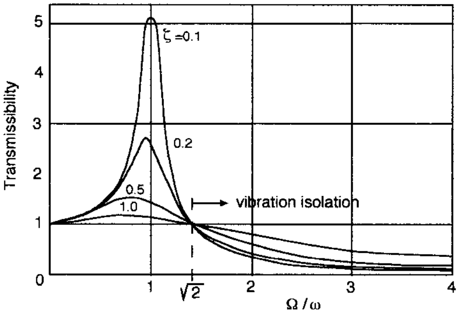

FIGURE 1.4.4 Transmissibility patterns of a vibration isolator.

The effectiveness of vibration isolation is expressed by the *transmissibility TR*, the ratio of the force transmitted F_T to the disturbing force F_o. A simple isolation system is modeled as a spring and a dashpot in parallel, for which the transmissibility is given by Equation (1.4.12) and sketched in Figure 1.4.4.

$$TR = \frac{F_T}{F_o} = \frac{\sqrt{1 + 4\zeta^2(\Omega/\omega)^2}}{\sqrt{\left[1 - (\Omega/\omega)^2\right]^2 + 4\zeta^2(\Omega/\omega)^2}} \tag{1.4.12}$$

When damping is negligible,

$$TR \simeq \frac{1}{(\Omega/\omega)^2 - 1}$$

Note from the figure that

- Vibration isolation occurs at $\Omega/\omega > \sqrt{2}$.
- Isolation efficiency increases with decreasing stiffness of the isolation mounts.
- Damping reduces isolation efficiency. However, some damping is normally required if resonance may occur in a system even for short periods.
- The response curves are essentially independent of damping when Ω/ω is large ($\gtrsim 3$) and damping is low ($\zeta \lesssim 0.2$). Here $TR \simeq 1/[(\Omega/\omega)^2 - 1]$.
- For a system with more than one excitation frequency, the lowest excitation frequency is of primary importance.

The efficiency of an isolating system is defined by the reduction R in transmissibility,

$$R = 1 - TR$$

If a certain reduction R in transmissibility is desired, the appropriate stiffness k of an isolation system is obtained from $\omega = \sqrt{k/m}$ and

$$\frac{\Omega}{\omega} = \sqrt{\frac{2 - R}{1 - R}}$$

A small magnitude of stiffness k makes the reduction R in transmissibility large. It is difficult to achieve isolation for very low excitation frequencies because of the required large static deflections. To obtain highly efficient isolation at low excitation frequencies, a large supporting mass M may be utilized, with the value of

$$\omega = \sqrt{k/(m + M)}$$

Vibration Absorption

In some cases, a vibratory force is purposely generated in a system by a secondary spring-mass system to oppose a primary disturbing force and thereby reduce or eliminate the undesirable net effect. An interesting example of this is the "tuned-mass damper" in a few skyscrapers, designed to counter the oscillatory motions caused by wind. The secondary spring-mass system has disadvantages of its own, such as extra weight, complexity, and effectiveness limited to a single frequency.

Balancing of Rotating Components

The conditions of static or dynamic unbalance of rotating bodies have long been recognized. These can be analyzed by the methods of elementary mechanics; simple tests can be performed in many cases and adequate corrections can be made routinely to achieve balance, such as for the wheels of automotive vehicles. Three categories of increasing complexity are distinguished.

1. *Static unbalance.* The distributed or lumped masses causing unbalance are in a single axial plane and all on the same side of the axis of rotation (Figure 1.4.5). Thin disks are also in this category. Static unbalance is detected in a static test because the center of gravity of the body is not on the axis, and correction is made by adding or removing mass at a convenient radial distance from the axis.
2. *Static balance with dynamic unbalance.* This may be the case when the masses causing unbalance are in a single axial plane but on opposite sides of the axis of rotation (Figure 1.4.6a). Static balance is achieved if the center of gravity of the body is on the axis, but dynamic unbalance results from the couple of the unbalance forces ($m\omega^2 r$) during rotation, causing a shaking of the axle.
3. *Static and dynamic unbalance.* This is the general case of unbalance, which can be visualized by not allowing m_1 and m_2 and the axis of rotation to lie in the same plane (Figure 1.4.6b).

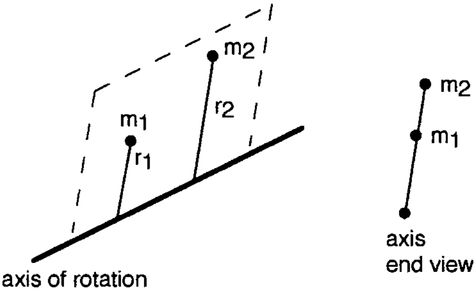

FIGURE 1.4.5 Schematic of static unbalance.

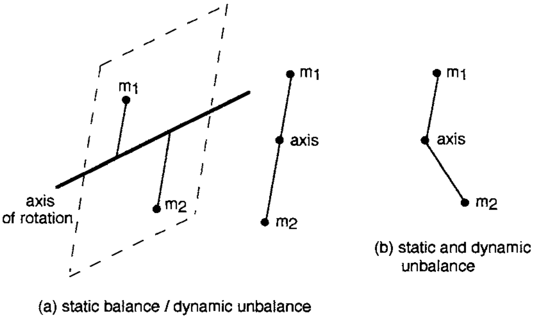

(a) static balance / dynamic unbalance

(b) static and dynamic unbalance

FIGURE 1.4.6 Schematic of two cases of dynamic unbalance.

The magnitude and angular position of a body's unbalance can be determined using a dynamic balancing machine. Here the shaking forces are measured by electronically sensing the small oscillations of the bearings that can be correlated with the position of the body.

Critical Speed of Rotating Shafts

A rotating shaft may become dangerously unstable and whirl with large lateral amplitudes of displacement at a critical speed of rotation. The critical speed, in revolutions per second, corresponds with the natural frequency of lateral vibration of the system. Thus, it can be analytically predicted fairly well and can be safely measured in a real but nonrotating machine with high precision. If unavoidable, as at startup, the critical speed should be passed over rapidly. Other ways of minimizing the problems of whirling shafts include the proper balancing of rotors and the replacing of bent shafts and worn bearings.

Random Vibrations. Shock Excitation

Many structures are subjected to nonharmonic excitations and respond with transient vibrations rather than steady-state motions. Random vibration is often caused by *shock* excitation, which implies that the loading occurs suddenly, in a short time with respect to the natural period of vibration of the system. Such a loading, typically caused by impact conditions, may be highly irregular in terms of amplitude, waveform, and repetition (Figure 1.4.7), but normally it is possible to extract practically uniform critical events from the loading history for purposes of future design and life prediction.

For most practical purposes, this plot represents aperiodic motion, in which the important quantities are the maximum and average large amplitudes and the projected total repetitions (in this case, at the rate of about 1000 per day) over the design life of the structure. The small-amplitude transient vibrations associated with the large events are likely to be negligible here in terms of dynamic behavior as well as fatigue damage, although the relatively large number of small oscillations may cause concern in some cases.

Random vibrations are difficult to deal with analytically. Numerical methods involving computers are advantageous to obtain response (or shock) spectrums of a system, assuming key parameters and simple models of nonharmonic excitations such as impulsive forces and force step functions. Because the

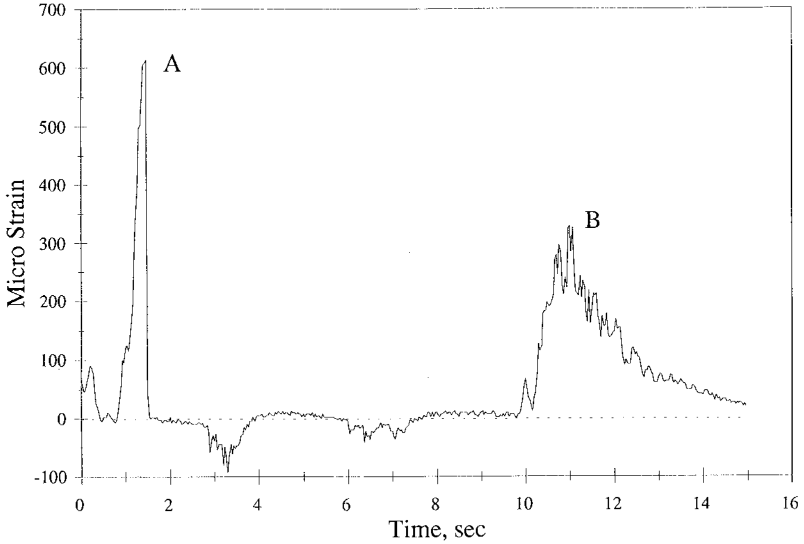

FIGURE 1.4.7 Strain-time history at one strain-gage location on a steel bridge caused by two trucks moving in opposite directions. (A) Garbage truck in the near lane; (B) tractor trailer in the far lane. Weights unknown. (Data courtesy Mark J. Fleming, University of Wisconsin–Madison.)

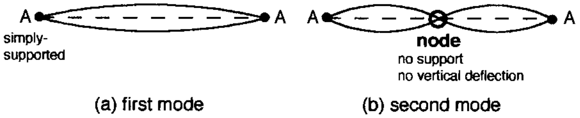

FIGURE 1.4.8 Simply supported beam in two modes of vibration.

maximum transient response is relatively insensitive to damping, an undamped system is useful in modeling response spectrums. Experimental techniques are needed to verify the analytical predictions, especially when the behavior of a multiple-degree-of-freedom system is determined from the response spectrum of a single-degree-of-freedom system.

Multiple-Degree-of-Freedom Systems. Modal Analysis

The analysis of a system with more than one degree of freedom requires an independent coordinate for each degree of freedom to describe the configurations. Thus, an n-degree-of-freedom system has n natural frequencies and n normal *modes* of vibration. Complex systems can be classified as (1) discrete and lumped-parameter systems with finite numbers of degrees of freedom; or (2) continuous elastic bodies of distributed mass with infinite number of degrees of freedom (in theory). A common example of the latter is a vibrating beam, with the first two modes of vibration shown in Figure 1.4.8. Each *nodal point* is a point of zero deflection. Usually the *fundamental natural frequency* (the lowest) is the most important, and only the lowest few frequencies are considered in practice.

A system's harmonic vibrations are its *principal modes*. The system can vibrate nonharmonically in many ways. Periodic motion of complex wave form can be analyzed as a combination of principal-mode vibrations.

The classical method of mathematical solution and the experimental techniques become increasingly cumbersome and sometimes inaccurate for a system of more than a few degrees of freedom. The recent emergence of sophisticated numerical (finite element; Figure 1.4.9) and experimental (electro-optics) techniques has resulted in significant progress in this area. The synergistic aspects of several new methods are especially remarkable. For example, damage caused by vibrations can significantly affect a system's own modal behavior and, consequently, the rate of damage evolution. Such nonlinear changes of a system can now be investigated and eventually predicted by the hybrid applications of computerized numerical methods; fatigue and fracture mechanics (Section 1.6); and high-speed, noncontacting, full-field vibration and stress imaging (Section 1.4, "Vibration-Measuring Instruments," and Section 1.5, "Experimental Stress Analysis and Mechanical Testing"). These enhance the already powerful modern methods of *modal analysis* for accurately describing the response of multiple-degree-of-freedom systems.

Vibration-Measuring Instruments

Many kinds of instruments can be used for the experimental investigation of vibrating systems. They range from simple, inexpensive devices to sophisticated electro-optics with lasers or infrared detectors, with the list still expanding in many areas.

The basic quantities of interest regarding a vibrating system are the displacement, velocity, acceleration, and frequency. A typical sensor (or pickup or transducer) for determining these is the piezoelectric accelerometer, which is attached to the vibrating machine or structure to be analyzed. The complete setup normally includes amplifiers, frequency analyzer, oscilloscope, and recorders. An instrumented impact hammer may be used to provide well-defined impulse excitation to determine the natural frequencies of structures. The frequency analyzer can display the accelerometer output in the time or the frequency domain. Other kinds of devices used for vibration sensing include seismic spring-mass systems, electrical-resistance strain gages, and electromagnetic transducers.

Care must be exercised in matching a transducer to the task at hand because reliable data can be obtained only if the transducer has a "flat-response" frequency region for the measurements of interest.

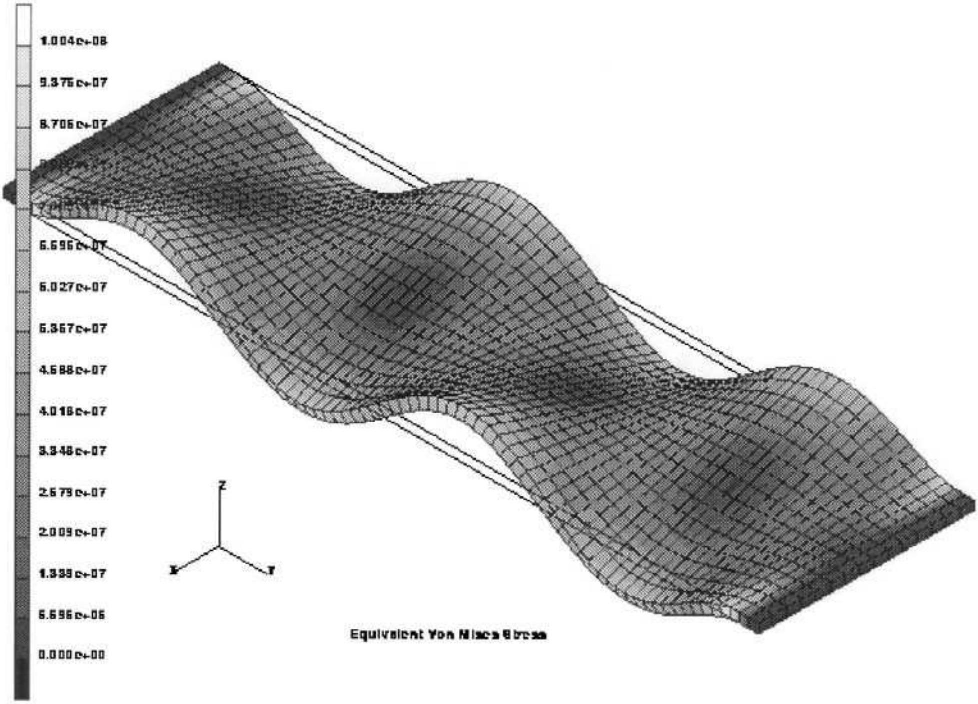

FIGURE 1.4.9 Modal analysis of a vibrating plate. (Photo courtesy David T. Corr, University of Wisconsin–Madison.)

For example, electromagnetic vibrometers (or seismometers) are low-frequency transducers that have low natural frequency compared to the frequency of the motion to be measured. At the other extreme, piezoelectric accelerometers are designed to have higher natural frequency than the frequency to be measured.

It is also important to use transducers of negligible mass compared to the mass of the vibrating system being measured. Very small, light-weight accelerometers are available to satisfy this condition in many cases. In some situations, however, only noncontacting means of motion measurement provide satisfactory results. Optical techniques are prominent in this area, offering several advantages besides the noncontacting measurement capability. They can be full-field techniques, which means that data may be obtained rapidly from many points on a body using one instrument. They have excellent resolution and precision, and some of them are easy to use. Three kinds of optical instruments are distinguished here for vibratory system analysis, depending on the primary quantity measured:

1. *Displacement measurement*. Holography and speckle pattern imaging have excellent resolution, but they are adversely affected by unstable measuring conditions. They are most useful in laboratory applications.
2. *Velocity measurement*. Laser Doppler systems provide time-resolved, accelerometer-like measurements. They are relatively unaffected by measuring conditions, and are simple and rugged enough to use in the laboratory or in the field. Several important capabilities of such a vibration pattern imaging system are worth mentioning (Color Figure 3 through Color Figure 7):
   - Noncontacting; the structure's response is not affected by the instrumentation; applicable in some hazardous environments (hot structures, etc.), and short or long range (over 200 m) on natural surfaces
   - Single-point or full-field data acquisition at high resolution from areas of 0.5 × 0.5 mm to 8 × 8 m; up to 500 individual points can be programmed
   - Wide frequency range; 0 to 100 kHz (for example, Figure 1.4.10)

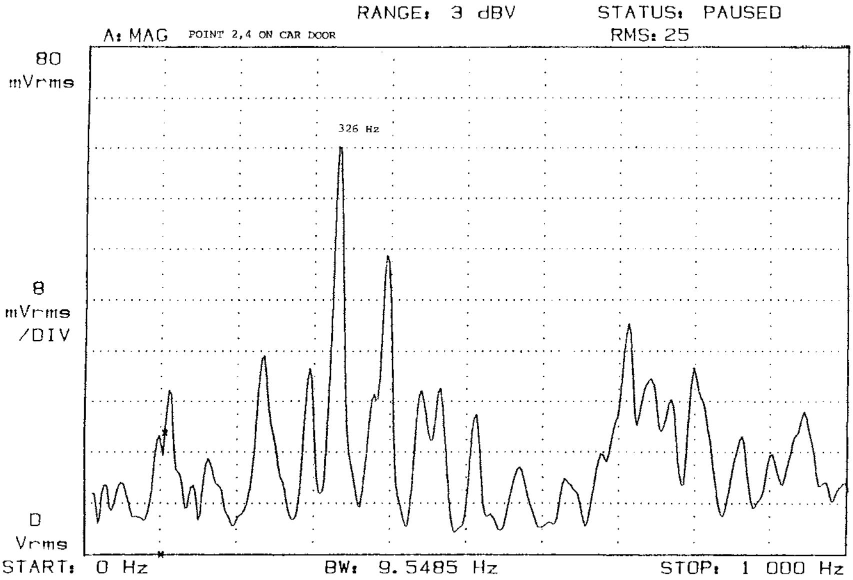

FIGURE 1.4.10 Laser-based, noncontacting vibration analysis of a point on a car door. (Data courtesy of Ometron Inc., Sterling, VA.)

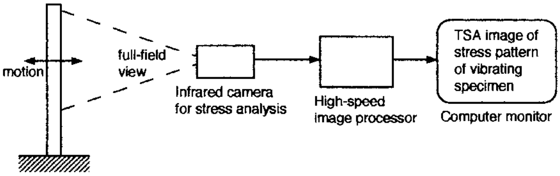

FIGURE 1.4.11 Schematic of modal analysis of a jet engine turbine blade by thermal imaging of the stress field caused by complex vibration. For sample data, see Color Figure 8.

- Sensitivity to a wide range of vibration velocities; 0.005 to 1000 mm/sec
- Large depth of focus; ±3 m at 10-m working distance
- Node spacing down to a few millimeters can be resolved
- Resolution of small displacements, down to the wavelength of the laser source (typically, ≈1 Å)
- Safe, class II laser system; <1 mW output
- Conventional signal processing is used to give multipoint modal parameters in familiar format for analytical comparisons

3. *Dynamic stress measurement.* Differential thermography via dynamic thermoelasticity (Figure 1.4.11) has recently become a powerful technique for measuring the modal response of vibrating structures and, uniquely, for directly assessing the structural integrity and durability aspects of the situation. This approach uses high-speed infrared electro-optics and has predictive capability because it can be quantitatively combined with modern fatigue and fracture mechanics methods. For example, it can effectively relate vibration modes to complex fracture modes and damage evolution rates of a real component even under arbitrary and unknown loading with unknown boundary conditions. See Section 1.5, "Experimental Stress Analysis and Mechanical Testing," for more on the dynamic thermoelasticity technique.

1.5 Mechanics of Materials

Bela I. Sandor, Stephen M. Birn, and Michael L. Brown

Mechanics of materials, also called strength of materials, provides quantitative methods to determine stresses (the intensity of forces) and strains (the severity of deformations), or overall deformations or load-carrying abilities of components and structures. The stress-strain behavior of materials under a wide range of service conditions must be considered in many designs. It is also crucial to base the analysis on correct modeling of component geometries and external loads. This can be difficult in the case of multiaxial loading, and even more so if time- or temperature-dependent material behaviors must be considered.

Proper modeling involves free-body diagrams and equations of equilibrium. However, it is important to remember that *the equilibrium equations of statics are valid only for forces or for moments of forces*, and not for stresses.

Stress

The intensity of a force is called stress and is defined as the force acting on an infinitesimal area. A normal stress σ is defined as

$$\sigma = \lim_{dA \to 0} \frac{dF}{dA} \tag{1.5.1}$$

where dF is a differential normal force acting on a differential area dA. It is often useful to calculate the average normal stress $\sigma = P/A$, where P is the resultant force on an area A. A shear stress τ caused by a shearing force V is defined likewise:

$$\tau = \lim_{dA \to 0} \frac{dV}{dA} \tag{1.5.2}$$

An average shear stress is obtained from V/A.

It is helpful to consider the general cases of stresses using rectangular elements in two and three dimensions, while ignoring the deformations caused by the stresses.

Plane Stress

In some relatively simple cases, all stress vectors lie in the same plane. This is represented by a two-dimensional element in Figure 1.5.1, where σ_x and/or σ_y may be tensile (pulling on the element as shown) or compressive (pushing on the element; not shown). Normal stresses are easy to visualize and set up correctly.

Shear stresses need to be discussed here in a little detail. The notation means that τ_{xy}, for example, is a shear stress acting in the y direction on a face perpendicular to the x axis. It follows that τ_{yx} is acting in the x direction on a face perpendicular to the y axis. The four shear stress vectors are pointed as they are because of the requirement that the element be in equilibrium: the net forces and moments of forces

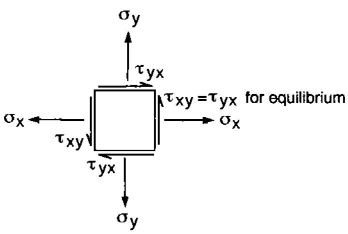

FIGURE 1.5.1 Generalized plane stress.

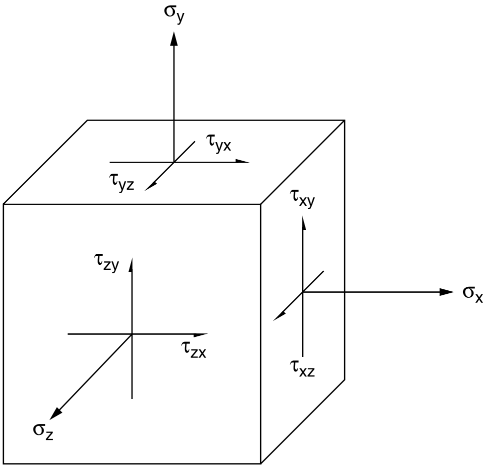

FIGURE 1.5.2 Three-dimensional general state of stress.

on it must be zero. Thus, reversing the direction of all four τs in Figure 1.5.1 is possible, but reversing less than four is not realistic.

Three-Dimensional State of Stress

The concept of plane stress can be generalized for a three-dimensional element as shown in Figure 1.5.2, working with the three primary faces of the cube and not showing stresses on the hidden faces, for clarity.

Again, the normal stresses are easy to set up, while the shear stresses may require considerable attention. The complex cases of stresses result from multiaxial loading, such as combined axial, bending, and torsional loading. Note that, even in complex situations, simplifications are possible. For example, if the right face in Figure 1.5.2 is a free surface, $\sigma_x = \tau_{xz} = \tau_{xy} = 0$. This leaves a plane stress state with σ_y, σ_z, and τ_{yz}, at most.

Stress Transformation

A free-body element with known stresses on it allows the calculation of stresses in directions other than the given *xyz* coordinates. This is useful when potentially critical welded or glued joints, or fibers of a composite, are along other axes. The stress transformations are simplest in the case of plane stress and can be done in several ways. In any case, at a given point in a material, only one state of stress is present at a particular instant. At the same time, the components of the stresses depend on the orientation of the chosen coordinate system.

The stress transformation equations depend on the chosen coordinate system and the sign convention adopted. A common arrangement is shown in Figure 1.5.3, where (a) is the known set of stresses and (b) is the unknown set, denoted by primes.

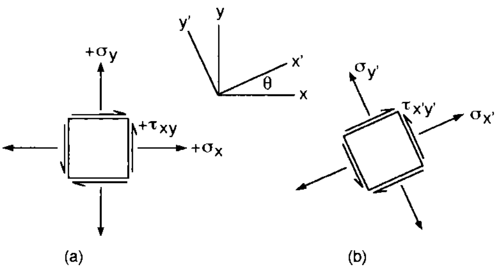

FIGURE 1.5.3 Elements for stress transformation.

In the present sign convention, an outward normal stress is positive and an upward shear stress on the right-hand face of the element is positive. The transformation equations are

$$\begin{aligned} \sigma_{x'} &= \frac{\sigma_x + \sigma_y}{2} + \frac{\sigma_x - \sigma_y}{2}\cos 2\theta + \tau_{xy}\sin 2\theta \\ \sigma_{y'} &= \frac{\sigma_x + \sigma_y}{2} - \frac{\sigma_x - \sigma_y}{2}\cos 2\theta - \tau_{xy}\sin 2\theta \\ \tau_{x'y'} &= -\frac{\sigma_x - \sigma_y}{2}\sin 2\theta + \tau_{xy}\cos 2\theta \end{aligned} \tag{1.5.3}$$

A negative result means that the actual direction of the stress is opposite to the assumed direction.

Principal Stresses

It is often important to determine the maximum and minimum values of the stress at a point and the orientations of the planes of these stresses. For plane stress, the maximum and minimum normal stresses, called **principal stresses**, are obtained from

$$\sigma_{1,2} = \frac{\sigma_x + \sigma_y}{2} \pm \sqrt{\left(\frac{\sigma_x - \sigma_y}{2}\right)^2 + \tau_{xy}^2} \tag{1.5.4}$$

No shear stress is acting on the principal planes on which the principal stresses are acting. However, shear stresses are on other planes. The maximum shear stress is calculated from

$$\tau_{\max} = \sqrt{\left(\frac{\sigma_x - \sigma_y}{2}\right)^2 + \tau_{xy}^2} \tag{1.5.5}$$

This stress acts on planes oriented 45° from the planes of principal stress. There is a normal stress on these planes of $\tau_{\max}$, the average of σ_x and σ_y:

$$\sigma_{ave} = \frac{\sigma_x + \sigma_y}{2} \tag{1.5.6}$$

Mohr's Circle for Plane Stress

The equations for plane stress transformation have a graphical solution, called Mohr's circle, which is convenient to use in engineering practice, including "back-of-the-envelope" calculations. Mohr's circle is plotted on an $\sigma - \tau$ coordinate system as in Figure 1.5.4, with the center C of the circle always on the σ axis at $\sigma_{\text{ave}} = (\sigma_x + \sigma_y)/2$ and its radius $R = \sqrt{[(\sigma_x - \sigma_y)/2]^2 + \tau_{xy}^2}$. The positive τ axis is downward for convenience in order to make θ on the element and the corresponding 2θ on the circle agree in sense (both counterclockwise here). The following aspects of Mohr's circle should be noted:

- The center C of the circle is always on the σ axis, but it may move left and right in a dynamic loading situation. This should be considered in failure prevention.
- The radius R of the circle is $\tau_{\max}$, and it may change, even pulsate, in dynamic loading. This is also relevant in failure prevention.
- Working back and forth between the rectangular element and the circle should be done carefully and consistently. An angle θ on the element should be represented by 2θ in the corresponding circle. If τ is positive downward for the circle, the sense of rotation is identical in the element and the circle.

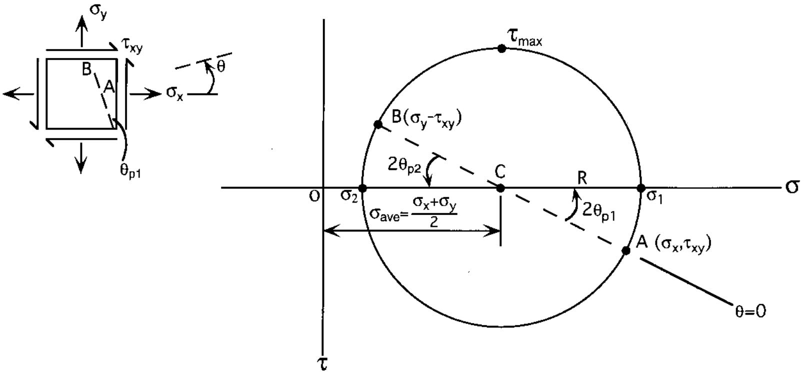

FIGURE 1.5.4 Mohr's circle.

- The principal stresses σ_1 and σ_2 are on the σ axis ($\tau = 0$).
- The planes on which σ_1 and σ_2 act are oriented at $2\theta_p$ from the planes of σ_x and σ_y (respectively) in the circle and at θ_p in the element.
- The stresses on an arbitrary plane can be determined by their σ and τ coordinates from the circle. These coordinates give magnitudes and signs of the stresses. The physical meaning of $+\tau$ vs. $-\tau$ regarding material response is normally not as distinct as $+\sigma$ vs. $-\sigma$ (tension vs. compression).
- To plot the circle, use the calculated center *C* coordinate and the radius *R* or directly plot the stress coordinates for two mutually perpendicular planes and draw the circle through the two points (*A* and *B* in Figure 1.5.4), which must be diametrically opposite on the circle.

Special Cases of Mohr's Circles for Plane Stress

See Figure 1.5.5 through Figure 1.5.9

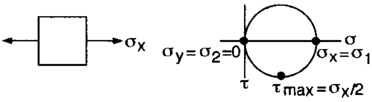

FIGURE 1.5.5 Uniaxial tension.

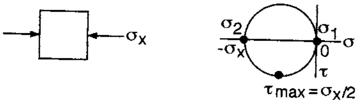

FIGURE 1.5.6 Uniaxial compression.

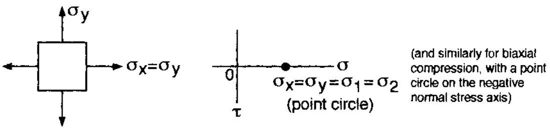

FIGURE 1.5.7 Biaxial tension: $\sigma_x = \sigma_y$ (and similarly for biaxial compression: $-\sigma_x = -\sigma_y$).

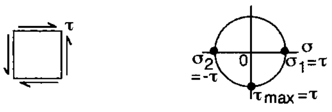

FIGURE 1.5.8 Pure shear.

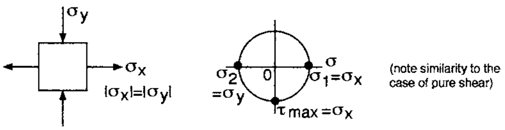

FIGURE 1.5.9 Biaxial tension-compression: $|\sigma_x| = |\sigma_y|$ (similar to the case of pure shear).

Absolute Maximum Shear Stress

In the case of a general three-dimensional state of stress, the transformations to arbitrary planes are complex and beyond the scope of this book. It is useful to note, however, that in general three principal stresses exist at any point in a material. (Plane stress is a special case with one of these stresses being zero.) If the three principal stresses are known, it is easy to determine the absolute maximum shear stress, which is valuable in assessing a material's performance in service. The idea is to view the element as three separate two-dimensional elements, each time from a different principal direction, and plot the Mohr's circles for them in the same diagram. This is illustrated schematically in Figure 1.5.10 for an element with three tensile principal stresses of maximum, minimum, and intermediate values.

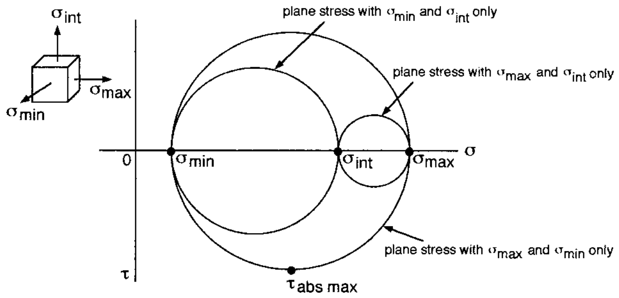

FIGURE 1.5.10 Principal stresses of three-dimensional element.

The Mohr's circles are interrelated because the three views of the element have common principal stresses associated with them. The absolute maximum shear stress is

$$\tau_{\text{abs max}} = \frac{\sigma_{\max} - \sigma_{\min}}{2} \tag{1.5.7}$$

Note that in calculating the absolute maximum shear stress for a state of plane stress, the actual third principal stress of $\sigma_3 = 0$ may be significant, if that is the minimum stress, and should be used in Equation (1.5.7) instead of a larger intermediate stress. For example, assume $\sigma_x = 200$ ksi and $\sigma_y = 100$ ksi in a case of plane stress. Using these as $\sigma_{\max}$ and $\sigma_{\min}$, $\tau_{\max} = (200 - 100)/2 = 50$ ksi. However, the fact that $\sigma_z = 0$ is important here. Thus, correctly, $\tau_{\text{abs max}} = (200 - 0)/2 = 100$ ksi. There is an important lesson here: apparently negligible quantities cannot always be ignored in mechanics of materials.

Strain

Solid materials deform when forces are acting on them. Large deformations are possible in some materials. Extremely small deformations are difficult to measure, but they still may be significant in critical geometry change or gradual damage evolution. Deformations are normally nonuniform even in apparently uniform components of machines and structures. The severity of deformation is called strain, which is separately defined for volumetric change and angular distortion of a body.

Normal Strain

The elongation or shortening of a line segment of unit length is called normal strain or axial strain. To define this quantitatively, consider a uniform bar of length L_o, and call this original length the gage length.

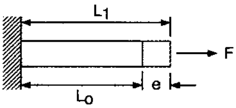

FIGURE 1.5.11 Model for calculating axial or normal strain.

Assume the bar elongates by an amount *e* to a new length L_1 under the action of a force *F* (Figure 1.5.11) or by thermal expansion. The normal strain ε is defined, with the gage length approaching zero in the limit, as

$$\varepsilon = \frac{e}{L_o} \tag{1.5.8}$$

The strain calculated this way is called engineering strain, which is useful and fairly accurate for small deformations. Elongation is considered positive.

Normal strain is a dimensionless quantity, but it is customary to label it in a way that indicates strain, such as in./in.; m/m; %; μ in./in.; or με (microstrain), depending on the system of units and the numerical representation.

True Strain

A difficulty of proper definition arises if the deformation *e* is not infinitesimal because, in a sense, the gage length is increasing. The correct definition in such a case is based on the instantaneous length *L* and infinitesimal changes *dL* in that length. Thus, the total true strain in a member axially deforming from length L_o to a final length L_f by an amount *e* is

$$\varepsilon = \int_{L_o}^{L_f} \frac{dL}{L} = \ell n \frac{L_f}{L_o} = \ell n(1+e) \tag{1.5.9}$$

True strain is practically identical to engineering strain up to a few percent of engineering strain. The approximate final length L_f of an axially deformed, short line segment of original length L_o is sometimes expressed as

$$L_f \approx (1+\varepsilon)L_o \tag{1.5.10}$$

Shear Strain

Angular distortions are called shear strains. More precisely, shear strain γ is the change in angle of two originally perpendicular ($\theta = \pi/2$) line segments. For consistency, assume that a decreasing angle represents positive shear strain, and an increasing angle is from negative shear strain. The angle γ is measured in radians. A useful way to show shear strain is given in Figure 1.5.12.

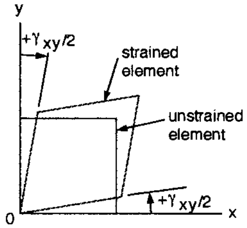

FIGURE 1.5.12 Shear strain in two dimensions.

Strain Transformation

The method of transforming strain at a point is similar to that for stress. In general, normal strain has three components: ε_x, ε_y, and ε_z, and shear strain has three: γ_{xy}, γ_{xz}, and γ_{yz}. Transformations of plane strain components are the simplest.

For a consistent approach, assume that strain transformation is desired from an *xy* coordinate system to an *x′y′* set of axes, where the latter is rotated counterclockwise (+θ) from the *xy* system. The transformation equations for plane strain are

$$\varepsilon_{x'} = \frac{\varepsilon_x + \varepsilon_y}{2} + \frac{\varepsilon_x - \varepsilon_y}{2}\cos 2\theta + \frac{\gamma_{xy}}{2}\sin 2\theta$$

$$\varepsilon_{y'} = \frac{\varepsilon_x + \varepsilon_y}{2} - \frac{\varepsilon_x - \varepsilon_y}{2}\cos 2\theta - \frac{\gamma_{xy}}{2}\sin 2\theta \tag{1.5.11}$$

$$\frac{\gamma_{x'y'}}{2} = -\frac{\varepsilon_x - \varepsilon_y}{2}\sin 2\theta + \frac{\gamma_{xy}}{2}\cos 2\theta$$

Note the similarity between the strain and stress transformation equations, as well as the differences.

Principal Strains

For isotropic materials only, principal strains (with no shear strain) occur along the principal axes for stress. In plane strain the principal strains ε_1 and ε_2 are expressed as

$$\varepsilon_{1,2} = \frac{\varepsilon_x + \varepsilon_y}{2} +/- \sqrt{\left(\frac{\varepsilon_x - \varepsilon_y}{2}\right)^2 - \left(\frac{\gamma_{xy}}{2}\right)^2} \tag{1.5.12}$$

The angular position θ_p of the principal axes (measured positive counterclockwise) with respect to the given *xy* system is determined from

$$\tan 2\theta_p = \frac{\gamma_{xy}}{\varepsilon_x - \varepsilon_y} \tag{1.5.13}$$

As in the case of stress, the maximum in-plane shear strain is

$$\frac{\gamma_{x'y'\max}}{2} = \sqrt{\left(\frac{\varepsilon_x - \varepsilon_y}{2}\right)^2 + \left(\frac{\gamma_{xy}}{2}\right)^2} \tag{1.5.14}$$

which occurs along axes at 45° from the principal axes, determined from

$$\tan 2\theta = -\frac{\varepsilon_x - \varepsilon_y}{\gamma_{xy}} \tag{1.5.15}$$

The corresponding average normal strain is

$$\varepsilon_{ave} = \frac{\varepsilon_x + \varepsilon_y}{2} \tag{1.5.16}$$

Mohr's Circle for Plane Strain

As in the case of stress, there is a graphical overview by Mohr's circle of the directional dependence of the normal and shear strain components at a point in a material. This circle has a center *C* at $\varepsilon_{\text{ave}} = (\varepsilon_x + \varepsilon_y)/2$, which is always on the *e* axis, but is shifting left and right in a dynamic loading situation. The radius *R* of the circle is

$$R = \sqrt{\left(\frac{\varepsilon_x - \varepsilon_y}{2}\right)^2 + \left(\frac{\gamma_{xy}}{2}\right)^2} \tag{1.5.17}$$

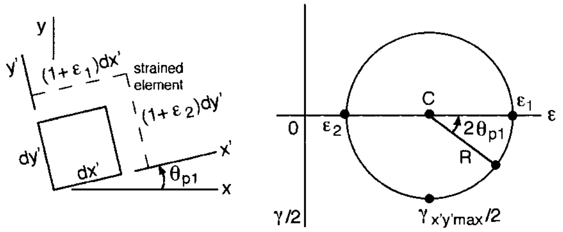

FIGURE 1.5.13 Mohr's circle for plane strain.

Note the proper labeling (ε vs. $\gamma/2$) and preferred orientation of the strain axes as shown in Figure 1.5.13. This sets up a favorable uniformity of angular displacement between the element ($+\theta$ counterclockwise) and the circle ($+2\theta$ counterclockwise).

Mechanical Behaviors and Properties of Materials

The stress–strain response of a material depends on its chemical composition, microstructure, geometry, magnitude and rate of change of stress or strain applied, and environmental factors. Numerous quantitative mechanical properties are used in engineering. Some of the basic properties and their common variations are described here because they are essential in mechanics of materials analyses.

Stress–Strain Diagrams

Uniaxial tension or compression stress–strain plots have several distinctive shapes, depending on the material, test conditions, and quantities plotted. The chosen representative schematic diagram here is a true stress vs. true strain curve for a ductile, nonferrous metal tested in tension (Figure 1.5.14). The important mechanical properties listed in Table 1.5.1 are obtained from such a test or a similar one in pure shear (not all are shown in Figure 1.5.14).

Another useful mechanical property (not measured from the $\sigma - \varepsilon$ plot) is hardness. This is a flow property, with some qualitative correlations to the other properties.

It is important to appreciate that the mechanical properties of a material depend on its chemical composition and its history of thermal treatment and plastic deformations (cold work; cyclic plasticity). For example, consider the wide ranges of monotonic and cyclic stress–strain curves for 1045 steel (a given chemical composition), at room temperature, as functions of its hardness resulting from thermal treatment (Figure 1.5.15). See Section 1.6, "Fatigue," for more on cycle-dependent material behaviors.

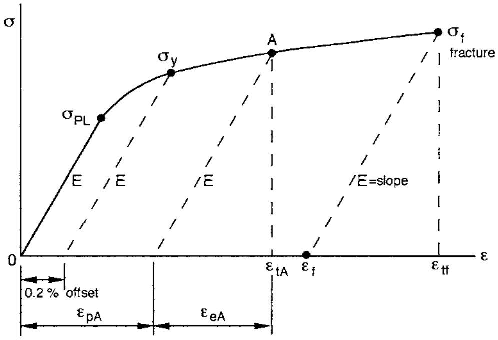

FIGURE 1.5.14 True stress vs. true strain for a ductile, nonferrous metal.

TABLE 1.5.1 Basic Mechanical Properties

Symbol	Definition	Remarks
E	Modulus of elasticity; Young's modulus; $E = \sigma/\varepsilon_e$	Hooke's law; T and ε_p effects small
G	Shear modulus of elasticity $G = \dfrac{\tau}{\gamma_e} = E/2(1+v)$	T and ε_p effects small
v	Poisson's ratio; $v = \dfrac{\varepsilon_{lateral}}{\varepsilon_{longit.}}$	T and ε_p effects small
σ_{PL}	Proportional limit; at onset of noticeable yielding (or at onset of nonlinear elastic behavior)	Flow property; inaccurate; T and ε_p effects large
σ_y	0.2% offset yield strength (but yielding can occur at $\sigma < \sigma_y$ if $\sigma_{PL} < \sigma_y$)	Flow property; accurate; T and ε_p effects large
σ_f	True fracture strength; $\sigma_f = \dfrac{P_f}{A_f}$	Fracture property; T and ε_p effects medium
ε_f	True fracture ductility; $\varepsilon_f = \ln\dfrac{A_O}{A_f} = \ln\dfrac{100}{100 - \%\text{RA}}$	Max. ε_p; fracture property; T and ε_p effects medium
% RA	Percent reduction of area; $\%\text{RA} = \dfrac{A_O - A_f}{A_O} \times 100$	Fracture property; T and ε_p effects medium
n	Strain hardening exponent; $\sigma = K\varepsilon_p^n$	Flow property; T and ε_p effects small to large
Toughness	Area under σ vs. ε_p curve	True toughness or intrinsic toughness; T and ε_p effects large
σ_u	Ultimate strength; $\dfrac{P_{\max}}{A_O}$	Fracture property; T and ε_p effects medium
M_r	Modulus of resilience; $M_r = \dfrac{\sigma_{PL}^2}{2E}$	Area under original elastic portion of $\sigma - \varepsilon$ curve

Notes: T is temperature; ε_p refers to prior plastic strain, especially cyclic plastic strain (fatigue). These are qualitative indicators here; exceptions are possible.

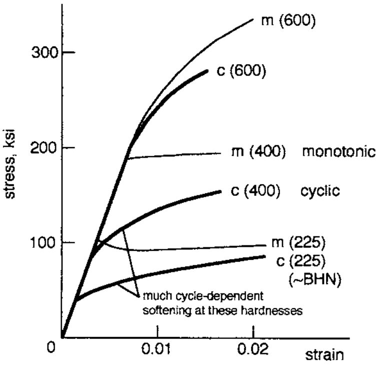

FIGURE 1.5.15 Influence of hardness and deformation history on the stress-strain response of SAE 1045 steel.

Generalized Stress–Strain Expressions. Hooke's Law

An important special case of stress–strain responses is when the material acts entirely elastically ($\varepsilon_p = 0$, $\varepsilon_t = \varepsilon_e$). In this case, for uniaxial loading, the basic **Hooke's law**, $\sigma = E\varepsilon$, can be used, and similarly for unidirectional shear, $\tau = G\gamma$. For multiaxial loading (Color Figure 9), the generalized Hooke's law is applicable,

$$\varepsilon_x = \frac{1}{E}\left[\sigma_x - v\left(\sigma_y + \sigma_z\right)\right]$$

$$\varepsilon_y = \frac{1}{E}\left[\sigma_y - v\left(\sigma_x + \sigma_z\right)\right] \tag{1.5.18}$$

$$\varepsilon_z = \frac{1}{E}\left[\sigma_z - v\left(\sigma_x + \sigma_y\right)\right]$$

Other useful expressions for ideally elastic behavior are as follows. Relating the axial and shear moduli,

$$G = \frac{E}{2(1+v)} \tag{1.5.19}$$

The change in volume per unit volume is the volumetric strain or dilatation,

$$e = \frac{1-2v}{E}\left(\sigma_x + \sigma_y + \sigma_z\right) \tag{1.5.20}$$

The bulk modulus k is the ratio of a uniform stress (hydrostatic) to the dilatation,

$$k = \frac{\sigma}{e} = \frac{E}{3(1-2v)} \tag{1.5.21}$$

For most metals, $v \approx 1/3$ and $k \approx E$.

Uniaxial Elastic Deformations

The total elastic deformation δ of axially loaded bars, columns, and wires is calculated with the aid of basic expressions. Using $\sigma = E\varepsilon$ and $\sigma = P(x)/A(x)$, where $P(x)$ and $A(x)$ are, respectively, the internal force and cross-sectional area of a bar at a distance x from one end,

$$\delta = \int_0^L \frac{P(x)}{A(x)E}\,dx \tag{1.5.22}$$

where L is the total length considered.

In most cases, $A(x)$ is a constant; $P(x)$ may also be a constant, except where several different axial forces are applied and, occasionally, for vertical bars and columns, where the member's own weight may cause $P(x)$ to vary significantly along the length. If $A(x)$, $P(x)$, and E are constants,

$$\delta = \frac{PL}{AE} \tag{1.5.23}$$

Thermally Induced Deformations

Thermal expansion or contraction is a linearly dependent, recoverable deformation as purely elastic deformations are. For a homogeneous and isotropic material, the thermally induced deformation from the original length L is calculated from

$$\delta_T = \alpha\Delta TL \tag{1.5.24}$$

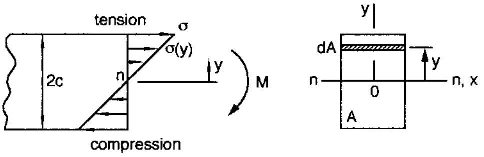

FIGURE 1.5.16 Internal normal stresses in a beam caused by bending.

where α is the linear coefficient of thermal expansion (strain per degree of temperature, a material property), and ΔT is the change in temperature. The thermal strain can be prevented or reduced by constraining a member. In that case, the stresses and strains can be calculated using the methods pertaining to statically indeterminate members.

Stresses in Beams

To calculate stresses in beams, one must first model the beam correctly in terms of its supports and loading (such as simply supported, with distributed loading); determine the appropriate unknown external reactions; and establish the corresponding shear and moment diagrams using a consistent sign convention. Normal and shear stresses may need to be calculated, but typically the normal stresses are the most significant.

Flexure Formula

The normal stresses at a particular cross section in a beam are caused by the bending moment that acts at that cross section, and are distributed by magnitude and sign (both tension and compression) so that the beam is in equilibrium. The basic concept for calculating the stresses is that a neutral axis *n-n* of $\varepsilon = \sigma = 0$ is in the beam, and that the longitudinal normal strain varies linearly with distance y from the neutral axis.

If the beam is behaving entirely elastically, the stress distribution is also linear, as in Figure 1.5.16. In this case, the stress at a distance y from the neutral axis is calculated from $M = \int \sigma(y) y \, dA$ and results in

$$\sigma(y) = \frac{My}{I} \tag{1.5.25}$$

where I = moment of inertia of the cross-sectional area about the neutral axis.

The maximum stress, with the appropriate sign, is

$$\sigma = \frac{Mc}{I} \tag{1.5.26}$$

Several special cases of bending require additional consideration and analysis as outlined next.

Inelastic Bending

A beam may plastically deform under an increasing moment, yielding first in its outer layers and ultimately throughout its depth. Such a beam is analyzed by assuming that the normal strains are still linearly varying from zero at the neutral axis to maximum values at the outer layers. Thus, the stress distributions depend on the stress–strain curve of the material. With the stress distribution established, the neutral axis can be determined from $\int \sigma(y) \, dA = 0$, and the resultant moment from $M = \int y \sigma(y) \, dA$. A fully plastic beam of rectangular cross section and flat-top yielding supports 50% more bending moment than its maximum elastic moment.

Neutral Axis of Semisymmetric Area

If the cross-sectional area is semisymmetric, such as a T-shape, and the loading is in a centroidal plane of symmetry, the neutral axis for elastic deformations is at the centroid *C* of the area as shown in Figure 1.5.17, and Equation (1.5.25) can be used. Note that the magnitudes of the maximum tensile and compressive stresses are not the same in this case.

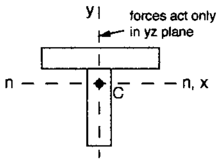

FIGURE 1.5.17 Neutral axis of a semisymmetric area.

Unsymmetric Bending

In the general case, the cross-sectional area has an arbitrary shape and the loading is arbitrarily applied. The problem of an arbitrary area is handled by choosing the centroidal *xy* coordinate system so that the axes are principal axes of inertia for the area. The principal axes can be determined by using inertia transformation equations or Mohr's circle of inertia. Having an axis of symmetry is a simple special case because the principal axes are the axis of symmetry and the axis perpendicular to it.

The **flexure formula** can be applied directly if the principal axes of inertia are known, and the bending moment is applied about one of these centroidal principal axes. A more complex case is if the moment is not about a principal axis as shown in Figure 1.5.18.

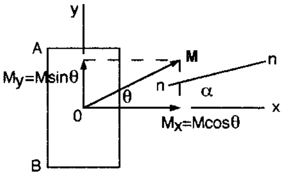

FIGURE 1.5.18 Schematic of arbitrary bending moment.

Different texts may present different formulas for calculating the bending stresses in such situations, depending on the choice of a coordinate system and the sign convention adopted. It is better not to rely on a cookbook formula, but to break down the problem into simple, easily visualized parts, and then reason out an algebraic superposition of the stress components. To illustrate this approach schematically, consider the stresses at points *A* and *B* in Figure 1.5.18. Instead of working directly with the applied moment **M**, resolve **M** into its components M_x and M_y. M_x causes a tensile stress $\sigma_{z_{A_1}}$ at *A* and a compressive stress $-\sigma_{z_{B_1}}$ at *B*. M_y causes tensile stresses at *A* and *B*, $\sigma_{z_{A_2}}$ and $\sigma_{z_{B_2}}$. The magnitudes of these stress components are readily calculated from the flexure formula with the appropriate dimensions and inertias for each. The resultant stresses are

$$\sigma_A = \sigma_{z_{A_1}} + \sigma_{z_{A_2}}$$

$$\sigma_B = -\sigma_{z_{B_1}} + \sigma_{z_{B_2}}$$

The neutral axis at angle α in the general case is not coincident with the direction of **M** (Figure 1.5.18). In the present case, α is defined by

$$\tan\alpha = \frac{I_x}{I_y}\tan\theta \tag{1.5.27}$$

Composite Beams

Nonhomogeneous beams are often designed to take advantage of the properties of two different materials. The approach for analyzing these is to imagine a transformation of the beam's cross section to an equivalent cross section of a different shape but of a single material, so that the flexure formula is usable. This is illustrated for a beam *A* with reinforcing plates *B*, as in Figure 1.5.19.

The transformation factor *n* is obtained from

$$n = \frac{E_B}{E_A} \tag{1.5.28}$$

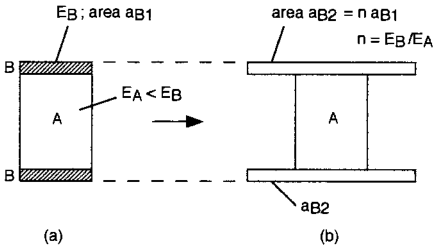

FIGURE 1.5.19 Equivalent area method for a symmetric composite beam.

Note that, in a composite beam, the strains vary linearly with distance from the neutral axis; however, the stresses do not because of the different elastic moduli of the components. The actual stress σ in the transformed area is determined by first calculating the "pretend" stress σ' for the uniform transformed area and then multiplying it by n:

$$\sigma = n\sigma' \tag{1.5.29}$$

Nonsymmetric composite beams (such as having only one reinforcing plate B in Figure 1.5.19) are analyzed similarly, but first require the location of the neutral axis.

Reinforced concrete beams are important special cases of composite beams. Their stress analysis is influenced by the fact that concrete is much weaker in tension than in compression. Empirical approaches are particularly useful in this area.

Curved Beams

The stress analysis of curved beams requires some additional considerations. For example, the flexure formula is about 7% in error (the calculated stresses are too low) when the beam's radius of curvature is five times its depth (hooks, chain links). The curved-beam formula provides realistic values in such cases.

Shear Stresses in Beams

Transverse loads on beams are common, and they cause transverse and complementary longitudinal shear stresses in the beams. Schematically, the transverse shear stresses are distributed on a rectangular cross section as shown in Figure 1.5.20. The shear stress is zero at free surfaces by definition.

The internal shear stress is calculated according to Figure 1.5.20 from

$$\tau = \frac{VQ}{It} \tag{1.5.30}$$

where

τ = shear stress value at any point on the line $\ell - \ell$ at a distance y' from the neutral axis
V = total shear force on cross-sectional area A
$Q = \bar{y}'A'$; A' = area above line $\ell - \ell$; $\bar{y}'$ = distance from neutral axis to centroid of A'
I = moment of inertia of entire area A about neutral axis
t = width of cross section where τ is to be determined

This shear formula gives $\tau_{max} = 1.5\ V/A$ if t is constant for the whole section (rectangle). Note that the magnitude of the shear stress distribution changes sharply when an abrupt change occurs in width t, such as in an I-beam (Figure 1.5.21).

Shear Flow

In the analysis of built-up members, such as welded, bolted, nailed, or glued box beams and channels, a useful quantity is the shear flow q measured in force per unit length along the beam:

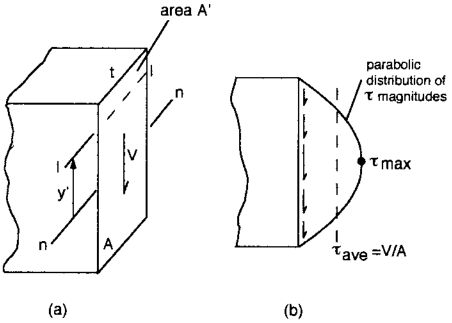

FIGURE 1.5.20 Transverse shear stress distribution.

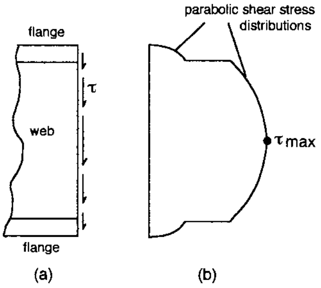

FIGURE 1.5.21 Shear stress distribution for I-beam.

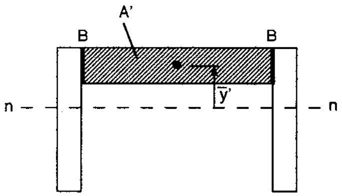

FIGURE 1.5.22 Critical joint regions of a built-up beam.

$$q = \frac{VQ}{I} \tag{1.5.31}$$

where all quantities are defined as for Equation (1.5.30).

Care must be taken to use the appropriate value for Q. For example, consider a channel section of three flat pieces glued together as in Figure 1.5.22. There are two critical joint regions B here, and the area A' is between them. The shear flow is carried by the two joints together, so the actual force per unit length on one joint is $q/2$ here.

Shear Flow in Thin-Walled Beams

The shear-flow distribution over the cross section of a thin-walled member is governed by equilibrium requirements. Schematic examples of this are given in Figure 1.5.23. Note the special case of unsymmetrical loading in part (c), which causes bending and twisting of the beam. The twisting is prevented if the vertical force V is applied at the shear center C, defined by the quantity e:

$$e = \frac{dH}{V} \tag{1.5.32}$$

where d is the centroidal distance between the two horizontal flanges and H is the shear force in the flanges (q_{ave} times width of flange).

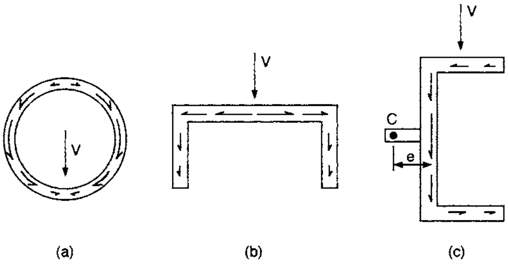

FIGURE 1.5.23 Shear flow distributions.

Deflections of Beams

Small deflections of beams can be determined relatively easily. The first step is to assess a beam's loading and support conditions and sketch an exaggerated elastic deflection curve as in Figure 1.5.24. The boundary conditions at the supports are useful in the solution for the whole beam. Here, at the fixed end *A*, no vertical displacement and no rotation occur, while at the roller support *B*, no vertical displacement is present, but rotation of the continuous beam occurs. The boundary and continuity conditions can be determined by inspection in simple cases.

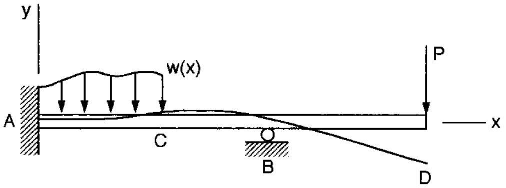

FIGURE 1.5.24 Exaggerated elastic curve of a beam in bending.

Moment vs. Curvature

For a homogeneous and elastic beam,

$$\frac{1}{\rho} = \frac{M}{EI} \tag{1.5.33}$$

where ρ = radius of curvature at a specific point on the elastic curve and 1/ρ is the curvature. The product *EI* is called the flexural rigidity; it is often a constant along the whole beam.

Integration Method for Slope and Displacement

For small displacements, $1/\rho = d^2y/dx^2$. In the general case, a distributed external loading *w*(*x*) should be included in the modeling of the problem. A set of expressions is available to solve for the deflections in rectangular coordinates:

$$-w(x) = \frac{dV}{dx} = EI\frac{d^4y}{dx^4}$$

$$V(x) = \frac{dM}{dx} = EI\frac{d^3y}{dx^3} \tag{1.5.34}$$

$$M(x) = EI\frac{d^2y}{dx^2}$$

TABLE 1.5.2

Beam	Slope: $\lvert dy/dx \rvert$	Max. deflection
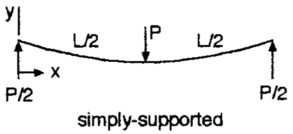	$PL^2 / 16EI$ at $x=0, L$	$PL^3 / 48EI$ at $x=L/2$
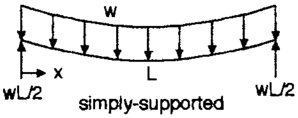	$wL^3 / 24EI$ at $x=0, L$	$5wL^4 / 384EI$ at $x=L/2$
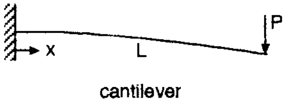	$PL^2 / 2EI$ at $x=L$	$PL^3 / 3EI$ at $x=L$
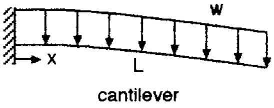	$wL^3 / 6EI$ at $x=L$	$wL^4 / 8EI$ at $x=L$
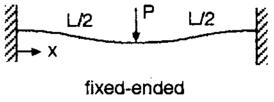	0 at $x=0, L/2, L$	$PL^3 / 192EI$ at $x=L/2$
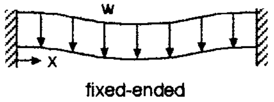	0 at $x=0, L/2, L$	$wL^4 / 384EI$ at $x=L/2$

The deflection y of the elastic curve is obtained by successive integrations, using appropriate constants of integration to satisfy the boundary and continuity conditions. In general, several functions must be written for the moment $M(x)$ — one for each distinct region of the beam — between loading discontinuities. For example, these regions in Figure 1.5.24 are AC, CB, and BD. Considerable care is required to set up a solution with a consistent sign convention and selection of coordinates for simple and efficient forms of $M(x)$.

In practice, even relatively complex problems of beam deflections are solved using the principle of superposition and handbook values of slopes and deflections for subsets of basic loadings and supports. The literature contains a large variety of such subsets, a sampling of which is given in Table 1.5.2.

Deflection Caused by Shear

The transverse shear acting on a beam causes a displacement that tends to be significant compared to bending deflections only in very short beams. The shear deflection over a length L is approximated by

$$y = \frac{\tau_{ave} L}{G} \tag{1.5.35}$$

Torsion

The simplest torsion members have circular cross sections. The main assumptions in their analysis are that cross-sectional circles remain plane circles during twisting of a shaft and that radial lines on any

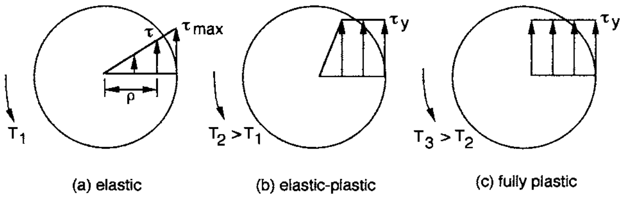

FIGURE 1.5.25 Shear stress distributions in a shaft.

cross section remain straight and rotate through the same angle. The length and diameter of the shaft are unchanged in small angular displacements. It is useful in the analysis that shear strain γ varies linearly along any radial line, from zero at the centerline of a solid or tubular shaft to a maximum at the outer surface:

$$\gamma = \frac{\rho}{r}\gamma_{\max} \tag{1.5.36}$$

where

ρ = radial distance to any element in the shaft
r = radius of the shaft.

Using $\tau = G\gamma$ for an elastically deforming material (Figure 1.5.25),

$$\tau = \frac{\rho}{r}\tau_{\max} \tag{1.5.37}$$

The torsion formula relating shear stress to the applied torque T is from $T = 2\pi \int \tau\rho^2\, d\rho$:

$$\tau_{\max} = \frac{Tr}{J} \quad \text{or} \quad \tau = \frac{T\rho}{J} \tag{1.5.38}$$

where J = the polar moment of inertia of the cross-sectional area; for a solid circle, $J = \pi r^4/2$; for a tube, $J = (\pi/2)(r_0^4 - r_i^4)$.

Power Transmission

The power P transmitted by a shaft under torque T and rotating at angular velocity w is

$$P = T\omega \tag{1.5.39}$$

where $\omega = 2\pi f$ and f = frequency of rotation or number of revolutions per second.

Angle of Twist

For a homogeneous shaft of constant area and G over a length L, under a torque T, the angular displacement of one end relative to the other is

$$\phi = \frac{TL}{JG} \tag{1.5.40}$$

For a shaft consisting of segments with various material and/or geometric properties, under several different torques in each, the net angular displacement is calculated from the vector sum of the individual twists:

$$\phi = \sum \frac{T_i L_i}{J_i G_i} \tag{1.5.41}$$

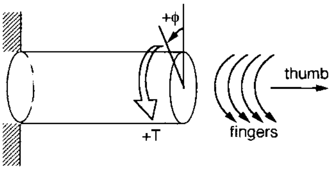

FIGURE 1.5.26 Right-hand rule for positive torque and angle.

The right-hand rule is used for a sign convention for torques and angles: T and ϕ are positive, with the thumb pointing outward from a shaft and the fingers curling in the direction of torque and/or rotation, as in Figure 1.5.26. Note that regardless of the number of torques applied to a shaft at various places along its length, only one torque is at a given cross section, and this torque is a constant in that segment of the shaft (until another external torque is encountered, requiring a different free-body diagram).

Inelastic Torsion

A shaft may plastically deform under an increasing torque, yielding first in its outer layers and ultimately throughout the cross section. Such a shaft is analyzed by assuming that the shear strains are still linearly varying from zero at the centerline to a maximum at the outer layers. Thus, the shear stress distribution depends on the shear stress–strain curve of the material. For example, an elastic, elastic–plastic, and fully plastic solid circular shaft is modeled in Figure 1.5.25, assuming flat-top yielding at τ_y. The torque T in any case is obtained by integrating the shear stresses over the whole area:

$$T = 2\pi \int_A \tau \rho^2 \, d\rho \tag{1.5.42}$$

The fully plastic torque in this case is 33% greater than the maximum elastic torque.

Noncircular Shafts

The analysis of solid noncircular members such as rectangles and triangles is beyond the scope of this book. The reason for the difficulty is that plane sections do not remain plane, but warp. It can be noted here, however, that a circular shaft utilizes material the most efficiently because it has a smaller maximum shear stress and a smaller angle of twist than a noncircular shaft of the same weight per unit length under the same torque.

Noncircular tubes with thin walls can be analyzed using the concept of shear flow that must be continuous and constant on the closed path of the cross-sectional area. The shear stress under a torque T is essentially constant over a uniformly thin wall (from inside to outside) and is given by

$$\tau = \frac{T}{2tA_m} \tag{1.5.43}$$

where t = thickness of the tube and A_m = mean area within the centerline of the wall thickness.

The angle of twist for an elastically deforming thin-walled tube of length L and constant thickness t is

$$\phi = \frac{TL}{4A_m^2 Gt} \oint ds \tag{1.5.44}$$

where the line integral represents the total length of the wall's centerline boundary in the cross section (for a circular tube, this becomes ≈$2\pi r$). For a tube with variable thickness t, the integrand becomes

$$\oint ds/t.$$

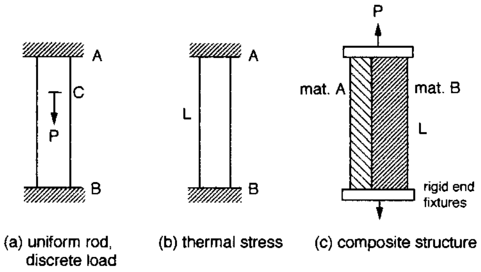

(a) uniform rod, discrete load (b) thermal stress (c) composite structure

FIGURE 1.5.27 Statically indeterminate axially loaded members.

Statically Indeterminate Members

Members that have more supports or constraints than the minimum required for static equilibrium are called statically indeterminate. They can be analyzed if a sufficient number of additional relationships are available. These are fundamentally similar to one another in terms of compatibility for displacements and are described separately for special cases.

Statically Indeterminate Axially Loaded Members

Several subsets of these are common; three are shown schematically in Figure 1.5.27.

1. From a free-body diagram of part (a), assuming upward forces F_A and F_B at ends A and B, respectively, the force equilibrium equation is

$$F_A + F_B - P = 0$$

The displacement compatibility condition is that both ends are fixed, so

$$\delta_{A/B} = 0$$

Then

$$\frac{F_A L_{AC}}{AE} - \frac{F_B L_{BC}}{AE} = 0, \quad F_A = P\frac{L_{BC}}{L_{AB}}, \quad F_B = P\frac{L_{AC}}{L_{AB}}$$

Alternatively, first assume that $F_B = 0$ and calculate the total downward displacement (tensile) of the free end B. Then calculate the required force F_B to compressively deform the rod upward so that after the superposition there is no net displacement of end B. The results are the same as previously for elastically deforming members.

2. Constrained thermal expansion or contraction of part (b) is handled as before, using the expression for thermally induced deformation:

$$\delta_T = \alpha\, \Delta T L \tag{1.5.45}$$

where α = linear coefficient of thermal expansion and ΔT = change in temperature.

3. The force equilibrium equation of part (c) is

$$P - F_A - F_B = 0$$

Here the two different component materials are deforming together by the same amount, so

$$\delta_A = \delta_B$$

$$\frac{F_A L}{A_A E_A} = \frac{F_B L}{A_B E_B}$$

providing two equations with two unknowns, F_A and F_B. Note that rigid supports are not necessarily realistic to assume in all cases.

Statically Indeterminate Beams

For axially loaded members, the redundant reactions of beams are determined from the given conditions of geometry (the displacement compatibility conditions). Various approaches can be used to solve problems of statically indeterminate beams, using the methods of integration, moment-areas, or superposition. Handbook formulas for the slopes and deflections of beams are especially useful; the boundary conditions must be well defined in any case. The method of superposition is illustrated in Figure 1.5.28.

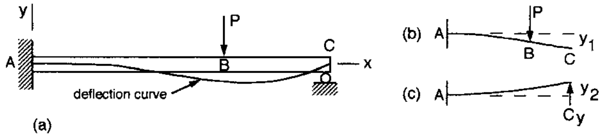

FIGURE 1.5.28 A statically indeterminate beam.

Choosing the reaction at C as the redundant support reaction (otherwise, the moment at A could be taken as redundant) and first removing the unknown reaction C_y, the statically determinate and stable primary beam is obtained in Figure 1.5.28b. Here the slope and deflection at A are zero. The slopes at B and C are the same because segment BC is straight. Next, the external load P is removed, and a cantilever beam fixed at A and with load C_y is considered in Figure 1.5.28c. From the original boundary conditions at C, $-y_1 + y_2 = 0$, and the problem can be solved easily using any appropriate method.

Statically Indeterminate Torsion Members

Torsion members with redundant supports are analyzed essentially the same way as other kinds of statically indeterminate members. The unknown torques, for example, are determined by setting up a solution to satisfy the requirements of equilibrium ($\Sigma T = 0$); angular displacement compatibility; and torque-displacement (angle = TL/JG) relationships. Again, the boundary conditions must be reasonably well defined.

Buckling

The elastic buckling of relatively long and slender members under axial compressive loading could result in sudden and catastrophic large displacements. The critical buckling load is the smallest for a given ideal column when it is pin supported at both ends; the critical load is larger than this for other kinds of supports. An ideal column is made of homogeneous material, is perfectly straight prior to loading, and is loaded only axially through the centroid of its cross-sectional area.

Critical Load. Euler's Equation

The buckling equation (Euler's equation) for a pin-supported column gives the critical or maximum axial load P_{cr} as

$$P_{cr} = \frac{\pi^2 EI}{L^2} \tag{1.5.46}$$

where

E = modulus of elasticity
I = smallest moment of inertia of the cross-sectional area
L = unsupported length of the pinned column

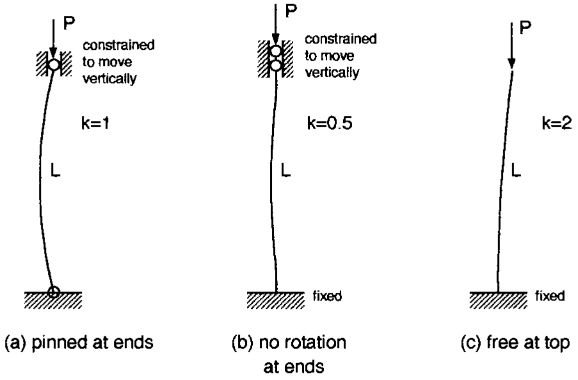

FIGURE 1.5.29 Common end conditions of slender columns.

A useful form of this equation gives the critical average stress prior to any yielding, for arbitrary end conditions,

$$\sigma_{cr} = \frac{\pi^2 E}{\left(k\,L/r\right)^2} \tag{1.5.47}$$

where

$r = \sqrt{I/A}$ = radius of gyration of cross-sectional area A
L/r = slenderness ratio
k = effective-length factor; constant, dependent on the end constraints
kL/r = effective-slenderness ratio

The slenderness ratio indicates, for a given material, the tendency for elastic buckling or failure by yielding (where the Euler formula is not applicable). For example, buckling is expected in mild steel if L/r is approximately 90 or larger, and in an aluminum alloy if $L/r > 60$. Yielding would occur first at smaller values of L/r. Ratios of 200 or higher indicate very slender members that cannot support large compressive loads. Several common end conditions of slender columns are shown schematically in Figure 1.5.29.

Secant Formula

Real columns are not perfectly straight and homogeneous and are likely to be loaded eccentrically. Such columns first bend and deflect laterally, rather than buckle suddenly. The maximum elastic compressive stress in this case is caused by the axial and bending loads and is calculated for small deflections from the secant formula,

$$\sigma_{\max} = \frac{P}{A}\left[1 + \frac{ec}{r^2}\sec\left(\frac{L}{2r}\sqrt{\frac{P}{EA}}\right)\right] \tag{1.5.48}$$

where e is the eccentricity of the load P (distance from the neutral axis of area A) and c is measured from the neutral axis to the outer layer of the column where $\sigma_{\max}$ occurs.

The load and stress are nonlinearly related; if several loads are on a column, the loads should be properly combined first before using the secant formula, rather than linearly superposing several individually determined stresses. Similarly, factors of safety should be applied to the resultant load.

Inelastic Buckling

For columns that may yield before buckling elastically, the generalized Euler equation, also called the Engesser equation, is appropriate. This involves substituting the tangent modulus E_T (tangent to the stress–strain curve) for the elastic modulus E in the Euler equation:

$$\sigma_{cr} = \frac{\pi^2 E_T}{(kL/r)^2} \tag{1.5.49}$$

Note that E_T must be valid for the stress σ_{cr}, but E_T is dependent on stress when the deformations are not entirely elastic. Thermal or plastic-strain events may even alter the stress–strain curve of the material, thereby further changing E_T. Thus, Equation (1.5.49) should be used with caution in a trial-and-error procedure.

Impact Loading

A mass impacting another object causes deformations that depend on the relative velocity between them. The simplest model for such an event is a mass falling on a spring. The maximum dynamic deformation d of a linearly responding spring is related to the static deformation d_{st} (the deformation caused by a weight W applied slowly) by a factor that depends on h, the height of free fall from a static position.

$$d = d_{st}\left(1 + \sqrt{1 + \frac{2h}{d_{st}}}\right) \tag{1.5.50}$$

The dynamic and static stresses are related in a similar way:

$$\sigma = \sigma_{st}\left(1 + \sqrt{1 + \frac{2h}{d_{st}}}\right) \tag{1.5.51}$$

The quantity in parentheses is called the impact factor and shows the magnification of deflection or stress in impacts involving free fall. Note that the real impact factor is somewhat smaller than what is indicated here because some energy is always dissipated by friction during the fall and deceleration of the body. This includes internal friction during plastic flow at the points of contact between the bodies. Other small errors may result from neglecting the mass and possible inelasticity of the spring.

A special value of the impact factor is worth remembering. When the load is applied suddenly without a prior free fall, $h = 0$, and

$$d = 2d_{st} \quad \text{and} \quad \sigma = 2\sigma_{st}$$

This means that the minimum impact factor is about two; it is likely to be larger than two, causing perhaps a "bottoming out" of the spring, or permanent damage somewhere in the structure or the payload supported by the spring.

Combined Stresses

Combinations of different kinds of loads on a member are common. The resultant states of stress at various points of interest can be determined by superposition if the material does not yield. The three-dimensional visualization and correct modeling of such a problem are typically the most difficult parts of the solution, followed by routine calculations of the stress components and resultants. No new methods of analysis are needed here.

The approach is to sketch an infinitesimal cube at each critical point in the member and determine the individual stresses (magnitudes and signs) acting on that element, generally caused by axial, shear, bending, torsion, and internal pressure loading. This is illustrated for a case of medium complexity in Figure 1.5.30.

Consider a solid circular rod of radius R, fixed at $z = 0$ (in the xy plane), and loaded by two forces at point B of a rigid arm. Set up the stress analysis at point A $(-R, 0, 0)$, assuming that no stress concentration is present at the wall fixture of the rod (Figure 1.5.30a).

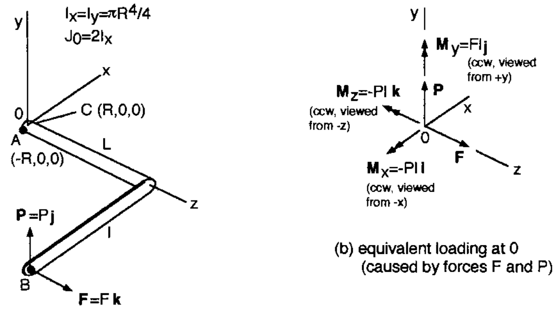

(a) problem modeling

(b) equivalent loading at 0 (caused by forces F and P)

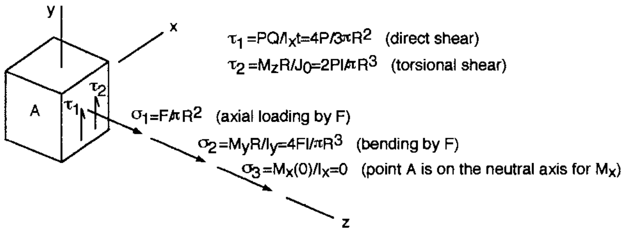

(c) superposition of stresses at point A

FIGURE 1.5.30 Illustration of stress analysis for combined axial, shear, bending, and torsion loading.

First, the equivalent loading at the origin 0 is determined (Figure 1.5.30b). This can be done most accurately in vector form. The individual stresses at point *A* are set up in the subdiagram (c). Check that each stress (even in symbolic form) has the proper units of force per area. The net normal force in this case is $\sigma_1 + \sigma_2$, and the net shear stress is $\tau_1 + \tau_2$.

The state of stress is different at other points in the member. Note that some of the stresses at a point could have different signs, reducing the resultant stress at that location. Such is the case at a point *C* diametrically opposite to point *A* in the present example (R, 0, 0), where the axial load **F** and $\mathbf{M}_y$ generate normal stresses of opposite signs. This shows the importance of proper modeling and setting up a problem of combined loads before finding the numerical solution.

Pressure Vessels

Pressure vessels, which are an important special category of combined stresses, are made in different shapes and sizes (Figure 1.5.31 and Color Figure 10) and are used in diverse applications. The applications range from air receivers in gasoline stations to nuclear reactors in submarines to heat exchangers in refineries. The required thicknesses for some commonly encountered pressure vessel components depend on the geometry as follows.

Cylindrical Shells

The force per unit length in the hoop (tangential) direction, N_t, required to contain a given pressure p in a cylindrical shell is obtained by taking a free-body diagram (Figure 1.5.32a) of the cross section. Assuming the thickness t to be much smaller than the radius R and summing forces in the vertical direction gives

$$2N_tL = 2RLp$$

or

$$N_t = pR \tag{1.5.52}$$

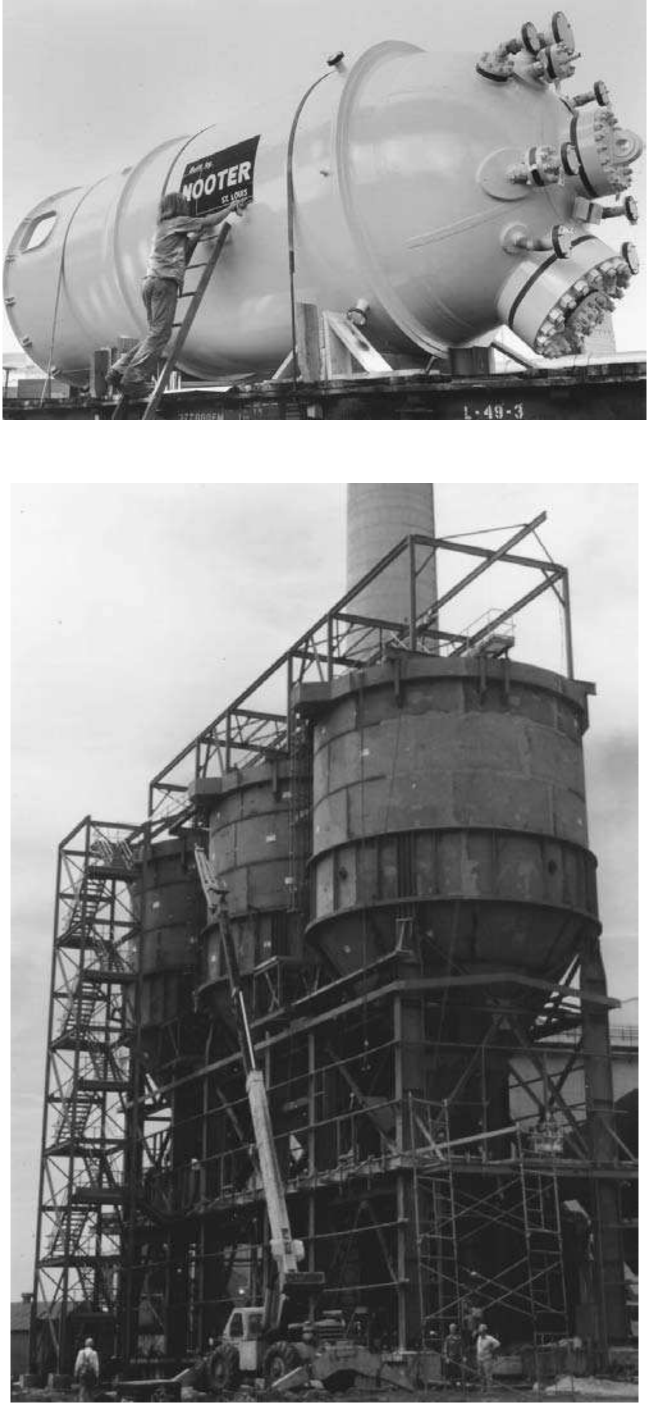

FIGURE 1.5.31 Various pressure vessels. (Photos courtesy Nooter Corp., St. Louis, MO.)

The corresponding hoop stress is $\sigma_t = pR/t$.

The longitudinal force per unit length, N_x, in the cylinder due to pressure is obtained by summing forces in the axial direction (Figure 1.5.32b),

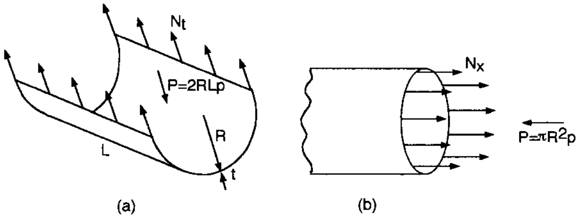

FIGURE 1.5.32 Analysis of cylindrical pressure vessels.

$$2\pi R N_x = \pi R^2 p$$

or

$$N_x = pR/2 \tag{1.5.53}$$

The corresponding axial stress is $\sigma_x = pR/2t$. It is seen that the magnitude of N_t (and σ_t) is twice that of N_x (and σ_x). If S is the allowable stress and t is the required minimum thickness,

$$t = pR/S \tag{1.5.54}$$

Spherical Shells

A free-body diagram of the spherical cross section is shown in Figure 1.5.33. Summation of forces gives

$$t = pR/2S \tag{1.5.55}$$

Example 10

Determine the required thickness of the shell and heads of the air receiver shown in Figure 1.5.34 if p = 100 psi and S = 15,000 psi.

Solution. From Equation (1.5.54), the required thickness for the cylindrical shell is

$$t = 100 \times 18/15{,}000 = 0.12 \text{ in.}$$

The required head thickness from Equation 1.5.55 is

$$t = 100 \times 18/2 \times 15{,}000 = 0.06 \text{ in.}$$

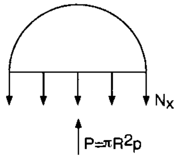

FIGURE 1.5.33 Analysis of spherical pressure vessels.

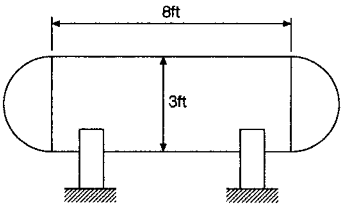

FIGURE 1.5.34 Sketch of a pressure vessel.

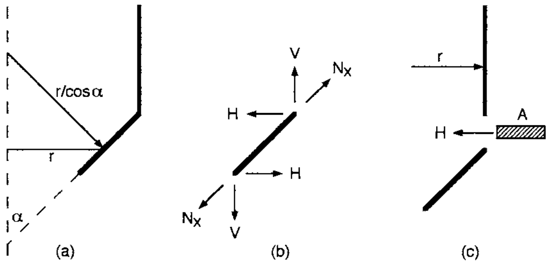

FIGURE 1.5.35 Analysis of conical shells.

Conical Shells

The governing equations for the longitudinal and circumferential forces in a conical shell (Figure 1.5.35a) due to internal pressure are similar to Equation (1.5.52) and Equation (1.5.53) for cylindrical shells, with the radius taken normal to the surface. Thus,

$$N_t = pr/\cos\alpha \tag{1.5.56}$$

$$N_x = pr/2\cos\alpha \tag{1.5.57}$$

where α is half the apex angle of the cone.

The junction between a conical and cylindrical shell, Figure 1.5.35b, is subjected to an additional force, *H*, in the horizontal direction due to internal pressure. The magnitude of this additional force per unit length can be obtained by taking a free-body diagram as shown in Figure 1.5.35b:

$$H = N_x \sin\alpha \tag{1.5.58}$$

A ring is usually provided at the cone-to-cylinder junction to carry the horizontal force *H*. The required area *A* of the ring is obtained from Figure 1.5.35c as

$$H2r = 2AS$$

or

$$A = Hr/S = \left(N_x \sin\alpha\right)r/S = \left(pr^2 \sin\alpha\right)/(2S\cos\alpha) \tag{1.5.59}$$

The stress in the ring is compressive at the large end of the cone and tensile at the small end due to internal pressure. This stress may reverse in direction due to other loading conditions such as weight of contents and end loads on the cone due to wind and earthquake loads.

Example 11

Determine the required thickness of the two cylindrical shells and cone shown in Figure 1.5.36a due to an internal pressure of 200 psi. Calculate the area of the rings required at the junctions. Assume the allowable stress to be 20 ksi in tension and 10 ksi in compression.

Solution. From Equation (1.5.54), the thickness of the large cylinder is

$$t = 200 \times 60/20{,}000 = 0.60 \text{ in.}$$

The thickness of the small cylinder is

$$t = 200 \times 30/20{,}000 = 0.30 \text{ in.}$$

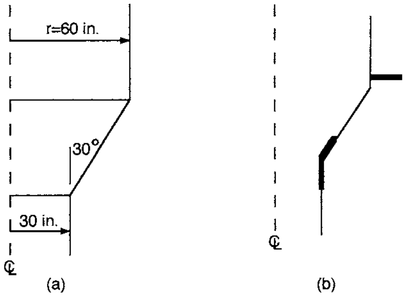

FIGURE 1.5.36 Cylindrical shells with cone connection.

The thickness of the cone is obtained from Equation (1.5.56) as

$$t = 200 \times 60/(20{,}000 \times \cos 30°) = 0.69 \text{ in.}$$

The required area of the ring at the large end of the cone is obtained from Equation (1.5.59) using the allowable compressive stress of 10 ksi:

$$A = 200 \times 60^2 \times \sin 30°/(2 \times 10{,}000 \times \cos 30°) = 20.78 \text{ in.}^2$$

The required area of the ring at the small end of the cone is obtained from Equation (1.5.59) using the allowable tensile stress of 20 ksi:

$$A = 200 \times 30^2 \times \sin 30°/(2 \times 20{,}000 \times \cos 30°) = 2.60 \text{ in.}^2$$

The rings at the junction are incorporated in a number of ways such as those shown in Figure 1.5.36b.

Nozzle Reinforcement

Reinforcements around openings in pressure vessels are needed to minimize the local stress in the area of the opening. The calculation for the needed reinforcement around an opening is based on the concept that pressure in a given area of a vessel is contained by the material in the vessel wall surrounding the pressure. Thus, in Figure 1.5.37, if one takes an infinitesimal length dL along the cylinder, the force caused by the pressure within this length is given by the quantity $pR\ dL$. The force in the corresponding vessel wall is given by $St\ dL$. Equating these two quantities results in the expression $t = pR/S$ that is given earlier as Equation (1.5.54). Similarly for the nozzle in Figure 1.5.37, $T = pr/S$. The intersection of the nozzle with the cylinder results in an opening where the pressure in area $ABCD$ is not contained by any material. Accordingly, an additional area must be supplied in the vicinity of the opening to prevent overstress of the vessel. The required area A is determined from Figure 1.5.37 as

$$A = pRr/S$$

Substituting Equation (1.5.54) into this expression gives

$$A = tr \tag{1.5.60}$$

This equation indicates that the needed additional area is equal to the removed area of the vessel wall.

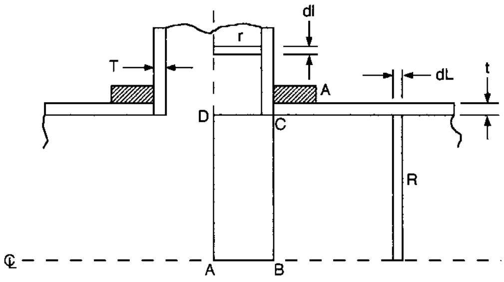

FIGURE 1.5.37 Nozzle reinforcement.

Creep–Fatigue of Boilers and Pressure Vessels

See Figure 1.6.27 in Section 1.6, "Fatigue."

Composite Materials for Pressure Vessels

Some pressure vessels can be made of fibrous composite materials with high strength-to-weight ratios. The advantages of using such a material are remarkable in the case of a tubular vessel, where the hoop stress is twice the longitudinal stress, if the fiber quantities and orientations are optimally designed to resist the applied load caused by internal pressure. Simplistically (because a basic element of a composite is strong along the fibers and weak perpendicular to the fibers), this requires twice as many fibers oriented circumferentially as axially. In practice, fibers are commonly laid at ± (a winding angle) at which the hoop and axial stress components are equal, to efficiently create an optimized configuration.

Example 12

Determine the minimum weight of the tube portion of a thin-walled cylindrical pressure vessel of $r = 8$ in. (20 mm), $\ell = 10$ ft (3.05 m), $p = 8$ ksi (55 MPa); $t = ?$ Assume using a typical graphite/epoxy composite of 60% fibers by volume with allowable tensile stress $\sigma_y = 300$ ksi (207 MPa) at 0.058 lb/in.^{3} (1600 kg/m^3). For comparison, consider a steel of $\sigma_y = 200$ ksi (138 MPa) at 0.285 lb/in.^{3} (7890 kg/m^3).

Solution.

Composite: $\sigma_y = pr/t$, $t = 0.213$ in. (5.41 mm) for circumferential plies and $\sigma_y = pr/2t$, $t = 0.107$ in. (2.72 mm) for axial plies

Total minimum wall thickness: 0.32 in. (8.13 mm)

Total material in tube: 112 lb (50.8 kg)

Steel: $\sigma_y = pr/t$, $t = 0.32$ in. (8.13 mm)

Total material in tube: 550 lb (249 kg) = 4.9 (composite material)

Note that additional considerations exist in practice, such as cost and potential problems in making adequate connections to the tube.

Thick-Walled Cylinders and Interference Fits

The previous section provided design considerations and analysis of thin-walled pressure vessels. However, some applications require thick-walled pressure vessel analysis, as is the case when $r/t > 10$, for example, when small diameter tubes are used to transport high pressure fluids. This section covers thick-walled pressure vessel analysis and a special case for interference fits.

Referring to Figure 1.5.38, the hoop and radial stress components (dependent on pressure and geometry) are shown without derivation in Equation (1.5.61a) and Equation (1.5.61b).

$$_{Hoop} = \overbrace{\frac{p_i R_i^2}{R_o^2 \quad R_i^2} \; 1 + \frac{R_o^2}{r^2}}^{\text{Internal Pressure Component}} \quad \overbrace{\frac{p_o R_o^2}{R_o^2 \quad R_i^2} \; 1 + \frac{R_i^2}{r^2}}^{\text{External Pressure Component}} \tag{1.5.61a}$$

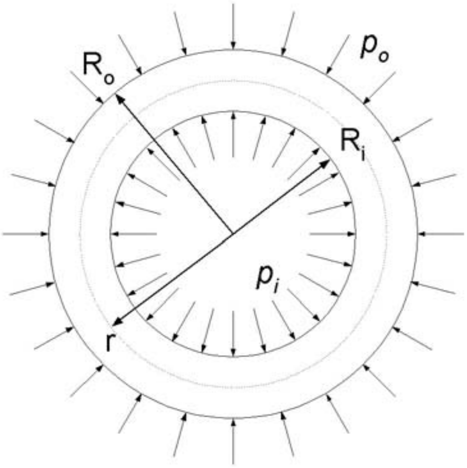

FIGURE 1.5.38 Thick-walled cylinder analysis nomenclature.

$$\sigma_{Radial} = \frac{p_i R_i^2}{R_o^2 - R_i^2}\left(1 - \frac{R_o^2}{r^2}\right) - \frac{p_o R_o^2}{R_o^2 - R_i^2}\left(1 - \frac{R_i^2}{r^2}\right) \tag{1.5.61b}$$

These equations can be simplified by setting the internal or external pressure to zero. As R_i approaches R_o, with $t = R_o - R_i$ the thin-wall pressure vessel equation, $\sigma_{Hoop} = pR/t$ (where $\sigma_{Hoop} = \sigma_t$ as stated in the pressure vessel section), is apparent.

A thick-walled cylinder with end caps exerts an axial force on the caps, thus applying a longitudinal stress component on the cylinder as given by

$$\sigma_z = \frac{p_i R_i^2 - p_o R_o^2}{R_o^2 - R_i^2} \tag{1.5.62}$$

The interference fit analysis is a special case that can be used for nesting pressure vessels (for example, to increase a pressure vessel's capacity) and for use as an assembly method (for example, to join an electric motor core to its output shaft). The interference fit equations are based on Equation (1.5.61a), Equation (1.5.61b), and Figure 1.5.39. An interface pressure p is generated by expanding the outer cylinder's inside diameter over the larger inner cylinder's outside diameter by a radial interference δ.

The first step in formulating the interference fit analysis is determining the hoop stress equations in the assembled inner and outer cylinders. These hoop stresses are calculated by recognizing that Figure 1.5.38 and Equation (1.5.61a) and Equation (1.5.61b) can be reduced by using p, the interface pressure, as the internal pressure on the outer cylinder and the external pressure on the inner cylinder (the internal and external pressures on the assembly are equal to zero).

$$\sigma_{Hoop_{Inner}} = -p\frac{b^2 + a^2}{b^2 - a^2} \tag{1.5.63a}$$

$$\sigma_{Hoop_{Outer}} = p\frac{c^2 + b^2}{c^2 - b^2} \tag{1.5.63b}$$

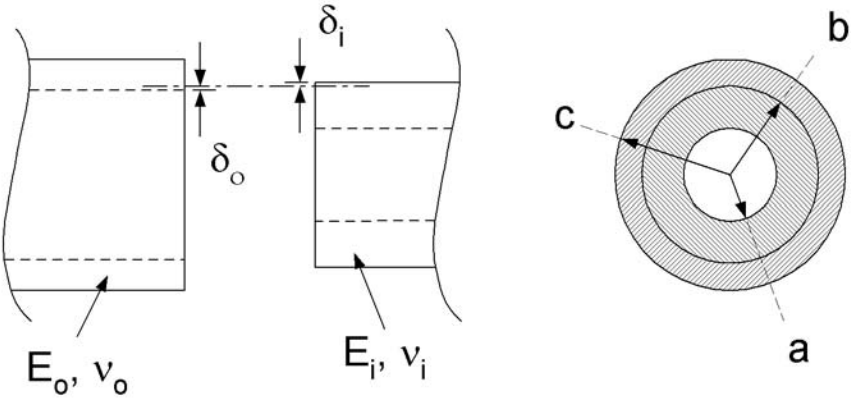

FIGURE 1.5.39 Interference fit schematic and analysis notations.

To solve Equation (1.5.63a) and Equation (1.5.63b), the interface pressure p must be determined. Referring to Figure 1.5.38 and using the strain relationships that result from the change in the interface diameters (from the change in circumference), the interferences are expressed as functions of radius,

$$\delta_o = \frac{pb}{E_o}\left(\frac{c^2+b^2}{c^2-b^2}+\nu_0^2\right) \tag{1.5.64a}$$

$$\delta_i = \frac{-pb}{E_i}\left(\frac{b^2+a^2}{b^2-a^2}-\nu_i^2\right) \tag{1.5.64b}$$

Recognizing that $\delta = \delta_o - \delta_i$, the interference fit equation is stated as

$$\delta = \frac{pb}{E_o}\left(\frac{c^2+b^2}{c^2-b^2}+\nu_0^2\right) - \frac{pb}{E_i}\left(\frac{b^2+a^2}{b^2-a^2}-\nu_i^2\right) \tag{1.5.65}$$

Given the geometry and material properties, the interface pressure p is calculated from Equation (1.5.65). This equation is useable for an assembly of two different materials, as is the case of a steel pin pressed into an aluminum housing. However, further simplification of Equation (1.5.65) is possible if both cylinders are of the same material; with $E_i = E_o$ and $\nu_i = \nu_o$,

$$p = \frac{E\delta}{b}\left(\frac{\left(c^2-b^2\right)\left(b^2-a^2\right)}{2b^2\left(c^2-a^2\right)}\right) \tag{1.5.66}$$

With the interface pressure p obtained, the hoop stresses at the interface can be found using Equation (1.5.63a) and Equation (1.5.63b). At this point, the design engineer should verify that the outer cylinder does not yield at this stress. Yielding of the outer cylinder leads to a reduced interference fit that may be detrimental to the assembly. If the stress at the interface is deemed too high, the assembly geometries should be iterated and the problem solved again. This process is to be repeated until the margins of safety are acceptable in the design.

The stress distributions across the thickness in the hoop and radial directions on the inner and outer cylinders are solved using Equation (1.5.61a) and Equation (1.5.61b), by recognizing the outer cylinder external pressure $p_o = 0$ and $p_i = p$, and the inner cylinder internal pressure $p_o = p$ and $p_i = 0$. The interference

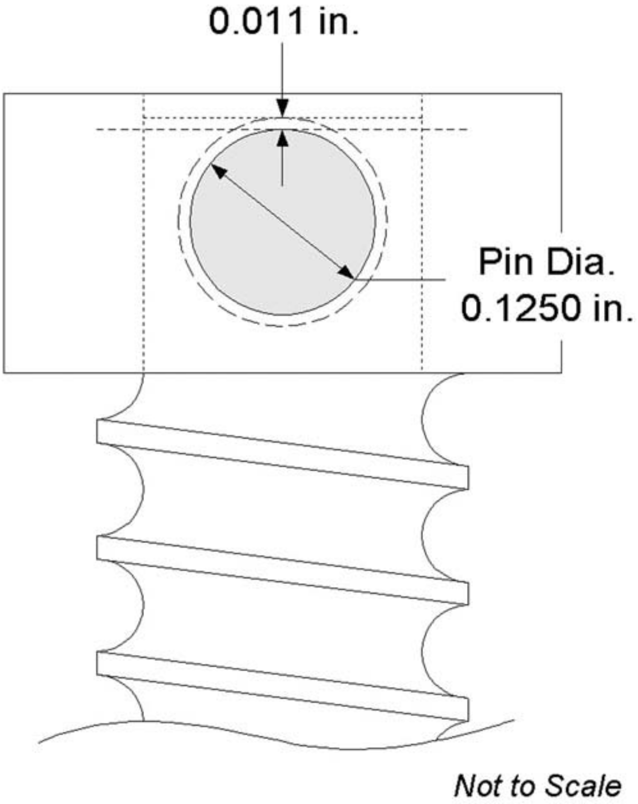

FIGURE 1.5.40 End-stop assembly.

fit equations presented previously are valid under the assumption that the inner and outer cylinders are of the same length. In the case of a hub fit over a shaft, a stress concentration should be employed.

It is worthwhile to note that a person must be able to assemble such a fit. This is usually accomplished by heating the outer cylinder and cooling the inner cylinder to develop a suitable clearance for assembly. It is important to understand the limits to which the cylinders can be heated and cooled with the available equipment and, possibly more importantly, without altering their material properties. Neglecting the practicality of the interference fit process often leads to unnecessary assembly problems.

Example 13

A mechanical stop is attached to a linear ballscrew assembly by pinning the stop to the screw as shown in Figure 1.5.40. The screw is recessed below the top surface of the end-stop. The minimum wall section between the pin outer edge and the top surface of the screw is 0.011 in. (the result of a complex and partially flawed design process that will not be discussed here). The pin of diameter 0.1250 in. is to be inserted into a reamed hole of 0.1240 in. Calculate the hoop stress in the "outer cylinder" for the screw.

Solution. Using Equation (1.5.65), $a = 0$ in., $b = 0.1250/2$ in., and $c = (0.1240 + 2 \times 0.011)/2$ in. The maximum interference fit is 0.0010 in. by completion of the tolerance analysis. Assuming both parts are steel ($E = 30 \times 10^6$ psi), the interface pressure is

$$p = \frac{\left(30\times10^6\right)\left(0.0005\right)}{\left(0.0625\right)}\left(\frac{\left(0.0730^2 - 0.0625^2\right)\left(0.0625^2 - 0^2\right)}{2\left(0.0625^2\right)\left(0.0730^2 - 0\right)}\right) = 32{,}000 \text{ psi (interface pressure)}$$

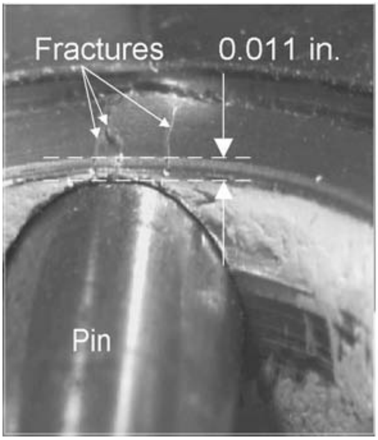

FIGURE 1.5.41 Assembled ballscrew end-stop with fractures. (Photo courtesy Moog Inc., Torrance, CA.)

With the interface pressure (also σ_{Radial} at b) solved, the hoop stress in the outer cylinder is calculated by using Equation (1.5.63b):

$$\sigma_{Hoop_{Outer}} = 32{,}000\frac{0.0730^2 + 0.0625^2}{0.0730^2 - 0.0625^2} = 207{,}700 \text{ psi}$$

The engineer should recognize that the hoop stress calculated here is above the yield strength and ultimate strength of most steels. The photograph of the assembly in Figure 1.5.41 shows the fractured thin-walled section.

This example illustrates that the engineer must check even seemingly benign loadings and geometries with respect to relevant material properties to assure structural integrity.

Experimental Stress Analysis and Mechanical Testing

Experimental stress analysis is based mostly on the measurement of strains, which may be transformed into stresses. A variety of techniques is available to measure strains. A few of these are described here.

Properties of Strain-Measuring Systems

Strain-measuring systems are based on a variety of sensors, including mechanical, optical, and electrical devices. Each has some special advantages but can usually be adapted for other needs as well. No one system is entirely satisfactory for all practical requirements, so it is necessary to optimize the gage system to each problem according to a set of desirable characteristics. Some of the common characteristics used to evaluate the system's adequacy for a typical application are

- The calibration constant for the gage should be stable; it should not vary with time, temperature, or other environmental factors.
- The gage should be able to measure strains with an accuracy of ±1 $\mu\varepsilon$ over a strain range of ±10%.
- The gage size, i.e., the gage length l_0 and width w_0, should be small so that strain at a point is approximated with small error.
- The response of the gage, largely controlled by its inertia, should be sufficient to permit recording of dynamic strains with frequency components exceeding 100 kHz.
- The gage system should permit on-location or remote readout.
- Both the gage and the associated auxiliary equipment should be inexpensive.
- The gage system should be easy to install and operate.
- The gage should exhibit a linear response to strain over a wide range.

Three of these basic characteristics deserve further mention here: the gage length l_0; gage sensitivity; and range of the strain gage. The gage length is often the most important because in nonlinear strain fields the error will depend on the gage length.

Sensitivity is the smallest value of strain that can be read on the scale associated with the strain gage and should not be mistaken for accuracy or precision. The sensitivity chosen should not be higher than necessary because it needlessly increases the complexity of the measuring method and introduces new problems.

The range of the strain gage refers to the maximum value of strain that can be recorded. Because the range and sensitivity of the gage are interrelated, it is often necessary to compromise between the two for optimal performance of both. Various compromises have resulted in two main kinds of strain gages: extensometers and electrical strain gages. Although electrical strain gage systems are numerous, only electrical-resistance strain gages will be considered here.

Extensometers

Various extensometers involving mechanical, electrical, magnetic, or optical devices are used in material test systems. A typical extensometer (Figure 1.5.42) is used in the conventional tensile test in which the stress-strain diagram is recorded. This kind of extensometer is attached to the specimen by knife edges and spring clips. Electrical-resistance strain gages are attached to the cross-flexural member and provide the strain output. The main advantage of extensometers is that they can be reused and recalibrated after each test. The disadvantages are that they are much larger and more expensive than electrical-resistance strain gages.

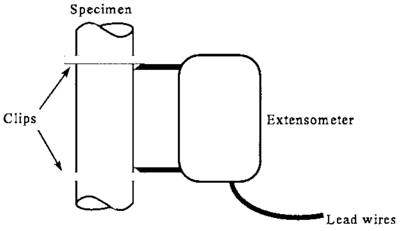

FIGURE 1.5.42 Extensometer attached to a tensile specimen.

Electrical-Resistance Strain Gages

The electrical-resistance strain gage fulfills most of the requirements of an optimum system and is widely used for experimental stress analysis. This gage consists of a metal-foil grid bonded to a polymer backing (Figure 1.5.43). A Wheatstone bridge is often used to enhance its ability to measure changes in resistance. As a specimen is deformed, the strain is transmitted to the grid, which has a current applied to it. The change in resistance of the grid is converted to a voltage signal output of the Wheatstone bridge. The basic equation used with this system is

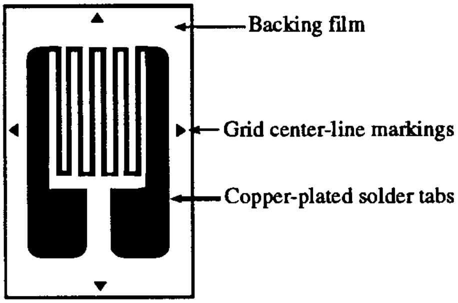

FIGURE 1.5.43 Model of metal-foil strain gages.

$$\frac{\Delta R}{R} = S_A \varepsilon \tag{1.5.67}$$

where R is the resistance of the gage; ε is the applied strain; and S_A is the sensitivity, or gage factor, of the metallic alloy used in the conductor. The most commonly used alloy is a copper–nickel alloy called Advance, for which the sensitivity is 2.1.

Electrical-Resistance Strain Gage Mounting Methods

For precision strain measurements, the correct adhesive and proper mounting procedures must be employed. The adhesive serves a vital function in the strain-measuring system: it must transmit the strain from the specimen to the sensing element without distortion. Bonding a strain gage to a specimen is one of the most critical steps in the entire process of measuring strain with an electric-resistance strain gage. When mounting a strain gage, it is important to prepare the surface of the component where the gage is to be located carefully. This includes sanding, degreasing, etching, cleaning, and, finally, neutralizing the surface where the gage is to be mounted. Next, the surface is marked to allow accurate orientation of the strain gage. The gage is then put in place and held with tape while the adhesive is allowed to dry.

Several of the adhesive systems commonly used for this are epoxy cements, cyanoacrylate cement, polyester adhesives, and ceramic adhesives. Once the adhesive has been placed, the drying process becomes vitally important because it can cause residual stresses in the grid work of the gage, which could influence the output. After allowing the adhesive to dry, the cure must be tested to ensure complete drying. Failure to do so will affect the stability of the gage and the accuracy of the output. The cure state of the adhesive can be tested by various resistance tests. Also, the bonded surface is inspected to determine if any voids are present between the gage and the specimen due to bubbling of the adhesive.

After the bonding process is complete, the lead wires are attached from the soldering tabs of the gage to an anchor terminal, which is also bonded to the test specimen. This anchoring terminal is used to protect the fragile metal-foil gages. Finally, wires are soldered from this anchor terminal to the instrumentation used to monitor the resistance changes.

Gage Sensitivities and Gage Factor

The electrical-resistance strain gage has a sensitivity to axial and transverse strain. The magnitude of the transverse strain transmitted to the grid depends on a number of factors, including the thickness and elastic modulus of the adhesive; the carrier material; the grid material; and the width-to-thickness ratio of the axial segments of the grid. Sometimes it is necessary to calculate the true value of strain that includes all contributions from

$$\varepsilon_a = \frac{(\Delta R/R)}{S_g}\frac{1-\nu_0 K_t}{1+K_t(\varepsilon_t/\varepsilon_a)} \qquad (1.5.68)$$

where

ε_a = the normal strain along the axial direction of the gage
ε_t = the normal strain along the transverse direction of the gage
ν_0 = 0.285 is Poisson's ratio for the calibration beam
K_t = the transverse-sensitivity factor of the gage

The strain gage sensitivity factor, S_g, is a calibration constant provided by the manufacturer. By using Equation (1.5.67) and Equation (1.5.68), the percent error involved in neglecting the transverse sensitivity can be calculated. These errors can be significant for large values of K_t and $\varepsilon_t/\varepsilon_a$, so it may be necessary to correct for the transverse sensitivity of the gage (Figure 1.5.44).

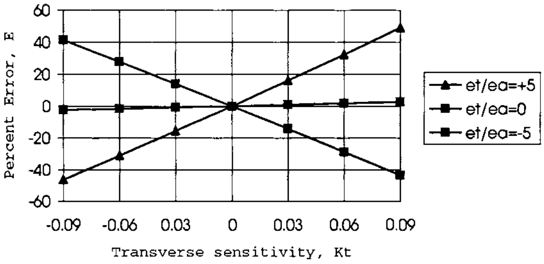

FIGURE 1.5.44 Error as a function of transverse-sensitivity factor with the biaxial strain ratio as a parameter.

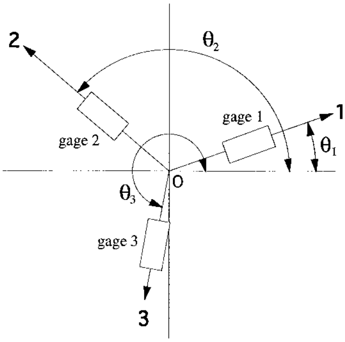

FIGURE 1.5.45 Three gage elements placed at arbitrary angles relative to the *x* and *y* axes.

Strain Analysis Methods

Electrical-resistance strain gages are normally employed on the free surface of a specimen to establish the stress at a particular point on this surface. In general, it is necessary to measure three strains at a point to define the stress or the strain field completely. For this general case in which nothing is known about the stress field or its directions before experimental analysis, three-element rosettes are required to establish the stress field. This is accomplished by using the three-element gage with orientations at arbitrary angles, as shown in Figure 1.5.45. Using this setup, the strains ε_x, ε_y, and γ_{xy} can be determined. These values can be used to determine the principal strains and principal directions:

$$\begin{aligned} \varepsilon_1 &= \frac{1}{2}\left(\varepsilon_{xx} + \varepsilon_{yy}\right) + \frac{1}{2}\sqrt{\left(\varepsilon_{xx} - \varepsilon_{yy}\right)^2 + \gamma_{xy}^2} \\ \varepsilon_2 &= \frac{1}{2}\left(\varepsilon_{xx} + \varepsilon_{yy}\right) - \frac{1}{2}\sqrt{\left(\varepsilon_{xx} - \varepsilon_{yy}\right)^2 + \gamma_{xy}^2} \\ \tan 2\phi &= \frac{\gamma_{xy}}{\varepsilon_{xx} - \varepsilon_{yy}} \end{aligned} \tag{1.5.69}$$

where ϕ is the angle between the principal axis (σ_1) and the *x* axis. The principal stresses can be computed using the principal strains:

$$\begin{aligned} \sigma_1 &= \frac{E}{1 - v^2}\left(\varepsilon_1 + v\varepsilon_2\right) \\ \sigma_2 &= \frac{E}{1 - v^2}\left(\varepsilon_2 + v\varepsilon_1\right) \end{aligned} \tag{1.5.70}$$

These expressions give the complete state of stress because the principal directions are known from Equation (1.5.69).

Optical Methods of Strain Analysis

Moiré Method of Strain Analysis. The moiré technique depends on an optical phenomenon of fringes caused by relative displacement of two sets of arrays of lines. The arrays used to produce the fringes may be a series of straight parallel lines; a series of radial lines emanating from a point; a series of concentric circles; or a pattern of dots. The straight parallel line “grids” are used most often for strain analysis work and consist of equal width lines with opaque spacing of the same width between them. These straight parallel lines are spaced in a “grating” scheme of typically 50 to 1000 lines per inch for moiré work.

In the cross-grid system of two perpendicular line arrays, the grid placed on the specimen is referred to as the model grid. The second grid is referred to as the reference grid and is overlaid on top of the model grid. Often a thin layer of oil or some other low-friction substance is placed between the model grid and the reference grid to keep them in contact while attempting to minimize the transmission of strains from the model to the reference grid.

To obtain a moiré fringe pattern, the grids are first aligned on the unloaded model so that no pattern is present. The model is loaded and light is transmitted through the two grids. Strain displacement is observed in the model grid while the reference grid remains unchanged. A moiré fringe pattern is formed each time the model grating undergoes a deformation in the primary direction equal to the pitch p of the reference grating. For a unit gage length, $\Delta L = np$, where ΔL is the change in length per unit length, p is the pitch of the reference grating, and n is the number of fringes in the unit gage length. In order to calculate ε_x, ε_y, and γ_{xy}, two sets of gratings must be applied in perpendicular directions. Then displacements u and v (displacements in the x and y directions, respectively) can be established and the Cartesian strain components can be calculated from slopes of the displacement surfaces: $\varepsilon_{xx} = \partial u/\partial x$, $\varepsilon_{yy} = \partial v/\partial y$, and $\gamma_{xy} = \partial v/\partial x + \partial u/\partial y$. The displacement gradients in the z direction, $\partial w/\partial x$ and $\partial w/\partial y$, have been neglected here because they are not considered in moiré analysis of in-plane deformation fields.

Photoelasticity. The method of photoelasticity is based on the physical behavior of transparent, noncrystalline, optically isotropic materials that exhibit optically anisotropic characteristics, referred to as temporary double refraction, while they are stressed. To observe and analyze these fringe patterns, a device called a polariscope is used. Two kinds of polariscope are common: the plane polariscope and the circular polariscope.

The plane polariscope (Figure 1.5.46) consists of a light source, two polarizing elements, and the model. The axes of the two polarizing elements are oriented at a 90° angle from each other. If the specimen is not stressed, no light passes through the analyzer and a dark field is observed. If the model is stressed, two sets of fringes — isoclinics and isochromatics — will be obtained. Black isoclinic fringe patterns are the loci of points where the principal-stress directions coincide with the axis of the polarizer. These fringe patterns are used to determine the principal stress directions at all points of a photoelastic model. When

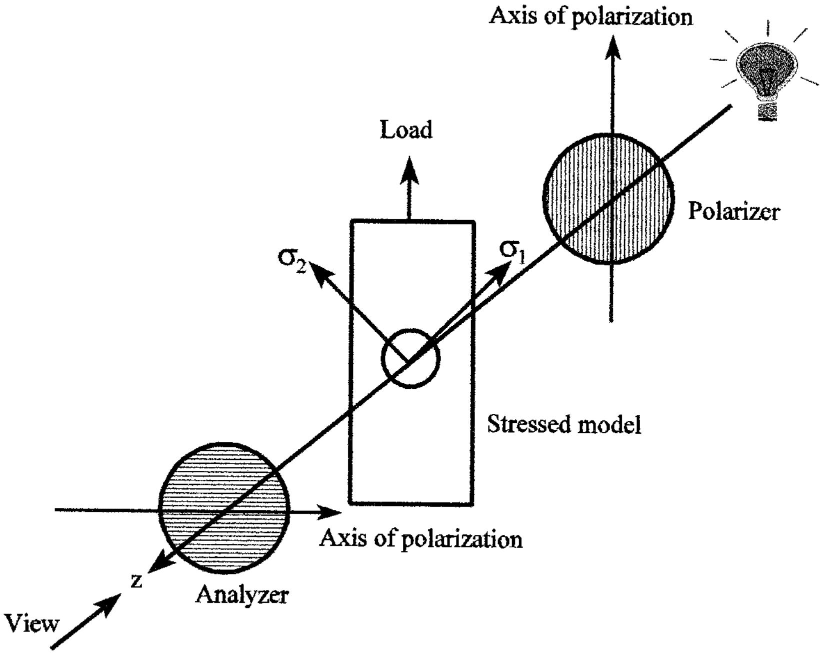

FIGURE 1.5.46 Schematic of a stressed photoelastic model in a plane polariscope.

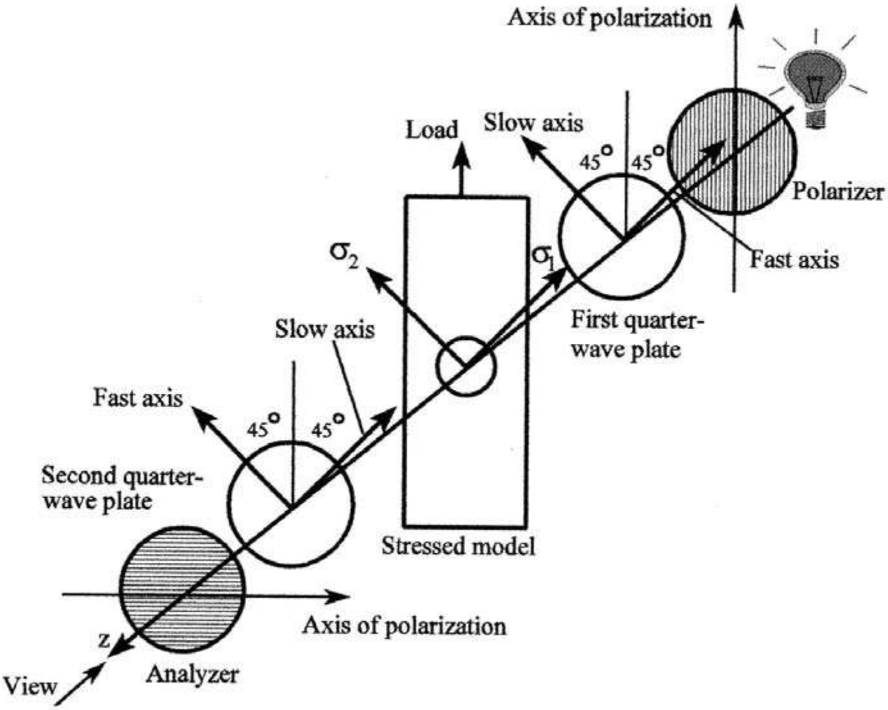

FIGURE 1.5.47 Schematic of a stressed photoelastic model in a circular polariscope.

the principal stress difference is zero ($n = 0$) or sufficient to produce an integral number of wavelengths of retardation ($n = 1, 2, 3, \ldots$), the intensity of light emerging from the analyzer is zero. This condition for extinction gives a second fringe pattern, called isochromatics, where the fringes are the loci of points exhibiting the same order of extinction ($n = 0, 1, 2, 3, \ldots$):

$$n = N = \frac{h}{f_\sigma}\left(\sigma_1 - \sigma_2\right) \tag{1.5.71}$$

where N is the isochromatic fringe order. The order of extinction n depends on the principal stress difference ($\sigma_1 - \sigma_2$), the thickness h of the model, and the material fringe value f_σ. When monochromatic light is used, the isochromatic fringes appear as dark bands. When white light is used, the isochromatic fringes appear as a series of colored bands. Black fringes appear in this case only where the principal stress difference is zero.

A circular polariscope is a plane polariscope with two additional polarizing plates, called quarter-wave plates, added between the model and the original polarizing plates (Figure 1.5.47). The two quarter-wave plates are made of a permanently doubly refracting material. The circular polariscope is used to eliminate the isoclinic fringes while maintaining the isochromatic fringes. To accomplish this, monochromatic light must be used because the quarter-wave plates are designed for a specific wavelength of light. For the dark-field arrangement shown, no light is passed through the polariscope when the model is unstressed. A light-field arrangement is achieved by rotating the analyzer 90°. The advantage of using light- and dark-field analysis is that twice as much data are obtained for the whole-field determination of $\sigma_1 - \sigma_2$. If a dark-field arrangement is used, n and N still coincide, as in Equation (1.5.71). If a light-field arrangement is used, they are not coincident. In this case, Equation (1.5.71) becomes

$$N = \frac{1}{2} + n = \frac{h}{f_\sigma}\left(\sigma_1 - \sigma_2\right) \qquad n = 0,\ 1,\ 2,\ 3,\ \ldots \tag{1.5.72}$$

By determining the isoclinic fringes and the isochromatic fringes, the principal-stress directions and the principal-stress difference can be obtained. In order to obtain the individual principal stresses, a stress separation technique would need to be employed.

The advantages of the photoelastic method are that it allows a full-field stress analysis and it makes it possible to determine the magnitude and direction of the principal stresses. The disadvantages are that it requires a plastic model of the actual component and it takes a considerable effort to separate the principal stresses.

Major advances have been made in this area recently, and a variety of special-purpose equipment is available to solve difficult engineering problems efficiently. Readers are encouraged to visit Internet sites such as www.stressphotonics.com for more information.

Thermoelastic Stress Analysis. Modern thermoelastic stress analysis (TSA) employs advanced differential thermography (or AC thermography) methods based on dynamic thermoelasticity and focal-plane-array infrared equipment capable of rapidly measuring small temperature changes (down to 0.001°C) caused by destructive or nondestructive alternating stresses. Stress resolutions comparable to those of strain gages can be achieved in a large variety of materials. The digitally stored data can be processed in near-real time to determine the gradient stress fields and related important quantities (such as combined-mode stress intensity factors) in complex components and structures, with no upper limit in temperature. The efficient, user-friendly methods can be applied in the laboratory, field, vehicles, and structures such as bicycles, automobiles, aircraft, surgical implants, welded bridges, and microelectronics. Optimum design, rapid prototyping, failure analysis, life prediction, and rationally accelerated testing can be facilitated with the new TSA methods (Color Figure 8 and Color Figure 11 through Color Figure 14).

Major advances have been made in this area recently, and a variety of special-purpose equipment is available to solve difficult engineering problems efficiently. Readers are encouraged to visit Internet sites, such as www.stressphotonics.com, for more information.

Brittle Coatings. If a coating is applied to a specimen that is thin in comparison with the thickness of the specimen, then the strains developed at the surface of the specimen are transmitted without significant change to the coating. This is the basis of the brittle coating method of stress analysis. The two kinds of coatings available are resin-based and ceramic-based coatings. The ceramic-based coatings are seldom used due to the high application temperatures (950 to 1100°F) required. The coatings are sprayed on the component until a layer approximately 0.003 to 0.010 in. thick has accumulated. It is also necessary to spray calibration bars with the coating at the same time in order to obtain the threshold strain at which the coating will crack. These calibration bars are tested in a cantilever apparatus and the threshold strain is calculated using the flexure formula and Hooke's law. Once the threshold strain is known and the actual specimen has been tested, the principal stress perpendicular to the crack can be determined by using Hooke's law. The procedure is to load the component, apply the coating, and then quickly release the loading in steps to observe any cracks.

The main advantages of this method are that magnitude and direction of the principal strains can be quickly obtained and that the coating is applied directly to the component. This also allows a quick analysis of where the maximum stress regions are located so that a better method can be used to obtain more accurate results. The main disadvantage is that the coatings are very sensitive to ambient temperature and might not have sufficiently uniform thickness.

Mechanical Testing

Standards. Many engineering societies have adopted mechanical testing standards; the most widely accepted are the standards published by the American Society for Testing and Materials. Standards for many engineering materials and mechanical tests (tension, compression, fatigue, plane strain fracture toughness, etc.) are available in the *Annual Book of ASTM Standards*.

Open-Loop Testing Machines. In an open-loop mechanical testing system, no feedback is offered to the control mechanism that would allow for continuous adjustment of the controlled parameter. Instead, the chosen parameter is "controlled" by the preset factory adjustments of the control mechanism. It is not possible for such a machine continually to adjust its operation to achieve a chosen (constant or not constant) displacement rate or loading rate. A human operator can be added to the control loop in some systems in an attempt to maintain some parameter, such as a loading rate, at a constant level. This is a poor means of obtaining improved equipment response and is prone to error.

Closed-Loop Testing Machines. In a closed-loop, most commonly electrohydraulic, testing system, a servo controller is used to control the chosen parameter continuously. When the difference between the desired value programmed in and the actual value measured is small, the servo controller adjusts the flow of hydraulic fluid to the actuator to reduce the difference (the error). This correction occurs at a rate much faster than any human operator could achieve. A standard system makes 10,000 adjustments per second automatically.

A typical closed-loop system (Color Figure 9, Color Figure 11, and Color Figure 15) allows the operator to control load, strain, or displacement as a function of time and can be adjusted to control other parameters as well. This makes it possible to perform many different kinds of tests, such as tension, compression, torsion, creep, stress relaxation, fatigue, and fracture.

Impact Testing. The most common impact testing machines utilize a pendulum hammer or a dropped weight. In the pendulum system, a hammer is released from a known height and strikes a small notched specimen, causing it to fracture. The hammer proceeds to some final height. The difference between the initial and final heights of the hammer is directly proportional to the energy absorbed by the specimen. For the Charpy test, the specimen is mounted horizontally with the ends supported so that the pendulum will strike the specimen in midspan, opposite the notch. In the Izod test, the specimen bottom is mounted in a vertical cantilever support so that the pendulum will strike the specimen at a specific distance above the notch, near the unsupported top end. A large variety of drop-weight tests is also available to investigate the behaviors of materials and packages during impact.

Hardness Testing. The major hardness tests are the Brinell, Rockwell, Vickers, and Shore scleroscope tests. The Brinell hardness test uses a hardened steel ball indenter that is pushed into the material under a specified force. The diameter of the indentation left in the surface of the material is measured and a Brinell hardness number is calculated from this diameter. The Rockwell hardness test differs from the Brinell test in that it uses a 120° diamond cone with a spherical tip for hard metals and a 1/16-in. steel ball for soft metals. The Rockwell tester gives a direct readout of the hardness number. The Rockwell scale consists of a number of different letter designators (B, C, etc.) based on the depth of penetration into the test material.

The Vickers hardness test uses a small pyramidal diamond indenter and a specified load. The diagonal length of the indentation is measured and used to obtain the Vickers hardness number. The Shore scleroscope uses a weight that is dropped on the specimen to determine the hardness. This hardness number is determined from the rebound height of the weight.

1.6 Structural Integrity and Durability

Bela I. Sandor

The engineer is often concerned about the long-term behavior and durability of machines and structures. Designs based only on statics, dynamics, and basic mechanics of materials are typically able to satisfy only minimal performance and reliability requirements. For realistic service conditions, numerous degradations may need to be considered. A simple and common approach is to use safety factors based on experience and judgment. The degradations could become severe and require sophisticated analyses if unfavorable interactions occur. For example, fatigue with corrosion or high temperatures is difficult to predict accurately, and much more so when corrosion is occurring at a high temperature.

There are many kinds of degradations and interactions between them, and a large (and still growing) technical literature is available in most of these areas. The present coverage cannot possibly do justice to the magnitude of the most serious problems and the available resources to deal with them. Instead, the material here highlights some common problems and provides fundamental concepts to prepare for more serious efforts. The reader is encouraged to study the technical literature (including that by technical societies such as ASM, ASME, ASNT, ASTM, SAE), attend specialized short courses, and seek consulting advice (ASM, ASTM, Teltech) as necessary.

Finite Element Analysis. Stress Concentrations

The most common problem in creating a machine or structure with good strength-to-weight ratio is to identify its critical locations and the corresponding maximum stresses or strains and to adjust the design optimally. This is difficult if a member's geometry, including the geometry and time dependence of the loading, is complex. The modern analytical tool for addressing such problems is finite element analysis (FEA) or finite element modeling (FEM).

Finite Element Analysis

The finite element (FE) method was developed by engineers using physical insight. In all applications, the analyst seeks to calculate a *field quantity*: in stress analysis, it is the displacement field or the stress field; in thermal analysis, it is the temperature field or the heat flux; and so on. Results of the greatest interest are usually peak values of the field quantity or its gradients. The FE method is a way of getting a *numerical* solution to a *specific* problem. An FEA does not produce a formula as a solution, nor does it solve a class of problems. Also, the solution is approximate unless the problem is so simple that a convenient exact formula is already available. Furthermore, it is important to validate the numerical solution instead of trusting it blindly.

The power of the FE method is its versatility. The structure analyzed may have arbitrary shape, arbitrary supports, and arbitrary loads. Such generality does not exist in classical analytical methods. For example, temperature-induced stresses are usually difficult to analyze with classical methods, even when the structure geometry and the temperature field are simple. The FE method treats thermal stresses as readily as stresses induced by mechanical load, and the temperature distribution can be calculated by FE. However, it is easy to make mistakes in describing a problem to the computer program. Therefore, *it is essential that the user have a good understanding of the problem and the modeling* so that errors in computed results can be detected by judgment.

Stress Concentrations

Geometric discontinuities cause localized stress increases above the average or far-field stress. A stress raiser's effect can be determined quantitatively in several ways, but not always readily. The simplest method, if applicable, is to use a known theoretical **stress concentration factor**, K_t, to calculate the peak stress from the nominal, or average, value:

$$\sigma_{\max} = K_t \sigma_{ave} \tag{1.6.1}$$

This is illustrated in Figure 1.6.1. The area under the true stress distribution always equals the area under the nominal stress level,

$$\int_A \sigma_{true}\, dA = \int_A \sigma_{ave}\, dA = \sigma_{ave} A \tag{1.6.2}$$

The factor K_t depends mainly on the geometry of the notch, not on the material, except when the material deforms severely under load. K_t values are normally obtained from plots such as in Figure 1.6.2 and are strictly valid only for ideally elastic, stiff members. K_t values can also be determined by FEA or by several experimental techniques. There are no K_t values readily available for sharp notches and cracks, but one can always assume that such discontinuities produce the highest stress concentrations, sometimes factors of tens. This is the reason why brittle, high-strength materials are extremely sensitive even to

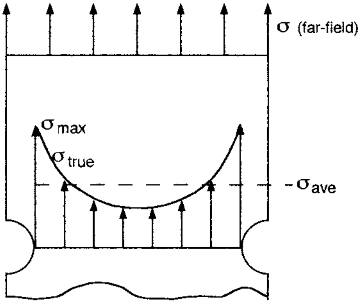

FIGURE 1.6.1 Stress distribution (simplistic) in a notched member under uniaxial load.

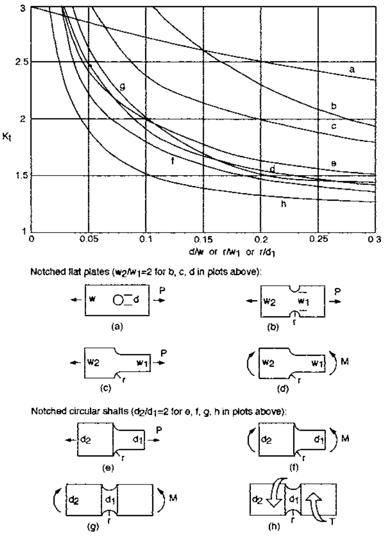

FIGURE 1.6.2 Samples of elastic stress concentration factors. (Condensed from Figure 10.1, Figure 10.2 and Figure 10.2, Dowling N.E., *Mechanical Behavior of Materials*, Prentice Hall, Englewood Cliffs, NJ, 1993. With permission.)

minor scratches. In fatigue, for example, invisible toolmarks may lead to premature, unexpected failures in strong steels.

Many other factors may seem similar to K_t, but they should be carefully distinguished. The first is the true stress concentration factor K_σ, defined as

$$K_\sigma = \frac{\sigma_{\max}}{\sigma_{ave}} \tag{1.6.3}$$

which means that $K_\sigma = K_t$ (by Equation 1.6.1) for ideally elastic materials. K_σ is most useful in the case of ductile materials that yield at the notch tip and lower the stress level from that indicated by K_t. Similarly, a true strain concentration factor, K_ε, is defined as

$$K_\varepsilon = \frac{\varepsilon_{\max}}{\varepsilon_{\text{ave}}} \tag{1.6.4}$$

where $\varepsilon_{\text{ave}} = \sigma_{\text{ave}}/E$.

Furthermore, a large number of **stress intensity factors** are used in fracture mechanics, and these (such as K, K_c, K_I, etc.) are easily confused with K_t and K_σ, but their definitions and uses are different as seen in the next section.

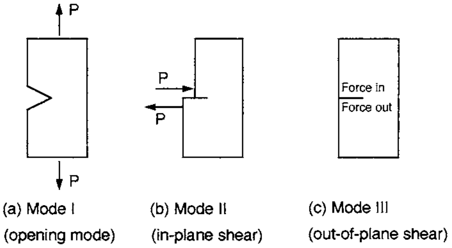

FIGURE 1.6.3 Modes of deformation.

Fracture Mechanics

Notches and other geometric discontinuities are common in solid materials, and they tend to facilitate the formation of cracks, which are in turn more severe stress raisers. Sharp cracks and their further growth are seldom simple to analyze and predict because the actual stresses and strains at a crack tip are not known with the required accuracy. In fact, this is the reason that classical failure theories (maximum normal stress, or Rankine, theory; maximum shear stress, or Tresca, theory; distortion energy, or von Mises or octahedral shear stress, theory), elegantly simple as they are, are not sufficiently useful in dealing with notched members. A powerful modern methodology in this area is fracture mechanics, which was originated by A. A. Griffith[2] in 1920 and has grown in depth and breadth enormously in recent decades. The space here is not adequate to list all of the significant references in this still expanding area. The purpose here is to raise the engineer's awareness to a quantitative, practically useful approach in dealing with stress concentrations as they affect structural integrity and durability.

Brittle and Ductile Behaviors. Embrittlements

Brittleness and ductility are often the first aspects of fracture considerations, but they often require some qualifications. Simplistically, a material that fractures in a tension test with 0% reduction of area (RA) is perfectly brittle (and very susceptible to fracture at stress raisers), while one with 100% RA is perfectly ductile (and quite tolerant of discontinuities). Between these extremes fall most engineering materials, with the added complication that embrittlement is often made possible by several mechanisms or environmental conditions. For example, temperature, microstructure, chemical environment, internal gases, and certain geometries are common factors in embrittlement. A few of these will be discussed later.

Linear-Elastic Fracture Mechanics (LEFM)

A major special case of fracture mechanics is when little or no plastic deformation occurs at the critical locations of notches and cracks. It is important that even intrinsically ductile materials may satisfy this condition in common circumstances.

Modes of Deformation. Three basic modes of deformation (or crack surface displacement) of cracked members are defined as illustrated schematically in Figure 1.6.3. Each of these modes is very common, but Mode I is the easiest to deal with analytically and experimentally, so most data available are for Mode I.

Stress Intensity Factors. The stresses on an infinitesimal element near a crack tip under Mode I loading are obtained from the theory of linear elasticity. Referring to Figure 1.6.4,

---

[2] The Griffith criterion of fracture states that a crack may propagate when the decrease in elastic strain energy is at least equal to the energy required to create the new crack surfaces. The available elastic strain energy must also be adequate to convert into other forms of energy associated with the fracture process (heat from plastic deformation, kinetic energy, etc.). The critical nominal stress for fracture according to the Griffith theory is proportional to $1/\sqrt{\text{crack length}}$. This is significant since crack length, even inside a member, is easier to measure nondestructively than stresses at a crack tip. Modern, practical methods of fracture analysis are sophisticated engineering tools on a common physical and mathematical basis with the Griffith theory.

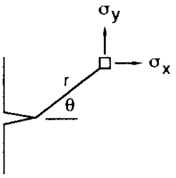

FIGURE 1.6.4 Coordinates for fracture analysis.

$$
\begin{aligned}
\sigma_x &= \frac{K_I}{\sqrt{2\pi r}} f_1(\theta) + \ldots \\
\sigma_y &= \frac{K_I}{\sqrt{2\pi r}} f_2(\theta) + \ldots \\
\tau_{xy} &= \frac{K_I}{\sqrt{2\pi r}} f_3(\theta) + \ldots \\
\tau_{xz} &= \tau_{zx} = 0
\end{aligned}
\tag{1.6.5}
$$

There are two special cases of σ_z:

1. $\sigma_z = 0$ for plane stress (thin members)
2. $\sigma_z = \nu(\sigma_x + \sigma_y)$ for plane strain, with $\varepsilon_z = 0$ (thick members)

The factor K in these and similar expressions characterizes the intensity or magnitude of the stress field near the crack tip. It is thus called the stress intensity factor, which represents a very useful concept different from that of the well-known stress concentration factor. K_I is a measure of the severity of a crack, and most conveniently it is expressed as

$$K_I = \sigma\sqrt{\pi a}\, f(\text{geometry}) \tag{1.6.6}$$

where a is the crack length and f is a function of the geometry of the member and of the loading (typically, $f \cong 1 \pm 0.25$). Sometimes f includes many terms, but all stress intensity factors have the same essential features and units of stress $\sqrt{\text{length}}$. In any case, expressions of K for many common situations are available in the literature, and numerical methods are presented for calculating special K values. Differential thermography via dynamic thermoelasticity is a powerful, efficient modern method for the measurement of actual stress intensity factors under a variety of complex conditions (Section 1.6, "Experimental Stress Analysis and Mechanical Testing"; Figure 1.6.12; Color Figure 8; Color Figure 11 through Color Figure 14).

Fracture Toughness of Notched Members

The stress intensity factor, simply K for now, is analogous to a stress-strain curve, as in Figure 1.6.5. K increases almost linearly from 0 at $\sigma = 0$, to a value K_c at a critical (fracture) event. K_c is called the *fracture*

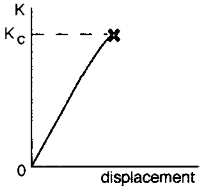

FIGURE 1.6.5 K_c = fracture toughness of a particular member.

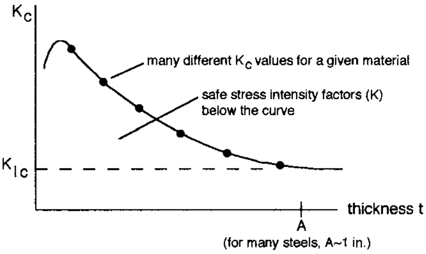

FIGURE 1.6.6 K_{Ic} = plane strain fracture toughness of material.

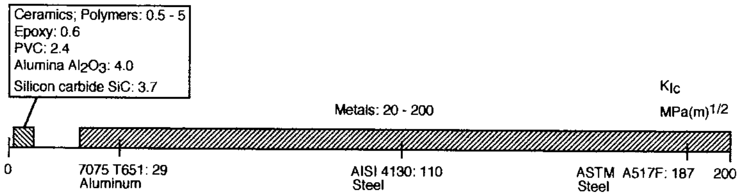

FIGURE 1.6.7 Plane strain fracture toughness ranges (approximate).

toughness of a particular member tested. It depends on the material, but it is not a reliable material property because it depends on the size of the member too much. This is illustrated in Figure 1.6.6 for plates of the same material but different thicknesses.

At very small thickness, K_c tends to drop. More significantly, K_c approaches a lower limiting value at large thickness (>A). This worst-case value of K_c is called K_{Ic}, the *plane strain fracture toughness* in Mode I. It may be considered a pseudomaterial property because it is independent of geometry at least over a range of thicknesses. It is important to remember that the thickness effect can be rather severe. An intrinsically ductile metal may fracture in an apparently brittle fashion if it is thick enough and has a notch.

Fracture Toughness Data. Certain criteria about crack sharpness and specimen dimensions must be satisfied in order to obtain reliable basic K_{Ic} data (see *ASTM Standards*). These data for many engineering materials are available in the technical literature. A schematic overview of various materials' K_{Ic} values is given in Figure 1.6.7. Note that particular expected values are not necessarily attained in practice. Poor material production or manufacturing shortcomings and errors could result in severely lowered toughness. On the other hand, special treatments or combinations of different but favorably matched materials (as in composites) could substantially raise the toughness.

Besides the thickness effect, there are a number of major influences on a given material's toughness, and they may occur in favorable or unfavorable combinations. Several of these are described here schematically, showing general trends. Note that some of the actual behavior patterns are not necessarily as simple or well defined as indicated.

Yield Strength. High yield strength results in a low fracture toughness (Figure 1.6.8); therefore, it should be chosen carefully, understanding the consequences.

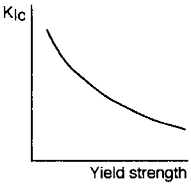

FIGURE 1.6.8 Yield strength effect on toughness.

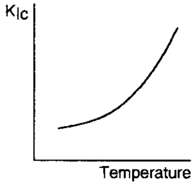

FIGURE 1.6.9 Temperature effect on toughness.

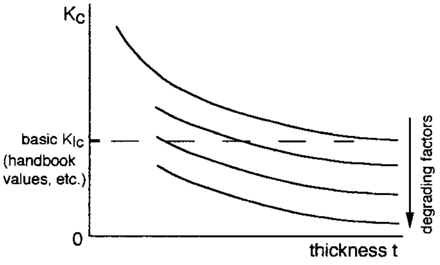

FIGURE 1.6.10 Trends of toughness degradations.

Temperature. Two kinds of temperature effect on toughness should be mentioned here. They may appear, at least for part of the data, as in Figure 1.6.9, with high temperature causing increased toughness. One temperature effect is by the increased ductility at higher temperature. This tends to lower the yield strength (except in low-carbon steels that strain-age at moderately elevated temperatures, about 100 to 500°C); increase the plastic zone at the notch tip; and effectively blunt the stress concentration. Another effect — the distinct temperature-transition behavior in low-carbon steels (BCC metals, in general; easily shown in Charpy tests) — is caused by microstructural changes in the metal and is relatively complex in mechanism.

Loading Rate. The higher the rate of loading, the lower the fracture toughness is in most cases. Note that toughness results obtained in notch-impact or explosion tests are most relevant to applications in which the rate of loading is high.

Microstructural Aspects. In some cases, apparently negligible variations in chemical composition or manufacturing processes may have a large effect on a material's fracture toughness. For example, carbon, sulfur, and hydrogen contents may be significant in several embrittling mechanisms. Also, the common mechanical processing of cold or hot working (rolling, extruding, forging) influences the grain structure (grain size and texture) and the corresponding toughness. Neutron radiation also tends to cause microscopic defects, increasing the yield strength and consequently lowering the ductility and toughness of the material.

Overview of Toughness Degradations. A multitude of mechanisms and situations must be considered singly and in realistic combinations, as illustrated schematically in Figure 1.6.10 (review Figure 1.6.6 for relevant toughness definitions).

Degrading Factors
Some chemical compositions
Sharper notch
Greater thickness
Faster loading
Lower temperature
Higher yield strength
Hostile chemical environment
Liquid metal embrittlement
Tensile residual stress
Neutron irradiation
Microstructural features
Moisture
Gases in solid solution
Surface hardening

Note that the toughness can drop essentially to zero in some cases.

Crack Propagation

Crack growth may be classified as stable (subcritical) or unstable (critical). Often stable cracks become unstable in time, although the opposite behavior, cracks decelerating and even stopping, is sometimes possible. Unstable cracks under load control are extremely dangerous because they propagate at speeds nearly 40% of the speed of sound in that particular solid. For example, in steels, this means a crack growth speed of about 1 mi/sec. Thus, warnings and even electronically activated, automated countermeasures during unstable propagation are useless. The only reasonable course is to provide, by design and proper manufacture, preventive measures such as ductile regions in a structure where cracks become stable and slow to grow, thus allowing for inspection and repair.

Each of the three kinds of stable crack growth is important in its own right; interactions among the three are possible. Under steady loads, environmentally assisted crack growth (also called stress corrosion cracking) and creep crack growth are commonly found. Under cyclic loading, fatigue crack growth is likely to occur. In each case the **rate of crack growth** tends to accelerate in time or with progressive cycles of load if the loads are maintained while the cracks reduce the load-bearing cross-sectional area. This common situation, caused by increasing true stresses, is illustrated schematically in Figure 1.6.11, where a_0 is an initial flaw's size, da/dN and da/dt are the fatigue and creep crack growth rates, respectively, and a_c is the critical crack size. The rate of stable crack growth is controlled by the stress intensity factor. This will be discussed later.

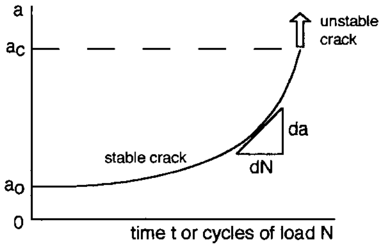

FIGURE 1.6.11 Crack growth rates under constant load.

Design and Failure Analysis Using Stress Intensity Concepts

The concept of stress intensity of cracked members is highly useful and practical. Three major possibilities are outlined here with respect to the essential framework of

$$K \propto \text{stress} \sqrt{\text{crack length}} \tag{1.6.7}$$

Here K may be an operating stress intensity factor or a K_{Ic} value, a material property (the units are the same). In design, the idea is to fix one or two quantities by some initial constraints of the case, then work with the results according to Equation (1.6.7).

- Operating stress and material (K_{Ic}) are predetermined. This forces one to measure crack length and set the maximum allowable size of cracks.
- Operating stress and detectable crack size are predetermined. This forces one to choose an appropriate material with the required K_{Ic} value.
- The material (K_{Ic} value) and the detectable crack size are predetermined. This forces one to limit the operating stress accordingly.

Similar thinking can be used in failure analysis and corresponding design iteration. For example, the critical crack size at the end of the stable propagation (and start of the unstable, high-speed growth) can

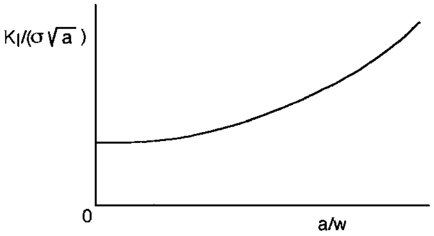

FIGURE 1.6.12 Practical fracture mechanics with NDE: nearly instantaneous measurement of crack size *and* the actual stress intensity factor via advanced thermoelastic stress analysis. The member's loading (including boundary conditions) need not be known to obtain reliable data using this method.

often be determined by looking at the broken parts. The material property, K_{Ic}, can also be estimated from the parts at hand, and thus the stress that caused the failure can be calculated. Whether the stress was within normal bounds or was an overload from misuse of the equipment can be determined. These are powerful, quantitative methods useful in improving designs and manufacturing.

Special Methods

The many other important and useful methods in fracture mechanics cannot even be listed here. For example, several methods in the area of elastic–plastic fracture mechanics are available. Within this area, mainly applicable to thin members of ductile materials, the J-integral approach alone has been covered in a large number of books and journal articles.

Nondestructive Evaluation

Because all of fracture mechanics is based on knowing the crack size and its location and orientation, nondestructive evaluation (NDE) is a major part of quantitative, predictive work in this area. Many techniques of NDE are available, and some are still rapidly evolving. Two major categories of NDE methods are defined here:

1. *Geometry-based methods.* At best, the size, shape, location, and orientation of a flaw are measured. Considerable additional effort is needed to estimate the effect of the flaw on structural integrity and durability. Common methods involve acoustic, magnetic, microwave, optical (including thermal), or x-ray instruments.
2. *Stress-based methods.* A flaw's effect on the stress–strain field is directly measured, which is often much more important than just finding that flaw (a flaw of a given geometry may be benign or malignant, depending on the stress field of the neighborhood). Only a few optical methods are readily available for stress-based NDE; the most effective one for laboratory and field applications is thermoelastic stress analysis by infrared means (Figure 1.6.12; Color Figure 8; Color Figure 11 through Color Figure 14; Section 1.5, "Experimental Stress Analysis and Mechanical Testing").

Creep and Stress Relaxation

Creep and stress relaxation are related time- and temperature-dependent phenomena, with creep occurring under load control and stress relaxation under deformation control. In both cases the material's temperature is a governing factor regarding what happens. Specifically, for most metals, the creep and relaxation regimes are defined as high homologous (relative, dimensionless) temperatures, normally those above half the melting point in absolute temperature for each metal. Thus, solder at room temperature creeps significantly under load, while steel and aluminum do not. However, some creep and relaxation may occur even at low homologous temperatures, and they are not always negligible. For polymers, the creep regime is above the glass transition temperature. This is typically not far from room temperature.

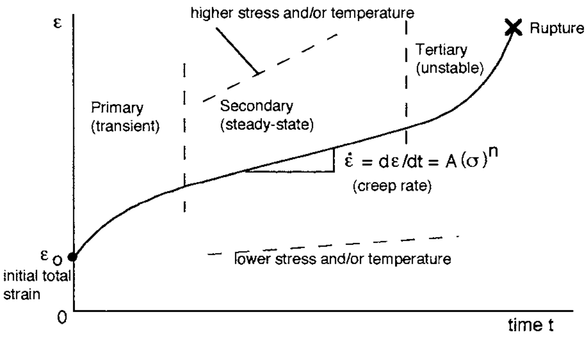

FIGURE 1.6.13 Creep under constant load. $d\varepsilon/dt = A(\sigma)^n$. A and n are material parameters.

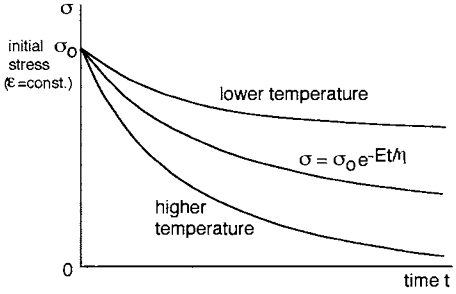

FIGURE 1.6.14 Stress relaxation under constant deformation. $\sigma = \sigma_0 e^{-Et/\eta}$. E and η are material parameters.

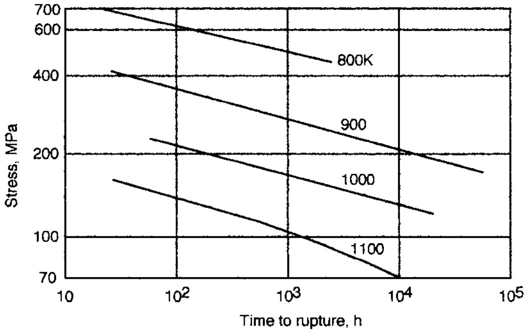

FIGURE 1.6.15 Approximate stress vs. rupture lives of S-590 alloy as functions of temperature. (After Figure 15.8, Dowling, N.E., *Mechanical Behavior of Materials.* Prentice Hall, Englewood Cliffs, NJ, 1993. With permission.)

Figure 1.6.13 and Figure 1.6.14 show trends of creep and stress relaxation in the large-scale phenomenon region. Stress vs. rupture life curves for creep may be nearly linear when plotted on log–log coordinates (Figure 1.6.15).

Mechanical Models of Viscoelastic Behaviors

Creep and stress relaxation appear to be combinations of behaviors of viscous liquids and elastic solids. The so-called viscoelastic phenomena are commonly modeled by simple mechanical components, springs and dashpots, as in Figure 1.6.16. The Maxwell model and related others are based on such elements.

The Maxwell model for creep under constant stress σ_0 is

$$\varepsilon = \varepsilon_1 + \varepsilon_2 = \frac{\sigma}{E} + \int_0^t \sigma_0 \, dt = \frac{\sigma_0}{E} + \frac{\sigma_0 t}{\eta} \tag{1.6.8}$$

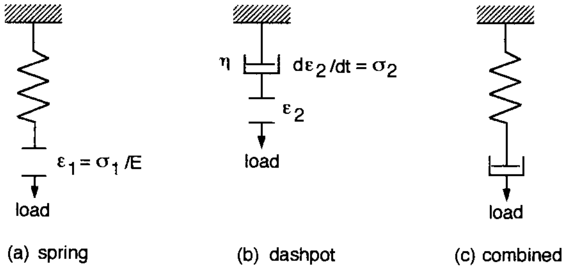

FIGURE 1.6.16 Viscoelastic elements.

For relaxation, ε = constant and σ varies, so

$$\frac{d\varepsilon}{dt} = 0 = \frac{1}{E}\frac{d\sigma}{dt} + \frac{\sigma}{\eta} \tag{1.6.9}$$

$$\int_{\sigma_0}^{\sigma} \frac{d\sigma}{\sigma} = -\frac{E}{\eta}\int_0^t dt, \quad \sigma = \sigma_0 e^{-Et/\eta}$$

Time–Temperature Parameters. Life Estimation

It is often necessary to extrapolate from laboratory creep test data, which are limited in time (from days to years), to real service lives, which tend to be from years to several decades. Time–temperature parameters are useful for this purpose. Three common parameters are outlined here. Note that no such parameter is entirely reliable in all cases; they are best if used consistently in direct comparisons of materials.

Sherby–Dorn Parameter (P_{SD})

$$P_{SD} = \log\theta_r = \log t_r - 0.217Q\left(\frac{1}{T}\right) \tag{1.6.10}$$

where, for steady-state creep,

θ_r = temperature-compensated time to rupture
t_r = rupture time, hours
Q = activation energy = constant
T = temperature, K

Stress-life data at high T and low t_r are needed to plot P_{SD} vs. stress, in order to predict a longer t_r at a lower T.

Larson–Miller Parameter (P_{LM})

This approach is analogous to the Sherby–Dorn approach, but is based on different assumptions and equations.

$$P_{LM} = 0.217Q = T\left(\log t_r + C\right) \tag{1.6.11}$$

where $C = -\log\theta_r \cong 20$ for steels. For using temperature in degrees Fahrenheit (as in most of the data):

$$P_{LM}\big|_{^\circ F} = 1.8 P_{LM}\big|_{K} \tag{1.6.12}$$

Manson–Haferd Parameter (P_{MH})

$$P_{MH} = \frac{T - T_a}{\log t_r - \log t_a} \tag{1.6.13}$$

where T_a and t_a are temperature and time constants representing a point of convergence for a family of data points. As shown previously, for different temperature scales:

$$P_{MH}\big|_{°F} = 1.8 P_{MH}\big|_{K} \tag{1.6.14}$$

Overview. The greater the extrapolation using any parameter, the greater the likelihood of error is. A factor of 10 or less extrapolation in life is often reasonable. At very large extrapolations, damage mechanisms may be different from those of the tests and unpredictable service loading and environmental conditions as well.

Fatigue

Fatigue is a process of damage evolving in a material due to repeated loads, also called cyclic loads. This is a common degradation that affects virtually all solid materials, and thus it is often the main (or a contributing) factor in the failure of vehicles, machinery, structures, appliances, toys, electronic devices, and surgical implants. Many apparently well-designed and -fabricated items that fail inexplicably have problems rooted in the fatigue area.

Nearly two centuries of fatigue studies and engineering efforts have resulted in a huge, and still expanding, technical literature. This brief review can cover only a few major topics, some old but valuable items of wisdom, and practical modern methods. Three important approaches are presented: the stress-based (useful for long lives), strain-based (useful for short lives), and fracture mechanics methods.

Definitions

Constant-amplitude, stress- or strain-controlled cycling is common in testing and some service situations. Figure 1.6.17 shows the stress (σ) quantities in such cycling. Similar notations are used for strains. In completely reversed stress, $\sigma_m = 0$ and $R = -1$. Zero-to-tension (a special case of pulsating tension) has $\sigma_{\min} = 0$ and $R = 0$.

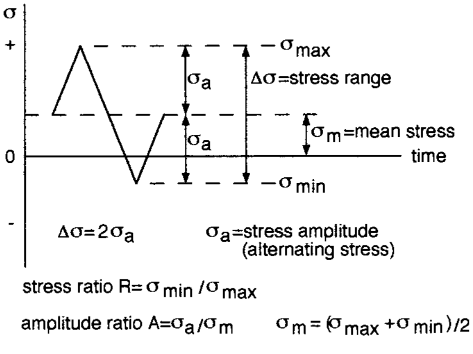

FIGURE 1.6.17 Notation for constant-amplitude stress cycling.

Material Properties in Cyclic Loading

The mechanical properties of some materials are gradually changed by cyclic plastic strains. The changes that occur are largest early in the fatigue life and become negligible beyond about 20 to 50% of the life. The most important material properties that could change significantly this way are the flow properties (yield strength, proportional limit, strain hardening exponent), while the modulus of elasticity is little affected. For metals, three initial conditions can be defined using the strain hardening exponent n as a key parameter. The concept of a cyclic stress–strain curve, as opposed to that in monotonic (static) loading, is also used to distinguish possible material behaviors in fatigue, as follows.

- **Stable**: $0.15 < n < 0.2$ (approx.)
  The monotonic and cyclic stress–strain curves are the same for most practical purposes (though seldom coincident).
  Examples: 7075-T6 Al; 4142 steel (550 BHN)
- **Cycle-dependent softening**: $n < 0.15$ (approx.) (means initially hard, cold-worked material)
  The cyclic stress-strain curve falls significantly below the monotonic curve, which means a gradually decreasing deformation resistance as cyclic loading progresses. The cyclic yield strength may be less than half the tensile yield strength in some cases.
  Examples: 4340 steel (350 BHN); 4142 steel (400 BHN)
- **Cycle-dependent hardening**: $n > 0.2$ (approx.) (means initially soft, annealed material)
  The cyclic stress–strain curve is significantly above the monotonic curve, which means a gradually increasing deformation resistance as cyclic loading progresses.
  Examples: 2024-T4 Al; 4142 steel (670 BHN)

Note that the hardest steels tend to harden further in cyclic loading. Thus, a given steel (such as 4142) may be stable, softening, or hardening, depending on its initial hardness.

In the technical literature, primes are normally used to denote cyclic material properties. For example, σ'_y is the yield strength obtained from a cyclic stress–strain curve.

Stress vs. Life (S-N) Curves

The most common and historical fatigue life plots present data of stress amplitude (simplistically, S or S_a) on a linear scale vs. cycles to failure (N or N_f) on a logarithmic scale as in Figure 1.6.18. Many steels (plain carbon or low alloy) appear to have a distinct fatigue limit. For other metals that do not have such a limit (aluminum, for example), an arbitrary fatigue limit is defined as a stress amplitude corresponding to a specified life, typically 10^7 or 10^8 cycles.

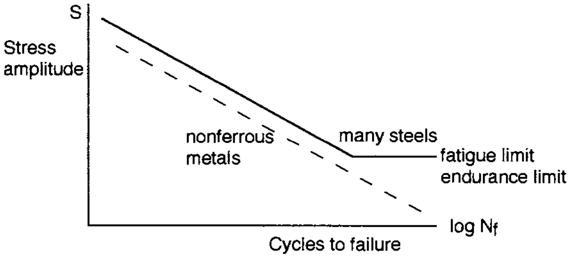

FIGURE 1.6.18 Schematic of S–N curves.

Trends in S-N Curves

There are many influences on the shape and position of a material's fatigue life curve as briefly discussed below.

Ultimate Strength. It is widely believed that, at least for steels, the fatigue limit σ_e is about one half of the ultimate strength σ_u. In fact, this is a gross oversimplification; actual values are lower or higher than that in many cases.

Mean Stress, Residual Stress. Several main points are worth remembering: residual stresses (also called self-stresses) are common, and they are to be treated as mean stresses (by sign and magnitude) in fatigue; a tensile mean stress lowers the life while a compressive one increases it. Simplistically, a tensile mean stress lowers the allowable cyclic stress amplitude, according to Figure 1.6.19 where

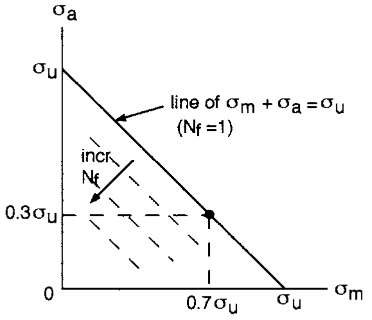

FIGURE 1.6.19 Schematic of tensile mean stress effect.

$$\sigma_m + \sigma_a \le \sigma_u \quad \text{or} \quad \sigma_y \qquad \text{(if yielding is to be prevented)}$$

For example, if $\sigma_m = 0.7\sigma_u$, then the maximum alternating stress for one cycle is $0.3\sigma_u$. This kind of graphical relationship is called a Goodman diagram. Several special expressions are used for dealing with the detrimental effects of tensile mean stresses. For example, the modified Goodman equation is

$$\frac{\sigma_a}{\sigma_e} + \frac{\sigma_m}{\sigma_u} = 1 \tag{1.6.15}$$

where σ_e is the fatigue limit for fully reversed loading.

Sometimes curved lines represent real behavior better than the linear theory shown in Figure 1.6.19. In that case, the Gerber parabola may be appropriate, in the form of

$$\frac{\sigma_a}{\sigma_e} + \left(\frac{\sigma_m}{\sigma_u}\right)^2 = 1 \qquad \text{for} \quad \sigma_m \ge 0 \tag{1.6.16}$$

Another approach worth mentioning is the mechanistically elegant and sensible Morrow expression, which will be presented later.

Note that tensile mean stresses are generally detrimental and that many approaches have been proposed to deal with them, although no single method is capable of good predictions in all cases. In practice, it is best to use a particular method that has a good track record for the material and situation at hand. Constant-life diagrams are useful, elaborate derivatives of the Goodman approach, if they include a broad data base (Figure 1.6.20).

Notch Effects. Stress raisers can be extremely detrimental in fatigue, except when they help create localized compressive residual stresses in ductile metals, delaying crack formation and growth. These are discussed in connection with the strain-based approach.

Microstructure. Large grain size (annealed metals) lowers the fatigue strength, and small grain size (by cold working) increases it, especially at long lives, under load control.

Surface Effects. The condition of a material's surface may influence the fatigue behavior in many ways, typically in combinations.

Toolmarks are common detrimental features, especially because they often are aligned perpendicular to the principal tensile stress in axial or bending loading. An example is a shaft cut in a lathe. Note that in the case of high-strength, hard materials even invisible scratches from grinding and buffing may be stress raisers. Machining also tends to create tensile or compressive residual stresses in surface layers.

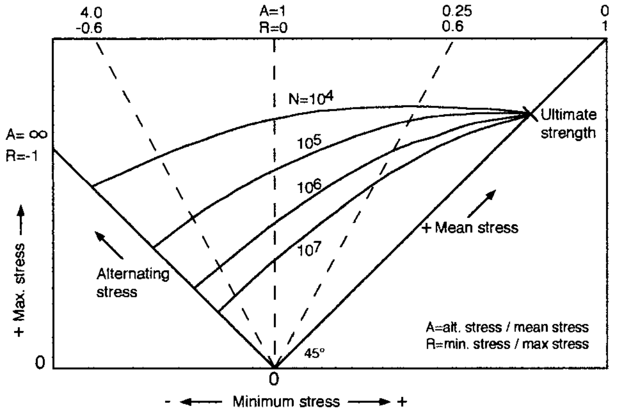

FIGURE 1.6.20 Constant-life diagram.

Surface treatments such as carburizing or nitriding of steels affect the fatigue life by changes in chemical composition, microstructure, hardness, or residual stress. Shot peening, surface rolling, or burnishing is done to introduce compressive residual stresses, which delay cracking in long-life service. Plating (chromium, nickel) tends to create layers of poor fatigue resistance and harmful tensile residual stresses. Shot peening after plating is a beneficial step.

Environment. Hostile chemical environments can severely reduce most materials' fatigue resistance. Common causes of problems are salt water, salt in the air, salt on the road, moisture, and even pollutants in the air. For example, sulfur in the air results in aggressive sulfuric acid on machines and structures.

Statistical Scatter. Statistical scatter is always in a material's fatigue life at any given stress level, especially at long lives. The scatter band may cover several orders of magnitude in life at a single stress level. Because of the scatter, there is no unique fatigue life curve for any material — the curve depends not only on physical factors such as environment, but also on the number of tests done. It is not sufficient to do a handful of tests and draw a curve somewhere through the data points. As a simple rule, to have a high level of confidence (>99%) in a fatigue life curve, at least six identical tests are needed to obtain a mean value at each of several levels of stresses in the general life range of interest. A curve through these mean values is fairly representative of the average life curve (50% probability of failure), but still may not be adequate to deal with scatter. Note that the minimum number of test specimens according to the ASTM Standard E 739 is 6 to 12 for preliminary, exploratory work or for research and development and component testing, and 12 to 24 for design allowables or reliability assessment.

Ideally, additional analysis is done, using Gaussian (normal) statistical distribution or some other model, such as the Weibull distribution. The latter is particularly informative in determining the probability of fatigue failure. The practical problem is that engineers may require very low probabilities of failure (less than 1%), but neither the necessary mathematical methods nor the data bases are available for that. A family of fatigue life curves for various probabilities of failure and other relevant considerations for one material are shown schematically in Figure 1.6.21 through Figure 1.6.23.

Variable Amplitude Loading

Many machines, vehicles, and structures experience random or blockwise changing loading. They can be simplistically modeled for life prediction using the Palmgren–Miner rule, illustrated in Figure 1.6.24. There are two major assumptions for this rule for completely reversed loading:

1. Every cycle at a given level of stress amplitude causes the same amount of damage, whether the cycle is early or late in the life.
2. The percentage of damage caused by a cycle of load at any level of stress is equivalent to the same percentage of damage at any other level of stress.

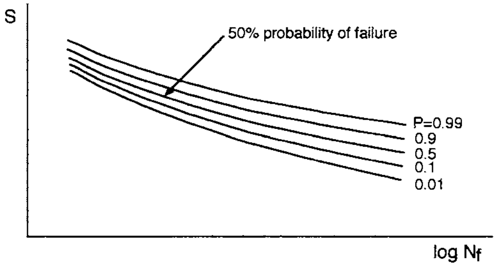

FIGURE 1.6.21 Schematic S–N curves with various probabilities of failure.

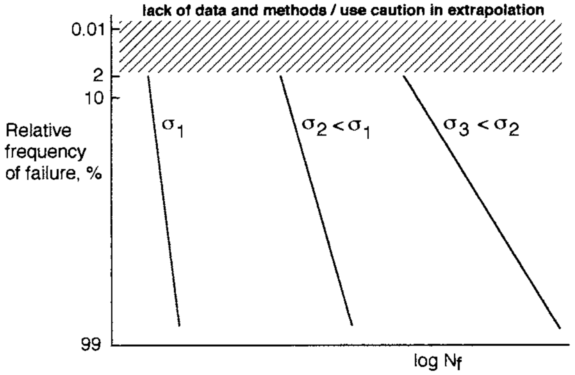

FIGURE 1.6.22 Probability aspects of fatigue depending on stress level.

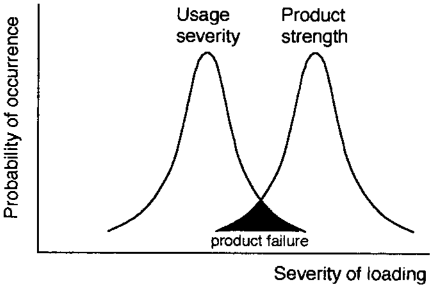

FIGURE 1.6.23 Probability aspects of fatigue depending on applied stress and product strength.

Thus, because 100% of the life N_{fi} is exhausted at failure at any single stress amplitude σ_i, in multilevel loading the life fractions sum to unity, as mathematically formulated here and illustrated in Figure 1.6.24:

$$\frac{N_1}{N_{f1}} + \frac{N_2}{N_{f2}} + \ldots = \sum \frac{N_i}{N_{fi}} = 1 \tag{1.6.17}$$

where N_i is the actual number of cycles at σ_i and N_{fi} is the life at σ_i.

In practice, summations of about 0.8 to 1.2 can be accepted, saying that the Palmgren–Miner rule is valid in that case. Gross deviations from summations of one are common, especially when the mean stress is not zero. Modified versions of the basic rule for such cases should be used with caution.

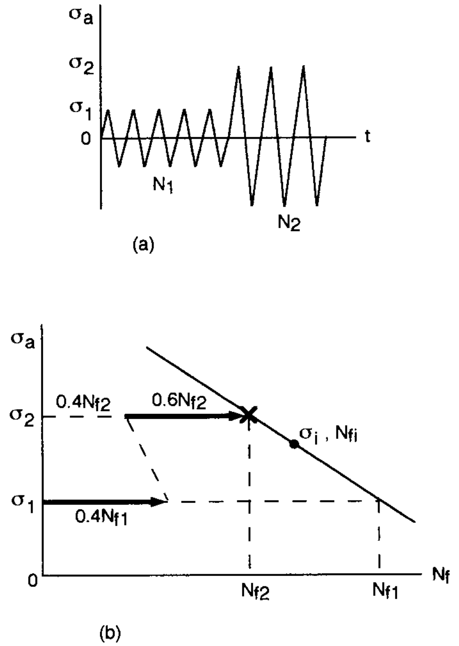

FIGURE 1.6.24 Schematic for Palmgren–Miner rule.

Cycle Counting. Highly irregular loading requires the use of special cycle counting methods, such as level crossing, range counting, or rainflow cycle counting. The latter is the best modern method, lending itself to efficient field data acquisition and computer work (ASTM Standard E1049; *SAE Fatigue Design Handbook*).

Multiaxial Fatigue

Complex states of stress are common in engineering components, and in fatigue analysis they may cause serious difficulties. Although many methods are available, none of them is adequate for all cases. The simplest situations that might be handled reasonably well involve fully reversed loading by in-phase or 180° out-of-phase proportional stresses at the same frequency. Multiaxial fatigue testing is difficult and expensive, so it is often desired to use uniaxial test data for predicting the multiaxial behavior. A typical approach for this is based on computing an effective stress amplitude *se* from the amplitudes of the principal stresses σ_{1a}, σ_{2a}, σ_{3a}. With the concept of the octahedral shear yield criterion,

$$\sigma_e = \frac{1}{\sqrt{2}}\sqrt{\left(\sigma_{1a}-\sigma_{2a}\right)^2+\left(\sigma_{2a}-\sigma_{3a}\right)^2+\left(\sigma_{3a}-\sigma_{1a}\right)^2} \tag{1.6.18}$$

where in-phase stresses are positive and 180° out-of-phase stresses are negative.

The life is estimated by entering σ_e on the appropriate S-N curve. Note that mean stresses, localized or general yielding, creep, and random frequencies of loading further complicate the problem and require more sophisticated methods than outlined here.

Strain vs. Life (ε-N) Curves

A strain-based approach is necessary in fatigue when measurable inelastic strains occur. In general, total strain consists of elastic, plastic, and creep strains, with the latter two in the category of inelastic strains:

$$\varepsilon_t = \varepsilon_e + \varepsilon_p + \varepsilon_c \tag{1.6.19}$$

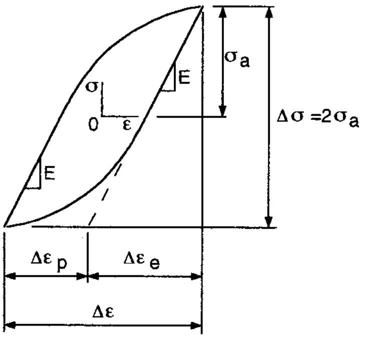

FIGURE 1.6.25 Hysteresis loop.

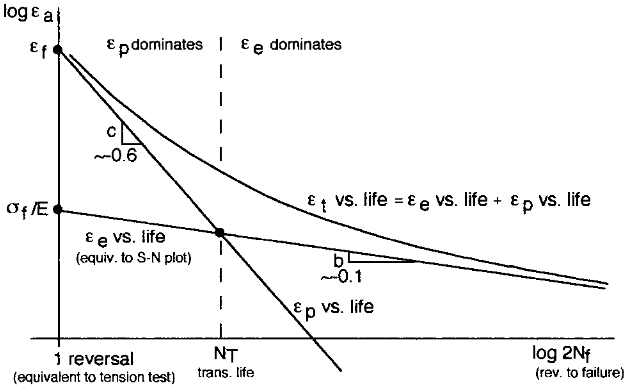

FIGURE 1.6.26 Schematic of strain vs. life curves.

When ε_p or/and ε_c are dominant, the life is relatively short and the situation is called low-cycle fatigue (LCF), as opposed to high-cycle fatigue (HCF), where ε_e is dominant. The mechanics of LCF can be understood by first considering hysteresis loops of elastic and plastic strains as defined in Figure 1.6.25.

Simplistically, HCF means a thin loop (a straight line at very long life) and LCF means a fat loop. Strain-life plots are especially useful in the LCF regime where material properties (ε_f, σ_f) obtained in monotonic tension tests are directly useful in fatigue life prediction as shown in Figure 1.6.26. Most commonly, the total strain amplitude ε_a is plotted vs. the life $2N_f$, with a corresponding equation (called Coffin–Manson equation) for fully reversed loading:

$$\varepsilon_a = \frac{\sigma_f}{E}\left(2N_f\right)^b + \varepsilon_f\left(2N_f\right)^c \tag{1.6.20}$$

It is remarkable that all metals are similar to one another in their values of the exponents b (≈ –0.1) and c (≈ –0.6), differing only in fracture strength σ_f and fracture ductility ε_f. These allow a simplistic fatigue life prediction if at least σ_f and ε_f are known.

If there is a mean stress, its effect is equivalent to an altered fracture strength. Using the Morrow approach in a simplified version,

$$\varepsilon_a = \frac{\sigma_f}{E}\left(1-\frac{\sigma_m}{\sigma_f}\right)\left(2N_f\right)^b + \varepsilon_f\left(2N_f\right)^c \tag{1.6.21}$$

where σ_m is positive for tensile and negative for compressive mean stress.

Notch Effects

The localized plastic strains of notched members complicate fatigue analysis considerably. It should be noted, first of all, that the theoretical stress concentration factor K_t is not entirely relevant to such members because yielding lowers the actual peak stresses from those predicted. This leads to the definitions of the true stress and strain concentration factors:

$$K_\sigma = \frac{\text{peak stress}}{\text{ave. stress}} \qquad K_\varepsilon = \frac{\text{peak strain}}{\text{ave. strain}} \tag{1.6.22}$$

According to Neuber's rule:

$$K_t = \sqrt{K_\sigma K_\varepsilon} \tag{1.6.23}$$

which is useful for notch analysis in fatigue. This expression is strictly true for ideally elastic behavior and is qualitatively evident for elastic–plastic deformations.

Residual Stresses at Notches. An extremely important, and somewhat surprising, phenomenon can occur in notched members if they yield locally under variable-amplitude loading. If a large load (called an overload) causes yielding at a notch and is followed only by smaller loads, a residual stress of the opposite sign to the overload's sign is generated at the root of the notch. Thus, a tensile overload (such as at one side of a shaft in a straightening operation) creates a compressive residual stress, and vice versa. These stresses may remain in the member for a long time or be relaxed by other plastic strain events or by annealing. Of course, such stresses are effective mean stresses and can alter the life greatly.

Creep–Fatigue Interactions

Inelastic strains (plastic and creep strains) are the basic causes of time- and cycle-dependent damage processes. When both kinds of strains occur during the life of a particular component, complex damage interactions may arise. The simplest and most elegant approach in such a case is to sum both of the different damages linearly (as in the Palmgren–Miner summation for pure fatigue), assuming that they are equivalent to one another. In other words, assume that X percentage of creep life exhausted is equivalent to the same X percentage of fatigue life exhausted. Thus, a linear expression involving time and cycle fractions can be stated:

$$\underset{\text{pure creep}}{\sum \frac{t_i}{t_{ri}}} + \underset{\text{pure fatigue}}{\sum \frac{n_j}{N_{fj}}} = \underset{\text{at failure}}{1} \tag{1.6.24}$$

where

t_i = actual time spent at stress level i in creep
t_{ri} = total time to rupture at stress level i
n_j = actual number of cycles at stress level j
N_{fj} = cycles to failure at stress level j

This idealized linear expression is plotted as a dashed line in Figure 1.6.27; in contrast, a more realistic ASME code and possible severe degradations are also plotted.

Many other methods (such as damage rate equations; strain-range partitioning) can be used to deal with creep–fatigue problems, but none of them is adequate for all situations. The difficulty is mainly because of the need to account for important, complex details of the loading cycle (frequency, hold times, temperature, and deformation wave shape).

Fracture Mechanics Method in Fatigue

Cyclic loading can cause crack growth with or without the presence of a hostile chemical environment. The rate of crack growth depends on the stress intensity factor $K \propto \sigma\sqrt{a}$. Investigations of this dependence

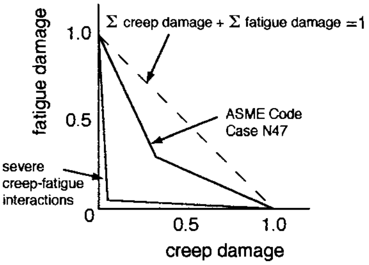

FIGURE 1.6.27 Schematic of creep–fatigue interactions. The bilinear damage rule is recommended in the ASME Boiler and Pressure Vessel Code, Section III, Code Case N47.

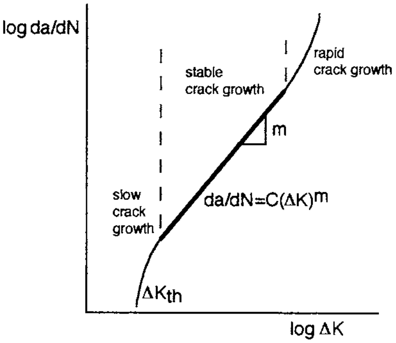

FIGURE 1.6.28 Schematic of fatigue crack propagation data.

have led to the development of powerful techniques in design and failure analysis. The fatigue crack growth behavior is quantified by the Paris equation:

$$\frac{da}{dN} = C(\Delta K)^m \tag{1.6.25}$$

where

da/dN = crack growth rate
C, m = material constants
$\Delta K = K_{\max} - K_{\min}$ = stress intensity factor range
$K_{\max} \propto \sigma_{\max}$
$K_{\min} \propto \sigma_{\min}$

Typical data for a wide range of crack growth rates have patterns as in Figure 1.6.28, where ΔK_{th} is a threshold value akin to a fatigue limit. The linear part of the curve is useful for life prediction and failure analysis.

Abridged Example of a Modern Fatigue Analysis

Many of the concepts mentioned earlier are applied in Sandia National Laboratories' "User's Manual for FAROW: Fatigue and Reliability of Wind Turbine Components," SAND94-2460, November 1994. FAROW is a computer program for the probabilistic analysis of large wind turbines, using structural reliability techniques to calculate the mean time to failure; probability of failure before a target lifetime; relative importance of each of the random inputs; and sensitivity of the reliability to all input parameters. The method is useful whether extensive data are available or not (showing how much can be gained by reducing the uncertainty in each input). It helps one understand the fatigue reliability of a component and indicates how to improve the reliability. The sample figures (Figure 1.6.29 through Figure 1.6.32) illustrate some of the key data and results for the machines and materials considered.

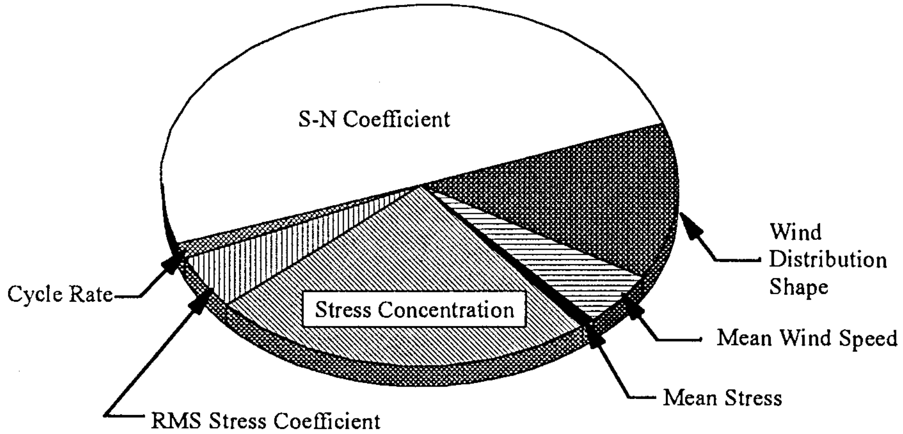

FIGURE 1.6.29 Relative importance factors as fractions of the total influence on the probability of failure. (Courtesy Sandia National Laboratories, Albuquerque, NM.)

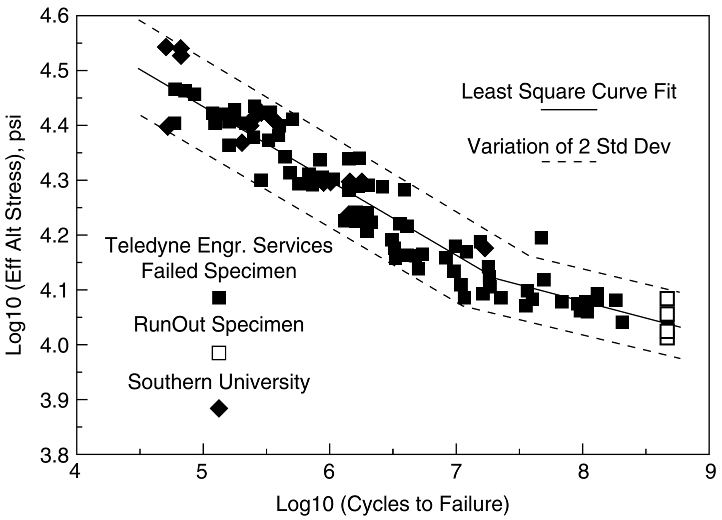

FIGURE 1.6.30 Fatigue life data for 6063 Al. (Courtesy Sandia National Laboratories, Albuquerque, NM.)

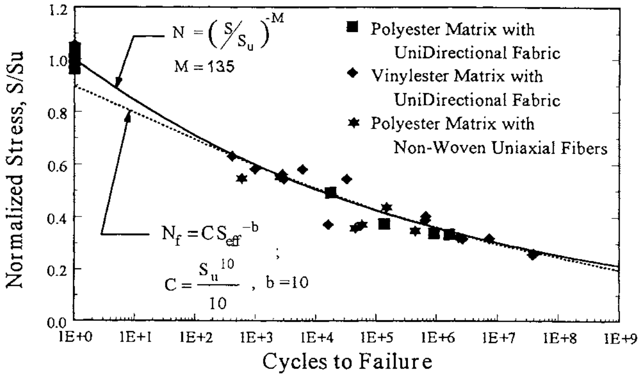

FIGURE 1.6.31 Fatigue life data for uniaxial fiberglass composite. (Courtesy Sandia National Laboratories, Albuquerque, NM.)

FIGURE 1.6.32 Example FAROW results for probability of premature failure as a function of target lifetime. (Courtesy Sandia National Laboratories, Albuquerque, NM.)

Note especially a large discrepancy between mean lifetime and probability of failure in a few years. A mean lifetime of 600 years was calculated for a critical component, using the median values for all the random variables considered and using the constant values for all the other input parameters. However, the probability of the component failing in less than 5 years is estimated at 7.6% (Figure 1.6.32). This shows the uncertainty — even in sophisticated fatigue life calculations — because of reasonable uncertainty in the inputs and the sensitivity of fatigue life to parameter variation.

1.7 Comprehensive Example of Using Mechanics of Solids Methods

Bela I. Sandor

A concise overview of an engineering project is presented to illustrate the relevance and coordinated application of several concepts and methods in this chapter. The sketchy outline is limited in breadth and depth, emphasizes modern methods, and is not aiming for completeness in any particular area.

The Project

Analyze the currently used A-shaped arm of the suspension system of a small, special-purpose ground vehicle. The goal is to redesign the component to save weight and, more importantly, reduce the cost of manufacturing while assuring the product's reliability over its expected service life.

Concepts and Methods

Statics

Vectors
Free-body diagrams. Equilibrium
Two-force member: shock absorber
Frame components
Beams. Bending moments
Moments of inertia
Center of mass

Dynamics

Velocity, acceleration
Rigid-body dynamics
General plane motion
Relative motion

Vibrations

Natural frequency
Damping. Logarithmic decrement

Mechanics of Materials

Stress and strain. Transformation equations. Principal stresses. Maximum shear stress
Material properties. Material selection
Bending stresses. Beam optimization
Strain gages. Mechanical testing with closed-loop equipment

Durability

Stress concentrations. Finite element analysis
Cumulative fatigue damage. Cycle counting in random loading. Mean stresses. Goodman diagrams. Life prediction
Thermoelastic stress analysis

Illustrations

A few aspects of the project are graphically illustrated in Color Figure 16 and Figure 1.7.1 through Figure 1.7.3.

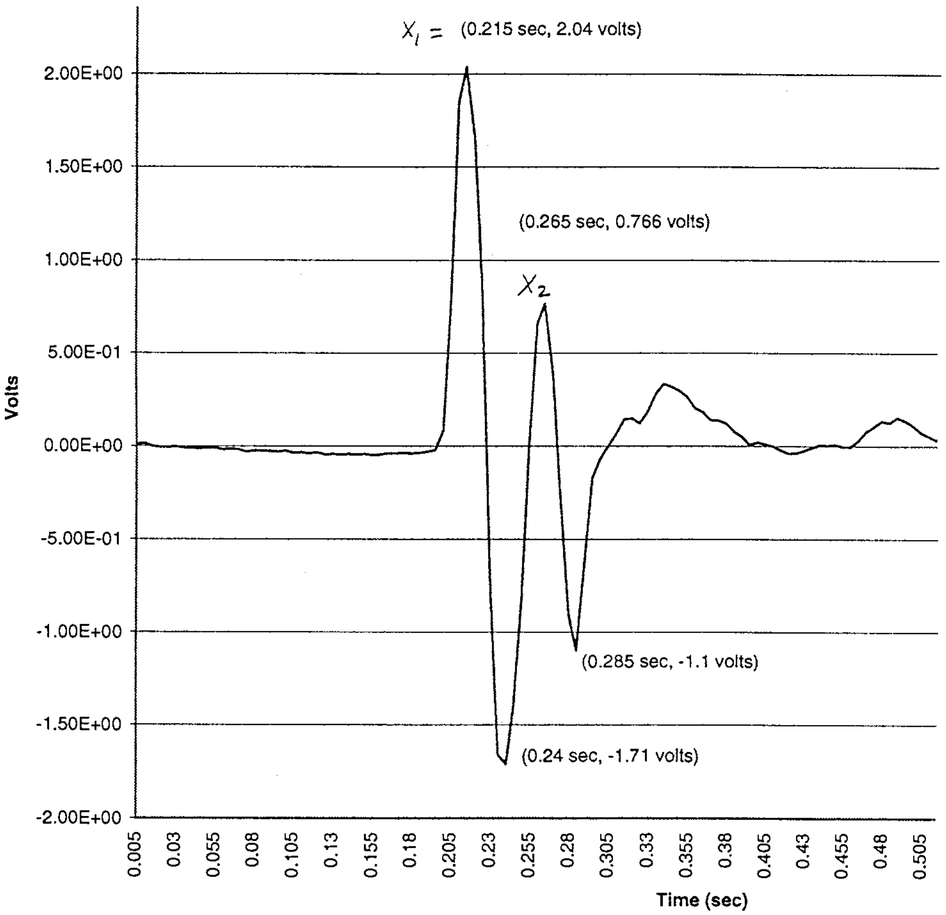

FIGURE 1.7.1 Accelerometer data from front suspension system of vehicle. Logarithmic decrement $\partial = \ln(x_1/x_2)$; damping ratio $\zeta = 0.16$.

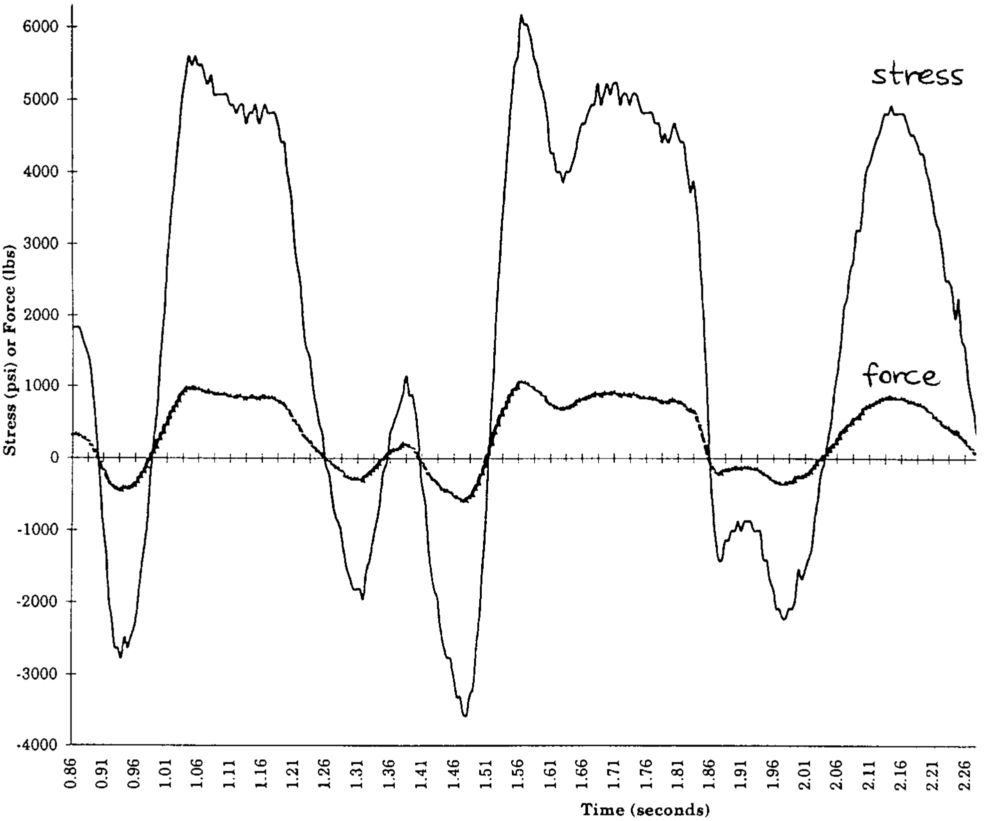

FIGURE 1.7.2 Axial stress and force vs. time in shock absorber shaft.

Defining Terms

Statics

Equilibrium: A concept used to determine unknown forces and moments. A rigid body is in equilibrium when the equivalent force-couple system of the external forces acting on it is zero. The general conditions of equilibrium are expressed in vector form ($\Sigma\mathbf{F} = 0$; $\Sigma\mathbf{M}_O = \Sigma[\mathbf{r} \times \mathbf{F}] = 0$) or scalar form ($\Sigma F_x = 0$; $\Sigma F_y = 0$; $\Sigma F_z = 0$; $\Sigma M_x = 0$; $\Sigma M_y = 0$; $\Sigma M_z = 0$).

Equivalent force-couple system: Any system of forces and moments acting on a rigid body can be reduced to a resultant force and a resultant moment. Transformations of a force-couple system involving chosen points of reference are easy to make. These are useful for determining unknown forces and moments and the critical locations in structural members.

Free-body diagram: A method of modeling and simplifying a problem for the efficient use of the equilibrium equations to determine unknown forces and moments. A body or group of bodies is imagined to be isolated from all other bodies, and all significant external forces and moments (known or unknown) are shown to act on the free-body model.

Dynamics

Equations of motion: Expressions of the acceleration of a body related to the forces acting on the body. The basic equation of motion for a particle of mass m is $\Sigma\mathbf{F} = m\mathbf{a}$. Many other equations of motion may be stated, depending on the dimensions of the body and its motion (such as two- or three-dimensional motion) and the coordinate system chosen.

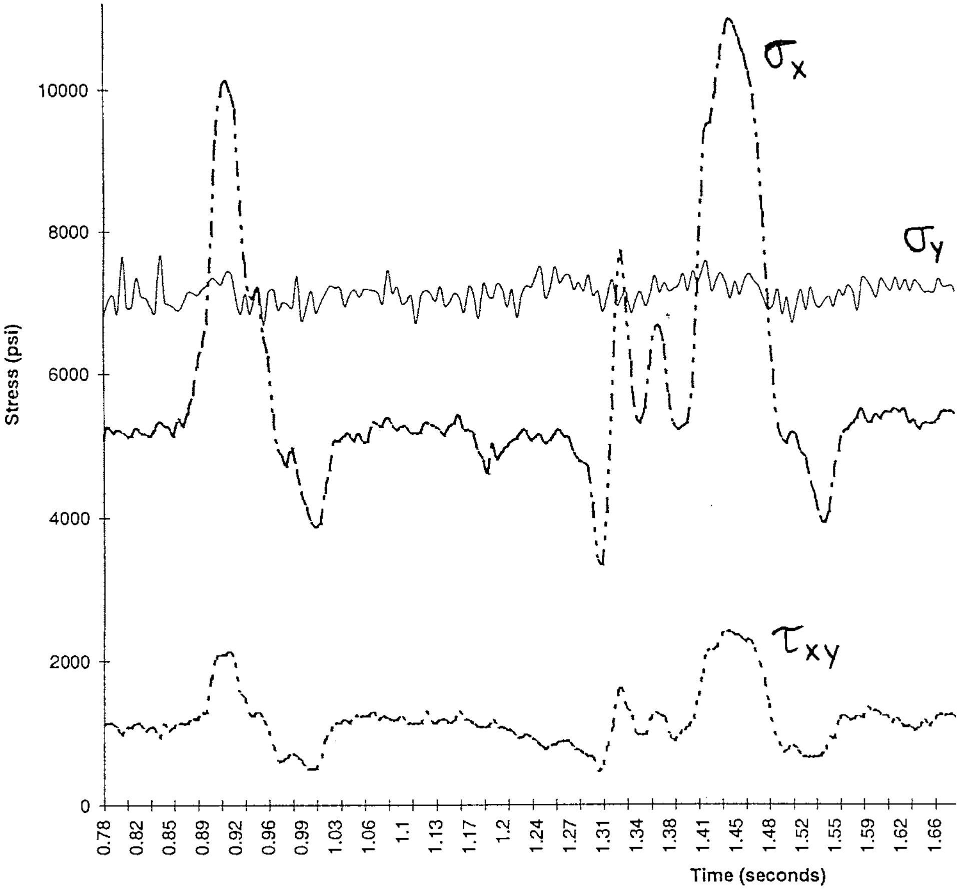

FIGURE 1.7.3 Stresses σ_x, σ_y, and τ_{xy} measured at one point of the A-arm by strain gages as the vehicle travels over bumps.

Kinematics: The analysis of motion based on geometry and time-dependent aspects. Forces may or may not be associated with the motion, but the analysis does not involve considerations of forces. The parameters of interest in kinematics are position, displacement, velocity, acceleration, and time.

Kinetics: The analysis of motion based on kinematics and the effects of forces on masses.

Vibrations

Forced vibration: Involves an exciting force applied periodically during the motion. A forced vibration may also be described in terms of the displacement of a foundation or primary mass that supports the vibrating system.

Free vibration: Occurs when only two kinds of forces are acting on a mass: (1) the elastic restoring force within the system; and (2) the force of gravity or other constant forces that cause no displacement from the equilibrium configuration of the system.

Resonance: A critical aspect of forced vibrations that occurs when the forcing frequency equals the system's natural frequency. In this condition, the amplitude of the displacements becomes infinite in theory or dangerously large in practice when the damping is small. Near-resonance conditions may also be undesirable.

Mechanics of Materials

Flexure formula: Used to calculate the bending stresses in beams. Must be applied with modifications if there are inelastic deformations or unsymmetric bending, or for composite beams and curved beams.

Hooke's law: Applicable for calculating uniaxial or multiaxial stress–strain responses when the material acts entirely elastically. Involves the modulus of elasticity E and Poisson's ratio ν.

Principal stresses: The maximum and minimum normal stresses at a point on an infinitesimal element. An important related quantity is the absolute maximum shear stress. These quantities can be determined (given an arbitrary state of applied stress) from stress transformation equations or from their graphical solution, Mohr's circle. Principal strains are determined in a similar way.

Stress–strain diagram: Shows the stress–strain response and many important mechanical properties for a material. These properties depend greatly on the material's chemical composition and several other factors of fabrication and service conditions. Monotonic (tension or compression) and cyclic loading conditions may result in grossly different mechanical behaviors, even for a given material.

Structural Integrity and Durability

Rate of crack growth: A measure of damage evolution and remaining life of a member. In fatigue, the crack propagation rate da/dN depends on the stress intensity factor range DK and material properties. This relationship is the basis of the powerful, well-established damage-tolerant design method.

Stress concentration factor: The localized stress-raising effect of a geometric discontinuity. Many potentially confusing forms of quantifying this effect exist. The most prominent factors are distinguished concisely:

- Theoretical stress concentration factor, $K_t = \sigma_{\max}/\sigma_{\text{ave}}$
  - Depends on geometry of notch, not on material
  - Has no engineering units
- True stress concentration factor, $K_\sigma = \sigma_{\max}/\sigma_{\text{ave}}$
  - Depends on geometry of notch and material; $K_\sigma = K_t$ for perfectly elastic material, $K_\sigma < K_t$ for ductile material
  - Has no engineering units
- True strain concentration factor, $K_\varepsilon = \varepsilon_{\max}/\varepsilon_{\text{ave}}$, $\varepsilon_{\text{ave}} = \sigma_{\text{ave}}/E$
  - Depends on geometry of notch and material; $K_\varepsilon = K_t$ for perfectly elastic material, $K_\varepsilon > K_t$ for ductile material
  - Has no engineering units

Stress intensity factor : A measure of the severity of a crack or the intensity of the stress field near the crack tip. Many potentially confusing forms of this factor exist; they have identical engineering units of stress $\sqrt{\text{length}}$, but a variety of definitions and applications. A few are listed concisely:

- Opening-mode stress intensity factor, K_I
  - Depends on geometry of a crack and applied stress, not on material
  - Units of stress $\sqrt{\text{length}}$
- Plane strain fracture toughness, K_{IC}
  - Depends on material but not on geometry above a certain thickness, and not on applied stress
  - Units of stress $\sqrt{\text{length}}$
- Stress intensity factor range, $\Delta K = K_{\max} - K_{\min}$
  - Depends on geometry of a crack and applied cyclic stress, not on material
  - Units of stress $\sqrt{\text{length}}$

References

Statics and Dynamics

Hibbeler, R.C. 2001. *Engineering Mechanics: Statics and Dynamics*, 9th ed. Prentice Hall, Inc., Upper Saddle River, NJ.

Sandor, B.I. 1987. *Engineering Mechanics: Statics and Dynamics*, 2nd ed. Prentice Hall, Englewood Cliffs, NJ.

Vibrations

Harris, C.M. and Crede, C.E. 1988. *Shock and Vibration Handbook*, 3rd ed. McGraw–Hill, New York.

James, M.L., Smith, G.M., Wolford, J.C., and Whaley, P.W. 1994. *Vibration of Mechanical and Structural Systems*, 2nd ed. Harper Collins College Publishers, New York.

Wowk, V. 1991. *Machinery Vibration: Measurement and Analysis*. McGraw–Hill, New York.

Wowk, V. 1993. *Machinery Vibration: Balancing*. McGraw–Hill, New York.

Mechanics of Materials

Cook, R.D. and Young, W.C. 1985. *Advanced Mechanics of Materials*. Macmillan, New York.

Dally, J.W. and Riley, W.F. 1991. *Experimental Stress Analysis*, 3rd ed. McGraw–Hill, New York.

Hibbeler, R.C. 1997. *Mechanics of Materials*, 3rd ed. Prentice Hall, Englewood Cliffs, NJ.

Jawad, M.H. and Farr, J.R. 1989. *Structural Analysis and Design of Process Equipment*, 2nd ed. John Wiley & Sons, New York.

Kobayashi, A.S. (Ed.). 1993. *Handbook on Experimental Mechanics*, 2nd ed. Society for Experimental Mechanics, Bethel, CT.

Pilkey, W.D., 1997. *Peterson's Stress Concentration Factors*, 2nd ed. John Wiley & Sons, New York.

Shigley, J.E. and Mischke, C.R. 1989. *Mechanical Engineering Design*, 5th ed. McGraw–Hill, New York.

Young, W.C. 1989. *Roark's Formulas for Stress and Strain*, 6th ed. McGraw–Hill, New York.

Structural Integrity and Durability

Anderson, T.L. 1994. *Fracture Mechanics: Fundamentals and Applications*, 2nd ed., CRC Press, Boca Raton, FL.

Boyer, J.E. 1986. *Atlas of Fatigue Curves*. American Society for Metals, Metals Park, OH.

Cook, R.D. 1995. *Finite Element Modeling for Stress Analysis*. John Wiley & Sons, New York.

Dowling, N.E. 1993. *Mechanical Behavior of Materials*. Prentice Hall, Englewood Cliffs, NJ.

Fuchs, H.O. and Stephens, R.I. 1980. *Metal Fatigue in Engineering*. John Wiley & Sons, New York.

Gallagher, J.P. (Ed). 1983. *Damage Tolerant Design Handbook*, 4 vols. Metals and Ceramics Information Ctr., Battelle Columbus Labs, Columbus, OH.

Murakami, Y. (Ed). 1987. *Stress Intensity Factors Handbook*, 2 vols. Pergamon Press, Oxford, U.K.

Rice, R.C. (Ed). 1988. *Fatigue Design Handbook*, 2nd ed. SAE Publ. No. AE-10. Society of Automotive Engineers, Warrendale, PA.

Further Information

Many technical societies are active in various areas of mechanics of solids, and they are excellent, steady sources of long-accepted and new information, some of which is available within hours. They also organize committee work, conferences, symposia, short courses, and workshops; establish codes and standards; and publish books, papers, journals, and proceedings covering the latest developments in numerous specialties. A short list of societies is given here; note that they tend to have international breadth, regardless of the name. It is wise to belong to several relevant societies and at least scan their announcements.

ASM International (formerly American Society for Metals) (800-336-5152)
ASME — American Society for Mechanical Engineers (800-843-2763)
ASNT — American Society for Nondestructive Testing (800-222-2768)
ASTM — American Society for Testing and Materials (215-299-5585)
SAE — Society of Automotive Engineers (412-776-4841)
SEM — Society for Experimental Mechanics (203-790-6373)
SES — Standards Engineering Society (513-223-2410)

As a hint of the scope and magnitude of what is available from the large technical societies, here are selected offerings of ASTM:

- ASTM staff access/tel: 215-299-5585; fax: 215-977-9679; e-mail: infoctr@local.astm.org
- *ASTM Standardization News*, a monthly magazine, regularly presents information on "the development of voluntary full consensus standards for materials, products, systems and services and the promotion of related knowledge… the research, testing and new activities of the ASTM standards-writing committees… the legal, governmental and international events impacting on the standards development process" (quotes from the masthead).
- Over 50 volumes of ASTM Standards

  Samples of standards:
    - Friction, wear, and abrasion (B611 on wear resistance of carbides; G77 on ranking of materials in sliding wear)
    - Fracture mechanics (E399 on fracture toughness testing of metals)
    - Fatigue (E466 on axial fatigue tests of metals; D671 on flexural fatigue of plastics)
- Training courses for ASTM Standards (215-299-5480)
- ASTM International Directory of Testing Laboratories
- ASTM Directory of Scientific & Technical Consultants & Expert Witnesses
- ASTM Special Technical Publications (STP) are books of peer-reviewed papers on recent research and developments

  Samples of STPs:
    - STP 1198 — *Nondestructive Testing of Pavements and Backcalculation of Moduli*, 2nd Vol.; 1995
    - STP 1231 — *Automation in Fatigue and Fracture: Testing and Analysis*; 1995.

2

Engineering Thermodynamics

Michael J. Moran
The Ohio State University

Although various aspects of what is now known as thermodynamics have been of interest since antiquity, formal study began only in the early 19th century through consideration of the motive power of *heat*: the capacity of hot bodies to produce *work*. Today the scope is larger, dealing generally with *energy and entropy*, and with relationships among the *properties* of matter. Moreover, in the past 25 years engineering thermodynamics has undergone a revolution, both in terms of the presentation of fundamentals and in the manner that it is applied. In particular, the second law of thermodynamics has emerged as an effective tool for engineering analysis and design.

0-8493-0866-6/05/$0.00+$1.50

2.1 Fundamentals

Classical thermodynamics is concerned primarily with the macrostructure of matter. It addresses the gross characteristics of large aggregations of molecules and not the behavior of individual molecules. The microstructure of matter is studied in kinetic theory and statistical mechanics (including quantum thermodynamics). In this chapter, the classical approach to thermodynamics is featured.

Basic Concepts and Definitions

Thermodynamics is both a branch of physics and an engineering science. The scientist is normally interested in gaining a fundamental understanding of the physical and chemical behavior of fixed, quiescent quantities of matter and uses the principles of thermodynamics to relate the *properties* of matter. Engineers are generally interested in studying *systems* and how they interact with their *surroundings.* To facilitate this, engineers have extended the subject of thermodynamics to the study of systems through which matter flows.

System

In a thermodynamic analysis, the *system is* the subject of the investigation. Normally the system is a specified quantity of matter and/or a region that can be separated from everything else by a well-defined surface. The defining surface is known as the *control surface* or *system boundary.* The control surface may be movable or fixed. Everything external to the system is the *surroundings.* A system of fixed mass is referred to as a *control mass* or as a *closed system.* When there is flow of mass through the control surface, the system is called a *control volume,* or *open, system.* An *isolated* system is a closed system that does not interact in any way with its surroundings.

State, Property

The condition of a system at any instant of time is called its *state.* The state at a given instant of time is described by the properties of the system. A *property is any* quantity whose numerical value depends on the state but not the history of the system. The value of a property is determined in principle by some type of physical operation or test.

Extensive properties depend on the size or extent of the system. Volume, mass, energy, and entropy are examples of extensive properties. An extensive property is additive in the sense that its value for the whole system equals the sum of the values for its parts. *Intensive* properties are independent of the size or extent of the system. Pressure and temperature are examples of intensive properties.

A mole is a quantity of substance having a mass numerically equal to its molecular weight. Designating the molecular weight by $\mathcal{M}$ and the number of moles by n, the mass m of the substance is $m = n\mathcal{M}$. One kilogram mole, designated kmol, of oxygen is 32.0 kg and one pound mole (lbmol) is 32.0 lb. When an extensive property is reported on a unit mass or a unit mole basis, it is called a *specific* property. An overbar is used to distinguish an extensive property written on a per-mole basis from its value expressed per unit mass. For example, the volume per mole is $\bar{v}$, whereas the volume per unit mass is v, and the two specific volumes are related by $\bar{v} = \mathcal{M}v$.

Process, Cycle

Two states are identical if, and only if, the properties of the two states are identical. When any property of a system changes in value there is a change in state, and the system is said to undergo a *process.* When a system in a given initial state goes through a sequence of processes and finally returns to its initial state, it is said to have undergone a *cycle.*

Phase and Pure Substance

The term *phase* refers to a quantity of matter that is homogeneous throughout in both chemical composition and physical structure. Homogeneity in physical structure means that the matter is all *solid,* or all *liquid*, or all *vapor* (or equivalently all *gas). A* system can contain one or more phases. For example, a system of liquid water and water vapor (steam) contains *two* phases. A *pure substance* is one that is uniform and invariable in chemical composition. *A* pure substance can exist in more than one phase, but its chemical composition must be the same in each phase. For example, if liquid water and water vapor form a system with two phases, the system can be regarded as a pure substance because each phase has the same composition. The nature of phases that coexist in equilibrium is addressed by the *phase rule* (Section 2.3, Multicomponent Systems).

Equilibrium

Equilibrium means a condition of balance. In thermodynamics the concept includes not only a balance of forces, but also a balance of other influences. Each kind of influence refers to a particular aspect of thermodynamic (complete) equilibrium. *Thermal* equilibrium refers to an equality of temperature, *mechanical* equilibrium to an equality of pressure, and *phase* equilibrium to an equality of chemical potentials (Section 2.3, Multicomponent Systems). *Chemical* equilibrium is also established in terms of chemical potentials (Section 2.4, Reaction Equilibrium). For complete equilibrium the several types of equilibrium must exist individually.

To determine if a system is in thermodynamic equilibrium, one may think of testing it as follows: isolate the system from its surroundings and watch for changes in its observable properties. If there are no changes, it may be concluded that the system was in equilibrium at the moment it was isolated. The system can be said to be at an *equilibrium state.* When a system is *isolated,* it cannot interact with its surroundings; however, its state can change as a consequence of spontaneous events occurring internally as its intensive properties, such as temperature and pressure, tend toward uniform values. When all such changes cease, the system is in equilibrium. At equilibrium. temperature and pressure are uniform throughout. If gravity is significant, a pressure variation with height can exist, as in a vertical column of liquid.

Temperature

A scale of temperature independent of the *thermometric substance* is called a *thermodynamic* temperature scale. The Kelvin scale, a thermodynamic scale, can be elicited from the second law of thermodynamics (Section 2.1, The Second Law of Thermodynamics, Entropy). The definition of temperature following from the second law is valid over all temperature ranges and provides an essential connection between the several *empirical* measures of temperature. In particular, temperatures evaluated using a *constant-volume gas thermometer* are identical to those of the Kelvin scale over the range of temperatures where gas thermometry can be used.

The empirical *gas scale* is based on the experimental observations that (1) at a given temperature level all gases exhibit the same value of the product $p\bar{v}$ (p is pressure and $\bar{v}$ the specific volume on a molar basis) if the pressure is low enough, and (2) the value of the product $p\bar{v}$ increases with the temperature level. On this basis the gas temperature scale is defined by

$$T = \frac{1}{\bar{R}} \lim_{p \to 0} \left(p\bar{v} \right)$$

where T is temperature and $\bar{R}$ is the *universal gas constant.* The absolute temperature at the *triple point of water* (Section 2.3, *P-v-T* Relations) is fixed by international agreement to be 273.16 K on the *Kelvin* temperature scale. $\bar{R}$ is then evaluated experimentally as $\bar{R} = 8.314$ kJ/kmol · K (1545 ft · lbf/lbmol · °R).

The *Celsius termperature scale* (also called the centigrade scale) uses the degree Celsius (°C), which has the same magnitude as the kelvin. Thus, temperature *differences* are identical on both scales. However, the zero point on the Celsius scale is shifted to 273.15 K, as shown by the following relationship between the Celsius temperature and the Kelvin temperature:

$$T(°\mathrm{C}) = T(\mathrm{K}) - 273.15 \tag{2.1}$$

On the Celsius scale, the triple point of water is 0.01°C and 0 K corresponds to –273.15°C.

Two other temperature scales are commonly used in engineering in the U.S. By definition, the *Rankine scale,* the unit of which is the degree rankine (°R), is proportional to the Kelvin temperature according to

$$T(°\mathrm{R}) = 1.8T(\mathrm{K}) \tag{2.2}$$

The Rankine scale is also an absolute thermodynamic scale with an absolute zero that coincides with the absolute zero of the Kelvin scale. In thermodynamic relationships, temperature is always in terms of the Kelvin or Rankine scale unless specifically stated otherwise.

A degree of the same size as that on the Rankine scale is used in the *Fahrenheit scale,* but the zero point is shifted according to the relation

$$T(°\mathrm{F}) = T(°\mathrm{R}) - 459.67 \tag{2.3}$$

Substituting Equation 2.1 and Equation 2.2 into Equation 2.3 gives

$$T(°\mathrm{F}) = 1.8T(°\mathrm{C}) + 32 \tag{2.4}$$

This equation shows that the Fahrenheit temperature of the *ice point* (0°C) is 32°F and of the *steam point* (100°C) is 212°F. The 100 Celsius or Kelvin degrees between the ice point and steam point corresponds to 180 Fahrenheit or Rankine degrees.

To provide a standard for temperature measurement taking into account both theoretical and practical considerations, the International Temperature Scale of 1990 (ITS-90) is defined in such a way that the temperature measured on it conforms with the thermodynamic temperature, the unit of which is the kelvin, to within the limits of accuracy of measurement obtainable in 1990. Further discussion of ITS-90 is provided by Preston-Thomas (1990).

The First Law of Thermodynamics, Energy

Energy is a fundamental concept of thermodynamics and one of the most significant aspects of engineering analysis. Energy can be *stored* within systems in various macroscopic forms: kinetic energy, gravitational potential energy, and internal energy. Energy can also be *transformed* from one form to another and *transferred* between systems. For closed systems, energy can be transferred by *work* and *heat transfer.* The total amount of energy is *conserved* in all transformations and transfers.

Work

In thermodynamics, the term *work* denotes a means for transferring energy. Work is an effect of one system on another that is identified and measured as follows: work is done by a system on its surroundings if the *sole effect* on everything external to the system *could have been* the raising of a weight. The test of whether a work interaction has taken place is not that the elevation of a weight is actually changed, nor that a force actually acted through a distance, but that the sole effect *could be* the change in elevation of a mass. The magnitude of the work is measured by the number of standard weights that could have been raised. Since the raising of a weight is in effect a force acting through a distance, the work concept of mechanics is preserved. This definition includes work effects such as is associated with rotating shafts, displacement of the boundary, and the flow of electricity.

Work done *by* a system is considered positive: $W > 0$. Work done *on* a system is considered negative: $W < 0$. The time rate of doing work, or *power,* is symbolized by $\dot{W}$ and adheres to the same sign convention.

Energy

A closed system undergoing a process that involves only work interactions with its surroundings experiences an *adiabatic* process. On the basis of experimental evidence, it can be postulated that *when a closed system is altered adiabatically, the amount of work is fixed by the end states of the system and is* *independent of the details of the process.* This postulate, which is one way the *first law of thermodynamics* can be stated, can be made regardless of the type of work interaction involved, the type of process, or the nature of the system.

As the work in an adiabatic process of a closed system is fixed by the end states, an extensive property called *energy* can be defined for the system such that its change between two states is the work in an adiabatic process that has these as the end states. In engineering thermodynamics the change in the energy of a system is considered to be made up of three macroscopic contributions: the change in *kinetic energy, KE,* associated with the motion of the system *as a whole* relative to an external coordinate frame, the change in gravitational *potential energy, PE,* associated with the position of the system *as a whole* in the Earth's gravitational field, and the change in *internal energy, U,* which accounts for all other energy associated with the system. Like kinetic energy and gravitational potential energy, internal energy is an extensive property.

In summary, the change in energy between two states of a closed system in terms of the work W_{ad} of an adiabatic process between these states is

$$\left(KE_2 - KE_1\right) + \left(PE_2 - PE_1\right) + \left(U_2 - U_1\right) = -W_{ad} \tag{2.5}$$

where 1 and 2 denote the initial and final states, respectively, and the minus sign before the work term is in accordance with the previously stated sign convention for work. Since any arbitrary value can be assigned to the energy of a system at a given state 1, no particular significance can be attached to the value of the energy at state 1 or at *any* other state. Only *changes* in the energy of a system have significance.

The specific energy (energy per unit mass) is the sum of the specific internal energy, u, the specific kinetic energy, $\mathrm{v}^2/2$, and the specific gravitational potential energy, gz, such that

$$\text{specific energy} = u + \frac{\mathrm{v}^2}{2} + \mathrm{gz} \tag{2.6}$$

where the velocity v and the elevation z are each relative to specified datums (often the Earth's surface) and g is the acceleration of gravity.

A property related to internal energy u, pressure p, and specific volume v is *enthalpy*, defined by

$$h = u + pv \tag{2.7a}$$

or on an extensive basis

$$H = U + pV \tag{2.7b}$$

Heat

Closed systems can also interact with their surroundings in a way that cannot be categorized as work, as, for example, a gas (or liquid) contained in a closed vessel undergoing a process while in contact with a flame. This type of interaction is called a *heat interaction,* and the process is referred to as *nonadiabatic.*

A fundamental aspect of the energy concept is that energy is conserved. Thus, since a closed system experiences precisely the same energy change during a nonadiabatic process as during an adiabatic process between the same end states, it can be concluded that the *net* energy transfer to the system in each of these processes must be the same. It follows that heat interactions also involve energy transfer. Denoting the amount of energy transferred *to* a closed system in heat interactions by Q, these considerations can be summarized by the *closed system energy balance:*

$$\left(U_2 - U_1\right) + \left(KE_2 - KE_1\right) + \left(PE_2 - PE_1\right) = Q - W \tag{2.8}$$

The closed system energy balance expresses the conservation of energy principle for closed systems of all kinds.

The quantity denoted by Q in Equation 2.8 accounts for the amount of energy transferred to a closed system during a process by means other than work. On the basis of experiments it is known that such an energy transfer is induced only as a result of a temperature difference between the system and its surroundings and occurs only in the direction of decreasing temperature. This means of energy transfer is called an *energy transfer by heat.* The following sign convention applies:

$Q > 0$: heat transfer *to* the system

$Q < 0$: heat transfer *from* the system

The time rate of heat transfer, denoted by $\dot{Q}$, adheres to the same sign convention.

Methods based on experiment are available for evaluating energy transfer by heat. These methods recognize two basic transfer mechanisms: *conduction* and *thermal radiation.* In addition, theoretical and empirical relationships are available for evaluating energy transfer involving *combined* modes such as *convection.* Further discussion of heat transfer fundamentals is provided in Chapter 4.

The quantities symbolized by W and Q account for *transfers* of energy. The terms *work* and *heat* denote different *means* whereby energy is transferred and not *what* is transferred. Work and heat are not properties, and it is improper to speak of work or heat "contained" in a system. However, to achieve economy of expression in subsequent discussions, W and Q are often referred to simply as work and heat transfer, respectively. This less formal approach is commonly used in engineering practice.

Power Cycles

Since energy is a property, over each cycle there is no net change in energy. Thus, Equation 2.8 reads for *any* cycle

$$Q_{cycle} = W_{cycle}$$

That is, for *any* cycle the net amount of energy received through heat interactions is equal to the net energy transferred out in work interactions. A *power cycle,* or *heat* engine, is one for which a net amount of energy is transferred out by work: $W_{cycle} > 0$. This equals the net amount of energy transferred in by heat.

Power cycles are characterized both by addition of energy by heat transfer, Q_A, and inevitable rejections of energy by heat transfer, Q_R:

$$Q_{cycle} = Q_A - Q_R$$

Combining the last two equations,

$$W_{cycle} = Q_A - Q_R$$

The *thermal efficiency* of a heat engine is defined as the ratio of the net work developed to the total energy added by heat transfer:

$$\eta = \frac{W_{cycle}}{Q_A} = 1 - \frac{Q_R}{Q_A} \tag{2.9}$$

The thermal efficiency is strictly less than 100%. That is, some portion of the energy Q_A supplied is invariably rejected $Q_R \neq 0$.

The Second Law of Thermodynamics, Entropy

Many statements of the second law of thermodynamics have been proposed. Each of these can be called a statement of the second law *or* a corollary of the second law since, if one is invalid, all are invalid. In every instance where a consequence of the second law has been tested directly or indirectly by experiment it has been verified. Accordingly, the basis of the second law, like every other physical law, is experimental evidence.

Kelvin-Planck Statement

The Kelvin-Planck statement of the second law of thermodynamics refers to a *thermal reservoir.* A thermal reservoir is a system that remains at a constant temperature even though energy is added or removed by heat transfer. A reservoir is an idealization, of course, but such a system can be approximated in a number of ways — by the Earth's atmosphere, large bodies of water (lakes, oceans), and so on. Extensive properties of thermal reservoirs, such as internal energy, can change in interactions with other systems even though the reservoir temperature remains constant, however.

The Kelvin-Planck statement of the second law can be given as follows: *It is impossible for any system to operate in a thermodynamic cycle and deliver a net amount of energy by work to its surroundings while receiving energy by heat transfer from a single thermal reservoir.* In other words, a *perpetual-motion machine of the second kind* is impossible. Expressed analytically, the Kelvin-Planck statement is

$$W_{cycle} \leq 0 \qquad \text{(single reservoir)}$$

where the words *single reservoir* emphasize that the system communicates thermally only with a single reservoir as it executes the cycle. The "less than" sign applies when *internal irreversibilities* are present as the system of interest undergoes a cycle and the "equal to" sign applies only when no irreversibilities are present.

Irreversibilities

A process is said to be *reversible* if it is possible for its effects to be eradicated in the sense that there is some way by which *both* the system and its surroundings can be *exactly restored* to their respective initial states. A process is *irreversible* if there is no way to undo it. That is, there is no means by which the system and its surroundings can be exactly restored to their respective initial states. A system that has undergone an irreversible process is not necessarily precluded from being restored to its initial state. However, were the system restored to its initial state, it would not also be possible to return the surroundings to their initial state.

There are many effects whose presence during a process renders it irreversible. These include, but are not limited to, the following: heat transfer through a finite temperature difference; unrestrained expansion of a gas or liquid to a lower pressure; spontaneous chemical reaction; mixing of matter at different compositions or states; friction (sliding friction as well as friction in the flow of fluids); electric current flow through a resistance; magnetization or polarization with hysteresis; and inelastic deformation. The term *irreversibility* is used to identify effects such as these.

Irreversibilities can be divided into two classes, *internal* and *external.* Internal irreversibilities are those that occur within the system, while external irreversibilities are those that occur within the surroundings, normally the immediate surroundings. As this division depends on the location of the boundary there is some arbitrariness in the classification (by locating the boundary to take in the immediate surroundings, all irreversibilities are internal). Nonetheless, valuable insights can result when this distinction between irreversibilities is made. When internal irreversibilities are absent during a process, the process is said to be *internally reversible.* At every intermediate state of an internally reversible process of a closed system, all intensive properties are uniform throughout each phase present: the temperature, pressure, specific volume, and other intensive properties do not vary with position. The discussions to follow compare the actual and internally reversible process concepts for two cases of special interest.

For a gas as the system, the work of expansion arises from the force exerted by the system to move the boundary against the resistance offered by the surroundings:

$$W = \int_1^2 F dx = \int_1^2 pA dx$$

where the force is the product of the moving area and the pressure exerted by the system there. Noting that *Adx* is the change in total volume of the system,

$$W = \int_1^2 p dV$$

This expression for work applies to both actual and internally reversible expansion processes. However, for an internally reversible process *p* is not only the pressure at the moving boundary but also the pressure of the entire system. Furthermore, for an internally reversible process the volume equals *mv*, where the specific volume *v* has a single value throughout the system at a given instant. Accordingly, the work of an internally reversible expansion (or compression) process is

$$W = m\int_1^2 p dv \tag{2.10}$$

When such a process of a closed system is represented by a continuous curve on a plot of pressure vs. specific volume, the area *under* the curve is the magnitude of the work per unit of system mass (area a-b-c′-d′ of Figure 2.3, for example).

Although improved thermodynamic performance can accompany the reduction of irreversibilities, steps in this direction are normally constrained by a number of practical factors often related to costs. For example, consider two bodies able to communicate thermally. With a *finite* temperature difference between them, a spontaneous heat transfer would take place and, as noted previously, this would be a source of irreversibility. The importance of the heat transfer irreversibility diminishes as the temperature difference narrows; and as the temperature difference between the bodies vanishes, the heat transfer approaches *ideality.* From the study of heat transfer it is known, however, that the transfer of a finite amount of energy by heat between bodies whose temperatures differ only slightly requires a considerable amount of time, a large heat transfer surface area, or both. To approach *ideality,* therefore, a heat transfer would require an exceptionally long time and/or an exceptionally large area, each of which has cost implications constraining what can be achieved practically.

Carnot Corollaries

The two corollaries of the second law known as *Carnot* corollaries state: (1) the thermal efficiency of an irreversible power cycle is always less than the thermal efficiency of a reversible power cycle when each operates between the same two thermal reservoirs; (2) all reversible power cycles operating between the same two thermal reservoirs have the same thermal efficiency. A cycle is considered *reversible* when there are no irreversibilities within the system as it undergoes the cycle, and heat transfers between the system and reservoirs occur ideally (that is, with a vanishingly small temperature difference).

Kelvin Temperature Scale

Carnot corollary 2 suggests that the thermal efficiency of a reversible power cycle operating between two thermal reservoirs depends only on the temperatures of the reservoirs and not on the nature of the substance making up the system executing the cycle or the series of processes. With Equation 2.9 it can be concluded that the ratio of the heat transfers is also related only to the temperatures, and is independent of the substance and processes:

$$\left(\frac{Q_C}{Q_H}\right)_{\substack{rev\\cycle}} = \psi\left(T_C, T_H\right)$$

where Q_H *is* the energy transferred to the system by heat transfer from a *hot* reservoir at temperature T_H, and Q_C is the energy rejected from the system to a *cold* reservoir at temperature T_C. The words *rev cycle* emphasize that this expression applies only to systems undergoing reversible cycles while operating between the two reservoirs. Alternative temperature scales correspond to alternative specifications for the function ψ in this relation.

The *Kelvin temperature scale is* based on $\psi(T_C, T_H) = T_C/T_H$. Then

$$\left(\frac{Q_C}{Q_H}\right)_{\substack{rev\\cycle}} = \frac{T_C}{T_H} \tag{2.11}$$

This equation defines only a ratio of temperatures. The specification of the Kelvin scale is completed by assigning a numerical value to one standard reference state. The state selected is the same used to define the *gas scale:* at the triple point of water the temperature is specified to be 273.16 K. If a reversible cycle is operated between a reservoir at the reference-state temperature and another reservoir at an unknown temperature T, then the latter temperature is related to the value at the reference state by

$$T = 273.16\left(\frac{Q}{Q'}\right)_{\substack{rev\\cycle}}$$

where Q is the energy received by heat transfer from the reservoir at temperature T, and Q' is the energy rejected to the reservoir at the reference temperature. Accordingly, a temperature scale is defined that is valid over all ranges of temperature and that is independent of the thermometric substance.

Carnot Efficiency

For the special case of a reversible power cycle operating between thermal reservoirs at temperatures T_H and T_C on the Kelvin scale, combination of Equation 2.9 and Equation 2.11 results in

$$\eta_{\max} = 1 - \frac{T_C}{T_H} \tag{2.12}$$

called the *Carnot efficiency.* This is the efficiency of *all* reversible power cycles operating between thermal reservoirs at T_H and T_C. Moreover, it is the *maximum theoretical* efficiency that any power cycle, real or ideal, could have while operating between the same two reservoirs. As temperatures on the Rankine scale differ from Kelvin temperatures only by the factor 1.8, the above equation may be applied with either scale of temperature.

The Clausius Inequality

The Clausius inequality provides the basis for introducing two ideas instrumental for quantitative evaluations of processes of systems from a second law perspective: *entropy* and *entropy generation.* The Clausius inequality states that

$$\oint\left(\frac{\delta Q}{T}\right)_b \le 0 \tag{2.13a}$$

where δQ represents the heat transfer at a part of the system boundary during a portion of the cycle, and T is the absolute temperature at that part of the boundary. The symbol δ is used to distinguish the differentials of *nonproperties,* such as heat and work, from the differentials of properties, written with the symbol *d*. The subscript *b* indicates that the integrand is evaluated at the boundary of the system executing the cycle. The symbol $\oint$ indicates that the integral is to be performed over all parts of the boundary and over the entire cycle. The Clausius inequality can be demonstrated using the Kelvin-Planck statement of the second law, and the significance of the inequality is the same: the equality applies when there are no internal irreversibilities as the system executes the cycle, and the inequality applies when internal irreversibilities are present.

The Clausius inequality can be expressed alternatively as

$$\oint \left(\frac{\delta Q}{T} \right)_b = -S_{gen} \tag{2.13b}$$

where S_{gen} can be viewed as representing the *strength* of the inequality. The value of S_{gen} is positive when internal irreversibilities are present, zero when no internal irreversibilities are present, and can never be negative. Accordingly, S_{gen} is a measure of the irreversibilities present within the system executing the cycle. In the next section, S_{gen} is identified as the *entropy* generated (or *produced*) by internal irreversibilities during the cycle.

Entropy and Entropy Generation

Entropy

Consider two cycles executed by a closed system. One cycle consists of an internally reversible process A from state 1 to state 2, followed by an internally reversible process C from state 2 to state 1. The other cycle consists of an internally reversible process B from state 1 to state 2, followed by the same process C from state 2 to state 1 as in the first cycle. For these cycles, Equation 2.13b takes the form

$$\left(\int_1^2 \frac{\delta Q}{T} \right)_A + \left(\int_2^1 \frac{\delta Q}{T} \right)_C = -S_{gen} = 0$$

$$\left(\int_1^2 \frac{\delta Q}{T} \right)_B + \left(\int_2^1 \frac{\delta Q}{T} \right)_C = -S_{gen} = 0$$

where S_{gen} has been set to zero since the cycles are composed of internally reversible processes. Subtracting these equations leaves

$$\left(\int_1^2 \frac{\delta Q}{T} \right)_A = \left(\int_1^2 \frac{\delta Q}{T} \right)_B$$

Since A and B are arbitrary, it follows that the integral of $\delta Q/T$ has the same value for *any* internally reversible process between the two states: the value of the integral depends on the end states only. It can be concluded, therefore, that the integral defines the change in some property of the system. Selecting the symbol *S* to denote this property, its change is given by

$$S_2 - S_1 = \left(\int_1^2 \frac{\delta Q}{T} \right)_{\substack{int \\ rev}} \tag{2.14a}$$

where the subscript *int rev* indicates that the integration is carried out for any internally reversible process linking the two states. This extensive property is called *entropy.*

Since entropy is a property, the change in entropy of a system in going from one state to another is the same for *all* processes, both internally reversible and irreversible, between these two states. In other words, once the change in entropy between two states has been evaluated, this is the magnitude of the entropy change for *any* process of the system between these end states.

The definition of entropy change expressed on a differential basis is

$$dS = \left(\frac{\delta Q}{T}\right)_{\substack{int \\ rev}} \tag{2.14b}$$

Equation 2.14b indicates that when a closed system undergoing an internally reversible process *receives* energy by heat transfer, the system experiences an *increase* in entropy. Conversely, when energy is *removed* from the system by heat transfer, the entropy of the system *decreases.* This can be interpreted to mean that an entropy transfer is *associated* with (or accompanies) heat transfer. The direction of the entropy transfer is the same as that of the heat transfer. In an *adiabatic* internally reversible process of a closed system the entropy would remain constant. A constant entropy process is called an *isentropic* process.

On rearrangement, Equation 2.14b becomes

$$(\delta Q)_{\substack{int \\ rev}} = TdS$$

Then, for an internally reversible process of a closed system between state 1 and state 2,

$$Q_{\substack{int \\ rev}} = m\int_1^2 Tds \tag{2.15}$$

When such a process is represented by a continuous curve on a plot of temperature vs. specific entropy, the area *under* the curve is the magnitude of the heat transfer per unit of system mass.

Entropy Balance

For a cycle consisting of an actual process from state 1 to state 2, during which internal irreversibilities are present, followed by an internally reversible process from state 2 to state 1, Equation 2.13b takes the form

$$\int_1^2 \left(\frac{\delta Q}{T}\right)_b + \int_2^1 \left(\frac{\delta Q}{T}\right)_{\substack{int \\ rev}} = -S_{gen}$$

where the first integral is for the actual process and the second integral is for the internally reversible process. Since no irreversibilities are associated with the internally reversible process, the term S_{gen} accounting for the effect of irreversibilities during the cycle can be identified with the actual process only.

Applying the definition of entropy change, the second integral of the foregoing equation can be expressed as

$$S_1 - S_2 = \int_2^1 \left(\frac{\delta Q}{T}\right)_{\substack{int \\ rev}}$$

Introducing this and rearranging the equation, the *closed system entropy balance* results:

$$\underbrace{S_2 - S_1}_{\substack{\text{entropy} \\ \text{change}}} = \underbrace{\int_1^2 \left(\frac{\delta Q}{T}\right)_b}_{\substack{\text{entropy} \\ \text{transfer}}} + \underbrace{S_{gen}}_{\substack{\text{entropy} \\ \text{generation}}} \tag{2.16}$$

When the end states are fixed, the entropy change on the left side of Equation 2.16 can be evaluated independently of the details of the process from state 1 to state 2. However, the two terms on the right side depend explicitly on the nature of the process and cannot be determined solely from knowledge of the end states. The first term on the right side is associated with heat transfer to or from the system during the process. This term can be interpreted as the *entropy transfer associated with (or accompanying) heat transfer.* The direction of entropy transfer is the same as the direction of the heat transfer, and the same sign convention applies as for heat transfer: a positive value means that entropy is transferred into the system, and a negative value means that entropy is transferred out.

The entropy change of a system is not accounted for solely by entropy transfer, but is also due to the second term on the right side of Equation 2.16 denoted by S_{gen}. The term S_{gen} is positive when internal irreversibilities are present during the process and vanishes when internal irreversibilities are absent. This can be described by saying that entropy is *generated* (or produced) within the system by the action of irreversibilities. The second law of thermodynamics can be interpreted as specifying that entropy is generated by irreversibilities and conserved only in the limit as irreversibilities are reduced to zero. Since S_{gen} measures the effect of irreversibilities present within a system during a process, its value depends on the nature of the process and not solely on the end states. Entropy generation is *not* a property.

When applying the entropy balance, the objective is often to evaluate the entropy generation term. However, the value of the entropy generation for a given process of a system usually does not have much significance by itself. The significance is normally determined through comparison. For example, the entropy generation within a given component might be compared to the entropy generation values of the other components included in an overall system formed by these components. By comparing entropy generation values, the components where appreciable irreversibilities occur can be identified and rank ordered. This allows attention to be focused on the components that contribute most heavily to inefficient operation of the overall system.

To evaluate the entropy transfer term of the entropy balance requires information regarding both the heat transfer and the temperature on the boundary where the heat transfer occurs. The entropy transfer term is not always subject to direct evaluation, however, because the required information is either unknown or undefined, such as when the system passes through states sufficiently far from equilibrium. In practical applications, it is often convenient, therefore, to enlarge the system to include enough of the immediate surroundings that the temperature on the boundary of the *enlarged system* corresponds to the ambient temperature, T_{amb}. The entropy transfer term is then simply Q/T_{amb}. However, as the irreversibilities present would not be just those for the system of interest but those for the enlarged system, the entropy generation term would account for the effects of internal irreversibilities within the system *and* external irreversibilities present within that portion of the surroundings included within the enlarged system.

A form of the entropy balance convenient for particular analyses is the *rate form:*

$$\frac{dS}{dt} = \sum_j \frac{\dot{Q}_j}{T_j} + \dot{S}_{gen} \tag{2.17}$$

where *dS/dt* is the time rate of change of entropy of the system. The term $\dot{Q}_j / T_j$ represents the time rate of entropy transfer through the portion of the boundary whose instantaneous temperature is T_j. The term $\dot{S}_{gen}$ accounts for the time rate of entropy generation due to irreversibilities within the system.

For a system *isolated* from its surroundings, the entropy balance is

$$\left(S_2 - S_1\right)_{isol} = S_{gen} \tag{2.18}$$

where S_{gen} is the total amount of entropy generated within the isolated system. Since entropy is generated in all actual processes, the only processes of an isolated system that actually can occur are those for which the entropy of the isolated system increases. This is known as the *increase of entropy principle.*

2.2 Control Volume Applications

Since most applications of engineering thermodynamics are conducted on a control volume basis, the control volume formulations of the mass, energy, and entropy balances presented in this section are especially important. These are given here in the form of *overall* balances. Equations of change for mass, energy, and entropy in the form of differential equations are also available in the literature (see, e.g., Bird et al., 1960).

Conservation of Mass

When applied to a control volume, the principle of mass conservation states: *The time rate of accumulation of mass within the control volume equals the difference between the total rates of mass flow in and out across the boundary.* An important case for engineering practice is one for which inward and outward flows occur, each through one or more ports. For this case the conservation of mass principle takes the form

$$\frac{dm_{cv}}{dt} = \sum_i \dot{m}_i - \sum_e \dot{m}_e \tag{2.19}$$

The left side of this equation represents the time rate of change of mass contained within the control volume, $\dot{m}_i$ denotes the mass flow rate at an inlet, and $\dot{m}_e$ is the mass flow rate at an outlet.

The *volumetric flow rate* through a portion of the control surface with area dA is the product of the velocity component normal to the area, $\mathrm{v_n}$, times the area: $\mathrm{v_n}\, dA$. The *mass* flow rate through dA is $\rho(\mathrm{v_n}\, dA)$. The mass rate of flow through a port of area A is then found by integration over the area

$$\dot{m} = \int_A \rho \mathrm{v_n}\, dA$$

For *one-dimensional* flow the intensive properties are uniform with position over area A, and the last equation becomes

$$\dot{m} = \rho \mathrm{v} A = \frac{\mathrm{v}A}{v} \tag{2.20}$$

where v denotes the specific volume and the subscript n has been dropped from velocity for simplicity.

Control Volume Energy Balance

When applied to a control volume, the principle of energy conservation states: *The time rate of accumulation of energy within the control volume equals the difference between the total incoming rate of energy transfer and the total outgoing rate of energy transfer.* Energy can enter and exit a control volume by work and heat transfer. Energy also enters and exits with flowing streams of matter. Accordingly, for a control volume with one-dimensional flow at a single inlet and a single outlet,

$$\frac{d(U + KE + PE)_{cv}}{dt} = \dot{Q}_{cv} - \dot{W} + \dot{m}\underline{\left(u_i + \frac{\mathrm{v}_i^2}{2} + \mathrm{g}z_i\right)} - \dot{m}\underline{\left(u_e + \frac{\mathrm{v}_e^2}{2} + \mathrm{g}z_e\right)} \tag{2.21}$$

where the underlined terms account for the specific energy of the incoming and outgoing streams. The terms $\dot{Q}_{cv}$ and $\dot{W}$ account, respectively, for the net rates of energy transfer by heat and work over the boundary (control surface) of the control volume.

Because work is always done on or by a control volume where matter flows across the boundary, the quantity $\dot{W}$ of Equation 2.21 can be expressed in terms of two contributions: one is the work associated with the force of the fluid pressure as mass is introduced at the inlet and removed at the exit. The other, denoted as $\dot{W}_{cv}$, includes *all other* work effects, such as those associated with rotating shafts, displacement of the boundary, and electrical effects. The work rate concept of mechanics allows the first of these contributions to be evaluated in terms of the product of the pressure force, *pA*, and velocity at the point of application of the force. To summarize, the work term $\dot{W}$ of Equation 2.21 can be expressed (with Equation 2.20) as

$$\begin{aligned} \dot{W} &= \dot{W}_{cv} + (p_e A_e)\mathrm{v}_e - (p_i A_i)\mathrm{v}_i \\ &= \dot{W}_{cv} + \dot{m}_e(p_e v_e) - \dot{m}_i(p_i v_i) \end{aligned} \tag{2.22}$$

The terms $\dot{m}_i$ (pv_i) and $\dot{m}_e$ $(p_e v_e)$ account for the work associated with the pressure at the inlet and outlet, respectively, and are commonly referred to as *flow work.*

Substituting Equation 2.22 into Equation 2.21, and introducing the specific enthalpy *h*, the following form of the control volume energy rate balance results:

$$\frac{d(U + KE + PE)_{cv}}{dt} = \dot{Q}_{cv} - \dot{W}_{cv} + \dot{m}_i\left(h_i + \frac{\mathrm{v}_i^2}{2} + \mathrm{g}z_i\right) - \dot{m}_e\left(h_e + \frac{\mathrm{v}_e^2}{2} + \mathrm{g}z_e\right) \tag{2.23}$$

To allow for applications where there may be several locations on the boundary through which mass enters or exits, the following expression is appropriate:

$$\frac{d(U + KE + PE)_{cv}}{dt} = \dot{Q}_{cv} - \dot{W}_{cv} + \sum_i \dot{m}_i\left(h_i + \frac{\mathrm{v}_i^2}{2} + \mathrm{g}z_i\right) - \sum_e \dot{m}_e\left(h_e + \frac{\mathrm{v}_e^2}{2} + \mathrm{g}z_e\right) \tag{2.24}$$

Equation 2.24 is an *accounting* rate balance for the energy of the control volume. It states that the time rate of accumulation of energy within the control volume equals the difference between the total rates of energy transfer in and out across the boundary. The mechanisms of energy transfer are heat and work, as for closed systems, and the energy accompanying the entering and exiting mass.

Control Volume Entropy Balance

Like mass and energy, entropy is an extensive property. And like mass and energy, entropy can be transferred into or out of a control volume by streams of matter. As this is the principal difference between the closed system and control volume forms, the control volume entropy rate balance is obtained by modifying Equation 2.17 to account for these entropy transfers. The result is

$$\underbrace{\frac{dS_{cv}}{dt}}_{\substack{\text{rate of}\\\text{entropy}\\\text{change}}} = \underbrace{\sum_j \frac{\dot{Q}_j}{T_j} + \sum_i \dot{m}_i s_i - \sum_e \dot{m}_e s_e}_{\substack{\text{rate of}\\\text{entropy}\\\text{transfer}}} + \underbrace{\dot{S}_{gen}}_{\substack{\text{rate of}\\\text{entropy}\\\text{generation}}} \tag{2.25}$$

where dS_{cv}/dt represents the time rate of change of entropy within the control volume. The terms $\dot{m}_i s_i$ and $\dot{m}_e s_e$ account, respectively, for rates of entropy *transfer* into and out of the control volume associated with mass flow. One-dimensional flow is assumed at locations where mass enters and exits. $\dot{Q}_j$ represents the time rate of heat transfer at the location on the boundary where the instantaneous temperature is T_j; and $\dot{Q}_j / T_j$ accounts for the associated rate of entropy *transfer.* $\dot{S}_{gen}$ denotes the time rate of entropy *generation* due to irreversibilities *within* the control volume. When a control volume comprises a number of components, $\dot{S}_{gen}$ is the sum of the rates of entropy generation of the components.

Control Volumes at Steady State

Engineering systems are often idealized as being at *steady state,* meaning that all properties are unchanging in time. For a control volume at steady state, the identity of the matter within the control volume change continuously, but the total amount of mass remains constant. At steady state, Equation 2.19 reduces to

$$\sum_i \dot{m}_i = \sum_e \dot{m}_e \tag{2.26a}$$

The energy rate balance of Equation 2.24 becomes, at steady state,

$$0 = \dot{Q}_{cv} - \dot{W}_{cv} + \sum_i \dot{m}_i \left(h_i + \frac{\mathrm{v}_i^2}{2} + \mathrm{g}\mathrm{z}_i \right) - \sum_e \dot{m}_e \left(h_e + \frac{\mathrm{v}_e^2}{2} + \mathrm{g}\mathrm{z}_e \right) \tag{2.26b}$$

At steady state, the entropy rate balance of Equation 2.25 reads

$$0 = \sum_j \frac{\dot{Q}_j}{T_j} + \sum_i \dot{m}_i s_i - \sum_e \dot{m}_e s_e + \dot{S}_{gen} \tag{2.26c}$$

Mass and energy are conserved quantities, but entropy is not generally conserved. Equation 2.26a indicates that the total rate of mass flow into the control volume equals the total rate of mass flow out of the control volume. Similarly, Equation 2.26b states that the total rate of energy transfer into the control volume equals the total rate of energy transfer out of the control volume. However, Equation 2.26c shows that the rate at which entropy is transferred out *exceeds* the rate at which entropy enters, the difference being the rate of entropy generation within the control volume owing to irreversibilities.

Applications frequently involve control volumes having a single inlet and a single outlet, as, for example, the control volume of Figure 2.1 where heat transfer (if any) occurs at T_b: the temperature, or a suitable average temperature, on the boundary where heat transfer occurs. For this case the mass rate balance, Equation 2.26a, reduces to $\dot{m}_i = \dot{m}_e$. Denoting the common mass flow rate by $\dot{m}$, Equation 2.26b and Equation 2.26c read, respectively,

$$0 = \dot{Q}_{cv} - \dot{W}_{cv} + \dot{m} \left[\left(h_i - h_e \right) + \left(\frac{\mathrm{v}_i^2 - \mathrm{v}_e^2}{2} \right) + \mathrm{g} \left(\mathrm{z}_i - \mathrm{z}_e \right) \right] \tag{2.27a}$$

$$0 = \frac{\dot{Q}_{cv}}{T_b} + \dot{m} \left(s_i - s_e \right) + \dot{S}_{gen} \tag{2.28a}$$

When Equation 2.27a and Equation 2.28a are applied to particular cases of interest, additional simplifications are usually made. The heat transfer term $\dot{Q}_{cv}$ is dropped when it is insignificant relative to other energy transfers across the boundary. This may be the result of one or more of the following: (1) the outer surface of the control volume is insulated; (2) the outer surface area is too small for there to be effective heat transfer; (3) the temperature difference between the control volume and its surroundings is small enough that the heat transfer can be ignored; (4) the gas or liquid passes through the control volume so quickly that there is not enough time for significant heat transfer to occur. The work term

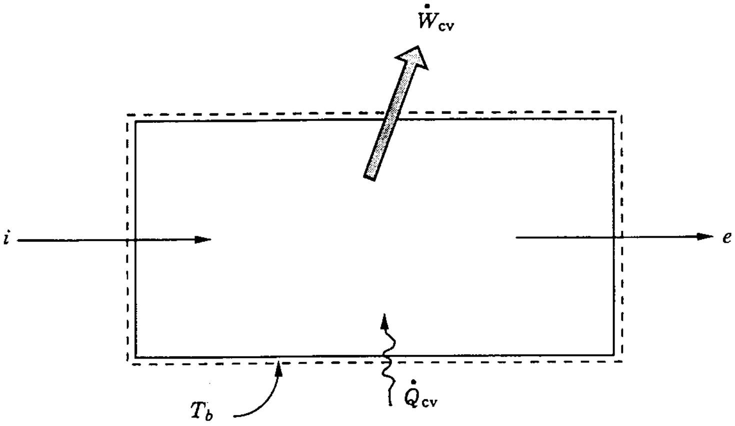

FIGURE 2.1 One-inlet, one-outlet control volume at steady state.

$\dot{W}_{cv}$ drops out of the energy rate balance when there are no rotating shafts, displacements of the boundary, electrical effects, or other work mechanisms associated with the control volume being considered. The changes in kinetic and potential energy of Equation 2.27a are frequently negligible relative to other terms in the equation.

The special forms of Equation 2.27a and Equation 2.28a listed in Table 2.1 are obtained as follows: when there is no heat transfer, Equation 2.28a gives

$$s_e - s_i = \frac{\dot{S}_{gen}}{\dot{m}} \geq 0 \tag{2.28b}$$

(no heat transfer)

Accordingly, when irreversibilities are present within the control volume, the specific entropy increases as mass flows from inlet to outlet. In the ideal case in which no internal irreversibilities are present, mass passes through the control volume with no change in its entropy — that is, *isentropically.*

For no heat transfer, Equation 2.27a gives

$$\dot{W}_{cv} = \dot{m}\left[\left(h_i - h_e\right) + \left(\frac{\mathrm{v}_i^2 - \mathrm{v}_e^2}{2}\right) + \mathrm{g}\left(\mathrm{z}_i - \mathrm{z}_e\right)\right] \tag{2.27b}$$

A special form that is applicable, at least approximately, to *compressors*, *pumps*, and *turbines* results from dropping the kinetic and potential energy terms of Equation 2.27b, leaving

$$\dot{W}_{cv} = \dot{m}\left(h_i - h_e\right) \tag{2.27c}$$

(*compressors*, *pumps*, and *turbines*)

In *throttling devices* a significant reduction in pressure is achieved simply by introducing a restriction into a line through which a gas or liquid flows. For such devices $\dot{W}_{cv} = 0$ and Equation 2.27c reduces further to read

TABLE 2.1 Energy and Entropy Balances for One-Inlet, One-Outlet Control Volumes at Steady State and No Heat Transfer

---

Energy balance

$$\dot{W}_{cv} = \dot{m}\left[\left(h_i - h_e\right) + \left(\frac{\mathrm{v}_i^2 - \mathrm{v}_e^2}{2}\right) + g\left(z_i - z_e\right)\right] \qquad (2.27b)$$

Compressors, pumps, and turbines[a]

$$\dot{W}_{cv} = \dot{m}\left(h_i - h_e\right) \qquad (2.27c)$$

Throttling

$$h_e \cong h_i \qquad (2.27d)$$

Nozzles, diffusers[b]

$$\mathrm{v}_e = \sqrt{\mathrm{v}_i^2 + 2\left(h_i - h_e\right)} \qquad (2.27f)$$

Entropy balance

$$s_e - s_i = \frac{\dot{S}_{gen}}{\dot{m}} \geq 0 \qquad (2.28b)$$

---

[a] For an ideal gas with constant c_p, Equation 1′ of Table 2.7 allows Equation 2.27c to be written as

$$\dot{W}_{cv} = \dot{m}c_p\left(T_i - T_e\right) \qquad (2.27c')$$

The power developed in an *isentropic process* is obtained with Equation 5′ of Table 2.7 as

$$\dot{W}_{cv} = \dot{m}c_p T_i\left[1 - \left(p_e/p_i\right)^{(k-1)/k}\right] \quad (s = c) \qquad (2.27c'')$$

where $c_p = kR/(k - 1)$.

[b] For an ideal gas with constant c_p, Equation 1′ of Table 2.7 allows Equation 2.27f to be written as

$$\mathrm{v}_e = \sqrt{\mathrm{v}_i^2 + 2c_p\left(T_i - T_e\right)} \qquad (2.27f')$$

The exit velocity for an *isentropic process* is obtained with Equation 5′ of Table 2.7 as

$$\mathrm{v}_e = \sqrt{\mathrm{v}_i^2 + 2c_p T_i\left[1 - \left(p_e/p_i\right)^{(k-1)/k}\right]} \quad (s = c) \qquad (2.27f'')$$

where $c_p = kR/(k - 1)$.

$$h_e \cong h_i \quad (\textit{throttling process}) \qquad (2.27d)$$

That is, upstream and downstream of the throttling device, the specific enthalpies are equal.

A *nozzle* is a flow passage of varying cross-sectional area in which the velocity of a gas or liquid increases in the direction of flow. In a *diffuser,* the gas or liquid decelerates in the direction of flow. For such devices, $\dot{W}_{cv} = 0$. The heat transfer and potential energy change are also generally negligible. Then Equation 2.27b reduces to

$$0 = h_i - h_e + \frac{\mathrm{v}_i^2 - \mathrm{v}_e^2}{2} \qquad (2.27e)$$

Solving for the outlet velocity

$$\mathrm{v}_e = \sqrt{\mathrm{v}_i^2 + 2(h_i - h_e)} \tag{2.27f}$$
$$(\textit{nozzle, diffuser})$$

Further discussion of the flow-through nozzles and diffusers is provided in Chapter 3.

The mass, energy, and entropy rate balances, Equations 2.26, can be applied to control volumes with multiple inlets and/or outlets, as, for example, cases involving heat-recovery steam generators, feedwater heaters, and counterflow and crossflow heat exchangers. Transient (or unsteady) analyses can be conducted with Equation 2.19, Equation 2.24, and Equation 2.25. Illustrations of all such applications are provided by Moran and Shapiro (1995).

Example 1

A turbine receives steam at 7 MPa, 440°C and exhausts at 0.2 MPa for subsequent process heating duty. If heat transfer and kinetic/potential energy effects are negligible, determine the steam mass flow rate, in kg/hr, for a turbine power output of 30 MW when (a) the steam quality at the turbine outlet is 95%, (b) the turbine expansion is internally reversible.

Solution. With the indicated idealizations, Equation 2.27c is appropriate. Solving, $\dot{m} = \dot{W}_{cv}/(h_i - h_e)$. Steam table data (Table A.5) at the inlet condition are h_i = 3261.7 kJ/kg, s_i = 6.6022 kJ/kg · K.

(a) At 0.2 MPa and $x = 0.95$, h_e = 2596.5 kJ/kg. Then

$$\dot{m} = \frac{30\ \text{MW}}{(3261.7 - 2596.5)\ \text{kJ/kg}}\left(\frac{10^3\ \text{kJ/sec}}{1\ \text{MW}}\right)\left(\frac{3600\ \text{sec}}{1\ \text{hr}}\right)$$
$$= 162{,}357\ \text{kg/hr}$$

(b) For an internally reversible expansion, Equation 2.28b reduces to give $s_e = s_i$. For this case, h_e = 2499.6 kJ/kg ($x = 0.906$), and $\dot{m}$ = 141,714 kg/hr.

Example 2

Air at 500°F, 150 lbf/in.^{2}, and 10 ft/sec expands adiabatically through a nozzle and exits at 60°F, 15 lbf/in.^{2}. For a mass flow rate of 5 lb/sec determine the exit area, in in.^{2}. Repeat for an isentropic expansion to 15 lbf/in.^{2}. Model the air as an ideal gas (Section 2.3, Ideal Gas Model) with specific heat c_p = 0.24 Btu/lb · °R ($k = 1.4$).

Solution. The nozle exit area can be evaluated using Equation 2.20, together with the ideal gas equation, v = RT/p:

$$A_e = \frac{\dot{m}v_e}{\mathrm{V}_e} = \frac{\dot{m}(RT_e/p_e)}{\mathrm{V}_e}$$

The exit velocity required by this expression is obtained using Equation 2.27f′ of Table 2.1,

$$\mathrm{v}_e = \sqrt{\mathrm{v}_i^2 + 2c_p(T_i - T_e)}$$
$$= \sqrt{\left(\frac{10\ \text{ft}}{s}\right)^2 + 2\left(0.24\frac{\text{Btu}}{\text{lb}\cdot\text{R}}\right)\left(\frac{778.17\ \text{ft}\cdot\text{lbf}}{1\ \text{Btu}}\right)(440°\text{R})\left(\frac{32.174\ \text{lb}\cdot\text{ft/sec}^2}{1\ \text{lbf}}\right)}$$
$$= 2299.5\ \text{ft sec}$$

Finally, with $R = \bar{R}/\mathcal{M}$ = 53.33 ft · lbf/lb · °R,

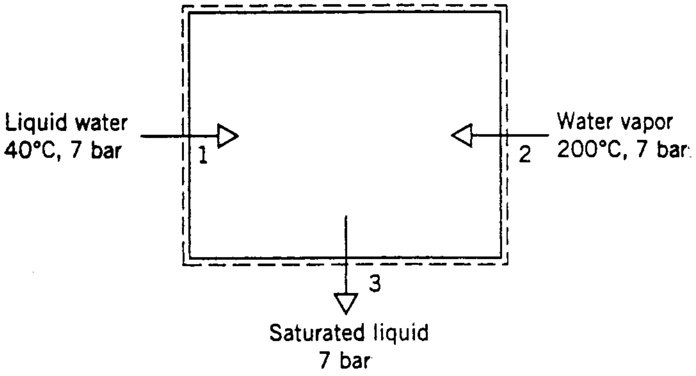

FIGURE 2.2 Open feedwater heater.

$$A_e = \frac{\left(5\frac{\text{lb}}{\text{sec}}\right)\left(53.3\frac{\text{ft}\cdot\text{lbf}}{\text{lb}\cdot{}^\circ\text{R}}\right)(520^\circ\text{R})}{\left(2299.5\frac{\text{ft}}{\text{sec}}\right)\left(15\frac{\text{lbf}}{\text{in.}^2}\right)} = 4.02 \text{ in.}^2$$

Using Equation 2.27f″ in Table 2.1 for the isentropic expansion,

$$\text{v}_e = \sqrt{(10)^2 + 2(0.24)(778.17)(960)(32.174)\left[1 - \left(\frac{15}{150}\right)^{0.4/1.4}\right]}$$

$$= 2358.3 \text{ ft/sec}$$

Then $A_e = 3.92$ in.^{2}.

Example 3

Figure 2.2 provides steady-state operating data for an open feedwater heater. Ignoring heat transfer and kinetic/potential energy effects, determine the ratio of mass flow rates, $\dot{m}_1/\dot{m}_2$.

Solution. For this case Equation 2.26a and Equation 2.26b reduce to read, respectively,

$$\dot{m}_1 + \dot{m}_2 = \dot{m}_3$$

$$0 = \dot{m}_1 h_1 + \dot{m}_2 h_2 - \dot{m}_3 h_3$$

Combining and solving for the ratio $\dot{m}_1/\dot{m}_2$,

$$\frac{\dot{m}_1}{\dot{m}_2} = \frac{h_2 - h_3}{h_3 - h_1}$$

Inserting steam table data, in kJ/kg, from Table A.5,

$$\frac{\dot{m}_1}{\dot{m}_2} = \frac{2844.8 - 697.2}{697.2 - 167.6} = 4.06$$

Internally Reversible Heat Transfer and Work

For one-inlet, one-outlet control volumes at steady state, the following expressions give the heat transfer rate and power in the absence of internal irreversibilities:

$$\left(\frac{\dot{Q}_{cv}}{\dot{m}}\right)_{\substack{int\\rev}} = \int_1^2 Tds \tag{2.29}$$

$$\left(\frac{\dot{W}_{cv}}{\dot{m}}\right)_{\substack{int\\rev}} = -\int_1^2 vdp + \frac{V_1^2 - V_2^2}{2} + g(z_1 - z_2) \tag{2.30a}$$

(see, e.g., Moran and Shapiro, 1995).

If there is no significant change in kinetic or potential energy from inlet to outlet, Equation 2.30a reads

$$\left(\frac{\dot{W}_{cv}}{\dot{m}}\right)_{\substack{int\\rev}} = -\int_1^2 vdp \qquad (\Delta ke = \Delta pe = 0) \tag{2.30b}$$

The specific volume remains approximately constant in many applications with liquids. Then Equation 30b becomes

$$\left(\frac{\dot{W}_{cv}}{\dot{m}}\right)_{\substack{int\\rev}} = -v(p_2 - p_1) \qquad (v = \text{constant}) \tag{2.30c}$$

When the states visited by a unit of mass flowing without irreversibilities from inlet to outlet are described by a continuous curve on a plot of temperature vs. specific entropy, Equation 2.29 implies that the area under the curve is the magnitude of the heat transfer per unit of mass flowing. When such an ideal process is described by a curve on a plot of pressure vs. specific volume, as shown in Figure 2.3, the magnitude of the integral $\int vdp$ of Equation 2.30a and Equation 2.30b is represented by the area a-b-c-d *behind* the curve. The area a-b-c′-d′ *under* the curve is identified with the magnitude of the integral $\int pdv$ of Equation 2.10.

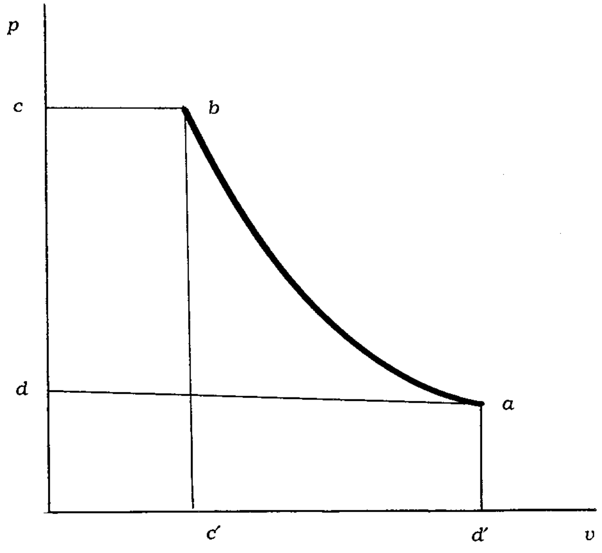

FIGURE 2.3 Internally reversible process on *p–v* coordinates.

2.3 Property Relations and Data

Pressure, temperature, volume, and mass can be found experimentally. The relationships between the specific heats c_v and c_p and temperature at relatively low pressure are also accessible experimentally, as are certain other property data. Specific internal energy, enthalpy, and entropy are among those properties that are not so readily obtained in the laboratory. Values for such properties are calculated using experimental data of properties that are more amenable to measurement, together with appropriate property relations derived using the principles of thermodynamics. In this section property relations and data sources are considered for *simple compressible systems*, which include a wide range of industrially important substances.

Property data are provided in the publications of the *National Institute of Standards and Technology* (formerly the U.S. Bureau of Standards), of professional groups such as the *American Society of Mechanical Engineering (ASME),* the *American Society of Heating. Refrigerating, and Air Conditioning Engineers (ASHRAE)*, and the *American Chemical Society,* and of corporate entities such as *Dupont* and *Dow Chemical.* Handbooks and property reference volumes such as included in the list of references for this chapter are readily accessed sources of data. Property data are also retrievable from various commercial online data bases. Computer software is increasingly available for this purpose as well.

Basic Relations for Pure Substances

An energy balance in differential form for a closed system undergoing an internally reversible process in the absence of overall system motion and the effect of gravity reads

$$dU = (\delta Q)_{\substack{int\\rev}} - (\delta W)_{\substack{int\\rev}}$$

From Equation 2.14b, $(\delta Q)_{\substack{int\\rev}} = TdS$. When consideration is limited to *simple compressible systems:* systems for which the only significant work in an internally reversible process is associated with volume change, $(\delta W)_{\substack{int\\rev}} = pdV$, the following equation is obtained:

$$dU = TdS - pdV \tag{2.31a}$$

Introducing enthalpy, $H = U + pV$, the Helmholtz function, $\Psi = U - TS$, and the Gibbs function, $G = H - TS$, three additional expressions are obtained:

$$dH = TdS + Vdp \tag{2.31b}$$

$$d\Psi = -pdV - SdT \tag{2.31c}$$

$$dG = Vdp - SdT \tag{2.31d}$$

Equations 2.31 can be expressed on a per-unit-mass basis as

$$du = Tds - pdv \tag{2.32a}$$

$$dh = Tds + vdp \tag{2.32b}$$

$$d\psi = -pdv - sdT \tag{2.32c}$$

$$dg = vdp - sdT \tag{2.32d}$$

Similar expressions can be written on a per-mole basis.

TABLE 2.2 Relations from Exact Differentials

Function	*Differential*	*Coefficients*	*Maxwell*
General:			
$z = z(x, y)$	$dz = M(x,y)dx + N(x,y)dy$	$\left(\frac{\partial z}{\partial x}\right)_y = M$	$\left(\frac{\partial M}{\partial y}\right)_x = \left(\frac{\partial N}{\partial x}\right)_y$
		$\left(\frac{\partial z}{\partial y}\right)_x = N$	
Internal energy:			
$u(s, v)$	$du = Tds - pdv$	$\left(\frac{\partial u}{\partial s}\right)_v = T$	$\left(\frac{\partial T}{\partial v}\right)_s = -\left(\frac{\partial p}{\partial s}\right)_v$
		$\left(\frac{\partial u}{\partial v}\right)_s = -p$	
Enthalpy:			
$h(s, p)$	$dh = Tds + vdp$	$\left(\frac{\partial h}{\partial s}\right)_p = T$	$\left(\frac{\partial T}{\partial p}\right)_s = \left(\frac{\partial v}{\partial s}\right)_p$
		$\left(\frac{\partial h}{\partial p}\right)_s = v$	
Helmholtz function:			
$\psi(v, T)$	$d\psi = -pdv - sdT$	$\left(\frac{\partial \psi}{\partial v}\right)_T = -p$	$\left(\frac{\partial p}{\partial T}\right)_v = \left(\frac{\partial s}{\partial v}\right)_T$
		$\left(\frac{\partial \psi}{\partial T}\right)_v = -s$	
Gibbs function:			
$g(T, p)$	$dg = vdp - sdT$	$\left(\frac{\partial g}{\partial p}\right)_T = v$	$\left(\frac{\partial v}{\partial T}\right)_p = -\left(\frac{\partial s}{\partial p}\right)_T$
		$\left(\frac{\partial g}{\partial T}\right)_p = -s$	

Maxwell Relations

Since only properties are involved, each of the four differential expressions given by Equations 2.32 is an *exact* differential exhibiting the general form $dz = M(x, y)dx + N(x, y)dy$, where the second mixed partial derivatives are equal: $(\partial M/\partial y) = (\partial N/\partial x)$. Underlying these exact differentials are, respectively, functions of the form $u(s, v)$, $h(s, p)$, $\psi(v, T)$, and $g(T, p)$. From such considerations the *Maxwell relations* given in Table 2.2 can be established.

Example 4

Derive the Maxwell relation following from Equation 2.32a.

Solution. The differential of the function $u = u(s, v)$ is

$$du = \left(\frac{\partial u}{\partial s}\right)_v ds + \left(\frac{\partial u}{\partial v}\right)_s dv$$

By comparison with Equation 2.32a,

$$T = \left(\frac{\partial u}{\partial s}\right)_v, \quad -p = \left(\frac{\partial u}{\partial v}\right)_s$$

In Equation 2.32a, T plays the role of M and $-p$ plays the role of N, so the equality of second mixed partial derivatives gives the Maxwell relation,

$$\left(\frac{\partial T}{\partial v}\right)_s = -\left(\frac{\partial p}{\partial s}\right)_v$$

Since each of the properties T, p, v, and s appears on the right side of two of the eight coefficients of Table 2.2, four additional property relations can be obtained by equating such expressions:

$$\left(\frac{\partial u}{\partial s}\right)_v = \left(\frac{\partial h}{\partial s}\right)_p, \quad \left(\frac{\partial u}{\partial v}\right)_s = \left(\frac{\partial \psi}{\partial v}\right)_T$$

$$\left(\frac{\partial h}{\partial p}\right)_s = \left(\frac{\partial g}{\partial p}\right)_T, \quad \left(\frac{\partial \psi}{\partial T}\right)_v = \left(\frac{\partial g}{\partial T}\right)_p$$

These four relations are identified in Table 2.2 by brackets. As any three of Equations 2.32 can be obtained from the fourth simply by manipulation, the 16 property relations of Table 2.2 also can be regarded as following from this single differential expression. Several additional first-derivative property relations can be derived; see, e.g., Zemansky, 1972.

Specific Heats and Other Properties

Engineering thermodynamics uses a wide assortment of thermodynamic properties and relations among these properties. Table 2.3 lists several commonly encountered properties.

Among the entries of Table 2.3 are the specific heats c_v and c_p. These intensive properties are often required for thermodynamic analysis, and are defined as partial derivations of the functions $u(T, v)$ and $h(T, p)$, respectively,

$$c_v = \left(\frac{\partial u}{\partial T}\right)_v \tag{2.33}$$

$$c_p = \left(\frac{\partial h}{\partial T}\right)_p \tag{2.34}$$

Since u and h can be expressed either on a unit mass basis or a per-mole basis, values of the specific heats can be similarly expressed. Table 2.4 summarizes relations involving c_v and c_p. The property k, the specific heat ratio, is

$$k = \frac{c_p}{c_v} \tag{2.35}$$

Values for c_v and c_p can be obtained via statistical mechanics using *spectroscopic* measurements. They can also be determined macroscopically through exacting property measurements. Specific heat data for

TABLE 2.3 Symbols and Definitions for Selected Properties

Property	Symbol	Definition	Property	Symbol	Definition
Pressure	p		Specific heat, constant volume	c_v	$(\partial u/\partial T)_v$
Temperature	T		Specific heat, constant pressure	c_p	$(\partial h/\partial T)_p$
Specific volume	v		Volume expansivity	β	$\frac{1}{v}(\partial v/\partial T)_p$
Specific internal energy	u		Isothermal compressivity	κ	$-\frac{1}{v}(\partial v/\partial p)_T$
Specific entropy	s		Isentropic compressibility	α	$-\frac{1}{v}(\partial v/\partial p)_s$
Specific enthalpy	h	$u + pv$	Isothermal bulk modulus	B	$-v(\partial p/\partial v)_T$
Specific Helmholtz function	ψ	$u - Ts$	Isentropic bulk modulus	B_s	$-v(\partial p/\partial v)_s$
Specific Gibbs function	g	$h - Ts$	Joule-Thomson coefficient	μ_J	$(\partial T/\partial p)_h$
Compressibility factor	Z	pv/RT	Joule coefficient	η	$(\partial T/\partial v)_u$
Specific heat ratio	k	c_p/c_v	Velocity of sound	c	$\sqrt{-v^2(\partial p/\partial v)_s}$

common gases, liquids, and solids are provided by the handbooks and property reference volumes listed among the Chapter 2 references. Specific heats are also considered in Section 2.3 as a part of the discussions of the *incompressible model* and the *ideal gas model.* Figure 2.4 shows how c_p for water vapor varies as a function of temperature and pressure. Other gases exhibit similar behavior. The figure also gives the variation of c_p with temperature in the limit as pressure tends to zero (the ideal gas limit). In this limit c_p increases with increasing temperature, which is a characteristic exhibited by other gases as well.

The following two equations are often convenient for establishing relations among properties:

$$\left(\frac{\partial x}{\partial y}\right)_z\left(\frac{\partial y}{\partial x}\right)_z = 1 \tag{2.36a}$$

$$\left(\frac{\partial y}{\partial z}\right)_x\left(\frac{\partial z}{\partial x}\right)_y\left(\frac{\partial x}{\partial y}\right)_z = -1 \tag{2.36b}$$

Their use is illustrated in Example 5.

Example 5

Obtain Equation 2 and Equation 11 of Table 2.4 from Equation 1.

Solution. Identifying x, y, z with s, T, and v, respectively, Equation 2.36b reads

$$\left(\frac{\partial T}{\partial v}\right)_s\left(\frac{\partial v}{\partial s}\right)_T\left(\frac{\partial s}{\partial T}\right)_v = -1$$

Applying Equation 2.36a to each of $(\partial T/\partial v)_s$ and $(\partial v/\partial s)_T$,

$$\left(\frac{\partial s}{\partial T}\right)_v = -\frac{1}{(\partial T/\partial v)_s(\partial v/\partial s)_T} = -\left(\frac{\partial v}{\partial T}\right)_s\left(\frac{\partial s}{\partial v}\right)_T$$

TABLE 2.4 Specific Heat Relations[a]

$c_v = \left(\frac{\partial u}{\partial T}\right)_v = T\left(\frac{\partial s}{\partial T}\right)_v$	(1)
$= -T\left(\frac{\partial p}{\partial T}\right)_v \left(\frac{\partial v}{\partial T}\right)_s$	(2)
$c_p = \left(\frac{\partial h}{\partial T}\right)_p = T\left(\frac{\partial s}{\partial T}\right)_p$	(3)
$= T\left(\frac{\partial v}{\partial T}\right)_p \left(\frac{\partial p}{\partial T}\right)_s$	(4)
$c_p - c_v = T\left(\frac{\partial p}{\partial T}\right)_v \left(\frac{\partial v}{\partial T}\right)_p$	(5)
$= -T\left(\frac{\partial v}{\partial T}\right)_p^2 \left(\frac{\partial p}{\partial v}\right)_T$	(6)
$= \frac{Tv\beta^2}{\kappa}$	(7)
$c_p = \frac{1}{\mu_J}\left[T\left(\frac{\partial v}{\partial T}\right)_p - v\right]$	(8)
$c_v = -\frac{1}{\eta}\left[T\left(\frac{\partial p}{\partial T}\right)_v - p\right]$	(9)
$k = \frac{c_p}{c_v} = \left(\frac{\partial v}{\partial p}\right)_T \left(\frac{\partial p}{\partial v}\right)_s$	10)
$\left(\frac{\partial c_v}{\partial v}\right)_T = T\left(\frac{\partial^2 p}{\partial T^2}\right)_v$	(11)
$\left(\frac{\partial c_p}{\partial p}\right)_T = -T\left(\frac{\partial^2 v}{\partial T^2}\right)_p$	(12)

[a] See, for example, Moran, M.J. and Shapiro, H.N. 1995. *Fundamentals of Engineering Thermodynamics*, 3rd ed. Wiley, New York, chap. 11.

Introducing the Maxwell relation from Table 2.2 corresponding to $\psi(T, v)$,

$$\left(\frac{\partial s}{\partial T}\right)_v = -\left(\frac{\partial v}{\partial T}\right)_s \left(\frac{\partial p}{\partial T}\right)_v$$

With this, Equation 2 of Table 2.4 is obtained from Equation 1, which in turn is obtained in Example 6. Equation 11 of Table 2.4 can be obtained by differentiating Equation 1 with repect to specific volume at fixed temperature, and again using the Maxwell relation corresponding to ψ.

P-v-T Relations

Considerable pressure, specific volume, and temperature data have been accumulated for industrially important gases and liquids. These data can be represented in the form $p = f(v, T)$, called an *equation of state*. Equations of state can be expressed in tabular, graphical, and analytical forms.

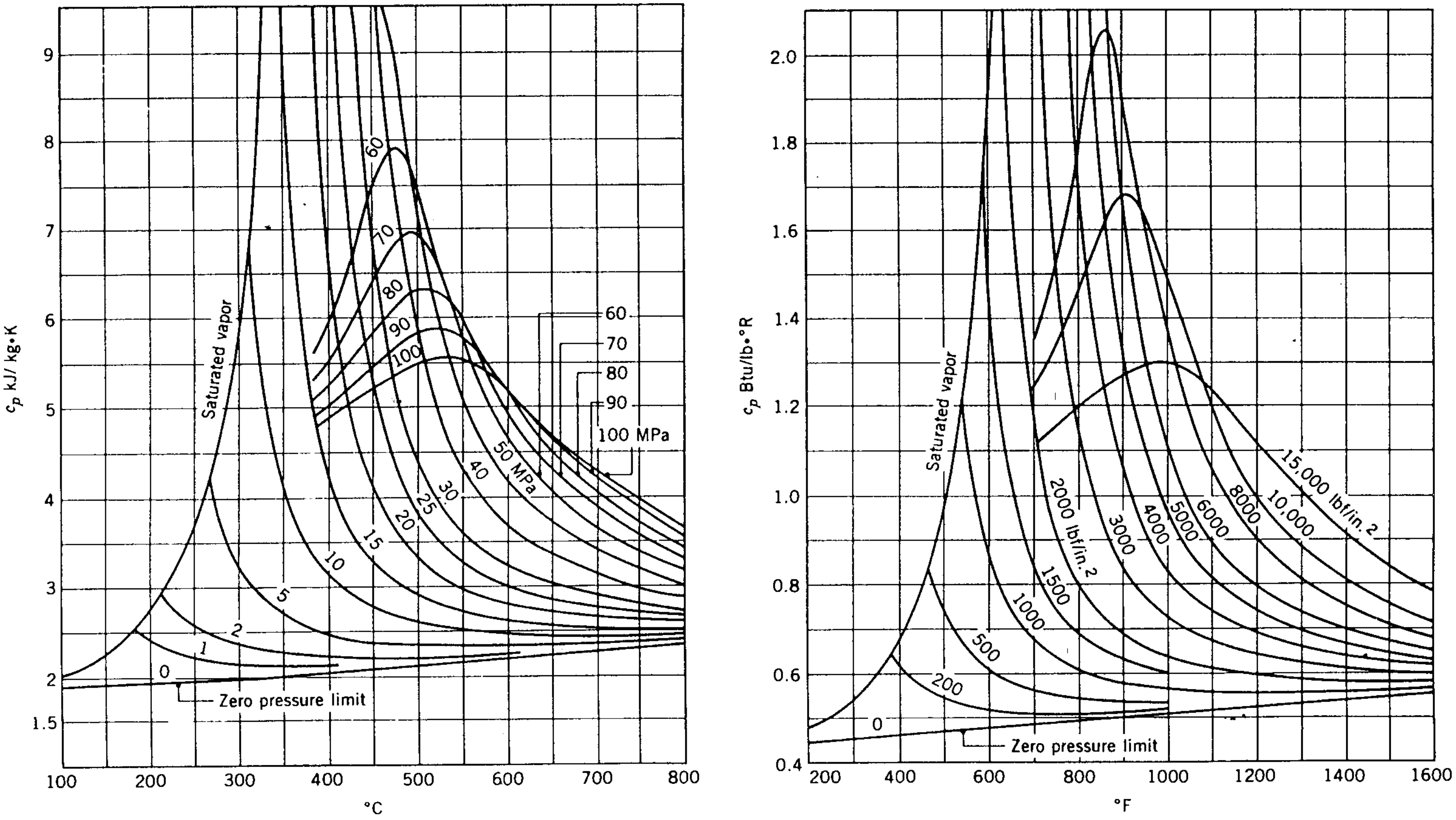

FIGURE 2.4 c_p of water vapor as a function of temperature and pressure. (Adapted from Keenan, J.H., Keyes, F.G., Hill, P.G., and Moore, J.G. 1969 and 1978. *Steam Tables — S.I. Units* (*English Units*). John Wiley & Sons, New York.)

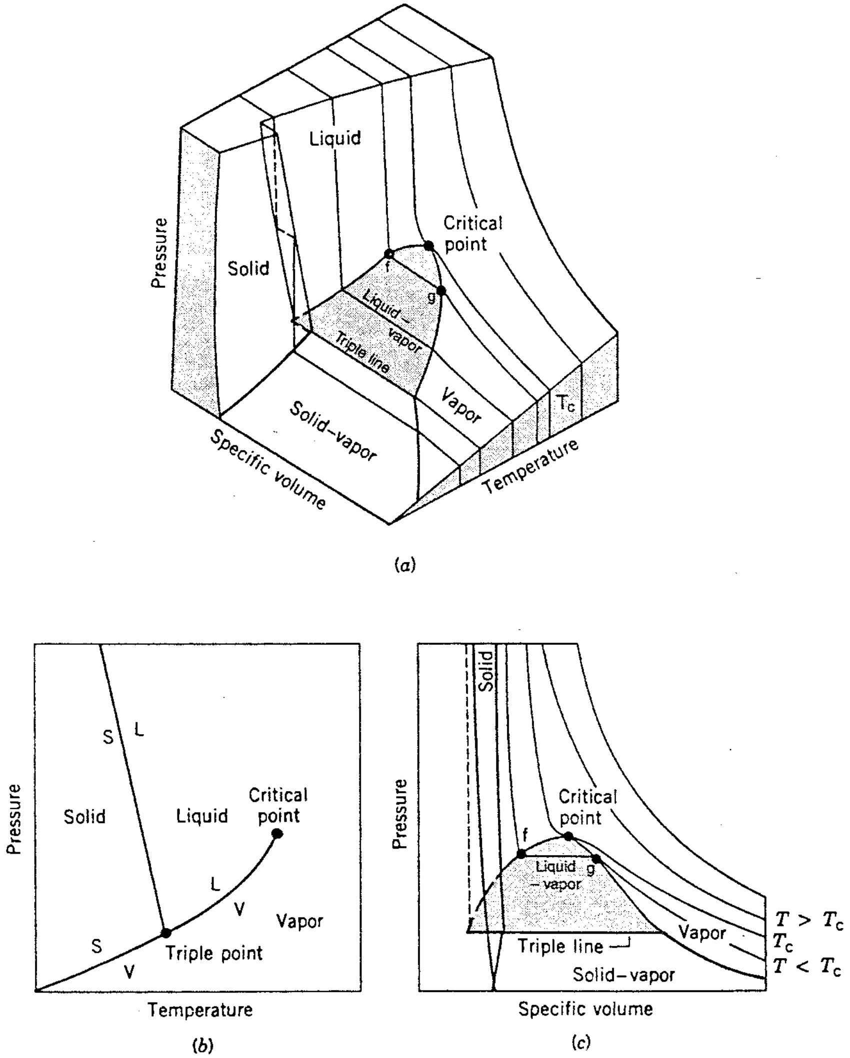

FIGURE 2.5 Pressure-specific volume-temperature surface and projections for water (not to scale).

P-v-T Surface

The graph of a function $p = f(v, T)$ is a surface in three-dimensional space. Figure 2.5 shows the *p-v-T* relationship for water. Figure 2.5b shows the projection of the surface onto the pressure-temperature plane, called the *phase diagram.* The projection onto the *p–v* plane is shown in Figure 2.5c.

Figure 2.5 has three regions labeled solid, liquid, and vapor where the substance exists only in a single phase. Between the single phase regions lie *two-phase* regions, where two phases coexist in equilibrium. The lines separating the single-phase regions from the two-phase regions are *saturation lines.* Any state represented by a point on a saturation line is a *saturation state.* The line separating the liquid phase and the two-phase liquid-vapor region is the saturated liquid line. The state denoted by f is a saturated liquid state. The saturated vapor line separates the vapor region and the two-phase liquid-vapor region. The state denoted by g is a saturated vapor state. The saturated liquid line and the saturated vapor line meet at the *critical point.* At the critical point, the pressure is the *critical pressure* p_c, and the temperature is the *critical temperature* T_c. Three phases can coexist in equilibrium along the line labeled *triple line.* The triple line projects onto a point on the phase diagram. The triple point of water is used in defining the Kelvin temperature scale (Section 2.1, Basic Concepts and Definitions; The Second Law of Thermodynamics, Entropy).

When a phase change occurs during constant pressure heating or cooling, the temperature remains constant as long as both phases are present. Accordingly, in the two-phase liquid-vapor region, a line of constant pressure is also a line of constant temperature. For a specified pressure, the corresponding temperature is called the *saturation temperature.* For a specified temperature, the corresponding pressure is called the *saturation pressure.* The region to the right of the saturated vapor line is known as the *superheated vapor region* because the vapor exists at a temperature greater than the saturation temperature for its pressure. The region to the left of the saturated liquid line is known as the *compressed liquid region* because the liquid is at a pressure higher than the saturation pressure for its temperature.

When a mixture of liquid and vapor coexists in equilibrium, the liquid phase is a saturated liquid and the vapor phase is a saturated vapor. The total volume of any such mixture is $V = V_f + V_g$; or, alternatively, $mv = m_f v_f + m_g v_g$, where m and v denote mass and specific volume, respectively. Dividing by the total mass of the mixture m and letting the *mass fraction* of the vapor in the mixture, m_g/m, be symbolized by x, called the *quality*, the apparent specific volume v of the mixture is

$$\begin{aligned} v &= (1-x)v_{\mathrm{f}} + xv_{\mathrm{g}} \\ &= v_{\mathrm{f}} + xv_{\mathrm{fg}} \end{aligned} \tag{2.37a}$$

where $v_{\mathrm{fg}} = v_{\mathrm{g}} - v_{\mathrm{f}}$. Expressions similar in form can be written for internal energy, enthalpy, and entropy:

$$\begin{aligned} u &= (1-x)u_{\mathrm{f}} + xu_{\mathrm{g}} \\ &= u_{\mathrm{f}} + xu_{\mathrm{fg}} \end{aligned} \tag{2.37b}$$

$$\begin{aligned} h &= (1-x)h_{\mathrm{f}} + xh_{\mathrm{g}} \\ &= h_{\mathrm{f}} + xh_{\mathrm{fg}} \end{aligned} \tag{2.37c}$$

$$\begin{aligned} s &= (1-x)s_{\mathrm{f}} + xs_{\mathrm{g}} \\ &= s_{\mathrm{f}} + xs_{\mathrm{fg}} \end{aligned} \tag{2.37d}$$

For the case of water, Figure 2.6 illustrates the phase change from solid to liquid (melting): *a-b-c*; from solid to vapor (sublimation): *a′-b′-c′*; and from liquid to vapor (vaporization): *a″-b″-c″*. During any such phase change the temperature and pressure remain constant and thus are not independent properties. The *Clapeyron equation* allows the change in enthalpy during a phase change at fixed temperature to be evaluated from *p-v-T* data pertaining to the phase change. For vaporization, the Clapeyron equation reads

$$\left(\frac{dp}{dT}\right)_{sat} = \frac{h_{\mathrm{g}} - h_{\mathrm{f}}}{T\left(v_{\mathrm{g}} - v_{\mathrm{f}}\right)} \tag{2.38}$$

where $(dp/dT)_{sat}$ is the slope of the saturation pressure-temperature curve at the point determined by the temperature held constant during the phase change. Expressions similar in form to Equation 2.38 can be written for sublimation and melting.

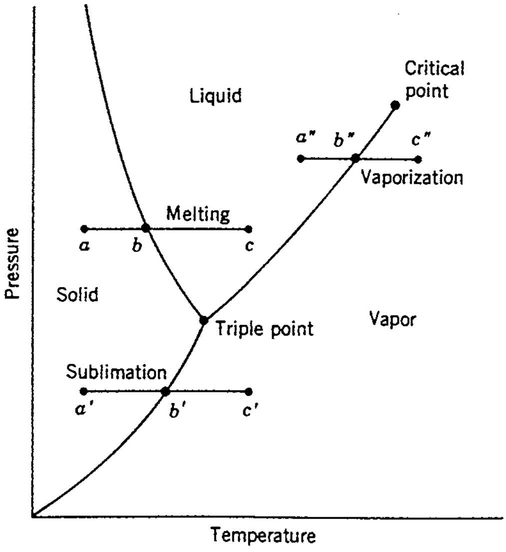

FIGURE 2.6 Phase diagram for water (not to scale).

The Clapeyron equation shows that the slope of a saturation line on a phase diagram depends on the signs of the specific volume and enthalpy changes accompanying the phase change. In most cases, when a phase change takes place with an increase in specific enthalpy, the specific volume also increases, and $(dp/dT)_{sat}$ is positive. However, in the case of the melting of ice and a few other substances, the specific volume decreases on melting. The slope of the saturated solid-liquid curve for these few substances is negative, as illustrated for water in Figure 2.6.

Graphical Representations

The intensive states of a pure, simple compressible system can be represented graphically with any two independent intensive properties as the coordinates, excluding properties associated with motion and gravity. While any such pair may be used, there are several selections that are conventionally employed. These include the p-T and p-v diagrams of Figure 2.5, the T-s diagram of Figure 2.7, the h-s (Mollier) diagram of Figure 2.8, and the p-h diagram of Figure 2.9. The compressibility charts considered next use the compressibility factor as one of the coordinates.

Compressibility Charts

The p-v-T relation for a wide range of common gases is illustrated by the generalized compressibility chart of Figure 2.10. In this chart, the compressibility factor, Z, is plotted vs. the *reduced* pressure, p_R, *reduced* temperature, T_R, and *pseudoreduced* specific volume, v_R', where

$$Z = \frac{p\bar{v}}{\bar{R}T} \tag{2.39}$$

and

$$p_R = \frac{p}{p_c}, \quad T_R = \frac{T}{T_c}, \quad v_R' = \frac{\bar{v}}{\left(\bar{R}T_c/p_c\right)} \tag{2.40}$$

In these expressions, $\bar{R}$ is the universal gas constant and p_c and T_c denote the critical pressure and temperature, respectively. Values of p_c and T_c are given for several substances in Table A.9. The reduced

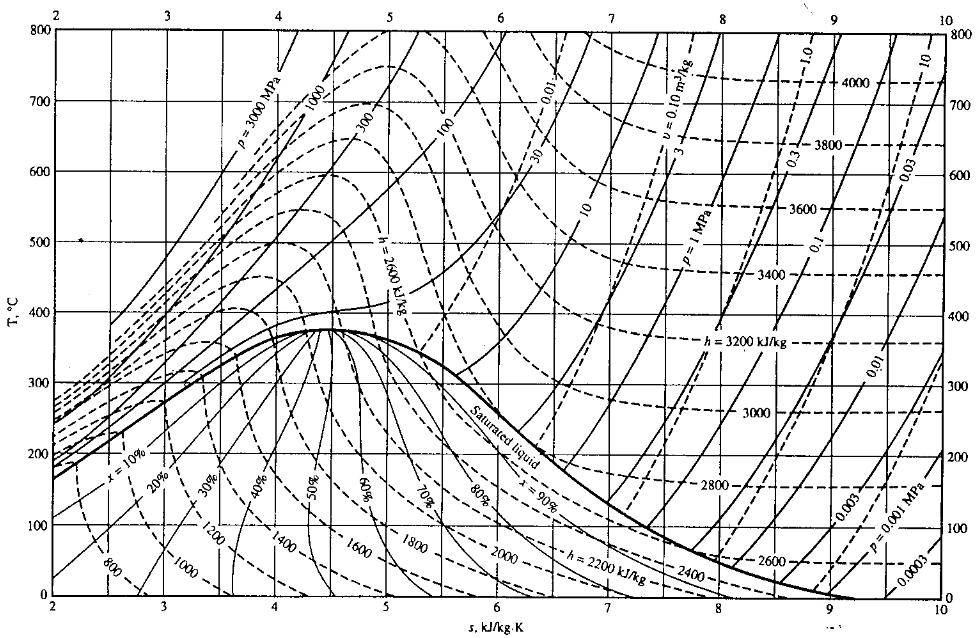

FIGURE 2.7 Temperature-entropy diagram for water. (*Source:* Jones, J.B. and Dugan, R.E. 1996. *Engineering Thermodynamics*, Prentice-Hall, Englewood Cliffs, NJ, based on data and formulations from Haar, L., Gallagher, J.S., and Kell, G.S. 1984. *NBS/NRC Steam Tables.* Hemisphere, Washington, D.C.)

isotherms of Figure 2.10 represent the best curves fitted to the data of several gases. For the 30 gases used in developing the chart, the deviation of observed values from those of the chart is at most on the order of 5% and for most ranges is much less.[1]

Figure 2.10 gives a common value of about 0.27 for the compressibility factor at the critical point. As the critical compressibility factor for different substances actually varies from 0.23 to 0.33, the chart is inaccurate in the vicinity of the critical point. This source of inaccuracy can be removed by restricting the correlation to substances having essentially the same Z_c values. which is equivalent to including the critical compressibility factor as an independent variable: $Z = f\,(T_R, p_R, Z_c)$. To achieve greater accuracy variables other than Z_c have been proposed as a third parameter — for example, the *acentric factor* (see, e.g., Reid and Sherwood, 1966).

Generalized compressibility data are also available in tabular form (see, e.g., Reid and Sherwood, 1966) and in equation form (see, e.g., Reynolds, 1979). The use of generalized data in any form (graphical, tabular, or equation) allows p, v, and T for gases to be evaluated simply and with reasonable accuracy. When accuracy is an essential consideration, generalized compressibility data should not be used as a substitute for p-v-T data for a given substance as provided by computer software, a table, or an equation of state.

Equations of State

Considering the isotherms of Figure 2.10, it is plausible that the variation of the compressibility factor might be expressed as an equation, at least for certain intervals of p and T. Two expressions can be written that enjoy a theoretical basis. One gives the compressibility factor as an infinite series expansion in pressure,

---

[1] To determine Z for hydrogen, helium, and neon above a T_R of 5, the reduced temperature and pressure should be calculated using $T_R = T/(T_c + 8)$ and $P_R = p/(p_c + 8)$, where temperatures are in K and pressures are in atm.

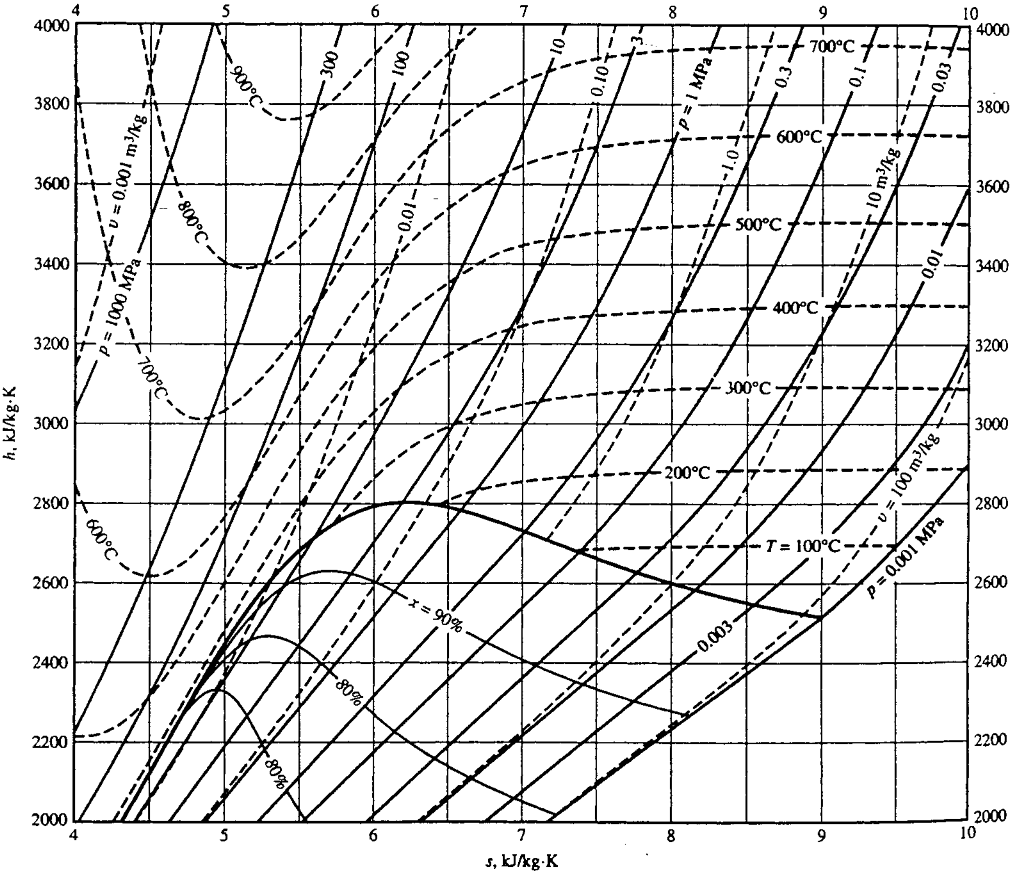

FIGURE 2.8 Enthalpy-entropy (Mollier) diagram for water. (*Source:* Jones, J.B. and Dugan, R.E. 1996. *Engineering Thermodynamics*. Prentice-Hall, Englewood Cliffs, NJ, based on data and formulations from Haar, L., Gallagher, J.S., and Kell, G.S. 1984. *NBS/NRC Steam Tables*. Hemisphere, Washington, D.C.)

$$Z = 1 + \hat{B}(T)p + \hat{C}(T)p^2 + \hat{D}(T)p^3 + \dots$$

and the other is a series in $1/\bar{v}$,

$$Z = 1 + \frac{B(T)}{\bar{v}} + \frac{C(T)}{\bar{v}^2} + \frac{D(T)}{\bar{v}^3} + \dots$$

These expressions are known as *virial expansions*, and the coefficients $\hat{B}$, $\hat{C}$ $\hat{D}$, … and B, C, D … are called *virial coefficients*. In principle, the virial coefficients can be calculated using expressions from statistical mechanics derived from consideration of the force fields around the molecules. Thus far only the first few coefficients have been calculated and only for gases consisting of relatively simple molecules. The coefficients also can be found, in principle, by fitting p-v-T data in particular realms of interest. Only the first few coefficients can be found accurately this way, however, and the result is a *truncated* equation valid only at certain states.

Over 100 equations of state have been developed in an attempt to portray accurately the p-v-T behavior of substances and yet avoid the complexities inherent in a full virial series. In general, these equations exhibit little in the way of fundamental physical significance and are mainly empirical in character. Most

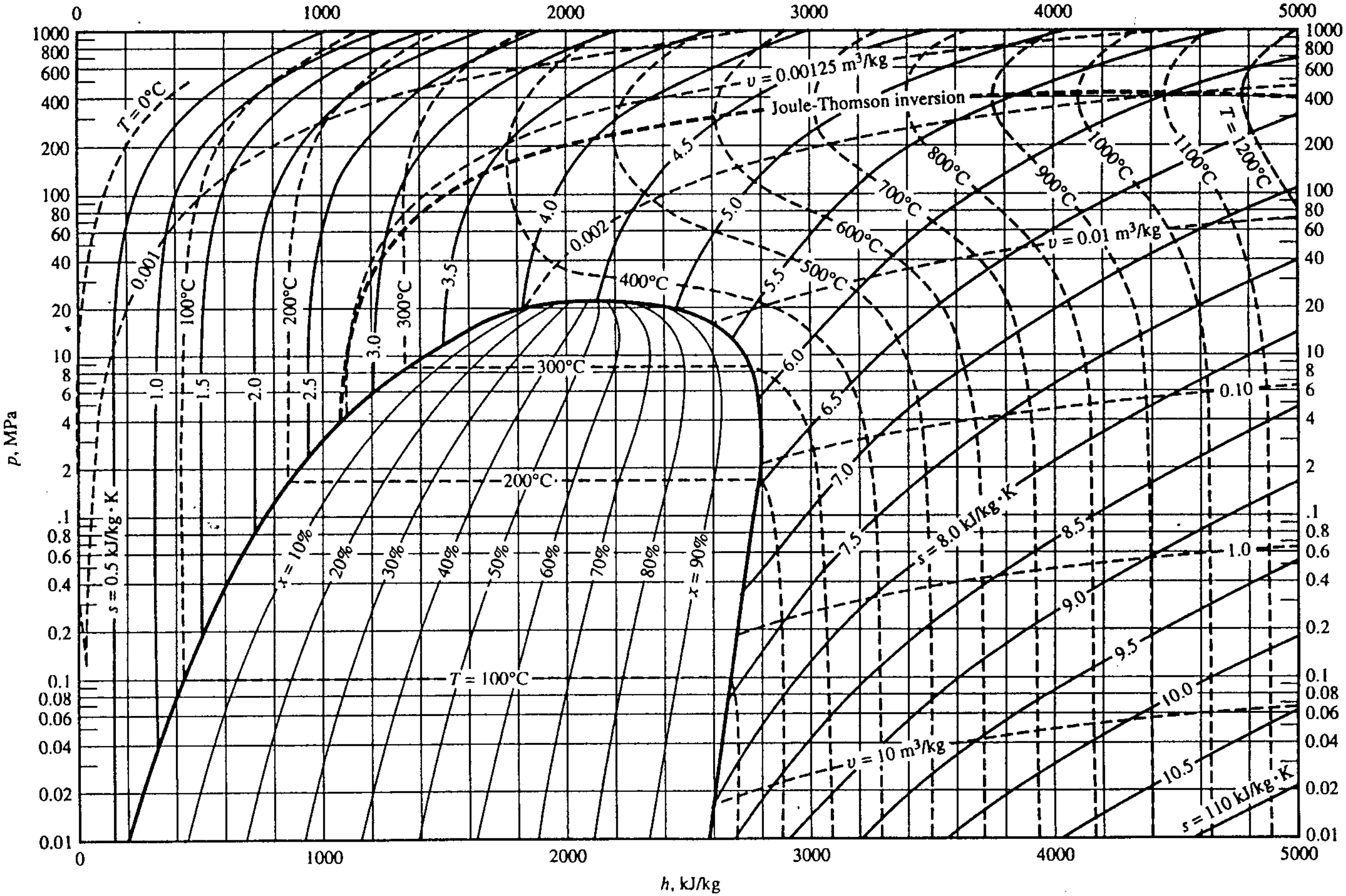

FIGURE 2.9 Pressure-enthalpy diagram for water. (*Source:* Jones, J.B. and Dugan, R.E. 1996. *Engineering Thermodynamics*. Prentice-Hall, Englewood Cliffs, NJ, based on data and formulations from Haar, L., Gallagher, J.S., and Kell, G.S. 1984. *NBS/NRC Steam Tables*. Hemisphere, Washington, D.C.)

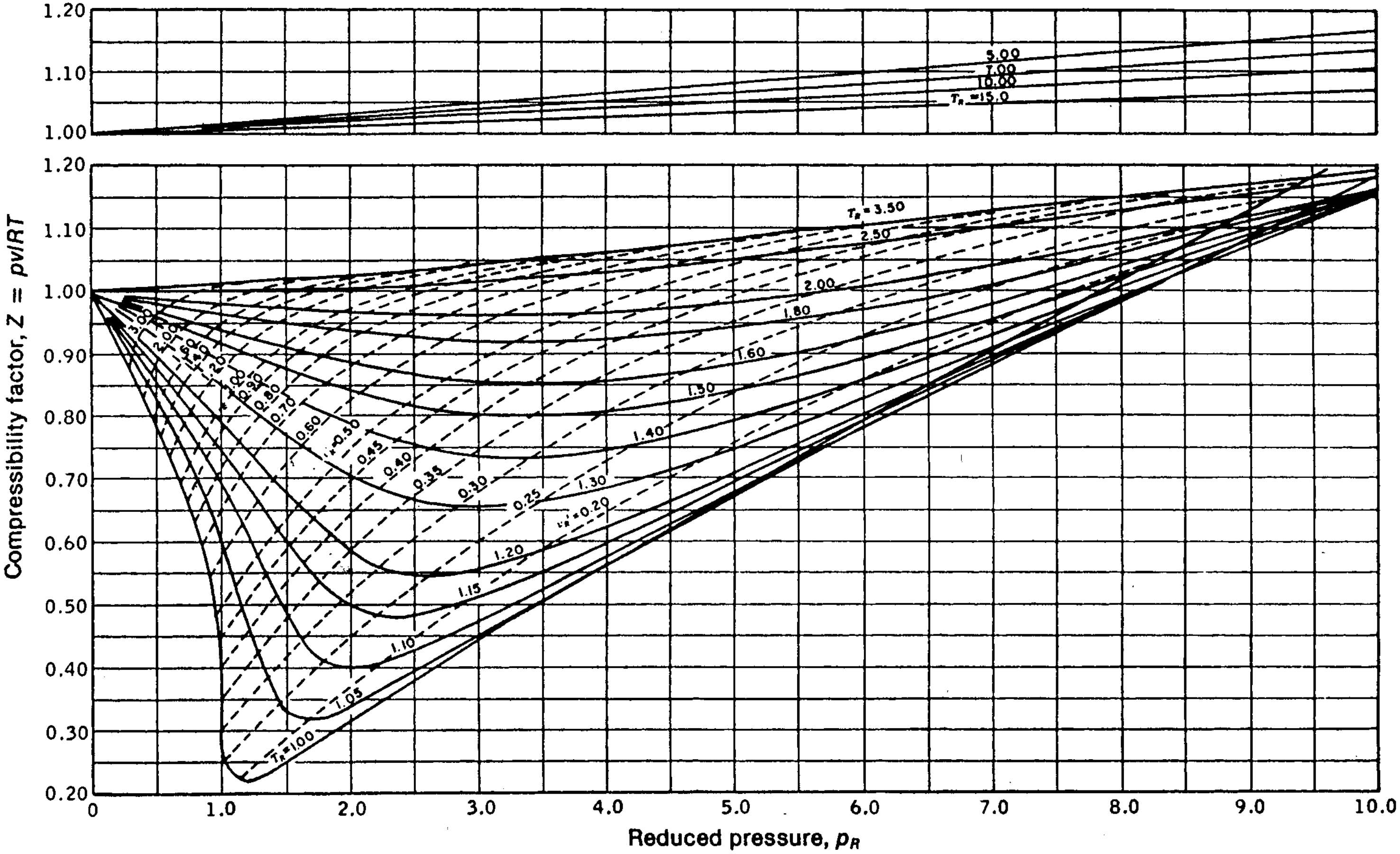

FIGURE 2.10 Generalized compressibility chart ($T_R = T/T_C$, $p_R = p/p_C$, $v_R' = \bar{v}p_C/RT_C$) for $p_R \leq 10$. (*Source:* Obert, E.F. 1960 *Concepts of Thermodynamics*. McGraw-Hill, New York.)

are developed for gases, but some describe the *p-v-T* behavior of the liquid phase, at least qualitatively. Every equation of state is restricted to particular states. The realm of applicability is often indicated by giving an interval of pressure, or density, where the equation can be expected to represent the *p-v-T* behavior faithfully. When it is not stated, the realm of applicability often may be approximated by expressing the equation in terms of the compressibility factor Z and the reduced properties, and superimposing the result on a generalized compressibility chart or comparing with compressibility data from the literature.

Equations of state can be classified by the number of adjustable constants they involve. The Redlich-Kwong equation is considered by many to be the best of the two-constant equations of state. It gives pressure as a function of temperature and specific volume and thus is *explicit* in pressure:

$$p = \frac{\bar{R}T}{\bar{v} - b} - \frac{a}{\bar{v}(\bar{v} + b)T^{1/2}} \tag{2.41}$$

This equation is primarily empirical in nature, with no rigorous justification in terms of molecular arguments. Values for the Redlich-Kwong constants for several substances are provided in Table A.9. Modified forms of the equation have been proposed with the aim of achieving better accuracy.

Although the two-constant Redlich-Kwong equation performs better than some equations of state having several adjustable constants, two-constant equations tend to be limited in accuracy as pressure (or density) increases. Increased accuracy normally requires a greater number of adjustable constants. For example, the Benedict-Webb-Rubin equation, which involves eight adjustable constants, has been successful in predicting the *p-v-T* behavior of *light hydrocarbons.* The Benedict-Webb-Rubin equation is also explicit in pressure,

$$p = \frac{\bar{R}T}{\bar{v}} + \left(B\bar{R}T - A - \frac{C}{T^2}\right)\frac{1}{\bar{v}^2} + \frac{\left(b\bar{R}T - a\right)}{\bar{v}^3} + \frac{a\alpha}{\bar{v}^6} + \frac{c}{\bar{v}^3T^2}\left(1 + \frac{\gamma}{\bar{v}^2}\right)\exp\left(-\frac{\gamma}{\bar{v}^2}\right) \tag{2.42}$$

Values of the Benedict-Webb-Rubin constants for various gases are provided in the literature (see, e.g., Cooper and Goldfrank, 1967). A modification of the Benedict-Webb-Rubin equation involving 12 constants is discussed by Lee and Kessler, 1975. Many multiconstant equations can be found in the engineering literature, and with the advent of high speed computers, equations having 50 or more constants have been developed for representing the *p-v-T* behavior of different substances.

Gas Mixtures

Since an unlimited variety of mixtures can be formed from a given set of pure components by varying the relative amounts present, the properties of mixtures are reported only in special cases such as air. Means are available for predicting the properties of mixtures, however. Most techniques for predicting mixture properties are empirical in character and are not derived from fundamental physical principles. The realm of validity of any particular technique can be established by comparing predicted property values with empirical data. In this section, methods for evaluating the *p-v-T* relations for pure components are adapted to obtain plausible estimates for gas mixtures. The case of ideal gas mixtures is discussed in Section 2.3, Ideal Gas Model. In Section 2.3, Multicomponent Systems, some general aspects of property evaluation for multicomponent systems are presented.

The total number of moles of mixture, n, *is* the sum of the number of moles of the components, n_i:

$$n = n_1 + n_2 + \ldots n_j = \sum_{i=1}^{j} n_i \tag{2.43}$$

The *relative* amounts of the components present can be described in terms of *mole fractions.* The mole fraction y_i of component i is $y_i = n_i/n$. The sum of the mole fractions of all components present is equal to unity. The apparent molecular weight $\mathcal{M}$ is the mole fraction average of the component molecular weights, such that

$$\mathcal{M} = \sum_{i=1}^{j} y_i \mathcal{M}_i \tag{2.44}$$

The *relative* amounts of the components present also can be described in terms of *mass fractions:* m_i/m, where m_i is the mass of component i and m is the total mass of mixture.

The p-v-T relation for a gas mixture can be estimated by applying an equation of state to the overall mixture. The constants appearing in the equation of state are *mixture values* determined with empirical combining rules developed for the equation. For example, mixture values of the constants a and b for use in the Redlich-Kwong equation are obtained using relations of the form

$$a = \left(\sum_{i=1}^{j} y_i a_i^{1/2} \right)^2, \quad b = \sum_{i=1}^{j} y_i b_i \tag{2.45}$$

where a_i and b_i are the values of the constants for component i. Combination rules for obtaining mixture values for the constants in other equations of state are also found in the literature.

Another approach is to regard the mixture as if it were a single pure component having critical properties calculated by one of several mixture rules. *Kay's rule is* perhaps the simplest of these, requiring only the determination of a mole fraction averaged critical temperature T_c and critical pressure p_c:

$$T_c = \sum_{i=1}^{j} y_i T_{c,i}, \quad p_c = \sum_{i=1}^{j} y_i p_{c,i} \tag{2.46}$$

where $T_{c,i}$ and $p_{c,i}$ are the critical temperature and critical pressure of component i, respectively. Using T_c and p_c, the mixture compressibility factor Z is obtained as for a single pure component. The unkown quantity from among the pressure p, volume V, temperature T, and total number of moles n of the gas mixture can then be obtained by solving $Z = pV/n\bar{R}T$.

Additional means for predicting the p-v-T relation of a mixture are provided by empirical mixture rules. Several are found in the engineering literature. According to the *additive pressure rule*, the pressure of a gas mixture is expressible as a sum of pressures exerted by the individual components:

$$p = p_1 + p_2 + p_3 \ldots \Big]_{T,V} \tag{2.47a}$$

where the pressures p_1, p_2, etc. are evaluated by considering the respective components to be at the volume V and temperature T of the mixture. The additive pressure rule can be expressed alternatively as

$$Z = \sum_{i=1}^{j} y_i Z_i \Bigg]_{T,V} \tag{2.47b}$$

where Z is the compressibility factor of the mixture and the compressibility factors Z_i are determined assuming that component i occupies the entire volume of the mixture at the temperature T.

The *additive volume rule* postulates that the volume V of a gas mixture is expressible as the sum of volumes occupied by the individual components:

$$V = V_1 + V_2 + V_3 \ldots \Big]_{p,T} \tag{2.48a}$$

where the volumes V_1, V_2, etc. are evaluated by considering the respective components to be at the pressure p and temperature T of the mixture. The additive volume rule can be expressed alternatively as

$$Z = \left.\sum_{i=1}^{j} y_i Z_i \right]_{p,T} \tag{2.48b}$$

where the compressibility factors Z_i are determined assuming that component i exists at the pressure p and temperature T of the mixture.

Evaluating Δh, Δu, and Δs

Using appropriate specific heat and p-v-T data, the changes in specific enthalpy, internal energy, and entropy can be determined between states of single-phase regions. Table 2.5 provides expressions for such property changes in terms of particular choices of the independent variables: temperature and pressure, and temperature and specific volume.

Taking Equation 1 of Table 2.5 as a representative case, the change in specific enthalpy between states 1 and 2 can be determined using the three steps shown in the accompanying property diagram. This requires knowledge of the variation of c_p with temperature at a fixed pressure p', and the variation of $[v - T(\partial v/\partial T)_p]$ with pressure at temperatures T_1 and T_2:

1-a: Since temperature is constant at T_1, the first integral of Equation 1 in Table 2.5 vanishes, and

$$h_a - h_1 = \int_{p_1}^{p'} \left[v - T\left(\partial v/\partial T\right)_p \right] dp$$

a-b: Since pressure is constant at p', the second integral of Equation 1 vanishes, and

$$h_b - h_a = \int_{T_1}^{T_2} c_p\left(T, p'\right) dT$$

b-2: Since temperature is constant at T_2, the first integral of Equation 1 vanishes, and

$$h_2 - h_b = \int_{p'}^{p_2} \left[v - T\left(\partial v/\partial T\right)_p \right] dp$$

Adding these expressions, the result is $h_2 - h_1$. The required integrals may be performed numerically or analytically. The analytical approach is expedited when an equation of state explicit in specific volume is known.

Similar considerations apply to Equation 2 to Equation 4 of Table 2.5. To evaluate $u_2 - u_1$ with Equation 3, for example, requires the variation of c_v with temperature at a fixed specific volume v', and the variation of $[T(\partial p/\partial T)_v - p]$ with specific volume at temperatures T_1 and T_2. An analytical approach to performing the integrals is expedited when an equation of state explicit in pressure is known.

As changes in specific enthalpy and internal energy are related through $h = u + pv$ by

$$h_2 - h_1 = \left(u_2 - u_1\right) + \left(p_2 v_2 - p_1 v_1\right) \tag{2.49}$$

only one of $h_2 - h_1$ and $u_2 - u_1$ need be found by integration. The other can be evaluated from Equation 2.49. The one found by integration depends on the information available: $h_2 - h_1$ would be found when an equation of state explicit in v and c_p as a function of temperature at some fixed pressure is known, $u_2 - u_1$ would be found when an equation of state explicit in p and c_v as a function of temperature at some specific volume is known.

TABLE 2.5 Δh, Δu, Δs Expressions

Independent properties:	temperature and pressure	temperature and specific volume
Preferred data:	$v(T, p)$, $c_p(T, p)$	$p(T, v)$, $c_v(T, v)$
Property diagram:	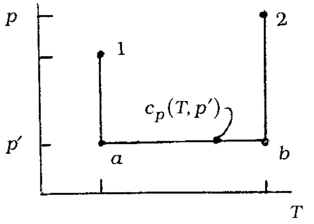	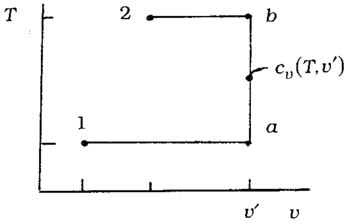
Property expressions:	$h(T, p)$: $dh = \underbrace{\left(\frac{\partial h}{\partial T}\right)_p}_{c_p} dT + \underbrace{\left(\frac{\partial h}{\partial p}\right)_T}_{\left[v - T\left(\frac{\partial v}{\partial T}\right)_p\right]} dp$ (1′) $\Delta h = \int c_p dT + \int \left[v - T\left(\frac{\partial v}{\partial T}\right)_p\right] dp$ (1) $s(T, p)$: $ds = \underbrace{\left(\frac{\partial s}{\partial T}\right)_p}_{\frac{c_p}{T}} dT + \underbrace{\left(\frac{\partial s}{\partial p}\right)_T}_{-\left(\frac{\partial v}{\partial T}\right)_p} dp$ (2′) $\Delta s = \int \frac{c_p}{T} dT - \int \left(\frac{\partial v}{\partial T}\right)_p dp$ (2)	$u(T, v)$: $du = \underbrace{\left(\frac{\partial u}{\partial T}\right)_v}_{c_v} dT + \underbrace{\left(\frac{\partial u}{\partial v}\right)_T}_{\left[T\left(\frac{\partial p}{\partial T}\right)_v - p\right]} dv$ (3′) $\Delta u = \int c_v dT + \int \left[T\left(\frac{\partial p}{\partial T}\right)_v - p\right] dv$ (3) $s(T, v)$: $ds = \underbrace{\left(\frac{\partial s}{\partial T}\right)_v}_{\frac{c_v}{T}} dT + \underbrace{\left(\frac{\partial s}{\partial v}\right)_T}_{\left(\frac{\partial p}{\partial T}\right)_v} dv$ (4′) $\Delta s = \int \frac{c_v}{T} dT + \int \left(\frac{\partial p}{\partial T}\right)_v dv$ (4)

Example 6

Obtain Equation 1 of Table 2.4 and Equation 3 and Equation 4 of Table 2.5.

Solution. With Equation 2.33 and the Maxwell relation corresponding to ψ(T, v) from Table 2.2, Equation 3′ and Equation 4′ of Table 2.5 become, respectively,

$$du = c_v dT + \left(\frac{\partial u}{\partial v}\right)_T dv$$

$$ds = \left(\frac{\partial s}{\partial T}\right)_v dT + \left(\frac{\partial p}{\partial T}\right)_v dv$$

Introducing these expressions for *du* and *ds* in Equation 2.32a, and collecting terms,

$$\left[T\left(\frac{\partial s}{\partial T}\right)_v - c_v\right]dT = \left[\left(\frac{\partial u}{\partial v}\right)_T + p - T\left(\frac{\partial p}{\partial T}\right)_v\right]dv$$

Since *T* and *v* are independent, the coefficients of *dT* and *dv* must vanish, giving, respectively,

$$\left(\frac{\partial s}{\partial T}\right)_v = \frac{c_v}{T}$$

$$\left(\frac{\partial u}{\partial v}\right)_T = T\left(\frac{\partial p}{\partial T}\right)_v - p$$

The first of these corresponds to Equation 1 of Table 2.4 and Equation 4 of Table 2.5. The second of the above expressions establishes Equation 3 of Table 2.5. With similar considerations, Equation 3 of Table 2.4 and Equation 1 and Equation 2 of Table 2.5 may be obtained.

Fundamental Thermodynamic Functions

A fundamental thermodynamic function is one that provides a complete description of the thermodynamic state. The functions $u(s, v)$, $h(s, p)$, $\psi(T, v)$, and $g(T, p)$ listed in Table 2.2 are fundamental thermodynamic functions.

In principle, all properties of interest can be determined from a fundamental thermodynamic function by differentiation and combination. Taking the function $\psi(T, v)$ as a representative case, the properties *v* and *T*, being the independent variables, are specified to fix the state. The pressure *p* and specific entropy *s* at this state can be determined by differentiation of $\psi(T, v)$, as shown in Table 2.2. By definition, $\psi = u - Ts$, so specific internal energy is obtained as

$$u = \psi + Ts$$

with *u*, *p*, and *v* known, the specific enthalpy can be found from the definition $h = u + pv$. Similarly, the specific Gibbs function is found from the definition $g = h - Ts$. The specific heat c_v can be determined by further differentiation $c_v = (\partial u/\partial T)_v$.

The development of a fundamental function requires the selection of a functional form in terms of the appropriate pair of independent properties and a set of adjustable coefficients that may number 50 or more. The functional form is specified on the basis of both theoretical and practical considerations. The coefficients of the fundamental function are determined by requiring that a set of selected property values and/or observed conditions be statisfied in a least-squares sense. This generally involves property data requiring the assumed functional form to be differentiated one or more times, for example *p-v-T* and specific heat data. When all coefficients have been evaluated, the function is tested for accuracy by using it to evaluate properties for which accepted values are known such as *velocity of sound* and *Joule-Thomson* data. Once a suitable fundamental function is established, extreme accuracy in and consistency among the thermodynamic properties are possible. The properties of water tabulated by Keenan et al. (1969) and by Haar et al. (1984) have been calculated from representations of the Helmholtz function.

Thermodynamic Data Retrieval

Tabular presentations of pressure, specific volume, and temperature are available for practically important gases and liquids. The tables normally include other properties useful for thermodynamic analyses, such as internal energy, enthalpy, and entropy. The various *steam tables* included in the references of this chapter provide examples. Computer software for retrieving the properties of a wide range of substances is also available, as, for example, the ASME Steam Tables (1993) and Bornakke and Sonntag (1996). Increasingly, textbooks come with computer disks providing thermodynamic property data for water, certain refrigerants, and several gases modeled as ideal gases — see, e.g., Moran and Shapiro (1996).

The sample *steam table* data presented in Table 2.6 are representative of data available for substances commonly encountered in mechanical engineering practice. Table A.5 and Figure 2.7 to Figure 2.9 provide *steam table* data for a greater range of states. The form of the tables and figures, and how they are used are assumed to be familiar. In particular, the use of *linear interpolation* with such tables is assumed known.

Specific internal energy, enthalpy, and entropy data are determined relative to arbitrary datums and such datums vary from substance to substance. Referring to Table 2.6a, the datum state for the specific internal energy and specific entropy of water is seen to correspond to saturated liquid water at 0.01°C (32.02°F), the triple point temperature. The value of each of these properties is set to zero at this state. If calculations are performed involving only differences in a particular specific property, the datum cancels. When there are changes in chemical composition during the process, special care should be exercised. The approach followed when composition changes due to chemical reaction is considered in Section 2.4.

Liquid water data (see Table 2.6d) suggests that at fixed temperature the variation of specific volume, internal energy, and entropy with pressure is slight. The variation of specific enthalpy with pressure at fixed temperature is somewhat greater because pressure is explicit in the definition of enthalpy. This behavior for v, u, s, and h is exhibited generally by liquid data and provides the basis for the following set of equations for estimating property data at liquid states from saturated liquid data:

$$v(T,p) \approx v_\mathrm{f}(T) \tag{2.50a}$$

$$u(T,p) \approx u_\mathrm{f}(T) \tag{2.50b}$$

$$h(T,p) \approx h_f(T) + \underline{v_\mathrm{f}\left[p - p_{sat}(T)\right]} \tag{2.50c}$$

$$s(T,p) \approx s_\mathrm{f}(T) \tag{2.50d}$$

As before, the subscript f denotes the saturated liquid state at the temperature T, and p_{sat} *is* the corresponding saturation pressure. The underlined term of Equation 2.50c is often negligible, giving $h(T, p) \approx h_\mathrm{f}(\mathrm{T})$, which is used in Example 3 to evaluate h_1.

In the absence of saturated liquid data, or as an alternative to such data, the *incompressible model* can be employed:

$$\text{Incompressible model: } \begin{cases} v = \text{constant} \\ u = u(T) \end{cases} \tag{2.51}$$

TABLE 2.6 Sample Steam Table Data

(a) Properties of Saturated Water (Liquid-Vapor): Temperature Table

		Specific Volume (m^3/kg)		Internal Energy (kJ/kg)		Enthalpy (kJ/kg)			Entropy (kJ/kg · K)	
Temp (°C)	Pressure (bar)	Saturated Liquid ($v_f \times 10^3$)	Saturated Vapor (v_g)	Saturated Liquid (u_f)	Saturated Vapor (u_g)	Saturated Liquid (h_f)	Evap. (h_{fg})	Saturated Vapor (h_g)	Saturated Liquid (s_f)	Saturated Vapor (s_g)
.01	0.00611	1.0002	206.136	0.00	2375.3	0.01	2501.3	2501.4	0.0000	9.1562
4	0.00813	1.0001	157.232	16.77	2380.9	16.78	2491.9	2508.7	0.0610	9.0514
5	0.00872	1.0001	147.120	20.97	2382.3	20.98	2489.6	2510.6	0.0761	9.0257
6	0.00935	1.0001	137.734	25.19	2383.6	25.20	2487.2	2512.4	0.0912	9.0003
8	0.01072	1.0002	120.917	33.59	2386.4	33.60	2482.5	2516.1	0.1212	8.9501

(b) Properties of Saturated Water (Liquid-Vapor): Pressure Table

		Specific Volume (m^3/kg)		Internal Energy (kJ/kg)		Enthalpy (kJ/kg)			Entropy (kJ/kg · K)	
Pressure (bar)	Temp (°C)	Saturated Liquid ($v_f \times 10^3$)	Saturated Vapor (v_g)	Saturated Liquid (u_f)	Saturated Vapor (u_g)	Saturated Liquid (h_f)	Evap. (h_{fg})	Saturated Vapor (h_g)	Saturated Liquid (s_f)	Saturated Vapor (s_g)
0.04	28.96	1.0040	34.800	121.45	2415.2	121.46	2432.9	2554.4	0.4226	8.4746
0.06	36.16	1.0064	23.739	151.53	2425.0	151.53	2415.9	2567.4	0.5210	8.3304
0.08	41.51	1.0084	18.103	173.87	2432.2	173.88	2403.1	2577.0	0.5926	8.2287
0.10	45.81	1.0102	14.674	191.82	2437.9	191.83	2392.8	2584.7	0.6493	8.1502
0.20	60.06	1.0172	7.649	251.38	2456.7	251.40	2358.3	2609.7	0.8320	7.9085

TABLE 2.6 (continued) Sample Steam Table Data

(c) Properties of Superheated Water Vapor

T(°C)	v(m^3/kg)	u(kJ/kg)	h(kJ/kg)	s(kJ/kg · K)	v(m^3/kg)	u(kJ/kg)	h(kJ/kg)	s(kJ/kg · K)
	p = 0.06 bar = 0.006 MPa (T_{sat} 36.16°C)				**p = 0.35 bar = 0.035 MPa (T_{sat} = 72.69°C)**			
Sat.	23.739	2425.0	2567.4	8.3304	4.526	2473.0	2631.4	7.7158
80	27.132	2487.3	2650.1	8.5804	4.625	2483.7	2645.6	7.7564
120	30.219	2544.7	2726.0	8.7840	5.163	2542.4	2723.1	7.9644
160	33.302	2602.7	2802.5	8.9693	5.696	2601.2	2800.6	8.1519
200	36.383	2661.4	2879.7	9.1398	6.228	2660.4	2878.4	8.3237

(d) Properties of Compressed Liquid Water

T(°C)	$v \times 10^3$ (m^3/kg)	u(kJ/kg)	h(kJ/kg)	s(kJ/kg · K)	$v \times 10^3$ (m^3/kg)	u(kJ/kg)	h(kJ/kg)	s(kJ/kg · K)
	p = 25 bar = 2.5 MPa (T_{sat} 223.99°C)				**p = 50 bar = 5.0 MPa (T_{sat} = 263.99°C)**			
20	1.0006	83.80	86.30	0.2961	0.9995	83.65	88.65	0.2956
80	1.0280	334.29	336.86	1.0737	1.0268	333.72	338.85	1.0720
140	1.0784	587.82	590.52	1.7369	1.0768	586.76	592.15	1.7343
200	1.1555	849.9	852.8	2.3294	1.1530	848.1	853.9	2.3255
Sat.	1.1973	959.1	962.1	2.5546	1.2859	1147.8	1154.2	2.9202

Source: Moran, M.J. and Shapiro, H.N. 1995. *Fundamentals of Engineering Thermodynamics*, 3rd ed. Wiley, New York, as extracted from Keenan, J. H., Keyes, F.G., Hill, P.G., and Moore, J.G. 1969. *Steam Tables*. Wiley, New York.

This model is also applicable to solids. Since internal energy varies only with temperature, the specific heat c_v is also a function of only temperature: $c_v(T) = du/dT$. Although specific volume is constant, enthalpy varies with both temperature and pressure, such that

$$h(T,p) = u(T) + pv \tag{2.52}$$

Differentiation of Equation 2.52 with respect to temperature at fixed pressure gives $c_p = c_v$. The common specific heat is often shown simply as c. Specific heat and density data for several liquids and solids are provided in Table B.2, Table C.1, and Table C.2. As the variation of c with temperature is slight, c is frequently taken as constant.

When the incompressible model is applied. Equation 2.49 takes the form

$$\begin{aligned} h_2 - h_1 &= \int_{T_1}^{T_2} c(T)dT + v(p_2 - p_1) \\ &= c_{ave}(T_2 - T_1) + v(p_2 - p_1) \end{aligned} \tag{2.53}$$

Also, as Equation 2.32a reduces to $du = Tds$, and $du = c(T)dT$, the change in specific entropy is

$$\begin{aligned} \Delta s &= \int_{T_1}^{T_2} \frac{c(T)}{T} dT \\ &= c_{ave} \ln \frac{T_2}{T_1} \end{aligned} \tag{2.54}$$

Ideal Gas Model

Inspection of the generalized compressibility chart, Figure 2.10, shows that when p_R is small, and for many states when T_R is large, the value of the compressibility factor Z is close to 1. In other words, for pressures that are low relative to p_c, and for many states with temperatures high relative to T_c, the compressibility factor approaches a value of 1. Within the indicated limits, it may be assumed with reasonable accuracy that $Z = 1$ — that is,

$$p\bar{v} = \bar{R}T \quad \text{or} \quad pv = RT \tag{2.55a}$$

where $R = \bar{R}/\mathcal{M}$ is the *specific* gas constant. Other forms of this expression in common use are

$$pV = n\bar{R}T, \qquad pV = mRT \tag{2.55b}$$

Referring to Equation 3′ of Table 2.5, it can be concluded that $(\partial u/\partial v)_T$ vanishes identically for a gas whose equation of state is *exactly* given by Equation 2.55, and thus the specific internal energy depends only on temperature. This conclusion is supported by experimental observations beginning with the work of Joule, who showed that the internal energy of air at low density depends primarily on temperature.

These considerations allow for an *ideal gas model* of each real gas: (1) the equation of state is given by Equation 2.55 and (2) the internal energy and enthalpy are functions of temperature alone. The real gas approaches the model in the limit of low reduced pressure. At other states the actual behavior may depart substantially from the predictions of the model. Accordingly, caution should be exercised when invoking the ideal gas model lest significant error is introduced.

Specific heat data for gases can be obtained by direct measurement. When extrapolated to zero pressure, ideal gas-specific heats result. Ideal gas-specific heats also can be calculated using molecular models of

TABLE 2.7 Ideal Gas Expressions for Δh, Δu, and Δs

Variable Specific Heats		Constant Specific Heats	
$h(T_2) - h(T_1) = \int_{T_1}^{T_2} c_p(T)dT$	(1)	$h(T_2) - h(T_1) = c_p(T_2 - T_1)$	(1′)
$s(T_2, p_2) - s(T_1, p_1) = \int_{T_1}^{T_2} \frac{c_p(T)}{T} dT - R\ln\frac{p_2}{p_1}$	(2)	$s(T_2, p_2) - s(T_1, p_1) = c_p \ln\frac{T_2}{T_1} - R\ln\frac{p_2}{p_1}$	(2′)
$u(T_2) - u(T_1) = \int_{T_1}^{T_2} c_v(T)dT$	(3)	$u(T_2) - u(T_1) = c_v(T_2 - T_1)$	(3′)
$s(T_2, v_2) - s(T_1, v_1) = \int_{T_1}^{T_2} \frac{c_v(T)}{T} dT + R\ln\frac{v_2}{v_1}$	(4)	$s(T_2, v_2) - s(T_1, v_1) = c_v \ln\frac{T_2}{T_1} + R\ln\frac{v_2}{v_1}$	(4′)
$s_2 = s_1$		$s_2 = s_1$	
$\frac{p_r(T_2)}{p_r(T_1)} = \frac{p_2}{p_1}$	(5)	$\frac{T_2}{T_1} = \left(\frac{p_2}{p_1}\right)^{(k-1)/k}$	(5′)
$\frac{v_r(T_2)}{v_r(T_1)} = \frac{v_2}{v_1}$	(6)	$\frac{T_2}{T_1} = \left(\frac{v_1}{v_2}\right)^{k-1}$	(6′)

matter together with data from spectroscopic measurements. Table A.9 provides ideal gas-specific heat data for a number of substances. The following ideal gas-specific heat relations are frequently useful:

$$c_p(T) = c_v(T) + R \tag{2.56a}$$

$$c_p = \frac{kR}{k-1}, \quad c_v = \frac{R}{k-1} \tag{2.56b}$$

where $k = c_p/c_v$.

With the ideal gas model, Equation 1 to Equation 4 of Table 2.5 give Equation 1 to Equation 4 of Table 2.7, respectively. Equation 2 of Table 2.7 can be expressed alternatively using $s°(T)$ defined by

$$s°(T) \equiv \int_0^T \frac{c_p(T)}{T} dT \tag{2.57}$$

as

$$s(T_2, p_2) - s(T_1, p_1) = s°(T_2) - s°(T_1) - R\ln\frac{p_2}{p_1} \tag{2.58}$$

Expressions similar in form to Equation 2.56 to Equation 2.68 can be written on a molar basis.

For processes of an ideal gas between states having the same specific entropy, $s_2 = s_1$, Equation 2.58 gives

$$\frac{p_2}{p_1} = \frac{\exp\left[s°(T_2)/R\right]}{\exp\left[s°(T_1)/R\right]}$$

or with $p_r = \exp[s°(T)/R]$

$$\frac{p_2}{p_1} = \frac{p_r(T_2)}{p_r(T_1)} \qquad (s_2 = s_1) \tag{2.59a}$$

A relation between the specific volume and temperatures for two states of an ideal gas having the same specific entropy can also be developed:

$$\frac{v_2}{v_1} = \frac{v_r(T_2)}{v_r(T_1)} \qquad (s_2 = s_1) \tag{2.59b}$$

Equations 2.59 are listed in Table 2.7 as Equation 5 and Equation 6, respectively.

Table A.8 provides a tabular display of h, u, $s°$, p_r, and v_r vs. temperature for air as an ideal gas. Tabulations of $\bar{h}$, $\bar{u}$, and $\bar{s}°$ for several other common gases are provided in Table A.2. Property retrieval software also provides such data; see, e.g., Moran and Shapiro (1996). The use of data from Table A.8 for the nozzle of Example 2 is illustrated in Example 7.

When the ideal gas-specific heats are assumed constant, Equation 1 to Equation 6 of Table 2.7 become Equation 1′ to Equation 6′, respectively. The specific heat c_p is taken as constant in Example 2.

Example 7

Using data from Table A.8, evaluate the exit velocity for the nozzle of Example 2 and compare with the exit velocity for an isentropic expansion to 15 lbf/in.^{2}.

Solution. The exit velocity is given by Equation 2.27f

$$\mathrm{v}_e = \sqrt{\mathrm{v}_i^2 + 2(h_i - h_e)}$$

At 960 and 520°R, Table A.8 gives, respectively, h_i = 231.06 Btu/lb and h_e = 124.27 Btu/lb. Then

$$\mathrm{v}_e = \sqrt{\left(\frac{10\ \text{ft}}{s}\right)^2 + 2(231.06 - 124.27)\left(\frac{\text{Btu}}{\text{lb}}\right)\left(\frac{778.17\ \text{ft}\cdot\text{lbf}}{1\ \text{Btu}}\right)\left(\frac{32.174\ \text{lb}\cdot\text{ft/sec}^2}{1\ \text{lbf}}\right)}$$
$$= 2312.5\ \text{ft sec}$$

Using Equation 2.59a and p_r data from Table A.8, the specific enthalpy at the exit for an isentropic expansion is found as follows:

$$p_r(T_e) = p_r(T_i)\frac{p_e}{p_i} = 10.61\left(\frac{15}{150}\right) = 1.061$$

Interpolating with p_r data, h_e = 119.54 Btu/lb. With this, the exit velocity is 2363.1 ft/sec. The actual exit velocity is about 2% less than the velocity for an isentropic expansion, the maximum theoretical value. In this particular application, there is good agreement in each case between velocities calculated using Table A.8 data and, as in Example 2, assuming c_p constant. Such agreement cannot be expected generally, however. See, for example, the Brayton cycle data of Table 2.15.

Polytropic Processes

An internally reversible process described by the expression pv^n = constant is called a *polytropic process* and n *is* the *polytropic exponent.* Although this expression can be applied with real gas data, it most generally appears in practice together with the use of the ideal gas model. Table 2.8 provides several expressions applicable to polytropic processes and the special forms they take when the ideal gas model is assumed. The expressions for $\int p dv$ and $\int v dp$ have application to work evaluations with Equation 2.10 and Equation 2.30, respectively. In some applications it may be appropriate to determine n by fitting pressure-specific volume data.

Example 8 illustrates both the polytropic process and the reduction in the compressor work achievable by cooling a gas as it is compressed.

TABLE 2.8 Polytropic Processes: pv^n = Constant[a]

General		Ideal Gas[b]	
$\frac{p_2}{p_1}=\left(\frac{v_1}{v_2}\right)^n$	(1)	$\frac{p_2}{p_1}=\left(\frac{v_1}{v_2}\right)^n=\left(\frac{T_2}{T_1}\right)^{n/(n-1)}$	(1′)
$n = 0$: constant pressure $n = \pm\infty$: constant specific volume		$n = 0$: constant pressure $n = \pm\infty$: constant specific volume $n = 1$: constant temperature $n = k$: constant specific entropy when k is constant	
$n = 1$		$n = 1$	
$\int_1^2 p\,dv = p_1v_1\ln\frac{v_2}{v_1}$	(2)	$\int_1^2 p\,dv = RT\ln\frac{v_2}{v_1}$	(2′)
$-\int_1^2 v\,dp = -p_1v_1\ln\frac{p_2}{p_1}$	(3)	$-\int_1^2 v\,dp = -RT\ln\frac{p_2}{p_1}$	(3′)
$n \neq 1$		$n \neq 1$	
$\int_1^2 p\,dv = \frac{p_2v_2-p_1v_1}{1-n}$ $=\frac{p_1v_1}{n-1}\left[1-\left(\frac{p_2}{p_1}\right)^{(n-1)/n}\right]$	(4)	$\int_1^2 p\,dv = \frac{R(T_2-T_1)}{1-n}$ $=\frac{RT_1}{n-1}\left[1-\left(\frac{p_2}{p_1}\right)^{(n-1)/n}\right]$	(4′)
$-\int_1^2 v\,dp = \frac{n}{1-n}(p_2v_2-p_1v_1)$ $=\frac{np_1v_1}{n-1}\left[1-\left(\frac{p_2}{p_1}\right)^{(n-1)/n}\right]$	(5)	$-\int_1^2 v\,dp = \frac{nR}{1-n}(T_2-T_1)$ $=\frac{nRT_1}{n-1}\left[1-\left(\frac{p_2}{p_1}\right)^{(n-1)/n}\right]$	(5′)

---

[a] For polytropic processes of closed systems where volume change is the only work mode, Equation 2, Equation 4, and Equation 2′, Equation 4′ are applicable with Equation 2.10 to evaluate the work. When each unit of mass passing through a one-inlet, one-exit control volume at steady state undergoes a polytropic process, Equation 3, Equation 5, and Equation 3′, Equation 5′ are applicable with Equation 2.30a and Equation 2.30b to evaluate the power. Also note that generally, $-\int_1^2 v\,dp = n\int_1^2 p\,dv$.

[b]

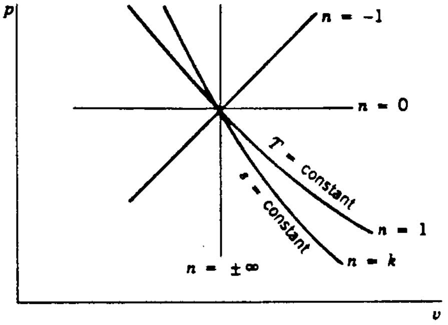

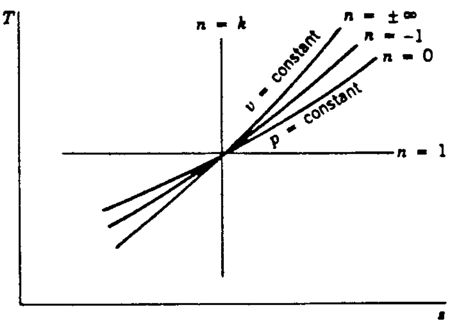

Example 8

A compressor operates at steady state with air entering at 1 bar, 20°C and exiting at 5 bar. (a) If the air undergoes a polytropic process with $n = 1.3$, determine the work and heat transfer, each in kJ/kg of air flowing. Repeat for (b) an isothermal compression and (c) an isentropic compression.

Solution. Using Equation 5′ of Table 2.8 together with Equation 2.30b,

$$\frac{\dot{W}_{cv}}{\dot{m}} = \frac{nRT_1}{n-1}\left[1 - \left(\frac{p_2}{p_1}\right)^{(n-1)/n}\right]$$

$$= \left(\frac{1.3}{0.3}\right)\left(\frac{8.314}{28.97}\frac{\text{kJ}}{\text{kg}\cdot\text{K}}\right)(293\ \text{K})\left[1-(5)^{0.3/1.3}\right]$$

$$= -163.9\ \frac{\text{kJ}}{\text{kg}}$$

(The area behind process 1-2 of Figure 2.11, area 1-2-a-b, represents the magnitude of the work required, per unit mass of air flowing.) Also, Equation 1′ of Table 2.8 gives T_2 = 425 K.

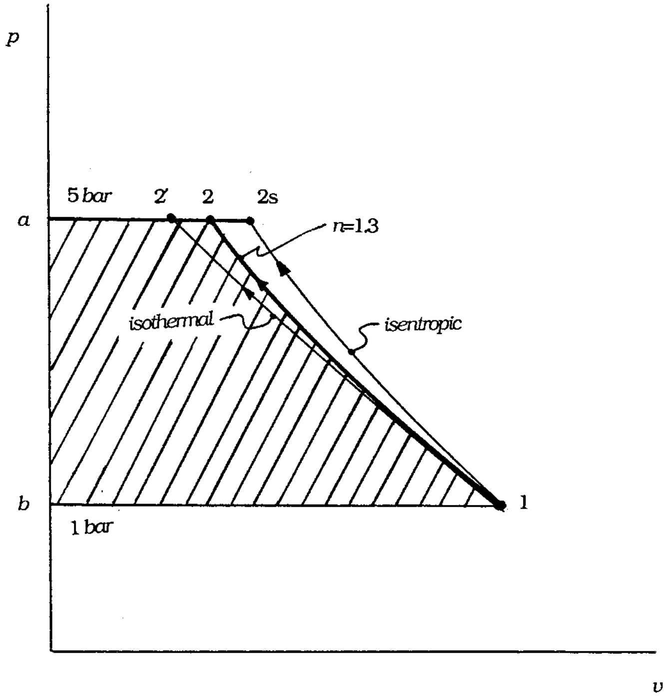

FIGURE 2.11 Internally reversible compression processes.

An energy rate balance at steady state and enthalpy data from Table A.8 gives

$$\frac{\dot{Q}_{cv}}{\dot{m}} = \frac{\dot{W}_{cv}}{\dot{m}} + h_2 - h_1$$

$$= -163.9 + (426.3 - 293.2) = -30.8\frac{\text{kJ}}{\text{kg}}$$

(b) Using Equation 3′ of Table 2.8 together with Equation 2.30b,

$$\frac{\dot{W}_{cv}}{\dot{m}} = -RT\ln\frac{p_2}{p_1}$$

$$= -\left(\frac{8.314}{28.97}\right)(293)\ln 5$$

$$= -135.3\frac{\text{kJ}}{\text{kg}}$$

Area 1-2′-*a*-*b* on Figure 2.11 represents the magnitude of the work required, per unit of mass of air flowing. An energy balance reduces to give $\dot{Q}_{cv}/\dot{m} = \dot{W}_{cv}/\dot{m} = -135.3$ kJ/kg. (c) For an isentropic compression, $\dot{Q}_{cv} = 0$ and an energy rate balance reduces to give $\dot{W}_{cv}/\dot{m} = -(h_{2s} - h_1)$, where 2*s* denotes the exit state. With Equation 2.59a and p_r data, $h_{2s} = 464.8$ kJ/kg ($T_{2s} = 463$K). Then $\dot{W}_{cv}/\dot{m} = -(464.8 - 293.2) = -171.6$ kJ/kg. Area 1-2s-*a*-*b* on Figure 2.11 represents the magnitude of the work required, per unit of mass of air flowing.

Ideal Gas Mixtures

When applied to an ideal gas mixture, the additive pressure rule (Section 2.3, *p*-*v*-*T* Relations) is known as the *Dalton model.* According to this model, each gas in the mixture acts as if it exists separately at the volume and temperature of the mixture. Applying the ideal gas equation of state to the mixture as a whole and to each component *i*, $pV = n\bar{R}T$, $p_iV = n_i\bar{R}T$, where p_i, the *partial pressure* of component *i*, is the pressure that component *i* would exert if n_i moles occupied the full volume *V* at the temperature *T*. Forming a ratio, the partial pressure of component *i* is

$$p_i = \frac{n_i}{n}p = y_i p \tag{2.60}$$

where y_i is the mole fraction of component *i*. The sum of the partial pressures equals the mixture pressure.

The internal energy, enthalpy, and entropy of the mixture can be determined as the sum of the respective properties of the component gases, provided that the contribution from each gas is evaluated at the condition at which the gas exists in the mixture. On a *molar* basis,

$$U = \sum_{i=1}^{j} n_i\bar{u}_i \quad \text{or} \quad \bar{u} = \sum_{i=1}^{j} y_i\bar{u}_i \tag{2.61a}$$

$$H = \sum_{i=1}^{j} n_i\bar{h}_i \quad \text{or} \quad \bar{h} = \sum_{i=1}^{j} y_i\bar{h}_i \tag{2.61b}$$

$$S = \sum_{i=1}^{j} n_i\bar{s}_i \quad \text{or} \quad \bar{s} = \sum_{i=1}^{j} y_i\bar{s}_i \tag{2.61c}$$

The specific heats $\bar{c}_v$ and $\bar{c}_p$ for an ideal gas mixture in terms of the corresponding specific heats of the components are expressed similarly:

$$\bar{c}_v = \sum_{i=1}^{j} y_i\bar{c}_{vi} \tag{2.61d}$$

$$\bar{c}_p = \sum_{i=1}^{j} y_i\bar{c}_{pi} \tag{2.61e}$$

When working on a *mass* basis, expressions similar in form to Equations 2.61 can be written using *mass* and *mass fractions* in place of *moles* and *mole fractions*, respectively, and using u, h, s, c_p, and c_v in place of $\bar{u}, \bar{h}, \bar{s}, \bar{c}_p$, and $\bar{c}_V$, respectively.

The internal energy and enthalpy of an ideal gas depend only on temperature, and thus the $\bar{u}_i$ and $\bar{h}_i$ terms appearing in Equations 2.61 are evaluated at the temperature of the mixture. Since entropy depends on *two* independent properties, the $\bar{s}_i$ terms are evaluated either at the temperature and the partial pressure p_i of component i, or at the temperature and volume of the mixture. In the former case

$$\begin{aligned} S &= \sum_{i=1}^{j} n_i \bar{s}_i(T, p_i) \\ &= \sum_{i=1}^{j} n_i \bar{s}_i(T, x_i p) \end{aligned} \tag{2.62}$$

Inserting the expressions for H and S given by Equation 2.61b and Equation 2.61c into the Gibbs function, $G = H - TS$,

$$\begin{aligned} G &= \sum_{i=1}^{j} n_i \bar{h}_i(T) - T \sum_{i=1}^{j} n_i \bar{s}_i(T, p_i) \\ &= \sum_{i=1}^{j} n_i \bar{g}_i(T, p_i) \end{aligned} \tag{2.63}$$

where the molar-specific Gibbs function of component i is $g_i(T, p_i) = h_i(T) - Ts_i(T, p_i)$. The Gibbs function of i can be expressed alternatively as

$$\begin{aligned} \bar{g}_i(T, p_i) &= \bar{g}_i(T, p') + \bar{R}T \ln(p_i/p') \\ &= \bar{g}_i(T, p') + \bar{R}T \ln(x_i p/p') \end{aligned} \tag{2.64}$$

were p' is some specified pressure. Equation 2.64 is obtained by integrating Equation 2.32d at fixed temperature T from pressure p' to p_i.

Moist Air

An ideal gas mixture of particular interest for many practical applications is *moist air.* Moist air refers to a mixture of dry air and water vapor in which the dry air is treated as if it were a pure component. Ideal gas mixture principles usually apply to moist air. In particular, the *Dalton model is* applicable, and so the mixture pressure p is the sum of the partial pressures p_a and p_v of the dry air and water vapor, respectively.

Saturated air is a mixture of dry air and saturated water vapor. For saturated air, the partial pressure of the water vapor equals $p_{sat}(T)$, which is the saturation pressure of water corresponding to the dry-bulb (mixture) temperature T. The makeup of moist air can be described in terms of the *humidity ratio* (*specific humidity*) and the *relative humidity.* The bulb of a *wet-bulb thermometer* is covered with a wick saturated with liquid water, and the *wet-bulb* temperature of an air-water vapor mixture is the temperature indicated by such a thermometer exposed to the mixture.

When a sample of moist air is cooled at constant pressure, the temperature at which the sample becomes saturated is called the *dew point temperature.* Cooling below the dew point temperature results in the condensation of some of the water vapor initially present. When cooled to a final equilibrium state at a temperature below the dew point temperature, the original sample would consist of a gas phase of dry air and saturated water vapor in equilibrium with a liquid water phase.

Psychrometric charts are plotted with various moist air parameters, including the dry-bulb and wet-bulb temperatures, the humidity ratio, and the relative humidity, usually for a specified value of the mixture pressure such as 1 atm. Further discussion of moist air and related psychrometric principles and applications is provided in Chapter 9.

Generalized Charts for Enthalpy, Entropy, and Fugacity

The changes in enthalpy and entropy between two states can be determined in principle by correcting the respective property change determined using the ideal gas model. The corrections can be obtained, at least approximately, by inspection of the generalized enthalpy correction and entropy correction charts, Figure 2.12 and Figure 2.13, respectively. Such data are also available in tabular form (see, e.g., Reid and Sherwood, 1966) and calculable using a generalized equation for the compressibility factor (Reynolds, 1979). Using the superscript * to identify ideal gas property values, the changes in specific enthalpy and specific entropy between states 1 and 2 are

$$\bar{h}_2 - \bar{h}_1 = \underline{\bar{h}_2^* - \bar{h}_1^*} - \underline{\bar{R}T_c\left[\left(\frac{\bar{h}^* - \bar{h}}{\bar{R}T_c}\right)_2 - \left(\frac{\bar{h}^* - \bar{h}}{\bar{R}T_c}\right)_1\right]} \tag{2.65a}$$

$$\bar{s}_2 - \bar{s}_1 = \underline{\bar{s}_2^* - \bar{s}_1^*} - \underline{\bar{R}\left[\left(\frac{\bar{s}^* - \bar{s}}{\bar{R}}\right)_2 - \left(\frac{\bar{s}^* - \bar{s}}{\bar{R}}\right)_1\right]} \tag{2.65b}$$

The first underlined term on the right side of each expression represents the respective property change assuming ideal gas behavior. The second underlined term is the correction that must be applied to the ideal gas value to obtain the actual value. The quantities $(\bar{h}^* - \bar{h})/\bar{R}T_c$ *and* $(\bar{s}^* - \bar{s})/\bar{R}$ at state 1 would be read from the respective correction chart or table or calculated, using the reduced temperature T_{R1} and reduced pressure p_{R1} corresponding to the temperature T_1 and pressure p_1 at state 1, respectively. Similarly, $(\bar{h}^* - \bar{h})/\bar{R}T_c$ *and* $(\bar{s}^* - \bar{s})/\bar{R}$ at state 2 would be obtained using T_{R2} and p_{R2}. Mixture values for T_c and p_c determined by applying Kay's rule or some other mixture rule also can be used to enter the generalized enthalpy correction and entropy correction charts.

Figure 2.14 gives the *fugacity* coefficient, *f/p*, as a function of reduced pressure and reduced temperature. The fugacity *f* plays a similar role in determining the specific Gibbs function for a real gas as pressure plays for the ideal gas. To develop this, consider the variation of the specific Gibbs function with pressure at fixed temperature (from Table 2.2)

$$\left.\frac{\partial g}{\partial p}\right)_T = v$$

For an ideal gas, integration at fixed temperature gives

$$g^* = RT\ln p + C(T)$$

where $C(T)$ is a function of integration. To evaluate g for a real gas, fugacity replaces pressure,

$$g = RT\ln f + C(T)$$

In terms of the fugacity coefficient the departure of the real gas value from the ideal gas value at fixed temperature is then

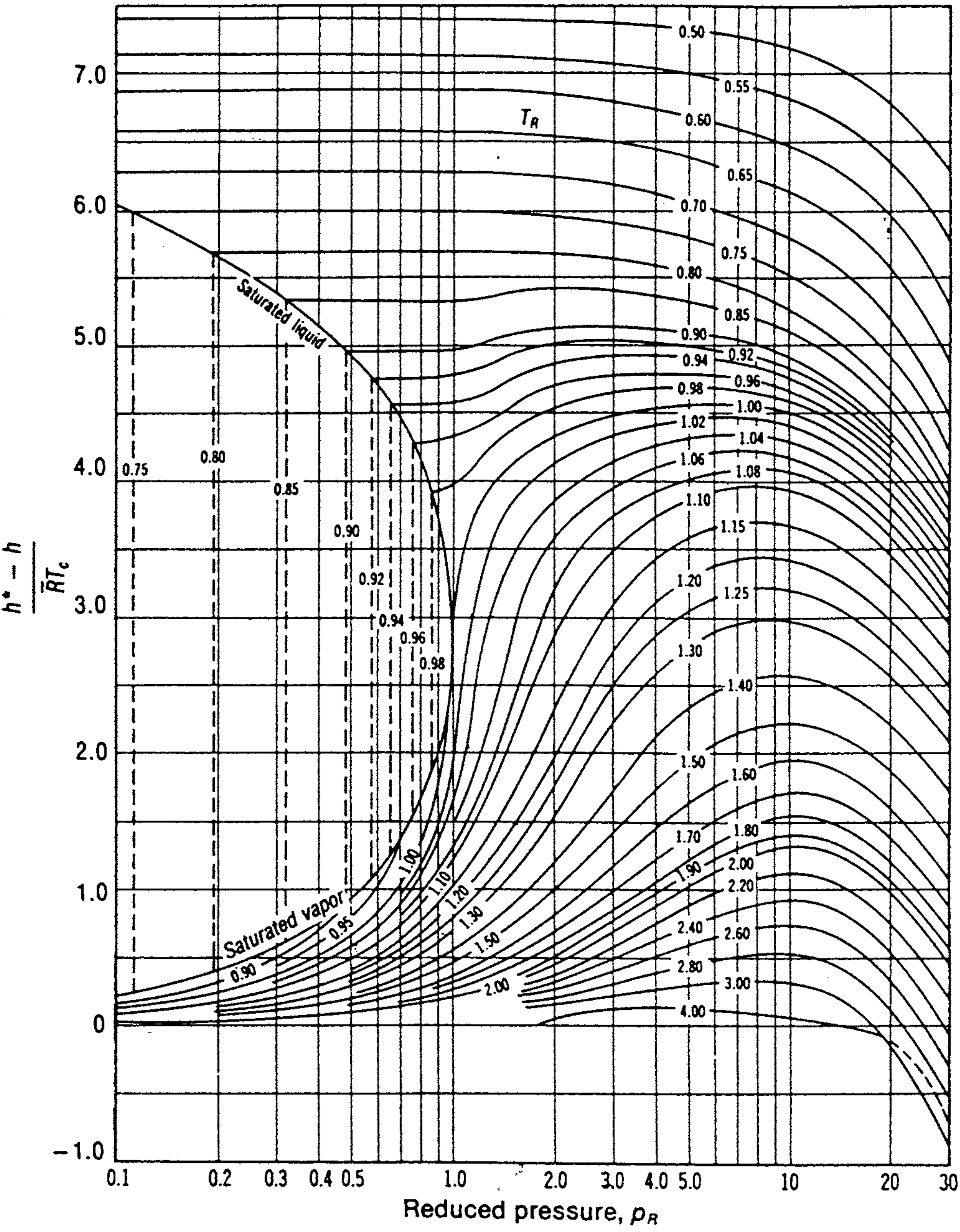

FIGURE 2.12 Generalized enthalpy correction chart. (*Source:* Adapted from Van Wylen, G. J. and Sonntag, R. E. 1986. *Fundamentals of Classical Thermodynamics*, 3rd ed., English/SI. Wiley, New York.)

$$g - g^* = RT \ln \frac{f}{p} \tag{2.66}$$

As pressure is reduced at fixed temperature, *f/p* tends to unity, and the specific Gibbs function is given by the ideal gas value.

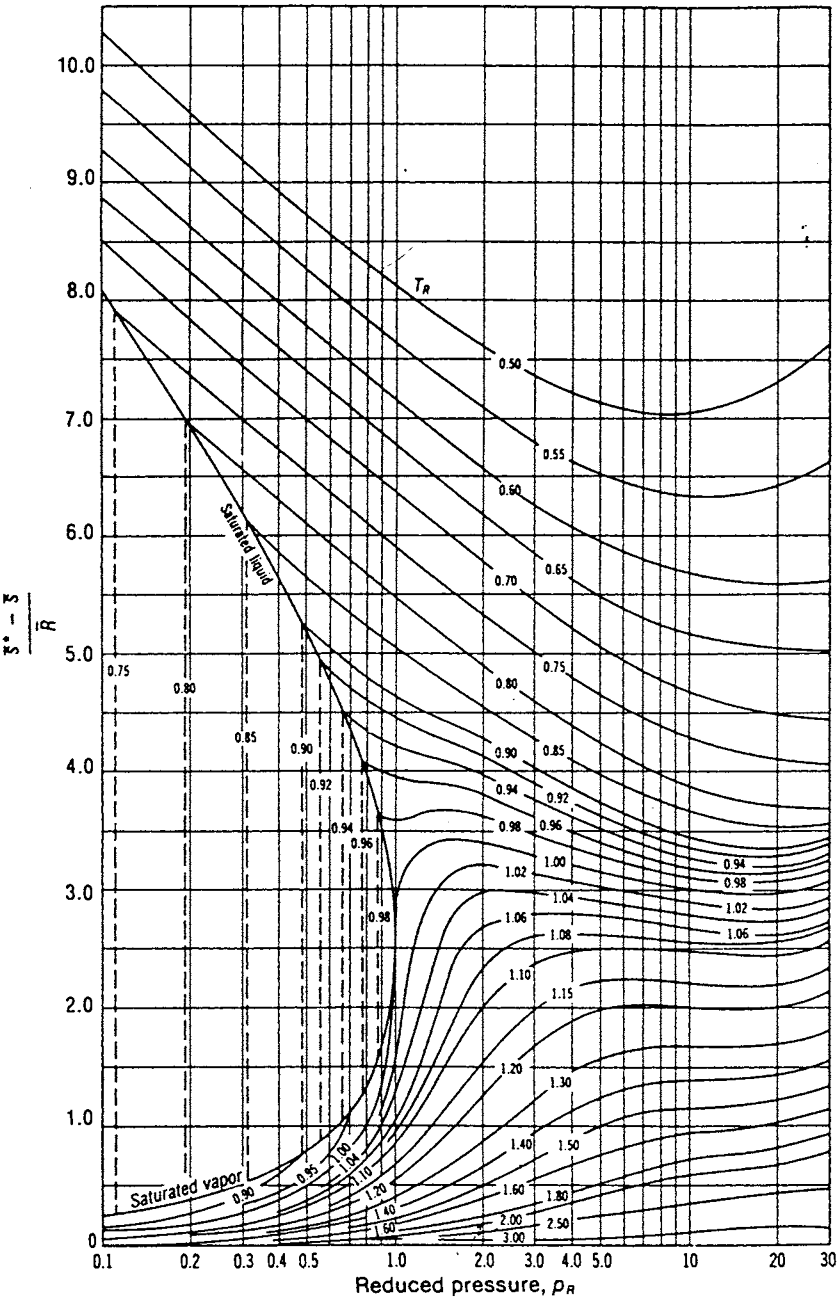

FIGURE 2.13 Generalized entropy correction chart. (*Source:* Adapted from Van Wylen, G. J. and Sonntag, R. E. 1986. *Fundamentals of Classical Thermodynamics*, 3rd ed., English/SI. Wiley, New York.)

Multicomponent Systems

In this section are presented some general aspects of the properties of multicomponent systems consisting of nonreacting mixtures. For a single phase *multicomponent* system consisting of *j* components, an extensive property *X* may be regarded as a function of temperature, pressure, and the number of moles

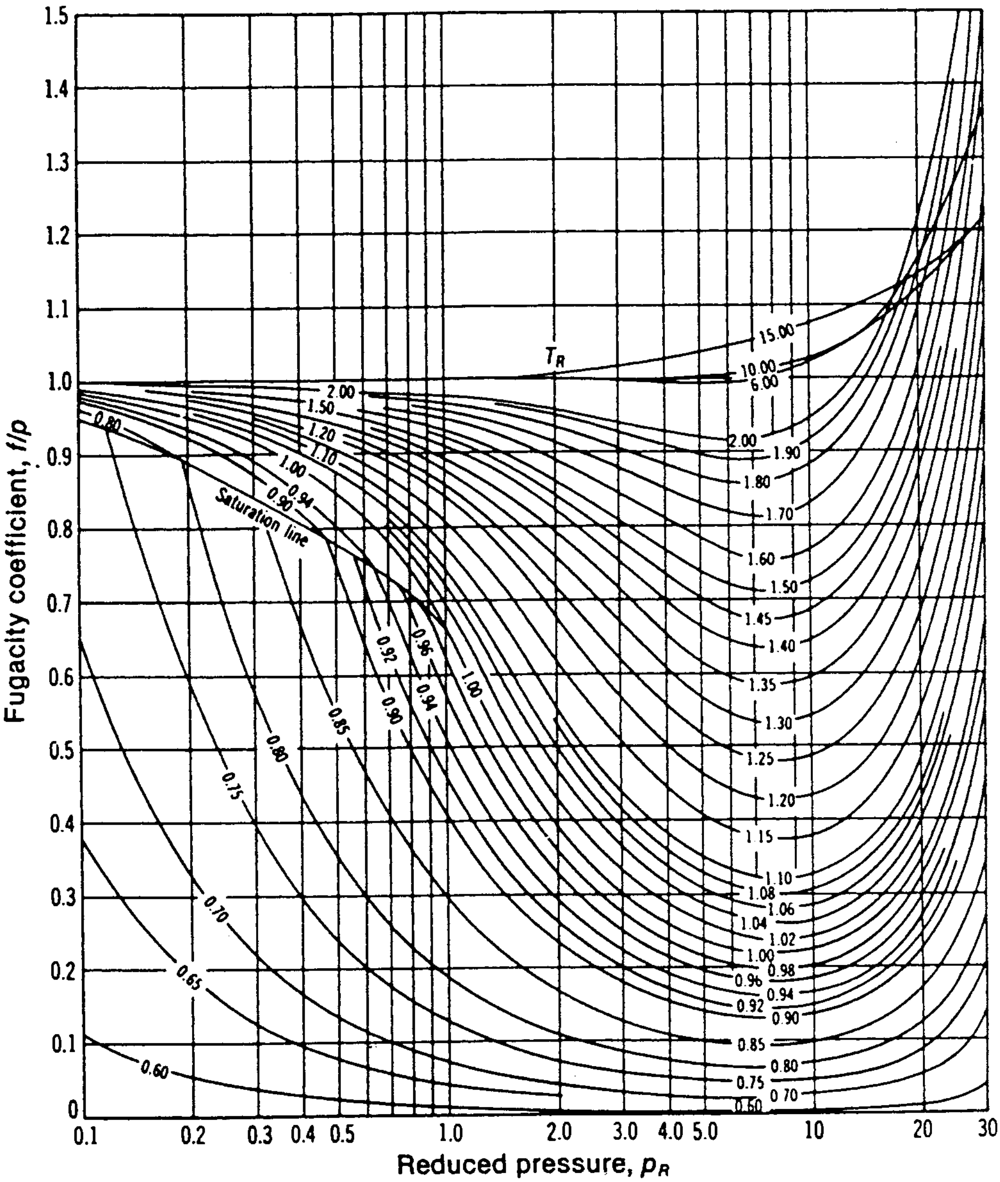

FIGURE 2.14 Generalized fugacity coefficient chart. (*Source:* Van Wylen, G. J. and Sonntag, R. E. 1986. *Fundamentals of Classical Thermodynamics*, 3rd ed., English/SI. Wiley, New York.)

of each component present in the mixture: $X = X(T, p, n_1, n_2, \ldots n_j)$. Since X is mathematically *homogeneous of degree one* in the n's, the function is expressible as

$$X = \sum_{i=1}^{j} n_i \overline{X}_i \tag{2.67}$$

where the *partial molar property* $\overline{X}_i$ is by definition

$$\overline{X}_i = \left.\frac{\partial X}{\partial n_i}\right)_{T,p,n_\ell} \tag{2.68}$$

and the subscript n_ℓ denotes that all n's except n_i are held fixed during differentiation. As $\overline{X}_i$ depends in general on temperature, pressure, and mixture composition: $\overline{X}_i\,(T, p, n_1, n_2, \ldots n_j)$, the partial molal property $\overline{X}_i$ is an intensive property of the mixture and not simply a property of the i*th* component.

Selecting the extensive property X to be volume, internal energy, enthalpy, entropy, and the Gibbs function, respectively, gives

$$\begin{aligned} V &= \sum_{i=1}^{j} n_i \overline{V}_i, \qquad & U &= \sum_{i=1}^{j} n_i \overline{U}_i \\ H &= \sum_{i=1}^{j} n_i \overline{H}_i, \qquad & S &= \sum_{i=1}^{j} n_i \overline{S}_i \\ G &= \sum_{i=1}^{j} n_i \overline{G}_i \end{aligned} \tag{2.69}$$

where $\overline{V}_i, \overline{U}_i, \overline{H}_i, \overline{S}_i$, and $\overline{G}_i$ denote the respective partial molal properties.

When pure components, each initially at the same temperature and pressure, are mixed, the changes in volume, internal energy, enthalpy, and entropy on mixing are given by

$$\Delta V_{\text{mixing}} = \sum_{i=1}^{j} n_i \left(\overline{V}_i - \bar{v}_i\right) \tag{2.70a}$$

$$\Delta U_{\text{mixing}} = \sum_{i=1}^{j} n_i \left(\overline{U}_i - \bar{u}_i\right) \tag{2.70b}$$

$$\Delta H_{\text{mixing}} = \sum_{i=1}^{j} n_i \left(\overline{H}_i - \bar{h}_i\right) \tag{2.70c}$$

$$\Delta S_{\text{mixing}} = \sum_{i=1}^{j} n_i \left(\overline{S}_i - \bar{s}_i\right) \tag{2.70d}$$

where $\bar{v}_i, \bar{u}_i, \bar{h}_i$, and $\bar{s}_i$ denote the molar-specific volume, internal energy, enthalpy, and entropy of pure component i.

Chemical Potential

The partial molal Gibbs function of the ith component of a multicomponent system is the *chemical potential*, μ_i,

$$\mu_i = \overline{G}_i = \left.\frac{\partial G}{\partial n_i}\right)_{T,p,n_\ell} \tag{2.71}$$

Like temperature and pressure, the chemical potential, μ_i is an *intensive* property.

When written in terms of chemical potentials, Equation 2.67 for the Gibbs function reads

$$G = \sum_{i=1}^{j} n_i \mu_i \tag{2.72}$$

For a *single component sysrem*, Equation 2.72 reduces to $G = n\mu$; that is, the chemical potential equals the molar Gibbs function. For an ideal gas mixture, comparison of Equation 2.63 and Equation 2.72 suggests $\mu_i = \bar{g}_i\ (T, p_i)$; that is, the chemical potential of component i in an ideal gas mixture equals its Gibbs function per mole of gas i evaluated at the mixture temperature and the partial pressure of the ith gas of the mixture.

The chemical potential is a measure of the *escaping tendency* of a substance in a multiphase system: a substance tends to move from the phase having the higher chemical potential for that substance to the phase having a lower chemical potential. A necessary condition for *phase equilibrium is* that the chemical potential of each component has the same value in every phase.

The *Gibbs phase rule* gives the number F of independent intensive properties that may be arbitrarily specified to fix the intensive state of a system at equilibrium consisting of N nonreacting components present in P phases: $F = 2 + N - P$. F is called the *degrees of freedom* (or the *variance*). For water as a single component, for example, $N = 1$ and $F = 3 - P$.

- For a single phase, $P = 1$ and $F = 2$: two intensive properties can be varied independently, say temperature *and* pressure, while maintaining a single phase.
- For two phases, $P = 2$ and $F = 1$: only one intensive property can be varied independently if two phases are maintained — for example, temperature *or* pressure.
- For three phases, $P = 3$ and $F = 0$: there are no degrees of freedom; each intensive property of each phase is fixed. For a system consisting of ice, liquid water, and water vapor at equilibrium, there is a unique temperature: 0.01°C (32.02°F) and a unique pressure: 0.6113 kPa (0.006 atm).

The phase rule does not address the relative amounts that may be present in the various phases.

With $G = H - TS$ and $H = U + pV$, Equation 2.72 can be expressed as

$$U = TS - pV + \sum_{i=1}^{j} n_i \mu_i \tag{2.73}$$

from which can be derived

$$dU = TdS - pdV + \sum_{i=1}^{j} \mu_i dn_i \tag{2.74}$$

When the mixture composition is constant, Equation 2.74 reduces to Equation 2.31a.

Ideal Solution

The *Lewis-Randall rule* states that the fugacity $\bar{f}_i$ of each component i in an *ideal solution* is the product of its mole fraction and the fugacity of the pure component, f_i, at the same temperature, pressure, and state of aggregation (gas, liquid, or solid) as the mixture:

$$\bar{f}_i = y_i f_i \qquad \text{(Lewis-Randall rule)} \tag{2.75}$$

The following characteristics are exhibited by an ideal solution: $\bar{V}_i = \bar{v}_i, \bar{U}_i = \bar{u}_i, \bar{H}_i = \bar{h}_i$. With these, Equation 2.70a, Equation 2.70b, and Equation 2.70c show that there is no change in volume, internal energy, or enthalpy on mixing pure components to form an ideal solution. The *adiabatic* mixing of different pure components would result in an increase in entropy, however, because such a process is irreversible.

The volume of an ideal solution is

$$V = \sum_{i=1}^{j} n_i \bar{v}_i = \sum_{i=1}^{j} V_i \qquad \text{(ideal solution)} \tag{2.76}$$

where V_i is the volume that pure component i would occupy when at the temperature and pressure of the mixture. Comparing Equation 2.48a and Equation 2.76, the *additive volume rule* is seen to be exact for ideal solutions. The internal energy and enthalpy of an ideal solution are

$$U = \sum_{i=1}^{j} n_i \bar{u}_i, \quad H = \sum_{i=1}^{j} n_i \bar{h}_i \qquad \text{(ideal solution)} \tag{2.77}$$

where $\bar{u}_i$ and $\bar{h}_i$ denote, respectively, the molar internal energy and enthalpy of pure component i at the temperature and pressure of the mixture. Many gaseous mixtures at low to moderate pressures are adequately modeled by the Lewis Randall rule. The ideal gas mixtures considered in Section 2.3, Ideal Gas Model, is an important special case. Some liquid solutions also can be modeled with the Lewis-Randall rule.

2.4 Combustion

The thermodynamic analysis of reactive systems is primarily an extension of principles presented in Sections 2.1 to 2.3. It is necessary, though, to modify the methods used to evaluate specific enthalpy and entropy.

Reaction Equations

In combustion reactions, rapid oxidation of combustible elements of the fuel results in energy release as combustion products are formed. The three major combustible chemical elements in most common fuels are carbon, hydrogen, and sulfur. Although sulfur is usually a relatively unimportant contributor to the energy released, it can be a significant cause of pollution and corrosion.

The emphasis in this section is on hydrocarbon fuels, which contain hydrogen, carbon, sulfur, and possibly other chemical substances. Hydrocarbon fuels may be liquids, gases, or solids such as coal. Liquid hydrocarbon fuels are commonly derived from crude oil through distillation and cracking processes. Examples are gasoline, diesel fuel, kerosene, and other types of fuel oils. The compositions of liquid fuels are commonly given in terms of mass fractions. For simplicity in combustion calculations, gasoline is often considered to be octane, C_8H_{18}, and diesel fuel is considered to be dodecane, $C_{12}H_{26}$. Gaseous hydrocarbon fuels are obtained from natural gas wells or are produced in certain chemical processes. Natural gas normally consists of several different hydrocarbons, with the major constituent being methane, CH_4. The compositions of gaseous fuels are commonly given in terms of mole fractions. Both gaseous and liquid hydrocarbon fuels can be synthesized from coal, oil shale, and tar sands. The composition of coal varies considerably with the location from which it is mined. For combustion calculations, the makeup of coal is usually expressed as an *ultimate analysis* giving the composition on a mass basis in terms of the relative amounts of chemical elements (carbon, sulfur, hydrogen, nitrogen, oxygen) and ash. Coal combustion is considered further in Chapter 8, Energy Conversion.

A fuel is said to have burned *completely* if all of the carbon present in the fuel is burned to carbon dioxide, all of the hydrogen is burned to water, and all of the sulfur is burned to sulfur dioxide. In practice, these conditions are usually not fulfilled and combustion is *incomplete.* The presence of carbon monoxide (CO) in the products indicates incomplete combustion. The products of combustion of *actual* combustion reactions and the relative amounts of the products can be determined with certainty only by experimental means. Among several devices for the experimental determination of the composition of products of combustion are the *Orsat analyzer*, *gas chromatograph*, *infrared analyzer*, and *flame ionization detector*. Data from these devices can be used to determine the makeup of the gaseous products of combustion. Analyses are frequently reported on a "dry" basis: mole fractions are determined for all gaseous products as if no water vapor were present. Some experimental procedures give an analysis including the water vapor, however.

Since water is formed when hydrocarbon fuels are burned, the mole fraction of water vapor in the gaseous products of combustion can be significant. If the gaseous products of combustion are cooled at constant mixture pressure, the *dew point temperature* (Section 2.3, Ideal Gas Model) is reached when water vapor begins to condense. Corrosion of duct work, mufflers, and other metal parts can occur when water vapor in the combustion products condenses.

Oxygen is required in every combustion reaction. Pure oxygen is used only in special applications such as cutting and welding. In most combustion applications, air provides the needed oxygen. Idealizations are often used in combustion calculations involving air: (1) all components of air other than oxygen (O_2) *are* lumped with nitrogen (N_2). On a molar basis air is then considered to be 21% oxygen and 79% nitrogen. With this idealization the molar ratio of the nitrogen to the oxygen in combustion air is 3.76; (2) the water vapor present in air may be considered in writing the combustion equation or ignored. In the latter case the combustion air is regarded as *dry*; (3) additional simplicity results by regarding the nitrogen present in the combustion air as inert. However, if high-enough temperatures are attained, nitrogen can form compounds, often termed NO_X, such as nitric oxide and nitrogen dioxide. Even trace amounts of oxides of nitrogen appearing in the exhaust of internal combustion engines can be a source of air pollution.

The minimum amount of air that supplies sufficient oxygen for the complete combustion of all the combustible chemical elements is the *theoretical*, or *stoichiometic*, amount of air. In practice, the amount of air actually supplied may be greater than or less than the theoretical amount, depending on the application. The amount of air is commonly expressed as the *percent of theoretical air* or the *percent excess* (or *percent deficiency*) of air. The *air-fuel ratio* and its reciprocal *the fuel-air ratio*, each of which can be expressed on a mass or molar basis, are other ways that fuel-air mixtures are described. Another is the *equivalence ratio:* the ratio of the actual fuel-air ratio to the fuel-air ratio for complete combustion with the theoretical amount of air. The reactants form a *lean* mixture when the equivalence ratio is less than unity and a *rich* mixture when the ratio is greater than unity.

Example 9

Methane, CH_4, is burned with dry air. The molar analysis of the products on a dry basis is CO_2, 9.7%; CO, 0.5%; O_2, 2.95%; and N_2, 86.85%. Determine (a) the air-fuel ratio on both a molar and a mass basis, (b) the percent of theoretical air, (c) the equivalence ratio, and (d) the dew point temperature of the products, in °F, if the pressure is 1 atm.

Solution.

(a) The solution is conveniently conducted on the basis of 100 lbmol of dry products. The chemical equation then reads

$$a\mathrm{CH_4} + b\left(\mathrm{O_2} + 3.76\mathrm{N_2}\right) \rightarrow 9.7\mathrm{CO_2} + 0.5\mathrm{CO} + 2.95\mathrm{O_2} + 86.85\mathrm{N_2} + c\mathrm{H_2O}$$

where N_2 is regarded as inert. Water is included in the products together with the assumed 100 lbmol of dry products. Balancing the carbon, hydrogen, and oxygen, the reaction equation is

$$10.2\mathrm{CH_4} + 23.1\left(\mathrm{O_2} + 3.76\mathrm{N_2}\right) \rightarrow 9.7\mathrm{CO_2} + 0.5\mathrm{CO} + 2.95\mathrm{O_2} + 86.85\mathrm{N_2} + 20.4\mathrm{H_2O}$$

The nitrogen also balances, as can be verified. This checks the accuracy of both the given product analysis and the calculations conducted to determine the unknown coefficients. Exact closure cannot be expected with measured data, however. On a molar basis, the air-fuel ratio is

$$\overline{\text{AF}} = \frac{23.1(4.76)}{10.2} = 10.78\frac{\text{lbmol(air)}}{\text{lbmol(fuel)}}$$

On a mass basis

$$\text{AF} = (10.78)\left(\frac{28.97}{16.04}\right) = 19.47\frac{\text{lb(air)}}{\text{lb(fuel)}}$$

(b) The balanced chemical equation for the complete combustion of methane with the *theoretical* amount of air is

$$CH_4 + 2(O_2 + 3.76N_2) \rightarrow CO_2 + 2H_2O + 7.52N_2$$

The theoretical air-fuel ratio on a molar basis is

$$\left(\overline{\text{AF}}\right)_{theo} = \frac{2(4.76)}{1} = 9.52\frac{\text{lbmol(air)}}{\text{lbmol(fuel)}}$$

The percent theoretical air is then

$$\begin{aligned}\%\text{ theoretical air} &= \frac{\left(\overline{\text{AF}}\right)}{\left(\overline{\text{AF}}\right)_{theo}} \\ &= \frac{10.78}{9.52} = 1.13(113\%)\end{aligned}$$

(c) Equivalence ratio = $(\overline{FA})/(\overline{FA})_{theo}$ = 9.52/10.78 = 0.88. The reactants form a lean mixture.

(d) To determine the dew point temperature requires the partial pressure p_v of the water vapor. The mole fraction of the water vapor is

$$y_v = \frac{20.4}{100 + 20.4} = 0.169$$

Since $p = 1$ atm, $p_v = 0.169$ atm = 2.48 lbf/in.^{2}. With $p_{sat} = 2.48$ lbf/in.^{2}, the corresponding saturation temperature from the steam tables is 134°F. This is the dew point temperature.

Property Data for Reactive Systems

Tables of thermodynamic properties such as the steam tables provide values for the specific enthalpy and entropy relative to some arbitrary datum state where the enthalpy (or alternatively the internal energy) and entropy are set to zero. When a chemical reaction occurs, however, reactants disappear and products are formed, and it is generally no longer possible to evaluate $\Delta\bar{h}$ and $\Delta\bar{s}$ so that these arbitrary datums cancel. Accordingly, special means are required to assign specific enthalpy and entropy for application to reacting systems.

Property data suited for the analysis of reactive systems are available from several sources. The encyclopedic *JANAF Thermochemical Tables* is commonly used. Data for a wide range of substances are retrievable from Knacke et al. (1991), which provides both tabular data and analytical expressions readily programmable for use with personal computers of the specific heat, enthalpy, entropy, and Gibbs function. Textbooks on engineering thermodynamics also provide selected data, as, for example, Moran and Shapiro (1995).

Enthalpy of Formation

An enthalpy datum for reacting systems can be established by assigning arbitrarily a value of zero to the enthalpy of the *stable elements* at a *standard reference state* where the temperature is $T_{ref} = 298.15$ K (25°C) and the pressure is p_{ref}, which may be 1 bar or 1 atm depending on the data source. The term stable simply means that the particular element is chemically stable. For example, at the standard state the stable forms of hydrogen, oxygen, and nitrogen are H_2, O_2, and N_2 and not the monatomic H, O, and N.

The molar enthalpy of a *compound* at the standard state equals its *enthalpy of formation*, symbolized here by $\bar{h}_f^\circ$. The enthalpy of formation is the energy released or absorbed when the compound is formed from its elements, the compound and elements all being at T_{ref} and p_{ref}. The enthalpy of formation may be determined by application of procedures from statistical thermodynamics using observed spectroscopic data. The enthalpy of formation also can be found in principle by measuring the heat transfer in a reaction in which the compound is formed from the elements. In this chapter, the superscript ° is used to denote p_{ref}. For the case of the enthalpy of formation, the reference temperature T_{ref} is also intended by this symbol. Table 2.9 gives the values of the enthalpy of formation of various substances at 298 K and 1 atm.

The molar enthalpy of a substance at a state other than the standard state is found by adding the molar enthalpy change $\Delta\bar{h}$ between the standard state and the state of interest to the molar enthalpy of formation:

$$\bar{h}(T,p) = \bar{h}_f^\circ + \left[\bar{h}(T,p) - \bar{h}\left(T_{ref}, p_{ref}\right)\right] = \bar{h}_f^\circ + \Delta\bar{h} \tag{2.78}$$

That is, the enthalpy of a substance is composed of $\bar{h}_f^\circ$, associated with the formation of the substance from its elements, and $\Delta\bar{h}$, associated with a change of state at constant composition. An arbitrarily chosen datum can be used to determine $\Delta\bar{h}$, since it is a *difference* at constant composition. Accordingly, $\Delta\bar{h}$ can be evaluated from sources such as the steam tables and the ideal gas tables.

The *enthalpy of combustion*, $\bar{h}_{RP}$, is the difference between the enthalpy of the products and the enthalpy of the reactants, each on a per-mole-of-fuel basis, when complete combustion occurs and both reactants and products are at the same temperature and pressure. For hydrocarbon fuels the enthalpy of combustion is negative in value since chemical internal energy is liberated in the reaction. The *heating value* of a fuel is a positive number equal to the magnitude of the enthalpy of combustion. Two heating values are recognized: the *higher* heating value and the *lower* heating value. The higher heating value is obtained when all the water formed by combustion is a liquid; the lower heating value is obtained when all the water formed by combustion is a vapor. The higher heating value exceeds the lower heating value by the energy that would be required to vaporize the liquid water formed at the specified temperature. Heating values are typically reported at a temperature of 25°C (77°F) and a pressure of 1 bar (or 1 atm). These values also depend on whether the fuel is a liquid or a gas. A sampling is provided on a unit-mass-of-fuel basis in Table 2.10.

In the absence of work $\dot{W}_{cv}$ and appreciable kinetic and potential energy effects, the energy liberated on combustion is transferred from a reactor at steady state in two ways: the energy accompanying the exiting combustion products and by heat transfer. The temperature that would be achieved by the products in the limit of adiabatic operation is the *adiabatic flame* or *adiabatic combustion* temperature.

For a specified fuel and specified temperature and pressure of the reactants, the *maximum* adiabatic flame temperature is realized for complete combustion with the theoretical amount of air. Example 10 provides an illustration. The measured value of the temperature of the combustion products may be several hundred degrees below the calculated maxunum adiabatic flame temperature, however, for several reasons including the following: (1) heat loss can be reduced but not eliminated; (2) once adequate oxygen has been provided to permit complete combustion, bringing in more air dilutes the combustion products, lowering the temperature; (3) incomplete combustion tends to reduce the temperature of the products, and combustion is seldom complete; (4) as result of the high temperatures achieved, some of the combustion products may dissociate. Endothermic dissociation reactions also lower the product temperature.

TABLE 2.9 Enthalpy of Formation, Gibbs Function of Formation, and Absolute Entropy of Various Substances at 298 K and 1 atm

$\bar{h}_f^\circ$ and $\bar{g}_f^\circ$ (kJ/kmol), $\bar{s}^\circ$ (kJ/kmol•K)

Substance	Formula	$\bar{h}_f^\circ$	$\bar{g}_f^\circ$	$\bar{s}^\circ$
Carbon	C(s)	0	0	5.74
Hydrogen	H_2(g)	0	0	130.57
Nitrogen	N_2(g)	0	0	191.50
Oxygen	O_2(g)	0	0	205.03
Carbon monoxide	CO(g)	–110,530	–137,150	197.54
Carbon dioxide	CO_2(g)	–393,520	–394,380	213.69
Water	H_2O(g)	–241,820	–228,590	188.72
	H_2O(l)	–285,830	–237,180	69.95
Hydrogen peroxide	H_2O_2(g)	–136,310	–105,600	232.63
Ammonia	NH_3(g)	–46,190	–16,590	192.33
Oxygen	O(g)	249,170	231,770	160.95
Hydrogen	H(g)	218,000	203,290	114.61
Nitrogen	N(g)	472,680	455,510	153.19
Hydroxyl	OH(g)	39,460	34,280	183.75
Methane	CH_4(g)	–74,850	–50,790	186.16
Acetylene	C_2H_2(g)	226,730	209,170	200.85
Ethylene	C_2H_4(g)	52,280	68,120	219.83
Ethane	C_2H_6(g)	–84,680	–32,890	229.49
Propylene	C_3H_6(g)	20,410	62,720	266.94
Propane	C_3H_8(g)	–103,850	–23,490	269.91
Butane	C_4H_{10}(g)	–126,150	–15,710	310.03
Pentane	C_5H_{12}(g)	–146,440	–8,200	348.40
Octane	C_8H_{18}(g)	–208,450	17,320	463.67
	C_8H_{18}(l)	–249,910	6,610	360.79
Benzene	C_6H_6(8)	82,930	129,660	269.20
Methyl alcohol	CH_3OH(g)	–200,890	–162,140	239.70
	CH_3OH(I)	–238,810	–166,290	126.80
Ethyl alcohol	C_2H_5OH(g)	–235,310	–168,570	282.59
	C_2H_5OH(I)	–277,690	174,890	160.70

Source: Adapted from Wark, K. 1983. *Thermodynamics*, 4th ed. McGraw-Hill, New York, as based on JANAF Thermochemical Tables, NSRDS-NBS-37, 1971; *Selected Values of Chemical Thermodynamic Properties*, NBS Tech. Note 270-3, 1968; and *API Research Project 44*, Carnegie Press, 1953.

TABLE 2.10 Heating Values in kJ/kg of Selected Hydrocarbons at 25°C

		Higher Value[a]		**Lower Value**[b]	
Hydrocarbon	Formula	Liquid Fuel	Gas. Fuel	Liquid Fuel	Gas. Fuel
Methane	CH_4	—	55,496	—	50,010
Ethane	C_2H_6	—	51,875	—	47,484
Propane	C_3H_8	49,973	50,343	45,982	46,352
n-Butane	C_4H_{10}	49,130	49,500	45,344	45,714
n-Octane	C_8H_{18}	47,893	48,256	44,425	44,788
n-Dodecane	$C_{12}H_{26}$	47,470	47,828	44,109	44,467
Methanol	CH_3OH	22,657	23,840	19,910	21,093
Ethanol	C_3H_5OH	29,676	30,596	26,811	27,731

[a] H_2O liquid in the products.

[b] H_2O vapor in the products.

Absolute Entropy

A common datum for assigning entropy values to substances involved in chemical reactions is realized through the *third law* of thermodynamics, which is based on experimental observations obtained primarily from studies of chemical reactions at low temperatures and specific heat measurements at temperatures approaching absolute zero. The third law states that the entropy of a pure crystalline substance is zero at the absolute zero of temperature, 0 K or 0°R. Substances not having a pure crystalline structure have a nonzero value of entropy at absolute zero.

The third law provides a datum relative to which the entropy of each substance participating in a reaction can be evaluated. The entropy relative to this datum is called the *absolute* entropy. The change in entropy of a substance between absolute zero and any given state can be determined from measurements of energy transfers and specific heat data or from procedures based on statistical thermodynamics and observed molecular data. Table 2.9, Table A.2 and Table A.8 provide absolute entropy data for various substances. In these tables, $p_{ref} = 1$ atm.

When the absolute entropy is known at pressure p_{ref} and temperature T, the absolute entropy at the same temperature and *any* pressure p can be found from

$$\bar{s}(T,p) = \bar{s}\left(T,p_{ref}\right) + \left[\bar{s}(T,p) - \bar{s}\left(T,p_{ref}\right)\right] \tag{2.79}$$

For an ideal gas, the second term on the right side of Equation 2.79 can be evaluated by using Equation 2.58, giving

$$\bar{s}(T,p) = \bar{s}^\circ(T) - \bar{R}\ln\frac{p}{p_{ref}} \qquad \text{(ideal gas)} \tag{2.80}$$

In this expression, $\bar{s}^\circ(T)$ denotes the absolute entropy at temperature T and pressure p_{ref}.

The entropy of the ith component of an *ideal gas mixture* is evaluated at the mixture temperature T and the *partial* pressure p_i: $\bar{s}_i(T, p_i)$. For the ith component, Equation 2.80 takes the form

$$\begin{aligned} \bar{s}_i\left(T,p_i\right) &= \bar{s}_i^\circ(T) - \bar{R}\ln\frac{p_i}{p_{ref}} \\ &= \bar{s}_i^\circ(T) - \bar{R}\ln\frac{y_i p}{p_{ref}} \qquad \text{(ideal gas)} \end{aligned} \tag{2.81}$$

where $\bar{s}_i^\circ(T)$ is the absolute entropy of component i at temperature T and p_{ref}.

Example 10

Liquid octane at 25°C, 1 atm enters a well insulated reactor and reacts with dry air entering at the same temperature and pressure. For steady-state operation and negligible effects of kinetic and potential energy, determine the temperature of the combustion products for complete combustion with the theoretical amount of air, and (b) the rates of entropy generation and exergy destruction, each per kmol of fuel.

Solution. For combustion of liquid octane with the theoretical amount of air, the chemical equation is

$$C_8H_{18}(l) + 12.5O_2 + 47N_2 \rightarrow 8CO_2 + 9H_2O(g) + 47N_2$$

(a) At steady state, the control volume energy rate balance reduces to read

$$0 = \cancel{\frac{\dot{Q}_{cv}}{\dot{n}_F}}^{\,0} - \cancel{\frac{\dot{W}_{cv}}{\dot{n}_F}}^{\,0} + \sum_R n_i\left(\bar{h}_f^\circ + \Delta\bar{h}\right)_i - \sum_P n_e\left(\bar{h}_f^\circ + \Delta\bar{h}\right)_e$$

where R denotes reactants, P denotes products, and the symbols for enthalpy have the same significance as in Equation 2.78. Since the reactants enter at 25°C, the corresponding $(\Delta\bar{h})_i$ terms vanish, and the energy rate equation becomes

$$\sum_P n_e\left(\Delta\bar{h}\right)_e = \sum_R n_i\bar{h}^\circ_{fi} - \sum_P n_e\bar{h}^\circ_{fe}$$

Introducing coefficients from the reaction equation, this takes the form

$$8\left(\Delta\bar{h}\right)_{CO_2} + 9\left(\Delta\bar{h}\right)_{H_2O(g)} + 47\left(\Delta\bar{h}\right)_{N_2} = \left[\left(\bar{h}^\circ_f\right)_{C_8H_{18}(l)} + 12.5\left(\bar{h}^\circ_f\right)_{O_2} + 47\left(\bar{h}^\circ_f\right)_{N_2}\right]$$

$$-\left[8\left(\bar{h}^\circ_f\right)_{CO_2} + 9\left(\bar{h}^\circ_f\right)_{H_2O(g)} + 47\left(\Delta\bar{h}^\circ_f\right)_{N_2}\right]$$

Using data from Table 2.9 to evaluate the right side,

$$8\left(\Delta\bar{h}\right)_{CO_2} + 9\left(\Delta\bar{h}\right)_{H_2O(g)} + 47\left(\Delta\bar{h}\right)_{N_2} = 5{,}074{,}630\ \text{kJ/kmol (fuel)}$$

Each $\Delta\bar{h}$ term on the left side of this equation depends on the temperature of the products, T_p, which can be solved for iteratively as $T_p = 2395$ K.

(b) The entropy rate balance on a per-mole-of-fuel basis takes the form

$$0 = \cancel{\sum_j \frac{\dot{Q}_j/T_j}{\dot{n}_F}}^{\,0} + \bar{s}_F + \left(12.5\bar{s}_{O_2} + 47\bar{s}_{N_2}\right) - \left(8\bar{s}_{CO_2} + 9\bar{s}_{H_2O(g)} + 47\bar{s}_{N_2}\right) + \frac{\dot{S}_{gen}}{\dot{n}_F}$$

or on rearrangement,

$$\frac{\dot{S}_{gen}}{\dot{n}_F} = \left(8\bar{s}_{CO_2} + 9\bar{s}_{H_2O(g)} + 47\bar{s}_{N_2}\right) - \bar{s}_F - \left(12.5\bar{s}_{O_2} + 47\bar{s}_{N_2}\right)$$

The absolute entropy of liquid octane from Table 2.9 is 360.79 kJ/mol · K. The oxygen and nitrogen in the combustion air enter the reactor as components of an ideal gas mixture at T_{ref}, p_{ref}. With Equation 2.81, where $p = p_{ref}$, and absolute entropy data from Table 2.9,

$$\begin{aligned}\bar{s}_{O_2} &= \bar{s}^\circ_{O_2}\left(T_{ref}\right) - \bar{R}\ln y_{O_2}\\ &= 205.03 - 8.314\ln 0.21 = 218.01\ \text{kJ/kmol}\cdot\text{K}\\ \bar{s}_{N_2} &= \bar{s}^\circ_{N_2}\left(T_{ref}\right) - \bar{R}\ln y_{N_2}\\ &= 191.5 - 8.314\ln 0.79 = 193.46\ \text{kJ/kmol}\cdot\text{K}\end{aligned}$$

The product gas exits as a gas mixture at 1 atm, 2395 K with the following composition: y_{CO_2} = 8/64 = 0.125, $y_{H_2O(g)}$ = 9/64 = 0.1406, y_{N_2} = 47/64 = 0.7344. With Equation 2.81, where $p = p_{ref}$, *an*d absolute entropy data at 2395 K from Table A.2,

$$\begin{aligned}\bar{s}_{CO_2} &= 320.173 - 8.314\ln 0.125 = 337.46\ \text{kJ/kmol}\cdot\text{K}\\ \bar{s}_{H_2O} &= 273.986 - 8.314\ln 0.1406 = 290.30\ \text{kJ/kmol}\cdot\text{K}\\ \bar{s}_{N_2} &= 258.503 - 8.314\ln 0.7344 = 261.07\ \text{kJ/kmol}\cdot\text{K}\end{aligned}$$

Inserting values, the rate of entropy generation is

$$\frac{\dot{S}_{gen}}{\dot{n}_F} = 8(337.46) + 9(290.30) + 47(261.07) - 360.79 - 12.5(218.01) - 47(193.46)$$

$$= 5404 \ \text{kJ/kmol} \cdot \text{K}$$

Using Equation 2.87 and assuming $T_0 = 298$ K, the rate of exergy destruction is $\dot{E}_D / \dot{n}_F = 1.61 \times 10^6$ kJ/kmol.

Gibbs Function of Formation

Paralleling the approach used for enthalpy, a value of zero is assigned to the Gibbs function of each stable element at the standard state. The *Gibbs function of formation* of a compound equals the change in the Gibbs function for the reaction in which the compound is formed from its elements. Table 2.9 provides Gibbs function of formation data of various substances at 298 K and 1 atm.

The Gibbs function at a state other than the standard state is found by adding to the Gibbs function of formation the change in the specific Gibbs function $\Delta\bar{g}$ between the standard state and the state of interest:

$$\bar{g}(T,p) = \bar{g}_f^\circ + \left[\bar{g}(T,p) - \bar{g}\left(T_{ref}, p_{ref}\right)\right] = \bar{g}_f^\circ + \Delta\bar{g} \tag{2.82a}$$

where

$$\Delta\bar{g} = \left[\bar{h}(T,p) - \bar{h}\left(T_{ref}, p_{ref}\right)\right] - \left[T\bar{s}(T,p) - T_{ref}\bar{s}\left(T_{ref}, p_{ref}\right)\right] \tag{2.82b}$$

The Gibbs function of component i in an ideal gas mixture is evaluated at the partial pressure of component i and the mixture temperature.

As an application, the maximum theoretical work that can be developed, per mole of fuel consumed, is evaluated for the control volume of Figure 2.15, where the fuel and oxygen each enter in separate streams and carbon dioxide and water each exit separately. All entering and exiting streams are at the same temperature T and pressure p. The reaction is complete:

$$C_aH_b + \left(a + \frac{b}{4}\right)\text{O}_2 \rightarrow a\text{CO}_2 + \frac{b}{2}\text{H}_2\text{O}$$

This control volume is similar to idealized devices such as a reversible fuel *cell* or a *van't Hoff equilibrium box.*

For steady-state operation, the energy rate balance reduces to give

$$\frac{\dot{W}_{cv}}{\dot{n}_F} = \frac{\dot{Q}_{cv}}{\dot{n}_F} + \bar{h}_F + \left(a + \frac{b}{4}\right)\bar{h}_{\text{O}_2} - a\bar{h}_{\text{CO}_2} - \frac{b}{2}\bar{h}_{\text{H}_2\text{O}}$$

where $\dot{n}_F$ denotes the molar flow rate of the fuel. Kinetic and potential energy effects are regarded as negligible. If heat transfer occurs only at the temperature T, an entropy balance for the control volume takes the form

$$0 = \frac{\dot{Q}_{cv}/\dot{n}_F}{T} + \bar{s}_F + \left(a + \frac{b}{4}\right)\bar{s}_{\text{O}_2} - a\bar{s}_{\text{CO}_2} - \frac{b}{2}\bar{s}_{\text{H}_2\text{O}} + \frac{\dot{S}_{gen}}{\dot{n}_F}$$

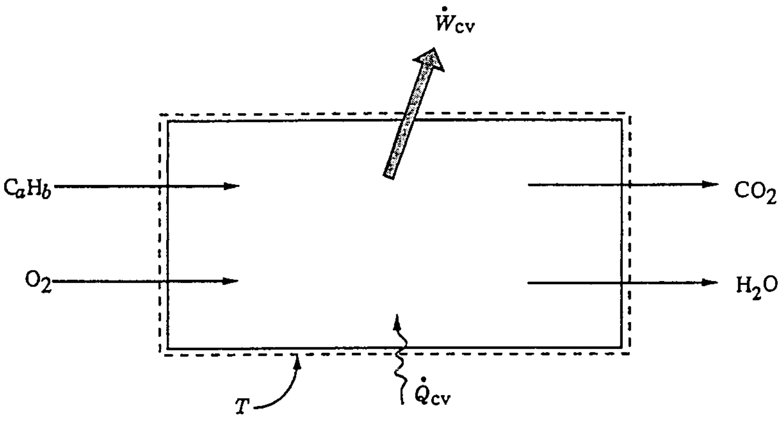

FIGURE 2.15 Device for evaluating maximum work.

Eliminating the heat transfer term from these expressions, an expression for the maximum theoretical value of the work developed per mole of fuel is obtained when the entropy generation term is set to zero:

$$\left(\frac{\dot{W}_{cv}}{\dot{n}_F}\right)_{\substack{int\\rev}} = \left[\bar{h}_F + \left(a+\frac{b}{4}\right)\bar{h}_{O_2} - a\bar{h}_{CO_2} - \frac{b}{2}\bar{h}_{H_2O}\right](T,p) - T\left[\bar{s}_F + \left(a+\frac{b}{4}\right)\bar{s}_{O_2} - a\bar{s}_{CO_2} - \frac{b}{2}\bar{s}_{H_2O}\right](T,p)$$

This can be written alternatively in terms of the enthalpy of combustion as

$$\left(\frac{\dot{W}_{cv}}{\dot{n}_F}\right)_{\substack{int\\rev}} = -\bar{h}_{RP}(T,p) - T\left[\bar{s}_F + \left(a+\frac{b}{4}\right)\bar{s}_{O_2} - a\bar{s}_{CO_2} - \frac{b}{2}\bar{s}_{H_2O}\right](T,p) \tag{2.83a}$$

or in terms of Gibbs functions as

$$\left(\frac{\dot{W}_{cv}}{\dot{n}_F}\right)_{\substack{int\\rev}} = \left[\bar{g}_F + \left(a+\frac{b}{4}\right)\bar{g}_{O_2} - a\bar{g}_{CO_2} - \frac{b}{2}\bar{g}_{H_2O}\right](T,p) \tag{2.83b}$$

Equation 2.83b is used in the solution to Example 11.

Example 11

Hydrogen (H_2) and oxygen (O_2), each at 25°C, 1 atm, enter a fuel cell operating at steady state, and liquid water exits at the same temperature and pressure. The hydrogen flow rate is 2×10^{-4} kmol/sec and the fuel cell operates isothermally at 25°C. Determine the maximum theoretical power the cell can develop, in kW.

Solution. The overall cell reaction is $H_2 + 1/2\ O_2 \rightarrow H_2O(\ell)$, and Equations 2.83 are applicable. Selecting Equation 2.83b, and using Gibbs function data from Table 2.9,

$$\left(\frac{\dot{W}_{cv}}{\dot{n}_F}\right)_{\substack{int\\rev}} = \left(\bar{g}_{H_2} + \frac{1}{2}\bar{g}_{O_2} - \bar{g}_{H_2O(\ell)}\right)(25°\text{C, 1 atm})$$

$$= 0 + \frac{1}{2}(0) - (-237{,}180) = 237{,}180 \text{ kJ/kmol}$$

Then

$$\left(\dot{W}_{cv}\right)_{\substack{int\\rev}} = \left(237{,}180\frac{\text{kJ}}{\text{kmol}}\right)\left(2\times10^{-4}\frac{\text{kmol}}{\text{s}}\right)\left(\frac{\text{kW}}{1\text{kJ/s}}\right) = 47.4\text{ kW}$$

Reaction Equilibrium

Let the objective be to determine the equilibrium composition of a system consisting of five gases A, B, C, D, and E, at a temperature T and pressure p, subject to a chemical reaction of the form

$$v_A A + v_B B \leftrightarrow v_C C + v_D D$$

where the v's are stoichiometric coefficients. Component E is assumed to be inert and thus does not appear in the reaction equation. The equation suggests that at equilibrium the tendency of A and B to form C and D is just balanced by the tendency of C and D to form A and B.

At equilibrium, the temperature and pressure would be uniform throughout the system. Additionally, the *equation of reaction equilibrium* must be satisfied:

$$v_A\mu_A + v_B\mu_B = v_C\mu_C + v_D\mu_D \tag{2.84a}$$

where the μ's are the chemical potentials (Section 2.3, Multicomponent Systems) of A, B, C, and D in the equilibrium mixture. In principle, the composition that would be present at equilibrium for a given temperature and pressure can be determined by solving this equation.

For ideal gas mixtures, the solution procedure is simplified by using the *equilibrium constant* $K(T)$ and the following equation:

$$\begin{aligned} K(T) &= \frac{y_C^{v_C} y_D^{v_D}}{y_A^{v_A} y_B^{v_B}}\left(\frac{p}{p_{ref}}\right)^{v_C+v_D-v_A-v_B} \\ &= \frac{n_C^{v_C} n_D^{v_D}}{n_A^{v_A} n_B^{v_B}}\left(\frac{p/p_{ref}}{n}\right)^{v_C+v_D-v_A-v_B} \end{aligned} \tag{2.84b}$$

where y_A, y_B, y_C, and y_D denote the mole fractions of A, B, C, and D in the equilibrium mixture and $n = n_A + n_B + n_C + n_D + n_E$, where the n's denote the molar amounts of the gases in the mixture. Tabulations of $K(T)$ for each of several reactions of the form Equation 2.84a are provided in Table 2.11. An application of Equation 2.84b is provided in Example 12.

Example 12

One kmol of CO reacts with the theoretical amount of dry air to form an equilibrium mixture of CO_2, CO, O_2, and N_2 at 2500 K, 1 atm. Determine the amount of CO in the equilibrium mixture, in kmol.

Solution. The reaction of CO with the theoretical amount of dry air to form CO_2, CO, O_2, and N_2 is

$$\text{CO} + \frac{1}{2}\text{O}_2 + 1.88\text{N}_2 \rightarrow z\text{CO} + \frac{z}{2}\text{O}_2 + (1-z)\text{CO}_2 + 1.88\text{N}_2$$

where z is the amount of CO, in kmol, present in the equilibrium mixture. The total number of moles n is

$$n = z + \frac{z}{2} + (1-z) + 1.88 = \frac{5.76 + z}{2}$$

TABLE 2.11 Logarithms to the Base 10 of the Equilibrium Constant K

	$\log_{10} K$								
Temp (K)	$H_2 \Leftrightarrow 2H$	$O_2 \Leftrightarrow 2O$	$N_2 \Leftrightarrow 2N$	$^1/_2O_2 + {}^1/_2N_2 \Leftrightarrow NO$	$H_2O \Leftrightarrow H_2 + {}^1/_2O_2$	$H_2O \Leftrightarrow OH + {}^1/_2H_2$	$CO_2 \Leftrightarrow CO + {}^1/_2 O_2$	$CO_2 + H_2 \Leftrightarrow CO + H_2O$	Temp (°R)
298	–71.224	–81.208	–159.600	–15.171	–40.048	–46.054	–45.066	–5.018	537
500	–40.316	–45.880	–92.672	–8.783	–22.886	–26.130	–25.025	–2.139	900
1000	–17.292	–19.614	–43.056	–4.062	–10.062	–11.280	–10.221	–0.159	1800
1200	–13.414	–15.208	–34.754	–3.275	–7.899	–8.811	–7.764	+0.135	2160
1400	–10.630	–12.054	–28.812	–2.712	–6.347	–7.021	–6.014	+0.333	2520
1600	–8.532	–9.684	–24.350	–2.290	–5.180	–5.677	–4.706	+0.474	2880
1700	–7.666	–8.706	–22.512	–2.116	–4.699	–5.124	–4.169	+0.530	3060
1800	–6.896	–7.836	–20.874	–1.962	–4.270	–4.613	–3.693	+0.577	3240
1900	–6.204	–7.058	–19.410	–1.823	–3.886	–4.190	–3.267	+0.619	3420
2000	–5.580	–6.356	–18.092	–1.699	–3.540	–3.776	–2.884	+0.656	3600
2100	–5.016	–5.720	–16.898	–1.586	–3.227	–3.434	–2.539	+0.688	3780
2200	–4.502	–5.142	–15.810	–1.484	–2.942	–3.091	–2.226	+0.716	3960
2300	–4.032	–4.614	–14.818	–1.391	–2.682	–2.809	–1.940	+0.742	4140
2400	–3.600	–4.130	–13.908	–1.305	–2.443	–2.520	–1.679	+0.764	4320
2500	–3.202	–3.684	–13.070	–1.227	–2.224	–2.270	–1.440	+0.784	4500
2600	–2.836	–3.272	–12.298	–1.154	–2.021	–2.038	–1.219	+0.802	4680
2700	–2.494	–2.892	–11.580	–1.087	–1.833	–1.823	–1.015	+0.818	4860
2800	–2.178	–2.536	–10.914	–1.025	–1.658	–1.624	–0.825	+0.833	5040
2900	–1.882	–2.206	–10.294	–0.967	–1.495	–1.438	–0.649	+0.846	5220
3000	–1.606	–1.898	–9.716	–0.913	–1.343	–1.265	–0.485	+0.858	5400
3100	–1.348	–1.610	–9.174	–0.863	–1.201	–1.103	–0.332	+0.869	5580
3200	–1.106	–1.340	–8.664	–0.815	–1.067	–0.951	–0.189	+0.878	5760
3300	–0.878	–1.086	–8.186	–0.771	–0.942	–0.809	–0.054	+0.888	5940
3400	–0.664	–0.846	–7.736	–0.729	–0.824	–0.674	+0.071	+0.895	6120
3500	–0.462	–0.620	–7.312	–0.690	–0.712	–0.547	+0.190	+0.902	6300

Source: Based on data from the JANAF Thermochemical Tables, NSRDS-NBS-37, 1971.

At equilibrium $CO_2 \leftrightarrow CO + 1/2\ O_2$; and Equation 2.84b takes the form

$$K = \frac{z(z/2)^{1/2}}{1-z}\left[\frac{p/p_{ref}}{(5.76+z)/2}\right]^{1/2}$$

where $p/p_{ref} = 1$. At 2500 K, Table 2.11 gives $K = 0.0363$. Solving iteratively, z = 0.175.

2.5 Exergy Analysis

The method of *exergy analysis* (*availability analysis*) presented in this section enables the location, cause, and true magnitude of energy resource waste and loss to be determined. Such information can be used in the design of new energy-efficient systems and for improving the performance of existing systems. Exergy analysis also provides insights that elude a purely first-law approach. For example, on the basis of first-law reasoning alone, the condenser of a power plant may be mistakenly identified as the component primarily responsible for the plant's seemingly low overall performance. An exergy analysis correctly reveals not only that the condenser loss is relatively unimportant (see the last two rows of the Rankine cycle values of Table 2.15), but also that the steam generator is the principal site of thermodynamic inefficiency owing to combustion and heat transfer irreversibilities within it.

When exergy concepts are combined with principles of engineering economy, the result is known as *thermoeconomics*. Thermoeconomics allows the real cost sources at the component level to be identified: capital investment costs, operating and maintenance costs, and the costs associated with the destruction and loss of exergy. Optimization of thermal systems can be achieved by a careful consideration of such cost sources. From this perspective thermoeconomics *is exergy-aided cost minimization.*

Discussions of exergy analysis and thermoeconomics are provided by Bejan et al. (1996), Moran (1989), and Moran and Shapiro (1995). In this section salient aspects are presented.

Defining Exergy

An opportunity for doing work exists whenever two systems at different states are placed in communication because, in principle, work can be developed as the two are allowed to come into equilibrium. When one of the two systems is a suitably idealized system called an *environment* and the other is some system of interest, *exergy* is the maximum theoretical useful work (shaft work or electrical work) obtainable as the systems interact to equilibrium, heat transfer occurring with the environment only. (Alternatively, exergy is the minimum theoretical useful work required to form a quantity of matter from substances present in the environment and to bring the matter to a specified state.) Exergy is a measure of the *departure* of the state of the system from that of the environment, and is therefore an attribute of the system and environment together. Once the environment is specified, however, a value can be assigned to exergy in terms of property values for the system only, so exergy can be regarded as an extensive property of the system.

Exergy can be destroyed and generally is not conserved. A limiting case is when exergy would be completely destroyed, as would occur if a system were to come into equilibrium with the environment *spontaneously* with no provision to obtain work. The capability to develop work that existed initially would be completely wasted in the spontaneous process. Moreover, since no work needs to be done to effect such a spontaneous change, the value of exergy can never be negative.

Environment

Models with various levels of specificity are employed for describing the environment used to evaluate exergy. Models of the environment typically refer to some portion of a system's surroundings, the intensive properties of each phase of which are uniform and do not change significantly as a result of any process under consideration. The environment is regarded as composed of common substances existing in abundance within the Earth's atmosphere, oceans, and crust. The substances are in their stable forms as they exist naturally, and there is no possibility of developing work from interactions — physical or chemical — between parts of the environment. Although the intensive properties of the environment are assumed to be unchanging, the extensive properties can change as a result of interactions with other systems. Kinetic and potential energies are evaluated relative to coordinates in the environment, all parts of which are considered to be at rest with respect to one another.

For computational ease, the temperature T_0 and pressure p_0 of the environment are often taken as standard-state values, such as 1 atm and 25°C (77°F). However, these properties may be specified differently depending on the application. T_0 and p_0 might be taken as the average ambient temperature and pressure, respectively, for the location at which the system under consideration operates. Or, if the system uses atmospheric air, T_0 might be specified as the average air temperature. If both air and water from the natural surroundings are used, T_0 would be specified as the lower of the average temperatures for air and water.

Dead States

When a system is in equilibrium with the environment, the state of the system is called the *dead state.* At the dead state, the conditions of mechanical, thermal, and chemical equilibrium between the system and the environment are satisfied: the pressure, temperature, and chemical potentials of the system equal those of the environment, respectively. In addition, the system has no motion or elevation relative to coordinates in the environment. Under these conditions, there is no possibility of a spontaneous change within the system or the environment, nor can there be an interaction between them. The value of exergy is zero.

Another type of equilibrium between the system and environment can be identified. This is a restricted form of equilibrium where only the conditions of mechanical and thermal equilibrium must be satisfied. This state of the system is called the *restricted dead state.* At the restricted dead state, the fixed quantity of matter under consideration is imagined to be sealed in an envelope impervious to mass flow, at zero velocity and elevation relative to coordinates in the environment, and at the temperature T_0 and pressure p_0.

Exergy Balances

Exergy can be transferred by three means: exergy transfer associated with work, exergy transfer associated with heat transfer, and exergy transfer associated with the matter entering and exiting a control volume. All such exergy transfers are evaluated relative to the environment used to define exergy. Exergy is also destroyed by irreversibilities within the system or control volume.

Exergy balances can be written in various forms, depending on whether a closed system or control volume is under consideration and whether steady-state or transient operation is of interest. Owing to its importance for a wide range of applications, an exergy rate balance for control volumes at steady state is presented next.

Control Volume Exergy Rate Balance

At steady state, the control volume exergy rate balance takes the form

$$0 = \underbrace{\sum_j \dot{E}_{q,j} - \dot{W}_{cv} + \sum_i \dot{E}_i - \sum_e \dot{E}_e}_{\substack{\text{rates of}\\ \text{exergy}\\ \text{transfer}}} - \underbrace{\dot{E}_D}_{\substack{\text{rate of}\\ \text{exergy}\\ \text{destruction}}} \tag{2.85a}$$

or

$$0 = \sum_j \left(1 - \frac{T_0}{T_j}\right)\dot{Q}_j - \dot{W}_{cv} + \sum_i \dot{m}_i e_i - \sum_e \dot{m}_e e_e - \dot{E}_D \tag{2.85b}$$

$\dot{W}_{cv}$ has the same significance as in Equation 2.22: the work rate excluding the flow work. $\dot{Q}_j$ is the time rate of heat transfer at the location on the boundary of the control volume where the instantaneous temperature is T_j. The associated rate of exergy transfer is

$$\dot{E}_{q,j} = \left(1 - \frac{T_0}{T_j}\right)\dot{Q}_j \tag{2.86}$$

As for other control volume rate balances, the subscripts *i* and *e* denote inlets and outlets, respectively. The exergy transfer rates at control volume inlets and outlets are denoted, respectively, as $\dot{E}_i = \dot{m}_i e_i$ and $\dot{E}_e = \dot{m}_e e_e$. Finally, $\dot{E}_D$ accounts for the time rate of exergy destruction due to irreversibilities within the control volume. The exergy destruction rate is related to the entropy generation rate by

$$\dot{E}_D = T_0 \dot{S}_{gen} \tag{2.87}$$

The specific exergy transfer terms e_i and e_e are expressible in terms of four components: physical exergy e^{PH}, kinetic exergy e^{KN}, potential exergy e^{PT}, and chemical exergy e^{CH}:

$$e = e^{PH} + e^{KN} + e^{PT} + e^{CH} \tag{2.88}$$

The first three components are evaluated as follows:

$$e^{PH} = \left(h - h_0\right) - T_0\left(s - s_0\right) \tag{2.89a}$$

$$e^{KN} = \frac{1}{2}\mathrm{v}^2 \tag{2.89b}$$

$$e^{PT} = gz \tag{2.89c}$$

In Equation 2.89a, h_0 and s_0 denote, respectively, the specific enthalpy and specific entropy at the restricted dead state. In Equation 2.89b and Equation 2.89c, v and z denote velocity and elevation relative to coordinates in the environment, respectively. The chemical exergy e^{CH} is considered next.

Chemical Exergy

To evaluate the chemical exergy, the exergy component associated with the departure of the chemical composition of a system from that of the environment, the substances comprising the system are referred to the properties of a suitably selected set of environmental substances. For this purpose, alternative models of the environment have been developed. For discussion, see, for example, Moran (1989) and Kotas (1995).

Exergy analysis is facilitated, however, by employing a *standard environment* and a corresponding table of *standard chemical exergies.* Standard chemical exergies are based on standard values of the environmental temperature T_0 and pressure p_0 — for example, 298.15 K (25°C) and 1 atm, respectively. A standard environment is also regarded as consisting of a set of reference substances with standard concentrations reflecting as closely as possible the chemical makeup of the natural environment. The reference substances generally fall into three groups: gaseous components of the atmosphere, solid substances from the lithosphere, and ionic and noninonic substances from the oceans. The chemical exergy data of Table 2.12 correspond to two alternative standard exergy reference environments, called here model I and model II, that have gained acceptance for engineering evaluations.

Although the use of standard chemical exergies greatly facilitates the application of exergy principles, the term *standard* is somewhat misleading since there is no one specification of the environment that suffices for all applications. Still, chemical exergies calculated relative to alternative specifications of the environment are generally in good agreement. For a broad range of engineering applications the simplicity and ease of use of standard chemical exergies generally outweigh any slight lack of accuracy that might result. In particular, the effect of slight variations in the values of T_0 and p_0 about the values used to determine the standard chemical exergies reported in Table 2.12 can be neglected.

The literature of exergy analysis provides several expressions allowing the chemical exergy to be evaluated in particular cases of interest. The molar chemical exergy of a gas mixture, for example, can be evaluated from

$$\bar{e}^{CH} = \sum_{i=1}^{j} y_i \bar{e}_i^{CH} + \bar{R}T_0 \sum_{i=1}^{j} y_i \ln y_i \tag{2.90}$$

where $\bar{e}_i^{CH}$ is the molar chemical exergy of the ith component.

TABLE 2.12 Standard Molar Chemical Exergy, e^{CH} (kJ/kmol), of Various Substances at 298 K and p_0

Substance	Formula	Model I[a]	Model II[b]
Nitrogen	$N_2(g)$	640	720
Oxygen	$O_2(g)$	3,950	3,970
Carbon dioxide	$CO_2(g)$	14,175	19,870
Water	$H_2O(g)$	8,635	9,500
	$H_2O(l)$	45	900
Carbon (graphite)	C(s)	404,590	410,260
Hydrogen	$H_2(g)$	235,250	236,100
Sulfur	S(s)	598,160	609,600
Carbon monoxide	CO(g)	269,410	275,100
Sulfur dioxide	$SO_2(g)$	301,940	313,400
Nitrogen monoxide	NO(g)	88,850	88,900
Nitrogen dioxide	$NO_2(g)$	55,565	55,600
Hydrogen sulfide	$H_2S(g)$	799,890	812,000
Ammonia	$NH_3(g)$	336,685	337,900
Methane	$CH_4(g)$	824,350	831,650
Ethane	$C_2H_6(g)$	1,482,035	1,495,840
Methanol	$CH_3OH(g)$	715,070	722,300
	$CH_3OH(l)$	710,745	718,000
Ethyl alcohol	$C_2H_5OH(g)$	1,348,330	1,363,900
	$C_2H_5OH(l)$	1,342,085	1,357,700

[a] Ahrendts, J. 1977. Die Exergie Chemisch Reaktionsfähiger Systeme, *VDI-Forschungsheft*. VDI-Verlag, Dusseldorf, 579. Also see Reference States, *Energy — The International Journal*, 5: 667–677, 1980. In Model I, p_0 = 1.019 atm. This model attempts to impose a criterion that the reference environment be in equilibrium. The reference substances are determined assuming restricted chemical equilibrium for nitric acid and nitrates and unrestricted thermodynamic equilibrium for all other chemical components of the atmosphere, the oceans, and a portion of the Earth's crust. The chemical composition of the gas phase of this model approximates the composition of the natural atmosphere.

[b] Szargut, J., Morris, D. R., and Steward, F. R. 1988. *Energy Analysis of Thermal, Chemical, and Metallurgical Processes*. Hemisphere, New York. In Model II, p_0 = 1.0 atm. In developing this model a reference substance is selected for each chemical element from among substances that contain the element being considered and that are abundantly present in the natural environment, even though the substances are not in completely mutual stable equilibrium. An underlying rationale for this approach is that substances found abundantly in nature have little economic value. On an overall basis, the chemical composition of the exergy reference environment of Model II is closer than Model I to the composition of the natural environment, but the equilibrium criterion is not always satisfied.

Example 13

Ignoring the kinetic and potential exergies, determine the exergy rate, in kJ/kg, associated with each of the following streams of matter:

(a) Saturated water vapor at 20 bar.
(b) Methane at 5 bar, 25°C.

Let T_0 = 298 K, p_0 = 1.013 bar (1 atm).

Solution. Equation 2.88 reduces to read

$$e = \left(h - h_0\right) - T_0\left(s - s_0\right) + e^{CH}$$

(a) From Table A.5, h = 2799.5 kJ/kg, s = 6.3409 kJ/kg · K. At T_0 = 298 K (25°C), water would be a liquid; thus with Equation 2.50c and Equation 2.50d, $h_0 \approx 104.9$ kJ/kg, $s_0 \approx 0.3674$ kJ/kg · K. Table 2.12 (model I) gives $e^{CH} = 45/18.02 = 2.5$ kJ/kg. Then

$$\begin{aligned} e &= (2799.5 - 104.9) - 298(6.3409 - 0.3674) + 2.5 \\ &= 914.5 + 2.5 = 917.0 \ \text{kJ/kg} \end{aligned}$$

Here the specific exergy is determined predominately by the physical component.

(b) Assuming the ideal gas model for methane, $h - h_0 = 0$. Also, Equation 2.58 reduces to give $s - s_0 = -R\ln p/p_0$. Then, Equation 2.88 reads

$$e = RT_0 \ln p/p_0 + e^{CH}$$

With $e^{CH} = 824{,}350/16.04 = 51{,}393.4$ kJ/kg from Table 2.12 (model I),

$$\begin{aligned} e &= \left(\frac{8.314}{16.04}\frac{\text{kJ}}{\text{kg} \cdot \text{K}}\right)(298 \text{ K})\ln\frac{5}{1.013} + 51{,}393.4\frac{\text{kJ}}{\text{kg}} \\ &= 246.6 + 51{,}393.4 \\ &= 51{,}640 \ \text{kJ/kg} \end{aligned}$$

Here the specific exergy is determined predominately by the chemical component.

The small difference between p_0 = 1.013 bar and the value of p_0 for model I has been ignored.

Exergetic Efficiency

The exergetic efficiency (second law efficiency, effectiveness, or rational efficiency) provides a true measure of the performance of a system from the thermodynamic viewpoint. To define the exergetic efficiency both a *product* and a *fuel* for the system being analyzed are identified. The product represents the desired result of the system (power, steam, some combination of power and steam, etc.). Accordingly, the definition of the product must be consistent with the purpose of purchasing and using the system. The fuel represents the resources expended to generate the product and is not necessarily restricted to being an actual fuel such as a natural gas, oil, or coal. Both the product and the fuel are expressed in terms of exergy.

For a control volume at steady state whose exergy rate balance reads

$$\dot{E}_F = \dot{E}_P + \dot{E}_D + \dot{E}_L$$

the exergetic efficiency is

$$\varepsilon = \frac{\dot{E}_P}{\dot{E}_F} = 1 - \frac{\dot{E}_D + \dot{E}_L}{\dot{E}_F} \tag{2.91}$$

where the rates at which the fuel is supplied and the product is generated are $\dot{E}_F$ and $\dot{E}_P$, respectively. $\dot{E}_D$ and $\dot{E}_L$ denote the rates of exergy destruction and exergy loss, respectively. Exergy is destroyed by irreversibilities within the control volume, and exergy is lost from the control volume via stray heat transfer, material streams vented to the surroundings, and so on. The exergetic efficiency shows the percentage of the fuel exergy provided to a control volume that is found in the product exergy. Moreover, the difference between 100% and the value of the exergetic efficiency, expressed as a percent, is the percentage of the fuel exergy wasted in this control volume as exergy destruction and exergy loss.

To apply Equation 2.91, decisions are required concerning what are considered as the fuel and the product. Table 2.13 provides illustrations for several common components. Similar considerations are used to write exergetic efficiencies for systems consisting of several such components, as, for example, a power plant.

Exergetic efficiencies can be used to assess the thermodynamic performance of a component, plant, or industry relative to the performance of *similar* components, plants, or industries. By this means the performance of a gas turbine, for instance, can be gauged relative to the typical present-day performance level of gas turbines. A comparison of exergetic efficiencies for *dissimilar* devices — gas turbines and heat exchangers, for example — is generally not significant, however.

The exergetic efficiency is generally more meaningful, objective, and useful than other efficiencies based on the first or second law of thermodynamics, including the thermal efficiency of a power plant, the isentropic efficiency of a compressor or turbine, and the effectiveness of a heat exchanger. The thermal efficiency of a cogeneration system, for instance, is misleading because it treats both work and heat transfer as having equal thermodynamic value. The isentropic turbine efficiency (Equation 2.95a) does not consider that the working fluid at the outlet of the turbine has a higher temperature (and consequently a higher exergy that may be used in the next component) in the actual process than in the isentropic process. The heat exchanger effectiveness fails, for example, to identify the exergy destruction associated with the pressure drops of the heat exchanger working fluids.

Example 14

Evaluate the exergetic efficiency of the turbine in part (a) of Example 1 for $T_0 = 298$ K.

Solution. The exergetic efficiency from Table 2.13 is

$$\varepsilon = \frac{\dot{W}}{\dot{E}_1 - \dot{E}_2} = \frac{\dot{W}}{\dot{m}\left(e_1 - e_2\right)}$$

Using Equation 2.88 and Equation 2.89a, and noting that the chemical exergy at 1 and 2 cancels,

$$\varepsilon = \frac{\dot{W}}{\dot{m}\left[\left(h_1 - h_2\right) - T_0\left(s_1 - s_2\right)\right]}$$

Since $\dot{W} = \dot{m}(h_1 - h_2)$,

$$\varepsilon = \frac{\dot{W}}{\dot{W} + \dot{m}T_0\left(s_2 - s_1\right)}$$

Finally, using data from Example 1 and $s_2 = 6.8473$ kJ/kg · K,

$$\varepsilon = \frac{30 \text{ MW}}{30 \text{ MW} + \left(\frac{162{,}357}{3600}\frac{\text{kg}}{\text{s}}\right)(298 \text{ K})(6.8473 - 6.6022)\left(\frac{\text{kJ}}{\text{kg} \cdot \text{K}}\right)\left(\frac{1 \text{ MW}}{10^3 \text{ kJ/sec}}\right)}$$

$$= \frac{30 \text{ MW}}{(30 + 3.29)\text{MW}} = 0.9(90\%)$$

TABLE 2.13 The Exergetic Efficiency for Selected Components at Steady State[a]

	Turbine or Expander	Extraction Turbine	Compressor, Pump, or Fan	Heat Exchanger[b]	Mixing Unit	Gasifier or Combustion Chamber	Boiler
Component	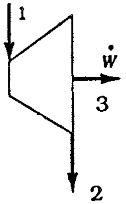	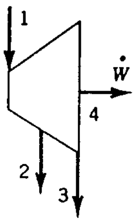	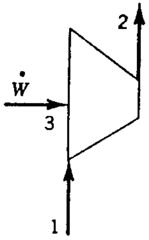	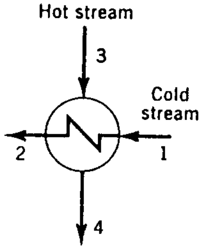	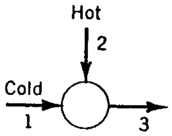	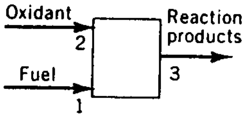	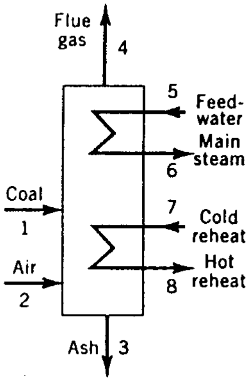
$\dot{E}_P$	$\dot{W}$	$\dot{W}$	$\dot{E}_2 - \dot{E}_1$	$\dot{E}_2 - \dot{E}_1$	$\dot{E}_3$	$\dot{E}_3$	$\left(\dot{E}_6 - \dot{E}_5\right) + \left(\dot{E}_8 - \dot{E}_7\right)$
$\dot{E}_F$	$\dot{E}_1 - \dot{E}_2$	$\dot{E}_1 - \dot{E}_2 - \dot{E}_3$	$\dot{W}$	$\dot{E}_3 - \dot{E}_4$	$\dot{E}_1 + \dot{E}_2$	$\dot{E}_1 + \dot{E}_2$	$\left(\dot{E}_1 + \dot{E}_2\right) + \left(\dot{E}_3 + \dot{E}_4\right)$
ε	$\dfrac{\dot{W}}{\dot{E}_1 - \dot{E}_2}$	$\dfrac{\dot{W}}{\dot{E}_1 - \dot{E}_2 - \dot{E}_3}$	$\dfrac{\dot{E}_2 - \dot{E}_1}{\dot{W}}$	$\dfrac{\dot{E}_2 - \dot{E}_1}{\dot{E}_3 - \dot{E}_4}$	$\dfrac{\dot{E}_3}{\dot{E}_1 + \dot{E}_2}$	$\dfrac{\dot{E}_3}{\dot{E}_1 + \dot{E}_2}$	$\dfrac{\left(\dot{E}_6 - \dot{E}_5\right) + \left(\dot{E}_8 - \dot{E}_7\right)}{\left(\dot{E}_1 + \dot{E}_2\right) - \left(\dot{E}_3 + \dot{E}_4\right)}$

---

[a] For discussion, see Bejan et al. (1996).

[b] This definition assumes that the purpose of the heat exchanger is to heat the cold stream ($T_1 \geq T_0$). If the purpose of the heat exchanger is to provide cooling ($T_3 \geq T_0$), then the following relations should be used: $\dot{E}_P = \dot{E}_4 - \dot{E}_3$ and $\dot{E}_F = \dot{E}_1 - \dot{E}_2$.

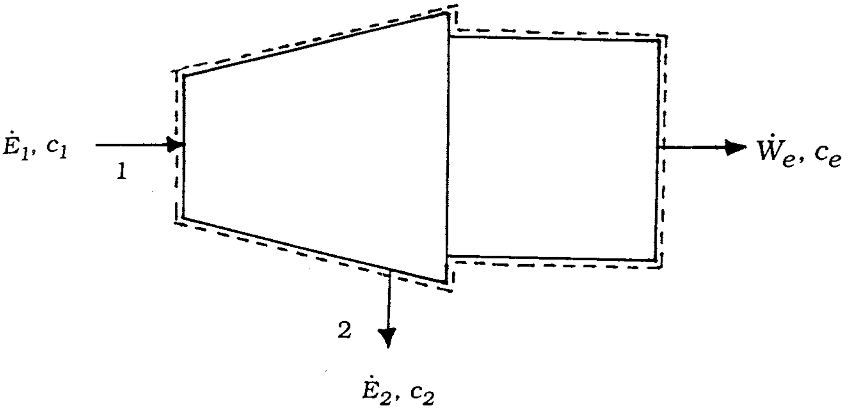

FIGURE 2.16 Steam turbine/electric generator used to discuss exergy costing.

Exergy Costing

Since exergy measures the true thermodynamic values of the work, heat, and other interactions between the system and its surroundings as well as the effect of irreversibilities within the system, exergy is a rational basis for assigning costs. This aspect of thermoeconomics is called *exergy costing.*

Referring to Figure 2.16 showing a steam turbine-electric generator at steady state, the total cost to produce the electricity and exiting steam equals the cost of the entering steam plus the cost of owning and operating the device. This is expressed by the *cost rate balance* for the turbine-generator:

$$\dot{C}_e + \dot{C}_2 = \dot{C}_1 + \dot{Z} \tag{2.92a}$$

where $\dot{C}_e$ is the cost rate associated with the electricity, $\dot{C}_1$ and $\dot{C}_2$ are the cost rates associated with the entering steam and exiting steam, respectively, and $\dot{Z}$ accounts for the cost rate associated with owning and operating the system, each *annualized* in \$ per year.

With exergy costing, the cost rates $\dot{C}_1$, $\dot{C}_2$, and $\dot{C}_e$ are evaluated in terms of the associated rate of exergy transfer and a *unit cost.* Equation 2.92a then appears as

$$c_e\dot{W}_e + c_2\dot{E}_2 = c_1\dot{E}_1 + \dot{Z} \tag{2.92b}$$

The coefficients c_1, c_2, and c_e in Equation 2.92b denote the *average* cost per unit of exergy for the associated exergy rate. The unit cost c_1 of the entering steam would be obtained from exergy costing applied to the components upstream of the turbine. Assigning the same unit cost to the exiting steam: $c_2 = c_1$ on the basis that the purpose of the turbine-generator is to generate electricity and thus all costs associated with owning and operating the system should be charged to the power, Equation 2.92b becomes

$$c_e\dot{W}_e = c_1\left(\dot{E}_1 - \dot{E}_2\right) + \dot{Z} \tag{2.92c}$$

The first term on the right side accounts for the cost of the net exergy used and the second term accounts for cost of the system itself. Introducing the exergetic efficiency from Table 2.13, the unit cost of the electricity is

$$c_e = \frac{c_1}{\varepsilon} + \frac{\dot{Z}}{\dot{W}_e} \tag{2.93}$$

This equation shows, for example, that the unit cost of electricity would increase if the exergetic efficiency were to decrease owing to a deterioration of the turbine with use.

Example 15

A turbine-generator with an exergetic efficiency of 90% develops 7×10^7 kW · hr of electricity annually. The annual cost of owning and operating the system is $\$2.5 \times 10^5$. If the average unit cost of the steam entering the system is \$0.0165 per kW · hr of exergy, evaluate the unit cost of the electricity.

Solution. Substituting values into Equation 2.93,

$$c_e = \frac{\$0.0165/\text{kW}\cdot\text{h}}{0.9} + \frac{\$2.5\times10^5/\text{year}}{7\times10^7\ \text{kW}\cdot\text{h/year}}$$

$$= 0.0183 + 0.0036 = \$0.0219/\text{kW}\cdot\text{h}$$

2.6 Vapor and Gas Power Cycles

Vapor and gas power systems develop electrical or mechanical power from energy sources of chemical, solar, or nuclear origin. In *vapor* power systems the *working fluid*, normally water, undergoes a phase change from liquid to vapor, and conversely. In *gas* power systems, the working fluid remains a gas throughout, although the composition normally varies owing to the introduction of a fuel and subsequent combustion. The present section introduces vapor and gas power systems. Further discussion is provided in Chapter 8. Refrigeration systems are considered in Chapter 9.

The processes taking place in power systems are sufficiently complicated that idealizations are typically employed to develop tractable thermodynamic models. The *air standard analysis* of gas power systems considered later in the present section is a noteworthy example. Depending on the degree of idealization, such models may provide only qualitative information about the performance of the corresponding real-world systems. Yet such information is frequently useful in gauging how changes in major operating parameters might affect actual performance. Elementary thermodynamic models can also provide simple settings to assess, at least approximately, the advantages and disadvantages of features proposed to improve thermodynamic performance.

Rankine and Brayton Cycles

In their simplest embodiments vapor power and gas turbine power plants are represented conventionally in terms of four components in series, forming, respectively, the Rankine cycle and the Brayton cycle shown schematically in Table 2.14. The thermodynamically ideal counterparts of these cycles are composed of four internally reversible processes in series: two isentropic processes alternated with two constant pressure processes. Table 2.14 provides property diagrams of the actual and corresponding ideal cycles. Each actual cycle is denoted 1-2-3-4-1; the ideal cycle is 1-2s-3-4s-1. For simplicity, pressure drops through the boiler, condenser, and heat exchangers are not shown. Invoking Equation 2.29 for the ideal cycles, the heat added per unit of mass flowing is represented by the area *under* the isobar from state 2s to state 3: area a-2s-3-b-a. The heat rejected is the area *under* the isobar from state 4s to state 1: area a-1-4s-b-a. Enclosed area 1-2s-3-4s-1 represents the net heat added per unit of mass flowing. For any power cycle, the net heat added equals the net work done.

Expressions for the principal energy transfers shown on the schematics of Table 2.14 are provided by Equation 1 to Equation 4 of the table. They are obtained by reducing Equation 2.27a with the assumptions of negligible heat loss and negligible changes in kinetic and potential energy from the inlet to the outlet of each component. All quantities are positive in the directions of the arrows on the figure. Using these expressions, the thermal efficiency is

$$\eta = \frac{(h_3 - h_4) - (h_2 - h_1)}{h_3 - h_2} \tag{2.94}$$

To obtain the thermal efficiency of the ideal cycle, h_{2s} replaces h_2 and h_{4s} replaces h_4 in Equation 2.94.

TABLE 2.14 Rankine and Brayton Cycles

Rankine Cycle

Brayton Cycle

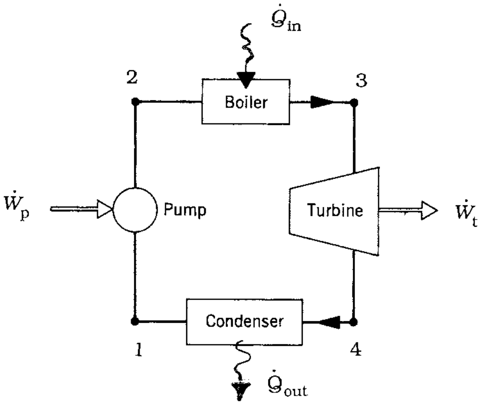

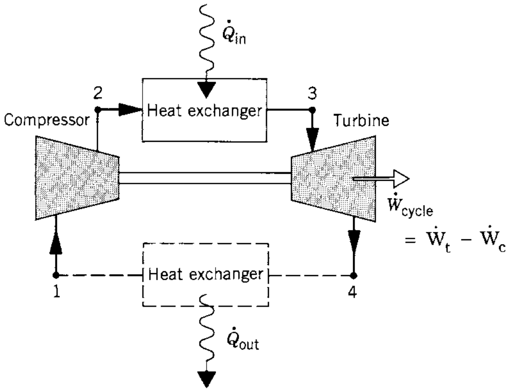

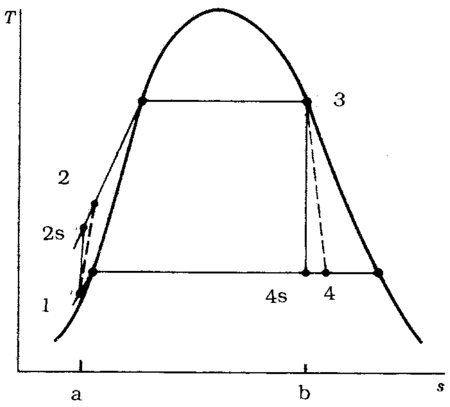

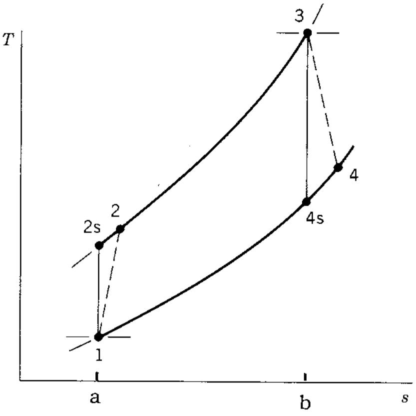

$$\left.\begin{matrix}\dot{W}_p\\ \dot{W}_c\end{matrix}\right\} = \dot{m}\left(h_2 - h_1\right) \qquad (>0) \tag{1}$$

$$\dot{Q}_{in} = \dot{m}\left(h_3 - h_2\right) \qquad (>0) \tag{2}$$

$$\dot{W}_t = \dot{m}\left(h_3 - h_4\right) \qquad (>0) \tag{3}$$

$$\dot{Q}_{out} = \dot{m}\left(h_1 - h_4\right) \qquad (>0) \tag{4}$$

Decisions concerning cycle operating conditions normally recognize that the thermal efficiency tends to increase as the average temperature of heat addition increases and/or the temperature of heat rejection decreases. In the Rankine cycle, a high average temperature of heat addition can be achieved by superheating the vapor prior to entering the turbine, and/or by operating at an elevated steam-generator pressure. In the Brayton cycle an increase in the compressor pressure ratio p_2/p_1 tends to increase the average temperature of heat addition. Owing to materials limitations at elevated temperatures and pressures, the state of the working fluid at the turbine inlet must observe practical limits, however. The turbine inlet temperature of the Brayton cycle, for example, is controlled by providing air far in excess of what is required for combustion. In a Rankine cycle using water as the working fluid, a low temperature of heat rejection is typically achieved by operating the condenser at a pressure below 1 atm. To reduce erosion and wear by liquid droplets on the blades of the Rankine cycle steam turbine, at least 90% quality should be maintained at the turbine exit: $x_4 > 0.9$.

The *back work ratio*, bwr, is the ratio of the work required by the pump or compressor to the work developed by the turbine:

$$bwr = \frac{h_2 - h_1}{h_3 - h_4} \tag{2.95}$$

As a relatively high specific volume vapor expands through the turbine of the Rankine cycle and a much lower specific volume liquid is pumped, the back work ratio is characteristically quite low in vapor power plants — in many cases on the order of 1 to 2%. In the Brayton cycle, however, both the turbine and compressor handle a relatively high specific volume gas, and the back ratio is much larger, typically 40% or more.

The effect of friction and other irreversibilities for flow-through turbines, compressors, and pumps is commonly accounted for by an appropriate *isentropic efficiency.* The isentropic turbine efficiency is

$$\eta_t = \frac{h_3 - h_4}{h_3 - h_{4s}} \tag{2.95a}$$

The isentropic compressor efficiency is

$$\eta_c = \frac{h_{2s} - h_1}{h_2 - h_1} \tag{2.95b}$$

In the isentropic pump efficiency, η_p, which takes the same form as Equation 2.95b, the numerator is frequently approximated via Equation 2.30c *as* $h_{2s} - h_1 \approx v_1 \Delta p$, where Δp is the pressure rise across the pump.

Simple gas turbine power plants differ from the Brayton cycle model in significant respects. In actual operation, excess air is continuously drawn into the compressor, where it is compressed to a higher pressure; then fuel is introduced and combustion occurs; finally the mixture of combustion products and air expands through the turbine and is subsequently discharged to the surroundings. Accordingly, the low-temperature heat exchanger shown by a dashed line in the Brayton cycle schematic of Table 2.14 is not an actual component, but included only to account formally for the cooling in the surroundings of the hot gas discharged from the turbine.

Another frequently employed idealization used with gas turbine power plants is that of an *air-standard analysis.* An air-standard analysis involves two major assumptions: (1) as shown by the Brayton cycle schematic of Table 2.14, the temperature rise that would be brought about by combustion is effected instead by a heat transfer from an external source; (2) the working fluid throughout the cycle is air, which behaves as an ideal gas. In a *cold* air-standard analysis the specific heat ratio k for air is taken as constant. Equation 1 to Equation 6 of Table 2.7 together with data from Table A.8 apply generally to air-standard analyses. Equation 1′ to Equation 6′ of Table 2.7 apply to cold air-standard analyses, as does the following expression for the turbine power obtained from Table 2.1 (Equation 27c″):

$$\dot{W}_t = \dot{m}\frac{kRT_3}{k-1}\left[1 - \left(p_4/p_3\right)^{(k-1)/k}\right] \tag{2.96}$$

(Equation 2.96 also corresponds to Equation 5′ of Table 2.8 when $n = k$.) An expression similar in form can be written for the power required by the compressor.

TABLE 2.15 Sample Calculations for the Rankine and Brayton Cycles of Table 2.14

Rankine Cycle

Given data: $p_1 = p_4 = 8$ kPa (saturated liquid at 1)
$T_3 = 480$°C (superheated vapor at 3)
$p_2 = p_3 = 8$ MPa
$\dot{W}_{net} = 100$ MW
Ideal cycle: $\eta_t = \eta_p = 100\%$
Actual cycle: $\eta_t = 85\%$, $\eta_p = 70\%$

Parameter	Ideal Cycle	Actual Cycle
x_4	0.794	0.873
h_2 (kJ/ kg)	181.9[a]	185.4
$\dot{m}$ (kg/h)	2.86×10^5	3.38×10^5
η (%)	39.7	33.6
$\dot{Q}_{out}$ (MW)	151.9	197.6
$\dot{E}_{q,out}$ (MW)[b]	8.2	10.7

[a] $h_{2s} \approx h_1 + v_1 \Delta p$

[b] Equation 2.86 with $T_0 = 298$ K, $T_j = T_{sat}$ (8 kPa) = 315 K

Brayton Cycle

Given data: $p_1 = p_4 = 1$ bar
$p_2 = p_3 = 10$ bar
$T_3 = 1400$ K
$\eta_t = \eta_c = 100\%$

Parameter	Air-Standard Analysis	Cold Air-Standard Analysis $k = 1.4$
T_2 (K)	574.1	579.2
T_4 (K)	787.7	725.1
$\dot{W}_{net}/\dot{m}$ (kJ/kg)	427.2	397.5
η (%)	45.7	48.2
bwr	0.396	0.414

For the simple Rankine and Brayton cycles of Table 2.14 the results of sample calculations are provided in Table 2.15. The Brayton cycle calculations are on an air-standard analysis basis.

Otto, Diesel, and Dual Cycles

Although most gas turbines are also internal combustion engines, the name is usually reserved to *reciprocating* internal combustion engines of the type commonly used in automobiles, trucks, and buses. Two principal types of reciprocating internal combustion engines are the *spark-ignition* engine and the *compression-ignition* engine. In a spark-ignition engine a mixture of fuel and air is ignited by a spark plug. In a compression ignition engine air is compressed to a high-enough pressure and temperature that combustion occurs spontaneously when fuel is injected.

In a *four-stroke* internal combustion engine, a piston executes four distinct strokes within a cylinder for every two revolutions of the crankshaft. Figure 2.17 gives *a* pressure-displacement diagram as it might

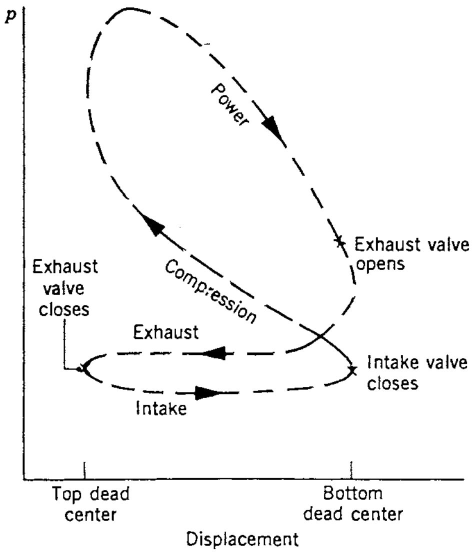

FIGURE 2.17 Pressure-displacement diagram for a reciprocating internal combustion engine.

be displayed electronically. With the intake valve open, the piston makes an *intake stroke* to draw a fresh charge into the cylinder. Next, with both valves closed, the piston undergoes a *compression stroke* raising the temperature and pressure of the charge. A combustion process is then initiated, resulting in a high-pressure, high-temperature gas mixture. A *power* stroke follows the compression stroke, during which the gas mixture expands and work is done on the piston. The piston then executes an *exhaust stroke* in which the burned gases are purged from the cylinder through the open exhaust valve. Smaller engines operate on *two-stroke* cycles. In two-stroke engines, the intake, compression, expansion, and exhaust operations are accomplished in one revolution of the crankshaft. Although internal combustion engines undergo *mechanical* cycles, the cylinder contents do not execute a *thermodynamic* cycle, since matter is introduced with one composition and is later discharged at a different composition.

A parameter used to describe the performance of reciprocating piston engines is the *mean effective pressure*, or mep. The mean effective pressure is the theoretical constant pressure that, if it acted on the piston during the power stroke, would produce the same *net* work as actually developed in one cycle. That is,

$$\text{mep} = \frac{\text{net work for one cycle}}{\text{displacement volume}} \tag{2.97}$$

where the displacement volume is the volume swept out by the piston as it moves from the top dead center to the bottom dead center. For two engines of equal displacement volume, the one with a higher mean effective pressure would produce the greater net work and, if the engines run at the same speed, greater power.

Detailed studies of the performance of reciprocating internal combustion engines may take into account many features, including the combustion process occurring within the cylinder and the effects of irreversibilities associated with friction and with pressure and temperature gradients. Heat transfer between the gases in the cylinder and the cylinder walls and the work required to charge the cylinder and exhaust the products of combustion also might be considered. Owing to these complexities, accurate modeling of reciprocating internal combustion engines normally involves computer simulation.

To conduct *elementary* thermodynamic analyses of internal combustion engines, considerable simplification is required. A procedure that allows engines to be studied *qualitatively* is to employ an *air-standard analysis* having the following elements: (1) a fixed amount of air modeled as an ideal gas is the system; (2) the combustion process is replaced by a heat transfer from an external source and generally represented in terms of elementary thermodynamic processes; (3) there are no exhaust and intake processes as in an actual engine: the cycle is completed by a constant-volume heat rejection process; (4) all processes are internally reversible.

The processes employed in air-standard analyses of internal combustion engines are selected to represent the events taking place within the engine simply and mimic the appearance of observed pressure-displacement diagrams. In addition to the constant volume heat rejection noted previously, the compression stroke and at least a portion of the power stroke are conventionally taken as isentropic. The heat addition is normally considered to occur at constant volume, at constant pressure, or at constant volume followed by a constant pressure process, yielding, respectively, the Otto, Diesel, and Dual cycles shown in Table 2.16.

Reducing the closed system energy balance, Equation 2.8, gives the following expressions for heat and work applicable in each case shown in Table 2.16:

$$\frac{W_{12}}{m} = u_1 - u_2 \qquad (< 0)$$

$$\frac{W_{34}}{m} = u_3 - u_4 \qquad (> 0)$$

$$\frac{Q_{41}}{m} = u_1 - u_4 \qquad (< 0)$$

Table 2.16 provides additional expressions for work, heat transfer, and thermal efficiency identified with each case individually. The thermal efficiency, evaluated from Equation 2.9, takes the form

$$\eta = 1 - \frac{\left|Q_{41}/m\right|}{Q_A/m}$$

Equation 1 to Equation 6 of Table 2.7 together with data from Table A.8, apply generally to air-standard analyses. In a *cold* air-standard analysis the specific heat ratio k for air is taken as constant. Equation 1′ to Equation 6′ of Table 2.7 apply to cold air-standard analyses, as does Equation 4′ of Table 2.8, with $n = k$ for the isentropic processes of these cycles.

Referring to Table 2.16, the ratio v_1/v_2 is the *compression ratio, r*. For the Diesel cycle, the ratio v_3/v_2 is the *cutoff ratio*, r_c. Figure 2.18 shows the variation of the thermal efficiency with compression ratio for an Otto cycle and Diesel cycles having cutoff ratios of 2 and 3. The curves are determined on a cold air-standard basis with $k = 1.4$ using the following expression:

$$\eta = 1 - \frac{1}{r^{k-1}}\left[\frac{r_c^k - 1}{k\left(r_c - 1\right)}\right] \qquad \text{(constant } k\text{)} \tag{2.98}$$

where the Otto cycle corresponds to $r_c = 1$.

As all processes are internally reversible, areas on the p-v and T-s diagrams of Table 2.16 can be interpreted, respectively, as work and heat transfer. Invoking Equation 2.10 and referring to the p-v diagrams, the areas under process 3-4 of the Otto cycle, process 2-3-4 of the Diesel cycle, and process x-3-4 of the Dual cycle represent the work done by the gas during the power stroke, per unit of mass. For each cycle, the area under the isentropic process 1-2 represents the work done on the gas during the compression stroke, per unit of mass. The enclosed area of each cycle represents the net work done per unit mass. With Equation 2.15 and referring to the T-s diagrams, the areas under process 2-3 of the Otto and Diesel cycles and under process 2-x-3 of the Dual cycle represent the heat added per unit of mass. For each cycle, the area under the process 4-1 represent the heat rejected per unit of mass. The enclosed area of each cycle represents the net heat added, which equals the net work done, each per unit of mass.

TABLE 2.16 Otto, Diesel, and Dual Cycles

(a) Otto Cycle	(b) Diesel Cycle	(c) Dual Cycle
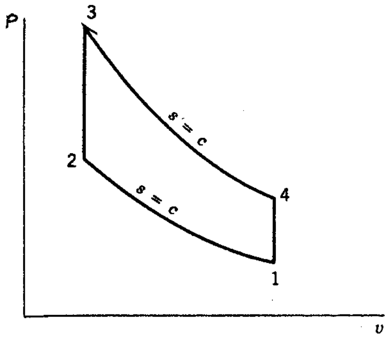	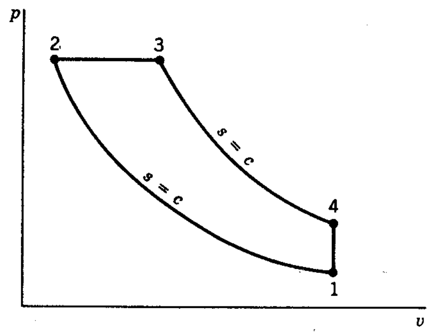	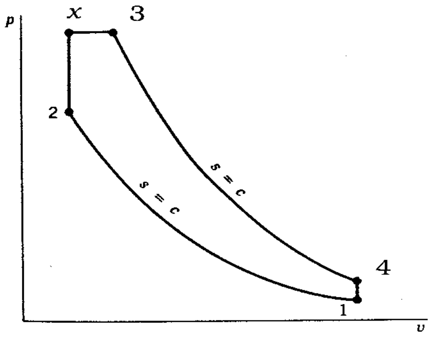
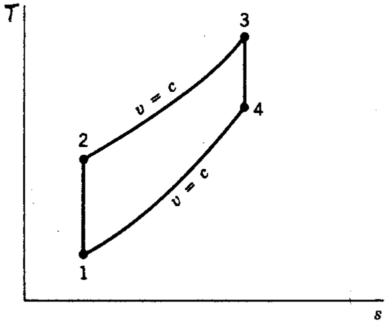	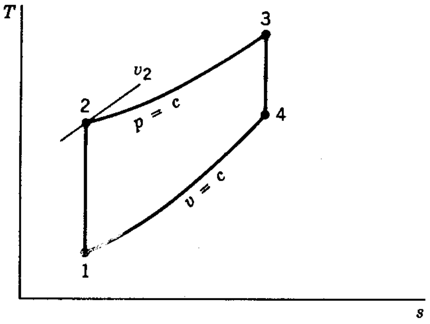	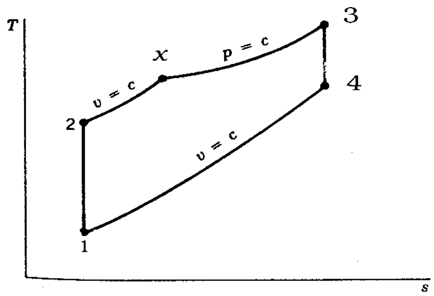
$\frac{W_{23}}{m} = 0$	$\frac{W_{23}}{m} = p_2\left(v_3 - v_2\right)$	$\frac{W_{2x}}{m} = 0, \quad \frac{Q_{2x}}{m} = u_x - u_2$
$\frac{Q_{23}}{m} = u_3 - u_2$	$\frac{Q_{23}}{m} = h_3 - h_2$	$\frac{W_{x3}}{m} = p_3\left(v_3 - v_2\right), \quad \frac{Q_{x3}}{m} = h_3 - h_x$
$\eta = 1 - \frac{u_4 - u_1}{u_3 - u_2}$	$\eta = 1 - \frac{u_4 - u_1}{h_3 - h_2}$	$\eta = 1 - \frac{u_4 - u_1}{\left(u_x - u_2\right) + \left(h_3 - h_x\right)}$

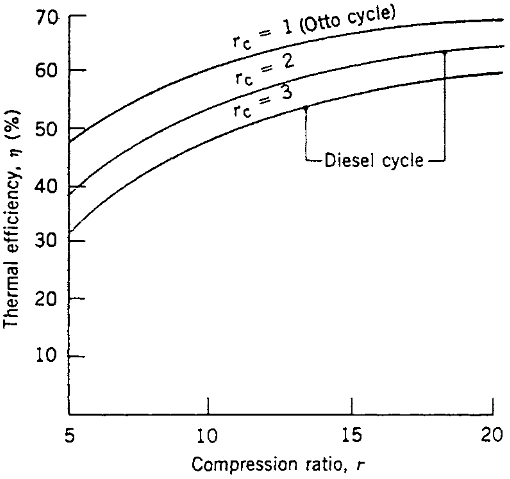

FIGURE 2.18 Thermal efficiency of the cold air-standard Otto and Diesel cycles, $k = 1.4$.

Carnot, Ericsson, and Stirling Cycles

Three thermodynamic cycles that exhibit the Carnot efficiency (Equation 2.12) are the Carnot, Ericsson, and Stirling cycles shown in Figure 2.19. Each case represents a reversible power cycle in which heat is added from an external source at a constant temperature T_H (process 2-3) and rejected to the surroundings at a constant temperature T_C (process 4-1). Carnot cycles can be configured both as vapor power cycles and as cycles executed by a gas in a piston-cylinder assembly (see, e.g., Moran and Shapiro, 1995). Carnot cycles also can be executed in systems where a capacitor is charged and discharged, a paramagnetic substance is magnetized and demagnetized, and in other ways. Regardless of the type of device and the working substance used, the Carnot cycle always has the same four internally reversible processes in series: two isentropic processes alternated with two isothermal processes.

The Ericsson and Stirling cycles also consist of four internally reversible processes in series: heating from state 1 to state 2 (at constant pressure in the Ericsson cycle and at constant volume in the Stirling cycle), isothermal heating from state 2 to state 3 at temperature T_H, cooling from state 3 to state 4 (at constant pressure in the Ericsson cycle and at constant volume in the Stirling cycle), and isothermal cooling from state 4 to state 1 at temperature T_C. An ideal regenerator allows the heat input required for process 1-2 to be obtained from the heat rejected in process 3-4. Accordingly, as in the Carnot cycle all the heat added externally occurs at T_H and all of the heat rejected to the surroundings occurs at T_C.

The Ericsson and Stirling cycles are principally of theoretical interest as examples of cycles that exhibit the same thermal efficiency as the Carnot cycle: Equation 2.12. However, a practical engine of the piston-cylinder type that operates on a closed regenerative cycle having features in common with the Stirling cycle has been under study in recent years. This engine, known as the *Stirling engine*, offers the opportunity for high efficiency together with reduced emissions from combustion products because the combustion takes place externally and not within the cylinder as in internal combustion engines. In the Stirling engine, energy is transferred to the working fluid from products of combustion, which are kept separate. It is an *external* combustion engine.

2.7 Guidelines for Improving Thermodynamic Effectiveness

Thermal design frequently aims at the most effective system from the cost viewpoint. Still, in the cost optimization process, particularly of complex energy systems, it is often expedient to begin by identifying a design that is nearly optimal thermodynamically; such a design can then be used as a point of departure for cost optimization. Presented in this section are guidelines for improving the use of fuels (natural gas,

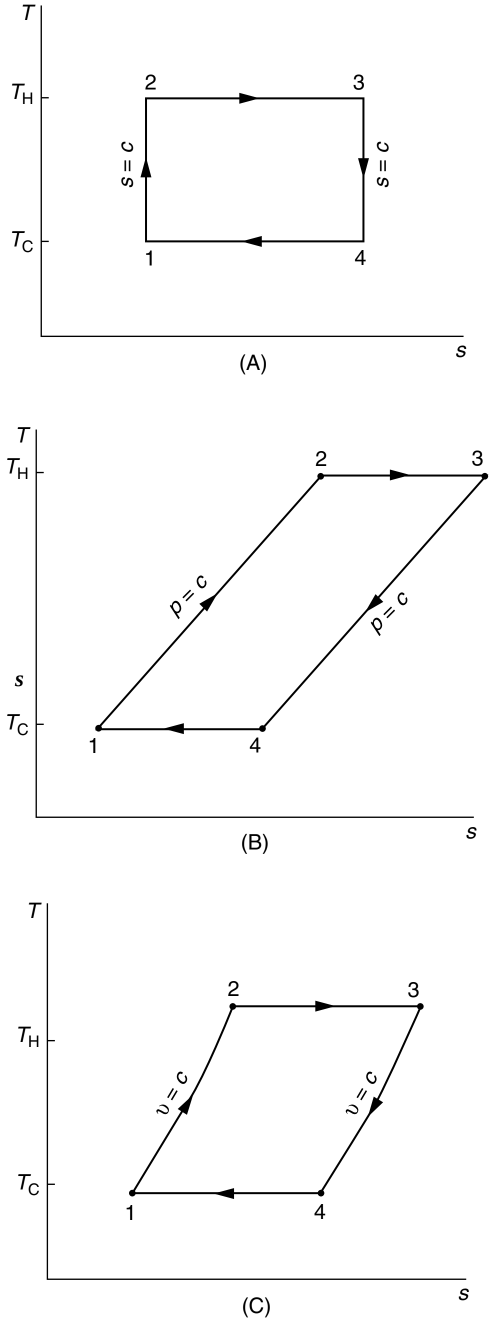

FIGURE 2.19 (A) Carnot, (B) Ericsson, and (C) Stirling cycles.

oil, and coal) by reducing sources of thermodynamic inefficiency in thermal systems. Further discussion is provided by Bejan et al. (1996).

To improve thermodynamic effectiveness it is necessary to deal directly with inefficiencies related to exergy destruction and exergy loss. The primary contributors to exergy destruction are chemical reaction, heat transfer, mixing, and friction, including unrestrained expansions of gases and liquids. To deal with them effectively, the principal sources of inefficiency not only should be understood qualitatively, but also determined quantitatively, at least approximately. Design changes to improve effectiveness must be done judiciously, however, for the cost associated with different sources of inefficiency can be different. For example, the unit cost of the electrical or mechanical power required to provide for the exergy destroyed owing to a pressure drop is generally higher than the unit cost of the fuel required for the exergy destruction caused by combustion or heat transfer.

Since chemical reaction is a significant source of thermodynamic inefficiency, it is generally good practice to minimize the use of combustion. In many applications the use of combustion equipment such as boilers is unavoidable, however. In these cases a significant reduction in the combustion irreversibility by conventional means simply cannot be expected, for the major part of the exergy destruction introduced by combustion is an inevitable consequence of incorporating such equipment. Still, the exergy destruction in practical combustion systems can be reduced by minimizing the use of excess air and by preheating the reactants. In most cases only a small part of the exergy destruction in a combustion chamber can be avoided by these means. Consequently, after considering such options for reducing the exergy destruction related to combustion, efforts to improve thermodynamic performance should focus on components of the overall system that are more amenable to betterment by cost-effective conventional measures. In other words, *some exergy destructions and energy losses can be avoided*, *others cannot. Efforts should be centered on those that can be avoided.*

Nonidealities associated with heat transfer also typically contribute heavily to inefficiency. Accordingly, unnecessary or cost-ineffective heat transfer must be avoided. Additional guidelines follow:

- The higher the temperature T at which a heat transfer occurs in cases where $T > T_0$, where T_0 denotes the temperature of the environment (Section 2.5), the more valuable the heat transfer and, consequently, the greater the need to avoid heat transfer to the ambient, to cooling water, or to a refrigerated stream. Heat transfer across T_0 should be avoided.
- The lower the temperature T at which a heat transfer occurs in cases where $T < T_0$, the more valuable the heat transfer and, consequently, the greater the need to avoid direct heat transfer with the ambient or a heated stream.
- Since exergy destruction associated with heat transfer between streams varies inversely with the temperature level, the lower the temperature level, the greater the need to minimize the stream-to-stream temperature difference.
- Avoid the use of intermediate heat transfer fluids when exchanging energy by heat transfer between two streams

Although irreversibilities related to friction, unrestrained expansion, and mixing are often secondary in importance to those of combustion and heat transfer, they should not be overlooked, and the following guidelines apply:

- Relatively more attention should be paid to the design of the lower temperature stages of turbines and compressors (the last stages of turbines and the first stages of compressors) than to the remaining stages of these devices.
- For turbines, compressors, and motors, consider the most thermodynamically efficient options.
- Minimize the use of throttling; check whether power recovery expanders are a cost-effective alternative for pressure reduction.
- Avoid processes using excessively large thermodynamic driving forces (differences in temperature, pressure, and chemical composition). In particular, minimize the mixing of streams differing significantly in temperature, pressure, or chemical composition.
- The greater the mass rate of flow, the greater the need to use the exergy of the stream effectively.
- The lower the temperature level, the greater the need to minimize friction.

Flowsheeting or *process simulation* software can assist efforts aimed at improving thermodynamic effectiveness by allowing engineers to readily model the behavior of an overall system, or system components, under specified conditions and do the required thermal analysis, sizing, costing, and optimization. Many of the more widely used flowsheeting programs: ASPEN PLUS, PROCESS, and CHEMCAD are of the *sequential-modular* type. SPEEDUP is a popular program of the *equation-solver* type. Since process simulation is a rapidly evolving field, vendors should be contacted for up-to-date information concerning the features of flowsheeting software, including optimization capabilities (if any). As background for further investigation of suitable software, see Biegler (1989) for a survey of the capabilities of 15 software products.

References

Ahrendts, J. 1980. Reference states. *Energy Int. J.* 5: 667–677.

ASHRAE Handbook 1993 Fundamentals. 1993. American Society of Heating, Refrigerating, and Air Conditioning Engineers, Atlanta.

ASME Steam Tables, 6th ed. 1993. ASME Press, Fairfield, NJ.

Bejan, A., Tsatsaronis, G., and Moran, M. 1996. *Thermal Design and Optimization*, John Wiley & Sons, New York.

Biegler, L.T. 1989. Chemical process simulation. *Chem. Eng. Progr.* October: 50–61.

Bird, R.B., Stewart, W.E., and Lightfoot, E.N. 1960. *Transport Phenomena*. John Wiley & Sons, New York.

Bolz, R.E. and Tuve, G.L. (eds.). 1973. *Handbook of Tables for Applied Engineering Science*, 2nd ed. CRC Press, Boca Raton, FL.

Bornakke, C. and Sonntag, R.E. 1996. *Tables of Thermodynamic and Transport Properties*. John Wiley & Sons, New York.

Cooper, H.W. and Goldfrank, J.C. 1967. B-W-R constants and new correlations. *Hydrocarbon Processing*. 46(12): 141–146.

Gray, D.E. (ed.). 1972. *American Institute of Physics Handbook*. McGraw-Hill, New York.

Haar, L. Gallagher, J.S., and Kell, G.S. 1984. *NBS/NRC Steam Tables*. Hemisphere, New York.

Handbook of Chemistry and Physics, annual editions. CRC Press, Boca Raton, FL.

JANAF Thermochemical Tables, 3rd ed. 1986. American Chemical Society and the American Institute of Physics for the National Bureau of Standards.

Jones, J.B. and Dugan, R.E. 1996. *Engineering Thermodynamics*. Prentice-Hall, Englewood Cliffs, NJ.

Keenan, J.H., Keyes, F.G., Hill, P.G., and Moore, J.G. 1969 and 1978. *Steam Tables*. John Wiley & Sons, New York (1969, English Units; 1978, SI Units).

Keenan, J.H., Chao, J., and Kaye, J. 1980 and 1983. *Gas Tables — International Version*, 2nd ed. John Wiley & Sons, New York (1980, English Units; 1983, SI Units).

Knacke, O., Kubaschewski, O., and Hesselmann, K. 1991. *Thermochemical Properties of Inorganic Substances*, 2nd ed. Springer-Verlag, Berlin.

Kotas, T.J. 1995. *The Exergy Method of Thermal Plant Analysis*, Krieger, Melbourne, FL.

Lee, B.I. and Kessler, M.G. 1975. A generalized thermodynamic correlation based on three-parameter corresponding states. *AIChE J.* 21: 510–527.

Liley, P.E. 1987. Thermodynamic properties of substances. In *Marks' Standard Handbook for Mechanical Engineers*, E.A. Avallone and T. Baumeister, (eds.). 9th ed. McGraw-Hill, New York, Sec. 4.2.

Liley, P.E., Reid, R.C., and Buck, E. 1984. Physical and chemical data. In *Perrys' Chemical Engineers, Handbook*, R.H. Perry and D.W. Green, (eds.). 6th ed. McGraw-Hill, New York, Sec. 3.

Moran, M.J. 1989. *Availability Analysis — A Guide to Efficient Energy Use*. ASME Press, New York.

Moran, M.J. and Shapiro, H.N. 2004. *Fundamentals of Engineering Thermodynamics*, 5th ed. John Wiley & Sons, New York.

Moran, M.J. and Shapiro, H.N. 2004. *IT: Interactive Thermodynamics*. Computer software to accompany *Fundamentals of Engineering Thermodynamics*, 5th ed. developed by Intellipro Inc., John Wiley & Sons, New York.

Obert, E.F. 1960. *Concepts of Thermodynamics*. McGraw-Hill, New York.

Preston-Thomas, H. 1990. The International Temperature Scale of 1990 (ITS-90). *Metrologia*. 27: 3–10.

Reid, R.C. and Sherwood, T.K. 1966. *The Properties of Gases and Liquids*, 2nd ed. McGraw-Hill, New York.

Reid, R.C., Prausnitz, J.M., and Poling, B.E. 1987. *The Properties of Gases and Liquids*, *4th ed.* McGraw-Hill, New York.

Reynolds, W.C. 1979. *Thermodynamic Properties in SI — Graphs, Tables and Computational Equations for 40 Substances*. Department of Mechanical Engineering, Stanford University, Palo Alto, CA.

Stephan, K. 1994. Tables. In *Dubbel Handbook of Mechanical Engineering*, W. Beitz and K.-H. Kuttner, (eds.). Springer-Verlag, London, Sec. C11.

Szargut, J., Morris, D.R., and Steward, F.R. 1988. *Exergy Analysis of Thermal, Chemical and Metallurgical Processes*. Hemisphere, New York.

Van Wylen, G.J., Sonntag, R.E., and Bornakke, C. 1994. *Fundamentals of Classical Thermodynamics*, 4th ed. John Wiley & Sons, New York.

Wark, K. 1983. *Thermodynamics*, 4th ed. McGraw-Hill, New York

Zemansky, M.W. 1972. Thermodynamic symbols, definitions, and equations. In *American Institute of Physics Handbook*, D.E. Gray, (ed.). McGraw-Hill, New York, Sec. 4b.

Frank Kreith
University of Colorado, Boulder

Stanley A. Berger
University of California, Berkeley

Stuart W. Churchill
University of Pennsylvania

J. Paul Tullis
Tullis Engineering Consultants

Blake P. Tullis
Utah State University

Frank M. White
University of Rhode Island

Ajay Kumar
NASA Langley Research Center

Jessica Todd
University of Colorado, Boulder

John C. Chen
Lehigh University

Thomas F. Irvine, Jr. (Deceased)
State University of New York, Stony Brook

Massimo Capobianchi
Gonzaga University

Francis E. Kennedy
Dartmouth College

E. Richard Booser
Consultant

Donald F. Wilcock (Deceased)
Tribolock, Inc.

Robert F. Boehm
University of Nevada, Las Vegas

Rolf D. Reitz
University of Wisconsin

Jungho Kim
University of Maryland

Alan T. McDonald
Purdue University

Sherif A. Sherif
University of Florida

Bharat Bhushan
The Ohio State University

3

Fluid Mechanics

3.1 Fluid Statics

Stanley A. Berger

Equilibrium of a Fluid Element

If the sum of the external forces acting on a fluid element is zero, the fluid will be at rest or moving as a solid body — in either case, the fluid element is in *equilibrium*. This section considers fluids in such an equilibrium state. For fluids in equilibrium, the only internal stresses acting will be normal forces because the shear stresses depend on velocity gradients, and all such gradients, by the definition of equilibrium, are zero. If one then carries out a balance between the body forces, assumed proportional to volume or mass — such as gravity — and the normal surface stresses acting on an elementary prismatic fluid volume, the resulting equilibrium equations, after shrinking the volume to zero, show that the normal stresses at a point are the same in all directions; because they are known to be negative, this common value, called the pressure, is denoted by $-p$.

Hydrostatic Pressure

Carrying out an equilibrium of forces on an elementary volume element $dxdydz$, the forces being pressures acting on the faces of the element and gravity acting in the $-z$ direction, one obtains

$$\frac{\partial p}{\partial x} = \frac{\partial p}{\partial y} = 0, \text{ and } \frac{\partial p}{\partial z} = -\rho g \equiv -\gamma \tag{3.1.1}$$

where γ is the specific weight of the fluid. The first two of these imply that the pressure is the same in all directions at the same vertical height in a gravitational field. The third shows that the pressure increases with depth in a gravitational field, the variation depending on $\rho(z)$. For homogeneous fluids, for which ρ = const., this last equation can be integrated, yielding

$$p_2 - p_1 = -\rho g\left(z_2 - z_1\right) = -\rho g\left(h_2 - h_1\right) \tag{3.1.2}$$

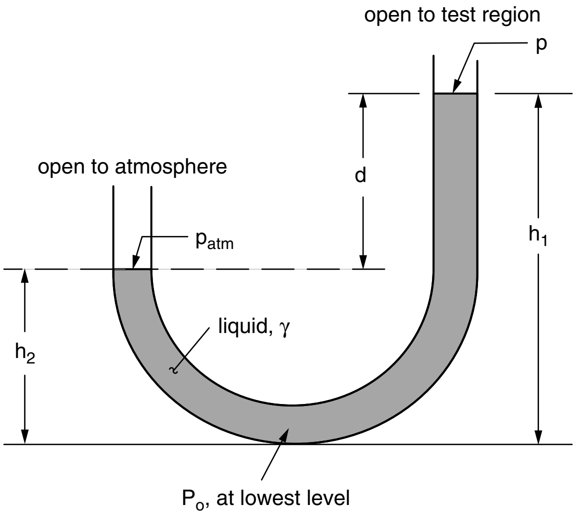

FIGURE 3.1.1 U-tube manometer.

or

$$p_2 + \rho g h_2 = p_1 + \rho g h_1 = \text{const.} \tag{3.1.3}$$

where h denotes the elevation. These are the equations for the *hydrostatic pressure variation*.

When applied to problems in which a liquid, such as the ocean, lies below the atmosphere, with constant pressure p_{atm}, h is usually measured from the ocean/atmosphere interface; p at any distance h below this interface differs from p_{atm} by an amount

$$p - p_{\text{atm}} = \rho g h \tag{3.1.4}$$

Pressures may be given as *absolute pressure*, which is pressure measured relative to absolute vacuum, or *gauge pressure*, pressure measured relative to atmospheric pressure.

Manometry

The hydrostatic pressure variation may be employed to measure pressure differences in terms of heights of liquid columns, Such devices are called *manometers* and are commonly used in wind tunnels and in a host of other applications and devices. Consider, for example, the U-tube manometer shown in Figure 3.1.1 filled with liquid of specific weight γ, the left leg open to the atmosphere and the right to the region whose pressure p is to be determined. In terms of the quantities shown in the figure:

$$\text{in left leg:} \qquad p_0 - \rho g h_2 = p_{\text{atm}} \tag{3.1.5a}$$

$$\text{in right leg:} \quad p_0 - \rho g h_1 = p \tag{3.1.5b}$$

The difference is

$$p - p_{\text{atm}} = -\rho g\left(h_1 - h_2\right) = -\rho g d = -\gamma d \tag{3.1.6}$$

and p is determined in terms of the height difference $d = h_1 - h_2$ between the levels of the fluid in the two legs of the manometer.

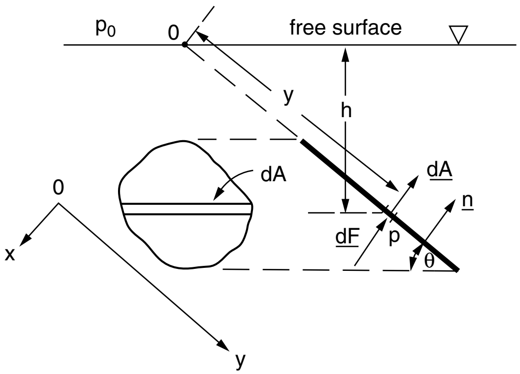

FIGURE 3.1.2 Hydrostatic force on a plane surface.

Hydrostatic Forces on Submerged Objects

Now consider the force acting on a submerged object due to the hydrostatic pressure. This is given by

$$\boldsymbol{F} = \iint p\, \boldsymbol{dA} = \iint p \cdot \boldsymbol{n}\, dA = \iint \rho g h\, \boldsymbol{dA} + p_0 \iint \boldsymbol{dA} \tag{3.1.7}$$

where h is the variable vertical depth of the element $\boldsymbol{dA}$; $\boldsymbol{n}$ is the local (outward) normal to this elemental area, and p_0 is the pressure at the surface. In turn, consider plane and nonplanar surfaces.

Forces on Plane Surfaces

Consider the planar surface A at an angle θ to a free surface shown in Figure 3.1.2. The force on one side of the planar surface, from Equation (3.1.7), is

$$\boldsymbol{F} = \rho g \boldsymbol{n} \iint_A h\, dA + p_0 A \boldsymbol{n} \tag{3.1.8}$$

but $h = y \sin\theta$, so

$$\iint_A h\, dA = \sin\theta \iint_A y\, dA = y_c A \sin\theta = h_c A \tag{3.1.9}$$

where the subscript c indicates the distance measured to the centroid of the area A. Thus, the total force (on one side) is

$$\boldsymbol{F} = \gamma h_c \boldsymbol{A} + p_0 \boldsymbol{A} \tag{3.1.10}$$

Thus, the magnitude of the force is independent of the angle θ and is equal to the pressure at the centroid, $\gamma h_c + p_0$, times the area. If gauge pressure is used, the term $p_0 A$ in Equation (3.1.10) is dropped.

Because p is not evenly distributed over A, but varies with depth, $\boldsymbol{F}$ does not act through the centroid. The point of action of $\boldsymbol{F}$, called the *center of pressure*, can be determined by considering moments in Figure 3.1.2. The moment of the hydrostatic force acting on the elementary area $\boldsymbol{dA}$ about the axis perpendicular to the page passing through the point 0 on the free surface is

$$y\, dF = y(\gamma\, y \sin\theta\, dA) = \gamma\, y^2 \sin\theta\, dA \tag{3.1.11}$$

so, if y_{cp} denotes the distance to the center of pressure,

$$y_{\mathrm{cp}} F = \gamma \sin\theta \iint y^2 \, dA = \gamma \sin\theta \, I_x \tag{3.1.12}$$

where I_x is the moment of inertia of the plane area with respect to the axis formed by the intersection of the plane containing the planar surface and the free surface (e.g., 0x). Dividing by $F = \gamma h_c A = \gamma y_c \sin\theta A$ gives

$$y_{\mathrm{cp}} = \frac{I_{\mathrm{x}}}{y_c A} \tag{3.1.13}$$

By using the parallel axis theorem $I_{\mathrm{x}} = I_{\mathrm{xc}} + A y_{\mathrm{c}}^2$, where I_{xc} is the moment of inertia with respect to an axis parallel to 0x passing through the centroid, Equation (3.1.13) becomes

$$y_{\mathrm{cp}} = y_{\mathrm{c}} + \frac{I_{\mathrm{xc}}}{y_{\mathrm{c}} A} \tag{3.1.14}$$

which shows that, in general, the center of pressure lies below the centroid.

Similarly, x_{cp} can be found by taking moments about the y axis, specifically

$$x_{\mathrm{cp}} F = \gamma \sin\theta \iint xy \, dA = \gamma \sin\theta \, I_{xy} \tag{3.1.15}$$

or

$$x_{\mathrm{cp}} = \frac{I_{\mathrm{xy}}}{y_{\mathrm{c}} A} \tag{3.1.16}$$

where I_{xy} is the product of inertia with respect to the x and y axes. Again, the parallel axis theorem, $I_{xy} = I_{xyc} + A x_c y_c$, where the subscript c denotes the value at the centroid, allows Equation (3.1.16) to be written

$$x_{\mathrm{cp}} = x_{\mathrm{c}} + \frac{I_{\mathrm{xyc}}}{y_{\mathrm{c}} A} \tag{3.1.17}$$

This completes the determination of the center of pressure (x_{cp}, y_{cp}). Note that if the submerged area is symmetrical with respect to an axis passing through the centroid and parallel to the x or y axis, $I_{xyc} = 0$ and $x_{\mathrm{cp}} = x_c$; also, as y_c increases, $y_{\mathrm{cp}} \to y_c$. Centroidal moments of inertia and centroidal coordinates for some common areas are shown in Figure 3.1.3.

Forces on Curved Surfaces

The most convenient approach to calculating the pressure force on a curved surface is by separating it into its horizontal and vertical components. A free-body diagram of the forces acting on the volume of fluid lying above a curved surface together with the conditions of static equilibrium of such a column shows that:

- The *horizontal* components of force on a curved submerged surface are equal to the forces exerted on the planar areas formed by the projections of the curved surface onto vertical planes normal to these components; the lines of action of these forces are calculated as described earlier for planar surfaces.
- The *vertical* component of force on a curved submerged surface is equal in magnitude to the weight of the entire column of fluid lying above the curved surface and acts through the center of mass of this volume of fluid.

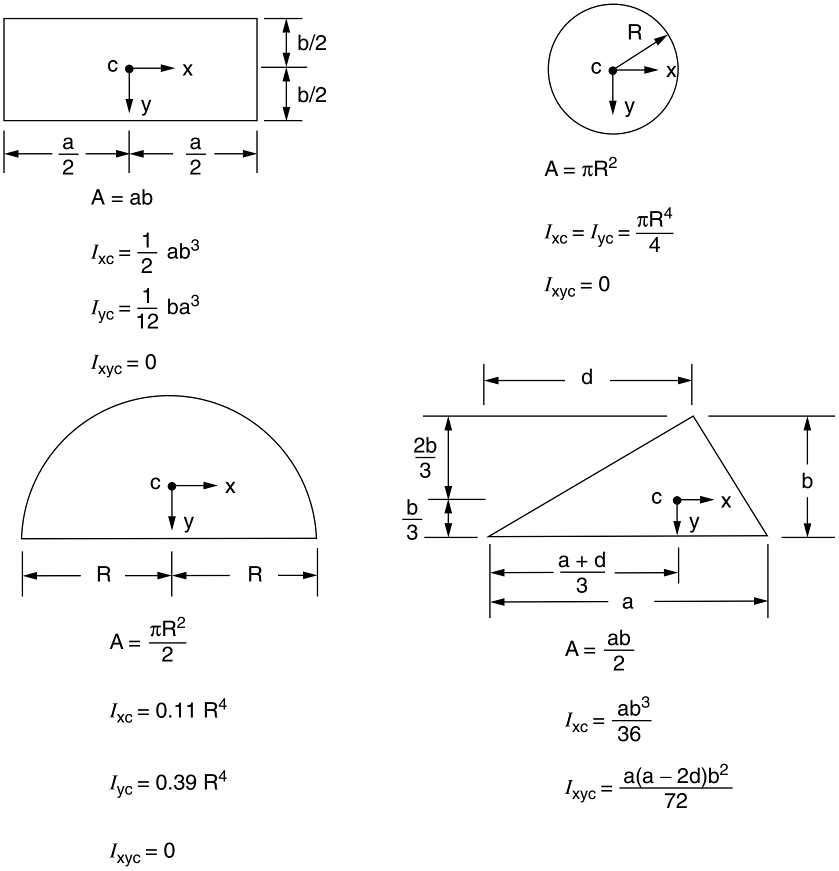

FIGURE 3.1.3 Centroidal moments of inertia and coordinates for some common areas.

These three components of force, two horizontal and one vertical, need not meet at a single point, so there is, in general, no single resultant force. They may, however, be combined into a single force at any arbitrary point of application together with a moment about that point.

Hydrostatic Forces in Layered Fluids

The preceding results employing the linear hydrostatic variation of pressure are valid only for homogeneous fluids. In heterogeneous fluids consisting of individual layers, each of constant density, the pressure varies linearly, with a different slope in each layer. The preceding analyses must be carried out by computing and summing the separate contributions to forces and moments.

Buoyancy

The principles used to compute hydrostatic forces may be used to determine the net pressure force acting on completely submerged or floating bodies. These laws of buoyancy, the *principles of Archimedes*, are:

- A completely submerged body experiences a vertical upward force equal to the weight of the displaced fluid.
- A floating or partially submerged body displaces its own weight in the fluid in which it floats (i.e., the vertical upward force is equal to the body weight).

The line of action of the buoyancy force in both these principles passes through the centroid of the displaced volume of fluid. This point, the *center of buoyancy,* need not correspond to the center of mass of the body (the body may be of nonuniform density). Previously, it has also been assumed that the displaced fluid has a constant γ. If this is not so, e.g., as in a layered fluid, the magnitude of the buoyant force is still equal to the weight of the displaced fluid, but its line of action passes through the center of gravity of the displaced volume, not the centroid. A body whose weight is exactly equal to that of the volume of fluid it displaces is said to be *neutrally buoyant* and will remain at rest at any point of immersion in a (homogeneous) fluid.

Pressure Variation in Rigid-Body Motion of a Fluid

In rigid-body motion of a fluid, all the particles translate and rotate as a whole; there is no relative motion between particles and thus no viscous stresses because these are proportional to velocity gradients. The equation of motion is then a balance among pressure, gravity, and the fluid acceleration, specifically:

$$\nabla p = \rho(\boldsymbol{g} - \boldsymbol{a}) \tag{3.1.18}$$

where $\boldsymbol{a}$ is the uniform acceleration of the body. Equation (3.1.18) shows that the lines of constant pressure, including a free surface if any, are perpendicular to the direction $\boldsymbol{g} - \boldsymbol{a}$. Two important applications of this are to fluids in uniform linear translation and rigid-body rotation. Although such problems are not, strictly speaking, fluid statics problems, their analysis and the resulting pressure variation are similar to those for static fluids.

Uniform Linear Acceleration

For a fluid partially filling a large container moving to the right with constant acceleration $\boldsymbol{a} = (a_x, a_y)$, the geometry of Figure 3.1.4 shows that the magnitude of the pressure gradient in the direction $\boldsymbol{n}$ normal to the accelerating free surface, in the direction $\boldsymbol{g} - \boldsymbol{a}$, is

$$\frac{dp}{dn} = \rho\left[a_x^2 + \left(g + a_y\right)^2\right]^{\frac{1}{2}} \tag{3.1.19}$$

and the angle to the horizontal of the free surface is

$$\theta = \tan^{-1}\left[\frac{a_x}{g + a_y}\right] \tag{3.1.20}$$

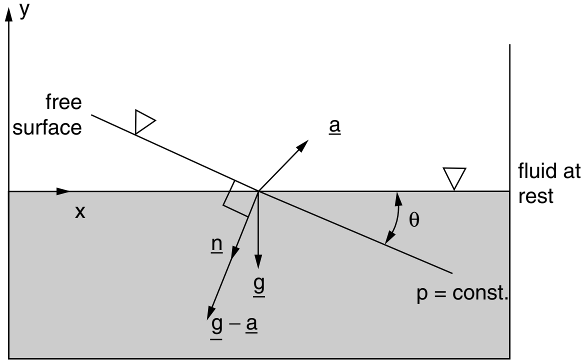

FIGURE 3.1.4 A fluid with a free surface in uniform linear acceleration.

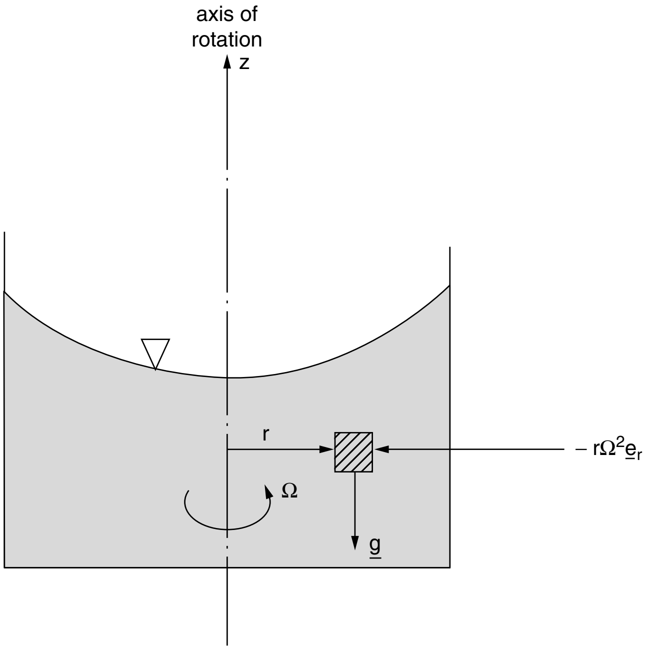

FIGURE 3.1.5 A fluid with a free surface in rigid-body rotation.

Rigid-Body Rotation

Consider a fluid-filled circular cylinder rotating uniformly with angular velocity $\boldsymbol{\Omega} = \Omega \boldsymbol{e}_z$ (Figure 3.1.5). The only acceleration is the centripetal acceleration $\boldsymbol{\Omega} \times (\boldsymbol{\Omega} \times \boldsymbol{r}) = -r\Omega^2 \boldsymbol{e}_r$, so Equation 3.1.18 becomes:

$$\nabla p = \frac{\partial p}{\partial r}\boldsymbol{e}_r + \frac{\partial p}{\partial z}\boldsymbol{e}_z = \rho(\boldsymbol{g} - \boldsymbol{a}) = \rho\left(r\Omega^2 \boldsymbol{e}_r - g\boldsymbol{e}_z\right) \tag{3.1.21}$$

or

$$\frac{\partial p}{\partial r} = \rho r \Omega^2, \qquad \frac{\partial p}{\partial z} = -\rho g = -\gamma \tag{3.1.22}$$

Integration of these equations leads to

$$p = p_0 - \gamma z + \frac{1}{2}\rho r^2 \Omega^2 \tag{3.1.23}$$

where p_0 is a reference pressure (at $r = z = 0$). Thus, at any fixed r, the pressure varies hydrostatically in the vertical direction, and the constant pressure surfaces, including the free surface, are paraboloids of revolution.

Further Information

The reader may find more detail and additional information on the topics in this section in any of the many excellent introductory texts on fluid mechanics, such as

White, F.M. 2003. *Fluid Mechanics*, 5th ed., McGraw–Hill, Boston.

Munson, B.R., Young, D.F., and Okiishi, T.H. 2003. *Fundamentals of Fluid Mechanics*, 4th ed., John Wiley & Sons, New York.

3.2 Equations of Motion and Potential Flow

Stanley A. Berger

Integral Relations for a Control Volume

Like most physical conservation laws, those governing motion of a fluid apply to (*moving*) material particles or systems of such particles. This so-called *Lagrangian viewpoint* is generally not as useful in practical fluid flows as an analysis using *fixed* (deformable) control volumes — the *Eulerian viewpoint*. The relationship between these two viewpoints can be deduced from the Reynolds transport theorem, from which one also most readily derives the governing integral and differential equations of motion.

Reynolds Transport Theorem

An *extensive* quantity *B*, which can be a scalar, vector, or tensor, is defined as any physical property of the fluid (e.g., momentum, energy) and *b* as the corresponding value per unit mass (the *intensive value*). The *Reynolds transport theorem* for a moving and arbitrarily deforming control volume *CV*, with boundary *CS* (see Figure 3.2.1), states that

$$\frac{d}{dt}\left(B_{\text{system}}\right)=\frac{d}{dt}\iiint_{\text{CV}}\rho b\,d\upsilon+\iint_{\text{CS}}\rho b\left(\boldsymbol{V}_r\cdot\boldsymbol{n}\right)dA \tag{3.2.1}$$

where B_{system} is the total quantity of *B* in the system (any mass of fixed identity); $\boldsymbol{n}$ is the outward normal to the CS, $\boldsymbol{V}_r = \boldsymbol{V}(\boldsymbol{r},t) - \boldsymbol{V}_{\text{CS}}(\mathbf{r},t)$, the velocity of the fluid particle, $\boldsymbol{V}(\boldsymbol{r},t)$, relative to that of the CS, $\boldsymbol{V}_{\text{CS}}(\mathbf{r},t)$; and *d/dt* on the left-hand side is the derivative following the fluid particles, i.e., the fluid mass comprising the system.

The theorem states that the time rate of change of the total *B* in the system is equal to the rate of change within the *CV* plus the net flux of *B* through the CS. To distinguish between the *d/dt* that appear on the two sides of Equation (3.2.1) but which have different interpretations, the derivative on the left-hand side, following the system, is denoted by *D/Dt* and is called the *material derivative*. This notation is used in what follows. For any function *f(x, y, z, t),*

$$\frac{Df}{Dt}=\frac{\partial f}{\partial t}+\boldsymbol{V}\cdot\nabla f$$

For a CV fixed with respect to the reference frame, Equation (3.2.1) reduces to

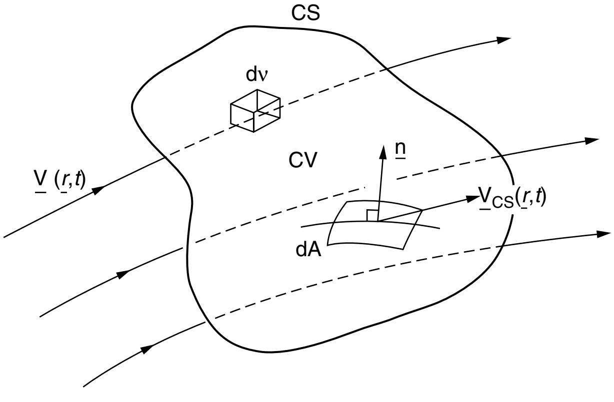

FIGURE 3.2.1 Control volume.

$$\frac{D}{Dt}\left(B_{\text{system}}\right)=\frac{d}{dt}\iiint\limits_{\substack{\text{CV}\\ \text{(fixed)}}}\rho b\,d\upsilon+\iint\limits_{\text{CS}}\rho \mathrm{b}\left(\boldsymbol{V}\cdot\boldsymbol{n}\right)dA \tag{3.2.2}$$

(In addition, for this case, the time derivative operator in the first term on the right-hand side may be moved inside the integral, in which case it is then to be interpreted as the partial derivative $\partial/\partial t$.)

Conservation of Mass

Applying Equation (3.2.2) for a fixed control volume, with B_{system} the total mass in the system, then, because conservation of mass requires that $DB_{\text{system}}/Dt = 0$, it follows, because $b = B_{\text{system}}/m = 1$, that

$$\iiint\limits_{\substack{\text{CV}\\ \text{(fixed)}}}\frac{\partial\rho}{\partial t}\,d\upsilon+\iint\limits_{\text{CS}}\rho\left(\boldsymbol{V}\cdot\boldsymbol{n}\right)dA=0 \tag{3.2.3}$$

This is the *integral form* of the *conservation of mass law* for a *fixed control volume*. For steady flow, Equation (3.2.3) reduces to

$$\iint\limits_{\text{CS}}\rho\left(\boldsymbol{V}\cdot\boldsymbol{n}\right)dA=0 \tag{3.2.4}$$

whether *compressible* or *incompressible*. For an incompressible flow, ρ = constant, so

$$\iint\limits_{\text{CS}}\left(\boldsymbol{V}\cdot\boldsymbol{n}\right)dA=0 \tag{3.2.5}$$

whether the flow is steady or unsteady.

Conservation of Momentum

The *conservation of (linear) momentum* states that

$$\boldsymbol{F}_{\text{total}}\equiv\sum\left(\text{external forces acting on the fluid system}\right)=\frac{D\boldsymbol{M}}{Dt}\equiv\frac{D}{Dt}\iiint\limits_{\text{system}}\rho\boldsymbol{V}\,d\upsilon \tag{3.2.6}$$

where $\boldsymbol{M}$ is the total system momentum. For an arbitrarily moving, deformable control volume, it then follows from Equation (3.2.1) with b set to $\boldsymbol{V}$, that

$$\boldsymbol{F}_{\text{total}}=\frac{d}{dt}\iiint\limits_{\text{CV}}\rho\boldsymbol{V}\,d\upsilon+\iint\limits_{\text{CS}}\rho\boldsymbol{V}\left(\boldsymbol{V}_r\cdot\boldsymbol{n}\right)dA \tag{3.2.7}$$

This expression is only valid in an *inertial coordinate frame*. For the equivalent expression in a *noninertial frame*, the relationship between the acceleration $\boldsymbol{a}_I$ in an inertial frame and that in a noninertial frame, $\boldsymbol{a}_R$, is used:

$$\boldsymbol{a}_I=\boldsymbol{a}_R+\frac{d^2\boldsymbol{R}}{dt^2}+2\boldsymbol{\Omega}\times\boldsymbol{V}+\boldsymbol{\Omega}\times\left(\boldsymbol{\Omega}\times\boldsymbol{r}\right)+\frac{d\boldsymbol{\Omega}}{dt}\times\boldsymbol{r} \tag{3.2.8}$$

where $\boldsymbol{R}$ is the position vector of the origin of the noninertial frame with respect to that of the inertial frame; $\boldsymbol{\Omega}$ is the angular velocity of the noninertial frame; and $\boldsymbol{r}$ and $\boldsymbol{V}$ the position and velocity vectors in the noninertial frame. The third term on the right-hand side of Equation (3.2.8) is the *Coriolis acceleration* and the fourth term is the *centrifugal acceleration*. In a noninertial frame, Equation (3.2.7) is

$$\begin{aligned}\boldsymbol{F}_{\text{total}} - \iiint_{\text{system}} \left[\frac{d^2\boldsymbol{R}}{dt^2} + 2\boldsymbol{\Omega}\times\boldsymbol{V} + \boldsymbol{\Omega}\times(\boldsymbol{\Omega}\times\boldsymbol{r}) + \frac{d\boldsymbol{\Omega}}{dt}\times\boldsymbol{r}\right]\rho\, d\upsilon &= \frac{D}{Dt}\iiint_{\text{system}} \rho\boldsymbol{V}\, d\upsilon \\ &= \frac{d}{dt}\iiint_{\text{CV}} \rho\boldsymbol{V}\, d\upsilon + \iint_{\text{CS}} \rho\boldsymbol{V}(\boldsymbol{V}_r\cdot\boldsymbol{n})\, dA\end{aligned} \tag{3.2.9}$$

where the frame acceleration terms of Equation (3.2.8) have been brought to the left-hand side because, to an observer in the noninertial frame, they act as “apparent” body forces.

For a *fixed control volume* in an *inertial frame for steady flow*, it follows from the preceding that

$$\boldsymbol{F}_{\text{total}} = \iint_{\text{CS}} \rho\boldsymbol{V}(\boldsymbol{V}\cdot\boldsymbol{n})\, dA \tag{3.2.10}$$

This expression is the basis of many control volume analyses for fluid flow problems.

The cross product of $\boldsymbol{r}$, the position vector with respect to a convenient origin, with the momentum Equation (3.2.6) written for an elementary particle of mass dm, noting that $(d\boldsymbol{r}/dt)\times\boldsymbol{V} = 0$, leads to the *integral moment of momentum equation*:

$$\sum \boldsymbol{M} - \boldsymbol{M}_I = \frac{D}{Dt}\iiint_{\text{system}} \rho(\boldsymbol{r}\times\boldsymbol{V})\, d\upsilon \tag{3.2.11}$$

where $\Sigma\boldsymbol{M}$ is the sum of the moments of all the external forces acting on the system about the origin of $\boldsymbol{r}$, and $\boldsymbol{M}_I$ is the moment of the apparent body forces (see Equation 3.2.9). The right-hand side can be written for a control volume using the appropriate form of the Reynolds transport theorem.

Conservation of Energy

The conservation of energy law follows from the first law of thermodynamics for a moving system

$$\dot{Q} - \dot{W} = \frac{D}{Dt}\iiint_{\text{system}} \rho e\, d\upsilon \tag{3.2.12}$$

where $\dot{Q}$ is the rate at which heat is added to the system; $\dot{W}$ the rate at which the system works on its surroundings; and e the total energy per unit mass, the specific energy.

For a particle of mass dm, the contributions to e are the internal energy u; the kinetic energy $V^2/2$; and the potential energy, which, in the case of gravity (the only body force to be considered here) is gz, where z is the vertical displacement opposite to the direction of gravity. (No energy transfer due to chemical reaction, as well as no magnetic or electric fields, is assumed.) For a fixed control volume, it follows from Equation (3.2.2) and Equation (3.2.12) (with $b = e = u + (V^2/2) + gz$) that

$$\dot{Q} - \dot{W} = \frac{d}{dt}\iiint_{\text{CV}} \rho\left[u + \frac{1}{2}V^2 + gz\right] d\upsilon + \iint_{\text{CS}} \rho\left[u + \frac{1}{2}V^2 + gz\right](\boldsymbol{V}\cdot\boldsymbol{n})\, dA \tag{3.2.13}$$

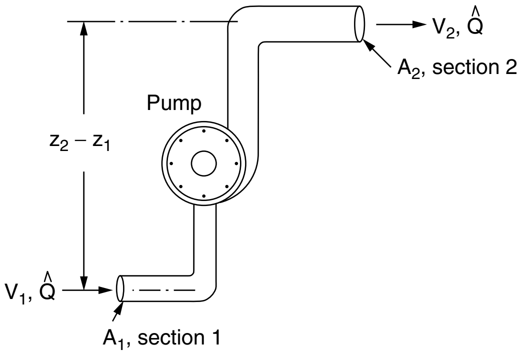

FIGURE 3.2.2 Pump producing pressure increase.

Problem

An incompressible fluid flows through a pump at a volumetric flow rate $\hat{Q}$. The (head) loss between sections 1 and 2 (see Figure 3.2.2) is equal to $\beta\rho V_1^2/2$ (V is the average velocity at the section). Calculate the power that must be delivered by the pump to the fluid to produce a given increase in pressure, $\Delta p = p_2 - p_1$.

Solution: The principal equation needed is the energy equation (Equation 3.2.13). The term $\dot{W}$, the rate at which the system does work on its surroundings, for such problems has the form:

$$\dot{W} = -\dot{W}_{\text{shaft}} + \iint_{\text{CS}} p\boldsymbol{V}\cdot\boldsymbol{n}\,dA \tag{P.3.2.1}$$

where $\dot{W}_{\text{shaft}}$ represents the work done on the fluid by a moving shaft, such as by turbines, propellers, fans, etc., and the second term on the right side represents the rate of working by the normal stress, the pressure, at the boundary. For steady flow in a control volume coincident with the physical system boundaries and bounded by sections 1 and 2, Equation (3.2.13) reduces to ($u \equiv 0$),

$$\dot{Q} + \dot{W}_{\text{shaft}} - \iint_{\text{CS}} p\boldsymbol{V}\cdot\boldsymbol{n}\,dA = \iint_{\text{CS}} \left[\frac{1}{2}\rho V^2 + \gamma z\right](\boldsymbol{V}\cdot\boldsymbol{n})\,dA \tag{P.3.2.2}$$

Using average quantities at sections 1 and 2, and the continuity equation (Equation 3.2.5), which reduces in this case to

$$V_1A_1 = V_2A_2 = \hat{Q}, \tag{P.3.2.3}$$

Equation (P.3.2.2) can be written as

$$\dot{Q} + \dot{W}_{\text{shaft}} - (p_2 - p_1)\hat{Q} = \left[\frac{1}{2}\rho\left(V_2^2 - V_1^2\right) + \gamma(z_2 - z_1)\right]\hat{Q} \tag{P.3.2.4}$$

$\dot{Q}$, the rate at which heat is added to the system, is here equal to $-\beta\rho V_1^2/2$, the head loss between sections 1 and 2. Equation (P.3.2.4) then can be rewritten

$$\dot{W}_{\text{shaft}} = \beta\rho\frac{V_1^2}{2} + (\Delta p)\hat{Q} + \frac{1}{2}\rho\left(V_2^2 - V_1^2\right)\hat{Q} + \gamma(z_2 - z_1)\hat{Q}$$

or, in terms of the given quantities,

$$\dot{W}_{\text{shaft}} = \frac{\beta\rho\hat{Q}^2}{A_1^2} + (\Delta p)\hat{Q} + \frac{1}{2}\rho\frac{\hat{Q}^3}{A_2^2}\left(1 - \frac{A_2^2}{A_1^2}\right) + \gamma(z_2 - z_1)\hat{Q} \tag{P.3.2.5}$$

Thus, for example, if the fluid is water ($\rho \approx 1000$ kg/m^3, $\gamma = 9.8$ kN/m^3), $\hat{Q} = 0.5$ m^3/sec, the heat loss is $0.2\rho V_1^2/2$, and $\Delta p = p_2 - p_1 = 2 \times 10^5$ N/m^2 = 200 kPa, $A_1 = 0.1$ m^2 = $A_2/2$, $(z_2 - z_1) = 2$ m, we find, using Equation (P.3.2.5),

$$\begin{aligned}\dot{W}_{\text{shaft}} &= \frac{0.2(1000)(0.5)^2}{(0.1)^2} + (2\times10^5)(0.5) + \frac{1}{2}(1000)\frac{(0.5)^3}{(0.2)^2}(1-4) + (9.8\times10^3)(2)(0.5)\\ &= 5{,}000 + 10{,}000 - 4{,}688 + 9{,}800 = 20{,}112\,\text{Nm/sec}\\ &= 20{,}112\ \text{W} = \frac{20{,}112}{745.7}\text{hp} = 27\,\text{hp}\end{aligned}$$

Differential Relations for Fluid Motion

In the previous section, the conservation laws were derived in integral form. These forms are useful in calculating, generally using a control volume analysis, gross features of a flow. Such analyses usually require some *a priori* knowledge or assumptions about the flow. In any case, an approach based on integral conservation laws cannot be used to determine the point-by-point variation of the dependent variables, such as velocity, pressure, temperature, etc. To do this requires the use of the differential forms of the conservation laws, which are presented next.

Mass Conservation — Continuity Equation

Applying Gauss's theorem (the divergence theorem) to Equation (3.2.3) yields

$$\underset{\substack{\text{CV}\\ \text{(fixed)}}}{\iiint}\left[\frac{\partial\rho}{\partial t} + \nabla\cdot(\rho\boldsymbol{V})\right]d\upsilon = 0 \tag{3.2.14}$$

which, because the control volume is arbitrary, immediately yields

$$\frac{\partial\rho}{\partial t} + \nabla\cdot(\rho\boldsymbol{V}) = 0 \tag{3.2.15}$$

This can also be written as

$$\frac{D\rho}{Dt} + \rho\nabla\cdot\boldsymbol{V} = 0 \tag{3.2.16}$$

using the fact that

$$\frac{D\rho}{Dt} = \frac{\partial\rho}{\partial t} + \boldsymbol{V}\cdot\nabla\rho \tag{3.2.17}$$

Special cases:

1. Steady flow $[(\partial/\partial t)\,() \equiv 0]$

$$\nabla\cdot(\rho\boldsymbol{V})=0 \tag{3.2.18}$$

2. Incompressible flow $(\mathrm{D}\rho/\mathrm{Dt} \equiv 0)$

$$\nabla\cdot\boldsymbol{V}=0 \tag{3.2.19}$$

Momentum Conservation

As a consequence of mass conservation for a system, the right-hand side of Equation (3.2.6) can be written as

$$\frac{D}{Dt}\underset{\text{system}}{\iiint}\rho\boldsymbol{V}\,d\upsilon \equiv \underset{\text{system}}{\iiint}\rho\frac{D\boldsymbol{V}}{Dt}\,d\upsilon \tag{3.2.20}$$

The total force acting on the system is the sum of the *body forces* $\boldsymbol{F}_b$ and *surface forces* $\boldsymbol{F}_s$. Body forces are often given as forces per unit mass (e.g., gravity) and thus can be written

$$\boldsymbol{F}_b = \underset{\text{system}}{\iiint}\rho\boldsymbol{f}\,d\upsilon \tag{3.2.21}$$

The surface forces are represented in terms of the second-order *stress tensor*[1] $\underline{\underline{\sigma}} = \{\sigma_{ij}\}$, where σ_{ij} is defined as the force per unit area in the i direction on a planar element whose normal lies in the j direction.[2] From elementary *angular momentum* considerations for an infinitesimal volume, it can be shown that σ_{ij} is a *symmetric tensor* and therefore has only six independent components. The total surface force exerted on the system by its surroundings is

$$\boldsymbol{F}_s = \underset{\substack{\text{system}\\\text{surface}}}{\iint}\underline{\underline{\sigma}}\cdot\boldsymbol{n}\,dA,\ \text{with } i-\text{component } \mathrm{F}_{s_i} = \iint\sigma_{ij}\boldsymbol{n}_j\,dA \tag{3.2.22}$$

The integral momentum conservation law, Equation (3.2.6), can then be written

$$\underset{\text{system}}{\iiint}\rho\frac{D\boldsymbol{V}}{Dt}d\upsilon = \underset{\text{system}}{\iiint}\rho\boldsymbol{f}\,d\upsilon + \underset{\substack{\text{system}\\\text{surface}}}{\iint}\underline{\underline{\sigma}}\cdot\boldsymbol{n}\,dA \tag{3.2.23}$$

The application of the divergence theorem to the last term in Equation (3.2.23) leads to

$$\underset{\text{system}}{\iiint}\rho\frac{D\boldsymbol{V}}{Dt}d\upsilon = \underset{\text{system}}{\iiint}\rho\boldsymbol{f}\,d\upsilon + \underset{\text{system}}{\iiint}\nabla\cdot\underline{\underline{\sigma}}\,d\upsilon \tag{3.2.24}$$

---

[1] It is assumed that the reader is familiar with elementary Cartesian tensor analysis and the associated subscript notation and conventions. The reader for whom this is not true should skip the details and concentrate on the final principal results and equations given at the ends of the next few subsections.

[2] This assignment of roles to the first and second subscripts of the stress tensor is a convention that is far from universal. Frequently, their roles are reversed: the first subscript denotes the direction of the normal to the planar element and the second denotes the direction of the force.

where $\nabla \cdot \underline{\underline{\sigma}} \equiv \{\partial\sigma_{ij}/\partial x_j\}$. Because Equation (3.2.24) holds for any material volume, it follows that

$$\rho \frac{D\boldsymbol{V}}{Dt} = \rho \boldsymbol{f} + \nabla \cdot \underline{\underline{\sigma}} \tag{3.2.25}$$

[With the preceding decomposition of $\boldsymbol{F}_{\text{total}}$, Equation (3.2.10) can be written

$$\iiint\limits_{\text{CV}} \rho \boldsymbol{f}\, d\upsilon + \iint\limits_{\text{CS}} \underline{\underline{\sigma}} \cdot \boldsymbol{n}\, dA = \iint\limits_{\text{CS}} \rho \boldsymbol{V}(\boldsymbol{V} \cdot \boldsymbol{n})\, dA \tag{3.2.26}$$

If ρ is uniform and $\boldsymbol{f}$ is a *conservative body force*, i.e., $\boldsymbol{f} = -\nabla\Psi$, where Ψ is the *body force potential*, then Equation (3.2.26), after application of the divergence theorem to the body force term, can be written

$$\iint\limits_{\text{CS}} \left(-\rho\Psi\boldsymbol{n} + \underline{\underline{\sigma}} \cdot \boldsymbol{n}\right) dA = \iint\limits_{\text{CS}} \rho \boldsymbol{V}(\boldsymbol{V} \cdot \boldsymbol{n})\, dA \tag{3.2.27}$$

This integral form of the momentum equation, involving integrals only over the surface of the control volume, is commonly used in control volume analyses, particularly when the body force term is absent.]

Analysis of Rate of Deformation

The principal aim of the following two subsections is to derive a relationship between the *stress* and the *rate of strain* to be used in the momentum equation (Equation 3.2.25). The reader less familiar with tensor notation may skip these sections, apart from noting some of the terms and quantities defined therein, and proceed directly to Equation (3.2.38) or Equation (3.2.39).

The relative motion of two neighboring points P and Q, separated by a distance η, can be written (**u** is the local velocity)

$$\boldsymbol{u}(Q) = \boldsymbol{u}(P) + (\nabla \boldsymbol{u})\boldsymbol{\eta}$$

or, equivalently, writing $\nabla \boldsymbol{u}$ as the sum of antisymmetric and symmetric tensors,

$$\boldsymbol{u}(Q) = \boldsymbol{u}(P) + \frac{1}{2}\left((\nabla \boldsymbol{u}) - (\nabla \boldsymbol{u})^*\right)\boldsymbol{\eta} + \frac{1}{2}\left((\nabla \boldsymbol{u}) + (\nabla \boldsymbol{u})^*\right)\boldsymbol{\eta} \tag{3.2.28}$$

where $\nabla \boldsymbol{u} = \{\partial u_i/\partial x_j\}$, and the superscript * denotes transpose, so $(\nabla \boldsymbol{u})^* = \{\partial u_j/\partial x_i\}$. The second term on the right-hand side can be rewritten in terms of the *vorticity*, $\nabla \times \boldsymbol{u}$, so Equation (3.2.28) becomes

$$\boldsymbol{u}(Q) = \boldsymbol{u}(P) + \frac{1}{2}(\nabla \times \boldsymbol{u}) \times \boldsymbol{\eta} + \frac{1}{2}\left((\nabla \boldsymbol{u}) + (\nabla \boldsymbol{u})^*\right)\boldsymbol{\eta} \tag{3.2.29}$$

which shows that the *local rate of deformation* consists of a *rigid-body translation*, a *rigid-body rotation* with *angular velocity* $\frac{1}{2}(\nabla \times \boldsymbol{u})$ and a *velocity or rate of deformation*. The coefficient of η in the last term in Equation (3.2.29) is defined as the *rate-of-strain tensor* and is denoted by $\underline{\underline{e}}$, in subscript form

$$e_{ij} = \frac{1}{2}\left(\frac{\partial u_i}{\partial x_j} + \frac{\partial u_j}{\partial x_i}\right) \tag{3.2.30}$$

From $\underline{\underline{e}}$, one can define a *rate-of-strain central quadric*, along the *principal axes* of which the deforming motion consists of a *rate of pure extension* or *contraction*.

Relationship between Forces and Rate of Deformation

Now the required relationship between the stress tensor and the rate of deformation is considered. Assuming that in a static fluid the stress reduces to a (negative) hydrostatic or thermodynamic pressure, equal in all directions, one can write

$$\underline{\underline{\sigma}} = -p\underline{\underline{\boldsymbol{I}}} + \underline{\underline{\tau}} \quad \text{or} \quad \sigma_{ij} = -p\delta_{ij} + \tau_{ij} \tag{3.2.31}$$

where $\underline{\underline{\tau}}$ is the viscous part of the total stress and is called the *deviatoric stress tensor*; $\underline{\underline{\boldsymbol{I}}}$ is the *identity tensor*, and δ_{ij} is the *Kronecker delta* ($\delta_{ij} = 0$ if $i \neq j$; $\delta_{ij} = 1$ if $i = j$). It is further assumed that (1) the fluid exhibits no preferred directions; (2) the stress is independent of any previous history of distortion; and (3) the stress depends only on the local thermodynamic state and the kinematic state of the immediate neighborhood. Specifically, $\underline{\underline{\tau}}$ is assumed to be linearly proportional to the first spatial derivatives of $\boldsymbol{u}$, the coefficient of proportionality depending only on the local thermodynamic state.

These assumptions, and the relations below that follow from them, are appropriate for a *Newtonian fluid*. Most common fluids, such as air and water under most conditions, are Newtonian, but many other fluids, including many that arise in industrial applications, exhibit so-called *non-Newtonian* properties. The study of such non-Newtonian fluids, such as viscoelastic fluids, is the subject of the field of *rheology*.

With the preceding Newtonian fluid assumptions and the *symmetry* of $\underline{\underline{\tau}}$, which follows from the symmetry of $\underline{\underline{\sigma}}$, one can show that the viscous part $\underline{\underline{\tau}}$ of the stress can be written as

$$\underline{\underline{\tau}} = \lambda(\nabla \cdot \boldsymbol{u})\underline{\underline{\boldsymbol{I}}} + 2\mu\underline{\underline{e}} \tag{3.2.32}$$

Thus, the total stress for a Newtonian fluid is

$$\underline{\underline{\sigma}} = -p\underline{\underline{\boldsymbol{I}}} + \lambda(\nabla \cdot \boldsymbol{u})\underline{\underline{\boldsymbol{I}}} + 2\mu\underline{\underline{e}} \tag{3.2.33}$$

or, in subscript notation

$$\sigma_{ij} = -p\delta_{ij} + \lambda\left(\frac{\partial u_k}{\partial x_k}\right)\delta_{ij} + \mu\left(\frac{\partial u_i}{\partial x_j} + \frac{\partial u_j}{\partial x_i}\right) \tag{3.2.34}$$

(The *Einstein summation convention* is assumed here: namely, that in any expression containing a repeated subscript, such as in the second term on the right-hand side above, that subscript is to be given all its possible values and the results then summed; note also that $\nabla \cdot \boldsymbol{u} = \partial u_k/\partial x_k = e_{kk}$.)

The coefficient λ is called the *second viscosity* and μ the *absolute viscosity* or, more commonly, the *dynamic viscosity*, or simply the "viscosity." For a Newtonian fluid, λ and μ depend only on local thermodynamic state, primarily on the temperature.

Note that, from Equation (3.2.34), whereas in a fluid at rest the pressure is an isotropic normal stress (equal to p in all directions), this is not the case for a moving fluid because, in general, $\sigma_{11} \neq \sigma_{22} \neq \sigma_{33}$. To have a quantity analogous to p for a moving fluid we define the pressure in a moving fluid as the negative mean normal stress, denoted, say, by $\bar{p}$, thusly:

$$\bar{p} = -\frac{1}{3}\sigma_{ii} \tag{3.2.35}$$

(σ_{ii} is the *trace* of $\underline{\underline{\sigma}}$ and an *invariant* of $\underline{\underline{\sigma}}$, independent of the orientation of the axes.) From Equation (3.2.34)

$$\bar{p} = -\frac{1}{3}\sigma_{ii} = p - \left(\lambda + \frac{2}{3}\mu\right)\nabla \cdot \boldsymbol{u} \tag{3.2.36}$$

For an incompressible fluid, $\nabla \cdot \boldsymbol{u} = 0$ and thus $\bar{p} \equiv p$. The quantity $(\lambda + \tfrac{2}{3}\mu)$ is called the *bulk viscosity.* If one assumes that the deviatoric stress tensor τ_{ij} makes no contribution to the mean normal stress, it follows that $\lambda + \tfrac{2}{3}\mu = 0$, so again $\bar{p} = p$. This condition, $\lambda = -\tfrac{2}{3}\mu$, is called the *Stokes assumption* or *hypothesis.* If neither the incompressibility nor the Stokes assumptions are made, the difference between $\bar{p}$ and p is usually negligibly small because generally $(\lambda + \tfrac{2}{3}\mu)\nabla \cdot \boldsymbol{u} << p$. If the Stokes hypothesis is made, as is often done, Equation (3.2.34) becomes

$$\sigma_{ij} = -p\delta_{ij} + 2\mu\left(e_{ij} - \frac{1}{3}e_{kk}\delta_{ij}\right) \tag{3.2.37}$$

The Navier–Stokes Equations

Substitution of Equation (3.2.33) into Equation (3.2.25), because $\nabla \cdot (\phi \underline{\underline{\boldsymbol{I}}}) = \nabla\phi$, for any scalar function ϕ, yields (replacing $\mathbf{u}$ in Equation (3.2.33) by $\boldsymbol{V}$)

$$\rho\frac{D\boldsymbol{V}}{Dt} = \rho\boldsymbol{f} - \nabla p + \nabla(\lambda\nabla \cdot \boldsymbol{V}) + \nabla \cdot \left(2\mu\underline{\underline{e}}\right) \tag{3.2.38}$$

These are the *Navier–Stokes equations* (although the name is as often given to the full set of governing conservation equations). With the Stokes assumption $(\lambda = -\tfrac{2}{3}\mu)$, Equation (3.2.38) becomes

$$\rho\frac{D\boldsymbol{V}}{Dt} = \rho\boldsymbol{f} - \nabla p + \nabla \cdot \left[2\mu\left(\underline{\underline{e}} - \frac{1}{3}e_{kk}\underline{\underline{\boldsymbol{I}}}\right)\right] \tag{3.2.39}$$

If the Eulerian frame is not an inertial frame, one can transform to an inertial frame using Equation (3.2.8) or the “apparent” body force formulation, Equation (3.2.9).

Energy Conservation — Mechanical and Thermal Energy Equations

The derivation of the differential form of the energy equation using Equation (3.2.12) begins by assuming that heat enters or leaves the material or control volume by heat conduction across the boundaries, the *heat flux per unit area* being $\boldsymbol{q}$, so

$$\dot{Q} = -\iint \boldsymbol{q} \cdot \boldsymbol{n}\, dA = -\iiint \nabla \cdot \boldsymbol{q}\, d\upsilon \tag{3.2.40}$$

The work-rate term $\dot{W}$ can be decomposed into the rate of work done against body forces

$$-\iiint \rho\boldsymbol{f} \cdot \boldsymbol{V}\, d\upsilon \tag{3.2.41}$$

and the rate of work done against surface stresses

$$-\iint_{\substack{\text{system}\\ \text{surface}}} \boldsymbol{V} \cdot \left(\underline{\underline{\sigma}}\boldsymbol{n}\right) dA \tag{3.2.42}$$

Substitution of these expressions for $\dot{Q}$ and $\dot{W}$ into Equation (3.2.12), use of the divergence theorem, and conservation of mass lead to

$$\rho\frac{D}{Dt}\left(u + \frac{1}{2}V^2\right) = -\nabla \cdot \boldsymbol{q} + \rho\boldsymbol{f} \cdot \boldsymbol{V} + \nabla \cdot \left(\boldsymbol{V}\underline{\underline{\sigma}}\right) \tag{3.2.43}$$

(The potential energy term no longer appears in *e*, the total specific energy, because it is accounted for by the body force rate-of-working term $\rho \boldsymbol{f} \cdot \boldsymbol{V}$.)

Equation (3.2.43), the total energy equation,[3] shows how the energy changes as a result of working by the body and surface forces, and heat transfer. It is useful to have an equation purely for the thermal energy. This is obtained by subtracting from Equation (3.2.43) the dot product of $\boldsymbol{V}$ with the momentum Equation (3.2.25), after expanding the last term in Equation (3.2.43); this results in

$$\rho \frac{Du}{Dt} = \frac{\partial V_i}{\partial x_j} \boldsymbol{\sigma}_{ij} - \nabla \cdot \boldsymbol{q} \tag{3.2.44}$$

With $\sigma_{ij} = -p\delta_{ij} + \tau_{ij}$, and the continuity equation, Equation (3.2.16), the first term on the right-hand side of Equation (3.2.44) may be written

$$\frac{\partial V_i}{\partial x_j} \sigma_{ij} = -\rho \frac{D(p/\rho)}{Dt} + \frac{Dp}{Dt} + \Phi \tag{3.2.45}$$

where Φ is the *rate of dissipation of mechanical energy per unit mass* due to *viscosity*, given by

$$\Phi \equiv \frac{\partial V_i}{\partial x_j} \tau_{ij} = 2\mu \left(e_{ij} e_{ij} - \frac{1}{3} e_{kk}^2 \right) = 2\mu \left(e_{ij} - \frac{1}{3} e_{kk} \delta_{ij} \right)^2 \tag{3.2.46}$$

With the introduction of Equation (3.2.45), Equation (3.2.44) becomes

$$\rho \frac{De}{Dt} = -p \nabla \cdot \boldsymbol{V} + \Phi - \nabla \cdot \boldsymbol{q} \tag{3.2.47}$$

or

$$\rho \frac{Dh}{Dt} = \frac{Dp}{Dt} + \Phi - \nabla \cdot \boldsymbol{q} \tag{3.2.48}$$

where $h = e + (p/\rho)$ is the *specific enthalpy*. Unlike the other terms on the right-hand side of Equation (3.2.47), which can be negative or positive, Φ is always non-negative and represents the increase in internal energy (or enthalpy) owing to irreversible degradation of mechanical energy.

Finally, from elementary thermodynamic considerations

$$\frac{Dh}{Dt} = T \frac{DS}{Dt} + \frac{1}{\rho} \frac{Dp}{Dt}$$

where *S* is the *entropy*, so Equation (3.2.48) can be written

$$\rho T \frac{DS}{Dt} = \Phi - \nabla \cdot \boldsymbol{q} \tag{3.2.49}$$

---

[3] There may be energy production, source, terms not included in this energy equation, which, depending on circumstances, should be included. The irreversible degradation of mechanical energy into heat by viscosity is accounted for (see Equation 3.2.48), but other contributions — chemical, electromagnetic, nuclear, etc. — may be important and their roles in the energy balance equation should then be taken into account. (See Bird et al., 2002.)

If the heat conduction is assumed to obey the *Fourier heat conduction law*, so that $\boldsymbol{q} = -k\nabla T$, where k is the *thermal conductivity*, then in the preceding equations

$$-\nabla \cdot \boldsymbol{q} = \nabla \cdot \left(k \nabla T\right) = k \nabla^2 T \tag{3.2.50}$$

the last of these equalities holding only if k = constant.

If the thermodynamic quantities vary little, the coefficients of the constitutive relations for $\underline{\underline{\sigma}}$ and $\boldsymbol{q}$ may be taken to be constant and the preceding equations simplified accordingly.

Incompressible Flow

If the flow is incompressible, then the mass conservation, or continuity, equation simplifies to

$$\nabla \cdot \boldsymbol{V} = 0 \tag{3.2.51}$$

and the momentum Equation (3.2.38) simplifies to

$$\rho \frac{D\boldsymbol{V}}{Dt} = \rho \boldsymbol{f} - \nabla p + \mu \nabla^2 \boldsymbol{V} \tag{3.2.52}$$

where ∇^2 is the Laplacian operator. Then the small temperature changes, compatible with the incompressibility assumption, are determined for a perfect gas with constant k and specific heats by the energy equation, rewritten for the temperature, in the form

$$\rho c_v \frac{DT}{Dt} = k \nabla^2 T + \Phi \tag{3.2.53}$$

where c_v is the *specific heat.*

Boundary Conditions

The appropriate boundary conditions to be applied at the boundary of a fluid in contact with another medium depend on the nature of this other medium — solid, liquid, or gas. A few of the more important cases are discussed here:

- *At a solid–fluid interface*: $\boldsymbol{V}$ and T are continuous. Contained in this boundary condition is the "no-slip" condition: namely, that the tangential velocity of the fluid in contact with the boundary of the solid is equal to that of the boundary. For an *inviscid* fluid, the no-slip condition does not apply, and only the normal component of velocity is continuous. If the wall is *permeable*, the tangential velocity is continuous and the normal velocity is arbitrary; the temperature boundary condition for this case depends on the nature of the injection or suction at the wall.
- *At a liquid–liquid interface*: The velocity components are continuous across the interface, as are the normal and tangential stress components.
- *At a liquid–gas interface*: For such cases the appropriate boundary conditions depend on what can be assumed about the gas in contact with the liquid. In the classical liquid-free surface problem, the tangential stresses in the gas, often atmospheric air, are generally negligible and the boundary conditions imposed are that (1) the normal velocity in the liquid at the interface is equal to the normal velocity of the interface; and (2) the pressure in the liquid at the interface is equal to that in the gas or, if *surface tension* is important, exceeds the atmospheric pressure by an amount equal to

$$\nabla p = p_{\text{liquid}} - p_{\text{atm}} = \sigma \left(\frac{1}{R_1} + \frac{1}{R_2} \right) \tag{3.2.54}$$

where R_1 and R_2 are the radii of curvature of the intercepts of the interface by two orthogonal planes containing the normal to the interface, and σ is the *surface tension*. (If the gas is a vapor that undergoes non-negligible interaction and exchanges with the liquid in contact with it, the boundary conditions can be more complex.) If surface tension is important in the liquid–liquid interfacial case, then Equation (3.2.54) is used with the left-hand side replaced by the difference in the normal stress instead of p alone.

For interfaces in general, the boundary conditions are derived from continuity conditions for each "transportable" quantity — namely, continuity of the appropriate intensity across the interface and continuity of the normal component of the flux vector. Fluid momentum and heat are two such transportable quantities; the associated intensities are velocity and temperature, and the associated flux vectors are stress and heat flux. Such general considerations are relative to more complex flow situations in which material passes through the interface (the discussion of the preceding three cases assumed this did not occur), such as when absorption; adsorption; evaporation; change of phase; or chemical reaction occur at the interface. (In the case of a rarefied gas in contact with a solid surface the boundary conditions must allow for velocity slip and temperature jump along the contact surface.) For situations in which heat and/or mass transfer are involved, see the section on heat and mass transfer. For consideration of a wide spectrum of important physical situations, see the updated transport classic by Bird, Stewart, and Lightfoot (2002).

Vorticity in Incompressible Flow

With μ and ρ constants, and $\boldsymbol{f} = -\boldsymbol{g} = -g\boldsymbol{k}$, the momentum equation, Equation (3.2.52), reduces to

$$\rho\frac{D\boldsymbol{V}}{Dt} = -\nabla p - \rho g\boldsymbol{k} + \mu\nabla^2\boldsymbol{V} \tag{3.2.55}$$

The vector identities

$$(\boldsymbol{V}\cdot\nabla)\boldsymbol{V} = \nabla\left(\frac{V^2}{2}\right) - \boldsymbol{V}\times(\nabla\times\boldsymbol{V}) \tag{3.2.56}$$

$$\nabla^2\boldsymbol{V} = \nabla(\nabla\cdot\boldsymbol{V}) - \nabla\times(\nabla\times\boldsymbol{V}) \tag{3.2.57}$$

together with the definition of *vorticity*

$$\boldsymbol{\zeta} \equiv \nabla\times\boldsymbol{V} \tag{3.2.58}$$

and the incompressible flow continuity equation, $\nabla\cdot\boldsymbol{V} = 0$, allow Equation (3.2.55) to be written

$$\rho\frac{\partial\boldsymbol{V}}{\partial t} + \nabla\left(p + \frac{1}{2}\rho V^2 + \rho g z\right) = \rho\boldsymbol{V}\times\boldsymbol{\zeta} - \mu\nabla\times\boldsymbol{\zeta} \tag{3.2.59}$$

The flow is said to be *irrotational* if

$$\boldsymbol{\zeta} \equiv \nabla\times\mathbf{V} = 0 \tag{3.2.60}$$

from which it follows that a *velocity potential* Φ can be defined

$$\boldsymbol{V} = \nabla\Phi \tag{3.2.61}$$

Setting $\boldsymbol{\zeta} = 0$ in Equation (3.2.59), using Equation (3.2.61), and integrating with respect to all the spatial variables leads to

$$\rho\frac{\partial\Phi}{\partial t}+\left(p+\frac{1}{2}\rho V^2+\rho gz\right)=F(t) \tag{3.2.62}$$

(The arbitrary function *F(t)* introduced by the integration can be absorbed into $\boldsymbol{\Phi}$, or is determined by the boundary conditions.)

Equation (3.2.62) is the unsteady *Bernoulli equation* for irrotational, incompressible flow. *Irrotational flows* are always *potential flows*, even if the flow is compressible. Because the viscous term in Equation (3.2.59) vanishes identically for $\boldsymbol{\zeta} = 0$, it would appear that the preceding Bernoulli equation is valid even for viscous flow. Potential solutions of hydrodynamics are in fact exact solutions of the full Navier–Stokes equations. Such solutions, however, are not valid near solid boundaries or bodies because the no-slip condition generates vorticity and causes nonzero $\boldsymbol{\zeta}$; the potential flow solution is invalid in all those parts of the flow field that have been "contaminated" by the spread of the vorticity by convection and diffusion. (See following discussion.)

The curl of Equation (3.2.59), noting that the curl of any gradient is zero, leads to

$$\rho\frac{\partial\boldsymbol{\zeta}}{\partial t}=\rho\nabla\times\left(\boldsymbol{V}\times\boldsymbol{\zeta}\right)-\mu\nabla\times\nabla\times\boldsymbol{\zeta} \tag{3.2.63}$$

but

$$\nabla^2\boldsymbol{\zeta}=\nabla(\nabla\cdot\boldsymbol{\zeta})-\nabla\times\nabla\times\boldsymbol{\zeta}=-\nabla\times\nabla\times\boldsymbol{\zeta} \tag{3.2.64}$$

because div curl () ≡ 0, and therefore also

$$\nabla\times\left(\boldsymbol{V}\times\boldsymbol{\zeta}\right)\equiv\boldsymbol{\zeta}\left(\nabla\boldsymbol{V}\right)+\boldsymbol{V}\nabla\cdot\boldsymbol{\zeta}-\boldsymbol{V}\nabla\boldsymbol{\zeta}-\boldsymbol{\zeta}\nabla\cdot\boldsymbol{V} \tag{3.2.65}$$

$$=\boldsymbol{\zeta}\left(\nabla\boldsymbol{V}\right)-\boldsymbol{V}\nabla\boldsymbol{\zeta} \tag{3.2.66}$$

Equation (3.2.63) can then be written

$$\frac{D\boldsymbol{\zeta}}{Dt}=\left(\boldsymbol{\zeta}\cdot\nabla\right)\boldsymbol{V}+\nu\nabla^2\boldsymbol{\zeta} \tag{3.2.67}$$

where $\nu = \mu/\rho$ is the *kinematic viscosity.*

Equation (3.2.67) is the vorticity equation for incompressible flow. The first term on the right, an inviscid term, represents the rate of change of vorticity by stretching and tilting of vortex lines. For $\nu \neq 0$, the second term on the right-hand side represents the rate of change of $\boldsymbol{\zeta}$ due to diffusion of vorticity, which may have been present in the flow from the beginning, or generated, for example, at solid boundaries due to the no-slip condition. (Vorticity can also be generated by *Coriolis effects* in a rotating frame and by *baroclinicity.*[4] For the vorticity equation including these effects, see Kundu and Cohen, 2004.)

In inviscid, two-dimensional flow both terms on the right-hand side vanish, and the equation reduces to $D\boldsymbol{\zeta}/Dt = 0$, from which it follows that the vorticity of a fluid particle remains constant as it moves.

---

[4] A flow is called *barotropic* if ρ is a function of p only, i.e., $\rho = f(p)$. Flows that are not barotropic are called *baroclinic.*

This is *Helmholtz's theorem.* As a consequence, it also follows that if $\boldsymbol{\zeta} = 0$ initially, $\boldsymbol{\zeta} = 0$ always; i.e., *initially irrotational flows remain irrotational* (for inviscid flows). Similarly, it can be proved that $D\Gamma/Dt = 0$; i.e., the *circulation* around a material closed circuit remains constant, which is *Kelvin's theorem.*

Also, for steady flow, the Bernoulli equation (Equation 3.2.62) reduces to

$$p + \frac{1}{2}\rho V^2 + \rho g z = \text{constant} \tag{3.2.68}$$

which is valid for steady, irrotational, incompressible flow.

Stream Function

For two-dimensional planar, incompressible flows [$\boldsymbol{V} = (u, v)$], the continuity equation,

$$\frac{\partial u}{\partial x} + \frac{\partial v}{\partial y} = 0 \tag{3.2.69}$$

is identically satisfied by introducing a *stream function* ψ, defined by

$$u = \frac{\partial \psi}{\partial y}, \qquad v = -\frac{\partial \psi}{\partial x} \tag{3.2.70}$$

Physically, ψ is a measure of the volume flow rate between streamlines. (Stream functions can be similarly defined to satisfy identically the continuity equations for incompressible cylindrical and spherical axisymmetric flows and for these flows, as well as the preceding planar flow, also when they are *compressible*, but then only if they are *steady.*)

Continuing with the planar case, note that, in such flows, there is only a single nonzero component of vorticity, given by

$$\boldsymbol{\zeta} = (0, 0, \zeta_z) = \left(0, 0, \frac{\partial v}{\partial x} - \frac{\partial u}{\partial y}\right) \tag{3.2.71}$$

With Equation (3.2.70), this sole nonzero component of vorticity is related to ψ by

$$\zeta_z = -\frac{\partial^2 \psi}{\partial x^2} - \frac{\partial^2 \psi}{\partial y^2} = -\nabla^2 \psi \tag{3.2.72}$$

For this two-dimensional flow, Equation (3.2.67) reduces to the single scalar equation:

$$\frac{\partial \zeta_z}{\partial t} + u\frac{\partial \zeta_z}{\partial x} + v\frac{\partial \zeta_z}{\partial y} = v\left(\frac{\partial^2 \zeta_z}{\partial x^2} + \frac{\partial^2 \zeta_z}{\partial y^2}\right) \equiv v\nabla^2 \zeta_z \tag{3.2.73}$$

Substitution of Equation (3.2.72) into Equation (3.2.73) yields an equation for the stream function alone:

$$\frac{\partial(\nabla^2 \psi)}{\partial t} + \frac{\partial \psi}{\partial y}\frac{\partial(\nabla^2 \psi)}{\partial x} - \frac{\partial \psi}{\partial x}\frac{\partial(\nabla^2 \psi)}{\partial y} = v\nabla^4 \psi \tag{3.2.74}$$

where $\nabla^4 \equiv \nabla^2 (\nabla^2)$. For uniform flow (aligned with the x-axis) past a solid body, for example, this equation for ψ would be solved subject to the boundary conditions:

$$\begin{aligned} &\frac{\partial}{\partial x} = 0, \quad \frac{\partial}{\partial y} = V_\bullet \quad \text{at infinity} \\ &\frac{\partial}{\partial x} = 0, \quad \frac{\partial}{\partial y} = 0 \quad \text{at the body (no penetration, no slip)} \end{aligned} \tag{3.2.75}$$

For the special case of irrotational flow, it follows immediately from Equation (3.2.70) and Equation (3.2.71) with $\zeta_z = 0$, that ψ satisfies the *Laplace equation*:

$$\nabla^2 \psi = \frac{\partial^2 \psi}{\partial x^2} + \frac{\partial^2 \psi}{\partial y^2} = 0 \tag{3.2.76}$$

Inviscid Irrotational Flow: Potential Flow

For irrotational flows, it has already been noted that a velocity potential Φ can be defined such that $\boldsymbol{V} = \nabla\Phi$. If the flow is also incompressible, so that $\nabla \cdot \boldsymbol{V} = 0$, it then follows that

$$\nabla \cdot (\nabla \Phi) = \nabla^2 \Phi = 0 \tag{3.2.77}$$

so Φ satisfies Laplace's equation. Note that unlike the stream function ψ, which can only be defined for two-dimensional flows, the preceding considerations for Φ apply to flows in two and three dimensions. On the other hand, the existence of ψ does not require the flow to be irrotational, whereas the existence of Φ does.)

Because Equation (3.2.77), with appropriate conditions on $\boldsymbol{V}$ at boundaries of the flow, completely determines the velocity field, and the momentum equation plays no role in this determination, inviscid irrotational flow — *potential theory* — is a purely *kinematic theory*. The momentum equation is used after Φ is known to calculate the pressure field consistent with the velocity field $\boldsymbol{V}$.

For two- as well as three-dimensional flows, the determination of Φ makes use of the powerful techniques of potential theory, well developed in the mathematical literature. For two-dimensional planar flows, the techniques of complex variable theory are available because Φ may be considered as the real or the imaginary part of an *analytic function*. (The same is true for ψ because, for such two-dimensional flows, Φ and ψ are conjugate variables.)

Because the Laplace equation, obeyed by Φ and ψ, is linear, complex flows may be built up from the *superposition* of *simple flows*; this property of inviscid irrotational flows is the basis of many of the solution techniques in this area of fluid mechanics.

Problem

A two-dimensional inviscid irrotational flow has the velocity potential

$$\Phi = x^2 - y^2 \tag{P.3.2.6}$$

What two-dimensional potential flow does this represent?

Solution. It follows from Equation (3.2.61) and Equation (3.2.70) that, for two-dimensional flows in general,

$$u = \frac{\partial \Phi}{\partial x} = \frac{\partial \psi}{\partial y}, \quad v = \frac{\partial \Phi}{\partial y} = -\frac{\partial \psi}{\partial x} \tag{P.3.2.7}$$

From Equation (P.3.2.6)

$$u = \frac{\partial \psi}{\partial y} = 2x, \quad v = -\frac{\partial \psi}{\partial x} = -2y \tag{P.3.2.8}$$

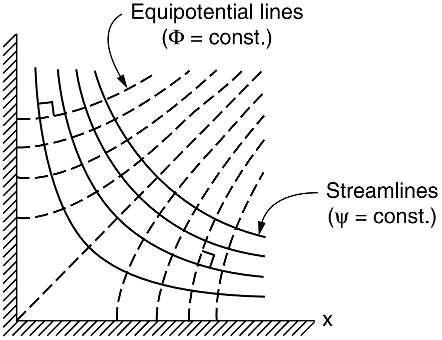

FIGURE 3.2.3 Potential flow in a 90° corner.

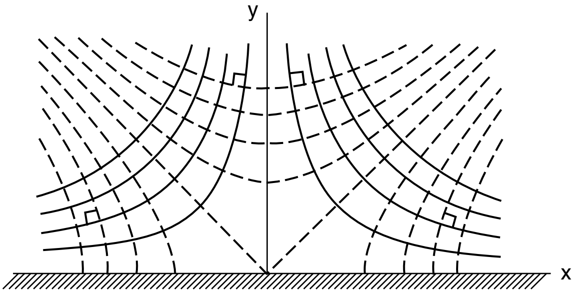

FIGURE 3.2.4 Potential flow impinging against a flat (180°) wall (plane stagnation-point flow).

integration of which yields

$$\psi = 2xy \tag{P.3.2.9}$$

The streamlines, ψ = constant, and equipotential lines, Φ = constant, both families of hyperbolas and each family the orthogonal trajectory of the other, are shown in Figure 3.2.3. Because the x and y axes are streamlines, Equation (P.3.2.6) and Equation (P.3.2.9) represent the inviscid irrotational flow in a right-angle corner. By symmetry, they also represent the planar flow in the upper half-plane directed toward a stagnation point at $x = y = 0$ (Figure 3.2.4). In polar coordinates (r,θ), with corresponding velocity components (u_r,u_θ), this flow is represented by

$$\Phi = r^2 \cos 2\theta, \quad \psi = \mathrm{r}^2 \sin 2\theta \tag{P.3.2.10}$$

with

$$u_r = \frac{\partial \Phi}{\partial r} = \frac{1}{r}\frac{\partial \psi}{\partial \theta} = 2r\cos 2\theta, \quad u_\theta = \frac{1}{r}\frac{\partial \Phi}{\partial \theta} = -\frac{\partial \psi}{\partial r} = -2r\sin 2\theta \tag{P.3.2.11}$$

For two-dimensional planar potential flows, one may also use *complex variables*, writing the *complex potential* $f(z) = \Phi + i\psi$ as a function of the complex variable $z = x + iy$, where the *complex velocity* is given by $f'(\mathrm{z}) = \mathrm{w}(\mathrm{z}) = u - \mathrm{i}\nu$. For the flow above

$$f(z) = z^2 \tag{P.3.2.12}$$

Expressions such as Equation (P.3.2.12), where the right-hand side is an analytic function of z, may also be regarded as a *conformal mapping*, which makes available as an aid in solving two-dimensional potential problems all the tools and techniques of that branch of mathematics.

References

Bird, R.B., Stewart, W.E., and Lightfoot, E.N. 2002. *Transport Phenomena*, 2nd ed., John Wiley & Sons, New York.

Kundu, P.K. and Cohen, I.M. 2004. *Fluid Mechanics*, 3rd ed., Elsevier Academic Press, San Diego.

Further Information

More detail and additional information on the topics in this section may be found in the following books:

Batchelor, G.K. 1967. *An Introduction to Fluid Dynamics*, Cambridge University Press, Cambridge, England.

Panton, R.L. 1996. *Incompressible Flow*, 2nd ed., John Wiley & Sons, New York.

Pozrikidis, C. 1997. *Introduction to Theoretical and Computational Fluid Dynamics,* Oxford University Press, New York.

Sherman, F.S. 1990. *Viscous Flow*, McGraw–Hill, New York.

Warsi, Z.U.A. 1999. *Fluid Dynamics: Theoretical and Computational Approaches*, 2nd ed., CRC Press, Boca Raton, FL.

3.3 Similitude: Dimensional Analysis and Data Correlation

Stuart W. Churchill

Dimensional Analysis

Similitude refers to the formulation of a description for physical behavior that is general and independent of the individual dimensions, physical properties, forces, etc. In this subsection the treatment of similitude is restricted to *dimensional analysis*; for a more general treatment see Zlokarnik (1991). The full power and utility of dimensional analysis is often underestimated and underutilized by engineers. This technique may be applied to a complete mathematical model or to a simple listing of the variables that define the behavior. Only the latter application is described here. For a description of the application of dimensional analysis to a mathematical model see Hellums and Churchill (1964).

General Principles

Dimensional analysis is based on the principle that all additive or equated terms of a complete relationship between the variables must have the same net dimensions. The analysis starts with the preparation of a list of the individual dimensional variables (dependent, independent, and parametric) that are presumed to define the behavior of interest. The performance of dimensional analysis in this context is reasonably simple and straightforward; the principal difficulty and uncertainty arise from the identification of the variables to be included or excluded. If one or more important variables are inadvertently omitted, the reduced description achieved by dimensional analysis will be incomplete and inadequate as a guide for the correlation of a full range of experimental data or theoretical values. The familiar band of plotted values in many graphical correlations is more often a consequence of the omission of one or more variables than of inaccurate measurements. If, on the other hand, one or more irrelevant or unimportant variables are included in the listing, the consequently reduced description achieved by dimensional analysis will result in one or more unessential dimensionless groupings. Such excessive dimensionless groupings are generally less troublesome than missing ones because the redundancy will ordinarily be revealed by the process of correlation. Excessive groups may, however, suggest unnecessary experimental work or computations, or result in misleading correlations. For example, real experimental scatter may inadvertently and incorrectly be correlated in all or in part with the variance of the excessive grouping.

In consideration of the inherent uncertainty in selecting the appropriate variables for dimensional analysis, it is recommended that this process be interpreted as a *speculative* and subject to correction of the basis of experimental data or other information. Speculation may also be utilized as a formal technique to identify the effect of eliminating a variable or of combining two or more. The latter aspect of speculation, which may be applied either to the original listing of dimensional variables or to the resulting set of dimensionless groups, is often of great utility in identifying possible limiting behavior or dimensionless groups of marginal significance. The systematic speculative elimination of all but the most certain variables, one at a time, followed by regrouping, is recommended as a general practice. The additional effort as compared with the original dimensional analysis is minimal, but the possible return is very high. A general discussion of this process may be found in Churchill (1981).

The minimum number of independent dimensionless groups i required to describe the fundamental and parametric behavior is (Buckingham, 1914)

$$i = n - m \tag{3.3.1}$$

where n is the number of variables and m is the number of fundamental dimensions such as mass M, length L, time θ, and temperature T that are introduced by the variables. The inclusion of redundant dimensions such as force F and energy E that may be expressed in terms of mass, length, time, and temperature is at the expense of added complexity and is to be avoided. (Of course, mass could be replaced by force or temperature by energy as alternative fundamental dimensions.) In some rare cases i is actually greater than $n - m$. Then

$$i = n - k \tag{3.3.2}$$

where k is the maximum number of the chosen variables that cannot be combined to form a dimensionless group. Determination of the minimum number of dimensionless groups is helpful if the groups are to be chosen by inspection, but is unessential if the algebraic procedure described below is utilized to determine the groups themselves since the number is then obvious from the final result.

The *particular* minimal set of dimensionless groups is arbitrary in the sense that two or more of the groups may be multiplied together to any positive, negative, or fractional power as long as the number of independent groups is unchanged. For example, if the result of a dimensional analysis is

$$\phi\left\{XY^{1/2}, Z/Y^2, Z\right\} = 0 \tag{3.3.3}$$

where X, Y, and Z are independent dimensionless groups, an equally valid expression is

$$\phi\{X, Y, Z\} = 0 \tag{3.3.4}$$

Dimensional analysis itself does not provide any insight as to the best choice of equivalent dimensionless groupings, such as between those of Equation (3.3.3) and Equation (3.3.4). However, isolation of each of the variables that are presumed to be the most important in a separate group may be convenient in terms of interpretation and correlation. Another possible criterion in choosing between alternative groupings may be the relative invariance of a particular one. The functional relationship provided by Equation (3.3.3) may equally well be expressed as

$$X = \phi\{Y, Z\} \tag{3.3.5}$$

where X is implied to be the dependent grouping and Y and Z to be independent or parametric groupings.

Three primary methods of determining a minimal set of dimensionless variables are (1) by inspection; (2) by combination of the residual variables, one at a time, with the set of chosen variables that cannot be combined to obtain a dimensionless group; and (3) by an algebraic procedure. These methods are illustrated in the examples that follow.

Example 3.3.1: Fully Developed Flow of Water Through a Smooth Round Pipe

Choice of Variables. The shear stress τ_w on the wall of the pipe may be postulated to be a function of the density ρ and the dynamic viscosity μ of the water, the inside diameter D of the pipe, and the space-mean of the time-mean velocity u_m. The limitation to fully developed flow is equivalent to a postulate of independence from distance x in the direction of flow, and the specification of a smooth pipe is equivalent to the postulate of independence from the roughness e of the wall. The choice of τ_w rather than the pressure drop per unit length $-dP/dx$ avoids the need to include the acceleration due to gravity g and the elevation z as variables. The choice of u_m rather than the volumetric rate of flow V, the mass rate of flow w, or the mass rate of flow per unit area G is arbitrary but has some important consequences as noted below. The postulated dependence may be expressed functionally as $\phi\{\tau_w, \rho, \mu, D, u_m\} = 0$ or $\tau_w = \phi\{\rho, \mu, D, u_m\}$.

Tabulation

Next prepare a tabular listing of the variables and their dimensions:

	τ_w	ρ	μ	D	u_m
M	1	1	1	0	0
L	–1	–3	–1	1	1
θ	–2	0	–1	0	–1
T	0	0	0	0	0

Minimal Number of Groups

The number of postulated variables is 5. Since the temperature does not occur as a dimension for any of the variables, the number of fundamental dimensions is 3. From Equation (3.3.1), the minimal number of dimensionless groups is 5 – 3 = 2. From inspection of the above tabulation, a dimensionless group cannot be formed from as many as three variables such as D, μ, and ρ. Hence, Equation (3.3.2) also indicates that $i = 5 - 3 = 2$.

Method of Inspection

By inspection of the tabulation or by trial and error it is evident that only two independent dimensionless groups may be formed. One such set is

$$\phi\left\{\frac{\tau_w}{\rho u_m^2}, \frac{Du_m\rho}{\mu}\right\} = 0$$

Method of Combination

The residual variables τ_w and μ may be combined in turn with the noncombining variables ρ, D, and u_m to obtain two groups such as those above.

Algebraic Method

The algebraic method makes formal use of the postulate that the functional relationship between the variables may in general be represented by a power series. In this example such a power series may be expressed as

$$\tau_w = \sum_{i=1}^{N} A_i \rho^{a_i} \mu^{b_i} D^{c_i} u_m^{d_i}$$

where the coefficients A_i are dimensionless. Each additive term on the right-hand side of this expression must have the same net dimensions as τ_w. Hence, for the purposes of dimensional analysis, only the first term need be considered and the indexes may be dropped. The resulting highly restricted expression is $\tau_w = A\rho^a\mu^bD^c u_m^d$. Substituting the dimensions for the variables gives

$$\frac{M}{L\theta^2} = A\left(\frac{M}{L^3}\right)^a\left(\frac{M}{L\theta}\right)^b L^c\left(\frac{L}{\theta}\right)^d$$

Equating the sum of the exponents of M, L, and θ on the right-hand side of the above expression with those of the left-hand side produces the following three simultaneous linear algebraic equations: $1 = a + b$; $-1 = -3a - b + c + d$; and $-2 = -b - d$, which may be solved for a, c, and d in terms of b to obtain $a = 1 - b$, $c = -b$, and $d = 2 - b$. Substitution then gives $\tau_w = A\rho^{1-b}\mu^b D^{-b} u_m^{2-b}$ which may be regrouped as

$$\frac{\tau_w}{\rho u_m^2} = A\left(\frac{\mu}{Du_m\rho}\right)^b$$

Since this expression is only the first term of a power series, it should *not* be interpreted to imply that $\tau_w/\rho u_m^2$ is necessarily proportional to some power at $\mu/Du_m\rho$ but instead only the equivalent of the expression derived by the method of inspection. The inference of a power dependence between the dimensionless groups is the most common and serious error in the use of the algebraic method of dimensional analysis.

Speculative Reductions

Eliminating ρ as a variable on speculative grounds to

$$\phi\left\{\frac{\tau_w D}{\mu u_m}\right\} = 0$$

or its exact equivalent:

$$\frac{\tau_w D}{\mu u_m} = A$$

The latter expression with $A = 8$ is actually the exact solution for the laminar regime ($Du_m\rho/\mu < 1800$). A relationship that does not include ρ may alternatively be derived directly from the solution by the method of inspection as follows. First, ρ is eliminated from one group, say $\tau_w/\rho u_m^2$, by multiplying it with $Du_m\rho/\mu$ to obtain

$$\phi\left\{\frac{\tau_w D}{\mu u_m}, \frac{Du_m\rho}{\mu}\right\} = 0$$

The remaining group containing ρ is now simply dropped. Had the original expression been composed of three independent groups each containing ρ, that variable would have to be eliminated from two of them before dropping the third one.

The relationships that are obtained by the speculative elimination of μ, D, and u_m, one at a time, do not appear to have any range of physical validity. Furthermore, if w or G had been chosen as the independent variable rather than u_m, the limited relationship for the laminar regime would not have been obtained by the elimination of ρ.

Alternative Forms

The solution may also be expressed in an infinity of other forms such as

$$\phi\left\{\frac{\tau_w D^2\rho}{\mu^2}, \frac{Du_m\rho}{\mu}\right\} = 0$$

If τ_w is considered to be the principal dependent variable and u_m the principal independent variable, this latter form is preferable in that these two quantities do not then appear in the same grouping. On the other hand, if D is considered to be the principal independent variable, the original formulation is preferable. The variance of $\tau_w/\rho u_m^2$ is less than that of $\tau_w D/\mu u_m$ and $\tau_w D^2\rho/\mu^2$ in the turbulent regime while that of $\tau_w D/\mu u_m$ is zero in the laminar regime. Such considerations may be important in devising convenient graphical correlations.

Alternative Notations

The several solutions above are more commonly expressed as

$$\phi\left\{\frac{f}{2}, \mathrm{Re}\right\} = 0$$

$$\phi\left\{\frac{f\,\mathrm{Re}}{2}, \mathrm{Re}\right\} = 0$$

or

$$\phi\left\{\frac{f\,\mathrm{Re}^2}{2}, \mathrm{Re}\right\} = 0$$

where $f = 2\,\tau_w/\rho u_m^2$ is the *Fanning friction factor* and $Re = Du_m\rho/\mu$ is the *Reynolds number.*

The more detailed forms, however, are to be preferred for purposes of interpretation or correlation because of the explicit appearance of the individual, physically measurable variables.

Addition of a Variable

The above results may readily be extended to incorporate the roughness e of the pipe as a variable. If two variables have the same dimensions, they will always appear as a dimensionless group in the form of a ratio, in this case e appears most simply as e/D. Thus, the solution becomes

$$\phi\left\{\frac{\tau_w}{\rho u_m^2}, \frac{Du_m\rho}{\mu}, \frac{e}{D}\right\} = 0$$

Surprisingly, as contrasted with the solution for a smooth pipe, the speculative elimination of μ and hence of the group $Du_m\rho/\mu$ now results in a valid asymptote for $Du_m\rho/\mu \rightarrow \infty$ and all finite values of e/D, namely,

$$\phi\left\{\frac{\tau_w}{\rho u_m^2}, \frac{e}{D}\right\} = 0$$

Example 3.3.2: Fully Developed Forced Convection in Fully Developed Flow in a Round Tube

It may be postulated for this process that $h = \phi\{D, u_m, \rho, \mu, k, c_p\}$, where here h is the local heat transfer coefficient, and c_p and k are the specific heat capacity and thermal conductivity, respectively, of the fluid. The corresponding tabulation is

	h	D	u_m	ρ	μ	k	c_p
M	1	0	0	1	1	1	0
L	0	1	1	–3	–1	1	2
θ	–3	0	–1	0	–1	–3	–2
T	–1	0	0	0	0	–1	–1

The number of variables is 7 and the number of independent dimensions is 4, as is the number of variables such as D, u_m, ρ, and k that cannot be combined to obtain a dimensionless group. Hence, the minimal number of dimensionless groups is 7 – 4 = 3. The following acceptable set of dimensionless groups may be derived by any of the procedures illustrated in Example 1:

$$\frac{hD}{k} = \phi\left\{\frac{Du_m\rho}{\mu}, \frac{c_p\mu}{k}\right\}$$

Speculative elimination of μ results in

$$\frac{hD}{k} = \phi\left\{\frac{Du_m\rho c_p}{k}\right\}$$

which has often erroneously been inferred to be a valid asymptote for $c_p\mu/k \to 0$. Speculative elimination of D, u_m, ρ, k, and c_p individually also does not appear to result in expressions with any physical validity. However, eliminating c_p and ρ or u_m gives a valid result for the laminar regime, namely,

$$\frac{hD}{k} = A$$

The general solutions for flow and convection in a smooth pipe may be combined to obtain

$$\frac{hD}{k} = \phi\left\{\frac{\tau_w D^2\rho}{\mu^2}, \frac{c_p\mu}{k}\right\}$$

which would have been obtained directly had u_m been replaced by τ_w in the original tabulation. This latter expression proves to be superior in terms of speculative reductions. Eliminating D results in

$$\frac{h\mu}{k(\tau_w\rho)^{1/2}} = \phi\left\{\frac{c_p\mu}{k}\right\}$$

which may be expressed in the more conventional form of

$$\text{Nu} = \text{Re}\left(\frac{f}{2}\right)^{1/2}\phi\{\text{Pr}\}$$

where Nu = hD/k is the *Nusselt number* and Pr = $c_p\mu/k$ is the *Prandtl number*. This result appears to be a valid asymptote for Re → ∞ and a good approximation for even moderate values (>5000) for large values of Pr. Elimination of μ as well as D results in

$$\frac{h}{c_p(\tau_w\rho)^{1/2}} = A$$

or

$$\mathrm{Nu} = A\,\mathrm{Re}\,\mathrm{Pr}\left(\frac{f}{2}\right)^{1/2}$$

which appears to be an approximate asymptote for Re → ∞ and Pr → 0. Elimination of both c_p and ρ again yields the appropriate result for laminar flow, indicating that ρ rather than u_m is the meaningful variable to eliminate in this respect.

The numerical value of the coefficient A in the several expressions above depends on the mode of heating, a true variable, but one from which the purely functional expressions are independent. If j_w the heat flux density at the wall, and $T_w - T_m$, the temperature difference between the wall and the bulk of the fluid, were introduced as variables in place of $h \equiv j_w/(T_w - T_m)$, another group such as $c_p(T_w - T_m)(D\rho/\mu)^2$ or $\rho c_p(T_w - T_m)/\tau_w$ or $c_p(T_w - T_m)/u_m^2$, which represents the effect of viscous dissipation, would be obtained. This effect is usually but not always negligible. (See Chapter 4.)

Example 3.3.3: Free Convection from a Vertical Isothermal Plate

The behavior for this process may be postulated to be represented by

$$h = \phi\left\{g, \beta, T_w - T_\infty, x, \mu, \rho, c_p, k\right\}$$

where g is the acceleration due to gravity, β is the volumetric coefficient of expansion with temperature, T_∞ is the unperturbed temperature of the fluid, and x is the vertical distance along the plate. The corresponding tabulation is

	h	g	β	$T_w - T_\infty$	x	μ	ρ	c_p	k
M	1	0	0	0	0	1	1	0	1
L	0	1	0	0	1	–1	–3	2	1
θ	–3	–2	0	0	0	–1	0	–2	–3
T	–1	0	–1	1	0	0	0	–1	1

The minimal number of dimensionless groups indicated by both methods is 9 – 4 = 5. A satisfactory set of dimensionless groups, as found by any of the methods illustrated in Example 1 is

$$\frac{hx}{k} = \phi\left\{\frac{\rho^2 g x^3}{\mu^2}, \frac{c_p\mu}{k}, \beta(T_w - T_\infty), c_p(T_w - T_\infty)\left(\frac{\rho x}{\mu}\right)^2\right\}$$

It may be reasoned that the buoyant force which generates the convective motion must be proportional to $\rho g\beta(T_w - T_\infty)$, thus, g in the first term on the right-hand side must be multiplied by $\beta(T_w - T_\infty)$, resulting in

$$\frac{hx}{k} = \phi\left\{\frac{\rho^2 g\beta(T_w - T_\infty)x^3}{\mu^2}, \frac{c_p\mu}{k}, \beta(T_w - T_\infty), c_p(T_w - T_\infty)\left(\frac{\rho x}{\mu}\right)^2\right\}$$

The effect of expansion other than on the buoyancy is now represented by $\beta(T_w - T_\infty)$, and the effect of viscous dissipation by $c_p(T_w - T_\infty)(\rho x/\mu)^2$. Both effects are negligible for all practical circumstances. Hence, this expression may be reduced to

$$\frac{hx}{k} = \phi\left\{\frac{\rho^2 g\beta(T_w - T_\infty)x^3}{\mu^2}, \frac{c_p\mu}{k}\right\}$$

or

$$\mathrm{Nu}_x = \phi\left\{\mathrm{Gr}_x, \mathrm{Pr}\right\}$$

where $\mathrm{Nu}_x = hx/k$ and $\mathrm{Gr}_x = \rho^2 g\beta(T_w - T_\infty)x^3/\mu^2$ is the *Grashof number.*

Elimination of x speculatively now results in

$$\frac{hx}{k} = \left(\frac{\rho^2 g\beta(T_w - T_\infty)x^3}{\mu^2}\right)^{1/3} \phi\{\mathrm{Pr}\}$$

or

$$\mathrm{Nu}_x = \mathrm{Gr}_\mathrm{x}^{1/3}\phi\{\mathrm{Pr}\}$$

This expression appears to be a valid asymptote for $\mathrm{Gr}_x \to \infty$ and a good approximation for the entire turbulent regime. Eliminating μ speculatively rather than x results in

$$\frac{hx}{k} = \phi\left\{\frac{\rho^2 c_p^2 g\beta(T_w - T_\infty)x^3}{k^2}\right\}$$

or

$$\mathrm{Nu}_x = \phi\left\{\mathrm{Gr}_x \mathrm{Pr}^2\right\}$$

The latter expression appears to be a valid asymptote for $\mathrm{Pr} \to 0$ for all Gr_x, that is, for both the laminar and the turbulent regimes. The development of a valid asymptote for large values of Pr requires more subtle reasoning. First $c_p\mu/k$ is rewritten as $\mu/\rho\alpha$ where $\alpha = k/\rho c_p$. Then ρ is eliminated speculatively except as it occurs in $\rho g\beta(T_w - T_\infty)$ and $k/\rho c_p$. The result is

$$\frac{hx}{k} = \phi\left\{\frac{c_p\rho^2 g\beta(T_w - T_\infty)x^3}{\mu k}\right\}$$

or

$$\mathrm{Nu}_x = \phi\left\{\mathrm{Ra}_x\right\}$$

where

$$\mathrm{Ra}_x = \frac{c_p\rho^2 g\beta(T_w - T_\infty)x^3}{\mu k} = \mathrm{Gr}_x\,\mathrm{Pr}$$

is the *Rayleigh number.* The expression appears to be a valid asymptote for $\mathrm{Pr} \to \infty$ and a reasonable approximation for even moderate values of Pr for all Gr_x, that is, for both the laminar and the turbulent regimes.

Eliminating x speculatively from the above expressions for small and large values of Pr results in

$$\mathrm{Nu}_x = A\left(\mathrm{Gr}_x\,\mathrm{Pr}^2\right)^{1/3} = A\left(\mathrm{Ra}_x\,\mathrm{Pr}\right)^{1/3}$$

and

$$\mathrm{Nu}_x = B\left(\mathrm{Gr}_x\,\mathrm{Pr}\right)^{1/3} = B\left(\mathrm{Ra}_x\right)^{1/3}$$

The former appears to be a valid asymptote for Pr → 0 and $\mathrm{Gr}_x \to \infty$ and a reasonable approximation for very small values of Pr in the turbulent regime, while the latter is well confirmed as a valid asymptote for Pr → ∞ and $\mathrm{Gr}_x \to \infty$ and as a good approximation for moderate and large values of Pr over the entire turbulent regime. The expressions in terms of Gr_x are somewhat more complicated than those in terms of Ra_x, but are to be preferred since Gr_x is known to characterize the transition from laminar to turbulent motion in natural convection just as Re_D does in forced flow in a channel. The power of speculation combined with dimensional analysis is well demonstrated by this example in which valid asymptotes are thereby attained for several regimes.

Correlation of Experimental Data and Theoretical Values

Correlations of experimental data are generally developed in terms of dimensionless groups rather than in terms of the separate dimensional variables in the interests of compactness and in the hope of greater generality. For example, a complete set of graphical correlations for the heat transfer coefficient h of Example 3.3.2 above in terms of each of the six individual independent variables and physical properties might approach book length, whereas the dimensionless groupings both imply that a single plot with one parameter should be sufficient. Furthermore, the reduced expression for the turbulent regime implies that a plot of $\mathrm{Nu}/\mathrm{Re}\, f^{1/2}$ vs. Pr should demonstrate only a slight parametric dependence on Re or $\mathrm{Re}\, f^{1/2}$. Of course, the availability of a separate correlation for f as a function of Re is implied.

Theoretical values, that is, ones obtained by numerical solution of a mathematical model in terms of either dimensional variables or dimensionless groups, are presumably free from imprecision. Even so, because of their discrete form, the construction of a correlation or correlations for such values may be essential for the same reasons as for experimental data.

Graphical correlations have the merit of revealing general trends, of providing a basis for evaluation of the choice of coordinates, and most of all of displaying visually the scatter of the individual experimental values about a curve representing a correlation or their behavior on the mean. (As mentioned in the previous subsection, the omission of a variable may give the false impression of experimental error in such a plot.) On the other hand, correlating equations are far more convenient as an input to a computer than is a graphical correlation. These two formats thus have distinct and complementary roles; both should generally be utilized. The merits and demerits of various graphical forms of correlations are discussed in detail by Churchill (1979), while the use of logarithmic and arithmetic coordinates, the effects of the appearance of a variable in both coordinates, and the effects of the distribution of error between the dependent and independent variable are further illustrated by Wilkie (1985).

Churchill and Usagi (1972; 1974) proposed general usage of the following expression for the formulation of correlating equations:

$$y^n\{x\} = y_0^n\{x\} + y_\infty^n\{x\} \tag{3.3.6}$$

where $y_o\{x\}$ and $y_\infty\{x\}$ denote asymptotes for small and large values of x, respectively, and n is an arbitrary exponent. For convenience and simplicity, Equation (3.3.6) may be rearranged in either of the following two forms:

$$\left(Y(x)\right)^n = 1 + Z^n\{x\} \tag{3.3.7}$$

or

$$\left(\frac{Y\{x\}}{Z\{x\}}\right)^n = 1 + \frac{1}{Z^n\{x\}} \tag{3.3.8}$$

where $Y\{x\} \equiv y\{x\}/y_o\{x\}$ and $Z\{x\} \equiv y_\infty\{x\}/y_o\{x\}$. Equation (3.3.6), Equation (3.3.7), and Equation (3.3.9) are hereafter denoted collectively as the CUE (Churchill–Usagi equation). The principle merits of the CUE as a canonical expression for correlation are its simple form, generality, and minimal degree of explicit empiricism, namely, only that of the exponent n, since the asymptotes $y_o\{x\}$ and $y_\infty\{x\}$ are ordinarily known in advance from theoretical considerations or well-established correlations. Furthermore, as will be shown, the CUE is quite insensitive to the numerical value of n. Although the CUE is itself very simple in form, it is remarkably successful in representing closely very complex behavior, even including the dependence on secondary variables and parameters, by virtue of the introduction of such dependencies through $y_o\{x\}$ and $y_\infty\{x\}$. In the rare instances in which such dependencies are not represented in the asymptotes, n may be correlated as a function of the secondary variables and/or parameters. Although the CUE usually produces very close representations, it is empirical and not exact. In a few instances, numerical values of n have been derived or rationalized on theoretical grounds, but even then some degree of approximation is involved. Furthermore, the construction of a correlating expression in terms of the CUE is subject to the following severe limitations:

1. The asymptotes $y_o\{x\}$ and $y_\infty\{x\}$ must intersect once and only once;
2. The asymptotes $y_o\{x\}$ and $y_\infty\{x\}$ must be free of singularities. Even though a singularity occurs beyond the asserted range of the asymptote, it will persist and disrupt the prediction of the CUE, which is intended to encompass all values of the independent variable x; and
3. The asymptotes must both be upper or lower bounds.

In order to avoid or counter these limitations it may be necessary to modify or replace the asymptotes with others. Examples of this process are provided below. A different choice for the dependent variable may be an option in this respect. The suitable asymptotes for use in Equation (3.3.6) may not exist in the literature and therefore may need to be devised or constructed. See, for example, Churchill (1988b) for guidance in this respect. Integrals and derivatives of the CUE are generally awkward and inaccurate, and may include singularities not present or troublesome in the CUE itself. It is almost always preferable to develop a separate correlating equation for such quantities using derivatives or integrals of $y_o\{x\}$ and $y_\infty\{x\}$, simplified or modified as appropriate.

The Evaluation of *n*

Equation (3.3.6) may be rearranged as

$$n = \frac{\ln\left\{1 + \left(\frac{y_\infty\{x\}}{y_0\{x\}}\right)^n\right\}}{\ln\left\{\frac{y\{x\}}{y_0\{x\}}\right\}} \tag{3.3.9}$$

and solved for n by iteration for any known value of $y\{x\}$, presuming that $y_o\{x\}$ and $y_\infty\{x\}$ are known. If $y\{x^*\}$ is known, where x^* represents the value of x at the point of intersection of the asymptotes, that is, for $y_o\{x\} = y_\infty\{x\}$, Equation (3.3.9) reduces to

$$n = \frac{\ln\{2\}}{\ln\left\{\frac{y\{x^*\}}{y_0\{x^*\}}\right\}} \tag{3.3.10}$$

and iterative determination of n is unnecessary.

A graphical and visual method of evaluation of n is illustrated in Figure 3.3.1 in which $Y\{Z\}$ is plotted vs. Z for $0 \le Z \le 1$ and $Y\{Z\}/Z$ vs. $1/Z$ for $0 \le 1/Z \le 1$ in arithmetic coordinates with n as a parameter. Values of $y\{x\}$ may be plotted in this form and the best overall value of n selected visually (as illustrated in Figure 3.3.2). A logarithmic plot of $Y\{Z\}$ vs. Z would have less sensitivity relative to the dependence on n. (See, for example, Figure 1 of Churchill and Usagi, 1972.) Figure 3.3.1 explains in part the success of the CUE. Although y and x may both vary from 0 to ∞, the composite variables plotted in Figure 3.3.1

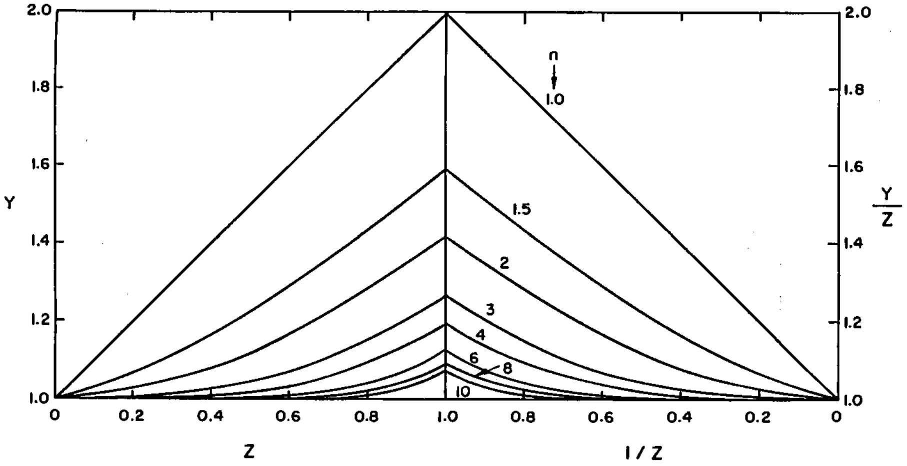

FIGURE 3.3.1 Arithmetic, split-coordinate plot of Equation 3.3.10. (From Churchill, S.W. and Usagi, R. *AIChE J.* 18(6), 1123, 1972. With permission from the American Institute of Chemical Engineers.)

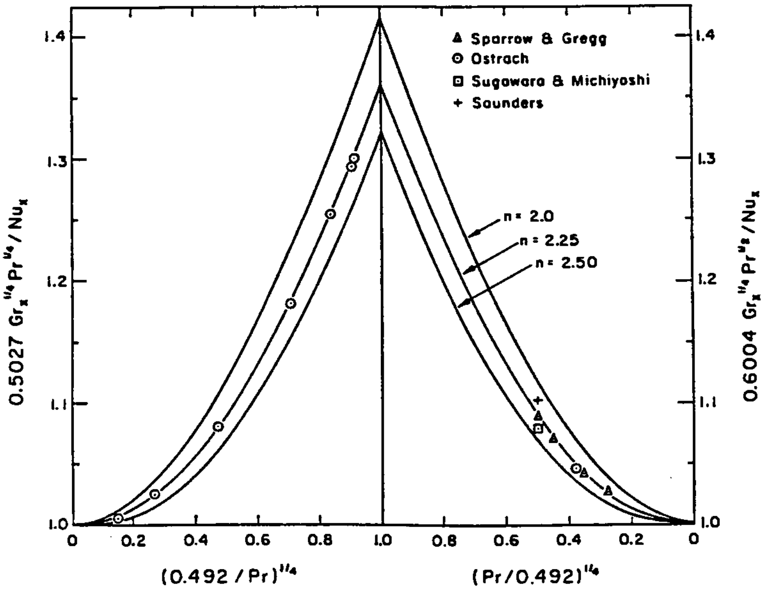

FIGURE 3.3.2 Arithmetic, split-coordinate plot of computed values and experimental data for laminar free convection from an isothermal vertical plate. (From Churchill, S.W. and Usagi, R. *AIChE J.* 18(6), 1124, 1972. With permission from the American Institute of Chemical Engineers.)

are highly constrained in that the compound independent variables Z and $1/Z$ vary only between 0 and 1, while for $n \geq 1$, the compound dependent variables $Y\{Z\}$ and $Y\{Z\}/Z$ vary only from 1 to 2.

Because of the relative insensitivity of the CUE to the numerical value of n, an integer or a ratio of two small integers may be chosen in the interest of simplicity and without significant loss of accuracy. For example, the maximum variance in Y (for $0 \leq Z \leq 1$) occurs at $Z = 1$ and increases only $100(2^{1/20} - 1) = 3.5\%$ if n is decreased from 5 to 4. If $y_o\{x\}$ and $y_\infty\{x\}$ are both lower bounds, n will be positive, and if they are both upper bounds, n will be negative. To avoid extending Figure 3.3.1 for negative values of n, $1/y\{x\}$ may simply be interpreted as the dependent variable.

Intermediate Regimes

Equation (3.3.6), Equation (3.3.7), and Equation (3.3.8) imply a slow, smooth transition between $y_o\{x\}$ and $y_\infty\{x\}$ and, moreover, one that is symmetrical with respect to $x^*(Z = 1)$. Many physical systems demonstrate instead a relatively abrupt transition, as for example from laminar to turbulent flow in a channel or along a flat plate. The CUE may be applied serially as follows to represent such behavior if an expression $y_i\{x\}$ is postulated for the intermediate regime. First, the transition from the initial to the intermediate regime is represented by

$$y_1^n = y_0^n + y_i^n \tag{3.3.11}$$

Then the transition from this combined regime to the final regime by

$$y^m = y_1^m + y_\infty^m = \left(y_0^n + y_i^n\right)^{m/n} + y_\infty^m \tag{3.3.12}$$

Here, and throughout the balance of this subsection, in the interests of simplicity and clarity, the functional dependence of all the terms on x is implied rather written out explicitly. If y_o is a lower bound and y_i is implied to be one, y_1 and y_∞ must be upper bounds. Hence, n will then be positive and m negative. If y_o and y_i are upper bounds, y_1 and y_∞ must be lower bounds; then n will be negative and m positive. The reverse formulation starting with y_∞ and y_1 leads by the same procedure to

$$y^n = y_0^n + \left(y_i^m + y_\infty^m\right)^{n/m} \tag{3.3.13}$$

If the intersections of y_i with y_o and y_∞ are widely separated with respect to x, essentially the same pair of values for n and m will be determined for Equation (3.3.12) and Equation (3.3.13), and the two representations for y will not differ significantly. On the other hand, if these intersections are close in terms of x, the pair of values of m and n may differ significantly and one representation may be quite superior to the other. In some instances a singularity in y_o or y_∞ may be tolerable in either Equation (3.3.12) or (3.3.13) because it is overwhelmed by the other terms. Equation (3.3.12) and Equation (3.3.13) have one hidden flaw. For $x \to 0$, Equation (3.3.12) reduces to

$$y \to y_0\left[1 + \left(\frac{y_\infty}{y_0}\right)^m\right]^{1/m} \tag{3.3.14}$$

If y_o is a lower bound, m is necessarily negative, and values of y less than y_o are predicted. If y_o/y_∞ is sufficiently small or if m is sufficiently large in magnitude, this discrepancy may be tolerable. If not, the following alternative expression may be formulated, again starting from Equation (3.3.11):

$$\left(y^n - y_0^n\right)^m = y_i^{nm} + \left(y_\infty^n - y_0^n\right)^m \tag{3.3.15}$$

Equation (3.3.15) is free from the flaw identified by means of Equation (3.3.14) and invokes no additional empiricism, but a singularity may occur at $y_\infty = y_o$, depending on the juxtapositions of y_o, y_i, and y_∞. Similar anomalies occur for Equation (3.3.13) and the corresponding analog of Equation (3.3.14), as well as for behavior for which $n < 0$ and $m > 0$. The preferable form among these four is best chosen by trying each of them.

One other problem with the application of the CUE for a separate transitional regime is the formulation of an expression for $y_i\{x\}$, which is ordinarily not known from theoretical considerations. Illustrations of the empirical determination of such expressions for particular cases may be found in Churchill and Usagi (1974), Churchill and Churchill (1975), and Churchill (1976; 1977), as well as in Example 3.3.5 below.

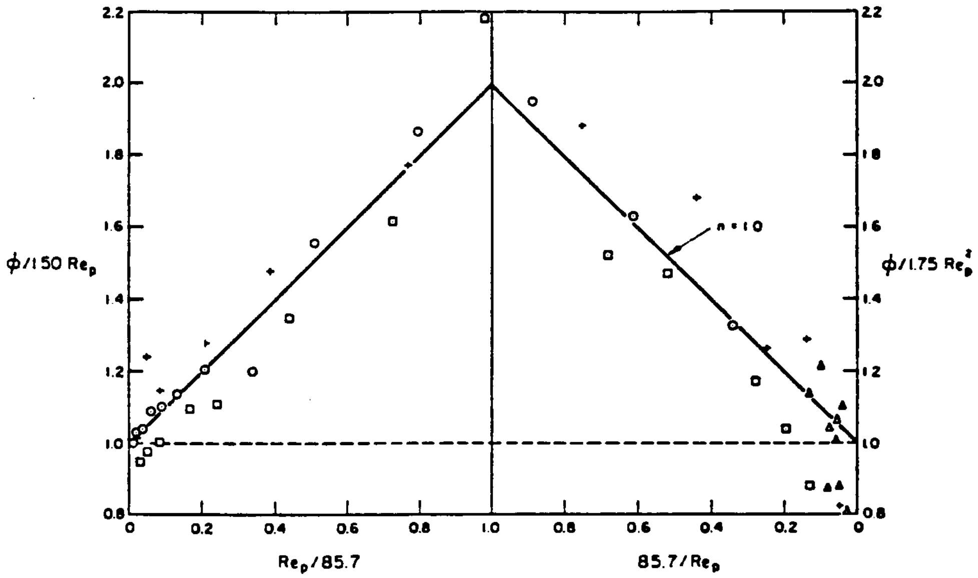

FIGURE 3.3.3 Arithmetic, split-coordinate plot of experimental data for the pressure drop in flow through a packed bed of spheres. (From Churchill, S.W. and Usagi, R. *AIChE J.* 18(6), 1123, 1972. With permission from the American Institute of Chemical Engineers.)

Example 3.3.4: The Pressure Gradient in Flow through a Packed Bed of Spheres

The pressure gradient at asymptotically low rates of flow (the creeping regime) can be represented by the Kozeny–Carman equation, $\Phi = 150\ \mathrm{Re}_p$, and at asymptotically high rates of flow (the inertial regime) by the Burke–Plummer equation, $\Phi = 1.75\ (\mathrm{Re}_p)^2$, where $\Phi = \rho\varepsilon^2 d_p(-dP_f/dx)\mu^2(1-\varepsilon)$, $\mathrm{Re}_p = d_p u_o \rho/\mu(1-\varepsilon)$, d_p = diameter of spherical particles, m, ε = void fraction of bed of spheres, dP_f/dx = dynamic pressure gradient (due to friction), Pa/m, and u_o = superficial velocity (in absence of the spheres), m/sec. For the origin of these two asymptotic expressions see Churchill (1988a). They both have a theoretical structure, but the numerical coefficients of 150 and 1.75 are basically empirical. These equations are both lower bounds and have one intersection. Experimental data are plotted in Figure 3.3.3, which has the form of Figure 3.3.1 with $Y = \Phi/150\ \mathrm{Re}_p$, $Y/Z = \Phi/(1.75\ \mathrm{Re}_p)^2$ and $Z = 1.75\ \mathrm{Re}_p^2/150\,\mathrm{Re}_p = \mathrm{Re}_p/85.7$. A value of $n = 1$ is seen to represent these data reasonably well on the mean, resulting in

$$\Phi = 150\mathrm{Re}_p + 1.75\left(\mathrm{Re}_p\right)^2$$

which was originally proposed as a correlating equation by Ergun (1952) on the conjecture that the volumetric fraction of the bed in "turbulent" flow is proportional to Re_p. The success of this expression in conventional coordinates is shown in Figure 3.3.4. The scatter, which is quite evident in the arithmetic split coordinates of Figure 3.3.3, is strongly suppressed in a visual sense in the logarithmic coordinates of Figure 3.3.4.

Example 3.3.5: The Friction Factor for Commercial Pipes for All Conditions

The serial application of the CUE is illustrated here by the construction of a correlating equation for both smooth and rough pipes in the turbulent regime followed by combination of that expression with ones for the laminar and transitional regimes.

The Turbulent Regime

The Fanning friction factor, f_F, for turbulent flow in a smooth round pipe for asymptotically large rates of flow (say $\mathrm{Re}_D > 5000$) may be represented closely by the empirical expression:

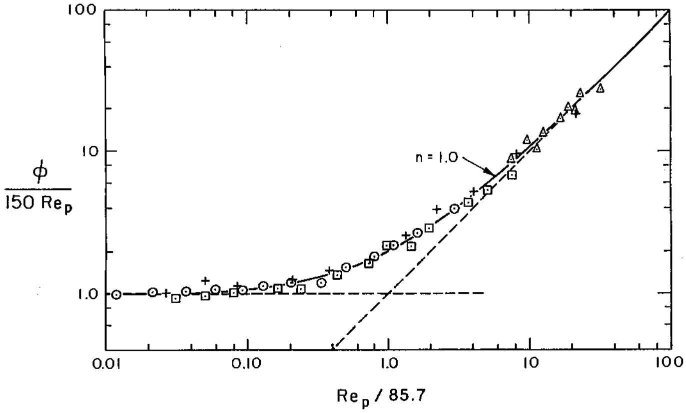

FIGURE 3.3.4 Logarithmic correlation of experimental data for the pressure drop in flow through a packed bed of spheres. (From Churchill, S.W. and Usagi, R. *AIChE J.* 18(6), 1123, 1972. With permission from the American Institute of Chemical Engineers.)

$$\left(\frac{2}{f_F}\right)^{1/2} = 0.256 + 2.5\ln\left\{\left(\frac{f_F}{2}\right)^{1/2}\mathrm{Re}_D\right\}$$

A corresponding empirical representation for naturally rough pipe is

$$\left(\frac{2}{f_F}\right)^{1/2} = 3.26 + 2.5\ln\left\{\frac{D}{e}\right\}$$

Direct combination of these two expressions in the form of the CUE does not produce a satisfactory correlating equation, but their combination in the following rearranged forms:

$$e^{(1/2.5)(2/f_F)^{1/2}} = 1.108\left(\frac{f_F}{2}\right)^{1/2}\mathrm{Re}_D$$

and

$$e^{(1/2.5)(2/f_F)^{1/2}} = 3.68\left(\frac{D}{e}\right)$$

with $n = -1$ results in, after the reverse rearrangement,

$$\left(\frac{2}{f_F}\right)^{1/2} = 0.256 + 2.5\ln\left\{\frac{\left(\frac{f_F}{2}\right)^{1/2}\mathrm{Re}_D}{1 + 0.3012\left(\frac{e}{D}\right)\left(\frac{f_F}{2}\right)^{1/2}\mathrm{Re}_D}\right\}$$

The exact equivalent of this expression in structure but with the slightly modified numerical coefficients of 0.300, 2.46, and 0.304 was postulated by Colebrook (1938–1939) to represent his own experimental data. The coefficients of the expression given here are presumed to be more accurate, but the difference in the predictions of f_F with the two sets of coefficients is within the band of uncertainty of the experimental data. The turbulent regime of the “friction-factor” plot in most current textbooks and handbooks is simply a graphical representation of the Colebrook equation. Experimental values are not included in such plots since e, the effective roughness of commercial pipes, is simply a correlating factor that forces agreement with the Colebrook equation. Values of e for various types of pipe in various services are usually provided in an accompanying table, that thereby constitutes an integral part of the correlation.

The Laminar Region

The Fanning friction factor in the laminar regime of a round pipe ($\mathrm{Re}_d < 1800$) is represented exactly by the following theoretical expression known as Poiseuille’s law: $f_F = 16/\mathrm{Re}_D$. This equation may be rearranged as follows for convenience in combination with that for turbulent flow:

$$\left(\frac{2}{f_F}\right)^{1/2} = \frac{\mathrm{Re}_D\left(f_F/2\right)^{1/2}}{8}$$

The Transitional Regime

Experimental data as well as semitheoretical computed values for the limiting behavior in the transition may be represented closely by $(f_F/2) = (\mathrm{Re}_D/37500)^2$. This expression may be rewritten, in terms of $(2/f_F)^{1/2}$ and $\mathrm{Re}_D(f_F/2)^{1/2}$, as follows:

$$\left(\frac{f_F}{2}\right)^{1/2} = \left(\frac{37500}{\mathrm{Re}_D\left(f_F/2\right)^{1/2}}\right)^{1/2}$$

Overall Correlation

The following correlating equation for all $\mathrm{Re}_D(f_F/2)^{1/2}$ and e/D may now be constructed by the combination of the expressions for the turbulent and transition regimes in the form of the CUE with $n = 8$, and then that expression and that for the laminar regime with $n = -12$, both components being chosen on the basis of experimental data and predicted values for the full regime of transition:

$$\left(\frac{2}{f_F}\right)^{1/2} = \left[\left(\frac{8}{\mathrm{Re}_D\left(f_F/2\right)^{1/2}}\right)^{12} + \left(\left[\frac{37500}{\mathrm{Re}_D\left(f_F/2\right)^{1/2}}\right]^4 + \left|2.5\ln\left\{\frac{1.108\,\mathrm{Re}_D\left(f_F/2\right)^{1/2}}{1+0.3012\left(\frac{e}{a}\right)\mathrm{Re}_D\left(f_F/2\right)^{1/2}}\right\}\right|^8\right)^{-3/2}\right]^{-1/12}$$

The absolute value signs are only included for aesthetic reasons; the negative values of the logarithmic term for very small values of $\mathrm{Re}_D(f_F/2)^{1/2}$ do not affect the numerical value of $(2/f_F)^{1/2}$ in the regime in which they occur. This overall expression appears to have a complicated structure, but it may readily be recognized to reduce to its component parts when the corresponding term is large with respect to the other two. It is insensitive to the numerical values of the two arbitrary exponents. For example, doubling their values would have almost no effect on the predictions of $(f_F/2)^{1/2}$. The principal uncertainty is associated with the expression for the transition regime, but the overall effect of the corresponding term is very small. The uncertainties associated with this correlating equation are common to most graphical correlations and algebraic expressions for the friction factor, and are presumed to be fairly limited in magnitude and to be associated primarily with the postulated value of e. Although the overall expression is explicit in $\mathrm{Re}_D(f_F/2)^{1/2}$ rather than Re_D, the latter quantity may readily be obtained simply by multiplying the postulated value of $\mathrm{Re}_D(f_F/2)^{1/2}$ by the computed values of $(2/f_F)^{1/2}$.

References

Buckingham, E. 1914. On physically similar systems; illustrations of the use of dimensional equations. *Phys. Rev., Ser. 2,* 4(4):345–375.

Churchill, S.W. 1976. A comprehensive correlating equation for forced convection from plates. *AIChE J.* 22(2):264–268.

Churchill, S.W. 1977. Comprehensive correlating equation for heat, mass and momentum transfer in fully developed flow in smooth tubes. *Ind. Eng. Chem. Fundam.* 16(1):109–116.

Churchill, S.W. 1979. *The Interpretation and Use of Rate Data. The Rate Process Concept,* rev. printing, Hemisphere Publishing Corp., Washington, D.C.

Churchill, S.W. 1981. The use of speculation and analysis in the development of correlations. *Chem. Eng. Commun.* 9:19–38.

Churchill, S.W. 1988a. Flow through porous media, Chapter 19 in *Laminar Flows. The Practical Use of Theory,* pp. 501–538, Butterworths, Boston.

Churchill, S.W. 1988b. Derivation, selection, evaluation and use of asymptotes. *Chem. Eng. Technol.* 11:63–72.

Churchill, S.W. and Churchill, R.U. 1975. A general model for the effective viscosity of pseudoplastic and dilatant fluids. *Rheol. Acta.* 14:404–409.

Churchill, S.W. and Usagi, R. 1972. A general expression for the correlation of rates of transfer and other phenomena. *AIChE J.* 18(6):1121–1128.

Churchill, S.W. and Usagi, R. 1974. A standardized procedure for the production of correlations in the form of a common empirical equation. *Ind. Eng. Chem. Fundam.* 13(1):39–44.

Colebrook, C.R. 1938–1939. Turbulent flow in pipes with particular reference to the transition region between the smooth and rough pipe laws. *J. Inst. Civ. Eng.* 11(5024):133–156.

Ergun, S. 1952. Fluid flow through packed beds. *Chem. Eng. Prog.* 48(2):81–96.

Hellums, J.D. and Churchill, S.W. 1964. Simplifications of the mathematical description of boundary and initial value problems. *AIChE J.* 10(1):110–114.

Wilkie, D. 1985. The correlation of engineering data reconsidered. *Int. J. Heat Fluid Flow.* 8(2):99–103.

Zlokarnik, M. 1991. *Dimensional Analysis and Scale-Up in Chemical Engineering.* Springer-Verlag, Berlin.

3.4 Hydraulics of Pipe Systems

J. Paul Tullis and Blake P. Tullis

Principles involved in the design and operation of pipelines include:

- Establish the required flow for present and future demands, determining the route, profile, and elevation differences, as well as need for and benefits of storage capabilities.
- Determine whether the flow will be supplied by gravity, pumps, or a combination.
- Select the appropriate pipe material and pressure class, considering fluid type; soil conditions; system pressure; pipe size; whether the pipe will be buried; etc.
- Consider the possibility of crushing from external loads and collapse due to internal vacuum pressures.
- Select the optimum pipe diameter.
- Select valves and pumps that have performance characteristics compatible with the system.
- Establish operating procedures for the pumps and valves to avoid excessive hydraulic transients.
- Analyze the cavitation potential of the valves and pumps.
- Select appropriate type, size, and location of air valves and check valves.
- Establish procedures for filling, flushing, and draining the system.

Basic Equations

Solving fluid flow problems involves the application of one or more of the three basic equations: continuity, momentum, and energy. These three basic tools are developed from the law of conservation of mass, Newton's second law of motion, and the first law of thermodynamics. The simplest form of the continuity equation is for one-dimensional incompressible steady flow in a closed conduit. Applying continuity between any two sections gives:

$$A_1V_1 = A_2V_2 = Q \tag{3.4.1}$$

For a variable density, the equation can be written:

$$\rho_1A_1V_1 = \rho_2A_2V_2 - \dot{m} \tag{3.4.2}$$

in which A is the cross-sectional area of the pipe; V is the mean velocity at that same location; Q is the flow rate; ρ is the fluid density; and $\dot{m}$ is the mass flow rate. The equations are valid for steady flow in any rigid conduit as long as there is no addition or loss of liquid between sections 1 and 2.

For steady-state pipe flow, the momentum equation relates the sum of forces in a given direction acting on a control volume (a section of the fluid inside the pipe), to the net momentum flux through the control volume in the same direction. The most common forces are pressure and friction.

$$\Sigma F_x = \rho_2A_2V_2V_{2x} - \rho_1A_1V_1V_{1x} \tag{3.4.3}$$

For incompressible flow, this equation can be reduced to:

$$\Sigma F_x = \rho Q\left(V_{2x} - V_{1x}\right) \tag{3.4.4}$$

These equations can easily be applied to a three-dimensional flow problem by adding equations in the y and z directions.

A general form of the energy equation applicable to incompressible pipe flow is:

$$\frac{P_I}{\gamma} + Z_1 + \frac{V_1^2}{2g} = \frac{P_2}{\gamma} + Z_2 + \frac{V_2^2}{2g} - H_p + H_t + H_f \tag{3.4.5}$$

The units are energy per unit weight of liquid: ft-lb/lb or $N\text{-}m/N$, or simply length.

The first three terms are pressure head (P/γ); elevation head (Z) (above some datum); and velocity head ($V^2/2g$). The last three terms on the right side of the equation are the total dynamic head added by a pump (H_p), removed by a turbine (H_t), and the total friction and minor head losses (H_f). The sum of the first three terms in Equation (3.4.5) is defined as the total head and the sum of the pressure and elevation heads is referred to as the piezometric head.

Fluid Friction

This subsection discusses pressure changes resulting from incompressible flow for pipes with circular geometry. However, the results can be generalized for a pipe of noncircular geometry by substituting for the diameter D in any of the equations, the hydraulic diameter, D_h, defined as $D_h = A/P$. A is the cross-sectional area of the conduit and P is the wetted perimeter (πD for a circular pipe flowing full).

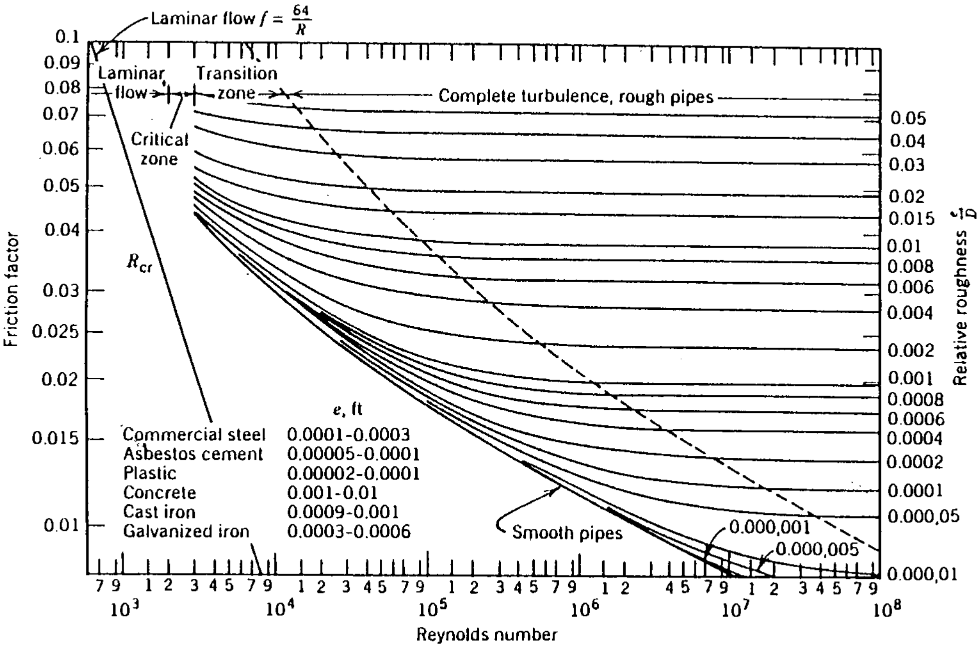

FIGURE 3.4.1 The Moody diagram.

The analysis in this subsection can also be applied to gases and vapors, provided the Mach number in the duct does not exceed 0.3. For greater values of the Mach number, the compressibility effect becomes significant and the reader should see Section 3.7 on compressible flow.

Friction loss (H_f) depends on pipe diameter (D); length (L); pipe roughness (e); fluid density (ρ) or specific weight (γ); viscosity (ν); and flow velocity (V). Dimensional analysis can be used to provide a functional relationship among the friction loss H_f, pipe dimensions, fluid properties, and flow parameters. The resulting equation is called the Darcy-Weisbach equation:

$$H_f = \frac{fLV^2}{2gD} = \frac{fLQ^2}{1.23gD^5} \tag{3.4.6}$$

The friction factor f is a measure of pipe roughness and has been evaluated experimentally for numerous pipes. The data were used to create the Moody friction factor chart shown as Figure 3.4.1. The friction factor f and the subsequent friction loss of a flowing liquid depend on whether the flow is laminar or turbulent. Laminar flow exists when viscous forces are large compared to inertial forces. The Reynolds number is the ratio of inertia forces to viscous forces and is a convenient parameter for determining whether a flow condition will be laminar or turbulent. The Reynolds number is defined as:

$$\mathrm{Re} = \frac{\rho V d}{\mu} = \frac{Vd}{\nu} \tag{3.4.7a}$$

V is the mean flow velocity; d is diameter; ρ is fluid density; μ is dynamic viscosity; and ν is kinematic viscosity.

For laminar flow (Re < 2000), f is only a function of Re and is calculated by $f = 64/\mathrm{Re}$. Laminar flow in pipes is unusual for practical applications. To illustrate this, the velocity of water flowing in a 1-m diameter pipe at 20°C would need to be less than or equal to 2 mm/sec to be laminar. Most practical pipe flow problems are in the turbulent region.

At Reynolds numbers between about 2000 and 4000, the flow is unstable as a result of the onset of turbulence (critical zone in Figure 3.4.1). In this range, friction loss calculations are difficult because it is impossible to determine a unique value of *f*. Fortunately, few pipe flow problems involve Reynolds numbers below 4000. For Re > 4000, the flow becomes turbulent and *f* is a function of Re and relative pipe roughness (e/D), where *e* is the equivalent roughness height and *D* is pipe diameter. At high Re, *f* eventually depends only on the relative roughness height, e/D. This region is defined as fully turbulent flow. The Reynolds number at which this occurs depends on the relative roughness of the pipe

Using the Moody chart in Figure 3.4.1 to get *f* requires that Re and e/D be known. Calculating Re is direct if the water temperature, flow, and pipe diameter are known. The problem then reduces to one of obtaining a good value for *e*. The values of *e* listed in Figure 3.4.1 should be considered as approximate and used only if more accurate values cannot be obtained from the pipe supplier.

For noncircular pipes, the only change in the friction loss equation is replacing the diameter with the hydraulic radius (R). R is the ratio of the flow area to the wetter perimeter. For a circular pipe, $D = 4R$,

The Moody diagram (Figure 3.4.1) is a graphical representation of the Colebrook and White equation:

$$\frac{1}{\sqrt{f}} = 1.74 - 0.869 \ln\left(\frac{2e}{D} + \frac{18.7}{\mathrm{Re}\sqrt{f}}\right) \tag{3.4.7b}$$

The Colebrook and White equation requires a trial-and-error or iterative solution because *f* appears on both sides of the equation.

Haaland (1983) developed an explicit relationship that approximates the Colebrook and White equation. The relationship provides reasonable accuracy in the range of $4000 < \mathrm{Re} < 10^8$ and $0 < e/d < 0.05$

$$\frac{1}{\sqrt{f}} = -0.782 \ln\left[\frac{6.9}{\mathrm{Re}} + \left(\frac{e}{3.7D}\right)^{1.11}\right] \tag{3.4.8}$$

If the flow or pipe diameter is not known, the solution to the Darcy–Weisbach or Haaland equations becomes a trial-and-error or iterative process.

For long gravity flow pipelines, the criterion for selecting the pipe diameter is simply finding the smallest pipe that can pass the required flow without the friction and minor losses exceeding the available head. For pumped systems, optimizing the pipe diameter is based on an economic analysis that compares the installed pipe cost with the cost of building and operating the pumping plant. Pipe cost is proportional to *D* and pumping cost is inversely proportional to *D*. The optimum pipe diameter is selected as the one that provides the lowest total cost.

The pipe roughness usually varies with time due to buildup of solid deposits or organic growths. Manufacturing methods and tolerances also cause variations in the surface roughness. Consequently, the friction factor for any pipe can only be approximated and proper allowance should be made for these uncertainties.

Minor Losses

Flow through valves, orifices, elbows, transitions, etc. causes flow separation, which results in the generation and dissipation of turbulent eddies. The resulting head loss, H_m, referred to as a minor loss, is proportional to the velocity head:

$$H_m = K_l \frac{Q^2}{\left(2gA_m^2\right)} \tag{3.4.9}$$

in which K_l is the minor loss coefficient and A_m is the flow area at the inlet to the minor loss element. Although these types of losses are referred to as minor, in short piping systems; long piping systems with small velocity heads; or other systems in which the friction loss is relatively small, the minor losses can be responsible for the majority of the system head loss. The minor loss coefficient K_l is analogous to fL/D in Equation (3.4.6).

The summation of all friction and minor losses in a pipe system can be expressed as:

$$H_l = H_f + H_m \tag{3.4.10}$$

$$H_l = \left[\sum \left(\frac{fL}{2gDA_p^2} \right) + \sum \left(\frac{K_l}{2gA_m^2} \right) \right] Q^2 = CQ^2 \tag{3.4.11}$$

in which:

$$C = \sum \left(\frac{fL}{2gDA_p^2} \right) + \sum \left(\frac{K_l}{2gA_m^2} \right) \tag{3.4.12}$$

It is important to use the correct pipe inside diameter for each pipe section and minor loss. The variation of the actual inside pipe diameters from the nominal is a function of size and pressure class.

In an effort to simplify calculations, some have expressed the minor losses as an equivalent pipe length parameter: $L_{\text{equ}} = K_l D/f$. It represents the length of pipe that produces the same head loss as the local or minor loss. This is a simple, but potentially inaccurate, method of including minor losses. The problem is that the friction coefficient varies from pipe to pipe, so the equivalent length will not have a unique value. When minor losses are truly minor, this problem becomes academic. However, when local losses are an important part of the analysis, it is recommended that the minor loss coefficients K_l be used rather than an equivalent length.

The following summarizes the testing programs conducted to evaluate the loss coefficients of pipe fittings. The documents are only available from ASHRAE.

- Reducing Ells, and Pipe Reducers (ASHRAE 2002 H-1405)
  Number: 250
  Radius: short and long
  Sizes: 2 and 4 in. (5 and 10 cm)
  Materials: threaded iron and welded steel
  Manufacturers: 11
- Threaded and Forged Weld Pipe Tees (ASHRAE 2002 H-1404)
  Number: 142
  Sizes: 2 and 4 in. (5 and 10 cm)
  Materials: threaded iron and welded steel
  Manufacturers: 11
- Large Pipe Ells, Reducers and Expansions (ASHRAE 2002 H-1672a)
  Number: 32
  Radius: long
  Sizes: 12, 16, 20, and 24 in. (30.5, 40.6, 50.8, and 61 cm)
  Materials: welded steel
  Manufacturers: 4
- Large Pipe Tees (ASHRAE 2002 H-1672b)
  Number: 328
  Sizes: 12 and 16 in. (30.5 and 40.6 cm)
  Materials: welded steel
  Manufacturers: 4

- Close Coupled Pipe Ells (ASHRAE 2002 H-1673)
    Sizes: 2 and 4 in. (5 and 10 cm)
    Radius: Short
    Spacing: 0, 1, 2, 3, 4, 5, 10, 20, and 50 pipe dia.
    Materials: threaded iron and welded steel
- PVC Pipe Elbows, Reducers and Expansions, RP-1193 (ASHRAE 2003,TECH-00034-2003)
    Number: 170
    Schedule: 80
    Sizes: 2, 4, 6, and 8 in. (5.08, 10.16, 15.25, and 20.32 cm)
    Materials: injection molded and fabricated PVC
    Manufacturers: 7
- PVC Pipe Tees, RP-1193 (ASHRAE 2003 TECH-00035-2003)
    Number: 61
    Schedule: 80
    Sizes: 2, 4, 6, and 8 in. (5.08, 10.16, 15.25, 20.32 cm)
    Materials: injection molded and fabricated PVC
    Manufacturers: 7

Test results show that the loss coefficients for fittings vary with material; manufacturer; method of fabrication; accuracy of installation; and, for tees, with the percent flow distribution between the branches. The loss coefficient consistently reduced as the size of the fitting increased. Currently, such variations in minor loss coefficients are not accounted for in published minor loss data.

The ASHRAE study also looked at the effect of closely spaced elbows in series (Rahmeyer, 2002e, Technical Paper H-1673). The testing included two sizes of elbows, four different alignments, and spacing from 0 to 20 pipe diameters. The results showed that the combined loss coefficient for the two elbows was never greater than the sum of the individual loss coefficients. At a spacing of 20 diameters, there was no effect. At 10 diameters, the combined loss coefficients were between 2 and 6% lower than the sum of the individual coefficients. At 3 diameters, the combined coefficient was 10 to15% lower. For close-coupled elbows, the combined loss coefficient was between 5 and 28% lower, depending on the orientation of the elbows.

Comparing the magnitude of ($\Sigma(fL/2gA_p^2)$ to $\Sigma(K_l/2gA_m^2)$) will determine how much care should be given to the selection of the K_l values. Typical values of K_l are listed in Table 3.4.1 with a range of values from the recent ASHRAE studies. For details on the loss coefficient for a specific fitting and for loss coefficients not found in the table, the reader is referred to Rahmeyer (2002a,b,c; 2003a,b) and Miller (1990).

Pipe Selection

Materials commonly used for pressure pipe transporting liquids are ductile iron; concrete; steel; fiberglass; PVC; and polyolefin (polyethylene and polypropylene). For each of these pipe materials, national committees have developed specifications that discuss external loads; internal design pressure; available sizes; quality of materials; corrosive environments; installation practices; and linings. Standards are available from the following organizations:

- American Water Works Association (AWWA)
- American Society of Mechanical Engineers (ASME)
- American Society for Testing and Materials (ASTM)
- American National Standards Institute (ANSI)
- Canadian Standards Association (CSA)
- Federal Specifications (FED)
- Plastic Pipe Institute (PPI)

In addition, manuals and other standards have been published by various manufacturers and manufacturers' associations. These specifications and standards should be used to guide the selection of pipe

TABLE 3.4.1 Minor Loss Coefficients

Item	K_l
Pipe inlets	
Projecting pipe	0.5–0.9
Sharp corner-flush	0.50
Slightly rounded	0.04–0.5
Bell mouth	0.03–0.1
Sudden expansions[a] (based on inlet velocity, V_1)	$(1\text{-}A_1/A_2)^2$
Sudden contractions[b] (based on outlet velocity, V_2)	$(1/C_c\text{-}1)^2$

A_2/A_1	0.1	0.2	0.3	0.4	0.5	0.6	0.7	0.8	0.9
C_c	0.624	0.632	0.643	0.659	0.681	0.712	0.755	0.813	0.892

Item	K_l
Steel bell reducers[e] (welded, $D1/D2$ = 1.2–1.33)	0.053–0.23
Steel bell expanders[e] (welded, $D2/D1$ = 1.2–1.33)	0.02–0.11
PVC fabricated reducers[e] ($D1/D2$ = 1.33–1.5)	0.12–0.68
PVC fabricated expanders[e] ($D2/D1$ = 1.2–1.33)	0.07–1.19

Bends	ASHRAE[e]	Typical Values[c]
Short radius, r/d = 1		
90	0.33–0.74	0.3–0.6
45		0.10
30		0.06
Long radius, r/d = 1.5		
90	0.089–0.26	0.07–0.33
45		0.09
30		0.06
Mitered (one miter)		
90	1.10	
60	0.40–0.59	
45	0.35–0.44	
30	0.11–0.19	
PVC injection molded elbows[e]	0.68–1.00	
PVC fabricated type I elbows[e]	0.40–0.42	
PVC fabricated type II elbows[e]	0.73–0.76	
Tees[e]		

Valves	Average Values	Range
Check valves[d]		
Swing check	1.0	0.29–2.2
Tilt disc	1.2	0.27–2.62
Lift	4.6	0.85–9.1
Double door	1.32	1.0–1.8
Full open gate	0.15	0.1–0.3
Full open butterfly	0.40	0.2–0.6
Full open globe	4.0	3–10

Sources:

[a] Streeter, V.L., and Wylie, E.B. (1975). *Fluid Mechanics*, 6th ed., McGraw–Hill, New York, p. 304.

[b] Streeter, V.L., and Wylie, E.B. (1975). *Fluid Mechanics*, 6th ed., McGraw–Hill, New York, p. 305.

[c] Miller, D.S. (1990). Internal Flow Systems — Design and Performance Prediction, 2nd ed., Gulf Publishing Company, Houston, TX.

[d] Kalsi Engineering and Tullis Engineering Consultants (1993). Application Guide for Check Valves in Nuclear Power Plants, Revision 1, NP-5479. Prepared for Nuclear Maintenance Applications Center, Charlotte, NC.

[e] Rahmeyer, W. (2002a). Pressure loss coefficients of threaded and forged weld pipe fittings for ells, reducing ells, and pipe reducers. Technical paper H-1405, American Society of Heating, Refrigeration and Air Conditioning Engineering, Atlanta, GA.

TABLE 3.4.1 (continued) Minor Loss Coefficients

Rahmeyer, W. (2002b). Pressure loss coefficients of pipe fittings for threaded and forged weld pipe tees. Technical paper H-1404, American Society of Heating, Refrigeration and Air Conditioning Engineering, Atlanta, GA.

Rahmeyer, W. (2002c). Pressure loss data for large pipe ells, reducers and expansions. Technical paper H-1672a, American Society of Heating, Refrigeration and Air Conditioning Engineering, Atlanta, GA.

Rahmeyer, W. (2002d). Pressure loss data for large pipe tees. Technical paper H-1672b, American Society of Heating, Refrigeration and Air Conditioning Engineering, Atlanta, GA.

Rahmeyer, W. (2002e). Pressure loss coefficients for close coupled pipe ells. Technical paper H-1673, American Society of Heating, Refrigeration and Air Conditioning Engineering, Atlanta, GA.

Rahmeyer, W. (2003a). Pressure loss data for PVC pipe elbows, reducers and expansions RP-1193. Technical paper TECH-00034-2003, American Society of Heating, Refrigeration and Air Conditioning Engineering, Atlanta, GA.

Rahmeyer, W. (2003b). Pressure loss data for PVC pipe tees RP-119. Technical paper TECH-00035-2003, American Society of Heating, Refrigeration and Air Conditioning Engineering, Atlanta, GA.

material. ASCE (1992) contains a description of most of these pipe materials and a list of the specifications for the various organizations, which apply to each material. The document also discusses the various pipe-linings available for corrosion protection. The following are relevant publications for selecting the proper type and pressure class of pipe: (ASCE 1992, 1993; AWWA 1995 (M9), 1989 (M11), 2003 (M41); PPI 1980 (M23).

For air and low-pressure liquid applications, available pipe materials include unreinforced concrete; corrugated steel; smooth sheet metal; spiral rib (sheet metal); and HDPE (high-density polyethylene). The choice of a material for a given application depends on pipe size, pressure requirements, resistance to collapse from internal vacuums or external loads, resistance to internal and external corrosion, ease of handling and installing, useful life, and economics.

Valve Selection

Valves serve a variety of functions; including, isolation; flow control; pressure regulation; preventing reverse flow; limiting maximum pressures; and releasing/admitting air. This section discusses characteristics of and principles for selecting and operating control valves, check valves, air valves, and pressure relief valves. For a description of various types of valves and details regarding their function, see Tullis 2005.

Control Valves

Valve selection and operation rarely receive the same detailed engineering attention given to other components of piping systems. Their function is often not demanding and detailed attention to valve selection may not be necessary. However, in some applications, the lack of attention to selecting the proper type and size valve can lead to excessive maintenance, poor performance, and other serious consequences.

To find the right valve, the user often relies on the valve vendors for engineering advice, and rightly so, because they should be the most familiar with their product. However, when the system requirements are nonstandard, or severe, few vendors have enough engineering experience or performance data on their valves to enable them to provide reliable information. To minimize valve problems, one must identify the valves in the system that need special attention. For such valves, the engineer needs tools for making a correct analysis. The following subsections provide information for selecting and operating valves when special engineering is required to avoid problems.

When analyzing a flow control valve, the following criteria should be considered:

- The valve should not produce excessive pressure drop when full open.
- The valve should control the flow rate over approximately 50% of its movement.
- The maximum operating torque must not exceed the capacity of the operator or valve shaft and connections for any flow condition.
- The cavitation intensity should be limited to the appropriate level.
- The valve should be operated so that the resulting pressure transients do not exceed the safe limits of the system.

Excessive Pressure Drop

What constitutes excessive pressure drop for a control valve depends on the overall purpose of the piping system and on the magnitude of the other losses in the system. A valve considered to have an excessive loss in one system might be totally acceptable in another. To determine the acceptability of the full open pressure loss of the control valve, the magnitude of the loss valve coefficient ($K_l/2gA_m^2$) should be compared to the total system loss coefficient C (Equation 3.4.12). For example, the loss coefficient for a full-open globe valve can be 10 times higher than a full-open butterfly valve. However, if the loss coefficient for the globe valve is small compared to the total system loss coefficient, the globe valve would be an acceptable choice.

Controllability

For many flow control applications, it is desirable to select a valve that has linear control characteristics. Some valve vendors advertise that their valves are linear. The problem with such a claim is that the linearity of a control valve depends on the system in which it is installed. In a short pipe, a valve may linearly control the flow. However, the same valve installed in a long pipe will only control the flow near the closed position.

The flow in a pipeline can be calculated using the energy equation (Equation 3.4.5) and the system loss equation (Equation 3.4.11). The result is:

$$Q = \sqrt{\frac{\Delta Z}{\left[\Sigma\left(\frac{fL}{2gDA_p^2}\right) + \Sigma\left(\frac{K_l}{2gA_m^2}\right)\right]}} \qquad (3.4.13)$$

The ability of the valve to control flow depends on the relative values of the valve's loss coefficient ($K_l/2gA_m^2$) compared to the pipe's friction coefficient ($fL/2gdA_p^2$). For a short system, a valve can almost linearly reduce the flow because the valve loss becomes large compared to the friction loss as the valve closes. In contrast, for a long pipeline $K_l/2gA_m^2$ will be small compared to $fL/2gdA_p^2$ until the valve is near its closed position.

To demonstrate the relationship between a valve and system, consider a butterfly valve that will be used to control the flow between two reservoirs with an elevation difference of ΔZ. System A is a short pipe (0.3 m dia., 100 m long, $\Delta Z = 10$ m, $f = 0.0138$) where pipe friction is small ($fL/2gdA_p^2 = 46.9$). System B is a long pipe (0.3 m dia., 10,000 m long, $\Delta Z = 200$ m, $f = 0.0138$) with high friction ($fL/2gdA_p^2 = 4690$). Initially, assume that the same butterfly valve will be used in both pipes and it will be the same size as the pipe diameter.

For the valve, assume that the K_l full open is 0.187 and at 50% open it is 8.4. Correspondingly, $K_l/2gA_m^2 = 1.905$ and 85.7. For system A, the flow with the valve full open will be 0.453 m^3/sec and at 50% open 0.275 m^3/sec, a reduction of 39%. Repeating these calculations over the full range of valve openings would show that the flow for system A reduces almost linearly as the valve closes.

For system B, the flow with the valve full open will be 0.206 m^3/sec and at 50% open 0.205 m^3/sec, a reduction of less than 1%. The valve in system B will not start to control the flow until it has closed more than 50%. A line-size butterfly valve is obviously not a good choice for a control valve in system B. One solution to this problem is to use a smaller valve. If the butterfly valve installed in system B were half the pipe diameter, it would control the flow over most of its stroke.

The range of opening over which the valve controls the flow also has a significant effect on the magnitude of the transient pressures caused by closing the valve. The valve closure time must be long enough to avoid excessive transient pressures. If the valve is oversized and does not start reducing the flow until it is more than 50% closed, over half of the closing time is wasted and the effective valve closure time is less than half the actual closing time. The solution to this problem is to reduce the valve size so it provides control over most of its movement.

The size of the control valve, as well as its associated open/close time, can also have an impact on the overall system control logic. The closing time for the valve must be fast enough to match the changing flow requirements for the rest of the system without generating excessive transient pressures. For example, if the valve controls the water level in a storage tank and is actuated by a level sensor, the valve must close fast enough that the tank does not overfill.

A case study of a pipeline rupture illustrates the need for selecting the proper size of control valve. The pipeline was 6 ft (2 m) in diameter, about 30 miles (51 km) long, and supplied water to two storage tanks. The pipes to the storage tanks each contained a 5-ft (1.52-m) diameter butterfly valve. The combined area of the two 5-ft (1.52-m) valves is equivalent to one 7-ft (2.13-m) valve. Because the valves were oversized, they only controlled flow over the last 25% of their movement. The pipeline ruptured due to a pressure transient that resulted from closing the valves too fast. If smaller control valves had been installed, the pipeline may not have ruptured during initial flow tests.

Torque

Selection of the correct operator for a specific quarter-turn valve and application requires knowing the maximum torque that the operator will be required to supply. This requires analyzing the system for the entire range of expected flow conditions so that the maximum flow torque can be identified. The maximum torque is also needed when selecting the valve to be sure that the valve shaft and connections are adequately designed. It is the responsibility of the valve manufacturer to provide the flow and torque characteristics and limits for their valve. It is the responsibility of the system engineers and/or operators to see that the valves are operated within these limits.

The four primary sources of torques for quarter-turn valves are seating torque; bearing friction torque; packing friction torque; and hydrodynamic (flow) torque. These torque values are usually determined experimentally and should be available from the valve manufacturer. All four torques should be evaluated to determine the maximum torque for a given valve.

Seating friction torque develops when the plug or disk moves in or out of the seat (sealing surface). For small valves with soft seats, the seating torque can be larger than the other three torques combined. Bearing friction torque develops when a load is placed on the bearing surface by the valve shaft when there is a pressure differential across the valve. Because the pressure drop significantly increases as a valve closes, the bearing torque is greatest at small openings. Packing friction torque is caused by the valve shaft rubbing against the packing material. Packing is the material placed between the valve shaft and valve body to prevent leakage. Packing friction torque can be particularly troublesome because the packing conditions can be modified in the field. If a packing leaks, the normal procedure is to tighten the packing until the leak stops. This can significantly increase the packing torque and may prevent the operator from opening the valve. When valve packing is adjusted, the ability of the actuator to close the valve under all operating conditions should be confirmed.

Forces induced by the fluid flowing through the valve cause a hydrodynamic torque, which usually acts to close the valve. The magnitude of the torque varies with flow rate, pressure drop, and valve opening. The valve opening, where maximum hydrodynamic torque occurs, depends on the valve design and system characteristics. In short systems, in which friction loss is low and velocities are high, a quarter-turn valve will see maximum torques at large openings where the flow rate is high. In long systems with high friction losses and lower velocities, the same valve will see maximum torque at smaller openings where the pressure drop is high. The hydrodynamic forces should be evaluated over the entire valve operating range and corresponding system flow conditions to identify the maximum operating torque. Operating torque is normally greater when the valve is being opened because the hydrodynamic torque usually acts to close the valve and the bearing and packing torques oppose the direction of valve motion. During closure, the bearing and packing torques act in the direction opposite to that of the hydrodynamic torque.

Cavitation

Cavitation is a process in which vapor bubbles form, grow, become unstable, and collapse. This causes excessive noise, vibrations, erosion damage; the valve can lose capacity if subjected to the most severe stage of cavitation. Evaluating the intensity of cavitation and limiting it to an acceptable level are important in control valve selection.

The first step in a cavitation evaluation is to decide on the acceptable level of cavitation. Three cavitation limits typically used to quantify the intensity of cavitation for a control valve are: critical, incipient damage, and choking cavitation. The cavitation design limit appropriate for a given application varies with valve type, valve function, details of the piping layout and location, and the frequency and duration of operation.

Critical cavitation is typically considered a conservative design limit. It corresponds to the onset of light but constant cavitation noise and is appropriate as a design limit for valves that need to operate essentially free of adverse cavitation effects. Incipient damage corresponds to onset of pitting (material removal). It is an appropriate design limit when significant noise and vibrations can be tolerated but no damage is desired. Choking cavitation (sometimes called flashing) represents the condition in which the mean pressure immediately downstream from the valve drops to vapor pressure and the flow rate is at its maximum for a given upstream pressure. Between critical and incipient damage, the noise level can become objectionable. Between incipient damage and choking cavitation, the erosion damage and vibration levels can be severe. Using choking as a design condition may be appropriate for a pressure relief valve, where valve operation is short lived and infrequent; maximum flow rate through the valve is required; and cavitation damage can be tolerated for short periods of time. It should not be used for valves intended for long-term, low-maintenance operation.

One of the challenges with cavitation has been a lack of consistent terminology between industries. For example, some industries define the onset of cavitation as the condition in which the performance of the valve begins to drop off due to heavy cavitation. This is a correct definition for onset of choking cavitation, but it is misleading to imply that it represents onset of cavitation. Choking is, in fact, the final stage of cavitation — well beyond the point at which damage begins. Promoting this incorrect definition of "onset of cavitation" has resulted in many valves suffering extensive damage. A similar definition of onset of cavitation exists in the pump industry, where the cavitation index NPSHr is often assumed to be the point at which cavitation begins. In reality, it represents onset of choking cavitation. Pump cavitation is discussed in more detail later in the chapter.

The intensity of cavitation and the corresponding noise, vibration, and erosion damage at the valve are at their maximum just before a valve chokes. If the valve operates at a flow condition beyond choking (sometimes referred to as supercavitation), the cavitation events create one large vapor cavity and the mean pressure in the pipe is essentially vapor pressure. The collapse of the large vapor cavity usually occurs at the first significant downstream flow disturbance — such as an elbow, tee, valve, or orifice — or when the frictional forces in the pipe are sufficient to generate the necessary pressure recovery. During supercavitation, damage may not occur inside the valve, but there will be serious vibration and material erosion problems farther downstream where the collapse occurs.

The cavitation intensity for valves is quantified with a cavitation index σ, which represents the ratio of forces preventing cavitation (high local pressure) to forces causing cavitation (high pressure differential).

$$\sigma = \frac{(Pd + Pb - Pv)}{(Pu - Pd)} \tag{3.4.14}$$

Pu and *Pd* are the gage pressures upstream and downstream from the valve; *Pb* is the barometric pressure; and *Pv* is the absolute vapor pressure.

The smaller the σ value is, the greater the chance that cavitation will occur. To evaluate the potential for cavitation of a valve or other minor loss element at a particular flow condition, the value of the system σ (Equation 3.4.14 evaluated at system pressure conditions) must be calculated and compared with σ values corresponding to the various cavitation intensity levels, i.e., critical, incipient damage, and choking. These cavitation intensity level values vary with valve type and valve opening and must be determined experimentally.

Numerous valves have been tested to evaluate critical cavitation and onset of choking. Consequently, many valve manufacturers should be able to provide experimental data for these limits. Only limited data, however, are available identifying onset of cavitation damage because of the difficulty and labor-intensive nature of laboratory damage testing. This is unfortunate because onset of damage is the most important cavitation limit. Experimental data for several types of valves are available in the literature (Tullis, 1989, 1993). Information from these sources can be used if information from the valve manufacturer is not available. It is important to note that most valves have unique cavitation characteristics and that valve-specific cavitation data should be used for design purposes.

As an example, if an incipient damage level of cavitation intensity were selected as the limiting operating condition, the experimentally determined σ-incipient damage would be compared with the σ-system. If the σ-system is larger than σ-incipient damage, then the level of cavitation for that condition is acceptable. Because some level of uncertainty is associated with the experimentally determined cavitation intensity parameters, designers may wish to include a factor of safety when limiting the cavitation intensity of the valve or other minor loss device. Cavitation characteristics of a valve can be and typically are subject to size and pressure scale effects. A discussion on cavitation scale effects is presented by Tullis (1989, 1993).

If the cavitation analysis indicates that the valve, orifice, or other device will be operating at a cavitation level greater than can be tolerated, various techniques can be used to limit the level of cavitation. One is to select a different type of valve. Recent developments have produced several new valves better suited for limiting the levels of cavitation or reducing the potential for cavitation damage. Some of these valves operate on the principle of dropping the pressure in stages. They have multiple paths with numerous sharp turns or sudden expansions in series and are sometimes referred to as “stack valves.” The number of restrictions depends on the total pressure drop required and the system pressure downstream from the last restriction. Because the pressure downstream from each restriction is progressively smaller, for cavitation purposes, each stage is designed so the pressure drop across each subsequent restriction is less than the preceding one (by approximately 50%). Consequently, the first stage (on the high-pressure inlet side) will be able to provide a pressure drop many times the pressure drop at the last stage, with both stages operating near the same level of cavitation intensity. As a result, these types of valves can operate at very large pressure differentials without experiencing cavitation damage. One limitation of stack valves is that they are only usable in clean systems.

For untreated water systems, the stack valve is not appropriate because of plugging problems. As an alternative, conventional valves and orifices can be installed in series to reduce the cavitation in stages. Proper spacing of valves and orifices is important. The spacing between valves depends upon the type. For most quarter-turn valves, a spacing of five to eight pipe diameters is needed for pressure recovery and uniform flow re-establishment between each valve. This prevents disk flutter and ensures normal pressure drop characteristics at each valve. Globe valves, however, can be installed with no piping between them and have satisfactory operation. The primary disadvantages of locating conventional valves in series are the space requirement, increased complexity of the control logic, and cost. For details on this type of application, see Tullis (1989, 1993).

Another recent advance in the fight against cavitation is the development of the sleeve valve. These valves use a perforated cylindrical sleeve to create multiple jets that discharge radially inward. An external sliding collar controls the number of holes exposed. These have excellent cavitation characteristics because they can operate at fairly heavy cavitation levels without damaging the valve or outlet pipe. The valve’s success is attributed to two things. Small holes discharging into a large chamber is the optimum configuration to suppress cavitation in a single-stage device. The other factor is that the jets from the multiple holes converge toward the center of the outlet sleeve, keeping the collapsing cavitation events away from the boundary until just before the valve chokes. These valves can operate at σ values below 0.2 without damage. Conventional valves typically experience cavitation damage at σ values greater than 1.0.

The cavitation performance of conventional valves varies considerably. For example, skirted cone valves and solid ball valves generate significantly less cavitation than unskirted cone and nonsolid ball valves. This is because, for valves with a solid plug, all the flow goes through two ports in series (one at the inlet side and one at the outlet side of the plug). Similarly to stack valves, reducing the pressure in stages provides superior cavitation performance, compared to a single-stage control valve. The unskirted cone and nonsolid ball valves have two throttling ports in series, but they also allow flow to pass around the plug. The flow passage around the plug experiences only a single-stage pressure drop, resulting in increased cavitation potential. Skirted cone and solid ball valves also have better cavitation performance than butterfly, gate, and segmented ball valves because those valves only have a single stage of pressure drop. See Tullis (1989, 1993, 2003) for descriptions of the different types of valves and their cavitation characteristics.

For some applications, cavitation can be avoided by using a free discharge valve. Fixed cone valves are specifically designed for this application. However, these are specially designed valves and are relatively expensive. Some conventional valves can also be used for free discharge, if they can be adequately vented.

Injecting air to suppress cavitation is a technique that has been used for many years with varying degrees of success to suppress cavitation damage. If an adequate amount of air is injected into the proper region, noise, vibrations, and erosion damage can be significantly reduced. For systems that can tolerate some air injection, aeration is often the cheapest and most effective remedy for cavitation.

If all else fails, cavitation damage can be suppressed by plating critical areas of the pipe and valve with cavitation-resistant materials. The final option is simply to replace damaged valves as needed. For additional information on valve cavitation, see AWWA (2001, M49); Knapp et al. (1970); ISA (2000); and Tullis (1989, 1993).

Transients

Hydraulic transients refer to the dynamic pressure waves that result from rapid acceleration or deceleration of flow and are common in pipeline operation. They can be generated as a result of pipeline filling and air-flushing techniques; valve operation techniques, pump startup and shutdown, and pipe ruptures. Transient pressures can exceed the safe operating limit of the pipe if adequate design provisions and operational procedures are not established. The larger the incremental velocity change is and the faster the changes occur, the larger the resulting pressure change will be.

Transients caused by slow velocity changes, such as the rise and fall of the water level in a tank, are called surges. Surge analysis, or "rigid column theory," involves the numerical solution of a simple ordinary differential equation (force = mass × acceleration). The compressibility of the fluid and the elasticity of the conduit are ignored and the entire column of fluid is assumed to move as a rigid body. When changes in velocity occur rapidly, the compressibility of the liquid and the elasticity of the pipe become important and must be included in the analysis. This procedure is often called "elastic" or "water hammer" analysis and involves tracking acoustic pressure waves through the pipe. The analysis requires solving partial differential equations.

An equation predicting the head rise ΔH caused by a sudden change of velocity $\Delta V = V2 - V1$ can be derived by applying the unsteady momentum equation to a control volume of a section of the pipe at which the change of flow occurred. Consider a partial valve closure, which instantly reduces the velocity by an amount ΔV. Reduction of the velocity can only be accomplished by an increase in the pressure upstream of the valve of magnitude ΔH. The pressure wave of magnitude ΔH travels in the upstream direction of the pipe at the acoustic velocity, $\boldsymbol{a}$, which is a function of the fluid and pipe material properties. The increased pressure compresses the liquid and slightly expands the pipe. The transient head rise due to an incremental change in velocity is described as

$$\Delta H = -\boldsymbol{a}\,\Delta V/g, \text{ for } \boldsymbol{a} >> \Delta V \tag{3.4.15}$$

This equation can be used to account for the accumulative effect of multiple incremental changes of velocity until the initial pressure wave returns to the point of origin.

The wave speed depends on the pipe material, wall thickness, diameter, type of liquid, and the amount of air in the system. For a steel pipe with no entrained or trapped air, the wave speed is typically about 3000 fps (1000 m/sec). Based on this wave speed, Equation (3.4.15) predicts that an instant velocity change of 3 fps (1 m/sec) causes a transient pressure of about 300 ft (100 m). This illustrates why transient pressures can easily damage pipes.

The derivation of Equation (3.4.15) was based on an assumption of an instantaneous incremental velocity change or an instant valve closure. Instant closure actually refers to a finite time. It is the longest time over which a valve can be closed and still cause a pressure rise equal to that of an instant closure. It is the time required for the initial transient pressure wave to travel from the point of origin to the next upstream (or downstream) boundary condition and return to the point of origin. This wave travel time equals $2L/\boldsymbol{a}$ seconds, where L is the pipe length between the point of origin and the adjacent boundary condition and $\boldsymbol{a}$ is the acoustic wave speed. The maximum transient pressure rise associated with an instant valve closer will occur at the valve if the closure time is less than or equal to $2L/\boldsymbol{a}$ seconds.

Computational techniques for estimating transient pressures are too complex to be done with simple hand calculations. The solution involves solving partial differential equations derived from the equations of motion and continuity. These partial differential equations are normally solved by the method of characteristics — a technique that transforms the equations into ordinary differential equations. After integration, the equations can be solved numerically by finite differences (Tullis, 1989; Wiley and Streeter, 1993).

To complete the analysis, equations describing the boundary conditions are required. Typical boundary conditions are the connection of a pipe to a reservoir, a valve, changes in pipe diameter or material, pipe junctions, etc. Friction loss is included in the development of the basic equations and minor losses are handled as boundary conditions.

Every pipe system should have at least a cursory transient analysis performed to identify the possibility of serious transients and decide whether a detailed analysis is necessary. If an analysis indicates that transients are a problem, methods of controlling them include:

- Increasing the closing time of the control valve
- Using a smaller valve to provide better control
- Designing special facilities for filling, flushing, and removing air from pipelines
- Increasing the pressure class of the pipeline
- Using pressure relief valves, surge tanks, air chambers, etc.

Restricted Valve Opening

Many conventional control valves cannot safely and/or accurately regulate flow near the closed and full-open positions. Near the closed position, two of the potential problems are seat damage due to high velocities and inability to set the valve opening accurately when the connections between the control element and the operator are loose.

Near full open, some valves lose control, meaning that flow does not change as the valve position is changed. For globe style valves, this occurs when the stroke is too long. For a butterfly valve, it is due to the shape of the disk and changes in the flow pattern around the disk at large openings. For some disk shapes, the flow can actually decrease at valve openings greater than about 90%. This problem is magnified when the valve is installed in a long system in which the valve loss is small compared to the system friction loss (see the section on "Controllability").

Another reason that some quarter-turn valves should not be operated at large openings is that some valves experience torque reversals, which result in disk flutter that can lead to fatigue of the shaft and/or connections. Torque reversals are a function of the plug or disk design and usually only occur for flow in one direction. Valve vendors usually indicate a preferred flow direction for valve installation to avoid torque reversal problems.

Check Valves

Selecting the wrong type or size of check valve can result in poor performance, severe transients, and frequent repairs (Kalsi Engineering and Tullis Engineering Consultants, 1993). Proper check valve selection requires understanding the characteristics of the various types of check valves and analyzing how they will function as a part of the system in which they will be installed. For a description of the characteristics of common types of check valves, see Kalsi Engineering and Tullis Engineering Consultants (1993) and Tullis (2003). A check valve that operates satisfactorily in one system may be totally inadequate in another. Each type has unique characteristics that give it advantages or disadvantages compared with the others. The characteristics of check valves that should be considered in the selection process include:

- Closure speed of check valves relative to the rate of flow reversal of the system
- Stability of the disk and its sensitivity to upstream disturbances
- The flow required to fully open and firmly backseat the disc
- The pressure drop at maximum flow
- Sealing effectiveness and ease of maintenance

Disk stability varies with flow rate, disk position, and upstream disturbances and is an important factor in determining the useful life of a check valve. For most applications, it is preferable to size the check valve (especially swing check valve) so that the disk is fully open and firmly back-seated at normal flow rates. It is a mistake to oversize a swing check valve that is located just downstream from a disturbance such as a pump, elbow, or control valve. The disk will not firmly back seat and it will be subjected to severe motion and accelerate wear. Reducing the valve size reduces this problem.

The transient pressure rise generated at check valve closure is another important consideration. The pressure rise is a function of how fast the check valve closes compared to the speed of flow reversal (Thorley, 1989). Systems in which rapid flow reversals occur include parallel pumps, where one pump is stopped while the others are still operating; systems that have air chambers or surge tanks close to the check valve; and short systems with high elevation heads. For these systems, a high-energy source downstream from the check valve causes the flow to reverse quickly. As the disk nears its seat, it starts to restrict the reverse flow. This builds the pressure, accelerates the disk, and slams it into the seat.

Results of laboratory experiments, field tests, and computer simulations show that dramatic reductions in the transient pressures can be achieved by replacing a slow-closing swing check valve with a fast-acting check valve. For example, in a system containing parallel pumps in which the transient was generated by stopping one of the pumps, the peak transient pressure was reduced from 745 to 76 kPa when the swing check was replaced with a nozzle check valve.

The closing speed of a valve is determined by the mass of the disk, the forces closing the disk, and the travel distance from fully open to fully closed. Fast-closing valves have the following properties: the disk (including all moving parts) is lightweight, closure is assisted by springs, and the full stroke of the disk is short. Swing check valves are the slowest closing valves because they violate all three of these criteria: they have heavy disks, no springs, and long disk travel. The nozzle check valve is one of the fastest closing valves because the closing element is light, spring loaded, and has a short stroke. The silent, duo, double door, and lift check valves with springs are similar to nozzle valves in their closing times, mainly because of the closing force of the spring.

Air Valves

There are three types of automatic air valves:

- *Air/vacuum valves* are designed for releasing large quantities of air while the pipe is being filled and for admitting air when the pipe is being drained. Air/vacuum valves typically contain a float, which rises and closes the orifice as the valve body fills with water. Once the line is pressurized, the float cannot reopen to remove air that may subsequently accumulate. If the pressure becomes negative during a transient or while draining, the float drops and admits air into the line. At least

one of the air/vacuum valves should be sized for maximum flow from a full pipe break. It must be large enough for its air flow rate under vacuum conditions to equal the maximum drainage rate of the water from a pipe break and at an internal pipe pressure above the pipe collapse pressure. When sized for vacuum service, the air/vacuum valves will actually be oversized for filling the pipe. However, this does not cause any problems because the filling rate must be controlled by the water inflow rate and not by the discharge capacity of the air/vacuum valves.
- *Air release valves* contain a small orifice and are designed to release small quantities of pressurized air not released by the air/vacuum valves and small quantities of air that accumulate after initial filling and pressurization. The small orifice is controlled by a plunger activated by a float at the end of a lever arm. As air accumulates in the valve body, the float drops and opens the orifice. As the air is expelled, the float rises and closes off the orifice.
- *Combination valves* are made up of two valves, a large valve that functions as an air/vacuum valve and a small one that functions as an air release valve. The installation can consist of an air/vacuum valve and an air release valve plumbed in parallel, or the two can be housed in a single valve body. Most air valve installations require combination valves. Guidelines for sizing air valves are available from valve manufacturers and AWWA (2001, M51).

The use of large manual air release valves should be avoided because they can cause severe transients. If the pipeline is filled with the manual air valves closed, the trapped air will be pressurized to full system pressure. When the manual air valve is manually opened, the pressurized air escapes at sonic velocity, causing rapid acceleration of the liquid toward the air valve. When the last of the air is released and the water hits the air valve, the velocity of the water is suddenly reduced and high transient pressures can be generated. If manual air valves are installed, they should be small so that the air release rate is properly controlled.

Air valves should be placed at prominent high points or at intervals if there are few or no high points. The pipe profile needs to be studied relative to possible pipe ruptures so that the largest air/vacuum valves can be located at the high points where they can protect against pipe collapse. At other high points, smaller air/vacuum valves can be installed.

Velocity of the flow during filling is important. A safe way to fill a pipe is to limit the fill rate to an average flow velocity of about 0.3 m/sec (1 ft/sec) until the air/vacuum valves close. Once they are closed, the fill rate can be increased to about 1 m/sec (3 ft/sec), keeping the system pressure as low as possible. This will move the remaining air to the air release valve. When possible, the system should not be pressurized until all of the air has been removed. Trapped air at high pressure can generate severe transients if the air is allowed to pass through a control valve or manual air release valve.

Relief Valves

Pressure relief valves (PRVs) are installed to limit maximum system pressures. They can automatically open when the system pressure exceeds a set pressure or they can be programmed to open in anticipation of a transient or surge. The two general types of relief valves are: nonpilot activated and pilot activated. The selection of which type is appropriate depends on the size of valve required and if the opening and/or closing rate needs to be controlled.

The characteristics of nonpilot-activated valves are:

- They are only available in small sizes.
- The valve is held closed with a spring.
- The valve opens when line pressure exceeds the spring setting.
- They are fast acting but the speed of opening and closing is not controlled.
- They automatically close when the pressure drops below the spring setting.
- Only small changes can be made in the pressure setting by adjusting the compression of the spring.

Pilot-activated relief valves are opened and closed by system pressure and a restoring spring. The characteristics of pilot-activated valves are:

- The main valve is generally a globe-style valve that is controlled by a small pilot valve.
- There is no size limitation.
- The valves are held closed by a spring and fluid pressure.
- The pilot valve is a miniature PRV and opens the main PRV by bleeding fluid from the hydraulic pressure chamber of the main valve.
- Opening and closing speeds are controlled by throttling valves in the pilot system.
- The range of pressures can be adjusted by changing the pilot PRV.
- They are generally slow acting, so they do not protect against rapid pressure transients.
- They can be programmed to be "surge anticipators."

The pressure setting of the PRV can be adjusted over a small range by changing the compression of the spring in the pilot valve. However, it is important that the spring not be overcompressed. It is possible to compress the pilot spring completely if the adjusting rod is screwed in all the way. If this is done, the pilot PRV will remain closed and the main PRV cannot open. It was this type of improper adjustment that caused the failure of a major pipeline. Large pressure range changes require changing the spring and piston size of the pilot valve.

For added safety, multiple PRVs should be installed. Typical options include two identical valves, each with 100% capacity, or three valves, each with 50% capacity. PRVs need to be serviced periodically to ensure that they are functional. Foreign matter in the liquid can plug the pilot valves and render them inoperable.

Centrifugal Pump Selection and Performance

Optimizing the life of a piping system requires proper selection, operation, and maintenance of the pumps. During the selection process, the designer must be concerned about matching the pump performance to the system requirements and anticipate problems that will be encountered when the pumps are started or stopped and when the pipe is filled and drained. The design should also consider the effect of variations in present and future flow demands. Selection of the pumps should not be based on the least initial cost but rather on the least total cost, considering pump performance and reliability. This subsection deals with pump selection and selected operational problems.

Single Pump Selection

Selecting a pump for a particular service requires matching the system requirements to the capabilities of the pump. The process consists of developing a system equation by applying the energy equation to evaluate the pumping head required to overcome the elevation difference between reservoirs friction, and minor losses. For a pump supplying water between two reservoirs or tanks, the pump head required to produce a given discharge can be expressed as

$$H_p = \Delta Z + H_l \text{ or } H_p = \Delta Z + CQ^2 \tag{3.4.16}$$

in which Q is flow rate, ΔZ is the downstream reservoir elevation minus the upstream reservoir elevation, and the constant C is defined by Equation (3.4.12).

The total dynamic head of a pump is defined by:

$$H_p = \frac{(V_2^2 - V_1^2)}{2g} + \frac{(P_2 - P_1)}{\gamma} + Z_2 - Z_1 + H_l \tag{3.4.17}$$

Figure 3.4.2 shows a system curve for a pipe having an elevation lift of 82 ft (25 m) and moderate friction losses. When the elevations of the upstream and/or downstream reservoirs are variable, a family of system curves can be developed using different values of ΔZ.

The three pump curves shown in Figure 3.4.2 represent different impeller diameters. The intersections of the system curve with the pump curves identify the flow rate that each impeller would supply if

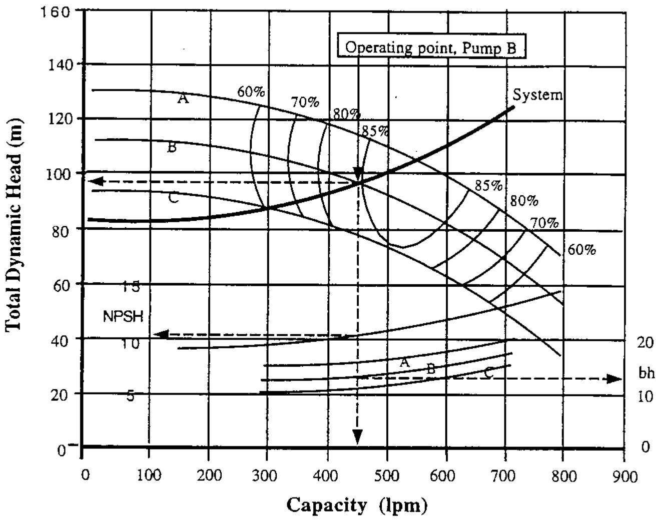

FIGURE 3.4.2 Pump selection for a single pump.

installed in that system. For this system, A and B impellers would be a good choice because they operate at or near their best efficiency range. Figure 3.4.2 shows the head and flow produced by the B pump when operating in that system are 97 ft (30 m) and 450 gpm (28.4 l/s), respectively. The net positive suction head (NPSH) and brake horsepower (bhp) are obtained as shown in the figure.

Multiple Pump Selection

The selection process is more complex when the system demand varies due to variations in reservoir elevation or to changing flow requirements. If the system must operate over a range of reservoir elevations, the pump should be selected so that the system curve, based on the mean water level (or that most frequently encountered), intersects the pump curve to the right of the midpoint of the best efficiency range. If the water level variation is not too great, the pump may not be able to operate efficiently over the complete flow range.

If the flow range is large, multiple pumps or variable-speed drives may be needed. Selection of multiple pumps and the decision about installing them in parallel or in series depend on the amount of friction in the system. Parallel installations are most effective for low-friction systems. Series pumps work best in high-friction systems.

For parallel constant speed pump operation, the combined two-pump curve is constructed by adding the flow of each pump. Such a curve is shown in Figure 3.4.3 (labeled 2 pumps). The intersection of the two-pump curve with the system curve identifies the head and combined flow for the two pumps. The pump efficiency for each pump is determined by projecting horizontally to the left to intersect the single-pump curve. For this example, a C pump, when operating by itself, will have an efficiency of 83%. With two C pumps operating, the efficiency of each will be about 72%. For the pumps to operate most efficiently for a one- or two-pump operation, the pump curve should intersect the system curve to the right of its best efficiency point.

Variable-Speed Pumps

Recent improvements in reliability and reductions in cost have made variable-speed pumps a viable option for installations in which a wide range of flow is required. Several variable speed technologies are available. One that is increasing in popularity, especially in the water and wastewater industries, is the variable-frequency drive (VFD). These are electronic controllers that adjust the speed of the electric pump motor by modulating the power delivered. VFD units can be retrofitted to existing pumps, as well as being supplied with new units.

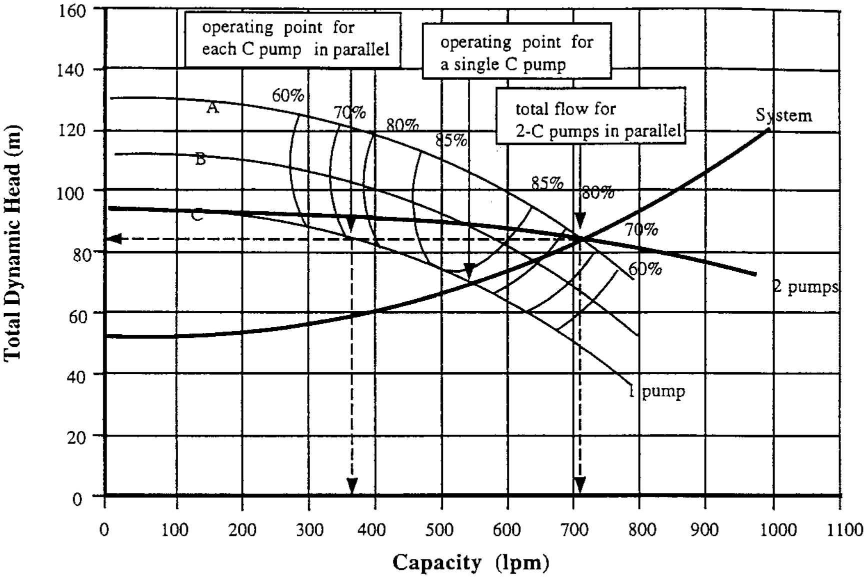

FIGURE 3.4.3 Selection of parallel pumps.

For a specific centrifugal pump, head/capacity curves for different motor speeds and/or different diameter impellers (shaved impellers) for noncavitating conditions can be estimated using the following affinity laws (Karassik et al., 1976). (Note: *D* represents impeller diameter, not pump diameter.)

$$Q_2 = Q_1 \left(\frac{N_2}{N_1} \right) \left(\frac{D_2}{D_1} \right) \tag{3.4.18}$$

$$H_2 = H_1 \left(\frac{N_2}{N_1} \right)^2 \left(\frac{D_2}{D_1} \right)^2 \tag{3.4.19}$$

$$P_2 = P_1 \left(\frac{N_2}{N_1} \right)^3 \left(\frac{D_2}{D_1} \right)^3 \tag{3.4.20}$$

To approximate pump curves for a family of geometrically similar pumps for noncavitating conditions, the following set of affinity equations can be used:

$$Q_2 = Q_1 \left(\frac{N_2}{N_1} \right) \left(\frac{D_2}{D_1} \right)^3 \tag{3.4.21}$$

$$H_2 = H_1 \left(\frac{N_2}{N_1} \right)^2 \left(\frac{D_2}{D_1} \right)^2 \tag{3.4.22}$$

$$P_2 = P_1 \left(\frac{N_2}{N_1} \right)^3 \left(\frac{D_2}{D_1} \right)^5 \tag{3.4.23}$$

The D ratios in Equation (3.4.21) through Equation (3.4.23) can be the pump or the impeller diameter. This is because the equations are only valid for geometrically similar pumps where the ratio of pump diameter to impeller diameter is constant. Either set of equations can be used to compute changes due to motor speed variations.

Figure 3.4.4 and Figure 3.4.5 show pump curves for different motor speeds and different systems for a pump with a constant impeller diameter but operating at different motor speeds. The curves for the different speeds are generated by scaling Q and H values from the 1770-rpm curve and using Equation (3.4.18) and Equation (3.4.19) or Equation (3.4.20) and Equation (3.4.22) to obtain the adjusted values of Q and H.

The variable-speed drive can operate at any speed from almost zero to full motor speed (and even higher). Assume that a 10:1 flow range is desired. The speed range required by the pump to provide a given flow range is controlled by the system. Figure 3.4.4 shows a system with a significant elevation change and relatively low friction. The pump can provide a 10:1 flow range at motor speeds between 1770 and 1310 rpm. For the high-friction system with a small elevation change shown in Figure 3.4.5, the speed variation will be between 1770 and 800 rpm for a flow range of 10:1.

Variable-speed drives offer several advantages. Single-speed drives start the motor abruptly, subjecting the rotating element to high torque and electrical current surges several times the full load current. For a constant speed deep well pump, rapid start of the motor can also cause transient and vibration problems related to compression and release of air trapped in the pump column between the water level and check valve. In contrast, variable-speed drives provide a "soft" start, gradually ramping up the motor to operating speed. This allows the air to be released slowly and reduces electrical and mechanical stress on the rotating elements, reduces maintenance, and extends motor and pump life. Because the speed can be controlled to a fraction of a percent variation, variable-speed units provide fine control of the system operating conditions.

One of the primary justifications for using a variable speed drive is cost savings resulting from reduced power demands and reduced maintenance of the motor, pump, and discharge control valves. For constant-speed pumps, reduced flow is achieved by throttling the discharge valve. This can be compared to operating an automobile at full throttle and trying to control speed by braking. The pressure drop across the valve required to reduce the flow results in wasted energy and creates the possibility of cavitation. Cavitation problems are more problematic for high-friction systems with small elevation changes due to the lack of back pressure at small flows and high-pressure differentials across the valve. Figure 3.4.4 and Figure 3.4.5 demonstrate the difference in cavitation potential and energy wasted by the throttled discharge control valve in two systems.

In the figures, the lines labeled "throttled" represent conditions in which the discharge control valve is throttled to provide a flow of 400 gpm (25.2 l/s) with the motor at full speed. The pump and system curves show that the head upstream from the valve will be 194 ft (59 m) and the back pressure provided by the system to the downstream side of the valve will be 108 ft (33 m). The head loss across the valve is therefore 194 – 108 = 86 ft (26.2 m). Using Equation (3.4.14) with $P_V = 32$ ft (9.8 m) gives $\sigma = 1.63$.

For the system shown in Figure 3.4.5, the head upstream from the valve is again 194 ft (59 m) and the back pressure provided by the system is 47 ft (14.3 m), so the head loss across the valve is 147 ft (44.8 m) and $\sigma = 0.54$. Because σ for the valve installed in the high-friction system (Figure 3.4.5) is one-third as much as the σ for the valve in the low-friction system, the valve in the high-head system will experience considerably more cavitation.

For the high-friction system (Figure 3.4.5), a variable speed pump provides more power savings than the system with low friction. In the former, the variable-speed pump would operate at a head of 47 ft (14.3 m) (compared to 194 ft (59.1 m) for a constant-speed pump), so the power consumption at a flow rate of 400 gpm (25.2 l/s) would be only 24% of the power consumption of a constant-speed pump.

Pump Operation

Starting a constant-speed pump with the pipeline empty can result in filling at a rapid rate because there is little frictional resistance initially to build back pressure. As a result, the pump will operate at a flow

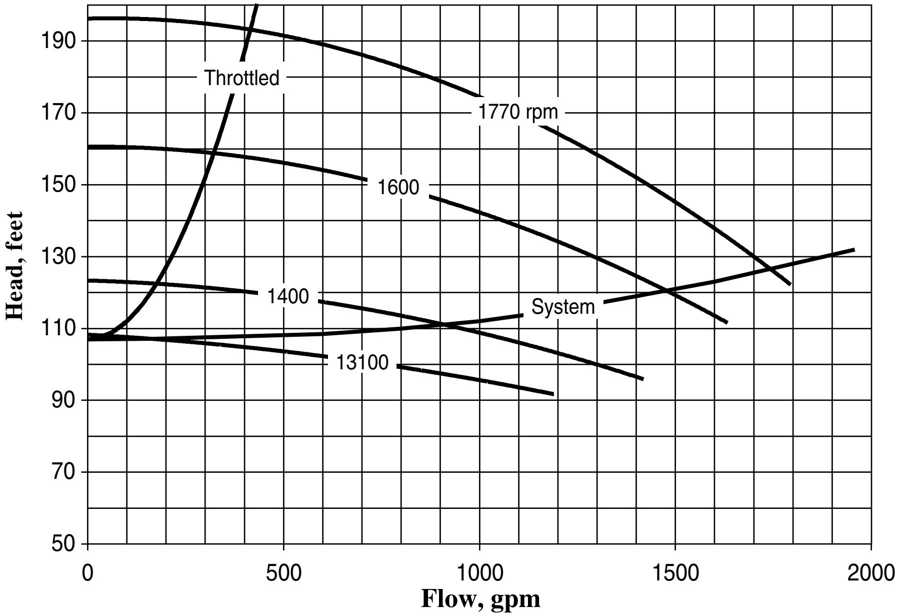

FIGURE 3.4.4 Variable-speed pump operating in a low-friction system.

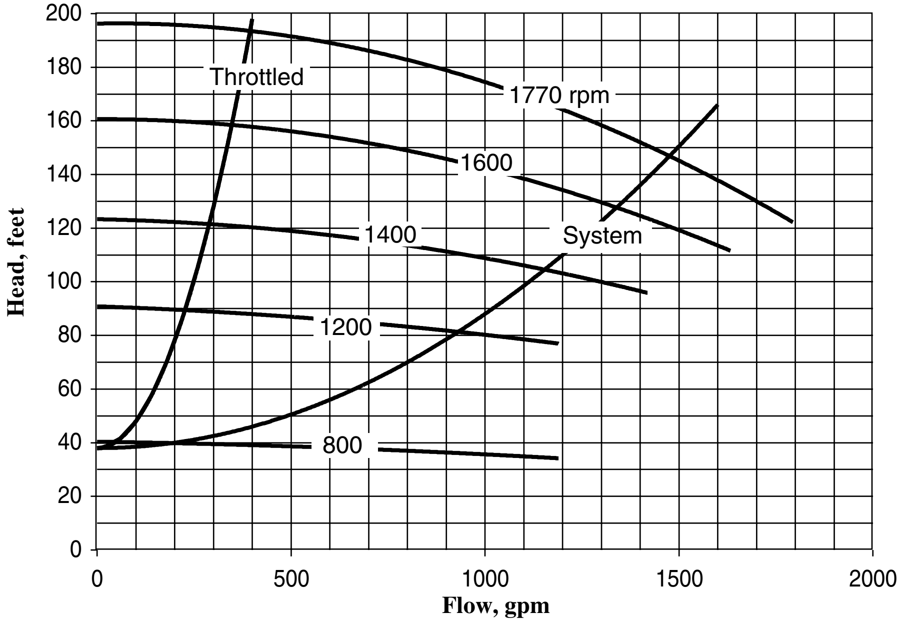

FIGURE 3.4.5 Variable-speed pump operating in a high-friction system.

greater than its design flow. This may cause the pump to cavitate, but the more serious problem is the possibility of high pressures generated by the rapid filling of the pipe. Provisions should be made to control the rate of filling. This can be done by starting the pump against a partially open discharge control valve and bypassing some of the flow around the pump, which allows the system to be filled slowly and safely. If the pipe remains full after a pump is shut down and no air is trapped in the pipe, subsequent start-up of the pumps generally does not create serious transient problems. If the pump has a VFD drive, the pipeline can be filled slowly without throttling the discharge valve and using a bypass.

For some systems, uncontrolled shutdown of the pumps due to power failures can generate high transient pressures. The problem is more severe for pipelines that have a large elevation change and multiple high points. The magnitude of the transient is related to the pipe length, the magnitude of the elevation change, the pump characteristics, and the type of check valve used. Computer simulations are needed to develop solutions to this transient problem.

Numerous mechanical devices and techniques have been used to suppress pump shut-down transients. These include increasing the rotational inertia of the pump, using surge tanks or air chambers near the pump, pressure relief valves, vacuum-breaking valves, and surge-anticipating valves. Selection of the proper transient control device will improve reliability, extend the economic life of the system, and reduce maintenance.

Pump Cavitation

The cavitation potential of a pump is quantified by a term referred to as the net positive suction head (NPSH). The available NPSH (NPSHa) is the total head at the pump suction relative to the liquid vapor pressure. For a wet-pit pump installation, NPSHa can be calculated by:

$$\text{NPSHa} = H_b - H_v + Z_s - H_l \tag{3.4.24}$$

in which, H_b is the barometric pressure at the pump installation; H_v is the absolute vapor pressure head of the liquid; Z_s is the elevation of the water level in the wet well; and H_l is the friction loss in the suction piping. Note that Z_s is negative if the liquid level in the wet well is below the elevation of the pump.

For dry-pit pumps, NPSHa can be calculated by:

$$\text{NPSHa} = H_b + H_v + \frac{P_s}{} + \frac{V_s^2}{2g} \tag{3.4.25}$$

The NPSH required by the pump (NPSHr), as defined by ANSI/HI (1998), corresponds to the flow condition in which the pump efficiency is reduced by 3% due to heavy cavitation. NPSHr is evaluated experimentally by maintaining a constant flow and reducing the pressure in the suction pipe (or lowering the level in the wet well) until the pump's efficiency is reduced by 3%. NPSHr varies with flow rate; for some pumps, NPSHr increases with flow rate and, for others, it decreases with flow rate. The intensity of cavitation generally increases when the pump is operated significantly above or below the best efficiency point even if the NPSHr reduces.

It is important to understand the intensity of the cavitation when a pump is operating at or near NPSHr. It is common practice to assume that if NPSHa > NPSHr, no cavitation will occur. This is not true. In order for the pump's efficiency to reduce by 3%, the cavitation must be heavy enough that part of the impeller is engulfed in a large vapor cavity.

Research has shown that, for some pumps, cavitation begins when the NPSH is several times higher than NPSHr (Grist, 1974). When cavitation first begins, it is manifest by individual cavitation events that create a light crackling sound. The noise is not objectionable and the cavitation does not cause vibrations or damage to the pump. As NPSH is reduced, the noise and vibrations increase. At some point, the cavitation is heavy enough that it causes erosion damage to the impeller and pump casing. Once the cavitation is in the damaging region, it often sounds like gravel passing through the pump.

As the suction pressure reduces and the system NPSH approaches NPSHr, the cavitation no longer consists of individual events. It has entered the most advanced stage in which so many cavitation events occur that they form into large vapor cavities that envelope part of the impeller. This condition is similar to the choked-flow or super-cavitating condition described in the section on control valves, in which a large vapor cavity extends into the downstream pipe. When choking cavitation occurs in a pump, the efficiency reduces because the pump is no longer pumping just a liquid but is pumping a mixture of liquid and vapor.

Consequently, even if NPSHa > NPSHr, the pump may not be operating cavitation-damage free. Adding a factor of safety of at least 5 to 10 ft (1.5 to 3 m) to the published NPSHr values is recommended to reduce the risk of severe vibrations and cavitation damage. There is a relationship between vibrations and cavitation. First, the forces caused by implosion of the cavitation events induce vibrations. Second, once measurable erosion damage occurs on the impeller, it becomes unbalanced. This further increases the intensity of the vibrations and accelerates bearing wear. The cavitation damage is also progressive. Once material is removed from the leading edge or from the impeller surface, the resulting roughened areas become sources of additional cavitation.

Suction Conditions

Pump installations can be classified as booster, dry pit, or wet pit. Booster pump installations refer to systems in which no wet well is close to the pump and suction conditions are controlled by the suction piping. Dry pit refers to installations in which the liquid is supplied from a wet well or vessel and the pump is connected via a short length of pipe and fittings. Wet pit identifies installations in which the impeller or the entire pump is submerged. Such installations are also commonly referred to as wet wells, pump sumps, or pumping pits.

Pump impellers are designed assuming that the approach flow will be relatively steady, uniform, and one-dimensional. Consequently, for acceptable pump operation, the flow needs to enter the pump free of undesirable flow conditions. Standards have been developed that identify the amount of circulation, degree of flow nonuniformity, unsteadiness of the flow, and strength of vortices acceptable for pump installations (IR, 1985; ANSI/HI, 1998).

Circulation and nonuniform flow distribution can cause the flow to approach the impeller blades at the wrong velocity and/or the wrong angle, thus causing flow separation on the impeller blades. Organized vortices and high levels of turbulence cause the impeller blades to respond much like the wings of an aircraft flying through a storm. These undesirable flow conditions can result in vibrations, cavitation, accelerated wear, and loss of efficiency. Considerable care should be used to provide good suction flow conditions to the pumps.

Hydraulic model studies are routinely performed for large wet-well pump installations to develop modifications to improve the flow approaching the pump (Sweeney and Rockwell, 1982; Tullis, 1979). These studies have shown that designing pumping pits based only on published guidelines does not guarantee acceptable suction conditions. Modifications to the pumping pits are usually required to provide acceptable flow conditions, even if the sump meets the ANSI/HI guidelines.

On the other hand, field experience has shown that some pumps with suction conditions that do not meet the ANSI/HI standards still operate without problems. This seems to be a function of the quality of the pump. For example, the authors are aware of one installation in which two variable-speed dry-pit pumps (built by different manufacturers) were installed side by side and connected to the same wet well with similar piping. The larger of the two pumps had higher suction velocities but operated normally. The smaller pump experienced severe cavitation and vibrations at all motor speeds. The difference in performance was attributed to differences in the quality of the two pumps.

Other Considerations

External Loads

In some situations, the external load is the controlling factor determining whether the pipe will collapse. The magnitude of the external load and the resistance of the pipe to collapse depend on numerous factors, including:

- Pipe diameter
- Pipe material
- Pipe deformation (deviation from circular cross section)
- Trench width
- Depth of cover
- Specific weight of the soil
- Degree of soil saturation

- Type of backfill material
- Method used to backfill
- Degree of compaction
- Live loads

The cumulative effect of all these sources of external loading requires considerable study and analysis, beyond the scope of this chapter. Because no simple guidelines for evaluating external pipe loads are available, the reader is referred to Watkins and Anderson (2000) and Spangler and Handy (1973) for details on how to perform calculations of earth loading.

Limiting Velocities

There are concerns about maximum and minimum velocity limits. If the velocity is too low, problems may develop due to settling of suspended solids and air being trapped at high points and along the crown of the pipe. The safe lower velocity limit to avoid collecting air and sediment depends on the amount and type of sediment and on the pipe diameter and pipe profile. Generally, velocities greater than about 1 m/sec (3 ft/sec) are sufficient to move trapped air to air release valves and keep the sediment in suspension.

Problems associated with high velocities are:

- Erosion of the pipe wall or liner (especially if coarse, abrasive suspended sediment is present)
- Cavitation at control valves and other restrictions
- Increased pumping costs
- Removal of air at air release valves
- Increased operator size requirements and concern about valve shaft failures due to excessive flow torques
- Increased risk of hydraulic transients

Each of these should be considered before making the final pipe diameter selection. A typical upper velocity for many applications is 20 ft/sec (6 m/sec). However, with proper pipe design and analysis, higher velocities can be tolerated.

Nomenclature

$\dot{m}$	Mass flow rate
ρ	Density
γ	Specific weight
μ	Dynamic viscosity
υ	Kinematic viscosity
ΔH	Transient head rise
ΔV	Velocity change
A	Area
a	Wave speed
A_m	Area at inlet to pipe fitting for minor losses
A_p	Area of pipe
C	Total system loss coefficient, (Equation 3.4.12)
C_c	Contraction coefficient
D	Diameter
e	Pipe roughness
F	Momentum force
f	Friction factor
g	Acceleration of gravity
H	Pressure head
H_b	Barometric pressure head

H_f	Total head loss, friction and local
h_f	Friction loss
h_l	Minor loss
H_p	Pump head
H_t	Turbine head
H_v	Absolute vapor pressure head of liquid
k	Relative roughness, e/D
K_l	Minor loss coefficient
L	Pipe length
L_{equ}	Equivalent length for minor loss
N	Motor speed
NPSHa	Available net positive suction head
NPSHr	Required net positive suction head
P	Pressure
P_b	Barometric pressure
P_d	Pressure downstream from valve
P_u	Pressure upstream from valve
P_v	Absolute vapor pressure
Q	Flow rate
R	Hydraulic radius, ratio of the flow area to the wetted perimeter
r	Radius
Re	Reynolds number
V	Velocity
Z	Elevation
Z_s	Elevation of liquid level in pump suction well (negative when below pump)
ΔZ	Elevation change
σ	Cavitation index

References

ANSI/HI 9.8-1998 (1998). Pump intake design. Hydraulic Institute and American National Standards Institute Inc., Parsippany, NJ.

ASCE (1992). Pressure pipeline design for water and wastewater. Prepared by the Committee on Pipeline Planning of the Pipeline Division of the American Society of Civil Engineers.

ASCE (1993). Steel penstocks. Prepared by the ASCE Task Committee on Manual of Practice for Steel Penstocks No. 79, Energy Division, American Society of Civil Engineers.

AWWA (1989). Steel pipe — a guide for design and installation (M11), ED. 1989. American Water Works Association.

AWWA (2003). Ductile iron pipe and fitting (M41), Second ed. 2003. American Water Works Association.

AWWA (1995). Concrete pressure pipe (M9), 1995 ED. American Water Works Association.

AWWA (2001). Butterfly valves: torque, head loss and cavitation analysis (M49). American Water Works Association.

AWWA (2001). Air-release, air/vacuum and combination air valves (M51). American Water Works Association.

Grist, E. (1974). Net positive suction head requirements for avoidance of unacceptable cavitation erosion in centrifugal pumps. Proceedings of the Conference on Cavitation, Edinburgh, Scotland, Sept. 3–5, 1974, Institute of Mechanical Engineers, London.

Haaland, S. (1983). Simple and explicit formulas for the friction factor in turbulent pipe flow. *ASME J. Fluids Eng.*, 105, March 1983, 89–90.

IR (1985). Test standards for pump intake models. Engineered Pump Division, Ingersoll–Rand Co., Atlanta GA.

ISA-RP75.23 (2000). Considerations for evaluating control valve cavitation. Instrument Society of America, Research Triangle Park, NC.

Kalsi Engineering and Tullis Engineering Consultants (1993). *Application Guide for Check Valves in Nuclear Power Plants*, Revision 1, NP-5479. Prepared for Nuclear Maintenance Applications Center, Charlotte, NC.

Karassik, I.J., Krutzsch, W.C., and Fraser, W.H. (1976), *Pump Handbook*. McGraw–Hill, New York.

Knapp, R.T., Daily, J.W., and Hammitt, F.G. (1970). *Cavitation*. McGraw–Hill, New York.

Miller, D.S. (1990). *Internal Flow Systems — Design and Performance Prediction*, 2nd ed. Gulf Publishing Company, Houston, TX.

Morrison, E.B. (1969). Monograph for the design of thrust blocks. *Civil Eng*., 39, June, 50–51, American Society of Civil Engineers.

PPI (1980). PVC pipe design and installation (M23). Plastics Pipe Institute, Inc.

Rahmeyer, W. (2002a). Pressure loss coefficients of threaded and forged weld pipe fittings for ells, reducing ells, and pipe reducers. Technical paper H-1405, American Society of Heating, Refrigeration and Air Conditioning Engineering, Atlanta, GA.

Rahmeyer, W. (2002b). Pressure loss coefficients of pipe fittings for threaded and forged weld pipe tees. Technical paper H-1404, American Society of Heating, Refrigeration and Air Conditioning Engineering, Atlanta, GA.

Rahmeyer, W. (2002c). Pressure loss data for large pipe ells, reducers and expansions. Technical paper H-1672a, American Society of Heating, Refrigeration and Air Conditioning Engineering, Atlanta, GA.

Rahmeyer, W. (2002d). Pressure loss data for large pipe tees. Technical paper H-1672b, American Society of Heating, Refrigeration and Air Conditioning Engineering, Atlanta, GA.

Rahmeyer, W. (2002e). Pressure loss coefficients for close coupled pipe ells. Technical paper H-1673, American Society of Heating, Refrigeration and Air Conditioning Engineering, Atlanta, GA.

Rahmeyer, W. (2003a). Pressure loss data for PVC pipe elbows, reducers and expansions, RP-1193. Technical paper TECH-00034-2003, American Society of Heating, Refrigeration and Air Conditioning Engineering, Atlanta, GA.

Rahmeyer, W. (2003b). Pressure loss data for PVC pipe tees, RP-119. Technical paper TECH-00035-2003, American Society of Heating, Refrigeration and Air Conditioning Engineering, Atlanta, GA.

Spangler, M.G. and Handy, R.L. (1973). *Soil Engineering*, 3rd ed. Intext Educational Publishers, New York, Chaps. 25 and 26.

Streeter, V.L. and Wylie, E.B. (1975). *Fluid Mechanics*, 6th ed., McGraw–Hill, New York.

Sweeney, C.E. and Rockwell, G.E. (1982). Pump sump design acceptance through hydraulic model testing. *Proc. IAHR Symp. Operating Probl. Pump Stations Power Plants*, Amsterdam, September 1982.

Thorley, A.R.D. (1989). *Check Valve Behavior under Transient Flow Conditions: A State-of-the-Art Review.* vol. 111. ASME, June.

Tullis, J.P. (1979). Modeling in design of pumping pits. *J. Hydraulics Division*, ASCE, 105(HY9), Proc. paper 14812, September, 1979, 1053–1063.

Tullis, J.P. (1989). *Hydraulics of Pipelines – Pumps, Valves, Cavitation, Transients.* John Wiley & Sons, New York.

Tullis, J.P. (1993). Cavitation guide for control valves. NUREG/CR-6031, U.S. Nuclear Regulatory Commission, Washington, D.C.

Tullis, J.P. (2005). Valves, in *The Engineering Handbook,* 2nd ed., Dorf, R.C., Ed. CRC Press, Boca Raton, FL.

Watkins, R.K. and Anderson, L.R. (2000). *Structural Mechanics of Buried Pipes*. CRC Press, Boca Raton, FL.

Wylie, E.B. and Streeter, V.L. (1993). *Fluid Transients in Systems*. Prentice Hall, Englewood Cliffs, NJ.

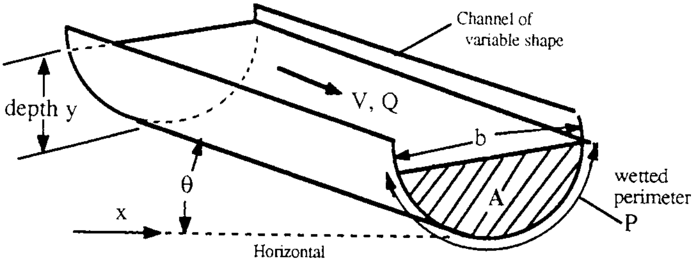

FIGURE 3.5.1 Definition sketch for an open channel.

3.5 Open Channel Flow

Frank M. White

Definition

The term *open channel flow* denotes the gravity-driven flow of a liquid with a free surface. Technically, we may study any flowing liquid and any gas interface. In practice, the vast majority of open channel flows concern water flowing beneath atmospheric air in artificial or natural channels.

The geometry of an arbitrary channel is shown in Figure 3.5.1. The area A is for the water cross section only, and b is its top width. The wetted perimeter P covers only the bottom and sides, as shown, not the surface (whose air resistance is neglected). The water depth at any location is y, and the channel slope is θ, often denoted as $S_o = \sin\theta$. All of these parameters may vary with distance x along the channel. In unsteady flow (not discussed here) they may also vary with time.

Uniform Flow

A simple reference condition, called *uniform flow,* occurs in a long straight prismatic channel of constant slope S_o. There is no acceleration, and the water flows at constant depth with fluid weight exactly balancing the wetted wall shear force: $\rho gLA \sin\theta = \tau_w PL$, where L is the channel length. Thus, $\tau_w = \rho g R_h S_o$, where $R_h = A/P$ is called the *hydraulic radius* of the channel. If we relate wall shear stress to the Darcy friction factor f, $\tau_w = (f/8)\rho V^2$, we obtain the basic uniform flow open channel relation:

$$\text{Uniform flow:}\quad V = \sqrt{\frac{8g}{f}}\sqrt{R_h S_o}\,,\quad \text{where}\quad \sqrt{\frac{8g}{f}} = C = \text{Chézy coefficient} \tag{3.5.1}$$

Antoine Chézy first derived this formula in 1769. It is satisfactory to base f upon the pipe-flow Moody diagram (Figure 3.4.1) using the hydraulic diameter, $D_h = 4R_h$, as a length scale. That is, $f = fcn\ (VD_h/\nu, \varepsilon/D_h)$ from the Moody chart. In ordinary practice, however, engineers assume fully rough, high-Reynolds-number flow and use Robert Manning's century-old correlation:

$$C \approx \frac{\zeta}{n} R_h^{1/6},\quad \text{or}\quad V_{\text{uniform}} \approx \frac{\zeta}{n} R_h^{2/3} S_o^{1/2}\quad \text{and}\quad Q = VA \tag{3.5.2}$$

where ζ is a conversion factor equal to 1.0 in SI units and 1.486 in English units. The quantity n is Manning's roughness parameter, with typical values, along with the associated roughness heights ε, listed in Table 3.5.1.

TABLE 3.5.1 Average Roughness Parameters for Various Channel Surfaces

		Average Roughness Height ε	
	n	ft	mm
Artificial lined channels			
Glass	0.010 ± 0.002	0.0011	0.3
Brass	0.011 ± 0.002	0.0019	0.6
Steel; smooth	0.012 ± 0.002	0.0032	1.0
Painted	0.014 ± 0.003	0.0080	2.4
Riveted	0.015 ± 0.002	0.012	3.7
Cast iron	0.013 ± 0.003	0.0051	1.6
Cement; finished	0.012 ± 0.002	0.0032	1.0
Unfinished	0.014 ± 0.002	0.0080	2.4
Planed wood	0.012 ± 0.002	0.0032	1.0
Clay tile	0.014 ± 0.003	0.0080	2.4
Brickwork	0.015 ± 0.002	0.012	3.7
Asphalt	0.016 ± 0.003	0.018	5.4
Corrugated metal	0.022 ± 0.005	0.12	37
Rubble masonry	0.025 ± 0.005	0.26	80
Excavated earth channels			
Clean	0.022 ± 0.004	0.12	37
Gravelly	0.025 ± 0.005	0.26	80
Weedy	0.030 ± 0.005	0.8	240
Stony; cobbles	0.035 ± 0.010	1.5	500
Natural channels			
Clean and straight	0.030 ± 0.005	0.8	240
Sluggish, deep pools	0.040 ± 0.010	3	900
Major rivers	0.035 ± 0.010	1.5	500
Floodplains			
Pasture, farmland	0.035 ± 0.010	1.5	500
Light brush	0.05 ± 0.02	6	2000
Heavy brush	0.075 ± 0.025	15	5000
Trees	0.15 ± 0.05	?	?

Critical Flow

Since the surface is always atmospheric, pressure head is not important in open channel flows. Total energy *E* relates only to velocity and elevation:

$$\text{Specific energy } E = y + \frac{V^2}{2g} = y + \frac{Q^2}{2gA^2}$$

At a given volume flow rate *Q*, the energy passes through a minimum at a condition called *critical flow*, where $dE/dy = 0$, or $dA/dy = b = gA^3/Q^2$:

$$A_{\text{crit}} = \left(\frac{bQ^2}{g}\right)^{1/3} \qquad V_{\text{crit}} = \frac{Q}{A_{\text{crit}}} = \left(\frac{gA_{\text{crit}}}{b}\right)^{1/2} \tag{3.5.3}$$

where *b* is the top-surface width as in Figure 3.5.1. The velocity V_{crit} equals the speed of propagation of a surface wave along the channel. Thus, we may define the Froude number *Fr* of a channel flow, for any cross section, as $Fr = V/V_{\text{crit}}$. The three regimes of channel flow are

Fr < 1: subcritical flow; Fr = 1: critical flow; Fr > 1: supercritical flow

There are many similarities between Froude number in channel flow and Mach number in variable-area duct flow (see Section 3.6).

For a rectangular duct, $A = by$, we obtain the simplified formulas

$$V_{\text{crit}} = \sqrt{gy} \qquad \text{Fr} = \frac{V}{\sqrt{gy}} \tag{3.5.4}$$

independent of the width of the channel.

Example 3.5.1

Water ($\rho = 998$ kg/m^3, $\mu = 0.001$ kg/m · sec) flows uniformly down a half-full brick 1-m-diameter circular channel sloping at 1°. Estimate (a) Q; and (b) the Froude number.

Solution 3.5.1 (a). First compute the geometric properties of a half-full circular channel:

$$A = \frac{\pi}{8}(1\text{ m})^2 = 0.393\text{ m}^2; \quad P = \frac{\pi}{2}(1\text{ m}) = 1.57\text{ m}; \quad R = \frac{A}{P} = \frac{0.393}{1.57} = 0.25\text{ m}$$

From Table 3.5.1, for brickwork, $n \approx 0.015$. Then, Manning's formula, Equation (3.5.2) predicts

$$V = \frac{\zeta}{n}R_h^{1/6}S_o^{1/2} = \frac{1.0}{0.015}(0.25)^{1/6}(\sin 1°)^{1/2} \approx 3.49\frac{\text{m}}{\text{sec}}; \quad Q = 3.49(0.393) \approx \mathbf{1.37}\frac{\mathbf{m^3}}{\mathbf{sec}} \quad \textit{Solution 3.5.1(a)}$$

The uncertainty in this result is about ±10%. The flow rate is quite large (21,800 gal/min) because 1°, although seemingly small, is a substantial slope for a water channel.

One can also use the Moody chart. with $V \approx 3.49$ m/sec, compute $\text{Re} = \rho V D_h/\mu \approx 3.49$ E6 and $\varepsilon/D_h \approx 0.0037$, then compute $f \approx 0.0278$ from the Moody chart. Equation (3.5.1) then predicts

$$V = \sqrt{\frac{8g}{f}R_h S_o} = \sqrt{\frac{8(9.81)}{0.0278}(0.25)(\sin 1°)} \approx 3.51\frac{\text{m}}{\text{sec}}; \quad Q = VA \approx \mathbf{1.38}\frac{\mathbf{m^3}}{\mathbf{sec}}$$

Solution 3.5.1 (b). With Q known from part (a), compute the critical conditions from Equation (3.5.3):

$$A_{\text{crit}} = \left(\frac{bQ^2}{g}\right)^{1/3} = \left[\frac{1.0(1.37)^2}{9.81}\right]^{1/3} = 0.576\text{ m}^2, \quad V_{\text{crit}} = \frac{Q}{A_{\text{crit}}} = \frac{1.37}{0.576} = 2.38\ \frac{\text{m}}{\text{sec}}$$

Hence

$$\text{Fr} = \frac{V}{V_{\text{crit}}} = \frac{3.49}{2.38} \approx \mathbf{1.47}\ \ (\text{supercritical}) \quad \textit{Solution 3.5.1(b)}$$

Again the uncertainty is approximately ±10%, primarily because of the need to estimate the brick roughness.

Hydraulic Jump

In gas dynamics (Section 3.6), a supersonic gas flow may pass through a thin normal shock and exit as a subsonic flow at higher pressure and temperature. By analogy, a supercritical open channel flow may pass through a *hydraulic jump* and exit as a subcritical flow at greater depth, as in Figure 3.5.2. Application of continuity and momentum to a jump in a rectangular channel yields

$$V_2 = V_1\frac{y_1}{y_2} \qquad y_2 = \frac{y_1}{2}\left[-1 + \sqrt{1 + 8\text{Fr}_1^2}\right] \text{ where } \text{Fr}_1 = \frac{V_1}{\sqrt{gy_1}} > 1 \tag{3.5.5}$$

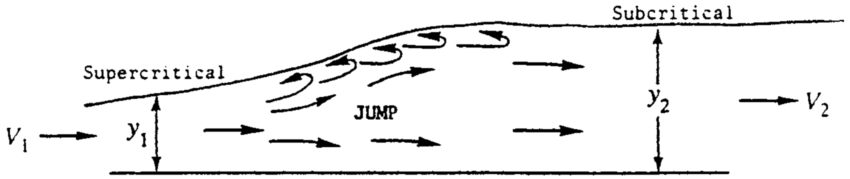

FIGURE 3.5.2 A two-dimensional hydraulic jump.

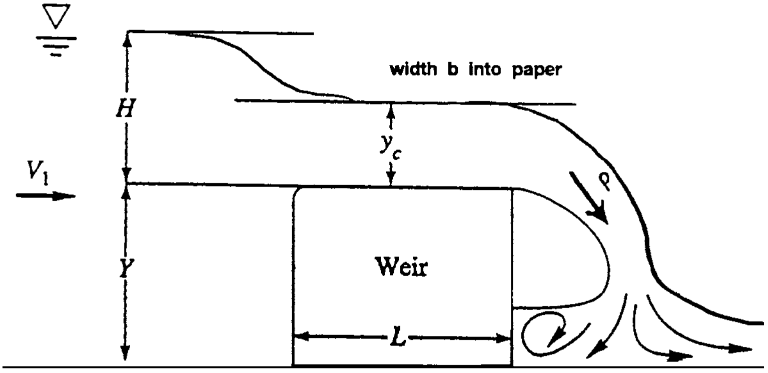

FIGURE 3.5.3 Geometry and notation for flow over a weir.

Both the normal shock and the hydraulic jump are dissipative processes: the entropy increases and the effective energy decreases. For a rectangular jump,

$$\Delta E = E_1 - E_2 = \frac{(y_2 - y_1)^3}{4y_1y_2} > 0 \tag{3.5.6}$$

For strong jumps, this loss in energy can be up to 85% of E_1. The second law of thermodynamics requires $\Delta E > 0$ and $y_2 > y_1$ or, equivalently, $\mathrm{Fr}_1 > 1$,

Note from Figure 3.5.2 that a hydraulic jump is not thin. Its total length is approximately four times the downstream depth. Jumps also occur in nonrectangular channels, and the theory is much more algebraically laborious.

Weirs

If an open channel flow encounters a significant obstruction, it will undergo rapidly varied changes which are difficult to model analytically but can be correlated with experiment. An example is the *weir* in Figure 3.5.3 (colloquially called a *dam*), which forces the flow to deflect over the top. If $L << Y$, the weir is termed *sharp-crested*; if $L = O(Y)$ it is *broad-crested*. Small details, such as the upper front corner radius or the crest roughness, may be significant. The crest is assumed level and of width b into the paper.

If there is a free overfall, as in Figure 3.5.3, the flow accelerates from subcritical upstream to critical over the crest to supercritical in the overfall. There is no flow when the excess upstream depth $H = 0$. A simple Bernoulli-type analysis predicts that the flow rate Q over a wide weir is approximately proportional to $bg^{1/2}H^{3/2}$. An appropriate correlation is thus

$$Q_{\text{weir}} = C_d b g^{1/2} H^{3/2}, \quad \text{where} \quad C_d = \text{dimensionless weir coefficient} \tag{3.5.7}$$

If the upstream flow is turbulent, the weir coefficient depends only upon geometry, and Reynolds number effects are negligible. If the weir has sidewalls and is narrow, replace width b by $(b - 0.1H)$.

Two recommended empirical correlations for Equation (3.5.7) are as follows:

$$\begin{aligned} &\text{Sharp-crested:} \quad C_d \approx 0.564 + 0.0846\frac{H}{Y} \quad \text{for} \quad \frac{L}{Y} < 0.07 \\ &\text{Broad-crested:} \quad C_d \approx 0.462 \quad \text{for} \quad 0.08 < \frac{H}{L} < 0.33 \end{aligned} \tag{3.5.8}$$

These data are for wide weirs with a sharp upper corner in front. Many other weir geometries are discussed in the references for this section. Of particular interest is the sharp-edged vee-notch weir, which has no length scale b. If 2θ is the total included angle of the notch, the recommended correlation is

$$\text{Vee-notch, angle } 2\theta: \quad Q \approx 0.44 \tan\theta\, g^{1/2} H^{5/2} \quad \text{for} \quad 10° < \theta \le 50° \tag{3.5.9}$$

The vee-notch is more sensitive at low flow rates (large H for a small Q) and thus is popular in laboratory measurements of channel flow rates.

A weir in the field will tend to spring free and form a natural *nappe*, or air cavity, as in Figure 3.5.3. Narrow weirs, with sidewalls, may need to be aerated artificially to form a nappe and keep the flow from sliding down the face of the weir. The correlations above assume nappe formation.

Gradually Varied Flow

Return to Figure 3.5.1 and suppose that (y, A, b, P, S_o) are all variable functions of horizontal position x. If these parameters are slowly changing, with no hydraulic jumps, the flow is termed *gradually varied* and satisfies a simple one-dimensional first-order differential equation if Q = constant:

$$\frac{dy}{dx} \approx \frac{S_o - S}{1 - \dfrac{V^2 b}{gA}}, \quad \text{where} \quad V = \frac{Q}{A} \quad \text{and} \quad S = \frac{f}{D_h}\frac{V^2}{2g} = \frac{n^2 V^2}{\zeta^2 R_h^{4/3}} \tag{3.5.10}$$

The conversion factor $\zeta^2 = 1.0$ for SI units and 2.208 for English units. If flow rate, bottom slope, channel geometry, and surface roughness are known, we may solve for $y(x)$ for any given initial condition $y = y_o$ at $x = x_o$. The solution is computed by any common numerical method, e.g., Runge–Kutta.

Recall from Equation (3.5.3) that the term $V^2b/(gA) \equiv \mathrm{Fr}^2$, so the sign of the denominator in Equation (3.5.10) depends upon whether the flow is sub- or supercritical. The mathematical behavior of Equation (3.5.10) differs also. If Fr is near unity, the change dy/dx will be very large, which probably violates the basic assumption of "gradual" variation.

For a given flow rate and local bottom slope, two reference depths are useful and may be computed in advance:

(a) The *normal* depth y_n for which Equation (3.5.2) yields the flow rate:
(b) The *critical* depth y_c for which Equation (3.5.3) yields the flow rate.

Comparison of these two, and their relation to the actual local depth y, specifies the type of solution curve being computed. The five bottom-slope regimes (mild M, critical C, steep S, horizontal H, and adverse A) create 12 different solution curves, as illustrated in Figure 3.5.4. All of these may be readily generated by a computer solution of Equation 3.5.10. The following example illustrates a typical solution to a gradually varied flow problem.

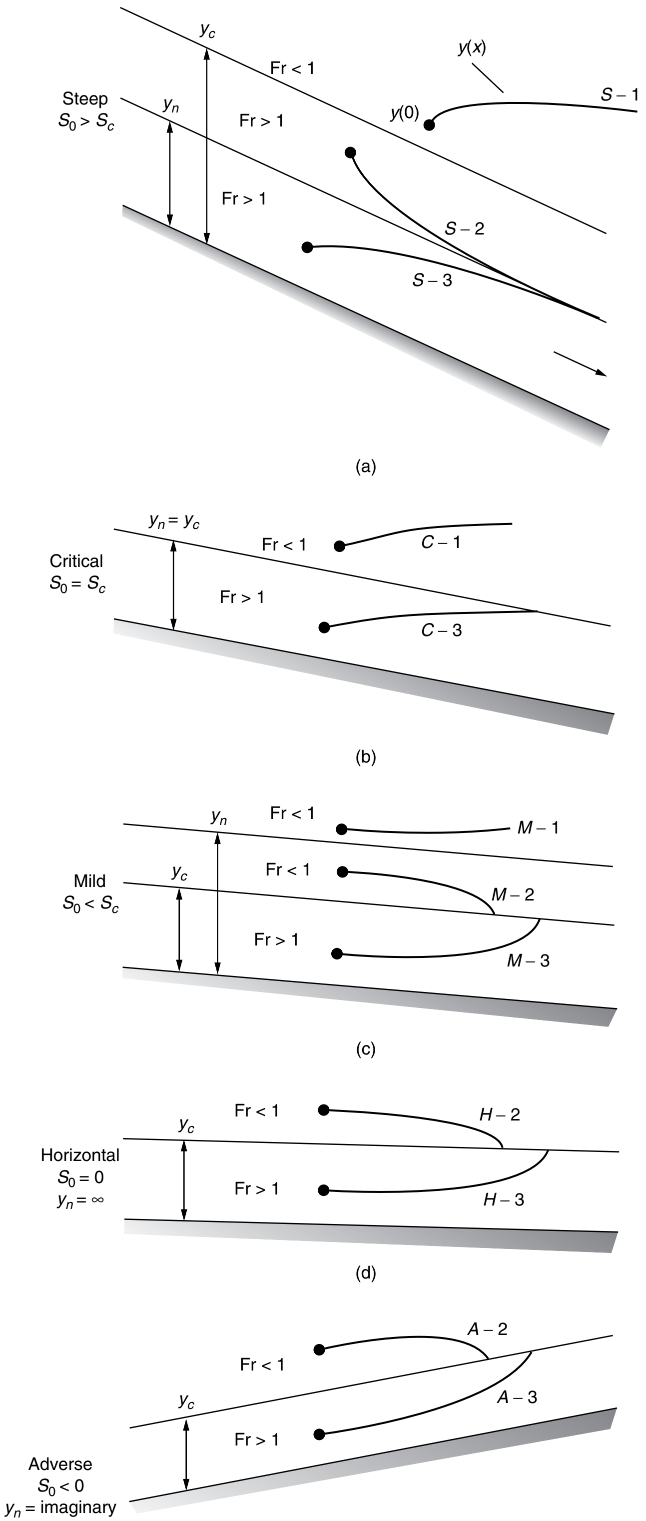

FIGURE 3.5.4 Classification of solution curves for gradually varied flow.

Example 3.5.2

Water, flowing at 2.5 m^3/sec in a rectangular gravelly earth channel 2 m wide, encounters a broad-crested weir 1.5 m high. Using gradually varied theory, estimate the water depth profile back to 1 km upstream of the weir. The bottom slope is 0.1^0.

Solution. We are given Q, $Y = 1.5$ m, and $b = 2$ m. We may calculate excess water level H at the weir (see Figure 3.5.3) from Equation (3.5.7) and Equation (3.5.8):

$$Q = 2.5\frac{\text{m}^3}{\text{sec}} = C_d b_{\text{eff}} g^{1/2} H^{3/2} = 0.462(2.0 - 0.1H)(9.81)^{1/2} H^{3/2}, \quad \text{solve for} \quad H \approx \mathbf{0.94}\ \text{m}$$

Since the weir is not too wide, we have subtracted 0.1 H from b as recommended. The weir serves as a "control structure" which sets the water depth just upstream. This is our initial condition for gradually varied theory: $y(0) = Y + H = 1.5 + 0.94 \approx 2.44$ m at $x = 0$. Before solving Equation (3.5.10), we find the normal and critical depths to get a feel for the problem:

$$\text{Normal depth:} \qquad Q = 2.5\frac{\text{m}^3}{\text{sec}} = \frac{1.0}{0.025}(2.0y_n)\left(\frac{2.0y_n}{2.0 + 2y_n}\right)^{3/2}\sqrt{\sin 0.1°}, \quad \text{solve} \quad y_n \approx \mathbf{1.14}\ \text{m}$$

$$\text{Critical depth:} \qquad A_c = 2.0y_c - \left(\frac{bQ^2}{g}\right)^{1/3} = \left[\frac{2.0(2.5)^2}{9.81}\right]^{1/3}, \quad \text{solve} \quad y_c \approx \mathbf{0.54}\ \text{m}$$

We have taken $n \approx 0.025$ for gravelly earth, from Table 3.5.1. Since $y(0) > y_n > y_c$, we are on a mild slope $M - 1$ "backwater" curve, as in Figure 3.5.4. For our data, Equation (3.5.10) becomes

$$\frac{dy}{dx} \approx \frac{S_o - n^2Q^2/\left(\zeta^2 A^2 R_h^{4/3}\right)}{1 - Q^2 b/\left(gA^3\right)}$$

where $Q = 2.5$, $b = 2$, $\zeta = 1$, $A = 2y$, $S_o = \sin 0.1°$, $R_h = 2y/(2 + 2y)$, $g = 9.81$, $y(0) = 2.44$ at $x = 0$.

Integrate numerically backward, that is, for $\Delta x < 0$, until $x = -1$ km $= -1000$ m. The complete solution curve is shown in Figure 3.5.5. The water depth decreases upstream and is approximately $y \approx 1.31$ m at $x = -1000$ m. If slope and channel width remain constant, the water depth asymptotically approaches the normal depth y_n far upstream.

Nomenclature

English symbols

A = water cross section area
b = channel upper-surface width
C = Chézy coefficient, Equation (3.5.1)
C_d = weir discharge coefficient, Equation (3.5.7)
D_h = hydraulic diameter, $= 4R_h$
E = specific energy, $= y + V^2/2g$
f = Moody friction factor
Fr = Froude number, $= V/V_{\text{crit}}$
g = acceleration of gravity
H = excess water level above weir, Figure 3.5.3
L = weir length, Figure 3.5.3
n = Manning roughness factor, Table 3.5.1
P = wetted perimeter

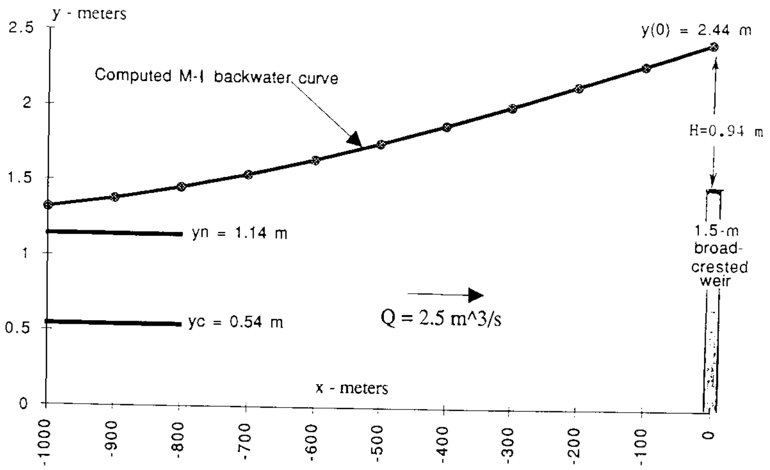

FIGURE 3.5.5 Backwater solution curve for Example 3.5.2.

Q = volume flow rate
R_h = hydraulic radius, = A/P
S = frictional slope, Equation (3.5.10)
S_o = bottom slope
V = average velocity
x = horizontal distance along the channel
y = water depth
Y = weir height, Figure (3.5.3)

Greek Symbols

ε = wall roughness height, Table 3.5.1
ρ = fluid density
μ = fluid viscosity
ν = fluid kinematic viscosity, = μ/ρ
ζ = conversion factor, = 1.0 (SI) and 1.486 (English)

Subscripts

c,crit = critical, at Fr = 1
n = normal, in uniform flow

References

Ackers, P. et al. 1978. *Weirs and Flumes for Flow Measurement*, John Wiley, New York.

Bos, M.G. 1985. *Long-Throated Flumes and Broad-Crested Weirs,* Martinus Nijhoff (Kluwer), Dordrecht, The Netherlands.

Bos, M.G., Replogle, J.A., and Clemmens, A.J. 1984. *Flow-Measuring Flumes for Open Channel Systems,* John Wiley, New York.

Brater, E.F. 1976. *Handbook of Hydraulics,* 6th ed., McGraw-Hill, New York.

Chow, V.T. 1959. *Open Channel Hydraulics,* McGraw-Hill, New York.

French, R.H. 1985. *Open Channel Hydraulics,* McGraw-Hill, New York.

Henderson, F.M. 1966. *Open Channel Flow,* Macmillan, New York.

Sellin, R.H.J. 1970. *Flow in Channels*, Gordon & Breach, London.

Spitzer, D.W. (Ed.). 1991. *Flow Measurement: Practical Guides for Measurement and Control*, Instrument Society of America, Research Triangle Park, NC.

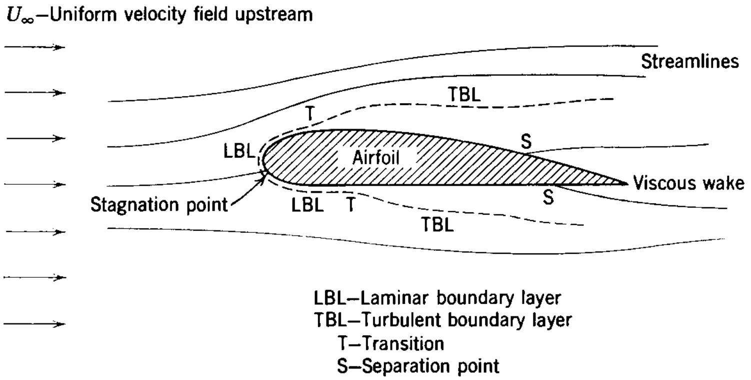

FIGURE 3.6.1 Viscous flow around an airfoil (boundary layer thickness exaggerated for clarity).

3.6 External Incompressible Flows

Alan T. McDonald

Introduction and Scope

Potential flow theory (Section 3.2) treats an incompressible *ideal fluid* with zero viscosity. There are no shear stresses; pressure is the only stress acting on a fluid particle. Potential flow theory predicts no drag force when an object moves through a fluid; this is obviously incorrect because all real fluids are viscous and cause drag forces. The objective of this section is to consider the behavior of viscous, incompressible fluids flowing over objects.

A number of phenomena that occur in external flow at high Reynolds number over an object are shown in Figure 3.6.1. The freestream flow divides at the stagnation point and flows around the object. Fluid at the object surface takes on the velocity of the body as a result of the no-slip condition. Boundary layers form on the upper and lower surfaces of the body; flow in the boundary layers is initially laminar, then **transition** to turbulent flow may occur (points "T").

Boundary layers thickening on the surfaces cause only a slight displacement of the streamlines of the external flow (their thickness is greatly exaggerated in the figure). **Separation** may occur in the region of increasing pressure on the rear of the body (points "S"); after separation, boundary layer fluid no longer remains in contact with the surface. Fluid that was in the boundary layers forms the viscous *wake* behind the object.

The Bernoulli equation is valid for steady, incompressible flow without viscous effects. It may be used to predict pressure variations outside the boundary layer. Stagnation pressure is constant in the uniform inviscid flow far from an object, and the Bernoulli equation reduces to

$$p_\infty + \frac{1}{2}\rho V^2 = \text{constant} \tag{3.6.1}$$

where p_∞ is pressure far upstream, ρ is density, and V is velocity. Therefore, the local pressure can be determined if the local freestream velocity, U, is known.

Boundary Layers

The Boundary Layer Concept

The **boundary layer** is the thin region near the surface of a body in which viscous effects are important. By recognizing that viscous effects are concentrated near the surface of an object, Prandtl showed that only the Euler equations for inviscid flow need be solved in the region outside the boundary layer. Inside

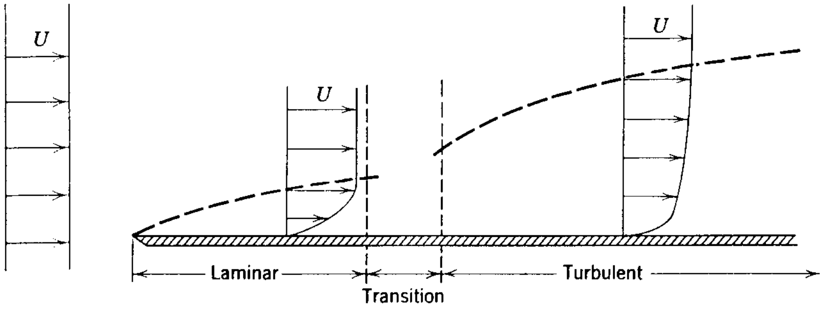

FIGURE 3.6.2 Boundary layer on a flat plate (vertical thickness exaggerated for clarity).

the boundary layer, the elliptic Navier–Stokes equations are simplified to boundary layer equations with parabolic form that are easier to solve. The thin boundary layer has negligible pressure variation across it; pressure from the freestream is impressed upon the boundary layer.

Basic characteristics of all laminar and turbulent boundary layers are shown in the developing flow over a flat plate in a semi-infinite fluid. Because the boundary layer is thin, disturbance of the inviscid flow outside the boundary layer is negligible, and the **pressure gradient** along the surface is close to zero. Transition from laminar to turbulent boundary layer flow on a flat plate occurs when Reynolds number based on x exceeds $\mathrm{Re}_x = 500{,}000$. Transition may occur earlier if the surface is rough, pressure increases in the flow direction, or separation occurs. Following transition, the turbulent boundary layer thickens more rapidly than the laminar boundary layer as a result of increased shear stress at the body surface.

Boundary Layer Thickness Definitions

Boundary layer disturbance thickness, δ, is usually defined as the distance, y, from the surface to the point where the velocity within the boundary layer, u, is within 1% of the local freestream velocity, U. As shown in Figure 3.6.2, the boundary layer velocity profile merges smoothly and asymptotically into the freestream, making δ difficult to measure. For this reason and for their physical significance, two integral measures of boundary layer thickness are defined. Displacement thickness, δ^*, is defined as

$$\frac{\delta^*}{\delta} = \int_0^\infty \left(1 - \frac{u}{U}\right) d\left(\frac{y}{\delta}\right) \tag{3.6.2}$$

Physically, δ^*, is the distance the solid boundary would need to be displaced into the freestream in a frictionless flow to produce the mass flow deficit caused by the viscous boundary layer. Momentum thickness, θ, is defined as

$$\frac{\theta}{\delta} = \int_0^\infty \frac{u}{U}\left(1 - \frac{u}{U}\right) d\left(\frac{y}{\delta}\right) \tag{3.6.3}$$

Physically, θ is the thickness of a fluid layer with velocity U, for which the momentum flux is the same as the deficit in momentum flux within the boundary layer (momentum flux is momentum per unit time passing a cross section).

Because δ^* and θ are defined in terms of integrals for which the integrand vanishes in the freestream, they are easier to evaluate experimentally than disturbance thickness δ.

Exact Solution of the Laminar Flat-Plate Boundary Layer

Blasius obtained an exact solution for laminar boundary layer flow on a flat plate. He assumed a thin boundary layer to simplify the streamwise momentum equation. He also assumed *similar* velocity profiles in the boundary layer so that, when written as $u/U = f(y/\delta)$, velocity profiles do not vary with x. He used a similarity variable to reduce the partial differential equations of motion and continuity to a single third-order ordinary differential equation.

Blasius used numerical methods to solve the ordinary differential equation. Unfortunately, the velocity profile must be expressed in tabular form. The principal results of the Blasius solution may be expressed as

$$\frac{\delta}{x} = \frac{5}{\sqrt{\mathrm{Re}_x}} \tag{3.6.4}$$

and

$$C_f = \frac{\tau_w}{\frac{1}{2}\rho U^2} = \frac{0.664}{\sqrt{\mathrm{Re}_x}} \tag{3.6.5}$$

These results characterize the laminar boundary layer on a flat plate; they show that laminar boundary layer thickness varies as $x^{1/2}$ and wall shear stress varies as $1/x^{1/2}$.

Approximate Solutions

The Blasius solution cannot be expressed in closed form and is limited to laminar flow. Therefore, approximate methods that give solutions for laminar and turbulent flow in closed form are desirable. One such method is the *momentum integral equation* (MIE), which may be developed by integrating the boundary layer equation across the boundary layer or by applying the streamwise momentum equation to a differential control volume (Fox et al., 2004). The result is the ordinary differential equation

$$\frac{d\theta}{dx} = \frac{\tau_w}{\rho U^2} - \left(\frac{\delta^*}{\theta} + 2\right)\frac{\theta}{U}\frac{dU}{dx} \tag{3.6.6}$$

The first term on the right side of Equation (3.6.6) contains the influence of wall shear stress. Because τ_w is always positive, it always causes θ to increase. The second term on the right side contains the pressure gradient, which can have either sign. Therefore, the effect of the pressure gradient can be to increase or to decrease the rate of growth of boundary layer thickness.

Equation (3.6.6) is an ordinary differential equation that can be solved for θ as a function of x on a flat plate (zero pressure gradient), provided a reasonable shape is assumed for the boundary layer velocity profile and shear stress is expressed in terms of the other variables. Results for laminar and turbulent flat-plate boundary layer flows are discussed next.

Laminar Boundary Layers — A reasonable approximation to the laminar boundary layer velocity profile is to express u as a polynomial in y. The resulting solutions for δ and τ_w have the same dependence on x as the exact Blasius solution. Numerical results are presented in Table 3.6.1. Comparing the approximate and exact solutions shows remarkable agreement in view of the approximations used in the analysis. The trends are predicted correctly and the approximate values are within 10% of the exact values.

Turbulent Boundary Layers — The turbulent velocity profile may be expressed well using a power law, $u/U = (y/\delta)^{1/n}$, where n is an integer between 6 and 10 (frequently 7 is chosen). For turbulent flow, it is not possible to express shear stress directly in terms of a simple velocity profile; an empirical correlation is required. Using a pipe flow data correlation gives

$$\frac{\delta}{x} = \frac{0.382}{\mathrm{Re}_x^{1/5}} \tag{3.6.7}$$

TABLE 3.6.1 Exact and Approximate Solutions for Laminar Boundary Layer Flow over a Flat Plate at Zero Incidence

Velocity Distribution $\frac{u}{U}=f\left(\frac{y}{\delta}\right)=f(\eta)$	$\frac{\theta}{\delta}$	$\frac{\delta^*}{\delta}$	$a=\frac{\delta}{x}\sqrt{\mathrm{Re}_x}$	$b=C_f\sqrt{\mathrm{Re}_x}$
$f(\eta) = 2\eta - \eta^2$	2/15	1/3	5.48	0.730
$f(\eta) = 3/2\,\eta - 1/2\,\eta^3$	39/280	3/8	4.64	0.647
$f(\eta) = \sin(\pi/2\,\eta)$	$(4-\pi)/2\pi$	$(\pi-2)/\pi$	4.80	0.654
Exact	0.133	0.344	5.00	0.664

TABLE 3.6.2 Thickness and Skin Friction Coefficient for Laminar and Turbulent Boundary Layers on a Flat Plate

Reynolds	Boundary Layer Thickness/x		Skin Friction Coefficient		Turbulent/Laminar Ratio	
Number	Laminar BL	Turbulent BL	Laminar BL	Turbulent BL	BL thickness	Skin friction
2E + 05	0.0112	0.0333	0.00148	0.00517	2.97	3.48
5E + 05	0.00707	0.0277	0.000939	0.00431	3.92	4.58
1E + 06	0.00500	0.0241	0.000664	0.00375	4.82	5.64
2E + 06	0.00354	0.0210	0.000470	0.00326	5.93	6.95
5E + 06	0.00224	0.0175	0.000297	0.00272	7.81	9.15
1E + 07	0.00158	0.0152	0.000210	0.00236	9.62	11.3
2E + 07	0.00112	0.0132	0.000148	0.00206	11.8	13.9
5E + 07	0.000707	0.0110	0.0000939	0.00171	15.6	18.3

Note: BL = boundary layer.

and

$$C_f = \frac{\tau_w}{\frac{1}{2}\rho U^2} = \frac{0.0594}{\mathrm{Re}_x^{1/5}} \tag{3.6.8}$$

These results characterize the turbulent boundary layer on a flat plate. They show that turbulent boundary layer thickness varies as $x^{4/5}$ and wall shear stress varies as $1/x^{1/5}$.

Approximate results for laminar and turbulent boundary layers are compared in Table 3.6.2. At a Reynolds number of 1 million, wall shear stress for the turbulent boundary layer is nearly six times as large as for the laminar layer. For a turbulent boundary layer, thickness increases five times faster with distance along the surface than for a laminar layer. These approximate results give a physical feel for relative magnitudes in the two cases.

The MIE cannot be solved in closed form for flows with nonzero pressure gradients. However, the role of the pressure gradient can be understood qualitatively by studying the MIE.

Effect of Pressure Gradient

Boundary layer flow with favorable, zero, and adverse pressure gradients is depicted schematically in Figure 3.6.3. (Assume a thin boundary layer, so that flow on the lower surface behaves as external flow on a surface, with the pressure gradient impressed on the boundary layer.) The pressure gradient is favorable when $\partial p/\partial x < 0$; zero when $\partial p/\partial x = 0$; and adverse when $\partial p/\partial x > 0$, as indicated for regions 1, 2, and 3.

Viscous shear always causes a net retarding force on any fluid particle within the boundary layer. For zero pressure gradient, shear forces alone can never bring the particle to rest. (Recall that for laminar and turbulent boundary layers, the shear stress varied as $1/x^{1/2}$ and $1/x^{1/5}$, respectively; shear stress never becomes zero for finite x.) Because shear stress is given by $\tau_w = \mu\, \partial u/\partial y)_{y=0}$, the velocity gradient cannot

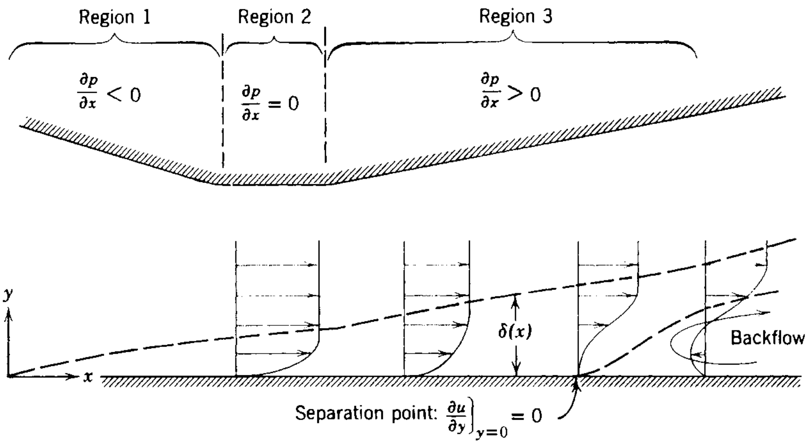

FIGURE 3.6.3 Boundary layer flow with pressure gradient (thickness exaggerated for clarity).

be zero. Therefore, flow cannot separate in a zero pressure gradient; shear stresses alone can never cause flow separation.

In the favorable pressure gradient of region 1, pressure forces tend to maintain the motion of the particle, so flow cannot separate. In the adverse pressure gradient of region 3, pressure forces oppose the motion of a fluid particle. An adverse pressure gradient is a necessary condition for flow separation.

Velocity profiles for laminar and turbulent boundary layers are shown in Figure 3.6.2. It is easy to see that the turbulent velocity profile has much more momentum than the laminar profile. Therefore, the turbulent velocity profile can resist separation in an adverse pressure gradient better than the laminar profile.

The freestream velocity distribution must be known before the MIE can be applied. A first approximation is obtained by applying potential flow theory to calculate the flow field around the object. Much effort has been devoted to calculation of velocity distributions over objects of known shape (the "direct" problem) and to determination of shapes to produce a desired pressure distribution (the "inverse" problem). Detailed discussion of such calculation schemes is beyond the scope of this section; the state of the art continues to progress rapidly.

Drag

Any object immersed in a viscous fluid flow experiences a net force from the shear stresses and pressure differences caused by the fluid motion. *Drag* is the force component parallel to, and *lift* is the force component perpendicular to, the flow direction. *Streamlining* is the art of shaping a body to reduce fluid dynamic drag. Airfoils (hydrofoils) are designed to produce lift in air (water); they are streamlined to reduce drag and thus to attain high lift–drag ratios.

In general, lift and drag cannot be predicted analytically for flows with separation, but progress continues on computational fluid dynamics methods. For many engineering purposes, drag and lift forces are calculated from experimentally derived coefficients, discussed next.

Drag coefficient is defined as

$$C_D = \frac{F_D}{\frac{1}{2}\rho V^2 A} \tag{3.6.9}$$

where $\frac{1}{2}\rho V^2$ is dynamic pressure and A is the area upon which the coefficient is based. Common practice is to base drag coefficients on projected *frontal area* (Fox et al., 2004).

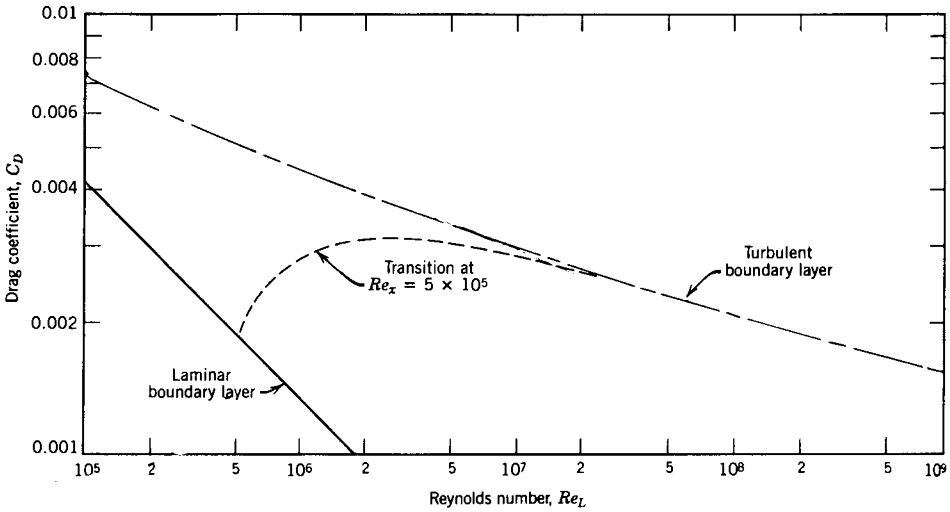

FIGURE 3.6.4 Drag coefficient vs. Reynolds number for a smooth flat plate parallel to the flow.

Similitude was treated in Section 3.3. In general, the drag coefficient may be expressed as a function of Reynolds number; Mach number; Froude number; relative roughness; submergence divided by length; and so forth. This section considers neither high-speed flow nor free-surface effects; only Reynolds number and roughness effects on drag coefficient will be considered.

Friction Drag

The total friction drag force acting on a plane surface aligned with the flow direction can be found by integrating the shear stress distribution along the surface. The drag coefficient for this case is defined as friction force divided by dynamic pressure and *wetted area* in contact with the fluid. Because shear stress is a function of Reynolds number, so is drag coefficient (see Figure 3.6.4). In Figure 3.6.4, transition occurs at $\mathrm{Re}_x = 500{,}000$; the dashed line represents the drag coefficient at larger Reynolds numbers. A number of empirical correlations may be used to model the variation in C_D shown in Figure 3.6.4 (Schlichting, 1979).

Extending the laminar boundary layer line to higher Reynolds numbers shows that it is beneficial to delay transition to the highest possible Reynolds number. Some results are presented in Table 3.6.3; drag is reduced more than 50% by extending laminar boundary layer flow to $\mathrm{Re}_L = 10^6$.

TABLE 3.6.3 Drag Coefficients for Laminar, Turbulent, and Transition Boundary Layers on a Flat Plate

Reynolds	Drag Coefficient			Laminar/	% Drag
Number	Laminar BL	Turbulent BL	Transition	Transition	Reduction
2E + 05	0.00297	0.00615	—	—	—
5E + 05	0.00188	0.00511	0.00189	—	—
1E + 06	0.00133	0.00447	0.00286	0.464	53.6
2E + 06	0.000939	0.00394	0.00314	0.300	70.0
5E + 06	0.000594	0.00336	0.00304	0.195	80.5
1E + 07	0.000420	0.00300	0.00284	0.148	85.2
2E + 07	0.000297	0.00269	0.00261	0.114	88.6
5E + 07	0.000188	0.00235	0.00232	0.081	9.19

Note: BL = boundary layer.

TABLE 3.6.4 Drag Coefficient Data for Selected Objects ($Re > 1000$)

Object	Diagram		CD(RE ≥ 10^3)
Square prism	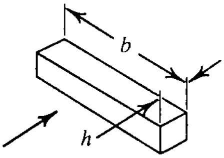	$b/h = \infty$	2.05
		$b/h = 1$	1.05
Disk	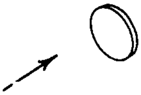		1.17
Ring			1.20[a]
Hemisphere (open end facing flow)	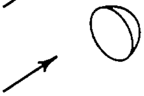		1.42
Hemisphere (open end facing downstream)	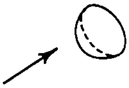		0.38
C-section (open side facing flow)	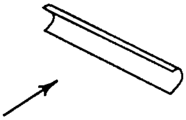		2.30
C-section (open side facing downstream)	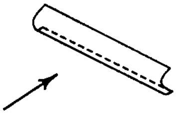		1.20

[a] Based on ring area.

Source: Data from Hoerner, S.F. 1965. *Fluid-Dynamic Drag*, 2nd ed. Published by the author, Midland Park, NJ.

Pressure Drag

A thin flat surface normal to the flow has no area parallel to the flow direction. Therefore, there can be no friction force parallel to the flow; all drag is caused by pressure forces. Drag coefficients for objects with sharp edges tend to be independent of Reynolds number (for Re > 1000) because the separation points are fixed by the geometry of the object. Drag coefficients for selected objects are shown in Table 3.6.4.

Rounding the edges that face the flow reduces drag markedly. Compare the drag coefficients for the hemisphere and C-section shapes facing into and away from the flow. Also note that the drag coefficient for a two-dimensional object (long square cylinder) is about twice that for the corresponding three-dimensional object (square cylinder with $b/h = 1$).

Friction and Pressure Drag: Bluff Bodies

Friction and pressure forces contribute to the drag of *bluff bodies* (see Shapiro, 1960, for a good discussion of the mechanisms of drag). As an example, consider the drag coefficient for a smooth sphere shown in Figure 3.6.5. Transition from laminar to turbulent flow in the boundary layers on the forward portion of the sphere causes a dramatic dip in drag coefficient at the *critical Reynolds number* ($\mathrm{Re}_D \approx 2 \times 10^5$). The turbulent boundary layer is better able to resist the adverse pressure gradient on the rear of the

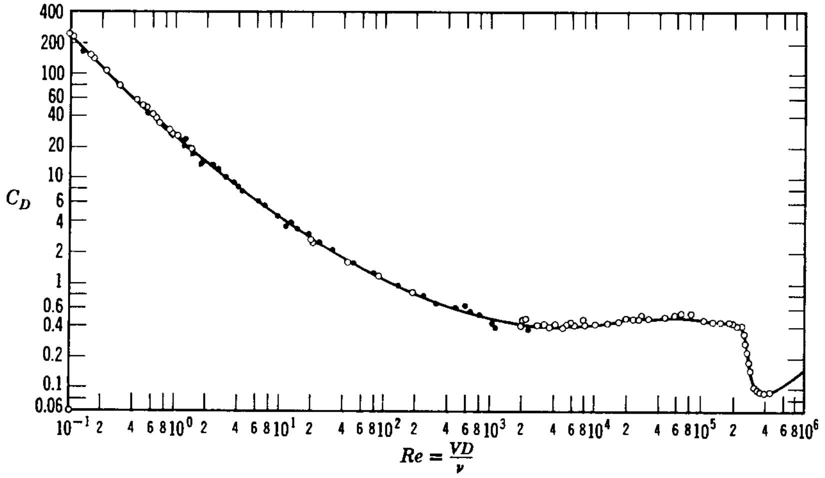

FIGURE 3.6.5 Drag coefficient vs. Reynolds number for a smooth sphere. (From Schlichting, H. 1979. *Boundary Layer Theory,* 7th ed., McGraw–Hill, New York. With permission.)

sphere, so separation is delayed and the wake is smaller, causing less pressure drag. Surface roughness (or freestream disturbances) can reduce the critical Reynolds number. For example, dimples on a golf ball cause the boundary layer to become turbulent and, therefore, lower the drag coefficient in the range of speeds encountered in a drive.

Streamlining

Streamlining is adding a faired tail section to reduce the extent of separated flow on the downstream portion of an object (at high Reynolds number where pressure forces dominate drag). The adverse pressure gradient is taken over a longer distance, delaying separation. However, adding a faired tail increases surface area, causing skin friction drag to increase. Thus, streamlining must be optimized for each shape. For example, front contours are of principal importance in road vehicle design; the angle of the back glass also is important (in most cases the entire rear end cannot be made long enough to control separation and reduce drag significantly).

Lift

Lift coefficient is defined as

$$C_L = \frac{F_L}{\frac{1}{2}\rho V^2 A} \tag{3.6.10}$$

Note that lift coefficient is based on projected *planform area.*

Airfoils

Airfoils are shaped to produce lift efficiently by accelerating flow over the upper surface to produce a low-pressure region. Because the flow must again decelerate, inevitably a region of adverse pressure gradient must be near the rear of the upper surface (pressure distributions are shown clearly in Hazen, 1965).

Lift and drag coefficients for airfoil sections depend on Reynolds number and *angle of attack* between the chord line and the undisturbed flow direction. The *chord line* is the straight line joining the leading and trailing edges of the airfoil (Abbott and von Doenhoff, 1959). As the angle of attack is increased, the minimum pressure point moves forward on the upper surface and the minimum pressure becomes lower. This increases the adverse pressure gradient. At some angle of attack, the adverse pressure gradient is strong enough to cause the boundary layer to separate completely from the upper surface, causing the airfoil to *stall*. The separated flow alters the pressure distribution, reducing lift sharply.

Increasing the angle of attack also causes the drag coefficient to increase. At some angle of attack below "stall," the ratio of lift to drag — the *lift–drag* ratio — reaches a maximum value.

Drag Due to Lift

For wings (airfoils of finite span), lift and drag also are functions of aspect ratio. Lift is reduced and drag increased compared with infinite span because end effects cause the lift vector to rotate rearward. For a given geometric angle of attack, this reduces effective angle of attack, reducing lift. The additional component of lift acting in the flow direction increases drag; the increase in drag due to lift is called *induced drag*.

The effective aspect ratio includes the effect of planform shape. When written in terms of effective aspect ratio, the drag of a finite-span wing is

$$C_D = C_{D,\infty} + \frac{C_L^2}{\pi ar} \tag{3.6.11}$$

where ar is effective aspect ratio and the subscript ∞ refers to the infinite section drag coefficient at C_L. For further details consult the references.

The lift coefficient must increase to support aircraft weight as speed is reduced. Therefore, induced drag can increase rapidly at low flight speeds. For this reason, minimum allowable flight speeds for commercial aircraft are closely controlled by the FAA.

Boundary Layer Control

The major part of the drag on an airfoil or wing is caused by skin friction. Therefore, it is important to maintain laminar flow in the boundary layers as far aft as possible; laminar flow sections are designed to do this. It also is important to prevent flow separation and to achieve high lift to reduce takeoff and landing speeds. These topics fall under the general heading of boundary layer control.

Profile Shaping

Boundary layer transition on a conventional airfoil section occurs almost immediately after the minimum pressure at about 25% chord aft the leading edge. Transition can be delayed by shaping the profile to maintain a favorable pressure gradient over more of its length. The U.S. National Advisory Committee for Aeronautics (NACA) has developed several series of profiles that delayed transition to 60 or 65% of chord, reducing drag coefficients (in the design range) 60% compared with conventional sections of the same thickness ratio (Abbott and von Doenhoff, 1959).

Flaps and Slats

Flaps are movable sections near the trailing edge of a wing. They extend and/or deflect to increase wing area and/or increase wing camber (curvature), to provide higher lift than the clean wing. Many aircraft also are fitted with leading edge slats that open to expose a slot from the pressure side of the wing to the upper surface. The open slat increases the effective radius of the leading edge, improving maximum lift coefficient. The slot allows energized air from the pressure surface to flow into the low-pressure region atop the wing, energizing the boundary layers and delaying separation and stall.

Suction and Blowing

Suction removes low-energy fluid from the boundary layer, reducing the tendency for early separation. Blowing via high-speed jets directed along the surface reenergizes low-speed boundary layer fluid. The objective of both approaches is to delay separation, thus increasing the maximum lift coefficient the wing can achieve. Powered systems add weight and complexity; they also require bleed air from the engine compressor, reducing thrust or power output.

Moving Surfaces

Many schemes have been proposed to utilize moving surfaces for boundary layer control. Motion in the direction of flow reduces skin friction and thus the tendency to separate; motion against the flow has the opposite effect. The aerodynamic behavior of sports balls — baseballs, golf balls, and tennis balls — depends significantly on aerodynamic side force (lift, down force, or side force) produced by spin. These effects are discussed at length in Fox et al. (2004) and its references.

Computation vs. Experiment

Experiments cannot yet be replaced completely by analysis. Progress in modeling, numerical techniques, and computer power continues to be made, but the role of the experimentalist likely will remain important for the foreseeable future.

Computational Fluid Dynamics (CFD)

Computation of fluid flow requires accurate mathematical modeling of flow physics and accurate numerical procedures to solve the equations. The basic equations for laminar boundary layer flow are well known. For turbulent boundary layers, it is not generally possible to resolve the solution space into sufficiently small cells to allow direct numerical simulation. Instead, empirical models for the turbulent stresses must be used. Advances in computer memory storage capacity and speed (e.g., through use of massively parallel processing) continue to increase the resolution that can be achieved.

A second source of error in CFD work results from the numerical procedures required to solve the equations. Even if the equations are exact, approximations must be made to discretize and solve them using finite-difference or finite-volume methods. Whichever is chosen, the solver must guard against introducing numerical instability, round-off errors, and numerical diffusion (Hoffman, 2001).

Role of the Wind Tunnel

Traditionally, wind tunnel experiments have been conducted to verify the design and performance of components and complete aircraft. Design verification of a modern aircraft may require expensive scale models, several thousand hours of wind tunnel time at many thousands of dollars an hour, and additional full-scale flight testing. New wind tunnel facilities continue to be built and old ones refurbished. This indicates a need for continued experimental work in developing and optimizing aircraft configurations.

Many experiments are designed to produce baseline data to validate computer codes. Such systematic experimental data can help to identify the strengths and weaknesses of computational methods. CFD tends to become only indicative of trends when massive zones of flow separation are present. Takeoff and landing configurations of conventional aircraft, with landing gear, high-lift devices, and flaps extended, tend to need final experimental confirmation and optimization. Many studies of vertical takeoff and vectored thrust aircraft require testing in wind tunnels.

Defining Terms

Boundary layer: Thin layer of fluid adjacent to a surface where viscous effects are important; viscous effects are negligible outside the boundary layer.

Drag coefficient: Force in the flow direction exerted on an object by the fluid flowing around it, divided by dynamic pressure and area.

Lift coefficient: Force perpendicular to the flow direction exerted on an object by the fluid flowing around it, divided by dynamic pressure and area.

Pressure gradient: Variation in pressure along the surface of an object. For a *favorable* pressure gradient, pressure *decreases* in the flow direction; for an *adverse* pressure gradient, pressure *increases* in the flow direction.

Separation: Phenomenon that occurs when fluid layers adjacent to a solid surface are brought to rest and boundary layers depart from the surface contour, forming a low-pressure *wake* region. Separation can occur only in an *adverse pressure gradient*.

Transition: Change from laminar to turbulent flow within the boundary layer. The location depends on distance over which the boundary layer has developed; pressure gradient; surface roughness; freestream disturbances; and heat transfer.

References

Abbott, I.H. and von Doenhoff, A.E. 1959. *Theory of Wing Sections, Including a Summary of Airfoil Data*. Dover, New York.

Fox, R.W., McDonald, A.T. and Pritchard, P.J. 2004. *Introduction to Fluid Mechanics*, 6th ed. John Wiley & Sons, New York.

Hazen, D.C. 1965. Boundary Layer Control, film developed by the National Committee for Fluid Mechanics Films (NCFMF) and available on videotape from Encyclopedia Britannica Educational Corporation, Chicago.

Hoerner, S.F. 1965. *Fluid-Dynamic Drag*, 2nd ed. Published by the author, Midland Park, NJ.

Hoffman, J.D. 2001. *Numerical Methods for Engineers and Scientists*, 2nd ed. Marcel Dekker, New York.

Schlichting, H. 1979. *Boundary-Layer Theory*, 7th ed. McGraw–Hill, New York.

Shapiro, A.H. 1960. *The Fluid Dynamics of Drag*, film developed by the National Committee for Fluid Mechanics Film (NCFMF) and available on videotape from Encyclopedia Britannica Educational Corporation, Chicago.

Further Information

A comprehensive source of basic information is the *Handbook of Fluid Dynamics*, V.L. Streeter, Ed., McGraw–Hill, New York, 1960.

Timely reviews of important topics are published in the *Annual Review of Fluid Mechanics* series (Annual Reviews, Inc., Palo Alto, CA.). Each volume contains a cumulative index.

ASME (American Society of Mechanical Engineers, New York, NY) publishes the *Journal of Fluids Engineering* quarterly, which contains fluid machinery and other engineering applications of fluid mechanics.

The monthly *AIAA Journal* and bimonthly *Journal of Aircraft* (American Institute for Aeronautics and Astronautics, New York, NY) treat aerospace applications of fluid mechanics.

3.7 Compressible Flow

Ajay Kumar and Jessica Todd

Introduction

This section deals with compressible flow. Only one- or two-dimensional steady, inviscid flows under perfect gas assumption are considered. Readers are referred to other sources of information for unsteady effects, viscous effects, and three-dimensional flows.

The term *compressible flow* is routinely used to define variable density flow which is in contrast to incompressible flow, where the density is assumed to be constant throughout. In many cases, these density variations are principally caused by the pressure changes from one point to another. Physically, the *compressibility* can be defined as the fractional change in volume of the gas element per unit change in pressure. It is a property of the gas and, in general, can be defined as

$$\tau = \frac{1}{\rho}\frac{d\rho}{dp}$$

where τ is the compressibility of the gas, ρ is the density, and p is the pressure being exerted on the gas. A more precise definition of compressibility is obtained if we take into account the thermal and frictional losses. If during the compression the temperature of the gas is held constant, it is called the isothermal compressibility and can be written as

$$\tau_T = \frac{1}{\rho}\left(\frac{\partial \rho}{\partial p}\right)_T$$

However, if the compression process is reversible, it is called the isentropic compressibility and can be written as

$$\tau_s = \frac{1}{\rho}\left(\frac{\partial \rho}{\partial p}\right)_s$$

Gases in general have high compressibility (τ_T for air is 10^{-5} $\mathrm{m^2/N}$ at 1 atm) as compared with liquids (τ_T for water is 5×10^{-10} $\mathrm{m^2/N}$ at 1 atm).

Compressibility is a very important parameter in the analysis of compressible flow and is closely related to the *speed of sound*, a, which is the velocity of propagation of small pressure disturbances and is defined as

$$a^2 = \left(\frac{\partial p}{\partial \rho}\right)_s \quad \text{or} \quad a = \sqrt{\left(\frac{\partial p}{\partial \rho}\right)_s}$$

In an isentropic process of a perfect gas, the pressure and density are related as

$$\frac{p}{\rho^\gamma} = \text{constant}$$

Using this relation along with the perfect gas relation $p = \rho RT$, we can show that for a perfect gas

$$a = \sqrt{\gamma RT} = \sqrt{\frac{\gamma p}{\rho}}$$

where γ is the ratio of specific heats at constant pressure and constant volume, R is the gas constant, and T is the temperature. For air under normal conditions, γ is 1.4 and R is 287 $\mathrm{m^2/sec^2\ K}$ so that the speed of sound for air becomes $a = 20.045\sqrt{T}$ m/sec where T is in kelvin.

Another important parameter in compressible flows is the *Mach number, M,* which is defined as the ratio of the gas velocity to the speed of sound or

$$M = \frac{V}{a}$$

where V is the velocity of gas. Depending upon the Mach number of the flow, we can define the following flow regimes:

$M \ll 1$ Incompressible flow

$M < 1$ Subsonic flow

$M \approx 1$ Transonic flow

$M > 1$ Supersonic flow

$M \gg 1$ Hypersonic flow

Subsonic through hypersonic flows are compressible in nature. In these flows, the velocity is appreciable compared with the speed of sound, and the fractional changes in pressure, temperature, and density are all of significant magnitude. We will restrict ourselves in this section to subsonic through flows only.

Before we move on to study these flows, let us define one more term. Let us consider a gas with static pressure p and temperature T, traveling at some velocity V and corresponding Mach number M. If this gas is brought isentropically to stagnation or zero velocity, the pressure and temperature which the gas achieves are defined as *stagnation pressure* p_0 and *stagnation temperature* T_0 (also called total pressure and total temperature). The speed of sound at stagnation conditions is called the *stagnation speed of sound* and is denoted as a_0.

One-Dimensional Flow

In one-dimensional flow, the flow properties vary only in one coordinate direction. Figure 3.7.1 shows two streamtubes in a flow. In a *truly one-dimensional flow* illustrated in Figure 3.7.1(a), the flow variables are a function of x only and the area of the stream tube is constant. On the other hand, Figure 3.7.1(b) shows a flow where the area of the stream tube is also a function of x but the flow variables are still a function of x only. This flow is defined as the *quasi-one-dimensional flow.* We will first discuss the truly one-dimensional flow.

In a steady, truly one-dimensional flow, conservation of mass, momentum, and energy leads to the following simple algebraic equations.

$$\begin{gathered}\rho u = \text{constant}\\ p + \rho u^2 = \text{constant}\\ h + \frac{u^2}{2} + q = \text{constant}\end{gathered} \tag{3.7.1}$$

where q is the heat added per unit mass of the gas. These equations neglect body forces, viscous stresses, and heat transfer due to thermal conduction and diffusion. These relations given by Equation 3.7.1, when applied at points 1 and 2 in a flow with no heat addition, become

$$\begin{gathered}\rho_1 u_1 = \rho_2 u_2\\ p_1 + \rho_1 u_1^2 = p_2 + \rho_2 u_2^2\\ h_1 + \frac{u_1^2}{2} = h_2 + \frac{u_2^2}{2}\end{gathered} \tag{3.7.2}$$

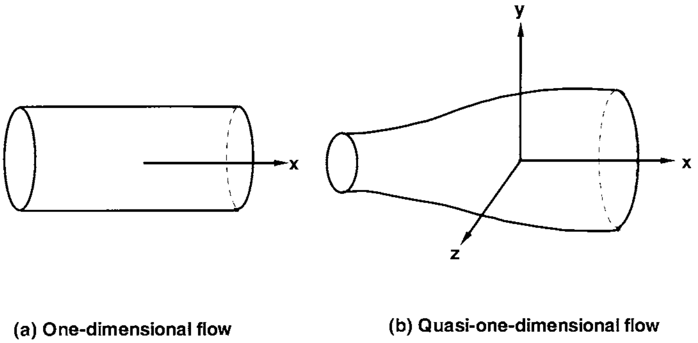

(a) One-dimensional flow

(b) Quasi-one-dimensional flow

FIGURE 3.7.1 (a) One-dimensional flow; (b) quasi-one-dimensional flow.

The energy equation for a calorically perfect gas, where $h = c_pT$, becomes

$$c_pT_1 + \frac{u_1^2}{2} = c_pT_2 + \frac{u_2^2}{2}$$

Using $c_p = \gamma R/(\gamma - 1)$ and $a^2 = \gamma RT$, the above equation can be written as

$$\frac{a_1^2}{\gamma - 1} + \frac{u_1^2}{2} = \frac{a_2^2}{\gamma - 1} + \frac{u_2^2}{2} \tag{3.7.3}$$

Since Equation (3.7.3) is written for no heat addition, it holds for an adiabatic flow. If the energy equation is applied to the stagnation conditions, it can be written as

$$c_pT + \frac{u^2}{2} = c_pT_0$$

$$\frac{T_0}{T} = 1 + \frac{\gamma - 1}{2}M^2 \tag{3.7.4}$$

It is worth mentioning that in arriving at Equation (3.7.4), only adiabatic flow condition is used whereas stagnation conditions are defined as those where the gas is brought to rest isentropically. Therefore, the definition of stagnation temperature is less restrictive than the general definition of stagnation conditions. According to the general definition of isentropic flow, it is a reversible adiabatic flow. This definition is needed for the definition of stagnation pressure and density. For an isentropic flow,

$$\frac{p_0}{p} = \left(\frac{\rho_0}{\rho}\right)^{\gamma} = \left(\frac{T_0}{T}\right)^{\gamma/(\gamma-1)} \tag{3.7.5}$$

From Equation (3.7.4) and Equation (3.7.5), we can write

$$\frac{p_0}{p} = \left(1 + \frac{\gamma - 1}{2}M^2\right)^{\gamma/(\gamma-1)} \tag{3.7.6}$$

$$\frac{\rho_0}{\rho} = \left(1 + \frac{\gamma - 1}{2}M^2\right)^{1/(\gamma-1)} \tag{3.7.7}$$

Values of stagnation conditions are tabulated in Anderson (1982) as a function of M for $\gamma = 1.4$.

Normal Shock Wave

A shock wave is a very thin region (of the order of a few molecular mean free paths) across which the static pressure, temperature, and density increase whereas the velocity decreases. If the shock wave is perpendicular to the flow, it is called a *normal shock wave*. The flow is supersonic ahead of the normal shock wave and subsonic behind it. Figure 3.7.2 shows the flow conditions across a normal shock wave which is treated as a discontinuity. Since there is no heat added or removed, the flow across the shock wave is adiabatic. By using Equations (3.7.2) the normal shock equations can be written as

$$\begin{gathered} \rho_1u_1 = \rho_2u_2 \\ p_1 + \rho_1u_1^2 = p_2 + \rho_2u_2^2 \\ h_1 + \frac{u_1^2}{2} = h_2 + \frac{u_2^2}{2} \end{gathered} \tag{3.7.8}$$

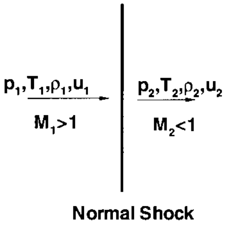

FIGURE 3.7.2 Flow conditions across a normal shock.

Equations (3.7.8) are applicable to a general type of flow; however, for a calorically perfect gas, we can use the relations $p = \rho RT$ and $h = c_p T$ to derive a number of equations relating flow conditions downstream of the normal shock to those at upstream. These equations (also known as Rankine–Hugoniot relations) are

$$\frac{p_2}{p_1} = 1 + \frac{2\gamma}{\gamma+1}\left(M_1^2 - 1\right)$$

$$\frac{\rho_2}{\rho_1} = \frac{u_1}{u_2} = \frac{(\gamma+1)M_1^2}{2+(\gamma-1)M_1^2} \tag{3.7.9}$$

$$\frac{T_2}{T_1} = \frac{h_2}{h_1} = \left[1 + \frac{2\gamma}{\gamma+1}\left(M_1^2 - 1\right)\right]\left[\frac{2+(\gamma-1)M_1^2}{(\gamma+1)M_1^2}\right]$$

$$M_2^2 = \frac{1 + \frac{\gamma-1}{2}M_1^2}{\gamma M_1^2 - \frac{\gamma-1}{2}}$$

Again, the values of p_2/p_1, ρ_2/ρ_1, T_2/T_1, etc. are tabulated in Anderson (1982) as a function of M_1 for $\gamma = 1.4$. Let us examine some limiting cases. As $M_1 \to 1$, Equations (3.7.9) yield $M_2 \to 1$, $p_2/p_1 \to 1$, $\rho_2/\rho_1 \to 1$, and $T_2/T_1 \to 1$. This is the case of an extremely weak normal shock across which no finite changes occur. This is the same as the sound wave. On the other hand, as $M_1 \to \infty$, Equations (3.7.9) yield

$$M_2 \to \sqrt{\frac{\gamma-1}{2\gamma}} = 0.378; \quad \frac{\rho_2}{\rho_1} \to \frac{\gamma+1}{\gamma-1} = 6; \quad \frac{p_2}{p_1} \to \infty; \quad \frac{T_2}{T_1} \to \infty$$

However, the calorically perfect gas assumption no longer remains valid as $M_1 \to \infty$.

Let us now examine why the flow ahead of a normal shock wave must be supersonic even though Equations (3.7.8) hold for $M_1 < 1$ as well as $M_1 > 1$. From the second law of thermodynamics, the entropy change across the normal shock can be written as

$$s_2 - s_1 = c_p \ln\frac{T_2}{T_1} - R\ln\frac{p_2}{p_1}$$

By using Equations (3.7.9) it becomes

$$s_2 - s_1 = c_p \ln\left\{\left[1 + \frac{2\gamma}{\gamma+1}\left(M_1^2 - 1\right)\right]\left[\frac{2+(\gamma-1)M_1^2}{(\gamma+1)M_1^2}\right]\right\} - R\ln\left[1 + \frac{2\gamma}{\gamma+1}\left(M_1^2 - 1\right)\right] \tag{3.7.10}$$

Equation (3.7.10) shows that the entropy change across the normal shock is also a function of M_1 only. Using Equation (3.7.10) we see that

$$\begin{aligned} s_2 - s_1 &= 0 \quad \text{for} \quad M_1 = 1 \\ &< 0 \quad \text{for} \quad M_1 < 1 \\ &> 0 \quad \text{for} \quad M_1 > 1 \end{aligned}$$

Since it is necessary that $s_2 - s_1 \geqslant 0$ from the second law, $M_1 \geq 1$. This, in turn, requires that $p_2/p_1 \geqslant 1$, $\rho_2/\rho_1 \geqslant 1$, $T_2/T_1 \geqslant 1$, and $M_2 \leqslant 1$.

We now examine how the stagnation conditions change across a normal shock wave. For a calorically perfect gas, the energy equation in Equations (3.7.9) gives

$$c_p T_{01} = c_p T_{02} \quad \text{or} \quad T_{01} = T_{02}$$

In other words, the total temperature remains constant across a stationary normal shock wave.

Let us now apply the entropy change relation across the shock using the stagnation conditions.

$$s_2 - s_1 = c_p \ln \frac{T_{02}}{T_{01}} - R \ln \frac{p_{02}}{p_{01}}$$

Note that entropy at stagnation conditions is the same as at the static conditions since to arrive at stagnation conditions, the gas is brought to rest isentropically. Since $T_{02} = T_{01}$,

$$s_2 - s_1 = -R \ln \frac{p_{02}}{p_{01}}$$

$$\frac{p_{02}}{p_{01}} = e^{-(s_2 - s_1)/R} \tag{3.7.11}$$

Since $s_2 > s_1$ across the normal shockwave, Equation (3.7.11) gives $P_{02} < P_{01}$ or, in other words, the total pressure decreases across a shock wave.

One-Dimensional Flow with Heat Addition

Consider one-dimensional flow through a control volume as shown in Figure 3.7.3. Flow conditions going into this control volume are designated by 1 and coming out by 2. A specified amount of heat per unit mass, q, is added to the control volume. The governing equations relating conditions 1 and 2 can be written as

$$\begin{gathered} \rho_1 u_1 = \rho_2 u_2 \\ p_1 + \rho_1 u_1^2 = p_2 + \rho_2 u_2^2 \\ h_1 + \frac{u_1^2}{2} + q = h_2 + \frac{u_2^2}{2} \end{gathered} \tag{3.7.12}$$

The following relations can be derived from Equation (3.7.12) for a calorically perfect gas

$$q = c_p \left(T_{02} - T_{01} \right) \tag{3.7.13}$$

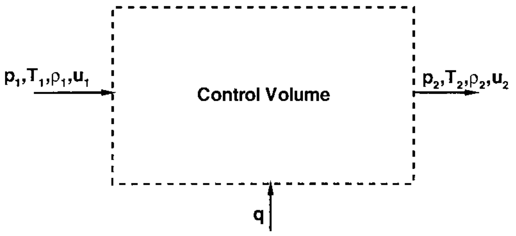

FIGURE 3.7.3 One-dimensional control volume with heat addition.

$$\frac{p_2}{p_1} = \frac{1+\gamma M_1^2}{1+\gamma M_2^2} \tag{3.7.14}$$

$$\frac{T_2}{T_1} = \left(\frac{1+\gamma M_1^2}{1+\gamma M_2^2}\right)^2 \left(\frac{M_2}{M_1}\right)^2 \tag{3.7.15}$$

$$\frac{\rho_2}{\rho_1} = \left(\frac{1+\gamma M_2^2}{1+\gamma M_1^2}\right)^2 \left(\frac{M_1}{M_2}\right)^2 \tag{3.7.16}$$

Equation (3.7.13) indicates that the effect of heat addition is to directly change the stagnation temperature T_0 of the flow. Table 3.7.1 shows some physical trends which can be obtained with heat addition to subsonic and supersonic flow. With heat extraction the trends in Table 3.7.1 are reversed.

Figure 3.7.4 shows a plot between enthalpy and entropy, also known as the Mollier diagram, for one-dimensional flow with heat addition. This curve is called the Rayleigh curve and is drawn for a set of

TABLE 3.7.1 Effect of Heat Addition on Subsonic and Supersonic Flow

	$M_1 < 1$	$M_1 > 1$
M_2	Increases	Decreases
p_2	Decreases	Increases
T_2	Increases for $M_1 < \gamma^{-1/2}$ and decreases for $M_1 > \gamma^{-1/2}$	Increases
u_2	Increases	Decreases
T_{02}	Increases	Increases
p_{02}	Decreases	Decreases

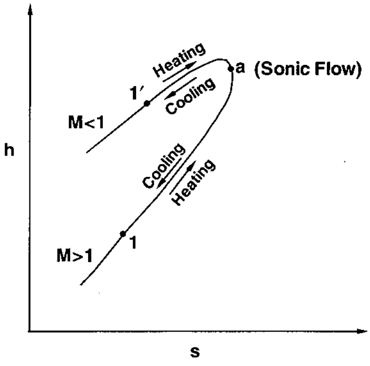

FIGURE 3.7.4 The Rayleigh curve.

given initial conditions. Each point on this curve corresponds to a different amount of heat added or removed. It is seen from this curve that heat addition always drives the Mach numbers toward 1. For a certain amount of heat addition, the flow will become sonic. For this condition, the flow is said to be *choked*. Any further increase in heat addition is not possible without adjustment in initial conditions. For example, if more heat is added in region 1, which is initially supersonic, than allowed for attaining Mach 1 in region 2, then a normal shock will form inside the control volume which will suddenly change the conditions in region 1 to subsonic. Similarly, in case of an initially subsonic flow corresponding to region 1′, any heat addition beyond that is needed to attain Mach 1 in region 2, the conditions in region 1′ will adjust to a lower subsonic Mach number through a series of pressure waves.

Similar to the preceding heat addition or extraction relationships, we can also develop relationships for one-dimensional steady, adiabatic flow but with frictional effects due to viscosity. In this case, the momentum equation gets modified for frictional shear stress. For details, readers are referred to Anderson (1982).

Quasi-One-Dimensional Flow

In quasi-one-dimensional flow, in addition to flow conditions, the area of duct also changes with *x*. The governing equations for quasi-one-dimensional flow can be written in a differential form as follows using an infinitesimal control volume shown in Figure 3.7.5.

$$d(\rho u A) = 0 \tag{3.7.17}$$

$$dp + \rho u\, du = 0 \tag{3.7.18}$$

$$dh + u\, du = 0 \tag{3.7.19}$$

Equation (3.7.17) can be written as

$$\frac{d\rho}{\rho} + \frac{du}{u} + \frac{dA}{A} = 0 \tag{3.7.20}$$

which can be further written as follows for an isentropic flow:

$$\frac{dA}{A} = \left(M^2 - 1\right)\frac{du}{u} \tag{3.7.21}$$

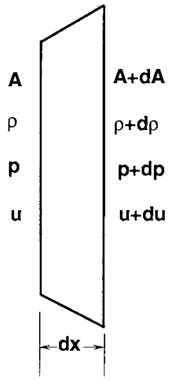

FIGURE 3.7.5 Control volume for quasi-one-dimensional flow.

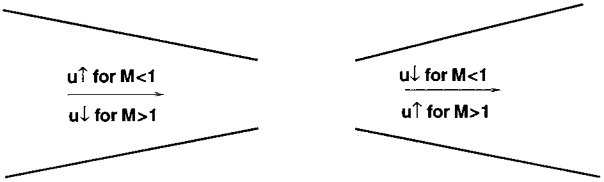

FIGURE 3.7.6 Compressible flow in converging and diverging ducts.

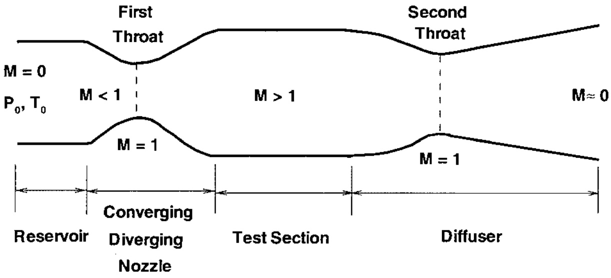

FIGURE 3.7.7 Schematic of a typical supersonic wind tunnel.

Some very useful physical insight can be obtained from this area–velocity relation.

- For subsonic flow ($0 \le M < 1$), an increase in area results in decrease in velocity, and vice versa.
- For supersonic flow ($M > 1$), an increase in area results in increase in velocity, and vice versa.
- For sonic flow ($M = 1$), $dA/A = 0$, which corresponds to a minimum or maximum in the area distribution, but it can be shown that a minimum in area is the only physical solution.

Figure 3.7.6 shows the preceding results in a schematic form.

It is obvious from this discussion that for a gas to go isentropically from subsonic to supersonic, and vice versa, it must flow through a convergent–divergent nozzle, also known as the de Laval nozzle. The minimum area of the nozzle at which the flow becomes sonic is called the throat. This physical observation forms the basis of designing supersonic wind tunnels shown schematically in Figure 3.7.7. In general, in a supersonic wind tunnel, a stagnant gas is first expanded to the desired supersonic Mach number. The supersonic flow enters the test section where it passes over a model being tested. The flow then is slowed down by compressing it through a second convergent–divergent nozzle, also known as a diffuser, before it is exhausted to the atmosphere.

Now, using the equations for quasi-one-dimensional flow and the isentropic flow conditions, we can derive a relation for the area ratio that is needed to accelerate or decelerate the gas to sonic conditions. Denoting the sonic conditions by an asterisk, we can write $u^* = a^*$. The area is denoted as A^*, and it is obviously the minimum area for the throat of the nozzle. From Equation (3.7.17) we have

$$\rho u A = \rho^* u^* A^*$$

$$\frac{A}{A^*} = \frac{\rho^* u^*}{\rho u} = \frac{\rho^*}{\rho_0} \frac{\rho_0}{\rho} \frac{u^*}{u} \qquad (3.7.22)$$

Under isentropic conditons,

$$\frac{\rho_0}{\rho} = \left(1 + \frac{\gamma - 1}{2} M^2\right)^{1/(\gamma-1)} \qquad (3.7.23)$$

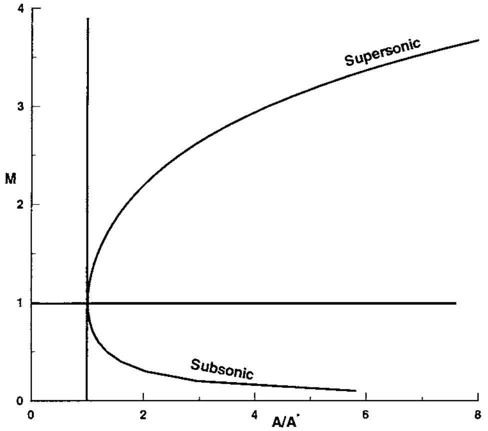

FIGURE 3.7.8 Variation of area ratio A/A* as a function of Mach number for a quasi-one-dimensional flow.

$$\frac{\rho_0}{\rho^*} = \left(1 + \frac{\gamma - 1}{2}\right)^{1/(\gamma-1)} = \left(\frac{\gamma + 1}{2}\right)^{1/(\gamma-1)} \tag{3.7.24}$$

Also, $u^*/u = a^*/u$. Let us define a Mach number $M^* = u/a^*$. M^* is known as the *characteristic Mach number* and it is related to the local Mach number by the following relation:

$$M^{*2} = \frac{\frac{\gamma+1}{2}M^2}{1 + \frac{\gamma - 1}{2}M^2} \tag{3.7.25}$$

Using Equation (3.7.23) through Equation (3.7.25) in Equation (3.7.22) we can write

$$\left(\frac{A}{A^*}\right)^2 = \frac{1}{M^2}\left[\left(\frac{2}{\gamma+1}\right)\left(1 + \frac{\gamma-1}{2}M^2\right)\right]^{(\gamma+1)/(\gamma-1)} \tag{3.7.26}$$

Equation (3.7.26) is called the area Mach number relation. Figure 3.7.8 shows a plot of A/A^* against Mach number. A/A^* is always ≥ 1 for physically viable solutions.

The area Mach number relation says that for a given Mach number, there is only one area ratio A/A^*. This is a very useful relation and is frequently used to design convergent–divergent nozzles to produce a desired Mach number. Values of A/A^* are tabulated as a function of M in Anderson (1982).

Equation (3.7.26) can also be written in terms of pressure as follows:

$$\frac{A}{A^*} = \frac{\left[1 - \left(\frac{p}{p_0}\right)^{(\gamma-1)/\gamma}\right]^{1/2}\left(\frac{p}{p_0}\right)^{1/\gamma}}{\left(\frac{\gamma-1}{2}\right)^{1/2}\left(\frac{2}{\gamma+1}\right)^{(\gamma+1)/2(\gamma-1)}} \tag{3.7.27}$$

Nozzle Flow

Using the area relations, we can now plot the distributions of Mach number and pressure along a nozzle. Figure 3.7.9 shows pressure and Mach number distributions along a given nozzle and the wave config-

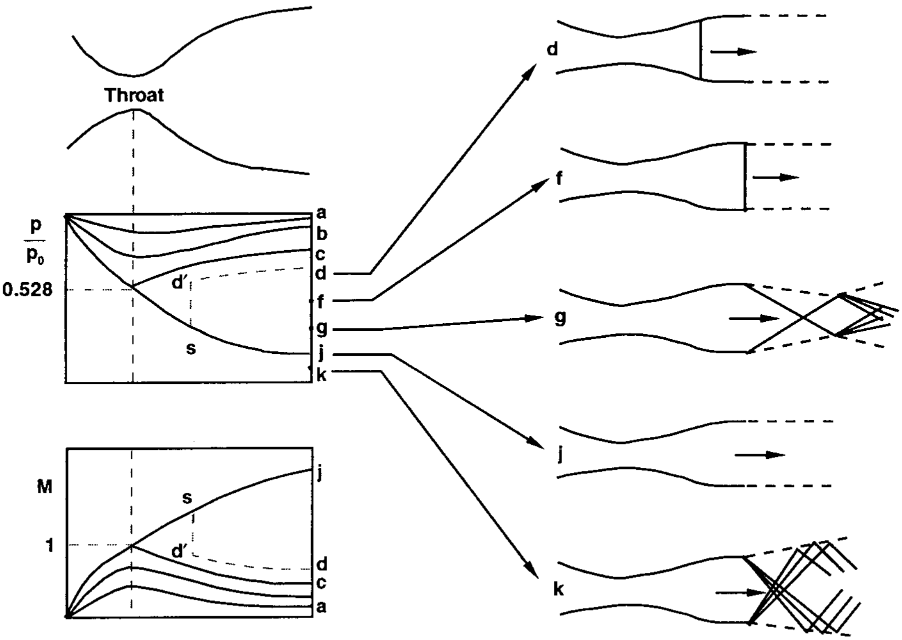

FIGURE 3.7.9 Effect of exit pressure on flow through a nozzle.

urations for several exit pressures. For curves a and b, the flow stays subsonic throughout and the exit pressure controls the flow in the entire nozzle. On curve c, the throat has just become sonic, and so the pressure at the throat, and upstream of it, can decrease no further. There is another exit pressure corresponding to curve j ($p_j < p_c$) for which a supersonic isentropic solution exists. But if the pressure lies between p_c and p_j, there is no isentropic solution possible. For example, for an exit pressure p_d, a shock will form in the nozzle at location *s* which will raise the pressure to $p_{d'}$ and turn the flow subsonic. The pressure will then rise to p_d as the subsonic flow goes through an increasing area nozzle. The location, *s*, depends on the exit pressure. Various possible situations are shown in Figure 3.7.9. It is clear that if the exit pressure is equal to or below p_f, the flow within the nozzle is fully supersonic. This is the principle used in designing supersonic wind tunnels by operating from a high-pressure reservoir or into a vacuum receiver, or both.

Diffuser

If a nozzle discharges directly into the receiver, the minimum pressure ratio for full supersonic flow in the test section is

$$\left(\frac{p_0}{p_E}\right)_{\min} = \frac{p_0}{p_f}$$

where p_f is the value of p_E at which the normal shock stands right at the nozzle exit. However, by adding an additional diverging section, known as a diffuser, downstream of the test section as shown in Figure 3.7.10 it is possible to operate the tunnel at a lower pressure ratio than p_0/p_f. This happens because the diffuser can now decelerate the subsonic flow downstream of the shock isentropically to a stagnation pressure p_0'. The pressure ratio required then is the ratio of stagnation pressures across a normal shock wave at the test section Mach number. In practice, the diffuser gives lower than expected recovery as a result of viscous losses caused by the interaction of shock wave and the boundary layer which are neglected here.

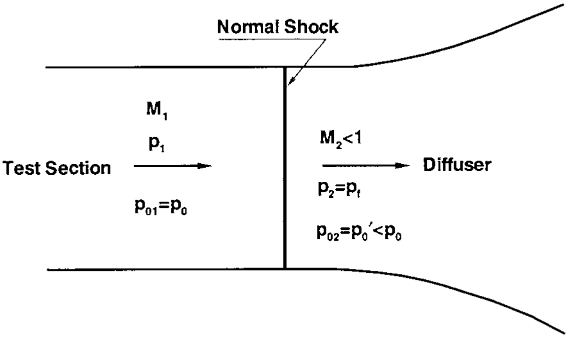

FIGURE 3.7.10 Normal shock diffuser.

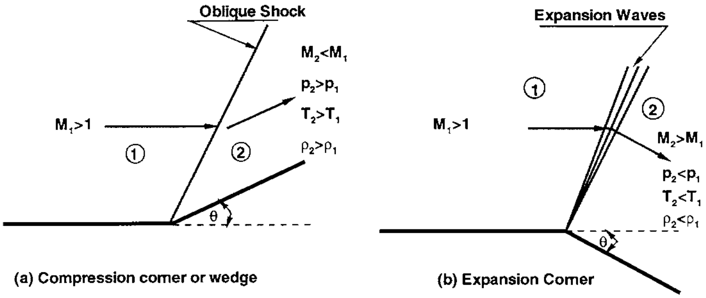

(a) Compression corner or wedge

(b) Expansion Corner

FIGURE 3.7.11 Supersonic flow over a corner.

The operation of supersonic wind tunnels can be made even more efficient; i.e., they can be operated at even lower pressure ratios than p_0/p_0', by using the approach shown in Figure 3.7.7 where the diffuser has a second throat. It can slow down the flow to subsonic Mach numbers isentropically and, ideally, can provide complete recovery, giving $p_0' = p_0$. However, due to other considerations, such as the starting process of the wind tunnel and viscous effects, it is not realized in real life.

Two-Dimensional Supersonic Flow

When supersonic flow goes over a wedge or an expansion corner, it goes through an oblique shock or expansion waves, respectively, to adjust to the change in surface geometry. Figure 3.7.11 shows the two flow situations. In Figure 3.7.11(a) an oblique shock abruptly turns the flow parallel to the wedge surface. The Mach number behind the shock is less than ahead of it, whereas the pressure, temperature, and density increase. In the case of an expansion corner, oblique expansion waves smoothly turn the flow to become parallel to the surface downstream of the expansion corner. In this case, the Mach number increases, but the pressure, temperature, and density decrease as the flow goes through the expansion corner. Oblique shocks and expansion waves occur in two- and three-dimensional supersonic flows. In this section, we will restrict ourselves to steady, two-dimensional supersonic flows only.

Oblique Shock Waves

The oblique shock can be treated in the same way as the normal shock by accounting for the additional velocity component. If a uniform velocity v is superimposed on the flow field of the normal shock, the resultant velocity ahead of the shock can be adjusted to any flow direction by adjusting the magnitude and direction of v. If v is taken parallel to the shock wave, as shown in Figure 3.7.12, the resultant velocity ahead of the shock is $w_1 = \sqrt{u_1^2 + v_1^2}$ and its direction from the shock is given by $\beta = \tan^{-1}(u_1/v)$. On the downstream side of the shock, since u_2 is less than u_1, the flow always turns toward the shock. The magnitude of u_2 can be determined by the normal shock relations corresponding to velocity u_1 and the

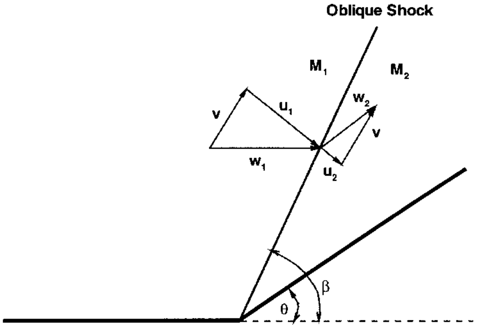

FIGURE 3.7.12 Oblique shock on a wedge.

magnitude of v is such that the flow downstream of the shock turns parallel to the surface. Since imposition of a uniform velocity does not affect the pressure, temperature, etc., we can use normal shock relations with Mach number replaced in them to correspond to velocity u_1 or u_1/a_1, which is nothing but $M_1 \sin\beta$. Thus, oblique shock relations become

$$\frac{p_2}{p_1} = 1 + \frac{2\gamma}{\gamma+1}\left(M_1^2 \sin^2\beta - 1\right) \tag{3.7.28}$$

$$\frac{\rho_2}{\rho_1} = \frac{(\gamma+1)M_1^2 \sin^2\beta}{(\gamma-1)M_1^2 \sin^2\beta + 2} \tag{3.7.29}$$

$$\frac{T_2}{T_1} = \frac{a_2^2}{a_1^2} = \left[1 + \frac{2\gamma}{\gamma+1}\left(M_1^2 \sin^2\beta - 1\right)\right]\left[\frac{2 + (\gamma-1)M_1^2 \sin^2\beta}{(\gamma+1)M_1^2 \sin^2\beta}\right] \tag{3.7.30}$$

The Mach number M_2 (= w_2/a_2) can be obtained by using a Mach number corresponding to velocity u_2 (= $w_2 \sin(\beta - \theta)$) in the normal shock relation for the Mach number. In other words,

$$M_2^2 \sin^2(\beta-\theta) = \frac{1 + \frac{\gamma-1}{2}M_1^2 \sin^2\beta}{\gamma M_1^2 \sin^2\beta - \frac{\gamma-1}{2}} \tag{3.7.31}$$

To derive a relation between the wedge angle θ and the wave angle β, we have from Figure 3.7.12

$$\tan\beta = \frac{u_1}{v} \quad \text{and} \quad \tan(\beta-\theta) = \frac{u_2}{v}$$

so that

$$\frac{\tan(\beta-\theta)}{\tan\beta} = \frac{u_2}{u_1} = \frac{\rho_1}{\rho_2} = \frac{(\gamma-1)M_1^2 \sin^2\beta + 2}{(\gamma+1)M_1^2 \sin^2\beta}$$

This can be simplified to

$$\tan\theta = 2\cot\beta \frac{M_1^2 \sin^2\beta - 1}{M_1^2(\gamma + \cos 2\beta) + 2} \tag{3.7.32}$$

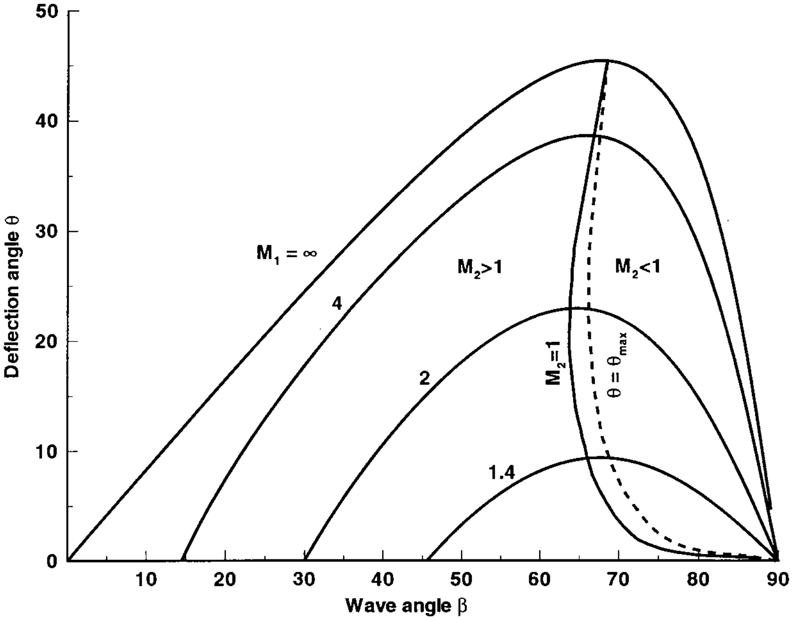

FIGURE 3.7.13 Oblique shock characteristics.

Dennard and Spencer (1964) have tabulated oblique shock properties as a function of M_1. Let us now make some observations from the preceding relations.

From the normal shock relations, $M_1 \sin\beta \geqslant 1$. This defines a minimum wave angle for a given Mach number. The maximum wave angle, of course, corresponds to the normal shock or $\beta = \pi/2$. Therefore, the wave angle β has the following range

$$\sin^{-1}\frac{1}{M} \leq \beta \leq \frac{\pi}{2} \tag{3.7.33}$$

Equation (3.7.32) becomes zero at the two limits of β. Figure 3.7.13 shows a plot of θ against β for various values of M_1. For each value of M_1, there is a maximum value of θ. For $\theta < \theta_{max}$, there are two possible solutions having different values of β. The larger value of β gives the stronger shock in which the flow becomes subsonic. A locus of solutions for which $M_2 = 1$ is also shown in the figure. It is seen from the figure that with weak shock solution, the flow remains supersonic except for a small range of θ slightly smaller than θ_{max}.

Let us now consider the limiting case of θ going to zero for the weak shock solution. As θ decreases to zero, β decreases to the limiting value μ, given by

$$M_1^2 \sin^2\mu - 1 = 0$$

$$\mu = \sin^{-1}\frac{1}{M_1} \tag{3.7.34}$$

For this angle, the oblique shock relations show no jump in flow quantities across the wave or, in other words, there is no disturbance generated in the flow. This angle μ is called the *Mach angle* and the lines at inclination μ are called *Mach lines.*

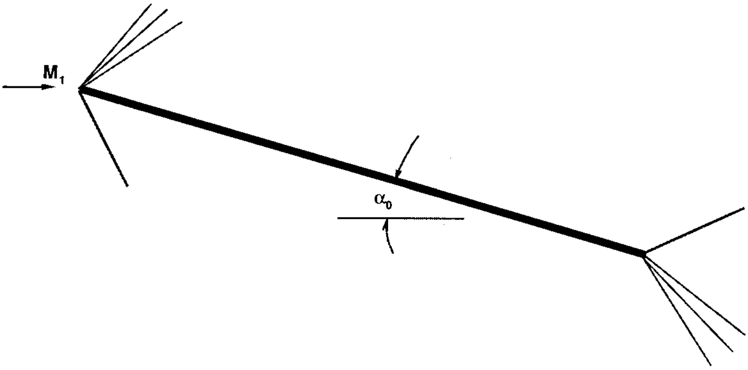

FIGURE 3.7.14 Lifting flat plate.

Thin-Airfoil Theory

For a small deflection angle $\Delta\theta$, it can be shown that the change in pressure in a flow at Mach M_1 is given approximately by

$$\frac{\Delta p}{p_1} \approx \frac{\gamma M_1^2}{\sqrt{M_1^2 - 1}} \Delta\theta \tag{3.7.35}$$

This expression holds for both compression and expansion. If Δp is measured with respect to the freestream pressure, p_1, and all deflections to the freestream direction, we can write Equation (3.7.35) as

$$\frac{p - p_1}{p_1} = \frac{\gamma M_1^2}{\sqrt{M_1^2 - 1}} \theta \tag{3.7.36}$$

where θ is positive for a compression and negative for expansion. Let us define a pressure coefficient C_p, as

$$C_p = \frac{p - p_1}{q_1}$$

where q_1 is the dynamic pressure and is equal to $\gamma p_1 M_1^2/2$. Equation (3.7.36) then gives

$$C_p = \frac{2\theta}{\sqrt{M_1^2 - 1}} \tag{3.7.37}$$

Equation (3.7.37) states that the pressure coefficient is proportional to the local flow deflection. This relation can be used to develop supersonic thin-airfoil theory. As an example, for a flat plate at angle of attack α_0 (shown in Figure 3.7.14), the pressure coefficients on the upper and lower surfaces are

$$C_p = \mp \frac{2\alpha_0}{\sqrt{M_1^2 - 1}}$$

The lift and drag coefficients can be written as

$$C_L = \frac{\left(p_L - p_U\right) c \cos\alpha_0}{q_1 c} = \left(C_{p_L} - C_{p_U}\right)\cos\alpha_0$$

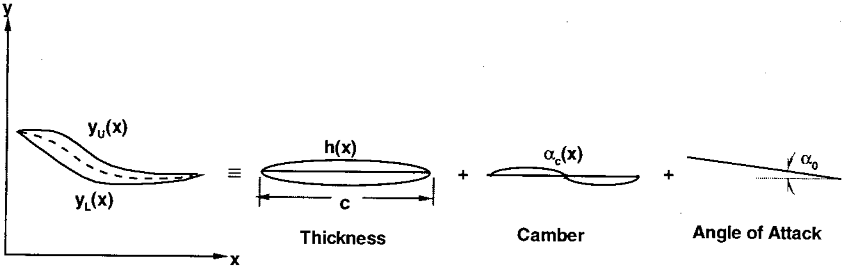

FIGURE 3.7.15 Arbitrary thin airfoil and its components.

$$C_D = \frac{(p_L - p_U)c\sin\alpha_0}{q_1 c} = \left(C_{p_L} - C_{p_U}\right)\sin\alpha_0$$

where c is the chord length of the plate. Since α_0 is small, we can write

$$C_L = \frac{4\alpha_0}{\sqrt{M_1^2 - 1}}, \qquad C_D = \frac{4\alpha_0^2}{\sqrt{M_1^2 - 1}} \tag{3.7.38}$$

A similar type of expression can be obtained for an arbitrary thin airfoil that has thickness, camber, and angle of attack. Figure 3.7.15 shows such an airfoil. The pressure coefficients on the upper and lower surfaces can be written as

$$C_{p_U} = \frac{2}{\sqrt{M_1^2 - 1}}\frac{dy_U}{dx}, \qquad C_{p_L} = \frac{2}{\sqrt{M_1^2 - 1}}\left(-\frac{dy_L}{dx}\right) \tag{3.7.39}$$

For the thin airfoil, the profile may be resolved into three separate components as shown in Figure 3.7.15. The local slope of the airfoil can be obtained by superimposing the local slopes of the three components as

$$\frac{dy_U}{dx} = -\left(\alpha_0 + \alpha_c(x)\right) + \frac{dh}{dx} = -\alpha(x) + \frac{dh}{dx}$$

$$\frac{dy_L}{dx} = -\left(\alpha_0 + \alpha_c(x)\right) - \frac{dh}{dx} = -\alpha(x) - \frac{dh}{dx} \tag{3.7.40}$$

where $\alpha = \alpha_0 + \alpha_c(x)$ is the local total angle of attack of the camber line. The lift and drag for the thin airfoil are given by

$$L = q_1 \int_0^c \left(C_{p_L} - C_{p_U}\right) dx$$

$$D = q_1 \int_0^c \left[C_{p_L}\left(-\frac{dy_L}{dx}\right) + C_{p_U}\left(\frac{dy_U}{dx}\right)\right] dx$$

Let us define an average value of $\alpha(x)$ as

$$\bar{\alpha} = \frac{1}{c}\int_0^c \alpha(x)\, dx$$

Using Equation (3.7.40) and the fact that $\overline{\alpha}_0 = \alpha$ and $\overline{\alpha}_c = 0$ by definition, the lift and drag coefficients for the thin airfoil can be written as

$$C_L = \frac{4\alpha_0}{\sqrt{M_1^2 - 1}}$$

$$C_D = \frac{4}{\sqrt{M_1^2 - 1}}\left[\overline{\left(\frac{dh}{dx}\right)^2} + \overline{\alpha_C^2(x)} + \alpha_0^2\right] \qquad (3.7.41)$$

Equations (3.7.41) show that the lift coefficient depends only on the mean angle of attack whereas the drag coefficient is a linear combination of the drag due to thickness, drag due to camber, and drag due to lift (or mean angle of attack).

References

Anderson, J.D. 2002. *Modern Compressible Flow: With Historical Perspective,* McGraw-Hill, New York.

Dennard, J.S. and Spencer, P.B. 1964. *Ideal-Gas Tables for Oblique-Shock Flow Parameters in Air at Mach Numbers from 1.05 to 12.0.* NASA TN D-2221.

Liepmann, H.W. and Roshko, A. 2002. *Elements of Gas Dynamics,* Dover Publications.

Further Information

This section discussed only one- or two-dimensional steady, inviscid compressible flows under perfect gas assumption. Further reading on this topic can be found in the following.

Kentfield, J.A.C. 1992. *Nonsteady, One-Dimensional, Internal, Compressible Flows: Theory and Application,* Oxford University Press.

Carscallen, W.E. and Oosthuizen, P. H. 1997. *Compressible Fluid Flow,* McGraw-Hill.

Information on advanced topics such as three-dimensional flows, viscous effects, and unsteady flows can be found in the following.

Ghrist, R. W., Holmes, P., and Sullivan, M. C. 1997. *Knots and Links in Three-Dimensional Flows*, Vol. 165, Springer Verlag, New York.

Golovachov, Y. P. and Ioffe, A. F. 1995. *Numerical Simulation of Viscous Shock Layer Flows: Fluid Mechanics and Its Applications*, Vol. 33, Kluwer Academic Publishers, Dordrecht, the Netherlands.

Pironneau, O., Rodi, W., Ryhming, I. L. Savill, A. M., and Troung, T. V., (Eds.) 1992. *Numerical Simulation of Unsteady Flows and Transition to Turbulence*, Cambridge University Press.

Spriggs, S. 1976. *Three-Dimensional Boundary Layer Flow, 1960–1975,* Gec Power Engineering Ltd. Library.

A reference for fundamentals of numerical methods with programming code is

Chapra, S. C. and Canale, R. P. 2001. *Numerical Methods for Engineers: With Software and Programming Application*, 4th ed., McGraw-Hill.

Numerous sources for programming codes are available on the World Wide Web, most of which is free, and can be found by using a search engine such as www.google.com.

Matrix Solvers for C++: www.vector-space.com/free.htm
Fortran and MatLab codes: www.unige.ch/math/folks/hairer/software.html

3.8 Multiphase Flow

John C. Chen

Introduction

Classic study of fluid mechanics concentrates on the flow of a single homogeneous phase, e.g., water, air, steam. However, many industrially important processes involve simultaneous flow of multiple phases, e.g., gas bubbles in oil, wet steam, dispersed particles in gas or liquid. Examples include vapor–liquid flow in refrigeration systems, steam–water flows in boilers and condensers, vapor–liquid flows in distillation columns, and pneumatic transport of solid particulates. In spite of their importance, multiphase flows are often neglected in standard textbooks. Fundamental understanding and engineering design procedures for multiphase flows are not nearly so well developed as those for single-phase flows. An added complexity is the need to predict the relative concentrations of the different phases in the multiphase flows, a need that doesn't exist for single-phase flows.

Inadequate understanding not withstanding, a significant amount of data have been collected and combinations of theoretical models and empirical correlations are used in engineering calculations. This knowledge base is briefly summarized in this section and references are provided for additional information. While discussions are provided of solid–gas flows and solid–liquid flows, primary emphasis is placed on multiphase flow of gas–liquids since this is the most often encountered class of multiphase flows in industrial applications.

A multiphase flow occurs whenever two or more of the following phases occur simultaneously: gas/vapor, solids, single-liquid phase, multiple (immiscible) liquid phases. Every possible combination has been encountered in some industrial process, the most common being the simultaneous flow of vapor/gas and liquid (as encountered in boilers and condensers). All multiphase flow problems have features which are characteristically different from those found in single-phase problems. First, the relative concentration of different phases is usually a dependent parameter of great importance in multiphase flows, while it is a parameter of no consequence in single-phase flows. Second, the spatial distribution of the various phases in the flow channel strongly affects the flow behavior, again a parameter that is of no concern in single-phase flows. Finally, since the density of various phases can differ by orders of magnitude, the influence of gravitational body force on multiphase flows is of much greater importance than in the case of single-phase flows. In any given flow situation, the possibility exists for the various phases to assume different velocities, leading to the phenomena of slip between phases and consequent interfacial momentum transfer. Of course, the complexity of laminar/turbulent characteristics occurs in multiphase flows as in single-phase flows, with the added complexity of interactions between phases altering the laminar/turbulent flow structures. These complexities increase exponentially with the number of phases encountered in the multiphase problem. Fortunately, a large number of applications occur with just two phase flows, or can be treated as pseudo-two-phase flows.

Two types of analysis are used to deal with two-phase flows. The simpler approach utilizes homogeneous models which assume that the separate phases flow with the same identical local velocity at all points in the fluid. The second approach recognizes the possibility that the two phases can flow at different velocities throughout the fluid, thereby requiring separate conservation equations for mass and momentum for each phase. Brief descriptions of both classes of models are given below.

Fundamentals

Consider *n* phases in concurrent flow through a duct with cross-sectional area A_c. Fundamental quantities that characterize this flow are

$\dot{m}_i$ = mass flow rate of ith phase

u_i = velocity of ith phase

α_i = volume fraction of ith phase in channel

Basic relationships between these and related parameters are

$$G_i = \text{mass flux of } i\text{th phase}$$

$$= \frac{\dot{m}_i}{A_c} \tag{3.8.1}$$

$$v_i = \text{superficial velocity of } i\text{th phase}$$

$$= \frac{G_i}{\rho_i} \tag{3.8.2}$$

$$u_i = \text{actual velocity of } i\text{th phase}$$

$$= \frac{v_i}{\alpha_i} \tag{3.8.3}$$

$$x_i = \text{flow quality of } i\text{th phase}$$

$$= \frac{\dot{m}_i}{\sum_i^n m_i} = \frac{G_i}{\sum_{i=1}^n G_i} \tag{3.8.4}$$

$$\alpha_i = \text{volume fraction of } i\text{th phase}$$

$$= \frac{\left(\dfrac{x_i}{\rho_i u_i}\right)}{\sum_{i=1}^n \left(\dfrac{x_i}{\rho_i u_i}\right)} \tag{3.8.5}$$

In most engineering calculations, the above parameters are defined as average quantities across the entire flow area, A_c. It should be noted, however, that details of the multiphase flow could involve local variations across the flow area. In the latter situation, G_i, v_i, and α_i are often defined on a local basis, varying with transverse position across the flow area.

Pressure drop along the flow channel is associated with gravitational body force, acceleration forces, and frictional shear at the channel wall. The total pressure gradient along the flow axis can be represented as

$$\frac{dP}{dz} = \left(\frac{dP}{dz}\right)_g + \left(\frac{dP}{dz}\right)_a + \left(\frac{dP}{dz}\right)_f \tag{3.8.6}$$

where

$$\left(\frac{dP}{dz}\right)_g = -g\cos\theta \cdot \sum_{i=1}^n \alpha_i \rho_i \tag{3.8.7}$$

θ = angle of channel from vertical

and

$$\left(\frac{dP}{dz}\right)_a = -\sum_{i=1}^{n} G_i \frac{du_i}{dz} \tag{3.8.8}$$

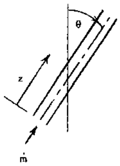

$$\left(\frac{dP}{dz}\right)_f = -\frac{\rho u^2}{2D} f \tag{3.8.9}$$

ρ = density of multiphase mixture

$$= \sum_{i=1}^{n} \rho_i \alpha_i \tag{3.8.10}$$

u = an average mixture velocity

$$= \frac{1}{\rho} \sum_{i=1}^{n} G_i \tag{3.8.11}$$

f = equivalent Darcy friction factor for the multiphase flow

In applications, the usual requirement is to determine pressure gradient (*dP*/*dz*) and the volume fractions (α_i). The latter quantities are of particular importance since the volume fraction of individual phases affects all three components of the pressure gradient, as indicated in Equation (3.8.7) to Equation (3.8.11). Correlations of various types have been developed for prediction of the volume fractions, all but the simplest of which utilize empirical parameters and functions.

The simplest flow model is known as the homogeneous equilibrium model (HEM), wherein all phases are assumed to be in neutral equilibrium. One consequence of this assumption is that individual phase velocities are equal for all phases everywhere in the flow system:

$$u_i = u \quad \text{for all} \quad i \tag{3.8.12}$$

This assumption permits direct calculation of the volume fractions from known mass qualities:

$$\alpha_i = \frac{x_i}{\rho_i \sum_{i=1}^{n} \left(\frac{x_i}{\rho_i}\right)} \tag{3.8.13}$$

The uniform velocity for all phases is the same as mixture velocity:

$$u = \frac{1}{\rho} \sum_{i=1}^{n} G_i \tag{3.8.14}$$

where

$$\frac{1}{\rho} = \sum_{i=1}^{n} \left(\frac{x_i}{\rho_i}\right) \tag{3.8.15}$$

This homogeneous model permits direct evaluation of all three components of axial pressure gradient, if flow qualities (x_i) are known:

$$\left(\frac{dP}{dz}\right)_g = -\frac{g\cos\theta}{\sum_{i=1}^{n}\left(\frac{x_i}{\rho_i}\right)} \tag{3.8.16}$$

$$\left(\frac{dP}{dz}\right)_a = -\left(\sum_{i=1}^{n} G_i\right)\cdot\frac{du}{dz} \tag{3.8.17}$$

$$\left(\frac{dP}{dz}\right)_f = -\frac{\rho u^2}{2D_f}\cdot f \tag{3.8.18}$$

where u and ρ are given by Equation (3.8.14) and Equation (3.8.15).

Predicting the coefficient of friction (f to clear) remains a problem, even in the homogeneous model. For cases of fully turbulent flows, experience has shown that a value of 0.02 may be used as a first-order approximation for (f to clear). More-accurate estimates require empirical correlations, specific to particular classes of multiphase flows and subcategories of flow regimes.

The following parts of this section consider the more common situations of two-phase flows and describe improved design methodologies specific to individual situations.

Gas–Liquid Two-Phase Flow

The most common case of multiphase flow is two-phase flow of gas and liquid, as encountered in steam generators and refrigeration systems. A great deal has been learned about such flows, including delineation of flow patterns in different flow regimes, methods for estimating volume fractions (gas void fractions), and two-phase pressure drops.

Flow Regimes

A special feature of multiphase flows is their ability to assume different spatial distributions of the phases. These different flow patterns have been classified in flow regimes, which are themselves altered by the direction of flow relative to gravitational acceleration. Figure 3.8.1 and Figure 3.8.2 (Delhaye, 1981) show the flow patterns commonly observed for co-current flow of gas and liquid in vertical and horizontal channels, respectively. For a constant liquid flow rate, the gas phase tends to be distributed as small bubbles at low gas flow rates. Increasing gas flow rate causes agglomeration of bubbles into larger slugs and plugs. Further increasing gas flow rate causes separation of the phases into annular patterns wherein liquid concentrates at the channel wall and gas flows in the central core for vertical ducts. For horizontal ducts, gravitational force tends to drain the liquid annulus toward the bottom of the channel, resulting in stratified and stratified wavy flows. This downward segregation of the liquid phase can be overcome by kinetic forces at high flow rates, causing stratified flows to revert to annular flows. At high gas flow rates, more of the liquid tends to be entrained as dispersed drops; in the limit one obtains completely dispersed mist flow.

Flow pattern maps are utilized to predict flow regimes for specific applications. The first generally successful flow map was that of Baker (1954) for horizontal flow, reproduced here in Figure 3.8.3. For vertical flows, the map of Hewitt and Roberts (1969), duplicated in Figure 3.8.4, provides a simple method for determining flow regimes. Parameters used for the axial coordinates of these flow maps are defined as follows:

$$\lambda = \left(\frac{\rho_g \rho_\ell}{\rho_a \rho_w}\right)^{1/2} \tag{3.8.19}$$

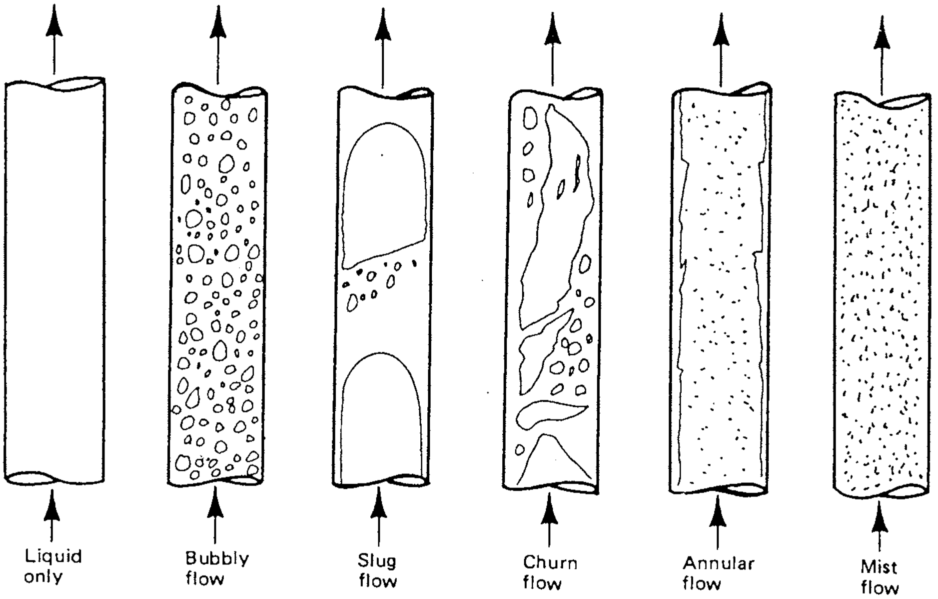

FIGURE 3.8.1 Flow patterns in gas–liquid vertical flow. (From Lahey, R.T., Jr. and Moody, F.I. 1977. *The Thermal Hydraulics of a Boiling Water Nuclear Reactor,* The American Nuclear Society, LaGrange, IL. With permission.)

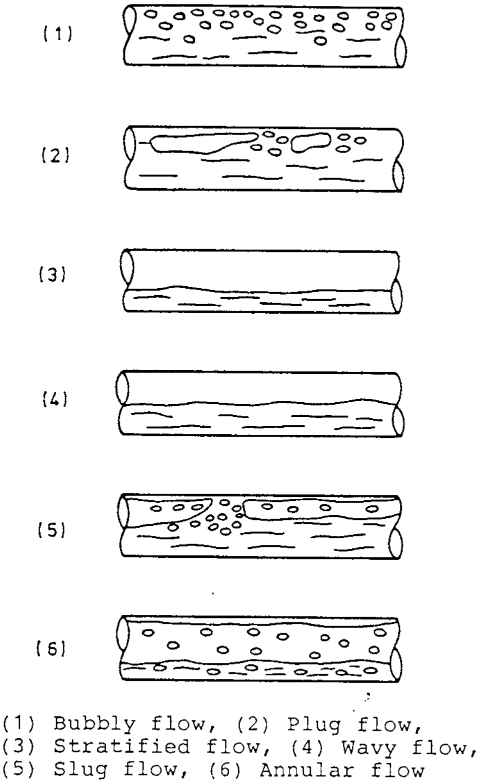

FIGURE 3.8.2 Flow patterns in gas–liquid horizontal flow.

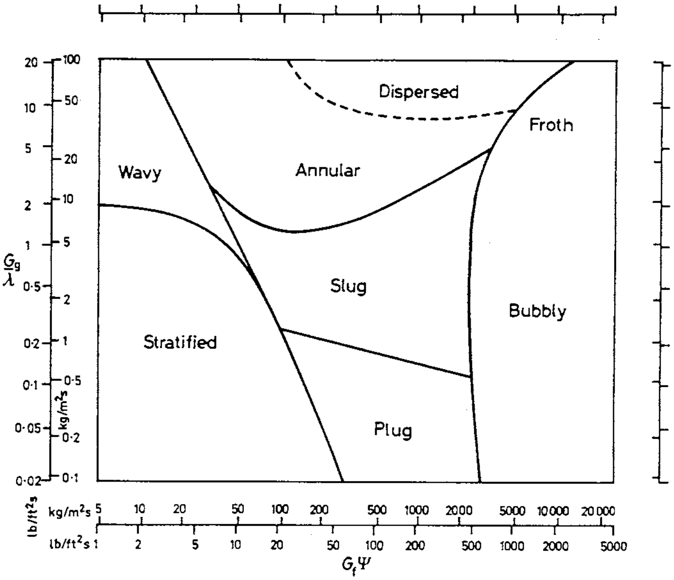

FIGURE 3.8.3 Flow pattern map for horizontal flow (Baker, 1954). (From Collier, J.G. 1972. *Convective Boiling and Condensation,* McGraw-Hill, London. With permission.)

$$\psi = \left(\frac{\sigma_w}{\sigma}\right)\left[\left(\frac{\mu_\ell}{\mu_w}\right)\left(\frac{\rho_w}{\rho_\ell}\right)^2\right]^{1/3} \tag{3.8.20}$$

$$j = \text{volumetric flux, } \frac{G}{\rho} \tag{3.8.21}$$

Void Fractions

In applications of gas–liquid flows, the volume fraction of gas (α_g) is commonly called “void fraction” and is of particular interest. The simplest method to estimate void fraction is by the HEM. From Equation (3.8.13), the void fraction can be estimated as

$$\alpha_g = \frac{x_g}{x_g + \left(1 - x_g\right)\dfrac{\rho_g}{\rho_\ell}} \tag{3.8.22}$$

where α_g, x_g, ρ_g, ρ_ℓ are cross-sectional averaged quantities.

In most instances, the homogenous model tends to overestimate the void fraction. Improved estimates are obtained by using separated-phase models which account for the possibility of slip between gas and liquid velocities. A classic separated-phase model is that of Lockhart and Martinelli (1949). The top portion of Figure 3.8.5 reproduces the Lockhart–Martinelli correlation for void fraction (shown as α) as a function of the parameter X which is defined as

$$X = \left[\left(\frac{dP}{dz}\right)_{f\ell} \div \left(\frac{dP}{dz}\right)_{fg}\right]^{1/2} \tag{3.8.23}$$

where

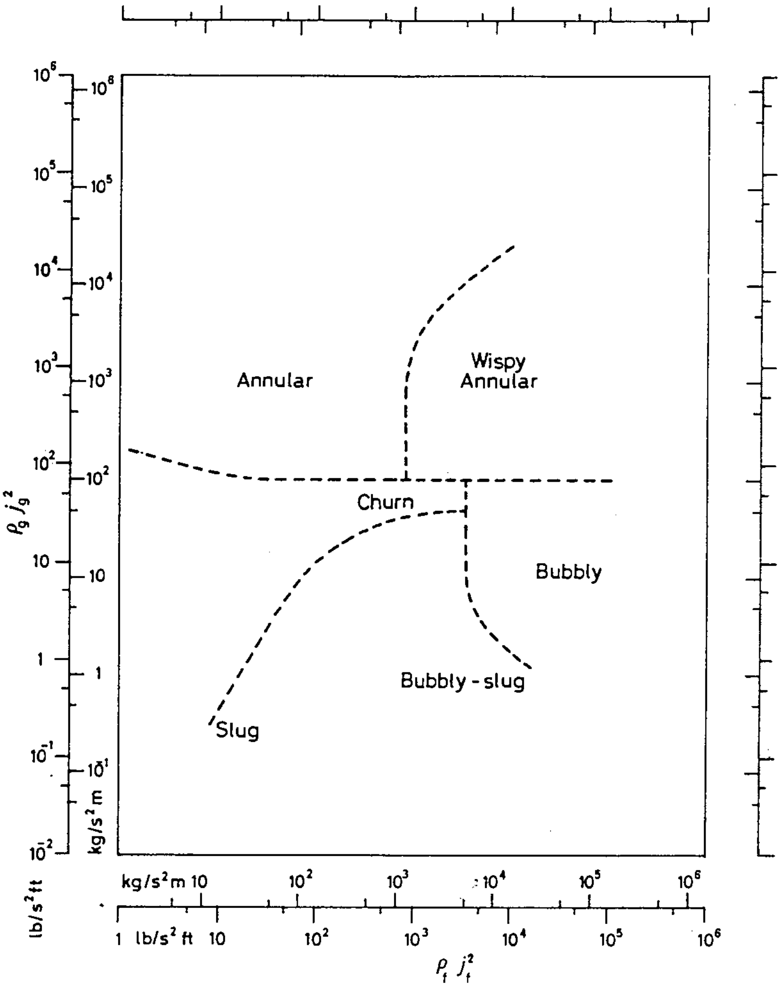

FIGURE 3.8.4 Flow pattern map for vertical flow (Hewitt and Roberts, 1969). (From Collier, J.G. 1972. *Convective Boiling and Condensation,* McGraw-Hill, London. With permission.)

$\left(\frac{dP}{dz}\right)_{f\ell}$ = frictional pressure gradient of liquid phase flowing alone in channel

$\left(\frac{dP}{dz}\right)_{fg}$ = frictional pressure gradient of gas phase flowing alone in channel

Often, flow rates are sufficiently high such that each phase if flowing alone in the channel would be turbulent. In this situation the parameter X can be shown to be

$$X_{tt} = \left(\frac{1-x_g}{x_g}\right)^{0.9}\left(\frac{\rho_g}{\rho_\ell}\right)^{0.5}\left(\frac{\mu_\ell}{\mu_g}\right)^{0.1} \tag{3.8.24}$$

Another type of separated-phase model is the drift-flux formulation of Wallis (1969). This approach focuses attention on relative slip between phases and results in slightly different expressions depending

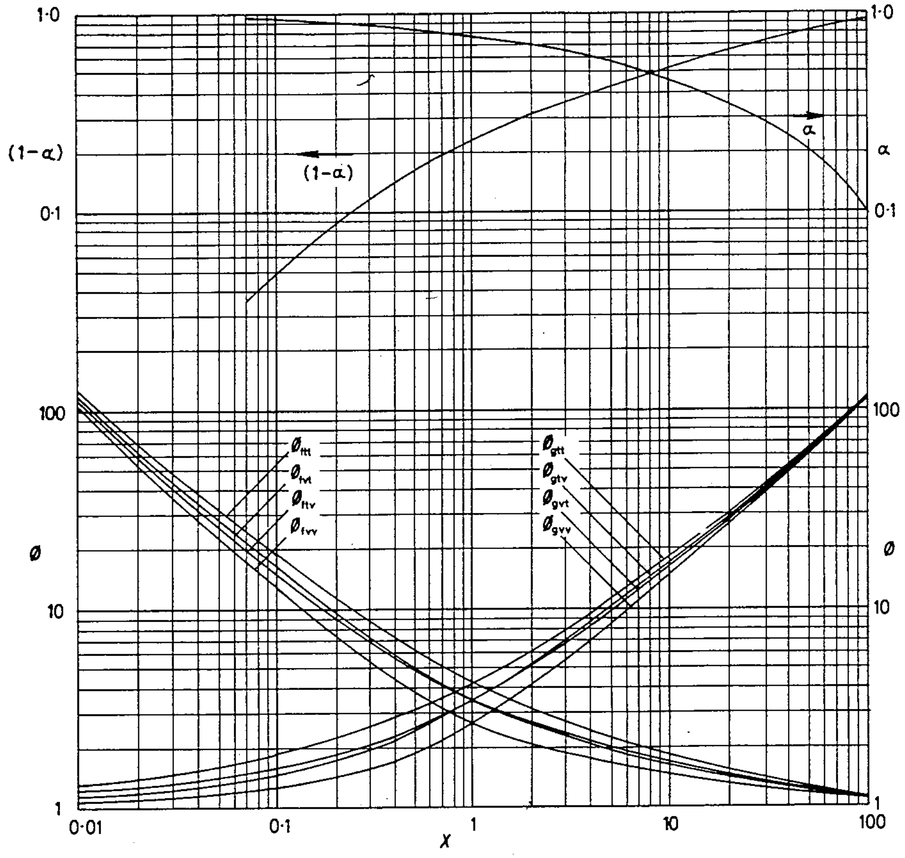

FIGURE 3.8.5 Correlations for void fraction and frictional pressure drop (Lockhart and Martinelli, 1949). (From Collier, J.G. 1972. *Convective Boiling and Condensation,* McGraw-Hill, London. With permission.)

on the flow regime. For co-current upflow in two of the more common regimes, the drift-flux model gives the following relationships between void fraction and flow quality:

Bubbly flow or churn-turbulent flow:

$$\alpha_g = \frac{x_g}{\left(\frac{u_o \rho_g}{G}\right) + C_o\left[x_g + \left(1 - x_g\right)\frac{\rho_g}{\rho_\ell}\right]} \tag{3.8.25}$$

Dispersed drop (mist) flow:

$$x_g = \frac{1 - \left(1 - \alpha_g\right)\left(\frac{u_o \rho_\ell}{G}\alpha_g^2 + 1\right)}{1 - \left(1 - \alpha_g\right)\left(1 - \frac{\rho_\ell}{\rho_g}\right)} \tag{3.8.26}$$

where

u_o = terminal rise velocity of bubble, in bubbly flow, or terminal fall velocity of drop in churn-turbulent flow

C_o = an empirical distribution coefficient $\simeq$ 1.2

Pressure Drop

Equation (3.8.16) through Equation (3.8.18) permit calculation of two-phase pressure drop by the homogeneous model, if the friction coefficient (f) is known. One useful method for estimating (f) is to treat the entire two-phase flow as if it were all liquid, except flowing at the two-phase mixture velocity. By this approach the frictional component of the two-phase pressure drop becomes

$$\left(\frac{dP}{dz}\right)_f = \left[1 + x_g\left(\frac{\rho_\ell}{\rho_g} - 1\right)\right] \cdot \left(\frac{dP}{dz}\right)_{f\ell G} \tag{3.8.27}$$

where $(dP/dz)_{f\ell G}$ = frictional pressure gradient if entire flow (of total mass flux G) flowed as liquid in the channel.

The equivalent frictional pressure drop for the entire flow as liquid, $(dP/dz)_{f\ell g}$, can be calculated by standard procedures for single-phase flow. In using Equation (3.8.16) through Equation (3.8.18), the void fraction would be calculated with the equivalent homogeneous expression Equation (3.8.13).

A more accurate method to calculate two-phase pressure drop is by the separated-phases model of Lockhart and Martinelli (1949). The bottom half of Figure 3.8.5 shows empirical curves for the Lockhart–Martinelli frictional multiplier, ϕ:

$$\phi_i = \left[\left(\frac{dP}{dz}\right)_f \div \left(\frac{dP}{dz}\right)_{fi}\right]^{1/2} \tag{3.8.28}$$

where (i) denotes either the fluid liquid phase (f) or gas phase (g). The single-phase frictional gradient is based on the ith phase flowing alone in the channel, in either viscous laminar (v) or turbulent (t) modes. The most common case is where each phase flowing alone would be turbulent, whence one could use Figure 3.8.5 to obtain

$$\begin{aligned}\left(\frac{dP}{dz}\right)_f &= \text{frictional pressure gradient for two-phase flow}\\ &= \phi_{gtt}^2 \cdot \left(\frac{dP}{dz}\right)_{fg}\end{aligned} \tag{3.8.29}$$

where $(dP/dz)_{fg}$ is calculated for gas phase flowing alone and $X = X_{tt}$ as given by Equation (3.8.24).

The correlation of Lockhart–Martinelli has been found to be adequate for two-phase flows at low-to-moderate pressures, i.e., with reduced pressures less than 0.3. For applications at higher pressures, the revised models of Martinelli and Nelson (1948) and Thom (1964) are recommended.

Gas–Solid, Liquid–Solid Two-Phase Flows

Two-phase flows can occur with solid particles in gas or liquid. Such flows are found in handling of granular materials and heterogeneous reaction processing. Concurrent flow of solid particulates with a fluid phase can occur with various flow patterns, as summarized below.

Flow Regimes

Consider vertical upflow of a fluid (gas or liquid) with solid particles. Figure 3.8.6 illustrates the major flow regimes that have been identified for such two-phase flows. At low flow rates, the fluid phase percolates between stationary particles; this is termed flow through a fixed bed. At some higher velocity a point is reached when the particles are all suspended by the upward flowing fluid, the drag force between particles and fluid counterbalancing the gravitational force on the particles. This is the point of minimum

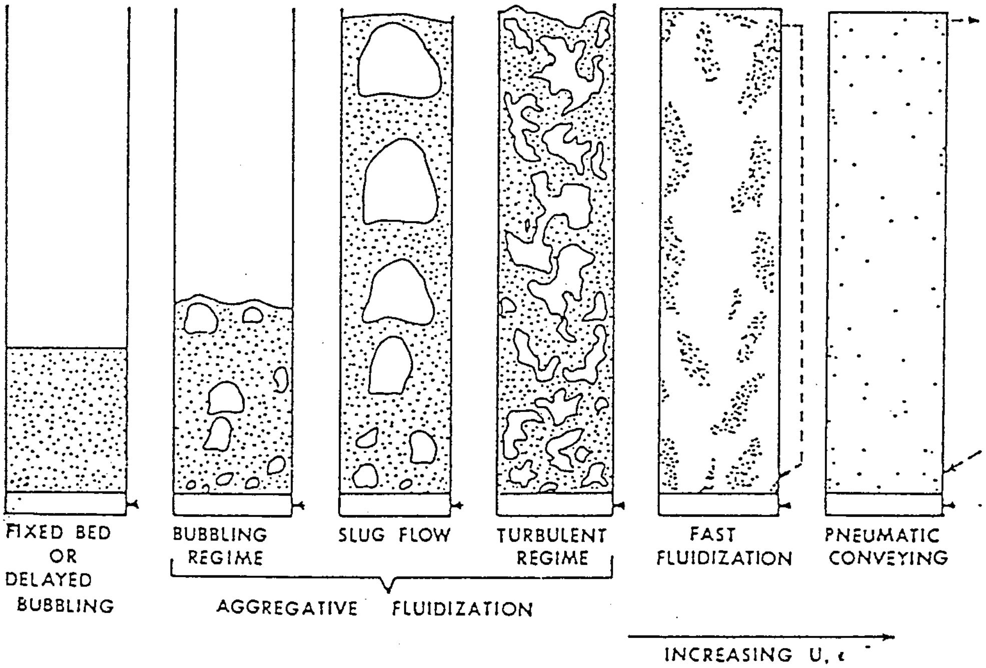

FIGURE 3.8.6 Flow patterns for vertical upflow of solid particles and gas or liquid. (From Chen, J.C. 1994. *Proc. Xth Int. Heat Transfer Conf.*, Brighton, U.K., 1:369–386. With permission.)

fluidization, marking the transition from fixed to fluidized beds. Increase of fluid flow rate beyond minimum fluidization causes instabilities in the two-phase mixture, and macroscopic bubbles or channels of fluid are observed in the case of gaseous fluids. In the case of liquid fluids, the two-phase mixture tends to expand, often without discrete bubbles or channels. Further increase of fluid velocity causes transition to turbulent fluidization wherein discrete regions of separated phases (fluid slugs or channels and disperse suspensions of particles) can coexist. Depending on specific operating conditions (e.g., superficial fluid velocity, particle size, particle density, etc.), net transport of solid particles with the flowing fluid can occur at any velocity equal to or greater than that associated with slug flow and turbulent flow. Further increases in fluid velocity increase the net transport of solid particles. This can occur with large-scale clusters of solid particles (as exemplified by the fast fluidization regime) or with dilute dispersions of solid particles (as often utilized in pneumatic conveying). For engineering application of fluid–solid two-phase flows, the important thresholds between flow regimes are marked by the fluid velocity for minimum fluidization, terminal slip, and saltation threshold.

Minimum Fluidization

The transition from flow through packed beds to the fluidization regime is marked by the minimum fluidization velocity of the fluid. On a plot pressure drop vs. superficial fluid velocity, the point of minimum fluidization is marked by a transition from a linearly increasing pressure drop to a relatively constant pressure drop as shown in Figure 3.8.7 for typical data, for two-phase flow of gas with sand particles of 280 μm mean diameter (Chen, 1996). The threshold fluid velocity at minimum fluidization is traditionally derived from the Carman–Kozeny equation,

$$U_{mf} = \frac{\left(\rho_s - \rho_f\right)\left(\phi\, dp\right)^2 g}{150\mu_f} \cdot \frac{\alpha_{mf}^2}{\left(1 - \alpha_{mf}\right)} \qquad (3.8.30)$$

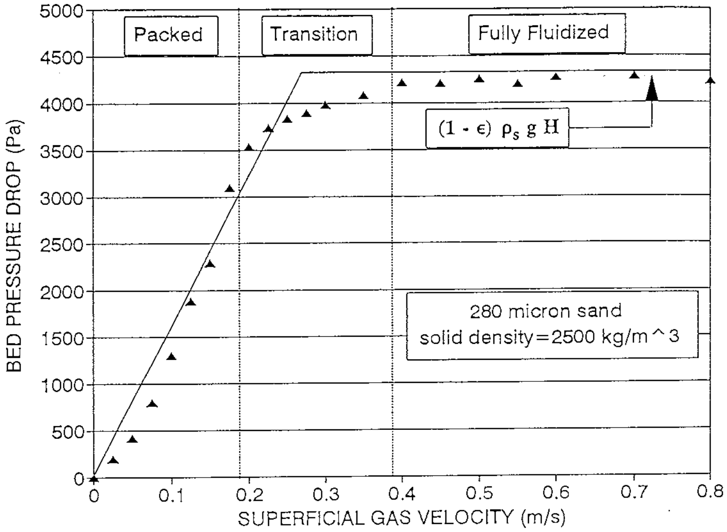

FIGURE 3.8.7 Transition at minimum fluidization. (From Chen, J.C. 1996. In *Annual Review of Heat Transfer*, Vol. VII, Begal House, Washington, D.C. With permission.)

where

ϕ = sphericity of particles (unity for spherical particles)
α_{mf} = volumetric fraction of fluid at minimum fluidization

Small, light particles have minimum fluidization voidage (α_{mf}) of the order 0.6, while larger particles such as sand have values closer to 0.4.

An alternative correlation for estimating the point of minimum fluidization is that of Wen and Yu (1966):

$$\frac{U_{mf} d_p \rho_f}{\mu_f} = (33.7 + 0.041 Ga)^{0.5} - 33.7 \tag{3.8.31}$$

where $Ga = \rho_f d_p^3 (\rho_s - \rho_f) g / \mu_f^2$.

When the fluid velocity exceeds U_{mf}, the two-phase mixture exists in the fluidized state in which the pressure gradient is essentially balanced by the gravitational force on the two-phase mixture:

$$\frac{dP}{dz} = g\left[\alpha_s \rho_s + \alpha_f \rho_f\right] \tag{3.8.32}$$

This fluidized state exists until the fluid velocity reaches a significant fraction of the terminal slip velocity, beyond which significant entrainment and transport of the solid particles occur.

Terminal Slip Velocity

For an isolated single particle the maximum velocity relative to an upflowing fluid is the terminal slip velocity. At this condition, the interfacial drag of the fluid on the particle exactly balances the gravitational body force on the particle:

$$U_t = \left(U_f - U_s\right)_t = \left[\frac{4 d_p \left(\rho_s - \rho_f\right)}{3 \rho_f} \cdot \frac{1}{C_D}\right]^{1/2} \tag{3.8.33}$$

where C_D = coefficient of drag on the particle.

The coefficient of drag on the particle (C_D) depends on the particle Reynolds number:

$$\mathrm{Re}_p = \frac{\rho_f d_p \left(U_f - U_s\right)}{\mu_f} \tag{3.8.34}$$

The following expressions may be used to estimate C_D as appropriate:

$$\begin{aligned} C_D &= \frac{32}{\mathrm{Re}_p}, && \mathrm{Re}_p \le 1 \\ C_D &= \frac{18.5}{\mathrm{Re}_p^{0.67}}, && 1 \le \mathrm{Re}_p \le 10^3 \end{aligned} \tag{3.8.35}$$

Pneumatic Conveying

A desirable mode of pneumatic conveying is two-phase flow with solid particles dispersed in the concurrent flowing fluid. Such dispersed flows can be obtained if the fluid velocity is sufficiently high. For both horizontal and vertical flows, there are minimum fluid velocities below which saltation of the solid particles due to gravitational force occurs, leading to settling of the solid particles in horizontal channels and choking of the particles in vertical channels. Figure 3.8.8 and Figure 3.8.9 for Zenz and Othmer (1960) show these different regimes of pneumatic conveying for horizontal and vertical transport, respectively. Figure 3.8.8 shows that for a given rate of solids flow (W) there is a minimum superficial fluid velocity below which solid particles tend to settle into a dense layer at the bottom of the horizontal channels. Above this saltation threshold, fully dispersed two-phase flow is obtained. In the case of vertical

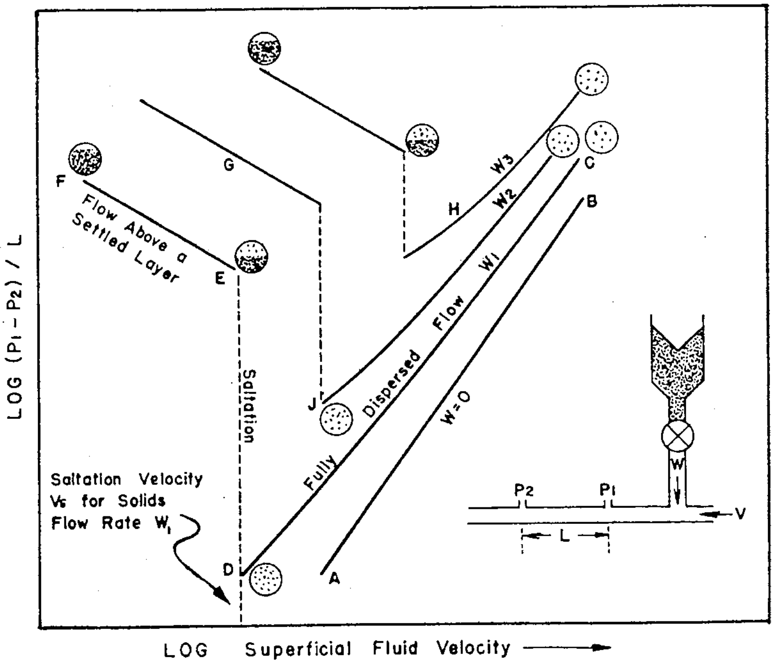

FIGURE 3.8.8 Flow characteristics in horizontal pneumatic conveying. (From Zeng, F.A. and Othmer, D.F. 1960. *Fluidization and Fluid-Particle Systems,* Reinhold, New York. With permission.)

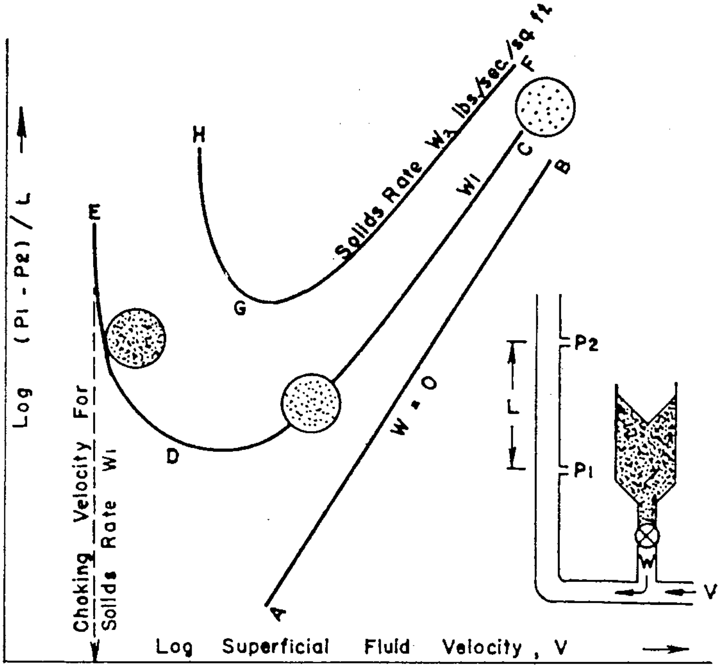

FIGURE 3.8.9 Flow characteristics in vertical pneumatic conveying. (From Zeng, F.A. and Othmer, D.F. 1960. *Fluidization and Fluid-Particle Systems,* Reinhold, New York. With permission.)

transport illustrated in Figure 3.8.9, there is a minimum fluid velocity below which solid particles tend to detrain from the two-phase suspension. This choking limit varies not only with particle properties but also with the actual rate of particle flow. Well-designed transport systems must operate with superficial fluid velocities greater than these limiting saltation and choking velocities.

Zenz and Othmer (1960) recommend the empirical correlations represented in Figure 3.8.10 estimating limiting superficial fluid velocities at incipient saltation or choking, for liquid or gas transport of uniformly sized particles. Note that these correlations are applicable for either horizontal or vertical concurrent flow. Figure 3.8.10 is duplicated from the original source and is based on parameters in engineering units, as noted in the figure. To operate successfully in dispersed pneumatic conveying of solid particles, the superficial fluid velocity must exceed that determined from the empirical correlations of Figure 3.8.10.

Nomenclature

A_c	cross-sectional flow area of channel
C_o	Wallis' distribution coefficient
d_p	diameter of solid particles
f_D	Darcy friction factor
G	mass flow flux, kg/m^2 · sec
j	volumetric flow flux, m/sec
$\dot{m}$	mass flow rate, kg/sec
P	pressure, N/m^2
u	velocity in axial flow direction, m/sec
v	superficial velocity in axial flow direction, m/sec
x	mass flow quality
z	axial coordinate

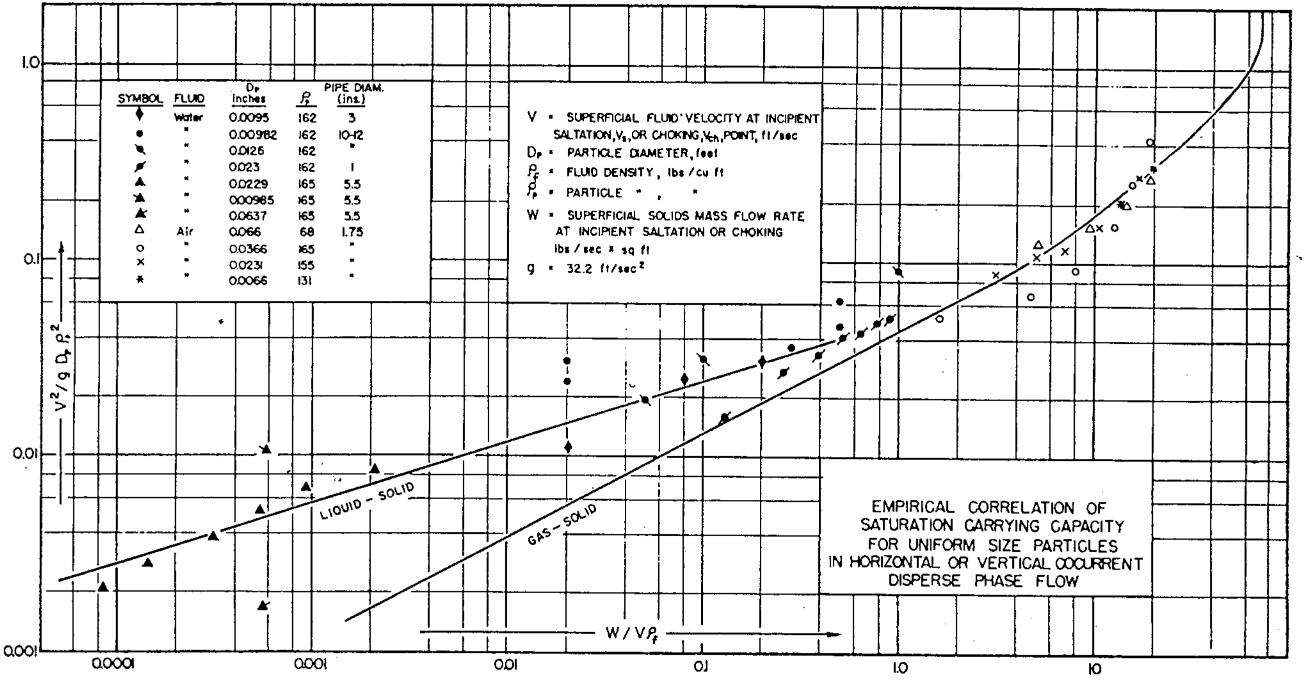

FIGURE 3.8.10 Correlations for limiting velocities in pneumatic conveying. (From Zeng, F.A. and Othmer, D.F. 1960. *Fluidization and Fluid-Particle Systems,* Reinhold, New York. With permission.)

Greek Letters

α	volume fraction
λ	parameter in Baker flow map
ϕ	sphericity of solid particles
ϕ_i	frictional multiphase for pressure drag, Equation (3.8.28)
ψ	parameter in Baker flow map
σ	surface tension
θ	angle from vertical

Subscripts

a	air
f	fluid phase
g	gas phase
l	liquid phase
mf	minimum fluidization
p	particle
s	solid phase
t	terminal slip
w	water

References

Baker, O. 1954. Design of pipelines for simultaneous flow of oil and gas, *Oil Gas J.*

Chen, J.C. 1994. Two-phase flow with and without phase changes: suspension flows. Keynote lecture, *Proc. Xth Int. Heat Transfer Conf.,* Brighton, U.K., 1:369–386.

Chen, J.C. 1996. Heat transfer to immersed surfaces in bubbling fluidized beds, in *Annual Review of Heat Transfer*, Vol. VII, Bengel House, Washington, D.C.

Collier, J.G. 1972. *Convective Boiling and Condensation,* McGraw-Hill, London.

Delhaye, J.M. 1981. Two-phase flow patterns, in *Two-Phase Flow and Heat Transfer,* A.E. Bergles, J.G. Collier, J.M. Delhaye, G.F. Newitt, and F. Mayinger, Eds., Hemisphere Publishing, McGraw-Hill, New York.

Hewitt, G.F. and Roberts, D.N. 1969. Studies of Two-Phase Flow Patterns by Simultaneous X-Ray and Flash Photography, Report AERE-M 2159.

Lahey, R.T., Jr. and Moody, F.I. 1977. *The Thermal Hydraulics of a Boiling Water Nuclear Reactor,* The American Nuclear Society, La Grange, IL.

Lockhart, R.W. and Martinelli, R.C. 1949. Proposed correlation of data for isothermal two-phase two-component flow in pipes, *Chem. Eng. Progr.,* 45:39.

Martinelli, R.C. and Nelson, D.B. 1984. Prediction of pressure drop during forced-circulation boiling of water, *Trans. ASME,* 70:695–702.

Thom, J.R.S. 1964. Prediction of pressure drop during forced circulation boiling of water, *Int. J. Heat Mass Transfer,* 7:709–724.

Wallis, G.B. 1969. *One-Dimensional Two-Phase Flow,* McGraw-Hill, New York.

Wen, C.Y. and Yu, Y.H. 1966. A generalized method of predicting the minimum fluidization velocity, *AIChE J.,* 12:610–612.

Zenz, F.A. and Othmer, D.F. 1960. *Fluidization and Fluid-Particle Systems,* Reinhold, New York.

3.9 New-Newtonian Flows

Thomas F. Irvine Jr. and Massimo Capobianchi

Introduction

An important class of fluids exists which differ from Newtonian fluids in that the relationship between the shear stress and the flow field is more complicated. Such fluids are called non-Newtonian or rheological fluids. Examples include various suspensions such as coal–water or coal–oil slurries, food products, inks, glues, soaps, polymer solutions, etc.

An interesting characteristic of rheological fluids is their large "apparent viscosities". This results in laminar flow situations in many applications, and consequently the engineering literature is concentrated on laminar rather than turbulent flows. It should also be mentioned that knowledge of non-Newtonian fluid mechanics and heat transfer is still in an early stage and many aspects of the field remain to be clarified.

In the following sections, we will discuss the definition and classification of non-Newtonian fluids, the special problems of thermophysical properties, and the prediction of pressure drops in both laminar and turbulent flow in ducts of various cross-sectional shapes for different classes of non-Newtonian fluids.

Classification of Non-Newtonian Fluids

It is useful to first define a Newtonian fluid since all other fluids are non-Newtonian. Newtonian fluids possess a property called viscosity and follow a law analogous to the Hookian relation between the stress applied to a solid and its strain. For a one-dimensional Newtonian fluid flow, the shear stress at a point is proportional to the rate of strain (called in the literature the *shear rate*) which is the velocity gradient at that point. The constant of proportionality is the dynamic viscosity, i.e.,

$$\tau_{y,x} = \mu \frac{du}{dy} = \mu \dot{\gamma} \tag{3.9.1}$$

where x refers to the direction of the shear stress y the direction of the velocity gradient, and $\dot{\gamma}$ is the shear rate. The important characteristic of a Newtonian fluid is that the dynamic viscosity is independent of the shear rate.

Equation (3.9.1) is called a constitutive equation, and if $\tau_{x,y}$ is plotted against $\dot{\gamma}$, the result is a linear relation whose slope is the dynamic viscosity. Such a graph is called a *flow curve* and is a convenient way to illustrate the viscous properties of various types of fluids.

Fluids which do not obey Equation (3.9.1) are called non-Newtonian. Their classifications are illustrated in Figure 3.9.1 where they are separated into various categories of purely viscous time-independent or time-dependent fluids and viscoelastic fluids. Viscoelastic fluids, which from their name possess both viscous and elastic properties (as well as memory), have received considerable attention because of their ability to reduce both drag and heat transfer in channel flows. They will be discussed in a later subsection.

Purely viscous time-dependent fluids are those in which the shear stress in a function only of the shear rate but in a more complicated manner than that described in Equation (3.9.1). Figure 3.9.2 illustrates the characteristics of purely viscous time-independent fluids. In the figure, (a) and (b) are fluids where the shear stress depends only on the shear rate but in a nonlinear way. Fluid (a) is called pseudoplastic (or shear thinning), and fluid (b) is called dilatant (or shear thickening). Curve (c) is one which has an initial yield stress after which it acts as a Newtonian fluid, called Buckingham plastic, and curve (d), called Hershel-Buckley, also has a yield stress after which it becomes pseudoplastic. Curve (e) depicts a Newtonian fluid.

Figure 3.9.3 shows flow curves for two common classes of purely viscous time-dependent non-Newtonian fluids. It is seen that such fluids have a hysteresis loop or memory whose shape depends upon

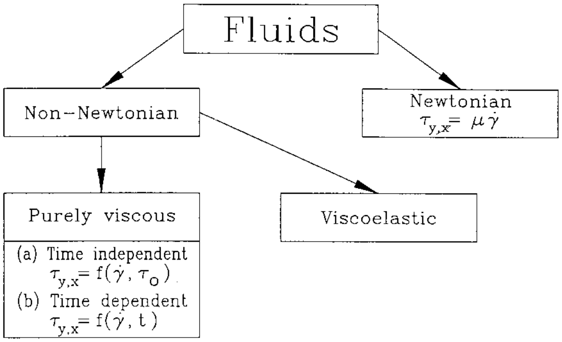

FIGURE 3.9.1 Classification of fluids.

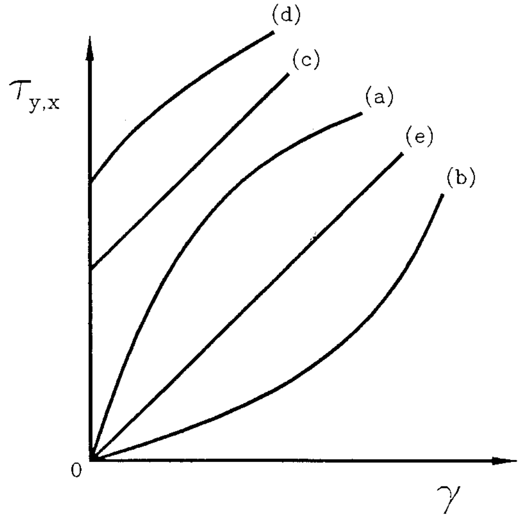

FIGURE 3.9.2 Flow curves of purely viscous, time-independent fluids: (a) pseudoplastic; (b) dilatant; (c) Bingham plastic; (d) Hershel–Buckley; (e) Newtonian.

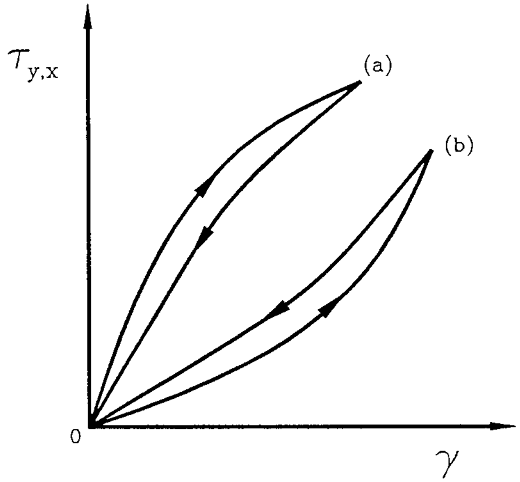

FIGURE 3.9.3 Flow curves for purely viscous, time-dependent fluids: (a) thixotropic; (b) rheopectic.

the time-dependent rate at which the shear stress is applied. Curve (a) illustrates a pseudoplastic time-dependent fluid and curve (b) a dilatant time-dependent fluid. They are called, respectively, thixotropic and rheopectic fluids and are complicated by the fact that their flow curves are difficult to characterize for any particular application.

Apparent Viscosity

Although non-Newtonian fluids do not have the property of viscosity, in the Newtonian fluid sense, it is convenient to define an apparent viscosity which is the ratio of the local shear stress to the shear rate at that point.

$$\mu_a = \frac{\tau}{\dot{\gamma}} \tag{3.9.2}$$

The apparent viscosity is not a true property for non-Newtonian fluids because its value depends upon the flow field, or shear rate. Nevertheless, it is a useful quantity and flow curves are often constructed with the apparent viscosity as the ordinate and shear rate as the abscissa. Such a flow curve will be illustrated in a later subsection.

Constitutive Equations

A constitutive equation is one that expresses the relation between the shear stress or apparent viscosity and the shear rate through the rheological properties of the fluid. For example, Equation (3.9.1) is the constitutive equation for a Newtonian fluid.

Many constitutive equations have been developed for non-Newtonian fluids with some of them having as many as five rheological properties. For engineering purposes, simpler equations are normally satisfactory and two of the most popular will be considered here.

Since many of the non-Newtonian fluids in engineering applications are pseudoplastic, such fluids will be used in the following to illustrate typical flow curves and constitutive equations. Figure 3.9.4 is a qualitative flow curve for a typical pseudoplastic fluid plotted with logarithmic coordinates. It is seen in the figure that at low shear rates, region (a), the fluid is Newtonian with a constant apparent viscosity of μ_o (called the *zero shear rate viscosity*). At higher shear rates, region (b), the apparent viscosity begins to decrease until it becomes a straight line, region (c). This region (c) is called the power law region and is an important region in fluid mechanics and heat transfer. At higher shear rates than the power law region, there is another transition region (d) until again the fluid becomes Newtonian in region (e). As discussed below, regions (a), (b), and (c) are where most of the engineering applications occur.

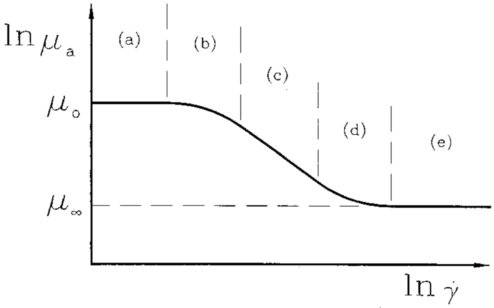

FIGURE 3.9.4 Illustrative flow curve for a pseudoplastic fluid (a) Newtonian region; (b) transition region I; (c) power law region; (d) transition region II; (e) high-shear-rate Newtonian region.

Power Law Constitutive Equation

Region (c) in Figure 3.9.4, which was defined above as the power law region, has a simple constitutive equation:

$$\tau = K\dot{\gamma}^{n} \tag{3.9.3}$$

or, from Equation (3.9.2):

$$\mu_a = K\dot{\gamma}^{n-1} \tag{3.9.4}$$

Here, K is called the fluid consistency and n the flow index. Note that if $n = 1$, the fluid becomes Newtonian and K becomes the dynamic viscosity. Because of its simplicity, the power law constitutive equation has been most often used in rheological studies, but at times it is inappropriate because it has several inherent flaws and anomalies. For example, if one considers the flow of a pseudoplastic fluid ($n < 1$) through a circular duct, because of symmetry at the center of the duct the shear rate (velocity gradient) becomes zero and thus the apparent viscosity from Equation (3.9.4) becomes infinite. This poses conceptual difficulties especially when performing numerical analyses on such systems. Another difficulty arises when the flow field under consideration is not operating in region (c) of Figure 3.9.4 but may have shear rates in region (a) and (b). In this case, the power law equation is not applicable and a more general constitutive equation is needed.

Modified Power Law Constitutive Equation

A generalization of the power law equation which extends the shear rate range to regions (a) and (b) is given by

$$\mu_a = \frac{\mu_o}{1 + \dfrac{\mu_o}{K}\dot{\gamma}^{1-n}} \tag{3.9.5}$$

Examination of Equation (3.9.5) reveals that at low shear rates, the second term in the denominator becomes small compared with unity and the apparent viscosity becomes a constant equal to μ_O. This represents the Newtonian region in Figure 3.9.4. On the other hand, as the second term in the denominator becomes large compared with unity, Equation (3.9.5) becomes Equation (3.9.4) and represents region (c), the power law region. When both denominator terms must be considered, Equation (3.9.5) represents region (b) in Figure 3.9.4.

An important advantage of the modified power law equation is that it retains the rheological properties K and n of the power law model plus the additional property μ_o. Thus, as will be shown later, in the flow and heat transfer equations, the same dimensionless groups as in the power law model will appear plus an additional dimensionless parameter which describes in which of the regions (a), (b), or (c) a particular system is operating. Also, solutions using the modified power law model will have Newtonian and power law solutions as asymptotes.

Equation (3.9.5) describes the flow curve for a pseudoplastic fluid ($n < 1$). For a dilatant fluid, ($n > 1$), an appropriate modified power law model is given by

$$\mu_a = \mu_o\left[1 + \frac{K}{\mu_o}\dot{\gamma}^{n-1}\right] \tag{3.9.6}$$

Many other constitutive equations have been proposed in the literature (Skelland, 1967; Cho and Hartnett, 1982; Irvine and Karni, 1987), but the ones discussed above are sufficient for a large number of engineering applications and agree well with the experimental determinations of rheological properties.

TABLE 3.9.1 Rheological Properties Used in the Modified Power Law Equations in Figure 3.9.5 for Three Polymer Solutions of CMC-7H4

CMC	K (N · sec^n/m^2)	n	μ_o (N · sec/m^2)n
5000 wppm	2.9040	0.3896	0.21488
2500 wppm	1.0261	0.4791	0.06454
1500 wppm	0.5745	0.5204	0.03673

Source: Park, S. et al., *Proc. Third World Conf. Heat Transfer, Fluid Mechanics, and Thermodynamics,* Vol. 1, Elsevier, New York, 1993, 900–908.

Rheological Property Measurements

For non-Newtonian fluids, specifying the appropriate rheological properties for a particular fluid is formidable because such fluids are usually not pure substances but various kinds of mixtures. This means that the properties are not available in handbooks or other reference materials but must be measured for each particular application. A discussion of the various instruments for measuring rheological properties is outside the scope of the present section, but a number of sources are available which describe different rheological property measurement techniques and instruments: Skelland (1967), Whorlow (1980), Irvine and Karni (1987), and Darby (1988). Figure 3.9.5 is an illustration of experimental flow curves measured with a falling needle viscometer and a square duct viscometer for polymer solutions of different concentrations. Also known in the figure as solid lines is the modified power law equation used to represent the experimental data. It is seen that Equation (3.9.5) fits the experimental data within ±2%. Table 3.9.1 lists the rheological properties used in the modified power law equations in Figure 3.9.5. It must be emphasized that a proper knowledge of these properties is vital to the prediction of fluid mechanics and heat transfer phenomena in rheological fluids.

Fully Developed Laminar Pressure Drops for Time-Independent Non-Newtonian Fluids

Modified Power Law Fluids

This important subject will be considered by first discussing modified power law fluids. The reason is that such solutions include both friction factor–Reynolds number relations and a shear rate parameter. The latter allows the designer to determine the shear rate region in which his system is operating and thus the appropriate solution to be used, i.e., regions (a), (b), or (c) in Figure 3.9.4.

For laminar fully developed flow of a modified power law fluid in a circular duct, the product of the friction factor and a certain Reynolds number is a constant depending on the flow index, n, and the shear rate parameter, β.

$$f_D \cdot \mathrm{Re}_m = \mathrm{constant}(n,\beta) \tag{3.9.7}$$

where f_D is the Darcy friction factor and Re_m the modified power law Reynolds number, i.e.,

$$f_D = \frac{2\dfrac{\Delta p}{L}D_H}{\rho \bar{u}^2} \quad \text{(Darcy friction factor)}^5$$

$$\mathrm{Re}_m = \frac{\rho \bar{u} D_H}{\mu^*}$$

---

[5] It should be noted that the Fanning friction factor is also used in the technical literature. The Fanning friction factor is ¼ of the Darcy friction factor, and will be characterized by the symbol f_F.

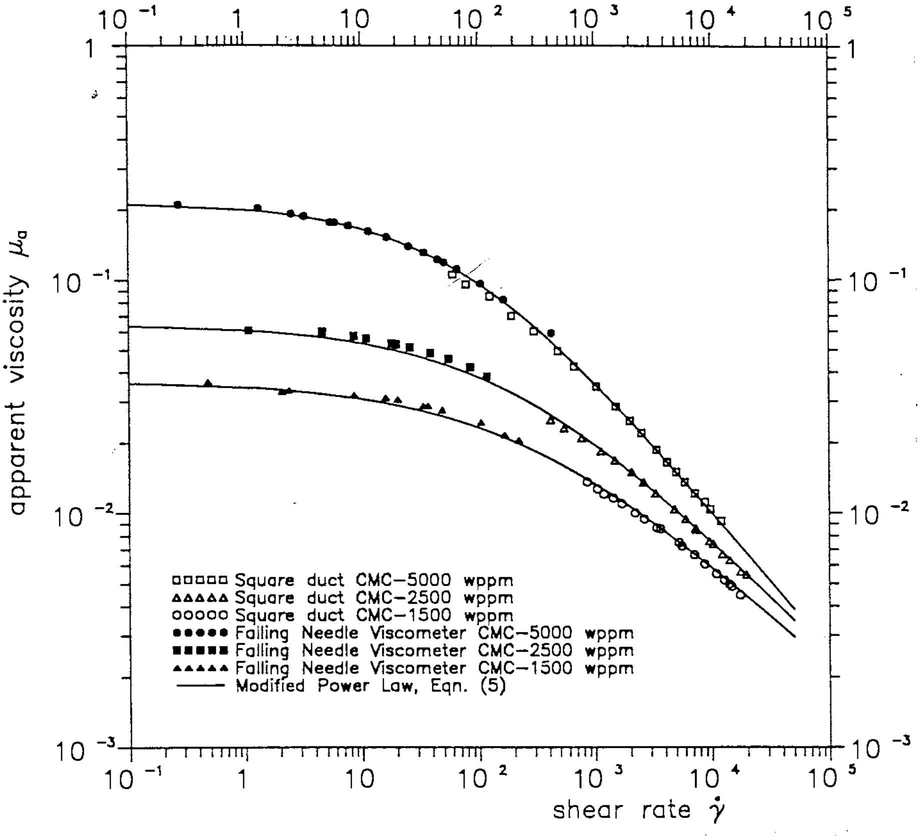

FIGURE 3.9.5 Experimental measurements of apparent viscosity vs. shear rate for polymer solutions (CMC-7H4) at different concentrations. (From Park, S. et al., in *Proc. Third World Conf. Heat Transfer, Fluid Mechanics, and Thermodynamics,* Vol. 1, Elsevier, New York, 1993, 900–908.

$$\mu^* = \frac{\mu_o}{1+\beta}$$

$$\beta = \frac{\mu_o}{K}\left(\frac{\bar{u}}{D_H}\right)^{1-n}$$

where β is the shear rate parameter mentioned previously which can be calculated by the designer for a certain operating duct ($\bar{u}$ and d) and a certain pseudoplastic fluid (μ_o, K, n). The solution for a circular tube has been calculated by Brewster and Irvine (1987) and the results are shown in Figure 3.9.6 and in Table 3.9.2. Referring to 3.9.6, we can see that when the $\log_{10} \beta$ is less than approximately –2, the duct is operating in region (a) of Figure 3.9.4 which is the Newtonian region and therefore classical Newtonian solutions can be used. Note that in the Newtonian region, Re_m reverts to the Newtonian Reynolds number given by

$$\mathrm{Re}_N = \frac{\rho \bar{u} D_H}{\mu_o} \tag{3.9.8}$$

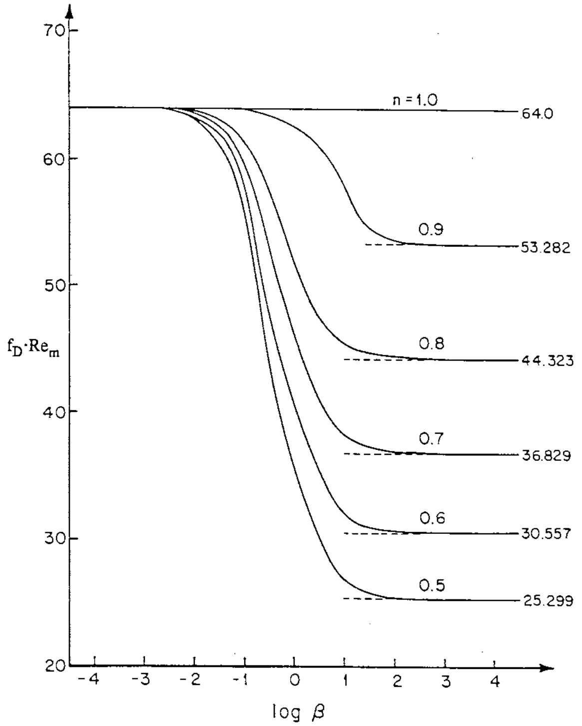

FIGURE 3.9.6 Product of friction factor and modified Reynolds number vs. $\log_{10} \beta$ for a circular duct. (From Brewster, R.A. and Irvine, T.F., Jr., *Wärme und Stoffübertragung,* 21, 83–86, 1987.

TABLE 3.9.2 Summary of Computed Values of $f_D \cdot Re_m$ for Various Values of n and β for a Circular Duct

b	$f_D \cdot Re_m$ for Flow Index: n =					
	1.0	0.9	0.8	0.7	0.6	0.5
10^{-5}	64.000	64.000	64.000	64.000	63.999	63.999
10^{-4}	64.000	63.999	63.997	63.995	63.993	63.990
10^{-3}	64.000	63.987	63.972	63.953	63.930	63.903
10^{-2}	64.000	63.873	63.720	63.537	63.318	63.055
10^{-1}	64.000	62.851	61.519	59.987	58.237	56.243
10^{0}	64.000	58.152	52.377	46.761	41.384	36.299
10^{1}	64.000	54.106	45.597	38.308	32.082	26.771
10^{2}	64.000	53.371	44.458	36.985	30.716	25.451
10^{3}	64.000	53.291	44.336	36.845	30.573	25.314
10^{4}	64.000	53.283	44.324	36.831	30.559	25.300
10^{5}	64.000	53.282	44.323	36.830	30.557	25.299
Exact solution	64.000	53.282	44.323	36.829	30.557	25.298

Source: Brewster, R.A. and Irvine, T.F., Jr., *Wärme und Stoffübertragung,* 21, 83–86, 1987. With permission.

When the value of $\log_{10} \beta$ is approximately in the range $-2 \leq \log_{10} \beta \leq 2$, the duct is operating in the transition region (b) of Figure 3.9.4 and the values of $f_D \cdot \mathrm{Re}_m$ must be obtained from Figure 3.9.6 or from Table 3.9.2.

When $\log_{10} \beta$ is greater than approximately 2, the duct is operating in the power law region (c) of Figure 3.9.4 and power law friction factor Reynolds number relations can be used. They are also indicated in Figure 3.9.6 and Table 3.9.2. In this region, Re_m becomes the power law Reynolds number given by

$$\mathrm{Re}_g = \frac{\rho \bar{u}^{2-n} D_H^n}{K} \tag{3.9.9}$$

For convenience, Brewster and Irvine (1987) have presented a correlation equation which agrees within 0.1% with the results tabulated in Table 3.9.2.

$$f_D \cdot \mathrm{Re}_m = \frac{1+\beta}{\dfrac{1}{64} + \dfrac{\beta}{2^{3n+3}\left(\dfrac{3n+1}{4n}\right)^n}} \tag{3.9.10}$$

Thus, Equation (3.9.10) contains all of the information required to calculate the circular tube laminar fully developed pressure drop for a pseudoplastic fluid depending upon the shear rate region(s) under consideration, i.e., regions (a), (b), or (c) of Figure 3.9.4. Note that in scaling such non-Newtonian systems, both Re_m and β must be held constant. Modified power law solutions have been reported for two other duct shapes. Park et al. (1993) have presented the friction factor–Reynolds number relations for rectangular ducts and Capobianchi and Irvine (1992) for concentric annular ducts.

Power Law Fluids

Since the power law region of modified power law fluids ($\log_{10} \beta \geq 2$) is often encountered, the friction factor–Reynolds number relations will be discussed in detail in this subsection.

An analysis of power law fluids which is most useful has been presented by Kozicki et al. (1967). Although the method is approximate, its overall accuracy (±5%) is usually sufficient for many engineering calculations. His expression for the friction factor–Reynolds number product is given by

$$f_D \cdot \mathrm{Re}^* = 2^{6n} \tag{3.9.11}$$

where

$$\mathrm{Re}^* = \text{Kozicki Reynolds number}, \quad \mathrm{Re}^* = \frac{\mathrm{Re}_g}{\left[\dfrac{a+bn}{n}\right]^n 8^{n-1}} \tag{3.9.12}$$

and a and b are geometric constants which depend on the cross-sectional shape of the duct. For example, for a circular duct, $a = 0.25$ and $b = 0.75$. Values of a and b for other duct shapes are tabulated in Table 3.9.3. For additional duct shapes in both closed and open channel flows, Kozicki et al. (1967) may be consulted.

Fully Developed Turbulent Flow Pressure Drops

In a number of engineering design calculations for turbulent flow, the shear rate range falls in region (c) of Figure 3.9.4. Thus, power law relations are appropriate for such pressure drop calculations.

TABLE 3.9.3 Constants *a* and *b* for Various Duct Geometrics Used in the Method Due to Kozicki et al. (1967)

Geometry	α^*	a	b
Concentric annuli 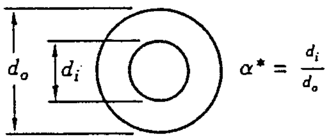	0.1	0.4455	0.9510
	0.2	0.4693	0.9739
	0.3	0.4817	0.9847
	0.4	0.4890	0.9911
	0.5	0.4935	0.9946
	0.6	0.4965	0.9972
	0.7	0.4983	0.9987
	0.8	0.4992	0.9994
	0.9	0.4997	1.0000
	1.0[a]	0.5000	1.0000
Rectangular 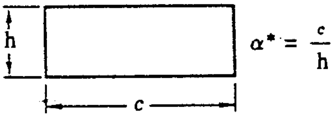	0.0	0.5000	1.0000
	0.25	0.3212	0.8482
	0.50	0.2440	0.7276
	0.75	0.2178	0.6866
	1.00	0.2121	0.8766
Elliptical 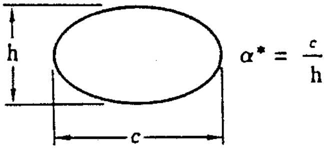	0.00	0.3084	0.9253
	0.10	0.3018	0.9053
	0.20	0.2907	0.8720
	0.30	0.2796	0.8389
	0.40	0.2702	0.8107
	0.50	0.2629	0.7886
	0.60	0.2575	0.7725
	0.70	0.2538	0.7614
	0.80	0.2515	0.7546
	0.90	0.2504	0.7510
	1.00[b]	0.2500	0.7500
Isosceles triangular 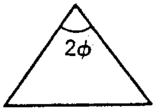	2ϕ (deg)		
	10	0.1547	0.6278
	20	0.1693	0.6332
	40	0.1840	0.6422
	60	0.1875	0.6462
	80	0.1849	0.6438
	90	0.1830	0.6395
Regular polygon (*N* sides) 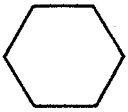	N		
	4	0.2121	0.6771
	5	0.2245	0.6966
	6	0.2316	0.7092
	8	0.2391	0.7241

[a] Parallel plates.

[b] Circle.

Source: Irvine, T.F., Jr. and Karni, J., in *Handbook of Single Phase Convective Heat Transfer,* John Wiley and Sons, New York, 1987, pp 20-1–20-57.

Hartnett and Kostic (1990) have investigated the various correlations which have appeared in the literature for circular tubes and have concluded that for a circular tube the relation proposed by Dodge and Metzner (1959) is the most reliable for pseudoplastic fluids. It is given by

$$\frac{1}{f_F^{1/2}} = \frac{4.0}{n^{0.75}} \cdot \log_{10}\left[\mathrm{Re}'_g \left(f_F\right)^{1-(1/2n)}\right] - \frac{0.40}{n^{1.2}} \tag{3.9.13}$$

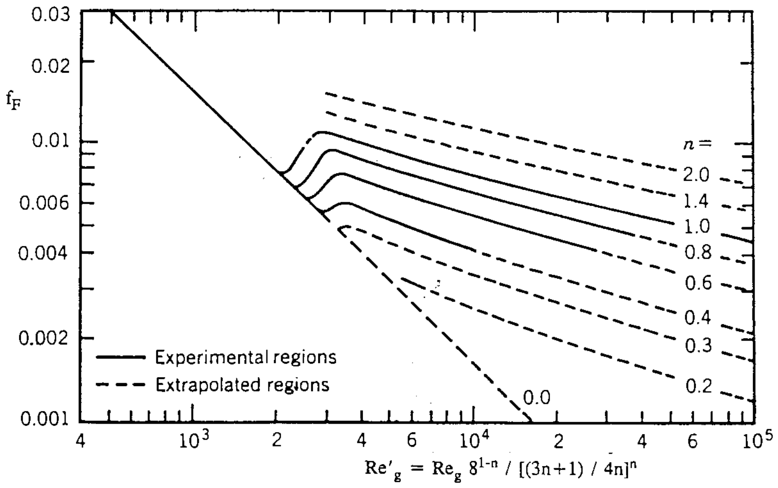

FIGURE 3.9.7 Dodge and Metzner relation between Fanning friction factor and Re'_g. (From Dodge, D.W. and Metzner, A.B., *AIChE J.*, 5, 189–204, 1959.)

where f_F is the Fanning friction factor and

$$\mathrm{Re}'_g = \mathrm{Re}_g \left[\frac{8^{1-n}}{\left[\dfrac{3n+1}{4n}\right]^n} \right] \tag{3.9.14}$$

Figure 3.9.7 is a graphical representation of Equation (3.9.13) which indicates the Dodge and Metzner experimental regions by solid lines, and by dashed lines where the data are extrapolated outside of their experiments.

For noncircular ducts in turbulent fully developed flow, only a limited amount of experimental data are available. Kostic and Hartnett (1984) suggest the correlation:

$$\frac{1}{f_F^{1/2}} = \frac{4}{n^{0.75}} \cdot \log_{10}\left[\mathrm{Re}^*\left(f_F\right)^{1-(1/2n)}\right] - \frac{0.40}{n^{0.5}} \tag{3.9.15}$$

where f_F is again the Fanning friction factor and Re^* is the Kozicki Reynolds number:

$$\mathrm{Re}^* = \frac{\mathrm{Re}_g}{\left[\dfrac{a+bn}{n}\right]^n 8^{n-1}} \tag{3.9.16}$$

and a and b are geometric constants given in Table 3.9.3.

Viscoelastic Fluids

Fully Developed Turbulent Flow Pressure Drops

Viscoelastic fluids are of interest in engineering applications because of reductions of pressure drop and heat transfer which occur in turbulent channel flows. Such fluids can be prepared by dissolving small amounts of high-molecular-weight polymers, e.g., polyacrylamide, polyethylene oxide (Polyox), etc., in

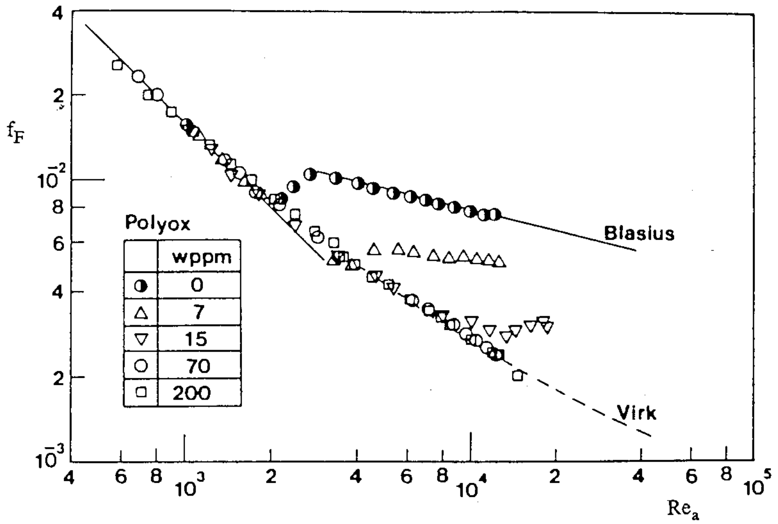

FIGURE 3.9.8 Reduction in friction factors for polyethylene oxide (Polyox) solutions in a small-diameter capillary tube. (From Cho, Y.I. and Harnett, J.P., *Adv. Heat Transfer,* 15, 59–141, 1982. With permission.)

water. Concentrations as low as 5 parts per million by weight (wppm) result in significant pressure drop reductions. Figure 3.9.8 from Cho and Hartnett (1982) illustrates the reduction in friction factors for Polyox solutions in a small-diameter capillary tube. It is seen that at zero polymer concentration the data agree with the Blasius equation for Newtonian turbulent flow. With the addition of only 7 wppm of Polyox, there is a significant pressure drop reduction and for concentrations of 70 wppm and greater all the data fall on the Virk line which is the maximum drag-reduction asymptote. The correlations for the Blasius and Virk lines as reported by Cho and Hartnett (1982) are

$$f_F = \frac{0.079}{\text{Re}^{1/4}} \quad \text{(Blasius)} \tag{3.9.17}$$

$$f_F = 0.20\,\text{Re}_a^{-0.48} \quad \text{(Virk)} \tag{3.9.18}$$

At the present time, no generally accepted method exists to predict the drag reduction between the Blasius and Virk lines. Kwack and Hartnett (1983) have proposed that the amount of drag reduction between those two correlations is a function of the Weissenberg number, defined as

$$w_s = \frac{\lambda \bar{u}}{D_H} \tag{3.9.19}$$

where λ = characteristic time of the viscoelastic fluid. They present correlations which allow the friction factor to be estimated at several Reynolds numbers between the Blasius and Virk lines.

Fully Developed Laminar Flow Pressure Drops

The above discussion on viscoelastic fluids has only considered fully developed turbulent flows. Laminar fully developed flows can be considered as nonviscoelastic but purely viscous non-Newtonian. Therefore, the method of Kozicki et al. (1967) may be applied to such situations once the appropriate rheological properties have been determined.

Nomenclature

a = duct shape geometric constant
b = duct shape geometric constant
c = duct width (see Table 3.9.3) (m)
d_i = concentric annuli inner diameter (see Table 3.9.3) (m)
d_o = concentric annuli outer diameter (see Table 3.9.3) (m)
f_D = Darcy friction factor
f_F = Fanning friction factor
h = duct height (see Table 3.9.3) (m)
K = fluid consistency ($\mathrm{Ns^n/m^2}$)
n = flow index
N = number of sides in polygon (see Table 3.9.3)
Re_g = generalized Reynolds number,

$$\mathrm{Re}_g = \frac{\rho \bar{u}^{2-n} D_H^n}{K}$$

Re_m = modified power law Reynolds number,

$$\mathrm{Re}_m = \frac{\rho \bar{u} D_H}{\mu^*}$$

Re_N = modified power law Reynolds number Newtonian asymptote,

$$\mathrm{Re}_N = \frac{\rho \bar{u} D_H}{\mu_o}$$

Re_a = apparent Reynolds number

$$\mathrm{Re}_a = \frac{\mathrm{Re}_g}{\left(\frac{3n+1}{4n}\right)^{n-1} 8^{n-1}}$$

Re^* = Kozicki Reynolds number

$$\mathrm{Re}^* = \frac{\rho \bar{u}^{2-n} D_H^n}{K\left[\frac{a+bn}{n}\right]^n 8^{n-1}}$$

Re'_g = Metzner Reynolds number

$$\mathrm{Re}'_g = \mathrm{Re}_g\left[\frac{8^{1-n}}{\left[\frac{3n+1}{4n}\right]^n}\right]$$

$\bar{u}$ = average streamwise velocity (m/sec)
t = time (sec)
w_s = Weissenberg number
x = direction of shear stress (m)
y = direction of velocity gradient (m)

Greek

α^* = duct aspect ratio in Table 3.9.3
β = shear rate parameter

$$\beta = \frac{\mu_o}{K}\left(\frac{\bar{u}}{D_H}\right)^{1-n}$$

$\dot{\gamma}$ = shear rate (L/sec)
ΔP = presure drop (N/m^2)
λ = characteristic time of viscoelastic fluid (sec)
μ_a = apparent viscosity (N · sec/m^2)
μ_o = zero shear rate viscosity (N · sec/m^2)
μ_∞ = high shear rate viscosity (N · sec/m^2)
μ^* = reference viscosity

$$\mu^* = \frac{\mu_o}{1+\beta} \quad \left(\mathrm{N\cdot sec/m^2}\right)$$

τ_o = yield stress (N/m^2)
$\tau_{y,x}$ = shear stress (N/m^2)
ϕ = half apex angle (see Table 3.9.3) (°)

References

Brewster, A.A. and Irvine, T.F. Jr. 1987. Similtude considerations in laminar flow of power law fluids in circular ducts, *Wärme und Stoffübertagung,* 21:83–86.

Capobianchi, M. and Irvine, T.F. Jr. 1992. Predictions of pressure drop and heat transfer in concentric annular ducts with modified power law fluids, *Wärme und Stoffübertagung,* 27:209–215.

Cho, Y.I. and Hartnett, J.P. 1982. Non-Newtonian fluids in circular pipe flow, in *Adv. Heat Transfer,* 15:59–141.

Darby, R. 1988. Laminar and turbulent pipe flows of non-Newtonian fluids, in *Encyclopedia of Fluid Mechanics,* Vol. 7, Gulf Publishing, Houston, 7:20–53.

Dodge, D.W. and Metzner, A.B. 1959. Turbulent flow of non-Newtonian systems, *AIChE J.,* 5:189–204.

Harnett, J.P. and Kostic, M. 1990. Turbulent Friction Factor Correlations for Power Law Fluids in Circular and Non-Circular Channels, *Int. Comm. Heat and Mass Transfer,* 17:59–65.

Irvine, T.F. Jr. and Karni, J. 1987. Non-Newtonian fluid flow and heat transfer, in *Handbook of Single Phase Convective Heat Transfer,* pp. 20-1–20-57, John Wiley and Sons, New York.

Kostic, M. and Hartnett, J.P. 1984. Predicting turbulent friction factors of non-Newtonian fluids in noncircular ducts, *Int. Comm. Heat and Mass Transfer,* 11:345–352.

Kozicki, W., Chou, C.H., and Tiu, C. 1967. Non-Newtonian flow in ducts of arbitrary cross-sectional shape, *Can. J. Chem. Eng.,* 45:127–134.

Kwack, E.Y. and Hartnett, J.P. 1983. Empirical correlations of turbulent friction factors and heat transfer coefficients for viscoelastic fluids, *Int. Comm. Heat and Mass Transfer,* 10:451–461.

Park, S., Irvine, T.F. Jr., and Capobianchi, M. 1993. Experimental and numerical study of friction factor for a modified power law fluid in a rectangular duct, *Proc. Third World Conf. Heat Transfer, Fluid Mechanics, and Thermodynamics,* Vol. 1, Elsevier, New York, 1:900–908.

Skelland, A.H.P. 1967. *Non-Newtonian Flow and Heat Transfer,* John Wiley and Sons, New York.

Whorlow, R.W. 1980. *Rheological Techniques,* Halsted Press, New York.

Further Information

It is not possible to include all of the interesting non-Newtonian topics in a section of this scope. Other items which may be of interest and importance are listed below along with appropriate references: hydrodynamic and thermal entrance lengths, Cho and Hartnett (1982); non-Newtonian flow over external surfaces, Irvine and Karni (1987); chemical, solute, and degradation effects in viscoelastic fluids, Cho and Harnett (1982); general references, Skelland (1967), Whorlow (1980), and Darby (1988).

3.10 Tribology, Lubrication, and Bearing Design

Francis E. Kennedy, E. Richard Booser, and Donald F. Wilcock

Introduction

Tribology — the science and technology of contacting surfaces involving friction, wear, and lubrication — is extremely important in nearly all mechanical components. A major focus of the field is on friction, its consequences, especially wear, and its reduction through lubrication and material surface engineering. The improper solution of tribological problems is responsible for huge economic losses in society, including shortened component lives, excessive equipment down time, and large expenditures of energy. It is particularly important that engineers use appropriate means to reduce friction and wear in mechanical systems through the proper selection of bearings, lubricants, and materials for all contacting surfaces. The aim of this chapter is to assist in that endeavor.

Sliding Friction and Its Consequences

Coefficient of Friction

If two stationary contacting bodies are held together by a normal force W, and if a tangential force is applied to one of them, the tangential force can be increased until it reaches a magnitude sufficient to initiate sliding. The ratio of the friction force at incipient sliding to the normal force is known as the static coefficient of friction, f_s. After sliding begins, the friction force always acts in the direction opposing motion and the ratio between that friction force and the applied normal force is the kinetic coefficient of friction, f_k.

Generally, f_k is slightly smaller than f_s and both coefficients are independent of the size or shape of the contacting surfaces. Both coefficients are very much dependent on the materials and cleanliness of the two contacting surfaces. For ordinary metallic surfaces, the friction coefficient is not very sensitive to surface roughness. For ultrasmooth or very rough surfaces, however, the friction coefficient can be larger. Typical friction coefficient values are given in Table 3.10.1. Generally, friction coefficients are greatest

TABLE 3.10.1 Some Typical Friction Coefficients[a]

Material Pair	Static Friction Coefficient, f_s		Kinetic Friction Coefficient, f_k	
	In Air	In Vacuo	In Air, Dry	Oiled
Mild steel vs. mild steel	0.75		0.57	0.16
Mild steel vs. copper	0.53	0.5 (oxidized) 2.0 (clean)	0.36	0.18
Copper vs. copper	1.3	21.0	0.8	0.1
Tungsten carbide vs. copper	0.35		0.4	
Tungsten carbide vs. tungsten carbide	0.2	0.4	0.15	
Mild steel vs. PTFE	0.04		0.05	0.04

[a] The friction coefficient values listed in this table were compiled from several of the references listed at the end of this section.

when the two surfaces are identical metals, slightly lower with dissimilar but mutually soluble metals, still lower for metal against nonmetal, and lowest for dissimilar nonmetals.

The kinetic coefficient of friction, f_k, for metallic or ceramic surfaces is relatively independent of sliding velocity at low and moderate velocities, although often a slight decrease occurs in f_k at higher velocities. With polymers and soft metals, the friction coefficient may increase with increasing velocity until a peak is reached, after which the friction may decrease with further increases in velocity or temperature. The decrease in kinetic friction coefficient with increasing velocity, which may become especially pronounced at higher sliding velocities, can be responsible for friction-induced vibrations (stick-slip oscillations) of the sliding systems. Such vibrations are an important design consideration for clutches and braking systems; they can also be important in the accurate control and positioning of robotic mechanisms and precision manufacturing systems.

Wear

Wear is the unwanted removal of material from solid surfaces by mechanical means; it is one of the leading reasons for the failure and replacement of manufactured products. It has been estimated that the costs of wear, which include repair and replacement along with equipment downtime, constitute up to 6% of the U.S. gross national product (Rabinowicz, 1995). Wear can be classified into four primary types: sliding wear, abrasion, erosion, and corrosive wear. Owing to its importance, wear and its control have been the subject of several handbooks (Peterson and Winer, 1980; Blau, 1992) that the interested reader may consult for further information.

Types of Wear

Sliding wear occurs to some degree whenever solid surfaces are in sliding contact; the two predominant sliding wear mechanisms are adhesion and surface fatigue. *Adhesive wear* is caused by strong adhesive forces between the two surfaces within the real area of contact. It results in the removal of small particles from at least one of the surfaces, usually the softer one. These particles can then transfer to the other surface or mix with other material from both surfaces before being expelled as loose wear debris. Adhesive wear can be particularly severe for surfaces that have a strong affinity for each other, such as those made from identical metals. *Surface fatigue wear* occurs when repeated sliding or rolling/sliding over a wear track results in the initiation of surface or subsurface cracks and the propagation of those cracks produces wear particles in ductile materials by a process called delamination. With brittle materials, sliding wear often occurs by a *surface fracture* process.

After an initial transition or "running-in" period, sliding wear tends to reach a steady-state rate, which is approximated by the following Archard (or Holm–Archard) wear equation:

$$V = K * W * s/H \tag{3.10.1}$$

where V = volume of worn material; K = dimensionless wear coefficient; s = sliding distance; W = normal load between the surfaces; and H = hardness of the softer of the two contacting surfaces.

The dimensionless wear coefficient gives an indication of the tendency of a given material combination to wear; relative wear coefficient values are given in Figure 3.10.1. In general, wear coefficients are highest for identical metals sliding without lubrication, and wear is decreased by adding a lubricant and by having dissimilar material pairs.

Abrasive wear occurs when a hard, rough surface slides against a softer surface (*two-body abrasion*) or when hard particles slide between softer surfaces (*three-body abrasion*). This process usually results in material removal by plowing or chip formation, especially when the abraded surface is metallic; surface fracture can occur during abrasion of brittle surfaces. In fact, abrasion mechanisms are similar to those of grinding and lapping, which could be considered intentional abrasion. Consideration of the cutting and plowing processes shows that abrasive wear obeys the same equation (Equation 3.10.1) as sliding wear does (Archard, 1980; Rabinowicz, 1995). Typical wear coefficients for abrasive wear are given in Figure 3.10.1. Because the relative size, hardness, and sharpness of the abrading particles, or surface

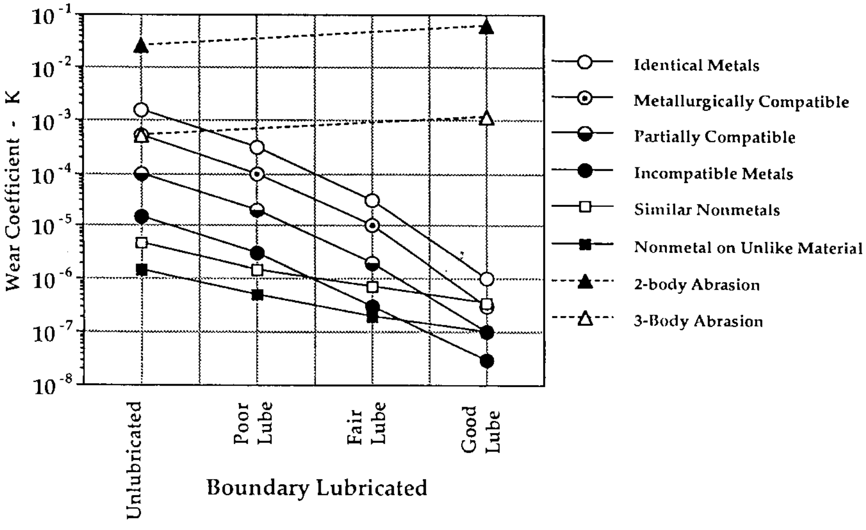

FIGURE 3.10.1 Typical values of wear coefficient for sliding and abrasive wear. (Modified from Rabinowicz, E., in *Wear Control Handbook*, M.B. Peterson and W.O. Winder, Eds., 475–506, ASME, New York, 1980, and Rabinowicz, E., *Friction and Wear of Materials*, 2nd ed., John Wiley & Sons, New York, 1995.)

asperities, also affect abrasive wear rates, the wear coefficients for abrasion must include recognition of those factors (Rabinowicz, 1995).

Erosion occurs when solid particles or liquid droplets impinge on a solid surface. When impingement is on a ductile metallic surface, the wear process is similar to that caused by abrasion and is dominated by plastic deformation. Brittle surfaces, on the other hand, tend to erode by surface fracture mechanisms. The material removal rate is dependent on the angle of attack of the particles, with erosion reaching a peak at low angles (about 20°) for ductile surfaces and at high angles (90°) for brittle materials. In either case, the wear rate is proportional to the mass rate of flow of the particles and to their kinetic energy; it is inversely proportional to the hardness of the surface and the energy-absorbing potential (or toughness) of the impinged surface (Schmitt, 1980). Although erosion is usually detrimental, it can be used beneficially in such material removal processes as sand blasting and abrasive water-jet machining.

Corrosive wear results from a combination of chemical and mechanical action. It involves the synergistic effects of chemical attack (corrosion) of the surface, followed by removal of the corrosion products by a wear mechanism to expose the metallic surface, and then repetition of those processes. Because many corrosion products act to protect the surfaces from further attack, the removal of those films by wear acts to accelerate the rate of material removal. Corrosive wear can become particularly damaging when it acts in a low-amplitude oscillatory contact, which may be induced by vibration, in which case it is called *fretting corrosion.*

Means for Wear Reduction

The following actions can be taken to limit *sliding wear*:

- Ensure that the sliding surfaces are well lubricated. This can best be accomplished by a liquid lubricant; however, grease or solid lubricants such as graphite or molybdenum disulfide can sometimes be effective when liquid lubricants cannot be used.
- Choose dissimilar materials for sliding pairs.
- Use hardened surfaces.
- Add wear-resistant coatings to the contacting surfaces (see the following subsection).
- Reduce normal loads acting on the contact.
- Reduce surface temperatures (particularly important for polymer surfaces).

To reduce *abrasive wear*:

- Use hardened surfaces.
- Add a hard surface coating.
- Reduce the roughness of hard surfaces in contact with softer surfaces.
- Provide for the removal of abrasive particles from contacting surfaces. This can be done by flushing surfaces with liquid and/or filtering liquid coolants and lubricants.
- Reduce the size of abrasive particles.

To reduce *erosion*:

- Modify the angle of impingement of solid particles or liquid droplets.
- Provide for the removal of solid particles from the impinging stream of fluid.
- Use hardened surfaces.
- Use tough materials for surfaces.
- Add protective coating to surfaces.

Surface Engineering for Friction and Wear Reduction

Surface treatments have long been an important remedy for wear problems —an importance that has grown in recent years with the introduction of new techniques to harden surfaces or apply hard surface coatings (Bhushan, 1999). Available processes and characteristics for treating a steel substrate are listed in Table 3.10.2.

Thermal transformation hardening processes are used to harden ferrous (primarily steel) surfaces by heating the surface rapidly, transforming it to austenite, and then quenching it to form martensite. The source of heat can be one of the following: an oxyacetylene or oxypropane flame (*flame hardening*); eddy currents induced by a high-frequency electric field (*induction hardening*); a beam from a high-power laser (*laser hardening*); or a focused electron beam (*electron beam hardening*). The depth and uniformity of the hard layer depend on the rate and method of heating. These processes are characterized by a short process time and all except electron beam hardening (which requires a moderate vacuum) can be done in air.

Thermal diffusion processes involve the diffusion of atoms into surfaces to create a hard layer. In the most widely used of these processes — *carburizing* (or case hardening) — carbon diffuses into a low-carbon steel surface to produce a hard, carbon-rich “case.” The hardness and thickness of the case depend

TABLE 3.10.2 Characteristics of Surface Treatment Processes for Steel

	Coating or Treated Layer		Substrate
Process	Hardness (HV)	Thickness (μm)	Temperature (°C)
Surface hardening			
Flame or induction hardening	500–700	250–6000	800–1000
Laser or electron beam hardening	500–700	200–1000	950–1050
Carburizing	650–900	50–1500	800–950
Carbonitriding	650–900	25–500	800–900
Citriding	700–1200	10–200	500–600
Boronizing	1400–1600	50–100	900–1100
Coating			
Chrome plating	850–1250	1–500	25–100
Electroless nickel	500–700	0.1–500	25–100
Hardfacing	800–2000	500–50000	1300–1400
Thermal spraying	400–2000	50–1500	<250
PVD	100–3000	0.05–10	100–300
CVD	1000–3000	0.5–100	150–2200
PACVD	1000–5000	0.5–10	<300
Ion implantation	750–1250	0.01–0.25	<200

on the temperature, exposure time, and source of carbon (a hydrocarbon gas, salt bath, or packed bed of carbon). *Carbonitriding* is a process similar to carburizing that involves simultaneous diffusion of carbon and nitrogen atoms into carbon steel surfaces. In the *nitriding* process, nitrogen atoms diffuse into the surface of steel that contains nitride-forming elements (such as Al, Cr, Mo, V, W, or Ti) and form fine precipitates of nitride compounds in a near-surface layer. The hardness of the surface layer depends on the types of nitrides formed. The source of nitrogen can be a hot gas (usually ammonia) or a plasma. *Nitrocarburizing* and *boronizing* are related processes in which nitrogen or boron atoms diffuse into steel surfaces and react with the iron to form a hard layer of iron carbonitride or iron boride, respectively.

Thin, hard metallic coatings can be very effective in friction and wear reduction and can be applied most effectively by *electroplating processes* (Weil and Sheppard, 1992). The most common of such coatings are *chromium*, which is plated from a chromic acid bath, and *electroless nickel*, which is deposited without electric current from a solution containing nickel ions and a reducing agent. Chromium coatings generally consist of fine-grained chromium with oxide inclusions, while electroless nickel coatings contain up to 10% of phosphorus or boron, depending on the reducing agent used.

Thermal spray processes (Kushner and Novinski, 1992) enable a large variety of coating materials, including metals, ceramics, and polymers, to be deposited rapidly on a wide range of substrates. Four different thermal spray processes are commercially available: *oxyfuel* (or flame) spraying of metallic wire or metallic or ceramic powder; *electric arc* spraying of metallic wire; *plasma* arc spraying of powder (metallic or ceramic); and *high-velocity oxyfuel* (or detonation gun) powder spray. In each of the thermal spray processes, the coating material, in wire or powder form, is heated to a molten or plastic state, and the heated particles are propelled toward the surface to be coated where they adhere and rapidly solidify to form a coating. The hardness of the coating depends on the sprayed material and the process parameters.

Weld hardfacing processes (Crook and Farmer, 1992) involve the application of a wear-resistant material to the surface of a part by means of a weld overlay. Weld overlay materials include ferrous alloys (such as martensitic air-hardening steel or high chromium cast iron); nonferrous alloys (primarily cobalt- or nickel-based alloys containing hard carbide, boride, or intermetallic particles); and cemented carbides (usually tungsten carbide/cobalt cermets). In each case, the surface being coated is heated to the same temperature as the molten weld layer, thus posing a limitation to the process. Weld hardfacing is best used when abrasion or sliding wear cannot be avoided (as with earthmoving or mining equipment) and the goal is to limit the wear rate.

Vapor deposition processes for wear-resistant coatings include *physical vapor deposition* (PVD), *chemical vapor deposition* (CVD), and several variants of those basic processes (Bhushan and Gupta, 1991; Holmberg and Matthews, 1994). Each of the processes consists of three steps:

1. Creation of a vapor phase of the coating material
2. Transportation of the vapor from source to substrate
3. Condensation of the vapor phase on the substrate and growth of a thin solid film

In PVD processes, the vapor is produced by evaporation (by heating of the coating source) or sputtering (in which coating material is dislodged and ejected from the source due to bombardment by energetic particles). In some PVD processes, the vapor becomes ionized or reacts with a gas or plasma en route to the substrate, thus modifying the structure or composition of the deposited film. In CVD processes, a gas composed of a volatile component of the coating material is activated thermally or by other means in the vicinity of the substrate, and it reacts to form a solid deposit on the surface of the hot substrate.

PVD and CVD methods can be used to produce a wide variety of coatings, including metals, alloys, and refractory compounds. Among the most popular vapor-deposited hard coatings for wear resistance are titanium nitride, titanium carbide, and hard amorphous carbon (diamond-like carbon). Deposition rates are relatively low compared to some other coating processes, ranging from <0.1 μm/min for some ion beam sputtering or ion plating processes, up to 25 μm/min or more for activated reactive evaporation or CVD processes.

Most PVD processes are done in a vacuum, while CVD processes are done in a reaction chamber that may be at atmospheric pressure. *Plasma-assisted chemical vapor deposition* (PACVD) is a hybrid process in which the constituents of the vapor phase react to form a solid film when assisted by a glow discharge plasma. The advantages of PACVD over other CVD processes include lower substrate temperatures, higher deposition rates, and a wider variety of coating possibilities.

Ion implantation (Fenske, 1992) is a process in which charged particles are created in an ion source, accelerated toward the surface at high velocity, and then injected into the substrate surface. The most commonly implanted ions for surface engineering are nitrogen, carbon, boron, and titanium, although virtually any element could be implanted. The microstructure of the near-surface region is changed by the presence of the implanted ions and the result can be high near-surface hardness and wear resistance. The affected layer is very thin (<1 μm).

Effect of Lubrication on Friction and Wear

Whenever lubricated surfaces slide together at low sliding speeds or with a high applied normal load, the lubricant may not separate the two solid surfaces completely. However, it can still significantly reduce the friction coefficient by reducing the shear strength of adhesive junctions between the two surfaces. In this so-called "boundary lubrication" regime, the effectiveness of the lubricant can be improved if the lubricant molecules adhere well to the solid surfaces. This is best accomplished by introducing a lubricant or additive that forms a surface film through adsorption, chemisorption, or chemical reaction with the surface. The ensuing reduced shear strength of the surface film can lower the friction coefficient by as much as an order of magnitude from the dry friction value.

When a good supply of a viscous lubricant is available, the separation between the surfaces will increase as the sliding speed increases or the normal load decreases. As the separation increases, the amount of solid–solid contact between the surfaces will decrease, as will the friction coefficient and wear rate. In this "mixed friction" regime, friction is determined by the amount of plowing deformation on the softer surface by the harder surface asperities and by adhesion within the solid–solid contacts. When the surfaces become completely separated by a self-acting or externally pressurized lubricant film, the lubricating regime is hydrodynamic, wear is reduced to nearly zero, and friction reaches a low value governed by viscous shear of the lubricant. Friction coefficients in such cases can be 0.001 or lower, depending on the surface velocities and the lubricant viscosity. This is the case for most journal or thrust bearings (see the subsection on fluid film bearings).

Bearings for Friction Reduction

Most mechanical systems contain moving components, such as shafts, which must be supported and held in position by stationary members. This is best done by appropriate design or selection of bearings to be used wherever the moving member is to be supported. Most bearings may be classified as fluid film bearings, dry or semilubricated bearings, or rolling element bearings.

Fluid film bearings (see subsection below) have a conformal geometry, with a thin film of fluid separating the two surfaces. The fluid lubricant could be a liquid, such as oil, or a gas, such as air. Fluid film bearings are commonly used to support rotating cylindrical shafts, and the load on such a bearing could be radial, in which case the bearing is called a journal bearing, or axial, for a thrust bearing. In most cases, the fluid film is generated by the motion within the bearing, so the bearing is called self-acting or hydrodynamic.

Whether a self-acting bearing can develop a fluid film sufficient to separate and support the two surfaces is determined by magnitude of the quantity $\mu U/W$, where μ is the (absolute) fluid viscosity; U is the relative sliding velocity; and W is the normal load. If that quantity is too small, the fluid film will be too thin and high friction will occur. Although this can be a problem during start-up of equipment when sliding velocities are low, it can be overcome by pressurizing the fluid film from an external pressure source to create a hydrostatic bearing. Whether the fluid film is externally pressurized (hydrostatic) or self-acting (hydrodynamic), separation of the solid surfaces allows wear to be essentially eliminated and friction to be very low, even when very large loads are carried by the pressurized lubricant.

TABLE 3.10.3 Bearing Characteristics

	Fluid Film Bearings	Dry Bearings	Semilubricated	Rolling Element Bearings
Start-up friction coefficient	0.25	0.15	0.10	0.002
Running friction coefficient	0.001	0.10	0.05	0.001
Velocity limit	High	Low	Low	Medium
Load limit	High	Low	Low	High
Life limit	Unlimited	Wear	Wear	Fatigue
Lubrication requirements	High	None	Low/none	Low
High temperature limit	Lubricant	Material	Lubricant	Lubricant
Low temperature limit	Lubricant	None	None	Lubricant
Vacuum	Not applicable	Good	Lubricant	Lubricant
Damping capacity	High	Low	Low	Low
Noise	Low	Medium	Medium	High
Dirt/dust	Need seals	Good	Fair	Need seals
Radial space requirement	Small	Small	Small	Large
Cost	High	Low	Low	Medium

Dry and semilubricated bearings (see subsection below) have conformal surfaces in direct contact with each other. This category includes bearings that run dry (without liquid lubrication) or those that have been impregnated with a lubricant. Dry bearings are made of a material such as a polymer or carbon-graphite, which has a low friction coefficient; they are generally used in low-load and low-speed applications. Semilubricated bearings are made of a porous material, usually metal, and are impregnated with a lubricant that resides within the pores. The lubricant, which could be oil or grease, cannot provide a complete fluid film, but usually acts as a boundary lubricant. Semilubricated bearings can carry greater loads at greater speeds than dry bearings, but not as high as fluid film or rolling element bearings. The failure mechanism for dry and semilubricated bearings is wear.

Rolling element bearings (see subsection below) take advantage of the fact that rolling friction is usually lower than sliding friction. These bearings include rolling elements, either balls or rollers, between hardened and ground rings or plates. Their main advantage over fluid film bearings is that they have low friction during startup and at operating velocities, although the friction can be higher than that of fluid film bearings during steady-state operation. Ball and roller bearings are most commonly lubricated by oil or grease. In either case, the lubricating film at the concentrated contacts between rolling elements and rings is very thin and the pressures in the film are very high; this is a condition known as elastohydrodynamic lubrication. Rolling element bearings fail by a number of mechanisms, often stemming from improper installation, use, or poor lubrication, but the overriding failure mechanism is rolling contact fatigue.

Each type of bearing has advantages and disadvantages, which are summarized in Table 3.10.3. The Engineering Sciences Data Unit (1965, 1967) has developed some general guides to the selection of bearing type for different load and speed conditions. Those guides for journal and thrust bearing selection are given in Figure 3.10.2 and Figure 3.10.3.

Lubricant Properties

Petroleum Oils

The vast majority of lubricants in use today are mineral oils obtained through the distillation of crude petroleum. Mineral oils are composed primarily of three types of hydrocarbon structures: paraffinic, aromatic, and alicyclic (naphthenic). The molecular weights of the hydrocarbons range from about 250, for low viscosity grades, up to nearly 1000 for more viscous lubricants. Mineral oils by themselves do not have all of the properties required of modern lubricants. For that reason, almost all current lubricants are fortified with a chemical additive package consisting of some of the following (Rudnick, 2003; Totten, 2003):

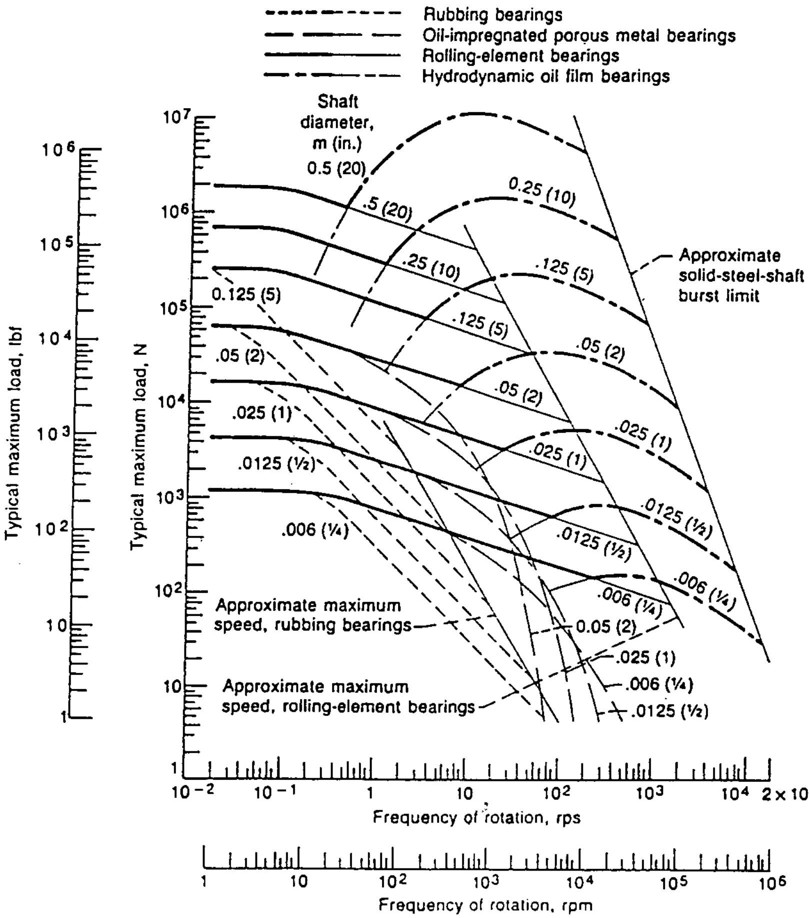

FIGURE 3.10.2 General guide to journal bearing type selection. Except for rolling element bearings, curves are drawn for bearings with width/diameter = 1. A medium viscosity mineral oil is assumed for hydrodynamic bearings. (ESDU, *General Guide to the Choice of Journal Bearing Type*, item 65007, Institution of Mechanical Engineers, London, 1965.)

- *Oxidation inhibitors* limit oxidation of hydrocarbon molecules by interrupting the hydroperoxide chain reaction.
- *Rust inhibitors* are surface-active additives that preferentially adsorb on iron or steel surfaces and prevent their corrosion by moisture.
- *Antiwear and extreme pressure agents* form low shear strength films on metallic surfaces, which limit friction and wear, particularly in concentrated contacts.
- *Friction modifiers* form adsorbed or chemisorbed surface films that are effective in reducing friction of bearings during low-speed operation (boundary lubrication regime).
- *Detergents* and *dispersants* reduce deposits of oil-insoluble compounds (e.g., sludge) in internal combustion engines.
- *Pour-point depressants* lower the temperature at which petroleum oils become immobilized by crystallized wax.
- *Foam inhibitors* are silicone polymers, which enhance the separation of air bubbles from the oil.
- *Viscosity-index improvers* are long chain polymer molecules that reduce the effect of temperature on viscosity. They are used in multigrade lubricants.

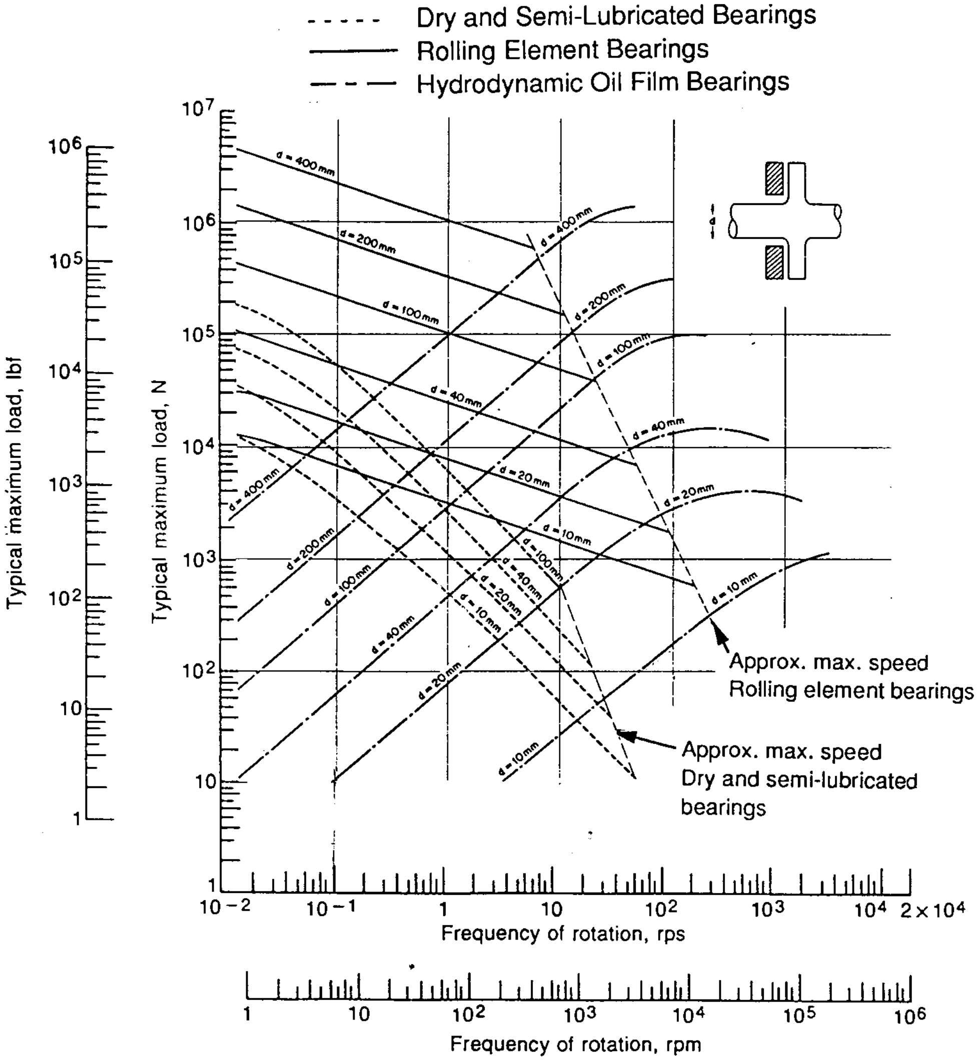

FIGURE 3.10.3 General guide to thrust bearing type selection. Except for rolling element bearings, curves are drawn for a ratio of inside diameter to outside diameter equal to 2 and for a nominal life of 10,000 h. A medium viscosity mineral oil is assumed for hydrodynamic bearings. (Based on ESDU, *General Guide to the Choice of Thrust Bearing Type*, item 67073, Institution of Mechanical Engineers, London, 1967, and Neale, M.J., *Bearings*, Butterworth–Heinemann, Oxford, U.K., 1993.)

Properties of Petroleum Oils

The lubricating oil property of most significance to bearing performance is viscosity. The absolute viscosity, designated as μ, could be given in SI units as Pascal second (Pa·sec = N•sec/m^2) or centiPoise (1 cP = 0.001 Pa·sec) or in English units as lb·sec/in.^{2} or reyn. Kinematic viscosity, designated here as ν, is defined as absolute viscosity divided by density. It is given in SI units as m^2/sec or centiStokes (1 cSt = 10^{-6} m^2/sec) and in English units as in.^{2}/sec.

Viscosity data in Table 3.10.4 are representative of typical petroleum “turbine” and “hydraulic” oils widely used in industry; they closely correspond to properties of most other commercially available petroleum oils. Table 3.10.5 gives equivalent viscosity grades for common automotive (SAE); gear (SAE

TABLE 3.10.4 Representative Oil Properties

	Viscosity				Density	
	Centistokes		10^{-6} reyns (lb·sec/in.^{2})		gm/cc	lb/in.^{3}
	40°C	100°C	104°F	212°F	40°C	104°F
ISO Grade (Equivalent SAE)						
32 (10W)	32.0	5.36	3.98	0.64	0.857	0.0310
46 (20)	46.0	6.76	5.74	0.81	0.861	0.0311
68 (20W)	68.0	8.73	8.53	1.05	0.865	0.0313
100 (30)	100.0	11.4	12.60	1.38	0.869	0.0314
150 (40)	150.0	15.0	18.97	1.82	0.872	0.0315
220 (50)	220.0	19.4	27.91	2.36	0.875	0.0316
SAE Multigrade						
5W-30	64.2	11.0	8.15	0.99	0.860	0.0311
10W-30	69.0	11.0	8.81	1.08	0.865	0.0312
10W-40	93.5	14.3	11.9	1.45	0.865	0.0312
20W-50	165.5	18.7	21.3	2.74	0.872	0.0315

TABLE 3.10.5 Equivalent Viscosity Grades for Industrial Lubricants

ISO-VG Grade	Viscosity (cSt) (at 40°C)		SAE Crankcase Oil Grades[a]	SAE Aircraft Oil Grades[a]	SAE Gear Lube Grades[a]	AGMA Gear Lube Grades	
	Minimum	Maximum				Regular	EP
2	1.98	2.42	—	—	—	—	—
3	2.88	3.52	—	—	—	—	—
5	4.14	5.06	—	—	—	—	—
7	6.12	7.48	—	—	—	—	—
10	9.00	11.0	—	—	—	—	—
15	13.5	16.5	—	—	—	—	—
22	19.8	24.2	5W	—	—	—	—
32	28.8	35.2	10W	—	—	—	—
46	41.4	50.6	15W	—	75W	1	—
68	61.2	74.8	20W	—	—	2	2 EP
100	90.0	110	30	65	80W-90	3	3 EP
150	135	165	40	80	—	4	4 EP
220	198	242	50	100	90	5	5 EP
320	288	352	60	120	—	6	6 EP
460	414	506	—	—	85W-140	7 Comp	7 EP
680	612	748	—	—	—	8 Comp	8 EP
1000	900	1100	—	—	—	8A comp	8A EP
1500	1350	1650	—	—	250	—	—

[a] Comparisons are nominal because SAE grades are not specified at 40°C vis; VI of lubes could change some of the comparisons.

and AGMA); and reciprocating aircraft engine (SAE) oils (Booser, 1995). Equivalent ISO viscosity grades are listed for the single-graded SAE automotive oils such as SAE 10W and SAE 30. For multigrade oils such as SAE 10W-30, however, the added viscosity-index improvers provide unique viscosity-temperature characteristics. Typical properties of a number of these multigrade SAE oils are included in Table 3.10.4.

ISO viscosity grade 32 and the equivalent SAE 10W are most widely used industrially. Lower viscosity oils often introduce evaporation and leakage problems, along with diminished load capacity. Higher viscosity may lead to high temperature rise, unnecessary power loss, and start-up problems at low temperature. For low-speed machines, however, higher viscosity oils ranging up to ISO 150, SAE 40, and sometimes higher are often used to obtain higher load capacity.

Oil viscosity decreases significantly with increasing temperature as shown in Figure 3.10.4. Although this figure provides viscosity data suitable for most bearing calculations, oil suppliers commonly provide

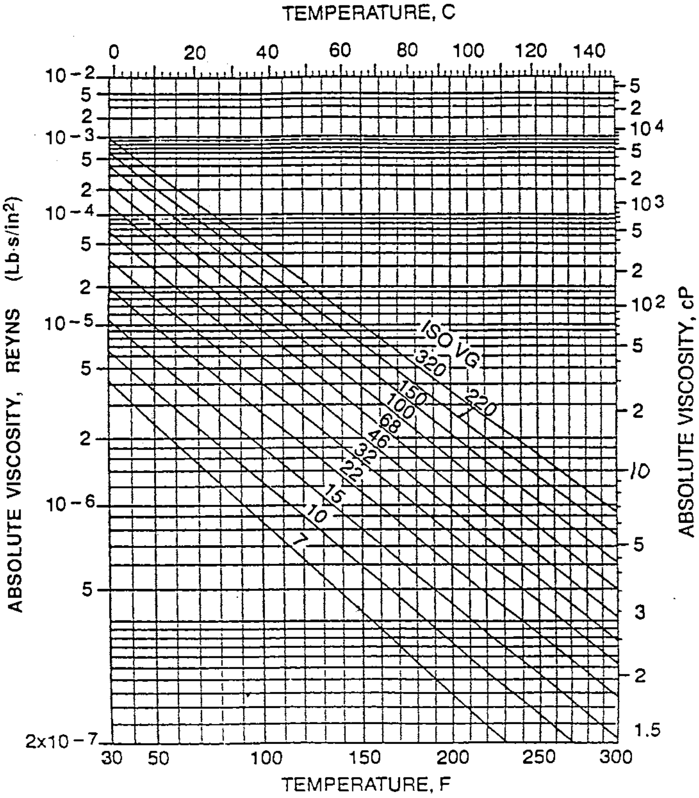

FIGURE 3.10.4 Viscosity-temperature chart for industrial petroleum oils. (Based on Raimondi, A.A. and Szeri, A.A., in *Handbook of Lubrication*, vol. 2, 413–462, CRC Press, Boca Raton, FL, 1984.)

only the 40 and 100°C values of kinematic viscosity in centistokes (mm²/sec). The viscosity at other temperatures can be found by the following ASTM D341 equation relating kinematic viscosity ν in centistokes (mm²/sec) to temperature T in degrees F:

$$\text{loglog}\,(\nu + 0.7) = A - B\log\,(460 + T) \tag{3.10.2}$$

where A and B are constants for any particular (petroleum or synthetic) oil. For ISO VG-32 oil in Table 3.10.4, for example, $A = 10.54805$ and $B = 3.76834$, based on the 104 and 212°F (40 and 100°C) viscosities. This gives a viscosity of 10.78 cSt at a bearing operating temperature of 160°F.

Conversion of kinematic to absolute viscosity requires use of density, which also varies with temperature. A coefficient of expansion of 0.0004/°F is typical for most petroleum oils, so the variation of density with temperature is in accordance with the following relation:

$$\rho_T = \rho_{104}\,[1 - 0.0004\,(T - 104)] \tag{3.10.3}$$

For the ISO-VG-32 oil with its density of 0.857 gm/cc at 100°F (40°C), this equation gives 0.838 gm/cc at 160°F. Multiplying 10.78 cSt by 0.838 then gives an absolute viscosity of 9.03 cP. Multiplying by the conversion factor of 1.45×10^{-7} gives 1.31×10^{-6} lb·sec/in.² (Reyns).

Heat capacity C_p of petroleum oils used in bearing calculations is given by (Klaus and Tewksbury, 1984):

$$C_p = 3860 + 4.5(T) \quad \text{in-lb/lb-°F} \tag{3.10.4}$$

The viscosity of petroleum oils is also affected significantly by pressure, and that increase can become important in concentrated contacts such as rolling element bearings where elastohydrodynamic lubrication occurs. The following relationship can be used for many oils to find the viscosity at elevated pressure:

$$\mu_p = \mu_o \, e^{\alpha p} \tag{3.10.5}$$

where μ_o is the viscosity at atmospheric pressure; μ_p is the viscosity at pressure p; and α is the pressure-viscosity exponent. This exponent, available from lubricant suppliers, generally ranges from about 1.0×10^{-4} psi^{-1} for low viscosities up to about 2.0×10^{-4} psi^{-1} at higher viscosities for many mineral and synthetic oils.

Synthetic Oils

Synthetic oils of widely varying characteristics are finding increasing use for applications at extreme temperatures and for their unique physical and chemical characteristics (Rudnick and Shubkin, 1999). Table 3.10.6 gives a few representative examples of commercially available synthetic oils. Cost of the synthetics, ranging up to many times that of equivalent petroleum oils, is a common deterrent to their use in situations in which petroleum products give satisfactory performance.

TABLE 3.10.6 Properties of Representative Synthetic Oils

	Viscosity, cSt					
Type	100°C	40°C	–54°C	Pour Point (°C)	Flash Point (°C)	Typical Uses
Synthetic hydrocarbons						
Mobil 1, 5W-30[a]	11	58		–54	221	Auto engines
SHC 824[a]	6.0	32		–54	249	Gas turbines
SHC 629[a]	19	141		–54	238	Gears
Organic esters						
MIL-L-7808	3.2	13	12,700	–62	232	Jet engines
MIL-L-23699	5.0	24	65,000	–56	260	Jet engines
Synesstic 68[b]	7.5	65		–34	266	Air compressors; hydraulics
Polyglycols						
LB-300-X[c]	11	60		–40	254	Rubber seals
50-HB-2000[c]	70	398		–32	226	Water solubility
Phosphates						
Fyrquel 150[d]	4.3	29		–24	236	Fire-resistant fluids for die casting; air compressors and hydraulic systems
Fyrquel 220[d]	5.0	44		–18	236	
Silicones						
SF-96 (50)	16	37	460	–54	316	Hydraulic and damping
SF-95 (1000)	270	650	7,000	–48	316	Fluids
F-50	16	49	2,500	–74	288	Aircraft and missiles
Fluorochemical						
Halocarbon 27[g]	3.7	30		–18	None	Oxygen compressors; liquid-oxygen systems
Krytox 103[h]	5.2	30		–45	None	

[a] Mobil Oil Corp.
[b] Exxon Corp.
[c] Union Carbide Chemicals Co.
[d] Akzo Chemicals.
[f] General Electric Co.
[g] Halocarbon Products Corp.
[h] DuPont Co.

Greases

Grease is essentially a suspension of oil in a thickening agent, along with appropriate additives. The oil generally makes up between 75 and 90% of a grease's weight, and it is held in place by the gel structure of the thickener to carry out its lubricating function. The simplicity of the lubricant supply system, ease of sealing, and corrosion protection make grease the first choice for many ball and roller bearings, small gear drives, and slow-speed sliding applications (Booser, 1995). Consistencies of greases vary from soap-thickened oils that are fluid at room temperature to hard brick types that may be cut with a knife. Greases of NLGI grade 2 stiffness (ASTM D217) are most common. Softer greases down to grade 000 provide easier feeding to multiple row roller bearings and gear mechanisms. Stiffer grade 3 is used in some prepacked ball bearings to avoid mechanical churning as the seals hold the grease in close proximity with the rotating balls.

Petroleum oils are used in most greases; the oils generally are in the SAE 30 range, with a viscosity of about 100 to 130 cSt at 40°C. Lower viscosity oil grades are used for some high-speed applications and for temperatures below about –20°C. Higher viscosity oils are used in greases for high loads and low speeds. Synthetic oils are used only when their higher cost is justified by the need for special properties, such as capability for operation below –20°C or above 125 to 150°C.

The most common gelling agents are the fatty acid metallic soaps of lithium, calcium, sodium, or aluminum in concentrations of 8 to 25%. Of these, the most popular is lithium 12-hydroxystearate; greases based on this lithium thickener are suitable for use at temperatures up to 110°C, where some lithium soaps undergo a phase change. Greases based on calcium or aluminum soaps generally have an upper temperature limit of 65 to 80°C, but this limit can be significantly raised to the 120 to 125°C range through new complex soap formulations. Calcium complex soaps with improved high temperature stability, for instance, are prepared by reacting a high molecular weight fatty acid (e.g., stearic acid) and at a low molecular weight fatty acid (acetic acid) with calcium hydroxide dispersed in mineral oil.

Inorganic thickeners, such as fine particles of bentonite clay, are inexpensively applied by simple mixing with oil to provide nonmelting greases for use up to about 140°C. Polyurea nonmelting organic powders are used in premium petroleum greases for applications up to about 150 to 170°C.

Additives, such as those mentioned in the subsection on petroleum oils, are added to grease to improve oxidation resistance, rust protection, or extreme pressure properties. Owing to the incompatibility of oils, thickeners, and additives, greases of different types should be mixed with caution.

Solid Lubricants

Solid lubricants provide thin solid films on sliding or rolling/sliding surfaces to reduce friction and wear. They are particularly useful for applications involving high operating temperatures, vacuum, nuclear radiation, or other environments that limit the use of oils or greases. Solid lubricant films do not prevent moving surfaces from contacting each other, so they cannot eliminate wear and their lives are limited by wear. The properties of some of the most common solid lubricants are given in Table 3.10.7.

The most important inorganic solid lubricants are layer-lattice solids such as molybdenum disulfide (MoS_2) and graphite. These materials are characterized by strong covalent or ionic bonding between atoms in individual layers, but relatively weak van der Waals' bonds between layers, thus enabling the layers to slide easily relative to one another. Graphite is a very effective lubricant film when moisture or water vapor is present because adsorbed water vapor lubricates the sliding layers; however, it has poor friction properties in vacuum or other low-humidity applications. Molybdenum disulfide does not require the presence of adsorbed water vapor, so it is widely used in vacuum or space applications.

The most commonly used organic solid lubricant is polytetrafluoroethylene (PTFE), which can be used as a fused surface coating or as a self-lubricating material (see subsection on plastics). Its low friction is attributed to the smooth profile of the PTFE molecule. The chemical inertness of PTFE makes it attractive for chemical and food processing applications.

TABLE 3.10.7 Properties of Selected Solid Lubricants

Material	Acceptable Usage Temperature, °C				Average Friction Coefficient, f		Remarks
	Minimum		Maximum				
	In Air	In N_2 or Vacuum	In Air	In N_2 or Vacuum	In Air	In N_2 or Vacuum	
Molybedenum disulfide, MoS_2	–240	–240	370	820	0.10–0.25	0.05–0.10	Low f, carries high load, good overall lubricant, can promote metal corrosion
Graphite	–240	—	540	Unstable in vacuum	0.10–0.30	0.02–0.45	Low f and high load capacity in air, high f and wear in vacuum, conducts electricity
PTFE	–70	–70	290	290	0.02–0.15	0.02–0.15	Lowest f of solid lubricants, load capacity moderate and decreases at elevated temperature
Calcium flouride–barium fluoride eutectic, CaF_2-BaF_2	430	430	820	820	0.10–0.25 above 540°C 0.25–0.40 below 540°C	Same as in air	Can be used at higher temperature than other solid lubricants, high f below 540°C

Source: Modified from Booser, E.R., in *Encyclopedia of Chemical Technology*, 4th ed., Vol. 15, 463–517, John Wiley & Sons, New York, 1995.

New ceramic-based solid lubricants have been developed for high-temperature applications, such as heat engines or space uses. One of the most promising of these is a calcium fluoride–barium fluoride eutectic, which can be used at temperatures exceeding 800°C.

Fluid Film Bearings

Journal Bearings

A journal bearing consists of an approximately cylindrical bearing body or sleeve around a rotating cylindrical shaft. In general, journal bearings are found in motors, pumps, generators, appliances, and internal combustion engines in which a fluid lubricant is used; they are also in smaller mechanisms such as switches, clocks, small motors, and circuit breakers in which a solid lubricant such as graphite, grease, or certain plastics serves to reduce friction. Air (gas) bearings are designed to utilize both fluid mechanics principles when operating, and solid lubricant surfaced materials for start, stop, and emergency operations.

A hydrodynamic journal bearing maintains separation of shaft from bearing because the lubricant viscosity and the speed of the shaft create pressure in the converging portion of the fluid film that carries load. The governing equations were first developed by Reynolds (1886). Their solution has led to numerous computer solutions, including those used for this chapter.

Journal Bearing Design

Figure 3.10.5 shows schematics of frequently used types of journal bearing in which one or more lobes of cylindrical shape are positioned around the shaft; their axis is assumed to be parallel to the shaft axis. The features of each design as well as applications in which it is often found are listed in Table 3.10.8. Noncontact journal bearings are designed to assure a continuous supply of lubricant to the load-carrying section, and the bearing grooves in Figure 3.10.5 are designed for that purpose. Oil must be resupplied to the bearing because of the continuous loss of lubricant as it is forced from the bearing by the load-carrying pressures generated within it. The subsection on lubricant supply methods describes some of the many systems designed to assure this supply and to cool the lubricant at the same time.

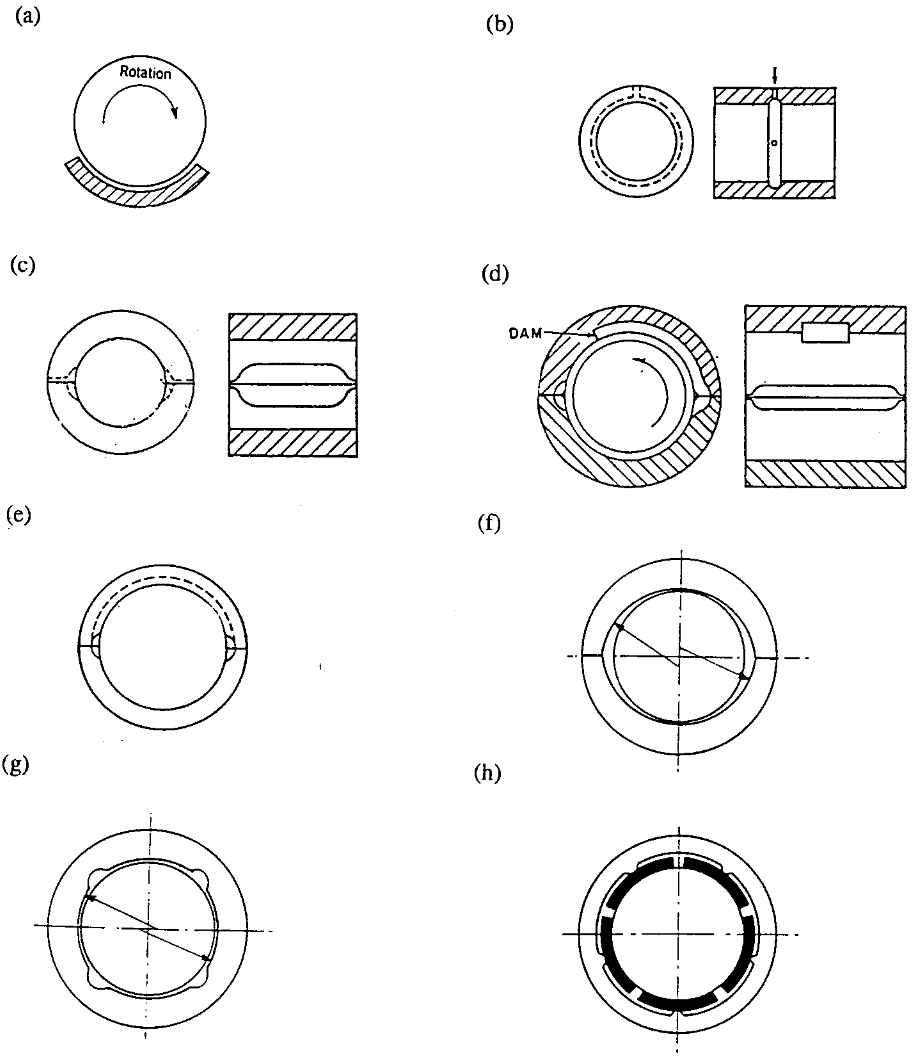

FIGURE 3.10.5 Types of pressure-fed journal bearings: (a) partial arc; (b) circumferential groove; (c) cylindrical bearing — axial groove; (d) pressure dam; (e) cylindrical overshot; (f) elliptical; (g) multilobe; (h) tilting pad.

TABLE 3.10.8 Journal Bearing Designs

Type	Typical Loading	Applications
Partial arc	Unidirectional load	Shaft guides, dampers
Circumferential groove	Variable load direction	Internal comb. engines
Axial groove types		
Cylindrical	Medium to heavy unidirectional load	General machinery
Pressure dam	Light loads, unidirectional	High speed turbines, compressors
Overshot	Light loads, unidirectional	Steam turbines
Multilobe	Light loads, variable direction	Gearing, compressors
Preloaded	Light loads, unidirectional	Minimize vibration
Tilt pad	Moderate variable loads	Minimize vibration

TABLE 3.10.9 Journal Bearing Parameters

B	Bearing damping coefficient	lb/in./sec
C	Radial clearance	in.
C_α	Adiabatic constant	—
C_p	Heat capacity	in.·lb/lb/°F
D	Diameter	in.
H_p	Power loss	in.·lb/sec
K	Bearing stiffness	lb/in.
L	Bearing length	in.
N	Shaft velocity	rpm
Q	Lubricant flow rate	in.^{3}/sec
R	Shaft radius	in.
R_e	Reynolds number	—
T_e	Entrance temperature	°F
T_f	Feed temperature	°F
T_q	Torque	in.·lb
ΔT_t	Temperature rise coeff., top half	°F
ΔT_b	Temperature rise coeff., bottom half	°F
U	Velocity	in./sec
W	Load	lb
e	Shaft eccentricity	in.
h	Film thickness	in.
j	Ratio: power loss/shaft-centered loss	—
p	Pressure	psi
q	Flow coefficient	—
w	Load coefficient	—
x	Coordinate in direction of load	in.
y	Coordinate orthogonal to load	in.
β	Exponential temp. coeff. of viscosity	—
ε	Shaft eccentricity, nondimensional	—
γ	Angular extent of film	—
ϕ	Attitude angle	—
ρ	Density	lb/in.^{3}
μ	Viscosity	lb·sec/in.^{2}
ω	Shaft velocity	rad/sec
θ	Angle in direction of rotation, from BDC	—
Φ	Energy dissipation	in.·lb/sec

Controlling variables. Definitions of the variables involved in journal bearing analysis are contained in Table 3.10.9. Because of the large range of many variables, nondimensional quantities are often used that are independent of the dimensional unit system involved. Examples are given are in the English system unless otherwise stated.

Calculating Bearing Performance

Journal bearing performance can be calculated directly from dedicated computer codes, which take account of load, speed, oil type, and delivery system as well as bearing dimensions. This subsection presents two approximate solutions: a simple thermal approach and a set of interpolation tables based on computer solutions.

Thermal Approach. It is assumed that the bearing is operating at a constant but elevated temperature. A predicted operating temperature can then be found as a function of an assumed viscosity. A solution is found when the assumed viscosity equals the lubricant viscosity at that temperature.

Three equations are used for this method. For radial loads, the power dissipation is:

$$H_p = j\pi^3 \mu \left(N/60\right)^2 D^3 L/C \text{ in}\cdot\text{lb/s} \tag{3.10.6}$$

where j = 1 for a shaft-centered design. The lubricant flow rate is:

$$Q = Q_o + q\,CR^2\omega/2 \text{ in.}^3/\text{s} \tag{3.10.7}$$

where q is the proportion of side flow to circulating flow, and the zero speed flow, Q_o (gpm), represents other flows such as from the ends of feed grooves not related to the load-carrying film. Q_o can usually be neglected for rough estimation, and this approximation is useful for eccentricities as high as 0.7. Note that q and j are functions of specific design as well as load and speed. The average operating temperature for a given viscosity is:

$$T_2 = T_f + \frac{\left(H_p - \Phi\right)}{\left(\rho C_p Q\right)} \ {}^\circ\text{F} \tag{3.10.8}$$

where T_f is the feed temperature and Φ is the energy loss due to conduction and radiation. For diameters of 2 in. or more, Φ can usually be assumed to be 0. Plotting T_2 vs. viscosity for several values of μ on a plot of the viscosity vs. T for the lubricant shows the operating temperature for the bearing as the intersection.

Flow dynamics solution. A more general solution for journal bearing performance is based on prediction of flow characteristics in the bearing and of physical behavior of the bearing based on Reynolds equation. A common two-pad journal bearing with pressurized oil feed will be used to provide specific design information.

Reynolds equation is the differential equation expressing the physical behavior of the fluid film between shaft and bearing, as written for cylindrical bearings:

$$1/R^2\left[\partial/\partial\theta\left(h^3/\mu\right)\partial p/\partial\theta\right] + \partial/\partial z\left(h^3/\mu\right)\partial p/\partial z = 6\left(U/R\right)\partial h/\partial\theta \tag{3.10.9}$$

where z is the axial coordinate and θ is the angular coordinate.

Bearing configuration. A cross section through a common type of two-pad cylindrical bearing is shown in Figure 3.10.6. Two pads having a radius of $R + C$ and an angular extent of 150°, and, with load applied vertically to the lower half through a shaft, comprise the bearing. Lubricant is admitted under moderate feed pressure to the two 30° grooves formed at the split as shown in Figure 3.10.6. The shaft rotates counterclockwise, and lubricant pressures are balanced when the shaft center is displaced down and to the right.

Lubricant properties. Pressures in the lubricant film are generated as a function of the local shear rates and the local viscosities as described by Reynolds equation.

The local temperature rise is given by the local energy dissipation divided by the local flow rate:

$$\Delta T = \left[2\mu\omega R^2\Delta\theta\right]/\left[h^2\rho C_p\right] \tag{3.10.10}$$

As an alternative to Equation (3.10.2), an exponential relation between viscosity and temperature is used:

$$\mu = \mu_0 e^{-\beta\left(T - T_0\right)} \tag{3.10.11}$$

Assuming an ISO 32 oil of viscosity μ_o at 104°F is 3.98 Reyns, density is 0.0310, and β is 0.0170 for the range from 104 to 212°F. The value for β may be determined from Figure 3.10.4.

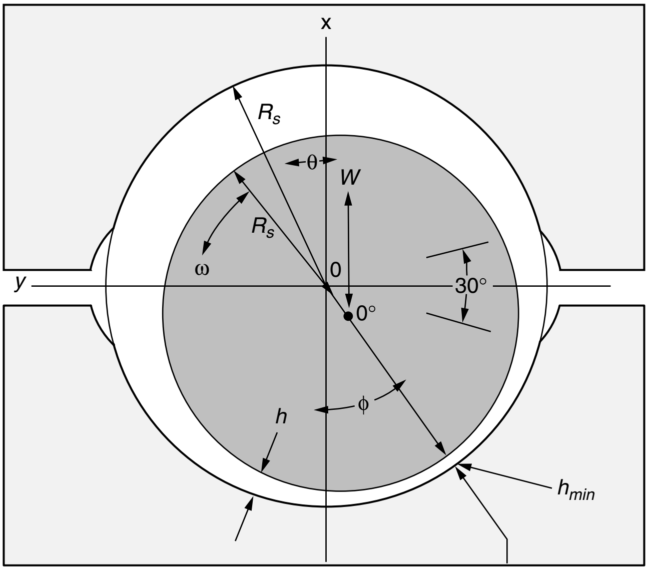

FIGURE 3.10.6 Geometry of split cylindrical journal bearing.

A nondimensional coefficient, C_α, the *adiabatic coefficient*, is used as an indicator of the severity of thermal heating in a design. It contains the several factors responsible for temperature rise.

$$C_\alpha = 2\mu_f \beta\omega \left(R/C\right)^2 \big/ \rho C_p \tag{3.10.12}$$

Bearing performance tables. Using computer-generated solutions of the Reynolds equation for the pressure field over the bearing surface, the relevant performance properties of the bearing/lubricant system can be determined. A number of programs are commercially available for this purpose. In order to illustrate how the behavior of a journal bearing can be determined, a two-pad split cylindrical bearing with an *L*/*D* of 0.5 has been selected, and a proprietary computer code has been used to develop a group of performance quantities for such a bearing. The code accounts for the internal lubricant circulation, including mixing in the inlet groove of feed lubricant with warm lubricant from the upper half, resulting in the viscosity μ_f.

The primary characteristics of the bearing are load, stiffness, and damping. Each of these factors is presented in nondimensional terms in Table 3.10.10; the corresponding dimensional and other quantities are given as follows:

Film thickness (in.): $$h = C\left(1 + e\cos\Theta\right) \tag{3.10.13a}$$

Shaft eccentricity (in.): $$e = \varepsilon C \tag{3.10.13b}$$

Load (lb): $$W = w\left[6\mu\omega\left(R/C\right)^2 DL\right] \tag{3.10.13c}$$

Flow (in.^{3}/sec): $$Q = q\left(CR^2\omega/2\right) \tag{3.10.13d}$$

Power loss (in.·lb/sec): $$H_p = j\left(2\pi\,\mu\omega^2 R^3 L/C\right) \tag{3.10.13e}$$

Stiffness (lb/in.): $$S_{xx} = K_{xx}\, 6\mu\omega R\left(R/C\right)^2 \qquad (3.10.13f)$$

Damping (lb·sec/in.): $$D_{xx} = B_{xx}\, 12\mu R\left(R.C\right)^3 \qquad (3.10.13g)$$

The axial length/diameter ratio also influences the performance of a journal bearing. To illustrate this, Table 3.10.11 presents the performance of longer bearings (L/D = 0.75 and 1.00) for comparison to the more common L/D = 1/2 results in Table 3.10.10. Comparing Table 3.10.10 and Table 3.10.11, the use of longer bearings has several important effects on operation and performance. Comparing key variables, the effects at an eccentricity of ratio of 0.7 are as follows:

Variable	$L/D = 0.5$	$L/D = 0.75$	$L/D = 1.00$
Load, w	0.28	0.69	1.21
Flow, q	0.69	0.82	0.88
Attitude angle, ϕ	36.4	36.1	35.8
Power ratio, j	1.00	1.15	1.17
Stiffness, K_{xx}	1.38	3.06	5.03
Damping, B_{xx}	0.99	2.52	4.31

Effect of Turbulence

Turbulence is a mixing phenomenon that occurs in larger high-speed bearings. When this behavior occurs, the simple viscous drag behavior assumed previously is broken up by numerous eddies which increase the drag. The Reynolds number is a nondimensional quantity that expresses this factor:

$$R_e = h\, U\, \rho/\mu \qquad (3.10.14)$$

where h is the local film thickness; U is the relative velocity of one surface with respect to the other; ρ is the fluid density; and μ is the local viscosity. The influence of turbulence on an L/D = 0.5 bearing is shown in Table 3.10.12.

Examination of Table 3.10.12 shows that the principal effects of operation in the turbulent regime with Reynolds number above about 1000 are in the greater power required (j) and the maximum bearing temperature. Load capacity and flow are only moderately affected.

Example Calculation

The problem is to design a two-pad cylindrical bearing for support of a rotor having a bearing load of 8000 lb, a shaft diameter of 6 in., and a speed of 3600 rpm. Assume use of ISO VG-32 oil fed at a temperature of 120°F. Compute operating characteristics for a 3-in. long bearing. Assume a radial clearance of 0.0044 in.

Feed viscosity: $\mu_f = 3.98 \times 10^{-6} e^{-0.00170(120-104)} = 3.03 \times 10^{-6}$ Reyn
Angular velocity: $\omega = 3600 \times 2\pi/60 = 377$ rad/sec
Adiabatic coefficient: $C_\alpha = 2 \times 3.03 \times 10^{-6} \times 0.0170 \times 377 \times (3/0.0044)^2/0.0310/4320 = 0.1345$
Load coefficient (from Equation 3.10.13c): $w = 8000/[6 \times 3.03 \times 10^{-6} \times 377 \times 3 \times 6 \times (33/0.0044)^2] = 0.139$

The desired solution lies between part 2 and part 3 of Table 3.10.10. Using linear interpolation between the tabulated values for C_α of 0.1 and 0.2, and values for ε of 0.7 and 0.8, an approximate operating point of $C_\alpha = 0.1345$ yields the following coefficients: $\varepsilon = 0.729$; $w = 0.279$; $q = 0.733$; $j = 0.860$; and $\Delta T_b = 0.915$.

Using Equation 13.10.13a through Equation 13.10.13g, the dimensional operating results are:

Shaft velocity: $\omega = 3600 \times 2\pi/60 = 377$ rad/sec
Flow: $Q = 0.733 \times .0044 \times 3^2 \times 377 = 5.47$ in.^{3}/sec
Power loss: $H_p = 0.860 \times 2\pi \times 3.03 \times 10^{-6} \times 377^2 \times 3^3 \times 3/0.0044 = 42.8$ in.·lb/sec
Oil temperature: $T_b = 120 + 0.915/0.0170 = 174$°F

TABLE 3.10.10 Performance of L/D = 0.5 Bearing

Part 1. $C_\alpha = 0.0$

ε	0.2	0.5	0.7	0.8	0.9	0.95
ϕ	66.5	48.01	36.44	30.07	22.18	16.46
w	0.0246	0.0997	0.2784	0.5649	1.6674	4.4065
q	0.3037	0.6014	0.6927	0.6946	0.6487	0.588
j	0.7779	0.8534	1.1005	1.3905	2.008	3.084
ΔT_b	0	0	0	0	0	0
ΔT_t	0	0	0	0	0	0
K_{xx}	0.041	0.2805	1.379	4.063	22.67	
K_{xy}	0.1465	0.3745	1.063	2.476	9.390	34.47
K_{yx}	–0.055	–0.072	0.0063	0.193	1.710	8.002
K_{yy}	0.046	0.170	0.4235	0.883	2.622	7.555
B_{xx}	0.142	0.352	0.989	2.311	8.707	32.30
B_{xy}, B_{yx}	0.023	0.094	0.236	0.522	1.547	4.706
B_{yy}	0.056	0.105	0.174	0.302	0.630	1.390

Part 2. $C_\alpha = 0.1$

ε	0.2	0.5	0.7	0.8	0.9	0.95
ϕ	69.9	50.2	38.7	32.35	24.83	19.8
w	0.022	0.087	0.233	0.451	1.184	2.621
q	0.312	0.620	0.721	0.728	0.692	0.642
j	0.686	0.723	0.863	0.997	1.253	1.545
ΔT_b	0.274	0.4030	0.642	0.907	1.519	2.346
ΔT_t	0.243	0.211	0.183	0.168	0.151	0.142
K_{xx}	0.038	0.2365	1.041	2.935	13.66	50.44
K_{xy}	0.126	0.3135	0.870	1.851	3.078	18.30
K_{yx}	–0.047	–0.061	–0.021	0.139	1.068	3.961
K_{yy}	0.037	0.140	0.3585	0.669	1.784	4.327
B_{xx}	0.121	0.286	0.776	1.592	4.97	14.00
B_{xy}, B_{yx}	0.016	0.071	0.195	0.341	0.850	2.10
B_{yy}	0.047	0.086	0.156	0.216	0.394	0.757

Part 3. $C_\alpha = 0.2$

ε	0.2	0.5	0.7	0.8	0.9	0.95
ϕ	73.4	52.2	40.8	34.55	27.23	22.5
w	0.020	0.077	0.198	0.368	0.890	1.779
q	0.320	0.639	0.747	0.759	0.730	0.760
j	0.613	0.628	0.712	0.791	0.933	1.092
ΔT_b	0.520	0.7520	1.162	1.594	2.521	3.651
ΔT_t	0.472	4.415	0.363	0.333	0.301	0.284
K_{xx}	0.035	0.1925	0.830	2.156	8.86	28.6
K_{xy}	0.111	0.272	0.704	1.477	4.515	11.72
K_{yx}	–0.041	–0.062	–0.018	0.074	0.640	2.371
K_{yy}	0.029	0.125	0.2895	0.551	1.375	2.932
B_{xx}	0.104	0.242	0.596	1.21	3.90	7.830
B_{xy}, B_{yx}	0.011	0.061	0.140	0.212	0.634	1.21
B_{yy}	0.040	0.080	0.121	0.187	0.326	0.501

Part 4. $C_\alpha = 0.4$

ε	0.2	0.5	0.7	0.8	0.9	0.95
ϕ	80.2	56.0	44.5	38.4	31.3	26.7
w	0.016	0.061	0.148	0.260	0.562	1.000
q	0.331	0.6720	0.795	0.815	0.797	0.760
j	0.504	0.498	0.534	0.570	0.637	0.716
ΔT_b	0.946	1.33	1.97	2.61	3.87	5.26
ΔT_t	0.898	0.801	0.712	0.658	0.597	0.562
K_{xx}	0.029	0.137	0.538	1.295	4.56	12.6

TABLE 3.10.10 (continued) Performance of L/D = 0.5 Bearing

K_{xy}	0.085	0.206	0.503	0.985	2.67	6.17
K_{yx}	–0.0315	–0.0548	0.0298	0.0233	0.321	1.136
K_{yy}	0.019	0.094	0.214	0.382	0.860	1.68
B_{xx}	0.079	0.175	0.397	0.734	1.75	3.44
B_{xy}, B_{yx}	0.0041	0.042	0.094	0.166	0.329	0.55
B_{yy}	0.030	0.064	0.092	0.131	0.120	0.276

TABLE 3.10.11 Performance of Long Bearings

Part 1. $L/D = 0.75$; $C_\alpha = 0.0$

ε	0.2	0.5	0.7	0.8	0.9	0.95
ϕ	64.74	46.54	36.13	30.17	22.64	17.03
w	0.0705	0.2714	0.6947	1.311	3.440	8.241
q	0.392	0.738	0.825	0.811	0.737	0.6545
j	0.777	0.871	1.145	1.450	2.184	3.233
ΔT_b	0	0	0	0	0	0
ΔT_t	0	0	0	0	0	0
K_{xx}	0.121	0.706	3.065	8.506	41.5	
K_{xy}	0.418	0.992	2.517	5.228	18.1	59.0
K_{yx}	–0.123	–0.189	0.052	0.404	3.18	16.2
K_{yy}	0.113	0.429	1.012	1.891	5.33	13.49
B_{xx}	0.423	0.982	2.52	5.16	17.7	54.4
B_{xy}, B_{yx}	0.057	0.249	0.609	1.10	3.24	7.58
B_{yy}	0.127	0.263	0.444	0.641	1.35	2.32

Part 2. $L/D = 1.00$; $C_\alpha = 0.0$

ε	0.2	0.5	0.7	0.8	0.9	0.95
ϕ	63.2	45.3	35.8	30.3	22.9	17.4
w	0.138	0.506	1.214	2.18	5.34	12.15
q	0.444	0.800	0.879	0.856	0.769	0.679
j	0.782	0.886	1.174	1.768	2.250	3.323
ΔT_b	0	0	0	0	0	0
ΔT_t	0	0	0	0	0	0
K_{xx}	0.234	1.254	5.026	13.24	60.9	
K_{xy}	0.818	1.795	4.142	8.12	26.8	83.5
K_{yx}	–0.201	–0.313	–0.075	0.671	4.96	24.9
K_{yy}	0.198	0.732	1.64	2.95	8.04	19.5
B_{xx}	0.82	1.87	4.31	8.27	26.5	75.9
B_{xy}, B_{yx}	0.10	0.45	0.97	1.68	4.78	10.36
B_{yy}	0.21	0.46	0.70	0.98	2.02	3.24

Thrust Bearings

Types of Thrust Bearings

Oil film thrust bearings range from coin-size flat washers to sophisticated assemblies many feet in diameter (Khonsari and Booser, 2002). Of the six common types of thrust bearings shown in Table 3.10.13, the first five are hydrodynamic. As with journal bearings, each of these generates oil film pressure when a rotating thrust face pumps oil by shear into a zone of reduced downstream clearance. When thrust load increases, film thickness drops until a new balance is reached between inflow and outflow, raising pressure until the higher bearing load is balanced. The hydrostatic bearing uses a separate oil pump to supply the pressurized flow.

TABLE 3.10.12 Influence of Turbulence[a]

R_e	0	1000	2000	4000
ϕ	40.8	43.8	46.4	49.2
ω	0.198	0.171	0.197	0.221
q	0.747	0.809	0.862	0.914
j	0.712	0.983	1.459	2.124
ΔT_b	1.162	0.585	0.918	1.404
K_{xx}	0.830	0.627	0.634	0.647
K_{xy}	0.704	0.575	0.577	0.645
K_{yx}	–0.018	–0.034	–0.047	–0.078
K_{yy}	0.289	0.257	0.282	0.330
B_{xx}	0.596	0.483	0.513	0.534
B_{xy}, B_{yx}	0.140	0.125	0.132	0.136
B_{yy}	0.121	—	—	0.104

[a] $\varepsilon = 0.7$; $C_\alpha = 0.2$; arc = 150°.

Flat-land bearings, simplest to fabricate and least costly, are the first choice for simple positioning of a rotor and for light loads in electric motors, appliances, pumps, crankshafts, and other machinery. They carry less of a load than the other types because flat parallel planes do not directly provide the required pumping action. Instead, their action depends on thermal expansion of the oil and warping of the bearing material induced by heating from the passing oil film. The resulting slight oil wedge then gives a load rating of about 10 to 20% of that for the other types.

Step bearings also offer relatively simple design. With a coined or etched step, they lend themselves to mass production as small-size bearings and thrust washers. Step height for optimum load capacity approximately equals the minimum film thickness, often 0.001 in. or less. Circumferential length beyond the step is ideally 45% of the total bearing segment (Wilcock and Booser, 1956).

Step thrust bearings are well suited for low-viscosity fluids such as water, gasoline, fuels, and solvents. Minimum film thickness in these applications is so small that features such as pivots and tapers are usually impractical. Step height must be small enough for good load capacity, yet large enough to accommodate some wear without becoming worn away. Step erosion by contaminants is sometimes a problem.

Tapered-land bearings provide reliable, compact designs for mid- to large-size high-speed machines such as turbines, compressors, and pumps. Taper height normally should be about one to three times the minimum film thickness. For greater load capacity and to minimize wear during starting, stopping, and at low speeds, a flat land is commonly machined at the trailing edge to occupy from 10 to 30% of the circumferential length of each segment. Because operation of these bearings is sensitive to load, speed, and lubricant viscosity, they are typically designed for the rated range of operating conditions for specific machines.

Tilting-pad thrust bearings are used increasingly in turbines, compressors, pumps, and marine drives in much the same range of applications as tapered-land designs. They usually have a central supporting pivot for each of their three to ten bearing segments. Each of these thrust pad segments is free to adjust its position to form a nearly optimum oil wedge with widely varying loads, speeds, and lubricants, and with rotation in both directions. A secondary leveling linkage system is commonly introduced to support the individual pads; this provides a further advantage over tapered-land designs by accommodating some misalignment. Off-the-shelf units are available to match rotor shaft diameters from about 2 to 12 in., and custom designs range from 120 to 170 in. outside diameter.

Recent trends to increase load capacity have led to offsetting pivots from the circumferential midpoint of a pad to about 60% beyond the leading edge; to substituting copper for steel as the backing for a tin babbitt bearing surface; and to nonflooded lubrication to minimize parasitic power loss from useless churning of oil passing through the bearing housing.

Springs or other flexible supports for thrust segments are employed for bearings ranging up to 10 ft or more in outside diameter and carrying millions of pounds of thrust. This flexible mounting avoids the

TABLE 3.10.13 Common Thrust Bearings and Their Range of Application

Type	O.D. in.	Unit load, psi
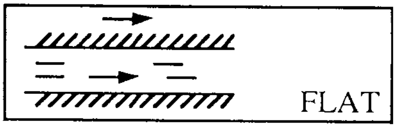	0.5–20	20–100
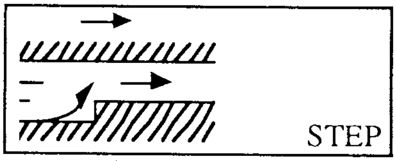	0.5–10	100–300
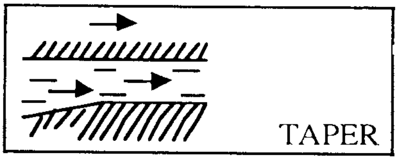	2–35	150–300
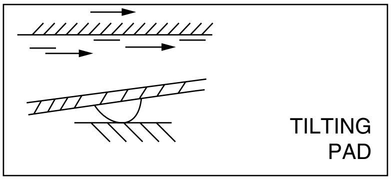	4–120	250–700
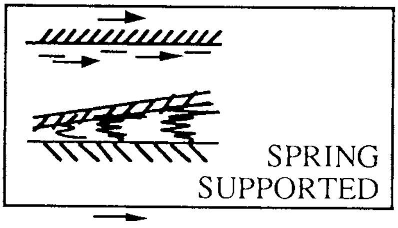	50–120	350–700
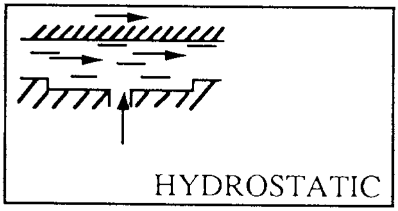	3–50	500–3000

Source: Booser, E.R. and Wilcock, D.F., *Machine Design*, June 20, 69–72, 1991.

high load concentration encountered by pivots in supporting large tilting-pads. Rubber backing can provide this flexible mounting for smaller thrust pads.

Hydrostatic thrust bearings are used when sufficient load support cannot be generated by oil film action within the bearing. This may be the case with low viscosity fluids, or for load support on an oil film at standstill and very low speeds. The fluid is first pressurized by an external pump and then introduced into pockets in the bearing surface to float the load.

A compact hydrostatic thrust bearing can sometimes be constructed with a single pocket at the end of a rotor. Larger bearings usually use three or more pressurized pockets to resist misalignment or to support off-center loads. Hydraulic flow resistance in the supply line to each pocket or constant flow to each pocket (as with ganged gear pumps) then provides any asymmetric pressure distribution needed to support an off-center load. Bearing unit load is commonly limited to about 0.5 (0.75 with fixed flow systems) times the hydrostatic fluid supply pressure — up to 5000 psi with conventional lubricating oils.

Design Factors for Thrust Bearings

In preliminary sizing, the inside diameter *d* of a thrust bearing is made sufficiently larger than the shaft to allow for assembly and to provide for any required oil flow to the thrust bearing inside diameter. This clearance typically ranges from about 1/8 in. for a 2-in. shaft to 1/2 in. for a 10-in. shaft. Bearing outside diameter *D* is then set to provide bearing area sufficient to support total thrust load *W* (pounds or Newtons) with an average loading *P* (psi or N/m²), using typical values from Table 3.10.13:

$$D = \left(\frac{4W}{\pi k_g P} + d^2 \right)^{0.5} \tag{3.10.15}$$

where k_g (typically 0.80 to 0.85) is the fraction of area between *d* and *D* not occupied by oil-distributing grooves. This bearing area is then divided by radial oil-feed groove passages, usually into "square" sectors with circumferential breadth *B* at their mean diameter equal to their radial length *L*.

Although square pads usually produce optimum oil film performance, other proportions may be advantageous. With very large bearing diameters, for instance, square sectors may involve such a long circumferential dimension that the oil film overheats before reaching the next oil-feed groove. On a radially narrow thrust face, on the other hand, square sectors may become so numerous as to introduce excessive oil groove area; thus, their short circumferential length would interfere with hydrodynamic oil film action.

Performance Analysis

Performance analyses for sector thrust bearings using a fixed taper also hold approximately for most thrust bearing shapes (other than flat lands) with the same ratio of inlet to outlet oil film thickness (Wilcock and Booser, 1956; Khonsari and Booser, 2002; Fuller, 1984). For centrally pivoted-pad thrust bearings and for spring-supported thrust bearings, use of an inlet-to-outlet film thickness ratio of two is usually appropriate in such an analysis.

Computer analyses in polar coordinates and with local oil film viscosity calculated over the whole oil film area give more exact solutions; however, the following constant viscosity approximations are made by relating a rectangular bearing sector (width B, length L) to the circular configuration of Figure 3.10.7.

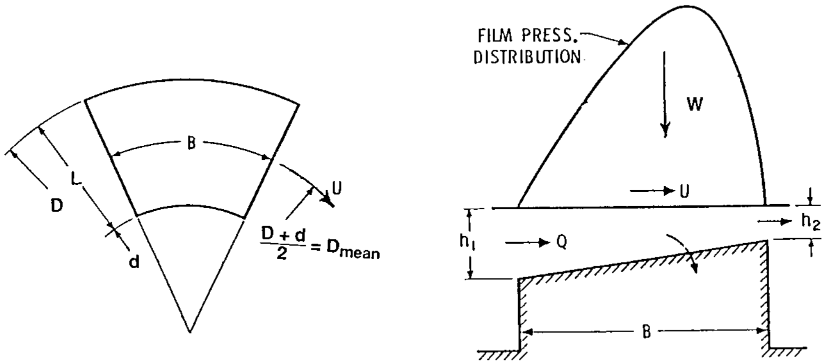

FIGURE 3.10.7 Sector for tapered land thrust bearing.

TABLE 3.10.14 Thrust Bearing Performance Characteristics

L/B:	0.25	0.5	0.75	1.0	1.5	2.0	∞
				$h_1/h_2 = 1.2$			
K_h	0.064	0.115	0.153	0.180	0.209	0.225	0.266
K_f	0.912	0.913	0.914	0.915	0.916	0.917	0.919
K_q	0.593	0.586	0.579	0.574	0.567	0.562	0.549
				$h_1/h_2 = 1.5$			
K_h	0.084	0.151	0.200	0.234	0.275	0.296	0.351
K_f	0.813	0.817	0.821	0.825	0.830	0.833	0.842
K_q	0.733	0.714	0.696	0.680	0.659	0.647	0.610
				$h_1/h_2 = 2$			
K_h	0.096	0.170	0.223	0.261	0.305	0.328	0.387
K_f	0.698	0.708	0.718	0.727	0.739	0.747	0.768
K_q	0.964	0.924	0.884	0.849	0.801	0.772	0.690
				$h_1/h_2 = 3$			
K_h	0.100	0.173	0.225	0.261	0.304	0.326	0.384
K_f	0.559	0.579	0.600	0.617	0.641	0.655	0.696
K_q	1.426	1.335	1.236	1.148	1.024	0.951	0.738
				$h_1/h_2 = 4$			
K_h	0.098	0.165	0.212	0.244	0.282	0.302	0.352
K_f	0.476	0.503	0.529	0.551	0.581	0.598	0.647
K_q	1.888	1.745	1.586	1.444	1.242	1.122	0.779
				$h_1/h_2 = 6$			
K_h	0.091	0.148	0.186	0.211	0.241	0.256	0.294
K_f	0.379	0.412	0.448	0.469	0.502	0.521	0.574
K_q	2.811	2.560	2.273	2.013	1.646	1.431	0.818
				$h_1/h_2 = 10$			
K_h	0.079	0.121	0.148	0.165	0.185	0.195	0.221
K_f	0.283	0.321	0.353	0.377	0.408	0.426	0.474
K_q	4.657	4.182	3.624	3.118	2.412	2.001	0.834

After Khonsari, M.M., *Tribology Data Handbook*, CRC Press, Boca Raton, FL, 1997.

This rectangular representation allows more ready evaluation of a range of variables and gives results quite similar to those of a more accurate polar coordinate analysis.

Employing the nomenclature of Figure 3.10.7, the following relations give minimum film thickness h_2, frictional power loss H, and oil flow into a sector Q. The dimensionless coefficients involved are given in Table 3.10.14 for a range of sector proportions L/B and ratios of inlet-to-outlet film thicknesses h_1/h_2.

$$h_2 = K_h \left(\mu UB/P\right)^{0.5} \qquad \text{in. (m)} \tag{3.10.16a}$$

$$H = K_f \, \mu U^2 BL/h_2 \qquad \text{lb} - \text{in./sec (N} - \text{m/sec)} \tag{3.10.16b}$$

$$Q = K_q ULh_2 \qquad \text{in.}^3\text{/sec (m}^3\text{/sec)} \tag{3.10.16c}$$

$$\Delta T = H\Big/\left(Q\rho C_p\right) = \frac{K_f}{K_q K_h^2 \rho C_p} P \qquad {}^\circ\text{F (}^\circ\text{C)} \tag{3.10.16d}$$

where:

B = circumferential breadth of sector at mean radius, in (m).
K_h, K_f, K_q = dimensionless coefficients.
L = radial length of sector, in (m).
P = unit loading on projected area of sector, W/BL, lb/in.^{2} (N/m^2).
U = surface velocity at mean diameter of sector, in./sec (m/sec).
W = load on a sector, lb. (N).
C_p = oil specific heat, in. – lb/(lb – °F) (J(kg – °C))
h_1, h_2 = leading edge and trailing edge film thicknesses, in (m)
ρ = oil density, lb/in.^{3} (N/m^3)
μ = oil viscosity at the operating temperature, lb·sec/in.^{2} (N·sec/m^2)

Example

The following example involves a bearing for 25,000 lb thrust load in a 1200 rpm compressor whose rotor has a 5-in. diameter journal. ISO-32 viscosity grade oil is to be fed at 120°F. Allowing 3/8-in. radial clearance along the shaft sets thrust bearing bore d = 5.75 in. Taking unit loading P = 300 psi allows a margin for uncertainty in expected thrust load; outside diameter D is given by Equation (3.10.14):

$$D=\left(\frac{4\times 25000}{\pi(0.85)(300)}+5.75^2\right)^{0.5}=12.6\text{ in.}$$

With 15% of the area used for oil feed passages, k_g= 0.85. Thrust bearing segment radial length L = (12.6 – 5.75)/2 = 3.425 in. With mean diameter (5.75 + 12.6)/2 = 9.175 in., total circumferential breadth of all pads at the mean diameter = $\pi D_m k_g$ = 24.5 in. The number of sectors (and grooves) for $B = L$ is then 24.5/3.425 = 7.2. Using seven lands, adjusted circumferential breadth B for each sector = 24.5/7 = 3.5 in. (For simpler fabrication, six or eight sectors should also be considered.) Runner velocity at the mean diameter, $U = \pi(9.175(1200/60)$ = 576.5 in./sec.

For square pads (L/B = 1) in a pivoted-pad bearing with h_1/h_2 = 2, which represents experience with centrally pivoted pads, Table 3.10.14 gives the following performance coefficients:

$$K_h = 0.261;\ K_f = 0.727;\ K_q = 0.849$$

The rise in temperature is given by Equation (3.10.16d), which assumes that the total frictional power loss H goes into heating the total oil flow Q passing over the pad.

$$\Delta T=\frac{K_f P}{K_q K_h^2 \rho C_p}=\frac{0.727(300)}{0.849(0.261)^2(0.0313)(4535)}=27^\circ\text{F}$$

Adding this ΔT to the 120°F feed temperature gives 147°F as the representative oil-operating temperature with a viscosity of 1.6×10^{-6} lb·sec/in.^{2} from Figure 3.10.4. Temperature rise to the maximum oil film temperature would be expected to be about 53°F, twice the 27°F. If this bearing were in a housing fully flooded with oil, feed temperature to each pad would become the housing oil temperature — essentially, the same as oil draining from the housing.

Minimum film thickness h_2 becomes from Equation (3.10.16a):

$$h_2=0.261\left[\left(1.6\times 10^{-6}\right)(576.5)(3.5)/300\right]^{0.5}=0.00086\text{ in.}$$

With a fixed tapered land, rather than a centrally pivoted pad for which it could be assumed that h_1/h_2 = 2, several iterations might be required with different assumed values of the h_1/h_2 ratio in order to determine the performance coefficients in Table 3.10.14. The proper value of h_1/h_2 will be the one that gives the same final calculated value of h_2 from the preceding equation as was assumed in the preliminary selection of K_h, K_f, and K_q.

After finding the values for h_2 and K_f, the power loss H can be determined using Equation (3.10.16b). For this example, the power loss would be $H = 5510$ lb·in./sec.

The total oil feed to the bearing should satisfy two requirements: (1) provide a full oil film over the bearing segment; and (2) maintain reasonably cool operation with no more than 30 to 40°F rise in the oil temperature from feed to drain. Equation (3.10.16c) can be used to find the oil feed Q needed at the sector inlet to form a full film. The oil feed needed for a 40°F rise is given by the following heat balance using typical density and specific heat values for petroleum oil:

$$Q = H\left(\rho C_p \, \Delta T\right) \tag{3.10.17}$$

The required oil feed will be the larger of the values determined by Equation (3.10.16c) and Equation (3.10.17).

The preceding calculations are for a single sector; power loss and oil feed would be multiplied by the number of sectors (seven) to obtain values for the total bearing. Consideration would normally follow for other pad geometries, and possibly other lubricants and oil flow patterns, in a search for the most promising design. More detailed calculations of film thickness, film temperatures, oil flow, and power loss could then be obtained by one of a number of computer codes available from bearing suppliers or other sources.

Oil-Film Bearing Materials

Selection of the material for use in a journal or thrust bearing depends on matching its properties to the load, temperature, contamination, lubricant, and required life.

Babbitts. Of the common bearing materials listed in Table 3.10.15, first consideration for rotating machines is usually a babbitt alloy containing about 85% tin or lead together with suitable alloying elements. With their low hardness, they have excellent ability to embed dirt, conform to shaft misalignment, and rate highest for compatibility with steel journals. Tin babbitts, which contain about 3 to 8% copper and 5 to 8% antimony, are usually the first choice for their excellent corrosion resistance. SAE

TABLE 3.10.15 Characteristics of Oil-Film Bearing Materials

Material	Brinell Hardness	Load Capacity, psi	Max Operating Temp., °F	Compatibility[a]	Conformability and Embedability[a]	Corrosion Resistance[a]	Fatigue Strength[a]
Tin babbitt	20–30	800–1500	300	1	1	1	5
Lead babbitt	15–25	800–1200	300	1	1	3	5
Copper lead	20–30	1500–2500	350	2	2	5	4
Leaded bronze	60–65	3000–4500	450	3	4	4	3
Tin bronze	65–80	5000+	500	5	5	2	2
Aluminum alloy	45–65	4000+	300	4	3	1	2
Zinc alloy	90–125	3000	250	4	5	5	3
Silver overplated		5000+	300	2	4	2	1
Two-component, babbitt surfaced		3000+	300	2	4	2	3
Three-component, babbitt surfaced		4000+	300	1	2	2	1

[a] Arbitrary scale: 1 = best, 5 = worst.

12 (ASTM grade 2) tin babbitt is widely used in automotive and industrial bearings. The much lower cost of lead babbitt, however, with 9 to 16% antimony and up to 12% tin for improved corrosion resistance, brings SAE 13, 14, and 15 grades into wide use for general automotive and industrial applications (Booser, 1992).

To achieve the high fatigue strength needed in reciprocating engines, only a very thin layer (commonly 0.001 in.) of babbitt is used so that much of the reciprocating load is taken on a stronger backing material (Kingsbury, 1992; DeHart, 1983). For bimetal bushings such as those used in automobile engines, oil grooves and feed holes are formed in continuous steel strip coated with babbitt. The strip is then cut to size and the individual segments are rolled into finished bearings.

For heavy-duty reciprocating engines, three-layer bearings are common. Using a steel strip backing, a thin overlay of SAE 19 or 190 lead babbitt is electroplated or precision cast on an intermediate layer about 0.1 to 0.3 in. thick of copper–nickel, copper–lead, leaded bronze, aluminum, or electroplated silver.

Copper Alloys. Copper–lead alloys containing 20 to 50% lead, cast or sintered on a steel back, provide good fatigue resistance for heavy-duty main and connecting rod bearings for auto, truck, diesel, and aircraft engines. The 10% lead–10% tin leaded bronze has been a traditional selection for bearings in steel mills, appliances, pumps, automotive piston pins, and trunions. This has been replaced in many applications by CA932 (SAE 660) containing 3% zinc for easier casting. The harder tin bronzes require reliable lubrication, good alignment, and 300 to 400 Brinell minimum shaft hardness. Cast tin bronze bushings are used at high loads and low speeds in farm machinery, earth-moving equipment, rolling mills, and in automotive engines for connecting rod bearings.

Utility of copper alloy bearings is limited to relatively low surface speeds by the tendency to form a copper transfer film on a steel shaft. Above about 1500 to 3000 ft/min, selective plucking of softer copper material from hotter load zones in the bearing may result in welded lumps forming on the cooler, stronger transfer layer on the mating steel shaft.

Zinc Alloys. Zinc alloys containing about 10 to 30% aluminum find some use for lower cost and better wear life in replacing leaded bronzes. They are used for oscillating and rotating applications involving speeds up to 1400 ft/min and temperatures up to 250°F.

Aluminum Alloys. Although finding only minor use in general industrial applications because of their limited compatibility with steel journals, aluminum alloys containing 6.5% tin, 1% copper, and up to 4% silicon are used as solid, bimetal, and trimetal bearings in automotive engines, reciprocating compressors, and aircraft equipment. Good journal finish and shaft hardness of Rockwell B 85 or higher are required. The good fatigue and corrosion resistance of aluminum alloys have led to use of a number of unique alloys containing major additions of silicon, lead, or tin to provide better compatibility characteristics (DeHart, 1983; Shabel et al., 1992).

Dry and Semilubricated Bearings

Various plastics, porous bronze and porous iron, carbon–graphite, rubber, and wood are widely used for bearings operating dry or with sparse lubrication (Booser, 1992). Unique properties of these materials have led to their broad use in applications once employing oil-film and ball and roller bearings. Although these materials provide good performance under conditions of poor or nonexistent lubrication at low speeds, performance commonly improves the closer the approach to full-film lubrication.

Plastics

Most commercial plastics find some dry or lubricated use in slow-speed bearings at light loads (Jamison, 1994). The most commonly used thermoplastics for bearings are polytetrafluorethylene (PTFE), nylon, and acetal resins. Thermosetting plastics used for bearings include phenolics, polyesters, and polyimides. Table 3.10.16 compares characteristics of typical plastic bearings with those of carbon–graphite, wood, and rubber, which are used in similar applications.

TABLE 3.10.16 Representative Limiting Conditions for Nonmetallic Bearing Materials

Material	Max Temperature, °C	$P\nu$ Limit, $MN/(m \cdot sec)$[a]	Max Pressure, P, MN/m^2 [b]	Max Speed, ν m/sec
Thermoplastics				
Nylon	90	0.90	5	3
Filled	150	0.46	10	
Acetal	100	0.10	5	3
Filled	—	0.28	—	—
PTFE	250	0.04	3.4	0.3
Filled	250	0.53	17	5
Fabric	—	0.88	400	0.8
Polycarbonate	105	0.03	7	5
Polyurethane	120	—	—	—
Polysulfone	160	—	—	—
Thermosetting				
Phenolics	120	0.18	41	13
Filled	160	0.53	—	—
Polyimides	260	4	—	8
Filled	260	5	—	8
Others				
Carbon–graphite	400	0.53	4.1	13
Wood	70	0.42	14	10
Rubber	65	—	0.3	20

[a] See Table 3.10.18.

[b] To convert MN/m^2 to psi, multiply by 145.

TABLE 3.10.17 Wear Factors for Plastic Bearings[a]

Material	Wear Factor k, m^2/N	
	No Filler	Filled[b]
Nylon-6, 6	4.0	0.24
PTFE	400	0.14[c]
Acetal resin	1.3	4.9
Polycarbonate	50	3.6
Polyester	4.2	1.8
Poly(phenylene oxide)	60	4.6
Polysulfone	30	3.2
Polyurethane	6.8	3.6

[a] See Booser (1992).

[b] With 30 wt% glass fiber, unless otherwise noted.

[c] 15% glass fiber.

In addition to the maximum temperature that can be tolerated, three operating limits shown in Table 3.10.16 are normally defined for plastic bearings (Blanchet, 1997): (1) maximum load at low speed, which reflects the compressive yield strength; (2) maximum speed for running under very light load; and (3) a $P\nu$ load-speed limit at intermediate speeds, which serves as a measure of the maximum tolerable surface temperature. Because wear volume in dry sliding is approximately proportional to total load and the distance of sliding, $P\nu$ also gives a measure of wear depth d in the modified form of Archard's relation (3.10.1), $d = k(P\nu)t$, where t is the operating time and wear factor k = wear coefficient K/hardness H.

Typical values of this wear factor k are given in Table 3.10.17. Because k values involve substantial variability, prototype tests are highly desirable for any planned application. Added fillers can reduce the wear factor for the base polymer by a factor of 10 to 1000 and more (Blanchet and Kennedy, 1992). Common fillers include inorganic powders such as clay, glass fibers, graphite, molybdenum disulfide, and powdered metal, and also silicone fluid as an internally available lubricant.

TABLE 3.10.18 Operating Limits for Porous Metal Bearings

Porous Metal	Nominal Composition, wt%	Pressure Limit, P, MN/m^2 Static	Dynamic	Speed Limit, v, m/sec	Pv Limit $MN/(m.sec)$
Bronze	Cu 90, Sn 10	59	28	6.1	1.8[a]
Iron		52	25	2.0	1.3
Iron-copper	Fe 90, Cu 10	140	28	1.1	1.4
Iron-copper-carbon	Fe 96, Cu 3, C 0.7	340	56	0.2	2.6
Bronze-iron	Fe 60, Cu36, Sn 4	72	17	4.1	1.2
Aluminum		28	14	6.1	1.8

Note: To convert MN/m^2 to psi, multiply by 145.

[a] Approximately equivalent to 50,000 psi × ft/min limit often quoted by U.S. suppliers.

Porous Metals

Bearings of compressed and sintered bronze, iron, and aluminum alloy powder are produced at the rate of millions per week for shaft sizes ranging from about 1.6 to 150 mm. These sleeve bearings and thrust washers are used in a wide variety of small electric motors, appliances, business machines, machine tools, automotive accessories, and farm and construction equipment (Cusano, 1994; Morgan, 1984). Traditional powder metal bearings consist of 90% copper and 10% tin (Table 3.10.18). The common pore volume of 20 to 30% is usually impregnated with a petroleum oil of SAE 30 viscosity. To promote formation of an oil film, high porosity with its high oil content is employed for higher speeds, often with an oil wick or grease providing a supplementary lubricant supply. Lower porosity with up to 3.5% added graphite is used for lower speeds and oscillation where oil film formation is difficult.

Porous iron bearings are used for lower cost, often with some copper and graphite added for high load capacity at low speed. Iron with up to 40% of added 90-10 bronze powder provides many of the characteristics of porous bronze bearings while enjoying the lower cost of the iron. Porous aluminum containing 3 to 5% copper, tin, and lead finds limited use for providing cooler operation, better conformability, and lower weight.

Table 3.10.18 gives approximate operating limits for porous metal bearings. Generally, maximum Pv values for sleeve bearings range up to 50,000 psi·ft/min. Pv levels for thrust bearings should generally not exceed about 20% of this value.

Rolling Element Bearings

Types of Rolling Element Bearings

Rolling element bearings may be classified according to the type of rolling element, i.e., ball or roller, and the loading direction. Ball and roller bearings can be designed to carry radial or thrust loads, or a combination of the two. Standard rolling element bearing configurations are shown in Figure 3.10.8, and the capabilities of the different types are summarized in Figure 3.10.9.

Ball bearings usually consist of a number of hardened and precisely ground balls interposed between two grooved and hardened rings or races. A cage or separator is used to keep the balls equally spaced around the groove. The most common *radial ball bearing* is a deep groove, or Conrad, type designed to carry large radial loads, with a small thrust load capability. The radial capacity of a deep groove bearing can be increased by inserting more balls in the bearing by means of a face-located filling notch (which decreases the thrust capacity) or a split inner or outer ring (which requires a means to hold the ring halves axially together). The thrust capability of a radial ball bearing can be increased by inducing angular contact between ball and rings. A single-row angular contact bearing can carry thrust load in only one direction; the thrust load capacity is dependent on the contact angle (angle between the line of action of the force and the plane perpendicular to the shaft axis). Duplex angular contact bearings consist of two angular contact bearings mounted together so they can carry thrust loads in either direction with little axial play, or they can be mounted in tandem to double the axial and radial load-carrying capacity.

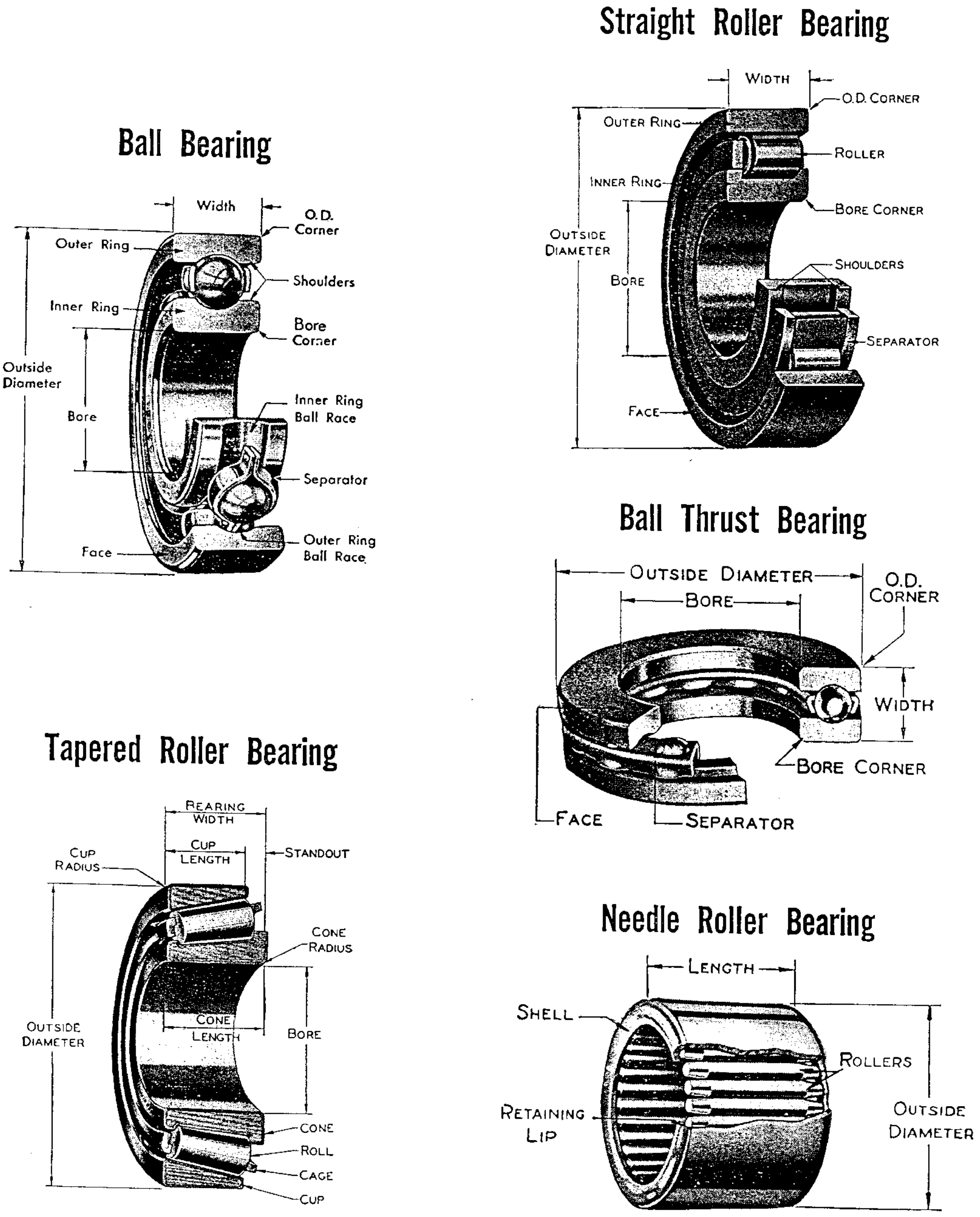
Ball Bearing

Straight Roller Bearing

Tapered Roller Bearing

Ball Thrust Bearing

Needle Roller Bearing

FIGURE 3.10.8 Major types of rolling element bearings.

Self-aligning ball bearings are designed to accommodate more shaft misalignment than is possible with other radial ball bearings.

Thrust ball bearings are used primarily in machinery with a vertically oriented shaft, which requires a stiff axial support. Many such bearings have a 90° contact angle and as a result can carry essentially no radial load; they also have limited high speed capability. If thrust loads in both directions are to be carried, a second row of balls must be added.

Roller bearings can be made with cylindrical, tapered, or spherical rollers. As with ball bearings, the rollers are contained between two rings, with a cage or separator used to keep the rollers separated. The

	TYPE	SIZE RANGE IN INCHES		AVERAGE RELATIVE RATINGS				DIMENSIONS	
				Capacity		Limiting Speed	Permissible Misalign-ment	Metric	Inch
		Bore	O.D.	Radial	Thrust				
BALL BEARINGS	CONRAD TYPE 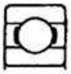	.1181 to 41.7323	.3750 to 55.1181	Good	Fair ↔	Conrad is basis for comparison 1.00	± 0° 8′	X	X
	MAXIMUM TYPE 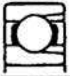	.6693 to 4.3307	1.5748 to 8.4645	Excellent	Poor ↔	1.00	± 0° 3′	X	
	ANGULAR CONTACT 15°/40°  15°/40°	.3937 to 7.4803	1.0236 to 15.7480	Good	Good (15°) Excellent (40°) ←	1.00/0.70	± 0° 2′	X	
	ANGULAR CONTACT 35° 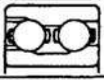	.3937 to 4.3307	1.1811 to 9.4488	Excellent	Good ←	0.70	0°	X	
	SELF-ALIGNING 	.1969 to 4.7244	.7480 to 9.4488	Fair	Fair ↔	1.00	± 4°	X	
CYLIN-DRICAL ROLLER BEARINGS	SEPARABLE INNER RING NON-LOCATING 	.4724 to 19.6850	1.2598 to 28.3465	Excellent	0	1.00	± 0° 4′	X	
	SEPARABLE INNER RING ONE DIR. LOCATING 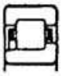	.4724 to 12.5984	1.2598 to 22.8346	Excellent	Fair ←	1.00	± 0° 4′	X	
	SELF-CONTAINED TWO DIR. LOCATING 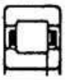	.4724 to 3.9370	1.4567 to 8.4646	Excellent	Fair ↔	1.00	± 0° 4′	X	
TAPERED ROLLER BEARINGS	SEPARABLE 	.6205 to 6.0000	1.5700 to 10.0000	Good	Good →	0.60	± 0° 2′	X	X
SPHERICAL ROLLER BEARINGS	SELF-ALIGNING 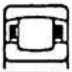	.9843 to 12.5984	2.0472 to 22.8346	Good	Fair ↔	0.50	± 4°	X	
	SELF-ALIGNING 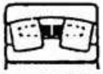	.9843 to 35.4331	2.0472 to 46.4567	Excellent	Good ↔	0.75	± 1°	X	
NEEDLE BEARINGS	COMPLETE BEARINGS  with or without locating rings & lubricating groove	.2362 to 14.1732	.6299 to 17.3228	Good	0	0.60	± 0° 2′	X	X
	DRAWN CUP 	.1575 to 2.3622	.3150 to 2.6772	Good	0	0.30	± 0° 2′	X	X
THRUST BEARINGS	SINGLE DIRECTION BALL Grooved Race 	.2540 to 46.4567	.8130 to 57.0866	Poor	Excellent →	0.30	0°	X	X
	SINGLE DIRECTION CYL. ROLLER 	1.1811 to 23.6220	1.8504 to 31.4960	0	Excellent →	0.20	0°	X	
	SELF-ALIGNING SPHERICAL ROLLER 	3.3622 to 14.1732	4.3307 to 22.0472	Poor	Excellent →	0.50	± 3°	X	

FIGURE 3.10.9 Characteristics of standard rolling element bearing configurations.

cage can be guided by the rollers or one of the rings. Because roller bearings operate with line contacts, as opposed to the point (or elliptical) contacts that occur in ball bearings, roller bearings are stiffer (less radial displacement per unit load) and have a greater load-carrying capacity than a ball bearing of similar size. Roller bearings are more expensive than ball bearings of comparable size.

Radial cylindrical roller bearings are designed to carry primarily radial loads. Cylindrical roller bearings have a high radial load capacity and low friction, so they are suitable for high speed operation. Their thrust load capacity is limited to that which can be carried by contact (sliding) between the ends of the rollers and the flange or shoulder on the ring that contains them.

The rollers in many cylindrical roller bearings are actually slightly crowned to relieve stress concentrations that would otherwise occur at the ends of the rollers and to compensate for misalignment of the bearing. In order to increase the load-carrying capacity of roller bearings, a second row of rollers is added instead of using longer rollers. This is because long rollers (i.e., length/diameter > 1.7) tend to skew in the roller path, thus limiting their high speed capability and sometimes shortening their life. Needle bearings have long rollers, however, and they are useful when there are severe radial space limitations and when neither high load capacity nor high speeds are required.

Spherical roller bearings usually have an outer ring with a spherical inside diameter, within which are barrel-shaped rollers. This makes these bearings self-aligning and also gives them a contact area between roller and ring larger than those of other rolling element bearings. Because of this, spherical roller bearings have a very high radial load-carrying capacity, along with some ability to carry thrust loads. They have higher friction between roller and ring and this limits their high-speed capability.

Tapered roller bearings have tapered rollers, ideally shaped like truncated cones, contained between two mating cones of different angles: the inner cone and the outer cup. The contact angle of the bearing determines its thrust load capability; a steeper angle is chosen for more thrust capacity. If a single row of rollers is used, the bearing is separable and can carry thrust loads in only one direction. If the thrust is double-acting, a second bearing can be mounted in a back-to-back configuration or a double row bearing can be selected. In tapered roller bearings there is sliding contact between the ends of the rollers and the guide flange on the inner cone; this requires lubrication to prevent wear and reduce friction.

Thrust roller bearings can be cylindrical, needle, tapered, or spherical (Figure 3.10.9). In each case, load-carrying capacity is high; however, the sliding that occurs between rollers and rings requires lubrication and cooling.

Rolling Element Bearing Materials

Ball and roller bearings require materials with excellent resistance to rolling contact fatigue and wear, as well as good dimensional stability and impact resistance. The rolling elements are subjected to cyclic contact pressures that can range from 700 to 3500 MPa (100 to 500 ksi) or more, and the bearing materials must be hard enough to resist surface fatigue under those conditions. Of the through-hardening steels that meet these requirements, the most popular is AISI 52100, which contains about 1% carbon and 1.5% chromium. In general, balls and rollers made from 52100 are hardened to about Rockwell C60.

Standard bearings made from 52100 may suffer from unacceptable dimensional changes resulting from metallurgical transformations at operating temperatures above 140°C (285°F). Special stabilization heat treatments enable operation at higher temperatures, with successful operation at temperatures as high as 200°C (390°F) achieved in cases involving low loads. However, the material's strength and fatigue resistance diminish if the bearing temperature increases above about 175°C (350°F), so above that temperature materials with better hot-hardness, such as M50 tool steel, are required. Carburizing steels such as AISI 8620 have been developed for tapered roller bearings and other heavily loaded types that benefit from the tougher core and case compressive residual stress developed during carburizing. For applications in oxidative or corrosive environments, a hardened martensitic stainless steel such as SAE 440C may be chosen.

For the highest operating temperatures, ceramic materials may be used in bearings. The most promising of the ceramics for rolling element bearing applications is silicon nitride. Its major use so far in

TABLE 3.10.19 Temperature Limits for Rolling Element Bearing Materials

Material	Maximum Operating Temperature °C	Maximum Operating Temperature °F
AISI 52100	140–175	285–350
AISI 8620 (carburized)	150	300
440C stainless steel	170	340
M50 tool steel	315	600
Hybrid Si_3N_4–M50	425	800
All-ceramic (Si_3N_4)	650	1200

bearings has been in hybrid bearings with ceramic balls or rollers and metallic rings, but all-ceramic bearings have also been developed.

The temperature limits of these bearing materials are given in Table 3.10.19. For all bearing materials, great care must be taken in the processing and production stages to ensure that no defects or inclusions are present that could serve as an initiation site for fatigue cracks. For most high-performance metallic bearings, this requires a very clean steel production process, such as vacuum arc remelting. Heat treatment of the material is also important to produce the required dimensional stability. The production process for ceramic bearings is even more critical because a defect in a ceramic bearing element could result in catastrophic fracture of the brittle material.

Bearing cages or retainers have the separation of the rolling elements as their primary purpose. In some cases, they also provide some solid lubrication to the bearing. Low carbon steel is the most common cage material, but bronze (silicon iron bronze or aluminum bronze) and polymers (particularly nylon 6-6) are used in many applications.

Selection of Rolling Element Bearings

It has been stated that if a rolling element bearing in service is properly lubricated; properly aligned; kept free of abrasive particles, moisture, and corrosive agents; and properly loaded, then all causes of damage will be eliminated except one — contact fatigue (Harris, 2000). The fatigue process results in a spall, which may originate on or just beneath the contact surface. Studies of rolling contact fatigue life by Lundberg and Palmgren (1947, 1952) and others showed that most rolling element bearings have fatigue lives that follow a Weibull statistical distribution: the dependence of strength on volume is explained by the dispersion in material strength. Most bearings today are designed according to the Lundberg–Palmgren model, which has been standardized by international (ISO, 2000) and national (e.g., ANSI/AFBMA, 1990) standards.

The basic rating life of rolling element bearings is the L_{10} life, which is the number of revolutions at constant speed for which there is a 10% probability of failure (or 90% reliability). The basic dynamic load-carrying capacity, or load rating, of a bearing is the constant load C, which corresponds to an L_{10} life of 1 million revolutions. For any other bearing load F, the L_{10} life can be determined by the following relationship:

$$L_{10} = (C/F)^n \tag{3.10.18}$$

where the load-life exponent $n = 3$ for ball bearings, and $n = 10/3$ for roller bearings.

For light loads, fatigue life may extend well beyond that predicted by Equation (3.10.18) (Ioannides and Harris, 1985). Even infinite fatigue life is possible with Hertz elastic contact stresses below 150 ksi (ASME 2003), or with oil film thickness in loaded contacts greater than about six times the composite surface roughness. This limiting stress varies with different steels, drops for operating temperatures above 80°C, and reaches 258 ksi with silicon nitride ceramics.

The equivalent bearing load includes contributions from radial as well as thrust loads and can be calculated by the following expression:

$$F = XF_r + YF_a \tag{3.10.19}$$

where X is a radial load factor; Y is a thrust load factor; F_r is the radial load applied to the bearing; and F_a is the applied thrust (or axial) load.

Values for the dynamic load rating C, as well as the load factors X and Y for any bearing configuration, can be found in manufacturers' catalogs, or they can be calculated according to formulas given in bearing texts by Harris (2000) or Brandlein et al. (2002). Life adjustment factors can be used to adjust the desired L_{10} life to account for special operating conditions, special material selections, special lubrication conditions, or reliability different from 90% (ASME, 2003).

The bearing user will generally select a commercially available bearing by the following procedure:

1. Determine the axial and thrust loads acting at the bearing location.
2. Determine the required bearing life (L_{10}).
3. Select the most appropriate bearing type from among those given in Figure 3.10.9.
4. Use the X and Y values appropriate to the type of bearing and loading conditions in Equation (3.10.19) to find the equivalent dynamic bearing load F.
5. Determine the required dynamic load capacity C from Equation (3.10.18).
6. Select a bearing with a dynamic load capacity at least as large as the required value from a manufacturer's catalog.
7. Provide an appropriate mounting arrangement for the bearing. Manufacturers' catalogs can be consulted for guidance in designing the mounting and selecting appropriate fits for the bearing. The importance of the fit cannot be overemphasized; improper fit can result in considerable reduction in bearing life.
8. Provide adequate lubrication for the bearing (see below). Seals and/or shields may be integrated into the bearing to retain or protect the lubricant in the bearing.

Despite their selection on the basis of fatigue life, lives of most ball bearings in industrial service appear to be limited by wear from factors such as misalignment, dried grease, or contamination (Khonsari and Booser, 2002).

Rolling Bearing Lubrication

The primary load-carrying contacts between rolling elements and rings exhibit nearly pure rolling. There are many sliding contacts in rolling element bearings, however, including those in which roller ends contact the internal flanges of rings; rolling elements contact separator/cage; and the separator contacts the guiding (piloting) ring of the bearing. All of those contacts must be lubricated to limit friction and wear; a grease or an oil can be used for that purpose.

Under most normal operating conditions, rolling element bearings can be grease lubricated. *Greases* coat surfaces with a thin boundary lubricant film of oil, thickener, and additive molecules, thus providing protection against sliding wear, and provide oil to lubricate the concentrated rolling contacts (see below). The selection of a grease depends on its effective temperature range, oil viscosity, consistency, and rust-inhibiting properties. For normal applications, a bearing should be filled with grease up to 30 to 50% of its free volume. Overfilling will cause overheating, particularly at high speeds. Grease will deteriorate with time and leak out. For that reason, a relubrication schedule should be developed, with grease added at intervals that can be estimated by the following expression (Neale, 1993):

$$\text{relubrication interval}\left(\text{hours}\right)=\left(k/d^{1/2}\right)\left[\left(14\times10^{-6}/n\right)-4d^{1/2}\right] \tag{3.10.20}$$

where k = 10 for radial ball bearings, = 5 for cylindrical roller bearings, and = 1 for spherical or tapered roller bearings; d = bearing bore diameter (mm); and n = speed (rpm).

Oil lubrication is required when high speed or high operating temperatures preclude the use of grease. It is necessary to choose an oil of proper viscosity and appropriate viscosity–temperature characteristics

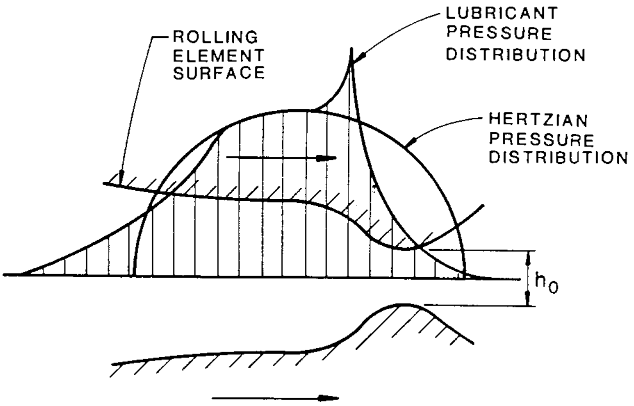

FIGURE 3.10.10 Typical pressure and film thickness distributions in elastohydrodynamic contact.

in order to ensure sufficient thickness of oil film in the lubricated concentrated contacts. If viscosity is too low, the film thickness will not prevent metal–metal contact; if the viscosity is too high, excessive friction will occur. Oil can be applied to a bearing by one of several methods (listed in order of increasing effectiveness at increasing bearing speed):

- *Oil bath* — the rolling elements carry the oil through the bearing.
- *Oil circulating system* — the oil is pumped from the bearing through an external filter and heat exchanger and back to the bearing.
- *Oil mist* — an air stream carries oil droplets to the bearing.
- *Oil jets* — the oil is injected into the bearing through carefully positioned nozzles.

The quantity and entry velocity of the oil must be carefully selected and controlled in order to dissipate the heat generated in the bearing.

The lubrication mechanism in the concentrated contacts of rolling element bearings is *elastohydrodynamic lubrication* (EHL). EHL typically occurs in lubricated, nonconforming elastic contacts, such as the elliptical contact that occurs between ball and raceway or the rectangular contact between roller and ring. These lubricated contacts have a very small area and the pressures are very high. Because of those high pressures, the contacting surfaces deform and the lubricant viscosity increases, thereby aiding its ability to sustain heavy loading without oil-film breakdown. A diagram of these phenomena is shown in Figure 3.10.10. The most important parameter of the concentrated contact, from the point of view of rolling-element bearing performance, is minimum EHL film thickness, h_o. The following expression can be used to find minimum film thickness in most rolling-element bearing contacts (Hamrock and Dowson, 1977):

$$h_o = 3.63\, R_x\, U^{0.68}\, G^{-0.49}\, W_p^{-0.73} \left(1 - e^{-0.68\kappa}\right) \tag{3.10.21}$$

where $R_x = (R_{x1}\, R_{x2})/(R_{x1} + R_{x2})$, $R_y = (R_{y1}\, R_{y2})/(R_{y1} + R_{y2})$, ellipticity parameter $\kappa = R_x/R_y$, $U = \mu\,(u_1 + u_2)/2E'R_x$, μ = absolute viscosity, u_1 and u_2 = velocities of rolling element and ring, respectively, $E' = E/(1 - \nu^2)$, E = modulus of elasticity, ν = Poisson's ratio, $G = \alpha E'$, α =pressure-viscosity exponent, $W_p = W/E'R_x^2$, and W = radial load.

The minimum film thickness must be large enough to prevent metal–metal contact within the lubricated conjunctions. The criterion for this is stated as:

$$h_0 \geq 1.5\left(r_{q1}^2 + r_{q2}^2\right)^{0.5} \tag{3.10.22}$$

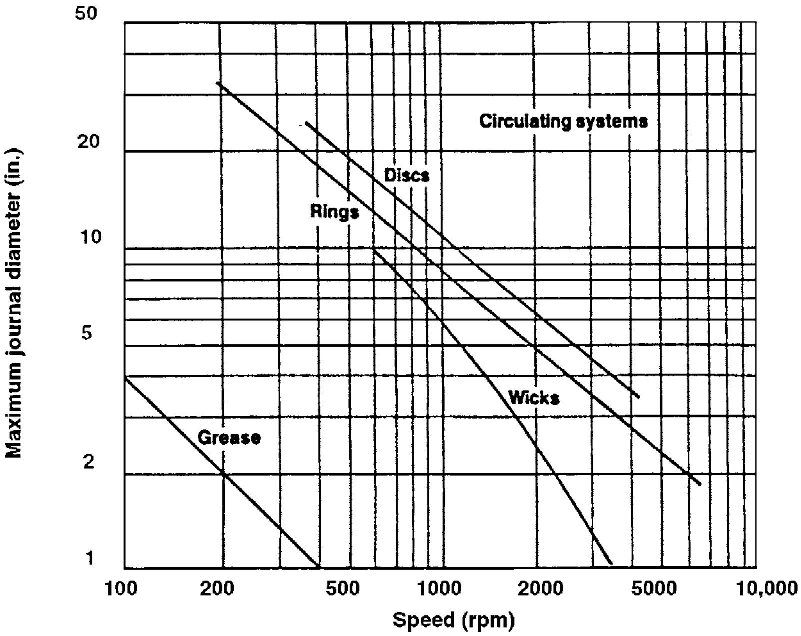

FIGURE 3.10.11 Upper limits for journal bearing lubrication methods. (From Wilcock, D.F. and Booser, E.R., *Bearing Design and Application*, McGraw–Hill, New York, 1987.)

where r_{q1} and r_{q2} are the rms surface roughness of the rolling element and ring, respectively. If the minimum film thickness is less than this value, complete elastohydrodynamic lubrication will not occur, and this could result in wear, surface fatigue, and eventual early bearing failure (i.e., well before the predicted L_{10} life). This drop in life can be minimized at low speeds with oils and greases incorporating certain antiwear additives.

An alternative to oil or grease lubrication for rolling element bearings operating under severe conditions is *solid lubrication*. Solid lubricants can be used effectively in high temperatures or vacuum conditions in which liquid lubricants are impractical or would provide marginal performance. Solid lubricants do not prevent solid–solid contact, so wear of the lubricant coating can be expected; bearing life is governed by the depletion of the solid lubricant film.

Lubricant Supply Methods

Lubrication systems for oil-film bearings can generally be grouped into three classifications: self-contained devices for small machines; centralized systems (common in manufacturing plants); and circulating systems dedicated to a single piece of equipment such as a motor, turbine, or compressor. Upper speed limits for common journal bearing lubrication methods are indicated in Figure 3.10.11 (Wilcock and Booser, 1987). Submerging the bearing directly in an oil bath is a common alternative for vertical machines.

Self-Contained Units

Lifting oil by *capillary action* from a small reservoir is used to feed small bearings in business machines, household appliances, electrical instruments, controls, and timer motors. In capillary tubes, the height h to which oil will rise is (Wilcock and Booser, 1987; Khonsari and Booser, 2002):

$$h = 2\sigma\cos\theta/(r\rho) \tag{3.10.23}$$

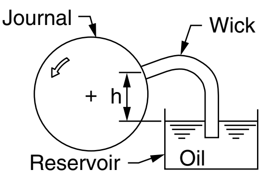

FIGURE 3.10.12 Wick-lubricated journal bearing. (From Elwell, R.C., in *Handbook of Lubrication and Tribology*, Vol. III, 515–533, CRC Press, Boca Raton, FL, 1994.)

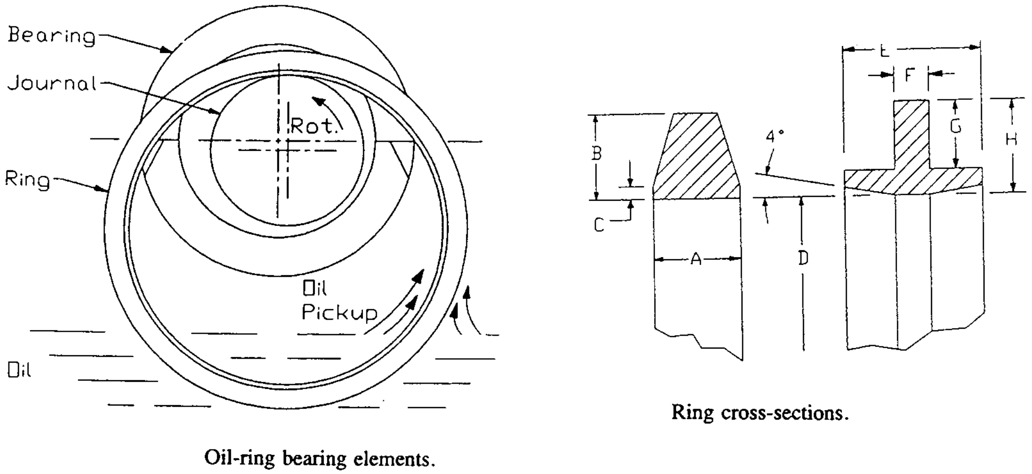

FIGURE 3.10.13 Oil-ring bearing elements and ring cross-sections. (From Elwell, R.C., in *Handbook of Lubrication and Tribology*, Vol. III, 515–533, CRC Press, Boca Raton, FL, 1994.)

where σ = surface tension, lb/in.; r = capillary radius (or spacing between two parallel plates), in.; and ρ =oil density, lb/in.^{3}. Because oils wet most surfaces readily, the cosine of the contact angle can be taken as unity. As an example, with $\sigma = 1.7 \times 10^{-4}$ lb/in. for a petroleum oil, the rise in an 0.005-in. radius capillary will be: $h = 2(1.7 \times 10^{-4})(1)/(0.005)(0.0307) = 2.2$ in.

Wick lubrication is applied in millions of fractional horsepower motors annually. Although wicks generally are not efficient at raising oil more than about 2 in., lift may be up to 5 in. in railway journal bearings. Referring to Figure 3.10.12, petroleum oil delivery by a typical wick can be estimated by the following equation (Elwell, 1994):

$$Q = kAF_o\left(h_u - h\right)/\left(\mu L\right) \quad \text{in.}^3/\text{min} \tag{3.10.24}$$

where the constant k reflects the capillary spacing in the wick and the surface tension of the oil; A is the wick cross section area, in.^{2}; F_o is volume fraction of oil in the saturated wick (often about 0.75); h_u is the ultimate wicking height, about 7.5 in. for SAE Grade F-1 felt; h is oil delivery height above the reservoir surface, in; L is wick length, in.; μ is viscosity at the wick temperature, lb.sec/in.$^2 \times 10^6$; k is approximately 0.26 for SAE Grade F-1 felt.

Oil rings hanging over a journal, as illustrated in Figure 3.10.13 and Table 3.10.20, are used to lift oil to journal bearings in electric motors, pumps, and medium-size industrial machines (Elwell, 1994). At very low journal surface speeds below about 2 to 3 ft/sec, the ring will run synchronously with its journal. At higher speeds, increasing viscous drag on the ring in its reservoir will slow the ring surface velocity; oil ring rpm at higher speeds is often in the range of 1/10 the journal rpm. Above about 45 ft/sec journal surface velocity, oil delivery drops to an unusably low level as centrifugal throw-off and windage interfere.

TABLE 3.10.20 Typical Oil-Ring Dimensions[a]

A	B	C	D	E	F	G	H
6 (0.24)	6 (0.24)	1 (0.04)	100 (3.94)				
7 (0.28)	7 (0.28)	1 (0.04)	135 (5.31)				
8 (0.31)	8 (0.31)	2 (0.08)	165 (6.50)				
16 (0.63)	13 (0.51)	2 (0.08)	200 (7.87)	16 (0.63)	5 (0.20)	11 (0.43)	10 (0.39)
			335 (13.2)	21 (0.83)	6 (0.24)	13 (0.51)	14 (0.55)
			585 (23.0)	25 (1.0)	7 (0.28)	14 (0.55)	20 (0.79)
			830 (32.7)	32 (1.3)	8 (0.31)	16 (0.63)	27 (1.06)

[a] mm (in.).

TABLE 3.10.21 Typical Oil Circulating Systems

Application	Duty	Oil Viscosity at 40°C (cSt)	Oil Feed (gpm)	Pump Type	Reservoir Dwell Time (min)	Type	Rating (μm)
Electrical machinery	Bearings	32–68	2	Gear	5	Strainer	50
General	Bearings	68	10	Gear	8	Dual cartridge	100
Paper mill dryer section	Bearings, gears	150–220	20	Gear	40	Dual cartridge	120
Steel mill	Bearings	150–460	170	Gear	30	Dual cartridge	150
	Gears	68–680	240	Gear	20	Dual cartridge	
Heavy duty gas turbines	Bearings, controls	32	600	Gear	5	Pleated paper	5
Steam turbine-generators	Bearings	32	1000	Centrifugal	5	By-pass 15%/h	10

These self-contained systems usually supply much less oil to a bearing than needed to form a full hydrodynamic oil film (Elwell, 1994). With the starved oil supply generating an oil wedge of reduced circumferential extent, power loss will be lowered at the expense of reduced load capacity (smaller minimum film thickness).

Centralized Distribution Systems

Limitations with individual localized lubricating devices have led to widespread use of centralized systems for factory production-line equipment, construction and mining machines, and similar applications. Oil or soft grease is pumped from a central reservoir in pulses or as metered continuous feed. Oil mist is piped for distances up to 300 ft for machines in petrochemical plants and steel mills. Polymer additives in the 50,000 to 150,000 mol wt range greatly reduce the escape of stray oil mist into the atmosphere.

Circulating Systems

When bearing design, reliability requirements, or equipment considerations preclude use of simpler oil feed, a circulating system involving an oil reservoir, pump, cooler, and filter (Twidale and Williams, 1984) is employed. These systems become quite compact with the space limitations in aircraft, marine, or automobile engines — the reservoir may simply be the machine sump with capacity to hold only a 20 to 60-sec oil supply. Characteristics of typical oil-circulating systems for industrial use are given in Table 3.10.21 (Wilcock and Booser, 1987).

Dynamic Seals

To control leakage of lubricating oil and process fluids and to minimize contamination, fluid seals commonly accompany bearings in a wide variety of machinery. Static seals, such as O-rings and gaskets,

TABLE 3.10.22 Characteristics of Dynamic Seals

Type of Seal	Type of Motion		Extent	Friction of Use	Leakage	Life
	Rotating	Reciprocating				
Contact						
Face seals	x		H	L	L	M–H
Lip seals	x		H	L	L	L–M
Piston rings		x	H	H	L	L–M
O-rings	x	x	M	H	L	L
Packings	x	x	H	M	M	L
Diaphragms		x	L	L	L	H
Controlled clearance						
Hydrodynamic	x		L	L	M	H
Hydrostatic	x		L	L	M	H
Floating bushing	x	x	M	M	M–H	H
Fixed geometry clearance						
Labyrinth	x		H	H	H	H
Bushing	x	x	M	H	H	M–H
Special						
Magnetic fuid	x	x	L	L	L	M
Centrifugal	x		L	M	L	H

Note: H = high; M = moderate; L = low.

Source: Modified from Stair, W., in *Handbook of Lubrication*, vol. 2, 581–622, CRC Press, Boca Raton, FL, 1984.

provide sealing between surfaces that do not move relative to each other. Dynamic seals, which will be the focus of this discussion, restrain flow of fluid between surfaces in relative motion. Most dynamic seals could be classified as contact or as clearance seals. Contact seals are used when surfaces are in sliding contact, while clearance seals imply that surfaces are in close proximity to each other but do not contact. The major types of dynamic seals are listed in Table 3.10.22. Further details about the design and analysis of dynamic sealing elements can be found in the handbook article by Stair (1984) and in the book by Lebeck (1991).

As an example of a contact seal, ball bearings are often sealed to retain their lubricant and to keep out contaminants over a long lifetime. For small grease-lubricated bearings, the sealing function is often accomplished by lightly loaded contact between a rubber lip seal component and the bearing ring. For shafts ranging up to about 2 in. (5 cm) in diameter, the lip seal may be replaced by a closely fitted, but noncontacting, shield; this helps contain the grease and restricts intrusion of dirt and other contaminants. For more severe sealing requirements in rolling element bearings, labyrinth clearance seals may be used (Harris, 2000).

The most common seals for rotating shafts passing through fixed housings, such as pumps or gearboxes, are radial lip seals and mechanical face seals. These contact seals can be designed to handle a wide range of sealed fluids, temperatures, velocities, and pressures (Lebeck, 1991; Stair, 1984). Material selection and surface finish considerations are similar to those discussed in the subsections on sliding friction and its consequences and on dry and semilubricated bearings.

When high surface speeds are encountered, wear and frictional heating may prohibit use of rubbing contact seals. For such applications, clearance seals such as close-fitting labyrinth seals or controlled-clearance fluid-film seals can be used. Fluid-film seals can be hydrostatic or hydrodynamic; both types have a pressurized film of fluid that prevents contact between the sealed surfaces and uses pressure balancing to restrain leakage. The principles governing their operation are similar to those discussed in the subsection on fluid film bearings. Details of fluid-film seals can be found in the article by Shapiro (1995).

References

ANSI/AFBMA, 1990. *Load Ratings and Fatigue Life for Ball Bearings*, ANSI/AFBMA 9-1990, AFBMA, Washington, D.C.

Archard, J.F., 1980. Wear theory and mechanisms, in *Wear Control Handbook*, M.B. Peterson and W.O. Winer, Eds., ASME, New York.

ASME, 2003. *Life Ratings for Modern Rolling Bearings*, TRIB-Vol, 14, ASME, New York.

Bhushan, B. and Gupta, B.K., 1991. *Handbook of Tribology*, McGraw–Hill, New York.

Bhushan, B., 1999. *Principles and Applications of Tribology*, John Wiley & Sons, New York.

Blanchet, T.A. and Kennedy, F.E.,1992. Sliding wear mechanism of polytetrafluoroethylene (PTFE) and PTFE composites, *Wear,* 153:229–243.

Blanchet, T.A., 1997. Friction, wear and PV limits of polymers and their composites, in *Tribology Data Handbook*, Booser, E.R., Ed., 547–562, CRC Press, Boca Raton, FL.

Blau, P.J., Ed.,1992. *Friction, Lubrication and Wear Technology, Metals Handbook*, v. 18, 10th ed., ASM International.

Booser, E.R., 1992. Bearing Materials, in *Encyclopedia of Chemical Technology*, v. 4, 1–21, John Wiley & Sons, New York.

Booser, E.R., 1995. Lubricants and Lubrication, in *Encyclopedia of Chemical Technology*, 4th ed., v. 15, 463–517, John Wiley & Sons, New York.

Booser, E.R. and Wilcock, D.F., 1987. New technique simplifies journal bearing design, *Machine Design*, April 23, 101–107.

Booser, E.R. and Wilcock, D.F., 1991. Selecting thrust bearings, *Machine Design*, June 20, 69–72.

Brandlein, J., Eschmann, P., Hasbargen, L., and Weigand, K., 2002. *Ball and Roller Bearings*, John Wiley & Sons, New York.

Crook, P. and Farmer, H.N., 1992. Friction and wear of hardfacing alloys, in *Friction, Lubrication and Wear Technology, Metals Handbook*, v. 18, 758–765, ASM International, Metals Park, OH.

Cusano, C., 1994. Porous metal bearings, in *Handbook of Lubrication and Tribology*, v. III, Booser, E.R., Ed., 491–513, CRC Press, Boca Raton, FL.

DeHart, A.O., 1983. Sliding bearing materials, in *Handbook of Lubrication*, Vol. II, Booser, E.R., Ed., 463–476, CRC Press, Boca Raton, FL.

Derner, W.J. and Pfaffenberger, E.E., 1983. Rolling element bearings, in *Handbook of Lubrication*, v. II, Booser, E.R., Ed., 495, CRC Press, Boca Raton, FL.

Elwell, R.C., 1994. Self-contained bearing lubrication: rings, disks, and wicks, in *Handbook of Lubrication and Tribology*, Vol. III, Booser, E.R., Ed., 515–533, CRC Press, Boca Raton, FL.

Engineering Sciences Data Unit (ESDU), 1965. *General Guide to the Choice of Journal Bearing Type*, Item 65007, Institution of Mechanical Engineers, London.

Engineering Sciences Data Unit (ESDU), 1967. *General Guide to the Choice of Thrust Bearing Type*, Item 67073, Institution of Mechanical Engineers, London.

Fenske, G.R., 1992. Ion implantation, in *Friction, Lubrication and Wear Technology, Metals Handbook*, v. 18, Blau, P.J., Ed., 850–860, ASM International, Metals Park, OH.

Fuller, D.D., 1984. *Theory and Practice of Lubrication for Engineers*, 2nd ed., John Wiley & Sons, New York.

Hamrock, B. and Dowson, D., 1977. Isothermal elastohydrodynamic lubrication of point contacts, *ASME J. Lubr. Tech.,* 99(2):264–276.

Harris, T.A., 2000. *Rolling Bearing Analysis*, 4th ed., John Wiley & Sons, New York.

Holmberg, K. and Matthews, A., 1994. *Coatings Tribology,* Elsevier, Amsterdam, The Netherlands.

Ioannides, S. and Harris, T.A., 1985. A new fatigue life model for rolling bearings, *ASME J. Tribology*, 107:367–378.

ISO, 2000. Rolling bearings — dynamic load ratings and rating life, amendment 2: life modification factor, International Standard ISO 281/2.

Jamison, W.E., 1994. Plastics and plastic matrix composites, in *Handbook of Lubrication and Tribology*, v. III, Booser, E.R., Ed., 121–147, CRC Press, Boca Raton, FL.

Khonsari, M.M., 1997. *Tribology Data Handbook*, Booser, E.R., Ed., CRC Press, Boca Raton, FL.

Khonsari, M.M. and Booser, E.R., 2002. *Applied Tribology: Bearing Design and Lubrication*, John Wiley & Sons, New York.

Kingsbury, G.R., 1992. Friction and wear of sliding bearing materials, in *Friction, Lubrication and Wear Technology, Metals Handbook*, v. 18, 741–757, ASM International, Ohio.

Klaus, E.E. and Tewksbury, E.J., 1984, *Handbook of Lubrication*, v. II, 229–254, CRC Press, Boca Raton, FL.

Kushner, B.A. and Novinski, E.R., 1992. Thermal spray coatings, in *Friction, Lubrication and Wear Technology, Metals Handbook*, v. 18, 829–833, ASM International, Ohio.

Lebeck, A.O., 1991. *Principles and Design of Mechanical Face Seals*, John Wiley & Sons, New York.

Lundberg, G. and Palmgren, A., 1947. Dynamic capacity of rolling bearings, *Acta Polytech. Mech. Eng. Ser.*, 1(3), IVAH no. 196.

Lundberg, G. and Palmgren, A., 1952. Dynamic capacity of roller bearings, *Acta Polytech. Mech. Eng. Ser.*, 2(4):96.

Morgan, V.T., 1984. *Porous Metal Bearings and Their Application*, MEP-213, Mechanical Engineering Publications, Ltd., Workington, U.K.,

Neale, M.J., 1993. *Bearings*, Butterworth–Heinemann, Oxford.

Peterson, M.B. and W.O. Winer, W.O., Eds., 1980. *Wear Control Handbook*, ASME, New York.

Rabinowicz, E., 1980. Wear coefficients — metals, in *Wear Control Handbook*, M.B. Peterson and W.O. Winer, Eds., 475–506, ASME, New York.

Rabinowicz, E., 1995. *Friction and Wear of Materials*, 2nd ed., John Wiley & Sons, New York.

Raimondi, A.A. and Szeri, A.Z, 1984. Journal and thrust bearings, in *Handbook of Lubrication*, v. II, Booser, E.R., Ed., 413–462, CRC Press, Boca Raton, FL.

Reynolds, O., 1886. On the theory of lubrication and its application to Mr. Beauchamp Tower's experiments, *Phil. Trans. R. Soc.*, 177, 157–234.

Rudnick, L.R., Ed., 2003. *Lubricant Additives*, Marcel Decker, New York.

Rudnick, L.R. and Shubkin, R.L., 1999. *Synthetic Lubricants and High Performance Functional Fluids*, Marcel Decker, New York.

Schmitt, G.F., 1980. Liquid and solid particle impact erosion, in *Wear Control Handbook*, M.B. Peterson and W.O. Winer, Eds., 231–282, ASME, New York.

Shabel, B.S., Granger, D.A., and Tuckner, W.G., 1992, Friction and wear of aluminum–silicon alloys, in *ASM Handbook*, v. 18, Blau, P.J., Ed., 785–794, ASM International, Ohio.

Shapiro, W., 1995. Hydrodynamic and hydrostatic seals, in *Handbook of Lubrication*, v. III, Booser, E.R., Ed., 445–468, CRC Press, Boca Raton, FL.

Stair, W., 1984. Dynamic seals, in *Handbook of Lubrication*, v. II, Booser, E.R., Ed., 581–622, CRC Press, Boca Raton, FL.

Totten, G.E., Ed., 2003. *Fuels and Lubricants Handbook*, ASTM, West Conshohocken, PA.

Twidale, A.J. and Williams, D.C.J., 1984. Circulating oil systems, in *Handbook of Lubrication*, v. II, Booser, E.R., Ed., 395–409, CRC Press, Boca Raton, FL.

Weil, R. and Sheppard, K., 1992. Electroplated coatings, in *Friction, Lubrication and Wear Technology, Metals Handbook*, v. 18, Blau, P.J., Ed., 834–839, ASM International, Ohio.

Wilcock, D.F. and Booser, E.R., 1956. *Bearing Design and Application*, McGraw–Hill, New York.

Wilcock, D.F. and Booser, E.R., 1987. Lubrication techniques for journal bearings, *Machine Design*, April 23, 101–107.

3.11 Pumps and Fans

Robert F. Boehm

Introduction

Pumps are devices that impart a pressure increase to a liquid. Fans are used to increase the velocity of a gas, but this is also accomplished through an increase in pressure. The pressure rise found in pumps can vary tremendously, and this is a very important design parameter, along with the liquid flow rate. This pressure rise can range from simply increasing the elevation of the liquid to increasing the pressure by hundreds of atmospheres. Fan applications, on the other hand, generally deal with small pressure increases. In spite of this seemingly significant distinction between pumps and fans, the fundamentals of certain types of these machines, as well as their applications and theories of operation, share many similarities.

Pumps or fans can be used as a means of forcing flows into a region of interest or, alternatively, exhausting flows from a region of interest. For example, induced draft fans are those in which the inlet to the fan is attached to the region of interest. Forced draft fans are hooked with their exhaust side to the region of interest. Pumps are usually not denoted with this distinction except for vacuum pumps, which are always used to exhaust a fluid from a volume of interest.

The appropriate use of pumps and fans depends upon the satisfactory choice of device and the proper design and installation for the application. A check of sources of commercial equipment shows that varieties of pumps and fans are many. Each of these has special characteristics that must be appreciated for achieving proper function. Preliminary design criteria for choosing between different types are given by Boehm (1987).

As to be expected, the wise applications of pumps and fans require knowledge of fluid flow fundamentals. Unless the fluid mechanics of a particular application is understood, the design could be less than desirable.

In this section, pump and fan types are briefly defined. In addition, typical application information is given. Also, some ideas from fluid mechanics that are especially relevant to pump and fan operation are reviewed. For more details on this latter topic, see the section of this book that discusses fluid mechanics fundamentals.

Pumps

Raising water from wells and cisterns was the earliest form of pumping (a very detailed history of early applications is given by Ewbank, 1842). Modern applications are much broader, and these find a wide variety of machines in use. Modern pumps function on one of two principles. By far the majority of pump installations are of the *velocity head* type. In these devices, the pressure rise is achieved by giving the fluid movement. At the exit of the machine, this movement is translated into a pressure increase by slowing down the fluid. The other major type of pump is called *positive displacement*. These devices are designed to increase the pressure on the liquid while essentially trying to compress the volume. A categorization of pump types (with the exception of vacuum pumps) has been given by Krutzsch (1986); an adaptation is shown below.

- I. Velocity head
  - A. Centrifugal
    - 1. Axial flow (single or multistage)
    - 2. Radial flow (single or double suction)
    - 3. Mixed flow (single or double suction)
    - 4. Peripheral (single or multistage)
  - B. Special effect
    - 1. Gas lift
    - 2. Jet
    - 3. Hydraulic ram
    - 4. Electromagnetic
- II. Positive displacement
  - A. Reciprocating
    - 1. Piston, plunger
      - a. Direct acting (simplex or duplex)
      - b. Power (single or double acting, simplex, duplex, triplex, multiplex)
    - 2. Diaphragm (mechanically or fluid driven, simplex or multiplex)

B. Rotary
  1. Single rotor (vane, piston, screw, flexible member, peristaltic)
  2. Multiple rotor (gear, lobe, screw, circumferential piston)

In the next subsections, some of the more common pumps are described.

Centrifugal and Other Velocity-Head Pumps

Centrifugal pumps are used in more industrial applications than any other kind of pump, primarily because these pumps offer low initial and upkeep costs. Traditionally, pumps of this type have been limited to low-pressure-head applications; however, modern pump designs have overcome this problem unless very high pressures are required. Some of the other good characteristics of these types of devices include smooth (nonpulsating) flow and the ability to tolerate nonflow conditions.

The most important parts of the centrifugal pump are the *impeller* and *volute*. An impeller can take on many forms, ranging from essentially a spinning disc to designs with elaborate vanes. The latter is usual. Impeller design tends to be somewhat unique to each manufacturer, as well as finding a variety of designs for a range of applications. An example of an impeller is shown in Figure 3.11.1. This device imparts a radial velocity to the fluid that has entered the pump perpendicular to the impeller. The volute (there may be one or more) performs the function of slowing the fluid and increasing the pressure. A good discussion of centrifugal pumps is given by Lobanoff and Ross (1992).

The design of a pump and its performance are dependent upon a number of applicable variables. These will be noted in more detail later; they include the pump operating speed, flow rate, and developed head. Pump engineers generally combine these variables together into a parameter called the *specific speed*, N_s. This is given as

$$N_s = Q^{0.5}N/H^{0.75}$$

where

Q = volume rate of flow, gpm
N = operating speed of pump, rpm
H = pump head, ft

Historically, the efficiency is related to this parameter in a general way, showing a maximum efficiency of over 90% at a specific speed of about 2500 and very high flow rates (Yedidiah, 1996). For lower flows, the maximum efficiency is decreased and occurs at smaller values of N_s. Rishel (2000) reported on the results of a study of actual installations of “wire-to-water” efficiencies for pumps. These ranged from 20% for small systems (20 gpm) to 84% for systems at 2000 gpm. The head was varied in the study. A plot of his data is given in Figure 3.11.2.

An important factor in the specification of a centrifugal pump is the casing orientation and type. For example, the pump can be oriented vertically or horizontally. Horizontal mounting is most common.

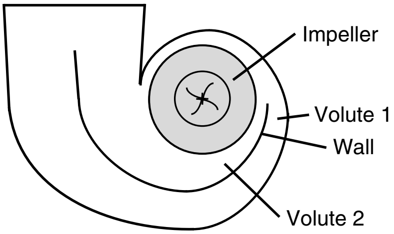

FIGURE 3.11.1 A schematic of a centrifugal pump is shown. The liquid enters perpendicular to the figure, and a radial velocity is imparted by clockwise spin of the impeller.

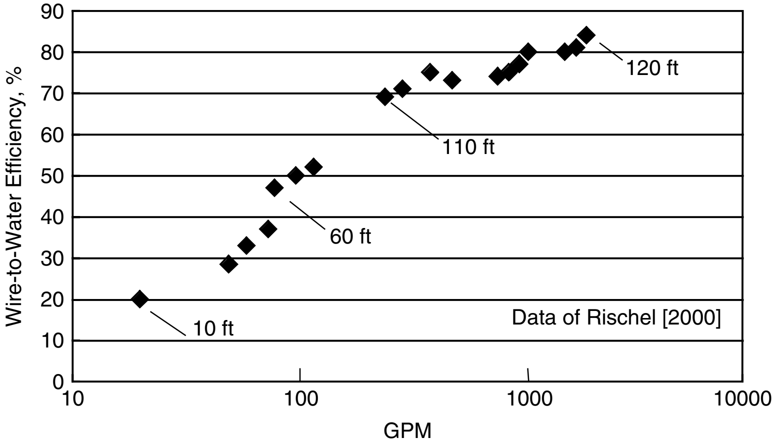

FIGURE 3.11.2 "Wire-to-water" efficiencies for centrifugal pumps are given. (Based upon the data of Rishel, J.B., 2000. *ASHRAE J.*, March, 48.) The head varies throughout the data within the range shown.

Vertical pumps usually offer benefits related to ease of priming and reduction in required NPSH (see discussion later). This type also requires less floor space. Submersible and immersible pumps are always of the vertical type. Another design factor is the way in which the casing is split, which has implications about ease of manufacture and repair. Casings split perpendicular to the shaft are called radially split, while those split parallel to the shaft axis are denoted as axially split. The latter can be horizontally split or vertically split. The number of stages in the pump greatly affects the pump-output characteristics. Several stages can be incorporated into the same casing, with an associated increase in pump output. Multistage pumps are often used for applications with total developed head over (about) 50 atm.

It can be important whether a pump is self-priming (the impeller of the pump must be immersed in the fluid to be pumped). In general, a centrifugal pump cannot begin pumping unless it is primed. If a centrifugal pump is filled with air when it is turned on, the initiation of pumping action may not be sufficient to bring the fluid into the pump. Pumps can be specified with features that can minimize priming problems.

Although not applicable to centrifugal pumps only, a major application here is the use of a *variable speed drive* (*VSD*). In many situations, the design condition is not the only one at which the pump may need to operate. For example, if the flow decreased for some reason, the head would go up, and vice versa. This may cause problems with the particular pump installation. A VSD will allow these situations, as well as part load operation, to be accommodated. Without VSD, for example, this would be accomplished by mechanical devices in order to throttle the flow. A VSD can greatly enhance system operational efficiency.

Other types of velocity-head pumps are available. *Gas lifts* accomplish a pumping action by a drag on gas bubbles that rise through a liquid. *Jet pumps* (eductors) increase pressure by imparting momentum from a high-velocity liquid stream to a low-velocity or stagnant body of liquid. The resulting flow then goes through a diffuser to achieve an overall pressure increase. Related designs that use a gas or a vapor to impart the momentum are called *jet ejectors*. An excellent summary of these types of devices has been given by Power (1994). In all cases in which eductors or ejectors are used, a separate high-pressure fluid stream needs to be available to power the device.

Positive-Displacement Pumps

Positive-displacement pumps demonstrate high discharge pressures and low flow rates. Usually, this is accomplished by some type of pulsating action. A piston pump is a classical example of a positive-displacement machine. Rotary pumps are one type of positive displacement device that does not impart pulsations to the exiting flow (a full description of these types of pumps is given by Turton, 1994). Several techniques are available for dealing with pulsating flows, including use of double-acting pumps (usually of the reciprocating type) and installation of pulsation dampeners.

Positive displacement pumps usually require special seals to contain the fluid. Costs are higher initially, as well as for maintenance, compared to most pumps that operate on the velocity-head basis. Positive-displacement pumps demonstrate an efficiency nearly independent of flow rate, in contrast to the velocity-head type.

Reciprocating pumps offer very high efficiencies, reaching 90% in larger sizes. These types of pumps are more appropriate for pumping abrasive liquids (e.g., slurries) than are centrifugal pumps.

Piston pumps are commonly applied positive-displacement devices. The piston-cylinder arrangement is familiar to most people who have used pumps. These pumps can be *single acting* or *double acting.* In the latter classification, the design is such that pumping takes place on both sides of the piston. Many application engineers recommend a maximum duty pressure of about 2000 psi. Higher pressures can be handled by a plunger-rod pump; a plunger rod moves inside a pipe of the same diameter. Because fluctuations are inherent in most positive displacement devices, a pulsation dampener may have to be used (Vandall and Foerg, 1993).

A possibly valuable characteristic of positive displacement pumps is that the output flow is proportional to pump speed. This allows this type of pump to be used for metering applications. Also, a positive aspect of these pumps is that they are self-priming, except at initial startup. *Very high head pressures (often damaging to the pump) can be developed in positive displacement pumps if the downstream flow is blocked.* For this reason, a pressure-relief-valve bypass must always be used with positive displacement pumps. Some designers recommend a bypass even for centrifugal pumps.

Selecting a Pump Based upon Flow Considerations

Performance characteristics of the pump must be considered in system design. Simple diagrams of pump applications are shown in Figure 3.11.3. First consider the left-hand figure, which represents a flow circuit; the pressure drops related to the piping, fittings, valves, and any other flow devices found in the circuit must be estimated using laws of fluid mechanics. Usually these resistances (pressure drops) are found to vary approximately with the square of the liquid flow rate.

Most pumps demonstrate a flow vs. pressure rise variation that is a positive value at zero flow and decreases to zero head at some larger flow. A variation typical of centrifugal pumps is shown on the left-hand side of Figure 3.11.4. One exception to this — an important one related to these types of pumps — is the so-called “drooping head” behavior. In this situation, the head at zero flow is less than the heads achieved at small positive flows. Described in some detail by Paugh (1994), this phenomenon is a result of high-efficiency design.

Positive displacement pumps, as shown on the right-hand side of Figure 3.11.4, are an exception to this characteristic behavior in that these devices usually cannot tolerate a zero flow. An important aspect

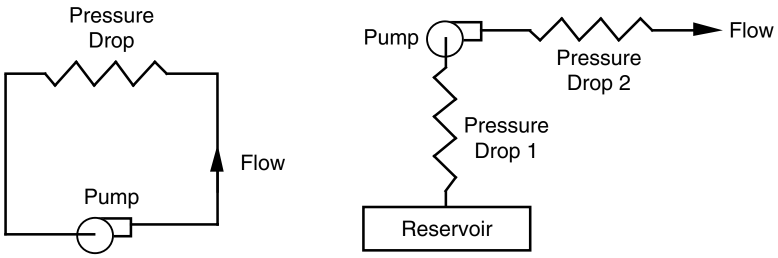

FIGURE 3.11.3 Typical pump applications, whether in circuits or once-through arrangements, can be represented as combined fluid resistances. The resistances are determined from fluid mechanics analyses.

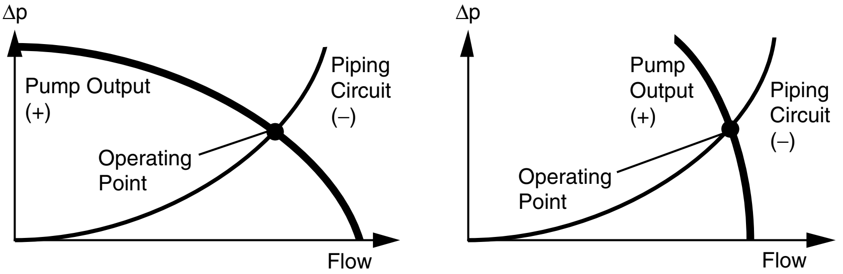

FIGURE 3.11.4 An overlay of the pump flow vs. head curve with the circuit piping characteristics gives the operating state of the circuit. A typical velocity-head pump characteristic is shown on the left, while a positive-displacement pump curve is shown on the right.

to note is that a closed system can presumably be pressurized by the pump to the detriment of the system and the pump.

The piping diagram shown on the right-hand side of Figure 3.11.3 is a once-through system, another frequently encountered installation. However, the leg of piping through "pressure drop 1" shown here can have some very important implications related to *net positive suction head*, often denoted as *NPSH*. In simple terms, NPSH indicates the difference between the local pressure and the thermodynamic saturation pressure at the fluid temperature. If NPSH = 0, the liquid can vaporize, thus resulting in a variety of outcomes from noisy pump operation to outright failure of components. This condition, called *cavitation*, must be eliminated by proper design.

Cavitation, if it occurs, will first take place at the lowest pressure point within the piping arrangement. Often this point is located at, or inside, the inlet to the pump. Most manufacturers specify how much NPSH is required for satisfactory operation of their pumps. Thus, the *actual NPSH* (often denoted as *NPSHA*) experienced by the pump must be larger than the manufacturer's *required NPSH* (which may be called *NPSHR*).

If a design indicates insufficient NPSH, changes should be made in the system, possibly including alternative piping layout. This might include lowering the pump location relative to the feed, changing sizes of the inlet piping and fittings, or slowing the pump speed. Some pumps have smaller NPSH requirements than others, possibly as a result of adding inducers to the inlet. Sometimes it is possible to cool the pump inlet fluid and this will increase the NPSHA. More extreme solutions could find a smaller pump installed prior to the inlet of the main pump whose purpose is to increase the NPSHA of the latter. Of course, if a pump is fed from a tank and vortices form there at typical flow conditions, this could greatly decrease the NPSHA beyond what would appear to be present.

Fluid properties can have a major impact on the choice of pump. One variable of concern is viscosity. This property can have high or extremely variable values in a given circuit. At the minimum, increases in viscosity will require more pumping power. However, the value of the viscosity may influence the type of pump used. For viscosities up to slightly over 3000 cP, centrifugal pumps will work quite well. Rotary pumps can handle less frequently encountered situations with considerably higher viscosities.

The manufacturer should be consulted for a map of operational information for a given pump. A typical set of these is shown in Figure 3.11.5 through Figure 3.11.7. This information will allow the designer to select a pump that satisfies the circuit operational requirements while meeting the necessary NPSH and most efficient operation criteria.

First consider Figure 3.11.5. This gives a map of overall performance for a given family of pumps. The specific operational ranges for each model within the family are shown. This range is due to use of various impeller sizes, pump speeds, and other design parameters in a particular configuration.

Once the general design conditions are located on an overall performance map, they will generally indicate a particular model for the application. This can then be referred to go determine the performance

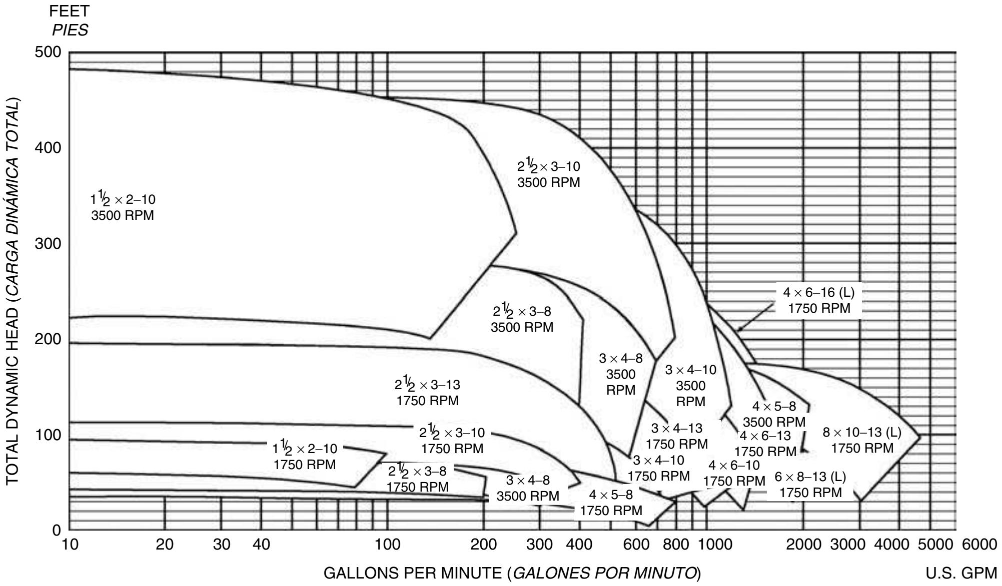

FIGURE 3.11.5 When a pump is selected for a given application, the starting point is a performance coverage map. From this, the model required to achieve a given performance can be selected. (Compliments of Goulds Pumps.)

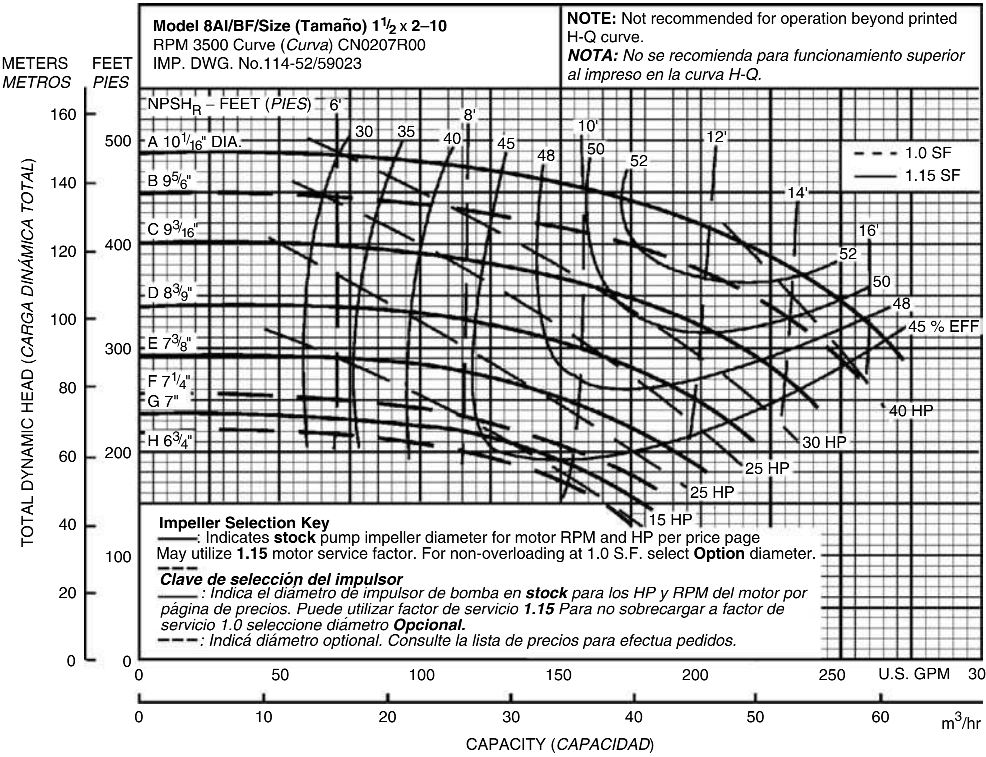
Model 8AI/BF/Size (Tamaño) 1½ x 2–10
RPM 3500 Curve (*Curva*) CN0207R00
IMP. DWG. No.114-52/59023

NOTE: Not recommended for operation beyond printed H-Q curve.
NOTA: *No se recomienda para funcionamiento superior al impreso en la curva H-Q.*

Impeller Selection Key
——: Indicates **stock** pump impeller diameter for motor RPM and HP per price page
May utilize **1.15** motor service factor. For non-overloading at 1.0 S.F. select **Option** diameter.
– – –
Clave de selección del impulsor
*——: Indica el diámetro de impulsor de bomba en **stock** para los HP y RPM del motor por página de precios. Puede utilizar factor de servicio **1.15** Para no sobrecargar a factor de servicio 1.0 seleccione diámetro **Opcional**.*
– – –: Indicá diámetro optional. Consulte la lista de precios para efectua pedidos.

FIGURE 3.11.6 Once the particular model of pump is determined (see Figure 3.11.5), the actual performance of that model can be examined from a plot of this type. This is given here for a particular speed. (Compliments of Goulds Pumps.)

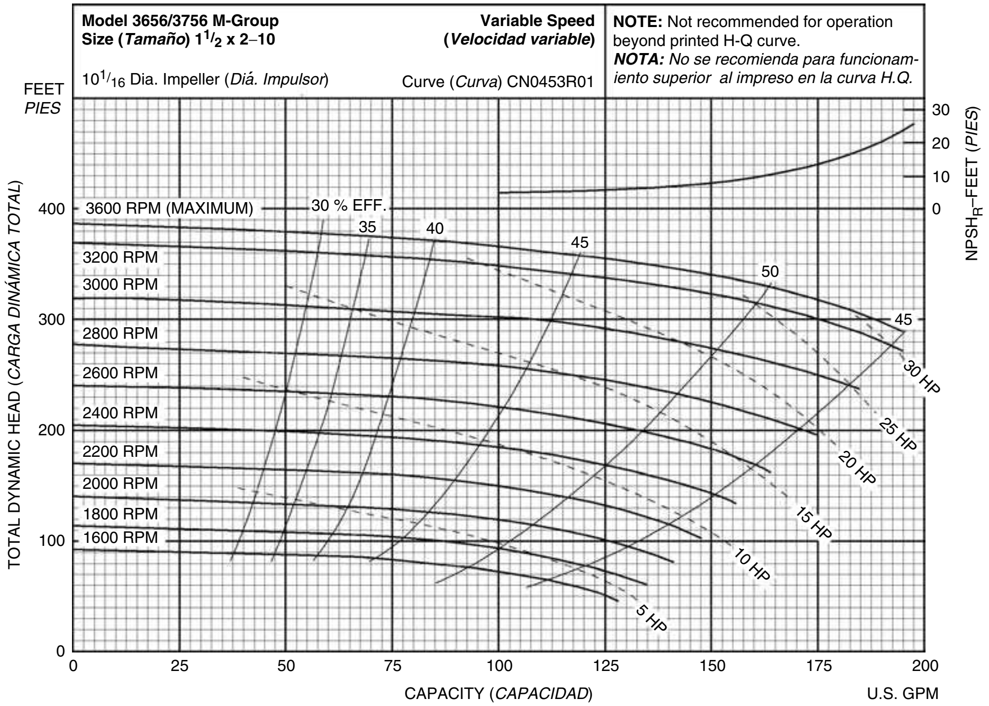

FIGURE 3.11.7 Impeller speed for a given model will have an impact on the pump performance (compare to Figure 3.11.6). (Compliments of Goulds Pumps.)

of the specific model. For example, if design conditions had fallen in the range of model 1½ × 2 – 10 3500 rpm, the details of this one would be examined (see Figure 3.11.6).

Note the following generally typical characteristics of centrifugal pumps. The produced head decreases with increasing flow over the specific range for this pump. Larger diameter impellers are required to move to higher level curves, and these conditions are associated with higher power requirements. NPSH requirements increase generally with increasing flow. Sometimes manufacturers give this information as a simple function of flow, or it can be specified in more definitive terms as shown in Figure 3.11.6. Pumping efficiency curves are also shown. It is desirable to operate near the maximum values of efficiency if that can be accommodated between the design requirements and the characteristics of the specific pumps. This is a lower-flow pump and, as was shown in Figure 3.11.2, this one demonstrates lower efficiencies than some larger units would be able to furnish within the same family of pumps.

Finally, consider Figure 3.11.7. This shows the impact of drive speed on the operation of the pump. Figure 3.11.6 was developed for a single speed; Figure 3.11.7 shows the effects of various speeds. Here the NPSH is shown as a simple function increasing with flow rate.

Several options are available to the designer for combining pumps in systems. Consider a comparison of the net effect between operating pumps in series or operating the same two pumps in parallel. Examples of this for pumps with characteristics like centrifugal units are shown in Figure 3.11.8. It is clear that one way to achieve high pumping pressures with centrifugal pumps is to place a number of units in series. This effect is related to what is found in multistage designs.

Vacuum Pumps

When pressures significantly below atmospheric are required, a vacuum pump should be applied. In fact, *vacuum* is defined as being a pressure below the surrounding atmosphere. These pumps are often used

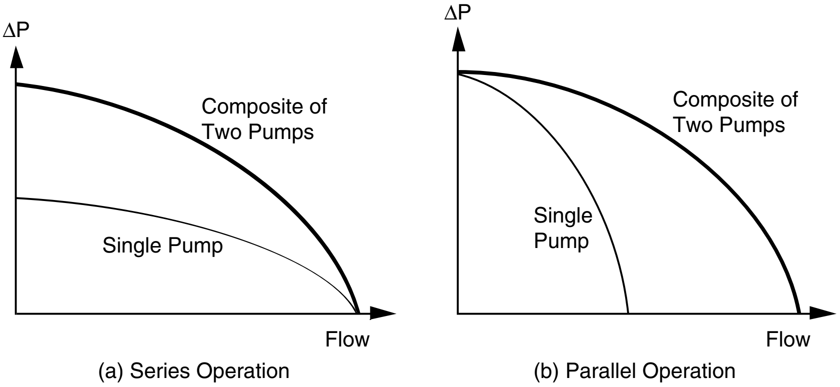

FIGURE 3.11.8 Series and parallel operations of centrifugal pumps are possible. The resultant characteristics for two identical pumps.

to remove a vapor or a gas from within a volume of interest. If most of the vapor or gas is removed, this is often called a "hard" or "high" vacuum.

Even though the pressure differential across a vacuum pump is typically less than 1 atm, the small value of pressure at the inlet to the pump complicates the performance of the device. A resulting high-pressure ratio usually exists across a vacuum pump. Because of this factor, as well as the characteristics of gases and vapors as they become rarefied, a large amount of vacuum is usually accomplished by using a sequence of vacuum pumps. To see how this is achieved, consider the general types of vacuum pumps available.

At coarse vacuums (not large pressure differences from atmospheric) a mechanical pump or blower might be used. These have designs very much like those of other pump and fan systems discussed in this chapter.

At higher vacuums, a *vapor jet* (or *diffusion*) pump may find a cost-effective application. The basic idea behind this approach is a concept illuminated by kinetic theory: gases can be pumped by the molecular drag effect. A separate pumping fluid is used to remove the vapor or gas of interest. Devices built on this concept demonstrate high pumping speeds at low pressures.

Using high-speed rotating machinery in several stages to accomplish necessary evacuation, *turbo* pumps reach levels of vacuums similar to those achieved by diffusion pumps.

Ion-getter and *sputter-ion pumps* are used for high- and ultrahigh-vacuum situations. In this approach, *gettering* is used, which denotes a concept of a chemical combination between a surface and the pumped gas. Although many types of gettering materials are available, a commonly used one is titanium. When chemically active gas atoms strike a getter surface, stable, solid compounds are formed there.

To achieve high- or ultrahigh-vacuums, a series of these pumps might be used. At moderate vacuums, a *roughing* pump is a good choice. As the absolute pressure decreases, a switch is made to another type of pump, for example, a cryopump or a diffusion pump. Finally, the very small pressures can then be reached using a getter or ion pump. Approximate ranges for each of these pumps are shown in Figure 3.11.9. Figure 3.11.10 shows the performance range of various types of coarse vacuum pumps. These figures were developed from information given by Hablanian (1997), whose text is an excellent source of information on all of these types of devices.

Fans

As noted earlier, fans are devices that cause air to move. This definition is broad and can even include a flapping palm branch, but the discussion here deals only with devices that impart air movement due to rotation of an impeller inside a fixed casing. In spite of this limiting definition, it includes a large variety of commercial designs.

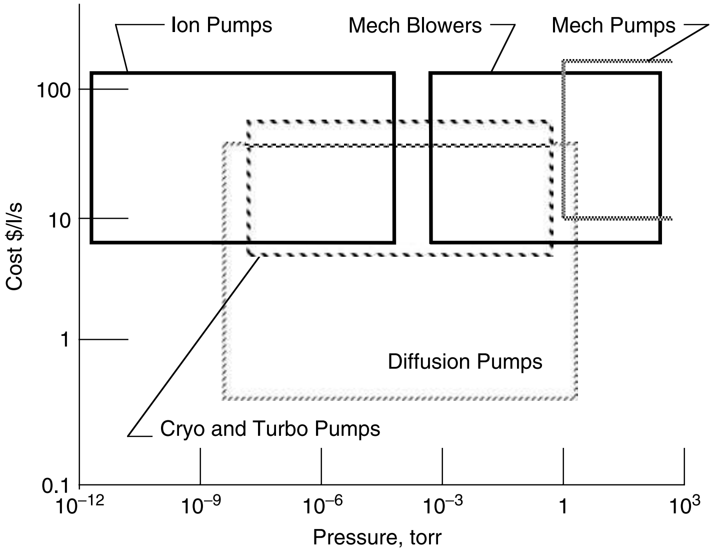

FIGURE 3.11.9 Approximate operational ranges in which various types of vacuum pumps are most cost effective (in 1985 prices). (Adapted from Hablanian, M., 1997. *High-Vacuum Technology — A Practical Guide*, 2nd ed., Marcel Dekker, New York.)

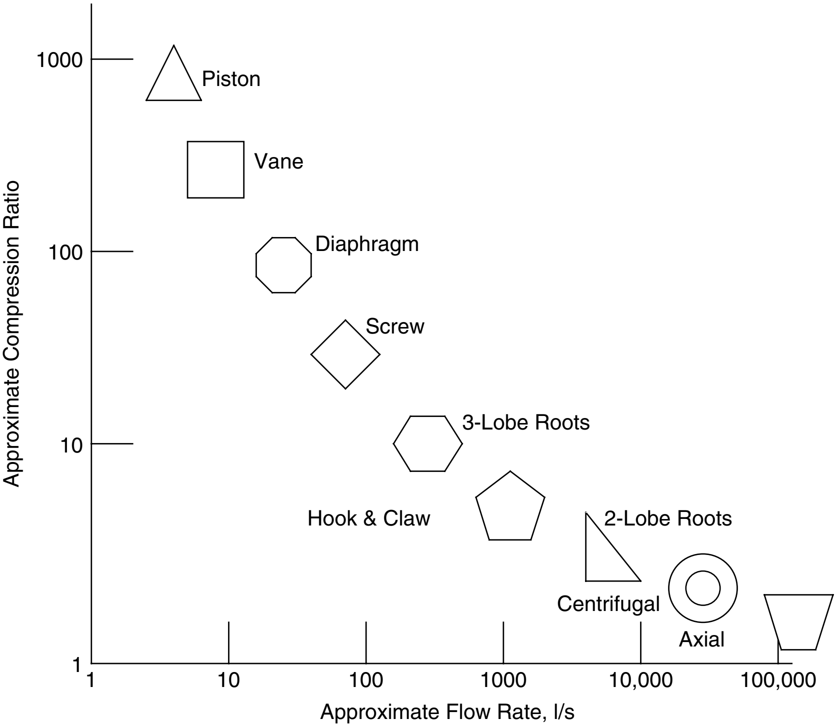

FIGURE 3.11.10 The operational ranges of coarse vacuum pumps. (Adapted from Hablanian, M., 1997. *High-Vacuum Technology — A Practical Guide*, 2nd ed., Marcel Dekker, New York.)

Fans find application in many engineering systems. Along with the chillers and boilers, they are the heart of heating, ventilating, and air conditioning (HVAC) systems. When large physical dimensions of a unit are not a design concern (usually the case), centrifugal fans are favored over axial flow units for

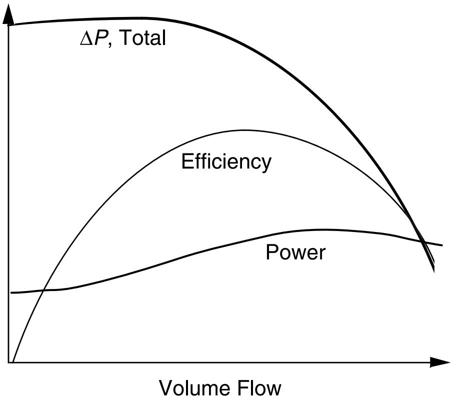

FIGURE 3.11.11 Characteristics of a centrifugal fan. The drawbacks to operating away from optimal conditions are obvious from the efficiency variation.

HVAC applications. Many types of fans are found in power plants (Stultz and Kitto, 1992). Very large fans are used to furnish air to the boiler as well to draw or force air through cooling towers and pollution control equipment. Electronic cooling finds applications for small units — automobiles have several fans in them. Because of the great engineering importance of fans, several organizations publish rating and testing criteria (see, for example, ASME, 1995).

Generally, fans are classified according to how the air flows through the impeller. These flows may be axial (essentially a propeller in a duct), radial (conceptually much like the centrifugal pumps discussed earlier), mixed, and cross. Although many other fan designations exist, all industrial units are one of these classifications. Mixed-flow fans are so named because axial and radial flow occurs on the vanes. Casings for these devices are essentially like those for axial flow machines, but the inlet has a radial flow component. On cross-flow impellers, the gas traverses the blading twice.

Generic characteristics of fans are shown in Figure 3.11.11. Because velocities can be high in fans, often the total and the static pressure increases are considered. Although both are not shown in this figure, the curves have similar variations. Of course, the total ΔP is greater than the static value; the difference is the velocity head and it increases as the volume flow increases. At zero flow (the *shut-off point*), the static and total pressure difference values are the same. Efficiency variation shows a sharp optimum value at the design point. For this reason, it is critical that fan designs be carefully tuned to the required conditions.

A variety of vane types are found on fans and the type of vane is also used for fan classification. Axial fans usually have vanes of airfoil shape or vanes of uniform thickness. Some vane types that might be found on a centrifugal (radial flow) fan are shown in Figure 3.11.12.

One issue in choosing fans for a particular application is fan efficiency. Typical efficiency comparisons of the effect of blade type on a centrifugal fan are shown in Figure 3.11.13. Because velocities can be high, the value of aerodynamic design is clear. Weighing against this is the increased cost.

An additional aspect that may be important in the choice of fans is noise generation, which may be most critical in HVAC applications. It is difficult to describe noise characteristics in brief terms because of the frequency-dependent nature of these phenomena. However, comparison of specific sound power levels (usually denoted by K_w) shows that backward-curved centrifugal fans with aerodynamic blades are among the best performing designs. Details of noise characteristics are given elsewhere (ASHRAE, 1999). Although each type of fan has some specific qualities for certain applications, most installations use centrifugal (radial flow) fans. A primary exception is for very-high-flow, low-pressure-rise situations in which axial (propeller) fans are used.

Similarities exist between fans and pumps because the fluid density essentially does not vary through either type of machine. Of course in pumps this is because a liquid can be assumed to be incompressible. In fans, a gas (typically air) is moved with little pressure change. As a result, the gas density can be taken

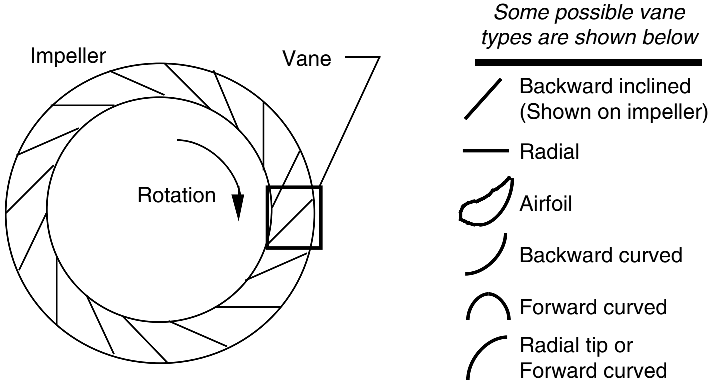

FIGURE 3.11.12 A variety of vane types that might be used on a centrifugal fan.

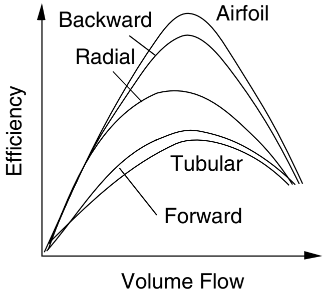

FIGURE 3.11.13 Efficiency variations with volume flow of centrifugal fans for a variety of vane types.

to be constant. Because most fans operate near atmospheric pressure, the ideal gas assumptions can be used in determining gas properties.

Flow control in fan applications, where needed, is a very important design concern. Methods for accomplishing this involve use of dampers (on the inlet or the outlet of the fan), variable pitch vanes, or variable speed control. Dampers are the least expensive to install but also the most inefficient in terms of energy use. Modern solid-state control for providing variable frequency power to the drive motor is becoming the preferred control method when a combination of initial and operating costs are considered.

References

ASHRAE, 1999. *ASHRAE Handbook 1999, HVAC Applications*, American Society of Heating, Refrigerating, and Air Conditioning Engineers, Atlanta, Chapter 42.

ASME, 1995. *ASME Performance Test Codes, Code on Fans*, ASME PTC 11-1984 (reaffirmed 1995), American Society of Mechanical Engineers, New York.

Boehm, R.F., 1987. *Design Analysis of Thermal Systems*, John Wiley & Sons, New York, pp. 17–26.

Ewbank, T., 1842. *A Description and Historical Account of Hydraulic and Other Machines for Raising Water*, 2nd ed., Greeley and McElrath, New York.

Hablanian, M., 1997. *High-Vacuum Technology — A Practical Guide*, 2nd ed., Marcel Dekker, New York.

Krutzsch, W.C., 1986, Introduction: classification and selection of pumps, in *Pump Handbook*, 2nd ed. (Eds., I. Karassik et al.), McGraw–Hill, New York, chapter 1.

Lobanoff, V. and Ross, R., 1992. *Centrifugal Pumps: Design & Application*, 2nd ed., Gulf Publishing Company, Houston, TX.

Paugh, J.J., 1994. Head vs. capacity characteristics of centrifugal pumps, in *Fluid Movers, Second Edition*, (Ed., N.P. Chopey), Chemical Engineering/McGraw–Hill, New York, 123–125.

Power, R.B., 1994. *Steam Jet Ejectors for the Process Industries,* McGraw–Hill, New York.

Rishel, J.B., 2000. 40 Years of fiddling with pumps, *ASHRAE J.*, March, 48.

Stulz, S.C. and Kitto, J.B., 1992. Fans, in *Steam Its Generation and Use*, Babcock and Wilcox, 23–16 to 23–25.

Turton, R.K., 1994. *Rotodynamic Pump Design*, Cambridge University Press, Cambridge, England.

Vandell, C. and Foerg, W., 1993. The pluses of positive displacement, *Chem. Eng.*, January, 74–86.

Yedidiah, S., 1996. *Centrifugal Pump User's Guidebook — Problems and Solutions*, Chapman & Hall, New York, 27.

3.12 Liquid Atomization and Spraying

Rolf D. Reitz

Sprays are involved in many practical applications, including in the process industries (e.g., spray drying, spray cooling, powdered metals); treatment applications (e.g., humidification, gas scrubbing); coating applications (e.g., surface treatment, spray painting and crop spraying); spray combustion (e.g., burners, furnaces, rockets, gas turbines, diesel and port fuel injected engines); and medicinal and printing applications. To be able to describe sprays it is necessary to obtain a detailed understanding of spray processes.

In the simplest case, the liquid to be sprayed is injected at a high velocity through a small orifice. Atomization is the process during which the injected liquid is broken up into droplets; it has a strong influence on spray vaporization rates because it increases the total surface area of the injected liquid greatly. Fast vaporization may be desirable in certain applications, but undesirable in others where the liquid is required to impinge on a target. The trajectories of the spray drops are governed by the drops' injected momentum, drag forces, and interactions between the drops and the surrounding gas. Control of these and other spray processes can lead to significant improvements in performance, quality of product, and reduction of emission of pollutants.

Spray Characterization

Practical atomizers generate sprays with a distribution of drop sizes with average sizes in the diameter range from a few microns (1 $\mu = 10^{-6}$ m) to as large as 0.5 mm. It is important to quantify the details of the distribution depending on the application. For example, the smaller drops in a spray vaporize fast, and this is helpful to control ignition processes in some combustion systems. On the other hand, the large drops carry most of the mass and momentum of the injected liquid; these drops are able to penetrate into the high-pressure gases in engine combustion chambers. Typical average drop sizes for broad classes of sprays are shown schematically in Figure 3.12.1. It should be noted that the terminology used to describe sprays in Figure 3.12.1 is qualitative and not universally agreed upon.

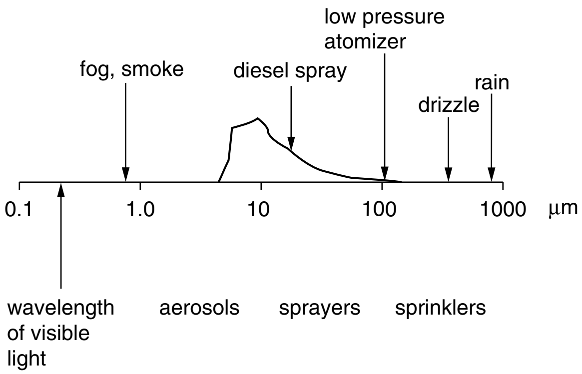

FIGURE 3.12.1 Typical average spray drop sizes for various classes of sprays. A representative size distribution is depicted for the diesel spray.

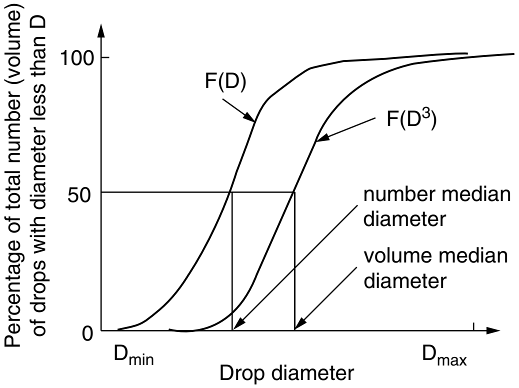

FIGURE 3.12.2 Cumulative spray drop number and volume distributions.

Methods for characterizing the size distribution of spray drops are discussed in American Society for Testing Materials (ASTM) Standard E799[1] and Mugele and Evans[2]. A probability distribution function, $F(D)$, is introduced that represents the fraction of drops per unit diameter range about the diameter, D, as shown in Figure 3.12.2. The spray drop sizes span a range from a minimum diameter, $D_{\min}$, to a maximum diameter, $D_{\max}$. It is also convenient to introduce a mean or average drop diameter instead of specifying the complete drop size distribution. The number median drop diameter (NMD) represents that drop whose diameter is such that 50% of the drops in the spray have sizes less than this size. Spray drop size distribution data can also be represented as a volume (or mass) distribution function, $F(D^3)$; this gives more weight to the large drops in the distribution. In this case a volume median diameter (VMD) or a mass median diameter (MMD) can also be defined, as indicated in Figure 3.12.2.

Various other mean diameters are also in common use. These are summarized using the standard notation of Mugele and Evens[2] as

$$\left(D_{jk}\right)^{j-k} = \frac{\int_{D_{\min}}^{D_{\max}} D^j f(D)dD}{\int_{D_{\min}}^{D_{\max}} D^k f(D)dD} \tag{3.12.1}$$

where $f(D) = dF(D)/dD$ is the drop size probability density function (usually normalized such that $\int_{D_{\min}}^{D_{\max}} f(D)dD = 1$).

Commonly used mean diameters are D_{10} (i.e., $j = 1$, $k = 0$, sometimes called the length mean diameter [3]) and D_{32} (i.e., $j = 3$, $k = 2$, called the Sauter mean diameter or SMD). The Sauter mean diameter has a useful physical interpretation in combustion applications because drop vaporization rates are proportional to the drop's surface area. It represents the size of the drop that has the same volume-to-surface area ratio as that of the entire spray.

Several distribution functions have been found to fit experimental data reasonably well. Among these are the Nukiyama–Tanasawa and the Rosin–Rammler distributions, which have the general form[3] $f(D) = cD^p \exp(-\{bD\}^q)$, where the constants c, p, b, and q characterize the size distribution. The higher the parameter, q, the more uniform the distribution is, and typically $1.5 < q < 4$. Other distributions have been proposed that consist of logarithmic transformations of the normal distribution, such as $f(D) = c\exp(-y^2/2)$, where $y = \delta \ln(\eta D/(D_{\max} - D))$, and c, δ, and η are constants. In this case, the smaller δ, is, the more uniform the size distribution. It should be noted that no theoretical justification for any of these size distributions exists. Spray drop size distributions can be measured nonintrusively by using optical laser diffraction and phase/Doppler instruments. A discussion of these techniques and their accuracy is reviewed by Chigier.[4]

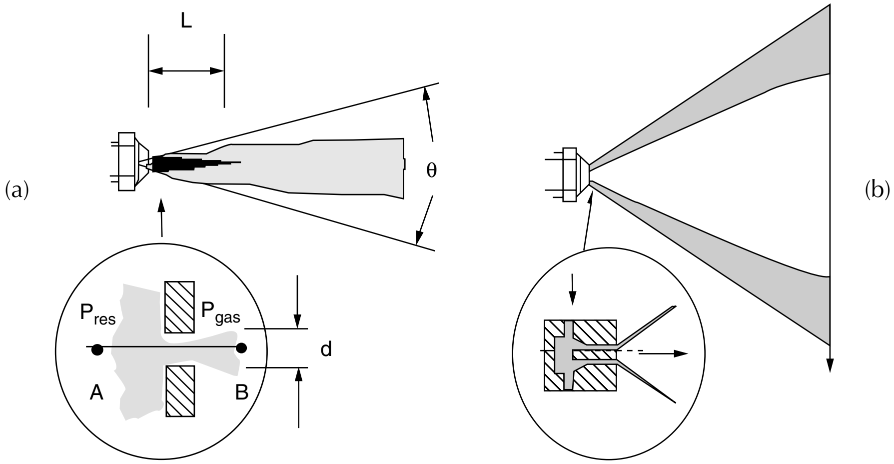

FIGURE 3.12.3 Schematic diagram of pressure atomizer sprays: (a) solid cone; and (b) hollow cone.

Atomizer Design Considerations

Atomization is generally achieved by forcing a liquid or a liquid–gas mixture through a small hole or slit under pressure to create thin liquid sheets or jets moving at a high relative velocity with respect to the surrounding ambient gas. Desirable characteristics of atomizers include: the ability to atomize the liquid over a wide range of flow rates, low power requirements, and low susceptibility to blockage or fouling. In addition, atomizers should produce consistent sprays with uniform flow patterns in operation.

Atomizers can be broadly characterized as those producing hollow cone or solid cone sprays, as depicted in Figure 3.12.3. In solid cone (or full cone) sprays, the spray liquid is concentrated along the spray axis (Figure 3.12.3a). These sprays are useful in applications requiring high spray penetration, such as in diesel engines. In hollow cone sprays, the axis region is relatively free of drops, giving wide spray dispersal (Figure 3.12.3b). These sprays are often used in furnaces, gas turbines, and spray coating applications.

Many different atomizer designs are found in applications. Common atomizer types include pressure; rotary; twin-fluid (air-assist, air-blast, effervescent); flashing; electrostatic; vibratory; and ultrasonic atomizers, as discussed next.

Atomizer Types

In *pressure atomizers* atomization is achieved by means of a pressure difference, $\Delta P = P_{\text{res}} - P_{\text{gas}}$, between the liquid in the supply reservoir pressure, P_{res}, and the ambient medium pressure, P_{gas}, across a nozzle. The simplest design is the plain orifice nozzle with exit hole diameter, *d*, depicted in Figure 3.12.3a. The liquid emerges at the theoretical velocity $U = \sqrt{2\Delta P / \rho_{liquid}}$ — the (Bernoulli) velocity along the streamline A–B in Figure 3.12.3a, where ρ_{liquid} is the density of the liquid. The actual injection velocity is less than the ideal velocity by a factor called the discharge coefficient, C_D, which is between 0.6 and 0.9 for plain hole nozzles. C_D accounts for flow losses in the nozzle.

Four main jet breakup regimes have been identified, corresponding to different combinations of liquid inertia, surface tension, and aerodynamic forces acting on the jet, as shown in Figure 3.12.4. At low injection pressures, the low velocity liquid jet breaks up due to the unstable growth of long wavelength waves driven by surface tension forces (Rayleigh regime). As the jet velocity is increased, the growth of disturbances on the liquid surface is enhanced due to the interaction between the liquid and the ambient gas (the first and second wind-induced breakup regimes). At high injection pressures, the high-velocity jet disintegrates into drops immediately after leaving the nozzle exit (atomization regime). Criteria for the boundaries between the regimes are available.[5] Aerodynamic effects have been found to become very

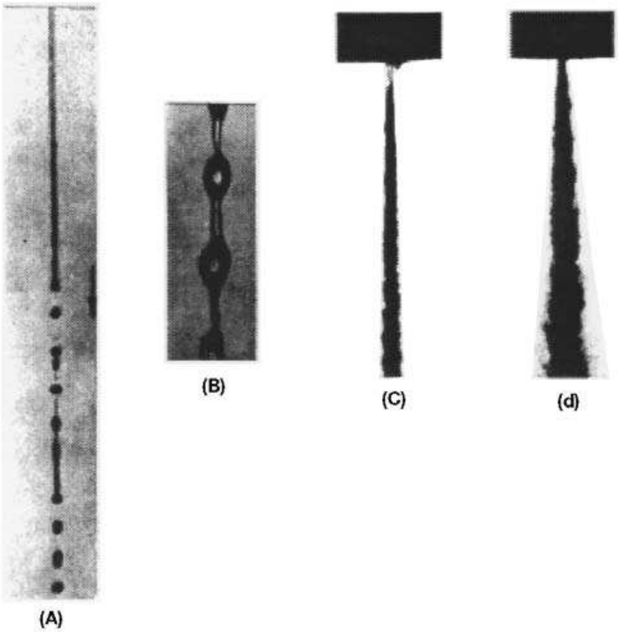

FIGURE 3.12.4 (a) Rayleigh breakup. Drop diameters are larger than the jet diameter. Breakup occurs many nozzle diameters downstream of nozzle. (b) First wind-induced regime. Drops with diameters of the order of jet diameter. Breakup occurs many nozzle diameters downstream of nozzle. (c) Second wind-induced regime. Drop sizes smaller than the jet diameter. Breakup starts some distance downstream of nozzle. (d) Atomization regime. Drop sizes much smaller than the jet diameter. Breakup starts at nozzle exit.‘

important relative to inertial effects when the jet Weber number, $\mathrm{We}_j > 40$, where $\mathrm{We}_j = \rho_{\mathrm{gas}} U^2 d/\sigma$; ρ_{gas} is the gas density; and σ is the liquid surface tension.

Experiments show that the unstable growth of surface waves is aided by high relative velocities between the liquid and the gas, high turbulence and other disturbances in the liquid and gas flows, and the use of spray liquids with low viscosity and low surface tension.

Liquid breakup characteristics such as the spray drop size, the jet breakup length, and spray angle have been related to the unstable wave growth mechanism. The wavelengths and growth rates of the waves can be predicted using results from a linear stability analysis, with[6]

$$\frac{\Lambda}{a} = 9.02\frac{\left(1+0.45Z^{0.5}\right)\left(1+0.4T^{0.7}\right)}{\left(1+0.87\,\mathrm{We}_2^{1.67}\right)^{0.6}} \tag{3.12.2a}$$

$$\Omega\left(\frac{\rho_1 a^3}{\sigma}\right)^{0.5} = \frac{0.34+0.38\ \mathrm{We}_2^{1.5}}{\left(1+Z\right)\left(1+1.4T^{0.6}\right)} \tag{3.12.2b}$$

where Λ is the wavelength and Ω is the growth rate of the most unstable surface wave, and a is the liquid jet radius. The maximum wave growth rate increases and the corresponding wavelength decreases with increasing Weber number, $\mathrm{We}_2 = \rho_{\mathrm{gas}} U^2 a/\sigma$, where U is the relative velocity between the liquid and the gas. The liquid viscosity appears in the Ohnesorge number, $Z = \mathrm{We}_1^{1/2}/\mathrm{Re}_1$. Here the Weber number We_1 is based on the liquid density; the Reynolds number is $\mathrm{Re}_1 = Ua/\nu_1$; ν_1 is the liquid viscosity; and the

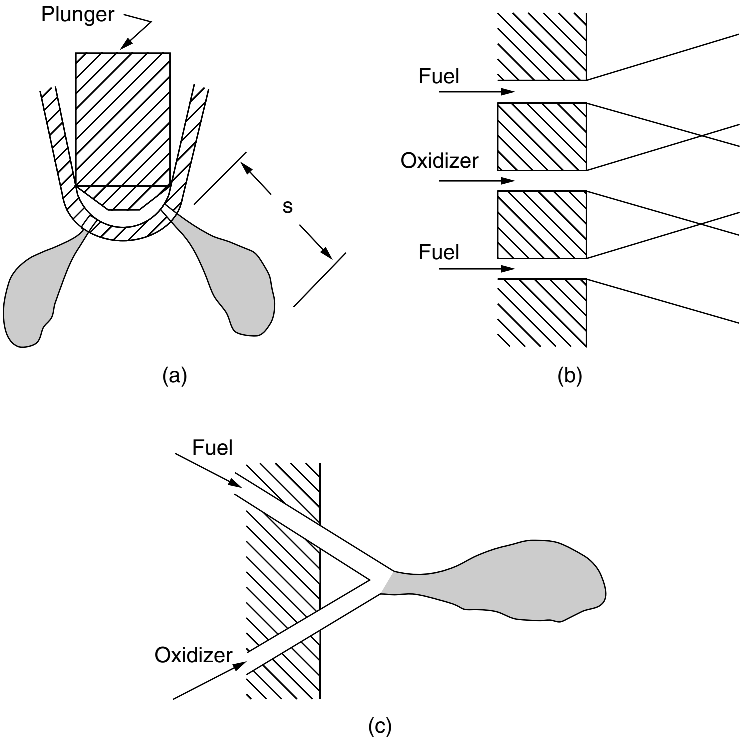

FIGURE 3.12.5 (a) Diesel injector multihole spray nozzle; (b) showerhead; and (c) doublet impingement nozzles.

parameter $T = Z\mathrm{We}_2^{1/2}$. The wave growth rate is reduced and the wave length is increased as the liquid viscosity increases.

The size of the drops formed from the breakup process is often assumed to be proportional to the wavelength of the unstable surface waves in modeling studies.[6] However, the drop sizes in the primary breakup region near the nozzle exit have also been found to be influenced by the length scale of the energy containing eddies in the turbulent liquid flow.[7]. There is uncertainty about atomization mechanisms because spray measurements are complicated by the high optical density of the spray in the breakup region (e.g., see Figure 3.12.4d). As the drops penetrate into the ambient gas, they interact with each other through collisions and coalescence, and the spray drop size changes dynamically within the spray due to secondary breakup and vaporization effects. The drop trajectories are determined by complex drop drag, breakup, and vaporization phenomena, and by interactions with the turbulent gas flow.[6]

High-pressure diesel sprays are intermittent and are required to start and stop quickly without dribble between injections. This is accomplished by means of a plunger arrangement actuated by a cam and spring system in mechanical "jerk" pump systems (see Figure 3.12.5a). Modern electronic injectors include electromagnetic solenoids that permit duration and injection pressure to be varied independently of each other and of engine speed. Experiments on diesel-type injector nozzles show that the penetration distance, S, of the tip of the spray at time, t, after the beginning of the injection is given by[8]

$$S = 0.39Ut \qquad \text{for} \quad t < t_b$$

$$S = 2.46\sqrt{U\,d\,t}\left(\rho_{liquid}/\rho_{gas}\right)^{1/4} \qquad \text{for} \quad t > t_b \tag{3.12.3}$$

where the "breakup time" is $t_b = 40.5d(\rho_{\text{liquid}}/\rho_{\text{gas}})^{1/2}/U$. The jet breakup length (see Figure 3.12.3a), $L = Ut_b$, is independent of the injection velocity. On the other hand, for low-speed jets, or for jets injected

TABLE 3.12.1 Representative Sauter Mean Diameter (SMD) Drop Size Correlations for Various Spray Devices

Device	Correlation	Notes
Plain orifice	$SMD = 3.08\nu_1^{0.385}\left(\rho_{liquid}\sigma\right)^{0.737}\rho_{gas}^{0.06}\Delta P^{-0.54}$	Use SI units
Fan spray	$SMD = 2.83\,d_h\left(\sigma\mu_{liquid}^2/\rho_{gas}d_h^3\Delta P^2\right)^{0.25}$ $+0.26d_h\left(\sigma\rho_{liquid}/\rho_{gas}d_h\Delta P\right)^{0.25}$	d_h = nozzle hydraulic diameter
Rotary atomizer	$SMD = 0.119Q^{0.1}\sigma^{0.5}/Nd^{0.5}\rho_{liquid}^{0.4}\mu_{liquid}^{0.1}$	N = rotational speed (rev/sec), Q = volumetric flow rate, A_{inj} U
Pressure swirl	$SMD = 4.52\left(\sigma\mu_{liquid}^2/\rho_{gas}\Delta P^2\right)^{0.25}\left(t\cos\theta\right)^{0.25}$ $+0.39\left(\sigma\rho_{liquid}/\rho_{gas}\Delta P\right)^{0.25}\left(t\cos\theta\right)^{0.75}$ $t = 0.0114\,A_{inj}\rho_{liquid}^{1/2}d\cos\theta$	t = film thickness, θ = cone angle, d = discharge orifice diameter
Twin fluid/air blast	$SMD = 0.48\,d\left(\sigma/\rho_{gas}U^2d\right)^{0.4}\left(1+1/ALR\right)^{0.4} +$ $0.15\,d\left(\mu_{liquid}^2/\sigma\rho_{liquid}d\right)^{0.5}\left(1+1/ALR\right)$	ALR = air-to-liquid mass ratio
Prefilming airblast	$SMD = \left(1+1/ALR\right)[0.33\,d_h\left(\sigma/\rho_{gas}U^2d_p\right)^{0.6} +$ $0.068\,d_h\left(\mu_{liquid}^2/\sigma\rho_{liquid}d_p\right)^{0.5}]$	d_h = hydraulic diameter, d_p = prefilmer diameter, Figure 3.12.7c
Ultrasonic	$SMD = \left(4\pi^3\sigma/\rho_{liquid}\omega^2\right)^{1/3}$	ω = vibration frequency

Note: Dimensional quantities are in SI units (kg, m, s).
Source: Lefebvre, A.H., *Atomization and Sprays*, Hemisphere Publishing Corp., New York, 1989.

into a low gas density environment, $t_b = 1.04C(\rho_{\text{liquid}}d^3/\sigma)^{1/2}$, where C is a constant typically between 12 and 16, and σ is the surface tension. In this case, L increases with the injection velocity.[9] The functional form of the preceding jet breakup time and length correlations can be derived for an inviscid liquid in the limits of large and small Weber number, We_2 from the unstable wave growth rate in Equation (3.12.2b) with $t_b \sim \Omega^{-1}$.

For high-speed diesel-type jets in the atomization regime, the resulting spray diverges in the form of a cone with cone angle, θ, that is usually in the range from 5 to 20°. θ increases with gas density following $\text{Tan}\theta = A(\rho_{\text{gas}}/\rho_{\text{liquid}})^{1/2}$, where A is a constant that depends on the nozzle passage length and (weakly) on the injection velocity.[9] Very high injection pressures are required to produce small drops. In diesel engines, ΔP is typically as high as 200 MPa and drops are produced with mean diameters of the order of 10 µm (see Figure 3.12.1). Drop size correlations such as that presented in Table 3.12.1 have been proposed for plain-orifice sprays.[3] Note, however, that these correlations do not account for the fact that the spray drop size varies with time and from place to place in the spray. Moreover, experimental correlations often do not include some parameters known to influence spray drop sizes, such as the nozzle passage length and its entrance geometry. Therefore, overall drop size correlations should only be used with caution.

The plain orifice design is also used in twin-fluid-type liquid rocket engines in showerhead and doublet designs (Figure 3.12.5b and Figure 3.12.5c). In the case of doublet nozzles, shown in Figure 3.12.5c, the impinging jets create unstable liquid sheets that break up to produce the sprays. Drop size correlations are available for liquid sheets such as those formed by discharging the liquid through a rectangular slit (see *fan sprays* in Table 3.12.1). Thin liquid sheets or slits lead to the production of small drops. The

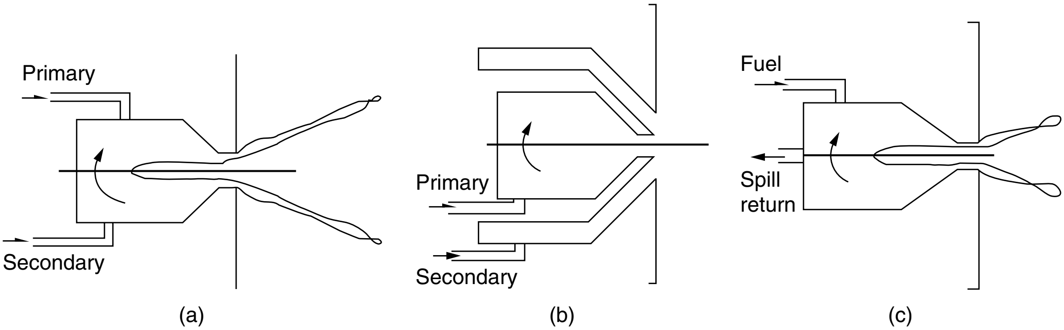

FIGURE 3.12.6 Nozzle designs: (a) duplex; (b) dual orifice; and (c) spill-return type.

breakup mechanism of liquid sheets is also thought to involve the unstable growth of surface waves due to surface tension and aerodynamic forces.[5]

In *rotary atomizers* centrifugal forces are used to further enhance the breakup process. In this case the liquid is supplied to the center of a spinning disk and liquid sheets or ligaments are thrown off the edges of the disk. The drop size depends on the rotational speed of the disk, as indicated in Table 3.12.1. A spinning wheel or cup (turbo-bell) is used in some spray-painting applications. The spray shape is controlled by supplying a coflowing stream of "shaping air."

Centrifugal forces also play a role in the breakup mechanism of *pressure swirl* atomizers (*simplex* nozzles). These atomizers give wider spray cone angles than plain-orifice nozzles and are available in hollow cone and solid cone designs. As depicted in Figure 3.12.3b, the spray liquid enters a swirl chamber tangentially to create a swirling liquid sheet. The air-core vortex within the swirl chamber plays an important role in determining the thickness of the liquid sheet or film at the nozzle exit. This type of nozzle produces relatively coarse sprays. A representative SMD correlation is listed in Table 3.12.1. The spray cone angle depends on the ratio of the axial and tangential liquid velocity components at the exit of the nozzle. This type of atomizer is not well suited for use in transient applications because it tends to dribble at startup and shut down when the air core is not fully formed.

The basic drawback of all pressure atomizers is that the flow rate depends on the square-root of ΔP. The volumetric flow rate is $Q = A_{inj}\, U$, where A_{inj} is the liquid flow area at the nozzle exit, so that a factor of 20 increase in flow rate (a typical turn-down ratio from idle- to full-load operation of a gas turbine engine) requires a factor of 400 increase in injection pressure.

This difficulty has led to so-called "wide-range" atomizer designs such as those shown in Figure 3.12.6. The *duplex* nozzle features two sets of tangential swirl ports: the primary (or pilot) supplies fuel at low flow rates, while the secondary ports become operational at high flow rates. Another variation is the *dual-orifice* nozzle, which is conceptually two simplex nozzles arranged concentrically, one supplying the primary flow and the other supplying the secondary flow. The *spill-return* nozzle is a simplex nozzle with a rear passage that returns fuel to the injection pump. In this design, the flow rate is controlled by the relative spill amount, and there are no small passages to become plugged. However, the fuel is always supplied at the maximum pressure, which increases the demands on the injection pump. However, high swirl is always maintained in the swirl chamber and good atomization is achieved even at low flow rates.

In *twin-fluid injectors* atomization is aided by a flow of high-velocity gas through the injector passages. The high-velocity gas stream impinges on a relatively low-velocity liquid internally (in *internal-mixing* nozzles, Figure 3.12.7a) or externally (in *external-mixing* designs, Figure 3.12.7b). The liquid and gas flows are typically swirled in opposite directions by means of swirl vanes to improve atomization. *Air-assist* refers to designs that use a relatively small amount of air at high (possibly sonic) velocities. *Air-blast* refers to designs that use large quantities of relatively low-velocity air that often supplies some of the air to help decrease soot formation in combustion systems.[3]

In *flashing* and *effervescent* atomizers, a two-phase flow is passed through the injector nozzle exit. In the former, the bubbles are generated by means of a phase change that occurs as the liquid, containing

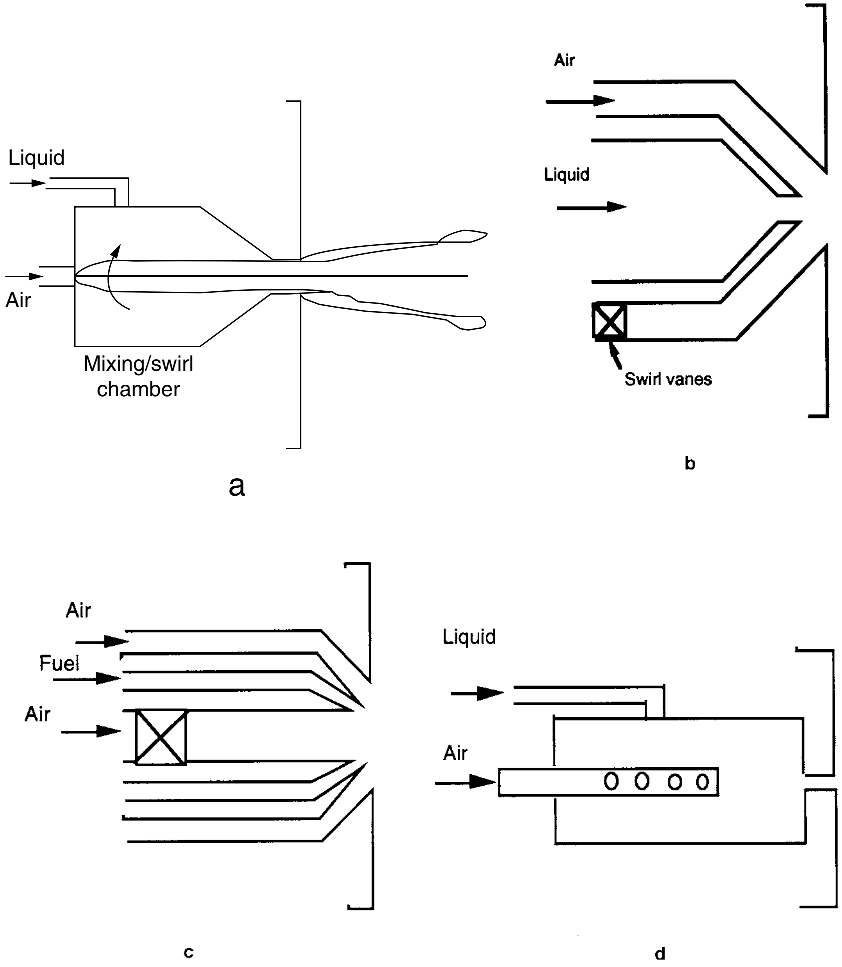

FIGURE 3.12.7 Twin-fluid injector designs: (a) internal mixing; and (b) external-mixing. Atomizers: (c) prefilming air blast; and (d) internal-mixing, effervescent atomizer.

a dissolved propellant gas or vapor, undergoes the pressure drop through the nozzle. This process is exploited in many household spray cans, but has the disadvantage of releasing the propellant gas required for atomization into the atmosphere. In the so-called effervescent atomizer, air bubbles are introduced into the liquid upstream of the exit orifice, as depicted in Figure 3.12.7d. The spray quality is found to depend weakly on the air bubble size and is independent of the nozzle exit diameter. This makes internal mixing, air-assist atomizers very attractive for use with high-viscosity fluids and slurries for which nozzle plugging would otherwise be a problem.[3]

In *electrostatic* atomizers, the spray liquid is charged by applying a high-voltage drop across the nozzle. The dispersion of the spray drops is increased by exploiting electrical repulsive forces between the droplets. An electrostatic charge on the drops is also helpful in spray-coating applications, such as in automotive spray painting using electrostatic turbo-bell sprayers, because the charged drops are attracted to an oppositely charged target surface.

Other atomizer types include *vibratory* and *ultrasonic* atomizers (or *nebulizers*) win which the drops are formed by vibrating the injector nozzle at high frequencies and at large amplitudes to produce short wavelength disturbances to the liquid flow. Ultrasonic atomizers are used in inhalation therapy where very fine sprays (submicron sizes) are required; an available representative drop size correlation is also listed in Table 3.12.1.

Nomenclature

a	liquid jet radius
A	spray angle constant, flow area
ALR	air-to-liquid mass ratio
b	Rosin–Rammler size distribution parameter
c	Rosin–Rammler size distribution parameter
C	jet breakup time constant
C_D	nozzle discharge coefficient
d	nozzle orifice exit diameter
D	drop diameter
f	drop probability density function
F	drop probability distribution function
L	jet breakup length
MMD	mass median drop diameter
N	rotational speed
NMD	number median diameter
p	Rosin–Rammler size distribution parameter
P	pressure
q	Rosin–Rammler size distribution parameter
Re	Reynolds number Ud/ν
Q	volumetric flow rate
S	spray tip penetration distance
SMD	Sauter mean drop diameter
t	time, liquid film thickness
T	Taylor number $Z\,\mathrm{We}^{1/2}$
U	liquid injection velocity, gas-liquid relative velocity
We	Weber number $\rho\, U^2\, d/\sigma$
y	normal drop size distribution parameter
Z	Ohnesorge number $\mathrm{We}^{1/2}/\mathrm{Re}$
δ	normal drop size distribution parameter
ΔP	liquid injection pressure
η	normal drop size distribution parameter
θ	spray cone angle
Λ	surface wave wavelength
μ	liquid kinematic viscosity
ν	liquid dynamic viscosity
ρ	density
σ	surface tension
ω	vibration frequency
Ω	surface wave growth rate

Subscripts

1	liquid phase
2	gas phase
b	breakup
gas	ambient gas conditions
h	hydraulic
j	jet
liq	liquid
max	maximum

min	minimum
p	prefilmer
res	reservoir conditions

References

1. American Society for Testing Materials (ASTM) Standard E799, Data Criteria and Processing for Liquid Drop Size Analysis.
2. Mugele, R. and Evans, H.D., Droplet size distributions in sprays, *Ind. Eng. Chem.*, 43, 1317–1324, 1951.
3. Lefebvre, A.H., *Atomization and Sprays*, Hemisphere Publishing Corp., New York, 1989.
4. Chigier, N.A., Drop size and velocity instrumentation, *Prog. Energy Combust. Sci.*, 9, 155–177, 1983.
5. Chigier, N. and Reitz, R.D., Regimes of jet breakup, *AIAA Progress in Astronautics and Aeronautics Series*, K. Kuo, Ed., AIAA, New York, 1995, chapter 4.
6. Reitz, R.D., Modeling atomization processes in high-pressure vaporizing sprays, *Atomization Spray Technol.*, 3, 309–337, 1988.
7. Wu, P.-K., Miranda, R.F., and Faeth, G.M., Effects of initial flow conditions on primary breakup of nonturbulent and turbulent round liquid jets, *Atomization Sprays*, 5, 175–196, 1995.
8. Hiroyasu, H., and Arai, M., Fuel spray penetration and spray angle in diesel engines, *Trans. JSAE*, 34, 3208, 1978.
9. Reitz, R.D. and Bracco, F.V., Mechanisms of breakup of round liquid jets, *The Encyclopedia of Fluid Mechanics*, N. Cheremisnoff, Ed., Gulf Publishing, New Jersey, vol. 3, chapter 10, 233–249, 1986.

3.13 Flow Measurement

Jungho Kim, Sherif A. Sherif, and Alan T. McDonald

Introduction

Flow measurements are perhaps the most common type of measurements made. Many types of flow measuring devices are available. The choice of meter type depends on the required accuracy, range, cost, ease of reading or data reduction, and service life. The simplest and cheapest device that gives the required accuracy should be chosen.

Flow measurement can be classified into four broad types: (1) direct methods, (2) flow restriction methods, (3) linear flow meters, and (4) traversing methods. Each of these are discussed in the subsections below.

Direct Methods

Tanks can be used to determine the flow rate for steady liquid flows by measuring the volume or mass of liquid collected during a known time interval. If the time interval is long enough, flow rates may be determined precisely by using tanks. Compressibility must be considered in gas volume measurements. It is not practical to measure the mass of gas, but a volume sample can be collected by placing an inverted "bell" over water and holding the pressure constant by counterweights. No calibration is required when volume measurements are set up carefully; this is a great advantage of direct methods.

Restriction Flow Meters for Flow in Ducts

Most restriction flow meters for internal flow (except the laminar flow element) are based on acceleration of a fluid stream through some form of nozzle, shown schematically in Figure 3.13.1. Flow separating from the sharp edge of the nozzle throat forms a recirculation zone shown by the dashed lines downstream

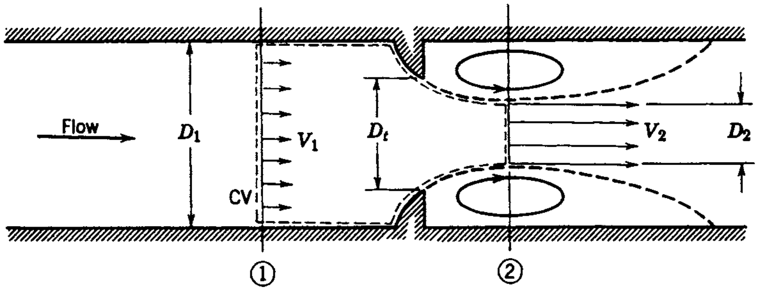

FIGURE 3.13.1 Internal flow through a generalized nozzle, showing control volume used for analysis.

from the nozzle. The main flow stream continues to accelerate from the nozzle throat to form a vena contracta at Section 2 and then decelerates again to fill the duct. At the vena contracta, the flow area is a minimum, the flow streamlines are essentially straight, and the pressure is uniform across the channel section. The theoretical flow rate is

$$\dot{m}_{\text{theoretical}} = \frac{A_2}{\sqrt{1-\left(A_2/A_2\right)^2}}\sqrt{2\rho\left(p_1-p_2\right)} \tag{3.13.1}$$

Equation 3.13.1 shows the general relationship for a restriction flow meter: Mass flow rate is proportional to the square root of the pressure differential across the meter taps. This relationship limits the flow rates that can be measured accurately to approximately a 4:1 range.

Several factors limit the utility of Equation 3.13.1 for calculating the actual mass flow rate through a meter. The actual flow area at Section 2 is unknown when the vena contracta is pronounced (e.g., for orifice plates when D_t is a small fraction of D_1). The velocity profiles approach uniform flow only at large Reynolds numbers. Frictional effects can become important (especially downstream from the meter) when the meter contours are abrupt. Finally, the location of the pressure taps influences the differential pressure reading, $p_1 - p_2$.

The actual mass flow rate is given by

$$\dot{m}_{\text{actual}} = \frac{CA_t}{\sqrt{1-\left(A_2/A_2\right)^2}}\sqrt{2\rho\left(p_1-p_2\right)} \tag{3.13.2}$$

where C is an empirical discharge coefficient.

If $\beta = D_t/D_1$, then $(A_t/A_1)^2 = (D_t/D_1)^4 = \beta^4$, and

$$\dot{m}_{\text{actual}} = \frac{CA_t}{\sqrt{1-\beta^4}}\sqrt{2\rho\left(p_1-p_2\right)} \tag{3.13.3}$$

where $1/(1 - \beta^4)^{1/2}$ is the velocity correction factor. Combining the discharge coefficient and velocity correction factor into a single *flow coefficient*,

$$K \equiv \frac{C}{\sqrt{1-\beta^4}} \tag{3.13.4}$$

TABLE 3.13.1 Characteristics of Orifice, Flow Nozzle, and Venturi Flow Meters

Flow Meter Type	Diagram	Head Loss	Cost
Orifice	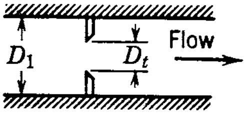	High	Low
Flow nozzle	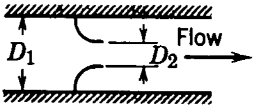	Intermediate	Intermediate
Venturi	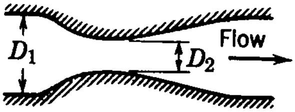	Low	High

yields the mass flow rate in the form:

$$\dot{m}_{\text{actual}} = KA_t\sqrt{2\rho(p_1 - p_2)} \tag{3.13.5}$$

Test data can be used to develop empirical equations to predict flow coefficients vs. pipe diameter and Reynolds numbers for standard metering systems. The accuracy of the equations (within specified ranges) is often adequate enough to use the meter without calibration. Otherwise, the coefficients must be measured experimentally.

For the turbulent flow regime ($\text{Re}_\text{D} > 4000$), the flow coefficient may be expressed by an equation of the form:

$$K = K_\infty + \frac{1}{\sqrt{1-\beta^4}}\frac{b}{\text{Re}_{D_1}^n} \tag{3.13.6}$$

where subscript ∞ denotes the flow coefficient at infinite Reynolds numbers and constants b and n allow for scaling to finite Reynolds numbers. Correlating equations and curves of flow coefficients vs. Reynolds number are given for specific metering elements in the next three subsections following the general comparison of the characteristics of the orifice plate, flow nozzle, and venturi meters in Table 3.13.1 (see Fox and McDonald, 1992).

Flow meter coefficients reported in the literature have been measured with fully developed turbulent velocity distributions at the meter inlet. When a flow meter is installed downstream from a valve, elbow, or other disturbance, a straight section of pipe must be placed in front of the meter. Approximately 10 diameters of straight pipe upstream are required for venturi meters, and up to 40 diameters for orifice plate or flow nozzle meters. Some design data for incompressible flow are given below. The same basic methods can be extended to compressible flows.

Orifice Plates

The orifice plate (Figure 3.13.2) may be clamped between pipe flanges. Since its geometry is simple, it is low in cost and easy to install or replace. The sharp edge of the orifice will not foul with scale or suspended matter. However, suspended matter can build up at the inlet side of a concentric orifice in a horizontal pipe; an eccentric orifice may be placed flush with the bottom of the pipe to avoid this difficulty. The primary disadvantages of the orifice are its limited capacity and the high permanent head loss caused by uncontrolled expansion downstream from the metering element.

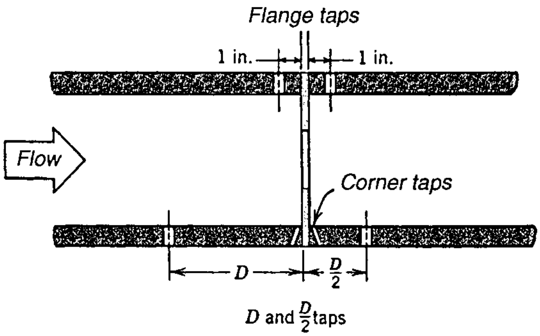

FIGURE 3.13.2 Orifice geometry and pressure tap locations. (From Miller, R.W., *Flow Measurement Engineering Handbook,* 3rd ed., McGraw-Hill, New York, 1996. With permission.)

Pressure taps for orifices may be placed in several locations as shown in Figure 3.13.2 (see Miller, 1996 for additional details). Since the location of the pressure taps influences the empirically determined flow coefficient, one must select handbook values of K consistent with the pressure tap locations.

The correlating equation recommended for a concentric orifice with corner taps is

$$C = 0.5959 + 0.0312\,\beta^{2.1} - 0.184\,\beta^{8} + \frac{91.71\,\beta^{2.5}}{\mathrm{Re}_{D_1}^{0.75}} \tag{3.13.7}$$

Equation 3.13.7 predicts orifice discharge coefficients within ±0.6% for $0.2 < \beta < 0.75$ and for $10^4 < \mathrm{Re}_{D1} < 10^7$. Some flow coefficients calculated from Equation 3.13.7 are presented in Figure 3.13.3. Flow coefficients are relatively insensitive to Reynolds number for $\mathrm{Re}_{D1} > 10^5$ when $\beta > 0.5$.

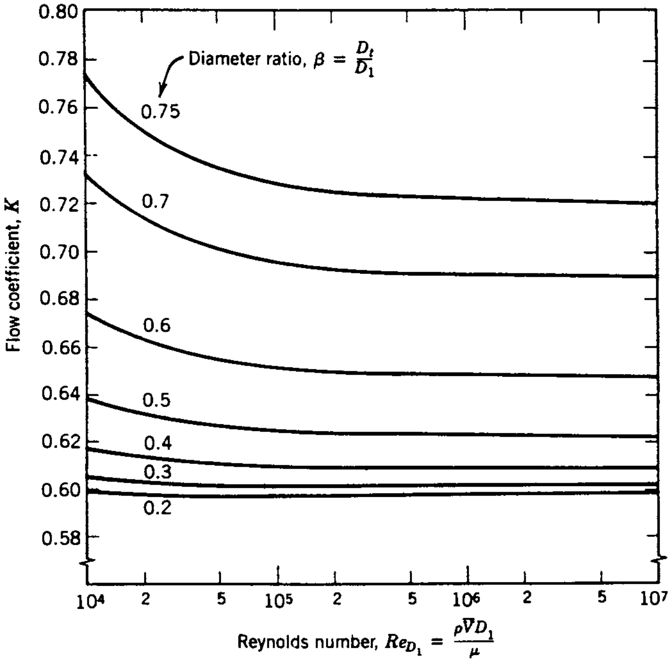

FIGURE 3.13.3 Flow coefficients for concentric orifices with corner taps.

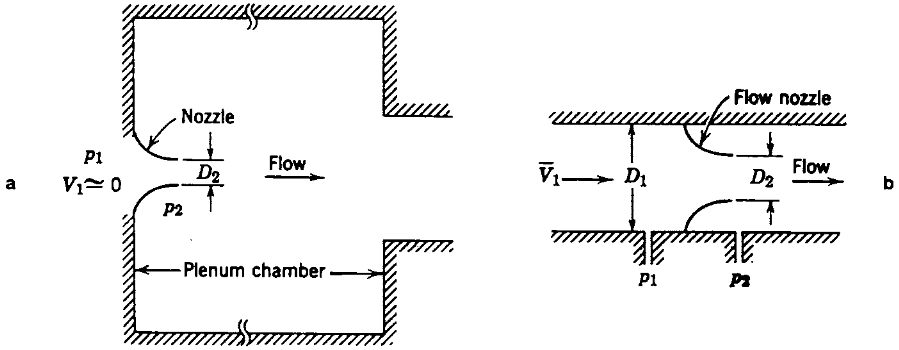

FIGURE 3.13.4 Typical installations of nozzle flow meters: (a) plenum, (b) in duct.

Flow Nozzles

Flow nozzles may be used as metering elements in either plenums or ducts, as shown in Figure 3.13.4; the nozzle section is approximately a quarter ellipse. Design details and recommended locations for pressure taps are given in *ASHRAE Handbook Fundamentals* (1981).

A similar correlating equation is available for orifice plates with D and D/2 taps. Flange taps require a different correlation for every line size. Pipe taps, located at 2 – 1/2 D and 8D, no longer are recommended. The correlating equation recommended for ASME long-radius flow nozzles is

$$C = 0.9975 - \frac{6.53\,\beta^{0.5}}{\mathrm{Re}_{D_1}^{0.5}} \tag{3.13.8}$$

Equation 3.13.8 predicts discharge coefficients for flow nozzles within ± 2.0% for $0.25 < \beta < 0.75$ for $10^4 < \mathrm{Re}_{D1} < 10^7$. Some flow coefficients calculated from Equation 3.13.8 are presented in Figure 3.13.5. (K can be greater than 1 when the velocity correction factor exceeds 1.) For plenum installation, nozzles may be fabricated from spun aluminum, molded fiberglass, or other inexpensive materials. Typical flow coefficients are in the range $0.95 < K < 0.99$; the larger values apply at high Reynolds numbers. Thus, the mass flow rate can be computed within approximately ±2% using $K = 0.97$.

Venturi Meters

Venturi meters are generally made from castings machined to close tolerances to duplicate the performance of the standard design, so they are heavy, bulky, and expensive. The conical diffuser section downstream from the throat gives excellent pressure recovery; overall head loss is low. Venturi meters are self-cleaning because of their smooth internal contours.

Experimentally measured discharge coefficients for venturi meters range from 0.980 to 0.995 at high Reynolds numbers ($\mathrm{Re}_{D1} > 2 \times 10^5$). Thus, $C = 0.99$ can be used to calculate mass flow rate within about ±1% at high Reynolds numbers. Consult manufacturers' literature for specific information at Reynolds numbers below 10^5.

Orifice plates, flow nozzles, and venturis all produce pressure drops proportional to the flow rate squared, according to Equation 3.13.4. In practice, a meter must be sized to accommodate the largest flow rate expected. Because the pressure drop vs. flow rate relationship is nonlinear, a limited range of flow rates can be measured accurately. Flow meters with single throats usually are considered for flow rates over a 4:1 range.

Unrecoverable head loss across a metering element may be expressed as a fraction of the differential pressure across the element. Unrecoverable head losses are shown in Figure 3.13.6.

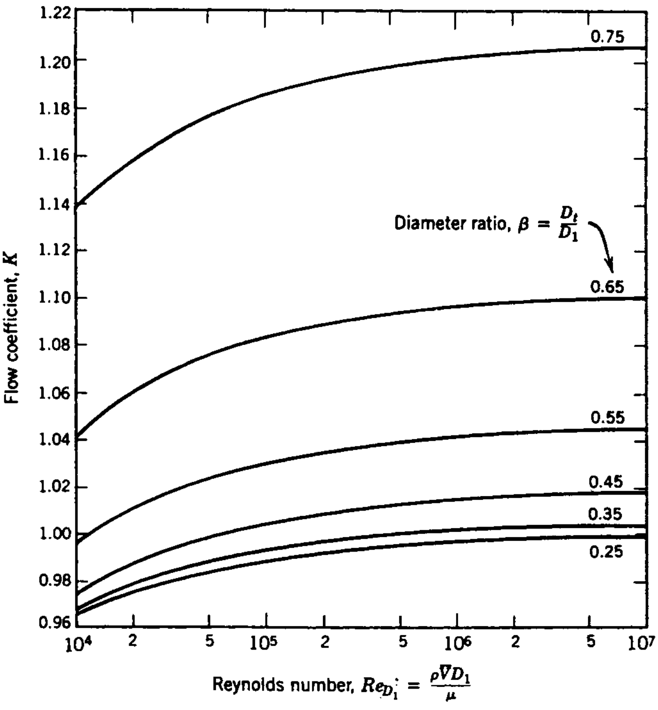

FIGURE 3.13.5 Flow coefficients for ASME long-radius flow nozzles.

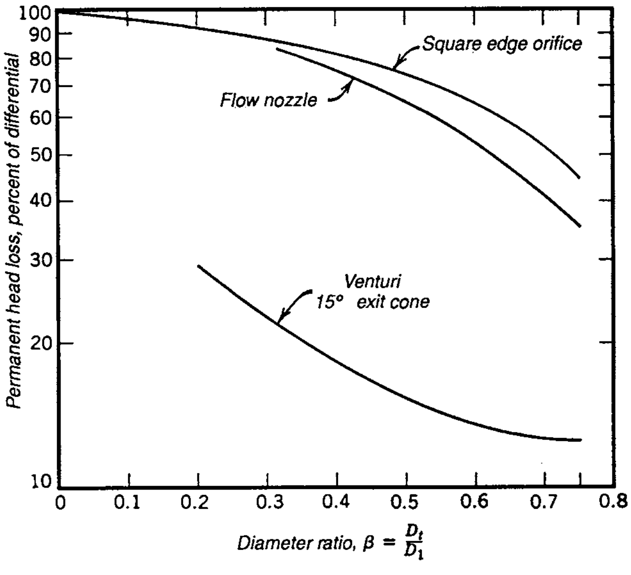

FIGURE 3.13.6 Permanent head loss produced by various flow metering elements. (From Miller, R.W., *Flow Measurement Engineering Handbook,* 3rd ed., McGraw-Hill, New York, 1996. With permission.)

Linear Flow Meters

The output of flow meters is typically calibrated to read a volume flow rate of a specified liquid or gas under certain conditions. For example, the volume flow rate of a liquid could be expressed in terms of liters per minute (LPM) of water, while that of a gas could be expressed in terms of standard cubic feet per minute (SCFM) of air. When using flow meters to determine flow rate at conditions different from the calibration conditions, corrections to the output must be made to obtain the true flow rate.

Rotameters

A typical rotameter consists of a float contained within a diverging tube (Figure 3.13.7). The float is raised by a combination of drag and buoyancy. The height to which the float rises in the tube can be made to vary by varying the shape of the diverging tube — tubes with linear or logarithmic variations can easily be fabricated.

Glass tube rotameters can be used to temperatures as high as 200°C and pressures up to 20 atm, depending on the diameter of the tube. Plastic tube rotameters are also available for use at lower temperatures and pressures. Flow rates at very high temperatures and pressures can be measured using metal tubes — detectors mounted on the outside of the tube are used to determine the float position.

Rotameters usually come with calibrations based on water or air at STP. The output is generally in SCFM of air or LPM of water. For measuring flow at other conditions or for other fluids, corrections must be made to determine the flow rate. The response of a rotameter can be determined by performing a force balance on the float. The height of the float is determined by a balance between the drag force on the float and the effective weight of the float:

$$F_D = \left(\rho_{float} - \rho_{fluid}\right) g V_{float} \tag{3.13.9}$$

where the drag force is given by

$$F_D = C_D A_{float} \frac{\rho_{fluid} u_{fluid}^2}{2} \tag{3.13.10}$$

Combining Equations 3.13.9 and 3.13.10 and solving for the fluid velocity u_{fluid} yields

$$u_{fluid} = \sqrt{\frac{2g\left(\rho_{float} - \rho_{fluid}\right)V_{float}}{C_d A_p \rho_{fluid}}} \tag{3.13.11}$$

The mass flow rate is given by

$$\dot{m} = \rho_{fluid} A_{meter} u_{fluid} \tag{3.13.12}$$

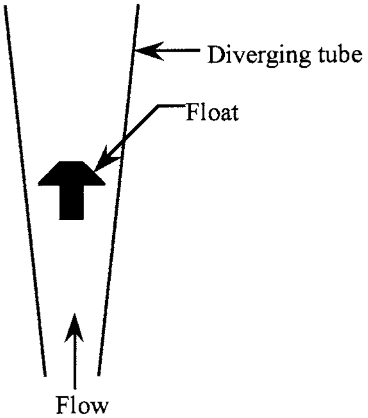

FIGURE 3.13.7 Schematic of rotameter operation.

where A_{meter} is the area between the float and the tube. Combining Equations 3.13.11 and 3.13.12 yields

$$\dot{m} = C\rho_{fluid} A_{meter} \sqrt{\frac{\rho_{float}}{\rho_{fluid}} - 1} \tag{3.13.13}$$

where it has been assumed that the drag coefficient, C_D, is constant. Many floats are designed for constant C_D over a wide flow range.

Consider now the case where a given flow meter indicates the same flow rate for two different fluid flows, i.e., A_{meter} is constant for both cases. Then,

$$\frac{\dot{m}_1}{\dot{m}_2} = \frac{\rho_{fluid,1}}{\rho_{fluid,2}} \frac{\sqrt{\rho_{float}/\rho_{fluid,1} - 1}}{\sqrt{\rho_{float}/\rho_{fluid,2} - 1}} \tag{3.13.14}$$

Since $\dot{m} = \rho_{fluid} \dot{V}$,

$$\frac{\dot{V}_1}{\dot{V}_2} = \frac{\sqrt{\rho_{float}/\rho_{fluid,1} - 1}}{\sqrt{\rho_{float}/\rho_{fluid,2} - 1}} \tag{3.13.15}$$

For cases where $\rho_{float} >> \rho_{fluid}$ (gas flows), the above equation reduces to

$$\frac{\dot{V}_1}{\dot{V}_2} = \frac{\sqrt{\rho_{fluid,2}}}{\sqrt{\rho_{fluid,1}}} \tag{3.13.16}$$

Example: Assume we have oil with a specific gravity of 0.8 flowing through a rotameter with a float made of steel. The steel has a specific gravity of 8.0. If the meter was calibrated for water, what is the correction that must be made to the indicated flow rate in order to obtain the true flow rate of oil?

Solution: Because the fluid density is not negligible compared to the float density, Equation 3.13.15 must be used.

$$\frac{\dot{V}_{oil}}{\dot{V}_{water}} = \frac{\sqrt{\rho_{float}/\rho_{oil} - 1}}{\sqrt{\rho_{float}/\rho_{water} - 1}} = \frac{\sqrt{8.0/0.8 - 1}}{\sqrt{8.0/1.0 - 1}} = 1.13$$

The true flow rate of oil, therefore, would be 1.13 times that indicated.

Target Flow Meters

These meters measure the drag force on a disk or target placed in the flow. The meter may consist simply of a hinged disk in the flow with a dial indicator showing the amount of deflection. More sophisticated meters use a strain gauge or a bellows to measure the force. Target meters can be used in dirty flows, and can also be used to sense the flow direction. Target meters are subject to the same corrections as for rotameters.

Turbine Flow Meters

Turbine flow meters consist of a free-running, vaned impeller mounted in a cylindrical section of tube. A cutaway of some turbine flow meters is shown in Figure 3.13.8. The rate of angular rotation is determined by counting the number of blade passages per unit time magnetically, mechanically, optically, or by some other method. No penetrations or seals in the duct are usually required, enabling turbine flow meters to measure flow rates in corrosive or toxic liquids. They are generally used for liquid flows,

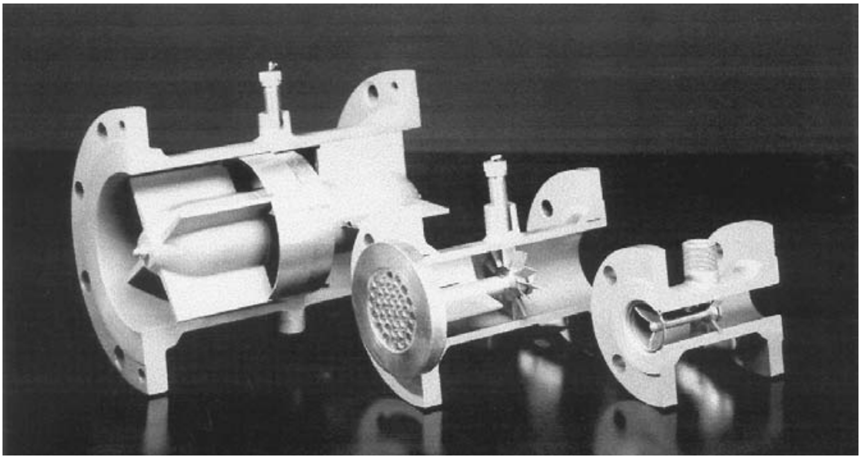

FIGURE 3.13.8 Some turbine flow meters. (Courtesy of Smith Meter, Erie, PA.)

and are characterized by high accuracy and wide dynamic range. Reading accuracies of 0.5% over a 30:1 range are common. If units with ball bearings are used, they should be inspected occasionally to check for bearing wear. The life of the unit can be dramatically increased by operating the unit well below the maximum rated speed, however. The response of turbine flow meters can be affected by viscosity. A field calibration should be performed when the working fluid has a viscosity significantly higher than that for water.

Paddlewheel flow meters are an inexpensive alternative to turbine flow meters when extreme accuracies are not required. The rate of rotation of a paddlewheel partially immersed in the flow is used as a measure of the flow rate. Unlike turbine flow meters, paddlewheels can be used in dirty flows.

Positive Displacement Meters

Positive displacement meters measure flow rate by separating the flow into discrete increments that are moved from one side of the flow meter to the other. An example of a positive displacement meter is shown in Figure 3.13.9. Positive displacement meters can be used to measure the flow rate of high-viscosity fluids.

Vortex Shedding Meters

When a bluff body is placed in a flow, vortices can be shed downstream of the body (Figure 3.13.10). Vortex shedding meters measure the frequency of the asymmetric pressure variations that occur on the body as the vortices are shed and relate this to the flow rate. The vortex shedding frequency is governed by the Strouhal number (St)

$$St = \frac{f_s d}{V} \tag{3.13.17}$$

where f_s = vortex shedding frequency
d = characteristic dimension of the body
V = velocity of the flow

Experiments have shown that St is constant within 1% for Reynolds numbers between 10^4 and 10^6. The frequency is directly proportional to the velocity (and thus the flow rate) around the body in this range. These flow meters are insensitive to dirty flows and can be used under a wide variety of conditions because they have no moving parts.

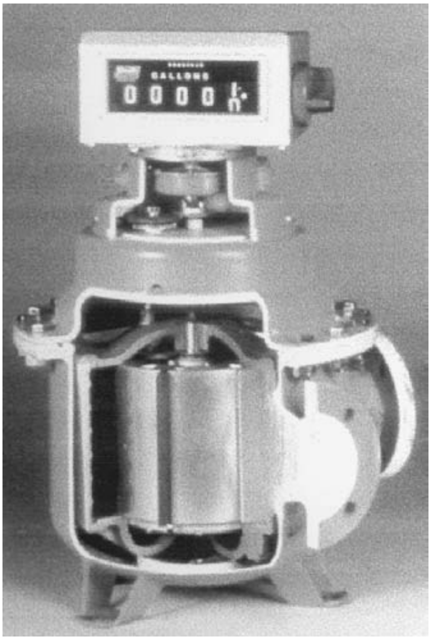

FIGURE 3.13.9 A cutaway of a positive displacement meter. (Courtesy of Smith Meter, Erie, PA.)

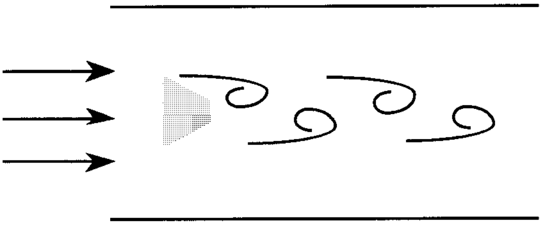

FIGURE 3.13.10 Vortices shedding off a body placed in a moving stream.

Thermal Mass Flow Meters

These determine flow rate of clean gases by passing the fluid through a precision tube that is heated in one section, and the temperature of the tube wall upstream and downstream of the heated section is measured (Figure 3.13.11). The difference in temperature between the two sensors is a measure of the mass flow rate. Calibration is usually performed using nitrogen and a correction factor is applied for other gases.

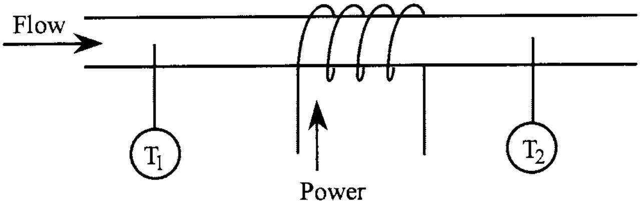

FIGURE 3.13.11 Schematic of thermal mass flow meter operation.

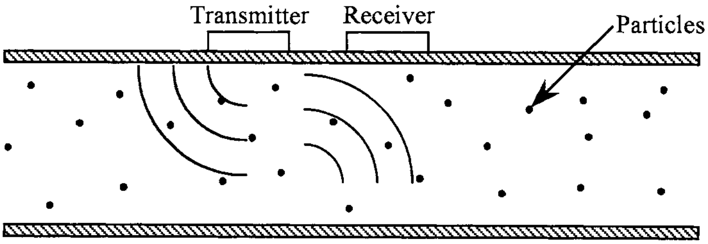

FIGURE 3.13.12 Schematic of ultrasonic flow meter.

An alternate scheme measures the temperature of the gas, and power is supplied to the downstream sensor such that its temperature is kept a fixed amount above the upstream sensor. The feedback circuit needed to do this is similar to that used in hot-wire anemometry. The amount of power supplied to the downstream sensor is a measure of the gas flow rate. The advantages of these meters are that they give a direct indication of the flow rate without requiring corrections for temperature or pressure variations, they have no moving parts, and are noninvasive.

Ultrasonic Flow Meters

These meters determine flow rate by measuring the Doppler shift of an ultrasonic signal due the movement of particles in the flow (Figure 3.13.12). Particles or bubbles in the fluid are usually required. Recently, meters have been developed that can measure the flow of clean fluids by measuring the velocity of turbulent swirls in the liquid. The meter is noninvasive, and can measure flow rate of dirty fluids or slurries.

The transit time method relies on measuring the difference in the time it takes for a signal to traverse the flow in one direction compared to a signal traveling in the opposite direction. Because the difference in transit times are so small, the time difference is usually measured as a phase difference between the two sound signals. When the particles move at flow speed, the frequency shift is proportional to flow speed. For a suitably chosen path, output is proportional to volume flow rate. Ultrasonic meters may require calibration in place. One or two transducers may be used.

Laminar Flow Elements (LFE)

Laminar flow meters operate by passing a gas through a bundle of tubes or a honeycomb (Figure 3.13.13). The small diameter of these flow passages in the matrix laminarize the flow, and the pressure drop between the inlet and exit of the tubes is measured. If the flow passages were circular, the pressure drop across the element would be

$$\Delta P = \frac{128\mu l\dot{V}}{\pi D^4} \tag{3.13.18}$$

and is linear with the volumetric flow rate. Because the flow passages are not necessarily circular, calibration of the flow meter is usually required. Corrections are also needed for changes in fluid viscosity and temperature. The gas must be clean. The LFE may be used with reasonable accuracy over a 10:1 flow rate range. A LFE costs approximately as much as a venturi, but is much lighter and smaller. Thus, the LFE is widely used in applications where compactness and extended range are important.

Coriolis Meters

These meters are true mass flow meters. The concept behind coriolis meters is shown in Figure 3.13.14. Consider the case where the flow moves through a U-tube that is vibrated at its resonant frequency using an electromagnetic coil. If fluid flows into the tube when the tube is moving upward, the fluid needs to be accelerated and will cause the tube to bend down. The fluid that has traveled around the bend at this

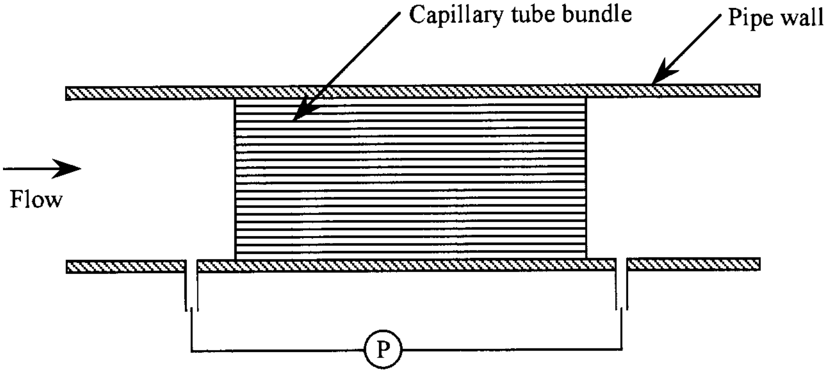

FIGURE 3.13.13 Schematic of laminar flow element.

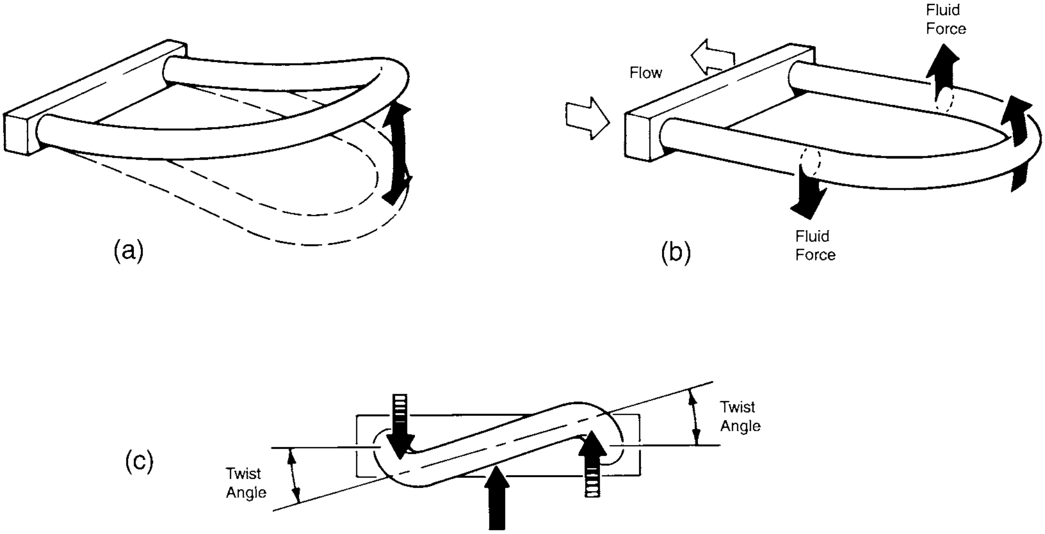

FIGURE 3.13.14 Principle of operation of a coriolis meter: (a) vibrating flow tube, (b) fluid forces reacting to vibration of flow tube, (c) end view of flow tube showing twist. (Courtesy of Micro Motion Inc., Boulder, CO.)

time already has an upward momentum and needs to be decelerated, causing this part of the tube to bend upward. The tube, therefore, will twist in the opposite direction during the downward motion. The difference in velocity of the two legs of the vibrating tubes is a measure of the mass flow rate. The density of the fluid flowing in the tube can be measured by measuring the change in resonant frequency of the tube. The instrument measures mass flow rate directly and, thus, is ideal for two-phase or liquid–solid flow measurements. Pressure drop across the coriolis meter may be high, but its useful flow rate range is 100:1.

Electromagnetic Flow Meters

Electromagnetic flow meters create a magnetic field across a pipe. When a conductive fluid passes through the field, a voltage is generated at right angles to the field and velocity vectors. Electrodes placed on a pipe detect the resulting signal voltage, which is proportional to the average axial velocity when the profile is axisymmetric. The minimum flow speed should be above about 0.3 m/s, but there are no restrictions on the Reynolds number. The flow rate range normally quoted is 10:1.7

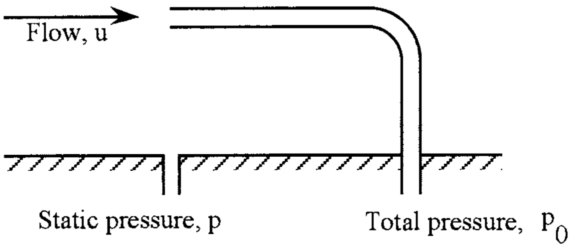

FIGURE 3.13.15 Basic total pressure probe setup.

Traversing Methods

In situations such as in air handling or refrigeration equipment, it may be impractical or impossible to install a fixed flow meter, but it may be possible to measure flow rate using a traversing technique. To measure flow rate by traverse, the duct cross section is subdivided into segments of equal area. The fluid velocity is measured at the center of each area segment, and the volume flow rate for each segment is approximated by the product of the measured velocity and segment area. Flow rate through the entire duct is the sum of these segmental flow rates. Methods for measuring the flow velocity are discussed below.

Pressure Probes

Perhaps the simplest and least expensive method of measuring velocity is through the use of Pitot probes. Consider the stagnating flow shown in Figure 3.13.15. Applying Bernoulli's equation to the flow between a point far upstream of the probe and the probe tip, assuming an incompressible flow, yields

$$p_0 = p + \frac{1}{2}\rho u^2 \tag{3.13.19}$$

The total pressure sensed by the tube (p_0) is greater than the freestream pressure (p) by the dynamic head $1/2\rho u^2$. The freestream velocity (u) thus can be determined by measuring the static and total pressures. Equation 3.13.19 can be applied to flows whose Mach number ($M = u/a$) is less than 0.2 with less than 0.5% uncertainty. The speed of sound is given by

$$a = \sqrt{\gamma R_g T} \tag{3.13.20}$$

where T is the static absolute temperature of the flow, R_g is the real gas constant, and γ is the ratio of specific heats. When the flow Mach number exceeds 0.2, the density of the fluid along the stagnation streamline changes and compressibility effects must be taken into account. For $0.2 < M < 1.0$, the relation between velocity and pressure difference is given by:

$$M^2 = \frac{2}{\gamma - 1}\left[\left(\frac{p_0}{p}\right)^{\frac{\gamma-1}{\gamma}} - 1\right] \tag{3.13.21}$$

When the flow is supersonic, the flow adjusts to the stagnation condition through a bow shock off the tip of the Pitot probe (Figure 3.13.16). The relationship between the static pressure ahead of the shock (measured by a static pressure tap) to the total pressure behind the shock (indicated by the probe) is given by

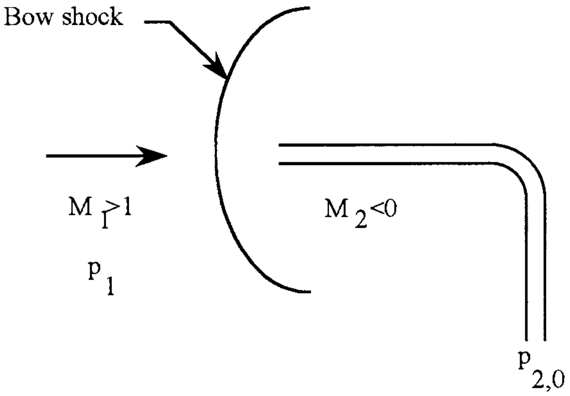

FIGURE 3.13.16 Supersonic flow around a total pressure probe.

$$\frac{p_1}{p_{2,0}} = \frac{\left(\frac{2\gamma}{\gamma+1} M_1^2 - \frac{\gamma-1}{\gamma+1}\right)^{\frac{1}{\gamma-1}}}{\left(\frac{\gamma+1}{2} M_1^2\right)^{\frac{\gamma}{\gamma-1}}} \tag{3.13.22}$$

The above equation can be solved to determine the Mach number and, hence, the flow velocity ahead of the shock.

Although the measurement of velocity using pressure probes is relatively straightforward, there are many situations where the ideal situation indicated in Figure 3.13.15 does not occur. Some factors that influence the measurement are

- Alignment of the probe with the flow
- Wall effects
- Turbulence effects
- Pitot probe design
- Static pressure tap geometry
- Streamline curvature

Each of these effects is briefly discussed below.

Alignment Effects

The change in stagnation pressure due to flow misalignment for various probes is shown in Figure 3.13.17. It is seen that an open-ended tube can be misaligned by up to ±10° without error in the pressure reading, while a tube with a chamfered opening can tolerate misalignments up to ±30°.

Wall Effects

The presence of a wall changes the flow around the probe, and this can result in pressure readings that are lower than when a wall is not present. For a round probe touching the wall, the velocity indicated can be up to 1.5% low (Moffatt).

Turbulence Effects

The effects of turbulence on velocity measurements are dependent on many factors such as turbulence scale and structure, fluctuation frequency, and internal geometry of the probe. The few studies that have been performed were inconclusive, with some studies indicating a decrease in the measured velocity with increasing turbulence and others indicating the opposite trend. A first-order analysis indicates that 20% turbulence intensities can result in a 2% increase in the measured velocity.

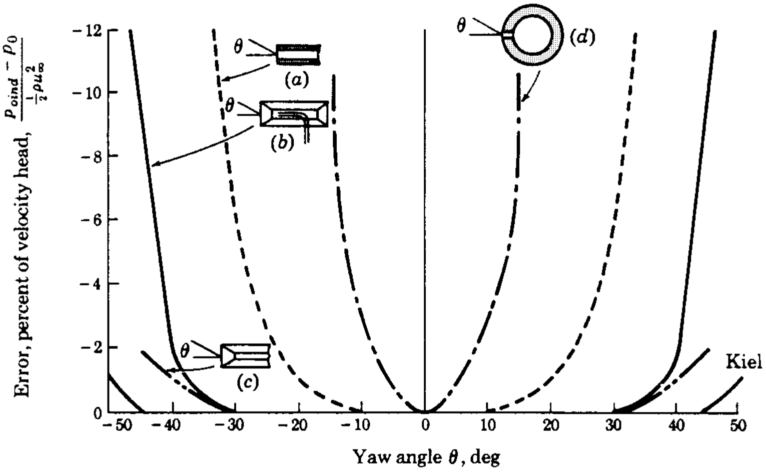

FIGURE 3.13.17 Error in stagnation pressure with changes in yaw angle for (a) open-ended tube, (b) channel tube, (c) chamfered tube, and (d) tube with orifice in side. (From Krause, L.N. and Gettleman, C.C., *ISA Proc.,* 7, 134, 1952. With permission.)

Static Pressure Taps

Static pressure taps should be drilled perpendicular to the wall, and no burrs or chamfers should be present. The holes should be made as small as possible without causing excessively slow response times at the transducer.

Streamline Curvature

If the streamlines in a flow are curved (perhaps due to obstacles in the flow), then velocity and pressure gradients can occur across the channel and the static pressure obtained from a wall pressure tap may not be representative of that where the total pressure is being measured. The local static pressure at the measuring location must either be measured or computed.

Design of Pitot-Static Probes

Pitot-static probes combine the measurement of total and static pressure in one unit. A commercially available Pitot-static probe is shown in Figure 3.13.18. The location of the static pressure taps is important. The static pressure taps should be located sufficiently far downstream of the tip so that flow acceleration effects can be ignored, and sufficiently far upstream of the support so that blockage effects are small. If the static pressure taps are located eight tube diameters downstream of the tip and eight tube diameters upstream of the support, then the effects of both acceleration and blockage will be below 1%.

Measurement of Flow Direction

The flow direction can be obtain by using prizm probes or probes with multiple sensing holes. Additional reading regarding the various types of pressure probes and the errors associated with them is given in Moffatt.

Hot-Wire Anemometry

Hot-wire anemometry is used when one wishes to measure rapidly varying velocities with good spatial resolution. Velocity fluctuations up to 50 kHz can easily be obtained. Typically a heated, thin wire is held in the flow, and the cooling effect on the wire due to velocity is measured. The disadvantages compared to pressure probes are that they are relatively expensive, they use frail wires, and they need to be calibrated in a known flow environment. Corrections also need to be made to account for freestream temperature variations and for flow along the wire for slanted wires. There are two types of hot-wire anemometry — constant temperature and constant current.

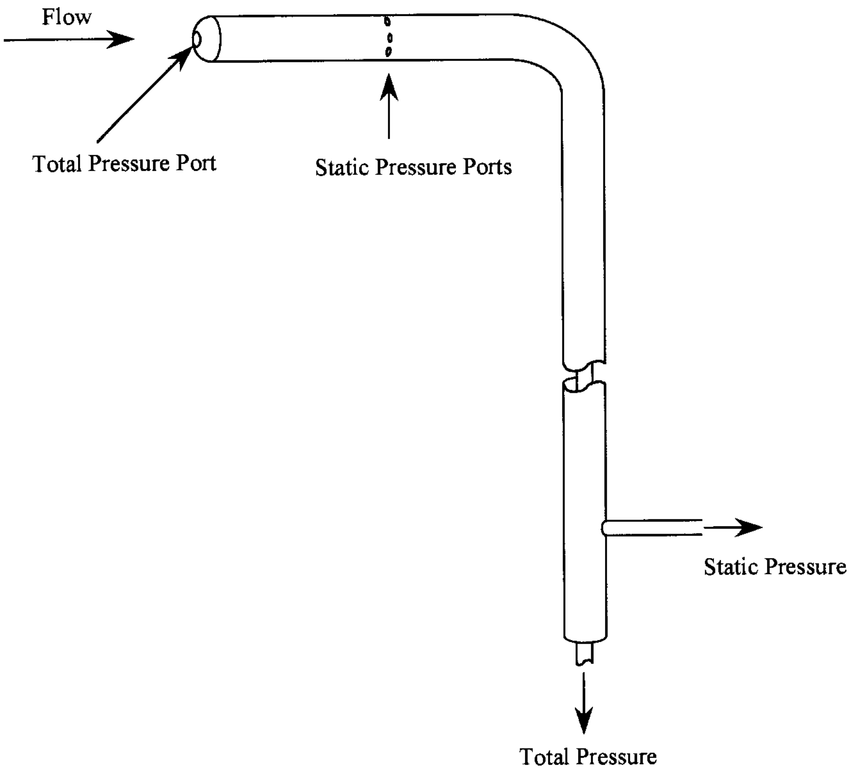

FIGURE 3.13.18 A pitot-static probe.

Constant Current Anemometry

This method consists of sending a constant current through a thin wire and measuring the change in resistance of the wire with velocity. Although much simpler than constant temperature anemometry, constant current anemometry has several disadvantages that has resulted in almost exclusive use of constant temperature anemometry today. These disadvantages include relatively low frequency response and the possibility of wire burnout at large currents and low velocities. However, they can be used when many channels of data need to be acquired, when turbulence information is not needed, or when the flow temperature needs to be measured. Numerous schemes for treating the resulting data have been published. Digital processing techniques, including fast Fourier transforms, can be used to obtain mean values and moments, and to analyze signal frequency content and correlations.

Constant Temperature Anemometry Fundamentals

The basic circuit is shown on Figure 3.13.19. The wire is represented by resistance R_w in a Wheatstone bridge. Resistors R_1, R_2, and R_c are very stable with temperature. The imbalance in the bridge is measured using an op-amp, and the op-amp outputs whatever voltage is necessary to bring the bridge back into balance. For example, consider the case where the bridge is balanced at a given flow velocity, i.e., $R_w/R_1 = R_c/R_2$ and $V_1 = V_2$. If the velocity over the wire increases, the wire temperature (and therefore its resistance) will decrease, causing the bridge to become unbalanced ($R_w/R_1 < R_c/R_2$ and $V_1 < V_2$). The op-amp senses this imbalance in the bridge and increases its output voltage causing more current to flow through the wire, bringing the bridge back into balance. The operating temperature of the wire is controlled by changing the value of R_c. The output voltage of the op-amp is a measure of the amount of cooling the wire experiences. Because the temperature of the wire does not change, the frequency response is not limited by the thermal mass of the wires and high frequency responses are possible.

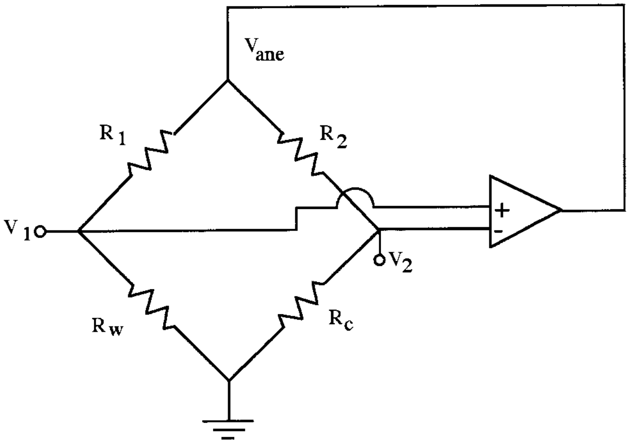

FIGURE 3.13.19 Schematic of hot-wire circuit.

Equations Governing Hot-Wire Anemometry

The cooling law is assumed to be of the form

$$Nu = A_0 + B_0 \operatorname{Re}^{0.5} \tag{3.13.23}$$

where Nu is the Nusselt number and Re is the Reynolds number; both are based on the wire diameter. The above equation is commonly known as King's law (King, 1914). Substituting in the definition of Nu and Re and solving for the heat transferred from the wire yields

$$q = A_1 \left(T_w - T_\infty\right) k + B_1 \left(\frac{P_\infty u_\infty}{T_\infty \mu}\right)^{0.5} \left(T_w - T_\infty\right) k \tag{3.13.24}$$

The heat transferred from the wire to the gas is balanced by the energy supplied by the anemometer:

$$q = i_w^2 R_w = \frac{V_{ane}^2 R_w}{\left(R_w + R_{ane}\right)^2} \tag{3.13.25}$$

or, since R_w and R_{ane} are constant,

$$q \propto V_{ane}^2 \tag{3.13.26}$$

Combining Equations 3.13.24 and 3.13.26 and solving for $P_\infty u_\infty$ yields

$$\left(P_\infty u_\infty\right)^{0.5} = A T_\infty^{0.5} \mu^{0.5} + B \frac{V_{ane}^2}{\left(T_w - T_\infty\right)} \frac{T_\infty^{0.5} \mu^{0.5}}{k} \tag{3.13.27}$$

For isothermal flows, the response equation reduces to

$$u^{0.5} = A + B V_{ane}^2 \tag{3.13.28}$$

Although it is theoretically possible to obtain the response curve without doing a calibration, the uncertainty in the wire diameter, wire length, and other errors make calibration of the wire mandatory at the conditions at which one wishes to operate.

Probe Design

Shown on Figure 3.13.20 are some typical probes used in anemometry. The curved prongs on the boundary layer probe (Figure 3.13.20b) are designed to minimize flow disturbance in the near-wall region. The two wires on this probe are used to obtain both u and v components of velocity.

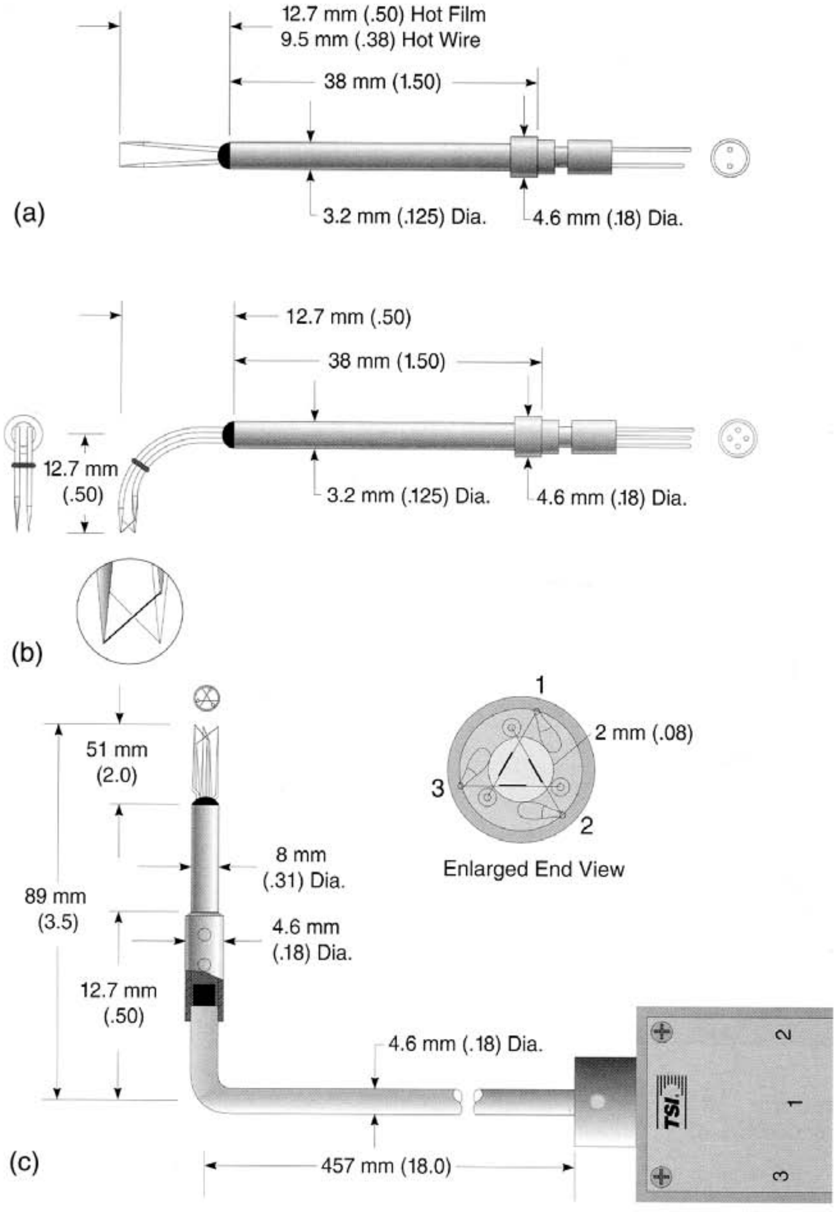

FIGURE 3.13.20 Some hot-wire probe configurations: (a) single-wire probe, (b) boundary layer cross-wire probe, (c) triple sensor cross-flow probe. (Courtesy of TSI Inc., St. Paul, MN.)

Platinum-plated tungsten wires 4 μm thick are typically used. Platinum is used to prevent oxidation of the wires during operation. The operating temperature for these wires is typically 250°C. Pure platinum wires are also used with the advantage of being able to operate at high temperatures (about 1000°C), thereby minimizing drift with ambient temperature changes, but they tend to be quite frail and their use is limited to low velocities. The ends of the wires where they attach to the prongs are usually copper-plated and the unplated length defines the sensitive portion of the wire. This is performed to isolate the sensing length from the disturbing effects of the prongs on the flow. The l/d of the sensing length is typically 200.

Platinum thin film probes are also available. These are made by depositing a thin layer of platinum onto a quartz substrate, typically a 50-μm-diameter quartz rod. The probe can be coated with a thin layer of oxide for use in electrically conductive liquids. The advantages of film sensors are their rigidity and strength. Rigidity is important for multisensor applications since the data reduction algorithms typically assume straight sensors. Film sensors are more resistant to damage by particles in the flow.

Multicomponent Probes

More than one component of velocity can be measured if multiple wires are present. Consider the case where a wire is inclined relative to the axis of the flow, as shown in Figure 3.13.21. Cross-wires (Figure 3.13.20b) inclined at θ_1 and θ_2 from the normal can be used to obtain the instantaneous U and V components of velocity. The cross-correlation between u′ and v′ (u′v′), also known as the turbulent shear stress, can be obtained if the instantaneous velocities U and V are known. The wires will be sensitive to the velocities according to

$$U_{eff,1} = U\cos(\theta_1) + V\sin(\theta_1) \tag{3.13.29}$$

$$U_{eff,2} = U\cos(\theta_2) - V\sin(\theta_2) \tag{3.13.30}$$

If the effective velocities over the two wires are known along with the probe geometry, then the velocities U and V can be determined. The instantaneous velocity can be broken down into the mean and fluctuating components:

$$U = \overline{U} + u' \tag{3.13.31}$$

$$V = \overline{V} + v' \tag{3.13.32}$$

Since

$$\overline{uv} = \overline{(\overline{U} + u')(\overline{V} + v')} = \overline{U}\overline{V} + \overline{u'v'} \tag{3.13.33}$$

the turbulent shear stress can be written as

$$\overline{u'v'} = \overline{uv} - \overline{U}\overline{V} \tag{3.13.34}$$

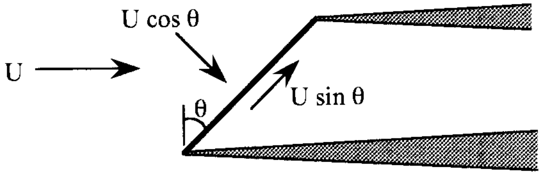

FIGURE 3.13.21 Normal and tangential components of velocity for a wire inclined to the flow.

The above results must be corrected to take into account the directional response of the wire, as discussed below. Three-wire probes to measure three components of velocity are also available (Figure 3.13.20c).

Directional Response

For small inclinations θ to the flow, the hot-wire will only respond to the velocity component normal to the wire or *Ucos*θ. For large inclinations, a significant axial flow develops along the wire resulting in additional cooling as a result of the finite length of the wire. The equation usually used to describe this effect is based on work by Champagne et al. (1967) and is given by

$$U_{eff}^2 = U^2\left(\cos^2\theta + k^2\sin^2\theta\right) \tag{3.13.35}$$

where k is a constant that varies linearly from 0.2 for a wire with $l/d = 200$ to zero for $l/d = 600$. Champagne et al. (1967) applied these results to estimate the overall error for a 45° cross-wire operated at constant temperature. They found that

$$\left(\frac{\overline{u'^2}}{U^2}\right)_m = \left(\frac{\overline{u'^2}}{U^2}\right)_i \tag{3.13.36}$$

$$\left(\frac{\overline{u'v'}}{U^2}\right)_m = \frac{1+k^2}{1-k^2}\left(\frac{\overline{u'v'}}{U^2}\right)_i \tag{3.13.37}$$

$$\left(\frac{\overline{v'^2}}{U^2}\right)_m = \frac{1+k^2}{1-3k^2+4k^4}\left(\frac{\overline{v'^2}}{U^2}\right)_i \tag{3.13.38}$$

where the subscript m is the measured value and the subscript i is the ideal value for a wire of infinite length.

Corrections Due to Temperature

Probably the most significant source of error when using a properly calibrated hot-wire occurs as a result of drifts in the flow temperature from the calibration temperature. If the flow temperature is higher than the calibration temperature, less energy is required to keep the wire at a constant temperature for a given velocity, and the indicated flow velocity will be lower than the true flow velocity. A first-order correction can be made to account for the drift in flow temperature as described below, however. The energy dissipated by the wire is proportional to the wire-to-flow temperature difference, and is also proportional to the voltage across the wire:

$$q_w \sim \Delta T \sim V^2 \tag{3.13.39}$$

The following equation can be used to correct for small changes in temperature:

$$V_{corr} = V_m\sqrt{\frac{T_w - T_{ref}}{T_w - T_\infty}} \tag{3.13.40}$$

where V_{corr} = corrected voltage
V_m = measured voltage
T_w = wire temperature
T_{ref} = temperature of the calibration flow
T_∞ = temperature of the flow

It should be noted that the sensitivity to ambient temperature changes decreases with higher wire temperatures — the wire should be operated at the highest possible temperature.

Laser Doppler Anemometry

LDV uses light to measure the velocity of particles in a flow through a small volume. If the particles faithfully follow the flow, then the velocity of the particle can be assumed to be the velocity of the flow itself. LDV has numerous advantages over other methods of measuring velocity. First, it is nonintrusive so it can be used in environments that are hostile to probes or where probes excessively disturb the flow. Second, it does not depend on temperature or pressure changes in the flow. Third, it can detect flow reversals. Fourth, it can measure very high velocities if sufficiently fast electronics are available. Fifth, velocity is measured directly and is unaffected by changes in temperature, density, or composition in the flow field. LDV has been used in flows ranging from natural convection to flows in IC engines and gas turbines. The disadvantages include the need for particles (seeded or naturally occurring) that follow the fluid motion, high cost, the need for optical access to the test section, and the need for careful alignment.

Principle of Operation

The basic setup for a popular type of LDV system is shown on Figure 3.13.22. A single, polarized, continuous-wave laser is split into two parallel beams using a beam splitter. The beams pass through a focusing lens that causes the beams to intersect in the focal plane of the lens, simultaneously reducing the beam diameter. The light beams approximate cylinders in the intersection region. The two beams constructively and destructively interfere with each other in the intersection regions, setting up alternating bright and dark fringes that are parallel to the axis of the laser beams. A particle moving through the measuring volume will scatter light, with the intensity of the scattered light depending on whether or not the particle is in a bright or dark fringe. Only the component of velocity perpendicular to the fringes and to the axis of the laser beams will be measured. The collecting lens collects some of the scattered light and focuses it onto a photodetector which outputs a signal dependent on the light intensity. Since the spacing between the fringes can be calculated or measured, the velocity of the particle traversing the measuring volume can be determined by measuring the frequency of the signal from the photomultiplier.

Measuring Volume Dimensions

The dimensions of the measuring volume can be computed from the following relations:

$$d_m = \frac{4 f \lambda}{\pi D_{e}^{-2}} \tag{3.13.41}$$

$$l_m = \frac{d_m}{\tan \kappa} \tag{3.13.42}$$

$$d_f = \frac{\lambda}{2 \sin \kappa} \tag{3.13.43}$$

where d_m = measuring volume diameter
l_m = measuring volume length
d_f = fringe spacing
f = focal length of the transmitting lens
D_{e}^{-2} = diameter of the laser beam at the e^{-2} intensity point entering the transmitting lens
λ = wavelength of the laser light
κ = half angle between the beams

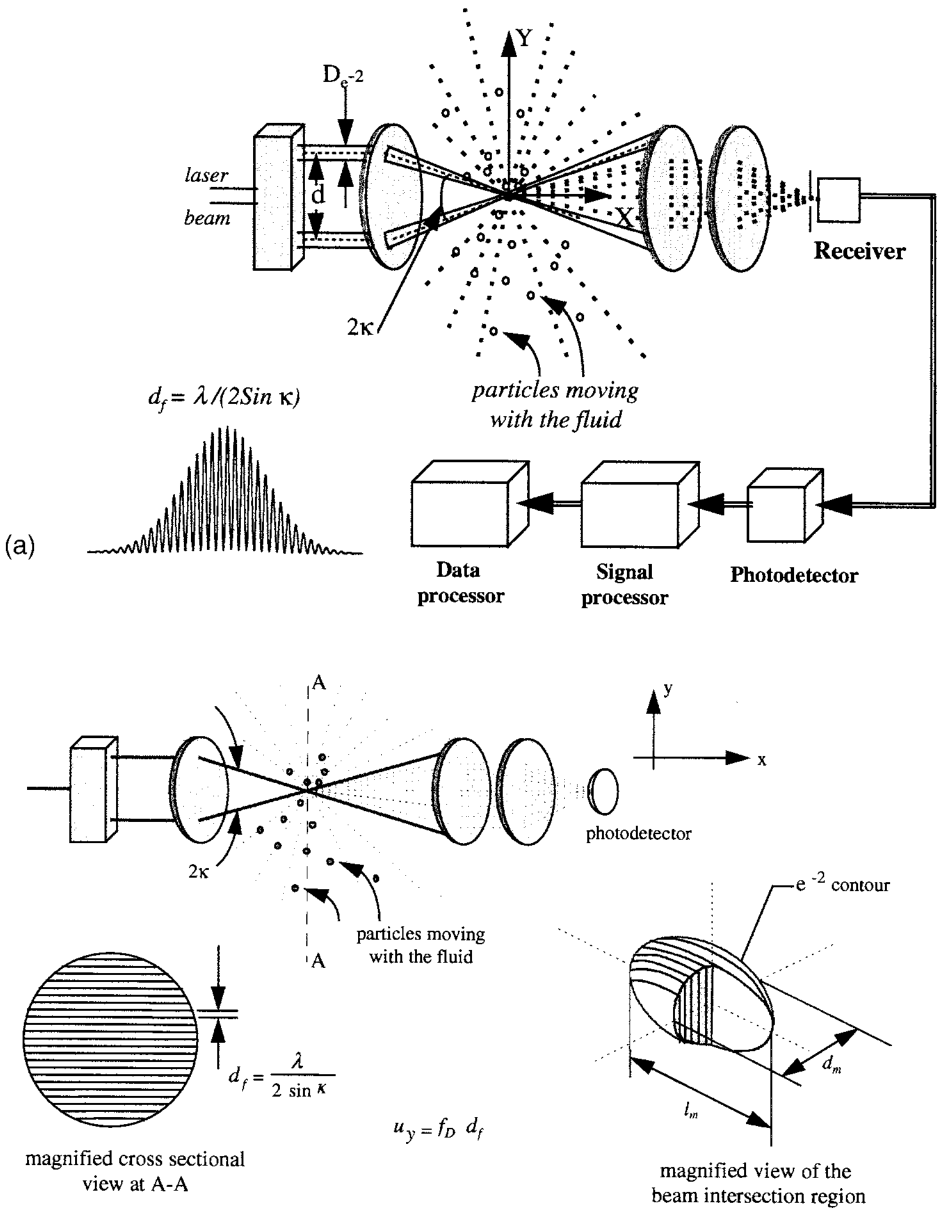

FIGURE 3.13.22 Basic setup for two-component LDV: (a) schematic of a dual beam system, (b) details of the beam crossing. (Courtesy of TSI Inc., St. Paul, MN.)

HeNe or argon-ion lasers are typically used. Note that in order to get a small measuring volume diameter, the focal length needs to be short, or the beam diameter needs to be large. Similar effects are seen for the measurement volume length. Ideally, one would like to have a measuring volume that is small compared to the scales of interest, with at least 10 fringes in the measuring volume.

Backscatter Mode

A configuration that is often used is shown in Figure 3.13.23. The backscatter configuration has the advantage that the optics can be made very compact, and because all the optics can be put in a single housing the optics need to be aligned only once. Much less light is scattered in the backward direction

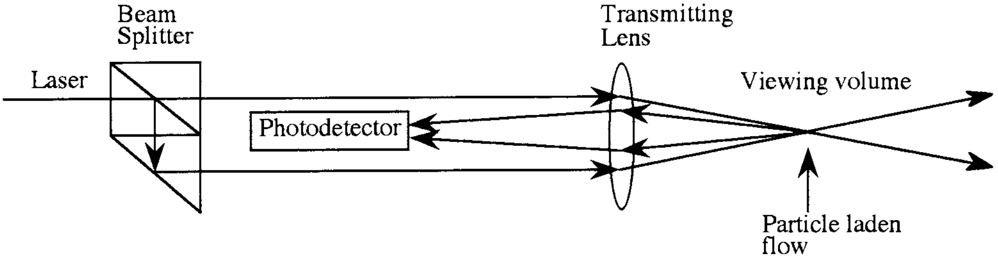

FIGURE 3.13.23. LDV configuration for backscatter.

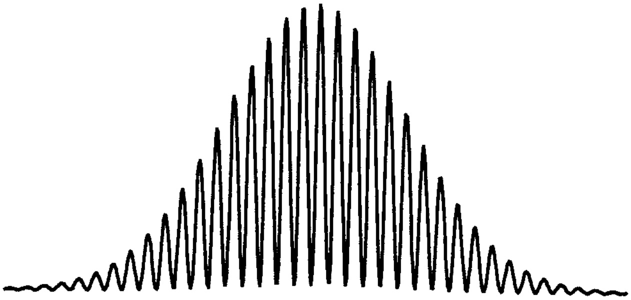

FIGURE 3.13.24 Typical photodetector signal due to scattering from a single particle. (Courtesy of TSI Inc., St. Paul, MN.)

than in the forward direction, however, so much more sensitive photodetectors are required to detect the weaker signal.

Photodetectors

Two types of photodetectors are generally used to convert the scattered light collected by the collecting lens to an electronic signal. In the photomultiplier, photons strike a coating of photoemissive material causing electrons to be emitted. These electrons are accelerated by a high-voltage field and impact onto a dynode that emits even more electrons. This amplification process is repeated, resulting in final gains of 10^3 to 10^7. Frequency responses up to 200 MHz can be obtained using photomultipliers.

Photodiodes are light-sensitive semiconductor junctions. An amplification process similar to that in PMTs occurs in photodiodes, but gains are limited to about 10^3. The frequency response tends to be lower as well. Photodiodes are much less expensive than photomultipliers, however.

Signal Processing

A typical output signal from a photodetector is shown on Figure 3.13.24. It is seen to consist of a pedestal along with the Doppler signal. Most commercial LDV systems currently on the market use FFT or correlation methods to determine the frequency.

Particle Tracking

It is important that the particles be able to follow the flow. Consider a spherical particle placed in a uniform flow. The drag force on the particle is due to the difference in speed between the particle and the carrier fluid, i.e.,

$$Force = ma = m\frac{dU_\infty}{dt} = \rho_P \frac{\pi D_P^3}{6}\frac{dU_\infty}{dt} = Drag \qquad (3.13.44)$$

The drag on a spherical particle is given by

$$Drag = C_d \frac{1}{2} \rho_\infty \frac{\pi D_P^2}{4} \left(U_\infty - U_P\right)^2 \tag{3.13.45}$$

where

$$C_d = \frac{24}{\text{Re}_P} = \frac{24\nu}{D_P\left(U_\infty - U_P\right)} \tag{3.13.46}$$

for $0 < Re_P < 100$. Combining Equations 3.13.44, 3.13.45, and 3.13.46 and integrating yields

$$\frac{\left(U_\infty - U_P\right)}{U_\infty} = \exp\left(-t/K\right) \tag{3.13.47}$$

where

$$K = \frac{D_P^2}{18\nu} \frac{\rho_P}{\rho_\infty} \tag{3.13.48}$$

Here, K is the time constant, and represents the time it takes for the initial velocity difference between the particle and the fluid to decay by $1/e$. Particles with K small compared to the time scales of interest will faithfully follow the flow.

Flow Reversal Measurements

If the fringes are stationary, as was assumed until now, one cannot tell the direction from which the particle passes the fringes, i.e., a particle moving with a velocity U will produce the same signal as a particle moving with velocity $-U$. While the direction of the flow is unambiguous in many cases, there are other flows (recirculating flows, flows with high turbulence intensity, impinging jets, shear flows) where the flow direction is not known. This problem can be easily rectified by shifting the frequency of one of the laser beams. If one of the beams is shifted in frequency, this will cause the fringes to move as well. If the fringes move at a speed faster than the maximum absolute flow velocity, then the indicated velocity will be the flow velocity plus the fringe velocity. Zero flow velocity would correspond to the fringe velocity, negative flow velocities would correspond to indicated velocities lower than the fringe velocity, and positive flow velocities would correspond to indicated velocities higher than the fringe velocity.

Frequency shifting is usually accomplished by inserting an acoustic-optic Bragg cell in one of the split beams. Typical shifts are 40 MHz, i.e., a 40-MHz signal would be seen at the output of the photodetector at zero flow velocity.

Multicomponent Systems

Measurement of more than one component of velocity is more difficult than simply having two one-component systems because the signals from the two beams interfere with each other. It is necessary to be able to distinguish which pair of beams the signal came from. One can either use two pairs of beams of different color or different polarities. In the two-color method, four beams consisting of two different colors are usually used. An argon-ion laser produces both blue and green lines. This light is split and converged to form two mutually orthogonal dual-beam systems. The scattered light is collected by a pair of receiving optics/photodetector systems, one of which accepts only blue light and one of which only accepts green light. The scattered light is separated using a dichroic mirror that transmits the blue light and reflects the green light.

Particle Image Velocimetry

A relatively new method of measuring velocity at many points in the flow is by particle image velocimetry (PIV). This method enables simultaneous measurement of velocity at many points in the flow by measuring the distance that particles carried by the flow travel over a known time interval. Accuracy and spatial resolution can be comparable to LDV.

Typical applications of PIV are to obtain the turbulent flow structure of complex steady flow fields where mapping is too difficult and time-consuming, and periodic flow fields where the velocity field can be obtained at different phases. An example of flow field velocity vectors obtained using PIV is shown on Figure 3.13.25.

The fundamental principle of PIV by optical imaging is the measurement of displacements δx, δy of image markers which travel with the fluid. In PIV, the time between the marks is fixed, while the distance between fringes is fixed in LDV. The time interval between marks in PIV must be small compared to the time scales of interest in the flow. Typical markers that have been used are H_2 bubbles, fluorescent particles, and naturally occurring small particles in liquids. The two main components of a PIV system are the imaging system which produces a double-exposed photographic image of the particles in the flow field, and the interrogation system which extracts and presents the velocity field information contained in the photograph.

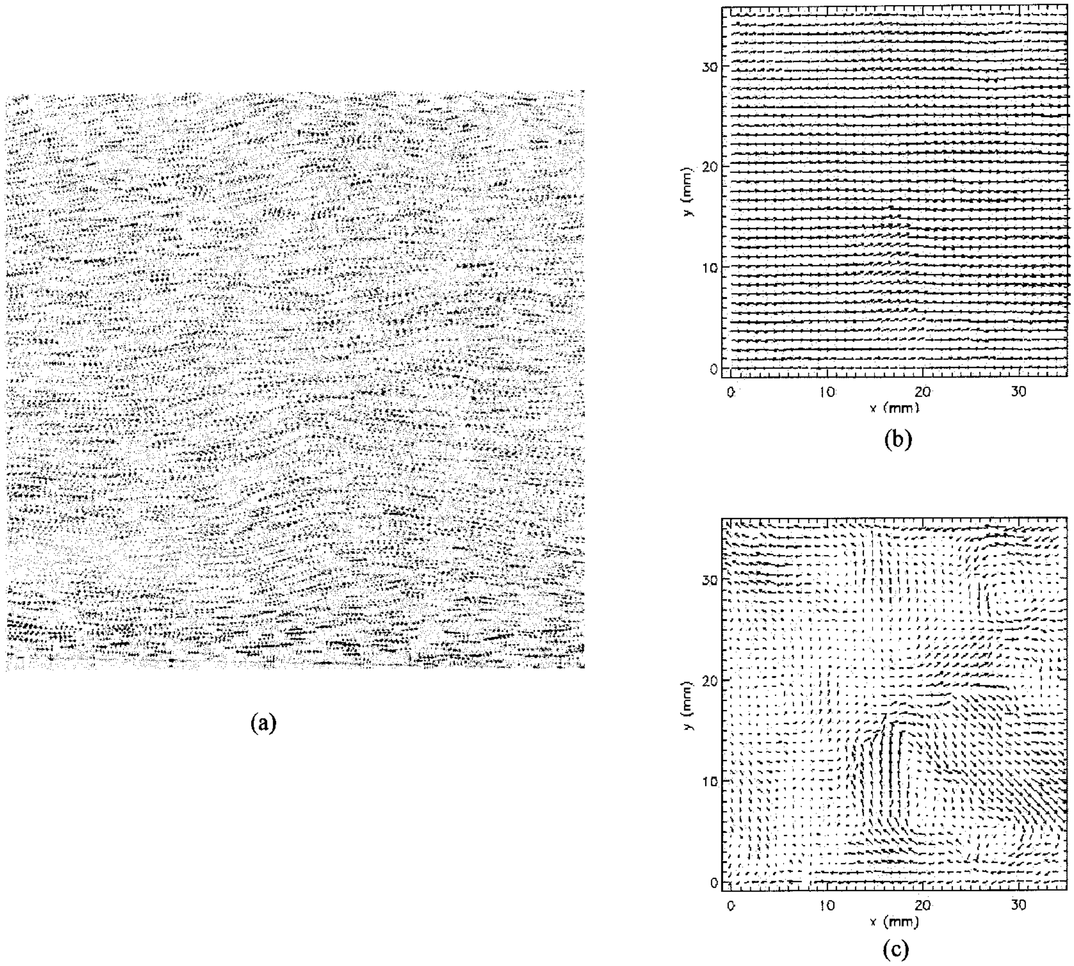

(a)

(b)

(c)

FIGURE 3.13.25 Example of velocity vectors obtained using PIV: (a) double exposure of particles in flowfield, (b) velocity vectors, (c) velocity vectors with mean velocity subtracted out. (Courtesy of Ken Kiger, University of Maryland, College Park, MD.)

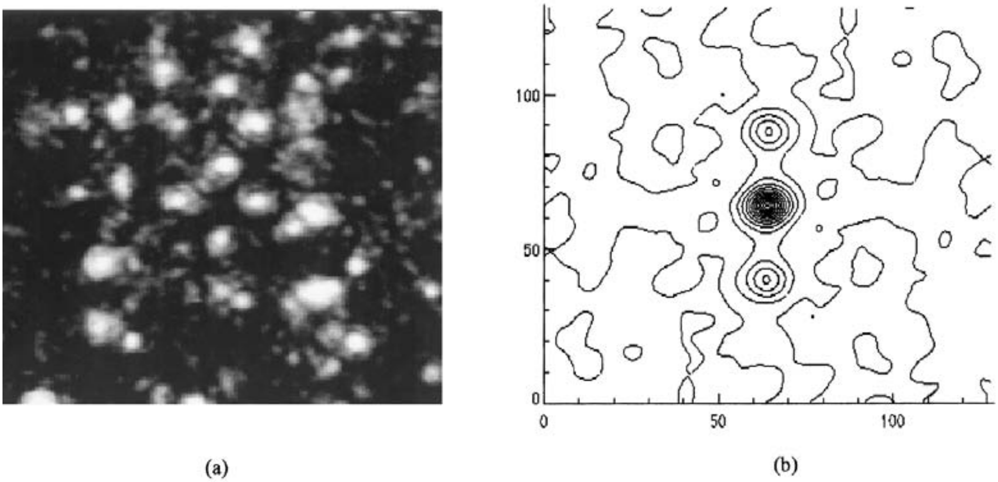

(a) (b)

FIGURE 3.13.26 Example of (a) double-exposed image of particle shifted from one another, (b) the corresponding spatial autocorrelation. (Courtesy of Ken Kiger, University of Maryland, College Park, MD.)

Imaging System

Typically, the beam from a doubly pulsed laser is converted into a sheet of laser light using a cylindrical lens, which is then used to illuminate the markers in the flow. A camera located perpendicular to the flow records the doubly exposed image onto film. Typical light sources are pulsed lasers or shuttered continuous wave (CW) lasers. Because pulsed lasers have larger energy output than CW lasers, they are generally used to illuminate small particles in the flow. Single CW laser beams swept across the flow using a rotating, faceted mirror produce a pseudo light sheet and can also be used to illuminate particles.

Film is usually necessary to resolve the markers if reasonable spatial resolution is desired. Larger markers in conjunction with high-resolution video cameras can be used, but care must be taken to ensure that the markers faithfully follow the flow. High-resolution cameras do have the advantage that near on-line processing of the data can be performed, however, with the appropriate digitizing and computing equipment.

The result of the imaging system is to produce two sets of markers that are displaced in time. The two sets can be on a single sheet of film, or can be recorded separately on different frames of a video camera. An example of two sets of markers is shown on Figure 3.13.26a.

Interrogation System

To obtain the velocity vectors, the doubly exposed image is first divided up into small sub-areas over which the average velocity vector will be computed. The size of the sub-areas should be as small as possible to obtain the highest number of velocity vectors, but they should not be so small that an insufficient number of particle pairs results. A good rule of thumb is to choose a sub-area size that contains about 10 particle pairs. The position of each of the particles is then determined, and a spatial autocorrelation performed (Figure 3.13.26b). The location of the peaks in the spatial correlation plane yields the average particle displacement over that sub-area. The largest peak results from a self-correlation and is not of interest. Two other peaks, one in the positive direction and the other in the negative direction, indicate the possible average particle displacement over that sub-area.

Flow Direction

It is not possible to determine the *direction* of the velocity vector from a doubly exposed photograph alone. This is not a problem if the main flow direction is known *a priori*, but it does present problems in highly turbulent flows or if flow reversals occur. Image shifting of the second set of particles relative to the first can be used to resolve this directional ambiguity. Suppose the second set of images is shifted by a positive amount. A stationary marker will be displaced by this amount. A moving marker will have an additional displacement as a result of its movement. A shift greater than that expected at the largest negative flow velocity then eliminates ambiguity regarding flow direction, since the second image is always on the positive side of the first image. This technique is analogous to using frequency shifting in LDV measurements to determine the direction of the particle movement.

Rotating mirrors and crystals have been used to produce this shift in images. More recently, cameras have been developed specifically for PIV that electronically shift the first set of images by a certain number of pixels before acquiring the second set, eliminating any additional mechanical complexity.

Viscosity Measurements

Viscometry is the technique of measuring the viscosity of a fluid. Viscometers are classified as rotational, capillary, or miscellaneous, depending on the technique employed. Rotational viscometers use the principle that a rotating body immersed in a liquid experiences a viscous drag which is a function of the viscosity of the liquid, the shape and size of the body, and the speed of its rotation. Rotational viscometers are widely used because measurements can be carried out for extended periods of time.

Capillary viscometry uses the principle that when a liquid passes in laminar flow through a tube, the viscosity of the liquid can be determined from measurements of the volume flow rate, the applied pressure, and the tube dimensions. Viscometers that cannot be classified either as rotational or capillary include the falling ball viscometer. Its method of operation is based on Stokes' law which relates the viscosity of a Newtonian fluid to the velocity of a sphere falling through it. Falling-ball viscometers are often employed for reasonably viscous fluids. Rising bubble viscometers utilize the principle that the rise of an air bubble through a liquid medium gives a visual measurement of liquid viscosity. Because of their simplicity, rising bubble viscometers are commonly used to estimate the viscosity of varnish, lacquer, and other similar media.

Defining Terms

Flow meter: Device used to measure mass flow rate or volume flow rate of fluid flowing in a duct.

Restriction flow meter: Flow meter that causes flowing fluid to accelerate in a nozzle, creating a pressure change that can be measured and related to flow rate.

Thermal anemometer: Heated sensor used to infer local fluid velocity by sensing changes in heat transfer from a small electrically heated surface exposed to the fluid flow.

Traverse: Systematic procedure used to traverse a probe across a duct cross section to measure flow rate through the duct.

References

Adrian, R.J., *Selected Papers on Particle Image Velocimetry,* SPIE Optical Engineering Press, Bellingham, WA, 1993.

ASHRAE, *Handbook Fundamentals*, American Society of Heating, Refrigerating, and Air-Conditioning Engineers, Atlanta, GA, 1981.

Champagne, F.H., Sleicher, C.A., and Wehrman, O.H., Turbulence measurements with inclined hot-wires, I. and II. *J. Fluid Mech.,* 28, 153-182, 1967.

Fox, R.W. and McDonald, A.T., *Introduction to Fluid Mechanics*, 4th ed., John Wiley & Sons, New York, 1992.

Goldstein, R.J., Ed., *Fluid Mechanics Measurements*, 2nd ed., Taylor & Francis, Bristol, PA, 1996.

Grant, I., *Selected Papers on Particle Image Velocimetry,* SPIE Optical Engineering Press, Bellingham, WA, 1994.

King, L.V., On the convection of heat from small cylinders in a stream of fluid: determination of the convection constants of small platinum wires with applications to hot-wire anemometry, *Philos. Trans. R. Soc. (London), Ser. A,* 214, 373-432, 1914.

Krause, L.N. and Gettleman, C.C., Considerations Entering into the Selection of Probes for Pressure Measurement in Jet Engines, *ISA Proc.,* 7, 134, 1952.

Miller, R.W., *Flow Measurement Engineering Handbook*, 3rd ed., McGraw-Hill, New York, 1996.

Moffatt, R.J., Experimental Methods in the Thermosciences, Department of Mechanical Engineering, Stanford University, Stanford, CA 94305, Copies available from Moffat Thermosciences, Inc. 2333 Eastridge Ave, #2, Menlo Park, CA 94025.

Further Information

This section presents only an overview of flow measurement methods. The references below contain a wealth of further information. Baker[1] surveys the field and discusses precision, calibration, probe, and tracer methods, and likely developments. Spitzer[4] presents an excellent practical discussion of flow measurement.

1. Baker, R.C., *An Introductory Guide to Flow Measurement*. Institution of Mechanical Engineers, London, 1989.
2. Bruun, H.H., *Hot-Wire Anemometry: Principles and Signal Analysis*, Oxford University Press, New York, 1995.
3. ISO 7145, Determination of Flowrate of Fluids in Closed Conduits or Circular Cross Sections Method of Velocity Determination at One Point in the Cross Section, ISO UDC 532.57.082.25:532.542. International Standards Organization, Geneva, 1982.
4. Spitzer, R.W., Ed., *Flow Measurement: A Practical Guide for Measurement and Control*, Instrument Society of America, Research Triangle Park, NC, 1991.
5. White, F.M., *Fluid Mechanics*, 3rd ed., McGraw-Hill, New York, 1994.
6. Van Wazer, J.R., Lyons, J.W., Kim, K.Y., and Colwell, R.E., *Viscosity and Flow Measurement: A Laboratory Handbook of Rheology*, Interscience, New York, 1963.

3.14 Pressure Measurements

Jungho Kim

Pressure is defined as force per unit area. Pressure transducers measure pressure relative to an absolute pressure p_a (relative to vacuum) or gage pressure p_g (relative to atmosphere). Gage pressure can be positive or negative depending on whether the measured pressure is above or below atmospheric. This atmospheric pressure can change depending on location. In some cases, pressure is measured relative to a sealed cavity which is at 1 bar regardless of the local atmospheric pressure. Some common units of pressure are Pa, mmHg, inches of water, torr, and bars. There are many types of pressure gages. Some can be considered standards which are accurate, repeatable, and fundamental pressure measuring instruments. Other gages must be calibrated against the standards.

Standards

Pressure standards use as force the weight of a solid or liquid mass. The two most common pressure standards are manometers and deadweight gages.

Manometers. A manometer (Figure 3.14.1) uses the deflection of a liquid column to measure pressure. A U-tube manometer measures pressure differences by balancing the forces on a liquid column in a U-shaped tube. A static force balance on the liquid gives

$$p_1 - p_2 = \rho_m g h$$

where ρ_m is the density of the manometer fluid column and h is the difference in the heights of the column. Because of surface tension and capillary effects, the meniscus (the liquid/air interference) is curved and the same point on the meniscus should be used when reading capillary height. The most common fluids are water, oil, alcohol, and mercury. Mercury is attractive because of its high density. Oil is good because evaporation losses and corrosion effects are minimized. Alcohol is attractive because the meniscus is flatter than with other fluids.

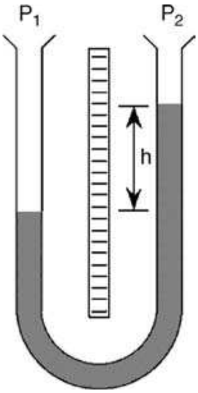

FIGURE 3.14.1 Manometer.

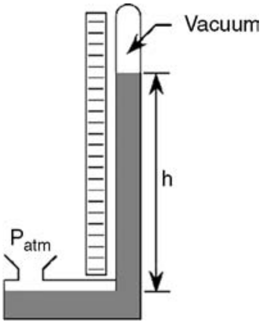

FIGURE 3.14.2 Barometer.

The manometer should be oriented along with the gravity vector, and the local gravitational acceleration must be known accurately. Corrections should be made that take into difference the recording temperature and the temperature at which the scale was calibrated since temperature variations can affect the manometer reading by causing the scale to expand and the density of the manometer fluid to change. The tube walls must be clean so that the meniscus shape does not change along the tube.

There are many variations on the U-tube manometer. A barometer (Figure 3.14.2) is used to measure atmospheric pressure by effectively connecting one side of a U-tube manometer to a vacuum and exposing the other side to the atmosphere. The evacuated space cannot be at zero pressure due to the vapor pressure of the fluid, so corrections are made for this. Inclined manometers have one leg tilted, and are used to increase the sensitivity of the measurement by decreasing the uncertainty in measurement of the liquid height. Systems that allow very small pressure differences to be measured are called micromanometers. In one scheme, the fluid level is found precisely using an electric circuit. A micrometer mounted on a pointer is lowered until it contacts the manometer fluid level, closing a circuit. Fluid level changes can be measured with a precision of 0.01 mm. Manometers can be used to measure pressures about 1 atm and lower, but the height of the liquid column becomes excessive at higher pressures and deadweight gages must be used.

Deadweight gages. A deadweight gage (Figure 3.14.3) consists of a piston-cylinder arrangement upon which standard weights are placed, and is used primary to calibrate other pressure transducers. Readings are taken when the piston is floating, and the pressure below the piston is equal to the sum of the weight of the piston and the added standard weights, divided by the piston area. Friction between the piston and cylinder is eliminated by rotating the piston. For absolute gages, the atmospheric pressure needs to be accurately measured and added to the reading. Pressures up to 350 atmospheres can be produced using deadweight gages.

FIGURE 3.14.3 Deadweight gage tester. (Courtesy of SI Pressure Instruments, Los Osos, CA.)

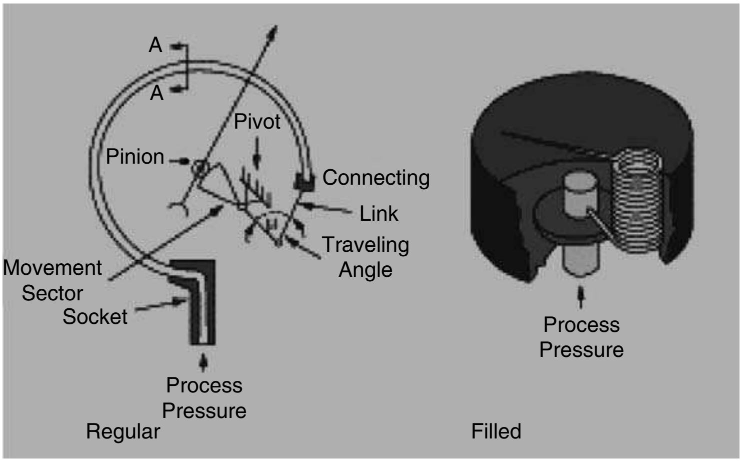

FIGURE 3.14.4 Bourdon gage (Omega). AMATEK: 727-536-7831 (Call on Monday)

Other Pressure Gages

Factors that need to be taken into consideration when choosing a pressure transducer include the pressure range, compatibility between the fluid and the transducer, the temperature, size, output type, and cost.

Bourdon tubes. The Bourdon tube (Figure 3.14.4) consists of a flattened tube bent into a circular arc. A pressure difference between the inside and outside of the tube tends to straighten the tube, and causes the free end to deflect and rotate a pointer. The angular position of the pointer is proportional to the pressure applied. A wide range of pressures from vacuum to over 10,000 atmospheres can be measured using Bourdon tubes. C-type Bourdon tubes with a tube bent over a 270° arc are used for higher pressures while spiral and helical type tubes are typically used below 70 bars in order to amplify the motion. Typical accuracies range from 0.1% to 5% full scale. Temperature change must be accounted for in order to obtain accurate measurements. Variations in indicated pressure are typically 0.3% to 0.4% over 10 K.

Bellows gages. These use elastic deformation to measure pressure. The deflection of the free end of the bellows is read on a dial driven by linkages and gears. Since small pressure difference can cause large forces when applied over a large area, bellows gages can be used to measure very low pressures or where high sensitivity is needed. Bellows can be made from bronze, copper, stainless steel, brass, or rubber.

Diaphragm gages. Diaphragm gages measure the deflection of a diaphragm when subjected to a pressure difference. Flat-diaphragm pressure elements can have strain gages attached to them to measure the amount of deflection the diaphragm undergoes for a given pressure. Very small gages in silicon with very high frequency response (100 kHz) have been made using VLSI technology. The strain in a micromachined silicon diaphragm is measured by four piezoresistive transducers arranged in a Wheatstone bridge. Transducers with pressure ranges up to 2000 atm are available.

Piezoelectric transducers. When a force is applied across a piezoelectric material, displaced electrical charges accumulate on the faces. The voltage produced is approximately proportional to the force applied. Because of charge leakage, piezoelectric transducers can only be used to make dynamic measurements. A static pressure will produce a signal initially, but this signal will slowly decay. These transducers are very rugged, hare high frequency response, and very low pressures (microphones) to very large pressures (e.g., pressure in gun barrels or shock tubes) can be measured. Typical frequency response is on the order of 100 kHz.

Capacitive transducers. These record movement of plates separated by a dielectric. Changes in capacitance are detected by change in resonance of a RC oscillator. Advantages include high sensitivity to diaphragm movement, minimum hysteresis due to friction, nd relatively fast response. Disadvantages include nonlinearity of output, charge leakage, and cost of the output sensing equipment. They are also somewhat sensitive to temperature changes.

Bridgeman-type gages. These gages measure the resistance change of a wire (manganin or gold with 2.1% chromium) when subjected to high pressure. A thin wire is wound into a coil, and the resistance change is measured using a Wheatstone bridge. A second coil that is not subject to the high pressure is used as an adjacent arm in the bridge and compensates for large temperature variations. Care must be taken to make sure the wire is free of internal stresses and corrections should be made for changes in temperature. These gages have been used to measure very high pressures (up to 27,000 bar).

Vacuum measurements. the unit of pressure commonly used in vacuum measurements is torr (1 mmHg) or microns (10^{-6} m Hg). Broudon gages can be used to about 10 torr, manometers and bellows gages down to about 0.1 torr, and diaphragm gages down to about 10^{-3} torr. At lower pressures, gages built specifically for vacuum measurements are needed. The McLeod gage is a standard for vacuum measurements because the pressure can be computed from the gage dimensions. It can be used to measure pressures as low as 0.01 microns when used tilted. In this gage, a low-pressure gas sample is sealed in a container, then compressed through a liquid seal to a pressure high enough that it can be read with a manometer.

Thermal conductivity gages utilize the finding that a linear relationship exists between thermal conductivity and pressure for pressures below 10^{-2} torr. Above 10^{-2} torr, the thermal conductivity varies approximately logarithmically until about 1 torr, after which it remains constant. The gages have an element which is electrically heated with a constant energy input. This element will attain a temperature at which the energy input balances the heat transfer away by conduction and radiation. For a given gas composition, this equilibrium temperature is a measure of the gas pressure. the emissivity of the surface is minimized to maximize the sensitivity. In the Pirani-type (Figure 3.14.5) thermal conductivity gage, two elements consisting of tungsten wires inside glass tubes are used One element is exposed to the gas,

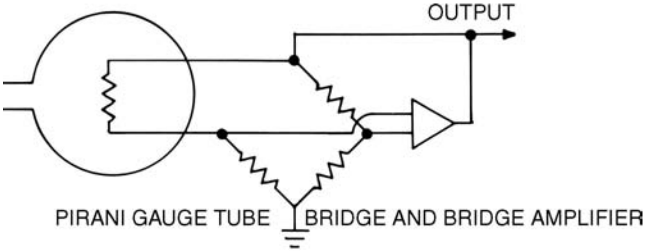

FIGURE 3.14.5 Schematic of Pirani gage. (Courtesy of MKS Instruments.)

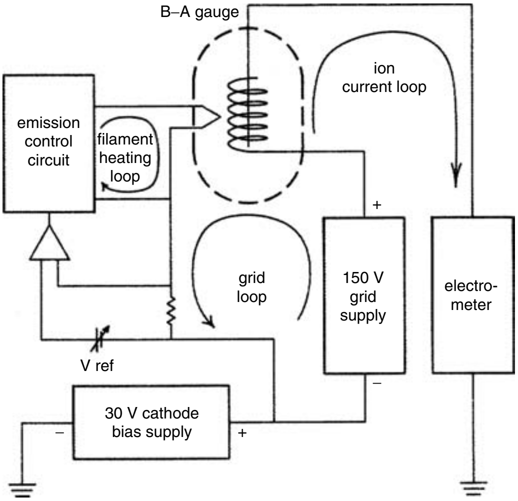

FIGURE 3.14.6 Schematic of ionization gage. (Courtesy of MKS Instruments.)

while the other is sealed in an evacuated tube. These two elements form adjacent arms in a Wheatstone bridge. When a voltage is applied to the bridge, the wires will be heated. The wire in the tube with the gas sample will be cooled by gas conduction and radiation, while the wire in the evacuated tube is cooled by radiation only. The imbalance of the Wheatstone bridge serves as a measure of gas pressure. Because gases vary in thermal conductivity, calibration must be performed for each gas that is tested.

the ionization gage (Figure 3.14.6) is one of the oldest and most widely used gages to measure gas pressure under high-vacuum conditions. Electrons emitted from a hot cathode into the vacuum is used to create ions when they collide with gas molecules. If the electron strikes a gas molecule, a positive ion can be created, freeing a secondary electron. These positive ions are accelerated to a collector where they combine with electrons. Recombination produces a current that is proportional the gas pressure. Conventional ionization gages are suitable for use below 1 torr. Cold cathodes replace the hot cathode with a voltage potential that accelerates electrons. Problems with decomposition of filament gases and filament burnout are thus avoided. A magnetic filed is sometimes used to deflect the electrons causing them to spiral as they move across the field, increasing their chances of colliding with a gas molecule and increasing the sensitivity of the instrument.

3.15 Micro/Nanotribology

Bharat Bhushan

Introduction

The emerging field of micro/nanotribology is concerned with processes ranging from atomic and molecular scales to microscale, occurring during adhesion, friction, wear, and thin-film lubrication at sliding surfaces (Bhushan, 1995, 1997; Bhushan et al., 1995). The differences between conventional tribology or macrotribology and micro/nanotribology are contrasted in Figure 3.15.1. In macrotribology, tests are conducted on components with relatively large mass under heavily loaded conditions. In these tests, wear is inevitable and the bulk properties of mating components dominate the tribological performance. In micro/nanotribology, measurements are made on at least one of the mating components, with relatively small mass under lightly loaded conditions. In this situation, negligible wear occurs and the surface properties dominate the tribological performance.

Micro/nanotribological investigations are needed to develop fundamental understanding of interfacial phenomena on a small scale and to study interfacial phenomena in the micro- and nanostructures used

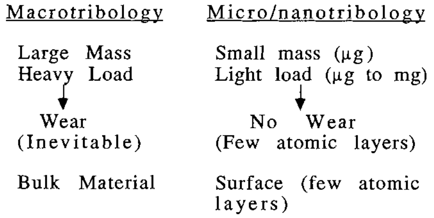

FIGURE 3.15.1 Comparison between macrotribology and microtribology.

in magnetic storage systems, microelectromechanical systems (MEMS), and other industrial applications (Bhushan, 1995, 1996, 1997). Friction and wear of lightly loaded micro/nanocomponents are highly dependent on the surface interactions (few atomic layers). These structures are generally lubricated with molecularly thin films. Micro- and nanotribological studies are also valuable in fundamental understanding of interfacial phenomena in macrostructures to provide a bridge between science and engineering (Bowden and Tabor, 1950, 1964; Bhushan and Gupta, 1997; Bhushan, 1996).

In 1985, Binnig et al. (1986) developed an "atomic force microscope" (AFM) to measure ultrasmall forces (less than 1 μN) present between the AFM tip surface and the sample surface. AFMs can be used for measurement of *all engineering surfaces* of any surface roughness, which may be either electrically conducting or insulating. AFM has become a popular surface profiler for topographic measurements on micro- to nanoscale. These are also used for scratching, wear, and nanofabrication purposes. AFMs have been modified in order to measure both normal and friction forces and this instrument is generally called a friction force microscope (FFM) or a lateral force microscope (LFM). New transducers in conjunction with an AFM can be used for measurements of elastic/plastic mechanical properties (such as load-displacement curves, indentation hardness, and modulus of elasticity) (Bhushan et al., 1996). A surface force apparatus (SFA) was first developed in 1969 (Tabor and Winterton, 1969) to study both static and dynamic properties of molecularly thin liquid films sandwiched between two molecularly smooth surfaces. SFAs are being used to study rheology of molecularly thin liquid films; however, the liquid under study has to be confined between molecularly smooth surfaces with radii of curvature on the order of 1 mm (leading to poorer lateral resolution as compared with AFMs) (Bhushan, 1995). Only AFMs/FFMs can be used to study *engineering surfaces* in the *dry and wet conditions* with *atomic resolution*. The scope of this section is limited to the applications of AFMs/FFMs.

At most solid–solid interfaces of technological relevance, contact occurs at numerous asperities with a range of radii; a sharp AFM/FFM tip sliding on a surface simulates just one such contact. Surface roughness, adhesion, friction, wear, and lubrication at the interface between two solids with and without liquid films have been studied using the AFM and FFM. The status of current understanding of micro/nanotribology of engineering interfaces follows.

Experimental Techniques

An AFM relies on a scanning technique to produce very high resolution, three-dimensional images of sample surfaces. The AFM measures ultrasmall forces (less than 1 nN) present between the AFM tip surface and a sample surface. These small forces are measured by measuring the motion of a very flexible cantilever beam having an ultrasmall mass. The deflection can be measured to with ±0.02 nm, so for a typical cantilever force constant of 10 N/m, a force as low as 0.2 nN can be detected. An AFM is capable of investigating surfaces of both conductors and insulators on an atomic scale. In the operation of a high-resolution AFM, the sample is generally scanned; however, AFMs are also available where the tip is scanned and the sample is stationary. To obtain atomic resolution with an AFM, the spring constant of the cantilever should be weaker than the equivalent spring between atoms. A cantilever beam with a spring constant of about 1 N/m or lower is desirable. Tips have to be sharp as possible. Tips with a radius ranging from 10 to 100 nm are commonly available.

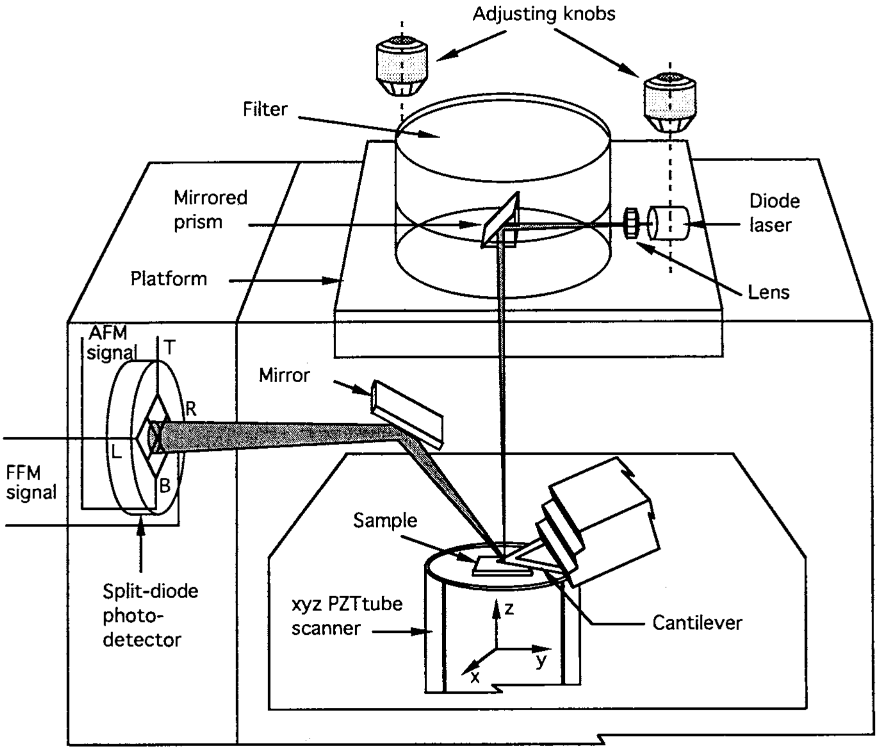

FIGURE 3.15.2 Schematic of a commercial AFM/FFM using laser beam deflection method.

In the AFM/FFM shown in Figure 3.15.2, the sample is mounted on a PZT tube scanner which consists of separate electrodes to precisely scan the sample in the *X–Y* plane in a raster pattern and to move the sample in the vertical (*Z*) direction. A sharp tip at the end of a flexible cantilever is brought in contact with the sample. Normal and frictional forces being applied at the tip–sample interface are measured simultaneously, using a laser beam deflection technique.

Topographic measurements are typically made using a sharp tip on a cantilever beam with normal stiffness on the order of 0.5 N/m at a normal load of about 10 nN, and friction measurements are carried out in the load range of 10 to 150 nN. The tip is scanned in such a way that its trajectory on the sample forms a triangular pattern. Scanning speeds in the fast and slow scan directions depend on the scan area and scan frequency. A maximum scan size of 125 × 125 μm and scan rate of 122 Hz typically can be used. Higher scan rates are used for small scan lengths.

For nanoscale boundary lubrication studies, the samples are typically scanned over an area of 1 × 1 μm at a normal force of about 300 nN, in a direction orthogonal to the long axis of the cantilever beam (Bhushan, 1997). The samples are generally scanned with a scan rate of 1 Hz and the scanning speed of 2 μm/sec. The coefficient of friction is monitored during scanning for a desired number of cycles. After the scanning test, a larger area of 2 × 2 μm is scanned at a normal force of 40 nN to observe for any wear scar.

For microscale scratching, microscale wear, and nano-scale indentation hardness measurements, a sharp single-crystal natural diamond tip mounted on a stainless steel cantilever beam with a normal stiffness on the order of 25 N/m is used at relatively higher loads (1 to 150 μN). For wear studies, typically an area of 2 × 2 μm is scanned at various normal loads (ranging from 1 to 100 μN) for a selected number of cycles. For nanoindentation hardness measurements the scan size is set to zero and then normal load is applied to make the indents. During this procedure, the diamond tip is continuously pressed against the sample surface for about 2 sec at various indentation loads. The sample surface is scanned before and after the scratching, wear, or indentation to obtain the initial and the final surface topography, at a low normal load of about 0.3 μN using the same diamond tip. An area larger than the indentation region is scanned to observe the indentation marks. Nanohardness is calculated by dividing the indentation load by the projected residual area of the indents.

In measurements using conventional AFMs, the hardness value is based on the projected residual area after imaging the incident. Identification of the boundary of the indentation mark is difficult to accomplish with great accuracy, which makes the direct measurement of contact area somewhat inaccurate. A capacitive transducer with the dual capability of depth sensing as well as *in situ* imaging is used in conjunction with an AFM (Bhushan et al., 1996). This indentation system, called nano/picoindention, is used to make load-displacement measurements and subsequently carry out *in situ* imaging of the indent, if necessary. Indenter displacement at a given load is used to calculate the projected indent area for calculation of the hardness value. Young's modulus of elasticity is obtained from the slope of the unloading portion of the load-displacement curve.

Surface Roughness, Adhesion, and Friction

Solid surfaces, irrespective of the method of formation, contain surface irregularities or deviations from the prescribed geometrical form. When two nominally flat surfaces are placed in contact, surface roughness causes contact to occur at discrete contact points. Deformation occurs in these points and may be either elastic or plastic, depending on the nominal stress, surface roughness, and material properties. The sum of the areas of all the contact points constitutes the real area that would be in contact, and for most materials at normal loads this will be only a small fraction of the area of contact if the surfaces were perfectly smooth. In general, real area of contact must be minimized to minimize adhesion, friction, and wear (Bhushan and Gupta, 1997; Bhushan, 1996). Characterizing surface roughness is therefore important for predicting and understanding the tribological properties of solids in contact.

Surface roughness most commonly refers to the variations in the height of the surface relative to a reference plane (Bowden and Tabor, 1950; Bhushan, 1996). Commonly measured roughness parameters, such as standard deviation of surface heights (rms), are found to be scale dependent and a function of the measuring instrument, for any given surface, Figure 3.15.3 (Poon and Bhushan, 1995). The topography of most engineering surfaces is fractal, possessing a self-similar structure over a range of scales. By using fractal analysis one can characterize the roughness of surfaces with two scale-independent fractal parameters *D* and *C* which provide information about roughness at all length scales (Ganti and Bhushan, 1995; Bhushan, 1995). These two parameters are instrument independent and are unique for each surface. *D* (generally ranging from 1 to 2) primarily relates to distribution of different frequencies in the surface profile, and *C* to the amplitude of the surface height variations at all frequencies. A fractal model of elastic plastic contact has been used to predict whether contacts experience elastic or plastic deformation and to predict the statistical distribution of contact points.

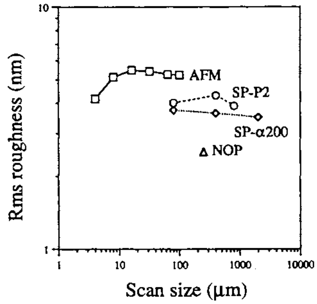

FIGURE 3.15.3 Scale dependence of standard deviation of surface heights (rms) for a glass–ceramic substrate, measured using an AFM, a stylus profiler (SP-P2 and SP-α200), and a noncontact optical profiler (NOP). (From Poon, C.Y. and Bhushan, B., *Wear*, 190, 76–88, 1995. With permission.)

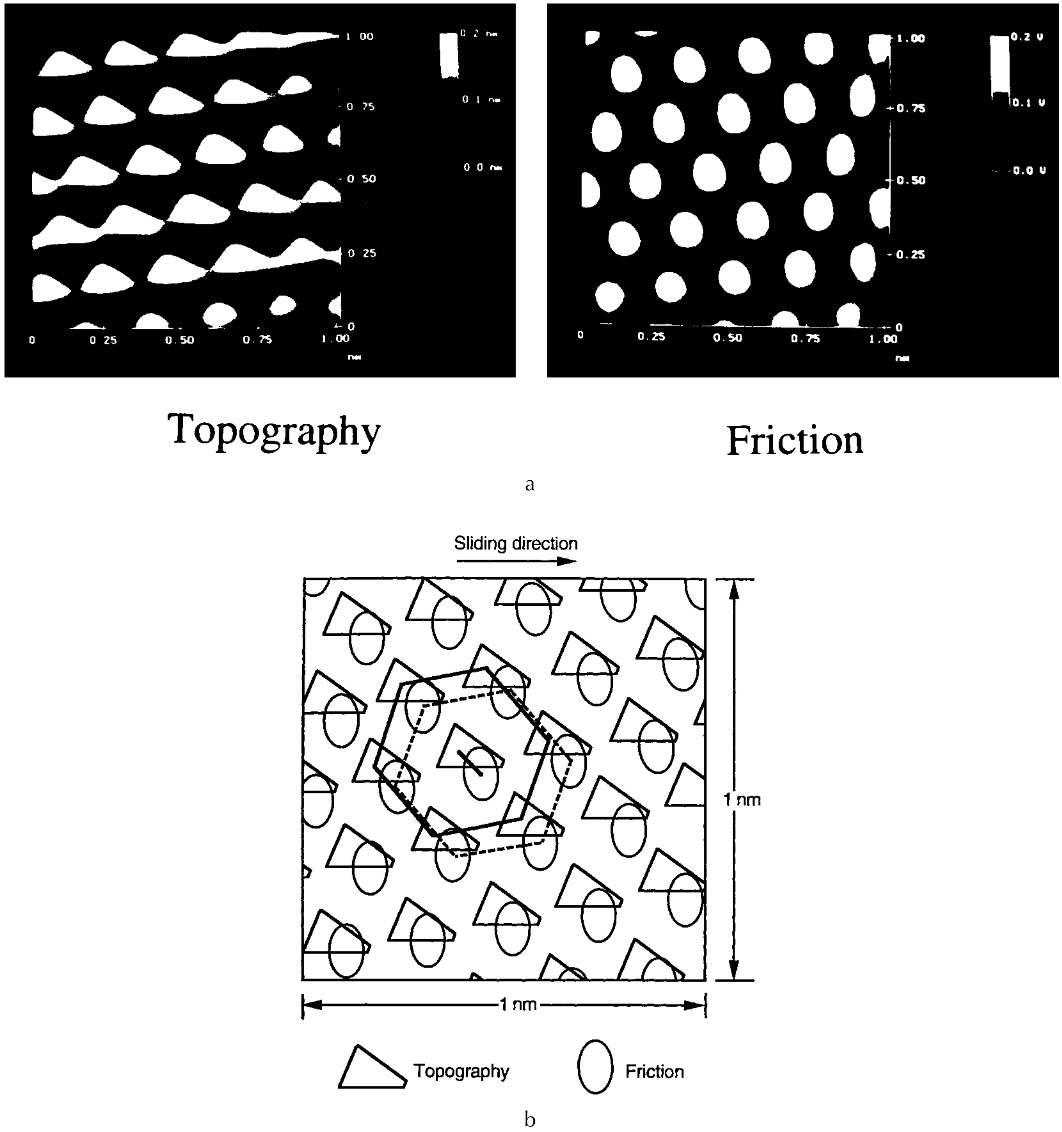

FIGURE 3.15.4 (a) Gray-scale plots of surface topography (left) and friction profiles (right) of a 1 × 1 nm area of freshly cleaved HOPG, showing the atomic-scale variation of topography and friction, (b) diagram of superimposed topography and friction profiles from (a); the symbols correspond to maxima. Note the spatial shift between the two profiles. (From Bhushan, B., *Handbook of Micro/Nanotribology*, CRC Press, Boca Raton, FL, 1995. With permission.)

Based on atomic-scale friction measurements of a well-characterized freshly cleaved surface of highly oriented pyrolytic graphite (HOPG), the atomic-scale friction force of HOPG exhibits the same periodicity as that of corresponding topography (Figure 3.15.4(a)), but the peaks in friction and those in topography were displaced relative to each other (Figure 3.15.4(b)). A Fourier expansion of the interatomic potential has been used to calculate the conservative interatomic forces between atoms of the FFM tip and those of the graphite surface. Maxima in the interatomic forces in the normal and lateral directions do not occur at the same location, which explains the observed shift between the peaks in the lateral force and those in the corresponding topography. Furthermore, the observed local variations in friction force were explained by variation in the intrinsic lateral force between the sample and the FFM tip, and these variations may not necessarily occur as a result of an atomic-scale stick–slip process.

TABLE 3.15.1 Surface Roughness and Micro- and Macroscale Coefficients of Friction of Various Samples

Material	rms Roughness, nm	Microscale Coefficient of Friction vs. Si_3N_4 Tip[a]	Macroscale Coefficient of Friction vs. Alumina Ball[b]
Si(111)	0.11	0.03	0.18
C^+-implanted Si	0.33	0.02	0.18

[a] Tip radius of about 50 nm in the load range of 10 to 150 nN (2.5 to 6.1 GPa), a scanning speed of 5 m/sec and scan area of 1 × 1 μm.

[b] Ball radius of 3 mm at a normal load of 0.1 N (0.3 GPa) and average sliding speed of 0.8 mm/sec.

Friction forces of HOPG have also been studied. Local variations in the microscale friction of cleaved graphite are observed, which arise from structural changes that occur during the cleaving process. The cleaved HOPG surface is largely atomically smooth, but exhibits line-shaped regions in which the coefficient of friction is more than an order of magnitude larger. Transmission electron microscopy indicates that the line-shaped regions consist of graphite planes of different orientation, as well as of amorphous carbon. Differences in friction can also be seen for organic mono- and multilayer films, which again seem to be the result of structural variations in the films. These measurements suggest that the FFM can be used for structural mapping of the surfaces. FFM measurements can be used to map chemical variations, as indicated by the use of the FFM with a modified probe tip to map the spatial arrangement of chemical functional groups in mixed organic monolayer films. Here, sample regions that had stronger interactions with the functionalized probe tip exhibited larger friction. For further details, see Bhushan (1995).

Local variations in the microscale friction of scratched surfaces can be significant and are seen to depend on the local surface slope rather than on the surface height distribution (Bhushan, 1995). Directionality in friction is sometimes observed on the macroscale; on the microscale this is the norm (Bhushan, 1995). This is because most "engineering" surfaces have asymmetric surface asperities so that the interaction of the FFM tip with the surface is dependent on the direction of the tip motion. Moreover, during surface-finishing processes material can be transferred preferentially onto one side of the asperities, which also causes asymmetry and directional dependence. Reduction in local variations and in the directionality of frictional properties therefore requires careful optimization of surface roughness distributions and of surface-finishing processes.

Table 3.15.1 shows the coefficient of friction measured for two surfaces on micro- and macroscales. The coefficient of friction is defined as the ratio of friction force to the normal load. The values on the microscale are much lower than those on the macroscale. When measured for the small contact areas and very low loads used in microscale studies, indentation hardness and modulus of elasticity are higher than at the macroscale. This reduces the degree of wear. In addition, the small apparent areas of contact reduce the number of particles trapped at the interface, and thus minimize the "ploughing" contribution to the friction force.

At higher loads (with contact stresses exceeding the hardness of the softer material), however, the coefficient of friction for microscale measurements increases toward values comparable with those obtained from macroscale measurements, and surface damage also increases (Bhushan et al., 1995; Bhushan and Kulkarni, 1996). Thus, Amontons' law of friction, which states that the coefficient of friction is independent of apparent contact area and normal load, does not hold for microscale measurements. These findings suggest that microcomponents sliding under lightly loaded conditions should experience very low friction and near zero wear.

Scratching, Wear, and Indentation

The AFM can be used to investigate how surface materials can be moved or removed on micro- to nanoscales, for example, in scratching and wear (Bhushan, 1995) (where these things are undesirable) and, in nanomachining/nanofabrication (where they are desirable). The AFM can also be used for measurements of mechanical properties on micro- to nanoscales. Figure 3.15.5 shows microscratches

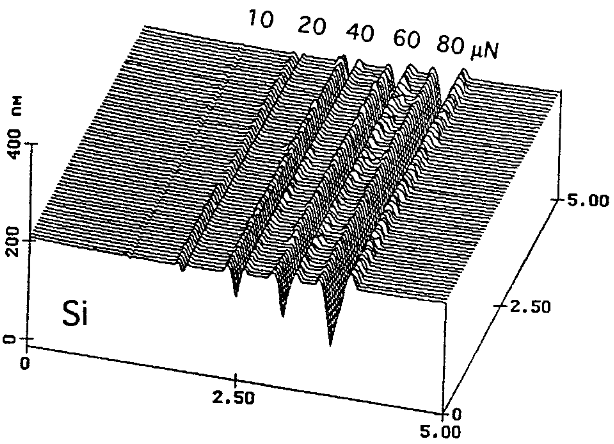

FIGURE 3.15.5 Surface profiles of Si(111) scratched at various loads. Note that the *x* and *y* axes are in micrometers and the *z* axis is in nanometers. (From Bhushan, B., *Handbook of Micro/Nanotribology*, CRC Press, Boca Raton, FL, 1995. With permission.)

made on Si(111) at various loads after 10 cycles. As expected, the depth of scratch increases with load. Such microscratching measurements can be used to study failure mechanisms on the microscale and to evaluate the mechanical integrity (scratch resistance) of ultrathin films at low loads.

By scanning the sample in two dimensions with the AFM, wear scars are generated on the surface. The evolution of wear of a diamond-like carbon coating on a polished aluminum substrate is showing in Figure 3.15.6 which illustrates how the microwear profile for a load of 20 μN develops as a function of the number of scanning cycles. Wear is not uniform, but is initiated at the nanoscratches indicating that surface defects (with high surface energy) act as initiation sites. Thus, scratch-free surfaces will be relatively resistant to wear.

Mechanical properties, such as load-displacement curves, hardness, and modulus of elasticity can be determined on micro- to picoscales using an AFM and its modifications (Bhushan, 1995; Bhushan et al., 1995, 1996). Indentability on the scale of picometers can be studied by monitoring the slope of cantilever deflection as a function of sample traveling distance after the tip is engaged and the sample is pushed against the tip. For a rigid sample, cantilever deflection equals the sample traveling distance; but the former quantity is smaller if the tip indents the sample. The indentation hardness on nanoscale of bulk materials and surface films with an indentation depth as small as 1 nm can be measured. An example of hardness data as a function of indentation depth is shown in Figure 3.15.7. A decrease in hardness with an increase in indentation depth can be rationalized on the basis that, as the volume of deformed materials increases, there is a higher probability of encountering material defects. AFM measurements on ion-implanted silicon surfaces show that ion implantation increases their hardness and, thus, their wear resistance (Bhushan, 1995). Formation of surface alloy films with improved mechanical properties by ion implantation is growing in technological importance as a means of improving the mechanical properties of materials.

Young's modulus of elasticity is calculated from the slope of the indentation curve during unloading (Bhushan, 1995; Bhushan et al., 1996). AFM can be used in a *force modulation mode* to measure surface elasticities: an AFM tip is scanned over the modulated sample surface with the feedback loop keeping the average force constant. For the same applied force, a soft area deforms more, and thus causes less cantilever deflection, than a hard area. The ratio of modulation amplitude to the local tip deflection is then used to create a *force modulation image*. The force modulation mode makes it easier to identify soft areas on hard substrates.

Detection of the transfer of material on a nanoscale is possible with the AFM. Indentation of C_{60}-rich fullerene films with an AFM tip has been shown to result in the transfer of fullerene molecules to the

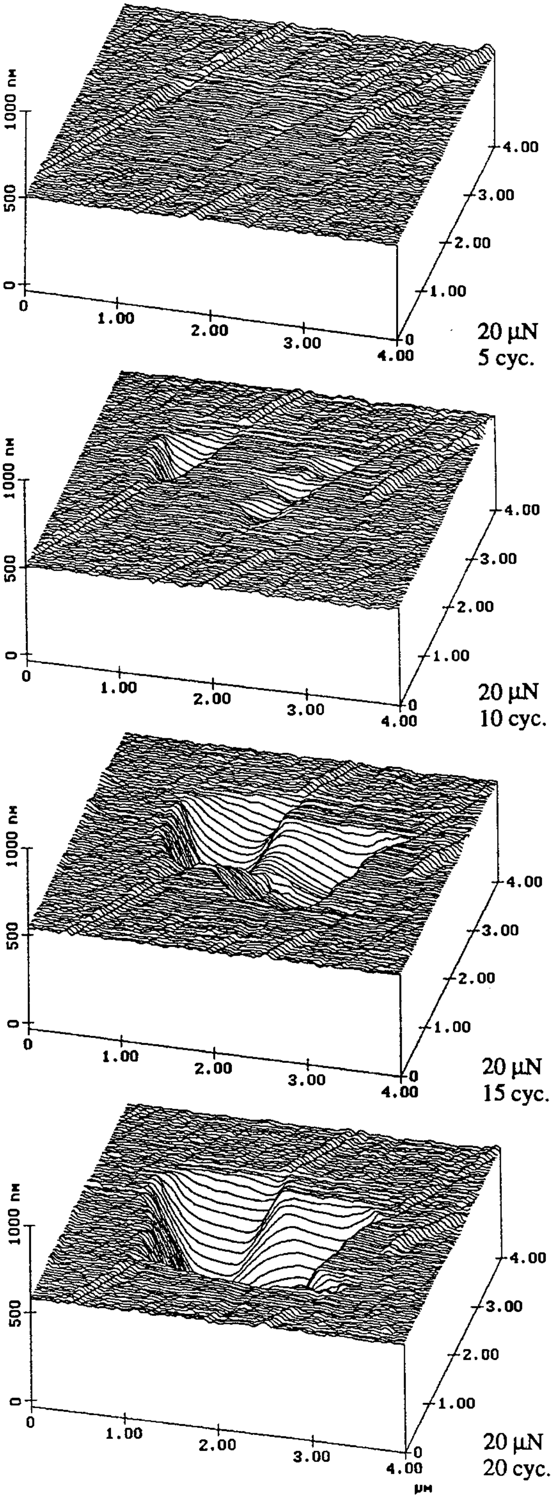

FIGURE 3.15.6 Surface profiles of diamond-like carbon-coated thin-film disk showing the worn region; the normal load and number of test cycles are indicated. (From Bhushan, B., *Handbook of Micro/Nanotribology*, CRC Press, Boca Raton, FL, 1995. With permission.)

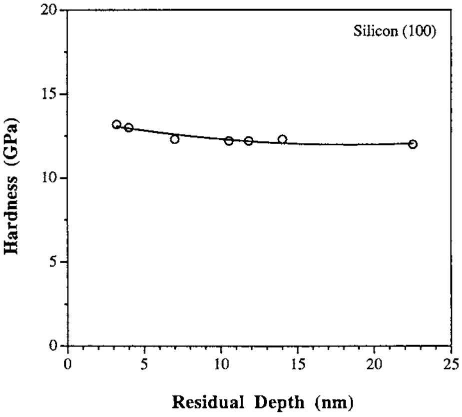

FIGURE 3.15.7 Indentation hardness as a function of residual indentation depth for Si(100). (From Bhushan, B. et al., *Philos. Mag.*, A74, 117–1128, 1996. With permission.)

AFM tip, as indicated by discontinuities in the cantilever deflection as a function of sample traveling distance in subsequent indentation studies (Bhushan, 1995).

Boundary Lubrication

The "classical" approach to lubrication uses freely supported multimolecular layers of liquid lubricants (Bowden and Tabor, 1950, 1964; Bhushan, 1996). The liquid lubricants are chemically bonded to improve their wear resistance (Bhushan, 1995, 1996). To study depletion of boundary layers, the microscale friction measurements are made as a function of the number of cycles. For an example of the data of virgin Si(100) surface and silicon surface lubricated with about 2-nm-thick Z-15 and Z-Dol perfluoropolyether (PEPE) lubricants, see Figure 3.15.8. Z-Dol is PFPE lubricant with hydroxyl end groups. Its lubricant film was thermally bonded. In Figure 3.15.8, the unlubricated silicon sample shows a slight increase in friction force followed by a drop to a lower steady state value after some cycles. Depletion of native oxide and possible roughening of the silicon sample are responsible for the decrease in this friction force. The initial friction force for the Z-15-lubricated sample is lower than that of the unlubricated silicon and

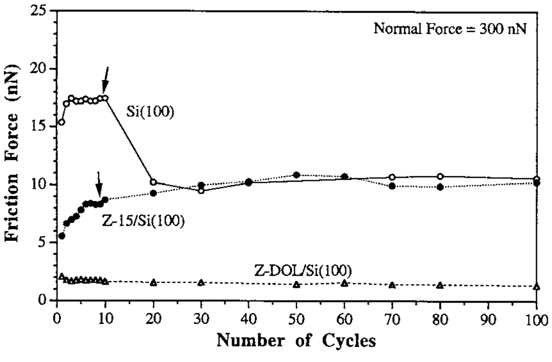

FIGURE 3.15.8 Friction force as a function of number of cycles using a silicon nitride tip at a normal force of 300 nN for the unlubricated and lubricated silicon samples. (From Bhushan, B., *Micro/Nanotribology and Its Applications*, Kluwer, Dordrecht, The Netherlands, 1997. With permission.)

increases gradually to a friction force value comparable with that of the silicon after some cycles. This suggests the depletion of the Z-15 lubricant in the wear track. In the case of the Z-Dol-coated silicon sample, the friction force starts out to be low and remains low during the entire test. It suggests that Z-Dol does not get displaced/depleted as readily as Z-15. Additional studies of freely supported liquid lubricants showed that either increasing the film thickness or chemically bonding the molecules to the substrate with a mobile fraction improves the lubrication performance (Bhushan, 1997).

For lubrication of microdevices, a more effect approach involves the deposition of organized, dense molecular layers of long-chain molecules on the surface contact. Such monolayers and thin films are commonly produced by Langmuir–Blodgett (LB) deposition and by chemical grafting of molecules into self-assembled monolayers (SAMs). Based on the measurements, SAMs of octodecyl (C_{18}) compounds based on aminosilanes on a oxidized silicon exhibited a lower coefficient of friction of (0.018) and greater durability than LB films of zinc arachidate adsorbed on a gold surface coated with octadecylthiol (ODT) (coefficient of friction of 0.03) (Bhushan et al., 1995). LB films are bonded to the substrate by weak van der Waals attraction, whereas SAMs are chemically bound via covalent bonds. Because of the choice of chain length and terminal linking group that SAMs offer, they hold great promise for boundary lubrication of microdevices.

Measurement of ultrathin lubricant films with nanometer lateral resolution can be made with the AFM (Bhushan, 1995). The lubricant thickness is obtained by measuring the force on the tip as it approaches, contacts, and pushes through the liquid film and ultimately contacts the substrate. The distance between the sharp “snap-in” (owing to the formation of a liquid of meniscus between the film and the tip) at the liquid surface and the hard repulsion at the substrate surface is a measure of the liquid film thickness. This technique is now used routinely in the information-storage industry for thickness measurements (with nanoscale spatial resolution) of lubricant films, a few nanometers thick, in rigid magnetic disks.

References

Bhushan, B. 1995. *Handbook of Micro/Nanotribology*, CRC Press, Boca Raton, FL.

Bhushan, B. 1996. *Tribology and Mechanics of Magnetic Storage Devices*, 2nd ed., Springer, New York.

Bhushan, B. 1997. *Micro/Nanotribiology and Its Applications*, NATO ASI Series E: Applied Sciences, Kluwer, Dordrecht, Netherlands.

Bhushan, B. and Gupta, B.K. 1997. *Handbook of Tribology: Materials, Coatings and Surface Treatments*, McGraw-Hill, New York (1991); Reprint with corrections, Kreiger, Malabar, FL.

Bhushan, B. and Kulkarni, A.V. 1996. Effect of normal load on microscale friction measurements, *Thin Solid Films*, 278, 49–56.

Bhushan, B., Israelachvili, J.N., and Landman, U. 1995. Nanotribology: friction, wear and lubrication at the atomic scale, *Nature*, 374, 607–616.

Bhushan, B., Kulkarni, A.V., Bonin, W., and Wyrobek, J.T. 1996. Nano-indentation and pico-indentation measurements using capacitive transducer system in atomic force microscopy, *Philos. Mag.*, A74, 1117–1128.

Binning, G., Quate, C.F., and Gerber, Ch. 1986. Atomic force microscopy, *Phys. Rev. Lett.*, 56, 930–933.

Bowden, F.P. and Tabor, D. 1950; 1964. *The Friction and Lubrication of Solids*, Parts I and II, Clarendon, Oxford.

Ganti, S. and Bhushan, B. 1995. Generalized fractal analysis and its applications to engineering surfaces, *Wear*, 180, 17–34.

Poon, C.Y. and Bhushan, B. 1995. Comparison of surface roughness measurements by stylus profiler, AFM and non-contact optical profiler, *Wear*, 190, 76–88.

Tabor, D. and Winterton, R.H.S. 1969. The direct measurement of normal and retarded van der Walls forces, *Proc. R. Soc. London*, A312, 435–450.

Nomenclature for Fluid Mechanics

Symbol	Quantity	Unit		Dimensions (*MLtT*)
		SI	English	
a	Velocity of sound	m/sec	ft/sec	Lt^{-1}
a	Acceleration	m/sec^2	ft/sec^2	Lt^{-2}
A	Area	m^2	ft^2	L^2
b	Distance, width	m	ft	L
c_p	Specific heat, constant pressure	J/kg·K	ft·lb/lb$_m$·°R	$L^2t^{-2}T^{-1}$
c_v	Specific heat, constant volume	J/kg·K	ft·lb/lb$_m$·°R	$L^2t^{-2}T^{-1}$
C	Concentration	No./m^3	No./ft^3	L^{-3}
C	Coefficient	—	—	—
C	Empirical constant	—	—	—
D	Diameter	m	ft	L
D_H	Hydraulic diameter	m	ft	L
e	Total energy per unit mass	J/kg	ft·lb/lb$_m$	L^2t^{-2}
E	Total energy	J	ft·lb or Btu	ML^2t^{-2}
E	Modulus of leasticity	Pa	lb/ft^2	ML^1t^{-2}
Eu	Euler number	—	—	—
f	Friction factor	—	—	—
F	Force	N	lb	MLt^{-2}
Fr	Froude number	—	—	—
F_B	Buoyant force	N	lb	MLt^{-2}
g	Acceleration of gravity	m/sec^2	ft/sec^2	Lt^{-2}
g_0	Gravitation constant	kg·m/N·sec^2	lb$_m$·ft/lb·sec^2	—
G	Mass flow rate per unit area	kg/sec·m^2	lb$_m$/sec·ft^2	$ML^{-2}t^{-1}$
h	Head, vertical distance	m	ft	L
h	Enthalpy per unit mass	J/kg	ft·lb/lb$_m$	L^2t^{-2}
H	Head, elevation of hydraulic grade line	m	ft	L
I	Moment of inertia	m^4	ft^4	L^4
k	Specific heat ratio	—	—	—
K	Bulk modulus of elasticity	Pa	lb/ft^2	ML^1t^{-2}
K	Minor loss coefficient	—	—	—
L	Length	m	ft	L
L	Lift	N	lb	MLt^{-2}
l	Length, mixing length	m	ft	L
ln	Natural logarithm	—	—	—
m	Mass	kg	lb$_m$	M
$\dot{m}$	Strength of source	m^3/sec	ft^3/sec	L^3t^{-1}
m	Mass flow rate	kg/sec	lb$_m$/sec	Mt^{-1}
M	Molecular weight	—	—	—
$\dot{M}$	Momentum per unit time	N	lb	MLt^{-2}
M	Mach number	—	—	—
n	Exponent, constant	—	—	—
n	Normal direction	m	ft	L
n	Manning roughness factor	—	—	—
n	Number of moles	—	—	—
N	Rotation speed	1/sec	1/sec	t^{-1}
NPSH	Net positive suction head	m	ft	L
p	Pressure	Pa	lb/ft^2	$ML^{-1}t^{-2}$
P	Height of weir	m	ft	L
P	Wetted perimeter	m	ft	L
q	Discharge per unit width	m^2/sec	ft^2/sec	L^2t^{-1}
q	Heat transfer per unit time	J/sec	Btu	ML^2t^{-3}
r	Radial distance	m	ft	L
R	Gas constant	J/kg·K	ft·lb/lb$_m$·°R	$L^2t^{-2}T^{-1}$
Re	Reynolds number	—	—	—
s	Distance	m	ft	L
s	Entropy per unit mass	J/kg·K	ft·lb/lb$_m$·°R	$L^2t^{-2}T^{-1}$

Symbol	Quantity	Unit		Dimensions (*MLtT*)
		SI	English	
S	Entropy	J/K	ft·lb/°R	$ML^2t^{-2}T^{-1}$
S	Specific gravity, slope	—	—	—
t	Time	sec	sec	t
t	Distance, thickness	m	ft	L
T	Temperature	K	°R	T
T	Torque	N·m	lb·ft	ML^2t^{-2}
u	Velocity, Velocity component	m/sec	ft/sec	Lt^{-1}
u	Peripheral speed	m/sec	ft/sec	Lt^{-1}
u	Internal energy per unit mass	J/kg	ft·lb/lb$_m$	L^2t^{-2}
u_*	Shear stress velocity	m/sec	ft/sec	Lt^{-1}
U	Internal energy	J	Btu	ML^2t^{-2}
v	Velocity, velocity component	m/sec	ft/sec	Lt^{-1}
v_s	Specific volume	m^3/kg	ft^3/lb$_m$	$M^{-1}L^3$
V	Volume	m^3	ft^3	L^3
V	Volumetric flow rate	m^3/sec	ft^3/sec	L^3t^{-1}
V	Velocity	m/sec	ft/sec	Lt^{-1}
w	Velocity component	m/sec	ft/sec	Lt^{-1}
w	Work per unit mass	J/kg	ft·lb/lb$_m$	L^2t^{-2}
W	Work per unit time	J/sec	ft·lb/sec	ML^2t^{-3}
W_s	Shaft work	m·N	ft·lb	ML^2t^{-2}
W	Weight	N	lb	MLt^{-2}
We	Weber number	—	—	—
x	Distance	m	ft	L
y	Distance, depth	m	ft	L
Y	Weir height	m	ft	L
z	Vertical distance	m	ft	L

Greek Symbols

a	Angle, coefficient	—	—	—
b	Blade angle	—	—	—
G	Circulation	m^2	ft^2	L^2t^{-1}
u	Vector operator	1/m	1/ft	L^{-1}
g	Specific weight	N/m^3	lb/ft^3	$ML^{-2}t^{-2}$
d	Boundary layer thickness	m	ft	L
e	Kinematic eddy viscosity	m^2/sec	ft^2/sec	L^2t^{-1}
e	Roughness height	m	ft	L
h	Eddy viscosity	N·sec/m^2	lb·sec/ft^2	$ML^{-1}t^{-1}$
h	Head ratio	—	—	—
h	Efficiency	—	—	—
Q	Angle	—	—	—
k	Universal constant	—	—	—
l	Scale ratio, undetermined multiplier	—	—	—
m	Viscosity	N·sec/m^2	lb·sec/ft^2	$ML^{-1}t^{-1}$
n	Kinematic viscosity (= μ/ρ)	m^2/sec	ft^2/sec	L^2t^{-1}
F	Velocity potential	m^2/sec	ft^2/sec	L^2t^{-1}
F	Function	—	—	—
p	Constant	—	—	—
P	Dimensionless constant	—	—	—
r	Density	kg/m^3	lb$_m$/ft^3	ML^{-3}
s	Surface tension	N/m	lb/ft	Mt^{-2}
s	Cavitation index	—	—	—
t	Shear stress	Pa	lb/ft^2	ML^1t^2
y	Stream function, two dimensions	m/sec	ft/sec	L^2t^{-1}
y	Stokes' stream function	m^3/sec	ft^3/sec	L^3t^{-1}
w	Angular velocity	rad/sec	rad/sec	t^{-1}

Subscripts

c	Critical condition
u	Unit quantities
c.s.	Control surface
c.v.	Control volume
o	Stagnation or standard state condition
1, 2	Inlet and outlet, respectively, of control volume or machine rotor
∞	Upstream condition far away from body, free stream
T	Total pressure
J	Static pressure

4

Heat and Mass Transfer

Frank Kreith
University of Colorado, Boulder

Robert F. Boehm
University of Nevada-Las Vegas

George D. Raithby
University of Waterloo

K. G. T. Hollands
University of Waterloo

N. V. Suryanarayana
Michigan Technological University

Michael F. Modest
Pennsylvania State University

Van P. Carey
University of California at Berkeley

John C. Chen
Lehigh University

Noam Lior
University of Pennsylvania

Ramesh K. Shah
Rochester Institute of Technology

Kenneth J. Bell
Oklahoma State University

Robert J. Moffat
Stanford University

Jungho Kim
University of Michigan

Anthony F. Mills
University of California at Los Angeles

Arthur E. Bergles
Rensselaer Polytechnic Institute

Larry W. Swanson
GEER

Vincent W. Antonetti
Poughkeepsie, New York

Thomas F. Irvine, Jr. (Deceased)
State University of New York, Stony Brook

Massimo Capobianchi
Gonzaga University

Kenneth R. Diller
University of Texas

Jonathan W. Valvano
University of Texas

John A. Pearce
University of Texas

4.1 Conduction Heat Transfer

Robert F. Boehm

Introduction

Conduction heat transfer phenomena are found throughout virtually all of the physical world and the industrial domain. The analytical description of this heat transfer mode is one of the best understood. Some of the bases of understanding of conduction date back to early history. It was recognized that by invoking certain relatively minor simplifications, mathematical solutions resulted directly. Some of these were very easily formulated. What transpired over the years was a very vigorous development of applications to a broad range of processes. Perhaps no single work better summarizes the wealth of these studies than does the book by Carslaw and Jaeger (1996). They gave solutions to a broad range of problems, from topics related to the cooling of the Earth to the current-carrying capacities of wires. The general analyses given there have been applied to a range of modern-day problems, from laser heating to temperature-control systems.

Today conduction heat transfer is still an active area of research and application. A great deal of interest has developed in recent years in topics like contact resistance, where a temperature difference develops between two solids that do not have perfect contact with each other. Additional issues of current interest include non-Fourier conduction, where the processes occur so fast that the equation described below does not apply. Also, the problems related to transport in miniaturized systems are garnering a great deal of interest. Increased interest has also been directed to ways of handling composite materials, where the ability to conduct heat is very directional.

Much of the work in conduction analysis is now accomplished by use of sophisticated computer codes. These tools have given the heat transfer analyst the capability of solving problems in nonhomogeneous media, with very complicated geometries, and with very involved boundary conditions. It is still important to understand analytical ways of determining the performance of conducting systems. At the minimum these can be used as calibrations for numerical codes.

Fourier's Law

The basis of conduction heat transfer is **Fourier's Law**. This law involves the idea that the heat flux is proportional to the temperature gradient in any direction *n*. **Thermal conductivity**, *k*, a property of materials that is temperature dependent, is the constant of proportionality.

$$q_k = -kA\frac{\partial T}{\partial n} \tag{4.1.1}$$

In many systems the area *A* is a function of the distance in the direction *n*. One important extension is that this can be combined with the first law of thermodynamics to yield the **heat conduction equation**. For constant thermal conductivity, this is given as

$$\nabla^2 T + \frac{\dot{q}_G}{k} = \frac{1}{\alpha}\frac{\partial T}{\partial t} \tag{4.1.2}$$

In this equation, α is the thermal diffusivity and $\dot{q}_G$ is the internal heat generation per unit volume. Some problems, typically steady-state, one-dimensional formulations where only the heat flux is desired, can be solved simply from Equation (4.1.1). Most conduction analyses are performed with Equation (4.1.2). In the latter, a more general approach, the temperature distribution is found from this equation and appropriate boundary conditions. Then the heat flux, if desired, is found at any location using Equation (4.1.1). Normally, it is the temperature distribution that is of most importance. For example, it may be desirable to know through analysis if a material will reach some critical temperature, like its melting point. Less frequently the heat flux is desired.

While there are times when it is simply desired to understand what the temperature response of a structure is, the engineer is often faced with a need to increase or decrease heat transfer to some specific level. Examination of the thermal conductivity of materials gives some insight into the range of possibilities that exist through simple conduction.

Of the more common engineering materials, pure copper exhibits one of the higher abilities to conduct heat with a thermal conductivity approaching 400 W/mK. Aluminum, also considered to be a good conductor, has a thermal conductivity a little over half that of copper. To increase the heat transfer above values possible through simple conduction, more-involved designs are necessary that incorporate a variety of other heat transfer modes like convection and phase change.

Decreasing the heat transfer is accomplished with the use of insulations. A separate discussion of these follows.

Insulations

Insulations are used to decrease heat flow and to decrease surface temperatures. These materials are found in a variety of forms, typically *loose fill*, *batt*, and *rigid*. Even a gas, like air, can be a good insulator if it can be kept from moving when it is heated or cooled. A vacuum is an excellent insulator. Usually, though, the engineering approach to insulation is the addition of a low-conducting material to the surface. While there are many chemical forms, costs, and maximum operating temperatures of common forms of insulations, it seems that when a higher operating temperature is required, many times the thermal conductivity and cost of the insulation will also be higher.

Loose-fill insulations include such materials as milled alumina-silica (maximum operating temperature of 1260°C and thermal conductivities in the range of 0.1 to 0.2 W/mK) and perlite (maximum operating temperature of 980°C and thermal conductivities in the range of 0.05 to 1.5 W/mK). Batt-type insulations include one of the more common types — glass fiber. This type of insulation comes in a variety of densities, which, in turn, have a profound affect on the thermal conductivity. Thermal conductivities for glass fiber insulations can range from about 0.03 to 0.06 W/mK. Rigid insulations show a very wide range of forms and performance characteristics. For example, a rigid insulation in foam form, polyurethane, is very lightweight, shows a very low thermal conductivity (about 0.02 W/mK), but has a maximum operating temperature only up to about 120°C. Rigid insulations in refractory form show quite different characteristics. For example, high-alumina brick is quite dense, has a thermal conductivity of about 2 W/mK, but can remain operational to temperatures around 1760°C. Many insulations are characterized in the book edited by Guyer (1999).

Often, commercial insulation systems designed for high-temperature operation use a layered approach. Temperature tolerance may be critical. Perhaps a refractory is applied in the highest temperature region, an intermediate-temperature foam insulation is used in the middle section, and a high-performance, low-temperature insulation is used on the outer side near ambient conditions.

Analyses can be performed including the effects of temperature variations of thermal conductivity. However, the most frequent approach is to assume that the thermal conductivity is constant at some temperature between the two extremes experienced by the insulation.

The Plane Wall at Steady State

Consider steady-state heat transfer in a plane wall of thickness L, but of very large extent in both other directions. The wall has temperature T_1 on one side and T_2 on the other. If the thermal conductivity is considered to be constant, then Equation (4.1.1) can be integrated directly to give the following result:

$$q_k = \frac{kA}{L}\left(T_1 - T_2\right) \tag{4.1.3}$$

This can be used to determine the steady-state heat transfer through slabs.

An electrical circuit analog is widely used in conduction analyses. This is realized by considering the temperature difference to be analogous to a voltage difference, the heat flux to be like current flow, and the remainder of Equation (4.1.3) to be like a thermal resistance. The latter is seen to be

$$R_k = \frac{L}{kA} \tag{4.1.4}$$

Heat transfer through walls made of layers of different types of materials can be easily found by summing the resistances in series or parallel form, as appropriate.

In the design of systems, seldom is a surface temperature specified or known. More often, the surface is in contact with a bulk fluid, whose temperature is known at some distance from the surface. Convection from the surface is then represented by Newton's law of cooling:

$$q = \bar{h}_c A\left(T_s - T_\infty\right) \tag{4.1.5}$$

This equation can also be represented as a temperature difference divided by a thermal resistance, which is $1/\bar{h}_c A$. It can be shown that a very low surface resistance, as might be represented by phase change phenomena, has the effect of imposing the fluid temperature directly on the surface. Hence, usually a *known* surface temperature results from a fluid temperature being imposed directly on the surface through a very high heat transfer coefficient. For this reason, in the later results given here, particularly those for transient systems, a convective boundary will be assumed. For steady results this is less important because of the ability to add resistances through the circuit analogy.

Long, Cylindrical Systems at Steady State

For long (L) annular systems at steady-state conditions with constant thermal conductivities, the following two equations are the appropriate counterparts to Equation (4.1.3) and Equation (4.1.4). The heat transfer can be expressed as

$$q_k = \frac{2\pi Lk}{\ln\left[r_2/r_1\right]}\left(T_1 - T_2\right) \tag{4.1.6}$$

Here, r_1 and r_2 represent the radii of annular section. A thermal resistance for this case is as shown below.

$$R_k = \frac{\ln\left[r_2/r_1\right]}{2\pi Lk} \tag{4.1.7}$$

The Overall Heat Transfer Coefficient

The **overall heat transfer coefficient** concept is valuable in several aspects of heat transfer. It involves a modified form of Newton's law of cooling, as noted above, and it is written as

$$Q = \bar{U}A\Delta T \tag{4.1.8}$$

In this formulation $\bar{U}$ is the overall heat transfer coefficient based upon the area A. Because the area for heat transfer in a problem can vary (as with a cylindrical geometry), it is important to note that the $\bar{U}$ is dependent upon which area is selected. The overall heat transfer coefficient is usually found from a combination of thermal resistances. Hence, for a common series-combination-circuit analog, the $\bar{U}A$ product is taken as the sum of resistances.

$$\bar{U}A = \frac{1}{\sum_{i=1}^{n} R_i} = \frac{1}{R_{\text{total}}} \tag{4.1.9}$$

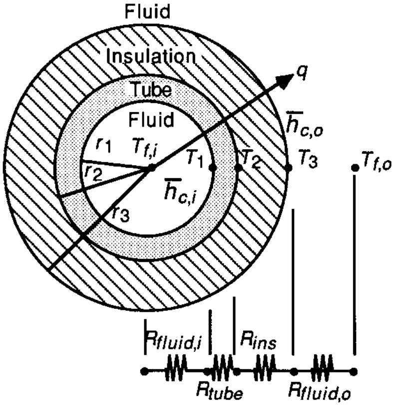

FIGURE 4.1.1 An insulated tube with convective environments on both sides.

To show an example of the use of this concept, consider Figure 4.1.1.

For steady-state conditions, the product $\bar{U}A$ remains constant for a given heat transfer and overall temperature difference. This can be written as

$$\bar{U}_1 A_1 = \bar{U}_2 A_2 = \bar{U}_3 A_3 = \bar{U}A \tag{4.1.10}$$

If the inside area, A_1, is chosen as the basis, the overall heat transfer coefficient can then be expressed as

$$\bar{U}_1 = \frac{1}{\dfrac{1}{\bar{h}_{c,i}} + \dfrac{r_1 \ln(r_2/r_1)}{k_{\text{pipe}}} + \dfrac{r_1 \ln(r_3/r_2)}{k_{\text{ins}}} + \dfrac{r_1}{r_3 \bar{h}_{c,o}}} \tag{4.1.11}$$

Critical Thickness of Insulation

Sometimes insulation can cause an increase in heat transfer. This circumstance should be noted in order to apply it when desired and to design around it when an insulating effect is needed. Consider the circumstance shown in Figure 4.1.1. Assume that the temperature is known on the outside of the tube (inside of the insulation). This could be known if the inner heat transfer coefficient is very large and the thermal conductivity of the tube is large. In this case, the inner fluid temperature will be almost the same as the temperature of the inner surface of the insulation. Alternatively, this could be applied to a coating (say an electrical insulation) on the outside of a wire. By forming the expression for the heat transfer in terms of the variables shown in Equation (4.1.11), and examining the change of heat transfer with variations in r_3 (that is, the thickness of insulation) a maximum heat flow can be found. While simple results are given many texts (showing the critical radius as the ratio of the insulation thermal conductivity to the heat transfer coefficient on the outside), Sparrow (1970) has considered a heat transfer coefficient that varies as $\bar{h}_{c,o} \sim r_3^{-m} |T_3 - T_{f,o}|^n$. For this case, it is found that the heat transfer is maximized at

$$r_3 = r_{\text{crit}} = \left[(1-m)/(1+n)\right]\frac{k_{\text{ins}}}{\bar{h}_{c,o}} \tag{4.1.12}$$

By examining the order of magnitudes of m, n, k_{ins}, and $\bar{h}_{c,o}$ the critical radius is found to be often on the order of a *few millimeters*. Hence, additional insulation on small-diameter cylinders such as small-gauge electrical wires could actually increase the heat dissipation. On the other hand, the addition of insulation to large-diameter pipes and ducts will almost always decrease the heat transfer rate.

Internal Heat Generation

The analysis of temperature distributions and the resulting heat transfer in the presence of volume heat sources is required in some circumstances. These include phenomena such as nuclear fission processes, joule heating, and microwave deposition. Consider first a slab of material $2L$ thick but otherwise very large, with internal generation. The outside of the slab is kept at temperature T_1. To find the temperature distribution within the slab, the thermal conductivity is assumed to be constant. Equation (4.1.2) reduces to the following:

$$\frac{d^2T}{dx^2} + \frac{\dot{q}_G}{k} = 0 \tag{4.1.13}$$

Solving this equation by separating variables, integrating twice, and applying boundary conditions gives

$$T(x) - T_1 = \frac{\dot{q}_G L^2}{2k}\left[1 - \left(\frac{x}{L}\right)^2\right] \tag{4.1.14}$$

A similar type of analysis for a long, cylindrical element of radius r_1 gives

$$T(r) - T_1 = \frac{\dot{q}_G r_1^2}{4k}\left[1 - \left(\frac{r}{r_1}\right)^2\right] \tag{4.1.15}$$

Two additional cases will be given. Both involve the situation when the heat generation rate is dependent upon the local temperature in a linear way (defined by a slope β), according to the following relationship:

$$\dot{q}_G = \dot{q}_{G,o}\left[1 + \beta\left(T - T_o\right)\right] \tag{4.1.16}$$

For a plane wall of $2L$ thickness and a temperature of T_1 specified on each surface

$$\frac{T(x) - T_o + 1/\beta}{T_1 - T_o + 1/\beta} = \frac{\cos \mu x}{\cos \mu L} \tag{4.1.17}$$

For a similar situation in a long cylinder with a temperature of T_1 specified on the outside radius r_1

$$\frac{T(r) - T_o + 1/\beta}{T_1 - T_o + 1/\beta} = \frac{J_o(\mu r)}{J_o(\mu r_1)} \tag{4.1.18}$$

In Equation (4.1.18), the J_o is the typical notation for the Bessel function. Variations of this function are tabulated in Abramowitz and Stegun (1964). In both cases the following holds:

$$\mu \equiv \sqrt{\frac{\beta \dot{q}_{G,o}}{k}}$$

Fins

Fins are widely used to enhance the heat transfer (usually convective, but it could also be radiative) from a surface. This is particularly true when the surface is in contact with a gas. Fins are used on air-cooled engines, electronic cooling forms, as well as for a number of other applications. Since the heat transfer coefficient tends to be low in gas convection, area is added in the form of fins to the surface to decrease the convective thermal resistance.

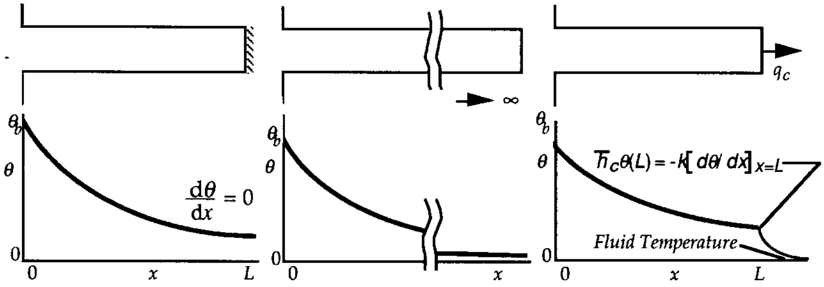

CASE I: Insulated Tip CASE II: Infinitely Long CASE III: Convecting Tip

FIGURE 4.1.2 Three typical cases for one-dimensional, constant-cross-section fins are shown.

The simplest fins to analyze, and which are usually found in practice, can be assumed to be one-dimensional and constant in cross section. In simple terms, to be one-dimensional, the fins have to be long compared with a transverse dimension. Three cases are normally considered for analysis, and these are shown in Figure 4.1.2. They are the insulated tip, the infinitely long fin, and the convecting tip fin.

For Case, I, the solution to the governing equation and the application of the boundary conditions of the known temperature at the base and the insulated tip yields

$$\text{Case I:} \qquad \theta = \theta_b = \frac{\cosh m(L-x)}{\cosh mL} \tag{4.1.19}$$

For the infinitely long case, the following simple form results:

$$\text{Case II:} \qquad \theta(x) = \theta_b e^{-mx} \tag{4.1.20}$$

The final case yields the following result:

$$\text{Case III:} \qquad \theta(x) = \theta_b \frac{mL\cosh m(L-x) + \mathrm{Bi}\sinh m(L-x)}{mL\cosh mL + \mathrm{Bi}\sinh mL} \tag{4.1.21}$$

where

$$\mathrm{Bi} \equiv \bar{h}_c L/k$$

In all three of the cases given, the following definitions apply:

$$\theta \equiv T(x) - T_\infty, \quad \theta_b \equiv T(x=0) - T_\infty, \quad \text{and} \quad m^2 \equiv \frac{\bar{h}_c P}{kA}$$

Here A is the cross section of the fin parallel to the wall; P is the perimeter around that area.

To find the heat removed in any of these cases, the temperature distribution is used in Fourier's law, Equation (4.1.1). For most fins that truly fit the one-dimensional assumption (i.e., long compared with their transverse dimensions), all three equations will yield results that do not differ widely.

Two performance indicators are found in the fin literature. The **fin efficiency** is defined as the ratio of the actual heat transfer to the heat transfer from an ideal fin.

$$\eta \equiv \frac{q_{\text{actual}}}{q_{\text{ideal}}} \tag{4.1.22}$$

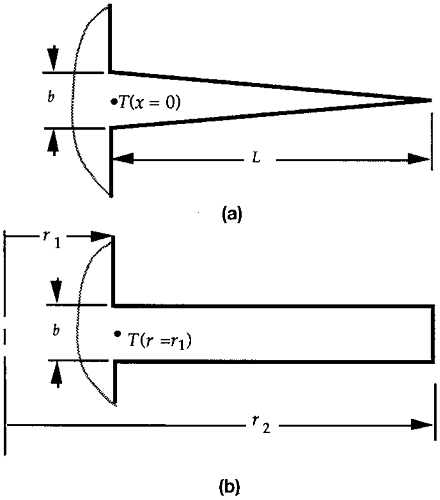

FIGURE 4.1.3 Two examples of fins with a cross-sectional area that varies with distance from the base. (a) Straight triangular fin. (b) Annular fin of constant thickness.

The ideal heat transfer is found from convective gain or loss from an area the same size as the fin surface area, all at a temperature T_b. Fin efficiency is normally used to tabulate heat transfer results for various types of fins, including ones with nonconstant area or which do not meet the one-dimensional assumption. An example of the former can be developed from a result given by Arpaci (1966). Consider a straight fin of triangular profile, as shown in Figure 4.1.3. The solution is found in terms of modified Bessel functions of the first kind. Tabulations are given in Abramowitz and Stegun (1964).

$$\eta = \frac{I_1\left(2\tilde{m}L^{1/2}\right)}{\tilde{m}L^{1/2}I_o\left(2\tilde{m}L^{1/2}\right)} \tag{4.1.23}$$

Here, $\tilde{m} \equiv \sqrt{2\bar{h}_c L/kb}$.

The **fin effectiveness**, ε, is defined as the heat transfer from the fin compared with the bare-surface transfer through the same base area.

$$\varepsilon = \frac{q_{\text{actual}}}{q_{\text{bare base}}} = \frac{q_f}{\bar{h}_c A\left(T_b - T_\infty\right)} \tag{4.1.24}$$

Carslaw and Jaeger (1959) give an expression for the effectiveness of a fin of constant thickness around a tube (see Figure 4.1.3) This is given as $(\tilde{\mu} \equiv \sqrt{2\bar{h}_c/kb})$.

$$\varepsilon = \frac{2}{\tilde{\mu}b}\,\frac{I_1\left(\tilde{\mu}r_2\right)K_1\left(\tilde{\mu}r_1\right) - K_1\left(\tilde{\mu}r_2\right)I_1\left(\tilde{\mu}r_1\right)}{I_o\left(\tilde{\mu}r_1\right)K_1\left(\tilde{\mu}r_2\right) + K_o\left(\tilde{\mu}r_1\right)I_1\left(\tilde{\mu}r_2\right)} \tag{4.1.25}$$

Here the notations I and K denote Bessel functions that are given in Abramowitz and Stegun (1964).

Fin effectiveness can be used as one indication whether or not fins should be added. A rule of thumb indicates that if the effectiveness is less than about three, fins should not be added to the surface.

Transient Systems

Negligible Internal Resistance

Consider the transient cooling or heating of a body with surface area A and volume V. This is taking place by convection through a heat transfer coefficient $\bar{h}_c$ to an ambient temperature of T_∞. Assume the thermal resistance to conduction inside the body is significantly less than the thermal resistance to convection (as represented by Newton's law of cooling) on the surface of the body. This ratio is denoted by the **Biot number**, Bi.

$$\mathrm{Bi} = \frac{R_k}{R_c} = \frac{\bar{h}_c (V/A)}{k} \tag{4.1.26}$$

The temperature (which will be uniform throughout the body at any time for this situation) response with time for this system is given by the following relationship. Note that the shape of the body is not important — only the ratio of its volume to its area matters.

$$\frac{T(t) - T_\infty}{T_o - T_\infty} = e^{-\bar{h}_c A t/\rho V c} \tag{4.1.27}$$

Typically, this will hold for the Biot number being less than (about) 0.1.

Bodies with Significant Internal Resistance

When a body is being heated or cooled transiently in a convective environment, but the internal thermal resistance of the body cannot be neglected, the analysis becomes more complicated. Only simple geometries (a symmetrical plane wall, a long cylinder, a composite of geometric intersections of these geometries, or a sphere) with an imposed step change in ambient temperature are addressed here.

The first geometry considered is a large slab of minor dimension $2L$. If the temperature is initially uniform at T_o, and at time 0+ it begins convecting through a heat transfer coefficient to a fluid at T_∞, the temperature response is given by

$$\theta = 2\sum_{n=1}^{\infty} \left(\frac{\sin \lambda_n L}{\lambda_n L + \sin \lambda_n L \cos \lambda_n L} \right) \exp\left(-\lambda_n^2 L^2 \mathrm{Fo}\right) \cos\left(\lambda_n x\right) \tag{4.1.28}$$

and the λ_n are the roots of the transcendental equation: $\lambda_n L \tan \lambda_n L = \mathrm{Bi}$. The following definitions hold:

$$\mathrm{Bi} \equiv \frac{\bar{h}_c L}{k} \qquad \mathrm{Fo} \equiv \frac{\alpha t}{L^2} \qquad \theta \equiv \frac{T - T_\infty}{T_o - T_\infty}$$

The second geometry considered is a very long cylinder of diameter $2R$. The temperature response for this situation is

$$\theta = 2\mathrm{Bi} \sum_{n=1}^{\infty} \frac{\exp\left(-\lambda_n^2 R^2 \mathrm{Fo}\right) J_o\left(\lambda_n r\right)}{\left(\lambda_n^2 R^2 + \mathrm{Bi}^2\right) J_o\left(\lambda_n R\right)} \tag{4.1.29}$$

Now the λ_n are the roots of $\lambda_n R\, J_1(\lambda_n R) + \mathrm{Bi}\, J_o(\lambda_n R) = 0$, and

$$\mathrm{Bi} = \frac{\bar{h}_c R}{k} \qquad \mathrm{Fo} = \frac{\alpha t}{R^2} \qquad \theta = \frac{T - T_\infty}{T_o - T_\infty}$$

The common definition of Bessel's functions applies here.

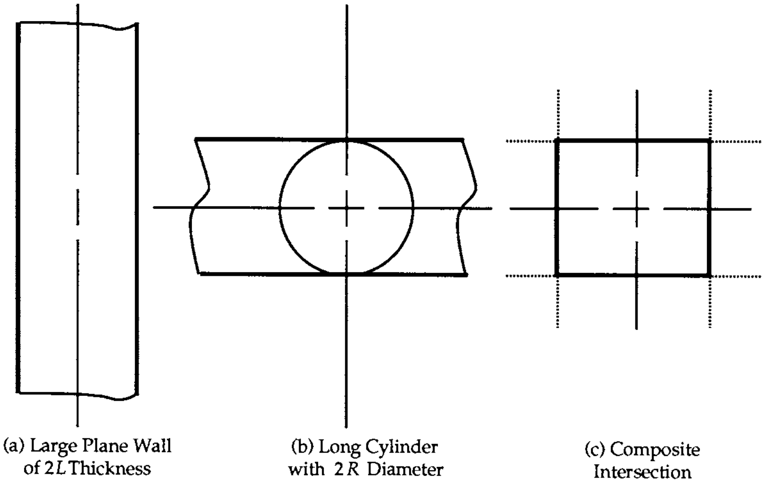

FIGURE 4.1.4 Three types of bodies that can be analyzed with results given in this section. (a) Large plane wall of 2*L* thickness; (b) long cylinder with 2*R* diameter; (c) composite intersection.

For the similar situation involving a solid sphere, the following holds:

$$\theta = 2\sum_{n=1}^{\infty} \frac{\sin(\lambda_n R) - \lambda_n R\cos(\lambda_n R)}{\lambda_n R - \sin(\lambda_n R)\cos(\lambda_n R)} \exp\left(-\lambda_n^2 R^2 \text{Fo}\right) \frac{\sin(\lambda_n r)}{\lambda_n r} \tag{4.1.30}$$

and the λ_n are found as the roots of $\lambda_n R \cos \lambda_n R = (1 - \text{Bi}) \sin \lambda_n R$. Otherwise, the same definitions as were given for the cylinder hold.

Solids that can be envisioned as the geometric intersection of the simple shapes described above can be analyzed with a simple product of the individual-shape solutions. For these cases, the solution is found as the product of the dimensionless temperature functions for each of the simple shapes with appropriate distance variables taken in each solution. This is illustrated as the right-hand diagram in Figure 4.1.4. For example, a very long rod of rectangular cross section can be seen as the intersection of two large plates. A short cylinder represents the intersection of an infinitely long cylinder and a plate. The temperature at any location within the short cylinder is

$$\theta_{2R,2L\text{ Rod}} = \theta_{\text{Infinite }2R\text{ Rod}}\,\theta_{2L\text{ Plate}} \tag{4.1.31}$$

Details of the formulation and solution of the partial differential equations in heat conduction are found in the text by Arpaci (1966).

Finite-Difference Analysis of Conduction

Today, numerical solution of conduction problems is the most-used analysis approach. Two general techniques are applied for this: those based upon finite-difference ideas and those based upon finite-element concepts. General numerical formulations are introduced in other sections of this book. In this section, a special, physical formulation of the finite-difference equations to conduction phenomena is briefly outlined.

Attention is drawn to a one-dimensional slab (very large in two directions compared with the thickness). The slab is divided across the thickness into smaller subslabs, and this is shown in Figure 4.1.5. All subslabs are thickness Δx except for the two boundaries where the thickness is $\Delta x/2$. A characteristic temperature for each slab is assumed to be represented by the temperature at the slab

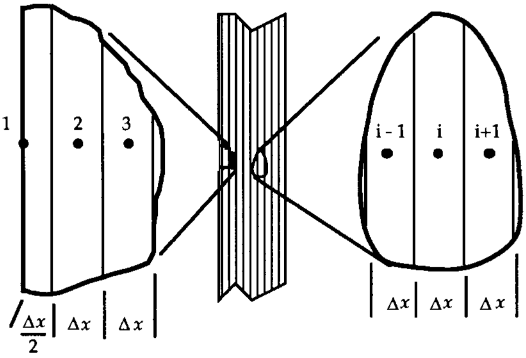

FIGURE 4.1.5 A one-dimensional finite differencing of a slab with a general interior node and one surface node detailed.

center. Of course, this assumption becomes more accurate as the size of the slab becomes smaller. With the two boundary-node centers located exactly on the boundary, a total of n nodes are used ($n - 2$ full nodes and one half node on each of the two boundaries).

In the analysis, a general interior node i (this applies to all nodes 2 through $n - 1$) is considered for an overall energy balance. Conduction from node $i - 1$ and from node $i + 1$ as well as any heat generation present is assumed to be energy per unit time flowing into the node. This is then equated to the time rate of change of energy within the node. A backward difference on the time derivative is applied here, and the notation $T_i' \equiv T_i(t + \Delta t)$ is used. The balance gives the following on a per-unit-area basis:

$$\frac{T_{i-1}' - T_i'}{\Delta x/k_-} + \frac{T_{i+1}' - T_i'}{\Delta x/k_+} + \dot{q}_{G,i}\Delta x = \rho \Delta x c_p \frac{T_i' - T_i}{\Delta t} \tag{4.1.32}$$

In this equation different thermal conductivities have been used to allow for possible variations in properties throughout the solid.

The analysis of the boundary nodes will depend upon the nature of the conditions there. For the purposes of illustration, convection will be assumed to be occurring off of the boundary at node 1. A balance similar to Equation (4.1.32) but now for node 1 gives the following:

$$\frac{T_\infty' - T_1'}{1/\bar{h}_c} + \frac{T_2' - T_1'}{\Delta x/k_+} + \dot{q}_{G,1}\frac{\Delta x}{2} = \rho \frac{\Delta x}{2} c_p \frac{T_1' - T_1}{\Delta t} \tag{4.1.33}$$

After all n equations are written, it can be seen that there are n unknowns represented in these equations: the temperature at all nodes. If one or both of the boundary conditions are in terms of a specified temperature, this will decrease the number of equations and unknowns by one or two, respectively. To determine the temperature as a function of time, the time step is arbitrarily set, and all the temperatures are found by simultaneous solution at $t = 0 + \Delta t$. The time is then advanced by Δt and the temperatures are then found again by simultaneous solution.

The finite difference approach just outlined using the backward difference for the time derivative is termed the *implicit* technique, and it results in an $n \times n$ system of linear simultaneous equations. If the forward difference is used for the time derivative, then only one unknown will exist in each equation. This gives rise to what is called an *explicit* or "marching" solution. While this type of system is more straightforward to solve because it deals with only one equation at a time with one unknown, a *stability criterion* must be considered which limits the time step relative to the distance step.

Two- and three-dimensional problems are handled in conceptually the same manner. One-dimensional heat fluxes between adjoining nodes are again considered. Now there are contributions from each of the dimensions represented. Details are outlined in the book by Jaluria and Torrance (2003).

Defining Terms

Biot number: Ratio of the internal (conductive) resistance to the external (convective) resistance from a solid exchanging heat with a fluid.

Fin: Additions of material to a surface to increase area and thus decrease the external thermal resistance from convecting and/or radiating solids.

Fin effectiveness: Ratio of the actual heat transfer from a fin to the heat transfer from the same cross-sectional area of the wall without the fin.

Fin efficiency: Ratio of the actual heat transfer from a fin to the heat transfer from a fin with the same geometry but completely at the base temperature.

Fourier's law: The fundamental law of heat conduction. Relates the local temperature gradient to the local heat flux, both in the same direction.

Heat conduction equation: A partial differential equation in temperature, spatial variables, time, and properties that, when solved with appropriate boundary and initial conditions, describes the variation of temperature in a conducting medium.

Overall heat transfer coefficient: The analogous quantity to the heat transfer coefficient found in convection (Newton's law of cooling) that represents the overall combination of several thermal resistances, both conductive and convective.

Thermal conductivity: The property of a material that relates a temperature gradient to a heat flux. Dependent upon temperature.

References

Abramowitz, M. and Stegun, I. 1964. *Handbook of Mathematical Functions with Formulas, Graphs, and Mathematical Tables*. National Bureau of Standards, Applied Mathematics Series 55, U.S. Government Printing Office, Washington, D.C.

Arpaci, V. 1966. *Conduction Heat Transfer*, Addison-Wesley, Reading, MA.

Carslaw, H.S. and Jaeger, J.C. 1996. *Conduction of Heat in Solids*, 2nd ed., Oxford University Press, London.

Guyer, E., Ed. 1999. Part 3, Thermal insulations, in *Handbook of Applied Thermal Design*, Taylor & Francis, New York.

Jaluria, Y. and Torrance, K. 2003. *Computational Heat Transfer*, 2nd ed., Taylor & Francis, New York.

Sparrow, E. 1970. Reexamination and correction of the critical radius for radial heat conduction, *AIChE J.* 16, 1, 149.

Further Information

The references listed above will give the reader an excellent introduction to analytical formulation and solution (Arpaci), material properties (Guyer), and numerical formulation and solution (Jaluria and Torrance). There are also several convenient heat transfer textbooks and books that provide further information about conduction heat transfer:

Bejan, A. and Kraus, A. 2003. *Heat Transfer Handbook*, Interscience, New York.

Incropera, F.P. and DeWitt, D.P. 2001. *Fundamentals of Heat and Mass Transfer*, 5th ed., John Wiley & Sons.

Jiji, L.M. 2003. *Heat Conduction*, 2nd ed., The City College of the City University of New York, New York.

Kreith, F. and Bohn, M.S. 2000. *Principles of Heat Transfer*, 6th ed., Brooks Cole.

A reference for fundamentals of numerical methods with programming code:

Chapra, S.C. and Canale, R.P. 2001. *Numerical Methods for Engineers: With Software and Programming Application*, 4th ed., McGraw-Hill.

For applications of conduction heat transfer see:

Kreith, F. (Ed.) 1999. *CRC Handbook of Thermal Engineering*, CRC Press, Boca Raton, FL.

Numerous sources for programming codes are available on the World Wide Web, most of which are free, and can be found by using a search engine such as www.google.com.

Matrix Solvers for C++: www.vector-space.com/free.htm
Fortran and MatLab codes: www.unige.ch/math/folks/hairer/software.html

Current developments in conduction heat transfer appear in several publications, including:

Journal of Heat Transfer, International Journal of Heat and Mass Transfer, International Journal for Computer-Aided Engineering and Software, and *Numerical Heat Transfer.*

4.2 Convection Heat Transfer

Natural Convection

George D. Raithby and K.G. Terry Hollands

Introduction

Natural convection heat transfer occurs when the convective fluid motion is induced by density differences that are themselves caused by the heating. An example is shown in Figure 4.2.1(A), where a body at surface temperature T_s transfers heat at a rate q to ambient fluid at temperature $T_\infty < T_s$.

In this section, correlations for the average Nusselt number are provided from which the heat transfer rate q from surface area A_s can be estimated. The Nusselt number is defined as

$$\mathrm{Nu} = \frac{\bar{h}_c L}{k} = \frac{qL}{A_s \Delta T k} \tag{4.2.1}$$

where $\Delta T = T_s - T_\infty$ is the temperature difference driving the heat transfer. A dimensional analysis leads to the following functional relation:

$$\mathrm{Nu} = f(\mathrm{Ra},\ \mathrm{Pr},\ \text{geometric shape, boundary conditions}) \tag{4.2.2}$$

For given thermal boundary conditions (e.g., isothermal wall and uniform T_∞), and for a given geometry (e.g., a cube), Equation (4.2.2) states that Nu depends only on the Rayleigh number, Ra, and Prandtl number, Pr. The length scales that appear in Nu and Ra are defined, for each geometry considered, in a separate figure. The fluid properties are generally evaluated at T_f, the average of the wall and ambient

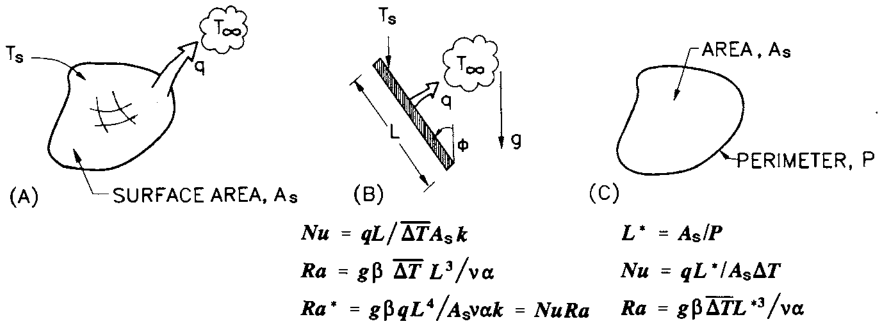

FIGURE 4.2.1 (A) Nomenclature for external heat transfer. (A) General sketch; (B) is for a tilted flat plate, and (C) defines the length scale for horizontal surfaces.

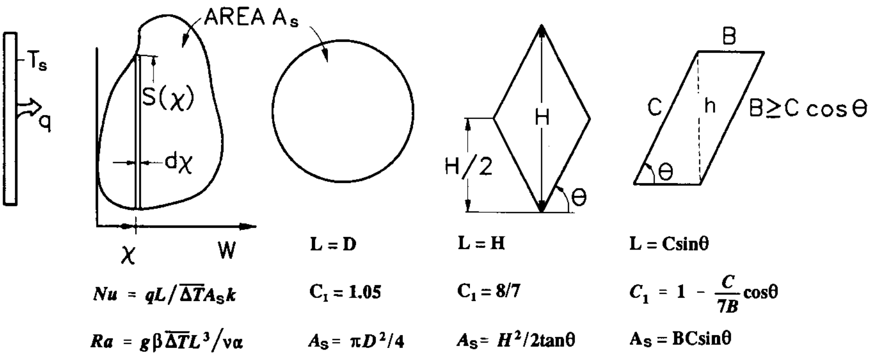

FIGURE 4.2.2 Nomenclature for heat transfer from planar surfaces of different shapes.

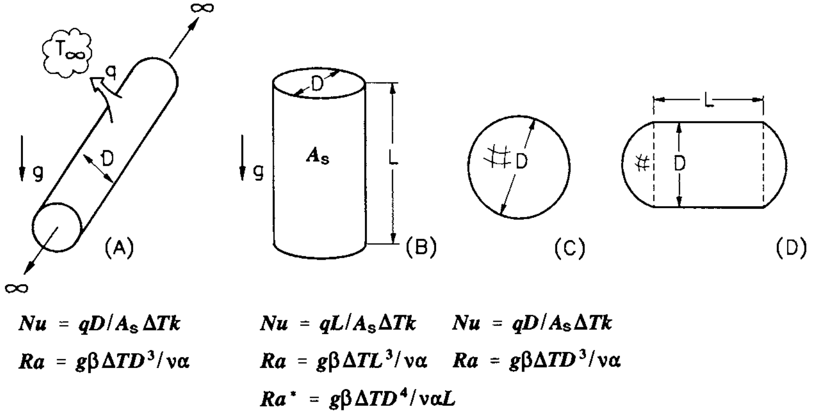

FIGURE 4.2.3 Definitions for computing heat transfer from a long horizontal circular cylinder (A), from the lateral surface of a vertical circular cylinder (B), from a sphere (C), and from a compound body (D).

temperatures. The exception is that β, the temperature coefficient of volume expansion, is evaluated at T_∞ for external natural convection(Figure 4.2.1 to Figure 4.2.3) in a *gaseous* medium.

The functional dependence on Pr is approximately independent of the geometry, and the following Pr-dependent function will be useful for laminar heat transfer (Churchill and Usagi, 1972):

$$\overline{C}_\ell = 0.671\Big/\left(1+(0.492/\mathrm{Pr})^{9/16}\right)^{4/9} \tag{4.2.3}$$

C_t^V and C_t^H are functions that will be useful for turbulent heat transfer:

$$C_t^V = 0.13\mathrm{Pr}^{0.22}\Big/\left(1+0.61\mathrm{Pr}^{0.81}\right)^{0.42} \tag{4.2.4}$$

$$C_t^H = 0.14\left(\frac{1+0.0107\mathrm{Pr}}{1+0.01\mathrm{Pr}}\right) \tag{4.2.5}$$

The superscripts *V* and *H* refer to the vertical and horizontal surface orientation.

The Nusselt numbers for fully laminar and fully turbulent heat transfer are denoted by Nu_ℓ and Nu_t, respectively. Once obtained, these are blended (Churchill and Usagi, 1972) as follows to obtain the equation for Nu:

$$\mathrm{Nu} = \left(\left(\mathrm{Nu}_\ell \right)^m + \left(\mathrm{Nu}_t \right)^m \right)^{1/m} \tag{4.2.6}$$

The blending parameter m depends on the body shape and orientation.

The equation for Nu_ℓ in this section is usually expressed in terms of Nu^T, the Nusselt number that would be valid if the thermal boundary layer were thin. The difference between Nu_ℓ and Nu^T accounts for the effect of the large boundary layer thicknesses encountered in natural convection.

It is assumed that the wall temperature of a body exceeds the ambient fluid temperature ($T_s > T_\infty$). For $T_s < T_\infty$ the same correlations apply with ($T_\infty - T_s$) replacing ($T_s - T_\infty$) for a geometry that is rotated 180° relative to the gravitational vector; for example, the correlations for a horizontal heated upward-facing flat plate applies to a cooled downward-facing flat plate of the same planform.

Correlations for External Natural Convection

This section deals with problems where the body shapes in Figure 4.2.1 to Figure 4.2.3 are heated while immersed in a quiescent fluid. Different *cases* are enumerated below.

1. *Isothermal Vertical (ϕ = 0) Flat Plate, Figure 4.2.1B.* For heat transfer from a vertical plate (Figure 4.2.1B), for $1 < \mathrm{Ra} < 10^{12}$,

$$\mathrm{Nu}^T = \overline{C}_\ell \mathrm{Ra}^{1/4} \qquad \mathrm{Nu}_\ell = \frac{2.0}{\ln\left(1 + 2.0/\mathrm{Nu}^T\right)} \tag{4.2.7}$$

$$\mathrm{Nu}_t = C_t^V \mathrm{Ra}^{1/3} \Big/ \left(1 + 1.4 \times 10^9 \,\mathrm{Pr}/\mathrm{Ra}\right)$$

$\overline{C}_\ell$ and C_t^V are given by Equation (4.2.3) and Equation (4.2.4). Nu is obtained by substituting Equation (4.2.7) expressions for Nu_ℓ and Nu_t into Equation (4.2.6) with $m = 6$.

2. *Vertical Flat Plate with Uniform Heat Flux, Figure 4.2.1B.* If the plate surface has a constant (known) heat flux, rather than being isothermal, the objective is to calculate the average temperature difference, $\overline{\Delta T}$, between the plate and fluid. For this situation, and for $15 < \mathrm{Ra}^* < 10^5$,

$$\mathrm{Nu}^T = \overline{G}_\ell \left(\mathrm{Ra}^*\right)^{1/5} \qquad \mathrm{Nu}_\ell = \frac{1.83}{\ln\left(1 + 1.83/\mathrm{Nu}^T\right)} \qquad \mathrm{Nu}_t = \left(C_t^V\right)^{3/4} \left(\mathrm{Ra}^*\right)^{1/4} \tag{4.2.8a}$$

$$\overline{G}_\ell = \frac{6}{5}\left(\frac{\mathrm{Pr}}{4 + 9\sqrt{\mathrm{Pr}} + 10\mathrm{Pr}} \right)^{1/5} \tag{4.2.8b}$$

Ra^* is defined in Figure 4.2.1B and C_t^V is given by Equation (4.2.4). Find Nu by inserting these expressions for Nu_ℓ and Nu_t into Equation (4.2.6) with $m = 6$. The $\overline{G}_\ell$ expression is due to Fujii and Fujii (1976).

3. *Horizontal Upward-Facing (ϕ = 90°) Plates, Figure 4.2.1C.* For horizontal isothermal surfaces of various platforms, correlations are given in terms of a lengthscale L^* (Goldstein et al., 1973), defined in Figure 4.2.1C. For $\mathrm{Ra} \geq 1$,

$$\mathrm{Nu}^T = 0.835\overline{C}_\ell \mathrm{Ra}^{1/4} \qquad \mathrm{Nu}_\ell = \frac{1.4}{\ln\left(1 + 1.4/\mathrm{Nu}^T\right)} \qquad \mathrm{Nu}_t = C_t^H \mathrm{Ra}^{1/3} \tag{4.2.9}$$

Nu is obtained by substituting Nu_ℓ and Nu_t from Equation 4.2.9 into Equation 4.2.6 with $m = 10$. For non-isothermal surfaces, replace ΔT by $\overline{\Delta T}$.

4. *Horizontal Downward-Facing ($\phi = -90°$) Plates, Figure 4.2.1C*. For horizontal downward-facing plates of various planforms, the main buoyancy force is into the plate so that only a very weak force drives the fluid along the plate; for this reason, only laminar flows have been measured. For this case, the following equation applies for Ra < 10^{10}, Pr ≥ 0.7:

$$\mathrm{Nu}^T = H_\ell \mathrm{Ra}^{1/5} \qquad \mathrm{H}_\ell = \frac{0.527}{\left[1+(1.9/\mathrm{Pr})^{9/10}\right]^{2/9}} \qquad \mathrm{Nu} = \frac{2.45}{\ln\left(1+2.45/\mathrm{Nu}^T\right)} \tag{4.2.10}$$

   H_ℓ fits the analysis of Fujii et al. (1973).

5. *Inclined Plates, Downward Facing ($-90° \le \phi \le 0$), Figure 4.2.1B*. First calculate q from *Case 1* with g replaced by $g \cos \phi$; then calculate q from *Case 4* (horizontal plate) with g replaced by $g \sin(-\phi)$, and use the maximum of these two values of q.
6. *Inclined Plates, Upward Facing ($0 \le \phi \le 90$), Figure 4.2.1B*. First calculate q from *Case 1* with g replaced by $g \cos \phi$; then calculate q from *Case 3* with g replaced by $g \sin \phi$, and use the maximum of these two values of q.
7. *Vertical and Tilted Isothermal Plates of Various Planform, Figure 4.2.2.* The line of constant χ in Figure 4.2.2 is the line of steepest ascent on the plate. Provided all such lines intersect the plate edges just twice, as shown in the figure, the thin-layer (Nu^T) heat transfer can be found by subdividing the body into strips of width $\Delta\chi$, calculating the heat transfer from each strip, and adding. For laminar flow from an isothermal vertical plate, this results in

$$\mathrm{Nu}^T = C_1 \bar{C}_\ell \mathrm{Ra}^{1/4} \qquad C_1 \equiv \left(\frac{L^{1/4}}{A}\int_0^W S^{3/4}\, d\chi\right) \tag{4.2.11}$$

   Symbols are defined in Figure 4.2.2, along with L and calculated C_1 values for some plate shapes. If the plate is vertical, follow the procedure in *Case 1* above (isothermal vertical flat plate) except replace the expression for Nu^T in Equation (4.2.7) by Equation (4.2.11). If the plate is tilted, follow the procedure described in *Case 5* or *6* (as appropriate) but again use Equation (4.2.11) for Nu^T in Equation (4.2.7)
8. *Horizontal Cylinders, Figure 4.2.3A*. For a long, horizontal circular cylinder use the following expressions for Nu_ℓ and Nu_t:

$$\mathrm{Nu}^T = 0.772 \bar{C}_\ell \mathrm{Ra}^{1/4} \qquad \mathrm{Nu}_\ell = \frac{2f}{\left(1+2f/\mathrm{Nu}^T\right)} \qquad \mathrm{Nu}_t = \bar{C}_t \mathrm{Ra}^{1/3} \tag{4.2.12}$$

   $\bar{C}_t$ is given in the table below. For Ra > 10^{-2}, $f = 0.8$ can be used, but for 10^{-10} < Ra < 10^{-2} use $f = 1 - 0.13/(\mathrm{Nu}^T)^{0.16}$. To find Nu, the values of Nu_ℓ and Nu_t from Equation (4.2.12) are substituted into Equation (4.2.6) with $m = 15$ (Clemes et al., 1994).

   $\bar{C}_t$ for Various Shapes and Prandtl Numbers

Pr→	0.01	0.022	0.10	0.71	2.0	6.0	50	100	2000
Horizontal cylinder	0.077	0.81	0.90	0.103	0.108	0.109	0.100	0.097	0.088
Spheres	0.074	0.078	0.088	0.104	0.110	0.111	0.101	0.097	0.086

9. *Vertical Cylinders ($\phi = 90°$), Figure 4.2.3B*. For high Ra values and large diameter, the heat transfer from a vertical cylinder approaches that for a vertical flat plate. Let the Nu^T and Nu_ℓ equations for a vertical flat plate of height L, Equation (4.2.7), be rewritten here as Nu_p^T and Nu_p, respectively.

At smaller Ra and diameter, transverse curvature plays a role which is accounted for in the following equations:

$$\mathrm{Nu}_{\ell} = \frac{0.9\xi \mathrm{Nu}_p}{\ln(1+0.9\xi)} \qquad \xi = \frac{2L/D}{Nu_p^T} \tag{4.2.13}$$

These equations are valid for purely laminar flow. To obtain Nu, blend Equation (4.2.13) for Nu_ℓ with Equation (4.2.7) for Nu_t using Equation (4.2.6) with $m = 10$.

10. *Spheres, Figure 4.2.3C.* For spheres use Equation (4.2.6), with $m = 6$, and with

$$\mathrm{Nu}_{\ell} = 2 + 0.878\overline{C}_{\ell}\mathrm{Ra}^{1/4} \quad \text{and} \quad \mathrm{Nu}_t = \overline{C}_t\mathrm{Ra}^{1/3} \tag{4.2.14}$$

The table above contains $\overline{C}_t$ values.

11. *Combined Shapes, Figure 4.2.3D.* For combined shapes, such as the cylinder in Figure 4.2.3D with spherical end caps, calculate the heat transfer from the cylinder of length L (*Case 8*), the heat transfer from a sphere of diameter D (*Case 10*) and add to obtain the total transfer. Other shapes can be treated in a similar manner.

Correlations for Open Cavities

Examples of this class of problem are shown in Figure 4.2.4. Walls partially enclose a fluid region (cavity) where boundary openings permit fluid to enter and leave. Upstream from its point of entry, the fluid is at the ambient temperature, T_∞. Since access of the ambient fluid to the heated surfaces is restricted, some of the heated surface is starved of cool ambient to which heat can be transferred. As the sizes of the boundary openings are increased, the previous class of problems is approached; for example, when the plate spacing in Figure 4.2.4A (*Case 12*) becomes very large, the heat transfer from each vertical surface is given by *Case 1*.

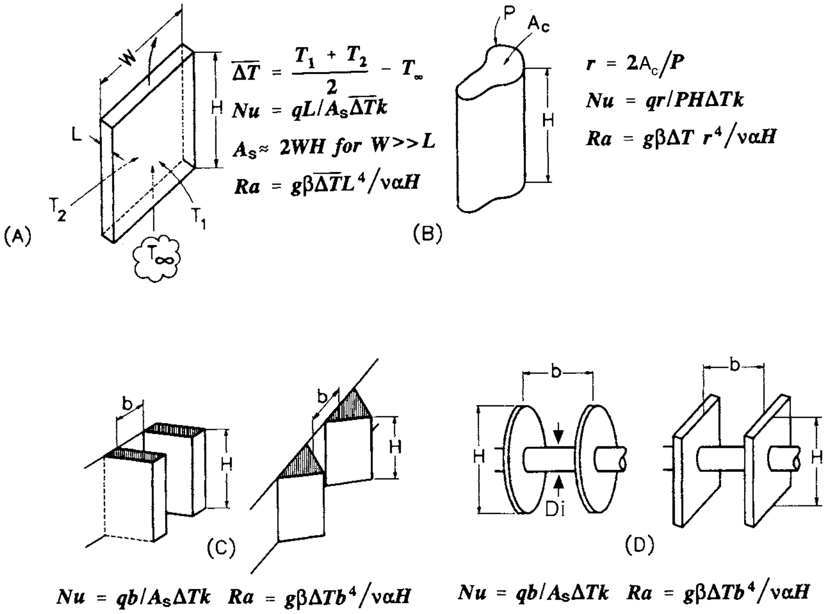

FIGURE 4.2.4 Nomenclature for various open-cavity problems.

12. *Isothermal Vertical Channels, Figure 4.2.4A and B.* Figure 4.2.4A shows an open cavity bounded by vertical walls and open at the top and bottom. The large opposing plates are isothermal, at temperatures T_1 and T_2, respectively, and the spacing between these plates is small. $\overline{\Delta T}$ is the average temperature difference between the plates and T_∞, as shown in Figure 4.2.4A, but T_1 and T_2 must not straddle T_∞. For this case

$$\mathrm{Nu} = \left(\left(\frac{\mathrm{Ra}}{f\mathrm{Re}} \right)^m + \left(C_1 \bar{C}_\ell \mathrm{Ra}^{1/4} \right)^m \right)^{1/m} \qquad \mathrm{Ra} \le 10^5 \tag{4.2.15}$$

where fRe is the product of friction factor and Reynolds number for fully developed channel flow, and C_1 is a constant that accounts for the augmentation of heat transfer, relative to a vertical flat plate (*Case 1*), due to the chimney effect. The fRe factor accounts for the cross-sectional shape (Elenbaas, 1942a). Symbols are defined in Figure 4.2.4A and B; in the Nu equation, q is the total heat transferred to the ambient fluid from all heated surfaces.

For the parallel plate channel shown in Figure 4.2.4(A), use $f\mathrm{Re} = 24$, $m = -1.9$, and for gases $C_1 \approx 1.2$. It should be noted, however, that C_1 must approach 1.0 as Pr increases or as the plate spacing increases. For channels of circular cross section (Figure 4.2.4B) $f\mathrm{Re} = 16$, $m = -1.03$, and for gases $C_1 \approx 1.17$. For other cross-sectional shapes like the square ($f\mathrm{Re} = 14.23$), hexagonal ($f\mathrm{Re} = 15.05$), or equilateral triangle ($f\mathrm{Re} = 13.3$), use Equation (4.2.15) with the appropriate fRe, and with $m = -1.5$, and $C_1 \approx 1.2$ for gases.

The heat transfer per unit cross-sectional area, q/A_c, for a given channel length H and temperature difference, passes through a maximum at approximately $\mathrm{Ra}_{\max}$, where

$$\mathrm{Ra}_{\max} = \left(\frac{f\mathrm{Re}\, C_1 \bar{C}_\ell}{2^{1/m}} \right)^{4/3} \tag{4.2.16}$$

$\mathrm{Ra}_{\max}$ provides the value of hydraulic radius $r = 2A_c/P$ at this maximum.

13. *Isothermal Triangular Fins, Figure 4.2.4C.* For a large array of triangular fins (Karagiozis et al., 1994) in air, for $0.4 < \mathrm{Ra} < 5 \times 10^5$

$$\mathrm{Nu} = \bar{C}_\ell \mathrm{Ra}^{1/4} \left[1 + \left(\frac{3.26}{\mathrm{Ra}^{0.21}} \right)^3 \right]^{-1/3} \qquad 0.4 < \mathrm{Ra} < 5 \times 10^6 \tag{4.2.17}$$

In this equation, b is the average fin spacing (Figure 4.2.4C), defined such that bL is the cross-sectional flow area between two adjacent fin surfaces up to the plane of the fin tips. For $\mathrm{Ra} < 0.4$, Equation (4.2.17) underestimates the convective heat transfer. When such fins are mounted horizontally (vertical baseplate, but the fin tips are horizontal), there is a substantial reduction of the convective heat transfer (Karagiozis et al., 1994).

14. *U-Channel Fins, Figure 4.2.4C.* For the fins most often used as heat sinks, there is uncertainty about the heat transfer at low Ra. By using a conservative approximation applying for $\mathrm{Ra} < 100$ (that underestimates the real heat transfer), the following equation may be used:

$$\mathrm{Nu} = \left[\left(\frac{\mathrm{Ra}}{24} \right)^{-2} + \left(C_1 \bar{C}_\ell \mathrm{Ra} \right)^{-2} \right]^{-0.5} \tag{4.2.18}$$

For air C_1 depends on aspect ratio of the fin as follows (Karagiozis, 1991):

$$C_1 = \left[1 + \left(\frac{H}{b}\right), 1.16\right]_{\min} \tag{4.2.19}$$

Equation (4.2.18) agrees well with measurements for Ra > 200, but for smaller Ra it falls well below data because the leading term does not account for heat transfer from the fin edges and for three-dimensional conduction from the entire array.

15. *Circular Fins on a Horizontal Tube, Figure 4.24D.* For heat transfer from an array of circular fins (Edwards and Chaddock, 1963), for $H/D_i = 1.94$, $5 < \text{Ra} < 10^4$, and for air,

$$\text{Nu} = 0.125\text{Ra}^{0.55}\left[1 - \exp\left(-\frac{137}{\text{Ra}}\right)\right]^{0.294} \tag{4.2.20}$$

A more general, but also more complex, relation is reported by Raithby and Hollands (1998).

16. *Square Fins on a Horizontal Tube, Figure 4.2.4D.* Heat transfer (Elenbaas, 1942b) from the square fins (excluding the cylinder that connects them) is correlated for gases by

$$\text{Nu} = \left[\left(\text{Ra}^{0.89}/18\right)^m + \left(0.62\text{Ra}^{1/4}\right)^m\right]^{1/m} \qquad m = -2.7 \tag{4.2.21}$$

Heat Transfer in Enclosures

This section deals with cavities where the bounding walls are entirely closed, so that no mass can enter or leave the cavity. The fluid motion inside the cavity is driven by natural convection, which enhances the heat transfer among the interior surfaces that bound the cavity.

17. *Extensive Horizontal Layers, Figure 4.2.5A.* If the heated plate, in a horizontal parallel-plate cavity, is on the top (θ = 180°), heat transfer is by conduction alone, so that Nu = 1. For heat transfer from below, θ = 0° (Hollands, 1984):

$$\text{Nu} = 1 + \left[1 - \frac{1708}{\text{Ra}}\right]^{\bullet}\left[k_1 + 2\left(\frac{\text{Ra}^{1/3}}{k_2}\right)^{1-\ln\left(\text{Ra}^{1/3}/k_2\right)}\right] + \left[\left(\frac{\text{Ra}}{5830}\right)^{1/3} - 1\right]^{\bullet} \tag{4.2.22}$$

where

$$[x]^{\bullet} = (x,0)_{\max} \qquad k_1 = \frac{1.44}{1 + 0.018/\text{Pr} + 0.00136/\text{Pr}^2} \qquad k_2 = 75\exp\left(1.5\text{Pr}^{-1/2}\right) \tag{4.2.23}$$

The equation has been validated for $\text{Ra} < 10^{11}$ for water, $\text{Ra} < 10^8$ for air, and over a smaller Ra range for other fluids. Equation (4.2.22) applies to extensive layers: $W/L \geq 5$. Correlations for nonextensive layers are provided by Raithby and Hollands (1998).

18. *Vertical Layers, Figure 4.2.5(A), with $\theta = 90°$.* W/L > *5*. For a vertical, gas-filled (Pr ≈ 0.7) cavity with $H/L \geq 5$, the following equation closely fits the data, for example that of Shewen et al. (1996) for $\text{Ra}(H/L)^3 \leq 5 \times 10^{10}$ and $H/L \geq 40$.

$$\text{Nu}_1 = \left[1 + \left(\frac{0.0665\text{Ra}^{1/3}}{1 + \left(\frac{9000}{\text{Ra}}\right)^{1.4}}\right)^2\right]^{1/2} \qquad \text{Nu}_2 = 0.242\left(\text{Ra}\frac{L}{H}\right)^{0.273} \qquad \text{Nu} = \left[\text{Nu}_1, \text{Nu}_2\right]_{\max} \tag{4.2.24}$$

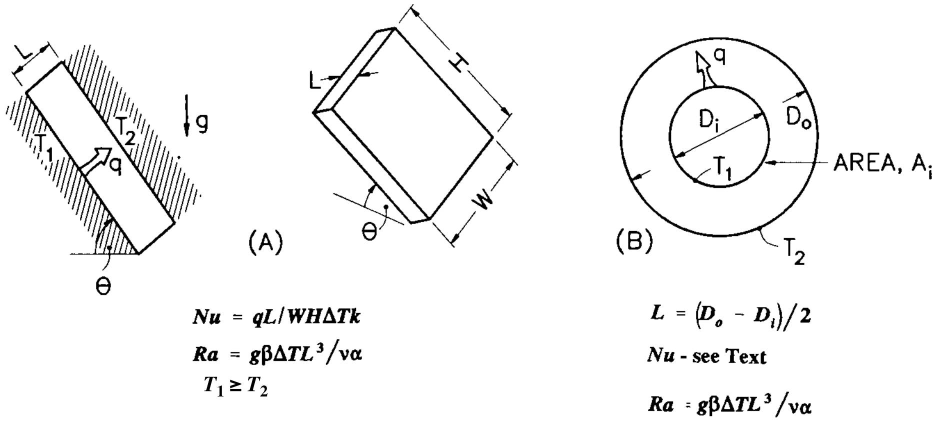

FIGURE 4.2.5 Nomenclature for enclosure problems.

For Pr ≥ 4, the following equation is recommended (Seki et al., 1978) for $\mathrm{Ra}(H/L)^3 < 4 \times 10^{12}$

$$\mathrm{Nu} = \left[1, 0.36\mathrm{Pr}^{0.051}\left(\frac{L}{H}\right)^{0.36}\mathrm{Ra}^{0.25}, 0.084\mathrm{Pr}^{0.051}\left(\frac{L}{H}\right)^{0.1}\mathrm{Ra}^{0.3}\right]_{\max} \tag{4.2.25a}$$

and for $\mathrm{Ra}\,(H/L)^3 > 4 \times 10^{12}$

$$\mathrm{Nu} = 0.039\mathrm{Ra}^{1/3} \tag{4.2.25b}$$

19. *Tilted Layers, Figure 4.25A, with 0 ≤ θ ≤ 90°,* W/L *> 8.* For gases (Pr ≈ 0.7), 0 ≤ θ ≤ 60° and $\mathrm{Ra} \le 10^5$ (Hollands et al., 1976), use

$$\mathrm{Nu} = 1 + 1.44\left[1 - \frac{1708}{\mathrm{Ra}\cos\theta}\right]^{\bullet}\left[1 - \frac{1708(\sin 1.8\theta)^{1.6}}{\mathrm{Ra}\cos\theta}\right] + \left[\left(\frac{\mathrm{Ra}\cos\theta}{5830}\right)^{1/3} - 1\right]^{\bullet} \tag{4.2.26}$$

See equation (4.2.23) for definition of $[x]^{\bullet}$. For 60° ≤ θ ≤ 90° linear interpolation is recommended using Equation (4.2.24) for θ = 90° and Equation (4.2.26) for θ = 60°.

20. *Concentric Cylinders, Figure 4.2.5B.* For heat transfer across the gap between horizontal concentric cylinders, the Nusselt number is defined as $\mathrm{Nu} = q' \ln(D_o/D_i)/2\pi k \Delta T$ where q' is the heat transfer per unit length of cylinder. For $\mathrm{Ra} \le 8 \times 10^7$, $0.7 \le \mathrm{Pr} \le 6000$, $1.15 \le D/D_i \le 8$ (Raithby and Hollands, 1975)

$$\mathrm{Nu} = \left[0.603\bar{C}_\ell \frac{\ln(D_o/D_i)\mathrm{Ra}^{1/4}}{\left[(L/D_i)^{3/5} + (L/D_o)^{3/5}\right]^{5/4}}, 1\right]_{\max} \tag{4.2.27}$$

For eccentric cylinders, see Raithby and Hollands (1998).

21. *Concentric Spheres, Figure 4.2.5B.* The heat transfer between concentric spheres is given by the following equation (Raithby and Hollands, 1975) for $\mathrm{Ra} \le 6 \times 10^8$, $5 \le \mathrm{Pr} \le 4000$, $1.25 < D_o/D_i \le 2.5$,

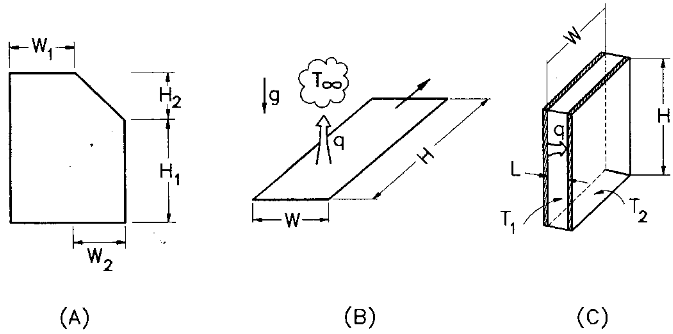

FIGURE 4.2.6 Sketches for example problems.

$$\mathrm{Nu} = \frac{qL}{\pi D_i D_o k \Delta T} = \left[1.16\bar{C}_\ell \left(\frac{L}{D_i}\right)^{1/4} \frac{\mathrm{Ra}^{1/4}}{\left[\left(D_i/D_o\right)^{3/5} + \left(D_o/D_i\right)^{4/5}\right]^{5/4}}, 1 \right]_{\max} \tag{4.2.28}$$

For eccentric spheres, see Raithby and Hollands (1985).

Example Calculations

Problem 1. Heat Transfer from Vertical Plate, Figure 4.2.6A. For the vertical isothermal surface in Figure 4.2.6A with $T_s = 40°\text{C}$, $H_1 = 1$ m, $H_2 = 1$ m, $W_1 = 1$ m, $W_2 = 1$ m and for an ambient air temperature of $T_\infty = 20°\text{C}$ (at 1 atm), find the heat transfer from one side of the plate.

Properties. At $T_f = (T_w + T_\infty)/2 = 30°\text{C}$ and atmospheric pressure for air: $\nu = 1.59 \times 10^{-5}$ m²/sec, $\alpha = 2.25\times10^{-5}$ m²/sec, Pr = 0.71, k = 0.0263 W/mK. At T_∞, $\beta \approx 1/T_\infty = 1/(273 + 20) = 0.00341\ \text{K}^{-1}$.

Solution. For the geometry shown in Figure 4.2.6A and using Equation (4.2.11):

$$A_s = \left(H_1 + H_2\right)W_1 + \left(H_1 + \frac{H_2}{2}\right)W_2 = 3.5\ \text{m}^2 \quad \text{(plate surface area)}$$

$$\int_0^{W_1+W_2} S^{3/4}\, d\chi = \left(H_1 + H_2\right)^{3/4} W_1 + \frac{4}{7}\frac{W_2}{H_2}\left[\left(H_1 + H_2\right)^{7/4} - H_1^{7/4}\right] = 3.03\ \text{m}^{7/4}$$

$$\mathrm{L}^{1/4} = \left(H_1 + H_2\right)^{1/4} = 1.19\ \text{m}^{1/4} \quad \text{(see comments below)}$$

$$C_1 = \frac{\mathrm{L}^{1/4}\displaystyle\int_0^{W_1+W_2} S^{3/4}\, d\chi}{A_s} = \frac{1.19\times3.03}{3.5} = 1.03$$

$$\mathrm{Ra} = \frac{g\beta_\infty L^3\left(T_w - T_\infty\right)}{\nu\alpha} = \frac{9.81\times0.00341\times2^3\times(40-20)}{1.59\times10^{-5}\times2.25\times10^{-5}} = 1.50\times10^{10}$$

$\bar{C}_\ell = 0.514$ from Equation (4.2.3); $C_t = C_t^V = 0.103$ from Equation (4.2.4). $\mathrm{Nu}^T = C_1\,\bar{C}_\ell\,\mathrm{Ra}^{1/4} = 185$ from Equation (4.2.11).

$$\left.\begin{aligned}\mathrm{Nu}_\ell &= \frac{2.0}{\ln\left(1+2.0/\mathrm{Nu}^T\right)} = 186\\ \mathrm{Nu}_t &= C_t^V \mathrm{Ra}^{1/3}\Big/\left(1+1.4\times10^9\,\mathrm{Pr/Ra}\right) = 238\end{aligned}\right\}\text{(from Equation (4.2.7))}$$

$$\mathrm{Nu} = \frac{qL}{A\Delta Tk} = \left(\mathrm{Nu}_\ell^6 + \mathrm{Nu}_t^6\right)^{1/6} = 246$$

from Equation (4.2.6) with $m = 6$.

$$q = \frac{A_s \Delta Tk\mathrm{Nu}}{\mathrm{L}} = \frac{3.5\times20\times0.0263\times246}{2} = 226W$$

Comments on Problem 1: Results are independent of the length scale L. Since $\mathrm{Nu}_\ell < \mathrm{Nu}_t$, the heat transfer is primarily turbulent. Do not neglect radiation. Had the surface been specified to be at constant heat flux, rather than isothermal, the equations in this section can be used to find the approximate average temperature difference between the plate and fluid.

Problem 2. Heat Transfer from Horizontal Strip, Figure 4.2.6B. Find the rate of heat loss per unit length from a very long strip (H → ∞) of width W = 0.1 m with a surface temperature of $T_s = 70°\mathrm{C}$ in water at $T_\infty = 30°\mathrm{C}$.

Properties. At $T_f = (T_s + T_\infty)1/2 = 50°\mathrm{C}$

$$v = 5.35\times10^{-7}\ \mathrm{m^2/sec} \qquad \alpha = 1.56\times10^{-7}\ \mathrm{m^2/sec} \qquad \mathrm{Pr} = 3.42$$

$$k = 0.645\ \mathrm{W/mK} \qquad \beta = 2.76\times10^{-4}\ \mathrm{K^{-1}}$$

Solution. This problem corresponds to *Case 3* and Figure 4.2.1C.

$$C_t^H = 0.14$$

from Equation 4.2.5 and $\overline{C}_l = 0.590$ from Equation (4.2.3).

$$L^* = \lim_{H\to\infty}\left(\frac{WH}{2W+2H}\right) = \frac{W}{2} = 0.05\ \mathrm{m}$$

from Figure 4.2.1C.

$$\mathrm{Ra} = \frac{g\beta\Delta TL^{*3}}{v\alpha} = 1.62\times10^8 \quad \mathrm{Nu}^T = 0.835\overline{C}_\ell \mathrm{Ra}^{1/4} = 55.6$$

$$\mathrm{Nu}_\ell = \frac{1.4}{\ln\left(1+1.4/\mathrm{Nu}^T\right)} = 54.2 \qquad \mathrm{Nu}_t = C_t^H \mathrm{Ra}^{1/3} = 76.3$$

$$\mathrm{Nu} = \frac{1}{WH\Delta T}\frac{L^*}{k} = \left(\mathrm{Nu}_\ell^{10} + \mathrm{Nu}_t^{10}\right)^{0.1} = 76.6$$

$$q/H = \frac{W\Delta Tk\mathrm{Nu}}{L^*} = 3950\ \text{W/m-length}$$

Comments: Turbulent heat transfer is dominant. Radiation can be ignored (since it lies in the far infrared region where it is not transmitted by the water).

Problem 3. Heat Loss across a Window Cavity, Figure 4.2.6C. The interior glazing is at temperature T_1 = 10°C, the exterior glazing at $T_2 = -10°C$, the window dimensions are W = 1 m, H = 1.7 m, and the air gap between the glazings is L = 1 cm and is at atmospheric pressure. Find the heat flux loss across the window.

Properties. At $\bar{T} = T_1 + T_2/2 = 0°C = 273K$

$$v = 1.35 \times 10^{-5} \text{ m}^2/\text{sec} \qquad \alpha = 1.89 \times 10^{-5} \text{ m}^2/\text{sec} \qquad \text{Pr} = 0.71$$

$$k = 0.024 \text{ W/mK} \qquad \beta = 1/273 = 3.66 \times 10^{-3} \text{ K}^{-1}$$

Solution. The appropriate correlations are given in *Case 18* and by Equation (4.2.24).

$$\text{Ra} = \frac{g\beta(T_1 - T_2)L^3}{v\alpha} = \frac{9.81 \times 3.66 \times 10^{-3} \times 20 \times (0.01)^3}{1.35 \times 10^{-5} \times 1.89 \times 10^{-5}} = 2.81 \times 10^3$$

$$\text{Nu}_1 = \left[1 + \left\{\frac{0.0665\text{Ra}^{1/3}}{1 + \left(\frac{9000}{\text{Ra}}\right)^{1.4}}\right\}^2\right]^{1/2} = 1.01$$

$$\text{Nu}_2 = 0.242\left(\text{Ra}\frac{L}{H}\right)^{0.273} = 0.242\left(2.81 \times 10^3 \times \frac{0.01}{1.7}\right)^{0.273} = 0.520$$

$$\text{Nu} = \frac{qL}{WH(T_1 - T_2)k} = \left(\text{Nu}_1, \text{Nu}_2\right)_{\max} = 1.01$$

$$q/WH = \frac{\text{Nu}(T_1 - T_2)k}{L} = \frac{1.01 \times 20 \times 0.024}{0.01} = 48.5 \text{ W/m}^2$$

Comments. For pure conduction across the air layer, Nu = 1.0. For the calculated value of Nu = 1.01, convection must play little role. For standard glass, the heat loss by radiation would be roughly double the natural convection value just calculated.

Special Nomenclature

Note that nomenclature for each geometry considered is provided in the figures that are referred to in the text.

$\bar{C}_\ell$ = function of Prandtl number, Equation (4.2.3)
C_t^V = function of Prandtl number, Equation (4.2.4)
C_t^H = function of Prandtl number, Equation (4.2.5)
$\underline{C}_t$ = surface averaged value of C_t, page 4–38
$\underline{\Delta T}$ = surface averaged value of $T_w - T_\infty$

References

Churchill, S.W. 1983. *Heat Exchanger Design Handbook*, Sections 2.5.7 to 2.5.10, E.V. Schlinder, Ed., Hemisphere Publishing, New York.

Churchill S.W. and Usagi, R. 1972. A general expression for the correlation of rates of transfer and other phenomena, *AIChE J.*, 18, 1121–1128.

Clemes, S.B., Hollands, K.G.T., and Brunger, A.P. 1994. Natural convection heat transfer from horizontal isothermal cylinders, *J. Heat Transfer*, 116, 96–104.

Edwards, J.A. and Chaddock, J.B. 1963. An experimental investigation of the radiation and free-convection heat transfer from a cylindrical disk extended surface, *Trans., ASHRAE*, 69, 313–322.

Elenbaas, W. 1942a. The dissipation of heat by free convection: the inner surface of vertical tubes of different shapes of cross-section, *Physica*, 9(8), 865–874.

Elenbaas, W. 1942b. Heat dissipation of parallel plates by free convection, *Physica*, 9(1), 2–28.

Fujii, T. and Fujii, M. 1976. The dependence of local Nusselt number on Prandtl number in the case of free convection along a vertical surface with uniform heat flux, *Int. J. Heat Mass Transfer*, 19, 121–122.

Fujii, T., Honda, H., and Morioka, I. 1973. A theoretical study of natural convection heat transfer from downward-facing horizontal surface with uniform heat flux, *Int. J. Heat Mass Transfer*, 16, 611–627.

Goldstein, R.J., Sparrow, E.M., and Jones, D.C. 1973. Natural convection mass transfer adjacent to horizontal plates, *Int. J. Heat Mass Transfer*, 16, 1025–1035.

Hollands, K.G.T. 1984. Multi-Prandtl number correlations equations for natural convection in layers and enclosures, *Int. J. Heat Mass Transfer*, 27, 466–468.

Hollands, K.G.T., Unny, T.E., Raithby, G.D., and Konicek, K. 1976. Free convection heat transfer across inclined air layers, *J. Heat Transfer*, 98, 189–193.

Incropera, F.P. and DeWitt, D.P. 2001. *Fundamentals of Heat and Mass Transfer*, 5th ed., John Wiley & Sons, New York.

Karagiozis, A. 1991. An Investigation of Laminar Free Convection Heat Transfer from Isothermal Finned Surfaces, Ph.D. Thesis, Department of Mechanical Engineering, University of Waterloo.

Karagiozis, A., Raithby, G.D., and Hollands, K.G.T. 1994. Natural convection heat transfer from arrays of isothermal triangular fins in air, *J. Heat Transfer*, 116, 105–111.

Kreith, F. and Bohn, M.S. 2000. *Principles of Heat Transfer*, 6th ed. Brooks Cole.

Raithby, G.D. and Hollands, K.G.T. 1975. A general method of obtaining approximate solutions to laminar and turbulent free convection problems, in *Advances in Heat Transfer*, Irvine, T.F. and Hartnett, J.P., Eds., Vol. 11, Academic Press, New York, 266–315.

Raithby, G.D. and Hollands, K.G.T. 1998. *Handbook Heat Transfer*, Chap. 4: Natural Convection, Rohsenow, W.M., Hartnett, J.P., and Ganic, E.H., Eds., McGraw-Hill, New York.

Seki, N., Fukusako, S., and Inaba, H. 1978. Heat transfer of natural convection in a rectangular cavity with vertical walls of different temperatures, *Bull. JSME.*, 21(152), 246–253.

Shewan, E., Hollands, K.G.T., and Raithby, G.D. 1996. Heat transfer by natural convection across a vertical air cavity of large aspect ratio, *J. Heat Transfer*, 118, 993–995.

Further Information

There are several heat transfer textbooks that provide fundamental information and correlations for natural convection heat transfer (e.g., Kreith and Bohn, 2000; Incropera and DeWitt, 2001). The correlations in this section closely follow the recommendations of Raithby and Hollands (1998), but that reference considers many more problems. Alternative equations are provided by Churchill (1983).

Other sources for more detailed information about natural convective heat transfer are:

Bejan, A. 1995. *Convection Heat Transfer*, 2nd ed., John Wiley & Sons, New York.

Kakac, S. and Yener, Y. 1994. *Convection Heat Transfer*, 2nd ed., CRC Press, Boca Raton, FL.

Figliola, R.A. and Catton, I. 1986. Natural convection in enclosures–1986. Presented at the Winter Annual Meeting of the American Society of Mechanical Engineers, Anaheim, California, December 7–12, 1986, American Society of Mechanical Engineers, New York.

A source for computational methods focusing on finite-difference methods is:

Tannehill, J.C., Anderson, D.A., and Pletcher, R.H. 1997. *Computational Fluid Mechanics and Heat Transfer*, 2nd ed., Taylor & Francis, Washington, D.C.

Numerous sources for programming codes are available on the World Wide Web, most of which are free, and can be found by using a search engine such as www.google.com.

Finite difference method: www.vector-space.com/free.hml
Fortran and MatLab codes: www.unige.ch/math/folks/hairer/software.html

Forced Convection — External Flows

N.V. Suryanarayana

Introduction

In this section we consider heat transfer between a solid surface and an adjacent fluid which is in motion relative to the solid surface. If the surface temperature is different from that of the fluid, heat is transferred as forced convection. If the bulk motion of the fluid results solely from the difference in temperature of the solid surface and the fluid, the mechanism is natural convection. The velocity and temperature of the fluid far away from the solid surface are the free-stream velocity and free-stream temperature. Both are usually known or specified. We are then required to find the heat flux from or to the surface with specified surface temperature or the surface temperature if the heat flux is specified. The specified temperature or heat flux either may be uniform or may vary. The convective heat transfer coefficient *h* is defined by

$$q'' = h\left(T_s - T_\infty\right) \tag{4.2.29}$$

In Equation (4.2.29) with the local heat flux, we obtain the local heat transfer coefficient, and with the average heat flux with a uniform surface temperature we get the average heat transfer coefficient. For a specified heat flux the local surface temperature is obtained by employing the local convective heat transfer coefficient.

Many correlations for finding the convective heat transfer coefficient are based on experimental data which have some uncertainty, although the experiments are performed under carefully controlled conditions. The causes of the uncertainty are many. Actual situations rarely conform completely to the experimental situations for which the correlations are applicable. Hence, one should not expect the actual value of the heat transfer coefficient to be within better than ±10% of the predicted value.

Many different correlations to determine the convective heat transfer coefficient have been developed. In this section only one or two correlations are given. For other correlations and more details, refer to the books given in the bibliography at the end of this section.

Flat Plate

With a fluid flowing parallel to a flat plate, changes in velocity and temperature of the fluid are confined to a thin region adjacent to the solid boundary — the boundary layer. Several cases arise:

1. Flows without or with pressure gradient
2. Laminar or turbulent boundary layer
3. Negligible or significant viscous dissipation (effect of frictional heating)
4. $\mathrm{Pr} \geq 0.7$ or $\mathrm{Pr} \ll 1$

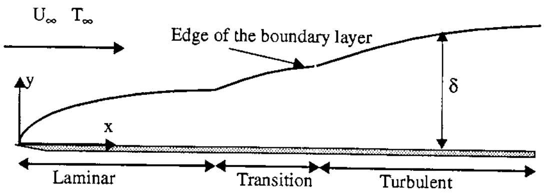

FIGURE 4.2.7 Flow of a fluid over a flat plate with laminar, transition, and turbulent boundary layers.

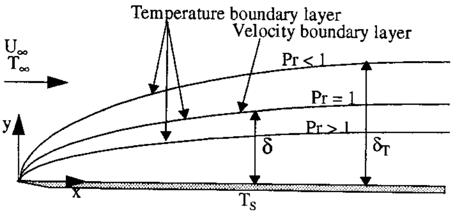

FIGURE 4.2.8 Temperature boundary layer thickness relative to velocity boundary layer thickness.

Flows with Zero Pressure Gradient and Negligible Viscous Dissipation

When the free-stream pressure is uniform, the free-stream velocity is also uniform. Whether the boundary layer is laminar or turbulent depends on the Reynolds number Re_X ($\rho U_\infty x/\mu$) and the shape of the solid at entrance. With a sharp edge at the leading edge (Figure 4.2.7) the boundary layer is initially laminar but at some distance downstream there is a transition region where the boundary layer is neither totally laminar nor totally turbulent. Farther downstream of the transition region the boundary layer becomes turbulent. For engineering applications the existence of the transition region is usually neglected and it is assumed that the boundary layer becomes turbulent if the Reynolds number, Re_X, is greater than the critical Reynolds number, Re_{cr}. A typical value of 5×10^5 for the critical Reynolds number is generally accepted, but it can be greater if the free-stream turbulence is low and lower if the free-stream turbulence is high, the surface is rough, or the surface does not have a sharp edge at entrance. If the entrance is blunt, the boundary layer may be turbulent from the leading edge.

Temperature Boundary Layer

Analogous to the velocity boundary layer there is a temperature boundary layer adjacent to a heated (or cooled) plate. The temperature of the fluid changes from the surface temperature at the surface to the free-stream temperature at the edge of the temperature boundary layer (Figure 4.2.8).

The velocity boundary layer thickness δ depends on the Reynolds number Re_X. The thermal boundary layer thickness δ_T depends both on Re_X and Pr

$\mathrm{Re}_x < \mathrm{Re}_{cr}$:

$$\frac{\delta}{x} = \frac{5}{\sqrt{\mathrm{Re}_x}} \qquad \mathrm{Pr} > 0.7 \qquad \frac{\delta}{\delta_T} = \mathrm{Pr}^{1/3}$$
$$\mathrm{Pr} \ll 1 \qquad \frac{\delta}{\delta_T} = \mathrm{Pr}^{1/2} \tag{4.2.30}$$

$\mathrm{Re}_{cr} < \mathrm{Re}_x$:

$$\frac{\delta}{x} = \frac{0.37}{\mathrm{Re}_x^{0.2}} \qquad \delta \approx \delta_T \tag{4.2.31}$$

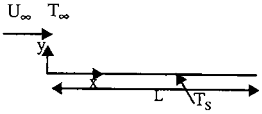

FIGURE 4.2.9 Heated flat plate with heating from the leading edge.

Viscous dissipation and high-speed effects can be neglected if $\Pr^{1/2}\,\mathrm{Ec}/2 \ll 1$. For heat transfer with significant viscous dissipation see the section on flow over flat plate with zero pressure gradient: Effect of High Speed and Viscous Dissipation. The Eckert number Ec is defined as $\mathrm{Ec} = U_\infty^2 / C_p(T_s - T_\infty)$.

With a rectangular plate of length L in the direction of the fluid flow the average heat transfer coefficient h_L with uniform surface temperature is given by

$$h_L = \frac{1}{L}\int_0^L h_x \, dx$$

Laminar Boundary Layer ($Re_x < Re_{cr}$, $Re_L < Re_{cr}$): With heating or cooling starting from the leading edge the following correlations are recommended. Note: in all equations evaluate fluid properties at the film temperature defined as the arithmetic mean of the surface and free-stream temperatures unless otherwise stated (Figure 4.2.9).

Local Heat Transfer Coefficient (Uniform Surface Temperature)
The Nusselt number based on the local convective heat transfer coefficient is expressed as

$$\mathrm{Nu}_x = f_{\Pr}\mathrm{Re}_x^{1/2} \tag{4.2.32}$$

The classical expression for $f_{\Pr}$ is $0.564\,\Pr^{1/2}$ for liquid metals with very low Prandtl numbers, $0.332\Pr^{1/3}$ for $0.7 < \Pr < 50$ and $0.339\Pr^{1/3}$ for very large Prandtl numbers. Correlations valid for all Prandtl numbers developed by Churchill (1976) and Rose (1979) are given below.

$$\mathrm{Nu}_x = \frac{0.3387\mathrm{Re}_x^{1/2}\Pr^{1/3}}{\left[1+\left(\frac{0.0468}{\Pr}\right)^{2/3}\right]^{1/4}} \tag{4.2.33}$$

$$\mathrm{Nu}_x = \frac{\mathrm{Re}^{1/2}\Pr^{1/2}}{\left(27.8+75.9\Pr^{0.306}+657\Pr\right)^{1/6}} \tag{4.2.34}$$

In the range $0.001 < \Pr < 2000$, Equation (4.2.33) is within 1.4% and Equation (4.2.34) is within 0.4% of the exact numerical solution to the boundary layer energy equation.

Average Heat Transfer Coefficient
The average heat transfer coefficient is given by

$$\mathrm{Nu}_L = 2\mathrm{Nu}_{x=L} \tag{4.2.35}$$

From Equation 4.2.35 it is clear that the average heat transfer coefficient over a length L is twice the local heat transfer coefficient at x = L.

Uniform Heat Flux

Local Heat Transfer Coefficient

Churchill and Ozoe (1973) recommend the following single correlation for all Prandtl numbers.

$$\mathrm{Nu}_x = \frac{0.886\,\mathrm{Re}_x^{1/2}\,\mathrm{Pr}^{1/2}}{\left[1+\left(\dfrac{\mathrm{Pr}}{0.0207}\right)^{2/3}\right]^{1/4}} \tag{4.2.36}$$

Note that for surfaces with uniform heat flux the local convective heat transfer coefficient is used to determine the local surface temperature. The total heat transfer rate being known, an average heat transfer coefficient is not needed and not defined.

Turbulent Boundary Layer ($Re_x > Re_{cr}$, $Re_L > Re_{cr}$): For turbulent boundary layers with heating or cooling starting from the leading edge use the following correlations:

Local Heat Transfer Coefficient

$\mathrm{Re}_{cr} < \mathrm{Re}_x < 10^7$:

$$\mathrm{Nu}_x = 0.0296\,\mathrm{Re}_x^{4/5}\,\mathrm{Pr}^{1/3} \tag{4.2.37}$$

$10^7 < \mathrm{Re}_x$:

$$\mathrm{Nu}_x = 1.596\,\mathrm{Re}_x\left(\ln \mathrm{Re}_x\right)^{-2.584}\mathrm{Pr}^{1/3} \tag{4.2.38}$$

Equation (4.2.38) is obtained by applying Colburn's *j* factor in conjunction with the friction factor suggested by Schlicting (1979).

In laminar boundary layers, the convective heat transfer coefficient with uniform heat flux is approximately 36% higher than with uniform surface temperature. With turbulent boundary layers, the difference is very small and *the correlations for the local convective heat transfer coefficient can be used for both uniform surface temperature and uniform heat flux.*

Average Heat Transfer Coefficient

If the boundary layer is initially laminar followed by a turbulent boundary layer at $\mathrm{Re}_x = \mathrm{Re}_{cr}$, the following correlations for $0.7 < \mathrm{Pr} < 60$ are suggested:

$\mathrm{Re}_{cr} < \mathrm{Re}_L < 10^7$:

$$\mathrm{Nu}_L = \left[0.664\,\mathrm{Re}_L^{1/2} + 0.037\left(\mathrm{Re}_L^{4/5} - \mathrm{Re}_{cr}^{4/5}\right)\right]\mathrm{Pr}^{1/3} \tag{4.2.39}$$

If $\mathrm{Re}_{cr} < \mathrm{Re}_L < 10^7$ and $\mathrm{Re}_{cr} = 10^5$, Equation 4.2.39 simplifies to

$$\mathrm{Nu}_L = \left(0.037\,\mathrm{Re}_L^{4/5} - 871\right)\mathrm{Pr}^{1/3} \tag{4.2.40}$$

$10^7 < \mathrm{Re}_L$ and $\mathrm{Re}_{cr} = 5 \times 10^5$:

$$\mathrm{Nu}_L = \left[1.963\,\mathrm{Re}_L\left(\ln \mathrm{Re}_L\right)^{-2.584} - 871\right]\mathrm{Pr}^{1/3} \tag{4.2.41}$$

Uniform Surface Temperature — Pr > 0.7: Unheated Starting Length

If heating does not start from the leading edge as shown in Figure 4.2.10, the correlations have to be modified. Correlation for the local convective heat transfer coefficient for laminar and turbulent boundary

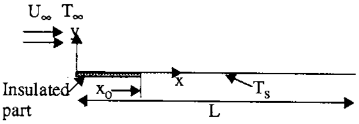

FIGURE 4.2.10 Heated flat plate with unheated starting length.

layers are given by Equation (4.2.42) and Equation (4.2.43) (Kays and Crawford, 1993) — the constants in Equation (4.2.42) and Equation (4.2.43) have been modified to be consistent with the friction factors. These correlations are also useful as building blocks for finding the heat transfer rates when the surface temperature varies in a predefined manner. Equation (4.2.44) and Equation (4.2.45), developed by Thomas (1977), provide the average heat transfer coefficients based on Equation (4.2.42) and Equation (4.2.43).

Local Convective Heat Transfer Coefficient

$\mathrm{Re}_x < \mathrm{Re}_{\mathrm{cr}}$:

$$\mathrm{Nu}_x = \frac{0.332\mathrm{Re}_x^{1/2}\mathrm{Pr}^{1/3}}{\left[1-\left(\frac{x_o}{x}\right)^{3/4}\right]^{1/3}} \tag{4.2.42}$$

$\mathrm{Re}_x > \mathrm{Re}_{\mathrm{cr}}$:

$$\mathrm{Nu}_x = \frac{0.0296\mathrm{Re}_x^{4/5}\mathrm{Pr}^{3/5}}{\left[1-\left(\frac{x_o}{x}\right)^{9/10}\right]^{1/9}} \tag{4.2.43}$$

Average Heat Transfer Coefficient over the Length (L – x_o)

$\mathrm{Re}_L < \mathrm{Re}_{\mathrm{cr}}$:

$$\begin{aligned} h_{L-x_o} &= \frac{0.664\mathrm{Re}_L^{1/2}\mathrm{Pr}^{1/3}\left[1-\left(\frac{x_o}{L}\right)^{3/4}\right]^{2/3} k}{L-x_o} \\ &= 2\frac{1-\left(\frac{x_o}{L}\right)^{3/4}}{1-x_o/L} h_{x=L} \end{aligned} \tag{4.2.44}$$

In Equation (4.2.44) evaluate $h_{x=L}$ from Equation (4.2.42).

$\mathrm{Re}_{\mathrm{cr}} = 0$:

$$\begin{aligned} h_{L-x_o} &= \frac{0.037\mathrm{Re}_L^{4/5}\mathrm{Pr}^{3/5}\left[1-\left(\frac{x_o}{L}\right)^{9/10}\right]^{8/9} k}{L-x_o} \\ &= 1.25\frac{1-\left(x_o/L\right)^{9/10}}{1-x_o/L} h_{x=L} \end{aligned} \tag{4.2.45}$$

In Equation (4.2.45) evaluate $h_{x=L}$ from Equation (4.2.43).

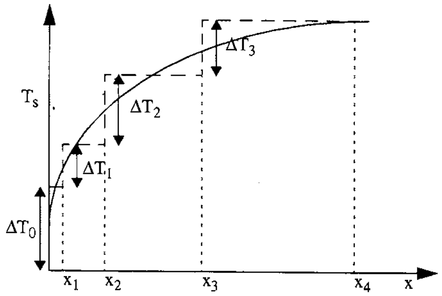

FIGURE 4.2.11 Arbitrary surface temperature approximated as a finite number of step changes.

Flat Plate with Prescribed Nonuniform Surface Temperature

The linearity of the energy equation permits the use of Equation (4.2.42) through Equation (4.2.45) for uniform surface temperature with unheated starting length to find the local heat flux and the total heat transfer rate by the principle of superposition when the surface temperature is not uniform. Figure 4.2.11 shows the arbitrarily prescribed surface temperature with a uniform free-stream temperature of the fluid. If the surface temperature is a differentiable function of the coordinate *x*, the local heat flux can be determined by an expression that involves integration (refer to Kays and Crawford, 1993). If the surface temperature can be approximated as a series of step changes in the surface temperature, the resulting expression for the local heat flux and the total heat transfer rate is the summation of simple algebraic expressions. Here the method using such an algebraic simplification is presented.

The local convective heat flux at a distance *x* from the leading edge is given by

$$q_x'' = \sum_1^n h_{xi} \Delta T_{si} \tag{4.2.46}$$

where h_{xi} denotes the local convective heat transfer coefficient at x due to a single step change in the surface temperature ΔT_{si} at location $x_i (x_i < x)$. Referring to Figure 4.2.11, the local convective heat flux at x ($x_3 < x < x_4$) is given by

$$q_x'' = h_x(x,0)\Delta T_o + h_x(x,x_1)\Delta T_1 + h_x(x,x_2)\Delta T_2 + h_x(x,x_3)\Delta T_3$$

where $h_x(x, x_1)$ is the local convective heat transfer coefficient at x with heating starting from x_1; the local convective heat transfer is determined from Equation (4.2.42) if the boundary layer is laminar and Equation (4.2.43) if the boundary layer is turbulent from the leading edge. For example, $h_x(x, x_2)$ in the third term is given by

$$\mathrm{Re}_x < \mathrm{Re}_{\mathrm{cr}} \qquad h_x(x,x_2) = \frac{0.332\left(\dfrac{\rho U_\infty x}{\mu}\right)^{1/2} \mathrm{Pr}^{1/3}}{\left[1-\left(\dfrac{x_2}{x}\right)^{3/4}\right]^{1/3}} \frac{k}{x}$$

$$\mathrm{Re}_{\mathrm{cr}} = 0 \qquad h_x(x,x_2) = \frac{0.0296\left(\dfrac{\rho U_\infty x}{\mu}\right)^{4/5} \mathrm{Pr}^{3/5}}{\left[1-\left(\dfrac{x_2}{x}\right)^{9/10}\right]^{1/9}} \frac{k}{x}$$

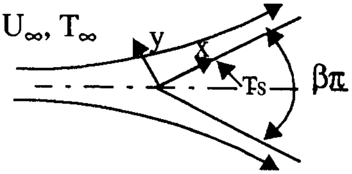

FIGURE 4.2.12 Flow over a wedge. βπ is the wedge angle.

The procedure for finding the total heat transfer rate from $x = 0$ to $x = L$ is somewhat similar. Denoting the width of the plate by W,

$$\frac{q}{W} = \sum h_{L-x_i} \Delta T_i \left(L - x_i\right) \tag{4.2.47}$$

where h_{L-x_i} is the average heat transfer coefficient over the length $L - x_i$ due to a step change ΔT_i in the surface temperature at x_i. For example, the heat transfer coefficient in the third term in Equation (4.2.47) obtained by replacing x_o by x_2 in Equation (4.2.44) or (4.2.45) depending on whether $\mathrm{Re}_L < \mathrm{Re}_{\mathrm{cr}}$ or $\mathrm{Re}_{\mathrm{cr}} = 0$.

Flows with Pressure Gradient and Negligible Viscous Dissipation

Although correlations for flat plates are for a semi-infinite fluid medium adjacent to the plate, most applications of practical interest deal with fluid flowing between two plates. If the spacing between the plates is significantly greater than the maximum boundary layer thickness, the medium can be assumed to approach a semi-infinite medium. In such a case if the plates are parallel to each other and if the pressure drop is negligible compared with the absolute pressure, the pressure gradient can be assumed to be negligible. If the plates are nonparallel and if the boundary layer thickness is very much smaller than the spacing between the plates at that location, the medium can still be considered as approaching a semi-infinite medium with a non-negligible pressure gradient. In such flows the free-stream velocity (core velocity outside the boundary layer) is related to the pressure variation by the Bernoulli equation:

$$\frac{p}{\rho} + \frac{U_\infty^2}{2} + zg = \text{constant}$$

Another situation where the free-stream velocity varies in the direction of flow giving rise to a pressure gradient is flow over a wedge. For the family of flows for which the solutions are applicable, the free-stream velocity at the edge of the boundary layer is related to the x-coordinate by a power law, $U_\infty = cx^m$. Flows over semi-infinite wedges (Figure 4.2.12) satisfy that condition. The exponent m is related to the wedge angle βπ

$$\beta = \frac{2m}{1+m} \qquad m = \frac{\beta}{2-\beta}$$

With laminar boundary layers, the boundary layer thickness, friction factor, and Nusselt numbers are defined by

$$\frac{\delta}{x} = \frac{c_1}{\sqrt{\mathrm{Re}_x}} \qquad \frac{C_{fx}}{2} = \frac{\tau_w}{\rho U_\infty^2} = \frac{c_2}{\sqrt{\mathrm{Re}_x}} \qquad \mathrm{Nu}_x = c_3 \mathrm{Re}_x^{1/2}$$

The values of c_1, c_2, and c_3 are available in Burmeister (1993). For example, for $\beta = 0.5$ (wedge angle = 90°), $m = 1/3$, $c_1 = 3.4$, $c_2 = 0.7575$, and $c_3 = 0.384$ for $\mathrm{Pr} = 0.7$, and $c_3 = 0.792$ for $\mathrm{Pr} = 5$. Re_x is based on $U_\infty = cx^m$; the free-stream velocity is not uniform.

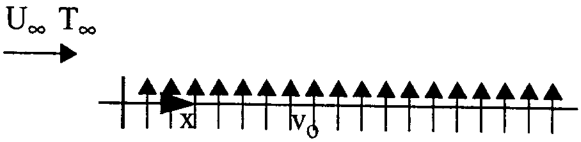

FIGURE 4.2.13 Flat plate with transpiration injection.

Uniform Temperature: Flat Plate with Injection or Suction with External Flows of a Fluid Parallel to the Surface

Injection or suction has engineering applications. When the free-stream temperature of the fluid is high, as in gas turbines, a cooling fluid is introduced into the mainstream to cool the surface. If the cooling fluid is introduced at discrete locations (either perpendicular to the surface or at an angle), it is known as film cooling. If a fluid is introduced or withdrawn through a porous medium, it is known as transpiration (Figure 4.2.13). An application of suction is to prevent boundary layer separation (Figure 4.2.13).

Analytical solutions for a laminar boundary layer with transpiration suction or blowing are available if the velocity perpendicular to the surface varies in the following manner:

$$\mathbf{v}_o = \text{constant } x^{(m-1)/2}$$

Solutions are limited to the cases of the injected fluid being at the same temperature as the surface and the injected fluid being the same as the free-stream fluid. Positive values of v_o indicate blowing and negative values indicate suction. Values of $\text{Nu}_x/\text{Re}_x^{1/2}$ for different values of Pr and for different values of blowing or suction parameter are given in Kays and Crawford (1993).

For example, for a laminar boundary layer over a flat plate with a fluid (Pr = 0.7) the value of $\text{Nu}_x/\text{Re}_x^{1/2}$ is 0.722 for $(v_o/U_\infty)\sqrt{\rho U_\infty x/\mu} = -0.75$ (suction) and 0.166 for $(v_o/U_\infty)\sqrt{\rho U_\infty x/\mu} = 0.25$ (blowing). Heat transfer coefficient increases with suction which leads to a thinning of the boundary layer. Blowing increases the boundary layer thickness and decreases the heat transfer coefficient.

For *turbulent boundary layers* Kays and Crawford (1993) suggest the following procedure for finding the friction factor and convective heat transfer coefficient. Define friction blowing parameter B_f and heat transfer blowing parameter B_h as

$$B_f = \frac{\mathbf{v}_o/U_\infty}{C_f/2} \tag{4.2.48}$$

$$B_h = \frac{\mathbf{v}_o/U_\infty}{\text{St}} = \frac{\dot{m}''/G_\infty}{\text{St}} \tag{4.2.49}$$

where

v_o = velocity normal to the plate
U_∞ = free-stream velocity
$\dot{m}''$ = mass flux of the injected fluid at the surface (ρv_o)
G_∞ = mass flux in the free stream (ρU_∞)
St = Stanton number = $\text{Nu}_x/\text{Re}_x\text{Pr} = h/\rho U_\infty c_p$

The friction factors and Stanton number with and without blowing or suction are related by

$$\frac{C_f}{C_{fo}} = \frac{\ln\left(1 + B_f\right)}{B_f} \tag{4.2.50}$$

$$\frac{\mathrm{St}}{\mathrm{St}_o} = \frac{\ln\left(1 + B_h\right)}{B_h} \tag{4.2.51}$$

In Equation (4.2.50) and Equation (4.2.51) C_{fo} and St_o are the friction factor and Stanton number with $v_o = 0$ (no blowing or suction), and C_f and St are the corresponding quantities with blowing or suction at the same $\mathrm{Re}_x(\rho U_\infty x/\mu)$.

For the more general case of variable free-stream velocity, temperature difference, and transpiration rate, refer to Kays and Crawford (1993).

Flow over Flat Plate with Zero Pressure Gradient: Effect of High-Speed and Viscous Dissipation

In the boundary layer the velocity of the fluid is reduced from U_∞ to zero at the plate leading to a reduction in the kinetic energy of the fluid. Within the boundary layer there is also the work done by viscous forces; the magnitude of the such viscous work is related to the velocity of the fluid, the velocity gradient, and the viscosity of the fluid. The effect of such a reduction in the kinetic energy and the viscous work is to increase the internal energy of the fluid in the boundary layer. The increase in the internal energy may be expected to lead to an increase in the temperature; but because of the heat transfer to the adjacent fluid the actual increase in the internal energy (and the temperature) will be less than the sum of the decrease in the kinetic energy and viscous work transfer; the actual temperature increase depends on the decrease in the kinetic energy, the viscous work transfer, and the heat transfer from the fluid. The maximum temperature in the fluid with an adiabatic plate is known as the adiabatic wall temperature (which occurs at the wall) and is given by

$$T_{aw} = T_\infty + r\frac{U_\infty^2}{2C_p} \tag{4.2.52}$$

In Equation (4.2.52) r is the recovery factor and is given by Eckert and Drake (1986).

Laminar boundary layer	$0.6 < \mathrm{Pr} < 15$	$r = \mathrm{Pr}^{1/2}$
Turbulent boundary layer		$r = \mathrm{Pr}^{1/3}$

Equation (4.2.52) can be recast as

$$\frac{T_{aw} - T_\infty}{T_s - T_\infty} = \frac{r}{2}\frac{U_\infty^2}{C_p\left(T_s - T_\infty\right)} \tag{4.2.53}$$

From Equation (4.2.53) the maximum increase in the fluid temperature as a fraction of the difference between the plate and free-stream temperatures is given by $r\,\mathrm{Ec}/2$. With air flowing over a plate at 500 m/sec, the increase in the temperature of the air can be as high as 105°C. With $T_s = 40°\mathrm{C}$ and $T_\infty = 20°\mathrm{C}$, the temperature of the air close to the plate can be higher than the plate temperature. It is thus possible that although the plate temperature is higher than the free-stream temperature, the heat transfer is from the air to the plate. At a Mach number greater than 0.1 for gases, viscous dissipation becomes significant.

The temperature profiles for high-speed flows for different values of T_s are shown in Figure 4.2.14. In high-speed flows, as heat transfer can be to the plate even if the plate temperature is greater than the fluid temperature, the definition of the convective heat transfer coefficient given in Equation (4.2.29) is not adequate. On the other hand, as the heat transfer is always from the plate if $T_s > T_{aw}$, the adiabatic wall temperature is more appropriate as the reference temperature. Thus, in high-speed flows the definition of the convective heat transfer coefficient is given by

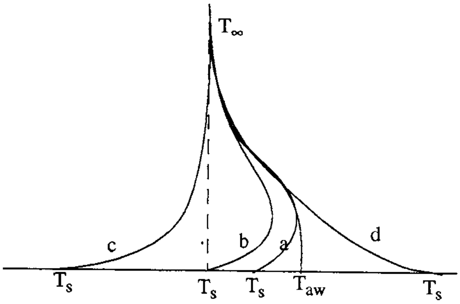

FIGURE 4.2.14 Temperature profiles for high-speed flows: (a) $T_\infty < T_s < T_{aw}$; (b) $T_s = T_\infty$; (c) $T_s \ll T_\infty$; (d) $T_s > T_{aw}$.

$$q'' = h\left(T_s - T_{aw}\right) \tag{4.2.54}$$

Equation (4.2.54) is consistent with Equation (4.2.29) as the adiabatic wall temperature equals the free-stream temperature if the effects of viscous dissipation and reduced kinetic energy in the boundary layer are neglected. With the adiabatic wall temperature as the fluid reference temperature for the definition of the convective heat transfer coefficient, equations for low speeds can also be used for high-speed flows. Because of the greater variation in the fluid temperature in the boundary layer, the variation of properties due to temperature variation becomes important. It is found that the correlations are best approximated if the properties are evaluated at the reference temperature T^* defined by Eckert (1956):

$$T^* = 0.5\left(T_s + T_\infty\right) + 0.22\left(T_{aw} - T_\infty\right) \tag{4.2.55}$$

With properties evaluated at the reference temperature given by Equation (4.2.55), Equation (4.2.56) through (4.2.61) are applicable to high-speed flows with Prandtl numbers less than 15. It should be noted that the adiabatic wall temperatures in the laminar and turbulent regions are different affecting both the temperature at which the properties are evaluated and the temperature difference for determining the local heat flux. Therefore, when the boundary layer is partly laminar and partly turbulent, an average value of the heat transfer coefficient is not defined as the adiabatic wall temperatures in the two regions are different. In such cases the heat transfer rate in each region is determined separately to find the total heat transfer rate.

Evaluate properties at reference temperature given by Equation (4.2.55):

Laminar Local: $\mathrm{Re}_x < \mathrm{Re}_{cr}$ $$\mathrm{Nu}_x = 0.332\mathrm{Re}_x^{1/2}\mathrm{Pr}^{1/3} \tag{4.2.56}$$

Average: $\mathrm{Re}_L < \mathrm{Re}_{cr}$ $$\mathrm{Nu}_L = 0.664\mathrm{Re}_L^{1/2}\mathrm{Pr}^{1/3} \tag{4.2.57}$$

Turbulent Local: $10^7 > \mathrm{Re}_x > \mathrm{Re}_{cr}$ $$\mathrm{Nu}_x = 0.0296\mathrm{Re}_x^{4/5}\mathrm{Pr}^{1/3} \tag{4.2.58}$$

Local: $10^7 < \mathrm{Re}_x < 10^9$ $$\mathrm{Nu}_x = 1.596\mathrm{Re}_x\left(\ln\mathrm{Re}_x\right)^{-2.584}\mathrm{Pr}^{1/3} \tag{4.2.59}$$

Average: $\mathrm{Re}_{cr} = 0,\ \mathrm{Re}_L < 10^7$ $$\mathrm{Nu}_L = 0.037\mathrm{Re}_L^{4/5}\mathrm{Pr}^{1/3} \tag{4.2.60}$$

Average: $\mathrm{Re}_{cr} = 0,\ 10^7 < \mathrm{Re}_L < 10^9$ $$\mathrm{Nu}_L = 1.967\mathrm{Re}_L\left(\ln\mathrm{Re}_L\right)^{-2.584}\mathrm{Pr}^{1/3} \tag{4.2.61}$$

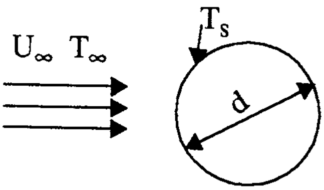

FIGURE 4.2.15 A fluid stream in cross flow over a cylinder.

When the temperature variation in the boundary layer is large, such that the assumption of constant specific heat is not justified, Eckert (1956) suggests that the properties be evaluated at a reference temperature corresponding to the specific enthalpy i^* given by

$$i^* = 0.5(i_s + i_\infty) + 0.22(i_s - i_\infty) \tag{4.2.62}$$

where i is the specific enthalpy of the fluid evaluated at the temperature corresponding to the subscript. Equation (4.2.62) gives the same values as Equation (4.2.55) if C_p is constant or varies linearly with temperature.

At very high speeds the gas temperature may reach levels of temperatures that are sufficient to cause disassociation and chemical reaction; these and other effects need to be taken into account in those cases.

Flow over Cylinders, Spheres, and Other Geometries

Flows over a flat plate and wedges were classified as laminar or turbulent, depending on the Reynolds number, and correlations for the local and average convective heat transfer coefficients were developed. But flows over cylinders (perpendicular to the axis) and spheres are more complex. In general, the flow over cylinders and spheres may have a laminar boundary layer followed by a turbulent boundary layer and a wake region depending on the Reynolds number with the diameter as the characteristic length. Because of the complexity of the flow patterns, only correlations for the average heat transfer coefficients have been developed (Figure 4.2.15).

Cylinders: Use the following correlation proposed by Churchill and Bernstein (1977): $\mathrm{Re}_d\,\mathrm{Pr} > 0.2$. Evaluate properties at $(T_s + T_\infty)/2$:

$$\mathrm{Re}_d > 400{,}000: \qquad \mathrm{Nu}_d = 0.3 + \frac{0.62\mathrm{Re}_d^{1/2}\mathrm{Pr}^{1/3}}{\left[1+(0.4/\mathrm{Pr})^{2/3}\right]^{1/4}}\left[1+\left(\frac{\mathrm{Re}_d}{282{,}000}\right)^{5/8}\right]^{4/5} \tag{4.2.63}$$

$$10{,}000 < \mathrm{Re}_d < 400{,}000: \quad \mathrm{Nu}_d = 0.3 + \frac{0.62\mathrm{Re}_d^{1/2}\mathrm{Pr}^{1/3}}{\left[1+(0.4/\mathrm{Pr})^{2/3}\right]^{1/4}}\left[1+\left(\frac{\mathrm{Re}_d}{282{,}000}\right)^{1/2}\right] \tag{4.2.64}$$

$$\mathrm{Re}_d < 10{,}000: \qquad \mathrm{Nu}_d = 0.3 + \frac{0.62\mathrm{Re}_d^{1/2}\mathrm{Pr}^{1/3}}{\left[1+(0.4/\mathrm{Pr})^{2/3}\right]^{1/4}} \tag{4.2.65}$$

For flow of liquid metals, use the following correlation suggested by Ishiguro et al. (1979):

$$1 < \mathrm{Re}_d\mathrm{Pr} < 100 \qquad \mathrm{Nu}_d = 1.125(\mathrm{Re}_d\mathrm{Pr})^{0.413} \tag{4.2.66}$$

For more information on heat transfer with flow over cylinders, refer to Morgan (1975) and Zukauskas (1987).

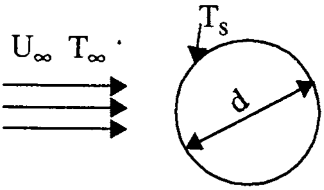

FIGURE 4.2.16 A fluid flowing over a sphere.

Spheres: For flows over spheres (Figure 4.2.16) use one of the following two correlations.

1. Whitaker (1972): Evaluate properties at T_∞ except μ_s at T_s.

$$3.5 < \mathrm{Re}_d < 76{,}000 \qquad 0.71 < \mathrm{Pr} < 380 \qquad 1 < \mu/\mu_s < 3.2$$

$$\mathrm{Nu}_d = 2.0 + \left(0.4\mathrm{Re}_d^{1/2} + 0.06\mathrm{Re}_d^{2/3}\right)\mathrm{Pr}^{2/5}\left(\frac{\mu}{\mu_s}\right)^{1/4} \tag{4.2.67}$$

2. Achenbach (1978): Evaluate properties at $(T_s + T_\infty)/2$:

$$100 < \mathrm{Re}_d < 2\times10^5 \qquad \mathrm{Pr} = 0.71$$

$$\mathrm{Nu}_d = 2 + \left(0.25\mathrm{Re}_d + 3\times10^{-4}\mathrm{Re}_d^{1.6}\right)^{1/2} \tag{4.2.68}$$

$$4\times10^5 < \mathrm{Re}_d < 5\times10^6 \qquad \mathrm{Pr} = 0.71$$

$$\mathrm{Nu}_d = 430 + 5\times10^{-3}\mathrm{Re}_d + 0.25\times10^{-9}\mathrm{Re}_d^2 - 3.1\times10^{-17}\mathrm{Re}_d^3 \tag{4.2.69}$$

3. Liquid Metals: From experimental results with liquid sodium, Witte (1968) proposed

$$3.6\times10^4 < \mathrm{Re}_d < 1.5\times10^5 \qquad \mathrm{Nu}_d = 2 + 0.386\left(\mathrm{Re}_d\mathrm{Pr}\right)^{1/2} \tag{4.2.70}$$

Other Geometries: For geometries other than cylinders and spheres, use Equation (4.2.71) with the characteristic dimensions and values of the constants given in the Table 4.2.1.

$$\mathrm{Nu}_D = c\mathrm{Re}_D^m \tag{4.2.71}$$

Although Equation (4.2.71) is based on experimental data with gases, its use can be extended to fluids with moderate Prandtl numbers by multiplying Equation (4.2.71) by $(\mathrm{Pr}/0.7)^{1/3}$.

Heat Transfer across Tube Banks

When tube banks are used in heat exchangers, the flow over the tubes in the second subsequent rows of tubes is different from the flow over a single tube. Even in the first row the flow is modified by the presence of the neighboring tubes. The extent of modification depends on the spacing between the tubes. If the spacing is very much greater than the diameter of the tubes, correlations for single tubes can be used. Correlations for flow over tube banks when the spacing between tubes in a row and a column is not much greater than the diameter of the tubes have been developed for use in heat-exchanger applications. Two arrangements of the tubes are considered — aligned and staggered as shown in Figure 4.2.17. The nomenclature used in this section is shown in the figure.

TABLE 4.2.1 Values of *c* and *m* in Equation (4.2.71)

Geometry	Re_D	c	m
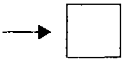	5000-100 000	0.092	0.675
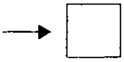	2500-8000	0.160	0.699
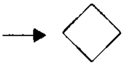	5000-100 000	0.222	0.588
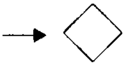	2500-7500	0.261	0.624
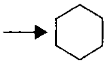	5000-19500 19 500-100 000	0.144 0.035	0.638 0.782
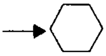	5000-100 000	0.138	0.638
	2500-15 000	0.224	0.612
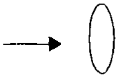	3000-15 000	0.085	0.804
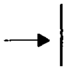	4000-15 000	0.205	0.731

Charcteristic dimension is the equivalent circular diameter = Perimeter/π
For example, for a square rod with each side a, D = 4a/π

From Jakob, 1949. With permission.

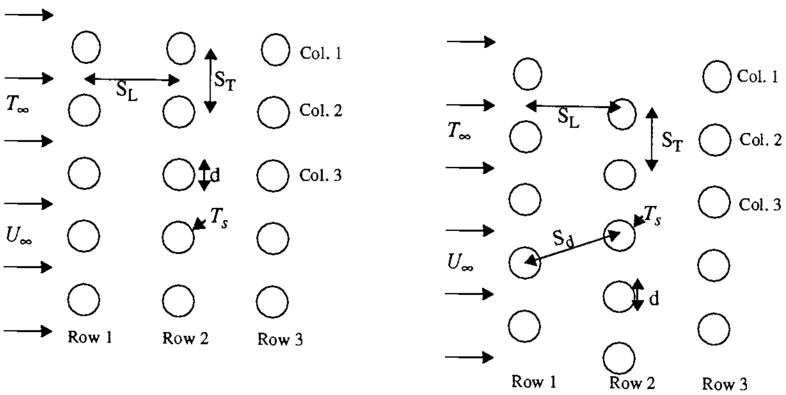

FIGURE 4.2.17 Two arrangements of tube banks. In-line or aligned arrangement on the left and staggered arrangement on the right. ($a = S_T/d$; $b = S_L/d$.)

TABLE 4.2.2 In-Line Arrangement — Values of Constants in Equation (4.2.72) ($p = 0$ in all cases)

Re_d	c	m	n
1–100	0.9	0.4	0.36
100–1000	0.52	0.5	0.36
10^3–2×10^5	0.27	0.63	0.36
$2 \times 10^5 - 2 \times 10^6$	0.033	0.8	0.4

TABLE 4.2.3 Staggered Arrangement — Values of Constants in Equation (4.2.72)

Re_d	c	p	m	n
1–500	1.04	0	0.4	0.36
500–1000	0.71	0	0.5	0.36
10^3–2×10^5	0.35	0.2	0.6	0.36
$2 \times 10^5 - 2 \times 10^6$	0.031	0.2	0.8	0.36

For the average convective heat transfer coefficient with tubes at uniform surface temperature, from experimental results, Zukauskas (1987) recommends correlations of the form:

$$\mathrm{Nu}_d = c\left(\frac{a}{b}\right)^p \mathrm{Re}_d^m \mathrm{Pr}^n \left(\frac{\mathrm{Pr}}{\mathrm{Pr}_s}\right)^{0.25} \tag{4.2.72}$$

In Equation (4.2.72) all properties are evaluated at the arithmetic mean of the inlet and exit temperatures of the fluid, except Pr_s which is evaluated at the surface temperature T_s. The values of the constants c, p, m, and n are given in Table 4.2.2 for in-line arrangement and in Table 4.2.3 for staggered arrangement.

In computing Re_d, the maximum average velocity between tubes is used. The maximum velocities for the in-line and staggered arrangements are given by

$$\text{In-line:} \qquad U_{\max} = \frac{U_\infty S_T}{S_T - d} \tag{4.2.73}$$

$$\text{Staggered:} \qquad S_d > \frac{S_T + d}{2} \qquad U_{\max} = \frac{U_\infty S_T}{S_T - d} \tag{4.2.74}$$

$$\text{Staggered:} \qquad S_d < \frac{S_T + d}{2} \qquad U_{\max} = \frac{U_\infty S_T}{2(S_d - d)}$$

$$S_d = \left[S_L^2 + \left(\frac{S_T}{2}\right)^2\right]^{1/2} \tag{4.2.75}$$

Equation (4.2.72) is for tube banks with 16 or more rows. When there are fewer than 16 rows, the heat transfer coefficient given by Equation (4.2.72) is multiplied by the correction factor c_1 defined by Equation (4.2.76) and given in Table 4.2.4.

$$\frac{h_N}{h_{16}} = c_1 \tag{4.2.76}$$

TABLE 4.2.4 Correction Factor c_1 to Be Used with Equation (4.2.76)

Tube Arrangement	Number of Rows (N) 1	2	3	4	5	7	10	13
In-line	0.70	0.80	0.86	0.90	0.93	0.96	0.98	0.99
Staggered	0.64	0.76	0.84	0.89	0.93	0.96	0.98	0.99

where

h_N = heat transfer coefficient with N rows (fewer than 16)
h_{16} = heat transfer coefficient with 16 or more rows

Pressure Drop: With tube banks, pressure drop is a significant factor, as it determines the fan power required to maintain the fluid flow. Zukauskas (1987) recommends that the pressure drop be computed from the relation

$$\Delta p = p_i - p_e = N\chi \frac{\rho U_{\max}^2}{2} f \tag{4.2.77}$$

where p_i and p_e are the fluid pressures at inlet and exit of the tube banks. The values of χ and f are presented in Figure 4.2.18A. In Figure 4.2.18A the friction factor f for in-line arrangement is presented for different values of b (S_L/d) for $S_L = S_T$. For values of S_L/S_T other than 1, the correction factor χ is given in the inset for different values of $(a - 1)/(b - 1)$. Similarly, the friction factor for staggered arrangement (for equilateral triangle arrangement) and a correction factor for different values of a/b are also given in Figure 4.2.18b. The value of f is for one row of tubes; the total pressure drop is obtained by multiplying the pressure drop for one row by the number of rows, N.

The temperature of the fluid varies in the direction of flow, and, therefore, the value of the convective heat transfer coefficient (which depends on the temperature-dependent properties of the fluid) also varies in the direction of flow. However, it is common practice to compute the total heat transfer rate with the assumption of uniform convective heat transfer coefficient evaluated at the arithmetic mean of the inlet and exit temperatures of the fluid. With such an assumption of uniform convective heat transfer coefficient, uniform surface temperature and constant specific heat (evaluated at the mean fluid temperature), the inlet and exit fluid temperatures are related by

$$\ln\left(\frac{T_s - T_e}{T_s - T_i}\right) = -\frac{hA_s}{\dot{m}c_p} \tag{4.2.78}$$

The heat transfer rate to the fluid is related by the equation

$$q = \dot{m}c_p\left(T_i - T_e\right) \tag{4.2.79}$$

Example

A heat exchanger with aligned tubes is used to heat 40 kg/sec of atmospheric air from 10 to 50°C with the tube surfaces maintained at 100°C. Details of the heat exchanger are

Diameter of tubes	25 mm
Number of columns	20
Length of each tube	3 m
$S_L = S_T$	75 mm

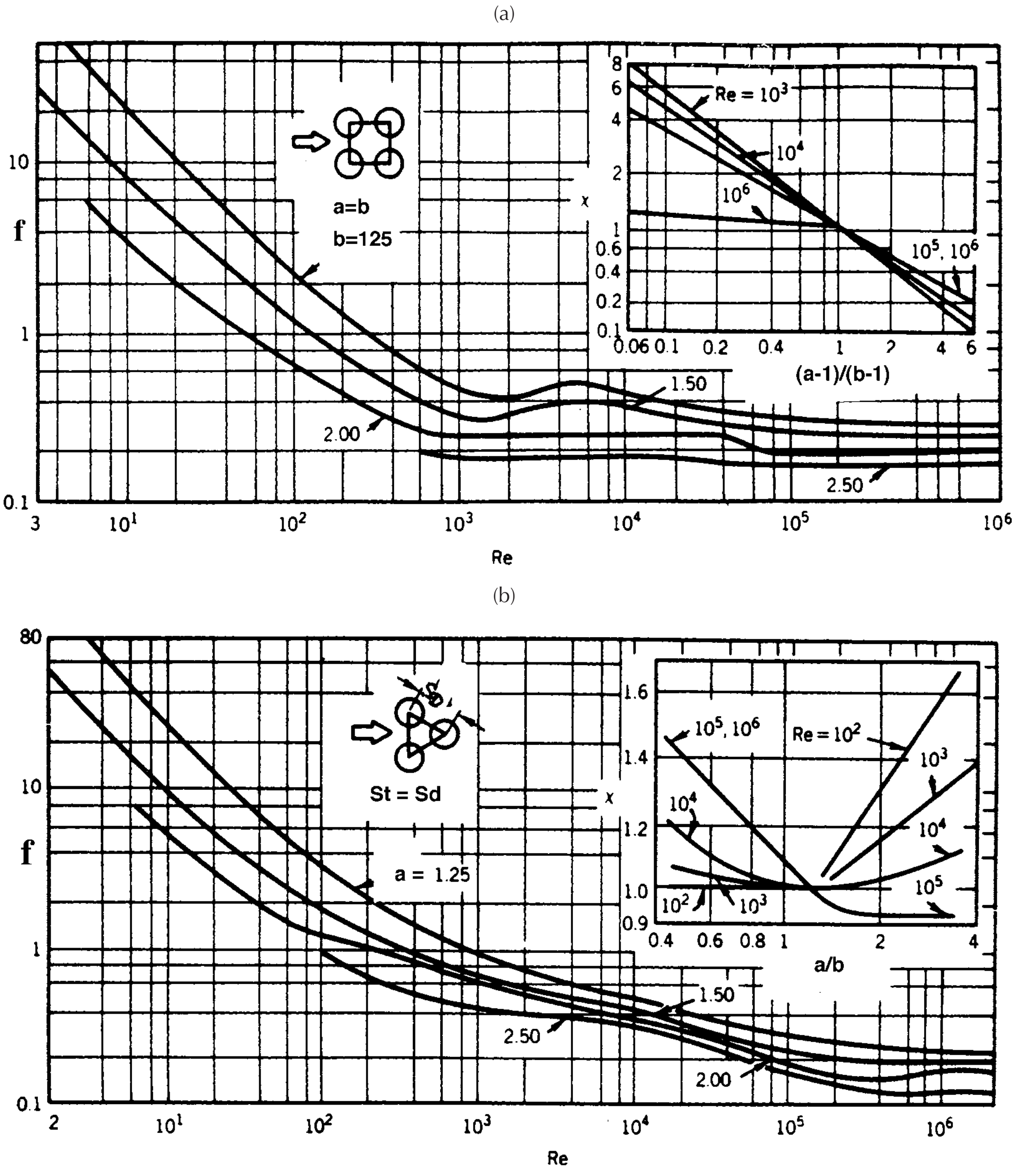

FIGURE 4.2.18 Friction factors for tube banks. (a) In-line arrangement; (b) Staggered arrangement. (From Zukauskas, A., in *Handbook of Single-Phase Convective Heat Transfer*, Kakac, S. et al., Eds., Wiley Interscience, New York, 1987. With permission.)

Determine the number of rows required.

Solution. Average air temperature = $(T_i + T_e)/2 = 30°\text{C}$. Properties of atmospheric air (from Suryanarayana, 1995):

$$\rho = 1.165 \text{ kg/m}^3 \qquad c_p = 1007 \text{ J/kg K}$$

$$\mu = 1.865 \times 10^{-5} \text{ N sec/m}^3 \qquad k = 0.0264 \text{ W/mK}$$

$$\text{Pr} = 0.712 \qquad \text{Pr}_s(\text{at } 100°\text{C}) = 0.705$$

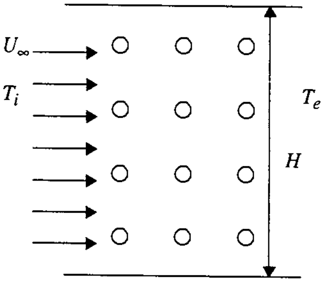

FIGURE 4.2.19 Aligned tube heat exchanger (only a few of the 20 columns and rows are shown).

To find $U_{\max}$ we need the minimum area of cross section for fluid flow (Figure 4.2.19).

$$H = 20 \times 0.075 = 1.5 \text{ m}$$

$$A_{\min} = 20(0.075 - 0.025) \times 3 = 3 \text{ m}^2$$

$$U_{\max} = \frac{\dot{m}}{\rho A_{\min}} = \frac{40}{1.165 \times 3} = 11.44 \text{ m/sec}$$

$$\text{Re}_d = \frac{\rho U_{\max} d}{\mu} = \frac{1.165 \times 11.44 \times 0.025}{1.865 \times 10^{-5}} = 17{,}865$$

With values from Table 4.2.2,

$$\text{Nu}_d = 0.27 \times 17{,}865^{0.63} \times 0.712^{0.36} \left(\frac{0.712}{0.705}\right)^{0.25} = 114.3$$

$$h = \frac{114.3 \times 0.0264}{0.025} = 120.7 \text{ W/m}^2 \text{ K}$$

From Equation 4.2.78,

$$\ln\left(\frac{100-50}{100-10}\right) = -\frac{120.7 \times A_s}{40 \times 1007} \qquad A_s = \pi \times 0.025 \times 3 \times 20 \times N$$

$$\underline{N = \text{number of rows} = 42}$$

Fan Power: From the first law of thermodynamics (see Chapter 2), the fan power is

$$\dot{W}_F = \dot{m}\left(\frac{p_i}{\rho_i} + \frac{p_e}{\rho_e} + \frac{\mathbf{v}_e^2}{2}\right)$$

p_i and p_e are the pressures at inlet and exit of the heat exchanger and $\mathbf{v}_e$ is the fluid velocity at exit. Assuming constant density evaluated at $(T_i + T_e)/2$ the pressure drop is found from Figure 4.2.18a.

$$\text{Re}_p = 17{,}865: \qquad a = b = S_T/d = 75/25 = 3$$

In Figure 4.2.18, although the friction factor is available for values of b up to 2.5, we will estimate the value of f for $b = 3$. From Figure 4.2.18, $f \approx 0.11$. The correction factor $c = 1$.

$$p_i - p_e = N\chi \frac{\rho U_{\max}^2}{2} f = 42 \times 1 \frac{1.165 \times 11.44^2}{2} \times 0.11 = 352.2 \text{ kPa}$$

$$\mathbf{v}_e = \frac{11.44 \times 50}{75} = 7.63 \text{ m/sec}$$

$$\dot{W}_F = 40\left(352.2 + \frac{7.63^2}{2}\right) = \underline{15{,}250 \text{ W}}$$

Heat Transfer with Jet Impingement

Jet impingement (Figure 4.2.20) on a heated (or cooled) surface results in high heat transfer rates, and is used in annealing of metals, tempering of glass, cooling of electronic equipment, internal combustion engines, and in a wide variety of industries — textiles, paper, wood, and so on. Usually, the jets are circular, issuing from a round nozzle of diameter d, or rectangular, issuing from a slot of width w. They may be used singly or in an array. The jets may impinge normally to the heated surface or at an angle. If there is no parallel solid surface close to the heated surface, the jet is said to be free; in the presence of a parallel surface close to the heated surface, the jet is termed confined. In this section only single, free jets (round or rectangular) impinging normally to the heated surface are considered.

Jets may be submerged with the fluid from the nozzle exiting into a body of a fluid (usually the same fluid), for example, air impinging on a surface surrounded by atmospheric air. In submerged jets entrained fluid (the part of the surrounding fluid dragged by the jet) has a significant effect on the flow and heat transfer characteristics of the jet, but the effect of gravity is usually negligible. In free-surface jets — a liquid jet in an atmosphere of air is a good approximation to a free-surface jet — the entrainment effect is usually negligible, but the effect of gravity may be significant.

A jet is usually divided into three regions, a free-jet region, a stagnation region, and a wall-jet region. In the free-jet region the effect of the target surface on the flow is negligible. In the stagnation region the target surface affects the flow field, and the velocity parallel to the surface increases while the velocity component normal to the surface decreases. At the beginning of the stagnation region, the axial velocity of the fluid is very much greater than the radial component (or the x-component) of the velocity. The stagnation region is followed by the wall-jet region where the radial component (or the x-component) of the velocity is much greater than the axial velocity.

The heat transfer coefficient is a function of H/d (or H/w), $\mathrm{Re}_d(\rho v_j d/\mu)$ or $(\rho v_j 2w/\mu)$, and Pr and depends on the region (stagnation or wall jet), whether it is submerged or nonsubmerged and whether

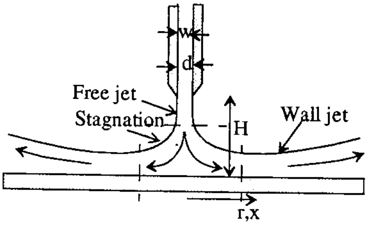

FIGURE 4.2.20 Circular jet of diameter d or a rectangular jet of width w.

the flow adjacent to the plate is laminar or turbulent. Some of the heat transfer correlations suggested by different researchers are given below. All the correlations are for single jets.

Submerged Jets: Single Circular Jets

$$\mathrm{Re}_d = \frac{4\dot{m}}{\pi d \mu} \qquad \mathrm{Nu}_d = \frac{hd}{k} \qquad \dot{m} = \text{mass rate of flow of fluid}$$

Average heat transfer coefficients up to radius r (Martin, 1990):

$$\mathrm{Nu}_d = 2\frac{d}{r}\frac{1-1.1d/r}{1+0.1(H/d-6)d/r}\left[\mathrm{Re}_d\left(1+\frac{\mathrm{Re}_d^{0.55}}{200}\right)\right]^{1/2}\mathrm{Pr}^{0.42} \tag{4.2.80}$$

Range of validity:

$$2000 \le \mathrm{Re}_d \le 400{,}000 \qquad 2.5 \le r/d \le 7.5 \qquad 2 \le H/d \le 12$$

Local convective heat transfer coefficient at radius r (Webb and Ma, 1995):

$$\mathrm{Nu}_d = 1.29\mathrm{Re}_d^{1/2}\mathrm{Pr}^{0.4}\left\{\left[\frac{\tanh(0.88r/d)}{r/d}\right]^{-8.5}+\left[1.69\left(\frac{r}{d}\right)^{-1.07}\right]^{-17}\right\}^{-1/17} \tag{4.2.81}$$

Submerged Jets: Single Rectangular Jet

$$\mathrm{Re}_w = \frac{\rho \mathbf{v}_j 2w}{\mu} = \frac{2\dot{m}}{\mu} \qquad \dot{m} = \text{mass rate of flow per unit length of jet}$$

$$\mathrm{Nu}_w = \frac{h2w}{k}$$

Average heat transfer coefficient (Martin, 1990):

$$\mathrm{Nu}_w = \frac{1.53\mathrm{Pr}^{0.42}\mathrm{Re}_w^m}{\dfrac{x}{2w}+\dfrac{H}{2w}+1.39} \tag{4.2.82}$$

$$m = 0.695 - \left[\frac{x}{2w}+\left(\frac{H}{2w}\right)^{1.33}+3.06\right]^{-1}$$

Free-Surface Jets: Single Circular Jet. Correlations are given in Table 4.2.5 (Liu et al., 1991 and Webb and Ma, 1995).

For more information on jet impingement heat transfer, refer to Martin (1977) and Webb and Ma (1995) and the references in the two papers.

TABLE 4.2.5 Correlations for Free-Surface Jets $r_v/d = 0.1773\,\text{Re}_d^{1/3}$

		Nu_d	
$r/d < 0.787$	$0.15 \le \text{Pr} \le 3$	$0.715\text{Re}_d^{1/2}\text{Pr}^{0.4}$	(4.2.83)
	$\text{Pr} > 3$	$0.797\text{Re}_d^{1/2}\text{Pr}^{1/3}$	(4.2.84)
$0.787 < r/d < r_v/d$		$0.632\text{Re}_d^{1/2}\text{Pr}^{1/3}\left(\dfrac{d}{r}\right)^{1/2}$	(4.2.85)
$r_v/d < r/d < r_t/d$		$\dfrac{0.407\text{Re}_d^{1/3}\text{Pr}^{1/3}(d/r)^{2/3}}{\left[\dfrac{0.1713}{(r/d)^2}+\dfrac{5.147}{\text{Re}_d}\dfrac{r}{d}\right]^{2/3}\left[\dfrac{(r/d)^2}{2}+C\right]^{1/3}}$ where $C = -5.051\times10^{-5}\text{Re}_d^{2/3}$ $\dfrac{r_t}{d} = \left\{-\dfrac{s}{2}+\left[\left(\dfrac{s}{2}\right)^2+\left(\dfrac{p}{3}\right)^3\right]^{1/2}\right\}^{1/3} + \left\{-\dfrac{s}{2}+\left[\left(\dfrac{s}{2}\right)^2-\left(\dfrac{p}{3}\right)^3\right]^{1/2}\right\}^{1/3}$ $p = \dfrac{-2C}{0.2058\text{Pr}-1} \qquad s = \dfrac{0.00686\text{Re}_d\text{Pr}}{0.2058\text{Pr}-1}$	(4.2.86)
$r > r_t$	$\text{Pr} < 4.86$	$\dfrac{0.25}{\dfrac{1}{\text{Re}_d\text{Pr}}\left[1-\left(\dfrac{r_t}{r}\right)^2\right]\left(\dfrac{r}{d}\right)^2+0.13\dfrac{h}{d}+0.0371\dfrac{h_t}{d}}$ where $h_t = h$ at r_t and $\dfrac{h}{d} = \dfrac{0.1713}{r/d}+\dfrac{5.147}{\text{Re}_d}\left(\dfrac{r}{d}\right)^2$	(4.2.87)

Bibliography

ASHRAE *Handbook of Fundamentals*, 1993. American Society of Heating, Ventilating and Air Conditioning Engineers, Atlanta, GA.

Hewitt, G.F., Ed. 1990. *Handbook of Heat Exchanger Design*, Hemisphere Publishing, New York.

Incropera, F.P. and Dewitt, D.P. 1990. *Fundamentals of Heat and Mass Transfer*, 3rd ed., John Wiley & Sons, New York.

Kakaç, S., Shah, R.K., and Win Aung, Eds. 1987. *Handbook of Single Phase Convective Heat Transfer*, Wiley-Interscience, New York.

Kreith, F. and Bohn, M.S. 1993. *Principles of Heat Transfer*, 5th ed., PWS, Boston.

Suryanarayana, N.V. 1995. *Engineering Heat Transfer*, PWS, Boston.

References

Achenbach, E. 1978. *Heat Transfer from Spheres up to Re = 6 × 10^6*, in *Proc. 6th Int. Heat Transfer Conf.,* Vol. 5, Hemisphere Publishing, Washington, D.C.

Burmeister, L.C. 1993. *Convective Heat Transfer*, Wiley-Interscience, New York.

Churchill, S.W. 1976. A comprehensive correlation equation for forced convection from a flat plate, *AIChE J.* 22(2), 264.

Churchill, S.W. and Bernstein, M. 1977. A correlating equation for forced convection from gases and liquids to a circular cylinder in cross flow, *J. Heat Transfer,* 99, 300.

Churchill, S.W. and Ozoe, H. 1973. Correlations for laminar forced convection with uniform heating in flow over a plate and in developing and fully developed flow in a tube, *J. Heat Transfer,* 18, 78.

Eckert, E.R.G. 1956. Engineering relations for heat transfer and friction in high-velocity laminar and turbulent boundary-layer flow over surfaces with constant pressure and temperature, *Trans. ASME*, 56, 1273.

Eckert, E.R.G. and Drake, M., Jr. 1986. *Analysis of Heat and Mass Transfer*, Hemisphere Publishers.

Ishiguro, R., Sugiyama, K., and Kumada, T. 1979. Heat transfer around a circular cylinder in a liquid-sodium cross flow, *Int. J. Heat Mass Transfer*, 22, 1041.

Jakob, H., 1949. *Heat Transfer*, John Wiley and Sons, London.

Kays, W.M. and Crawford, M.E. 1993. *Convective Heat and Mass Transfer*, 3rd ed., McGraw-Hill, New York.

Liu, X., Lienhard, v., J.H., and Lombara, J.S. 1991. Convective heat transfer by impingement of circular liquid jets, *J. Heat Transfer*, 113, 571.

Martin, H. 1977. Heat and mass transfer between impinging gas jets and solid surfaces, in *Advances in Heat Transfer*, Hartnett, J.P. and Irvine, T.F., Eds., 13, 1, Academic Press, New York.

Martin, H. 1990. Impinging jets, in *Handbook of Heat Exchanger Design*, Hewitt, G.F., Ed., Hemisphere, New York.

Morgan, Vincent T., 1975. The overall convective heat transfer from smooth circular cylinders, in *Advances in Heat Transfer*, Irvine, T.F. and Hartnett, J.P., Eds., 11, 199, Academic Press, New York.

Rose, J.W. 1979. Boundary layer flow on a flat plate, *Int. J. Heat Mass Transfer*, 22, 969.

Schlichting, H. 1979. *Boundary Layer Theory*, 7th ed., McGraw-Hill, New York.

Suryanarayana, N.V. 1995. *Engineering Heat Transfer*, West Publishing, Minneapolis.

Thomas, W.C. 1977. Note on the heat transfer equation for forced-convection flow over a flat plate with an unheated starting length, *Mech. Eng. News* (*ASEE*), 9(1), 19.

Webb, B.W. and Ma, C.F. 1995. Single-phase liquid jet impingement heat transfer, in *Advances in Heat Transfer*, Hartnett, J.P. and Irvine, T.F., Eds., 26, 105, Academic Press, New York.

Witte, L.C. 1968. An experimental study of forced-convection heat transfer from a sphere to liquid sodium, *J. Heat Transfer*, 90, 9.

Zukauskas, A. 1987. Convective heat transfer in cross flow, in *Handbook of Single-Phase Convective Heat Transfer*, Kakaç, S., Shah, R.K., and Win Aung, Eds., Wiley-Interscience, New York.

Further Information

Other sources for more detailed information about forced convection—external flows are:

Bejan, A. 1995. *Convection Heat Transfer*, 2nd ed., John Wiley & Sons, New York.

Bejan, A. and Kraus, A. 2003. *Heat Transfer Handbook,* Interscience, New York.

De Vahl Davis, G. and Leonardi, E. 2001. *Advances in Computational Heat Transfer II CHT'01: Proceedings of a Symposium*, Palm Cove, Queensland, Australia, Begell House, New York.

Incropera, F.P. and DeWitt, D.P. 2001. *Fundamentals of Heat and Mass Transfer*, 5th ed., John Wiley & Sons, New York.

Kakac, S. and Yener, Y. 1994. *Convection Heat Transfer*, 2nd ed., CRC Press, Boca Raton, FL.

Kreith, F. and Bohn, M.S. 2000. *Principles of Heat Transfer*, 6th ed., Brooks Cole.

Pelekasis, N.A. 1995. *Forced Convection and Sedimentation Past a Flat Plate*, National Aeronautics and Space Administration, Washington, D.C.

For applications of forced convection–external flow, see:

Kreith, F. (Ed.) 1999. *CRC Handbook of Thermal Engineering*, CRC Press, Boca Raton, FL.

A source for computational methods focusing on finite-difference methods is:

Tannehill, J.C., Anderson, D.A., and Pletcher, R.H. 1997. *Computational Fluid Mechanics and Heat Transfer*, 2nd ed., Taylor & Francis, Washington, D.C.

Numerous sources for programming codes are available on the World Wide Web, most of which are free, and can be found by using a search engine such as www.google.com.

Finite difference method: www.vector-space.com/free.hml
Fortran and MatLab codes: www.unige.ch/math/folks/hairer/software.html

Forced Convection — Internal Flows

N.V. Suryanarayana

Introduction

Heat transfer to (or from) a fluid flowing inside a tube or duct is termed *internal forced convection*. The fluid flow may be laminar or turbulent. If the Reynolds number based on the average velocity of the fluid and diameter of the tube ($\rho vd/\mu$) is less than 2100 (Reynolds numbers in the range of 2000 to 2300 are cited in different sources), the flow is laminar. If the Reynolds number is greater than 10,000, the flow is turbulent. The flow with a Reynolds number in the range 2100 to 10,000 is considered to be in the transitional regime. With heating or cooling of the fluid, there may or may not be a change in the phase of the fluid. Here, only heat transfer to or from a single-phase fluid is considered.

Fully Developed Velocity and Temperature Profiles. When a fluid enters a tube from a large reservoir, the velocity profile at the entrance is almost uniform as shown in Figure 4.2.21. The fluid in the immediate vicinity of the tube surface is decelerated and the velocity increases from zero at the surface to u_c at a distance δ from the surface; in the region $r = 0$ to $(R - \delta)$ the velocity is uniform. The value of δ increases in the direction of flow and with constant fluid density the value of the uniform velocity u_c increases. At some location downstream, δ reaches its maximum possible value, equal to the radius of the tube, and from that point onward the velocity profile does not change.

The region where δ increases, i.e., where the velocity profile changes, is known as the entrance region or hydrodynamically developing region. The region downstream from the axial location where δ reaches its maximum value and where the velocity profile does not change is the fully developed velocity profile or hydrodynamically fully developed region. Similarly, downstream of the location where heating or cooling of the fluid starts, the temperature profile changes in the direction of flow. But beyond a certain distance the dimensionless temperature profile does not change in the direction of flow. The region where

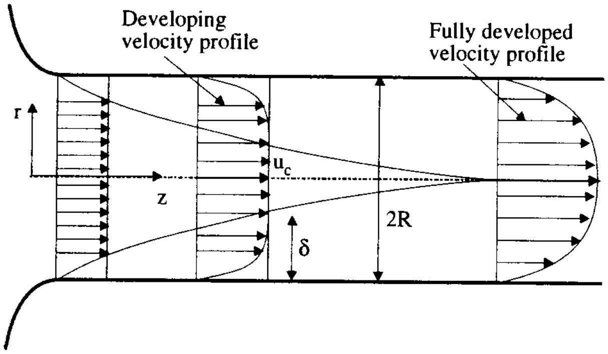

FIGURE 4.2.21 Developing and fully developed velocity profiles.

the dimensionless temperature profile changes is the thermally developing region or the thermal entrance region, and the region where the dimensionless temperature profile does not change is the thermally fully developed region. For simultaneously developing velocity and temperature profiles in laminar flows, the hydrodynamic and thermal entrance lengths are given by

$$\frac{L_e}{d} = 0.0565\text{Re}_d \tag{4.2.88}$$

$$\frac{L_{e,th}}{d} = 0.053\text{Re}_d\text{Pr} \qquad \text{Uniform heat flux} \tag{4.2.89}$$

$$\frac{L_{e,th}}{d} = 0.037\text{RePr} \qquad \text{Uniform surface temperature} \tag{4.2.90}$$

In most engineering applications, with turbulent flows, correlations for fully developed conditions can be used after about 10 diameters from where the heating starts.

Convective Heat Transfer Coefficient and Bulk Temperature. The reference temperature for defining the convective heat transfer coefficient is the bulk temperature T_b and the convective heat flux is given by

$$q'' = h\left(T_s - T_b\right) \tag{4.2.91}$$

The bulk temperature T_b is determined from the relation

$$T_b = \frac{\int_{A_c} \rho v C_p T dA_c}{\int_{A_c} \rho v C_p dA_c} \tag{4.2.92}$$

where A_c is the cross-sectional area perpendicular to the axis of the tube.

If the fluid is drained from the tube at a particular axial location and mixed, the temperature of the mixed fluid is the bulk temperature. It is also know as the mixing cup temperature. With heating or cooling of the fluid the bulk temperature varies in the direction of flow. In some cases we use the term *mean fluid temperature*, T_m, to represent the arithmetic mean of the fluid bulk temperatures at inlet and exit of the tube.

Heat Transfer Correlations

Laminar Flows — Entrance Region. For laminar flows in a tube with uniform surface temperature, in the entrance region the correlation of Sieder and Tate (1936) is

$$\overline{\text{Nu}_d} = 1.86\left(\frac{\text{Re}_d\text{Pr}}{L/d}\right)^{1/3}\left(\frac{\mu}{\mu_s}\right)^{0.14} \tag{4.2.93}$$

valid for

$$\frac{L}{d} < \frac{\text{Re}_d\text{Pr}}{8}\left(\frac{\mu}{\mu_s}\right)^{0.42} \qquad 0.48 < \text{Pr} < 16{,}700 \qquad 0.0044 < \frac{\mu}{\mu_s} < 9.75$$

The overbar in the Nusselt number indicates that it is formed with the average heat transfer coefficient over the entire length of the tube. Properties of the fluid are evaluated at the arithmetic mean of the inlet and exit bulk temperatures. In Equation (4.2.93) the heat transfer coefficient was determined from

$$q = \bar{h}\pi dL\left(T_s - \frac{T_{bi} + T_{be}}{2}\right) \tag{4.2.94}$$

Therefore, to find the total heat transfer rate with $\bar{h}$ from Equation (4.2.93) employ Equation (4.2.94).

Laminar Flows — Fully Developed Velocity and Temperature Profiles. Evaluate properties at the bulk temperature

$$\text{Uniform Surface Temperature} \qquad \text{Nu}_d = 3.66 \tag{4.2.95}$$

$$\text{Uniform Surface Heat Flux} \qquad \text{Nu}_d = 4.36 \tag{4.2.96}$$

Turbulent Flows. If the flow is turbulent, the difference between the correlations with uniform surface temperature and uniform surface heat flux is not significant and the correlations can be used for both cases. For turbulent flows, Gnielinsky (1976, 1990) recommends:

Evaluate properties at the bulk temperature.

$0.6 < \text{Pr} < 2000 \qquad 2300 < \text{Re}_d < 10^6 \qquad 0 < d/L < 1$

$$\text{Nu}_d = \frac{(f/2)(\text{Re}_d - 1000)\text{Pr}}{1 + 12.7(f/2)^{1/2}\left(\text{Pr}^{2/3} - 1\right)}\left[1 + \left(\frac{d}{L}\right)^{2/3}\right] \tag{4.2.97}$$

$$f = \left[1.58\ln(\text{Re}_d) - 3.28\right]^{-2} \tag{4.2.98}$$

f = friction factor = $2\tau_w/\rho v^2$.

To reflect the effect of variation of fluid properties with temperature, multiply the Nusselt numbers in Equation (4.2.97) by $(T_b/T_s)^{0.45}$ for gases and $(\text{Pr}/\text{Pr}_s)^{0.11}$ for liquids where the temperatures are absolute, and T and Pr with a subscript s are to be evaluated at the surface temperature. The equations can be used to evaluate the heat transfer coefficient in the developing profile region. To determine the heat transfer coefficient in the fully developed region set $d/L = 0$. A simpler correlation (fully developed region) is the Dittus–Boelter (1930) equation. Evaluate properties at T_b.

$0.7 \le \text{Pr} \le 160 \qquad \text{Re}_d > 10{,}000 \qquad d/L > 10$

$$\text{Nu}_d = 0.023\text{Re}_d^{4/5}\text{Pr}^n \tag{4.2.99}$$

where $n = 0.4$ for heating ($T_s > T_b$) and $n = 0.3$ for cooling ($T_s < T_b$).

For liquid metals with $\text{Pr} \ll 1$ the correlations due to Sleicher and Rouse (1976) are

Uniform surface temperature:

$$\text{Nu}_{d,b} = 4.8 + 0.0156\text{Re}_{d,f}^{0.85}\text{Pr}_s^{0.93} \tag{4.2.100}$$

Uniform heat flux:

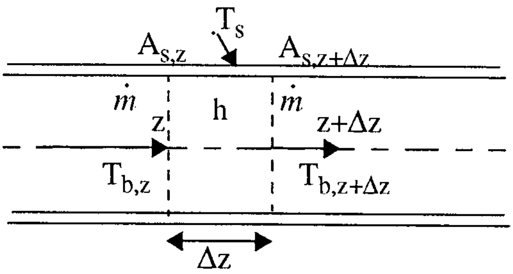

FIGURE 4.2.22 Elemental length of a tube for determining heat transfer rate.

$$\mathrm{Nu}_{d,b} = 6.3 + 0.0167\mathrm{Re}_{d,f}^{0.85}\mathrm{Pr}_s^{0.93} \tag{4.2.101}$$

Subscripts *b*, *f*, and *s* indicate that the variables are to be evaluated at the bulk temperature, film temperature (arithmetic mean of the bulk and surface temperatures), and surface temperature, respectively.

In the computations of the Nusselt number the properties (evaluated at the bulk temperature) vary in the direction of flow and hence give different values of *h* at different locations. In many cases a representative average value of the convective heat transfer coefficient is needed. Such an average value can be obtained either by taking the arithmetic average of the convective heat transfer coefficients evaluated at the inlet and exit bulk temperatures or the convective heat transfer coefficient evaluated at the arithmetic mean of the inlet and exit bulk temperatures. If the variation of the convective heat transfer coefficient is large, it may be appropriate to divide the tube into shorter lengths with smaller variation in the bulk temperatures and evaluating the average heat transfer coefficient in each section.

Uniform Surface Temperature — Relation between the Convective Heat Transfer Coefficient and the Total Heat Transfer Rate: With a uniform surface temperature, employing an average value of the convective heat transfer coefficient the local convective heat flux varies in the direction of flow. To relate the convective heat transfer coefficient to the temperatures and the surface area, we have, for the elemental length Δ*z* (Figure 4.2.22).

$$\dot{m}C_p \frac{dT_b}{dz} = h\frac{dA_s}{dz}\left(T_s - T_b\right) \tag{4.2.102}$$

Assuming a suitable average convective heat transfer coefficient over the entire length of the tube, separating the variables, and integrating the equation from $z = 0$ to $z = L$, we obtain

$$\ln\frac{T_s - T_{be}}{T_s - T_{bi}} = -\frac{hA_s}{\dot{m}C_p} \tag{4.2.103}$$

Equation (4.2.103) gives the exit temperature. For a constant-density fluid or an ideal gas, the heat transfer rate is determined from

$$q = \dot{m}C_p\left(T_{be} - T_{bi}\right) \tag{4.2.104}$$

Equation (4.2.103) was derived on the basis of uniform convective heat transfer coefficient. However, if the functional relationship between *h* and T_b is known, Equation (4.2.102) can be integrated by substituting the relationship. The convective heat transfer coefficient variation with T_b for water in two tubes of different diameters for two different flow rates is shown in Figure 4.2.23. From the figure it is clear that *h* can be very well approximated as a linear function of *T*. By substituting such a linear function relationship into Equation (4.2.102), it can be shown that

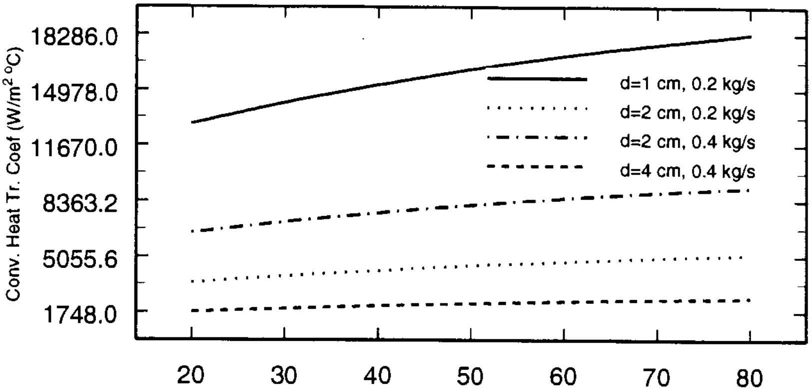

FIGURE 4.2.23 Variation of h with T_b in 1-, 2-, and 4-cm-diameter tubes with water flow rates of 0.2 kg/sec and 0.4 kg/sec with uniform surface temperature.

$$\ln \frac{h_i}{h_e} \frac{T_s - T_{be}}{T_s - T_{bi}} = -\frac{h_s A_s}{\dot{m} C_p} \tag{4.2.105}$$

where h_i, h_e, and h_s are the values of the convective heat transfer coefficient evaluated at bulk temperatures of T_{bi}, T_{be}, and T_s, respectively. Although it has been demonstrated that h varies approximately linearly with the bulk temperature with water as the fluid, the variation of h with air and oil as the fluid is much smaller and is very well approximated by a linear relationship. For other fluids it is suggested that the relationship be verified before employing Equation (4.2.105). [**Note:** It is tempting to determine the heat transfer rate from the relation

$$q = hA_s \frac{(T_s - T_{be}) + (T_s - T_{bi})}{2}$$

Replacing q by Equation (4.2.104) and solving for T_{be} for defined values of the mass flow rate and tube surface area, the second law of thermodynamics will be violated if $hA_s / \dot{m}C_p > 2$. Use of Equation (4.2.103) or (4.2.105) ensures that no violation of the second law occurs however large A_s is.]

Uniform Surface Heat Flux: If the imposed heat flux is known, the total heat transfer rate for a defined length of the tube is also known. From Equation (4.2.104) the exit temperature of the fluid is determined. The fluid temperature at any location in the pipe is known from the heat transfer rate up to that location ($q = q''A_s$) and Equation (4.2.104). The convective heat transfer coefficient is used to find the surface temperature of the tube.

Temperature Variation of the Fluid with Uniform Surface Temperature and Uniform Heat Flux: The fluid temperature variations in the two cases are different. With the assumption of uniform heat transfer coefficient, with a uniform surface temperature the heat flux decreases in the direction of flow leading to a progressively decreasing rate of temperature change in the fluid with axial distance. With uniform heat flux, the surface and fluid temperatures vary linearly except in the entrance region where the higher heat transfer coefficient leads to a smaller difference between the surface and fluid temperatures. The variation of the fluid temperature in the two cases is shown in Figure 4.2.24.

Convective Heat Transfer in Noncircular Tubes

Laminar Flows: The Nusselt numbers for laminar flows have been analytically determined for different noncircular ducts. Some of them can be found in Kakac et al. (1987), Kays and Crawford (1993), and Burmeister (1993). A few of the results are given below. The characteristic length for forming the Reynolds number and Nusselt number is the hydraulic mean diameter defined as

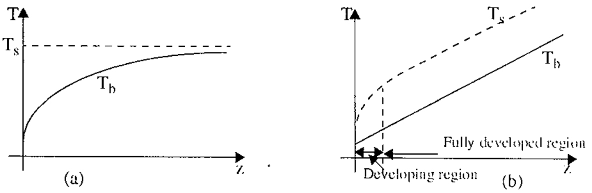

FIGURE 4.2.24 Variation of fluid temperature in a tube with (a) uniform surface temperature and (b) uniform heat flux.

$$d_h = \frac{4 \text{ cross-sectional area}}{\text{wetted perimeter}}$$

Infinite parallel plates: a = spacing between plates, $d_h = 2a$

Both plates maintained at uniform and equal temperatures: Nu = 7.54
Both plates with imposed uniform and equal heat fluxes: Nu = 8.24

Rectangular ducts: a = longer side, b = shorter side, $d_h = 2ab/(a + b)$

b/a	1	0.7	0.5	0.25	0.125
Uniform surface temperature	2.98	3.08	3.39	4.44	5.6
Uniform heat flux*	3.61	3.73	4.12	5.33	6.49

Equilateral triangle: $d_h = a/3^{1/2}$, a = length of each side

Uniform surface temperature: Nu = 2.35
Uniform surface heat flux:* Nu = 3.0

Coaxial tubes: With coaxial tubes many different cases arise — each tube maintained at uniform but different temperatures, each tube subjected to uniform but different heat fluxes (an insulated surface is a special case of imposed heat flux being zero), or a combinations of uniform surface temperature of one tube and heat flux on the other. The manner in which the heat transfer coefficient is determined for uniform but different heat fluxes on the two tubes is described below. Define:

$$d_h = 2(r_o - r_i) \qquad r^* = r_i/r_o$$

$$q_i'' = h_i(T_i - T_b) \qquad \mathrm{Nu}_i = \frac{h_i d_h}{k} \qquad q_o'' = h_o(T_o - T_b) \qquad \mathrm{Nu}_o = \frac{h_o d_h}{k}$$

$$q_o'' = 0 \qquad \mathrm{Nu}_{ii} = \frac{h_i d_h}{k} \quad \text{and} \quad q_i'' = 0 \qquad \mathrm{Nu}_{oo} = \frac{h_o d_h}{k}$$

Then

$$\mathrm{Nu}_i = \frac{\mathrm{Nu}_{ii}}{1 - \dfrac{q_o''}{q_i''}\theta_i^*} \quad \text{and} \quad \mathrm{Nu}_o = \frac{\mathrm{Nu}_{oo}}{1 - \dfrac{q_i''}{q_o''}\theta_o^*} \tag{4.2.106}$$

Some of the values needed for the computations of Nu_i and Nu_o (taken from Kays and Crawford, 1993) are given in the Table 4.2.6.

---

* Uniform axial heat flux but circumferentially uniform surface temperature.

TABLE 4.2.6 Values for Use with Equation (4.2.106)

r^*	Nu_{ii}	Nu_{oo}	θ_i^*	θ_o^*
0.05	17.81	4.792	2.18	0.0294
0.1	11.91	4.834	1.383	0.0562
0.2	8.499	4.883	0.905	0.1041
0.4	6.583	4.979	0.603	0.1823
0.6	5.912	5.099	0.473	0.2455
0.8	5.58	5.24	0.401	0.299
1.0	5.385	5.385	0.346	0.346

For a more detailed information on heat transfer and friction factors for laminar flows in noncircular tubes refer to Kakac et al. (1987).

Turbulent Flows: For noncircular tubes, estimates of the convective heat transfer coefficient can be obtained by employing equations for circular tubes with d_h replacing d in the computations of the Reynolds and Nusselt numbers. To determine the heat transfer coefficients in developing regions and for more-accurate values with turbulent flows in noncircular tubes refer to Kakac et al. (1987) and the references in that book.

Mixed Convection

If the fluid velocity is low, the effect of natural convection becomes significant and the heat transfer rate may be increased or decreased by natural convection. From a review of experimental results, Metais and Eckert (1964) developed maps to delineate the different regimes where one or the other mode is dominant and where both are significant. Figure 4.2.25 and Figure 4.2.26 show the relative significance of natural and forced convection in vertical and horizontal tubes. The maps are applicable for $10^{-2} < \Pr(d/L) < 1$ where d and L are the diameter and the axial length of the tube. The maps show the limits of forced and natural convection regimes. The limits are delineated "in such a way that the actual heat flux under the combined influence of the forces does not deviate by more than 10 percent from the heat flux that would be caused by the external forces alone or by the body forces alone." The Grashof number is based on the diameter of the tube.

For flows in horizontal tubes, correlations were developed for the mixed convection regime in isothermal tubes by Depew and August (1971) and for uniform heat flux by Morcos and Bergles (1975).

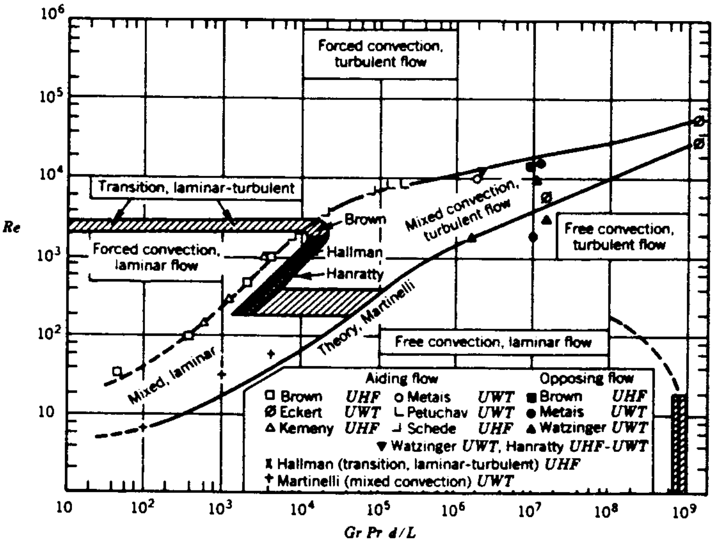

FIGURE 4.2.25 Map delineating forced, mixed, and natural convection — vertical tubes.

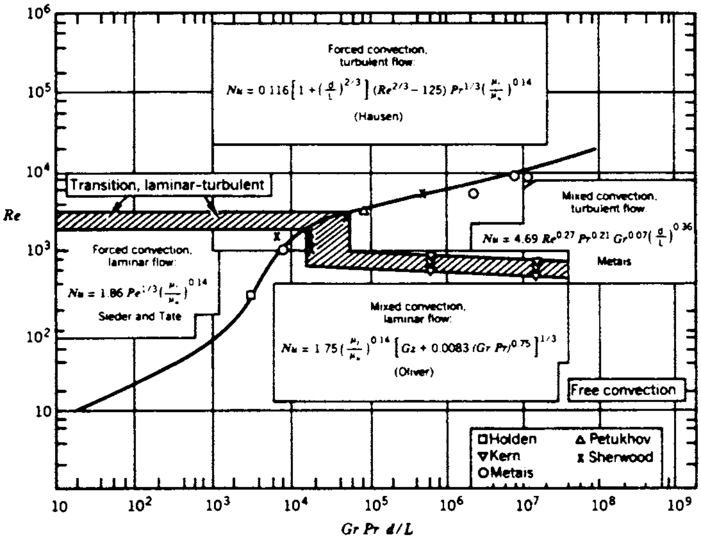

FIGURE 4.2.26 Map delineating forced, mixed, and natural convection — horizontal tubes.

Uniform Surface Temperature. Fully developed velocity profile, developing temperature profile:

$L/d < 28.4$ $\quad$ $25 < \text{Gz} < 712$ $\quad$ $0.7 \times 10^5 < \text{Gr} < 9.9 \times 10^5$
μ_s = dynamic viscosity, evaluated at the wall temperature
All other properties at the average bulk temperature of the fluid

$$\text{Gz} = \frac{\dot{m}C_p}{kL} \qquad \text{Gr} = g\beta\Delta T\, d^3/\nu^2$$

$$\text{Nu}_d = 1.75\left[\text{Gz} + 0.12\left(\text{Gz}\text{Gr}^{1/3}\text{Pr}^{0.36}\right)^{0.88}\right]^{1/3}\left(\mu_b/\mu_s\right)^{0.14} \tag{4.2.107}$$

Uniform Heat Flux. Properties at $(T_s + T_b)/2$: $3 \times 10^4 < \text{Ra} < 10^6$, $4 < \text{Pr} < 175$, $2 < hd^2/(k_w t) < 66$, k_w = tube wall thermal conductivity, t = tube wall thickness.

$$\text{Gr}_d^* = g\beta d^4 q_w''/\left(\nu^2 k\right) \qquad P_w = kd/\left(k_w t\right) \qquad \text{Ra}_d = g\beta\Delta T\, d^3\text{Pr}/\nu^2$$

$$\text{Nu}_d = \left\{4.36^2 + \left[0.145\left(\frac{\text{Gr}_d^*\text{Pr}^{1.35}}{P_w^{0.25}}\right)^{0.265}\right]^2\right\}^{0.5} \tag{4.2.108}$$

In Equation (4.2.107) and (4.2.108) evaluate fluid properties at the arithmetic mean of the bulk and wall temperatures.

Nomenclature

A_s	surface area
d	diameter
d_h	hydraulic mean diameter
f	friction factor

h	convective heat transfer coefficient
k	fluid thermal conductivity
$\mathrm{L_e}$	hydrodynamic entrance length
$\mathrm{L_{e,th}}$	thermal entrance length
Nu_d	Nusselt number
Nu_{ii}	Nusselt number with only inner tube heated
Nu_{oo}	Nusselt number with only outer tube heated
Pr	Prandtl number
q''	heat flux
q_i''	heat flux on the inner tube surface
q_o''	heat flux on the outer tube surface
Re_d	Reynolds number ($\rho vd/\mu$)
$\mathrm{T_b}$	bulk temperature
$\mathrm{T_s}$	surface temperature
v	average fluid velocity
μ	dynamic viscosity
μ_s	dynamic viscosity at surface temperature
ρ	fluid density

References

Burmeister, L.C. 1993. *Convective Heat Transfer*, 2nd ed., Wiley-Interscience, New York.

Depew, C.A. and August, S.E. 1971. Heat transfer due to combined free and forced convection in a horizontal and isothermal tube, *Trans. ASME* 93C, 380.

Dittus, F.W. and Boelter, L.M.K. 1930. Heat transfer in automobile radiators of the tubular type, *Univ. Calif. Pub. Eng.*, 13, 443.

Gnielinsky, V. 1976. New equations for heat and mass transfer in turbulent pipe channel flow, *Int. Chem. Eng.*, 16, 359.

Gnielinsky, V. 1990. Forced convection in ducts, in *Handbook of Heat Exchanger Design*, Hewitt, G.F., Ed., Begell House/Hemisphere, New York.

Kakac, S., Shah, R.K., and Win Aung, Eds. 1987. *Handbook of Single-Phase Convective Heat Transfer*, Wiley-Interscience, New York.

Kays, W.M. and Crawford, M.E. 1993. *Convective Heat and Mass Transfer*, 3rd ed., McGraw-Hill, New York.

Metais, B. and Eckert, E.R.G. 1964. Forced, mixed, and free convection regimes, *Trans. ASME* 86C, 295.

Morcos, S.M. and Bergles, A.E. 1975. Experimental investigation of combined forced and free laminar convection in a horizontal tube, *Trans. ASME* 97C, 212.

Sieder, E.N. and Tate, C.E. 1936. Heat transfer and pressure drop of liquids in tubes, *Ind. Eng. Chem.*, 28, 1429.

Sleicher, C.A. and Rouse, M.W. 1976. A convenient correlation for heat transfer to constant and variable property fluids in turbulent pipe flow, *Int. J. Heat Mass Transfer,* 18, 677.

Further Information

Other sources for more detailed information about forced convection—internal flows are:

Bejan, A. 1995. *Convection Heat Transfer*, 2nd ed., John Wiley & Sons, New York.

Bejan, A. and Kraus, A. 2003. *Heat Transfer Handbook*, Interscience, New York.

De Vahl Davis, G. and Leonardi, E. 2001. *Advances in Computational Heat Transfer II CHT'01: Proceedings of a Symposium*, Palm Cove, Queensland, Australia, Begell House, New York.

Incropera, F.P. and DeWitt, D.P. 2001. *Fundamentals of Heat and Mass Transfer*, 5th ed., John Wiley & Sons, New York.

Kakac, S. and Yener, Y. 1994. *Convection Heat Transfer*, 2nd ed., CRC Press, Boca Raton, FL.
Kreith, F. and Bohn, M.S. 2000. *Principles of Heat Transfer*, 6th ed., Brooks Cole.
Manglik, R.M. 1996. *Process, Enhanced, and Multiphase Heat Transfer*, Begell House, New York.
Vasiliev, L.L. 1993. *Heat Pipe Technology*, Begell House, New York.

For applications of forced convection–internal flows, see:

Kreith, F. (Ed.) 1999. *CRC Handbook of Thermal Engineering*, CRC Press, Boca Raton, FL.

A source for computational methods focusing on finite-difference methods is:

Tannehill, J.C., Anderson, D.A., and Pletcher, R.H. 1997. *Computational Fluid Mechanics and Heat Transfer*, 2nd ed., Taylor & Francis, Washington, D.C.

Numerous sources for programming codes are available on the World Wide Web, most of which are free, and can be found by using a search engine such as www.google.com.

Finite difference method: www.vector-space.com/free.hml
Fortran and MatLab codes: www.unige.ch/math/folks/hairer/software.html

4.3 Radiation

Michael F. Modest

Nature of Thermal Radiation

All materials continuously emit and absorb radiative energy by lowering or raising their molecular energy levels. This thermal radiative energy may be viewed as consisting of electromagnetic waves or of massless energy parcels, called **photons**. Electromagnetic waves travel through any medium at the speed of light c, which is $c_0 = 2.998 \times 10^8$ m/sec in vacuum and approximately the same in most gases such as air and combustion products. They are characterized by their wavelength λ (usually measured in $\mu\text{m} = 10^{-6}$ m) or frequency ν (usually measured in cycles/s = Hz), which are related by

$$\nu = c/\lambda \tag{4.3.1}$$

The strength and wavelengths of **emission** and **absorption** depend on the temperature and nature of the material.

The ability of photons to travel unimpeded through vacuum and gases makes thermal radiation the dominant mode of heat transfer in vacuum, low-pressure environments and outer space applications (due to the near absence of conduction and convection). Its temperature dependence (as given by Equation 4.3.3), on the other hand, guarantees that radiative heat transfer is of utmost importance in high-temperature applications (including solar radiation with the sun a high-temperature heat source at an effective temperature of $T_{\text{sun}} = 5777$ K).

When an electromagnetic wave traveling through a gas (or vacuum) strikes the surface of a medium, the wave may be partly or totally reflected, and any nonreflected part will penetrate into the medium. If a wave passes through a medium without any attenuation, the material is called **transparent**. A body with partial attenuation is known as **semitransparent**, and a body through which none of the incoming radiation penetrates is called **opaque**. Most gases are rather transparent to radiation (except for narrow spectral regions, called absorption bands) and most solids tend to be strong absorbers for most wavelengths, making them opaque over a distance of a few nanometers (electrical conductors, i.e., metals) to a few micrometers (ceramics, semiconductors), or more (dielectrics).

Blackbody Radiation

The total amount of radiative energy emitted from a surface into all directions above it is termed emissive power; a distinction is made between spectral (at a given wavelength λ per unit wavelength) and total (encompassing all wavelengths) emissive power. The magnitude of emissive power depends on wavelength λ, temperature T, and a surface property, called emittance ε, that relates the ability of a surface to emit radiative energy to that of an ideal surface, which emits the maximum possible energy (at a given wavelength and temperature). Such an ideal surface is known as a "blackbody" or "black surface" because it absorbs all incoming radiation; i.e., it reflects no radiation and is, therefore, invisible (black) to the human eye. The spectral distribution of the emissive power of a black surface (i.e., its dependence on the spectral variable, for example, λ) is given by Planck's law as

$$E_{b\lambda} = \frac{C_1}{\lambda^5\left[e^{C_2/\lambda T} - 1\right]}, \quad C_1 = 3.7419 \times 10^{-16}\ \mathrm{Wm}^2, \quad C_2 = 14,388\ \mu\mathrm{mK} \tag{4.3.2}$$

where C_1 and C_2 are sometimes called Planck function constants, or the first and second radiation constant, respectively. The total emissive power of a blackbody is given by

$$E_b = \int_0^\infty E_{b\lambda}\, d\lambda = \sigma T^4, \quad \sigma = 5.670 \times 10^{-8}\ \mathrm{W/m^2K^4} \tag{4.3.3}$$

with σ known as the Stefan–Boltzmann constant. Figure 4.3.1 shows the spectral solar irradiation that impinges on Earth, which closely resembles the spectrum of a blackbody at 5777 K. The general behavior of Planck's law is depicted in Figure 4.3.2, together with the fractional emissive power, $f(\lambda T)$, defined as

$$f(\lambda T) = \frac{1}{E_b}\int_0^\lambda E_{b\lambda}(\lambda, T)\, d\lambda \tag{4.3.4}$$

Note that 80% of all blackbody emission takes place between the wavelengths of $\lambda T > 2200\ \mu$mK and $\lambda T < 9400\ \mu$mK. This implies that, for typical high-temperature heat transfer applications in the range between 1000 and 2000 K, infrared wavelengths in the range 1 μm < λ < 10 μm govern the heat transfer

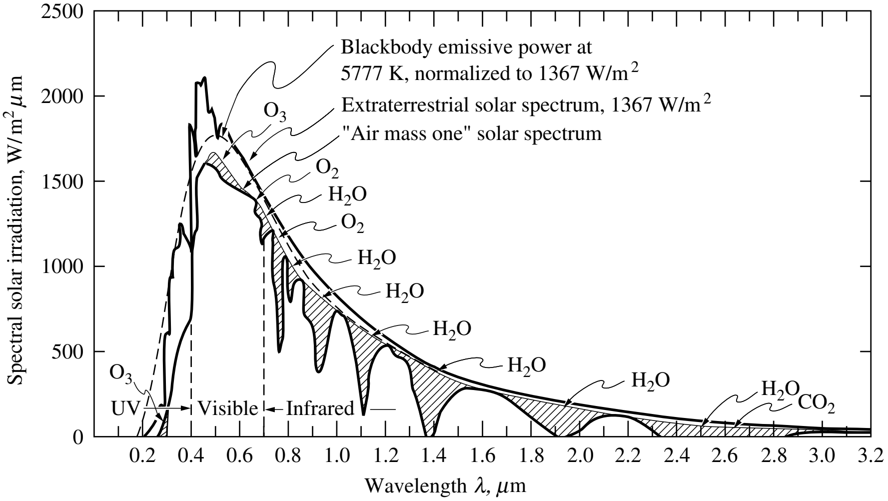

FIGURE 4.3.1 Solar irradiation onto Earth.

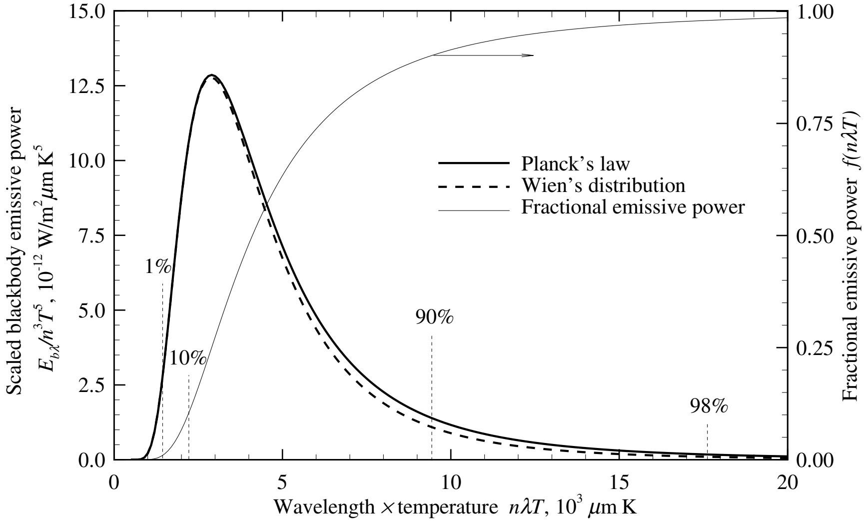

FIGURE 4.3.2 Normalized blackbody emissive power spectrum.

rates. For solar applications, shorter wavelengths, down to λ ≅ 0.4 μm, are also important. Also shown in Figure 4.3.2 is Wien's law:

$$E_{b\lambda} = \frac{C_1}{\lambda^5} e^{-C_2/\lambda T} \tag{4.3.5}$$

which approximates Planck's law accurately over the part of the spectrum that is important to heat transfer and easier to manipulate mathematically.

Example 4.3.1

What fraction of total solar emission falls into the visible spectrum (0.4 to 0.7 μm)?

Solution. With a solar temperature of 5777 K, it follows that for

$$\lambda_1 = 0.4\ \mu\text{m}, \qquad \lambda_1 T_{\text{sun}} = 0.4 \times 5777 = 2311\ \mu\text{mK}$$

and for

$$\lambda_2 = 0.7\ \mu\text{m}, \qquad \lambda_2 T_{\text{sun}} = 0.7 \times 5777 = 4044\ \mu\text{mK}$$

From Figure 4.3.2, one can estimate $f(\lambda_1 T_{\text{sun}}) \cong 12\%$ and $f(\lambda_2 T_{\text{sun}}) \cong 49\%$. Thus, the visible fraction of sunlight is 49 – 12 ≅ 37%: with a bandwidth of only 0.3 μm, the human eye responds to approximately 37% of all emitted sunlight.

Radiative Exchange between Opaque Surfaces

Radiative Properties of Surfaces

Strictly speaking, the surface of an enclosure wall can only reflect radiative energy and allow a part of it to penetrate into the substrate. A surface cannot absorb or emit photons; attenuation takes place inside the solid, as does emission of radiative energy (with some of the emitted energy escaping through the surface into the enclosure). In practical systems, the thickness of the surface layer over which absorption of **irradiation** from inside the enclosure occurs is very small compared with the overall dimension of an enclosure — usually a few nanometers for metals and a few micrometers for most nonmetals. The same may be said about emission from within the walls that escapes into the enclosure. Thus, in the case of opaque walls, it is customary to speak of absorption by and emission from a "surface," although a thin surface layer is implied.

Four fundamental radiative properties are defined:

Reflectance, $$\rho \equiv \frac{\text{reflected part of incoming radiation}}{\text{total incoming radiation}} \tag{4.3.6a}$$

Absorptance, $$\alpha \equiv \frac{\text{absorbed part of incoming radiation}}{\text{total incoming radiation}} \tag{4.3.6b}$$

Transmittance, $$\tau \equiv \frac{\text{transmitted part of incoming radiation}}{\text{total incoming radiation}} \tag{4.3.6c}$$

Emittance, $$\varepsilon \equiv \frac{\text{energy emitted from a surface}}{\text{energy emitted by a black surface at same temperature}} \tag{4.3.6d}$$

Because all incoming radiation must be reflected, absorbed, or transmitted, it follows that

$$\rho + \alpha + \tau = 1 \tag{4.37}$$

In most practical applications, surface layers are thick enough to be opaque ($\tau = 0$, leading to $\rho + \alpha = 1$. All four properties may be functions of wavelength, temperature, incoming direction (except emittance), and outgoing direction (except absorptance).

Directional Behavior. For heat transfer applications, the dependence on incoming direction for absorptance (as well as ρ and τ) and outgoing direction for emittance is generally weak and is commonly neglected; i.e., it is assumed that the surface absorbs and emits **diffusely**. Then, for an opaque surface, at any given wavelength

$$\varepsilon_\lambda = \alpha_\lambda = 1 - \rho_\lambda \tag{4.38}$$

Published values of emittance are generally "normal emittance" (the directional value of ε_λ in the direction perpendicular to the surface) or "hemispherical emittance" (an average value over all outgoing directions). The difference between these two values is often smaller than experimental accuracy and/or repeatability.

Reflected energy (due to a single, distinct incoming direction) may leave the surface in a single direction ("specular" reflection, similar to reflection from a mirror for visible light), or the reflection may spread out over all possible outgoing directions. In the extreme case of equal amounts going into all directions, "diffuse" reflection takes place. Smooth surfaces (as compared with the wavelength of radiation) tend to be specular reflectors, while rough surfaces tend to be more or less diffusely reflecting. Analysis is vastly simplified if diffuse reflections are assumed. Research has shown that — except for some extreme geometries and irradiation conditions susceptible to beam channeling (irradiated open cavities, channels with large aspect ratios) — radiative heat transfer rates are only weakly affected by the directional distribution of reflections. Therefore, it is common practice to carry out radiative heat transfer calculations assuming only diffuse reflections.

Spectral Dependence. The emittance of a surface generally varies strongly and in complex ways with wavelength, depending on the material, surface layer composition, and surface structure (roughness).

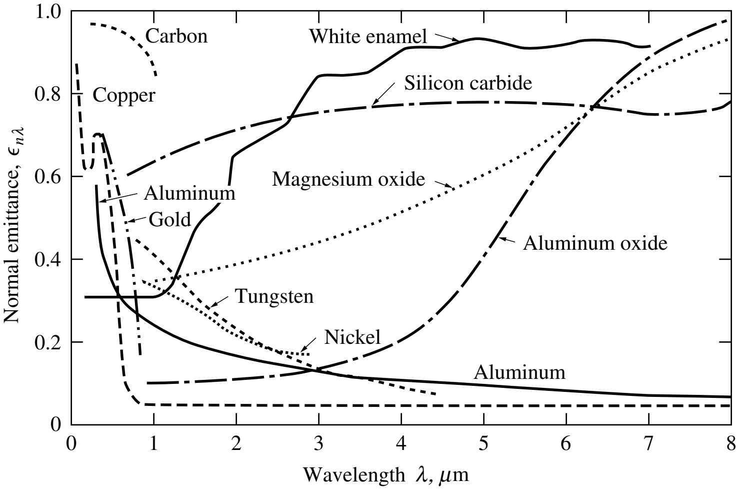

FIGURE 4.3.3 Normal, spectral emittances for selected materials.

Therefore, unlike bulk material properties (such as thermal conductivity), the surface emittance may display significant differences between two ostensibly identical samples, and even for the same sample measured at different times (due to surface roughness and contamination). Despite these difficulties, surfaces may be loosely grouped into two categories — metals and nonconductors (dielectrics) — and some generalizations can be made.

Polished Metals. Smooth, purely metallic surfaces (i.e., without any nonmetallic surface contamination, such as metal oxides) tend to have very low emittances in the infrared. For many clean metals, $\varepsilon_\lambda < 0.1$ for $\lambda > 2$ µm, and spectral as well as temperature dependence is generally well approximated by the proportionality $\varepsilon_\lambda \propto \sqrt{T/\lambda}$ in the infrared. However, for shorter wavelengths ($\lambda < 1$ µm), emittance values may become quite substantial, and temperature dependence is usually reversed (decreasing, rather than increasing, with temperature). Typical room temperature behavior of several metals is shown in Figure 4.3.3. Caution needs to be exercised when choosing an emittance value for a metal surface; unless extraordinary care is taken to keep a polished metal clean (i.e., free from oxidation and/or surface contamination), its emittance may soon become several times the value of the original, polished specimen (for example, consider the formation of aluminum oxide on top of aluminum, Figure 4.3.3).

Ceramics and Refractories. Smooth ceramics tend to have fairly constant and intermediate emittance over the near- to mid-infrared, followed by a sharp increase somewhere between 4 and 10 µm. At short wavelengths, these materials display strong decreases in emittance, so a number of them may appear white to the human eye even though they are fairly black in the infrared. The temperature dependence of the emittance of ceramics is rather weak; generally, a slight increase with temperature is observed in the infrared. The spectral emittance of a few ceramics is also shown in Figure 4.3.3.

Other Nonconductors. The behavior of most electrically nonconducting materials is governed by surface structure, nonhomogeneity, dopants, porosity, flaws, surface films, etc. The emittance may vary irregularly across the spectrum because of various emission bands, influence of flaws, etc., thus making any generalization impossible. This irregularity may be exploited to obtain surfaces of desired spectral behavior, so-called selective surfaces. Some selective surfaces (as compared with a common steel) are depicted in Figure 4.3.4. For a solar collector, it is desirable to have a high spectral emittance for short wavelengths $\lambda < 2.5$ µm (strong absorption of solar irradiation) and a low value for $\lambda > 2.5$ µm (to minimize re-emission from the collector). The opposite is true for a spacecraft radiator panel used to reject heat into space.

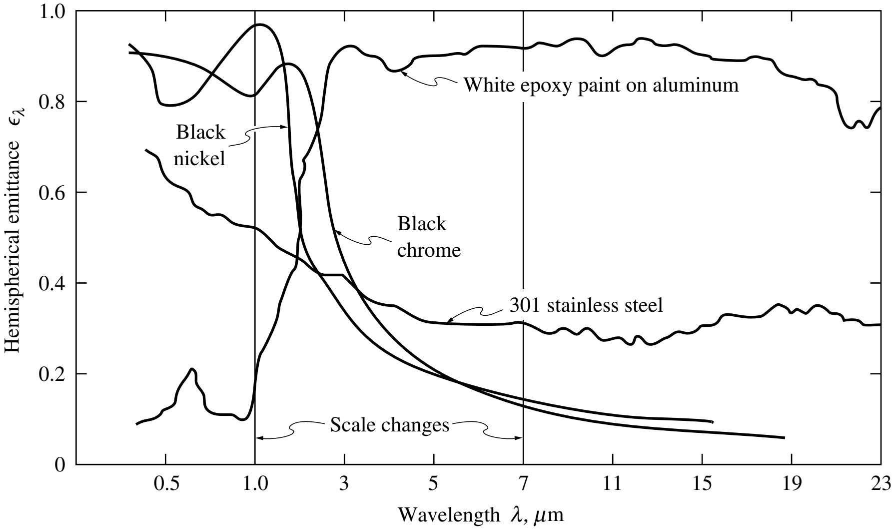

FIGURE 4.3.4 Spectral, hemispherical emittance of several spectrally selective surfaces.

It is clear that (1) values of spectral surface emittance are subject to great uncertainty; and (2) only a relatively small range of infrared wavelengths are important. Therefore, it is often assumed that the surfaces are "**gray**," i.e., the emittance is constant across (the important fraction of) the spectrum, $\varepsilon_\lambda \neq \varepsilon_\lambda(\lambda)$, because this assumption also vastly simplifies analysis. Table 4.3.1 gives a fairly detailed listing of total emittances of various materials, defined as

$$\varepsilon(T) = \frac{1}{E_b(T)} \int_0^\infty \varepsilon_\lambda(\lambda, T) E_{b\lambda}(T)\, d\lambda \tag{4.3.9}$$

which may be enlisted for a gray analysis.

View Factors

In many engineering applications, the exchange of radiative energy between surfaces is virtually unaffected by the medium that separates them. Such (radiatively) *nonparticipating media* include vacuum as well as monatomic and most diatomic gases (including air) at low to moderate temperature levels (i.e., before ionization and dissociation occurs). Examples include spacecraft heat rejection systems, solar collector systems, radiative space heaters, illumination problems, and so on.

It is common practice to simplify the analysis by making the assumption of an *idealized enclosure* and/or *ideal surface properties*. The greatest simplification arises if all surfaces are black: for such a situation, no reflected radiation needs to be accounted for, and all emitted radiation is diffuse (i.e., the radiative energy leaving a surface does not depend on direction). The next level of difficulty arises if surfaces are assumed to be gray diffuse emitters (and thus absorbers) as well as gray diffuse reflectors. The vast majority of engineering calculations are limited to such ideal surfaces, particularly because the effects of nondiffuse reflections are usually weak (see discussion in previous section).

Thermal radiation is generally a long-range phenomenon. This is always the case in the absence of a participating medium because photons will travel unimpeded from surface to surface. Therefore, performing a thermal radiation analysis for one surface implies that all surfaces, no matter how far removed, that can exchange radiative energy with one another must be considered simultaneously. How much energy any two surfaces exchange depends in part on their size, separation, distance, and orientation; this leads to geometric functions known as **view factors**, which are defined as

TABLE 4.3.1 Total Emittance and Solar Absorptance of Selected Surfaces

	Temperature (°C)	Total Normal Emittance	Extraterrestrial Solar Absorptance
Alumina, Flame Sprayed	–25	0.80	0.28
Aluminum foil			
As received	20	0.04	
Bright dipped	20	0.025	0.10
Aluminum, vacuum deposited	20	0.025	0.10
Hard-anodized	–25	0.84	0.92
Highly polished plate, 98.3% pure	225–575	0.039–0.057	
Commercial sheet	100	0.09	
Rough polish	100	0.18	
Rough plate	40	0.055–0.07	
Oxidized at 600°C	200–600	0.11–0.19	
Heavily oxidized	95–500	0.20–0.31	
Antimony, polished	35–260	0.28–0.31	
Asbestos	35–370	0.93–0.94	
Beryllium	150	0.18	0.77
	370	0.21	
	600	0.30	
Beryllium, anodized	150	0.90	
	370	0.88	
	600	0.82	
Bismuth, bright	75	0.34	
Black paint			
Parson's optical black	–25	0.95	0.975
Black silicone	–25–750	0.93	0.94
Black epoxy paint	–25	0.89	0.95
Black enamel paint	95–425	0.81–0.80	
Brass, polished	40–315	0.10	
Rolled plate, natural surface	22	0.06	
Dull plate	50–350	0.22	
Oxidized by heating at 600˚C	200–600	0.61–0.59	
Carbon, graphitized	100–320	0.76–0.75	
	320–500	0.75–0.71	
Candle soot	95–270	0.952	
Graphite, pressed, filed surface	250–510	0.98	
Chromium, polished	40–1100	0.08–0.36	
Copper, electroplated	20	0.03	0.47
Carefully polished electrolytic copper	80	0.018	
Polished	115	0.023	
Plate heated at 600˚C	200–600	0.57	
Cuprous oxide	800–1100	0.66–0.54	
Molten copper	1075–1275	0.16–0.13	
Glass, Pyrex, lead, and soda	260–540	0.95–0.85	
Gypsum	20	0.903	
Gold, pure, highly polished	225–625	0.018–0.035	
Inconel X, oxidized	–25	0.71	0.90
Lead, pure (99.96%), unoxidized	125–225	0.057–0.075	
Gray oxidized	25	0.28	
Oxidized at 150°C	200	0.63	
Magnesium oxide	275–825	0.55–0.20	
	900–1705	0.20	
Magnesium, polished	35–260	0.07–0.13	
Mercury	0–100	0.09–0.12	
Molybdenum, polished	35–260	0.05–0.08	
	540–1370	0.10–0.18	
	2750	0.29	

TABLE 4.3.1 (continued) Total Emittance and Solar Absorptance of Selected Surfaces

	Temperature (°C)	Total Normal Emittance	Extraterrestrial Solar Absorptance
Nickel, electroplated	20	0.03	0.22
Polished	100	0.072	
Platinum, pure, polished	225–625	0.054–0.104	
Silica, sintered, powdered, fused silica	35	0.84	0.08
Silicon carbide	150–650	0.83–0.96	
Silver, polished, pure	40–625	0.020–0.032	
Stainless steel			
Type 312, heated 300 h at 260°C	95–425	0.27–0.32	
Type 301 with Armco black oxide	–25	0.75	0.89
Type 410, heated to 700°C in air	35	0.13	0.76
Type 303, sandblasted	95	0.42	0.68
Titanium, 75A	95–425	0.10–0.19	
75A, oxidized 300 h at 450°C	35–425	0.21–0.25	0.80
Anodized	–25	0.73	0.51
Tungsten, filament, aged	27–3300	0.032–0.35	
Zinc, pure, polished	225–325	0.045–0.053	
Galvanized sheet	100	0.21	

$$F_{i-j} = \frac{\text{diffuse energy leaving } A_i \text{ directly toward and intercepted by } A_j}{\text{total diffuse energy leaving } A_i} \tag{4.3.10}$$

In order to make a radiative energy balance, it is always necessary to consider an entire *enclosure* rather than an infinitesimal control volume (as is normally done for other modes of heat transfer, i.e., conduction or convection). The enclosure must be closed so that irradiation from all possible directions can be accounted for, and the enclosure surfaces must be *opaque* so that all irradiation is accounted for, for each direction. In practice, an incomplete enclosure may be closed by introducing artificial surfaces.

An enclosure may be idealized in two ways, as indicated in Figure 4.3.5: by replacing a complex geometric shape with a few simple surfaces and by assuming surfaces to be isothermal with constant (i.e., average) heat flux values across them. Obviously, the idealized enclosure approaches the real enclosure for sufficiently small isothermal subsurfaces.

Mathematically, the view factor needs to be determined from a double surface integral, i.e.,

$$F_{i-j} = \frac{1}{A_i} \int_{A_i} \int_{A_j} \frac{\cos\theta_i \cos\theta_j}{\pi S_{ij}^{\;2}} dA_j dA_i \tag{4.3.11}$$

where θ_i and θ_j are the angles between the surface normals on A_i and A_j, respectively, and the line (of length S_{ij}) connecting two points on the two surfaces.

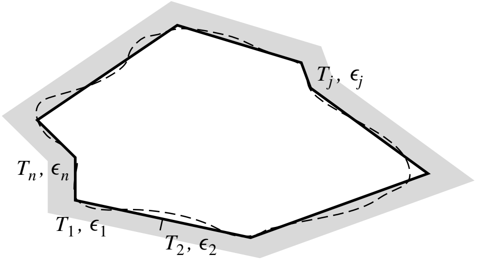

FIGURE 4.3.5 Real and ideal enclosures for radiative transfer calculations.

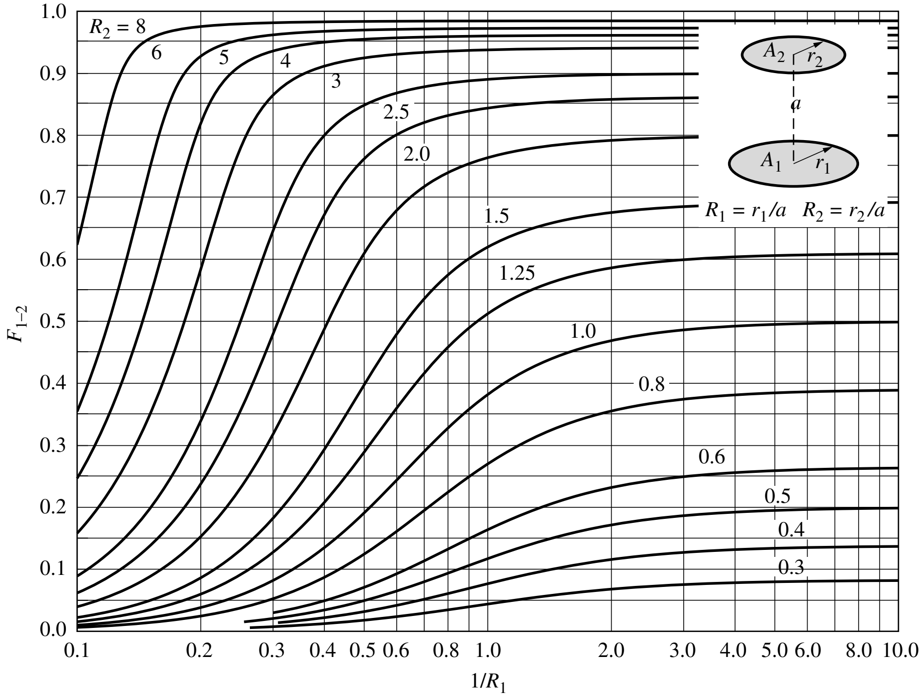

FIGURE 4.3.6 View factor between parallel, coaxial disks of unequal radius.

Analytical solutions to Equation (4.3.11) may be found for relatively simple geometries. A few graphical results for important geometries are shown in Figure 4.3.6 to Figure 4.3.8. More extensive tabulations, as well as analytical expressions, may be found in textbooks on the subject area (Modest, 2003; Siegel and Howell, 2002) as well as view factor catalogs (Howell, 1982). For nontrivial geometries, view factors must be calculated numerically, by (1) numerical quadrature of the double surface integral in Equation (4.3.11); or (2) converting Equation (4.3.11) into a double-line integral, followed by numerical quadrature; or (3) a Monte Carlo method (statistical sampling and tracing of selected light rays).

View Factor Algebra. For simple geometries, analytical values can often be found by expressing the desired view factor in terms of other, known ones. This method is known as view factor algebra, by manipulating the two relations,

Reciprocity rule:

$$A_i F_{i-j} = A_j F_{j-i} \tag{4.3.12}$$

Summation rule:

$$\sum_{j=1}^{N} F_{i-j} = 1, \quad i = 1, N \qquad (4.3.13$$

assuming that the (closed) configuration consists of N surfaces. The reciprocity rule follows immediately from Equation (4.3.11), while the summation rule simply states that the fractional energies leaving surface A_i must add up to a whole.

Example 4.3.2

Assuming the view factor for a finite corner as shown in Figure 4.3.8 is known, determine the view factor F_{3-4}, between the two perpendicular strips as shown in Figure 4.3.9.

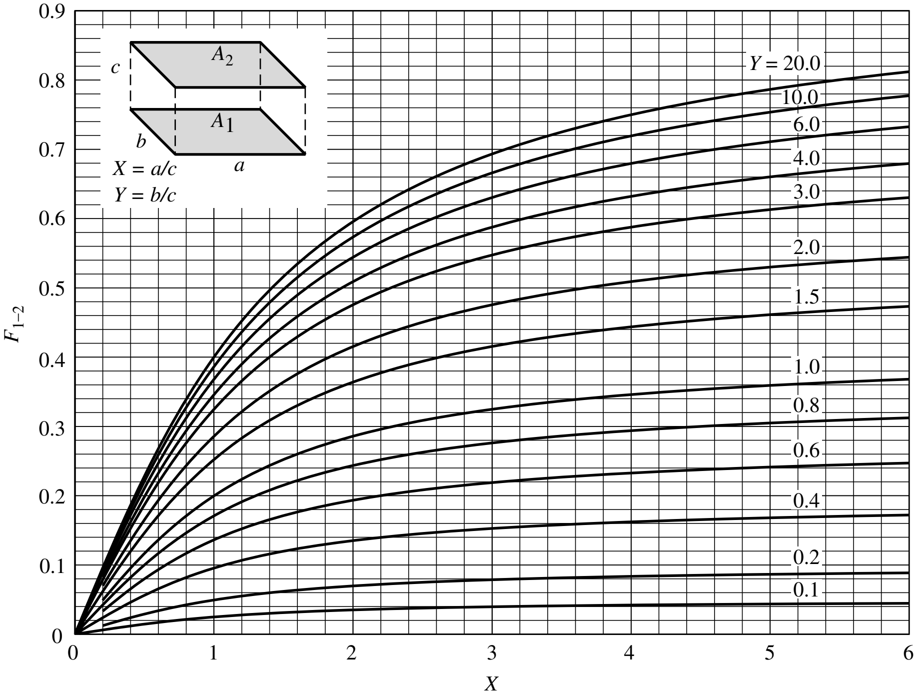

FIGURE 4.3.7 View factor between identical, parallel, directly opposed rectangles.

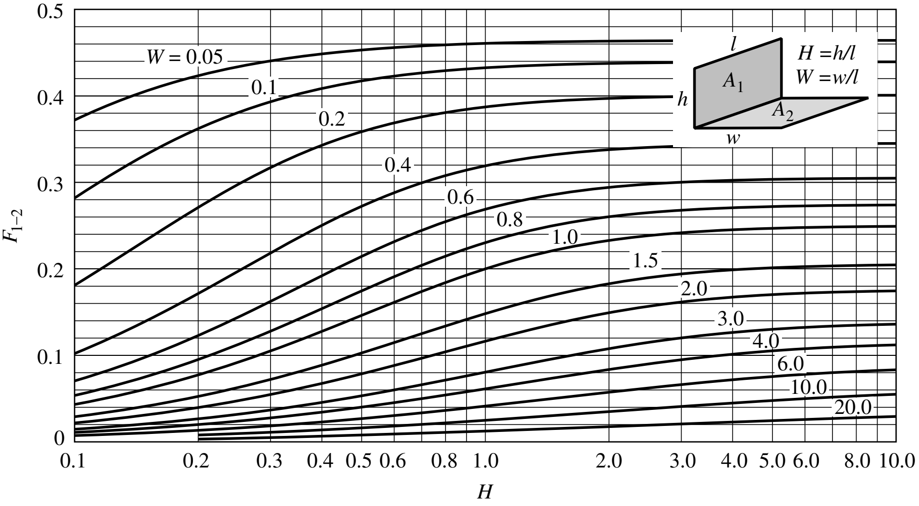

FIGURE 4.3.8 View factor between perpendicular rectangles with common edge.

Solution. From the definition of the view factor, and because the energy traveling to A_4 is the energy going to A_2 and A_4 minus the one going to A_2, it follows that

$$F_{3-4} = F_{3-(2+4)} - F_{3-2}$$

and, using reciprocity,

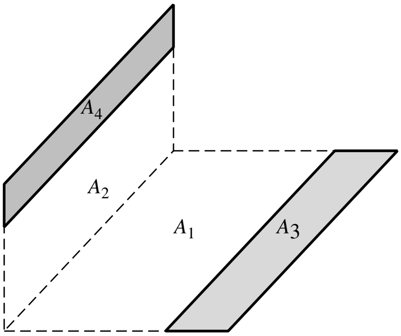

FIGURE 4.3.9 Configuration for Example 4.3.2 (strips on a corner piece).

$$F_{3-4} = \frac{1}{A_3}\left[\left(A_2 + A_4\right)F_{(2+4)-3} - A_2 F_{2-3}\right]$$

Similarly,

$$F_{3-4} = \frac{A_2 + A_4}{A_3}\left(F_{(2+4)-(1+3)} - F_{(2+4)-1}\right) - \frac{A_2}{A_3}\left(F_{2-(1+3)} - F_{2-1}\right)$$

All view factors on the right-hand side are corner pieces and thus are known from Figure 4.3.8.

Crossed-Strings Method. A special type of view factor algebra may be used to determine all the view factors in long enclosures with constant cross section. The method is called the crossed-strings method because the view factors can be determined experimentally with four pins, a roll of string, and a yardstick. Consider the configuration in Figure 4.3.10, which shows the cross section of an infinitely long enclosure, continuing into and out of the plane of the figure. Repeatedly applying reciprocity and summation rules allows the evaluation of F_{1-2} as

$$F_{1-2} = \frac{\left(A_{bc} + A_{ad}\right) - \left(A_{ac} + A_{bd}\right)}{2A_1} \tag{4.3.14}$$

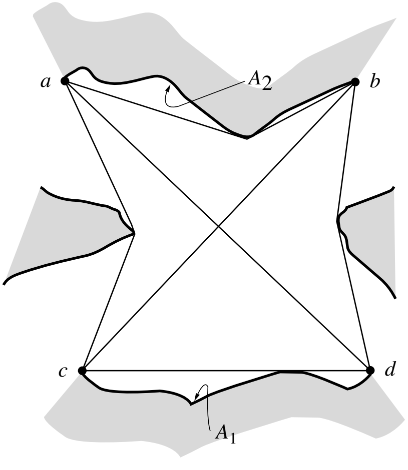

FIGURE 4.3.10 The crossed-strings method for arbitrary two-dimensional configurations.

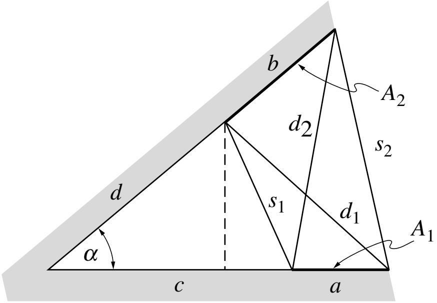

FIGURE 4.3.11 Infinitely long wedge-shaped groove for Example 4.3.3.

where A_{ab} is the area (per unit depth) defined by the length of the string between points *a* and *b*, etc. This formula is easily memorized by looking at the configuration between any two surfaces as a generalized "rectangle," consisting of A_1, A_2, and the two sides A_{ac} and A_{bd}. Then

$$F_{1-2} = \frac{\text{diagonals} - \text{sides}}{2 \times \text{originating area}} \tag{4.3.15}$$

Example 4.3.3

Calculate F_{1-2} for the configuration shown in Figure 4.3.11.

Solution. From the figure, it is obvious that

$$s_1^2 = (c - d\cos\alpha)^2 + d^2\sin^2\alpha = c^2 + d^2 - 2cd\cos\alpha$$

Similarly,

$$s_2^2 = (a+c)^2 + (b+d)^2 - 2(a+c)(b+d)\cos\alpha$$

$$d_1^2 = (a+c)^2 + d^2 - 2(a+c)d\cos\alpha$$

$$d_2^2 = c^2 + (b+d)^2 - 2c(b+d)\cos\alpha$$

and

$$F_{1-2} = \frac{d_1 + d_2 - (s_1 + s_2)}{2a}$$

Radiative Exchange between Opaque Surfaces (Net Radiation Method)

Consider an enclosure consisting of *N* opaque surfaces. The enclosure is closed or, if not, no surface external to the surface reflects or emits radiation into the enclosure (i.e., the open configuration may be artificially closed by replacing openings with cold black surfaces); any external radiation entering the enclosure is dealt with individually for each surface (see Equation 4.3.17). All surfaces are assumed to be gray and emit and reflect diffusely. Traditionally, the **radiosity** *J* of the surfaces is determined, defined as the total diffuse radiative energy leaving a surface (by emission and reflection),

$$J_i = \varepsilon_i E_{bi} + \rho_i H_i, \qquad i = 1, N \tag{4.3.16}$$

where H_i is the incoming radiative flux per unit area (irradiation) onto surface A_i. This leads to *N* simultaneous equations for the unknown radiosities, specifically,

$$J_i = \varepsilon_i E_{bi} + (1-\varepsilon_i)\left[\sum_{j=1}^{N} J_j F_{i-j} + H_{oi}\right] \tag{4.3.17a}$$

or

$$J_i = q_i + \sum_{j=1}^{N} J_j F_{i-j} + H_{oi} \tag{4.3.17b}$$

depending on whether surface temperature or surface flux is known on surface A_i. In Equation (4.3.17), H_{oi} is irradiation onto surface A_i from outside the enclosure, if any; H_{oi} is always zero for closed configurations, but is useful in the presence of external light sources (such as solar energy, lasers, etc.). The radiosity is not a useful quantity to determine, nor is there a need to determine it. Eliminating the radiosities from Equation (4.3.17a) and Equation (4.3.17b) leads to N simultaneous equations in temperature (E_{bi}) and heat flux (q_i):

$$\frac{q_i}{\varepsilon_i} - \sum_{j=1}^{N}\left(\frac{1}{\varepsilon_j} - 1\right) F_{i-j} q_j + H_{oi} = E_{bi} - \sum_{j=1}^{N} F_{i-j} E_{bj} \tag{4.3.18}$$

Note that no artificial closing surfaces ($j > N$) appear in Equation (4.3.18) because, for these surfaces, $\varepsilon_j = 1$ and $E_{bj} = 0$. Thus, such closing surfaces may simply be ignored in the analysis.

Because Equation (4.3.18) is a set of N equations, this requires that N values of emissive power E_{bi} and/or flux q_i must be given as boundary conditions, in order to solve for the remaining N unknowns. For computer calculations, Equation (4.3.18) may be recast in matrix form

$$\mathbf{C} \cdot \mathbf{q} = \mathbf{A} \cdot \mathbf{e_b} - \mathbf{h_o} \tag{4.3.19a}$$

where

$$C_{ij} = \frac{\delta_{ij}}{\varepsilon_j} - \left(\frac{1}{\varepsilon_j} - 1\right) F_{i-j} \tag{4.3.19b}$$

$$A_{ij} = \delta_{ij} - F_{i-j} \tag{4.3.19c}$$

δ_{ij} is Kronecker's delta, i.e.,

$$\delta_{ij} = \begin{cases} 1 \text{ if } i = j \\ 0 \text{ if } i \neq j \end{cases} \tag{4.3.20}$$

and $\mathbf{q}$, $\mathbf{e_b}$, and $\mathbf{h_o}$ are vectors of the surface heat fluxes q_i, emissive powers E_{bi}, and external irradiations H_{oi} (if any). For example, if the temperatures are given for all the surfaces and the heat fluxes are to be determined, Equation (4.3.19) is solved by matrix inversion, and

$$\mathbf{q} = \left(\mathbf{C}^{-1} \cdot \mathbf{A}\right) \cdot \mathbf{e_b} - \left(\mathbf{C}^{-1} \cdot \mathbf{h_o}\right) \tag{4.3.21}$$

Example 4.3.4

A right-angled groove, consisting of two long black surfaces of width a, is exposed to solar radiation q_{sol} (Figure 4.3.12). The entire groove surface is kept isothermal at temperature T. Determine the net radiative heat transfer rate from the groove.

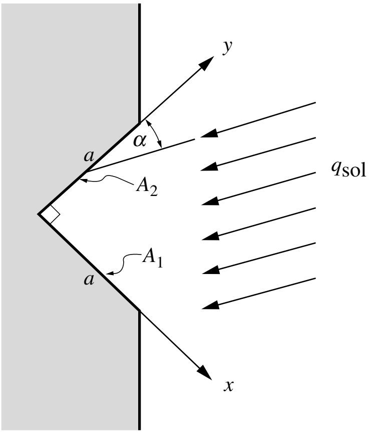

FIGURE 4.3.12 Right-angled groove exposed to solar irradiation, Example 4.3.4.

Solution. Equation (4.3.19) may be used. However, the enclosure is not closed and thus must be closed artificially. Note that any radiation leaving the cavity will not come back (barring any reflection from other surfaces nearby). Thus, the artificial surface should be black. It is also assumed that, with the exception of the (parallel) solar irradiation, no external radiation enters the cavity. Because the solar irradiation is best treated separately through the external irradiation term H_o, the artificial surface is nonemitting. Both criteria are satisfied by covering the groove with a black surface at 0 K (A_3). Even though one now has three surfaces, the last one does not really appear in Equation (4.3.18) (because $E_{b3} = 0$ and $1/\varepsilon_3 - 1 = 0$):

$$q_1 = E_{b1} - F_{1-2}E_{b2} - H_{o1} = \sigma T^4 (1 - F_{1-2}) - q_{\text{sol}} \cos\alpha$$

$$q_2 = E_{b2} - F_{2-1}E_{b1} - H_{o2} = \sigma T^4 (1 - F_{2-1}) - q_{\text{sol}} \sin\alpha$$

From the crossed-strings method, Equation (4.3.15),

$$F_{1-2} = \frac{a + a - \left(\sqrt{2}a + 0\right)}{2a} = \frac{1}{2}\left(2 - \sqrt{2}\right) = 0.293 = F_{2-1}$$

and

$$Q' = a(q_1 + q_2) = a\left[\sqrt{2}\sigma T^4 - q_{\text{sol}}(\cos\alpha + \sin\alpha)\right]$$

Example 4.3.5

Consider a very long duct as shown in Figure 4.3.13. The duct is 30 × 40 cm in cross section, and all surfaces are covered with a gray, diffuse surface material. Top and bottom walls are at $T_1 = T_3 = 1000$ K with $\varepsilon_1 = \varepsilon_3 = 0.3$, while the side walls are at $T_2 = T_4 = 600$ K with $\varepsilon_2 = \varepsilon_4 = 0.8$ as shown. Determine the net radiative heat transfer rates for each surface.

Solution. Using Equation (4.3.18) for $i = 1$ and $i = 2$ and noting that $F_{1-2} = F_{1-4}$ and $F_{2-1} = F_{2-3}$, as well as $q_1 = q_3$ and $q_2 = q_4$,

$$i = 1: \quad \frac{q_1}{\varepsilon_1} - 2\left(\frac{1}{\varepsilon_2} - 1\right)F_{1-2}q_2 - \left(\frac{1}{\varepsilon_1} - 1\right)F_{1-3}q_1 = 2F_{1-2}\left(E_{b1} - E_{b2}\right)$$

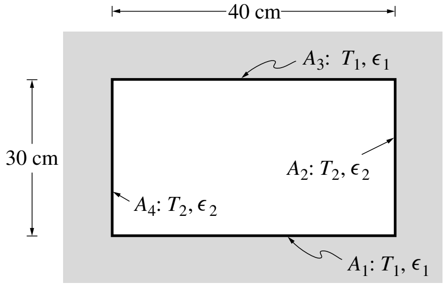

FIGURE 4.3.13 Two-dimensional gray, diffuse duct for Example 4.3.5.

$$i=2:\quad \frac{q_2}{\varepsilon_2}-2\left(\frac{1}{\varepsilon_1}-1\right)F_{2-1}q_1-\left(\frac{1}{\varepsilon_2}-1\right)F_{2-4}q_2=2F_{2-1}\left(E_{b1}-E_{b2}\right)$$

The view factors are readily evaluated from the crossed-strings method as $F_{1-2} = 1/4$, $F_{1-3} = 1 - 2F_{1-2} = 1/2$, $F_{2-1} = 4/3F_{1-2} = 1/3$, and $F_{2-4} = 1 - 2F_{2-1} = 1/3$. Substituting these as well as emissivity values into the relations reduces them to the simpler form of

$$\left[\frac{1}{0.3}-\left(\frac{1}{0.3}-1\right)\frac{1}{2}\right]q_1-2\left(\frac{1}{0.8}-1\right)\frac{1}{4}q_2=2\times\frac{1}{4}\left(E_{b1}-E_{b2}\right)$$

$$-2\left(\frac{1}{0.3}-1\right)\frac{1}{3}q_1+\left[\frac{1}{0.8}-\left(\frac{1}{0.8}-1\right)\frac{1}{3}\right]q_2=2\times\frac{1}{3}\left(E_{b1}-E_{b2}\right)$$

or

$$\frac{13}{6}q_1-\frac{1}{8}q_2=\frac{1}{2}\left(E_{b1}-E_{b2}\right)$$

$$-\frac{14}{9}q_1+\frac{7}{6}q_2=-\frac{2}{3}\left(E_{b1}-E_{b2}\right)$$

Thus,

$$\left(\frac{13}{6}\times\frac{7}{6}-\frac{14}{9}\times\frac{1}{8}\right)q_1=\left(\frac{1}{2}\times\frac{7}{6}-\frac{2}{3}\times\frac{1}{8}\right)\left(E_{b1}-E_{b2}\right)$$

$$q_1=\frac{3}{7}\times\frac{1}{2}\left(E_{b1}-E_{b2}\right)=\frac{3}{14}\sigma\left(T_1^4-T_2^4\right)$$

and

$$\left(-\frac{1}{8}\times\frac{14}{9}+\frac{7}{6}\times\frac{13}{6}\right)q_2=\left(\frac{1}{2}\times\frac{14}{9}-\frac{2}{3}\times\frac{13}{6}\right)\left(E_{b1}-E_{b2}\right)$$

$$q_2=-\frac{3}{7}\times\frac{2}{3}\left(E_{b1}-E_{b2}\right)=-\frac{2}{7}\sigma\left(T_1^4-T_2^4\right)$$

Finally, substituting values for temperatures,

$$Q_1' = 0.4\ \text{m} \times \frac{3}{14} \times 5.670 \times 10^{-8}\ \frac{\text{W}}{\text{m}^2\text{K}^4}\left(1000^4 - 600^4\right)\text{K}^4 = 4230\ \ \text{W/m}$$

$$Q_2' = -0.3\ \text{m} \times \frac{2}{7} \times 5.670 \times 10^{-8}\ \frac{\text{W}}{\text{m}^2\text{K}^4}\left(1000^4 - 600^4\right)\text{K}^4 = -4230\ \ \text{W/m}$$

Note that, for conservation of energy, both heat transfer rates must add up to zero.

Small Body Inside Isothermal Enclosure. An especially simple — but important — case occurs if a small, convex body A_1 (i.e., a surface that cannot "see" itself, or $F_{1-1} = 0$) is totally enclosed by an isothermal enclosure A_2. Then, with $N = 2$ and $F_{1-2} = 1$, Equation (4.3.18) reduces to

$$q_1 = \frac{E_{b1} - E_{b2}}{\dfrac{1}{\varepsilon_1} + \dfrac{A_1}{A_2}\left(\dfrac{1}{\varepsilon_2} - 1\right)} = \frac{\sigma\left(T_1^{\,4} - T_2^{\,4}\right)}{\dfrac{1}{\varepsilon_1} + \dfrac{A_1}{A_2}\left(\dfrac{1}{\varepsilon_2} - 1\right)} \tag{4.3.22}$$

If the enclosure is large, i.e., $A_1 \ll A_2$, then Equation (4.3.22) simplifies further to

$$q_1 = \varepsilon_1 \sigma\left(T_1^{\,4} - T_2^{\,4}\right) \tag{4.3.23}$$

Radiation Shields. If it is desired to minimize radiative heat transfer between two surfaces, it is common practice to place one or more radiation shields between them (usually thin metallic sheets of low emittance). If two surfaces A_i and A_j are close together, so that $A_i \cong A_j$ and $F_{i-j} \cong 1$, then the radiative exchange between them is, from Equation (4.3.22),

$$q = \frac{E_{bi} - E_{bj}}{R_{ij}}, \qquad R_{ij} = \frac{1}{\varepsilon_i} + \frac{1}{\varepsilon_j} - 1 \tag{4.3.24}$$

where R_{ij} is termed the *radiative resistance*. Equation (4.3.24) is seen to be analogous to an electrical circuit with "current" q and "voltage potential" $E_{bi} - E_{bj}$. Therefore, expressing radiative fluxes in terms of radiative resistances is commonly known as **network analogy**.

The network analogy is a very powerful method of solving one-dimensional problems (i.e., whenever only two isothermal surfaces see each other, such as infinite parallel plates, or when one surface totally encloses another). Consider, for example, two large parallel plates, A_1 and A_N, separated by $N - 2$ radiation shields, as shown in Figure 4.3.14. Let each shield have an emittance ε_S on both sides. Then, by applying Equation (4.3.24) to any two consecutive surfaces and using the fact that q remains constant throughout the gap,

$$q = \frac{E_{b1} - E_{b2}}{R_{12}} = \ldots = \frac{E_{bk-1} - E_{bk}}{R_{k-1,k}} = \ldots = \frac{E_{bN-1} - E_{bN}}{R_{N-1,N}} = \frac{E_{b1} - E_{bN}}{\sum_{j-2}^{N} R_{j-1,j}} \tag{4.3.25}$$

where

$$R_{j-1,j} = \frac{1}{\varepsilon_{j-1}} + \frac{1}{\varepsilon_j} - 1 \tag{4.3.26}$$

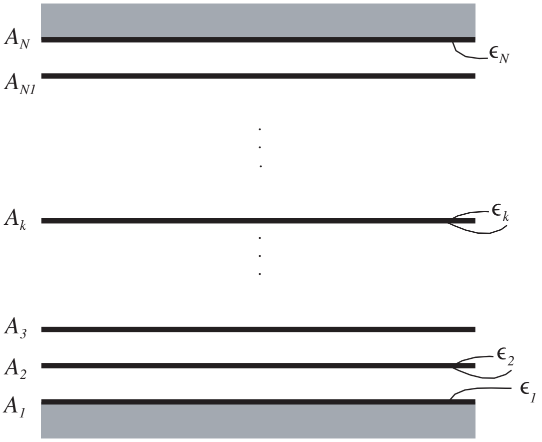

FIGURE 4.3.14 Placement of radiation shields between two large, parallel plates.

and, if $\varepsilon_2 = \varepsilon_3 \ldots = \varepsilon_{N-1} = \varepsilon_S$,

$$\sum_{j=2}^{N} R_{j-1,j} = \frac{1}{\varepsilon_1} + \frac{1}{\varepsilon_N} - 1 + (N-2)\left(\frac{2}{\varepsilon_S} - 1\right) \tag{4.3.27}$$

Equation (4.3.24) to Equation (4.3.27) are also valid for concentric cylinders, concentric spheres, and similar configurations, as long as $r_N - r_1 \ll r_1$. Also, the relations are readily extended to shields with nonidentical emittance.

Although the network analogy can be (and has been) applied to configurations with more than two surfaces seeing each other, this leads to very complicated circuits (because there is one resistance between any two surfaces). For such problems, the network analogy is not recommended, and the net radiation method, Equation (4.3.18), should be employed.

Radiative Exchange within Participating Media

In many high-temperature applications, when radiative heat transfer is important, the medium between surfaces is not transparent, but is "participating" — i.e., it absorbs, emits, and (possibly) scatters radiation. In a typical combustion process, this interaction results in (1) continuum radiation due to tiny, burning soot particles (of dimension < 1 μm) and also due to larger suspended particles, such as coal particles, oil droplets, and fly ash; (2) banded radiation in the infrared due to emission and absorption by molecular gaseous combustion products, mostly water vapor and carbon dioxide; and (3) chemiluminescence due to the combustion reaction. Chemiluminescence may normally be neglected; however, particulates as well as gas radiation generally must be accounted for.

Radiative Properties of Molecular Gases

When a photon (or an electromagnetic wave) interacts with a gas molecule, it may be absorbed, raising the energy level of the molecule. Conversely, a gas molecule may spontaneously lower its energy level by the emission of an appropriate photon. This leads to large numbers of narrow spectral lines, which partially overlap and together form so-called vibration–rotation bands. As such, gases tend to be transparent over most of the spectrum, but may be almost opaque over the spectral range of a band. The **absorption coefficient** κ_λ is defined as a measure of how strongly radiation is absorbed or emitted along a path of length L, leading to the spectral absorptivity and emissivity for this path, or

$$\alpha_\lambda = \varepsilon_\lambda = 1 - e^{-\kappa_\lambda L} \tag{4.3.28}$$

This exponential decay of incident radiation is often called *Beer's law*. Although gases are distinctly nongray, for simple heat transfer calculations it is often sufficient to determine the total emissivity for an isothermal path (compare Equation 4.3.9)

$$\varepsilon = \frac{1}{E_b} \int_0^{\infty} \left(1 - e^{-\kappa_\lambda L}\right) E_{b\lambda}\left(T_g\right) d\lambda \tag{4.3.29}$$

For a mixture of gases, the total emissivity is a function of path length L; gas temperature T_g; partial pressure(s) of the absorbing gas(es) p_a; and total pressure p. For the mixture of nitrogen with water vapor and/or carbon dioxide (in combustion applications most important), the total emissivity may be calculated from Leckner (1972). First, the individual emissivities for water vapor and carbon dioxide, respectively, are calculated separately from

$$\varepsilon\left(p_a L, p, T_g\right) = \varepsilon_0\left(p_a L, T_g\right)\left(\frac{\varepsilon}{\varepsilon_0}\right)\left(p_a L, p, T_g\right) \tag{4.3.30a}$$

$$\left(\frac{\varepsilon}{\varepsilon_0}\right)\left(p_a L, p, T_g\right) = \left[1 - \frac{(a-1)(1-P_E)}{a+b-1+P_E} \exp\left(-c\left[\log_{10}\frac{(p_a L)_m}{p_a L}\right]^2\right)\right] \tag{4.3.30b}$$

$$\varepsilon_0\left(p_a L, T_g\right) = \exp\left[\sum_{i=0}^{N} \sum_{j=0}^{N} c_{ji}\left(\frac{T_g}{T_0}\right)^j \left(\log_{10}\frac{p_a L}{(p_a L)_0}\right)^i\right] \tag{4.3.30c}$$

Here ε_0 is the total emissivity of a reference state, i.e., for the case of $p = 1$ bar and $p_a \to 0$ (but $p_a L > 0$); the correlation constants a, b, c, c_{ji}, P_E, $(p_a L)_0$, $(p_a L)_m$, and $(p_a L)_m$ are given in Table 4.3.2 for water vapor and carbon dioxide. (For convenience, plots of ε_0 are given in Figure 4.3.15 for CO_2 and Figure 4.3.16

TABLE 4.3.2 Correlation Constants for Determination of Total Emissivity for Water Vapor and Carbon Dioxide

Gas	Water Vapor			Carbon Dioxide			
M, N	2,2			2,3			
$\begin{matrix} c_{00} & \cdots & c_{N0} \\ \vdots & \ddots & \vdots \\ c_{0M} & \cdots & c_{NM} \end{matrix}$	−2.2118 0.85667 −0.10838	−1.1987 0.93048 −0.17156	0.035596 −0.14391 0.045915	−3.9893 1.2710 −0.23678	2.7669 1.1090 0.19731	−2.1081 1.0195 −0.19544	0.39163 −0.21897 0.044644
P_E	$\left(p + 2.56 p_a / \sqrt{t}\right) / p_0$			$(p + 0.28\, p_a)/p_0$			
$(p_a L)_m/(p_a L)_0$	$13.2t^2$			$0.054/t^2$, $t < 0.7$ $0.225t^2$, $t > 0.7$			
a	2.144, $t < 0.75$ $1.88 - 2.053 \log_{10} t$, $t > 0.75$			$1 + 0.1/t^{1.45}$			
b	$1.10/t^{1.4}$			0.23			
c	0.5			1.47			

Note: $T_0 = 1000$ K, $p_0 = 1$ bar, $t = T/T_0$, $(p_a L)_0 = 1$ bar cm.

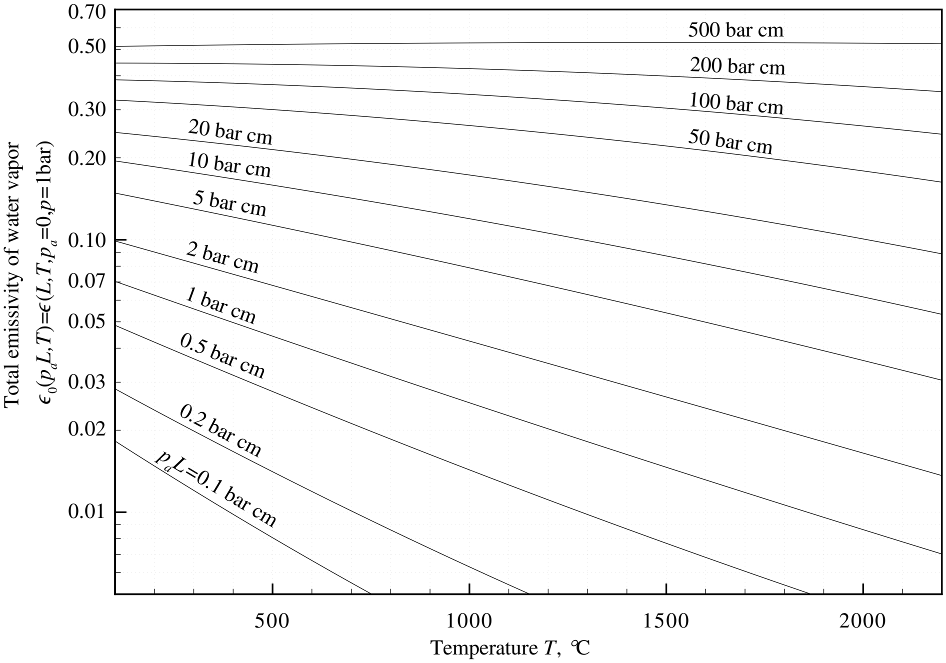

FIGURE 4.3.15 Total emissivity of water vapor at reference state (total gas pressure $p = 1$ bar, partial pressure of $H_2O p_a \rightarrow 0$).

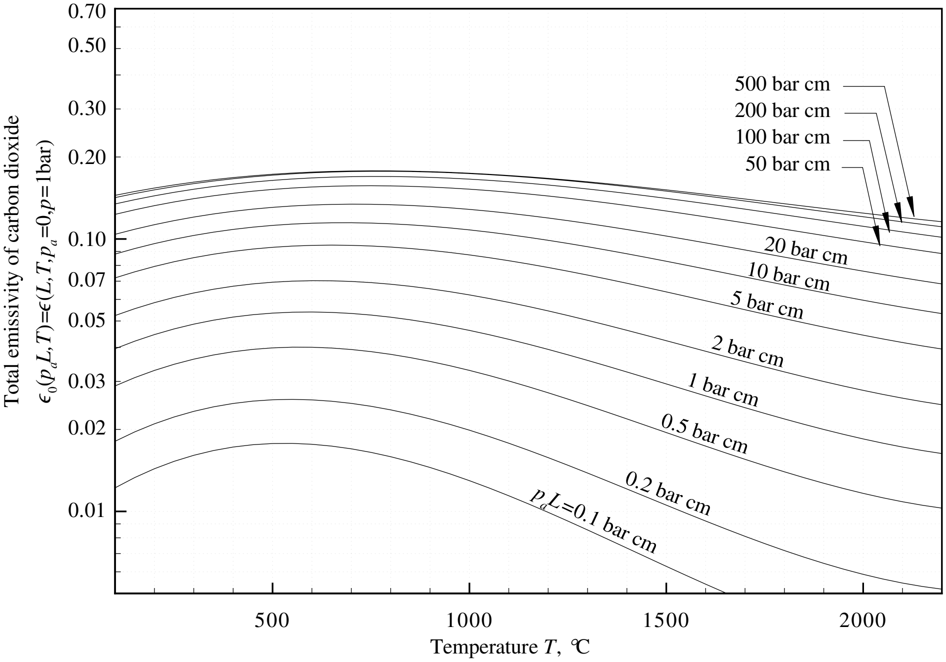

FIGURE 4.3.16 Total emissivity of carbon dioxide at reference state (total gas pressure $p = 1$ bar, partial pressure of $CO_2 p_a \rightarrow 0$).

for H_2O.) The total emissivity of a mixture of nitrogen with water vapor and carbon dioxide is calculated from

$$\varepsilon_{CO_2+H_2O} = \varepsilon_{CO_2} + \varepsilon_{H_2O} - \Delta\varepsilon \tag{4.3.31}$$

$$\Delta\varepsilon = \left(\frac{\zeta}{10.7+101\zeta} - 0.0089\zeta^{10.4}\right)\left(\log_{10}\frac{\left(p_{H_2O}+p_{CO_2}\right)L}{\left(p_a L\right)_0}\right)^{2.76} \tag{4.3.32a}$$

$$\zeta = \frac{p_{H_2O}}{p_{H_2O}+p_{CO_2}} \tag{4.3.32b}$$

where the $\Delta\varepsilon$ compensates for overlap effects between H_2O and CO_2 bands, and the ε_{CO_2} and ε_{H_2O} are calculated from Equation (4.3.30).

If radiation emitted externally to the gas (for example, by emission from an adjacent wall at temperature T_s) travels through the gas, the total amount absorbed by the gas is of interest. This leads to the absorptivity of a gas path at T_g with a source at T_s:

$$\alpha\left(p_a L, p, T_g, T_s\right) = \frac{1}{E_b(T_s)}\int_0^\infty \left(1-e^{-\kappa_\lambda(T_g)L}\right)E_{b\lambda}(T_s)\,d\lambda \tag{4.3.33}$$

which, for water vapor or carbon dioxide, may be estimated from

$$\alpha\left(p_a L, p, T_g, T_s\right) = \left(\frac{T_g}{T_s}\right)^{1/2} \varepsilon\left(p_a L\frac{T_s}{T_g}, p, T_s\right) \tag{4.3.34}$$

where ε is the emissivity calculated from Equation (4.3.30) evaluated at the temperature of the surface T_s, and using an adjusted pressure path length, $p_a L T_s/T_g$. For mixtures of water vapor and carbon dioxide, band overlap is again accounted for by taking

$$\alpha_{CO_2+H_2O} = \alpha_{CO_2} + \alpha_{H_2O} - \Delta\varepsilon \tag{4.3.35}$$

with $\Delta\varepsilon$ evaluated for a pressure path length of $p_a L T_s/T_g$.

Example 4.3.6

Consider a layer of a gas mixture at 1000 K and 5 bar that consists of 10% carbon dioxide and 70% nitrogen. What is its emissivity for a path length of 1.76 m, and its absorptivity (for the same path) if the layer is irradiated by a source at 1500 K?

Solution. First calculate the total emissivity of the CO_2 at the reference state (p = 1 bar, $p_a \to 0$) for a length of 1.76 m from Equation (4.3.30c) or Figure 4.3.15. With

$$T_g = 1000\text{ K} = 727°\text{C} \quad \text{and} \quad p_a L = 0.1\times 5\text{ bar}\times 1.76\text{m} = 88\text{ bar cm}$$

one gets, interpolating Figure 4.3.15, $\varepsilon_0 \cong 0.15$. The correction factor in Equation (4.3.30b) is calculated from Table 4.3.2 with $P_E = 5 + 0.28 \times 0.5 = 5.14$, $a = 1.1$, $b = 0.23$, $c = 1.47$, and $(p_a L)_m = 0.225$ bar cm. Thus,

$$\frac{\varepsilon}{\varepsilon_0} = 1 - \frac{0.1\times(-4.14)}{0.33+5.14}\exp\left(-1.47\left(\log_{10}\frac{0.225}{88}\right)^2\right) \cong 1$$

and

$$\varepsilon \cong 0.15$$

To calculate the absorptivity, ε_0 must be found for a temperature of

$$T_s = 1500\ \text{K} = 1227°\text{C} \quad \text{and} \quad p_a L \frac{T_s}{T_g} = 88 \times 1500/1000 = 132\ \text{bar cm}$$

From Figure 4.3.15, it follows that $\varepsilon_0 \cong 0.15$ again and, with $\varepsilon/\varepsilon_0$ relatively unchanged, from Equation (4.3.34),

$$\alpha \cong \left(\frac{1000}{1500}\right)^{1/2} \times 0.15 \times 1.00 = 0.122$$

Radiative Properties of Particle Clouds

Nearly all flames are visible to the human eye and are therefore called *luminous* (sending out light). Apparently, some radiative emission from within the flame takes place at wavelengths where no vibration–rotation bands for any combustion gases exist. This luminous emission is known today to come from tiny char (almost pure carbon) particles, called soot, which are generated during the combustion process. The "dirtier" the flame is (i.e., the higher the soot content), the more luminous it is.

Radiative Properties of Soot. Soot particles are produced in fuel-rich flames, or fuel-rich parts of flames, as a result of incomplete combustion of hydrocarbon fuels. As shown by electron microscopy, soot particles are generally small and spherical, ranging in size between approximately 50 and 800 Å (0.005 to 0.08 μm), and up to about 3000 Å in extreme cases. Although mostly spherical in shape, soot particles may also appear in agglomerated chunks and even as long agglomerated filaments. It has been determined experimentally in typical diffusion flames of hydrocarbon fuels that the volume percentage of soot generally lies in the range between 10^{-4} to 10^{-6}%.

Because soot particles are very small, they are generally at the same temperature as the flame and strongly emit thermal radiation in a continuous spectrum over the infrared region. Experiments have shown that soot emission often is considerably stronger than the emission from the combustion gases.

For a simplified heat transfer analysis it is desirable to use suitably defined mean absorption coefficients and emissivities. If the soot volume fraction, f_v, is known as well as an appropriate spectral average of the complex index of refraction of the soot, $m = n - ik$, one may approximate the spectral absorption coefficient by (Felske and Tien, 1977):

$$\kappa_\lambda = C_0 \frac{f_v}{\lambda} \qquad C_0 = \frac{36\pi nk}{\left(n^2 - k^2 + 2\right)^2 + 4n^2k^2} \tag{4.3.36}$$

and a total, or spectral-average value may be taken as

$$\kappa_m = 3.72 f_v C_0 T/C_2 \tag{4.3.37}$$

where C_2 = 1.4388 mK is the second Planck function constant. Substituting Equation (4.3.37) into Equation (4.3.29) gives a total soot cloud emissivity of

$$\varepsilon\left(f_v TL\right) = 1 - e^{-\kappa_m L} = 1 - e^{-3.72 C_0 f_v TL/C_2} \tag{4.3.38}$$

Pulverized Coal and Fly Ash Dispersions. To calculate the radiative properties of arbitrary size distributions of coal and ash particles, one must have knowledge of their complex index of refraction as a function of wavelength and temperature. Data for carbon and different types of coal indicate that its real part, n, varies little over the infrared and is relatively insensitive to the type of coal (e.g., anthracite, lignite, bituminous), while the absorptive index, k, may vary strongly over the spectrum and from coal to coal.

If the number and sizes of particles are known and if a suitable average value for the complex index of refraction can be found, then the spectral absorption coefficient of the dispersion may be estimated by a correlation given by Buckius and Hwang (1980). Substitution into Equation (4.3.29) can then provide an estimate of the total emissivity. If soot as well as larger particles are present in the dispersion, the absorption coefficients of all constituents must be added before applying Equation (4.3.29).

Mixtures of Molecular Gases and Particulates. To determine the total emissivity of a mixture, it is generally necessary to find the spectral absorption coefficient κ_λ of the mixture (i.e., the sum of the absorption coefficient of all contributors), followed by numerical integration of Equation (4.3.29). However, because the molecular gases tend to absorb only over a small part of the spectrum, to some degree of accuracy

$$\varepsilon_{\text{mix}} \cong \varepsilon_{\text{gas}} + \varepsilon_{\text{particulates}} \tag{4.3.39}$$

Equation (4.3.39) gives an upper estimate because overlap effects result in lower emissivity (compare Equation 4.3.31 for gas mixtures).

Heat Exchange in the Presence of a Participating Medium

The calculation of radiative heat transfer rates through an enclosure filled with a participating medium is a challenging task, to say the least. High-accuracy calculations are rare and a topic of ongoing research. However, several simple models are available that allow the estimation of radiative heat transfer rates and relatively accurate calculations for some simple cases.

Diffusion Approximation. A medium through which a photon can only travel a short distance without being absorbed is known as *optically thick*. Mathematically, this implies that $\kappa_\lambda L \gg 1$ for a characteristic dimension L, across which the temperature does not vary substantially. For such an optically thick nonscattering medium, the spectral radiative flux may be calculated from

$$\mathbf{q} = -\frac{4}{3\kappa_\lambda}\nabla E_{b\lambda} \tag{4.3.40}$$

similar to Fourier's diffusion law for heat conduction. Note that a medium may be optically thick at some wavelengths, but thin ($\kappa_\lambda L \ll 1$) at others (e.g., molecular gases). For a medium that is optically thick for all wavelengths, Equation (4.3.40) may be integrated over the spectrum, yielding the total radiative flux

$$\mathbf{q} = -\frac{4}{3\kappa_R}\nabla E_b = -\frac{4}{3\kappa_R}\nabla(\sigma T^4) = -\frac{16\sigma T^3}{3\kappa_R}\nabla T \tag{4.3.41}$$

where κ_R is the suitably averaged absorption coefficient, termed the *Rosseland-mean absorption coefficient*. For a cloud of soot particles, $\kappa_R \cong \kappa_m$ from Equation (4.3.37) is a reasonable approximation. Equation (4.3.41) may be rewritten by defining a "radiative conductivity" k_R,

$$\mathbf{q} = -k_R\nabla T \qquad k_R = \frac{16\sigma T^3}{3\kappa_R} \tag{4.3.42}$$

This form shows that the diffusion approximation is mathematically equivalent to conductive heat transfer with a (strongly) temperature-dependent conductivity.

More accurate calculations show that, in the absence of other modes of heat transfer (conduction, convection), there is generally a temperature discontinuity near the boundaries ($T_{\text{surface}} \neq T_{\text{adjacent medium}}$) and, unless boundary conditions that allow such temperature discontinuities are chosen, the diffusion approximation will do very poorly in the vicinity of bounding surfaces.

Example 4.3.7

A soot cloud is contained between two walls at T_1 = 1000 K and T_2 = 2000 K, spaced 1 m apart. The effective absorption coefficient of the medium is $\kappa_R = 10\ \text{m}^{-1}$ and the effective thermal conductivity is k_c = 0.1 W/mK. Estimate the total heat flux between the plates (ignoring convection effects).

Solution. For simplicity, one may want to assume a constant total conductivity $k = k_c + k_R$, leading to

$$q = -k\frac{dT}{dx} = k\frac{T_2 - T_1}{L}$$

where k_R must be evaluated at some effective temperature. Choosing, based on its temperature dependence,

$$k_R \cong \frac{8\sigma}{3\kappa_R}\left(T_1^3 + T_2^3\right) = \frac{8\times 5.670\times 10^{-8}\ \text{W/m}^2\text{K}^4}{3\times 10/\text{m}}\left(1000^3 + 2000^3\right)\text{K}^3 = 136\frac{\text{W}}{\text{mK}}$$

gives

$$q = (0.1 + 136)\frac{2000 - 1000}{1}\frac{\text{W}}{\text{m}^2} = 136\frac{\text{kW}}{\text{m}^2\text{K}}$$

Note that (1) conduction is negligible in this example; and (2) the surface emittances do not enter the diffusion approximation. Although a more accurate answer can be obtained by taking the temperature dependence of k_R into account, the method should be understood as a relatively crude approximation.

Mean Beam Length Method. Relatively accurate, yet simple, heat transfer calculations can be carried out if an isothermal absorbing–emitting, but not scattering, medium is contained in an isothermal black-walled enclosure. Although these conditions are, of course, very restrictive, they are met to some degree by conditions inside furnaces. For such cases, the local irradiation onto a point of the surface may be calculated from

$$H = \left[1 - \alpha(L_m)\right]E_{bw} - \varepsilon(L_m)E_{bg},\quad q_{\text{net}} = E_{bw} - H \tag{4.3.43}$$

where E_{bw} and E_{bg} are blackbody emissive powers for the walls and medium (gas and/or particulates), respectively, and $\alpha(L_m)$ and $\varepsilon(L_m)$ are the total absorptivity and emissivity of the medium for a path length L_m through the medium. The length L_m, known as the average mean beam length, is a directional average of the thickness of the medium as seen from the point on the surface.

On a spectral basis, Equation (4.3.43) is exact if the preceding conditions are met and an accurate value of the (spectral) mean beam length is known. It has been shown that spectral dependence of the mean beam length is weak (generally less than ±5% from the mean). Consequently, total radiative heat flux at the surface may be calculated very accurately from Equation (4.3.43) if the emissivity and absorptivity of the medium are also known accurately. The mean beam lengths for many important geometries have been calculated and are collected in Table 4.3.3. In this table, L_0 is known as the geometric mean beam length, which is the mean beam length for the optically thin limit ($\kappa_\lambda \to 0$), and L_m is a spectral average of the mean beam length. For geometries not listed in Table 4.3.3, the mean beam length may be estimated from

$$L_0 \cong 4\frac{V}{A} \qquad L_m \cong 0.9L_0 \cong 3.6\frac{V}{A} \tag{4.3.44}$$

where V is the volume of the participating medium and A is its entire bounding surface area.

TABLE 4.3.3 Mean Beam Lengths for Radiation from a Gas Volume to a Surface on Its Boundary

Geometry of Gas Volume	Characterizing Dimension, L	Geometric Mean Beam Length, L_0/L	Average Mean Beam Length, L_m/L	L_m/L_0
Sphere radiating to its surface	Diameter, $L = D$	0.67	0.65	0.97
Infinite circular cylinder to bounding surface	Diameter, $L = D$	1.00	0.94	0.94
Semi-infinite circular cylinder to:	Diameter, $L = D$			
Element at center of base		1.00	0.90	0.90
Entire base		0.81	0.65	0.80
Circular cylinder (height/diameter = 1) to:	Diameter, $L = D$			
Element at center of base		0.76	0.71	0.92
Entire surface		0.67	0.60	0.90
Circular cylinder (height/diameter = 2) to:	Diameter, $L = D$			
Plane base		0.73	0.60	0.82
Concave surface		0.82	0.76	0.93
Entire surface		0.80	0.73	0.91
Circular cylinder (height/diameter = 0.5) to:	Diameter, $L = D$			
Plane base		0.48	0.43	0.90
Concave surface		0.53	0.46	0.88
Entire surface		0.50	0.45	0.90
Infinite semicircular cylinder to center of plane rectangular face	Radius, $L = R$	—	1.26	—
Infinite slab to its surface	Slab thickness, L	2.00	1.76	0.88
Cube to a face	Edge L	0.67	0.6	0.90
Rectangular 1 × 1 × 4 parallelepipeds:	Shortest edge, L			
To 1 × 4 face		0.90	0.82	0.91
To 1 × 1 face		0.86	0.71	0.83
To all faces		0.89	0.81	0.91

Example 4.3.8

An isothermal mixture of 10% CO_2 and 90% nitrogen at 1000 K and 5 bar is contained between two large, parallel black plates, which are isothermal at 1500 K. Estimate the net radiative heat loss from the surfaces.

Solution. The heat loss may be calculated from Equation (4.3.43), after determining the mean beam length, followed by evaluation of $\varepsilon(L_m)$ and $\alpha(L_m)$. From Table 4.3.3, it is clear that $L_m = 1.76 \times$ thickness of slab = 1.76 m. It turns out that the necessary $\varepsilon(L_m) = 0.15$ and $\alpha(L_m) = 0.122$ have already been calculated in Example 4.3.6. Thus, the heat flux is immediately calculated from Equation (4.3.43) as

$$H = (1 - 0.122) 5.670 \times 10^{-8} \times 1500^4 - 0.15 \times 5.670 \times 10^{-8} \times 1000^4$$

$$= 2.44 \times 10^5 \frac{\mathrm{W}}{\mathrm{m}^2} = 244 \ \mathrm{kW/m^2}$$

$$q_{\mathrm{net}} = 5.670 \times 10^{-8} \times 1500^4 - 2.44 \times 10^5 = 43 \ \mathrm{kW/m^2}$$

Advanced Concepts

Radiative transfer in a participating medium is governed by the so-called *radiative transfer equation* (RTE), an energy balance for spectral radiative intensity I_λ traveling in a specific direction $\hat{s}$,

$$\frac{dI_\lambda}{ds} = \kappa_\lambda I_{b\lambda} - \beta_\lambda I_\lambda(\hat{s}) + \frac{\sigma_{s\lambda}}{4\pi} \int_{4\pi} I_\lambda(\hat{s}) \Phi_\lambda(\hat{s}, \hat{s}') d\Omega', \tag{4.3.45}$$

in which $I_{b\lambda} = E_{b\lambda}/\pi$ is the blackbody intensity; κ_λ is the *absorption coefficient* (the ability of a medium to absorb and emit radiation, as given in Equation 4.3.28); $\sigma_{s\lambda}$ is the *scattering coefficient* (the ability of a medium to scatter radiation); $\beta_\lambda = \kappa_\lambda + \sigma_{s\lambda}$ is called the *extinction coefficient*; and $\Phi_\lambda(\hat{s}, \hat{s}')$ is the scattering phase function (the probability that radiation traveling in the direction of $\hat{s}$ is scattered, i.e., redirected, into the direction of $\hat{s}'$).

The RTE states that the strength of a light beam traveling along a path s is augmented by emission from the medium (first term on the right-hand side), diminished by absorption and outscattering, i.e., scattering *away* from $\hat{s}$ (second term), and increased by inscattering, i.e., scattering from all other directions *into* direction $\hat{s}$ (last term). The RTE is a five-dimensional (three space coordinates, and two direction coordinates with local origins) integrodifferential equation, which is extremely difficult to solve. The problem is compounded by the complicated spectral behavior usually exhibited by the medium's radiation properties (κ_λ, $\sigma_{s\lambda}$, and Φ_λ). Therefore, numerous approximate and/or numerical techniques have been developed to solve the RTE and to deal with the complicated spectral behavior.

RTE Solution Methods. All RTE solution methods attempt to approximate the directional dependence of radiative intensity or express it numerically. The next level of sophistication beyond the diffusion and mean-beam-length approximations are the so-called *flux methods*. Assuming the intensity to have two constant but different values across two hemispheres of directions, the two-flux model has been successfully applied to one-dimensional problems (Modest, 2003); the six-flux method can be applied to more general geometries, but must be tailored toward each individual problem.

The most popular numerical methods are the *spherical harmonics* and the *discrete ordinates* methods. In the former, the directional dependence of intensity is expanded into a series of spherical harmonics, truncated at the *N*th level and resulting in the so-called *P-N* methods. Although higher order *P-N* methods are difficult to implement, its lowest order, the *P-1* approximation, is very popular because of its simplicity and surprising accuracy. Reducing the RTE into a single elliptical partial differential equation, it is easy to implement and has been incorporated into most modern commercial CFD codes. The *P-1* approximation assumes a near-isotropic intensity distribution and is, therefore, accurate in emission-dominated applications (such as combustion of fuels and high-temperature combustion products) and optically thick systems (large κ_λ); the method fails for predicting heat exchange between hot and cold surfaces separated by an optically thin medium (small κ_λ).

The *discrete ordinates* method (DOM) finite differences the directional dependence of intensity, requiring the simultaneous solution of many hyperbolic partial differential equations (Modest, 2003). Because it can be carried to arbitrary levels of accuracy (albeit at a steep computational price), this and its modern finite volume implementation (FVM) (Modest, 2003) are also incorporated into most CFD codes. Some commercial codes also offer the older *discrete transfer* method, which is today known to be less accurate and less efficient (Modest, 2003) and thus not recommended.

Spectral Models. As indicated earlier, the spectral variations of radiation properties of gases and particles are extremely difficult to predict and to deal with. Although particles tend to have a distribution of particle sizes and shapes, thus smoothing out spectral variations and allowing the assumption of gray or near-gray behavior, this is almost never the case for molecular gases (but may result in errors of hundreds, and even thousands, of percent). This has prompted the development of a number of approximate models, which may be loosely grouped into four groups: (1) line-by-line calculations; (2) narrow band models; (3) wide band models; and (4) global models.

In line-by-line calculations (LBL), the spectral variation of the gas absorption coefficient is followed in small steps across the entire spectrum, requiring 1 million RTE evaluations or more, making this method suitable only for benchmarking. Narrow band models take advantage of the fact that the gas absorption coefficient varies much more rapidly across the spectrum than other quantities, such as emissive power or surface emittance. The models predict gas transmissivities averaged across small spectral ranges; the most successful ones are the so-called *statistical narrow band models* (SNB), in particular the Malkmus model (Modest, 2003). Wide band models (WBM) are similar to narrow band models, but average over an entire vibration–rotation band and usually employ correlations of somewhat dated experimental data. Finally, global models look at the entire spectrum; the most successful is the *weighted sum of gray gases* (WSGG) first introduced by Hottel (Hottel and Sarofim, 1967).

The most modern, accurate, and efficient approach is the method of *correlated k-distributions*, in which the absorption coefficient is reordered across a spectral range into a monotonically increasing function. This method also exists in narrow band, wide band, and global forms and can result in (near) exact answers at a tiny fraction of the costs for LBL calculations. For more detailed information on spectral modeling, the reader is referred to Modest (2003). Apparently, as of 2003, none of the better known CFD packages includes a credible nongray spectral model.

Defining Terms

Absorptance: The ability of a solid material to absorb (i.e., trap and convert to other forms of energy) incoming radiation; gives the fraction of incoming radiation that is absorbed by the medium.

Absorptivity: The fraction of incoming radiation absorbed by a column of a radiatively participating medium (e.g., a gas or a particle cloud).

Absorption coefficient: The ability of a medium to absorb (i.e., trap and convert to other forms of energy) radiative energy over a unit path length; the reciprocal of the mean distance a photon travels before being absorbed.

Blackbody: Any material or configuration that absorbs all incoming radiation completely. A blackbody also emits the maximum possible amount of radiation as described by Planck's law.

Diffuse surface: A surface that emits and/or reflects equal amounts of radiative energy (photons) into all directions; a surface that absorbs and/or reflects equal amounts of radiation independent of incoming direction.

Emissive power: The rate of radiative energy leaving a surface through emission. The maximum amount of emissive power is emitted by a blackbody with a spectral strength described by Planck's law.

Emittance: The ability of a solid material to emit (i.e., convert internal energy into electromagnetic waves or photons) thermal radiation; gives the fraction of emission as compared with a blackbody.

Emissivity: The ability of a column of a radiatively participating medium (e.g., a gas or a particle cloud) to emit thermal radiation; gives the fraction of emission as compared with an opaque (i.e., infinitely long) column.

Gray: A medium whose radiative properties (such as absorptance, emittance, reflectance, absorption coefficient) do not vary with wavelength.

Irradiation: incoming radiative flux onto a surface from outside it.

Network analogy: Expressing radiative heat exchange between surfaces in terms of an electrical network, with heat flux as "current," differences in emissive power as "potentials," and defining radiative resistances.

Opaque medium: A medium of sufficient thickness that absorbs all nonreflected irradiation; no radiation is transmitted through the medium.

Photon: A massless particle carrying energy in the amount of $h\nu$; the quantum mechanical alternative view of an electromagnetic wave carrying radiative energy.

Planck's law: The law describing the spectral distribution of the radiative energy emitted (emissive power) of a blackbody.

Radiosity: Total radiative flux leaving a surface (diffusely), consisting of emitted as well as reflected radiation.

Reflectance: The ability of an interface, a medium, or a composite with a number of interfaces to reflect incoming radiation back into the irradiating medium.

Semitransparent: See transparent.

Spectral value: The value of a quantity that varies with wavelength at a given wavelength; for dimensional quantities, the amount per unit wavelength.

Transmittance: The fraction of incoming radiation transmitted through a layer of a solid material.

Transmissivity: The fraction of incoming radiation transmitted by a column of a radiatively participating medium (e.g., a gas or a particle cloud).

Transparent: The ability of a medium to let incoming radiation pass through it. A medium that lets all radiation pass through it is called transparent; a medium that only allows a part to pass through it is called *semitransparent*.

View factor: The fraction of diffuse radiant energy leaving one surface that is intercepted by another surface.

References

Brewster, M.Q. 1992. *Thermal Radiative Transfer & Properties*, John Wiley & Sons, New York.

Buckius, R.O. and Hwang, D.C. 1980. Radiation properties for polydispersions: application to coal, *J. Heat Transfer*, 102, 99–103.

Felske, J.D. and Tien, C.L. 1977. The use of the Milne–Eddington absorption coefficient for radiative heat transfer in combustion systems, *J. Heat Transfer*, 99(3), 458–465.

Hottel, H.C. and Sarofim, A.F. 1967. *Radiation Transfer*, McGraw–Hill, New York.

Howell, J.R. 1982. *Catalog of Radiation Configuration Factors*, McGraw–Hill, New York.

Leckner, B. 1972. Spectral and total emissivity of water vapor and carbon dioxide, *Combust. Flame*, 19, 33–48.

Modest, M.F. 2003. *Radiative Heat Transfer*, 2nd ed., Academic Press, New York.

Özisik, M.N. 1973. *Radiative Transfer and Interactions with Conduction and Convection*, John Wiley & Sons, New York.

Siegel, R. and Howell, J.R. 2002. *Thermal Radiation Heat Transfer*, 4th ed., Taylor & Francis, New York.

Sparrow, E.M. and Cess, R.D. 1978. *Radiation Heat Transfer*, Hemisphere, New York.

4.4 Phase-Change

Boiling and Condensation

Van P. Carey

Introduction

Liquid-vapor phase-change processes play an important role in many technological applications. The virtually isothermal heat transfer associated with boiling and condensation processes makes their inclusion in power and refrigeration processes highly advantageous from a thermodynamic efficiency standpoint. In addition, the high heat transfer coefficients associated with boiling and condensation have made the use of these processes increasingly attractive in the thermal control of compact devices that have high heat dissipation rates. Applications of this type include the use of boiling heat transfer to cool electronic components in computers and the use of compact evaporators and condensers for thermal control of aircraft avionics and spacecraft environments. Liquid-vapor phase-change processes are also of critical importance to nuclear power plant design, both because they are important in normal operating circumstances and because they dominate many of the accident scenarios that are studied as part of design evaluation.

The heat transfer and fluid flow associated with liquid-vapor phase-change processes are typically among the more complex transport circumstances encountered in engineering applications. These processes have all the complexity of single-phase convective transport, plus additional elements resulting from motion of the interface, nonequilibrium effects, and dynamic interactions between the phases. Due to the highly complex nature of these processes, development of methods to accurately predict the associated heat and mass transfer is often a formidable task.

In this section, commonly used variables not defined in the nomenclature are as follows: q'' = surface heat flux, μ_l = liquid viscosity, μ_v = vapor viscosity, Pr_l = liquid Prandtl number, T_w = wall surface temperature, T_{sat} = saturation temperature, c_{pl} = liquid specific heat, k_v = vapor thermal conductivity, g = gravitational acceleration, and x = mass quality.

Boiling

Three mechanisms that play important roles in boiling processes are (1) surface tension effects, (2) surface wetting characteristics of the liquid, and (3) metastable phase stability.

Anyone who has watched small bubbles rise in a carbonated beverage or a pot of boiling water has undoubtedly noticed that the bubbles are almost perfectly spherical, as if an elastic membrane were present at the interface to pull the vapor into a spherical shape. This apparent interfacial tension or *surface tension* σ is equivalent to an energy stored in the interface region per unit area. The energy excess in this region is due to the slightly larger separation of the liquid phase molecules adjacent to the gas phase.

The magnitude of the surface tension for a substance is directly linked to the strength of intermolecular forces in the material. Nonpolar liquids typically have the lowest surface tension. Water and other **polar molecules** have somewhat higher surface tension, and liquid metals, which exhibit metallic bond attraction, have very high surface tension. The surface tension of water at 20°C is 0.0728 N/m, whereas liquid mercury has a surface tension of 0.484 N/m at the same temperature. The surface tension for any pure liquid varies with temperature. It decreases almost linearly with increasing temperature, vanishing altogether at the critical point where the distinction between the phases disappears.

As a result of the surface tension at the interface, the pressure inside a spherical bubble of radius r must exceed that in the surrounding liquid by $2\sigma/r$:

$$P_v = P_l + \frac{2\sigma}{r} \tag{4.4.1}$$

By using the relation (1) between the pressure in the two phases it can be shown that for the bubble to be in equilibrium with the surrounding liquid, the liquid must actually be superheated above the saturation temperature for the ambient liquid pressure. The amount of required superheating increases as the radius of curvature of the bubble interface decreases.

The wetting characteristics of the liquid are generally quantified in terms of a *contact angle* between the solid surface and the tangent to the interface at the point where it contacts the solid. This angle is measured through the liquid phase, as shown in Figure 4.4.1. In some systems, the wetting angle established at equilibrium may depend on the fluid motion history. For some systems the contact angle established by liquid advancing over a solid surface is larger than that established when a liquid front recedes over the surface. This behavior is referred to as *contact angle hysteresis*. Contact angle hysteresis can have an important effect on boiling and condensation processes, particularly those involving water.

For a bubble with a specified vapor volume, the contact angle will dictate the radius of curvature of the bubble interface. The wetting behavior in combination with the surface tension effect, thus, determines the level of superheat required for the bubble to be in equilibrium with the surrounding liquid. The liquid must be heated above this superheat level for the bubble to grow. A steady boiling process can be sustained only if the liquid is heated above this threshold superheat level.

It can be shown from basic thermodynamic analysis that a necessary and sufficient condition for phase stability is that

$$\left(\frac{\partial P}{\partial v}\right)_T < 0 \tag{4.4.2}$$

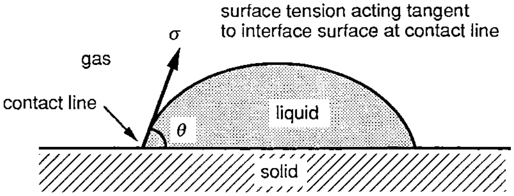

FIGURE 4.4.1 Definition of the contact angle θ.

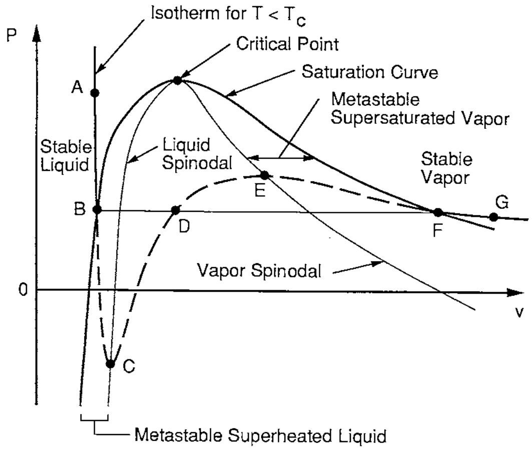

FIGURE 4.4.2 Spinodal lines and metastable regions on a *P*–$\boldsymbol{v}$ diagram.

where v is the specific volume. Below the critical temperature, extrapolation of the isotherms for the liquid and vapor phases consistent with an equation of state like the van de Waals equation results in an isotherm shape similar to that shown in Figure 4.4.2.

The locus of points where $(\partial P/\partial v)_T = 0$ are termed *spinodal curves*. Regions of metastable vapor and liquid exist between the saturation curve and the spinodal curves. The effects of surface tension discussed above require that fluid surrounding a vapor bubble be in the metastable superheated liquid region. Predictions of statistical thermodynamics imply that as $(\partial P/\partial v)_T$ approaches zero, the level of fluctuations in a fluid system increases. This, in turn, increases the probability that an embryonic new phase will form as a result of density fluctuations. Initiation of a phase change in this manner is termed *homogeneous nucleation*. Generally, a pure liquid must be heated to nearly 90% of its absolute critical temperature before homogeneous nucleation of vapor bubbles occurs.

In most physical systems of engineering interest, the bulk phase is in contact with solid walls of the containing structures, or solid particulate contaminants. These solid phases may provide nucleation sites where phase change may occur if the system state is driven into the metastable range. Nucleation of vapor bubbles may preferentially occur at low liquid superheat levels in crevices in the solid surface where gas is trapped. This type of nucleation at the solid surface of a containment wall is categorized as *heterogeneous nucleation*. Because solid containment walls usually contain microscopic crevice-type imperfections, heterogeneous nucleation is more common than homogeneous nucleation in systems where boiling occurs.

Vapor entrapment in crevices of the heated walls of evaporator heat exchangers usually makes it easier to initiate the vaporization process. Vapor bubbles grow from these crevices until buoyancy or drag on the bubbles exceeds the surface tension force holding the droplet to the solid surface. The bubble then releases into the bulk liquid. A small remnant of vapor remains in the crevice after a bubble releases, and this remnant grows in size as further vaporization occurs until the bubble grows out of the crevice again. The result is a cyclic process of bubble growth and release known as the *ebullition cycle*. Crevices at which the ebullition cycle is sustained are said to be active nucleation sites. When the ebullition process occurs at many sites over a heated surface, the overall process is referred to as **nucleate boiling**, which is one possible mode of **pool boiling**.

Pool Boiling

Vaporization of liquid at the surface of a body immersed in an extensive pool of motionless liquid is generally referred to as pool boiling. The nature of the pool boiling process varies considerably depending on the conditions at which boiling occurs. The level of heat flux, the thermophysical properties of the liquid and vapor, the surface material and finish, and the physical size of the heated surface all may have an effect on the boiling process.

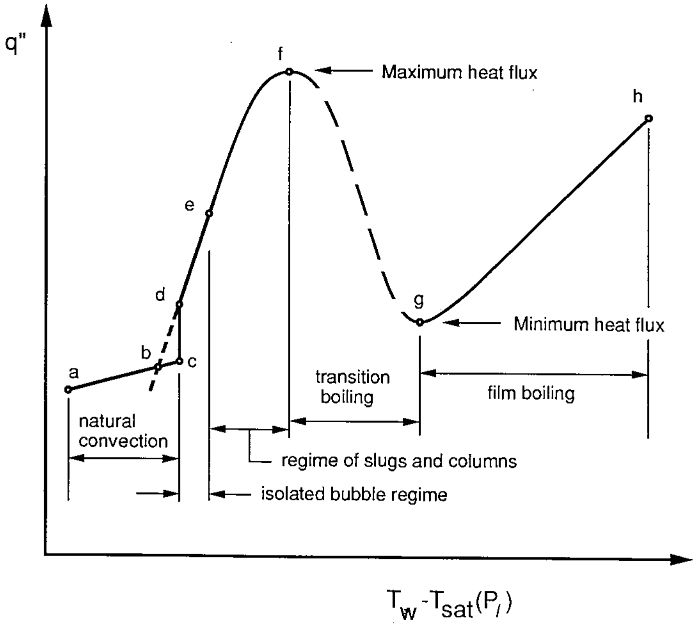

FIGURE 4.4.3 Pool boiling regimes for an independently controlled surface temperature.

The regimes of pool boiling are most easily understood in terms of the so-called boiling curve: a plot of heat flux q'' vs. wall superheat $T_w - T_{sat}$ for the circumstances of interest. Many of the features of the classic pool boiling curve were determined in the early investigations of pool boiling conducted by Nukiyama (1934). Strictly speaking, the classic pool boiling curve defined by the work of this investigator and others applies to well-wetted surfaces for which the characteristic physical dimension L is large compared to the bubble or capillary length scale L_b defined as

$$L_b = \sqrt{\frac{\sigma}{g(\rho_l - \rho_v)}} \tag{4.4.3}$$

The discussion in this section is limited to pool boiling of wetting liquids on surfaces with dimensions large compared with L_b. Additional information on features of the boiling curve when the liquid poorly wets the surface or when L/L_b is small can be found in Carey (1992). To make this discussion concrete, we will assume that the ambient liquid surrounding the immersed body is at the saturation temperature for the ambient pressure. If the surface temperature of the immersed body is controlled and slowly increased, the boiling curve will look similar to that shown in Figure 4.4.3. The axes in this plot are logarithmic scales. The regimes of pool boiling encountered for an upward-facing horizontal flat surface as its temperature is increased are also indicated in Figure 4.4.3. The lateral extent of the surface is presumed to be much larger than L_b. At very low wall superheat levels, no nucleation sites may be active and heat may be transferred from the surface to the ambient liquid by natural convection alone and q'' increases slowly with $T_w - T_{sat}$.

Eventually, the superheat becomes large enough to initiate nucleation at some of the cavities on the surface. This *onset of nucleate boiling* (ONB) condition occurs at point *c* in Figure 4.4.3. Once nucleate boiling is initiated, any further increase in wall temperature causes the system operating point to move upward along section *d-f* of the curve in Figure 4.4.3. This portion of the curve corresponds to the nucleate boiling regime. The active sites are few and widely separated at low wall superheat levels. This range of conditions, corresponding to segment *d-e* of the curve, is sometimes referred to as the *isolated bubble regime.*

With increasing surface superheat, more sites become active, and the bubble frequency at each site generally increases. Eventually, the active sites are spaced so closely that bubbles from adjacent sites merge together during the final stages of growth and release. Vapor is being produced so rapidly that bubbles merging together form columns of vapor slugs that rise upward in the liquid pool toward its free surface. This higher range of wall superheat, corresponding to segment *e-f* of the boiling curve in Figure 4.4.3, is referred to as the *regime of slugs and columns*.

Increasing the wall superheat and heat flux within the regime of slugs and columns produces an increase in the flow rate of vapor away from the surface. Eventually, the resulting vapor drag on the liquid moving toward the surface becomes so severe that liquid is unable to reach the surface fast enough to keep the surface completely wetted with liquid. Vapor patches accumulate at some locations and evaporation of the liquid between the surface and some of these patches dries out portions of the surface.

If the surface temperature is held constant and uniform, dry portions of the surface covered with a vapor film will locally transfer a much lower heat flux than wetted portions of the surface where nucleate boiling is occurring. Because of the reduction in heat flux from intermittently dry portions of the surface, the mean overall heat flux from the surface is reduced. Thus, increasing the wall temperature within the slugs and columns region ultimately results in a peaking and rollover of the heat flux. The peak value of heat flux is called the **critical heat flux** (CHF), designated as point *f* in Figure 4.4.3

If the wall temperature is increased beyond the critical heat flux condition, a regime is encountered in which the mean overall heat flux decreases as the wall superheat increases. This regime, which is usually referred to as the **transition boiling** regime, corresponds to segment *f-g* on the boiling curve shown in Figure 4.4.3. The transition boiling regime is typically characterized by rapid and severe fluctuations in the local surface heat flux and/or temperature values (depending on the imposed boundary condition). These fluctuations occur because the dry regions are generally unstable, existing momentarily at a given location before collapsing and allowing the surface to be rewetted.

The vapor film generated during transition boiling can be sustained for longer intervals at higher wall temperatures. Because the intermittent insulating effect of the vapor blanketing is maintained longer, the time-averaged contributions of the blanketed locations to the overall mean heat flux are reduced. The mean heat flux from the surface thus decreases as the wall superheat is increased in the transition regime. As this trend continues, eventually a point is reached at which the surface is hot enough to sustain a stable vapor film on the surface for an indefinite period of time. The entire surface then becomes blanketed with a vapor film, thus making the transition to the **film boiling** regime. This transition occurs at point *g* in Figure 4.4.3.

Within the film boiling regime, the heat flux monotonically increases as the superheat increases. This trend is a consequence of the increased conduction and/or convection transport due to the increased driving temperature difference across the vapor film. Radiative transport across the vapor layer may also become important at higher wall temperatures.

Once a surface is heated to a superheat level in the film boiling regime, if the surface temperature is slowly decreased, in general the system will progress through each of the regimes described above in reverse order. However, the path of the boiling curve may differ significantly from that observed for increasing wall superheat, depending on whether the surface heat flux or temperature is controlled.

Experimental evidence summarized by Witte and Lienhard (1982) implies that the path of the transition boiling curve is determined, to a large degree, by the wetting characteristics of the liquid on the solid surface. For a given wall superheat level in the transition boiling regime, a higher heat flux is generally obtained if the liquid wets the surface than if it poorly wets the surface. For systems that exhibit contact angle hysteresis, the transition boiling curves obtained for decreasing and increasing wall superheat may therefore be somewhat different. The transition boiling curve for decreasing wall superheat may be significantly below that for increasing superheat for such circumstances, as indicated in Figure 4.4.4.

For an electrically heated surface, the rise in temperature associated with the jump from nucleate to film boiling at the critical heat flux is very often large enough to melt component materials and burn out the component. As a result, the critical heat flux is often referred to as the *burnout heat flux* to

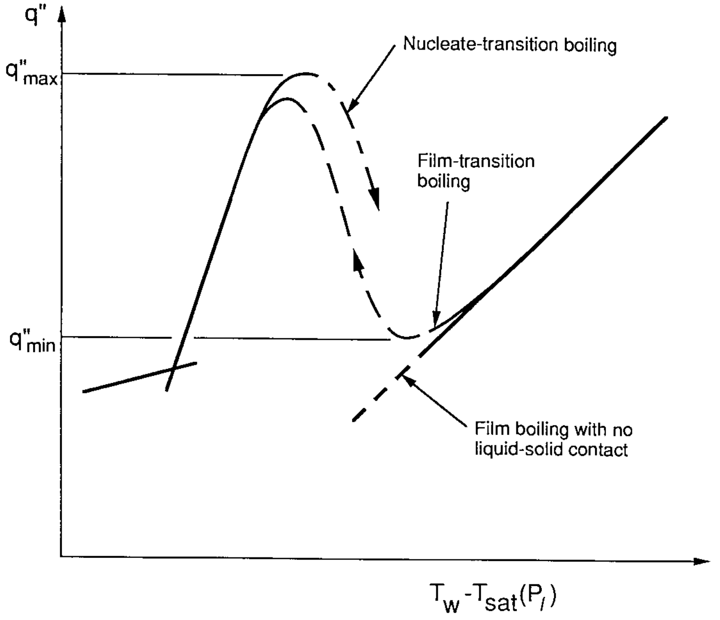

FIGURE 4.4.4 Relative locations of the nucleate transition and film transition portions of the pool boiling curve.

acknowledge the potentially damaging effects of applying this heat flux level to components cooled by nucleate boiling. Once the jump to film boiling has been made, any further increase in applied heat flux increases the wall superheat, and the system follows basically the same film boiling curve as in the temperature-controlled case.

Correlations of nucleate pool boiling heat transfer data have typically been used as tools to predict nucleate boiling heat transfer in engineering systems and heat exchangers. Many investigators have proposed methods of correlating data of this type; so many, in fact, that a complete discussion of them all could easily fill a major portion of this section. In this section, three of the more commonly used correlation methods will be mentioned. However, before proceeding, two aspects of the interpretation of such correlations are worth noting. First, experimental data indicate that the subcooling of the liquid pool has a negligible effect on the nucleate boiling heat transfer rate. Consequently, the pool boiling correlations are generally regarded as being valid for both subcooled and saturated nucleate boiling. Second, it has also been observed that at moderate to high heat flux levels, a pool boiling heat transfer correlation developed for one heated surface geometry in one specific orientation often works reasonably well for other geometries and/or other orientations. Hence, although a correlation was developed for a specific geometry and orientation, it may often be used for other geometries, at least at moderate to high heat flux levels.

Having taken note of the above points, a commonly used correlation for nucleate boiling heat transfer developed by Rohsenow (1962) is

$$\frac{q''}{\mu_l h_{fg}}\left[\frac{\sigma}{g(\rho_l-\rho_v)}\right]^{1/2}=\left(\frac{1}{C_{sf}}\right)^{1/r}\mathrm{Pr}_l^{-s/r}\left[\frac{c_{pl}\left[T_w-T_{sat}(P_l)\right]}{h_{fg}}\right]^{1/r} \tag{4.4.4}$$

Values of $r = 0.33$ and $s = 1.7$ are recommended for this correlation, but for water s should be changed to 1.0. The values of C_{sf} in this correlation vary with the type of solid surface and the type of fluid in the system. This empirically accounts for material property and/or wetting angle effects. Recommended values of C_{sf} for specific liquid–solid combinations are given by Rohsenow (1962), but whenever possible, an experiment should be conducted to determine the appropriate value of C_{sf} for the particular solid–liquid combination of interest. If this is not possible, a value of C_{sf} = 0.013 is recommended as a first approximation.

As noted previously, the pool boiling curve generally exhibits a maximum heat flux or CHF at the transition between nucleate and transition boiling. This peak value is the maximum level of heat flux from the surface which the system can provide in a nonfilm-boiling mode at a given pressure. The mechanism responsible for the CHF has been the subject of considerable investigation and debate over the past five decades. As the heat flux increases, bubbles generated at the surface coalesce to form vapor columns or jets. Perhaps the most widely cited CHF model postulates that the CHF condition occurs when Helmholtz instability of the large vapor jets leaving the surface distorts the jets, blocking liquid flow to portions of the heated surface. Continued vaporization of liquid at locations on the surface which are starved of replacement liquid than leads to formation of a vapor blanket over part or all of the surface. According to Zuber (1959) for a flat horizontal surface, the predicted maximum heat flux $q''_{\max}$ is

$$q''_{\max} = 0.131 \rho_v h_{fg} \left[\frac{\sigma_g (\rho_l - \rho_v)}{\rho_v^2} \right]^{1/4} \tag{4.4.5}$$

but Lienhard and Dhir (1973) recommend that the constant 0.131 in the above relation be replaced with 0.141. Other geometries are treated by Lienhard et al. (1973) and Lienhard and Dhir (1973b). An alternative model has been proposed by Haramura and Katto (1983).

Lienhard and Witte (1985) discuss the development and limitations of hydrodynamic CHF theories.

As shown in the Figure 4.4.3, the boundary between the transition boiling regime and the film boiling regime corresponds to a minimum in the heat flux vs. superheat curve. This condition is referred to as the **minimum heat flux** condition, referred to as the *Leidenfront point*. The minimum heat flux corresponds approximately to the lowest heat flux which will sustain stable film boiling.

For an infinite flat (upward-facing) heated surface, vapor generated at the interface during stable film boiling is released as bubbles at the nodes of a standing two-dimensional Taylor wave pattern. The following relation for the minimum heat flux $q''_{\min}$ derived by Zuber (1959) and Berenson (1961).

$$q''_{\min} = 0.09 \rho_v h_{fg} \left[\frac{\sigma_g (\rho_l - \rho_v)}{(\rho_l + \rho_v)^2} \right]^{1/4} \tag{4.4.6}$$

$q''_{\min}$ correlations have been developed by Lienhard and Wong (1964) for horizontal cylinders and Gunnerson and Cronenberg (1980) for spheres.

In film boiling, transport of heat across the vapor film from the wall to the interface may occur by convection, conduction, and radiation. The radiation contribution depends on the nature of the solid surface, but when the radiation effect is small, the heat transfer for film boiling is independent of the material properties and finish of the surface. For buoyancy-driven laminar film boiling over a vertical flat isothermal surface in a pool of saturated liquid, the local heat transfer coefficient from the surface can be obtained from the following relation:

$$h = \left[\frac{k_v^3 g \rho_v (\rho_l - \rho_v) h_{fg}}{4 \mu_v (T_w - T_{\text{sat}}) x} \right]^{1/4} \tag{4.4.7}$$

At low surface temperatures, radiation effects are negligible and consideration of convective transport alone is sufficient to predict the heat transfer. At higher temperatures radiation effects must also be included. If the vapor in the film absorbs and emits radiation at infrared wavelengths, a detailed treatment of the radiation interaction with the vapor may be necessary to accurately predict the film boiling heat transfer.

Additional information mechanisms such as interfacial waves, turbulence, and variable properties is summarized in Carey (1992).

Transition pool boiling has traditionally been interpreted as a combination of nucleate and film boiling alternately occurring over the heated surface, and a model of transition boiling that accounts for contact angle effects has been proposed by Ramilison and Lienhard (1987).

Internal Convective Boiling

Flow boiling in tubes is perhaps the most complex convective process encountered in applications. In most evaporator and boiler applications, the flow is either horizontal or vertically upward. Figure 4.4.5 schematically depicts a typical low-flux vaporization process in a horizontal round tube. In this example liquid enters as subcooled liquid and leaves as superheated vapor. As indicated in Figure 4.4.5, the flow undergoes transitions in the boiling regime and the two-phase flow regime as it proceeds down the tubes. The regimes encountered depend on the entrance conditions and the thermal boundary conditions at the tube wall. At low quality the vaporization process is dominated by nucleate boiling, with convective effects being relatively weak. As the quality increases, the flow quickly enters the annular film flow regime in which convective evaporation of the annular liquid film is the dominant heat transfer mechanism. Often the conditions are such that liquid droplets are often entrained in the core vapor flow during annular flow evaporation. Eventually, the annular film evaporates away, leaving the wall dry. Mist-flow evaporation of entrained liquid droplets continues in the post-dryout regime until only vapor remains. Similar, sequences of flow and boiling regimes occurring in vertical upward flow, as indicated in Figure 4.4.6.

The boiling regime trends shown in Figure 4.4.5 and Figure 4.4.6 are typical for low heat flux vaporization processes. At high wall superheat levels, transition boiling or film boiling can also occur. The transition from nucleate boiling to one of these regimes is termed a *departure from nucleate boiling* (DNB) or the CHF condition. However, the heat transfer performance of an evaporator under transition or film boiling conditions is so poor that equipment is not usually designed to operate under such conditions.

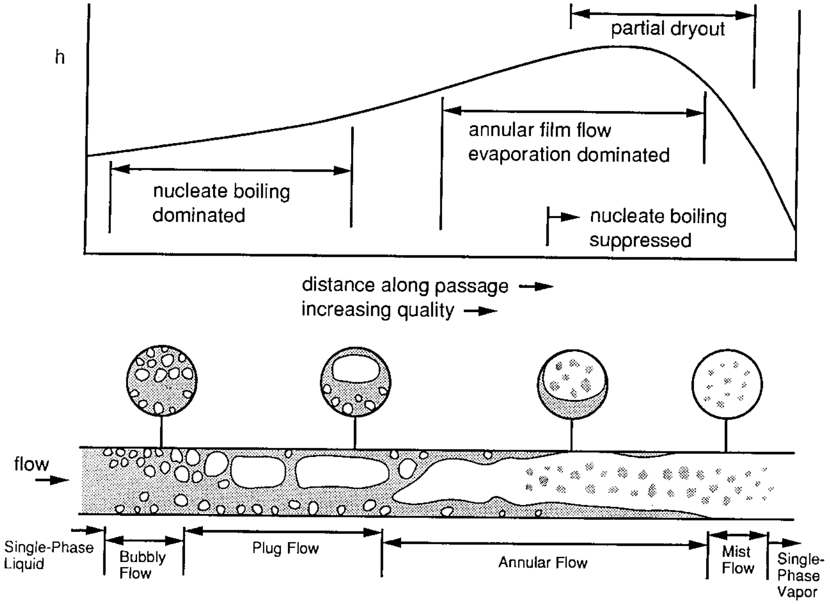

FIGURE 4.4.5 Qualitative variation of the heat transfer coefficient *h* and flow regime with quality for internal convective boiling in a horizontal tube at moderate wall superheat.

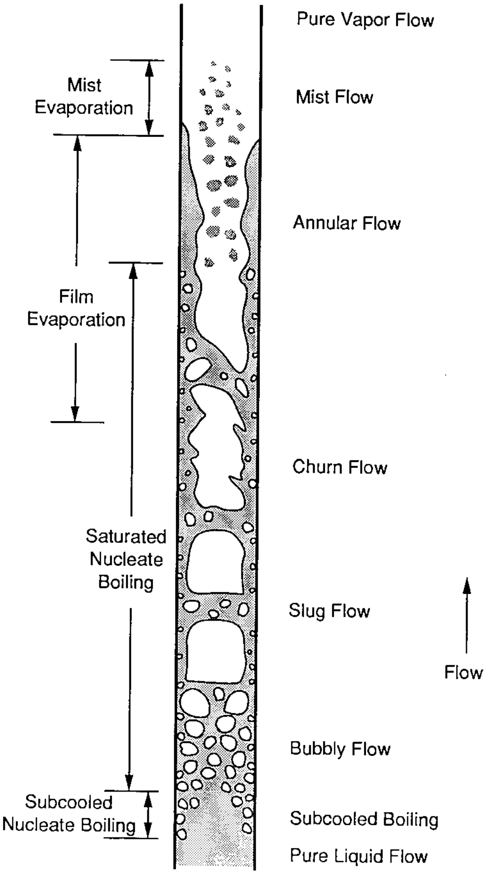

FIGURE 4.4.6 Flow regimes and boiling mechanisms for upflow convective boiling in a vertical tube at moderate wall superheat.

Because low-quality or subcooled flow boiling are nucleate boiling dominated, the heat transfer coefficient in these regimes is often predicted using a nucleate boiling correlation developed as a fit to pool boiling data. The usefulness of such an approach is a consequence of the fact that for most conditions of practical interest, nucleate boiling heat transfer is only weakly affected by liquid subcooling or liquid bulk convection.

For saturated convective boiling prior to dryout, relations to predict the heat transfer coefficient have typically been formulated to impose a gradual suppression of nucleate boiling and gradual increase in liquid film evaporation heat transfer as the quality increases. A number of correlations based on such an approach have been developed. An early correlation of this type developed by Chen (1966) has been widely used. One of the better methods of this type is the recently developed correlation of Kandlikar (1989) which has been fit to a broad spectrum of data for both horizontal and vertical tubes. For this method the heat transfer coefficient for a tube of diameter D is given by

$$h = h_l\left[C_1 Co^{C_2}\left(25\mathrm{Fr}_{le}\right)^{C_5} + C_3 Bo^{C_4} F_K\right] \tag{4.4.8}$$

where

$$Co = \left(\frac{1-x}{x}\right)^{0.8}\left(\frac{\rho_v}{\rho_l}\right)^{0.5} \tag{4.4.9}$$

TABLE 4.4.1 Constants for the Correlation of Kandlikar (1987)

	$Co < 0.65$ (Convective Region)	$Co \geq 0.65$ (Nucleate Boiling Region)
C_1	1.1360	0.6683
C_2	–0.9	–0.2
C_3	667.2	1058.0
C_4	0.7	0.7
C_5[a]	0.3	0.3

[a] $C_5 = 0$ for vertical tubes and horizontal tubes with $\mathrm{Fr}_{le} > 0.04$.

$$Bo = q''/Gh_{fg} \tag{4.4.10}$$

$$Fr_{le} = G^2/\rho_l^2 gD \tag{4.4.11}$$

and h_l is the single-phase heat transfer coefficient for the liquid phase flowing alone in the tube computed as

$$h_l = 0.023\left(\frac{k_l}{D}\right)\left(\frac{G(1-x)D}{\mu_l}\right)^{0.8} \mathrm{Pr}_l^{0.4} \tag{4.4.12}$$

The constants $C_1 - C_5$ are given in Table 4.4.1. The factor F_K is a fluid-dependent parameter. For water, $F_K = 1$. For R-12 and nitrogen, recommended values of F_K are 1.50 and 4.70, respectively. Values of F_K for a variety of other fluids can be obtained from Kandlikar (1989).

Methods for predicting the conditions at which dryout or a DNB transition occurs have typically been empirical in nature. Based on fits to extensive data, Levitan and Lantsman (1975) recommended the following relations for the DNB heat flux and the quality at which dryout occurs during flow boiling of water in a tube with an 8-mm diameter.

$$q''_{\text{crit}} = \left[10.3 - 7.8\left(\frac{P}{98}\right) + 1.6\left(\frac{P}{98}\right)^2\right]\left(\frac{G}{1000}\right)^{1.2\{[0.25(P-98)/98]-x\}} e^{-1.5x} \tag{4.4.13}$$

$$x_{\text{crit}} = \left[0.39 + 1.57\left(\frac{P}{98}\right) - 2.04\left(\frac{P}{98}\right)^2 + 0.68\left(\frac{P}{98}\right)^3\right]\left(\frac{G}{1000}\right)^{-0.5} \tag{4.4.14}$$

In the above relations, q''_{crit} is in MW/m², P is the pressure in bar, and G is in kg/m²sec. To obtain values of q''_{crit} and x_{crit} for diameters other than 8 mm, Levitan and Lantsman (1975) recommended that the 8-mm values from the above relations be corrected as follows:

$$q''_{\text{crit}} = \left(q''_{\text{crit}}\right)_{8\text{mm}}\left(\frac{8}{D}\right)^{1/2} \tag{4.4.15}$$

$$x_{\text{crit}} = \left(x_{\text{crit}}\right)_{8\text{mm}}\left(\frac{8}{D}\right)^{0.15} \tag{4.4.16}$$

where D is the diameter in millimeters. A good generalized empirical correlation for predicting dryout or CHF conditions in vertical uniformly heated tubes is that recently proposed by Katto and Ohno (1984).

In many cases, post-dryout mist flow evaporation is driven primarily by convective transport from the tube wall to the gas and then to the entrained droplets. In some circumstances, impingement of droplets onto the heat surface and radiation interactions may also be important. In cases where convection is dominant, predictions of the heat transfer coefficient have been developed by modifying a single-phase correlation for the entire flow as vapor with a correction factor which accounts for the presence of the entrained droplets. Often this correction factor has been presumed to be a function of property ratios. An example of such an approach is the correlation of Dougall and Rohsenow (1963) for which the heat transfer coefficient h is given by

$$\frac{hD}{k_v} = 0.023\left[\left(\frac{GD}{\mu_v}\right)\left(x + \frac{\rho_v}{\rho_l}(1-x)\right)\right]^{0.8} \mathrm{Pr}_{v,\mathrm{sat}}^{0.4} \tag{4.4.17}$$

For further information on mechanisms of convective boiling, see the texts of Collier (1996), Stephan (1992), and Carey (1992).

Condensation

As in the case of boiling, surface tension effects, surface wetting characteristics, and metastable phase stability also can play important roles in condensation processes. As a result of interfacial tension, the pressure inside a spherical liquid droplet of radius r must exceed that in the surrounding liquid by $2\sigma/r$. A consequence of this and basic thermodynamics is that at equilibrium the surrounding vapor must actually be slightly supersaturated. The amount of supersaturation required at equilibrium increases as the radius of curvature of the bubble interface decreases.

For a liquid droplet on a solid surface with a specified volume, the wetting contact angle dictates the radius of curvature of the droplet interface. Because of the linkage between the interface curvature and the required equilibrium supersaturation, the wetting behavior thus determines the level above which the vapor supersaturation must be raised for the droplet to grow. Steady condensation on the droplet interface can be sustained only if the vapor is driven beyond this supersaturation level by cooling or depressurization. For such conditions, the vapor is in the metastable supersaturated range indicated in Figure 4.4.2.

Condensation on external surfaces of a body immersed in a gas phase generally falls into one or two categories: **dropwise condensation** or **film condensation**. In dropwise condensation, the liquid-phase condensate collects as individual droplets which grow in size with time on the cold surface. This mode of condensation is most likely when the liquid poorly wets the solid surface. When the condensation rate is high or the liquid readily wets the surface, a film of liquid condensate covers the solid surface, and the process is referred to as film condensation.

Dropwise Condensation. Dropwise condensation may occur on a solid surface cooled below the saturation temperature of a surrounding vapor when the surface is poorly wetted except at locations where well-wetted contaminant nuclei exist. The poorly wetted surface condition can result from contamination or coating of the surface with a substance which is poorly wetted by the liquid phase of the surrounding vapor. In practice, this can be achieved for steam condensation by (1) injecting a nonwetting chemical into the vapor which subsequently deposits on the surface, (2) introducing a substance such as a fatty (i.e., oleic) acid or wax onto the solid surface, or (3) by permanently coating the surface with a low-surface-energy polymer or a noble metal. The effects of the first two methods are generally temporary, since the resulting surface films eventually are dissolved or eroded away.

During dropwise condensation, the condensate is usually observed to appear in the form of droplets which grow on the surface and coalesce with adjacent droplets. When droplets become large enough, they are generally removed from the surface by the action of gravity or drag forces resulting from the motion of the surrounding gas. As the drops roll or fall from the surface they merge with droplets in their path, effectively sweeping the surface clean of droplets. Droplets then begin to grow anew on the freshly-exposed solid surface. This sweeping and renewal of the droplet growth process is responsible for the high heat transfer coefficients associated with dropwise condensation. Theoretical aspects of dropwise condensation are described in two publications by Tanaka (1975, 1979). A discussion of correlations for the heat transfer coefficient associated with dropwise condensation is provided in the review article by Merte (1973).

External Film Condensation. If the liquid phase fully wets a cold surface in contact with a vapor near saturation conditions, the conversion of vapor to liquid will take the form of film condensation. As the name implies, the condensation takes place at the interface of a liquid film covering the solid surface. Because the latent heat of vaporization must be removed at the interface to sustain the process, the rate of condensation is directly linked to the rate at which heat is transported across the liquid film from the interface to the surface.

The classic integral analysis of Nusselt (1916) for laminar falling-film condensation on a vertical surface considers the physical circumstances shown in Figure 4.4.7. The surface exposed to a motionless ambient of saturated vapor is taken to be isothermal with a temperature below the saturation temperature. Note that although a vertical surface is considered here, the analysis is identical for an inclined surface, except that the gravitational acceleration g is replaced by $g \sin \Omega$, with Ω being the angle between the surface and the horizontal. Because the liquid film flows down the surface because of gravity, this situation is sometimes referred to as *falling-film condensation*.

In its simplest form, the classic Nusselt analysis incorporates the following idealizations: (1) laminar flow, (2) constant properties, (3) that subcooling of liquid is negligible in the energy balance, (4) that inertia effects are negligible in the momentum balance, (5) that the vapor is stationary and exerts no drag, (6) that the liquid-vapor interface is smooth, and (7) that heat transfer across film is only by conduction (convection is neglected). With these idealizations, the following relation for the local heat transfer coefficient h can be obtained

$$\frac{hz}{k_l} = \left[\frac{\rho_l(\rho_l - \rho_v) g h_{fg} z^3}{4 k_l \mu_\ell (T_{\text{sat}} - T_w)} \right]^{1/4} \tag{4.4.18}$$

Modified versions of this analysis have been subsequently developed which relax many of these assumptions. Laminar film condensation on a vertical surface can also be analyzed with a full boundary layer formulation. An example of this type of approach is the analysis presented by Sparrow and Gregg (1959).

The analyses described above do not include two physical mechanisms which can significantly affect the transport: (1) the effects of waves on the liquid-vapor interface and (2) interfacial vapor shear drag on the interface. The effects of interfacial shear have been studied analytically by numerous investigators. The effects of surface waves on laminar film condensation are more difficult to incorporate into theoretical analyses. In general, interfacial waves are expected to enhance convective heat transport in the film since it intermittently thins the film, increases the interfacial area, and induces mixing. Because of these effects,

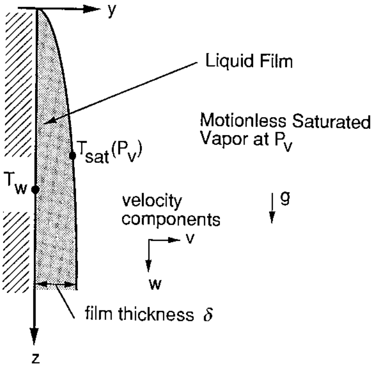

FIGURE 4.4.7 System model for the Nusselt analysis of falling-film condensation.

laminar film condensation heat transfer data are often significantly higher than the values predicted by simple boundary layer models.

As for any boundary layer flow, when the film Reynolds number becomes large enough, it is expected that a transition to turbulent flow will occur. Eddy diffusivity models of the resulting turbulent transport have been developed by Seban (1954), Dukler (1960), and others. This methodology was later extended to evaporation of a falling liquid film (see, for example, Mills and Chung, 1973).

Subsequent studies (see, for example, Mills and Chung, 1973) have suggested that the presence of the interface tends to damp larger turbulent eddies near the interface in the liquid film. This implies that a viscous sublayer exists at the interface as well as at the wall. Recent efforts to model turbulent falling-film evaporation and condensation processes have therefore included a variation of the eddy viscosity in which it goes to zero at both the wall and the interface. The analysis tools and correlations described above work reasonably well for values of liquid Prandtl number above 1. However, deviation of the predictions using these methods from heat transfer data for liquid metals can be quite significant.

Because of its importance to the design of tube-and-shell condensers, condensation on the outside of horizontal tubes has been the subject of numerous studies. The length of the tube perimeter over which the condensate flows is usually small for commonly used tubes. Consequently, the film Reynolds number is usually low and the flow in the liquid film is laminar.

With slight modification, the Nusselt (1916) analysis of laminar falling-film condensation over a flat plate can be adapted to film condensation on an isothermal horizontal cylinder. Doing so yields the following relation for the mean heat transfer coefficient:

$$\frac{\bar{h}D}{k_l} = 0.728\left[\frac{\left(\rho_l - \rho_v\right) g h_{fg} D^3 \mathrm{Pr}_l}{\rho_l \nu_l^2 c_{pl}\left(T_{\mathrm{sat}} - T_w\right)}\right]^{1/4} \tag{4.4.19}$$

Selin (1961) found that better agreement with film condensation data for horizontal tubes was obtained by replacing the constant factor in Equation (4.4.19) by 0.61. Correlations similar to the single-tube relation above have also been developed for the average condensation heat transfer coefficient for banks of round tubes.

Analytical treatment of laminar film condensation on a sphere is virtually the same as that for a horizontal cylinder. The only differences result from the angular variation of the body perimeter because of the spherical geometry. A general analytical prediction of the local heat transfer coefficient for laminar film condensation on arbitrary axisymmetric bodies has been developed by Dhir and Lienhard (1971).

Condensation in the Presence of a Noncondensable Gas. In nature and in a number of technological applications, condensation of one component vapor in a mixture may occur in the presence of other noncondensable components. The most common example is the condensation of water vapor in the air on a cold solid surface. If the component gases are considered to be a mixture of independent substances, condensation of one component vapor will occur if the temperature of the surface is below the saturation temperature of the pure vapor at its partial pressure in the mixture. This temperature threshold is referred to as the *dew point* of the mixture.

Because only the vapor is condensed, the concentration of the noncondensable gas at the interface is higher than its value in the far ambient. This, in turn, decreases the partial pressure of the vapor at the interface below its ambient value. The corresponding saturation temperature at the interface is therefore lower than the bulk temperature. The resulting depression of the interface temperature generally reduces the condensation heat transfer rate below that which would result for pure vapor alone under the same conditions. Space limitations here preclude a detailed discussion of the effects of noncondensable gases. The interested reader may find more-extensive discussions of this topic in the references by Collier (1996) and Carey (1992).

Internal Convective Condensation. In most power and refrigeration systems, the flow in the condenser is either horizontal or vertically downward. Figure 4.4.8 schematically depicts a typical condensation process

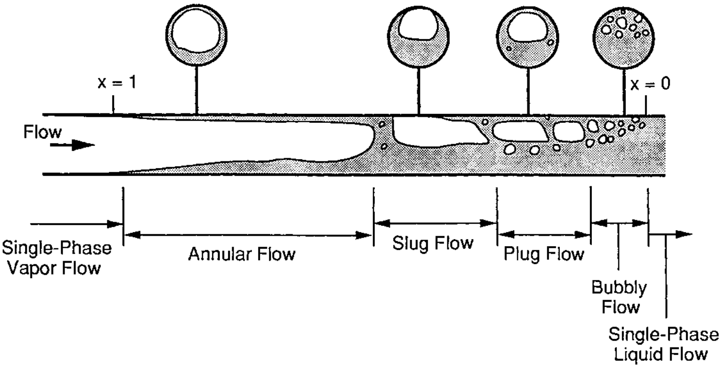

FIGURE 4.4.8 Flow regimes during horizontal cocurrent flow with condensation.

in a horizontal round tube. Superheated vapor enters the tube and at the exit end the liquid is subcooled. At a point some distance downstream of the entrance, vapor begins to condense on the walls of the tube. The location at which this occurs is at or slightly before the bulk flow reaches the equilibrium saturation condition. In most condensers, the liquid readily wets the interior of the tube and at high vapor volume fractions the liquid forms a thin liquid film on the interior wall of the tube.

The vapor velocity is generally high at the inlet end of the condenser tube, and the liquid film is driven along the tube by strong vapor shear on the film. At low vapor flow rates, some stratification may occur and the film may be thicker on the bottom of the horizontal tube. At high vapor flow rates, turbulent stresses acting on the liquid may tend to keep the thickness of the liquid film nominally uniform over the perimeter of the tube.

In most condenser applications, shear-dominated annular flow persists to very low qualities and the overwhelming majority of the heat transfer occurs in this regime. The very last stage of the condensation process, corresponding to qualities less than a few percent, may occur in slug, plug, or bubbly two-phase flow. Generally these regimes represent such a small portion of the overall heat transfer in the condenser that some inaccuracy in estimating the heat transfer coefficient for them is tolerated. As a first estimate, the heat transfer coefficient may be predicted using a correlation for pure single-phase liquid flow in the tube at the same total flow rate, or a correlation for annular flow condensation may simply be extrapolated to zero quality.

Because most of the heat duty occurs in the annular flow regime, accurate prediction of the overall heat transfer performance of the condenser requires a predictive methodology that accurately treats the transport in this regime. For this reason, the form of most correlation methods for predicting local convective condensation heat transfer coefficients are optimized to match data in the annular flow regime. One example of such a correlation is the following relation for the local heat transfer coefficient for annular flow condensation proposed by Traviss et al. (1973):

$$\frac{hD}{k_l} = \frac{0.15 \mathrm{Pr}_l \mathrm{Re}_l^{0.9}}{F_T} \left[\frac{1}{X_{tt}} + \frac{2.85}{X_{tt}^{0.476}} \right] \tag{4.4.20}$$

where

$$\mathrm{Re}_l = \frac{G(1-x)D}{\mu_l}, \qquad X_{tt} = \left(\frac{1-x}{x} \right)^{0.9} \left(\frac{\rho_v}{\rho_l} \right)^{0.5} \left(\frac{\mu_l}{\mu_v} \right)^{0.1}$$

and F_T is given by

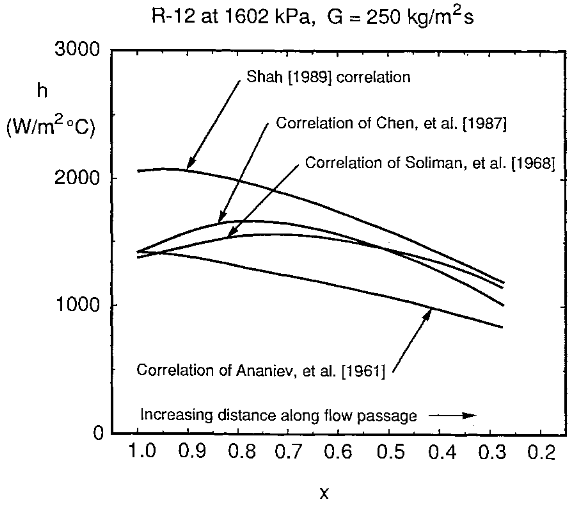

FIGURE 4.4.9 Comparison of the variation of *h* with *x* predicted by four correlation methods for internal convective condensation. References cited in this figure are listed in chapter 11 of Carey (1992).

$$
\begin{aligned}
F_T &= 5\mathrm{Pr}_l + 5\ln\left\{1 + 5\mathrm{Pr}_l\right\} + 2.5\ln\left\{0.0031\mathrm{Re}_l^{0.812}\right\} && \text{for} \quad \mathrm{Re}_l > 1125 \\
&= 5\mathrm{Pr}_l + 5\ln\left\{1 + \mathrm{Pr}_l\left(0.0964\mathrm{Re}_l^{0.585} - 1\right)\right\} && \text{for} \quad 50 < \mathrm{Re}_l < 1125 \\
&= 0.707\mathrm{Pr}_l\mathrm{Re}_l^{0.5} && \text{for} \quad \mathrm{Re}_l < 50
\end{aligned}
$$

Carey (1992) has shown that the generic form of this correlation can be derived from a theoretical model of annular flow condensation in a round tube. Several correlations of this general type have been developed as fits to experimental data; see Carey (1992) for a summary. The predictions of these correlations may vary significantly for a given set of conditions. When possible, a correlation should be selected which has been tested against data for conditions close to those for the application of interest.

A correlation methodology that can be used to predict internal convective condensation heat transfer for slug, plug, or wavy stratified flow has also been proposed by Rossen and Meyers (1965). To predict the overall heat transfer performance of a condenser, methods to predict the local heat transfer coefficient must be combined with a scheme to numerically integrate finite-difference forms of the energy, mass, and momentum balances in the tube. For further information on such schemes see the references by Collier (1996) and Carey (1992) (Figure 4.4.9).

Defining Terms

Critical heat flux (CHF): A maximum heat flux condition that characterizes the transition between nucleate boiling and transition boiling or film boiling.

Dropwise condensation: Condensation of vapor into liquid in discrete droplets, usually attained when a cold surface is poorly wetted by the liquid phase.

Film boiling: Generation of vapor at the interface of a vapor film which entirely covers the hot surface.

Film condensation: Condensation of vapor onto the interface of a liquid film that completely covers a cold surface.

Minimum heat flux: A minimum heat flux condition on the classic boiling curve that characterizes the transition between film boiling and transition boiling. Also, sometimes referred to as the Leidenfrost point, it is a lower bound for heat flux values at which stable film boiling may occur.

Nucleate boiling: Generation of vapor at a hot surface by formation of bubbles at discrete nucleation sites with full liquid wetting of the surface.

Polar molecules: Molecules which have a permanent electric dipole moment. Examples include water and ammonia.

Pool boiling: Generation of vapor at the surface of a hot body immersed in an extensive liquid pool.

Transition boiling: Generation of vapor at a hot surface with intermittent or partial liquid wetting of the surface.

References

Berenson, P.J. 1961. Film boiling heat transfer from a horizontal surface. *J. Heat Transfer*, 83, 351–356.

Carey, V.P. 1992. *Liquid-Vapor Phase Change Phenomena.* Taylor and Francis, Washington, D.C.

Chen, J.C. 1966. Correlation for boiling heat transfer to saturated fluids in convective flow. *Ind. Eng. Chem. Proc. Design and Dev.* 5(3), 322–339.

Collier, J.G. 1996. *Convective Boiling and Condensation*, 3rd ed. Oxford University Press, Oxford, U.K.

Dhir, V.K. and Lienhard, J. 1971. Laminar film condensation on plane and axisymmetric bodies in nonuniform gravity. *J. Heat Transfer* 93, 97–100.

Dougall, R.S. and Rohsenow, W.M. 1963. Film boiling on the inside of vertical tubes with upward flow of the fluid at low qualities. MIT Report No. 9079-26. MIT, Cambridge, MA.

Dukler, A.E. 1960. Fluid mechanics and heat transfer in vertical falling film systems. *Chem. Eng. Prog. Symp. Ser.* 56(30), 1–10.

Gunnerson, F.S. and Cronenberg, A.W. 1980. On the minimum film boiling conditions for spherical geometries. *J. Heat Transfer* 102,335–341.

Haramura, Y. and Katto, Y. 1983. A new hydrodynamic model of the critical heat flux, applicable widely to both pool and forced convective boiling on submerged bodies in saturated liquids. *Int. J. Heat Mass Transfer* 26, 389–399.

Kandlikar, S.G. 1989. A general correlation for saturated two-phase flow boiling heat transfer inside horizontal and vertical tubes. *J. Heat Transfer* 112, 219–228.

Katto, Y. and Ohno, H. 1984. An improved version of the generalized correlation of critical heat flux for the forced convective boiling in uniformly heated vertical tubes. *Int. Heat Mass Transfer* 21, 1527–1542.

Levitan, L.L. and Lantsman, F.P. 1975. Investigating burnout with flow of a steam-water mixture in a round tube, *Therm. Eng.* (USSR). English trans., 22, 102–105.

Lienhard, J.H. and Dhir, V.K. 1973. Extended hydrodynamic theory of the peak and minimum pool boiling heat fluxes. NASA CR-2270.

Lienhard, J.H. and Witte, L.C. 1985. A historical review of the hydrodynamic theory of boiling. *Rev. Chem. Eng.* 3, 187–277.

Lienhard, J.H. and Wong, P.T.Y. 1964. The dominant unstable wavelength and minimum heat flux during film boiling on a horizontal cylinder. *J. Heat Transfer* 86, 220–226.

Merte, H. 1973. Condensation heat transfer. *Adv. Heat Transfer* 9, 181–272.

Mills, A.F. and Chung, D.K. 1973. Heat transfer across turbulent falling films. *Int. J. Heat Mass Transfer* 16, 694–696.

Nukiyama, S. 1934. The maximum and minimum values of Q transmitted from metal to boiling water under atmospheric pressure. *J. Jpn. Soc. Mech. Eng.* 37, 367–374.

Nusselt, W. 1916. Die Oberflachenkondensation des Wasser dampfes. *Z. Ver. Dtsch. Ininuere* 60, 541–575.

Ramilison, J.M. and Lienhard, J.H. 1987. Transition boiling heat transfer and the film transition regime. *J. Heat Transfer* 109, 746–752.

Rohsenow, W.M. 1962. A method of correlating heat transfer data for surface boiling of liquids. *Trans. ASME* 84, 969–975.

Rossen, H.F. and Meyers, J.A. 1965. Point values of condensing film coefficients inside a horizontal tube. *Chem. Eng. Prog. Symp. Ser.* 61(59), 190–199.

Seban, R. 1954. Remarks on film condensation with turbulent flow. *Trans. ASME* 76, 299–303.

Selin, G. 1961. Heat transfer by condensing pure vapors outside inclined tubes, in *Proc. First Int. Heat Transfer Conf.*, University of Colorado, Boulder, Part II, 279–289.

Sparrow, E.M. and Gregg, J.L. 1959. A boundary-layer treatment of laminar film condensation. *J. Heat Transfer* 81, 13–23.

Stephen, K. 1992. *Heat Transfer in Condensation and Boiling*. Springer-Verlag, New York.

Tanaka, H. 1975. A theoretical study of dropwise condensation. *J. Heat Transfer* 97, 72–78.

Tanaka, H. 1979. Further developments of dropwise condensation theory. *J. Heat Transfer* 101, 603–611.

Traviss, D.P., Rohsenow, W.M., and Baron, A.B. 1973. Forced convection condensation in tubes: a heat transfer correlation for condenser design. *ASHRAE Trans.* 79(I), 157–165.

Witte, L.C. and Lienhard, J.H. 1982. On the existence of two "transition" boiling curves. *Int. J. Heat Mass Transfer* 25, 771–779.

Zuber, N. 1959. Hydrodynamic aspects of boiling heat transfer. AEC Rep. AECU-4439.

Further Information

The texts *Heat Transfer in Condensation and Boiling* by K. Stephan (Springer-Verlag, New York, 1992) and *Liquid-Vapor Phase Change Phenomena* by V.P. Carey (Taylor and Francis, Washington, D.C., 1992) provide an introduction to the physics of boiling and condensation processes. The text by J.G. Collier, *Convective Boiling and Condensation* (3rd ed., Oxford University Press, Oxford, U.K., 1996), summarizes more-advanced elements of convective boiling and condensation processes. The *ASHRAE Handbook of Fundamentals* (American Society of Heating, Refrigerating, and Air-Conditioning Engineers, Atlanta, GA, 2001) provides some information on boiling and condensation heat transfer and is a good source of thermophysical property data needed to analyze boiling and condensation processes.

There are also other convenient heat transfer textbooks and books that provide further information about phase-change:

Bejan, A. and Kraus, A. 2003. *Heat Transfer Handbook*, Interscience, New York.

De Vahl Davis, G. and Leonardi, E. 2001. *Advances in Computational Heat Transfer II CHT'01: Proceedings of a Symposium*, Palm Cove, Queensland, Australia, Begell House, New York.

Incropera, F.P. and DeWitt, D.P. 2001. *Fundamentals of Heat and Mass Transfer*, 5th ed., John Wiley & Sons, New York.

Kandlikar, S.G., Shoji, M., and Dhir, V.K. (Eds.) 1999. *Handbook of Phase Change: Boiling and Condensation*, Hemisphere, Washington, D.C.

Kreith, F. and Bohn, M.S. 2000. *Principles of Heat Transfer*, 6th ed., Brooks Cole.

Manglik, R.M. 1996. *Process, Enhanced, and Multiphase Heat Transfer*, Begell House, New York.

For applications of boiling and condensation heat transfer, see:

Kreith, F. (Ed.) 1999. *CRC Handbook of Thermal Engineering*, CRC Press, Boca Raton, FL.

Particle Gas Convection

John C. Chen

Introduction

Heat transfer in two-phase systems involving gas and solid particles are encountered in several types of operations important in chemical, power, and environmental technologies. Chief among these are gas fluidized beds which are widely used to achieve either physical processing or chemical reactions that require interfacial contact between gas and solid particles. Currently, fluidized beds operate in either the *bubbling regime* or the *fast-circulating regime*. In the first case, particles are retained in the fluidized bed while the gas passes upward past the particles, partially as rising bubbles. In the second case, gas velocities exceed terminal velocity for the individual particles and the two phases flow through the fluidized bed in cocurrent upward flow. For those applications which require thermal control, convective heat transfer between the fluidized medium and heat transfer surfaces (either immersed tubes or the vessel walls) is an essential element of the process design.

Bubbling Fluidized Beds

Bubbling fluidization occurs when the superficial gas velocity exceeds a critical value wherein the gravitational body force on the solid particles is balanced by the shear force between particles and flowing gas. The superficial gas velocity at this condition, commonly called the minimum fluidization velocity (U_{mf}), marks the boundary between gas flow through packed beds and gas flow in fluidized beds. Wen and Yu (1966) derived the following general equation to estimate U_{mf} for spherical particles:

$$\mathrm{Re}_{mf} = \left[(33.7)^2 + 0.0408\mathrm{Ar}\right]^{1/2} - 33.7 \qquad (4.4.21)$$

where

$$\mathrm{Re}_{mf} = \text{particle Reynolds number at } U_{\mathrm{mf}} = \frac{U_{\mathrm{mf}} d_p \rho_g}{\mu_g}$$

$$\mathrm{Ar} = \text{Archimedes number} = \frac{d_p^3 \rho_g \left(\rho_s - \rho_g\right) g}{\mu_g^2}$$

Increasing gas velocity beyond minimum fluidization causes the excess gas to collect into discrete bubbles that grow and rise through the fluidized matrix of solid particles. In this bubbling fluidization regime, the total pressure drop over the height of the fluidized bed, H, is equal to the hydrostatic pressure of the solid mass,

$$\Delta P = g\rho_s (1 - \varepsilon) H \qquad (4.4.22)$$

where ε = volume fraction of gas (void fraction).

Tubes carrying cooling or heating fluids are often immersed in bubbling fluidized beds to extract or add thermal energy. The effective heat transfer coefficient at the surface of such tubes has been the objective of numerous experimental and analytical investigations. Data for the circumferentially averaged heat transfer coefficient for horizontal tubes are shown in Figure 4.4.10 for various types of solid particles. Characteristics representative of such systems are

- The heat transfer coefficient increases sharply as the gas velocity exceeds minimum fluidization velocity,
- After the initial increase, the heat transfer coefficient remains fairly constant over a significant range of the gas velocity beyond minimum fluidization velocity,
- The absolute magnitude of the heat transfer coefficient is severalfold greater than single-phase gas convection at the same superficial velocity,
- The heat transfer coefficient increases as particle size decreases.

Kunii and Levenspiel (1991) have shown that increasing gas pressure and density significantly increases the magnitude of the heat transfer coefficient as well as promoting the occurrence of minimum fluidization at a lower value of superficial gas velocity. The effect of bundle spacing is insignificant at 1-atm pressure but becomes increasingly more important as gas pressure and density increase. The data of Jacob and Osberg (1957) indicate that the convective heat transfer coefficient in fluidized beds increases with increasing thermal conductivity of the gas phase, for any given particle size.

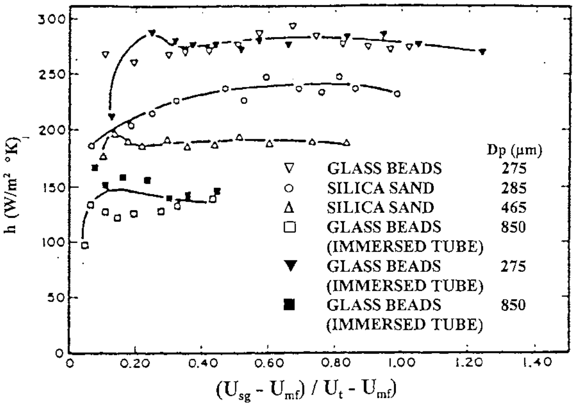

FIGURE 4.4.10 Average heat transfer coefficients for horizontal tubes immersed in bubbling fluidized beds. (From Biyikli, Tuzla and Chen, 1983.)

Several different types of correlations have been suggested for predicting convective heat transfer coefficients at submerged surfaces in bubbling fluidized beds. The first type attributes the enhancement of heat transfer to the scouring action of solid particles on the gas boundary layer, thus decreasing the effective film thickness. These models generally correlate a heat transfer Nusselt number in terms of the fluid Prandtl number and a modified Reynolds number with either the particle diameter or the tube diameter as the characteristic length scale. Examples are

Leva's correlation for vertical surfaces and larger particles (Leva and Gummer, 1952);

$$\mathrm{Nu}_{d_p} = \frac{h_c d_p}{k_g} = 0.525\left(\mathrm{Re}_p\right)^{0.75} \tag{4.4.23}$$

where

$$\mathrm{Re}_p = \frac{d_p \rho_g U}{\mu_g}$$

Vreedenberg's (1958) correlation for horizontal tubes refers to the particle of diameter D_t.

$$\mathrm{Nu}_{Dt} = \frac{h_c D_t}{k_g} = 420\left(\frac{\rho_s}{\rho_g}\mathrm{Re}_t\right)^{0.3}\left(\frac{\mu_g^2}{g\rho_s^2 d_p^3}\right)^{0.3}\left(\mathrm{Pr}_g\right)^{0.3} \tag{4.4.24}$$

for

$$\left(\frac{\rho_s}{\rho_g}\mathrm{Re}_t\right) > 2250$$

where

$$\mathrm{Re}_t = \frac{D_t \rho_g U}{\mu_g}$$

Molerus and Schweinzer (1989) developed an alternative type of correlation based on the supposition that the heat transfer is dominated by gas convection through the matrix of particles in the vicinity of the heat transfer surface. Their correlation takes the form:

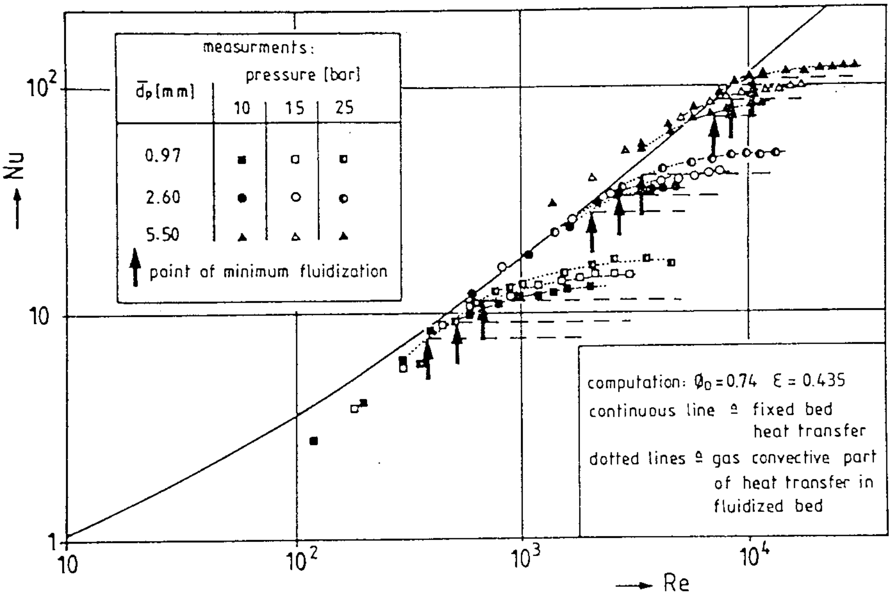

FIGURE 4.4.11 Correlation of Molerus and Schweinzer compared with experimental data (1989).

$$\mathrm{Nu} = \frac{h_c d_p}{k_g} = 0.0247(\mathrm{Ar})^{0.4304}(\mathrm{Pr})^{0.33} \tag{4.4.25}$$

Figure 4.4.11 shows comparison of this model with experimental data obtained at three different pressures. The solid curve represents the relationship for fixed beds, while the dashed lines represent the behavior for fluidized beds (i.e., Equation 4.4.25) upon exceeding minimum fluidization.

A third type of model considers the heat transfer surface to be contacted alternately by gas bubbles and packets of packed particles, leading to a surface renewal process for heat transfer. Mickley and Fairbanks (1955) provided the first analysis of this renewal mechanism. Ozkaynak and Chen (1980) showed that if experimentally measured values of the packet contact time and residence times are used in the packet model analysis, excellent agreement is obtained.

Fast-Circulating Fluidized Beds

Fast fluidization occurs when the superficial gas velocity exceeds the terminal velocity of the solid particles, causing the particles to be suspended in cocurrent upward flow with the gas. This upward flow occurs in “rise reactors” wherein desired physical or chemical reactions occur. In most applications, the two-phase flow exits the top of the riser into a cyclone where the gas phase is separated and exhausted while the solid particles are captured and returned for reinjection at the bottom of the riser. The volumetric concentration of solid particles in these fast fluidized beds (FFBs) tend to be fairly dilute, often with average concentrations of less than 2%. Heat exchange with the particle/gas suspension is usually accomplished through the vertical wall surfaces or through vertical tubes immersed in the duct.

The heat transfer coefficient at vertical surfaces FFBs has been found to increase with increasing solid concentration, aside from other second-order parametric effects. Figure 4.4.12 shows heat transfer coefficients experimentally measured by Dou et al. (1994) for an FFB operating with sand particles of 124 μm mean diameter. Figure 4.4.12b shows that the heat transfer coefficient increased with solid mass flux, for a constant superficial gas velocity. Figure 4.4.12a shows that the heat transfer coefficient decreased parametrically with superficial gas velocity for a constant solid mass flux. Both figures indicate that heat transfer coefficients decrease with increasing elevation in the riser duct. These three parametric trends

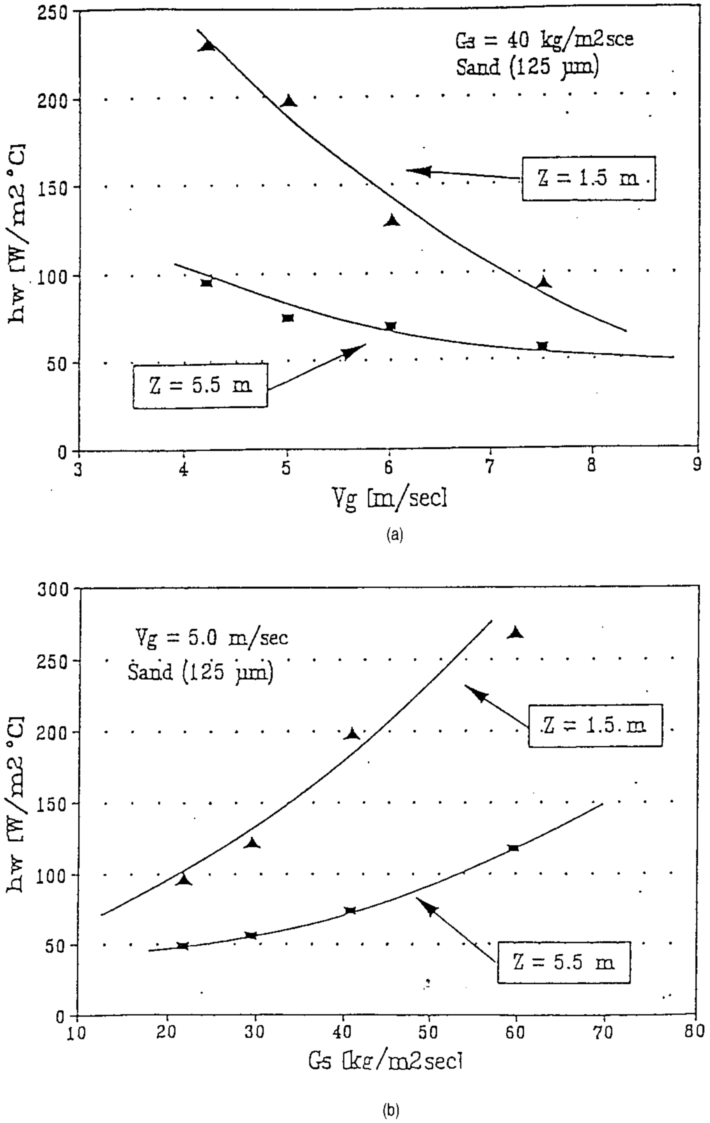

FIGURE 4.4.12 Heat transfer coefficients in fast fluidized beds; Vg is superficial gas velocity, Gs is mass flux of particles, and Z is elevation in FFB. (From Dou, Tuzla and Chen, 1992.)

are all consistent with the hypothesis that heat transfer in FFBs increases with increasing concentration of the solid phase.

It is generally accepted that the effective heat transfer coefficient for surfaces in FFBs have contributions for gas-phase convection, particle-induced convection, and radiation:

$$h = h_g + h_p + h_r \tag{4.4.26}$$

In contrast to the situation in dense-bubbling fluidized beds, the relatively dilute concentration of solid particles in FFBs often results in significant contributions from all three heat transfer mechanisms. The radiation coefficient can be obtained by a gray body model suggested by Grace (1985). The contribution of the gas phase convection (h_g) is commonly estimated based on correlations for gas flow alone at the same superficial gas velocity. Although the presence of particles may alter the turbulence characteristic of this gas flow, any errors caused by this procedure are usually small since h_g is generally smaller than the particle-phase convective coefficient h_p.

For most FFBs, the particle convective contribution to heat transfer is most important and the prediction of h_p is the major concern in thermal design. Unfortunately, mechanistically based models are still lacking and most design methods rely on empirical correlations which often combine the contributions of gas and particle phases into a single convective heat transfer coefficient (h_c). One such correlation proposed by Wen and Miller (1961) is

$$\mathrm{Nu}_{dp} = \frac{h_c d_p}{k_g} = \left(\frac{C_{pp}}{C_{pg}}\right)\left(\frac{\rho_{\mathrm{susp}}}{\rho_p}\right)^{0.3}\left(\frac{V_t}{g d_p}\right)^{0.21} \mathrm{Pr}_g \tag{4.4.27}$$

where V_t = terminal velocity of particle.

Other correlations have been proposed by Fraley (1992) and Martin (1984). These correlations are useful as a starting point but have not yet been verified over wide parametric ranges. Large deviations can occur when compared with measurements obtained outside of the experimental parametric ranges.

References

Biyikli, K., Tuzla, K., and Chen, J.C. 1983. Heat transfer around a horizontal tube in freeboard region of fluidized beds, *AIChE J.*, 29(5), 712–716.

Dou, S., Herb, B., Tuzla, K., and Chen, J.C. 1992. Dynamic variation of solid concentration and heat transfer coefficient at wall of circulating fluidized bed, in *Fluidization VII*, Eds. Potter and Nicklin, Engineering Foundation, 793–802.

Fraley, L.D., Lin, Y.Y., Hsiao, K.H., and Solbakken, A. 1983. ASME Paper 83-HT-92, National Heat Transfer Conference, Seattle.

Grace, J.R. 1985. Heat transfer in circulating fluidized beds, *Circulating Fluidized Bed Technology I*, Peramon Press, New York, 63–81.

Jacob, A. and Osberg, G.L. 1957. Effect of gas thermal conductivity on local heat transfer in a fluidized bed, *Can. J. Chem. Eng.*, 35(6), 5–9.

Kunii, D. and Levenspiel, O. 1991. *Fluidization Engineering*, 2nd ed., Butterworth-Heinemann, Boston.

Leva, M. and Grummer, M. 1952. A correlation of solids turnovers in fluidized systems, *Chem. Eng. Prog.*, 48(6), 307–313.

Martin, H. 1984. *Chem. Eng. Process*, 18, 157–223.

Mickley, H.S. and Fairbanks, D.F. 1955. Mechanism of heat transfer to fluidized beds, *AIChE J.*, 1(3), 374–384.

Molerus, O. and Scheinzer, J. 1989. Prediction of gas convective part of the heat transfer to fluidized beds, in *Fluidization IV*, Engineering Foundation, New York, 685–693.

Ozkaynak, T.F. and Chen, J.C. 1980. Emulsion phase residence time and its use in heat transfer models in fluidized bed, *AIChE J.*, 26(4), 544–550.

Vreedenberg, H.A. 1958. Heat transfer between a fluidized bed and a horizontal tube, *Chem. Eng. Sci.*, 9(1), 52–60.

Wen, C.Y. and Yu, Y.H. 1966. A generalized method for predicting the minimum fluidization velocity, *AIChE J.*, 12(2), 610–612

Wen, C.Y. and MIller, E.N. 1961. *Ind. Eng. Chem.*, 53, 51–53.

Further Information

There are also several convenient heat transfer textbooks and books that provide further information about phase-change:

De Vahl Davis, G. and Leonardi, E. 2001. *Advances in Computational Heat Transfer II CHT'01: Proceedings of a Symposium*, Palm Cove, Queensland, Australia, Begell House, New York.

Gibilaro, L.G. 2001. *Fluidization Dynamics*, Butterworth–Heinemann.

Gidaspow, D.1994. *Multiphase Flow and Fluidization,* Academic Press, Boston, MA.

Manglik, R.M. 1996. *Process, Enhanced, and Multiphase Heat Transfer*, Begell House, New York.

Yang, W. 2003. *Handbook of Fluidization and Fluid–Particle Systems*, Marcel Dekker, New York.

Melting and Freezing

Noam Lior

Introduction and Overview

Melting and freezing occur naturally (Lunardini, 1981) as with environmental ice in the atmosphere (hail, icing on aircraft), on water bodies and ground regions at the Earth surface, and in the molten Earth core (Figure 4.4.13). They are also a part of many technological processes, such as preservation of

FIGURE 4.4.13 Melting and freezing in nature. (a) A melting icicle. (b) Frozen lava in Hawaii.

foodstuffs (ASHRAE, 1990, 1993), refrigeration and air-conditioning (ASHRAE, 1990, 1993), snow and ice making for skiing and skating (ASHRAE, 1990), organ preservation and cryosurgery (Rubinsky and Eto, 1990), manufacturing (such as casting, molding of plastics, coating, welding, high-energy beam cutting and forming, crystal growth, electrodischarge machining, electrodeposition) (Flemings, 1974; Cheng and Seki, 1991; Tanasawa and Lior, 1992), and thermal energy storage using solid–liquid phase-changing materials (deWinter, 1991).

In simple thermodynamic systems (i.e., without external fields, surface tension, etc.) of a pure material, melting or freezing occurs at certain combinations of temperature and pressure. Since pressure typically has a relatively smaller influence, only the fusion (freezing or melting) temperature is often used to identify this phase transition. Fusion becomes strongly dependent on the concentration when the material contains more than a single species. Furthermore, melting and freezing are also sensitive to external effects, such as electric and magnetic fields, in more-complex thermodynamic systems.

The equilibrium thermodynamic system parameters during phase transition can be calculated from the knowledge that the partial molar Gibbs free energies or chemical potentials of each component in the two phases must be equal. One important result of using this principle for simple single-component systems is the Clapeyron equation relating the temperature (T) and pressure (P) during the phase transition, such that

$$\frac{dP}{dT} = \frac{h_{s\ell}}{T\Delta v} \tag{4.4.28}$$

where $h_{s\ell}$ is the enthalpy change from phase A to phase B ($=h_B - h_A$, the latent heat of fusion with appropriate sign) and Δv is the specific volume difference between phases A and B ($= v_B - v_A$). Considering for example that phase A is a solid and B a liquid ($h_{s\ell}$ is then positive), examination of Equation (4.4.28) shows that increasing the pressure will result in an increase in the melting temperature if $\Delta v > 0$ (i.e., when the specific volume of the liquid is higher than that of the solid, which is a property of tin, for example), but will result in a decrease of the melting temperature when $\Delta v < 0$ (for water, for example).

In some materials, called glassy, the phase change between the liquid and solid occurs with a gradual transition of the physical properties, from those of one phase to those of the other. When the liquid phase flows during the process, the flow is strongly affected because the viscosity increases greatly as the liquid changes to solid. Other materials, such as pure metals and ice, and eutectic alloys, have a definite line of demarcation between the liquid and the solid, the transition being abrupt. This situation is easier to analyze and is therefore more thoroughly addressed in the literature.

Gradual transition is most distinctly observed in mixtures. Consider the equilibrium phase diagram for a binary mixture (or alloy) composed of species a and b, shown in Figure 4.4.14. χ is the concentration of species b in the mixture, ℓ denotes the liquid, s the solid, s_a a solid with a lattice structure of species a in its solid phase but containing some molecules of species b in that lattice, and s_b a solid with a lattice structure of species b in its solid phase but containing some molecules of species a in that lattice. "Liquidus" denotes the boundary above which the mixture is just liquid, and "solidus" is the boundary separating the final solid mixture of species a and b from the solid–liquid mixture zones and from the other zones of solid s_a and solid s_b.

For illustration, assume that a liquid mixture is at point 1, characterized by concentration χ_1 and temperature T_1 (Figure 4.4.14), and is cooled (descending along the dashed line) while maintaining the concentration constant. When the temperature drops below the liquidus line, solidification starts, creating a mixture of liquid and of solid s_a. Such a two-phase mixture is called the **mushy zone**. At point 2 in that zone, the solid phase (s_a) portion contains a concentration χ_{2,s_a} of component b, and the liquid phase portion contains a concentration $\chi_{2,\ell}$ of component b. The ratio of the mass of the solid s_a to that of the liquid is determined by the lever rule, and is $(\chi_{2,\ell} - \chi_2)/(\chi_2 - \chi_{2,s_a})$ at point 2. Further cooling to below the solidus line, say to point 3, results in a solid mixture (or alloy) of s_a and s_b, containing concentrations χ_{3,s_A} and χ_{3,s_B} of species b, respectively. The ratio of the mass of the solid s_a to that of s_b is again determined by the lever rule, and is $(\chi_{3,s_b} - \chi_3)/(\chi_3 - \chi_{3,s_a})$ at point 3.

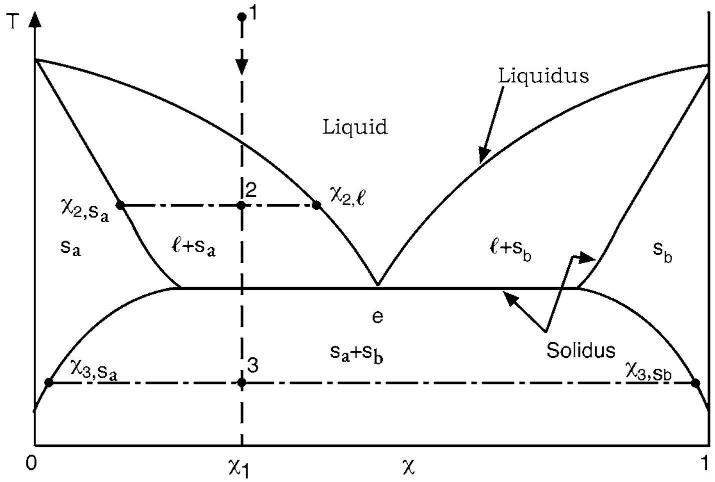

FIGURE 4.4.14 A liquid–solid phase diagram of a binary mixture.

A unique situation occurs if the initial concentration of the liquid is χ_e: upon constant-concentration cooling, the liquid forms the solid mixture $s_a + s_b$ having the same concentration and without the formation of a two-phase zone. χ_e is called the **eutectic concentration**, and the resulting solid mixture (or alloy) is called a *eutectic.*

The presence of a two-phase mixture zone with temperature-dependent concentration and phase proportion obviously complicates heat transfer analysis, and requires the simultaneous solution of both the heat and mass transfer equations. Furthermore, the liquid usually does not solidify on a simple planar surface. Crystals of the solid phase are formed at some preferred locations in the liquid, or on colder solid surfaces immersed in the liquid, and as freezing progesses the crystals grow in the form of intricately shaped fingers, called dendrites. This complicates the geometry significantly and makes mathematical modeling of the process very difficult. An introduction to such problems and further references are available in Hayashi and Kunimine (1992) and Poulikakos (1994).

Flow of the liquid phase often has an important role in the inception of, and during, melting and freezing (see Incropera and Viskanta, 1992). The flow may be forced, such as in the freezing of a liquid flowing through or across a cooled pipe, and/or may be due to natural convection that arises whenever there are density gradients in the liquid, here generated by temperature and possibly concentration gradients. It is noteworthy that the change in phase usually affects the original flow, such as when the liquid flowing in a cooled pipe gradually freezes and the frozen solid thus reduces the flow passage, or when the evolving dendritic structure gradually changes the geometry of the solid surfaces that are in contact with the liquid. Under such circumstances, strong coupling may exist between the heat transfer and fluid mechanics, and also with mass transfer when more than a single species is present. The process must then be modeled by an appropriate set of continuity, momentum, energy, mass conservation, and state equations, which need to be solved simultaneously.

More-detailed information about melting and freezing can be found in the monograph by Alexiades and Solomon (1993) and in the comprehensive reviews by Fukusako and Seki (1987) and Yao and Prusa (1989).

Melting and Freezing of Pure Materials

Thorough mathematical treatment of melting and freezing is beyond the scope of this section, but examination of the simplified one-dimensional case for a pure material and without flow effects provides important insights into the phenomena, identifies the key parameters, and allows analytical solutions and thus qualitative predictive capability for at least this class of problems.

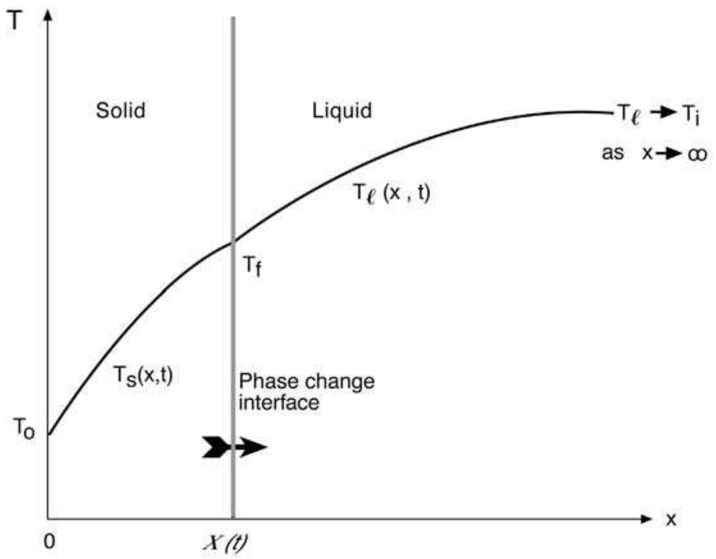

FIGURE 4.4.15 Freezing of semi-inifinite liquid with heat conduction in both phases.

In the freezing model, described in Figure 4.4.15, a liquid of infinite extent is to the right ($x > 0$) of the infinite surface at $x = 0$, initially at a temperature T_i higher than the fusion temperature T_f. At time $t = 0$ the liquid surface temperature at $x = 0$ is suddenly lowered to a temperature $T_0 < T_f$, and maintained at that temperature for $t > 0$. Consequently, the liquid starts to freeze at $x = 0$, and the freezing interface (separating in Figure 4.4.15 the solid to its left from the liquid on its right) located at the position $x = X(t)$ moves gradually to the right (in the positive x direction). We note that in this problem heat is conducted in both phases.

Assuming for simplification that heat transfer is by conduction only — although at least natural convection (Incropera and Viskanta, 1992) and sometimes forced convection and radiation also take place — the governing equations are

In the liquid: The transient heat conduction equation is

$$\frac{\partial T_\ell(x,t)}{\partial t} = \alpha_\ell \frac{\partial^2 T_\ell(x,t)}{\partial x^2} \quad \text{in} \quad X(t) < x < \infty \quad \text{for} \quad t > 0 \tag{4.4.29}$$

$$T_\ell(x,t) = T_i \quad \text{in} \quad x > 0, \quad \text{at} \quad t = 0 \tag{4.4.30}$$

where α_ℓ is the thermal diffusivity of the liquid, with the initial condition and the boundary condition

$$T_\ell(x \to \infty, t) \to T_i \quad \text{for} \quad t > 0 \tag{4.4.31}$$

In the solid: The transient heat conduction equation is

$$\frac{\partial T_s(x,t)}{\partial t} = \alpha_s \frac{\partial^2 T_s(x,t)}{\partial x^2} \quad \text{in} \quad 0 < x < X(t) \quad \text{for} \quad t > 0 \tag{4.4.32}$$

where α_s is the thermal diffusivity of the solid, with the boundary condition

$$T_s(0,t) = T_0 \quad \text{for} \quad t > 0 \tag{4.4.33}$$

The remaining boundary conditions are those of temperature continuity and heat balance at the solid–liquid phase-change interface $X(t)$,

$$T_\ell\left[X(t)\right] = T_s\left[X(t)\right] = T_f \quad \text{for} \quad t > 0 \tag{4.4.34}$$

$$k_s\left(\frac{\partial T_s}{\partial x}\right)_{[X(t)]} - k_\ell\left(\frac{\partial T_\ell}{\partial x}\right)_{[X(t)]} = \rho h_{s\ell}\frac{dX(t)}{dt} \quad \text{for} \quad t > 0 \tag{4.4.35}$$

where k_s and k_ℓ are the thermal conductivities of the solid and liquid, respectively, ρ is the density (here it is assumed for simplicity to be the same for the liquid and solid), and $h_{s\ell}$ is the latent heat of fusion. The two terms on the left-hand side of Equation (4.4.35) thus represent the conductive heat flux away from the phase-change interface, into the solid at left and the liquid at right, respectively. Energy conservation at the interface requires that the sum of these fluxes leaving the interface be equal to the amount of heat generated due to the latent heat released there, represented by the term on the right-hand side of the equation.

The analytical solution of Equation (4.4.29) to Equation (4.4.35) yields the temperature distributions in the liquid and solid phases,

$$T_\ell(x,t) = T_i - \left(T_i - T_f\right)\frac{\operatorname{erfc}\left(\dfrac{x}{2\sqrt{\alpha_\ell t}}\right)}{\operatorname{erfc}\left(\lambda\sqrt{\alpha_s/\alpha_\ell}\right)} \tag{4.4.36}$$

$$T_s(x,t) = T_0 + \left(T_f - T_0\right)\frac{\operatorname{erfc}\left(\dfrac{x}{2\sqrt{\alpha_s t}}\right)}{\operatorname{erfc}\lambda} \tag{4.4.37}$$

where erf and erfc are the *error function* and the *complementary error function*, respectively, and λ is a constant, obtained from the solution of the equation

$$\frac{e^{\lambda^2}}{\operatorname{erf}\lambda} - \frac{k_\ell}{k_s}\sqrt{\frac{\alpha_s}{\alpha_\ell}}\,\frac{T_i - T_f}{T_f - T_0}\,\frac{e^{(\alpha_s/\alpha_\ell)\lambda^2}}{\operatorname{erfc}\left(\lambda\sqrt{\alpha_s/\alpha_\ell}\right)} = \frac{\lambda\sqrt{\pi}}{\mathrm{Ste}_s} \tag{4.4.38}$$

where Ste is the Stefan number (dimensionless), here defined for the solid as

$$\mathrm{Ste}_s \equiv \frac{c_s\left(T_f - T_0\right)}{h_{s\ell}} \tag{4.4.39}$$

and c_s is the specific heat of the solid. Solutions of Equation (4.4.38) are available for some specific cases in several of the references, and can be obtained relatively easily by a variety of commonly used software packages.

The solution of Equation (4.4.29) to Equation (4.4.35) also gives an expression for the transient position of the freezing interface,

$$X(t) = 2\lambda\left(\alpha_s t\right)^{1/2} \tag{4.4.40}$$

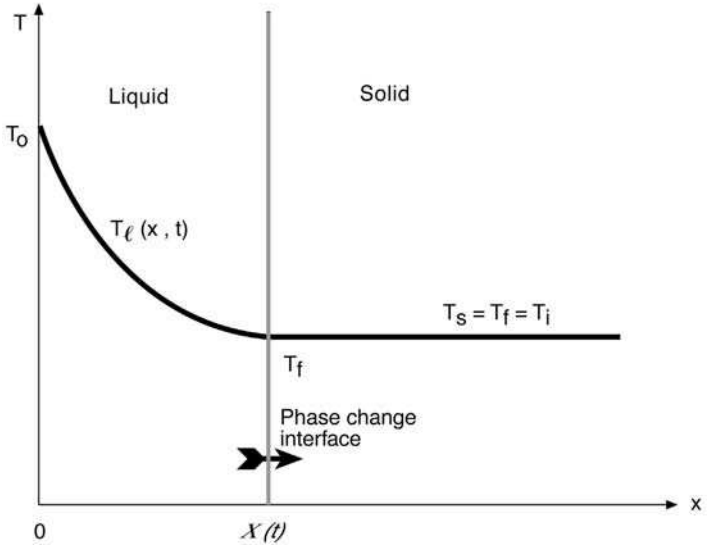

FIGURE 4.4.16 Melting of semi-infinite solid with conduction in the liquid phase only.

where λ is the solution of Equation 4.4.38, and thus the expression for the rate of freezing, i.e., the velocity of the motion of the solid liquid interface, is

$$\frac{dX(t)}{dt} = \lambda \alpha_s^{1/2} t^{1/2} \tag{4.4.41}$$

For a simple one-dimensional melting example of an analytical solution for melting, consider the semi-infinite solid described in Figure 4.4.16, initially at the fusion temperature T_f. For time $t > 0$ the temperature of the surface (at $x = 0$) is raised to $T_0 > T_f$, and the solid consequently starts to melt there. In this case the temperature in the solid remains constant, $T_s = T_f$, so the temperature distribution needs to be calculated only in the liquid phase. It is assumed that the liquid formed by melting remains motionless and in place. Very similarly to the above-described freezing case, the equations describing this problem are the heat conduction equation

$$\frac{\partial T_\ell(x,t)}{\partial t} = \alpha_\ell \frac{\partial^2 T_\ell(x,t)}{\partial x^2} \quad \text{in} \quad 0 < x < X(t) \quad \text{for} \quad t > 0 \tag{4.4.42}$$

with the initial condition

$$T_\ell(x,t) = T_f \quad \text{in} \quad x > 0, \quad \text{at} \quad t = 0 \tag{4.4.43}$$

the boundary condition

$$T_\ell(0,t) = T_0 \quad \text{for} \quad t > 0 \tag{4.4.44}$$

and the liquid–solid interfacial temperature and heat flux continuity conditions

$$T_\ell\left[X(t)\right] = T_f \quad \text{for} \quad t > 0 \tag{4.4.45}$$

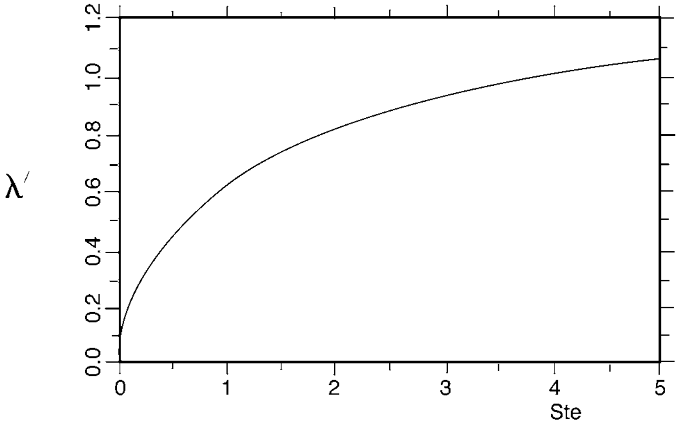

FIGURE 4.4.17 The root λ′ of Equation 4.4.48.

$$-k_\ell \left(\frac{\partial T_\ell}{\partial x}\right)_{[X(t)]} = \rho h_{\ell s} \frac{dX(t)}{dt} \quad \text{for} \quad t > 0 \tag{4.4.46}$$

The analytical solution of this problem yields the temperature distribution in the liquid,

$$T_\ell(x,t) = T_0 - \left(T_0 - T_f\right) \frac{\operatorname{erf}\left(\dfrac{x}{2\sqrt{\alpha_\ell t}}\right)}{\operatorname{erf}\lambda'} \quad \text{for} \quad t > 0 \tag{4.4.47}$$

where λ′ is the solution of the equation

$$\lambda' e^{\lambda'^2} \operatorname{erf}(\lambda') = \frac{\text{Ste}_\ell}{\sqrt{\pi}} \tag{4.4.48}$$

with Ste_ℓ here defined for the liquid as

$$\text{Ste}_\ell \equiv \frac{c_\ell\left(T_0 - T_f\right)}{h_{s\ell}} \tag{4.4.49}$$

λ′ as a function of Ste, for $0 \le \text{Ste} \le 5$, is given in Figure 4.4.17. The interface position is

$$X(t) = 2\lambda'\left(\alpha_\ell t\right)^{1/2} \tag{4.4.50}$$

The solution of the *freezing* problem under similar conditions, i.e., of a semi-infinite liquid initially at temperature T_f where $T(0,t)$ is abruptly reduced to $T_0 < T_f$ for $t > 0$, is identical to the above if every subscript ℓ is replaced by s and the latent heat $h_{s\ell}$ is replaced by $-h_{s\ell}$.

Example: The temperature of the vertical surface of a large volume of solid paraffin wax used for heat storage, initially at the fusion temperature, $T_i = T_f = 28$°C, is suddenly raised to 58°C. Any motion in the melt may be neglected. How long would it take for the paraffin to solidify to a depth of 0.1 m? Given properties: $\alpha_\ell = (1.09)\ 10^{-7}$ m²/sec, $\rho_s = \rho_\ell = 814$ kg/m³, $h_{s\ell} = 241$ kJ/kg, $c_\ell = 2.14$ kJ/kg°C. To find the required time we use Equation (4.4.50), in which the value of λ' needs to be determined. λ' is calculated from Equation (4.4.48), which requires the knowledge of Ste_ℓ. From Equation (4.4.49)

$$\mathrm{Ste}_\ell = \frac{(2.14\ \mathrm{kJ/kg°C})(58°\mathrm{C} - 28°\mathrm{C})}{241.2\ \mathrm{kJ/kg}} = 0.266$$

The solution of Equation (4.4.48) as a function of Ste_ℓ is given in Figure 4.4.17, yielding $\lambda \approx 0.4$. By using Equation (4.4.50), the time of interest is calculated by

$$t = \frac{[X(t)]^2}{4\lambda^2 \alpha_\ell} = \frac{(0.1\ \mathrm{m})^2}{4(0.4)^2\left[(1.09)10^7\ \mathrm{m^2/sec}\right]} = (1.43)10^5\ \mathrm{sec} = 39.8\ \mathrm{hr}$$

The axisymmetric energy equation in *cylindrical coordinates*, applicable to both the solid phase and immobile liquid phase (with appropriate assignment of the properties) is

$$\frac{\partial T(r,t)}{\partial t} = \frac{1}{\rho c}\frac{\partial}{\partial r}\left(\frac{k}{r}\frac{\partial T(r,t)}{\partial r}\right) \quad \text{for} \quad t > 0 \tag{4.4.51}$$

and the temperature and heat balance conditions at the solid–liquid phase-change interface $r = R(t)$ are

$$T_\ell[R(t)] = T_s[R(t)] \quad \text{for} \quad t > 0 \tag{4.4.52}$$

$$k_s\left(\frac{\partial T_s}{\partial r}\right)_{R(t)} - k_\ell\left(\frac{\partial T_\ell}{\partial r}\right)_{R(t)} = h_{s\ell}\frac{dR(t)}{dt} \tag{4.4.53}$$

Because of the nature of the differential equations describing nonplanar and multidimensional geometries, analytical solutions are available for only a few cases, such as line heat sources in cylindrical coordinate systems or point heat sources in spherical ones, which have very limited practical application. Other phase-change problems in nonplanar geometries, and in cases when the melt flows during phase change, are solved by approximate and numerical methods (Yao and Prusa, 1989; Alexiades and Solomon, 1993).

Some Approximate Solutions

Two prominent approximate methods used for the solution of melting and freezing problems are the integral method and the *quasi-static* approximation. The integral method is described in Goodman (1964), and only the quasi-static approximation is described here.

To obtain rough estimates of melting and freezing processes quickly, in cases where heat transfer takes place in only one phase, it is assumed in this approximation that effects of sensible heat are negligible relative to those of latent heat ($\mathrm{Ste} \to 0$), thus eliminating the sensible-heat left-hand side of the energy equations (such as (4.4.29), (4.4.32), and (4.4.51)). This is a significant simplification, since the energy equation then becomes independent of time, and solutions to the steady-state heat conduction problem are much easier to obtain. At the same time, the transient phase-change interface condition (such as Equation (4.4.35) and Equation (4.4.53)) 5 is retained, allowing the estimation of the transient interface position and velocity. This is hence a quasi-static approximation, and its use is shown below.

We emphasize that these are just approximations, without full information on the effect of specific problem conditions on the magnitude of the error incurred when using them. In fact, in some cases, especially with a convective boundary condition, they may produce incorrect results. It is thus necessary to examine the physical viability of the results, such as overall energy balances, when using these approximations.

All of the examples are for melting, but freezing problems have the same solutions when the properties are taken to be those of the solid and $h_{s\ell}$ is replaced everywhere by $-h_{s\ell}$. It is assumed here that the problems are one-dimensional, and that the material is initially at the fusion temperature T_f.

Examples of the Quasi-Static Approximation for Cartesian Coordinate Geometries. Given a semi-infinite solid (Figure 4.4.16), on which a *time-dependent temperature* $T_0(t) > T_f$ *is imposed at* $x = 0$, the above-described quasi-static approximation of Equation (4.4.42) to Equation (4.4.46) easily yields the solution

$$X(t) = \left[2 \frac{k_\ell}{\rho h_{s\ell}} \int_0^t \left[T_0(t) - T_f \right] dt \right]^{1/2} \quad \text{for} \quad t \geq 0 \tag{4.4.54}$$

$$T_\ell(x,t) = T_0(t) - \left[T_0(t) - T_f \right] \frac{x}{X(t)} \quad \text{in} \quad 0 \leq x \leq X(t) \quad \text{for} \quad t \geq 0 \tag{4.4.55}$$

The heat flux needed for melting, $q(x,t)$, can easily be determined from the temperature distribution in the liquid (Equation 4.4.55), which is linear because of the steady-state form of the heat conduction equation in this quasi-static approximation, so that

$$q(x,t) = -k_\ell \frac{dT_\ell(x,t)}{dx} = k_\ell \frac{T_0(t) - T_f}{X(t)} \tag{4.4.56}$$

For comparison of this approximate solution to the exact one (Equation (4.4.47) and Equation (4.4.50)), consider the case where $T_0(t) = T_0$ = constant. Rearranging to use the Stefan number, Equation (4.4.54) and Equation (4.4.55) become

$$X(t) = 2\left(\text{Ste}_\ell/2\right)^{1/2} \left(\alpha_\ell t\right)^{1/2} \quad \text{for} \quad t > 0 \tag{4.4.57}$$

$$T(x,t) = T_0 - \left[T_0 - T_f \right] \frac{x\Big/\left[2\left(\alpha_\ell t\right)^{1/2}\right]}{\left(\text{Ste}_\ell/2\right)^{1/2}} \quad \text{in} \quad 0 \leq x \leq X(t) \quad \text{for} \quad t \geq 0 \tag{4.4.58}$$

It is easy to show that λ' in the exact solution (Equation 4.4.48) approaches the value $(\text{Ste}_\ell/2)^{1/2}$ when $\text{Ste}_\ell \to 0$, and that otherwise $\lambda' < (\text{Ste}_\ell/2)^{1/2}$. The approximate solution is therefore indeed equal to the exact one when $\text{Ste}_\ell \to 0$, and it otherwise overestimates the values of both $X(t)$ and $T(x,t)$. While the errors depend on the specific problem, they are confined to about 10% in the above-described case (Alexiades and Solomon, 1993).

For the same melting problem but with the *boundary condition of an imposed time-dependent heat flux* $q_0(t)$,

$$-k_\ell \left(\frac{dT_\ell}{dx} \right)_{0,t} = q_0(t) \quad \text{for} \quad t > 0 \tag{4.4.59}$$

the quasi-static approximate solution is

$$X(t) \equiv \frac{1}{\rho h_{s\ell}} \int_0^t q_0(t)\, dt \quad \text{for} \quad t > 0 \tag{4.4.60}$$

$$T_\ell(x,t) = T_f + \left[\frac{q_0}{k_\ell} \frac{q_0}{\rho h_{s\ell}} t - x \right] \quad \text{in} \quad 0 \leq x \leq X(t) \quad \text{for} \quad t > 0 \tag{4.4.61}$$

For the same case if the *boundary condition is a convective heat flux* from an ambient fluid at the transient temperature $T_a(t)$, characterized by a heat transfer coefficient $\bar{h}$,

$$-k_\ell\left(\frac{dT_\ell}{dx}\right)_{0,t}=\bar{h}\left[T_a(t)-T_\ell(0,t)\right] \quad \text{for} \quad t\geq 0 \tag{4.4.62}$$

the quasi-static approximate solution is

$$X(t)=-\frac{k_\ell}{\bar{h}}+\left\{\left(\frac{k_\ell}{\bar{h}}\right)^2+2\frac{k_\ell}{\rho h_{s\ell}}\int_0^t\left[T_a(t)-T_f\right]dt\right\}^{1/2} \quad \text{for} \quad t\geq 0 \tag{4.4.63}$$

$$T_\ell(x,t)=T_f(t)\left[T_a(t)-T_f\right]\frac{\bar{h}\left[X(t)-x\right]}{\bar{h}X(t)+k_\ell} \quad \text{in} \quad 0\leq x\leq X(t) \quad \text{for} \quad t>0 \tag{4.4.64}$$

Examples of the Quasi-Static Approximation for Cylindrical Coordinate Geometries. It is assumed in these examples that the cylinders are very long and that the problems are axisymmetric. Just as in the Cartesian coordinate case, the energy equation (4.4.51) is reduced by the approximation to its steady-state form. Here

$$T_\ell\left(r_i,t\right)=T_0(t)>T_f \quad \text{for} \quad t>0 \tag{4.4.65}$$

Consider the *outward-directed melting* of a hollow cylinder due to a temperature imposed at the internal radius r_i. The solution is

$$T_\ell(r,t)=T_f+\left[T_0(t)-T_f\right]\frac{\ln\left[r/R(t)\right]}{\ln\left[r_i/R(t)\right]} \quad \text{in} \quad r_i\leq r\leq R(t) \quad \text{for} \quad t>0 \tag{4.4.66}$$

and the transient position of the phase front, $R(t)$, can be calculated from the transcendental equation

$$2R(t)^2\ln\frac{R(t)}{r_i}=R(t)^2-r_i^2+\frac{4k_\ell}{\rho h_{s\ell}}\int_0^t\left[T_0(t)-T_f\right]dt \tag{4.4.67}$$

If the melting for the same case occurs due to the imposition of a *heat flux* q_0 *at* r_p

$$-k_\ell\left(\frac{dT_\ell}{dx}\right)_{r_i,t}=q_0(t)>0 \quad \text{for} \quad t>0 \tag{4.4.68}$$

the solution is

$$T_\ell(r,t)=T_f-\frac{q_0(t)r_i}{k_\ell}\ln\frac{r}{R(t)} \quad \text{in} \quad r_i\leq r\leq R(t) \quad \text{for} \quad t>0 \tag{4.4.69}$$

$$R(t)=\left(r_i^2+2\frac{r_i}{\rho h_{s\ell}}\int_0^t q_0(t)\,dt\right)^{1/2} \quad \text{for} \quad t>0 \tag{4.4.70}$$

If the melting for the same case occurs due to the imposition of a *convective heat flux from a fluid at the transient temperature* $T_a(t)$, *with a heat transfer coefficient* $\bar{h}$, *at* r_i

$$-k_\ell \left(\frac{dT_\ell}{dr}\right)_{r_i,t} = \bar{h}\left[T_a(t) - T_f(r_i,t)\right] > 0 \quad \text{for} \quad t > 0 \tag{4.4.71}$$

The solution is

$$T_\ell(r,t) = T_f + \left[T_a(t) - T_f\right] \frac{\ln\left[r/R(t)\right]}{\ln\left[r_i/R(t)\right] - k_\ell/\bar{h}r_i} \quad \text{in} \quad r_i \le r \le R(t) \quad \text{at} \quad t > 0 \tag{4.4.72}$$

with $R(t)$ calculated from the transcendental equation

$$2R(t)^2 \ln\frac{R(t)}{r_i} = \left(1 - \frac{2k_\ell}{\bar{h}r_i}\right)\left[R(t)^2 - r_i^2\right] + \frac{4k_\ell}{\rho h_{s\ell}} \int_0^t \left[T_a(t) - T_f\right] dt \tag{4.4.73}$$

The solutions for *inward melting* of a cylinder, where heating is applied at the outer radius r_o, are the same as the above-described ones for the outward-melting cylinder, if the replacements $r_i \rightarrow r_o$, $q_0 \rightarrow -q_0$, and $\bar{h} \rightarrow -\bar{h}$ are made. If such a cylinder is not hollow, then $r_i = 0$ is used.

Estimation of Freezing and Melting Time

There are a number of approximate formulas for estimating the freezing and melting times of different materials having a variety of shapes. The American Society of Heating, Refrigerating, and Air-Conditioning Engineers (ASHRAE) provides a number of such approximations for estimating the freezing and thawing times of foods (ASHRAE, 1993). For example, if it can be assumed that the freezing or thawing occurs at a single temperature, the time to freeze or thaw, t_f, for a body that has shape parameters P and R (described below) and thermal conductivity k, initially at the fusion temperature T_f, and which is exchanging heat via heat transfer coefficient $\bar{h}$ with an ambient at the constant T_a, can be approximated by Planck's equation

$$t_f = \frac{h_{s\ell}\rho}{\left|T_f - T_a\right|}\left(\frac{Pd}{\bar{h}} + \frac{Rd^2}{k}\right) \tag{4.4.74}$$

where d is the diameter of the body if it is a cylinder or a sphere, or the thickness when it is an infinite slab, and where the shape coefficients P and R for a number of body forms are given in Table 4.4.2. Shape coefficients for other body forms are also available. To use Equation 4.4.74 for freezing, k and ρ should be the values for the food in its frozen state. In thawing, they should be for the unfrozen food. Other simple approximations for melting and thawing times can be found in Cleland et al. (1987).

TABLE 4.4.2 Shape Factors for Equation (4.4.74)

Forms	*P*	*R*
Slab	1/2	1/8
Cylinder	1/4	1/16
Sphere	1/6	1/24

From ASHRAE, in *Fundamentals*, ASHRAE, Atlanta, 1993, chap. 29. With permission.

Example of Using Planck's Equation (4.4.74) for Estimating Freezing Time. Estimate the time needed to freeze a fish, the shape of which can be approximated by a cylinder 0.5 m long having a diameter of 0.1 m. The fish is initially at its freezing temperature, and during the freezing process it is surrounded by air at $T_a = -25°C$, with the cooling performed with a convective heat transfer coefficient $\bar{h} = 68$ W/m^2 K. For the fish, $T_f = -1°C$, $h_{s\ell} = 200$ kJ/kg, $\rho_s = 992$ kg/m^3, and $_sk_s = 1.35$ W/m K.

By using Table 4.4.2, the geometric coefficients for the cylindrical shape of the fish are $P = {}^1/_2$ and $R = {}^1/_{16}$, while d is the cylinder diameter, = 0.1 m. Substituting these values into Equation (4.4.74) gives

$$t_f = \frac{200{,}000 \cdot 992}{-1-(-25)}\left(\frac{1/4(0.1)}{68} + \frac{1/16(0.1)^2}{1.35}\right) = 6866 \text{ sec} = 1.9 \text{ hr}$$

In fact, freezing or melting of food typically takes place over a range of temperatures, and approximate Planck-type formulas have been developed for various specific foodstuffs and shapes to represent reality more closely than Equation (4.4.74) (ASHRAE, 1993).

Alexiades and Solomon (1993) provide several easily computable approximate equations for estimating the time needed to melt a simple solid body initially at the fusion temperature T_f. It is assumed that conduction occurs in one phase (the liquid) only, that the problems are axi- and spherically symmetric for cylindrical and spherical bodies, respectively, and that the melting process for differently shaped bodies can be characterized by a single geometric parameter, r, in the body domain $0 \le r \le L$, using a shape factor, ω, defined by

$$\omega = \frac{LA}{V} - 1 \tag{4.4.75}$$

where A is the surface area across which the heat is transferred into the body and V is the body volume, to account for the specific body shape:

$$\omega = \begin{matrix} 0 & \text{for a slab insulated at one end} \\ 1 & \text{for a cylinder} \\ 2 & \text{for a sphere} \end{matrix} \tag{4.4.76}$$

$0 \le \omega \le 2$ always, and ω may be assigned appropriate values for shapes intermediate between the slab, cylinder, and sphere. For example, a football-shaped body, somewhere between a cylinder and sphere, may be assigned $\omega = 1.5$, and a short cylinder with a large diameter-to-height ratio may have $\omega = 0.5$.

For the case where the temperature $T_0 > T_f$ is imposed on the boundary at $t = 0$, the melt time, t_m can be estimated by

$$t_m = \frac{L^2}{2\alpha_\ell(1+\omega)\text{Ste}_\ell}\left[1 + \left(0.25 + 0.17\omega^{0.7}\right)\text{Ste}_\ell\right] \tag{4.4.77}$$

valid for $0 \le \text{Ste}_\ell \le 4$.

If the *heat input is convective*, with a heat transfer coefficient $\bar{h}$ from a fluid at temperature T_a, the approximate melt time is

$$t_m = \frac{L^2}{2\alpha_\ell(1+\omega)\text{Ste}_\ell}\left[1 + \frac{2k_\ell}{\bar{h}L} + \left(0.25 + 0.17\omega^{0.7}\right)\text{Ste}_\ell\right] \tag{4.4.78}$$

valid for $0 \le \text{Ste}_\ell \le 4$ and $\bar{h}L/k_\ell \ge 0.1$, and the temperature, $T(0,t)$, of the surface across which the heat is supplied can be estimated from the implicit time-temperature relationship:

$$t = \frac{\rho c_\ell k_\ell}{2\bar{h}^2 \mathrm{Ste}_\ell}\left[1.18\mathrm{Ste}_\ell \left(\frac{T(0,t) - T_f}{T_a - T(0,t)}\right)^{1.83} + \left(\frac{T_a - T_f}{T_a - T(0,t)}\right)^2 - 1\right] \tag{4.4.79}$$

Both equations (4.4.78) and (4.4.79) are claimed to be accurate within 10%.

The suitability of using several simplified analytical solutions for the estimation of freezing and melting times for more-realistic problems was assessed by Dilley and Lior (1986).

Defining Terms

Eutectic concentration: A concentration of a component of a multicomponent liquid at which the liquid would upon freezing form a solid containing the same concentration, and at which the freezing process is completed at a single temperature.

Mushy zone: The zone composed of both liquid and solid, bounded by the liquidus and solidus curves, in a freezing or melting process.

References

Alexiades, V. and Solomon, A.D. 1993. *Mathematical Modeling of Melting and Freezing Processes,* Hemisphere Publishing, Washington, D.C.

ASHRAE (American Society of Heating, Refrigerating, and Air-Conditioning Engineers). 1993. Cooling and freezing times of foods, in *Fundamentals*, ASHRAE, Atlanta, GA, chap. 29.

ASHRAE (American Society of Heating, Refrigerating, and Air-Conditioning Engineers). 1990. *Refrigeration*, ASHRAE, Atlanta, GA.

Cheng, K.C. and Seki, N., Eds. 1991. *Freezing and Melting Heat Transfer in Engineering,* Hemisphere Publishing, Washington, D.C.

Cleland, D.J., Cleland, A.C., and Earle, R.L. 1987. Prediction of freezing and thawing times for multidimensional shapes by simple formulae: Part 1, regular shapes; Part 2, irregular shapes. *Int. J. Refrig.,* 10, 156–166; 234–240.

DeWinter, F. 1991. Energy storage of solar systems; in *Solar Collectors, Energy Storage, and Materials*, MIT Press, Cambridge, MA, Section II.

Dilley, J.F. and Lior, N. 1986. The evaluation of simple analytical solutions for the prediction of freeze-up time, freezing, and melting. *Proc. 8th International Heat Transfer Conf.*, 4, 1727–1732, San Francisco.

Flemings, M.C. 1974. *Solidification Processes*, McGraw-Hill, New York.

Fukusako, S. and Seki, N. 1987. Fundamental aspects of analytical and numerical methods on freezing and melting heat-transfer problems, in *Annual Review of Numerical Fluid Mechanics and Heat Transfer*, Vol. 1, T.C. Chawla, Ed., Hemisphere, Publishing, Washington, D.C., chap. 7, 351–402.

Goodman, T.R. 1964. Application of integral methods to transient nonlinear heat transfer, in *Advances in Heat Transfer*, Vol. 1, T.F. Irvine and J.P. Hartnett, Eds., Academic Press, San Diego, 51–122.

Hayashi, Y. and Kunimine, K. 1992. Solidification of mixtures with supercooling, in *Heat and Mass Transfer in Materials Processing*, I. Tanasawa and N. Lior, Eds., Hemisphere Publishing, New York, 265–277.

Incropera, F.P. and Viskanta, R. 1992. Effects of convection on the solidification of binary mixtures, in *Heat and Mass Transfer in Materials Processing*, I. Tanasawa and N Lior, Eds., Hemisphere Publishing, New York, 295–312.

Lunardini, V.J. 1981. *Heat Transfer in Cold Climate*, Van Nostrand-Reinhold, Princeton, NJ.

Poulikakos, D. 1994. *Conduction Heat Transfer,* Prentice-Hall, Englewood Cliffs, NJ.

Tanasawa, I. and Lior, N., Ed. 1992. *Heat and Mass Transfer in Materials Processing*, Hemisphere Publishing, New York.

Yao, L.S. and Prusa, J. 1989. Melting and freezing, in *Advances in Heat Transfer*, Vol. 19, J.P. Hartnett and T.F. Irvine, Eds., Academic Press, San Diego, 1–95.

Further Information

In addition to the references above, there are also heat transfer textbooks and books that provide further information about melting and freezing:

De Vahl Davis, G. and Leonardi, E. 2001. *Advances in Computational Heat Transfer II CHT'01: Proceedings of a Symposium*, Palm Cove, Queensland, Australia, Begell House, New York.
Kroeger, P.G. and Bayazitoglu, Y. (Eds.) 1992. *Fundamentals of Phase Change: Freezing, Melting, & Sublimation — 1992,* American Society of Mechanical Engineers.
Manglik, R.M. 1996. *Process, Enhanced, and Multiphase Heat Transfer*, Begell House, New York.

Many technical journals contain articles about this subject. Some of the major journals, classified by orientation, are

General: *ASME Journal of Heat Transfer, International Journal of Heat & Mass Transfer, Numerical Heat Transfer, Canadian Journal of Chemical Engineering, AIChE Journal*
Refrigeration: *Transactions of the ASHRAE, International Journal of Refrigeration, Journal of Food Science, Bulletin of the International Institute of Refrigeration*
Manufacturing: *ASME Journal of Engineering for Industry, Journal of Crystal Growth, Materials Science and Engineering A*
Geophysical, climate, cold regions engineering: *Limnology and Oceanography, Journal of Geophysical Research, ASCE Journal of Cold Regions Engineering, Cold Regions Science and Technology*
Medical: *Cryobiology, ASME Journal of Biomechanical Engineering, Journal of General Physiology*

4.5 Heat Exchangers

Ramesh K. Shah and Kenneth J. Bell

The two major categories of heat exchangers are shell-and-tube exchangers and compact exchangers. Basic constructions of gas-to-gas compact heat exchangers are plate-fin, tube-fin and all prime surface recuperators (including polymer film and laminar flow exchangers), and compact regenerators. Basic constructions of liquid-to-liquid and liquid-to-phase-change compact heat exchangers are gasketed and welded plate-and-frame, welded stacked plate (without frames), spiral plate, printed circuit, and dimple plate heat exchangers.

Shell-and-tube exchangers are custom designed for virtually any capacity and operating condition, from high vacuums to ultrahigh pressures, from cryogenics to high temperatures, and for any temperature and pressure differences between the fluids, limited only by the materials of construction. They can be designed for special operating conditions: vibration, heavy fouling, highly viscous fluids, erosion, corrosion, toxicity, radioactivity, multicomponent mixtures, etc. They are made from a variety of metal and nonmetal materials, and in surface areas from less than 0.1 to 100,000 m^2 (1 to over 1,000,000 ft^2). They have generally an order of magnitude less surface area per unit volume than the compact exchangers, and require considerable space, weight, support structure, and footprint.

Compact heat exchangers have a large heat transfer surface area per unit volume of the exchanger, resulting in reduced space, weight, support structure and footprint, energy requirement and cost, as well as improved process design, plant layout and processing conditions, together with low fluid inventory compared with shell-and-tube exchangers. From the operating condition and maintenance point of view, compact heat exchangers of different constructions are used for specific applications, such as for high-temperature applications (up to about 850°C or 1550°F), high pressure applications (over 200 bars), and moderate fouling applications. However, applications do not involve both high temperature and pressure simultaneously. Plate-fin exchangers are generally brazed, and the largest size currently manufactured is $1.2 \times 1.2 \times 6$ m ($4 \times 4 \times 20$ ft). Fouling is one of the major potential problems in many compact exchangers except for the plate heat exchangers. With a large frontal area exchanger, flow maldistribution could be another problem. Because of short transient times, a careful design of controls is required for startup of some compact heat exchangers compared with shell-and-tube exchangers. Standards are available for compact heat exchangers used in cryogenics applications and process plants (ALPEMA, 2000).

This section is divided into two parts: Compact Heat Exchangers and Shell-and-Tube Exchangers, written by R. K. Shah and K. J. Bell, respectively. In the compact heat exchangers section, the following topics are covered: definition and description of exchangers, heat transfer and pressure drop analyses, heat transfer and flow friction correlations, exchanger design (rating and sizing) methodology, flow maldistribution, and fouling. In the shell-and-tube heat exchangers section, the following topics are covered: construction features, principles of design, and an approximate design method with an example.

Compact Heat Exchangers

Ramesh K. Shah

Introduction

A heat exchanger is a device to provide for transfer of thermal energy (enthalpy) between two or more fluids, between a solid surface and a fluid, or between solid particulates and a fluid, at different temperatures and in thermal contact without external heat and work interactions. The fluids may be single compounds or mixtures. Typical applications involve heating or cooling of a fluid stream of concern, evaporation or condensation of single or multicomponent fluid stream, and heat recovery or heat rejection from a system. In other applications, the objective may be to sterilize, pasteurize, fractionate, distill, concentrate, crystallize, or control process fluid. In some heat exchangers, the fluids transferring heat are in direct contact. In other heat exchangers, heat transfer between fluids takes place through a separating wall or into and out of a wall in a transient manner. In most heat exchangers, the fluids are separated by a heat transfer surface and do not mix. Such exchangers are referred to as *direct transfer type*, or simply *recuperators*. Exchangers in which there is an intermittent flow of heat from the hot to cold fluid (via heat storage and heat rejection through the exchanger surface or matrix) are referred to as *indirect transfer type* or simply *regenerators*.

The heat transfer surface is a surface of the exchanger core which is in direct contact with fluids and through which heat is transferred by conduction in a recuperator. The portion of the surface which also separates the fluids is referred to as a *primary* or *direct surface*. To increase heat transfer area, appendages known as fins may be intimately connected to the primary surface to provide an *extended*, *secondary*, or *indirect surface*. Thus, the addition of fins reduces the thermal resistance on that side and thereby increases the net heat transfer from the surface for the same temperature difference.

Heat exchangers may be classified according to transfer process, construction, flow arrangement, surface compactness, number of fluids, and heat transfer mechanisms as shown in Figure 4.5.1.

A gas-to-fluid heat exchanger is referred to as a compact heat exchanger if it incorporates a heat transfer surface having a surface area density above about 700 m^2/m^3 (213 ft^2/ft^3) on at least one of the fluid sides which usually has gas flow. It is referred to as a laminar flow heat exchanger if the surface area density is above about 3000 m^2/m^3 (914 ft^2/ft^3), and as a micro heat exchanger if the surface area density is above about 15,000 m^2/m^3 (4570 ft^2/ft^3). A liquid/two-phase heat exchanger is referred to as a compact heat exchanger if the surface area density on any one fluid side is above about 400 m^2/m^3 (122 ft^2/ft^3). A typical process industry shell-and-tube exchanger has a surface area density of less than 100 m^2/m^3 on one fluid side with plain tubes, and two to three times that with the high-fin-density low-finned tubing. Plate-fin, tube-fin, and rotary regenerators are examples of compact heat exchangers for gas flows on one or both fluid sides, and gasketed and welded plate heat exchangers are examples of compact heat exchangers for liquid flows and phase-change applications.

Types and Description

Gas-to-Fluid Exchangers.

The important design and operating considerations for compact extended surface exchangers are (1) usually at least one of the fluids is a gas or specific liquid that has low h; (2) fluids must be clean and

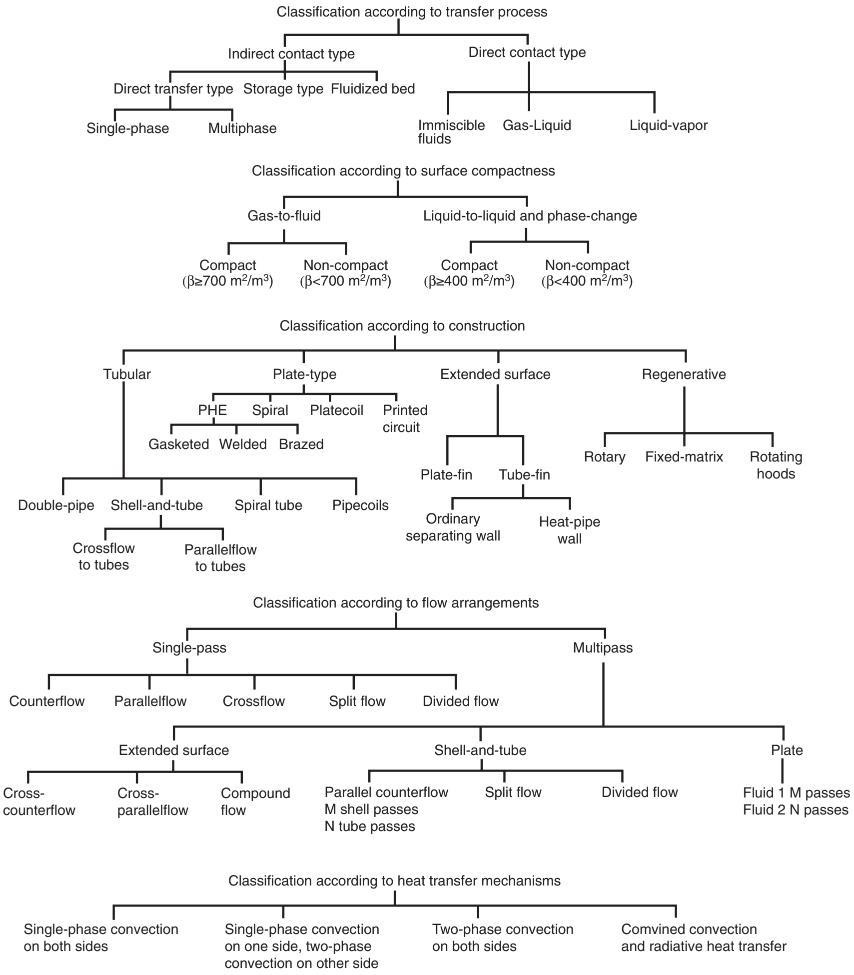

FIGURE 4.5.1 Classification of heat exchangers.

relatively noncorrosive because of small hydraulic diameter (D_h) flow passages and no easy techniques for mechanically cleaning them; (3) the fluid pumping power (i.e., pressure drop) design constraint is often equally as important as the heat transfer rate; (4) operating pressures and temperatures are somewhat limited compared with shell-and-tube exchangers as a result of the joining of the fins to plates or tubes by brazing, mechanical expansion, etc.; (5) with the use of highly compact surfaces, the resultant shape of a gas-to-fluid exchanger is one having a large frontal area and a short flow length (the header design of a compact heat exchanger is thus important for a uniform flow distribution among the very large number of small flow passages); (6) the market potential must be large enough to warrant the sizable manufacturing research and tooling costs for new forms to be developed.

Some advantages of plate-fin exchangers over conventional shell-and-tube exchangers are as follows. Compact heat exchangers, generally fabricated from thin metallic plates, yield large heat transfer surface area per unit volume (β), typically up to ten times greater than the 50 to 100 m^2/m^3 provided by a shell-and-tube exchanger for general process application and from 1000 to 6000 m^2/m^3 for highly compact gas side surfaces. Compact liquid or phase-change side surfaces have a β ratio ranging from 500 to 600 m^2/m^3. A compact exchanger provides a tighter temperature control; thus it is useful for heat-sensitive materials, improves the product (e.g., refining fats from edible oil) and its quality (such as a catalyst bed).

Also, a compact exchanger could provide rapid heating or cooling of a process stream, thus improving the product quality. The plate-fin exchangers can accommodate multiple (up to 12 or more) fluid streams in one exchanger unit with proper manifolding, thus allowing process integration and cost-effective compact solutions.

Fouling is one of the potential major problems in compact heat exchangers (except for plate-and-frame heat exchangers), particularly those having a variety of fin geometries or very fine circular or noncircular flow passages that cannot be cleaned mechanically. Chemical cleaning may be possible; thermal baking and subsequent rinsing is possible for small-size units. Hence, extended surface compact heat exchangers may not be used in heavy fouling applications.

Liquid-to-Liquid Exchangers.

Liquid-to-liquid and phase-change exchangers are plate-and-frame and welded plate heat exchangers (PHE), spiral plate, and printed circuit exchangers; plate-fin exchangers are also used in phase-change applications. Some of them are described next in some detail along with other compact heat exchangers and their applications.

Plate-Fin Heat Exchangers.

This type of exchanger has "corrugated" fins or spacers sandwiched between parallel plates (referred to as plates or parting sheets) as shown in Figure 4.5.2. Sometimes fins are incorporated in a flat tube with rounded corners (referred to as a formed tube), thus eliminating a need for the side bars. If liquid or phase-change fluid flows on the other side, the parting sheet is usually replaced by a flat tube with or without inserts/webs. Other plate-fin constructions include drawn-cup or tube-and-center configurations. Fins are die- or roll-formed and are attached to the plates by brazing, soldering, adhesive bonding, welding, mechanical fit, or extrusion. Fins may be used on both sides in gas-to-gas heat exchangers. In gas-to-liquid applications, fins are usually used only on the gas side; if employed on the liquid side, they are used primarily for structural strength and flow-mixing purposes. Fins are also sometimes used for pressure containment and rigidity.

Plate fins are categorized as (1) plain (i.e., uncut) and straight fins, such as plain triangular and rectangular fins; (2) plain but wavy fins (wavy in the main fluid flow direction); and (3) interrupted fins such as offset strip, louver, and perforated. Examples of commonly used fins are shown in Figure 4.5.3.

Plate-fin exchangers have been built with a surface area density of up to about 5900 m^2/m^3 (1800 ft^2/ft^3). There is a total freedom of selecting fin surface area on each fluid side, as required by the design, by

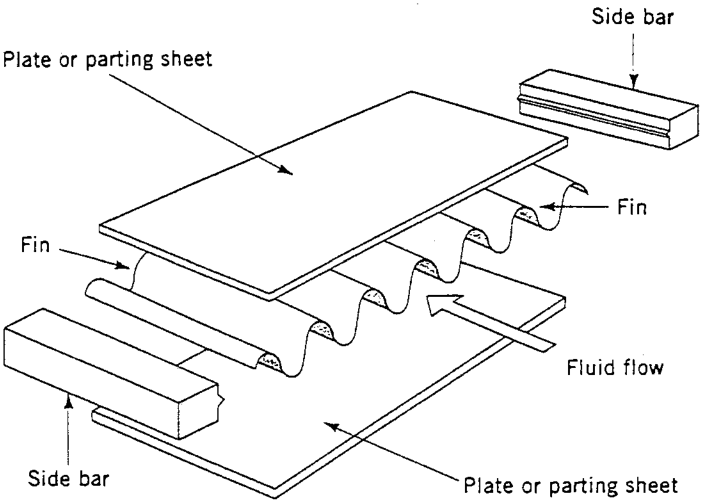

FIGURE 4.5.2 Typical components of a plate-fin exchanger.

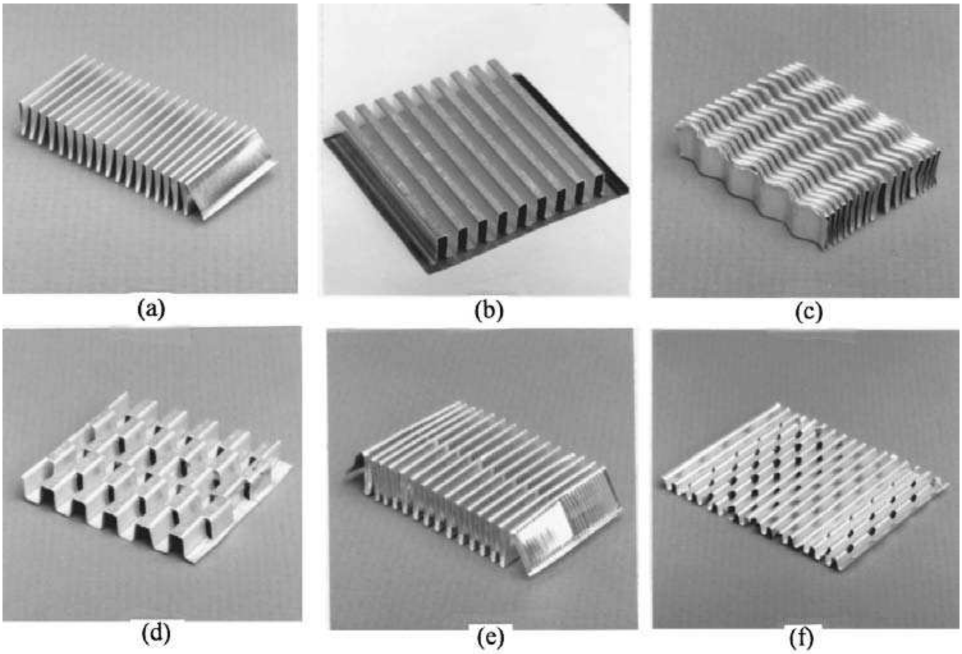

FIGURE 4.5.3 Fin geometries for plate-fin heat exchangers: (a) plain triangular fin, (b) plain rectangular fin, (c) wavy fin, (d) offset strip fin, (e) multilouver fin, and (f) perforated fin.

varying fin height and fin density. Although typical fin densities are 120 to 700 fins/m (3 to 18 fins/in.), applications exist for as many as 2100 fins/m (53 fins/in.). Common fin thicknesses range from 0.05 to 0.25 mm (0.002 to 0.010 in.). Fin heights range from 2 to 25 mm (0.08 to 1.0 in.). A plate-fin exchanger with 600 fins/m (15.2 fins/in.) provides about 1300 m^2 (400 ft^2/ft^3) of heat transfer surface area per cubic meter volume occupied by the fins. Plate-fin exchangers are manufactured in virtually all shapes and sizes, and made from a variety of materials.

Tube-Fin Heat Exchangers.

In this type of exchanger, round and rectangular tubes are the most common, although elliptical tubes are also used. Fins are generally used on the outside, but they may be used on the inside of the tubes in some applications. They are attached to the tubes by a tight mechanical fit, tension winding, adhesive bonding, soldering, brazing, welding, or extrusion. Fins on the outside of the tubes may be categorized as follows: (1) normal fins on individual tubes, referred to as individually finned tubes or simply as *finned tubes*, as shown in Figure 4.5.5 and Figure 4.5.4a; (2) flat or continuous (plain, wavy, or interrupted) external fins on an array of tubes, as shown in Figure 4.5.6 and Figure 4.5.4b; (3) longitudinal fins on individual tubes. The exchanger having flat (continuous) fins on tubes has also been referred to as a *plate-fin and tube* exchanger in the literature. In order to avoid confusion with plate-fin surfaces, we will refer to it as a tube-fin exchanger having flat (plain, wavy, or interrupted) fins. Individually finned tubes are probably more rugged and practical in large tube-fin exchangers. Shell-and-tube exchangers sometimes employ low-finned tubes to increase the surface area on the shell side when the shell-side heat transfer coefficient is low compared with the tube-side coefficient. The exchanger with flat fins is usually less expensive on a unit heat transfer surface area basis because of its simple and mass-production-type construction features. Longitudinal fins are generally used in condensing applications and for viscous fluids in double-pipe heat exchangers.

Tube-fin exchangers can withstand high pressures on the tube side. The highest temperature is again limited by the type of bonding, the materials employed, and the material thickness. Tube-fin exchangers with an area density of about 3300 m^2/m^3 (1000 ft^2/ft^2) are commercially available. On the fin side, the

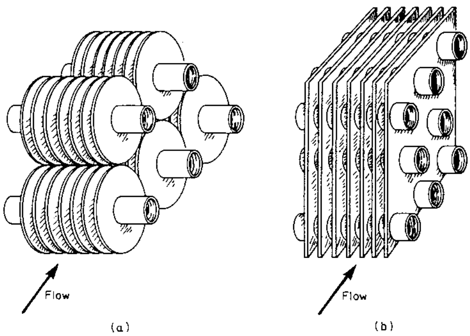

FIGURE 4.5.4 (a) Individually finned tubes, (b) flat or continuous fins on an array of tubes.

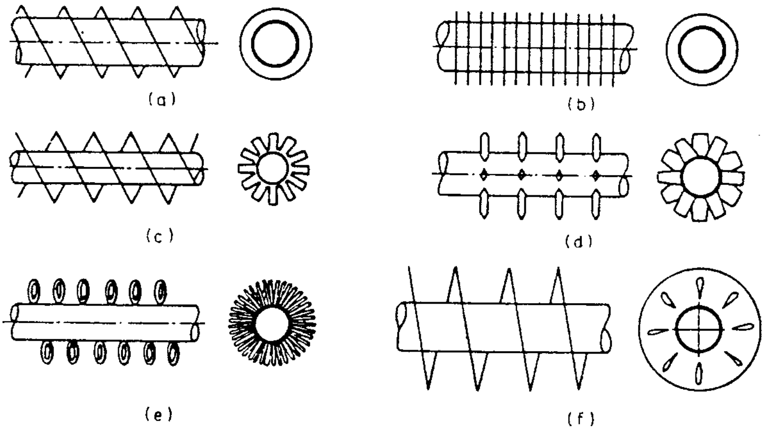

FIGURE 4.5.5 Individually finned tubes: (a) helical, (b) annular disk, (c) segmented, (d) studded, (e) wire loop, and (f) slotted helical.

desired surface area can be employed by using the proper fin density and fin geometry. The typical fin densities for flat fins vary from 250 to 800 fins/m (6 to 20 fins/in.), fin thicknesses vary from 0.08 to 0.25 mm (0.003 to 0.010 in.), and fin flow lengths from 25 to 250 mm (1 to 10 in.). A tube-fin exchanger having flat fins with 400 fins/m (10 fins/in.) has a surface area density of about 720 m^2/m^3(220 ft^2/ft^3). These exchangers are extensively used as condensers and evaporators in air-conditioning and refrigeration applications, as condensers in electric power plants, as oil coolers in propulsive power plants, and as air-cooled exchangers (also referred to as a fin-fan exchanger) in process and power industries.

Regenerators.

The regenerator is a storage-type exchanger. The heat transfer surface or elements are usually referred to as a matrix in the regenerator. In order to have continuous operation, either the matrix must be moved periodically into and out of the fixed streams of gases, as in a *rotary* regenerator (Figure 4.5.7a), or the gas flows must be diverted through valves to and from the fixed matrices as in a *fixed-matrix* regenerator (Figure 4.5.7b). The latter is also sometimes referred to as a *periodic-flow regenerator* or a *reversible heat accumulator*. A third type of regenerator has a fixed matrix (in the disk form) and the fixed stream of gases, but the gases are ducted through rotating hoods (headers) to the matrix as shown in Figure 4.5.7c. This Rothemuhle regenerator is used as an air preheater in some power-generating plants. The thermodynamically superior counterflow arrangement is usually employed in regenerators.

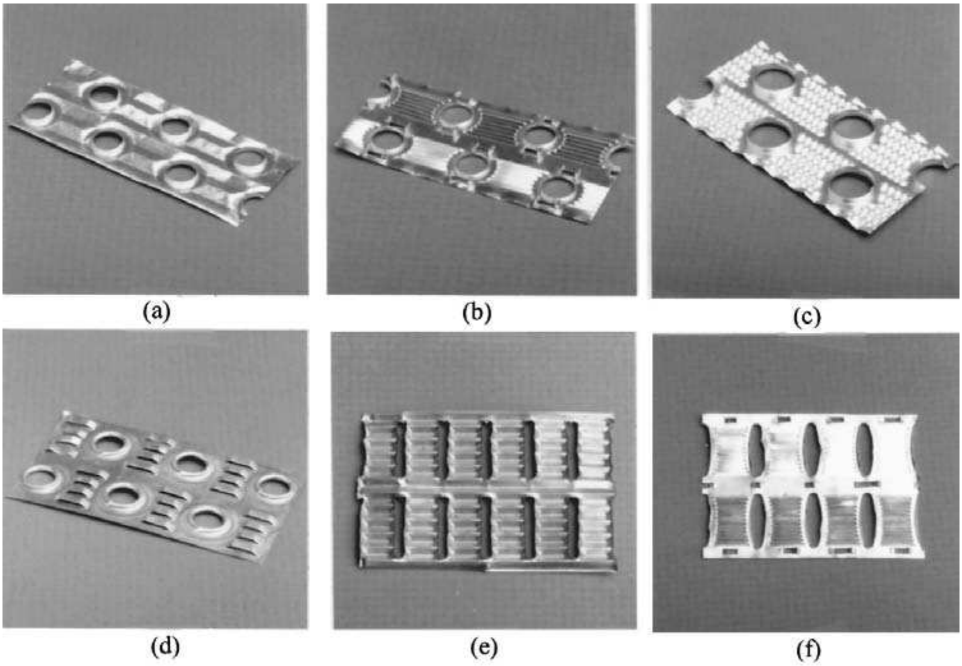

FIGURE 4.5.6 Flat or continuous fins on an array of tubes: On round tubes: (a) wavy fin, (b) multilouver fin, (c) fin with structured surface roughness (dimples), (d) parallel louver fin; (e) louver fin on flat tubes; (f) multilouver fin on elliptical tubes.

The **rotary regenerator** is usually a disk type in which the matrix (heat transfer surface) is in a disk form and fluids flow axially. It is rotated by a hub shaft or a peripheral ring gear drive. For a rotary regenerator, the design of seals to prevent leakage of hot to cold fluids and vice versa becomes a difficult task, especially if the two fluids are at significantly differing pressures. Rotating drives also pose a challenging mechanical design problem.

Major advantages of rotary regenerators are the following. For a highly compact regenerator, the cost of the regenerator surface per unit of heat transfer area is usually substantially lower than that for the equivalent recuperator. A major disadvantage of a regenerator is an unavoidable carryover of a small fraction of the fluid trapped in the passage to the other fluid stream just after the periodic flow switching. Since fluid contamination (small mixing) is prohibited with liquids, the regenerators are used exclusively for gas-to-gas heat or energy recovery applications. Cross contamination can be minimized significantly by providing a purge section in the disk and using double-labyrinth seals.

Rotary regenerators have been designed for a surface area density of up to about 6600 m^2/m^3 (2000 ft^2/ft^3), and exchanger effectivenesses exceeding 85% for a number of applications. They can employ thinner stock material, resulting in the lowest amount of material for a given effectiveness and pressure drop of any heat exchanger known today. The metal rotary regenerators have been designed for continuous inlet temperatures up to about 790°C (1450°F) and ceramic matrices for higher-temperature applications; these regenerators are designed up to 400 kPa or 60 psi pressure differences between hot and cold gases. Plastic, paper, and wool are used for regenerators operating below 65°C (150°F) inlet temperature of the hot gas and 1 atm pressure. Typical regenerator rotor diameters and rotational speeds are as follows: up to 10 m (33 ft) and 0.5 to 3 rpm for power plant regenerators, 0.25 to 3 m (0.8 to 9.8 ft) and up to 10 rpm for air-ventilating regenerators, and up to 0.6 m (24 in.) and up to 18 rpm for vehicular regenerators. Refer to Shah (1994) for the description of **fixed-matrix regenerator**, also referred to as a *periodic-flow*, *fixed bed*, *valved*, or *stationary* regenerator.

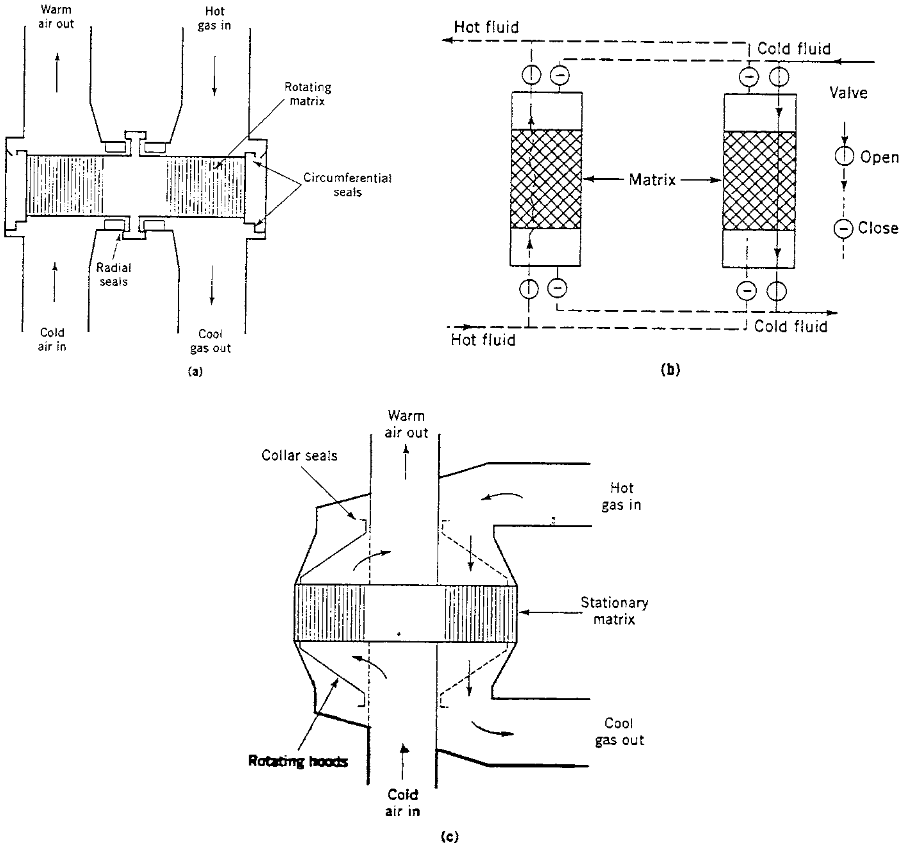

FIGURE 4.5.7 Regenerators: (a) rotary, (b) fixed-matrix, and (c) Rothemuhle.

Plate-Type Heat Exchangers.

These exchangers are usually built of thin plates (all prime surface). The plates are either smooth or have some form of corrugations, and they are either flat or wound in an exchanger. Generally, these exchangers cannot accommodate very high pressures, temperatures, and pressure and temperature differentials. These exchangers may be further classified as plate, spiral plate, lamella, and plate-coil exchangers as classified in Figure 4.5.1. The plate heat exchanger, being the most important of these, is described next.

The **plate-and-frame** or **gasketed PHE** consists of a number of thin rectangular corrugated or embossed metal plates sealed around the edges by gaskets and held together in a frame as shown in Figure 4.5.8. The plate pack with fixed and movable end covers is clamped together by long bolts, thus compressing the gaskets and forming a seal. Sealing between the two fluids is accomplished by elastomeric molded gaskets (typically 5 mm or 0.2 in. thick) that are fitted in peripheral grooves mentioned earlier. The most conventional flow arrangement is 1 pass –1 pass counterflow with all inlet and outlet connections on the fixed end cover. By blocking flow through some ports with proper gasketing, either one or both fluids could have more than one pass. Also more than one exchanger can be accommodated in a single frame with the use of intermediate connector plates such as up to five "exchangers" or sections to heat, cool, and regenerate heat between raw milk and pasteurized milk in a milk pasteurization application.

Typical PHE dimensions and performance parameters are given in Table 4.5.1 (Shah, 1994). Any metal which can be cold-worked is suitable for PHE applications. The most common plate materials are stainless steel (AISI 304 or 316) and titanium. Plates made from Incoloy 825, Inconel 625, Hastelloy C-276 are also available. Nickel, cupronickel, and monel are rarely used. Carbon steel is not used because of low

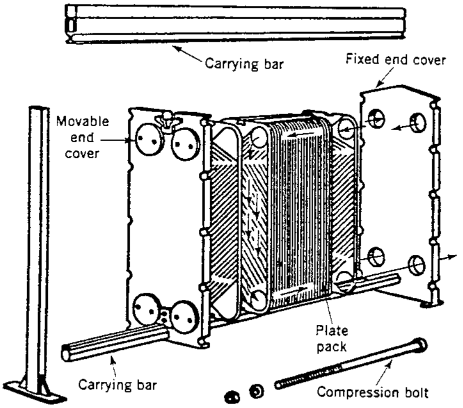

FIGURE 4.5.8 A plate-and-frame or gasketed PHE.

TABLE 4.5.1 Some Geometric and Operating Condition Characteristics of Plate-and-Frame Heat Exchangers

Unit		**Operation**	
Maximum surface area	2500 m^2	Pressure	0.1 to 3.0 MPa
Number of plates	3–700	Temperature	–40 to 260°C
Port size	Up to 400 mm	Maximum port velocity	6 m/sec (for liquids)
Plates		Channel flow rates	0.05 to 12.5 m^3/hr
Thickness	0.5–1.2 mm	Max unit flow rate	2500 m^3/hr
Size	0.03–3.6 m^2	**Performance**	
Spacing	1.5–7 mm	Temperature approach	As low as 1°C
Width	70–1200 mm	Heat exchanger efficiency	Up to 93%
Length	0.4–5 m	Heat transfer coefficients for water-water duties	3000 to 8000 W/m^2 K

Source: Modified from Shah, R.K., in *Encyclopedia of Energy Technology and the Environment*, A. Bision and S.G. Boots, Eds., John Wiley & Sons, New York, 1994, 1651–1670. With permission.

corrosion resistance for thin plates. The heat transfer surface area per unit volume for plate exchangers ranges from 120 to 660 m^2/m^3 (37 to 200 ft^2/ft^3).

In PHEs, the high turbulence due to plates reduces fouling from about 10 to 25% of that of a shell-and-tube exchanger. High thermal performance can be achieved in plate exchangers because the high degree of counterflow in PHEs makes temperature approaches of up to 1°C (2°F) possible. The high thermal effectiveness (up to about 93%) makes low-grade heat recovery economical. PHEs are most suitable for liquid-liquid heat transfer duties and high vapor density phase-change applications.

Welded PHEs. One of the limitations of gasketed PHE is the presence of the gaskets which restricts the use to compatible fluids and which limits operating temperatures and pressures. In order to overcome this limitation, a number of welded PHE designs have surfaced with a welded pair of plates for one or both fluid sides. However, the disadvantage of such design is the loss of disassembling flexibility on the fluid side where the welding is done. Essentially, welding is done around the complete circumference where the gasket is normally placed. A *stacked plate heat exchanger* is another welded PHE design from Pacinox in which rectangular plates are stacked and welded at the edges. The physical size limitations of PHEs (1.2 m wide × 4 m long max, 4 × 13 ft) are considerably extended to 1.5 m wide × 20 m long (5 × 66 ft) in this exchanger. A maximum surface area of (10,000 m^2 or over 100,000 ft^2) can be accommodated in one unit. The potential maximum operating temperature is 815°C (1500°F) with an operating pressure of up to 20 MPa (3000 psig) when the stacked plate assembly is placed in a cylindrical pressure vessel. For operating pressures below 2 MPa (300 psig) and operating temperatures below 200°C (400°F), the plate bundle is not contained in a pressure vessel, but is bolted between two heavy plates. Some of the applications of this exchanger are catalytic reforming, hydrosulfurization, crude distillation, synthesis converter feed effluent exchanger for methanol, propane condenser, etc.

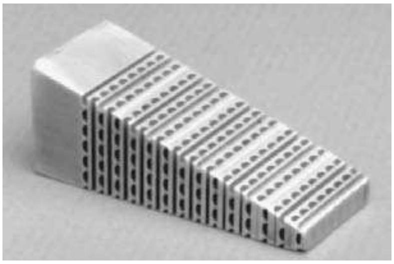

FIGURE 4.5.9 A section of a printed circuit heat exchanger. (Courtesy of Heatric Ltd., Dorset, U.K.)

A number of other PHE constructions have been developed to address some of the limitations of the conventional PHEs. A double-wall PHE is used to avoid mixing of the two fluids. A wide-gap PHE is used for fluids having high fiber content or coarse particles. Graphite and polymer plate PHEs are used for highly corrosive fluids. A flow-flex exchanger has plain fins on one fluid side between plates and the other fluid side has conventional plate channels, and is used to handle asymmetric duties (flow rate ratio of 2 to 1 and higher).

A vacuum **brazed PHE** is a compact PHE for high-temperature and high-pressure duties, and it does not have gaskets, tightening bolts, frame, or carrying and guide bars. It simply consists of stainless steel plates and two end plates. The brazed unit can be mounted directly on piping without brackets and foundations.

Printed Circuit Heat Exchangers. This exchanger, as shown in Figure 4.5.9, has only primary heat transfer surfaces as PHEs. Fine grooves are made in the plate by using the same techniques as those employed for making printed electrical circuits. High surface area densities (650 to 1350 m^2/m^3 or 200 to 400 ft^2/ft^3 for operating pressures of 500 to 20 bar respectively) are achievable. A variety of materials including stainless steel, titanium, copper, nickel, and nicket alloys can be used. It has been successfully used with relatively clean gases, liquids and phase-change fluids in chemical processing, fuel processing, waste heat recovery, and refrigeration industries. Again, this exchanger is a new construction with limited special applications currently.

Exchanger Heat Transfer and Pressure Drop Analysis

In this subsection, starting with the thermal circuit associated with a two-fluid exchanger, ε-NTU, P-NTU, and mean temperature difference (MTD) methods used for an exchanger analysis are presented, followed by the fin efficiency concept and various expressions. Finally, pressure drop expressions are outlined for various single-phase exchangers.

Two energy conservation differential equations for a two-fluid exchanger with any flow arrangement are (see Figure 4.5.10 for counterflow)

$$dq = q'' \, dA = -C_h \, dT_h = \pm C_c \, dT_c \tag{4.5.1}$$

where the ± sign depends upon whether dT_c is increasing or decreasing with increasing dA or dx. The local overall rate equation is

$$dq = q'' \, dA = U\left(T_h - T_c\right)_{\text{local}} \, dA = U \, \Delta T \, dA \tag{4.5.2}$$

Integration of Equation (4.5.1) and Equation (4.5.2) across the exchanger surface area results in

$$q = C_h\left(T_{h,i} - T_{h,o}\right) = C_c\left(T_{c,o} - T_{c,i}\right) \tag{4.5.3}$$

and

$$q = UA \, \Delta T_m = \Delta T_m / R_o$$

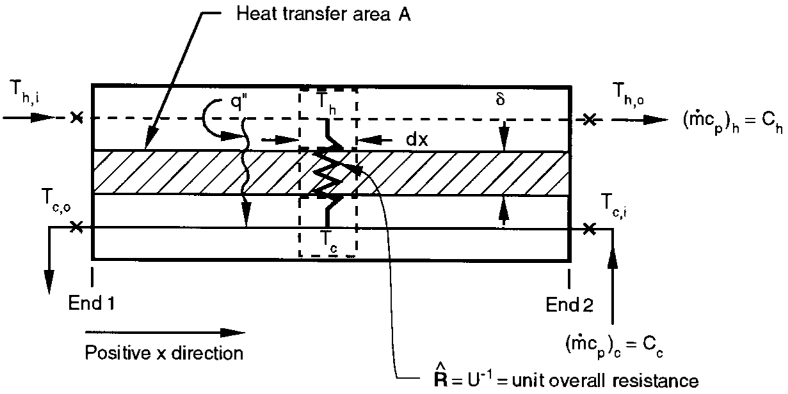

FIGURE 4.5.10 Nomenclature for heat exchanger variables.

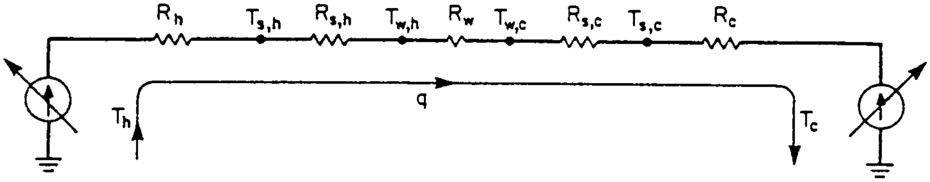

FIGURE 4.5.11 Thermal circuit for heat transfer in an exchanger.

where ΔT_m is the true mean temperature difference (or MTD) that depends upon the exchanger flow arrangement and degree of fluid mixing within each fluid stream. The inverse of the overall thermal conductance *UA* is referred to as the overall thermal resistance R_o as follows (see Figure 4.5.11).

$$R_o = R_h + R_{s,h} + R_w + R_{s,c} + R_c \tag{4.5.4}$$

where the subscripts *h*, *c*, *s*, and *w* denote hot, cold, fouling (or scale), and wall, respectively. In terms of the overall and individual heat transfer coefficients, Equation (4.5.4) is represented as

$$\frac{1}{UA} = \frac{1}{(\eta_o hA)_h} + \frac{1}{(\eta_o h_s A)_h} + R_w + \frac{1}{(\eta_o h_s A)_c} + \frac{1}{(\eta_o hA)_c} \tag{4.5.5}$$

where η_o = the overall extended surface efficiency and is related to the fin efficiency η_f, fin surface area A_f, and the total surface area *A* by Equation (4.5.19).

The wall thermal resistance R_w of Equation (4.5.4) is given by

$$R_w = \begin{cases} \delta / A_w k_w & \text{for a flat wall} \\ \dfrac{\ln(d_o/d_j)}{2\pi k_w L N_t} & \text{for } N_t \text{ circular tubes with a single-layer wall} \\ \dfrac{1}{2\pi L N_t}\left[\displaystyle\sum_j \frac{\ln(d_{j+1}/d_j)}{k_{w,j}}\right] & \text{for } N_t \text{ circular tubes with a multiple-layer wall} \end{cases}$$

TABLE 4.5.2 General Functional Relationships and Dimensionless Groups for ε-NTU, P-NTU, and MTD Methods

ε-NTU Method	P-NTU Method[a]	MTD Method[a]
$q = \varepsilon C_{\min}(T_{h,i} - T_{c,i})$	$q = \mathrm{P}_1 C_1 \lvert T_{1,i} - T_{2,i} \rvert$	$q = UAF\Delta T_{lm}$
$\varepsilon = \phi_1(\mathrm{NTU}, \mathrm{C}^*, \text{flow arrangement})$	$\mathrm{P}_1 = \phi_2(\mathrm{NTU}_1, \mathrm{R}_1, \text{flow arrangement})$	$F = \phi_3(\mathrm{P}, \mathrm{R}, \text{flow arrangement})^{\mathrm{b}}$
$\varepsilon = \dfrac{C_h(T_{h,i} - T_{h,o})}{C_{\min}(T_{h,i} - T_{c,i})} = \dfrac{C_c(T_{c,o} - T_{c,i})}{C_{\min}(T_{h,i} - T_{c,i})}$	$\mathrm{P}_1 = \dfrac{T_{1,o} - T_{1,i}}{T_{2,i} - T_{1,i}}$	$F = \dfrac{\Delta T_m}{\Delta T_{\mathrm{lm}}}$
$\mathrm{NTU} = \dfrac{UA}{C_{\min}} = \dfrac{1}{C_{\min}} \displaystyle\int_A U\, dA$	$\mathrm{NTU}_1 = \dfrac{UA}{C_1} = \dfrac{\lvert T_{1,o} - T_{1,i} \rvert}{\Delta T_m}$	$\mathrm{LMTD} = \Delta T_{\mathrm{lm}} = \dfrac{\Delta T_{\mathrm{I}} - \Delta T_{\mathrm{II}}}{\ln(\Delta T_{\mathrm{I}}/\Delta T_{\mathrm{II}})}$
$C^* = \dfrac{C_{\min}}{C_{\max}} = \dfrac{(\dot{m}c_p)_{\min}}{(\dot{m}c_p)_{\max}}$	$\mathrm{R}_1 = \dfrac{C_1}{C_2} = \dfrac{T_{2,i} - T_{2,o}}{T_{1,o} - T_{1,i}}$	$\Delta T_{\mathrm{I}} = T_{h,i} - T_{c,o} \quad \Delta T_{\mathrm{II}} = T_{h,o} - T_{c,i}$

[a] Although P_1, R_1, and NTU_1 are defined on fluid side 1, it must be emphasized that all the results of the P-NTU and MTD methods are valid if the definitions of P, NTU, and R are consistently based on C_c, C_s, C_h, C_t, *or* C_2.

[b] P and R are defined in the P-NTU method.

If one of the resistances on the right-hand side of Equation (4.5.4) or (4.5.5) is significantly higher than the other resistances, it is referred to as the *controlling thermal resistance*. A reduction in the controlling thermal resistance will have much more impact in reducing the exchanger surface area (A) requirement compared with the reduction in A as a result of the reduction in other thermal resistances.

UA of Equation (4.5.5) may be defined in terms of hot or cold fluid side surface area or wall conduction area as

$$UA = U_h A_h = U_c A_c = U_w A_w \tag{4.5.6}$$

When R_w is negligible, $T_{w,h} = T_{w,c} = T_w$ of Figure 4.5.11 is computed from

$$T_w = \frac{T_h + \left[\left(R_h + R_{s,h}\right)/\left(R_c + R_{s,c}\right)\right]T_c}{1 + \left[\left(R_h + R_{s,h}\right)/\left(R_c + R_{s,c}\right)\right]} \xrightarrow[R_{s,h}=R_{s,c}=0]{} T_w = \frac{T_h/R_h + T_c/R_c}{1/R_h + 1/R_c} = \frac{(\eta_o hA)_h T_h + (\eta_o hA)_c T_c}{(\eta_o hA)_h + (\eta_o hA)_c} \tag{4.5.7}$$

ε-NTU, P-NTU, and MTD Methods. If we consider the fluid outlet temperatures or heat transfer rate as dependent variables, they are related to independent variables/parameters of Figure 4.5.10 as follows.

$$T_{h,o},\ T_{c,o}, \ \text{ or } \ q = \phi\left\{T_{h,i},\ T_{c,i},\ C_c,\ C_h,\ U,\ A,\ \text{flow arrangement}\right\} \tag{4.5.8}$$

Six independent and three dependent variables of Equation (4.5.8) for a given flow arrangement can be transferred into two independent and one dependent dimensionless groups; three different methods are presented in Table 4.5.2 based on the choice of three dimensionless groups. The relationship among three dimensionless groups is derived by integrating Equation (4.5.1) and Equation (4.5.2) across the surface area for a specified exchanger flow arrangement. Such expressions are presented later in Table 4.5.4 for the industrially most important flow arrangements. Now we briefly describe the three methods.

In *the ε-NTU method*, the heat transfer rate from the hot fluid to the cold fluid in the exchanger is

$$q = \varepsilon C_{\min}\left(T_{h,i} - T_{c,i}\right) \tag{4.5.9}$$

Here the exchanger effectiveness ε is an efficiency factor. It is a ratio of the actual heat transfer rate from the hot fluid to the cold fluid in a given heat exchanger of any flow arrangement to the maximum possible heat transfer rate $q_{\max}$ thermodynamically permitted. The $q_{\max}$ is obtained in a *counterflow* heat exchanger (recuperator) of *infinite surface area* operating with the fluid flow rates (heat capacity rates) and fluid inlet temperatures equal to those of an actual exchanger (constant fluid properties are idealized). As noted in Table 4.5.2, the exchanger effectiveness ε is a function of NTU and C^* in this method. The number of transfer units NTU is a ratio of the overall conductance UA to the smaller heat capacity rate $C_{\min}$. NTU designates the dimensionless "heat transfer size" or "thermal size" of the exchanger. Other interpretations of NTU are given by Shah (1983). The heat capacity rate ratio C^* is simply a ratio of the smaller to the larger heat capacity rate for the two fluid streams. Note that $0 \leq \varepsilon \leq 1$, $0 \leq \text{NTU} \leq \infty$ and $0 \leq C^* \leq 1$.

The P-NTU method represents a variant of the ε-NTU method. The ε-NTU relationship is different depending upon whether the shell fluid is the $C_{\min}$ or $C_{\max}$ fluid in the stream asymmetric flow arrangements used for shell-and-tube exchangers. In order to avoid possible errors and to avoid keeping track of the $C_{\min}$ fluid side, an alternative is to present the temperature effectiveness P as a function of NTU and R, where P, NTU, and R are defined consistently either for Fluid 1 side or Fluid 2 side; in Table 4.5.2, they are defined for Fluid 1 side (regardless of whether that side is the hot or cold fluid side), and Fluid 1 side is clearly identified for each flow arrangement in Table 4.5.4; it is the shell side in a shell-and-tube exchanger. Note that

$$q = P_1 C_1 \left| T_{1,i} - T_{2,i} \right| = P_2 C_2 \left| T_{2,i} - T_{1,i} \right| \tag{4.5.10}$$

$$P_1 = P_2 R_2,\ P_2 = P_1 R_1,\ \text{NTU}_1 = \text{NTU}_2 R_2,\ \text{NTU}_2 = \text{NTU}_1 R_1,\ \text{and}\ R_1 = 1/R_2 \tag{4.5.11}$$

In *the MTD method*, the heat transfer rate from the hot fluid to the cold fluid in the exchanger is given by

$$q = UA\,\Delta T_m = UAF\,\Delta T_{\text{lm}} \tag{4.5.12}$$

where ΔT_m the log-mean temperature difference (LMTD), and F the LMTD correction factor, a ratio of true (actual) MTD to the LMTD, where

$$\text{LMTD} = \Delta T_{\text{lm}} = \frac{\Delta T_{\text{I}} - \Delta T_{\text{II}}}{\ln\left(\Delta T_{\text{I}} / \Delta T_{\text{II}}\right)} \tag{4.5.13}$$

Here ΔT_1 and ΔT_2 are defined as

$$\Delta T_{\text{I}} = T_{h,i} - T_{c,o} \quad \Delta T_{\text{II}} = T_{h,o} - T_{c,i} \qquad \text{for all flow arrangements except for parallel flow} \tag{4.5.14}$$

$$\Delta T_{\text{I}} = T_{h,i} - T_{c,i} \quad \Delta T_{\text{II}} = T_{h,o} - T_{c,o} \qquad \text{for parallel flow} \tag{4.4.15}$$

The LMTD represents a true MTD for a counterflow arrangement under the idealizations listed below. Thus, the LMTD correction factor F represents a degree of departure for the MTD from the counterflow LMTD; it does not represent the effectiveness of a heat exchanger. It depends on two dimensionless group P_1 and R_1 or P_2 and R_2 for a given flow arrangement.

The relationship among the dimensionless groups of the ε-NTU, P-NTU, and MTD methods are presented in Table 4.5.3. The closed-form formulas for industrially important exchangers are presented in terms of P_1, NTU_1, and R_1 in Table 4.5.4. These formulas are valid under idealizations which include: (1) steady-state conditions; (2) negligible heat losses to the surrounding; (3) no phase changes in the fluid streams flowing through the exchanger, or phase changes (condensation or boiling) occurring at constant temperature and constant effective specific heat; (4) uniform velocity and temperature at the entrance of the heat exchanger on each fluid side; (5) the overall extended surface efficiency η_o as uniform

TABLE 4.5.3 Relationships between Dimensionless Groups of the P-NTU and LMTD Methods and Those of the ε-NTU Method

$$\mathrm{P}_1 = \frac{C_{\min}}{C_1}\varepsilon = \begin{cases} \varepsilon & \text{for} \quad C_1 = C_{\min} \\ \varepsilon C^* & \text{for} \quad C_1 = C_{\max} \end{cases}$$

$$\mathrm{R}_1 = \frac{C_1}{C_2} = \begin{cases} C^* & \text{for} \quad C_1 = C_{\min} \\ 1/C^* & \text{for} \quad C_1 = C_{\max} \end{cases}$$

$$\mathrm{NTU}_1 = \mathrm{NTU}\frac{C_{\min}}{C_1} = \begin{cases} \mathrm{NTU} & \text{for} \quad C_1 = C_{\min} \\ \mathrm{NTU}\,C^* & \text{for} \quad C_1 = C_{\max} \end{cases}$$

$$F = \frac{\mathrm{NTU}_{\mathrm{cf}}}{\mathrm{NTU}} = \frac{1}{\mathrm{NTU}\left(1 - C^*\right)} \ln\left[\frac{1 - C^*\varepsilon}{1 - \varepsilon}\right] \xrightarrow[C^* = 1]{} \frac{\varepsilon}{\mathrm{NTU}(1 - \varepsilon)}$$

$$F = \frac{1}{\mathrm{NTU}_1\left(1 - \mathrm{R}_1\right)} \ln\left[\frac{1 - \mathrm{R}_1\mathrm{P}_1}{1 - \mathrm{P}_1}\right] \xrightarrow[\mathrm{R}_1 = 1]{} \frac{\mathrm{P}_1}{\mathrm{NTU}_1\left(1\text{-}\mathrm{P}_1\right)}$$

and constant; (6) constant individual and overall heat transfer coefficients; (7) uniformly distributed heat transfer area on each fluid side; (7) a large number of baffles in shell-and-tube exchangers; (8) no flow maldistribution; and (9) negligible longitudinal heat conduction in the fluid and exchanger wall.

The overall heat transfer coefficient can vary as a result of variations in local heat transfer coefficients due to two effects: (1) change in heat transfer coefficients in the exchanger as a result of changes in the fluid properties or radiation due to rise or drop of fluid temperatures and (2) change in heat transfer coefficients in the exchanger due to developing thermal boundary layers; it is referred to as the *length effect*. The first effect due to fluid property variations (or radiation) consists of two components: (1) distortion of velocity and temperature profiles at a given flow cross section due to fluid property variations — this effect is usually taken into account by the so-called property ratio method, with the correction scheme of Equation (4.5.45) and Equation (4.5.46) — and (2) variations in the fluid temperature along the axial and transverse directions in the exchanger depending upon the exchanger flow arrangement — this effect is referred to as the *temperature effect*. The resultant axial changes in the overall mean heat transfer coefficient can be significant; the variations in U_{local} could be nonlinear, dependent upon the type of the fluid. The effect of varying U_{local} can be taken into account by evaluating U_{local} at a few points in the exchanger and subsequently integrating U_{local} values by the Simpson or Gauss method (Shah, 1993). The temperature effect can increase or decrease mean U slightly or significantly, depending upon the fluids and applications. The length effect is important for developing laminar flows for which high heat transfer coefficients are obtained in the thermal entrance region. However, in general it will have less impact on the overall heat transfer coefficient because the other thermal resistances in series in an exchanger may be controlling. The length effect reduces the overall heat transfer coefficient compared with the mean value calculated conventionally (assuming uniform mean heat transfer coefficient on each fluid side). It is shown that this reduction is up to about 11% for the worst case (Shah, 1993).

Shah and Pignotti (1997) have shown that the following are the specific number of baffles beyond which the influence of the finite number of baffles on the exchanger effectiveness is not significantly larger than 2%: $N_b \geq 10$ for 1-1 TEMA E counterflow exchanger; $N_b \geq 6$ for 1-2 TEMA E exchanger for $\mathrm{NTU}_s \leq 2$, $R_s \leq 5$; $N_b \geq 9$ for 1-2 TEMA J exchanger for $\mathrm{NTU}_s \leq 2$, $R_s \leq 5$; $N_b \geq 5$ for 1-2 TEMA G exchanger for $\mathrm{NTU}_s \leq 3$, all R_s; $N_b \geq 11$ for 1-2 TEMA H exchanger for $\mathrm{NTU}_s \leq 3$, all R_s. Various shell-and-tube heat exchangers (such as TEMA E, G, H, J, etc.) are classified by the Tubular Exchanger Manufacturers' Association (TEMA, 1999).

If any of the basic idealizations are not valid for a particular exchanger application, the best solution is to work directly with either Equation 4.5.1 and Equation 4.5.2 or their modified form by including a particular effect, and to integrate them over a small exchanger segment numerically in which all of the idealizations are valid.

TABLE 4.5.4 $P_1 - NTU_1$ Formulas and Limiting Values of P_1 for $R_1 = 1$ and $NTU_1 \to \infty$ for Various Exchanger Flow Arrangements[a]

Flow Arrangement	Eq. no.	General formula	Value for $R_1 = 1$	Value for $NTU_1 \to \infty$
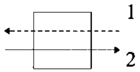	I.1.1	$P_1 = \dfrac{1-\exp[-NTU_1(1-R_1)]}{1-R_1\exp[-NTU_1(1-R_1)]}$	$P_1 = \dfrac{NTU_1}{1+NTU_1}$	$P_1 \to 1$ for $R_1 \le 1$ $P_1 \to 1/R_1$ for $R_1 \ge 1$
	I.1.2	$NTU_1 = \dfrac{1}{(1-R_1)}\ln\left[\dfrac{1-R_1P_1}{1-P_1}\right]$	$NTU_1 = \dfrac{P_1}{1-P_1}$	$NTU_1 \to \infty$
Counterflow exchanger, stream symmetric.	I.1.3	$F = 1$	$F = 1$	$F = 1$
	I.2.1	$P_1 = \dfrac{1-\exp[-NTU_1(1+R_1)]}{1+R_1}$	$P_1 = \dfrac{1}{2}[1-\exp(-2NTU_1)]$	$P_1 \to \dfrac{1}{1+R_1}$
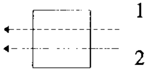	I.2.2	$NTU_1 = \dfrac{1}{1+R_1}\ln\left[\dfrac{1}{1-P_1(1+R_1)}\right]$	$NTU_1 = \dfrac{1}{2}\ln\left[\dfrac{1}{1-2P_1}\right]$	$NTU_1 \to \infty$
Parallel flow exchanger, stream symmetric.	I.2.3	$F = \dfrac{(R_1+1)\ln\left[\dfrac{1-R_1P_1}{1-P_1}\right]}{(R_1-1)\ln[1-P_1(1+R_1)]}$	$F = \dfrac{2P_1}{(P_1-1)\ln(1-2P_1)}$	$F \to 0$
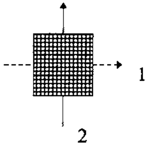	II.1	$P_1 = 1-\exp(NTU_1)$ $-\exp[-(1+R_1)NTU_1]$ $\cdot\sum_{n=1}^{\infty} R_1^n P_n(NTU_1)$	same as Eq. (II.1) with $R_1 = 1$	$P_1 \to 1$ for $R_1 \le 1$ $P_1 \to \dfrac{1}{R_1}$ for $R_1 \ge 1$
Single-pass crossflow exchanger, both fluids unmixed, stream symmetric		$P_n(y) = \dfrac{1}{(n+1)!}\sum_{j=1}^{n}\dfrac{(n+1-j)}{j!}y^{n+j}$	$P_1 \approx 1-\exp\left[\dfrac{NTU_1^{0.22}}{R_1}\left(e^{-P_1NTU_1^{0.78}}-1\right)\right]$ This approximate equation is accurate within ±1% for $1 < NTU_1 < 7$.	

TABLE 4.5.4 (continued) $P_1 - NTU_1$ Formulas and Limiting Values of P_1 for $R_1 = 1$ and $NTU_1 \to \infty$ for Various Exchanger Flow Arrangements[a]

Flow Arrangement	Eq. no.	General formula	Value for $R_1 = 1$	Value for $NTU_1 \to \infty$
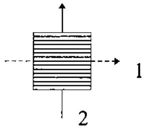	II.2.1	$P_1 = [1 - \exp(-KR_1)]/R_1$ $K = 1 - \exp(-NTU_1)$	$P_1 = 1 - \exp(-K)$ $K = 1 - \exp(-NTU_1)$	$P_1 \to \dfrac{1 - \exp(-R_1)}{R_1}$
	II.2.2	$NTU = \ln\left[\dfrac{1}{1 + \dfrac{1}{R_1}\ln(1 - R_1P_1)}\right]$	$NTU_1 = \ln\left[\dfrac{1}{1 + \ln(1 - P_1)}\right]$	$NTU_1 \to \infty$
Single-pass crossflow exchanger, fluid 1 unmixed, fluid 2 mixed.	II.2.3	$F = \dfrac{\ln[(1 - R_1P_1)/(1 - P_1)]}{(R_1 - 1)\ln\left[1 + \dfrac{1}{R_1}\ln(1 - R_1P_1)\right]}$	$F = \dfrac{P_1}{(P_1 - 1)\ln[1 + \ln(1 - P_1)]}$	$F \to 0$
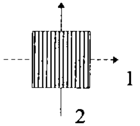	II.3.1	$P = 1 - \exp(-K/R_1)$ $K = 1 - \exp(-R_1NTU_1)$	$P = 1 - \exp(-K)$ $K = 1 - \exp(-NTU_1)$	$P_1 \to 1 - \exp(-1/R_1)$
	II.3.2	$NTU_1 = \dfrac{1}{R_1}\ln\left[\dfrac{1}{1 + R_1\ln(1 - P_1)}\right]$	$NTU_1 = \ln\left[\dfrac{1}{1 + \ln(1 - P_1)}\right]$	$NTU_1 \to \infty$
Single-pass crossflow exchanger, fluid 1 mixed, fluid 2 unmixed.	II.3.3	$F = \dfrac{\ln(1 - R_1P_1)/(1 - P_1)]}{(1 - 1/R_1)\ln[1 + R_1\ln(1 - P_1)]}$	$F = \dfrac{P_1}{(P_1 - 1)\ln[1 + \ln(1 - P_1)]}$	$F \to 0$
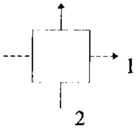	II.4	$P_1 = \left[\dfrac{1}{K_1} + \dfrac{R_1}{K_2} - \dfrac{1}{NTU_1}\right]^{-1}$	$P_1 = \left[\dfrac{2}{K_1} - \dfrac{1}{NTU_1}\right]^{-1}$	$P_1 \to \dfrac{1}{1 + R_1}$
Single-pass crossflow exchanger, both fluids mixed, stream symmetric.		$K_1 = 1 - \exp(-NTU_1)$ $K_2 = 1 - \exp(-R_1NTU_1)$		

TABLE 4.5.4 (continued) $P_1 - NTU_1$ Formulas and Limiting Values of P_1 for $R_1 = 1$ and $NTU_1 \to \infty$ for Various Exchanger Flow Arrangements[a]

Flow Arrangement	Eq. no.	General formula	Value for $R_1 = 1$	Value for $NTU_1 \to \infty$
	III.1.1	$P_1 = \frac{2}{1+R_1+E\coth(E\,NTU_1/2)}$	$P_1 = \frac{1}{1+\coth(NTU_1/\sqrt{2})/\sqrt{2}}$	$P_1 \to \frac{2}{1+R_1+E}$
		$E = \left[1+R_1^2\right]^{1/2}$		
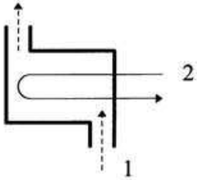	III.1.2	$NTU_1 = \frac{1}{E}\ln\left[\frac{2-P_1(1+R_1-E)}{2-P_1(1+R_1+E)}\right]$	$NTU_1 = \ln\left[\frac{2-P_1}{2-3P_1}\right]$	$NTU_1 \to \infty$
1-2 TEMA E shell-and-tube exchanger, shell fluid mixed, stream symmetric	III.1.3	$F = \frac{E\ln[(1-R_1P_1)/(1-P_1)]}{(1-R_1)\ln\left[\frac{2-P_1(1+R_1-E)}{2-P_1(1+R_1+E)}\right]}$	$F = \frac{P_1/(1-P_1)}{\ln[(2-P_1)/(2-3P_1)]}$	$F \to 0$
	IV.1.1	$P_1 = \frac{\prod_{i=1}^{n}(1-R_1P_{1,A_i}) - \prod_{i=1}^{n}(1-P_{1,A_i})}{\prod_{i=1}^{n}(1-R_1P_{1,A_i}) - R_1\prod_{i=1}^{n}(1-P_{1,A_i})}$	$P_1 = \frac{\sum_{i=1}^{n}\frac{P_{1,A_i}}{1-P_{1,A_i}}}{1+\sum_{i=1}^{n}\frac{P_{1,A_i}}{1-P_{1,A_i}}}$	same as Eq. (IV.1.1)
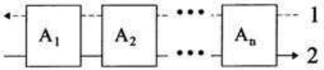	IV.1.2	$R_1 = R_{1,A_i}, \quad i = 1,\dots,n$	$1 = R_{1,A_i}, \quad i = 1,\dots,n$	same as Eq. (IV.1.2)
	IV.1.3	$NTU_1 = \sum_{i=1}^{n} NTU_{1,A_i}$	same as for Eq. (IV.1.3)	same as Eq. (IV.1.3)
Series coupling of n exchangers, overall counterflow arrangement. Stream symmetric if all A_1 are stream symmetric.	IV.1.4	$F = \frac{1}{NTU_1}\sum_{i=1}^{n} NTU_{1,A_i}F_{A_i}$	same as Eq. (IV.1.4)	same as Eq. (IV.1.4)

---

[a] In this table, all variables, except P_1, R_1, NTU_1 and F, are local or dummy variables not necessarily related to similar ones defined in the nomenclature and the text. Source: Shah, R.K. and Mueller, A.C., 1988. With permission.

Fin Efficiency and Extended Surface Efficiency.

Extended surfaces have fins attached to the primary surface on one or both sides of a two-fluid or a multifluid heat exchanger. Fins can be of a variety of geometries — plain, wavy, or interrupted — and can be attached to the inside, outside, or both sides of circular, flat, or oval tubes, or parting sheets. Fins are primarily used to increase the surface area (when the heat transfer coefficient on that fluid side is relatively low) and consequently to increase the total rate of heat transfer. In addition, enhanced fin geometries also increase the heat transfer coefficient compared to that for a plain fin. Fins may also be used on the high heat transfer coefficient fluid side in a heat exchanger primarily for structural strength purposes (for example, for high-pressure water flow through a flat tube) or to provide a thorough mixing of a highly viscous liquid (such as for laminar oil flow in a flat or a round tube). Fins are attached to the primary surface by brazing, soldering, welding, adhesive bonding, or mechanical expansion, or they are extruded or integrally connected to the tubes. Major categories of extended surface heat exchangers are plate-fin (Figure 4.5.2 to Figure 4.5.4) and tube-fin (Figure 4.5.5 to Figure 4.5.7) exchangers. Note that shell-and-tube exchangers sometimes employ individually finned tubes — low finned tubes (similar to Figure 4.5.5a but with low-height fins) (Shah, 1985).

The concept of fin efficiency accounts for the reduction in temperature potential between the fin and the ambient fluid due to conduction along the fin and convection from or to the fin surface depending upon the fin cooling or heating situation. The fin efficiency is defined as the ratio of the actual heat transfer rate through the fin base divided by the maximum possible heat transfer rate through the fin base which would be obtained if the entire fin were at the base temperature (i.e., its material thermal conductivity were infinite). Since most of the real fins are "thin", they are treated as one-dimensional (1-D) with standard idealizations used for the analysis (Huang and Shah, 1992). This 1-D fin efficiency is a function of the fin geometry, fin material thermal conductivity, heat transfer coefficient at the fin surface, and the fin tip boundary condition; it is not a function of the fin base or fin tip temperature, ambient temperature, and heat flux at the fin base or fin tip in general. Fin efficiency formulas for some common fins are presented in Table 4.5.5 (Shah, 1985). Huang and Shah (1992) also discuss the influence on η_f if any of the basic idealizations used in the fin analysis are violated.

The fin efficiency for flat fins (Figure 4.5.4b) is obtained by a sector method (Shah, 1985). In this method, the rectangular or hexagonal fin around the tube (Figure 4.5.6a and Figure 4.5.6b) or its smallest symmetrical section is divided into n sectors (Figure 4.5.12). Each sector is then considered as a circular

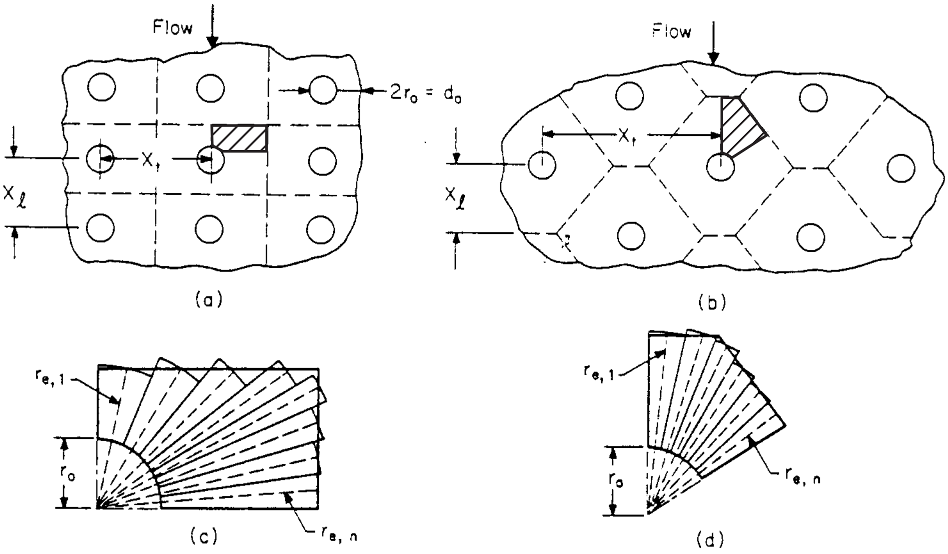

FIGURE 4.5.12 A flat fin over (a) an in-line and (b) staggered tube arrangement; the smallest representative segment of the fin for (c) an in-line and (d) a staggered tube arrangement.

TABLE 4.5.5 Fin Efficiency Expressions for Plate-Fin and Tube-Fin Geometries of Uniform Fin Thickness

Geometry	Fin Efficiency Formula $m_i = \left[\frac{2h}{k_f \delta_{f,i}}\left(1+\frac{\delta_{f,i}}{l_f}\right)\right]^{1/2} \quad E_i = \frac{\tanh(m_i l_i)}{m_i l_i} \quad i = 1, 2, 3$
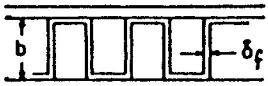 Plain, wavy, or offset strip fin of rectangular cross section	$\eta_f = E_1$ $l_1 = \frac{b}{2} - \delta_1 \quad \delta_1 = \delta_f$
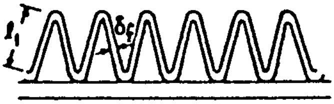 **Triangular fin heated/cooled from one side**	$\eta_f = \dfrac{hA_1(T_0 - T_a)\dfrac{\sinh(m_1 l_1)}{m_1 l_1} + q_e}{\cosh(m_1 l_1)\left[hA_1(T_0 - T_a) + q_e \dfrac{T_0 - T_a}{T_1 - T_a}\right]}$
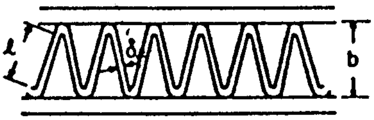 Plain, wavy, or louver fin of triangular cross section	$\eta_f = E_1$ $l_1 = \frac{l}{2} \quad \delta_1 = \delta_f$
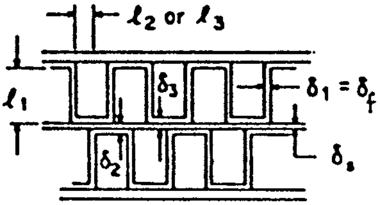 Double sandwich fin	$\eta_f = \frac{E_1 l_1 + E_2 l_2}{l_1 + l_2} \frac{1}{1 + m_1^2 E_1 E_2 l_1 l_2}$ $\delta_1 = \delta_f \quad \delta_2 = \delta_3 = \delta_f + \delta_s$ $l_1 = b - \delta_f + \frac{\delta_s}{2} \quad l_2 = l_3 = \frac{p_f}{2}$
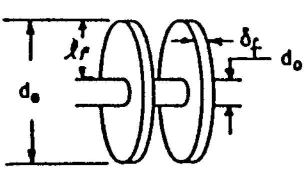 Circular fin	$\eta_j = \begin{cases} a(ml_e)^{-b} & \text{for } \Phi > 0.6 + 2.257(r^*)^{-0.445} \\ \dfrac{\tanh \Phi}{\Phi} & \text{for } \Phi \le 0.6 + 2.257(r^*)^{-0.445} \end{cases}$ $a = (r^*)^{-0.246} \quad \Phi = ml_e(r^*)^{\exp(0.13ml_e - 1.3863)}$ $b = \begin{cases} 0.9107 + 0.0893r^* & \text{for } r^* \le 2 \\ 0.9706 + 0.17125 \ln r^* & \text{for } r^* > 2 \end{cases}$ $m = \left(\frac{2h}{k_f \delta_f}\right)^{1/2} \quad l_e = l_j + \frac{\delta_f}{2} \quad r^* = \frac{d_e}{d_o}$
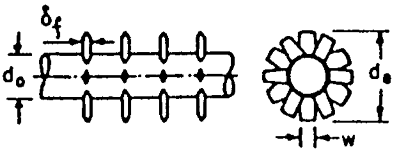 Studded fin	$\eta_j = \frac{\tanh(ml_e)}{ml_e}$ $m = \left[\frac{2h}{k_f \delta_f}\left(1+\frac{\delta_f}{w}\right)\right]^{1/2} \quad l_e = l_f + \frac{\delta_f}{2} \quad l_f = \frac{(d_e - d_o)}{2}$

fin with the radius $r_{e,i}$ equal to the length of the centerline of the sector. The fin efficiency of each sector is subsequently computed using the circular fin formula of Table 4.5.5. The fin efficiency η_f for the whole fin is then the surface area weighted average of $\eta_{f,i}$ of each sector.

$$\eta_f = \left(\sum_{i=1}^{n} \eta_{f,i} A_{f,i}\right) \Bigg/ \left(\sum_{i=1}^{n} A_{f,i}\right) \tag{4.5.16}$$

Since the heat flow seeks the path of least thermal resistance, actual η_f will be equal to or higher than that calculated by Equation (4.5.16); hence, Equation (4.5.16) yields a somewhat conservative value of η_f. For a further refinement in η_f of Figure 4.5.12, refer to Shah and Sekulić (2002).

The η_f values of Table 4.5.5 or Equation (4.5.16) are not valid in general when the fin is thick, when it is subject to variable heat transfer coefficients or variable ambient fluid temperature, or when it has a temperature depression at the fin base. See Huang and Shah (1992) for details for these cases. For a thin rectangular fin of constant cross section, the fin efficiency as presented in Table 4.5.5 is given by

$$\eta_f = \frac{\tanh(m\ell)}{m\ell} \tag{4.5.17}$$

where $m = [2h(1 + \delta_f/\ell_f)/k_f\delta_f]^{1/2}$. For a thick rectangular fin of constant cross section, the fin efficiency (a counterpart of Equation (4.5.17) is given by (Huang and Shah, 1992)

$$\eta_f = \frac{\left(\mathrm{Bi}^+\right)^{1/2}}{K\mathrm{Bi}} \tanh\left[K\left(\mathrm{Bi}^+\right)^{1/2}\right] \tag{4.5.18}$$

where $\mathrm{Bi}^+ = \mathrm{Bi}/(1 + \mathrm{Bi}/4)$, $\mathrm{Bi} = h\delta_f/2k_f$, $K = 2\ell/\delta_f$. Equation (4.5.17) is accurate (within 0.3%) for a "thick" rectangular fin having $\eta_f > 80\%$; otherwise, use Equation (4.5.18) for a thick fin.

In an extended-surface heat exchanger, heat transfer takes place from both the fins ($\eta_f < 100\%$) and the primary surface ($\eta_f = 100\%$). In that case, the total heat transfer rate is evaluated through a concept of extended surface efficiency η_o defined as

$$\eta_o = \frac{A_p}{A} + \eta_f \frac{A_f}{A} = 1 - \frac{A_f}{A}\left(1 - \eta_f\right) \tag{4.5.19}$$

where A_f is the fin surface area, A_p is the primary surface area, and $A = A_f + A_p$. In Equation (4.5.19), heat transfer coefficients over the finned and unfinned surfaces are idealized to be equal. Note that $\eta_o \geq \eta_f$ and η_o is always required for the determination of thermal resistances of Equation (4.5.5) in heat exchanger analysis.

Pressure Drop Analysis.

Usually a fan, blower, or pump is used to flow fluid through individual fluid sides of a heat exchanger. Due to potential initial and operating high cost, low fluid pumping power requirement is highly desired for gases and viscous liquids. The fluid pumping power $\wp$ is approximately related to the core pressure drop in the exchanger as (Shah, 1985).

$$\wp = \frac{\dot{m}\Delta p}{\rho\eta_p} = \begin{cases} \dfrac{1}{2g_c\eta_p}\dfrac{\mu}{\rho^2}\dfrac{4L}{D_h}\dfrac{\dot{m}^2}{D_h A_o} f\,\mathrm{Re} & \text{for fully developed laminar flow} \quad (4.5.20) \\[2ex] \dfrac{0.046}{2g_c\eta_p}\dfrac{\mu^{0.2}}{\rho^2}\dfrac{4L}{D_h}\dfrac{\dot{m}^{2.8}}{A_o^{1.8} D_h^{0.2}} & \text{for fully developed turbulent flow} \quad (4.5.21) \end{cases}$$

where η_f is pump/fan efficiency.

It is clear from Equation (4.5.20) and Equation (4.5.21) that the fluid pumping power is strongly dependent upon the fluid density ($\wp \propto 1/\rho^2$) particularly for low-density fluids in laminar and turbulent flows, and upon the viscosity in laminar flow. In addition, the pressure drop itself can be an important consideration when blowers and pumps are used for the fluid flow since they are head limited. Also for condensing and evaporating fluids, the pressure drop affects the heat transfer rate. Hence, the pressure drop determination in the exchanger is important.

The pressure drop associated with a heat exchanger consists of (1) core pressure drop, and (2) the pressure drop associated with the fluid distribution devices such as inlet and outlet manifolds, headers, tanks, nozzles, ducting, and so on, which may include bends, valves, and fittings. This second Δp component is determined from Idelchik (1994) and Miller (1990). The core pressure drop may consist of one or more of the following components depending upon the exchanger construction: (1) friction losses associated with fluid flow over heat transfer surface (this usually consists of skin friction, form (profile) drag, and internal contractions and expansions, if any); (2) the momentum effect (pressure drop or rise due to fluid density changes) in the core; (3) pressure drop associated with sudden contraction and expansion at the core inlet and outlet, and (4) the gravity effect due to the change in elevation between the inlet and outlet of the exchanger. The gravity effect is generally negligible for gases. For vertical flow through the exchanger, the pressure drop or rise ("static head") due to the elevation change is given by

$$\Delta p = \pm \frac{\rho_m g L}{g_c} \tag{4.5.22}$$

Here the "+" sign denotes vertical upflow (i.e., pressure drop), the "–" sign denotes vertical downflow (i.e., pressure rise). The first three components of the core pressure drop are now presented for plate-fin, tube-fin, plate, and regenerative heat exchangers.

Plate-fin heat exchangers. For the plate-fin exchanger (Figure 4.5.2), all three components are considered in the core pressure drop evaluation as follows:

$$\frac{\Delta p}{p_i} = \frac{G^2}{2g_c}\frac{1}{p_i\rho_i}\left[\left(1-\sigma^2+K_c\right)+f\frac{L}{r_h}\rho_i\left(\frac{1}{\rho}\right)_m+2\left(\frac{\rho_i}{\rho_o}-1\right)-\left(1-\sigma^2-K_e\right)\frac{\rho_i}{\rho_o}\right] \tag{4.5.23}$$

where f is the Fanning friction factor, K_c and K_e are flow contraction (entrance) and expansion (exit) pressure loss coefficients (see Figure 4.5.13), and σ is a ratio of minimum free flow area to frontal area. K_c and K_e for four different entrance flow passage geometries are presented by Kays and London (1998). The entrance and exit losses are important at low values of σ and L (short cores), high values of Re, and for gases; they are negligible for liquids. The values of K_c and K_e apply to long tubes for which flow is fully developed at the exit. For partially developed flows, K_c and K_e is higher than that for fully developed flows. For interrupted surfaces, flow is never a fully developed boundary layer type. For highly interrupted fin geometries, the entrance and exit losses are generally small compared to the core pressure drop and the flow is well mixed; hence, K_c and K_e for Re → ∞ should represent a good approximation. The mean specific volume v_m or $(1/\rho)_m$ in Equation (4.5.23) is given as follows. For liquids with any flow arrangement, or for a perfect gas with $C^* = 1$ and any flow arrangement (except for parallel flow),

$$\left(\frac{1}{\rho}\right)_m = v_m = \frac{v_i + v_o}{2} = \frac{1}{2}\left(\frac{1}{\rho_i}+\frac{1}{\rho_o}\right) \tag{4.5.24}$$

where v is the specific volume in m^3/kg. For a perfect gas with $C^* = 0$ and any flow arrangement,

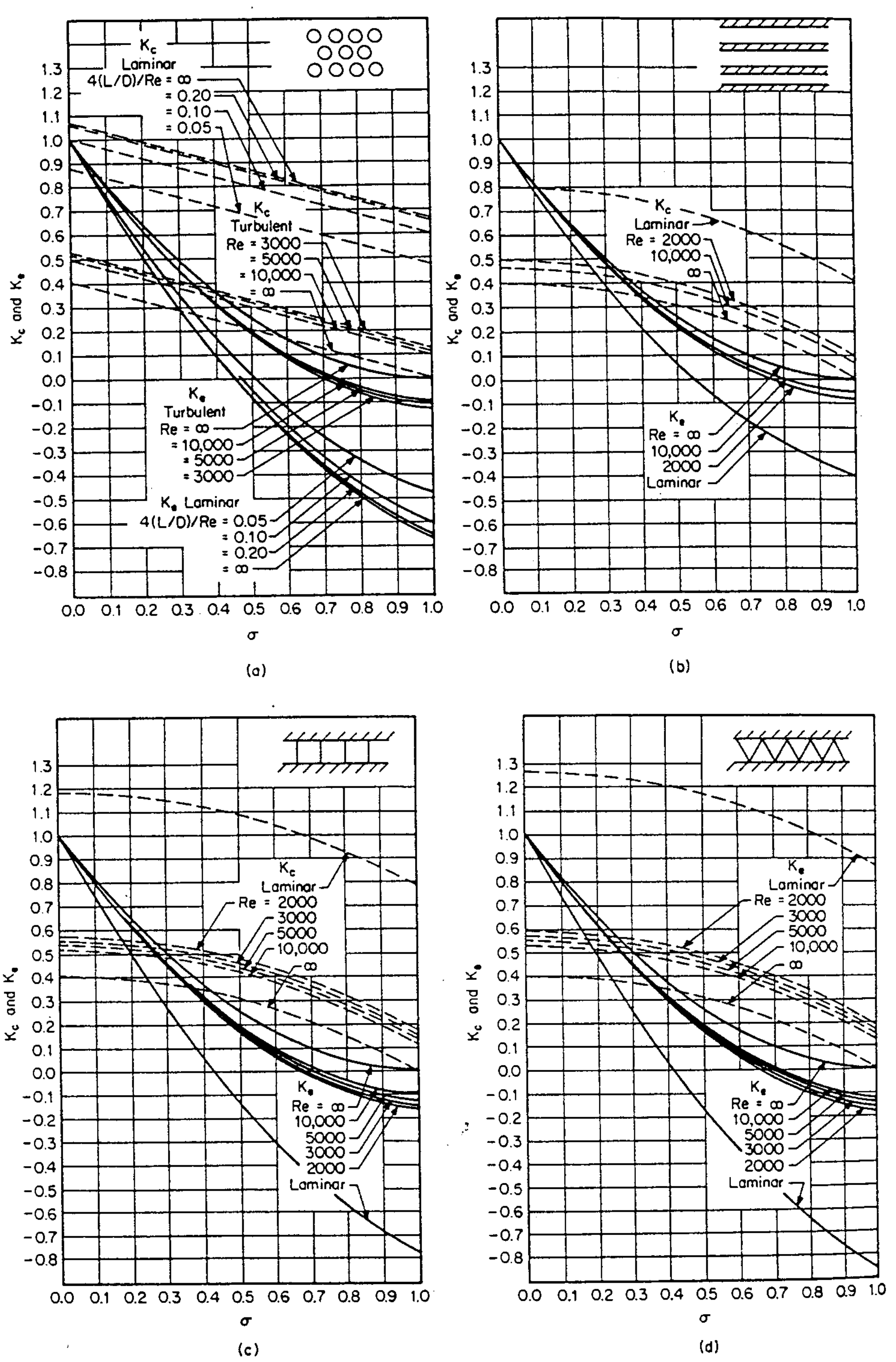

FIGURE 4.5.13 Entrance and exit pressure loss coefficients: (a) circular tubes, (b) parallel plates, (C) square passages, and (d) triangular passages. (From Kays, W.M. and London, A.L., *Compact Heat Exchangers*, 3rd ed., McGraw-Hill, New York, 1984. With permission.) For each of these flow passages, shown in the inset, the fluid flows perpendicular to the plane of the paper into the flow passages.

$$\left(\frac{1}{\rho}\right)_m = \frac{\tilde{R}}{p_{\text{ave}}} T_{\text{lm}} \tag{4.5.25}$$

Here $\tilde{R}$ is the gas constant in J/(kg K), $p_{\text{ave}} = (p_i + p_o)/2$, and $T_{\text{lm}} = T_{\text{const}} \pm \Delta T_{\text{lm}}$ where T_{const} is the mean average temperature of the evaporating (cold) or condensing (hot) fluid on the other side of the exchanger; the LMTD ΔT_{lm} is defined in Table 4.5.2. The core frictional pressure drop in Equation (4.5.23) may be approximated as

$$\Delta p = \frac{4fLG^2}{2g_c D_h}\left(\frac{1}{\rho}\right)_m \approx \frac{4fLG^2}{2g_c \rho_m D_h} \tag{4.5.26}$$

Tube-fin heat exchangers. The pressure drop inside a circular tube is computed using Equation (4.5.23) with proper values of f factors, and K_c and K_e from Figure 4.5.13 for circular tubes.

For flat fins on an array of tubes (see Figure 4.5.4b), the components of the core pressure drop (such as those in Equation 4.5.23) are the same with the following exception: the core friction and momentum effect take place within the core with $G = \dot{m}/A_o$, where A_o is the minimum free-flow area within the core, and the entrance and exit losses occur at the leading and trailing edges of the core with the associated flow area A_o' such that

$$\dot{m} = GA_o = G'A_o' \quad \text{or} \quad G'\sigma' = G\sigma \tag{4.5.27}$$

where σ' is the ratio of free-flow area to frontal area at the fin leading edges. The pressure drop for flow normal to a tube bank with flat fins is then given by

$$\frac{\Delta p}{p_i} = \frac{G^2}{2g_c}\frac{1}{p_i\rho_i}\left[f\frac{L}{r_h}\rho_i\left(\frac{1}{\rho}\right)_m + 2\left(\frac{\rho_i}{\rho_o} - 1\right)\right] + \frac{G'^2}{2g_c}\frac{1}{p_i\rho_i}\left[\left(1-\sigma'^2+K_c\right) - \left(1-\sigma'^2-K_e\right)\frac{\rho_i}{\rho_o}\right] \tag{4.5.28}$$

For individually finned tubes as shown in Figure 4.5.4a, flow expansion and contraction take place along each tube row, and the magnitude is of the same order as that at the entrance and exit. Hence, the entrance and exit losses are generally lumped into the core friction factor. Equation (4.5.23) then reduces for individually finned tubes to

$$\frac{\Delta p}{p_i} = \frac{G^2}{2g_c}\frac{1}{p_i\rho_i}\left[f\frac{L}{r_h}\rho_i\left(\frac{1}{\rho}\right)_m + 2\left(\frac{\rho_i}{\rho_o} - 1\right)\right] \tag{4.5.29}$$

Regenerators. For regenerator matrices having cylindrical passages, the pressure drop is computed using Equation (4.5.23) with appropriate values of f, K_c, and K_e. For regenerator matrices made up of any porous material (such as checkerwork, wire, mesh, spheres, copper wools, etc.), the pressure drop is calculated using Equation (4.5.29) in which the entrance and exit losses are included in the friction factor f.

Plate heat exchangers. Pressure drop in a PHE consists of three components: (1) pressure drop associated with the inlet and outlet manifolds and ports, (2) pressure drop within the core (plate passages), and (3) pressure drop due to the elevation change. The pressure drop in the manifolds and ports should be kept as low as possible (generally < 10%, but it is found as high as 25 to 30% or higher in some designs). Empirically, it is calculated as approximately 1.5 times the inlet velocity head per pass. Since the entrance and exit losses in the core (plate passages) cannot be determined experimentally, they are included in the friction factor for the given plate geometry. The pressure drop (rise) caused by the elevation change for liquids is given by Equation (4.5.22). Hence, the pressure drop on one fluid side in a PHE is given by

$$\Delta p = \frac{1.5 G_p^2 N_p}{2 g_c \rho_i} + \frac{4 f L G^2}{2 g_c D_e}\left(\frac{1}{\rho}\right)_m + \left(\frac{1}{\rho_o} - \frac{1}{\rho_i}\right)\frac{G^2}{g_c} \pm \frac{\rho_m g L}{g_c} \tag{4.5.30}$$

where $G_p = \dot{m}/(\pi/4)D_p^2$ is the fluid mass velocity in the port, N_p is the number of passes on the given fluid side and D_e is the equivalent diameter of flow passages (usually twice the plate spacing). Note that the third term on the right-hand side of the equality sign of Equation (4.5.30) is for the momentum effect which is generally negligible in liquids.

Heat Transfer and Flow Friction Correlations

Accurate and reliable surface heat transfer and flow friction characteristics are a key input to the exchanger heat transfer and pressure drop analyses or to the rating and sizing problems (Shah, 1985). Some important analytical solutions and empirical correlations are presented next for selected exchanger geometries.

The heat transfer rate in laminar duct flow is very sensitive to the thermal boundary condition. Hence, it is essential to identify carefully the thermal boundary condition in laminar flow. The heat transfer rate in turbulent duct flow is insensitive to the thermal boundary condition for most common fluids (Pr > 0.7); the exception is liquid metals (Pr < 0.03). Hence, there is generally no need to identify the thermal boundary condition in turbulent flow for all fluids except liquid metals.

Fully developed laminar flow analytical solutions for some duct shapes of interest in compact heat exchangers are presented in Table 4.5.6 for three important thermal boundary conditions denoted by the subscripts *H*1, *H*2, and *T* (Shah and London, 1978; Shah and Bhatti, 1987). Here, *H*1 denotes constant axial wall heat flux with constant peripheral wall temperature, *H*2 denotes constant axial and peripheral wall heat flux, and *T* denotes constant wall temperature. The entrance effects, flow maldistribution, free convection, property variation, fouling, and surface roughness all affect fully developed analytical solutions. In order to account for these effects in real plate-fin plain fin geometries having fully developed flows, it is best to reduce the magnitude of the analytical Nu by at least 10% and to increase the value of the analytical *f*Re by 10% for design purposes.

The initiation of transition flow, the lower limit of the critical Reynolds number ($\mathrm{Re}_{\mathrm{crit}}$), depends upon the type of entrance (e.g., smooth vs. abrupt configuration at the exchanger flow passage entrance). For a sharp square inlet configuration, $\mathrm{Re}_{\mathrm{crit}}$ is about 10 to 15% lower than that for a rounded inlet configuration. For most exchangers, the entrance configuration would be sharp. Some information on $\mathrm{Re}_{\mathrm{crit}}$ is provided by Ghajar and Tam (1994).

Transition flow and fully developed turbulent flow Fanning friction factors (within ±2% accuracy) are given by Bhatti and Shah (1987) as

$$f = \begin{cases} 0.0054 + 2.3\times10^{-8}\,\mathrm{Re}^{3/2} & \text{for } 2100 \le \mathrm{Re} \le 4000 \\ 0.00128 + 0.1143\,\mathrm{Re}^{0.3111} & \text{for } 4000 < \mathrm{Re} \le 10^7 \end{cases} \tag{4.5.31}$$

The transition flow and fully developed turbulent flow Nusselt number correlation for a circular tube is given by Gnielinski as reported in Bhatti and Shah (1987) as

$$\mathrm{Nu} = \frac{(f/2)(\mathrm{Re} - 1000)\,\mathrm{Pr}}{1 + 12.7(f/2)^{1/2}\left(\mathrm{Pr}^{2/3} - 1\right)} \tag{4.5.32}$$

which is accurate within about ±10% with experimental data for $2300 \le \mathrm{Re} \le 5 \times 10^6$ and $0.5 \le \mathrm{Pr} \le 2000$.

A careful observation of accurate experimental friction factors for all noncircular smooth ducts reveals that ducts with laminar *f*Re < 16 have turbulent *f* factors lower than those for the circular tube; whereas ducts with laminar *f*Re > 16 have turbulent *f* factors higher than those for the circular tube (Shah and

TABLE 4.5.6 Solutions for Heat Transfer and Friction for Fully Developed Laminar Flow Through Specified Ducts

Geometry ($L/D_h > 100$)	Nu_{H1}	Nu_{H2}	Nu_T	$f\mathrm{Re}$	j_{H1}/f [a]	$\mathrm{Nu}_{H1}/\mathrm{Nu}_T$
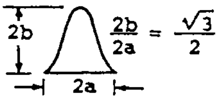 $\frac{2b}{2a} = \frac{\sqrt{3}}{2}$	3.014	1.474	2.39[b]	12.630	0.269	1.26
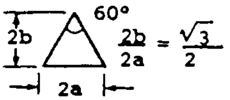 60°, $\frac{2b}{2a} = \frac{\sqrt{3}}{2}$	3.111	1.892	2.47	13.333	0.263	1.26
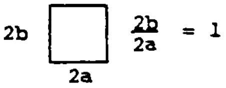 $\frac{2b}{2a} = 1$	3.608	3.091	2.976	14.227	0.286	1.21
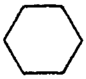	4.002	3.862	3.34[b]	15.054	0.299	1.20
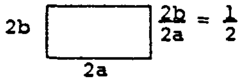 $\frac{2b}{2a} = \frac{1}{2}$	4.123	3.017	3.391	15.548	0.299	1.22
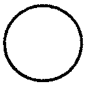	4.364	4.364	3.657	16.000	0.307	1.19
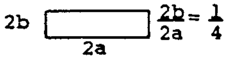 $\frac{2b}{2a} = \frac{1}{4}$	5.331	2.94	4.439	18.233	0.329	1.20
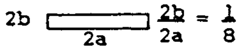 $\frac{2b}{2a} = \frac{1}{8}$	6.490	2.94	5.597	20.585	0.355	1.16
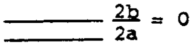 $\frac{2b}{2a} = 0$	8.235	8.235	7.541	24.000	0.386	1.09
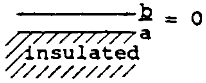 $\frac{b}{a} = 0$, insulated	5.385	—	4.861	24.000	0.253	1.11

[a] This heading is the same as $\mathrm{Nu}_{H1}\,\mathrm{Pr}^{-1/3}/f\,\mathrm{Re}$ with $\mathrm{Pr} = 0.7$.

[b] Interpolated values.

Source: Shah, R.K. and London, A.L., *Laminar Flow Forced Convection in Ducts,* Academic Press, New York, 1978. With permission.

Bhatti, 1988). Similar trends are observed for the Nusselt numbers. Within ±15% accuracy, Equation (4.5.31) and Equation (4.5.32) for f and Nu can be used for noncircular passages with the hydraulic diameter as the characteristic length in f, Nu, and Re; otherwise, refer to Bhatti and Shah (1987) for more accurate results for turbulent flow.

For hydrodynamically and thermally developing flows, the analytical solutions are boundary condition dependent (for laminar flow heat transfer only) and geometry dependent. The hydrodynamic entrance length for developing laminar flow is given by Shah and Bhatti (1987) as $L_{hy}/D_h = 0.0565\ \mathrm{Re}$; it is for developing turbulent flow given by Bhatti and Shah (1987) as $L_{hy}/D_h = 1.359\ \mathrm{Re}^{1/4}$.

Analytical results are useful for well-defined constant-cross-sectional surfaces with essentially unidirectional flows. The flows encountered in heat exchangers are generally very complex having flow separation, reattachment, recirculation, and vortices. Such flows significantly affect Nu and f for the specific exchanger surfaces. Since no analytical or accurate numerical solutions are available, the information is derived experimentally. Kays and London (1998) and Webb (1994) present most of the experimental results reported in the open literature. In the following, empirical correlations for only some important surfaces are summarized due to space limitations. Refer to Section 4.2, subsection "Heat Transfer across Tube Banks" or Shah and Sekulić (2003) for correlations for tube bundles.

Plate-Fin Extended Surfaces.

Offset strip fins. This is one of the most widely used enhanced fin geometries (Figure 4.5.14) in aircraft, cryogenics, and many other industries that do not require mass production. This surface has one of the highest heat transfer performances relative to the friction factor. The most comprehensive correlations for j and f factors for the offset strip fin geometry is provided by Manglik and Bergles (1995) as follows.

$$\begin{aligned} j = {} & 0.6522\mathrm{Re}^{-0.5403}\left(\frac{s}{h'}\right)^{-0.1541}\left(\frac{\delta_f}{l_f}\right)^{0.1499}\left(\frac{\delta_f}{s}\right)^{-0.0678} \\ & \times\left[1+5.269\times10^{-5}\,\mathrm{Re}^{1.340}\left(\frac{s}{h'}\right)^{0.504}\left(\frac{\delta_f}{l_f}\right)^{0.456}\left(\frac{\delta_f}{s}\right)^{-1.055}\right]^{0.1} \end{aligned} \tag{4.5.33}$$

$$\begin{aligned} f = {} & 9.6243\mathrm{Re}^{-0.7422}\left(\frac{s}{h'}\right)^{-0.1856}\left(\frac{\delta_f}{l_f}\right)^{0.3053}\left(\frac{\delta_f}{s}\right)^{-0.2659} \\ & \times\left[1+7.669\times10^{-8}\,\mathrm{Re}^{4.429}\left(\frac{s}{h'}\right)^{0.920}\left(\frac{\delta_f}{l_f}\right)^{3.767}\left(\frac{\delta_f}{s}\right)^{0.236}\right]^{0.1} \end{aligned} \tag{4.5.34}$$

where

$$D_h = 4A_o\Big/\left(A/l_f\right) = 4sh'l_f\Big/\left[2\left(sl_f + h'l_f + \delta_f h'\right) + \delta_f s\right] \tag{4.5.35}$$

Geometric symbols in Equation (4.5.35) are shown in Figure 4.5.14. Note that $h' = b - \delta_f$.

These correlations predict the experimental data of 18 test cores within ±20% for $120 \le \mathrm{Re} \le 10^4$. Although all the experimental data for these correlations are obtained for air, the j factor takes into consideration minor variations in the Prandtl number, and the above correlations should be valid for $0.5 < \mathrm{Pr} < 15$.

Louver fins. Louver or multilouver fins are extensively used in the auto industry because of their mass production manufacturability and hence lower cost. The louver fin has generally higher j and f factors than those for the offset strip fin geometry, and also the increase in the friction factors is in general higher than the increase in the j factors. However, the exchanger can be designed for higher heat transfer and the same pressure drop compared to that with the offset strip fins by a proper selection of exchanger frontal area, core depth, and fin density. Wang (2000) and his co-researchers have correlated experimental data of 91 test cores published in the literature and presented correlations for j and f data that are accurate within ±15% with a mean deviation of 9%.

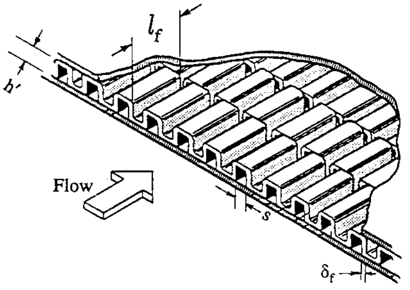

FIGURE 4.5.14 An offset strip fin geometry.

Tube-Fin Extended Surfaces.

Two major types of tube-fin extended surfaces as shown in Figure 4.5.4 are (a) individually finned tubes and (b) flat fins (also sometimes referred to as plate fins) with or without enhancements/interruptions on an array of tubes. An extensive coverage of the published literature and correlations for these extended surfaces are provided by Webb (1994), Kays and London (1984), and Rozenman (1976). Empirical correlations for some important geometries are summarized below.

Individually finned tubes. This fin geometry, helically wrapped (or extruded) circular fins on a circular tube as shown in Figure 4.5.4a, is commonly used in process and waste heat recovery industries. The following correlation for j factors is recommended by Briggs and Young (see Webb, 1994) for individually finned tubes on staggered tube banks.

$$j = 0.134\mathrm{Re}_d^{-0.319}\left(s/l_f\right)^{0.2}\left(s/\delta_f\right)^{0.11} \tag{4.5.36}$$

where l_f is the radial height of the fin, δ_f the fin thickness, $s = p_f - \delta_f$ is the distance between adjacent fins and p_f is the fin pitch. Equation (4.5.36) is valid for the following ranges: $1100 \le \mathrm{Re}_d \le 18{,}000$, $0.13 \le s/l_f \le 0.63$, $1.01 \le s/\delta_f \le 6.62$, $0.09 \le l_f/d_o \le 0.69$, $0.011 \le \delta_f/d_o \le 0.15$, $1.54 \le X_t/d_o \le 8.23$, fin root diameter d_o between 11.1 and 40.9 mm, and fin density N_f $(= 1/p_f)$ between 246 and 768 fin/m. The standard deviation of Equation (4.5.36) with experimental results was 5.1%.

For friction factors, Robinson and Briggs (see Webb, 1994) recommended the following correlation:

$$f_{tb} = 9.465\mathrm{Re}_d^{-0.316}\left(X_t/d_o\right)^{-0.927}\left(X_t/X_d\right)^{0.515} \tag{4.5.37}$$

Here $X_d = (X_t^2 + X_l^2)^{1/2}$ is the diagonal pitch, and X_t and X_l are the transverse and longitudinal tube pitches, respectively. The correlation is valid for the following ranges: $2000 \le \mathrm{Re}_d \le 50{,}000$, $0.15 \le s/l_f \le 0.19$, $3.75 \le s/\delta_f \le 6.03$, $0.35 \le l_f/d_o \le 0.56$, $0.011 \le \delta_f/d_o \le 0.025$, $1.86 \le X_t/d_o \le 4.60$, $18.6 \le d_o \le 40.9$ mm, and $311 \le N_f \le 431$ fin/m. The standard deviation of Equation (4.5.37) with correlated data was 7.8%

For crossflow over low-height finned tubes, a simple but accurate correlation for heat transfer is given by Ganguli and Yilmaz (1987) as

$$j = 0.255\mathrm{Re}_d^{-0.3}\left(d_e/s\right)^{-0.3} \tag{4.5.38}$$

A more accurate correlation for heat transfer is given by Rabas and Taborek (1987). Chai (1988) provides the best correlation for friction factors:

$$f_{tb} = 1.748\mathrm{Re}_d^{-0.233}\left(\frac{l_f}{s}\right)^{0.552}\left(\frac{d_o}{X_t}\right)^{0.599}\left(\frac{d_o}{X_1}\right)^{0.1738} \tag{4.5.39}$$

This correlation is valid for $895 < \mathrm{Re}_d < 713{,}000$, $20 < \theta < 40°$, $X_t/d_o < 4$, $N \ge 4$, and θ is the tube layout angle. It predicts 89 literature data points within a mean absolute error of 6%; the range of actual error is from –16.7 to 19.9%. Refer to Shah and Sekulić (2003) for better correlations.

Plain flat fins on a staggered tubebank. This geometry, as shown in Figure 4.5.4b, is used in air-conditioning/refrigeration industry as well as where the pressure drop on the fin side prohibits the use of enhanced/interrupted flat fins. An inline tubebank is generally not used unless very low fin side pressure drop is the essential requirement. Heat transfer correlation for Figure 4.5.4b plain flat fins on staggered tubebanks is provided by Gray and Webb (see Webb, 1994) as follows for four or more tube rows.

$$j_4 = 0.14\mathrm{Re}_d^{-0.328}\left(X_t/X_l\right)^{-0.502}\left(s/d_o\right)^{0.031} \tag{4.5.40}$$

For the number of tube rows N from 1 to 3, the j factor is lower and is given by

$$\frac{j_N}{j_4} = 0.991\left[2.24\,\mathrm{Re}_d^{-0.092}\left(N/4\right)^{-0.031}\right]^{0.607(4-N)} \tag{4.5.41}$$

Gray and Webb (see Webb, 1994) hypothesized the friction factor consisting of two components: one associated with the fins and the other associated with the tubes as follows.

$$f = \left(0.508\,\mathrm{Re}_d^{-0.521}\left(X_t/d_o\right)^{1.318}\right)\frac{A_f}{A} + f_t\left(1-\frac{A_f}{A}\right)\left(1-\frac{d_f}{p_f}\right) \tag{4.5.42}$$

and f_t (defined the same way as f) is the Fanning friction factor associated with the tube and can be determined from Eu of Figure 19 of Zukaukas (1987) as $f_t = \mathrm{Eu}N(X_t - d_o)/\pi d_o$. Equation (4.5.42) correlated 90% of the data for 19 heat exchangers within ±20%. The range of dimensionless variables of Equation (4.5.42) are $500 \le \mathrm{Re} \le 24{,}700$, $1.97 \le X_t/d_o \le 2.55$, $1.7 \le X_l/d_o \le 2.58$, and $0.08 \le s/d_o \le 0.64$.Wang (2000) and his co-researchers have presented improved correlations for j and f factors for flat fins on a staggered tubebank based on experimental data of 74 test cases. Refer to Shah and Sekulić (2003) for better correlations.

Exchanger Design Methodology

The problem of heat exchanger design is complex and multidisciplinary (Shah, 1991). The major design considerations for a new heat exchanger include process/design specifications, thermal and hydraulic design, mechanical design, manufacturing and cost considerations, and trade-offs and system-based optimization, as shown in Figure 4.5.15 with possible strong interactions among these considerations as indicated by double-sided arrows. The thermal and hydraulic design methods are mainly analytical, and the structural design is analytical to some extent. Most of the other major design considerations involve qualitative and experience-based judgments, trade-offs, and compromises. Therefore, there is no unique solution to designing a heat exchanger for given process specifications. Further details on this design methodology is given by Shah (1991) and Shah and Sekulić (2003).

Two important heat exchanger design problems are the rating and sizing problems. Determination of heat transfer and pressure drop performance of either an existing exchanger or an already sized exchanger is referred to as the rating problem. The objective here is to verify vendor's specifications or to determine the performance at off-design conditions. The rating problem is also sometimes referred to as the performance problem. In contrast, the design of a new or existing type of exchanger is referred to as the sizing problem. In a broad sense, it means the determination of the exchanger construction type, flow arrangement, heat transfer surface geometries and materials, and the physical size of an exchanger to meet the specified heat transfer and pressure drops. However, from the viewpoint of quantitative thermal-hydraulic analysis, we will consider that the selection of the exchanger construction type, flow arrangement, and materials has already been made. Thus, in the sizing problem, we will determine the physical size (length, width, height) and surface areas on each side of the exchanger. The sizing problem is also sometimes referred to as the design problem.

The step-by-step solution procedures for the rating and sizing problems for counterflow and crossflow single-pass plate-fin heat exchangers have been presented with a detailed illustrative example by Shah (1981). Shah (1988a) presented further refinements in these procedures as well as step-by-step procedures for two-pass cross-counterflow plate-fin exchangers, and single-pass crossflow and two-pass cross-counterflow tube-fin exchangers. Also, step-by-step solution procedures for the rating and sizing problems for rotary regenerators (Shah, 1988b), heat pipe heat exchangers (Shah and Giovannelli, 1988) and PHEs (Shah and Wanniarachchi, 1991) are available. As an illustration, the step-by-step solution procedures will be covered here for a single-pass crossflow exchanger.

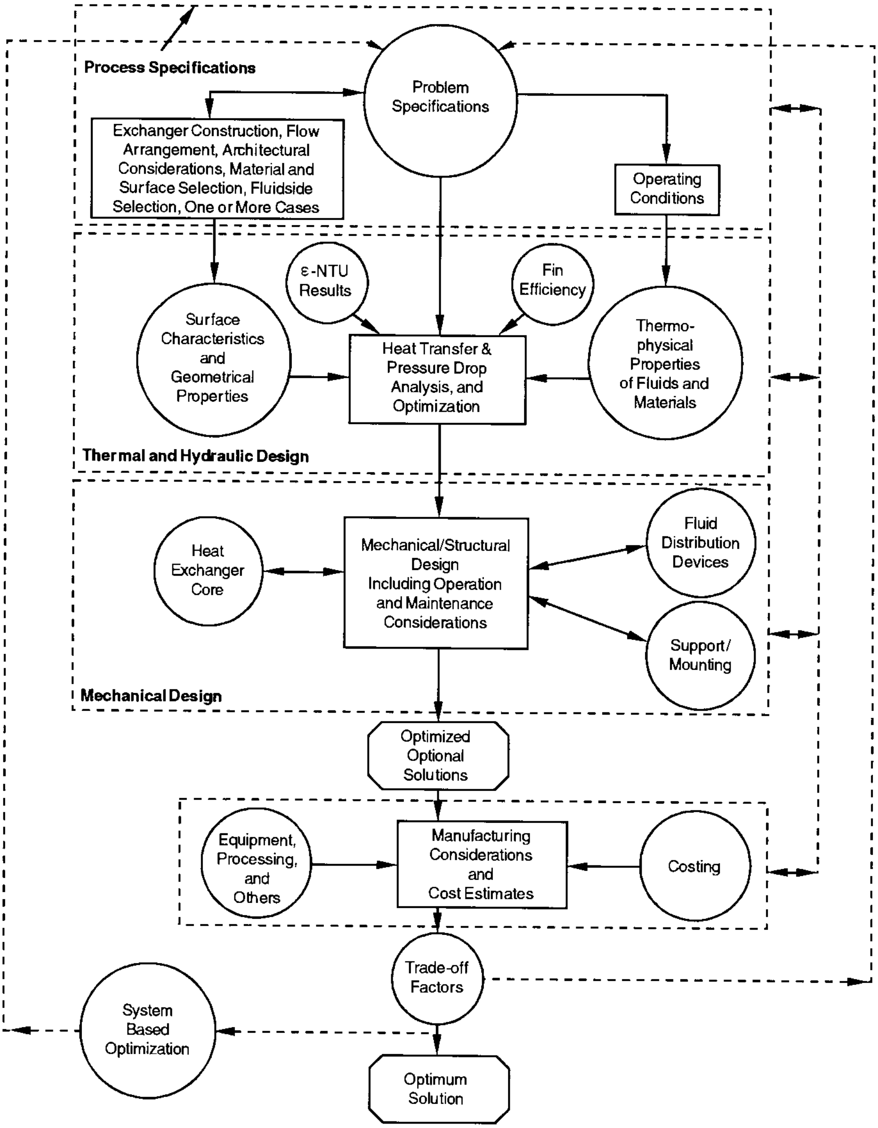

FIGURE 4.5.15 Heat exchanger design methodology.

Rating Problem for a Crossflow Plate-Fin Exchanger.

Following is a step-by-step procedure for rating a crossflow plate-fin exchanger. Inputs to the rating problem for a two-fluid exchanger are the exchanger construction, flow arrangement and overall dimensions, complete details on the materials and surface geometries on both sides including their nondimensional heat transfer and pressure drop characteristics (j and f vs. Re), fluid flow rates, inlet temperatures, and fouling factors. The fluid outlet temperatures, total heat transfer rate, and pressure drops on each side of the exchanger are then determined as the rating problem solution.

1. Determine the surface geometric properties on each fluid side. This includes the minimum free-flow area A_o, heat transfer surface area A (both primary and secondary), flow lengths L, hydraulic diameter D_h, heat transfer surface area density β, the ratio of minimum free-flow area to frontal area σ, fin length l_f, and fin thickness δ_f for fin efficiency determination, and any specialized dimensions used for heat transfer and pressure drop correlations.

2. Compute the fluid bulk mean temperature and fluid thermophysical properties on each fluid side. Since the outlet temperatures are not known for the rating problem, they are estimated initially. Unless it is known from past experience, assume an exchanger effectiveness as 50 to 75% for most single-pass crossflow exchangers, or 75 to 85% for single-pass counterflow exchangers. For the assumed effectiveness, calculate the fluid outlet temperatures.

$$T_{h,o} = T_{h,i} - \varepsilon\left(C_{\min}/C_h\right)\left(T_{h,i} - T_{c,i}\right) \qquad T_{c,o} = T_{c,i} + \varepsilon\left(C_{\min}/C_c\right)\left(T_{h,i} - T_{c,i}\right) \tag{4.5.43}$$

Initially, assume $C_c/C_h = \dot{m}_c/\dot{m}_h$ for a gas-to-gas exchanger, or $C_c/C_h = \dot{m}_c c_{p,c}/\dot{m}_h c_{p,h}$ for a gas-to-liquid exchanger with very approximate values of c_p for the fluids in question.

For exchangers with $C^* < 0.5$ (usually gas-to-gas exchangers), the bulk mean temperatures on each fluid side will be the arithmetic mean of the inlet and outlet temperatures on each fluid side (Shah, 1981). For exchangers with $C^* < 0.5$ (usually gas-to-gas exchangers), the bulk mean temperature on the $C_{\max}$ side will be the arithmetic mean of inlet and outlet temperatures; the bulk mean temperature on the $C_{\min}$ side will be the log-mean average temperature obtained as follows:

$$T_{m,C_{\min}} = T_{m,C_{\max}} \pm \Delta T_{\mathrm{lm}} \tag{4.5.44}$$

where ΔT_{lm} is the LMTD based on the terminal temperatures (see Equation 4.5.13). Use the plus sign if the $C_{\min}$ side is hot; otherwise, use the negative sign.

Once the bulk mean temperature is obtained on each fluid side, obtain the fluid properties from thermophysical property books or from handbooks. The properties needed for the rating problem are μ, c_p, k, Pr, and ρ. With this c_p, one more iteration may be carried out to determine $T_{h,o}$ or $T_{c,o}$ from Equation (4.5.43) on the $C_{\max}$ side, and subsequently T_m on the $C_{\max}$ side, and refine fluid properties accordingly.

3. Calculate the Reynolds number $\mathrm{Re} = GD_h/\mu$ and/or any other pertinent dimensionless groups (from the basic definitions) needed to determine the nondimensional heat transfer and flow friction characteristics (e.g., j or Nu and f) of heat transfer surfaces on each fluid side of the exchanger. Subsequently, compute j or Nu and f factors. Correct Nu (or j) for variable fluid property effects (Shah, 1981) in the second and subsequent iterations from the following equations.

$$\text{For gases:} \qquad \frac{\mathrm{Nu}}{\mathrm{Nu}_{\mathrm{cp}}} = \left[\frac{T_w}{T_m}\right]^{n'} \qquad \frac{f}{f_{\mathrm{cp}}} = \left[\frac{T_w}{T_m}\right]^{m'} \tag{4.5.45}$$

$$\text{For liquids:} \qquad \frac{\mathrm{Nu}}{\mathrm{Nu}_{\mathrm{cp}}} = \left[\frac{\mu_w}{\mu_m}\right]^{n'} \qquad \frac{f}{f_{\mathrm{cp}}} = \left[\frac{\mu_w}{\mu_m}\right]^{m'} \tag{4.5.46}$$

where the subscript cp denotes constant properties, and m' and n' are empirical constants provided in Table 4.5.7. Note that T_w and T_m in Equation (4.5.45) and in Table 4.5.7a and Table 4.5.7b are absolute temperatures, and T_w is computed from Equation (4.5.7).

4. From Nu or j, compute the heat transfer coefficients for both fluid streams.

$$h = \mathrm{Nu}\, k/D_h = jGc_p \mathrm{Pr}^{-2/3} \tag{4.5.47}$$

Subsequently, determine the fin efficiency η_f and the extended surface efficiency η_o

$$\eta_f = \frac{\tanh m\ell}{m\ell} \qquad \text{where} \qquad m^2 = \frac{h\tilde{P}}{k_f A_k} \tag{4.5.48}$$

TABLE 4.5.7a Property Ratio Method Exponents of Equation (4.5.45) and Equation (4.5.46) for Laminar Flow

Fluid	Heating	Cooling
Gases	$n' = 0.00$, $m' = 1.00$ for $1 < T_w/T_m < 3$	$n' = 0.0$, $m' = 0.81$ for $0.5 < T_w/T_m < 1$
Liquids	$n' = -0.14$, $m' = 0.58$ for $\mu_w/\mu_m < 1$	$n' = -0.14$, $m' = 0.54$ for $\mu_w/\mu_m > 1$

Source: Shah, R.K., in *Heat Exchangers: Thermal-Hydraulic Fundamentals and Design*, S. Kakaç et al., Eds., Hemisphere Publishing, Washington, D.C., 1981. With permission.

TABLE 4.5.7b Property Ratio Method Correlations of Exponents of Equation (4.5.45) and Equation (4.5.46) for Turbulent Flow

Fluid	Heating	Cooling
Gases	$\mathrm{Nu} = 5 + 0.012\,\mathrm{Re}^{0.83}\,(\mathrm{Pr} + 0.29)\,(T_w/T_m)^n$ $n = -[\log_{10}(T_w/T_m)]^{1/4} + 0.3$ for $1 < T_w/T_m < 5$, $0.6 < \mathrm{Pr} < 0.9$, $10^4 < \mathrm{Re} < 10^6$, and $L/D_h > 40$	$n' = 0$
	$m' = -0.1$ for $1 < T_w/T_m < 2.4$	$m' = -0.1$ (tentative)
Liquids	$n' = -0.11$[a] for $0.08 < \mu_w/\mu_m < 1$	$n' = -0.25$[a] for $1 < \mu_w/\mu_m < 40$
	$f/f_{cp} = (7 - \mu_m/\mu_w)/6$[b] or $m' = 0.25$ for $0.35 < \mu_w/\mu_m < 1$	$m' = 0.24$[b] for $1 < \mu_w/\mu_m < 2$

[a] Valid for $2 \le \mathrm{Pr} \le 140$, $10^4 \le \mathrm{Re} \le 1.25 \times 10^5$.

[b] Valid for $1.3 \le \mathrm{Pr} \le 10$, $10^4 \le \mathrm{Re} \le 2.3 \times 10^5$.

Source: Shah, R.K., in *Handbook of Heat Transfer Applications,* 2nd ed., W.M. Rohsenow, J.P. Hartnett, and E.N. Ganić, Eds., McGraw-Hill, New York, Chap. 4, Part 3, 1985.

where $\tilde{P}$ is the wetted perimeter of the fin surface. Refer to Table 4.5.5 for the η_f formulas for some additional fin geometries for a plate-fin exchanger. The extended surface efficiency η_o is then given by Equation (4.5.19). Also calculate the wall thermal resistance $R_w = \delta/A_w k_w$. Finally, compute the overall thermal conductance UA from Equation (4.5.5) knowing the individual convective film resistances, wall thermal resistances, and fouling resistances, if any.

5. From the known heat capacity rates on each fluid side, compute $C^* = C_{\mathrm{min}}/C_{\mathrm{max}}$. From the known UA, determine $\mathrm{NTU} = UA/C_{\mathrm{min}}$. Also calculate the longitudinal conduction parameter λ. With the known NTU, C^*, λ, and the flow arrangement, determine the exchanger effectiveness ε or P from either closed-form equations of Table 4.5.4 or tabular/graphical results from Kays and London (1998).
6. With this ε, finally compute the outlet temperatures from Equation (4.5.43). If these outlet temperatures are significantly different from those assumed in Step 2, use these outlet temperatures in Step 2 and continue iterating Steps 2 to 6, until the assumed and computed outlet temperatures converge within the desired degree of accuracy. For a gas-to-gas exchanger, most probably one or two iterations will be sufficient.
7. Finally, compute the heat duty q from Equation (4.5.9).
8. For the pressure drop calculations, first we need to determine the fluid densities at the exchanger inlet and outlet (ρ_i and ρ_o) for each fluid. The mean specific volume on each fluid side is then computed from Equation (4.5.24).

   Next, the entrance and exit loss coefficients, K_c and K_e, are obtained from Figure 4.5.13 for known σ, Re, and the flow passage entrance geometry.

The friction factor on each fluid side is corrected for variable fluid properties using Equation (4.5.45) or (4.5.46). Here, the wall temperature T_w is computed from

$$T_{w,h} = T_{m,h} - \left(R_h + R_{s,h}\right)q \qquad T_{w,c} = T_{m,c} + \left(R_c + R_{s,c}\right)q \tag{4.5.49}$$

where the various resistance terms are defined by Equation (4.5.5).

The core pressure drops on each fluid side are then calculated from Equation (4.5.23). This then completes the procedure for solving the rating problem.

Sizing Problem for a Crossflow Plate-Fin Exchanger.

As defined earlier, we will concentrate here to determine the physical size (length, width, and height) of a single-pass crossflow exchanger for specified heat duty and pressure drops. More specifically, inputs to the sizing problem are surface geometries (including their nondimensional heat transfer and pressure drop characteristics), fluid flow rates, inlet and outlet fluid temperatures, fouling factors, and pressure drops on each fluid side.

For the solution to this problem, there are four unknowns — two mass velocities or Reynolds numbers (to determine correct heat transfer coefficients and friction factors) and two surface areas — for the two-fluid crossflow exchanger. The following four equations (Equation (4.5.50), Equation (4.5.52), and Equation (4.5.54) are used to solve iteratively the surface areas on each fluid side: UA in Equation (4.5.50) is determined from NTU computed from the known heat duty or ε and C^*; G in Equation (4.5.52) represents two equations, for Fluids 1 and 2 (Shah, 1988a); and the volume of the exchanger in Equation (4.5.54) is the same based on the surface area density of Fluid 1 or Fluid 2.

$$\frac{1}{UA} \approx \frac{1}{\left(\eta_o hA\right)_h} + \frac{1}{\left(\eta_o hA\right)_c} \tag{4.5.50}$$

Here we have neglected the wall and fouling thermal resistances. This equation in nondimensional form is given by

$$\frac{1}{\text{NTU}} = \frac{1}{\text{ntu}_h\left(C_h/C_{\min}\right)} + \frac{1}{\text{ntu}_c\left(C_c/C_{\min}\right)} \tag{4.5.51}$$

$$G_i = \left[\frac{2g_c \Delta p}{\text{Deno}}\right]_i^{1/2} \qquad i = 1,2 \tag{4.5.52}$$

where

$$\text{Deno}_i = \left[\frac{f}{j}\frac{\text{ntu}}{\eta_o}\text{Pr}^{2/3}\left(\frac{1}{\rho}\right)_m + 2\left(\frac{1}{\rho_o} - \frac{1}{\rho_i}\right) + \left(1 - \sigma^2 + K_c\right)\frac{1}{\rho_i} - \left(1 - \sigma^2 - K_e\right)\frac{1}{\rho_o}\right]_i \tag{4.5.53}$$

$$V = \frac{A_1}{\alpha_1} = \frac{A_2}{\alpha_2} \tag{4.5.54}$$

In the iterative solutions, the first time one needs ntu_h and ntu_c to start the iterations. These can be either determined from the past experience or by estimations. If both fluids are gases or both fluids are liquid, one could consider that the design is "balanced," i.e., that the thermal resistances are distributed approximately equally on the hot and cold sides. In that case, $C_h = C_c$, and $\text{nut}_h \approx \text{ntu}_c \approx 2\text{NTU}$. Alternatively, if we have liquid on one side and gas on the other side, consider 10% thermal resistance on the liquid side, i.e., $1/(\eta_o hA)_{\text{liq}} = 0.10(1/UA)$. Then, from Equation (4.5.50) and Equation (4.5.51) with $C_{\text{gas}} = C_{\min}$, we can determine the ntu values on each side as follows: $\text{ntu}_{\text{gas}} = 1.11\text{NTU}$, $\text{ntu}_{\text{liq}} = 10C^*\text{NTU}$.

Also note that initial guesses of η_o and j/f are needed for the first iteration to solve Equation (4.5.53). For a good design, consider $\eta_o = 0.80$ and determine an approximate value of j/f from the plot of j/f vs. Re curve for the known j and f vs. Re characteristics of each fluid side surface. The specific step-by-step design procedure is as follows:

1. In order to compute the fluid mean temperature and fluid thermophysical properties on each fluid side, determine the fluid outlet temperatures from the specified heat duty

$$q = \left(\dot{m}c_p\right)_h \left(T_{h,i} - T_{h,o}\right) = \left(\dot{m}c_p\right)_c \left(T_{c,o} - T_{c,i}\right) \tag{4.5.55}$$

   or from the specified exchanger effectiveness using Equation (4.5.43). For the first time, estimate the values of c_p.

   For exchangers with $C^* \geq 0.5$, the mean temperature on each fluid side will be the arithmetic mean of inlet and outlet temperatures on each fluid side. For exchangers with $C^* < 0.5$, the mean temperature on the $C_{\max}$ side will be the arithmetic mean of the inlet and outlet temperatures on that side and the mean temperature on the $C_{\min}$ side will be the log-mean average as given by Equation (4.5.44). With these mean temperatures, determine c_p and iterate one more time for the outlet temperatures if warranted. Subsequently, determine μ, c_p, k, Pr, and ρ on each fluid side.
2. Calculate C^* and ε (if q is given), and determine NTU from the ε-NTU expression, tables, or graphical results for the selected flow arrangement (in this case, it is unmixed–unmixed crossflow, Table 4.5.4). The influence of longitudinal heat conduction, if any, is ignored in the first iteration since we don't know the exchanger size yet.
3. Determine ntu on each side by the approximations discussed in the paragrapgh after Equation (4.5.54) unless it can be estimated from the past experience.
4. For the selected surfaces on each fluid side, plot j/f vs. Re curve from the given surface characteristics and obtain an approximate value of j/f. If fins are employed, assume $\eta_o = 0.80$ unless a better value can be estimated.
5. Evaluate G from Equation (4.5.52) on each fluid side using the information from Steps 1 to 4 and the input value of Δp.
6. Calculate Reynolds number Re, and determine j and f on each fluid side from the given design data for each surface.
7. Compute h, η_f, and η_o using Equation (4.5.47), Equation (4.5.48), and Equation (4.5.19). For the first iteration, determine U_1 on Fluid 1 side from the following equation derived from Equation (4.5.5) and Equation (4.5.54).

$$\frac{1}{U_1} = \frac{1}{\left(\eta_o h\right)_1} + \frac{1}{\left(\eta_o h_s\right)_1} + \frac{\alpha_1/\alpha_2}{\left(\eta_o h_s\right)_2} + \frac{\alpha_1/\alpha_2}{\left(\eta_o h\right)_2} \tag{4.5.56}$$

   where $\alpha_1/\alpha_2 = A_1/A_2$, $\alpha = A/V$, V is the exchanger total volume, and subscripts 1 and 2 denote Fluid 1 and 2 sides. For a plate-fin exchanger, α terms are given by Shah (1981) and Kays and London (1998):

$$\alpha_1 = \frac{b_1\beta_1}{b_1 + b_2 + 2\delta} \qquad \alpha_2 = \frac{b_2\beta_2}{b_1 + b_2 + 2\delta} \tag{4.5.57}$$

Note that the wall thermal resistance in Equation (4.5.56) is ignored in the first iteration. In second and subsequent iterations, compute U_1 from

$$\frac{1}{U_1} = \frac{1}{(\eta_o h)_1} + \frac{1}{(\eta_o h_s)_1} + \frac{\delta A_1}{k_w A_w} + \frac{A_1/A_2}{(\eta_o h_s)_2} + \frac{A_1/A_2}{(\eta_o h)_2} \tag{4.5.58}$$

where the necessary geometry information A_1/A_2 and A_1/A_w is determined from the geometry calculated in the previous iteration.

8. Now calculate the core dimensions. In the first iteration, use NTU computed in Step 2. For subsequent iterations, calculate longitudinal conduction parameter λ (and other dimensionless groups for a crossflow exchanger). With known ε, C^*, and λ, determine the correct value of NTU using either a closed-form equation or tabular/graphical results (Kays and London, 1998). Determine A_1 from NTU using U_1 from the previous step and known $C_{\min}$.

$$A_1 = \text{NTU}\, C_{\min}/U_1 \tag{4.5.59}$$

and hence

$$A_2 = (A_2/A_1)A_1 = (\alpha_2/\alpha_1)A_1 \tag{4.5.60}$$

A_o from known $\dot{m}$ and G is given by

$$A_{o,1} = (\dot{m}/G)_1 \qquad A_{o,2} = (\dot{m}/G)_2 \tag{4.5.61}$$

so that

$$A_{fr,1} = A_{o,1}/\sigma_1 \qquad A_{fr,2} = A_{o,2}/\sigma_2 \tag{4.5.62}$$

where σ_1 and σ_2 are generally specified for the surface or can be computed for plate-fin surfaces from Shah (1981) and Kays and London (1998):

$$\sigma_1 = \frac{b_1\beta_1 D_{h,1}/4}{b_1 + b_2 + 2\delta} = \frac{\alpha_1 D_{h,1}}{4} \qquad \sigma_2 = \frac{b_2\beta_2 D_{h,2}/4}{b_1 + b_2 + 2\delta} = \frac{\alpha_2 D_{h,2}}{4} \tag{4.5.63}$$

Now compute the fluid flow lengths on each fluid side (see Figure 4.5.16) from the definition of the hydraulic diameter of the surface employed on each fluid side.

$$L_1 = \left(\frac{D_h A}{4A_o}\right)_1 \qquad L_2 = \left(\frac{D_h A}{4A_o}\right)_2 \tag{4.5.64}$$

Since $A_{fr,1} = L_2 L_3$ and $A_{fr,2} = L_1 L_3$, we can obtain

$$L_3 = \frac{A_{fr,1}}{L_2} \quad \text{or} \quad L_3 = \frac{A_{fr,2}}{L_1} \tag{4.5.65}$$

Theoretically, L_3 calculated from both expressions of Equation (4.5.65) should be identical. In reality, they may differ slightly because of the round-off error. In that case, consider an average value for L_3.

9. Finally, compute the pressure drop on each fluid side, after correcting f factors for variable property effects, in a manner similar to Step 8 of the Rating Problem for a Crossflow Plate-Fin Exchanger.

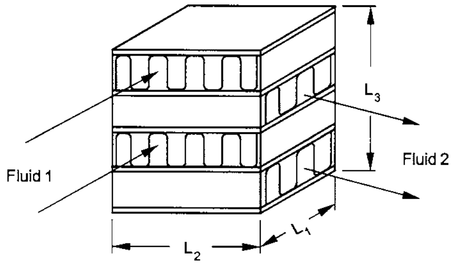

FIGURE 4.5.16 A single-pass crossflow exchanger.

10. If the calculated values of Δp are within and close to input specifications, the solution to the sizing problem is completed. Finer refinements in the core dimensions, such as integer numbers of flow passages, etc., may be carried out at this time. Otherwise, compute the new value of G on each fluid side using Equation (4.5.23) in which Δp is the input-specified value, and f, K_c, K_e, and geometric dimensions are from the previous iteration.
11. Repeat (iterate) Steps 6 to 10 until both transfer and pressure drops are met as specified. It should be emphasized that since we have imposed no constraints on the exchanger dimensions, the above procedure will yield L_1, L_2, and L_3 for the selected surfaces such that the design will meet exactly the heat duty and pressure drops on both fluid sides.

Flow Maldistribution

In the previously presented heat transfer (ε-NTU, MTD, etc. methods) and pressure drop analyses, it is presumed that the fluid is uniformly distributed through the core. In practice, flow maldistribution does occur to some extent and often severely, and may result in a significant reduction in exchanger heat transfer performance and an increase in pressure drop. Hence, it may be necessary for the designer to take into account the effect of flow maldistribution causing undesirable performance deterioration up front while designing a heat exchanger.

Some maldistributions are geometry-induced (i.e., the result of exchanger fabrication conditions, such as header design or manufacturing tolerances, or the duct geometry/structure upstream of the exchanger), and other maldistributions are the result of exchanger operating conditions. Gross, passage-to-passage and manifold-induced flow maldistributions are examples of the former category, while viscosity, natural convection, and density-difference-induced flow maldistributions are of the latter category. Flow maldistributions associated with two-phase and multiphase flow are too complex, with only limited information available in the literature. The analysis methods and results for some of the above flow maldistributions for single-phase flows are given by Shah (1985), Mueller and Chiou (1987), and Putnam and Rohsenow (1985).

Fouling in Heat Exchangers

Fouling, Its Effect, and Mechanisms.

Fouling refers to undesired accumulation of solid material (by-products of the heat transfer processes) on heat exchanger surfaces which results in additional thermal resistance to heat transfer, thus reducing exchanger performance. The fouling layer also blocks the flow passage/area and increases surface roughness, thus either reducing the flow rate in the exchanger or increasing the pressure drop or both. The foulant deposits may be loose such as magnetite particles or hard and tenacious such as calcium carbonate scale; other deposits may be sediment, polymers, coking or corrosion products, inorganic salts, biological growth, etc. Depending upon the fluids, operating conditions, and heat exchanger construction, the maximum fouling layer thickness on the heat transfer surface may result in a few hours to a number of years.

Fouling could be very costly depending upon the nature of fouling and the applications. It increases capital costs: (1) oversurfacing heat exchanger, (2) provisions for cleaning, and (3) use of special materials and constructions/surface features. It increases maintenance costs: (1) cleaning techniques, (2) chemical additives, and (3) troubleshooting. It may cause a loss of production: (1) reduced capacity and (2) shutdown. It increases energy losses: (1) reduced heat transfer, (2) increased pressure drop, and (3) dumping dirty streams. Fouling promotes corrosion, severe plugging, and eventual failure of uncleaned heat exchangers. In a fossil-fired exhaust environment, gas-side fouling produces a potential fire hazard in heat exchangers.

The following are the major fouling mechanisms:

- *Crystallization or precipitation fouling* results from the deposition/formation of crystals of dissolved substances from the liquid onto heat transfer surface due to solubility changes with temperature beyond the saturation point. If the deposited layer is hard and tenacious, it is often referred to as scaling. If it is porous and mushy, it is called sludge.
- *Particulate fouling* results from the accumulation of finely divided substances suspended in the fluid stream onto heat transfer surface. If the settling occurs as a result of gravity, it is referred to as sedimentation fouling.
- *Chemical reaction fouling* is defined as the deposition of material produced by chemical reaction (between reactants contained in the fluid stream) in which the heat transfer surface material does not participate.
- *Corrosion fouling* results from corrosion of the heat transfer surface that produces products fouling the surface and/or roughens the surface, promoting attachment of other foulants.
- *Biological fouling* results from the deposition, attachment, and growth of biological organisms from liquid onto a heat transfer surface. Fouling due to microorganisms refers to microbial fouling and fouling due to macroorganisms refers to macrobial fouling.
- *Freezing fouling* results from the freezing of a single-component liquid or higher-melting-point constituents of a multicomponent liquid onto a subcooled heat transfer surface.

Biological fouling occurs only with liquids since there are no nutrients in gases. Also crystallization fouling is not too common with gases since most gases contain few dissolved salts (mainly in mists) and even fewer inverse-solubility salts. All other types of fouling occur in both liquid and gas. More than one mechanism is usually present in many fouling situations, often with synergetic results. Liquid-side fouling generally occurs on the exchanger side where the liquid is being heated, and gas-side fouling occurs where the gas is being cooled; however, reverse examples can be found.

Importance of Fouling.

Fouling in liquids and two-phase flows has a significant detrimental effect on heat transfer with some increase in fluid pumping power. In contrast, fouling in gases reduces heat transfer somewhat (5 to 10% in general) in compact heat exchangers, but increases fluid pumping power significantly up to several hundred percent. For example, consider U = 1400 W/m^{2}K as in a process plant liquid-to-liquid heat exchanger. Hence, $R = 1/U = 0.00072$ m^{2}K/W. If the fouling factors ($r_{s,h} + r_{s,c}$) together amount to 0.00036 (considering a typical TEMA value of the fouling factor as 0.00018), 50% of the heat transfer area requirement A for given q is chargeable to fouling. However, for gas flows on both sides of an exchanger, $U \approx 280$ W/m^{2}K, and the same fouling factor of 0.00036 would represent only about 10% of the total surface area. Thus, one can see a significant impact on the heat transfer surface area requirement due to fouling in heat exchangers having high U values (such as having liquids or phase-change flows).

Considering the core frictional pressure drop (Equation (4.5.26) as the main pressure drop component, the ratio of pressure drops of fouled and cleaned exchangers is given by

$$\frac{\Delta p_F}{\Delta p_C} = \frac{f_F}{f_C}\left(\frac{D_{h,C}}{D_{h,F}}\right)\left(\frac{u_{m,F}}{u_{m,C}}\right)^2 = \frac{f_F}{f_C}\left(\frac{D_{h,C}}{D_{h,F}}\right)^5 \tag{4.5.68}$$

where the term after the second equality sign is for a circular tube and the mass flow rates under fouled and clean conditions remain the same. Generally, $f_F > f_C$ due to the fouled surface being rough. Thus, although the effect of fouling on the pressure drop is usually neglected, it can be significant, particularly for compact heat exchangers with gas flows. If we consider $f_F = f_C$, and the reduction in the tube inside diameter due to fouling by only 10 and 20%, the resultant pressure drop increase will be 69 and 205%, respectively, according to Equation (4.5.68) regardless of whether the fluid is liquid or gas! However, the resultant fluid pumping power increase will be very small for liquids compared to gases in general since now the density ratio comes into picture (water-to-air density ratio over 800:1 at ambient conditions) as found from the first equality of Equation (4.5.20).

TABLE 4.5.8 Fouling Factors and Design Parameters for Finned Tubes in Fossil Fuel Exhaust Gases

Type of Flue Gas	Fouling Factor, $m^2 K/W$	Minimum Spacing between Fins, m	Maximum Gas Velocity to Avoid Erosion, m/sec
Clean Gas (Cleaning Devices Not Required)			
Natural Gas	0.0000881–0.000528	0.00127–0.003	30.5–36.6
Propane	0.000176–0.000528	0.00178	—
Butane	0.000176–0.000528	0.00178	—
Gas turbine	0.000176	—	—
Average Gas (Provisions for Future Installation of Cleaning Devices)			
No. 2 oil	0.000352–0.000704	0.00305–0.00384	25.9–30.5
Gas turbine	0.000264	—	—
Diesel engine	0.000528	—	—
Dirty Gas (Cleaning Devices Required)			
No. 6 oil	0.000528–0.00123	0.00457–0.00579	18.3–24.4
Crude oil	0.000704–0.00264	0.00508	—
Residual oil	0.000881–0.00352	0.00508	—
Coal	0.000881–0.00881	0.00587–0.00864	15.2–21.3

Source: Weierman, R.C., 1982. Design of Heat Transfer Equipment for Gas-Side Fouling Service, Workshop on an Assessment of Gas-Side Fouling in Fossil Fuel Exhaust Environments, W.J. Marner and R.L. Webb, Eds., JPL Publ. 82-67, Jet Propulsion Laboratory, California Institute of Technology, Pasadena. With permission.

Accounting of Fouling in Heat Exchangers.

Fouling is an extremely complex phenomenon characterized by a combined heat, mass, and momentum transfer under transient condition. Fouling is affected by a large number of variables related to heat exchanger surfaces, operating conditions, and fluids. Fouling is time dependent, zero at $\tau = 0$; after the induction or delay period τ_d, the fouling resistance is either pseudolinear, falling rate, or asymptotic.

Fouling is characterized by all or some of the following sequential events: initiation, transport, attachment, removal, and aging (Epstein, 1983). Research efforts are concentrated on quantifying these events by semitheoretical models (Epstein, 1978) with very limited success on specific fouling situations. Hence, the current heat exchanger design approach is to use a constant (supposedly an asymptotic) value of the *fouling factor* or *fouling resistance* $r_s = 1/h_s$. Equation (4.5.5) presented earlier includes the fouling resistances on the hot and cold fluid sides for a tubular or nontubular extended-surface exchanger. Fouling factors for some common fluids are presented in Table 4.5.8 and Table 4.5.9.

The specification of fouling effects in a process heat exchanger is usually presented in terms of the combined fouling factor $r_{s,t}$, the cleanliness factor CF or percentage oversurface (%OS) as follows:

$$r_{s,t} = \frac{1}{U_C} - \frac{1}{U_F} \tag{4.5.69}$$

$$\mathrm{CF} = U_F / U_C \tag{4.5.70}$$

$$\%\mathrm{OS} = \left(\frac{A_F}{A_C} - 1\right)100 \tag{4.5.71}$$

Here the subscripts F and C denote fouled and clean exchanger values. From Equation (4.5.5) with $A_h = A_c = A$, $\eta_o = 1$, $\Delta T_{m,F} = \Delta T_{m,C}$, it can be shown that

$$\frac{A_F}{A_C} = \frac{U_C}{U_F} = 1 + U_C r_{s,t} \qquad r_{s,t} = \frac{1}{U_F} - \frac{1}{U_C} \tag{4.5.72}$$

In heat exchanger design, constant (supposedly an asymptotoic) values of $r_{s,h}$ and $r_{s,c}$ are used. Accordingly, extra heat transfer surface area is provided to take into account the deleterious effect of fouling. Thus, the heat exchanger will be "oversized" for the initial clean condition, "correctly sized" for asymptotic fouling (if it occurs in practice), and "undersized" just before the cleaning operation for nonasymptotic fouling.

Influence of Operating and Design Variables.

Based on operational experience and research over the last several decades, many variables have been identified that have a significant influence on fouling. The most important variables are summarized next.

Flow velocity. Flow velocity is one of the most important variables affecting fouling. Higher velocities increase fluid shear stress at the fouling deposit–fluid interface and increase the heat transfer coefficient, pressure drop and fluid pumping power. However, at the same time, increased velocity may erode the surface and may accelerate the corrosion of the surface by removing the protective oxide layer. The fouling buildup in general is inversely proportional to $u_m^{1.5}$. For water, the velocity should be kept above 2 m/sec to suppress fouling, and the absolute minimum should be above 1 m/sec to minimize fouling.

Surface temperature. Higher surface temperatures promote chemical reaction, corrosion, crystal formation (with inverse solubility salts), and polymerization, but reduce biofouling for temperatures above the optimum growth, avoid potential freezing fouling, and avoid precipitation of normal-solubility salts. It is highly recommended that the surface temperature be maintained below the reaction temperature; it should be kept below 60°C for cooling tower water.

Tube material. The selection of the tube material is important from the corrosion point of view which in turn could increase crystallization and biological fouling. Copper alloys can reduce certain biofouling, but their use is limited by environmental concerns with river, ocean, and lake waters.

There are many other variables that affect fouling. It is beyond the scope here, but the reader may refer to TEMA (1999).

Fouling Control and Cleaning Techniques.

Control of fouling should be attempted first before any cleaning method is attempted. For gas-side fouling, one should verify that fouling exists, identify the sequential event that dominates the foulant accumulation, and characterize the deposit. For liquid-side fouling, fouling inhibitors/additives should be employed while the exchanger is in operation; for example, use antidispersant polymers to prevent sedimentation fouling, "stabilizing" compounds to prevent polymerization and chemical reaction fouling, corrosion inhibitors to prevent corrosion fouling, biocide/germicide to prevent biofouling, softeners, acids, and polyphosphates to prevent crystallization fouling.

If the foulant control is not effective, the exchanger must be cleaned either on-line or off-line. On-line cleaning includes flow-driven brushes/sponge balls inside tubes, power-driven rotating brushes inside tubes, acoustic horns/mechanical vibrations for tube banks with gases, soot blowers, and shutting off of the cold gas supply, flowing hot gas, or reversing of the fluids. Off-line cleaning methods, without dismantling the exchanger include chemical cleaning (circulate acid/detergent solutions), circulating of particulate slurry (such as sand and water), and thermal melting of frost layers. Off-line cleaning with a heat exchanger opened includes high-pressure steam or water cleaning, and thermal baking of an exchanger and then rinsing for small heat exchanger modules removed from the container of the modular exchangers.

Nomenclature

A	total heat transfer area (primary + fin) on one fluid side of a heat exchanger, A_p: primary surface area, A_f: fin surface area, m^2
A_{fr}	frontal area on one fluid side of an exchanger, m^2
A_k	total wall cross-sectional area for heat conduction in fin or for longitudinal conduction in the exchanger, m^2
A_o	minimum free-flow area on one fluid side of a heat exchanger, m^2
b	plate spacing, $h' + \delta_f$, m
C	flow stream heat capacity rate with a subscript c or h, $\dot{m}c_p$, W/°C
C^*	heat capacity rate ratio, $C_{\min}/C_{\max}$, dimensionless
c_p	specific heat of a fluid at constant pressure, J/kg K
D_h	hydraulic diameter of flow passages, $4A_oL/A$, m
d_e	fin tip diameter of an individually finned tube, m
d_i, d_o	tube inside and outside diameters, respectively, m
Eu	N-row average Euler number, $\Delta p/(\rho\, u_m^2 N/2g_c)$, $\rho\Delta p g_c/(NG^2/2)$, dimensionless
F	log-mean temperature difference correction factor, dimensionless
f	Fanning friction factor, $\rho\Delta p g_c D_h/(2LG^2)$, dimensionless
f_{tb}	Row average Fanning friction factor per tube for crossflow to tubes, $\rho\Delta p g_c/(2NG^2)$, dimensionless
G	mass velocity based on the minimum free flow area, $\dot{m}/A_o$, kg/m²sec
g	gravitational acceleration, m²/sec
g_c	proportionality constant in Newton's second law of motion, $g_c = 1$ and dimensionless in SI units
h	heat transfer coefficient, W/m²K
h'	height of the offset strip fin for the η_f calculation, $b - \delta_f$, m
j	Colburn factor, $\mathrm{NuPr}^{-1/3}/\mathrm{Re}$, $\mathrm{StPr}^{2/3}$, dimensionless
k	fluid thermal conductivity, W/m K
k_f	thermal conductivity of the fin material, W/m K
k_w	thermal conductivity of the matrix (wall) material, W/m K
L	fluid flow (core or tube) length on one fluid side of an exchanger, m
ℓ	fin length for heat conduction from primary surface to the midpoint between plates for symmetric heating, see Table 4.5.5 for other definitions of ℓ, m
l_f	offset trip fin length (see Figure 4.5.14) or fin height for individually finned tubes (see circular fin in Table 4.5.5), l_f represents the fin length in the fluid flow direction for an uninterrupted fin with $l_f = L$ in most cases, m
m	fin parameter, see Table 4.5.5 for specific definitions, 1/m
$\dot{m}$	mass flow rate, kg/sec
N	number of tube rows
N_f	number of fins per meter, 1/m
N_t	total number of tubes in an exchanger
NTU	number of heat transfer units, $UA/C_{\min}$, it represents the total number of transfer units in a multipass unit, $\mathrm{NTU}_s = UA/C_{\mathrm{shell}}$, dimensionless
Nu	Nusselt number, hD_h/k, dimensionless
ntu_c	number of heat transfer units based on the cold fluid side, $(\eta_o hA)_c/C_c$, dimensionless
ntu_h	number of heat transfer units based on the hot fluid side, $(\eta_o hA)_h/C_h$, dimensionless
P	temperature effectiveness of one fluid, dimensionless
$\wp$	fluid pumping power, W
Pr	fluid Prandtl number, $\mu c_p/k$, dimensionless
p	fluid static pressure, Pa
Δp	fluid static pressure drop on one fluid side of heat exchanger core, Pa
p_f	fin pitch, m

q	heat duty, W
q_e	heat transfer rate (leakage) at the fin tip, W
q''	heat flux, W/m^2
R	heat capacity rate ratio used in the P-NTU method, $R_1 = C_1/C_2$, $R_2 = C_2/C_1$, dimensionless
R	thermal resistance based on the surface area A, compare Equation 4.5.4 and Equation 4.5.5 for definitions of specific thermal resistances, K/W
Re	Reynolds number, GD_h/μ, dimensionless
Re$_d$	Reynolds number based on the tube outside diameter, $\rho u_m d_o/\mu$, dimensionless
r_h	hydraulic radius, $D_h/4$, $A_o L/A$, m
r_s	fouling factor or fouling resistance, $1/h_s$, m^{2}K/W
St	Stanton number, h/Gc_p, dimensionless
s	distance between adjacent fins, $p_f - \delta_f$, m
T	fluid static temperature to a specified arbitrary datum, °C
T_a	ambient temperature, °C
T_o	fin base temperature, °C
T_l	fin tip temperature, °C
U	overall heat transfer coefficient, W/m^2 K
u_m	mean axial velocity in the minimum free flow area, m/sec
V	heat exchanger total volume, m^3
X_d	diagonal tube pitch, m
X_l	longitudinal tube pitch, m
X_t	transverse tube pitch, m
α	ratio of total heat transfer area on one fluid side of an exchanger to the total volume of an exchanger, A/V, m^2/m^3
β	heat transfer surface area density, a ratio of total transfer area on one fluid side of a plate-fin heat exchanger to the volume between the plates on that side, m^2/m^3
ε	heat exchanger effectiveness, it represents an overall exchanger effectiveness for a multiplass unit, dimensionless
δ	wall thickness, m
δ_f	fin thickness, m
η_f	fin efficiency, dimensionless
η_o	extended surface efficiency, defined by Equation (4.5.19), dimensionless
λ	longitudinal wall heat conduction parameter based on the total conduction area, $\lambda = k_w A_{k,t}/C_{\min} L$, $\lambda_c = k_w A_{k,c}/C_c L_c$, $\lambda_h = k_w A_{k,h}/C_h L_h$, dimensionless
μ	fluid dynamic viscosity, Pa·s
ρ	fluid density, kg/m^3
σ	ratio of free flow area to frontal area, A_o/A_{fr}, dimensionless

Subscripts

C	clean surface value
c	cold fluid side
F	fouled surface value
f	fin
h	hot fluid side
i	inlet to the exchanger
o	outlet to the exchanger
s	scale or fouling
w	wall or properties at the wall temperature
1	one section (inlet or outlet) of the exchanger
2	other section (outlet or inlet) of the exchanger

References

Bhatti, M.S. and Shah, R.K. 1987. Turbulent and transition flow convective heat transfer in ducts, in *Handbook of Single-Phase Convective Heat Transfer,* S. Kakaç, R. K. Shah, and W. Aung, Eds., John Wiley & Sons, New York, chap. 4, 166 pp.

Chai, H.C. 1988. A simple pressure drop correlation equation for low finned tube crossflow heat exchangers, *Int. Commun. Heat Mass Transfer*, 15, 95–101.

Epstein, N. 1978. Fouling in heat exchangers, in *Heat Transfer 1978*, Vol. 6, Hemisphere Publishing, New York, 235–254.

Epstein, N. 1983. Thinking about heat transfer fouling: a 5×5 matrix, *Heat Transfer Eng.*, 4(1), 43–56.

Foumeny, E.A. and Heggs, P.J. 1991. *Heat Exchange Engineering*, Vol. 2, *Compact Heat Exchangers: Techniques for Size Reduction*, Ellis Horwood Ltd., London.

Ganguli, A. and Yilmaz, S.B. 1987. New heat transfer and pressure drop correlations for crossflow over low-finned tube banks, *AIChE Symp. Ser. 257*, 83, 9–14.

Ghajar, A.J. and Tam, L.M. 1994. Heat transfer measurements and correlations in the transition region for a circular tube with three different inlet configurations, *Exp. Thermal Fluid Sci.*, 8, 79–90.

Hesselgreaves, J.E. 2001. *Compact Heat Exchangers — Selection, Design, and Operation,* Elsevier Science, Oxford, U.K.

Huang, L.J. and Shah, R.K. 1992. Assessment of calculation methods for efficiency of straight fins of rectangular profiles, *Int. J. Heat Fluid Flow*, 13, 282–293.

Idelchik, I.E. 1994. *Handbook of Hydraulics Resistance*, 3rd ed., CRC Press, Boca Raton, FL.

Kakaç, S., Ed. 1991. *Boilers, Evaporators, and Condensers*, John Wiley & Sons, New York.

Kakaç, S., Bergles, A.E., and Mayinger, F. 1981. *Heat Exchangers: Thermal-Hydraulic Fundamentals and Design*, Hemisphere Publishing, Washington, D.C.

Kakaç, S., Shah, R.K., and Bergles, A.E. 1983. *Low Reynolds Number Flow Heat Exchangers*, Hemisphere Publishing, Washington, D.C.

Kakaç, S., Bergles, A.E., and Fernandes, E.O. 1988. *Two-Phase Flow Heat Exchangers: Thermal Hydraulic Fundamentals and Design*, Kluwer Academic Publishers, Dordrecht, Netherlands.

Kays, W.M. and London, A.L. 1998. *Compact Heat Exchangers*, Reprint 3rd ed., Krieger Publishing, Malabar, FL.

Manglik, R.M. and Bergles, A.E. 1995. Heat transfer and pressure drop correlations for the rectangular offset-strip-fin compact heat exchanger, *Exp. Thermal Fluid Sci.*, 10, 171–180.

Miller, D.S. 1990. *Internal Flow Systems, 2nd ed., BHRA (Information Services),* Cranfield, Bedford, U.K.

Mueller, A.C. and Chiou, J.P. 1987. *Review of Various Types of Flow Maldistribution in Heat Exchangers*, Book No. H00394, HTD-Vol. 75, ASME, New York, 3–16.

Putnam, G.R. and Rohsenow, W.M. 1985. Viscosity induced nonuniform flow in laminar flow heat exchangers, *Int. J. Heat Mass Transfer*, 28, 1031–1038.

Rabas, T.J. and Taborek, J. 1987. Survey of turbulent forced-convection heat transfer and pressure drop characteristics of low-finned tube banks in cross flow, *Heat Transfer Eng.*, 8(2), 49–62.

Roetzel, W., Heggs, P.J., and Butterworth, D., Eds. 1991. *Design and Operation of Heat Exchangers*, Springer-Verlag, Berlin.

Rozenman, T. 1976. Heat transfer and pressure drop characteristics of dry cooling tower extended surfaces, Part I: Heat transfer and pressure drop data, Report BNWL-PFR 7-100; Part II: Data analysis and correlation, Report BNWL-PFR 7-102, Battelle Pacific Northwest Laboratories, Richland, WA.

Shah, R.K. 1981. Compact heat exchangers, in *Heat Exchangers: Thermal-Hydraulic Fundamentals and Design*, S. Kakaç, A.E. Bergles, and F. Mayinger, Eds., Hemisphere Publishing, Washington, D.C., 111–151.

Shah, R.K. 1983. Heat Exchanger Basic Design Methods, in *Low Reynolds Number Flow Heat Exchanger*, S. Kakaç, R.K. Shah and A.E. Bergles, Eds., pp. 21–72, Hemisphere, Washington, D.C.

Shah, R.K. 1985. Compact heat exchangers, in *Handbook of Heat Transfer Applications*, 2nd ed., W.M. Rohsenow, J.P. Hartnett, and E.N. Ganić, Eds., McGraw-Hill, New York, Chap. 4, Part 3.

Shah, R.K. 1988a. Plate-fin and tube-fin heat exchanger design procedures, in *Heat Transfer Equipment Design*, R.K. Shah, E.C. Subbarao, and R.A. Mashelkar, Eds., Hemisphere Publishing, Washington, D.C., 255–266.

Shah, R.K. 1988b. Counterflow rotary regenerator thermal design procedures, in *Heat Transfer Equipment Design*, R.K. Shah, E.C. Subbarao, and R.A. Mashelkar, Eds., Hemisphere Publishing, Washington, D.C., 267–296.

Shah, R.K. 1991. Multidisciplinary approach to heat exchanger design, in *Industrial Heat Exchangers*, J.-M. Buchlin, Ed., Lecture Series No. 1991-04, von Kármán Institute for Fluid Dynamics, Rhode Saint Genèse, Belgium.

Shah, R.K. 1993. Nonuniform heat transfer coefficients for heat exchanger thermal design, in *Aerospace Heat Exchanger Technology 1993*, R.K. Shah and A. Hashemi, Eds., Elsevier Science, Amsterdam, Netherlands, 417–445.

Shah, R.K. 1994. Heat exchangers, in *Encyclopedia of Energy Technology and The Environment*, A. Bision and S.G. Boots, Eds., John Wiley & Sons, New York, 1651–1670.

Shah, R.K., Bell, K.J., Mochizuki, S., and Wadekar, V. V., Eds., 1997. *Compact Heat Exchangers for the Process Industries*, Begell House, New York.

Shah, R.K. and Bhatti, M.S. 1987. Laminar convective heat transfer in ducts, in *Handbook of Single-Phase Convective Heat Transfer*, S. Kacaç, R.K. Shah, and W. Aung, Eds., John Wiley, New York, Chap. 3, 137 pp.

Shah, R.K. and Bhatti, M.S. 1988. Assessment of correlations for single-phase heat exchangers, in *Two-Phase Flow Heat Exchangers: Thermal-Hydraulic Fundamentals and Design*, S. Kakaç, A.E. Bergles, and E.O. Fernandes, Eds., Kluwer Academic Publishers, Dordrecht, The Netherlands, 81–122.

Shah, R.K. and Giovannelli, A.D. 1988. Heat pipe heat exchanger design theory, in *Heat Transfer Equipment Design*, R.K. Shah, E.C. Subbarao, and R.A. Mashelkar, Eds., Hemisphere Publishing, Washington, D.C., 609–653.

Shah, R.K. and Hashemi, A., Eds. 1993. *Aerospace Heat Exchanger Technology*, Elsevier Science, Amsterdam.

Shah, R.K., Kraus, A.D., and Metzger, D.E., Eds., 1990. *Compact Heat Exchangers — A Festschrift for Professor A.L. London*, Hemisphere, Washington, D.C.

Shah, R.K. and London, A.L. 1978. Laminar flow forced convection in ducts, Suppl. 1 to *Advances in Heat Transfer*, Academic Press, New York.

Shah, R.K. and Mueller, A.C. 1988. Heat Exchange, in *Ullmann's Encyclopedia of Industrial Chemistry*, Unit Operations II, vol. B3, chap. 2, 108 pages, VCH, Weinheim, Germany.

Shah, R.K. and Pignotti, A. 1997. The influence of a finite number of baffles on the shell-and-tube heat exchanger performance, *Heat Transfer Eng.*, 18(1), 82–94.

Shah, R.K. and Sekulić, D.P. 2003. *Fundamentals of Heat Exchanger Design*, John Wiley & Sons, New York.

Shah, R.K., Subbarao, E.C., and Mashelkar, R.A., Eds. 1988. *Heat Transfer Equipment Design*, Hemisphere Publishing, Washington, D.C.

Shah, R.K. and Wanniarachchi, A.S. 1991. Plate heat exchanger design theory, in *Industrial Heat Exchangers*, J.-M. Buchlin, Ed., Lecture Series No. 1991-04, von Kármán Institute for Fluid Dynamics, Rhode Saint Genèse, Belgium.

Taylor, M.A. 1987. *Plate-Fin Heat Exchangers: Guide to Their Specificaitons and Use*, 1st ed., HTFS, Harwell Laboratory, Oxon, U.K., rev. 1990.

TEMA, 1999. *Standards of the Tubular Exchanger Manufacturers Association*, 8th ed., Tubular Exchanger Manufacturers Association, New York.

Wang, C.C. 2000. Recent progress on the air-side performance of fin-and-tube heat exchangers, *Int. J. Heat Exchangers*, 1, 49–76.

Webb, R.L. 1994. *Principles of Enhanced Heat Transfer*, John Wiley & Sons, New York.

Weierman, R.C. 1982. Design of Heat Transfer Equipment for Gas-Side Fouling Service, Workshop on an Assessment of Gas-Side Fouling in Fossil Fuel Exhaust Environments, W.J. Marner and R.L. Webb, Eds., JPL Publ. 82-67, Jet Propulsion Laboratory, California Institute of Technology, Pasadena.

Zukauskas, A. 1987. Convective heat transfer in cross flow, in *Handbook of Single-Phase Convective Heat Transfer*, S. Kacaç, R.K. Shah, and W. Aung, Eds., John Wiley, New York, Chap. 6.

Further Information

Heat exchangers play a crucial and dominant role in many developments related to energy conservation, recovery, utilization, economic development of new energy sources, fuel cell technology, and environmental issues such as air and water pollution control, thermal pollution, waste disposal, etc. Many new and innovative heat exchangers have been developed for these and many other applications worldwide. A broad overview is provided for various heat exchangers and basic design theory for single-phase heat exchangers. For further details and study, the reader may refer to the following references: Kakaç et al. (1981; 1983; 1988), Taylor (1987), Shah et al. (1990), Foumeny and Heggs (1991), Kakaç (1991), Roetzel et al. (1991), Shah and Hashemi (1993), Shah et al. (1997), Hesselgreaves (2001), and Shah and Sekulić (2003).

Shell-and-Tube Heat Exchangers

Kenneth J. Bell

Introduction

A shell-and-tube heat exchanger is essentially a bundle of tubes enclosed in a shell and so arranged that one fluid flows through the tubes and another fluid flows across the outside of the tubes, heat being transferred from one fluid to the other through the tube wall. A number of other mechanical components are required to guide the fluids into, through, and out of the exchanger, to prevent the fluids from mixing, and to ensure the mechanical integrity of the heat exchanger. A typical shell-and-tube heat exchanger is shown in Figure 4.5.18 (TEMA, 1988), but the basic design allows many modifications and special features, some of which are described below.

1. Stationary Head-Channel
2. Stationary Head Flange-Channel or Bonnet
3. Channel Cover
4. Stationary Head Nozzle
5. Stationary Tubesheet
6. Tubes
7. Shell
8. Shell Cover
9. Shell Flange-Stationary Head End
10. Shell Flange-Rear Head End
11. Shell Nozzle
12. Shell Cover Flange
13. Floating Tubesheet
14. Floating Head Cover
15. Floating Head Cover Flange
16. Floating Head Backing Device
17. Tierods and Spacers
18. Transverse Baffles or Support Plates
19. Impingement Plates
20. Pass Partition
21. Vent Connection
22. Drain Connection
23. Instrument Connection
24. Support Saddle
25. Lifting Lug

Nomenclature of Heat Exchanger Components

For the purpose of establishing standard terminology, Figure 4.5.17 illustrates various types of heat exchangers. Typical parts and connections, for illustrative purposes only, are numbered for identification:

Shell-and-tube heat exchangers have been constructed with heat transfer areas from less than 0.1 m^2 (1 ft^2) to over 100,000 m^2 (1,000,000 ft^2), for pressures from deep vacuum to over 1000 bar (15,000 psi), for temperatures from near 0 to over 1400 K (2000°F), and for all fluid services including single-phase heating and cooling and multiphase vaporization and condensation. The key to such flexibility is the wide range of materials of construction, forming and joining methods, and design features that can be built into these exchangers (see Schlünder, Vol. 4, 1983; Saunders, 1988; and Yokell, 1990). Most shell-

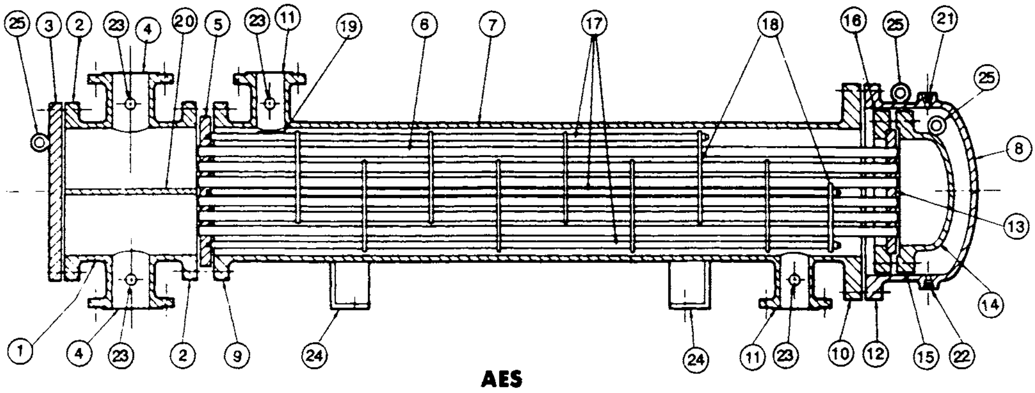

FIGURE 4.5.17 Longitudinal section of a typical shell-and-tube heat exchanger (TEMA AES) with nomenclature. (Modified from TEMA, *Standards* 7th ed., Tubular Exchanger Manufacturers Association, Tarrytown, NY, 1988.)

and-tube heat exchangers are manufactured in conformity with TEMA *Standards* (1988) and the *ASME Boiler and Pressure Vessel Code* (latest edition), but other codes and standards may apply.

Construction Features

In the design process, it is important to consider the mechanical integrity under varying operational conditions and the maintainability (especially cleaning) of the exchanger as equally important with the thermal-hydraulic design.

Tubes. Tubes used in shell-and-tube exchangers range from 6.35 mm ($^1/_4$ in.) to 50.8 mm (2 in.) and above in outside diameter, with the wall thickness usually being specified by the Birmingham wire gauge (BWG). Tubes are generally available in any desired length up to 30 m (100 ft) or more for plain tubes. While plain tubes are widely used, a variety of internally and/or externally enhanced tubes is available to provide special heat transfer characteristics when economically justified (see subsection on enhancement in Section 4.8). Low fin tubes having circumferential fins typically 0.8 to 1.6 mm (0.032 to 0.062 in.) high, spaced 630 to 1260 fins/m (16 to 32 fins/in.) are often employed, especially when the shell-side heat transfer coefficient is substantially smaller than the tube-side coefficient. The outside heat transfer area of a low fin tube is three to six times the inside area, resulting in a smaller heat exchanger shell for the same service, which may offset the higher cost of the tube per unit length.

The tubes are inserted into slightly oversized holes drilled (or, occasionally, punched) through the tubesheets (items 5 and 13, Figure 4.5.17). The tubes are secured by several means, depending upon the mechanical severity of the application and the need to avoid leakage between the streams. In some low-severity applications, the tubes are roller-expanded into smooth holes in the tubesheet. For a stronger joint, two shallow circumferential grooves are cut into the wall of the hole in the tubesheet and the tube roller-expanded into the grooves; to eliminate the possibility of leakage, a seal weld can be run between the outer end of the tube and the tubesheet. Alternatively, the tubes may be strength-welded into the tubesheet.

Tube Supports. It is essential to provide periodic support along the length of the tubes to prevent sagging and destructive vibration caused by the fluid flowing across the tube bank. A secondary role played by the tube supports is to guide the flow back and forth across the tube bank, increasing the velocity and improving the heat transfer on the shell side (but also increasing the pressure drop). The tube support is usually in the form of single segmental baffles (item 18 in Figure 4.5.17) — circular plates with holes drilled to accommodate the tubes and with a segment sheared off to form a “window” or “turnaround” to allow the shell-side fluid to pass from one cross-flow section to the next. The baffles must overlap at least one full row of tubes to give the bundle the necessary rigidity against vibration. When minimizing shell-side pressure drop is not a priority, a baffle cut of 15 to 25% of the shell inside diameter is customary. Baffle spacing is determined first by the necessity to avoid vibration and secondarily to approximately match the free cross-flow area between adjacent baffles to the flow area in the window; i.e., small baffle cuts correspond to closer baffle spacing.

In situations such as low-pressure gas flows on the shell side where pressure drop is severely limited, double segmental and strip baffle arrays can be used. More recently, a helical baffle arrangement has been introduced (Kral et al., 1996) which causes the shell-side fluid to spiral through the exchanger giving improved heat transfer vs. pressure drop characteristics. Where vibration prevention and/or minimum pressure drop are the main concerns, grids of rods or strips can be used (Gentry et al., 1982).

Shells. The shell is the cylinder which confines the shell-side fluid (item 7 in Figure 4.5.17), fitted with nozzles for fluid inlet and exit. Diameters range from less than 50 mm (2 in.) to 3.05 m (10 ft) commonly, and at least twice that value for special applications. In diameters up to 610 mm (24 in.), shells are usually made from standard pipe or tubular goods by cutting to the desired length; in larger sizes, metal plates are rolled to the desired diameter and welded.

A variety of nozzle arrangements are used for special purposes, and TEMA has a standard code to identify the major types, as well as the various front and rear head configurations on the tube side. Figure 4.5.18 shows these configurations with the corresponding code letters.

The E shell (center column, top) has the nozzles on opposite ends of the shell and is the most common configuration. It is used for any of the thermal services (single-phase heating or cooling, vaporization, and condensation). The nozzles may be on opposite sides of the shell as shown, or on the same side; the choice is largely determined by plumbing convenience. The E shell allows countercurrent flow (see below) of the two streams if there is one tube-side pass (i.e., the tube-side fluid flows through all of the tubes in parallel).

The F shell has both nozzles at one end of the shell and uses a longitudinal baffle on the shell side (shown dashed in the drawing) to force the shell-side fluid to flow to the far end of the heat exchanger and then back to the exit nozzle on the other side of the longitudinal baffle. Ideally, this allows countercurrent flow of the two streams if there are two tube-side passes (i.e., the tube-side fluid flows through half of the tubes in one direction, is turned around in the rear head, and returns through the other half of the tubes — see discussion of head types below). However, the longitudinal baffle must be carefully sealed to the shell to prevent leakage of the shell-side fluid across it; this is done by welding the longitudinal baffle to the shell and front tubesheet (which limits some design options) or by using mechanical seals. The F shell is mainly used for sensible heat transfer services.

The G shell has both nozzles at the center of the shell, with a centrally located longitudinal baffle to force the fluid to the ends of the shell before returning. While the G shell is used for all services, its main application is as a shellside vaporizer with either forced or natural (thermosiphon) convection of the boiling fluid; in the latter service, limited leakage across the baffle generally does not greatly degrade the thermal performance and the longitudinal baffle does not need to be perfectly sealed against the shell.

The H shell is effectively a double G shell and is employed in the same services. It is considered when the calculated shell-side pressure drop for a G arrangement is too high and threatens to limit the circulation rate.

The J shell, with one nozzle on top of the shell and two on the bottom, or vice versa, is commonly used in vacuum-condensing applications because of its low pressure drop. Two J shells (one inverted) may be mated in series for long-condensing-range mixtures. The nozzles are usually different diameters, with the large diameter accommodating the inlet vapor. The baffles are vertically cut.

The K shell (or kettle reboiler or flooded chiller) is exclusively intended for vaporization of liquid on the shell side, with a condensing vapor (usually steam) or a hot liquid on the tube side as the heating medium. The tubesheet diameter is large enough to accommodate the tube bundle, but the shell transitions to a larger diameter to allow the vapor to disengage from the liquid pool and exit from the top nozzle. A weir or other level control is used to maintain the liquid level, usually just above the top tubes in the bundle.

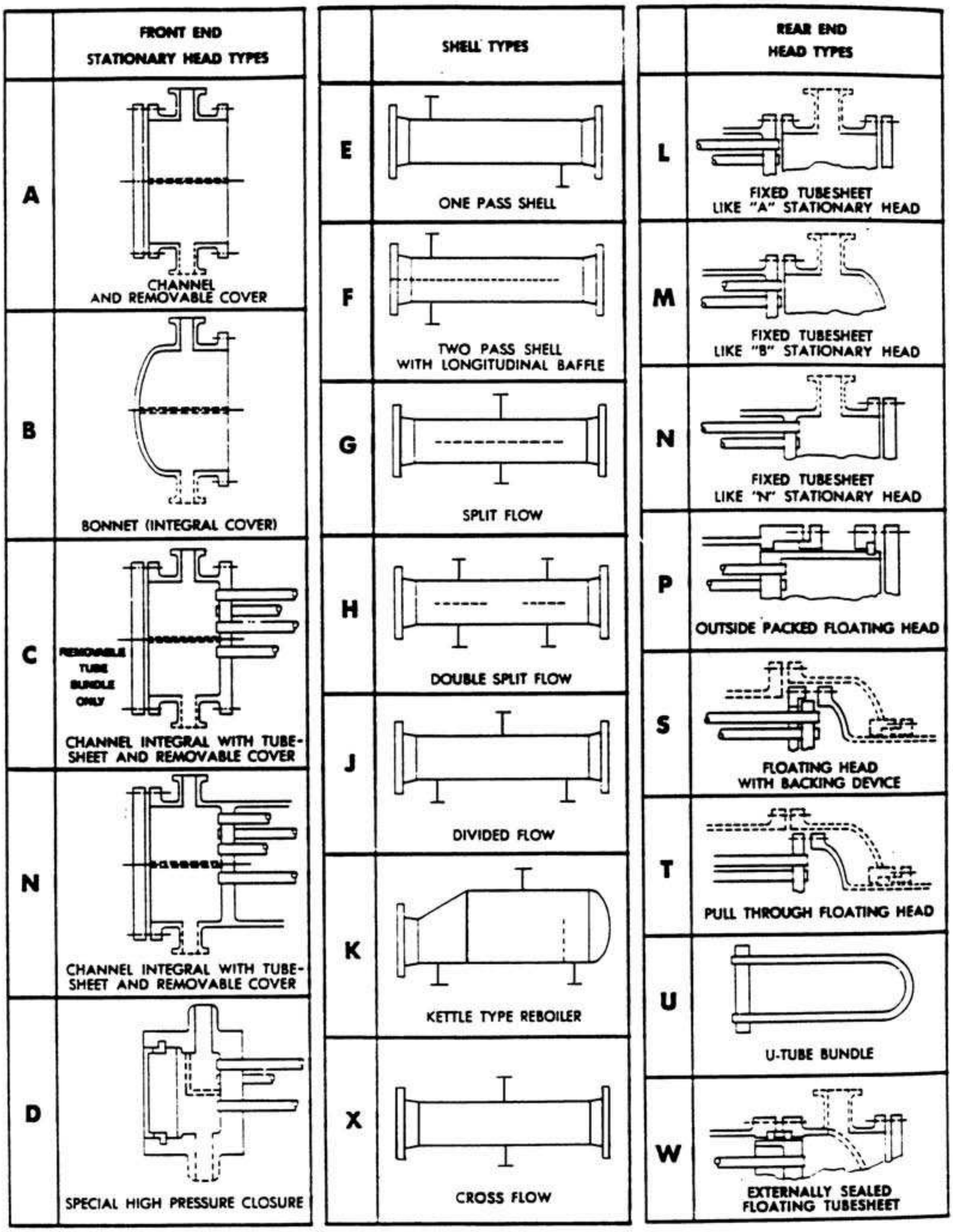

FIGURE 4.5.18 TEMA nomenclature for shell and tube configurations. (From TEMA, *Standards,* 7th ed., Tubular Exchanger Manufacturers Association, Tarrytown, NY, 1988. With permission.)

The X shell is intended to provide a well-distributed cross flow of the shell-side fluid, the fluid usually entering at the top and exiting at the bottom but occasionally used for upflow or horizontal cross flow. To obtain good distribution, multiple nozzles from a properly designed manifold may be required. Alternatively, the upper tubes in the bundle may be omitted to allow internal redistribution, or a large plenum chamber may be welded to the top of the shell ("vapor dome" or "bathtub nozzle"), or a diverging transition section may be placed between the inlet piping and the top of the shell. The tube supports may be complete circles since there is little or no longitudinal shell-side flow. The X shell gives the lowest shell-side pressure drop of any configuration and is often used for low-pressure vapor condensers.

Front Head. TEMA recognizes several front head designs as shown in the first column of Figure 4.5.18. Any of these designs will get the tube-side fluid into the tubes, but each has special features which recommend it to meet special needs. In Figure 4.5.18 the dashed lines indicate optional features depending upon need.

The A head, a channel with removable cover, bolts directly to the shell flange as shown in Figure 4.5.17, the tubesheet in that case being held between them and sealed with gaskets. Alternatively, the tubesheet may be integral with the shell (see the L rear head in Figure 4.5.18). A removable channel cover permits inspection, cleaning, removal, and replacement of tubes without disturbing the piping. The dashed lines at the center and the lower nozzle indicate that a pass partition plate may be welded in the channel (and gasketed against the tubesheet and channel cover) to provide for two tube-side passes (as shown in Figure 4.5.17 and required by the F shell design). Additional pass partitions may be provided to allow four, six, or any even number of tube-side passes. This permits the designer to utilize the available tube-side pressure drop to increase velocity, improve the heat transfer coefficient, and possibly reduce fouling. A second nozzle is required on the channel for multipass designs.

The B, or bonnet, front head reduces the number of gasketed joints and thus the opportunity for leakage, but it does not permit inspection of the tubes without breaking the piping connection. It is generally less expensive than the A head.

C and N heads retain the removable cover feature of the A head but, respectively, replace the channel-to-tubesheet and the tubesheet-to-shell gasketed connections with welds to minimize leakage possibilities. The N head is particularly used in nuclear services.

The D head is mainly used in feed-water heater applications where tube-side pressures are in the 100 to 400 bar range. The internal partition (optional) need only withstand the 1 to 2 bar pressure drop through the tubes so it can be of lightweight construction. The high-pressure closure against the atmosphere uses a shear key ring to lock the main closure in place.

Rear Head. A variety of rear head designs are used in shell-and-tube exchangers, primarily because of the need to accommodate thermally induced stresses. During operation, the tubes and the shell have different temperatures and therefore will expand (or try to) different amounts, even if there were no residual stresses in the exchanger before start-up and even if the entire exchanger is made out of the same material. The thermal stress problem is exacerbated if there are residual stresses, or if the exchanger is made of different materials, or during transient operation (including start-up and shutdown). If the temperature differences are small, the structure may be able to accommodate the thermal stresses safely; usually, however, it is necessary to make specific provision to allow the shell and the tubes to expand or contract independently. Failure to do so can result in buckling, bending, or even rupture of the shell or the tubes, or destruction of the tube-to-tubesheet joint.

A simple solution is to incorporate an expansion joint or a bellows into the shell (or in certain special applications, into the tube-side piping internal to the shell cover). However, this solution cannot cover the entire range of pressures and temperature differences encountered in practice. Further, it is usually possible to incorporate other desirable features, such as removable bundles, with thermal stress relief in the variety of rear head designs available. These are shown in the last column of Figure 4.5.18.

The L and M rear heads correspond to the A and B front heads previously described. As shown, they require a fixed tubesheet design; that is, the tubesheets are rigidly fastened to the shell, and thermal stress relief, if necessary, must be provided by a shell-side expansion joint or bellows. The tube bundle cannot be removed for inspection or mechanical cleaning on the shell side. However, the outer tube limit (OTL) — the diameter of the tube field circumscribing the outermost tubes in the bundle — can be as little as 0.4 in. (10 mm) less than the inside diameter of a pipe shell and 0.5 in. (12.7 mm) for a rolled shell. Therefore, the tube field can be very full, giving more tubes and minimizing bypass flow. Similar comments apply to the N rear head, except that more clearance must be left between the outermost tubes and the shell.

The type P head uses packing between the skirt on the rear tubesheet and the shell extension to seal the shell-side fluid against leakage. The compression on the packing has to be adjusted to prevent excessive leakage on the one hand and to allow limited movement of the tube-side head on the other, so the shell-side fluid must be benign and cheap (not surprisingly, it is often cooling water). On the other hand, leakage between the two fluids can occur only through tube hole leaks. Because of the tubesheet skirt, clearance between the outermost tubes and the shell must increase compared with types L or M; accordingly, fewer tubes are possible in a given shell, and sealing strips to partially block the bundle-to-shell bypass stream are recommended. When the floating head cover and packing gland are removed, the tube bundle can be pulled out of the shell for inspection and cleaning.

The TEMA S split-ring floating head design uses a split backing ring to hold the floating head cover and its gasket to the tubesheet. The split backing ring is bolted to the cover with a bolt circle outside the diameter of the tubesheet. Therefore, when the split ring is removed, the entire tube bundle may be pulled out of the shell. Tube count is similar to type P design and sealing strips are recommended. Usually, the split-ring floating head is used with an even number of tube passes so that a plain bonnet-type shell cover can be used. However, as shown by the dashed lines in Figure 4.5.18, single tube-side pass design (and counter-current flow) can be achieved by use of a packing gland on the exit piping through the bonnet; alternatively, a deep bonnet can be used together with an expansion joint or bellows on the tube-side exit piping.

The pull-through floating head, type T, uses a floating head cover that flanges directly to the tubesheet, reducing the possibility of internal leakage compared with type S, but also eliminating more tubes around the periphery. Sealing strips are a virtual necessity. Single tube-side pass design is similar to type S, but is rarely used.

TEMA type U uses a bundle of U tubes and hence requires no rear head at all. The U-tube bundle effectively eliminates the thermal stress problem between shell and tubes, because each tube is free to expand or contract independently. The U bundle is also the cheapest construction because the cost of a second tubesheet is avoided. However, there are a number of drawbacks: designs must have an even number of tube-side passes, mechanical cleaning of the smaller bend radius tubes in the U bend is impossible, individual tubes cannot be replaced except in the outer row, some tube count is lost because of minimum bend limits, and the U bend must be carefully supported against vibration or kept out of the cross-flow stream by placing the shell nozzle upstream of the bend. The tube side in the U bend is susceptible to erosion, especially with two-phase or particulate-containing fluids.

Type W uses two sets of packing, often with a lantern ring in between. This construction is generally limited to benign fluids and low to very moderate pressures and temperatures.

Other Features. Numerous other components are necessary or optional to construction of shell-and-tube exchangers. Probably the most complete discussion is given by Yokell (1990).

Principles of Design

Design Logic. The design of a shell-and-tube exchanger involves the following steps:

1. Selection of a set of design features which are required for mechanical integrity and ease of maintenance, and which will likely lead to satisfying the thermal requirements within the allowable pressure drops, and at lowest cost.
2. Selection of a set of dimensions for the actual exchanger.
3. For the dimensions selected in (2), calculation of the thermal performance of the heat exchanger and both tube-side and shell-side pressure drops, using available rating procedures.
4. Comparison of the thermal performance calculated in (3) with that required and examination of the pressure drops calculated in (3) to ensure that the allowed pressure drops are reasonably used but not exceeded.
5. Adjustment of the dimensions selected in (2) and repetition of steps (3) and (4) until the criteria are satisfied.
6. Completion of the mechanical design to satisfy code requirements.
7. Cost estimation.

Basic Design Equations. The basic design equation for a shell-and-tube exchanger in steady-state service is

$$A^* = \int_0^{q_T} \frac{dq}{U^*\left(T_h - T_c\right)} \tag{4.5.73}$$

where A^* is the heat transfer area required in the heat exchanger, m^2 (ft^2); q_T is the heat transfer rate of the heat exchanger, W (Btu/hr); U^* is the local overall heat transfer coefficient referenced to area A^*, W/m^2 K (Btu/hr ft^2 °F); and T_h and T_c are the local hot and cold stream temperatures, K (°F). The * superscript on A^* and U^* only means that a consistent reference area must be used in defining these terms. For example, for an exchanger with plain tubes, it is customary to use the total outside heat transfer area of all of the tubes in the exchanger, A_o, as the reference area, and then U_o is the overall heat transfer coefficient referenced to A_o. If the exchanger has low-finned tubes, A^* may refer either to the total outside area including fins or to the inside tube heat transfer area; the choice is optional, but must be spelled out. Since T_h and T_c generally vary with the amount of heat transferred (following the first law of thermodynamics, and excepting isobaric phase transition of a pure component) and U^* may vary with local heat transfer conditions, in principle Equation 4.5.73 must be numerically integrated with T_h, T_c, and U^* calculated along the path of integration, and this process is performed by the most-advanced computer-based design methods.

For many applications, certain reasonable assumptions can be made allowing the analytical integration of Equation 4.5.73 to give (Schlünder, Vol. 1, 1983; Hewitt et al., 1994)

$$A^* = \frac{q_T U^*}{(\mathrm{MTD})} \tag{4.5.74}$$

where MTD is the mean temperature difference for the particular flow conditions and configuration. The key assumptions are that there is no significant bypassing of fluid around the heat transfer surface, that the overall heat transfer coefficient is constant, and that the specific heats of the two streams are constant over their temperature ranges in the exchanger; isothermal phase transitions, such as vaporizing or condensing a pure component at constant pressure, are also allowed.

If the two streams are in countercurrent flow, i.e., if they flow always in the opposite direction to one another,

$$\mathrm{MTD} = (\mathrm{LMTD})_{\text{countercurrent}} = \frac{\left(T_{h,i} - T_{c,o}\right) - \left(T_{h,o} - T_{c,i}\right)}{\ln\left(\dfrac{T_{h,i} - T_{c,o}}{T_{h,o} - T_{c,i}}\right)} \tag{4.5.75}$$

where $(\mathrm{LMTD})_{\text{countercurrent}}$ is the "logarithmic mean temperature difference for countercurrent flow" and the subscripts i and o indicate "inlet" and "outlet," respectively. E shells with a single tube-side pass and F shells with two tube-side passes are almost always designed for countercurrent flow. (While the flow between adjacent baffles is basically cross flow, it can be shown that the total shell-side flow pattern is equivalent to countercurrent flow if there are more than three or four baffles).

Very occasionally, usually when close control of tube wall temperatures is required, cocurrent flow is specified, with the two streams flowing in the same direction through the exchanger. For this case,

$$\mathrm{MTD} = (\mathrm{LMTD})_{\text{cocurrent}} = \frac{\left(T_{h,i} - T_{c,i}\right) - \left(T_{h,o} - T_{c,o}\right)}{\ln\left(\dfrac{T_{h,i} - T_{c,i}}{T_{h,o} - T_{c,o}}\right)} \tag{4.5.76}$$

where the symbols have the same meaning as before. $(\text{LMTD})_{\text{countercurrent}}$ is always equal to or greater than $(\text{LMTD})_{\text{cocurrent}}$, so wherever possible, countercurrent design and operation is preferred.

However, most shell-and-tube exchangers have nozzle and tube pass configurations which lead to mixed countercurrent and cocurrent flow regions (as well as cross flow in the X shell). For these cases,

$$\text{MTD} = F(\text{LMTD})_{\text{countercurrent}} \tag{4.5.77}$$

where $(\text{LMTD})_{\text{countercurrent}}$ is calculated from Equation (4.5.75) and F is the "configuration correction factor" for the flow configuration involved. F has been found as a function of dimensionless temperature ratios for most flow configurations of interest and is given in analytical and/or graphical form in the earlier part of this section by Shah and in many heat transfer references (e.g., Schlünder, Vol. 1, 1983). F is equal to unity for pure countercurrent flow and is less than unity for all other cases; practical considerations limit the range of interest to values above 0.7 at the lowest and more comfortably to values above 0.8. Values of zero or below indicate conditions that violate the second law of thermodynamics.

The Overall Heat Transfer Coefficient. The overall heat transfer coefficient U^*, referenced to the heat transfer area A^*, is related to the individual (film) heat transfer coefficients and the fouling resistances by

$$U^* = \frac{1}{\dfrac{A^*}{h_i A_i} + R_{fi}\dfrac{A^*}{A_i} + \dfrac{A^* \ln\left(d_o/d_i\right)}{2\pi N_t L k_w} + R_{fo}\dfrac{A^*}{A_o} + \dfrac{A^*}{h_o A_o}} \tag{4.5.78}$$

where h_i and h_o are, respectively, the tube-side and shell-side film heat transfer coefficients, W/m^{2}K (Btu/hr ft^2 °F), each referenced to its corresponding heat transfer area; R_{fi} and R_{fo} the corresponding fouling resistances (see below), m^{2}K/W (hr ft^2 °F/Btu); N_t the total number of tubes in the heat exchanger; L the effective tube length between the inside surfaces of the tubesheets, m (ft); d_o and d_i the outside and inside tube diameters, m (ft); and k_w the thermal conductivity of the tube wall material, W/m K (Btu/hr ft°F). For the special but important case of plain tubes

$$A^* = A_o = N_t\left(\pi d_o L\right) \tag{4.5.79}$$

and Equation (4.5.78) reduces to

$$U_o = \frac{1}{\dfrac{d_o}{h_i d_i} + R_{fi}\dfrac{d_o}{d_i} + \dfrac{d_o \ln\left(d_o/d_i\right)}{2k_w} + R_{fo} + \dfrac{1}{h_o}} \tag{4.5.80}$$

If finned tubes are used, the root diameter d_r of the fins replaces d_o in Equation (4.5.78) and A_o includes the surface area of the fins as well as the bare tube surface between the fins; it is also necessary to include a fin efficiency (typically about 0.8 to 0.95) multiplier in the numerators of the last two terms on the right side of Equation (4.5.78) to account for resistance to conduction in the fins. The treatment of fin efficiency is fully developed in Kern and Kraus (1972). Efficiencies of some of the important geometries are given in the earlier half of this section.

Film Heat Transfer Coefficients. Calculation of single-phase tube-side heat transfer coefficients for plain tubes is discussed in Section 4.1; special correlations are required for internally enhanced tubes, see discussion of enhancement in Section 4.8. Intube condensation and vaporization are covered in the subsection on boiling and condensation in Section 4.4.

Shell-side heat transfer calculations are more complex owing to the large number and range of design variables and process conditions that can occur. The most accurate methods are proprietary and computer based. The best known of these methods are those of Heat Transfer Research, Inc. (HTRI), College Station, TX; Heat Transfer and Fluid Flow Services (HTFS), Harwell, U.K.; and B-JAC, Midlothian, VA. For single-phase flow, the Delaware method appears to be the best in the open literature, and it is feasible for both had and computer use; various presentations of the method appear in many references, including Schlünder, Vol. 3 (1983) and Hewitt et al. (1994). These references also give methods for shell-side vaporizing and condensing design. An approximate design procedure is given in the next subsection.

Fouling. Fouling is the formation of any undesired deposit on the heat transfer surface, and it presents an additional resistance to the flow of heat. Several different types of fouling are recognized:

Sedimentation: deposition of suspended material on the surface.
Crystallization: precipitation of solute from supersaturated solutions.
Corrosion: formation of corrosion products on the surface.
Thermal degradation/polymerization: formation of insoluble products by oxidation, charring, and/or polymerization of a process stream.
Biofouling: growth of large organisms (e.g., barnacles) that interfere with flow to or past a heat transfer surface ("macrobiofouling") or small organisms (e.g., algae) that form a fouling layer on the surface ("microbiofouling").

The effect of fouling on design is twofold: Extra surface must be added to the heat exchanger to overcome the additional thermal resistance, and provision must be made to allow cleaning either by chemical or mechanical means. The fouling resistances included in Equation (4.5.78) result in requiring extra surface by reducing U^* (though they do not properly account for the time-dependent nature of fouling) and should be chosen with care. Ranges of typical values for major classes of service are included in Table 4.5.9.

Other things being equal, a fouling stream that requires mechanical cleaning should be put in the tubes because it is easier to clean the tube side. If this is not possible or desirable, then a removable bundle with a rotated square tube layout should be chosen to facilitate cleaning.

Pressure Drop. Tube-side pressure drop in plain tubes is discussed in Section 3.4. These calculations are straightforward and quite accurate as long as the tubes are smooth and clean; however, even a small amount of roughening due to corrosion or fouling (sometimes with a significant reduction of flow area) can double or triple tube-side pressure drop. Special correlations are required for internally enhanced tubes.

Calculation of shell-side pressure drop is implicit in the design methods mentioned above for heat transfer. Roughness has less effect on shell-side pressure drop than on tube side, but fouling still may have a very substantial effect if the deposits fill up the clearances between the baffles and the shell and between the tubes and the baffles, or if the deposits are thick enough to narrow the clearances between adjacent tubes. Existing design methods can predict these effects if the thickness of the fouling layer can be estimated.

Limitations of Design. It should be recognized that even under the best of conditions — new, clean exchangers with conventional construction features — heat exchanger design is not highly accurate. The best methods, when compared with carefully taken test data, show deviations of ±20% on overall heat transfer and ±40% on shell-side pressure drop (Palen and Taborek, 1969). These ranges are considerably worsened in fouling services. In these cases, the thermal *system* should be designed for operational flexibility, including carefully chosen redundancy of key components, and easy maintenance.

Approximate Design Method

Because of the complexity of rigorous design methods, it is useful to have an estimation procedure that can quickly give approximate dimensions of a heat exchanger for a specified service. Such a method is given here for purposes of preliminary cost estimation, plant layout, or checking the results of computer

TABLE 4.5.9 Typical Film Heat Transfer Coefficients for Shell-and-Tube Heat Exchangers

Fluid Conditions		h, W/m^{2}K[a,b]	Fouling resistance, m^2 K/W[a]
Sensible heat transfer			
Water[c]	Liquid	5000–7500	1–2.5 × 10^{-4}
Ammonia	Liquid	6000–8000	0–1 × 10^{-4}
Light organics[d]	Liquid	1500–2000	0–2 × 10^{-4}
Medium organics[e]	Liquid	750–1500	1–4 × 10^{-4}
Heavy organics[f]	Liquid		
	Heating	250–750	2–10 × 10^{-4}
	Cooling	150–400	2–10 × 10^{-4}
Very heavy organics[g]	Liquid		
	Heating	100–300	4–30 × 10^{-3}
	Cooling	60–150	4–30 × 10^{-3}
Gas[h]	Pressure 100–200 kN/m^2 abs	80–125	0–1 × 10^{-4}
Gas[h]	Pressure 1 MN/m^2 abs	250–400	0–1 × 10^{-4}
Gas[h]	Pressure 10 MN/m^2 abs	500–800	0–1 × 10^{-4}
Condensing heat transfer			
Steam, ammonia	Pressure 10 kN/m^2 abs, no noncondensables[i,j]	8000–12000	0–1 × 10^{-4}
Steam, ammonia	Pressure 10 kN/m^2 abs, 1% noncondensables[k]	4000–6000	0–1 × 10^{-4}
Steam, ammonia	Pressure 10 kN/m^2 abs, 4% noncondensables[k]	2000–3000	0–1 × 10^{-4}
Steam, ammonia	Pressure 100 kN/m^2 abs, no noncondensables[i,j,k,l]	10000–15000	0–1 × 10^{-4}
Steam, ammonia	Pressure 1 MN/m^2 abs, no noncondensables[i,j,k,l]	15000–25,000	0–1 × 10^{-4}
Light organics[d]	Pure component, pressure 10 kN/m^2 abs, no noncondensables[i]	1500–2000	0–1 × 10^{-4}
Light organics[d]	Pressure 10 kN/m^2 abs, 4% noncondensables[k]	750–1000	0–1 × 10^{-4}
Light organics[d]	Pure component, pressure 100 kN/m^2 abs, no noncondensables	2000–4000	0–1 × 10^{-4}
Light organics[d]	Pure component, pressure 1 MN/m^2 abs	3000–4000	0–1 × 10^{-4}
Medium organics[e]	Pure component or narrow condensing range, pressure 100 kN/m^2 abs[m,n]	1500–4000	1–3 × 10^{-4}
Heavy organics	Narrow condensing range pressure 100 kN/m^2 abs[m,n]	600–2000	2–5 × 10^{-4}
Light multicomponent mixtures, all condensable[d]	Medium condensing range, pressure 100 kN/m^2 abs[k,m,o]	1000–2500	0–2 × 10^{-4}
Medium multicomponent mixtures, all condensable[e]	Medium condensing range, pressure 100 kN/m^2 abs[k,m,o]	600–1500	1–4 × 10^{-4}
Heavy multicomponent mixtures, all condensable[f]	Medium condensing range, pressure 100 kN/m^2 abs[k,m,o]	300–600	2–8 × 10^{-4}
Vaporizing heat transfer[p,q]			
Water[r]	Pressure < 0.5 MN/m^2 abs, $\Delta T_{SH,max}$ = 25 K	3000–10000	1–2 × 10^{-4}
Water[r]	Pressure < 0.5 MN/m^2 abs, pressure < 10 MN/m^2 abs, $\Delta T_{SH,max}$ = 20 K	4000–15000	1–2 × 10^{-4}

TABLE 4.5.9 (continued) Typical Film Heat Transfer Coefficients for Shell-and-Tube Heat Exchangers

Fluid Conditions		h, W/m^{2}K[a,b]	Fouling resistance, m^2 K/W[a]
Ammonia	Pressure < 3 MN/m^2 abs, $\Delta T_{SH,max} = 20$ K	3000–5000	0–2 × 10^{-4}
Light organics[d]	Pure component, pressure < 2 MN/m^2 abs, $\Delta T_{SH,max} = 20$ K	1000–4000	1–2 × 10^{-4}
Light organics[d]	Narrow boiling range,[s] pressure < 2 MN/m^2 abs, $\Delta T_{SH,max} = 15$ K	750–3000	0–2 × 10^{-4}
Medium organics[e]	Pure component, pressure < 2 MN/m^2 abs, $\Delta T_{SH,max} = 20$ K	1000–3500	1–3 × 10^{-4}
Medium organics[e]	Narrow boiling range,[s] pressure < 2 MN/m^2 abs, $\Delta T_{SH,max} = 15$ K	600–2500	1–3 × 10^{-4}
Heavy organics[f]	Pure component, pressure < 2 MN/m^2 abs, $\Delta T_{SH,max} = 20$ K	750–2500	2–5 × 10^{-4}
Heavy organics[g]	Narrow boiling range,[s] pressure < 2 MN/m^2 abs, $\Delta T_{SH,max} = 15$ K	400–1500	2–8 × 10^{-4}
Very heavy organics[h]	Narrow boiling range,[s] pressure < 2 MN/m^2 abs, $\Delta T_{SH,max} = 15$ K	300–1000	2–10 × 10^{-4}

Source: Schlünder, E.U., Ed., *Heat Exchanger Design Handbook*, Begell House, New York, 1983. With permision.

[a] Heat transfer coefficients and fouling resistances are based on area in contact with fluid. Ranges shown are typical, not all encompassing. Temperatures are assumed to be in normal processing range; allowances should be made for very high or low temperatures.

[b] Allowable pressure drops on each side are assumed to be about 50–100 kN/m^2 except for (1) low-pressure gas and two-phase flows, where the pressure drop is assumed to be about 5% of the absolute pressure; and (2) very viscous organics, where the allowable pressure drop is assumed to be about 150–250 kN/m^2.

[c] Aqueous solutions give approximately the same coefficients as water.

[d] Light organics include fluids with liquid viscosities less than about 0.5×10^{-3} Nsec/m^2, such as hydrocarbons through C_8, gasoline, light alcohols and ketones, etc.

[e] Medium organics include fluids with liquid viscosities between about 0.5×10^{-3} and 2.5×10^{-3} Nsec/m^2, such as kerosene, straw oil, hot gas oil, and light crudes.

[f] Heavy organics include fluids with liquid viscosities greater than 2.5×10^{-3} Nsec/m^2, but not more than 50×10^{-3} Nsec/m^2, such as cold gas oil, lube oils, fuel oils, and heavy and reduced crudes.

[g] Very heavy organics include tars, asphalts, polymer melts, greases, etc., having liquid viscosities greater than about 50×10^{-3} Nsec/m^2. Estimation of coefficients for these materials is very uncertain and depends strongly on the temperature difference, because natural convection is often a significant contribution to heat transfer in heating, whereas congelation on the surface and particularly between fins can occur in cooling. Since many of these materials are thermally unstable, high surface temperatures can lead to extremely severe fouling.

[h] Values given for gases apply to such substances as air, nitrogen, carbon dioxide, light hydrocarbon mixtures (no condensation), etc. Because of the very high thermal conductivities and specific heats of hydrogen and helium, gas mixtures containing appreciable fractions of these components will generally have substantially higher heat transfer coefficients.

[i] Superheat of a pure vapor is removed at the same coefficient as for condensation of the saturated vapor if the exit coolant temperature is less than the saturation temperature (at the pressure existing in the vapor phase) and if the (constant) saturation temperature is used in calculating the MTD. But see note k for vapor mixtures with or without noncondensable gas.

[j] Steam is not usually condensed on conventional low-finned tubes; its high surface tension causes bridging and retention of the condensate and a severe reduction of the coefficient below that of the plain tube.

[k] The coefficients cited for condensation in the presence of noncondensable gases or for multicomponent mixtures are only for very rough estimation purposes because of the presence of mass transfer resistances in the vapor (and to some extent, in the liquid) phase. Also, for these cases, the vapor-phase temperature is not constant, and the coefficient given is to be used with the MTD estimated using vapor-phase inlet and exit temperatures, together with the coolant temperatures.

[l] As a rough approximation, the same relative reduction in low-pressure condensing coefficients due to noncondensable gases can also be applied to higher pressures.

[m] Absolute pressure and noncondensables have about the same effect on condensing coefficients for medium and heavy organics as for light organics. For large fractions of noncondensable gas, interpolate between pure component condensation and gas cooling coefficients.

[n] Narrow condensing range implies that the temperature difference between dew point and bubble point is less than the smallest temperature difference between vapor and coolant at any place in the condenser.

[o] Medium condensing range implies that the temperature difference between dew point and bubble point is greater than the smallest temperature difference between vapor and coolant, but less than the temperature difference between inlet vapor and outlet coolant.

[p] Boiling and vaporizing heat transfer coefficients depend very strongly on the nature of the surface and the structure of the two-phase flow past the surface in addition to all of the other variables that are significant for convective heat transfer in other modes. The flow velocity and structure are very much governed by the geometry of the equipment and its connecting piping. Also, there is a maximum heat flux from the surface that can be achieved with reasonable temperature differences between surface and saturation temperatures of the boiling fluid; any attempt to exceed this maximum heat flux by increasing the surface temperature leads to partial or total coverage of the surface by a film of vapor and a sharp decrease in the heat flux.

Therefore, the vaporizing heat transfer coefficients given in this table are only for very rough estimating purposes and assume the use of plain or low-finned tubes without special nucleation enhancement.

$\Delta T_{\text{SH,max}}$ is the maximum allowable temperature difference between surface and saturation temperature of the boiling liquid. No attempt is made in this table to distinguish among the various types of vapor-generation equipment, since the major heat transfer distinction to be made is the propensity of the process stream to foul. Severely fouling streams will usually call for a vertical thermosiphon or a forced-convection (tube-side) reboiler for ease of cleaning.

[q] Subcooling heat load is transferred at the same coefficient as latent heat load in kettle reboilers, using the saturation temperature in the MTD. For horizontal and vertical thermosiphons and forced-circulation reboilers, a separate calculation is required for the sensible heat transfer area, using appropriate sensible heat transfer coefficients and the liquid temperature profile for the MTD.

[r] Aqueous solutions vaporize with nearly the same coefficient as pure water if attention is given to boiling-point elevation, if the solution does not become saturated, and if care is taken to avoid dry wall conditions.

[s] For boiling of mixtures, the saturation temperature (bubble point) of the final liquid phase (after the desired vaporization has taken place) is to be used to calculate the MTD. A narrow-boiling-range mixture is defined as one for which the difference between the bubble point of the incoming liquid and the bubble point of the exit liquid is less than the temperature difference between the exit hot stream and the bubble point of the exit boiling liquid. Wide-boiling-range mixtures require a case-by-case analysis and cannot be reliably estimated by these simple procedures.

output. This method is based upon Equation (4.5.74) with $A^* = A_o$ and $U^* = U_o$ and depends upon rapidly estimating values for q_T, MTD, and U_o. The procedure is as follows:

Estimation of q_T. For sensible heat transfer,

$$q_T = \dot{m}_h c_{p,h}\left(T_{h,i} - T_{h,o}\right) = \dot{m}_c c_{p,c}\left(T_{c,o} - T_{c,i}\right) \tag{4.5.83}$$

where $\dot{m}$ is the mass flow rate, c_p the specific heat, and T the stream temperature, with subscripts h and c denoting the hot and cold streams, respectively, and i and o inlet and outlet, respectively.

For isothermal phase change,

$$q_T = \dot{m} h_{fg} \tag{4.5.84}$$

where $\dot{m}$ is the mass rate of condensation or vaporization and h_{fg} is the latent heat of phase transformation.

For more complex cases, such as partial or multicomponent condensation, more elaborate analyses are required, although this method can still be used with care to give rough estimates.

Estimation of MTD. The first step is to calculate or estimate $\text{LMTD}_{\text{countercurrent}}$ from Equation (4.5.75) and then estimate F as follows:

1. If the two streams are in countercurrent flow, $F = 1$.
2. If the two streams are in a combination of countercurrent and cocurrent flows (i.e., multiple tube passes) and the outlet temperatures of the two streams are equal, $F = 0.8$.

3. If the exchanger has multiple passes and $T_{h,o} > T_{c,o}$, then $0.8 < F < 1.0$, with the actual value depending upon the temperature ranges of the two streams and $(T_{h,o} - T_{c,o})$. It is usually sufficiently accurate to take $F = 0.9$ in this case, but a more accurate value can be obtained from the earlier half of this section by Shah.
4. Design of a multiple tube pass exchanger with $T_{h,o} < T_{c,o}$ (i.e., a temperature cross) leads to $F < 0.8$, which is inefficient, of uncertain inaccuracy, and perhaps even thermodynamically impossible. The problem can be handled with multiple shells in series. Consult Shah's discussion.
5. Then, $\text{MTD} = F(\text{LMTD})_{\text{countercurrent}}$, (Equation 4.5.77).

Estimation of U_o. The best way to estimate U_o is to use Equation (4.5.80), together with values of h_o, h_i, $R_{f,o}$, and $R_{f,i}$, chosen from Table 4.5.9. This table includes ranges of values that are typical of the fluids and services indicated assuming normally allowable pressure drops, exchanger construction, and fouling. However, care should be taken in selecting values to consider possible unusual conditions, e.g., especially high or low velocities (implying correspondingly high or low allowable pressure drops), and especially fouling. In selecting values from the table, the user should carefully read the footnotes for each entry.

Calculation of A_o. The total outside tube heat transfer area required in the heat exchanger is now found from Equation (4.5.74).

Estimation of Exchanger Dimensions. Figure 4.5.19 shows the relationship among A_o, effective tube length L, and inside shell diameter for a fully tubed, fixed tubesheet heat exchanger with one tube-side pass, with $^3/_4$ in. (19.05 mm) plain tubes on a $^{15}/_{16}$ in. (23.8 mm) pitch equilateral triangular tube layout. These curves are constructed using tube count tables (e.g., Saunders, 1988). The dashed lines marked 3:1, 6:1,

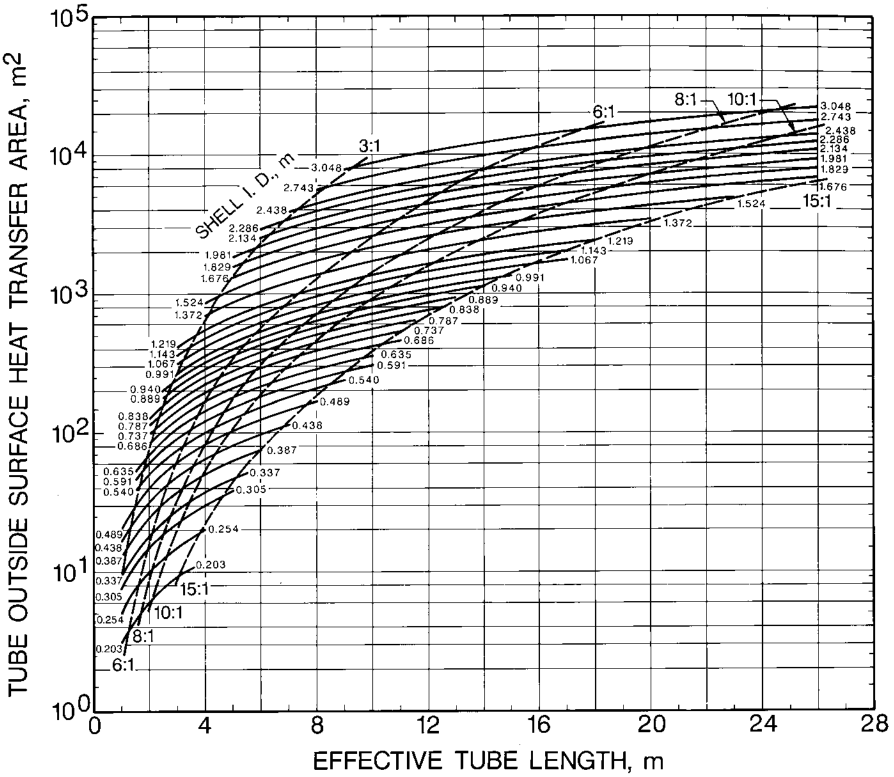

FIGURE 4.5.19 Heat transfer area as a function of shell inside diameter and effective tube length for 19.05 mm ($^3/_4$ in.) tubes on a 23.8 mm ($^{15}/_{16}$ in.) equilateral triangular tube layout, fixed tubesheet, one tube-side pass, fully tubed shell. (From Schlünder, E. U., Ed. *Heat Exchanger Design Handbook*, Begell House, New York, 1983. With permission.)

8:1, 10:1, and 15:1 indicate ratios of tube length to shell inside diameter for guidance in selection. Exchangers of less than 3:1 ratio are expensive because of the large-diameter shell and tubesheet, with more holes to be drilled and tubes rolled and/or welded, and shell-side flow distribution is likely to be poor and lead to excessive fouling. Exchangers greater than 15:1 ratio are probably beyond the point of saving money by reducing shell diameter and number of tubes and may require excessive clear way for pulling the bundle; the bundles may be springy and difficult to handle during maintenance. Most heat exchangers fall into the 6:1 to 10:1 range.

Figure 4.5.19 is a very specific case which is used as a reference. In order to extend its usefulness to other tube diameters, layouts, bundle constructions, etc., Equation (4.5.83) is used:

$$A'_o = A_o F_1 F_2 F_3 \tag{4.5.83}$$

where A'_o is the value to be used with Figure 4.5.19, A_o is the required area calculated from Equation (4.5.74), and

F_1 is the correction factor for the tube layout. F_1 = 1.00 for $^3/_4$ in. (19.05 mm) outside diameter tubes on a $^{15}/_{16}$ in. (23.8 mm) triangular pitch. Values of F_1 for other tube diameters and pitches are given in Table 4.5.10.

F_2 is the correction factor for the number of tube-side passes. F_2 = 1.00 for one tube-side pass, and Table 4.5.11 gives values of F_2 for more passes.

F_3 is the correction factor for shell construction/tube bundle configuration. F_3 = 1.00 for fixed tubesheet, fully tubed shells, and Table 4.5.12 gives values of F_3 for the standard TEMA types.

TABLE 4.5.10 Values of F$_1$ for Various Tube Diameters and Layouts

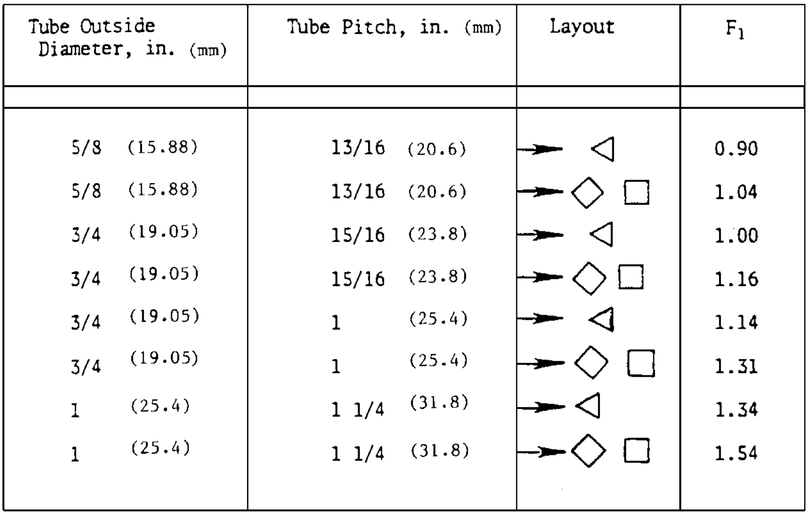

Tube Outside Diameter, in. (mm)	Tube Pitch, in. (mm)	Layout	F$_1$
5/8 (15.88)	13/16 (20.6)	→ ◁	0.90
5/8 (15.88)	13/16 (20.6)	→ ◇ □	1.04
3/4 (19.05)	15/16 (23.8)	→ ◁	1.00
3/4 (19.05)	15/16 (23.8)	→ ◇ □	1.16
3/4 (19.05)	1 (25.4)	→ ◁	1.14
3/4 (19.05)	1 (25.4)	→ ◇ □	1.31
1 (25.4)	1 1/4 (31.8)	→ ◁	1.34
1 (25.4)	1 1/4 (31.8)	→ ◇ □	1.54

$$F_1 = \frac{(\text{Heat transfer area / cross-sectional area of unit cell})_{\text{Reference}}}{(\text{Heat transfer area / cross-sectional area of unit cell})_{\text{New Case}}}$$

This table may also be used for low-finned tubing in the following way. The value estimated for h_o from Table 4.5.9 should be multiplied by the fin efficiency (usually between 0.75 and 1 for a good application; 0.85 is a good estimate) and used in Equation 4.5.78 with $A^* = A_o$, the total outside heat transfer area including fins. Then this value of A_o is divided by the ratio of the finned tube heat transfer area to the plain tube area (per unit length). The result of this calculation is used as A_o in Equation 4.5.82 to find A'_o to enter Figure 4.5.19.

Source: Schlünder, E.U., Ed., *Heat Exchanger Design Handbook*, Begell House, New York, 1983. With permission.

TABLE 4.5.11 Values of F_2 for Various Numbers of Tube Side Passes[a]

Inside Shell Diameter, in. (mm)	F_2 Number of Tube-Side Passes			
	2	4	6	8
Up to 12 (305)	1.20	1.40	1.80	—
$13^1/_4$ to $17^1/_4$ (337 to 438)	1.06	1.18	1.25	1.50
$19^1/_4$ to $23^1/_4$ (489 to 591)	1.04	1.14	1.19	1.35
25 to 33 (635 to 838)	1.03	1.12	1.16	1.20
35 to 45 (889 to 1143)	1.02	1.08	1.12	1.16
48 to 60 (1219 to 1524)	1.02	1.05	1.08	1.12
Above 60 (above 1524)	1.01	1.03	1.04	1.06

[a] Since U-tube bundles must always have at least two passes, use of this table is essential for U-tube bundle estimation. Most floating head bundles also require an even number of passes.

Source: Schlünder, E.U., Ed., *Heat Exchanger Design Handbook*, Begell House, New York, 1985. With permission.

TABLE 4.5.12 F_3 for Various Tube Bundle Constructions

Type of Tube Bundle Construction	F_3 Inside Shell Diameter, in. (mm)				
	Up to 12 (305)	13–22 (330–559)	23–36 (584–914)	37–48 (940–1219)	Above 48 (1219)
Split backing ring (TEMA S)	1.30	1.15	1.09	1.06	1.04
Outside packed floating heat (TEMA P)	1.30	1.15	1.09	1.06	1.04
U-Tube* (TEMA U)	1.12	1.08	1.03	1.01	1.01
Pull-through floating head (TEMA T)	—	1.40	1.25	1.18	1.15

[a] Since U-tube bundles must always have at least two tube-side passes, it is essential to use Table 4.5.11 also for this configuration.

Source: Schlünder, E.U., Ed., *Heat Exchanger Design Handbook*, Begell House, New York, 1983. With permission.

Once a value of A_o' has been calculated from Equation (4.5.83), enter the ordinate of Figure 4.5.19 at that value and move horizontally, picking off the combinations of shell inside diameter and tube length that meet that requirement. The final choice can then be made from among those possibilities.

Example of the Approximate Design Method

Problem Statement. Estimate the dimensions of a shell-and-tube heat exchanger to cool 100,000 lb_m/hr (12.6 kg/sec) of liquid toluene from 250 to 110°F (121.1 to 43.3°C) using cooling tower water available at 80°F (26.7°C). Use split-ring floating head construction (TEMA S) with $^3/_4$ in. (19.05 mm) outside diameter × 14 BWG (0.083 in. = 2.11 mm wall) low-carbon steel tubes on $^{15}/_{16}$ in. (23.8 mm) equilateral triangular pitch. This construction implies one shell-side pass and an even number of tube-side passes — assume two for the present. Choose cooling water exit temperature of 100°F (37.8°C). Specific heat of toluene is 0.52 Btu/lb_m°F (2177 J/kgK) and viscosity at 180°F (82.2°C) is 0.82 lb/$_\text{m}$/ft hr (0.34×10^{-3} Nsec/m^2 or 0.34 cP).

Solution.

$$q_T = \left(100{,}000\ \text{lb}_\text{m}/\text{hr}\right)\left(0.52\ \text{Btu}/\text{lb}_\text{m}{}^\circ\text{F}\right)(250-110)^\circ\text{F}$$

$$= 7.28\times10^6\ \text{Btu/hr} = 2.14\times10^6\ \text{W}$$

$$\text{LMTD}_{\text{countercurrent}} = \frac{(250-100)-(110-80)}{\ln\dfrac{250-100}{110-80}} = 74.6^\circ\text{F} = 41.4^\circ\text{C}$$

Since there are at least two tube-side passes, flow is not countercurrent, and $T_{h_o} > T_{c_o}$, estimate $F \approx 0.9$. Therefore, MTD = 0.9 (74.6°F) = 67.1°F = 37.3°C.

Estimation of U_o. Light organic liquid cooled by liquid water. (Note that 1 Btu/hr ft² °F = 5.678 W/m²K).

Water (in tubes) h_i	1000 Btu/hr ft² °F	5700 W/m²K
Toluene (in shell) h_o	300 Btu/hr ft² °F	1700 W/m²K
Tube-side fouling R_{f_i}	0.001 hr ft² °F/Btu	1.8×10^{-4} m²K/W
Shell-side fouling R_{f_o}	0.0005 hr ft² °F/Btu	8.8×10^{-5} m²K/W

Tube wall resistance (for estimation purposes, this term can be approximated by x_w/k_w, where x_w is the wall thickness):

$$\frac{x_w}{k_w} = \frac{0.083 \text{ in.}}{(12 \text{ in./ft})(26 \text{ Btu/hr ft °F})} = 2.7 \times 10^{-4} \frac{\text{hr ft}^2 \text{ °F}}{\text{Btu}} = 4.6 \times 10^{-5} \frac{\text{m}^2\text{K}}{\text{W}}$$

Then,

$$U_o = \frac{1}{\dfrac{0.750}{1000(0.584)} + \dfrac{0.001(0.750)}{0.584} + 2.7 \times 10^{-4} + 0.0005 + \dfrac{1}{300}}$$

$$= 150 \text{ Btu/hr ft °F} = 848 \text{ W/m}^2\text{K}$$

$$A_o = \frac{7.28 \times 10^6 \text{ Btu/hr}}{(150 \text{ Btu/hr ft}^2 \text{ °F})(67.1\text{°F})} = 723 \text{ ft}^2 = 67.7 \text{ m}^2$$

Correct for changes in construction features (preliminary examination of Figure 4.5.19 indicates shell inside diameter will be in the range of 500 mm, or 20 in.):

F_1: F_1 = 1.00 since the same tube size and layout is used;
F_2: F_2 = 1.04, assuming two passes;
F_3: F_3 = 1.15, TEMA S construction;
A_o' = (723 ft²) (1.00)(1.04)(1.15) = 865 ft² = 81 m².

From Figure 4.5.19, entering at A_o', pick off the following combinations of shell inside diameter and tube length:

Shell Inside Diameter		Effective Tube Length		L/D_s
in.	mm	ft	m	
27	686	6.6	2.0	2.9
25	635	7.5	2.3	3.6
23 1/4	591	9.2	2.8	4.7
21 1/4	540	10.8	3.3	6.1
19 1/4	489	13.1	4.0	8.2
17 1/4	438	16.7	5.1	11.6

Any of these combinations would supply the desired area; the 21 1/4 in. (540 mm) and 19 1/4 in. (489 mm) would appear to be likely choices.

References

American Society of Mechanical Engineers. 1995. *ASME Boiler and Pressure Vessel Code*, Section VIII. New editions published every 3 years. ASME, New York.

Gentry, C.C., Young, R.K., and Small, W.M. 1982. RODbaffle heat exchanger thermal-hydraulic predictive methods, in *Proceedings of the Seventh International Heat Transfer Conference*, Munich, Germany, 6, 197–202.

Hewitt, G.F., Shires, G.L., and Bott, T.R. 1994. *Process Heat Transfer*, CRC/Begell House, Boca Raton, FL.

Kern, D.Q. and Kraus, A.D. 1972. *Extended Surface Heat Transfer*, McGraw-Hill, New York.

Kral, D., Stehlik, P., Van der Ploeg, H.J., and Master, B.I., 1996. Helical baffles in shell and tube heat exchangers. Part I: Experimental verification, *Heat Transfer Eng.*, 17(1), 93–101.

Palen, J.W. and Taborek, J. 1969. Solution of shell side flow pressure drop and heat transfer by stream analysis method, *Chem. Eng. Prog. Symp. Ser. No. 92, Heat Transfer-Philadelphia*, 65, 53–63.

Saunders, E.A.D. 1988. *Heat Exchangers: Selection, Design, and Construction,* Longman Scientific & Technical/John Wiley & Sons, New York.

Schlünder, E.U., Ed. 1983. *Heat Exchanger Design Handbook*, Begell House, New York.

Singh, K.P. and Soler, A.I. 1984. *Mechanical Design of Heat Exchangers and Pressure Vessel Components*, Arcturus, Cherry Hill, NJ.

TEMA. 1988. *Standards*, 7th ed., Tubular Exchanger Manufacturers Association, Tarrytown, NY.

Yokell, S. 1990. *A Working Guide to Shell and Tube Heat Exchangers*, McGraw-Hill, New York.

4.6 Temperature and Heat Transfer Measurements

Robert J. Moffat and Jungho Kim

There are two different kinds of material to consider with respect to experimental methods: the unit operations of measurement (transducers and their environmental errors) and the strategy of experimentation. This section deals only with the unit operations: transducers, their calibrations, and corrections for environmental errors.

Temperature Measurement

An International Practical Temperature Scale (IPTS) has been defined in terms of a set of fixed points (melting points of pure substances) along with a method for interpolating between the fixed points. The IPTS agrees with the thermodynamic temperature scale within a few degrees Kelvin over most of its range. The IPTS is the basis for all commerce and science, and all calibrations are made with respect to the IPTS temperature. The scale is revised periodically.

Accurate calibrations are not enough to ensure accurate data, however. If a sensor has been installed to measure a gas temperature or a surface temperature, any difference between the sensor temperature and the measurement objective due to heat transfer with the environment of the sensor is an “error.” In most temperature-measuring applications, the environmental errors are far larger than the calibration tolerance on the sensor and must be dealt with just as carefully as the calibration.

Thermocouples

Any pair of thermoelectrically dissimilar materials can be used as a thermocouple. The pair need only be joined together at one end and connected to a voltage-measuring instrument at the other to form a usable system. A thermocouple develops its signal in response to the temperature difference from one end of the pair to the other. The temperature at one end, known as the *reference junction* end, must be known accurately before the temperature at the other end can be deduced from the voltage.

Thermocouples are the most commonly used electrical output sensors for temperature measurement. With different materials for different ranges, thermocouples have been used from cryogenic temperatures (a few Kelvin) to over 3000 K. In the moderate temperature range, ambient to 1200°C, manufacturer’s quoted calibration accuracy can be as good as ±3/8% of reading (referred to 0°C) for precision-grade base metal thermocouples. Broader tolerances apply at very high temperature and very low temperatures. Thermocouple signals are DC voltages in the range from a few microvolts to a few tens of microvolts per degree C. Because of their low signal levels, thermocouple circuits must be protected from ground loops, galvanic effects, and from pickup due to electrostatic or electromagnetic interactions with their surroundings. Thermocouples are low-impedance devices. Multiple channels of thermocouples can be fed to a single voltage reader using low-noise-level scanners or preamplifiers and electronic multiplexers.

The alloys most frequently used for temperature measurement are listed in Table 4.6.1. These alloys have been developed, over the years, for the linearity, stability, and reproducibility of their EMF vs. temperature characteristics and for their high-temperature capability.

Calibration data for thermocouples are periodically reviewed by the National Institutes of Science and Technology based on the then-current IPTS. Values in Table 4.6.1 illustrate the approximate levels which can be expected, and are from the National Bureau of Standards Monograph 125. Maximum temperatures listed in this table are estimates consistent with a reasonable service lifetime. Allowable atmosphere refers to the composition in contact with the thermoelements themselves. Accuracy estimates are provided for two levels of precision: standard grade and precision grade where these data are available.

Noble metal and refractory metal thermocouples are often used with substitute lead wires, as a cost-saving measure. These lead wires, described in Table 4.6.2 are cheaper and easier to handle than the high temperature thermocouples. They have the same temperature–EMF characteristics as their primary thermoelements, but only over the range of temperatures the lead wires will usually encounter (up to a few hundred degrees C). Except for the substitute alloys, thermocouple extension wires have the same composition as thermocouple wires, differing only in the type of insulation and the accuracy of calibration, which is not held as closely for extension wire as for thermocouple-grade wire.

Any instrument capable of reading low DC voltages (on the order of millivolts) with 5 to 10 μV resolution will suffice for temperature measurements. *Galvanometric measuring instruments* can be used, but, since they draw current, the voltage available at the terminals of the instrument depends not only on the voltage output of the thermocouple loop but also on the resistance of the instrument and the loop together. Such instruments are normally marked to indicate the external resistance for which they have been calibrated. *Potentiometric instruments*, either manually balanced or automatically balanced, draw no current when in balance, hence can be used with thermocouple loops of any arbitrary resistance without error. High-input impedance *voltmeters* draw very low currents and, except for very high resistance circuits, are not affected by the loop resistance.

Thermocouple Theory. Equation (4.6.1) is the general form describing the EMF generated in a two-wire thermocouple (Moffat, 1962). The same form can be derived from either the free-electron theory of metals or from thermodynamic arguments alone: the output of a thermocouple can be described as the sum of a set of terms, one arising in each wire in the circuit.

The junctions do not generate the EMF: they are merely electrical connections between the wires. For a two-wire circuit,

$$\text{EMF} = \int_0^L \varepsilon_1 \frac{dT}{dx} dx + \int_L^0 \varepsilon_2 \frac{dT}{dx} dx \tag{4.6.1}$$

where

ε_1 and ε_2 = the total thermoelectric power of materials 1 and 2, respectively, mV/C. The value of ε is equal to the sum of the Thomson coefficient and the temperature derivative of the Peltier coefficient for the material.

T = temperature, C

x = distance along the wire, m

L = length of the wire, m

This form for expressing the output of a two-wire circuit applies regardless of whether the wires are uniform in composition or not. If a circuit contained four wires (two thermocouple wires and two extension wires), then Equation (4.6.1) would be written with four terms, one for each length of wire.

When the wire is uniform in composition and both wires begin at (T_o) and both end at (T_L) the two terms can be collected into one integral:

$$\text{EMF} = \int_{T_0}^{T_L} \left(\varepsilon_1 - \varepsilon_2\right) dT \tag{4.6.2}$$

TABLE 4.6.1 Application Characteristics of Some Common Thermocouple Alloys

Max T °F	Max T °C	Allowable Atmos. (Hot)	Material Names	ANSI Type[a]	Color Code	Output mV/100°F	Accuracy, %	
							Standard[a]	Precision[a]
5072	2800	Inert, H_2, vacuum	Tungsten/tungsten 26% rhenium	—	—	0.86	—	—
5000	2760	Inert, H_2, vacuum	Tungsten 5% rhenium/tungsten 26% rhenium	—	—	0.76	—	—
4000	2210	Inert, H_2	Tungsten 3% rhenium/tungsten 35% rhenium	—	—	0.74	—	—
3720	1800	Oxidizing[b]	Platinum 30% rhodium/platinum 6% rhodium	B	—	0.43	1/2	1/4
2900	1600	Oxidizing[b]	Platinum 13% rhodium/platinum	R	—	0.64	1/4	1/4
2800	1540	Oxidizing[b]	Platinum 10% rhodium/platinum	S	—	0.57	1/4	1/4
2372	1300	Oxidizing[b,c]	Platinel II (5355)/Platinel II (7674)	—	—	2.20	5/8	—
2300	1260	Oxidizing	Chromel/Alumel,[d] Tophel/Nial,[e] Advance T1/T2,[f] Thermo-Kanathal P/N[g]	K	Yellow red	2.20	4°F, or 3/4%	2°F, or 3/8%
1800	980	Reducing[a]	Chromel/constantan	E	Purple red	4.20	1/2	3/8
1600	875	Reducing	Iron/constantan	J	White red	3.00	4°F, or 3/4%	2°F, or 3/8%
750	400	Reducing	Copper/constantan	T	Blue red	2.50	3/4	3/8

[a] Per ANSI C96.1 Standard.

[b] Avoid contact with carbon, hydrogen, metallic vapors, silica, reducing atmosphere.

[c] @ Engelhard Corp.

[d] @ Hoskins Mfg. Co.

[e] Wilber B. Driver Co.

[f] Driver-Harris Co.

[g] The Kanthal Corp.

TABLE 4.6.2 Substitute Material Extension Wires for Thermocouples

Thermocouple Material	Thermocouple Type[a]	Extension Wire, Type[a]	Color for (+) Wire	Color for (–) Wire	Overall Color
Tungsten/tungsten 26% rhenium	—	Alloys 200/226[b]	—	—	—
Tungsten 5% rhenium/tungsten 26% rhenium	—	Alloys (405/426)[b]	White	Red	Red[b]
Tungsten 3% rhenium/tungsten 25% rhenium	—	Alloys (203/225)[b]	White/yellow	White/red	Yellow/red[b]
Platinum/platinum rhodium	S, R	SX, SR	Black	Red	Green
Platinel II-5355/Platinel II-7674	—	P2X[d]	Yellow	Red	Black[d]
Chromel/Alumel, Tophel/Nial, Advance, Thermokanthal[c]	K	KX	Yellow	Red	Yellow
Chromel/constantan	E	EX	Purple	Red	Purple
Iron/constantan	J	JX	White	Red	Black
Copper/constantan	T	TX	Blue	Red	Blue

[a] ANSI, except where noted otherwise.
[b] Designations affixed by Hoskins Mfg. Co.
[c] Registered trade mark names.
[d] Engelhard Mfg. Co.

The EMF–temperature (E–T) tables produced by NIST and others are "solutions" to Equation (4.6.2) and can be used only when the following three conditions are met:

1. The thermoelectric power, ε, is not a function of position; i.e., the wires are homogeneous;
2. There are only two wires in the circuit;
3. Each wire begins at T_o and ends at T_L

When the circuit consists entirely of pairs of materials, Equation 4.6.2 can be used directly as the basis for understanding the source of the EMF. As an example, consider the three-pair system shown in Figure 4.6.1. For that circuit, Equation (4.6.2) would have three terms: one for each pair. The total EMF generated by the circuit would be the sum of the EMFs generated in the thermocouple pair and in the extension wire pair. The pair of copper wires would not contribute to the net EMF, assuming the two copper wires were perfectly matched. The EMF contributed by each pair would be proportional to the temperature difference from end to end of that pair, as shown in Equation (4.6.3) and (4.6.4).

$$\text{EMF} = \int_{T_1}^{T_2} \left(\varepsilon_{\text{cu}} - \varepsilon_{\text{cu}}\right) dT + \int_{T_2}^{T_3} \left(\varepsilon_+ - \varepsilon_-\right)_{\text{LEADS}} dT + \int_{T_3}^{T_4} \left(\varepsilon_+ - \varepsilon_-\right)_{\text{TC}} dT \tag{4.6.3}$$

$$\text{EMF} = 0 + (T3 - T2)\left(\varepsilon_+ - \varepsilon_-\right)_{\text{LEADS}} + (T4 - T3)\left(\varepsilon_+ - \varepsilon_-\right)_{\text{TC}} \tag{4.6.4}$$

Most thermocouple circuits consist only of pairs of wires and can be understood in terms of these two equations, but some require a more detailed treatment. A graphical method of analysis is available, based on Equation (4.6.1).

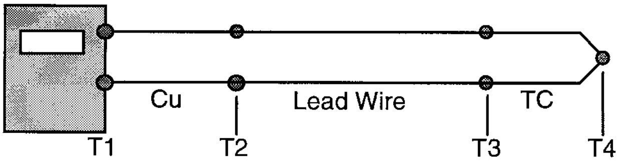

FIGURE 4.6.1 A three-pair circuit.

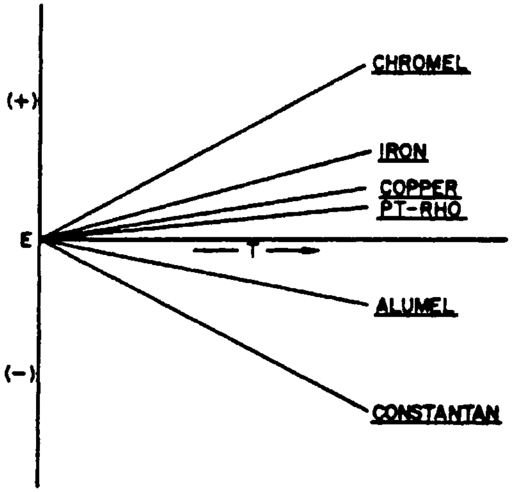

FIGURE 4.6.2 E–T calibrations for several common thermocouple materials.

The temperature–EMF calibrations of the more common materials are shown in Figure 4.6.2 derived from NBS Monograph 125 and other sources. This figure provides the input data for a simple graphical technique for describing the EMF generation in a circuit. Each curve in Figure 4.6.2 represents the output which would be derived from a thermocouple made of material X used with platinum when the cold end is held at 0°C and the hot end is held at *T*.

Those elements commonly used as "first names" for thermocouple pairs, i.e., Chromel (Chromel-Alumel), iron (-constantan), copper (-constantan), have positive slopes in Figure 4.6.2.

The simplest thermocouple circuit for temperature measurement consists of two wires joined together at one end (forming the "measuring junction") with their other ends connected directly to a measuring instrument, as shown in the upper portion of Figure 4.6.3. The EMF generation in this circuit is graphically represented in the lower portion, an E–T diagram, using the data in Figure 4.6.2. The E–T diagram is used for examining the EMF generated in the circuit, to be certain that it arises only from the desired thermocouple materials, and that all segments of the circuit are properly connected. The E–T diagram is not used for evaluating the output — that is done using the tables after the circuit has been shown to be correctly wired.

To construct an E–T diagram, first sketch the physical system considered and assign a number to each "point of interest" on that sketch and a temperature. On E–T coordinates, locate point 1 at 0/mV and at its assigned temperature. Then start a line from point 1, moving toward the temperature of point 2, and copying the shape of the calibration curve of the iron wire (see Figure 4.6.2). From 2 to 3, use the constantan calibration curve. The difference in elevation of points 1 and 3 describes the net EMF generated in the circuit between points 1 and 3, and describes the polarity. When point 3 lies physically above point 1 in the E–T diagram, it is, by convention, electrically negative with respect to point 1.

The simple triangular shape shown in Figure 4.6.3 identifies a proper circuit. Any thermocouple circuit whose E–T diagram is equivalent to that is appropriate for temperature measurement and its EMF may be interpreted using the conventional tables. Any circuit whose E–T diagram is not equivalent to the pattern circuit should be rewired.

Thermocouples generate their signal in response to the temperature difference between the two ends of the loop. For accurate measurements, the temperature of the "reference junction" must be known. Laboratory users often use an ice bath made from a good-quality Dewar flask or vacuum-insulated bottle of at least 1 pt capacity, as shown in Figure 4.6.4. The flask should be filled with finely crushed ice and then flooded with water to fill the interstices between the ice particles. The reference thermocouple is inserted into a thin-walled glass tube containing a small amount of silicone oil and submerged six or eight diameters into the ice pack. The oil assures good thermal contact between the thermocouple junction

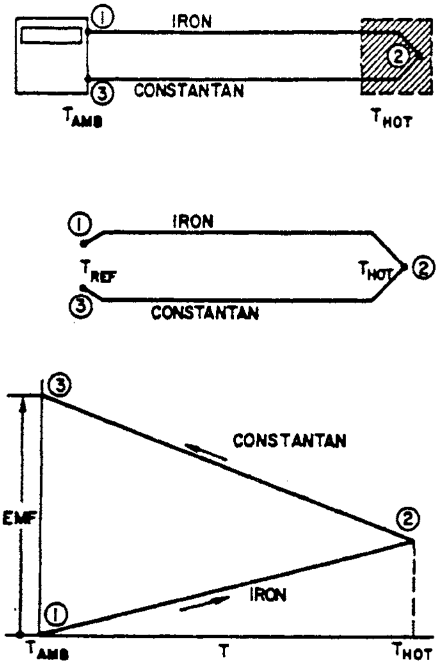

FIGURE 4.6.3 E–T diagram of a thermocouple using an ambient reference.

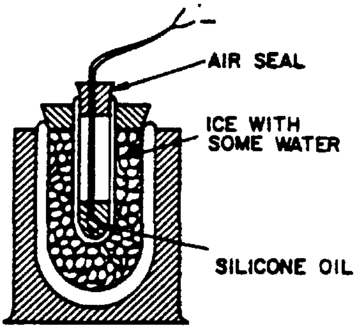

FIGURE 4.6.4 Characteristics of a good ice bath

and the ice/water mixture. The tube should be sealed at the top to prevent atmospheric moisture from condensing inside it, which would cause corrosion when using iron-constantan thermocouples. Figure 4.6.5 shows in iron-constantan thermocouple circuit with an ice bath. The individual thermocouple wires are connected to copper wires in the ice bath, and the two copper wires taken to the voltmeter. The lower portion of this figure shows the E–T diagram for this circuit, and proves that the output of this circuit is entirely due to the temperature difference from end to end of the iron-constantan loop: the two copper wires do not contribute to the output.

Calibration. Thermocouple calibrations are provided by the wire manufacturers to tolerances agreed upon industry-wide, as summarized in Table 4.6.1. These tolerances include two components: the uncertainty in the average slope of the calibration curve of the wire, and the effects of local inhomogeneities in the wire. It is difficult to improve the accuracy of a thermocouple by calibrating it. For a truly significant calibration, the thermocouple would have to be exposed to the same temperature during calibration, at every point along it, that it would encounter in service. In an oven calibration, most of the signal is generated in the material at the mouth of the oven, as could be recognized by considering the temperature gradient distribution along the wire. The material inside the oven contributes little or nothing to the signal.

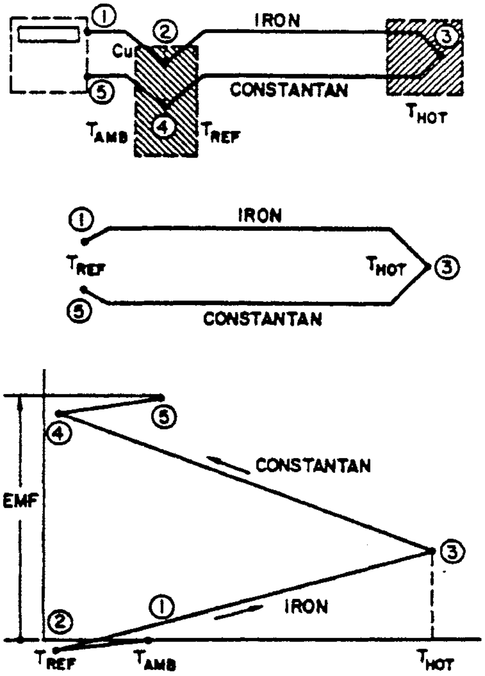

FIGURE 4.6.5 A thermocouple circuit using an ice bath reference, and its E–T diagram.

Thermistors

Thermistors are electrical resistance temperature transducers whose resistance varies inversely, and exponentially, with temperature. The resistance of a 5000 Ω thermistor may go down by 200 Ω for each degree C increase in temperature in the vicinity of the initial temperature. Interrogated by a 1.0 mA current source, this yields a signal of 200 mV/°C. As a consequence of this large signal, thermistors are frequently used in systems where high sensitivity is required. It is not uncommon to find thermistor data logged to the nearest 0.001°C. This does not mean that the data are accurate to 0.001°C, simply that the data are readable to that precision. A thermistor probe is sensitive to the same environmental errors which afflict any immersion sensor: its accuracy depends on its environment.

Thermistor probes can be used between –183°C (the oxygen point) and +327°C (the lead point) but most applications are between –80 and +150°C. The sensitivity of a thermistor (i.e., the percent change in resistance per degree C change in thermistor temperature) varies markedly with temperature, being highest at cryogenic temperatures.

Thermistor probes range in size from 0.25-mm spherical beads (glass covered) to 6-mm-diameter steel-jacketed cylinders. Lead wires are proportionately sized. Disks and pad-mounted sensors are available in a wide range of shapes, usually representing a custom design "gone commercial." Aside from the unmounted spherical probes and the cylindrical probes, there is nothing standard about the probe shapes.

Calibration. Thermistor probes vary in resistance from a few hundred ohms to megohms. Probe resistance is frequently quoted at 25°C, with no power dissipation in the thermistor. The commercial range is from about 2000 to 30,000 Ω. Representative values of the sensitivity coefficient (% change in resistance per degree C) is given in Table 4.6.3 and resistance values themselves, in Table 4.6.4.

Proprietary probes are available which "linearize" thermistors by placing them in combination with other resistors to form a circuit whose overall resistance varies linearly with temperature over some range. These compound probes can be summed, differenced, and averaged as can any linear sensor. Modern manufacturing practices allow matched sets to be made, interchangeable within +/–0.1°C.

TABLE 4.6.3 Thermistor Temperature Coefficient Variations with Temperature

Temp. °C	Condition	ΔR/R, %
–183	Liquid oxygen	–61.8
–80	Dry ice	–13.4
–40	Frozen mercury	–9.2
0	Ice point	–6.7
25	Room temperature	–5.2
100	Boiling water	–3.6
327	Melting lead	–1.4

TABLE 4.6.4 Thermistor Resistance Variation with Temperature

Temp., °C	Res., Ω	Temp., °C	Res., Ω
–80	1.66 M	0	7355
–40	75.79 K	25	2252
–30	39.86 K	100	152.8
–20	21.87 K	120	87.7
–10	12.46 K	150	41.9

TABLE 4.6.5 Representative Thermal Dissipation Constants for Two Thermistor Probe Designs

Environment	1.0-cm Disk	5.0-cm Cylinder
Still air	8 mW/C	1 mW/C
Still oil	55	—
Still water	—	3.5
Oil at 1 m/sec	250	—

Thermal Characteristics. Thermistor probes are generally interrogated using a low current, either AC or DC. A level of about 10 μA would be typical. With a probe resistance of 10 K Ω, 0.01 W must be dissipated into its surrounding material. This current results in the probe running slightly above the temperature of the medium into which it is installed: the "self-heating" effect. Since thermistors are often used where very small changes in temperature are important, even small amounts of self-heating may be important.

The self-heating response is discussed in terms of the "dissipation constant" of the probe, in milliwatts per degree C. The dissipation constant depends on the thermal resistance between the thermistor and its surroundings. For fluid-sensing probes, the self-heating varies with velocity and thermal conductivity, while for solid immersion probes, it varies with the method of attachment and type of substrate.

Dissipation constants for representative probes are given in Table 4.6.5. The self-heating effect must be considered in calibration as well as in use.

The transient response of a thermistor is more complex than that of a thermocouple and, size for size, they are not as well suited to transient measurements.

Thermistor probes are sold with calibration tables of resistance vs. temperature at some specified accuracy, on the order of +/–0.1 or 0.2 K, depending on the grade of probe purchased. These tables are typically in increments of 1 K. For computer interpretation, they should be fit to the Steinhart-Hart form[2] and the coefficients determined for least error.

$$\frac{1}{T} = A_0 + A_1 \ln(R) + A_3 \ln\left(R^3\right) \qquad (4.6.5)$$

Resistance Temperature Detectors

The terms *resistance temperature detector* (RTD) and *resistance thermometer* are used interchangeably to describe temperature sensors containing either a fine wire or a thin film metallic element whose resistance increases with temperature. In use, a small current (AC or DC) is passed through the element, and its resistance measured. The temperature of the element is then deduced from the measured resistance using a calibration equation or table lookup.

RTDs are used both for standards and calibration laboratories and for field service. Field-service probes are generally encased in stainless steel protective tubes with either wire or film elements bonded to sturdy support structures. They are made to take considerable physical abuse. Laboratory standard-grade probes are often enclosed in quartz tubes, with the resistance wire mounted in a strain-free manner on a delicate mandrel.

High-quality resistance thermometers have been used as defining instruments over part of the range of the IPTS. Because of this association with high-precision thermometry, resistance thermometers in general have acquired a reputation for high precision and stability. Commercial probes, however, are far different in design from the standards-grade probes, and their stability and precision depend on their design and manufacture.

RTDs are often recommended for single-point measurements in steady-state service at temperatures below 1000°C where longtime stability and traceable accuracy are required and where reasonably good heat transfer conditions exist between the probe and its environment.

They are not recommended for use in still air, or in low-conductivity environments. RTDs self-heat, which causes an error when the probes are used in a situation with poor heat transfer. They are not recommended for transient service or dynamic temperature measurements unless specifically designed for such service. The probes tend to have complex transient characteristics and are not amenable to simple time-constant compensation.

Physical Characteristics. The physical characteristics of any given resistance thermometer represent a compromise between two opposing sets of requirements. For accuracy, repeatability, and speed of response, a delicate, low-mass sensing element is desired, supported in a strain-free manner in good thermal contact with its surroundings. For durability, a rugged sensor is indicated, mounted firmly to a sturdy structure inside a robust, sealed protection tube.

Both the short-term calibration (resistance vs. specimen temperature) and the long-term stability (drift) are directly affected by the mechanical configuration of the probe. The electrical resistance of the sensing element is a function of its temperature and state of mechanical strain (Figure 4.6.6).

The sensing elements used in field-service RTD probes range from thin metallic films deposited on rectangular ceramic wafers (0.5 × 1.0 × 2.0 mm) with pigtail leads (0.25 mm diameter and 2.5 cm long) to glass-encapsulated, wire-wound mandrels (4 mm in diameter and 2.0 cm long), again with pigtail leads.

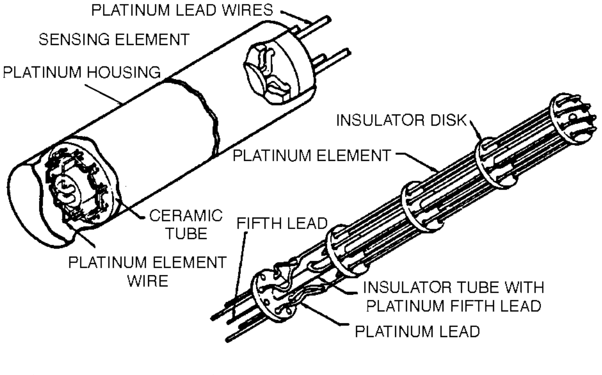

FIGURE 4.6.6 Slack-wire platinum resistance thermometer.

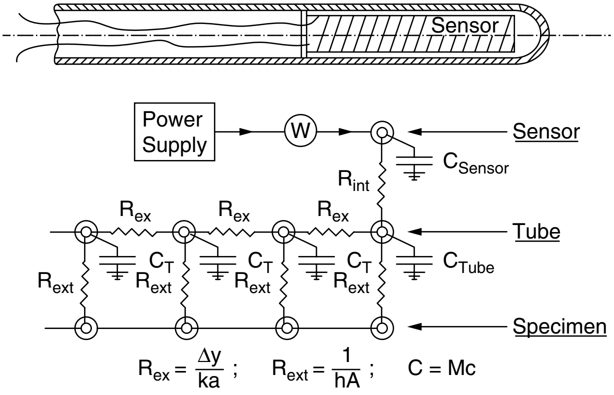

FIGURE 4.6.7 Thermal circuit representation of a typical resistance thermometer.

Bonding the sensor to its support provides good mechanical protection to the element, but subjects the element to strain due to thermal expansion. As long as this process is repeatable, the calibration is stable.

Electrical Characteristics. RTDs are available commercially with resistances from 20 to 20,000 Ω with 100 Ω being common. Bifilar windings are frequently used in wire-wound elements, to reduce the electrical noise pickup. This is more important in the quartz-jacketed probes than in those with stainless steel protection tubes. Twisted pair lead wires are recommended.

Thermal Characteristics. Figure 4.6.7 shows a simplified cross section of a typical resistance thermometer and a thermal circuit which can be used to discuss its behavior. In forming such a thermal circuit model, each element of the probe is described by its resistive and capacitive attributes following conventional heat transfer practice. The principal components are

- The external thermal resistance per unit length;
- The thermal capacitance of the protective tube per unit length, C_T;
- The radial internal thermal resistance between the sensor and the protective tube, R_{int};
- The capacitance of the sensor element and its support, C_{sensor};
- The axial internal thermal resistance of the stem, per unit length, R_T.

This circuit can be used to predict the temperature distribution within the probe both at steady state and during transients and can be refined, if needed, by subdividing the resistance and capacitance entities.

Steady-State Self-Heating. Interrogating an RTD by passing a current through it dissipates power in the element, shown in Figure 4.6.7 as W, which goes off as heat transfer through the internal and external resistances. This self-heating causes the sensing element to stabilize at a temperature higher than its surroundings and constitutes an "error" if the intent is to measure the surrounding temperature. The amount of the self-heating error depends on three factors:

- The amount of power dissipated in the element,
- The internal thermal resistance of the probe, as a consequence of its design, and
- The external thermal resistance between the surface of the probe and the surrounding material.

The self-heating temperature rise is given by Equation (4.6.6):

$$T_{\text{sens}} - T_{\text{surr}} = W\left(R_{\text{int}} + R_{\text{ext}}\right) \tag{4.6.6}$$

The internal thermal resistance of a probe, R_{int}, measured in degree C per watt, describes the temperature rise of the sensing element above the surface temperature of the probe, per unit of power dissipated. The internal thermal resistance can be deduced from measurements of the sensor temperature at several different current levels when the probe is maintained in a well-stirred ice bath, where the external thermal resistance is very low. The slope of the apparent temperature vs. power dissipated line, °C/W, is the internal thermal resistance. When an RTD is used in a gas or liquid, the external resistance between the probe and its surroundings must be estimated from standard heat transfer data. The external resistance is 1/(hA), °C/W.

A typical cylindrical probe exposed to still air will display self-heating errors on the order of 0.1 to 1.0°C per mW (commercial probes of 1.5 to 5 mm in diameter). At 1 m/sec air velocity, the self-heating error is reduced to between 0.03 and 0.3°C. In water at 1 m/sec velocity, the self-heating effect would be reduced by a factor of four or five compared to the values in moving air, depending on the relative importance of the internal and the external thermal resistances.

Calibration and Drift. The relationship between resistance and temperature must be determined for each probe or acquired from the manufacturer. Generally speaking, the reported values will require interpolation.

The resistance–temperature characteristic of a probe may drift (i.e., change with time) while the probe is in service. Manufacturers of laboratory-grade probes will specify the expected drift rate, usually in terms of the expected error in temperature over an interval of time. Two sample specifications are "0.01 C per 100 hours" for a low-resistance, high-temperature probe (0.22 Ω at 0°C, 1100°C maximum service temperature) and "0.01 C per year" for a moderate-resistance, moderate-temperature probe (25.5 Ω at 0°C, 250°C maximum service temperature). Drift of the resistance-temperature relationship takes place more rapidly at high temperatures.

Radiation Devices

Surface temperatures and gas temperatures can be deduced from radiation measurements. Surface-temperature measurements are based on the emitted infrared energy, while gas-temperature measurements use specific emission lines from the gas itself or from a tracer inserted into the gas.

Commercial surface-temperature measurement systems (single-point) are available, at low cost, which can measure temperature to +/–1% of reading, above 38°C, if the emissivity of the surface is known. The device referenced requires a spot size of 1.25 cm diameter, viewed from 75 cm. Spectroscopic gas-temperature measurements can be accurate to +/–3 or 4% of reading, but require a significant investment in effort as well as equipment (on the order of 1 to 2 years and $100,000 to $200,000). Several techniques based on Raman scattering have been used in combustion systems. Planar-lasar-induced fluorescence has shown considerable promise as one of the newer methods.

Infrared emission from a surface is described by two laws: the Stefan Boltzmann law describing the total emitted radiation as a function of temperature, and Planck's law describing its distribution as a function of temperature. These laws form the basis for all radiation-based surface-temperature detectors.

Early radiometers focused the total infrared energy on a thermopile bolometer and used the temperature rise across its calibrated heat loss path to measure the incident energy flux. Solid-state photon detectors have replaced thermopile bolometers as the detector of choice. Such a detector will respond to any photon having energy above a certain level (specific to the detector). Since the energy of a photon is inversely proportional to its wavelength, detectors respond to all wavelengths below some value. Modern detectors use band-pass filters to limit the wavelength band of photons admitted to the detector and rely on Planck's law to infer the temperature from the energy flux:

$$E_{b,\lambda} = \frac{C_1 \lambda^{-5}}{e^{C_2/\lambda T} - 1} \tag{4.6.7}$$

Commercial radiation temperature detectors use different wave bands for different temperature ranges, with different detectors for each band. The emissivity of the surface must be known, as a function of temperature, in the wavelength band used by the detector.

Many IR thermometers have an emissivity compensator that is used to correct for non-blackbody behavior. This compensator amplifies the detector output to compensate for emissivities less than 1, but can also be used to correct for transmission losses due to smoke, dust, or windows. If the emissivity of the material is less than 1, then the emissivity multiplied by the transmissivity must be entered into the instrument. Some ways of determining emissivity are as follows.

1. Heat a sample of the material to a known temperature, and dial in the emissivity required to get that temperature reading on the instrument.
2. Cover the material with a *thin* layer of another material that does not affect the surface temperature but is of known emissivity, and measure the temperature. Remove the thin layer or go to another section, and dial in the emissivity to get that temperature again.
3. Drill a hole in the surface (depth should be at least six times the diameter) and measure the temperature of the hole. The hole simulates a blackbody since much of the energy is absorbed after multiple reflections. Measure the temperature of another area on the surface, and dial in the emissivity to get the hole temperature.

Radiation detectors are vulnerable to interference from many sources. if it is desired to measure the temperature of materials that can transmit radiation, then a wavelength must be chosen so that the material appears opaque. One could use a wavelength that is semi-opaque, but care must be taken so that radiation that is transmitted *throught* the material does not bias the readings. Often, it is desired to measure the temperature behind a glass or quartz window. In this case, an appropriate wavelength must be chosen so that the radiation readily travels through the window (shorter wavelengths). For reflective surfaces, it is important that the surface not see sources of heat that can be reflected into the instrument. Reflective sources can usually be removed using shields.

Because the atmosphere contains components that absorb infrared radiation (CO_2, water vapor, methane) at certain wavelengths, care must be taken to operate outside of these wavelengths or to compensate for them. If one does operate at the absorption wavelengths, then the measurement will be distance dependent, or may be affected by changes in humidity. There are “windows” in the IR spectrum which allow these absorption bands to be avoided, however. A good choice for many low temperature applications is 8 to 14 microns. Higher temperatures require that one use narrowband filters at shorter wavelengths.

Filters are used to determine the portion of the spectrum that is used for the measurement. For low temperatures (less than 500°C), the most popular band is 8 to 14 microns. This is a wide range (resulting in much energy emitted from the surface), is free of atmospheric absorption, and can even be used at temperatures below ambient. For temperatures between 100°C and 800°C, wavelengths around 3.8 microns are preferred. This allows for no atmospheric absorption, and allows for penetraiton of flames. At high temperatures (above 300°C), 2.2 microns is popular. Again, this allows for no atmospheric absorption. These are more expensive, however, since relatively little energy is available at this wavelength and a high-gain amplifier is required to amplify the weak signal.

Since IR thermometers determine the average temperature of everything in their field of view (FOV), then a temperature between the object temperature and the surroundings will be indicated if the desired object does not fill the filed of view. One must either decrease the distance between the thermometer and the object, or use the emissivity compensator to correct for the loss in energy.

Two color interferometers determine the temperature by measuring the ratio of the energies at two wavelengths. If the change in the emissivity is the same (which occurs if the body is gray), then the unit does not depend on the absolute value of emissivity. Another advantage of this instrument is that it is often not affected by dust or smoke obscuring the target since it usually results in the same decrease in energy at both wavelengths. In reality, however, one must be sure that the emissivity at both wavelenghts change equally. These units are much more expensive, and they may not provide superior performance under certain circumstances.

A fiber-optic blackbody temperature detector system is offered by the Luxtron Corporation for standards room and field service above 300°C. The unit consists of a blackbody capsule fiber-optically coupled to a filtered, band-limited photon detector. Accuracy of 0.01 to 0.1°C is claimed, depending on temperature level.

A fluoroptic temperature-measuring system is also offered by the same company, for use only at lower temperatures (–200 to +450°C). This system uses an ultraviolet-stimulated phosphor on the end of an optical fiber as its sensor. The fluorescent signal from the phosphor decays with time, and its "time constant" is a function of temperature. Accuracy of +/–0.5°C is claimed for measurements within +/–50°C of a calibration point, or +/–1°C within 100°C.

Temperature-Sensitive Paints, Crayons, and Badges

Temperature-sensitive paints, crayons, and badges are available from several suppliers (Omega Engineering, Inc., Stamford, CT, and others in Germany and Japan). Each undergoes an irreversible change (e.g., a change in color or a change from solid to liquid) at one specified temperature. With a range of paints, temperatures from ambient to about 1500°C can be covered. The accuracy generally quoted is about +/–1% of level, although melting standards are available to +/–0.5°C.

The phase-change materials melt at well-defined temperatures, yielding easily discernible evidence that their event temperature has been exceeded. When more than one phase-change paint is applied to the same specimen, there can be interference if the melt from the low-melting paint touches the high-melting material. Color change materials do not interfere, but are more difficult to interpret. The calibration of high-temperature paints (both phase change and color change) may shift when they are used on heavily oxidized materials, due to alloying of the oxide with the paint. Recommended practice is to calibrate the paints on specimens of the application material. The event temperature which will cause transformation depends on the time at temperature: short exposure to a high temperature often has the same effect as long exposure to a lower temperature.

The paints and crayons are nonmetallic and, therefore, tend to have higher emissivities for thermal radiation than metals. They should be used only over small areas of metallic surfaces, compared with the metal thickness, or else their different emissivities may lead to a shift in the operating temperature of the parts.

The principal disadvantages of the paints and crayons are that they require visual interpretation, which can be highly subjective, and they are one-shot, irreversible indicators which respond to the highest temperature encountered during the test cycle. They cannot record whether the peak was reached during normal operation or during soak-back.

Liquid crystals can be divided into three groups, depending on their molecular arrangements: (1) smectic, (2) nematic, and (3) cholesteric. Most of the temperature-sensitive liquid crystals now in use are cholesteric: made from esters of cholesterol. Their molecules are arranged in planar layers of molecules with their long axes parallel and in the plane of the layer. The molecules in each layer are rotated with respect to those in its neighboring layers by about 15 min of arc in a continuous, helical pattern along an axis normal to the layers.

The colors reflected from cholesteric liquid crystals are thought to be due to Bragg diffraction from the aligned layers. The "wrap angle" between adjacent layers increases with temperature; hence, the color of the liquid crystal shifts toward short wavelengths (toward blue) as the temperature is raised. The color can also be affected by electric fields, magnetic fields, pressure, shear stress, and some chemical vapors.

Warm cholesterics are colorless liquids and they pass through a series of bright colors as they are heated through their "color-play" temperature band. The first color to appear is a deep red, followed by yellow, green, blue, and violet. Further heating yields a colorless liquid again. This cycle is reversible and repeatable, and the color–temperature relationship can be calibrated.

Liquid crystals selectively reflect only a small fraction of the incident light; hence, to enhance the brightness of the color image, they must be backed up with black paint or a nonreflecting surface.

A typical calibration is shown in Figure 4.6.8 for liquid crystals painted over black paint on an aluminum calibration strip. The upper part of Figure 4.6.8 describes the color variation, while the lower part shows the imposed linear temperature distribution. The hot end is blue, the cold end is red. Color-play intervals range from 0.5 to 10.0°C. Liquid crystals whose color-play interval is on the order of 0.5 to 2.0°C are often referred to as *narrow-band* materials, while those whose interval extends to 5.0 to 10°C are called *wide band*. Narrow-band images are easy to interpret by eye. Wide-band images show only

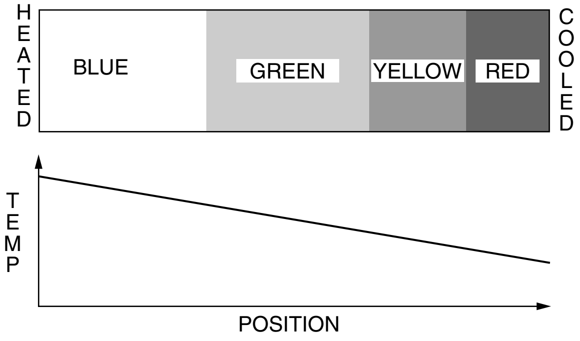

FIGURE 4.6.8 Schematic representation of a calibration strip.

subtle variations of color for small changes in temperature, and accurate work requires digital image handling or multiple images taken with different filters.

Several different narrow-band liquid crystals can be mixed together to make a single, multi-event paint covering a wide range of temperatures, provided their color-play intervals do not overlap. Such a mixture yields a set of color-play bands, one for each component.

Calibration. Liquid crystals are sold by event temperature and color-play bandwidth, with a nominal accuracy of +/–1°C on the event temperature. In many applications, especially if the image is to be visually interpreted, no further calibration is needed.

The accuracy attainable with a liquid crystal is related to the width of the color-play interval. With narrow-band material (a color-play interval of about 1.0°C), visual interpretation can be done with an uncertainty of 0.25 to 0.5°C. With digital image interpretation, spectrally controlled lighting and appropriate corrections for reflected light interference, the uncertainty can be held below 0.25°C.

Early users reported that the perceived color of a liquid crystal depended on both the lighting angle and the viewing angle. This dependence can be eliminated by using a light source along the line of sight (coaxial viewing and illumination).

Multiple-Event Paints. Several narrow-band paints can be mixed together to make a single paint with all the characteristics of each component, if their color-play intervals do not overlap. Each component retains its original calibration and acts independently of the other components.

Figure 4.6.9 shows the image from a five-event paint used to map the adiabatic wall temperature isotherms around a heated block in mixed convection. The outermost isotherm is 30°C, and the events are spaced apart at 5°C intervals. Determination of the temperatures from a multiple-event image requires that the temperature be known at one point in the image.

Liquid Crystals in Water. Liquid crystals can be used to mark the temperature distribution in water and some other liquids by adding a small quantity of encapsulated liquid crystal material to the liquid and photographing the color distribution using planar lighting. Velocity and temperature distributions can be determined by photographing the liquid crystal particles using a known exposure time. The temperature is deduced from the particle color, and the velocity by the length of the streak its image forms. Figure 4.6.10 shows the velocity and temperature distributions in a shear-driven, water-filled cavity 30 sec after the impulsive start of belt motion. In this view, the belt is at the top of the image, and moved from left to right. The water was stably stratified initially, with the top being 4°C hotter than the bottom. This technique was demonstrated by Rhee et al. (1984) and has been used by several workers.

Image Processing. Several schemes have been proposed to remove the subjectivity from interpretation of liquid crystal images. Akino et al. (1989), and others, have processed RGB video images of narrow-band images using multiple filters to extract images of specified isochromes, related to temperatures through a calibration. Hollingsworth et al. (1989) processed RGB images of wide-band images using chromaticity

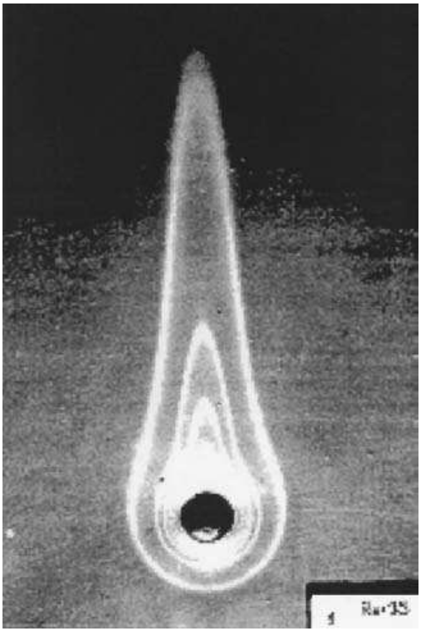

FIGURE 4.6.9 Multi-event liquid crystal used to visualize the isotherm pattern above a heated spot in mixed convection.

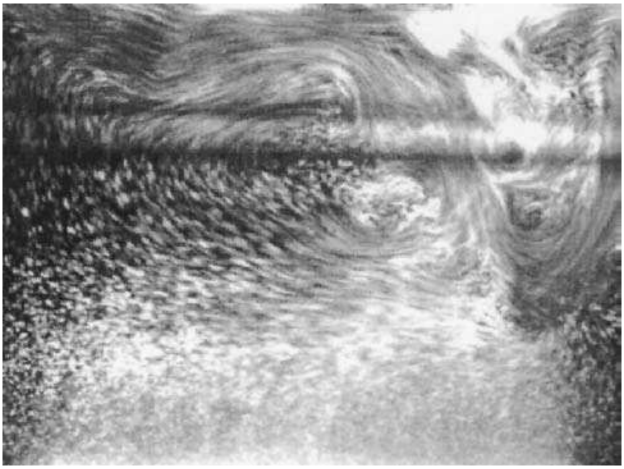

FIGURE 4.6.10 Liquid crystal visualization of the velocity and temperature distribution in a water-filled tank.

coordinates (hue, saturation, and intensity) and extracted temperature at each pixel, rather than along isochromes.

Heat Flux

Heat flux to or from a surface can be measured directly, using heat flux meters, or inferred from an overall energy balance, or inferred from temperature–time measurements at the surface or within the body. There are no primary standards for heat flux measurement.

Three general classes of heat flux meters are in common use: slug calorimeters, planar heat flux gauges (sometimes called Schmidt–Boelter gauges), and circular foil gauges (sometimes called Gardon gauges).

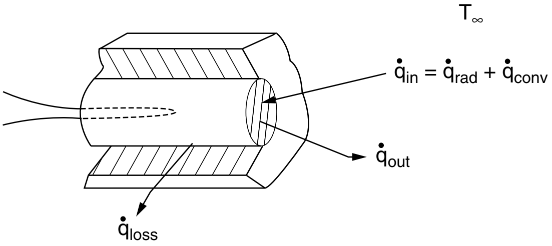

FIGURE 4.6.11 A simple slug calorimeter.

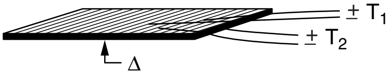

FIGURE 4.6.12 A typical planar heat flux gauge.

Sensitivities range from microvolts per kW/m² to millivolts per W/m². Planar gauges can be used for radiant or convective heat loads. Circular foil gauges should be used only for radiant loads.

Slug Calorimeter

The slug calorimeter is an energy balance transducer consisting of a known mass of material instrumented so that its temperature can be measured. A simple version is shown in Figure 4.6.11. If losses are negligibly small and the mass and the specific heat are constant, the instantaneous heat flux is deduced from

$$\dot{q}''_{\text{in}} A = Mc \frac{\partial T}{\partial t} \tag{4.6.8}$$

The variation of slug temperature with time is used to infer net heat transfer rate to the gauge. Slug calorimeters are used mainly when the heat flux, or the heat transfer coefficient, is expected to be relatively constant. They are of less value when the input flux changes arbitrarily because of the inaccuracies inherent in differentiating the signals.

Planar Heat Flux Gauge

Planar heat flux gauges use Fourier's law to deduce the heat flux from a steady-state measurement of the temperature difference across a thin sheet of thermally insulating material. The planar gauge geometry is shown in Figure 4.6.12. The working equation for a planar gauge is

$$\text{EMF} = N\varepsilon \Delta T = \frac{N\varepsilon t}{k} \dot{q}'' \tag{4.6.9}$$

where

N = number of junction pairs,
e = thermoelectric power of the thermoelement, mV/C
t = thickness of the insulator, m
k = conductivity of the insulator, W/m·C
q'' = heat flux through the gauge, W/m²

The figure shows one thermocouple junction on the top and one on the bottom surface of the insulator. Most gauges use multiple junctions. The thermoelements may be wire (down to 0.025 mm diameter) or thin films deposited on the insulator (10 to 20 Å). The assembly is usually sandwiched between two sheets of protective material to form an integral unit. Up to 150°C application temperature, these units are often made of Kapton, and provided with a contact adhesive. They may be as thin as 0.15 mm overall.

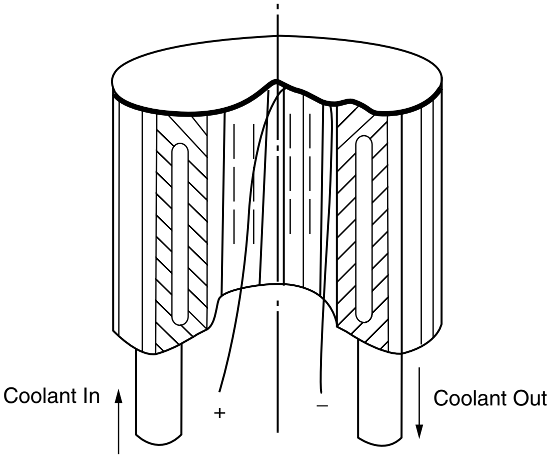

FIGURE 4.6.13 A water-cooled circular foil gauge (Gardon gauge).

Gauges should not be removed and reinstalled without recalibration, as the act of removing them from the surface may delaminate the gauge, changing its thermal resistance, and therefore its calibration.

Circular Foil Gauges

A circular foil gauge consists of a thin circular disk of metal supported by its edge from a structure of constant and uniform temperature. The circular foil gauge is often called a Gardon gauge. A constantan foil is often used, with a copper support structure. Two copper wires complete the circuit: one attached to the center of the foil disk and one to the support structure. The copper–constantan thermocouple thus formed produces an EMF determined by the temperature difference from the center of the foil disk to its rim. That temperature difference is directly proportional to the average heat flux on the disk. A cross-sectional view of a circular foil gauge is shown in Figure 4.6.13.

The working equation for a circular foil gauge is

$$\text{EMF} = \varepsilon \frac{R^2}{4kt}\dot{q}'' \tag{4.6.10}$$

The output signal is thus directly proportional to the heat flux on the disk. Cooling passages are frequently built into the support structure to maintain the edge of the disk (the heat sink for the foil disk) at constant temperature.

Fast Response Heat Flux Gages

The bulk of heat flux measuring devices on the market are for use where the heat flux varies slowly with time. Heat flux gages with frequency response up to 100 kHz are required for applications such as gas turbines, shock tubes, and IC engines.

A heat flux microsensor has been developed at Virginia Polytechnic University and marketed by Vatell Corporation (Diller and Onishi, 1988; Hager et al., 1991; Hager et al., 1993). This device consists of a thermopile manufactured on a substrate using VLSI techniques (see Figure 4.6.14). One set of thermocouple junctions are deposited onto an electrically insulating substrate. A thin layer of insulation (typically an oxide) is then deposited on top of the thermocouple junctions. A second layer of thermocouple junctions is deposited on the previous layers such that a thermopile is formed. Finally, a protective oxide layer is deposited. Because of the thinness of the insulator, a small temperature difference will result. Many thermocouple junctions are therefore needed to obtain a measurable signal. Between 40 and 90 junctions per device is not uncommon. The device size is on the order of millimeters (typically 3 mm × 3 mm sensing area). A temperature level since the thermopile only outputs temperature differences. The

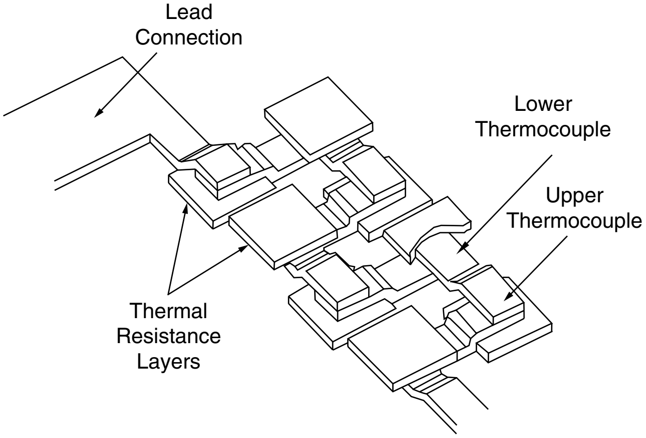

FIGURE 4.6.14 Schematic of heat flux microsensor. (From Hager, J.M., Simmons, S., Smith, D., Onishi, S., Langley, L.W., and Diller, T.E., Experimental performance of a heat flux microsensor. *ASME Journal of Engineering for Gas Turbines and Power,* 113, 246–250, 1991.)

advantage of this device is that the layers are very thin, resulting in frequency responses as high as 100 kHz and minimal thermal and flow disruption to the surface. The device is able to operate at temperature as high as 800°C, depending on the type of thermocouple used, with a precision of up to 0.1 W/cm^2. Because of the high frequency response of the device, calibration can be performed in the steady state.

The second device developed at MIT by Epstein et al. (1986) consists of a polyimide substrate with resistance thermometers deposited on each side. The substrate is relatively thick, about 25 μm (0.001″), which result sin a low inherent frequency response (about 100 Hz). The frequency response can be increased up to 100 kHz through numerical processing as follows. Since the temperature at the boundaries of the substrate are measured using the resistance thermometers, the temperature profile within the substrate as a function of time can be obtained by numerically solving the transient conduction equation. The heat flux is then calculated by taking the derivative of this numerically constructed temperature profile to obtain the slope at the surface at every time step. The density, specific heat, and the substrate thickness are needed to perform this calculation. Because the substrate is quite thick, measurable signals can be obtained easily making the device quite small (about 1 mm × 1 mm sensing area). The flexible substrate allows the gages to be applied to curved surfaces. A disadvantage of the device is the numerical processing associated with the device if high frequency response is desired. Also, an unsteady calibration of the device must be performed to determine the density and specific heat of the substrate. High temperature capabilities are obtainable depending on the substrate material. The device as described by MIT (resistance thermometers of nickel on a polyimide substrate) has a maximum temperature capability of about 300°C.

Button type heat flux gages have been used in shock tubes to measure heat flux transients (Hartunian and Varwig, 1962; Skinner, 1961). This gage consists of an insulating Pyrex substrate about 1 mm in diameter and a few millimeters thick that is mounted within a gas turbine blade. A thin platinum film is hand painted onto this substrate, and is used as a resistance thermometer to measure the surface temperature of the substrate as a function of time. The instantaneous heat flux into the substrate can then be obtained by assuming the substrate acts as a semi-infinite solid and numerically reconstructing the instantaneous temperature profile at the surface (George et al., 1987). The low thermal diffusivity of the Pyrex substrate relative to the surrounding metal is critical to the successful performance of these gages because they "hold the heat at the surface," producing a large increase in temperature and enabling a measurable signal to be obtained.

An active heat transfer measurement technique has recently been developed that can measure heat transfer at many points on the surface at frequencies up to 15 kHz (Rule and Kim, 1999). An array of

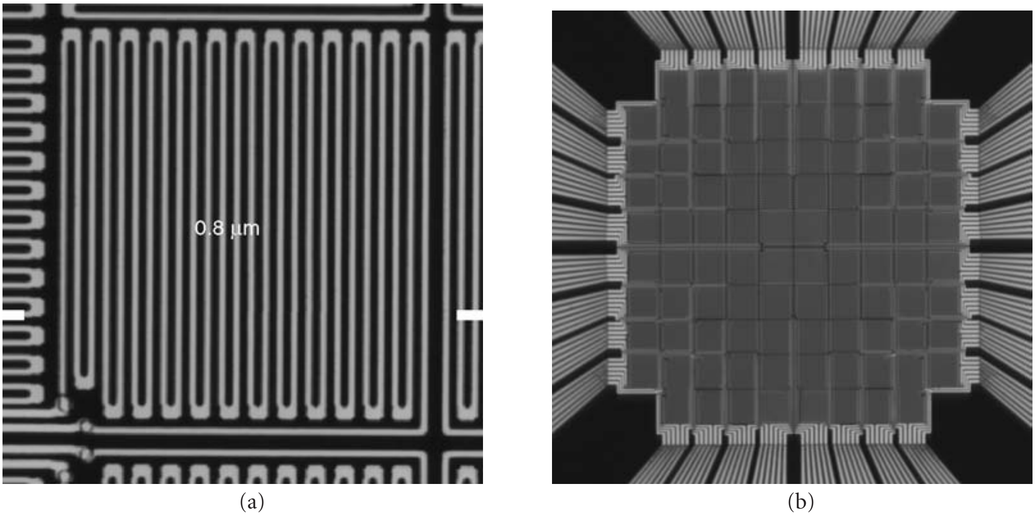

(a) (b)

FIGURE 4.6.15 Photograph of (a) a single heater element and (b) an array of 96 heaters.

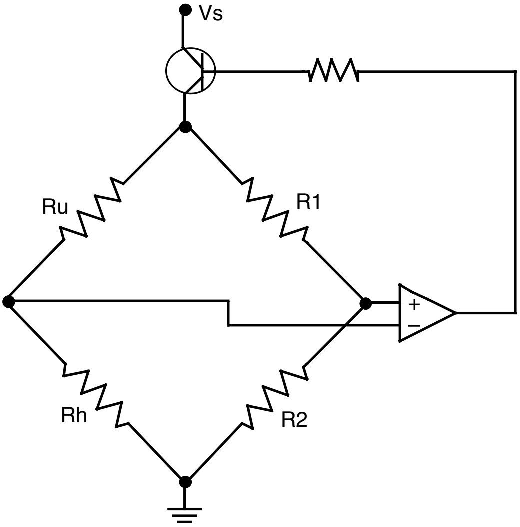

FIGURE 4.6.16 Simplified schematic of control circuit.

platinum resistance heater elements is deposited onto a quartz substrate. Pictures of a single heater element and the array are shown in Figure 4.6.15. Each element is nominally 0.25 mm × 0.25 mm in size. Aluminum lines supply power to the heaters, and are routed between the heaters to the edge of the array. A 1 micron layer of SiO_2 is deposited over the heater array to protect the heaters and to provide the surface with a uniform surface energy. The temperature of each heater in the array is regulated by a series of feedback control circuits similar to those used in constant-temperature hot-wire anemometry. Figure 4.6.16 shows a simplified schematic of the feedback control circuit that is used to maintain each heater at a constant temperature. The voltage difference across a Wheatstone bridge is sensed by an amplifier which provides enough power to the heater to keep the bridge in balance. This condition is satisfied if the ratio of $R_h/R_u = R_2/R_1$. This technique has been used to measure time resolved heat flux distributions beneath growing and departing bubbles during boiling (Yaddanapudi and Kim, 2001) as well as during droplet evaporation (Lee et al., 2001).

Sensor Environmental Errors

Temperature sensors generate signals in response to their own temperatures, but are usually installed to measure the temperature of some fluid or solid. There is heat transfer between the sensor and all of its surroundings, with the result that the sensor usually equilibrates at some temperature different from the fluid or solid it is installed in. This difference is considered an error in the measurement.

Similarly, heat flux gauges are generally installed so one can infer the heat flux which would have been there had the gauge not altered the system behavior. But heat flux gauges do disturb the system, and the heat flux at the gauge location, when the gauge is there, may be significantly different from that which would have been there without the gauge. This system disturbance effect must also be considered an error.

Steady-State Errors in Gas-Temperature Measurement

All immersion-type temperature sensors (thermocouples, resistance detectors, and thermistors) are subject to the same environmental errors, which are frequently larger than the calibration errors of the sensors. Large probes are usually affected more than small ones; hence, RTDs and thermistors (selected by investigators who wish to claim high accuracy for their data) are more vulnerable to environmental errors (due to their larger size and their self-heating errors). This aspect of accuracy is sometimes overlooked.

Sensor installations for gas-temperature measurements should be checked for all three of the usual steady-state environmental errors: velocity error, radiation error, and conduction error. The same equations apply to all sensors, with appropriate dimensions and constants.

$$\text{velocity error:} \qquad E_v = (1-\alpha)\frac{V^2}{2g_c J c_p} \tag{4.6.11}$$

$$\text{radiation error:} \qquad E_r = \frac{\sigma\varepsilon}{h}\left(T_{\text{sens}}^4 - T_{\text{surr}}^4\right) \tag{4.6.12}$$

$$\text{conduction error:} \qquad E_c = \frac{T_{\text{gas}} - T_{\text{mount}}}{\cosh\left[L\sqrt{\dfrac{hA_c}{kA_k}}\right]} \tag{4.6.13}$$

Velocity error depends upon the recovery factor, which varies with the Prandtl number of the fluid. The Prandtl numbers of most liquids are greater than 1; hence, the recovery factor α is greater than 1 and probes tend to read higher than the stagnation temperature in high-speed liquid flows. With thermistors and RTDs in liquids, the self-heating effect and the velocity error both tend to cause high readings. In gases, where the Prandtl number is less than 1, the two effects are of opposite sign and may partly cancel each other.

Radiation and conduction errors vary inversely with the heat transfer coefficient. Both tend to be larger for larger-diameter probes since, all other factors remaining the same, the heat transfer coefficient will be lower for a large-diameter probe. This results in larger radiation and conduction errors. In liquids, radiation error is not a problem, but velocity error and conduction error may both be significant. Conduction error becomes a problem in liquid-temperature measurements when thermowells are used. The depth of immersion of the well is frequently too short to eliminate conduction error.

Steady-State Errors in Solid and Surface-Temperature Measurements

When probes are used to measure solid temperature by inserting them into a hole in the specimen, they are subject to conduction errors proportional to their size and conductivity. A general rule of thumb is to keep the insertion depth at least 20 times the diameter (or wall thickness) of the probe. This assumes a close-fitting hole, backfilled with a material with higher thermal conductivity than air. For more-exact

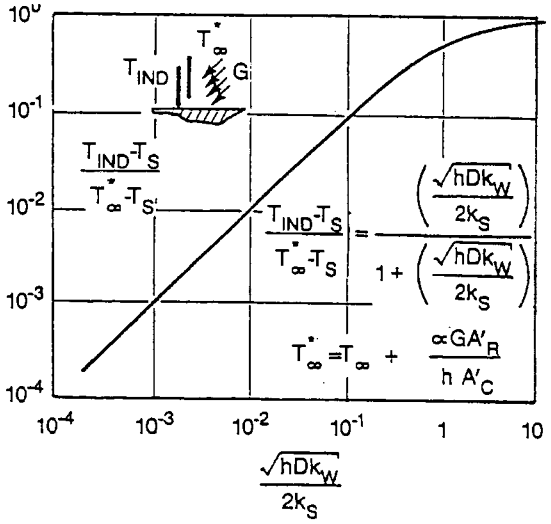

FIGURE 4.6.17 System disturbance errors caused by an attached thermocouple (worst case).

advice regarding a specific installation, a careful thermal circuit analysis of the installation should be developed, and its results used to guide the selection of diametrical clearance, backfill materials, and penetration depth.

A thermocouple attached to a hot surface surrounded by cooler fluid will exchange heat with the fluid by convection and with the surrounding solids by radiation. Heat lost from the thermocouple must be made up from the surface by conduction, which will result in a cold spot at the point of attachment.

Figure 4.6.17 shows the system disturbance error caused by a surface-attached thermocouple, as a fraction of the maximum possible error for the installation. If the surface is irradiated (e.g., by heating lamps), the irradiation will raise the surface temperature, but will also affect the system disturbance error. The effect on the system disturbance error caused by turning on the irradiation is similar to that of raising the temperature of the surrounding fluid to a new value, T_∞°.

The effective gas temperature is defined in terms of the incident irradiation and the heat transfer coefficient as

$$T_\infty^* = T_\infty + \frac{\alpha G A_R}{h A_C} T_\infty^* \tag{4.6.14}$$

Steady-State Errors in Heat Flux Gauges for Convective Heat Transfer

If the gauge is not flush with the surface, it may disturb the flow, and if it is not at the same temperature as the surface, it will disturb the heat transfer. Thus, the gauge may properly report the heat flux which is present when the gauge is present, but that may be significantly different from the heat flux which would have been there if the gauge had not been there.

For planar gauges, both effects are usually small. The thermal resistance of such a gauge is generally small, and they are thin enough to avoid disturbing most flows. Circular foil gauges pose a more serious problem, since they are often cooled significantly below the temperature of the surrounding surface. Dropping the wall temperature at the gauge location can significantly increase the local heat load in two ways: one due to the fact that, for a given value of *h*, a cold spot receives a higher heat load from the gas stream. The second effect arises because the value of the heat transfer coefficient itself depends on the local wall temperature distribution: a local cold spot under a hot gas flow will experience a higher heat transfer coefficient than would have existed had the surface been of uniform temperature.

Evaluating the Heat Transfer Coefficient

The heat transfer coefficient is a defined quantity, given by

$$h = \frac{\dot{q}''_{\text{conv}}}{\left(T_o - T_{\text{ref}}\right)} \tag{4.6.15}$$

Different reference temperatures are conventionally used for different situations:

- T_∞: The free-stream temperature. Used for isolated objects of uniform temperature in a uniform free stream, where an average value of h is desired which describes the overall heat transfer between the object and the flow. Also used in boundary layer heat transfer analyses where local values of h are needed to deal with locally varying conditions.
- T_m: The mixed mean fluid temperature. Used for internal flows where the intent of the calculation is to describe the changes in mixed mean fluid temperature (e.g., heat exchangers).
- $T_{\text{adiabatic}}$: The adiabatic surface temperature. Used for isolated objects or small regions of uniform temperature in either internal or external flows, where the overall thermal boundary conditions are neither uniform heat flux nor uniform temperature.

For a given data set, the value of the heat transfer coefficient will depend on the reference temperature chosen, and h should be subscripted to inform later users which reference was used: e.g., h_∞, h_m, or $h_{\text{adiabatic}}$.

Direct Methods

The two most commonly used methods for measuring the heat transfer coefficient are both derived from the same energy balance equation:

$$hA\left(T_o - T_{\text{ref}}\right) = \dot{e}_{\text{in}} + \dot{q}_{\text{cond,in}} + \dot{q}_{\text{rad,in}} - Mc\frac{dT}{d\tau} \tag{4.6.16}$$

Steady State. In the steady-state method, the transient term is zero (or nearly so), and h is determined by measuring the input power and the operating temperature, and correcting for losses. Equation (4.6.16) can be applied to differentially small elements or to whole specimens. The considered region must be reasonably uniform in temperature, so the energy storage term and the convective heat transfer term use the same value.

For tests of isolated objects, or embedded calorimeter sections, steady-state tests usually use high-conductivity specimens (e.g., copper or aluminum) with embedded electric heaters. The resulting value of h is the average over the area of the specimen. The Biot number, hL/k, for the specimen should be low (on the order of 0.01 or less) if only one temperature sensor is used in the specimen, so the surface temperature can be determined from the embedded sensor.

If a single heated element is used within an array of unheated elements, the resulting heat transfer coefficient is implicitly defined as $h_{\text{adiabatic}}$ and should be identified as such. Heat transfer coefficients measured with single-active-element tests cannot be used with the mixed mean fluid temperature.

When the variation of h over a surface is required, one common steady-state technique is to stretch a thin foil (stainless steel, or carbon impregnated paper, or gold deposited on polycarbonate) over an insulating substrate, and electrically heat the foil surface. Liquid crystals or infrared techniques can be used to map the surface temperature, from which the heat transfer coefficient distribution can be determined. The "heated foil with liquid crystal" approach was used by Cooper et al. in 1975 to measure heat transfer coefficients, and has since been used by many others. Hippensteele et al. (1985) have made extensive use of the foil technique in studies of gas turbine heat transfer. An example of their work on the end wall of a turbine cascade is shown in Figure 4.6.18.

Hollingsworth et al. (1989) used a stainless steel foil heater for a study in air for an electronics cooling application, illustrated in Figure 4.6.19.

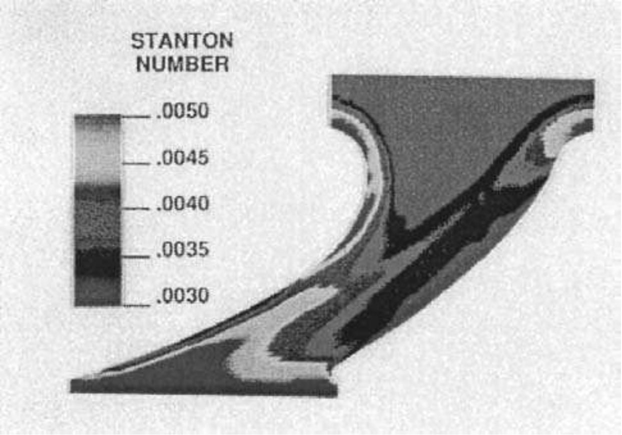

FIGURE 4.6.18 Heat transfer coefficient distribution on the end wall of a turbine cascade. (From Hippensteele, S.A. et al., NASA Technical Memorandum 86900, March, 1985. With permission.)

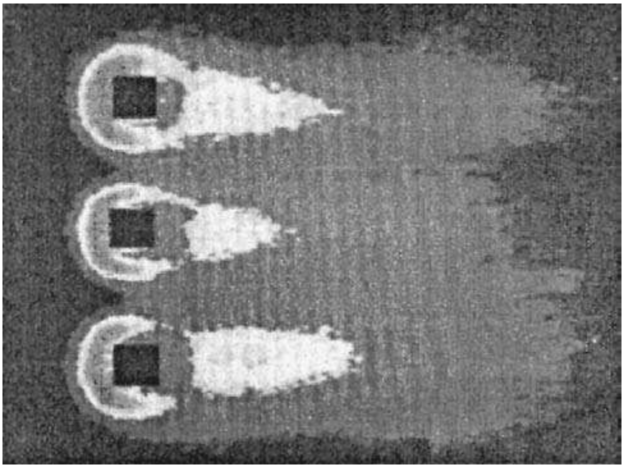

FIGURE 4.6.19 Visualization of the heat transfer coefficient distribution on a heated plate around three unheated cubes.

Another steady-state technique which reveals the distribution of *h* on the surface was introduced by den Ouden and Hoogendoorn (1974) and is currently in use by Meinders (1996). It uses a uniform and constant-temperature substrate (originally, a tank of warm water, now a copper block) covered with a layer of known thermal resistance (originally, a plate of glass, now a thin layer of epoxy). The surface was painted with liquid crystals (now visualized using infrared imaging) and the surface-temperature distribution determined. The inner (uniform) and outer (measured) temperature distributions are then used as boundary conditions to a three-dimensional conduction solver which calculates the total heat flux at each point on the surface. The total heat flux is corrected for radiation to yield the net convective transport at each point, from which *h* can be determined.

This method appears to have an advantage in accuracy over the heated foil technique because of the more accurate handling of substrate conduction.

Transient Lumped Parameter Systems. In the lumped parameter transient method, the specimen is assumed to be uniform in temperature at every instant through the transient. The power, $\dot{e}_{\text{in}}$, in Equation

(4.6.16) is usually zero, although that is not necessary (one could simply change the power level at time zero to initiate the transient). At time zero, a transient is initiated, and the response curve recorded.

The data can be interpreted, and the validity of the first-order assumption tested at the same time by plotting $(T - T_{\text{final}})/(T_{\text{initial}} - T_{\text{final}})$ on the log scale of semilog coordinates, with time on the algebraic scale. If the line is straight, then the system is first order and the characteristic time can be determined from any two points on the line by

$$\tau = \frac{\left(t_2 - t_1\right)}{\ln\left\{\dfrac{T_{\text{fin}} - T_1}{T_{\text{fin}} - T_2}\right\}} \tag{4.6.17}$$

The heat transfer coefficient is extracted from the time-constant definition.

Indirect Methods

An increasingly popular method is the extraction of *h* from surface-temperature variations after a step in flow temperature using an inverse calculation method (see the section on inferential methods of heat flux measurement). The simplest inverse method assumes one-dimensional conduction into an infinitely thick plate of constant material properties. Even highly irregular geometries can be studied with this technique, if the streamwise extent of the specimen is small and the testing time is short. A short time interval is necessary so the penetration of the thermal wave is limited to a thin layer near the surface. The short streamwise extent is necessary so the temperature response of the surface upstream does not alter the thermal step applied to the downstream surface. This technique has been used to determine the heat transfer coefficient distribution on the inside walls of passages of irregular shape, by making the passage in a transparent material.

Naphthalene Sublimination. The equations for mass diffusion are similar to those for heat transfer, except for replacing the Prandtl number in the heat transfer equation by the Schmidt number in the diffusion equation. Thus, one could expect that the distribution of the mass transfer coefficients on a surface would mimic the distribution of the heat transfer coefficients.

The most commonly used analog technique is naphthalene sublimination. As early as 1940, the mass transfer/heat transfer similarity was used to estimate the heat transfer coefficient distribution. Naphthalene is a solid material which sublimes at a reasonable rate in air at ambient temperature. Specimens can be cast in naphthalene with good precision, and the recession of the surface mapped as a function of position and time using automated or semiautomated measuring equipment. The surface recession over a known interval of time is a measure of the mass transfer rate, from which the mass transfer coefficient can be deduced.

Naphthalene experiments are generally done at uniform temperature; hence, a uniform vapor pressure exists at the surface. This corresponds to the heat transfer situation of heat transfer from a uniform temperature surface. No counterpart of the uniform heat flux situation has been produced using naphthalene, nor have there been experiments corresponding to variable wall temperature.

Naphthalene sublimation experiments do not suffer from any counterpart of the conduction heat transfer in the substrate. Conduction makes it difficult to work near discontinuities in wall temperature in a heat transfer experiment. Details of the fine structure of mass transfer near obstructions and discontinuities can be resolved in naphthalene experiments, but those details might not exist in a heat transfer process. The Prandtl number of air is much lower than the Schmidt number of naphthalene diffusing in air; hence, thermal conduction would tend to blur out sharp gradients in the temperature field more than diffusion would blur out gradients in naphthalene concentration.

The Schmidt number of naphthalene in air is about 2.5, far different than the Prandtl number of air (0.71); hence, the mass transfer coefficient deduced from a naphthalene experiment is not numerically equal to the heat transfer coefficient which would have existed at those conditions. The usual recommendation is to adjust for the Prandtl number of Schmidt number using a relation of the form:

$$\mathrm{St}\,\mathrm{Pr}^{2/3} = f\{\mathrm{Re}\} = \mathrm{Sh}_j \mathrm{Sc}_j^{2/3} \qquad (4.6.18)$$

based on laminar results. That recommendation has not been seriously tested by experiments in turbulent and separated flows. By using nominal values of the Schmidt number and Prandtl number, the heat transfer Stanton number would be 2.3 times higher than the measured Sherwood number and an uncertainty of 10% in that ratio would alter the inferred heat transfer coefficient by 23%.

System Performance Matching. Sometimes the "effective average heat transfer coefficient" for a system is inferred from the overall behavior of the system, e.g., estimating h from the effectiveness of a heat exchanger. Values deduced by this means cannot be expected to agree well with direct measurements unless a very sophisticated system description model is used.

References

Akino, N. and Kunugi, T., *ASME HTD,* Vol. 112, 1989.

Cooper, T.E., Field, R.J., and Meyer, J.F., Liquid crystal thermography and its application to the study of convective heat transfer, *J. Heat Transfer*, 97, 442–450, 1975.

den Ouden, C. and Hoogendoorn, C.J., Local convective heat transfer coefficients for jets impinging on a plate: experiments using a liquid crystal technique, in *Proc. of the 5th Int. Heat Transfer Conf.,* Vol. 5, AIChE, New York, 1974, 293–297.

Diller, T.E. and Onishi, S., Heat Flux Gage, U.S. Patent No. 4,779,994, Issued 25 October 1988.

Epstein, A.H., Guenette, G.R., Norton, R.J.G., and Yazhang, C., High-frequency response heat-flux gage, *Rev. Sci. Instruments,* 57(4), 639–649, 1986.

George, W.K., Rae, W.J., Seymour, P.J., and Sonnenmeir, J.K., An evaluation of analog and numerical techniques for unsteady heat transfer measurements with thin-film gages in transient facilities, *Proc. of the 1987 ASME-JSME Thermal Engineering Joint Conf.,* 1987, pp. 611–617.

Hager, J.M., Onishi, S., Langley, L.W., and Diller, T.E., High temperature heat flux measurements, *AIAA Journal of Thermophysics and Heat Transfer,* 7, 531–534, 1993.

Hager, J.M., Simmons, S., Smith, D., Onishi, S., Langley, L.W., and Diller, T.E., Experimental performance of a heat flux microsensor. *ASME Journal of Engineering for Gas Turbines and Power,* 113, 246–250, 1991.

Hartunian, R.A. and Varwig, R.L., On thin-film heat-transfer measurements in shock tubes and shock tunnels, *The Physics of Fluids,* 5(2), 169–174, 1962.

Hippensteele, S.A., Russell, L.M., and Torres, F.J., Local Heat Transfer Measurements on a Large Scale Model Turbine Blade Airfoil Using a Composite of a Heater Element and Liquid Crystals, NASA Technical Memorandum 86900, March 1985.

Hollingsworth, K., Boehman, A.L., Smith, E.G., and Moffat, R.J., Measurement of temperature and heat transfer coefficient distributions in a complex flow using liquid crystal thermography and true-color image processing, in *Coll. Pap. Heat Transfer, ASME HTD*, 123, 35–42, Winter Annual Meeting, 1989.

Lee, J., Kim, J., and Kiger, K.T., Time and space resolved heat transfer characteristics of single droplet cooling using microscale heater arrays, *International Journal of Heat and Fluid Flow,* 22, 188–200, 2001.

Moffat, R.J., The gradient approach to thermocouple circuitry, *Temperature, Its Measurement and Control in Science and Industry*, Rienhold, New York, 1962.

Personal Communication from Erwin Meinders, March 1996. Work in progress at the Technical University of Delft under Prof. Hanjalic.

Rhee, H.S., Koseff, J.R., and Street, R.L., Flow visualization of a recirculating flow by rheoscopic liquid and liquid crystal techniques, *Exp. Fluids*, 2, 57–64, 1984.

Rule, T.D. and Kim, J., Heat transfer behavior on small horizontal heaters during pool boiling of FC-72, *Journal of Heat Transfer,* 121(2), 386–393, 1999.

Skinner, G.T., Calibration of thin-film backing materials, *J. of the American Rocket Society,* 31(5), 671–672, 1961.

Steinhart, J.S. and Hart, S.R., Calibration curves for thermistors, *Deep Sea Res.*, 15, 497, 1968.

Yaddanapudi, N. and Kim, J., Single bubble heat transfer in saturated pool boiling of FC-72, *Multiphase Science and Technology*, 12, 47–63, 2001.

4.7 Mass Transfer

Anthony F. Mills

Introduction

Mass transfer may occur in a gas mixture, a liquid solution, or a solid solution. There are several physical mechanisms that can transport a chemical species through a phase and transfer it across phase boundaries. The two most important mechanisms are ordinary diffusion and convection. Mass diffusion is analogous to heat conduction and occurs whenever there is a gradient in the concentration of a species. Mass convection is essentially identical to heat convection: a fluid flow that transports heat may also transport a chemical species. The similarity of mechanisms of heat transfer and mass transfer results in the mathematics often being identical, a fact that can be exploited to advantage. But there are some significant differences between the subjects of heat and mass transfer. One difference is the much greater variety of physical and chemical processes that require mass transfer analysis. Another difference is the extent to which the essential details of a given process may depend on the particular chemical system involved, and on temperature and pressure.

In the next subsection, concentrations, velocities, and fluxes are defined, and special attention is paid to phase interfaces where the concentration of a chemical species is almost always discontinuous. Fick's law of ordinary diffusion is introduced in the third section, where other diffusion phenomena are also discussed. The fourth section presents various forms of the species conservation equation. Results for diffusion in a stationary medium are given in the fifth section, and include steady diffusion across a plane wall, transient diffusion in a semi-infinite solid, and diffusion in a porous catalyst. Results for diffusion in a moving medium are given in the sixth section, and the Stefan flow is introduced for diffusion with one component stationary. Also considered are particle combustion, droplet evaporation, and combustion of a volatile liquid hydrocarbon fuel droplet. The last section deals with mass convection. Low mass transfer rate theory is presented and how to exploit the analogy between convective heat and mass transfer is shown. Particular attention is given to situations involving simultaneous heat and mass transfer associated with evaporation or condensation. The section closes by presenting high mass transfer rate theory for convection, and gives engineering calculation methods for boundary layer flows that account for variable property effects.

Concentrations, Velocities, and Fluxes

Definitions of Concentrations

In a gas mixture, or liquid or solid solution, the local *concentration* of a mass species can be expressed in a number of ways. The *number density* of species *i* in a mixture or solution of *n* species is defined as

$$\begin{aligned}\text{Number density of species } i &\equiv \text{Number of molecules of } i \text{ per unit volume}\\ &\equiv \mathcal{N}_i \text{ molecules/m}^3\end{aligned} \tag{4.7.1}$$

Alternatively, if the total number of molecules of all species per unit volume is denoted as $\mathcal{N}$, then we define the *number fraction* of species *i* as

$$n_i \equiv \frac{\mathcal{N}_i}{\mathcal{N}}; \qquad \mathcal{N} = \sum \mathcal{N}_i \tag{4.7.2}$$

where the summation is over all species present, $i = 1, 2, \ldots, n$. Equation (4.7.1) and Equation (4.7.2) describe *microscopic* concepts and are used, for example, when the kinetic theory of gases is used to describe transfer processes.

Whenever possible, it is more convenient to treat matter as a continuum. Then the smallest volume considered is sufficiently large for macroscopic properties such as pressure and temperature to have their usual meanings. For this purpose we also require *macroscopic* definitions of concentration. First, on a mass basis,

$$\begin{aligned} &\textit{Mass concentration} \text{ of species } i \equiv \text{partial density of species } i \\ &\equiv \rho_i \text{ kg/m}^3 \end{aligned} \tag{4.7.3}$$

The total mass concentration is the total mass per unit volume, that is, the density $\rho = \sum\rho_i$. The *mass fraction* of species i is defined as

$$m_i = \frac{\rho_i}{\rho} \tag{4.7.4}$$

Second, on a molar basis,

$$\begin{aligned} &\textit{Molar concentration} \text{ of species } i \equiv \text{number of moles of } i \text{ per unit volume} \\ &\equiv c_i \text{ kmol/m}^3 \end{aligned} \tag{4.7.5}$$

If M_i (kg/kmol) is the molecular weight of species i, then

$$c_i = \frac{\rho_i}{M_i} \tag{4.7.6}$$

The total molar concentration is the molar density $c = \sum c_i$. The *mole fraction* of species i is defined as

$$x_i \equiv \frac{c_i}{c} \tag{4.7.7}$$

A number of important relations follow directly from these definitions. The mean molecular weight of the mixture of solution is denoted M and may be expressed as

$$M = \frac{\rho}{c} = \sum x_i M_i \tag{4.7.8a}$$

or

$$\frac{1}{M} = \sum \frac{m_i}{M_i} \tag{4.7.8b}$$

There are summation rules

$$\sum m_i = 1 \tag{4.7.9a}$$

$$\sum x_i = 1 \tag{4.7.9b}$$

It is often necessary to have the mass fraction of species *i* expressed explicitly in terms of mole fractions and molecular weights; this relation is

$$m_i = \frac{x_i M_i}{\sum x_j M_j} = x_i \frac{M_i}{M} \tag{4.7.10a}$$

and the corresponding relation for the mole fraction is

$$x_i = \frac{m_i / M_i}{\sum m_j / M_j} = m_i \frac{M}{M_i} \tag{4.7.10b}$$

Dalton's law of partial pressures for an ideal gas mixture states that

$$P = \sum P_i, \qquad \text{where} \quad P_i = \rho_i R_i T \tag{4.7.11}$$

Dividing partial pressure by total pressure and substituting $R_i = \mathcal{R}/M_i$ gives

$$\frac{P_i}{P} = \frac{\rho_i}{M_i}\frac{\mathcal{R}T}{P} = c_i \frac{\mathcal{R}T}{P} = x_i \frac{c\mathcal{R}T}{P} = x_i \tag{4.7.12}$$

Thus, for an ideal gas mixture, the mole fraction and partial pressure are equivalent measures of concentration (as also is the number fraction).

A commonly used specification of the composition of dry air is 78.1% N_2, 20.9% O_2, and 0.9% Ar, by volume. (The next largest component is CO_2, at 0.3%.) Since equal volumes of gases contain the same number of moles, specifying composition on a volume basis is equivalent to specifying mole fractions, namely,

$$x_{N_2} = 0.781; \qquad x_{O_2} = 0.209; \qquad x_{Ar} = 0.009$$

The corresponding mass fractions are calculated to be

$$m_{N_2} = 0.755; \qquad m_{O_2} = 0.231; \qquad m_{Ar} = 0.014$$

Concentrations at Interfaces

Although temperature is continuous across a phase interface, concentrations are usually discontinuous. In order to define clearly concentrations at interfaces, we introduce imaginary surfaces, denoted *u* and *s*, on both sides of the real interface, each indefinitely close to the interface, as shown in Figure 4.7.1 for water evaporating into an airstream. Thus, the liquid-phase quantities at the interface are subscripted *u*, and gas-phase quantities are subscripted *s*. If we ignore the small amount of air dissolved in the water, $x_{H_2O,u} = 1$. Notice that the subscript preceding the comma denotes the chemical species, and the subscript following the comma denotes location. To determine $x_{H_2O,s}$ we make use of the fact that, except in extreme circumstances, the water vapor and air mixture at the *s*-surface must be in thermodynamic equilibrium with water at the *u*-surface. Equilibrium data for this system are found in conventional steam tables: the saturation vapor pressure of steam at the water temperature, T_s, ($T_s = T_u$), is the required partial pressure

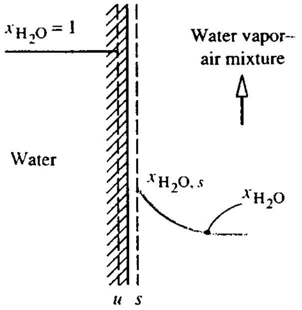

FIGURE 4.7.1 Concentrations at a water-air interface.

$P_{H_2O,s}$. With the total pressure P known, $x_{H_2O,s}$ is calculated as $P_{H_2O,s}/P$. If $m_{H_2O,s}$ is required, Equation (4.7.10a) is used.

For example, at $T_s = 320$ K, the saturation vapor pressure is obtained from steam tables as 0.10535×10^5 Pa. If the total pressure is 1 atm = 1.0133×10^5,

$$x_{H_2O,s} = \frac{0.10535 \times 10^5}{1.0133 \times 10^5} = 0.1040$$

$$m_{H_2O,s} = \frac{(0.1040)(18)}{(0.1040)(18) + (1 - 0.1040)(29)} = 0.06720$$

For a gas or solid dissolving in a liquid, equilibrium data are often referred to simply as solubility data, found in chemistry handbooks. Many gases are only sparingly soluble, and for such dilute solutions solubility data are conveniently represented by *Henry's law*, which states that the mole fraction of the gas at the *s*-surface is proportional to its mole fraction in solution at the *u*-surface, the constant of proportionality being the *Henry number*, He. For species *i*,

$$x_{i,s} = \mathrm{He}_i x_{i,u} \tag{4.7.13}$$

The Henry number is inversely proportional to total pressure and is also a function of temperature. The product of Henry number and total pressure is the *Henry constant*, C_{He}, and for a given species is a function of temperature only:

$$\mathrm{He}_i P = C_{\mathrm{He}_i}(T) \tag{4.7.14}$$

Solubility data are given in Table 4.7.1.

TABLE 4.7.1 Henry Constants C_{He} for Dilute Aqueous Solutions at Moderate Pressures ($P_{i,s}/x_{i,u}$ in atm, or in bar = 10^5 Pa, within the accuracy of the data)

Solute	290 K	300 K	310 K	320 K	330 K	340 K
H_2S	440	560	700	830	980	1,140
CO_2	1,280	1,710	2,170	2,720	3,220	—
O_2	38,000	45,000	52,000	57,000	61,000	65,000
H_2	67,000	72,000	75,000	76,000	77,000	76,000
CO	51,000	60,000	67,000	74,000	80,000	84,000
Air	62,000	74,000	84,000	92,000	99,000	104,000
N_2	16,000	89,000	101,000	110,000	118,000	124,000

For example, consider absorption of carbon dioxide from a stream of pure CO_2 at 2 bar pressure into water at 310 K. From Table 4.7.1, C_{He} = 2170 bar; thus

$$\mathrm{He}_{CO_2} = \frac{2170}{2} = 1085; \qquad x_{CO_{2,u}} = \frac{1}{1085} = 9.22 \times 10^{-4}$$

Dissolution of gases into metals is characterized by varied and rather complex interface conditions. Provided temperatures are sufficiently high, hydrogen dissolution is reversible (similar to CO_2 absorption into water); hence, for example, titanium-hydrogen solutions can exist only in contact with a gaseous hydrogen atmosphere. As a result of hydrogen going into solution in atomic form, there is a characteristic square root relation

$$m_{H_2,u} \alpha P_{H_2,s}^{1/2}$$

The constant of proportionality is strongly dependent on temperature, as well as on the particular titanium alloy: for Ti-6Al-4V alloy it is twice that for pure titanium. In contrast to hydrogen, oxygen dissolution in titanium is irreversible and is complicated by the simultaneous formation of a rutile (TiO_2) scale on the surface. Provided some oxygen is present in the gas phase, the titanium-oxygen *phase diagram* (found in a metallurgy handbook) shows that $m_{O_2,u}$ in alpha-titanium is 0.143, a value essentially independent of temperature and O_2 partial pressure. Dissolution of oxygen in zirconium alloys has similar characteristics to those discussed above for titanium.

All the preceding examples of interface concentrations are situations where thermodynamic equilibrium can be assumed to exist at the interface. Sometimes thermodynamic equilibrium does not exist at an interface: a very common example is when a chemical reaction occurs at the interface, and temperatures are not high enough for equilibrium to be attained. Then the concentrations of the reactants and products at the *s*-surface are dependent both on the rate at which the reaction proceeds — that is, the *chemical kinetics* — as well as on mass transfer considerations.

Definitions of Fluxes and Velocities

The mass (or molar) flux of species *i* is a vector quantity giving the mass (or moles) of species *i* that pass per unit time through a unit area perpendicular to the vector (Figure 4.7.2). We denote the absolute mass and molar fluxes of species *i*, that is, relative to stationary coordinate axes, as $\boldsymbol{n}_i$ (kg/m²sec) and $\boldsymbol{N}_i$ (kmol/m²sec), respectively. The absolute mass flux of the mixture (mass velocity) is

$$\boldsymbol{n} = \sum \boldsymbol{n}_i \tag{4.7.15}$$

and the local mass-average velocity is

$$\boldsymbol{v} = \frac{\boldsymbol{n}}{\rho} \text{ m/sec} \tag{4.7.16}$$

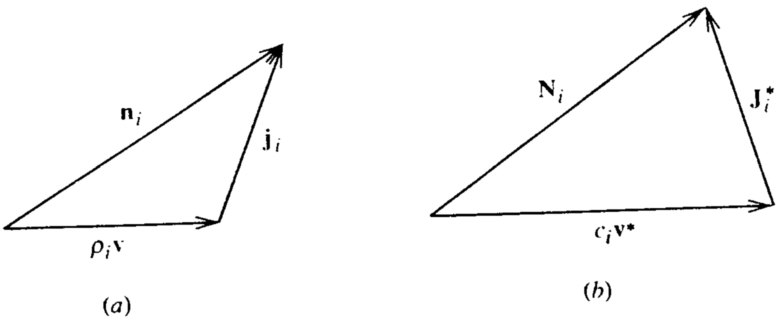

FIGURE 4.7.2 Flux vectors: (a) mass basis, (b) molar basis.

The velocity $\boldsymbol{v}$ is the velocity that would be measure by a Pitot tube and corresponds to the velocity used in considering pure fluids. On a molar basis, the absolute molar flux of the mixture is

$$\boldsymbol{N} = \sum \boldsymbol{N}_i \tag{4.7.17}$$

and the local molar-average velocity is

$$\boldsymbol{v}^* = \frac{\boldsymbol{N}}{c} \text{ m/sec} \tag{4.7.18}$$

The absolute fluxes at species *i* have two components. On a mass basis we write

$$\boldsymbol{n}_i = \rho_i \mathbf{v} + \boldsymbol{j}_i \tag{4.7.19}$$

where $\rho_i \boldsymbol{n}$ is transport of species *i* by bulk motion of the fluid at velocity $\boldsymbol{v}$ and is the *convective* component. Thus, $\boldsymbol{j}_i$ is transport of species *i* relative to the mass average velocity; it is called the *diffusive* component because most commonly it is due to ordinary (concentration) diffusion of the species. On a molar basis the corresponding relation is

$$N_i = c_i \mathbf{v}^* + \boldsymbol{J}_i^* \tag{4.7.20}$$

Some important relations follow from these definitions:

$$\sum \boldsymbol{j}_i = \sum \boldsymbol{J}_i^* = 0 \tag{4.7.21}$$

$$\boldsymbol{N}_i = \frac{\boldsymbol{n}_i}{M_i} \tag{4.7.22}$$

$$\boldsymbol{n}_i = \rho_i \boldsymbol{v} + \boldsymbol{j}_i = m_i \sum \boldsymbol{n}_i + \boldsymbol{j}_i \tag{4.7.23a}$$

$$\boldsymbol{N}_i = c_i \boldsymbol{v}^* + \boldsymbol{J}_i^* = x_i \sum \boldsymbol{N}_i + \boldsymbol{J}_i^* \tag{4.7.23b}$$

Mechanisms of Diffusion

Ordinary Diffusion

Fick's law of ordinary diffusion is a linear relation between the rate of diffusion of a chemical species and the local concentration gradient of that species. It is exact for a binary gas mixture, for which the kinetic theory of gases gives

$$\boldsymbol{j}_1 = -\rho \mathcal{D}_{12} \nabla m_1 \text{ kg/m}^2 \text{ sec} \tag{4.7.24a}$$

on a mass basis, and

$$\boldsymbol{J}_1^* = -c \mathcal{D}_{12} \nabla x_1 \text{ kg/m}^2 \text{ sec} \tag{4.7.24b}$$

on a molar basis; $\mathcal{D}_{12}$ (m^2/sec) is the binary diffusion coefficient (or mass diffusivity), and $\mathcal{D}_{21} = \mathcal{D}_{21}$. Equation (4.7.24a) and Equation (4.7.24b) are mathematically equivalent; however, notice that it is incorrect to write

$$\boldsymbol{j}_i = -\mathcal{D}_{12} \nabla \rho_1 \tag{4.7.25}$$

since $\nabla \rho_1 \neq \rho \nabla m_1$ in general. Fick's law in the form of Equation (4.7.24a) and Equation (4.7.24b) is also valid for dilute liquid and solid solutions, for which it is often possible to assume ρ (or c) constant, and then Equation (4.7.25) or its molar equivalent are good approximations.

Ordinary diffusion in multicomponent systems is described by the Stefan–Maxwell equations (Hirschfelder et al., 1954). These equations are difficult to use for engineering analysis. In gas mixtures containing species that do not have widely varying molecular weights, it is possible to model approximately the diffusion process by using an effective binary diffusion coefficient in Fick's law. This coefficient is a suitable average over the species in the mixture, and may be calculated from

$$\mathcal{D}_{1m} = \frac{\left(1 - x_1\right)}{\sum_{i=2}^{n} \left(x_i / \mathcal{D}_{1i}\right)}; \qquad x_1 \ll 1 \tag{4.7.26}$$

This equation works well for most mixtures of combustion gases (except those containing appreciable concentrations of H or H_2).

Binary diffusion coefficients at 300 K are of the order of 10^{-5} m^2/sec in gases at 1 atm, 10^{-9} m^2/sec in aqueous solutions, and 10^{-10} to 10^{-13} m^2/sec in solids. However, the product $\rho\mathcal{D}$ or $(c\mathcal{D})$ is, at most, one order of magnitude different for gases and liquids. Data for diffusion coefficients may be found in Table 4.7.2 through Table 4.7.5.

Molecules in a gas mixture, and in a liquid or solid solution, can diffuse by mechanisms other than ordinary diffusion governed by Fick's law. *Thermal diffusion* is diffusion due to a temperature gradient and is often called the *Soret effect*. Thermal diffusion is usually negligible compared with ordinary diffusion, unless the temperature gradient is very large. However, there are some important processes that depend on thermal diffusion, the most well known being the large-scale separation of uranium isotopes. *Pressure diffusion* is diffusion due to a pressure gradient and is also usually negligible unless the pressure gradient is very large. Pressure diffusion is the principle underlying the operation of a centrifuge. Centrifuges are used to separate liquid solutions and are increasingly being used to separate gaseous isotopes as well. *Forced diffusion* results from an external force field acting on a molecule. Gravitational force fields do not cause separation since the force per unit mass of a molecule is constant. Forced diffusion occurs when an electrical field is imposed on an electrolyte (for example, in charging an automobile battery), on a semiconductor, or on an ionized gas (for example, in a neon tube or metal-ion laser). Depending on the strength of the electric field, rates of forced diffusion can be very large.

Some interesting diffusion phenomena occur in porous solids. When a gas mixture is in a porous solid, such as a catalyst pellet or silica–gel particle, the pores can be smaller than the mean free path of the molecules. Then, the molecules collide with the wall more often than with other molecules. In the limit of negligible molecule collisions we have *Knudsen diffusion*, also called *free molecule flow* in the fluid mechanics literature. If the pore size approaches the size of a molecule, then Knudsen diffusion becomes negligible and *surface diffusion*, in which adsorbed molecules move along the pore walls, becomes the dominant diffusion mechanism.

Very small particles of 10^{-3} to 10^{-1} μm size — for example, smoke, soot, and mist — behave much like large molecules. Ordinary diffusion of such particles is called *Brownian motion* and is described in most elementary physics texts. Diffusion of particles due to a temperature gradient is called *thermophoresis* and plays an important role for larger particles, typically in the size range 10^{-1} to 1 μm. Diffusion of particles in a gas mixture due to concentration gradients of molecular species is called *diffusiophoresis.*

TABLE 4.7.2 Diffusion Coefficients in Air at 1 atm (1.013×10^5 Pa)[a]

	Binary Diffusion Coefficient (m^2/sec $\times 10^4$)							
T(K)	O_2	CO_2	CO	C_7H_6	H_2	NO	SO_2	He
200	0.095	0.074	0.098	0.036	0.375	0.088	0.058	0.363
300	0.188	0.157	0.202	0.075	0.777	0.180	0.126	0.713
400	0.325	0.263	0.332	0.128	1.25	0.303	0.214	1.14
500	0.475	0.385	0.485	0.194	1.71	0.443	0.326	1.66
600	0.646	0.537	0.659	0.270	2.44	0.603	0.440	2.26
700	0.838	0.684	0.854	0.364	3.17	0.782	0.576	2.91
800	1.05	0.857	1.06	0.442	3.93	0.978	0.724	3.64
900	1.26	1.05	1.28	0.538	4.77	1.18	0.887	4.42
1000	1.52	1.24	1.54	0.641	5.69	1.41	1.060	5.26
1200	2.06	1.69	2.09	0.881	7.77	1.92	1.440	7.12
1400	2.66	2.17	2.70	1.13	9.90	2.45	1.870	9.20
1600	3.32	2.75	3.37	1.41	12.5	3.04	2.340	11.5
1800	4.03	3.28	4.10	1.72	15.2	3.70	2.850	13.9
2000	4.80	3.94	4.87	2.06	18.0	4.48	3.360	16.6

[a] Owing to the practical importance of water vapor-air mixtures, engineers have used convenient empirical formulas for $\mathcal{D}_{H_2O\,\text{air}}$. A formula that has been widely used for many years is

$$\mathcal{D}_{H_2O\,\text{air}} = 1.97 \times 10^{-5} \left(\frac{P_0}{P}\right)\left(\frac{T}{T_0}\right)^{1.685} \text{m}^2/\text{sec}; \quad 273 \text{ K} < T < 373 \text{ K}$$

where $P_0 = 1$ atm; $T_0 = 256$ K. More recently, the following formula has found increasing use. (Marrero, T.R. and Mason, E.A. 1992. Gaseous diffusion coefficients, *J. Phys. Chem. Ref. Data*, 1, 3–118):

$$\mathcal{D}_{H_2O\,\text{air}} = 1.87 \times 10^{-10} \frac{T^{2.072}}{P}; \quad 280 \text{ K} < T < 450 \text{ K}$$

$$= 2.75 \times 10^{-9} \frac{T^{1.632}}{P}; \quad 450 \text{ K} < T < 1070 \text{ K}$$

for P in atmospheres and T in kelvins. Over the temperature range 290 to 330 K, the discrepancy between the two formulas is less than 2.5%. For small concentrations of water vapor in air, the older formula gives a constant value of $\text{Sc}_{H_2O\,\text{air}} = 0.61$ over the temperature range 273 to 373 K. On the other hand, the Marrero and Mason formula gives values of $\text{Sc}_{H_2O\,\text{air}}$ that vary from 0.63 at 280 K to 0.57 at 373 K.

Forced diffusion of a charged particle in an electrical field is similar to that for an ionized molecular species. Thermal and electrostatic precipitators are used to remove particles from power plant and incinerator stack gases, and depend on thermophoresis and forced diffusion, respectively, for their operation. Diffusion phenomena are unimportant for particles of size greater than about 1 μm in air at 1 atm; the motion of such particles is governed by the laws of Newtonian mechanics. Transport of particles is dealt with in the *aerosol science* literature.

Species Conservation Equation

The principle of conservation of a chemical species is used to derive the *species conservation equation.* On a mass basis this equation is

$$\frac{\partial \rho_i}{\partial t} + \nabla \cdot \boldsymbol{n}_i = \dot{r}_i''' \tag{4.7.27}$$

and on a molar basis

$$\frac{\partial c_i}{\partial t} + \nabla \cdot \boldsymbol{N}_i = \dot{R}_i''' \tag{4.7.28}$$

TABLE 4.7.3 Schmidt Number for Vapors in Dilute Mixture in Air at Normal Temperature, Enthalpy of Vaporization, and Boiling Point at 1 atm[a]

Vapor	Chemical Formula	Sc[b]	h_{fg}, J/kg × 10^{-6}	T_{BP}, K
Acetone	CH_3COCH_3	1.42	0.527	329
Ammonia	NH_3	0.61	1.370	240
Benzene	C_6H_6	1.79	0.395	354
Carbon dioxide	CO_2	1.00	0.398	194
Carbon monoxide	CO	0.77	0.217	81
Chlorine	Cl_2	1.42	0.288	238
Ethanol	CH_3CH_2OH	1.32	0.854	352
Helium	He	0.22	—	4.3
Heptane	C_7H_{16}	2.0	0.340	372
Hydrogen	H_2	0.20	0.454	20.3
Hydrogen sulfide	H_2S	0.94	0.548	213
Methanol	CH_3OH	0.98	1.110	338
Naphthalene	$C_{10}H_8$	2.35[c]	—	491
Nitric oxide	NO	0.87	0.465	121
Octane	C_8H_{18}	2.66	0.303	399
Oxygen	O_2	0.83	0.214	90.6
Pentane	C_5H_{12}	1.49	0.357	309
Sulfur dioxide	SO_2	1.24	0.398	263
Water vapor	H_2O	0.61	2.257	373

[a] With the Clausius-Clapeyron relation, one may estimate vapor pressure as

$$P_{\text{sat}} \simeq \exp\left\{-\frac{Mh_{fg}}{\mathcal{R}}\left(\frac{1}{T}-\frac{1}{T_{BP}}\right)\right\} \text{ atm} \quad \text{for } T \sim T_{BP}$$

[b] The Schmidt number is defined as Sc = $\mu/\rho\mathcal{D} = \nu/\mathcal{D}$. Since the vapors are in small concentrations, values for μ, ρ, and ν can be taken as pure air values.

[c] From a recent study by Cho, C., Irvine, T.F., Jr., and Karni, J. 1992. Measurement of the diffusion coefficient of naphthalene into air, *Int. J. Heat Mass Transfer*, 35, 957–966. Also, $h_{sg} = 0.567 \times 10^6$ J/kg at 300 K.

where $\dot{r}_i'''$ and $\dot{R}_i'''$ are the mass and molar rates of production of species i due to chemical reactions. Summing Equation 4.7.27 over all species gives the mass conservation or continuity equation,

$$\frac{\partial \rho}{\partial t} + \nabla \cdot \rho \boldsymbol{v} = 0 \tag{4.7.29}$$

The molar form is

$$\frac{\partial c}{\partial t} + \nabla \cdot c\boldsymbol{v}^* = \sum_i \dot{R}_i''' \tag{4.7.30}$$

since, in general, moles are not conserved in chemical reactions. A useful alternative form to Equation 4.7.27 can be obtained using Equation (4.7.23a) and Equation (4.7.29) and is

$$\rho \frac{Dm_i}{Dt} = \nabla \cdot \boldsymbol{j}_i + \dot{r}_i''' \tag{4.7.31}$$

where D/Dt is the substantial derivative operator.

If we consider a binary system of species 1 and 2 and introduce Fick's law, Equation (4.7.24a) into Equation (4.7.31), then

$$\rho \frac{Dm_i}{Dt} = \nabla \cdot \left(\rho \mathcal{D}_{12} \nabla m_1\right) + \dot{r}_1''' \tag{4.7.32}$$

TABLE 4.7.4 Schmidt Numbers for Dilute Solution in Water at 300 K[a]

Solute	Sc	M
Helium	120	4.003
Hydrogen	190	2.016
Nitrogen	280	28.02
Water	340	18.016
Nitric oxide	350	30.01
Carbon monoxide	360	28.01
Oxygen	400	32.00
Ammonia	410	17.03
Carbon dioxide	420	44.01
Hydrogen sulfide	430	34.08
Ethylene	450	28.05
Methane	490	16.04
Nitrous oxide	490	44.02
Sulfur dioxide	520	64.06
Sodium chloride	540	58.45
Sodium hydroxide	490	40.00
Acetic acid	620	60.05
Acetone	630	58.08
Methanol	640	32.04
Ethanol	640	46.07
Chlorine	670	70.90
Benzene	720	78.11
Ethylene glycol	720	62.07
n-Propanol	730	60.09
i-Propanol	730	60.09
Propane	750	44.09
Aniline	800	93.13
Benzoic acid	830	122.12
Glycerol	1040	92.09
Sucrose	1670	342.3

[a] Schmidt number $\mathrm{Sc} = \mu/\rho\mathcal{D}$; since the solutions are dilute, μ and ρ can be taken as pure water values. For other temperatures use $\mathrm{Sc}/\mathrm{Sc}_{300\,\mathrm{K}} \simeq (\mu^2/\rho T)/(\mu^2\rho T)_{300\,\mathrm{K}}$, where μ and ρ are for water, and T is absolute temperature. For chemically similar solutes of different molecular weights use $\mathrm{Sc}_2/\mathrm{Sc}_1 \simeq (M_2/M_1)^{0.4}$. A table of $(\mu^2/\rho T)/(\mu^2\rho T)_{300\,\mathrm{K}}$ for water follows.

T(K)	$(\mu^2/\rho T)/(\mu^2/\rho T)_{300\,\mathrm{K}}$
290	1.66
300	1.00
310	0.623
320	0.429
330	0.296
340	0.221
350	0.167
360	0.123
370	0.097

From Spalding, D.B. 1963. *Convective Mass Transfer*, McGraw-Hill, New York. With permission.

When working on a mass basis we define a stationary medium as one in which the mass average velocity $\boldsymbol{v}$ is zero everywhere. Substituting in Equation (4.7.32) with no chemical reactions and assuming constant properties,

$$\frac{\partial m_1}{\partial t} = \mathcal{D}_{12}\nabla^2 m_1 \tag{4.7.33}$$

TABLE 4.7.5 Diffusion Coefficients in Solids, $\mathcal{D} = \mathcal{D}_o \exp(-E_a/\mathcal{R}T)$

System	$\mathcal{D}_o$, m^2/sec	E_a, kJ/kmol
Oxygen-Pyrex glass	6.19×10^{-8}	4.69×10^{4}
Oxygen-fused silica glass	2.61×10^{-9}	3.77×10^{4}
Oxygen-titanium	5.0×10^{-3}	2.13×10^{5}
Oxygen-titanium alloy (Ti-6Al-4V)	5.82×10^{-2}	2.59×10^{5}
Oxygen-zirconium	4.68×10^{-5}	7.06×10^{5}
Hydrogen-iron	7.60×10^{-8}	5.60×10^{3}
Hydrogen-α-titanium	1.80×10^{-6}	5.18×10^{4}
Hydrogen-β-titanium	1.95×10^{-7}	2.78×10^{4}
Hydrogen-zirconium	1.09×10^{-7}	4.81×10^{4}
Hydrogen-Zircaloy^{-4}	1.27×10^{-5}	6.05×10^{5}
Deuterium-Pyrex glass	6.19×10^{-8}	4.69×10^{4}
Deuterium-fused silica glass	2.61×10^{-9}	3.77×10^{4}
Helium-Pyrex glass	4.76×10^{-8}	2.72×10^{4}
Helium-fused silica glass	5.29×10^{-8}	2.55×10^{4}
Helium-borosilicate glass	1.94×10^{-9}	2.34×10^{4}
Neon-borosilicate glass	1.02×10^{-10}	3.77×10^{4}
Carbon-FCC iron	2.3×10^{-5}	1.378×10^{5}
Carbon-BCC iron	1.1×10^{-6}	8.75×10^{4}

Various sources.

which is the *diffusion* equation, and is the mass transfer analog to Fourier's equation for heat conduction. For steady diffusion, Equation (4.7.33) reduces to Laplace's equation

$$\nabla^2 m_1 = 0 \qquad (4.7.34)$$

Notice that since properties have been assumed constant, any measure of concentration can be used in Equation (4.7.33) and Equation (4.7.34), for example ρ_1, c_1, and x_1.

Diffusion in a Stationary Medium

Many problems involving diffusion in a stationary medium are governed by the diffusion equation (Equation 4.7.33). Often solutions may be obtained from their heat conduction analogs. Some important cases follow.

Steady Diffusion through a Plane Wall

The mass flow of species 1 across a plane wall of thickness L and cross-sectional area A is

$$\dot{m}_1 = \frac{\rho \mathcal{D}_{12} A}{L}\left(m_{1,u} - m_{1,u'}\right) \text{ kg/m}^2 \text{ sec} \qquad (4.7.35)$$

where the u- and u'-surfaces are shown in Figure 4.7.3. Solubility data are required to relate the u- and u'-surface concentrations to s- and s'-surface concentrations. Alternatively for systems that obey Henry's law, a solubility $\mathcal{S}$ can be defined as the volume of solute gas (at STP of 0°C and 1 atm) dissolved in unit volume when the gas is at a partial pressure of 1 atm. Then, defining permeability $\mathcal{P}_{12}$ as the product $\mathcal{D}_{12}\mathcal{S}$, the volume flow of species 1 is

$$\dot{V}_1 = \frac{\mathcal{P}_{12} A}{L}\left(P_{1,s} - P_{1,s'}\right) \text{ m}^3 \text{ (STP)/sec} \qquad (4.7.36)$$

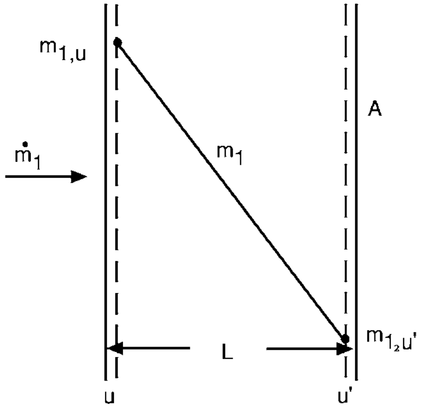

FIGURE 4.7.3 Steady diffusion across a plane wall.

where the partial pressures P_1 are in atmospheres. The SI units for permeability are m^3 (STP)/m^2sec(atm/m). Permeability and solubility data are given in Table 4.7.6. For example, consider helium at 10^5 Pa contained in a 7056-glass vessel with a 1-mm-thick wall at 680 K. For a surface area of 0.01 m^2, the leakage rate into ambient air is

$$\dot{V} = \frac{\left(1.0\times 10^{-12}\right)(0.01)}{(0.001)}\left(10^5 - 0\right) = 1.0\times 10^{-6}\ \text{m}^3\ \text{(STP)/sec}$$

where the value $\mathcal{P}_{12}$ was obtained from Table 4.7.6.

In general, mass fractions are discontinuous across phase interfaces. Hence, Equation (4.7.35) cannot be generalized to a number of walls in series by simply adding diffusion resistances. However, equilibrium partial pressures P_1 are continuous, and for two walls *A* and *B*, Equation 4.7.36 becomes

$$\dot{V}_1 = \frac{P_{1,s} - P_{1,s'}}{\dfrac{L_A}{\mathcal{P}_{1A}A} + \dfrac{L_B}{\mathcal{P}_{1B}A}}\ \text{m}^3\ \text{(STP)/sec} \qquad (4.7.37)$$

Transient Diffusion in a Semi-Infinite Solid

The typically low diffusion coefficients characterizing solids result in many situations where concentration changes are limited to a thin region near the surface (of thickness $\delta_c \sim (\mathcal{D}_{12}t)^{1/2}$). Examples include case-hardening of mild steel and coloring of clear sapphires. Details of the geometry are then unimportant and semi-infinite solid model can be used (Figure 4.7.4). For an initial concentration $m_{1,0}$ and a *u*-surface concentration suddenly changed to $m_{1,u}$ at time $t = 0$, the concentration distribution $m_1(z,t)$ is

$$\frac{m_1 - m_{1,0}}{m_{1,u} - m_{1,0}} = erfc\frac{z}{\left(4\mathcal{D}_{12}t\right)^{1/2}} \qquad (4.7.38)$$

and the dissolution rate is

$$\dot{m}_1 = j_{1,u}A = \rho A\left(\frac{\mathcal{D}_{12}}{\pi t}\right)^{1/2}\left(m_{1,u} - m_{1,0}\right)\ \text{kg/sec} \qquad (4.7.39)$$

TABLE 4.7.6 Solubility and Permeability of Gases in Solids

Gas	Solid	Temperature, K	$\mathscr{S}$ (m^3(STP)/m^3 atm) or $\mathscr{S}'$[a]	Permeability[b] m^3(STP)/m^2 sec (atm/m)
H_2	Vulcanized rubber	300	$\mathscr{S} = 0.040$	0.34×10^{-10}
	Vulcanized neoprene	290	$\mathscr{S} = 0.051$	0.053×10^{-10}
	Silicone rubber	300		4.2×10^{-10}
	Natural rubber	300		0.37×10^{-10}
	Polyethylene	300		0.065×10^{-10}
	Polycarbonate	300		0.091×10^{-10}
	Fused silica	400	$\mathscr{S}' \simeq 0\ 035$	
		800	$\mathscr{S}' \simeq 0.030$	
	Nickel	360	$\mathscr{S}' = 0.202$	
		440	$\mathscr{S}' = 0.192$	
He	Silicone rubber	300		2.3×10^{-10}
	Natural rubber	300		0.24×10^{-10}
	Polycarbonate	300		0.11×10^{-10}
	Nylon 66	300		0.0076×10^{-10}
	Teflon	300		0.047×10^{-10}
	Fused silica	300	$\mathscr{S}' \simeq 0.018$	
		800	$\mathscr{S}' \simeq 0.026$	
	Pyrex glass	300	$\mathscr{S}' \simeq 0.006$	
		800	$\mathscr{S}' \simeq 0.024$	
	7740 glass	470	$\mathscr{S} = 0.0084$	4.6×10^{-13}
	(94% $SiO_2 + B_2O_3 + P_2O_5$,	580	$\mathscr{S} = 0.0038$	1.6×10^{-12}
	5% $Na_2O + Li_2 + K_2O$,	720	$\mathscr{S} = 0.0046$	6.4×10^{-12}
	1% other oxides)			
	7056 glass	390	$\mathscr{S}' = 0.0039$	1.2×10^{-14}
	(90% $SiO_2 + B_2O_3 + P_2O_5$,	680	$\mathscr{S}' = 0.0059$	1.0×10^{-12}
	8% $Na_2O + Li_2 + K_2O$,			
	1% PbO, 5% other oxides)			
O_2	Vulcanized rubber	300	$\mathscr{S} = 0.070$	0.15×10^{-10}
	Silicone rubber	300		3.8×10^{-10}
	Natural rubber	300		0.18×10^{-10}
	Polyethylene	300		4.2×10^{-12}
	Polycarbonate	300		0.011×10^{-10}
	Silicone-polycarbonate copolymer (57% silicone)	300		1.2×10^{-10}
	Ethyl cellulose	300		0.09×10^{-10}
N_2	Vulcanized rubber	300	$\mathscr{S} = 0.035$	0.054×10^{-10}
	Silicone rubber	300		1.9×10^{-12}
	Natural rubber	300		0.062×10^{-10}
	Silicone-polycarbonate copolymer (57% silicone)	300		0.53×10^{-10}
	Teflon	300		0.019×10^{-10}
CO_2	Vulcanized rubber	300	$\mathscr{S} = 0.090$	1.0×10^{-10}
	Silicone rubber	290		21×10^{-10}
	Natural rubber	300		1.0×10^{-10}
	Silicone-polycarbonate copolymer (57% silicone)	300		7.4×10^{-10}
	Nylon 66	300		0.0013×10^{-10}
H_2O	Silicone rubber	310		$0.91–1.8 \times 10^{-10}$
Ne	Fused silica	300–1200	$\mathscr{S} \simeq 0.002$	
Ar	Fused silica	900–1200	$\mathscr{S} \simeq 0.01$	

[a] Solubility $\mathscr{S}$ = volume of solute gas (0°C, 1 atm) dissolved in unit volume of solid when the gas is at 1 atm partial pressure. Solubility coefficient $\mathscr{S}' = c_{1,u}/c_{1,s}$.

[b] Permeability $\mathcal{P}_{12} = \mathcal{D}_{12}\mathscr{S}$.

From various sources, including Geankoplis, C.J. 1993. *Transport Processes and Unit Operations*, 3rd ed., Prentice-Hall; Englewood Cliffs, N.J.; Doremus, R.H. 1973. *Glass Science*, Wiley, New York; Altemose, V.O. 1961. Helium diffusion through glass, *J. Appl. Phys.*, 32, 1309–1316. With permission.

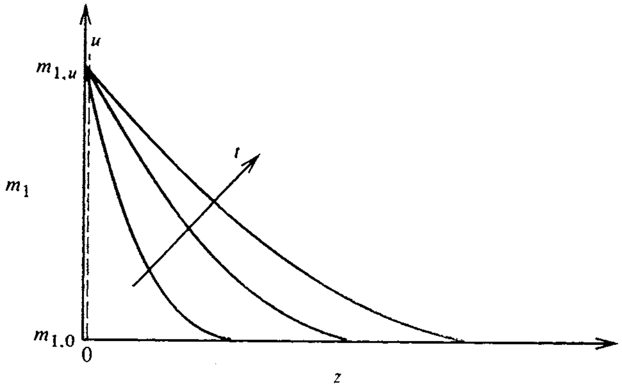

FIGURE 4.7.4 Transient diffusion in a plane slab.

For example, consider a Pyrex glass slab at 800 K suddenly exposed to helium at 10^4 Pa. The molar equivalent to Equation (4.7.39) for an assumed constant solid phase molar concentration c is

$$\frac{\dot{M}_1}{A} = \left(\frac{\mathcal{D}_{12}}{\pi t}\right)^{1/2} \left(c_{1,u} - c_{1,0}\right)$$

From Table 4.7.6, $\mathcal{S}' = c_{1,u}/c_{1,s} \cong 0.024$; hence, $c_{1,u} = (0.024)(10^4)/(8314)(800) = 3.61 \times 10^{-5}$ kmol/m^3. From Table 4.7.4, $\mathcal{D}_{12} = 4.76 \times 10^{-8} \exp[-(2.72 \times 10^4)(10^3)/(8314)(800)] = 7.97 \times 10^{-10}$ m^2/sec. Hence,

$$\frac{\dot{M}_1}{A} = \left(\frac{7.97 \times 10^{-10}}{\pi t}\right)^{1/2} \left(3.61 \times 10^{-5} - 0\right) = 5.75 \times 10^{-10}/t \text{ kmol/sec}$$

Transient Diffusion in Slabs, Cylinders, and Spheres

Transient heat conduction in slates, cylinders, and spheres with surface convection is dealt with in Section 4.1. The analogous mass diffusion problem for the slab $-L < z < L$ is now considered. On a molar basis the governing differential equation is

$$\frac{\partial x_1}{\partial t} = \mathcal{D}_{12} \frac{\partial^2 x_1}{\partial z^2} \tag{4.7.40}$$

with initial condition $x_1 = x_{1,0}$ at $t = 0$. Boundary conditions are $\partial x_1/\partial z = 0$ at $z = 0$, and at the surface $z = L$,

$$-c\mathcal{D}_{12} \left.\frac{\partial x_1}{\partial z}\right|_{z=L} = \mathcal{G}_{m1}\left(y_{1,s} - y_{1,e}\right) \tag{4.7.41}$$

The convective boundary condition is of the same form as Newton's law of cooling, and defines the mole transfer conductance $\mathcal{G}_{m1}$ (kmol/m^{2}sec) (see also the section on mass and mole transfer conductances). Also, we have followed chemical engineering practice and denoted mole fraction x in the solid (or liquid) phase and y in the liquid (or gas) phase, to emphasize that generally mole fraction is not continuous across a phase interface. For example, consider absorption of a sparingly soluble gas into a liquid for which Henry's law, Equation (4.7.13), applies: then $y_{1,s} = \text{He}x_{1,u}$.

In using heat conduction charts for mass diffusion problems, particular care must be taken with the evaluation of the Biot number. For heat conduction Bi = h_cL/k, where k is the solid conductivity. For mass diffusion the Biot number accounts for the discontinuity in concentration across the phase interface.

Using gas absorption into a plane layer of liquid, for example, when Equation (4.7.41) is put into an appropriate dimensionless form, the mass transfer Biot number is seen to be

$$\mathrm{Bi}_m = \frac{\mathcal{G}_{m1}\mathrm{He}L}{c\mathcal{D}_{12}} \tag{4.7.42}$$

For sparingly soluble gases, e.g., O_2 or CO_2 in water, He, and hence Bi_m, are very large, and the absorption process is liquid-side controlled; that is, a uniform gas-phase composition can be assumed. Often interface equilibrium data are in graphical or tabular form; then an effective Biot number at the concentration of concern must be used.

For example, consider a 2-mm-diameter droplet of water at 300 K entrained in an air flow at 1 atm pressure containing 1% by volume CO_2. From Table 4.7.5, He = C_{He}= 1710. The liquid phase molar density can be approximated by the pure water value of $c = \rho/M = 996/18 = 55.3$ kmol/m^3. The liquid phase diffusion coefficient is obtained from Table 4.7.4 as $\mathcal{D}_{12} = \nu_{H_2O}/Sc_{12} = 0.87 \times 10^{-6}/420 = 2.07 \times 10^{-9}$ m^2/sec. For negligible relative motion between the droplet and gas, the Sherwood number (see the section on dimensionless groups) is approximately 2.0, and hence the gas phase mole transfer conductance is $\mathcal{G}_{m1} = 2c\mathcal{D}_{12}/\mathcal{D}$. For the gas phase, the molar density $c = \mathcal{P}/\mathcal{R}T = (1.0133 \times 10^5)/(8314)(300) = 0.0406$ kmol/m^3 and $\mathcal{D}_{12} = 0.157 \times 10^{-4}$ m^2/sec from Table 4.7.2. Thus,

$$\mathcal{G}_{m1} = \frac{(2)(0.0406)\left(0.157\times10^{-4}\right)}{(0.002)} = 6.37\times10^{-4}\ \mathrm{kmol/m^2\,sec}$$

From Equation 4.7.42 with $L = R$ the droplet radius, the mass transfer Biot number is

$$\mathrm{Bi}_m = \frac{\left(6.37\times10^{-4}\right)(1710)(0.001)}{(55.3)\left(2.07\times10^{-9}\right)} = 9520$$

Thus, even for a small droplet with a relatively large gas-side mole transfer conductance, the absorption process is liquid-side controlled.

Diffusion in a Porous Catalyst

Porous catalysts are used to give a large surface area per unit volume of catalyst surface. Current practice for automobile catalytic convertors is to use a ceramic matrix as a support for a thin porous alumina layer that is impregnated with the catalyst (called a *washcoat*). A typical matrix has passages of hydraulic diameter 1 mm, and the washcoat may be about 20 μm thick. Pore sizes are of the order of 1 μm for which ordinary and Knudsen diffusion resistances are important. A simple model for diffusion in a porous catalyst is

$$\mathbf{J}_1 = -c\mathcal{D}_{1,\mathrm{eff}}\nabla x_1\ \mathrm{kmol/m^2\,sec} \tag{4.7.43}$$

where the subscript eff denotes an effective diffusivity that accounts for the presence of the solid material. Assuming additive resistances,

$$\frac{1}{\mathcal{D}_{1,\mathrm{eff}}} = \frac{1}{\mathcal{D}_{12,\mathrm{eff}}} + \frac{1}{\mathcal{D}_{K1,\mathrm{eff}}} \tag{4.7.44}$$

and

$$\mathcal{D}_{12,\mathrm{eff}} = \frac{\varepsilon_v}{\tau}\mathcal{D}_{12}; \qquad \mathcal{D}_{K1,\mathrm{eff}} = \frac{\varepsilon_v}{\tau}\mathcal{D}_{K1,\mathrm{eff}} \tag{4.7.45}$$

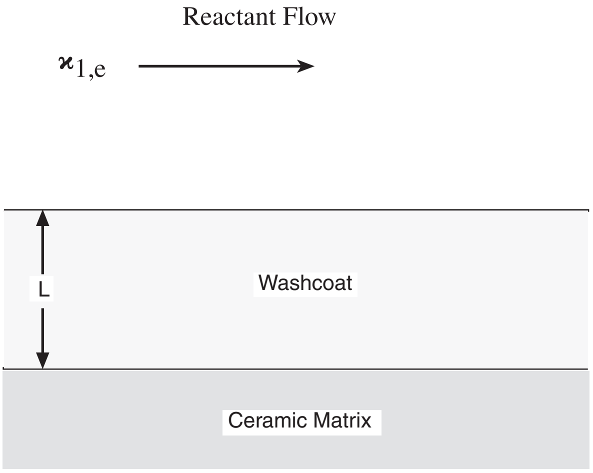

FIGURE 4.7.5 A catalyst layer.

where ε_v is the volume void fraction and τ is the tortuosity factor (usually between 4 and 8). From the kinetic theory of gases the Knudsen diffusion coefficient is

$$\mathcal{D}_{K1} = 97 r_e \left(T/M_1\right)^{1/2} \text{ m}^2/\text{sec} \tag{4.7.46}$$

for effective pore radius r_e in meters and T in kelvins.

When a chemical reaction takes place within a porous layer, a concentration gradient is set up, and surfaces on pores deep within the pellet are exposed to lower reactant concentrations than surfaces near the pore openings. For a first-order reaction it is straightforward to obtain the concentration distribution. The results of such an analysis are conveniently given in the form of an effectiveness η_p, which is defined as the actual consumption rate of the reactant divided by that for an infinite diffusion coefficient. For a layer of thickness L exposed to reactants on one side, as shown in Figure 4.7.5.

$$\eta_p = \frac{\tanh bL}{bL}; \qquad b = \left(\frac{k'' a_P}{\mathcal{D}_{1,\text{eff}}}\right)^{1/2} \tag{4.7.47}$$

where k'' (m/sec) is the rate constant for a first-order reaction and a_p (m^{-1}) is the catalyst area per unit volume. Notice that this effectiveness is analogous to the efficiency of a heat transfer fin.

For example, consider a 30-μm-thick porous alumina washcoat with a volume void fraction $\varepsilon_v = 0.8$, a tortuosity factor $\tau = 4.0$, average pore radius $r_e = 1$ μm, and catalytic surface area per unit volume $a_p = 7.1 \times 10^5$ cm^2/cm^3. For carbon monoxide oxidation by copper oxide at 800 K, 1 atm, the rate constant is approximately 4.2×10^{-4} m^2/sec. To calculate the effectiveness of the washcoat, we first need to calculate the effective diffusion coefficient $\mathcal{D}_{1,\text{eff}}$:

$$\mathcal{D}_{12,\text{eff}} = \frac{\varepsilon_v}{\tau}\mathcal{D}_{12} = \frac{0.8}{4.0}\left(1.06 \times 10^{-4}\right) = 2.12 \times 10^{-5} \text{ m}^2/\text{sec}$$

where $\mathcal{D}_{12}$ is approximated as the CO-air value from Table 4.7.2.

$$\mathcal{D}_{K1,\text{eff}} = \frac{\varepsilon_v}{\tau}\mathcal{D}_{12} = \frac{0.8}{4.0}(97)\left(1 \times 10^{-6}\right)(800/28)^{1/2} = 1.04 \times 10^{-4} \text{ m}^2/\text{sec}$$

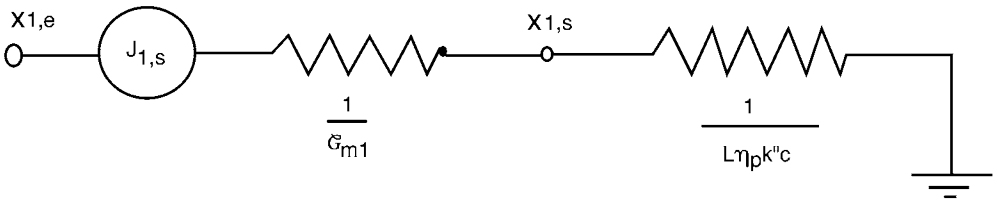

FIGURE 4.7.6 Equivalent circuit for mass transfer in an automobile catalytic convertor.

$$\frac{1}{\mathcal{D}_{1,\mathrm{eff}}} = \frac{1}{2.12\times10^{-5}} + \frac{1}{1.04\times10^{-4}}; \qquad \mathcal{D}_{1,\mathrm{eff}} = 1.76\times10^{-5}\ \mathrm{m^2/sec}$$

$$b = \left[\frac{\left(4.2\times10^{-4}\right)\left(7.1\times10^{5}\right)\left(10^{2}\right)}{1.76\times10^{-5}}\right]^{1/2} = 4.2\times10^{4}\ \mathrm{m^{-1}}; \qquad bL = \left(4.2\times10^{4}\right)\left(30\times10^{-6}\right) = 1.236$$

$$\eta_P = \frac{\tanh 1.236}{1.236} = 68.3\%$$

In an automobile catalytic convertor, Equation 4.7.47 applies to the catalyst washcoat. However, the mass transfer problem also involves a convective process for transport of reactants from the bulk flow. Referring to Figure 4.7.6 there are two mass transfer resistances in series, and the consumption rate of species 1 per unit surface area of the washcoat is

$$J_{1,s} = \frac{-x_{1,e}}{\dfrac{1}{L\eta_p k''c} + \dfrac{1}{\mathcal{G}_{m1}}}\ \mathrm{kmol/m^2\ sec} \tag{4.7.48}$$

where $\mathcal{G}_{m1}$ is the mole transfer conductance describing convective transport to the washcoat surface (see the section on mass and mole transfer conductances). Notice that when $\mathcal{G}_{m1} \lll L\eta_p k''c$ the reaction rate is controlled by mass transfer from the gas stream to the washcoat surface; when $L\eta_p k''c \lll \mathcal{G}_{m1}$, the reaction rate is controlled by diffusion within the washcoat and the kinetics of the reaction.

Diffusion in a Moving Medium

Net mass transfer across a surface results in a velocity component normal to the surface, and an associated convective flux in the direction of mass transfer. This convective flow is called a *Stefan flow*. The solutions of a number of mass transfer problems, involving a Stefan flow induced by the mass transfer process itself, follow. When necessary to obtain an analytical result, properties are assumed constant. Thus, use of these results requires evaluation of properties at a suitable reference state.

Diffusion with One Component Stationary

As an example, consider the simple heat pipe shown in Figure 4.7.7 with the evaporator and condenser located at the ends only (a bad design!). Then, if the working fluid is species 1, and a noncondensable gas is species 2, the concentration distribution is

$$\left(\frac{1-x_1}{1-x_{1,s}}\right) = \left(\frac{1-x_{1,e}}{1-x_{1,s}}\right)^{z/L} \tag{4.7.49}$$

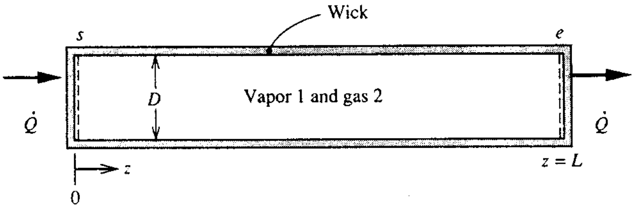

FIGURE 4.7.7 A simple heat pipe with the evaporator and condenser located at its ends.

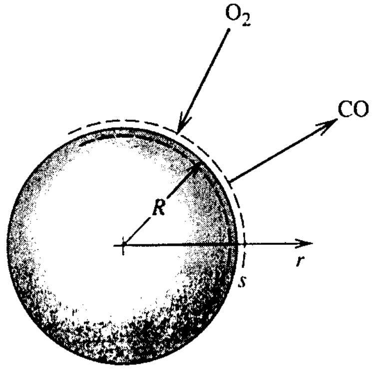

FIGURE 4.7.8 Combustion of a carbon particle in high-temperature air. The surface reaction is 2C + $O_2 \rightarrow$ 2CO.

and the vapor flux along the heat pipe is

$$N_1 = \frac{c\mathcal{D}_{12}}{L} \ln \frac{1 - x_{1,e}}{1 - x_{1,s}} \text{ kmol/m}^2 \text{ sec} \tag{4.7.50}$$

Notice that $N_2 = 0$; that is, the gas is stationary. The rate of heat flow for a heat pipe of cross-sectional area of A_c is $\dot{Q} = N_1 M_1 h_{fg} A_c$. Evaluation of the $c\mathcal{D}$ product at a reference temperature $T_r = (1/2)(T_s + T_e)$ is adequate for most applications. Equation (4.7.50) applies to any situation where a one-dimensional model of mass transport is appropriate.

Heterogeneous Combustion

As an example, consider a small carbon particle entrained in a high-temperature airstream, as shown in Figure 4.7.8. The surface reaction is 2C + $O_2 \rightarrow$ 2CO and there are no reactions in the gas phase. The stoichiometric ratio for the reaction is $r = 4/3$ kg oxygen/kg carbon. The reaction is diffusion controlled at the temperatures under consideration, that is, $m_{O_2,s} \simeq 0$. The mass transfer rate is n_s, which we give the distinctive symbol $\dot{m}''$ since it is usually the desired result of an analysis; in this situation $\dot{m}'' = n_{C,u}$ is the combustion rate of carbon, and for a spherical particle of radius R is given by

$$\dot{m}'' = \frac{\rho\mathcal{D}_{O_2,m}}{R} \ln\left[1 + \frac{m_{O_2,e} - m_{O_2,s}}{m_{O_2,s} + 4/3}\right] = 0.160 \frac{\rho\mathcal{D}_{O_2,m}}{R} \text{ kg/m}^2 \text{ sec} \tag{4.7.51}$$

The carbon particle temperature depends on its radius, and it is required to evaluate the property product $\rho\mathcal{D}$ at an appropriate reference temperature: an energy balance on the particle should be performed by this purpose. The resulting particle lifetime τ is

$$\tau = \frac{\rho_{\text{solid}} D_O^2}{1.28\left(\rho\mathcal{D}_{O_2,m}\right)_r} \text{ sec} \tag{4.7.52}$$

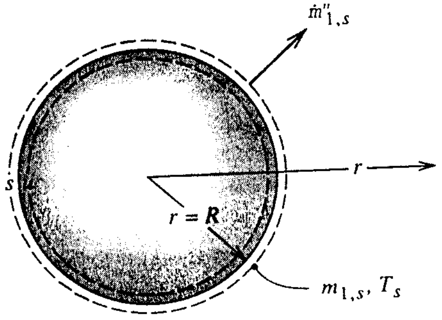

FIGURE 4.7.9 Evaporation of a droplet.

for an initial particle diameter of D_0. Air properties at an average mean film temperature can be used to evaluate $\rho\mathcal{D}_{O_2,m}$.

Consider a 10-μm-diameter carbon particle ignited in an airstream at 1500 K and 1 atm. An energy balance on the particle (including radiation to surroundings at 1500 K) shows that the average temperature of the particle is approximately 2550 K, and, thus, $T_r = (1/2)(1500 + 2550) = 2025$ K or $\rho \simeq \rho_{air} = 0.175$ kg/m^3 and $\mathcal{D}_{O_2,m} \simeq \mathcal{D}_{O_2,air} = 4.89 \times$ m^2/sec (from Table 4.7.1). Then

$$\tau = \frac{(1810)\left(10\times 10^{-6}\right)^2}{(1.28)(0.175)\left(4.89\times 10^{-4}\right)} = 1.65\times 10^{-3} \text{ sec}$$

Droplet Evaporation

Consider a small droplet of species 1 entrained in a gas stream, species 2 (Figure 4.7.9). This is a simultaneous heat and mass transfer problem, and the mass transfer rate can be obtained by solving simultaneously

$$\dot{m}'' = \frac{\rho\mathcal{D}_{12}}{R}\ln\left(1+\frac{m_{1,e}-m_{1,s}}{m_{1,s}-1}\right) = \frac{k/c_{p1}}{R}\ln\left(1+\frac{c_{p1}\left(T_e-T_s\right)}{h_{fg}}\right) \text{kg/m}^2 \text{ sec} \tag{4.7.53a}$$

$$m_{1,s} = m_{1,s}(T,P) \qquad \text{(from vapor−pressure data)} \tag{4.7.53b}$$

Temperature T_s is the adiabatic vaporization temperature and is essentially the psychrometric wet-bulb temperature. Properties can be evaluated at mean film temperature and composition; alternatively, c_{p1} can be set equal to the reference specific heat and all properties evaluated using Hubbard's $^1/_3$ rule, namely,

$$m_{1,r} = m_{1,s} + (1/3)\left(m_{1,e} - m_{1,s}\right) \tag{4.7.54a}$$

$$T_r = T_s + (1/3)\left(T_e - T_s\right) \tag{4.7.54b}$$

Droplet Combustion

Figure 4.7.10 shows a schematic of a volatile liquid hydrocarbon fuel droplet burning in air at zero gravity. The flame diameter is typically four to six times the droplet diameter. Heat is transferred from the flame to the droplet and serves to vaporize the fuel. In the flame the vapor reacts with oxygen to form gaseous products, primarily CO_2 and H_2O. When a fuel droplet ignites, there is a short initial transient during which the droplet heats up, until further conduction into the droplet is negligible and the droplet attains a steady temperature (approximately the wet-bulb temperature, which is very close to the boiling point

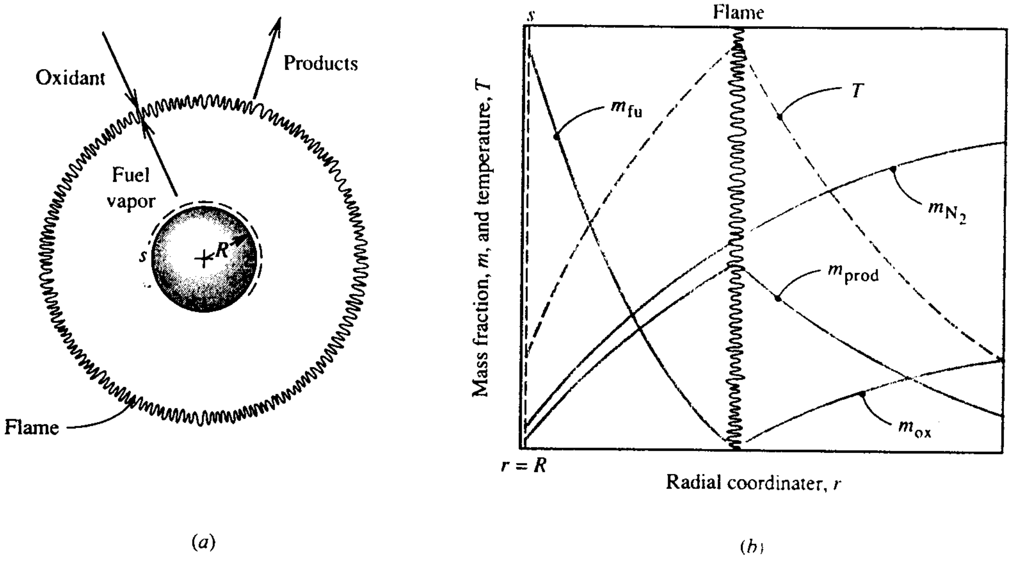

FIGURE 4.7.10 Combustion of a volatile fuel droplet burning in air: (a) schematic showing the flame, (b) concentration and temperature profiles.

for a typical hydrocarbon fuel). The reaction in the flame can be modeled as a single-step reaction with a constant stoichiometric ratio, r, and heat of combustion Δh_c J/kg of fuel.

The burning (mass transfer) rate of the droplet is given by the Godsave–Spalding formula,

$$\dot{m}'' = \frac{k/c_p}{R} \ln[1 + \mathcal{B}] \text{ kg/m}^2 \text{ sec} \tag{4.7.55}$$

where

$$\mathcal{B} = \frac{m_{ox,e}\,\Delta h_c / r + c_p\left(T_e - T_s\right)}{h_{fg}}$$

is the *mass transfer driving force* (or *transfer number*). The droplet lifetime is then

$$\tau = \frac{\rho_l D_O^2}{8\left(k/c_p\right)\ln(1 + \mathcal{B})} \text{ sec} \tag{4.7.56}$$

Based on experimental data for alkane droplets burning in air, Law and Williams (1972) recommend that properties be evaluated at a reference temperature $T_r = (1/2)(T_{BP} + T_{\text{flame}})$ where T_{flame} is the adiabatic flame temperature. The reference specific heat is $c_{pr} = c_{pfu}$, and the reference thermal conductivity is $k_r = 0.4k_{fu} + 0.6k_{\text{air}}$. Radiation has been ignored in the analysis leading to Equation (4.7.55) but is accounted for in using the Law and Williams reference-property scheme.

For example, consider a 1-mm-diameter n-octane droplet burning in air at 1 atm and 300 K, at near zero gravity. For n-octane (n-C_8H_{18}), $\rho_l = 611$ kg/m^3, $h_{fg} = 3.03 \times 10^5$ J/kg, $\Delta h_c = 4.44 \times 10^7$ J/kg, and $T_{BP} = 399$ K. The flame temperature is $T_{\text{flame}} = 2320$ K. At a reference temperature of (1/2) ($T_{\text{flame}} + T_{BP}$) = 1360 K, property values of n-octane vapor include $k = 0.113$ W/m K, $c_p = 4280$ J/kg K. The reaction is

$$C_8H_{18} + 12.5O_2 \rightarrow 8CO_2 + 9H_2O$$

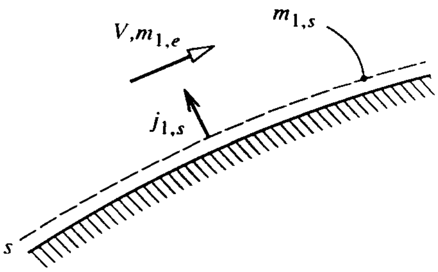

FIGURE 4.7.11 Notation for convective mass transfer into an external flow.

Hence, the stoichiometric ratio $r = 400/114.2 = 3.50$. Also $m_{ox,e} = 0.231$ and $T_s \cong T_{BP} = 399$ K. Thus, the transfer number is

$$\mathcal{B} = \frac{(0.231)\left(4.44\times10^7\right)/(3.50) + 4280(300-399)}{3.03\times10^5} = 8.27$$

At $T_r = 1360$ K, $k_{\text{air}} = 0.085$ W/m K. Hence,

$$k_r = 0.4k_{fu} + 0.6k_{\text{air}} = (0.4)(0.113) + (0.6)(0.085) = 0.096 \text{ W/m K}$$

and the droplet lifetime is

$$\tau = \frac{(611)\left(1\times10^{-3}\right)^2}{(8)(0.096/4280)\ln(1+8.27)} = 1.53 \text{ sec}$$

Mass Convection

The terms *mass convection* or *convective mass transfer* are generally used to describe the process of mass transfer between a surface and a moving fluid, as shown in Figure 4.7.11. The surface may be that of a falling water film in an air humidifier, of a coke particle in a gasifier, or of a silica-phenolic heat shield protecting a reentry vehicle. As is the case for heat convection, the flow can be *forced* or *natural, internal* or *external,* and *laminar* or *turbulent*. In addition, the concept of whether the mass transfer rate is *low* or *high* plays an important role: when mass transfer rates are low, there is a simple analogy between heat transfer and mass transfer that can be efficiently exploited in the solution of engineering problems.

Mass and Mole Transfer Conductances

Analogous to convective heat transfer, the rate of mass transfer by convection is usually a complicated function of surface geometry and *s*-surface composition, the fluid composition and velocity, and fluid physical properties. For simplicity, we will restrict our attention to fluids that are either binary mixtures or solutions, or situations in which, although more than two species are present, diffusion can be adequately described using effective binary diffusion coefficients, as was discussed in the section on ordinary diffusion. Referring to Figure 4.7.11, we define the *mass transfer conductance* of species 1, g_{m1}, by the relation

$$j_{1,s} = g_{m1}\,\Delta m_1; \qquad \Delta m_1 = m_{1,s} - m_{1,e} \tag{4.7.57}$$

and the units of g_{m1} are seen to be the same as for mass flux (kg/m^{2}sec). Equation (4.7.57) is of a similar form to Newton's law of cooling, which defines the heat transfer coefficient h_c. Why we should not use a similar name and notation (e.g., mass transfer coefficient and h_m) will become clear later. On a molar basis, we define the *mole transfer conductance* of species 1, $\mathcal{G}_{m1}$, by a corresponding relation,

$$J_{1,s} = \mathcal{G}_{m1}\,\Delta x_1; \qquad \Delta x_1 = x_{1,s} - x_{1,e} \tag{4.7.58}$$

where $\mathcal{G}_{m1}$ has units (kmol/m^{2}sec).

Low Mass Transfer Rate Theory

Consider, as an example, the evaporation of water into air, as shown in Figure 4.7.12. The water–air interface might be the surface of a water reservoir, or the surface of a falling water film in a cooling tower or humidifier. In such situations the mass fraction of water vapor in the air is relatively small; the highest value is at the s-surface, but even if the water temperature is as high as 50°C, the corresponding value of $m_{H_2O,s}$ at 1 atm total pressure is only 0.077. From Equation 4.7.54 the driving potential for diffusion of water vapor away from the interface is $\Delta m_1 = m_{1,s} - m_{1,e}$, and is small compared to unity, even if the free-stream air is very dry such that $m_{1,e} \simeq 0$. We then say that the mass transfer rate is *low* and the rate of evaporation of the water can be approximated as $j_{1,s}$; for a surface area A,

$$\dot{m}_1 = \left(m_{1,s} n_s + j_{1,s}\right) A \simeq j_{1,s} A \text{ kg/sec} \tag{4.7.59}$$

In contrast, if the water temperature approaches its boiling point, $m_{1,s}$ is no longer small, and of course, in the limit of $T_s = T_{BP}$, $m_{1,s} = 1$. The resulting driving potential for diffusion Δm_1 is then large, and we say that the mass transfer rate is *high*. Then, the evaporation rate cannot be calculated from Equation 4.7.59, as will be explained in the section on high mass transfer rate theory. For water evaporation into air, the error incurred in using low mass transfer rate theory is approximately $(^1/_2)\ \Delta m_1$, and a suitable criterion for application of the theory to engineering problems is $\Delta m_1 < 0.1$ or 0.2.

A large range of engineering problems can be adequately analyzed assuming low mass transfer rates. These problems include cooling towers and humidifiers as mentioned above, gas absorbers for sparingly soluble gases, and catalysis. In the case of catalysis, the *net* mass transfer rate is actually zero. Reactants diffuse toward the catalyst surface and the products diffuse away, but the catalyst only promotes the reaction and is not consumed. On the other hand, problems that are characterized by high mass transfer rates include condensation of steam containing a small amount of noncondensable gas, as occurs in most power plant condensers; combustion of volatile liquid hydrocarbon fuel droplets in diesel engines and oil-fired power plants, and ablation of phenolic-based heat shields on reentry vehicles.

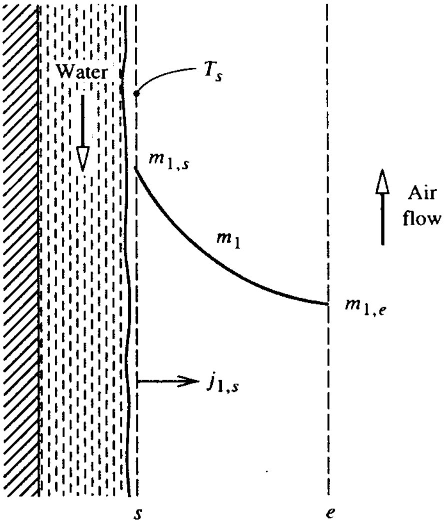

FIGURE 4.7.12 Evaporation of water into an air flow.

Dimensionless Groups

Dimensional analysis of convective mass transfer yields a number of pertinent dimensionless groups that are, in general, analogous to dimensionless groups for convective heat transfer. The most important groups are as follows.

1. The Schmidt number, $\mathrm{Sc}_{12} = \mu/\rho\mathcal{D}_{12}$, which is a properties group analogous to the Prandtl number. For gas mixtures, $\mathrm{Sc}_{12} = O(1)$, and for liquid solutions, $\mathrm{Sc}_{12} = O(100)$ to $O(1000)$. There are not fluids for which $\mathrm{Sc}_{12} \ll 1$, as is the case of Prandtl number for liquid metals.
2. The Sherwood number (or mass transfer Nusselt number). $\mathrm{Sh} = g_{m1}L/\rho\mathcal{D}_{12}$ $(= \mathcal{G}_{m1}L/c\mathcal{D}_{12})$ is a dimensionless conductance.
3. The mass transfer Stanton number $\mathrm{St}_m = g_{\mathrm{m1}}/\rho V$ $(= \mathcal{G}_{m1}/cV)$ is an alternative dimensionless conductance.

As for convective heat transfer, forced convection flows are characterized by a Reynolds number, and natural convection flows are characterized by a Grashof or Rayleigh number. In the case of Gr or Ra it is not possible to replace $\Delta\rho$ by $\beta\Delta T$ since density differences can result from concentration differences (and both concentration and temperature differences for simultaneous heat and mass transfer problems).

Analogy between Convective Heat and Mass Transfer

A close analogy exists between convective heat and convective mass transfer owing to the fact that conduction and diffusion in a fluid are governed by physical laws of identical form, that is, Fourier's and Fick's laws, respectively. As a result, in many circumstances the Sherwood or mass transfer Stanton number can be obtained in a simple manner from the Nusselt number or heat transfer Stanton number for the same flow conditions. Indeed, in most gas mixtures Sh and St_m are nearly equal to their heat transfer counterparts. For dilute mixtures and solutions and low mass transfer rates, the rule for exploiting the analogy is simple: The *Sherwood or Stanton number is obtained by replacing the Prandtl number by the Schmidt number in the appropriate heat transfer correlation*. For example, in the case of fully developed turbulent flow in a smooth pipe

$$\mathrm{Nu}_D = 0.023\mathrm{Re}_D^{0.8}\mathrm{Pr}^{0.4}; \qquad \mathrm{Pr} > 0.5 \tag{4.7.60a}$$

which for mass transfer becomes

$$\mathrm{Sh}_D = 0.023\mathrm{Re}_D^{0.8}\mathrm{Sc}^{0.4}; \qquad \mathrm{Sc} > 0.5 \tag{4.7.60b}$$

Also, for natural convection from a heated horizontal surface facing upward,

$$\overline{\mathrm{Nu}} = 0.54\left(\mathrm{Gr}_L\mathrm{Pr}\right)^{1/4}; \qquad 10^5 < \mathrm{Gr}_L\mathrm{Pr} < 2\times10^7 \quad \text{(laminar)} \tag{4.7.61a}$$

$$\overline{\mathrm{Nu}} = 0.14\left(\mathrm{Gr}_L\mathrm{Pr}\right)^{1/3}; \qquad 2\times10^7 < \mathrm{Gr}_L\mathrm{Pr} < 3\times10^{10} \quad \text{(turbulent)} \tag{4.7.61b}$$

which for isothermal mass transfer with $\rho_s < \rho_e$ become

$$\overline{\mathrm{Sh}} = 0.54\left(\mathrm{Gr}_L\mathrm{Sc}\right)^{1/4}; \qquad 10^5 < \mathrm{Gr}_L\mathrm{Sc} < 2\times10^7 \quad \text{(laminar)} \tag{4.7.62a}$$

$$\overline{\mathrm{Sh}} = 0.14\left(\mathrm{Gr}_L\mathrm{Sc}\right)^{1/3}; \qquad 2\times10^7 < \mathrm{Gr}_L\mathrm{Sc} < 3\times10^{10} \quad \text{(turbulent)} \tag{4.7.62b}$$

With evaporation, the condition, $\rho_s < \rho_e$ will be met when the evaporating species has a smaller molecular weight than the ambient species, for example, water evaporating into air. Mass transfer correlations can be written down in a similar manner for almost all the heat transfer correlations given in Section 4.2. There are some exceptions: for example, there are no fluids with a Schmidt number much less than unity, and thus there are no mass transfer correlations corresponding to those given for heat transfer to liquid metals with $\mathrm{Pr} \ll 1$. In most cases it is important for the wall boundary conditions to be of analogous form, for example, laminar flow in ducts. A uniform wall temperature corresponds to a uniform concentration $m_{1,s}$ along the *s*-surface, whereas a uniform heat flux corresponds to a uniform diffusive flux $j_{1,s}$. In chemical engineering practice, the analogy between convective heat and mass transfer is widely used in a form recommended by Chilton and Colburn in 1934, namely, $\mathrm{St}_m/\mathrm{St} = (\mathrm{Sc}/\mathrm{Pr})^{-2/3}$. The Chilton-Colburn form is of adequate accuracy for most external forced flows but is inappropriate for fully developed laminar duct flows.

For example, air at 1 atm and 300 K flows inside a 3-cm-inside-diameter tube at 10 m/sec. Using pure-air properties the Reynolds number is $VD/\nu = (10)(0.03)/15.7 \times 10^{-6} = 1.911 \times 10^4$. The flow is turbulent. Using Equation (4.7.60b) with $\mathrm{Sc}_{12} = 0.61$ for small concentrations of H_2O in air,

$$\mathrm{Sh}_D = (0.023)\left(1.911\times 10^4\right)^{0.8}(0.61)^{0.4} = 50.2$$

$$g_{m1} = \rho\mathcal{D}_{12}\mathrm{Sh}/D = \rho\nu\mathrm{Sh}/\mathrm{Sc}_{12}D = \frac{(1.177)\left(15.7\times 10^{-6}\right)(50.2)}{(0.61)(0.03)} = 5.07\times 10^{-2}\ \mathrm{kg/m^2\ sec}$$

Further insight into this analogy between convective heat and mass transfer can be seen by writing out Equation (4.7.60a) and Equation (4.7.60b) as, respectively,

$$\frac{\left(h_c/c_p\right)D}{k/c_p} = 0.023\mathrm{Re}_D^{0.8}\left(\frac{\mu}{k/c_p}\right)^{0.4} \tag{4.7.63a}$$

$$\frac{g_m D}{\rho\mathcal{D}_{12}} = 0.023\mathrm{Re}_D^{0.8}\left(\frac{\mu}{\rho\mathcal{D}_{12}}\right)^{0.4} \tag{4.7.63b}$$

When cast in this form, the correlations show that the property combinations k/c_p and $\rho\mathcal{D}_{12}$ play analogous roles; these are *exchange coefficients* for heat and mass, respectively, both having units kg/m sec, which are the same as those for dynamic viscosity μ. Also, it is seen that the ratio of heat transfer coefficient to specific heat plays an analogous role to the mass transfer conductance, and has the same units (kg/m^2 sec). Thus, it is appropriate to refer to the ratio h_c/c_p as the *heat transfer conductance*, g_h, and for this reason we should not refer to g_m as the mass transfer *coefficient*.

Simultaneous Heat and Mass Transfer

Often problems involve simultaneous convective heat and mass transfer, for which the surface energy balance must be carefully formulated. Consider, for example, evaporation of water into air, as shown in Figure 4.7.13. With H_2O denoted as species 1, the steady-flow energy equation applied to a control volume located between the *u*- and *s*-surfaces requires that

$$\dot{m}\left(h_{1,s} - h_{1,u}\right) = A\left(q''_{\mathrm{cond}} - q''_{\mathrm{conv}} - q''_{\mathrm{rad}}\right)\ \mathrm{W} \tag{4.7.64}$$

where it has been recognized that only species 1 crosses the *u*- and *s*-surfaces. Also, the water has been assumed to be perfectly opaque so that all radiation is emitted or absorbed between the *u*-surface and the interface.

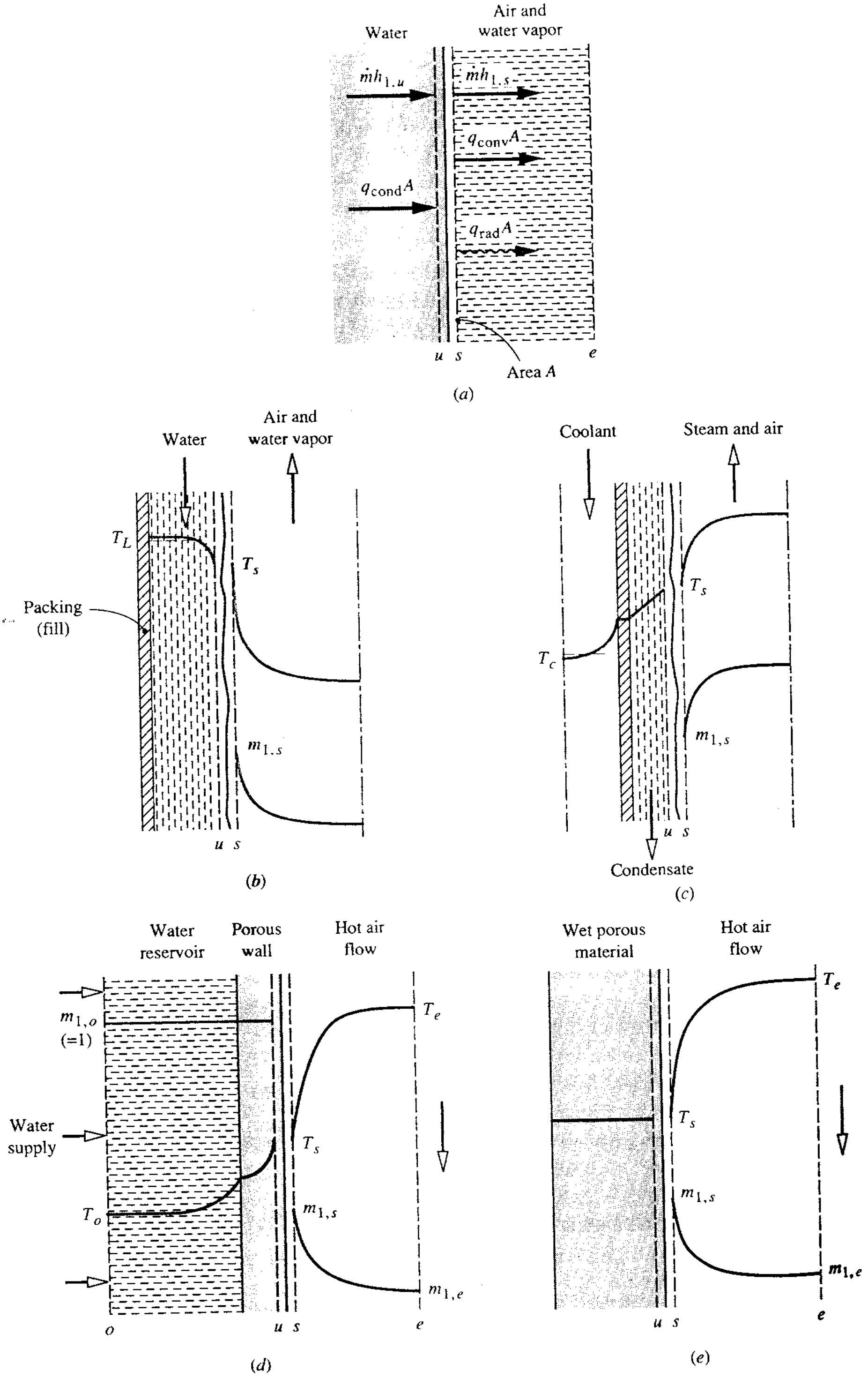

FIGURE 4.7.13 The surface energy balance for evaporation of water into an air stream.

If we restrict our attention to conditions for which low mass transfer rate theory is valid, we can write $\dot{m}/A \simeq j_{1,s} = g_{m1}\,(m_{1,s} - m_{1,e})$. Also, we can then calculate the convective heat transfer as if there were no mass transfer, and write $q_{\text{conv}} = h_c(T_s - T_e)$. Substituting in Equation (4.7.64) with $q_{\text{conv}} = -k\partial T/\partial y|_u$, $h_{1,s} - h_{1,u} = h_{fg}$, and rearranging, gives

$$-k\frac{\partial T}{\partial y}\bigg|_u = h_c\left(T_s - T_e\right) + g_{m1}\left(m_{1,s} - m_{1,e}\right)h_{fg} + q''_{\text{rad}} \text{ W/m}^2 \tag{4.7.65}$$

It is common practice to refer to the convective heat flux $h_c(T_s - T_e)$ as the *sensible* heat flux, whereas the term $g_{m1}\,(m_{1,s} - m_{1,e})\,h_{fg}$ is called the *evaporative* or *latent* heat flux. Each of the terms in Equation 4.7.65 can be positive or negative, depending on the particular situation. Also, the evaluation of the conduction heat flux at the u-surface, $-k\partial T/\partial y|_u$, depends on the particular situation. Four examples are shown in Figure 4.7.13. For a water film flowing down a packing in a cooling tower (Figure 4.7.13b), this heat flux can be expressed in terms of convective heat transfer from the bulk water at temperature T_L to the surface of the film, $-k\partial T/\partial y|_u = h_{cL}\,(T_L - T_s)$. If the liquid-side heat transfer coefficient h_{cL} is large enough, we can simply set $T_s \simeq T_L$, which eliminates the need to estimate h_{cL}. The evaporation process is then *gas-side controlled*. Figure 4.7.13c shows film condensation from a steam-air mixture on the outside of a vertical tube. In this case we can write $k\partial T/\partial y|_u = U(T_s - T_c)$, where T_c is the coolant bulk temperature. The overall heat transfer coefficient U includes the resistances of the condensate film, the tube wall, and the coolant. Sweat cooling is shown in Figure 4.7.13d, with water from a reservoir (or *plenum chamber*) injected through a porous wall at a rate just sufficient to keep the wall surface wet. In this case, the conduction across the u-surface can be related to the reservoir conditions by application of the steady-flow energy equation to a control volume located between the o- and u-surfaces. Finally, Figure 4.7.13e shows drying of a wet porous material (e.g., a textile or wood). During the constant-rate period of the process, evaporation takes place from the surface with negligible heat conduction into the solid; then $-k\partial T/\partial y|_u \simeq 0$. The term *adiabatic vaporization* is used to describe evaporation when $q_{\text{cond}} = 0$; constant-rate drying is one example, and the wet-bulb psychrometer is another.

Consider a 1-m-square wet towel on a washline on a day when there is a low overcast and no wind. The ambient air is at 21°C, 1 atm, and 50.5% RH. In the constant-rate drying period the towel temperature is constant, and $q_{\text{cond}} = 0$. An iterative calculation is required to obtain the towel temperature using correlations for natural convection on a vertical surface to obtain h_c and g_{m1}; q_{rad} is obtained as $q_{\text{rad}} = \sigma\varepsilon(T_s^4 - T_e^4)$ with $\varepsilon = 0.90$. The results are $T_s = 17.8$°C, $h_c = 1.69$ W/m²K, $g_{m1} = 1.82 \times 10^{-3}$ kg/m²sec, and the energy balance is

$$q_{\text{cond}} = h_c\left(T_s - T_e\right) + g_{m1}\left(m_{1,s} - m_{1,e}\right)h_{fg} + q_{\text{rad}}$$

$$0 = -5.4 + 21.7 - 16.3 \text{ W/m}^2$$

Evaluation of composition-dependent properties, in particular the mixture specific heat and Prandtl number, poses a problem. In general, low mass transfer rates imply small composition variations across a boundary layer, and properties can be evaluated for a mixture of the free-stream composition at the mean film temperature. In fact, when dealing with evaporation of water into air, use of the properties of dry air at the mean film temperature gives results of adequate engineering accuracy. If there are large composition variations across the boundary layer, as can occur in some catalysis problems, properties should be evaluated at the mean film composition and temperature.

The Wet- and Dry-Bulb Psychrometer

The wet- and dry-bulb psychrometer is used to measure the moisture content of air. In its simplest form, the air is made to flow over a pair of thermometers, one of which has its bulb covered by a wick whose

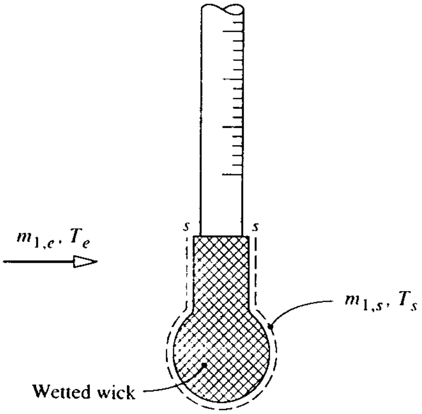

FIGURE 4.7.14 Wet bulb of a wet- and dry-bulb psychrometer.

other end is immersed in a small water reservoir. Evaporation of water from the wick causes the wet bulb to cool and its steady-state temperature is a function of the air temperature measured by the dry bulb and the air humidity. The wet bulb is shown in Figure 4.7.14. In order to determine the water vapor mass fraction $m_{1,e}$, the surface energy balance Equation (4.7.66) is used with conduction into the wick and q''_{rad} set equal to zero. The result is

$$m_{1,e} = m_{1,s} - \frac{c_p}{h_{fg}}\left(\frac{\text{Pr}}{\text{Sc}_{12}}\right)^{-2/3}\left(T_e - T_s\right) \qquad (4.7.66)$$

Usually $m_{1,e}$ is small and we can approximate $c_p = c_{p\text{ air}}$ and $(\text{Pr}/\text{Sc}_{12})^{-2/3} = 1/1.08$. Temperatures T_s and T_e are the known measured wet- and dry-bulb temperatures. With T_s known, $m_{1,s}$ can be obtained using steam tables in the usual way. For example, consider an air flow at 1000 mbar with measured wet- and dry-bulb temperatures of 305.0 and 310.0 K, respectively. Then $P_{1,s} = P_{\text{sat}}(T_s) = P_{\text{sat}}(305.0\text{ K}) = 4714$ Pa from steam tables. Hence, $x_{1,s} = P_{1,s}/P = 4714/10^5 = 0.04714$, and

$$m_{1,s} = \frac{0.04714}{0.04714 + (29/18)(1 - 0.04714)} = 0.02979$$

Also, h_{fg} (305 K) = 2.425×10^6 J/kg, and $c_{p\text{ air}} = 1005$ J/kg K; thus

$$m_{1,e} = 0.02979 - \frac{1005}{(1.08)\left(2.425 \times 10^6\right)}(310 - 305) = 0.02787$$

$$x_{1,e} = \frac{0.02787}{0.02787 + (18/29)(1 - 0.02787)} = 0.04415$$

$$P_{1,e} = x_{1,e}P = (0.04415)\left(10^5\right) = 4412\text{ Pa}$$

By definition, the relative humidity is RH = $P_{1,e}/P_{\text{sat}}(T_e)$; RH = 4415/6224 = 70.9%.

In the case of other adiabatic vaporization processes, such as constant-rate drying or evaporation of a water droplet, $m_{1,e}$ and T_e are usually known and Equation (4.7.66) must be solved for T_s. However, the thermodynamic wet-bulb temperature obtained from psychrometric charts or software is accurate enough for engineering purposes.

High Mass Transfer Rate Theory

When there is net mass transfer across a phase interface, there is a convective component of the absolute flux of a species across the *s*-surface. From Equation (4.7.23a) for species 1,

$$n_{1,s} = \rho_{1,s} \mathrm{v}_s + j_{1,s} \text{ kg/m}^2 \text{ sec} \tag{4.7.67}$$

During evaporation the convection is directed in the gas phase, with a velocity normal to the surface v_s. When the convective component cannot be neglected, we say that the mass transfer rate is *high*. There are two issues to consider when mass transfer rates are high. First, the rate at which species 1 is transferred across the *s*-surface is not simply the diffusive component $j_{1,s}$ as assumed in low mass transfer rate theory, but is the sum of the convective and diffusive components shown in Equation 4.7.67. Second, the normal velocity component v_s has a *blowing* effect on the concentration profiles, and hence on the Sherwood number. The Sherwood number is no longer analogous to the Nusselt number of conventional heat transfer correlations, because those Nusselt numbers are for situations involving impermeable surfaces, e.g., a metal wall, for which $v_s = 0$.

Substituting for $j_{1,s}$ from Equation (4.7.57) into Equation (4.7.67) gives

$$\dot{m}'' = \mathcal{g}_{m1} \frac{m_{1,e} - m_{1,s}}{m_{1,s} - n_{1,s}/\dot{m}''} = \mathcal{g}_{m1} \mathcal{B}_{m1} \tag{4.7.68}$$

where $\dot{m}'' = n_s$ is the mass transfer rate introduced in the section on heterogeneous combustion and $\mathcal{B}_{m1}$ is the *mass transfer driving force*. In the special case where only species 1 is transferred, $n_{1,s}/\dot{m}'' = 1$, for example, when water evaporates into air, and dissolution of air in the water is neglected. It is convenient to rewrite Equation (4.7.68) as

$$\dot{m}'' = \mathcal{g}^*_{m1} \left(\mathcal{g}_{m1} / \mathcal{g}^*_{m1} \right) \mathcal{B}_{m1} \text{ kg/m}^2 \text{ sec} \tag{4.7.69a}$$

where

$$\mathcal{g}^*_{m1} = \lim_{\mathcal{B}_m \to 0} \mathcal{g}_{m1} \tag{4.7.69b}$$

Now $\mathcal{g}^*_{m1}$ is the limit value of $\mathcal{g}_{m1}$ for zero mass transfer (i.e., $v_s = 0$), and Sh^* can be obtained from conventional heat transfer Nusselt number correlations for impermeable surfaces. The ratio $(\mathcal{g}_{m1}/\mathcal{g}^*_{m1})$ is termed a *blowing factor* and accounts for the effect of v_s on the concentration profiles. Use of Equation (4.7.69) requires appropriate data for the blowing factor. For the constant-property laminar boundary layer on a flat plate, Figure 4.7.15 shows the effect of the Schmidt number on the blowing factor. The abscissa is a *blowing parameter* $B_m = \dot{m}''/\mathcal{g}^*_m$.

The blowing velocity also affects the velocity and temperature profiles, and hence the wall shear stress and heat transfer. The curve for $\mathrm{Sc} = 1$ in Figure 4.7.15 also gives the effect of blowing on shear stress as τ_s/τ^*_s, and the curve for $\mathrm{Sc} = 0.7$ gives the effect of blowing on heat transfer for air injection into air as h_c/h^*_c (since $\mathrm{Pr} = 0.7$ for air).

Variable Property Effects of High Mass Transfer Rates

High mass transfer rate situations are usually characterized by large property variations across the flow, and hence property evaluation for calculating $\mathcal{g}_m$ and h_c is not straightforward. An often-encountered situation is transfer of a single species into an inert laminar or turbulent boundary layer flow. The effect

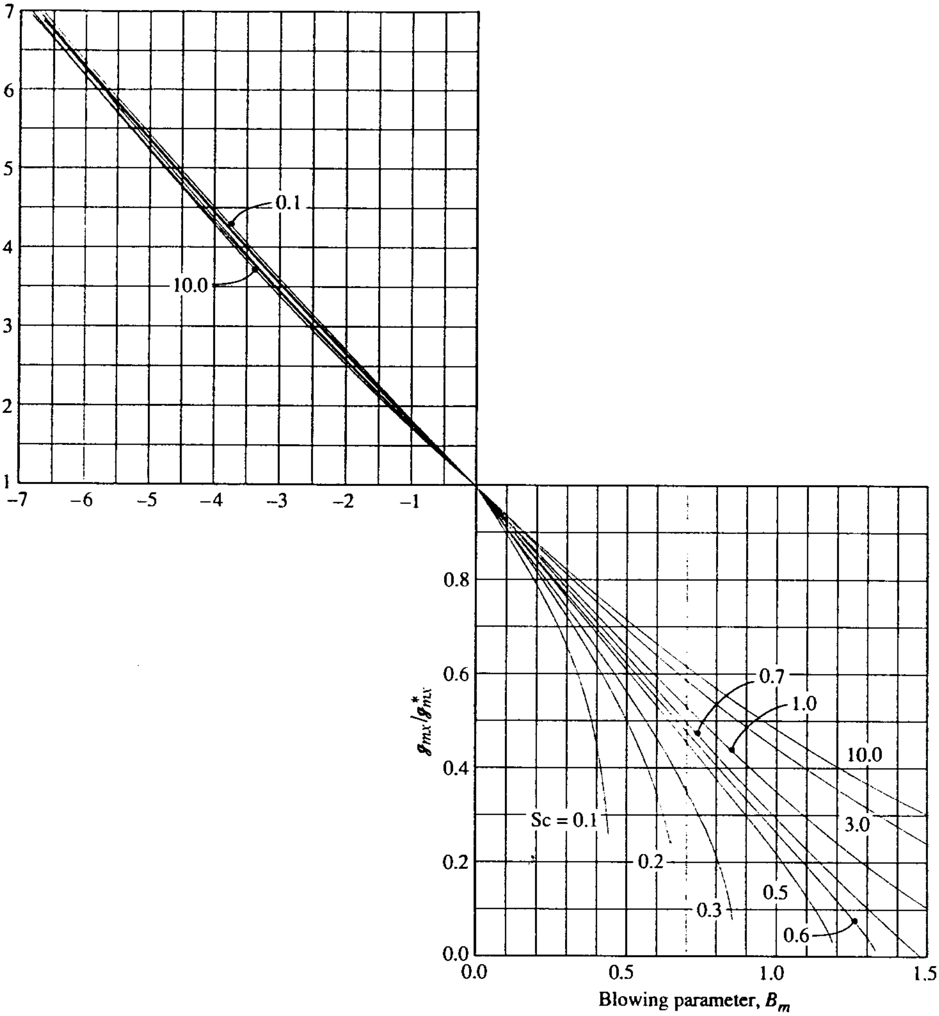

FIGURE 4.7.15 Effect of mass transfer on the mass transfer conductance for a laminar boundary layer on a flat plate: g_m / g^*_m vs. blowing parameter $B_m = \dot{m}'' / g^*_m$.

of variable properties can be very large as shown in Figure 4.7.16 for laminar boundary layers, and Figure 4.7.17 for turbulent boundary layers.

A simple procedure for correlating the effects of flow type and variable properties is to use weighting factors in the exponential functions suggested by a constant-property Couette-flow model (Mills, 1995). Denoting the injected species as species i, we have

$$\frac{g_{m1}}{g^*_{m1}} = \frac{a_{mi} B_{mi}}{\exp(a_{mi} B_{mi}) - 1}; \qquad B_{mi} = \frac{\dot{m}''}{g^*_{mi}} \tag{4.7.70a}$$

or

$$\frac{g_{m1}}{g^*_{mi}} = \frac{\ln(1 + a_{mi} \mathcal{B}_{mi})}{a_{mi} \mathcal{B}_{mi}}; \qquad \mathcal{B}_{mi} = \frac{\dot{m}''}{g_{mi}} = \frac{m_{i,e} - m_{i,e}}{m_{i,s} - 1}$$

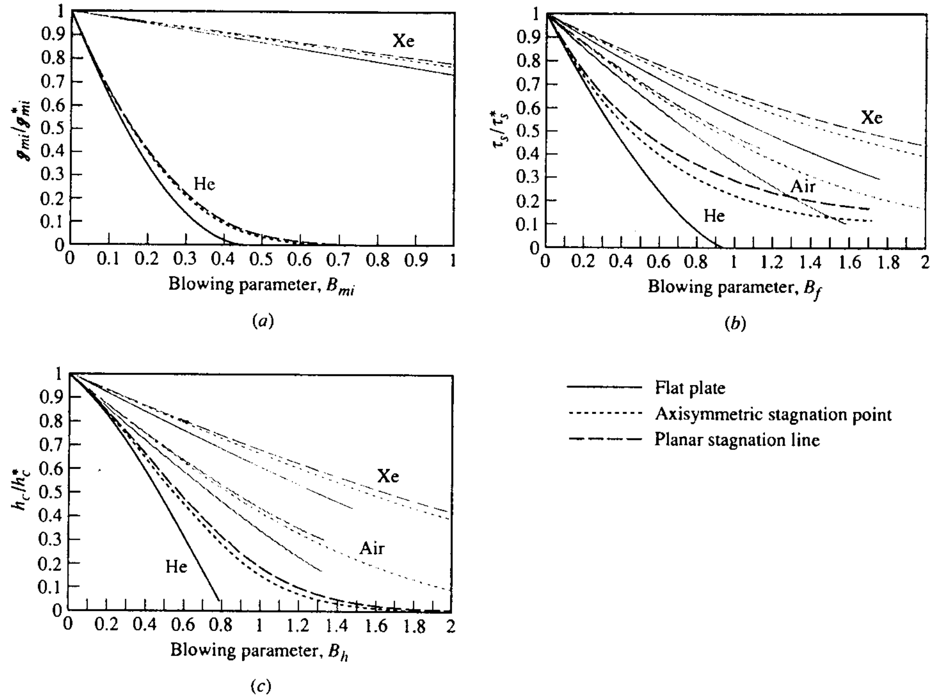

FIGURE 4.7.16 Numerical results for the effect of pressure gradient and variable properties on blowing factors for laminar boundary layers: low-speed air flow over a cold wall ($T_s/T_e = 0.1$) with foreign gas injection: (a) mass transfer conductance, (b) wall shear stress, (c) heat transfer coefficient. (From Wortman, A., Ph.D. dissertation, University of California, Los Angeles, 1969. With permission.)

$$\frac{\tau_s}{\tau_s^*} = \frac{a_{fi} B_f}{\exp\left(a_{fi} B_f\right) - 1}; \qquad B_f = \frac{\dot{m}'' u_e}{\tau_s^*} \tag{4.7.70b}$$

$$\frac{h_c}{h_c^*} = \frac{a_{hi} B_h}{\exp\left(a_{hi} B_h\right) - 1}; \qquad B_h = \frac{\dot{m}'' c_{pe}}{h_c^*} \tag{4.7.70c}$$

Notice that g^*_{mi}, τ^*_s, h^*_c, and c_{pe} are evaluated using properties of the free-stream gas at the mean film temperature. The weighting factor a may be found from exact numerical solutions of boundary layer equations or from experimental data. Some results for laminar and turbulent boundary layers follow.

1. *Laminar Boundary Layers.* We will restrict our attention to low-speed air flows, for which viscous dissipation and compressibility effects are negligible, and use exact numerical solutions of the self-similar laminar boundary layer equations (Wortman, 1969). Least-squares curve fits of the numerical data were obtained using Equation (4.7.70a) to Equation (4.7.70c). Then, the weighting factors for axisymmetric stagnation-point flow with a cold wall ($T_s/T_e = 0.1$) were correlated as

$$a_{mi} = 1.65\left(M_{\text{air}}/M_i\right)^{10/12} \tag{4.7.71a}$$

$$a_{fi} = 1.38\left(M_{\text{air}}/M_i\right)^{5/12} \tag{4.7.71b}$$

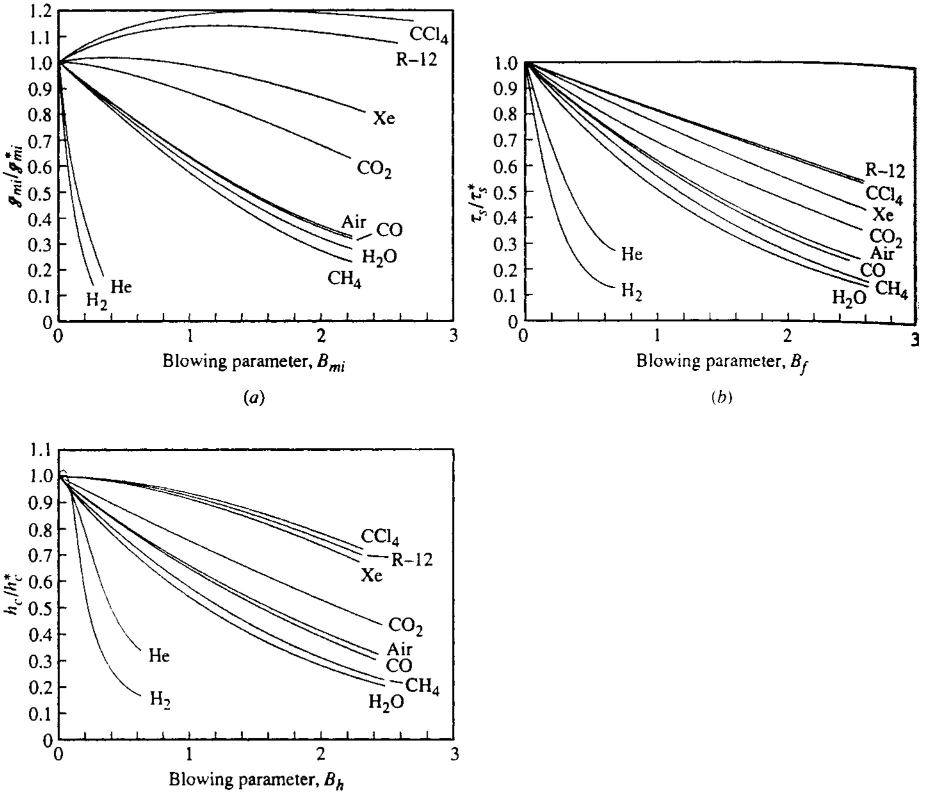

FIGURE 4.7.17 Numerical results for the effect of variable properties on blowing factors for a low-speed turbulent air boundary layer on a cold flat plate ($T_s/T_e = 0.2$) with foreign gas injection: (a) mass transfer conductance, (b) wall shear stress, (c) heat transfer coefficient. (From Landis, R.B., Ph.D. dissertation, University of California, Los Angeles, 1971. With permission.)

$$a_{hi} = 1.30\left(M_{\text{air}}/M_i\right)^{3/12}\left[c_{pi}/\left(2.5\mathcal{R}/M_i\right)\right] \tag{4.7.71c}$$

Notice that $c_{pi}/2.5\mathcal{R}/M_i)$ is unity for a monatomic species. For the planar stagnation line and the flat plate, and other values of the temperature ratio T_s/T_e, the values of the species weighting factors are divided by the values given by Equations (4.7.71a,b,c) to give correction factors G_{mi}, G_{fi}, and G_{hi}, respectively. The correction factors are listed in Table 4.7.7.

The exponential relation blowing factors cannot accurately represent some of the more anomalous effects of blowing. For example, when a light gas such as H_2 is injected, Equation (4.7.70c) indicates that the effect of blowing is always to reduce heat transfer, due to both the low density and high specific heat of hydrogen. However, at very low injection rates, the heat transfer is actually increased, as a result of the high thermal conductivity of H_2. For a mixture, $k \approx \sum x_i k_i$ whereas $c_p = \sum m_i c_{pi}$. At low rates of injection, the mole fraction of H_2 near the wall is much larger than its mass fraction; thus, there is a substantial increase in the mixture conductivity near the wall, but only a small change in the mixture specific heat. An increase in heat transfer results. At higher injection rates, the mass fraction of H_2 is also large, and the effect of high mixture specific heat dominates to cause a decrease in heat transfer.

TABLE 4.7.7 Correction Factors for Foreign Gas Injection into Laminar Air Boundary Layers

		G_{mi} T_s/T_e			G_{fi} T_s/T_e			G_{hi} T_s/T_e		
Geometry	Species	0.1	0.5	0.9	0.1	0.5	0.9	0.1	0.5	0.9
	H	1.14	1.36	1.47	1.30	1.64	1.79	1.15	1.32	—
	H_2	1.03	1.25	1.36	1.19	1.44	1.49	1.56	1.17	1.32
	He	1.05	1.18	1.25	1.34	1.49	1.56	1.18	1.32	—
	Air	—	—	—	1.21	1.27	1.27	1.17	1.21	—
	Xe	1.21	1.13	1.15	1.38	1.34	1.34	1.19	1.18	—
	CCl_4	1.03	0.95	1.00	1.00	1.03	1.03	1.04	1.04	—
Axisymmetric stagnation point	H	1.00	1.04	1.09	1.00	0.62	0.45	1.00	0.94	0.54
	H_2	1.00	1.06	1.06	1.00	0.70	0.62	1.00	1.00	1.01
	He	1.00	1.04	1.03	1.00	0.66	0.56	1.00	1.00	0.95
	C	1.00	1.01	1.00	1.00	0.79	0.69	1.00	0.99	0.87
	CH_4	1.00	1.01	1.00	1.00	0.88	0.84	1.00	1.00	1.00
	O	1.00	0.98	0.97	1.00	0.79	0.70	1.00	0.98	0.95
	H_2O	1.00	1.01	1.00	1.00	0.82	0.73	1.00	1.00	0.99
	Ne	1.00	1.00	0.98	1.00	0.83	0.75	1.00	0.97	0.95
	Air	—	—	—	1.00	0.87	0.82	1.00	0.99	0.97
	A	1.00	0.97	0.94	1.00	0.93	0.91	1.00	0.96	0.95
	CO_2	1.00	0.97	0.95	1.00	0.96	0.94	1.00	0.99	0.97
	Xe	1.00	0.98	0.96	1.00	0.96	1.05	1.00	1.06	0.99
	CCl_4	1.00	0.90	0.83	1.00	1.03	1.07	1.00	0.96	0.93
	I_2	1.00	0.91	0.85	1.00	1.02	1.05	1.00	0.97	0.94
Planar stagnation line	He	0.96	0.98	0.98	0.85	0.53	0.47	0.93	0.91	0.92
	Air	—	—	—	0.94	0.84	0.81	0.94	0.94	—
	Xe	0.92	0.87	0.83	0.90	0.93	0.95	0.93	0.93	—

Based on numerical data of Wortman (1969). Correlations developed by Dr. D.W. Hatfield.

2. *Turbulent Boundary Layers.* Here we restrict our attention to air flow along a flat plate for Mach numbers up to 6, and use numerical solutions of boundary layer equations with a mixing length turbulence model (Landis, 1971). Appropriate species weighting factors for $0.2 < T_s/T_e < 2$ are

$$a_{mi} = 0.79\left(M_{\text{air}}/M_i\right)^{1.33} \tag{4.7.72a}$$

$$a_{fi} = 0.91\left(M_{\text{air}}/M_i\right)^{0.76} \tag{4.7.72b}$$

$$a_{hi} = 0.86\left(M_{\text{air}}/M_i\right)^{0.73} \tag{4.7.72c}$$

In using Equation (4.7.70), the limit values for $\dot{m}'' = 0$ are elevated at the same location along the plate. Whether the injection rate is constant along the plate or varies as $x^{-0.2}$ to give a self-similar boundary layer has little effect on the blowing factors. Thus, Equation (4.7.72) has quite general applicability. Notice that the effects of injectant molecular weight are greater for turbulent boundary layers than for laminar ones, which is due to the effect of fluid density on turbulent transport. Also, the injectant specific heat does not appear in a_{hi} as it did for laminar flows. In general, c_{pi} decreases with increasing M_i and is adequately accounted for in the molecular weight ratio.

Reference State Schemes. The reference state approach, in which constant-property data are used with properties evaluated at some reference state, is an alternative method for handling variable-property effects. In principle, the reference state is independent of the precise property data used and of the combination of injectant and free-stream species. A reference state for a boundary layer on a flat plate that can be used in conjunction with Figure 4.7.14 is (Knuth, 1963)

$$m_{1,r} = 1 - \frac{M_2}{M_2 - M_1} \frac{\ln\left(M_e / M_s\right)}{\ln\left(m_{2,e} M_e / m_{2,s} M_s\right)} \tag{4.7.73}$$

$$T_r = 0.5\left(T_e + T_s\right) + 0.2 r^* \left(u_e^2 / 2c_{pr}\right) + 0.1\left[B_{hr} + \left(B_{hr} + B_{mr}\right) \frac{c_{p1} - c_{pr}}{c_{pr}}\right]\left(T_s - T_e\right) \tag{4.7.74}$$

where species 1 is injected into species 2 and r^* is the recovery factor for an impermeable wall. Use of the reference state method is impractical for hand calculations: a computer program should be used to evaluate the required mixture properties.

References

Hirschfelder, J.O., Curtiss, C.F., and Bird, R.B. 1954. *Molecular Theory of Gases and Liquids*, John Wiley & Sons, New York.

Knuth, E.L. 1963. Use of reference states and constant property solutions in predicting mass-, momentum-, and energy-transfer rates in high speed laminar flows, *Int. J. Heat Mass Transfer*, 6, 1–22.

Landis, R.B. 1972. Numerical solution of variable property turbulent boundary layers with foreign gas injection, Ph.D. dissertation, School of Engineering and Applied Science, University of California, Los Angeles.

Law, C.K. and Williams, F.A. 1972. Kinetics and convection in the combustion of alkane droplets, *Combustion and Flame*, 19, 393–405.

Mills, A.F. 2001. *Mass Transfer*, Prentice-Hall, Upper Saddle River, NJ.

Wortman, A. 1969. Mass transfer in self-similar boundary-layer flows, Ph.D. dissertation, School of Engineering and Applied Science, University of California, Los Angeles.

Further Information

Geankoplis, C.J. 2003. *Transport Processes and Unit Operations*, 4th ed., Prentice-Hall, Upper Saddle River, NJ. This text gives a chemical engineering perspective on mass transfer.

Mills, A.F. 2001. *Mass Transfer*, Prentice-Hall, Upper Saddle River, NJ. Chapter 3 treats mass transfer equipment.

Strumillo, C. and Kudra, T. 1986. *Drying: Principles, Applications and Design*, Gordon and Breach, New York.

Mujamdar, A.S.. Ed. 1987. *Handbook of Industrial Drying*, Marcel Dekker, New York.

4.8 Applications

Enhancement

Arthur E. Bergles

Introduction

Energy- and materials-saving considerations, as well as economic incentives, have led to efforts to produce more efficient heat exchange equipment. Common thermal-hydraulic goals are to reduce the size of a

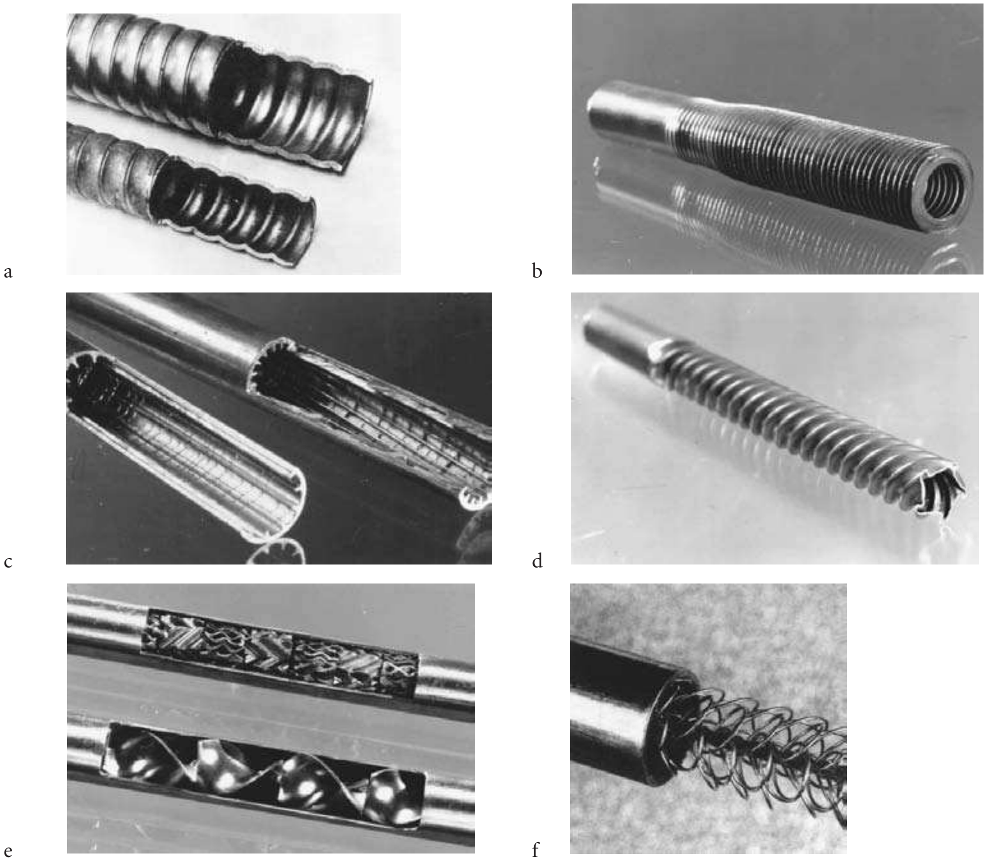

FIGURE 4.8.1 Enhanced tubes for augmentation of single-phase heat transfer. (a) Corrugated or spirally indented tube with internal protuberances. (b) Integral external fins. (c) Integral internal fins. (d) Deep spirally fluted tube. (e) Static mixer inserts. (f) Wire-wound insert.

heat exchanger required for a specified heat duty, to upgrade the capacity of an existing heat exchanger, to reduce the approach temperature difference for the process streams, or to reduce the pumping power.

The study of improved heat transfer performance is referred to as heat transfer *enhancement*, *augmentation*, or *intensification*. In general, this means an increase in heat transfer coefficient. Attempts to increase "normal" heat transfer coefficients have been recorded for more than a century, and there is a large store of information. A bibliographic survey (Bergles et al., 1995) lists 5676 technical publications, excluding patents and manufacturers' literature. An update for 2001 by Manglik and Bergles (2004) indicates that new literature is being added to this field at the rate of about 400 references per year.

Enhancement techniques can be classified either as passive methods, which require no direct application of external power (Figure 4.8.1), or as active methods, which require external power. The effectiveness of both types of techniques is strongly dependent on the mode of heat transfer, which may range from single-phase free convection to dispersed-flow film boiling. Brief descriptions of these methods follow.

Treated surfaces involve fine-scale alternation of the surface finish or coating (continuous or discontinuous). They are used for boiling and condensing; the roughness height is below that which affects single-phase heat transfer.

Rough surfaces are produced in many configurations ranging from random sand-grain-type roughness to discrete protuberances. See Figure 4.8.1a. The configuration is generally chosen to disturb the viscous sublayer rather than to increase the heat transfer surface area. Application of rough surfaces is directed primarily toward single-phase flow.

Extended surfaces are routinely employed in many heat exchangers. See Figure 4.8.1a to d. Work of special interest to enhancement is directed toward improvement of heat transfer coefficients on extended surfaces by shaping or perforating the surfaces.

Displaced enhancement devices are inserted into the flow channel so as indirectly to improve energy transport at the heated surface. They are used with forced flow. See Figure 4.8.1e and f.

Swirl-flow devices include a number of geometric arrangements or tube inserts for forced flow that create rotating and/or secondary flow: coiled tubes, inlet vortex generators, twisted-tape inserts, and axial-core inserts with a screw-type winding.

Surface-tension devices consist of wicking or grooved surfaces to direct the flow of liquid in boiling and condensing.

Additives for liquids include solid particles and gas bubbles in single-phase flows and liquid trace additives for boiling systems.

Additives for gases are liquid droplets or solid particles, either dilute-phase (gas-solid suspensions) or dense-phase (fluidized beds).

Mechanical aids involve stirring the fluid by mechanical means or by rotating the surface. Surface "scraping," widely used for batch processing of viscous liquids in the chemical process industry, is applied to the flow of such diverse fluids as high-viscosity plastics and air. Equipment with rotating heat exchanger ducts is found in commercial practice.

Surface vibration at either low or high frequency has been used primarily to improve single-phase heat transfer.

Fluid vibration is the practical type of vibration enhancement because of the mass of most heat exchangers. The vibrations range from pulsations of about 1 Hz to ultrasound. Single-phase fluids are of primary concern.

Electrostatic fields (DC or AC) are applied in many different ways to dielectric fluids. Generally speaking, electrostatic fields can be directed to cause greater bulk mixing or fluid or disruption of fluid flow in the vicinity of the heat transfer surface, which enhances heat transfer.

Injection is utilized by supplying gas to a stagnant or flowing liquid through a porous heat transfer surface or by injecting similar fluid upstream of the heat transfer section. Surface degassing of liquids can produce enhancement similar to gas injection. Only single-phase flow is of interest.

Suction involves vapor removal, in nucleate or film boiling, or fluid withdrawal, in single-phase flow, through a porous heated surface.

Two or more of the above techniques may be utilized simultaneously to produce an enhancement that is larger than either of the techniques operating separately. This is termed *compound enhancement*.

It should be emphasized that one of the motivations for studying enhanced heat transfer is to assess the effect of an inherent condition on heat transfer. Some practical examples include roughness produced by standard manufacturing, degassing of liquids with high gas content, surface vibration resulting from rotating machinery or flow oscillations, fluid vibration resulting from pumping pulsation, and electrical fields present in electrical equipment.

The surfaces in Figure 4.8.1 have been used for both single-phase and two-phase heat transfer enhancement. The emphasis is on effective and cost-competitive (proved or potential) techniques that have made the transition from the laboratory to commercial heat exchangers.

Single-Phase Free Convection

With the exception of the familiar technique of providing extended surfaces, the passive techniques have little to offer in the way of enhanced heat transfer for free convection. This is because the velocities are usually too low to cause flow separation or secondary flow.

The restarting of thermal boundary layers in interrupted extended surfaces increases heat transfer so as to more than compensate for the lost area.

Mechanically aided heat transfer is a standard technique in the chemical and food industries when viscous liquids are involved. The predominant geometry for surface vibration has been the horizontal cylinder, vibrated either horizontally or vertically. Heat transfer coefficients can be increased tenfold for both low-frequency/high-amplitude and high-frequency/low-amplitude situations. It is, of course, equally effective and more practical to provide steady forced flow. Furthermore, the mechanical designer is concerned that such intense vibrations could result in equipment failures.

Since it is usually difficult to apply surface vibrations to practical equipment, an alternative technique is utilized whereby vibrations are applied to the fluid and focused toward the heated surface. With proper transducer design, it is also possible to improve heat transfer to simple heaters immersed in gases or liquids by several hundred percent.

Electric fields are particularly effective in increasing heat transfer coefficients in free convection. Dielectrophoretic or electrophoretic (especially with ionization of gases) forces cause greater bulk mixing in the vicinity of the heat transfer surface. Heat transfer coefficients may be improved by as much as a factor of 40 with electrostatic fields up to 100,000 V. Again, the equivalent effect could be produced at lower capital cost and without the voltage hazard by simply providing forced convection with a blower or fan.

Single-Phase Forced Convection

The present discussion emphasizes enhancement of heat transfer *inside* ducts that are primarily of circular cross section. Typical data for turbulence promoters inserted inside tubes are shown in Figure 4.8.2. As shown in Figure 4.8.2a, the promoters produce a sizable elevation in the Nusselt number, or heat transfer coefficient, at constant Reynolds number, or velocity. However, as shown in Figure 4.8.2b, there is an accompanying large increase in the friction factor.

Surface roughness has been used extensively to enhance forced convection heat transfer. Integral roughness may be produced by the traditional manufacturing processes of machining, forming, casting, or welding. Various inserts can also provide surface protuberances. In view of the infinite number of possible geometric variations, it is not surprising that, even after more than 300 studies, no completely satisfactory unified treatment is available.

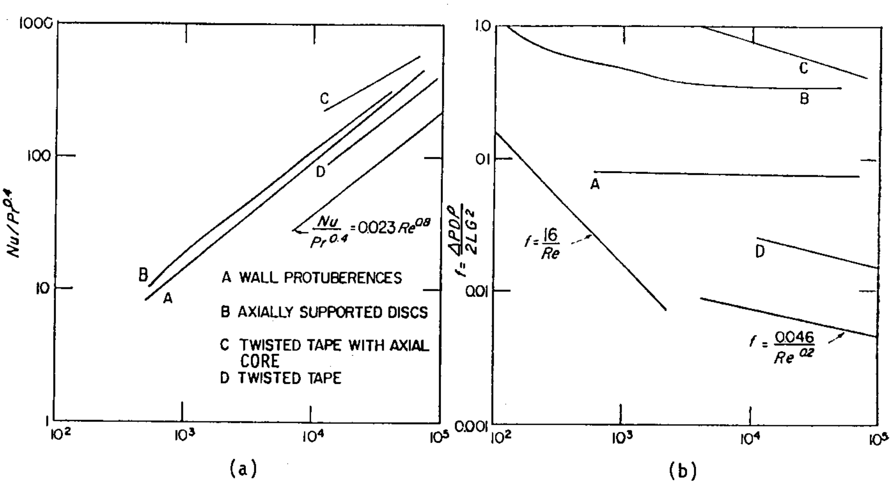

FIGURE 4.8.2 Typical data for turbulence promoters inserted inside tubes: (a) heat transfer data, (b) friction data. (From Bergles, 1969. With permission.)

In general, the maximum enhancement of laminar flow with many of the techniques is the same order of magnitude, and seems to be independent of the wall boundary condition. The enhancement with some rough tubes, corrugated tubes, inner-fin tubes, various static mixers, and twisted-type inserts is about 200%. The improvements in heat transfer coefficient with turbulent flow in rough tubes (based on nominal surface area) are as much as 250%. Analogy solutions for sand-grain-type roughness and for square-repeated-rib roughness have been proposed. A statistical correlation is also available for heat transfer coefficient and friction factor.

The following correlations are recommended for tubes with transverse or helical repeated ribs (Figure 4.8.1a) with turbulent flow (Ravigururajan and Bergles, 1996):

$$\mathrm{Nu}_{D_i,a}/\mathrm{Nu}_{D_i,s} = \left\{1+\left[2.64\mathrm{Re}^{0.036}\left(e/D_i\right)^{0.212}\left(\left(p/D_i\right)^{-0.21}\right)\left(\alpha/90\right)^{0.29}(\mathrm{Pr})^{-0.024}\right]^7\right\}^{1/7} \tag{4.8.1}$$

$$f_a/f_s = \left\{1+\left[29.1\mathrm{Re}_{D_i}^{\left(0.67-0.06\,p/D_i-0.49\,a/90\right)}\times\left(e/D_i\right)^{\left(1.37-0.157\,p/D_i\right)}\times\left(p/D_i\right)^{\left(-1.66\times10^{-6}\,\mathrm{Re}_{D_i}-0.33\,\alpha/90\right)}\left(\alpha/90\right)^{\left(4.59+4.11\times10^{-6}\,\mathrm{Re}_{D_i}-0.15\,p/D_i\right)}\times\left(1+\frac{2.94}{n}\right)\sin\beta\right]^{15/16}\right\}^{16/15} \tag{4.8.2}$$

where the subscript a refers to the enhanced tube and the subscript s refers to the smooth tube. The special symbols are given as follows: e = protuberance height; p = repeated-rib pitch; α = spiral angle for helical ribs, °; n = number of sharp corners facing the flow; and β = contact angle of rib profile, °.

Also,

$$\mathrm{Nu}_s = 0.125 f\,\mathrm{Re}_{D_i}\mathrm{Pr}\Big/\left(1+12.7(0.125f)^{0.5}\,\mathrm{Pr}^{0.667}-1\right)$$

and

$$f_s = \left(1.58\ln\,\mathrm{Re}_{D_i}-3.28\right)^{-2}\,{}^{*}$$

Much work has been done to obtain the enhanced heat transfer of parallel angled ribs in short rectangular channels, simulating the interior of gas turbine blades. Jets are frequently used for heating, cooling, and drying in a variety of industrial applications. A number of studies have reported that roughness elements of the transverse-repeated-rib type mitigate the deterioration in heat transfer downstream of stagnation.

In the case of rough surfaces, Champagne and Bergles (2001) have proposed and tested a novel variable roughness that can provide enhancement "on demand" for single-phase flows. This is based on a shape-memory coil. At low wall temperature (efficient heat transfer), the roughness coil is closely pitched. An excessive tube-wall temperature (low heat transfer coefficient) results in extension of the coil, which has been shown to provide considerable heat transfer enhancement. Current limitations in material processing and training techniques of shape-memory alloys impose a manual resetting of the coil once it is extended; thus, this should perhaps be considered an active enhancement technique rather than a passive one.

---

[*] The Fanning friction factor is used in all equations in this section, but the Darcy friction factor appears in Figure 4.8.2(b).

Extended surfaces can be considered "old technology" as far as most applications are concerned. The real interest now is in increasing heat transfer coefficients on the extended surface. Compact heat exchangers of the plate-fin or tube-and-center variety use several enhancement techniques: offset strip fins, louvered fins, perforated fins, or corrugated fins. Coefficients are several hundred percent above the smooth-tube values; however, the pressure drop is also substantially increased, and there may be vibration and noise problems.

For the case of offset strip fins the following correlations are recommended for calculating the *j* and *f* characteristics (Manglik and Bergles, 1990)

$$j_h = 0.6522\mathrm{Re}_h^{-0.5403}\,\alpha^{-0.1541}\,\delta^{0.1499}\,\gamma^{-0.0678}\times\left[1+5.269\times10^{-5}\,\mathrm{Re}_h^{1.340}\,\alpha^{0.504}\,\delta^{0.456}\,\gamma^{-1.055}\right]^{0.1} \quad (4.8.3)$$

$$f_h = 9.6243\mathrm{Re}_h^{-0.7422}\,\alpha^{-0.1856}\,\delta^{0.3053}\,\gamma^{-0.2659}\times\left[1+7.669\times10^{-8}\,\mathrm{Re}_h^{4.429}\,\alpha^{0.920}\,\delta^{3.767}\,\gamma^{0.236}\right]^{0.1} \quad (4.8.4)$$

where j_H (the heat transfer *j*-factor $\mathrm{Nu}_H/\mathrm{Re}_H\mathrm{Pr}^{1/3}$), and f_h, and Re_h are based on the hydraulic diameter given by

$$D_h = 4shl\big/\left[2(sl+hl+th)+ts\right] \quad (4.8.5)$$

Special symbols are α = aspect ratio s/h, δ = ratio t/l, γ = ratio t/s, s = lateral spacing of strip fin, h = strip fin height, l = length of one offset module of strip fins, and t = fin thickness.

These equations are based on experimental data for 18 different offset strip-fin geometries, and they represent the data continuously in the laminar, transition, and turbulent flow regions.

Internally finned circular tubes are available in aluminum and copper (or copper alloys). Correlations (for heat transfer coefficient and friction factor) are available for laminar flow, for both straight and spiral continuous fins.

Turbulent flow in tubes with straight or helical fins (Figure 4.8.1c) was correlated by (Carnavos, 1979)

$$\mathrm{Nu}_h = 0.023\mathrm{Pr}^{0.4}\mathrm{Re}_h^{0.8}\left[\frac{A_c}{A_{ci}}\right]^{0.1}\left[\frac{A_{s,i}}{A_s}\right]^{0.5}(\sec\alpha)^3 \quad (4.8.6)$$

$$f_h = 0.046\mathrm{Re}_h^{-0.2}\left[\frac{A_c}{A_{c,i}}\right]^{0.5}(\sec\alpha)^{0.75} \quad (4.8.7)$$

where $A_{c,i}$ is based on the maximum inside (envelope) flow area, $A_{s,i}$ is based on the maximum inside (envelope) surface area, and α the spiral angle for helical fins, °.

A numerical analysis of turbulent flow in tubes with idealized straight fins was reported. The necessary constant for the turbulence model was obtained from experimental data for air. Further improvements in numerical techniques are expected, so that a wider range of geometries and fluids can be handled without resort to extensive experimental programs.

Many proprietary surface configurations have been produced by deforming the basic tube. The "convoluted," "corrugated," "spiral," or "spirally fluted" tubes (Figure 4.8.1a) have multiple-start spiral corrugations, which add area, along the tube length. A systematic survey of the single-tube performance of condenser tubes indicates up to 400% increase in the nominal inside heat transfer coefficient (based on diameter of a smooth tube of the same maximum inside diameter); however, pressure drops on the water side are about 20 times higher.

Displaced enhancement devices are typically in the form of inserts, within elements arranged to promote transverse mixing (static mixers, Figure 4.8.1e). They are used primarily for viscous liquids, to promote either heat transfer or mass transfer. Displaced promoters are also used to enhance the radiant heat transfer in high-temperature applications. In the flue-tube of a hot-gas-fired hot water heater, there is a trade-off between radiation and convection. Another type of displaced insert generates vortices, which enhance the downstream flow. Delta-wing and rectangular wing promoters, both co-rotating and counterrotating, have been studied. Wire-loop inserts (Figure 4.8.1f) have also been used for enhancement of laminar and turbulent flow.

Twisted-tape inserts have been widely used to improve heat transfer in both laminar and turbulent flow. Correlations are available for laminar flow, for both uniform heat flux and uniform wall temperature conditions. Turbulent flow in tubes with twisted-tape inserts has also been correlated. Several studies have considered the heat transfer enhancement of a decaying swirl flow, generated, say, by a short twisted-tape insert.

Performance Evaluation Criteria for Single-Phase Forced Convection in Tubes

Numerous, and sometimes conflicting, factors enter into the ultimate decision to use an enhancement technique: heat duty increase or area reduction that can be obtained, initial cost, pumping power or operating cost, maintenance cost (especially cleaning), safety, and reliability, among others. These factors are difficult to quantitize, and a generally acceptable selection criterion may not exist. It is possible, however, to suggest some performance criteria for preliminary design guidance. As an example, consider the basic geometry and the pumping power fixed, with the objective of increasing the heat transfer. The following ratio is then of interest

$$R_3 = \left(\frac{h_a}{h_s}\right)_{D_i,L,N,P,T_{\text{in}},\Delta T} = \frac{\left(\text{Nu}/\text{Pr}^{0.4}\right)_a}{\left(\text{Nu}/\text{Pr}^{0.4}\right)_s} = \frac{q_a}{q_s} \tag{4.8.8}$$

where P = pumping power, T_{in} = inlet bulk temperature of fluid, and ΔT = average wall-fluid temperature difference.

With the pumping power (neglecting entrance and exit losses) given as

$$P = NVA_c 4f(L/D)\rho V^2/2 \tag{4.8.9}$$

and

$$f_s = 0.046/\text{Re}_s^{0.2} \tag{4.8.10}$$

$$A_{c,a} f_a \text{Re}_a^3 = 0.046\, A_{c,s} \text{Re}_s^{2.8} \tag{4.8.11}$$

The calculation best proceeds by picking $\text{Re}_{D_i,a}$, and reading $\text{Nu}_{D_i,a}/\text{Pr}^{0.4}$ and f_a. $\text{Re}_{D_i,s}$ is then obtained from Equation (4.8.11) and $\text{Nu}_{D_i,s}/\text{Pr}^{0.4}$ obtained from a conventional, empty-tube correlation. The desired ratio of Equation (4.8.8) is then obtained. Typical results are presented in Figure 4.8.3 for a repeated-rib roughness (Bergles et al., 1974).

Active and Compound Techniques for Single-Phase Forced Convection

Under active techniques, mechanically aided heat transfer in the form of surface scraping can increase forced convection heat transfer. Surface vibration has been demonstrated to improve heat transfer to both laminar and turbulent duct flow of liquids. Fluid vibration has been extensively studied for both air (loudspeakers and sirens) and liquids (flow interrupters, pulsators, and ultrasonic transducers). Pulsations are relatively simple to apply to low-velocity liquid flows, and improvements of several hundred percent can be realized.

Some very impressive enhancements have been recorded with electrical fields, particularly in the laminar-flow region. Improvements of at least 100% were obtained when voltages in the 10-kV range were applied to transformer oil. It is found that even with intense electrostatic fields, the heat transfer enhancement disappears as turbulent flow is approached in a circular tube with a concentric inner electrode.

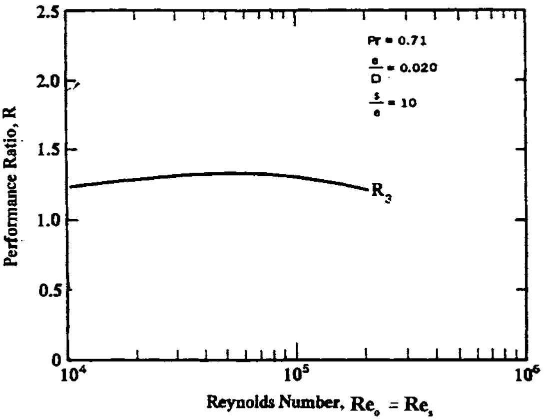

FIGURE 4.8.3 Constant pumping power performance criterion applied to repeated rib roughness.

Compound techniques are a slowly emerging area of enhancement that holds promise for practical applications, since heat transfer coefficients can usually be increased above each of the several techniques acting along. Some examples that have been studied are as follows: rough tube wall with twisted-tape inserts, rough cylinder with acoustic vibrations, internally finned tube with twisted-tape inserts, finned tubes in fluidized beds, externally finned tubes subjected to vibrations, rib-roughened passage being rotated, gas-solid suspension with an electrical field, fluidized bed with pulsations of air, and a rib-roughened channel with longitudinal vortex generation.

Pool Boiling

Selected passive and active enhancement techniques have been shown to be effective for pool boiling and flow boiling/evaporation. Most techniques apply to nucleate boiling; however, some techniques are applicable to transition and film boiling.

It should be noted that phase-change heat transfer coefficients are relatively high. The main thermal resistance in a two-fluid heat exchanger often lies on the non-phase-change side. (Fouling of either side can, of course, represent the dominant thermal resistance.) For this reason, the emphasis is often on enhancement of single-phase flow. On the other hand, the overall thermal resistance may then be reduced to the point where significant improvement in the overall performance can be achieved by enhancing the two-phase flow. Two-phase enhancement would also be important in double-phase-change (boiling/condensing) heat exchangers.

As discussed elsewhere, surface material and finish have a strong effect on nucleate and transition pool boiling. However, reliable control of nucleation on plain surfaces is not easily accomplished. Accordingly, since the earliest days of boiling research, there have been attempts to relocate the boiling curve through use of relatively gross modification of the surface. For many years, this was accomplished simply by area increase in the form of low helical fins. The subsequent tendency was to structure surfaces to improve the nucleate boiling characteristics by a fundamental change in the boiling process. Many of these advanced surfaces are being used in commercial shell-and-tube boilers.

Several manufacturing processes have been employed: machining, forming, layering, and coating. In Figure 4.8.4a standard low-fin tubing is shown. Figure 4.8.4c depicts a tunnel-and-pore arrangement produced by rolling, upsetting, and brushing. An alternative modification of the low fins is shown in Figure 4.8.4d, where the rolled fins have been split and rolled to a T shape. Further modification of the internal, Figure 4.8.4e, or external, Figure 4.8.4f, surface is possible. Knurling and rolling are involved in producing the surface shown in Figure 4.4.8g. The earliest example of a commercial structured surface, shown in Figure 4.8.4b is the porous metallic matrix produced by sintering or brazing small particles. Wall superheat reductions of up to a factor of ten are common with these surfaces. The advantage is not

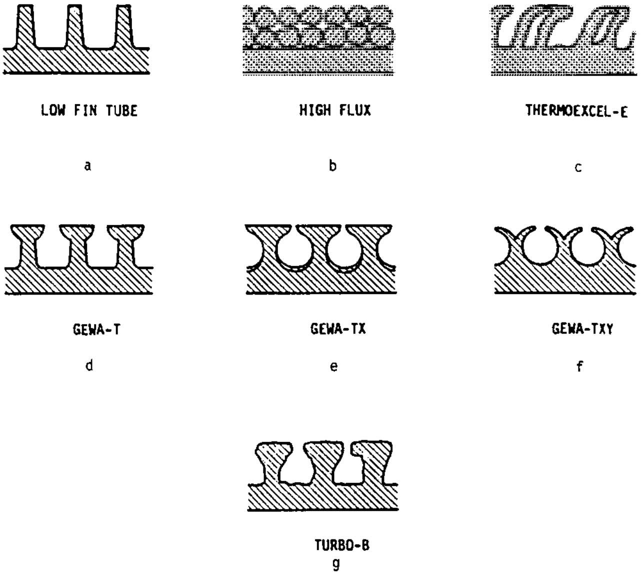

FIGURE 4.8.4 Examples of commercial structured boiling surfaces. (From Pate, M.B. et al., in *Compact Heat Exchangers*, Hemisphere Publishing, New York, 1990. With permission.)

only a high nucleate boiling heat transfer coefficient, but the fact that boiling can take place at very low temperature differences.

These structured boiling surfaces, developed for refrigeration and process applications, have been used as "heat sinks" for immersion-cooled microelectronic chips.

The behavior of tube bundles is often different with structured-surface tubes. The enhanced nucleate boiling dominates, and the convective boiling enhancement, found in plain tube bundles, does not occur.

Active enhancement techniques include heated surface rotation, surface wiping, surface vibration, fluid vibration, electrostatic fields, and suction at the heated surface. Although active techniques are effective in reducing the wall superheat and/or increasing the critical heat flux, the practical applications are very limited, largely because of the difficulty of reliably providing the mechanical or electrical effect.

Compound enhancement, which involves two or more techniques applied simultaneously, has also been studied. Electrohydrodynamic enhancement was applied to a finned tube bundle, resulting in nearly a 200% increase in the average boiling heat transfer coefficient of the bundle, with a small power consumption for the field.

Convective Boiling/Evaporation

The structured surfaces described in the previous section are generally not used for in-tube vaporization, because of the difficulty of manufacture. One notable exception is the high-flux surface in a vertical thermosiphon reboiler. The considerable increase in the low-quality, nucleate boiling coefficient is desirable, but it is also important that more vapor is generated to promote circulation.

Helical repeated ribs and helically coiled wire inserts have been used to increase vaporization coefficients and the dry-out heat flux in once-through boilers.

Numerous tubes with internal fins, either integral or attached, are available for refrigerant evaporators. Original configurations were tightly packed, copper, offset strip fin inserts soldered to the copper tube or aluminum, star-shaped inserts secured by drawing the tube over the insert. Examples are shown in Figure 4.8.5. Average heat transfer coefficients (based on surface area of smooth tube of the same diameter) for typical evaporator conditions are increased by as much as 200%. A cross-sectional view of a typical "microfin" tube is included in Figure 4.8.5. The average evaporation boiling coefficient is increased 30

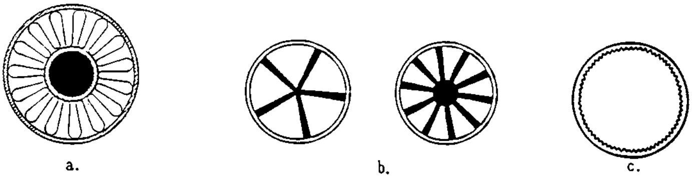

FIGURE 4.8.5 Inner-fin tubes for refrigerant evaporators: (a) Strip-fin inserts, (b) Star-shaped inserts, (c) Microfin.

to 80%. The pressure drop penalties are less; that is, lower percentage increases in pressure drop are frequently observed.

Twisted-tape inserts are generally used to increase the burnout heat flux for subcooled boiling at high imposed heat fluxes $10^7 - 10^8$ W/m^2, as might be encountered in the cooling of fusion reactor components. Increases in burnout heat flux of up to 200% were obtained at near atmospheric pressure.

Vapor-Space Condensation

As discussed elsewhere, condensation can be either filmwise or dropwise. In a sense, dropwise condensation is enhancement of the normally occurring film condensation by surface treatment. The only real application is for steam condensers, because nonwetting coatings are not available for most other working fluids. Even after much study, little progress has been made in developing permanently hydrophobic coatings for practical steam condensers. The enhancement of dropwise condensation is pointless, because the heat transfer coefficients are already so high.

Surface extensions are widely employed for enhancement of condensation. The integral low fin tubing (Figure 4.8.4a), used for kettle boilers, is also used for horizontal tube condensers. With proper spacing of the fins to provide adequate condensate drainage, the average coefficients can be several times those of a plain tube with the same base diameter. These fins are normally used with refrigerants and other organic fluids that have low condensing coefficients, but which drain effectively, because of low surface tension.

The fin profile can be altered according to mathematical analysis to take full advantage of the Gregorig effect, whereby condensation occurs mainly at the tops of convex ridges. Surface tension forces then pull the condensate into concave grooves, where it runs off. The average heat transfer coefficient is greater than that for an axially uniform film thickness. The initial application was for condensation of steam on vertical tubes used for reboilers and in desalination. According to numerical solutions, the optimum geometry is characterized by a sharp fin tip, gradually changing curvature of the fin surface from tip to root, wide grooves between fins to collect condensate, and periodic condensate strippers. Figure 4.8.6 schematically presents the configuration.

Recent interest has centered on three-dimensional surfaces for horizontal-tube condensers. The considerable improvement relative to low fins or other two-dimensional profiles is apparently due to multidimensional drainage at the fin tips. Other three-dimensional shapes include circular pin fins, square pins, and small metal particles that are bonded randomly to the surface.

Convective Condensation

This final section on enhancement of the various modes of heat transfer focuses on in-tube condensation. The applications include horizontal kettle-type reboilers, moisture separator reheaters for nuclear power plants, and air-conditioner condensers.

Internally grooved or knurled tubes, deep spirally fluted tubes, random roughness, conventional inner-fin tubes have been shown to be effective for condensation of steam and other fluids.

The microfin tubes mentioned earlier have also been applied successfully to in-tube condensing. As in the case of evaporation, the substantial heat transfer improvement is achieved at the expense of a lesser percentage increase in pressure drop. By testing a wide variety of tubes, it has been possible to suggest some guidelines for the geometry, e.g., more fins, longer fins, and sharper tips; however, general correlations are not yet available. Fortunately for heat-pump operation, the tube that performs best for evaporation also performs best for condensation.

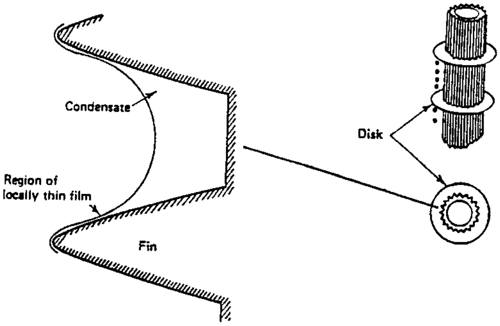

FIGURE 4.8.6 Recommended flute profile and schematic of condensate strippers.

Twisted-tape inserts result in rather modest increases in heat transfer coefficient for complete condensation of either steam or refrigerant. The pressure drop increases are large because of the large wetted surface. Coiled tubular condensers provide a modest improvement in average heat transfer coefficient.

References

Bergles, A.E. 1969. Survey and evaluation of techniques to augment convective heat and mass transfer, in *Progress in Heat and Mass Transfer*, Vol. 1, Pergamon, Oxford, England.

Bergles, A.E. 1988. Some perspectives on enhanced heat transfer — second generation heat transfer technology, *J. Heat Transfer*, 110, 1082–1096.

Bergles, A.E. 1997. Heat transfer enhancement — the encouragement and accommodation of high heat fluxes. *J. Heat Transfer*, 119, 8–19.

Bergles, A.E. 1998. Techniques to enhance heat transfer, in *Handbook of Heat Transfer,* 3rd ed., W.M. Rohsenow, J.P. Hartnett, and Y.I. Cho, Eds., McGraw-Hill, New York, 11.1–11.76.

Bergles, A.E. 2002. ExHFT for fourth generation heat transfer technology, *Experimental Thermal and Fluid Science,* 26, 335–344.

Bergles, A.E., Blumenkrantz, A.R., and Taborek, J. 1974. Performance evaluation criteria for enhanced heat transfer surfaces, in *Heat Transfer 1974*, The Japan Society of Mechanical Engineers, Tokyo, Vol. II, 234–238.

Bergles, A.E., Jensen, M.K., and Shome, B. 1995. Bibliography on enhancement of convective heat transfer, Heat Transfer Laboratory Report No. HTL-23, Rensselaer Polytechnic Institute, Troy, NY.

Carnavos, T.C. 1979. Heat transfer performance of internally finned tubes in turbulent flow, in *Advances in Advanced Heat Transfer*, ASME, New York, 61–67.

Champagne, P.R. and Bergles, A.E. 2001. Development and testing of a novel, variable-roughness technique to enhance, on demand, heat transfer in a single-phase heat exchanger, *J. Enhanced Heat Transfer,* 8, 341–352.

Manglik, R.M. 2003. Heat transfer enhancement, in *Heat Transfer Handbook,* A Bejan and A.D. Kraus, Eds., Wiley, Hoboken, NJ, chap. 14.

Manglik, R.M. and Bergles, A.E. 1990. The thermal-hydraulic design of the rectangular offset-strip-fin compact heat exchanger, in *Compact Heat Exchangers*, Hemisphere Publishing, New York, 123–149.

Manglik, R.M. and Bergles, A.E. 2004. Enhanced heat and mass transfer in the new millenium: a review of the 2001 literature, to be published in *Journal of Enhanced Heat Transfer.*

Pate, M.B., Ayub, Z.H., and Kohler, J. 1990. Heat exchangers for the air-conditioning and refrigeration industry: state-of-the-art design and technology, in *Compact Heat Exchangers*, Hemisphere Publishing, New York, 567–590.

Revigururajan, T.S. and Bergles, A.E. 1996. Development and verification of general correlations for pressure drop and heat transfer in single-phase turbulent flow in enhanced tubes, *Experimental Thermal and Fluid Science,* 13, 55–70.

Thome, J.R. 1990. *Enhanced Boiling Heat Transfer*, Hemisphere Publishing, New York.

Webb, R.L. 1994. *Principles of Enhanced Heat Transfer*, John Wiley & Sons, New York.

Further Information

This section gives some indication as to why heat transfer enhancement is one of the fastest growing areas of heat transfer. Many techniques are available for improvement of the various modes of heat transfer. Fundamental understanding of the transport mechanism is growing, but, more importantly, design correlations are being established. Many effective and cost-competitive enhancement techniques have made the transition from the laboratory to commercial heat exchangers.

Broad reviews of developments in enhanced heat transfer are available (Bergles, 1988, 1997, 1998, 2002; Thome, 1990; Webb, 1994; Manglik, 2003). Also, several journals, especially *Heat Transfer Engineering, Enhanced Heat Transfer,* and *International Journal of Heating, Ventilating, Air-Conditioning and Refrigerating Research*, feature this technology.

Cooling Towers

Anthony F. Mills

Introduction

In a wet cooling tower, water is evaporated into air with the objective of cooling the water stream. Both natural- and mechanical-draft towers are popular, and examples are shown in Figure 4.8.7. Large natural-draft cooling towers are used in power plants for cooling the water supply to the condenser. Smaller mechanical-draft towers are preferred for oil refineries and other process industries, as well as for central air-conditioning systems and refrigeration plant. Figure 4.8.7a shows a natural draft *counterflow* unit in which the water flows as thin films down over a suitable packing, and air flows upward. In a natural-draft tower the air flows upward due to the buoyancy of the warm, moist air leaving the top of the packing. In a mechanical-draft tower, the flow is forced or induced by a fan. Since the air inlet temperature is usually lower than the water inlet temperature, the water is cooled both by evaporation and by sensible heat loss. For usual operating conditions the evaporative heat loss is considerably larger than the sensible heat loss. Figure 4.8.7b shows a mechanical draft cross-flow unit. Figure 4.8.8 shows a natural-draft cross-flow tower for a power plant.

Packing Thermal Performance

Counterflow units. Merkel's method (Merkel, 1925) for calculating the number of transfer units required to cool the water stream, for specified inlet and outlet water temperatures and inlet air condition is (Mills, 1995)

$$N_{tu} = \frac{g_m S}{\dot{m}_L} = \int_{h_{L,\text{in}}}^{h_{L,\text{out}}} \frac{dh_L}{h_s - h_G} \tag{4.8.12}$$

$$h_G = h_{G,\text{in}} + \left(\dot{m}_L/\dot{m}_G\right)\left(h_L - h_{L,\text{out}}\right) \tag{4.8.13}$$

$$h_s\left(P, T_s\right) = h_s\left(P, T_L\right) \tag{4.8.14}$$

It is imperative that the usual enthalpy datum states be used, namely, zero enthalpy for dry air and liquid water at 0°C. Table 4.8.1 gives enthalpy data for 1 atm pressure. The important assumptions required to obtain this result include

1. A Lewis number of unity;
2. Low mass transfer rate theory is valid;
3. The liquid-side heat transfer resistance is negligible, that is, $T_s \simeq T_L$;
4. The amount of water evaporated is small compared with the water and air flow rates.

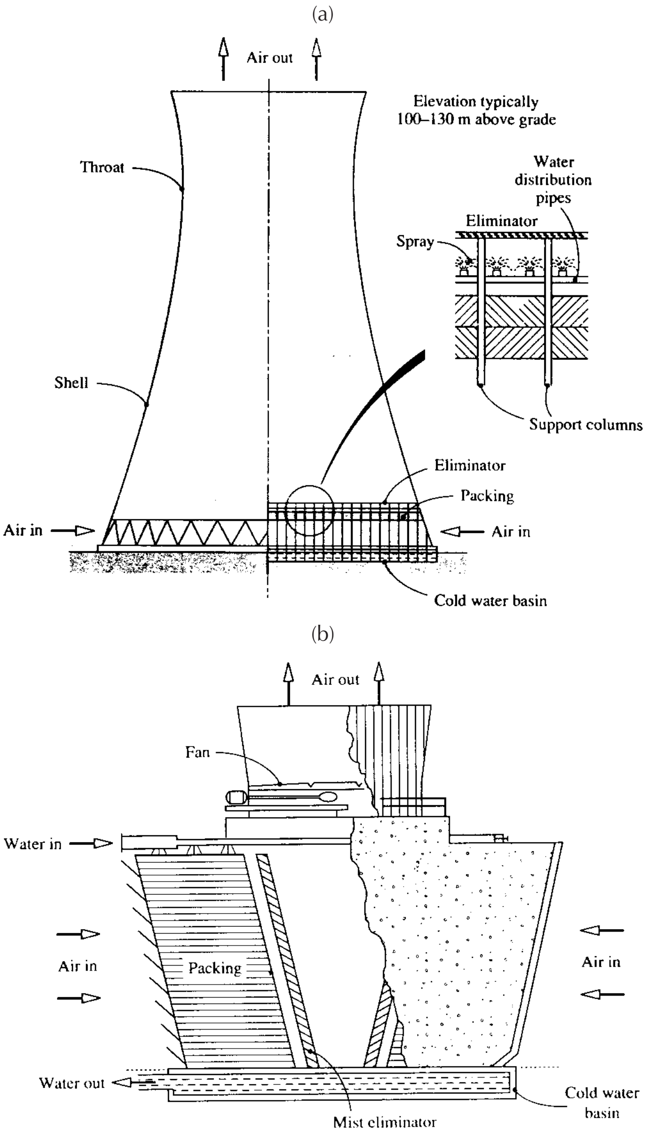

FIGURE 4.8.7 (a) A natural-draft counterflow cooling tower for a power plant. (b) A cross-flow cooling tower for an air-conditioning system.

The method is accurate up to temperatures of about 60°C; comparisons with more exact results are usually within 3 to 5%, and seldom show errors greater than 10%. Notice that the method does not give the outlet state of the air; however, in situations encountered in practice, the outlet air can be assumed to be saturated for the purposes of calculating its density. It is possible to extend Merkel's method to include a finite liquid-side heat transfer resistance, but such refinement is seldom warranted. For typical operating conditions the bulk liquid temperature is seldom more than 0.3 K above the interface temperature.

Cross-flow units. Figure 4.8.9 shows a schematic of a cross-flow packing. If we assume that both the liquid and gas streams are unidirectional, and that there is no mixing in either stream, then use of Merkel's assumptions leads to the following pair of differential equations (Mills, 2001):

FIGURE 4.8.8 A natural-draft cross-flow cooling tower for a power plant.

$$\frac{\partial h_G}{\partial x} = \frac{g_m a}{G}\left(h_s - h_G\right) \tag{4.8.15}$$

$$\frac{\partial h_L}{\partial y} = -\frac{g_m a}{L}\left(h_s - h_G\right) \tag{4.8.16}$$

Also $h_s = h_s(h_L)$ for a negligible liquid-side heat transfer resistance and the required boundary conditions are the inlet enthalpies of both streams. Equation (4.8.15) and Equation (4.8.16) are solved numerically and the solution used to evaluate the average enthalpy of the outlet liquid,

$$\bar{h}_{L,\text{out}} = \frac{1}{X}\int_0^X h_{L,\text{out}}\; dx \tag{4.8.17}$$

Substituting in an exchanger energy balance on the liquid stream gives the heat transfer as

$$q = \dot{m}_L\left(h_{L,\text{in}} - h_{L,\text{out}}\right) \tag{4.8.18}$$

TABLE 4.8.1 Thermodynamic Properties of Water Vapor-Air Mixtures at 1 atm

Temp., °C	Saturation Mass Fraction	Specific Volume, m^3/kg		Enthalpy[a,b] kJ/kg		
		Dry Air	Saturated Air	Liquid Water	Dry Air	Saturated Air
10	0.007608	0.8018	0.8054	42.13	10.059	29.145
11	0.008136	0.8046	0.8086	46.32	11.065	31.481
12	0.008696	0.8075	0.8117	50.52	12.071	33.898
13	0.009289	0.8103	0.8148	54.71	13.077	36.401
14	0.009918	0.8131	0.8180	58.90	14.083	38.995
15	0.01058	0.8160	0.8212	63.08	15.089	41.684
16	0.01129	0.8188	0.8244	67.27	16.095	44.473
17	0 01204	0.8217	0.8276	71.45	17.101	47.367
18	0 01283	0.8245	0.8309	75.64	18.107	50.372
19	0.01366	0.8273	0.8341	79.82	19.113	53.493
20	0.01455	0.8302	0.8374	83.99	20.120	56.736
21	0.01548	0.8330	0.8408	88.17	21.128	60.107
22	0.01647	0.8359	0.8441	92.35	22.134	63.612
23	0.01751	0.8387	0.8475	96.53	23.140	67.259
24	0.01861	0.8415	0.8510	100.71	24.147	71.054
25	0.01978	0.8444	0.8544	104.89	25.153	75.004
26	0.02100	0.8472	0.8579	109.07	26.159	79.116
27	0.02229	0.8500	0.8615	113.25	27.166	83.400
28	0.02366	0.8529	0.8650	117.43	28.172	87.862
29	0.02509	0.8557	0.8686	121.61	29.178	92.511
30	0.02660	0.8586	0.8723	125.79	30.185	97.357
31	0.02820	0.8614	0.8760	129.97	31.191	102.408
32	0.02987	0.8642	0.8798	134.15	32.198	107.674
33	0.03164	0.8671	0.8836	138.32	33.204	113.166
34	0.03350	0.8699	0.8874	142.50	34.211	118.893
35	0.03545	0.8728	0.8914	146.68	35.218	124.868
36	0.03751	0.8756	0.8953	150.86	36.224	131.100
37	0.03967	0.8784	0.8994	155.04	37.231	137.604
38	0.04194	0.8813	0.9035	159.22	38.238	144.389
39	0.04432	0.8841	0.9077	163.40	39.245	151.471
40	0.04683	0.8870	0.9119	167.58	40.252	158.862
41	0.04946	0.8898	0.9162	171.76	41.259	166.577
42	0.05222	0.8926	0.9206	175.94	42.266	174.630
43	0.05512	0.8955	0.9251	180.12	43.273	183.037
44	0.05817	0.8983	0.9297	184.29	44.280	191.815
45	0.06137	0.9012	0.9343	188.47	45.287	200.980
46	0.06472	0.9040	0.9391	192.65	46.294	210.550
47	0.06842	0.9068	0.9439	196.83	47.301	220.543
48	0.07193	0.9097	0.9489	201.01	48.308	230.980
49	0.07580	0.9125	0.9539	205.19	49.316	241.881

[a] The enthalpies of dry air and liquid water are set equal to zero at a datum temperature of 0°C.

[b] The enthalpy of an unsaturated water vapor-air mixture can be calculated as $h = h_{\text{dry air}} + (m_1/m_{1,\text{sat}})(h_{\text{sat}} - h_{\text{dry air}})$.

Sample calculation. Consider a counterflow unit that is required to cool water from 40 to 26°C when the inlet air is at 10°C, 1 atm, and saturated. We will calculate the number of transfer units required for balanced flow, that is, $\dot{m}_G/\dot{m}_L = 1$. Equation (4.8.12) is to be integrated numerically, with h_G obtained from Equation 4.8.13. The required thermodynamic properties can be obtained from Table 4.8.1. Using Table 4.8.1, $h_{G,\text{in}} = h_{\text{sat}}$ (10°C) = 29.15 kJ/kg, $h_{L,\text{out}} = h_L(26°\text{C}) = 109.07$ kJ/kg. Substituting in Equation (4.8.13),

$$h_G = 29.15 + \left(h_L - 109.07\right)$$

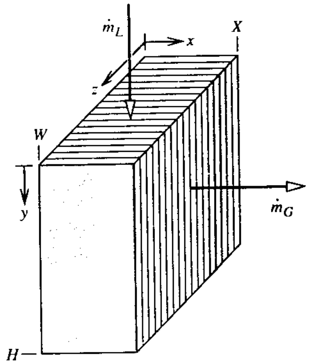

FIGURE 4.8.9 Schematic of a cross-flow cooling tower packing showing the coordinate system.

T_L, °C	h_L, kJ/kg	h_G, kJ/kg	h_s, kJ/kg	$h_s - h_g$, kJ/kg	$\dfrac{1}{h_s - h_g}$
26	109.07	29.15	79.12	49.97	0.02001
28	117.43	37.51	87.86	50.35	0.01986
30	125.79	45.87	97.36	51.49	0.01942
32	134.15	54.23	107.67	53.44	0.01871
34	142.50	62.58	118.89	56.31	0.01776
36	150.86	70.94	131.10	60.16	0.01662
38	159.22	79.30	144.39	65.09	0.01536
40	167.58	87.66	158.86	71.20	0.01404

Choosing 2°C intervals for convenient numerical integration, the above table is constructed, with h_L and $h_s = h_s(T_L)$ also obtained from Table 4.8.1.
Using the trapezoidal rule,

$$\begin{aligned}\int_{h_{L,\text{out}}}^{h_{L,\text{in}}} \frac{dh_L}{h_s - h_G} &= \frac{8.36}{2}\Big[0.02001 + 2(0.01986 + 0.01942 + 0.01871 + 0.01776 \\ &\quad + 0.01662 + 0.01536) + 0.01404\Big] \\ &= 1.043\end{aligned}$$

From Equation (4.8.12), $N_{tu} = 1.043$. Also, by using Table 4.8.1, $T_{G,\text{out}} = 27.9°$ for saturated outlet air.

Thermal-Hydraulic Design of Cooling Towers

The thermal-hydraulic design of a mechanical-draft cooling tower is relatively straightforward. The flow rate ratio $\dot{m}_L / \dot{m}_G$ can be specified and varied parametrically to obtain an optimal design, for which the size and cost of the packing is balanced against fan power requirements and operating cost. Data are required for mass transfer conductances and friction for candidate packings. Table 4.8.2a and Table 4.8.2b give correlations for a selection of packings. In Table 4.8.2b, the mass transfer conductance is correlated as $g_m a/L$, where a is the transfer area per unit volume and $L = \dot{m}_L / A_{fr}$ is the superficial mass velocity of the water flow (also called the *water loading* on the packing). Similarly, we define $G = \dot{m}_G / A_{fr}$. Typical water loadings are 1.8 to 2.7 kg/m^2 sec, and superficial air velocities fall in the range 1.5 to 4 m/sec. No attempt is made to correlate g_m and a separately. The number of transfer units of a packing of height H is then

$$N_{tu} = \frac{g_m S}{\dot{m}_L} = \frac{g_m a H}{L} \tag{4.8.19}$$

TABLE 4.8.2a Packings for Counterflow and Cross-Flow Cooling Towers: Designations and Descriptions

Counterflow Packings

1. Flat asbestos sheets, pitch 4.45 cm
2. Flat asbestos sheets, pitch 3.81 cm
3. Flat asbestos sheets, pitch 3.18 cm
4. Flat asbestos sheets, pitch 2.54 cm
5. 60° angle corrugated plastic, Munters M12060, pitch 1.17 in.
6. 60° angle corrugated plastic, Munters M19060, pitch 1.8 in.
7. Vertical corrugated plastic, American Tower Plastics Coolfilm, pitch 1.63 in.
8. Horizontal plastic screen, American Tower Plastics Cooldrop, pitch 8 in. 2 in. grid
9. Horizontal plastic grid, Ecodyne shape 10, pitch 12 in.
10. Angled corrugated plastic, Marley MC67, pitch 1.88 in.
11. Dimpled sheets, Toschi Asbestos-Free Cement, pitch 0.72 in.
12. Vertical plastic honeycomb, Brentwood Industries Accu-Pack, pitch 1.75 in.

Cross-Flow Packings

1. Doron V-bar, 4 × 8 in. spacing
2. Doron V-bar, 8 × 8 in. spacing
3. Ecodyne T-bar, 4 × 8 in. spacing
4. Ecodyne T-bar, 8 × 8 in. spacing
5. Wood lath, parallel to air flow, 4 × 4 in. spacing
6. Wood lath, perpendicular to air flow, 4 × 4 in. spacing
7. Marley α-bar, parallel to air flow, 16 × 4 in. spacing
8. Marley ladder, parallel to air flow, 8 × 2 in. spacing

The correlations are in terms of dimensionless mass velocities L^+ and G^+, and a *hot water correction* T^+_{HW}. The hot water correction accounts for a number of factors, such as errors associated with Merkel's method, deviations from low mass transfer rate theory at higher values of T_s, and fluid property dependence on temperature. Frictional resistance to air flow through the packings is correlated as a *loss coefficient* $N = \Delta P/(\rho V^2/2)$ per unit height or depth of packing, as a function of L^+ and G^+. The velocity V is superficial gas velocity. No hot water correction is required.

In a natural-draft tower, the thermal and hydraulic performance of the tower are coupled, and the flow rate ratio $\dot{m}_L/\dot{m}_G$ cannot be specified *a priori*. The buoyancy force producing the air flow depends on the state of the air leaving the packing which in turn depends on $\dot{m}_L/\dot{m}_G$ and the inlet air and water states. An iterative solution is required to find the operating point of the tower. The buoyancy force available to overcome the shell and packing pressure drops is

$$\Delta P^B = g\left(\rho_a - \rho_{G,\mathrm{out}}\right)H \qquad (4.8.20)$$

where ρ_a is the ambient air density and H is usually taken as the distance from the bottom of the packing to the top of the shell. The various pressure drops are conveniently expressed as

$$\Delta P_i = N_i \frac{\rho_{Gi} V_i^2}{2} \qquad (4.8.21)$$

Where N_i is the loss coefficient and V_i is the air velocity at the corresponding location. The pressure drops are associated with the shell, the packing, the mist eliminators, supports and pipes, and the water spray below the packing. Some sample correlations are given in Table 4.8.3.

Water loadings in counterflow natural-draft towers typically range from 0.8 to 2.4 kg/m^2 sec, and superficial air velocities range from 1 to 2 m/sec. The ratio of base diameter to height may be 0.75 to 0.85, and the ratio of throat to base diameter 0.55 to 0.65. The height of the air inlet is usually 0.10 to

TABLE 4.8.2b Mass Transfer and Pressure Drop Correlations for Cooling Towers

Packing Number	C_1, m^{-1}	n_1	n_2	n_3	C_2, m^{-1}	n_4	n_5
Counterflow Packings: $L_0 = G_0 =$ 3.391 kg/m^2 sec							
1	0.289	–0.70	0.70	0.00	2.72	0.35	–0.35
2	0.361	–0.72	0.72	0.00	3.13	0.42	–0.42
3	0.394	–0.76	0.76	0.00	3.38	0.36	–0.36
4	0.459	–0.73	0.73	0.00	3.87	0.52	–0.36
5	2.723	–0.61	0.50	–0.34	19.22	0.34	0.19
6	1.575	–0.50	0.58	–0.40	9.55	0.31	0.05
7	1.378	–0.49	0.56	–0.35	10.10	0.23	–0.04
8	0.558	–0.38	0.48	–0.54	4.33	0.85	–0.60
9	0.525	–0.26	0.58	–0.45	2.36	1.10	–0.64
10	1.312	–0.60	0.62	–0.60	8.33	0.27	–0.14
11	0.755	–0.51	0.93	–0.52	1.51	0.99	0.04
12	1.476	–0.56	0.60	–0.38	6.27	0.31	0.10
Cross-Flow Packings: L_0 = 8.135 kg/m^2 sec, G_0 = 2.715 kg/m^2 sec							
1	0.161	–0.58	0.52	–0.44	1.44	0.66	–0.73
2	0.171	–0.34	0.32	–0.43	1.97	0.72	–0.82
3	0.184	–0.51	0.28	–0.31	1.38	1.30	0.22
4	0.167	–0.48	0.20	–0.29	1.25	0.89	0.07
5	0.171	–0.58	0.28	–0.29	3.18	0.76	–0.80
6	0.217	–0.51	0.47	–0.34	4.49	0.71	–0.59
7	0.213	–0.41	0.50	–0.42	3.44	0.71	–0.85
8	0.233	–0.45	0.45	–0.48	4.89	0.59	0.16

Correlations (SI units)

$$\text{Mass transfer: } \frac{g_m a}{L\left[\text{kg/m}^2\ \text{sec}\right]} = C_1\left(L^+\right)^{n_1}\left(G^+\right)^{n_2}\left(T^+_{\text{HW}}\right)^{n_3};\ \text{Pressure drop: } \frac{N}{H \text{ or } X} = C_2\left(L^+\right)^{n} + \left(G^+\right)^{n_s}$$

$$\text{where } L^+ = \frac{L}{L_0}, \quad G^+ = \frac{G}{G_0}, \quad T^+_{\text{HW}} = \frac{1.8T_{L,\text{in}}[°\text{C}] + 32}{110}$$

Sources: Lowe, H.J. and Christie, D.G. 1961. "Heat transfer and pressure drop data on cooling tower packings, and model studies of the resistance of natural draft towers to airflow" Paper 113, *International Developments in Heat Transfer, Proc. of the International Heat Transfer Conference*, Boulder, CO, ASME, New York; Johnson, B.M., Ed. 1990. *Cooling Tower Performance Prediction and Improvement*, Vols. 1 and 2, EPRI GS-6370, Electric Power Research Institute, Palo Alto, CA. With permission.

0.12 times the base diameter to facilitate air flow into the tower. In practice the air flow distribution in natural-draft towers is not very uniform. However, the assumption of uniform air and water flows in our model of counterflow packing is adequate for most design purposes.

Cost-optimal design of cooling towers requires consideration of the complete power or refrigeration system. For refrigeration, the economics are determined mainly by the operating cost of the chiller (Kintner-Meyer and Emery, 1955).

Cooling Tower Behavior

There are a number of computer programs available that use variations of Merkel's method to calculate the cooling tower performance, for example, TEFRI (Bourillot, 1983), VERA2D-84 (Mujamdar et al., 1985), CTOWER (Mills, 2001). These programs can be used to perform parametric studies to obtain the response of cooling towers to environmental, duty, and design changes. However, before using such programs, some thought should be given to the important characteristics of cooling tower behavior. For this purpose, it is useful to consider a graphical representation of Merkel's theory for a counterflow tower. Figure 4.8.10 shows a chart with moist air enthalpy plotted vs. water enthalpy (or, equivalently, water

TABLE 4.8.3 Pressure Drop Correlations for Cooling Tower Shells, Sprays, Supports, and Mist Eliminators

1. Shell (natural draft counterflow):

   $$N = 0.167\left(\frac{D_B}{b}\right)^2$$

   where D_B *is* the diameter of the shell base and b is the height of the air inlet.
2. Spray (natural-draft counterflow):

   $$N = 0.526(Z_p[\mathrm{m}] + 1.22)\ (\dot{m}_L/\dot{m}_G)^{1.32}$$
3. Mist eliminators:
   $N = 2–4$
4. Support columns, pipes, etc. (natural-draft counterflow):
   $N = 2–6$
5. Fan exit losses for mechanical-draft towers (velocity based on fan exit area):

   $$N = 1.0,\ \text{forced draft}$$
   $$\simeq 0.5,\ \text{induced draft, depending on diffuser design}$$
6. Miscellaneous losses for mechanical-draft towers (velocity based on packing crosssectional area):
   $N \simeq 3$

Note: N is the loss coefficient defined by Equation 4.8.21, with velocity based on cross-sectional area for air flow underneath the packing in items 1 through 4.

Sources: Lowe, H.J. and Christie, D.G. 1961. Heat transfer and pressure drop data on cooling tower packings, and model studies of the resistance of natural draft towers to airflow. Paper 113, *International Developments in Heat Transfer Proc. of the International Heat Transfer Conference*, Boulder, CO, ASME, New York; Singham, J.R. 1990. Natural draft towers, in *Hemisphere Handbook of Heat Exchanger Design,* Sec. 3.12.3, Hewitt, G.E., Coord. Ed., Hemisphere, New York. With permission.

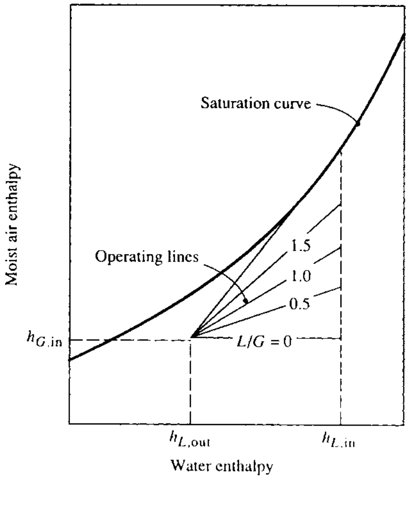

FIGURE 4.8.10 Counterflow cooling tower operating lines for various water-to-air flow-rate ratios shown on an enthalpy chart.

temperature) at 1 atm pressure. The *saturation curve* $h_s(T_s)$ is the enthalpy of saturated air. The *operating lines* $h_G(h_L)$ are given by Equation (4.8.13) and relate the air enthalpy to the water enthalpy at each location in the packing. The slope of an operating line is L/G. Since the assumption $T_s = T_L$ is made in Merkel's method, vertical lines on the chart connect h_s and h_G at each location in the packing. The driving force for enthalpy transfer, $(h_s - h_G)$, is the vertical distance between the saturation curve and the operating line. The integral in Equation (4.8.12) averages the reciprocal of this distance. By using this chart, a number of observations about cooling tower behavior can be made.

1. Figure 4.8.10 shows the effect of L/G for fixed water inlet and outlet temperatures, and fixed inlet air temperature and humidity. If we imagine L to be fixed as well, we see that as G decreases, the driving forces decrease, and so a larger NTU is required.
2. The minimum NTU required corresponds to $L/G = 0$, that is, an infinite air flow rate, for which the operating line is horizontal.
3. Due to the curvature of the operating line, it is possible for the operating line to be tangent to the saturation curve. The indicated NTU is then infinite, which tells us that the air flow rate must be increased in order to achieve the desired water cooling range.
4. For a mechanical-draft tower, the optimal value of L/G lies between the two limits described in items 2 and 3 above. If L/G is large, the required height of packing is large, and the capital cost will be excessive. If L/G is small, the fan power will be excessive (since fan power is proportional to air volume flow rate times pressure drop).

Range and Approach

Cooling tower designers and utility engineers have traditionally used two temperature differences to characterize cooling tower operation. The *range* is the difference between the water inlet and outlet temperatures (also called simply the hot and cold water temperatures). The *approach* is the difference between the outlet water temperature and the wet-bulb temperature of the entering (ambient) air. The approach characterizes cooling tower performance; for a given inlet condition, a larger packing will produce a smaller approach to the ambient wet-bulb temperature, and hence a lower water outlet temperature. (The water cannot be cooled below the ambient wet-bulb temperature.) The approach concept is useful because the ambient dry-bulb temperature has little effect on performance at usual operating conditions (for a specified wet-bulb temperature).

Cooling Demand Curves

Electrical utility engineers have found it convenient to use charts of *cooling demand curves* to evaluate packing specifications. Figure 4.8.11 is an example of such a chart, on which the required NTU, for a given inlet air wet-bulb temperature and range, is plotted vs. L/G with the approach as a parameter. Such a plot is possible since the inlet air dry-bulb temperature has only a small effect under usual operating conditions. Now, if it is possible to correlate the mass transfer conductance as

$$\frac{g_m a}{L} = C\left(\frac{L}{G}\right)^{-n} \tag{4.8.22}$$

the NTU of a packing of height H is

$$\frac{g_m S}{\dot{m}_L} = \frac{g_m a H}{L} = C\left(\frac{L}{G}\right)^{-n} H \tag{4.8.23}$$

Equation (4.8.23) can also be plotted on the chart to give the *packing capability line*. For a required approach, the *operating point* of the tower is the intersection of the cooling demand curve and packing capability line. Charts of cooling demand curves are available (Cooling Tower Institute, 1967; Kelly, 1976). Correlations of the form of Equation (4.8.22) do not necessarily fit experimental data well. A dependence $g_m a \; \alpha L^{1-n} G^n$ is implied and, in the past, experimental data were often forced to fit such a relation. If the $g_m a$ correlation does not have the form of Equation (4.8.22), the NTU cannot be plotted as a line on a cooling demand chart.

With the almost universal use of computers and the availability of suitable computer programs, one can expect less use of cooling demand charts in the future. The major sources of error in the predictions made by these programs are related to nonuniform air and water flow, and the correlations of packing mass transfer and pressure drop experimental data. The experimental data are obtained in small-scale test rigs, in which it is impossible to simulate many features of full-size towers — for example, nonuniform

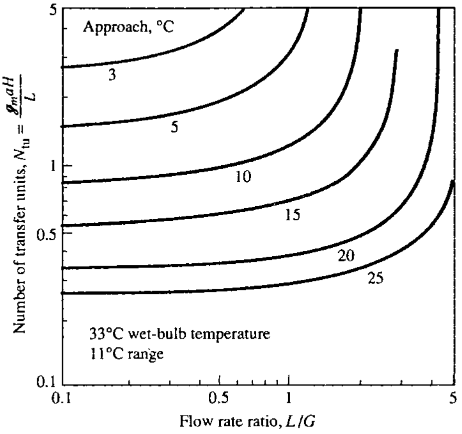

FIGURE 4.8.11 Example of cooling demand curves for a specified wet-bulb temperature and range: NTU vs. flow rate ratio for a fixed approach.

flow due to entrance configuration, nonuniform wetting of the packing, and, in the case of counterflow towers, the effect of spray above the packing and rain below the packing. Furthermore, since testing of packings in small-scale test rigs is itself not easy, considerable scatter is seen in such test data. Correlations of the data typically have root mean square errors of 10 to 20%.

Legionnaires' Disease

Legionnaires' disease is a form of pneumonia caused by a strain of legionnella bacteria (sero group I). Smokers and sick people are particularly vulnerable to the disease. Major outbreaks have occurred at conventions and in hospitals, for which the source of the bacteria has been traced to cooling towers of air-conditioning systems. The bacteria require nutrients such as algae or dead bacteria in sludge, and thrive if iron oxides are present. However, properly designed, installed, and maintained cooling towers have never been implicated in an outbreak of the disease. Key requirements to be met include the following:

1. Mist (drift) eliminators should be effective.
2. The tower should be located so as to minimize the possibility of mist entering a ventilation system.
3. Corrosion in the tower and water lines should be minimized by use of glass fiber, stainless steel, and coated steel.
4. The design should facilitate inspection and cleaning, to allow early detection and remedy of sludge buildup.
5. Water treatment and filtration procedures should meet recommended standards.

References

Bourillot, C. 1983. *TEFRI: Numerical Model for Calculating the Performance of an Evaporative Cooling Tower*, EPRI CS-3212-SR, Electric Power Research Institute, Palo Alto, CA.

Cooling Tower Institute, 1967. *Cooling Tower Performance Curves*, the Institute, Houston.

Kelly, N.W. 1976. *Kelly's Handbook of Cross-Flow Cooling Tower Performance*, Neil W. Kelly and Associates, Kansas City, MO.

Kintner-Meyer, M. and Emery, A.F. 1995. Cost-optimal design of cooling towers, *ASHRAE J.*, April, 46–55.

Merkel, F. 1925. Verdunstungskühlung, *Forschungsarb. Ing. Wes.*, no. 275.

Mills, A.F. 2001. *Mass Transfer*, Prentice-Hall, Upper Saddle River, NJ.

Majumdar, A.K., Singhal, A.K., and Spalding, D.B. 1985. *VERA2D-84: A Computer Program for 2-D Analysis of Flow, Heat and Mass Transfer in Evaporative Cooling Towers*, EPRI CS-4073, Electric Power Research Institute, Palo Alto, CA.

Further Information

Baker, D. 1984. *Cooling Tower Performance*, Chemical Publishing Company, New York.

Johnson, B.M. Ed. 1990. *Cooling Tower Performance Prediction and Improvement*, Vols. 1 and 2, EPRI GS-6370, Electric Power Research Institute, Palo Alto, CA.

Singham, J.R. 1990. Natural draft towers, in *Hemisphere Handbook of Heat Exchanger Design*, Section 3.12.3, Hewitt, G.E., Coord Ed., Hemisphere Publishing, New York.

Stoeker, W.F. and Jones, J.W. 1982. *Refrigeration and Air Conditioning*, 2nd ed., McGraw-Hill, New York.

Webb, R.L. 1988. A critical review of cooling tower design methods, in *Heat Transfer Equipment Design*, Shah, R.K., Subba Rao, E.C., and Mashelkar, R.A., Eds., Hemisphere Publishing, Washington, D.C.

Heat Pipes

Larry W. Swanson

Introduction

The heat pipe is a vapor-liquid phase-change device that transfers heat from a hot reservoir to a cold reservoir using **capillary forces** generated by a **wick** or porous material and a working fluid. Originally conceived by Gaugler in 1944, the operational characteristics of heat pipes were not widely publicized until 1963 when Grover and his colleagues at Los Alamos Scientific Laboratory independently reinvented the concept. Since then many types of heat pipes have been developed and used by a wide variety of industries.

Figure 4.8.12 shows a schematic of a heat pipe aligned at angle ψ relative to the vertical axis (gravity vector). The heat pipe is composed of a container lined with a wick that is filled with liquid near its saturation temperature. The vapor-liquid interface, usually found near the inner edge of the wick, separates the liquid in the wick from an open vapor core. Heat flowing into the evaporator is transferred through the container to the liquid-filled wicking material, causing the liquid to evaporate and vapor to flow into the open core portion of the evaporator. The capillary forces generated by the evaporating interface increase the pressure difference between the vapor and liquid. The vapor in the open core flows out of the evaporator through the adiabatic region (insulated region) and into the condenser. The vapor then condenses, generating capillary forces similar, although much less in magnitude, to those in the evaporator. The heat released in the condenser passes through the wet wicking material and container out into the cold reservoir. The condensed liquid is then pumped, by the liquid pressure difference due to the net capillary force between the evaporator and condenser, out of the condenser back into the evaporator. Proper selection and design of the pipe container, working fluid, and wick structure are essential to the successful operation of a heat pipe. The **heat transfer limitations, effective thermal conductivity**, and axial temperature difference define the operational characteristics of the heat pipe.

Heat Pipe Container, Working Fluid, and Wick Structures

The container, working fluid, and wick structure of a heat pipe determine its operational characteristics. One of the most important considerations in choosing the material for the heat pipe container and wick is its compatibility with the working fluid. Degradation of the container or wick and contamination of the working fluid due to chemical reaction can seriously impair heat pipe performance. For example, noncondensable gas created during a chemical reaction eventually can accumulate near the end of the condenser, decreasing the condensation surface area. This reduces the ability of the heat pipe to transfer heat to the external heat sink. The material and geometry of the heat pipe container also must have a high burst strength, low weight, high thermal conductivity, and low porosity.

Using the proper working fluid for a given application is another critical element of proper heat pipe operation. The working fluid must have good thermal stability properties at the specified operational temperature and pressure. The operational temperature range of the working fluid has to lie between its triple point and its critical point for liquid to exist in the wicking material. The **wettability** of the working

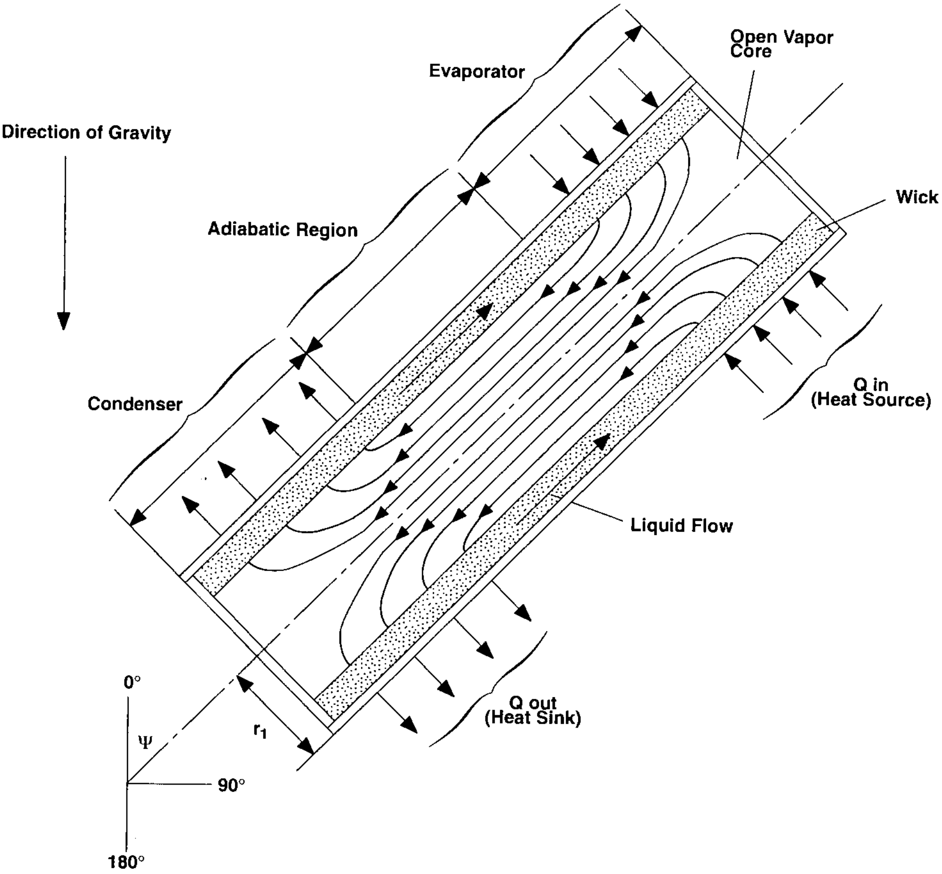

FIGURE 4.8.12 Schematic of a typical heat pipe.

fluid contributes to its capillary pumping and priming capability. High-surface-tension fluids are commonly used in heat pipes because they provide the capillary pumping and wetting characteristics necessary for proper operation. Other desirable thermophysical properties include a high liquid thermal conductivity, high latent heat of vaporization, low liquid viscosity, and a low vapor viscosity. Table 4.8.4 gives the thermophysical properties for three typical heat pipe working fluids that span a fairly wide operating temperature range. The thermophysical properties for other heat pipe working fluids can be obtained from Dunn and Reay (1982) and Peterson (1994).

The wick structure and working fluid generate the capillary forces required to (1) pump liquid from the condenser to the evaporator and (2) keep liquid evenly distributed in the wicking material. Heat pipe wicks can be classified as either homogeneous wicks or composite wicks. Homogeneous wicks are composed of a single material and configuration. The most common types of homogeneous wicks include wrapped screen, sintered metal, axial groove, annular, crescent, and arterial. Composite wicks are composed of two or more materials and configurations. The most common types of composite wicks include variable screen mesh, screen-covered groove, screen slab with grooves, and screen tunnel with grooves. Regardless of the wick configuration, the desired material properties and structural characteristics of heat pipe wick structures are a high thermal conductivity, high wick porosity, small capillary radius, and high wick permeability. Table 4.8.2 gives the geometric properties of some commonly used homogeneous wicks. The properties of other wick structures, including nonhomogenous types, can be obtained from Peterson (1994). The container, wick structure, and working fluid are used to determine the heat transfer limitations of heat pipes.

TABLE 4.8.4 Thermophysical Properties of Some Heat-Pipe Fluids

Temperature (°C)	Latent Heat (kJ /kg)	Liquid Density (kg/m^3)	Vapor Density (kg/m^3)	Liquid Thermal Conductivity (W/m°C)	Liquid Viscosity (cP)	Vapor Viscosity (cP, ×10^2)	Vapor Pressure (bars)	Vapor Specific Heat (kJ/kg°C)	Liquid Surface Tension (N/m × 10^2)
Methanol									
–50	1194	843.5	0.01	0.210	1.700	0.72	0.01	1.20	3.26
–30	1187	833.5	0.01	0.208	1.300	0.78	0.02	1.27	2.95
–10	1182	818.7	0.04	0.206	0.945	0.85	0.04	1.34	2.63
10	1175	800.5	0.12	0.204	0.701	0.91	0.10	1.40	2.36
30	1155	782.0	0.31	0.203	0.521	0.98	0.25	1.47	2.18
50	1125	764.1	0.77	0.202	0.399	1.04	0.55	1.54	2.01
70	1085	746.2	1.47	0.201	0.314	1.11	1.31	1.61	1.85
90	1035	724.4	3.01	0.199	0.259	1.19	2.69	1.79	1.66
110	980	703.6	5.64	0.197	0.211	1.26	4.98	1.92	1.46
130	920	685.2	9.81	0.195	0.166	1.31	7.86	1.92	1.25
150	850	653.2	15.90	0.193	0.138	1.38	8.94	1.92	1.04
Water									
20	2448	998.0	0.02	0.603	1.00	0.96	0.02	1.81	7.28
40	2402	992.1	0.05	0.630	0.65	1.04	0.07	1.89	7.00
60	2359	983.3	0.13	0.649	0.47	1.12	0.20	1.91	6.66
80	2309	972.0	0.29	0.668	0.36	1.19	0.47	1.95	6.26
100	2258	958.0	0.60	0.680	0.28	1.27	1.01	2.01	5.89
120	2200	945.0	1.12	0.682	0.23	1.34	2.02	2.09	5.50
140	2139	928.0	1.99	0.683	0.20	1.41	3.90	2.21	5.06
160	2074	909.0	3.27	0.679	0.17	1.49	6.44	2.38	4.66
180	2003	888.0	5.16	0.669	0.15	1.57	10.04	2.62	4.29
200	1967	865.0	7.87	0.659	0.14	1.65	16.19	2.91	3.89
Potassium									
350	2093	763.1	0.002	51.08	0.21	0.15	0.01	5.32	9.50
400	2078	748.1	0.006	49.08	0.19	0.16	0.01	5.32	9.04
450	2060	735.4	0.015	47.08	0.18	0.16	0.02	5.32	8.69
500	2040	725.4	0.031	45.08	0.17	0.17	0.05	5.32	8.44
550	2020	715.4	0.062	43.31	0.15	0.17	0.10	5.32	8.16
600	2000	705.4	0.111	41.81	0.14	0.18	0.19	5.32	7.86
650	1980	695.4	0.193	40.08	0.13	0.19	0.35	5.32	7.51
700	1960	685.4	0.314	38.08	0.12	0.19	0.61	5.32	7.12
750	1938	675.4	0.486	36.31	0.12	0.20	0.99	5.32	6.72
800	1913	665.4	0.716	34.81	0.11	0.20	1.55	5.32	6.32
850	1883	653.1	1.054	33.31	0.10	0.21	2.34	5.32	5.92

Heat Transfer Limitations

Heat pipes undergo various heat transfer limitations depending on the working fluid, the wick structure, the dimensions of the heat pipe, and the heat pipe operational temperature. Figure 4.8.13 gives a qualitative description of the various heat transfer limitations, which include vapor-pressure, sonic, entrainment, capillary, and boiling limitations. The composite curve enclosing the shaded region in Figure 4.8.13 gives the maximum heat transfer rate of the heat pipe as a function of the operational temperature. The figure shows that as the operational temperature increases, the maximum heat transfer rate of the heat pipe is limited by different physical phenomena. As long as the operational heat transfer rate falls within the shaded region, the heat pipe will function properly.

The vapor-pressure limitation (or viscous limitation) in heat pipes develops when the pressure drop in the vapor core reaches the same order of magnitude as the vapor pressure in the evaporator. Under

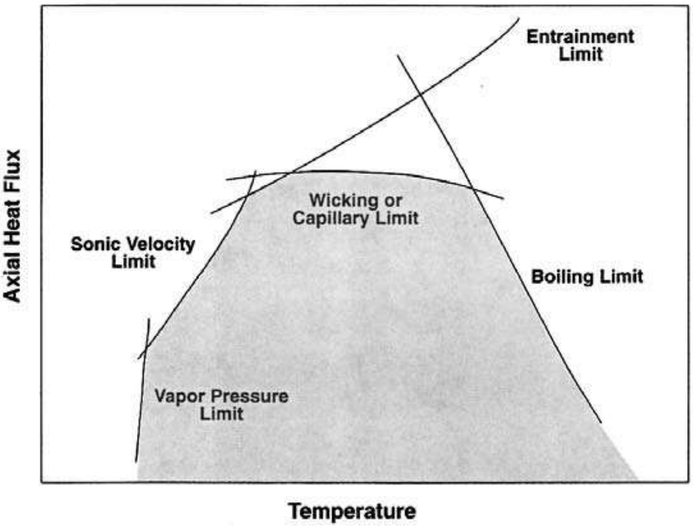

FIGURE 4.8.13 Heat transfer limitations in heat pipes.

these conditions, the pressure drop due to flow through the vapor core creates an extremely low vapor pressure in the condenser preventing vapor from flowing in the condenser. A general expression for the vapor-pressure limitation is (Dunn and Reay, 1982)

$$Q_{\mathrm{v}p,\max} = \frac{\pi r_{\mathrm{v}}^4 h_{fg} \rho_{v,e} P_{\mathrm{v},e}}{12 \mu_{v,e} l_{\mathrm{eff}}} \tag{4.8.24}$$

where r_v is the cross-sectional radius of the vapor core (m), h_{fg} is the latent heat of vaporization (J/kg), $\rho_{v,e}$ is the vapor density in the evaporator (kg/m^3), P_{ve} is the vapor pressure in the evaporator (Pa), and $\mu_{v,e}$ is the vapor viscosity in the evaporator (N sec/m^2). l_{eff} is the effective length of the heat pipe (m) equal to $l_{\mathrm{eff}} = 0.5(l_e + 2l_a + l_c)$. The vapor-pressure limitation can occur during the start-up of heat pipes at the lower end of the working-fluid-temperature range.

The sonic limitation also can occur in heat pipes during start-up at low temperatures. The low temperature produces a low vapor density, thereby reducing the speed of sound in the vapor core. Thus, a sufficiently high mass flow rate in the vapor core can cause sonic flow conditions and generate a shock wave that chokes the flow and restricts the pipes ability to transfer heat to the condenser. Dunn and Reay (1982) give an expression for the sonic limitation that agrees very well with experimental data,

$$Q_{s,\max} = 0.474 A_{\mathrm{v}} h_{fg} \left(\rho_v P_v\right)^{1/2} \tag{4.8.25}$$

where A_v is the cross-sectional area of the vapor core (m^2). The sonic limitation should be avoided because large temperature gradients occur in heat pipes under choked-flow conditions.

The entrainment limitation in heat pipes develops when the vapor mass flow rate is large enough to shear droplets of liquid off the wick surface causing dry-out in the evaporator. A conservative estimate of the maximum heat transfer rate due to entrainment of liquid droplets has been given by Dunn and Reay (1982) as

$$Q_{e,\max} = A_{\mathrm{v}} h_{fg} \left[\frac{\rho_v \sigma_l}{2 r_{c,\mathrm{ave}}}\right]^{1/2} \tag{4.8.26}$$

where σ_l is the surface tension (N/m) and $r_{c,\mathrm{ave}}$ is the average capillary radius of the wick. Note that for many applications $r_{c,\mathrm{ave}}$ is often approximated by $r_{c,e}$.

The capillary limitation in heat pipes occurs when the net capillary forces generated by the vapor-liquid interfaces in the evaporator and condenser are not large enough to overcome the frictional pressure losses due to fluid motion. This causes the heat pipe evaporator to dry out and shuts down the transfer of heat from the evaporator to the condenser. For most heat pipes, the maximum heat transfer rate due to the capillary limitation can be expressed as (Chi, 1976).

$$Q_{c,\max} = \left[\frac{\rho_l \sigma_l h_{fg}}{\mu_l}\right]\left[\frac{A_w K}{l_{\mathrm{eff}}}\right]\left(\frac{2}{r_{c,e}} - \left[\frac{\rho_l}{\sigma_l}\right] g L_t \cos\Psi\right) \tag{4.8.27}$$

where K is the wick permeability (m^2), A_w is the wick cross-sectional area (m^2), ρ_l is the liquid density (m^3), μ_l is the liquid viscosity (N sec/m^2), $r_{c,e}$ is the wick capillary radius in the evaporator (m), g is the acceleration due to gravity (9.8 m/sec^2), and L_t is the total length of the pipe (m). For most practical operating conditions, this limitation can be used to determine maximum heat transfer rate in heat pipes.

The boiling limitation in heat pipes occurs when the degree of liquid superheat in the evaporator is large enough to cause the nucleation of vapor bubbles on the surface of the wick or the container. Boiling is usually undesirable in heat pipes because local hot spots can develop in the wick, obstructing the flow of liquid in the evaporator. An expression for the boiling limitation is (Chi, 1976)

$$Q_{b,\max} = \frac{4\pi l_{\mathrm{eff}} k_{\mathrm{eff}} T_v \sigma_v}{h_{fg} \rho_l \ln\left(r_i / r_v\right)}\left(\frac{1}{r_n} - \frac{1}{r_{c,e}}\right) \tag{4.8.28}$$

where k_{eff} is the effective thermal conductivity of the composite wick and working fluid (W/m K), T_v is the vapor saturation temperature (K), r_i is the inner container radius (m), r_n is the nucleation radius (equal to 2.00×10^{-6} m in the absence of noncondensable gas).

Effective Thermal Conductivity and Heat Pipe Temperature Difference

One key attribute of the heat pipe is that it can transfer a large amount of heat while maintaining nearly isothermal conditions. The temperature difference between the external surfaces of the evaporator and the condenser can be determined from the following expression

$$\Delta T = R_t Q \tag{4.8.29}$$

where R_t is the total thermal resistance (K/W) and Q is the heat transfer rate (W). Figure 4.8.14 shows the thermal resistance network for a typical heat pipe and the associated thermal resistances. In most cases, the total thermal resistance can be approximated by

$$R_t = R_1 + R_2 + R_3 + R_5 + R_7 + R_8 + R_9 \tag{4.8.30}$$

The reader is referred to Peterson (1994) for the specific mathematical relationships used to calculate each thermal resistance. The effective thermal conductivity of the heat pipe is defined as the heat transfer rate divided by the temperature difference between the heat source and heat sink,

$$k_{\mathrm{eff}} = \frac{L_t}{R_t A_t} \tag{4.8.31}$$

where A_t is the overall cross-sectional area of the pipe (m^2). Under normal operating conditions, the total thermal resistance is relatively small, making the external surface temperature in the evaporator approx-

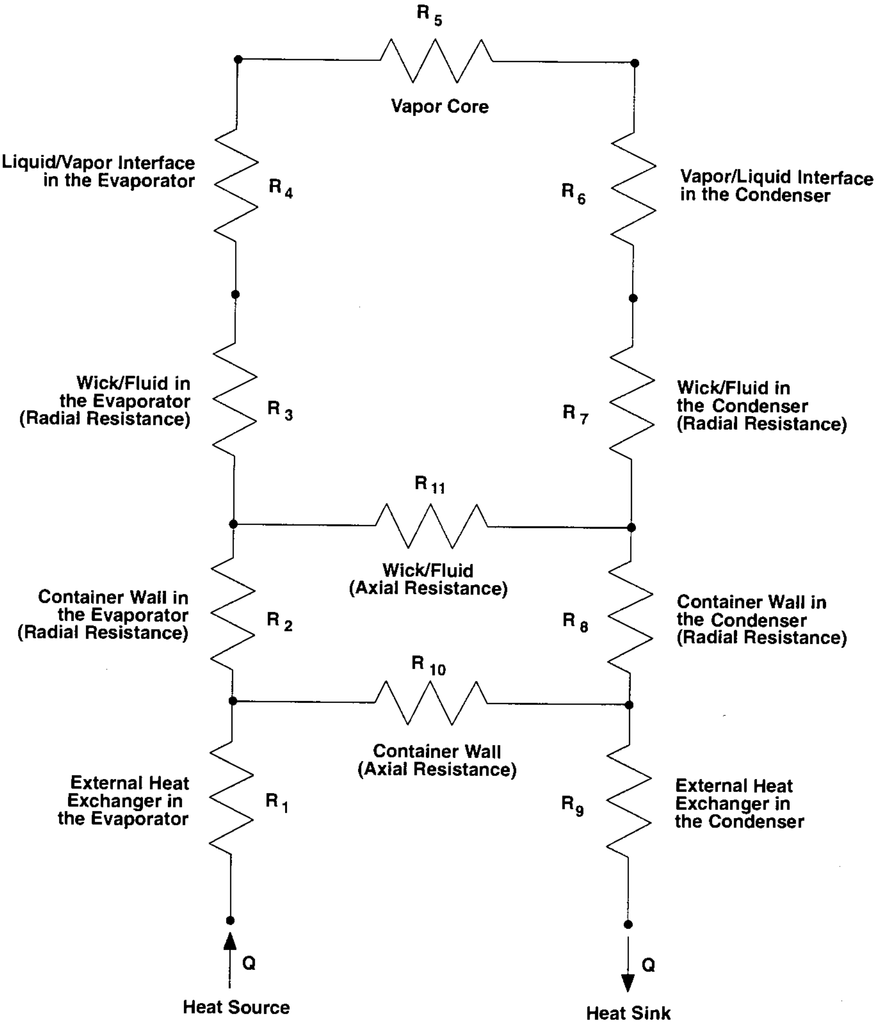

FIGURE 4.8.14 Thermal resistance network in a heat pipe.

imately equal to that in the condenser. Thus, the effective thermal conductivity in a heat pipe can be very large (at least an order of magnitude larger than that of aluminum).

Design Example

Design a water heat pipe to transport 80 W of waste heat from an electronics package to cooling water. The heat pipe specifications are

1. Axial orientation — complete gravity-assisted operation (condenser above the evaporator; ψ = 180°)
2. Maximum heat transfer rate — 80 W
3. Nominal operating temperature — 40°C
4. Inner pipe diameter — 3 cm
5. Pipe length — 25 cm evaporator length, 50 cm adiabatic section, and 25 cm condenser length

The simplest type of wick structure to use is the single-layer wire mesh screen wick shown in Table 4.8.5. The geometric and thermophysical properties of the wick have been selected as (this takes some forethought)

- $d = 2.0 \times 10^{-5}$ m
- $w = 6.0 \times 10^{-5}$ m
- $\dfrac{1}{2N} = r_c = {}^1/_2(2.0 \times 10^{-5} + 6 \times 10^{-5}) = 4.0 \times 10^{-5}$ m
- $\varepsilon = 1$
- $k_{\text{eff}} = k_1 = 0.630 \ \dfrac{\text{W}}{\text{mK}}$
- $t_w = 1.0 \times 10^{-3}$ m
- $K = \dfrac{t_w^2}{12} = \dfrac{\left(1\times 10^{-3}\right)^2}{12} = 8.33\times 10^{-8}\ \text{m}^2$

The other heat pipe geometric properties are

- $r_v = r_i - t_w = 0.015 - 0.001 = 0.014$ m
- $l_{\text{eff}} = \dfrac{0.25+0.25}{2} + 0.5 = 0.75$ m
- $L_t = 0.25 + 0.50 + 0.25 + 1.0$ m
- $A_w = \pi(r_i^2 - r_v^2) = \pi[(0.015)^2 - (0.014)^2] = 9.11 \times 10^{-5}\ \text{m}^2$
- $A_v = \pi r_v^2 = \pi(0.014)^2 = 6.16 \times 10^{-4}\ \text{m}^2$

The thermophysical properties of water at 40°C are (see Table 4.8.4):

- $\rho_l = 992.1\ \text{kg/m}^3$
- $\rho_v = 0.05\ \text{kg/m}^3$
- $\sigma_l = 2.402 \times 10^6$ J/kg
- $\mu_l = 6.5 \times 10^{-3}$ kg/m sec
- $\mu_v = 1.04 \times 10^{-4}$ kg/m sec
- $P_v = 7000$ Pa

The various heat transfer limitations can now be determined to ensure the heat pipe meets the 80 W heat transfer rate specification. The vapor-pressure limitation is

$$Q_{vp,\max} = \frac{\pi(0.014)^4\left(2.402\times 10^6\right)(0.05)(7000)}{12\left(1.04\times 10^{-4}\right)(0.75)} = 1.08\times 10^5\ \text{W} \tag{4.8.32}$$

The sonic limitation is

$$\begin{aligned} Q_{s,\max} &= 0.474\left(6.16\times 10^{-4}\right)\left(2.402\times 10^6\right)\left[(0.05)(7000)\right]^{1/2} \\ &= 1.31\times 10^4\ \text{W} \end{aligned} \tag{4.8.33}$$

The entrainment limitation is

$$\begin{aligned} Q_{e,\max} &= \left(6.16\times 10^{-4}\right)\left(2.402\times 10^6\right)\left[\frac{(0.05)(0.07)}{2\left(4.0\times 10^{-5}\right)}\right]^{1/2} \\ &= 9.79\times 10^3\ \text{W} \end{aligned} \tag{4.8.34}$$

Noting that cos ψ = −1, the capillary limitation is

$$Q_{c,\max} = \left[\frac{(992.1)(0.07)\left(2.402\times10^{6}\right)}{6.5\times10^{-3}}\right]\left[\frac{\left(9.11\times10^{-5}\right)\left(8.33\times10^{-8}\right)}{0.75}\right]\left[\frac{2}{4.0\times10^{-5}}+\frac{992.1}{0.07}9.8(1.0)\right] \tag{4.8.35}$$

$$= 4.90\times10^{4}\ \text{W}$$

Finally, the boiling limitation is

$$Q_{b,\max} = \frac{4\pi(0.75)(0.63)(313)(0.07)}{\left(2.402\times10^{6}\right)(992.1)\ln\left(\dfrac{0.015}{0.014}\right)}\left[\frac{1}{2.0\times10^{-6}}-\frac{1}{4.0\times10^{-5}}\right] \tag{4.8.36}$$

$$= 0.376\ \text{W}$$

All of the heat transfer limitations, with the exception of the boiling limitation, exceed the specified heat transfer rate of 80 W. The low value of 0.376 W for the boiling limitation strongly suggests that the liquid will boil in the evaporator and possibly cause local dry spots to develop. The reason the liquid boils is because the effective thermal conductivity of the wick is equal to the conductivity of the liquid, which is very low in this case. Because the liquid is saturated at the vapor-liquid interface, a low effective thermal conductivity requires a large amount of wall superheat which, in turn, causes the liquid to boil. This problem can be circumvented by using a high conductivity wire mesh or sintered metal wick, which greatly increases the effective conductivity. It should be noted, however, that because porous wicks have lower permeabilities, the capillary limitation should be lower as well. Let's try a sintered particle wick made of copper with the following properties (see Table 4.8.5):

- $d = 1.91 \times 10^{-4}$ m
- $r_{c,3} = 0.21d = 4.0 \times 10^{-5}$ m (same as before)
- $\varepsilon = 0.48$
- $K = \dfrac{\left(1.91\times10^{-4}\right)^{2}(0.48)}{150(1-0.48)^{2}} = 2.07\times10^{-10}\ \text{m}^{2}$
- $k_s = 400\ \dfrac{\text{W}}{\text{mK}}$ (copper)
- $k_1 = 0.630\ \dfrac{\text{W}}{\text{mK}}$ (water)
- $k_{\text{eff}} = \dfrac{400\left[2(400)+0.63-2(0.48)(400-0.63)\right]}{2(400)+0.63+0.48(400-0.63)} = 168\ \text{W/mK}$

All other geometric and thermophysical properties are the same. The heat transfer limitations affected by the change in wick structure are the capillary and boiling limitations. The sintered metal wick produces a capillary limitation of

$$Q_{c,\max} = \left[\frac{(992.1)(0.07)\left(2.402\times10^{6}\right)}{6.5\times10^{-3}}\right]\left[\frac{\left(9.11\times10^{-5}\right)\left(2.07\times10^{-10}\right)}{0.75}\right]\left[\frac{2}{4.0\times10^{-5}}+\frac{992.1}{0.07}9.8(1.0)\right] \tag{4.8.37}$$

$$= 122\ \text{W}$$

The boiling limitation for the sintered wick is

TABLE 4.8.5 Physical Properties of Wick Structures

	Wick Type[a]	Thermal Conductivity	Porosity	Minimum Capillary Radius	Permeability
Single-layer wire mesh screens (heat-pipe axis in the plane of the paper in this sketch) 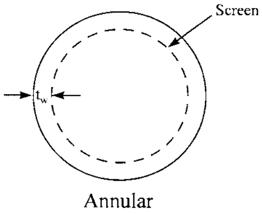 $1/N = d + w$ N = number of aperatures per unit length	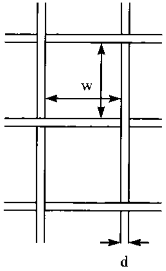	$k_{\text{eff}} = k_e$	$\varepsilon = 1$	$r_c = {}^1/_{(2N)}$	$K = t_w^2/12$
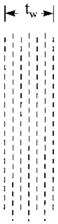	Multiple wire mesh screens,[b] plain or sintered (screen dimensions as for single layers illustrated above)	$k_{\text{eff}} = \dfrac{k_e\left[k_e + k_s - (1-\varepsilon)(k_e - k_s)\right]}{k_e + k_s + (1-\varepsilon)(k_e - k_s)}$	Estimated from $\varepsilon = 1 - (\pi N d)/4$	$r_c = {}^1/_{(2N)}$	$k = \dfrac{d^2\varepsilon^2}{122(1-\varepsilon)^2}$

TABLE 4.8.5 Physical Properties of Wick Structures (continued)

	Wick Type[a]		Thermal Conductivity	Porosity	Minimum Capillary Radius	Permeability
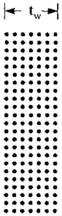	Unconsolidated packed spherical particles (d = average particle diameter)	Plain	$k_{\text{eff}} = \dfrac{k_e\left[2k_e + k_s - 2(1-\varepsilon)(k_e - k_s)\right]}{2k_e + k_s + (1-\varepsilon)(k_e - k_s)}$	Estimated from (assuming cubic packing) ε = 0.48	$r_c = 0.21d$	$k = \dfrac{d^2\varepsilon^2}{150(1-\varepsilon)^2}$
		Sintered	$k_{\text{eff}} = \dfrac{k_e\left[2k_s + k_e - 2\varepsilon(k_s - k_e)\right]}{2k_s + k_e + \varepsilon(k_s - k_e)}$			
	Sintered metal fibers (d = fiber diameter)		$k_{\text{eff}} = \varepsilon^2 k_e (1-\varepsilon)^2 k_s + \dfrac{4\varepsilon(1-\varepsilon)k_e k_s}{k_e + k_s}$	Use manufacturers data	$r_c = \dfrac{d}{2(1-\varepsilon)}$	$k = C_1 \dfrac{y^2 - 1}{y^2 - 1}$ where $y = 1 + \dfrac{C_2 d^2 \varepsilon^3}{(1-\varepsilon)^2}$ $C_1 = 6.0 \times 10^{-10}\ \text{m}^2$ $C_2 = 3.3 \times 10^7\ \text{l/m}^2$

[a] The axis of the pipe and direction of fluid flow are normal to the paper.

[b] These wicks are positioned so that the layers follow the contours of the iner surface of the pipe wall.

Revised from Peterson, G.P., *An Introduction to Heat Pipes Modeling, Testing, and Applications*, John Wiley & Sons, New York, 1994.

$$Q_{b,\max} = \frac{4\pi(0.75)(168)(313)(0.07)}{\left(2.402\times10^{6}\right)(992.1)\ln\left(\dfrac{0.015}{0.014}\right)}\left[\frac{1}{2.0\times10^{-6}}-\frac{1}{4.0\times10^{-5}}\right] \tag{4.8.38}$$

$$= 100 \text{ W}$$

This design now meets all the specifications defined in the problem statement.

Application of Heat Pipes

Heat pipes have been applied to a wide variety of thermal processes and technologies. It would be an impossible task to list all the applications of heat pipes; therefore, only a few important industrial applications are given in this section. In the aerospace industry, heat pipes have been used successfully in controlling the temperature of vehicles, instruments, and space suits. Cryogenic heat pipes have been applied in (1) the electronics industry for cooling various devices (e.g., infrared sensors, parametric amplifiers) and (2) the medical field for cryogenic eye and tumor surgery. Heat pipes have been employed to keep the Alaskan tundra frozen below the Alaskan pipeline. Other cooling applications include (1) turbine blades, generators, and motors; (2) nuclear and isotope reactors; and (3) heat collection from exhaust gases, solar and geothermal energy.

In general, heat pipes have advantages over many traditional heat-exchange devices when (1) heat has to be transferred isothermally over relatively short distances, (2) low weight is essential (the heat pipe is a passive pumping device and therefore does not require a pump), (3) fast thermal-response times are required, and (4) low maintenance is mandatory.

Defining Terms

Capillary force: The force caused by a curved vapor-liquid interface. The interfacial curvature is dependent on the surface tension of the liquid, the contact angle between the liquid wick structure, the vapor pressure, and the liquid pressure.

Effective thermal conductivity: The heat transfer rate divided by the temperature difference between the evaporator and condenser outer surfaces.

Heat transfer limitations: Limitations on the axial heat transfer capacity imposed by different physical phenomena (i.e., vapor pressure, sonic, entrainment, capillary, and boiling limitations).

Wettability: The ability of a liquid to spread itself over a surface. A wetting liquid spreads over a surface whereas a nonwetting liquid forms droplets on a surface.

Wick: A porous material used to generate the capillary forces that circulate fluid in a heat pipe.

References

Chi, S.W. 1976. *Heat Pipe Theory and Practice*, Hemisphere Publishing, Washington, D.C.

Dunn, P.D. and Reay, D.A. 1982. *Heat Pipes*, 3rd ed., Pergamon Press, Oxford, U.K.

Gaugler, R.S. 1944. Heat Transfer Device. U.S. Patent No. 2350348.

Grover, G.M. 1963. Evaporation-Condensation Heat Transfer Device. U.S. Patent No. 3229759.

Peterson, G.P. 1994. *An Introduction to Heat Pipes Modeling, Testing, and Applications*, John Wiley & Sons, New York.

Further Information

Recent developments in heat pipe research and technology can be found in the proceedings from a number of technical conferences: (1) The International Heat Pipe Conference (2) The National Heat Transfer Conference, (3) The ASME Winter Annual Meeting, (4) The AIAA Thermophysics Conference.

Books particularly useful for the design of heat pipes include (1) *Heat Pipe Design Handbook* by Brennan and Kroliczek available from B&K Engineering in Baltimore, M.D. (2) *The Heat Pipe* by Chisholm available from Mills and Boon Limited in London, England, and (3) *Heat Pipes: Construction and Application* by Terpstra and Van Veen available from Elsevier Applied Science in New York, N.Y.

An additional book particularly strong in heat pipe theory is *The Principles of Heat Pipes* by Ivanovskii, Sorokin, and Yagodkin available from Clarendon Press in Oxford, England.

Cooling Electronic Equipment

Vincent W. Antonetti

Introduction

In electronic packages, the thermal resistances to heat transfer from heat source to heat sink are often grouped into an internal resistance and an external resistance. The **internal thermal resistance** R_{int} is conductive and exists between the chip and the module case:

$$R_{\text{int}} = \frac{T_{\text{chip}} - T_{\text{case}}}{P_{\text{chip}}} \tag{4.8.39}$$

where P_{chip} is the chip power.

The **external thermal resistance** R_{ext} is primarily convective and exists between the surface of the case of the module and some reference point, typically the temperature of the cooling fluid near the module. In a multichip module, the module power P_m is the sum of the individual chip powers, and the external resistance is

$$R_{\text{ext}} = \frac{T_{\text{case}} - T_{\text{coolant}}}{P_m} \tag{4.8.40}$$

The internal and external resistances are related to the chip junction temperature T_j through the following expression:

$$T_j = \Delta T_{j-\text{chip}} + P_{\text{chip}} R_{\text{int}} + P_m R_{\text{ext}} + \Delta T_{\text{coolant}} + T_{\text{coolant in}} \tag{4.8.41}$$

Many factors are involved in determining the appropriate cooling mode to be used. If the component junction temperature is constrained to approximately 85°C, Table 4.8.6 may be used to make a preliminary selection of the cooling mode. Extended surfaces can often be used to increase the allowable heat fluxes.

Free Convection Air Cooling of Vertical Printed Circuit Boards

Data have been collected from rack-mounted simulated printed circuit boards (PCBs) (see Figure 4.8.15) and from several actual electronic systems at AT&T Bell Laboratories. Results indicated that existing parallel plate correlations for symmetric isoflux plates (separated by distance "b") could be adapted to

TABLE 4.8.6 Maximum Component Heat Flux for Various Cooling Modes

Cooling Mode	W/cm^2
Free convection air	0.05
Forced convection air	0.5
Impingement air	1.0
Free convection immersion	1.0
Forced convection immersion	50
Pool boiling	20
Forced convection boiling	100
Jet immersion (single phase)	40
Boiling jet immersion	90

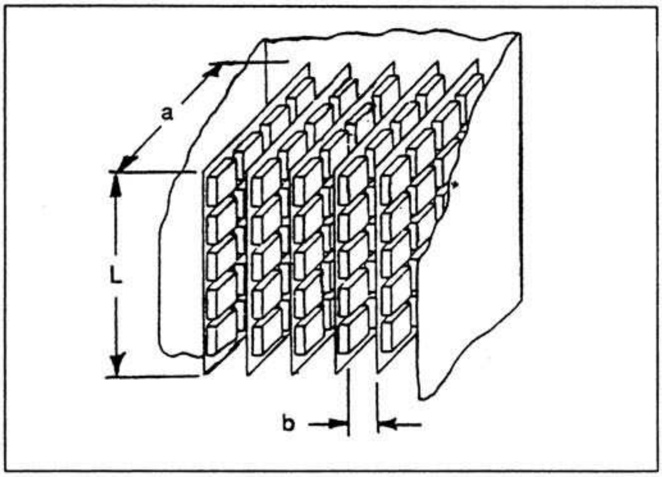

FIGURE 4.8.15 Typical PCB array. (From Antonetti, V.W., in *Heat Transfer and Fluid Flow Data Books*, F. Kreith, Ed., Genium Publishing, Schenectady, NY, 1993. With permission.)

PCB conditions. Specifically, for $\mathrm{Ra}_b < 10$ use the equation corresponding to the fully developed laminar boundary layer condition:

$$\mathrm{Nu}_b = 0.144\mathrm{Ra}_b^{0.5} \tag{4.8.42}$$

For $10 < \mathrm{Ra}_b < 1000$, use

$$\mathrm{Nu}_b = \left[\frac{48}{\mathrm{Ra}_b} + \frac{2.5}{\mathrm{Ra}_b^{0.4}}\right]^{-0.5} \tag{4.8.43}$$

where

$$\mathrm{Ra}_b = \frac{g\beta c_p \rho^2 b^5 q''}{\mu k L}$$

For Ra > 1000, the expression for an isolated plate in infinite media is recommended:

$$\mathrm{Nu}_b = 0.524\mathrm{Ra}_b^{0.2} \tag{4.8.44}$$

In the previous three expressions air properties are evaluated at the average of the module case and ambient temperatures.

The PCB spacing $b_{\max}$ for a given power dissipation which yields the lowest PCB component case temperatures (or which maximizes the rate of heat transfer while maintaining PCB temperatures below the maximum allowable) occurs when the developing boundary layers from adjacent PCBs do not interfere, i.e., so the isolated plate condition is approached as follows: If heat is transferred from both sides of the PCB, let $\mathrm{Ra}_{ab} = 17{,}000$ and the recommended PCB spacing is $b_{\max} = 7.02\xi^{-0.2}$. If heat is transferred from only one side of the PCB, let $\mathrm{Ra}_{ab} = 5400$ and the recommended PCB spacing is $b_{\max} = 5.58\xi^{-0.2}$. In both cases

$$\xi = \frac{g\beta\rho^2 \mathrm{Pr} q''}{\mu^2 k L} \tag{4.8.45}$$

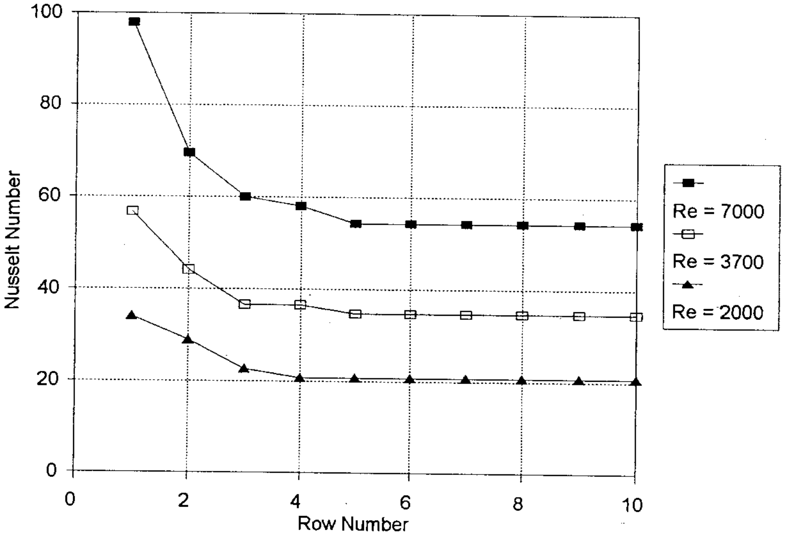

FIGURE 4.8.16 Nusselt number for fully populated array of modules. (From Sparrow, E.M. et al., *Int. J. Heat Mass Transfer*, 25, 961–973, 1982. With permission.)

Forced Convection Air Cooling of Vertical PCBs

Sparrow et al. (1982, 1984) studied vertical arrays with simulated modules of uniform size, which was 4 modules wide by 17 module rows deep in the flow direction; the modules were 26.7 mm square and 10 mm high; the space between modules was 6.67 mm, and the distance from the top of the module to the adjoining card Hc = 16.7 mm. The Nusselt number as a function of module row position for a fully populated array may be determined from Figure 4.8.16. Correction factors to the fully developed Nusselt numbers for the effect of missing modules and the presence of modules whose height differs from others in the array are presented in the cited references.

In actual electronic packages, conditions differ from the relatively ideal setups in laboratories because in real packages the flow is disturbed by the PCB supporting hardware and may extend the entry region effect.

Data from actual computer hardware with PCBs containing a 6 × 4 array of 28 mm modules (4 in the flow direction) were used to develop the following expressions:

$$\mathrm{Nu}_x = C\left\{\mathrm{Re}_{D_h}\left[1 + x/\left(D_h\right)^{-0.836}\right]\right\}^m \tag{4.8.46}$$

For Re < 2000, $C = 0.072$ and $m = 0.70$, and for 2000 < Re < 10,000, $C = 0.056$ and $m = 1.02$, where x is the distance in the flow direction. Because the array was only 4 modules deep, all the modules on the PCB were in the entry region.

Tests have been conducted on a 9 × 7 array of 25-mm-square by 6.4-mm-high blocks cooled by a 3 × 3 array of air jets directed normal to the face of each block. The spent flow exited along the channel formed by the orifice plate and the heat transfer surfaces. Test results were correlated by the relation:

$$N_d = 0.213(z/d)^{-0.376}\,\mathrm{Re}_d^{0.743} \tag{4.8.47}$$

where d is the jet orifice diameter, s is the orifice-to-orifice spacing, and z is the distance from the orifice outlet to the face of the module.

Immersion Cooling

The highly inert perfluorinated liquids, called FC coolants by the 3M Company, are frequently used in **immersion cooling** applications. FC coolants are available with boiling points from 30 to 172°C at atmospheric pressure. FC-75 are FC-77 with boiling points of 100°C are often used in single-phase applications, while FC-72 and FC-87, with boiling points of 56 and 30°C, respectively, are used in systems involving phase change.

Data exist for free convection immersion cooling of a 3 × 3 array of simulated chips mounted on a vertical wall in an enclosure filled with FC-75. Each heat source was 8 mm high by 24 mm wide by 6 mm thick. With the Nusselt and modified Rayleigh numbers based on the heater height, L, the best fit to the data is

$$\mathrm{Nu}_L = 0.279\mathrm{Ra}_b^{0.224} \tag{4.8.48}$$

Air cooling expressions have been modified to make them applicable to free convection immersion cooling of vertical PCB arrays with FC coolants. The Nusselt number (based on PCB spacing "b") at the top of the PCB is

$$\mathrm{Nu}_L = \left[\frac{C}{\mathrm{Ra}_b} + \frac{2.78}{\mathrm{Ra}_b^{0.4}}\right]^{-0.5} \tag{4.8.49}$$

$C = 24$ when heat transfer is from one side of the PCB, and $C = 48$ when from both sides.

Nucleate Pool Boiling

A number of investigators have tested small flush heat sources boiling in a pool of dielectric liquid. The heaters ranged from 4 × 4 mm to 12.7 × 12.7 mm. Typical saturated pool boiling data for FC-72 and FC-87 are shown in Figure 4.8.17. Note that a temperature overshoot up to 25°C has been regularly observed for silicon chips in dielectric liquid pools. To estimate the temperature excursion at boiling incipience (q_i''), the following approximation is recommended

$$\Delta T_{\mathrm{ex}} = T_{\mathrm{sat}}\left(p - \frac{2\sigma}{r_b} - p_g\right) - T_{\mathrm{sat}} - C\left(q_i''\right)^n \tag{4.8.50}$$

where

$$C = \mu h_{fg}\left[\frac{c_p}{h_{fg}\mathrm{Pr}^b C_{sf}}\right]^{1/a}\left[\frac{\alpha}{g\left(\rho - \rho_g\right)}\right]^{0.5} \tag{4.8.51}$$

with $r_b = 0.25$ µm, $C_{sf} = 0.003$, $a = 0.33$, and $b = 1.7$. (Note that $n = 1/a = 3$.)

Park and Bergles (1988) determined the critical heat flux (CHF) as a function of size for flush heaters operating in a saturated pool of R-113. For a 5-mm-wide heater, and for heater heights from 5 to 80 mm, use

$$\frac{q''_{c_{\mathrm{sat}}}}{q''_{c_z}} = 0.86\left[1 + \frac{152}{L^{*3.29}}\right]^{0.14} \tag{4.8.52}$$

where the CHF prediction of Zuber, $q''_{c_z} = \rho_g^{0.5} h_{fg}[\sigma g(\rho_f - \rho_g)]^{0.5}$, and $L^* = L[g(\rho_f - \rho_g)/\sigma]^{0.5}$.

For a 5-mm-high heater, and for heater widths from 2.5 to 70 mm, use

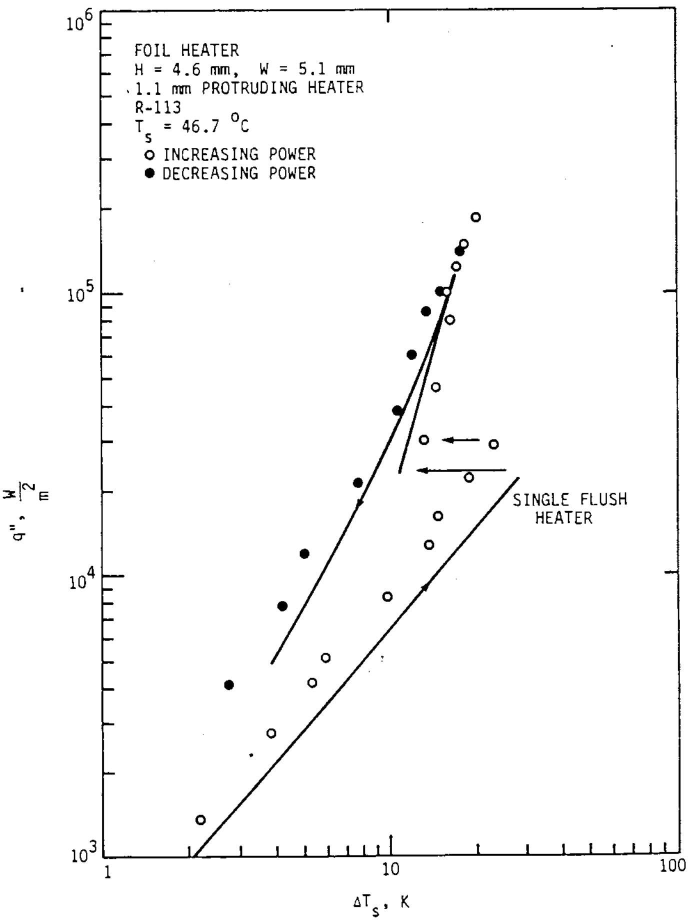

FIGURE 4.8.17 Typical pool boiling curve for small heater. (From Park, K.A. and Bergles, A.E. *J. Heat Transfer*, 110, 728–734, 1988. With permission.)

$$\frac{q''_{c_{\text{sat}}}}{q''_{c_z}} = 0.93\left[1 + \frac{52}{I^{1.02}}\right]^{0.14} \tag{4.8.53}$$

where the induced convection parameter is $I = (\rho_f W\sigma/\mu^2)^{0.5}$.

For flush 12.7 × 12.7 mm heaters in FC-72, test data yield $q''_{c_{\text{sat}}}/q''_{c_z} \approx 1.45$. These subcooling data were correlated by

$$\frac{q''_{c_{\text{sub}}}}{q''_{c_{\text{sat}}}} = 1 + \frac{0.0643\rho_f c_{p,f}}{\rho_g h_{fg}}\left[\frac{\rho_g}{\rho_f}\right]^{1/4} \Delta T_{\text{sub}} \tag{4.8.54}$$

Single-Phase and Boiling Forced Convection in Channel Flow

The average Nusselt numbers for 12 flush 12.7 × 12.7 mm heaters (4 rows of 3 sources per row) operating in FC-77 has been correlated by the following expression:

$$\overline{\text{Nu}_L} = C\left(\text{Re}_{D_h}\right)^m \text{Pr}^{0.11} \tag{4.8.55}$$

For row 1: $C = 0.194$ and $m = 0.60$; for row 2: $C = 0.069$ and $m = 0.69$; for row 3: $C = 0.041$ and $m = 0.74$; and for row 4: $C = 0.029$ and $m = 0.78$. All properties are determined at the inlet temperature except for μ_h, which is evaluated at the heater temperature. Note that when heat sinks are employed, forced convection immersion cooling can support a heat flux of approximately 50 W/cm^2.

Test data have been obtained for a vertical column of ten 6.4 mm × 6.4 mm heaters, with subcooled R-113 flowing in the upward direction. In general, CHF occurred first at the last downstream element in the array, and that CHF values of 100 W/cm^2 were easily attained. The CHF data yielded the following equation:

$$q_c'' = C_5 \mathrm{We}^n V \rho_f h_{fg} \left(\frac{\rho_f}{\rho_g}\right)^{15/23} \left(\frac{L}{D_h}\right)^{1/23} \left[1 + \frac{c_{pf}\Delta T_{\mathrm{sub}}}{h_{fg}}\right]^{7/23} \left[1 + \frac{0.021\rho_f c_{pf}\Delta T_{\mathrm{sub}}}{\rho_g h_{fg}}\right] \tag{4.8.56}$$

where the Weber number, $\mathrm{We} = \rho_f V^2 L/\sigma$. Note that for $\mathrm{We} > 100$, $C_5 = 0.125$ and $n = -8/23$, and for $\mathrm{We} < 10$, $C_5 = 0.254$ and $n = -^1/_2$.

Immersion Cooling Using Jets

Two modes have been studied. In the first, a dielectric liquid jet discharges into a miscible liquid and is said to be submerged; in the second, a liquid jet discharges into an immiscible gas (air) and is said to be free. In general, the average Nusselt number can be expressed as

$$\overline{\mathrm{Nu}} = f\left(\mathrm{Re}^m, \mathrm{Pr}^n, L/d, z/d\right) \tag{4.8.57}$$

where L/d is the ratio of the chip length to orifice diameter, and z/d is the ratio of the jet to heat source distance to the orifice diameter. A free jet is virtually unaffected by the orifice-to-chip distance, and as a consequence the (z/d) term drops out.

Data for single-phase forced convection cooling with free jets are available for 2 × 2 and 3 × 3 heat source arrays. The heat sources were 12.7 × 12.7 mm and the cooling fluid was FC-77. Each heat source was cooled either by a single jet or by a 2 × 2 or 3 × 3 array of jets per source. For all the configurations tested, the average Nusselt number was correlated by a single expression:

$$\overline{\mathrm{Nu}_L} = 3.84\left(0.008\frac{L}{d}n + 1\right)\mathrm{Re}^{1/2}\mathrm{Pr}^{1/3} \tag{4.8.58}$$

where fluid properties are to be evaluated at an average of the heat source and jet inlet temperatures.

Data for single-phase forced convection using submerged jets are available for a 5 × 5 mm vertical heat source cooled by a 1.0-mm-diameter submerged jet of R-113. The Nusselt number at the stagnation point was correlated by

$$\mathrm{Nu}_d = 1.29\mathrm{Re}_d^{1/2}\mathrm{Pr}^{0.4} \tag{4.8.59}$$

Also note that the performance of a submerged liquid jet should be approximately equivalent to gas jet impingement.

Data for two-phase forced convection using free jets have been collected for a single 12.7 × 12.7 mm heat source cooled by either a single jet or a 2 × 2 or 3 × 3 array of jets. The jet diameter, velocity, and jet-to-source distance were varied. The CHF data was correlated by

$$q_c'' = 0.0742\mathrm{We}^{-0.365} V \rho_f h_{fg} \left(\frac{\rho_g}{\rho_f}\right)^{0.239} \left[1 + 0.952\left(\frac{\rho_f}{\rho_g}\right)^{0.118} \left(\frac{c_{pf}\Delta T_{\mathrm{sub}}}{h_{fg}}\right)\right]^{1.414} \tag{4.8.60}$$

Experimental evidence in two-phase forced convection using submerged jets indicates that (1) the temperature overshoot at incipient boiling was very small compared with pool or forced boiling; (2) the boiling curves at various velocities merge to a single curve and that this curve coincides approximately with an upward extrapolation of the pool boiling curve; (3) the CHF varies as the cube of the jet velocity; (4) the CHF is greatly improved by increasing the subcooling; and (5) powers in excess of 20 W (5×5-mm chip) could be accommodated within a 85°C chip temperature.

Defining Terms

External thermal resistance: The thermal resistance from a convenient reference point on the outside of the electronic package to the local ambient.

Internal thermal resistance: The thermal resistance from the device junction inside an electronic package to a convenient reference point on the outside surface of the package.

Immersion cooling: Concerns applications where the coolant is in direct physical contact with the electronic components.

References

Antonetti, V.W. 1993. Cooling electronic equipment — section 517, *Heat Transfer and Fluid Flow Data Books*, Kreith, F., Ed., Genium Publishing, Schenectady, NY.

Antonetti, V.W. and Simons, R.E. 1985. Bibliography of heat transfer in electronic equipment, *IEEE Trans. Components, Hybrids, Manuf. Tech.*, CHMT-8(2), 289–295.

Park, K.A. and Bergles, A.E. 1988. Effects of size of simulated microelectron chips on boiling and critical heat flux, *J. Heat Transfer*, 110, 728–734.

Simons, R.E. 1988. Bibliography of heat transfer in electronic equipment, in *Advances in Thermal Modeling of Electronic Components and Systems*, Vol. 1, Bar-Cohen, A. and Kraus, A.D., Eds., Hemisphere Publishing, New York, 413–441.

Simons, R.E. 1990. Bibliography of heat transfer in electronic equipment, in *Advances in Thermal Modeling of Electronic Components and Systems*, Vol. 2, Bar-Cohen, A. and Kraus, A.D., Eds., ASME Press, New York, 343–412.

Sparrow, E.M., Niethammer, J.E., and Chaboki, A. 1982. Heat transfer and pressure-drop characteristics of arrays of rectangular modules in electronic equipment, *Int. J. Heat Mass Transfer*, 25, 961–973.

Sparrow, E.M., Yanezmoreno, A.A., and Otis, D.R. 1984. Convective heat transfer response to height differences in an array of block-like electronic components, *Int. J. Heat Mass Transfer*, 27, 469–473.

4.9 Non-Newtonian Fluids — Heat Transfer

Thomas F. Irvine, Jr., and Massimo Capobianchi

Introduction

The general characteristics of non-Newtonian fluids are described in Section 3.9 and will not be repeated here. Topics to be included in this section are laminar and turbulent heat transfer in fully developed duct flow, and laminar free convection heat transfer in vertical channels and plates and several other common geometries.

For non-Newtonian flows, except for certain classes of fluids which exhibit a slip phenomenon at solid boundaries, the boundary condition is taken as no-slip or zero velocity at all solid surfaces. For heat transfer analyses, however, the situation is more complicated because there are many different ways to heat a wall, which in turn affects the type of thermal boundary conditions.

In general, the rate of heat transfer from a surface, or the temperature difference between the wall and the fluid, is calculated using the equation $q_c = h_c A_q \Delta T$. Since the heat transfer coefficient can vary

TABLE 4.9.1 Thermal Boundary Conditions for Duct Heat Transfer

1.	Constant wall temperature in both the flow and circumferential direction	Nu_T
2.	Constant heat flux in the flow direction and constant temperature in the circumferential direction	Nu_{H1}
3.	Constant heat flux in the flow and circumferential directions	Nu_{H2}
4.	Constant heat flux per unit volume in the wall with circumferential wall heat conduction	Nu_{H4}

considerably for different thermal boundary conditions, it is important that the boundary conditions be specified correctly. Although the number of thermal boundary conditions is in principle infinite, several classical types have been identified and are in common use. They are usually identified in terms of the Nusselt number, $\mathrm{Nu} = h_c L/k$, with a particular subscript. For example, for duct flow, the symbol Nu_T is used to specify the Nusselt number when the wall temperature is constant in both the flow and peripheral directions. Other thermal boundary conditions are described in Table 4.9.1 for duct heat transfer and will be used throughout this section.

It should be noted that because of the symmetry in circular and parallel plate ducts, Nu_{H1} and Nu_{H2} are identical and are referred to simply as Nu_H. Nu_{H4} with wall conduction is a more-complicated problem where the energy equations must be solved simultaneously in both the wall and the fluid. Such problems are called conjugated. In the Nu_{H4} situation, the designer has the flexibility of affecting the heat transfer by varying either or both the characteristics of the duct wall or the convective fluid. In the heat transfer relations to be considered later, care will be taken to identify the proper thermal boundary conditions using the nomenclature in Table 4.9.1.

Laminar Duct Heat Transfer — Purely Viscous, Time-Independent Non-Newtonian Fluids

As discussed in Section 3.9, a convenient and comprehensive constitutive equation for pseudoplastic fluids (flow index, $n < 1$) is the modified power law equation:

$$\mu_a = \frac{\mu_o}{1 + \frac{\mu_o}{K}(\dot{\gamma})^{1-n}} \tag{4.9.1}$$

Equation (4.9.1) has the characteristic that at low shear rates, the equation approaches that for a Newtonian fluid while at large shear rates it describes a power law fluid. In addition, solutions using Equation (4.9.1) generate a shear rate parameter, β, which describes whether any particular system is in the Newtonian, transitional, or power law region. For duct flow, β is given by

$$\beta = \frac{\mu_o}{K}\left(\frac{\bar{u}}{D_H}\right)^{1-n} \tag{4.9.2}$$

If $\log_{10} \beta > 2$: Power law region
If $\log_{10} \beta < -2$: Newtonian region
If $-2 \le \log_{10} \beta \le 2$: Transition region

For fully developed flow, the characteristic length is the hydraulic diameter, D_H, and the fluid temperature is the “bulk” temperature defined as

$$T_b = \frac{1}{A_c \bar{u}} \int_{A_c} uT dA_c \tag{4.9.3}$$

Figure 4.9.1 illustrates the values of Nu_T vs. β for a circular duct with the flow index, n, as a parameter. It is seen from the figure that the effect of β on Nu_T is only moderate, but for some applications it may

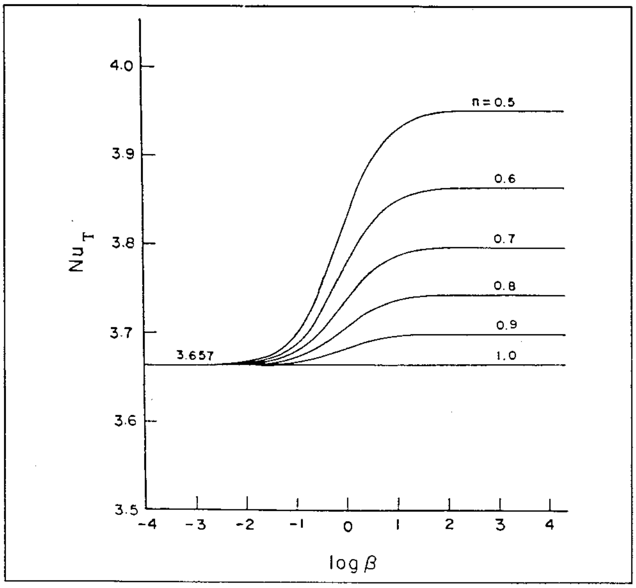

FIGURE 4.9.1 Variation of the fully developed circular duct Nusselt numbers, Nu_T, with the shear rate parameter β and *n*. (From Irvine, T.F., Jr. et al., in *ASME Symposium on Fundamentals of Forced Convection Heat Transfer*, ASME publ. HTD 101, 1988, 123–127. With permission.)

be important to know at what value of β the system is operating. The situation is similar for boundary condition Nu_H.

Although Figure 4.9.1 shows the Nusselt number relation graphically, it is convenient to have simple correlation equations to represent the solutions for both boundary conditions. For fully developed Nusselt numbers with values of $0.5 \le n \le 1.0$ and $10^{-4} \le \beta \le 10^4$, Irvine et al. (1988) present the following equation which represents both solutions with a maximum difference of 1.5%:

$$Nu = \frac{Nu_N (1+\beta)}{1 + \dfrac{Nu_N \beta}{Nu_P}} \tag{4.9.4}$$

The Newtonian Nusselt numbers are $Nu_N = 3.6568$ for Nu_T, and $Nu_N = 4.3638$ for Nu_H. In addition, Table 4.9.2 lists the power law Nusselt numbers, Nu_{TP} and Nu_{HP}, for $\log_{10} \beta = 4$.

Graetz solutions for the thermal entrance lengths are also available. They assume that the velocity profile is fully developed at the duct entrance and present the duct lengths required for the Nusselt

TABLE 4.9.2 Power Law Nu_T and Nu_H Solutions for a Circular Duct ($\log_{10} \beta = 4$)

n	Nu_{TP}	Nu_{HP}
1.0 (Newtonian)	3.6568	4.3638
0.9	3.6934	4.4109
0.8	3.7377	4.4679
0.7	3.7921	4.5385
0.6	3.8605	4.6281
0.5	3.9494	4.7456

Source: Irvine, T.F., Jr. et al., in *ASME Symposium on Fundamentals of Forced Convection Heat Transfer*, ASME publ. HTD 101, 1988, 123–127.

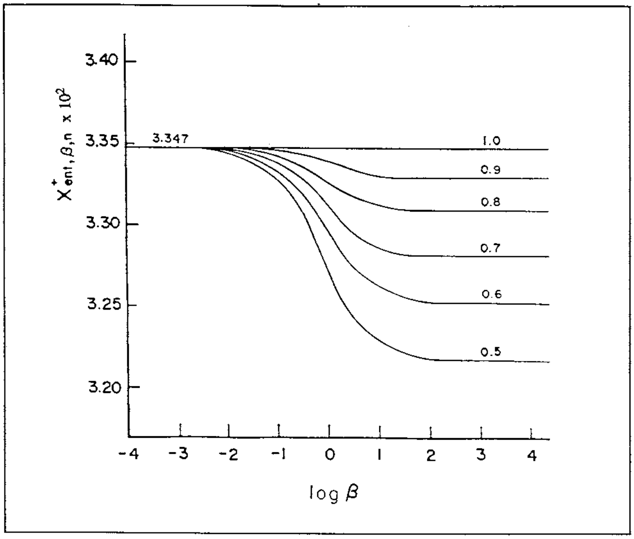

FIGURE 4.9.2 Thermal entrance lengths vs. shear rate parameter β and n for Nu_T in circular ducts. (From Irvine, T.F., Jr. et al., in *ASME Symposium on Fundamentals of Forced Convection Heat Transfer*, ASME publ. HTD 101, 1988, 123–127. With permission.)

TABLE 4.9.3 Values of Circular Duct Thermal Entrance Lengths for Nu_T and Nu_H for Use in Equation 4.9.5

n	Nu_T, $x^+_{\mathrm{ent},P} \times 10^2$	Nu_H, $x^+_{\mathrm{ent},P} \times 10^2$
1.0 (Newtonian)	3.347	4.309
0.9	3.326	4.281
0.8	3.306	4.248
0.7	3.279	4.210
0.6	3.250	4.166
0.5	3.213	4.114

Source: Irvine, T.F., Jr., et al., in *ASME Symposium on Fundamentals of Forced Convection Heat Transfer*, ASME publ. HTD 101, 1988, 123–127.

numbers to reach within 1% of the fully developed values. Figure 4.9.2 shows these thermal entrance lengths for Nu_T thermal boundary condition. The situation is similar for boundary condition Nu_H.

A correlation equation for the thermal entrance lengths for both the Nu_T and Nu_H boundary conditions by Irvine et al. (1988) represents the numerical solutions within 0.5% for $0.5 \le n \le 1.0$ and $-4 \le \log_{10} \beta \le 4$. Table 4.9.3 lists the power law thermal entrance lengths which are needed to evaluate the following correlation equation:

$$x^+_{\mathrm{ent},\beta,n} = \frac{x^+_{\mathrm{ent},N}(1+\beta)}{1+\dfrac{x^+_{\mathrm{ent},N}(\beta)}{x^+_{\mathrm{ent},P}}} \tag{4.9.5}$$

where $x^+_{\mathrm{ent},\beta,n}$ is the modified power law dimensionless entrance length defined as $x^+_{\mathrm{ent},\beta,n} = (x_{\mathrm{ent},\beta,n}/D_H)/Pe$, and $x^+_{\mathrm{ent},N}$ and $x^+_{\mathrm{ent},P}$ are the Newtonian and power law values, respectively. The Newtonian dimensionless entrance lengths are $x^+_{\mathrm{ent},N} = 0.03347$ for Nu_T and $x^+_{\mathrm{ent},N} = 0.04309$ for Nu_H.

Only one noncircular geometry using the modified power law equation has been published in the archival literature for laminar fully developed heat transfer (Capobianchi and Irvine, 1992). A correlation equation for Nu_{H1} for annuli with constant heat flux at the inner wall and the outer wall insulated is

$$n<1 \qquad \mathrm{Nu}_{H1}=\frac{1+\beta}{\dfrac{1}{\mathrm{Nu}_{H1,N}}+\dfrac{\beta}{\mathrm{Nu}_{H1,P}}} \tag{4.9.6}$$

Nusselt numbers for square ducts and power law fluids can be found in Chandrupatla and Sastri (1977) and, for isosceles triangular ducts, in Cheng (1984). Thermally developing and thermally developed laminar heat transfer in rectangular channels has been studied by Hartnett and Kostic (1989).

For other cross-sectional shapes, a power law approximate correlation has been proposed by Cheng (1984):

$$\mathrm{Nu}_P=\mathrm{Nu}_N\left[\frac{(a+bn)}{(a+b)n}\right]^{1/3} \tag{4.9.7}$$

where a and b are the Kozicki geometric constants listed in Table 3.9.3 in the section on non-Newtonian flows. Equation (4.9.7) applies to any thermal boundary condition. For circular ducts, Equation 4.9.7 predicts the correct solution for both Nu_T and Nu_H.

Turbulent Duct Flow for Purely Viscous Time-Independent Non-Newtonian Fluids

It is known that in turbulent flow, the type of thermal boundary conditions has much less effect than in laminar flow. Therefore, turbulent flow heat transfer investigations are often reported without specifying the thermal boundary conditions. Yoo (1974) has presented an empirical correlation for turbulent heat transfer in circular ducts for purely viscous time-independent power law fluids.

$$\mathrm{St}\,\mathrm{Pr}_a^{2/3}=0.0152\,\mathrm{Re}_a^{-0.155} \tag{4.9.8}$$

Equation (4.9.8) describes all of the experimental data available in the literature at the time with a mean deviation of 2.3%. Equation (4.9.8) is recommended in order to predict the turbulent fully developed heat transfer in the ranges $0.2 \le n \le 0.9$ and $3000 \le \mathrm{Re}_a \le 90{,}000$. The Reynolds number and Prandtl numbers in Equation (4.9.8) are based on the apparent viscosity at the wall, μ_a, i.e.,

$$\mathrm{Re}_a=\frac{\rho\bar{u}D_H}{\mu_a} \tag{4.9.9}$$

$$\mathrm{Pr}_a=\frac{\mu_a c_p}{k} \tag{4.9.10}$$

In order to evaluate Equation (4.9.9) and Equation (4.9.10) in terms of the rheological properties and operating parameters, an expression must be obtained for μ_a in terms of these quantities. The value of μ_a is evaluated by considering that μ_a is determined from fully developed laminar circular tube power law fluid flow for which it can be shown that (Irvine and Karni, 1987)

$$\mu_a=K\left(\frac{3n+1}{4n}\right)^{n-1}\left(\frac{8\bar{u}}{D_H}\right)^{n-1} \tag{4.9.11}$$

assuming that the quantities K, n, c_p, and k are constant. It is also of interest that the Prandtl number is no longer a thermophysical property for power law fluids but depends upon the average velocity, $\bar{u}$, and the hydraulic diameter, D_H.

Hartnett and Rao (1987) have investigated fully developed turbulent heat transfer for a rectangular duct with a 2:1 aspect ratio and propose the following equation which generally agreed with their experimental data within ±20%:

$$\mathrm{Nu} = (0.0081 + 0.0149n)\mathrm{Re}_a^{0.8}\mathrm{Pr}_a^{0.4} \tag{4.9.12}$$

Viscoelastic Fluids

An important characteristic of viscoelastic fluids is their large hydrodynamic and thermal entrance lengths. Cho and Hartnett (1982) have reported hydrodynamic entrance lengths of up to 100 diameters and thermal entrance lengths up to 200 to 800 diameters depending upon the Reynolds and Prandtl numbers. These can be compared with Newtonian fluids entrance lengths which are of the order of 10 to 15 diameters. Therefore, care must be used in applying fully developed relations to practical situations.

Cho et al. (1980) reported heat transfer measurements in the thermal entrance region and recommend the following empirical equation for saturated aqueous polymer solutions for $6000 \le \mathrm{Re}_a$ and x/D_H values up to 450:

$$J_H = 0.13\left(x/D_H\right)^{-0.24}\mathrm{Re}_a^{-0.45} \tag{4.9.13}$$

where $J_H = \mathrm{St}\,\mathrm{Pr}_a^{2/3}$ and $\mathrm{St} - h_c/\rho c_p\,\bar{u}$.

All of the reported fully developed turbulent flow heat transfer measurements have been plagued by solute and solvent, thermal entrance, and degradation effects, and thus there is considerable scatter in the results. Degradation effects can be reduced or eliminated by using large amounts of polymer (500 to 10,000 wppm) so that the solution becomes saturated. Cho and Hartnett (1982) attempted to eliminate these effects by using a thermal entrance length of 430 diameters and saturated polymer solutions which should yield maximum heat transfer reductions. Their experimental results for fully developed heat transfer were correlated for a Reynolds number range $3500 \le \mathrm{Re}_a \le 40{,}000$ and concentration solutions of 500 to 5000 wppm of polyacrylamide and polyethylene oxide by

$$J_H = 0.03\mathrm{Re}_a^{-0.45} \tag{4.9.14}$$

For viscoelastic fluids in fully developed (hydrodynamically and thermally) *laminar flow in circular ducts* there is no apparent viscoelastic effect. Thus, the heat transfer relations are the same as those for time-independent fluids such as power law or modified power law fluids. The same situation holds for thermal entrance region heat transfer (Graetz problem). Relations for laminar Nusselt numbers in thermal entrance regions are presented by Cho and Hartnett (1982).

Free Convection Flows and Heat Transfer

Free convection information available in the heat transfer literature up to the present time is concentrated on heat transfer to power law fluids for vertical plates and parallel plate channels. For free convection flows, however, the velocities and thus the shear rates are low and care must be taken that the flow for a particular fluid is in the power law shear rate region before using power law solutions or correlations. Comprehensive review articles on free convection with non-Newtonian fluids have been presented by Shenoy and Mashelkar (1982) and Irvine and Karni (1987).

For a single vertical plate with a modified power law fluid and a thermal boundary condition $\overline{Nu}_T$, in laminar flow, the following relation is recommended by Shenoy and Mashelkar (1982):

$$\overline{Nu}_{TL} = T(n)Gr_{TL}^{1/(2n+2)}\mathrm{Pr}_{TL}^{n/(3n+1)} \tag{4.9.15}$$

where $\overline{Nu}_{TL}$ is the average Nusselt number and

$$\mathrm{Gr}_{TL} = \frac{\rho^2 L^{n+2}}{K^2}\left[g\alpha\left(T_s - T_\infty\right)\right]^{2-n} \tag{4.9.16}$$

$$\mathrm{Pr}_{TL} = \frac{\rho c_p}{k}\left(\frac{K}{\rho}\right)^{2/(n+1)} L^{(n-1)/(2n+2)}\left[g\alpha\left(T_s - T_\infty\right)\right]^{(3n-3)/(2n+2)} \tag{4.9.17}$$

where α is the isobaric thermal expansion coefficient.

In the range $0.5 \le n \le 1$, $T(n)$ can be approximated by

$$T(n) = 0.1636n + 0.5139 \tag{4.9.18}$$

The characteristic dimension in the Nusselt and Grashof numbers is the plate height, L.

For thermal boundary conditions Nu_H, the following relation is also recommended by Shenoy and Mashelkar (1982). Since the heat flux, q_w is specified in this case, the local plate temperature at any x (measured from the bottom of the plate) can be obtained from the local Nusselt number Nu_{Hx}. The heat transfer coefficient is defined in terms of the difference between the wall and free-stream temperatures.

$$\mathrm{Nu}_{Hx} = 0.619\left[\mathrm{Gr}_{Hx}^{(3n+2)/(n+4)}\mathrm{Pr}_{Hx}^{n}\right]^{0.213} \tag{4.9.19}$$

where

$$\mathrm{Gr}_{Hx} = \frac{\rho^2 x^4}{k^2}\left(\frac{g\alpha q_w}{k}\right)^{2-n} \tag{4.9.20}$$

$$\mathrm{Pr}_{Hx} = \frac{\rho c_p}{K}\left(\frac{K}{\rho}\right)^{5/(n+4)} x^{(2n-2)/(n+4)}\left(\frac{g\alpha q_w}{k}\right)^{(3n-3)/(n+4)} \tag{4.9.21}$$

Vertical Parallel Plates

For *power law fluids* and laminar flow, Figure 4.9.3 presents the graphical results of a numerical solution. Of interest are the average Nusselt number $\overline{Nu}_{Tb}$ and the dimensionless average flow velocity between the plates, U_o^+. These are shown on the left and right ordinates respectively in Figure 4.9.3 (Irvine et al., 1982). The characteristic dimension in the Nusselt and Grashof numbers is the plate spacing, b. The dimensionless quantities used in Figure 4.9.3 are defined as follows:

$$\overline{Nu}_{Tb} = \frac{\bar{h}_c b}{k} \qquad U_o^+ = \frac{b u_o}{L u^*}$$

$$\mathrm{Pr}_g = \frac{\rho c_p}{k}\left[\frac{\nu_k^{1/(2-n)}}{\left(\frac{L}{b}\right)^{(1-n)/(2-n)} b^{(2n-2)/(2-n)}}\right] \qquad \nu_K = \frac{K}{\rho}$$

$$\mathrm{Gr}_g = \frac{g\alpha\left(T_s - T_\infty\right) b^{(n+2)/(2-n)}}{\nu_K^{2/(2-n)}\left(\frac{L}{b}\right)^{n/(2-n)}} \qquad u^* = \frac{\nu_K^{1/(2-n)}\, b^{(1-2n)/(2-n)}}{L^{(1-n)/(2-n)}}$$

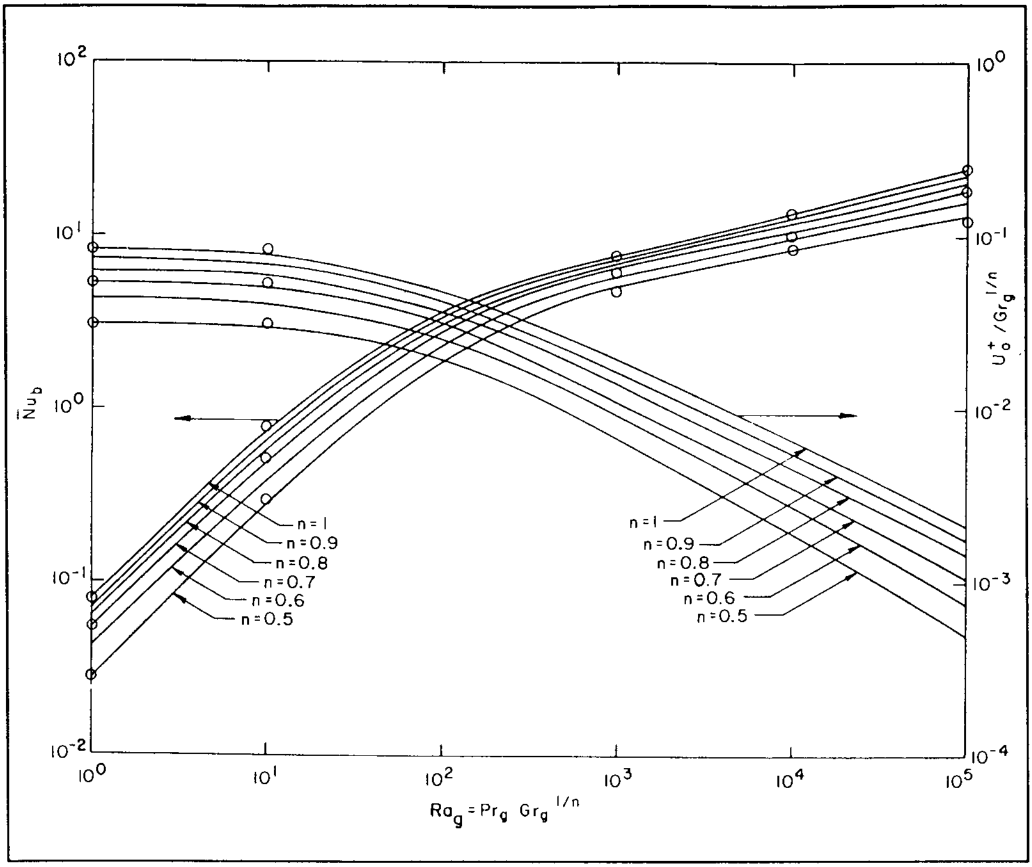

FIGURE 4.9.3 Free convection average Nusselt number, $\overline{Nu}_b$ and dimensionless average velocity U_o^+ between vertical plates for a power law fluid vs. generalized Raleigh number for the Nu_T boundary condition. (From Irvine, T.F., Jr. et al., ASME Paper 82-WA/HT-69, 1982. With permission.)

For vertical parallel plates for the average Nusselt number, $\overline{Nu}_{Hb}$, and the between plate average velocity, Schneider and Irvine (1984) have presented graphical results similar to Figure 4.9.3.

Lee (1992) has presented a numerical solution for laminar flow of a *modified power law fluid* between vertical plates. Lee has also calculated thermal entrance regions and shown that if a parallel plate system is actually operating in the transition region and if the power law solution is used, both the total heat transfer and the velocity between plates can differ by over an order of magnitude. It is important to consider the shear rate parameter in order to determine which free convection solution to use.

Sphere and Horizontal Cylinder — Power Law Fluids

For flow over a sphere, the correlation for power law fluids by Amato and Tien (1976) is

$$\overline{Nu}_{Tr} = CZ^D \tag{4.9.22}$$

where

$$Z = \mathrm{Gr}_{Tr}^{1/(2n+2)}\,\mathrm{Pr}_{Tr}^{n/(3n+1)} \tag{4.9.23}$$

and

$$C = 0.996 \pm 0.120, \quad D = 0.682 \qquad \text{for } Z < 10$$

$$C = 0.489 \pm 0.005, \quad D = 1.10 \qquad \text{for } 10 \le Z \le 40$$

where the characteristic dimension in all dimensionless variables is the sphere radius, r, and Gr_{Tr} and Pr_{Tr} are defined in Equation (4.9.16) and Equation (4.9.17).

For pseudoplastic fluids flowing over a cylinder, an experimental correlation proposed by Gentry and Worllersheim (1974) for the average Nusselt number, $\overline{Nu}_{TD}$, is

$$\overline{Nu}_{TD} = \frac{\bar{h}_c D}{k} = 1.19\left(\mathrm{Gr}_{TD}\,\mathrm{Pr}_{TD}\right)^{0.2} \tag{4.9.24}$$

where Gr_{TD} and Pr_{TD} are defined as in Equation (4.9.16) and Equation (4.9.17) with the cylinder diameter, D, being used instead of L.

References

Acrivos, A. 1960. A theoretical analysis of laminar natural convection heat transfer to non-Newtonian fluids, *AIChE J.*, 6, 584–590.

Amato, W.S. and Tien, C. 1976. Free convection heat transfer from isothermal spheres in polymer solutions, *Int. J. Heat Mass Transfer*, 19, 1257–1266.

Capobianchi, M. and Irvine, T.F., Jr. 1992. Predictions of pressure drop and heat transfer in concentric annular ducts with modified power law fluids, *Wärme Stoffübertragung*, 27,209–215.

Chandrupatla, A.R. and Sastri, V.M. 1977. Laminar forced convection heat transfer of a non-Newtonian fluid in a square duct, *Int. J. Heat Mass Transfer*, 20, 1315–1324.

Cheng, J.A. 1984. Laminar Forced Convection Heat Transfer of Power Law Fluids in Isosceles Triangular Ducts, Ph.D. Thesis, Mechanical Engineering Department, State University of New York at Stony Brook.

Cho, Y.I. and Hartnett, J.P. 1982. Non-Newtonian fluids in circular pipe flow, *Adv. Heat Transfer*, 15, 59–141.

Cho, Y.I., Ng, K.S., and Hartnett, J.P. 1980. Viscoelastic fluids in turbulent pipe flow — a new heat transfer correlation, *Lett. Heat Mass Transfer*, 7, 347.

Gentry, C.C. and Wollersheim, D.E. 1974. Local free convection to non-Newtonian fluids from a horizontal isothermal cylinder, *ASME J. Heat Transfer*, 96, 3–8.

Hartnett, J.P. and Kostic, M. 1989. Heat transfer to Newtonian and non-Newtonian fluids in rectangular ducts, *Adv. Heat Transfer*, 19, 247–356.

Hartnett, J.P. and Rao, B.K. 1987. Heat transfer and pressure drop for purely viscous non-Newtonian fluids in turbulent flow through rectangular passages, *Wärme Stofffüberetragung*, 21, 261.

Irvine, T.F., Jr. and Karni, J. 1987. Non-Newtonian flow and heat transfer, in *Handbook of Single Phase Convective Heat Transfer*, John Wiley & Sons, New York, 20-1–20-57.

Irvine, T.F., Jr., Wu, K.C., and Schneider, W.J. 1982. Vertical Channel Free Convection to a Power Law Fluid, ASME Paper 82-WA/HT-69.

Irvine, T.F., Jr., Kim, S.C., and Gui, F.L. 1988. Graetz problem solutions for a modified power law fluid, in *ASME Symposium on Fundamentals of Forced Convection Heat Transfer*, ASME publ. HTD 101, pp. 123–127.

Lee, S.R. 1992, A Computational Analysis of Natural Convection in a Vertical Channel with a Modified Power Law Fluid, Ph.D. Thesis, Mechanical Engineering Department, State University of New York at Stony Brook.

Schneider, W.J. and Irvine, T.F., Jr. 1984. Vertical Channel Free Convection for a Power Law Fluid with Constant Heat Flux, ASME Paper 84-HT-16.

Shenoy, A.V. and Mashelkar, R.A. 1982 Thermal convection in non-Newtonian fluids, *Adv. Heat Transfer*, 15, 143–225.

Yoo, S.S. 1974. Heat Transfer and Friction Factors for Non-Newtonian Fluids in Turbulent Pipe Flow, Ph.D. Thesis, University of Illinois at Chicago Circle.

Further Information

Other sources which may be consulted for more detailed information are Cho and Hartnett (1982), Shenoy and Mashelkar (1982), Irvine and Karni (1987), and Hartnett and Kostic (1989).

4.10 Bioheat Transfer

Kenneth R. Diller, Jonathan W. Valvano, and John A. Pearce

Introduction

Analysis and control of heat transfer processes in living systems involves phenomena not encountered in systems that are not alive. For example, there is a continuous flow of blood through tissues and organs via a complex network of branching vessels. Heat exchange processes are influenced by vascular geometry, which consists of arteries and veins with countercurrent flow over large portions of the network of pairs. For some physiological conditions, arterial and venous blood temperatures are different — neither is equal to the local tissue temperature — and these temperature differences may vary as a function of many transient physiological and physical parameters. Mechanisms of regulation for the thermal state in tissue are quite nonlinear and have presented a major challenge to understand and model. Nonetheless, thermoregulatory processes are critical to the maintenance of life and must be accounted for in the design of many types of systems that interface with humans and animals.

Although considerable progress has been made in defining and modeling thermal processes in living systems, especially so over the past 15 years, many important problems remain. This chapter provides a brief discussion of the present state of knowledge of some of the more active areas of bioheat transfer. Greater detail and additional areas of application of bioheat transfer may be found among the references cited.

Coupling Temperature History to Rate Processes

Although the processes of life are observed at the system (macroscopic) and microscopic levels of resolution, the true essence of life lies in the multitudinous biochemical phenomena that occur continuously throughout all organisms. Over the past 50 years the science of biochemistry has elucidated many of the governing life processes at the molecular level. Today, the major frontier of knowledge in the life sciences is associated with molecular biology. Increasingly, bioengineers are collaborating with molecular biologists to understand and manipulate the molecules and biochemical processes that constitute the basis of life.

Temperature is a primary controlling parameter in the regulation of these rate processes. The study of thermal biology has identified that the rates of nearly all physiological functions are altered by 6 to 10% per degree Celsius over a wide a range of thermal states produced in response to environment conditions [1]. Likewise, temperature is often altered during therapeutic or diagnostic procedures to produce or measure a targeted effect, based on the fact that a change in local temperature will have a large effect on biochemical process rates. Thus, knowledge of how temperature can be monitored and/or controlled in living tissues is of great value in the assessment of normal physiological function and treatment of pathological states.

In assessing the effects of temperature alterations on biochemical rate processes, two broad categories of state changes can be considered: temperatures above and below the normal physiological thermal state. An extensive review of these thermal domains has been published recently, to which the reader is referred for further details and bibliography [2]. A summary of some of the most important and recent advances in bioheat transfer will be discussed in this chapter.

Tissue Thermal Transport Properties

The transport of thermal energy in living tissue is a complex process involving multiple phenomenological mechanisms including conduction; convection; radiation; metabolism; evaporation; and phase change. The equilibrium thermal properties presented in this chapter were measured after temperature stability had been achieved.

Thermal probe techniques are used frequently to determine the thermal conductivity and the thermal diffusivity of biomaterials [3–6]. Common to these techniques is the use of a thermistor bead as a heat source or a temperature sensor. Various thermal diffusion probe techniques [7] have been developed from Chato's first practical use of the thermal probe [3]. Physically, for all of these techniques, heat is introduced to the tissue at a specific location and is dissipated by conduction through the tissue and by convection with blood perfusion.

Thermal probes are constructed by placing a miniature thermistor at the tip of a plastic catheter. The volume of tissue over which the measurement occurs depends on the surface area of the thermistor. Electrical power is delivered simultaneously to a spherical thermistor positioned invasively within the tissue of interest. The tissue is assumed to be homogeneous within the milliliter surrounding the probe. The electrical power and the resulting temperature rise are measured by a microcomputer-based instrument. When the initial tissue temperature is just below the freezing point, the thermistor heat is removed by conduction and by latent heat. In this situation, the instrument measures effective thermal properties that are the combination of conduction and latent heat.

By taking measurements over a range of temperatures, the processes of conduction and latent heat can be separated. When the tissue is perfused by blood, the thermistor heat is removed by conduction and by heat transfer due to blood flow near the probe. *In vivo*, the instrument measures effective thermal properties that are the combination of conductive and convective heat transfer. Thermal properties are derived from temperature and power measurements using equations that describe heat transfer in the integrated probe/tissue system.

The following five complexities make the determination of thermal properties a technically challenging task:

- Tissue heat transfer includes conduction, convection, radiation, metabolism, evaporation, and phase change. It is difficult but necessary to decouple these different heat transfer mechanisms.
- Mechanical and thermal interactions between the probe and tissue are complex and must be properly modeled to achieve accurate measurements. When the probe is inserted into living tissue, a fluid pool may form around the probe because of the mechanical trauma. Because the probe is most sensitive to the tissue closest to it, the presence of a pool of blood and other fluids will significantly alter the results. Tissue damage due to probe insertion may also occur *in vitro*.
- Tissue structure is quite heterogeneous within each sample. Thus, the probe (which returns a single measurement value) measures a spatial average of the tissue properties surrounding the active elements. Unfortunately, the spatial average is very nonuniform [8]; the probe is most sensitive to the tissue immediately adjacent to it. It is important to control this effective measurement volume. If the effective volume is too small, the measurement is highly sensitive to the mechanical/thermal contact between the probe and tissue. If the effective volume is too large, then the measurement is sensitive to the boundary conditions at the surface of the tissue sample.
- Significant sample-to-sample and species-to-species variabilities exist. One must be careful when extrapolating results obtained in one situation to different situations.
- Tissue handling is critical. Thermal properties are dependent on temperature and water content [9–12]. Blood flow, extracellular water, and local metabolism are factors that strongly affect heat transfer in living tissue, but are difficult to determine or control experimentally. Once a tissue dies, if handled improperly significant water fluxes that will affect tissue thermal properties will occur. Tissues should be stored in a slightly hypertonic saline buffer or on a saline-moistened surgical gauzepad and wrapped in aluminum foil and kept at 4°C to minimize tissue mass transfer.

Currently, no method can simultaneously quantify the major three parameters: intrinsic tissue thermal conductivity, k_m; the tissue thermal diffusivity, α_m; and perfusion, w. The knowledge of k_m is required prior to the perfusion measurement or, even when k_m is measured in the presence of perfusion, the thermal diffusivity cannot be measured [6, 13].

Background

There are many good reviews of techniques to measure thermal properties [10, 14–16]. *Thermophysical Properties of Matter* is a 10-volume set that catalogs thermal properties. Volumes 1 and 3 contain thermal conductivity data, and volume 10 contains thermal diffusivity data. Extensive reviews of measurement techniques exist as prefaces to each volume of the set. Additional thermal property data can be found in Kreith and Bohn [17]. Chato has written an excellent chapter in *Heat Transfer in Medicine and Biology*, which reviews techniques to measure thermal properties of biologic materials [10]. Valvano has documented the temperature dependence of tissue thermal properties [11, 12] and Duck has written an excellent review chapter on this subject [18].

The thermal diffusion probe was conceived by Chato [3, 10]. Significant developments were obtained by Balasubramaniam, Bowman, Chen, Holmes, and Valvano [4,19–27]. Patel and Walsh have applied the self-heated thermistor technique to nondestructive surface measurements [8, 24–26]. Unfortunately, surface probes are unreliable due to poor probe–tissue contact and uncertain boundary conditions at the tissue surface [8, 24].

Self-heated thermistors have been used to measure perfusion [4, 9, 19, 20, 22–24]. Effective thermal conductivity, k_{eff}, is the total ability of perfused tissue to transfer heat in the steady state. k_{eff} is the combination of conduction (due to intrinsic thermal conductivity, k_m) and convection (due to perfusion.) Measurements of k_{eff} are very sensitive to perfusion. The limitation of most techniques is that the intrinsic tissue thermal conductivity must be known in order to measure perfusion accurately. Holmes and Chen use a combination of steady state and transient heating modes to determine perfusion without requiring a no-flow calibration measurement [13, 19, 20]. The uncertainty of k_m significantly limits the perfusion accuracy [9].

Measurement of Thermal Conductivity and Diffusivity

Methods

In the constant temperature heating technique, the instrument first measures the baseline tissue temperature, T_0. Then, an electronic feedback circuit applies a variable voltage, $V(t)$, in order to maintain the average thermistor temperature at a predefined constant, T_h. The electrical circuit used to implement the constant temperature heating technique is shown in Figure 4.10.1. Three high-quality, gold-plated, electromagnetic relays are used to switch the thermistor (R_s) between "heat" and "sense" mode. The figure shows the position of the three relays in "heat" mode.

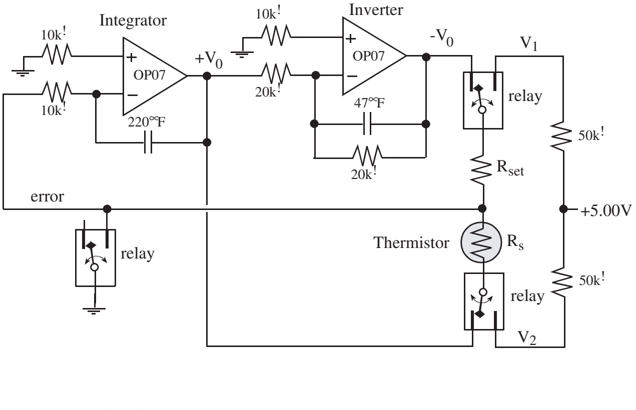

FIGURE 4.10.1 Electrical circuit for the constant temperature heating technique.

Initially, the instrument places the circuit in "sense" mode with the three relays in the opposite position as shown in Figure 4.10.1. A precision +5.00 V reference (PMI REF02) supplies voltage to the four-resistor bridge, formed by the two 50-kΩ, R_{set} and R_s resistors. The voltage difference $V_2 - V_1$ is fed to a differential amplifier, passed through a low-pass filter, then fed to a 12-bit ADC. Resistance calibration is performed to determine the relationship between the ADC sample and the unknown R_s. Next, temperature calibration is performed by placing the thermistor adjacent to an accurate temperature monitor and placing the combination in a temperature-controlled water bath. The thermistor resistance varies nonlinearly with its temperature. For small temperature ranges, Equation (4.10.1) can be used for temperature calibration:

$$R_s = R_o e^{\beta/(T_s+273.15)} \tag{4.10.1}$$

where T_s is the temperature in °C, and R_s is the thermistor resistance in ohms. Equation (4.10.2) yields an accurate fit over a wide range of temperatures:

$$T = \frac{1}{H_0 + H_1 \ln(R) + H_3\left[\ln(R)\right]^3} - 273.15 \tag{4.10.2}$$

In "heat" mode, the integrator/inverter circuit varies the voltage across the thermistor until the thermistor resistance, R_s, matches the fixed resistor, R_{set}. It takes just a few milliseconds for the electrical control circuit to stabilize. Once stable, R_s is equal to R_{set}, meaning the volume average thermistor temperature is equal to a constant. The instrument uses the calibration temperature vs. resistance curve, Equation (4.10.2), to determine the heated temperature T_h from the fixed resistor R_{set}. The power applied to the thermistor is calculated from $(V_0)^2/R_{set}$.

The applied thermistor power includes a steady state and a transient term:

$$P(t) = A + Bt^{-1/2} \tag{4.10.3}$$

where A and B are system constants that depend on the characteristics of the probe and the thermal interaction with the tissue in which it is embedded.

In order to measure thermal conductivity, thermal diffusivity, and tissue perfusion, the relationship between applied thermistor power, P, and resulting thermistor temperature rise, $T(t)=T_h - T_0$, must be known. In the constant temperature method, T is constant. The thermistor bead is treated as a sphere of radius "a" embedded in a homogeneous medium. Because all media are considered to have constant parameters with respect to time and space, the initial temperature will be uniform when no power is supplied to the probe:

$$T_b = T_m = T_0 = T_a + \frac{Q_{met}}{wc_{bl}} \text{ at } t = 0 \tag{4.10.4}$$

where w is the rate of perfusion of blood through the local tissue (ml blood/ml tissue–s) and c_{bl} is the specific heat of blood (kJ/kg.K).

Let V be the temperature rise above baseline, $V = T - T_s$. The thermistor bead temperature rise (V_b) and the tissue temperature rise (V_m) are initially zero.

$$V_b = V_m = 0 \text{ at } t = 0 \tag{5}$$

Assuming the venous blood temperature equilibrates with the tissue temperature and that the metabolic heat is uniform in time and space, the Pennes' bioheat transfer equation in spherical coordinates is given by [28]:

$$\rho_b c_b \frac{\partial V_b}{\partial t} = k_b \frac{1}{r^2}\frac{\partial}{\partial r}\left(r^2 \frac{\partial V_b}{\partial r}\right) + \frac{A + Bt^{-1/2}}{\frac{4}{3}\pi a^3} \quad r < a \tag{4.10.6}$$

$$\rho_m c_m \frac{\partial V_m}{\partial t} = k_m \frac{1}{r^2}\frac{\partial}{\partial r}\left(r^2 \frac{\partial V_m}{\partial r}\right) - wc_{bl} V_m \quad r > a \tag{4.10.7}$$

Perfect thermal contact is assumed between the finite-sized spherical thermistor and the infinite homogeneous perfused tissue. At the interface between the bead and the tissue, continuity of thermal flux and temperature leads to the following boundary conditions:

$$V_b = V_m \text{ at } r = a \tag{4.10.8}$$

$$k_b \frac{\partial V_b}{\partial r} = k_m \frac{\partial V_m}{\partial r} \text{ at } r = a \tag{4.10.9}$$

The other boundary conditions are necessary at positions $r \rightarrow 0$ and $r \rightarrow \infty$. Because no heat is gained or lost at the center of the thermistor:

$$V_b = \text{finite (or } k_b \frac{\partial V_b}{\partial r} = 0) \text{ as } r \rightarrow 0 \tag{4.10.10}$$

Because thermistor power is finite and tissue is infinite, the tissue temperature rise at infinity goes to zero:

$$V_m \rightarrow 0 \text{ as } r \rightarrow \infty \tag{4.10.11}$$

It is this last initial condition that allows the Laplace transform to be used to solve the coupled partial differential equations. The Laplace transform converts the partial differential equations into ordinary differential equations that are independent of time *t*. The steady state solution allows for the determination of thermal conductivity and perfusion [20]:

$$V_b(r) = \frac{A}{4\pi a k_b}\left\{\frac{k_b}{k_m\left(1+\sqrt{z}\right)}\right\} + \frac{1}{2}\left[1 - \left(\frac{r}{a}\right)^2\right] \tag{4.10.12}$$

$$V_m(r) = \frac{A}{4\pi r k_m}\left(\frac{e^{\left(1-r/a\right)\sqrt{z}}}{1+\sqrt{z}}\right) \tag{4.10.13}$$

where *z* is a dimensionless Pennes' model perfusion term ($wc_{bl}a^2/k_m$). The measured thermistor response, ΔT, is assumed be the simple volume average of the thermistor temperature:

$$\Delta T = \frac{\int_0^a V_b\left(r\right) 4\pi r^2 \, dr}{\frac{4}{3}\pi a^3} \tag{4.10.14}$$

Inserting Equation (4.10.12) into Equation (4.10.14) yields the relationship used to measure thermal conductivity, assuming no perfusion [4]:

$$k_m = \frac{1}{\frac{4\pi a\Delta T}{A} - \frac{0.2}{k_b}} \tag{4.10.15}$$

A similar equation allows the measurement of thermal diffusivity from the transient response, again assuming no perfusion [22]:

$$\alpha_m = \left[\frac{a}{\sqrt{\pi}\, B/A\left(1+0.2\frac{k_m}{k_b}\right)}\right]^2 \tag{4.10.16}$$

Rather than using the actual probe radius (a) and probe thermal conductivity (k_b), the following empirical equations are used to calculate thermal properties:

$$k_m = \frac{1}{\frac{c_1\ T}{A} + c_2} \tag{4.10.17}$$

$$\alpha_m = \left[\frac{c_3}{\sqrt{\pi}\, B/A\left(1+0.2\frac{k_m}{c_4}\right)}\right]^2 \tag{4.10.18}$$

The coefficients c_1, c_2, c_3, and c_4 are determined by operating the probe in two materials of known thermal properties. Typically, agar-gelled water and glycerol are used as thermal standards. This empirical calibration is performed at the same temperatures at which the thermal property measurements will be performed.

It is assumed that the baseline tissue temperature, T_0, is constant during the 30-sec transient. Patel has shown that if the temperature drift, dT_0/dt, is larger than 0.1°C/min, then significant errors will occur [8]. The electronic feedback circuit forces T_h to a constant. Thus, if T_0 is constant, ΔT does not vary during the 30-sec transient perod.

The applied power, $P(t)$, varies during the 30-sec transient. Linear regression is used to calculate the steady state and transient terms in Equation (4.10.3). Figure 4.10.2 shows some typical responses. The steady state response (time equals infinity) is a measure of the thermal conductivity. The transient response (slope) indicates the thermal diffusivity.

The time of heating can vary from 10 to 60 s. Shorter heating times are better for small tissue samples and for situations in which baseline tissue temperature drift is present. Another advantage of shorter heating times is the reduction in the total time required to make one measurement. Longer heating times increase the measurement volume and reduce the effect of imperfect thermistor–tissue coupling. Typically, shorter heating times are used *in vivo* because more measurements may be taken over the same time period. On the other hand, longer heating times are used *in vitro* because accuracy is more important than measurement speed.

Probe Design

Thermal probes must be specially constructed in order to measure thermal properties. The two important factors for the thermal probe are thermal contact and transducer sensitivity. The shape of the probe should be chosen in order to minimize trauma during insertion. Any boundary layer between the

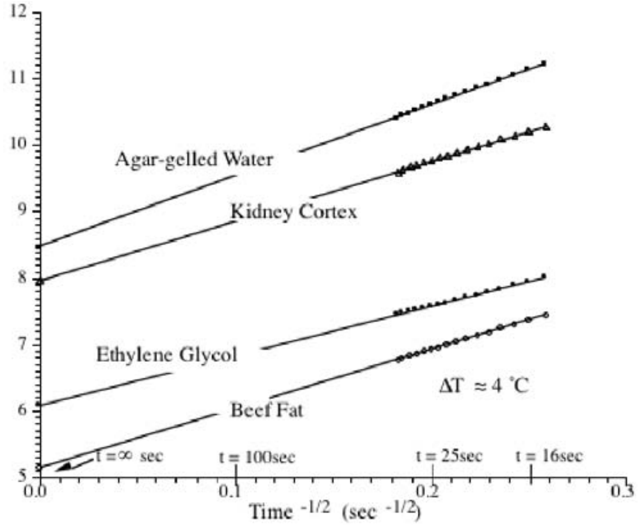

FIGURE 4.10.2 Typical P/T vs. time$^{-1/2}$ data for the constant temperature heating technique.

thermistor and the tissue of interest will cause a significant measurement error. The second factor is transducer sensitivity that is the slope of the thermistor voltage vs. tissue thermal conductivity. Equation (4.10.15) shows for a fixed ΔT, k_m and k_b, the thermistor power (A) increases linearly with probe size (a). Therefore, larger probes are more sensitive to thermal conductivity.

Thermometrics P60DA102M and Fenwal 121-102EAJ-Q01 are glass probe thermistors that make excellent transducers. The glass-coated spherical probes provide a large bead size and a rugged, stable transducer. The Thermometrics BR55KA102M and Fenwal 112-102EAJ-B01 bead thermistors also provide excellent results. For large tissue samples, multiple thermistors can be wired in parallel so that they act electrically and thermally as one large device.

Using multiple thermistors has two advantages. The effective radius, $a = c_1/4\pi$, is increased from about 0.1 cm for a typical single P60DA102M probe to about 0.5 cm for a configuration of three P60DA102M thermistors. The second advantage is that the three thermistors are close enough to each other that the tissue between the probes will be heated by all three thermistors. This cooperative heating tends to increase the effective measurement volume and reduce the probe–tissue contact error. Good mechanical/thermal contact is critical. The probes are calibrated after they are constructed so that the thermistor geometry is incorporated into the coefficients c_1, c_2, c_3, and c_4. The same water bath and probe configuration should be used during the calibration and during the tissue measurements.

Calibration

Calibration is a critical factor when using an empirical technique. For temperatures below 0°C, ice and ethylene glycol are used as thermal standards. For temperatures between 0 and 15°C, agar-gelled water and ethylene glycol can be used as thermal standards. For temperatures between 15 and 75°C, agar-gelled water and glycerol were used. One gram of agar per 100 mL of water should be added to prevent convection. The instrument has been used to measure k_m and α_m of various concentrations of agar-gelled water at 37°C.

A mixture of water and glycerol can be used to estimate the accuracy of the technique. The mass fraction, m, can be used to determine the true thermal properties of the mixture [29]:

$$k_m = m\, k_g + (1 - m)k_w + 1.4\, m\,(m - 1)(k_w - \mathrm{k_g} - 2) - 0.014\, m\,(m - 1)(T - 20°\mathrm{C}) \quad (4.10.19)$$

$$\alpha_m = m\, \alpha_g + (1 - m)\, \alpha_w \quad (4.10.20)$$

Estimation of Heat Transfer Coefficient

Introduction

Heat-flux transducers measure net heat transfer rate at the transducer surface. These sensors can be classified according to their principle of operation [30] as follows:

- Time rate change of thermal energy at the surface
- Temperature difference across a known thermal resistance
- Electric power dissipated in a heater at steady-state

The first type of gauge is too slow to measure unsteady heat transfer flux [30] as found in the body. Moreover, it requires that the surrounding temperature be constant. Unfortunately, the temperature *in vivo* can vary during an experiment. The second type requires a heater and at least two temperature sensors to measure the difference of temperature across a known thermal resistance. This would make the sensor apparatus difficult to realize due to uncertainties in the placement of the sensors and in the thermal resistance. The third has some advantages over the others. First, only one sensor is necessary in order to measure h. Second, the sensor can be a conventional thermistor found in regular Swan–Ganz catheters. Third, the frequency response of the sensor placed in a feedback circuit is typically 10 to 100 Hz, which is high enough to measure the instantaneous h in the ventricles.

Several researchers have addressed the use of the heat flux gauges of the third type for measurements of the heat flux:

- Van Heiningen and colleagues [31] acknowledged that it is possible to use thin-film gauges with constant-temperature anemometer control for heat flux measurements without guard heater. In this case, the sensor overheat ratio must be kept small in order to be calibrated correctly.
- Kraabel et al. [32] used a self-heated thermistor embedded in a conical shape sensor to measure heat flux. In this study, they did not use guard heaters, but rather used their probe for measurements in air. Consequently, they did not cover the sensor with a protective layer.
- Campbell and Diller [33] used a thin film gauge placed in a constant-temperature anemometer to keep the sensor at constant temperature under fluctuating condition. In one of their steady-state calibrations, they calibrate the gauge against the predictable value of Nusselt numbers for cylinders in crossflow.
- Fitzgerald et al. [34] used a small gauge with small overheat ratio (above 2°C) to measure instantaneous heat transfer coefficient in immersed tubes in fluidized beds.
- Wu and colleagues [35] developed an instantaneous heat transfer probe to measure local heat convection coefficients. They used a platinum film as a heater element as well as a temperature sensor. To minimize heat loss due to conduction, they used a guard heater. Despite the fact that they used their probe in the air, they coated the sensor with a plastic film. During their experiments, the average probe temperature was set to be 3°C above the surrounding temperature for the purpose of keeping the stability of the instrumentation.
- Pflum and coworkers [36] used a resistance wire to measure heat convection coefficient in fluidized beds. They pointed out two systematic errors inherent to heated-wire technique: temperature gradients between wires and heat conduction through the sensor substrate and proposed a finite-difference model to correct these errors.
- Beasley and Figliola [37] found that the probe effective area differs from that of the actual film sensor surface area. However, it keeps nearly constant for a wide range of heat convection coefficient for large values of k_c/k_s, where k_c is the thermal conductivity of the coating and k_s is the thermal conductivity of the substrate.
- Figliola and Swaminathan [38] analyzed the influence of thermal boundary conditions around the sensor perimeter during steady state conditions. They found that boundary conditions alter the static calibration of the probe and that this influence is linear. Moreover, they concluded that, for high-convection conditions, the results tend toward those of perfect boundary conditions.

- Griffth et al. [39] measured heat convection coefficients using a small platinum coil. To account for conduction losses, they used a one-dimensional model.
- Holmberg and Womeldorf [40] compared the calibration of three types of sensors in the NIST (National Institute of Standards and Technology — U.S.) convective heat flux calibration facility. Because the sensor disturbs the thermal and velocity boundary layer, they calibrated the sensor output as a function of the heat flux through the surrounding surface. In other words, they did not assume that the heat fluxes through the sensor and through the surroundings are the same. This opened the possibility of calibrating a sensor against predicted values of h.

These works suggest that, in order to measure the heat convection coefficient correctly, one should be aware of the sensor behavior. In addition, they also suggest that: (1) guard heaters are not necessary to correctly evaluate h; (2) a one-dimensional model can correctly account for probe behavior; (3) it is possible to calibrate the sensor output against the environment predicted or known values of h; and (4) a calibration is more useful when it is performed in conditions similar to the conditions to be found in the actual measurement site.

The topologies of the inner surfaces of the heart and blood vessels are very complex. Consequently, it is very difficult to model the heat transfer at the wall analytically. Any attempt to estimate the heat transfer coefficient analytically will be inaccurate because of the complex contours of structures like the endocardium. Thus, the experimental method presented in this section to estimate the heat transfer coefficient is very appropriate. In order to measure the h, a thermoresistive sensor is employed as heating element and temperature sensor. The probe is placed in close contact with the endocardium and self-heated by electric power above the temperature of the circulating blood pool. The power lost by convection can then be used to measure h on the endocardial surface. This method can also be applied to blood vessels.

In this configuration, the instrumentation has two modes of operation: the sensing and the heating modes. The probe can be switched from one mode to another anytime using a circuit similar to that in Figure 4.10.1 [41, 42]. In the sensing mode, the probe measures the surrounding temperature, T_s. In the heating mode, the electrical resistance of the probe and thus its volume-averaged temperature, T_h, is kept constant by a feedback circuit like the one described in dos Santos et al. [41]. In order to measure h, in principle one could use the so-called Newton's law of cooling, Equation (4.10.21):

$$P = hA(T_h - T_s) \tag{4.10.21}$$

where P is the power dissipated by the probe, which can be calculated from the voltage across its terminal and its resistance; T_h is the temperature at the surface of the sensor that is ideally kept constant by the anemometer circuitry in the heating mode; T_s is the fluid temperature measured in the sensing mode; and A is the surface area in contact with the fluid. Because the probe is meant to be used inside the heart, a Swan–Ganz catheter, which has a thermistor embedded close to its tip that can be used to measure h, was chosen as a suitable instrument to make the measurements. However, one should be aware that using this instrument to measure h is complicated by the following factors:

- A portion of the heat is conducted through the back of the sensor.
- The catheter surface temperature depends on h.
- The catheter surface temperature is not the temperature measured by the instrument.
- The sensor area is not easy to measure because the sensor is mounted in the catheter.

Consequently, an empirical calibration technique is used [41].

Calibration

The calibration method consists of using empirical equations to predict h on the wall in circular tubes. The predicted value is then used to calibrate the instrument. Besides the fact that the calibration environment closely matches the environment where the measurement will be performed, turbulent flow was chosen for three reasons. First, it facilitates calibration because the values of h can be easily controlled under this condition by simply changing the flow rate. Second, the fully developed velocity profile is attained for small tube lengths. Third, long-time and widely used empirical equations are available to evaluate h under this condition. Thus, knowing the tube diameter and shape and the mean flow velocity and thermal properties of the water, the evaluation of the heat transfer coefficient from the wall to the circulating flow inside the tube is possible. This means that the sensor output can be calibrated vs. the evaluated average heat convection coefficient (h).

The following empirical equation [41–43] was proposed by dos Santos. Let ΔT be the temperature difference, $T_h - T_s$, between the heated thermistor and the circulating blood.

$$h - c_1\left(\frac{P}{\Delta T}\right)^3 + c_2\left(\frac{P}{\Delta T}\right)^2 + c_3\left(\frac{P}{\Delta T}\right) + c_4 \tag{4.10.22}$$

where c_1, c_2, c_3, and c_4 are calibration constants; dos Santos [42] showed the accuracy of this curve to be 7.4%. The key to accurate measurements lies in how close the calibration configuration matches the actual experimental conditions.

A second calibration equation can be derived analytically, assuming a spherical thermistor of radius a and having a uniform convective boundary condition around its entire surface area [43]. The voltage average temperature rise is ΔT and P is the total steady state power, which is uniformly applied throughout the entire thermistor volume:

$$\frac{\Delta T}{P} = \left(\frac{1}{8\pi a k_i} - \frac{3}{40\pi a k_i}\right) + \left(\frac{1}{4\pi a^2}\right)\frac{1}{h} \tag{4.10.23}$$

This analytic solution suggests the following empirical equation:

$$h = \frac{1}{c_1\dfrac{\Delta T}{P} + c_2} \tag{4.10.24}$$

where c_1 and c_2 are calibration constants.

For a smooth tube of cylindrical cross section, the relation among Nu, Re, and Pr, for turbulent flow conditions, is given by

$$\mathrm{Nu}_D = \frac{(f/8)(\mathrm{Re}_D - 1000)\mathrm{Pr}}{1 + 12.7(f/8)^{1/2}\left(\mathrm{Pr}^{2/3} - 1\right)} \tag{4.10.25}$$

where the friction factor, f, is

$$f = (0.79 \ln \mathrm{Re}_D - 1.64)^{-2} \tag{4.10.26}$$

This correlation is valid for $0.5 < \mathrm{Pr} < 2000$ and $2300 < \mathrm{Re}_D < 5 \times 10^6$. The setup was calibrated with a tube of 1.46 cm diameter and then tested with a tube of 1.27 cm. The flow rates were selected to give a range of h values from 800 to 4000 W/m^{2}K. The average accuracy is about 10%.

In Vivo *Measurements*

The heat convection coefficient was measured in several locations in the right atrium and right ventricle of two pigs [42]. Figure 4.10.3 illustrates that the cylindrical shape of catheter matches the contour of the endocardial surface of the ventricle. For each location, three sets of measurements were taken and the standard deviation of the average values was calculated. For a short period of time (up to 15 heart

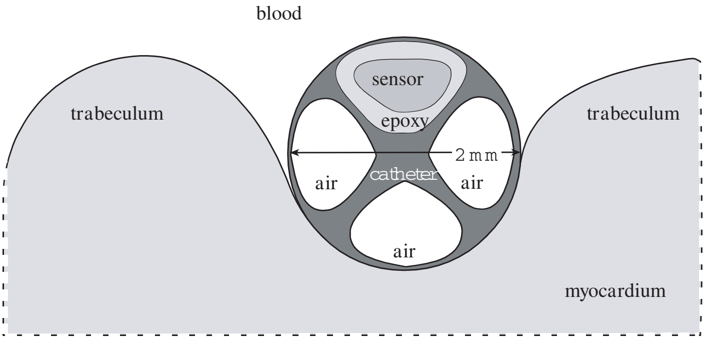

FIGURE 4.10.3 Schematic view of the catheter placed between trabecula of the endocardium.

TABLE 4.10.1 Experimental Measurements of Convective Heat Transfer Coefficient

Position	Average h (W m^2 K^1)	Standard Deviation (W m^2 K^1)	Cardiac Rate (bpm)
A1 (RA)	511	214	120
A2 (RA)	2520	494	110
A3 (RV)	4500	477	120
A4 (RV)	2200	61	120
B1 (RA)	1010	360	120
B2 (RV)	570	170	120
B3 (RV)	4890	381	110
B4 (RV)	1510	107	110

Source: dos Santos, I., Will, J.A., da Rocha, A.F., de O. Nascimento, F.A., Webster, J.G., and Valvano, J.W., *Physiol. Meas.*, 24, 793–804, 2003.42

beats), no changes occurred in h because the temperature, heart rate, cardiac output, and ejection fraction are unlikely to change in such a short period of time. This means that the standard deviation of the average values can be used as an assessment of the performance of the instrument.

Positions A1 and B1 are on the anterior surface of the right atrium located midway between superior vena cava inlet and the tricuspid valve. Position A2 is on the anterolateral surface of the right atrium, just above the tricuspid valve. Position B5 is on the anterior surface of the right ventricle just below the pulmonary valve. Positions A3 and B3 are at the midpoint of the anterolateral surface of the right ventricle. Position A4 and B4 are on the intraventricular septal surface of the right ventricle. Table 4.10.1 gives the measured convective coefficient values.

Temperature-Dependent Thermal Properties

Temperature Dependence of Organ Tissue

When modeling heat transfer in situations in which the temperature range exceeds 10°C, it is important to consider the temperature dependence of the tissue thermal properties. Valvano and colleagues [11] and Valvano and Chitsabesan [12] measured tissue thermal properties as a function of temperature using the constant ΔT thermistor heating technique. The results shown in Table 4.10.2 were derived from *in vitro* measurements taken at 3, 10 17, 23, 30, 37, and 45°C.

The animal tissues were measured from freshly sacrificed dogs, rabbits, and pigs. The normal human tissues were obtained from autopsy. The human cancers were freshly excised. The k_0, k_1, α_0, and α_1 values are the linear fit of the thermal properties as a function of temperature.

$$k = k_0 + k_1\ T \tag{4.10.27}$$

TABLE 4.10.2 Thermal Properties as a Function of Temperature

Tissue	Species	k_0 (mW/cm°C)	k_1 (mW/cm°C^2)	α_0 (cm^2/s)	α_1 (cm^2/s°C)
Adenocarinoma of the breast	Human	4.194	0.03911	0.001617	–0.000049
Cerebral cortex	Human	5.043	0.00296	0.001283	0.000050
Colon cancer	Human	5.450	(at 19°C)	0.001349	(at 19°C)
Fat of spleen	Human	3.431	–0.00254	0.001321	–0.000002
Liver	Human	4.692	0.01161	0.001279	0.000036
Liver	Pig	4.981	0.00800	0.001240	0.000053
Liver	Rabbit	4.668	0.02601	0.001370	0.000178
Lung	Human	3.080	0.02395	0.001071	0.000082
Lung	Human	4.071	0.01176	0.001192	0.000031
Lung	Pig	2.339	0.02216	0.000695	0.000080
Myocardium	Dog	4.869	0.01332	0.001296	0.000058
Myocardium	Human	4.925	0.01195	0.001289	0.000050
Myocardium	Pig	4.841	0.01333	0.001270	0.000051
Pancreas	Dog	4.790	0.00849	0.001287	0.000062
Pancreas	Human	4.365	0.02844	0.001391	0.000084
Pancreas	Pig	4.700	0.00194	0.001530	0.000130
Renal cortex	Dog	4.905	0.01280	0.001333	0.000039
Renal cortex	Human	4.989	0.01288	0.001266	0.000055
Renal cortex	Pig	4.967	0.01176	0.001284	0.000039
Renal cortex	Rabbit	4.945	0.01345	0.001311	0.000027
Renal medulla	Dog	5.065	0.01298	0.001305	0.000063
Renal medulla	Human	4.994	0.01102	0.001278	0.000055
Renal pelvis	Dog	4.930	0.01055	0.001334	0.000052
Renal pelvis	Human	4.795	0.01923	0.001329	0.000011
Spleen	Human	4.913	0.01300	0.001270	0.000047
Spleen	Rabbit	4.863	0.01267	0.001257	0.000042

Source: Pearce, J.S. and Thomsen, S., in *Optical–Thermal Response of Laser-Irradiated Tissue*, Welch, A.J. and van Germert, M.M.C., Eds., Plenum Press, New York, 1995. With permission.

$$\alpha = \alpha_0 + \alpha_1 T \tag{4.10.28}$$

The average thermal properties of these data are

$$k = 4.574 + 0.01403\ T \tag{4.10.29}$$

$$\alpha = 0.001284 + 0.000053\ T \tag{4.10.30}$$

where conductivity is in mW/cm°C; diffusivity is in cm^2/sec and temperature is in °C.

Temperature Dependence of Human Arterial Tissue

Aortic tissue was obtained from a local pathology lab. The thermal probes were placed on the endothelial surface of the aortic wall, and the tissue–probe combination was wrapped in plastic. The tissue surface was kept wet to improve the thermal contact and to prevent drying. The samples were placed in a breaker of saline and the breaker was put into a temperature-controlled water bath. Thermal conductivity and thermal diffusivity were measured 10 times at each temperature 35, 55, 75, and 90°C. The measurement order was varied among 35, 55, 75, and 90°C; 95, 75, 55, and 35°C; 75, 90, 55, and 35°C; and 55, 35, 90, and 75°C. Measurements were obtained from normal and diseased tissue and the plaques were categorized by gross visual observation. The calcified plaques were hard and bony; the fibrous plaques were firm but pliable and the fatty plaques were loose and buttery. The results from 54 tissues are presented in Table 4.10.3 and Table 4.10.4. The column *n* refers to the number of tissue samples. The standard deviation is given in parentheses.

The two-sample *t*-test with $p = 0.05$ was used to determine significant differences. Tissue thermal properties increased with temperature and were significantly less than those of water. The measurement order did

TABLE 4.10.3 Thermal Conductivity[a] of Human Aorta and Atherosclerotic Plaque

Tissue	n	at 35°C	at 55°C	at 75°C	at 90°C
Normal aorta	12	4.76 (0.41)	5.03 (0.60)	5.59 (0.37)	6.12 (0.12)
Fatty plaque	13	4.84 (0.44)	4.97 (0.49)	5.46 (0.54)	5.88 (0.81)
Fibrous plaque	12	4.85 (0.22)	5.07 (0.30)	5.38 (0.38)	5.77 (0.56)
Calcified plaque	17	5.02 (0.59)	5.26 (0.73)	5.81 (0.82)	6.19 (0.85)

[a] mW/cm–°C.

Source: Pearce, J.S. and Thomsen, S., in *Optical–Thermal Response of Laser-Irradiated Tissue*, Welch, A.J. and van Germert, M.M.C., Eds., Plenum Press, New York, 1995. With permission.

TABLE 4.10.4 Thermal Diffusivity[a] of Human Aorta and Atherosclerotic Plaque

Tissue	n	at 35°C	at 55°C	at 75°C	at 90°C
Normal aorta	12	1.27 (0.07)	1.33 (0.11)	1.44 (0.10)	1.56 (0.05)
Fatty plaque	13	1.28 (0.05)	1.32 (0.06)	1.41 (0.11)	1.46 (0.15)
Fibrous plaque	12	1.29 (0.03)	1.36 (0.07)	1.41 (0.10)	1.52 (0.20)
Calcified plaque	17	1.32 (0.07)	1.37 (0.12)	1.53 (0.17)	1.66 (0.20)

[a] 1000 cm^2/s.

Source: Pearce, J.S. and Thomsen, S., in *Optical–Thermal Response of Laser-Irradiated Tissue*, Welch, A.J. and van Germert, M.M.C., Eds., Plenum Press, New York, 1995. With permission.

not affect the measured thermal properties and no difference was found among the thermal conductivity of normal aorta, fatty plaque, and fibrous plaque. The thermal conductivity and thermal diffusivity of calcified plaque were slightly higher than normal aorta, fatty plaque, and fibrous plaque.

Temperature Dependence of Canine Arterial Tissue

Carotid and femoral arteries were harvested immediately *post mortem*. The thermal probes were placed on the endothelial surface of the arterial wall. Thermal conductivity and thermal diffusivity were measured 10 times at each temperature: 25, 35, 45, 55, 65, 75, 85, and 95°C. Measurements were obtained only from normal tissue. The results from 18 tissues are summarized in Equation (4.1031) through Equation (4.10.35).

Canine femoral artery:

$$k\ (\text{mW/cm–°C}) = 3.688 + 0.0062014\ T\ (°\text{C}) \tag{4.10.31}$$

$$\alpha\ (\text{cm}^2/\text{sec}) = 0.001003 + 0.000001381\ \text{T}\ (°\text{C}) \tag{4.10.32}$$

Canine carotid artery:

$$k\ (\text{mW/cm–°C}) = 4.480 + 0.0000164\ T\ (°\text{C}) \tag{4.10.33}$$

$$\alpha\ (\text{cm}^2/\text{sec}) = 0.001159 + 0.000003896\ T\ (°\text{C}) \tag{4.10.34}$$

The two-sample t-test with $p = 0.01$ shows that thermal conductivity and thermal diffusivity are larger in carotid vs. femoral artery. These results could be explained from the fact that the carotid artery contains more collagen than femoral artery does. A tissue with a higher percentage of collagen would have lower thermal properties because collagen is a thermal insulator.

Temperature Dependence of Swine Left Ventricle

Swine myocardial samples were harvested immediately *post mortem*. The thermal probes were placed on the left ventricular muscle. Thermal conductivity and thermal diffusivity were measured 10 times at each temperature: 25, 37. 50, 62, and 76°C. Measurements were obtained only from normal tissue. The results are summarized in Table 4.10.5 andTable 4.10.6.

TABLE 4.10.5 Thermal Conductivity[a] of Myocardial Tissue

Temperature				
25°C	37°C	50°C	62°C	76°C
5.23	5.14	5.17	4.39	5.24
5.07	5.12	4.75	3.30	4.29
5.30	5.21	5.61	5.67	4.83
5.43	5.54	4.22	4.16	5.89
4.68	5.35	4.93	5.33	5.23
5.25	5.08	4.84	5.70	5.39
5.27	5.48	4.42	5.11	4.75
5.28	4.57	4.93	4.99	3.25
5.86	5.76	5.52	5.03	2.69
4.78	5.10	5.88	5.30	5.28
4.75	5.35	5.35	4.67	5.60
4.92	6.02	5.60	5.49	4.68
Mean				
5.15	5.31	5.1	4.93	4.76
Standard deviation				
0.33	0.37	0.51	0.70	0.95

[a] mW•cm^{-1}•K^{-1}.

TABLE 4.10.6 Thermal Diffusivity[a] of Myocardial Tissue

Temperature				
25°C	37°C	50°C	62°C	76°C
0.00151	0.00170	0.00165	0.00159	0.00167
0.00154	0.00147	0.00203	0.00235	0.00249
0.00143	0.00165	0.00151	0.00169	0.00166
0.00146	0.00143	0.00116	0.00191	0.00229
0.00159	0.00160	0.00176	0.00167	0.00173
0.00141	0.00178	0.00179	0.00163	0.00185
0.00165	0.00149	0.00235	0.00143	0.00185
0.00132	0.00206	0.00179	0.00170	0.00199
0.00141	0.00144	0.00147	0.00143	0.00062
0.00168	0.00179	0.00160	0.00180	0.00167
0.00154	0.00156	0.00173	0.00161	0.00173
0.00164	0.00138	0.00171	0.00169	0.00192
Mean				
0.00152	0.00161	0.00171	0.00171	0.00179
Standard deviation				
0.00012	0.00020	0.00031	0.00025	0.00047

[a] cm^2•s^{-1}.

TABLE 4.10.7 Average Thermal Properties

T (°C)	N	M	Species	Tissue	k_m(mW/cm°C)	α_m(1000*cm^2/s)
+0.1	45	6	Bovine	Kidney Cortex	4.54 (±0.16)	1.18 (±0.09)
–5	15	4	Bovine	Kidney Cortex	15.35 (±1.09)	4.71 (±0.99)
–18	18	3	Bovine	Kidney Cortex	13.72 (±0.73)	6.84 (±0.83)
+0.1	66	9	Bovine	Liver	4.17 (±0.13)	1.05 (±0.09)
–5	66	9	Bovine	Liver	13.96 (±2.49)	4.77 (±0.58)
–18	56	8	Bovine	Liver	9.89 (±0.44)	5.71 (±0.74)
+0.1	48	6	Bovine	Muscle	4.25 (±0.37)	1.05 (±0.11)
—	42	7	Bovine	Muscle	13.93 (±1.23)	5.37 (±0.97)
–18	60	8	Bovine	Muscle	10.76 (±1.14)	6.84 (±1.10)
+0.1	21	3	Bovine	Fat	1.93 (±0.12)	0.59 (±0.13)
–5	32	4	Bovine	Fat	2.66 (±0.38)	0.98 (±0.19)
–8	24	4	Bovine	Fat	2.80 (±0.53)	1.54 (±0.57)

Notes: N is the number of measurements and M is the number of tissues. (±0.xx) is the standard deviation of the average.

Source: Pearce, J.S. and Thomsen, S., in *Optical–Thermal Response of Laser-Irradiated Tissue*, Welch, A.J. and van Germert, M.M.C., Eds., Plenum Press, New York, 1995. With permission.

Thermal Properties of Frozen Tissue

The thermal properties of frozen tissue are significantly different from those of normal tissue. Valvano measured frozen tissue thermal properties using the constant ΔT thermistor heating technique [44]. The results shown in Table 4.10.7 were derived from *in vitro* measurements taken at –18, –5, and +0.1°C.

Thermal Properties as a Function of Water and Fat Content

In a global sense, the thermal properties of tissue are determined by the relative concentrations of its constituate parts. Spells found a linear relationship between tissue thermal conductivity and water content [45]:

$$k\ (\text{mW/cm–°C}) = 0.54 + 5.73\ m_{water} \text{ for } m_{water} > 0.2 \tag{4.10.35}$$

where m_{water} is the mass fraction of water in the tissue. Cooper and Trezek found an empirical relationship between thermal conductivity and mass fractions of water, protein, and fat [46]:

$$k\ (\text{mW/cm–°C}) = \rho \sum_n \frac{k_n m_n}{\rho_n} = \rho\left(6.28 m_{water} + 1.17 m_{protein} + 2.31 m_{fat}\right) \tag{4.10.36}$$

Cooper and Trezek [46] found similar relationships for specific heat and density:

$$c\ (\text{J/g-°C}) = \sum_n c_n m_n = 4.2\ m_{water} + 1.09\ m_{protein} + 2.3\ m_{fat} \tag{4.10.37}$$

$$\rho\ (\text{g/cm}^3) = \frac{1}{\sum_n \frac{m_n}{\rho_n}} = \frac{1}{m_{water} + 0.649 m_{protein} + 1.227 m_{fat}} \tag{4.10.38}$$

Effect of Blood Flow on Temperature

Introduction

Bioheat transfer processes in living tissues are often affected by the influence of blood perfusion through the vascular network on the local temperature distribution. When the difference between the temperature of blood and the tissue through which it flows is significant, convective heat transport will occur, altering the temperatures of blood and tissue. Perfusion-based heat transfer interaction is critical to a number of physiological processes such as thermoregulation and inflammation.

The blood–tissue thermal interaction is a function of several parameters, including the rate of perfusion and the vascular anatomy, which vary widely among the different tissues, organs of the body, and pathology. Appendix B contains an extensive compilation of perfusion rate data for many tissues and organs and for many species. The literature on mathematical modeling of the influence of blood perfusion on bioheat transfer phenomena has been reviewed recently by Charney [47]; his paper is highly recommended for readers desiring an in-depth presentation of the topic.

The rate of perfusion of blood through different tissues and organs varies over the time course of a normal day's activities, depending on factors such as physical activity, physiological stimulus, and environmental conditions. Furthermore, many disease processes are characterized by alterations in blood perfusion, and some therapeutic interventions result in an increase or decrease in blood flow in a target tissue. For these reasons, it is very useful in a clinical context to know the absolute level of blood perfusion within a given tissue. Numerous techniques have been developed for this purpose over the past several decades. In some of these techniques, the coupling between vascular perfusion and local tissue temperature is applied to advantage to assess the flow through local vessels via inverse solution of equations that model the thermal interaction between perfused blood and the surrounding tissue.

Pennes [28] published the seminal work on developing a quantitative basis for describing the thermal interaction between tissue and perfused blood. His work consisted of a series of experiments to measure temperature distribution as a function of radial position in the forearms of nine human subjects. A butt-junction thermocouple was passed completely through the arm via a needle inserted as a temporary guideway, with the two leads exiting on opposite sides of the arm. The subjects were unanesthetized so as to avoid the effects of anesthesia on blood perfusion. Following a period of normalization, the thermocouple was scanned transversely across the mediolateral axis to measure the temperature as a function of radial position within the interior of the arm. The environment in the experimental suite was kept thermally neutral during experiments. Pennes' data showed a temperature differential of 3 to 4° between the skin and the interior of the arm; he attributed this to the effects of metabolic heat generation and heat transfer with arterial blood perfused through the microvasculature.

Pennes proposed a model to describe the effects of metabolism and blood perfusion on the energy balance within tissue. These two effects were incorporated into the standard thermal diffusion equation, which is written in its simplified form as:

$$\rho c \frac{\partial T}{\partial t} = \nabla \cdot k \nabla T + (\rho c)_b \omega_b (T_a - T) + q_{met} \tag{4.10.39}$$

Metabolic heat generation, q_{met}, is assumed to be homogeneously distributed throughout the tissue of interest as rate of energy deposition per unit volume. It is assumed that the blood perfusion effect is homogeneous and isotropic and that thermal equilibration occurs in the microcirculatory capillary bed. In this scenario, blood enters capillaries at the temperature of arterial blood, T_a, where heat exchange occurs to bring the temperature to that of the surrounding tissue, T. There is assumed to be no energy transfer before or after the blood passes through the capillaries, so that the temperature at which it enters the venous circulation is that of the local tissue. The total energy exchange between blood and tissue is directly proportional to the density, ρ_b, specific heat, c_b, and perfusion rate, ω_b, of blood through the tissue, and is described in terms of the change in sensible energy of the blood. This thermal transport model is analogous to the process of mass transport between blood and tissue, which is confined primarily to the capillary bed.

A major advantage of the Pennes' model is that the added term to account for perfusion heat transfer is linear in temperature, which facilitates the solution of Equation (4.10.39). Since the publication of this work, the Pennes' model has been adapted by many researchers for the analysis of a variety of bioheat transfer phenomena. These applications vary in physiological complexity from a simple homogeneous volume of tissue to thermal regulation of the entire human body [48, 49]. As more scientists have evaluated the Pennes' model for application in specific physiological systems, it has become increasingly clear that many of the assumptions foundational to the model are not valid.

For example, Chato [50], Chen and Holmes [51], and Weinbaum et al. [52–64] have demonstrated very convincingly that thermal equilibration between perfused blood and local tissue occurs in the precapillary arterioles and that, by the time blood flows into vessels 60 μm in diameter and smaller, the equilibration process is complete. Therefore, no significant heat transfer occurs in the capillary bed; the exchange of heat occurs in the larger components of the vascular tree. The vascular morphology varies considerably among the various organs of the body, which contributes to the need for specific models for the thermal effects of blood flow (as compared to the Pennes' model that incorporates no information concerning vascular geometry). As a consequence of these physiological realities, it would appear that the validity of the Pennes' model is questionable.

Many investigators have developed alternative models for the exchange of heat between blood and tissue. These models have accounted for the effects of vessel size [50, 51, 65]; countercurrent heat exchange [65–69]; and a combination of partial countercurrent exchange and bleed-off perfusion [52–64]. All of these models provided a larger degree of rigor in the analysis, but at the compromise of greater complexity and reduced generality. Some of these models have been the subject of considerable debate concerning their validity and range of appropriate application [70–73]. These studies also led to an increased appreciation of the necessity for a more explicit understanding of the local vascular morphology as it governs bioheat transfer, which has given rise to experimental studies to measure and characterize the three-dimensional architecture of the vasculature in tissues and organs of interest.

It is quite interesting that, in the context of the preceding studies to improve on the widely applied but questioned Pennes' model, the 50th anniversary of the publication of Pennes' paper was recognized recently [74]. For this occasion Wissler [73] returned to Pennes' original data and analysis and reevaluated his work. Given the hindsight of five decades of advances in bioheat transfer plus greatly improved computational tools and better constitutive property data, Wissler's analysis pointed out further flaws in Pennes' work that had not been appreciated previously. However, he also showed that much of the criticism directed toward the Pennes' model is not justified, in that his improved computations with the model demonstrated a good standard of agreement with the experimental data. Thus, Wissler's conclusion is that "those who base their theoretical calculations on the Pennes' model can be somewhat more confident that their starting equations are valid." The quantitative analysis of the effects of blood perfusion on the internal temperature distribution in living tissue remains a topic of active research after a half century of study.

Limitations of Pennes' Model

Pennes' model was the first major effort in quantifying the heat transfer contribution of perfusion. It was developed for describing the transverse temperature profile in the human forearm. The model is unique in that the perfusion term is very simple. The "bioheat equation" was previously shown as Equation (4.10.39).

The limitations of this model arise from the erroneous view of the heat transfer process and its anatomical location. Chen and Holmes' analysis of blood vessel thermal equilibration lengths showed that Pennes' concept is incorrect [51]. The thermal equilibration length is defined as the length at which the difference between the blood and tissue temperature decreases to $1/e$ of the initial value. They indicated that thermal equilibration occurs predominantly within the terminal arterioles and venules, and that blood is essentially equilibrated prior to the capillaries. In considering the contribution of perfusion as a nondirectional term, the directional convective mechanism is neglected. The model also does not account for specific vascular architecture such as countercurrent arteries and veins. The limitations of Pennes' model have motivated subsequent investigators to develop their own models.

Despite its erroneous concept, the perfusion term of Pennes' model has been widely used and found to be valid for situations other than the forearm. Its wide usage has been mainly due to its simplicity of implementation, especially in analyses in which a closed form analytical solution is sought [22, 75]. Investigators have obtained good temperature predictions for the following circumstances:

- Porcine kidney cortex in the absence of large vessels (diameter > 300 μm) [76]
- Rat liver [5, 22]
- Capillary bleed-off from large vessels [56]

In the last case, Charny compared Weinbaum–Jiji's countercurrent model and Pennes' model against the experimental results of Pennes. The simulations found that Pennes' model is valid in the initial branchings of the largest microvessels from the countercurrent vessels (diameter > 500 μm) in deep tissue. In this case, the microvessel blood temperature is close to arterial temperature. Arkin et al. [77] provide an explanation of the inconsistencies between the two anatomical sites. They suggest that because blood typically travels down successive generations of the vascular branches before equilibrating with the tissue temperature, Charny's claim actually refers to the collective contribution of numerous smaller thermally significant vessels in a region dominated by the large microvessels. The distinction of being thermally significant is based upon the ratio of thermal equilibration length to actual vessel length (ε):

$$\varepsilon = \frac{L_e}{L} \tag{4.10.40}$$

Along with Xu's observations on porcine kidney [76], Pennes' model appears to be applicable to regions in which the vasculature comprises numerous small thermally significant vessels ($\varepsilon \approx 1$).

Continuum Models

Among the continuum formulations of bioheat transfer, the Chen–Holmes model is the most developed. Prior to Chen–Holmes, continuum formulations by Wulff [78] and Klinger [79] addressed the isotropicity of Pennes' perfusion term. However, they did not challenge Pennes' concept of the site of heat exchange. Chen and Holmes [51] formulated their model after analyzing the significance of blood vessel thermal equilibration length. Through this analysis, they quantitatively showed that the major heat transfer processes occur in the 50- to 500-μm diameter vessels and refuted Pennes' paradigm.

In their model, they proposed that larger vessels be modeled separately from smaller vessels and tissue. Larger vessels were distinguished using the ratio of equilibration length to actual vessel length of about one ($\varepsilon \approx 1$) as the criteria. The smaller vessels and tissue were then modeled as a continuum. In a differential control volume of this continuum, they further separated solid tissue from the blood within the vascular space (Figure 4.10.4).

Subsequently, the heat transfer mechanisms can be divided into the contributions from (1) nonequilibrated blood in the thermally significant vessels; (2) blood that has equilibrated with the surrounding tissue; and (3) nearly equilibrated blood. The perfusion term of Pennes is then replaced with three terms:

$$\rho c \frac{\partial T}{\partial t} = \nabla \cdot k \nabla T + (\rho c)_b \, \omega^* \left(T_a^* - T\right) - (\rho c)_b \, \vec{u} \cdot \nabla T + \nabla \cdot k_p \nabla T + q_m \tag{4.10.41}$$

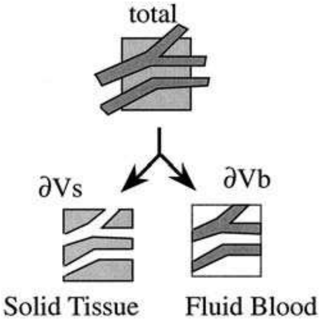

FIGURE 4.10.4 Schematic representation of tissue control volume as used by Chen–Holmes. (From Chen, M.M. and Holmes, K.R., *Ann. NY Acad. Sci.*, 335, 137–150, 1980.)

The second through the fourth terms on the right-hand side arise from each of the three categories described earlier. The second term, $(\rho c)_b \omega^*(T_a^* - T)$, is similar to Pennes except the perfusion and the arterial temperature are specific to the volume being considered. The $\nabla\ (\rho c)_b\ \vec{u} \cdot \nabla T$ term is a directional convective term due to the net flux of equilibrated blood. Finally, the $\nabla \cdot k_p \nabla T$ term is to account for the contribution of the nearly equilibrated blood in a tissue temperature gradient. The nearly equilibrated blood contributes to small temperature fluctuations within the tissue and the effect is modeled as a tensor "perfusion conductivity":

$$k_p = n(\rho c)_b \pi r_b^2\ \vec{V} \cos^2 \gamma \sum_{i=1}^{\infty} \frac{L_e}{L_e^2 \beta_i^2 + 1} \tag{4.10.42}$$

which is a function of local average blood flow velocity vector within the vessel ($\vec{V}$); relative angle (γ) between blood vessel direction and the tissue temperature gradient; the number of vessels (n); and vessel radius (r_b). The Fourier integral spectral wave number (β) can be approximated as the inverse of vessel length. The contribution of this conductivity is minimal except when vessels with large equilibration lengths are considered. However, for this situation, Chen and Holmes recommend that these vessels be treated separately. The assumptions made for their model include: (1) neglecting the mass transfer between vessel and tissue space; and (2) treating the thermal conductivity and temperature within the tissue–blood continuum as that of the solid tissue because the vascular volume is much smaller than that of the solid tissue.

The limitation of this model is that, given the detail required, the model is not easy to implement. Also, the perfusion conductivity term is difficult to evaluate, and distinction within the continuum model is not well defined. Furthermore, the model does not explicitly address the effect of closely spaced countercurrent artery–vein pairs. This model has been applied to the porcine kidney and found to predict temperatures similar to Pennes' model; thus, given the simplicity of the latter, Xu et al. [76] recommended that Pennes be used. Arkin et al. [77] claim that the Chen–Holmes model can be essentially applied to the same tissue region as that for Pennes.

Vasculature-Based Models

Weinbaum–Jiji–Lemons [52–64]

The modeling of countercurrent vasculature, which was not explicitly addressed by the Chen–Holmes model, developed separately from that of the continuum models. Bazett et al. [80] initially presented the countercurrent structure from observations of large arteries and veins in human limbs. The first major quantitative analysis was presented by Mitchell and Myers [69]. It was then followed by the work of Keller and Seiler [68], which became the predecessor to the Weinbaum–Jiji models. In 1979, Weinbaum and Jiji [57] proposed the initial model of the artery–vein pair as two parallel cylinders of equal diameters with collateral bleedoff in the plane normal to the cylinders. The anatomical configuration is a schematic of an artery and vein pair with branches to the peripheral skin layer (Figure 4.10.5).

The contribution of perfusion to heat transfer in tissue was treated as heat transfer in a porous medium and was considered a unidirectional convective term normal to the artery–vein pair. Knowledge of vessel density, diameter, and blood velocity was required at the different blood vessel generations.

In 1984, Weinbaum and Jiji presented a more thorough model based upon anatomical observations with Lemons [52, 53]. This model analyzed three tissue layers of a limb: (1) deep; (2) intermediate; and (3) superficial or cutaneous. For the countercurrent structure of the deep tissue layer, they proposed a system of three coupled equations:

$$(\rho c)_b \pi r_b^2\ \overline{V} \cdot \frac{dT_a}{ds} = -q_a \tag{4.10.43}$$

$$(\rho c)_b \pi r_b^2\ \overline{V} \cdot \frac{dT_v}{ds} = -q_v \tag{4.10.44}$$

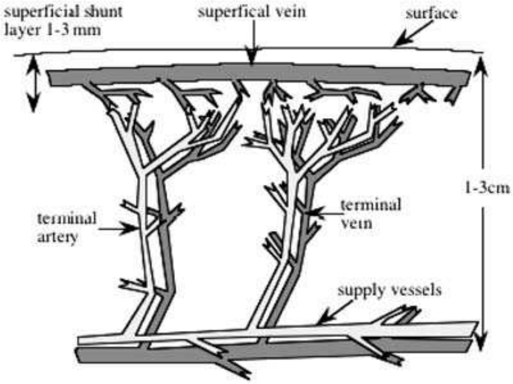

FIGURE 4.10.5 Schematic of artery and vein pair in peripheral skin layer. (From Weinbaum, S. and Jiji, L.M., *Advan. Bioeng.*, ASME WA/HT-72: 179–182, 1979.)

$$\rho c\frac{\partial T}{\partial t} = \nabla \cdot k\nabla T + n\, g\left(\rho c\right)_b \cdot \left(T_a - T_v\right) - n\,\pi\, r_b^2\left(\rho c\right)_b \overline{V} \cdot \frac{d\left(T_a - T_v\right)}{ds} + q_m \tag{4.10.45}$$

The first two equations describe the heat transfer of the thermally significant artery and vein, respectively. The third equation refers to the tissue surrounding the artery–vein pair. For this equation, the middle two right-hand side terms represent the capillary bleed-off energy exchange and the net heat exchange between the tissue and artery–vein pair, respectively. The capillary bleed-off term is similar to Pennes' perfusion term except the bleed-off mass flow (g) is used. Their analysis showed that the major heat transfer is due to the imperfect countercurrent heat exchange between artery–vein pairs. They quantified the effect of perfusion bleedoff associated with this vascular structure and showed that Pennes' perfusion formulation is negligible due to the temperature differential.

Assumptions include the following:

- Neglecting the lymphatic fluid loss so that the mass flow rate in the artery is equal to that of the vein
- Spatially uniform bleed-off perfusion
- Heat transfer in the plane normal to the artery–vein pair greater than that along the vessels (in order to apply the approximation of superposition of a line sink and source in a pure conduction field)
- Linear relationship for the temperature along the radial direction in the plane normal to the artery and vein
- Artery–vein border temperature equal to the mean of the artery and vein temperature
- Blood exiting the bleed-off capillaries and entering the veins at the venous blood temperature

The last assumption has drawn criticism based on studies that indicate the temperature is closer to tissue [72, 77]. Limitations of this model include the difficulty of implementation and identical artery and vein diameters. These two issues have lead to the development of the models described in subsequent sections. Studies using this model have been applied to the peripheral muscle tissue of a limb [68–70], and the model is accepted as valid for vasculature with diameters < 300 μm and $\varepsilon < 0.3$ [77].

Simplified Weinbaum–Jiji (W–J) [54]

In response to the criticism that their previous model is difficult and complex to apply, Weinbaum and Jiji simplified the three-equation model to a single equation:

$$\rho c\frac{\partial T}{\partial t} = \frac{\partial}{\partial x}\left(k_{eff}\frac{\partial T}{\partial x}\right) + q_{met} \tag{4.10.46}$$

In their simplification, they derived an equation based on the temperature of tissue only. The imperfect countercurrent heat exchange is embodied in an effective conductivity tensor term:

$$k_{eff} = k\left\{1 + \frac{n\left[(\rho c)_b \pi r_b^2 \overline{V} \cos\gamma\right]^2}{\sigma_\Delta \cdot k^2}\right\} + q_{met} \tag{4.10.47}$$

The k_{eff} term has similar parameters to the tissue and artery–vein pair heat exchange term in Equation (4.10.47), and a shape factor term (σ_Δ). In order to eliminate the blood temperature from their previous formulation, two major assumptions (the closure conditions) were used:

- Mean tissue temperature = $(T_a + T_v)/2$
- Heat from paired artery is mostly conducted to the corresponding vein:

$$q_a \approx q_v \approx \sigma_\Delta k\,(T_a - T_v). \tag{4.10.48}$$

Both these assumptions were based upon studies in rabbit thigh muscle from their previous formulation. However, to respond to criticism of these assumptions, Weinbaum and Jiji performed further mathematical analysis on ε and provided insights into the limits for applying these assumptions [61]. An obvious limitation of this model is that the local temperatures along the countercurrent artery and vein cannot be calculated. Another limitation is that the model is applicable only in situations in which $L_e/L \ll 1$.

In the example of analyzing the peripheral tissue in the arm, L is equal to the characteristic radius of the arm [62]. Weinbaum and Lemons [62] admit that this assumption breaks down under the following conditions: (1) if blood flow rates significantly increased in the larger vessel pairs of the peripheral tissue layer; and (2) if deeper muscle tissue, where the diameters of the countercurrent pair vessels are less than 300 μm, are included. This model has been tested in the porcine [76] and canine kidney [81] and continues to be verified by the Weinbaum group [55, 64] and other investigators [82].

Small Artery Model [83, 84]

The small artery model was developed by Anderson in studies of the canine kidney cortex [83, 84]. The model considers the energy balance in a control volume (i, j, k) that contains an arterial (Q_a) or venous (Q_v) vessel. For a volume with an artery parallel to the z coordinate axis, the equation is

$$Q_a = N(VA)_a(\rho c)_b(1+\lambda-2\lambda\xi)\left(\frac{T_z - T_{z-\Delta z}}{\Delta z}\right) \tag{4.10.49}$$

For a volume with a vein:

$$Q_v = M(VA)_v(\rho c)_b(1+\lambda-2\lambda\xi)\left(\frac{T_{z+\Delta z} - T_z}{\Delta z}\right) \tag{4.10.50}$$

where N and M are the density of the interlobular arteries and veins in the kidney cortex, respectively. Zeta refers to the fraction of the total interlobular artery flow within the control volume; in the kidney cortex, $\xi = 1$ at the corticomedullary junction and decreases to $\xi = 0$ at the outer capsule. The total flow within this region accounts for bleedoff from the interlobular arteries through the λ term, where $\lambda = 1$ represents complete bleedoff. The discrete representation provides for straightforward numerical implementation when the vessel density within the tissue region of interest is known. Model assumptions include:

- Thermal equilibration length within the volume is much less than vessel length.
- There is a linear relation between the effect of bleedoff on arterial flow and location along the length of the vessel.
- Bleedoff is modeled as change in the arterial flow.
- Bleed-off heat transfer is negligible.
- No major thermally significant vessels (i.e., $\varepsilon \ll 1$) are in the region of interest.

In its initial formulation, arbitrarily oriented vessels that would cause more than one vessel to occupy a control volume were not considered. Branching vessels are also not addressed. Even though this is not an inherent limitation of the model, implementation would be more difficult. Due to its discrete representation, the model cannot solve the inverse problem. The model has been shown to be valid in the canine kidney cortex in which there is uniformly oriented countercurrent artery vein architecture of 70 μm diameters.

Hybrid Models

The lack of an encompassing model that can account for the various tissue structures has lead researchers to propose and apply hybrid models. The substantial amount of effort related to the application and investigation of the major models discussed has shown that no one model applies to all the different vascular structures in tissue [72, 77]. Wissler [72, 73] points to the unlikelihood of a single equation providing a complete description of the heat transfer process in tissue and thus suggests using a combination of equations. The realization of this suggestion is found in Charny's work [56] in which W–J's and Pennes' models are used to describe peripheral and deep muscle tissue, respectively. When the applicability of each of the major models has been conclusively defined, an algorithm that would enable users to arrive at the appropriate choice of equations, given the tissue vasculature of interest, would be beneficial.

The applicability of the models discussed requires an understanding of the validity and development of each model. A comparison of the models discussed has been summarized by Charney [47].

Thermal Measurements of Perfusion

Introduction

Perfusion, the transmission of blood in the microcirculation, is an important factor in surgery, tissue transplants, heart disease, and cancer therapy. Despite its importance, no clinical method of measuring perfusion is currently available for a majority of applications. One technique that shows considerable promise involves the use of self-heated thermistors [6–13]. In this method, a miniature thermistor (0.5 to 2.5 mm diameter) is placed invasively in the tissue of interest and heated with a predetermined applied power. Because tissue conduction and perfusion act to carry heat away from the thermistor, the resulting volumetric-average temperature rise in the thermistor bead, ΔT, is related to the tissue thermal conductivity and perfusion. When the intrinsic tissue conductivity and the apparent conductivity of the tissue (due to blood flow and conduction) are known, the perfusion rate can be calculated.

At least two difficulties exist with this technique. The first is that the intrinsic tissue conductivity of perfused tissue must be known in order to calculate the perfusion rate. Although one could stop the blood flow to a tissue and measure its conductivity, this is clearly not desirable and is not always practical. In order to overcome this problem, Holmes and Chen have proposed techniques that measure perfusion without interrupting blood flow [13, 20].

Perfusion Resolution

The perfusion resolution, δw, is defined as the smallest change in perfusion that can be detected by the instrument. It can be determined theoretically:

$$\delta w = \delta k \bullet \frac{\partial w}{\partial k} = \delta k \bullet c_{15} \tag{4.10.51}$$

For the constant temperature heating technique using a P60 thermistor, δk is about 0.02 mW/cm-°C, and the sensitivity is about 100 (mL/100 g-min)/(mW/cm-°C). Using Equation (4.10.51) gives a perfusion resolution of about 2 mL/100 g-min. Due to fluctuations in the baseline tissue temperature, the practical resolution is about 10 mL/100 g-min. Because so many experimental and tissue variables exist, it is extremely important to test these techniques in preparations in which the perfusion is known.

Measurement Volume

The measurement volume of a thermistor is a complex function of many factors, including the perfusion rate and vascular anatomy of the tissue of interest. One problem with small thermistors is their small measurement volume. A boundary layer (decoupler) between the thermistor and the tissue causes a significant measurement error. This unwanted boundary layer is often caused by the probe during insertion. The larger probes exhibit a smaller error, but are likely to cause a larger decoupler because of the increased trauma during insertion.

Temperature Dependence of Perfusion

Perfusion depends on a wide variety of factors: some are local to the tissue (pH, temperature, O_2); some are external but directly control local flow (parasympathetic, hormones); and some indirectly affect local flow (heart rate, blood pressure, skin temperature, needs of other organs). A simple experiment studied the effect of local tissue temperature on muscle perfusion. The constant ΔT method was used to measure perfusion in an anesthetized rat. The muscle temperature was manipulated by placing the hind limb into a water bath. Insulation was carefully placed so as to minimize changes to the body temperature. The rectal and neck temperatures were constant while the muscle in the hind limb was heated.

Figure 4.10.6 shows the perfusion as a function of tissue temperature for a typical experiment. The dip in perfusion as a function of temperature as shown in Figure 4.10.6 consistently occurred, but did not always occur at the same temperature. This dip may be due to an anastomotic shunt attempting to regulate the core body temperature.

Figure 4.10.7 presents the averaged results for 10 rats. Because the dip occurred at different temperatures for the various rats, it does not appear in the average. The large standard deviations are due to perfusion differences from one rat to the next. A linear fit to this averaged data gives the following approximation:

$$w = 1.9720\,(1 + 0.059\,T) \tag{4.10.52}$$

where w has units of mL/100 g-min and T has units of °C.

Yuan et al. [85] measured perfusion and temperatures at various locations within each of four canine prostates subjected to a transurethral microwave thermal source. The total number of the perfusion sampling points coupled with temperature is 15. Colored microspheres were used to measure perfusion due to its simplicity compared with radioactively labeled microspheres and because the microsphere trapping method is regarded as a standard. Temperatures were measured using miniature thermistors. The prostate temperatures were raised to 40 ~ 45°C by 5-W step increments of the microwave power at

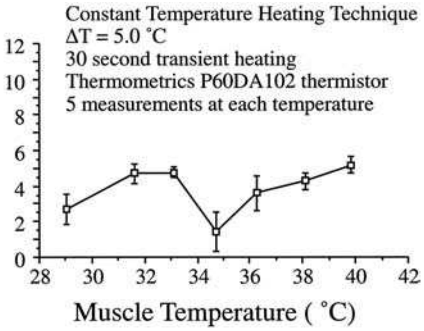

FIGURE 4.10.6 Perfusion vs. muscle temperature during a typical experiment.

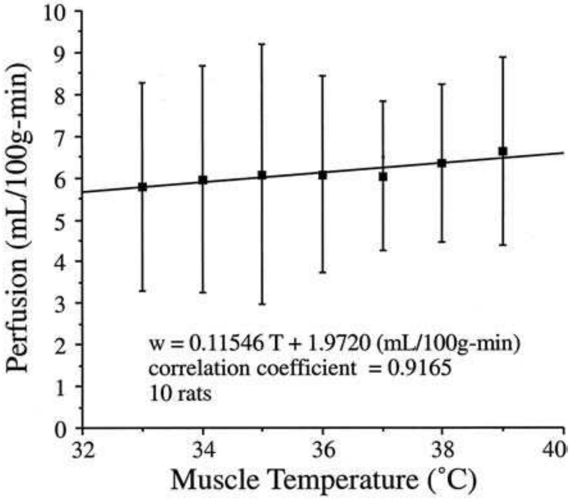

FIGURE 4.10.7 Perfusion vs. muscle temperature averaged over 10 experiments.

hourly intervals to 15 W. Temperatures and perfusion were measured at baseline and at the beginning and end of each heating interval. Thus, the periods between perfusion samples were approximately 5 or 60 minutes. Under baseline conditions, the temperature fluctuations within the prostate were approximately ±0.3°C. A relative dispersion estimate of 15% was derived from one dog for the fluctuations in baseline perfusion. Thus, changes in absolute perfusion and temperature greater than 15% and 0.3°C, respectively, were considered to be substantial changes.

As heating progressed, a variety of substantial changes were observed, but no uniform pattern emerged. However, the measurements included changes typically expected for hyperthermia: (1) an initial perfusion increase associated with elevating the baseline temperature; (2) a perfusion return toward baseline after this initial increase; and (3) a dramatic increase in perfusion at elevated temperatures. The initial perfusion increases were observed in three dogs when the temperatures exceeded 38 ± 3°C (mean ± 1 s.d., $N = 8$). The perfusion increased 34% from a baseline value of 0.59 ± 0.26 ml/g-min over a temperature rise of 1.7 ± 1.3°C. Half of the measurements in the three dogs subsequently showed a decrease in perfusion ranging from 16 to 25%. In two dogs, dramatic perfusion increases as high as 364% were observed with a corresponding decrease in tissue temperature.

The mean perfusion and temperature measured from all dogs at similar instances during the experimental protocol were calculated. Figure 4.10.8 shows the changes as the experiment progressed from

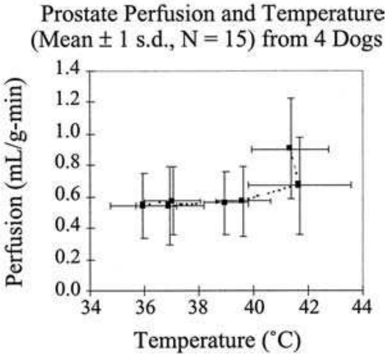

FIGURE 4.10.8 Perfusion vs. prostate temperature. (From Yuan, D.Y., Xu, L.X., Zhu, L., Holmes, K.R., and Valvano, J.W., *17th S. Biomed. Engr. Conf.*, 85, 1998.)

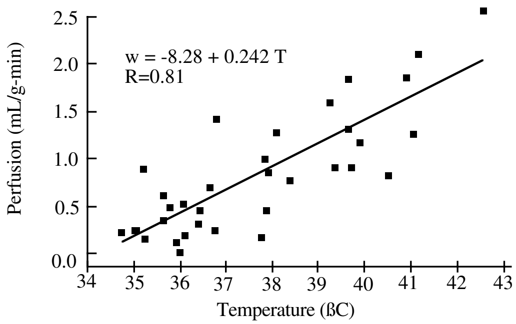

FIGURE 4.10.9 Perfusion vs. prostate temperature. (From Xu, L.X., Zhu, L., and Holmes, K.R., *Int. J. Hyperthermia.* 14, 65–73, 1998.)

baseline conditions. The mean behavior indicates no substantial change in perfusion until the tissue temperature exceeded 39.6°C, after which the perfusion increased 17%. This occurred over a 5-min period as the nominal microwave power was stepped from 10 to 15 W. The perfusion increased another 35% when the tissue temperature exceeded 41.7°C and appeared to affect a slight lowering of tissue temperature.

Xu et al. [86] measured perfusion using the pulse-decay self-heated thermistor technique [13, 20] in these dog prostates during the same transurethral microwave hyperthermia treatments. Interestingly, the perfusion response to temperature measured with the thermal technique was roughly linear with temperature in the same dogs at roughly the same locations, as shown in Figure 4.10.9.

The interdependence between perfusion and temperature was observed in these studies. Most notably, a decrease in tissue temperature was associated with a dramatic increase of perfusion. Such changes have been modeled previously with Pennes' bioheat equation using assumed perfusion values and changes for the prostate. The data from this study will provide more realistic estimates of perfusion values and thermoregulation models in hyperthermic canine prostates. Two hypotheses explain the differences between the perfusion responses to hyperthermia as measured by microspheres and the thermal decay probe. The first possibility is that one or both methods have significant measurement errors. A second possibility is that perfusion as measured by spheres trapped in the capillaries is a different parameter than perfusion as measured by enhanced heat transfer within the 70- to 200-μm diameter vessels.

Human Thermoregulation

Humans possess an elaborate thermal control (thermoregulation) system that ensures maintenance of internal body temperatures near a physiological set point under a large spectrum of environmental conditions and metabolic rate activities. After many years of research, much has been learned of the operation of the human thermoregulatory system, although it remains a topic of active investigation. A number of reviews on specific aspects of the physiological basis of thermoregulation are recommended for further background detail [87–92].

Internal and boundary heat transfer processes are key to thermoregulation. As the operational mechanisms have been understood, it has been possible to model these functions in an attempt to simulate and predict thermoregulatory behavior and to be able to design systems to interact thermally with the human body (e.g., an environmental protective garment or a space suit) without compromising the health and safety of the subject.

Physiological Processes of Thermoregulation

The prevailing thermal physiology theory is that the human thermoregulation system operates to maintain the body core temperature at a constant value consistent with that required for regular body function, regardless of the environmental temperature and energy loading. Alternatively, it has been suggested that thermoregulation serves the purpose of maintaining the body's energy balance, with body temperatures a *result*, not a cause, of the regulation process [87, 93, 94].

Many general observations of the thermal characteristics of human thermoregulation are consistent, even if alternative explanations of the underlying operative mechanisms are preferred. For example, temperature and internal energy storage of the human body vary with time of day, metabolic activity, and individuality of the human [95]. The body incorporates a number of energy production and dissipation mechanisms to preserve thermal homeostasis, many of which are controlled by feedback signals based on specific physiological states. Examples of thermoregulatory processes governed by feedback are sweating, shivering, and variable localized blood flow.

According to the theory of thermoregulation by control of the body core temperature, the main control center is located in the hypothalamus of the brain, from which multiple reflex responses operate to maintain the body temperature within a narrow range [96]. The signals that activate the hypothalamic temperature-regulating centers come largely from two sources: temperature-sensitive cells in the anterior hypothalamus and cutaneous temperature receptors. The cells in the anterior hypothalamus sense the temperature of the body core or, specifically, the temperature of arterial blood that passes through the head.

Webb has presented a theory of thermoregulation to maintain an energy balance within the body, as demonstrated by the existence of temperature sensors at several levels in the skin enabling the sensing of heat flow within and from the body [94]. Evidence also supports neurological sensing of thermal gradients that direct thermoregulation behavior. The hypothesis in support of the theory of energy content regulation based on Webb's experimental observations is [94]:

> Heat (energy) regulation achieves heat (energy) balance over a wide range of heat (energy) loads. Heat flow to or from the body is sensed, and physiological responses defend the body heat (energy) content. Heat (energy) content varies over a range that is related to heat (energy) load. Changes in body heat (energy) content drive deep body temperatures.

The proposed mechanism of energy-driven thermoregulation balances constantly changing metabolic energy production and the adjustment of heat losses to maintain the body as a system in equilibrium. In contrast, the proposed mechanism of temperature-driven thermoregulation effects a coordination of physiological processes to maintain the body core temperature at a set point.

Thermoregulatory Processes

Conservation of energy for the human body must account for internal metabolic energy production plus multiple mechanisms of environmental heat and work exchange:

$$\Delta E = M - (W + Q_{conv} + Q_{cond} + Q_{rad} + Q_{evap} + Q_{resp}) \tag{4.10.53}$$

where

ΔE = rate of energy storage in the body (W)
M = metabolic energy production (W)
W = external work (W)
Q_{conv} = surface heat loss by convection (W)
Q_{cond} = surface heat loss by conduction (W)
Q_{rad} = surface heat loss by radiation (W)
Q_{evap} = surface heat loss by evaporation (W)
Q_{resp} = respiratory heat loss (W)

The human body produces energy, exchanges heat with the environment, and loses heat by evaporation of body fluids. Energy is produced in the body by basal, or resting, metabolism, defined as the minimal metabolism measured at a temperature of thermal neutrality in a resting homeotherm with normal body temperature several hours after a meal and not immediately after hypothermia. It is also produced at an increased rate due to muscle activity, including physical exercise and shivering, and by food intake. Therefore, the total energy production in the body is determined by the energy needed for basic body processes plus any external work.

Because the body operates with less than 100% efficiency, only a fraction of the metabolic rate is applied to work, with the remainder dissipated as heat [95, 96]. The mechanical efficiency, η, associated with metabolic energy utilization is zero for most activities except when the person is performing external mechanical work such as walking upstairs, lifting something to a higher level, or cycling on an ergometer [97]. When work transferred from the environment is dissipated as heat in the human body, η is negative. An example of this case is walking downstairs.

Convection, radiation, conduction, and evaporation of sweat at the skin surface facilitate heat transfer from the body. Heat transfer also occurs via the respiratory tract and lungs, although to a minor extent in human beings compared with many mammals and reptiles. Storage of energy takes place whenever production and dissipation mechanisms are not in balance. In many instances, such as astronauts in space suits or military personnel in chemical defense garments, energy storage is forced due to the lack of appropriate heat exchange with the environment [98].

The human thermoregulatory system is quite complex and behaves mathematically in a highly nonlinear manner. It contains multiple sensors, multiple feedback loops, and multiple outputs [99]. The primary mechanisms by which the body responds to control the storage of energy (positive or negative) include the evaporation of sweat, shivering of the muscles, and vasoconstriction and vasodilatation of the blood vessels.

Heat transfer internal to the body is due to the conductance that governs the flow of energy between the core, through the tissue, and the surface. This transport process is governed significantly by peripheral blood flow, the core–skin temperature gradient, and the conductivity of the various body tissues. Transient blood perfusion provides an effective variable path of peripheral energy transport via convection between blood and tissue and countercurrent heat exchange between the arteries and the veins. Blood flow distribution is controlled according to metabolic needs of the body, local tissue temperature, and the need to maintain the appropriate core temperature.

When the core becomes too hot, the blood vessels in the skin dilate to allow increased perfusion to the body surface. The blood is cooled by the environment, and the cooler blood is returned to the core. Increased blood flow to the skin surface also enables greater sweat production, adding to the cooling process. In contrast, when the core becomes too cold, blood flow to the skin is constricted to conserve the body's internal energy. Sweating occurs when the arterial blood is elevated in temperature, causing the hypothalamus to increase nerve impulses to the sweat glands. Shivering, on the other hand, is an involuntary response of the skeletal muscles when passive body cooling exceeds metabolic energy production [96].

Human thermoregulation mechanisms can be divided into two main categories: autonomic and behavioral [99]. Autonomic thermoregulation is controlled primarily by the hypothalamus, whereas behavioral thermoregulation is controlled consciously by man and includes active movement and adjustment of clothing. Behavioral thermoregulation is associated with conscious temperature sensation as well as with thermal comfort or discomfort. Some engineered systems are designed to interact with the body to enhance it ability to maintain thermoregulation in harsh or hazardous environments. Examples range from the common HVAC systems encountered in buildings and vehicles to sophisticated garments worn during certain military and space missions.

Wissler Model of Human Thermoregulation

Models that incorporate accurately the transient whole body behavior during thermoregulation for a wide range of states and environmental challenges may be quite useful in describing and predicting this important human physiological function. Moreover, such a model can be used as a design tool in the development of systems with which humans must interact for a variety of work, pathological, and recreational circumstances. The development of models of human thermoregulation has proved to be a daunting task that has been addressed by many researchers. The complexity of the coupling among

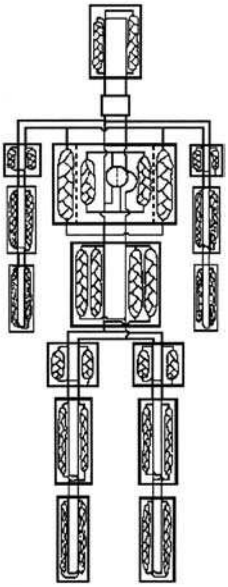

FIGURE 4.10.10 Multi-element model representing the human body in the Wissler model.

physiological processes involved in thermoregulation and of the control algorithms has dictated that models incorporating these multiple effects be solved numerically. Thus, the first realistic thermoregulation models appeared in the 1960s and 1970s from the studies of Wissler [100, 101]; Stolwijk [102]; Nadel et al. [103]; Mitchell et al. [104]; Hayward [105, 106]; and Kuznetz [107]. An important early application of modeling human thermoregulation was the design and development of active thermal control garments to be worn under the space suit during extravehicular activity [95, 98, 108, 109]. Over the intervening years, the Wissler model has been improved and updated on a continuous basis; it is now applied to a very broad spectrum of human thermal control scenarios [107–113].

The Wissler human thermoregulation model is a transient-state mathematical formulation used to describe human physiological responses to various levels and combinations of exercise and thermal stress. The model computes thermal, cardiovascular, ventilatory, and metabolic changes that occur during a specified period of time. The values for the independent physiological and environmental variables, such as metabolic rate, environmental conditions, and liquid cooling garment flow rate, are specified as inputs to the model. A finite-difference scheme is applied to compute tissue and blood temperatures throughout the body numerically as a function of time.

The model represents the human body as 15 cylindrical elements for the head, thorax, abdomen, and proximal, medial, and distal portions of each arm and leg. A schematic representation of the multielement model of the human body is shown in Figure 4.10.10. Each body element is composed of cylindrical shells defined by physical and physiological properties for composite layers of viscera, bone, muscle, fat, and skin. In each of the elements, metabolic energy may be generated as appropriate due to basal metabolism, exercise, and shivering. The generated energy is conducted to adjacent body regions, convected to circulating blood, or stored in the element. Each body element contains an arterial and venous pool and a capillary bed. The pools are interconnected serially between adjacent elements. As venous blood is returned to the heart, it passes through the lungs for exchange of gases before entering the arterial system.

A number of signal feedback loops are used to account for thermoregulation within the body. Feedback data are the differences between skin and central head temperatures and their respective specified set point values. Error signals specified by these differences drive sweat secretion, shivering, and vasomotion responses. The algorithm equations have the general format of a proportional controller that is activated when a defined threshold condition is satisfied. The control equations do not all have the same level of response to error signals. For example, sweating and vasodilation are more responsive to an increase in central head temperature than in cutaneous temperature, while vasoconstriction is more responsive to cutaneous temperature.

Thermoregulation is also affected via heat exchange during the venous return flow of blood. Venous flow occurs through deep or superficial veins, thus influencing the rate of countercurrent heat exchange. Modeling the venous return provides a realistic simulation of the countercurrent heat exchange that takes place in the extremities during exercise in hot environments and immersion in cold water.

Blood flow rates are simulated to satisfy the level of local metabolic need for oxygen in the tissues. Therefore, a lower limit is set for extremity blood perfusion during cold exposure. The model also incorporates material balances for oxygen, carbon dioxide, and lactate as defined for cardiovascular response. In addition to physiological factors, conditions of the environment with which the subject interacts are accounted for. Physical properties of the environmental fluid and characteristics of the flow field in the vicinity of the subject are specified because they determine conductive and convective heat transfer.

The model allows the user to specify layers of clothing described by physical properties of annular shells outside and interacting with the skin layer. The physical properties of the garments may change with accumulation of unevaporated sweat, which may saturate the material.

Transient tissue and blood temperatures are calculated during simulated thermal scenarios by Crank–Nicolson type finite-difference equations. Undated temperatures and other physiological values are computed every 10 s. The model allows a simulation to be broken down into any number of scenario subintervals, with the following factors specified in each interval:

- Basal metabolic rate
- Kind and level of exercise performed
- Environmental conditions (pressure, temperature, dewpoint, etc.)
- Garment properties
- Use of a fluid-conditioned garment (FCG) (flow rates, inlet temperatures, etc.)

The equations needed to describe a liquid or air-cooled garment are derived from material and energy balances for the circulating fluid. Sensible heat transfer is treated the same for liquid- and air-cooling situations. However, the evaporation and condensation associated with latent heat transfer must be treated differently for the two fluids. In the case of the liquid-cooled garment, water from sweat and environmental moisture condenses on the cool surface of the garment. On the other hand, air cooling generally facilitates evaporation of sweat by removing water vapor from the garment.

In its early formulation, the Wissler model required a large main frame computer to perform simulations of thermal regulation. However, owing to advances in computational capabilities in recent years, it is now possible to run extensive simulations on a desktop personal computer in an order of magnitude less than real time. The thermoregulation model provides reliable predictions of changes in the human thermal state for many different types of environmental and metabolic stress, and it has been used for the design of new automated personal garments for application in hazardous environments [114].

Therapeutic Heating

Normal physiologic temperatures range from approximately 30 to 42°C. The average so-called “core” (central abdominal) temperature in mammals varies slightly among species between about 36 and 38°C (37°C for humans, 38°C for most canines). Thermal gradients are inherent in metabolically driven open systems at steady state and measured core temperatures will vary slightly depending on the relative metabolic rate, blood flow, and location of the various organs, as well as from point to point within an organ. Although core temperature is maintained close to a steady-state value, for example, skin surface temperature at rest in a controlled room environment varies between about 30 and 34°C depending on climate and season.

Elevation of body, appendage, or organ temperature to between 40 and 42°C can be used for analgesia (relief of pain) and to provide the most advantageous environment for injury-response (wound healing) processes. Note that no external intervention can be claimed to promote wound healing — one may only provide the best conditions under which the natural processes will heal wounds. Thermal intervention has been used for many years for these two purposes.

Heat Generation Modalities

Therapeutic heating can be obtained by surface heat transfer means (hot or cold packs), but the effectiveness is limited to surface injury. Nevertheless, contact heating is the method of choice for such injuries as sprains, muscle strain, and postoperative swelling. The standard response to elevated temperatures is to increase blood flow and thus perfusion. One applies cold heat sinks to reduce perfusion in the injured area during the first 12 or 24 h; warm hot packs or circulating water (up to 45°C) are then used to promote perfusion and thus increase the supply of neutrophils and other blood components related to the injury response and wound healing.

Deeper injuries require volumetric heating to attain adequate temperatures. The most effective volumetric heating methods to date have been: (1) electromagnetic fields at radio frequencies (RF) or microwave frequencies (MW); and (2) ultrasound (US). Assigned radio frequencies for industrial, medical, and scientific use (ISM) are: 6.78, 13.56, 27.12, and 40.68 MHz. Practical ISM frequencies for medical use in the microwave range are 915 MHz and 2.45 GHz. Typical ultrasound heating devices operate between about 500 kHz and 10 MHz. In all three cases, an engineering tradeoff takes place among local volumetric heat generation, q''', thermal heat generation field dimensions, and depth of penetration. Higher frequencies have shorter wavelengths and are, in general, absorbed more strongly and thus penetrate less deeply. Tissues are inhomogeneous and, with only a few exceptions, anisotropic. The electrical and acoustic properties of tissues can vary over several orders of magnitude. Consequently, electromagnetic and acoustic boundary conditions often determine the volume generation term in spite of efforts to shape the field by clever applicator design.

For electromagnetic heating in tissues, the volume generation term is essentially governed by the electrical conductivity, σ (S/m); the imaginary part of the electric permittivity, ε'' (F/m); and the magnitude of the local electric field, $|E|$ (V/m):

$$q''' = \left(\sigma + \omega\varepsilon''\right)\left|\mathbf{E}\right|^2 \tag{4.10.54}$$

where ω is the angular frequency (r/s). Heating due to direct absorption from a magnetic field, $\omega\mu''|\mathbf{H}|^2$, where μ is the magnetic permeability (H/m), is negligible except in the most unusual circumstances. Yet, RF and MW magnetic fields heat tissue very effectively, too. This is because, by Faraday's law of induction, a time-varying magnetic field will induce an electric field in the tissue, but the electric field actually generates the heat:

Integral form:

$$\oint \mathbf{E}\bullet d\mathbf{L} = -\frac{\partial}{\partial t}\left[\iint \mu\mathbf{H}\bullet d\mathbf{S}\right] \tag{4.10.55}$$

Point form:

$$\nabla\times\mathbf{E} = -\mu\frac{\partial \mathbf{H}}{\partial t} \tag{4.10.56}$$

A comprehensive discussion of these properties and effects in materials may be found in Roussy and Pearce [115]. Values of relevant electrical and acoustical properties of tissues are given in Table 4.10.8 and Table 4.10.9, respectively.

Acoustic waves are highly scattered in many tissues, so simple wave propagation models are inadequate to predict the local acoustic field strength. Nevertheless, a uniform plane wave description of the heating field often suffices to explain the distribution of the heat generation with acceptable accuracy. The volume

TABLE 4.10.8 Representative Electric Properties of Tissues

Tissue	Conductivity (*S*/*m*)	Real Part, ε_r'	Imaginary Part, ε_r''
Fat	0.05–0.09	3.9–7.2	0.67–1.4
Muscle	0.1–1.0	45–48	13–13.9
Bone	0.006–0.05	4.2–5.8 (marrow)	0.7–1.3 (marrow)

Notes: Muscle is highly anisotropic, with higher conductivity parallel to fibers. Electric permittivity is as measured at 3 GHz, and ε (*F*/*m*) = $\varepsilon_0[\varepsilon_r' - j\varepsilon_r'']$ where $j = \sqrt{(-1)}$ and ε_0 = free space permittivity, 8.85×10^{-12} *F*/*m*.

Sources: From Schwan, H.P., in *Therapeutic Heat and Cold*, E. Licht, Ed., Waverly Press, Baltimore, MD, chap. 3, 1972. Conductivity is from Geddes, L.A. and Baker, L.E., *Med. Biol. Eng.,* 5, 271–293, 1967.

TABLE 4.10.9 Representative Acoustic Properties of Tissues

Tissue	Velocity, *a* (m/s)	Absorption at 1 MHz (cm^{-1})
Fat	1450	0.06
Muscle	1585	0.2–0.7
Bone	4080	30

Source: From Schwan, H.P., in *Therapeutic Heat and Cold*, E. Licht, Ed., Waverly Press, Baltimore, MD, chap. 3, 1972.

heat generation term is determined by the acoustic absorption coefficient, α (m^{-1}), and the wave power density, E (W/m^2), approximately according to Beer's law:

$$q'''(z) = \alpha E_0 e^{-\alpha z} \tag{4.10.57}$$

where E_0 is the surface intensity (at $z = 0$) and α varies according to frequency, f (Hz) $\alpha \approx f^n$, where $1 < n < 2$. Table 4.10.9 units for α are cm^{-1}. In other references, α may be reported as dB/cm (dB = $10 \log_{10}\{E_{\text{out}}/E_{\text{in}}\}$).

Physiologic Effects of Local Heating

The general physiological effects of local heating comprise a cascade of response [118]. As noted in the previous subsection, systemic response is controlled from the hypothalamus by neuronal and hormonal signals. Appendage- and organ-level response to local heat may be spinal-cord mediated; however, local heating can trigger local release of bradykinins that induce vascular dilation or constriction, thus affecting temperature rise.

The increase in tissue temperature is accompanied by an increase in cellular metabolism. The arterioles (microscopic arteries typically about 40 to 200 μm inner diameter [118]) dilate in response to heating under smooth muscle control. The downstream capillary pressure increases above the homeostatic level of about 25 torr. Two consequences are increased capillary flow and capillary pressure.

First, at higher capillary pressures the gaps between the endothelial cells (thin epithelial cells comprising the vessel wall) tend to widen and, at higher pressures, edema may form (an increase in the fluid in the extracellular compartment) [119, 120]. Second, higher capillary flow results in rapid clearing of cellular metabolites and increases convection heat transfer, delivery of tissue oxygen, cellular nutrients, antibodies, and leukocytes (white blood cells) including the monocytes necessary in the healing response. Neutrophils are white blood cells that initially release proteolytic enzymes to digest dead tissue and, later, phagocytose (eat) the debris [121]. Monocytes are other leukocytes that remove damaged and dead cells by phagocytosis.

Tissue Effects: Elevated Temperatures

Exposure to temperatures above normal physiologic ranges (>42°C) can result in measurable irreversible changes in tissue structure or function. Cell death or tissue alterations may be detrimental — for example, skin burns — or beneficial, as in vessel sealing or tumor destruction. Tissues of the central nervous system are the most thermally sensitive, exhibiting irreversible changes for long-term exposures above about 42°C. The specific pathologic end point may be evaluated histologically, histochemically, and/or physiologically. Most assays of thermal alterations are qualitative in nature; however, several end points that are inherently quantitative lend themselves well to rate process descriptions of their thermal kinetics. Even for qualitative processes, thermal kinetic models often provide useful descriptions and thus provide helpful insights into the underlying principles of tissue thermal damage.

Here, "damage" is used in a generic sense to denote all kinds of irreversible alterations, therapeutic or not. In the Arrhenius models, irreversible thermal damage is exponentially dependent on temperature and linearly dependent on time of exposure. Many damage processes can be modeled as first-order rate processes for which two experimentally derived coefficients are sufficient. Second-order processes require four parameters, again derived from experiment. The first-order rate process models often apply well to the prediction of damage thresholds and less well as the damage becomes complete or severe because several of the fundamental assumptions are violated. In order to be useful in evaluating thermal insult, the kinetic model must be coupled to quantitative pathological analysis. This subsection describes several quantitative markers of thermal damage and experimental methods for estimating relevant kinetic coefficients in constant temperature and in transient thermal history experiments. As expected, transient *in vivo* thermal history data yield a noisy kinetic plot; nevertheless, estimates of the appropriate rate coefficients can be made.

Theory of Rate Process Descriptions

The original work on the application of rate process models to thermal damage was reported by Moritz and Henriques in a series of seminal papers entitled "Studies of Thermal Injury" in 1947 [122–125]. They applied flowing water at elevated temperatures to pig skin and measured exposure times required to create first-, second-, and third-degree burns. In their work, the damage was quantified using a single parameter, Ω, which ranges on the positive real axis and is calculated from an Arrhenius integral:

$$\Omega(\tau) = \int_0^{\tau} A\, e^{\left[\frac{-E}{RT}\right]} dt \qquad (4.10.58)$$

where

A = a frequency factor (s^{-1})
τ = the total heating time (s)
E = an activation energy barrier (J/mol)
R = the universal gas constant (8.32 J–mol^{-1}–K^{-1})
T = the absolute temperature (K).

Over the ensuing 50 years many subsequent investigators have modeled this process [126–129] and made experimental measurements of threshold burn conditions in human [130–132]; animal [133–134]; and cellular and molecular [135–137] systems. Although a considerable body of literature has been accrued, there is by no means a consensus on how to predict the occurrence of thermal injury accurately over the wide range of conditions that cause burns.

One difficulty with this model is that a single damage parameter inherently lumps all damage processes into one global measure. In multiple process cases, such as in the case of a skin burn, the lowest temperature process saturates the damage measure, Ω, early during an exposure. In this discussion, we review the underlying assumptions and origin of the terms in Equation (4.10.58) are reviewed and the traditional thermal damage parameter, Ω, recast into a form suitable for evaluation of multiple-process thermal damage effects.

Kinetic Models of Reaction Product Formation Rates

The basis for rate process models of thermal damage may be obtained from chemical reaction kinetics (see, for example, Maron and Lando [138]). In a typical reaction process, thermally active reactants jump an activation barrier to form products, as illustrated in Figure 4.10.11, in which E is the energy barrier

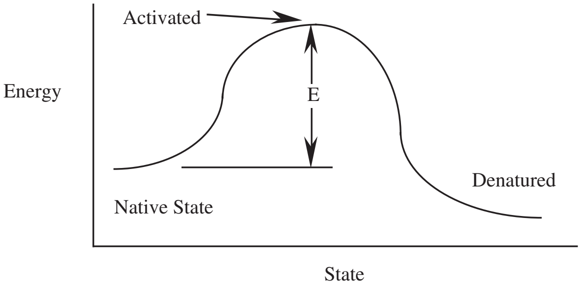

FIGURE 4.10.11 Energy-state diagram of a bimolecular process.

in Equation (4.10.58). The collision theory description of ordinary first-order bimolecular reaction kinetics holds that the reactants are activated by collisions; n^* are activated out of n total molecules, and the probability of activation is:

$$\frac{n^*}{n} = e^{-\left[\frac{E}{RT}\right]} \tag{4.10.59}$$

In such a process, activated reactants are considered to form an activated "complex" that may relax to inactivated single reactants or irreversibly progress to form product molecules. The complex has some of the properties of an ordinary molecule and is at least temporarily stable. For reactant molecules A and B the sequence of formation is:

$$\left[A\right]+\left[B\right] \underset{k_b}{\overset{k_a}{\rightleftarrows}} \left[AB\right]^* \xrightarrow{k} \text{Pr}\mathit{oducts} \tag{4.10.60}$$

The overall reaction velocity, k (s^{-1}), determines the rate of formation of product and is related to the equilibrium constant for formation of activated complex, K^*, by:

$$k = \frac{RT}{Nh} K^* = \frac{RT}{Nh} e^{-\frac{\Delta G^*}{RT}} \tag{4.10.61}$$

where

N = Avogadro's number (6.023×10^{23})
h = Planck's constant (6.627×10^{-34} J-s)
ΔG^* = the Gibb's free energy of formation of activated complex

In turn, the free energy of formation is given by:

$$\Delta G^* = \Delta H^* - T\Delta S^* \tag{4.10.62}$$

where ΔH^* is the enthalpy of activation (J/mol) and ΔS^* is the entropy of activation (J/mol–K).

The activation entropy is not calculable except for the simplest possible reactions in the gas phase and is therefore usually determined from experimental measurements of the reaction velocity and activation enthalpy. The activation enthalpy, ΔH^*, is determined from the observed activation energy, E by:

$$\Delta H^* = E - iRT \tag{4.10.63}$$

where i is 1 for first-order reactions in solution and gases; 2 for second order; and 3 for third-order reactions.

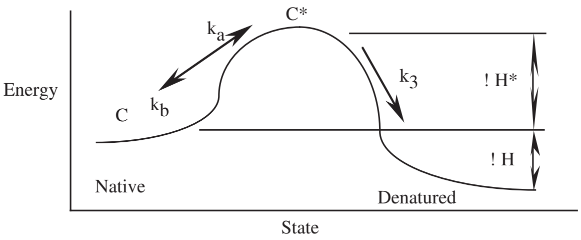

FIGURE 4.10.12 Unimolecular process activation and denaturization.

Unimolecular Process Descriptions

Thermal damage in tissue is a unimolecular process — tissue constituents transition from the native state to the damaged state (Figure 4.10.12). Absolute reaction rate theory can also be used to explain the rate of formation for this process if one assumes that a time lag exists between molecular activation and denaturization [138]. During this time lag, the molecules may denature or relax back to the native state, as illustrated in Figure 4.10.10. Here, ΔH is the enthalpy (internal thermal energy) difference between native state and denatured molecules. The relative barriers are such that, in the thermal damage of tissue, ΔH^* is almost always smaller than ΔH.

Thus, the activation process may be regarded as reasonably likely, and the probability of denatured tissue relaxing back to native state tissue is near enough to zero that it may be regarded as an impossible event in the absence of an energy-consuming healing process. The rate of damage formation is then proportional to only molecules that remain activated. For a unimolecular process in the native state C, with an activated state, C^*, and velocity constants k_a, and k_b:

$$[C] \underset{k_b}{\overset{k_a}{\rightleftarrows}} [C]+[C^*] \tag{4.10.64}$$

The activated complex, $[C^*]$ progresses to the damaged state at k_c:

$$[C^*] \xrightarrow{k_c} \text{Damaged state} \tag{4.10.65}$$

so that the rate of disappearance of native state molecules, $[C]$, is given by:

$$-\frac{d[C]}{dt} = k_c[C^*] \tag{4.10.66}$$

Generally $[C^*]$ is neither known nor calculable; however, at sufficiently low concentrations of C^*, the steady-state principle asserts that for short-lived activated states, the rate of formation can be considered equal to the rate of disappearance. The activated state, $[C^*]$, forms at a rate $k_a\,[C]^2$, relaxes back to inactivated at rate $k_b\,[C][C^*]$; and denatures at the rate $k_c\,[C^*]$. Consequently:

$$k_a[C]^2 = k_b[C][C^*] + k_c[C^*] \tag{4.10.67}$$

and so:

$$[C^*] = \frac{k_a[C]^2}{k_c + k_b[C]} \tag{4.10.68}$$

An overall reaction velocity, k, which relates $[C]$ to its rate of disappearance, is needed:

$$-\frac{d[C]}{ct}=k[C] \tag{4.10.69}$$

There are two limiting cases for Equation (4.10.68):

- The concentration of remaining undamaged material, $[C]$, may be large enough that deactivation at k_b dominates the k_c pathway, so $[C^*] \cong [C]\ k_a/k_b$ for which the overall formation rate, $k = k_c\ k_a/k_b$ and a first-order process result.
- If the remaining undamaged material concentration, $[C]$, is small, $k_c \gg k_b\ [C]$ and the process is second-order because, from Equation (4.10.68), $k = k_a\ [C]$.

In liquid-phase systems with appreciable concentrations of native state molecules, the first condition should apply, so the first-order approximation applies. After a long time of exposure at damaging temperatures so that $[C]$ is very small, $k_c \gg k_b\ C$ and a second-order process results:

$$-\frac{d[C]}{dt}=k[C]^2 \tag{4.10.70}$$

where for simplicity the $[C]$ dependence has been removed from k.

First-Order Solution

Equation (4.10.69), then, is a Bernoulli differential equation with the solution:

$$C(\tau)=C(0)e^{\{\int k dt\}} \tag{4.10.71}$$

Equation (4.10.61) and Equation (4.10.62) may be used to relate k to $\Delta H*$ and $\Delta S*$. It should be noted at this point that the energy barrier, E, (Figure 4.10.8) is in fact $\Delta H* + \mathrm{RT}$; however, in practice $\{\Delta H^* \cong 5 \times 10^5\} \gg \{\mathrm{RT} \cong 3 \times 10^3\}$, so it may be assumed that $E \cong \Delta H^*$.

The pre-exponential term in Equation (4.10.61) suggests that it is temperature dependent; however, the linear dependence of A on $1/T$ is extremely weak compared to the exponential dependence in the final term.

Second-Order Solution

The second-order process of Equation (4.10.69) can be solved by dividing both sides by C^2 and using the substitution that $y = 1/C$. With that substitution:

$$\frac{dy}{dt}=\frac{dy}{dC}\frac{dC}{dt}= \quad \frac{1}{C^2}\frac{dC}{dt}=k \tag{4.10.72}$$

and the solution is straightforward:

$$y(\tau)=\int_0^\tau k\,dt+y(0) \tag{4.10.73}$$

or:

$$\frac{1}{C(\tau)}-\frac{1}{C(0)}=\int_0^\tau k\,dt \tag{4.10.74}$$

Application of Kinetic Formulations in Thermal Damage Studies

When a quantitative thermal damage phenomenon has been identified, it can be studied as a first-order or combined first- and second-order process. This subsection inspects the more common first-order analysis in some detail and introduces one form of combined process analysis to extend the usefulness of the method. The specific example of Henriques and Moritz original data is also studied. When the damage end point is a qualitative measure, application of these kinetic models is closer to a curve-fitting exercise than to a fundamental study of the underlying phenomena. Therefore, precise identification and strict definition of quantifiable damage end points are required for meaningful analysis.

First-Order Process Analysis

A more useful form of Equation (4.10.58) may obtained by recasting the result into a volume fraction model. In this formulation, C signifies the remaining concentration of native state (undamaged) tissue constituent. Therefore, the physical significance of the traditional damage measure, Ω, is the logarithm of the ratio of the original concentration of native tissue to the remaining native state tissue:

$$\Omega(\tau) = \ln\left\{\frac{C(0)}{C(\tau)}\right\} = \int_0^\tau A\, e^{-\left[\frac{E}{RT}\right]} dt \qquad (4.10.75)$$

This form of the damage integral has the advantage that it is easily compared to quantitative pathologic endpoints such as collagen and muscle birefringence loss; collagen hyaline damage; leakage of fluorescent dyes; or cell survival in culture. Using this description, direct comparisons can be made between computer models of $T(x, y, z, \tau)$ and measured histologic damage. A set of coefficients, A and E, is required for each damage process considered in the computer model. For tissue damage processes studied to date, A varies from about 10^{40} to 10^{105} s^{-1} while E usually ranges from about 10^5 to 10^6 J/mol.

Each damage process is then allowed to progress in parallel, driven by the calculated thermal field. This formulation assumes that the individual processes are thermodynamically independent, a reasonable description for identifiable thermal damage processes. The concentration of each of the damage markers, $C(\tau)_i$, is accumulated; a distributed field description of the predicted histologic endpoint may be generated.

Functional Behavior of the First-Order Model — The characteristic behavior of the kinetic damage model is that, below a threshold temperature, the rate of damage accumulation is negligible and it increases precipitously when this value is exceeded. For purposes of discussion, it is useful to define the critical temperature as the temperature at which the damage accumulation rate, $d\Omega/dt$, is 1.0:

$$T_{crit} = \frac{E}{R\ln\{A\}} \qquad (4.10.76)$$

A damage process with representative coefficients of $A = 1.0 \times 10^{75}$ and $\Delta E = 5 \times 10^5$ has a critical temperature of 74.8°C. Figure 4.10.13 illustrates the damage accumulation rate dependence on temperature for the example process.

Constant temperature exposures of the example process will result in a decrease in concentration of native state material depending on the time of exposure. Figure 4.10.14 shows the remaining concentration for this process for constant temperature exposures of $\tau = 0.1$, 1.0, and 10 s; the concentration is seen to decrease gradually with increasing temperature for fixed exposure times, as expected. The strong exponential nature of the process is evident as well. Applying this model framework relies heavily on identifying independent damage processes that can be quantitatively measured.

From plots of the form of Figure 4.10.14, estimates of A and E may be made. Each curve will give one point on an Arrhenius plot (see above), where $\Omega = 1$. Note the necessity of using exposure times that span several orders of magnitude in order to separate the curves sufficiently to give acceptable accuracy in determination of the kinetic coefficients.

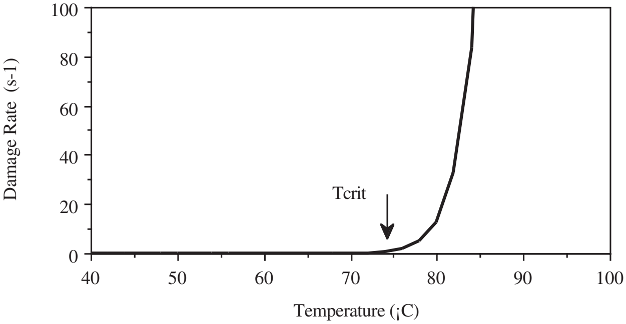

FIGURE 4.10.13 Hypothetical example damage accumulation process has $A = 1.0 \times 10^{75}$ and $\Delta E = 5 \times 10^5$, which gives the damage rate, $d\Omega/dt$, and a critical temperature of 74.8°C.

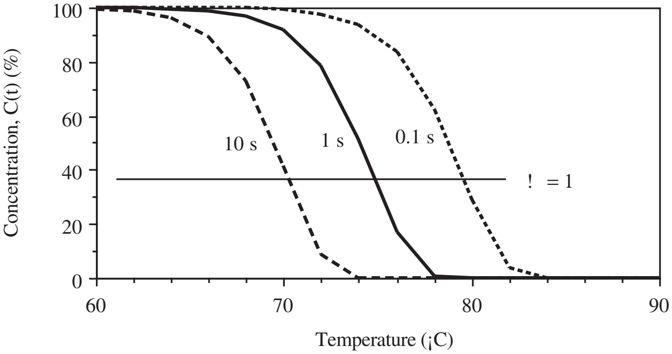

FIGURE 4.10.14 Concentration vs. temperature at various durations of exposure for the hypothetical example process.

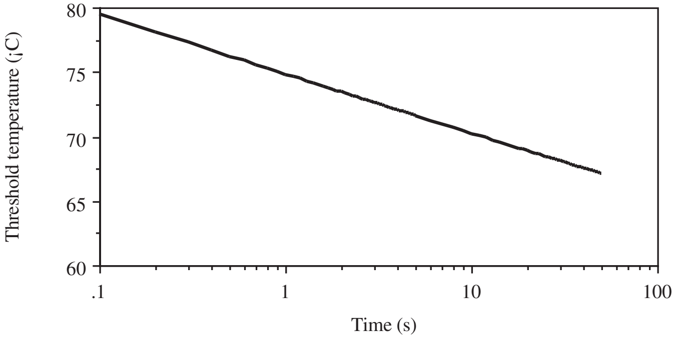

FIGURE 4.10.15 Threshold temperature, T_{TH}, (where $\Omega = 1$) as a function of duration, τ, for constant temperature exposures for the hypothetical example damage process.

Though the damage parameter, Ω, cannot be measured directly in histologic section, often a clearer picture of the functional behavior can be obtained from it. The exponential dependence of damage on the inverse of absolute temperature means that the temperature required to obtain comparable damage levels is quite sensitive to time of exposure. For example, a threshold temperature, T_{TH}, may be defined as the temperature at which the damage parameter, Ω, is 1 for a given duration, τ. Assuming a constant temperature exposure, the integral of Equation (4.10.74) reduces to a simple multiplication and the threshold temperature is

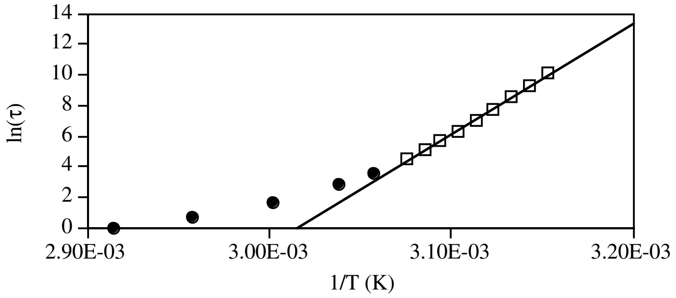

$$\ln(\tau) = 72504\ (1/T) - 218.610; \quad r^2 = 0.997$$

FIGURE 4.10.16 Plot of Henriques and Moritz data on Arrhenius axes with curve fit line for data at 52°C and lower (open diamonds). For the fit E/R = 72,504 and $\ln\{A\}$ = 218.61.

TABLE 4.10.10 Henriques and Moritz Skin Burn Threshold Data[a]

Exposure Time (s)	Temperature (°C)
25,000	44
11,000	45
5,000	46
2,400	47
1,100	48
570	49
300	50
160	51
90	52
35	54
16	56
5	60
2	65
1	70

[a] $\Omega = 1$ means a second-degree burn was observed.

Source: Henriques, F.C., *Arch. Pathol.*, 23, 489–502, 1947.

$$T_{TH} = \frac{E}{R\left[\ln\{\tau\} - \ln\left\{{}^{1}\!/\!_{A}\right\}\right]} \tag{4.10.77}$$

Figure 4.10.15 is a plot of the threshold temperature as a function of duration for the example damage process of Figure 4.10.13 and Figure 4.10.14. Note that threshold temperature is approximately exponentially dependent on duration, as expected, with (in this case) a slope of about –4.65°C/decade. Thus, although 79.5°C is sufficient to result in $\Omega = 1$ at 0.1 s, 102.3°C would be required for a 1-µs exposure for the example process.

Application to Henriques and Moritz Data — A study of the original skin burn data reported by Henriques and Moritz [125] (Figure 4.10.16 and Table 4.10.10) shows that the fit to a first-order process is weak for the higher temperature–shorter exposure time experiments [139], and that the original values of $A = 3.1 \times 10^{98}$ and $E = 6.27 \times 10^5$ (J/mol) [125] do not fit the data as well as their values of $A = 1.3 \times 10^{95}$ and $E = 6.04 \times 10^5$ (for temperatures less than 52°C). In Figure 4.10.17, the skin burn data are fit well with $A = 87.3 \times 10^{93}$ and $E = 6.03 \times 10^5$ when the last reasonable datum is included (at 52°C).

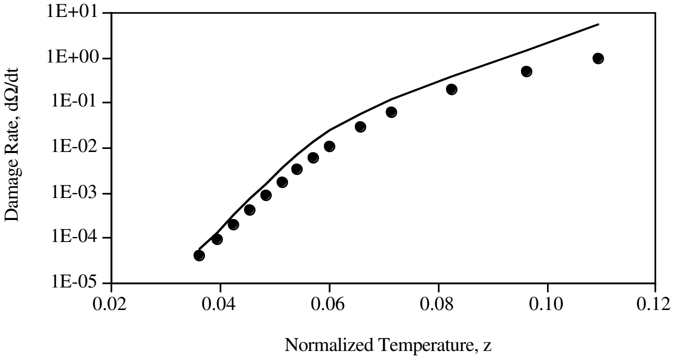

FIGURE 4.10.17 Plot of damage rate for the original Henriques and Moritz data (solid circles) and the enzyme deactivation model of Xu and Qian vs. normalized temperature. (From Henriques, F.C., and Moritz, A.R., *Am. J. Pathol.,* 23, 531–549, 1947, and Xu, Y. and Qian, R., *Trans. ASME J. Biomech. Eng.*, 117, 462–465, 1995.)

Enzyme Deactivation Model

Xu and Qian [140] presented an enzyme deactivation model for skin burn data that combines some of the first- and second-order aspects in a single calculation. The method is based on a general simple enzyme catalyzed reaction sequence from substrates, *S*, to products, *P*:

$$E_a + S \underset{k^-}{\overset{k^+}{\rightleftarrows}} E_aS \xrightarrow{k} E_a + P \tag{4.10.78}$$

and:

$$E_a \xrightarrow{k_d} E_i \tag{4.10.79}$$

where E_a is activated enzyme; E_i is inactivated denatured enzyme (at velocity k_d); and E_aS is the enzyme–substrate complex. The analysis is completed by assuming that the enzyme inactivation process is slow compared to the main reaction sequence. Nondimensional temperature, *z*, is used in the analysis, where:

$$z = 1 - \frac{T_0}{T} \tag{4.10.80}$$

The reference temperature, T_0, as used by Xu and Qian, was representative of the average resting skin temperature: $T_0 = 32.49°\text{C} = 305.65\text{K}$.

$$\Omega(\tau) = \ln\left\{\frac{C(0)}{C(\tau)}\right\} = \ln\left\{\frac{E_a(0)}{E_a(\tau)}\right\} = \int_0^\tau \frac{Ae^{-\alpha z}}{1 + Be^{-\beta z}}\,dt \tag{4.10.81}$$

This combined formulation fits the Henriques and Moritz data (Table 4.10.10) quite well over its entire range if $A = 1.0 \times 10^{-4}$; $\alpha = 100$, $B = 8.0 \times 10^4$; and $\beta = 195$ [123] (see Figure 4.10.17).

Histologic Markers of Thermal Damage*

Tissue and cell heating produce several pathologic alterations that can be directly attributed to thermal damage mechanisms. Many of these are measurable using quantitative pathologic techniques and thus

---

* The authors acknowledge contributions to this section by Sharon Thomsen, M.D.

are amenable to description by kinetic rate process models. As discussed earlier, it is important to recognize that several independent damage processes can occur at the same time. Therefore, it is imperative to describe precisely which particular end point will be measured for kinetic analysis. Depending on the tissue, some end points are more easily identified and measured than others. From the pragmatic biological standpoint, cellular and tissue thermal damage end points are divided into two general categories: lethal and nonlethal thermal injury.

Nonlethal Low-Temperature Tissue Effects

Most living cells and tissues can tolerate and survive modest temperature elevations for limited time periods depending on the species and the metabolic status of the individual. Recovery after heating is marked by restoration of normal functions. Most nonlethal thermal injuries of individual cells are secondary to: (1) heat-induced acceleration of metabolism; (2) thermal inactivation of particular enzymes; and/or (3) rupture of cellular membranes. These alterations lead to disruption of several physiologic reactions of which the most critical are respiration and energy-generating metabolic functions [140, 141]. The best indicators of reversible, nonlethal thermal injury in the living cell or organism are physiological tests that monitor heat-sensitive biochemical and metabolic changes rather than morphologic alterations.

Immediate Effects — Routine light microscopic techniques applied immediately after heating are not useful for the detection of histologic markers of nonlethal thermal injury. However, enzyme histochemistry, a laborious, somewhat capricious methodology, can be used to reveal inactivation of a few heat-labile enzymes [142]. Additionally, transmission electron microscopy (TEM) provides sufficient magnification and resolution to show ruptured cellular membranes and distorted organelles; however, if the ruptures and distortions are frequently seen, the damage is not likely to be lethal. Over time, recovery occurs with synthesis of replacement enzyme proteins and new membranes to patch the holes and reconstitute the normal functions of the organelle and cell.

On the other hand, tissues and organs are composed of a diverse population of cells that have: (1) varying levels of heat sensitivity; (2) different types of metabolic functions and repair capabilities; and (3) various contributions to the function of the tissue or organ. Unlike single cells, reversible thermal damage of tissues can and usually does involve some cell death; however, it occurs at a level that does not impair the function of the organ or tissues. Similarly to the situation in single cells, histologic assessment of reversible tissue thermal injury immediately after heating requires enzyme histochemistry and TEM to determine the degree and distribution of thermal damage because this damage is not detectable with routine light microscopic techniques.

Delayed Effects — Depending on the tissue, intracellular edema, tissue edema, and hyperemia occur within seconds to hours. These are easily identified, delayed organismal responses to nonlethal thermal damage in single cells as well as living tissues. Intracellular edema is due to abnormal accumulation of fluids secondary to thermally induced metabolic dysfunction; resolution of the edema upon repair is a marker of healing. Heat-induced tissue edema and transient hyperemia (increased blood flow and blood vessel dilatation) are mediated by release of vasoactive polypeptides from local inflammatory cells within several seconds of injury. The action of the polypeptides causes blood fluids (primarily plasma) to escape through gaps between the endothelial cells lining the vessel. On the other hand, prolonged hyperemia like that associated with sunburn is a delayed response associated with direct endothelial damage. In this case, the histologic indicators of the more severe vascular damage are dilated blood vessels stuffed with red blood cells and, not infrequently, microscopic leakage of the red blood cells through the damaged vessel wall into the adjacent tissue spaces. Recovery, which is secondary to endothelial regeneration and repair, is seen in a few days [143].

Lethal Low-Temperature Thermal Effects

Cell and Tissue Death and Necrosis — Cell death and subsequent necrosis result when the damage is so severe that the usual repair mechanisms cannot cope and/or the mediators of the repair mechanisms (DNA and RNA transcription enzymes) are thermally destroyed. Again, routine light microscopic techniques cannot be used to identify dead cells immediately after heating except in the case of severe damage. However, within minutes of lethal thermal damage, TEM reveals accumulation of chromatin (the DNA containing chromosomes) at the margins of the nuclei (a recognized TEM marker of cell death) plus more extensive disruption of cellular organelles and limiting cell membranes that are incompatible with survival [144]. Enzyme histochemistry demonstrates enzyme inactivation but, as discussed previously, enzyme inactivation by itself cannot be used as a hallmark of cell death.

After death, cells and tissues undergo necrosis, which is a natural process of disintegration that follows a predictable course over time. Tissue necrosis, the "gold standard" marker of death, is easily recognized in light microscopic sections of lesions 24 to 72 h after the lethal event and, for most tissues, histologic evaluation of the maximal extent of tissue necrosis is seen at about 3 to 5 days for most tissues [145–147]. After 5 days, the boundaries of necrosis and other markers of thermal coagulation are obscured by the healing processes and precise measurement of the extent of lethal heating can no longer be done.

In Vivo *Red Zone Thermal Damage* — When localized electromagnetic, acoustic, or optical heating results in deep zones of necrosis, as when laser light is delivered through an optical fiber or ultrasound or electromagnetic waves are focused, concentric zones of thermal damage form around the source during heating and immediately thereafter. The boundaries between these zones are often distinct and measurable. Depending on the power density and duration of exposure, the three major zones in the lesion that can be seen by the naked eye are: (1) a central ablation hole (at high-power densities); (2) a whitish zone of coagulation; and (3) when the blood supply is intact, a surrounding peripheral red zone. The red zone is formed as a result of hemostasis, hemorrhage, and hyperemia (increased blood flow). The vascular responses are intermixed; however, hemostasis — due to direct damage to blood cells and vessels — tends to occur at the inner boundary between the surrounding red zone and the more central white coagulation zone. Studies performed in rat liver and goat breast show that the outer boundary of the red zone corresponds to the maximum extent of lethal thermal damage as determined by tissue necrosis evaluated in surviving animals 3 days after treatment [145, 146].

Microscopically, additional distinct zones of thermal damage can be detected in the white coagulum. Advancing radially inward from the boundary between the red and white zones, the following quantitative histopathological markers of thermal damage can be observed:

- Lethal cellular injury manifested by cell shrinkage, spindling, and hyperchromasia
- Collagen hyalinization
- Collagen birefringence changes
- Muscle birefringence changes
- Water-dominated effects

The changes intensify as the hotter center of the lesion is approached. Additionally, a mass defect created by ablation of the tissue is observed in cases of intense heating, but is not considered in this chapter.

Thermal Coagulation

As temperatures rise and/or heating times are prolonged, cellular and tissue structural proteins, which are thermally more stable than the vital, energy-producing enzymes, undergo denaturization and conformational changes, a process defined as thermal coagulation. Coagulation is immediately apparent and always indicates lethal thermal effect. For most tissues, coagulation can be seen with the naked eye as whitening of the tissue associated with increased turgor and opacity. The changes of the egg white while the egg is fried is an obvious example of thermal coagulation. On the other hand, coagulation of collagen-rich tissues such as tendon and skin can be signaled by increasing transparency, apparently due to decreased optical scattering by the denatured collagen fibrils.

Microscopically, thermal coagulation of cellular and extracellular structural proteins includes an array of morphological alterations that mark a large range of temperatures and exposure times. As tissue temperatures and/or exposure times increase, the coagulative changes become more obvious and light microscopic analysis becomes the investigative tool of choice.

The most useful histologic markers of coagulative thermal damage in tissues are structural alterations of cells and collagens. Thermally coagulated cells and intracellular organelles shrink and undergo characteristic conformational changes. Collagens are a widely dispersed biochemical class of extracellular fibrous proteins that form the supporting scaffolding of nearly all soft tissues and the organic strut system of bone, cartilage, and teeth. These fibrillar proteins swell and form amorphous masses as a unique response to heat.

Cellular Shrinkage and Conformational Changes — Thermally coagulated cells shrink due to denaturation of the elongate cytoplasmic and nuclear proteins that form the three-dimensional scaffolding system of these structures [147, 148]. Coagulated surface epithelial cells — such as those that line the gut, bladder, and numerous glands of the body — tend to become elongate (spindle shaped). The boundary between this change and the normal epithelium can be quite distinct and thus potentially useful for kinetic analysis.

In contrast, the epithelial cells of the solid organs — such as the liver, pancreas, and kidney — just shrink and do not undergo noticeable conformational change at the light microscopic level. The cellular shrinkage is also due to loss of intracellular water. The coagulated proteins of the desiccated cells become more densely packed, as reflected by dark cytoplasmic and nuclear staining (hyperchromasia) in routinely prepared histologic sections. Unfortunately, these histologic changes are very subtle and, frequently, cannot be distinguished from technical artifacts due to poor fixation. Therefore, they are not reliable markers of thermal damage, especially in the hands of an inexperienced observer.

Collagen Coagulation — Thermal denaturization of extracellular fibrous structural proteins, the collagens, is marked histologically by swelling and an amorphous, glassy transformation of the fibers (hyalinization) [145, 146, 149, 150]. This transformation is easily seen in tissues composed of loose networks of collagen fibers, such as the cornea, skin, submucosa of the stomach, intestines, and urinary bladder. However, some collagen fibers, such as those found in arterial media and liver sinusoids, are very thin ("reticulin fibers"); thus, detection of hyalinization is beyond the resolution of the light microscope. Additionally, at the other end of the fiber size spectrum, mild hyalinization and fiber swelling are equally difficult to see in tissues composed of thick, densely packed collagen fibers, such as those found in blood vessel adventitia and dermis. Changes of birefringence of thermally coagulated collagen (described later) are sometimes easier to detect than hyalinization in these circumstances.

Thermally Induced Loss of Birefringence

Birefringence is an optical property of some tissues that rotates incident polarized light. Thermal coagulation is associated with partial and total loss of the native birefringence of muscle tissues and certain fibrillar collagens as revealed by transmission polarizing microscopy (TPM) [146, 150]. The birefringence of muscle is due to the very regular arrangement of the fibrillar contractile protein macromolecules, actin and myosin, that form the contractile unit of the muscle. Collagen birefringence is the result of the molecular structure and regimentation of the tropocollagen molecules from which collagen fibrils are built.

Tissue birefringence has two components: intrinsic and form birefringence. Intrinsic birefringence is secondary to the α-helical conformation of the polypeptides that form the individual contractile proteins of muscle and tropocollagen molecules; it accounts for 12 to 30% of the total birefringence of these tissues. The remaining birefringence, form birefringence, is related to the crystalline-like array of the actin and myosin molecules in the sarcomere and the regimented longitudinal array of tropocollagens within the collagen fibrils [148, 150–163].

Thermally induced changes of muscle birefringence are associated with dissociation and disruption of the molecules, as revealed by TEM. Partial loss of birefringence in skeletal and cardiac muscle has been identified with the breakdown of the relationships of actin and myosin in the sarcomere (loss of form birefringence). The source of the birefringence of striated muscle is the central portion of the sarcomere, the A or anisotropic band, in which the actin and myosin are arranged in parallel crystalline-like array. The I, or isotropic, band of the sarcomere includes portions of adjacent sarcomeres that contain actin molecules attached to the Z band, an attachment zone for the actin molecules. Total loss of birefringence is associated with increased temperature–time histories and is probably related to reduction of the individual fibrillar contractile proteins to thermally denatured granular profiles (loss of intrinsic birefringence) as shown in TEM of heated myocardium [164, 165].

Thermally induced birefringence changes in collagen involve decreasing intensity of the birefringent image until it is totally lost at higher temperatures. TEM of heated collagens shows a gradual unraveling of the fibers with disappearance of the characteristic periodicity of collagen reflecting the dissolution of the regimented organization of native collagen as it is heated [146, 163].

The onset of the birefringence changes of collagens varies depending on the experimental conditions, anatomic site, and the age of the organism. Native tissue collagens reside in complex environments of different proteins, glycoproteins, and cells that are greatly influenced by the local and systemic physiology of the living organism. The intimate relationships of the collagens with these tissue constituents are regulated by water and salt concentrations; ionic and covalent bonds; and hormonal and metabolic effects. Collagens extracted from tissues are not in their natural environment; therefore, *in vitro* experiments testing molecular relationships including measurements of birefringence will not predict the native behavior of collagen *in situ* or *in vivo* [159–161]. In addition, as the organism ages, the collagens, especially the Type I collagen found in most tissues, form more molecular cross links that alter the temperature–time thresholds of fiber dissociation [160].

Polarizing microscopy can be performed on paraffin sections prepared for routine light microscopy; thus, the birefringent images can be correlated directly to morphologic structure. The intensity of the birefringent images is governed by the thickness of the section, the types of dyes used, and, in the case of collagens, the collagen fiber thickness [145, 166].

Water-Dominated Effects

The role of water vaporization becomes dominant as tissue temperatures approach 100°C. The tissue effects depend on: (1) the rate of water vapor formation; (2) the temperature of the water vapor; (3) the rate of diffusion (escape) of the vapor from the tissue; and (4) the tissue mechanical properties [167–176]. All tissues exposed to air will lose water vapor to the atmosphere because of the differences between the partial pressure of water vapor across the tissue–air boundary. Below 100°C, water vaporization is a surface phenomenon. As tissues are heated, water vapor will be generated and the vapor will diffuse toward the surface to escape. The water vapor is in thermodynamic equilibrium with liquid water; in tissues deep beneath the surface, the relatively low partial pressure gradients favor the liquid over the vapor phase. Meanwhile, at the surface, the tissues dry out as the water vapor escapes leaving the hard, not infrequently brittle, solid tissue components behind.

At or just above 100°C, water vapor is generated volumetrically, equilibrium is pushed toward the vapor phase, and, for sufficiently high-volume generation rates, q''', more vapor is produced than can escape by simple diffusion. The excess vapor is trapped within the cell and in the extracellular tissue layers forming vacuoles or dissections along planes of mechanical weakness [176–178]. The surface desiccates rapidly because diffusion lengths are short. The temperatures of the tissues that still contain liquid water will remain close to 100°C or the pressure will rise.

The vapor in the vacuoles will expand quickly, compressing the surrounding, rapidly drying tissues that form the vacuolar walls. As the vacuoles expand, the walls separating the vapor pockets from each other or the tissue surface become thin. The walls rupture as the force of the increasing pressures of expanding vapor overcomes the mechanical strength of the tissue. The vacuoles coalesce to become larger holes within the tissues or form irregular defects on the surface. When this process takes place over relatively long heating times, the tissue defects are formed as the result of tissue compression, desiccation, and shrinkage but *not* to loss of dry mass. On the other hand, rapid heating times result in explosive rupture, which causes tissue fragments to be ejected from the surface, thus creating irregular craters formed secondary to dry tissue mass loss. These water-dominated events are the same as those when popcorn is made; thus, the tissue changes have been called the “popcorn” effect [168–171, 177–179].

The kinetics of water vaporization will not be treated here; see the chapter on nucleate boiling for a kinetic discussion of this phenomenon. Histologically, the zone of water vapor formation manifests as a distinct region populated by vacuoles adjacent to ablation craters formed from volume heat sources. In some experiments — for example, electrosurgical cutting and laser ablation at water-absorbed wavelengths — the vacuolized zone usually has a distinct and measurable border.

Damage Rate Process Coefficients

Thermal damage kinetic coefficients are usually determined from constant temperature exposures of relatively long duration. Threshold damage results are selected out of a set of damaged tissue samples for analysis from which estimates of A and E are obtained.

Constant Temperature Exposures

Because of the sensitivity of the damage integral to small changes in temperature, the typical approach in obtaining A and ΔE is to expose the tissue to a constant temperature; identify experiments in which the damage is threshold — i.e., for which $\Omega = 1$ or $C(t) = 36.8\%$ of $C(0)$ — and obtain A from the intercept and E from the slope of an Arrhenius plot of $\ln(t)$ vs. $1/T$ for the threshold experiments. If the temperature is held constant, the integral reduces to a simple multiplication, and $C(t) = 0.368\ C(0)$; then Equation (4.10.71) becomes:

$$\ln\{\tau\} = \frac{E}{R}\frac{1}{T} - \ln\{A\} \tag{4.10.82}$$

The usual experimental method is to expose thin slices of tissue to constant temperature in a water bath, by surface application of heated water [122–125] or on a heated metallic plate for desired time intervals. Table 4.10.11 lists rate coefficients obtained in various experiments and the relative damage rates ($d\Omega/dt$) are compared for several of them in Figure 4.10.18.

When using the kinetic models and measured coefficients, it is imperative that an adequate description of the particular end point be given. This is because different end points in the same tissue will have widely varying critical temperatures and damage accumulation rates. For example, in addition to the variation in tissue, the end points in the various studies listed in Table 4.10.11 differ markedly.

Retina — The measurements of Welch and Polhamus [180] used the diameter of the edge of the visible lesion formed in bovine retina under argon laser irradiation as the end point. The temperatures were not measured directly, but were determined in separate experiments on retinas in which a correlation between temperature and radius was established using microthermocouples (about 5 μm in diameter) advanced from the posterior surface of the eye to a point just below the retina. The correlates were used to estimate the retinal temperature, given laser beam power and duration. The critical temperature for these coefficients is 56.0°C.

Takata et al. [181] used a similar decision criterion for retinal damage for shorter exposure times. They fit the data with three sets of coefficients because a single first-order model was not sufficient. It would appear that because several parallel damage processes were at work in their study, a set of coefficients was required. The critical temperature for the high-temperature set of coefficients is 59.9°C. Birngruber et al. [182, 183] estimated a frequency factor and activation energy from consideration of the thermodynamics of protein and enzyme denaturization processes. Their estimates have a critical temperature of 74.5°C.

Skin — The end point for $\Omega = 1$ in the original studies of Henriques and Moritz [122–125] corresponded to a continuum of cascaded effects. In their study, the skin of pigs was exposed, *in vivo*, to flowing water at a controlled temperature for exposure times varying over several orders of magnitude. They calibrated their coefficients so that $\Omega = 0.53$ corresponded to the onset of erythema (characterized as first degree in their paper). Then, $\Omega = 1.0$ corresponded to a second-degree, or partial-thickness, burn and $\Omega = 10^4$ to a full-thickness, or third-degree, burn. Their coefficients, $A = 3.1 \times 10^{98}$ and $E = 6.27 \times 10^5$, have a critical temperature of 59.7°C. Weaver and Stoll [128] used similar criteria to those of Henriques and Moritz and applied two sets of coefficients (the upper values applicable above 50°C, as in the Takata et al.

TABLE 4.10.11 Experimentally Determined Rate Coefficients

A (s^{-1})	E (J/mol)	Conditions	Ref.
Retina			
0		T ≤ 316 K	181
4.3×10^{64}	4.2×10^{5}	$316 < T \leq 323$	
9.3×10^{104}	6.7×10^{5}	$T > 323$	
3.1×10^{99}	6.28×10^{5}		180
10^{44}	2.93×10^{5}		182, 183
Skin			
3.1×10^{98}	6.27×10^{5}		125
2.2×10^{124}	7.83×10^{5}	$317 < T < 323$ K	128
1.8×10^{51}	3.27×10^{5}	$T \geq 323$	
Egg			
White: 3.8×10^{57}	3.85×10^{5}		184
Yolk: 3.05×10^{56}	3.89×10^{5}		
Aorta (collagen)			
5.6×10^{63}	4.3×10^{5}		185
Calcein leakage, AT-1 cells			
1.14×10^{5}	4.78×10^{4}	$300 < T < 328$ K	137
2.7×10^{11}	8.78×10^{4}	$T > 328$ K	
50% Cell survival, AT-1 cells			
1.16×10^{48}	6.58×10^{6}	$300 < T < 328$ K	137
6.11×10^{12}	9.22×10^{4}	$T > 328$ K	

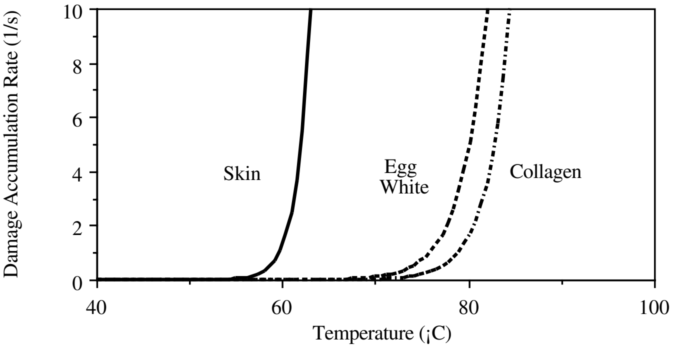

FIGURE 4.10.18 Comparison of selected damage processes from Table 4.10.11: damage rate, $d\Omega/dt$, vs. temperature.

study) to match the experimental data. The critical temperature for their highest temperature coefficient set is 59.4°C.

Egg White and Egg Yolk — Egg white and yolk were exposed to constant temperature (±0.2°C) in a water bath for varying exposure times [184]. Coagulation was defined as the onset of whiteness (coagulum formation apparently due to increased scattering in the clear liquid egg white) observed by the naked eye. Water bath temperatures ranged from 60 to 90°C in 4°C increments. At each temperature, the time to threshold was measured and plotted in accordance with Equation (4.10.24) and rate coefficients determined from linear regression, as described. Approximately 3 to 5 s were required to obtain whitening in the egg white at 70°C; in the egg yolk, 82°C was required for the same exposure time. The table values have critical temperatures of 76.0°C for egg white and 86.6°C for egg yolk.

Aorta — Coefficients for collagen damage have been measured in excised human aorta wherein the specific damage end point was a measurable and repeatable weakening of the connection between collagen and elastin in the medial layers [185]. The experiments consisted of variable exposure time (15 to 1500 s) contact of the intimal surface with a heated copper block controlled to ±1°C; the adventitial surface was insulated. The weakening was reflected as a tearing between these fibers in histologic section. Of course, tearing in a histologic section can be due to a number of processing variables. In order for an experiment to be acceptable as a damage measure, the tearing region had to be specifically associated with the region of heated block application in multiple adjacent sections. Ten thresholds were obtained in 90 experiments, from which the damage coefficients were estimated to be: $A = 5.6 \times 10^{63}$ (s^{-1}) and $E = 4.3 \times 10^5$ (J/mol). The critical temperature for these coefficients is 78.9°C.

The kinetic nature of thermal damage means that the time of exposure is critically important when discussing threshold temperatures. For example, it is commonly stated that thermal damage occurs above 45°C — and, in fact, 45°C was identified by Moritz and Henriques as the long-term exposure asymptote for threshold damage. However, at that temperature, it would require 9.7 h of exposure to get a burn ($\Omega = 1$). To get a skin burn in 1 s, a temperature of 59°C would be required; over the 0.1 s typical of the laser activations, 63°C is required. Similarly, using the coefficients for collagen, at 45°C, it would require about 73 days of exposure to get $\Omega = 1$; for damage in 1 s, 79°C is necessary; and in 0.1 s a constant temperature of 84.5°C is required.

Thus, when comparing the higher temperatures required to obtain collagen denaturization in laser experiments (above about 80°C), for example, to published values of collagen temperature thresholds (which range from 50 to 60°C), it is important to note that: (1) the times of exposure used in published collagen damage reports are usually in terms of hours; and (2) it is entirely likely that collagen in dilute solution has a different set of kinetic coefficients than collagen *in situ* because of complex structural interrelationships inherent in the tissue.

Calcein Leakage — Bhowmick and Bischof [137] measured calcein leakage rates from type AT-1 prostate tumor cells exposed to elevated temperatures. Calcein is a fluorescent dye that leaks out of cell membranes at varying rates depending on membrane integrity. The coefficients in Table 4.10.11 correspond to 50% decrease in intracellular calcein fluorescence intensity. These researchers also reported cell survival rates (again, for 50% survival). These data are reasonably close to $\Omega = 1$ point (36.8% survival or remaining fluorescence intensity). Many other cell survival studies have been reported in the literature (see, for example, Mixter et al. [186] and Padanilam et al. [187]).

Transient Thermal History Experiments

Problems with the standard constant temperature approach to determining A and ΔE are that

- With only a very few exceptions, the tissue must be excised to perform the experiments, thus disrupting its blood perfusion and activating autolytic (*postmortem* degeneration and necrosis) processes.
- No exposure is truly constant temperature and rise time segments must necessarily be short compared to total exposure time in order to be negligible (restricting one to the study of very slow processes).
- It is difficult to obtain trustworthy estimates of A because the temperature axis is hyperbolic ($1/T$) and, even if the exposure times vary over several orders of magnitude, small uncertainties in the slope ($\Delta E/R$) create very large uncertainties in A.
- The methods are difficult to use in laser damage studies because constant temperature exposures are not possible to obtain.

Working with transient thermal data adds a high level of uncertainty to the damage coefficients because the time of exposure is problematic. Nevertheless, estimates of rate coefficients can be made upon which treatment protocols can be evaluated. An approximate method has been applied with some limited success [188, 189], and is described here.

As can be seen from Table 4.10.11, most of the damage processes have activation enthalpies on the order of 10^5 J/mol. For the hypothetical example damage process, with $E = 5.0 \times 10^5$ J/mol, at 60°C the rate of damage formation would double if the temperature increased to 61.3°C (about 0.4% temperature increase on the absolute scale). The rate of rise of laser spot heating experiments is usually many degrees per second; therefore, the exposure time is assigned as the time during which the tissue temperature is within 2°C of the maximum value. Of course, noise in the determination of temperature creates significant uncertainty in the determination of exposure time, τ, for a calculation; however, technically acceptable experiments can be extracted by inspection of the temperature history.

Note that the temperature history at the location of threshold damage is required, so the surface location of threshold damage in the histologic section is determined, using the methods previously outlined, and then the thermographic record of temperature at that location is analyzed. This method has been used to make preliminary estimates of damage coefficients for birefringence loss in rabbit myocardium and purpura formation in pig skin irradiated with an argon laser. By referring directly to the recorded thermographic image data, the uncertainty associated with optical models and properties of the tissue can be avoided.

Purpura Formation — When using lasers for the clinical treatment of dermatologic anomalies such as port wine stain, a variable of major importance in dosimetry planning is the purpura threshold. The purpura threshold is determined by optical and thermal properties of the skin because purpura generation is of photothermal rather than photochemical origin. In controlling the dose, thermal feedback can be used to limit the laser irradiance if the damage process is known. Direct use of thermal feedback has the additional advantage that variations in the tissue optical properties are not important to the control algorithm. Therefore, useful thermodynamic models of purpura formation could provide additional information to be used in treatment planning and will likely facilitate thermal feedback approaches to dosimetry control.

An argon laser was used to conduct 20 experiments on porcine skin *in vivo* [188]. The spot size was nominally 2 mm and activation times and beam powers ranged from 0.2 to 20 s and 1 to 11 W, respectively. Skin surface temperature was recorded thermographically and transient thermal histories for the radius of purpura formation were determined *a posteriori* at locations determined from gross and histologic observation. The 2°C criterion was used to estimate the exposure time at the threshold radius. The time and temperature were plotted on an Arrhenius plot and A and ΔE determined by linear regression.

It should be noted that the purpura coefficients were derived by measuring surface temperature and the active thermal damage process is occurring subsurface at the capillary level. Also, the Argon laser wavelength is significantly scattered in dermis and epidermis, so one would expect that the deep temperatures were higher than the skin surface temperatures. Consequently, the coefficients apply to measured surface temperature, not the capillary damage process per se. Of course, when feedback control based on surface temperature is desired, this is the variable of choice. For these data, $A = 4.11 \times 10^{53}\ \mathrm{s}^{-1}$ and $\Delta E = 3.39 \times 10^5$ J/mol and the critical temperature is 56.9°C. Not unexpectedly, the data are quite noisy, as can be seen in Figure 4.10.19.

Birefringence Loss in Myocardium — A similar series of experiments was conducted on freshly excised rabbit myocardium less than 10 min after sacrifice [189]. The epicardial surface of the excised left ventricle was exposed to argon laser light. Again, the spot size was 2 mm with durations and beam powers from 0.2 to 20 s and 1 to 12 W, respectively. After exposure, the visible lesion was measured and marked across the diameter to guide the histologic sections. Stained sections (Mallory's trichrome and H&E) were analyzed to determine the depth and surface diameter of the zones of partial and total birefringence loss. The temperature histories of the radii of the threshold of birefringence loss were calculated from the recorded thermal imagery.

Figure 4.10.20 is an Arrhenius plot of the resulting data. Damage coefficients for this process were estimated to be: $A = 3.12 \times 10^{20}$ (s^{-1}) and $\Delta E = 1.28 \times 10^5$ (J/mol) with a critical temperature of 52.9°C.

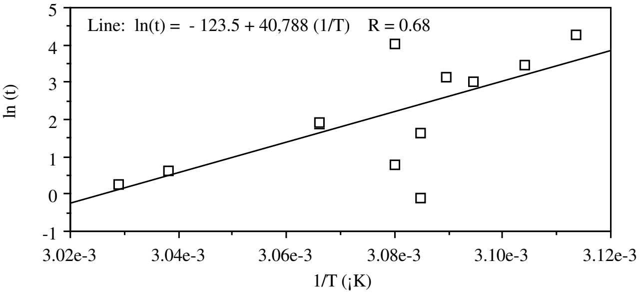

FIGURE 4.10.19 Arrhenius plot for purpura formation *in vivo* in porcine skin. Data derived from surface measurement of temperature resulting from coagulation of deeper blood vessels.

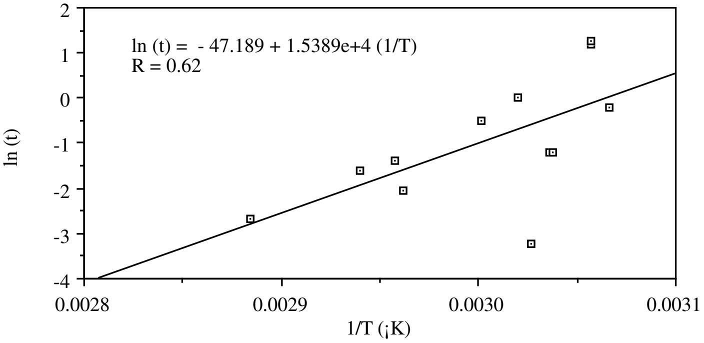

FIGURE 4.10.20 Arrhenius plot for birefringence loss in rabbit myocardium *in vitro.*

Interestingly, in this data set the diameters of the visible lesions equaled those of the birefringence loss zones within the accuracy of the measurements.

Summary

First-order kinetic models for tissue damage are useful for predicting trends in damage experiments. Unfortunately, the frequency factor and energy have been determined *in situ* for only a few damage processes; critical temperatures for known processes range from about 50 to 90°C. Nevertheless, these models can be used to make direct comparisons between numerical predictions of damage and histologic results — something that cannot, as yet, be achieved any other way.

A very careful definition of the particular histologic end point is necessary. To avoid the arbitrariness that characterizes much of the early damage studies, the end point should: (1) be clearly recognizable and defined; (2) be reproducible under varying experimental conditions; (3) be easily measured; and (4) involve relatively homogeneous and readily available test tissues. For example, thermally induced birefringence image intensity decrease in skeletal and cardiac muscle is easily seen and measured using polarizing microscopy and optical detectors. Beef and pork loin cuts, chicken breasts, and canine or beef hearts can provide the numerous tissue slices required to accumulate adequate data.

In part because of the effects of biologic inhomogeneities and random fluctuations in tissue characteristics, and in part due to the difficulty of resolving small temperature differences, thermal damage data are inherently noisy. Consequently, the prediction of observed damage boundaries in very long exposure experiments (on the order of minutes to hours) in the presence of substantial spatial thermal gradients may be frustrating. However, in small spot size exposures of relatively short duration (up to fractions of seconds), the predicted boundaries compare favorably to those observed. This is probably due to the very steep thermal gradients typical of small spot experiments — that is, a rather large error in actual critical temperature may be swamped out by the very steep thermal gradient so that the location of the predicted damage contour may, in fact, agree fairly well with experimental histologic observation.

Certainly, even though the results of a particular experiment may eventually prove impossible to duplicate in numerical models, a rather careful analysis of the trends, which could be obtained from changing power, contact temperature, spot size, and duration, can be studied in detail in the numerical model and on a spatial scale similar to microscopic observation. Also, the numerical model allows dissection of the transient development of thermal damage — something that cannot be achieved in any other way. Thus, although many uncertainties are associated with kinetic models of thermal damage, they can be extremely illuminating and helpful in dosimetry planning.

Tissue Effects: Subzero Temperatures

An important area of bioheat transfer application is in the domain of subzero temperatures. As was noted previously, biochemical rate processes are governed by the local system temperature. Lowering the temperature has the effect of reducing reaction rates and, at sufficiently low temperatures, a state of suspended animation can be achieved. Owing to the major aqueous component of physiological fluids, temperatures low enough to effect suspended animation normally result in freezing. The freezing of native biomaterials is nearly always lethal to the affected tissue upon thawing. The effected injury can be used to benefit in cryosurgery for the purpose of destroying a target tissue such as cancer.

Alternatively, the tissue can be modified prior to freezing by the introduction of a chemical cryoprotective agent (CPA) to afford protection from freeze–thaw injury. Techniques have been developed for the successful long-term cryopreservation of many biomaterials for subsequent applications, including human transplantation. The response of living biomaterials to freezing and thawing is intimately tied to thermal history during processing, especially at subzero temperatures. Thus, bioheat transfer analysis has played a key role in the design and development of low-temperature bioprocessing protocols.

Cryopreservation

Living tissues may be frozen to deep subzero temperatures to create a state of suspended animation for indefinite periods and recovered with very minimal loss of viability and function. It is necessary to store tissues at below approximately –120°C so that the kinetics of chemical reactions and ice nucleation become infinitesimally small. Successful cryopreservation protocols require that subject tissue be modified prior to cooling to subzero (°C) temperatures by addition of a CPA to protect against the injurious effects of ice formation or to block the formation of ice so that a glassy state results (vitrification).

Widespread interest has developed in exploiting cryopreservation as a means for reversibly banking a broad spectrum of tissues for transplantation. The seminal paper that first reported this work described the use of glycerol to freeze fowl sperm 50 years ago [190]. Successes were then reported for other types of tissues having rather simple cell structures, such as erythrocytes, gametes, and various cells obtained from primary cultures [191–193]. Most of these cryopreservation techniques were derived via largely empirical methods. Starting in the 1970s, it was realized that cryopreservation of more complex systems such as multicellular tissues and whole organs required a more rigorous scientific understanding of the mechanisms of the governing biophysical processes and cellular response to freezing and thawing. Since that time, engineers have made significant contributions to the developing science of cryobiology — not the least of which has been to identify some of the key biophysical problems to be solved [194].

Biophysical Basis of Freezing Processes in Cells

Analysis of cryopreservation by freeze–thaw processes is based on addressing phenomena associated with the solidification of aqueous solutions and their resulting effects on embedded living cells surrounded by semipermeable membranes. When an aqueous solution freezes, water is sequestered into the solid ice phase, resulting in concentration of solutes in the residual liquid phase solution. If equilibrium is maintained between the liquid and solid phases, the coupling between temperature and solute concentration is described by the phase diagram for the solution. As shown in Figure 4.10.21, as the temperature is depressed below 0°C, the amount of solute in the liquid increases according to a function

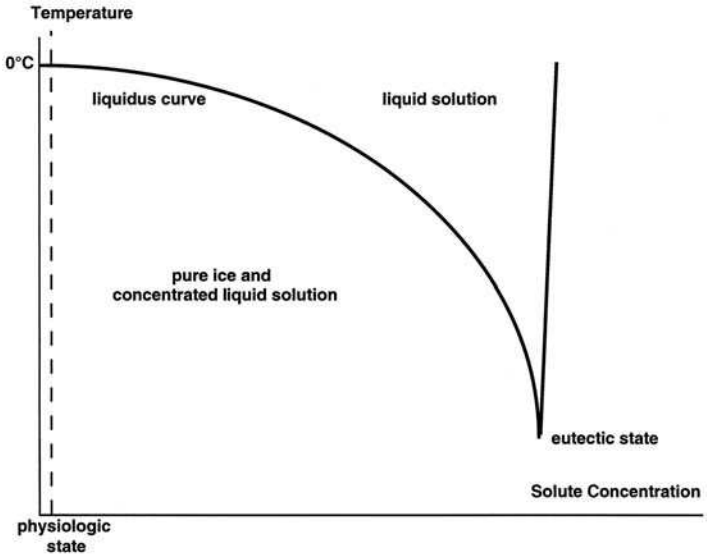

FIGURE 4.10.21 Simplified representation of an aqueous equilibrium phase diagram. Physiological solutions have solute concentrations that are quite small (about 300 mOsm) in comparison with the eutectic state. As freezing progresses, the liquid phase concentration may increase by more than 20-fold, subjecting cells to intense osmotic stress

defined by the liquidus curve until the eutectic state is reached. Thus, cooling a biological tissue until ice is nucleated imposes osmotic as well as thermal stress.

A consequence of the osmotic stress is that the individual cells in a tissue will lose intracellular water to the solute-enriched environment. (It is assumed that, at subzero temperatures, the time scales for transport of other molecular species will be negligible in comparison to that for water.) The rate at which this mass transport occurs across the cell membrane is governed by the membrane's permeability to water. This process was modeled initially by Mazur as a simple transport phenomenon [195]:

$$\frac{\partial \Psi}{\partial T} = -\frac{L_p S B \Re T}{v} \ln\left(\frac{p_{in}}{p_{ex}}\right) \tag{4.10.83}$$

The Mazur equation predicts the change in the volume, Ψ, of a cell with temperature during freezing at a cooling rate of B in conjunction with the transport of water from within the cell in response to the osmotic differential developed across the membrane as solutes are concentrated during the solidification process. The rate of transport is dependent on the surface area, S, of the cell; the membrane permeability to water, L_p; the molar volume of water, v; and the ratio of intracellular to extracellular vapor pressures of water. Although the latter term is not a rigorous description of the driving potential for the transport process, it is easily replaced by the transmembrane differential in chemical potential or solution concentration.

Dehydration is not the only process by which equilibrium can be achieved between intracellular and extracellular water during freezing. Ice crystals may nucleate within the cell, forming intracellular ice (IIF) [196]. The occurrence of IIF is nearly always lethal to cells, with certain explicit exceptions [197] and is therefore to be avoided during cryopreservation. The balance between equilibration of water across the cell membrane by osmotic dehydration and by IIF is governed primarily by the magnitude of the cooling rate [198]. As depicted in Figure 4.10.22, at rapid cooling rates, water has little opportunity to escape from the interior of the cell as the extracellular solute concentration increases with progressive freezing.

Eventually, the conditions are satisfied for intracellular nucleation of ice crystals. At slow cooling rates, the cells are able to dehydrate as the extracellular solute concentration increases, and the intracellular

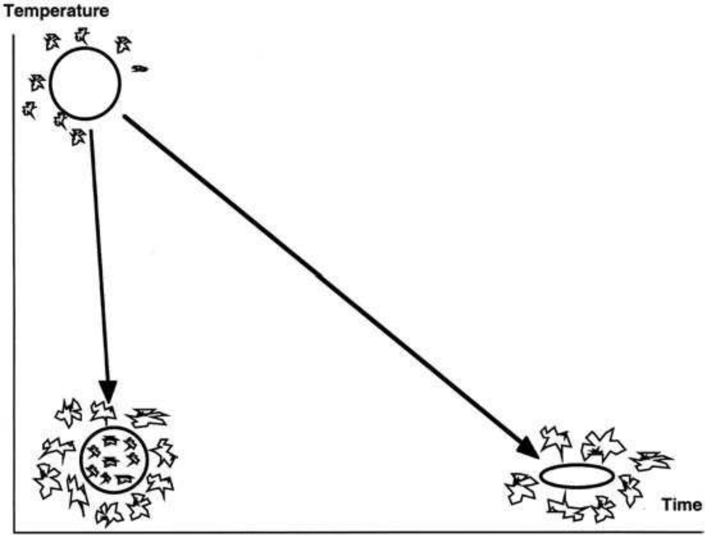

FIGURE 4.10.22 Schematic of the reaction of individual cells to extreme variations in the cooling rate during freezing. At rapid cooling rates dehydration of the cell is minimal, and intracellular ice forms. At slow cooling rate, dehydration is extensive, resulting in loss of intracellular water and morphological distortion.

water becomes frozen in the extracellular space. The resulting shrinkage of the cell can give rise to injurious chemical and mechanical stresses. In general, optimal survival from cryopreservation is achieved at intermediate cooling rates, the magnitude of which are dictated by the membrane's permeability at subzero temperatures [199].

Cryoprotective Additives (CPA)

The sensitivity of cells and tissues to IIF and osmotic stress and dehydration can be modified substantially by the prefreezing additions of a CPA. As a consequence, virtually all practical cryopreservation procedures are based on the use of a CPA to which the cell membrane is permeable. Interestingly, recent research has demonstrated that some cell species damaged by typical freezing and thawing processes can be cryopreserved successfully via microinjection of small amounts of sugars into the intracellular volume [200, 201] and by addition of sugars into the extracellular solution along with common permeating CPAs [202].

During the CPA addition and removal procedures and the freezing and thawing processes, the applied osmotic stress results in coupled transport between the CPA and water. This coupled process is typically described in terms of irreversible thermodynamics using a format defined by Kedem and Katchalsky in which the phenomenological coefficients are related directly to physically measurable properties of a cell membrane [203, 204]. These equations are written as

$$J_V = L_p \Delta p - \sum_{i=1}^{n} \sigma_i \Delta \pi_i \tag{4.10.84}$$

$$J_S = C_S (1 - \sigma) J_V + \omega_S \Delta \pi \tag{4.10.85}$$

L_p is the membrane permeability to water; ω is the permeability to solute (CPA for applications in cryopreservation); and σ is the coupling between the two flows (reflection coefficient). The average concentration of permeable solute between the extracellular and intracellular solutions is given by C_S, and the total volume flux and solute fluxes by J_V and J_S, respectively. Equation (4.10.84) shows a provision for volume flow occurring under the action of multiple solutes. Evidence is growing that in at least some cell systems the movements of water and CPA across the plasma membrane are uncoupled [205, 206], thus obviating the need for an irreversible thermodynamic formulation of the process [207].

An alternative, more generalized formulation of this type of phenomenon was also posed by Katchalsky in terms of network thermodynamics [208]. The network thermodynamic model has been applied successfully to the analysis of the cellular response to freezing processes [209, 211]. It can readily be applied for inverse solution to quantify the transport coefficients from freezing data or CPA addition data [210, 212].

Cryoprotective additives may also have a significant effect on IIF and the general mechanical properties of ice growing in biological systems. In particular, various antifreeze proteins (AFP) isolated from cold weather organisms have been demonstrated to influence damage processes to living cells during freezing and thawing [213, 214]. Long-standing evidence indicates that one mechanism of cryoinjury derives from a mechanical interaction between cells and the growing extracellular ice phase in which they are enmeshed [215–217].

The presence of a CPA can strongly modify the structure of ice growth through a cell suspension, as observed and measured by cryomicroscopy [218]. Decoupling the cooling rate into the product of the temperature gradient and interface velocity and then controlling these parameters independently on a directional solidification cryomicroscope allows demonstration that identical cooling rates can produce very different ice crystal morphologies and concomitant cell damage, thereby implicating ice–cell interaction as a damage mechanism [219, 220]. Further studies have shown the ability of AFP to alter ice crystal structure [221, 222] dramatically; these results are being applied to design cryopreservation protocols, including the use of synthetic polymers for specific applications [223].

Multicellular Systems, Tissues, and Organs

The preceding models hold for the analysis of individual cells. However, many important biological systems of interest for cryopreservation consist of organized tissues that have a two- or three-dimensional geometry that may exert a significant effect on the system osmotic behavior and on processes sensitive to cell–cell interactions. For these systems, transport not only occurs across the individual cell membranes, but the interstitial volume is also involved in the transport and storage of water and CPA. In this case, the model must be expanded to include parallel and serial transport and storage for all mobile chemical species. Network thermodynamics provides an effective modeling format for describing these processes [211].

The cryopreservation of whole organs, which is still in the research stage, will demand even more complex coupled thermal and chemical transport analyses. CPAs are added and removed via perfusion through the vascular network; this hydrodynamic flow is coupled to the osmotic, diffusional, and viscoelastic energy domains of the organ. The network thermodynamic approach to modeling is very well suited to analysis of these coupled multidomain processes and has been applied successfully to the design of CPA perfusion protocols [224].

Cell–cell contact has been shown to affect IIF in a number of different experimental systems, generally by enhancing the ability of ice crystals to nucleate on the cell interior [225–227]. This rate of propagation of intracellular ice is greater in a cell culture grown to confluence and is dimished when a gap junction blocker is introduced [228]. The phenomenon is explained by modification of an IIF nucleation model [229].

The Influence of Cell Membrane Permeability

It is well documented that the permeability of cell membranes to water and to CPA is a strong function of the cell species, and that for all species it is a function of temperature [204]. For example, the water permeability among various species may vary by a factor of 10^3 or greater. In general, membranes are significantly more permeable to water than to common CPAs, although the opposite case may also occur under unusual conditions [206]. As the temperature is reduced, the permeability is depressed dramatically. For most practical purposes, at temperatures below the range of about –20 to –30°C, the impedance to membrane transport becomes so high that very little molecular exchange can take place between the intracellular and extracellular compartments.

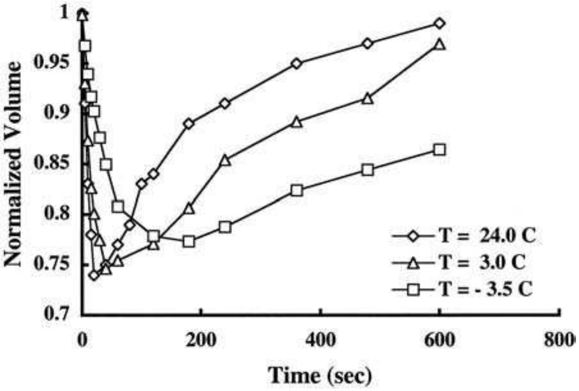

FIGURE 4.10.23 Osmotic response of human pancreas islets to exposure to a 2-*M* solution of dimethylsulfoxide at the indicated temperatures. (From Acker, J.P., Larese, A., Yang, H., Petrenko, A., and McGann, L.E., *Cryobiology*, 38, 363–371, 1999.)

One of the major challenges in applying models for cell membrane transport during freezing has been to develop instrumentation to measure the permeability to water and CPAs at subzero temperatures, in the presence as well as in the absence of ice. The most successful approach is to follow visually on a light microscope the transient size of individual cells or tissues when they are subjected to controlled osmotic stress created by freezing the specimen [230–232] or by changing the chemical environment [233, 234]. An effective step change in the concentration of the extracellular solution is produced when ice is nucleated in the extracellular medium and the temperature is subsequently held constant for the duration of the experiment, or when a new bathing medium is perfused rapidly through the specimen chamber on the stage while the cells or tissues are physically immobilized. Both procedures cause the concentration of the environmental solution to be altered from an initial value to a final well-defined state, and the change in cell volume with time can be measured by direct microscopic observation.

The two-dimensional cross-sectional areas of the cells in the micrographs are quantified via digital image analysis and extrapolated to three-dimensional volumes based on an assumption of a consistent geometric morphology throughout the process. These experiments are repeated serially at different temperatures to generate a series of transient volume curves as shown in Figure 4.10.23 for pancreas islets [235], a multicellular mammalian tissue.

A 2-*M* solution of the CPA dimethyl sulfoxide (Me_2SO) was introduced stepwise into the perfusion cryostage to control the osmotic environment of the islets. An initial shrinkage is measured because water leaves the cells more rapidly than the Me_2SO can enter. As time progresses, the islet reaches a minimum volume and then begins to swell as Me_2SO and water enter the cell. The design of protocols for addition and removal of CPAs to tissues is an important and challenging step in developing effective cryopreservation methods. A rational design process is dependent on the ability to measure the constitutive transport properties of the tissue of interest and have a model that can be applied to optimize the osmotic process, minimizing stresses (which are potentially lethal) on the cells.

Thus, the utility of the transient volume data is to provide a database from which Equation (4.10.81) through Equation (4.10.83) can be applied to determine the constitutive transport properties for a cell or tissue of interest by inverse solution techniques. Property values are identified at each temperature for which experimental data exist, and the data for each property are used to fit an Arrhenius type function to characterize the temperature coefficient [204]. Equation (4.10.86) shows a typical formulation used for this purpose:

$$L_p(T) = L_{p,g}(T_g)\exp\left[\frac{\Delta E}{\Re}\left(\frac{1}{T} - \frac{1}{T_g}\right)\right] \tag{4.10.86}$$

Experiments for many different cell types have shown that the Arrhenius expression provides a model that describes the temperature dependence of the tissue transport properties well [204].

In order to fully interpret the transient osmotic data described earlier, it is necessary to determine the fraction of the cell contents unable to cross the cell membrane under the types of osmotic stress encountered during cryopreservation. This component of the cytoplasm is often referred to as the osmotically inactive volume. It can be measured by conducting a series of experiments in which cells are exposed to increasing concentrations of impermeable solute and measuring the equilibrium volume at each state. These volumes are then plotted as a function of reciprocal solute concentration and extrapolated to the intercept of the ordinate, which indicates the volume that the cell would assume without injury when exposed to an infinitely large solute concentration. The complementary normalized fraction is a measure of the initial amount of intracellular water that can participate in the response to extracellular osmotic stress. The data are displayed on a Boyle–van't Hoff plot [236].

A fundamental issue in the analysis of cryopreservation processes that has only recently begun to be addressed via rigorous quantitative modeling is the osmotic behavior of frozen cells during the thawing process. It has now been demonstrated by application of a model based on Equation (4.10.83) that, for some combinations of freeze–thaw protocols, the warming rate may be the governing component of the thermal history in determining the mechanism and extent of injury [237]. The design of optimal cryoprocessing protocols may therefore require an analysis of the effect on a tissue of interest of the complete thermal history, including cooling and warming.

Cryopreservation by Vitrification

Ice nucleation can be avoided by doping the biological specimen with a high concentration of chemicals to induce a vitreous state [238]. The chemicals act to raise the glass transition temperature to a high value, which can be reached at cooling rates consistent with standard refrigeration systems. By vitrifying the system injury, mechanisms associated with freeze-concentration of solutes and with IIF are avoided. Major problems involving transport processes remain to be solved before vitrification can be applied to the cryopreservation of whole organs.

In order to achieve a vitrified state, a 4- to 5-*M* solution must be equilibrated with the entire volume of an organ, including all the constituent cells. Because this high concentration of CPA can be toxic to cells, the addition process is preferably effected at a low temperature such as 4°C to reduce the rates of injurious chemical reactions. In addition, the duration of exposure to the CPA prior to further cooling should be minimized to limit the accrued reaction time. However, the tradeoff to lowering the temperature is caused by the thermal coefficient of viscosity, which makes it much more difficult to effect the perfusion of CPA solution through the vascular systems of an organ and the diffusion from the vascular lumen through the interstitial tissue and into the individual cells. Optimal design is dependent upon balancing the coupled hydrodynamic, osmotic and viscoelastic reaction of the organ to the perfusion process with the biochemical toxic reactions [239].

Although increasing numbers of biological systems are being identified that are compatible with cryopreservation by vitrification, widespread application will require that the technique become easier to use in practical clinical and biological environments. To this end, there is an ongoing search for CPAs that render the vitrification process less sensitive to accurate control of thermal history; to toxic injury to the biological specimen; and to devitrification (crystal nucleation) during rewarming. This process involves gaining a better understanding of the phase change and vitrification kinetics of various CPA solutions [240, 241] and of identifying new and more effective CPAs [223].

Optimization of Heat Transfer during Cryopreservation

The foregoing discussion indicates the importance of the combined osmotic and thermal history at the local cellular level in determining the response to cryopreservation, including the type and extent of injury that may occur. For a given combination of cell type and CPA composition and concentration, the post-thaw viability achieved is governed by the thermal history of the process. The cooling rate determines the frozen state for storage, and the warming rate determines the manifestation of the frozen state on the final level of viability.

In general, there are two extremes of behavior during freezing [242]. For relatively slow cooling rates the rate at which the extracellular solute concentration increases will have a time scale comparable with that for the osmotic dehydration of the cell at high subzero temperatures. Therefore, the cell will lose a considerable fraction of its water and experience extensive dehydration as indicated in Figure 4.10.22. This large loss of volume is known to damage cells by one or more molecular level mechanisms, which have not been fully identified [199]. Increasing the concentration of CPA will provide an osmotic buffer against this type of dehydration-induced injury, as well as possibly providing other means of protection.

Alternatively, when the cooling rate is rapid, the temperature is reduced much more rapidly than the cell can respond osmotically (because the membrane permeability becomes greatly reduced at low temperatures as will be explained subsequently). Therefore, no opportunity exists for intracellular water to osmotically equilibrate with the extracellular water being progressively diminished in concentration. When the transmembrane water disequilibrium (as manifested in terms of liquid phase supercooling) reaches a critical value, the conditions will be satisfied for nucleation of ice in the intracellular volume. It is important to note that the cell membrane acts as a barrier to the growth of a continuous ice phase between the intracellular and extracellular compartments. The crystalline structure of intracellular ice will be considerably smaller than that of extracellular ice because of the greater extent of supercooling prior to nucleation. Consequently, the propensity for recrystallization will be relatively large in the intracellular volume, and this process has been demonstrated to be nearly universally lethal to cells.

The combination of different injury mechanisms associated with rapid and slow cooling rates during freezing gives rise to a two-factor theory of cryoinjury [242, 243]. Between the extremes of rapid and slow cooling will be a range of intermediate rates at which survival will be maximized. The magnitude and breadth of this range are defined uniquely for each cell type as a function of its membrane permeability and sensitivity to injury. Cryopreservation protocols are targeted to produce a cooling process lying within the optimal range of this survival signature that will produce the highest possible biological function following thawing. The design of a cryopreservation protocol for a given cell type must take into account the combined effects of the CPA composition and concentration plus the cooling and warming rates [244, 245]. A true optimal process design can be conducted based on the availability of relevant constitutive properties of cell species of interest and models for the behavior of cells during the ice nucleation, freezing, and thawing events [246].

The preceding analysis of the freezing process is presented from the perspective of the local thermal history for an individual cell. However, practical cryopreservation procedures are conducted on tissues and organs of finite macroscopic dimensions or on containers of solutions of cells or microscopic tissue suspensions. The consequence is that, although the governing mass transport processes occur across microscopic scale dimensions (a single membrane and the associated boundary layers may be less than 0.1 μm), the governing heat transport occurs on a scale measured in millimeters or centimeters. It is this macroscopic heat transfer that drives all components of the cryopreservation process. Because of the macroscopic dimensions and the restriction that the refrigeration source be applied only at the external boundary of the systems during cooling, significant spatial gradients in cooling rate can be manifested within the system.

Also, in general the cooling rate will not be constant over the entire cooling process; it should be defined over the range of temperatures most important to determining the frozen state of a cell. The critical temperature range is defined as that for which transport occurs across the cell membrane and for which intracellular ice formation (IIF) is most probable. Analysis of this process involves solution of the classic Stefan moving boundary problem. For the freezing of biological systems, it is most important to determine the cooling at high subzero temperatures accurately within the mushy zone [247] during which the primary membrane transport processes occur.

It is precisely this range of temperatures for which simplifying assumptions concerning the pattern of latent heat release are frequently made in order to render the mathematical solution more tractable. Therefore, it is important to match as well as possible the coupling between temperature and changing solute concentration as defined by the phase diagram. Only when the actual process physics are matched can the cooling rate for the critical temperature range be described accurately. The combination of a nonlinear pattern of latent heat release with temperature and the often complex system geometry dictates that the governing heat transport equations be solved via numerical methods. The thermal histories calculated may then be correlated with the cooling rates on the survival signature and with the membrane mass transport equations, such as Equation (4.10.83), to predict the biological response of a given tissue to a defined boundary cooling protocol [248].

Thermal Stress Effects

Another analysis problem to be addressed in cryopreservation is that of thermal stresses in a frozen or vitrified organ. The paucity of constitutive property data for the thermal expansion of biological tissues and solutions in the subzero temperature range has been long standing. Recently, intial experiments have been conducted to make these measurements [249, 250]. It is apparent that a biological tissue with dimensions on the order of several centimeters will be subject to fracture at even moderate cooling rates below –120°C after a glass phase has formed [251]. A mechanical fracture of a whole organ will render it useless for subsequent transplantation. It is important to measure the viscoelastic properties of biological materials loaded with high concentrations of CPA over the temperature range between the glass transition and storage temperatures (usually at or near liquid nitrogen temperature at –196°C).

Complementary to the property measurements is a need for a thermal stress analysis that can be applied with versatility of geometric details. Rubinsky et al. [252] have developed a model for how mechanical stresses may develop in the interior of an organ during solidification and the subsequent cooling process. Different organs have widely divergent shapes and sizes, and constitutive property data for frozen and vitrified tissues are practically nonexistent. In addition, an organ is likely to be preserved in a container of fluid with which it will be coupled thermally and mechanically. Factors to be considered in a process design are: manipulation of the boundary thermal protocol; shape of the overall container into which an organ is placed; and coordination of the pattern of distributed internal deposition with cooling at the boundary.

Recent Developments and Innovations

Recent innovative experiments by Fowler and Toner [253] have demonstrated that it is possible at the micro (cellular) scale to melt and recool cells containing intracellular ice at a rate that can produce a vitrified state without the introduction of the CPA to block the initial ice nucleation event. The frozen specimen is irradiated with a laser wavelength that is absorbed preferentially by the cell cytoplasm over the extracellular solution. For a solution of individual cells having characteristic diameters of about 6 μm, warming rates on the order of 10^{11}°C/s can be achieved within the cells, while the extracellular matrix remains frozen.

When the heating process is terminated in an approximate step-wise manner after 7 ns, heat transfer from the extracellular matrix to the cells produces an intracellular cooling rate of about 10^{6}°C/s, which is adequate to produce a glass state in an aqueous solution. The vitrified cells may then be warmed rapidly to suprafreezing temperatures (>0°C) without nucleation and with no measured injury. If this process is to realize broad clinical or commercial application, considerable engineering work must be accomplished in scale-up from these microscopic level processes to applications in larger tissue and organ systems.

Since the initial achievements in the cryopreservation of cells, many applications have been developed in the biological and medical fields. Numerous for-profit concerns have now developed successful techniques for preserving human tissues for subsequent transplantation. Many of these corporations use proprietary processing protocols to preserve specific tissues; the number of commercial participants in this field has been growing steadily over the past 10 years. In like manner, many for-profit and not-for-profit groups are marketing the cryopreservation of a very broad spectrum of nonhuman tissues. Some of the more prominent applications involve mammalian and amphibian gametes, tissue culture collections, and plant germplasm.

A potentially important new area of application will be the cryopreservation of living materials manufactured by tissue engineering techniques being developed [254]. Bioartificial systems such as skin and organs that contain living cells will require a technology for maintaining them in a viable but latent state between the time of manufacture and implementation in a clinical setting. Cryopreservation provides a tool of suitable potential for meeting this unique need, but the processing protocols will need to be designed to ensure successful storage and recovery for each type of manufactured tissue.

Studies are progressing on the cryopreservation of numerous types of engineered cells and tissues [255–258]. Realization of the potential for cryopreservation in these new application arenas will be facilitated by parallel developments in instrumentation and analaysis techniques that enable more accurate and subtle measurements of the processes and properties that govern cellular and tissue response to freezing and thawing. An example is the identification and measurement of the energy associated with the subzero transport of water across cell membranes [259–262].

Cryosurgery

All of the foregoing discussion has been devoted to cryopreservation, for which the objective is to maximize the survival of cells from the frozen state to ensure their living function after thawing. The antithesis of this work is cryosurgery, for which the objective is to maximize destruction of a target tissue *in situ* [263]. Cryosurgery has long been practiced as an effective means for killing surface lesions; recently, it has been adopted more widely as a tool for treating internal tumors that are difficult to resect mechanically [264].

Many of the recent gains in the successful application of cryosurgery are due to the development of new imaging methods that enable the surgeon to follow the growth of the solid–liquid interface, to which the zone of cellular destruction is coupled, in real time during the freezing process. The initial imaging methodology adapted for this purpose was ultrasonography [265]. Subsequently, other imaging modalities that can be coupled to the transient temperature field are being developed, including NMR [266–268]; spectroscopy [269]; and electrical impedance [270]. Advances in cryosurgical probes that provide more effective removal of heat from tissues via enhanced thermal transport mechanisms have also contributed to the recent growth in cryosurgery [271]. Finally, over the past decade there has been a steady advance in understanding the mechanisms by which freezing and thawing act to cause tissue death as a function of the thermal parameters of the solidification process and tissue properties. Many of these fundamental advances have resulted from the application of bioengineering analysis of the tissue freezing process [272–276], which portends the potential for engineering to contribute further to the field of cryosurgery.

A new approach to improving the efficacy of cryosurgery is derived from techniques long applied to enhance cryopreservation processes. Namely, the tissue is modified by adding a chemical agent prior to the initiation of freezing. However, for applications in cryosurgery, the desired result is an increased level of cell killing. Antifreeze proteins (AFP) are proving to be effective for this purpose [277–279]. AFPs are chemical compounds synthesized by many differing types of plants and animals to provide protection against freezing injury at high subzero temperatures [280, 281]. It has also been demonstrated that AFPs modify ice crystals to needle-like shapes that can destroy cells during freezing to deeper subzero temperatures [282].

In summary, clearly there continue to be many opportunities for contributions in low-temperature biological heat transfer with the potential for substantial positive impact on health care delivery.

Acknowledgments

This paper was prepared with the support of National Science Foundation grants no. CTS-9632378 to KRD and no. DBI-9512746 to KRD; NIH grant #1 R01 HL56143-01 to JWV, and the Joe J. King Professorship in Engineering at the University of Texas at Austin. The perfusion measurements were supported in part by a grant to JWV from Urologix Inc. The sections on convective heat transfer and thermal properties of swine myocardium were derived from N.C. Bhavaraju's [283] and I. dos Santos' Ph.D. dissertations [43]. In a similar fashion, the sections on thermal models and microsphere perfusion measurements in the canine prostate were derived from D. Yuan's Ph.D. dissertation [284]. Collaborations with colleagues in writing prior reviews in bioheat transfer are acknowledged. In particular, we note

Dr. Sharon Thomsen's contribution to the subsection on histologic markers of thermal damage and Dr. Thomas Ryan's broad review [285].

Nomenclature

σ (S/m)	electrical conductivity
ε'' (F/m)	electric permittivity
$\lvert E \rvert$ (V/m)	magnitude of local electric field
ω	angular frequency (r/s)
μ	magnetic permeability (H/m)
α (m^{-1})	acoustic absorption coefficient
E (W/m^2)	wave power density
f (Hz)	frequency
A	a frequency factor (s^{-1})
τ	the total heating time (s)(s^{-1}) frequency factor
E	activation energy barrier (J/mol)

References

1. Johnston, K.A. and Bennett, A.F., Eds. *Animals and Temperature: Phenotypic and Evolutionary Adaptation*, Cambridge University Press, Cambridge, 1996.
2. Diller, K.R., Modeling of bioheat transfer processes at high and low temperatures, *Adv. Heat Trans.*, 22, 157–357, 1992.
3. Chato, J.C., A method for the measurement of thermal properties of biologic materials, *Symposium on Thermal Problems in Biotechnology*, ASME, New York, LCN068-58741, 16–25, 1968.
4. Balasubramaniam, T.A. and Bowman, H.F., Thermal conductivity and thermal diffusivity of biomaterials: a simultaneous measurement technique, *J. Biomech. Eng.*, 99, 148–154, 1977.
5. Valvano, J.W. et al., An isolated rat liver model for the evaluation of thermal techniques to measure perfusion, *J. Biomech. Eng.*, 106, 187–191, 1984.
6. Arkin, H. et al., Thermal pulse decay method for simultaneous measurement of local thermal conductivity and blood perfusion: a theoretical analysis *J. Biomech. Eng.*, 108, 208–214, 1986.
7. Kress, R., A comparative analysis of thermal blood perfusion measurement techniques, *J. Biomech. Eng.*, 109, 218–225, 1987.
8. Patel, P.A. et al., A finite element analysis of a surface thermal probe, *Thermodynamics, Heat, and Mass Transfer in Biotech.*, ASME HTD-Vol. 90, BED. Vol. 5, 95–102, 1987.
9. Bowman, H.F., Estimation of tissue blood flow, in *Heat Transfer in Medicine and Biology: Analysis and Applications, Vol. 1*, Shitzer, A. and Eberhart, R.C., Eds., Plenum Press, New York, 1985, chap. 9, 193–230.
10. Chato, J.C., Measurement of thermal properties of biological materials, in *Heat Transfer in Medicine and Biology: Analysis and Applications, Vol. 1*, Shitzer, A. and Eberhart, R.C., Eds., Plenum Press, New York, 1985, chap. 8, 167–192.
11. Valvano, J.W., Cochran, J.R., and Diller, K.R., Thermal conductivity and diffusivity of biomaterials measured with self-heated thermistors, *Int. J. Thermophys.,* 6, 301–311, 1985.
12. Valvano, J.W. and Chitsabesan, B., Thermal conductivity and diffusivity of arterial wall and atherosclerotic plaque, *Lasers Life Sci.*, 1, 219–229, 1987.
13. Holmes, K.R. and Chen, M.M., *In vivo* tissue thermal conductivity and local blood perfusion measured with heat pulse-decay method, *Advan. Bioeng.*, 113–115, 1980.
14. Touloukian, Y.S. et al., *Thermophysical Properties of Matter: Thermal Conductivity*, IFI/ Plenum, New York, Vo1. 3, 1970, 120, 209.
15. Touloukian, Y.S. et al., *Thermophysical Properties of Matter: Thermal Conductivity*, IFI/ Plenum, New York, Vo1. 3, 1970, preface.

16. Touloukian, Y.S. et al., *Thermophysical Properties of Matter: Thermal Diffusivity*, IFI/ Plenum, New York, Vo1. 10, 1973, 15a–42a.
17. Kreith, F. and Bohn, M.S. *Principles of Mass Transfer,* 5th ed., West Publishing Co., St. Paul, MN, 1993.
18. Duck, F.A., *Physical Properties of Tissue: A Comprehensive Reference Book*, Academic Press, London, 1991.
19. Chen, M.M. et al., Pulse-decay method for measuring the thermal conductivity of living tissue, *J. Biomech. Eng.,* 103, 253–260, 1981.
20. Holmes, K.R. and Chen, M.M., Local tissue heating, microbead pulse decay technique for heat transfer parameter evaluation, *Measurement of Blood Flow and Local Tissue Energy Production by Thermal Methods*, Muller–Schenburg (Ed.), Thieme–Stratton Inc., New York, 1983, 50–56.
21. Valvano, J.W. et al., A finite element analysis of self-heated noninvasive thermistors, *Advances in Bioengineering*, ASME, 1983.
22. Valvano, J.W. et al., The simultaneous measurement of thermal conductivity, thermal diffusivity and perfusion in small volume of tissue, *J. Biomech. Eng.,* 106, 192–197, 1984.
23. Valvano, J.W., Badeau, A.F., and Pearce, J.A., Simultaneous measurement of intrinsic and effective thermal conductivity, *Heat Transfer in Bioengineering and Medicine*, ASME HTD-Vol 95, BED. Vol. 7, 31–36, 1987.
24. Patel, P.A. et al., A self-heated thermistor technique to measure effective thermal properties from the tissue surface, *J. Biomech. Eng.,* 109, 330–335, 1987.
25. Patel, P.A., Valvano, J.W., and Hayes, L.J., Perfusion measurement by a surface thermal probe, IEEE Engineering in Medicine and Biology, Boston, 1987.
26. Walsh, J.T., A noninvasive thermal method for the quantification of tissue perfusion, M.S. Thesis, M.I.T., Cambridge, 1984.
27. Patera et al., Prediction of tissue perfusion from measurement of the phase shift between heat flux and temperature, *AMSE*, Paper #79-WA/HT-71, 1979.
28. Pennes, H.H., Analysis of tissue and arterial blood temperatures in the resting forearm, *J. Appl. Physiol.*, 1, 93–122, 1948 (republished for 50th anniversary issue of *J. Appl. Physiol*, 85, 5–34, 1998).
29. Rastorguev, Y.L. and Ganiev, Y.A., Thermal conductivity of aqueous solutions or organic materials, *Russ. J. Phys. Chem.*, 40, 869–871, 1966.
30. Hager, J.M., Onishi, S., Lagley, L.W., and Diller, T.E., Heat flux microsensors, Ntl. Heat Trans. Conf. — Heat Transfer Measurements and Flow Visualization, 112, 1–7, 1989.
31. van Heiningen, A.R.P., Mujumdar, A.S., and Douglas, W.J.M., On the use of hot film and cold film sensors for skin friction and heat transfer measurements in impingement flows, *Lett. Heat Mass Trans*, 3, 532–528, 1976.
32. Kraabel, J.S., Baughn, J.W., and McKillop, A.A., An instrument for the measurement of heat flux from a surface with uniform temperature, *J. Heat Trans.*, 102, 576–578, 1980.
33. Campbell D.S. and Diller, T.E., Design and calibration of a local-heat flux measurement system for unsteady flows, *ASME Fundamentals of Forced and Mixed Convection*, HTD 42, 73–80, 1985.
34. Fitzgerald, T.J., Catipovic, N.M., and Jovanovic, G.N., Instrumented cylinder for studying heat transfer to immersed tubes in fluidized beds, *Ind. Eng. Chem. Fund.*, 20, 82–88, 1981.
35. Wu, R.L., Lim, C.J., and Grace, J.R., The measurement of instantaneous local heat transfer coefficients in a circulating fluidized bed, *Can. J. Chem. Eng.*, 67 301–307, 1989.
36. Pflum, D.L., Brown, R.C., and Maxwell, G.M., A resistance wire technique applied to heat transfer measurements in high aspect ration fluidized beds, Ntl. Heat Trans. Conf. — Heat Transfer Measurements and Flow Visualization, 112, 39–45, 1989.
37. Beasley, D.E. and Figliola, R.S., Analysis of a local heat flux probe heat transfer, *Proc. Int. Heat Trans. Conf.*, 2, 467–472, 1986.
38. Figliola, R.S. and Swaminathan, M., Boundary condition influences on the effective area of a local heat flux probe, *Meas. Sci. Technol.*, 7, 1439–1443, 1996.

39. Griffith, A.E., Louge, M., and Mohd–Yusof, J., Simultaneous, noninvasive measurements of convective heat transfer and solid volume at the wall of an entrained gas–solid suspension, *Rev. Sci. Instr.*, 71, 2922–2927, 2000
40. Holmberg, D.G. and Womeldorf, C.A., Performance and modeling of heat flux sensors in different environments, *Proc. ASME* HTD, 4, 71–77, 1999.
41. dos Santos, I., da Rocha, A.F., Webster, J.G., and Valvano, J.W., An instrument to measure the heat convection coefficient on the endocardial surface, *Physiol. Meas.*, 24, 321–335, 2003.
42. dos Santos, I., Will, J.A., da Rocha, A.F., de O. Nascimento, F.A., Webster, J.G., and Valvano, J.W., *In vivo* measurements of heat transfer on the endocardial surface, *Physiol. Meas.*, 24, 793–804, 2003.
43. dos Santos, I., *In vivo* measurements of heat transfer on the endocardial surface, Ph.D. Thesis, Univ. Texas Austin, Dept. Elect. Comput. Engr., 2003.
44. Valvano, J.W., Low temperature tissue thermal properties, in *Low Temperature Biotechnology: Emerging Applications and Engineering Contributions*, J.J. McGrath and K.R. Diller, Eds., ASME, New York, 331–346, 1988.
45. Spells, K.E., The thermal conductivities of some biological fluids, *Phys. Med. Biol.*, 5, 139–153, 1960.
46. Cooper, T.E., and Trezck, G.J., Correlation of thermal properties of some human tissues with water content, *Aerospace. Med.*, 42, 24–27, 1971.
47. Charney, C.K., Mathematical models of bioheat transfer, *Adv. Heat Trans.*, 22, 19–155, 1992.
48. Wissler, E.H., Steady-state temperature distribution in man. *J. Appl. Physiol.*, 16, 734–740, 1961.
49. Wissler, E.H., Mathematical simulation of human thermal behavior using whole body models, in *Heat Transfer in Medicine and Biology: Analysis and Applications, Vol. 1*, Shitzer, A. and Eberhart, R.C., Eds., Plenum Press, New York, 1985, chap. 13, 325–373.
50. Chato, J.C., Heat transfer to blood vessels, *J. Biomech. Eng.,* 102, 110–118, 1980.
51. Chen, M.M. and Holmes, K.R., Microvascular contributions in tissue heat transfer, *Ann. NY Acad. Sci.*, 335, 137–150, 1980.
52. Weinbaum, S., Jiji, L., and Lemons, D.E., Theory and experiment for the effect of vascular temperature on surface tissue heat transfer — part 1: anatomical foundation and model conceptualization, *J. Biomech. Eng.*, 106, 246–251, 1984.
53. Weinbaum, S., Jiji, L., and Lemons, D.E., Theory and experiment for the effect of vascular temperature on surface tissue heat transfer – part 2: model formulation and solution, *J. Biomech. Eng.*, 106, 331–341, 1984.
54. Weinbaum, S. and Jiji, L.M., A new simplified bioheat equation for the effect of blood flow on average tissue temperature, *J. Biomech. Eng.*, 107 131–139, 1985.
55. Zhu, L., Lemons, D.E., and Weinbaum, S., A new approach for predicting the enhancement in the effective conductivity of perfused tissue due to hyperthermia, ASME HTD 288, 37–43, 1994.
56. Charny, C.K., Weinbaum, S., and Levin, R.L., An evaluation of the Weinbaum–Jiji bioheat equation for normal and hyperthermic conditions, *J. Biomech. Eng.*, 112, 80–87, 1990.
57. Weinbaum, S. and Jiji, L.M., A two phase theory for the influence of circulation on the heat transfer in surface tissue, *Advan. Bioeng.*, ASME WA/HT-72: 179–182, 1979.
58. Dagan, Z., Weinbaum, S., and Jiji, L.M., Parametric study of the three layer microcirculatory nodel for surface tissue energy exchange, *J. Biomech. Eng.*, 108, 89–96, 1986.
59. Song, W.J., Weinbaum, S., and Jiji, L.M., A combined macro and microvascular model for whole limb heat transfer, *J. Biomech. Eng.*, 110, 259–267, 1988.
60. Song, W.J., Weinbaum, S.. and Jiji, L.M., A theoretical model for peripheral geat transfer using the bioheat equation of Weinbaum and Jiji, *J. Biomech. Eng.*, 109, 72–78, 1987.
61. Weinbaum, S. and Jiji, L.M., The matching of thermal fields surrounding countercurrent microvessels and the closure approximation in the Weinbaum–Jiji equation, *J. Biomech. Eng.*, 111, 271–275, 1989.
62. Weinbaum, S. and Lemons, D.E., Heat transfer in living tissue: the search for a blood–tissue energy equation and the local thermal microvascular control mechanism, *BMES Bull.*, 16, 38–43, 1992.

63. Zhu, M., Weinbaum, S., and Lemons, D.E., On the generalization of the Weinbaum–Jiji equation to microvessels of unequal size: the relation between the near field and local average tissue temperatures, *J. Biomech. Eng.*, 110, 74–81, 1988.
64. Lemons, D.E., Weinbaum, S., and Jiji, L.M., Experimental studies on the role of the micro and macro vascular system in tissue heat transfer, *Am J. Physiol.*, 253, R128, 1987.
65. Mooibroek, J. and Lagendijk, J.J.W., A fast and simple algorithm for the calculation of convective heat transfer by large vessels in three-dimensional inhomogeneous tissue, *IEEE Trans. Biomed. Eng.*, 38, 490–501, 1991.
66. Baish, J.W., Heat transport by countercurrent blood vessels in the presence of an arbitrary temperature gradient, *J. Biomech. Eng.*, 112, 207–211, 1990.
67. Huang, H.W., Chen, Z.P., and Roemer, R.B., A countercurrent vascular network model of heat transfer in tissues, *J. Biomech. Eng.*, 118, 120–129, 1996.
68. Keller, K.H. and Seiler, L., An analysis of peripheral heat transfer in man, *J. Appl. Physiol.*, 30, 779, 1971.
69. Mitchell, J.W. and Myers, G.E., An analytical model of the countercurrent heat exchange phenomena, *Biophys. J.*, 8, 897–911, 1968.
70. Baish, J.W., Ayyaswamy, P.S., and Foster, K.R., Heat transport mechanisms in vascular tissues: a model comparison, *J. Biomech. Eng.*, 108, 324–331, 1986.
71. Weinbaum, S. and Jiji, L.M., Discussion of papers by Wissler and Baish et al. concerning the Weinbaum–Jiji bioheat equation, *J. Biomech. Eng.*, 109, 234–237, 1987.
72. Wissler, E.H., Comments on Weinbaum and Jiji's discussion of their proposed bioheat equation, *J. Biomech. Eng.*, 109, 355–356, 1987.
73. Wissler, E.H., Pennes' 1948 paper revisited, *J. Appl. Physiol.*, 85, 35–41, 1998.
74. Pennes, H.H., Analysis of tissue and arterial blood temperatures in the resting forearm, *J. Appl. Physiol.*, 1, 93–122, 1948 (republished for 50th anniversary issue of *J. Appl. Physiol*, 85, 5–34, 1998).
75. Huang, H.W., Chan, C.L., and Roemer, R.B., Analytical solutions of Pennes' bioheat transfer equation with a blood vessel, *J. Biomech. Eng.*, 116, 208–212, 1994.
76. Xu, L.X., Chen, M.M., Holmes, K.R., and Arkin, H., The evaluation of the Pennes, the Chen–Holmes, the Weinbaum–Jiji bioheat transfer models in the pig kidney vortex, ASME HTD 189: 15–21, 1991.
77. Arkin, H., Xu, L.X., and Holmes, K.R., Recent developments in modeling heat transfer in blood perfused tissues, *IEEE Trans. Biomed. Eng.*, BME-41, 97–107, 1994.
78. Wulff, W.,The energy conservation equation for living tissue, *IEEE Trans. Biomed. Eng.*, BME–21, 494–495, 1974.
79. Klinger, H.G., Heat transfer in perfused biological tissue — I: general theory, *Bull. Math. Biol.*, 36, 403–415, 1974.
80. Bazett, H.C. and McGlone, B., Temperature gradients in the tissue in man, *Am. J. Physiol.*, 82, 415, 1927.
81. Valvano, J.W., Nho, S., and Anderson, G.T., Analysis of the Weinbaum–Jiji model of blood flow in the canine kidney cortex for self-heated thermistors, *J. Biomech Eng.*, 116: 201–207, 1994.
82. Brinck, H. and Werner, J., Estimation of the thermal effect of blood flow in a branching countercurrent network using a three-dimensional vascular model, *J. Biomech Eng.*, 116, 324–330, 1994.
83. Anderson, G.T. and Valvano, J.W., An interlobular artery and vein based model for self-heated thermistor measurements of perfusion in the canine kidney cortex, in *Bioheat Transfer — Applications in Hyperthermia, Emerging Horizons in Instrumentation and Modeling*. ASME HTD Vol. 126, BED Vol. 12, 29–35, 1989.
84. Anderson, G.T. and Valvano, J.W., A small artery heat transfer model for self-heated thermistor measurements of perfusion in the canine kidney cortex, *J. Biomech Eng.*, 116, 71–78, 1994.
85. Yuan, D.Y., Xu, L.X., Zhu, L., Holmes, K.R., and Valvano, J.W., Perfusion and temperature measurements in hyperthermic canine prostates, *17th S. Biomed. Engr. Conf.*, 85, 1998.
86. Xu, L.X., Zhu, L., and Holmes, K.R., Thermoregulation in canine prostate during transurethral microwave hyperthermia, part II: blood flow response, *Int. J. Hyperthermia*. 14, 65–73, 1998.

87. Bligh, J., Regulation of body temperature in man and other mammals, in *Heat Transfer in Medicine and Biology: Analysis and Applications, Vol. 1*, Shitzer, A. and Eberhart, R.C., Eds., Plenum Press, New York, 1985, chap. 2, 15–52.
88. Rowell, L.B. and Wyss, C.R., Temperature regulation in exercising and heat-stressed man, in *Heat Transfer in Medicine and Biology: Analysis and Applications, Vol. 1*, Shitzer, A. and Eberhart, R.C., Eds., Plenum Press, New York, 1985, chap. 3, 53–78.
89. Lipton, J.M, Thermoregulation in pathological states, in *Heat Transfer in Medicine and Biology: Analysis and Applications, Vol. 1*, Shitzer, A. and Eberhart, R.C., Eds., Plenum Press, New York, 1985, chap. 4, 79–106.
90. Heller, H.C. and Glotzbach, S.F., Thermoregulation and sleep, in *Heat Transfer in Medicine and Biology: Analysis and Applications, Vol. 1*, Shitzer, A. and Eberhart, R.C., Eds., Plenum Press, New York, 1985, chap. 5, 107–134.
91. Hissa, R., Central control of body temperature: a review, *Arctic Med. Res.,* 49, 3–15, 1990.
92. Florez–Duquet, M. and McDonald, R.B., Cold-induced thermoregulation and biological aging, *Physiol. Rev.,* 78, 339–358, 1998.
93. Chappuis, P., Pittet, P., and Jequier, E., Heat storage regulation in exercise during thermal transients, *J. Appl. Physiol.*, 40, 384–392, 1976.
94. Webb, P., The physiology of heat regulation, *Am. J. Physiol.*, 268, R838–R850, 1995.
95. Nunneley, S.A., Water cooled garments: a review, *Space Life Sci.*, 2, 335–360, 1970.
96. Ganong, W.F., *Review of Medical Physiology,* 16th ed., Appleton & Lange, Norwalk, CT, 1993.
97. Fanger, P.O., *Thermal Comfort: Analysis and Applications in Environmental Engineering*, McGraw–Hill, New York, 1970.
98. Fulcher, C.W.G., Control of a liquid cooling garment for extravehicular astronauts by cutaneous and external auditory meatus temperatures, Ph.D. Dissertation, University of Houston, 1970.
99. Hensen, J.L.M., Literature review on thermal comfort in transient conditions, *Build. Envir.*, 25, 309–316, 1990.
100. Wissler, E.H., Steady-state temperature distribution in man. *J. Appl. Physiol.*, 16, 734–740, 1961.
101. Wissler, E.H., Comparison of resutls obtained from two mathematical models — A simple 14-node model and a complex 250-node model, *J. Physiol. (Paris)*, 63, 455–458, 1970.
102. Stolwijk, J.A.J. and Hardy, J.D., Temperature regulation in man — a theoretical study, *Pflugers Arch.*, 291, 129–162, 1966.
103. Nadel, E.R., Mitchell, J.W., Saltin, B., and Stolwijk, J.A.J., Peripheral modifications to the central drive for sweating, *J. Appl. Physiol.*, 31, 828–833, 1971.
104. Mitchell, J.W., Galvez, T.L., Hengle, J., Myers, G.E., and Siebecker, K.L., Thermal response of human legs during cooling, *J. Appl. Physiol.*, 29, 859–865, 1970.
105. Hayward, J.S., Thermal balance and survival time prediction of man in cold water, *Can. J. Physiol. Pharmacol.*, 53, 21–32, 1975.
106. Hayward, J.S., Eckerson, J.D., and Collis, M.L., Thermoregulatory heat production in man: prediction equation based on skin and core temperatures, *J. Appl. Physiol.*, 42, 377–384, 1977.
107. Kuznetz, L.H., A Two-dimensional transient mathematical model of human thermoregulation, *Am. J. Physiol.*, 6, R266–R277, 1979.
108. Shitzer, A., Chato, J.C., and Hertig, B.A., Thermal protective garment using independent regional control of coolant temperature, *Aerospace Med.*, 44, 49–59, 1973.
109. Shitzer, A. and Chato, J.C., Thermal interaction with garments, in *Heat Transfer in Medicine and Biology: Analysis and Applications, Vol. 1*, Shitzer, A. and Eberhart, R.C., Eds., Plenum Press, New York, 1985, chap. 14, 375–394.
110. Wissler, E.H., Mathematical simulation of human thermal behavior using whole body models, in *Heat Transfer in Medicine and Biology: Analysis and Applications, Vol. 1*, Shitzer, A. and Eberhart, R.C., Eds., Plenum Press, New York, 1985, chap. 13, 325–373.
111. Wissler, E., Simulation of fluid-cooled or heated garments that allow man to function in hostile environments, *Chem. Eng. Sci.*, 41, 1689–1698, 1986.

112. Wissler, E. H., A review of human thermal models, in *Environmental Ergonomics*, Mekjavic, I.B., Banister, E.W., and Morrison., J.B., Eds., Taylor and Francis, New York, 1988, 267–285.
113. Nyberg. K.L., Diller, K.R., and Wissler, E.H., Automatic control of thermal neutrality for space suit applications using a liquid cooling garment, *Aviat., Space, Environ. Med.*, 71, 904–915, 2001.
114. Nyberg, K.L., Diller, K.R., and Wissler, E.H., Model of human/liquid cooling garment interaction for space suit automatic thermal control, *J. Biomech. Eng.*, 123, 114–120, 2001.
115. Roussy, G. and Pearce, J. *Foundations and Industrial Applications of Microwaves and Radio Frequency Fields,* Wiley–Interscience, Chichester, U.K., 1985.
116. Geddes, L.A. and Baker, L.E. The specific resistance of biological material — a compendium of data for the biomedical engineer and physiologist, *Med. Biol. Eng.,* 5, 271–293, Pergammon Press, 1967.
117. Schwan, H.P., Biophysics of diathermy, in *Therapeutic Heat and Cold*, E. Licht, Ed., Waverly Press, Baltimore, MD, chap. 3, 1972.
118. Fawcett, D.W., *Textbook of Histology,* 12th ed., 368–409, Chapman & Hall, New York, 1994.
119. Stillwell, G.K., General principles of thermal therapy, in *Therapeutic Heat and Cold,* E. Licht, Ed., Waverly Press, Baltimore, MD, chap. 7, 1972.
120. Green, D.M. and Diller, K.R., Measurement of burn-induced leakage of macromolecules in living tissue, *Trans. ASME J. Biomech. Eng.,* 100, 153–158, 1978.
121. Cotran, R.S., Kumar, V., and Collins, T., *Pathologic Basis of Disease,* 6th ed., 1–112, W.B. Saunders Co., Philadelphia, 1999.
122. Moritz, A.R. and Henriques, F.C., Studies of thermal injury II. The relative importance of time and surface temperature in the causation of cutaneous burns, *Am. J. Pathol.,* 23, 695–720, 1947.
123. Moritz, A.R., Studies of thermal injury, III. The pathology and pathogenesis of cutaneous burns: an experimental study, *Am. J. Pathol.*, 23, 915–934, 1947.
124. Henriques, F.C., and Moritz, A.R., Studies of thermal injury, I. The conduction of heat to and through skin and the temperatures attained therein. A theoretical and experimental investigation, *Am. J. Pathol.,* 23, 531–549, 1947.
125. Henriques, F.C., Studies of thermal injury, V. The predictability and the significance of thermally induced rate processes leading to irreversible epidermal injury, *Arch. Pathol.,* 23, 489–502, 1947.
126. Büttner, K., Effects of extreme heat and cold on human skin, I. Analysis of temperature changes caused by different kinds of heat application, *J. Appl. Physiol.*, 3, 691–702, 1951.
127. Stoll, A.M., A computer solution for determination of thermal tissue damage integrals from experimental data, *I.R.E. Trans. Med. Electron.*, 7, 355–358, 1960.
128. Weaver, J.A. and Stoll, A.M., Mathematical model of skin exposed to thermal radiation, *Aerospace Med.*, 40, 24–30, 1967.
129. Takata, A.N., Development of criterion for skin burns, *Aerospace Med.*, 45, 634–637, 1974.
130. Stoll, A.M. and Green, L.C., Relationship between pain and tissue damage due to thermal radiation, *J. Appl. Physiol.*, 14, 373–382, 1959.
131. Stoll, A.M. and Chianta, M.A., Burn production and prevention in convective and radiant heat transfer, *Aerospace Med.*, 39, 1232–1238, 1968.
132. Lawrence, J.C. and Bull, J.P., Thermal conditions which cause skin burns, *J. Instit. Mech. Engrs., Eng. Med.*, 5, 61–63, 1976.
133. Büttner, K., Effects of extreme heat and cold on human skin. II. Surface temperature, pain and heat conductivity in experiments with radiant heat, *J. Appl. Physiol*, 3, 691–702, 1951.
134. Ross, D.C. and Diller, K.R., An experimental investigation of burn injury in living tissue, *J. Heat Trans.*, 98, 292–296, 1976.
135. Moussa, N.A., McGrath, J.J., Cravalho, E.G., and Asimacopoulos, P.J., Kinetics of thermal injury in cells, *J. Biomech. Eng.*, 99, 155–159, 1977.
136. Moussa, N.A., Tell, E.N., and Cravalho, E.G., Time progression of hemolysis of erythrocyte populations exposed to supraphysiological temperatures, *J. Biomech. Eng.*, 101, 213–217, 1979.

137. Bhowmick, S. and Bischof, J.C. Supraphysiological thermal injury in Dunning AT-1 prostate tumor cells, *Advances in Heat and Mass Transfer in Biotechnology*, HTD-362, ASME, 77–78, 1998.
138. Maron, S.H. and Lando, J.B., *Fundamentals of Physical Chemistry,* McMillan, New York, 1974.
139. Diller, K.R. and Klutke, G.A., Accuracy analysis of the Henriques model for predicting burn injury, *Advances in Bioheat and Mass Transfer*, HTD-268, ASME, 1993.
140. Xu, Y. and Qian, R., Analysis of thermal injury process based on enzyme deactivation mechanisms, *Trans. ASME J. Biomech. Eng.*, 117, 462–465, 1995.
141. Anghileri, L.J. and Robert, J., *Hyperthermia in Cancer Treatment* CRC Press. Boca Raton, FL, 1986.
142. Pearse, A.G.E. *Histochemistry: Theoretical and Applied*. 4th ed. Churchill Livingstone, New York, NY, Vols.1 and 2, 1980; Vol. 3, 1992.
143. Cotran, S., Kumar, V., and Collins, T. *Pathologic Basis of Disease.* 4th ed., W. B. Saunders Company. Philadelphia, 1999.
144. Ghadially, F.N., *Ultrastructural Pathology of the Cell and Matrix*. 3rd. ed., Butterworths, Boston, 1988.
145. Thomsen, S., Mapping thermal injury in biologic tissues using quantitative pathologic techniques, *Proc. SPIE* 3594, 1999.
146. Thomsen, S., Identification of lethal thermal injury at the time of photothermal treatment, in *Laser-induced Interstitial Thermotherapy,* Muller, G. and Roggan, A., Eds., 459–467, SPIE Publishing, Bellingham, WA, 1995.
147. Ingber, D.E., The architecture of life, *Sci. Am.*, 278, 48–57, 1998.
148. Fawcett, D., *A Textbook of Histology,* 12th ed. W.B. Saunders, Philadelphia, 1994.
149. Schober, R., Ullrich, F., Sander, T., Dunselen, H., and and Hessel, S., Laser-induced alteration of collagen substructures allows microsurgical tissue welding, *Science*, 232, 1421–1422, 1986.
150. Thomsen, S., Pearce, J.A., and Cheong, W.-F., Changes in birefringence as markers of thermal damage in tissues, *IEEE Trans. Biomed. Eng.*, BME-36, 1174–1179, 1989.
151. Schmidt, S.J. Die Doppelbrechung von karyoplasma, zytoplasma und metaplasma in *Protoplasma-Monographien. Vol. II* Verlag von Gebruder Borntraeger, 154–267, Berlin, 1937.
152. Fisher, E., The birefringence of striated and smooth muscles, *J. Cell Comp.Physiol.* 23, 110–130, 1944.
153. Ramachandran, G.N. and Ramakrishnan, C., Molecular structure, In *Biochemistry of Collagen.* Eds. Ramachandran G.N. and Reddi, A.H. Plenum Press, New York, NY, 45–84, 1976.
154. Miller, E.J. and Gay, S., *Collagens In Structural and Contractile Proteins: Part D, Extracellular Matrix (Methods in Enzymology),* Cunningham, L.W., Ed., 144, 3–171, 1987.
155. Cohen, K.I., Diegelmann, R.F., and Linblad, W.J., Eds. Structural and regulatory components of wound healing, In *Wound Healing: Biochemical and Clinical Aspects*, W.B. Saunders Co. Philadelphia, PA, 130–237, 1992.
156. Peckham, M. and Irving, M., Myosin crossbridge orientation in demembranated muscle fibres studied by birefringence and x-ray diffraction measurements, *J. Mol Biol.,* 210, 113–126, 1989.
157. Harris, P. and Heath, D., Structure and function of vascular smooth muscle, in *The Human Pulmonary Circulation: Its Form and Function in Health and Disease,* Churchill Livingstone, New York, 161–82, 1986.
158. Canham, P.B., Finlay, H.M., Whittaker, P., and Starkey, J., The tunica musclularis of human brain arteries: three dimensional measurements of alignment of the smooth muscle mechanical axis by polarized light and the universal stage, *Neurol. Res.,* 8, 66–74, 1986.
159. Hulmes, D.J.S., Miller, A., Parry, D.A.D., Piez, K.A., and Woodhead–Galloway, J., Crystalline regions in collagen fibrils, *J. Mol. Biol.,* 184, 473–477, 1985.
160. Flory, P. and Garrett, R.R., Phase transition in collagen and gelatin systems, *J. Am. Chem. Soc.,* 80, 4836–4845, 1958.
161. Wood, G.C., Spectral changes accompanying the thermal denaturation of collagen, *Biochem. Biophys. Res. Commun.,* 13, 95–99, 1963.

162. Deak, Gy. and Romhanyi, Gy., The thermal shrinkage process of collagen fibers as revealed by polarization optical analysis of topo-optical staining reactions, *Acta Morphol.* Acad. Sci./Hung/ 15, 195–200, 1967.
163. Lim, J.J., Transition temperature and enthalpy change dependence on stabilizing and destabilizing ions in the helix-coil transition in native tendon collagen, *Biopolymers.* 15, 2371–2381, 1976.
164. Bosman, S., Pickering, J.W., vanMarle, J., and vanGemert, M.J.C., Ultrastructural alterations in heated canine myocardium, *Lasers Surg. Med.*, 17, 39–48, 1995.
165. Thomsen, S., Jacques, S.L., and Flock, S., Microscopic correlates of macroscopic optical property changes during thermal coagulation of myocardium, *Proc. SPIE Laser-Tissue Interactions,* 1202, 2–11, 1990.
166. Junqueira, L.C.U., Bignolas, G., and Brentani, R.R., Picrosirius staining plus polarization microscopy, a specific method for collagen detection in tissue sections, *Histochem. J.*, 11, 447–455, 1979.
167. McKenzie, A.L., A three-zone model of soft-tissue damage by a CO_2 laser, *Phys. Med. Biol.,* 31, 967–983, 1986.
168. Partovi, F., Izatt, J.A., Cothren, R.M., Kittrell, C., Thomas, J.E., S. Strikwerda, Kramer, J.R., and Feld, M.S., A model for thermal ablation of biological tissue using laser radiation, *Lasers Surg. Med.,* 7, 141–154, 1987.
169. Rastegar, S., Motamedi, M., Welch, A.J., and Hayes, L.J., A theoretical study of the effect of optical properties in laser ablation of tissue, *IEEE Trans. Biomed. Eng.,* BME-36, 1180–1187, 1989.
170. LeCarpentier, G.L., Motamedi, M., Rastegar, S., and Welch, A.J., Simultaneous analysis of thermal and mechanical events during cw laser ablation of biological media, *Proc. SPIE*, 1064, 107–113, 1989.
171. Verdaasdonk, R.M., Borst, C., and vanGemert, M.J.C., Explosive onset of continuous wave laser tissue ablation, *Phys. Med. Biol.,* 1991.
172. Van Leeuwen, T.G., van der Veen, J.J., Verdaasdonk, R.M., and Borst, C., Noncontact tissue ablation by holmium: YAG laser pulsed in blood, *Lasers Surg. Med.,* 11, 26–34, 1991.
173. Gijsbers, G.H.M., Selten, F.M., and vanGemert, M.J.C., CW laser ablation velocities as a function of absorption in and experimental one dimensional tissue model, *Lasers Surg. Med.,* 11, 287–296, 1991.
174. Zweig, A.D., Infrared tissue ablation: consequences of liquefaction, *Proc. SPIE Laser-Tissue Interactions,* 1427, 2–8, 1991.
175. Frenz, M.C., Greber, M., Romano, V., Forrer, M., and Weber, H.P., Damage induced by pulsed IR laser radiation at transitions between different tissues, *Proc. SPIE Laser–Tissue Interactions,* 1427, 9–15, 1991.
176. Pearce, J.A. and Thomsen, S., Kinetic models of tissue fusion processes, *Proc. SPIE Laser Tissue Interactions III,* 1643, 1992.
177. Zweig, A.D., Meierhofer, B., Muller, O.M., Mischler, C., Romano, V., Frenz, M., and Weber, H.P., Lateral damage along pulsed laser incisions, *Lasers Surg. Med.,* 10, 262–274, 1990.
178. Van Leeuwen, T.G., L. Van Erven, L., Meertens, J.H., Motamedi, M., Post, M.J., and Borst, C., Origin of wall dissections induced by pulsed excimer and mid-infrared laser ablation in the pig, *J. Am. Col. Cardiol.,* 1992.
179. Dabby, F.W. and Paek, U., High-intensity laser-induced vaporization and explosion of solid material, *IEEE J. Quant. Electron.,* QE8, 106–111, 1972.
180. Welch, A.J. and Polhamus, G.D., Measurement and prediction of thermal injury in the retina of Rhesus monkey, *IEEE Trans. Biomed. Eng.,* BME-31, 633–644, 1984.
181. Takata, A.N. et al., Thermal model of laser induced eye damage, Final Rept. USAF School of Aerospace Medicine, Brooks AFB TX, Contract F41609-74-C-0005, IIT Research Institute, Chicago, IL. 1974.
182. Birngruber, R., Hillenkamp, F., and Gabel, V.-P., Theoretical investigations of laser thermal retinal injury, *Health Phys.,* 48(6), 781–796, 1985.

183. Birngruber, R., Thermal modeling in biological tissue, in *Lasers in Biology and Medicine,* F. Hillenkamp, R. Pratesi, and C.A. Sacchi, Eds., Plenum Publishing Corp., New York 77–97, 1980.
184. Yang, Y., Welch, A.J., and Rylander, H.G., III, Rate process parameters of albumen, *Lasers Surg. Med.,*11, 188–190, 1991.
185. Agah, R., Quantitative characterization of arterial tissue thermal damage, M.SE thesis, The University of Texas at Austin, 1988.
186. Mixter, G., Delhry, G.P., Derksen, W.L., and Monahan, T. The Influence of time on the death of HeLa cells at elevated temperature, in *Temperature: Its Measurement and Control in Science and Industry,* Ed., Hardy, J.D., vol. 3, Reinhold, 1963.
187. Padanilam, J., Bischof, J.C., Lee, R.C., Cravalho, E.G., Tompkins, R.G., Yarmush, M.L., and Toner, M., Effectiveness of poloxamer 188 in arresting calcein leakage from thermally damaged isolated skeletal muscle cells, *Ann. NY Acad. Sci.*, 720, 111–123, 1994.
188. Pearce, J.A., Cheong W.F., Pandit, K., McMurray,T., and Thomsen S., Kinetic models for coagulation processes: determination of rate coefficients *in vivo*, *Proc. Lasers Dermatol. Tissue Welding* (SPIE), 1422, 27–32, 1991.
189. Pearce, J.A., Han, A., Gutierrez, T., and Thomsen, S., Argon laser coagulation of myocardium: the effect of pulse width on threshold temperature, *Lasers Surg. Med.* suppl. 2 (Proc. ASLMS meeting), 16, 1990.
190. Polge, C., Smith, A.U., and Parkes, A.S., Revival of spermatozoa after vitrificaiton and dehydration at low temperatures, *Nature*, 164, 666, 1949.
191. Lovelock, J.E., The mechanism of the protective action of glycerol against haemolysis by freezing and thawing, *Biochim. Biophys. Acta*, 11, 28–36, 1953.
192. Strumia, M.M., Clawell, L.S., and Strumia, P.V., The preservation of blood for transfusion, *J. Lab. Clin. Med.*, 56, 576–593, 1960.
193. Whittingham, D.G., Leibo, S.P., and Mazur, P., Survival of mouse embryos frozen to –196°C and –296°C, *Science*, 178, 411–414, 1972.
194. McGrath, J.J. and Diller, K.R., Eds., *Low Temperature Biotechnology: Emerging Applications and Engineering Contributions*, ASME, New York, 1–380, 1988.
195. Mazur, P., Kinetics of water loss from cells at subzero temperatures and the likelihood of intracellular freezing, *J. Gen. Physiol.*, 47, 347–369, 1963.
196. Toner, M., Nucleation of ice crystals in biological cells, in *Advances in Low Temperature Biology.* Steponkus, P.L., Ed., JAI Press, London, 1993, 1–52.
197. Acker, J.P. and McGann, L.E., Protective effect of intracellular ice during freezing? *Cryobiology*, 46, 197–202, 2003.
198. Mazur, P., Freezing of animal cells: mechanisms and implications, *Am. J. Physiol.,* 247, C125–C142, 1984.
199. Mazur, P., Equilibrium, quasi-equilibrium and nonequilibrium freezing of mammalian embryos, *Cell Biophys*., 17, 53–92, 1990.
200. Eroglu, A., Russon M.J., Bieganski, R., Fowler, A., Cheley, S., Bayley, H., and Toner, M., Intracellular trehalose improves the survival of cryopreserved mammalian cells, *Nature Biotech.*, 18, 163–167, 2000.
201. Eroglu, A., Toner, M., and Toth, T.L., Beneficial effect of microinjected trehalose on the cryosurvival of human oocytes, *Fertil. Steril.*, 77, 152–158, 2002.
202. Erdag, G., Eroglu, A., Morgan, J.R., and Toner, M., Cryopreservation of fetal skin is improved by extracellular trehalose, *Cryobiology,* 44, 218–228, 2002.
203. Kedem, O. and Katchalsky, A., Thermodynamic analysis of permeability of biological membranes to nonelectrolytes, *Biochim. Biophys. Acta*, 27, 229–246, 1958.
204. McGrath, J.J., Membrane transport properties, in *Low Temperature Biotechnology: Emerging Applications and Engineering Contributions*, J.J. McGrath and K.R. Diller, Eds., ASME, New York, 273–330, 1988.

205. Hertel, A. and Steudle, E., The function of water channels in *Chara*: the temperature dependence of water and solute flows provides evidence for composite membrane transport and for a slippage of small organic solutes across water channels, *Planta*, 202, 1997, 324–335.
206. Walsh, J.R., Diller, K.R., and Brand, J.J., Measurement and simulation of water transport in algal cells, *J. Biomech. Eng.*, 126, 167–179, 2004.
207. Kleinhans, F.W., Membrane permeability modeling: Kedem–Katchalsky vs. a two-parameter formalism, *Cryobiology*, 37, 1998, 271–289.
208. Oster, G.F., Perelson, A.S., and Katchalsky, A., Network thermodynamic modelling of biophysical systems, *Q. Rev. Biophys.*, 6, 1–134, 1973.
209. Diller, K.R., Energy based network modeling for cryobiology, in *Low Temperature Biotechnology: Emerging Applications and Engineering Contributions*, J.J. McGrath and K.R. Diller, Eds., ASME, New York, 189–202, 1988.
210. Diller, K.R., Beaman, J.J., Montoya, J.P., and Breedfeld, P.C., Network thermodynamic modeling with bond graphs for membrane transport during cell freezing, *J. Heat Trans.*, 110, 938–945, 1988.
211. deFreitas, R.C., Diller, K.R., Lachenbruch, C.A., and Merchant, F.A., Network thermodynamic model of coupled transport in a multicellular tissue — the islet of Langerhans, *Ann. N.Y. Acad. Sci.*, 858, 191–204, 1998.
212. Walsh, J.R., Diller, K.R., and Brand, J.J., Osmomechanical behavior of plant cells across regions of elastic and osmotic stress, *Adv. Heat Mass Transfer Biotechnol.*, ASME HTD 355, BED 37, 15–23, 1997.
213. Devries, A.L. and Wohlschlag, D.E., Freezing resistance in some Antarctic fishes, *Science*, 163, 1074–1075, 1969.
214. Yeh, Y. and Feeney, R.E.F., Antifreeze proteins: structures and mechanisms of function, *Chem. Rev.*, 96, 601–617, 1996.
215. Mazur, P. and Cole, K.W., Roles of unfrozen fraction, salt concentration and changes in cell volume in the survival of frozen human erythrocytes, *Cryoobiology*, 26, 1–29, 1989.
216. Pegg, D.E. and Daiper, M.P. The unfrozen factor hypothesis of freezing injury to human erythrocytes: a critical examination of evidence, *Cryobiology*, 26, 30–38, 1989.
217. Takamatsu, H. and Rubinsky, B., Viability of deformed cells, *Cryobiology*, 39, 243–251, 1999.
218. Körber, Ch., Phenomena at the advancing ice–liquid interface: solutes, particles and biological cells, *Q. Rev. Biophys.*, 21, 229–298, 1988.
219. Beckman, J., Körber, Ch., Rau, G., Hubel, A., and Cravalho, E.G., Redefining cooling rates in terms of ice front velocity and thermal gradient: First evidence of relevance to freezing injury of lymphocytes, *Cryobiology*, 27, 279–287, 1990.
220. Hubel, A., Cravalho, E.G., Nunner, B., and Körber, Ch., Survival of directional solidified B-lymphoblasts under various crystal growth conditions, *Cryobiology*, 29, 183–190, 1992.
221. Ishiguro, H. and Rubinsky, B., Mechanical interactions between ice crystals and red blood cells during directional solidification, *Cryobiology,* 31, 483–500, 1994.
222. Ishiguro, H. and Rubinsky, B., Influence of fish antifreeze proteins on the freezing of cell suspensions with cryoprotectants penetrating cells, *Int. J. Heat Mass Trans.*, 41, 1907–1915, 1998.
223. Wowk, B., Leitl, E., Rasch, C.M., Mesbah–Karimi, N., Harris, S.B., and Fahy, G.M., Vitrification enhancement by synthetic ice blocking agents, *Cryobiology*, 40, 228–236, 2000.
224. Lachenbruch, C.A. and Diller K.R., A network thermodynamic model of kidney perfusion with a cryoprotective agent, *J. Biomech. Eng.*, 121, 574–583, 1999.
225. Acker, J.P., Larese, A., Yang, H., Petrenko, A., and McGann, L.E., Intracellular ice formation is affected by cell interactions, *Cryobiology*, 38, 363–371, 1999.
226. Acker, J.P. and McGann, L.E., Cell–cell contact affects membrane integrity after intracellular freezing, *Cryobiology*, 40, 54–63, 2000.
227. deFreitas, R.C. and Diller, K.R., Intracellulas ice formation in three dimensional tissues: pancreas islets, *Cell Preserv. Tech.*, 2, 19–28, 2004.

228. Irimia, D. and Karlsson, J.O.M., Kinetics and mechanism of intercellular ice propagation in a micropatterned tissue construct, *Biophys. J.*, 82, 1858–1868, 2002.
229. Karlsson, J.O.M., Cravalho, E.G., and Toner, M., A model of diffusion-limited ice growth inside biological cells during freezing, *J. Appl. Physics*, 75, 4442–4455, 1994.
230. Diller, K.R. and Cravalho, E.G., A cryomicroscope for the study of freezing and thawing processes in biological cells, *Cryobiology*, 7, 191–199, 1970.
231. Diller, K.R., Quantitative low temperature optical microscopy of biological systems, *J. Micros.*, 126, 9–28, 1982.
232. Diller, K.R., Cryomicroscopy, in *Low Temperature Biotechnology: Emerging Applications and Engineering Contributions*, J.J. McGrath and K.R. Diller, Eds., ASME, New York, 347–362, 1988.
233. McGrath, J.J., A microscope diffusion chamber for the determination of the equilibrium and nonequilibrium response of individual cells, *J. Micros.*, 139, 249–263, 1985.
234. Walcerz, D.B. and Diller, K.R., Quantitative light microscopy of combined perfusion and freezing processes, *J. Micros.*, 161, 297–311, 1991.
235. deFreitas, R.C., Diller, K.R., Lakey, J.R.T., and Rajotte, R.V. Osmotic behavior and transport properties of human islets in a dimethyl sulfoxide solution, *Cryobiology*, 35, 230–239, 1997.
236. Levin, R.L., Osmotic behavior of cells during freezing and thawing, in *Low Temperature Biotechnology: Emerging Applications and Engineering Contributions*, J.J. McGrath and K.R. Diller, Eds., ASME, New York, 177–188, 1988.
237. Kasharin, A.V. and Karlsson, J.O.M., Analysis of mass transport during warming of cryopreserved cells, *Ann. N.Y. Acad. Sci.*, 858, 163–174, 1998.
238. Fahy, G.M., MacFarlance, D.R., Angell, C.A., and Meryman, H.T. Vitrification as an approach to cryopreservation, *Cryobiology*, 21, 407–426, 1984
239. Fahy, G.M., Vitrification, in *Low Temperature Biotechnology: Emerging Applications and Engineering Contributions*, J.J. McGrath and K.R. Diller, Eds., ASME, New York, 113–146, 1988.
240. Baudot, A, Agler, L., and Boutron, P., Glass-forming tendency in the system water-dimethyl sulfoxide, *Cryobiology*, 40 151–158, 2000.
241. Chen, T., Bhowmick, S., Sputtek, A., Fowler, A., and Toner, M., The glass formation temperature of mixtures of trehalose and hydroxyethyl starch, *Cryobiology*, 44, 301–306, 2002.
242. Mazur, P., Leibo, S.P., and Chu, E.H.Y., A two-factor hypothesis of freezing injury: evidence from Chinese hamster tissue-culture cells, *Exp. Cell Res.*, 71, 345–355, 1972.
243. Steponkus, P.L., The role of the plasma membrane in freezing injury and cold acclimation, *Ann. Rev. Plant Physiol.*, 35, 543–584, 1984.
244. Kasharin, A.V. and Karlsson, J.O.M., Analysis of mass transport during warming of cryopreserved cells, *Ann. NY Acad. Sci.*, 858, 160–171, 1998.
245. Koshimoto, C. and Mazur, P., Effects of warming rate, temperature, and antifreeze proteins on the survival of mouse spermatozoa frozen at an optimal rate, *Cryobiology*, 45, 49–59, 2002.
246. Toner, M., Cravalho, E.G., Stachecki, J., Fitzgerald, T., Tompkins, R.G., Yarmush, M.L., and Armant, D.R., Nonequilibrium freezing of one-cell mouse embryos: membrane integrity and developmental potential. *Biohpys. J.,* 64: 1908–1921, 1993.
247. Kurz, W. and Fisher, D.J., *Fundamentals of Solidification*, 3rd ed., Trans Tech Publications, Aedermannsdorf, Switzerland, 1992.
248. Hayes, L.J., Diller, K.R., Chang, H.J., and Lee, H.S., Prediction of local cooling rates and cell survival during the freezing of cylindrical specimens, *Cryobiology*, 25, 67–82, 1988.
249. Rabin, Y. and Bell, E., Thermal expansion measurements of cryoprotective agents. Part I: a new experimental apparatus, *Cryobiology*, 46, 254–263, 2003.
250. Rabin, Y. and Bell, E., Thermal expansion measurements of cryoprotective agents. Part II: measurements of DP6 and VS55, and comparison with DMSO, *Cryobiology*, 46, 264–270, 2003.
251. Fahy, G.M., Physical problems with the vitrification of large biological systems, *Cryobiology*, 27, 492–510, 1990.

252. Rubinsky, B., Cravalho, E.G., and Mikic, B., Thermal stresses in frozen organs, *Cryobiology*, 17, 66–73, 1980.
253. Fowler, A.J. and Toner, M., Prevention of hemolysis in rapidly frozen erythrocytes by using a laser pulse, *Ann. NY Acad. Sci.*, 858, 245–252, 1998.
254. Nerem, R.M. and Sambanis, A., Tissue engineering: from biology to biological substitutes, *Tissue Eng.*, 1, 3–13, 1995.
255. Hubel, A., Horman, J., and Darr, T.B., Cryobiophysical characteristics of genetically modified hematopoietic progenitor cells, *Cryobiology*, 38, 140–153, 1999.
256. Bidault, N.P., Hammer, B.E., and Hubel, A., Rapid MR imaging of cryoprotectants permeation in an engineered dermal replacement, *Cryobiology*, 40, 13–26, 2000.
257. Oegema, T.R., Jr., Deloria, L.B., Fedewa, M.M., Bischof, J.C., and Lewis, J.L., A simple cryopreservation method for the maintenance of cell viability and mechanical integrity of a cultured cartilage analog, *Cryobiology*, 40, 370–375, 2000.
258. Ebertz, S.L. and McGann, L.E., Osmotic parameters of cells from a bioengineered human corneal equivalent and consequences for cryopreservation, *Cryobiology*, 45, 109–117, 2002.
259. Devireddy. R.V. and Bischof, J.C., Measurement of water transport during freezing in cell suspensions using a differential scanning calorimeter, *Cryobiology*, 36, 124–155, 1998.
260. Devireddy, R.V. and Bischof, J.C., Measurement of water transport during freezing in mammalian liver tissue. II. The use of differential scanning calorimetry, *J. Biomech. Eng.*, 12–, 559–569, 1998.
261. Devireddy, R.V., Barratt, P.R., Storey, K.B., and Bishcof, J.C., Liver freezing response to the freeze-tolerant wood frog, *Rana sylvatica*, in the presence and absence of glucose. I. experimental measurements, *Cryobiology*, 38, 310–326, 1999.
262. Devireddy, R.V., Barratt, P.R., Storey, K.B., and Bishcof, J.C., Liver freezing response to the freeze-tolerant wood frog, *Rana sylvatica*, in the presence and absence of glucose. II. mathematical modeling, *Cryobiology*, 38, 327–338, 1999.
263. Rubinsky, B., Biophysical and bioengineering aspects of cryosurgery, *Cryobiol. Cryotechnol.*, 41, 67–81, 1995.
264. Onik, G. and Rubinsky, B., Cryosurgery: new developments in understanding and technique, in *Low Temperature Biotechnology: Emerging Applications and Engineering Contributions*, J.J. McGrath and K.R. Diller, Eds., ASME, New York, 57–80, 1988.
265. Onik, G., Gilbert, J., Hoddick, W., Filly, R., Callen, P., Rubinsky, B., and Christianson, M., Ultrasonic characteistics of frozen liver, *Cryobiology*, 21, 331–335, 1984.
266. Rubinsky, B., Gilbert, J.C., Onik, G.M., Roos, H.S., Wong, S.T.S., and Brennan, K.M., Monitoring cryosurgery in the brain and in the prostate with proton NMR, *Cryobiology*, 30, 191–199, 1993.
267. Tacke, J., Speetzen, R., Heschel, I., Hunter, D.W., Rau, G., and Günther, R.W., Imaging of interstitial cryotherapy-an *in Vitro* comparison of ultrasound, computed tomography, and magnetic resonance imaging, *Cryobiology*, 38, 250–259, 1999.
268. Mala, T., Samset, E., Aurdal, L., Gladhaug, I., Edwin, B., and Søreide, O., Magnetic resonance imaging-estimated three-dimensional temperature distribution in liver cryolesions: a study of cryolesion characteristics assumed necessary for tumor ablation, *Cryobiology*, 43, 268–275, 2001.
269. Otten, D.M., Rubinsky, B., Cheong, W-F., and Benaron, D.A., Ice front propagation monitoring in tissue by the use of visible-light spectroscopy, *Appl. Optics*, 37, 6006–6010, 1998.
270. Radai, M.M., Abboud, S., and Rubinsky, B., Evaluation of the impedance technique for cryosurgery in a theoretical model of the head, *Cryobiology*, 38, 51–59, 1999.
271. Baust, J.G. and Chang, Z., Underlying mechanisms of damage and new concept in cryosurgical instrumentation, *Cryosurgery: Mechanism and Applications*, IIR Press, Paris, 21–36, 1995.
272. Rubinsky, B. and Pegg, D.E., A mathematical model for the freezing process in biological tissue, *Proc. R. Soc. London*, B234, 343–358, 1989.
273. Bischof, J.C. and Rubinsky, B., Microscale heat and mass transfer of vascular and intracellular freezing in the liver, *J. Heat Trans.*, 115, 1029–1035, 1993.

274. Pazhayannur, P.V., and Bischof, J.C., Measurement and simulation of water transport during freezing in mammalian liver tissue, *J. Biomech. Eng.*, 119, 269–277, 1997.
275. Rupp, C.C., Hoffmann, N.E., Schmidlin, F.R., Swanlund, D.J., Bischof, J.C., and Coad, J.E., Cryosurgical changes I the porcine kidney: histologic analyisis with thermal history correlation, *Cryobiology*, 45, 167–182, 2002.
276. Rabin, Y., A general model for the propagation of uncertainty in measurements into heat transfer simulations and its application to cryosurgery, *Cryobiology*, 46, 109–120, 2003.
277. Koushafar, H. and Rubinsky, B., Effect of antifreeze proteins on frozen primary prostatic adenocarcinoma cells, *Urology*, 49, 421–425, 1997.
278. Koushafar, H., Pham, L., Lee, C., and Rubinsky, B., Chemical adjuvant cryosurgery with antifreeze proteins, *J. Surg. Oncol.*, 66, 114–121, 1997.
279. Pham, L., Dahiya, R., and Rubinsky, B., An *in vivo* study of antifreeze protein adjuvant cryosurgery, *Cryosurgery*, 38, 169–175, 1999.
280. DeVries, A.L., The role of antifreeze glycopeptides and peptides in the freezing avoidance of antarctic fishes, *Comp. Biochem. Physiol.*, 90, 611–621, 1988.
281. Ananthanarayanan, V.S., Antifreeze proteins: structural diversity and mechanism of action, *Life Chem. Rep.*, 7, 1–32, 1989.
282. Ishiguro, H. and Rubinsky, B., Influence of fish antifreeze proteins on the freezing of cell suspensions with cryoprotectant penetrating cells, *Int. J. Heat Mass Trans.*, 41, 1907–1915, 1998.
283. Bhavaraju, N.C., Heat transfer modeling during cardiac ablation in swine myocardium, Ph.D. Thesis, Univ. Texas Austin, Dept. Biomed. Eng., 1999.
284. Yuan, D., Perfusion heat transfer in the canine prostate parenchyma, Ph.D. Thesis, Univ. Texas Austin, Dept. Biomed. Eng., 2002.
285. Diller, K.R. and Ryan, T.P., Heat transfer in living systems: current opportunities, *J. Heat Trans.*, 120, 810–829, 1998.
286. Holmes, K.R., Thermal conductivity of selected tissues, in *Biotransport: Heat and Mass Transfer in Living Systems*, Diller, K.R., Ed., *Ann. NY Acad. Sci.*, 858, 18–20, 1998.

The following physiological properties were compiled by Kenneth R. Holmes <krholmes@ux1.cso.uiuc.edu> and were published in part previously [286]. The tabulation includes values for the native thermal conductivity of biomaterials (Appendix A) and the blood perfusion rates for specific tissues and organs (Appendix B). Original sources are documented in the dedicated list of references at the end of each appendix. Knowledge of the perfusion behavior of tissues is important in that the flow of blood can have a direct quantitative effect on the temperature distribution within living tissue.

Appendix A

Thermal Conductivity Data for Specific Tissues and Organs for Humans and Other Mammalian Species

Tissue	k (W/mK)	%H_2O	Ref.
Kidney			
Whole (rabbit)	.502	81	6
Whole (rabbit)	.495		16
Whole (human)	.543	84	4
Cortex (rabbit)	.465–.490 ($n = 7$)	76.6–79.81	
Cortex (dog)	.491		16
Cortex (human)	.499		16
Medulla (rabbit)	.502–.544 ($n = 7$)	82.0–86.0	1
Medulla (dog)	.507		16
Medulla (human)	.499		16
Aorta			
Human	.476 ± .041 (SD) ($n = 12$)		2

Tissue	k (W/mK)	%H_2O	Ref.
Arterial plaque			
Fatty	.484 ± .044 (SD) (n = 13)		2
Fibrous	.485 ± .022 (SD) (n = 12)		2
Calcified	.502 ± .059 (SD) (n = 17)		2
Artery			
Femoral (dog)	.391		2
Carotid (dog)	.448		2
Blood			
Whole	.505		10
Whole (human)	.492 ± .009 (SD) (n = 10)		5
Plasma	.582		10
Plasma (human)	.570 ± .010 (SD) (n = 10)		5
Spleen			
Human	.543	80	4
Liver			
Rabbit	.493	72	6
Rat	.498–.528 (n = 4)		3
Sheep	.495 ± .017 (SD) (n = 9)		5
Dog	.550 ± .010 (SD) (n = 7)		5
Dog	.574		11
Pig	.498		16
Human	.469		16
Human	.564	77	4
Heart			
Rat	.521–.531 (n = 2)		3
Dog	.527		11
Dog	.487		16
Pig	.484		
Human	.493		16
Human	.585	81	4
Muscle			
Rat	.505–.530 (n = 7)		3
Cow	.410–.426		7
Pig	.518–.618		7
Pig	.460		17
Sheep	.478 ± .019 (SD) (n = 10)		5
Fat			
Cow	.185–.233		7
Cow	.222		17
Pig	.317–.402		
Pig	.159		
Blubber (Minke whale)	.200–.280	3–30	
Blubber (Harp seal)	.190 ± .010		8
Human	.201–.217		17
Brain			
Whole	.527	78	4
Cerebral cortex	.564	83	4
Cerebral cortex	.504		16
White matter	.502	71	4
Tumor			
Periphery	.511		11
Core	.561		
Colon cancer (human)	.545		
Bone	.410–.630		15
Skin	.210–.410		
Crocodile, middle of back	.432		12
Crocodile, tail, ventral	.334		12

Tissue	k (W/mK)	%H_2O	13
Epidermis (elephant; freeze/thaw)	.475	62.5	14
Epidermis (rhinoceros; freeze/thaw)	.452	60.1	14
Giraffe (formalin fixed)	.442	60.0	14
Epidermis (human)	.209		17
Epidermis (pig)	.209		17
Dermis (human)	.293–.322		17
Pure water	.627		17

Notes: $c = [\%H_2O + 0.4 * (100 - \%H_2O)] * 41.9$ J/kg K; $\rho = 1.05(10^3)$ kg/m^3. (From Balasubramaniam, T.A. and Bowman, H.F., Biomech. Eng., 99, 148–154, 1977.

References

1. Holmes, K.R., Ryan, R., and Chen. M.M., Thermal conductivity and H_2O content in rabbit kidney cortex and medulla. *J. Therm. Biol.* 8, 311–313, 1983.
2. Valvano, J.W. and Chitsabesan, B., Thermal conductivity and diffusivity of arterial wall and atherosclerotic plaque. *Lasers Life Sci.*, 1, 219–229, 1987.
3. Valvano, J.W., Allen, J.T., and Bowman, H.F. The simultaneous measurement of thermal conductivity, thermal diffusivity, and perfusion in small volumes of tissue. *ASME 81-WA/HT-21*, 1981.
4. Cooper, T.E. and Trezek, G.J., Correlation of thermal properties of some human tissue with water content. *Aerospace Med.* 42, 24–27, 1971.
5. Balasubramaniam, T.A. and Bowman, H.F., Thermal conductivity and thermal diffusivity of biomaterials: a simultaneous measurement technique. *J. Biomech. Eng.* 99, 148–154, 1977.
6. Grayson, J., Internal calorimetry in the determination of thermal conductivity and blood flow. *J. Physiol.* 118, 54–72, 1952.
7. Chato, J.C., A method for the measurement of the thermal properties of biological materials. In *Thermal Problems in Biotechnology*, J.C. Chato, Ed., ASME symposium series, American Society of Mechanical Engineers, New York, 1968.
8. Kvadsheim, P.H., Folkow, L.P., and Blix, A.S., Thermal conductivity of Minke whale blubber. *J. Therm. Biol.* 21, 123–128, 1996.
9. Kvadsheim, P.H., Folkow, L.P., and Blix, A.S., A new device for measurement of the thermal conductivity of fur and blubber. *J. Therm. Biol.* 19, 431–435, 1994.
10. Dumas, A. and Barozzi, G.S., Laminar heat transfer to blood flowing in a circular duct. *Int. J. Heat Mass Trans.* 27, 391–398, 1984.
11. Holmes, K.R. and Chen, M.M., Local thermal conductivity of Para-7 fibrosarcoma in hamster. *1979 Advances in Bioengineering*, ASME, New York, 147–149, 1979.
12. Drane, C.R., The thermal conductivity of the skin of crocodilians. *Comp. Biochem. Physiol.* 68A, 107–110, 1981.
13. Holmes, K.R. and Adams, T., Epidermal thermal conductivity and stratum corneum hydration in cat footpad. *Am. J. Physiol.* 228, 1903–1908, 1975.
14. Holmes, K.R., Unpublished data.
15. Chato, J.C., Fundamentals of bioheat transfer. In *Thermal Dosimetry and Treatment Planning*, M. Gautherie, Ed., Springer–Verlag, New York, 1990, p. 51.
16. Valvano, J.W., Cochran, J.R., and Diller, K.R., Thermal conductivity and diffusivity of biomaterials measured with self-heated thermistors. *Int. J. Thermophys.* 6, 301–311, 1985.
17. Cohen, M.L., Measurement of the thermal properties of human skin. a review. *J. Invest. Dermatol.* 69, 333–338, 1977 (and its references).

Appendix B

Blood Perfusion Data for Specific Tissues and Organs for Humans and Other Mammalian Species

Organ	Blood flow (ml/min/gm)	Species[a]	Ref.	Technique
Brain	0.36 ± 0.04 (SE)	Dog (n = 11)	36	µs (pentobarbital)
Brain	0.78 ± 0.06 (SE)	Rat (*n* = 7)	30	µs
Brain	1.52 ± 0.23 (SE)	Fetal sheep[a] (*n* = 12)	32	µs
Brain	0.82 ± 0.06 (SE)	Neonatal sheep[a] (*n* = 13)	37	µs
Brain	0.64 ± 0.03 (SE)	Sheep[a] (*n* = 7)	37	µs
Brain	1.14 ± 0.14 (SD)	Rat[a] (12 mo old)(*n* = 5)	33	µs
Brain	0.65 ± 0.07 (SD)	Rat (*n* = 10)	33	µs (pentobarbital)
Brain	1.31 ± 0.22 (SD)	Rat[a] (24 mo old)(*n* = 5)	33	µs
Brain	0.43 ± 0.14 (SD)	Rat (*n* = 7)	33	µs (decerebrate)
Mean Cerebral	0.373 ± 0.062	Dog	2	
Mean Cerebral	0.491 ± 0.078	Baboon	2	
Cerebrum	0.48 ± 0.03	Cat	18	
Cerebrum	0.53 ± 0.06	Cat	18	
Cerebrum	0.32 ± 0.06	Monkey	18	
Cerebrum	0.39 ± 0.03	Monkey	18	
Cerebrum	0.79 ± 0.12	Pig[¶]	19	
Cerebrum	1.17 ± 0.11 (SE)	Rat[a] (*n* = 8)	31	µs
Cerebrum	0.61 ± 0.06 (SE)	Rat (*n* = 7)	31	µs (pentobarbital)
Cerebrum	0.72 ± 0.05 (SE)	Rat (*n* = 7)	31	µs (chlor.-urethan)
Cerebrum	0.50 ± 0.04 (SE)	Rat (*n* = 7)	31	µs (decerebrate)
Cerebrum	0.60 ± 0.06 (SE)	Cat (*n* = 8)	34	µs (α-chloralose)
Cerebrum	1.29 ± 0.03 (SE)	Cat (*n* = 8) (hypercapnic)	34	µs (α-chloralose)
Cerebral cortex	0.446 ± 0.061	Dog	2	
Cerebral cortex	0.447 ± 0.036	Dog	3	
Cerebral cortex	0.64 ± 0.05	Cat	18	
Cerebral cortex	0.75 ± 0.11	Cat	18	
Cerebral cortex	0.40 ± 0.11	Monkey	18	
Cerebral cortex	0.50 ± 0.11	Monkey	18	
Frontal cortex	1.06 ± 0.05	Rat	4	
Parietal cortex	1.07 ± 0.05	Rat	4	
Occipital cortex	0.98 ± 0.08	Rat	4	
Cerebral white	0.240 ± 0.037	Dog	2	
Cerebral white	0.305 ± 0.022	Dog	3	
Cerebral white	0.20 ± 0.05	Monkey	18	
Cerebral white	0.21 ± 0.06	Monkey	18	
Cerebral white	0.29 ± 0.03	Cat	18	
Cerebral white	0.20 ± 0.03 (SE)	Cat (*n* = 8)	34	µs (α-chloralose)
Cerebral white	0.35 ± 0.09 (SE)	Cat (*n* = 8) (hypercapnic)	34	µs (α-chloralose)
White matter	0.164 ± 0.022	Baboon	2	
Corpus callosum	0.249 ± 0.035	Dog	3	
Corpus callosum	0.62 ± 0.03	Rat	4	
Gray matter	0.552 ± 0.077	Baboon	2	
Cortical grey	0.87 ± 0.11 (SE)	Cat (n = 8)	34	µs (α-chloralose)
Cortical gray	1.94 ± 0.37 (SE)	Cat (*n* = 8) (hypercapnic)	34	µs (α-chloralose)
Caudate nucleus	0.88 ± 0.03	Rat	4	
Caudate nucleus	0.65 ± 0.06	Cat	18	
Caudate nucleus	0.87 ± 0.11	Cat	18	
Caudate nucleus	0.39 ± 0.05	Monkey	18	
Caudate nucleus	0.47 ± 0.05	Monkey	18	
Caudate nucleus	0.85 ± 0.10 (SE)	Cat (*n* = 8)	34	µs (α-chloralose)
Caudate nucleus	1.31 ± 0.19 (SE)	Cat (*n* = 8) (hypercapnic)	34	µs (α-chloralose)
Choroid plexus	4.18 ± 0.60 (SE)	Neonatal sheep[a] (*n* = 13)	37	µs
Choroid plexus	7.53 ± 1.11 (SE)	Sheep[a] (*n* = 7)	37	µs
Hypothalamus	1.03 ± 0.06	Rat	4	
Pituitary	1.08 ± 0.24 (SE)	Neonatal sheep[a] (*n* = 13)	37	µs

Organ	Blood flow (ml/min/gm)	Species[a]	Ref.	Technique
Pituitary	1.13 ± 0.16 (SE)	Sheep[a] ($n = 7$)	37	
Thalamus	0.92 ± 0.07	Rat	4	
Thalamus-midbrain	0.62 ± 0.07 (SE)	Cat ($n = 8$)	34	μs (α-chloralose)
Thalamus-midbrain	1.64 ± 0.32 (SE)	Cat ($n = 8$) (hypercapnic)	34	μs (α-chloralose)
Hippocampus	0.68 ± 0.06	Rat	4	
Cerebellum	0.63 ± 0.04	Cat	18	
Cerebellum	0.70 ± 0.07	Cat	18	
Cerebellum	0.60 ± 0.08 (SE)	Cat ($n = 8$)	34	μs (α-chloralose)
Cerebellum	1.63 ± 0.31 (SE)	Cat ($n = 8$) (hypercapnic)	34	μs (α-chloralose)
Cerebellum	0.40 ± 0.08	Monkey	18	
Cerebellum	0.50 ± 0.02	Monkey	18	
Cerebellum	0.78 ± 0.06	Pig[a]	19	
Cerebellum	1.31 ± 0.19 (SE)	Rat[a] ($n = 8$)	31	μs
Cerebellum	1.02 ± 0.12 (SE)	Rat ($n = 7$)	31	μs (pentobarbital)
Cerebellum	1.04 ± 0.08 (SE)	Rat ($n = 7$)	31	μs (chlor.-urethan)
Cerebellum	0.78 ± 0.07 (SE)	Rat ($n = 7$)	31	μs (decerebrate)
Pons	0.50 ± 0.03 (SE)	Cat ($n = 8$)	34	
Pons	1.18 ± 0.25 (SE)	Cat ($n = 8$) (hypercapnic)	34	
Medulla	0.37 ± 0.06 (SE)	Cat ($n = 8$)	34	μs (α-chloralose)
Medulla	1.07 ± 0.20 (SE)	Cat ($n = 8$) (hypercapnic)	34	μs (α-chloralose)
Medulla	0.84 ± 0.04	Rat	4	
Brain stem	0.52 ± 0.03	Cat	18	
Brain stem	0.58 ± 0.03	Cat	18	
Brain stem	0.33 ± 0.06	Monkey	18	
Brain stem	0.36 ± 0.03	Monkey	18	
Brain stem	0.46 ± 0.06	Pig[a]	19	
Brain stem	0.55 ± 0.05 (SE)	Cat ($n = 8$)	34	μs (α-chloralose)
Brain stem	1.44 ± 0.28 (SE)	Cat ($n = 8$) (hypercapnic)	34	μs (α-chloralose)
Spinal cord	0.22 ± 0.02	Cat	18	
Spinal cord	0.31 ± 0.03	Cat	18	
Spinal cord	0.20 ± 0.03	Monkey	18	
Spinal cord	0.21 ± 0.03	Monkey	18	
Nerve, sciatic	0.27 ± 0.03 (SE)	Rat ($n = 14$)	29	[^{14}C]iodoantipyrine
Kidney	3.018 ± 0.412 (SE)	Dog ($n = 11$)	36	μs (pentobarbital)
Kidney	3.99 ± 0.88 (SD)	Rat[a] (12 mo old)($n = 5$)	33	μs
Kidney	3.64 ± 0.92 (SD)	Rat ($n = 10$)	33	μs (pentobarbital)
Kidney	4.82 ± 1.39 (SD)	Rat[a] (24 mo old)($n = 5$)	33	μs
Kidney	2.31 ± 0.82 (SD)	Rat ($n = 7$)	33	μs (decerebrate)
Kidney	1.54 ± 0.12 (SE)	Fetal sheep[a] ($n = 12$)	32	μs
Kidney	3.00 ± 0.14 (SE)	Neonatal sheep[a] ($n = 13$)	37	μs
Kidney	4.19 ± 0.32 (SE)	Sheep[a] ($n = 7$)	37	μs
Kidney	4.32 ± 0.30	Dog	3	
Kidney	3.2 ± 0.3	Rabbit	17	
Kidney	2.80 ± 0.05	Pig[a]	19	
Kidney	4.7 ± 0.3	Rat	13	
Kidney	5.55 (4.87-8.76)	Rat ($n = 14$)	26	
Kidney	6.23 ± 0.49	Rat ($n = 9$)	27	
Kidney	4.38 ± 0.51 (SE)	Rat ($n = 7$)	30	μs
Kidney	4.38 ± 0.44 (SE)	Rat ($n = 7$)	30	μs
Kidney	7.63 ± 0.46 (SE)	Rat[a] ($n = 8$)	31	μs
Kidney	6.16 ± 0.39 (SE)	Rat ($n = 7$)	31	μs (pentobarbital)
Kidney	5.96 ± 0.42 (SE)	Rat ($n = 7$)	31	μs (chlor.-urethan)
Kidney	5.46 ± 0.53 (SE)	Rat ($n = 7$)	31	μs (decerebrate)
Whole cortex	4.0–5.0	human[a]	6	
Whole cortex	3.63 ± 0.54 (range = 3.0–4.4)	Pig	8	
Whole cortex	3.71 ± 0.284	Pig ($n = 4$)	25	
Whole cortex	4.69 ± 0.347	Pig ($n = 6$)	25	

Organ	Blood flow (ml/min/gm)	Species[a]	Ref.	Technique
Whole cortex	5.06 ± 0.251	Pig (*n* = 6)	25	
Whole cortex	3.25 ± 0.20 (SE)	Sheep[a] (*n* = 6)	40	μs
Outer cortex	3.81 ± 0.23 (SE)	Sheep[a] (*n* = 6)	40	μs
Outer cortex	6.32 ± 0.33	Dog	3	
Outer cortex	7.56 ± 0.70	Dog	11	
Outer cortex	4.62	Dog	7	
Outer cortex	8.84 ± 0.014	Rabbit	5	
Outer cortex	8.7 ± 0.6	Rat	13	
Middle cortex	9.53 ± 0.013	Rabbit	5	
Inner cortex	2.57 ± 0.22 (SE)	Sheep[a] (*n* = 6)	40	μs
Inner cortex	4.38 ± 1.19	Dog	11	
Inner cortex	3.35 ± 0.42	Dog	3	
Inner cortex	3.96	Dog	7	
Inner cortex	3.24 ± 0.004	Rabbit	5	
Inner cortex	4.7 ± 0.4	Rat	13	
Outer 1/4 cortex	4.24 ± 0.40	Dog	12	
Next 1/4	6.24 ± 0.61	Dog	12	
Next 1/4	3.55 ± 0.45	Dog	12	
Next 1/4	1.73 ± 0.13	Dog	12	
Medulla	0.35 ± 0.09 (SE)	Sheep[a] (*n* = 6)	40	
Medulla	0.77 ± 0.064	Dog	3	
Outer medulla	1.2	human[a]	6	
Outer medulla	1.30	Dog	7	
Outer medulla	2.10 ± 0.28	Dog	11	
Inner medulla	0.25	human[a]	6	
Adrenal gland	7.62 ± 2.55 (SE)	Fetal sheep[a] (*n* = 12)	32	μs
Adrenal gland	1.83 ± 0.12 (SE)	Neonatal sheep (*n* = 13)	37	μs
Adrenal gland	1.99 ± 0.13 (SE)	Sheep[a] (*n* = 7)	37	μs
Adrenal gland	1.341 ± 0.297 (SE)	Dog (*n* = 11)	36	μs (pentobarbital)
Muscle				
Skeletal	0.027 (average)	human[a]	16	
Skeletal	0.12 ± 0.02 (SE)	Neonatal sheep[a] (*n* = 13)	37	μs
Skeletal	0.04 ± 0.01 (SE)	Sheep[a] (*n* = 7)	37	ms
Skeletal	0.18 ± 0.07 (SD)	Rat[a] (12 mo old)(*n* = 5)	33	ms
Skeletal	0.03 ± 0.01 (SD)	Rat (*n* = 10)	33	ms (pentobarbital)
Skeletal	0.22 ± 0.12 (SD)	Rat[a] (24 mo old)(*n* = 5)	33	ms
Skeletal	0.05 ± 0.02 (SD)	Rat (*n* = 7)	33	ms (decerebrate)
Skeletal	0.39 ± 0.20 (SD)	Rat (*n* = 12)	41	^{133}Xe (ether)
Resing thigh 1.5 cm Depth	0.018 ± 0.011	Human[a]	14	
Resting thigh 3.0 cm Depth	0.026 ± 0.013	Human[a]	14	
Resting thigh	0.020-0.022	Human[a]	15	
Vastus medialis and triceps	0.14 ± 0.03	Pig[a]	19	
Gracilis	0.049 ± 0.064	Dog	2	
Masseter	0.09 ± 0.01 (SE)	Rat (*n* = 7)	30	ms
Cremaster	0.16 ± 0.03 (SE)	Rat (*n* = 7)	30	ms
Cremaster	0.07 ± 0.018 (SE)	Rat[a] (*n* = 8)	31	ms
Cremaster	0.06 ± 0.008 (SE)	Rat (*n* = 7)	31	ms (pentobarbital)
Cremaster	0.05 ± 0.013 (SE)	Rat (*n* = 7)	31	ms (chlor.-urethan)
Cremaster	0.04 ± 0.012 (SE)	Rat (*n* = 7)	31	ms (decerebrate)
Diaphragm	0.93 ± 0.19 (SE)	Rat[a] (*n* = 8)	31	ms
Diaphragm	0.22 ± 0.02 (SE)	Rat (*n* = 7)	31	ms (pentobarbital)
Diaphragm	0.24 ± 0.04 (SE)	Rat (*n* = 7)	31	ms (chlor.-urethan)
Diaphragm	0.35 ± 0.04 (SE)	Rat (*n* = 7)	31	ms (decerebrate)
Diaphragm	0.144 ± 0.017 (SE)	Dog (*n* = 11)	36	ms (pentobarbital)
Rectus abdominus	0.18 ± 0.029 (SE)	Rat[a] (*n* = 8)	31	ms
Rectus abdominus	0.04 ± 0.008 (SE)	Rat (*n* = 7)	31	ms (pentobarbital)
Rectus abdominus	0.09 ± 0.025 (SE)	Rat (*n* = 7)	31	ms (chlor.-urethan)
Rectus abdominus	0.09 ± 0.027 (SE)	Rat (*n* = 7)	31	ms (decerebrate)

Organ	Blood flow (ml/min/gm)	Species[a]	Ref.	Technique
gastrocnemius	0.11 ± 0.022 (SE)	Rat[a] ($n = 8$)	31	ms (decerebrate)
Gastrocnemius	0.04 ± 0.003 (SE)	Rat ($n = 7$)	31	ms (decerebrate)
Gastrocnemius	0.15 ± 0.084 (SE)	Rat ($n = 7$)	31	ms (decerebrate)
Gastrocnemius	0.06 ± 0.019 (SE)	Rat ($n = 7$)	31	ms (decerebrate)
Tibialis anterior	0.36 ± 0.068 (SE)	Rat[a] ($n = 8$)	31	ms (decerebrate)
Tibialis anterior	0.03 ± 0.004 (SE)	Rat ($n = 7$)	31	ms (decerebrate)
Tibialis anterior	0.17 ± 0.11 (SE)	Rat ($n = 7$)	31	ms (decerebrate)
Tibialis anterior	0.08 ± 0.03 (SE)	Rat ($n = 7$)	31	ms (decerebrate)
Psoas	0.26 ± 0.034 (SE)	Rat[a] ($n = 8$)	31	ms (decerebrate)
Psoas	0.04 ± 0.004 (SE)	Rat ($n = 7$)	31	ms (decerebrate)
Psoas	0.09 ± 0.037 (SE)	Rat ($n = 7$)	31	ms (decerebrate)
Psoas	0.07 ± 0.022 (SE)	Rat ($n = 7$)	31	ms (decerebrate)
Heart	3.72 ± 0.45 (SE)	Fetal sheep[a] ($n = 12$)	32	ms
Heart	2.16 ± 0.23 (SE)	Neonatal sheep[a] ($n = 13$)	37	ms
Heart	1.13 ± 0.09 (SE)	Sheep[a] ($n = 7$)	37	ms
Heart	5.45 ± 0.59 (SE)	Rat ($n = 7$)	30	ms
Heart	5.31 ± 0.59 (SE)	Rat[a] ($n = 8$)	31	ms
Heart	2.83 ± 0.60 (SE)	Rat ($n = 7$)	31	ms (pentobarbital)
Heart	2.23 ± 0.37 (SE)	Rat ($n = 7$)	31	ms (chlor.-urethan)
Heart	3.19 ± 0.55 (SE)	Rat ($n = 7$)	31	ms (decerebrate)
Heart	6.61 ± 2.20 (SD)	Rat[a] (12 mo old)($n = 5$)	33	ms
Heart	5.45 ± 1.62 (SD)	Rat ($n = 10$)	33	ms (pentobarbital)
Heart	8.66 ± 2.74 (SD)	Rat[a] (24 mo old)($n = 5$)	33	ms
Heart	3.67 ± 1.03 (SD)	Rat ($n = 7$)	33	ms (decerebrate)
Right ventricle	0.92 ± 0.12	Pig[a]	19	
Left ventricle	1.45 ± 0.09	Pig[a]	19	
Left ventricle	1.58 ± 0.13	Dog	20	
Left ventricle	1.09 ± 0.35	Dog	21	
Left ventricle	0.61 ± 0.41	Dog	22	
Left ventricle	0.88 ± 0.14	Dog	23	
Epicardium	0.89 ± 0.14	Dog	24	
Epicardium	0.86 ± 0.14	Dog	24	
Epicardium	1.14 ± 0.18	Dog	24	
Epicardium	1.08 ± 0.18	Dog	24	
GI				
Intestine	0.47 ± 0.05 (SE)	Fetal sheep[a] ($n = 12$)	32	ms
Intestine	0.389 ± 0.04	Dog	3	
Tract	2.05 ± 0.25	Rat[a] ($n = 8$)	31	ms
Tract	1.31 ± 0.11	Rat ($n = 7$)	31	ms (pentobarbital)
Tract	1.26 ± 0.09	Rat ($n = 7$)	31	ms (chlor.-urethan)
Tract	1.19 ± 0.14	Rat ($n = 7$)	31	ms (decerebrate)
Stomach	1.27 ± 0.21 (SE)	Rat[a] ($n = 8$)	31	ms
Stomach	0.46 ± 0.04 (SE)	Rat ($n = 7$)	31	ms (pentobarbital)
Stomach	0.53 ± 0.05 (SE)	Rat ($n = 7$)	31	ms (chlor.-urethan)
Stomach	0.52 ± 0.07 (SE)	Rat ($n = 7$)	31	ms (decerebrate)
Stomach	1.31 ± 0.30 (SD)	Rat[a] (12 mo old)($n = 5$)	33	ms
Stomach	0.55 ± 0.21 (SD)	Rat ($n = 10$)	33	ms (pentobarbital)
Stomach	1.50 ± 0.45 (SD)	Rat[a] (24 mo old)($n = 5$)	33	ms
Stomach	0.42 ± 0.21 (SD)	Rat ($n = 7$)	33	ms (decerebrate)
Stomach	0.53 ± 0.26 (SD)	Dog ($n = 12$)	39	Rb^{86}(pentobarbital)
Duodenum	1.11 ± 0.46 (SD)	Dog ($n = 12$)	39	Rb^{86}(pentobarbital)
Duodenum	0.901 ± 0.132 (SE)	Dog ($n = 11$)	36	ms (pentobarbital)
Duodenum	3.63 ± 0.70 (SD)	Rat[a] (12 mo old)($n = 5$)	33	ms
Duodenum	2.33 ± 0.89 (SD)	Rat ($n = 10$)	33	ms (pentobarbital)
Duodenum	3.31 ± 0.64 (SD)	Rat[a] (24 mo old)($n = 5$)	33	ms
Duodenum	2.00 ± 0.76 (SD)	Rat ($n = 7$)	33	ms (decerebrate)
Jejunum	0.642 ± 0.086 (SE)	Dog ($n = 11$)	36	ms (pentobarbital)
Jejunum	0.263 ± 0.034 (SE)	Cat ($n = 12$	35	ms (pentobarbital)

Organ	Blood flow (ml/min/gm)	Species[a]	Ref.	Technique
Ileum	0.498 ± 0.083 (SE)	Dog (*n* = 11)	36	ms (pentobarbital)
Small bowel	1.00 ± 0.45 (SD)	Dog (*n* = 12)	39	Rb^{86}(pentobarbital)
Small bowel	2.09 ± 0.17 (SE)	Neonatal sheep[a] (*n* = 13)	37	ms
Small bowel	0.81 ± 0.06 (SE)	Sheep[a] (*n* = 7)	37	ms
Small bowel	2.81 ± 0.46 (SE)	Rat[a] (*n* = 8)	31	ms
Small bowel	1.73 ± 0.18 (SE)	Rat (*n* = 7)	31	ms (pentobarbital)
Small bowel	1.67 ± 0.13 (SE)	Rat (*n* = 7)	31	ms (chlor.-urethan)
Small bowel	1.52 ± 0.20 (SE)	Rat (*n* = 7)	31	ms (decerebrate)
Cecum	1.89 ± 0.19 (SE)	Rat[a] (*n* = 8)	31	ms
Cecum	1.52 ± 0.08 (SE)	Rat (*n* = 7)	31	ms (pentobarbital)
Cecum	1.51 ± 0.15 (SE)	Rat (*n* = 7)	31	ms (chlor.-urethan)
Cecum	1.55 ± 0.22 (SE)	Rat (*n* = 7)	31	ms (decerebrate)
Colon	1.24 ± 0.57 (SD)	Dog (*n* = 12)	39	Rb^{86}(pentobarbital)
Colon	0.711 ± 0.065 (SE)	Dog (*n* = 11)	36	ms (pentobarbital)
Large bowel	0.92 ± 0.06 (SE)	Neonatal sheep[a] (*n* = 13)	37	ms
Large bowel	0.55 ± 0.09 (SE)	Sheep[a] (*n* = 7)	37	ms
Large bowel	1.33 ± 0.29 (SE)	Rat[a] (*n* = 8)	31	ms
Large bowel	0.66 ± 0.09 (SE)	Rat (*n* = 7)	31	ms (pentobarbital)
Large bowel	0.59 ± 0.07 (SE)	Rat (*n* = 7)	31	ms (chlor.-urethan)
Large bowel	0.70 ± 0.13 (SE)	Rat (*n* = 7)	31	ms (decerebrate)
Pancreas	0.008-0.016	Dog	1	
Pancreas	0.545 ± 0.070 (SE)	Dog (*n* = 11)	36	ms (pentobarbital)
Pancreas	0.652 ± 0.26 (SD)	Dog (*n* = 12)	39	Rb^{86}(pentobarbital)
Liver				
Hep art. + portal	2.65 ± 0.530	Pig (*n* = 4)	25	
Hep art. + portal	2.53 ± 0.184	Pig (*n* = 6)	25	
Hep art. + portal	3.17 ± 0.228	Pig (*n* = 6)	25	
Hep art. + portal	1.40 ± 0.15 (SE)	Rat[a] (*n* = 8)	31	µs
Hep art. + portal	1.19 ± 0.07 (SE)	Rat (*n* = 7)	31	µs (pentobarbital)
Hep art. + portal	1.22 ± 0.09 (SE)	Rat (*n* = 7)	31	µs (chlor-urethan)
Hep art. + portal	1.25 ± 0.16 (SE)	Rat (*n* = 7)	31	µs (decerebrate)
Via portal vein	1.25	Rat	25	
Via portal vein	1.19 ± 0.12 (SE)	Rat[a] (*n* = 8)	31	µs
Via portal vein	0.98 ± 0.05 (SE)	Rat (*n* = 7)	31	µs (pentobarbital)
Via portal vein	0.98 ± 0.10 (SE)	Rat (*n* = 7)	31	µs (chlor.-urethan)
Via portal vein	0.93 ± 0.12 (SE)	Rat (*n* = 7)	31	µs (decerebrate)
Via portal vein	0.24 ± 0.04	Pig	3	
Via portal vein	0.22 ± 0.04	Pig[a]	19	
Via hepatic art.	0.15 ± 0.03	Rat (*n* = 9)	27	
Via hepatic art.	0.22 ± 0.05 (SE)	Rat[a] (*n* = 8)	31	µs
Via hepatic art.	0.21 ± 0.05 (SE)	Rat (*n* = 7)	31	µs (pentobarbital)
Via hepatic art.	0.23 ± 0.02 (SE)	Rat (*n* = 7)	31	µs (pentobarbital)
Via hepatic art.	0.31 ± 0.07 (SE)	Rat (*n* = 7)	31	µs (pentobarbital)
Via hepatic art.	0.10 ± 0.05 (SE)	Fetal sheep[a] (*n* = 12)	32	µs
Via hepatic art.	0.10 ± 0.03 (SE)	Neonatal sheep[a] (*n* = 13)	37	µs
Via hepatic art.	0.14 ± 0.05 (SE)	Sheep[a] (*n* = 7)	37	µs
Via hepatic art.	0.02 ± 0.02 (SD)	Rat[a] (12 mo old)(*n* = 5)	33	µs
Via hepatic art.	0.07 ± 0.04 (SD)	Rat (*n* = 10)	33	µs (pentobarbital)
Via hepatic art.	0.03 ± 0.01 (SD)	Rat[a] (24 mo old)(*n* = 5)	33	µs
Via hepatic art.	0.11 ± 0.07 (SD)	Rat (*n* = 7)	33	µs (decerebrate)
Via hepatic art.	0.178 ± 0.050 (SE)	Dog (*n* = 11)	36	µs (decerebrate)
Via hepatic art.	0.31 ± 0.30 (SD)	Rabbit (*n* = 5)	42	µs
Spleen	1.46 ± 0.14	Dog	3	
Spleen	1.381 ± 0.199 (SE)	Dog (*n* = 11)	36	µs (pentobarbital)
Spleen	3.60 ± 0.16	Pig[a]	19	
Spleen	1.64 ± 0.14 (SE)	Rat[a] (*n* = 8)	31	µs
Spleen	1.52 ± 0.22 (SE)	Rat (*n* = 7)	31	µs (pentobarbital)
Spleen	2.35 ± 0.49 (SE)	Rat (*n* = 7)	31	µs (chlor.-urethan)

Organ	Blood flow (ml/min/gm)	Species[a]	Ref.	Technique
Spleen	2.01 ± 0.22 (SE)	Rat ($n = 7$)	31	µs (decerebrate)
Spleen	5.43 ± 1.13 (SE)	Fetal sheep[a] ($n = 12$)	32	µs
Spleen	4.03 ± 0.73 (SE)	Neonatal sheep[a] ($n = 13$)	37	µs
Spleen	1.88 ± 0.27 (SE)	Sheep[a] ($n = 7$)	37	µs
Spleen	1.51 ± 0.54 (SD)	Rat[a] (12 mo old)($n = 5$)	33	µs
Spleen	0.75 ± 0.37 (SD)	Rat ($n = 10$)	33	µs (pentobarbital)
Spleen	1.13 ± 0.38 (SD)	Rat[a] (24 mo old)($n = 5$)	33	µs
Spleen	0.40 ± 0.15 (SD)	Rat ($n = 7$)	33	µs (decerebrate)
Prostate	0.17 (.11–.21)	Rat ($n = 14$)	26	
Prostate	0.18 ± 0.02	Rat ($n = 9$)	27	
Prostate	0.31–0.79	Dog ($n = 11$)	38	(pentobarb, halothane, or nembutal)
Bone				
Femur	0.096 ± 0.039	Rat	9	
Tibia	0.083 ± 0.032	Rat	9	
Femur	0.14 ± 0.01	Pig[a]	19	
Skin	0.20 ± 0.02 (SE)	Neonatal sheep[a] ($n = 13$)	37	µs
Skin	0.09 ± 0.01 (SE)	Sheep[a] ($n = 7$)	37	µs
Skin	0.18 ± 0.03 (SE)	Rat[a] ($n = 8$)	31	µs
Skin	0.12 ± 0.03 (SE)	Rat ($n = 7$)	31	µs (pentobarbital)
Skin	0.15 ± 0.02 (SE)	Rat ($n = 7$)	31	µs (chlor.-urethan)
Skin	0.17 ± 0.02 (SE)	Rat ($n = 7$)	31	µs (decerebrate)
Skin				
In the cold	Approx. 0.02	Human forearm[a]	10	
Thermoneutral	0.04–0.05	Human forearm[a]	10	
Hyperthermic	Near or >0.20	Human forearm[a]	10	
Thermoneutral	0.9 ± 0.09	Pig[a]	19	
Subcutaneous tissue	0.48 ± 0.15	Rat ($n = 29$)	41	^{133}Xe (ether)
Tumor	0.25 ± 0.11	Rat ($n = 12$)	41	^{133}Xe (ether)
	1.79 ± 0.70	Rabbit ($n = 5$)	42	
Fat	0.21 ± 0.06	pig[a]	19	
Testes	0.45 ± 0.06	Rat ($n = 9$)	27	
Lungs	1.14 ± 0.14 (SE)	Fetal sheep[a] ($n = 12$)	32	µs

[a] Unanesthetized.

References

1. Rappaport, A.M., Kawamura, T., Davidson, J.K., Lin, B.J., Ohira, S., Zeigler, M., Coddling, J.A., Henderson, M.J., and Haist, R.E., Effects of hormones and blood flow on insulin output of isolated pancreas *in situ*, *Am. J. Physiol.*, 221, 343, 1971.
2. Marcus, M.L., Bischof, C.J., and Heistad, D.D., Comparison of microsphere and xenon-133 clearance method in measuring skeletal muscle and cerebral blood flow, *Circ. Res.*, 48, 748–761, 1981.
3. Fan, F-C., Schuessler, G.B., Chen, R.Y.Z., and S. Chien, S., Determinations of blood flow and shunting of 9- and 15-µm spheres in regional beds, *Am. J. Physiol.*, 237, H25–H33, 1979.
4. Mraovitch, S., Iadecola, C., and Reis, D.J., Vasoconstriction unassociated with metabolism in cerebral cortex elicited by electrical stimulation of the parabrachial nucleus in rat, *J. Cerebral Blood Flow Metab.*, 3 (Suppl. 1), S196–S197, 1983.
5. Bhattacharya, J., and Beilin, L.J., Left ventricular cannulation for microsphere estimation of rabbit renal blood flow, *Am. J. Physiol.*, 238, H736–H739, 1980.
6. Thurau, K. and D.Z. Levine, D.Z., The renal circulation, in *The Kidney: Morphology, Biochemistry, Physiology*. C. Rouiller and A.F. Muller, Eds., Academic Press, New York, chap. 1, 1–70, 1971.
7. Passmore, J.C., Neiberger, R.E., and Eden, S.W., Measurement of intrarenal anatomic distribution of krypton-85 in endotoxic shock in dogs, *Am. J. Physiol.*, 232, H54–58, 1977.
8. Gyrd–Hansen, N., Renal clearances in pigs, *Acta Vet. Scand.*, 9, 183–198, 1968.

9. Schoutens, A., Bergmann, P., and M. Verhas, M., Bone blood flow measured by ^{85}Sr microspheres and bone seeker clearances in the rat, *Am. J. Physiol.*, 236, H1–H6, 1979.
10. Johnson, J.M., Brengelmann, G.L., Hales, J.R.S., Vanhoutte, P.M., and Wenger, C.B., Regulation of the cutaneous circulation, *Fed. Proc.*, 45, 2841–2850, 1986.
11. Neiberger, R.E. and Passmore, J.C., Effects of dopamine on canine intrarenal blood flow distribution during hemorrhage, *Kidney Int.*, 15, 219–226, 1979.
12. Youichi, A., Okahara, T., Kishimoto, T., Yamamoto, K., and Ueda, J., Relationship between intrarenal distribution of blood flow and renin secretion, *Am. J. Physiol.*, 225, 319–323, 1973.
13. Mimran, A., and Casellas, D., Microsphere size and determination of intrarenal blood flow distribution in the rat, *Pflugers Arch.*, 382, 233–240, 1979.
14. Sekins, K.M., Dundore, D., Emery, A.F., Lehmann, J.F., McGrath, P.W., and Nelp, W.B., Muscle blood flow changes in response to 915 MHz diathermy with surface cooling as measured by Xe^{133} clearance, *Arch Phys. Med. Rehabil.*, 61, 105–113, 1980.
15. Lassen, N.A., Lindbjerg, J., and Munck, O., Measurement of bloodflow through skeletal muscle by intramuscular injection of xenon–133, *Lancet*, 1, 686–689, 1964.
16. Keele, C.A. and E. Neil, E., Eds., *Samson Wright's Applied Physiology.* ed. 12, Oxford Press, London, 62, 1971.
17. Ott, C.E., and Vari, R.C., Renal autoregulation of blood flow and filtration rate in the rabbit, *Am. J. Physiol.*, 237, F479–F482, 1979.
18. Haws, C.W., and Heistad, D.D., Effects of nimodipine on cerebral vasoconstrictor responses, *Am. J. Physiol.*, 247, H170–H176, 1984.
19. Tranquilli, W.J., Parks, C.M., Thurmon, J.C., Benson, G.J., Koritz, G.D., Manohar, M., and Theodorakis, M.C., Organ blood flow and distribution of cardiac output in nonanesthetized swine, *Am. J. Vet. Res.*, 43, 895–897, 1982.
20. Hernandez, E.J., Hoffman, J.K., Fabian, M., Siegel, J.H., and Eberhart, R.C., Thermal quantification of regional myocardial perfusion and heat generation, *Am. J. Physiol.*, 236, H345–H355, 1979.
21. Drake, A.J., and Noble, M.I.M., Myocardial blood flow measured by carbonized microspheres before and after cardiac denervation, *9th Eur. Conf. Microcirculation,* Antwerp, Bibl. Anat., 15, 53–56, 1976.
22. Baer, R.W., Payne, B.D., Verrier, E.D., Vlahakes, G.J., Molodowitch, D., Uhlig, P.N., and Hoffman, J.I.E., Increased number of myocardial blood flow measurements with radionuclide-labeled microspheres, *Am. J. Physiol.*, 246, H418–434, 1984.
23. Crystal, G.J., Boatwright, R.B., Downey, H.F., and Bashour, F.A., Shunting of microspheres across the canine coronary circulation, *Am. J. Physiol.*, 236, H7–H12, 1979.
24. Capurro, N.L., Goldstein, R.E., Aamodt, R., Smith, H.J., and Epstein, S.E., Loss of microspheres from ischemic canine cardiac tissue, *Circ. Res.*, 44, 223–227, 1979.
25. Lovell, R.A., The toxicity of microcystin-LR in swine and mice. Ph.D. Thesis. University of Illinois, 1989.
26. Damber, J.-E., Bergh, A., Daehlin, L., Petrow, V., and M. Landstrom, M., Effects of 6-methylene progesterone on growth, morphology, and blood flow of the Dunning R3327 prostatic adenocarcinoma, *Prostate*, 20, 187–197, 1992.
27. Jonsson, O., Widmark, A., Grankvist, K., Damber, J.-E., and Henriksson, R., Effects of clonidine-induced hypertension on blood flows in prostatic adenocarcinoma (Dunning R3327) and normal tissue, *Prostate*, 20, 225–232, 1992.
28. Gores, G.J., Kost, L.J., and LaRusso, N.F., The isolated perfused rat liver: conceptual and practical considerations, *Hepatology*, 6, 511–517, 1986.
29. Rundquist, I., Smith, Q.R., Michel, M.E., Ask, P., Öberg, P.A., and Rapoport, S.I., Sciatic nerve blood flow measured by laser Doppler flowmetry and [^{14}C] iodoantipyrine, *Am. J. Physiol.*, 248, H311–H317, 1985.
30. Proctor, K.G. and Busija, D.W., Relationships among arteriolar, regional, and whole organ blood flow in cremaster muscle, *Am. J. Physiol.*, 249, H34–H41, 1985.

31. Seyde, W.C., McGowan, L., Lund, N., Duling, B., and Longnecker, D.E., Effects of anesthetics on regional hemodynamics in normovolemic and hemorrhaged rats, *Am. J. Physiol.*, 249, H164–H173, 1985.
32. Crandell, S.S., Fisher, D.J., and Morriss, F.H., Jr., Effects of ovine maternal hyperglycemia on fetal regional blood flows and metabolism, *Am. J. Physiol.*, 249, E454–E460, 1985.
33. Tuma, R.F., Irion, G.L., Vasthare, U.S., and Heinel, L.A., Age-related changes in regional blood flow in the rat, *Am. J. Physiol.*, 249, H485–H491, 1985.
34. Baumbach, G.I. and Heistad, D.D., Heterogeneity of brain blood flow and permeability during acute hypertension, *Am. J. Physiol.*, 249, H629–H637, 1985.
35. Kvietys, P.R., Shepherd, A.P., and Granger, D.N., Laser-Doppler, H_2 clearance, and microsphere estimates of mucosal blood flow, *Am. J. Physiol.*, 249, G221–G227, 1985.
36. Kapin, M.A. and Ferguson, J.L., Hemodynamic and regional circulatory alterations in dog during anaphylactic challenge, *Am. J. Physiol.*, 249, H430–H437, 1985.
37. Koehler, R.C., Traystman, R.J., and Jones, M.D., Jr., Regional blood flow and O_2 transport during hypoxic and CO hypoxia in neonatal and adult sheep, *Am. J. Physiol.*, 248, H118–H124, 1985.
38. Andersson, L., Dahn, I., Nelson, K.E., and Norgren, A., Method for measuring prostate blood flow with Xenon^{133} in the dog, *Invest. Urol.*, 5, 140–148, 1967.
39. Goodhead, B., Accute pancreatitis and pancreatic blood flow, *Surg. Gynecol. Obstet.*, 129, 331–340, 1969.
40. Reddy, V.K., Zamora, C.S., Frandle, K.A., and Samson, M.D., Regional renal blood flow in ewes, *Am. J. Vet. Res.* 42, 1802–1803, 1981.
41. Mattsson, J., Alpsten, M., Appelgren, L., and Peterson, H.-I., Influence of Noradrenalin on local tumor blood flow, *Eur. J. Cancer,* 16, 99–102, 1980.
42. Burton, M.A., Kelleher, D.K., Gray, B.N., and Morgan, C.K., Effect of temperature on liver tumour blood flow, *Eur. J. Cancer.* 26, 999, 1990.

5

Electrical Engineering

Giorgio Rizzoni
Ohio State University

5.1 Introduction

The role played by electrical and electronic engineering in mechanical systems has dramatically increased in importance in the past two decades, thanks to advances in integrated circuit electronics and in materials that have permitted the integration of sensing, computing, and actuation technology into industrial systems and consumer products. Examples of this integration revolution, which has been referred to as a new field called *Mechatronics*, can be found in consumer electronics (auto-focus cameras, printers, microprocessor-controlled appliances), in industrial automation, and in transportation systems, most notably in passenger vehicles. The aim of this chapter is to review and summarize the foundations of electrical engineering for the purpose of providing the practicing mechanical engineer a quick and useful reference to the different fields of electrical engineering. Special emphasis has been placed on those topics that are likely to be relevant to product design.

5.2 Fundamentals of Electric Circuits

This section presents the fundamental laws of circuit analysis and serves as the foundation for the study of electrical circuits. The fundamental concepts developed in these first pages will be called on through the chapter.

The fundamental electric quantity is **charge**, and the smallest amount of charge that exists is the charge carried by an electron, equal to

$$q_e = -1.602 \times 10^{-19} \text{ coulomb} \tag{5.2.1}$$

As you can see, the amount of charge associated with an electron is rather small. This, of course, has to do with the size of the unit we use to measure charge, the **Coulomb** (C), named after Charles Coulomb. However, the definition of the coulomb leads to an appropriate unit when we define electric current, since current consists of the flow of very large numbers of charge particles. The other charge-carrying particle in an atom, the proton, is assigned a positive sign and the same magnitude. The charge of a proton is

$$q_p = +1.602 \times 10^{-19} \text{ coulomb} \tag{5.2.2}$$

Electrons and protons are often referred to as **elementary charges**.

Electric current is defined as the time rate of change of charge passing through a predetermined area. If we consider the effect of the enormous number of elementary charges actually flowing, we can write this relationship in differential form:

$$i = \frac{dq}{dt} \frac{\text{C}}{\text{s}} \tag{5.2.3}$$

The units of current are called **amperes** (A), where 1 A = 1 C/sec. The electrical engineering convention states that the positive direction of current flow is that of positive charges. In metallic conductors, however, current is carried by negative charges; these charges are the free electrons in the conduction band, which

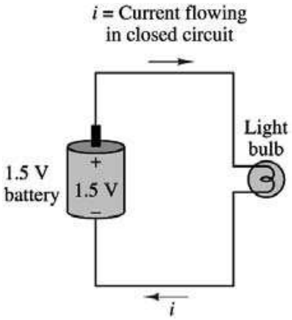

FIGURE 5.2.1 A simple electrical circuit.

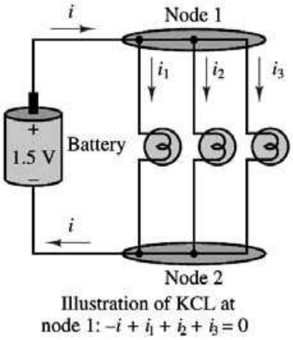

FIGURE 5.2.2 Illustration of Kirchhoff's current law.

are only weakly attracted to the atomic structure in metallic elements and are therefore easily displaced in the presence of electric fields.

In order for current to flow there must exist a closed circuit, Figure 5.2.1 depicts a simple circuit, composed of a battery (e.g., a dry-cell or alkaline 1.5-V battery) and a light bulb.

Note that in the circuit of Figure 5.2.1, the current, *i*, flowing from the battery to the resistor is equal to the current flowing from the light bulb to the battery. In other words, no current (and therefore no charge) is "lost" around the closed circuit. This principle was observed by the German scientist G.R. Kirchhoff and is now known as **Kirchhoff's current law** (KCL). KCL states that because charge cannot be created but must be conserved, *the sum of the currents at a node must equal zero* (in an electrical circuit, a **node** is the junction of two or more conductors). Formally:

$$\sum_{n=1}^{N} i_n = 0 \qquad \text{Kirchhoff' s current law} \tag{5.2.4}$$

The significance of KCL is illustrated in Figure 5.2.2, where the simple circuit of Figure 5 has been augmented by the addition of two light bulbs (note how the two nodes that exist in this circuit have been emphasized by the shaded areas). In applying KCL, one usually defines currents entering a node as being negative and currents exiting the node as being positive. Thus, the resulting expression for the circuit of Figure 5.2.2 is

$$-i + i_1 + i_2 + i_3 = 0$$

Charge moving in an electric circuit gives rise to a current, as stated in the preceding section. Naturally, it must take some work, or energy, for the charge to move between two points in a circuit, say, from point *a* to point *b*. The total *work per unit charge* associated with the motion of charge between two points is called **voltage**. Thus, the units of voltage are those of energy per unit charge:

$$1 \text{ volt} = \frac{1 \text{ joule}}{\text{coulomb}} \tag{5.2.5}$$

- The voltage, or **potential difference,** between two points in a circuit indicates the energy required to move charge from one point to the other. As will be presently shown, the direction, or polarity, of the voltage is closely tied to whether energy is being dissipated or generated in the process. The seemingly abstract concept of work being done in moving charges can be directly applied to the analysis of electrical circuits; consider again the simple circuit consisting of a battery and a light bulb. The circuit is drawn again for convenience in Figure 5.2.3, and nodes are defined by the letters *a* and *b*. A series of carefully conducted experimental observations regarding the nature of voltages in an electric circuit led Kirchhoff to the formulation of the second of his laws, **Kirchhoff's voltage law,** or KVL. The principle underlying KVL is that no energy is lost or created in an electric circuit; in circuit terms, the sum of all voltages associated with sources must equal the sum of the load voltages, so that *the net voltage around a closed circuit is zero.* If this were not the case, we would need to find a physical explanation for the excess (or missing) energy not accounted for in the voltages around a circuit. KVL may be stated in a form similar to that used for KCL:

$$\sum_{n=1}^{N} v_n = 0 \quad \text{Kirchhoff's voltage law} \tag{5.2.6}$$

where the v_n are the individual voltages around the closed circuit. Making reference to Figure 5.2.3, we can see that it must follow from KVL that the work generated by the battery is equal to the energy dissipated in the light bulb to sustain the current flow and to convert the electric energy to heat and light:

$$v_{ab} = -v_{ba}$$

or

$$v_1 = v_2$$

One may think of the work done in moving a charge from point *a* to point *b* and the work done moving it back from *b* to *a* as corresponding directly to the *voltages across individual circuit elements.* Let *Q* be the total charge that moves around the circuit per unit time, giving rise to the current *i.* Then the work done in moving *Q* from *b* to *a* (i.e., across the battery) is

$$W_{ba} = Q \times 1.5 \text{ V} \tag{5.2.7}$$

Similarly, work is done in moving *Q* from *a* to *b*, that is, across the light bulb. Note that the word *potential* is quite appropriate as a synonym of voltage, in that voltage represents the potential energy between two points in a circuit: if we remove the light bulb from its connections to the battery, there still exists a voltage across the (now disconnected) terminals *b* and *a*.

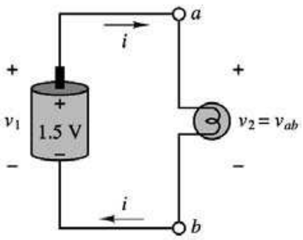

Illustration of Kirchhoff's voltage law: $v_1 = v_2$

FIGURE 5.2.3 Voltages around a circuit.

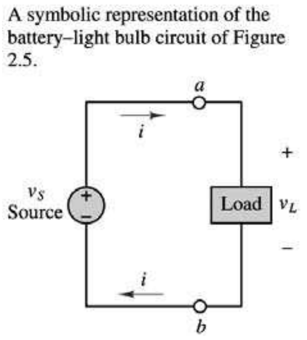
A symbolic representation of the battery–light bulb circuit of Figure 2.5.

FIGURE 5.2.4 Sources and loads in an electrical circuit.

A moment's reflection upon the significance of voltage should suggest that it must be necessary to specify a sign for this quantity. Consider, again, the same dry-cell or alkaline battery, where, by virtue of an electrochemically induced separation of charge, a 1.5-V potential difference is generated. The potential generated by the battery may be used to move charge in a circuit. The rate at which charge is moved once a closed circuit is established (i.e., the current drawn by the circuit connected to the battery) depends now on the circuit element we choose to connect to the battery. Thus, while the voltage across the battery represents the potential for *providing energy* to a circuit, the voltage across the light bulb indicates the amount of work done in *dissipating energy*. In the first case, energy is generated; in the second, it is consumed (note that energy may also be stored, by suitable circuit elements yet to be introduced). This fundamental distinction required attention in defining the sign (or polarity) of voltages.

We shall, in general, refer to elements that provide energy as **sources**, and to elements that dissipate energy as **loads**. Standard symbols for a generalized source-and-load circuit are shown in Figure 5.2.4. Formal definitions will be given in a later section.

Electric Power and Sign Convention

The definition of voltage as work per unit charge lends itself very conveniently to the introduction of power. Recall that power is defined as the work done per unit time. Thus, the power, *P*, either generated or dissipated by a circuit element can be represented by the following relationship:

$$\text{Power} = \frac{\text{Work}}{\text{Time}} = \frac{\text{Work}}{\text{Unit charge}}\frac{\text{Charge}}{\text{Time}} = \text{Voltage} \times \text{Current} \tag{5.2.8}$$

Thus, the electrical power generated by an active element, or that dissipated or stored by a passive element, is equal to the product of the voltage across the element and the current flowing through it.

$$P = VI \tag{5.2.9}$$

It is easy to verify that the units of voltage (joules/coulomb) times current (coulombs/second) are indeed those of power (joules/second, or watts).

It is important to realize that, just like voltage, power is a signed quantity, and that it is necessary to make a distinction between *positive* and *negative power*. This distinction can be understood with reference to Figure 5.2.5, in which a source and a load are shown side by side. The polarity of the voltage across the source and the direction of the current through it indicate that the voltage source *is doing work in moving charge from a lower potential to a higher potential*. On the other hand, the load is dissipating energy, because the direction of the current indicates that *charge is being displaced from a higher potential to a lower potential*. To avoid confusion with regard to the sign of power, the electrical engineering community uniformly adopts the **passive sign convention**, which simply states that *the power dissipated by a load is a positive quantity* (or, conversely, that the power generated by a source is a positive quantity). Another way of phrasing the same concept is to state that if current flows from a higher to a lower voltage (+ to –), the power dissipated will be a positive quantity.

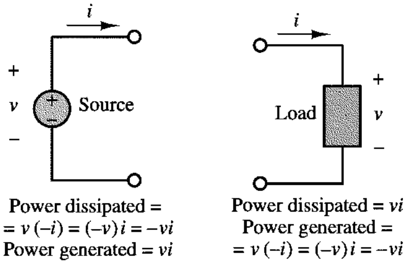

FIGURE 5.2.5 The passive sign convention.

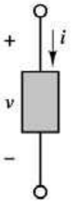

FIGURE 5.2.6 Generalized representation of circuit elements.

Circuit Elements and Their *i-v* Characteristics

The relationship between current and voltage at the terminals of a circuit element defines the behavior of that element within the circuit. In this section, we shall introduce a graphical means of representing the terminal characteristics of circuit elements. Figure 5.2.6 depicts the representation that will be employed throughout the chapter to denote a generalized circuit element: the variable i represents the current flowing through the element, while v is the potential difference, or voltage, across the element.

Suppose now that a known voltage were imposed across a circuit element. The current that would flow as a consequence of this voltage, and the voltage itself, form a unique pair of values. If the voltage applied to the element were varied and the resulting current measured, it would be possible to construct a functional relationship between voltage and current known as the ***i-v* characteristic** (or **volt-ampere characteristic**). Such a relationship defines the circuit element, in the sense that if we impose any prescribed voltage (or current), the resulting current (or voltage) is directly obtainable from the *i-v* characteristic. A direct consequence is that the power dissipated (or generated) by the element may also be determined from the *i-v* curve.

The *i-v* characteristics of ideal current and voltage sources can also be useful in visually representing their behavior. An ideal voltage source generates a prescribed voltage independent of the current drawn from the load; thus, its *i-v* characteristic is a straight vertical line with a voltage axis intercept corresponding to the source voltage. Similarly, the *i-v* characteristic of an ideal current source is a horizontal line with a current axis intercept corresponding to the source current. Figure 5.2.7 depicts this behavior.

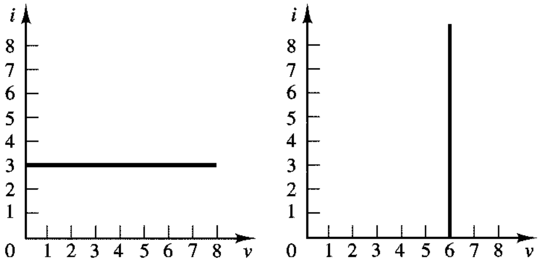

i-v characteristic of a 3 A current source

i-v characteristic of a 6 V voltage source

FIGURE 5.2.7 *i-v* characteristics of ideal sources.

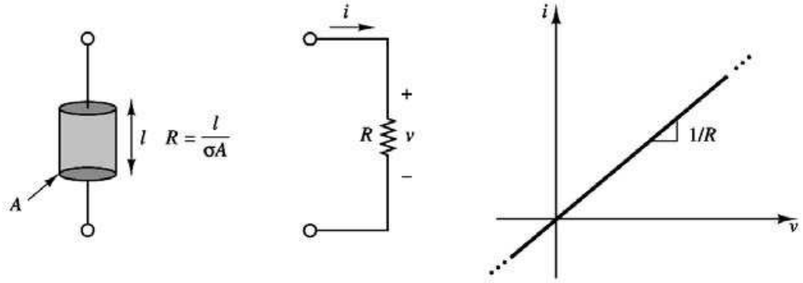

Physical resistors with resistance *R*. Typical materials are carbon, metal film.

Circuit symbol

i-*v* characteristic

FIGURE 5.2.8 The resistance element.

Resistance and Ohm's Law

When electric current flows through a metal wire or through other circuit elements, it encounters a certain amount of **resistance,** the magnitude of which depends on the electrical properties of the material. Resistance to the flow of current may be undesired — for example, in the case of lead wires and connection cable — or it may be exploited in an electrical circuit in a useful way. Nevertheless, practically all circuit elements exhibit some resistance; as a consequence, current flowing through an element will cause energy to be dissipated in the form of heat. An ideal **resistor** is a device that exhibits linear resistance properties according to **Ohm's law,** which states that

$$V = IR \tag{5.2.10}$$

that is, that the voltage across an element is directly proportional to the current flow through it. *R* is the value of the resistance in units of **ohms** (Ω), where

$$1\,\Omega = 1\ \text{V/A} \tag{5.2.11}$$

The resistance of a material depends on a property called **resistivity,** denoted by the symbol ρ; the inverse of resistivity is called **conductivity** and is denoted by the symbol σ. For a cylindrical resistance element (shown in Figure 5.2.8), the resistance is proportional to the length of the sample, *l*, and inversely proportional to its cross-sectional area, A, and conductivity, σ.

$$v = \frac{l}{\sigma A} i \tag{5.2.12}$$

It is often convenient to define the **conductance** of a circuit element as the inverse of its resistance. The symbol used to denote the conductance of an element is *G*, where

$$G = \frac{1}{R}\ \text{siemens (S)} \quad \text{where} \quad 1\ \text{S} = 1\ \text{A/V} \tag{5.2.13}$$

Thus, Ohm's law can be rested in terms of conductance, as

$$I = GV \tag{5.2.14}$$

Ohm's law is an empirical relationship that finds widespread application in electrical engineering because of its simplicity. It is, however, only an approximation of the physics of electrically conducting materials. Typically, the linear relationship between voltage and current in electrical conductors does not

TABLE 5.2.1 Common Resistor Values ($^1/_8$-, $^1/_4$-, $^1/_2$-, 1-, 2-W Rating)

Ω	Code	Ω	Multiplier	kΩ	Multiplier	kΩ	Multiplier	kΩ	Multiplier
10	Brn-blk-blk	100	Brown	1.0	Red	10	Orange	100	Yellow
12	Brn-red-blk	120	Brown	1.2	Red	12	Orange	120	Yellow
15	Brn-grn-blk	150	Brown	1.5	Red	15	Orange	150	Yellow
18	Brn-gry-blk	180	Brown	1.8	Red	18	Orange	180	Yellow
22	Red-red-blk	220	Brown	2.2	Red	22	Orange	220	Yellow
27	Red-vlt-blk	270	Brown	2.7	Red	27	Orange	270	Yellow
33	Org-org-blk	330	Brown	3.3	Red	33	Orange	330	Yellow
39	Org-wht-blk	390	Brown	3.9	Red	39	Orange	390	Yellow
47	Ylw-vlt-blk	470	Brown	4.7	Red	47	Orange	470	Yellow
56	Grn-blu-blk	560	Brown	5.6	Red	56	Orange	560	Yellow
68	Blu-gry-blk	680	Brown	6.8	Red	68	Orange	680	Yellow
82	Gry-red-blk	820	Brown	8.2	Red	82	Orange	820	Yellow

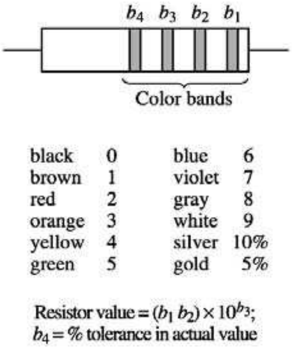

FIGURE 5.2.9 Resistor color code.

apply at very high voltages and currents. Further, not all electrically conducting materials exhibit linear behavior even for small voltages and currents. It is usually true, however, that for some range of voltages and currents, most elements display a linear *i-v characteristic.*

The typical construction and the circuit symbol of the resistor are shown in Figure 5.2.8. Resistors made of cylindrical sections of carbon (with resistivity $\rho = 3.5 \times 10^{-5}$ Ω-m) are very common and are commercially available in a wide range of values for several power ratings (as will be explained shortly). Another commonly employed construction technique for resistors employs metal film. A common power rating for resistors used in electronic circuits (e.g., in most consumer electronic appliances such as radios and television sets) is $^1/_4$ W. Table 5.2.1 lists the standard values for commonly used resistors and the color code associated with these values (i.e., the common combinations of the digits $b_1 b_2 b_3$ as defined in Figure 5.2.9. For example, if the first three color bands on a resistor show the colors red ($b_1 = 2$), violet ($b_2 = 7$), and yellow ($b_3 = 4$), the resistance value can be interpreted as follows:

$$R = 27 \times 10^4 = 270{,}000\ \Omega = 270\ \text{k}\Omega$$

In Table 5.2.1, the leftmost column represents the complete color code; columns to the right of it only show the third color, since this is the only one that changes. For example, a 10-Ω resistor has the code brown-black-*black*, while a 100-Ω resistor has brown-black-*brown.*

In addition to the resistance in ohms, the maximum allowable power dissipation (or **power rating**) is typically specified for commercial resistors. Exceeding this power rating leads to overheating and can cause the resistor to literally start on fire. For a resistor R, the power dissipated is given by

$$P = VI = I^2 R = \frac{V^2}{R} \tag{5.2.15}$$

That is, the power dissipated by a resistor is proportional to the square of the current flowing through it, as well as the square of the voltage across it. The following example illustrates how one can make use of the power rating to determine whether a given resistor will be suitable for a certain application.

Example 5.2.1 Resistance Strain Gauges

A common application of the resistance concept to engineering measurements is the resistance **strain gauge**. Strain gauges are devices that are bonded to the surface of an object, and whose resistance varies as a function of the surface strain experienced by the object. Strain gauges may be used to perform measurements of strain, stress, force, torque, and pressure. Recall that the resistance of a cylindrical conductor of cross-sectional area A, length L, and conductivity σ is given by the expression

$$R = \frac{L}{\sigma A}$$

If the conductor is compressed or elongated as a consequence of an external force, its dimensions will change, and with them its resistance. In particular, if the conductor is stretched, its cross-sectional area will decrease and the resistance will increase. If the conductor is compressed, its resistance decreases, since the length, L, will decrease. The relationship between change in resistance and change in length is given by the gauge factor, G, defined by

$$\mathrm{G} = \frac{\Delta R/R}{\Delta L/L}$$

and since the strain ε is defined as the fractional change in length of an object by the formula

$$\varepsilon = \frac{\Delta L}{L}$$

the change in resistance due to an applied strain ε is given by the expression

$$\Delta R = R_0 G\varepsilon$$

where R_0 is the resistance of the strain gauge under no strain and is called the zero strain resistance. The value of G for resistance strain gauges made of metal foil is usually about 2.

Figure 5.2.10 depicts a typical foil strain gauge. The maximum strain that can be measured by a foil gauge is about 0.4 to 0.5%; that is , $\Delta L/L = 0.004$ to 0.005. For a 120-Ω gauge, this corresponds to a change in resistance of the order of 0.96 to 1.2 Ω. Although this change is resistance is very small, it can be detected by means of suitable circuitry. Resistance strain gauges are usually connected in a circuit called the Wheatstone bridge, which we analyze later in this section.

Open and Short Circuits

Two convenient idealizations of the resistance element are provided by the limiting cases of Ohm's law as the resistance of a circuit element approaches zero or infinity. A circuit element with resistance approaching zero is called a **short circuit**. Intuitively, one would expect a short circuit to allow for unimpeded flow of current. In fact, metallic conductors (e.g., short wires of large diameter) approximate the behavior of a short circuit. Formally, a short circuit is defined as a circuit element across which the voltage is zero, regardless of the current flowing through it. Figure 5.2.11 depicts the circuit symbol for an ideal short circuit.

Physically, any wire or other metallic conductor will exhibit some resistance, though small. For practical purposes, however, many elements approximate a short circuit quite accurately under certain conditions.

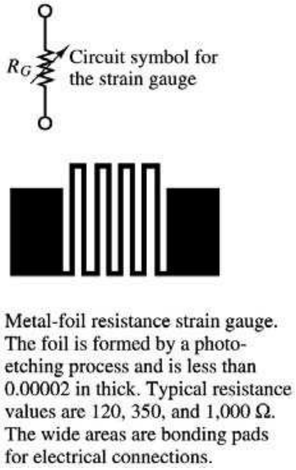

FIGURE 5.2.10 The resistance strain gauge.

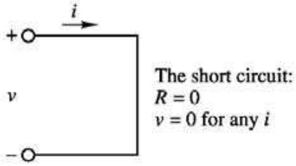

FIGURE 5.2.11 The short circuit.

TABLE 5.2.2 Resistance of Copper Wire

AWG Size	Number of Strands	Diameter per Strand	Resistance per 1000 ft (Ω)
24	Solid	0.0201	28.4
24	7	0.0080	28.4
22	Solid	0.0254	18.0
22	7	0.0100	19.0
20	Solid	0.0320	11.3
20	7	0.0126	11.9
18	Solid	0.0403	7.2
18	7	0.0159	7.5
16	Solid	0.0508	4.5
16	19	0.0113	4.7

For example, a large-diameter copper pipe is effectively a short circuit in the context of a residential electrical power supply, while in a low-power microelectronic circuit (e.g., an FM radio) a short length of 24 gauge wire (refer to Table 5.2.2 for the resistance of 24 gauge wire) is a more than adequate short circuit.

A circuit element whose resistance approaches infinity is called an **open circuit**. Intuitively, one would expect no current to flow through an open circuit, since it offers infinite resistance to any current. In an open circuit, we would expect to see zero current regardless of the externally applied voltage. Figure 5.2.12 illustrates this idea.

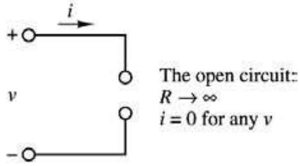

FIGURE 5.2.12 The open circuit.

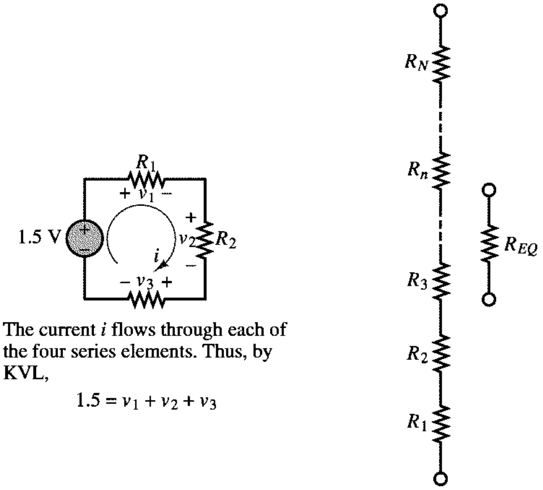

The current i flows through each of the four series elements. Thus, by KVL,

$$1.5 = v_1 + v_2 + v_3$$

N series resistors are equivalent to a single resistor equal to the sum of the individual resistances.

FIGURE 5.2.13 Voltage divider rule.

In practice, it is not too difficult to approximate an open circuit; any break in continuity in a conducting path amounts to an open circuit. The idealization of the open circuit, as defined in Figure 5.2.12 does not hold, however, for very high voltages. The insulating material between two insulated terminals will break down at a sufficiently high voltage. If the insulator is air, ionized particles in the neighborhood of the two conducting elements may lead to the phenomenon of arcing; in other words, a pulse of current may be generated that momentarily jumps a gap between conductors (thanks to this principle, we are able to ignite the air-fuel mixture in a spark-ignition internal combustion engine by means of spark plugs). The ideal open and short circuits are useful concepts and find extensive use in circuit analysis.

Series Resistors and the Voltage Divider Rule

Although electrical circuits can take rather complicated forms, even the most involved circuits can be reduced to combinations of circuit elements *in parallel* and *in series*. Thus, it is important that you become acquainted with parallel and series circuits as early as possible, even before formally approaching the topic of network analysis. Parallel and series circuits have a direct relationship with Kirchhoff's laws. The objective of this section and the next is to illustrate two common circuits based on series and parallel combinations of resistors: the voltage and current dividers. These circuits form the basis of all network analysis; it is therefore important to master these topics as early as possible.

For an example of a series circuit, refer to the circuit of Figure 5.2.13, where a battery has been connected to resistors R_1, R_2, and R_3. The following definition applies.

Definition. Two or more circuit elements are said to be in series if the same current flows through each of the elements.

The three resistors could thus be replaced by a single resistor of value R_{EQ} without changing the amount of current required of the battery. From this result we may extrapolate to the more general relationship defining the equivalent resistance of N series resistors:

$$R_{EQ} = \sum_{n=1}^{N} R_n \tag{5.2.16}$$

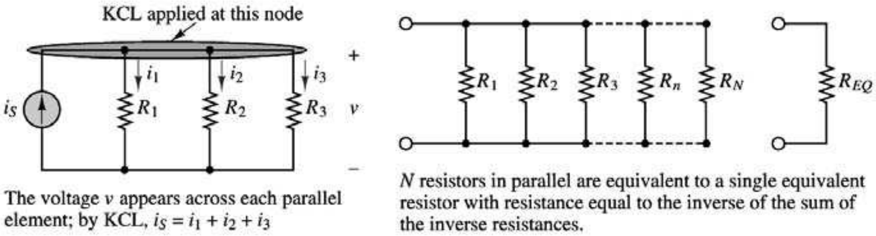

The voltage v appears across each parallel element; by KCL, $i_S = i_1 + i_2 + i_3$

N resistors in parallel are equivalent to a single equivalent resistor with resistance equal to the inverse of the sum of the inverse resistances.

FIGURE 5.2.14 Parallel circuits.

which is also illustrated in Figure 5.2.13. A concept very closely tied to series resistors is that of the **voltage divider**.

The general form of the voltage divider rule for a circuit with N series resistors and a voltage source is

$$v_n = \frac{R_n}{R_1 + R_2 + \ldots + R_n + \ldots + R_N} v_S \tag{5.2.17}$$

Parallel Resistors and the Current Divider Rule

A concept analogous to that of the voltage may be developed by applying Kirchhoff's current law to a circuit containing only parallel resistances.

Definition. Two or more circuit elements are said to be in parallel if the same voltage appears across each of the elements. (See Figure 5.2.14.)

N resistors in parallel act as a single equivalent resistance, R_{EQ}, given by the expression

$$\frac{1}{R_{EQ}} = \frac{1}{R_1} + \frac{1}{R_2} + \ldots + \frac{1}{R_N} \tag{5.2.18}$$

or

$$R_{EQ} = \frac{1}{1/R_1 + 1/R_2 + \ldots + 1/R_N} \tag{5.2.19}$$

Very often in the remainder of this book we shall refer to the parallel combination of two or more resistors with the following notation:

$$R_1 \parallel R_2 \parallel \cdots$$

where the symbol $\parallel$ signifies "in parallel with."

The general expression for the current divider for a circuit with N parallel resistors is the following:

$$i_n = \frac{1/R_n}{1/R_1 + 1/R_2 + \ldots + 1/R_n + \ldots + 1/R_N} i_S \quad \text{Current divider} \tag{5.2.20}$$

Example 5.2.2 The Wheatstone Bridge

The **Wheatstone bridge** is a resistive circuit that is frequently encountered in a variety of measurement circuits. The general form of the bridge is shown in Figure 5.2.15(a), where R_1, R_2, and R_3 are known, while R_x is an unknown resistance, to be determined. The circuit may also be redrawn as shown in Figure 5.2.15(b). The latter circuit will be used to demonstrate the use of the voltage divider rule in a mixed series-parallel circuit. The objective is to determine the unknown resistance R_x.

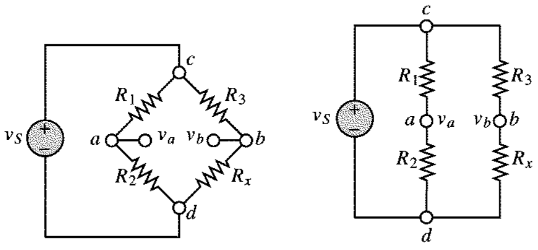

(a) (b)

FIGURE 5.2.15 Wheatstone bridge circuits.

1. Find the value of the voltage $v_{ad} = v_{ad} - v_{bd}$ in terms of the four resistances and the source voltage, v_s. Note that since the reference point d is the same for both voltages, we can also write $v_{ab} = v_a - v_b$.
2. If $R_1 = R_2 = R_3 = 1\ \text{k}\Omega$, $v_s = 12$ V, and $v_{ab} = 12$ mV, what is the value of R_x?

Solution.

1. First, we observe that the circuit consists of the parallel combination of three subcircuits: the voltage source, the series combination of R_1 and R_2, and the series combination of R_3 and R_x. Since these three subcircuits are in parallel, the same voltage will appear across each of them, namely, the source voltage, v_s.

   Thus, the source voltage divides between each resistor pair, R_1-R_2 and R_3-R_x, according to the voltage divider rule: v_a is the fraction of the source voltage appearing across R_2, while v_b is the voltage appearing across R_x:

$$v_a = v_S \frac{R_2}{R_1 + R_2} \quad \text{and} \quad v_b = v_S \frac{R_x}{R_3 + R_x}$$

   Finally, the voltage difference between points a and b is given by:

$$v_{ab} = v_a - v_b = v_S \left(\frac{R_2}{R_1 + R_2} - \frac{R_x}{R_3 + R_x} \right)$$

   This result is very useful and quite general, and it finds application in numerous practical circuits.
2. In order to solve for the unknown resistance, we substitute the numerical values in the preceding equation to obtain

$$0.012 = 12 \left(\frac{1{,}000}{2{,}000} - \frac{R_x}{1{,}000 + R_x} \right)$$

   which may be solved for R_x to yield

$$R_x = 996\ \Omega$$

Practical Voltage and Current Sources

Idealized models of voltage and current sources fail to take into consideration the finite-energy nature of practical voltage and current sources. The objective of this section is to extend the ideal models to

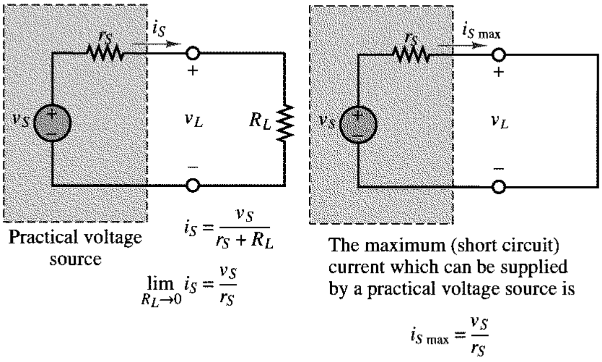

Practical voltage source

$i_S = \frac{v_S}{r_S + R_L}$

$\lim_{R_L \to 0} i_S = \frac{v_S}{r_S}$

The maximum (short circuit) current which can be supplied by a practical voltage source is

$i_{S\,\max} = \frac{v_S}{r_S}$

FIGURE 5.2.16 Practical voltage source.

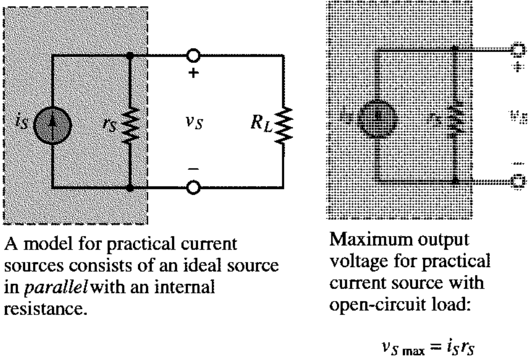

A model for practical current sources consists of an ideal source in *parallel* with an internal resistance.

Maximum output voltage for practical current source with open-circuit load:

$v_{S\,\max} = i_S r_S$

FIGURE 5.2.17 Practical current source.

models that are capable of describing the physical limitations of the voltage and current sources used in practice. Consider, for example, the model of an ideal voltage source. As the load resistance (R) decreases, the source is required to provide increasing amounts of current to maintain the voltage $v_s(t)$ across its terminal:

$$i(t) = \frac{v_S(t)}{R} \tag{5.2.21}$$

This circuit suggests that the ideal voltage source is required to provide an infinite amount of current to the load, in the limit as the load resistance approaches zero.

Figure 5.2.16 depicts a model for a practical voltage source; this is composed of an ideal voltage source, v_s, in series with a resistance, r_s. The resistance r_s in effect poses a limit to the maximum current the voltage source can provide:

$$i_{S\,\max} = \frac{v_S}{r_S} \tag{5.2.22}$$

It should be apparent that a desirable feature of an ideal voltage source is a very small internal resistance, so that the current requirements of an arbitrary load may be satisfied.

A similar modification of the ideal current source model is useful to describe the behavior of a practical current source. The circuit illustrated in Figure 5.2.17 depicts a simple representation of a practical current source, consisting of an ideal source in parallel with a resistor. Note that as the load resistance approaches infinity (i.e., an open circuit), the output voltage of the current source approaches its limit,

$$v_{S\max} = i_S r_S \tag{5.2.23}$$

A good current source should be able to approximate the behavior of an ideal current source. Therefore, a desirable characteristic for the internal resistance of a current source is that it be as large as possible.

Measuring Devices

The Ammeter

The **ammeter** is a device that, when connected in series with a circuit element, can measure the current flowing through the element. Figure 5.2.18 illustrates this idea. From Figure 5.2.18, two requirements are evident for obtaining a correct measurement of current:

1. The ammeter must be placed in series with the element whose current is to be measured (e.g., resistor R_2).
2. The ammeter should not resist the flow of current (i.e., cause a voltage drop), or else it will not be measuring the true current flowing the circuit. *An ideal ammeter has zero internal resistance.*

The Voltmeter

The **voltmeter** is a device that can measure the voltage across a circuit element. Since voltage is the difference in potential between two points in a circuit, the voltmeter needs to be connected across the element whose voltage we wish to measure. A voltmeter must also fulfill two requirements:

1. The voltmeter must be placed in parallel with the element whose voltage it is measuring.
2. The voltmeter should draw no current away from the element whose voltage it is measuring, or else it will not be measuring the true voltage across that element. Thus, *an ideal voltmeter has infinite internal resistance.*

Figure 5.2.19 illustrates these two points.

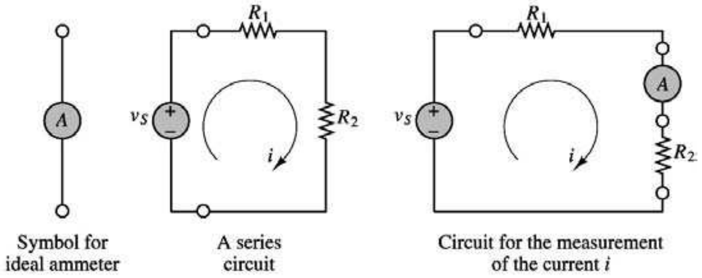

FIGURE 5.2.18 Measurement of current.

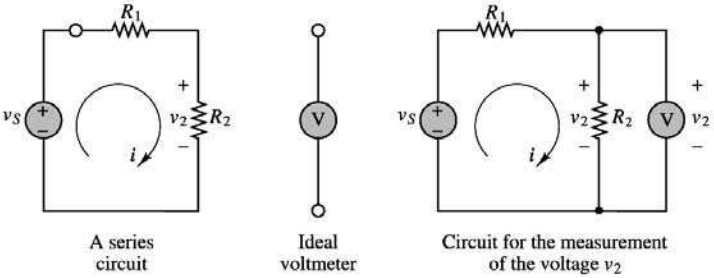

FIGURE 5.2.19 Measurement of voltage.

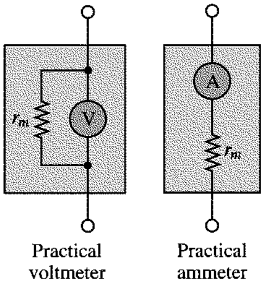

FIGURE 5.2.20 Models for practical ammeter and voltmeter.

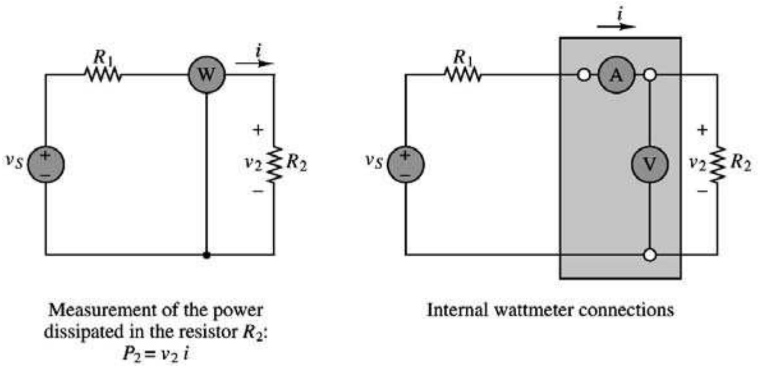

FIGURE 5.2.21 Measurement of power.

Once again, the definitions just stated for the ideal voltmeter and ammeter need to be augmented by considering the practical limitations of the devices. A practical ammeter will contribute some series resistance to the circuit in which it is measuring current; a practical voltmeter will not act as an ideal open circuit but will always draw some current from the measured circuit. Figure 5.2.20 depicts the circuit models for the practical ammeter and voltmeter.

All of the considerations that pertain to practical ammeters and voltmeters can be applied to the operation of a **wattmeter**, a measuring instrument that provides a measurement of the power dissipated by a circuit element, since the wattmeter is in effect made up of a combination of a voltmeter and an ammeter.

Figure 5.2.21 depicts the typical connection of a wattmeter in the same series circuit used in the preceding paragraphs. In effect, the wattmeter measures the current flowing through the load and, simultaneously, the voltage across it and multiplies the two to provide a reading of the power dissipated by the load.

5.3 Resistive Network Analysis

This section will illustrate the fundamental techniques for the analysis of resistive circuits. The methods introduced are based on Kirchhoff's and Ohm's laws. The main thrust of the section is to introduce and illustrate various methods of circuit analysis that will be applied throughout the book.

The Node Voltage Method

Node voltage analysis is the most general method for the analysis of electrical circuits. In this section, its application to linear resistive circuits will be illustrated. The **node voltage method** is based on defining the voltage at each node as an independent variable. One of the nodes is selected as a **reference node**

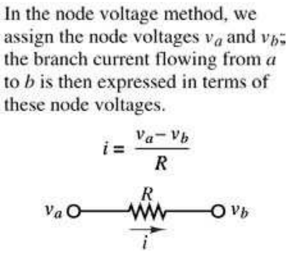

In the node voltage method, we assign the node voltages v_a and v_b; the branch current flowing from a to b is then expressed in terms of these node voltages.

$$i = \frac{v_a - v_b}{R}$$

FIGURE 5.3.1 Branch current formulation in nodal analysis.

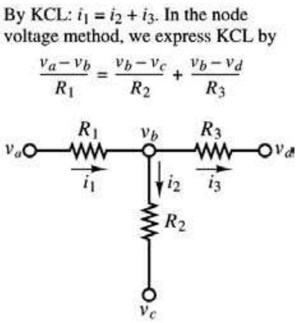

By KCL: $i_1 = i_2 + i_3$. In the node voltage method, we express KCL by

$$\frac{v_a - v_b}{R_1} = \frac{v_b - v_c}{R_2} + \frac{v_b - v_d}{R_3}$$

FIGURE 5.3.2 Use of KCL in nodal analysis.

(usually — but not necessarily — ground), and each of the other node voltages is referenced to this node. Once each node voltage is defined, Ohm's law may be applied between any two adjacent nodes in order to determine the current flowing in each branch. In the node voltage method, *each branch current is expressed in terms of one or more node voltages;* thus, currents do not explicitly enter into the equations. Figure 5.3.1 illustrates how one defines branch currents in this method.

Once each branch current is defined in terms of the node voltages, Kirchhoff's current law is applied at each node. The particular form of KCL employed in the nodal analysis equates the sum of the currents into the node to the sum of the currents leaving the node:

$$\sum i_{\text{in}} = \sum i_{\text{out}} \tag{5.3.1}$$

Figure 5.3.2 illustrates this procedure.

The systematic application of this method to a circuit with n nodes would lead to writing n linear equations. However, one of the node voltages is the reference voltage and is therefore already known, since it is usually assumed to be zero. Thus, we can write $n - 1$ *independent linear equations* in the $n - 1$ independent variables (the node voltages). Nodal analysis provides the minimum number of equations required to solve the circuit, since any branch voltage or current may be determined from knowledge of nodal voltages.

The nodal analysis method may also be defined as a sequence of steps, as outlined below.

Node Voltage Analysis Method

1. Select a reference node (usually ground). All other node voltages will be referenced to this node.
2. Define the remaining $n - 1$ node voltages as the independent variables.
3. Apply KCL at each of the $n - 1$ nodes, expressing each current in terms of the adjacent node voltages.
4. Solve the linear system of $n - 1$ equations in $n - 1$ unknowns.

In a circuit containing n nodes we can write at most $n - 1$ independent equations.

The current i, defined as flowing from left to right, establishes the polarity of the voltage across R.

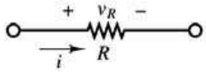

FIGURE 5.3.3 Basic principle of mesh analysis.

Once the direction of current flow has been selected, KVL requires that $v_1 = v_2 + v_3$.

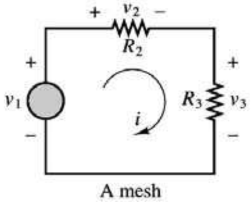

FIGURE 5.3.4 Use of KVL in mesh analysis.

The Mesh Current Method

In the mesh current method, we observe that a current flowing through a resistor in a specified direction defines the polarity of the voltage across the resistor, as illustrated in Figure 5.3.3, and that the sum of the voltages around a closed circuit must equal zero, by KVL. Once a convention is established regarding the direction of current flow around a mesh. Simple application of KVL provides the desired equation. Figure 5.3.4 illustrates this point.

The number of equations one obtains by this technique is equal to the number of meshes in the circuit. All branch currents and voltages may subsequently be obtained from the mesh currents, as will presently be shown. Since meshes are easily identified in a circuit, this method provides a very efficient and systematic procedure for the analysis of electrical circuits. The following section outlines the procedure used in applying the mesh current method to a linear circuit.

Mesh Current Analysis Method

1. Define each mesh current consistently. We shall always define mesh currents clockwise, for convenience.
2. Apply KVL around each mesh, expressing each voltage in terms of one or more mesh currents.
3. Solve the resulting linear system of equations with mesh currents as the independent variables.

In mesh analysis, it is important to be consistent in choosing the direction of current flow. To avoid confusion in writing the circuit equations, mesh currents will be defined exclusively clockwise when we are using this method.

One-Port Networks and Equivalent Circuits

This general circuit representation is shown in Figure 5.3.5. This configuration is called a **one-port network** and is particularly useful for introducing the notion of equivalent circuits. Note that the network of Figure 5.3.5 is completely described by its *i*-*v* characteristic.

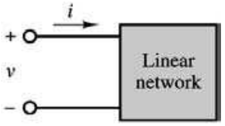

FIGURE 5.3.5 One-port network.

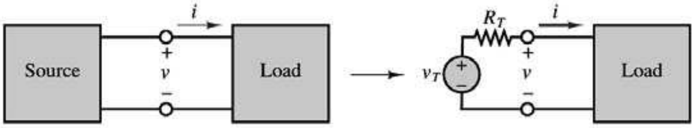

FIGURE 5.3.6 Illustration of Thévenin theorem.

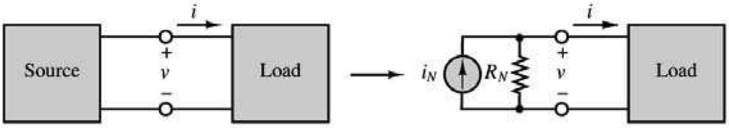

FIGURE 5.3.7 Illustration of Norton theorem.

Thévenin and Norton Equivalent Circuits

This section discusses one of the most important topics in the analysis of electrical circuits: the concept of an **equivalent circuit.** It will be shown that it is always possible to view even a very complicated circuit in terms of much simpler *equivalent* source and load circuits, and that the transformations leading to equivalent circuits are easily managed, with a little practice. In studying node voltage and mesh current analysis, you may have observed that there is a certain correspondence (called **duality**) between current sources and voltage sources, on the one hand, and parallel and series circuits, on the other. This duality appears again very clearly in the analysis of equivalent circuits: it will shortly be shown that equivalent circuits fall into one of two classes, involving either voltage or current sources and (respectively) either series or parallel resistors, reflecting this same principle of duality. The discussion of equivalent circuits begins with the statement of two very important theorems, summarized in Figure 5.3.6 and Figure 5.3.7.

The Thévenin Theorem. As far as a load is concerned, any network composed of ideal voltage and current sources, and of linear resistors, may be represented by an equivalent circuit consisting of an ideal voltage source, v_T, in series with an equivalent resistance, R_T.

The Norton Theorem. As far as a load is concerned, any network composed of ideal voltage and current sources, and of linear resistors, may be represented by an equivalent circuit consisting of an ideal current source, i_N, in parallel with an equivalent resistance, R_N.

Determination of Norton or Thévenin Equivalent Resistance

The first step in computing a Thévenin or Norton equivalent circuit consists of finding the equivalent resistance presented by the circuit at its terminals. This is done by setting all sources in the circuit equal to zero and computing the effective resistance between terminals. The voltage and current sources present in the circuit are set to zero as follows: voltage sources are replaced by short circuits, current sources by open circuits. We can produce a set of simple rules as an aid in the computation of the Thévenin (or Norton) equivalent resistance for a linear resistive circuit.

Computation of Equivalent Resistance of a One-Port Network:

1. Remove the load.
2. Zero all voltage and current sources
3. Compute the total resistance between load terminals, *with the load removed.* This resistance is equivalent to that which would be encountered by a current source connected to the circuit in place of the load.

These rules are summarized in Figure 5.3.8.

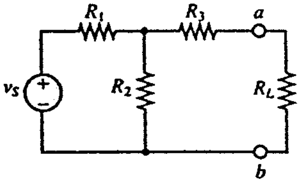

Complete circuit

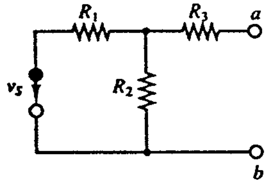

Circuit with load removed for computation of R_T. The voltage source is replaced by a short circuit.

FIGURE 5.3.8 Computation of Thévenin resistance.

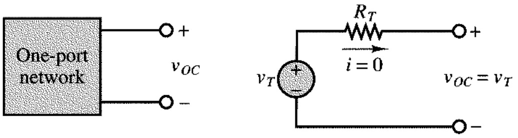

FIGURE 5.3.9 Equivalence of open-circuit and Thévenin voltage.

Computing the Thévenin Voltage

The Thévenin equivalent voltage is defined as follows: the equivalent (Thévenin) source voltage is equal to the **open-circuit voltage** present at the load terminals with the load removed.

This states that in order to compute v_T, it is sufficient to remove the load and to compute the open-circuit voltage at the one-port terminals. Figure 5.3.9 illustrates that the open-circuit voltage, v_{OC}, and the Thévenin voltage, v_T, must be the same if the Thévenin theorem is to hold. This is true because in the circuit consisting of v_T and R_T, the voltage v_{OC} must equal v_T, since no current flows through R_T and therefore the voltage across R_T is zero. Kirchhoff's voltage law confirms that

$$v_T = R_T(0) + v_{OC} = v_{OC} \tag{5.3.2}$$

Computing the Norton Current

The computation of the Norton equivalent current is very similar in concept to that of the Thévenin voltage. The following definition will serve as a starting point.

Definition. The Norton equivalent current is equal to the short-circuit current that would flow were the load replaced by a short circuit.

An explanation for the definition of the Norton current is easily found by considering, again, an arbitrary one-port network, as shown in Figure 5.3.10, where the one-port network is shown together with its Norton equivalent circuit.

It should be clear that the current, i_{SC}, flowing through the short circuit replacing the load is exactly the Norton current, i_N, since all of the source current in the circuit of Figure 5.3.10 must flow through the short circuit.

Experimental Determination of Thévenin and Norton Equivalents

Figure 5.3.11 illustrates the measurement of the open-circuit voltage and short-circuit current for an arbitrary network connected to any load and also illustrates that the procedure requires some special

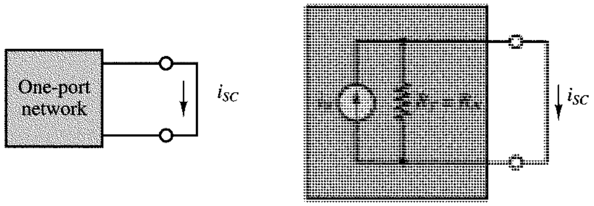

FIGURE 5.3.10 Illustration of Norton equivalent circuit.

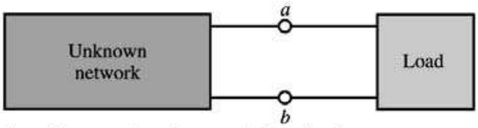

An unknown network connected to a load

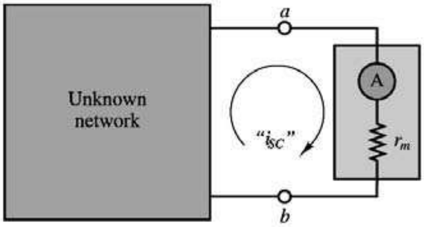

Network connected for measurement of short-circuit current

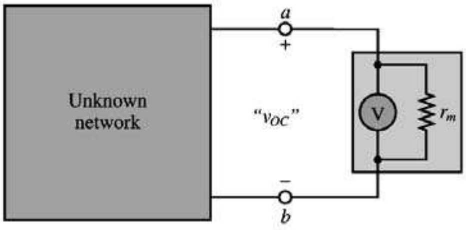

Network connected for measurement of open-circuit voltage

FIGURE 5.3.11 Measurement of open-circuit voltage and short-circuit current.

attention, because of the nonideal nature of any practical measuring instrument. The figure clearly illustrates that in the presence of finite meter resistance, r_m, one must take this quantity into account in the computation of the short-circuit current and open-circuit voltage; v_{OC} and i_{SC} appear between quotation marks in the figure specifically to illustrate that the measured "open-circuit voltage" and "short-circuit current" are, in fact, affected by the internal resistance of the measuring instrument and are not the true quantities.

The following are expressions for the true short-circuit current and open-circuit voltage.

$$
\begin{aligned}
i_N &= "i_{SC}"\left(1+\frac{r_m}{R_T}\right) \\
v_T &= "v_{OC}"\left(1+\frac{R_T}{r_m}\right)
\end{aligned}
\tag{5.3.3}
$$

where i_N is the ideal Norton current, v_T the Thévenin voltage, and R_T the true Thévenin resistance.

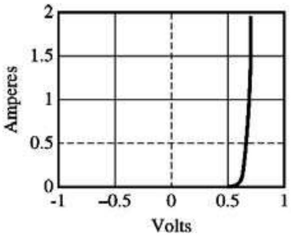

FIGURE 5.3.12 *i*-*v* characteristic of exponential resistor.

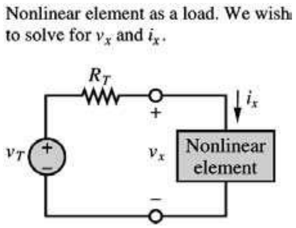

FIGURE 5.3.13 Representation of nonlinear element in a linear circuit.

Nonlinear Circuit Elements

Description of Nonlinear Elements

There are a number of useful cases in which a simple functional relationship exists between voltage and current in a nonlinear circuit element. For example, Figure 5.3.12 depicts an element with an exponential *i*-*v* characteristic, described by the following equations:

$$\begin{aligned} i &= I_0 e^{\alpha v} \qquad v > 0 \\ i &= -I_0 \qquad v \le 0 \end{aligned} \tag{5.3.4}$$

There exists, in fact, a circuit element (the semiconductor diode) that very nearly satisfies this simple relationship. The difficulty in the *i*-*v* relationship of Equation (5.3.4) is that it is not possible, in general, to obtain a closed-form analytical solution, even for a very simple circuit.

One approach to analyzing a circuit containing a nonlinear element might be to treat the nonlinear element as a load, and to compute the Thévenin equivalent of the remaining circuit, as shown in Figure 5.3.13. Applying KVL, the following equation may then be obtained:

$$v_T = R_T i_x + v_x \tag{5.3.5}$$

To obtain the second equation needed to solve for both the unknown voltage, v_x, and the unknown current, i_x, it is necessary to resort to the *i*-*v* description of the nonlinear element, namely, Equation (5.3.4). If, for the moment, only positive voltages are considered, the circuit is completely described by the following system:

$$\begin{aligned} i_x &= I_0 e^{\alpha v_x} \qquad v > 0 \\ v_T &= R_T i_x + v_x \end{aligned} \tag{5.3.6}$$

The two parts of Equation (5.3.6) represent a system of two equations in two unknowns. Any numerical method of choice may now be applied to solve the system of Equations (5.3.6).

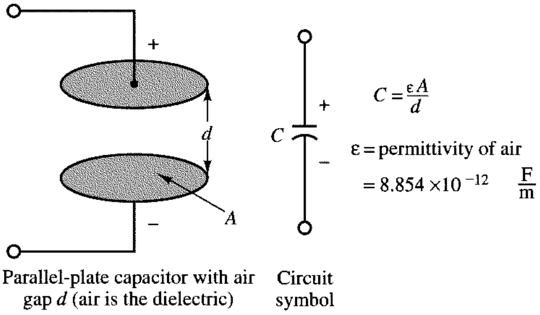

FIGURE 5.4.1 Structure of parallel-plate capacitor.

5.4 AC Network Analysis

In this section we introduce energy-storage elements, dynamic circuits, and the analysis of circuits excited by sinusoidal voltages and currents. Sinusoidal (or AC) signals constitute the most important class of signals in the analysis of electrical circuits. The simplest reason is that virtually all of the electric power used in households and industries comes in the form of sinusoidal voltages and currents.

Energy-Storage (Dynamic) Circuit Elements

The ideal resistor was introduced through Ohm's law in Section 5.2 as a useful idealization of many practical electrical devices. However, in addition to resistance to the flow of electric current, which is purely a dissipative (i.e., an energy-loss) phenomenon, electric devices may also exhibit energy-storage properties, much in the same way a spring or a flywheel can store mechanical energy. Two distinct mechanisms for energy storage exist in electric circuits: **capacitance** and **inductance**, both of which lead to the storage of energy in an electromagnetic field.

The Ideal Capacitor

A physical capacitor is a device that can store energy in the form of a charge separation when appropriately polarized by an electric field (i.e., a voltage). The simplest capacitor configuration consists of two parallel conducting plates of cross-sectional area A, separated by air (or another **dielectric**[1] material, such as mica or Teflon). Figure 5.4.1 depicts a typical configuration and the circuit symbol for a capacitor.

The presence of an insulating material between the conducting plates does not allow for the flow of DC current; thus, *a capacitor acts as an open circuit in the presence of DC currents*. However, if the voltage present at the capacitor terminals changes as a function of time, so will the charge that has accumulated at the two capacitor plates, since the degree of polarization is a function of the applied electric field, which is time-varying. In a capacitor, the charge separation caused by the polarization of the dielectric is proportional to the external voltage, that is, to the applied electric field:

$$Q = CV \tag{5.4.1}$$

where the parameter C is called the *capacitance* of the element and is a measure of the ability of the device to accumulate, or store, charge. The unit of capacitance is the coulomb/volt and is called the **farad** (F). The farad is an unpractically large unit; therefore, it is common to use microfarads (1 μF = 10^{-6} F) or picofarads (1 pF = 10^{-12} F). From Equation (5.4.1) it becomes apparent that if the external voltage applied to the capacitor plates changes in time, so will the charge that is internally stored by the capacitor:

---

[1] A dielectric material contains a large number of electric dipoles, which become polarized in the presence of an electric field.

$$q(t) = Cv(t) \tag{5.4.2}$$

Thus, although no current can flow through a capacitor if the voltage across it is constant, a time-varying voltage will cause charge to vary in time. The change with time in the stored charge is analogous to a current. The relationship between the current and voltage in a capacitor is as follows:

$$i(t) = C\frac{dv(t)}{dt} \tag{5.4.3}$$

If the above differential equation is integrated, one can obtain the following relationship for the voltage across a capacitor:

$$v_C(t) = \frac{1}{C}\int_{-\infty}^{t_0} i_C \, dt \tag{5.4.4}$$

Equation (5.4.4) indicates that the capacitor voltage depends on the past current through the capacitor, up until the present time, *t*. Of course, one does not usually have precise information regarding the flow of capacitor current for all past time, and so it is useful to define the initial voltage (or *initial condition*) for the capacitor according to the following, where t_0 is an arbitrary initial time:

$$V_0 = v_C(t = t_0) = \frac{1}{C}\int_{-\infty}^{t} i_C \, dt \tag{5.4.5}$$

The capacitor voltage is now given by the expression

$$v_C(t) = \frac{1}{C}\int_{t_0}^{t} i_C \, dt + V_0 \qquad t \geq t_0 \tag{5.4.6}$$

The significance of the initial voltage, V_0, is simply that at time t_0 some charge is stored in the capacitor, giving rise to a voltage, $v_c\,(t_0)$, according to the relationship $Q = CV$. Knowledge of this initial condition is sufficient to account for the entire past history of the capacitor current. (See Figure 5.4.2.)

From the standpoint of circuit analysis, it is important to point out that capacitors connected in series and parallel can be combined to yield a single equivalent capacitance. The rule of thumb, which is illustrated in Figure 5.4.3, is the following: capacitors in parallel add; capacitors in series combine according to the same rules used for resistors connected in parallel.

Physical capacitors are rarely constructed of two parallel plates separated by air, because this configuration yields very low values of capacitance, unless one is willing to tolerate very large plate areas. In

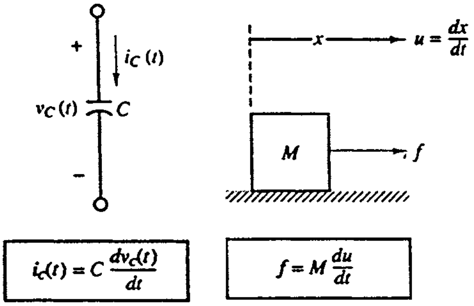

FIGURE 5.4.2 Defining equation for the ideal capacitor, and analogy with force-mass system.

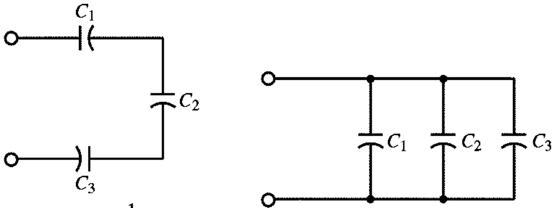

$$C_{EQ} = \frac{1}{\frac{1}{C_1} + \frac{1}{C_2} + \frac{1}{C_3}}$$

Capacitances in series combine like resistors in parallel

$$C_{EQ} = C_1 + C_2 + C_3$$

Capacitances in parallel add

FIGURE 5.4.3 Combining capacitors in a circuit.

TABLE 5.4.1 Capacitors

Material	Capacitance Range	Maximum Voltage (V)	Frequency Range (Hz)
Mica	1 pF to 0.1 μF	100–600	10^3–10^{10}
Ceramic	10 pF to 1 μF	50–1000	10^3–10^{10}
Mylar	0.001 to 10 μF	50–500	10^2–10^8
Paper	1,000 pF to 50 μF	100–105	10^2–10^8
Electrolytic	0.1 μF to 0.2 F	3–600	10–10^4

order to increase the capacitance (i.e., the ability to store energy), physical capacitors are often made of tightly rolled sheets of metal film, with a dielectric (paper or Mylar) sandwiched in-between. Table 5.4.1 illustrates typical values, materials, maximum voltage ratings, and useful frequency ranges for various types of capacitors. The voltage rating is particularly important, because any insulator will break down if a sufficiently high voltage is applied across it.

The energy stored in a capacitor is given by:

$$W_C(t) = \frac{1}{2} C v_C^2(t) \quad \text{(J)}$$

Example 5.4.1 Capacitive Displacement Transducer and Microphone

As shown in Figure 5.3.5, the capacitance of a parallel-plate capacitor is given by the expression

$$C = \frac{\varepsilon A}{d}$$

where ε is the **permittivity** of the dielectric material, A the area of each of the plates, and d their separation. The permittivity of air is $\varepsilon_0 = 8.854 \times 10^{-12}$ F/m, so that two parallel plates of area 1 m^2, separated by a distance of 1 mm, would give rise to a capacitance of 8.854×10^{-3} μF, a very small value for a very large plate area. This relative inefficiency makes parallel-plate capacitors impractical for use in electronic circuits. On the other hand, parallel-plate capacitors find application as *motion transducers*, that is, as devices that can measure the motion or displacement of an object. In a capacitive motion transducer, the air gap between the plates is designed to be variable, typically by fixing one plate and connecting the other to an object in motion. Using the capacitance value just derived for a parallel-plate capacitor, one can obtain the expression

$$C = \frac{8.854 \times 10^{-3}\ A}{x}$$

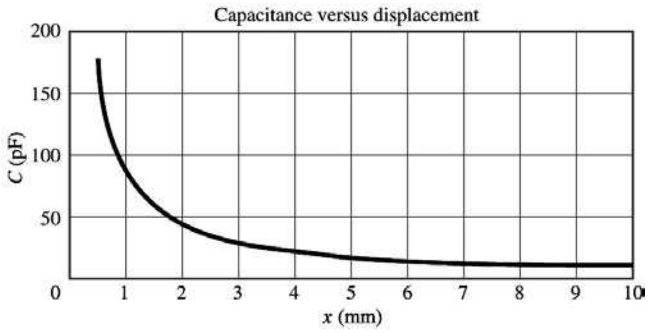

FIGURE 5.4.4 Response of a capacitive displacement transducer.

where C is the capacitance in pF, A is the area of the plates in mm^2, and x is the (variable) distance in mm. It is important to observe that the change in capacitance caused by the displacement of one of the plates is nonlinear, since the capacitance varies as the inverse of the displacement. For small displacements, however, the capacitance varies approximately in a linear fashion.

The *sensitivity, S,* of this motion transducer is defined as the slope of the change in capacitance per change in displacement, x, according to the relation

$$S = \frac{dC}{dx} = -\frac{8.854 \times 10^{-3}\ A}{2x^2} \frac{\text{pF}}{\text{mm}}$$

Thus, the sensitivity increases for small displacements. This behavior can be verified by plotting the capacitance as a function of x and noting that as x approaches zero, the slope of the nonlinear $C(x)$ curve becomes steeper (thus the greater sensitivity). Figure 5.4.4 depicts this behavior for a transducer with area equal to 10 mm^2.

This simple capacitive displacement transducer actually finds use in the popular *capacitive (or condenser) microphone*, in which the sound pressure waves act to displace one of the capacitor plates. The change in capacitance can then be converted into a change in voltage or current by means of a suitable circuit. An extension of this concept that permits measurement of differential pressures is shown in simplified form in Figure 5.4.5. In the figure, a three-terminal variable capacitor is shown to be made up of two fixed surfaces (typically, spherical depressions ground into glass disks and coated with a conducting material) and of a deflecting plate (typically made of steel) sandwiched between the glass disks. Pressure inlet orifices are provided, so that the deflecting plate can come into contact with the fluid whose pressure it is measuring. When the pressure on both sides of the deflecting plate is the same, the capacitance between terminals b and d, C_{bd}, will be equal to that between terminals b and c, C_{bc}. If any pressure differential exists, the two capacitances will change, with an increase on the side where the deflecting plate has come closer to the fixed surface and a corresponding decrease on the other side.

This behavior is ideally suited for the application of a bridge circuit, similar to the Wheatstone bridge circuit illustrated in Example 5.3.1, and also shown in Figure 5.4.5. In the bridge circuit, the output voltage, v_{out}, is precisely balanced when the differential pressure across the transducer is zero, but it will deviate from zero whenever the two capacitances are not identical because of a pressure differential across the transducer. We shall analyze the bridge circuit later in Example 5.4.2.

The Ideal Inductor

The ideal inductor is an element that has the ability to store energy in a magnetic field. Inductors are typically made by winding a coil of wire around a core, which can be an insulator or a ferromagnetic material, shown in Figure 5.4.6. When a current flows through the coil, a magnetic field is established, as you may recall from early physics experiments with electromagnets. In an ideal inductor, the resistance of the wire is zero, so that a constant current through the inductor will flow freely without causing a

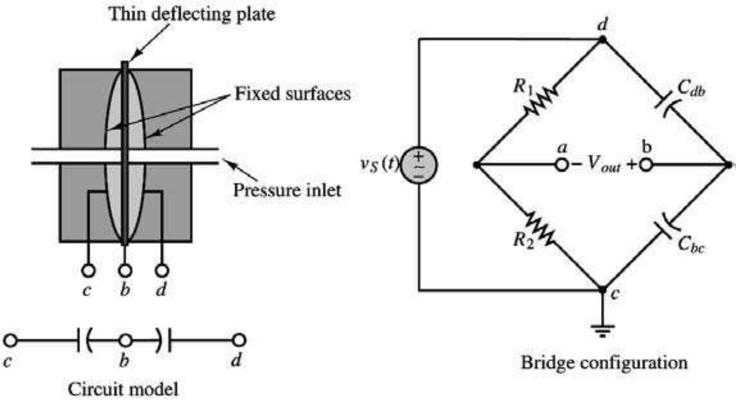

FIGURE 5.4.5 Capacitive pressure transducer and related bridge circuit.

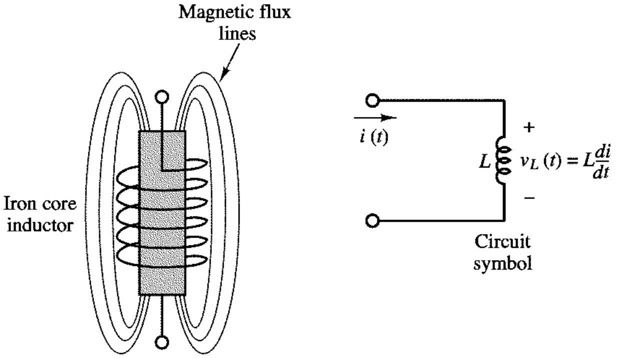

FIGURE 5.4.6 Iron-core inductor.

voltage drop. In other words, *the ideal inductor acts as a short circuit in the presence of DC currents.* If a time-varying voltage is established across the inductor, a corresponding current will result, according to the following relationship:

$$v_L(t) = L\frac{di_L}{dt} \tag{5.4.7}$$

where L is called the *inductance* of the coil and is measured **henry** (H), where

$$1\text{ H} = 1\text{ V-sec/A} \tag{5.4.8}$$

Henrys are reasonable units for practical inductors; millihenrys (mH) and microhenrys (μH) are also used.

The inductor current is found by integrating the voltage across the inductor:

$$i_L(t) = \frac{1}{L}\int_{-\infty}^{t} v_L\, dt \tag{5.4.9}$$

If the current flowing through the inductor at time $t = t_0$ is known to be I_0, with

$$I_0 = i_L(t = t_0) = \frac{1}{L}\int_{-\infty}^{t_0} v_L\, dt \tag{5.4.10}$$

then the inductor current can be found according to the equation

$$i_L(t) = \frac{1}{L}\int_{t_0}^{t} v_L \, dt + I_0 \qquad t \ge t_0 \tag{5.4.11}$$

Inductors in series add. Inductors in parallel combine according to the same rules used for resistors connected in parallel. See Figure 5.4.7 to Figure 5.4.9.

Table 5.4.2 and Figure 5.4.2, Figure 5.4.7, and Figure 5.4.9 illustrate a useful analogy between ideal electrical and mechanical elements.

The defining equation for the inductance circuit element is analogous to the equation of motion of a spring acted upon by a force.

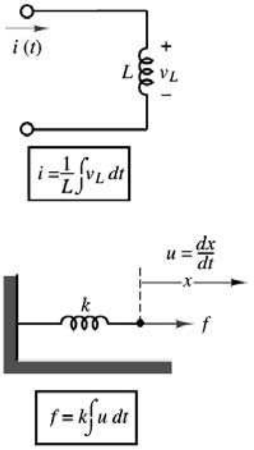

FIGURE 5.4.7 Defining equation for the ideal inductor and analogy with force-spring system.

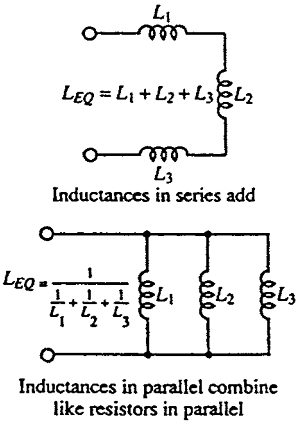

FIGURE 5.4.8 Combining inductors in a circuit.

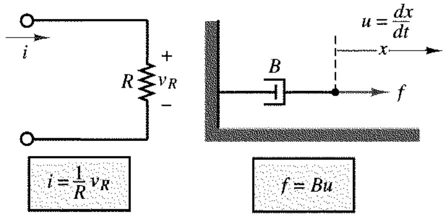

FIGURE 5.4.9 Analogy between electrical and mechanical elements.

TABLE 5.4.2 Analogy Between Electrical and Mechanical Variables

Mechanical System	Electrical System
Force, *f* (N)	Current, *i* (A)
Velocity, µ (m/sec)	Voltage, *v* (V)
Damping, *B* (N-sec/m)	Conductance, 1/R (S)
Compliance, 1/k (m/N)	Inductance, *L* (H)
Mass, *M* (kg)	Capacitance, *C* (F)

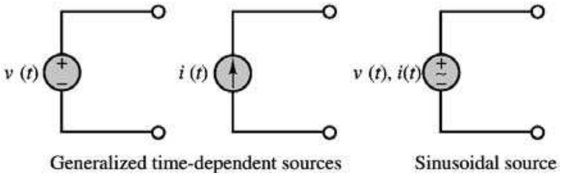

FIGURE 5.4.10 Time-dependent signal sosurces.

Time-Dependent Signal Sources

Figure 5.4.10 illustrates the convention that will be employed to denote time-dependent signal sources.

One of the most important classes of time-dependent signals is that of **periodic signals**. These signals appear frequently in practical applications and are a useful approximation of many physical phenomena. A periodic signal $x(t)$ is a signal that satisfies the following equation:

$$x(t) = x(t + nT) \qquad n = 1, 2, 3, \ldots \tag{5.4.12}$$

where T is the **period** of $x(t)$. Figure 5.4.11 illustrates a number of the periodic waveforms that are typically encountered in the study of electrical circuits. Waveforms such as the sine, triangle, square, pulse, and sawtooth waves are provided in the form of voltages (or, less frequently, currents) by commercially available **signal** (or **waveform**) **generators**. Such instruments allow for selection of the waveform peak amplitude, and of its period.

As stated in the introduction, sinusoidal waveforms constitute by far the most important class of time-dependent signals. Figure 5.4.12 depicts the relevant parameters of a sinusoidal waveform. A generalized sinusoid is defined as follows:

$$x(t) = A\cos(\omega t + \phi) \tag{5.4.13}$$

where A is the **amplitude**, ω the **radian frequency**, and ϕ the **phase**. Figure 5.4.12 summarizes the definitions of A, ω, and ϕ for the waveforms

$$x_1(t) = A\cos(\omega t) \quad \text{and} \quad x_2(t) = A\cos(\omega t + \phi)$$

where

$$\begin{aligned} f &= \text{natural frequency} = \frac{1}{T}(\text{cycles/sec, or Hz}) \\ \omega &= \text{radian frequency} = 2\pi f(\text{radians/sec}) \\ \phi &= 2\pi\frac{\Delta T}{T}(\text{radians}) = 360\frac{\Delta T}{T}(\text{degrees}) \end{aligned} \tag{5.4.14}$$

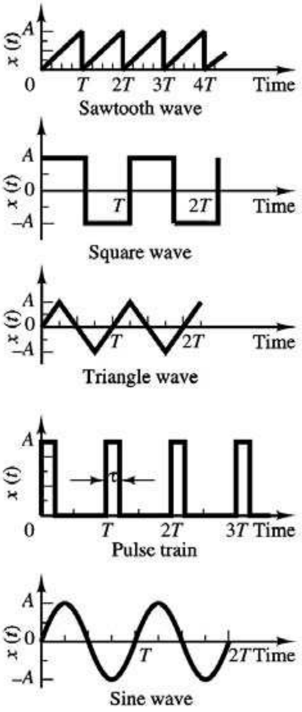

FIGURE 5.4.11 Periodic signal waveforms.

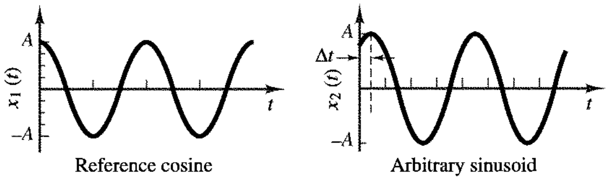

FIGURE 5.4.12 Sinusoidal waveforms.

The phase shift, ϕ, permits the representation of an arbitrary sinusoidal signal. Thus, the choice of the reference cosine function to represent sinusoidal signals — arbitrary as it may appear at first — does not restrict the ability to represent all sinusoids. For example, one can represent a sine wave in terms of a cosine wave simply by introducing a phase shift of π/2 radians:

$$A\sin(\omega t) = A\cos\left(\omega t - \frac{\pi}{2}\right) \tag{5.4.15}$$

It is important to note that, although one usually employs the variable ω (in units of radians per second) to denote sinusoidal frequency, it is common to refer to natural frequency, *f*, in units of cycles per second, or **hertz** (Hz). The relationship between the two is the following:

$$\omega = 2\pi f \tag{5.4.16}$$

Average and RMS Values

Now that a number of different signal waveforms have been defined, it is appropriate to define suitable measurements for quantifying the strength of a time-varying electrical signal. The most common types of measurements are the **average** (or **DC**) **value** of a signal waveform — which corresponds to just

FIGURE 5.4.13 Averaging a signal waveform.

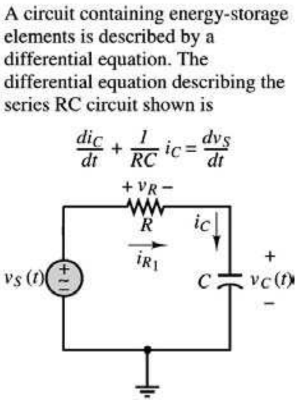
A circuit containing energy-storage elements is described by a differential equation. The differential equation describing the series RC circuit shown is

$$\frac{di_C}{dt}+\frac{1}{RC}i_C=\frac{dv_S}{dt}$$

FIGURE 5.4.14 Circuit containing energy-storage element.

measuring the mean voltage or current over a period of time — and the **root-mean-square** (or **rms**) **value**, which takes into account the fluctuations of the signal about its average value. Formally, the operation of computing the average value of a signal corresponds to integrating the signal waveform over some (presumably, suitably chosen) period of time. We define the time-averaged value of a signal $x(t)$ as

$$\langle x(t)\rangle=\frac{1}{T}\int_0^T x(t)\,dt \tag{5.4.17}$$

where T is the period of integration. Figure 5.4.13 illustrates how this process does, in fact, correspond to computing the average amplitude of $x(t)$ over a period of T seconds.

$$\langle A\cos(\omega t+\phi)\rangle=0$$

A useful measure of the voltage of an AC waveform is the root-mean-square, or rms, value of the signal, $x(t)$, defined as follows:

$$x_{rms}\sqrt{\frac{1}{T}\int_0^T x^2(t)\,dt} \tag{5.4.18}$$

Note immediately that if $x(t)$ is a voltage, the resulting x_{rms} will also have units of volts. If you analyze Equation (5.4.18), you can see that, in effect, the rms value consists of the square root of the average (or mean) of the square of the signal. Thus, the notation *rms* indicates exactly the operations performed on $x(t)$ in order to obtain its rms value.

Solution of Circuits Containing Dynamic Elements

The major difference between the analysis of the resistive circuits and circuits containing capacitors and inductors is now that the equations that result from applying Kirchhoff's laws are differential equations, as opposed to the algebraic equations obtained in solving resistive circuits. Consider, for example, the circuit of Figure 5.4.14 which consists of the series connection of a voltage source, a resistor, and a capacitor. Applying KVL around the loop, we may obtain the following equation:

$$v_S(t) = v_R(t) + v_C(t) \tag{5.4.19}$$

Observing that $i_R = i_C$, Equation (5.4.19) may be combined with the defining equation for the capacitor (Equation 4.6.6) to obtain

$$v_S(t) = Ri_C(t) + \frac{1}{C}\int_{-\infty}^{t} i_C \, dt \tag{5.4.20}$$

Equation (5.4.20) is an integral equation, which may be converted to the more familiar form of a differential equation by differentiating both sides of the equation, and recalling that

$$\frac{d}{dt}\left(\int_{-\infty}^{t} i_C \, dt\right) = i_C(t) \tag{5.4.21}$$

to obtain the following differential equation:

$$\frac{di_C}{dt} + \frac{1}{RC} i_C = \frac{1}{R}\frac{dv_S}{dt} \tag{5.4.22}$$

where the argument (t) has been dropped for ease of notation.

Observe that in Equation (5.4.22), the independent variable is the series current flowing in the circuit, and that this is not the only equation that describes the series *RC* circuit. If, instead of applying KVL, for example, we had applied KCL at the node connecting the resistor to the capacitor, we would have obtained the following relationship:

$$i_R = \frac{v_S - v_C}{R} = i_C = C\frac{dv_C}{dt} \tag{5.4.23}$$

or

$$\frac{dv_C}{dt} + \frac{1}{RC} v_C = \frac{1}{RC} v_S \tag{5.4.24}$$

Note the similarity between Equation (5.4.22) and Equation (5.4.24). The left-hand side of both equations is identical, except for the dependent variable, while the right-hand side takes a slightly different form. The solution of either equation is sufficient, however, to determine all voltages and currents in the circuit.

We can generalize the results above by observing that any circuit containing a single energy-storage element can be described by a differential equation of the form

$$a_1 \frac{dy(t)}{dt} + a_0(t) = F(t) \tag{5.4.25}$$

where $y(t)$ represents the capacitor voltage in the circuit of Figure 5.4.14 and where the constants a_0 and a_1 consist of combinations of circuit element parameters. Equation (5.4.25) is a **first-order ordinary differential equation** with constant coefficients.

Consider now a circuit that contains two energy-storage elements, such as that shown in Figure 5.4.15. Application of KVL results in the following equation:

$$Ri(t) + L\frac{di(t)}{dt} + \frac{1}{C}\int_{-\infty}^{t} i(t) \, dt = v_S(t) \tag{5.4.26}$$

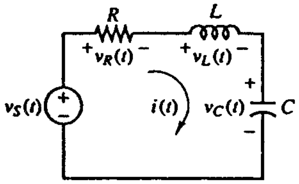

FIGURE 5.4.15 Second-order circuit.

Equation (5.4.26) is called an integro-differential equation because it contains both an integral and a derivative. This equation can be converted into a differential equation by differentiating both sides, to obtain:

$$R\frac{di(t)}{dt} + L\frac{d^2i(t)}{dt^2} + \frac{1}{C}i(t) = \frac{dv_S(t)}{dt} \tag{5.4.27}$$

or, equivalently, by observing that the current flowing in the series circuit is related to the capacitor voltage by $i(t) = Cdv_C/dt$, and that Equation (5.4.26) can be rewritten as:

$$RC\frac{dv_C}{dt} + LC\frac{d^2v_C(t)}{dt^2} + v_C(t) = v_S(t) \tag{5.4.28}$$

Note that although different variables appear in the preceding differential equations, both Equation (5.4.26) and Equation (5.4.28) can be rearranged to appear in the same general form, as follows:

$$a_2\frac{d^2y(t)}{dt^2} + a_1\frac{dy(t)}{dt} + a_0y(t) = F(t) \tag{5.4.29}$$

where the general variable $y(t)$ represents either the series current of the circuit of Figure 5.4.15 or the capacitor voltage. By analogy with Equation (5.4.25), we call Equation (5.4.29) a **second-order ordinary differential equation** with constant coefficients. As the number of energy-storage elements in a circuit increases, one can therefore expect that higher-order differential equations will result.

Phasors and Impedance

In this section, we introduce an efficient notation to make it possible to represent sinusoidal signals as *complex numbers*, and to eliminate the need for solving differential equations.

Phasors

Let us recall that it is possible to express a generalized sinusoid as the real part of a complex vector whose **argument**, or **angle**, is given by $(\omega t + \phi)$ and whose length, or **magnitude**, is equal to the peak amplitude of the sinusoid. The **complex phasor** corresponding to the sinusoidal signal $A\cos(\omega t + \phi)$ is therefore defined to be the complex number $Ae^{j\phi}$:

$$Ae^{j\phi} = \text{complex phasor notation for } A\cos(\omega t + \phi) \tag{5.4.30}$$

1. Any sinusoidal signal may be mathematically represented in one of two ways: a **time-domain form,**

$$v(t) = A\cos(\omega t + \phi)$$

   and a **frequency-domain** (or **phasor**) **form**.

$$\mathbf{V}(j\omega) = Ae^{j\phi}$$

2. A phasor is a complex number, expressed in polar form, consisting of a *magnitude* equal to the peak amplitude of the sinusoidal signal and a *phase angle* equal to the phase shift of the sinusoidal signal *referenced to a cosine signal.*
3. When using phasor notation, it is important to make a note of the specific frequency, ω, of the sinusoidal signal, since this is not explicitly apparent in the phasor expression.

Impedance

We now analyze the *i-v* relationship of the three ideal circuit elements in light of the new phasor notation. The result will be a new formulation in which resistors, capacitors, and inductors will be described in the same notation. A direct consequence of this result will be that the circuit theorems of Section 5.3 will be extended to AC circuits. In the context of AC circuits, any one of the three ideal circuit elements defined so far will be described by a parameter called **impedance**, which may be viewed as a *complex resistance*. The impedance concept is equivalent to stating that capacitors and inductors act as *frequency-dependent resistors*, that is, as resistors whose resistance is a function of the frequency of the sinusoidal excitation. Figure 5.4.16 depicts the same circuit represented in conventional form (top) and in phasor-impedance form (bottom); the latter representation explicitly shows phasor voltages and currents and treats the circuit element as a generalized "impedance". It will presently be shown that each of the three ideal circuit elements may be represented by one such impedance element.

Let the source voltage in the circuit of Figure 5.4.16 be defined by

$$v_S(t) = A\cos\omega t \quad \text{or} \quad \mathbf{V}_S(j\omega) = Ae^{j0^\circ} \tag{5.4.31}$$

without loss of generality. Then the current $i(t)$ is defined by the *i-v* relationship for each circuit element. Let us examine the frequency-dependent properties of the resistor, inductor, and capacitor, one at a time.

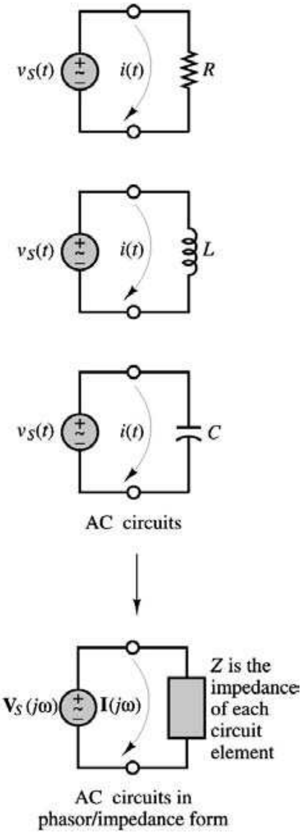

FIGURE 5.4.16 The impedance element.

The *impedance* of the resistor is defined as the ratio of the phasor voltage across the resistor to the phasor current flowing through it, and the symbol Z_R is used to denote it:

$$Z_R(j\omega) = \frac{\mathbf{V}_S(j\omega)}{\mathbf{I}(j\omega)} = R \tag{5.4.32}$$

The impedance of the inductor is defined as follows:

$$Z_L(j\omega) = \frac{\mathbf{V}_S(j\omega)}{\mathbf{I}(j\omega)} = \omega L e^{j90^\circ} = j\omega L \tag{5.4.33}$$

Note that the inductor now appears to behave like a *complex frequency-dependent resistor*, and that the magnitude of this complex resistor, ωL, is proportional to the signal frequency, ω. Thus, an inductor will "impede" current flow in proportion to the sinusoidal frequency of the source signal. This means that at low signal frequencies, an inductor acts somewhat like a short circuit, while at high frequencies it tends to behave more as an open circuit. Another important point is that *the magnitude of the impedance of an inductor is always positive*, since both L and ω are positive numbers. You should verify that the units of this magnitude are also ohms.

The impedance of the ideal capacitor, $Z_C(j\omega)$, is therefore defined as follows:

$$Z_C(j\omega) = \frac{\mathbf{V}_S(j\omega)}{\mathbf{I}(j\omega)} = \frac{1}{\omega C} e^{-j90^\circ} = \frac{-j}{\omega C} = \frac{1}{j\omega C} \tag{5.4.34}$$

where we have used the fact that $1/j = e^{-j90^\circ} = -j$. Thus, the impedance of a capacitor is also a frequency-dependent complex quantity, with the impedance of the capacitor varying as an inverse function of frequency; and so a capacitor acts like a short circuit at high frequencies, whereas it behaves more like an open circuit at low frequencies. Another important point is that *the impedance of a capacitor is always negative*, since both C and ω are positive numbers. You should verify that the units of impedance for a capacitor are ohms. Figure 5.4.17 depicts $Z_C(j\omega)$ in the complex plane, alongside $Z_R(j\omega)$ and $Z_L(j\omega)$.

The impedance parameter defined in this section is extremely useful in solving AC circuit analysis problems, because it will make it possible to take advantage of most of the network theorems developed

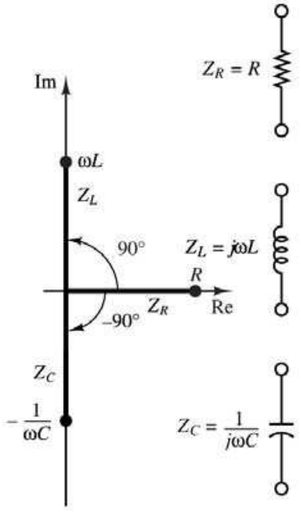

FIGURE 5.4.17 Impedances of *R*, *L*, and *C* in the complex plane.

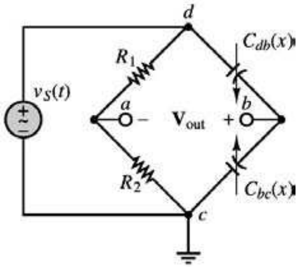

FIGURE 5.4.18 Bridge circuit for capacitive displacement transducer.

for DC circuits by replacing resistances with complex-valued impedances. In its most general form, the impedance of a circuit element is defined as the sum of a real part and an imaginary part:

$$Z(j\omega) = R(j\omega) + jX(j\omega) \tag{5.4.35}$$

where R is called the **AC resistance** and X is called the **reactance**. The frequency dependence of R and X has been indicated explicitly, since it is possible for a circuit to have a frequency-dependent resistance. The examples illustrate how a complex impedance containing both real and imaginary parts arises in a circuit.

Example 5.4.2 Capacitive Displacement Transducer

In Example 5.4.1, the idea of a capacitive displacement transducer was introduced when we considered a parallel-plate capacitor composed of a fixed plate and a movable plate. The capacitance of this variable capacitor was shown to be a *nonlinear* function of the position of the movable plate, x (see Figure 5.4.5). In this example, we show that under certain conditions the impedance of the capacitor varies as a *linear* function of displacement — that is, the movable-plate capacitor can serve as a linear transducer.

Recall the expression derived in Example 5.4.1:

$$C = \frac{8.854 \times 10^{-3} A}{x}$$

where C is the capacitance in pF, A is the area of the plates in mm^2, and x is the (variable) distance in mm. If the capacitor is placed in an AC circuit, its impedance will be determined by the expression

$$Z_C = \frac{1}{j\omega C}$$

so that

$$Z_C = \frac{x}{j\omega 8.854 A}$$

Thus, at a fixed frequency ω, the impedance of the capacitor will vary linearly with displacement. This property may be exploited in the bridge circuit of Example 5.4.1, where a differential pressure transducer was shown as being made of two movable-plate capacitors, such that if the capacitance of one increased as a consequence of a pressure differential across the transducer, the capacitance of the other had to decrease by a corresponding amount (at least for small displacements). The circuit is shown again in Figure 5.4.18 where two resistors have been connected in the bridge along with the variable capacitors (denoted by $C(x)$). The bridge is excited by a sinusoidal source.

Using phasor notation, we can express the output voltage as follows:

$$\mathbf{V}_{\text{out}}(j\omega) = \mathbf{V}_S(j\omega)\left(\frac{Z_{C_{bc}(x)}}{Z_{C_{db}(x)} + Z_{C_{bc}(x)}} - \frac{R_2}{R_1 + R_2}\right)$$

If the nominal capacitance of each movable-plate capacitor with the diaphragm in the center position is given by

$$C = \frac{\varepsilon A}{d}$$

where d is the nominal (undisplaced) separation between the diaphragm and the fixed surfaces of the capacitors (in mm), the capacitors will see a change in capacitance given by

$$C_{db} = \frac{\varepsilon A}{d - x} \quad \text{and} \quad C_{bc} = \frac{\varepsilon A}{d + x}$$

when a pressure differential exists across the transducer, so that the impedances of the variable capacitors change according to the displacement:

$$Z_{C_{db}} = \frac{d - x}{j\omega 8.854A} \quad \text{and} \quad Z_{C_{bc}} = \frac{d + x}{j\omega 8.854A}$$

and we obtain the following expression for the phasor output voltage, if we choose $R_1 = R_2$.

$$\begin{aligned}\mathbf{V}_{\text{out}}(j\omega) &= \mathbf{V}_S(j\omega)\left(\frac{\dfrac{d+x}{j\omega 8.854A}}{\dfrac{d-x}{j\omega 8.854A} + \dfrac{d+x}{j\omega 8.854A}} - \frac{R_2}{R_1 + R_2}\right) \\ &= \mathbf{V}_S(j\omega)\left(\frac{1}{2} + \frac{x}{2d} - \frac{R_2}{R_1 + R_2}\right) \\ &= \mathbf{V}_S(j\omega)\frac{x}{2d}\end{aligned}$$

Thus, the output voltage will vary as a scaled version of the input voltage in proportion to the displacement.

5.5 AC Power

The aim of this section is to introduce the student to simple AC power calculations, and to the generation and distribution of electric power.

Instantaneous and Average Power

The most general expressions for the voltage and current delivered to an arbitrary load are as follows:

$$\begin{aligned} v(t) &= V\cos(\omega t + \theta_v) \\ i(t) &= I\cos(\omega t + \theta_I) \end{aligned} \tag{5.5.1}$$

where V and I are the peak amplitudes of the sinusoidal voltage and current, respectively, and θ_V and θ_I are their angles. Two such waveforms are plotted in Figure 5.5.1, with unit amplitude and with phase angles $\theta_V = \pi/6$ and $\theta_I = \pi/3$.

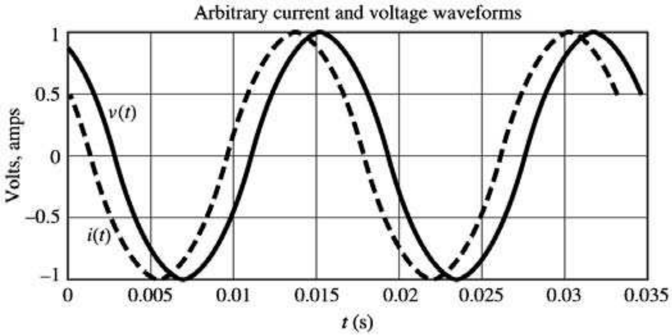

FIGURE 5.5.1 Current and voltage waveforms for illustration of AC power.

Since the **instantaneous power** dissipated by a circuit element is given by the product of the instantaneous voltage and current, it is possible to obtain a general expression for the power dissipated by an AC circuit element:

$$\begin{aligned} p(t) &= v(t)i(t) \\ &= VI\cos\left(\omega t + \theta_v\right)\cos\left(\omega t + \theta_I\right) \end{aligned} \tag{5.5.2}$$

Equation (5.5.2) can be further simplified with the aid of trigonometric identities to yield

$$p(t) = \frac{VI}{2}\cos(\theta) + \frac{VI}{2}\cos(2\omega t + \theta) \tag{5.5.3}$$

Equation (5.5.3) illustrates how the instantaneous power dissipated by an AC circuit element is equal to the sum of an average component, $VI/2\cos(\theta)$, plus a sinusoidal component, $VI/2\cos(2\omega t + \theta)$, oscillating at a frequency double that of the original source frequency.

The **average power** corresponding to the voltage and current signals of Equation (5.5.1) can be obtained by integrating the instantaneous power over one cycle of the sinusoidal signal.

$$P_{\text{av}} = \frac{VI}{2}\cos(\theta)$$

AC Power Notation

It has already been noted that AC power systems operate at a fixed frequency; in North America, this frequency is 60 cycles per second (Hz), corresponding to a radian frequency

$$\omega = 2\pi \cdot 60 = 377 \text{ rad/sec} \quad \text{AC power frequency} \tag{5.5.4}$$

In Europe and most other parts of the world, AC power is generated at a frequency of 50 Hz (this is the reason why some appliances will not operate under one of the two systems). It will therefore be understood that for the remainder of this section the radian frequency, ω, is fixed at 377 rad/sec. With knowledge of the radian frequency of all voltages and currents, it will always be possible to compute the exact magnitude and phase of any impedance in a circuit.

Power Factor

The phase angle of the load impedance plays a very important role in the absorption of power by a load impedance. As illustrated in Equation (5.5.3) and in the preceding examples, the average power dissipated by an AC load is dependent on the cosine of the angle of the impedance. To recognize the importance of this factor in AC power computations, the term cos(θ) is referred to as the **power factor** (pf). Note that the power factor is equal to 0 for a purely inductive or capacitive load and equal to 1 for a purely resistive load; in every other case,

$$0 < \text{pf} < 1 \tag{5.5.5}$$

Two equivalent expressions for the power factor are given in the following:

$$\text{pf} = \cos(\theta) = \frac{P_{\text{av}}}{\tilde{V}\tilde{I}} \quad \text{Power factor} \tag{5.5.6}$$

where $\tilde{V}$ and $\tilde{I}$ are the rms values of the load voltage and current.

Complex Power

The expression for the instantaneous power given in Equation (5.5.3) may be further expanded to provide further insight into AC power.

$$p(t) = \tilde{I}^2R + \tilde{I}^2R\cos(2\omega t) - \tilde{I}^2X\sin(2\omega t) \tag{5.5.7}$$

The physical interpretation of this expression for the instantaneous power should be intuitively appealing at this point. As Equation (5.5.7) suggests, the instantaneous power dissipated by a complex load consists of the following three components:

1. An average component, which is constant; this is called the *average power* and is denoted by the symbol P_{av}:

   $$P_{\text{av}} = \tilde{I}^2R \tag{5.5.8}$$

   where R = Re (Z).
2. A time-varying (sinusoidal) component with zero average value that is contributed by the power fluctuations in the resistive component of the load and is denoted by $p_R(t)$:

   $$\begin{aligned} p_R(t) &= \tilde{I}^2R\cos(2\omega t) \\ &= P_{\text{av}}\cos 2\omega t \end{aligned} \tag{5.5.9}$$

3. A time-varying (sinusoidal component with zero average value, due to the power fluctuation in the reactive component of the load and denoted by $p_X(t)$:

   $$\begin{aligned} p_X(t) &= -\tilde{I}^2X\sin(2\omega t) \\ &= Q\sin 2\omega t \end{aligned} \tag{5.5.10}$$

   where X = Im (Z) and Q is called the **reactive power**. *Note that since reactive elements can only store energy and not dissipate it, there is no net average power absorbed by X.*

Since P_{av} corresponds to the power absorbed by the load resistance, it is also called the **real power**, measured in units of watts (W). On the other hand, Q takes the name of *reactive power*, since it is associated with the load reactance. Table 5.5.1 shows the general methods of calculating P and Q.

TABLE 5.5.1 Real and Reactive Power

Real Power, P_{av}	Reactive Power, Q
$\tilde{V}\tilde{I}\cos(\theta)$	$\tilde{V}\tilde{I}\sin(\theta)$
I^2R	I^2X

The units of Q are **volt-amperes reactive**, or VAR. Note that Q represents an exchange of energy between the source and the reactive part of the load; thus, no net power is gained or lost in the process since the average reactive power is zero. In general, it is desirable to minimize the reactive power in a load.

The computation of AC power is greatly simplified by defining a fictitious but very useful quantity called the **complex power**, S:

$$S = \mathbf{VI}^* \quad \text{Complex power} \tag{5.5.11}$$

or

$$S = P_{\text{av}} + jQ$$

The complex power S may be interpreted graphically as a vector in the complex plane, as shown in Figure 5.5.2.

The magnitude of S, $|S|$, is measured in units of **volt-amperes** (VA) and is called **apparent power**, because this is the quantity one would compute by measuring the rms load voltage and currents without regard for the phase angle of the load. The complex power may also be expressed by the product of the square of the rms current through the load and the complex load impedance:

$$S = \tilde{I}^2 Z$$

or

$$\tilde{I}^2 R + j\tilde{I}^2 R = \tilde{I}^2 Z \tag{5.5.12}$$

or, equivalently, by the ratio of the rms voltage across the load to the complex conjugate of the load impedance:

$$S = \frac{\tilde{V}^2}{Z^*} \tag{5.5.13}$$

Although the reactive power does not contribute to any average power dissipation in the load, it may have an adverse effect on power consumption because it increases the overall rms current flowing in the circuit. The presence of any source resistance (typically, the resistance of the line wires in AC power circuits) will cause a loss of power; the power loss due to this line resistance is unrecoverable and constitutes a net loss for the electric company, since the user never receives this power.

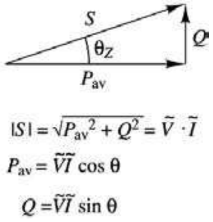

$$|S| = \sqrt{P_{\text{av}}^2 + Q^2} = \tilde{V}\cdot\tilde{I}$$

$$P_{\text{av}} = \tilde{V}\tilde{I}\cos\theta$$

$$Q = \tilde{V}\tilde{I}\sin\theta$$

FIGURE 5.5.2 The complex power triangle.

Power Factor, Revisited

The power factor, defined earlier as the cosine of the angle of the load impedance, plays a very important role in AC power. A power factor close to unity signifies an efficient transfer from the AC source to the load, while a small power factor corresponds to inefficient use of energy. It should be apparent that if a load requires a fixed amount of real power, *P*, the source will be providing the smallest amount of current when the power factor is the greatest, that is, when $\cos\theta = 1$. If the power factor is less than unity, some additional current will be drawn from the source, lowering the efficiency of power transfer from the source to the load. However, it will be shown shortly that it is possible to correct the power factor of a load by adding an appropriate reactive component to the load itself.

Since the reactive power, *Q*, is related to the reactive part of the load, its sign depends on whether the load reactance in inductive or capacitive. This leads to the following important statement:

> If the load has an inductive reactance, then θ is positive and the current *lags* (or *follows*) the voltage. Thus, when θ and *Q* are positive, the corresponding power factor is termed *lagging*. Conversely, a capacitive load will have a negative *Q*, and hence a negative θ. This corresponds to a *leading* power factor, meaning that the load current *leads* the load voltage.

Table 5.5.2 illustrates the concept and summarizes all of the important points so far. In the table, the phasor voltage *V* has a zero phase angle and the current phasor is referenced to the phase of *V*.

The distinction between leading and lagging power factors made in Table 5.5.2 is important because it corresponds to opposite signs of the reactive power: *Q* is positive if the load is inductive ($\theta > 0$) and the power factor is lagging: *Q* is negative if the load is capacitive and the power factor is leading ($\theta < 0$). It is therefore possible to improve the power factor of a load according to a procedure called **power factor correction** — that is, by placing a suitable reactance in parallel with the load so that the reactive power component generated by the additional reactance is of opposite sign to the original load reactive power. Most often the need is to improve the power factor of an inductive load because many common industrial loads consist of electric motors, which are predominantly inductive loads. This improvement may be accomplished by placing a capacitance in parallel with the load. The following example illustrates a typical power factor correction for an industrial load.

TABLE 5.5.2 Important Facts Related to Complex Power

	Resistive load	**Capacitive load**	**Inductive load**
Ohm's law	$\mathbf{V}_L = Z_L\mathbf{I}_L$	$\mathbf{V}_L = Z_L\mathbf{I}_L$	$\mathbf{V}_L = Z_L\mathbf{I}_L$
Complex impedance	$Z_L = R_L$	$Z_L = R_L - jX_L$	$Z_L = R_L + jX_L$
Phase angle	$\theta_V - \theta_I = \theta = 0$	$\theta_V - \theta_I = \theta < 0$	$\theta_V - \theta_I = \theta > 0$
Complex plane sketch	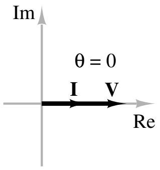	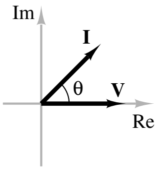	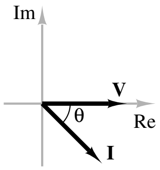
Explanation	The current is in phase with the voltage.	The current "leads" the voltage.	The current "lags" the voltage.
Power factor	Unity	Leading, < 1	Lagging, < 1
Reactive power	0	Negative	Positive

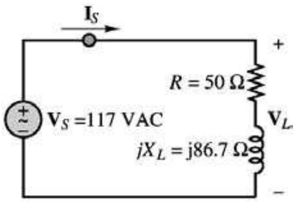

FIGURE 5.5.3 Circuit for Example 5.5.1.

Example 5.5.1

For the circuit shown in Figure 5.5.3:

1. Calculate the complex power for the load.
2. Correct the power factor by adding a suitable reactance in parallel with the load.

Solution.

1. The circuit of Figure 5.5.4 is an inductive load. The total impedance is

$$Z = R + jX_L = 50 + j86.7\ \Omega = 100\angle 60^\circ$$

The power factor is then

$$\text{pf} = \cos\theta = \cos 60^\circ = 0.5\ (\text{lagging})$$

The current drawn from the source by the load is

$$\mathbf{I}_S = \frac{\mathbf{V}_S}{Z} = \frac{117\angle 0^\circ}{100\angle 60^\circ} = 1.17\angle -60^\circ$$

and the average power is found to be

$$P = \tilde{V}_S \tilde{I}_S \cos\theta = 117 \times 1.17 \cos 60^\circ = 68.4\ \text{W}$$

while the reactive power is

$$Q_L = \tilde{V}_S \tilde{I}_S \sin\theta = 117 \times 1.17 \sin 60^\circ = 119\ \text{VAR}$$

Figure 5.5 shows the power triangle for the circuit.

2. The unity power factor for the circuit can be obtained by simply reducing the power factor angle θ to 0°. This can be accomplished by adding a capacitor to the circuit that requires –119 VAR of reactive power. The capacitive power and the inductive power will then cancel each other in the power triangle, resulting in a unity power factor, as shown in Figure 5.5.5.

   The value of capacitive reactance, X_c, required to cancel the reactive power due to the inductance is found most easily by observing that the total reactive power in the circuit must be the sum of the reactive power due to the capacitance and that due to the inductance. Observing that the capacitor sees the same voltage as the RL load, because of the parallel connection, we can write

$$X_C = \frac{\tilde{V}_S^2}{Q_C} = \frac{117^2}{119} 115\ \Omega$$

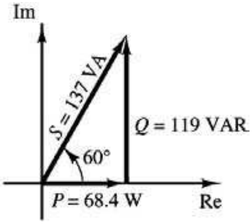

FIGURE 5.5.4 Power triangle for the circuit.

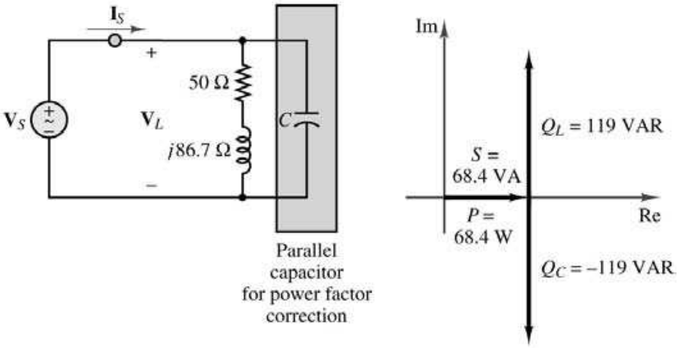

FIGURE 5.5.5 Power factor correction.

From the expression for the reactance, it is then possible to compute the value of the capacitor that will cancel the reactive power due to the inductor:

$$C = \frac{1}{\omega X_C} = \frac{1}{377 \times 115} = 23.1\ \mu\text{F}$$

The reactive component of power needed by the inductance is now balanced by the capacitance, and all the power delivered by the source is real power. The power factor is 1.

Example 5.5.2

The instrument used to measure power is called a *wattmeter.* The external part of a wattmeter consists of four connections and a metering mechanism that displays the amount of real power dissipated by a circuit. The external and internal appearances of a wattmeter are depicted in Figure 5.5.6. Inside the wattmeter are two coils: a current-sensing coil and a voltage-sensing coil. In this example, we assume for simplicity that the impedance of the current-sensing coil, C_I, is zero and the impedance of the voltage-sensing coil, C_V, is infinite. In practice, this will not necessarily be true; some correction mechanism will be required to account for the impedance of the sensing coils.

A wattmeter should be connected as shown in Figure 5.5.7, to provide both current and voltage measurements. We see that the current-sensing coil is placed in series with the load and the voltage-sensing coil is placed in parallel with the load. In this manner, the wattmeter is seeing the current through and the voltage across the load. Remember that the power dissipated by a circuit element is related to these two quantities. The wattmeter, then, is constructed to provide a readout of the product of the rms values of the load current and the voltage, which is the real power absorbed by the load: $P = \text{Re}\ (\text{S}) = \text{Re}\ (\mathbf{VI}^*)$.

1. For the circuit shown in Figure 5.5.8, show the connections of the wattmeter, and find the power dissipated by the load.
2. Show the connections that will determine the power dissipated by R_2. What should the meter read?

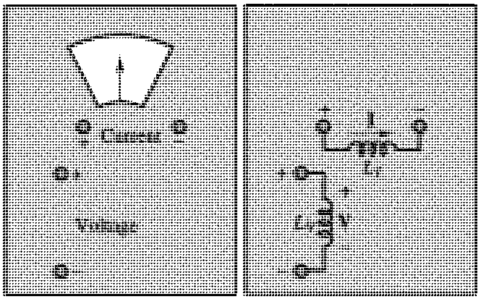

External connections

Wattmeter coils (inside)

FIGURE 5.5.6 Wattmeter.

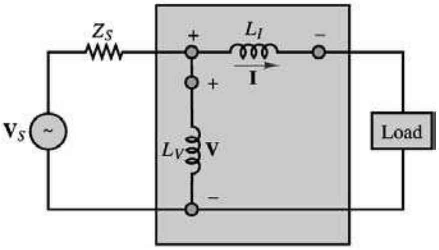

FIGURE 5.5.7 Circuit for Example 5.5.2.

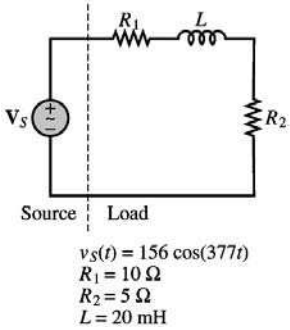

FIGURE 5.5.8 Circuit for Example 5.5.2.

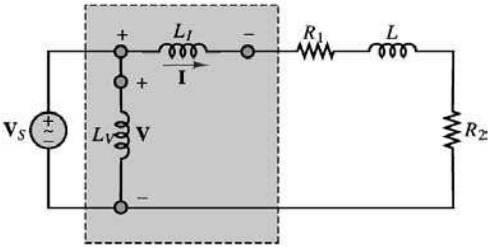

FIGURE 5.5.9 Circuit for Example 5.5.2.

Solution.

1. To measure the power dissipated by the load, we must know the current through and the voltage across the entire load circuit. This means that the wattmeter must be connected as shown in Figure 5.5.9. The wattmeter should read:

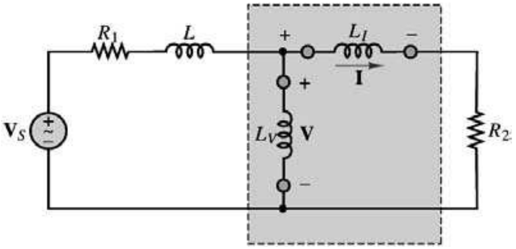

FIGURE 5.5.10 Circuit for Example 5.5.2.

$$
\begin{aligned}
P &= \mathrm{Re}\left(\mathbf{V}_S\mathbf{I}^*\right) \\
&= \mathrm{Re}\left\{\left(\frac{156}{\sqrt{2}}\angle 0^\circ\right)\left(\frac{\frac{156}{\sqrt{2}}\angle 0^\circ}{R_1 + R_2 + j\omega L}\right)^*\right\} \\
&= \mathrm{Re}\left\{110\angle 0^\circ\left(\frac{110\angle 0^\circ}{15 + j7.54}\right)^*\right\}
\end{aligned}
$$

$$
\begin{aligned}
\mathrm{Re}\left\{110\angle 0^\circ\left(\frac{110\angle 0^\circ}{16.79\angle 26.69^\circ}\right)^*\right\} &= \mathrm{Re}\left(\frac{110^2}{16.79\angle -26.69^\circ}\right) \\
&= \mathrm{Re}(720.67\angle 26.69^\circ) \\
&= 643.88 \text{ W}
\end{aligned}
$$

2. To measure the power dissipated by R_2 alone, we must measure the current through R_2 and the voltage across R_2 *alone*. The connection is shown in Figure 5.5.10. The meter will read:

$$
\begin{aligned}
P &= \tilde{I}^2 R_2 \\
&= \left(\frac{110}{\left(15^2 + 7.54^2\right)^{1/2}}\right)^2 \times 5 \\
&= \left(\frac{110^2}{\left(15^2 + 7.54^2\right)}\right)^2 \times 5 = 215 \text{ W}
\end{aligned}
$$

The measurement and correction of the power factor for the load are an extremely important aspect of any engineering application in industry that requires the use of substantial quantities of electric power. In particular, industrial plants, construction sites, heavy machinery, and other heavy users of electric power must be aware of the power factor their loads present to the electric utility company. As was already observed, a low power factor results in greater current draw from the electric utility and in greater line losses. Thus, computations related to the power factor of complex loads are of great practical utility to any practicing engineer.

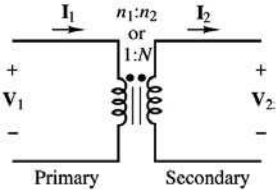

FIGURE 5.5.11 Ideal transformer.

Transformers

AC circuits are very commonly connected to each other by means of **transformers**. A transformer is a device that couples two AC circuits magnetically rather than through any direct conductive connection and permits a "transformation" of the voltage and current between one circuit and the other (for example, by matching a high-voltage, low-current AC output to a circuit requiring a low-voltage, high-current source). Transformers play a major role in electric power engineering and are a necessary part of the electric power distribution network. The objective of this section is to introduce the ideal transformer and the concepts of impedance reflection and impedance matching.

The Ideal Transformer

The ideal transformer consists of two coils that are coupled to each other by some magnetic medium. There is no electrical connection between the coils. The coil on the input side is termed the **primary**, and that on the output side the **secondary**. The primary coil is wound so that it has n_1 turns, while the secondary has n_2 turns. We define the **turns ratio** N as

$$N = \frac{n_2}{n_1} \tag{5.5.14}$$

Figure 5.5.11 illustrates the convention by which voltages and currents are usually assigned at a transformer. The dots in Figure 5.5.11 are related so the polarity of the coil voltage: coil terminals marked with a dot have the same polarity.

Since an ideal inductor acts as a short circuit in the presence of DC currents, transformers do not perform any useful function when the primary voltage is DC. However, when a time-varying current flows in the primary winding, a corresponding time-varying voltage is generated in the secondary because of the magnetic coupling between the two coils. This behavior is due to Faraday's law, as will be explained in Section 5.12. The relationship between primary and secondary current in an ideal transformer is very simply stated as follows:

$$\begin{aligned} \mathbf{V}_2 &= N\mathbf{V}_1 \\ \mathbf{I}_2 &= \frac{\mathbf{I}_1}{N} \end{aligned} \tag{5.5.15}$$

An ideal transformer multiplies a sinusoidal input voltage by a factor of N and divides a sinusoidal input current by a factor of N. If N is greater than 1, the output voltage is greater than the input voltage and the transformer is called a **step-up transformer**. If N is less than 1, then the transformer is called a **step-down transformer**, since V_2 is now smaller than V_1.

An ideal transformer can be used in either direction (i.e., either of its coils may be viewed as the input side or primary). Finally, a transformer with $N = 1$ is called an **isolation transformer** and may perform a very useful function if one needs to electrically isolate two circuits from each other; note that any DC currents at the primary will not appear at the secondary coil. An important property of ideal transformers is conservation of power; one can easily verify that an ideal transformer conserves power, since

$$S_1 = \mathbf{I}_1^*\mathbf{V}_1 = N\mathbf{I}_2^*\frac{\mathbf{V}_2}{N} = \mathbf{I}_2^*\mathbf{V}_2 = S_2 \tag{5.5.16}$$

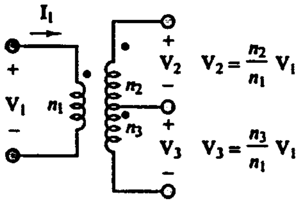

FIGURE 5.5.12 Center-tapped transformer.

That is, the power on the primary side equals that on the secondary.

In many practical circuits, the secondary is tapped at two different points, giving rise to two separate output circuits, as shown in Figure 5.5.12. The most common configuration is the **center-tapped transformer**, which splits the secondary voltage into two equal voltages of half the original amplitude. The most common occurrence of this type of transformer is found at the entry of a power line into a household, where the 240-VAC line is split into two 120-VAC lines (this may help explain why both 240- and 120-VAC power are present in your house).

Three-Phase Power

The material presented so far in this chapter has dealt exclusively with **single-phase AC power**, that is, with single sinusoidal sources. In fact, most of the AC power used today is generated and distributed as **three-phase power**, by means of an arrangement in which three sinusoidal voltages are generated out of phase with each other. The primary reason is efficiency: the weight of the conductors and other components in a three-phase system is much lower than in a single-phase system delivering the same amount of power. Further, while the power produced by a single-phase system has a pulsating nature, a three-phase system can deliver a steady, constant supply of power. A three-phase generator producing three **balanced voltages** — that is, voltages of equal amplitude and frequency displaced in phase by 120° — has the property of delivering constant instantaneous power.

Another important advantage of three-phase power is that, as will be explained in Section 5.12, three-phase motors have a nonzero starting torque, unlike their single-phase counterpart. The change to three-phase AC power system from the early DC system proposed by Edison was therefore due to a number of reasons: the efficiency resulting from transforming voltages up and down to minimize transmission losses over long distances; the ability to deliver constant power (an ability not shared by single- and two-phase AC systems); a more efficient use of conductors; and the ability to provide starting torque for industrial motors.

To begin the discussion of three-phase power, consider a three-phase source connected in the **wye** (or **Y**) **configuration**, as shown in Figure 5.5.13. Each of the three voltages is 120° out of phase with the others, so that, using phasor notation, we may write:

$$\begin{aligned} V_{an} &= \tilde{V}_{an}\angle 0^\circ \\ V_{bn} &= \tilde{V}_{bn}\angle -120^\circ \\ V_{cn} &= \tilde{V}_{cn}\angle -240^\circ = \tilde{V}_{cn}\angle 120^\circ \end{aligned} \tag{5.5.17}$$

where the quantities $\tilde{V}_{an}$, $\tilde{V}_{bn}$, and $\tilde{V}_{cn}$ are rms values and are equal to each other. To simplify the notation, it will be assumed from here on that

$$\tilde{V}_{an} = \tilde{V}_{bn} = \tilde{V}_{cn} = \tilde{V} \tag{5.5.18}$$

Section 5.12 will discuss how three-phase AC electric generators may be constructed to provide such balanced voltages. In the circuit of Figure 5.5.13, the resistive loads are also wye-connected and balanced

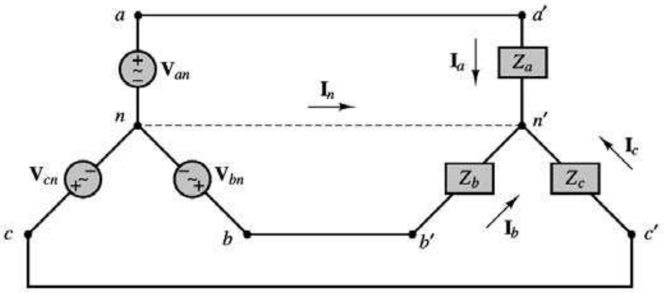

FIGURE 5.5.13 Balanced three-phase AC circuit.

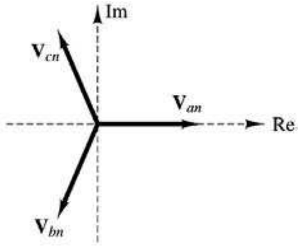

FIGURE 5.5.14 Positive, or *abc*, sequence for balanced three-phase voltages.

(i.e., equal). The three AC sources are all connected together at a node called the *neutral node*, denoted by *n*. The voltages $\tilde{V}_{an}$, $\tilde{V}_{bn}$, and $\tilde{V}_{cn}$ are called the *phase voltages* and form a balanced set in the sense that

$$\mathbf{V}_{an} + \mathbf{V}_{bn} + \mathbf{V}_{cn} = 0 \tag{5.5.19}$$

This last statement is easily verified by sketching the phasor diagram. The sequence of phasor voltages shown in Figure 5.5.14 is usually referred to as the **positive** (or *abc*) **sequence**.

Consider now the "lines" connecting each source to the load and observe that it is possible to also define **line voltages** (also called *line-to-line voltages*) by considering the voltages between the lines *aa′* and *bb′*, *aa′* and *cc′*, and *bb′* and *cc′*. Since the line voltage, say, between *aa′* and *bb′* is given by

$$\mathbf{V}_{ab} = \mathbf{V}_{an} + \mathbf{V}_{nb} = \mathbf{V}_{an} - \mathbf{V}_{bn} \tag{5.5.20}$$

the line voltages may be computed relative to the phase voltages as follows:

$$\begin{aligned} \mathbf{V}_{ab} &= \tilde{V}\angle 0° - \tilde{V}\angle -120° = \sqrt{3}\tilde{V}\angle 30° \\ \mathbf{V}_{bc} &= \tilde{V}\angle -120° - \tilde{V}\angle 120° = \sqrt{3}\tilde{V}\angle -90° \\ \mathbf{V}_{ca} &= \tilde{V}\angle 120° - \tilde{V}\angle 0° = \sqrt{3}\tilde{V}\angle 150° \end{aligned} \tag{5.5.21}$$

It can be seen, then, that the magnitude of the line voltages is equal to $\sqrt{3}$ times the magnitude of the phase voltages. It is instructive, at least once, to point out that the circuit of Figure 5.5.13 can be redrawn to have the appearance of the circuit of Figure 5.5.15.

One of the important features of a balanced three-phase system is that it does not require a fourth wire (the neutral connection), since the current $\mathbf{I}_n$ is identically zero (for balanced load $Z_a = Z_b = Z_c = Z$). Another, more important characteristic of a balanced three-phase power system is that the total power delivered to the balanced load by the three-phase generator is constant.

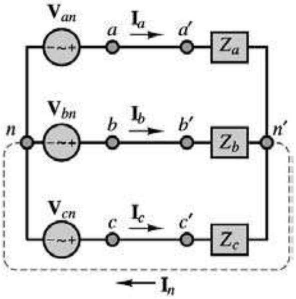

FIGURE 5.5.15 Balanced three-phase AC circuit (redrawn).

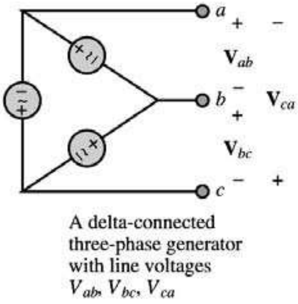

FIGURE 5.5.16 Delta-connected generators.

$$p(t) = p_a(t) + p_b(t) + p_c(t) = \frac{3\tilde{V}^2}{R}$$

It is also possible to connect the three AC sources in a three-phase system in a so-called **delta** (or Δ) **connection**, although in practice this configuration is rarely used. Figure 5.5.16 depicts a set of three delta-connected generators.

Balanced Wye Loads

Consider again the circuit of Figure 5.5.13, where now the balanced load consists of the three complex impedances

$$Z_a = Z_b = Z_c = Z_v = |Z_y|\angle\theta \tag{5.5.22}$$

From the diagram of Figure 5.5.13, it can be verified that each impedance sees the corresponding phase voltage across itself; thus, since the currents $\mathbf{I}_a$, $\mathbf{I}_b$, and $\mathbf{I}_c$ have the same rms value, $\tilde{I}$, the phase angles of the currents will differ by ±120°. It is therefore possible to compute the power for each phase by considering the phase voltage (equal to the load voltage) for each impedance, and the associated line current. Let us denote the complex power for each phase by S:

$$S = \mathbf{V} \cdot \mathbf{I}^* \tag{5.5.23}$$

so that

$$\begin{aligned} S &= P + jQ \\ &= \tilde{V}\tilde{I}\cos\theta + j\tilde{V}\tilde{I}\sin\theta \end{aligned} \tag{5.5.24}$$

where $\tilde{V}$ and $\tilde{I}$ denote, once again, the rms values of each phase voltage and line current. Consequently, the total real power delivered to the balanced wye load is $3P$, and the total reactive power is $3Q$. Thus, the total complex power, S_T, is given by

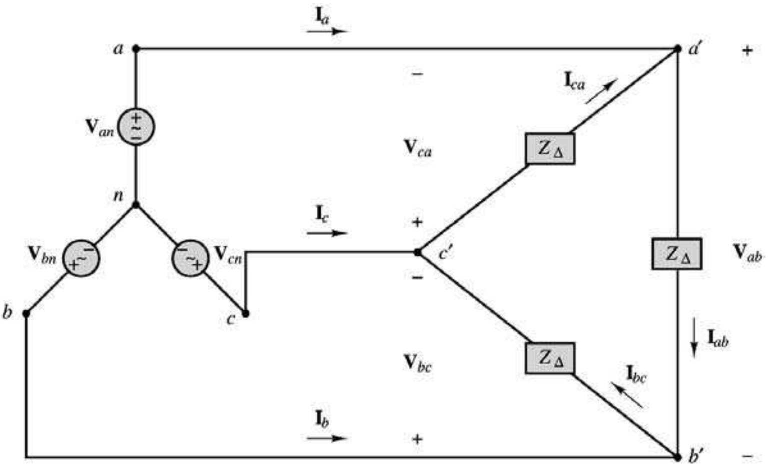

FIGURE 5.5.17 Balanced wye generators with balanced delta load.

$$
\begin{aligned}
S_T &= P_T + jQ_T = 3P + j3Q \\
&= \sqrt{(3P)^2 + (3Q)^2}\angle\theta
\end{aligned}
\tag{5.5.25}
$$

and the apparent power is

$$
\begin{aligned}
|S_T| &= 3\sqrt{(VI)^2\cos^2\theta + (VI)^2\sin^2\theta} \\
&= 3VI
\end{aligned}
$$

and the total real and reactive power may be expressed in terms of the apparent power:

$$
\begin{aligned}
P_T &= |S_T|\cos\theta \\
Q_T &= |S_T|\sin\theta
\end{aligned}
\tag{5.5.26}
$$

Balanced Delta Loads

In addition to a wye connection, it is also possible to connect a balanced load in the delta configuration. A wye-connected generator and a delta-connected load are shown in Figure 5.5.17.

It should be noted immediately that now the corresponding line voltage (not phase voltage) appears across each impedance. For example, the voltage across $Z_{c'a'}$ is $\mathbf{V}_{ca}$. Thus, the three load currents are given by the following expressions:

$$
\begin{aligned}
\mathbf{I}_{ab} &= \frac{\mathbf{V}_{ab}}{Z_\Delta} = \frac{\sqrt{3}V\angle 30^\circ}{|Z_\Delta|\angle\theta} \\
\mathbf{I}_{bc} &= \frac{\mathbf{V}_{bc}}{Z_\Delta} = \frac{\sqrt{3}V\angle -90^\circ}{|Z_\Delta|\angle\theta} \\
\mathbf{I}_{ca} &= \frac{\mathbf{V}_{ca}}{Z_\Delta} = \frac{\sqrt{3}V\angle 150^\circ}{|Z_\Delta|\angle\theta}
\end{aligned}
$$

One can readily verify that the two currents $(\mathbf{I}_a)_\Delta$ and $(\mathbf{I}_a)_y$ will be equal if the magnitude of the delta-connected impedance is three times larger than Z_y:

$$Z_\Delta = 3Z_y \tag{5.5.27}$$

This result also implies that a delta load will necessarily draw three times as much current (and therefore absorb three times as much power) as we wye load with the same branch impedance.

Generation and Distribution of AC Power

We now conclude the discussion of power systems with a brief description of the various elements of a power system. Electric power originates from a variety of sources; in Section 5.12, electric generators will be introduced as a means of producing electric power from a variety of energy-conversion processes. In general, electric power may be obtained from hydroelectric, thermoelectric, geothermal, wind, solar, and nuclear sources. The choice of a given source is typically dictated by the power requirement for the given application and by economic and environmental factors. In this section, the structure of an AC power network, from the power-generating station to the residential circuits discussed in the previous section, is briefly outlined.

A typical generator will produce electric power at 18 kV, as shown in the diagram of Figure 5.5.18. To minimize losses along the conductors, the output of the generators is processed through a step-up transformer to achieve line voltages of hundreds of kilovolts. Without this transformation, the majority of the power generated would be lost in the **transmission lines** that carry the electric current from the power station.

The local electric company operates a power-generating plant that is capable of supplying several hundred megavolt-amperes (MVA) on a three-phase basis. For this reason, the power company uses a three-phase step-up transformer at the generation plant to increase the line voltage to around 345 kV. One can immediately see that at the rated power of the generator (in MVA) there will be a significant reduction of current beyond the step-up transformer.

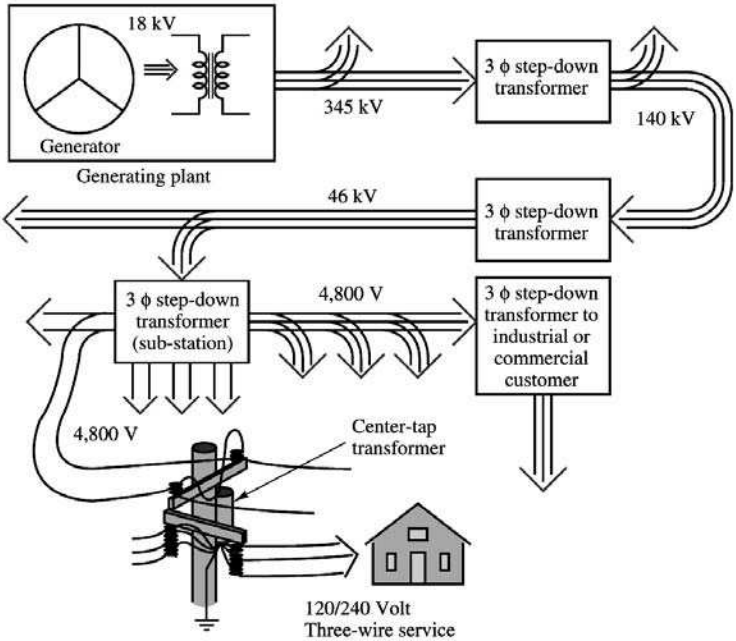

FIGURE 5.5.18 Structure of an AC power distribution network.

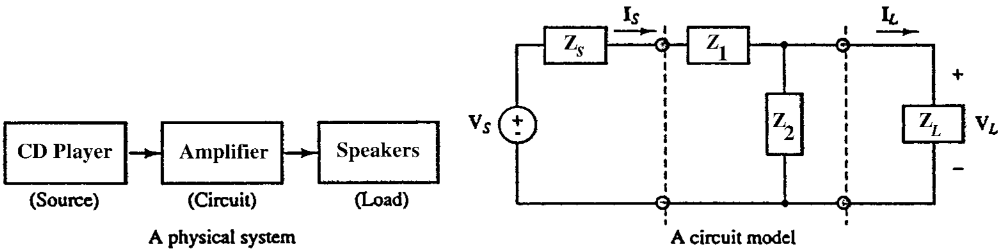

FIGURE 5.6.1 A circuit model.

Beyond the generation plant, an electric power network distributes energy to several **substations**. This network is usually referred to as the **power grid**. At the substations, the voltage is stepped down to a lower level (10 to 150 kV, typically). Some very large loads (for example, an industrial plant) may be served directly from the power grid, although most loads are supplied by individual substations in the power grid. At the local substations (one of which you may have seen in your own neighborhood), the voltage is stepped down further by a three-phase step-down transformer to 4800 V. These substations distribute the energy to residential and industrial customers. To further reduce the line voltage to levels that are safe for residential use, step-down transformers are mounted on utility poles. These drop the voltage to the 120/240-V three-wire single-phase residential service discussed in the previous section. Industrial and commercial customers receive 460- and/or 208-V three-phase service.

5.6 Frequency Response, Filters, and Transient Analysis

The aim of the present section is twofold: first, to exploit AC circuit analysis methods to study the frequency response of electric circuits; and second, to continue the discussion of dynamic circuit equations for the purpose of analyzing the transient response of electrical circuits.

The **sinusoidal frequency response** (or, simply, **frequency response**) of a circuit provides a measure of how the circuit responds to sinusoidal inputs of arbitrary frequency. In other words, given the input signal amplitude, phase, and frequency, knowledge of the frequency response of a circuit permits the computation of the output signal.

The frequency response of a circuit is a measure of the variation of a load-related voltage or current as a function of the amplitude, phase, and frequency of the excitation signal.

To express the frequency response of a circuit in terms of variation in output voltage as a function of source voltage, we use the general formula

$$H_V(j\omega) = \frac{\mathbf{V}_L(j\omega)}{\mathbf{V}_S(j\omega)} \tag{5.6.1}$$

One method that allows for representation of the load voltage as a function of the source voltage (this is, in effect, what the frequency response of a circuit implies) is to describe the source and attached circuit by means of the Thévenin equivalent circuit. The frequency response of the circuit shown in Figure 5.6.1 is given by the expression

$$\frac{\mathbf{V}_L}{\mathbf{V}_S}(j\omega) = H_V(j\omega) = \frac{Z_L Z_2}{Z_L\left(Z_S + Z_1 + Z_2\right) + \left(Z_S + Z_1\right)Z_2} \tag{5.6.2}$$

The expression for $H_V(j\omega)$ could be evaluated for any given $\mathbf{V}_S(j\omega)$ (i.e., for any given source signal amplitude, phase, and frequency) to determine what the resultant load voltage would be. Note that $H_V(j\omega)$

is a complex quantity (dimensionless, because it is the ratio of two voltages), and that it therefore follows that $\mathbf{V}_L(j\omega)$ is a phase-shifted and amplitude-scaled version of $\mathbf{V}_S(j\omega)$:

$$\mathbf{V}_L(j\omega) = H_V(j\omega) \cdot \mathbf{V}_S(j\omega) \tag{5.6.3}$$

$$V_L e^{j\phi_L} = \left|H_V\right| e^{j\phi_H} \cdot V_S e^{j\phi_S} \tag{5.6.4}$$

or

$$V_L e^{j\phi_L} = \left|H_V\right| \mathbf{V}_S\, e^{j(\phi_H + \phi_S)} \tag{5.6.5}$$

where

$$V_L = \left|H_V\right| \cdot V_S$$

and

$$\phi_L = \phi_H + \phi_S \tag{5.6.6}$$

The effect of inserting a linear circuit between a source and a load is best understood by considering that, at any given frequency, ω, the load voltage is a sinusoid at the same frequency as the source voltage, with amplitude given by $V_L = |H_V| \cdot V_S$ and phase equal to $\phi_L = \phi_H + \phi_S$, where $|H_V|$ is the magnitude of the frequency response and ϕ_H its phase angle. Both $|H_V|$ and ϕ_H are functions of frequency.

The importance and usefulness of the frequency response concept lies in its ability to summarize the response of a circuit in a single function of frequency, $H(j\omega)$, which can predict the load voltage or current at any frequency, given the input. Note that the frequency response of a circuit can be defined in four different ways:

$$\begin{aligned} H_V(j\omega) &= \frac{\mathbf{V}_L(j\omega)}{\mathbf{V}_S(j\omega)} \qquad & H_I(j\omega) &= \frac{\mathbf{I}_L(j\omega)}{\mathbf{I}_S(j\omega)} \\ H_Z(j\omega) &= \frac{\mathbf{V}_L(j\omega)}{\mathbf{I}_S(j\omega)} \qquad & H_Y(j\omega) &= \frac{\mathbf{I}_L(j\omega)}{\mathbf{V}_S(j\omega)} \end{aligned} \tag{5.6.7}$$

If $H_V(j\omega)$ and $H_I(j\omega)$ are known, one can directly derive the other two expressions:

$$H_Z(j\omega) = \frac{\mathbf{V}_L(j\omega)}{\mathbf{I}_S(j\omega)} = Z_L(j\omega)\frac{\mathbf{I}_L(j\omega)}{\mathbf{I}_S(j\omega)} = Z_L(j\omega)H_I(j\omega) \tag{5.6.8}$$

$$H_Y(j\omega) = \frac{\mathbf{I}_L(j\omega)}{\mathbf{V}_S(j\omega)} = \frac{1}{Z_L(j\omega)}\frac{\mathbf{V}_L(j\omega)}{\mathbf{V}_S(j\omega)} = \frac{1}{Z_L(j\omega)}H_V(j\omega) \tag{5.6.9}$$

With these definitions in hand, it is now possible to introduce one of the central concepts of electrical circuit analysis: **filters.** The concept of filtering an electrical signal will be discussed in the next section.

Filters

There are a host of practical, everyday applications that involve filters of one kind or another. Just to mention two, filtration systems are used to eliminate impurities from drinking water, and sunglasses are used to filter out eye-damaging ultraviolet radiation and to reduce the intensity of sunlight reaching the eyes. An analogous concept applies to electrical circuits: it is possible to *attenuate* (i.e., reduce in amplitude) or altogether eliminate signals of unwanted frequencies, such as those that may be caused by electrical noise or other forms of interference. This section will be devoted to the analysis of electrical filters.

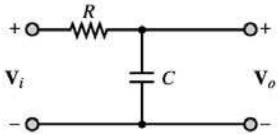

RC low-pass filter. The circuit preserves lower frequencies while attenuating the frequencies above the cutoff frequency, $\omega_0 = 1/RC$. The voltages V_i and V_0 are the filter input and output voltages respectively.

FIGURE 5.6.2 A simple RC filter.

Low-Pass Filters

Figure 5.6.2 depicts a simple **RC filter** and denotes its input and output voltages by $\mathbf{V}_i$ and $\mathbf{V}_o$. The frequency response for the filter may be obtained by considering the function.

$$H(j\omega) = \frac{\mathbf{V}_o}{\mathbf{V}_i}(j\omega) \tag{5.6.10}$$

and noting that the output voltage may be expressed as a function of the input voltage by means of a voltage divider, as follows:

$$\mathbf{V}_o(j\omega) = \mathbf{V}_i(j\omega)\frac{1/j\omega C}{R + 1/j\omega C} = \mathbf{V}_i(j\omega)\frac{1}{1 + j\omega RC} \tag{5.6.11}$$

$$H(j\omega) = \frac{\mathbf{V}_o}{\mathbf{V}_i}(j\omega) = \frac{1}{1 + j\omega CR}$$

or

$$H(j\omega) = \left|H(j\omega)\right| e^{j\phi_H(j\omega)} \tag{5.6.12}$$

with

$$\left|H(j\omega)\right| = \frac{1}{\sqrt{1 + (\omega CR)^2}} = \frac{1}{\sqrt{1 + \left(\omega/\omega_0\right)^2}} \tag{5.6.13}$$

and

$$\phi_H(j\omega) = -\arctan(\omega CR) = -\arctan\left(\frac{\omega}{\omega_0}\right) \tag{5.6.14}$$

with

$$\omega_0 = \frac{1}{RC} \tag{5.6.15}$$

The simplest way to envision the effect of the filter is to think of the phasor voltage $\mathbf{V}_i = V_i e^{j\phi_i}$ scaled by a factor of |**H**| and shifted by a phase angle ϕ_H by the filter *at each frequency*, so that the resultant output is given by the phasor $V_o e^{j\phi_o}$, with

$$\begin{aligned} V_o &= |H| \cdot V_i \\ \phi_o &= \phi_H + \phi_i \end{aligned} \tag{5.6.16}$$

and where $|H|$ and ϕ_H are functions of frequency. The frequency ω_0 is called the **cutoff frequency** of the filter and, as will presently be shown, gives an indication of the filtering characteristics of the circuit.

It is customary to represent $H(j\omega)$ in two separate plots, representing $|H|$ and ϕ_H as functions of ω. These are shown in Figure 5.6.3 in normalized form — that is, with $|H|$ and ϕ_H plotted vs. ω/ω_0, corresponding to a cutoff frequency $\omega_0 = 1$ rad/sec. Note that, in the plot, the frequency axis has been scaled logarithmically. This is a common practice in electrical engineering, because it allows viewing a very broad range of frequencies on the same plot without excessively compressing the low-frequency end of the plot. The frequency response plots of Figure 5.6.3 are commonly employed to describe the frequency response of a circuit, since they can provide a clear idea at a glance of the effect of a filter on an excitation signal. For example, the *RC* filter of Figure 5.6.2 has the property of "passing" signals at low frequencies ($\omega \ll 1/RC$) and of filtering out signals at high frequencies ($\omega \gg 1/RC$). This type of filter is called a **low-pass filter**. The cutoff frequency $\omega = 1/RC$ has a special significance in that it represents — approximately — the point where the filter begins to filter out the higher-frequency signals. The value of $H(j\omega)$ at the cutoff frequency is $1/\sqrt{2} = 0.707$. Note how the cutoff frequency depends exclusively on the values of *R* and *C*. Therefore, one can adjust the filter response as desired simply by selecting appropriate values for *C* and *R*, and therefore choose the desired filtering characteristics.

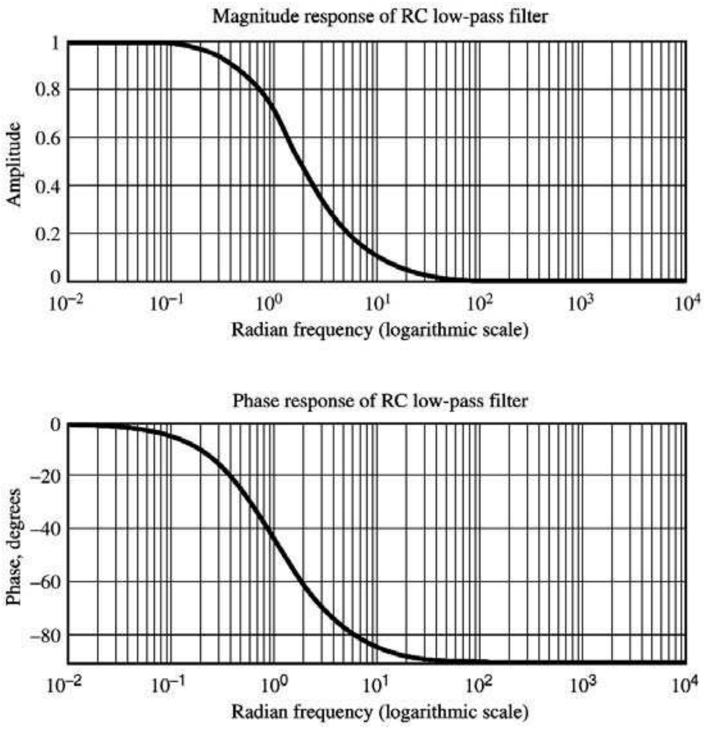

FIGURE 5.6.3 Magnitude and phase response plots for *RC* filter.

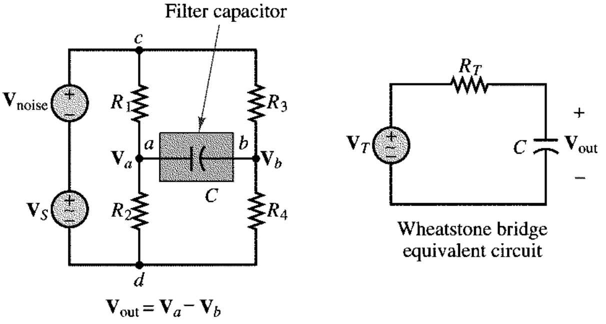

FIGURE 5.6.4 Wheatstone bridge with equivalent circuit and simple capacitive filter.

Example 5.6.1 Wheatstone Bridge Filter

The Wheatstone bridge circuit is used in a number of instrumentation applications, including the measurement of force (see Example 5.6.2, describing the strain gauge bridge). Figure 5.6.4 depicts the appearance of the bridge circuit. When undesired noise and interference are present in a measurement, it is often appropriate to use a low-pass filter to reduce the effect of the noise. The capacitor that is connected to the output terminals of the bridge in Figure 5.6.4 constitutes an effective and simple low-pass filter, in conjunction with the bridge resistance. Assume that the average resistance of each leg of the bridge is 350 Ω (a standard value for strain gauges) and that we desire to measure a sinusoidal force at a frequency of 30 Hz. From prior measurements, it has been determined that a filter with a cutoff frequency of 300 Hz is sufficient to reduce the effects of noise. Choose a capacitor that matches this filtering requirement.

Solution. By evaluating the Thévenin equivalent circuit for the Wheatstone bridge, calculating the desired value for the filter capacitor becomes relatively simple, as illustrated at the bottom of Figure 5.6.4. The Thévenin resistance for the bridge circuit may be computed by short-circuiting the two voltage sources and removing the capacitor placed across the load terminals:

$$R_T = R_1 \| R_2 + R_3 \| R_4 = 350 \| 350 + 350 \| 350 = 350\ \Omega$$

Since the required cutoff frequency is 300 Hz, the capacitor value can be computed from the expression

$$\omega_0 = \frac{1}{R_T C} = 2\pi \times 300$$

or

$$C = \frac{1}{R_T \omega_0} = \frac{1}{350 \times 2\pi \times 300} = 1.51\ \mu\text{F}$$

The frequency response of the bridge circuit is of the form

$$\frac{\mathbf{V}_{\text{out}}}{\mathbf{V}_T}(j\omega) = \frac{1}{1 + j\omega C R_T}$$

This response can be evaluated at the frequency of 30 Hz to verify that the attenuation and phase shift at the desired signal frequency are minimal:

$$\frac{\mathbf{V}_{\text{out}}}{\mathbf{V}_T}(j\omega = j2\pi \times 30) = \frac{1}{1 + j2\pi \times 30 \times 1.51 \times 10^{-6} \times 350}$$

$$= 0.9951\angle -5.7°$$

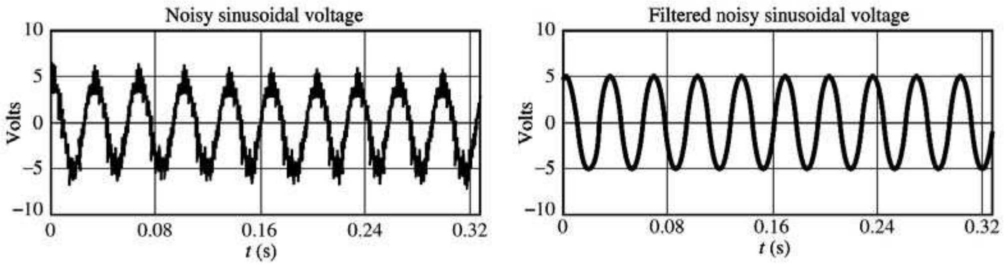

FIGURE 5.6.5 Unfiltered and filtered bridge output.

Figure 5.6.5 depicts the appearance of a 30-Hz sinusoidal signal before and after the addition of the capacitor to the circuit.

High-Pass Filters

Just as you can construct a simple filter that preserves low frequencies and attenuates higher frequencies, you can easily construct a **high-pass filter** that passes mainly those frequencies *above a certain cutoff frequency*. The analysis of a simple high-pass filter can be conducted by analogy with the preceding discussion of the low-pass filter. Consider the circuit shown in Figure 5.6.6.

The frequency response of the filter is

$$\frac{\mathbf{V}_o}{\mathbf{V}_i}(j\omega) = \frac{j\omega CR}{1 + j\omega CR}$$

or

$$H(j\omega) = |H| e^{j\phi_H}$$

with

$$H(j\omega) = \frac{\omega CR}{\sqrt{1 + (\omega CR)^2}}$$

$$\phi_H(j\omega) = 90° - \arctan(\omega CR)$$

Amplitude-and-phase response curves for the high-pass filter are shown in Figure 5.6.7. These plots have been normalized to have the filter cutoff frequency $\omega_0 = 1$ rad/sec. Note that, once again, it is possible to define a cutoff frequency at $\omega_0 = 1/RC$ in the same way as was done for the low-pass filter.

Band-Pass Filters

Building on the principles developed in the preceding sections, we can also construct a circuit that acts as a **band-pass filter**, passing mainly those frequencies *within a certain frequency range*. The analysis of

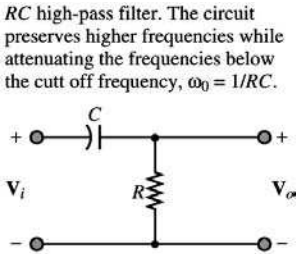

FIGURE 5.6.6 High-pass filter.

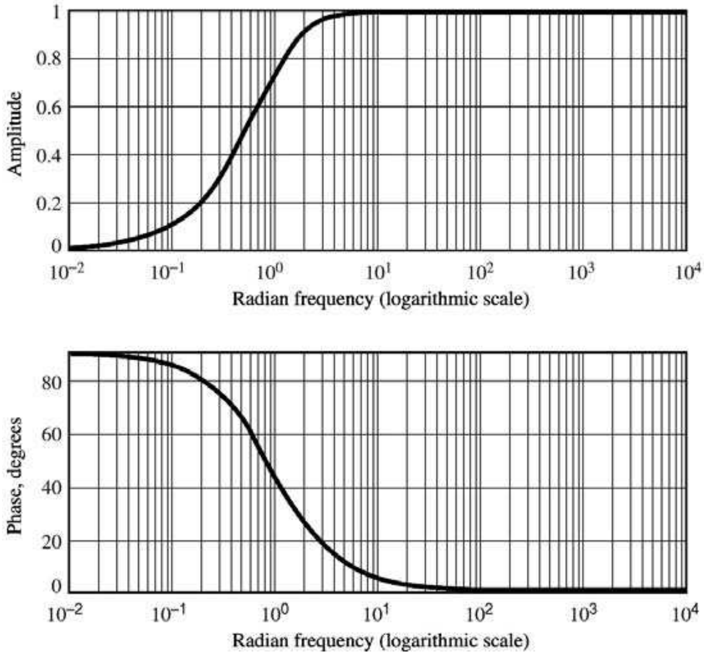

FIGURE 5.6.7 Frequency response of a high-pass filter.

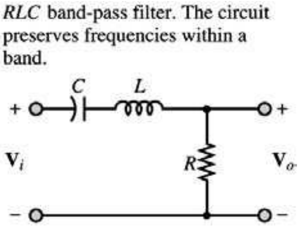
RLC band-pass filter. The circuit preserves frequencies within a band.

FIGURE 5.6.8 *RLC* band-pass filter.

a simple *second-order* band-pass filter (i.e., a filter with two energy-storage elements) can be conducted by analogy with the preceding discussions of the low-pass and high-pass filters. Consider the circuit shown in Figure 5.6.8, and the related frequency response function for the filter $H(j\omega) = (\mathbf{V}_o/\mathbf{V}_i)(j\omega)$.

We may write the frequency response of the filter as

$$\frac{\mathbf{V}_o}{\mathbf{V}_i}(j\omega) = \frac{j\omega CR}{1 + j\omega CR + (j\omega)^2 LC} \tag{5.6.17}$$

Equation (5.6.17) can often be factored into the following form:

$$\frac{\mathbf{V}_o}{\mathbf{V}_i}(j\omega) = \frac{jA\omega}{(j\omega/\omega_1 + 1)(j\omega/\omega_2 + 1)} \tag{5.6.18}$$

where ω_1 and ω_2 are the two frequencies that determine the **pass-band** (or **band-width**) of the filter — that is, the frequency over which the filter "passes" the input signal. The magnitude and phase plots for the frequency response of the band-pass filter of Figure 5.6.8 are shown in Figure 5.6.9. These plots have been normalized to have the filter pass-band centered at the frequency $\omega = 1$ rad/sec.

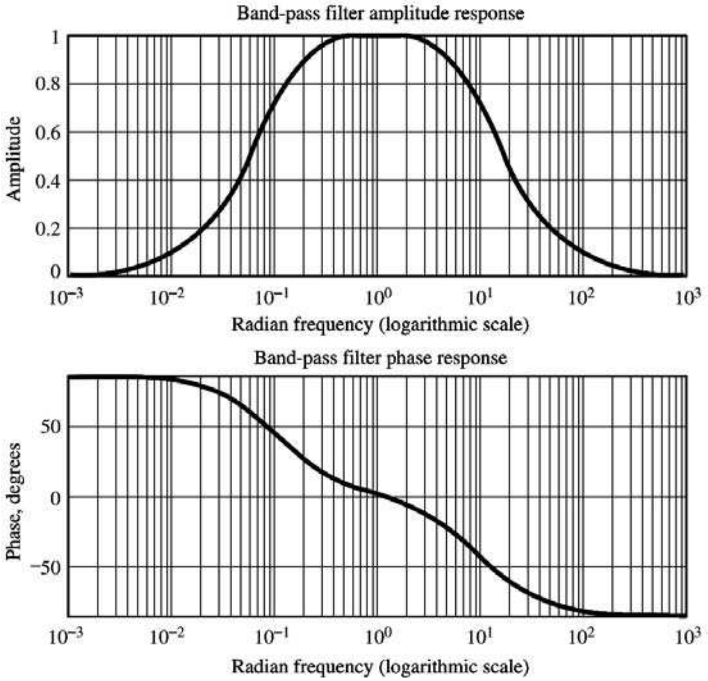

FIGURE 5.6.9 Frequency response of *RLC* band-pass filter.

The expression for the frequency response of a second-order band-pass filter (Equation (5.6.17)) can also be rearranged to illustrate two important features of this circuit: the **quality factor**, Q, and the **resonant frequency**, ω_0. Let

$$\omega_0 = \frac{1}{\sqrt{LC}} \quad \text{and} \quad Q = \omega_0 CR = \frac{R}{\omega_0 L} \tag{5.6.19}$$

Then we can write $\omega CR = \omega_0 CR(\omega/\omega_0) = Q(\omega/\omega_0)$ and rearrange Equation 5.6.18 as follows:

$$\frac{\mathbf{V}_o}{\mathbf{V}_i}(j\omega) = \frac{jQ\dfrac{\omega}{\omega_0}}{\left(\dfrac{j\omega}{\omega_0}\right)^2 + jQ\dfrac{\omega}{\omega_0} + 1} \tag{5.6.20}$$

In Equation (5.6.20), the resonant frequency, ω_0, corresponds to the center frequency of the filter, while Q, the quality factor, indicates the *sharpness* of the resonance, that is, how narrow or wide the shape of the pass-band of the filter is. The width of the pass-band is also referred to as the *bandwidth*, and it can easily be shown that the bandwidth of the filter is given by the expression

$$B = \frac{\omega_0}{Q} \tag{5.6.21}$$

Thus, a high-Q filter has a narrow bandwidth, while a low-Q filter has a large bandwidth and is therefore less selective. The quality factor of a filter provides an immediate indication of the nature of the filter.

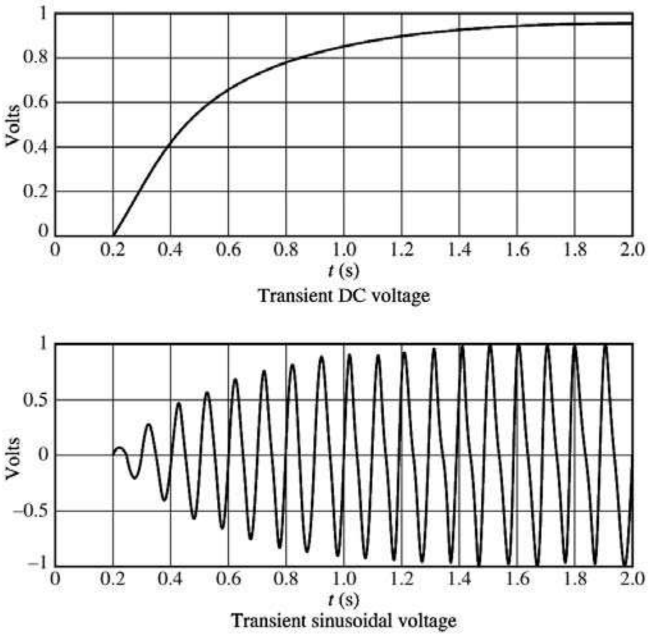

FIGURE 5.6.10 Examples of transient response.

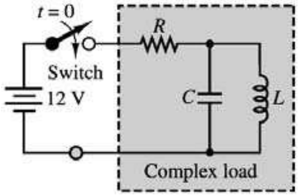

FIGURE 5.6.11 Circuit with switched DC excitation.

Transient Analysis

In analyzing the frequency response of AC circuits earlier in this chapter, we made the assumption that the particular form of the voltages and currents in the circuit was sinusoidal.

There are many signals, however, for which the steady-state sinusoidal representation is not adequate. In particular, the sinusoidal, or AC method of analysis does not apply to **transient signals**, that is, voltages and currents that vary as a function of time as a consequence of a sudden change in the input. Figure 5.6.10 illustrates the appearance of the voltage across some hypothetical load when a DC and an AC source, respectively, are abruptly switched on at time $t = 2$ sec. The waveforms in Figure 5.6.10 can be subdivided into three regions: a *steady-state region* for $0 \le t \le 0.2$ sec; a *transient region*, for 0.2 sec $\le t \le$ 2 sec (approximately); and a new steady-state region for $t > 2$ sec, where the waveform reaches a new steady-state DC or sinusoidal condition. The objective of **transient analysis** is to describe the behavior of a voltage or current during the transition that takes place between two different steady-state conditions.

You already know how to analyze circuits in a sinusoidal steady state by means of phasors. The material presented in the remainder of this chapter will provide the tools necessary to describe the *transient response* of circuits containing resistors, inductors, and capacitors. A general example of the type of circuit that will be discussed in this section is shown in Figure 5.6.11. The switch indicates that we turn the battery power on at time $t = 0$. Transient behavior may be expected whenever a source of electrical energy is switched on or off, whether it be AC or DC. A typical example of the transient response to a switched DC voltage would be what occurs when the ignition circuits in an automobile are turned on, so that a

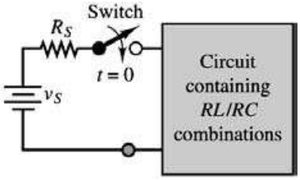

FIGURE 5.6.12 A general model of the transient analysis problem.

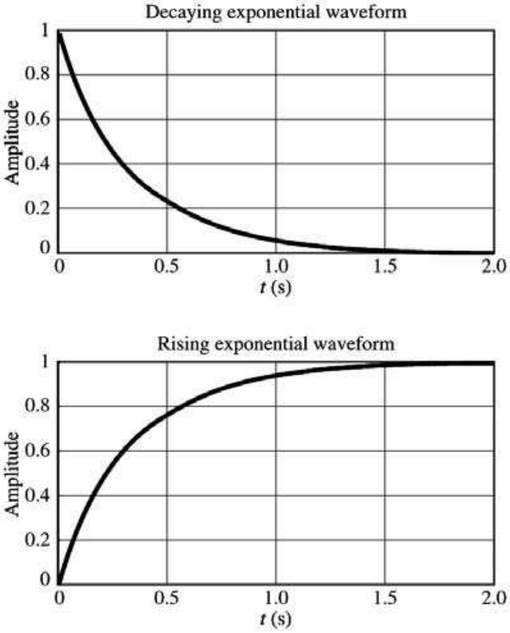

FIGURE 5.6.13 Decaying and rising exponential responses.

12-V battery is suddenly connected to a large number of electrical circuits. The degree of complexity in transient analysis depends on the number of energy-stored elements in the circuit; the analysis can become quite involved for high-order circuits. In this chapter, we shall analyze only first- and second-order circuits — that is, circuits containing one or two energy-storage elements, respectively. In electrical engineering practice, we would typically resort to computer-aided analysis for higher-order circuits.

A convenient starting point in approaching the transient response of electrical circuits is to consider the general model shown in Figure 5.6.12, where the circuits in the box consist of a combination of resistors connected to a *single energy-storage element*, either an inductor or a capacitor. Regardless of how many resistors the circuit contains, it is a **first-order circuit**. In general, the response of a first-order circuit to a switched DC source will appear in one of the two forms shown in Figure 5.6.13 which represent, in order, a **decaying exponential** and a **rising exponential** waveform. In the next sections, we will systematically analyze these responses by recognizing that they are exponential in nature and can be computed very easily once we have the proper form of the differential equation describing the circuit.

Example 5.6.2 Pulse Response

A problem of great practical importance is the transmission of voltage *pulses* along cables. Short voltage pulses are used to represent the two-level binary signals that are characteristic of digital computers; it is often necessary to transmit such voltage pulses over a long distance through **coaxial cables**, which are characterized by a finite resistance per unit length and by a certain capacitance per unit length, usually expressed in units of pF/m. A simplified model of a long coaxial cable is shown in Figure 5.6.14. It has the appearance of a low-pass filter. If a 100-m cable has a capacitance of 40 pF/m and a series resistance

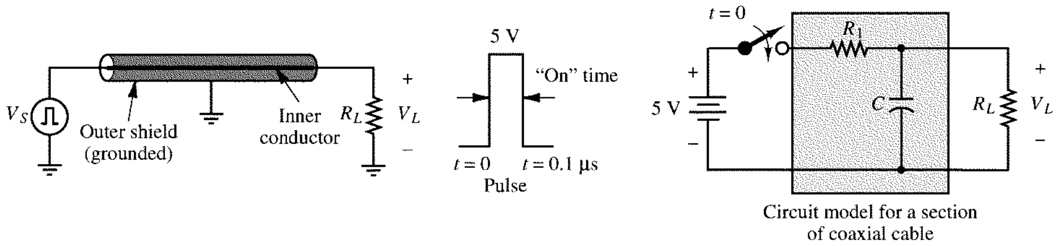

FIGURE 5.6.14 Pulse transmission in a coaxial cable.

of 0.2 Ω/m, what will the output pulse look like after traveling the length of the cable? Assume the input pulse has a duration of 0.1 μsec and has an amplitude of 5 V. The load resistance is 150 Ω.

Solution. The Thévenin equivalent circuit seen by the capacitor will vary, depending on whether the pulse is "on" or "off". In the former case, the equivalent resistance consists of the parallel combination of R_1 and R_L; in the latter case, since the switch is open, the capacitor is connected only to R_L. Thus, the effect of the pulse is to charge C through the parallel combination of R_1 and R_L during the "on" time ($0 \le t < 0.1$ μsec); the capacitor will then discharge through R_L during the "off" time. This behavior is depicted by the circuit model of Figure 5.6.14 in which the pulse signal is represented by a 5-V battery in series with a switch.

The charging time constant of the coaxial cable equivalent circuit when the switch is closed is therefore given by

$$\tau_{\text{on}} = \left(R_1 \| R_L\right)C = 17.65 \times 4000 \times 10^{-12} = 0.07\ \mu\text{sec}$$

and the transient response of the cable during the "on" time is

$$v_L(t) = 4.41\left(1 - e^{-t/\tau}\right) = 4.41\left(1 - e^{-1.42\times 10^{7} t}\right) \qquad 0 \le t \le 0.1\ \mu\text{sec}$$

where $V_T = R_L/(R_1 + R_L) \times 5 = 4.41$ V. At $t = 0.1$ μsec we calculate the load voltage to be

$$v_L(0.1\ \mu\text{sec}) = 4.41\left(1 - e^{-1.42}\right) = 3.35\ \text{V}$$

For $t \ge 0.1$ μsec, the output will naturally decay to zero, starting from the initial condition, v_L (0.1 μsec), with a time constant τ_{off} equal to

$$\tau_{\text{off}} = R_L C = 150 \times 4000 \times 10^{-12} = 0.6\ \mu\text{sec}$$

The load voltage will therefore decay according to the following expression:

$$v_L(t) = 3.35\left(e^{-1.67\times 10^{6}\left(t - 0.1\times 10^{-6}\right)}\right) \qquad t > 0.1\ \mu\text{sec}$$

The appearance of the response is shown in Figure 5.6.15. It should be apparent that as the cable becomes longer, both R_1 and C increase, and therefore the output voltage will respond more slowly to the input pulse; according to the simple model of a long coaxial cable given in this example, there is a limit to the maximum distance over which a voltage pulse can be transmitted by cable.

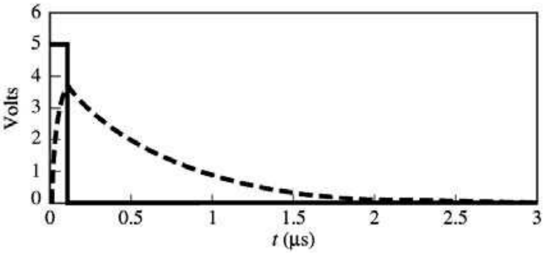

FIGURE 5.6.15 Pulse response of 100-m-long coaxial cable.

5.7 Electronics

This chapter introduces semiconductor-based electronic devices, and in so doing, it provides a transition between the fundamentals of electrical circuit analysis and the study of electronic circuits.

Semiconductors and *pn* Junctions

This section briefly introduces the mechanism of conduction in a class of materials called **semiconductors**. Semiconductors are typically materials consisting of elements from group IV of the periodic table and having electrical properties falling somewhere between those of conducting and of insulating materials. As an example, consider the conductivity of three common materials. Copper, a good conductor, has a conductivity of 0.59×16^6 S/cm; glass, a common insulator, may range between 10^{-16} and 10^{-13} S/cm; while silicon, a semiconductor, has a conductivity that varies from 10^{-8} to 10^{-1} S/cm. You see, then, that the name *semiconductor* is an appropriate one.

A conducting material is characterized by a large number of conduction-band electrons, which have a very weak bond with the basic structure of the material. Thus, an electric field easily imparts energy to the outer electrons in a conductor and enables the flow of electric current.

The free valence electrons are not the only mechanism of conduction in a semiconductor, however, Whenever a free electron leaves the lattice structure, it creates a corresponding positive charge within the lattice. The vacancy caused by the departure of a free electron is called a **hole**. Note that whenever a hole is present, we have, in effect, a positive charge. The positive charges also contribute to the conduction process, in the sense that if a valence-band electron "jumps" to fill a neighboring hole, thereby neutralizing a positive charge, it correspondingly creates a new hole at a different location. Thus, the effect is equivalent to that of a positive charge moving.

Semiconductor technology rarely employs pure, or intrinsic, semiconductors. To control the number of charge carriers in a semiconductor, the process of **doping** is usually employed. Doping consists of adding impurities to the crystalline structure of the semiconductor. The amount of these impurities is controlled, and the impurities can be of one of two types.

Semiconductors doped with donor elements conduct current predominantly by means of free electrons and are therefore called ***n*-type semiconductors**. When an acceptor element is used as the dopant, holes constitute the most common carrier, and the resulting semiconductor is said to be a ***p*-type semiconductor**. Doping usually takes place at such levels that the concentration of carriers due to the dopant is significantly greater than the intrinsic concentration of the original semiconductor. If n is the total number of free electrons and p that of holes, then in an n-type doped semiconductor, we have

$$n \gg n_i$$

and

$$p \ll p_i$$

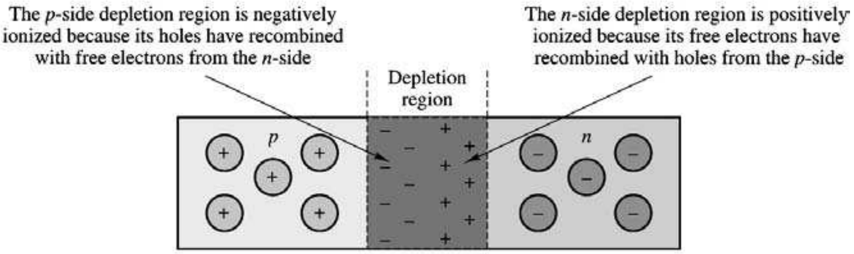

FIGURE 5.7.1 A *pn* junction.

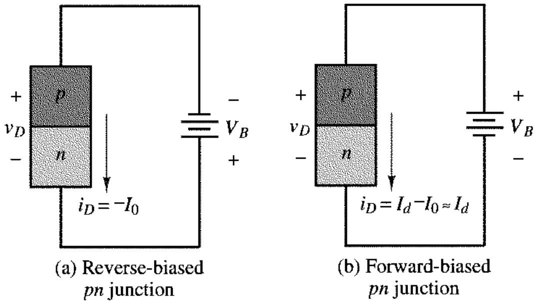

(a) Reverse-biased *pn* junction

(b) Forward-biased *pn* junction

FIGURE 5.7.2 Forward- and reverse-biased *pn* junctions.

Thus, free electrons are the **majority carriers** in an *n*-type material, while holes are the **minority carriers**. In a *p*-type material, the majority and minority carriers are reversed.

A simple section of semiconductor material does not in and of itself possess properties that make it useful for the construction of electronic circuits. However, when a section of *p*-type material and a section of *n*-type material are brought in contact to form a ***pn* junction**, a number of interesting properties arise. The *pn* junction forms the basis of the **semiconductor diode**, a widely used circuit element.

Figure 5.7.1 depicts an idealized *pn* junction, where on the *p* side, we see a dominance of positive charge carriers, or holes, and on the *n* side, the free electrons dominate. The charge separation causes a **contact potential** to exist at the junction. This potential is typically on the order of a few tenths of a volt and depends on the material (about 0.6 to 0.7 V for silicon). The contact potential is also called the *offset voltage*, V_γ.

Consider the diagrams of Figure 5.7.2, where a battery has been connected to a *pn* junction in the **reverse-biased** direction (Figure 5.7.2(a)), and in the **forward-biased** direction (Figure 5.7.2(b)). We assume that some suitable form of contact between the battery wires and the semiconductor material can be established (this is called an **ohmic contact**). The effect of a reverse bias is to increase the contact potential at the junction. Now, the majority carriers trying to diffuse across the junction need to overcome a greater barrier (a larger potential) and a wider depletion region. Thus, the diffusion current becomes negligible. The only current that flows under reverse bias is the very small reverse saturation current, so that the diode current, i_D (defined in the figure), is

$$i_D = -I_0$$

When the *pn* junction is forward-biased, the contact potential across the junction is lowered (note that V_B acts in opposition to the contact potential). Now, the diffusion of majority carriers is aided by the external voltage source; in fact, the diffusion current increases as a function of the applied voltage, according to the expression

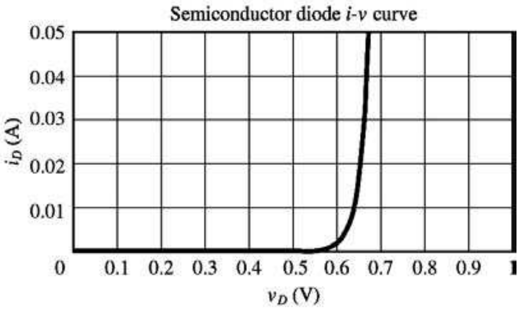

FIGURE 5.7.3 Semiconductor diode *i*-*v* characteristic.

$$I_d = I_0 e^{qv_D/kT} \tag{5.7.1}$$

where v_D is the voltage across the *pn* junction, $k = 1.381 \times 10^{-23}$ j/K is Boltzmann's constant, q the charge of one electron, and T the temperature of the material in kelvins (K). The quantity kT/q is constant at a given temperature and is approximately equal to 25 mV at room temperature. The net diode current under forward bias is given by the expression

$$i_D = I_d - I_0 = I_0\left(e^{qv_D/kT} - 1\right) \tag{5.7.2}$$

which is known as the **diode equation**. Figure 5.7.3 depicts the diode *i*-*v* characteristic described by the diode equation for a fairly typical silicon diode for positive diode voltages. Since the reverse saturation current, I_0, is typically very small (10^{-9} to 10^{-15} A), the expression

$$i_D = I_0 e^{qv_D/kT} \tag{5.7.3}$$

is a good approximation if the diode voltage, v_D, is greater than a few tenths of a volt.

The ability of the *pn* junction to essentially conduct current in only one direction — that is, to conduct only when the junction is forward-biased — makes it valuable in circuit applications. A device having a single *pn* junction and ohmic contacts at its terminals, as described in the preceding paragraphs, is called a *semiconductor diode,* or simply *diode*. As will be shown later in this chapter, it finds use in many practical circuits. The circuit symbol for the diode is shown in Figure 5.7.4, alongside with a sketch of the *pn* junction.

Circuit Models for the Semiconductor Diode

From the viewpoint of a *user* of electronic circuits (as opposed to a *designer*), it is often sufficient to characterize a device in terms of its *i*-*v* characteristic, using appropriate circuit models to determine the operating currents and voltages.

Ideal Diode Model

The large-signal model treats the diode as a simple on–off device (much like a check valve in hydraulic circuits). Figure 5.7.5 illustrates how, on a large scale, the *i*-*v* characteristic of a typical diode may be approximated by an open circuit when $v_D < 0$ and by a short circuit when $v_D \geq 0$ (recall the *i*-*v* curves of the ideal short and open circuits presented in Section 5.2). The analysis of a circuit containing a diode may be greatly simplified by using the short-circuit–open-circuit model. From here on, this diode model will be known as the **ideal diode model**. In spite of its simplicity, the ideal diode model (indicated by the symbol shown in Figure 5.7.5 can be very useful in analyzing diode circuits.

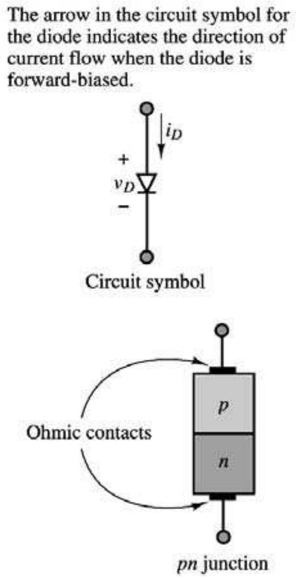

FIGURE 5.7.4 Semiconductor diode circuit symbol.

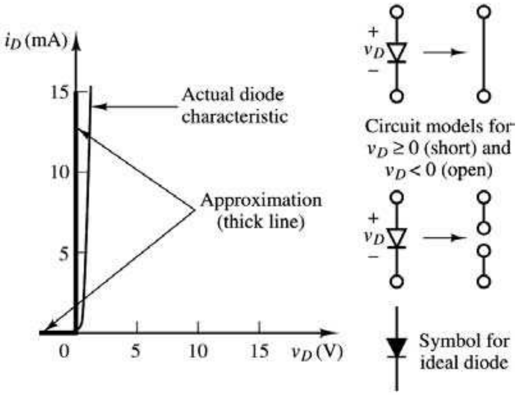

FIGURE 5.7.5 Large-signal on–off diode model.

One of the important applications of the semiconductor diode is **rectification** of AC signals, that is, the ability to convert an AC signal with zero average (DC) value to a signal with a nonzero DC value. The application of the semiconductor diode as a rectifier is very useful in obtaining DC voltage supplies from the readily available AC line voltage. Here we illustrate the basic principle of rectification using an ideal diode, for simplicity, and also because the large-signal model is appropriate when the diode is used in applications involving large AC voltage and current levels.

Consider the circuit of Figure 5.7.6, where an AC source, $v_i = 155.56 \cdot \sin \omega t$, is connected to a load by means of a series ideal diode. The diode will conduct only during the positive half-cycle of the sinusoidal voltage — that is, that the condition $v_D \geq 0$ will be satisfied only when the AC source voltage is positive — and that it will act as an open circuit during the negative half-cycle of the sinusoid ($v_D < 0$). Thus, the appearance of the load voltage will be as shown in Figure 5.7.7 with the negative portion of the sinusoidal waveform cut off. The rectified waveform clearly has a nonzero DC (average) voltage, whereas the average input waveform voltage was zero. When the diode is conducting, or $v_D \geq 0$, the unknowns v_L and i_D can be found by using the following equations:

$$i_D = \frac{v_i}{R_L} \quad \text{when} \quad v_i > 0 \tag{5.7.4}$$

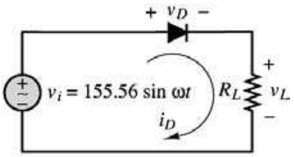

FIGURE 5.7.6

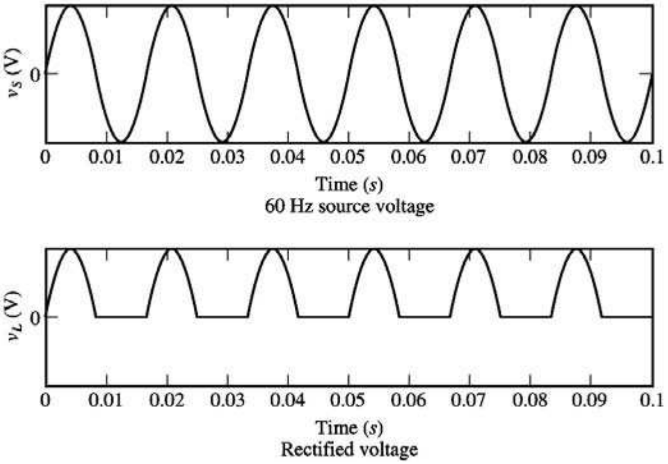

FIGURE 5.7.7 Ideal diode rectifier input and output voltages.

and

$$v_L = i_D R_L \tag{5.7.5}$$

The load voltage, v_L and the input voltage, v_i, are sketched in Figure 5.7.7. From Equation (5.7.5) it is obvious that the current waveform has the same shape as the load voltage. The average value of the load voltage is obtained by integrating the load voltage over one period and dividing by the period:

$$v_{\text{load,DC}} = \frac{\omega}{2\pi}\int_0^{\pi/\omega} 155.56 \sin \omega t \, dt = \frac{155.56}{\pi} = 49.52 \text{ V} \tag{5.7.6}$$

The circuit of Figure 5.7.6 is called a **half-wave rectifier**, since it preserves only half of the waveform. This is not usually a very efficient way of rectifying an AC signal, since half the energy in the AC signal is not recovered. It will be shown in a later section that it is possible to recover also the negative half of the AC waveform by mans of a *full-wave rectifier.*

Offset Diode Model

While the ideal diode model is useful in approximating the large-scale characteristics of a physical diode, it does not account for the presence of an offset voltage, which is an unavoidable component in semiconductor diodes. The **offset diode model** consists of an ideal diode in series with a battery of strength equal to the offset voltage (we shall use the value $V_\gamma = 0.6$ V for silicon diodes, unless otherwise indicated). The effect of the battery is to shift the characteristic of the ideal diode to the right on the voltage axis, as shown in Figure 5.93. This model is a better approximation of the large-signal behavior of a semiconductor diode than the ideal diode model.

According to the offset diode model, the diode of Figure 5.7.8 acts as an open circuit for $v_D < 0.6$ V, and it behaves like a 0.6-V battery for $v_D \geq 0.6$ V. The equations describing the offset diode model are as follows:

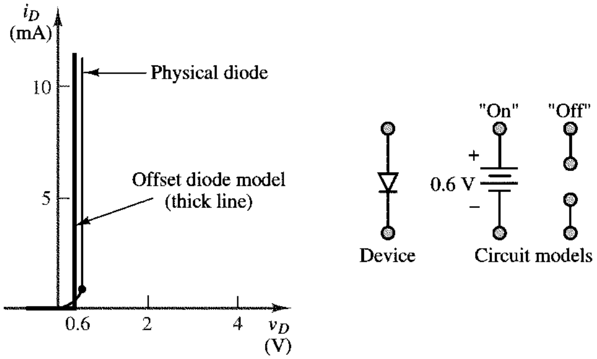

FIGURE 5.7.8

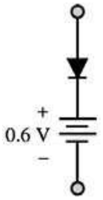

FIGURE 5.7.9 Offset diode as an extension of ideal diode model.

$$\begin{array}{ll} v_D \geq 0.6 \text{ V} & \text{Diode} \rightarrow 0.6\text{-V battery} \\ v_D < 0.6 \text{ V} & \text{Diode} \rightarrow \text{Open circuit} \end{array} \tag{5.7.7}$$

The diode offset model may be represented by an ideal diode in series with a 0.6-V ideal battery, as shown in Figure 5.7.9.

Practical Diode Circuits

The Full-Wave Rectifier

The half-wave rectifier discussed earlier is one simple method of converting AC energy to DC energy. The need for converting one form of electrical energy into the other arises frequently in practice. The most readily available form of electric power is AC (the standard 110- or 220-V rms AC line power), but one frequently needs a DC power supply, for applications ranging from the control of certain types of electric motors to the operation of electronic circuits.

The half-wave rectifier, however, is not a very efficient AC–DC conversion circuit, because it fails to utilize half the energy available in the AC waveform by not conducting current during the negative half-cycle of the AC waveform. The full-wave rectifier shown in Figure 5.7.10 offers a substantial improvement

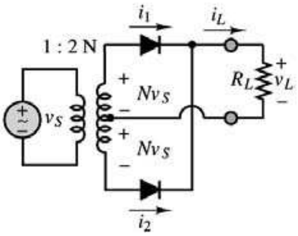

FIGURE 5.7.10 Full-wave rectifier.

in efficiency over the half-wave rectifier. The first section of the full-wave rectifier circuit includes an AC source and a center-tapped transformer (see Section 5.5) with 1:2 N turns ratio. The purpose of the transformer is to obtain the desired voltage amplitude prior to rectification. Thus, if the peak amplitude of the AC source voltage is v_s, the amplitude of the voltage across each half of the output side of the transformer will be Nv_s; this scheme permits scaling the source voltage up or down (depending on whether N is greater or less than 1), according to the specific requirements of the application. In addition to scaling the source voltage, the transformer also isolates the rectifier circuit from the AC source voltage, since there is no direct electrical connection between the input and output of a transformer.

The Bridge Rectifier

Another rectifier circuit commonly available "off the shelf" as a single *integrated circuit package* is the *bridge rectifier*, which employs four diodes in a bridge configuration, similar to the Wheatstone bridge already explored in Section 5.2. Figure 5.7.11 depicts the bridge rectifier, along with the associated integrated circuit (IC) package.

The analysis of the bridge rectifier is simple to understand by visualizing the operation of the rectifier for the two half-cycles of the AC waveform separately. The key is that, as illustrated in Figure 5.7.12, diodes D_1 and D_3 conduct during the positive half-cycle, while diodes D_2 and D_4 conduct during the negative half-cycle. Because of the structure of the bridge, the flow of current through the load resistor is in the same direction (from c to d) during both halves of the cycle; hence, the full-wave rectification of the waveform.

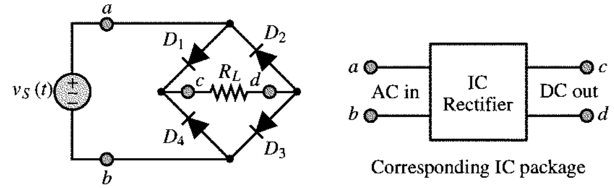

Bridge rectifier

Corresponding IC package

FIGURE 5.7.11 Full-wave bridge rectifier.

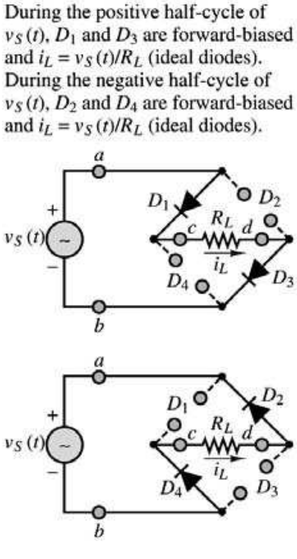
During the positive half-cycle of $v_S(t)$, D_1 and D_3 are forward-biased and $i_L = v_S(t)/R_L$ (ideal diodes).
During the negative half-cycle of $v_S(t)$, D_2 and D_4 are forward-biased and $i_L = v_S(t)/R_L$ (ideal diodes).

FIGURE 5.7.12 Diodes conduct.

DC Power Supplies and Voltage Regulation

The principal application of rectifier circuits is in the conversion of AC to DC power. A circuit that accomplishes this conversion is usually called a **DC power supply**. In power supply applications, transformers are employed to obtain an AC voltage that is reasonably close to the desired DC supply voltage. DC power supplies are very useful in practice: many familiar electrical and electronic appliances (e.g., radios, personal computers, TVs) require DC power to operate. For most applications, it is desirable that the DC supply be as steady and ripple-free as possible. To ensure that the DC voltage generated by a DC supply is constant, the DC supply is made up of voltage regulators, that is, devices that can hold a DC load voltage relatively constant in spite of possible fluctuations in the DC supply. This section will describe the fundamentals of voltage regulators.

A typical DC power supply is made up of the components shown in Figure 5.7.13. In the figure, a transformer is shown connecting the AC source to the rectifier circuit to permit scaling of the AC voltage to the desired level. For example, one might wish to step the 110-V rms line voltage down to 24 V rms by means of a transformer prior to rectification and filtering, to eventually obtain a 12-VDC regulated supply (*regulated* here means that the output voltage is a DC voltage that is constant and independent of load and supply variations). Following the step-down transformer are a bridge rectifier, a filter capacitor, a voltage regulator, and, finally, the load.

The most common device employed in voltage regulation schemes is the Zener diode. Zener diodes function on the basis of the reverse portion of the *i-v* characteristic of the diode with forward offset voltage V_γ and **reverse Zener voltage** V_Z.

The operation of the Zener diode may be analyzed by considering three modes of operation:

1. For $v_D \geq V_\gamma$, the device acts as a conventional forward-biased diode (Figure 5.7.14).
2. For $V_Z < v_D < V_\gamma$, the diode is reverse-biased but Zener breakdown has not taken place yet. Thus, it acts as an open circuit.
3. For $v_D \leq V_Z$, Zener breakdown occurs and the device holds a nearly constant voltage, $-V_Z$ (Figure 5.7.15).

To illustrate the operation of a Zener diode as a voltage regulator, consider the circuit of Figure 5.7.16, where the unregulated DC source, v_S, is regulated to the value of the Zener voltage, V_Z. Note how the diode must be connected "upside down" to obtain a positive regulated voltage. Note also that if v_S is greater than V_Z, it follows that the Zener diode is in its reverse-breakdown mode. Thus, one need not worry whether the diode is conducting or not in simple voltage regulator problems, provided that the unregulated supply voltage is guaranteed to stay above V_Z (a problem arises, however, if the unregulated

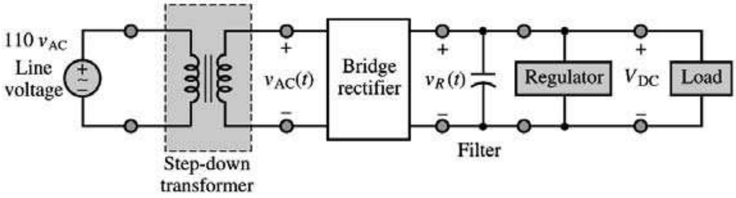

FIGURE 5.7.13 DC power supply.

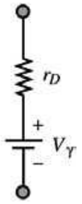

FIGURE 5.7.14 Zener diode model for forward bias.

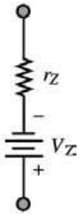

FIGURE 5.7.15 Zener diode model for reverse bias.

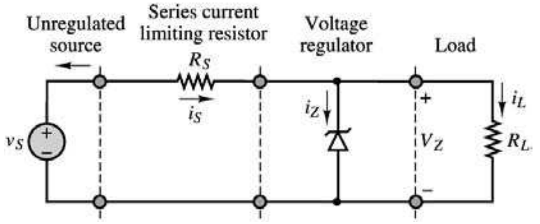

FIGURE 5.7.16 A Zener diode voltage regulator.

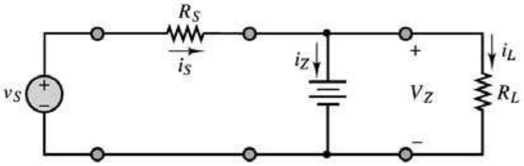

FIGURE 5.7.17 Simplified circuit for Zener regulator.

supply can drop below the Zener voltage). Assuming that the resistance r_Z is negligible with respect to R_S and R_L, we replace the Zener diode with the simplified circuit mode of Figure 5.7.17 consisting of a battery of strength V_Z.

Three simple observations are sufficient to explain the operation of this voltage regulator:

1. The load voltage must equal V_Z, as long as the Zener diode is in the reverse-breakdown mode. Then,

$$i_L = \frac{V_Z}{R_L} \tag{5.7.10}$$

2. The load current (which should be constant if the load voltage is to be regulated to sustain V_Z) is the difference between the unregulated supply current, i_s, and the diode current i_z:

$$i_L = i_S - i_Z \tag{5.7.11}$$

   This second point explains intuitively how a Zener diode operates: any current in excess of that required to keep the load at the constant voltage V_Z is "dumped" to ground through the diode. Thus, the Zener diode acts as a sink to the undesired source current.

3. The source current is given by

$$i_S \frac{v_S - V_Z}{R_S} \tag{5.7.12}$$

The Zener diode is usually rated in terms of its maximum allowable power dissipation. The power dissipated by the diode, P_Z, may be computed from

$$P_Z = i_Z V_Z \tag{5.7.13}$$

Thus, one needs to worry about the possibility that i_Z will become too large. This may occur either if the supply current is very large (perhaps because of an unexpected upward fluctuation of the unregulated supply), or if the load is suddenly removed and all of the supply current sinks through the diode. The latter case, of an open-circuit load, is an important design consideration.

Another significant limitation occurs when the load resistance is small, thus requiring large amounts of current from the unregulated supply. In this case, the Zener diode is hardly taxed at all in terms of power dissipation, but the unregulated supply may not be able to provide the current required to sustain the load voltage. In this case, regulation fails to take place. Thus, in practice, the range of load resistances for which load voltage regulation may be attained is constrained to a finite interval:

$$R_{L\,\min} \le R_L \le R_{L\,\max} \tag{5.7.14}$$

where $R_{L\max}$ is typically limited by the Zener diode power dissipation and $R_{L\min}$ by the maximum supply current.

Example 5.7.1

This example illustrates the calculation of the range of allowable load resistances for a Zener regulator design. For the Zener regulator shown in Figure 5.7.18, we want to maintain the load voltage at 14 V. Find the range of load resistances for which regulation can be obtained if the Zener diode is rated at 14 V, 5 W.

Solution. The minimum load resistance for which a regulated load voltage of 14 V may be attained is found by requiring that the load voltage be 14 V and applying KVL subject to this constraint:

$$50\left(\frac{R_{L\,\min}}{R_{L\,\min}+30}\right) = 14$$

$$\begin{aligned} R_{L\,\min} &= \frac{14}{50}\left(R_{L\,\min}+30\right) \\ &= 11.7\ \Omega \end{aligned}$$

The maximum current through the Zener diode that does not exceed the diode power rating may be computed by considering the 5-W power rating:

$$i_{Z\,\max} = \frac{5}{14} = 0.357\ \text{A}$$

The current through the 20-Ω resistor will be

$$\frac{50-14}{30} = 1.2\ \text{A}$$

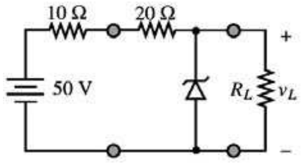

FIGURE 5.7.18 Circuit for example.

so that the maximum load resistance for which regulation occurs is

$$R_{L\max} = \frac{14}{1.2 - 0.357}$$
$$= 16.6\ \Omega$$

Finally, the range of allowable load resistances is:

$$16.6\ \Omega \geq R_L \geq 11.7\ \Omega$$

Photodiodes

Another property of semiconductor materials that finds common application in measurement systems is their response to light energy. In appropriately fabricated diodes, called **photodiodes**, when light reaches the depletion region of a *pn* junction, photons cause hole-electron pairs to be generated by a process called *photo-ionization*. This effect can be achieved by using a surface material that is transparent to light. As a consequence, the reverse saturation current depends on the light intensity (i.e., on the number of incident photons), in addition to the other factors mentioned earlier. In a photodiode, the reverse current is given by $-(I_0 + I_p)$, where I_p is the additional current generated by photo-ionization. The result is depicted in the family of curves of Figure 5.7.19, where the diode characteristic is shifted downward by an amount related to the additional current generated by photo-ionization. Figure 5.7.19 depicts the appearance of the *i-v* characteristic of a photodiode for various values of I_p, where the *i-v* curve is shifted to lower values for progressively larger values of I_p. The circuit symbol is depicted in Figure 5.7.20.

As displayed in Figure 5.7.19 are three load lines, which depict the three modes of operation of a photodiode. Curve L_1 represents normal diode operation, under forward bias. Note that the operating point of the device is in the positive *i*, positive *v* (first) quadrant of the *i-v* plane; thus, the diode dissipates positive power in this mode, and is therefore a passive device, as we already know. On the other hand, load line L_2 represents operation of the photodiode as a **solar cell**; in this mode, the operating point is in the negative *i*, positive *v*, or fourth, quadrant, and therefore the power dissipated by the diode is *negative*. In other words, the photodiode is generating power by converting light energy to electrical

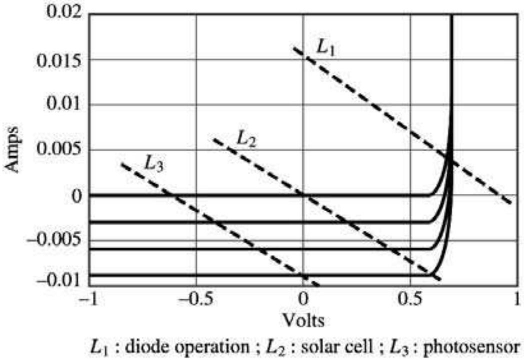

FIGURE 5.7.19 Photodiode *i-v* curves.

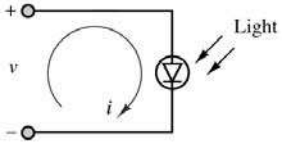

FIGURE 5.7.20 Photodiode circuit symbol.

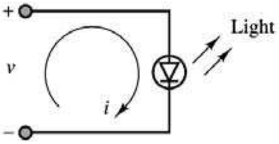

FIGURE 5.7.21 Light-emitting diode (LED) circuit symbol.

TABLE 5.7.1 LED Materials and Wavelengths

Material	Dopant	Wavelength (nm)	Color
GaAs	Zn	900	Infrared
GaAs	Si	910–1020	Infrared
GaP	N	570	Green
GaP	N	590	Yellow
GaP	Zn,O	700	Red
$GaAs_{0.6}P_{0.4}$		650	Red
$GaAs_{0.35}P_{0.65}$	N	632	Orange
$GaAs_{0.15}P_{0.85}$	N	589	Yellow

energy. Note further that the load line intersects the voltage axis at zero, meaning that no supply voltage is required to bias the photodiode in the solar-cell mode. Finally, load line L_3 represents the operation of the diode as a light sensor: when the diode is reverse-biased, the current flowing through the diode is determined by the light intensity; thus, the diode current changes in response to changes in the incident light intensity.

The operation of the photodiode can also be reversed by forward-biasing the diode and causing a significant level of recombination to take place in the depletion region. Some of the energy released is converted to light energy by emission of photons. Thus, a diode operating in this mode emits light when forward-biased. Photodiodes used in this way are called **light-emitting diodes** (LEDs); they exhibit a forward (offset) voltage of 1 to 2 volts. The circuit symbol for the LED is shown in Figure 5.7.21.

Gallium arsenide (GaAs) is one of the more popular substrates for creating LEDs; gallium phosphide (GaP) and the alloy $GaAs_{1-x}P_x$ are also quite common. Table 5.7.1 lists combinations of materials and dopants used for common LEDs and the colors they emit. The dopants are used to create the necessary *pn* junction.

Example 5.7.2 Opto-Isolators

One of the common applications of photodiodes and LEDs is the **opto-coupler**, or **opto-isolator**. This device, which is usually enclosed in a sealed package, uses the light-to-current and current-to-light conversion property of photodiodes and LEDs to provide signal connection between two circuits without any need for electrical connections. Figure 5.7.22 depicts the circuit symbol for the opto-isolator.

Because diodes are nonlinear services, the opto-isolator is not used in transmitting analog signals: the signals would be distorted because of the nonlinear diode *i-v* characteristic. However, opto-isolators find a very important application when on–off signals need to be transmitted from high-power machinery to delicate computer control circuitry. The optical interface ensures that potentially damaging large currents cannot reach delicate instrumentation and computer circuits.

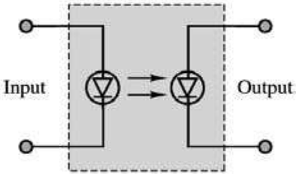

FIGURE 5.7.22 Opto isolator.

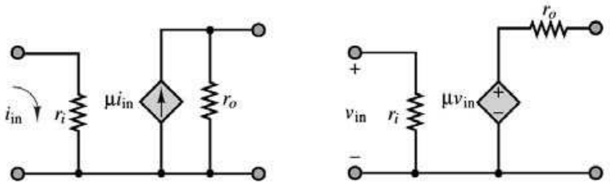

(a) Current-controlled current source (b) Voltage-controlled voltage source

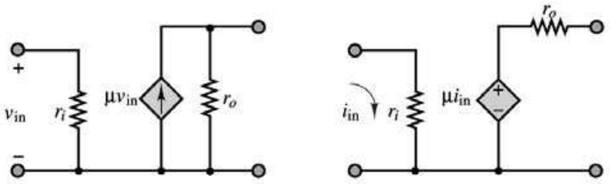

(c) Voltage-controlled current source (d) Current-controlled voltage source

FIGURE 5.7.23 Controlled-source models of linear amplifier transistor operation.

Transistors

A transistor is a three-terminal semiconductor device that can perform two functions that are fundamental to the design of electronic circuits: **amplification** and **switching**. Put simply, amplification consists of magnifying a signal by transferring energy to it from an external source; whereas a transistor switch is a device for controlling a relatively large current between or voltage across two terminals by means of a small control current or voltage applied at a third terminal. In this chapter, we provide an introduction to the two major families of transistors: *bipolar junction transistors*, or *BJTs*; and *field-effect transistors*, or *FETs*.

The operation of the transistor as a linear amplifier can be explained qualitatively by the sketch of Figure 5.7.23 in which the four possible modes of operation of a transistor are illustrated by means of circuit models employing controlled sources. In Figure 5.7.23 controlled voltage and current sources are shown to generate an output proportional to an input current or voltage; the proportionality constant, μ, is called the internal *gain* of the transistor. As will be shown, the BJT acts essentially as a current-controlled device, while the FET behaves as a voltage-controlled device.

Transistors can also act in a nonlinear mode, as voltage- or current-controlled switches. When a transistor operates as a switch, a small voltage or current is used to control the flow of current between two of the transistor terminals in an on–off fashion. Figure 5.7.24 depicts the idealized operation of the transistor as a switch, suggesting that the switch is closed (on) whenever a control voltage or current is greater than zero and is open (off) otherwise. It will later become apparent that the conditions for the switch to be on or off need not necessarily be those depicted in Figure 5.7.24.

The Bipolar Junction Transistor (BJT)

The *pn* junction forms the basis of a large number of semiconductor devices. The semiconductor diode, a two-terminal device, is the most direct application of the *pn* junction. In this section, we introduce the **bipolar junction transistor** (BJT). As we did in analyzing the diode, we will introduce the physics of transistor devices as intuitively as possible, resorting to an analysis of their *i-v* characteristics to discover important properties and applications.

A BJT is formed by joining three sections of semiconductor material, each with a different doping concentration. The three sections can be either a thin *n* region sandwiched between p^+ and *p* layers, or a *p* region between *n* and n^+ layers, where the superscript "plus" indicates more heavily doped material. The resulting BJTs are called *pnp* and *npn* transistors, respectively; we shall discuss only the latter in this section. Figure 5.7.25 illustrates the approximate construction, symbols, and nomenclature for the two types of BJTs.

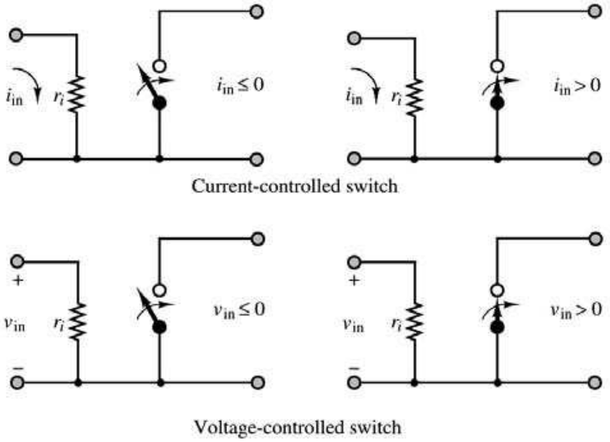

FIGURE 5.7.24 Models of ideal transistor switches.

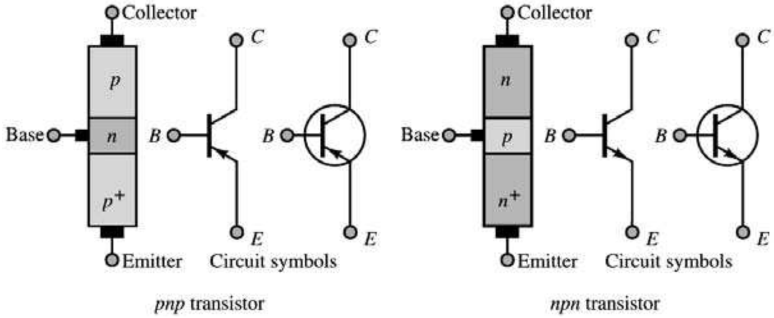

FIGURE 5.7.25 Bipolar junction transistors.

The most important property of the bipolar transistor is that the small base current controls the amount of the much larger collector current

$$I_C = \beta I_B \tag{5.7.15}$$

where β is a current amplification factor dependent on the physical properties of the transistor. Typical values of β range from 20 to 200.

The detailed operation of bipolar transistors can be explained by resorting to a detailed physical analysis of the *npn* or *pnp* structure of these devices. The reader interested in such a discussion of transistors is referred to any one of a number of excellent books on semiconductor electronics.

The focus of this section will be on the analysis of the *i-v* characteristic of the *npn* BJT, based on the circuit notation defined in Figure 5.7.26. The device *i-v* characteristics will be presented qualitatively, without deriving the underlying equations, and will be utilized in constructing circuit models for the device.

The number of independent variables required to uniquely define the operation of the transistor may be determined by applying KVL and KCL to the circuit of Figure 5.7.26. It should be apparent that two voltages and two currents are sufficient to specify the operation of the device. Note that, since the BJT is a three-terminal device, it will not be sufficient to deal with a single *i-v* characteristic; it will soon become apparent that two such characteristics are required to explain the operation of this device. One of these characteristics relates the base current, i_B, to the base-emitter voltage, v_{BE}; the other relates the collector current, i_C, to the collector-emitter voltage, v_{CE}. As will be shown, the latter characteristic actually

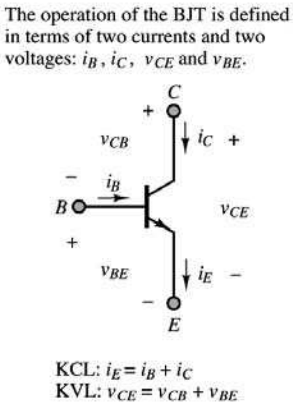

FIGURE 5.7.26 Definition of BJT voltages and currents.

consists of a *family* of curves. To determine these *i-v* characteristics, consider the *i-v* curves of Figure 5.7.27 and Figure 5.7.28 using the circuit notation of Figure 5.7.26. In Figure 5.7.27, the collector is open and the *BE* junction is shown to be very similar to a diode. The ideal current source, I_{BB}, injects a base current, which causes the junction to be forward-biased. By varying I_{BB}, one can obtain the open-collector *BE* junction *i-v* curve shown in the figure.

If a voltage source were now to be connected to the collector circuit, the voltage v_{CE} and, therefore, the collector current, i_C, could be varied, in addition to the base current, i_B. The resulting circuit is depicted in Figure 5.7.28(a). By varying both the base current and the collector-emitter voltage, one could then generate a plot of the device **collector characteristic**. This is also shown in Figure 5.7.28(b).

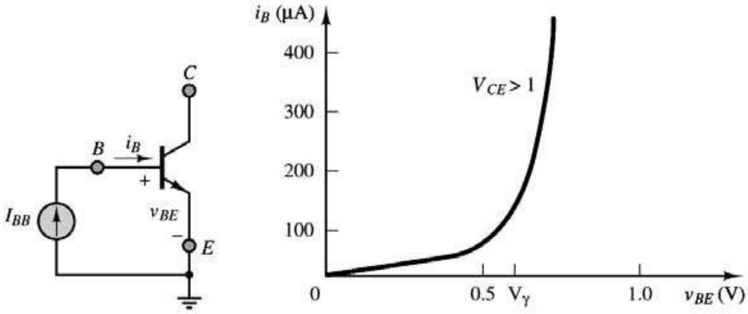

FIGURE 5.7.27 Determining the *BE* junction open-collector *i-v* characteristic.

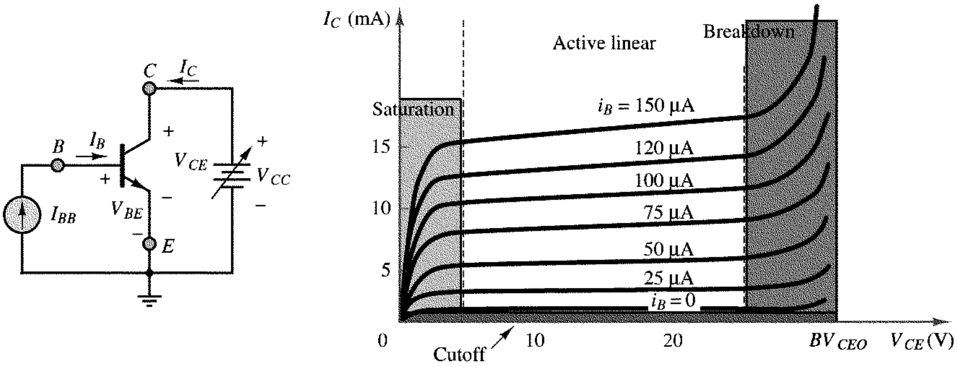

FIGURE 5.7.28 (a) Ideal test circuit to determine the *i-v* characteristic of a BJT; (b) the collector-emitter output characteristics of a BJT.

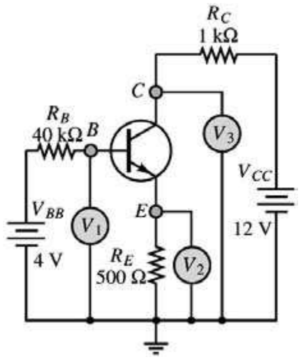

FIGURE 5.7.29 Determination of the operating state of a BJT.

Note that this figure depicts not just a single i_C-v_{CE} curve, but an entire family, since for each value of the base current, i_B, an i_C-v_{CE} curve can be generated. Four regions are identified in the collector characteristic:

1. The **cutoff region**, where both junctions are reverse-biased, the base current is very small, and essentially no collector current flows
2. The **active linear region**, in which the transistor can act as a linear amplifier, where the *BE* junction is forward-biased and the *CB* junction is reverse-biased
3. The **saturation region**, in which both junctions are forward-biased
4. The **breakdown region**, which determines the physical limit of operation of the device.

Large-Signal Model of the *npn* BJT

The large-signal model for the BJT recognizes three basic operating modes of the transistor (Figure 5.7.29). When the *BE* junction is reverse-biased, no base current (and therefore no forward collector current) flows, and the transistor acts (virtually as an open circuit; the transistor is said to be in the *cutoff region*. In practice, there is always a leakage current flowing through the collector, even when $V_{BE} = 0$ and $I_B = 0$. This leakage current is denoted by I_{CEO}. When the *BE* junction becomes forward-biased, the transistor is said to be in the *active region,* and the base current is amplified by a factor of β at the collector:

$$I_C = \beta I_B \tag{5.7.16}$$

Since the collector current is controlled by the base current, the controlled-source symbol is used to represent the collector current. Finally, when the base current becomes sufficiently large, the collector-emitter voltage, V_{CE}, reaches its saturation limit, and the collector current is no longer proportional to the base current; this is called the *saturation region*. The three conditions are described in Figure 5.7.30 in terms of simple circuit models.

Example 5.7.3 illustrates the application of this large-signal model in a practical circuit and illustrates how to determine which of the three states is applicable, using relatively simple analysis.

Example 5.7.3 LED Driver

The circuit shown in Figure 5.7.31 is being used to "drive" (i.e., provide power for) a light-emitting diode (LED) from a desktop computer. The signal available from the computer consists of a 5-V low-current output. The reason for using a BJT (rather than driving the LED directly with the signal available from the computer) is that the LED requires a substantial amount of current (at least 15 mA for the device used in this example) and the computer output is limited to 5mA. Thus, some current amplification is required. The LED has an offset voltage of 1.4 V and a maximum power dissipation rating of 280 mW. The circuit has been designed so that the transistor will be either in cutoff, when the LED is to be turned off, or in saturation, when the LED is to be turned on.

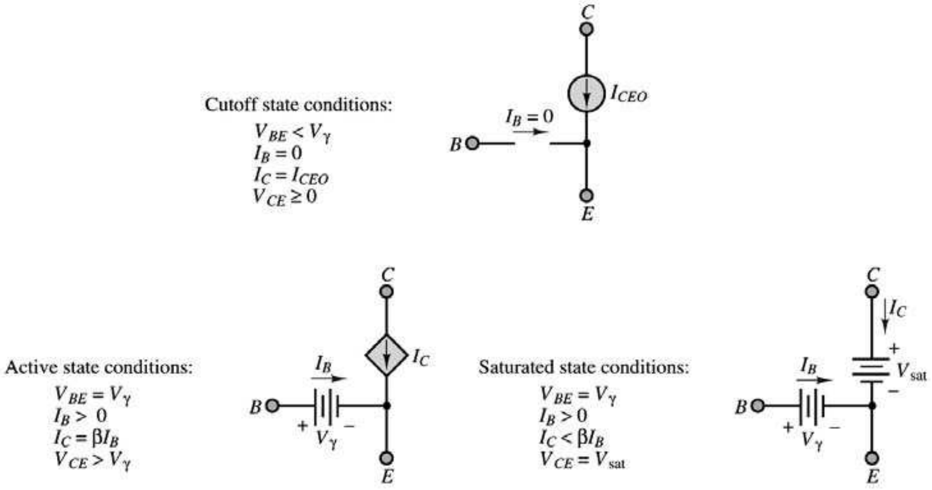

FIGURE 5.7.30 *npn* BJT large-signal model.

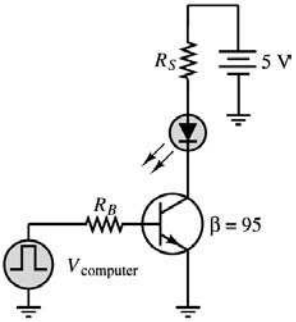

FIGURE 5.7.31 LED driver circuit.

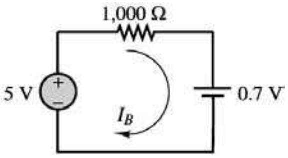

FIGURE 5.7.32 *BE* circuit for LED driver.

Assume that the base-emitter junction of the transistor has an offset voltage of 0.7 V and that R_B = 1 kΩ and R_S = 42.5 Ω.

1. When the computer is supplying 5 V to the circuit, is the transistor in cutoff, in saturation, or in the linear region of operation?
2. Determine the current in the LED when "turned on" and, thus, state whether the LED will exceed its power rating.

Solution. The base-emitter circuit is considered first, to determine whether the BE junction is forward-biased. The equivalent circuit is shown in Figure 5.7.32

Writing KVL around the base circuit, we obtain

$$(5 - 0.7) = I_B(1000)$$

or

$$I_B = 4.3 \text{ mA}$$

Since this current is greater than zero (i.e., since positive current flows into the base), the transistor is not in cutoff.

Next, we need to determine whether the transistor is in the linear active or in the saturation region. One method that can be employed to determine whether the device is in the active region is to assume that it is and to solve for the circuit that results from the assumed condition. If the resulting equations are consistent, then the assumption is justified. Assuming that the transistor is in its active region, the following equations apply:

$$I_C = \beta I_B$$

or

$$I_C = 95(4.3 \text{ mA}) = 408.5 \text{ mA}$$

With reference to the circuit of Figure 5.7.33, KVL may be applied around the collector circuit, to obtain

$$5 = 1.4 + V_{CE} + I_C R_S$$

or

$$(5 - 1.4) - 408.5(42.5) = V_{CE}$$

or

$$V_{CE} = -13.76 \text{ V}$$

This result is clearly not possible, since the supply voltage is only 5V! It must therefore be concluded that the transistor is not in the linear region and must be in saturation. To test this hypothesis, we can substitute the nominal saturation voltage for the BJT in place of V_{CE} (a typical saturation voltage would be V_{CE} sat = 0.2 V) and verify that in this case we obtain a consistent solution:

$$I_C = \frac{(5 - 1.4 - 0.2)}{42.5} = 80 \text{ mA}$$

This is a reasonable result, stating that the collector current in the saturation region for the given circuit is of the order of 80 mA.

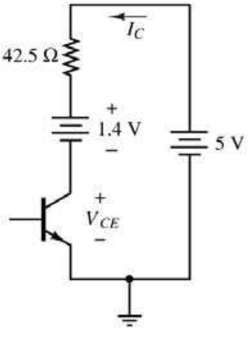

FIGURE 5.7.33 Equivalent collector circuit of LED driver, assuming that the BJT is in the linear active region.

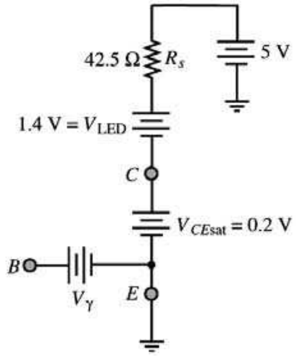

FIGURE 5.7.34 LED driver equivalent collector circuit, assuming that the BJT is in the saturation region.

In the above part, it was determined that the transistor was in saturation. Using the circuit model for saturation, we may draw the equivalent circuit of Figure 5.7.34. Since I_C = 80 mA, the power dissipated by the LED may be calculated as follows:

$$P_{\text{LED}} = I_C V_{\text{LED}} = 80 \text{ mA} \times 1.4 \text{ V} = 112 \text{ mW}$$

Thus, the power limitation of the LED will not be exceeded.

Field-Effect Transistors

The second transistor family discussed in this section operates on the basis of a principle that is quite different from that of the *pn* junction devices. The concept that forms the basis of the operation of the **field-effect transistor**, or FET, is that the width of a conducting channel in a semiconductor may be varied by the external application of an electric field. Thus, FETs behave as *voltage-controlled resistors*. This family of electronic devices can be subdivided into three groups, all of which will be introduced in the remainder of this chapter. Figure 5.7.35 depicts the classification of field-effect transistors, as well as the more commonly used symbols for these devices. These devices can be grouped into three major categories. The first two categories are both types of **metal-oxide-semiconductor field-effect transistors**, or MOSFETs: **enhancement-mode MOSFETs** and **depletion-mode MOSFETs**. The third category consists of **junction field-effect transistors**, or JFETs. In addition, each of these devices can be fabricated either as an ***n*-channel** device or as a ***p*-channel** device, where the *n* or *p* designation indicates the nature of the doping in the semiconductor channel.

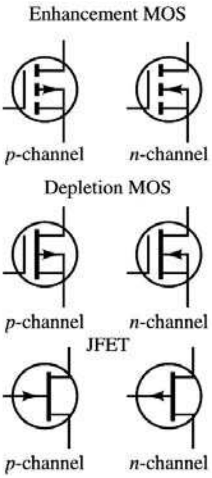

FIGURE 5.7.35 Classification of field-effect transistors.

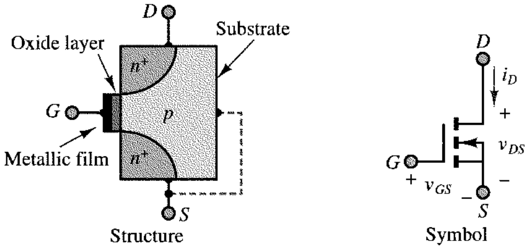

FIGURE 5.7.36 *n*-Channel enhancement MOSFET.

The construction of the MOSFET is shown in Figure 5.7.36, along with its circuit symbol. The device consists of a metal **gate**, insulated from the bulk of the *p*-type semiconductor material by an oxide layer (thus the terminology *metal-oxide-semiconductor*). Two n^+ regions on either side of the gate are called **source** and **drain**, respectively. An electric field can be applied between the gate and the *bulk* of the semiconductor by connecting the gate to a voltage source. The effect of the electric field, the intensity of which depends on the strength of the gate voltage, is to push positive charge carriers away from the surface of the bulk material. As a consequence of this effect, the *p*-type material has a lower concentration of positive charge carriers near its surface, and it behaves progressively more like intrinsic semiconductor material and then, finally, like *n*-type material as the electric field strength increases. Thus, in a narrow layer between n^+ regions, the *p*-type material is *inverted* and *n*-type charge carriers become available for conduction. This layer is called the *channel*. The device of Figure 5.7.36 takes the name *n-channel MOSFET*. It is also called an *enhancement-mode* device, because the applied electric field "enhances" the conduction in the channel by attracting *n*-type charge carriers. There are also *depletion-mode* devices, in which the application of an electric field "depletes" the channel of charge carriers, reducing the effective channel width. It is useful to think of enhancement-mode devices as being normally off: current cannot flow from drain to source unless a gate voltage is applied. On the other hand, depletion-mode devices are normally on; that is, the gate voltage is used to reduce the conduction of current from drain to source.

An analogous discussion could be carried out for *p-channel MOSFETs*. In a *p*-channel device, conduction in the channel occurs through positive charge carriers. The correspondence between *n*-channel and *p*-channel devices is akin to that between *npn* and *pnp* bipolar devices.

We are now ready to describe qualitatively the *i-v* characteristic of this enhancement-mode MOSFET, for small values of drain-to-source voltage, v_{DS}, and for constant v_{GS}, the channel has essentially constant width and therefore acts as a constant resistance. As the gate voltage is changed, this resistance can be varied over a certain range. This mode of operation, for small drain voltages, is called the **ohmic state**, and, as depicted in Figure 5.7.37, it corresponds to a linear *i-v* curve for fixed v_{GS}, as would be expected of a resistor. Thus, in the ohmic state the MOSFET acts as a **voltage-controlled resistor**.

As the drain voltage is increased, the gate-to-drain voltage, v_{GD}, decreases, reducing the electric field strength at the drain end of the device.

When $v_{GD} = v_{GS} - v_{DS} < v_T$ and $v_{DS} > v_{GS} - v_T$, the channel is *pinched down*, and the electron flow into the drain is physically limited, so that the drain current becomes essentially constant. This phenomenon

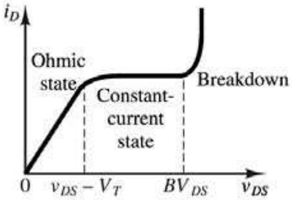

FIGURE 5.7.37 MOSFET *i-v* curve.

is clearly reflected in the curve of Figure 5.7.37, where it is shown that for drain-to-source voltages above $v_{DS} > v_{GS} - v_T$, the drain current becomes constant, independent of v_{DS}. This mode of operation is the **constant-current state.** If v_{DS} exceeds a given **drain breakdown voltage**, BV_{DS} (usually between 20 and 50 V), avalanche breakdown occurs and the drain current increases substantially. Operation in this **breakdown state** can lead to permanent damage because of the excessive heat caused by the large drain current. Finally, if v_{GS} exceeds the **gate breakdown voltage** (around 50 V), permanent damage to the oxide layer can occur. It is important to know that it is possible to generate *static* voltages of magnitude sufficient to exceed this breakdown voltage just by handling the device; thus, some attention must usually be paid to static voltage buildup in handling MOS circuits.

Transistor Gates and Switches

Transistor switching circuits form the basis of digital logic circuits. The objective of this section is to discuss the internal operation of these circuits and to provide the reader interested in the internal workings of digital circuits with an adequate understanding of the basic principles.

An **electronic gate** is a device that, on the basis of one or more input signals, produces one of two or more prescribed outputs; as will be seen shortly, one can construct both digital and analog gates. A word of explanation is required, first, regarding the meaning of the words *analog* and *digital.* An analog voltage or current — or, more generally, an analog signal — is one that varies in a continuous fashion over time, in *analogy* (hence the expression *analog*) with a physical quantity. An example of an analog signal is a sensor voltage corresponding to ambient temperature on any given day, which may fluctuate between, say, 30° and 50°F. A digital signal, on the other hand, is a signal that can take only a finite number of values; in particular, a commonly encountered class of digital signals consists of **binary signals**, which can take only one of two values (for example, 1 and 0). A typical example of a binary signal would be the control signal for the furnace in a home heating system controlled by a conventional thermostat, where one can think of this signal as being "on" (or 1) if the temperature of the house has dropped below the thermostat setting (desired value), or "off" (or 0) if the house temperature is greater than or equal to the set temperature (say, 68°F). Figure 5.7.38 illustrates the appearance of the analog and digital signals in this furnace example.

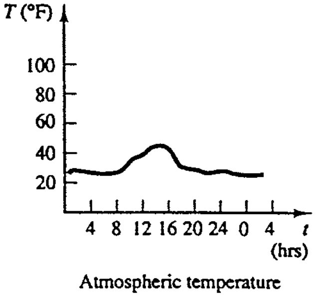

Atmospheric temperature over a 24-hour period

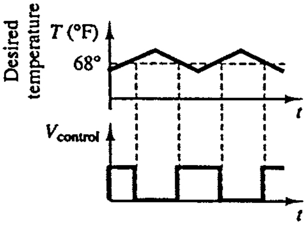

Average temperature in a house and related digital control voltage furnace

FIGURE 5.7.38 Illustration of analog and digital signals.

Analog Gates

A common form of analog gate — probably the most important, in practice — employs an FET and takes advantage of the fact that current can flow in either direction in an FET biased in the ohmic region. Recall that the drain characteristic of the MOSFET consists of three regions: ohmic, active, and breakdown. A MOSFET amplifier is operated in the active region, where the drain current is nearly constant for any given value of v_{GS}. On the other hand, a MOSFET biased in the ohmic state acts very much as a linear resistor. For example, for an *n*-channel enhancement MOSFET, the conditions for the transistor to be in the ohmic region are

$$v_{GS} > V_T \quad \text{and} \quad |v_{DS}| \le \frac{1}{4}\left(v_{GS} - V_T\right) \tag{5.7.17}$$

As long as the FET is biased within these conditions, it acts simply as a linear resistor, and it can conduct current in either direction (provided that v_{DS} does not exceed the limits stated in Equation (5.7.17). In particular, the resistance of the channel in the ohmic region is found to be

$$R_{DS} = \frac{V_T^2}{2I_{DSS}\left(v_{GS} - V_T\right)} \tag{5.7.18}$$

so that the drain current is equal to

$$i_D \approx \frac{v_{DS}}{r_{DS}} \quad \text{for} \quad |v_{DS}| \le \frac{1}{4}\left(v_{GS} - V_T\right) \quad \text{and} \quad v_{GS} > V_T \tag{5.7.19}$$

The most important feature of the MOSFET operating in the ohmic region, then, is that it acts as a voltage-controlled resistor, with the gate-source voltage, v_{GS}, controlling the channel resistance, R_{DS}. The use of the MOSFET as a switch in the ohmic region, then, consists of providing a gate-source voltage that can either hold the MOSFET in the cutoff region ($v_{GS} < V_T$) or bring it into the ohmic region. In this fashion, v_{GS} acts as a control voltage for the transistor.

Consider the circuit shown in Figure 5.7.39, where we presume that v_C can be varied externally and that v_{in} is some analog signal source that we may wish to connect to the load R_L at some appropriate time. The operation of the switch is as follows. When $v_C \le V_T$, the FET is in the cutoff region and acts as an open circuit. When $v_C > V_T$ (with a value of v_{GS} such that the MOSFET is in the ohmic region), the transistor acts as a linear resistance, R_{DS}. If $R_{DS} \ll R_L$, then $v_{\text{out}} \approx v_{\text{in}}$. By using a pair of MOSFETs, it is possible to improve the dynamic range of signals one can transmit through this analog gate.

MOSFET analog switches are usually produced in integrated circuit (IC) form and denoted by the symbol shown in Figure 5.7.40.

Digital Gates

BJT Gates. In discussing large-signal models for the BJT, we observed that the *i-v* characteristic of this family of devices includes a *cutoff* region, where virtually no current flows through the transistor. On the other hand, when a sufficient amount of current is injected into the base of the transistor, a bipolar transistor will reach *saturation*, and a substantial amount of collector current will flow. This behavior is quite well suited to the design of electronic gates and switches and can be visualized by superimposing a load line on the collector characteristic, as shown in Figure 5.7.41.

The operation of the simple **BJT switch** is illustrated in Figure 5.7.41 by means of load-line analysis. Writing the load-line equation at the collector circuit, we have

$$v_{CE} = V_{CC} - i_C R_C \qquad (5.7.20$$

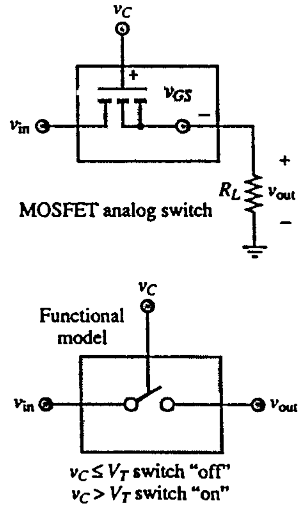

FIGURE 5.7.39 MOSFET analog switch.

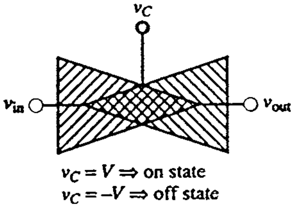

FIGURE 5.7.40 Symbol for bilateral FET analog gate.

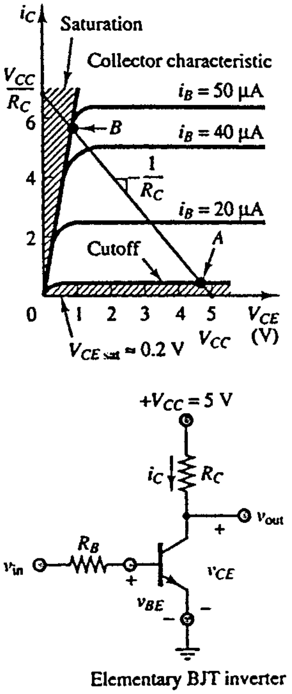

FIGURE 5.7.41 BJT switching characteristic.

and

$$v_{\text{out}} = v_{CE} \tag{5.7.21}$$

Thus, when the input voltage, v_{in}, is low (say, 0 V, for example) the transistor is in the cutoff region and little or no current flows, and

$$v_{\text{out}} = v_{CE} = V_{CC} \tag{5.7.22}$$

so that the output is "logic high."

When v_{in} is large enough to drive the transistor into the saturation region, a substantial amount of collector current will flow and the collector-emitter voltage will be reduced to the small saturation value, $V_{CE\,\text{sat}}$, which is typically a fraction of a volt. This corresponds to the point labeled B on the load line. For the input voltage v_{in} to drive the BJT of Figure 5.7.41 into saturation, a base current of approximately 50 mA will be required. Suppose, then, that the voltage v_{in} could take the values 0 or 5 V. Then, if $v_{\text{in}} =$ 0 V, v_{out} will be nearly equal to V_{CC} or, again, 5 V. If, on the other hand, $v_{\text{in}} = 5$ V and R_B is, say, equal to 85 kΩ [so that the base current required for saturation flows into the base: $i_B \approx (5\text{ V} - 0.7\text{ V})/R_B =$ 50.6 μA], we have the BJT in saturation, and $v_{\text{out}} = V_{CE\,\text{sat}} \approx 0.2$ V.

Thus, you see that whenever v_{in} corresponds to a logic high (or logic 1), v_{out} takes a value close to 0 V, or logic low (or 0); conversely, $v_{\text{in}} =$"0" (logic "low") leads to $v_{\text{out}} =$ "1". The values of 5 and 0 V for the two logic levels 1 and 0 are quite common in practice and are the standard values used in a family of logic circuits denoted by the acronym TTL, which stands for **transistor-transistor logic**. One of the more common TTL blocks is the **inverter** shown in Figure 5.7.41, so called because it "inverts" the input by providing a low output for a high input, and vice versa. This type of inverting, or "negative", logic behavior is quite typical of BJT gates (and of transistor gates in general).

MOSFET Logic Gates. Having discussed the BJT as a switching element, we might quite naturally suspect that FETs may similarly serve as logic gates. In fact, in some respects, FETs are better suited to be employed as logic stages than BJTs. The *n*-channel enhancement MOSFET serves as an excellent illustration: because of its physical construction, it is normally off (that is, it is off until a sufficient gate voltage is provided), and therefore it does not require much current from the input signal source. Further, MOS devices offer the additional advantage of easy fabrication into integrated circuit form, making production economical in large volume. On the other hand, MOS devices cannot provide as much current as BJTs, and their switching speeds are not quite as fast — although these last statements may not hold true for long, because great improvements are taking place in MOS technology. Overall, it is certainly true that in recent years it has become increasingly common to design logic circuits based on MOS technology. In particular, a successful family of logic gates called *CMOS* (for *complementary metal-oxide-semiconductor*) takes advantage of both *p*- and *n*-channel enhancement-mode MOSFETs to exploit the best features of both types of transistors. CMOS logic gates (and many other types of digital circuits constructed using the same technology) consume very little supply power and have become the mainstay in pocket calculators, wristwatches, portable computers, and many other consumer electronics products. Without delving into the details of CMOS technology, we shall briefly illustrate the properties of MOSFET logic gates and of CMOS gates in the remainder of this section.

Figure 5.7.42 depicts a MOSFET switch with its drain *i-v* characteristic. Note the general similarity with the switching characteristic of the BJT shown in the previous section. When the input voltage, v_{in}, is zero, the MOSFET conducts virtually no current and the output voltage, v_{out}, is equal to V_{DD}. When v_{in} is equal to 5 V, the MOSFET Q point moves from point A to point B along with the load line, with $v_{DS} = 0.5$ V. Thus, the circuit acts as an inverter. Much as in the case of the BJT, the inverter forms the basis of all MOS logic gates.

An elementary CMOS inverter is shown in Figure 5.7.43. Note first the simplicity of this configuration, which simply employs two enhancement-mode MOSFETs: *p*-channel at the top, denoted by the symbol Q_p, and *n*-channel at the bottom, denoted by Q_n. Recall from Chapter 8 that when v_{in} is low, transistor

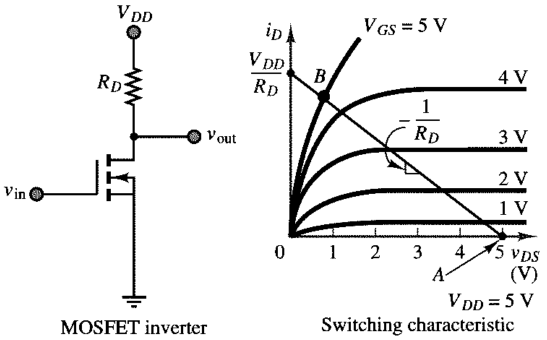

MOSFET inverter

Switching characteristic

FIGURE 5.7.42 MOSFET switching characteristic.

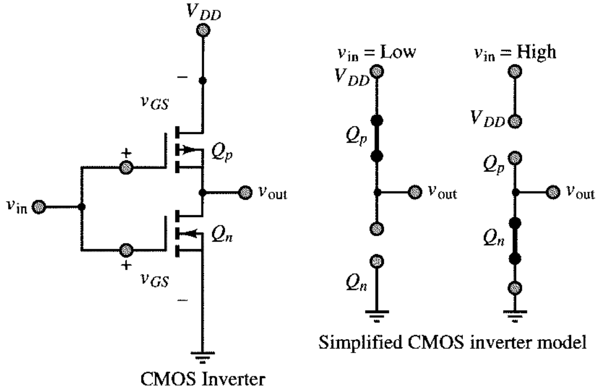

CMOS Inverter

Simplified CMOS inverter model

FIGURE 5.7.43 CMOS inverter.

Q_n is off. However, transistor Q_p sees a gate-to-source voltage $v_{GS} = v_{in} - V_{DD} = -V_{DD}$; in a *p*-channel device, this condition is the counterpart of having $v_{GS} = V_{DD}$ for an *n*-channel MOSFET. Thus, when Q_n is off, Q_p is on and acts very much as a small resistance. In summary, when v_{in} is low, the output is $v_{out} \approx V_{DD}$. When v_{in} is high, the situation is reversed: Qn is now on and acts nearly as a short circuit while Q_p is open (since $v_{GS} = 0$ for Q_p). Thus, $v_{in} \approx 0$. The complementary MOS operation is depicted in Figure 5.7.43 in simplified form by showing each transistor as either a short or an open circuit, depending on it state. This simplified analysis is sufficient for the purpose of a qualitative analysis.

5.8 Power Electronics

The objective of this section is to present a survey of power electronic devices and systems. Power electronic devices form the "muscle" of many electromechanical systems. For example, one finds such devices in many appliances, in industrial machinery, and virtually wherever an electric motor is found, since one of the foremost applications of power electronic devices is to supply and control the currents and voltages required to power electric machines, such as those introduced in Section 5.12.

Classification of Power Electronic Devices

Power semiconductors can be broadly subdivided into five groups: (1) power diodes, (2) thyristors, (3) power bipolar junction transistors (BJTs), (4) insulated-gate bipolar transistors (IGBTs), and (5) static induction transistors (SITs). Figure 5.8.1 depicts the symbols for the most common power electronic devices.

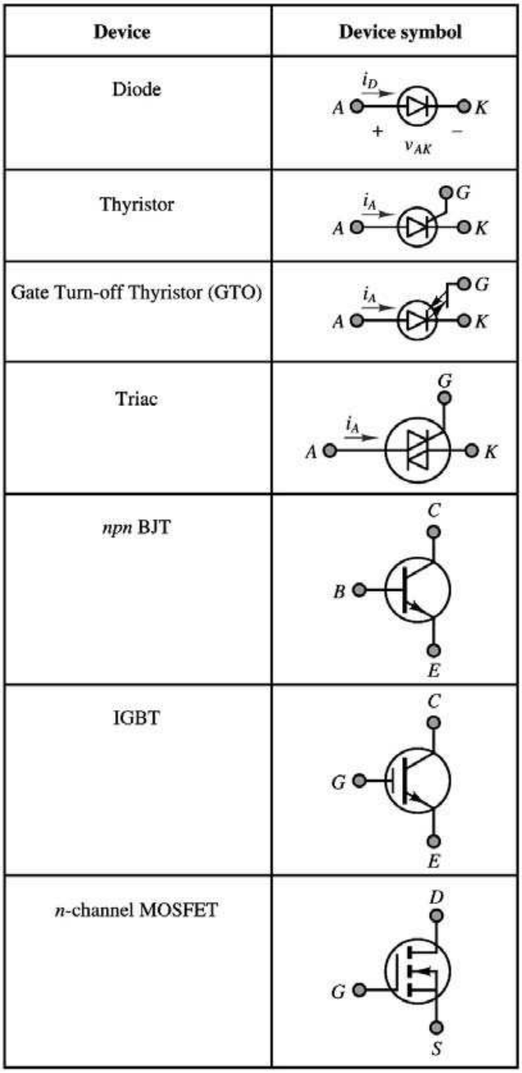

FIGURE 5.8.1 Classification of power electronic devices.

Power diodes are functionally identical to the diodes introduced in Section 5.7, except for their ability to carry much larger currents. A diode conducts in the forward-biased mode when the anode voltage (V_A) is higher than the cathode voltage (V_K). Three types of power diodes exist: general-purpose, high-speed (fast-recovery), and Schottky. Typical ranges of voltage and current are 3000 V and 3500 A for general-purpose diodes and 3000 V and 1000 A for high-speed devices. The latter have switching times as low as a fraction of a microsecond. Schottky diodes can switch much faster (in the nanosecond range) but are limited to around 100 V and 300 A. The forward voltage drop of power diodes is not much higher than that of low-power diodes, being between 0.5 and 1.2 V. Since power diodes are used with rather large voltages, the forward bias voltage is usually considered negligible relative to other voltages in the circuit, and the switching characteristics of power diodes may be considered near ideal. The principal consideration in choosing power diodes is their power rating.

Thyristors function like power diodes with an additional gate terminal that controls the time when the device begins conducting; a thyristor starts to conduct when a small gate current is injected into the gate terminal, provided that the anode voltage is greater than the cathode voltage (or $V_{AK} > 0$ V). The forward voltage drop of a thyristor is of the order of 0.5 to 2 V. Once conduction is initiated, the gate current has no further control. To stop conduction, the device must be reverse-biased; that is, one must ensure that $V_{AK} \leq 0$ V. Thyristors can be rated at up to 6000 V and 3500 A. The **turn-off time** is an important characteristic of thyristors; it represents the time required for the device current to return to zero after external switching of V_{AK}. The fastest turn-off times available are in the range of 10 μsec; however, such turn-off times are achieved only in devices with slightly lower power ratings (1200 V, 1000 A). Thyristors can be subclassified into the following groups: force-commutated and line-commutated thyristors, gate turn-off thyristors (GTOs), reverse-conducting thyristors (RCTs), static induction thyristors (SITHs), gate-assisted turn-off thyristors (GATTs), light-activated silicon-controlled rectifiers (LASCSRs), and MOS-controlled thyristors (MCTs). It is beyond the scope of this chapter to go into a detailed description of each of these types of devices; their operation is typically a slight modification of the basic operation of the thyristor. The reader who wishes to gain greater insight into this topic may refer to one of a number of excellent books specifically devoted to the subject of power electronics.

Two types of thyristor-based device deserve some more attention. The **triac**, as can be seen in Figure 5.8.1, consists of a pair of thyristors connected back to back, with a single gate; this allows for current control in either direction. Thus, a triac may be thought of as bidirectional thyristor. The **gate turn-off** thyristor (GTO), on the other hand, can be turned on by applying a short positive pulse to the gate, like a thyristor, and can also be turned off by application of a short negative pulse. Thus, GTOs are very convenient in that they do not require separate commutation circuits to be turned on and off.

Power BJTs can reach ratings up to 1200 V and 400 A, and they operate in much the same way as a conventional BJT. Power BJTs are used in power converter applications at frequencies up to around 10 kHz. **Power MOSFETs** can operate at somewhat higher frequencies (a few to several tens of kHz), but are limited in power (typically up to 1000 V, 50 A). **Insulated-gate bipolar transistors** (IGBTs) are voltage-controlled (because of their insulated gate, reminiscent of insulated-gate FETs) power transistors that offer superior speed with respect to BJTs but are not quite as fast as power MOSFETs.

Classification of Power Electronic Circuits

The devices that will be discussed in the present chapter find application in a variety of **power electronic circuits**. This section will briefly summarize the principal types of power electronic circuits and will qualitatively describe their operation. The following sections will describe the devices and their operation in these circuits in more detail.

One possible classification of power electronic circuits is given in Table 5.8.1. Many of the types of circuits are similar to circuits that were introduced in earlier chapters. Voltage regulators were introduced in Section 5.7. Power electronic switches function exactly like the transistor switches described in Section 5.7; their function is to act as voltage- or current-controlled switches to turn AC or DC supplies on and off. Transistor power amplifiers are the high-power version of the BJT and MOSFET amplifiers mentioned in Section 5.7.

TABLE 5.8.1 Power Electronic Circuits

Circuit Type	Essential Features
Voltage regulators	Regulate a DC supply to a fixed voltage output
Power amplifiers	Large-signal amplification of voltages and currents
Switches	Electronic switches (for example, transistor switches)
Diode rectifier	Converts fixed AC voltage (single- or multiphase) to fixed DC voltage
AC-DC converter (controlled rectifier)	Converts fixed AC voltage (single- or multiphase) to variable DC voltage
AC-AC converter (AC voltage controller)	Converts fixed AC voltage to variable AC voltage (single- or multiphase)
DC-DC converter (chopper)	Converts fixed DC voltage to variable DC voltage
DC-AC converter (inverter)	Converts fixed DC voltage to variable AC voltage (single- or multiphase)

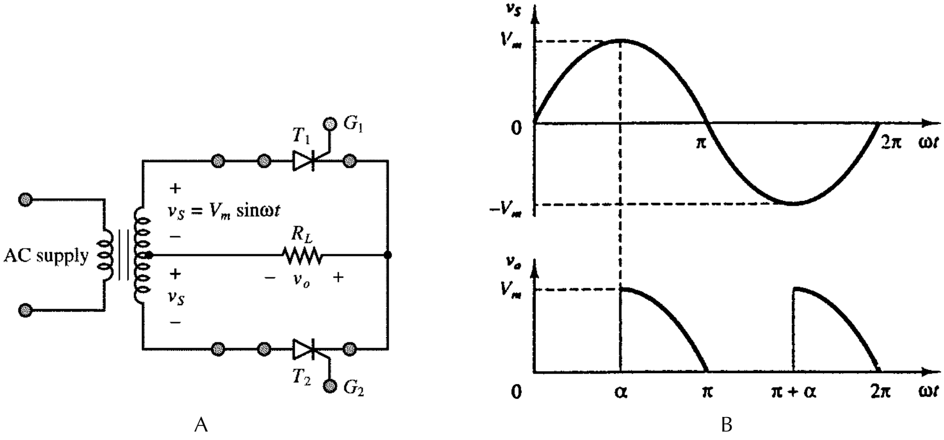

FIGURE 5.8.2 AC-DC converter circuit and waveform.

Diode rectifiers were discussed in Section 5.7 in their single-phase form; similar rectifiers can also be designed to operate with three-phase sources. The operation of a single-phase full-wave rectifier was summarized in Figure 5.8.2. AC-DC converters are also rectifiers, but they take advantage of the controlled properties of thyristors. The thyristor gate current can be timed to "fire" conduction at variable times, resulting in a variable DC output, as illustrated in Figure 5.8.2, which shows the circuit and behavior of a single-phase AC-DC converter. This type of converter is very commonly used as a supply for DC electric motors. In Figure 5.8.2 α is the firing angle of thyristor T_1, where the device starts to conduct.

AC-AC converters are used to obtain a variable AC voltage from a fixed AC source. Figure 5.8.3 shows a triac-based AC-AC converter, which takes advantage of the bidirectional capability of triacs to control the rms value of an alternating voltage. Note in particular that the resulting AC waveform is no longer a pure sinusoid even though its fundamental period (frequency) is unchanged. A DC-DC converter, also known as a *chopper*, or *switching regulator*, permits conversion of a fixed DC source to a variable DC supply. Figure 5.8.4 shows how such an effect may be obtained by controlling the base-emitter voltage of a bipolar transistor, enabling conduction at the desired time. This results in the conversion of the DC input voltage to a variable-duty-cycle output voltage, whose average value can be controlled by selecting the "on" time of the transistor. DC-DC converters find application as variable voltage supplies for DC electric motors used in electric vehicles.

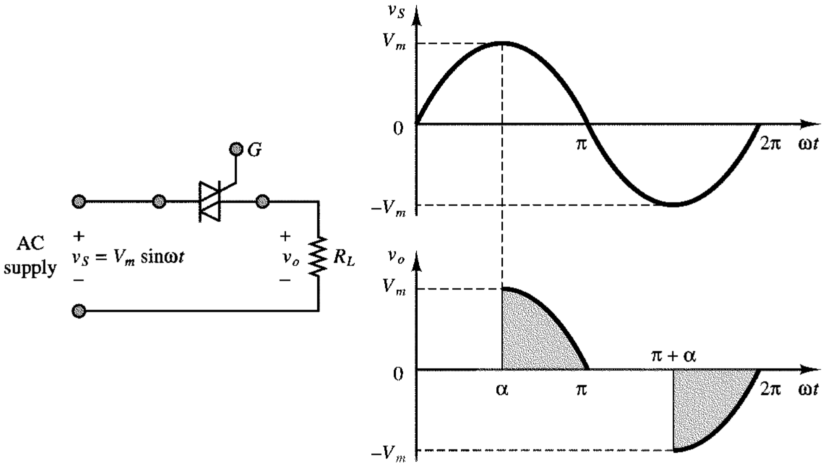

FIGURE 5.8.3 AC-AC converter circuit and waveform.

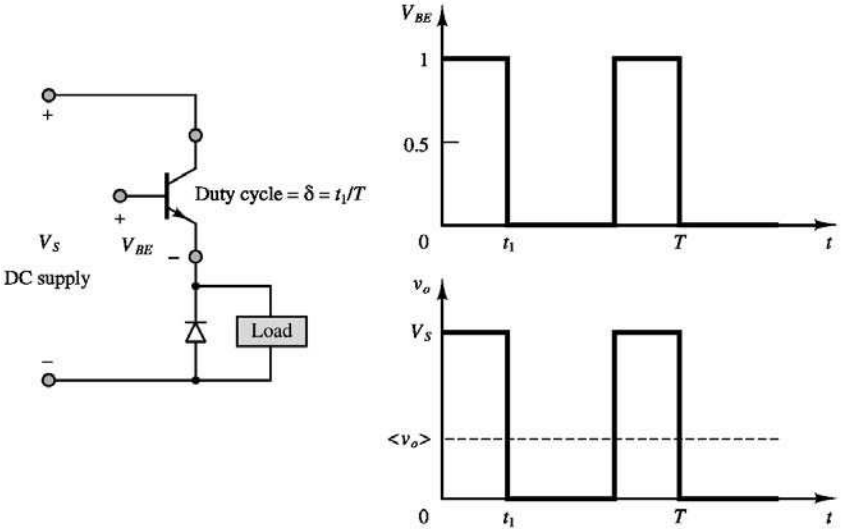

FIGURE 5.8.4 DC-DC converter circuit and waveform.

Finally, DC-AC supplies, or inverters, are used to convert a fixed DC supply to a variable AC supply; they find application in AC motor control. The operation of these circuits is rather complex; it is illustrated conceptually in the waveforms of Figure 5.8.5, where it is shown that by appropriately switching two pairs of transistors it is possible to generate an alternating current waveform (square wave).

Each of the circuits of Table 5.8.1 will now be analyzed in greater detail.

Rectifiers and Controlled Rectifiers (AC-DC Converters)

Thyristors and Controlled Rectifiers

In a number of applications, it is useful to be able to externally control the amount of current flowing from an AC source to the load. A family of power semiconductor devices called **controlled rectifiers** allows for control of the rectifiers state by means of a third input, called the gate. Figure 5.8.6 depicts the appearance of a **thyristor**, or **silicon-controlled rectifier** (SCR), illustrating how the physical structure of this device consists of four layers, alternating *p*-type and *n*-type material. Note that the circuit symbol for the thyristor suggests that this device acts as a diode, with provision for an additional external control signal.

The operation of the thyristor can be explained in an intuitive fashion as follows. When the voltage v_{AK} is negative (i.e., providing reverse bias), the thyristor acts just like a conventional *pn* junction in the off state. When v_{AK} is forward-biased *and* a small amount of current is injected into the gate, the thyristor conducts forward current. The thyristor then continues to conduct (even in the absence of gate current), provided that v_{AK} remains positive. Figure 5.8.7 depicts the *i-v* curve for the thyristor. Note that the thyristor has two stable states, determined by the bias v_{AK} and by the gate current. In summary, the thyristor acts as a diode with a control gate that determines the time when conduction begins.

A somewhat more accurate description of thyristor operation may be provided if we realize that the four-layer *pnpn* device can be modeled as a *pnp* transistor connected to an *npn* transistor. Figure 5.8.8 clearly shows that, physically, this is a realistic representation. Note that the anode current, i_A, is equal to the emitter current of the *pnp* transistor (labeled Q_p) and the base current of Q_p is equal to the collector current of the *npn* transistor, Q_n. Likewise, the base current of Q_n is the sum of the gate current and the collector current of Q_p. The behavior of this transistor model is explained as follows. Suppose, initially, i_G and i_{B_n} are both zero. Then it follows that Q_n is in cutoff, and therefore $i_{C_n} = 0$. But if $i_{C_n} = 0$, then the base current going into Q_p is also zero and Q_p is also in cutoff, and $i_{C_n} = 0$, consistent with our initial

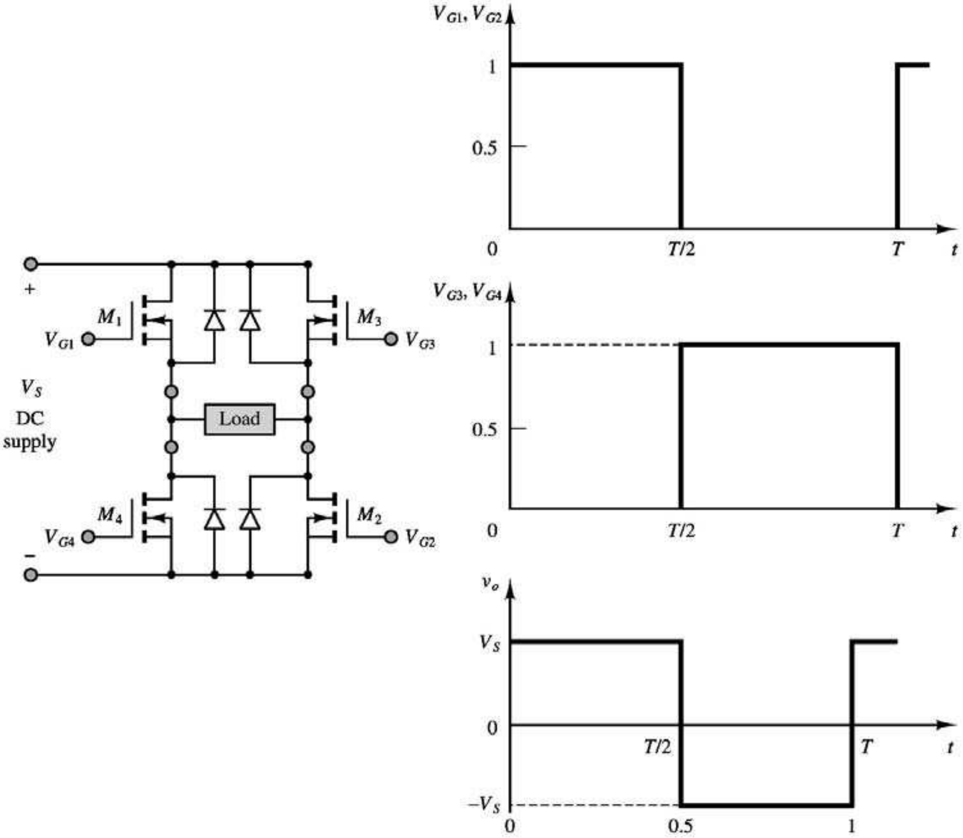

FIGURE 5.8.5 DC-AC converter circuit and waveform.

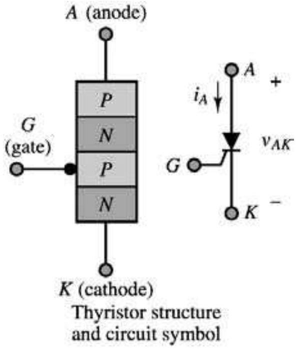

FIGURE 5.8.6 Thyristor structure and circuit symbol.

assumption. Thus, this is a stable state, in the sense that unless an external condition perturbs the thyristor, it will remain off.

Now, suppose a small pulse of current is injected at the gate. Then $i_{B_n} > 0$ and Q_n starts to conduct, provided, of course, that $v_{AK} > 0$. At this point, i_{C_n}, and therefore i_{B_p}, must be greater than zero, so that Q_p conducts. It is important to note that once the gate current has turned Q_n on, Q_p also conducts, so that $i_{C_p} > 0$. Thus, even though i_G may cease, once this "on" state is reached, $i_{C_p} = i_{B_n}$ continues to drive Q_n so that the on state is also self-sustaining. The only condition that will cause the thyristor to revert to the off state is the condition in which v_{AK} becomes negative; in this case, both transistors return to the cutoff state.

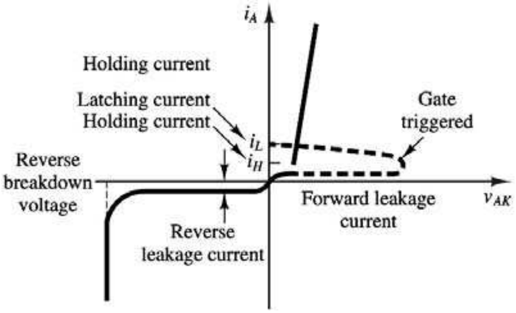

FIGURE 5.8.7 Thyristor *i*-*v* characteristic.

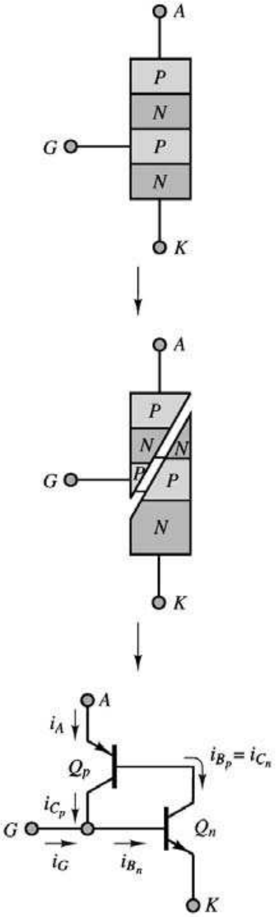

FIGURE 5.8.8 Thyristor two-transistor model.

In a typical controlled rectifier application, the device is used as a half-wave rectifier that conducts only after a trigger pulse is applied to the gate. Without concerning ourselves with how the trigger pulse is generated, we can analyze the general waveforms for the circuit of Figure 5.8.9 as follows. Let the voltage v_{trigger} be applied to the gate of the thyristor at $t = \tau$. The voltage v_{trigger} can be a short pulse, provided by a suitable trigger-timing circuit (Section 5.11 will discuss timing and switching circuits). At $t = \tau$, the thyristor begins to conduct, and it continues to do so until the AC source enters its negative cycle. Figure 5.8.10 depicts the relevant waveforms.

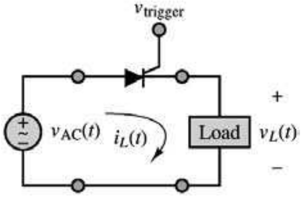

FIGURE 5.8.9 Controlled rectifier circuit.

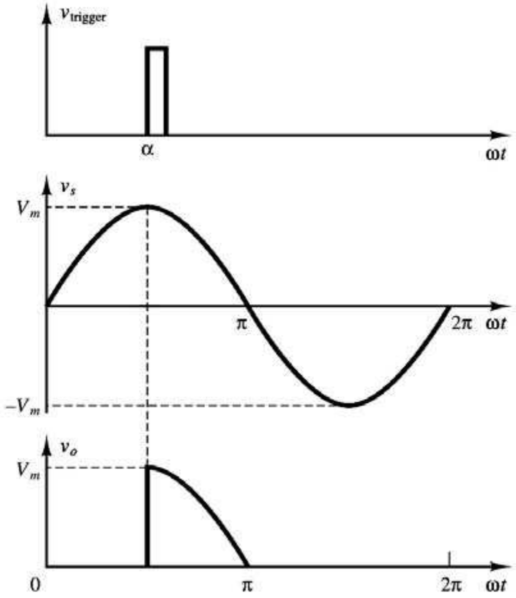

FIGURE 5.8.10 Half-wave controlled rectifier waveforms.

Note how the DC load voltage is controlled by the firing time τ, according to the following expression:

$$\langle v_L \rangle = V_L = \frac{1}{T}\int_{\tau}^{T/2} v_{\text{AC}}(t)\,dt \tag{5.8.1}$$

where T is the period of $v_{AC}(t)$, Now, if we let

$$v_{\text{AC}}(t) = A\sin\omega t \tag{5.8.2}$$

we can express the average (DC) value of the load voltage

$$V_L = \frac{1}{T}\int_{\tau}^{T/2} A\sin\omega t\,dt = (1+\cos\omega t)\frac{A}{2\pi} \tag{5.8.3}$$

in terms of the **firing angle**, α, defined as

$$\alpha = \omega t \tag{5.8.4}$$

By evaluating the integral of Equation (5.8.3), we can see that the (DC) load voltage amplitude depends on the firing angle, α:

$$V_L = (1+\cos\alpha)\frac{A}{2\pi} \tag{5.8.5}$$

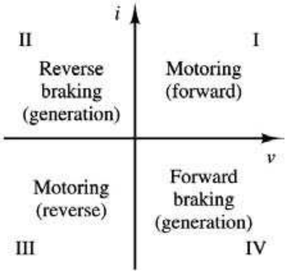

FIGURE 5.8.11 The four quadrants of an electric drive.

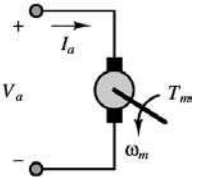

FIGURE 5.8.12 DC motor.

Electric Motor Drives

The advent of high-power semiconductor devices has made it possible to design effective and relatively low-cost electronic supplies that take full advantage of the capabilities of the devices introduced in this chapter. Electronic power supplies for DC and AC motors have become one of the major fields of application of power electronic devices. The last section of this chapter is devoted to an introduction to two families of power supplies, or **electric drives: choppers**, or **DC-DC converters**; and **inverters**, or **DC-AC converters**. These circuits find widespread application in the control of AC and DC motors in a variety of applications and power ranges.

Before we delve into the discussion of the electronic supplies, it will be helpful to introduce the concept of quadrants of operation of a drive. Depending on the direction of current flow and on the polarity of the voltage, an electronic drive can operate in one of four possible modes, as indicated in Figure 5.8.11.

Choppers (DC-DC Converters)

As the name suggests, a DC-DC converter is capable of converting a fixed DC supply to a variable DC supply. This feature is particularly useful in the control of the speed of a DC motor (described in greater detail in Section 5.12). In a DC motor, shown schematically in Figure 5.8.12, the developed torque, T_m, is proportional to the current supplied to the motor **armature**, I_a, while the **electromotive force** (emf), E_a, which is the voltage developed across the armature, is proportional to the speed of rotation of the motor, ω_m. A DC motor is an electromechanical energy-conversion system; that is, it converts electrical to mechanical energy (or vice versa if it is used as a generator); if we recall that the product of torque and speed is equal to power in the mechanical domain, and that current times voltage is equal to power in the electrical domain, we conclude that in the ideal case of complete energy conversion, we have

$$E_a \times I_a = T_m \times \omega_m \tag{5.8.6}$$

Naturally, such ideal energy conversion cannot take place; however, we can see that there is a correspondence between the four-electrical quadrants of Figure 5.8.11 and the mechanical power output of the motor: namely, if the voltage and current are both positive or both negative, the electrical power will be positive, and so will the mechanical power. This corresponds to the **forward** (*i*, *v* both positive) and **reverse** (*i*,*v* both negative) **motoring** operation. Forward motoring corresponds to quadrant I, and reverse motoring to quadrant III in Figure 5.8.12. If the voltage and current are of opposite polarity (quadrants II and IV), electrical energy is flowing back to the electric drive; in mechanical terms this corresponds to a braking condition. Operation in the fourth quadrant can lead to **regenerative braking**, so called

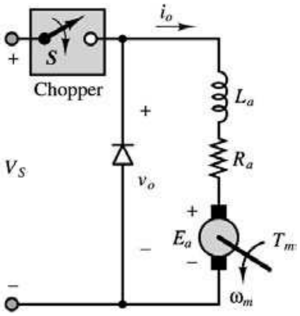

FIGURE 5.8.13 Step-down chopper (buck converter).

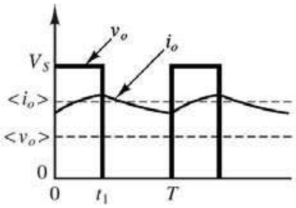

FIGURE 5.8.14 Step-down chopper waveforms.

because power is generated by making current flow back to the source. This mode could be useful, for example, to recharge a battery supply, because the braking energy can be regenerated by returning it to the electric supply.

A simple circuit that can accomplish the task of providing a variable DC supply from a fixed DC source is the **step-down chopper (buck converter)**, shown in Figure 5.8.13. The circuit consists of a "chopper" switch, denoted by the symbol S, and a free-wheeling diode. The switch can be any of the power switches described in this chapter, for example, a power BJT or MOSFET, or a thyristor; see, for example, the BJT switch of Figure 5.8.4. The circuit to the right of the diode is a model of a DC motor, including the inductance and resistance of the armature windings and the effect of the back emf E_a. When the switch is turned on (say, at $t = 0$), the supply V_s is connected to the load and $v_o = V_s$. The load current, i_o, is determined by the motor parameters. When the switch is turned off, the load current continues to flow through the free-wheeling diode, but the output voltage is now $v_o = 0$. At time T, the switch is turned on again, and the cycle repeats.

Figure 5.8.14 depicts the v_o and i_o waveforms. The average value of the output voltage, $\langle v_o \rangle$, is given by the expression

$$\langle v_o \rangle = \frac{t_1}{T} V_S = \delta V_S \tag{5.8.7}$$

where δ is the **duty cycle** of the chopper. The step-down chopper has a useful range,

$$0 \le \langle v_o \rangle \le V_S \tag{5.8.8}$$

It is also possible to increase the range of a DC-DC converter to above the supply voltage by making use of the energy-storage properties of an inductor; the resulting circuit is shown in Figure 5.8.15. When the chopper switch, S, is on, the supply current flows through the inductor and the closed switch, storing energy in the inductor; the output voltage, v_o, is zero, since the switch is a short circuit. When the switch is open, the supply current will flow through the load via the diode; but the inductor voltage is negative during the transient following the opening of the switch and therefore adds to the source voltage: the energy stored in the inductor while the switch was closed is now released and transferred to the load. This stored energy makes it possible for the output voltage to be higher than the supply voltage for a finite period of time.

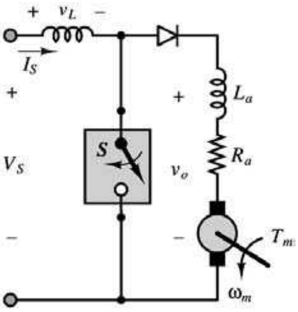

FIGURE 5.8.15 Step-up chopper (boost converter).

Let t_1 once again be the time during which the chopper conducts; neglecting for the moment the ripple in the supply current, the energy stored in the inductor during this period is

$$W_i = V_S I_S t_1 \tag{5.8.9}$$

When the chopper is off, the energy released to the load is

$$W_i = \left(\langle v_o \rangle - V_S\right) I_S \left(T - t_1\right) \tag{5.8.10}$$

If the system is lossless, the two energy expressions must be equal:

$$V_S I_S t_1 = \left(\langle v_o \rangle - V_S\right) I_S \left(T - t_1\right) \tag{5.8.11}$$

and we can determine the average output voltage to be

$$\langle v_o \rangle = V_S \frac{t_1 + T - t_1}{T - t_1} = V_S \frac{T}{T - t_1} = V_S \frac{1}{1 - \delta} \tag{5.8.12}$$

Since the duty cycle, δ, is always less than 1, the theoretical range of the supply is

$$V_S \le \langle v_o \rangle < \infty \tag{5.8.13}$$

The waveforms for the boost converter are shown in Figure 5.8.16.

A step-up chopper can also be used to provide regenerative braking: if the "supply" voltage is the motor armature voltage and the output voltage is the fixed DC supply (battery) voltage, then power can be made to flow from the motor to the DC supply (i.e., recharging the battery). This configuration is shown in Figure 5.8.17.

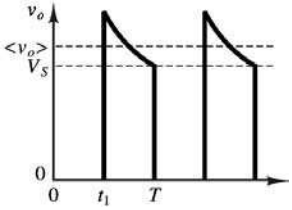

FIGURE 5.8.16 Step-up chopper output voltage waveform.

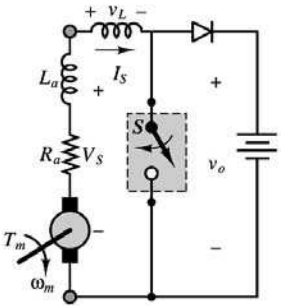

FIGURE 5.8.17 Step-up chopper used for regenerative braking.

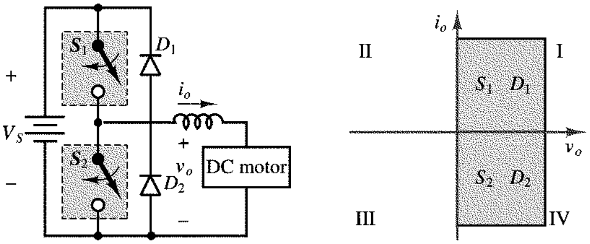

FIGURE 5.8.18 Two-quadrant chopper.

Finally, the operation of the step-down and step-up choppers can be combined into a **two-quadrant chopper**, shown in Figure 5.8.18. The circuit shown schematically in Figure 5.8.18 can provide both regenerative braking and motoring operation in a DC motor. When switch S_2 is open and switch S_1 serves as a chopper, the circuit operates as a step-down chopper, precisely as was described earlier in this section (convince yourself of this by redrawing the circuit with S_2 and D_2 replaced by open circuits). Thus, the drive and motor operate in the first quadrant (motoring operation). The output voltage, v_o, will switch between V_S and zero, as shown in Figure 5.8.14, and the load current will flow in the direction indicated by the arrow in Figure 5.8.18 diode D_1 free-wheels whenever S_1 is open. Since both output voltage and current are positive, the system operates in the first quadrant.

When switch S_1 is open and switch S_2 serves as a chopper, the circuit resembles a step-up chopper. The source is the motor emf, E_a, and the load is the battery; this is the situation depicted in Figure 5.8.17. The current will now be negative, since the sum of the motor emf and the voltage across the inductor (corresponding to the energy stored during the "on" cycle of S_2) is greater than the battery voltage. Thus, the drive operates in the fourth quadrant.

Inverters (DC-AC Converters)

As will be explained in Section 5.12, variable-speed drives for AC motors require a multiphase variable-frequency, variable-voltage supply. Such drives are called *DC-AC converters*, or *inverters*. Inverter circuits can be quite complex, so the objective of this section is to present a brief introduction to the subject, with the aim of illustrating the basic principles. A **voltage source inverter** (VSI) converts the output of a fixed DC supply (e.g., a battery) to a variable-frequency AC supply. Figure 5.8.19 depicts a **half-bridge VSI**; once again, the switches can be either bipolar or MOS transistors, or thyristors. The operation of this circuit is as follows. When switch S_1 is turned on, the output voltage is in the positive half-cycle, and $v_o = V_S/2$. The switching sequence of S_1 and S_2 is shown in Figure 5.8.20. It is important that each switch be turned off before the other is turned on; otherwise, the DC supply would be short-circuited. Since the load is always going to be inductive in the case of a motor drive, it is important to observe that the load current, i_o, will lag the voltage waveform, as shown in Figure 5.8.20. As shown in this figure, there will be some portions of the cycle in which the voltage is positive but the current is negative. The function of diodes D_1 and D_2 is precisely to conduct the load current whenever it is of direction opposite to the

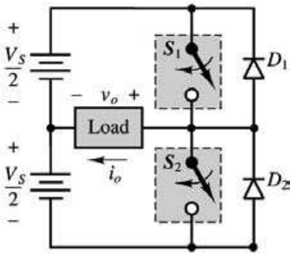

FIGURE 5.8.19 Half-bridge voltage source inverter.

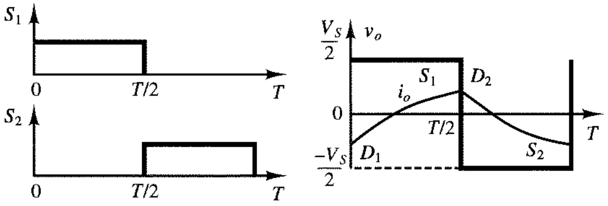

FIGURE 5.8.20 Half-bridge voltage source inverter waveforms.

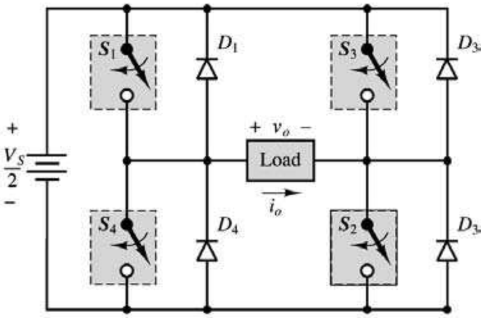

FIGURE 5.8.21 Full-bridge voltage source inverter.

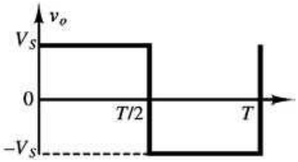

FIGURE 5.8.22 Half-bridge voltage source inverter output voltage waveform.

polarity of the voltage. Without these diodes, there would be no load current in this case. Figure 5.8.20 also shows which element is conducting in each portion of the cycle.

A full-bridge version of the VSI can also be designed as shown in Figure 5.8.21; the associated output voltage waveform is shown in Figure 5.8.22. A 3-phase VSI is shown in Figure 5.8.23.

5.9 Operational Amplifiers

In this section we will analyze the properties of a general-purpose amplifier circuit known as the *operational amplifier.*

The Operational Amplifier

An **operational amplifier** is an **integrated circuit**, that is, a large collection of individual electrical and electronic circuits integrated on a single silicon wafer. An operational amplifier — or op-amp — can perform a great number of operations, such as addition, filtering, or integration, which are all based on

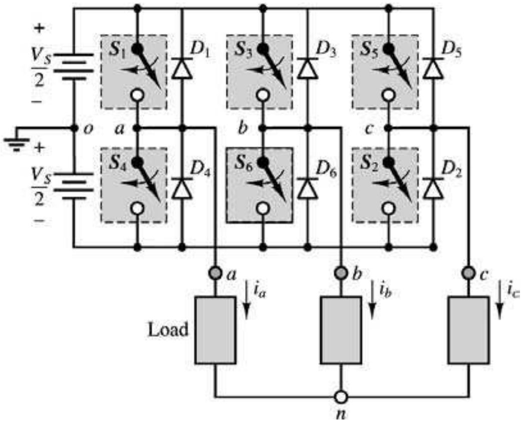

FIGURE 5.8.23 Three-phase voltage source inverter.

the properties of ideal amplifiers and of ideal circuit elements. The introduction of the operational amplifier in integrated circuit form marked the beginning of a new era in modern electronics. Since the introduction of the first IC op-amp, the trend in electronic instrumentation has been to move away from the discrete (individual-component) design of electronic circuits, toward the use of integrated circuits for a large number of applications. This statement is particularly true for applications of the type the nonelectrical engineer is likely to encounter: op-amps are found in most measurement and instrumentation applications, serving as extremely versatile building blocks for any application that requires the processing of electrical signals.

In the following pages, simple circuit models of the op-amp will be introduced. The simplicity of the models will permit the use of the op-amp as a circuit element, or building block, without the need to describe its internal workings in detail. Integrated circuit technology has today reached such an advanced stage of development that it can be safely stated that for the purpose of many instrumentation applications, the op-amp can be treated as an ideal device. Following the introductory material presented in this chapter, more advanced instrumentation applications will be explored in Section 5.11.

The Open-Loop Model

The ideal operational amplifier behaves very much as an ideal **differential amplifier**, that is, a device that amplifies the difference between two input voltages. Operational amplifiers are characterized by near-infinite input resistance and very small output resistance. As shown in Figure 5.9.1 the output of the op-amp is an amplified version of the difference between the voltages present at the two inputs:

$$v_{\text{out}} = A_{V(OL)}\left(v^{+} - v^{-}\right) \tag{5.9.1}$$

The input denoted by a positive sign is called the **noninverting input** (or terminal), while that represented with a negative sign is termed the **inverting input** (or terminal). The amplification factor, or gain, $A_{V(OL)}$, is called the **open-loop voltage gain** and is quite large by design, typically of the order of 10^5 to 10^7; it will soon become apparent why a large open-loop gain is a desirable characteristic. Together with the high input resistance and low output resistance, the effect of a large amplifier open-loop voltage gain, $A_{V(OL)}$, is such that op-amp circuits can be designed to perform very nearly as ideal voltage or current amplifiers. In effect, to analyze the performance of an op-amp circuit, only one assumption will be needed: that the current flowing into the input circuit of the amplifier is zero, or

$$i_{\text{in}} = 0 \tag{5.9.2}$$

This assumption is justified by the large input resistance and large open-loop gain of the operational amplifier. The model just introduced will be used to analyze three amplifier circuits in the next part of this section.

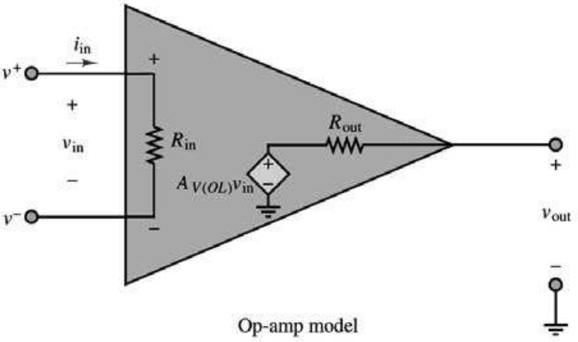

Op-amp model

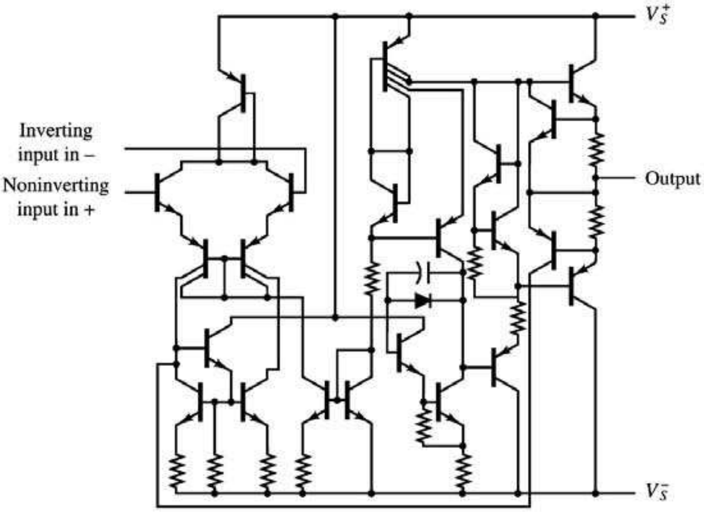

IC op-amp diagram

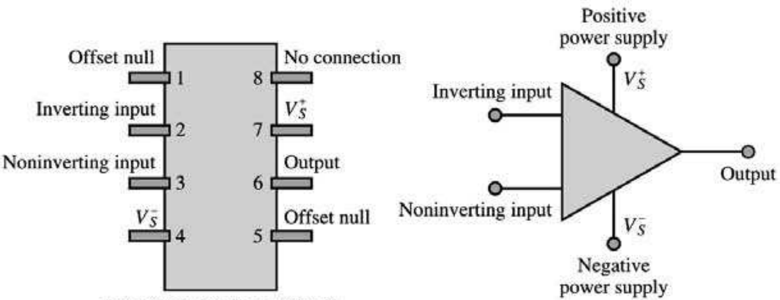

Integrated circuit operational amplifier (IC op-amp)

Simplified circuit symbol

FIGURE 5.9.1 Operational amplifier model symbols, and circuit diagram.

The Operational Amplifier in the Closed-Loop Mode

The Inverting Amplifier. One of the more popular circuit configurations of the op-amp, because of its simplicity, is the so-called inverting amplifier, shown in Figure 5.9.2.

$$v_S = -v_{\text{out}}\left(\frac{1}{R_F/R_S} + \frac{1}{A_{V(OL)}R_F/R_S} + \frac{1}{A_{V(OL)}}\right) \tag{5.9.3}$$

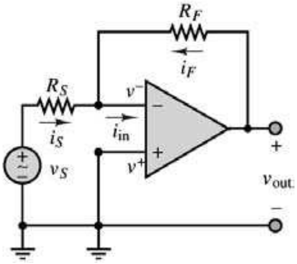

FIGURE 5.9.2 Inverting amplifier.

If the open-loop gain of the amplifier, $A_{V(OL)}$, is sufficiently large, the terms $1/(A_{V(OL)}R_F/R_S)$ and $1/A_{V(OL)}$, are essentially negligible, compared with $1/(R_F/R_S)$. As stated earlier, typical values of $A_{V(OL)}$ range from 10^5 to 10^7, and thus it is reasonable to conclude that, to a close approximation, the following expression describes the closed-loop gain of the inverting amplifier:

$$v_{out} = -\frac{R_F}{R_S}v_S \quad \text{Inverting amplifier closed-loop gain} \tag{5.9.4}$$

Next, we show that by making an additional assumption it is possible to simplify the analysis considerably. Consider that, as was shown for the inverting amplifier, the inverting terminal voltage is given by

$$v^- = -\frac{v_{out}}{A_{V(OL)}} \tag{5.9.5}$$

Clearly, as $A_{V(OL)}$ approaches infinity, the inverting-terminal voltage is going to be very small (practically, of the order of microvolts). It may then be assumed that *in the inverting amplifier*, v^- is virtually zero:

$$v^- \approx 0 \tag{5.9.6}$$

This assumption prompts an interesting observation (which may not yet appear obvious at this point): the effect of the feedback connection from output to inverting input is to force the voltage at the inverting input to be equal to that at the noninverting input.

This is equivalent to stating that for an op-amp *with negative feedback*,

$$v^- \approx v^+ \tag{5.9.7}$$

The analysis of the operational amplifier can now be greatly simplified if the following two assumptions are made:

$$\begin{aligned} &1. \quad i_{in} = 0 \\ &2. \quad v^- = v^+ \end{aligned} \tag{5.9.8}$$

This technique will be tested in the next subsection by analyzing a noninverting amplifier configuration.

A useful op-amp circuit that is based on the inverting amplifier is the **op-amp summer**, or **summing amplifier**. This circuit, shown in Figure 5.9.3, is used to add signal sources. The primary advantage of using the op-amp as a summer is that the summation occurs independently of load and source impedances, so that sources with different internal impedances will not interact with each other.

$$v_{out} = -\sum_{n=1}^{N} \frac{R_F}{R_{S_n}} v_{S_n} \tag{5.9.9}$$

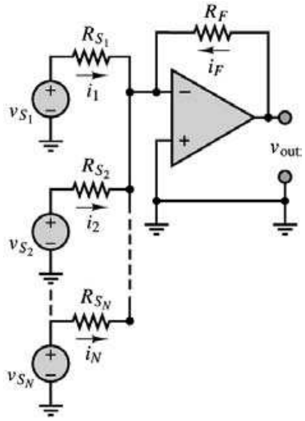

FIGURE 5.9.3 Summing amplifier.

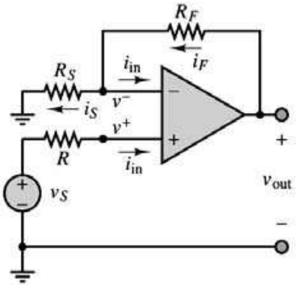

FIGURE 5.9.4 Noninverting amplifier.

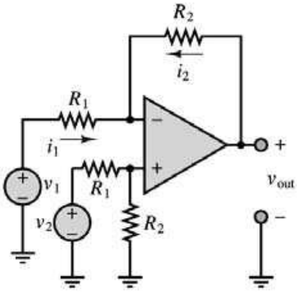

FIGURE 5.9.5 Differential amplifier.

That is, the output consists of the weighted sum of N input signal sources, with the weighting factor for each source equal to the ratio of the feedback resistance to the source resistance.

The Noninverting Amplifier. To avoid the negative gain (i.e., phase inversion) introduced by the inverting amplifier, a noninverting amplifier configuration is often employed. A typical noninverting amplifier is shown in Figure 5.9.4; note that the input signal is applied to the noninverting terminal this time.

$$\frac{v_{out}}{v_S} = 1 + \frac{R_F}{R_S} \quad \text{Noninverting amplifier closed-loop gain}$$

The Differential Amplifier. The third closed-loop model examined in this chapter is a combination of the inverting and noninverting amplifiers; it finds frequent use in situations where the difference between two signals needs to be amplified. The basic differential amplifier circuit is shown in Figure 5.9.5, where the two sources, v_1 and v_2, may be independent of each other, or may originate from the same process, as they do in Example 5.9.1.

The following expression for the output voltage is obtained:

$$v_{\text{out}} = R_2\left[\frac{-v_1}{R_1} + \frac{1}{R_1 + R_2}v_2 + \frac{R_2}{R_1(R_1 + R_2)}v_2\right]$$

$$= \frac{R_2}{R_1}(v_2 - v_1)$$

In practice, it is often necessary to amplify the difference between two signals that are both corrupted by noise or some other form of interference. In such cases, the differential amplifier provides an invaluable tool in amplifying the desired signal while rejecting the noise. Example 5.9.1 provides a realistic look at a very common application of the differential amplifier.

Example 5.9.1 An EKG Amplifier

This example illustrates the principle behind a two-lead electrocardiogram (EKG) measurement. The desired cardiac waveform is given by the difference between the potentials measured by two electrodes suitably placed on the patient's chest, as shown in Figure 5.9.6. A healthy, noise-free EKG waveform, $v_1 - v_2$, is shown in Figure 5.9.7.

Unfortunately, the presence of electrical equipment powered by the 60-Hz, 110-VAC line current causes undesired interference at the electrode leads: the lead wires act as antennas and pick up some of the 60-Hz signal in addition to the desired EKG voltage. In effect, instead of recording the desired EKG signals, v_1 and v_2, the two electrodes provide the following inputs to the EKG amplifier, shown in Figure 5.9.8.

Lead 1:

$$v_1(t) + v_n(t) = v_1(t) + V_n\cos(377t + \phi_n)$$

Lead 2:

$$v_2(t) + v_n(t) = v_2(t) + V_n\cos(377t + \phi_n)$$

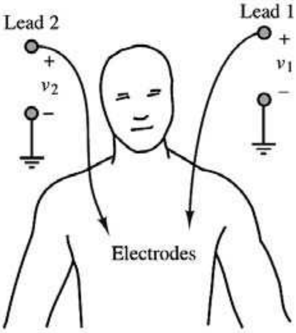

FIGURE 5.9.6 Two-lead electrocardiogram.

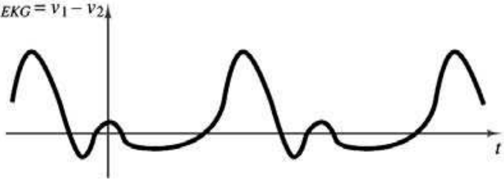

FIGURE 5.9.7 EKG waveform.

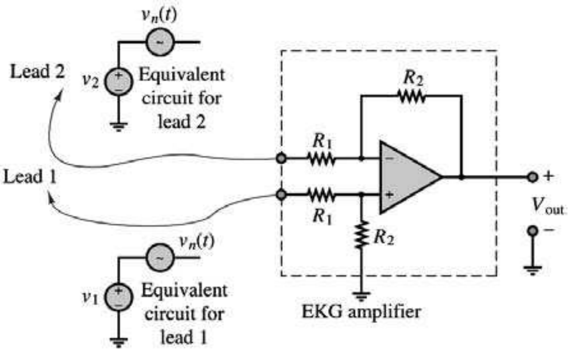

FIGURE 5.9.8 EKG amplifier.

The interference signal, $V_n \cos(377t + \phi n)$, is approximately the same at both leads, because the electrodes are chosen to be identical (e.g., they have the same lead lengths) and are in close proximity to each other. Further, the nature of the interference signal is such that it is common to both leads, since it is a property of the environment the EKG instrument is embedded in. On the basis of the analysis presented earlier, then,

$$v_{out} = \frac{R_2}{R_1}\left[\left(v_1 + v_n(t)\right) - \left(v_2 + v_n(t)\right)\right]$$

or

$$v_{out} = \frac{R_2}{R_1}\left(v_1 - v_2\right)$$

Thus, the differential amplifier nullifies the effect of the 60-Hz interference, while amplifying the desired EKG waveform.

The preceding example introduced the concept of so-called **common-mode** and **differential-mode signals**. In the EKG example, the desired differential-mode EKG signal was amplified by the op-amp while the common-mode disturbance was canceled. Thus, the differential amplifier provides the ability to reject common-mode signal components (such as noise or undesired DC offsets) while amplifying the differential-mode components. This is a very desirable feature in instrumentation systems. In practice, rejection of the common-mode signal is not always complete: some of the common-mode signal component will always appear in the output. This fact gives rise to a figure of merit called the *common-mode rejection ratio*, which is discussed later in this section.

Often, to provide impedance isolation between bridge transducers and the differential amplifier stage, the signals v_1 and v_2 are amplified separately. This technique gives rise to the so-called **instrumentation amplifier** (IA), shown in Figure 5.9.9. Example 5.9.2 illustrates the calculation of the closed-loop gain for a typical instrumentation amplifier.

Example 5.9.2 Instrumentation Amplifier

In this example, we compute the closed-loop gain of the instrumentation amplifier of Figure 5.9.9.

Solution. To carry out the desired analysis as easily as possible, it is helpful to observe that resistor R_1 is shared by the two input amplifiers. This corresponds to having each amplifier connected to a resistor equal to $R_1/2$, as shown in Figure 5.9.10(a). Because of the symmetry of the circuit, one can view the shared resistor as being connected to ground in the center, so that the circuit takes the form of a noninverting amplifier, with closed-loop gain given by

$$A = 1 + \frac{2R_2}{R_1} \tag{5.9.10}$$

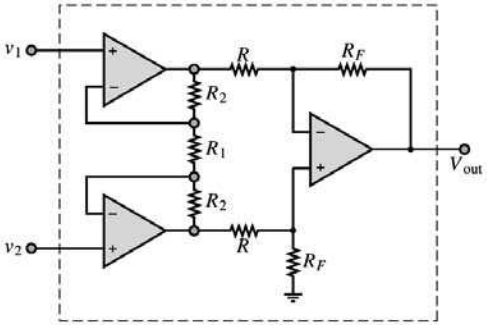

FIGURE 5.9.9 Instrumentation amplifier.

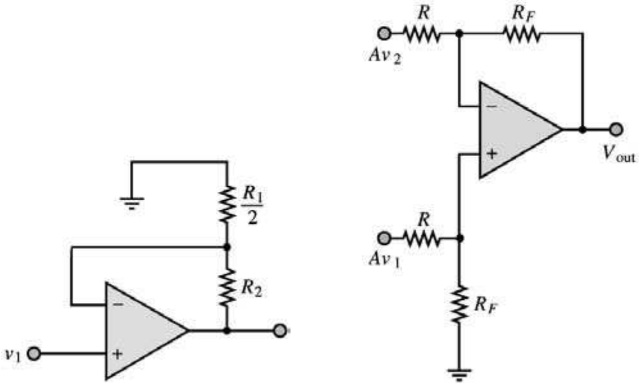

ab

FIGURE 5.9.10 (a) and (b).

Thus, each of the input voltages is amplified by this gain, and the overall gain of the instrumentation amplifier can then be computed by considering that the voltage difference ($Av_1 - Av_2$) is then amplified by the differential amplifier stage, with gain R_F/R, as shown in Figure 5.9.10(b):

$$v_{out} = \frac{R_F}{R}(Av_1 - v_2) = \frac{R_F}{R}\left(1 + \frac{2R_2}{R_1}\right)(v_1 - v_2) \tag{5.9.11}$$

Active Filters

The class of filters one can obtain by means of op-amp designs is called **active filters**, because op-amps can provide amplification (gain) in addition to the filtering effects already studied in Section 5.6 for passive circuits (i.e., circuits comprising exclusively resistors, capacitors, and inductors).

The easiest way to see how the frequency response of an op-amp can be shaped (almost) arbitrarily is to replace the resistors R_F and R_S in Figure 5.9.2 and Figure 5.9.4 with impedances Z_F and Z_S, as shown in Figure 5.9.11. It is a straightforward matter to show that in the case of the inverting amplifier, the expression for the closed loop gain is given by

$$\frac{\mathbf{V}_{out}}{\mathbf{V}_S}(j\omega) = -\frac{Z_F}{Z_S} \tag{5.9.12}$$

whereas for the noninverting case, the gain is

$$\frac{\mathbf{V}_{out}}{\mathbf{V}_S}(j\omega) = 1 + \frac{Z_F}{Z_S} \tag{5.9.13}$$

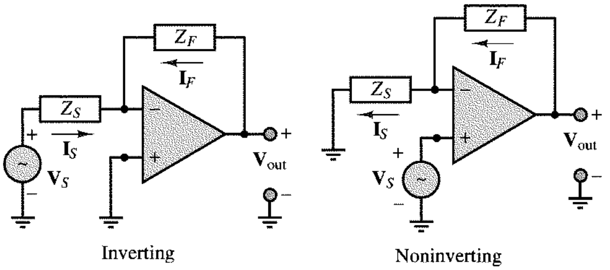

FIGURE 5.9.11 Op-amp circuits employing complex impedances.

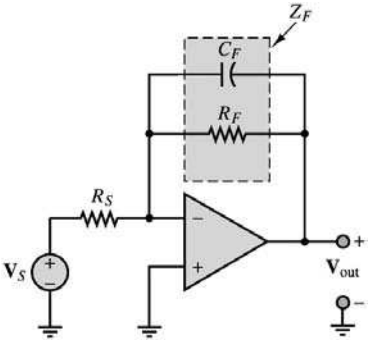

FIGURE 5.9.12 Active low-pass filter.

where Z_F and Z_S can be arbitrarily complex impedance functions and where $\mathbf{V}_S$, $\mathbf{V}_{out}$, $\mathbf{I}_F$, and $\mathbf{I}_S$ are all phasors. Thus, it is possible to shape the frequency response of an ideal op-amp filter simply by selecting suitable ratios of feedback impedance to source impedance. The simplest op-amp low-pass filter is shown in Figure 5.9.12. The closed-loop gain $A_{LP}(j\omega)$ is then computed to be

$$A_{LP}(j\omega) = -\frac{Z_F}{Z_S} = -\frac{R_F/R_S}{1 + j\omega C_F R_F}$$

It should be apparent that the response of this op-amp filter is just an amplified version of that of the passive filter. Figure 5.9.13 depicts the amplitude response of the active low-pass filter (in the figure, $R_F/R_S = 10$ and $1/R_F C_F = 1$) in two different graphs; the first two plots the amplitude ratio $\mathbf{V}_{out}/\mathbf{V}_S$ vs. radian frequency, ω, on a logarithmic scale, while the second plots the amplitude ratio $20 \log_{10} (\mathbf{V}_{out}/\mathbf{V}_S)$ (in units of dB), also vs. ω on a logarithmic scale.

A high-pass active filter can easily be obtained by using the circuit shown in Figure 5.9.14. The following gain function for the op-amp circuit can be derived:

$$\begin{aligned} A_{HP}(j\omega) &= -\frac{Z_F}{Z_S} = -\frac{R_F}{R_S + 1/j\omega C_S} \\ &= -\frac{j\omega C_S R_F}{1 + j\omega R_S C_S} \end{aligned} \tag{5.9.14}$$

The high-pass response is depicted in Figure 5.9.15 in both linear and dB plots (in the figure, $R_F/R_S = 10$, $1/R_S C = 1$).

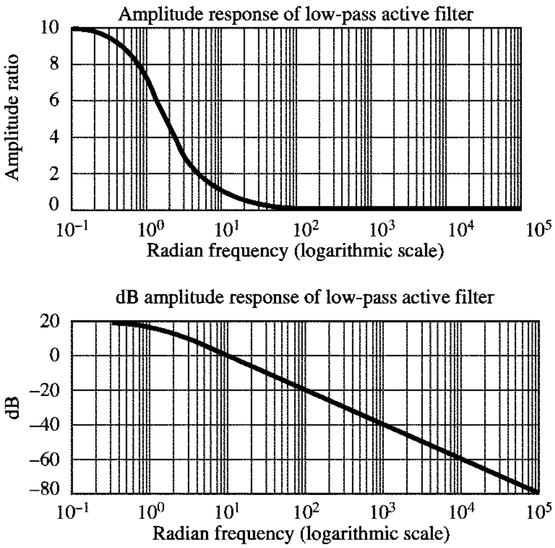

FIGURE 5.9.13 Normalized response of active low-pass filter.

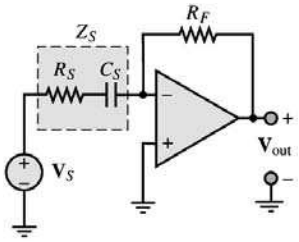

FIGURE 5.9.14 Active high-pass filter.

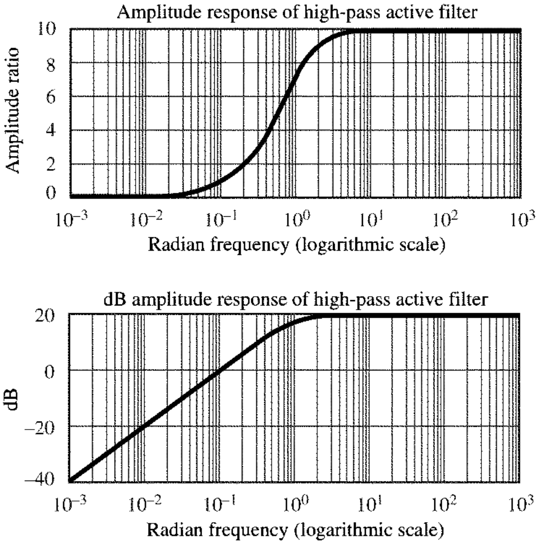

FIGURE 5.9.15 Normalized response of active high-pass filter.

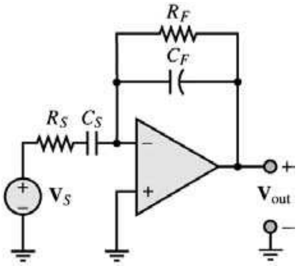

FIGURE 5.9.16 Active band-pass filter.

The band-pass filter of Figure 5.9.16 can be shown to have the following frequency response:

$$A_{BP}(j\omega) = -\frac{Z_F}{Z_S} = -\frac{j\omega C_S R_F}{\left(1 + j\omega C_F R_F\right)\left(1 + j\omega C_S R_S\right)} \tag{5.9.15}$$

The form of the op-amp response we just obtained should not appear as a surprise. It is very similar (although not identical) to the product of the low-pass and high-pass responses:

$$A_{LP}(j\omega) = -\frac{R_F / R_S}{1 + j\omega C_F R_F} \tag{5.9.16}$$

$$A_{HP}(j\omega) = -\frac{j\omega C_S R_F}{1 + j\omega R_S C_S} \tag{5.9.17}$$

In particular, the denominator of $A_{BP}(j\omega)$ is exactly the product of the denominators of $A_{LP}(j\omega)$ and $A_{HP}(j\omega)$. It is particularly enlightening to rewrite $A_{LP}(j\omega)$ in a slightly different form, after making the observation that each *RC* product corresponds to some "critical" frequency:

$$\omega_1 = \frac{1}{R_F C_S} \qquad \omega_{LP} = \frac{1}{R_F C_F} \qquad \omega_{HP} = \frac{1}{R_S C_S} \tag{5.9.18}$$

It is easy to verify that for the case where

$$\omega_{HP} > \omega_{LP} \tag{5.9.19}$$

the response of the op-amp filter may be represented as shown in Figure 5.9.17 in both linear and dB plots (in the figure, $\omega_1 = 1$, $\omega_{HP} = 1000$, $\omega_{HP} = 10$). The dB plot is very revealing, for its shows that, in effect, the band-pass response is the graphical superposition of the low-pass and high-pass responses shown earlier. The two 3-dB (or cutoff) frequencies are the same as in $A_{LP}(j\omega)$, $1/R_F C_F$; and in $A_{HP}(j\omega)$, $1/R_S C_S$. The third frequency, $\omega_1 = 1/R_F C_S$, represents the point where the response of the filter crosses the 0-dB axis (rising slope). Since 0 dB corresponds to a gain of 1, this frequency is called the **unity gain frequency**.

The ideas developed thus far can be employed to construct more complex functions of frequency. In fact, most active filters one encounters in practical applications are based on circuits involving more than one or two energy-storage elements. By constructing suitable functions for Z_F and Z_S, it is possible to realize filters with greater frequency selectivity (i.e., sharpness of cutoff), as well as flatter band-pass or band-rejection functions (that is, filters that either allow or reject signals in a limited band of frequencies). A few simple applications are investigated in the homework problems. One remark that should be made in passing, though, pertains to the exclusive use of capacitors in the circuits analyzed thus far.

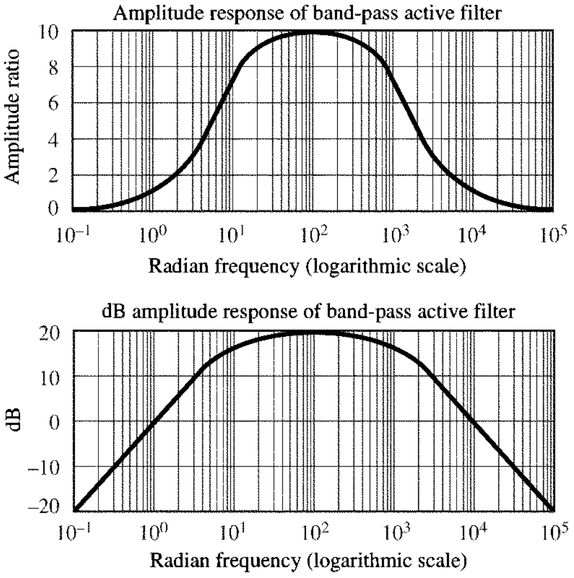

FIGURE 5.9.17 Normalized response of active band-pass filter.

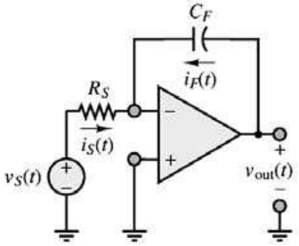

FIGURE 5.9.18 Op-amp integrator.

Integrator and Differentiator Circuits

The Ideal Integrator

Consider the circuit of Figure 5.9.18, where $v_s(t)$ is an arbitrary function of time (e.g., a pulse train, a triangular wave, or a square wave). The op-amp circuit shown provides an output that is proportional to the integral of $v_s(t)$.

$$v_{\text{out}} = -\frac{1}{R_S C_F}\int_{-\infty}^{t} v_S(t')\,dt' \tag{5.9.20}$$

This equation states that the output voltage is the integral of the input voltage.

There are numerous applications of the op-amp integrator, most notably the **analog computer**. The following example illustrates the operation of the op-amp integrator.

Example 5.9.3 Charge Amplifiers

One of the most common families of transducers for the measurement of force, pressure, and acceleration is that of **piezoelectric transducers**. These transducers contain a piezoelectric crystal, a crystal that generates an electric charge in response to deformation. Thus, if a force is applied to the crystal (leading to a displacement), a charge is generated within the crystal. If the external force generates a displacement x_i, then the transducer will generate a charge q according to the expression

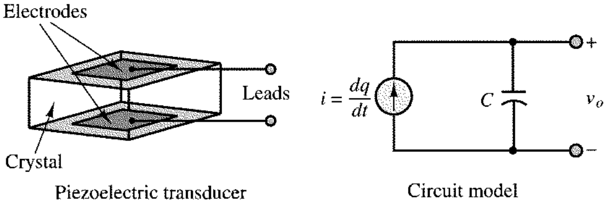

Piezoelectric transducer

Circuit model

FIGURE 5.9.19 Piezolectric transducer.

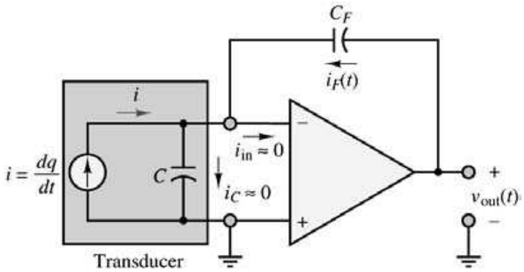

FIGURE 5.9.20 Charge amplifier.

$$q = K_p x_i$$

Figure 5.9.19 depicts the basic structure of the piezoelectric transducer and a simple circuit model. The model consists of a current source in parallel with a capacitor, where the current source represents the rate of change of the charge generated in response to an external force and the capacitance is a consequence of the structure of the transducer, which consists of a piezoelectric crystal (e.g., quartz or Rochelle salt) sandwiched between conducting electrodes (in effect, this is a parallel-plate capacitor).

Although it is possible, in principle, to employ a conventional voltage amplifier to amplify the transducer output voltage, v_o, given by

$$v_o = \frac{1}{C}\int i\,dt = \frac{1}{C}\int \frac{dq}{dt}\,dt = \frac{q}{C} = \frac{K_p x_i}{C}$$

it is often advantageous to use a **charge amplifier**. The charge amplifier is essentially an integrator circuit, as shown in Figure 5.9.20 characterized by an extremely high input impedance. The high impedance is essential; otherwise, the charge generated by the transducer would leak to ground through the input resistance of the amplifier.

Because of the high input impedance, the input current into the amplifier is negligible; further, because of the high open-loop gain of the amplifier, the inverting-terminal voltage is essentially at ground potential. Thus, *the voltage across the transducer is effectively zero*. As a consequence, to satisfy KCL, the feedback current, $i_F(t)$ must be equal and opposite to the transducer current, i:

$$i_F(t) = -i$$

and since

$$v_{\text{out}}(t) = \frac{1}{C_F} i_F(t)\,dt$$

it follows that the output voltage is proportional to the charge generated by the transducer, and therefore to the displacement:

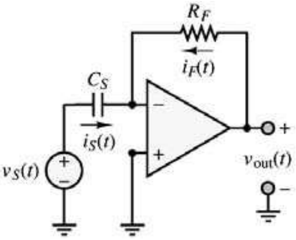

FIGURE 5.9.21 Op-amp differentiators.

$$v_{out}(t) = \frac{1}{C_F}\int -i\,dt = \frac{1}{C_F}\int -\frac{dq}{dt}\,dt = -\frac{q}{C_F} = -\frac{K_p x_i}{C_F}$$

Since the displacement is caused by an external force or pressure, this sensing principle is widely adopted in the measurement of force and pressure.

The Ideal Differentiator

Using an argument similar to that employed for the integrator, we can derive a result for the ideal differentiator circuit of Figure 5.9.21. The relationship between input and output is obtained by observing that

$$i_S(t) = C_S \frac{dv_S(t)}{dt} \tag{5.9.21}$$

and

$$i_F(t) = \frac{v_{out}(t)}{R_F} \tag{5.9.22}$$

so that the output of the differentiator circuit is proportional to the derivative of the input:

$$v_{out}(t) = -R_F C_S \frac{dv_S(t)}{dt} \tag{5.9.23}$$

Although mathematically attractive, the differentiation property of this op-amp circuit is seldom used in practice, because differentiation tends to simplify any noise that may be present in a signal.

Physical Limitations of Op-Amps

Thus far, the operational amplifier has been treated an ideal device, characterized by infinite input resistance, zero output resistance, and infinite open-loop voltage gain. Although this model is adequate to represent the behavior of the op-amp in a large number of applications, it is important to realize that practical operational amplifiers are not ideal devices, but exhibit a number of limitations that should be considered in the design of instrumentation. In particular, in dealing with relatively large voltages and currents, and in the presence of high-frequency signals, it is important to be aware of the nonideal properties of the op-amp. In the present section, we examine the principal limitations of the operational amplifier.

Voltage Supply Limits

The effect of limiting supply voltages is that amplifiers are capable of amplifying signals *only within the range of their supply voltages*;

$$V_S^- < v_{out} < V_S^+ \tag{5.9.24}$$

For most op-amps, the limit is actually approximately 1.5 V less than the supply voltages.

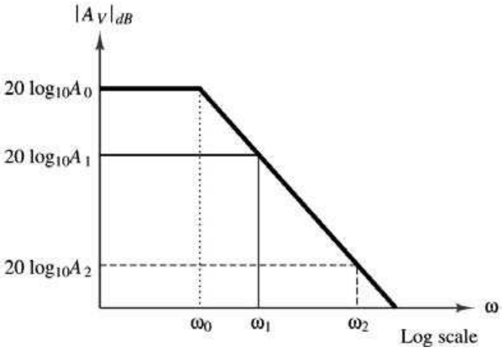

FIGURE 5.9.22

Frequency Response Limits

Another property of all amplifiers that may pose severe limitations to the op-amp is their finite bandwidth. We have so far assumed, in our ideal op-amp model, that the open-loop gain is a very large constant. In reality, $A_{V(OL)}$ is a function of frequency and is characterized by a low-pass response. For a typical op-amp,

$$A_{V(OL)}(j\omega) = \frac{A_0}{1 + j\omega/\omega_0} \tag{5.9.25}$$

The finite bandwidth of the practical op-amp results in a fixed **gain-bandwidth product** for any given amplifier. The effect of a constant gain-bandwidth product is that as the closed-loop gain of the amplifier is increased, its 3-dB bandwidth is proportionally reduced, until, in the limit, if the amplifier were used in the open-loop mode, its gain would be equal to A_0 and its 3-dB bandwidth would be equal to ω_0. Thus, *the product of gain and bandwidth in any given op-amp is constant*. That is,

$$A_0 \times \omega_0 = A_1 \times \omega_1 = A_2 \times \omega_2 = K \tag{5.9.26}$$

as is shown in Figure 5.9.22.

Input Offset Voltage

Another limitation of practical op-amps results because even in the absence of any external inputs, it is possible that an **offset voltage** will be present at the input of an op-amp. This voltage is usually denoted by $\pm V_{os}$ and it is caused by mismatches in the internal circuitry of the op-amp. The offset voltage appears as a differential input voltage between the inverting and noninverting input terminals. The presence of an additional input voltage will cause a DC bias error in the amplifier output, which can be modeled as shown in Figure 5.9.23.

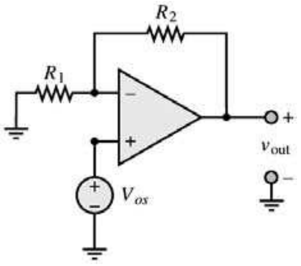

FIGURE 5.9.23 Op-amp input offset voltage.

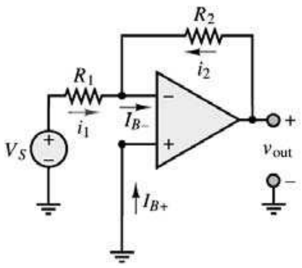

FIGURE 5.9.24

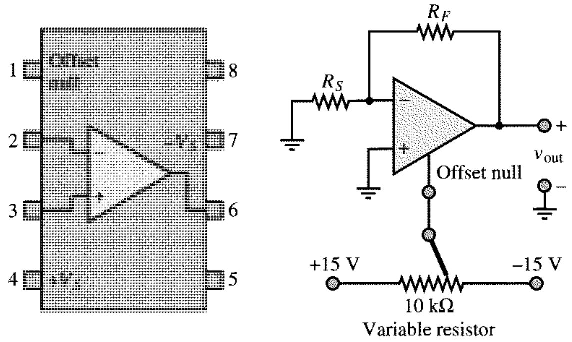

FIGURE 5.9.25 Output off-set voltage adjustment.

Input Bias Currents

Another nonideal characteristic of op-amps results from the presence of small input bias currents at the inverting and noninverting terminals. Once again, these are due to the internal construction of the input stage of an operational amplifier. Figure 5.9.24 illustrates the presence of nonzero input bias currents (I_B) going into an op-amp.

Typical values of I_B depend on the semiconductor technology employed in the construction of the op-amp. Op-amps with bipolar transistor input stages may see input bias currents as large as 1 μA, while for FET input devices, the input bias currents are less than 1 nA. Since these currents depend on the internal design of the op-amp, they are not necessarily equal. One often designates the **input offset current** I_{os} as

$$I_{os} = I_{B+} - I_{B-} \tag{5.9.27}$$

The latter parameter is sometimes more convenient from the standpoint of analysis.

Output Offset Adjustment

Both the offset voltage and the input offset current contribute to an output offset voltage $V_{out,os}$. Some op-amps provide a means for minimizing $V_{out,os}$. For example, the μA741 op-amp provides a connection for this procedure. Figure 5.9.25 shows a typical pin configuration for an op-amp in an eight-pin dual-in-line package (DIP) and the circuit used for nulling the output offset voltage. The variable resistor is adjusted until v_{out} reaches a minimum (ideally, 0 V). Nulling the output voltage in this manner removes the effect of both input offset voltage and current on the output.

Slew Rate Limit

Another important restriction in the performance of a practical op-amp is associated with rapid changes in voltage. The op-amp can produce only a finite rate of change at its output. This limit rate is called the **slew rate**. Consider an ideal step input, where at t = 0 the input voltage is switched from zero to V

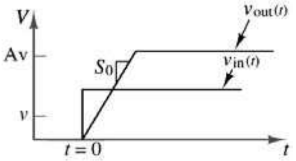

FIGURE 5.9.26 Slew rate limit in op-amps.

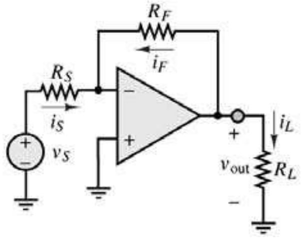

FIGURE 5.9.27

volts. Then we would expect the output to switch from 0 to $A \cdot V$ volts, where A is the amplifier gain. However, $v_{out}(t)$ can change at only a finite rate; thus,

$$\left|\frac{dv_{out}(t)}{dt}\right|_{max} = S_0 = \text{Slew rate} \tag{5.9.28}$$

Figure 5.9.26 shows the response of an op-amp to an ideal step change in input voltage, Here S_0, the slope of $v_{out}(t)$, represents the slew rate.

Short-Circuit Output Current

Recall the model for the op-amp, which represented the internal circuits of the op-amp in terms of an equivalent input resistance, R_{in}, and a controlled voltage source, $A_V\, v_{in}$. In practice, the internal source is not ideal, because it cannot provide an infinite amount of current (either to the load or to the feedback connection, or both). The immediate consequence of this nonideal op-amp characteristic is that the maximum output current of the amplifier is limited by the so-called short-circuit output current, I_{SC}:

$$|I_{out}| < I_{SC} \tag{5.9.29}$$

To further explain this point, consider that the op-amp needs to provide current to the feedback path (in order to "zero" the voltage differential at the input) and to whatever load resistance, R_L, may be connected to the output. Figure 5.9.27 illustrates this idea for the case of an inverting amplifier, where I_{SC} is the load current that would be provided to a short-circuit load ($R_L = 0$).

Common-Mode Rejection Ratio (CMRR)

Example 5.9.2 introduced the notion of differential-mode and common-mode signals. If we define A_{dm} as the **differential-mode gain** and A_{cm} as the **common-mode gain** of the op-amp, the output of an op-amp can then be expressed as follows:

$$v_{out} = A_{dm}(v_2 - v_1) + A_{cm}\left(\frac{v_2 - v_1}{2}\right) \tag{5.9.30}$$

Under ideal conditions, A_{cm} should be exactly zero, since the differential amplifier should completely reject common-mode signals. The departure from this ideal condition is a figure of merit for a differential amplifier and is measured by defining a quantity called the **common-mode rejection ratio** (CMRR).

The CMRR is defined as the ratio of the differential-mode gain to the common-mode gain and should ideally be infinite:

$$\mathrm{CMRR} = \frac{A_{dm}}{A_{cm}}$$

The CMRR is often expressed in units of decibels (dB).

5.10 Digital Circuits

The objective of this section is to discuss the essential features of digital logic circuits, which are at the heart of digital computers.

Analog and Digital Signals

One of the fundamental distinctions in the study of electronic circuits (and in the analysis of any signals derived from physical measurements) is that between analog and digital signals. As discussed in the preceding chapter, an **analog signal** is an electrical signal whose value varies in analogy with a physical quantity (e.g., temperature, force, or acceleration). For example, a voltage proportional to a measured variable pressure or to a vibration naturally varies in an analog fashion. Figure 5.10.1 depicts an arbitrary analog function of time, $f(t)$. We note immediately that for each value of time, t, $f(t)$ can take one value among any of the values in a given range. For example, in the case of the output voltage of an op-amp, we expect the signal to take any value between $+V_{\text{sat}}$ and $-V_{\text{sat}}$, where V_{sat} is the supply-imposed saturation voltage.

A **digital signal**, on the other hand, can take only a *finite number of values.* This is an extremely important distinction, as will be shown shortly. An example of a digital signal is a signal that allows display of a temperature measurement on a digital readout. Let us hypothesize that the digital readout is three digits long and can display numbers from 0 to 100, and let us assume that the temperature sensor is correctly calibrated to measure temperatures from 0 to 100°F. Further, the output of the sensor ranges from 0 to 5 V, where 0 V corresponds to 0°F and 5 V to 100°F. Therefore, the calibration constant of the sensor is $k_T = (100° - 0°)/(5 - 0) = 20°/\text{V}$. Clearly, the output of the sensor is an analog signal; however, the display can show only a finite number of readouts (101, to be precise). Because the display itself can only take a value out of a discrete set of states — the integers from 0 to 100 — we call it a digital display, indicating that the variable displayed is expressed in digital form.

Now, each temperature on the display corresponds to a *range of voltages:* each digit on the display represents one hundredth of the 5-V range of the sensor, or 0.05 V = 50 m V. Thus, the display will read 0 if the sensor voltage is between 0 and 49 mV, 1 if it is between 50 and 99 mV, and so on. Figure 5.10.2 depicts the staircase function relationship between the analog voltage and the digital readout. This **quantization** of the sensor output voltage is, in effect, an approximation. If one wished to know the temperature with greater precision, a greater number of display digits could be employed.

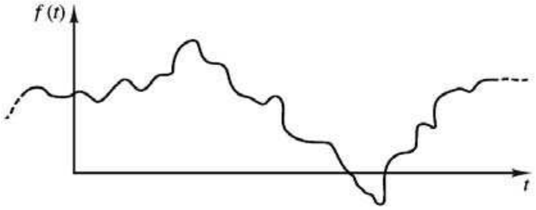

FIGURE 5.10.1 Analog signal.

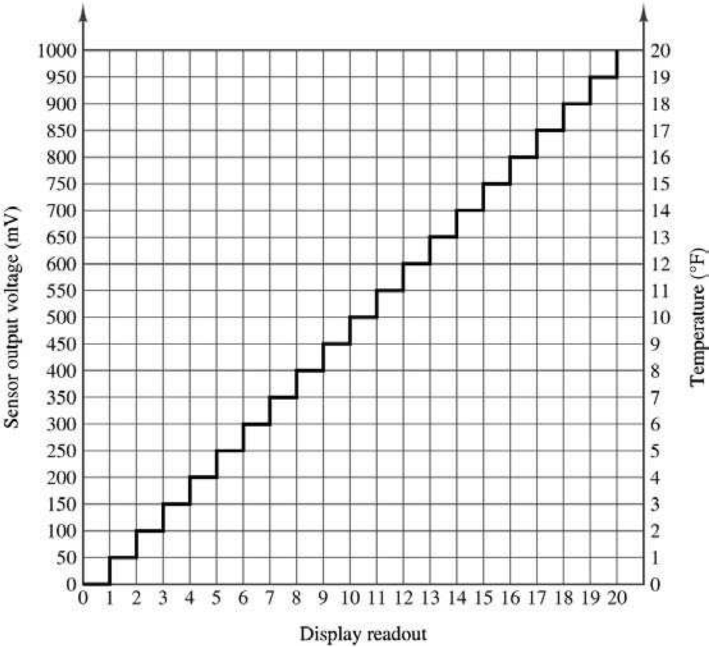

FIGURE 5.10.2 Digital representation of an analog signal.

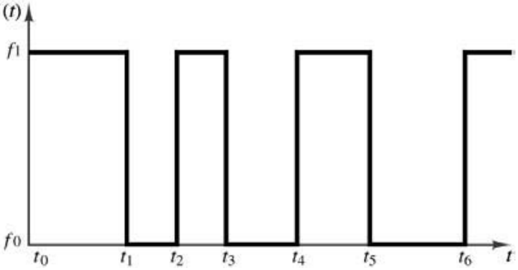

FIGURE 5.10.3 A binary signal.

The most common digital signals are binary signals. A **binary signal** is a signal that can take only one of two discrete values and is therefore characterized by transitions between two states. Figure 5.10.3 displays a typical binary signal. In binary arithmetic (which we discuss in the next section), the two discrete values f_1 and f_0 are represented by the numbers 1 and 0. In binary voltage waveforms, these values are represented by two voltage levels. For example, in the TTL convention, these values are (nominally) 5 and 0 V, respectively; in CMOS circuits, these values can vary substantially. Other conventions are also used, including reversing the assignment — for example, by letting a 0-V level represent a logic 1 and a 5-V level represent a logic 0. Note that in a binary waveform, knowledge of the transition between one stage and another (e.g., from f_0 to f_1 at $t = t_2$) is equivalent to knowledge of the state. Thus, digital logic circuits can operate by detecting transitions between voltage levels. The transitions are often called **edges** and can be positive (f_0 to f_1) or negative (f_1 to f_0). Virtually all of the signals handled by a computer are binary. From here on, whenever we speak of digital signals, you may assume that the text is referring to signals of the binary type, unless otherwise indicated.

TABLE 5.10.1 Conversion from Decimal to Binary

Decimal Number, n_{10}	Binary Number, n_2
0	0
1	1
2	10
3	11
4	100
5	101
6	110
7	111
8	1000
9	1001
10	1010
11	1011
12	1100
13	1101
14	1110
15	1111
16	10000

The Binary Number System

The binary number system is a natural choice for representing the behavior of circuits that operate in one of two states (on or off, 1 or 0, or the like). The diode and transistor gates and switches studied in Section 5.7 fall in this category. Table 5.10.1 shows the correspondence between decimal and binary number systems for decimal numbers up to 16.

Table 5.10.1 shows that it takes four binary digits, also called **bits**, to represent the decimal numbers up to 15. Usually, the rightmost bit is called the **least significant bit**, or LSB, and the leftmost bit is called the **most significant bit**, or MSB. Since binary numbers clearly require a larger number of digits than decimal numbers, the digits are usually grouped in sets of four, eight, or sixteen. Four bits are usually termed a **nibble**, eight bits are called a **byte**, and sixteen bits (or two bytes) form a **word**.

Addition and Subtraction

The operations of addition and subtraction are based on the simple rules shown in Table 5.10.2. Figure 5.10.4 provides three examples.

The procedure for subtracting binary numbers is based on the rules of Table 5.10.3. A few examples of binary subtraction are given in Figure 5.10.5, with their decimal counterparts.

TABLE 5.10.2 Rules for Addition

$0 + 0 = 0$
$0 + 1 = 1$
$1 + 0 = 1$
$1 + 1 = 0$ (with a carry of 1)

Decimal	Binary	Decimal	Binary	Decimal	Binary
5	101	15	1111	3.25	11.01
+6	+110	+20	+10100	+5.75	+101.11
11	1011	35	100011	9.00	1001.00

FIGURE 5.10.4 Examples of binary addition.

TABLE 5.10.3 Rules for Subtraction

$0 - 0 = 0$
$1 - 0 = 1$
$1 - 1 = 0$
$0 - 1 = 1$ (with a borrow of 1)

Decimal	Binary	Decimal	Binary	Decimal	Binary
9	1001	16	10000	6.25	110.01
−5	−101	−3	−11	−4.50	−100.10
4	0100	13	01101	1.75	001.11

FIGURE 5.10.5 Examples of binary subtraction.

Multiplication and Division

Whereas in the decimal system the multiplication table consists of $10^2 = 100$ entries, in the binary system we only have $2^2 = 4$ entries. Table 5.10.4 represents the complete multiplication table for the binary number system.

TABLE 5.10.4 Rules for Multiplication

$0 \times 0 = 0$
$0 \times 1 = 0$
$1 \times 0 = 0$
$1 \times 1 = 1$

Division in the binary system is also based on rules analogous to those of the decimal system, with the two basic laws given in Table 5.10.5. Once again, we need be concerned with only two cases, and just as in the decimal system, division by zero is not contemplated.

TABLE 5.10.5 Rules for Division

$0 \div 1 = 0$
$1 \div 1 = 1$

Conversion from Decimal to Binary

The conversion of a decimal number to its binary equivalent is performed by successive division of the decimal number by 2, checking for the remainder each time. Figure 5.10.6 illustrates this idea with an example.

Remainder
$49 \div 2 = 24 + 1$
$24 \div 2 = 12 + 0$
$12 \div 2 = 6 + 0$
$6 \div 2 = 3 + 0$
$3 \div 2 = 1 + 1$
$1 \div 2 = 0 + 1$
$49_{10} = 110001_2$

FIGURE 5.10.6 Example of conversion from decimal to binary.

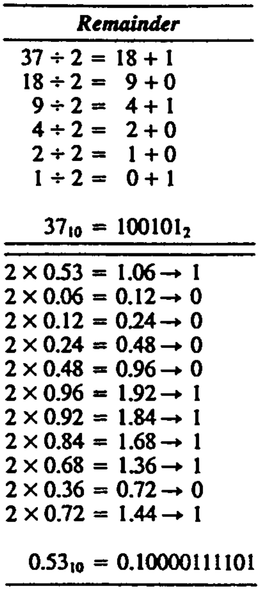

Remainder

$$\begin{array}{rcl}
37 \div 2 & = & 18 + 1 \\
18 \div 2 & = & 9 + 0 \\
9 \div 2 & = & 4 + 1 \\
4 \div 2 & = & 2 + 0 \\
2 \div 2 & = & 1 + 0 \\
1 \div 2 & = & 0 + 1
\end{array}$$

$$37_{10} = 100101_2$$

$$\begin{array}{rcl}
2 \times 0.53 & = & 1.06 \rightarrow 1 \\
2 \times 0.06 & = & 0.12 \rightarrow 0 \\
2 \times 0.12 & = & 0.24 \rightarrow 0 \\
2 \times 0.24 & = & 0.48 \rightarrow 0 \\
2 \times 0.48 & = & 0.96 \rightarrow 0 \\
2 \times 0.96 & = & 1.92 \rightarrow 1 \\
2 \times 0.92 & = & 1.84 \rightarrow 1 \\
2 \times 0.84 & = & 1.68 \rightarrow 1 \\
2 \times 0.68 & = & 1.36 \rightarrow 1 \\
2 \times 0.36 & = & 0.72 \rightarrow 0 \\
2 \times 0.72 & = & 1.44 \rightarrow 1
\end{array}$$

$$0.53_{10} = 0.10000111101$$

FIGURE 5.10.7 Conversion from decimal to binary.

The same technique can be used for converting decimal fractional numbers to their binary form, provided that the whole number is separated from the fractional part and each is converted to binary form (separately), with the results added at the end. Figure 5.10.7 outlines this procedure by converting the number 37.53 to binary form.

Complements and Negative Numbers

To simplify the operation of subtraction in digital computers, **complements** are used almost exclusively. In practice, this corresponds to replacing the operation $X - Y$ with operation $X + (-Y)$. This procedure results in considerable simplification, since the computer hardware need include only adding circuitry. Two types of complements are used with binary numbers: the **one's complement** and the **two's complement**.

The one's complement of an n-bit binary number is obtained by subtracting the number itself from $(2^n - 1)$. Two examples are as follows:

$$\begin{aligned}
a &= 0101 \\
\text{One' s complement of } a &= \left(2^4 - 1\right) - a \\
&= (1111) - (0101) \\
&= 1010 \\
b &= 101101 \\
\text{One' s complement of } b &= \left(2^6 - 1\right) - b \\
&= (111111) - (101101) \\
&= 010010
\end{aligned}$$

The two's complement of n-bit binary number is obtained by subtracting the number itself from 2^{n}. Two's complements of the same numbers a and b used in the preceding illustration are computed as follows:

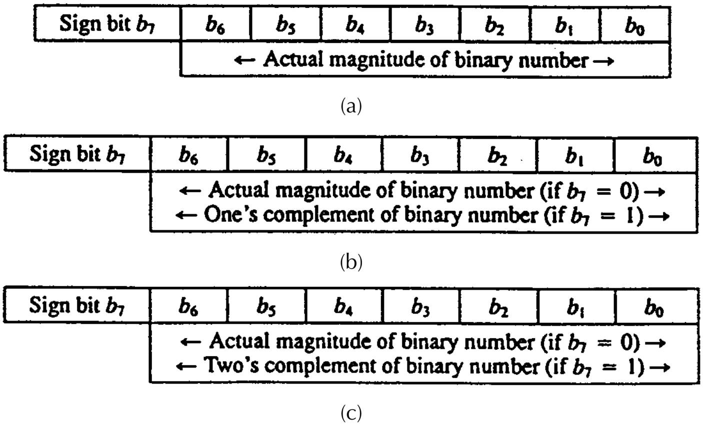

FIGURE 5.10.8 (a) Eight-bit sign-magnitude binary number; (b) eight-bit one's complement binary number; (c) eight-bit two's complement binary number.

$$a = 0101$$

$$\text{Two's complement of } a = 2^4 - a$$

$$= (10000) - (0101)$$

$$= 1011$$

$$b = 101101$$

$$\text{Two's complement of } b = 2^6 - b$$

$$= (1000000) - (101101)$$

$$= 010011$$

Different conventions exist in the binary system to represent whether a number is negative or positive. These are summarized in Figure 5.10.8.

The Hexadecimal System

It should be apparent by now that representing numbers in base 2 and base 10 systems is purely a matter of convenience, given a specific application. Another base frequently used is the **hexadecimal system**, a direct derivation of the binary number system. In the hexadecimal (or hex) code, the bits in a binary number are subdivided into groups of four. Since there are 16 possible combinations for a four-bit number, the natural digits in the decimal system (0 through 9) are insufficient to represent a hex digit. To solve this problem, the first six letters of the alphabet are used, as shown in Table 5.10.6. Thus, in hex code, an eight-bit word corresponds to just two digits; for example:

$$1010\ 0111_2 = A7_{16}$$

$$0010\ 1001_2 = 29_{16}$$

Binary Codes

In this subsection, we describe two common binary codes that are often used for practical reasons. The first is a method of representing decimal numbers in digital logic circuits that is referred to as **binary-coded decimal**, or BCD, **representation**. In effect, the simplest BCD representation is just a sequence of

TABLE 5.10.6 Hexadecimal Code

0	0000
1	0001
2	0010
3	0011
4	0100
5	0101
6	0110
7	0111
8	1000
9	1001
A	1010
B	1011
C	1100
D	1101
E	1110
F	1111

four-bit binary numbers that stops after the first ten entries, as shown in Table 5.10.7. There are also other BCD codes, all reflecting the same principle: that each decimal digit is represented by a fixed-length binary word. One should realize that although this method is attractive because of its direct correspondence with the decimal system, it is not efficient. Consider, for example, the decimal number 68. Its binary representation by direct conversion is the seven-bit number 1000100. On the other hand, the corresponding BCD representation would require eight bits:

$$68_{10} = 01101000_{\mathrm{BCD}}$$

TABLE 5.10.7 BCD Code

0	0000
1	0001
2	0010
3	0011
4	0100
5	0101
6	0110
7	0111
8	1000
9	1001

Another code that finds many applications is the **Gray code**. This is simply a reshuffling of the binary code with the property that any two consecutive numbers differ only by one bit. Table 5.10.8 illustrates the three-bit Gray code. The Gray code can be very useful in practical applications, because in counting up or down according to this code, the binary representation of a number changes only one bit at a time.

Boolean Algebra

The mathematics associated with the binary number system (and with the more general field of logic) is called *Boolean algebra*. The variables in a Boolean, or logic, expression can take only one of two values, usually represented by the numbers 0 and 1. These variables are sometimes referred to as true (1) and false (0). This convention is normally referred to as **positive logic**. There is also a **negative logic** convention in which the roles of logic 1 and logic 0 are reversed. In this book we shall employ only positive logic.

Analysis of **logic functions**, that is, functions of logical (Boolean) variables, can be carried out in terms of truth tables. A truth table is a listing of all the possible values each of the Boolean variables can take,

TABLE 5.10.8 Three-Bit Gray Code

Binary	Gray
000	000
001	001
010	011
011	010
100	110
101	111
110	101
111	100

and of the corresponding value of the desired function. In the following paragraphs we shall define the basic logic functions upon which Boolean algebra is founded, and we shall describe each in terms of a set of rules and a truth table; in addition, we shall also introduce **logic gates**. Logic gates are physical devices that can be used to implement logic functions. Elementary logic gates were introduced in Section 5.7.

AND and OR Gates

The basis of **Boolean algebra** lies in the operations of **logical addition**, or the **OR** operation; and **logical multiplication**, or the **AND** operation. Both of these find a correspondence in simple logic gates, as we shall presently illustrate. Logical addition, although represented by the symbol +, differs from conventional algebraic addition, as shown in the last rule listed in Table 5.10.9. Note that this rule also differs from the last rule of binary addition studied in the previous section. Logical addition can be represented by the logic gate called an **OR gate**, whose symbol and whose inputs and outputs are shown in Figure 5.10.9. The OR gate represents the following logical statement:

$$\text{If either } X \text{ or } Y \text{ is true (1), then } Z \text{ is true (1)} \tag{5.10.1}$$

This rule is embodied in the electronic gates discussed in Chapter 9, in which a logic 1 corresponds, say, to a 5-V signal and a logic 0 to a 0-V signal.

Logical multiplication is denoted by the center dot (·) and is defined by the rules of Table 5.10.10. Figure 5.10.10 depicts the **AND gate**, which corresponds to this operation. The AND gate corresponds to the following logical statement:

$$\text{If both } X \text{ and } Y \text{ are true (1), then } Z \text{ is true (1)} \tag{5.10.2}$$

TABLE 5.10.9 Rules for Logical Addition (OR)

$0 + 0 = 0$
$0 + 1 = 1$
$1 + 0 = 1$
$1 + 1 = 1$

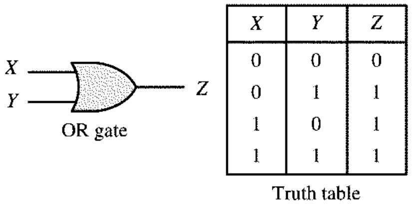

X	Y	Z
0	0	0
0	1	1
1	0	1
1	1	1

FIGURE 5.10.9 Logical addition and the OR gate.

TABLE 5.10.10 Rules for Logical Multiplication (AND)

$$0 \cdot 0 = 0$$
$$0 \cdot 1 = 0$$
$$1 \cdot 0 = 0$$
$$1 \cdot 1 = 1$$

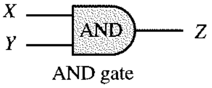

X	Y	Z
0	0	0
0	1	0
1	0	0
1	1	1

Truth table

FIGURE 5.10.10 Logical multiplication and the AND gate.

One can easily envision logic gates (AND and OR) with an arbitrary number of inputs; three- and four-input gates are not uncommon.

The rules that define a logic function are often represented in tabular form by means of a **truth table**. Truth tables for the AND and OR gates are shown in Figure 5.10.9 and Figure 5.10.10. A truth table is nothing more than a tabular summary of all of the possible outputs of a logic gate, given all the possible input values. If the number of inputs is 3, the number of possible combinations grows from 4 to 8, but the basic idea is unchanged. Truth tables are very useful in defining logic functions. A typical logic design problem might specify requirements such as "the output Z shall be logic 1 only when the condition ($X = 1$ AND $Y = 1$) OR ($W = 1$) occurs, and shall be logic 0 otherwise." The truth table for this particular logic function is shown in Figure 5.10.11 as an illustration. The design consists, then, of determining the combination of logic gates that exactly implements the required logic function. Truth tables can greatly simplify this procedure.

The AND and OR gates form the basis of all logic design in conjunction with the **NOT gate**. The NOT gate is essentially an inverter, and it provides the complement of the logic variable connected to its input. The complement of a logic variable X is denoted by $\overline{X}$. The NOT gate has only one input, as shown in Figure 5.10.12

Logic gate realization of the statement "the output Z shall be logic 1 only when the condition ($X = 1$ AND $Y = 1$) OR ($W = 1$) occurs, and shall be logic 0 otherwise."

X	Y	W	Z
0	0	0	0
0	0	1	1
0	1	0	0
0	1	1	1
1	0	0	0
1	0	1	1
1	1	0	1
1	1	1	1

Truth table

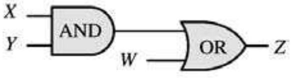

Solution using logic gates

FIGURE 5.10.11 Example of logic function implementation with logic gates.

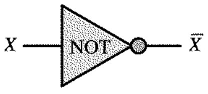

NOT gate

X	$\overline{X}$
1	0
0	1

Truth table for NOT gate

FIGURE 5.10.12 Complements and the NOT gate.

X	$\overline{X}$	Y	W	Z
0	1	0	0	0
0	1	0	1	1
0	1	1	0	1
0	1	1	1	1
1	0	0	0	0
1	0	0	1	1
1	0	1	0	0
1	0	1	1	1

(Required logic function)

Truth table

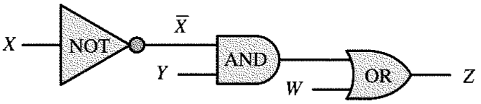

Solution using logic gates

FIGURE 5.10.13 Solution of a logic problem using logic gates.

To illustrate the use of the NOT gate, or inverter, we return to the design example of Figure 5.10.11, where we required that the output of a logic circuit be $Z = 1$ only if $X = 0$ AND $Y = 1$ OR if $W = 1$. We recognize that except for the requirement $X = 0$, this problem would be identical if we stated it as follows: "The output Z shall be logic 1 only when the condition ($\overline{X} = 1$ AND $Y = 1$) OR ($W = 1$) occurs, and shall be logic 0 otherwise." If we use an inverter to convert X to $\overline{X}$, we see that the required condition becomes $\overline{X} = 1$ AND $Y = 1$) OR ($W = 1$). The formal solution to this elementary design exercise is illustrated in Figure 5.10.13.

In the course of the discussion of logic gates, extensive use will be made of truth tables to evaluate logic expressions. A set of basic rules will facilitate this task. Table 5.10.11 lists some of the rules of Boolean algebra:

TABLE 5.10.11 Rules of Boolean Algebra

1.	$0 + X = X$	
2.	$1 + X = 1$	
3.	$X + X = X$	
4.	$X + \overline{X} = 1$	
5.	$0 \cdot X = 0$	
6.	$1 \cdot X = X$	
7.	$X \cdot X = X$	
8.	$X \cdot \overline{X} = 0$	
9.	$\overline{\overline{X}} = X$	
10.	$X + Y = Y + X$	Commutative law
11.	$X \cdot Y = Y \cdot X$	
12.	$X + (X + Z) = (X + Y) + Z$	Associative law
13.	$X \cdot (Y \cdot Z) = (X \cdot Y) \cdot Z$	
14.	$X \cdot (Y + Z) = X \cdot Y + X \cdot Z$	Distributive law
15.	$X + X \cdot Z = X$	Absorption law
16.	$X \cdot (X + Y) = X$	
17.	$(X + Y) \cdot (X + Z) = X + Y \cdot Z$	
18.	$X + \overline{X} \cdot Y = X + Y$	
19.	$X \cdot Y + Y \cdot Z + \overline{X} \cdot Z = X \cdot Y + \overline{X} \cdot Z$	

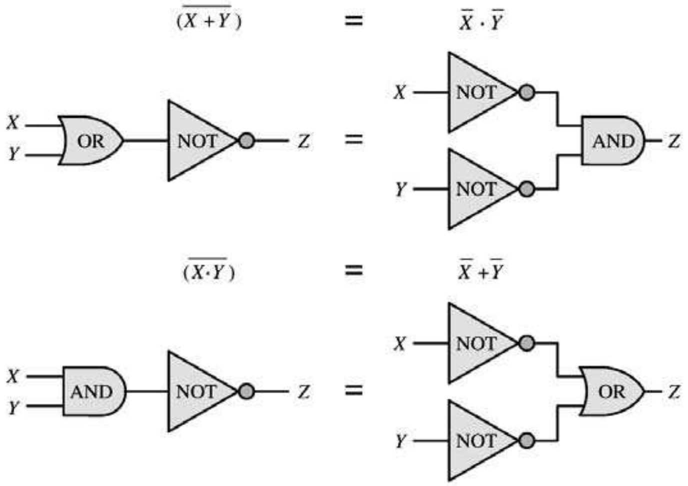

FIGURE 5.10.14 De Morgan's laws.

To complete the introductory material on Boolean algebra, a few paragraphs need to be devoted to two very important theorems, called **De Morgan's theorems**. These are stated here in the form of logic functions:

$$\left(\overline{X+Y}\right)=\bar{X}\cdot\bar{Y} \tag{5.10.3}$$

$$\left(\overline{X\cdot Y}\right)=\bar{X}+\bar{Y} \tag{5.10.4}$$

These two laws state a very important property of logic functions: any logic function can be implemented using only OR and NOT gates, or using only AND and NOT gates.

De Morgan's laws can easily be visualized in term of logic gates, as shown in Figure 5.10.14. The associated truth tables are proof of these theorems.

The importance of De Morgan's laws is in the statement of the **duality** that exists between AND and OR operations: any function can be realized by just one of the two basic operations, plus the complement operation. This gives rise to two families of logic functions: **sums of products** and **products of sums**, as shown in Figure 5.10.15. Any logical expression can be reduced to either one of these two forms. Although the two forms are equivalent, it may well be true that one of the two has a simpler implementation (fewer gates). Example 5.10.1 illustrates this point.

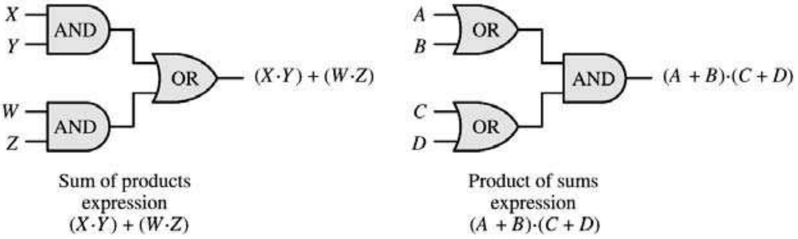

FIGURE 5.10.15 Sun-of-products and product-of-sums logic functions.

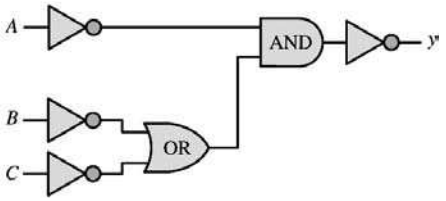

FIGURE 5.10.16 Figure for Example 5.10.1.

Example 5.10.1

Use De Morgan's theorem to realize the function $y = A + (B \cdot C)$ as a product-of-sums expression, and implement it using AND, OR, and NOT gates.

Solution. Knowing that $\overline{\overline{y}} = y$, we can apply the first of De Morgan's laws to the complement of the function y to obtain the expression

$$\overline{y} = \overline{A + (B \cdot C)} = \overline{A} \cdot \left(\overline{B \cdot C}\right) = \overline{A} \cdot \left(\overline{B} + \overline{C}\right)$$

Thus,

$$\overline{\overline{y}} = y = \overline{\overline{A} \cdot \left(\overline{B} + \overline{C}\right)}$$

Using logic gates, we can then implement the function as shown in Figure 5.10.16

NAND and NOR Gates

In addition to the AND and OR gates we have just analyzed, the complementary forms of these gates, called NAND and NOR, are very commonly used in practice. In fact, NAND and NOR gates form the basis of most practical logic circuits. Figure 5.10.17 depicts these two gates and illustrates how they can be easily interpreted in terms of AND, OR, and NOT gates by virtue of De Morgan's laws. You can readily verify that the logic function implemented by the NAND and NOR gates corresponds, respectively, to AND and OR gates followed by an inverter. It is very important to note that, by De Morgan's laws, the NAND gate performs a *logical addition* on the *complements* of the inputs. while the NOR gate performs a *logical multiplication* on the *complements* of the inputs. Functionally, then, any logic function could be implemented with either NOR or NAND gates only.

In the next section we shall learn how to systematically approach the design of logic functions. First, we provide a few examples to illustrate logic design with NAND and NOR gates.

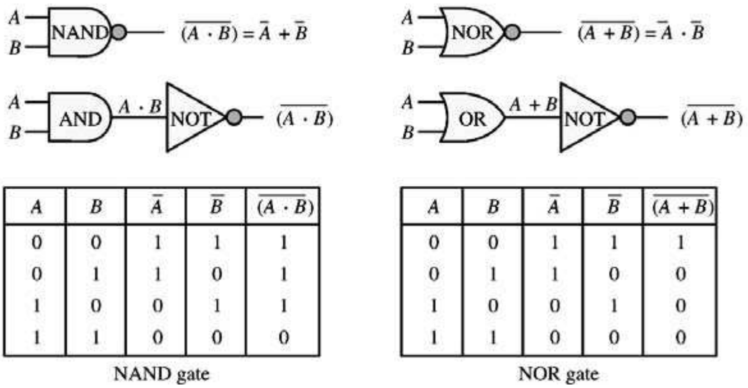

A	B	$\overline{A}$	$\overline{B}$	$(\overline{A \cdot B})$
0	0	1	1	1
0	1	1	0	1
1	0	0	1	1
1	1	0	0	0

NAND gate

A	B	$\overline{A}$	$\overline{B}$	$(\overline{A + B})$
0	0	1	1	1
0	1	1	0	0
1	0	0	1	0
1	1	0	0	0

NOR gate

FIGURE 5.10.17 Equivalence of NAND and NOR gates with AND and OR gates.

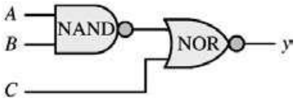

FIGURE 5.10.18 Figure for Example 5.10.2.

X	Y	Z
0	0	0
0	1	1
1	0	1
1	1	0

Truth table

FIGURE 5.10.19 XOR gate.

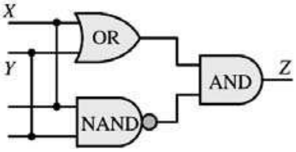

FIGURE 5.10.20 Realization of an XOR gate.

Example 5.10.2

Realize the following function using only NAND and NOR gates:

$$y = \overline{(A \cdot B) + C}$$

Solution. Since the term in parentheses appears as a complement product, it can be obtained by means of a NAND gate. Further, once the function $\overline{(A \cdot B)}$ has been realized, we can see that y is the complemented sum of two terms — that is, it can be obtained directly with a NOR gate. The resulting logic circuit is shown in Figure 5.10.18.

Can you find another solution to this problem that employs only two gates?

The XOR (Exclusive OR) Gate

It is rather common practice for a manufacturer of integrated circuits to provide common combinations of logic circuits in a single integrated circuit package. An example of this idea is provided by the **exclusive OR** (XOR) **gate**, which provides a logic function similar, but not identical, to the OR gate we have already studied. The XOR gate acts as an OR gate, except when its inputs are all logic 1s; in this case, the output is a logic 0 (thus the term *exclusive*). Figure 5.10.19 shows the logic circuit symbol adopted for this gate, and the corresponding truth table. The logic function implemented by the XOR gate is the following: "either X or Y, but not both." This description can be extended to an arbitrary number of inputs.

The symbol adopted for the exclusive OR operation is ⊕, and so we shall write

$$Z = X \oplus Y$$

to denote this logic operation. The XOR gate can be obtained by a combination of the basic gates we are already familiar with. For example, if we observe that the XOR function corresponds to $Z = X \oplus Y = (X + Y) \cdot X \cdot\ (\overline{X + Y})$, we can realize the XOR gate by means of the circuit shown in Figure 5.10.20.

Karnaugh Maps and Logic Design

In examining the design of logic functions by means of logic gates, we have discovered that more than one solution is usually available for the implementation of a given logic expression. It should also be clear by now that some combinations of gates can implement a given function more efficiently than

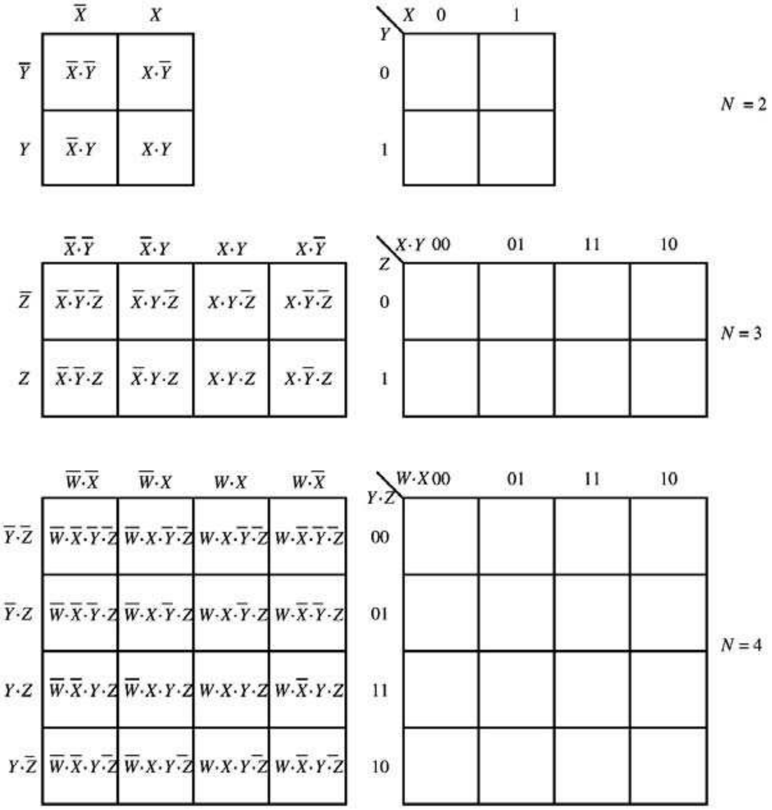

FIGURE 5.10.21 Two-, three-, and four-variable Karnaugh maps.

others. How can we be assured of having chosen the most efficient realization? Fortunately, there is a procedure that utilizes a map describing all possible combinations of the variables present in the logic function of interest. This map is called a **Karnaugh map**, after its inventor. Figure 5.10.21 depicts the appearance of Karnaugh maps for two-, three-, and four-variable expressions in two different forms. As can be seen, the row and column assignments for two or more variables are arranged so that all adjacent terms change by only one bit. For example, in the three- or four-variable map, the columns next to column 01 are columns 00 and 10. Also note that each map consists of 2^N **cells**, where N is the number of logic variables.

Each cell in a Karnaugh map contains a **minterm**, that is, a product of the N variables that appear in our logic expression (in either uncomplemented or complemented form). For example, for the case of three variables ($N = 3$), there are $2^3 = 8$ such combination, or minterms: $\overline{X} \cdot \overline{Y} \cdot \overline{Z}$, $\overline{X} \cdot \overline{Y} \cdot Z$, $\overline{X} \cdot Y \cdot \overline{Z}$, $\overline{X} \cdot Y \cdot Z$, $X \cdot \overline{Y} \cdot \overline{Z}$, $X \cdot \overline{Y} \cdot Z$, $X \cdot Y \cdot \overline{Z}$, and $X \cdot Y \cdot Z$. The content of each cell — that is, the minterm — is the product of the variables appearing at the corresponding vertical and horizontal coordinates. For example, in the three-variable map, $X \cdot Y \cdot \overline{Z}$ appears at the intersection of $X \cdot Y$ and $\overline{Z}$. The map is filled by placing a value of 1 for any combination of variables for which the desired output is a 1. For example, consider the function of three variables for which we desire to have an output of 1 whenever the variables X, Y, and Z have the following values:

$$\begin{array}{lll} X = 0 & Y = 1 & Z = 0 \\ X = 0 & Y = 1 & Z = 1 \\ X = 1 & Y = 1 & Z = 0 \\ X = 1 & Y = 1 & Z = 1 \end{array}$$

	$\overline{X}\overline{Y}$	$\overline{X}Y$	XY	$X\overline{Y}$
$\overline{Z}$	0	1	1	0
Z	0	1	1	0

Karnaugh map

X	Y	Z	Desired Function
0	0	0	0
0	0	1	0
0	1	0	1
0	1	1	1
1	0	0	0
1	0	1	0
1	1	0	1
1	1	1	1

Truth table

FIGURE 5.10.22 Truth table and Karnaugh map representations of a logic function.

W	X	Y	Z	Desired Function
0	0	0	0	1
0	0	0	1	1
0	0	1	0	0
0	0	1	1	0
0	1	0	0	0
0	1	0	1	1
0	1	1	0	1
0	1	1	1	0
1	0	0	0	0
1	0	0	1	1
1	0	1	0	1
1	0	1	1	0
1	1	0	0	0
1	1	0	1	0
1	1	1	0	0
1	1	1	1	1

Truth table for four-variable expression

	$\overline{W}\cdot\overline{X}$	$\overline{W}\cdot X$	$W\cdot X$	$W\cdot\overline{X}$
$\overline{Y}\cdot\overline{Z}$	1	0	0	0
$\overline{Y}\cdot Z$	1	1	0	1
$Y\cdot Z$	0	0	1	0
$Y\cdot\overline{Z}$	0	1	0	1

FIGURE 5.10.23 Karnaugh map for a four-variable expression.

The same truth table is shown in Figure 5.10.22 together with the corresponding Karnaugh map.

The Karnaugh map provides an immediate view of the values of the function in graphical form. Further, the arrangement of the cells in the Karnaugh map is such that any two adjacent cells contain minterms that vary in only one variable. This property, as will be verified shortly, is quite useful in the design of logic functions by means of logic gates, especially if we consider the map to be continuously wrapping around itself, as if the top and bottom, and right and left edges were touching each other. For the three-variable map given in Figure 5.10.21, for example, the cell $X \cdot \overline{Y} \cdot \overline{Z}$ is adjacent to $\overline{X} \cdot \overline{Y} \cdot \overline{Z}$ if we "roll" the map so that the right edge touches the left. Note that these two cells differ only in the variable X, a property we earlier claimed adjacent cells have.

Shown in Figure 5.10.23 is a more complex, four-variable logic function which will serve as an example in explaining how Karnaugh maps can be used directly to implement a logic function. First, we define a subcube as a set of 2^m adjacent cells, for $m = 1, 2, 3, \ldots, N$. Thus, a subcube can consist of 1, 2, 4, 8, 16, 32, … cells. All possible subcubes for the four-variable map of Figure 5.10.23 are shown in Figure 5.10.24. Note that there are no four-cell subcubes in this particular case. Note also that there is some overlap between subcubes.

Sum-of-Products Realizations

Although not explicitly stated, the logic functions of the preceding section were all in sum-of-products form. As you know, it is also possible to realize logic functions in product-of-sums form. This section

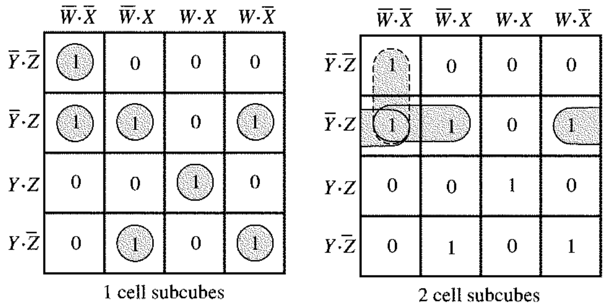

FIGURE 5.10.24 One- and two-cell subcubes for the Karnaugh map of Figure 5.10.23.

discusses the implementation of logic functions in sum-of-products form and gives a set of design rules. The next section will do the same for product-of-sums form logical expressions. The following rules are a useful aid in determining the minimal sum-of-products expression:

1. Begin with isolated cells. These must be used as they are, since no simplification is possible.
2. Find all cells that are adjacent to only one other cell, forming two-cell subcubes.
3. Find cells that form four-cell subcubes, eight-cell subcubes, and so forth.
4. The minimal expression is formed by the collection of the *smallest number of maximal subcubes.*

The following examples illustrate the application of these principles to a variety of problems.

Product-of-Sums Realizations

Thus far, we have exclusively worked with sum-of-products expressions, that is, logic functions of the form $A \cdot B + C \cdot D$. We know, however, that De Morgan's laws state that there is an equivalent form that appears as a product of sums, for example, $(W + Y) \cdot (Y + Z)$. The two forms are completely equivalent, logically, but one of the two forms may lead to a realization involving a smaller number of gates. When using Karnaugh maps, we may obtain the product-of-sums form very simply by following these rules:

1. Solve for the 0s exactly as for the 1s in sum-of-products expressions.
2. Complement the resulting expression.

The same principles stated earlier apply in covering the map with subcubes and determining the minimal expression. The following examples illustrate how one form may result in a more efficient solution than the other.

Example 5.10.3

This example illustrates the design of a logic function using both sum-of-products and product-of-sums implementations, thus showing that it may be possible to realize some savings by using one implementation rather than the other.

1. Realize the function *f* by a Karnaugh map using 0s.
2. Realize the function *f* by a Karnaugh map using 1s.

x	y	z	f
0	0	0	0
0	0	1	1
0	1	0	1
0	1	1	1
1	0	0	1
1	0	1	1
1	1	0	0
1	1	1	0

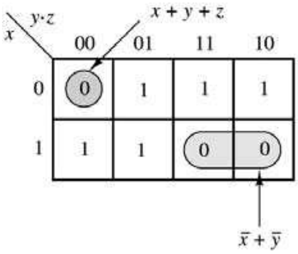

FIGURE 5.10.25 Figure for Example 5.10.3.

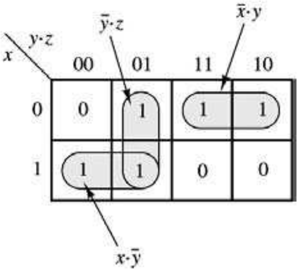

FIGURE 5.10.26 Figure for Example 5.10.3.

Solution.

1. Using 0s, we obtain the Karnaugh map of Figure 5.10.25, leading to the product-of-sums expression

$$f = (x + y + z) \cdot (\bar{x} + \bar{y})$$

which requires five gates.

2. If 1s are used, as shown in Figure 5.10.26, a sum-of-products expression is obtained, of the form

$$f = \bar{x} \cdot y + x \cdot \bar{y} + \bar{y} \cdot z$$

which requires seven gates.

Example 5.10.4 Safety Circuit for Operation of a Stamping Press

In this example, the techniques illustrated in the preceding example will be applied to a practical situation. To operate a stamping press, an operator must press two buttons (b_1 and b_2) 1 m apart from each other and away from the press (this ensures that the operator's hands cannot be caught in the press). When the buttons are pressed, the logical variables b_1 and b_2 are equal to 1. Thus, we can define a new variable $A = b_1 \cdot b_2$; when $A = 1$, the operator's hands are safely away from the press. In addition to the safety requirement, however, other conditions must be satisfied before the operator can activate the press. The press is designed to operate on one of two workpieces, part I and part II, but not both. Thus, acceptable logic states for the press to be operated are "part I is in the press, but not part II" and "part II is in the press, but not part I." If we denote the presence of part I in the press by the logical variable $B = 1$ and the presence of part II by the logical variable $C = 1$, we can then impose additional requirements on the operation of the press. For example, a robot used to place either part in the press could activate a pair of switches (corresponding to logical variables B and C) indicating which part, if any, is in the press. Finally, in order for the press to be operable, it must be "ready", meaning that it has to have completed any previous stamping operation. Let the logical variable $D = 1$ represent the ready condition. We have now represented the operation of the press in terms of four logical variables, summarized in the truth table of Table 5.10.12. Note that only two combinations of the logical variables will result in operation of the press: $ABCD = 1011$ and $ABCD = 1101$. You should verify that these two conditions correspond

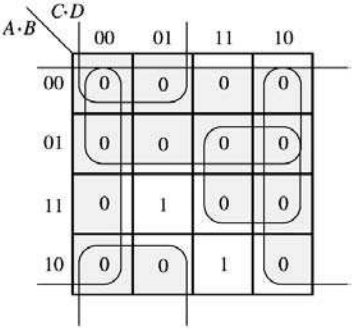

FIGURE 5.10.27 Figure for Example 5.10.4.

TABLE 5.10.12 Conditions for Operation of Stamping Press

(*A*) $b_1 \cdot b_2$	(*B*) Part I is in Press	(*C*) Part II is in Press	(*D*) Press is Operable	Press Operation 1 = Pressing; 0 = Not Pressing
0	0	0	0	0
0	0	0	1	0
0	0	1	0	0
0	0	1	1	0
0	1	0	0	0
0	1	0	1	0
0	1	1	0	0
0	1	1	1	0
1	0	0	0	0
1	0	0	1	0
1	0	1	0	0
1	0	1	1	1
1	1	0	0	0
1	1	0	1	1
1	1	1	0	0
1	1	1	1	0

Note: ↑ Both buttons (b_1, b_2) must be pressed for this to be a 1.

to the desired operation of the press. Using a Karnaugh map, realize the logic circuitry required to implement the truth table shown.

Solution. Table 5.10.12 can be converted to a Karnaugh map, as shown in Figure 5.10.27. Since there are many more 0s than 1s in the table, the use of 0s in covering the map will lead to greater simplification. This will result in a product-of-sums expression. The four subcubes shown in Figure 5.10.27 yield the equation

$$A \cdot D \cdot (C + B) \cdot \left(\overline{C} + \overline{B}\right)$$

By De Morgan's law, this equation is equivalent to

$$A \cdot D \cdot (C + B) \cdot \overline{(C \cdot B)}$$

which can be realized by the circuit of Figure 5.10.28.

For the purpose of comparison, the corresponding sum-of-products circuit is shown in Figure 5.10.29. Note that this circuit employs a greater number of gates and will therefore lead to a more expensive design.

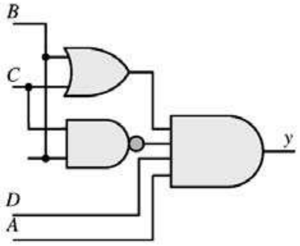

FIGURE 5.10.28 Figure for Example 5.10.4.

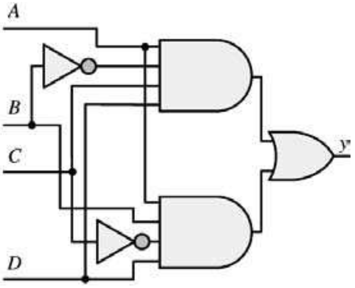

FIGURE 5.10.29 Figure for Example 5.10.4.

Don't Care Conditions

Another simplification technique may be employed whenever the value of the logic function to be implemented can be either a 1 or a 0. This condition may result from the specification of the problem and is not uncommon. Whenever it does not matter whether a position in the map is filled by a 1 or a 0, we use a so-called **don't care** entry, denoted by an x. Then the don't care can be used as either a 1 or a 0, depending on which results in a greater simplification (i.e., helps in forming the smallest number of maximal subcubes).

Combinational Logic Modules

The basic logic gates described in the previous section are used to implement more advanced functions and are often combined to form logic modules, which, thanks to modern technology, are available in compact integrated circuit (IC) packages. In this section and the next, we discuss a few of the more common **combinational logic modules**, illustrating how these can be used to implement advanced logic function.

Multiplexers

Multiplexers, or **data selectors**, are combinational logic circuits that permit the selection of one of many inputs. A typical multiplexer (MUX) has 2^n **data lines**, n **address lines**, and one output. In addition, other control inputs (e.g., enables) may exist. Standard, commercially available MUXs allow for n up to 4; however, two or more MUXs can be combined if a greater range is needed. The MUX allows for one of 2^n inputs to be selected as the data output; the selection of which input is to appear at the output is made by way of the address lines. Figure 5.10.30 depicts the block diagram of a four-input MUX. The input data lines are labeled D_0, D_1, D_2, and D_3; the **data select**, or address, **lines** are labeled I_0 and I_1; and the output is available in both complemented and uncomplemented form, and is thus labeled F, or $\overline{F}$. Finally, an **enable** input, labeled E, is also provided, as a means of enabling or disabling the MUX: if $E = 1$, the MUX is disabled; if $E = 0$, it is enabled. The negative logic (MUX off when $E = 1$ and on when $E = 0$) is represented by the small "bubble" at the enable input, which represents a complement operation (just as at the output of NAND and NOR gates). The enable input is useful whenever one is interested in a cascade of MUXs; this would be of interest if we needed to select a line from a large number, say $2^8 = 256$. Then two 4-input MUXs could be used to provide the data selection of 1 of 8.

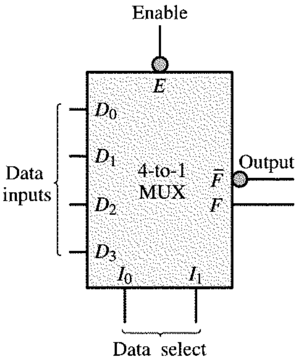

block diagram of 4-to-1 MUX

I_1	I_0	F
0	0	D_0
0	1	D_1
1	0	D_2
1	1	D_3

Truth table of 4-to-1 MUX

FIGURE 5.10.30 4:1 MUX.

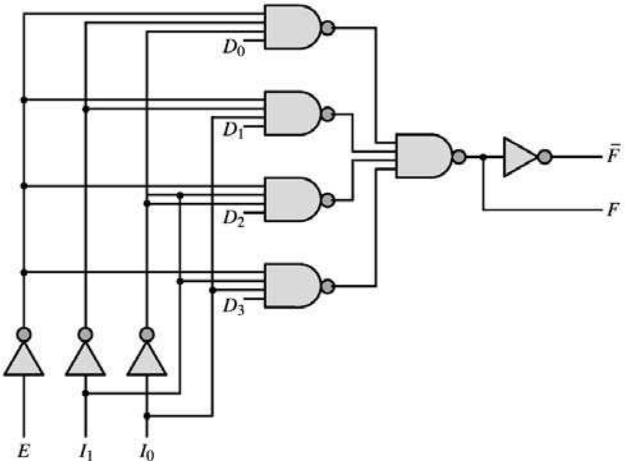

FIGURE 5.10.31 Internal structure of the 4:1 MUX.

The material described in the previous sections is quite adequate to describe the internal workings of a multiplexer. Figure 5.10.31 shows the internal construction of 4:1 MUX using exclusively NAND gates (inverters are also used, but the reader will recall that a NAND gate can act as an inverter if properly connected).

In the design of digital systems (for example, microcomputers), a single line is often required to carry two or more different digital signals. However, only one signal at a time can be placed on the line. A MUX will allow us to select, at different instants, the signal we wish to place on this single line. This property is shown here for a 4:1 MUX. Figure 5.10.32 depicts the functional diagram of a 4:1 MUX, showing four data lines, D_0 through D_3, and two select lines, I_0 and I_1.

The data selector function of a MUX is best understood in terms of Table 5.10.13. In this truth table, the x's represent don't care entries. As can be seen from the truth table, the output selects one of the data lines depending on the values of I_1 and I_0, assuming that I_0 is the least significant bit. As an example, $I_1I_0 = 10$ selects D_2, which means that the output, F, will select the value of the data line D_2. Therefore $F = 1$ if $D_2 = 1$ and $F = 0$ if $D_2 = 0$.

Read-Only Memory (ROM)

Another common technique for implementing logic functions uses a **read-only memory**, or ROM. As the name implies, a ROM is a logic circuit that holds in storage ("memory") information — in the form of binary numbers — that cannot be altered but can be "read" by a logic circuit. A ROM is an array of

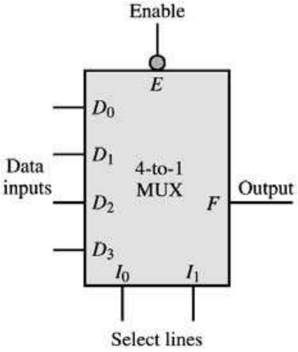

FIGURE 5.10.32 Functional diagram of four-input MUX.

TABLE 5.10.13

I_1	I_0	D_3	D_2	D_1	D_0	F
0	0	x	x	x	0	0
0	0	x	x	x	1	1
0	1	x	x	0	x	0
0	1	x	x	1	x	1
1	0	x	0	x	x	0
1	0	x	1	x	x	1
1	1	0	x	x	x	0
1	1	1	x	x	x	1

memory cells, each of which can store either a 1 or a 0. The array consists of $2^m \times n$ cells, where n is the number of bits in each word stored in ROM. To access the information stored in ROM, m address lines are required. When an address is selected, in a fashion similar to the operation of the MUX, the binary word corresponding to the address selected appears at the output, which consists of n bits, that is, the same number of bits as the stored words. In some sense, a ROM can be thought of as a MUX that has an output consisting of a word instead of a single bit.

Figure 5.10.33 depicts the conceptual arrangement of a ROM with $n = 4$ and $m = 2$. The ROM table has been filled with arbitrary 4-bit words, just for the purpose of illustration. In Figure 5.10.33, if one were to select an enable input of 0 (i.e., on) and values for the address lines of $I_0 = 0$ and $I_1 = 1$, the output word would be $W_2 = 0110$, so that $b_0 = 0$, $b_1 = 1$, $b_2 = 1$, $b_3 = 0$. Depending on the content of the ROM and the number of address and output lines, one could implement an arbitrary logic function.

Unfortunately, the data stored in read-only memories must be entered during fabrication and cannot be altered later. A much more convenient type of read-only memory is the **erasable programmable read-only memory** (EPROM), the content of which can be easily programmed and stored and may be changed if needed. EPROMs find use in many practical applications because of their flexibility in content and

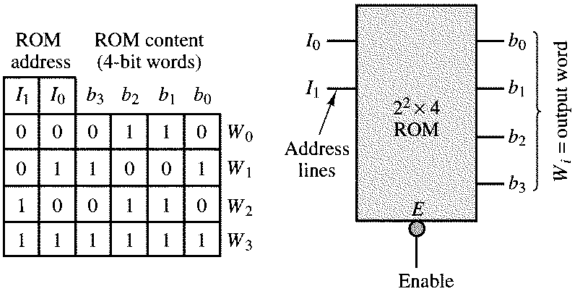

ROM address		ROM content (4-bit words)				
I_1	I_0	b_3	b_2	b_1	b_0	
0	0	0	1	1	0	W_0
0	1	1	0	0	1	W_1
1	0	0	1	1	0	W_2
1	1	1	1	1	1	W_3

FIGURE 5.10.33 Read-only memory.

ease of programming. The following example illustrates the use of an EPROM to perform the linearization of a nonlinear function.

Example 5.10.5 EPROM-Based Lookup Table

One of the most common applications of EPROMs is the *arithmetic lookup table*. A lookup table is similar in concept to the familiar multiplication table and is used to store precomputed values of certain functions, eliminating the need for actually computing the function. A practical application of this concept is present in every automobile manufactured in the U.S. since the early 1980s, as part of the exhaust emission control system. In order for the catalytic converter to minimize the emissions of exhaust gases (especially hydrocarbons, oxides of nitrogen, and carbon monoxide), it is necessary to maintain the *air-to-fuel ratio* (A/F) as close as possible to the stoichiometric value, that is, 14.7 parts of air for each part of fuel. Most modern-day engines are equipped with fuel injection systems that are capable of delivering accurate amounts of fuel to each individual cylinder; thus, the task of maintaining an accurate A/F amounts to measuring the mass of air that is aspirated into each cylinder and computing the corresponding mass of fuel. Many automobiles are equipped with a *mass airflow sensor*, capable of measuring the mass of air drawn into each cylinder during each engine cycle. Let the output of the mass airflow sensor be denoted by the variable M_A, and let this variable represent the mass of air (in g) actually entering a cylinder during a particular stroke. It is then desired to compute the mass of fuel, M_F (also expressed in g), required to achieve an A/F of 14.7. This computation is simply

$$M_F = \frac{M_A}{14.7}$$

Although the above computation is a simple division, its actual calculation in a low-cost digital computer (such as would be used on an automobile) is rather complicated. It would be much simpler to tabulate a number of values of M_A, to precompute the variable M_F, and then to store the result of this computation into an EPROM. If the EPROM address were made to correspond to the tabulated values of air mass and the content at each address to the corresponding fuel mass (according to the precomputed values of the expression $M_F = M_A/14.7$), it would not be necessary to perform the division by 14.7. For each measurement of air mass into one cylinder, an EPROM address is specified and the corresponding content is read. The content at the specific address is the mass of fuel required by the particular cylinder.

In practice, the fuel mass needs to be converted into a time interval corresponding to the duration of time during which the fuel injector is open. This final conversion factor can also be accounted for in the table. Suppose, for example, that the fuel injector is capable of injecting K_F g of fuel per second; then the time duration, T_F, during which the injector should be open in order to inject M_F g of fuel into the cylinder is given by

$$T_F = \frac{M_F}{K_F} \text{ s}$$

Therefore, the complete expression to be precomputed and stored in the EPROM is

$$T_F = \frac{M_A}{14.7 \times K_F} \text{ s}$$

Figure 5.10.34 illustrates this process graphically.

To provide a numerical illustration, consider a hypothetical engine capable of aspirating air in the range $0 < M_A < 0.51$ g and equipped with fuel injectors capable of injecting at the rate of 1.36 g/sec. Thus, the relationship between T_F and M_A is

$$T_F = 50 \times M_A \text{ msec} = 0.05 M_A \text{ sec}$$

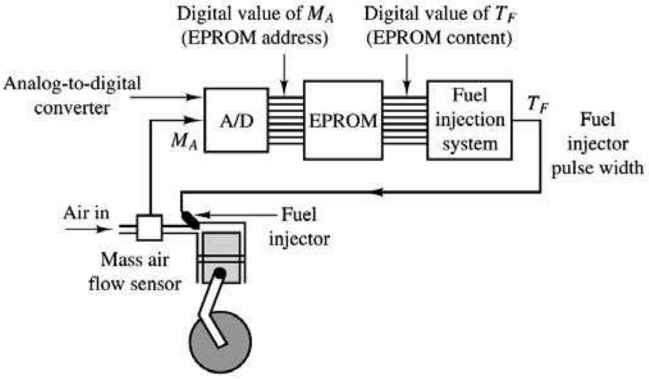

FIGURE 5.10.34 Use of EPROM lookup table in automotive fuel injection system.

M_A(g) × 10^{-2}	Address (digital value of M_A)	Content (digital value of T_F)	T_F(ms) × 10^{-1}
0.	00000000	00000000	0
1	00000001	00000101	5
2	00000010	00001010	10
3	00000011	00001111	15
4	00000100	00010100	20
5	00000101	00011001	25
⋮	⋮	⋮	⋮
51	00110011	11111111	255

FIGURE 5.10.35 Lookup table for automotive fuel injection application.

If the digital value of M_A is expressed in dg (decigrams, or tenths of g), the lookup table of Figure 5.10.35 can be implemented, illustrating the conversion capabilities provided by the EPROM. Note that in order to represent the quantities of interest in an appropriate binary format compatible with the 8-bit EPROM, the units of air mass and of time have been scaled.

Decorders and Read and Write Memory

Decoders, which are commonly used for applications such as address decoding or memory expansion, are combinational logic circuits as well. Our reason for introducing decoders is to show some of the internal organization of semiconductor memory devices.

Figure 5.10.36 shows the truth table for a 2:4 decoder. The decoder has an enable input, $\overline{G}$, and select inputs, B and A. It also has four outputs, Y_0 through Y_3. When the enable input is logic 1, all decoder outputs are forced to logic 1 regardless of the select inputs.

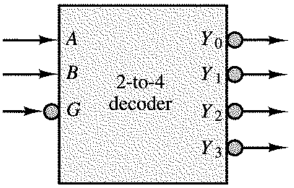

Inputs			Outputs			
Enable	Select					
$\overline{G}$	A	B	Y_0	Y_1	Y_2	Y_3
1	X	X	1	1	1	1
0	0	0	0	1	1	1
0	0	1	1	0	1	1
0	1	0	1	1	0	1
0	1	1	1	1	1	0

FIGURE 5.10.36 2:4 decoder.

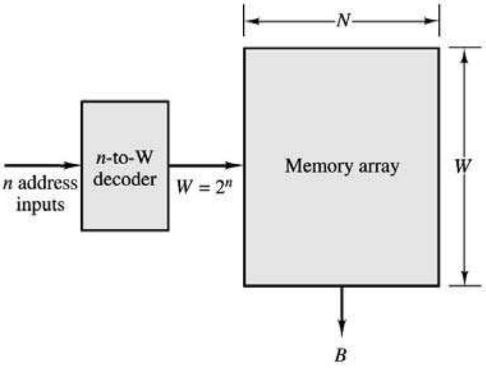

FIGURE 5.10.37 Internal organization of SRAM.

This simple description of decoders permits a brief discussion of the internal organization of an SRAM (**static random-access** or **read and write memory**). SRAM is internally organized to provide memory with high speed (i.e., short access time), a large bit capacity, and low cost. The memory array in this memory device has a column length equal to the number of words, W, and a row length equal to the number of bits per word, N. To select a word, an n-to-W decoder is needed. Since the address inputs to the decoder select only one of the decoder's outputs, the decoder selects one word in the memory array. Figure 5.10.37 shows the internal organization of a typical SRAM.

Thus, to choose the desired word from the memory array, the proper address inputs are required. As an example, if the number of words in the memory array is 8, a 3:8 decoder is needed. Data sheets for 2:4 and 3:8 decoders from a CMOS family data book are provided at the end of the chapter.

Sequential Logic Modules

Combinational logic circuits provide outputs that are based on a combination of present inputs only. On the other hand, sequential logic circuits depend on present and past input values. Because of this "memory" property, sequential circuits can store information; this capability opens a whole new area of application for digital logic circuits.

Latches and Flip-Flops

The basic information-storage device in a digital circuit is called a **flip-flop**. There are many different varieties of flip-flops; however, all flip-flops share the following characteristics:

1. A flip-flop is a **bistable device**; that is, it can remain in one of two stable states (0 and 1) until appropriate conditions cause it to change state. Thus, a flip-flop can serve as a memory element.
2. A flip-flop has two outputs, one of which is the complement of the other.

RS Flip-Flop. It is customary to depict flip-flops by their block diagram and a name — such as Q or X — representing the output variable. Figure 5.10.38 represents the so-called **RS flip-flop**, which has two inputs, denoted by S and R, and two outputs, Q and $\overline{Q}$. The value of Q is called the state of the flip-flop. If $Q = 1$, we refer to the device as *being in the 1 state*. Thus, we need define only one of the two outputs of the flip-flop. The two inputs, R and S, are used to change the state of the flip-flop, according to the following rules:

1. When $R = S = 0$, the flip-flop remains in its present state (whether 1 or 0).
2. When $S = 1$ and $R = 0$, the flip-flop is *set* to the 1 state (thus, the letter S, for **set**).
3. When $S = 0$ and $R = 1$, the flip-flop is *reset* to the 0 state (thus, the letter R, for **reset**).
4. It is not permitted for both S and R to be equal to 1. (This would correspond to requiring the flip-flop to set and reset at the same time.)

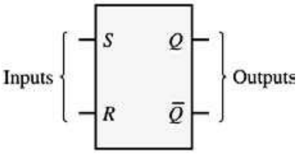

FIGURE 5.10.38 *RS* flip-flop.

S	*R*	*Q*
1	0	1
0	0	1
0	0	1
0	1	0
0	0	0
0	0	0
0	1	0
0	0	0
1	0	1
0	0	1

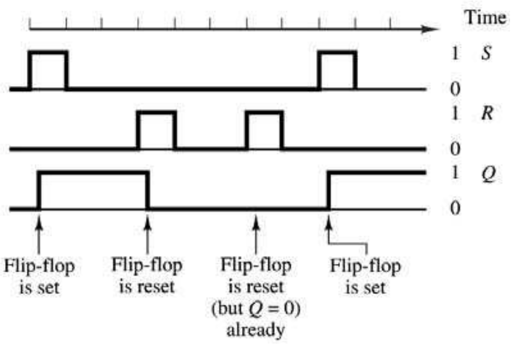

FIGURE 5.10.39 Timing diagram for the *RS* flip-flop.

The rules just described are easily remembered by noting that 1s on the *S* and *R* inputs correspond to the set and reset commands, respectively.

A convenient means of describing the series of transitions that occur as the signals sent to the flip-flop inputs change is the **timing diagram**. A timing diagram is a graph of the inputs and outputs of the *RS* flip-flop (or any other logic device) depicting the transitions that occur over time. In effect, one could also represent these transitions in tabular form; however, the timing diagram provides a convenient visual representation of the evolution of the state of the flip-flop. Figure 5.10.39 depicts a table of transitions for an *RS* flip-flop *Q*, as well as the corresponding timing diagram.

It is important to note that the *RS* flip-flop is **level-sensitive.** This means that the set and reset operations are completed only after the *R* and *S* inputs have reached the appropriate levels. Thus, in Figure 5.10.39 we show the transitions in the *Q* outputs as occurring with a small delay relative to the transitions in the *R* and *S* inputs.

It is instructive to illustrate how an *RS* flip-flop can be constructed using simple logic gates. For example, Figure 5.10.40 depicts a realization of such a circuit consisting of four gates: two inverters and two NAND gates (actually, the same result could be achieved with four NAND gates). Consider the case in which the circuit is in the initial state $Q = 0$ (and therefore $\overline{Q} = 1$). If the input $S = 1$ is applied, the top NOT gate will see inputs $\overline{Q} = 1$ and $\overline{S} = 0$, so that $Q = (\overline{\overline{S} \cdot \overline{Q}}) = (\overline{0 \cdot 1}) = 1$ — that is, the flip-flop is set. Note that when Q is set to 1, $\overline{Q}$ becomes 0. This, however, does not affect the state of the Q output, since replacing $\overline{Q}$ with 0 in the expression

$$Q = \left(\overline{\overline{S} \cdot \overline{Q}}\right)$$

does not change the result:

$$Q = \left(\overline{0 \cdot 0}\right) = 1$$

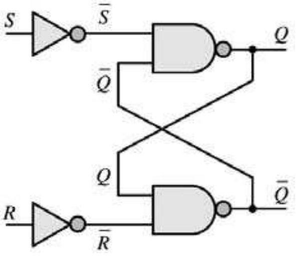

FIGURE 5.10.40 Logic gate implementation of the *RS* flip-flop.

Thus, the cross-coupled feedback from outputs Q and $\overline{Q}$ to the input of the NAND gates is such that the set condition sustains itself. It is straightforward to show (by symmetry) that a 1 input on the R line causes the device to reset (i.e., causes $Q = 0$) and that this condition is also self-sustaining.

An extension of the *RS* flip-flop includes an additional enable input that is *gated* into each of the other two inputs. Figure 5.10.41 depicts an *RS* flip-flop consisting of two NOR gates. In addition, an enable input is connected through two AND gates to the *RS* flip-flop, so that an input to the R and S line will be effective only when the enable input is 1. Thus, any transitions will be controlled by the enable input, which acts as a synchronizing signal. The enable signal may consist of a **clock**, in which case the flip-flop is said to be **clocked** and its operation is said to be **synchronous**.

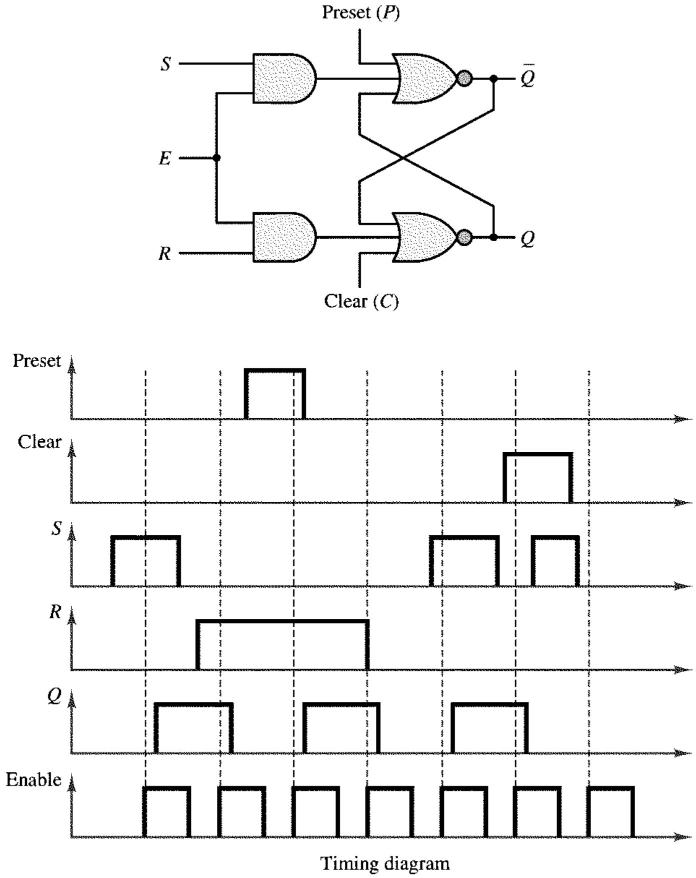

FIGURE 5.10.41 *RS* flip-flop with enable, preset, and clear lines.

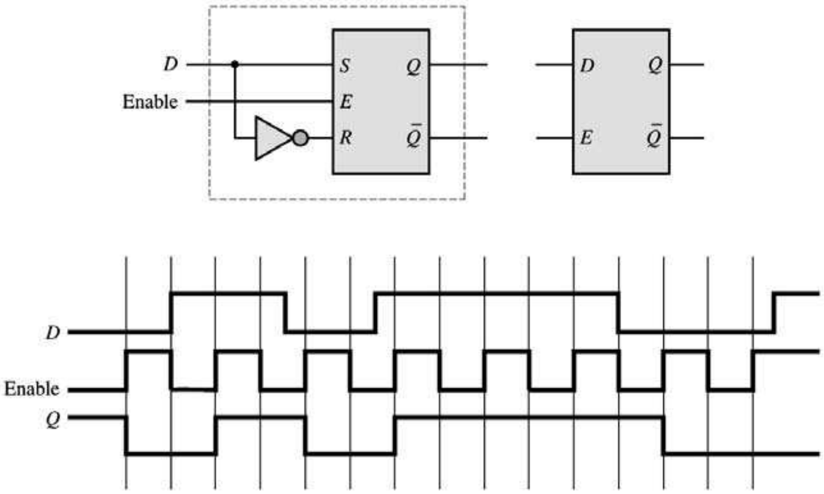

FIGURE 5.10.42 Data latch.

The same circuit of Figure 5.10.41 can be used to illustrate two additional features of flip-flops: the **preset** and **clear** functions, denoted by the inputs P and C, respectively. When P and C are 0, they do not affect the operation of the flip-flop. Setting $P = 1$ corresponds to setting $S = 1$, and therefore causes the flip-flop to go into the 1 state, thus, the term *preset*: this function allows the user to preset the flip-flop to 1 at any time. When C is 1, the flip-flop is reset, or *cleared* (i.e., Q is made equal to 0). Note that these direct inputs are, in general, asynchronous; therefore, they allow the user to preset or clear the flip-flop at any time. A set of timing waveforms illustrating the function of the enable, preset, and clear inputs is also shown in Figure 5.10.41. Note how transitions occur only when the enable input goes high (unless the preset or clear inputs are used to override the RS inputs).

Another extension of the RS flip-flop, called the **data latch**, is shown in Figure 5.10.42. In this circuit, the R input is always equal to the inverted S input, so that whenever the enable input is high, the flip-flop is set. This device has the dual advantage of avoiding the potential conflict that might arise if both R and S were high and reducing the number of input connections by eliminating the reset input. This circuit is called a data latch because once the enable input goes low, the flip-flop is latched to the previous value of the input. Thus this device can serve as a basic memory element.

D Flip-Flop. The ***D* flip-flop** is an extension of the data latch that utilizes two RS flip-flops, as shown in Figure 5.10.43. In this circuit, a clock is connected to the enable input of each flip-flop. Since Q_1 sees an inverted clock signal, the latch is enabled when the clock waveform goes low. However, since Q_2 is disabled when the clock is low, the output of the D flip-flop will not switch to the 1 state until the clock goes high, enabling the second latch and transferring the state of Q_1 to Q_2. It is important to note that the D flip-flop changes state only on the positive edge of the clock waveform: Q_1 is set on the negative edge of the clock, and Q_2 (and therefore Q) is set on the positive edge of the clock, as shown in the timing diagram of Figure 5.10.43. This type of device is said to be **edge-triggered**. This feature is indicated by the "knife edge" drawn next to the CLK input in the device symbol. The particular device described here is said to be positive edge-triggered, or **leading edge-triggered**, since the final output of the flip-flop is set on a positive-going clock transition.

On the basis of the rules stated in this section, the state of the D flip-flop can be described by means of the following truth table:

D	CLK	Q
0	≠	0
1	≠	1

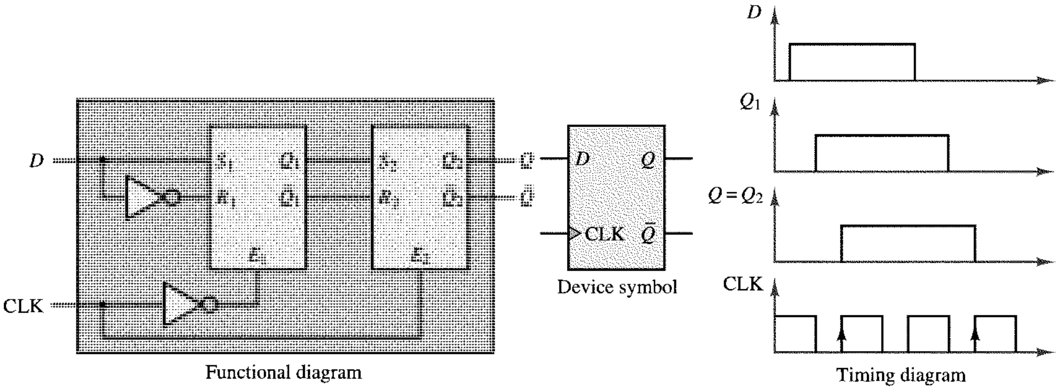

FIGURE 5.10.43 D flip-flop.

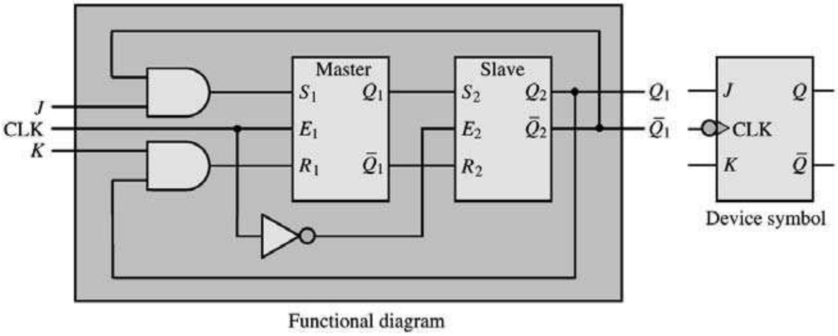

FIGURE 5.10.44 *JK* flip-flop.

where the symbol ↑ indicates the occurrence of a positive transition.

JK Flip-Flop. Another very common type of flip-flop is the ***JK* flip-flop**, shown in Figure 5.10.44. The *JK* flip-flop operates according to the following rules:

- When J and K are both low, no change occurs in the state of the flip-flop.
- When $J = 0$ and $K = \downarrow$, the flip-flop is reset to 0.
- When $J = \downarrow$ and $K = 0$, the flip-flop is set to 1.
- When both J and K are high, the flip-flop will toggle between states at every transition of the clock input.

The symbol ↓ denotes a negative transition.

Note that, functionally, the operation of the *JK* flip-flop can also be explained in terms of two *RS* flip-flops. When the clock waveform goes high, the "master" flip-flop is enabled; the "slave" receives the state of the master upon a negative clock transition. The "bubble" at the clock input signifies that the device is negative or **trailing edge-triggered**. This behavior is similar to that of an *RS* flip-flop, except for the $J = 1$, $K = 1$ condition, which corresponds to a toggle mode rather than to a disallowed combination of inputs.

Figure 5.10.45 depicts the truth table for the *JK* flip-flop. It is important to note that when both inputs are 0 the flip-flop remains in its previous state at the occurrence of a clock transition; when either input is high and the other is low, the *JK* flip-flop behaves like the *RS* flip-flop, whereas if both inputs are high, the output "toggles" between states every time the clock waveform undergoes a negative transition.

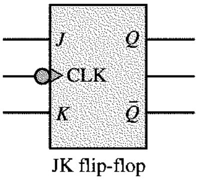

J_n	K_n	Q_{n+1}
0	0	Q_n
0	1	0 (reset)
1	0	1 (set)
1	1	$\bar{Q}_n$ (toggle)

FIGURE 5.10.45 Truth table for the *JK* flip-flop.

Digital Counters

One of the more immediate applications of flip-flops is in the design of **counters**. A counter is a sequential logic device that can take one of *N* possible states, stepping through these states in a sequential fashion. When the counter has reached its last state, it resets to zero and is ready to start counting again. For example, a three-bit **binary up counter** would have $2^3 = 8$ possible states, and might appear as shown in the functional block of Figure 5.10.46. The input clock waveform causes the counter to step through the eight states, making one transition for each clock pulse. We shall shortly see that a string of *JK* flip-flops can accomplish this task exactly. The device shown in Figure 5.10.46 also displays a reset input, which forces the counter to equal 0: $b_2b_1b_0 = 000$.

Although binary counters are very useful in many applications, one is often interested in a **decade counter**, that is, a counter that counts from 0 to 9 and then resets. A four-bit binary counter can easily be configured in principle to provide this function by means of simple logic that resets the counter when it has reached the count $1001_2 = 9_{10}$. As shown in Figure 5.10.47, if we connect bits b_3 and b_1 to a four-input AND gate, along with $\bar{b}_2$ and $\bar{b}_0$, the output of the AND gate can be used to reset the counter after a count of 10. Additional logic can provide a "carry" bit whenever a reset condition is reached,

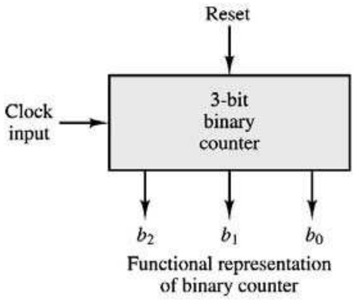

Functional representation of binary counter

Input pulses	State b_2	b_1	b_0
0	0	0	0
1	0	0	1
2	0	1	0
3	0	1	1
4	1	0	0
5	1	0	1
6	1	1	0
7	1	1	1

Timing table

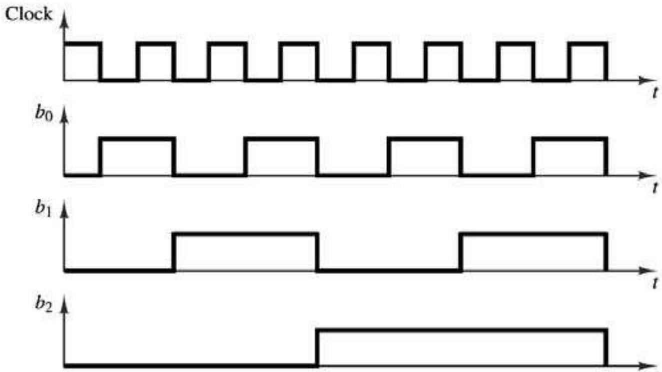

Timing diagram

FIGURE 5.10.46 Binary up counter.

Input pulses	b_3	b_2	b_1	b_0
0	0	0	0	0
1	0	0	0	1
2	0	0	1	0
3	0	0	1	1
4	0	1	0	0
5	0	1	0	1
6	0	1	1	0
7	0	1	1	1
8	1	0	0	0
9	1	0	0	1

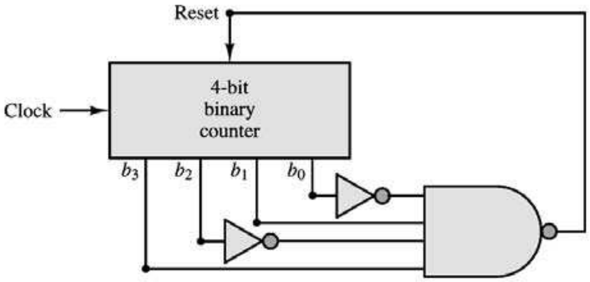

FIGURE 5.10.47 Decade counter.

which could be passed along to another decade counter, enabling counts up to 99. Decade counters can be cascaded so as to represent decimal digits in succession.

Although the decade counter of Figure 5.10.47 is attractive because of its simplicity, this configuration would never be used in practice because of the presence of **propagation delays**. These delays are caused by the finite response time of the individual transistors in each logic device and cannot be guaranteed to be identical for each gate and flip-flop. Thus, if the reset signal — which is presumed to be applied at exactly the same time to each of the four *JK* flip-flops in the four-bit binary counter — does not cause the *JK* flip-flops to reset at exactly the same time on account of different propagation delays, then the binary word appearing at the output of the counter will change from 1001 to some other number, and the output of the four-input NAND gate will no longer be high. In such a condition, the flip-flops that have not already reset will then not be able to reset, and the counting sequence will be irreparably compromised.

What can be done to obviate this problem? The answer is to use a systematic approach to the design of sequential circuits making use of **state transition diagrams**. This topic is discussed in the references.

A simple implementation of the binary counter we have described in terms of its functional behavior is shown in Figure 5.10.48. The figure depicts a three-bit binary **ripple counter**, which is obtained from a cascade of three *JK* flip-flops. The transition table shown in the figure illustrates how the *Q* output of each state becomes the clock input to the next stage, while each flip-flop is held in the toggle mode. The output transitions assume that the clock, CLK, is a simple square wave (all *JK*s are negative edge-triggered).

This 3-bit ripple counter can easily be configured as a divide-by-8 mechanism, simply by adding an AND gate. To divide the input clock rate by 8, one output pulse should be generated for every eight clock pulses. If one were to output a pulse every time a binary 111 combination occurs, a simple AND gate would suffice to generate the required condition. This solution is shown in Figure 5.10.49. Note that the

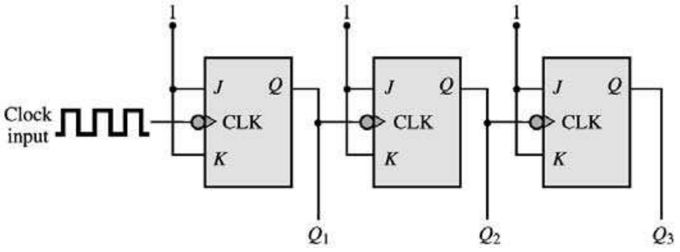

Input	Q_3	Q_2	Q_1
⎍	0	0	0
⎍	0	0	1
⎍	0	1	0
⎍	0	1	1
⎍	1	0	0
⎍	1	0	1
⎍	1	1	0
⎍	1	1	1

FIGURE 5.10.48 Ripple counter.

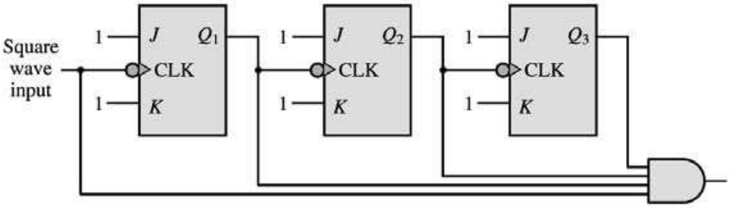

FIGURE 5.10.49 Divide-by-8 circuit.

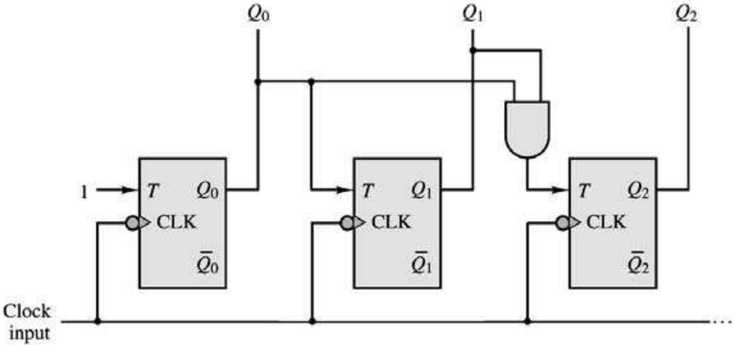

FIGURE 5.10.50 Three-bit synchronous counter.

square wave is also included as an input to the AND gate; this ensures that the output is only as wide as the input signal. This application of ripple counters is further illustrated in the following example.

A slightly more complex version of the binary counter is the so-called **synchronous counter**, in which the input clock drives all of the flip-flops simultaneously. Figure 5.10.50 depicts a three-bit synchronous counter. In this figure, we have chosen to represent each flip-flop as a *T* flip-flop. The clocks to all the flip-flops are incremented simultaneously. The reader should verify that Q_0 toggles to 1 first and then Q_1 toggles to 1, and that the AND gate ensures that Q_2 will toggle only after Q_0 and Q_1 have both reached the 1 state ($Q_0 \cdot Q_1 = 1$).

Other common counters are the **ring counter** and the **up-down counter**, which has an additional select input that determines whether the counter counts up or down.

Example 5.10.6 Measurement of Angular Position

One type of angular position encoder is the slotted encoder shown in Figure 5.10.51. This encoder can be used in conjunction with a pair of counters and a high-frequency clock to determine the speed of rotation of the slotted wheel. As shown in Figure 5.10.52, a clock of known frequency is connected to a counter while another counter records the number of slot pulses detected by an optical slot detector as the wheel rotates. Dividing the counter values, one could obtain the speed of the rotating wheel in radians per second. For example, assume a clocking frequency of 1.2 kHz. If both counters are started at zero and at some instant the timer counter reads 2850 and the encoder counter reads 3050, then the speed of the rotating encoder is found to be

$$1200\frac{\text{cycles}}{\text{second}}\cdot\frac{2850\text{ slots}}{3050\text{ cycles}} = 1121.3\frac{\text{slots}}{\text{second}}$$

and

$$1121.3\ \text{slots/sec} \times 1^\circ\ \text{per slot} \times 2\pi/360\ \text{rad/degree} = 19.6\ \text{rad/sec}$$

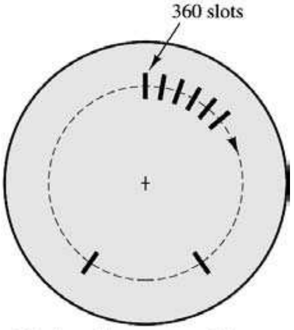

FIGURE 5.10.51

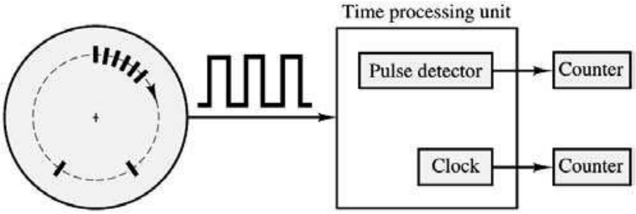

FIGURE 5.10.52 Calculating the speed of rotation of the slotted wheel.

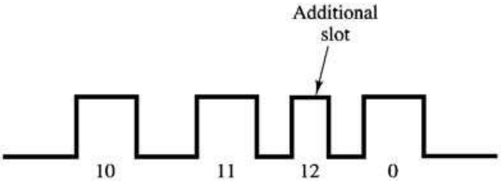

FIGURE 5.10.53 PMA pulse sequence.

If this encoder is connected to a rotating shaft, it is possible to measure the angular position and velocity of the shaft. Such shaft encoders are used in measuring the speed of rotation of electric motors, machine tools, engines, and other rotating machinery. A typical application of the slotted encoder is to compute the ignition and injection timing in an automotive engine. In an automotive engine, information related to speed is obtained from the camshaft and the flywheel, which have known reference points. The reference points determine the timing for the ignition firing points and fuel injection pulses and are identified by special slot patterns on the camshaft and crankshaft. Two methods are used to detect the special slots (reference points): *period measurement with additional transition detection* (PMA, and *period measurement with missing transition detection* (PMM). In the PMA method, an additional slot (reference point) determines a known reference position on the crankshaft or camshaft. In the PMM method, the reference position is determined by the absence of a slot. Figure 5.10.53 illustrates a typical PMA pulse sequence, showing the presence of an additional pulse. The additional slot may be used to determine the timing for the ignition pulses relative to a known position of the crankshaft. Figure 5.10.54 depicts a typical PMM pulse sequence. Because the period of the pulses is known, the additional slot of the missing slot can be easily detected and used as a reference position. How would you implement these pulse sequences using ring counters?

Registers

A register consists of a cascade of flip-flops that can store binary data, one bit in each flip-flop. The simplest type of register is the parallel input–parallel output register shown in Figure 5.10.55. In this register, the “load” input pulse, which acts on all clocks simultaneously, causes the parallel inputs $b_0b_1b_2b_3$

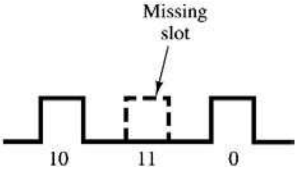

FIGURE 5.10.54 PMA pulse sequence.

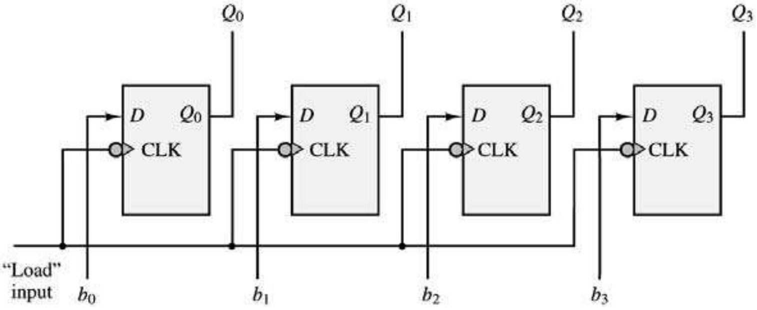

FIGURE 5.10.55 Four-bit parallel register.

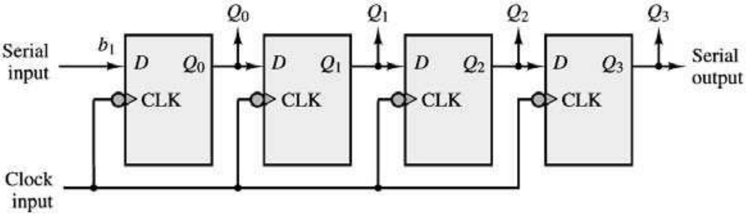

FIGURE 5.10.56 Four-bit shift register.

to be transferred to the respective flip-flops. The *D* flip-flop employed in this register allows the transfer from b_n to Q_n to occur very directly. Thus, *D* flip-flops are very commonly used in this type of application. The binary word $b_3b_2b_1b_0$ is now "stored", each bit being represented by the state of a flip-flop. Until the "load" input is applied again and a new word appears at the parallel inputs, the register will preserve the stored word.

The construction of the parallel register presumes that the *N*-bit word to be stored is available in parallel form. However, it is often true that a binary word will arrive in serial form, that is, one bit at a time. A register that can accommodate this type of logic signal is called a **shift register**. Figure 5.10.56 illustrates how the same basic structure of the parallel register applies to the shift register, except that the input is now applied to the first flip-flop and shifted along at each clock pulse. Note that this type of register provides both a serial and a parallel output.

5.11 Measurements and Instrumentation

Measurement Systems and Transducers

Measurement Systems

In virtually every engineering application there is a need for measuring some physical quantities, such as forces, stresses, temperatures, pressures, flows, or displacements. These measurements are performed by physical devices called **sensors** or **transducers**, which are capable of converting a physical quantity to a more readily manipulated electrical quantity. Most sensors, therefore, convert the change of a physical

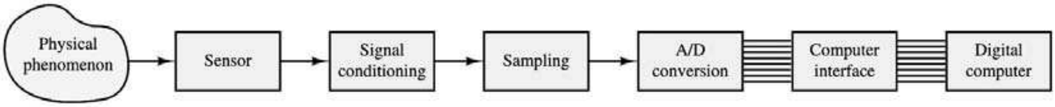

FIGURE 5.11.1 Measurement system.

quantity (e.g., humidity, temperature) to a corresponding (usually proportional) change in an electrical quantity (e.g., voltage or current). Often, the direct output of the sensor requires additional manipulation before the electrical output is available in a useful form. For example, the change in resistance resulting from a change in the surface stresses of a material — the quantity measured by the resistance strain gauges described in Section 5.2 — must first be converted to a change in voltage through a suitable circuit (the Wheatstone bridge) and then amplified from the millivolt to the volt level. The manipulations needed to produce the desired end result are referred to as *signal conditioning*. The wiring of the sensor to the signal conditioning circuitry requires significant attention to *grounding* and *shielding* procedures, to ensure that the resulting signal is as free from noise and interference as possible. Very often, the conditioned sensor signal is then converted to *digital* form and recorded in a computer for additional manipulation, or is displayed in some form. The apparatus used in manipulating a sensor output to produce a result that can be suitably displayed or stored is called a **measurement system**. Figure 5.11.1 depicts a typical computer-based measurement system in block diagram form.

Sensor Classification

There is no standard and universally accepted classification of sensors. Depending on one's viewpoint, sensors may be grouped according to their physical characteristics (e.g., electronic sensors, resistive sensors), or by the physical variable or quantity measured by the sensor (e.g., temperature, flow rate). Other classifications are also possible. Table 5.11.1 presents a partial classification of sensors grouped according to the variable sensed; we do not claim that the table is complete, but we can safely state that most of the engineering measurements of interest to the reader are likely to fall in the categories listed in Table 5.11.1. Also included in the table are section or example references to sensors described in this chapter.

A sensor is usually accompanied by a set of specifications that indicate its overall effectiveness in measuring the desired physical variable. The following definitions will help the reader understand sensor data sheets:

Accuracy: Conformity of the measurement to the true value, usually in percent of full-scale reading
Error: Difference between measurement and true value, usually in percent of full-scale reading
Precision: Number of significant figures of the measurement
Resolution: Smallest measurable increment
Span: Linear operating range
Range: The range of measurable values
Linearity: Conformity to an ideal linear calibration curve, usually in percent of reading or of full-scale reading (whichever is greater)

Motion and Dimensional Measurements

The measurement of motion and dimension is perhaps the most commonly encountered engineering measurement. Measurements of interest include absolute position, relative position (displacement), velocity, acceleration, and jerk (the derivative of acceleration). These can be either translational or rotational measurements; usually, the same principle can be applied to obtain both kinds of measurements. These measurements are often based on changes in elementary properties, such as changes in the resistance of an element (e.g., strain gauges, potentiometers), in an electric field (e.g., capacitive sensors), or in a magnetic field (e.g., inductive, variable-reluctance, or eddy current sensors). Other mechanisms may be based on special materials (e.g., piezoelectric crystals), or on optical signals and imaging systems.

TABLE 5.11.1 Sensor Classification

Sensed Variables	Sensors	Ref. in this Chapter
Motion and dimensional variables	Resistive potentiometers	
	Strain gauges	Example 5.2.1
	Differential transformers (LVDTs)	Example 5.12.1
	Variable-reluctance sensors	Example 5.12.2
	Capacitive sensors	Example 5.4.1 and 5.4.2
	Piezoelectric sensors	Example 5.9.2
	Electro-optical sensors	Example 5.10.6
	Moving-coil transducers	Example 5.12.4
	Seismic sensors	
Force, torque, and pressure	Strain gauges	Example 5.2.1
	Piezoelectric sensors	Example 5.9.2
	Capacitive sensors	Example 5.4.1 and 5.4.2
Flow	Pitot tube	
	Hot-wire anemometer	Section 5.11
	Differential pressure sensors	Section 5.11
	Turbine meters	Section 5.11
	Vortex shedding meters	
	Ultrasonic sensors	
	Electromagnetic sensors	
	Imaging systems	
Temperature	Thermocouples	Section 5.11
	Resistance thermometers (RTDs)	Section 5.11
	Semiconductor thermometers	
	Radiation detectors	
Liquid level	Motion transducers	
	Force transducers	
	Differential-pressure measurement devices	
Humidity	Semiconductor sensors	
Chemical composition	Gas analysis equipment	
	Solid-state gas sensors	

Force, Torque, and Pressure Measurements

Another very common class of measurements is that of pressure and force, and the related measurement of torque. Perhaps the single most common family of force and pressure transducers comprises those based on strain gauges (e.g., load cells, diaphragm pressure transducers). Also very common are piezoelectric transducers. Capacitive transducers again find application in the measurement of pressure.

Flow Measurementrs

In many engineering applications it is desirable to sense the flow rate of a fluid, whether compressible (gas) or incompressible (liquid). The measurement of fluid flow rate is a complex subject; in this section we simply summarize the concepts underlying some of the most common measurement techniques. Shown in Figure 5.11.2 are three different types of flow rate sensors. The sensor in Figure 5.11.2(a) is based on **differential pressure measurement** and on a **calibrated orifice**: the relationship between pressure across the orifice, $p_1 - p_2$, and flow rate through the orifice, q, is predetermined through the calibration; therefore, measuring the differential pressure is equivalent to measuring flow rate.

The sensor in Figure 5.11.2(b) is called a **hot-wire anemometer**, because it is based on a heated wire that is cooled by the flow of a gas. The resistance of the wire changes with temperature, and a Wheatstone bridge circuit converts this change in resistance to a change in voltage. Also commonly used are **hot-film anemometers**, where a heated film is used in place of the more delicate wire. A very common application of the latter type of sensor is in automotive engines, where control of the air-to-fuel ratio depends on measurement of the engine intake mass airflow rate.

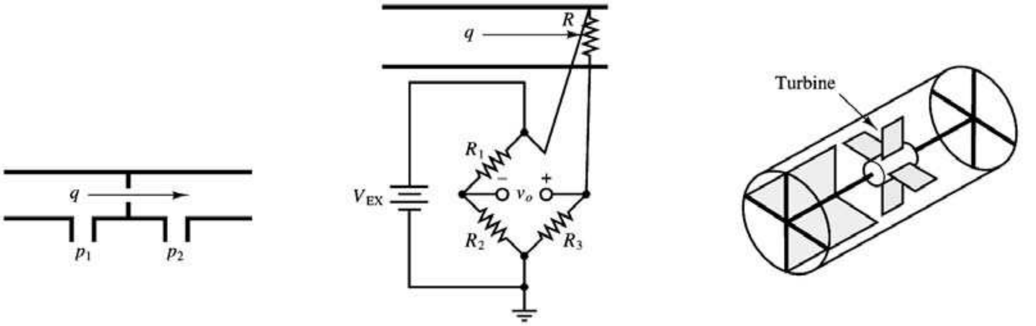

Differential-pressure flowmeter: A calibrated orifice and a pair of pressure transducers permit the measurement of flow rate.
(a)

Hot-wire anemometer: A heated wire is cooled by the gas flow. The resistance of the wire changes with temperature.
(b)

Turbine flowmeter: Fluid flow induces rotation of the turbine; measurement of turbine velocity provides an indication of flow rate.
(c)

FIGURE 5.11.2 Devices for the measurement of flow.

TABLE 5.11.2 Thermocouple Data

Type	Elements +/–	Seebeck Coefficient (μV/°C)	Range (°C)	Range (mV)
E	Chromel/constantan	58.70 at 0°C	–270 to 1000	–9.835 to 76.358
J	Iron/constantan	50.37 at 0°C	–210 to 1200	–8.096 to 69.536
K	Chromel/alumel	39.48 at 0°C	–270 to 1372	–6.548 to 54.874
R	Pt(10%)–Rh/Pt	10.19 at 600°C	–50 to 1768	–0.236 to 18.698
T	Copper/constantan	38.74 at 0°C	–270 to 400	–6.258 to 20.869
S	Pt(13%)–Rh/Pt	11.35 at 600°C	–50 to 1768	–0.226 to 21.108

Figure 5.11.2(c) depicts a **turbine flowmeter**, in which the fluid flow causes a turbine to rotate; the velocity of rotation of the turbine (which can be measured by a noncontact sensor — e.g., a magnetic pickup) is related to the flow velocity.

Besides the techniques discussed in this chapter, many other techniques exist for measuring fluid flow, some of significant complexity.

Temperature Measurements

One of the most frequently measured physical quantities is temperature. The need to measure temperature arises in just about every field of engineering. This subsection is devoted to summarizing two common temperature sensors — the **thermocouple** and the **resistance temperature detector** (RTD) — and their related signal conditioning needs.

Thermocouples. A thermocouple is formed by the junction of two dissimilar metals. This junction results on an open-circuit **thermoelectric voltage** due to the **Seebeck effect**, named after Thomas Seebeck, who discovered the phenomenon in 1821. Various types of thermocouples exist; they are usually classified according to the data of Table 5.11.2. The Seebeck coefficient shown in the table is specified at a given temperature because the output voltage of a thermocouple, v, has a nonlinear dependence on temperature. This dependence is typically expressed in terms of a polynomial of the following form:

$$T = a_0 + a_1 v + a_2 v^2 + a_3 v^3 + \ldots + a_n v^n \tag{5.11.1}$$

For example, the coefficients of the J thermocouple in the range –100 to + 1000°C are as follows:

$$a_0 = -0.048868252 \qquad a_1 = 19{,}873.14503 \qquad a_2 = -128{,}614.5353$$

$$a_3 = 11{,}569{,}199.78 \qquad a_4 = -264{,}917{,}531.4 \qquad a_5 = 2{,}018{,}441{,}314$$

The use of a thermocouple requires special connections, because the junction of the thermocouple wires with other leads (such as voltmeter leads, for example) creates additional thermoelectric junctions that in effect act as additional thermocouples. For example, in the J thermocouple circuit of Figure 5.11.3, junction J_1 is exposed to the temperature to be measured, but junctions J_2 and J_3 also generate a thermoelectric voltage, which is dependent on the temperature at these junctions, that is, the temperature at the voltmeter connections. One would therefore have to know the voltages at these junctions as well, in order to determine the actual thermoelectric voltage at J_1. To obviate this problem, a reference junction at known temperature can be employed; a traditional approach involves the use of a **cold junction**, so called because it consists of an ice bath, one of the easiest means of obtaining a known reference temperature. Figure 5.11.4 depicts a thermocouple measurement using an ice bath. The voltage measured in Figure 5.11.4 is dependent on the temperature difference $T_1 - T_{\text{ref}}$, where $T_{\text{ref}} = 0$°C. The connections to the voltmeter are made at an *isothermal block*, kept at a constant temperature; note that the same metal is used in both of the connections to the isothermal block. Thus (still assuming a J thermocouple), there is no difference between the thermoelectric voltages at the two copper-iron junctions; these will add to zero at the voltmeter. The voltmeter will therefore read a voltage proportional to $T_1 - T_{\text{ref}}$.

An ice bath is not always a practical solution. Other cold junction temperature compensation techniques employ an additional temperature sensor to determine the actual temperature of the junctions J_2 and J_3 of Figure 5.11.3

Resistance Temperature Detectors (RTDs). A resistance temperature detector (RTD) is a variable-resistance device whose resistance is a function of temperature. RTDs can be made with both positive and negative temperature coefficients and offer greater accuracy and stability than thermocouples. **Thermistors** are part of the RTD family. A characteristic of all RTDs is that they are *passive* devices, that is,

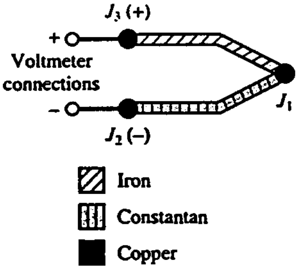

FIGURE 5.11.3 J thermocouple circuit.

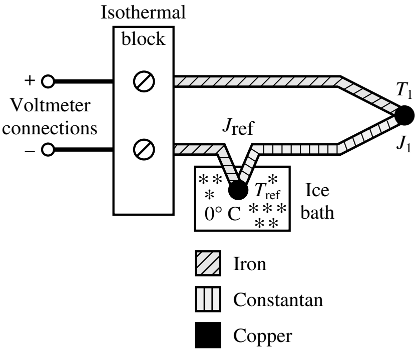

FIGURE 5.11.4 Cold-junction-compensated thermocouple circuit.

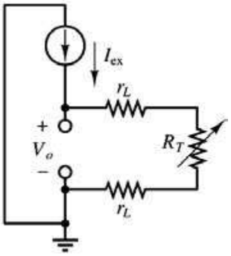

FIGURE 5.11.5 Effect of connection leads on RTD temperature measurement.

they do not provide a useful output unless excited by an external source. The change in resistance in an RTD is usually converted to a change in voltage by forcing a current to flow through the device. An indirect result of this method is a **self-heating error**, caused by the i^2 R heating of the device. Self-heating of an RTD is usually denoted by the amount of power that will raise the RTD temperature by 1°C. Reducing the excitation current can clearly help reduce self-heating, but it also reduces the output voltage.

The RTD resistance has a fairly linear dependence on temperature, a common definition of the **temperature coefficient** of an RTD is related to the change in resistance from 0 to 100°C. Let R_0 be the resistance of the device at 0°C and R_{100} the resistance at 100°C. Then the temperature coefficient, α, is defined to be

$$\alpha = \frac{R_{100} - R_0}{100 - 0} \frac{\Omega}{^\circ\mathrm{C}} \tag{5.11.2}$$

A more accurate representation of RTD temperature dependence can be obtained by using a nonlinear (cubic) equation and published tables of coefficients. As an example, a platinum RTD could be described either by the temperature coefficient $\alpha = 0.003911$, or by the equation

$$\begin{aligned} R_T &= R_0\left(1 + AT - BT^2 - CT^3\right) \\ &= R_0\left(1 + 3.6962\times10^{-3}T - 5.8495\times10^{-7}T^2 - 4.2325\times10^{-12}T^3\right) \end{aligned} \tag{5.11.3}$$

where the coefficient C is equal to zero for temperatures above 0°C.

Because RTDs have fairly low resistance, they are sensitive to error introduced by the added resistance of the lead wires connected to them; Figure 5.11.5 depicts the effect of the lead resistances, r_L, on the RTD measurement. Note that the measured voltage includes the resistance of the RTD as well as the resistance of the leads. If the leads used are long (greater than 3 m is a good rule of thumb), then the measurement will have to be adjusted for this error. Two possible solutions to the lead problems are the *four-wire* RTD measurement circuit and the *three-wire* Wheatstone bridge circuit, shown in Figure 5.11.6(a) and (b), respectively. In the circuit of Figure 5.11.6(a), the resistance of the lead wires from the excitation, r_{L1} and r_{L4}, may be arbitrarily large, since the measurement is affected by the resistance of only the output lead wires, r_{L2} and r_{L3}, which can be kept small by making these leads short. The circuit of Figure 5.11.6(b) takes advantage of the properties of the Wheatstone bridge to cancel out the unwanted effect of the lead wires while still producing an output dependent on the change in temperature.

Wiring, Grounding, and Noise

The importance of proper circuit connections cannot be overemphasized. Unfortunately, this is a subject that is rarely taught in introductory electrical engineering courses. The present section summarizes some important considerations regarding signal source connections, various types of input configurations, noise sources and coupling mechanisms, and means of minimizing the influence of noise on a measurement.

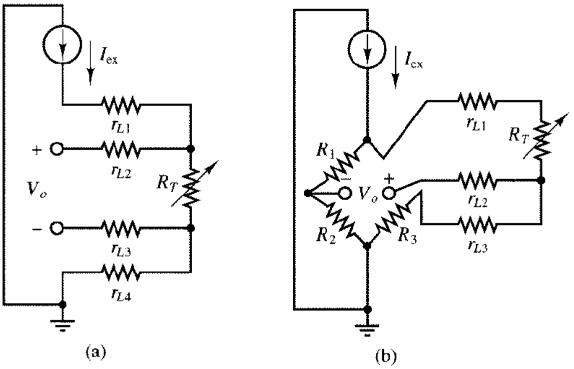

FIGURE 5.11.6 Four-wire RTD circuit (a) and three-wire Wheatstone bridge RTD circuit (b).

Signal Sources and Measurement System Configurations

Before proper connection and wiring techniques can be presented, we must examine the difference between **grounded** and **floating signal sources**. Every sensor can be thought of as some kind of signal source; a general representation of the connection of a sensor to a measurement system is shown in Figure 5.11.7(a). The sensor is modeled as an ideal voltage source in series with a source resistance. Although this representation does not necessarily apply to all sensors, it will be adequate for the purposes of the present section. Figure 5.7.11(b) and Figure 5.7.11(c) show two types of signal sources: grounded and floating. A grounded signal source is one in which a ground reference is established — for example, by connecting the *signal low* lead to a case or housing. A floating signal source is one in which neither signal lead is connected to ground; since ground potential is arbitrary, the signal source voltage levels (*signal low* and *signal high*) are at an unknown potential relative to the case ground. Thus, the signal is said to be *floating*. Whether a sensor can be characterized as a grounded or a floating signal source ultimately depends on the connection of the sensor to its case, but the choice of connection may depend on the nature of the source. For example, the thermocouple described earlier is *intrinsically* a floating signal source, since the signal of interest is a difference between voltages. The same thermocouple *could* become a grounded signal source if one or its two leads were directly connected to ground, but this is usually not a desirable arrangement for this particular sensor.

In analogy with a signal source, a measurement system can be either **ground-referenced** or **differential.** In a ground-referenced system, the signal low connection is tied to the instrument case ground; in a differential system, neither of the two signal connections is tied to ground. Thus, a differential measurement system is well suited to measuring the difference between two signal levels (such as the output of an ungrounded thermocouple).

One of the potential dangers in dealing with grounded signal sources is the introduction of **ground loops**. A ground loop is an undesired current path caused by the connection of two reference voltages to each other. This is illustrated in Figure 5.11.8, where a grounded signal source is shown connected to

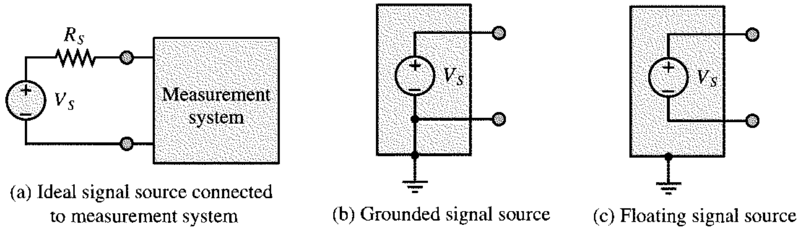

(a) Ideal signal source connected to measurement system

(b) Grounded signal source

(c) Floating signal source

FIGURE 5.11.7 Measurement system and types of signal sources.

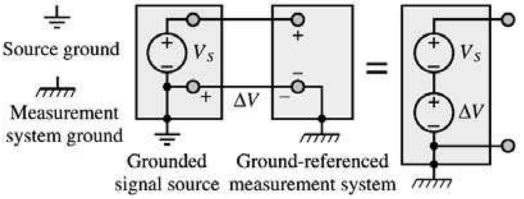

FIGURE 5.11.8 Ground loop in ground-referenced measurement system.

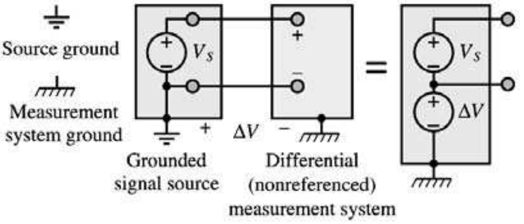

FIGURE 5.11.9 Differential (nonreferenced) measurement system.

a ground-referenced measurement system. Notice that we have purposely denoted the signal source ground and the measurement system ground by two distinct symbols, to emphasize that these are not necessarily at the same potential — as also indicated by the voltage difference ΔV. Now, one might be tempted to tie the two grounds to each other, but this would only result in a current flowing from one ground to the other, through the small (but nonzero) resistance of the wire connecting the two. The net effect of this ground loop would be that the voltage measured by the instrument would include the unknown ground voltage difference ΔV, as shown in Figure 5.11.8. Since this latter voltage is unpredictable, you can see that ground loops can cause substantial errors in measuring systems. In addition, ground loops are the primary cause of conducted noise, as explained later in this section.

A differential measurement system is often a way to avoid ground loop problems because the signal source and measurement system grounds are not connected to each other, and especially because the signal low input of the measuring instrument is not connected to either instrument case ground. The connection of a grounded signal source and a differential measurement system is depicted in Figure 5.11.9.

If the signal source connected to the differential measurement system is floating, as shown in Figure 5.11.10, it is often a recommended procedure to reference the signal to the instrument ground by means of two identical resistors that can provide a return path to ground for any currents present at the instrument. An example of such input currents could be the input bias currents inevitably present at the input of an operational or instrumentation amplifier.

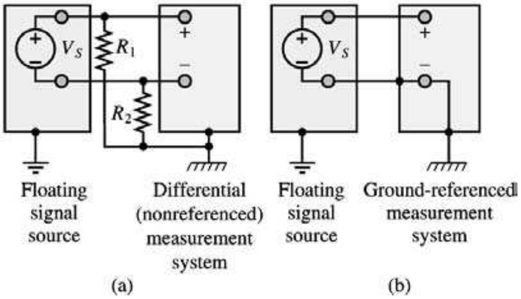

FIGURE 5.11.10 Measuring signals from a floating source: (a) differential input; (b) single-ended input.

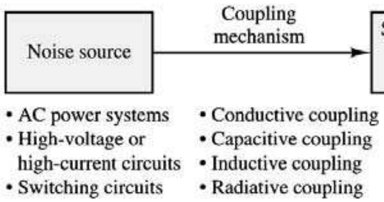

FIGURE 5.11.11 Noise sources and coupling mechanisms.

The simple concepts illustrated in the preceding paragraphs and figures can assist the user and designer of instrumentation systems in making the best possible wiring connections for a given measurement.

Noise Sources and Coupling Mechanisms

Noise — meaning any undesirable signal interfering with a measurement — is an unavoidable element of all measurements. Figure 5.11.11 depicts a block diagram of the three essential stages of a noisy measurement: **a noise source, a noise coupling mechanism**, and a sensor or associated signal-conditioning circuit. Noise sources are always present and are often impossible to eliminate completely; typical sources of noise in practical measurements are the electromagnetic fields caused by fluorescent light fixtures, video monitors, power supplies, switching circuits, and high-voltage (or current) circuits. Many other sources exist, of course, but often the simple sources in our everyday environment are the most difficult to defeat.

Figure 5.11.11 also indicates that various coupling mechanisms can exist between a noise source and an instrument. Noise coupling can be conductive; that is, noise currents may actually be conducted from the noise source to the instrument by physical wires. Noise can also be coupled capacitively, inductively and radiatively.

Figure 5.11.12 illustrates how interference can be **conductively coupled** by way of a ground loop. In the figure, a power supply is connected to both a load and a sensor. We shall assume that the load may be switched on and off, and that it carriers substantial currents. The top circuit contains a ground loop: the current i from the supply divides between the load and sensor; since the wire resistance is nonzero, a large current flowing through the load may cause the ground potential at point a to differ from the potential at point b. In this case, the measured sensor output is no longer, v_o, but it is now equal to $v_o + v_{ba}$, where v_{ba} is the potential difference from point b to point a. Now, if the load is switched on and off and its current is therefore subject to large, abrupt changes, these changes will be manifested in the voltage v_{ba} and will appear as noise on the sensor output.

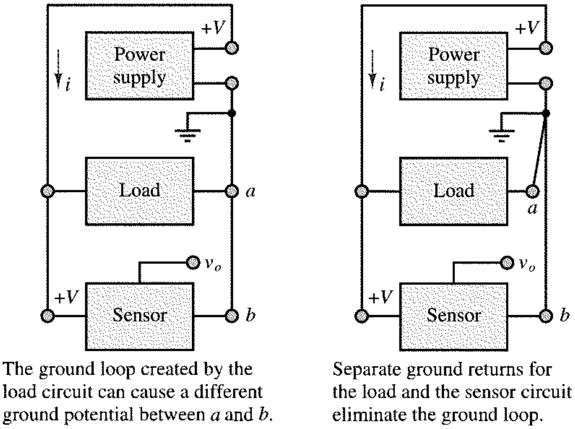

The ground loop created by the load circuit can cause a different ground potential between *a* and *b*.

Separate ground returns for the load and the sensor circuit eliminate the ground loop.

FIGURE 5.11.12 Conductive coupling: ground loop and separate ground returns.

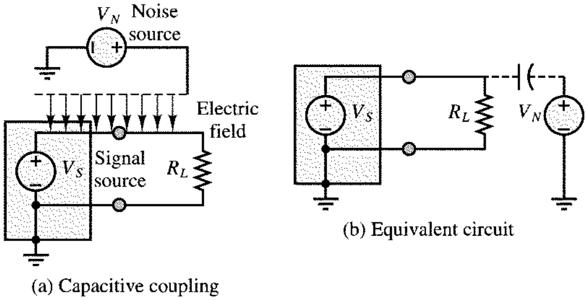

FIGURE 5.11.13 Capacitive coupling and equivalent-circuit representation.

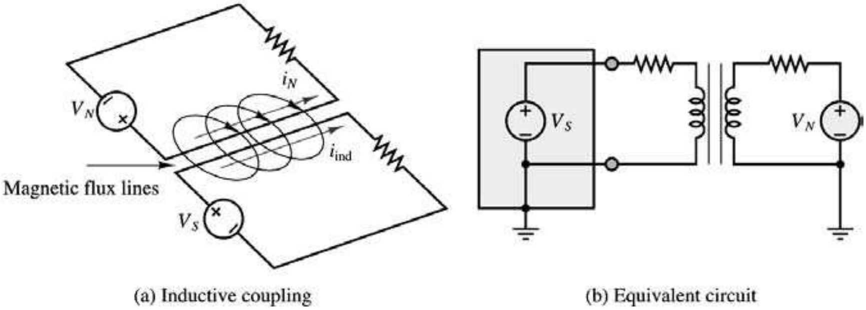

FIGURE 5.11.14 Inductive coupling and equalent-circuit representation.

This problem can be cured simply and effectively by providing separate *ground returns* for the load and sensor, thus eliminating the ground loop.

The mechanism of **capacitive coupling** is rooted in electric fields that may be caused by sources of interference. The detailed electromagnetic analysis can be quite complex, but to understand the principle, refer to Figure 5.11.13(a), where a noise source is shown to generate an electric field. If a noise source conductor is sufficiently close to a conductor that is part of the measurement system, the two conductors (separated by air, a dielectric) will form a capacitor, through which any time-varying currents can flow. Figure 5.11.13(b) depicts an equivalent circuit in which the noise voltage V_N couples to the measurement circuit through an imaginary capacitor, representing the actual capacitance of the noise path.

The dual of capacitive coupling is **inductive coupling**. This form of noise coupling is due to the magnetic field generated by current flowing through a conductor. If the current is large, the magnetic fields can be significant, and the **mutual inductance** between the noise source and the measurement circuit causes the noise to couple to the measurement circuit. Thus, inductive coupling, as shown in Figure 5.11.14 results when undesired (unplanned) magnetic coupling ties the noise source to the measurement circuit.

Noise Reduction

Various techniques exist for minimizing the effect of undesired interference, in addition to proper wiring and grounding procedures. The two most common methods are **shielding** and the use of **twisted-pair wire**. A shielded cable is shown in Figure 5.11.15. The shield is made of a copper braid or of foil and is usually grounded at the source end, *but not at the instrument end*, because this would result in a ground loop. The shield can protect the signal from a significant amount of electromagnetic interference, especially at lower frequencies. Shielded cables with various numbers of conductors are available commercially. However, shielding cannot prevent inductive coupling. The simplest method for minimizing inductive coupling is the use of twisted-pair wire; the reason for using twisted pair is that untwisted wire can offer

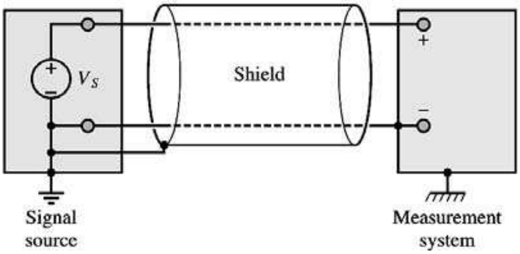

FIGURE 5.11.15 Shielding.

large loops that can couple a substantial amount of electromagnetic radiation. Twisting drastically reduces the loop area, and with it the interference. Twisted pair is available commercially.

Signal Conditioning

A properly wired, grounded, and shielded sensor connection is a necessary first stage of any well-designed measurement system. The next stage consists of any **signal conditioning** that may be required to manipulate the sensor output into a form appropriate for the intended use. Very often, the sensor output is meant to be fed into a digital computer, as illustrated in Figure 5.11.1. In this case, it is important to condition the signal so that it is compatible with the process of data acquisition. Two of the most important signal-conditioning functions are *amplification* and *filtering*. Both are discussed in the present section.

Instrumentation Amplifiers

An **instrumentation amplifier** (IA) is a differential amplifier with very high input impedance, low bias current, and programmable gain that finds widespread application when low-level signals with large common-mode components are to be amplified in noisy environments. This situation occurs frequently when a low-level transducer signal needs to be preamplified, prior to further signal conditioning (e.g., filtering).

The functional structure of an IC instrumentation amplifier is depicted in Figure 5.11.16. Specifications for a common IC instrumentation amplifier (and a more accurate circuit description) are shown in.

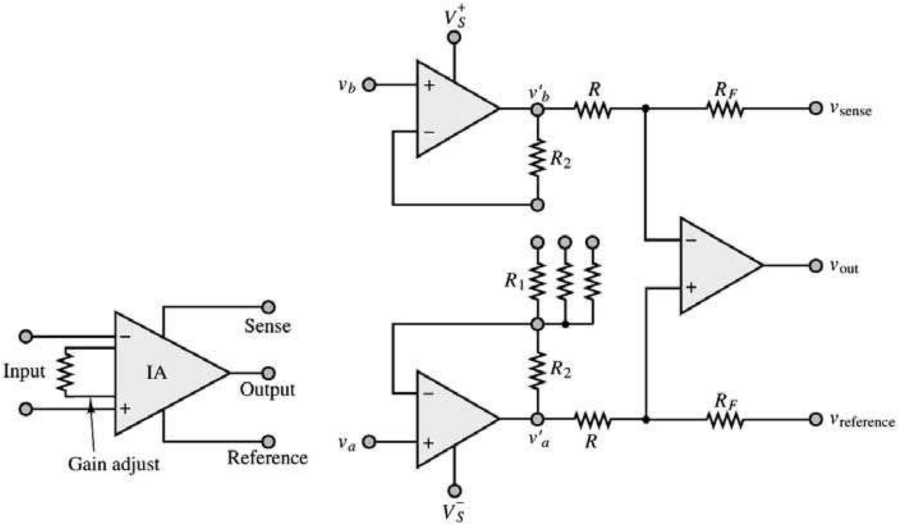

FIGURE 5.11.16 IC instrumentation amplifier.

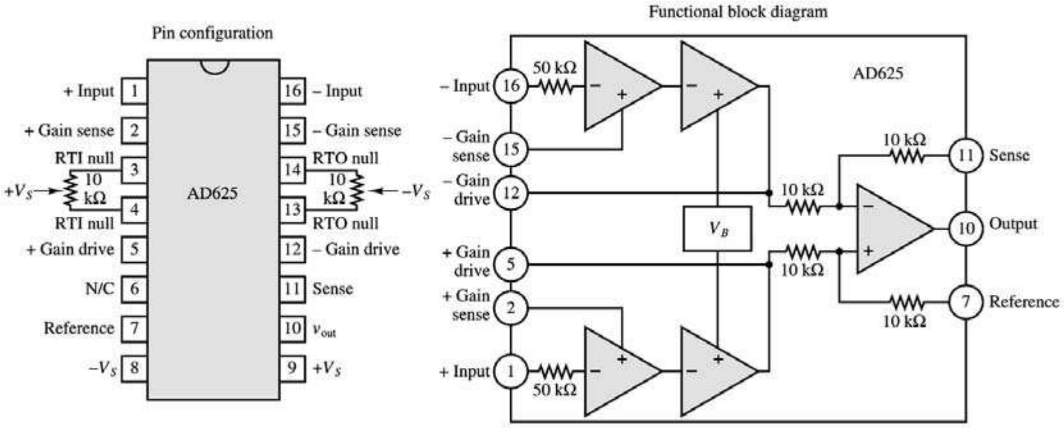

FIGURE 5.11.17 AD625 instrumentation amplifier data sheet.

Figure 5.11.17 Among the features worth mentioning here are the programmable gains, which the user can set by suitably connecting one or more of the resistors labeled R_1 to the appropriate connection. Note that the user may also choose to connect additional resistors to control the amplifier gain, without adversely affecting the amplifier's performance, since R_1 requires no matching. In addition to the pin connection that permits programmable gains, two additional pins are provided, called **sense** and **reference**. These additional connections are provided to the user for the purpose of referencing the output voltage to a signal other than ground, by means of the reference terminal, or of further amplifying the output current (e.g., with a transistor stage), by connecting the sense terminal to the output of the current amplifier.

Active Filters

The need to filter sensor signals that may be corrupted by noise or other interfering or undesired inputs has already been approached in two earlier chapters. In Section 5.6, simple passive filters made of resistors, capacitors, and inductors were analyzed. It was shown that three types of filter frequency response characteristics can be achieved with these simple circuits: low-pass, high-pass, and band-pass. In Section 5.9, the concept of active filters was introduced, to suggest that it may be desirable to exploit the properties of operational amplifiers to simplify filter design, to more easily match source and load impedances, and to eliminate the need for inductors. The aim of this section is to discuss more advanced active filter designs, which find widespread application in instrumentation circuits.

Figure 5.11.18 depicts the general characteristics of a low-pass active filter, indicating that within the pass-band of the filter, a certain deviation from the nominal filter gain, A, is accepted, as indicated by the minimum and maximum pass-band gains, $A + \varepsilon$ and $A - \varepsilon$. The width of the pass-band is indicated by the cutoff frequency, ω_c. On the other hand, the stop-band, starting at the frequency ω_s, does not

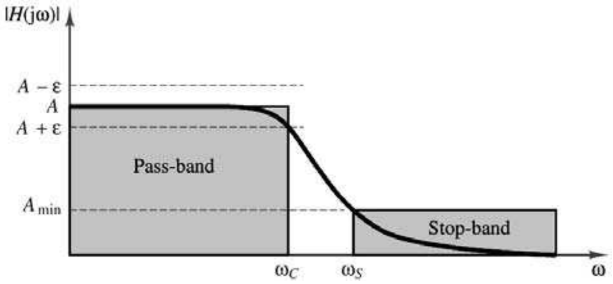

FIGURE 5.11.18 Prototype low-pass filter response.

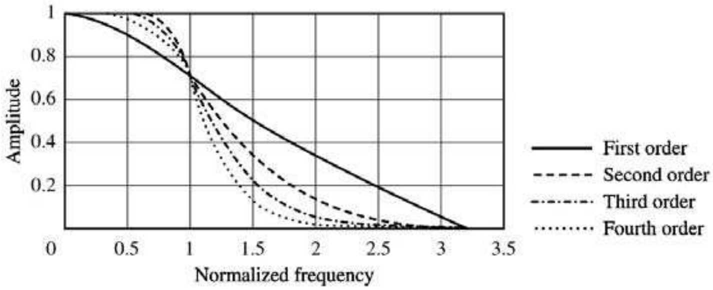

FIGURE 5.11.19 Butterworth low-pass filter frequency response.

TABLE 5.11.3 Butterworth Polynomials in Quadratic Form

Order, n	Quadratic Factors
1	$(s + 1)$
2	$(s^2 + \sqrt{2}s + 1)$
3	$(s + 1)\ (s^2 + s + 1)$
4	$(s^2 + 0.7654s + 1)\ (s^2 + 1.8478s + 1)$
5	$(s + 1)\ (s^2 + 0.6180s + 1)\ (s^2 + 1.6180s + 1)$

allow a gain greater than $A_{\min}$. Different types of filter designs achieve different types of frequency responses, which are typically characterized either by having a particularly flat pass-band frequency response (**Butterworth filters**) or by a very rapid transition between pass-band and stop-band (**Chebyshev filters**, and **Cauer**, or **elliptical, filters**), or by some other characteristic, such as a very linear phase response (**Bessel filters**). Achieving each of these properties usually involves trade-offs; for example, a very flat pass-band response will usually result in a relatively slow transition from pass-band to stop-band.

In addition to selecting a filter from a certain family, it is also possible to select the *order* of the filter; this is equal to the order of the differential equation that describes the input-output relationship of a given filter. In general, the higher the order, the faster the transition from pass-band to stop-band (at the cost of greater phase shifts and amplitude distortion, however). Although the frequency response of Figure 5.11.18 pertains to a low-pass filter, similar definitions also apply to the other types of filters.

Butterworth filters are characterized by a *maximally flat* pass-band frequency response characteristic; their response is defined by a magnitude-squared function of frequency:

$$\left|H(j\omega)\right|^2 = \frac{H_0^2}{1+\varepsilon^2\omega^{2n}} \tag{5.11.14}$$

where $\varepsilon = 1$ for maximally flat response and n is the order of the filter. Figure 5.11.19 depicts the frequency response (normalized to $\omega_c = 1$) of first-, second-, third-, and fourth-order Butterworth low-pass filters. The **Butterworth polynomials**, given in Table 5.11.3 in factored form, permit the design of the filter by specifying the denominator as a polynomial in s. For $s = j\omega$, one obtains the frequency response of the filter.

Figure 5.11.20 depicts the normalized frequency response of first- to fourth-order low-pass Chebyshev filters ($n = 1$ to 4), for $\varepsilon = 1.06$. Note that a certain amount of ripple is allowed in the pass-band; the amplitude of the ripple is defined by the parameter ε and is constant throughout the pass-band. Thus, these filters are also called **equiripple filters**. Cauer, or elliptical, filters are similar to Chebyshev filters, except for being characterized by equiripple both in the pass-band and in the stop-band. Design tables exist to select the appropriate order of Butterworth, Chebyshev, or Cauer filter for a specific application.

Three common configurations of second-order active filters, which can be used to implement **second-order** (or **quadratic**) **filter sections** using a single of op-amp, are shown in Figure 5.11.21. These filters

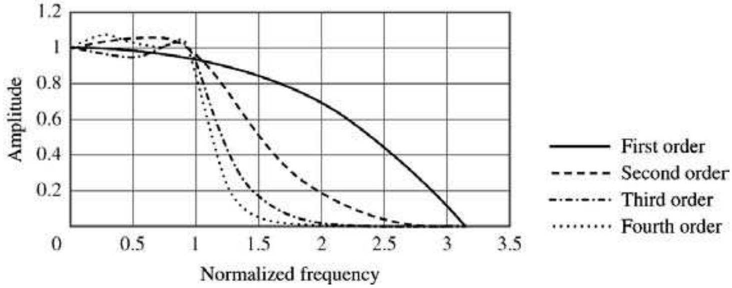

FIGURE 5.11.20 Chebyshev low-pass filter frequency response.

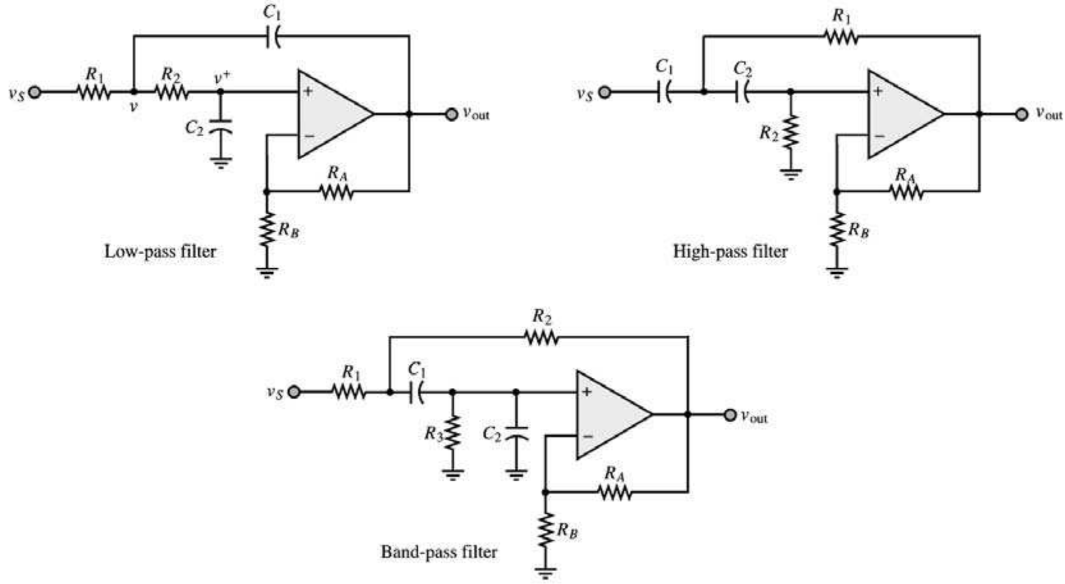

FIGURE 5.11.21 Sallen and Key active filters.

are called **constant-*K***, or **Sallen and Key, filters** (after the name of the inventors). The analysis of these active filters, although somewhat more involved than that of the active filters presented in the preceding chapter, is based on the basic properties of the ideal operational amplifier discussed earlier. Consider, for example, the low-pass filter of Figure 5.11.21. The first unusual aspect of the filter is the presence of both negative and **positive feedback**; that is, feedback connections are provided to both the inverting and the noninverting terminals of the op-amp. The analysis method consists of finding expressions for the input terminal voltages of the op-amp, V^+ and V^-, and using these expressions to derive the input-output relationship for the filter. The frequency response of the low-pass filter is given by

$$H(j\omega) = \frac{K\left(1/R_1R_2C_1C_2\right)}{(j\omega)^2 + \left[\frac{1}{R_1C_1} + \frac{1}{R_2C_1} + \frac{1}{R_2C_2}(1-K)\right] + \frac{1}{R_1R_2C_1C_2}} \tag{5.11.5}$$

This frequency response can be expressed in more general form as follows:

$$H(j\omega) = \frac{H_0 \omega_C^2}{(j\omega)^2 + (\omega_C/Q) j\omega + \omega_C^2}$$

where

$$H_0 = K \tag{5.11.6}$$

is the DC gain of the filter, and where

$$\omega_C = \sqrt{\frac{1}{R_1 R_2 C_1 C_2}}$$

is the cutoff frequency, and where

$$\frac{1}{Q} = \sqrt{\frac{R_2 C_1 C_2}{R_1 C_1}} + \sqrt{\frac{R_1 C_2}{R_2 C_1}} + (1-K)\sqrt{\frac{R_1 C_1}{R_2 C_2}} \tag{5.11.17}$$

is the inverse of the **quality factor**, Q. The Q of a filter is related to the overshoot in the transient response of the filter; and to the peaking (i.e., sharpness of the resonant peak) of the frequency response, a high-Q circuit will display more peaking, or overshoot, than a low-Q circuit.

Analog-to-Digital and Digital-to-Analog Conversion

To take advantage of the capabilities of a microcomputer, it is necessary to suitably interface signals to and from external devices with the microcomputer. Such signals may be analog or digital. Depending on the nature of the signal, either an analog or a digital interface circuit will be required. The advantages in memory storage, programming flexibility, and computational power afforded by today's digital computers are such that the instrumentation designer often chooses to convert an analog signal to an equivalent digital representation, to exploit the capabilities of a microprocessor in processing the signal. In many cases, the data converted from analog to digital form remain in digital form for ease of storage, or for further processing. In some instances it is necessary to convert the data back to analog form. The latter condition arises frequently in the context of control system design, where an analog measurement is converted to digital form and processed by a digital computer to generate a control action (e.g., raising or lowering the temperature of a process, or exerting a force or a torque); in such cases, the output of the digital computer is converted back to analog form, so that a continuous signal becomes available to the actuators. Figure 5.11.22 illustrates the general appearance of a digital measuring instrument and of a digital controller acting on a plant or process.

The objective of this section is to describe how the digital-to-analog (D/A) and analog-to-digital (A/D) conversion blocks of Figure 5.11.22 function. After illustrating discrete circuits that can implement simple A/D and D/A converters, we shall emphasize the use of ICs specially made for these tasks. Nowadays, it is uncommon (and impractical) to design such circuits using discrete components: the performance and ease of use of IC packages make them the preferred choice in virtually all applications.

Digital-to-Analog Converters

We discuss digital-to-analog conversion first because it is a necessary part of analog-to-digital conversion in many A/D conversion schemes. A **digital-to-analog converter** (DAC) will convert a binary word to an analog output voltage (or current). The binary word is represented in terms of 1s and 0s, where typically (but not necessarily) 1s correspond to a 5-V level and 0s to a 0-V signal. As an example, consider a four-bit binary word:

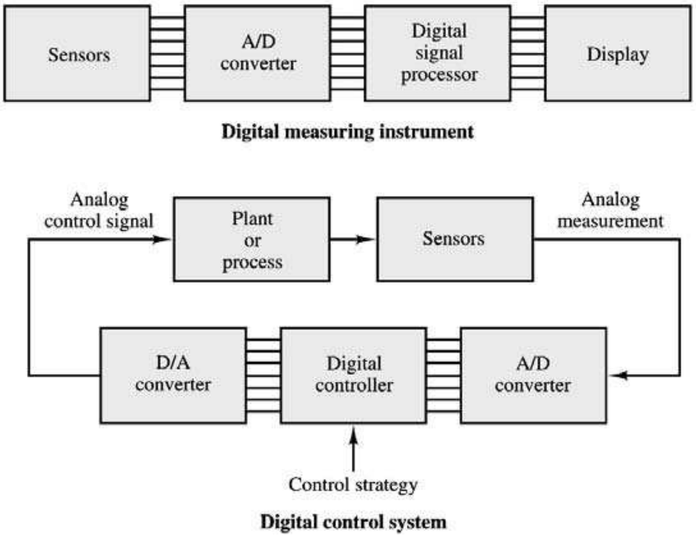

Digital measuring instrument

Digital control system

FIGURE 5.11.22 Block diagrams of a digital measuring instrument and a digital control system.

$$B = \left(b_3 b_2 b_1 b_0\right)_2 = \left(b_3 \cdot 2^3 + b_2 \cdot 2^2 + b_1 \cdot 2^1 + b_0 \cdot 2^0\right)_{10} \tag{5.11.8}$$

The analog voltage corresponding to the digital word *B* would be

$$v_a = \left(8b_3 + 4b_2 + 2b_1 + b_0\right)\delta v \tag{5.11.9}$$

where δv is the smallest *step size* by which v_a can increment. This least step size will occur whenever the least significant bit (LSB), b_0, changes from 0 to 1, and is the smallest increment the digital number can make. We shall also shortly see that the analog voltage obtained by the D/A conversion process has a "staircase" appearance because of the discrete nature of the binary signal.

The step size is determined on the basis of each given application and is usually determined on the basis of the number of bits in the digital word to be converted to an analog voltage. We can see that, by extending the previous example for an *n*-bit word, the maximum value v_a can attain is

$$\begin{aligned} v_{a\,\max} &= \left(2^{n-1} + 2^{n-2} + \ldots + 2^1 + 2^0\right)\delta v \\ &= \left(2^n - 1\right)\delta v \end{aligned} \tag{5.11.10}$$

It is relatively simple to construct a DAC by taking advantage of the summing amplifier illustrated in Section 5.9. Consider the circuit shown in Figure 5.11.23, where each bit in the word to be converted is represented by means of a 5-V source and a switch. When the switch is closed, the bit takes a value of 1 (5 V); when the switch is not closed, the bit has value 0. Thus, the output of the DAC is proportional to the word $b_{n-1} \ldots b_{n-2} \ldots b_1 b_0$.

If we select

$$R_i = \frac{R_0}{2^i} \tag{5.11.11}$$

we can obtain weighted gains for each bit so that

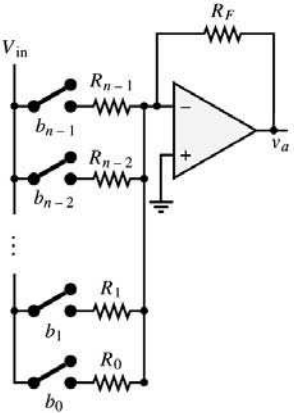

FIGURE 5.11.23 *n*-bit digital-to-analog converter (DAC).

$$v_a = -\frac{R_F}{R_0}\left(2^{n-1}b_{n-1} + \ldots + 2^1 b_1 + 2^0 b_0\right)\cdot 5\ \text{V} \tag{5.11.12}$$

and so that the analog output voltage is proportional to the decimal representation of the binary word.

The practical design of a DAC is generally not carried out in terms of discrete components, because of problems such as the accuracy required of the resistor value. Many of the problems associated with this approach can be solved by designing the complete DAC circuit in integrated circuit (IC) form. The specifications stated by the IC manufacturer include the resolution, that is, the minimum nonzero voltage; the full-scale accuracy; the output range; the output settling time; the power supply requirements; and the power dissipation. The following example illustrates the use of a common integrated circuit DAC.

Example 5.11.1

A typical DAC one would use in conjunction with the 8086 microprocessor is the AD558. This is an IC that can be used in a "stand-alone" configuration (without a microprocessor) or with a microprocessor interfaced to it.

1. If one were to set up the AD558 for an output swing of 0 to 10 V, what would be the smallest voltage output increment attainable?
2. On what is the maximum operating frequency (the largest frequency on which the DAC can perform conversion) of the AD558 dependent? Determine the maximum frequency attainable if the converter is to be run at full-scale input.

Solution.

1. Since this DAC is an eight-bit device, the total number of digital increments one could expect is 256. Thus, the finest voltage steps one could expect at the output would be

   $$\frac{10}{255} = 39.2\ \text{mV}$$

   This means that for every increment of one bit, the output would jump (in a stepwise fashion) by 39.2 mV.
2. The maximum frequency at which a DAC can run is dependent on the settling time. This is defined as the time it takes for the output to settle to within one half of the least significant bit of its final value. Thus, only one transition can be made per settling time. The settling time for the AD558 depends on the voltage range and is defined for a positive-going full-scale step to ±1/2 LSB. The settling time is 1 μsec, and the corresponding maximum conversion frequency is 1 MHz.

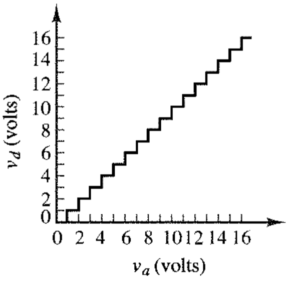

Quantized voltage v_d	Binary representation b_3	b_2	b_1	b_0
0	0	0	0	0
1	0	0	0	1
2	0	0	1	0
3	0	0	1	1
4	0	1	0	0
⋮		⋮		
14	1	1	1	0
15	1	1	1	1

FIGURE 5.11.24 A digital voltage representation of an analog voltage.

Analog-to-Digital Converters

You should by now have developed an appreciation for the reasons why it is convenient to process data in digital form. The device that makes conversion of analog signals to digital form is the **analog-to-digital converter** (ADC), and, just like the DAC, it is also available as a single IC package. In addition to discussing analog-to-digital conversion, we shall also introduce the *sample-and-hold amplifier.*

Quantization. The process of converting an analog voltage (or current) to digital form requires that the analog signal be quantized and encoded in binary form. The process of **quantization** consists of subdividing the range of the signal into a finite number of intervals; usually, one employs $2^n - 1$ intervals, where n is the number of bits available for the corresponding binary word. Following this quantization, a binary word is assigned to each interval (i.e., to each range of voltages or currents); the binary word is then the digital representation of any voltage (current) that falls within that interval. You will note that the smaller the interval, the more accurate the digital representation is. However, some error is necessarily always present in the conversion process; this error is usually referred to as **quantization error**. Let v_a represent the analog voltage and v_d its quantized counterpart, as shown in Figure 5.11.24 for an analog voltage in the range 0 to 0 16 V. In the figure, the analog voltage v_a takes on a value of $v_d = 0$ whenever it is in the range 0 to 1 V; for $1 \le v_a < 2$, the corresponding value is $v_d = 1$; for $2 \le v_a < 3$, $v_d = 2$; and so on, until, for $15 \le v_a < 16$, we have $v_d = 15$. You see that if we now represent the quantized voltage v_d by its binary counterpart, as shown in the table of Figure 5.11.24, each 1-V analog interval corresponds to a unique binary word. In this example, a four-bit word is sufficient to represent the analog voltage, although the representation is not very accurate. As the number of bits increases, the quantized voltage is closer and closer to the original analog signal; however, the number of bits required to represent the quantized value increases.

Tracking ADC. Although not the most efficient in all applications, the **tracking ADC** is an easy starting point to illustrate the operation of an ADC, in that it is based on the DAC presented in the previous section. The tracking ADC, shown in Figure 5.11.25, compares the analog input signal with the output of a DAC; the comparator output determines whether the DAC output is larger or smaller than the analog input to be converted to binary form. If the DAC output is smaller, then the comparator output will cause an up-down counter to count up, until it reaches a level close to the analog signal; if the DAC output is larger than the analog signal, then the counter is forced to count down. Note that the rate at which the up-down counter is incremented is determined by the external clock, and that the binary counter output corresponds to the binary representation of the analog signal. A feature of the tracking ADC is that it follows ("tracks") the analog signal by changing one bit at a time.

Integrating ADC. The **integrating ADC** operates by charging and discharging a capacitor, according to the following principle: if one can ensure that the capacitor charges (discharges) linearly, then the time it will take for the capacitor to discharge is linearly related to the amplitude of the voltage that has charged

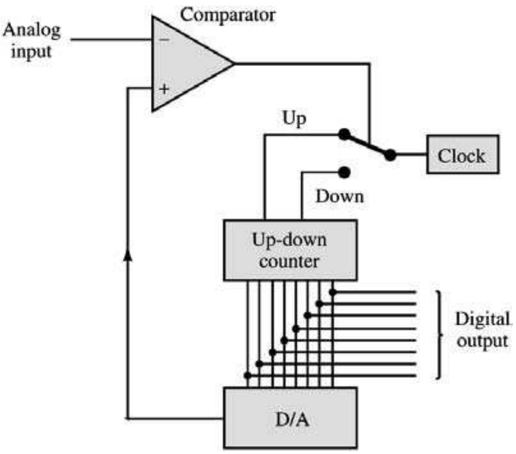

FIGURE 5.11.25 Tracking ADC.

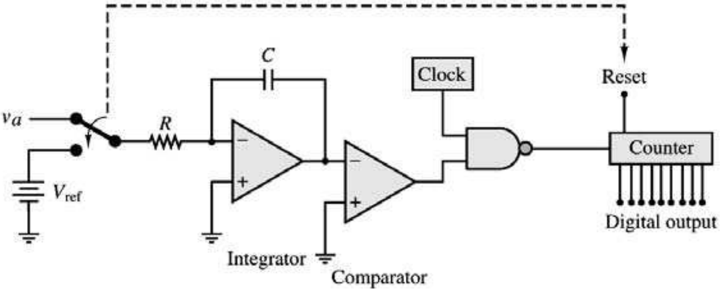

FIGURE 5.11.26 Integrating ADC.

the capacitor. In practice, to limit the time it takes to perform a conversion, the capacitor is not required to charge fully. Rather, a clock is used to allow the input (analog) voltage to charge the capacitor for a short period of time, determined by a fixed number of clock pulses. Then the capacitor is allowed to discharge through a known circuit, and the corresponding clock count is incremented until the capacitor is fully discharged. The latter condition is verified by a comparator, as shown in Figure 5.11.26. The clock count accumulated during the discharge time is proportional to the analog voltage.

In the figure, the switch causes the counter to reset when it is connected to the reference voltage, V_{ref}. The reference voltage is used to provide a known, linear discharge characteristic through the capacitor (see the material on the op-amp integrator in Section 5.9. When the comparator detects that the output of the integrator is equal to zero, it switches state and disables the NAND gate, thus stopping the count. The binary counter output is now the digital counterpart of the voltage v_a.

Other common types of ADC are the so-called successive-approximation ADC and the flash ADC.

Flash ADC. The **flash ADC** is fully parallel and is used for high-speed conversion. A resistive divider network of 2^n resistors divides the known voltage range into that many equal increments. A network of $2^n - 1$ comparators then compares the unknown voltage with that array of test voltages. All comparators with inputs exceeding the unknown are “on”; all others are “off”. This comparator code can be converted to conventional binary by a digital priority encoder circuit. For example, assume that the three-bit flash ADC of Figure 5.11.27 is set up with $V_{ref} = 8$ V. An input of 6.2 V is provided. If we number the comparators from the top of Figure 5.11.27, the state of each of the seven comparators is as given in Table 5.11.4.

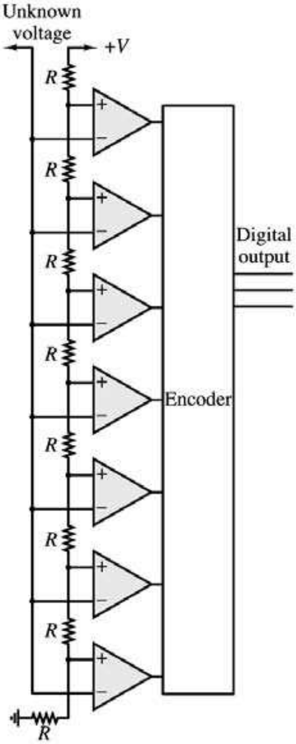

FIGURE 5.11.27 A three-bit flash ADC.

TABLE 5.11.4 State of Comparators in a 3-Bit Flash ADC

Comparator	Input on + Line	Input on – Line	Output
1	7 V	6.2 V	H
2	6 V	6.2 V	L
3	5 V	6.2 V	L
4	4 V	6.2 V	L
5	3 V	6.2 V	L
6	2 V	6.2 V	L
7	1 V	6.2 V	L

To resolve the uncertainty generated by the finite ADC conversion time of any practical converter, it is necessary to use a sample-and-hold amplifier. The objective of such an amplifier is to "freeze" the value of the analog waveform for a time sufficient for the ADC to complete its task.

A typical sample-and-hold amplifier is shown in Figure 5.11.28. It operates as follows. A MOSFET analog switch is used to "sample" the analog waveform. Recall that when a voltage pulse is provided to the sample input of the MOSFET switch (the gate), the MOSFET enters the ohmic region and in effect becomes nearly a short circuit for the duration of the sampling pulse. While the MOSFET conducts, the analog voltage, v_a, charges the "hold" capacitor, C, at a fast rate through the small "on" resistance of the MOSFET. The duration of the sampling pulse is sufficient to charge C to the voltage v_a. Because the MOSFET is virtually a short circuit for the duration of the sampling pulse, the charging (RC) time constant is very small, and the capacitor charges very quickly. When the sampling pulse is over, the MOSFET returns to its nonconducting state, and the capacitor holds the sampled voltage without discharging, thanks to the extremely high input impedance of the voltage-follower (buffer) stage. Thus, v_{SH} is the sampled-and-held value of v_a at any given sampling time.

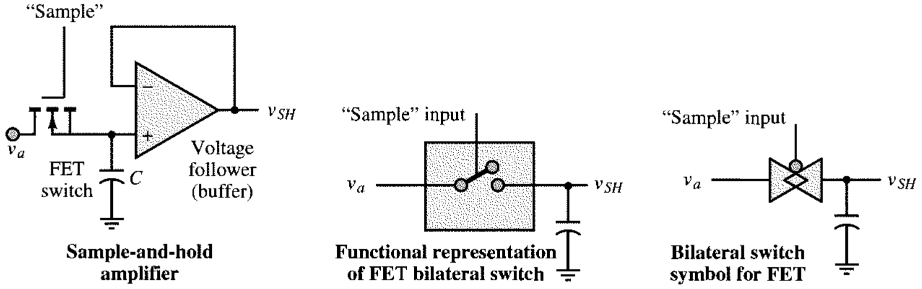

FIGURE 5.11.28 Description of the sample-and-hold process.

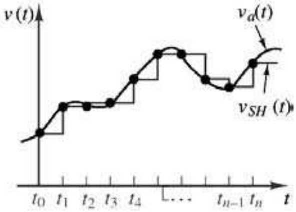

FIGURE 5.11.29 Sampled data.

The appearance of the output of a typical sample-and-hold circuit is shown in Figure 5.11.29, together with the analog signal to be sampled. The time interval between samples, or **sampling interval**, $t_n - t_{n-1}$, allows the ADC to perform the conversion and make the digital version of the sampled signal available, say, to a computer or to another data acquisition and storage system. The sampling interval needs to be at least as long as the A/D conversion time, of course, but it is reasonable to ask how frequently one needs to sample a signal to preserve its fundamental properties (e.g., peaks and valleys, "ringing", fast transition). One might instinctively be tempted to respond that it is best to sample as frequently as possible, within the limitations of the ADC, so as to capture all the features of the analog signal. In fact, this is not necessarily the best strategy. How should we select the appropriate sampling frequency for a given application? Fortunately, an entire body of knowledge exists with regard to sampling theory, which enables the practicing engineer to select the best sampling rate for any given application. Given the scope of this chapter, we have chosen not to delve into the details of sampling theory, but, rather, to provide the student with a statement of the fundamental result: the **Nyquist sampling criterion**. The Nyquist criterion states that to prevent aliasing[2] when sampling a signal, *the sample rate should be selected to be at least twice the highest-frequency component present in the signal.* Thus, if we were sampling an audio signal (say, music), we would have to sample at a frequency of at least 40 kHz (twice the highest audible frequency, 20 kHz). In practice, it is advisable to select sampling frequencies substantially greater than the Nyquist rate; a good rule of thumb is five to ten times greater. The following example illustrates how the designer might take the Nyquist criterion into account in designing a practical A/D conversion circuit.

Example 5.11.2

A typical ADC one would use in conjunction with the 8086 microprocessor is the AD574. This is a successive-approximation converter.

1. What is the accuracy (in volts) the AD574 can provide if $V_{CC} =$ 15.0 V and $0 \leq \text{Vin} \leq 15.0$ V?
2. On the basis of the data sheet, what is the highest-frequency signal you could convert using the AD574? (Assume that $V_{CC} =$ 15.0 V.)
3. If the maximum conversion time available were 40 msec, what would be the highest-frequency signal you could expect to sample on the basis of the Nyquist criterion?

---

[2] Aliasing is a form of signal distortion that occurs when an analog signal is sampled at an insufficient rate.

Solution.

1. According to the data sheet, the least significant bit (LSB) of this converter limits its accuracy, meaning that the output is accurate within ± 1 bit. For the 0- to 15-V swing, this gives a voltage accuracy of

$$\frac{V_{\max} - V_{\min}}{2^n - 1} \quad \text{or} \quad \frac{15}{2^{12} - 1} \times (\pm 1 \text{ bit}) = \pm 3.66 \text{ mV}$$

2. On the basis of the data sheet, the maximum conversion time is 35 μsec. Therefore, the highest frequency of data conversion using the AD574 is

$$f_{\max} = \frac{1}{35\ \mu\text{s}} = 28.57 \text{ kHz}$$

   Thus, the highest signal frequency that could be represented, according to the Nyquist principle, is

$$\frac{1}{2} f_{\max} = \frac{28.57 \times 10^3}{2} = 14.285 \text{ kHz}$$

   This is the maximum theoretical signal frequency that can be represented without distortion, according to the Nyquist principle.
3. Following the same procedure discussed in part 2,

$$\frac{1}{2} f_{\max} = \left(\frac{1}{40 \times 10^{-6}}\right)\left(\frac{1}{2}\right) = 12.5 \text{ kHz}$$

Data Acquisition Systems

A typical data acquisition system, shown in Figure 5.11.30, often employs an *analog multiplexer*, to process several different input signals. A bank of bilateral analog MOSFET switches provides a simple and effective means of selecting which of the input signals should be sampled and converted to digital form. Control logic, employing standard gates and counters, is used to select the desired *channel* (input-signal) and to trigger the sampling circuit and the ADC. When the A/D conversion is completed, the ADC sends an appropriate *end of conversion* signal to the control logic, thereby enabling the next channel to be sampled.

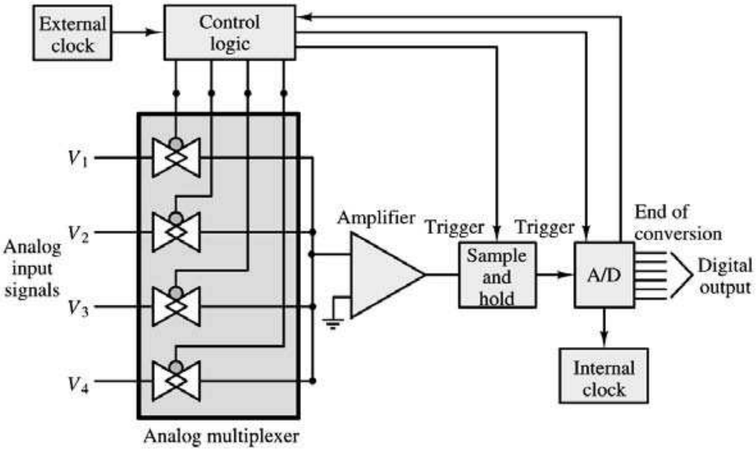

FIGURE 5.11.30 Data acquisition system.

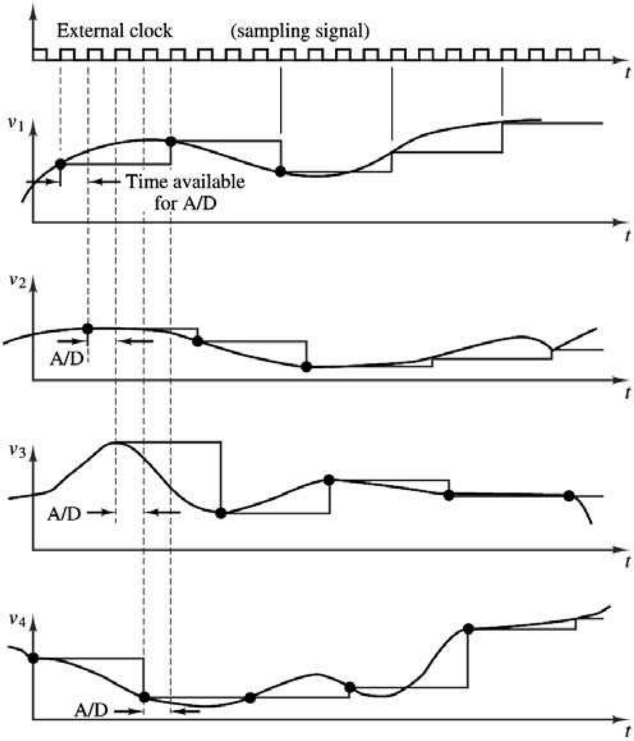

FIGURE 5.11.31 Multiplexed sampled data.

In the block diagram of Figure 5.11.30, four analog inputs are shown; if these were to be sampled at regular intervals, the sequence of events would appear as depicted in Figure 5.11.31. We notice, from a qualitative analysis of the figure, that the effective sampling rate for each channel is one fourth the actual external clock rate; thus, it is important to ensure that the sampling rate for each individual channel satisfies the Nyquist criterion. Further, although each sample is held for four consecutive cycles of the external clock, we must notice that the ADC can use only one cycle of the external clock to complete the conversion, since its services will be required by the next channel during the next clock cycle. Thus, the internal clock that times the ADC must be sufficiently fast to allow for a complete conversion of any sample within the design range.

Timer ICs: the NE555

This section introduces a multipurpose integrated circuit that can perform basic timing functions. The NE555 is a timer circuit capable of producing accurate time delays (pulses) or oscillation. In the time-delay, or monostable, mode, the time delay or pulse duration is controlled by an external RC network. In the astable, or clock generator, mode, the frequency is controlled by two external resistors and one capacitor. Figure 5.11.32 depicts typical circuits for monostable and astable operation of the NE555. Note that the threshold level and the trigger level can also be externally controlled. For the monostable circuit, the pulse width can be computed from the following equation:

$$T = 1.1 R_1 C \tag{5.11.13}$$

For the astable circuit, the positive pulse width can be computed from the following equation:

$$T_+ = 0.69\left(R_1 + R_2\right)C \tag{5.11.14}$$

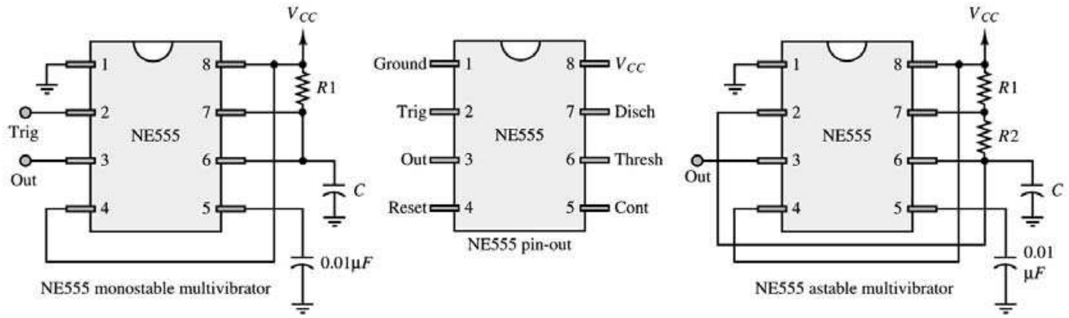

FIGURE 5.11.32 NE555 timer.

and the negative pulse width can be computed from

$$T_- = 0.69 R_2 C \tag{5.11.15}$$

Data Transmission in Digital Instruments

One of the necessary aspects of data acquisition and control systems is the ability to transmit and receive data. Often, a microcomputer-based data acquisition system is interfaced to other digital devices, such as digital instruments or other microcomputers. In these cases it is necessary to transfer data directly in digital form. In fact, it is usually preferable to transmit data that are already in digital form, rather than analog voltages or currents. Among the chief reasons for the choice of digital over analog is that digital data are less sensitive to noise and interference than analog signals: in receiving a binary signal transmitted over a data line, the only decision to be made is whether the value of a bit is 0 or 1. Compared with the difficulty in obtaining a precise measurement of an analog voltage or current, either of which could be corrupted by noise or interference in a variety of ways, the probability of making an error in discerning between binary 0s and 1s is very small. Further, as will be shown shortly, digital data are often coded in such a way that many transmission errors may be detected and corrected for. Finally, storage and processing of digital data are much more readily accomplished than would be the case with analog signals. This section explores a few of the methods that are commonly employed in transmitting digital data; both parallel and serial interfaces are considered.

Digital signals in a microcomputer are carried by a bus, consisting of a set of parallel wires each carrying one bit of information. In addition to the signal-carrying wires, there are also control lines that determine under what conditions transmission may occur. A typical computer data bus consists of eight parallel wires and therefore enables the transmission of one byte; digital data are encoded in binary according to one of a few standard codes, such as the BCD code described in Section 5.10, or the ASCII code, which is summarized in Table 5.11.5. This bus configuration is usually associated with **parallel transmission**, whereby all of the bits are transmitted simultaneously, along with some control bits.

Figure 5.11.33 depicts the general appearance of a parallel connection. Parallel data transmission can take place in one of two modes: **synchronous** or **asynchronous**. In synchronous transmission, a timing clock pulse is transmitted along with the data over a control line. The arrival of the clock pulse indicates that valid data have also arrived. While parallel synchronous transmission can be very fast, it requires the added complexity of a synchronizing clock and is typically employed only for internal computer data transmission. Further, this type of communication can take place only over short distances (approximately 4 m). Asynchronous data transmission, on the other hand, does not take place at a fixed clock rate, but requires a **handshake protocol** between sending and receiving ends. The handshake protocol consists of the transmission of *data ready* and *acknowledge* signals over two separate control wires. Whenever the sending device is ready to transmit data, it sends a pulse over the *data ready* line. When this signal reaches

TABLE 5.11.5 ASCII Code

Graphic or Control	ASCII (hex)	Graphic or Control	ASCII (hex)	Graphic or Control	ASCII (hex)
NUL	00	+	2B	V	56
SOH	01	,	2C	W	57
STX	02	-	2D	X	58
ETX	03	.	2E	Y	59
EOT	04	/	2F	Z	5A
ENQ	05	0	30	[	5B
ACK	06	1	31	\	5C
BEL	07	2	32	]	5D
BS	08	3	33	↑	5E
HT	09	4	34	←	5F
LF	0A	5	35	`	60
VT	0B	6	36	a	61
FF	0C	7	37	b	62
CR	0D	8	38	c	63
SO	0E	9	39	d	64
SI	0F	:	3A	e	65
DLE	10	;	3B	f	66
DCl	11	<	3C	g	67
DC2	12	=	3D	h	68
DC3	13	>	3E	i	69
DC4	14	?	3F	j	6A
NAK	15	@	40	k	6B
SYN	16	A	41	l	6C
ETB	17	B	42	m	6D
CAN	18	C	43	n	6E
EM	19	D	44	o	6F
SUB	1A	E	45	p	70
ESC	1B	F	46	q	71
FS	1C	G	47	r	72
GS	1D	H	48	s	73
RS	1E	I	49	t	74
US	1F	J	4A	u	75
SP	20	K	4B	v	76
!	21	L	4C	w	77
”	22	M	4D	x	78
#	23	N	4E	y	79
$	24	O	4F	z	7A
%	25	P	50	{	7B
&	26	Q	51	|	7C
’	27	R	52	}	7D
(	28	S	53	~	7E
)	29	T	54	DEL	7F
*	2A	U	55		

the receiver, and if the receiver is ready to receive the data, an *acknowledge* pulse is sent back, indicating that the transmission may occur; at this point, the parallel data are transmitted.

Perhaps the most common parallel interface is based on the **IEEE 488 standard**, leading to the so-called IEEE 488 bus, also referred to as GPIB (for **general-purpose instrument bus**).

The IEEE 488 Bus

The IEEE 488 bus, shown in Figure 5.11.34, is an eight-bit parallel asynchronous interface that has found common application in digital instrumentation applications. The physical bus consists of 16 lines, of which 8 are used to carry the data, 3 for the handshaking protocol, and the rest to control the data flow. The bus permits connection of up to 15 instruments and data rates of up to 1 Mbyte/sec. There is a

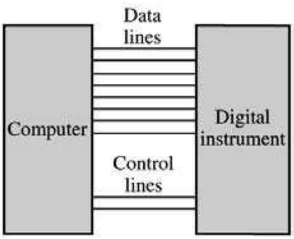

FIGURE 5.11.33 Parallel data transmission.

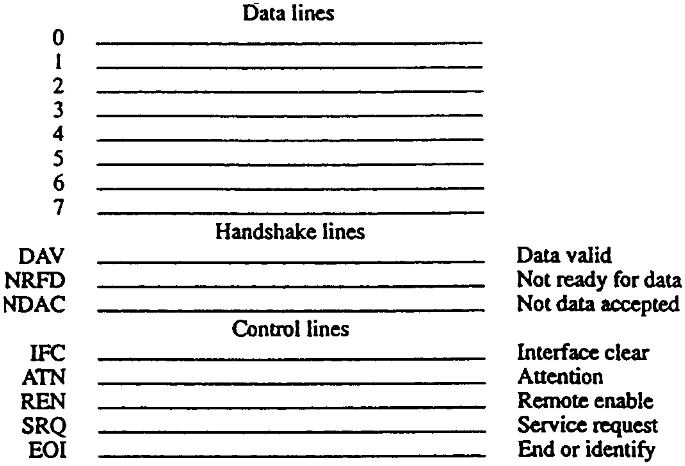

FIGURE 5.11.34 IEEE 488 bus.

limitation, however, in the maximum total length of the bus cable, which is 20 m. The signals transmitted are TTL-compatible and employ negative logic, whereby a logic 0 corresponds to a TTL high state (>2 V) and a logic 1 to a TTL low state (<0.8 V). Often, the eight-bit word transmitted over an IEEE 488 bus is coded in ASCII format (see Table 5.11.5).

In an IEEE 488 bus system, devices may play different roles and are typically classified as *controllers*, which manage the data flow; *talkers* (e.g., a digital voltmeter), which can only send data; *listeners* (e.g., a printer), which can only receive data; and *talkers/listeners* (e.g., a digital oscilloscope), which can receive as well as transmit data. The simplest system configuration might consist of just a talker and a listener. If more than two devices are present on the bus, a controller is necessary to determine when and how data transmission is to occur on the bus. For example, one of the key rules implemented by the controller is that only one talker can transmit at any one time; it is possible, however, for several listeners to be active on the bus simultaneously. If the data rates of the different listeners are different, the talker will have to transmit at the slowest rate, so that all of the listeners are assured of receiving the data correctly.

The set of rules by which the controller determines the order in which talking and listening are to take place is determined by a **protocol**. One aspect of the protocol is the handshake procedure, which enables the transmission of data. Since different devices (with different data rate capabilities) may be listening to the same talker, the handshake protocol must take into account these different capabilities. Let us discuss a typical handshake sequence that leads to transmission of data on an IEEE 488 bus. The three handshake lines used in the IEEE 488 have important characteristics that give the interface system wide flexibility, allowing interconnection of multiple devices that may operate at different speeds. The slowest active device controls the rate of data transfer, and more than one device can accept data simultaneously. The timing diagram of Figure 5.11.35 is used to illustrate the sequence in which the handshake and data transfer are performed:

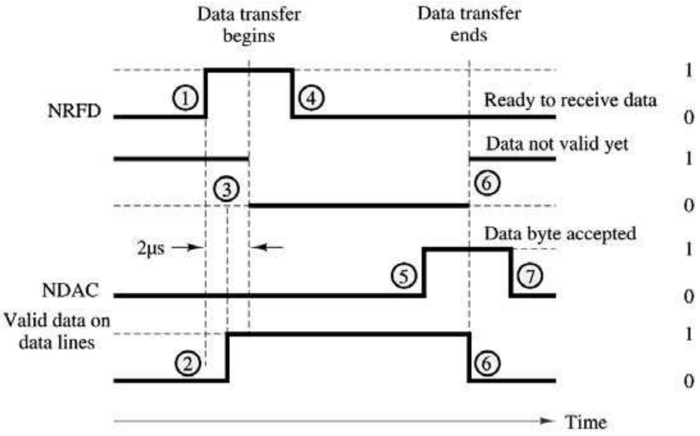

FIGURE 5.11.35 IEEE 488 data transmission protocol.

1. All active listeners use the not ready for data (NRFD) line to indicate their state of readiness to accept a new piece of information. Nonreadiness to accept data is indicated if the NRFD line is held at 0 V. If even one active listener is not ready, the NRFD line of the entire bus is kept at 0 V and the active talker will not transmit the next byte. When all active listeners are ready and they have released the NRFD line, it now goes high.
2. The designated talker drives all eight data input/output lines, causing valid data to be placed on them.
3. Two microseconds after putting valid data on the data lines, the active talker pulls the data valid (DAV) line to 0 V and thereby signals the active listeners to read the information on the data bus. The 2-μsec interval is required to allow the data put on the data lines to reach (settle to) valid logic levels.
4. After the DAV is asserted, the listeners respond by pulling the NRFD line back down to zero. This prevents any additional data transfers from being initiated. The listeners also begin accepting the data byte at their own rates.
5. When each listener has accepted the data, it releases the not data accepted (NDAC) line. Only when the last active listener has released its hold on the NDAC line will that line go to its high-voltage-level state.
6. (a) When the active talker sees that NDAC has come up to its high state, it stops driving the data line. (b) At the same time, the talker releases the DAV line, ending the data transfer. The talker may now put the next byte on the data bus.
7. The listeners pull down the NDAC line back to 0 V and put the byte “away”.

Each of the instruments present on the data bus is distinguished by its own address, which is known to the controller; thus, the controller determines who the active talkers and listeners are on the bus by *addressing* them. To implement this and other functions, the controller uses the five control lines. Of these, ATN (attention) is used as a switch to indicate whether the controller is addressing or instructing the devices on the bus, or whether data transmission is taking place: when ATN is logic 1, the data lines contain either control information or addresses; with ATN = 1, only the controller is enabled to talk. When ATN = 0, only the devices that have been addressed can use the data lines. The IFC (interface clear) line is used to initialize the bus, or to clear it and reset it to a known condition in case of incorrect transmission. The REN (remote enable) line enables a remote instrument to be controlled by the bus; thus, any function that might normally be performed manually on the instrument (e.g., selecting a range or mode of operation) is now controlled by the bus via the data lines. The SRQ (service request) line is used by instruments on the bus whenever the instrument is ready to send or receive data; however, it is the controller who decides when to service the request. Finally, the EOI (end or identify) line can be used in two modes; when it is used by a talker, it signifies the end of a message; when it is used by the controller, it serves as a *polling* line, that is, a line used to interrogate the instrument about its data output.

Although it was mentioned earlier that the IEEE 488 bus can be used only over distances of up to 20 m, it is possible to extend its range of operation by connecting remote IEEE 488 bus systems over telephone communication lines. This can be accomplished by means of *bus extenders*, or by converting the parallel data to serial form (typically, in RS-232 format) and by transmitting the serial data over the phone lines by means of a modem. Serial communications and the RS-232 standard are discussed in the next section.

The RS-232 Standard

The primary reason why parallel transmission of data is not used exclusively is the limited distance range over which it is possible to transmit data on a parallel bus. Although there are techniques which permit extending the range for parallel transmission, these are complex and costly. Therefore, **serial transmission** is frequently used whenever data is to be transmitted over a significant distance. Since serial data travel along one single path and are transmitted one bit at a time, the cabling costs for long distances are relatively low; further, the transmitting and receiving units are also limited to processing just one signal and are also much simpler and less expensive. Two modes of operation exist for serial transmission: **simplex**, which corresponds to transmission in one direction only; and **duplex**, which permits transmission in either direction. Simplex transmission requires only one receiver and one transmitter, at each end of the link; on the other hand, duplex transmission can occur in one of two manners: **half-duplex** and **full-duplex**. In the former, although transmission can take place in both directions, it cannot occur simultaneously in both directions; in the latter case, both ends can simultaneously transmit and receive. Full-duplex transmission is usually implemented by means of four wires.

The data rate of a serial transmission line is measured in bits per second, since the data are transmitted one bit at a time. The unit of 1 bit/sec is called a **baud**; thus, reference is often made to the baud rate of a serial transmission. The baud rate can be translated into a parallel transmission rate in words per second if the structure of the word is known; for example, if a word consists of 10 bits (start and stop bits plus an 8-bit data word) and the transmission takes place at 1200 baud, 120 words are being transmitted every second. Typical data rates for serial transmission are standardized; the most common rates (familiar to the users of personal computer modem connections) are 300, 600, 1200, and 2400 baud. Baud rates can be as low as 50 baud or as high as 19,200 baud.

Like parallel transmission, serial transmission can also occur either synchronously or asynchronously. In the serial case, it is also true that asynchronous transmission is less costly but not as fast. A handshake protocol is also required for asynchronous serial transmission, as explained in the following. The most popular data-coding scheme for serial transmission is, once again, the ASCII code, consisting of a 7-bit word plus a **parity bit**, for a total of 8 bits per character. The role of the parity bit is to permit error detection in the event of erroneous reception (or transmission) of a bit. To see this, let us discuss the sequence of handshake events for asynchronous serial transmission and the use of parity bits to correct for errors. In serial asynchronous systems, handshaking is performed by using start and stop bits at the beginning and end of each character that is transmitted. The beginning of the transmission of a serial asynchronous word is announced by the "start" bit, which is always a 0-state bit. For the next five to eight successive bit times (depending on the code and the number of bits that specify the word length in the code), the line is switched to the 1 and 0 states required to represent the character being sent. Following the last bit of the data and the parity bit (which will be explained next), there is 1 bit or more in the 1 state, indicating "idle". The time period associated with this transmission is called the "stop" bit interval.

If noise pulses affect the transmission line, it is possible that a bit in the transmission could be misread. Thus, following the 5 to 8 transmitted data bits, there is a party bit that is used for error detection. Here is how the parity bit works. If the transmitter keeps track of the number of 1s in the word being sent, it can send a parity bit, a 1 or a 0, to ensure that the total number of 1s sent is always even (even parity) or odd (odd parity). Similarly, the receiver can keep track of the 1s received to see whether there was an error with the transmission. If an error is detected, retransmission of the word can be repeated.

Serial data transmission occurs most frequently according to the **RS-232 standard**. The RS-232 standard is based on the transmission of voltage pulses at a preselected baud rate; the voltage pulses are in the range –3 to –15 V for a logic 0 and in the range of +3 to +15 V for a logic 1. It is important to note that this amounts to a negative logic convention and that the signals are *not* TTL-compatible. The distance over which such transmission can take place is up to approximately 17 m (50 ft). The RS-232 standard was designed to make the transmission of digital data compatible with existing telephone lines; since phone lines were originally designed to carry analog voice signals, it became necessary to establish some standard procedures to make digital transmission possible over them. The resulting standard describes the mechanical and electrical characteristics of the interface between *data terminal equipment* (DTE) and *data communication equipment* (DCE). DTE consists of computers, terminals, digital instruments, and related peripherals; DCE includes all of those devices that are used to encode digital data in a format that permits their transmission over telephone lines. Thus, the standard specified how data should be presented by the DTE to the DCE so that digital data can be transmitted over voice lines.

A typical example of DCE is the **modem**. A modern converts digital data to audio signals that are suitable for transmission over a telephone line and is also capable of performing the reverse function, by converting the audio signals back to digital form. The term *modem* stands for *mod*ulate-*dem*odulate, because a modem modulates to a sinusoidal carrier using digital pulses (for transmission) and demodulates the modulated sinusoidal signal to recover the digital pulses (at reception). Three methods are commonly used for converting digital pulses to an audio signal: **amplitude-shift keying, frequency-shift keying**, and **phase-shift keying**, depending on whether the amplitude, phase, or frequency of the sinusoid is modulated by the digital pulses. Figure 5.11.36 depicts the essential block of a data transmission system based on the RS-232 standard, as well as examples of digital data encouded for transmission over a voice line.

In addition to the function just described, however, the RS-232 standard also provides a very useful set of specifications for the direct transmission of digital data between computers and instruments. In other words, communication between digital terminal instruments may occur directly in digital form (i.e., without digital communication devices encoding the digital data with analog voice lines). Thus, this standard is also frequently used for direct digital communication.

The RS-232 standard can be summarized as follows:

- Data signals are encoded according to a negative logic convention using voltage levels of –3 to –15 V for logic 1 and +3 to +15 V for logic 0.
- Control signals use a positive logic convention (opposite to that of data signals).
- The maximum shunt capacitance of the load cannot exceed 2500 pF; this, in effect, limits the maximum length of the cables used in the connection.
- The load resistance must be between 300 Ω and 3 kΩ.
- Three wires are used for data transmission. One wire each is used for receiving and transmitting data; the third wire is a signal return line (signal ground). In addition, there are 22 wires that can be used for a variety of control purposes between the DTE and DCE.
- The male part of the connector is assigned to the DTE and the female part to the DCE. Figure 5.11.37 labels each of the wires in the 25-pin connector. Since each side of the connector has a *receive* and a *transmit* line, it has been decided by convention that the DCE transmits on the transmit line and receives on the receive line, while the DTE receives on the transmit line and transmits on the receive line.
- The baud rate is limited by the length of the cable; for a 17-m length, any rate from 50 baud to 19.2 kbaud is allowed. If a longer cable connection is desired, the maximum baud rate will decrease according to the length of the cable and **line drivers** can be used to amplify the signals, which are transmitted over twisted-air wires. Line drivers are simply signal amplifiers that are used directly

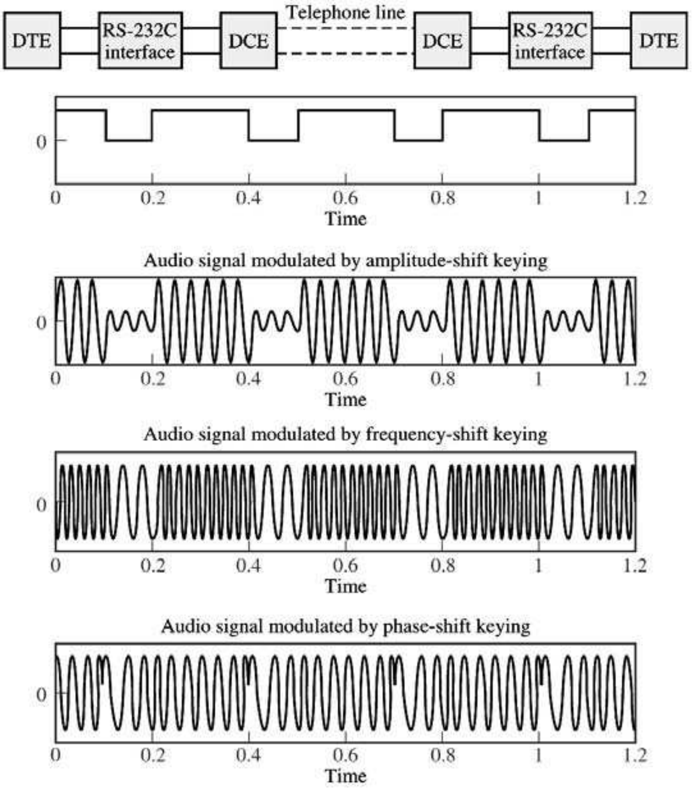

FIGURE 5.11.36 Digital data encoded for analog transmission.

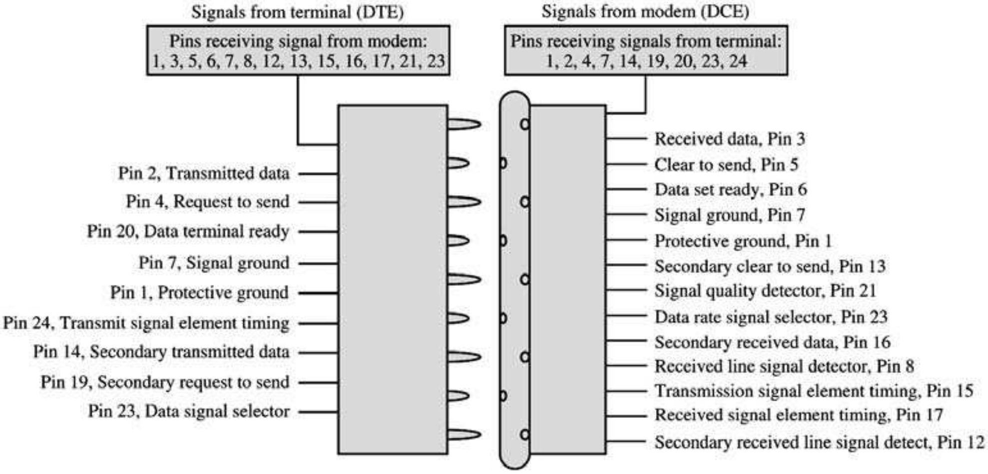

FIGURE 5.11.37 RS-232 connections.

on the digital signal, prior to encoding. For example, the signal generated by a DTE device (say, a computer) may be transmitted over a distance of up to 3300 m (at a rate of 600 baud) prior to being encoded by the DCE.

- The serial data can be encoded according to any code, although the ASCII code is by far the most popular.

Other Communication Network Standards

In addition to the popular RS-232 and IEEE bus standards we should mention other communication standards that have become or are rapidly becoming commonplace. One is the *Ethernet*, which operates at 10 Mb/sec and is based on IEEE Standard 802.3. This is commonly used in office networks. Higher speed networks include FDDI (fiber distributed data interface), which specifies an optical fiber ring with a data rate of 100 Mb/sec, and ATM (asynchronous transfer mode), a packet oriented transfer mode moving data in fixed-size packets called cells. ATM does not operate at a fixed speed. Typical speed is 155 Mb/sec, but there are implementations running as fast as 2 Gb/sec.

5.12 Electromechanical Systems

The objective of this section is to introduce the fundamental notions of electromechanical energy conversion, leading to an understanding of the operation of various electromechanical transducers

The Magnetic Field and Faraday's Law

The quantities used to measure the strength of a magnetic field are the **magnetic flux**, ϕ, in units of **webers** (Wb); and the **magnetic flux density**, B, in units of webers per square(Wb/m^2), or **teslas** (T). The latter quantity, as well as the associated **magnetic field intensity,** H (in units of amperes per meter, or A/m), are vectors. Thus, the density of the magnetic flux and its intensity are in general described in vector form, in terms of the components present in each spatial direction (e.g., on the x, y, and z axes). In discussing magnetic flux density and field intensity in this chapter and the next, we shall almost always assume that the field is a *scalar field*, that is, that it lies in a single spatial direction. This will simplify many explanations.

It is customary to represent the magnetic field by means of the familiar *lines of force* (a concept also due to Faraday); we visualize the strength of a magnetic field by observing the density of these lines in space. You probably know from a previous course in physics that such lines are closed in a magnitude field, that is, that they form continuous loops exiting at a magnetic north pole (by definition) and entering at a magnetic south pole. The relative strengths of the magnetic fields generated by two magnets could be depicted as shown in Figure 5.12.1.

Magnetic fields are generated by electric charge in motion, and their effect is measured by the force they exert on a moving charge. As you may recall from previous physics courses, the vector force **f** exerted on a charge of q moving at velocity **u** in the presence of a magnetic field with flux density **B** is given by the equation

$$\mathbf{f} = q\mathbf{u} \times \mathbf{B} \tag{5.12.1}$$

where the symbol × denotes the (vector) cross product. If the charge is moving at a velocity **u** in a direction that makes an angle θ with the magnetic field, then the magnitude of the force is given by

$$f = quB\sin\theta \tag{5.12.2}$$

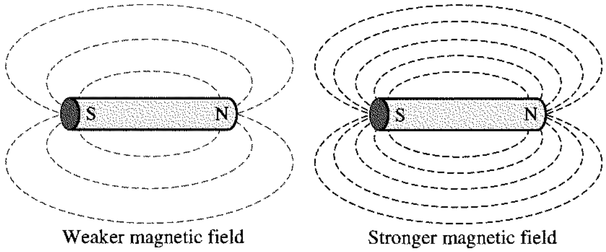

FIGURE 5.12.1 Lines of force in a magnetic field.

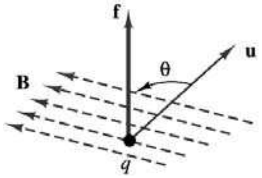

FIGURE 5.12.2 Charge moving in a constant magnetic field.

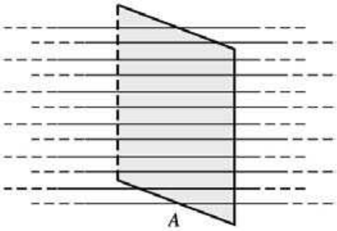

FIGURE 5.12.3 Magnetic flux lines crossing a surface.

and the direction of this force is at right angles with the plane formed by the vectors **B** and **u**. This relationship is depicted in Figure 5.12.2.

The magnetic flux, ϕ, is then defined as the integral of the flux density over some surface area. For the simplified (but often useful) case of magnetic flux lines perpendicular to a cross-sectional area A, we can see that the flux is given by the following integral:

$$\phi = \int_A B \, dA \tag{5.12.3}$$

in webers (Wb), where the subscript A indicates that the integral is evaluated over the surface A. Furthermore, if the flux were to be uniform over the cross-sectional area A (a simplification that will be useful), the preceding integral could be approximated by the following expression:

$$\phi = B \cdot A \tag{5.12.4}$$

Figure 5.12.3 illustrates this idea by showing hypothetical magnetic flux lines traversing a surface, delimited in the figure by a thin conducting wire.

Faraday's law states that if the imaginary surface A were bounded by a conductor — for example, the thin wire of Figure 5.12.3 — then a *changing* magnetic field would induce a voltage, and therefore a current, in the conductor. More precisely, Faraday's law states that a time-varying flux causes an induced **electromotive force**, or emf, e, as follows:

$$e = -\frac{d\phi}{dt} \tag{5.12.5}$$

In practical applications, the size of the voltages induced by the changing magnetic field can be significantly increased if the conducting wire is coiled many times around, so as to multiply the area crossed by the magnetic flux lines many times over. For an N-turn coil with cross-sectional area A, for example, we have the emf

$$e = N\frac{d\phi}{dt} \tag{5.12.6}$$

Figure 5.12.4 shows an N-turn coil *linking* a certain amount of magnetic flux; you can see that if N is very large and the coil is tightly wound (as is usually the case in the construction of practical devices),

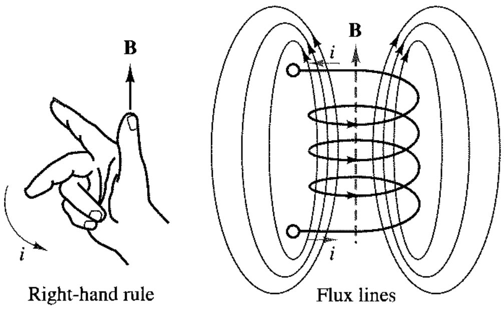

FIGURE 5.12.4 Concept of flux linkage.

it is not unreasonable to presume that each turn of the coil links the same flux. It is convenient, in practice, to define the **flux linkage**, λ, as

$$\lambda = N\phi \tag{5.12.7}$$

so that

$$e = \frac{d\lambda}{dt} \tag{5.12.8}$$

In the analysis of linear circuits, we implicitly assumed that the relationship between flux linkage and current was a linear one:

$$\lambda = Li \tag{5.12.9}$$

so that the effect of a time-varying current was to induce a transformer voltage across an inductor coil, according to the expression

$$v = L\frac{di}{dt} \tag{5.12.10}$$

This is, in fact, the defining equation for the ideal **self-inductance**, L. In addition to self-inductance, however, it is also important to consider the **magnetic coupling** that can occur between neighboring circuits. Self-inductance measures the voltage induced in a circuit by the magnetic field generated by a current flowing in the same circuit. It is also possible that a second circuit in the vicinity of the first may experience an induced voltage as a consequence of the magnetic field generated in the first circuit. This principle underlies the operation of all transformers.

Self- and Mutual Inductance

Figure 5.12.5 depicts a pair of coils, one of which, L_1, is excited by a current, i_1, and therefore develops a magnetic field and a resulting induced voltage, v_1, The second coil, L_2, is not energized by a current, but links some of the flux generated by the current i_1 and L_1 because of its close proximity to the first coil. The magnetic coupling between the coils established by virtue of their proximity is described by a quantity called **mutual inductance** and defined by the symbol M. The mutual inductance is defined by the equation

$$v_2 = M\frac{di_1}{dt} \tag{5.12.11}$$

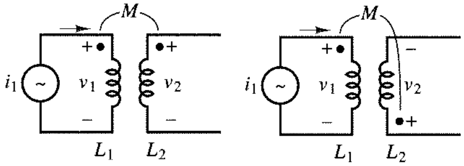

FIGURE 5.12.5 Mutual inductance.

The dots shown in the two figures indicate the polarity of the coupling between the coils. If the dots are at the same end of the coils, the voltage induced in coil 2 by a current in coil 1 has the same polarity as the voltage induced by the same current in coil 1; otherwise, the voltages are in opposition, as shown in the lower part of Figure 5.12.5. Thus, the presence of such dots indicates that magnetic coupling is present between two coils, It should also be pointed out that if a current (and therefore a magnetic field) were present in the second coil, an additional voltage would be induced across coil 1. The voltage induced across a coil is, in general, equal to the sum of the voltages induced by self-inductance and mutual inductance.

Example 5.12.1 Linear Variable Differential Transformer (LVDT)

The linear variable differential transformer (LVDT) is a displacement transducer based on the mutual inductance concept just discussed. Figure 5.12.6 shows a simplified representation of an LVDT, which consists of a primary coil, subject to AC excitation (v_{ex}) and of a pair of identical secondary coils, which are connected so as to result in the output voltage

$$v_{out} = v_1 - v_2$$

The ferromagnetic core between the primary and secondary coils can be displaced in proportion to some external motion, x, and determines the magnetic coupling between primary and secondary coils. Intuitively, as the core is displaced upward, greater coupling will occur between the primary coil and the top secondary coil, thus inducing a greater voltage in the top secondary coil. Hence, $v_{out} > 0$ for positive displacements. The converse is true for negative displacements. More formally, if the primary coil has resistance R_p and self-inductance L_p, we can write

$$iR_p + L_p \frac{di}{dt} = v_{ex}$$

and the voltages induced in the secondary coils are given by

$$v_1 = M_1 \frac{di}{dt}$$

$$v_2 = M_2 \frac{di}{dt}$$

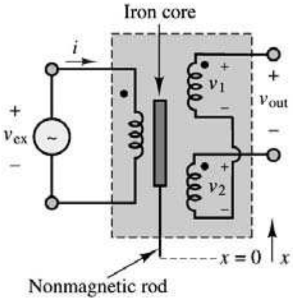

FIGURE 5.12.6 Linear variable differential transformer.

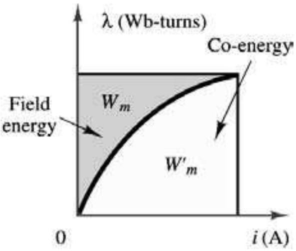

FIGURE 5.12.7

so that

$$v_{\text{out}} = (M_1 - M_2)\frac{di}{dt}$$

where M_1 and M_2 are the mutual inductances between the primary and the respective secondary coils, It should be apparent that each of the mutual inductances is dependent on the position of the iron core. For example, with the core at the *null position,* $M_1 = M_2$ and $v_{\text{out}} = 0$. The LVDT is typically designed so that $M_1 - M_2$ is linearly related to the displacement of the core, x.

Because the excitation is by necessity an AC signal, the output voltage is actually given by the difference of two sinusoidal voltages at the same frequency and is therefore itself a sinusoid, whose amplitude and phase depend on the displacement, x. Thus, v_{out} is an *amplitude-modulated* (AM) signal. To recover a signal proportional to the actual displacement, it is therefore necessary to use a demodulator circuit.

In practical electromagnetic circuits, the self-inductance of a circuit is not necessarily constant; in particular, the inductance parameter, L, is not constant, in general, but depends on the strength of the magnetic field intensity, so that it will not be possible to use such a simple relationship as $v = L\, di/dt$, with L constant. If we revisit the definition of the transformer voltage,

$$e = N\frac{d\phi}{dt} \tag{5.12.12}$$

We see that in an inductor coil, the inductance is given by

$$L = \frac{N\phi}{i} = \frac{\lambda}{i} \tag{5.12.13}$$

This expression implies that the relationship between current and flux in a magnetic structure is linear (the inductance being the slope of the line). In fact, the properties of ferromagnetic materials are such that the flux-current relationship is nonlinear, so that the simple linear inductance parameter used in electric circuit analysis is not adequate to represent the behavior of the magnetic circuits of the present chapter. In any practical situation, the relationship between the flux linkage, λ, and the current is nonlinear, and might be described by a curve similar to that shown in Figure 5.12.7. Wherever the i-λ curve is not a straight line, it is more convenient to analyze the magnetic system in terms of energy calculations, since the corresponding circuit equation would be nonlinear.

In a magnetic system, the energy stored in the magnetic field is equal to the integral of the instantaneous power, which is the product of voltage and current, just as in a conventional electrical circuit.

$$W_m = \int ei\, dt \tag{5.12.14}$$

However, in this case, the voltage corresponds to the induced emf, according to Faraday's law:

$$e = \frac{d\lambda}{dt} = N\frac{d\phi}{dt} \tag{5.12.15}$$

and is therefore related to the rate of change of the magnetic flux. The energy stored in the magnetic field could therefore be expressed in terms of the current by the integral

$$W_m = \int ei\,dt = \int \frac{d\lambda}{dt} i\,dt = \int i\,d\lambda \tag{5.12.16}$$

It should be straightforward to recognize that this energy is equal to the area above the λ-*i* curve of Figure 5.12.7. From the same figure, it is also possible to define a fictitious (but sometimes useful) quantity called **co-energy**, equal to the area under and identified by the symbol W'_m. From the figure, it is also possible to see that the co-energy can be expressed in terms of the stored energy by means of the following relationship:

$$W'_m = i\lambda - W_m \tag{5.12.17}$$

Ampère's Law

As explained in the previous section, Faraday's law is one of two fundamental laws relating electricity to magnetism. The second relationship, which forms a counterpart to Faraday's law, is **Ampère's law**. Qualitatively, Ampère's law states that the magnetic field intensity, **H**, in the vicinity of a conductor is related to the current carried by the conductor; thus Ampère's law establishes a dual relationship with Faraday's law.

In the previous section, we described the magnetic field in terms of its flux density, **B**, and flux ϕ, To explain Ampère's law and the behavior of magnetic materials, we need to define a relationship between the magnetic field intensity, **H**, and the flux density, **B**. These quantities are related by:

$$\begin{aligned}\mathbf{B} &= \mu\mathbf{H} \\ &= \mu_r\mu_0\mathbf{H} \quad \text{Wb/m}^2 \text{ or T}\end{aligned} \tag{5.12.18}$$

where the parameter μ is a scalar constant for a particular physical medium (at least, for the applications we consider here) and is called the **permeability** of the medium. The permeability of a material can be factored as the product of the permeability of free space, $\mu_0 = 4\pi \times 107$ H/m, times the relative permeability, μ_r, which varies greatly according to the medium. For example, for air and for most electrical conductors and insulators, μ_r is equal to 1. For ferromagnetic materials, the value of μ_r can take values in the hundreds or thousands. The size of μ_r represents a measure of the magnetic properties of the material. A consequence of Ampère's law is that the larger the value of μ, the smaller the current required to produce a large flux density in an electromagnetic structure. Consequently, many electromechanical devices make use of ferromagnetic materials, called iron cores, to enhance their magnetic properties. Table 5.12.1 gives approximate values of μ_r for some common materials.

Conversely, the reason for introducing the magnetic field intensity is that it is dependent of the properties of the materials employed in the construction of magnetic circuits. Thus, a given magnetic field intensity, **H**, will give rise to different flux densities in different materials. It will therefore be useful to define *sources* of magnetic energy in terms of the magnetic field intensity, so that different magnetic structures and materials can then be evaluated or compared for a given source. In analogy with electromotive force, this "source" will be termed **magnetomotive force** (mmf). As stated earlier, both the magnetic flux density and field intensity are vector quantities; however, for ease of analysis, scalar fields will be chosen by appropriately selecting the orientation of the fields, wherever possible.

TABLE 5.12.1 Relative Permeabilities for Common Materials

Material	μ_r
Air	1
Permalloy	100,000
Cast steel	1,000
Sheet steel	4,000
Iron	5,195

The field generated by a single conducting wire is not very strong; however, if we arrange the wire into a tightly wound coil with many turns, we can greatly increase the strength of the magnetic field. For such a coil with N turns, one can verify visually that the lines of force associated with the magnetic field link all of the turns of the conducting coil, so that we have effectively increased the current linked by the flux lines N-fold. The product $N \cdot i$ is a useful quantity in electromagnetic circuits and is called the magnetomotive force, $\mathcal{F}$ (often abbreviated mmf), in analogy with the electromotive force defined earlier:

$$\mathcal{F} = Ni \quad \text{ampere-turns } (A \cdot t) \tag{5.12.19}$$

Typical arrangements are the iron-core inductor and the toroid of Figure 5.12.8. The flux densities for these inductors are given by the expressions

$$B = \frac{\mu N i}{l} \quad \text{Flux density for tightly wound circular coil} \tag{5.12.20}$$

$$B = \frac{\mu N i}{2\pi r_2} \quad \text{Flux density for toroidal coil} \tag{5.12.21}$$

Intuitively, the presence of a high-permeability material near a source of magnetic flux causes the flux to preferentially concentrate in the high-μ material, rather than in air, much as a conducting path concentrates the current produced by an electric field in an electric circuit. Figure 5.12.9 depicts an example of a simple electromagnetic structure, which, as we shall see shortly, forms the basis of the practical transformer.

Table 5.12.2 summarizes the variables introduced thus far in the discussion of electricity and magnetism.

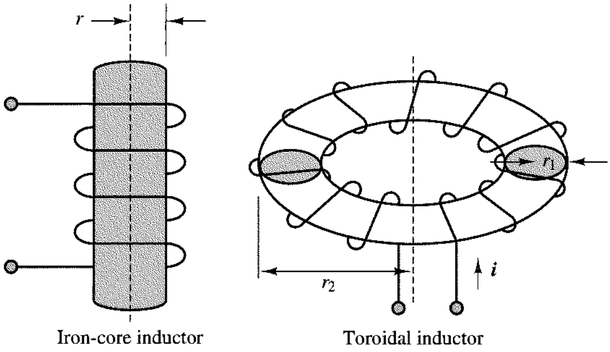

FIGURE 5.12.8 Practical inductors.

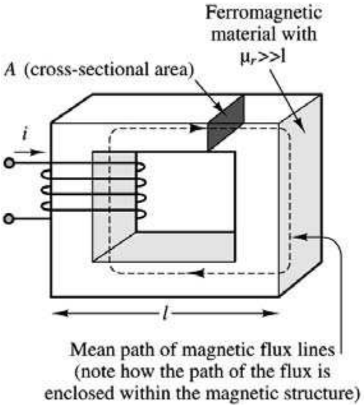

FIGURE 5.12.9 A simple electromagnetic structure.

TABLE 5.12.2 Magnetic Variables and Units

Variable	Symbol	Units
Current	I	A
Magnetic flux density	B	Wb/m² = T
Magnetic flux	ϕ	Wb
Magnetic field intensity	H	A/m
Electromotive force	e	V
Magnetomotive force	$\mathcal{F}$	A · t
Flux linkage	λ	Wb · t

Magnetic Circuits

It is possible to analyze the operation of electromagnetic devices such as the one depicted in Figure 5.12.9 by means of magnetic equivalent circuits, similar in many respects to the equivalent electrical circuits of the earlier chapters. Before we can present this technique, however, we need to make a few simplifying approximations. The first of these approximations assumes that there exists a **mean path** for the magnetic flux, and that the corresponding mean flux density is approximately constant over the cross-sectional area of the magnetic structure. Thus, a coil wound around a coil with cross-sectional area A will have flux density

$$B = \frac{\phi}{A} \qquad (5.12.22)$$

where A is assumed to be perpendicular to the direction of the flux lines. Figure 5.12.9 illustrates such a mean path and the cross-sectional area, A. Knowing the flux density, we obtain the field intensity:

$$H = \frac{B}{\mu} = \frac{\phi}{A\mu} \qquad (5.12.23)$$

But then, knowing the field intensity, we can relate the mmf of the coil, $\mathcal{F}$, to the product of the magnetic field intensity, H, and the length of the magnetic (mean) path, l, for one leg of the structure:

$$\mathcal{F} = N \cdot i = H \cdot l \qquad (5.12.24)$$

In summary, the mmf is equal to the magnetic flux times the length of the magnetic path, divided by the permeability of the material times the cross-sectional area:

TABLE 5.12.3 Analogy between Electric and Magnetic Circuits

Electrical Quantity	Magnetic Quantity
Electrical field intensity, E, V/m	Magnetic field intensity, H, A · t/m
Voltage, v, V	Magnetomotive force, $\mathcal{F}$, A · t
Current, i, A	Magnetic flux, ϕ, Wb
Current density, J, A/m^2	Magnetic flux density, B, Wb/m^2
Resistance, R, Ω	Reluctance, $\mathcal{R} = l/\mu A$, A · t/Wb
Conductivity, σ, l/Ω · m	Permeability, μ, Wb/A · m

$$\mathcal{F} = \phi \frac{l}{\mu A} \tag{5.12.25}$$

A review of this formula reveals that the magnetomotive force, $\mathcal{F}$, may be viewed as being analogous to the voltage source in a series electrical circuit, and that the flux, ϕ, is then equivalent to the electrical current in a series circuit and the term $l/\mu A$ to the *magnetic resistance* of one leg of the magnetic circuit. You will note that the term $l/\mu A$ is very similar to the term describing the resistance of a cylindrical conductor of length l and cross-sectional A, where the permeability, μ, is analogous to the conductivity, σ. The term $l/\mu A$ occurs frequently enough to be assigned the name of reluctance, and the symbol $\mathcal{R}$.

In summary, when an N-turn coil carrying a current i is wound around a magnetic core such as the one indicated in Figure 5.12.9, the mmf, $\mathcal{F}$, generated by the coil produces a flux, ϕ, that is *mostly* concentrated with the core and is assumed to be uniform across the cross section. Within this simplified picture, then, the analysis of a magnetic circuit is analogous to that of resistive electrical circuits. This analogy is illustrated in Table 5.12.3 and in the examples in this section.

The usefulness of the magnetic circuit analogy can be emphasized by analyzing a magnetic core similar to that of Figure 5.12.9, but with a slightly modified geometry. Figure 5.12.10 depicts the magnetic structure and its equivalent circuit analogy. In the figure, we see that the mmf, $\mathcal{F}$ = Ni, excites the magnetic circuit, which is composed of four legs: two of mean path length l_1 and cross-sectional area $A_1 = d_1 w$, and the other two of mean length l_2 and cross section $A_2 = d_2 w$. Thus, the reluctance encountered by the flux in its path around the magnetic core is given by the quantity $\mathcal{R}_{\text{series}}$, with

$$\mathcal{R}_{\text{series}} = 2\mathcal{R}_1 + 2\mathcal{R}_2$$

and

$$\mathcal{R}_1 = \frac{l_1}{\mu A_1} \qquad \mathcal{R}_2 = \frac{l_2}{\mu A_2} \tag{5.12.26}$$

It is important at this stage to review the assumptions and simplifications made in analyzing the magnetic structure of Figure 5.12.10:

1. All of the magnetic flux is linked by all of the turns of the coil.
2. The flux is confined exclusively within the magnetic core.
3. The density of the flux is uniform across the cross-sectional area of the core.

You can probably see intuitively that the first of these assumptions might not hold true near the ends of the coil, but that it might be more reasonable if the coil is tightly wound. The second assumption is equivalent to stating that the relative permeability of the core is infinitely higher than that of air (presuming that this is the medium surrounding the core): if this were the case, the flux would indeed be

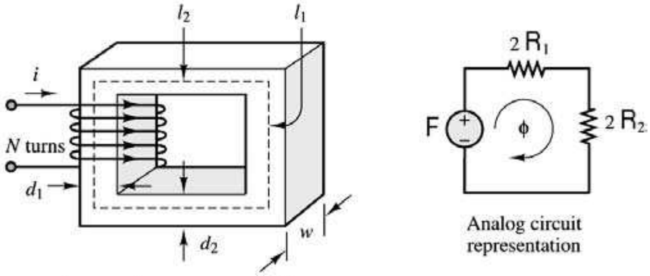

A magnetic structure excited by a magnetomotive force $F = Ni$

Analog circuit representation

FIGURE 5.12.10 Analogy between magnetic and electric circuits.

confined within the core. It is worthwhile to note that we made a similar assumption when we treat wires in electric circuits as perfect conductors: the conductivity of copper is substantially greater than that of free space, by a factor of approximately 10^{15}. In the case of magnetic materials, however, even for the best alloys, we have a relative permeability only on the order of 10^3 to 10^4. Thus, an approximation that is quite appropriate for electric circuits is not nearly as good in the case of magnetic circuits. Some of the flux in a structure such as those of Figure 5.12.9 and Figure 5.12.10 would thus not be confined within the core (this is usually referred to as **leakage flux**). Finally, the assumption that the flux is uniform across the core cannot hold for a finite-permeability medium, but it is very helpful in giving an approximate *mean* behavior of the magnetic circuit.

The magnetic circuit analogy is therefore far from being exact. However, short of employing the tools of electromagnetic field theory and of vector calculus, or advanced numerical simulation software, it is the most convenient tool at the engineer's disposal for the analysis of magnetic structures.

Example 5.12.2 Magnetic Reluctance Position Sensor

A simple magnetic structure, very similar to those examined in the previous examples, finds very common application in the so-called variable-reluctance position sensor, which, in turn, finds widespread application in a variety of configurations for the measurement of linear and angular position and velocity. Figure 5.12.11 depicts one particular configuration that is used in many applications. In this structure, a permanent magnet with a coil of wire wound around it forms the sensor; a steel disk (typically connected to a rotating shaft) has a number of tabs that pass between the pole pieces of the sensor. The area of the tab is assumed equal to the area of the cross section of the pole pieces and is equal to a^2. The reason for the name *variable-reluctance sensor* is that the reluctance of the magnetic structure is variable, depending on whether or not a ferromagnetic tab lies between the pole pieces of the magnet.

The principle of operation of the sensor is that an electromotive force, e_s, is induced across the coil by the change in magnetic flux caused by the passage of the tab between the pole pieces when the disk

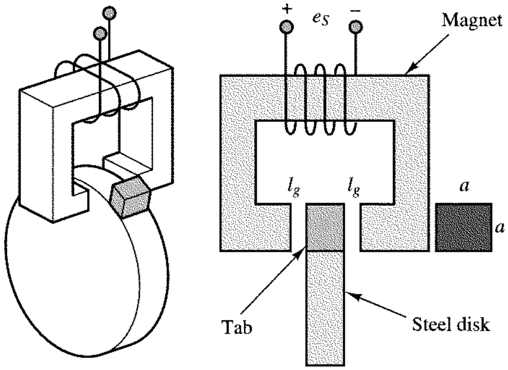

FIGURE 5.12.11 Variable-reluctance position sensor.

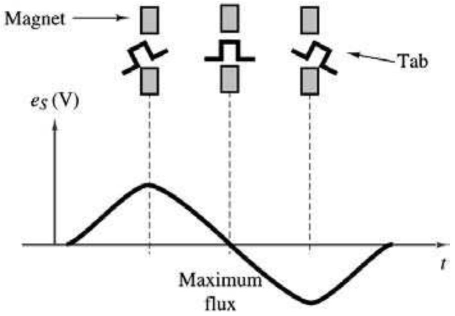

FIGURE 5.12.12 Variable-reluctance position sensor waveform.

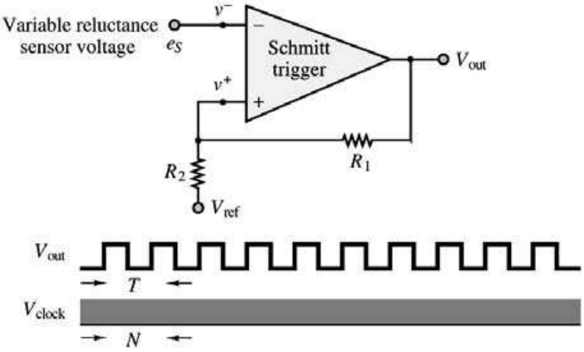

FIGURE 5.12.13 Signal processing for a 60-tooth wheel RPM sensor.

is in motion. As the tab enters the volume between the pole pieces, the flux will increase because of the lower reluctance of the configuration, until it reaches a maximum when the tab is centered between the poles of the magnet. Figure 5.12.12 depicts the approximate shape of the resulting voltage, which, according to Faraday's law, is given by

$$e_S = -\frac{d\phi}{dt}$$

The rate of change of flux is dictated by the geometry of the tab and of the pole pieces, and by the speed of rotation of the disk. It is important to note that, since the flux is changing only if the disk is rotating, this sensor cannot detect the static position of the disk.

One common application of this concept is in the measurement of the speed of rotation of rotating machines, including electric motors and internal combustion engines. In these applications, use is made of a *60-tooth wheel*, which permits the conversion of the speed rotation directly to units of revolutions per minute. The output of a variable-reluctance position sensor magnetically coupled to a rotating disk equipped with 60 tabs (teeth) is processed through a comparator or Schmitt trigger circuit. The voltage waveform generated by the sensor is nearly sinusoidal when the teeth are closely spaced, and it is characterized by one sinusoidal cycle for each tooth on the disk. If a negative zero-crossing detector is employed, the trigger circuit will generate a pulse corresponding to the passage of each tooth, as shown in Figure 5.12.13. If the time between any two pulses is measured by means of a high-frequency clock, the speed of the engine can be directly determined in units of rev/min by means of a digital counter.

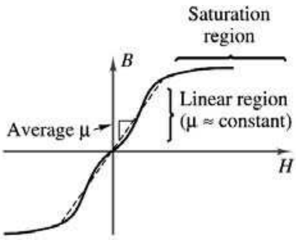

FIGURE 5.12.14 Permeability and magnetic saturation effects.

Magnetic Materials and *B-H* Curves

In the analysis of magnetic circuits presented in the previous sections, the relative permeability, μ_r, was treated as a constant. In fact, the relationship between the magnetic flux density, **B**, and the associated field intensity, **H**,

$$\mathbf{B} = \mu \mathbf{H} \tag{5.12.27}$$

is characterized by the fact that the relative permeability of magnetic materials is not a constant, but is a function of the magnetic field intensity. In effect, all magnetic materials exhibit a phenomenon called **saturation**, whereby the flux density increases in proportion to the field intensity until it cannot do so any longer. Figure 5.12.14 illustrates the general behavior of all magnetic materials. You will note that since the *B-H* curve shown in the figure is nonlinear, the value of μ (which is the slope of the curve) depends on the intensity of the magnetic field.

To understand the reasons for the saturation of a magnetic material, we need to briefly review the mechanism of magnetization. The basic idea behind magnetic materials is that the spin of electrons constitutes motion of charge and therefore leads to magnetic effects, as explained in the introductory section of this chapter. In most materials, the electron spins cancel out, on the whole, and no net effect remains. In ferromagnetic materials, on the other hand, atoms can align so that the electron spins cause a net magnetic effect. In such materials, there exist small regions with strong magnetic properties (called **magnetic domains**), the effects of which are neutralized in unmagnetized material by other, similar regions that are oriented differently, in a random pattern. When the material is magnetized, the magnetic domains tend to align with each other, to a degree that is determined by the intensity of the applied magnetic field.

In effect, the large number of miniature magnets within the material are *polarized* by the external magnetic field. As the field increases, more and more domains become aligned. When all of the domains have become aligned, any further increase in magnetic field intensity does not yield an increase in flux density beyond the increase that would be caused in a nonmagnetic material. Thus, the relative permeability, μ_r, approaches 1 in the saturation region. It should be apparent that an exact value of μ_r cannot be determined; the value of μ_r used in the earlier examples is to be interpreted as an average permeability, for intermediate values of flux density. As a point of reference, commercial magnetic steels saturate at flux densities around a few teslas. Figure 5.12.17, shown later in this section, will provide some actual *B-H* curves for common ferromagnetic materials.

The phenomenon of saturation carries some interesting implications with regard to the operation of magnetic circuits: the results of the previous section would seem to imply that an increase in the mmf (that is, an increase in the current driving the coil) would lead to a proportional increase in the magnetic flux. This is true in the *linear region* of Figure 5.12.14; however, as the material reaches saturation, further increases in the driving current (or, equivalently, in the mmf) do not yield further increases in the magnetic flux.

There are two more features that cause magnetic materials to further deviate from the ideal model of the linear *B-H* relationship: **eddy currents** and **hysteresis**. The first phenomenon consists of currents that are caused by any time-varying flux in the core material. As you know, a time-varying flux will

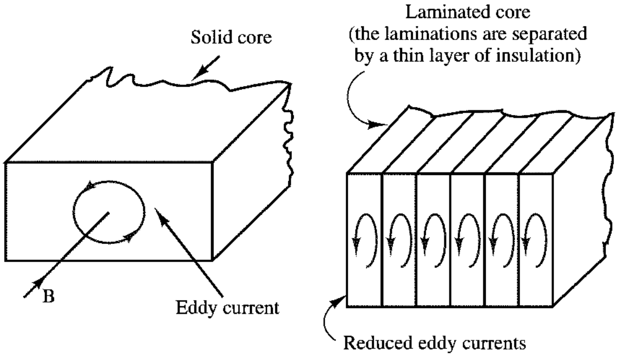

FIGURE 5.12.15 Eddy currents in magnetic structures.

induce a voltage, and therefore a current. When this happens inside the magnetic core, the induced voltage will cause "eddy" currents (the terminology should be self-explanatory) in the core, which depend on the resistivity of the core. Figure 5.12.15 illustrates the phenomenon of eddy currents. The effect of these currents is to dissipate energy in the form of heat. Eddy currents are reduced by selecting high-resistivity core materials, or by *laminating* the core, introducing tiny, discontinuous air gaps between core layers (see Figure 5.12.15). Lamination of the core reduces eddy currents greatly without affecting the magnetic properties of the core.

It is beyond the scope of this section to quantify the losses caused by induced eddy currents, but it will be important to be aware of this source of energy loss.

Hysteresis is another loss mechanism in magnetic materials; it displays a rather complex behavior, related to the magnetization properties of a material. The curve of Figure 5.12.16 reveals that the *B-H* curve for a magnetic material during magnetization (as *H* is increased) is displaced with respect to the curve that is measured when the material is demagnetized. To understand the hysteresis process, consider a core that has been energized for some time, with a field intensity of $H_1 A \cdot$ t/m. As the current required to sustain the mmf corresponding to H_1 is decreased, we follow the hysteresis curve from the point α to the point β. When the mmf is exactly zero, the material displays the **remanent** (or **residual**) **magnetization** B_r. To bring the flux density to zero, we must further decrease the mmf (i.e., produce a negative current), until the field intensity reaches the value $-H_0$ (point γ on the curve). As the mmf is made more negative, the curve eventually reaches the point α'. If the excitation current go the coil is now increased, the magnetization curve will follow the path $\alpha' = \beta' = \gamma' = \alpha$, eventually returning to the original point in the *B-H* plane, but via a different path.

The result of this process, by which an *excess magnetomotive force* is required to magnetize or demagnetize the material, is a net energy loss. It is difficult to evaluate this loss exactly; however, it can be shown that it is related to the area between the curves of Figure 5.2.16. There are experimental techniques that enable the approximate measurement of these losses.

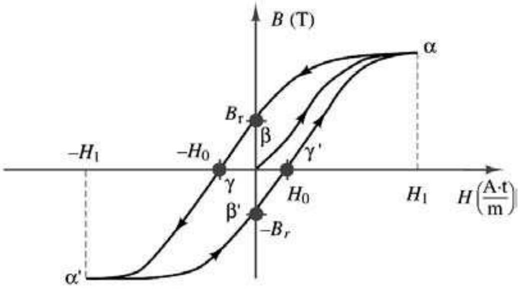

FIGURE 5.12.16 Hysteresis in magnetization curves.

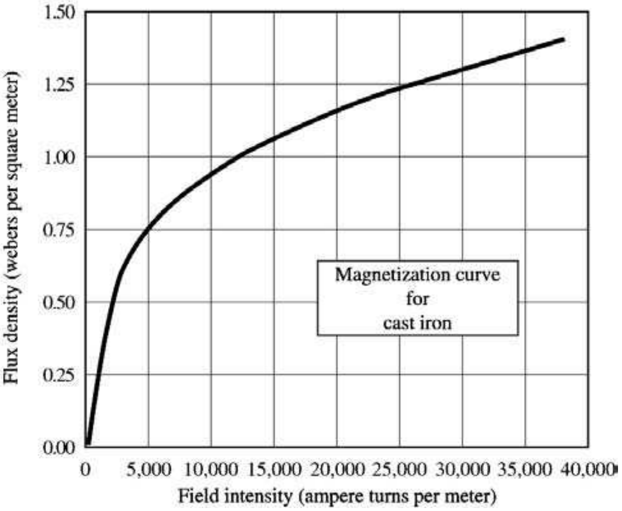

(a)

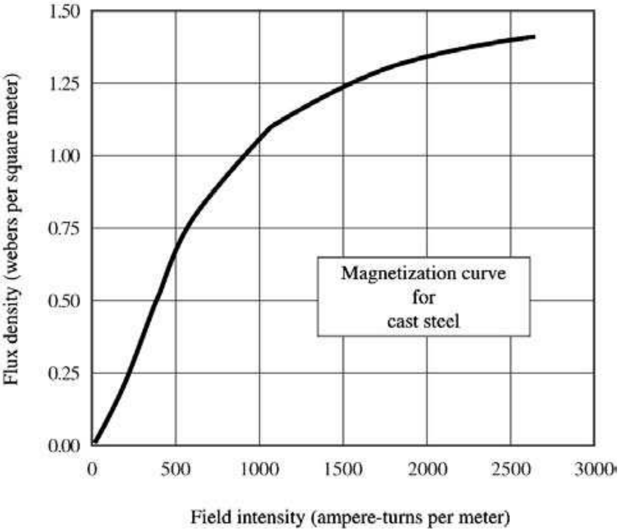

(b)

FIGURE 5.12.17 (a) Magnetization curve for cast iron; (b) magnetization curve for cast steel;

Figure 5.2.17(a) to Figure 5.2.17(c) depict magnetization curves for three very common ferromagnetic materials: cast iron, cast steel, and sheet steel.

Electromechanical Energy Conversion

From the material developed thus far, it should be apparent that electromagnetomechanical devices are capable of converting mechanical forces and displacements to electromagnetic energy, and that the converse is also possible. The objective of this section is to formalize the basic principles of energy conversion in electromagnetomechanical systems, and to illustrate its usefulness and potential for application by presenting several examples of **energy transducers**. A transducer is a device that can convert electrical to mechanical energy (in this case, it is often called an **actuator**), or vice versa (in which case it is called a sensor).

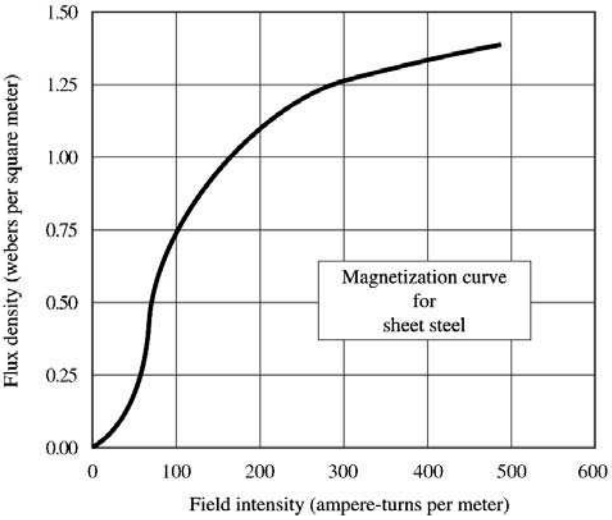

(c)

FIGURE 5.12.17 (c) magnetization curve for sheet steel.

Several physical mechanisms permit conversion of electrical to mechanical energy and back, the principal phenomena being the **piezoelectric effect**, consisting of the generation of a change in electric field in the presence of strain in certain crystals (e.g., quartz), and **electrostriction** and **magnetostriction**, in which changes in the dimension of certain materials lead to a change in their electrical (or magnetic) properties. Although these effects lead to some interesting applications, this chapter is concerned only with transducers in which electrical energy is converted to mechanical energy through the coupling of a magnetic field. It is important to note that all rotating machines (motors and generators) fit the basic definition of electromechanical transducers we have just given.

Forces in Magnetic Structures

It should be apparent by now that it is possible to convert mechanical forces to electrical signals, and vice versa, by means of the coupling provided by energy stored in the magnetic field. In this subsection, we discuss the computation of mechanical forces and of the corresponding electromagnetic quantities of interest; these calculations are of great practical importance in the design and application of electromechanical actuators. For example, a problem of interest is the computation of the current required to generate a given force in an electromechanical structure. This is the kind of application that is likely to be encountered by the engineer in the selection of an electromechanical device for a given task.

As already seen in this chapter, an electromechanical system includes an electrical system and a mechanical system, in addition to means through which the two can interact. The principal focus of this chapter has been the coupling that occurs through an electromagnetic field common to both the electrical and the mechanical system; to understand electromechanical energy conversion, it will be important to understand the various energy storage and loss mechanisms in the electromagnetic field. Figure 5.12.18 illustrates the coupling between the electrical and mechanical systems. In the mechanical system, energy loss can occur because of the heat developed as a consequence of *friction*, while in the electrical system, analogous losses are incurred because of *resistance*. Loss mechanisms are also present in the magnetic coupling medium, since *eddy current losses* and *hysteresis losses* are unavoidable in ferromagnetic materials. Either system can supply energy, and either system can store energy. Thus, the figure depicts the flow of energy from the electrical to the mechanical system, accounting for these various losses. The same flow could be reversed if mechanical energy were converted to electrical form.

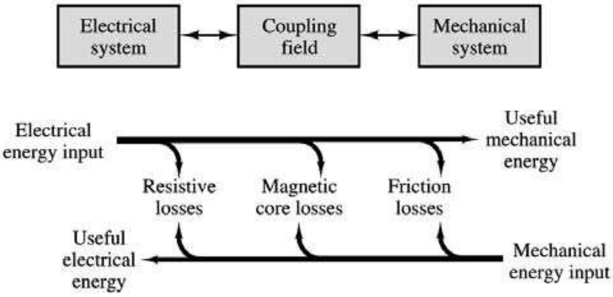

FIGURE 5.12.18 Electromechanical system.

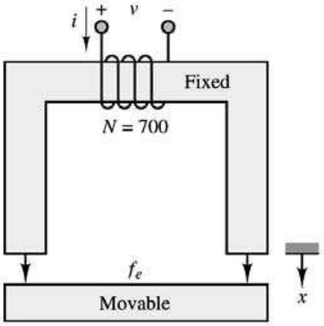

FIGURE 5.12.19 Simple electromagnet.

Moving-Iron Transducers

One important class of electromagnetomechanical transducers is that of **moving-iron transducers**. The aim of this section is to derive an expression for the magnetic forces generated by such transducers and to illustrate the application of these calculations to simple, yet common devices such as electromagnets, solenoids, and relays. The simplest example of a moving-iron transducer is the electromagnet of Figure 5.12.19, in which the U-shaped element is fixed and the bar is movable. In the following paragraphs, we shall derive a relationship between the current applied to the coil, the displacement of the movable bar, and the magnetic force acting in the air gap.

The principle that will be applied throughout the section is that in order for a mass to be displaced, some work needs to be done; this work corresponds to a change in the energy stored in the electromagnetic field, which causes the mass to be displaced. With reference to Figure 5.12.19, let f_e represent the magnetic force acting on the bar and x the displacement of the bar, in the direction shown. Then the net work into the electromagnetic field, W_m, is equal to the sum of the work done by the electrical circuit plus the work done by the mechanical system. On the basis of a linear approximation, it can be shown that the stored energy in a magnetic structure is given by the expression

$$W_m = \frac{\phi \mathcal{F}}{2} \tag{5.12.28}$$

and since the flux and the mmf are related by the expression

$$\phi = \frac{Ni}{\mathcal{R}} = \frac{\mathcal{F}}{\mathcal{R}} \tag{5.12.29}$$

the stored energy can be related to the reluctance of the structure according to

$$W_m = \frac{\phi^2 \mathcal{R}(x)}{2} \tag{5.12.30}$$

where the reluctance has been explicitly shown to be a function of displacement, as is the case in a moving-iron transducer. Finally, then, we shall use the following approximate expression to compute the magnetic force acting on the moving iron:

$$f = -\frac{dW_m}{dx} = -\frac{\phi^2}{2}\frac{d\mathcal{R}(x)}{dx} \tag{5.12.31}$$

Example 5.12.13 An Electromagnet

An electromagnet is used to support a solid piece of steel as shown in Figure 5.12.19. A force of 8900 N is required to support the weight. The cross-sectional area of the magnet core (the fixed part) is 0.01 m^2. Determine the minimum current that can keep the weight from falling for $x = 1.5$ mm. Assume negligible reluctance for the steel parts, and negligible fringing in the air gap.

Solution. We have already shown that in magnetic structures with air gaps, the reluctance is mostly due to the air gaps. This explains the assumption that the reluctance of the structure is negligible. For the structure of Figure 5.12.19, the reluctance is therefore given by

$$\mathcal{R}(x) = \frac{l}{\mu_0 A}$$

where $A = 0.01$ m^2 and $l = 2x$, and therefore

$$\mathcal{R}(x) = \frac{2x}{4\pi \times 10^{-7} \times 0.01} = \frac{x}{1.2566 \times 10^{-8}}$$

The magnitude of the force in the air gap is given by the expression

$$\begin{aligned}|f| &= \frac{\phi^2}{2}\frac{d\mathcal{R}(x)}{dx} = \frac{N^2 i^2}{2\mathcal{R}^2}\frac{d\mathcal{R}(x)}{dx} \\ &= \frac{i^2}{2}\frac{N^2}{\mathcal{R}^2}\frac{d\mathcal{R}}{dx} = \frac{i^2}{2}(700)^2\frac{6.2832 \times 10^{-9}}{x^2} = 8900 \text{ N}\end{aligned}$$

from which the current can be computed:

$$i^2 = 2 \times \frac{8900\left(1.5 \times 10^{-3}\right)^2}{(700)^2\left(6.2832 \times 10^{-9}\right)} 6.504 \text{ A}$$

or

$$i = 2.55 \text{ A}$$

You should recognize the practical importance of these calculations in determining approximate current requirements and force-generation capabilities of electromechanical transducers.

Moving-Coil Transducers

Another important class of electromagnetomechanical transducers is that of **moving-coil transducers**. This class of transducers includes a number of common devices, such as microphones, loudspeakers, and

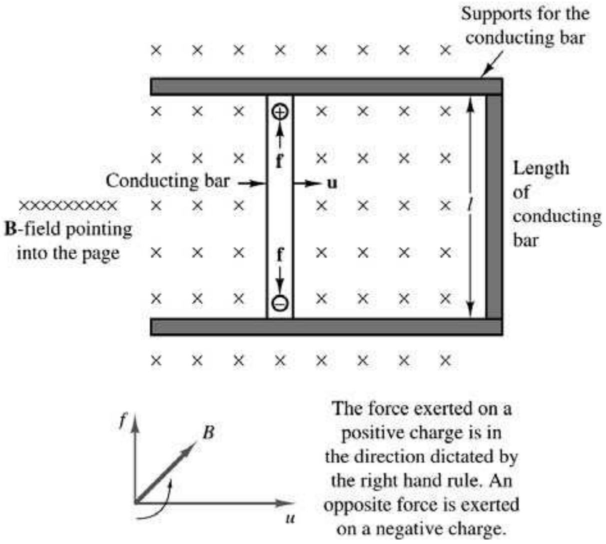

FIGURE 5.12.20 A simple electromechanical motion transducer.

all electric motors and generators. The aim of this section is to explain the relationship between a fixed magnetic field, the emf across the moving coil, and the forces and motions of the moving element of the transducer.

Motor Action. A moving-coil transducer can act as a motor when an externally supplied current flowing through the electrically conducting part of the transducer is converted into a force that can cause the moving part of the transducer to be displaced. Such a current would flow, for example, if the support of Figure 5.12.20 were made of conducting material, so that the conductor and the right-hand side of the support "rail" were to form a loop (in effect, a 1-turn coil).

The phenomenon we have just described is sometimes referred to as the "*Bli* law".

Generator Action. The other mode of operation of a moving-coil transducer occurs when an external force causes the coil (i.e., the moving bar, in Figure 5.12.20) to be displaced. This external force is converted to an emf across the coil, as will be explained in the following paragraphs.

It is important to observe that since positive and negative charges are forced in opposite directions in the transducer of Figure 5.12.20, a potential difference will appear across the conducting bar; this potential difference is the electromotive force, or emf. The emf must be equal to the force exerted by the magnetic field. In short, the electric force per unit charge (or electric field) e/l must equal the magnetic force per unit charge $f/q = Bu$. Thus, the relationship

$$e = Blu \tag{5.12.32}$$

which holds whenever **B, l,** and **u** are mutually perpendicular, as in Figure 5.12.20.

It was briefly mentioned that the *Blu* and *Bli* laws indicate that, thanks to the coupling action of the magnetic field, a conversion of mechanical to electrical energy — or the converse — is possible. The simple structure of Figures 5.12.20 can, again, serve as an illustration of this energy-conversion process, although we have not yet indicated how these idealized structures can be converted into a practical device. In this section we shall begin to introduce some physical considerations. Before we proceed any further, we should try to compute the power — electrical and mechanical — that is generated (or is required) by our ideal transducer. The electrical power is given by

$$P_E = ei = Blui \quad \text{(W)} \tag{5.12.33}$$

while the mechanical power required, say, to move the conductor from left to right is given by the product of force and velocity:

$$P_M - f_{\text{ext}}u = Bliu \quad (\text{W}) \tag{5.12.34}$$

Example 5.12.4 The Loudspeaker

A loudspeaker, shown in Figure 5.12.21, uses a permanent magnet and a moving coil to produce the vibrational motion that generates the pressure waves we perceive as sound. Vibration of the loudspeaker is caused by changes in the input current to a coil; the coil is, in turn, coupled to a magnetic structure that can produce time-varying forces on the speaker diaphragm. A simplified model for the mechanics of the speaker is also shown in Figure 5.12.21. The force exerted on the coil is also exerted on the mass of the speaker diaphragm, as shown in Figure 5.12.22, which depicts a free-body diagram of the forces acting on the loudspeaker diaphragm.

The force exerted on the mass, f_i, is the magnetic force due to current flow in the coil. The electrical circuit that describes the coil is shown in Figure 5.12.23, where L represents the inductance of the coil, R represents the resistance of the windings, and e is the emf induced by the coil moving through the magnetic field.

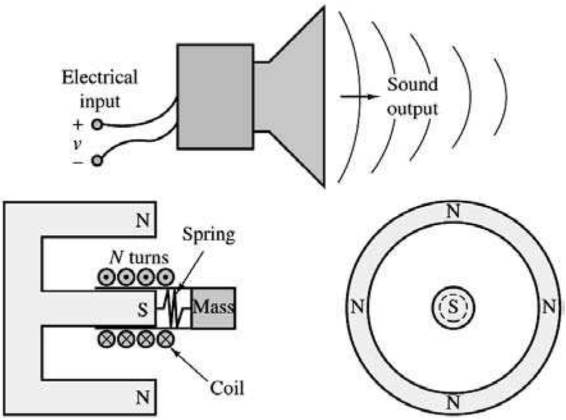

FIGURE 5.12.21 Loudspeaker.

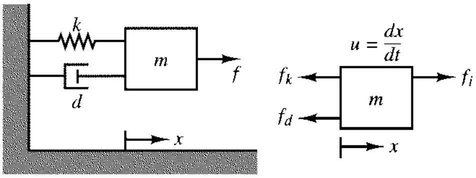

FIGURE 5.12.22 Forces acting on loudspeaker diaphragm.

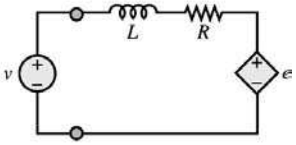

FIGURE 5.12.23 Model of transducer electrical field.

Determine the frequency response, (**U**/**V**)($j\omega$), of the speaker using phasor analysis if the model parameters are

$$L \approx 0 \text{ H} \qquad R = 8\ \Omega \qquad m = 0.001 \text{ kg} \qquad d = 22.75$$

$$k \approx 500{,}000 \text{ N/m} \qquad N = 47 \qquad B = 1T \qquad \text{Radius of coil} = 5 \text{ cm}$$

Solution: To determine the frequency response of the loudspeaker, we need to write the fundamental equations that describe the two subsystems that make up the loudspeaker. The electrical subsystem is described by the usual KVL relationship, applied to the circuit of Figure 5.12.23.

$$v = L\frac{di}{dt} + Ri + e$$

where e is the emf generated by the motion of the coil in the magnetic field. Next, according to Newton's law, we can write a force balance equation to describe the dynamics of the mechanical subsystem:

$$m\frac{du}{dt} = f_i - f_d - f_k = f_i - du - kx$$

Now, the coupling between the electrical and mechanical systems is expressed in each of the two preceding equations by the terms e and f_i:

$$e = Blu$$

$$f_i = Bli$$

Since we desire the frequency response, we use phasor techniques to represent the electrical and mechanical subsystem equations:

$$\mathbf{V}(j\omega) = j\omega L\mathbf{I}(j\omega) + R\mathbf{I}(j\omega) + Bl\mathbf{U}(j\omega) \qquad \text{Electrical equation}$$

$$(j\omega m + d)\mathbf{U}(j\omega) + \frac{K}{j\omega}\mathbf{U}(j\omega) = Bl\mathbf{I}(j\omega) \qquad \text{Mechanical equation}$$

Having assumed that the inductance of the coil is negligible, we are able to simplify the electrical equation and to solve for **I**($j\omega$):

$$\mathbf{I}(j\omega) = \frac{\mathbf{V}(j\omega) - Bl\mathbf{U}(j\omega)}{R}$$

Substituting this equivalence into the mechanical equation and accounting for the length of the coil, $l = 2\pi Nr$, the final expression for the frequency response of the loudspeaker is then given by

$$\frac{\mathbf{U}}{\mathbf{V}}(j\omega) = \frac{2\pi NBr}{Rm} \times \frac{j\omega}{(j\omega)^2 + j\omega\left(\dfrac{d + \dfrac{(2\pi)^2 B^2 N^2 r^2}{R}}{m}\right) + \dfrac{k}{m}}$$

or, numerically,

$$\frac{\mathbf{U}}{\mathbf{V}}(j\omega) = \frac{2\pi\times 47\times 1\times 0.05}{8(0.001)} \times \frac{j\omega}{(j\omega)^2 + j\omega\left(\dfrac{22.75+\dfrac{(2\pi)^2(1)^2(47)^2(0.05)^2}{8}}{0.001}\right)+\dfrac{500,000}{0.001}}$$

$$\approx \frac{1,845 j\omega}{\left(j\omega + 13.8\times 10^3\right)\left(j\omega + 36.2\times 10^3\right)}$$

$$= \frac{0.051\left(\dfrac{j\omega}{13.8\times 10^3}\right)}{\left(1+\dfrac{j\omega}{36.2\times 10^3}\right)\left(1+\dfrac{j\omega}{13.8\times 10^3}\right)}$$

This frequency response shows that the speaker has a lower cutoff frequency f_{ct} = 13,800/2π ≈ 2200 Hz and an upper cutoff frequency of f_{ch} = 36,000/2π ≈ 5800 Hz. In practice, a loudspeaker with such a frequency response would be useful only as a midrange speaker.

Rotating Electric Machines

The range of sizes and power ratings and the different physical features of rotating machines are such that the task of explaining the operation of rotating machines in a single chapter may appear formidable at first. Some features of rotating machines, however, are common to all such devices. This introductory section is aimed at explaining the common properties of all rotating electric machines. We begin our discussion with reference to Figure 5.12.24, in which a hypothetical rotating machine is depicted in a cross-sectional view. In the figure, a box with a cross inscribed in it indicates current flowing into the page, while a dot represents current out of the plane of the page.

In Figure 5.12.24, we identify a **stator**, of cylindrical shape, and a **rotor**, which, as the name indicates, rotates inside the stator, separated from the latter by means of an air gap. The rotor stator each consist of a magnetic core, some electrical insulation, and the windings necessary to establish a magnetic flux (unless this is created by a permanent magnet). The rotor is mounted on a bearing-supported shaft, which can be connected to *mechanical loads* (if the machine is a motor) or to a *prime mover* (if the machine is a generator) by means of belts, pulleys, chains, or other mechanical couplings. The windings carry the electric currents that generate the magnetic fields and flow to the electrical loads, and also provide the closed loops in which voltages will be induced (by virtue of Faraday's law, as discussed in the previous section).

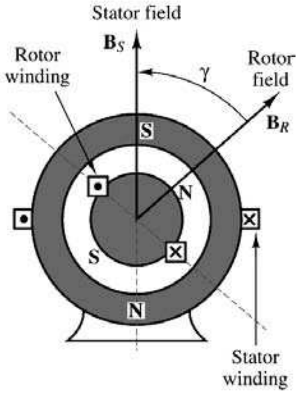

FIGURE 5.12.24 A rotating electric machine.

TABLE 5.12.4 Configurations of the Three Types of Electric Machines

Machine Type	Winding	Winding Type	Location	Current
DC	Input and output	Armature	Rotor	AC (winding) DC (at brushes)
	Magnetizing	Field	Stator	DC
Synchronous	Input and output	Armature	Stator	AC
	Magnetizing	Field	Rotor	DC
Induction	Input	Primary	Stator	AC
	Output	Secondary	Rotor	AC

Basic Classification of Electric Machines

An immediate distinction can be made between different types of windings characterized by the nature of the current they carry. If the current serves the sole purpose of providing a magnetic field and is independent of the load, it is called a *magnetizing*, or excitation, current, and the winding is termed a **field winding**. Field currents are nearly always DC and are of relatively low power, since their only purpose is to magnetize the core (recall the important role of high-permeability cores in generating large magnetic fluxes from relatively small currents). On the other hand, if the winding carries only the load current, it is called an **armature**. In DC and AC synchronous machines, separate windings exist to carry field and armature currents. In the induction motor, the magnetizing and load currents flow in the same winding, called the *input winding*, or *primary*; the output winding is then called the *secondary.* As we shall see, this terminology, which is reminiscent of transformers, is particularly appropriate for induction motors, which bear a significant analogy to the operation of the transformers. Table 5.12.4 characterizes the principal machines in terms of their field and armature configuration.

It is also useful to classify electric machines in terms of their energy-conversion characteristics. A machine acts as a **generator** if it converts mechanical energy from a prime mover — e.g., an internal combustion engine — to electrical form. Examples of generators are the large machines used in power-generating plants, or the common automotive alternator. A machine is classified as a **motor** if it converts electrical energy to mechanical form. The latter class of machines is probably of more direct interest to you, because of its widespread application in engineering practice. Electric motors are used to provide forces and torques to generate motion in countless industrial applications. Machine tools, robots, punches, presses, mills, and propulsion systems for electric vehicles are but a few examples of the application of electric machines in engineering.

Note that in Figure 5.12.24 we have explicitly shown the direction of two magnetic fields: that of the rotor, $\mathbf{B}_R$, and that of the stator, $\mathbf{B}_S$. Although these fields are generated by different means in differential machines (e.g., permanent magnets, AC currents, DC currents), the presence of these fields is what causes a rotating machine to turn and enables the generation of electric power. In particular, we see that in Figure 5.12.24 the north pole of the rotor field will seek to align itself with the south pole of the stator field. It is this magnetic attraction force that permits the generation of torque in an electric motor; conversely, a generator exploits the laws of electromagnetic induction to convert a changing magnetic field to an electric current.

To simplify the discussion in later sections, we shall presently introduce some basic concepts that apply to all rotating electric machines. Referring to Figure 5.12.25, we note that all machines the force on a wire is given by the expression

$$\mathbf{f} = i_w \mathbf{I} \times \mathbf{B} \tag{5.12.35}$$

where i_w is the current in the wire, $\mathbf{I}$ is a vector along the direction of the wire, and × denotes the cross product of two vectors. Then the torque for a multiturn coil becomes

$$T = KBi_w \sin\alpha \tag{5.12.36}$$

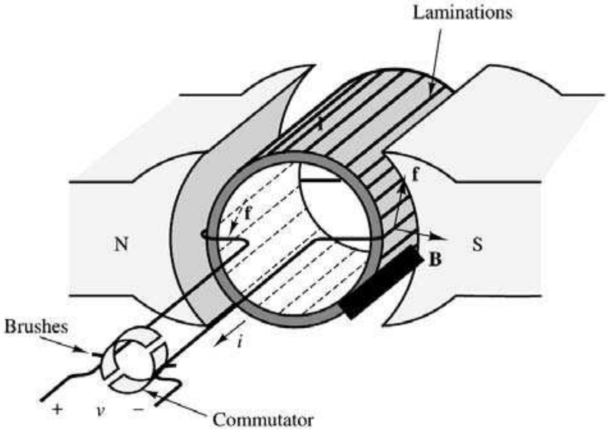

FIGURE 5.12.25 Stator and rotor fields and the force acting on a rotating machine.

where

B = magnetic flux density caused by the stator field
K = constant depending on coil geometry
α = angle between **B** and the normal to the plane of the coil

Other Characteristics of Electric Machines

As already stated earlier in this chapter, electric machines are **energy-conversion devices**, and we are therefore interested in their energy-conversion **efficiency**. Typical applications of electric machines as motors or generators must take into consideration the energy losses associated with these devices. Figure 5.12.26 represents the various loss mechanisms you must consider in analyzing the efficiency of an electric machine for the case of direct-current machines. It is important for you to keep in mind this conceptual flow of energy when analyzing electric machines. The sources of loss in a rotating machine can be separated into three fundamental groups: electrical (I^2R) losses, core losses, and mechanical losses.

I^2R losses are usually computed on the basis of the DC resistance of the windings at 75°C; in practice, these losses vary with operating conditions. The difference between the nominal and actual I^2R is usually lumped under the category of *stray-load loss*. In direct-current machines, it is also necessary to account for the *brush contact loss* associated with slip rings and commutators.

Mechanical losses are due to *friction* (mostly in the bearings) and *windage,* that is, the air drag force that opposes the motion of the rotor. In addition, if external devices (e.g., blowers) are required to circulate air through the machine for cooling purposes, the energy expended by these devices is also included in the mechanical losses.

Open-circuit core losses consist of hysteresis and eddy current losses, with only the excitation winding energized. Often these losses are summed with friction and windage losses to give rise to the *no-load rotational loss*. The latter quantity is useful if one simply wishes to compute efficiency. Since open-circuit core losses do not account for the changes in flux density caused by the presence of load currents, an additional magnetic loss is incurred that is not accounted for in this term. *Stray-load losses* are used to lump the effects of nonideal current distribution in the windings and of the additional core losses just mentioned. Stray-load losses are difficult to determine exactly and are often assumed to be equal to 1.0% of the output power for DC machines; these losses can be determined by experiment in synchronous and induction machines.

The performance of an electric machine can be quantified in a number of ways. In the case of an electric motor, it is usually portrayed in the form of a graphical **torque-speed characteristic.** The torque-speed characteristic of a motor describes how the torque supplied by the machine varies as a function of the speed of rotation of the motor for steady speeds. As we shall see in later sections, the torque-speed

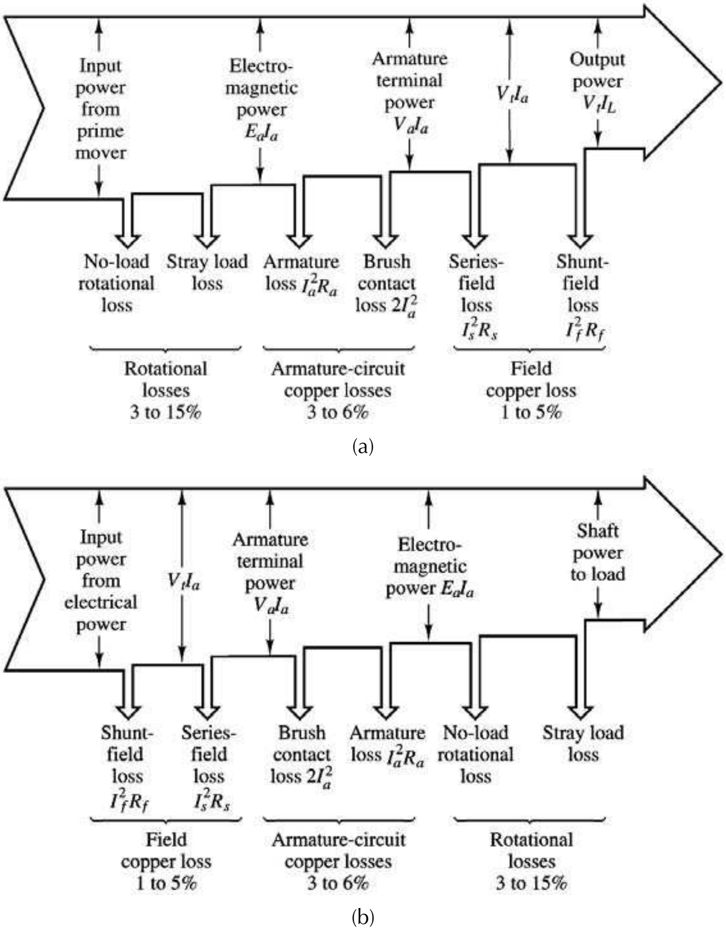

FIGURE 5.12.26 (a) Generator losses, direct current; (b) motor losses, direct current.

curves vary in shape with the type of motor (DC, induction, synchronous) and are very useful in determining the performance of the motor when connected to a mechanical load. Figure 5.12.27 depicts the torque-speed curve of a hypothetical motor. We shall presently describe the essential elements of such a graphical representation of motor performance, and we shall later return to analyze the typical performance curve of each type of motor we encounter in our discussion. It is quite likely that in most

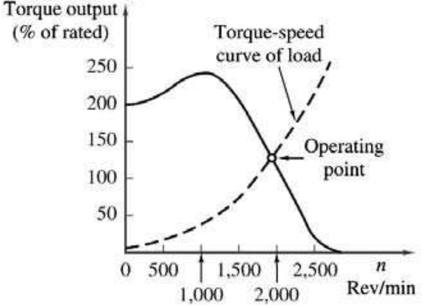

FIGURE 5.12.27 Torque-speed curve for an electric motor.

engineering applications, the engineer is required to make a decision regarding the performance characteristics of the motor best suited to a specified task. In this context, the torque-speed curve of a machine is a very useful piece of information.

The first feature we note of the torque-speed characteristic is that it bears a strong resemblance to the *i-v* characteristics used in earlier chapters to represent the behavior of electrical sources. It should be clear that, according to this torque-speed curve, the motor is not an ideal source of torque (if it were, the curve would appear as a horizontal line across the speed range). One can readily see, for example, that the hypothetical motor represented by the curves of Figure 5.12.27 would produce maximum torque in the range of speeds between approximately 800 and 1400 rev/min. What determines the actual speed of the motor (and therefore its output torque and power) is the torque-speed characteristic of the load connected to it, much as a resistive load determines the current drawn from a voltage source. In the figure, we display the torque-speed curve of a load, represented by the dashed line; the operating point of the motor-load pair is determined by the intersection of the two curves.

Another important observation pertains to the fact that the motor of Figure 5.12.27 produces a nonzero torque at zero speed. This fact implies that as soon as electric power is connected to the motor, the latter is capable of supplying a certain amount of torque; this zero-speed torque is called the **starting torque**. If the load the motor is connected to requires less than the starting torque the motor can provide, then the motor can accelerate the load, until the motor speed and torque settle to a stable value, at the operating point. The motor-load pair of Figure 5.12.27 would behave in the manner just described. However, there may well be circumstances in which a motor might not be able to provide a sufficient starting torque to overcome the static load torque that opposes its motion. Thus, we see that a torque-speed characteristic can offer valuable insight into the operation of a motor. As we proceed to discuss each type of machine in greater detail, we shall devote some time to the discussion of its torque-speed curve.

The most common means of conveying information regarding electric machines is the *nameplate*. Typical information conveyed by the nameplate is

1. Type of device (e.g., DC motor, alternator)
2. Manufacturer
3. Rated voltage and frequency
4. Rated current and volt-amperes
5. Rated speed and horsepower

The **rated voltage** is the terminal voltage for which the machine was designed, and which will provide the desired magnetic flux. Operation at higher voltages will increase magnetic core losses, because of excessive core saturation. The **rated current** and **rated volt-amperes** are an indication of the typical current and power levels at the terminal that will not cause undue overheating due to copper losses (I^2R losses) in the windings. These ratings are not absolutely precise, but they give an indication of the range of excitations for which the motor will perform without overheating. Peak power operation in a motor may exceed rated torque (horsepower) or currents by a substantial factor (up to as much as six or seven times the rated value); however, continuous operation of the motor above the rated performance will cause the machine to overheat, and possibly to sustain damage. Thus, it is important to consider both peak and continuous power requirements when selecting a motor for a specific application. An analogous discussion is valid for the speed rating: while an electric machine may operate above rated speed for limited periods of time, the large centrifugal forces generated at high rotational speeds will eventually cause undesirable mechanical stresses, especially in the rotor windings, leading eventually even to self-destruction.

Another important feature of electric machines is the **regulation** of the machine speed or voltage, depending on whether it is used as a motor or as a generator, respectively. Regulation is the ability to maintain speed or voltage constant in the face of load variations. The ability to closely regulate speed in a motor or voltage in a generator is an important feature of electric machines; regulation is often improved by means of feedback control mechanisms, some of which will be briefly introduced in this chapter. We shall take the following definitions as being adequate for the intended purpose of this chapter.

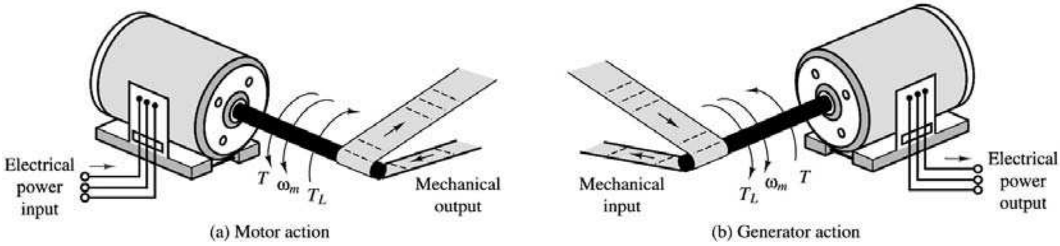

FIGURE 5.12.28 Generator and motor action in an electric machine.

$$\text{Speed regulation} = \frac{\text{Speed at no load} - \text{Speed at rated load}}{\text{Speed at rated load}} \tag{5.12.37}$$

$$\text{Voltage regulation} = \frac{\text{Voltage at no load} - \text{Voltage at rated load}}{\text{Voltage at rated load}} \tag{5.12.38}$$

Please note that the rated value is usually taken to be the nameplate value, and that the meaning of *load* changes depending on whether the machine is a motor, in which case the load is mechanical, or a generator, in which case the load is electrical.

Basic Operation of All Rotating Machines

We have already seen how the magnetic field in electromechanical devices provides a form of coupling between electrical and mechanical systems. Intuitively, one can identify two aspects of this coupling, both of which play a role in the operation of electric machines: (1) magnetic attraction and repulsion forces generate mechanical torque, and (2) the magnetic field can induce a voltage in the machine windings (coils) by virtue of Faraday's law. Thus, we may think of the operation of an electric machine in terms of either a motor or a generator, depending on whether the input power is electrical and mechanical power is produced (motor action), or the input power is mechanical and the output power is electrical (generator action). Figure 5.12.28 illustrates the two cases graphically.

The coupling magnetic field performs a dual role, which may be explained as follows. When a current i flow through conductors placed in a magnetic field, a force is produced on each conductor, according to Equation (5.12.35). If these conductors are attached to a cylindrical structure, a torque is generated, and if the structure is free to rotate, then it will rotate at an angular velocity ω_m. As the conductors rotate, however, they move through a magnetic field and cut through flux lines, thus generating an electromotive force in opposition to the excitation. This emf is also called "counter" emf; it opposes the source of the current i. If, on the other hand, the rotating element of the machine is driven by a prime mover (for example, an internal combustion engine), then an emf is generated across the coil that is rotating in the magnetic field (the armature). If a load is connected to the armature, a current i will flow to the load, and this current flow will in turn cause a reaction torque on the armature that opposes the torque imposed by the prime mover.

You see, then, that for energy conversion to take place, two elements are required: (1) a coupling field, **B**, usually generated in the field winding; and (2) an armature winding that supports the load current, i, and the emf, e.

Magnetic Poles in Electric Machines

Before discussing the actual construction of a rotating machine, we should spend a few paragraphs to illustrate the significance of **magnetic poles** in an electric machine. In an electric machine, torque is developed as a consequence of magnetic forces of attraction and repulsion between magnetic poles on the stator and on the rotor; these poles produce a torque that accelerates the rotor and a reaction torque on the stator. Naturally, we would like a construction such that the torque generated as a consequence

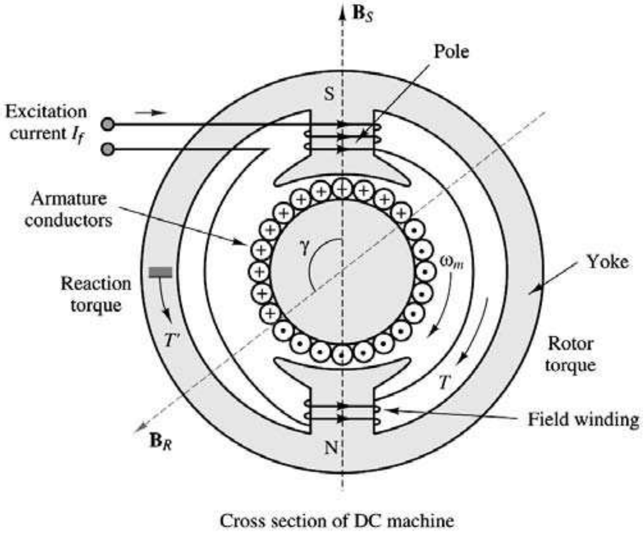

FIGURE 5.12.29 A two-pole machine with salient stator poles.

of the magnetic forces is continuous and in a constant direction. This can be accomplished if the number of rotor poles is equal to the number of stator poles. It is also important to observe that the number of poles must be even, since there have to be equal numbers of north and south poles.

Figure 5.12.29 depicts a two-pole machine in which the stator poles are constructed in such a way as to project closer to the rotor than to the stator structure. This type of construction is rather common, and poles constructed in this fashion are called **salient poles**. Note that the rotor could also be constructed to have salient poles.

To understand magnetic polarity, we need to consider the direction of the magnetic field in a coil carrying current. Figure 5.12.30 shows how the *right-hand rule* can be employed to determine the direction of the magnetic flux. If one were to grasp the coil with the right hand, with the fingers curling in the direction of current flow, then the thumb would be pointing in the direction of the magnetic flux. Magnetic flux is by convention viewed as entering the south pole and exiting from the north pole. Thus, to determine whether a magnetic pole is north or south, we must consider the direction of the flux. Figure 5.12.31 shows a cross section of a coil wound around a pair of salient rotor poles. In this case, one can readily identify the direction of the magnetic flux and therefore the magnetic polarity of the poles by applying the right-hand rule, as illustrated in the figure.

Often, however, the coil windings are not arranged as simply as in the case of salient poles. In many machines, the windings are embedded in slots cut into the stator or rotor, so that the situation is similar

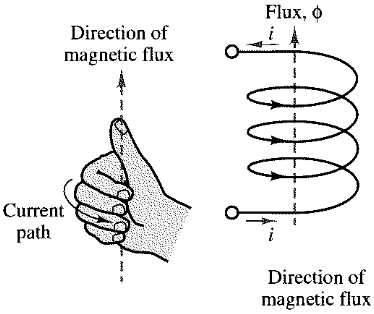

FIGURE 5.12.30 Right-hand rule.

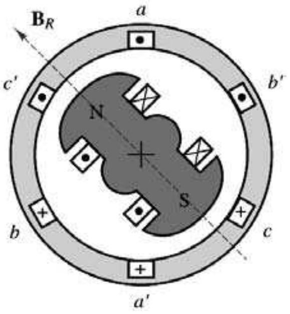

FIGURE 5.12.31 Magnetic field in a salient rotor winding.

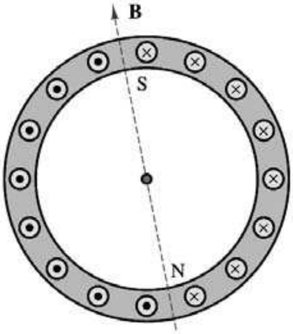

FIGURE 5.12.32 Magnetic field of stator.

to that of the stator depicted in Figure 5.12.32. This figure is a cross section in which the wire connections between "crosses" and "dots" have been cut away. In Figure 5.12.32, the dashed line indicates the axis of the stator flux according to the right-hand rule, indicating that the slotted stator in effect behaves like a pole pair. The north and south poles indicated in the figure are a consequence of the fact that the flux exits the bottom part of the structure (thus, the north pole indicated in the figure) and enters the top half of the structure (thus, the south pole). In particular, if you consider that the windings are arranged so that the current entering the right-hand side of the stator (to the right of the dashed line) flows through the back end of the stator and then flows outward from the left-hand side of the stator slots (left of the dashed line), you can visualize the windings in the slots as behaving in a manner similar to the coils of Figure 5.12.31, where the flux axis of Figure 5.12.32 corresponds to the flux axis of each of the coils of Figure 5.12.31. The actual circuit that permits current flow is completed by the front and back ends of the stator, where the wires are connected according to the pattern *a*-*a*′, *b*-*b*′, *c*-*c*′, as depicted in the figure.

Another important consideration that facilitates understanding the operation of electric machines pertains to the use of AC currents. It should be apparent by now that if the current flowing into the slotted stator is alternating, the direction of the flux will also alternate, so that in effect the two poles will reverse polarity every time the current reverses direction, that is, every half-cycle of the sinusoidal current. Further — since the magnetic flux is approximately proportional to the current in the coil — as the amplitude of the current oscillates in a sinusoidal fashion, so will the flux density in the structure. Thus, *the magnetic field developed in the stator changes both spatially and in time.*

This property is typical of AC machines, where a *rotating magnetic field* is established by energizing the coil with an alternating current. As we shall see in the next section, the principles underlying the operation of DC and AC machines are quite different: in a direct-current machine, there is no rotating field, but a mechanical switching arrangement (the *commutator*) makes it possible for the rotor and stator magnetic fields to always align at right angles to each other.

Direct-Current Machines

As explained in the introductory section, direct-current (DC) machines are easier to analyze than their AC counterparts, although their actual construction is made rather complex by the need to have a commutator, which reverses the direction of currents and fluxes to produce a net torque. The objective of this section is to describe the major construction features and the operation of direct-current machines, as well as to develop simple circuit models that are useful in analyzing the performance of this class of machines.

Physical Structure of DC Machines

A representative DC machine was depicted in Figure 5.12.29, with the magnetic poles clearly identified for both the stator and the rotor. Note the salient pole construction of the stator and the slotted rotor. As previously stated, the torque developed by the machine is a consequence of the magnetic forces between stator and rotor poles. This torque is maximum when the angle γ between the rotor and stator poles is 90°. Also, as you can see from the figure, in a DC machine the armature is usually on the rotor, and the field winding is on the stator.

To keep this torque angle constant as the rotor spins on its shaft, a mechanical switch, called a **commutator**, is configured so the current distribution in the rotor winding remains constant and therefore the rotor poles are consistently at 90° with respect to the fixed stator poles. In a DC machine, the magnetizing current is DC, so that there is no spatial alternation of the stator poles due to time-varying currents. To understand the operation of the commutator, consider the simplified diagram of Figure 5.12.33. In the figure, the brushes are fixed, and the rotor revolves at an angular velocity ω_m; the instantaneous position of the rotor is given by the expression $\theta = \omega_m t - \gamma$.

The commutator is fixed to the rotor and is made up in this example of six segments that are made of electrically conducting material but are insulated from each other. Further, the rotor windings are configured so that they form six coils, connected to the commutator segments as shown in Figure 5.12.33.

As the commutator rotates counterclockwise, the rotor magnetic field rotates with it up to $\theta = 30°$. At that point, the direction of the current changes in coils L_3 and L_6 as the brushes make contact with the next segment. Now the direction of the magnetic field is –30°. As the commutator continues to rotate, the direction of the rotor field will again change from –30° to +30°, and it will switch again when the brushes switch to the next pair of segments. In this machine, then, the torque angle, γ, is not always 90°, but can vary by as much as ±30°; the actual torque produced by the machine would fluctuate by as much as ±14%, since the torque is proportional to $\sin \gamma$. As the number of segments increases, the torque fluctuation produced by the commutation is greatly reduced. In a practical machine, for example, one might have as many as 60 segments, and the variation of γ from 90° would be only ±3°, with a torque fluctuation of less than 1%. Thus, the DC machine can produce a nearly constant torque (as a motor) or voltage (as a generator).

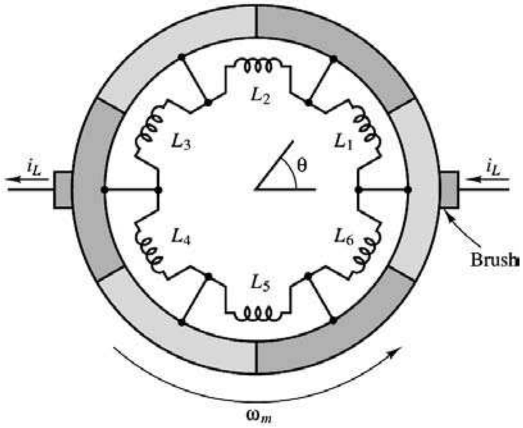

FIGURE 5.12.33 Rotor winding and commutator.

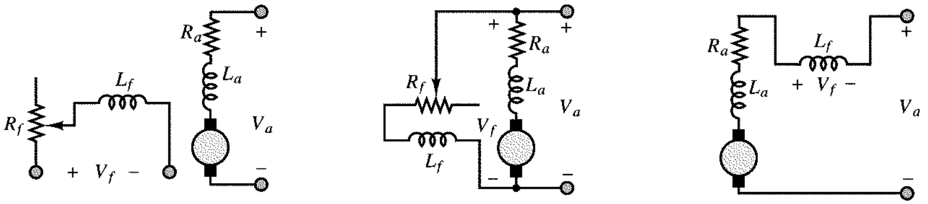

(a) Separately excited (b) Shunt connected (c) Series connected

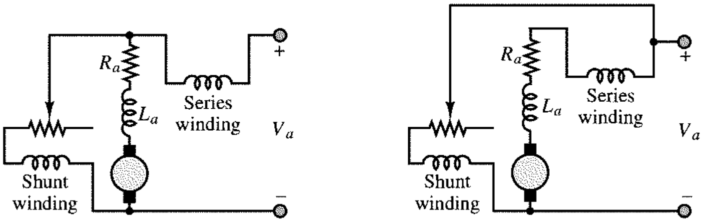

(d) Short-shunt compound connection (e) Long-shunt compound connection

FIGURE 5.12.34

Configuration of DC Machines

In DC machines, the field excitation that provides the magnetizing current is occasionally provided by an external source, in which case the machine is said to be **separately excited** (Figure 5.12.34(a)). More often, the field excitation is derived from the armature voltage and the machine is said to be **self-excited.** The latter configuration does not require the use of a separate source for the field excitation and is therefore frequently preferred. If a machine is in the separately excited configuration, an additional source, V_f, is required. In the self-excited case, one method used to provide the field excitation is to connect the field in parallel with the armature, since the field winding typically has significantly higher resistance than the armature circuit (remember that it is the armature that carries the load current), this will not draw excessive current from the armature. Further, a series resistor can be added to the field circuit to provide the means for adjusting the field current independent of the armature voltage. This configuration is called a **shunt-connected** machine and is depicted in Figure 5.12.34(b). Another method for self-exciting a DC machine consists of connecting the field in series with the armature, leading to the **series-connected** machine, depicted in Figure 5.12.34(c); in this case, the field winding will support the entire armature current, and thus the field coil must have low resistance (and therefore relatively few turns). This configuration is rarely used for generators, since the generated voltage and the load voltage must always differ by the voltage drop across the field coil, which varies with the load current. Thus, a series generator would have poor (large) regulation. However, series-connected motors are commonly used in certain applications, as will be discussed in a later section.

The third type of DC machine is the **compound-connected** machine, which consists of a combination of the shunt and series configurations. Figure 5.12.34(d) and Figure 5.12.34(e) show the two types of connections, called the **short shunt** and the **long shunt**, respectively. Each of these configurations may be connected so that the series part of the field adds to the shunt part (**cumulative compounding**) or so that it subtracts (**differential compounding**).

DC Machine Models

As stated earlier, it is relatively easy to develop a simple model of a DC machine, which is well suited to performance analysis, without the need to resort to the details of the construction of the machine itself. This section will illustrate the development of such models in two steps. First, steady-state models relating field and armature currents and voltages to speed and torque are introduced; second, the differential equations describing the dynamic behavior or DC machines are derived.

When a field excitation is established, a magnetic flux, ϕ, is generated by the field current, I_f. From Equation (5.12.36) we know that the torque acting on the rotor is proportional to the product of the magnetic field and the current in the load-carrying wire; the latter current is the armature current, I_a (i_w, in Equation 5.12.36). Assuming that, by virtue of the cummutator, the torque angle, γ, is kept very close to 90°, and therefore $\sin\gamma = 1$, we obtain the following expression for the torque (in units of N-m) in a DC machine:

$$T = k_T \phi I_a \qquad \text{for } \gamma = 90° \tag{5.12.39}$$

You may recall that this is simply a consequence of the *Bli* law of Chapter 15. The mechanical power generated (or absorbed) is equal to the product of the machine torque and the mechanical speed of rotation, ω_m (in rad/sec), and is therefore given by

$$P_m = \omega_m T = \omega_m k_T \phi I_a \tag{5.12.40}$$

Recall now that the rotation of the armature conductors in the field generated by the field excitation causes a **back emf**, E_b, in a direction that opposes the rotation of the armature. According to the *Blu* law then, this back emf is given by the expression.

$$E_b = k_a \phi \omega_m \tag{5.12.41}$$

where k_a is called the **armature constant** and is related to the geometry and magnetic properties of the structure. The voltage E_b represents a countervoltage (opposing the DC excitation) in the case of a motor, and the generated voltage in the case of a generator. Thus, the electric power dissipated (or generated) by the machine is given by the product of the back emf and the armature current:

$$P_e = E_b I_a \tag{5.12.42}$$

The constants k_T and k_a in Equation (5.12.39) and Equation (5.12.41) are related to geometry factors, such as the dimension of the rotor and the number of turns in the armature winding; and to properties of materials, such as the permeability of the magnetic materials. Note that in the ideal energy-conversion case, $P_m = P_e$, and therefore $k_a = k_T$. We shall, in general, assume such ideal conversion of electrical to mechanical (or vice versa) and will therefore treat the two constants as being identical: $k_a = k_T$. The constant k_a is given by

$$k_a = \frac{pN}{2\pi M} \tag{5.12.43}$$

where

p = number of magnetic poles
N = number of conductors per coil
M = number of parallel paths in armature winding

An important observation concerning the units of angular speed must be made at this point. The equality (under the no-loss assumption) between the constants k_a and k_T in Equation (5.12.39) and Equation (5.12.41) results from the choice of consistent units, namely, volts and amperes for the electrical quantities, and newton-meters and radians per second for the mechanical quantities. You should be aware that it is fairly common practice to refer to the speed of rotation of an electric machine in units of revolutions per minute (rev/min). In this book, we shall uniformly use the symbol n to denote angular speed in rev/min; the following relationship should be committed to memory:

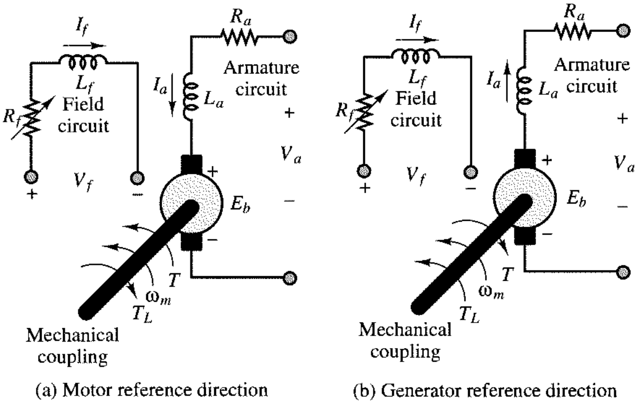

(a) Motor reference direction (b) Generator reference direction

FIGURE 5.12.35 Electrical circuit model of a separately excited DC machine.

$$n(\text{rev/min}) = \frac{60}{2\pi}\omega_m \ (\text{rad/sec}) \tag{5.12.44}$$

If the speed is expressed in rev/min, the armature constant changes as follows:

$$E_b = k'_a \phi n \tag{5.12.45}$$

where

$$k'_a = \frac{pN}{60M} \tag{5.12.46}$$

Having introduced the basic equations relating torque, speed, voltages, and currents in electric machines, we may now consider the interaction of these quantities in a DC machine at steady state, that is, operating at constant speed and field excitation. Figure 5.12.35 depicts the electrical circuit model of a separately excited DC machine, illustrating both motor and generator action. It is very important to note the reference direction of armature current flow and of the developed torque, in order to make a distinction between the two modes of operation. The field excitation is shown as a voltage, V_f, generating the field current, I_f, that flows through a variable resistor, R_f, and through the field coil, L_f. The variable resistor permits adjustment of the field excitation. The armature circuit, on the other hand, consists of a voltage source representing the back emf, E_b, the armature resistance, R_a, and the armature voltage, V_a. This model is appropriate both for motor and for generator action. When $V_a < E_b$, the machine acts as a generator (I_a flows out of the machine). When $V_a > E_b$, the machine acts as a motor (I_a flows into the machine). Thus, according to the circuit model of Figure 5.12.35, the operation of a DC machine at steady state (i.e., with the inductors in the circuit replaced by short circuits) is described by the following equations:

$$\begin{aligned} I_f &= \frac{V_f}{R_f} \quad \text{and} \quad V_a = R_a I_a + E_b \quad (\text{motor action}) \\ I_f &= \frac{V_f}{R_f} \quad \text{and} \quad V_a = -R_a I_a + E_b \quad (\text{generator action}) \end{aligned} \tag{5.12.47}$$

Equation pair (5.12.47) together with Equation (5.12.39) and Equation (5.12.41) may be used to determine the steady-state operating condition of a DC machine.

The circuit model of Figure 5.12.35 permits the derivation of a simple set of differential equations that describe the *dynamic* analysis of a DC machine. The dynamic equations describing the behavior of a separately excited DC machine are as follows:

$$V_a(t) = I_a(t)R_a + L_a \frac{dI_a(t)}{dt} + E_b(t) \qquad \text{(armature circuit)} \tag{5.12.48a}$$

$$V_f(t) = I_f(t)R_f + L_f \frac{dI_f(t)}{dt} \qquad \text{(field circuit)} \tag{5.12.48b}$$

These equations can be related to the operation of the machine in the presence of a load. If we assume that the motor is rigidly connected to an inertial load with moment of inertia J and that the friction losses in the load are represented by a viscous friction coefficient, b, then the torque developed by the machine (in the motor mode of operation) can be written as follows:

$$T(t) = T_L + b\omega_m(t) + J\frac{d\omega_m(t)}{dt} \tag{5.12.49}$$

where T_L is the load torque. T_L is typically either constant or some function of speed, ω_m, in a motor. In the case of a generator, the load torque is replaced by the torque supplied by a prime mover, and the machine torque, $T(t)$, opposes the motion of the prime mover, as shown in Figure 5.12.35. Since the machine torque is related to the armature and field currents by Equation (5.12.39), Equation (5.12.48) and Equation (5.12.49) are coupled to each other; this coupling may be expressed as follows:

$$T(t) = k_a\phi I_a(t) \tag{5.12.50}$$

or

$$k_a\phi I_a(t) = T_L + b\omega_m(t) + J\frac{d\omega_m(t)}{dt} \tag{5.12.51}$$

The dynamic equations described in this section apply to any DC machine. In the case of a *separately excited* machine, a further simplification is possible, since the flux is established by virtue of a separate field excitation, and therefore

$$\phi = \frac{N_f}{\mathcal{R}} I_f = k_f I_f \tag{5.12.52}$$

where N_f is the number of turns in the field coil, $\mathcal{R}$ is the reluctance of the structure, and I_f is the field current.

AC Machines

From the previous sections, it should be apparent that it is possible to obtain a wide range of performance characteristics from DC machines, as both motors and generators. A logical question at this point should be, would it not be more convenient in some cases to take advantage of the single- or multiphase AC power that is available virtually everywhere than to expend energy and use additional hardware to rectify and regulate the DC supplies required by direct-current motors? The answer to this very obvious question is certainly a resounding yes. In fact, the AC induction motor is the workhorse of many industrial applications, and synchronous generators are used almost exclusively for the generation of electric power worldwide. Thus, it is appropriate to devote a significant portion of this chapter to the study of AC machines, and of induction motors in particular. The objective if this section is to explain the basic operation of both synchronous and induction machines, and to outline their performance characteristics. In doing so, we shall also point out the relative advantages and disadvantages of these machines in comparison with direct-current machines.

Rotating Magnetic Fields

As mentioned in earlier, the fundamental principle of operation o AC machines is the generation of a rotating magnetic field, which causes the rotor to turn at a speed that depends on the speed of rotation of the magnetic field. We shall now explain how a rotating magnetic field can be generated in the stator and air gap of an AC machine by means of AC currents.

Consider the stator shown in Figure 5.12.36, which supports windings, *a-a′*, *b-b′*, and *c-c′*. The coils are geometrically spaced 120° apart, and a three-phase voltage is applied to the coils. As you may recall from the discussion of AC power in Section 5.5, the currents generated by a three-phase source are also spaced by 120°, as illustrated in Figure 5.12.37. The phase voltages referencing the neutral terminal would then be given by the expressions

$$v_a = A\cos(\omega_e t)$$

$$v_b = A\cos\left(\omega_e t - \frac{2\pi}{3}\right)$$

$$v_c = A\cos\left(\omega_e t + \frac{2\pi}{3}\right)$$

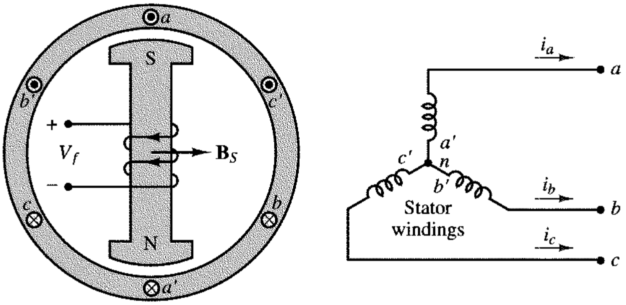

FIGURE 5.12.36 Two-pole three-phase stator.

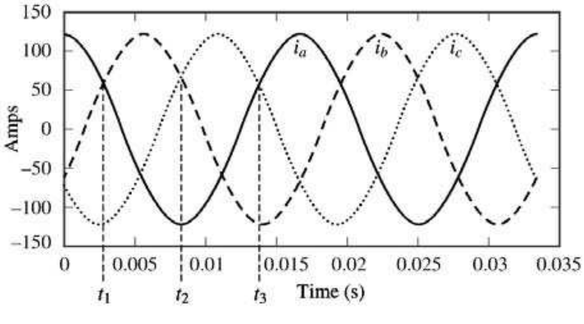

FIGURE 5.12.37 Three-phase stator winding currents.

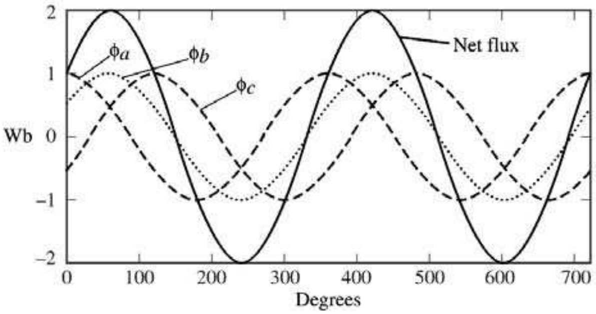

FIGURE 5.12.38 Flux distribution in a three-phase stator winding as a function of angle of rotation.

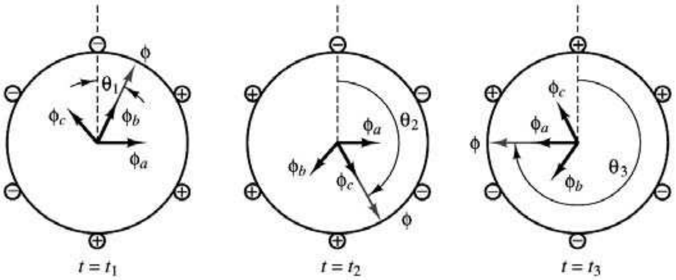

FIGURE 5.12.39 Rotating flux in a three-phase machine.

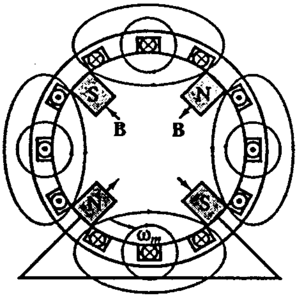

FIGURE 5.12.40 Four-pole stator.

where ω_e is the frequency of the AC supply, or line frequency. The coils in each winding are arranged in such a way that the flux distribution generated by any one winding is approximately sinusoidal. Such a flux distribution may be obtained by appropriately arranging groups of coils for each winding over the stator surface. Since the coils are spaced 120° apart, the flux distribution resulting from the sum of the contributions of the three windings is the sum of the fluxes due to the separate windings, as shown in Figure 5.12.38. Thus, the flux in a three-phase machine rotates in space according to the vector diagram of Figure 5.12.39, and is constant in amplitude. A stationary observer on the machine's stator would see a sinusoidally varying flux distribution as shown in Figure 5.12.38.

Since the resultant flux of Figure 5.12.38 is generated by the currents of Figure 5.12.37, the speed of rotation of the flux must be related to the frequency of the sinusoidal phase currents. In the case of the stator of Figure 5.12.36, the number of magnetic poles resulting from the winding configuration is two; however, it is also possible to configure the windings so that they have more poles. For example, Figure 5.12.40 depicts a simplified view of a four-pole stator.

In general, the speed of the rotating magnetic field is determined by the frequency of the excitation current, *f*, and by the number of poles present in the stator, *p*, according to the equation

$$n_s = \frac{120f}{p} \text{ rev/min}$$

or

$$\omega_s = \frac{2\pi n_s}{60} = \frac{2\pi \times 2f}{p} \tag{5.12.53}$$

where n_s (or ω_s) is usually called the **synchronous speed**.

The Induction Motor

The induction motor is the most widely used electric machine because of its relative simplicity of construction. The stator winding of an induction machine is similar to that of a synchronous machine; thus, the description of the three-phase winding of Figure 5.12.36 also applies to induction machines. The primary advantage of the induction machine, which is almost exclusively used as a motor (its performance as a generator is not very good), is that no separate excitation is required for the rotor. The rotor typically consists of one of two arrangements: **a squirrel cage** or a **wound rotor**. The former contains conducting bars short-circuited at the end and embedded within it; the latter consists of a multiphase winding similar to that used for the stator, but electrically short-circuited.

In either case, the induction motor operates by virtue of currents induced from the stator field in the rotor. In this respect, its operation is similar to that of a transformer, in that currents in the stator (which acts as a primary coil) induce currents in the rotor (acting as a secondary coil). In most induction motors, no external electrical connection is required for the rotor, thus permitting a simple, rugged construction, without the need for slip rings or brushes. Unlike the synchronous motor, the induction motor does not operate at synchronous speed, but at a somewhat lower speed, which is dependent on the load. Figure 5.12.41 illustrates the appearance of a squirrel-cage induction motor. The following discussion will focus mainly on this very common configuration.

You are by now acquainted with the notion of a rotating stator magnetic field. Imagine now that a squirrel-cage rotor is inserted in a stator in which such a rotating magnetic field is present. The stator field will induce voltages in the cage conductors, and if the stator field is generated by a three-phase source, the resulting rotor currents — which circulate in the bars of the squirrel cage, with the conducting path completed by the shorting rings at the end of the cage — are also three-phase, and are determined by the magnitude of the induced voltages and by the impedance of the rotor. Since the rotor currents are induced by the stator field, the number of poles and the speed of rotation of the induced magnetic field are the same as those of the stator field, *if the rotor is at rest.* Thus, when a stator field is initially applied, the rotor field is synchronous with it, and the fields are stationary with respect to each other. Thus, according to the earlier discussion, a *starting torque* is generated.

If the starting torque is sufficient to cause the rotor to start spinning, the rotor will accelerate up to its operating speed. However, an induction motor can never reach synchronous speed; if it did, the rotor would appear to be stationary with respect to the rotating stator field, since it would be rotating at the same speed. But in the absence of relative motion between the stator and rotor fields, no voltage would be induced in the rotor. Thus, an induction motor is limited to speeds somewhere below the synchronous speed, n_s. Let the speed of rotation of the rotor be n; then, the rotor is losing ground with respect to the rotation of the stator field at a speed $(n_s - n)$. In effect, this is equivalent to backward motion of the rotor at the **slip speed**, defined by $(n_s - n)$. The **slip**, s, is usually defined as a fraction of n_s:

$$s = \frac{n_s - n}{n_s} \tag{5.12.54}$$

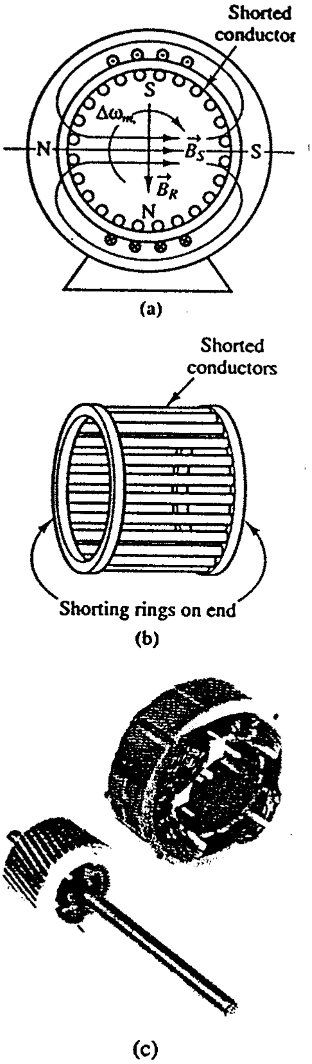

FIGURE 5.12.41 (a) Squirrel-cage induction motor; (b) conductors in rotor; (c) photo of squirrel-cage induction motor.

which leads to the following expression for the motor speed:

$$n = n_s(1 - s) \tag{5.12.55}$$

The slip, s, is a function of the load, and the amount of slip in a given motor is dependent on its construction and rotor type (squirrel cage or wound rotor). Since there is a relative motion between the stator and rotor fields, voltages will be induced in the rotor at a frequency called the **slip frequency**, related to the relative speed of the two fields. This gives rise to an interesting phenomenon: the rotor field travels relative to the rotor at the slip speed sn_s, but the rotor is mechanically traveling at the speed $(1 - s)n_s$, so that the net effect is that the rotor field travels at the speed

$$sn_s + (1 - s)n_s = n_s \tag{5.12.56}$$

that is, at synchronous speed. The fact that the rotor field rotates at synchronous speed — although the rotor itself does not — is extremely important, because it means that the stator and rotor fields will continue to be stationary with respect to each other, and therefore a net torque can be produced.

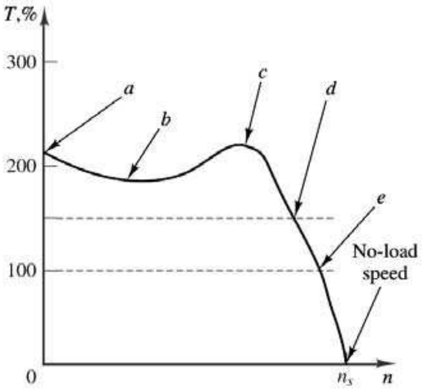

FIGURE 5.12.42 Performance curve for induction motor.

As in the case of DC and synchronous motors, important characteristics of induction motors are the starting torque, the maximum torque, and the torque-speed curve.

Performance of Induction Motors

The performance of induction motors can be described by torque-speed curves similar to those already used for DC motors. Figure 5.12.42 depicts an induction motor torque-speed curve, with five torque ratings marked *a* through *e*. Point *a* is the *starting torque*, also called **breakaway torque**, and is the torque available with the rotor "locked", that is, in a stationary position. At this condition, the frequency of the voltage induced in the rotor is highest, since it is equal to the frequency of rotation of the stator field; consequently, the inductive reactance of the rotor is greatest. As the rotor accelerates, the torque drops off, reaching a maximum value called the **pull-up torque** (point *b*); this typically occurs somewhere between 25 and 40% of synchronous speed. As the rotor speed continues to increase, the rotor reactance decreases further (since the frequency of the induced voltage is determined by the relative speed of rotation of the rotor with respect to the stator field). The torque becomes a maximum when the rotor inductive reactance is equal to the rotor resistance; maximum torque is also called **breakdown torque** (point *c*). Beyond this point, the torque drops off, until it is zero at synchronous speed, as discussed earlier. Also marked on the curve are the *150% torque* (point *d*), and the *rated torque* (point *e*).

A general formula for the computation of the induction motor steady-state torque-speed characteristic is

$$T = \frac{1}{\omega_e} \frac{m V_S^2 R_R / s}{\left[\left(R_S + \frac{R_R}{s}\right)^2 + \left(X_S + X_R\right)^2\right]} \tag{5.12.57}$$

where *m* is the number of phases.

Different construction arrangements permit the design of induction motors with different torque-speed curves, thus permitting the user to select the motor that best suits a given application. Figure 5.12.43 depicts the four basic classifications, classes A, B, C, and D, as defined by NEMA. The determining features in the classification are the locked-rotor torque and current, the breakdown torque, the pull-down torque, and the percent slip. Class A motors have a higher breakdown torque than class B motors, and a slip of 5% or less. Motors in this class are often designed for a specific application. Class B motors are general-purpose motors; this is the most commonly used type of induction motor, with typical values of slip of 3 to 5%. Class C motors have a high starting torque for a given starting current, and a low slip. These motors are typically used in applications demanding high starting torque but having relatively normal running loads, once running speed has been reached. Class D motors are characterized by high starting torque, high slip, low starting current, and low full-load speed. A typical value of slip is around 13%.

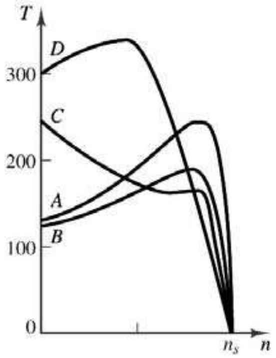

FIGURE 5.12.43 Induction motor classification.

Factors that should be considered in the selection of an AC motor for a given application are the *speed range*, both minimum and maximum, and the speed variation. For example, it is important to determine whether constant speed is required; what variation might be allowed, either in speed or in torque; or whether variable-speed operation is required, in which case a variable-speed drive will be needed. The torque requirements are obviously important as well. The starting and running torque should be considered; they depend on the type of load. Starting torque can vary from a small percentage of full-load to several times full-load torque. Furthermore, the excess torque available at start-up determines the *acceleration characteristics* of the motor. Similarly, *deceleration characteristics* should be considered, to determine whether external braking might be required.

Another factor to be considered is the *duty cycle* of the motor. The duty cycle, which depends on the nature of the application, is an important consideration when the motor is used in repetitive, noncontinuous operation, such as is encountered in some types of machine tools. If the motor operates at zero or reduced load for periods of time, the duty cycle — that is, the percentage of the time the motor is loaded — is an important selection criterion. Last, but by no means least, are the *heating properties* of a motor. Motor temperature is determined by internal losses and by ventilation; motors operating at a reduced speed may not generate sufficient cooling, and forced ventilation may be required.

Stepping Motors

Stepping, or **stepper, motors** are motors that convert digital information to mechanical motion. The principles of operation of stepping motors have been known since the 1920s; however, their application has seen a dramatic rise with the increased use of digital computers. Stepping motors, as the name suggests, rotate in distinct steps, and their position can be controlled by means of logic signals. Typical applications of stepping motors are line printers, positioning of heads in magnetic disks drives, and any other situation where continuous or stepwise displacements are required.

Stepping motors can generally be classified in one of three categories: variable-reluctance, permanent-magnet, and hybrid types. It will soon be shown that the principles of operation of each of these devices bear a definite resemblance to those of devices already encountered in this book. Stepping motors have a number of special features that make them particularly useful in practical applications. Perhaps the most important feature of a stepping motor is that the angle of rotation of the motor is directly proportional to the number of input pulses; further, the angle error per step is very small and does not accumulate. Stepping motors are also capable of rapid response to starting, stopping, and reversing commands, and can be driven directly by digital signals. Another important feature is a self-holding capability that makes it possible for the rotor to be held in the stopped position without the use of brakes. Finally, a wide range of rotating speeds — proportional to the frequency of the pulse signal — may be attained in these motors.

Figure 5.12.44 depicts the general appearance of three types of stepping motors. The **permanent-magnet-rotor stepping motor**, Figure 5.12.44(a), permits a nonzero holding torque when the motor is not energized. Depending on the construction of the motor, it is typically possible to obtain step angles

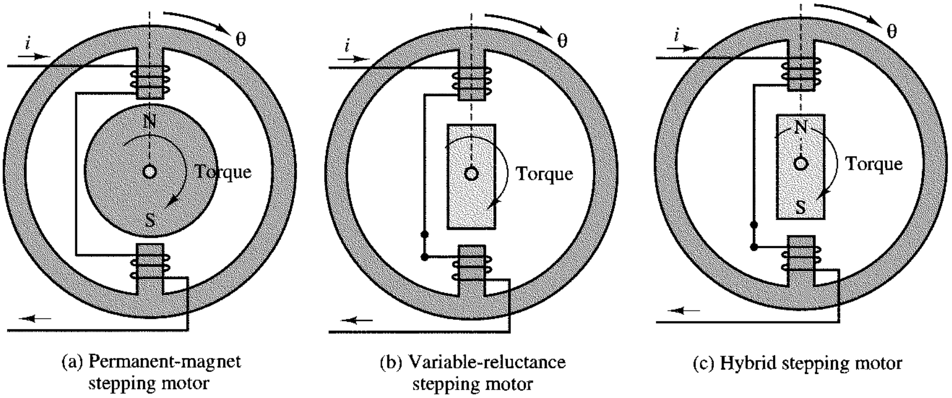

(a) Permanent-magnet stepping motor

(b) Variable-reluctance stepping motor

(c) Hybrid stepping motor

FIGURE 5.12.44 Stepping motor configurations.

of 7.5, 11.25, 15, 18, 45, or 90°. The angle of rotation is determined by the number of stator poles, as will be illustrated shortly in an example. The **variable-reluctance stepping motor,** Figure 5.12.44(b), has an iron multipole rotor and a laminated wound stator, and rotates when the teeth on the rotor are attracted to the electromagnetically energized stator teeth. The rotor inertia of a variable-reluctance stepping motor is low, and the response is very quick, but the allowable load inertia is small. When the windings are not energized, the static torque of this type of motor is zero. Generally, the step angle of the variable-reluctance stepping motor is 15°.

The **hybrid stepping motor**, Figure 5.12.44(c), is characterized by multitoothed stator and rotor, the rotor having an axially magnetized concentric magnet around its shaft. It can be seen that this configuration is a mixture of the variable-reluctance and permanent-magnet types. This type of motor generally has high accuracy and high torque and can be configured to provide a step angle as small as 1.8°.

For any of these configurations, the principle of operation is essentially the same: when the coils are energized, magnetic poles are generated in the stator, and the rotor will align in accordance with the direction of the magnetic field developed in the stator. By reversing the phase of the currents in the coils or by energizing only some of the coils (this is possible in motors with more than two stator poles), the alignment of the stator magnetic field can take one of a discrete number of positions; if the currents in the coils are pulsed in the appropriate sequence, the rotor will advance in a step-by-step fashion. Thus, this type of motor can be very useful whenever precise incremental motion must be attained. As mentioned earlier, typical applications are printer wheels, computer disk drives, and plotters. Other applications are found in the control of the position of valves (e.g., control of the throttle valve in an engine or of a hydraulic valve in a fluid power-system), and in drug-dispensing apparatus for clinical applications.

The Universal Motor

If it were possible to operate a DC motor from a single-phase AC supply, a wide range of simple applications would become readily available. Recall that the direction of the torque produced by a DC machine is determined by the direction of current flow in the armature conductors and by the polarity of the field; torque is developed in a DC machine because the commutator arrangement permits the field and armature currents to remain in phase, thus producing torque in a constant direction. A similar result can be obtained by using an AC supply, and by connecting the armature and field windings in series, as shown in Figure 5.12.45. A series DC motor connected in this configuration can therefore operate on a single-phase AC supply, and is referred to as a **universal motor**. An additional consideration is that, because of the AC excitation, it is necessary to reduce AC core losses by laminating the stator; thus, the universal motor differs from the series DC motor in its construction features. Typical torque-speed curves for AC and DC operation of a universal motor are shown in Figure 5.12.46. As shown in Figure 5.12.45,

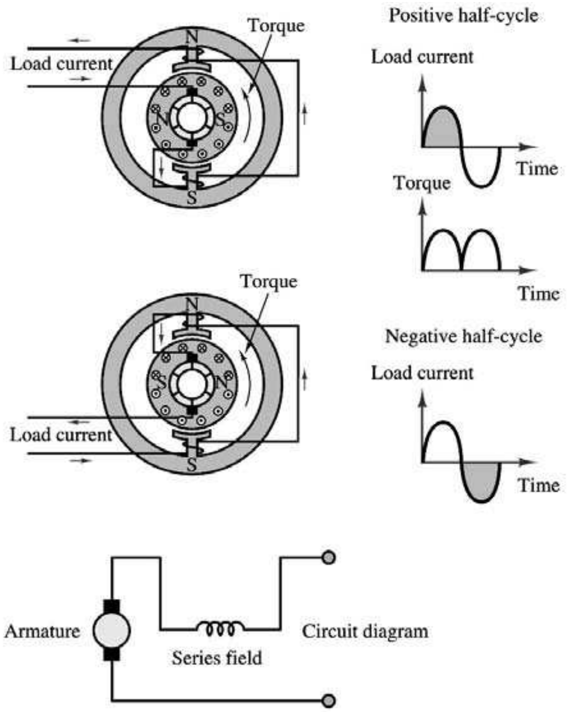

FIGURE 5.12.45 Operation and circuit diagram of a universal motor.

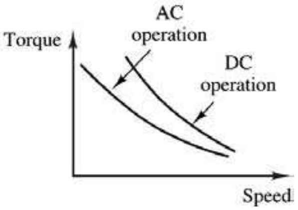

FIGURE 5.12.46 Torque-speed curve of a universal motor.

the load current is sinusoidal and therefore reverses direction each half-cycle; however, the torque generated by the motor is always in the same direction, resulting in a pulsating torque, with nonzero averaging value.

As in the case of a DC series motor, the best method for controlling the speed of a universal motor is to change its (rms) input voltage. The higher the rms input voltage, the greater the resulting speed of the motor. Approximate torque-speed characteristics of a universal motor as a function of voltage are shown in Figure 5.12.47.

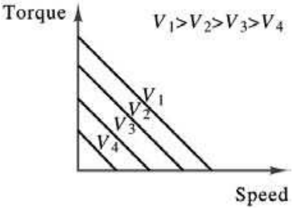

FIGURE 5.12.47 Torque-speed characteristics of a universal motor.

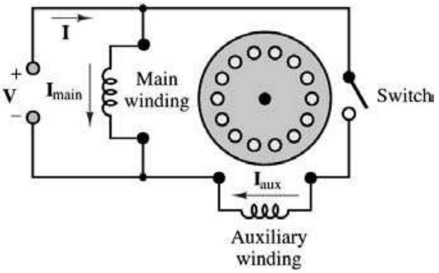

FIGURE 5.12.48 Split-phase motor.

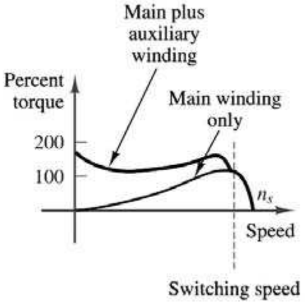

FIGURE 5.12.49 Torque-speed curve of split-phase motor.

Single-Phase Induction Motors

Thus far, we have not mentioned how the initial starting torque can be provided to a single-phase motor. In practice, single-phase motors are classified by their starting and running characteristics, and several methods exist to provide nonzero starting torque. The aim of this section is to classify single-phase motors by describing their configuration on the basis of the method of starting. For each class of motor, a torque-speed characteristic will also be described.

Split-Phase Motors

Split-phase motors are constructed with two separate stator windings, called **main** and **auxiliary windings**; the axes of the two windings are actually at 90° with respect to each other, as shown in Figure 5.12.48. The auxiliary winding current is designed to be out of phase with the main winding current, as a result of different reactances of the two windings. Different winding reactances can be attained by having a different ratio of resistance to inductance — for example, by increasing the resistance of the auxiliary winding. In particular, the auxiliary winding current, $\mathbf{I}_{aux}$, leads the main winding current, $\mathbf{I}_{main}$. The net effect is that the motor sees a two-phase (unbalanced) current that results in a rotating magnetic field, as in any polyphase stator arrangement. Thus, the motor has a nonzero starting torque, as shown in Figure 5.12.49. Once the motor, a centrifugal switch is used to disconnect the auxiliary winding, since a single winding is sufficient to sustain the motion of the rotor. The switching action permits the use of relatively high-resistance windings, since these are not used during normal operation and therefore one need not be concerned with the losses associated with a higher-resistance winding. Figure 5.12.49 also depicts the combined effect of the two modes of operation of the split-phase motor.

Split-phase motors have appropriate characteristics (at very low cost) for fans, blowers, centrifugal pumps, and other applications in the range of 1/20 to 1/2 hp.

Capacitor-Type Motors

Another method for obtaining a phase difference between currents that will give rise to a rotating magnetic field is by the addition of a capacitor. Motors that use this arrangement are termed **capacitor-type motors**. These motors make different use of capacitors to provide starting or running capabilities, or a combi-

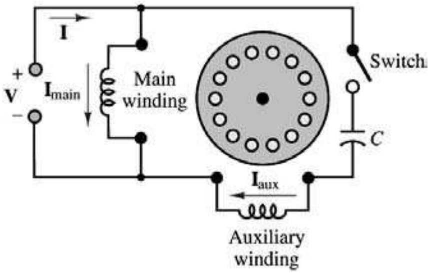

FIGURE 5.12.50 Capacitor-start motor.

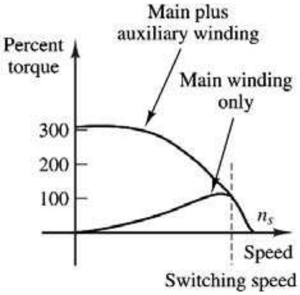

FIGURE 5.12.51 Torque-speed curve for a capacitor-start motor.

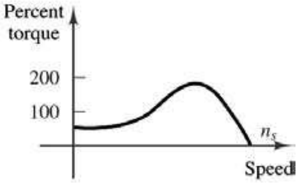

FIGURE 5.12.52 Torque-speed curve for a permanent split-capacitor motor.

nation of the two. The **capacitor-start motor** is essentially identical to the split-phase motor, except for the addition of a capacitor in series with the auxiliary winding, as shown in Figure 5.12.50. The addition of the capacitor changes the reactance of the auxiliary circuit in such a way as to cause the auxiliary current to lead the main current. The advantage of using the capacitor as a means for achieving a phase split is that greater starting torque may be obtained than with the split-phase arrangement. A centrifugal switching arrangement is used to disconnect the auxiliary winding above a certain speed, in the neighborhood of 75% of synchronous speed.

Figure 5.12.51 depicts the torque-speed characteristic of a capacitor-start motor. Because of their higher starting torque, these motors are very useful in connection with loads that present a high static torque. Examples of such loads are compressors, pumps, and refrigeration and air-conditioning equipment.

It is also possible to use the capacitor-start motor without the centrifugal switch, leading to a simpler design. Motors with this design are called **permanent split-capacitor motors**; they offer a compromise between running and starting characteristics. A typical torque-speed curve is shown in Figure 5.12.52.

A further compromise can be achieved by using two capacitors, one to obtain a permanent phase split and the resulting improvement in running characteristics, the other to improve the starting torque. A small capacitance is sufficient to improve the running performance, while a much larger capacitor provides the temporary improvement in starting torque. A motor with this design is called a **capacitor-start capacitor-run motor**; its schematic diagram is shown in Figure 5.12.53. Its torque-speed characteristic is similar to that of a capacitor-start motor.

Shaded-Pole Motors

The last type of single-phase induction motor discussed in this chapter is the **shaded-pole motor**. This type of motor operates on a different principle from the motors discussed thus far. The stator of a shaded-pole motor has a salient pole construction, as shown in Figure 5.12.54, that includes a shading coil

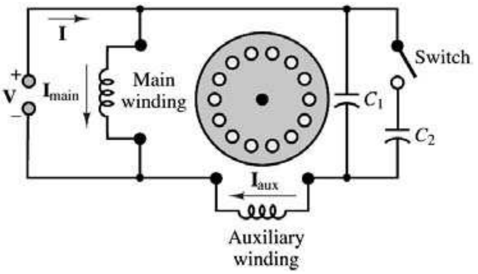

FIGURE 5.12.53 Capacitor-start capacitor-run motor.

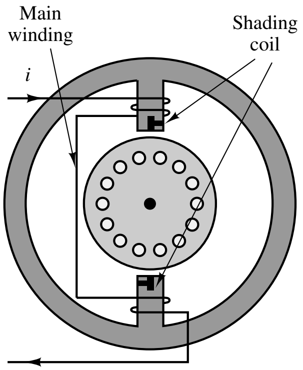

FIGURE 5.12.54 Shaded-pole motor.

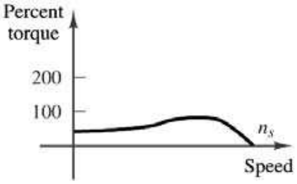

FIGURE 5.12.55 Torque-speed curve of a shaded-pole motor.

consisting of a copper band wound around part of each pole. The flux in the shaded portion of the pole lags behind the flux in the unshaded part, achieving an effect similar to a rotation of the flux in the direction of the shaded part of the pole. This flux rotation in effect produces a rotating field that enables the motor to have a starting torque. This construction technique is rather inexpensive and is used in motors up to about 1/20 hp.

A typical torque-speed characteristic for a shaded-pole motor is given in Figure 5.12.55.

Summary of Single-Phase Motor Characteristics

For basic classes of single-phase motors are commonly used:

1. Single-phase induction motors are used for the larger home and small business tasks, such as furnace oil burner pumps, or hot water or hot air circulators. Refrigerator compressors, lathes, and bench-mounted circular saws are also powered with induction motors.
2. Shaded-pool motors are used in the smaller sizes for quite, low-cost applications. The size range is for 1/30 hp (24.9 W) to 1/2 hp (373 W), particularly for fans and similar drives in which the starting torque is low.
3. Universal motors will operate on any household AC frequency or on DC without modification or adjustment. They can develop very high speed while loaded, and very high power for their size. Vacuum cleaners, sewing machines, kitchen food mixers, portable electric drills, portable circular saws, and home motion-picture projectors are examples of applications of universal motors.
4. The capacitor-type motor finds its widest field of application at low speeds (below 900 rev/min) and in ratings from 3/4 hp (0.5595 kW) to 3 hp (2.238 kW) at all speeds, especially in fan drives.

References

Section 2

Irwin, J.D., 1989. *Basic Engineering Circuit Analysis,* 3rd ed. Macmillan, New York.

Nilsson, J.W., 1989. *Electric Circuits,* 3rd ed. Addison-Wesley, Reading, MA.

Rizzoni, G., 1966. *Principles and Applications of Electrical Engineering,* 2nd ed. Richard D. Irwin, Burr Ridge, IL.

Smith, R.J. and Dorf, R.C., 1992. *Circuits, Devices and Systems,* 5th ed. John Wiley & Sons, New York.

1993. *The Electrical Engineering Handbook,* CRC Press, Boca Raton, FL.

Section 3

Irwin, J.D., 1989. *Basic Engineering Circuit Analysis,* 3rd ed. Macmillan, New York.

Nilsson, J.W., 1989. *Electric Circuits,* 3rd ed. Addison-Wesley, Reading, MA.

Rizzoni, G., 1966. *Principles and Applications of Electrical Engineering,* 2nd ed. Richard D. Irwin, Burr Ridge, IL.

Smith, R.J. and Dorf, R.C., 1992. *Circuits, Devices and Systems,* 5th ed. John Wiley & Sons, New York.

1993. *The Electrical Engineering Handbook,* CRC Press, Boca Raton, FL.

Section 4

Budak, A., *Passive and Active Network Analysis and Synthesis*, Houghton Mifflin, Boston.

Irwin, J.D., 1989. *Basic Engineering Circuit Analysis,* 3rd ed. Macmillan, New York.

Nilsson, J.W., 1989. *Electric Circuits,* 3rd ed. Addison-Wesley, Reading, MA.

Rizzoni, G., 1966. *Principles and Applications of Electrical Engineering,* 2nd ed. Richard D. Irwin, Burr Ridge, IL.

Smith, R.J. and Dorf, R.C., 1992. *Circuits, Devices and Systems,* 5th ed. John Wiley & Sons, New York.

Van Valkenburg, M.E., 1982, *Analog Filter Design,* Holt, Rinehart & Winston, New York.

1993. *The Electrical Engineering Handbook,* CRC Press, Boca Raton, FL.

Section 5

Del Toro, V., 1992. *Electric Power Systems,* Prentice-Hall, Englewood Cliffs, NJ.

Nilsson, J.W., 1989. *Electric Circuits,* 3rd ed. Addison-Wesley, Reading, MA.

Rizzoni, G., 1966. *Principles and Applications of Electrical Engineering,* 2nd ed. Richard D. Irwin, Burr Ridge, IL.

Smith, R.J. and Dorf, R.C., 1992. *Circuits, Devices and Systems,* 5th ed. John Wiley & Sons, New York.

1993. *The Electrical Engineering Handbook,* CRC Press, Boca Raton, FL.

Section 6

Irwin, J.D., 1989. *Basic Engineering Circuit Analysis,* 3rd ed. Macmillan, New York.

Nilsson, J.W., 1989. *Electric Circuits,* 3rd ed. Addison-Wesley, Reading, MA.

Rizzoni, G., 1966. *Principles and Applications of Electrical Engineering,* 2nd ed. Richard D. Irwin, Burr Ridge, IL.

Smith, R.J. and Dorf, R.C., 1992. *Circuits, Devices and Systems,* 5th ed. John Wiley & Sons, New York.

1993. *The Electrical Engineering Handbook,* CRC Press, Boca Raton, FL.

Section 7

Horowitz, P. and Hill, W., 1989. *The Art of Electronics,* 2nd ed. Cambridge University Press, New York.

Millman, J. and Grabel, A., 1987. *Microelectronics.* McGraw-Hill, New York.

Sedra, A.S. and Smith, K.C., 1991. *Microelectronic Circuits,* 3rd ed. W.B. Saunders, Philadelphia.

Neamen, D.A., 1994. *Semiconductor Physics and Devices.* Richard D. Irwin, Burr Ridge, IL.
Rizzoni, G., 1966. *Principles and Applications of Electrical Engineering,* 2nd ed. Richard D. Irwin, Burr Ridge, IL.
Streetman, B.G., 1990. *Solid State Electronic Devices,* 3rd ed. Prentice-Hall, Englewood Cliffs, NJ.
Sze, S.M., 1981. *Physics of Semiconductor Devices,* 2nd ed. Wiley, New York.
1993. *The Electrical Engineering Handbook,* CRC Press, Boca Raton, FL.

Section 8

Bose, B.K., 1986. *Power Electronics and AC Drives,* Prentice-Hall, Englewood Cliffs, NJ.
Mohan, N., Undeland, T.M., and Robbins, P., *Power Electronics*, Van Nostrand, New York.
Rashid, M.H., 1988. *Power Electronics,* Prentice-Hall, Englewood Cliffs, NJ.
Rizzoni, G., 1966. *Principles and Applications of Electrical Engineering,* 2nd ed. Richard D. Irwin, Burr Ridge, IL.
1993. *The Electrical Engineering Handbook,* CRC Press, Boca Raton, FL.

Section 9

Horowitz, P. and Hill, W., 1989. *The Art of Electronics,* 2nd ed. Cambridge University Press, New York.
Millman, J. and Grabel, A., 1987. *Microelectronics.* McGraw-Hill, New York.
Rizzoni, G., 1966. *Principles and Applications of Electrical Engineering,* 2nd ed. Richard D. Irwin, Burr Ridge, IL.
Kennedy, E.J., 1988. *Operational Amplifier Circuits,* Holt, Rinehart & Winston, New York.
1993. *The Electrical Engineering Handbook,* CRC Press, Boca Raton, FL.

Section 10

Breeding, K.J., 1992. *Digital Design Fundamentals,* 2nd ed. Prentice-Hall, Englewood Cliffs, NJ.
Horowitz, P. and Hill, W., 1989. *The Art of Electronics,* 2nd ed., Cambridge University Press, New York.
Mano, M.M., 1988. *Computer Engineering Hardware Design,* Prentice-Hall, Englewood Cliffs, NJ.
Rizzoni, G., 1966. *Principles and Applications of Electrical Engineering,* 2nd ed. Richard D. Irwin, Burr Ridge, IL.
Sandige, R.S., 1990. *Modern Digital Design.* McGraw-Hill, New York.
1993. *The Electrical Engineering Handbook,* CRC Press, Boca Raton, FL.

Section 11

Doebelin, E.O., 1990. *Measurement Systems: Application and Design,* 4th ed. McGraw-Hill, New York.
Annino, R. and Driver, R., 1986. *Scientific and Engineering Applications with Personal Computers.* Wiley-Interscience, New York.
Horowitz, P. and Hill, W., 1989. *The Art of Electronics,* 2nd ed., Cambridge University Press, New York.
Nachitgal, C. (ed.), 1990. *Instrumentation and Control: Fundamentals and Applications.* John Wiley & Sons, New York.
Rizzoni, G., 1966. *Principles and Applications of Electrical Engineering,* 2nd ed. Richard D. Irwin, Burr Ridge, IL.
Webster, J.G., 1992. *Medical Instrumentation: Application and Design,* 2nd ed. Houghton Mifflin, Boston.
1993. *The Electrical Engineering Handbook,* CRC Press, Boca Raton, FL.

Section 12

Del Toro, V., 1990. *Basic Electric Machines.* Prentice-Hall, Englewood Cliffs, NJ.
Fitzgerald, A.E., Kingsley, C., and Umans, S., 1990. *Electric Machinery*, 5th ed. McGraw-Hill, New York.

Krause, P. and Wasynczuk, O., 1989. *Electromechanical Motion Devices.* McGraw-Hill, New York.

Rizzoni, G., 1966. *Principles and Applications of Electrical Engineering,* 2nd ed. Richard D. Irwin, Burr Ridge, IL.

1993. *The Electrical Engineering Handbook,* CRC Press, Boca Raton, FL.

6

Mechanical System Controls

Thomas B. Sheridan
Massachussetts Institute of Technology

Peter S. Curtiss
Curtiss Engineering

Jan F. Kreider
Kreider & Associates

Ronald M. Nelson
Iowa State University

Shou-Heng Huang
Raytheon Co. Appliance Tech Center

6.1 Human–Machine Interaction

Thomas B. Sheridan

Over the years, machines of all kinds have improved and become more reliable. However, machines typically operate as components of larger systems, such as transportation, communication, manufacturing, defense, health care, and so on. Although many aspects of such systems can be and have been automated, the human operator is retained in many cases. This may be because of economics, tradition, cost, or (most likely) capabilities of the human to perceive patterns of information and weigh subtle factors in making control decisions, which the machine cannot match.

Although the public as well as those responsible for system operation usually demand a human operator, "human error" is a major reason for system failure. Aside from prevention of error, getting the best performance out of the system means that human and machine must be working together effectively — that they be properly "impedance matched." Therefore, the performance capabilities of the human relative to those of the machine must be taken into account in system design.

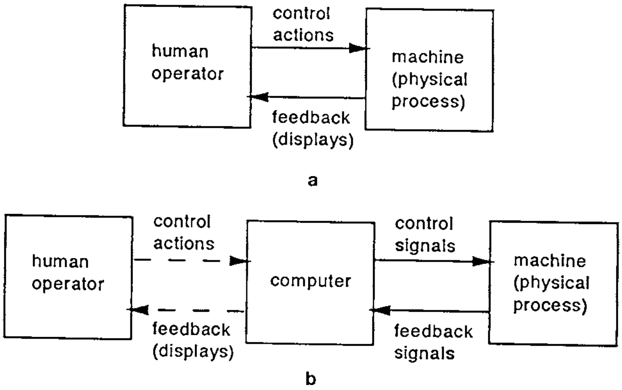

FIGURE 6.1.1 Direct manual control (a) and supervisory control (b).

Efforts to "optimize" the human–machine interaction are meaningless in the mathematical sense of optimization because most important interactions between human and machine cannot be reduced to a mathematical form, and the objective function (defining what is good) is not easily obtained in any given context. For this reason, engineering the human–machine interaction, much as in management or medicine, remains an art more than a science based on laboratory experiments and practical experience.

In the broadest sense, engineering the human–machine interface includes all of *ergonomics* or *human factors engineering,* and goes well beyond design of displays and control devices. Ergonomics includes not only questions of sensory physiology (whether the operator can see the displays or hear the auditory warnings), but also questions of *biomechanics* — how the body moves and whether the operator can reach and apply proper force to the controls. It further includes the fields of operator selection and training; human performance under stress; human factors in maintenance; and many other aspects of the relation of the human to technology. This section focuses primarily on human–machine interaction in control of systems.

The human–machine interactions in control are considered in terms of Figure 6.1.1. In Figure 6.1.1a, the human directly controls the machine, i.e., the control loop to the machine is closed through physical sensors; displays; human senses (visual, auditory, tactile); brain; human muscles; control devices; and machine actuators. Figure 6.1.1b illustrates what has come to be called a *supervisory control system*, wherein the human intermittently instructs a computer as to goals, constraints, and procedures, then turns a task over to the computer to perform automatic control for some period of time.

Displays and control devices can be *analogic* (movement signal directions and extent of control action; isomorphic with the world, such as an automobile steering wheel or computer mouse controls; or a moving needle or pictorial display element). On the other hand, they can be *symbolic* (dedicated buttons or general purpose keyboard controls, icons or alarm light displays). In normal human discourse, speech (symbolic) and gestures (analogic) are used and alphanumeric text (symbolic) and draw pictures (analogic) are written on paper. The system designer must decide which types of displays or controls best suit a particular application and/or what mix to use. The designer must be aware of important criteria such as whether, for a proposed design, changes in the displays and controls caused by the human operator correspond in a natural and common-sense way to "more" or "less" of some variable as expected by that operator and correspond to cultural norms (such as reading from left to right in western countries), and whether the movement of the display elements correspond geometrically to movements of the controls.

Direct Manual Control

In the 1940s, aircraft designers appreciated the need to characterize the transfer function of the human pilot in terms of a differential equation. Indeed, this is necessary for any vehicle or controlled physical process for which the human is the controller (see Figure 6.1.2). In this case, the human operator **H** and

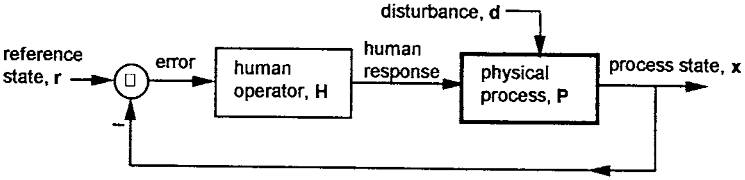

FIGURE 6.1.2 Direct manual control loop analysis.

the physical process **P** lie in the closed loop (where **H** and **P** are Laplace transforms of the component transfer functions), and the **HP** combination determines whether the closed loop is inherently stable (i.e., the closed loop characteristic equation $1 + HP = 0$ has only negative real roots).

In addition to the stability criterion are the criteria of rapid response of process state **x** to a desired or reference state **r** with minimum overshoot, zero steady state error between **r** and output **x**, and reduction to near zero of the effects of any disturbance input **d**. (The latter effects are determined by the closed loop transfer functions $\mathbf{x} = \mathbf{HP}/(1 + \mathbf{HP})\ \mathbf{r} + 1/(1 + \mathbf{HP})\ \mathbf{d}$, where, if the magnitude of **H** is large enough, $\mathbf{HP}/(1 + \mathbf{HP})$ approaches unity and $1/(1 + \mathbf{HP})$ approaches 0. Unhappily, some ingredients of **H** produce delays in combination with magnitude and thereby can cause instability. Therefore, **H** must be chosen carefully by the human for any given **P**.)

Research to characterize the pilot in these terms resulted in the discovery that the human adapts to a wide variety of physical processes so as to make $\mathbf{HP} = \mathbf{K}(1/\mathbf{s})(e^{-sT})$. In other words, the human adjusts **H** to make **HP** constant. The term **K** is an overall amplitude or gain; $(1/\mathbf{s})$ is the Laplace transform of an integrator; and (e^{-sT}) is a delay **T** long (the latter time delay is an unavoidable property of the nervous system). Parameters **K** and **T** vary modestly in a predictable way as a function of the physical process and the input to the control system. This model is now widely accepted and used, not only in engineering aircraft control systems, but also in designing automobiles, ships, nuclear and chemical plants, and a host of other dynamic systems.

Supervisory Control

Supervisory control may be defined by the analogy between a supervisor of subordinate staff in an organization of people, and the human overseer of a modern computer-mediated semiautomatic control system. The supervisor gives human subordinates general instructions that they in turn may translate into action. The supervisor of a computer-controlled system does the same.

Defined strictly, *supervisory control* means that one or more human operators are setting initial conditions for, intermittently adjusting, and receiving high-level information from a computer that closes a control loop in a well-defined process through artificial sensors and effectors. For some time period, the computer controls the process automatically.

By a less strict definition "supervisory control" is used when a computer transforms human operator commands to generate detailed control actions, or makes significant transformations of measured data to produce integrated summary displays. In this latter case the computer need not have the capability to commit actions based upon new information from the environment, whereas in the first it necessarily must. The two situations may appear similar to the human supervisor because the computer mediates human outputs and inputs, and the supervisor is thus removed from detailed events at the low level.

A supervisory control system is represented in Figure 6.1.3. Here the human operator issues commands to a *human-interactive* computer capable of understanding high-level language and providing integrated summary displays of process state information back to the operator. Typically located in a control room, cockpit, or office near the supervisor, this computer in turn communicates with at least one, and probably many (thus the dotted lines), *task-interactive* computers located with the equipment they are controlling. The task-interactive computers thus receive subgoal and conditional branching information from the

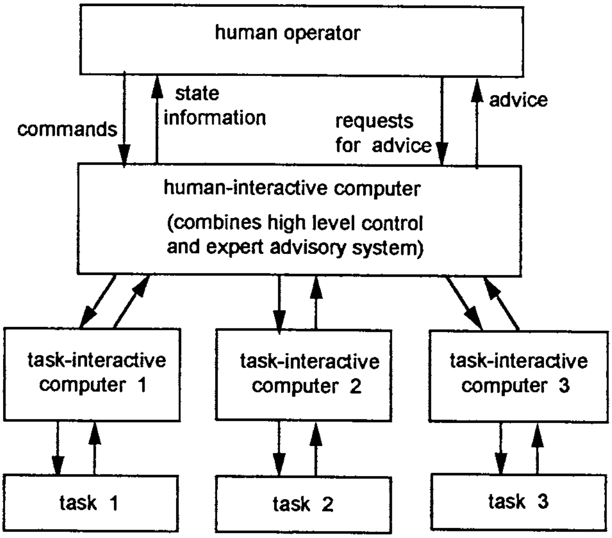

FIGURE 6.1.3 Supervisory control.

human-interactive computer. Using such information as reference inputs, task-interactive computers serve to close low-level control loops between artificial sensors and mechanical actuators, i.e., they accomplish the low-level automatic control.

The low-level task typically operates at some physical distance from the human operator and his human-friendly, display-control computer. Therefore, the communication channels between computers may be constrained by multiplexing, time delay, or limited bandwidth. The task-interactive computer, of course, sends analog control signals to and receives analog feedback signals from the controlled process, and the latter does the same with the environment as it operates (vehicles moving relative to air, sea, or Earth; robots manipulating objects; process plants modifying products; etc.).

Supervisory command and feedback channels for process state information are shown in Figure 6.1.3 to pass through the left side of the human-interactive computer. On the right side are represented decision-aiding functions, with requests of the computer for advice and displayed output of advice (from a data base, expert system, or simulation) to the operator. Many new developments in computer-based decision aids for planning, editing, monitoring, and failure detection are being used as an auxiliary part of operating dynamic systems. Reflection upon the nervous system of higher animals reveals a similar kind of supervisory control wherein commands are sent from the brain to local ganglia, and peripheral motor control loops are then closed locally through receptors in the muscles, tendons, or skin. The brain, presumably, does higher level planning based on its own stored data and "mental models," an internalized expert system available to provide advice and permit trial responses before commitment to actual response.

Theorizing about supervisory control began as aircraft and spacecraft became partially automated. It became evident that the human operator was being replaced by the computer for direct control responsibility and was moving to a new role of monitor and goal-constraint setter. An added incentive was the U.S. space program, which posed the problem of how a human operator on Earth could control a manipulator arm or vehicle on the Moon through a three-second communication round-trip time delay. The only solution that avoided instability was to make the operator a supervisory controller communicating intermittently with a computer on the moon, which in turn closed the control loop there. The rapid development of microcomputers has forced a transition from manual control to supervisory control in a variety of industrial and military applications (Sheridan, 1992).

Now, some examples of human–machine interaction will be considered, particularly those illustrating supervisory control in its various forms. First, three forms of vehicle control will be considered, namely,

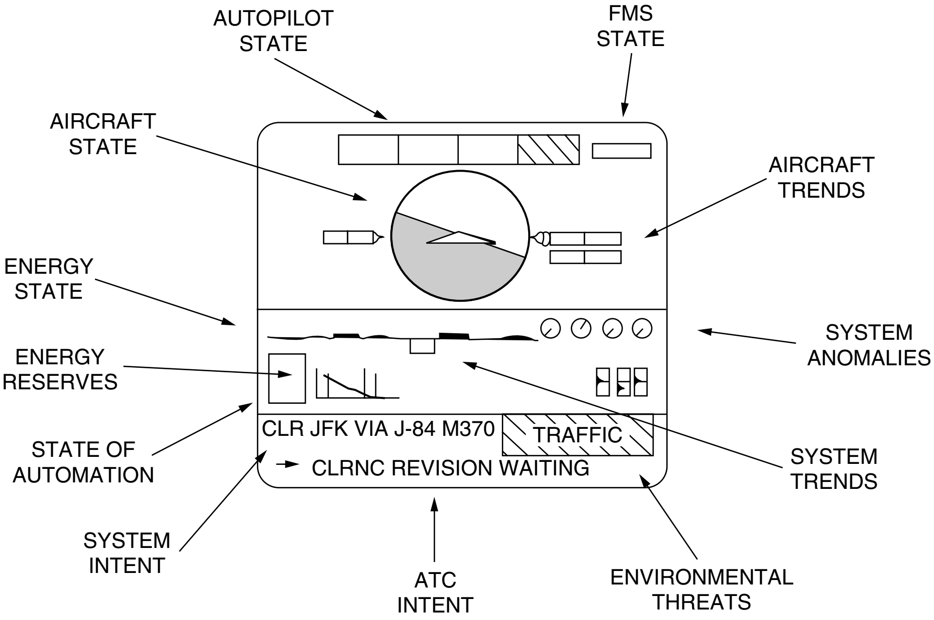

FIGURE 6.1.4 Pilot information requirements. (From Billings, 1991.)

control of modern aircraft, "intelligent" highway vehicles, and high-speed trains — all of which have human operators in the vehicles as well as humans in centralized traffic control centers. Second, telerobots for space, undersea, and medical applications will be discussed.

Advanced Control of Commercial Aircraft

Flight Management Systems

Aviation has appreciated the importance of human–machine interaction from its beginning, and today exemplifies the most sophisticated forms of such interaction. Although there have been many good examples of display and control design over the years, the current development of the flight management systems (FMSs) is the epitome. It also provides an excellent example of supervisory control in which the pilot flies the aircraft by communicating in high-level language through a computer intermediary.

The FMS is a centralized computer that interacts with a great variety of sensors and communication from the ground, as well as many displays and controls within the aircraft. It embodies many functions and mediates most of the pilot information requirements shown in Figure 6.1.4. Gone are the days when each sensor had its own display, operating independently of all other sensor-display circuits. The FMS, for example, brings together all of the various autopilot modes, from long-standing, low-level control modes wherein the aircraft is commanded to go to and hold a commanded altitude, heading, and speed, to more sophisticated modes in which the aircraft is instructed to fly a given course, consisting of a sequence of waypoints (latitudes and longitudes) at various altitudes, and even land automatically at a given airport on a given runway.

Figure 6.1.5 illustrates one type of display mediated by the FMS — in this case integrating many formerly separate components of information. Mostly, it is a multicolor plan-view map showing position and orientation of important objects relative to one's aircraft (the triangle at the bottom):

- Heading (compass arc at top, present heading 175°)
- Groundspeed plus wind speed and wind direction (upper left)
- Actual altitude relative to desired altitude (vertical scale on right side)
- Programmed course connecting various waypoints (OPH and FLT)

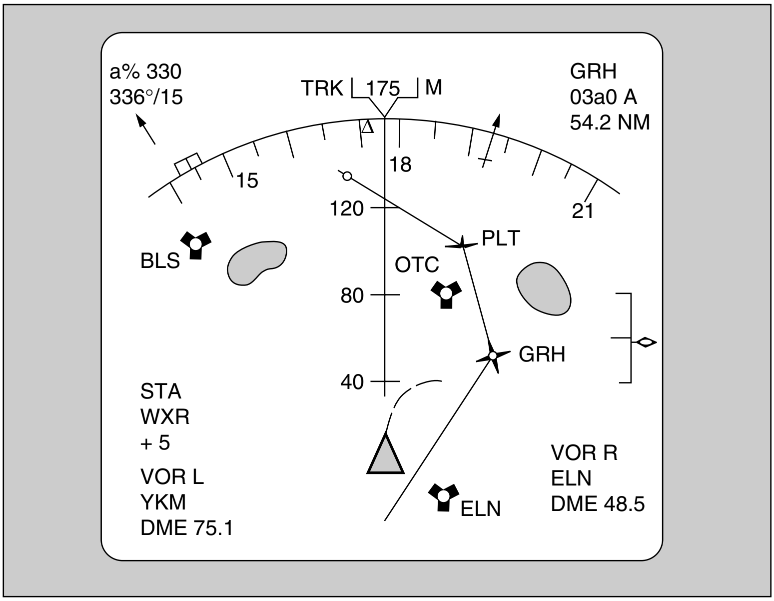

FIGURE 6.1.5 Integrated aircraft map display. (From Billings, 1991.)

- Salient VOR radar beacons to the right and left of present position/direction with their codes and frequencies (lower left and right corners)
- Location of key VORs along the course (three-cornered symbols)
- Location of weather to be avoided (two gray blobs)
- Predicted trajectory based on present turn rate, showing that the right turn is appropriately getting back on course

Programming the FMS is done through a specialized keyboard and text display unit (Figure 6.1.6) having all the alphanumeric keys plus a number of special function keys. The displays in this case are specialized to the different phases of a flight (taxi, takeoff, departure, en route approach, land, etc.), each phase with up to three levels of pages.

The FMS makes clear that designing displays and controls is no longer a matter of what can be built — the computer allows essentially any conceivable display or control to be realized. The computer can also provide a great deal of real-time advice, especially in emergencies, based on its many sensors and stored knowledge about how the aircraft operates. However, pilots are not sure that they need all the information that aircraft designers would like to give them and have an expression "killing us with kindness" to refer to this plethora of available information. The question is what should be designed based on the needs and capabilities of the pilot.

Boeing, McDonnell Douglas, and Airbus have different philosophies for designing the FMS. Airbus has been the most aggressive in automating, intending to make piloting easier and safer for pilots from countries with less well-established pilot training. Unfortunately, of the modern commercial jets, these most automated aircraft have had the most accidents — a fact that has precipitated vigorous debate about how far to automate.

Air Traffic Control

As demands for air travel continue to increase, so do demands for air traffic control. Given what is currently regarded as safe separation criteria, air space over major urban areas is already saturated, so simply adding more airports is not acceptable (in addition to which residents do not want more airports,

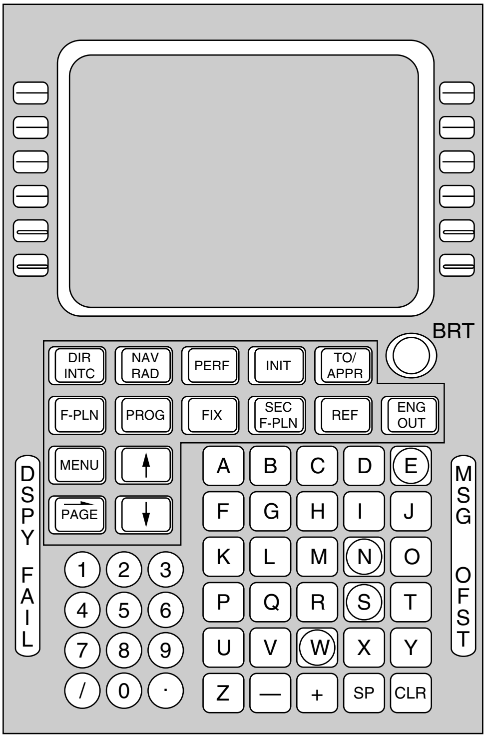

FIGURE 6.1.6 Flight management system control and display unit. (From Billings, 1991.)

with their noise and surface traffic). The need is to reduce separations in the air, as well as to land aircraft closer together or on parallel runways simultaneously. This puts much greater demands on air traffic controllers, particularly at the terminal area radar control centers (TRACONs); here trained operators stare at blips on radar screens and verbally guide pilots entering the terminal airspace from various directions and altitudes into orderly descent and landing patterns with proper separation between aircraft.

Currently, many changes being introduced into air traffic control have profound implications for human–machine interaction. Previously, communication between pilots and air traffic controllers was entirely by voice; now digital communication between aircraft and ground (a system called *datalink)* allows more, as well as more reliable, two-way communication so that weather and runway and wind information, clearances, etc. can be displayed to pilots visually. However, pilots are not so sure that they want this additional technology. They fear the demise of the "partyline" of voice communications with which they are so familiar that permits all pilots in an area to listen in on other pilots' conversations.

New aircraft-borne radar allows pilots to detect air traffic in their own vicinity. Improved ground-based radar detects microbursts or wind shear, which can easily put an aircraft out of control. Both types of radar pose challenges as to how best to warn the pilot and provide guidance as to how to respond. They also pose a cultural change in air traffic control because heretofore pilots have been dependent upon air traffic controllers to advise them of weather conditions and other air traffic. Furthermore, because of the new weather and collision avoidance technology, current plans call for radically altering the rules whereby high-altitude commercial aircraft must stick to well-defined traffic lanes. Instead, pilots will have great flexibility as to altitude (to find the most favorable winds and therefore save fuel) and be able to take great-circle routes straight to their destinations (also saving fuel). However, air traffic controllers are not sure they want to give up the power they have had and become passive observers and monitors who function only in emergencies.

Intelligent Highway Vehicles

Vehicle Guidance and Navigation Systems

The combination of GPS (global positioning system) satellites, high-density computer storage of map data, electronic compass, synthetic speech synthesis, and computer-graphic displays allows cars and trucks to know where they are located on the Earth to within 10 m or less, and can guide a driver to a programmed destination by a combination of a map display and speech. Some human factors challenges are in deciding how to configure the map (how much detail to present; whether to make the map north-up with a moving dot representing one's own vehicle position; or current heading up and rapidly changing with every turn). The computer graphics can also be used to show the turns to anticipate and which lane to get in.

Synthetic speech can reinforce these turn anticipations, caution the driver if he is perceived to be headed in the wrong direction or off-course, and even guide him or her back on course. An interesting question is what the computer should say in each situation to get the driver's attention, to be understood quickly and unambiguously but without being an annoyance. Another question is whether such systems will distract the driver's attention from the primary tasks, thereby reducing safety. The major vehicle manufacturers have developed such systems, which have been evaluated for reliability and human use and are beginning to be marketed in the U.S., Europe, and Japan.

Smart Cruise Control

Standard cruise control has a major deficiency in that it knows nothing about vehicles ahead, and one can easily collide with the rear end of another vehicle if not careful. In a smart cruise control system, a microwave or optical radar detects the presence of a vehicle ahead and measures that distance. The question is what to do with this information. Should the driver be warned with some visual or auditory alarm (auditory is better because the driver need not be looking in the right place)? Can a warning be too late to elicit braking, or surprise the driver so that he brakes too suddenly and causes a rear-end accident to his own vehicle? Should the computer automatically apply the brakes by some function of distance to the obstacle ahead, speed, and closing deceleration? If the computer did all the braking, would the driver become complacent and not pay attention, to the point that a serious accident would occur if the radar failed to detect an obstacle, say a pedestrian or bicycle, or the computer failed to brake? Should braking be some combination of human and computer braking, and if so by what algorithm? These are human factors questions currently being researched.

It is interesting to note that current developmental systems only decelerate and downshift, mostly because if the vehicle manufacturers sell vehicles that claim to perform braking, they would be open to a new and worrisome area of litigation. The same radar technology that can warn the driver or help control the vehicle can also be applied to cars overtaking from one side or the other. Another set of questions then arises as to how and what to communicate to the driver and whether to trigger some automatic control maneuver in certain cases.

Advanced Traffic Management Systems

Automobile congestion in major cities has become unacceptable, and advanced traffic management systems are being built in many of these cities to measure traffic flow at intersections (by some combination of magnetic loop detectors, optical sensors, and other means) and regulate stop lights and message signs. These systems can also issue advisories of accidents ahead by means of variable message signs or radio and give advice of alternate routings. In emergencies, they can dispatch fire, police, ambulances, or tow trucks, and in the case of tunnels, can shut down entering traffic completely if necessary. These systems are operated by a combination of computers and humans from centralized control rooms. The operators look at banks of video monitors, which let them see the traffic flow at different locations, and computer-graphic displays of maps, alarm windows, and textual messages. The operators get advice from computer-based "expert systems" that suggest best responses based on measured inputs, and the operator must decide whether to accept the computer's advice, whether to seek further information, and how to respond.

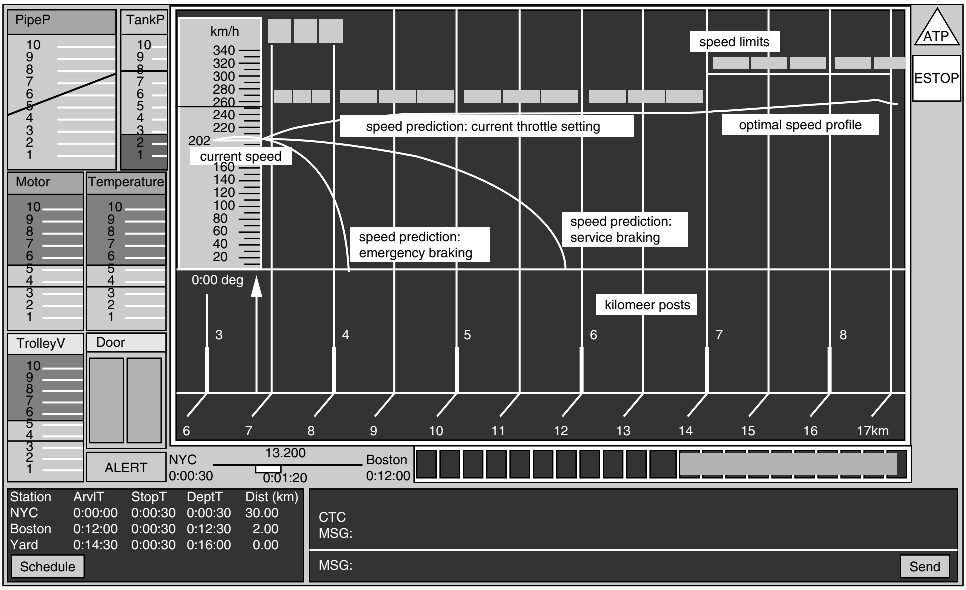

Station	ArvlT	StopT	DeptT	Dist (km)
NYC	0:00:00	0:00:30	0:00:30	30.00
Boston	0:12:00	0:00:30	0:12:30	2.00
Yard	0:14:30	0:00:30	0:16:00	0.00

FIGURE 6.1.7 Prototype of computer-generated display for high-speed trains. (From Askey, 1995.)

High-Speed Train Control

With respect to new electronic technology for information sensing, storage, and processing, railroad technology has lagged behind that of aircraft and highway vehicles, but currently is catching up. The role of the human operator in future rail systems is being debated because, for some limited right-of-way trains (e.g., in airports), one can argue that fully automatic control systems now perform safely and efficiently. The train driver's principal job is speed control (although he must perform many other monitoring duties); in a train this task is much more difficult than in an automobile because of the huge inertia of the train — it takes 2 to 3 km to stop a high-speed train.

Speed limits are fixed at reduced levels for curves, bridges, grade-crossings, and densely populated areas; while wayside signals temporarily command lower speeds if maintenance is being performed on the track; there are poor environmental conditions such as rock slides or deep snow are present; or, especially, if another train is ahead. The driver must obey all speed limits and reach the next station on time. Learning to maneuver the train with its long time constants can take months, given that the driver's only input currently for the speed control task is an indication of current speed.

The authors' laboratory has proposed a new computer-based display that helps the driver anticipate the future effects of current throttle and brake actions. Based on a dynamic model of the train, this approach gives an instantaneous prediction of future train position and speed based on current acceleration, so speed can be plotted on the display, assuming the operator holds to current brake–throttle settings. It also plots trajectories for maximum emergency braking and maximum service braking. In addition, the computer generates a speed trajectory that adheres to all (known) future speed limits, gets the train to the next station on time, and minimizes fuel/energy. Figure 6.1.7 shows the laboratory version of this display, which is currently being evaluated.

Telerobots for Space, under the Sea, and Medicine

When nuclear power was first adopted in the late 1940s, engineers began the development of master-slave remote manipulators, by which a human operator at one location could position and orient a device attached to his hand, and a servomechanism-controlled gripper would move in correspondence and

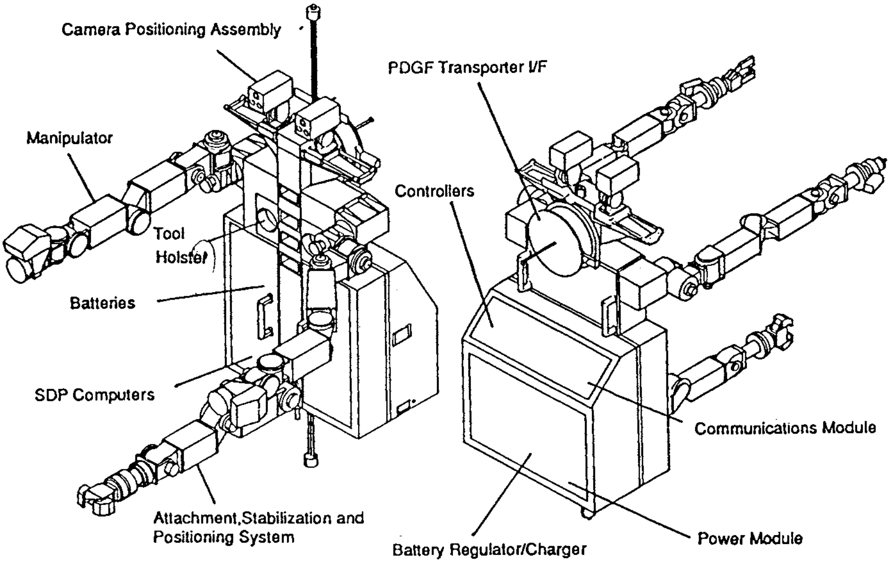

FIGURE 6.1.8 Flight telerobotic servicer prototype design. (Courtesy of NASA.)

handle objects at another location. At about the same time, remotely controlled wheeled vehicles, submarines, and aircraft began to be developed. Such manipulators and vehicles remotely controlled by humans are called *teleoperators.*

Teleoperator technology got a big boost from industrial robot technology, which came in a decade or so later and provided improved vision, force, and touch sensors, actuators, and control software. Large teleoperators were developed for rugged mining and undersea tasks and small teleoperators for delicate tasks such as eye surgery. Eventually, teleoperators were equipped with sensitive force feedback, so that the human operator can see the objects in the remote environment and also feel them in his grasp.

Supervisory controlled teleoperators were developed because, during the time of the Apollo flights to the Moon, the desire to control lunar manipulators and vehicles from Earth was stimulated and unavoidable round trip time delays of 3 sec (speed of light from Earth to Moon and back) would not permit simple closed loop control. The human could communicate a subgoal to be reached and a procedure for getting there, and the teleoperator would be turned loose for some short period to perform automatically. Such a teleoperator is called a *telerobot.*

Figure 6.1.8 shows the flight telerobotic servicer (FTS) developed by Martin Marietta for the U.S. Space Station Freedom. It has two seven-degree of freedom (DOF) arms (including gripper) and one five DOF “leg” for stabilizing itself while the arms work. It has two video “eyes” to present a stereo image to its human operator. It can be configured as a master–slave teleoperator (under direct human control) or as a telerobot (able to execute small programmed tasks using its own eyes and force sensors). Unfortunately the FTS project was canceled by Congress.

Figure 6.1.9 shows the remotely operated submersible *Jason* developed by Woods Hole Oceanographic Institution. It is the “big brother” of *Jason Junior*, which swam into the interior of the ship *Titanic* and made a widely viewed video record when the latter was first discovered. It has a single manipulator arm, sonar and photosensors, and four thrusters that can be oriented within limited range and enable it to move in any direction. It is designed for depths up to 6000 m — rather severe pressures. It, too, can be operated in direct teleoperator mode or as a telerobot.

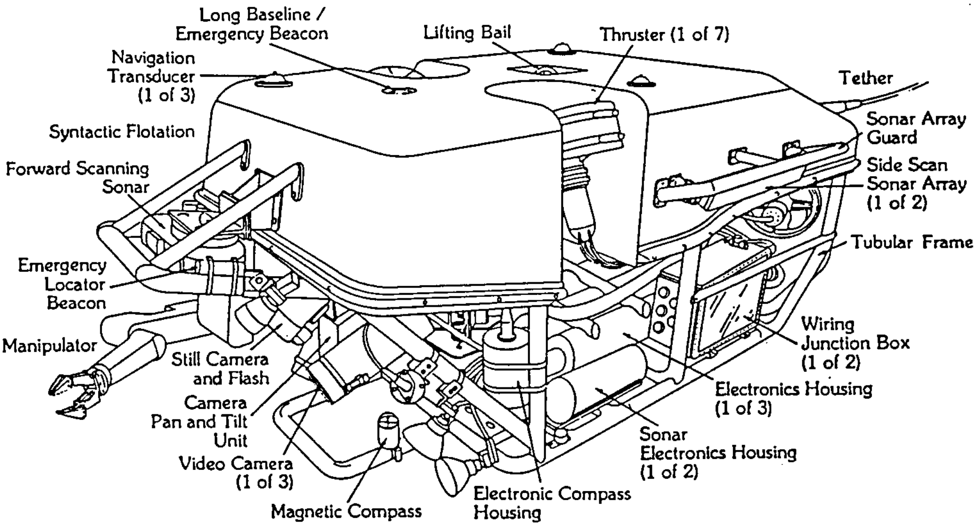

FIGURE 6.1.9 Deep ocean submersible Jason. (Courtesy of Woods Hole Oceanographic Institution.)

Common Criteria for Human Interface Design

Design of operator control stations for teleoperators poses the same types of problems as design of controls and displays for aircraft, highway vehicles, and trains. The displays must show the important variables unambiguously to whatever accuracy is required, but more than that must show the variables in relation to one another so as to portray the current "situation" clearly *(situation awareness* is currently a popular test of the human operator in complex systems). Alarms must get the operator's attention; indicate what is abnormal by text, symbol, or location on a graphic display; determine where in the system the failure occurred, what the urgency is, and if response is urgent; and even suggest what action to take. (For example, the ground proximity warning in an aircraft gives a loud "Whoop, whoop!" followed by a distinct spoken command, "Pull up, pull up!") Controls — whether analogic joysticks, master-arms, or knobs — or symbolic special-purpose buttons or general purpose keyboards must be natural and easy to use and require little memory of special procedures (computer icons and windows do well here). The placement of controls and instruments and their mode and direction of operation must correspond to the desired direction and magnitude of system response.

Human Workload and Human Error

As noted previously, new technology allows combination, integration, and simplification of displays compared to the intolerable plethora of separate instruments in older aircraft cockpits and plant control rooms. The computer has taken over more and more functions from the human operator. These changes potentially make the operator's task easier. However, they also allow for much more information to be presented, more extensive advice to be given, etc.

These advances have elevated the stature of the human operator from that of providing physical energy and control, to that of providing only continuous control, to finally serving as a supervisor or a robotic vehicle or system. "Expert systems" can now answer the operator's questions, much as does a human consultant, or whisper suggestions in his ear even if he does not request them. These changes seem to add many cognitive functions that were not present at an earlier time. They make the operator into a monitor of the automation who is supposed to step in when required to set things straight. Unfortunately, people are not always reliable monitors and interveners.

Mental Workload

Under such complexity, it is imperative to know whether the mental workload of the operator is too great for safety. Human–machine systems engineers have sought to develop measures of mental workload, the idea being that as mental load increases the risk of error increases; however, presumably measurable mental load comes before actual lapse into error. Three approaches have been developed for measuring mental workload:

1. Subjective rating scale, typically a 10-level category scale with descriptors for each category from no load to unbearable load
2. Use of physiological indices that correlate with subjective scales, including heart rate and the variability of heart rate; certain changes in the frequency spectrum of the voice; electrical resistance of the skin; diameter of the pupil of the eye; and certain changes in the evoked brain wave response to sudden sound or light stimuli
3. Use of what is called a secondary task, an easily measurable additional task that consumes all of the operator's attention remaining after the requirements of the primary task are satisfied

The latter technique has been used successfully in the laboratory, but has shortcomings in practice in that operators may refuse to cooperate.

Such techniques are now routinely applied to critical tasks such as aircraft landing, air traffic control, certain planned tasks for astronauts, and emergency procedures in nuclear power plants. The evidence suggests that supervisory control relieves mental load when things are going normally, but when automation fails, the human operator is subjected to a rapidly increased mental load.

Human Error

Human error has long been of interest, but only in recent decades has a serious effort been made to understand human error in terms of categories, causation, and remedy. Human errors can be classified in several ways. One is according to whether it is an error of *omission* (something not done that was supposed to have been done) or *commission* (something done that was not supposed to have been done). Another is *slip* (a correct intention for some reason not fulfilled) vs. a *mistake* (an incorrect intention that was fulfilled). Errors may also be classified according to whether they are in sensing, perceiving, remembering, deciding, or acting.

Some special categories of error worth noting are associated with following procedures in operation of systems. One, for example, is called a *capture error*, wherein the operator, who is very accustomed to a series of steps, say A, B, C, and D, intends at another time to perform E, B, C, F. However, he is "captured" by the familiar sequence B, C and does E, B, C, D.

As to effective therapies for human error, proper design to make operation easy and natural and unambiguous is surely the most important. If possible, the system design should allow for error correction before the consequences become serious. Active warnings and alarms are necessary when the system can detect incipient failures in time to take such corrective action. Training is probably next most important after design, but any amount of training cannot compensate for an error-prone design. Preventing exposure to error by guards, locks, or an additional "execute" step can help make sure that the most critical actions are not taken without sufficient forethought. Least effective are written warnings such as posted decals or warning statements in instruction manuals, although many tort lawyers would say the opposite.

Trust, Alienation, and How Far to Go with Automation

Trust

If an operator does not trust his sensors and displays, expert advisory system, or automatic control system, he will not use them or will avoid using them, if possible. On the other hand, if an operator comes to place too much trust in such systems, he will let down his guard, become complacent, and, when it fails, not be prepared. The question of operator trust in automation is an important current issue in human–machine interface design. It is desirable that operators trust their systems, but it is also desirable that they be alert, aware of the situation, and ready to take over.

Alienation

The new human–machine interaction can have a set of broader social effects that can be discussed under the rubric of *alienation*:

1. People worry that computers can do some tasks, such as memory and calculation, much better than they can. Surely, people should not try to compete in this arena.
2. Supervisory control tends to make people remote from the ultimate operations they are supposed to be overseeing — remote in space, desynchronized in time, and interacting with a computer instead of the end product or service.
3. People lose the perceptual–motor skills that, in many cases, gave them their identity. They become "deskilled" and, if ever called upon to use their previous well-honed skills, they cannot.
4. Increasingly, people who use computers in supervisory control or in other ways, whether intentionally or not, are denied access to the knowledge to understand what is going on inside the computer.
5. Partly as a result of the preceding factor, the computer becomes mysterious, and the untutored user comes to attribute more capability, wisdom, or blame to the computer than is appropriate.
6. Because computer-based systems are growing more complex and people are being "elevated" to roles of supervising larger and larger aggregates of hardware and software, the stakes naturally become higher. A human error before might have gone unnoticed and been easily corrected; now such an error could precipitate a disaster.
7. The last factor in alienation is similar to the first, but all encompassing — namely, the fear that a "race" of machines is becoming more powerful than the human race.

The preceding seven factors and the fears that they engender, whether justified or not, must be reckoned with. Computers must be made not only "human friendly" but also not alienating with respect to these broader factors. Operators and users must become computer literate at the level of sophistication with which they can deal.

How Far to Go with Automation

The trend toward supervisory control is definitely changing the role of the human operator, posing fewer requirements on continuous sensory–motor skill and more on planning, monitoring, and supervising the computer. As computers take over more sensory–motor skill functions, new questions are raised regarding how the interface should be designed to provide the best cooperation between human and machine. Among these questions are: To what degree should the system be automated? How much "help" from the computer is desirable? What are the points of diminishing returns?

Table 6.1.1 lists 10 levels of automation, from 0 to 100% computer control. Obviously, few tasks have achieved 100% computer control; however, new technology pushes relentlessly in that direction. It is

TABLE 6.1.1 Scale of Degrees of Automation

1	The computer offers no assistance; the human must do it all
2	The computer offers a complete set of action alternatives, and
3	Narrows the selection down to a few, or
4	Suggests one alternative, and
5	Executes that suggestion if the human approves, or
6	Allows the human a restricted time to veto before automatic execution, or
7	Executes automatically, then necessarily informs the human, or
8	Informs the human only if asked, or
9	Informs the human only if it, the computer, decides to do so
10	The computer decides everything and acts autonomously, ignoring the human

Source: From Sheridan, 1987.

instructive to consider the various intermediate levels of Table 6.1.1 not only in terms of how capable and reliable the technology is, but also in terms of what is desirable in terms of the human operators' and general public's safety and satisfaction. The current controversy about how much to automate large commercial transport aircraft is often couched in these terms.

6.2 The Need for Control of Mechanical Systems

Peter S. Curtiss

Process control typically involves some mechanical system that needs to be operated in such a fashion that the output of the system remains within its design operating range. The objective of a process control loop is to maintain the process at the setpoint under the following dynamic conditions:

- The setpoint is changed.
- The load on the process is changed.
- The transfer function of the process is changed or a disturbance is introduced.

Classical Control System Representation

Feedback-Loop System

A *feedback* (or *closed-loop*) system contains a process, a sensor, and a controller. Figure 6.2.1 shows some of the components and terms used when discussing feedback loop systems.

- *Process.* A process is a system that produces a motion, temperature change, flow, pressure, or many other actions as a function of the actuator position and external inputs. The output of the process is called the process value. If a positive action in the actuator causes an increase in the process value, the process is called *direct acting*. If positive action in the actuator decreases the process value, it is called reverse *acting*.
- *Sensor.* A sensor is a pneumatic, fluidic, electronic, or other device that produces some kind of signal indicative of the process value.
- *Setpoint.* The setpoint is the desired value for a process output. The difference between the setpoint and the process value is called the process error.
- *Controller.* A controller sends signals to an actuator to effect changes in a process. The controller compares the setpoint and the process value to determine the process error. It then uses this error to adjust the output and bring the process back to the setpoint. The controller gain dictates the amount that the controller adjusts its output for a given error.
- *Actuator.* An actuator is a pneumatic, fluidic, electric, or other device that performs any physical action that will control a process.
- *External disturbances.* An external disturbance is any effect that is unmeasured or unaccounted for by the controller.

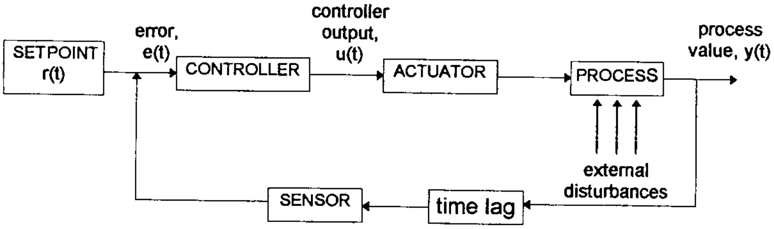

FIGURE 6.2.1 Typical feedback control schematic diagram.

- *Time constants*. The time constant of a sensor or process is a quantity that describes the dynamic response of the device or system. Often the time constant is related to the mass of an object or other dynamic effect in the process. For example, a temperature sensor may have a protective sheath around it that must first be warmed before the sensor registers a change of temperature. Time constants can range from seconds to hours.
- *Dead time*. The dead time or lag time of a process is the time between the change of a process and the time this change arrives at the sensor. The delay time is not related to the time constant of the sensor, although the effects of the two are similar. Large dead times must be properly treated by the control system to prevent unstable control.
- *Hysteresis*. Hysteresis is a characteristic response of positioning actuators that results in different positions, depending on whether the control signal is increasing or decreasing.
- *Dead band*. The dead band of a process is that range of the process value in which no control action is taken. A dead band is usually used in *two*-position control to prevent "chattering" or in split-range systems to prevent sequential control loops from fighting each other.
- *Control point*. The control point is the actual, measured value of a process (i.e., the setpoint + steady-state offset + compensation).
- *Direct/reverse action*. A direct-acting process will increase in value as the signal from the controller increases. A reverse-acting process will decrease in value as the signal from the controller increases.
- *Stability*. The *stability* of a feedback control loop is an indication of how well the process is controlled or, alternatively, how controllable the process is. The stability is determined by any number of criteria, including overshoot, settling time, correction of deviations due to external disturbances, etc.
- *Electric control*. Electric control is a method of using low voltages (typically 24 VAC) or line voltages (110 VAC) to measure values and effect changes in controlled variables.
- *Electronic control*. Electronic controls use solid-state electronic components *that are* used for measurement and amplification of measured signals and the generation of proportional control signals.
- *Pneumatic control*. Pneumatic controls use compressed air as the medium for measuring and controlling processes.
- *Open-loop systems*. An open-loop system is one in which no feedback *occurs, e.g., a* whole-house attic fan. It will continue to run even though the house may have already cooled off. Also, timed on/off devices are open loops.

Examples

Direct-Acting Feedback Control

A classic control example is a reservoir in which the fluid must be maintained at a constant level. Figure 6.2.2 shows this process schematically; the key features of this direct-acting system are labeled. The control action of this system will be referred to shortly after defining some terms are defined:

- *Cascaded (master–slave) control loops*. If a process consists of several subprocesses, each with a relatively different transfer function, it is often useful to use cascaded control loops. For example, consider a building housing a manufacturing line in which 100% outside air is used that must also have very strict control of room air temperature. The room temperature is controlled by changing the position of a valve on a coil at the main air-handling unit that supplies the zone. Typically, the time constant of the coil will be much smaller than the time constant of the room. A single feedback loop would probably result in poor control because both processes involve so much dead time. The solution is to use two controllers: the first (the master) compares the room temperature to the thermostat setting and sends a signal to the second (the slave), which uses that signal as its own setpoint for controlling the coil valve. The slave controller measures the output

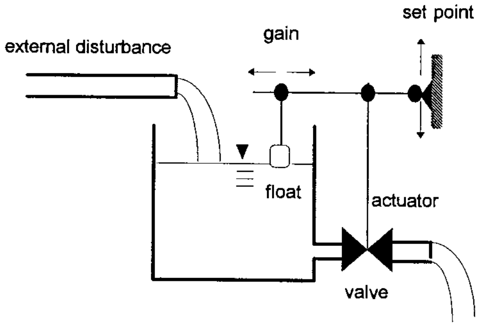

FIGURE 6.2.2 Example of a controlled process.

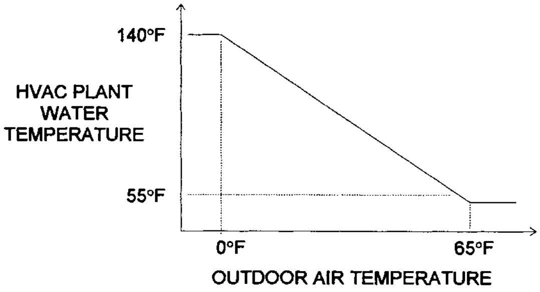

FIGURE 6.2.3 Example of the effect of compensation control.

of the coil, not the temperature of the room. The controller gain on the master can be set lower than that of the slave to prevent excessive cycling.

- *Sequential control loops.* Sometimes control action is needed at more than one point in a process. An example of this is an air-handling unit that contains heating and cooling coils in order to maintain a fixed outlet air temperature in any season. Typically, a *sequential* (or *split-range*) system in an air-handling unit will have three temperature ranges of operation: the first for heating mode; the last for cooling mode; and a middle dead-band region in which neither the cooling nor heating coils are operating. Most sequential loops are simply two different control loops acting from the same sensor. The term *sequential* refers to the fact that in most of these systems the components are in series in the air or water stream.
- *Combined feed-forward/feedback loops.* As pointed out earlier, feed-forward loops can be used when the effects of an external disturbance on a system are known. An example of this is outside air temperature reset control used to modify supply air temperatures. The control loop contains a discharge air temperature sensor (the *primary* sensor) and an outdoor air temperature sensor (the *compensation* sensor). The designer should have some idea about the influence of the outside temperature on the heating load and can then assign an *authority* to the effect of the outside air temperature on the controller setpoint. As the outdoor temperature increases, the control point decreases and vice versa (see Figure 6.2.3).
- *Predictive control.* Predictive control uses a model of the process to predict what the process value will be at some point in the future based upon current and past conditions. The controller then specifies a control action to be taken *in* the present that will reduce future process errors.
- *Adaptive control.* Adaptive controllers modify their gains dynamically in order to adapt to current process conditions.
- *Supervisory controllers.* Supervisory controllers are used to govern the operation of an entire plant and/or control system. These may be referred to as *distributed control systems* (DCSs), which can be used to govern the control of individual feedback loops and can also be used to ensure some

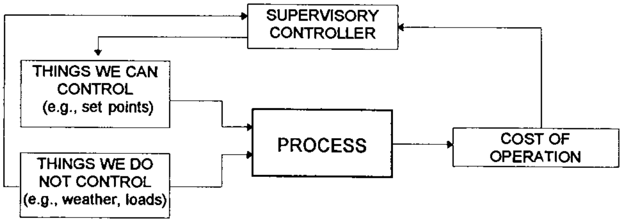

FIGURE 6.2.4 Typical supervisory controller.

kind of optimal performance of the entire plant. The controller will vary setpoints and operating modes in an attempt to minimize a cost function. Figure 6.2.4 shows a basic diagram of a supervisory controller.

6.3 Control System Analysis

Peter S. Curtiss

The Linear Process Approximation

To design controllers, it is necessary to have a dynamic process as well as control system representation. This section describes the key points of the most common such representation — that of linear processes and their controls. A process is basically a collection of mechanical equipment in which an input is changed or transformed somehow to produce an output. Many processes will be near steady state, while others may be in a more or less constant state of change. Building control systems are used as an illustration.

Steady-State Operation

The true response of a seemingly simple process can be, in fact, quite complex. It is very difficult to identify and quantify every single input due to the stochastic nature of life. However, practically any process can be approximated by an equation that takes into account the known input variables and produces a reasonable likeness to the actual process output.

It is convenient to use differential equations to describe the behavior of processes. For this reason, the "complexity" of the function will be denoted by the number of terms in the corresponding differential equation (i.e., the *order* or *degree* of the differential equation). In a linear system analysis, a step change in the control signal is usually considered and the response observed. The following descriptions will assume a step input to the function, as shown in Figure 6.3.1

Note that a step change such as this is usually unlikely in most fields of control outside of electronic systems and even then can only be applied to a digital event such as a power supply being switched on or a relay being energized. Zero-order system output has a one-to-one correspondence to the input:

$$y(t) = a_0 \cdot u(t)$$

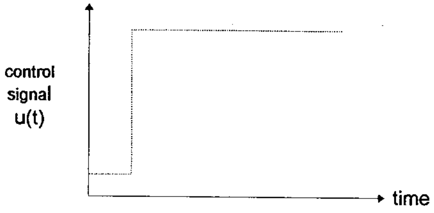

FIGURE 6.3.1 Step change in control signal.

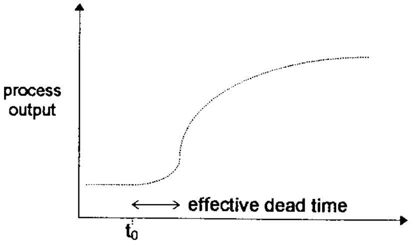

FIGURE 6.3.2 Effective dead time of a process subjected to a step change in controlled signal.

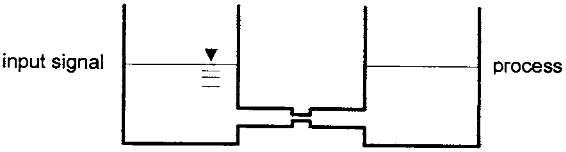

FIGURE 6.3.3 Connected water containers used for example of dynamic response.

First-order functions will produce a time-varying output with a step-change as input:

$$\frac{dy(t)}{dt} + a_1 \cdot y(t) = b_1 \cdot u(t)$$

and higher order functions will produce more complex outputs.

The function that relates the process value to the controller input is called the *transfer function* of the process. The time between the application of the step change, t_0, and the time at which the full extent of the change in the process value has been achieved is called the *transfer period*. A related phenomenon is process dead time. If sufficient physical distance is present between the process output and the sensor assigned to measuring it, then one observes dead time during which the process output is not affected by the control signal (as in Figure 6.3.2).

The *process gain* (or *static gain*) is the ratio of the percentage change of the process output to the corresponding percentage change of the control signal for a given response. For example, gain can be positive (as in a heating coil) or negative (as in a cooling coil).

Dynamic Response

In practice, very few processes are controlled in a step-wise fashion. Usually, the control signal is constantly modulating much the way that one makes small changes to the steering wheel of a car when driving down the highway. The dynamic process of level control in buckets filled with water is now considered. (See Figure 6.2.3.)

Imagine that the level of water in a bucket on the left is the control signal and the level of water in a bucket on the right is the process value. It is obvious that a step change in the control signal will bring about a first-order response of the process value. Suppose, however, that a periodic signal is applied to the level of the bucket on the left. If the frequency of the signal is small enough, a response in the level in the bucket on the right varies as a function of this driving force, but with a delay and a decrease in the amplitude.

Here the *dynamic process gain* is less than one even though the static process gain is 1. This process has no dead time; as soon as the control signal begins to increase, the process value will also begin to increase. The dynamic process gain, therefore, can be defined similarly to that of the static gain — it is the ratio of the amplitude of the two signals, comparable to the normalized ranges used in the static gain definition.

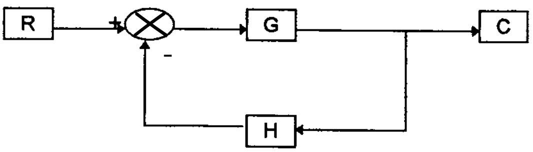

FIGURE 6.3.4 Generalized feedback loop.

The dynamic gain, as its name suggests, is truly dynamic. It will change according to the transfer function as well as to the frequency of the control signal. As the frequency increases, the output will lag even farther behind the input and the gain will continue to decrease. At one point, the frequency may be exactly right to cancel any past effects of the input signal (i.e., the phase shift is 180°) and the dynamic gain will approach zero. If the frequency rises further, the process output may decrease as the control signal increases (easily the case with a building cooling or heating coil due to the mass effects) and the dynamic gain will be negative. At this point, it is convenient to define a feedback loop mathematically. A general feedback loop is shown in Figure 6.3.4.

The controller, actuator, and process have been combined into the *forward transfer function* (or *open-loop transfer function*) **G** and the sensor and dead time have been combined into the *feedback path* transfer function **H**. The overall *closed-loop transfer function* is defined as

$$\frac{\mathrm{C}}{\mathrm{R}}=\frac{\mathrm{G}}{1+\mathrm{G}\cdot\mathrm{H}}$$

The right-hand side of this equation is usually a ratio of two polynomials when using Laplace or *z* transforms. The roots of the numerator are called the *zeros* of the transfer function and the roots of the denominator are called the *poles* (Shinners, 1978).

The denominator of the closed loop transfer function, $\mathbf{1 + G \cdot H}$, is called the *characteristic function.* When the characteristic function is set equal to zero, it yields the *characteristic equation*

$$1 + \mathrm{G} \cdot \mathrm{H} = 0$$

The characteristic equation can be used to assess process control stability during system design.

Representation of Processes in *t*, *s*, and *z* Domains

How a process truly behaves can never be known. The world is an inherently stochastic place and any model of a system is going to approximate at best. Nonetheless, it is necessary to choose some kind of representation in order to perform any useful analysis. This section will consider three different domains: the continuous time domain; the frequency domain; and the discrete time domain. The frequency domain is useful for certain aspects of controller design and the discrete time domain is used in digital controllers.

Continuous Time Domain Representation of a Process

In the time domain, a process is represented by a differential equation such as:

$$\frac{d^n y}{dt^n}+a_1\frac{d^{n-1}y}{dt^{n-1}}+a_2\frac{d^{n-2}y}{dt^{n-2}}+\ldots+a_{n-1}\frac{dy}{dt}+a_n y=b_0\frac{d^m u}{dt^m}+b_1\frac{d^{m-1}u}{dt^{m-1}}+\ldots+b_{m-1}\frac{du}{dt}+b_m u$$

This is just a generalization of the first-order system equation described earlier.

Frequency Domain Representation of a Process — Laplace Transforms

The solution of higher order system models, closed form solution, is difficult in the time domain. For this reason, process transfer functions are often written using Laplace transforms. A Laplace transform is a mapping of a continuous time function to the frequency domain and is defined as

$$F(s) = \int_0^{\infty} f(t)e^{-st}dt$$

This formulation allows one to greatly simplify problems involving ordinary differential equations that describe the behavior of systems. A transformed differential equation becomes purely algebraic and can be easily manipulated and solved. These solutions are not of great interest in modern control system design, but the transformed system + controller differential equation is very useful in assessing control stability. This is the single key aspect of Laplace transforms that is of most interest. Of course, it is possible to solve only the governing differential equation for the system directly and explore stability in that fashion.

The Laplace transform of the previous differential equation is

$$s^n Y(s) + A_1 s^{n-1} Y(s) + \ldots + A_{n-1} sY(s) + A_n Y(s) = B_0 s^m \mathrm{U}(s) + B_1 s^{n-1} \mathrm{U}(s) + \ldots + B_{n-1} s U(s) + B_\mathrm{n} \mathrm{U}(s)$$

This equation can be rewritten as

$$Y(s)\cdot(s^\mathrm{n} + A_1 s^{n-1} + \ldots + A_{n-1} s + A_\mathrm{n}) = U(s)\cdot(B_0 s^\mathrm{m} + B_1 s^{n-1} + \ldots + B_{n-1} s + B_n)$$

so that the transfer function is found from

$$\frac{Y(s)}{U(s)} = \frac{s^m + B_1 s^{m-1} + \ldots + B_{m-1}s + A_m}{s^n + A_1 s^{n-1} + \ldots + A_{n-1}s + A_n}$$

This is the expression used for stability studies.

Discrete Time Domain Representation of a Process

A process in the discrete time domain is described (Radke and Isermann, 1989) by

$$\begin{aligned} y(k) &= a_1 y(k-1) + a_2 y(k-2) + a_3 y(k-3) + \ldots \\ &\quad + b_1 u(k-1) + b_2 u(k-2) + b_3 u(k-3) + \ldots \end{aligned}$$

This representation is of use when one is designing and analyzing the performance of direct digital control (DDC) systems. Note that the vectors **a** and **b** are *not* the same as for the continuous time domain equation. The z-transform uses the backward shift operator and therefore the z-transform of the discrete time equation is given by

$$y\left(1 - a_1 z^{-1} - a_2 z^{-2} - a_3 z^{-3} + \ldots\right) = u\left(b_1 z^{-1} - b_2 z^{-2} - b_3 z^{-3} + \ldots\right)$$

The transfer function can now be found:

$$\frac{y}{u} = \frac{b_1 z^{-1} - b_2 z^{-2} - b_3 z^{-3} + \ldots}{1 - a_1 z^{-1} - a_2 z^{-2} - a_3 z^{-3} + \ldots}$$

z-Transform Details

Because z-transforms are important in modern control design and are not treated elsewhere in this handbook, some basics of their use are given next. More and more control applications are being turned over to computers and DDC systems. In such systems, the sampling is not continuous as required for a Laplace transform. The control loop schematic is shown in Figure 6.3.5.

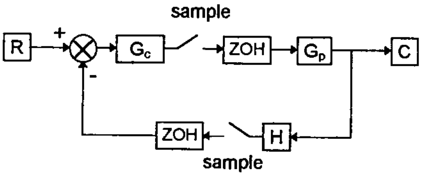

FIGURE 6.3.5 Sampled feedback loop.

It would be prohibitively expensive to include a voltmeter or ohmmeter on each loop; therefore, the controller employs what is called a *zero-order hold.* This basically means that the value read by the controller is "latched" until the next value is read in. This discrete view of the world precludes the use of Laplace transforms for analyses, thus making it necessary to find some other means of simplifying the simulation of processes and controllers. The following indicates briefly how *z*-transforms of controlled processes can be derived and how they are used in a controls application. In the design section of this chapter, the *z*-transform will be used to assess controller stability.

Recall that the Laplace transform is given as

$$\mathscr{L}\left\{f(t)\right\} = \int_0^\infty f(t)e^{-st}dt$$

Now suppose a process that is sampled at a discrete, constant time interval T. The index k will be used to count the intervals

At time $t = 0$, $k = 0$,
At time $t = T$, $k = 1$,
At time $t = 2T$, $k = 2$,
At time $t = 3T$, $k = 3$,

and so forth. The equivalent Laplace transform of a process that is sampled at a constant interval T can be represented as

$$\mathscr{L}\left\{f^*(t)\right\} = \sum_{k=0}^{\infty} f(kT)e^{-s\cdot kT}$$

Substituting the *backward-shift operator* z for e^{Ts} results in the definition of the *z*-transform:

$$Z\left\{f(t)\right\} = \sum_{k=0}^{\infty} f(kT)z^{-k}$$

6.4 Control System Design and Application

Peter S. Curtiss

Controllers

Controllers are akin to processes in that they have gains and transfer functions. Generally, there is no dead time in a controller or it is so small as to be negligible.

Steady-State Effects of Controller Gain

Recall that the process static gain can be viewed as the total change in the process value due to a 100% change in the controller output. A proportional controller acts like a multiplier between an *error signal* and this process gain. Under stable conditions, therefore, there must be some kind of error to yield any controller output. This is called the steady-state or static *offset*.

Dynamic Effects of Controller Gain

Ideally, a controller gain value is chosen that compensates for the dynamic gain of the process under normal operating conditions. The total loop dynamic gain can be considered as the product of the process, feedback, and controller gains. If the total dynamic loop gain is one, the process will oscillate continuously at the natural frequency of the loop with no change in amplitude of the process value. If the loop gain is greater than one, the amplitude will increase with each cycle until the limits of the controller or process are reached or until something fails. If the dynamic loop gain is less than one, the process will eventually settle down to stable control.

Controller Bias

The controller bias is a constant offset applied to the controller output. It is the output of the controller if the error is zero:

$$u = K \cdot e + M$$

where M is the bias. This is useful for processes that become nonlinear at the extremes or for processes in which the normal operating conditions are at a nonzero controller output.

PID Controllers

Many mechanical systems are controlled by proportional-integral-derivative (PID) controllers. Many permutations of such controllers use only certain portions of the PID controllers or use variations of this kind of controller. This subsection considers this very common type of controller.

Proportional Control

Proportional control results in action that is linear with the error. The proportional term, $K_p \cdot e$, has the greatest effect when the process value is far from the desired setpoint. However, very large values of K_p will tend to force the system into oscillatory response. The proportional gain effect of the controller goes to zero as the process approaches setpoint. Purely proportional control should therefore only be used when

- The time constant of the process is small and thus a large controller gain can be used.
- The process load changes are relatively small so that the steady-state offset is limited.
- The steady-state offset is within an acceptable range.

Integral Control

Integral makes a process adjustment based on the cumulative error, not its current value. The integral term K_i is the reciprocal of the reset time, T_r, of the system. The reset time is the duration of each error summing cycle. Integral control can cancel any steady-state offsets that would occur when using purely proportional control. This is sometimes called *reset* control.

Derivative Control

Derivative makes a process adjustment based on the current rate of change of the process control error. Derivative control is typically used in cases in which a large time lag occurs between the controlled device and the sensor used for the feedback. This term has the overall effect of preventing the actuator signal from going too far in one direction or another and can be used to limit excessive overshoot.

PID Controller in Time Domain

The PID controller can be represented in a variety of ways. In the time domain, the output of the controller is given by

$$u(t) = K_p\left[e(t) + K_i\int_0^t e(t)\,dt + K_d\frac{de(t)}{dt}\right]$$

PID Controller in the *s* Domain

It is relatively straightforward to derive the Laplace transform of the time domain PID equation. The transfer function of the controller is

$$\frac{U(s)}{E(s)} = \left[K_p + \frac{K_pK_i}{s} + K_pK_ds\right]$$

This controller transfer function can be multiplied by the process transfer function to yield the overall forward transfer function **G** of an *s*-domain process model. The criteria described earlier can then be used to assess overall system stability.

PID Controller in the *z* Domain

Process data are measured discretely at time intervals Δt, and the associated PID controller can be represented by

$$u(k) = K_p\left[e(k) + K_i\Delta t\sum_{i=0}^{k} e(i) + K_d\frac{e(k) - e(k-1)}{\Delta t}\right]$$

The change of the output from one time step to the next is given by $u(k) - u(k-1)$, so the PID *difference equation* is:

$$u(k) - u(k-1) = K_p\left[\left(1 + \frac{K_d}{\Delta t}\right)e(k) + \left(K_i\Delta t - 1 - 2\frac{K_d}{\Delta t}\right)e(k-1) + \left(\frac{K_d}{\Delta t}\right)e(k-2)\right]$$

and can be simplified as

$$u(k) - u(k-1) = q_0e(k) + q_1e(k-1) + q_2e(k-2)$$

where

$$q_0 = K_p\left(1 + \frac{K_d}{\Delta t}\right); \quad q_1 = K_p\left(K_i\Delta t - 1 - 2\frac{K_d}{\Delta t}\right); \quad q_2 = K_p\left(\frac{K_d}{\Delta t}\right)$$

Note that this can be written as

$$u\left(1 - z^{-1}\right) = e\left(q_0 + q_1z^{-1} + q_2z^{-2}\right)$$

The *z*-domain transfer function of the PID controller is then given as

$$\frac{u(z)}{e(z)} = \frac{q_0 + q_1z^{-1} + q_2z^{-2}}{1 - z^{-1}} = \frac{q_0z^2 + q_1z + q_2}{z^2 - z}$$

Controller Performance Criteria and Stability

Performance Indices

Obviously, in feedback loops one wishes to reduce the process error quickly and stably. The control systems engineer can use different cost functions in the design of a given controller depending on the criteria for the controlled process. Some of these cost functions (or *performance indices*) are listed here:

ISE	Integral of the square of the error	$\int e^2$
ITSE	Integral of the time and the square of the error	$\int te^2$
ISTAE	Integral of the square of the time and the absolute error	$\int t^2 \lvert e \rvert$
ISTSE	Integral of the square of the time and the square of the error	$\int t^2 e^2$

These indices are readily calculated in with DDC systems and can be used to compare the effects of different controller settings, gains, and even control methods.

Stability

Stability in a feedback loop means that the feedback loop will tend to converge on a value as opposed to exhibiting steady-state oscillations or divergence. Recall that the closed loop transfer function is given by

$$\frac{C}{R} = \frac{G}{1+GH}$$

and that the denominator, 1 + *GH*, when equated to zero, is called the characteristic equation. Typically, this equation will be a polynomial in *s* or *z* depending on the method of analysis of the feedback loop. Two necessary conditions for stability are that (1) all powers of *s* must be present in the characteristic equation from zero to the highest order; and (2) all coefficients in the characteristic equation must have the same sign. Note that the process may still be unstable even when these conditions are satisfied.

Roots of the Characteristic Equation

The roots of the characteristic equation play an important role in determining the stability of a process. These roots can be real and/or imaginary and can be plotted as shown in Figure 6.4.1. In the *s*-domain, if all the roots are in the left half-plane (i.e., to the left of the imaginary axis), then the feedback loop is guaranteed to be asymptotically stable and will converge to a single output value. If one or more roots are in the right half-plane, then the process is unstable. If one or more roots lie on the imaginary axis and none are in the right half-plane, then the process is considered to be marginally stable.

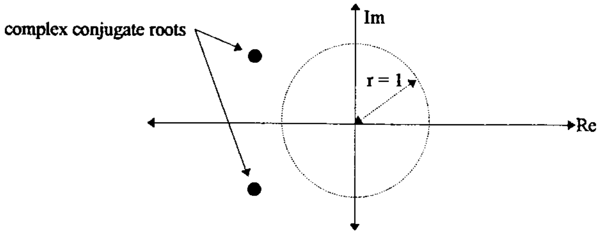

FIGURE 6.4.1 Placement of roots in the imaginary plane (showing unit circle).

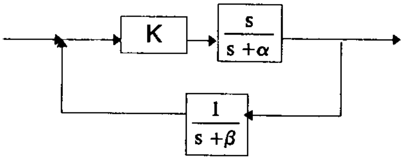

FIGURE 6.4.2 Simple feedback control loop.

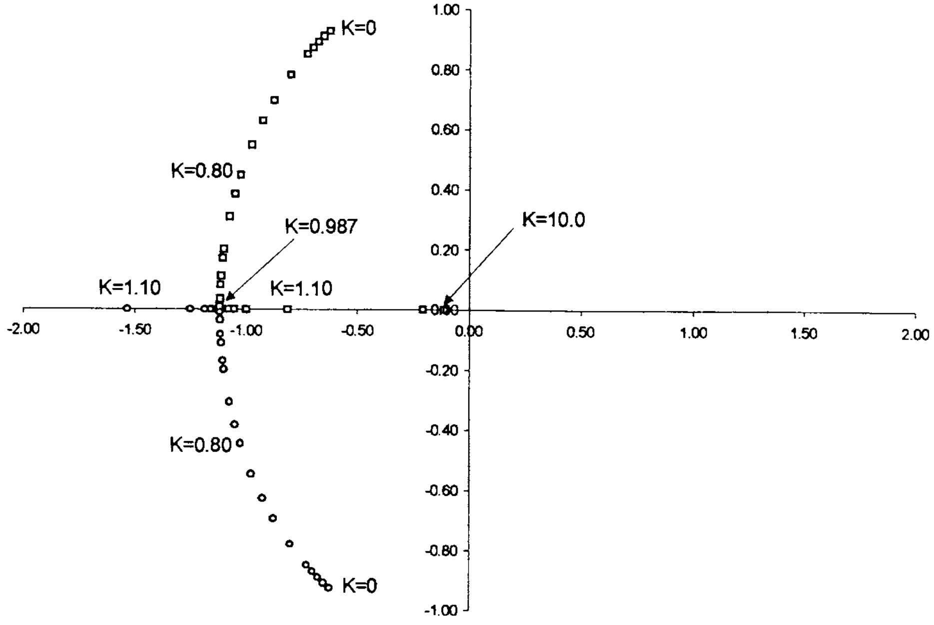

FIGURE 6.4.3 Root locus of $s^2 + (1.25 + K)s + 1.25 = 0$.

In the z-domain, if all the roots lie within the unit circle about the origin, then the feedback loop is asymptotically stable and will converge. If one or more roots lie outside the unit circle, then the process is unstable. If one or more roots lie on the unit circle and none are outside the unit circle, then the process is marginally stable.

Root locus example: Consider the feedback loop shown in Figure 6.4.2. The characteristic equation is given by $1 + GH = 0$, or

$$1+K\left(\frac{s}{s+\alpha}\right)\left(\frac{1}{s+\beta}\right)=0$$

For different values of K the roots of this equation can be plotted. The graph in Figure 6.4.3 shows an example plot when the characteristic equation is given by $s^2 + (1.25 + K)s + 1.25 = 0$. The plot shows that a system described by this characteristic demonstrates stable response for a process gain of $0.0 \leq K \leq 10.0$. For gains greater than 10, at least one root exists in the right half-plane and the process is not under stable control. Note that the root locus plot is always symmetric about the real axis and that the number of separate segments of the locus is equal to the number of roots of the characteristic equation (i.e., the number of poles of the closed-loop transfer function).

Routh–Hurwitz Stability Criteria

The Routh–Hurwitz method is an tabular manipulation of the characteristic equation in the frequency domain and is used to assess stability. If the characteristic equation is given by

$$a_0 s^n + a_1 s^{n-1} + \ldots + a_{n-1} s + a_n = 0$$

then the Routh–Hurwitz method constructs a table from the coefficients as follows:

$$\begin{array}{ccccc}
s^n & a_0 & a_2 & a_4 & \cdots \\
s^{n-1} & a_1 & a_3 & a_5 & \cdots \\
s^{n-2} & X_1 & X_2 & X_3 & \cdots \\
s^{n-3} & Y_1 & Y_2 & Y_3 & \cdots \\
\vdots & \vdots & \vdots & \vdots & \cdots
\end{array}$$

where

$$X_1 = \frac{a_1 a_2 - a_0 a_3}{a_1}; \qquad X_2 = \frac{a_1 a_4 - a_0 a_5}{a_1}; \qquad X_3 = \frac{a_1 a_6 - a_0 a_7}{a_1} \cdots$$

$$Y_1 = \frac{X_1 a_3 - a_1 X_2}{X_1}; \qquad Y_2 = \frac{X_1 a_5 - a_1 X_3}{X_1} \cdots$$

and so forth. The number of roots in the right-hand plane of the *s*-domain is equal to the number of sign changes in the first column, i.e., the column containing a_0, a_1, X_1, Y_1, etc. In other words, if all the elements in the first column have the same sign, then no roots are in the right-hand plane and the process is stably controlled. Also, for special cases of the characteristic equation:

- If the first element of any row is zero but the remaining elements are not, then use some small value ε and interpret the final results as $\varepsilon \to 0$.
- If one of the rows before the final row is entirely zeros, then (1) there is at least one pair of real roots of equal magnitude but opposite signs; or (2) there is at least one pair of imaginary roots that lie on the imaginary axis; or (3) there are complex roots symmetric about the origin.

Field Commissioning — Installation, Calibration, Maintenance

Tuning of Feedback Loops

The *tuning* of a controller involves finding controller gains that will ensure at least a critically damped response of the process to a change in setpoint or process disturbance. A good starting point for PID constants is that derived during the design phase by the stability assessment approaches described earlier. However, real processes do not necessarily behave as their models would suggest and actual field tuning of controls is needed during the system commissioning process.

Pole-Zero Cancellation

One method of obtaining the desired critically damped response of a process is to determine the closed-loop transfer function in the form

$$\frac{C}{R} = \frac{(s + A_1)(s + A_2)\ldots(s + A_m)}{(s + B_1)(s + B_2)\ldots(s + B_n)}$$

The coefficients *A* and *B* will depend on the process characteristics and the controller gains. The objective of pole-zero cancellation is to find values for the controller gains that will set some numerator

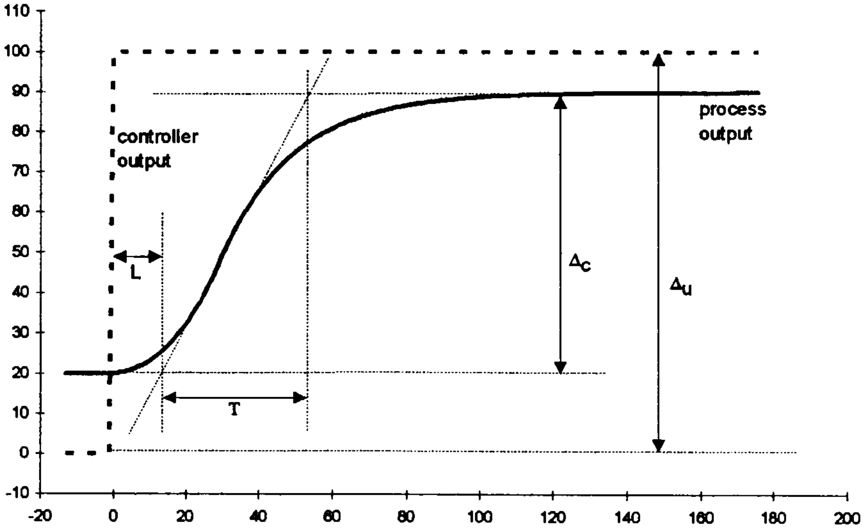

FIGURE 6.4.4 Reaction curve components.

coefficients equal to those in the denominator, effectively canceling terms. As can be imagined, however, this can be a very difficult exercise, particularly when working with complex roots of the equations. This method can only be used with very simple system models.

Reaction Curve Techniques

Often it is advisable to test a feedback loop *in situ*. Several techniques have been developed that allow for the derivation of "good" PID constants for a given open-loop response. Consider the process response shown in Figure 6.4.4 where Δ_c is the change of process output; Δ_u is the change of controller; L is the time between change and intersection; and T is the time between lower intersection and upper intersection. The following variables can be defined: $A = \Delta_u/\Delta_c$; $B = T/L$, and $R = L/T$. These values can be used with the equations given in Table 6.4.1 to estimate "decent" control constants. The users of these constants

TABLE 6.4.1 Equations for Finding PID Constants Using Zeigler–Nichols and Cohen and Coon Reaction Curve Tests

	Zeigler–Nichols			Cohen and Coon		
Controller Components	K_p	$\frac{K_p}{K_i}$	$\frac{K_d}{K_p}$	K_p	$\frac{K_p}{K_i}$	$\frac{K_d}{K_p}$
P	AB	—	—	$AB\left(1+\frac{R}{3}\right)$	—	—
P + I	$0.9AB$	$3.3L$	—	$AB\left(1.1+\frac{R}{12}\right)$	$L\frac{30+3R}{9+20R}$	—
P + D	—	—	—	$AB\left(1.25+\frac{R}{6}\right)$	—	$L\frac{6-2R}{22+3R}$
P + I + D	$1.2AB$	$2L$	$0.5L$	$AB\left(1.33+\frac{R}{4}\right)$	$L\frac{32+6R}{13+8R}$	$L\frac{4}{11+2R}$

TABLE 6.4.2 Equations for Estimating PID Constants Using the Ultimate Frequency Test

Controller Components	K_p	$\frac{K_p}{K_i}$	$\frac{K_d}{K_p}$
P	$0.5\ K_p^*$	—	—
P + I	$0.45\ K_p^*$	$0.8T^*$	—
P + I + D	$0.6\ K_p^*$	$0.5T^*$	$0.125T^*$

should be aware, however, that they are based on the typical response of second-order systems and may not provide good values for all processes.

Ultimate Frequency

The ultimate frequency test involves increasing the proportional gain of a process until it begins steady-state oscillations. K_p^* is defined as the proportional gain that results in steady oscillations of the controlled system and T^* is the period of the oscillations. The desired controller gains are given in Table 6.4.2. Note that the use of the ultimate period test is not always easy to do in practice and may be prohibited in certain cases by a process operations manager.

6.5 Advanced Control Topics

Peter S. Curtiss, Jan Kreider, Ronald M. Nelson, and Shou-Heng Huang

Neural Network-Based Predictive/Adaptive Controllers

Neural networks are powerful modeling tools used for predicting nonlinear behavior of processes and require a minimum of knowledge about the physical system involved. This approach can be used to predict the behavior of a process and can calculate the future value of the process variables. The effects of current modifications to the future value of the controlled process can be easily quantified and used to obtain the desired process response.

Overview of Neural Networks

The artificial neural network attempts to mimic a few aspects of the behavior of biological neural networks. Inputs to a biological nerve cell are carried along the dendrites of that cell. These inputs come from the positive impulse signals of other cells but may be converted to negative signals by the chemical interactions at the synapse between the cells. All of the inputs are then carried to the soma where they add or subtract from the overall potential difference between the interior of the soma and the surrounding fluid. Once the cell potential rises above a certain level, the cell “fires” and sends signals to other cells along its axon.

The artificial cell behaves in much the same way, except that the output signal is analog instead of digital. Signals from sending cells are passed along to a receiving cell through a series of connections. Each connection has an associated weighting factor that acts as a multiplier on the signal from the sending cell. All the inputs to a cell are summed (along with a cell bias, if included) and the resulting value is used to generate the output of the receiving cell. The output of the cell is referred to as the cell *activation* and the function that uses the net input to generate the cell activation is called the *activation function*. The latter can theoretically be of any form, although linear and sigmoidal functions are frequently used. Figure 6.5.1 shows a comparison between a biological cell and an artificial cell.

When many different cells are combined together into a richly connected network (Figure 6.5.2), the result can behave mathematically as a nonlinear regression capable of mapping inputs to outputs for complex relationships. The trick is to find a series of weights W that allow the network to provide the desired outputs using specific inputs. A number of references to network training are cited in the bibliography at the end of this chapter.

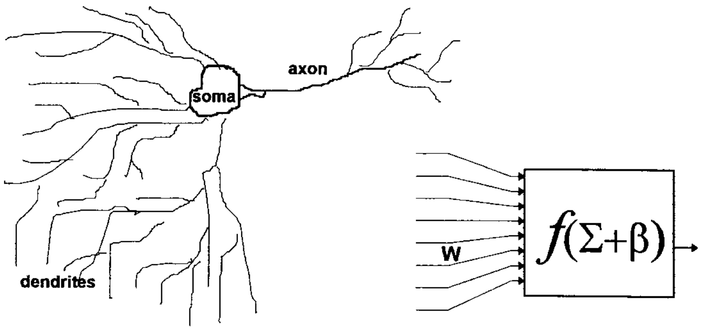

FIGURE 6.5.1 Biological cell vs. artificial cell.

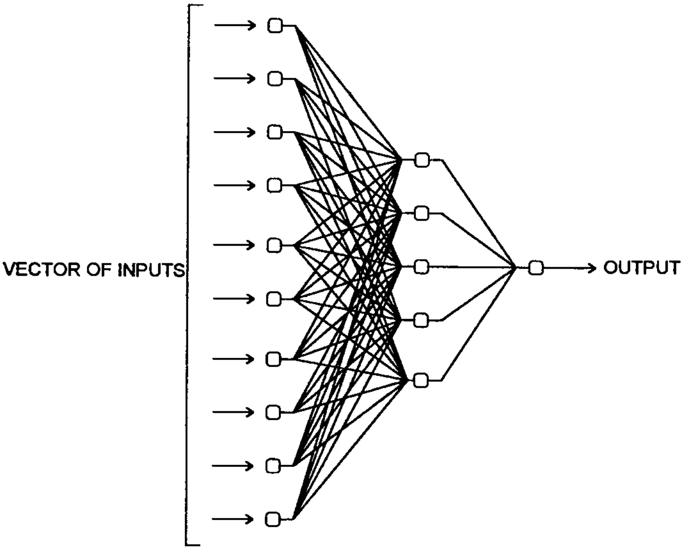

FIGURE 6.5.2 Artificial neural network consisting of several layers of mathematical models of biological neurons.

Using Networks for Controlling Feedback Loop Processes

Neural networks offer the potential for and have demonstrated improved control of processes through predictive techniques. The concept is fairly simple: train a network to predict the dynamic behavior of a process and then use these predictions to modify the controller output to place the process at a desired setpoint $R(t)$ at some time in the future. Initial results from computer simulations of such a controller are presented in Curtiss et al. (1993a, b, c). Anderson (1989) described a computer simulation in which a network was trained to recognize the dynamic properties of an inverted pendulum (e.g., a broom balanced on an open palm). A control system was developed in which the angle and position of the pendulum were used to move the supporting base in order to maintain the pendulum upright. A neural network-based predictive controller is outlined in the classic discussion by Nguyen and Widrow (1989) on the "truck backer-upper" problem in which a tractor-trailer is backed into position at a loading dock.

Properly tuned fixed-gain controllers will usually work over a relatively wide range of process operation provided that the external perturbations and influences are small or time invariant. With nonlinear processes, however, a conventional control algorithm can lead to unstable control if the gains were chosen for a range different from the current operating conditions.

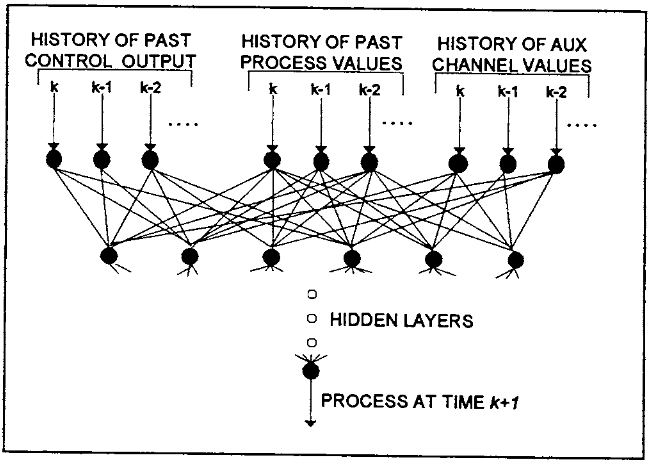

FIGURE 6.5.3 Network used for process prediction.

Architecture of the Network

With the neural network approach, it is possible to overcome these problems by using as many additional salient inputs (the *auxiliary* inputs) as necessary and by incorporating an inherently nonlinear model to accomplish the control objectives. The network is trained using examples of the time-dependent relationship between a value of the feedback and previous values of the feedback, the controller output, and the auxiliary inputs. An example of the network architecture required for this is shown in Figure 6.5.3. In practice, it is not necessary to limit the number of previous measurements of any of the inputs, although the final size of the network and the corresponding training time and memory requirements need to be taken into consideration.

The network, once trained, can predict the future feedback value for any controller output. The trick is to find the controller output that causes the future process value to match the setpoint. This is accomplished by finding the derivative of the future error with respect to the current controller signal. Starting with the current process conditions, the feedback value is predicted at each time step into the future over a preset time window as shown in Figure 6.5.4. During each step of the prediction, the values for the controller output and auxiliary inputs are held constant. This simulation is performed twice: the first time with a small increase in the controller output and the second time with a small decrease. This allows for calculation of the change of the future process value (and thus the change of the future error) as a function of the change in the current controller output. The controller output is then modified by

$$\Delta U(t) = -G_{net} \cdot E_f(t) \frac{\partial E_f(t)}{\partial U(t)}$$

where E_f is the future error and G_{net} is the network controller gain. For a multiple-output controller, the additional outputs are simply added as more outputs of the network and the future predictions repeated several times to find the correct partial derivatives.

Many different variations on this theme are possible — for example, using the sum of the absolute values of all the errors over the prediction window (or the sum of the square of the errors, etc.) instead of simply the future error. Computer simulated results of such tests are provided by Curtiss et al. (1993c).

Estimating Size of the Prediction Time Window

It is possible to use the network model to determine the size of the time window by estimating the amount of time required for the process to reach some future steady state after a simulated change in the controller output. An example of such an open-loop response is shown in Figure 6.5.5. Here the

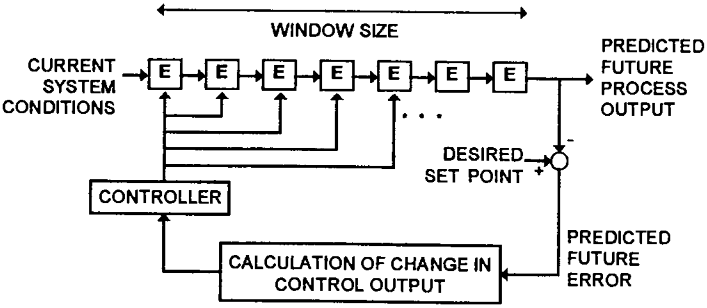

FIGURE 6.5.4 Schematic of procedure for determining future process value and error.

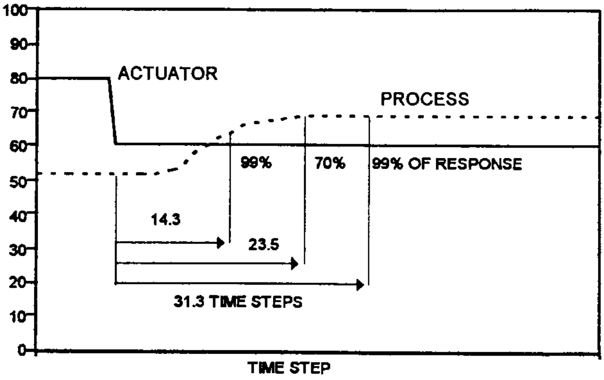

FIGURE 6.5.5 Example of computer-simulated process step change (used to determine size of time window.)

network is simulating the response of a reverse-acting process after a decrease in actuator position at time step 0. About 70% (ln2) of total rise time is achieved after 15 time steps. This kind of calculation can be performed during the control sequence and should indicate the proper time window size.

Example of PID vs. Network Controller

Figure 6.5.6 shows an example of a process under PID control that demonstrates nonlinearity at different ranges of actuator position. Figure 6.5.7 shows the same process under the influence of a predictive neural network controller that had been trained on the process. Note that the network-based controller does not show the same problems of unstable control in certain actuator ranges. The size of the time window (15 time steps) was determined using the method discussed in the previous subsection.

Using Networks as Supervisory Controllers

The previous section discussed the use of neural networks to minimize a predicted error of a feedback-loop process. It is possible to apply a similar methodology for supervisory plant control to optimize the process according to some cost function. A network is first trained to predict the cost function under a wide range of operating conditions. This network is then used to predict what will happen with different control strategies. Figure 6.5.8 shows a schematic of this technique. The left side of the figure shows the training mode, where the network is attempting to associate the various plant inputs with the cost function output. There can be multiple inputs, including uncontrollable variables (e.g., ambient conditions, plant loads, etc.) and controlled variables (i.e., the various process setpoints.)

Once the network is sufficiently trained, it is used to find values for the setpoints under any set of uncontrolled variables. The technique for doing so is similar to the back-propagation training technique of the network. The inputs corresponding to the controlled variables are replaced with *virtual nodes*

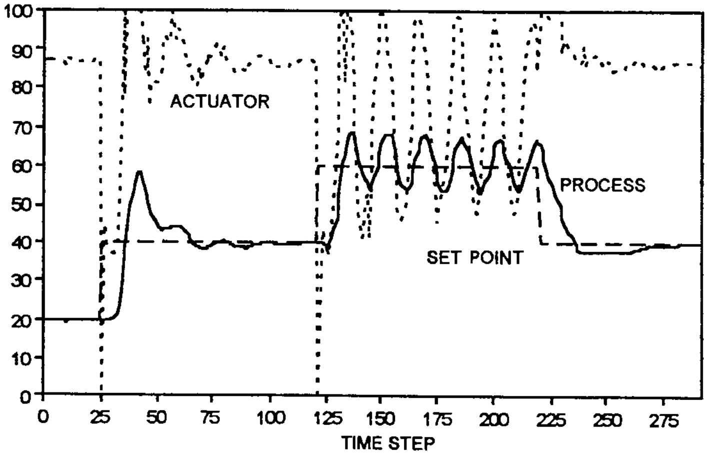

FIGURE 6.5.6 Example of computer simulation using PID controller.

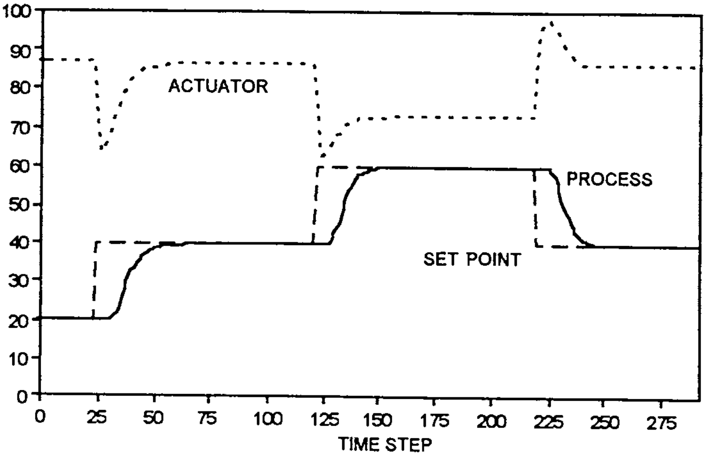

FIGURE 6.5.7 Example of computer simulation using neural network controller.

whose outputs are always unity. These nodes are connected to the predictor network through adjustable weights.

The optimization occurs by finding values for these weights that allow the model to predict a desired output. These weights can be found through any number of search methods, including the gradient descent technique used in back-propagation training. In this case, the predictor network is "trained" normally, except that all weights in the network are static except those connected to the virtual nodes. Once weights have been found that produce the desired output, the setpoints can be found from direct interpretation of these weights. Constraints can be imposed on the weights through physical limitations (e.g., freezing points) or from predictions from local-loop neural network controllers.

Fuzzy Logic Controllers

Fuzzy logic controllers use conditional relationships to analyze one or more inputs — that is, the inputs are subject to a series of *if…then* queries to produce some intermediate values. An example would be something like a simple cruise control on an automobile:

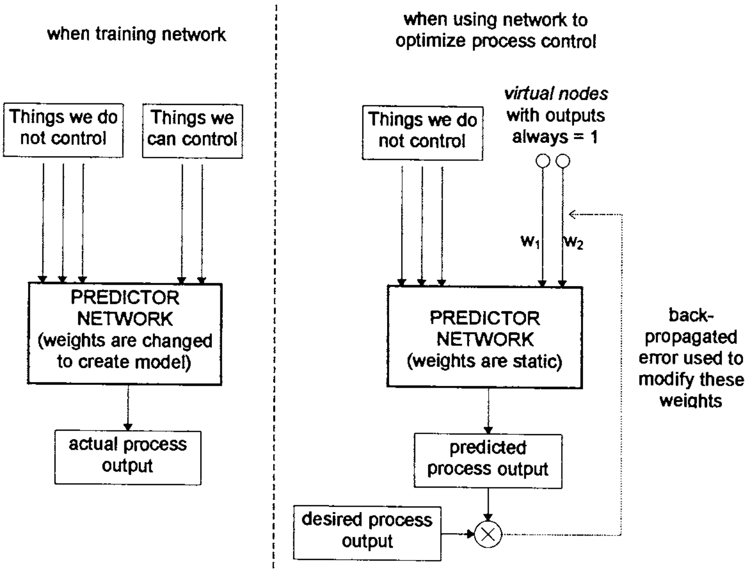

FIGURE 6.5.8 Using network model to optimize process control.

- *If* vehicle speed = much lower than setpoint, *then* need to increase speed = large
- *If* vehicle speed = slightly lower than setpoint, *then* need to increase speed = small

These intermediate values are then used to determine the actual change of speed in the car:

- *If* need to increase speed = large, *then* increase of throttle position = 10%
- *If* need to increase speed = small, *then* increase of throttle position = 3%

In fuzzy control, the satisfaction of a particular *if* statement may not lead to or be restricted by a true or false response. A range of weighting coefficients is assigned to a particular conditional, with the coefficients generally decreasing as the certainty of a specific condition decreases.

In the preceding example, "need to increase speed = large" may be assigned a certainty of 1 when the speed of the vehicle is less than 50% of the desired speed of the car. This certainty will decrease as the speed of the car increases, so that "need to increase speed = large" may be 0 when the speed of the car is greater than 90% of the desired speed, but the certainty of "need to increase speed = small" will be large. It is possible that, for a given speed of the car, two or more conditions may be satisfied with different magnitudes of certainty. These conditions can then be applied to the output rules along with their respective certainties to determine the actual increase (or decrease) in the controller output. When the speed of the car is below the desired speed, the initial rules may yield, for example:

- Need to increase speed = large with certainty = 0.3
- Need to increase speed = small with certainty = 0.7

The actual output would then be

$$\text{Increase of throttle position} = (0.3 \times 10\% + 0.7 \times 3\%)/(0.3 + 0.7) = 5.1\%$$

The following subsection formalizes some of these ideas and includes a detailed example. The chapter on mathematics contains the formalism underlying fuzzy set theory and fuzzy logic. The reader is referred to that chapter and one that follows for the technical basis for fuzzy logic controllers.

Fuzzy Logic Controllers for Mechanical Systems

Introduction

In the last decade, fuzzy logic controllers (FLCs) have been receiving more attention (Daley and Gill, 1985; Leigh and Wetton, 1983; Xu, 1989; Yasunobu and Miyamoto, 1985), not only in test cases but also in real industrial process control applications, including building mechanical systems (Meijer, 1992; Sakai and Ohkusa, 1985; Ono et al., 1989; Togai and Maski 1991; Huang and Nelson, 1991). The basic idea of this approach is to incorporate the experience of human operators in the design of controllers. From a set of linguistic rules describing operators' control strategies, a control algorithm can be constructed (Ralston and Ward, 1985).

Computer simulations and experiments have shown that FLCs may have better performance than those obtained by conventional controllers. In particular, FLCs appear very useful when the processes are too complex for analysis using conventional control algorithms or when the available information is qualitative, inexact, or uncertain. Thus, fuzzy logic control may be viewed as a compromise between conventional precise mathematical control and human-like decision making, as indicated by Gupta (Gupta and Tsukamoto, 1980).

However, fuzzy logic controllers sometimes fail to obtain satisfactory results with the initial rule set drawn from the operators' experiences. This is because some differences exist between the way a plant is operated by an experienced operator and by a fuzzy logic controller using the rules based directly on his experience. It is often difficult to express human experience exactly using linguistic rules in a simple form. Sometimes no experience is available that can be used to construct control rules for FLCs. In these cases, it is necessary to design, develop, and modify control rules for FLCs to obtain optimal performance. Few discussions have been undertaken about rule development and adjustment strategies for FLCs (Scharf and Mandic, 1985; Ollero and Williams, 1989; Sheridah, 1984; Wakileh and Gill, 1988).

Basic Aspects of an FLC

An FLC includes three parts: fuzzifier; fuzzy reasoning unit; and defuzzifier. The fuzzifier converts ordinary inputs into their fuzzy counterparts; the fuzzy reasoning unit creates fuzzy control signals based on these fuzzy variables and the defuzzifier converts the fuzzy control signals into the real control outputs. The block diagram of a fuzzy control system is shown in Figure 6.5.9, where e, d, and u are tracking error, derivative error, and output control action; $\tilde{e}$, $\tilde{d}$, and $\tilde{u}$ are their fuzzy counterparts, respectively; y is the controlled parameter; and r is the set point for y. K_p is the scale factor for e; K_d is the scale factor for d; and K_o is the output gain.

The control rules expressed in natural language are expressed in the following form:

$$\text{IF } (e \text{ is } A) \text{ AND } (d \text{ is } B) \text{ THEN } (u \text{ is } C)$$

where A, B, and C are fuzzy subsets defined on the universes of discourse of e, d, and u, respectively. Every rule is interpreted into a fuzzy reasoning matrix:

$$R_k = \left[A_k(e) \otimes B_k(d) \right]^{\Theta} \otimes C_k(u) \qquad k = (1, N)$$

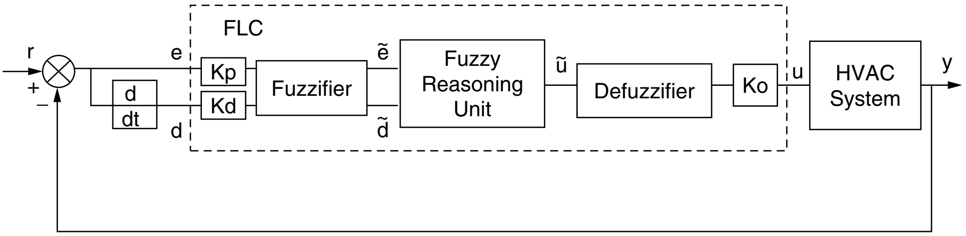

FIGURE 6.5.9 The block diagram of a fuzzy control system.

TABLE 6.5.1 The Membership Function of Input of FLC

$A(e)$, $B(d)$	–6	–5	–4	–3	–2	–1	0	1	2	3	4	5	6
PL	0.0	0.0	0.0	0.0	0.0	0.0	0.0	0.0	0.0	0.1	0.5	0.8	1.0
PM	0.0	0.0	0.0	0.0	0.0	0.0	0.0	0.1	0.5	0.8	1.0	0.8	0.5
PS	0.0	0.0	0.0	0.0	0.0	0.1	0.5	0.8	1.0	0.8	0.5	0.1	0.0
ZZ	0.0	0.0	0.0	0.1	0.5	0.8	1.0	0.8	0.5	0.1	0.0	0.0	0.0
NS	0.0	0.1	0.5	0.8	1.0	0.8	0.5	0.1	0.0	0.0	0.0	0.0	0.0
NM	0.5	0.8	1.0	0.8	0.5	0.1	0.0	0.0	0.0	0.0	0.0	0.0	0.0
NL	1.0	0.8	0.5	0.1	0.0	0.0	0.0	0.0	0.0	0.0	0.0	0.0	0.0

where N is the number of rules, the symbol $\otimes$ denotes aggregation operator, and the symbol Θ denotes an align-turning operator (see Chap. 19). The general fuzzy relation matrix R can be constructed as the union of the individual rules:

$$R = \bigcup_{k=1}^{N} R_k$$

This matrix represents the relationship between the fuzzy inputs and the fuzzy control output. The fuzzy control output can then be calculated from the known fuzzy input $\tilde{e}$ and $\tilde{d}$ by:

$$\tilde{u} = \left[\tilde{e} \otimes \tilde{d}\right]^{\Theta} \circ R$$

where the symbol $\circ$ denotes the max–min composition operator (see Chapter 19).

The input universe of discourse for tracking error e or derivative error d is divided into several degrees connected with a number of fuzzy subsets by membership functions. In this study, e and d can each range from –6 to +6, and 13 degrees are used:

–6, –5, –4, –3, –2, –1, 0, 1, 2, 3, 4, 5, 6.

Also, seven fuzzy subsets are defined as:

NL, NM, NS, ZZ, PS, PM, PL

where the first letters N and P mean negative and positive; the second letters L, M, and S mean large, middle, and small; and ZZ means zero.

These degrees and fuzzy subsets are shown in Table 6.5.1, which uses a 1.0-0.8-0.5-0.1 distribution. For example, if $e = 3$, then its membership in PL is 0.1, its membership in PM is 0.8, etc. A similar analysis is given to the outputs for the control action indicated in Table 6.5.2, which uses a 1.0-0.7-0.2 distribution.

The fuzzifier converts ordinary inputs into their fuzzy counterparts. In this study, a fuzzy singleton is used as a fuzzification strategy, which interprets an input, e (or d), into a fuzzy value, $\tilde{e}$ (or $\tilde{d}$), with membership function (μ) equal to zero except at the element nearest to the real input, where $\mu = 1.0$. For example, if $e = 3.2$ and the nearest element is 3, then the fuzzy singleton will be:

$$\tilde{d} = (0, 0, 0, 0, 0, 0, 0, 0, 0, 1, 0, 0, 0.)$$

This fuzzy singleton has membership function $\mu = 1.0$ at the point of element $e = 3$. The defuzzifier converts the fuzzy control output created by the rule-based fuzzy reasoning unit into a real control action. In this study, weighted combination method is used as defuzzification strategy, which can be explained by the following example:

TABLE 6.5.2 The Membership Function of Output of FLC

$C(u)$	–6	–5	–4	–3	–2	–1	0	1	2	3	4	5	6
VS (level 7)	0.0	0.0	0.0	0.0	0.0	0.0	0.0	0.0	0.0	0.0	0.2	0.7	1.0
ST (level 6)	0.0	0.0	0.0	0.0	0.0	0.0	0.0	0.0	0.2	0.7	1.0	0.7	0.2
SU (level 5)	0.0	0.0	0.0	0.0	0.0	0.0	0.2	0.7	1.0	0.7	0.2	0.0	0.0
ME (level 4)	0.0	0.0	0.0	0.0	0.2	0.7	1.0	0.7	0.2	0.0	0.0	0.0	0.0
SS (level 3)	0.0	0.0	0.2	0.7	1.0	0.7	0.2	0.0	0.0	0.0	0.0	0.0	0.0
SM (level 2)	0.2	0.7	1.0	0.7	0.2	0.0	0.0	0.0	0.0	0.0	0.0	0.0	0.0
TI (level 1)	1.0	0.7	0.2	0.0	0.0	0.0	0.0	0.0	0.0	0.0	0.0	0.0	0.0

Note: Abbreviations mean that the output control actions are Very Strong; Strong; SUbstrong; Medium; Slightly Small; Small; and TIny.

If

$$\tilde{u} = (0, 0, 0, 0, 0, 0, 0, 0.2, 0.4, 0.8, 0.7, 0.5, 0.1.)$$

then

$$u = [0.2(1) + 0.4(2) + 0.8(3) + 0.7(4) + 0.5(5) + 0.1(6)]/[0.2 + 0.4 + 0.8 + 0.7 + 0.5 + 0.1] = 3.4$$

Rule Refinement

An FLC is characterized by a set of linguistic statements that are usually in the form of "if–then"' rules. The initial set of rules is usually constructed based on the operators' experiences, or sometimes by analyzing the dynamic process of the controlled plant. Both approaches require modifying the initial set of rules to obtain an optimal rule set. This is called *rule refinement*.

Figure 6.5.10 shows an initial rule set analyzed on a "linguistic plane." The horizontal axis expresses the fuzzy subsets defined on the universe of discourse for the tracking error (e), and the vertical axis expresses the fuzzy subsets defined on the universe of discourse for the derivative error (d). Both have seven fuzzy "values": NL, NM, NS, ZZ, PS, PM, and PL. Output control action levels are on the cross points of these fuzzy values; these are also fuzzy subsets having seven values from level 1 (tiny) to level 7 (very strong). For example, the cross point of e = NM and d = PM indicates u = level 5. This corresponds to the rule:

IF (e is NM) AND (d is PM) THEN (u is level 5)

For example, the initial rule set could be based on the following control strategies. First, it tries to keep a proportional relationship between the control action (u) and the tracking error (e). Note that if the derivative error (d) is ZZ, then the output control action (u) increases from level 1 to level 7 when the tracking error (e) changes from NL to PL. Second, the influence of derivative error (d) is considered such that if it is positive, then the control action (u) is increased a little bit, and if it is negative, then the control action (u) is decreased. For example, if the tracking error (e) keeps PM, the control action (u) increases from level 6 to level 7 when the derivative error (d) is positive, and it decreases from level 6 to level 5 when the derivative error (d) is negative.

Consider a second order plant with a transfer function:

$$H(s) = \frac{1.0}{s^2 + 0.1s + 1.0}$$

that is controlled using the initial rule set to respond to a step input for computer simulation.

The performance trajectory of the FLC is shown by the arrows in Figure 6.5.10 and the dynamic process of the normalized controlled parameter (CP) is shown in Figure 6.5.11, where the horizontal axis indicates the number of sample period (SP). The dynamic process can be divided into two stages.

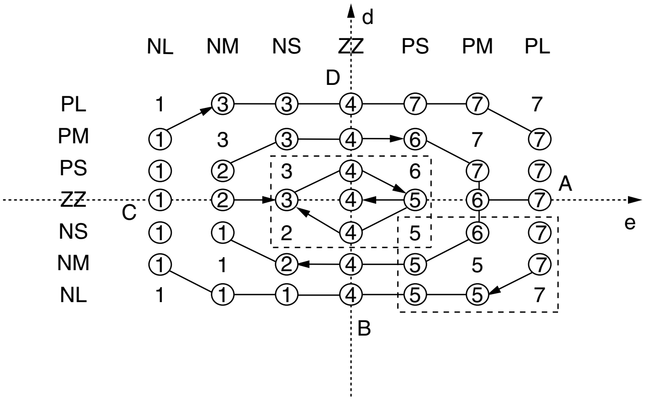

FIGURE 6.5.10 The initial rule set and performance trajectory on the linguistic plane.

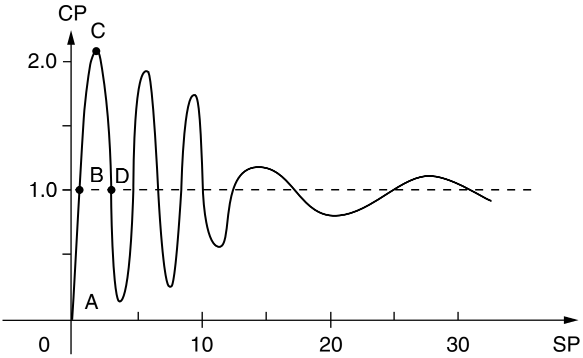

FIGURE 6.5.11 The dynamic process corresponding to Figure 6.5.10.

At the first stage, there is a strong oscillation with a higher frequency and, at the second stage, there is a moderate swing with a smaller frequency. Looking at the performance trajectory in the linguistic plane reveals that the stronger oscillation occurs at the out-cycle (points further from the center). As time increases, the state moves to the in-cycle near the center of the plane and becomes moderate. This shows that FLCs have the desirable property of a structure-variable controller. The rules at the out-cycle belong to one kind of structure for the first stage, and the rules at the in-cycle belong to another structure for the second stage.

If the initial rule set does not satisfy a good design for a controller, then it can be modified by intuitive reasoning. A rule set is often symmetrically positioned about the central point, which is the desired stable operating point at which the tracking error (e) and the derivative error (d) equal zero and the control action (u) is medium. When a positive step increase is imposed to the set point, the tracking error (e) has the biggest value and the derivative error (d) is zero at the beginning time (point A in the linguistic plane). With the regulating action, the tracking error (e) will decrease, the derivative error (d) will be negative, and the performance trajectory will enter into the right-bottom block in the linguistic plane. Thus, the rules in this area have the most important effect on the behavior of the first stage of the dynamic process. The most important area responsible for the behavior of the second stage is the central block.

To avoid strong oscillations, it is apparent that the control actions in the right-bottom block should be decreased. The modified rule set and its simulation of response to a step input are shown in Figure 6.5.12. The performance trajectory expressed in the linguistic plane is just like spiral (Figure 6.5.12). It can be seen that the performance of the control system has been improved, but a small oscillation still exists and a little overshoot is indicated by point C in Figure 6.5.13. Once again, the rule set is modified and the final rule set and its simulation of response to a step input are shown in Figure 6.5.16 and Figure 6.5.17.

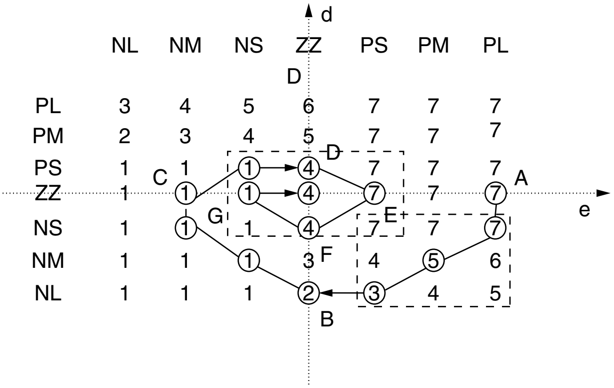

	NL	NM	NS	ZZ	PS	PM	PL
PL	3	4	5	6	7	7	7
PM	2	3	4	5	7	7	7
PS	1	1	①	④	7	7	7
ZZ	1	①	①	④	⑦	7	⑦
NS	1	①	1	④	7	7	⑦
NM	1	1	①	3	4	⑤	6
NL	1	1	1	②	③	4	5

FIGURE 6.5.12 The second rule set on the linguistic plane.

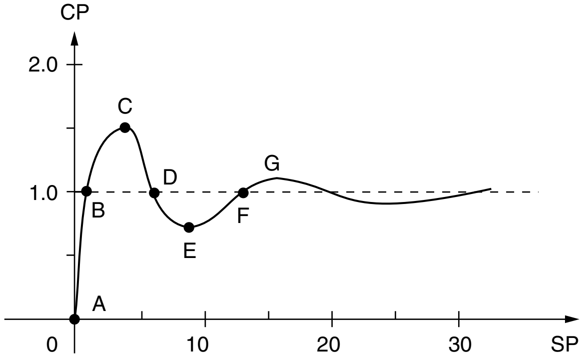

FIGURE 6.5.13 The dynamic process corresponding to Figure 6.5.12.

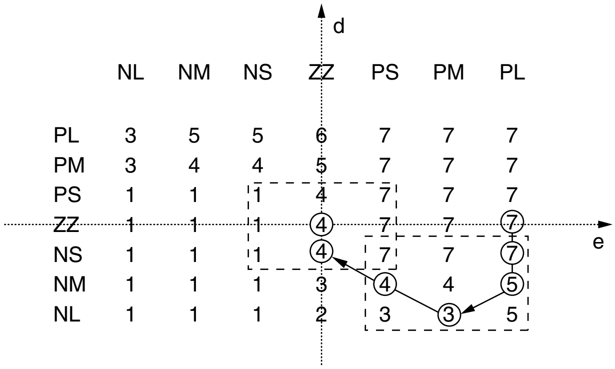

	NL	NM	NS	ZZ	PS	PM	PL
PL	3	5	5	6	7	7	7
PM	3	4	4	5	7	7	7
PS	1	1	1	4	7	7	7
ZZ	1	1	1	④	7	7	⑦
NS	1	1	1	④	7	7	⑦
NM	1	1	1	3	④	4	⑤
NL	1	1	1	2	3	③	5

FIGURE 6.5.14 The third rule set on the linguistic plane.

The final rule set gives good performance with a short rise time and a very small overshoot and is considered satisfactory.

By analyzing the performance trajectory on the linguistic plane, a rule set is refined. It relies heavily on intuitive reasoning when comparing the dynamic process of the controlled parameter for the present rule set with the desired one.

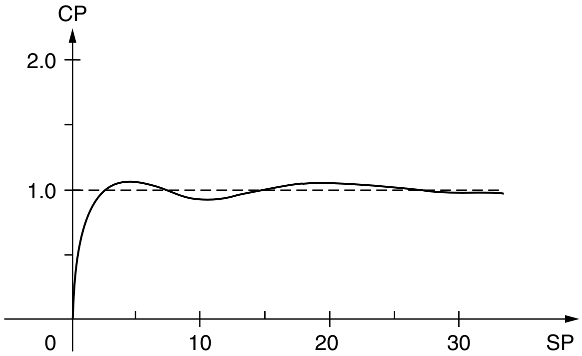

FIGURE 6.5.15 The dynamic process corresponding to Figure 6.5.14.

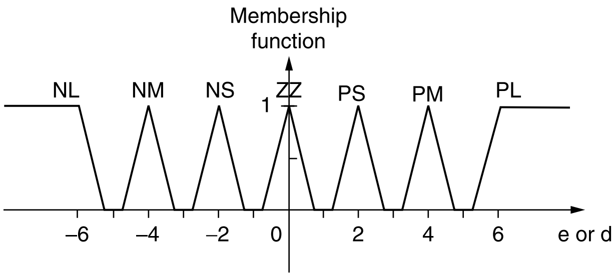

FIGURE 6.5.16 Noncomplete membership function.

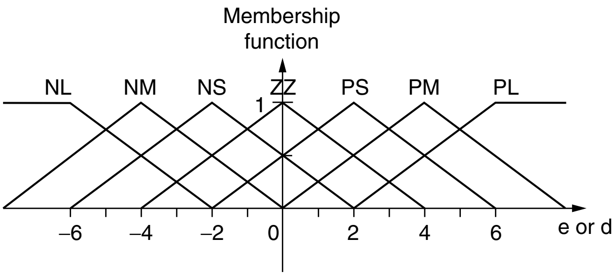

FIGURE 6.5.17 Heavy overlap membership function.

Completeness and Interaction of Rules and Selection of Membership Functions

The second significant influence on the behavior of an FLC is the membership functions. They should be chosen carefully in the adjustment process. As mentioned previously, the fuzzy subsets, language variables, NL, NM, NS, ZZ, PS, PM, and PL, are defined on the universe discourse of tracking error (e) or derivative error (d). Some possible membership functions are shown in Figure 6.5.16 through Figure 6.5.18. The membership functions should be chosen to make these language variables have suitable coverage on the universe of discourse.

For the case of Figure 6.5.16, the whole range is not covered by these language variables. For some values of e or d, the membership functions of all language variables are zero. In this case, an empty output control action could be created. This means that the control actions are lost for those points not covered by any input fuzzy subset. This is referred to as the noncompleteness of control rules. FLCs should satisfy the condition of completeness for their membership functions; the membership function shown in Figure 6.5.17 cannot be used for an effective fuzzy logic controller. In other words, the union of all fuzzy subsets, X_i, i = [1,7], should be greater than zero for all e $\in$ E, i.e.,

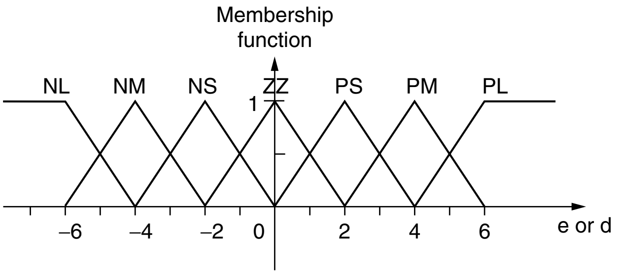

FIGURE 6.5.18 Moderate overlap membership function.

$$\forall e \in E \qquad \bigcup_{i=1}^{7} X_i(e) > 0$$

On the other hand, interaction can take place among the rules if the overlap of fuzzy subsets occurs on the range of the universe of discourse. In this case, the membership functions have the forms shown in Figure 6.5.17 and Figure 6.5.18. The interaction tends to smooth out the set of control rules. Consider the single-input–single-output case for simplicity. The rule set is:

$$\text{IF } (e \text{ is } A_i), \text{ THEN } (u \text{ is } C_i) \; i = [1,\mathrm{N}]$$

where N is the number of rules in the set. These rules are incorporated into a fuzzy relation matrix as follows:

$$R = \bigcup_{i=1}^{N} R_i = \bigcup_{i=1}^{N} \left(A_i \otimes C_i \right)$$

If the fuzzy value of input e is known as $\tilde{e}$, the fuzzy output $\tilde{u}$ then can be calculated as follows:

$$\tilde{u} = \tilde{e} \circ R$$

If $\tilde{e}$ is A_i, $\tilde{u}$ is expected to be C_i. However, now the interaction of rules due to overlap results in:

$$C_i \subseteq A_i \circ R$$

The equality is established only when no overlap occurs. This analysis is based on the fuzzy logic scheme including max–min composition operator. A more detailed example of the numeric calculation is given in the next subsection.

If the overlap is heavy, as shown in Figure 6.5.17, large deformation will occur and the control rules will lose their original shape. In the limit, as the membership functions become unity for all values, the output of the FLC will always be the same fuzzy quantity. This means that the fuzzy reasoning system conveys no valuable information and the FLC has lost its efficacy.

A moderate overlap, shown in Figure 6.5.18, is desirable to allow for reasoning with uncertainty and the need for completeness of the control rules. How does one determine the "size" of overlap? At present, intuitive judgment is used to choose membership functions when adjusting an FLC. There appears to be some latitude in choosing the amount of overlap on which the performance of an FLC does not change significantly. The quantitative analysis will be given after further research.

When the control rules are modified in the linguistic plane, the overlapping membership functions let the rules near the performance trajectory have an effect on the output control actions. This is because interactions occur among the neighboring rules.

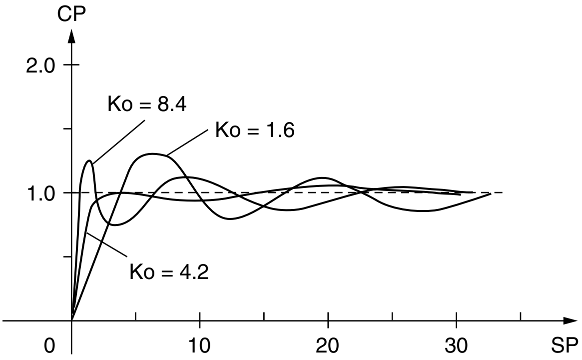

FIGURE 6.5.19 The influence of K_o on the behavior of FLCs.

Scale Factors and Output Gain

The scale factors, K_p and K_d, and the output gain, K_o, shown in Figure 6.5.19, also have significant influence on the behavior of an FLC. Their influence is not as complicated as those of rules and membership functions. The adjustment for the scale factors and output gain is comparatively simple.

The scale factor K_p relates the actual range of tracking error (e) to the universe of discourse (E) defined in the fuzzy logic system. In this work, E consists of 13 degrees as indicated earlier. Then K_p is determined as the ratio of the range of E to the range of the real variable:

$$K_p = \frac{E_{\max} - E_{\min}}{e_{\max} - e_{\min}}$$

For scale factor K_d, similar analysis leads to:

$$K_d = \frac{D_{\max} - D_{\min}}{d_{\max} - d_{\min}} \tag{6.5.1}$$

where D is the universe of discourse for derivative error (d) defined in the fuzzy logic system. Small K_p or K_d will narrow the control band, while large K_p or K_d will lead to loss of control for large inputs.

The output gain K_o is defined as follows:

$$K_o = \frac{u_{\max} - u_{\min}}{U_{\max} - U_{\min}} \tag{6.5.2}$$

This is the ratio of range of real output control action (u) to the range of its universe of discourse (U) defined in the fuzzy logic system. K_o acts as an amplification factor of the whole FLC.

Figure 6.5.19 shows the influence of K_o on the step response simulation of an FLC with the final rule set used in Figure 6.5.14. Increasing K_o results in a shorter rise time. The performance trajectory in the linguistic plane will become steeper for the first stage and oscillation occurs. Decreasing K_o results in a longer rise time and the performance trajectory in the linguistic plane will become moderate during the first stage. However, in this simulation, oscillation still occurred. This is because different K_o, larger or smaller, results in a new route of the performance trajectory, which will activate the different rules that might cause oscillation. Therefore, the influence of output gain, K_o, should be considered together with the change of the activated rules.

Conclusion

A fuzzy logic controller can perform much better than a conventional one, such as a PID controller, if the FLC has been well constructed. The main disadvantage of using FLCs today seems to be the lack of a systematic procedure for the design of FLCs. The general method for designing an FLC is to use trial and observation. No useful mathematical tool has yet been developed for the design of an FLC because of its fuzziness, complexity, and nonparameterization.

Three significant elements have notable influence on the behavior of a fuzzy logic controller:

- Control rules expressed in linguistic language
- Membership functions defined for fuzzy subsets
- Scale factors attached to the input and the output gains

The control rules play the main role in forming the dynamics of FLCs. The rule set can be analyzed and modified using the performance trajectory technique and evaluated using the dynamic process curve of the controlled parameter. The membership functions define the "shape" of fuzzy subsets. They should have appropriate width to avoid noncompleteness and suitable interaction among the fuzzy control rules. The scale factors (K_p and K_d) and output gain (K_o) serve as amplification factors.

At present, each application must be individually designed. The initial sets of rules are specifically set up for different applications. Work is now under way to develop a self-adaptive fuzzy logic controller, which will choose the initial set of rules automatically according to the process dynamics and refine it on the basis of the global performance evaluation.

6.6 Control of Distributed Generation Technologies

Peter S. Curtiss and Jan F. Kreider

Distributed power generation (DG) is any small-scale power generation technology that provides electric power at a site closer to customers than central station generation; it is usually interconnected to the distribution system or directly to the customer's facilities (Curtiss et al., 1999). Distributed generation technologies include small combustion turbine generators; internal combustion; reciprocating engines and generators; photovoltaic panels; wind turbines; and fuel cells. Table 6.6.1 provides an overview of feasible DG technologies using present or near-future technologies.

Distributed generation can provide a multitude of services to utilities and consumers, including standby generation; peak shaving capability; baseload generation; or cogeneration. Less well-understood benefits including ancillary services such as voltage/VAR support, network stability, and others may ultimately be of more economic benefit than simple energy-related benefits.

Electric restructuring has spurred the consideration of DG power because the buyers and sellers of electricity will need to be more responsive to market forces. Central utilities suffer from the burden of significant stranded costs; however, DG avoids this cost. DG is a priority in parts of the country where the spinning reserve margins are shrinking, where industrial and commercial users and transmission and distribution (T&D) constraints are limiting power flows (DCPA, 1998).

TABLE 6.6.1 Summary of Distributed Generation Technologies

	IC Engine	Turbine	PVs	Wind Turbine	Fuel Cells
Dispatchable	Yes	Yes	No	No	Yes
Capacity range (MW)	0.05–5	0.025–25	0.001–1	0.01–1	0.2–2
Efficiency	35%	15–35%	6–19%	25%	30–55%
Capital cost ($/kW)	200–350	450–850	~6000	~1000	~3500
O&M cost (¢/kWh)	~1	0.5–0.65	0.1–0.4	~1	0.1–0.2

Notes: Efficiencies of fossil and renewable DG technologies are not directly comparable. O&M costs do not include fuel.

Source: Adapted from Distributed Power Coalition of America (DCPA), 1998. URL: www.dcpa.org.

Control Techniques

The control techniques chosen for distributed generation will depend on the type of equipment installed (Curtiss, 2000). In the case of wind or solar power generation, the main goal is to get as much energy out of the system as possible in order to recoup the installation cost. For combustion-based processes, however, the cost of fuel and maintenance must also be taken into account. The goal of the control scheme is to determine whether the on-site generation should be operating during a particular hour. Generally, a simple hour-ahead control method is sufficient if the start-up transients of the generator are not too inefficient. Otherwise, it is necessary to develop methods that perform a certain degree of prediction to determine the effects of scheduled dispatch over the period of several hours or even several days.

Threshold Control

In threshold control, the turbines run whenever the building electrical load is greater than a predetermined threshold. The number of turbines initially installed is equal to the difference between the annual peak and the threshold, divided by the nominal power output of each installed unit:

$$Number\ installed = \frac{kW_{PEAK} - kW_{THRESHOLD}}{kW_{UNIT}}$$

If the electrical load of the building is greater than the threshold, then the number of turbines operating is equal to that required to reduce the grid load to the threshold limit:

$$Number\ operating = \frac{kW_{BUILDING} - kW_{THRESHOLD}}{kW_{UNIT}}$$

A problem with this control method is deciding where to assign the threshold limit. A high limit means the turbine is used for peak shaving and will reduce the number of operating hours. A low limit forces the generators to run more often and is akin to base loading. A threshold of zero indicates that the generators would try to operate whenever possible. This specific case is referred to as *always-on* control.

Buyback Priority

Buyback priority is used in cases in which the building operator wishes to produce electricity and sell any or all of the produced power back to the utility. There are two versions of buyback control; one takes advantage of a simple buyback rate and the other responds to net metering, in which the value of produced power is used to offset the traditional electrical bill.

Simple Buyback

In the case of simple buyback the generators would normally use the threshold control scheme as described previously. If the buyback cost is greater than the equivalent cost of gas, then all the generators run and the excess is sold to the utility. The number of turbines installed depends on the projected income the building operator expects to make from selling electricity. The control method finds the incremental sum of all fuel used to get the total cost for the hour:

$$\text{Total cost} = \Delta\$\text{kWh}_{\text{GRID}} + \Delta\$\text{Btu}_{\text{GRID}} - \Delta\$\text{kWh}_{\text{BUYBACK}}$$

The Δ$ term implies that the non-RTP gas and electric costs are evaluated on a monthly (i.e., billing period) incremental basis. For example, the change of the grid electricity bill is

$$\Delta\$\text{kWh}_{\text{GRID}} = \text{M}\$(\text{kWh}_1, \text{kWh}_2, \ldots, \text{kWh}_{N-1}) - \text{M}\$(\text{kWh}_1, \text{kWh}_2, \ldots, \text{kWh}_N)$$

where M$ is the monthly bill amount (including consumption and demand fees, surcharges, and taxes) based on *N* hourly electricity use values for that billing period. This allows the true bills to be calculated, including any time-of-use and block components.

Unfortunately, these latter components also affect the linearity of the cost function — the cost function is not necessarily linear under these conditions. The algorithm for determining whether to use buyback, therefore, should (1) determine the loads on the building for a given hour; (2) calculate the total cost function for all integral numbers of generators operating, from zero to the number installed; and (3) find the number of generators, which minimizes the total cost function.

Net Metering Control

In the net metering scenario, the electrical meter "runs backwards" if excess electricity is produced on site. Once the meter reaches zero, buyback rates apply. As with the buyback priority control, the incremental sum of all fuel uses is calculated to get the total cost for the hour:

$$\text{Total cost} = \Delta\$\text{kWh}_{\text{GRID}} + \Delta\$\text{Btu}_{\text{GRID}} - \Delta\$\text{kWh}_{\text{BUYBACK}}.$$

The Δ$ terms are the incremental costs as discussed in the buyback priority control. Consequently, the control algorithm is the same as in the buyback priority with the exception that the $\Delta\$\text{kWh}_{\text{GRID}}$ term here refers to the adjusted (i.e., rolled back) meter usage and the $\Delta\$\text{kWh}_{\text{BUYBACK}}$ amount is decreased by the kWh that go into reducing $\Delta\$\text{kWh}_{\text{GRID}}$.

If the monthly sum is positive (i.e., more electricity has been used from the grid than produced on site), then the monthly bill is based on simple effective aggregation of hourly consumption plus demand and fees. Otherwise, the customer is refunded the value of excess electricity produced as dictated by buyback rate.

Cooling/Heating Priority Control

In some cases, distributed generation will be applied to satisfy a cooling load (through auxiliary absorption cooling or direct electrical connection to conventional cooling equipment) or a heating load (through heat recovery). In this mode of control, the generators operate primarily to satisfy these loads and the satisfaction of the electrical load is a secondary benefit. The number of generators installed is sufficient to meet the annual peak thermal load and the control algorithm has the generators operating as required to meet the thermal load of the building. No consideration is given to the value of electricity.

Optimal Control

Ideally, distributed generation would be operated using an algorithm that reduces the operating cost over the lifetime of the equipment such that the cost to the building operator is minimized. If the building is subject to a real-time pricing rate schedule then the optimization can be trivial; the costs of grid electricity and locally produced electricity are compared at each hour and, when the former is more expensive, the on-site generators are operated. However, more conventional rate structures such as block rates and time-of-use rates as accumulated over a billing period can make the calculation of instantaneous "next kWh" costs much more difficult. In this case, the electricity bill C_{ELEC} at any given hour is

$$C_{ELEC} = \Phi_{KWH}\begin{bmatrix} kWh_{BLDG}(1) - kWh_{GEN}(1) \\ kWh_{BLDG}(2) - kWh_{GEN}(2) \\ \cdots \\ kWh_{BLDG}(k) - kWh_{GEN}(k) \end{bmatrix}$$

$$+\Phi_{KW}\begin{bmatrix} kW_{BLDG}(1) - kW_{GEN}(1) \\ kW_{BLDG}(2) - kW_{GEN}(2) \\ \cdots \\ kW_{BLDG}(k) - kW_{GEN}(k) \end{bmatrix}$$

where Φ_{KWH} is the utility function used to calculate the bill based on consumption; Φ_{KW} is the function used for demand; $kWh_{BLDG}(1)$ is the total electric load at hour 1; $kWh_{GEN}(1)$ is the kWh offset from the on-site generation equipment at hour 1; and so forth.

The calculation must be performed for each hour of the billing period to account for the hourly building load, any time-of-use components of the utility rate, and any ambient temperature or solar dependencies of the generation equipment. If the generators use natural gas to produce electricity (an internal combustion engine, microturbine, or fuel cell), then a similar calculation is performed for the gas consumption. Assuming no demand component for gas, the total gas bill up to hour k of the billing period is given as

$$C_{GAS} = \Phi_{GAS} \begin{bmatrix} Btu_{BLDG}(1) + Btu_{GEN}(1) \\ Btu_{BLDG}(2) + Btu_{GEN}(2) \\ \cdots \\ Btu_{BLDG}(k) + Btu_{GEN}(k) \end{bmatrix}$$

where $\mathrm{Btu}_{\mathrm{GEN}}$ is the incremental gas consumption of the generation equipment at each hour. Note that $\mathrm{kWh}_{\mathrm{GEN}}$, $\mathrm{kW}_{\mathrm{GEN}}$, and $\mathrm{Btu}_{\mathrm{GEN}}$ can have zero values at any hour, depending on whether the generation equipment is operating for that hour. To determine if the generators should operate at hour $k + 1$, the total cost $C_{\mathrm{ELEC}} + C_{\mathrm{GAS}}$ should be evaluated twice: once using values for the terms $\mathrm{kWh}_{\mathrm{GEN}}$, $\mathrm{kW}_{\mathrm{GEN}}$, and $\mathrm{Btu}_{\mathrm{GEN}}$ based on the estimated generator performance and then again with these values set to zero. If the former is greater than the latter, then the generators should not be run for that hour.

Complete Optimization

The procedure just described is sufficient for performing an optimization based on a single type of generation equipment without accounting for any other inputs. To be truly optimal, however, the algorithm should account for any different capacities of generators installed, any utility incentives, and the variable operation and maintenance costs experienced during operation. Such an optimization uses an algorithm similar to that described here.

The structure and calculation methods used for the electricity and gas utility rate schedules must be known. The optimization routine must also be able to keep track of all data acquired during a given billing period and provide cost estimates for the current hour. Any utility-sponsored incentives and rebates should be tallied, along with the method of their application (e.g., by kilowatt hours produced, kilowatts installed, etc.)

At each hour of the billing period, the optimization routine determines the number of generators that should run for that hour. This requires a prediction of the building load data for that hour, including:

- whole building kWh use
- whole building Btu use
- kWh used for domestic water heating
- Btu used for domestic water heating
- kWh used for space heating
- Btu used for space heating
- kWh used for space cooling

The electrical and thermal output from each generation device in the building must then be determined. This may require monitoring of the ambient temperature, wind speed, and insolation.

Parametrics are then run examining the benefit of operating each generator, accounting for any generators that may already be operating and for any part-load characteristics of generators that are not operating at full load. The cost function in the analysis is truly a cost function; the costs of providing on-site electrical and thermal costs are compared with those of grid consumption and the lowest-cost option is chosen. To assess these costs properly, the grid electricity consumption $\mathrm{kWh}_{\mathrm{GRID}}$ is adjusted by the decrease of grid electricity consumption due to distributed power generation:

$$\mathrm{kWh}_{\mathrm{GRID}} = \mathrm{kWh}_{\mathrm{BLDG}} - \mathrm{kWh}_{\mathrm{GEN}} - \mathrm{kWh}_{\mathrm{COOL}}$$

where kWh_{BLDG} is the building load and kWh_{GEN} is the amount of electricity from the generators. The term kWh_{COOL} is nonzero if the generator provides direct cooling through absorption cooling and must be corrected for the nominal efficiency of the conventional cooling equipment:

$$kWh_{COOL} = \frac{\sum \dot{Q}_{COOL}}{COP_{COOL}}$$

where the summation is taken over all devices that provide supplemental cooling.

If the distributed generation equipment includes any gas-fired devices, the incremental cost of natural gas consumption must also be taken into account,

$$\text{Btu}_{\text{GRID}} = \text{Btu}_{\text{BLDG}} + \text{Btu}_{\text{GEN}} - \text{Btu}_{\text{HEAT}}$$

where Btu_{BLDG} is the building load and Btu_{GEN} is the consumption of gas by the generators:

$$Btu_{GEN} = \sum W_{GEN}(PLR)$$

where the summation is taken over all devices that convert gas to electricity.

The work term must also be corrected by the part load efficiency of any generators that are not at full load. The term Btu_{HEAT} represents any credit that can be applied due to heat recovery from the generators that precludes the use of conventional space or water heating sources. As with the cooling term, this credit is adjusted by the nominal efficiency of the conventional sources:

$$Btu_{HEAT} = \frac{\sum \dot{Q}_{HEAT}}{\eta_{HEAT}}$$

The total operating cost can now be calculated from the incremental rates, incentives, and maintenance costs:

$$\begin{aligned}
C_{TOTAL} = \Phi_{KWH} &\begin{bmatrix} kWh_{BLDG}(1) - kWh_{GEN}(1) \\ kWh_{BLDG}(2) - kWh_{GEN}(2) \\ \vdots \\ kWh_{BLDG}(k) - kWh_{GEN}(k) \end{bmatrix} \\
+ \Phi_{KW} &\begin{bmatrix} kW_{BLDG}(1) - kW_{GEN}(1) \\ kW_{BLDG}(2) - kW_{GEN}(2) \\ \vdots \\ kW_{BLDG}(k) - kW_{GEN}(k) \end{bmatrix} \\
+ \Phi_{GAS} &\begin{bmatrix} Btu_{BLDG}(1) + Btu_{GEN}(1) \\ Btu_{BLDG}(2) + Btu_{GEN}(2) \\ \vdots \\ Btu_{BLDG}(k) + Btu_{GEN}(k) \end{bmatrix} \\
- \Phi_{CRED} &\left[\sum kWh_{GEN} \right] \\
+ \Phi_{O\&M} &\left[kW_{INST} + \sum kWh_{GEN} \right]
\end{aligned}$$

where Φ_{CRED} represents a positive cash flow based on any utility incentives that are provided, including transmission loss credits, wheeling charge credits, voltage support credits, etc. The term $\Phi_{O\&M}$ is used to account for any operation and maintenance costs that arise from operating the generation equipment.

Finally, a cost matrix is compiled that represents all reasonable combinations of generation available to that building. The combination with the lowest cost is chosen and implemented.

References

Anderson, C., 1989, Learning to control an inverted pendulum using neural networks, *IEEE Control Syst. Mag.*, April, 31–36.

Askey, S.Y. 1995. Design and Evaluation of Decision Aids for Control of High Speed Trains: Experiments and a Model, Ph.D. Thesis, Massachusetts Institute of Technology, Cambridge, MA, June.

Billings, C.E. 1991. *Human-Centered Aircraft Automation: A Concept and Guidelines,* NASA Ames Research Center, Moffet Field, CA.

Curtiss, P., 2000, Control of distributed electrical generation systems, *ASHRAE Trans.*, 106, Pt. 1.

Curtiss, P.S., Kreider, J.F., and Brandemuehl, M.J., 1993a, Artificial neural networks proof of concept for local and global control of commercial building HVAC systems, *Proc. ASME Int. Solar Energy Conf.*, Washington, D.C., pp. 429–443.

Curtiss, P.S., Kreider, J.F. and Brandemuehl, M.J., 1993b, Energy management in central HVAC plants using neural networks, *Proc. ASHRAE Annu. Winter Meeting*, Chicago, IL.

Curtiss, P.S., Brandemuehl, M.J. and Kreider, J.F., 1993c, Adaptive control of HVAC processes using predictive neural networks, *ASHRAE Trans.*, 99, Pt 1, pp. 496–504.

Curtiss, P., Cohen, D., and Kreider, J.F., 1999, A methodology for technical and financial assessment of distributed generation in the U.S., *Proc. ASME ISEC April 1999 Conf.* Maui, HI.

Daley, S. and Gill, K.F., 1985, The fuzzy logic controller: an alternative design scheme? *Computers Ind.*, 6, 3–14.

Gupta, M. M. and Tsukamoto, Y., 1980, Fuzzy logic controllers — a perspective, *Proc. Joint Automatic Control Conf.*, FA10-C, August 1980, San Francisco.

Huang, S.H. and Nelson, R.M., 1991., A PID-law-combining fuzzy controller for HVAC applications, *ASHRAE Trans.*, 97, Pt. 2, 768–774.

Leigh, R. and Wetton, M., 1983, Thinking clearly with fuzzy logic, *Process Eng.*, 64, 36–37.

Meijer, G., 1992, Fuzzy logic-controlled A/Cs heat pumps, *IEA Heat Pump Centre Newslett.*, 10(1).

Ollero, A. and Williams, J., 1989, Direct digital control, auto-tuning, and supervision using fuzzy logic, *Fuzzy Sets Syst.*, 30, 135–153.

Ono, H., Ohnish, T., and Terada, Y. ,1989, Combustion control of refuse incineration plant by fuzzy logic, *Fuzzy Sets Syst.*, 32, 193–206.

Nguyen, D.H. and Widrow, B., 1989, The truck backer-upper: an example of self learning in neural networks, *Proc. Int. Joint Conf. Neural Networks*, 2, 357–363.

Radke, F. and Isermann, R., 1987, A parameter-adaptive PID-controller with stepwise parameter optimization, *Automatica*, 23, 449–457.

Ralston, P.A. and Ward, T.L., 1985, Fuzzy control of industrial process, in *Appl. Fuzzy Set Methodol. Ind. Eng.*, 29–45. B.V., North Holland. Elsevier Science Publishers.

Sakai, Y. and Ohkusa, K., 1985, A fuzzy controller in turning process automation, in *Ind. Appl. Fuzzy Control*, 139–151. B.V., North Holland. Elsevier Science Publishers.

Scharf, E.M. and Mandic, N.J., 1985, The application of a fuzzy controller to the control of a multidegree-of-freedom robot arm, in *Ind. Appl. Fuzzy Control*, 1–18. B.V., North Holland. Elsevier Science Publishers.

Sheridan, S.E., 1984, Automatic kiln control at Oregon portland cement company's Durkee plant utilizing fuzzy logic, *IEEE Trans. Ind. Appl.*, 20, 562–568.

Sheridan, T.B. 1987. Supervisory control. In G. Salvendy, Ed., *Handbook of Human Factors/Ergonomics,* Wiley, New York.

Shinners, S. M., 1978, *Modern Control System Theory and Application*, Reading, MA: Addison–Wesley Publishing Co.

Togai and Maski, 1991, An example of fuzzy logic control, *Computer Design*, 30, 93–103.

Wakileh, B.A. and Gill, K.F., 1988, se of fuzzy logic in robotics, *Computers Ind.*, 10, 35–46.

Xu, C.W., 1989, Fuzzy system identification, *IEEE Proc.*, 136(4), Pt. D, 146–150.

Yasunobu, S. and Miyamoto, S., 1985, Automatic train operation system by predictive fuzzy control, *Ind. Appl. Fuzzy Control*, 1–18. B.V., North Holland. Elsevier Science Publishers.

Bibliography

Distributed Power Coalition of America (DCPA) (1998). URL: www.dcpa.org.

Huang, S.-H. and Nelson, R.M., 1993, Rule development and adjustment strategies of a fuzzy logic controller for an HVAC system: part two — experiment, *ASHRAE Trans.*, (Submitted for review.)

MacArthur, J.W., Grald, E.W., and Konar, A.F., 1989, An effective approach fir dynamically compensated adaptive control, *ASHRAE Trans.*, 95(2), 415–423.

Additional Reading

The following are suggested reading for those interested in learning more about neural networks and their use in control systems:

Helferty, J.J., Collins, J.B., Wong, L.C., and Kam, M., 1989, A learning strategy for the control of a one-legged hopping robot, *Proc. 1989 Am. Control Conf.*, 896–901.

Kuperstein, M. and Rubinstein, J., 1989, Implementation of an adaptive neural network controller for sensory-motor coordination, *IEEE Control Syst. Mag.*, April, 25–30.

Lan, M., 1989, Adaptive control of unknown dynamical systems via neural network approach, *Proc. 1989 Am. Control Conf.*, 910–915.

Liu, H., Iderall, T., and Bekey, G., 1989, Neural network architecture for robot hand control, *IEEE Control Syst. Mag.*, April, 38–41.

Miller, R.C. and Seem, J.E., 1991, Comparison of artificial neural networks with traditional methods of predicting return time from night or weekend setback, *ASHRAE Trans.*, 97(2), 500–508.

Psaltis, D., Sideris, A., and Yamamura, A.,1988, A multilayered neural network controller, *IEEE Control Syst. Mag.*, April, 17–21.

Rumelhart, D.E. and McClelland, J.L., 1986, *Parallel Distributed Processing: Explorations in the Microstructure of Cognition*, Cambridge, MA: MIT Press.

Wasserman, P.D., 1989, *Neural Computing: Theory and Practice*," New York: Van Nostrand Reinhold.

7

Energy Resouces

D. Yogi Goswami
University of Florida

Robert Reuther
U.S. Department of Energy

Richard Bajura
West Virginia University

Philip C. Crouse
Philip C. Crouse and Associates, Inc.

Ralph P. Overend
National Renewable Energy Laboratory

Lynn L. Wright
Oak Ridge National Laboratory

James S. Tulenko
University of Florida

Dale E. Berg
Sandia National Laboratories[1]

Joel L. Renner
Idaho National Engineering Laboratory

Marshall J. Reed
U.S. Department of Energy

This chapter describes the primary as well as derived energy sources. The objective is to provide information on the extent, availability, measurements and estimation, properties, and limitations of each type of resource. These considerations are important for an engineer to know and understand before attempting selection and design of an energy conversion system. The chapter also includes environmental impacts of energy resources since the environmental aspects are expected to play a major role in the selection of energy resources. In addition, there is a brief discussion of the costs associated with each resource to help in the economic analysis and comparison of the resources.

The chapter starts with an introduction and background of a historical perspective on energy use and projections of the future energy needs in the U.S., the industrialized countries, and the world. The primary energy sources described in this chapter include fossil fuels such as coal, natural gas, petroleum (including their synthetic derivatives), biomass (including refuse-derived biomass fuels), nuclear, solar radiation, wind, geothermal, and ocean. In addition there is a brief section on derived energy sources including electricity. So, the terminology and units used for each energy resource and their equivalence are provided.

---

[1] Sandia is a multiprogram laboratory operated by Sandia Corporation, a Lockheed Martin Company, for the United States Department of Energy under contract DE-AC04-94AL85000.

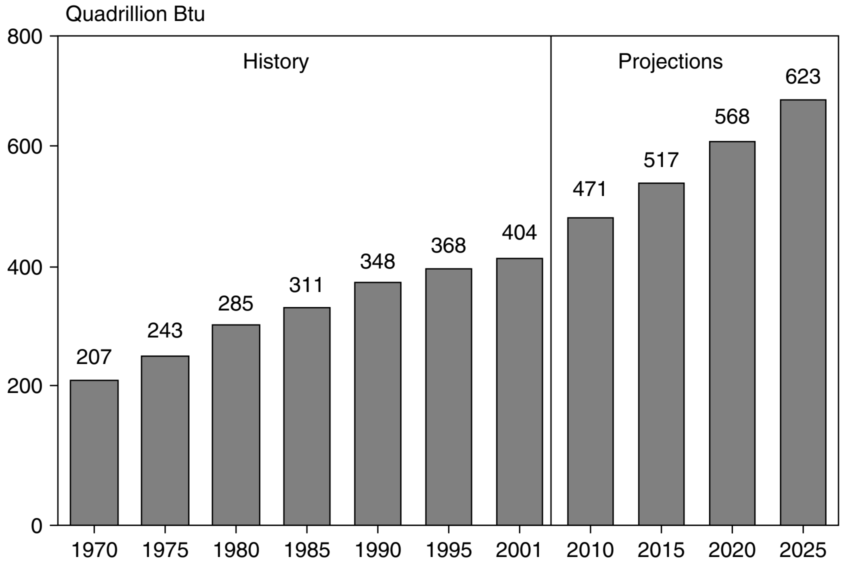

FIGURE 7.1.1 Historical and projected energy consumption. (From EIA. *International Energy Outlook 2001,* U.S. DOE, DOE/EIA-0484 (2001), Washington, D.C.)

7.1 Introduction

D. Yogi Goswami

Global energy consumption in the last 50 years has increased at a very rapid rate. Present trends in global population growth, rapid industrialization, and urbanization in major population centers of the world suggest that the world energy demand will continue to increase in the next 50 years (U.S. DOE, 2001). Figure 7.1.1 shows the historical and projected world energy consumption compiled by the Energy Information Agency.

The energy resources available to furfill the world demand include

Fossil fuels (oil, coal, natural gas)
Nuclear fuels
Geothermal
Solar radiation
Hydropower
Biomass (crops, wood, municipal solid waste)
Wind
Ocean

Out of all the energy resources, fossil fuels have been used the most (88% of total consumption) because of their extremely high energy densities and simplicity of conversion and use. Figure 7.1.2 shows the world energy consumption by resource.

Recent concerns about the environment are expected to increase the use of natural gas for power production. Renewable energy resources, such as solar energy, wind, and biomass, are also expected to increase their share of the energy use. There is a strong sentiment in the world in favor of exploiting renewable energy resources, especially because of environmental concerns. How far that sentiment translates into practical use will depend on the development of the renewable energy technologies and prices of the fossil fuels.

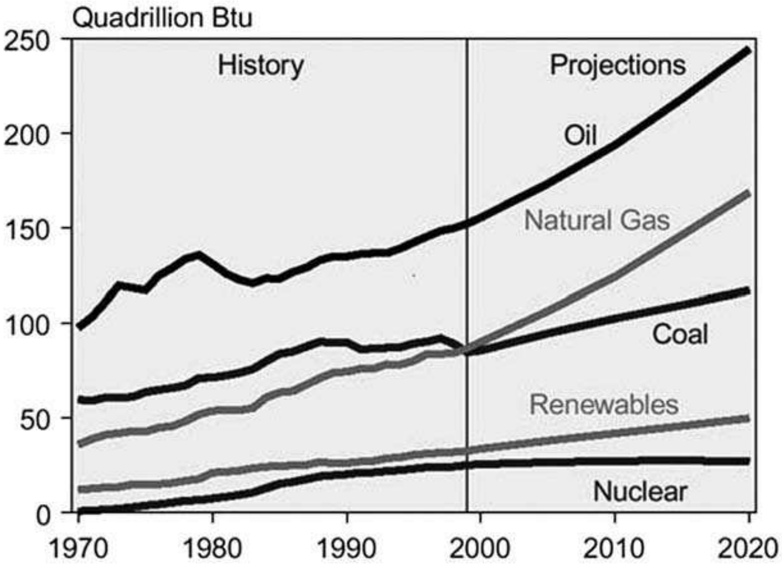

FIGURE 7.1.2 World energy consumption by resource. (From EIA. *International Energy Outlook 2001,* U.S. DOE, DOE/EIA-0484 (2001), Washington, D.C.)

Defining Terms

MTOE: Mega tons of oil equivalent; 1 MTOE = 42.63×10^{12} Btu.
Quadrillion Btu: 10^{15} British thermal units (Btu), also known as Quad; 1 Btu = 1055 joules).

References

EIA. *International Energy Outlook 2001,* International U.S. DOE, DOE/EIA-0484 (2001), Washington, D.C.

IEA. 1994. *World Energy Outlook,* Economic Analysis Division, International Energy Agency, Paris.

U.S. DOE. 1991. *National Energy Strategy — Powerful Ideas for America, 1991.* National Technical Information Service, U.S. Department of Commerce, Springfield, VA.

Further Information

Historial and projected energy consumption are published annually by the Energy Information Agency, U.S. Department of Energy, Washington, D.C., and International Energy Agency, Paris.

7.2 Types of Derived Energy

D. Yogi Goswami

Energy from renewable and nonrenewable fuels can be converted to the derived energy forms — thermal, mechanical, and electrical, which are useful for various end uses such as transportation, buildings (heating, cooling, lighting), agricultural, and industrial. The derived energy forms are easily transformed from one type to the other. Figure 7.2.1 shows the projected U.S. energy use by end-use sector.

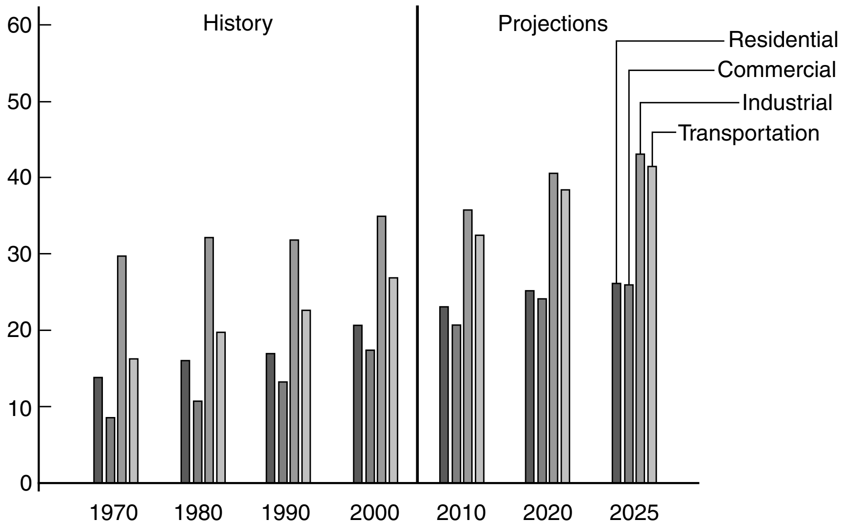

FIGURE 7.2.1 Projected U.S. energy use by end-use sector. (From EIA. *Annual Energy Outlook,* 2001, U.S. DOE, DOE/EIA-0383 (2001), Washington, D.C.)

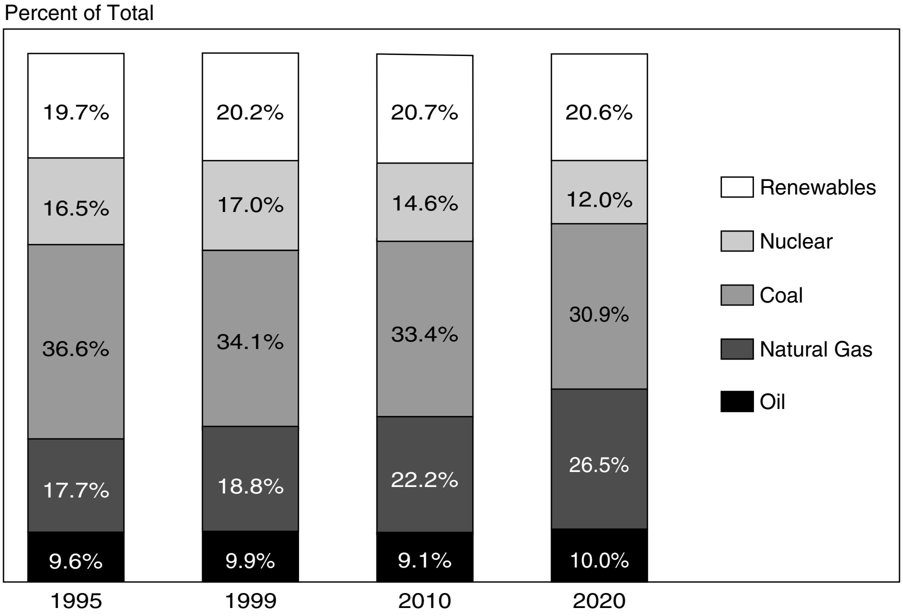

FIGURE 7.2.2 World electricity output. (From EIA. *International Energy Outlook,* 2001, U.S. DOE, DOE/EIA-0484 (2001), Washington, D.C.)

Transportation is mainly dependent on oil resources. Efforts to reduce urban air pollution are expected to increase the use of electricity as the preferred energy form for urban transportation. For most of the other end uses electricity will continue to be the preferred energy form. Therefore, it is important to understand the activity in the area of electricity production. Figure 7.2.2 shows the world installed electricity generation capacity by primary energy sources. The United States produces 770 GW (gigawatts), representing more than 25% of the world electricity capacity. Other major electricity producers are Russia, Europe, Japan, and China. It is expected that China, India, and Southeast Asian countries will add major electricity capacity in the next 20 years.

Integrated resource planning (IRP), or least-cost planning, is the process used to optimize the resource options and minimize the total consumer costs including environmental and health costs that may be attributed to the resource. IRP examines all of the options, including the demand-side options, to minimize the total costs. There is considerable emphasis on IRP in a number of states in United States for future electric capacity and on **demand-side management** (DSM) for the current capacity (Kreith and Burmeister, 1993). The IRP process generally includes some combination of the following steps (Kreith and Burmeister, 1993): development of a load forecast; inventory of existing resources; identification of additional electrical capacity needs; demand-side management programs; screening and identification of options that are feasible; uncertainty analysis in view of uncertainty of future load, fuel prices, capital costs, etc; and selection of a resource or a mix of resources.

Demand Side Management DSM refers to a mix of electrical utility-sponsored custom incentives and disincentives that influence the amount and timing of customer demand in order to better utilize the available resources. Kreith and Burmeister (1993) and SERI (1991) list a number of DSM strategies.

Defining Terms

Demand-side management (DSM): Refers to a mix of incentives and disincentives that influence the amount and timing of energy use in order to better utilize the available resources.

Integrated resource planning (IRP): The process to optimize the resource options and minimize the total consumer costs including environmental and health costs that may be all attributed to the resource.

References

EIA. *International Energy Outlook,* 2001, U.S. DOE, DOE/EIA-0484 (2001), Washington, D.C.

EIA. *Annual Energy Outlook,* 2001, U.S. DOE, DOE/EIA-0383 (2001), Washington, D.C.

Kreith, F. and Burmeister, G. 1993. *Energy Management and Conservation.* National Conference of State Legislatures, Denver, CO.

SERI. 1991. Demand Side Management Pocket Guide Book, Volume 1: Residential Technologies; and Volume 2: Commercial Technologies. SERI (Now National Renewable Energy Laboratory), Golden, CO.

Further Information

Annual reviews published by the EIA, U.S. Department of Energy, and the International Energy Agency (see References) provide a wealth of information on electricity capacity and energy consumption by end-use sectors.

7.3 Fossil Fuels

Coal

Robert Reuther

Coal Composition and Classification

Coal is a sedimentary rock formed by the accumulation and decay of organic substances, derived from plant tissues and exudates, which have been buried over periods of geological time, along with various mineral inclusions. Coal is classified by **type** and **rank.** Coal type classifies coal by the plant sources from which it was derived. Coal rank classifies coal by its degree of metamorphosis from the original plant sources and is therefore a measure of the age of the coal. The process of metamorphosis or aging is termed **coalification.**

The study of coal by type is known as coal petrography. Coal type is determined from the examination of polished sections of a coal sample using a reflected-light microscope. The degree of reflectance and the color of a sample are identified with specific residues of the original plant tissues. These various residues

TABLE 7.3.1 Coal Maceral Groups and Macerals

Maceral Group	Maceral	Derivation
Vitrinite	Collinite	Humic gels
	Telinite	Wood, bark, and cortical tissue
	Pseudovitrinite	? (Some observers place in the inertinite group)
Exinite	Sporinite	Fungal and other spores
	Cutinite	Leaf cuticles
	Alginite	Algal remains
Inertinite	Micrinite	Unspecified detrital matter, <0μ
	Macrinite	Unspecified detrital matter, 10–100 μ
	Semifusinite	"Burned" woody tissue, low reflectance
	Fusinite	"Burned" woody tissue, high reflectance
	Sclerotinite	Fungal sclerotia and mycelia

Source: Modified from Berkowitz, N., *An Introduction to Coal Technology*. Academic Press, New York, 1979. With permission.

are referred to as **macerals**. Macerals are collected into three main groups: vitrinite, inertinite, and exinite (sometimes referred to as liptinite). The maceral groups and their associated macerals are listed in Table 7.3.1, along with a description of the plant tissue from which each distinct maceral type is derived.

Coal rank is the most important property of coal because rank initiates the classification of coal for use. Coalification describes the process that the buried organic matter undergoes to become coal. When first buried, the organic matter has a certain elemental composition and organic structure. However, as the material becomes subjected to heat and pressure, the composition and structure slowly change. Certain structures are broken down, and others are formed. Some elements are lost through volatilization, while others are concentrated through a number of processes, including exposure to underground flows, which carry away some elements and deposit others. Coalification changes the values of various properties of coal. Thus, coal can be classified by rank through the measurement of one or more of these changing properties.

In the United States and Canada, the rank classification scheme defined by the American Society of Testing and Materials (ASTM) has become the standard. In this scheme, the properties of **gross calorific value** and **fixed carbon** or **volatile matter** content are used to classify a coal by rank. Gross calorific value is a measure of the energy content of the coal and is usually expressed in units of energy per unit mass. Calorific value increases as the coal proceeds through coalification. Fixed carbon content is a measure of the mass remaining after heating a dry coal sample under conditions specified by the ASTM.

Fixed carbon content also increases with coalification. The conditions specified for the measurement of fixed carbon content result in being able, alternatively, to use the volatile matter content of the coal, measured under dry, ash-free conditions, as a rank parameter. The rank of a coal proceeds from lignite, the "youngest" coal, through sub-bituminous, bituminous, and semibituminous, to anthracite, the "oldest" coal. The subdivisions within these rank categories are defined in Table 7.3.2. (Some rank schemes include meta-anthracite as a rank above, or "older" than, anthracite. Others prefer to classify such deposits as graphite — a minimal resource valuable primarily for uses other than as a fuel.)

According to the ASTM scheme, coals are ranked by calorific value up to the high-volatile A bituminous rank, which includes coals with calorific values (measured on a moist, mineral matter-free basis) greater than 14,000 Btu/lb (32,564 kJ/kg). At this point, fixed carbon content (measured on a dry, mineral matter-free basis) takes over as the rank parameter. Thus, a high-volatile A bituminous coal is defined as having a calorific value greater than 14,000 Btu/lb, but a fixed carbon content less than 69 wt%. The requirement for having two different properties with which to define rank arises because calorific value increases significantly through the lower-rank coals, but very little (in a relative sense) in the higher ranks; fixed carbon content has a wider range in higher rank coals, but little (relative) change in the lower ranks. The most widely used classification scheme outside North America is that developed under the jurisdiction of the International Standards Organization, Technical Committee 27, Solid Mineral Fuels.

TABLE 7.3.2 Classification of Coals by Rank

Class	Group	Fixed carbon limits, % (dmmf) Equal to or Greater Than	Fixed carbon limits, % (dmmf) Less Than	Volatile matter limits, % (dmmf) Greater Than	Volatile matter limits, % (dmmf) Equal to or Less Than	Gross calorific value limits, Btu/lb (moist, mmf) Equal to or Greater Than	Gross calorific value limits, Btu/lb (moist, mmf) Less Than	Agglomerating Character
Anthracitic	Meta-anthracite	98	…	…	2	…	…	Nonagglomerating
	Anthracite	92	98	2	8	…	…	Nonagglomerating
	Semianthracite	86	92	8	14	…	…	Nonagglomerating
Bituminous	Low-volatile bituminous	78	86	14	22	…	…	Commonly agglomerating
	Medium-volatile bituminous	69	78	22	31	…	…	Commonly agglomerating
	High-volatile A bituminous	…	69	31	…	14,000	…	Commonly agglomerating
	High-volatile B bituminous	…	…	…	…	13,000	14,000	Commonly agglomerating
	High-volatile C bituminous	…	…	…	…	11,500	13,000	Commonly agglomerating
	High-volatile C bituminous	…	…	…	…	10,500	11,500	Agglomerating
Subbituminous	Subbituminous A	…	…	…	…	10,500	11,500	Nonagglomerating
	Subbituminous B	…	…	…	…	9,500	10,500	Nonagglomerating
	Subbituminous C	…	…	…	…	8,300	9,500	Nonagglomerating
Lignitic	Lignite A	…	…	…	…	6,300	8,300	Nonagglomerating
	Lignite B	…	…	…	…	…	6,300	Nonagglomerating

Source: From the American Society for Testing and Materials' Annual Book of ASTM Standards. With permission.

Coal Analysis and Properties

The composition of a coal is typically reported in terms of its **proximate analysis** and its **ultimate analysis**. The proximate analysis of a coal is made up of four constituents: volatile matter content; fixed carbon content; moisture content; and ash content, all of which are reported on a weight percent basis. The measurement of these four properties of a coal must be carried out according to strict specifications codified by the ASTM. Note that the four constituents of proximate analysis do not exist, per se, in the coal, but are measured as analytical results upon treating the coal sample to various conditions.

ASTM volatile matter released from coal includes carbon dioxide, inorganic sulfur- and nitrogen-containing species, and organic compounds. The percentages of these various compounds or species released from the coal varies with rank. Volatile matter content can typically be reported on a number of bases, such as moist; dry, mineral matter-free (dmmf); moist, mineral matter-free; moist, ash-free; and dry, ash-free (daf), depending on the condition of the coal on which the measurements were made.

Mineral matter and ash are two distinct entities. Coal does not contain ash, even though the ash content of a coal is reported as part of its proximate analysis. Instead, coal contains mineral matter, which can be present as distinct mineral entities or inclusions and as material intimately bound with the organic matrix of the coal. Ash, on the other hand, refers to the solid inorganic material remaining *after combusting* a coal sample. Proximate ash content is the ash remaining after the coal has been exposed to air under specific conditions codified in ASTM Standard Test Method D 3174. It is reported as the mass percent remaining upon combustion of the original sample on a dry or moist basis.

Moisture content refers to the mass of water released from the solid coal sample when it is heated under specific conditions of temperature and residence time as codified in ASTM Standard Test Method D 3173.

The fixed carbon content refers to the mass of organic matter remaining in the sample after the moisture and volatile matter are released. It is primarily made up of carbon. However, hydrogen, sulfur, and nitrogen also are typically present. It is reported by difference from the total of the volatile matter, ash, and moisture contents on a mass percent of the original coal sample basis. Alternatively, it can be reported on a dry basis; a dmmf basis; or a moist, mineral matter-free basis.

The values associated with a proximate analysis vary with rank. In general, volatile matter content decreases with increasing rank, while fixed carbon content correspondingly increases. Moisture and ash also decrease, in general, with rank. Typical values for proximate analyses as a function of the rank of a coal are provided in Table 7.3.3.

The ultimate analysis provides the composition of the organic fraction of coal on an elemental basis. Like the proximate analysis, the ultimate analysis can be reported on a moist or dry basis and on an ash-containing or ash-free basis. The moisture and ash reported in the ultimate analysis are found from the corresponding proximate analysis. Nearly every element on Earth can be found in coal. However, the important elements that occur in the organic fraction are limited to only a few. The most important of these include carbon; hydrogen; oxygen; sulfur; nitrogen; and, sometimes, chlorine. The scope, definition of the ultimate analysis, designation of applicable standards, and calculations for reporting results on different moisture bases can be found in ASTM Standard Test Method D 3176M. Typical values for the ultimate analysis for various ranks of coal found in the U.S. are provided in Table 7.3.4. Other important properties of coal include swelling, caking, and coking behavior; ash fusibility; reactivity; and calorific value.

Calorific value measures the energy available in a unit mass of coal sample. It is measured by ASTM Standard Test Method D 2015M, Gross Calorific Value of Solid Fuel by the Adiabatic Bomb Calorimeter, or by ASTM Standard Test Method D 3286, Gross Calorific Value of Solid Fuel by the Isothermal-Jacket Bomb Calorimeter. In the absence of a directly measured value, the gross calorific value, Q, of a coal (in Btu/lb) can be estimated using the Dulong formula (Elliott and Yohe, 1981):

$$Q = 14{,}544C + 62{,}028\left[H - \left(O/8\right)\right] + 4{,}050S$$

where C, H, O, and S are the mass fractions of carbon, hydrogen, oxygen, and sulfur, respectively, obtained from the ultimate analysis.

TABLE 7.3.3 Calorific Values and Proximate Analyses of Ash-Free Coals of Different Rank

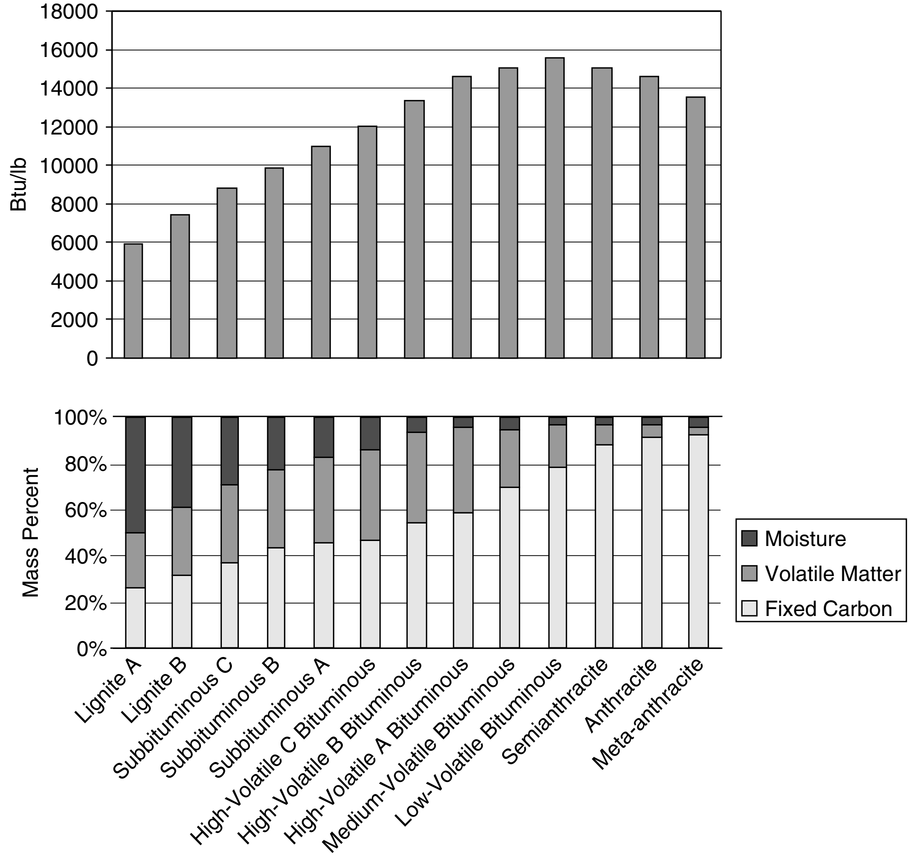

Source: From Averitt, P., Coal Resources of the United States, January 1, 1974. U.S. Geological Survey Bulletin 1412, Government Printing Office, Washington, D.C., 1975.

TABLE 7.3.4 Ultimate Analysis in Mass Percent of Representative Coals of the U.S.

Component	Fort Union Lignite	Powder River Subbituminous	Four Corners Subbituminous	Illinois C Bituminous	Appalachia Bituminous
Moisture	36.2	30.4	12.4	16.1	2.3
Carbon	39.9	45.8	47.5	60.1	73.6
Hydrogen	2.8	3.4	3.6	4.1	4.9
Nitrogen	0.6	0.6	0.9	1.1	1.4
Sulfur	0.9	0.7	0.7	2.9	2.8
Oxygen	11.0	11.3	9.3	8.3	5.3
Ash	8.6	7.8	25.6	7.4	9.7
Gross calorific value, Btu/lb	6700	7900	8400	10,700	13,400

Source: Modified from Probstein, R. and Hicks, R., *Synthetic Fuels*. McGraw–Hill, New York, 1982. With permission.

Swelling, caking, and coking all refer to the property of certain bituminous coals to change in size, composition, and, notably, strength, when slowly heated in an inert atmosphere to between 450 and 550 or 600°F. Under such conditions, the coal sample initially becomes soft and partially devolatilizes. With further heating, the sample takes on a fluid characteristic. During this fluid phase, further devolatilization causes the sample to swell. Still further heating results in the formation of a stable, porous, solid material with high strength. Several tests have been developed, based on this property, to measure the degree and suitability of a coal for various processes. Some of the more popular tests are the free swelling index (ASTM Test Method D 720); the Gray–King assay test (initially developed and extensively used in Great Britain); and the Gieseler plastometer test (ASTM Test Method D 2639), as well as a host of dilatometric methods (Habermehl et al., 1981).

The results of these tests are often correlated with the ability of a coal to form a coke suitable for iron making. In the iron-making process, the high carbon content and high surface area of the coke are used in reducing iron oxide to elemental iron. The solid coke must also be strong enough to provide the structural matrix upon which the reactions take place. Bituminous coals that have good coking properties are often referred to as metallurgical coals. (Bituminous coals without this property are, alternatively, referred to as steam coals because of their historically important use in raising steam for conversion to mechanical energy or electricity generation.)

Ash fusibility is another important property of coals. This is a measure of the temperature range over which the mineral matter in the coal begins to soften, eventually to melt into a slag, and to fuse together. This phenomenon is important in combustion processes; it determines if and at what point the resultant ash becomes soft enough to stick to heat exchanger tubes and other boiler surfaces or at what temperature it becomes molten so that it flows (as slag), making removal as a liquid from the bottom of a combustor possible.

Reactivity of a coal is a very important property fundamental to all coal conversion processes (such as combustion, gasification, and liquefaction). In general, lower rank coals are more reactive than higher rank coals. This is due to several different characteristics of coals, which vary with rank as well as with type. The most important characteristics are the surface area of the coal, its chemical composition, and the presence of certain minerals that can act as catalysts in the conversion reactions. The larger surface area present in lower rank coals translates into a greater degree of penetration of gaseous reactant molecules into the interior of a coal particle. Lower rank coals have a less aromatic structure than higher ranks. This corresponds to the presence of a higher proportion of lower energy, more reactive chemical bonds. Lower rank coals also tend to have higher proximate ash contents, and the associated mineral matter is more distributed, even down to the atomic level. Any catalytically active mineral matter is thus more highly dispersed.

However, the reactivity of a coal also varies depending upon what conversion is attempted. That is, the reactivity of a coal toward combustion (or oxidation) is not the same as its reactivity toward liquefaction, and the order of reactivity established in a series of coals for one conversion process will not necessarily be the same as that for another process.

Coal Reserves

Coal is found throughout the U.S. and the world. It is the most abundant fossil energy resource in the U.S. and the world, comprising 95% of U.S. fossil energy resources and 70% of world fossil energy resources on an energy content basis. All coal ranks can be found in the U.S. The largest resources in the U.S. are made up of lignite and sub-bituminous coals, which are found primarily in the western part of the country, including Alaska. Bituminous coals are found principally in the Midwest states, northern Alaska, and the Appalachian region. Principal deposits of anthracite coal are found in northeastern Pennsylvania.

The Alaskan coals have not been extensively mined because of their remoteness and the harsh climate. Of the other indigenous coals, the anthracite coals have been heavily mined to the point that little economic resource remains. The bituminous coals continue to be heavily mined in the lower 48 states, especially those with sulfur contents less than 2.5 wt%. The lignite and subbituminous coals in the western U.S. have been historically less heavily mined because of their distance from large population centers and because of their low calorific values and high moisture and ash contents. However, with the enactment of the 1990 Clean Air Act Amendments, these coals are now displacing high sulfur-containing

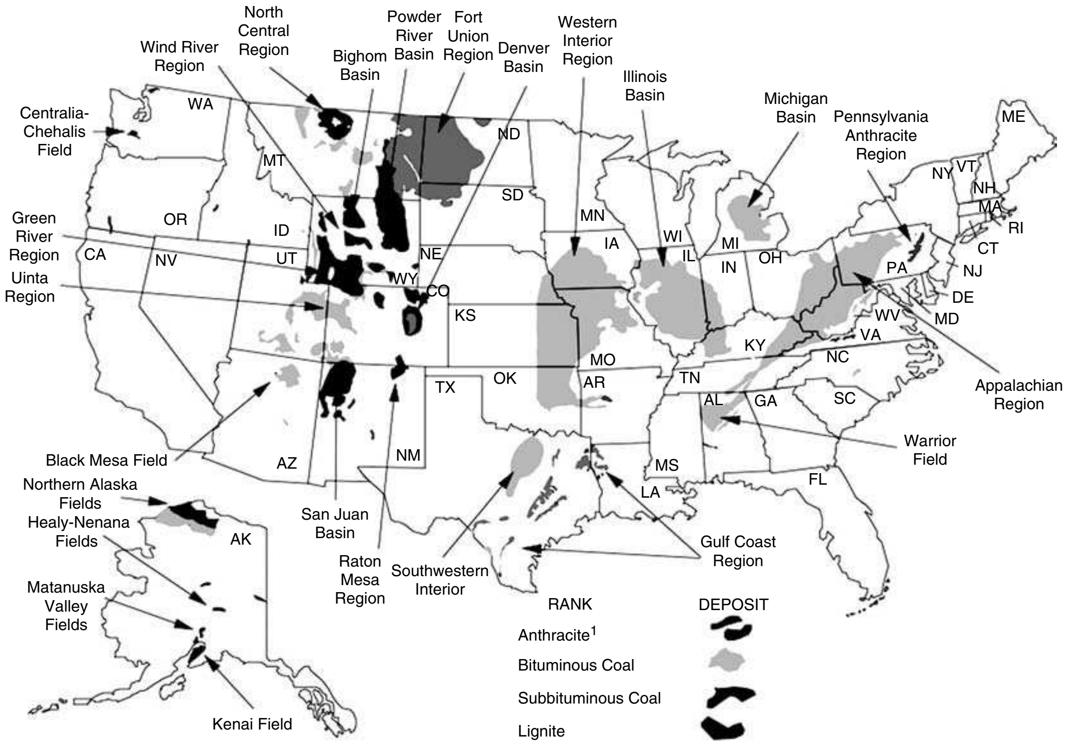

Note: Alaska not to scale of conterminous United States. Small fields and isolated occurrences are not shown.

1 Principal anthracite deposits are in Pennsylvania. Small deposits occur in Alaska, Arkansas, Colorado, Massachusetts-Rhode Island, New Mexico, Utah, Virginia, Washington, and West Virginia.

FIGURE 7.3.1 U.S. coal deposits.

coals for use in the eastern U.S. A map showing the general distribution of coal in the U.S. is included as Figure 7.3.1.

The amount of coal that exists is not known exactly and is continually changing as old deposits are mined out and new deposits are discovered or reclassified. Estimates are published by many different groups throughout the world. In the U.S., the Energy Information Administration (EIA), an office within the U.S. Department of Energy, gathers and publishes estimates from various sources. The most commonly used definitions for classifying the estimates are provided below.

Important Terminology: Resources, Reserves, and the Demonstrated Reserve Base[1]

Resources are naturally occurring concentrations or deposits of coal in the Earth's crust, in such forms and amounts that economic extraction is currently or potentially feasible.

Measured resources refers to coal for which estimates of the rank and quantity have been computed to a high degree of geologic assurance, from sample analyses and measurements from closely spaced and geologically well-known sample sites. Under the U.S. Geological Survey (USGS) criteria, the

---

[1] For a full discussion of coal resources and reserve terminology as used by EIA, USGS, and the Bureau of Mines, see U.S. Coal Reserves, 1996, Appendix A, "Specialized Resource and Reserve Terminology."

Sources: U.S. Department of the Interior, Coal Resource Classification System of the U.S. Bureau of Mines and the U.S. Geological Survey, Geological Survey Bulletin 1450-B (1976). U.S. Department of the Interior, Coal Resource Classification System of the U.S. Geological Survey, Geological Survey Circular 891 (1983) U.S. Department of the Interior, A Dictionary of Mining, Mineral, and Related Terms, Bureau of Mines (1968).

points of observation are no greater than ½ mile apart. Measured coal is projected to extend as a ¼-mile-wide belt from the outcrop or points of observation or measurement.

Indicated resources refers to coal for which estimates of the rank, quality, and quantity have been computed to a moderate degree of geologic assurance, partly from sample analyses and measurements and partly from reasonable geologic projections. Under the USGS criteria, the points of observation are from ½ to 1½ miles apart. Indicated coal is projected to extend as a ½-mile-wide belt that lies more than ¼ mile from the outcrop or points of observation or measurement.

Demonstrated resources are the sum of measured resources and indicated resources.

Demonstrated reserve base (DRB; or simply "reserve base" in USGS usage) is, in its broadest sense, defined as those parts of identified resources that meet specified minimum physical and chemical criteria related to current mining and production practices, including those for quality, depth, thickness, rank, and distance from points of measurement. The "reserve base" is the in-place demonstrated resource from which reserves are estimated. The reserve base may encompass those parts of a resource that have a reasonable potential for becoming economically recoverable within planning horizons that extend beyond those that assume proven technology and current economics.

Inferred resources refers to coal of a low degree of geologic assurance in unexplored extensions of demonstrated resources for which estimates of the quality and size are based on geologic evidence and projection. Quantitative estimates are based on broad knowledge of the geologic character of the bed or region from which few measurements or sampling points are available and on assumed continuation from demonstrated coal for which geologic evidence exists. The points of measurement are from 1½ to 6 miles apart. Inferred coal is projected to extend as a 2¼-mile-wide belt that lies more than ¾ mile from the outcrop or points of observation or measurement. Inferred resources are not part of the DRB.

Recoverable refers to coal that is, or can be, extracted from a coalbed during mining.

Reserves relates to that portion of demonstrated resources that can be recovered economically with the application of extraction technology available currently or in the foreseeable future. Reserves include only recoverable coal; thus, terms such as "minable reserves," "recoverable reserves," and "economic reserves" are redundant. Even though "recoverable reserves" is redundant, implying recoverability in both words, EIA prefers this term specifically to distinguish recoverable coal from in-ground resources, such as the demonstrated reserve base, that are only partially recoverable.

Minable refers to coal that can be mined using present-day mining technology under current restrictions, rules, and regulations.

The demonstrated reserve base for coals in the U.S. as of January 1, 2001, is approximately 501.1 billion (short) tons. It is broken out by rank, state, and mining method (surface or underground) in Table 7.3.5. As of December 31, 1999 (December 31, 2000, for the U.S.), the world recoverable reserves are estimated to be 1083 billion (short) tons. A breakdown by region and country is provided in Table 7.3.6. The recoverability factor for all coals can vary from approximately 40 to over 90%, depending on the individual deposit. The recoverable reserves in the U.S. represent approximately 54% of the demonstrated reserve base as of January 1, 2001. Thus, the U.S. contains approximately 25% of the recoverable reserves of coal in the world.

Transportation

Most of the coal mined and used domestically in the U.S. is transported by rail from the mine mouth to its final destination. In 1998, 1,119 million short tons of coal were distributed domestically. Rail constituted 58.3% of the tonnage, followed by water at 21.4%; truck at 11.0%; and tramway, conveyor, or slurry pipeline at 9.2%. The remaining 0.1% is listed as "unknown method." Water's share includes transportation on the Great Lakes, all navigable rivers, and on tidewaters (EIA, 1999).

In general, barge transportation is cheaper than rail transportation. However, this advantage is reduced for distances over 300 miles (Villagran, 1989). For distances less than 100 miles, rail is very inefficient, and trucks are used primarily, unless water is available as a mode of transport.

TABLE 7.3.5 U.S. Coal Demonstrated Reserve Base, January 1, 2001[a]

		Bituminous Coal		Subbituminous Coal		Lignite	Total		
Region and State	Anthracite	Underground	Surface	Underground	Surface	Surface[b]	Underground	Surface	Total
Appalachian	7.3	72.9	23.7	0.0	0.0	1.1	76.9	28.1	105.0
Appalachian	7.3	7.40	24.0	0.0	0.0	1.1	78.0	28.5	106.5
Alabama	0.0	1.2	2.1	0.0	0.0	1.1	1.2	3.2	4.4
Kentucky, eastern	0.0	1.7	9.6	0.0	0.0	0.0	1.7	9.6	11.3
Ohio	0.0	17.7	5.8	0.0	0.0	0.0	17.7	5.8	23.5
Pennsylvania	7.2	19.9	1.0	0.0	0.0	0.0	23.8	4.3	28.1
Virginia	0.1	1.2	0.6	0.0	0.0	0.0	1.3	0.6	2.0
West Virginia	0.0	30.1	4.1	0.0	0.0	0.0	30.1	4.1	34.2
Other[c]	0.0	1.1	0.4	0.0	0.0	0.0	1.1	0.4	1.5
Interior	0.1	117.8	27.5	0.0	0.0	13.1	117.9	40.7	158.6
Illinois	0.0	88.2	16.6	0.0	0.0	0.0	88.2	16.6	104.8
Indiana	0.0	8.8	0.9	0.0	0.0	0.0	8.8	0.9	9.7
Iowa	0.0	1.7	0.5	0.0	0.0	0.0	1.7	0.5	2.2
Kentucky, western	0.0	16.1	3.7	0.0	0.0	0.0	16.1	3.7	19.7
Missouri	0.0	1.5	4.5	0.0	0.0	0.0	1.5	4.5	6.0
Oklahoma	0.0	1.2	0.3	0.0	0.0	0.0	1.2	0.3	1.6
Texas	0.0	0.0	0.0	0.0	0.0	12.7	0.0	12.7	12.7
Other[e]	0.1	0.3	1.1	0.0	0.0	0.5	0.4	1.6	2.0
Western	(s)	22.3	2.3	121.3	61.8	29.6	143.7	93.7	237.4
Alaska	0.0	0.6	0.1	4.8	0.6	(s)	5.4	0.7	6.1
Colorado	(s)	8.0	0.6	3.8	0.0	4.2	11.8	4.8	16.6
Montana	0.0	1.4	0.0	69.6	32.8	15.8	71.0	48.5	119.5
New Mexico	(s)	2.7	0.9	3.5	5.2	0.0	6.2	6.1	12.3
North Dakota	0.0	0.0	0.0	0.0	0.0	9.2	0.0	9.2	9.2
Utah	0.0	5.4	0.3	0.0	0.0	0.0	5.4	0.3	5.6
Washington	0.0	0.3	0.0	1.0	(s)	(s)	1.3	0.0	1.4
Wyoming	0.0	3.8	0.5	38.7	23.2	0.0	42.5	23.7	66.2
Other[e]	0.0	0.1	0.0	(s)	(s)	0.4	0.1	0.4	0.5

TABLE 7.3.5 (continued) U.S. Coal Demonstrated Reserve Base, January 1, 2001[a]

		Bituminous Coal		Subbituminous Coal		Lignite	Total		
Region and State	Anthracite	Underground	Surface	Underground	Surface	Surface[b]	Underground	Surface	Total
U.S. total	7.5	213.1	53.5	121.3	61.8	43.8	338.5	162.5	501.1
States east of the Mississippi River	7.3	186.1	44.8	0.0	0.0	1.1	190.1	49.3	239.4
States west of the Mississippi River	0.1	27.0	8.7	121.3	61.8	42.7	148.4	113.3	261.7

[a] Billion short tons.

[b] Lignite resources are not mined underground in the U.S.

[c] Georgia, Maryland, North Carolina, and Tennessee.

[d] Arkansas, Kansas, Louisiana, and Michigan.

[e] Arizona, Idaho, Oregon, and South Dakota.

Notes: (s) = Less than 0.05 billion short tons. Data represent known measured and indicated coal resources meeting minimum seam and depth criteria, in the ground as of January 1, 2001. These coal resources are not totally recoverable. Net recoverability ranges from 0 percent to more than 90 percent. Fifty-four percent of the demonstrated reserve base of coal in the United States is estimated to be recoverable. Totals may not equal sum of components due to independent rounding.

Source: Energy Information Administration, Coal Reserves Data Base.

TABLE 7.3.6 World Recoverable Reserves of Coal[a]

Region/Country	Recoverable Anthracite and Bituminous	Recoverable Lignite and Subbituminous	Total Recoverable Coal
North America			
Canada	3,826	3,425	7,251
Greenland	0	202	202
Mexico	948	387	1,335
U.S.	126,804	146,852	273,656
Total	131,579	150,866	282,444
Central and South America			
Argentina	0	474	474
Bolivia	1	0	1
Brazil	0	13,149	13,149
Chile	34	1,268	1,302
Colombia	6,908	420	7,328
Ecuador	0	26	26
Peru	1,058	110	1,168
Venezuela	528	0	528
Total	8,530	15,448	23,977
Western Europe			
Austria	0	28	28
Croatia	7	36	43
France	24	15	40
Germany	25,353	47,399	72,753
Greece	0	3,168	3,168
Ireland	15	0	15
Italy	0	37	37
Netherlands	548	0	548
Norway	0	1	1
Portugal	3	36	40
Slovenia	0	303	303
Spain	220	507	728
Sweden	0	1	1
Turkey	306	3,760	4,066
United Kingdom	1,102	551	1,653
Yugoslavia	71	17,849	17,919
Total	27,650	73,693	101,343
Eastern Europe and former U.S.S.R.			
Bulgaria	14	2,974	2,988
Czech Republic	2,330	3,929	6,259
Hungary	0	1,209	1,209
Kazakhstan	34,172	3,307	37,479
Kyrgyzstan	0	895	895
Poland	22,377	2,050	24,427
Romania	1	1,605	1,606
Russia	54,110	118,964	173,074
Slovakia	0	190	190
Ukraine	17,939	19,708	37,647
Uzbekistan	1,102	3,307	4,409
Total	132,046	158,138	290,183
Middle East			
Iran	1,885	0	1,885
Total	1,885	0	1,885

TABLE 7.3.6 (continued) World Recoverable Reserves of Coal[a]

Region/Country	Recoverable Anthracite and Bituminous	Recoverable Lignite and Subbituminous	Total Recoverable Coal
Africa			
Algeria	44	0	44
Botswana	4,740	0	4,740
Central African Republic	0	3	3
Congo (Kinshasa)	97	0	97
Egypt	0	24	24
Malawi	0	2	2
Mozambique	234	0	234
Niger	77	0	77
Nigeria	23	186	209
South Africa	54,586	0	54,586
Swaziland	229	0	229
Tanzania	220	0	220
Zambia	11	0	11
Zimbabwe	553	0	553
Total	60,816	216	61,032
Far East and Oceania			
Afghanistan	73	0	73
Australia	46,903	43,585	90,489
Burma	2	0	2
China	68,564	57,651	126,215
India	90,826	2,205	93,031
Indonesia	871	5,049	5,919
Japan	852	0	852
Korea, North	331	331	661
Korea, South	86	0	86
Malaysia	4	0	4
Nepal	2	0	2
New Caledonia	2	0	2
New Zealand	36	594	631
Pakistan	0	2,497	2,497
Philippines	0	366	366
Taiwan	1	0	1
Thailand	0	1,398	1,398
Vietnam	165	0	165
Total	208,719	113,675	322,394
World total	571,224	512,035	1,083,259

[a] Millions of tons.

Notes: The estimates in this table are dependent on the judgment of each reporting country to interpret local economic conditions and its own mineral assessment criteria in terms of specified standards of the World Energy Council. Consequently, the data may not all meet the same standards of reliability, and some data may not represent reserves of coal known to be recoverable under current economic conditions and regulations. Some data represent estimated recovery rates for highly reliable estimates of coal quantities in the ground that have physical characteristics like those of coals currently being profitably mined. U.S. coal rank approximations are based partly on Btu content and may not precisely match borderline geologic ranks. Data for the U.S. represent recoverable coal estimates as of December 31, 2000. Data for other countries are as of December 31, 1999.

Sources: World Energy Council, Survey of Energy Resources 2001, October 2001. U.S. Energy Information Administration. Unpublished file data of the Coal Reserves Data Base (February 2002).

Prior to the signing of the 1990 Clean Air Act Amendments, most coal was transported to the closest power plant or other end-use facility to reduce transportation costs. Because most coal-fired plants are east of the Mississippi River, most of the coal was transported from eastern coal mines. However, once

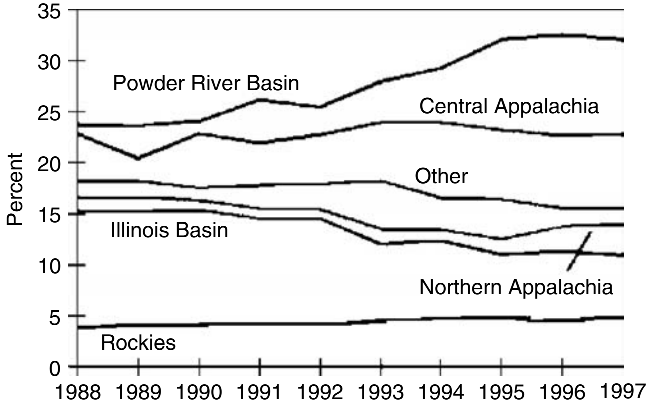

FIGURE 7.3.2 Supply region shares of domestic coal distribution. (From Energy Information Administration, EIA-6, "Coal Distribution Report.")

the Amendments, which required sulfur emissions to be more strictly controlled, began to be enforced, the potential economic advantage of transporting and using low-sulfur western coals compared to installing expensive cleanup facilities in order to continue to use high-sulfur eastern coals began to be considered. This resulted in increasing the average distance coal was shipped from 640 miles in 1988 to 793 miles in 1997.

In comparing shipments from coal-producing regions, the trend of Figure 7.3.2 shows that an increasing share of coal was shipped from the low-sulfur coal producing Powder River Basin between 1988 and 1997 and that less coal was shipped from the high-sulfur coal producing Central Appalachian Basin. Overall, coal use continued to increase at about 2.2% per year over this timeframe.

The cost of transporting coal decreased between 1988 and 1997, due to the increased competition from the low-sulfur western coals following passage of the Clean Air Act Amendments in 1990. This decrease held for all sulfur levels, except for a slight increase in medium sulfur B coals over the last couple of years, as shown in Figure 7.3.3.

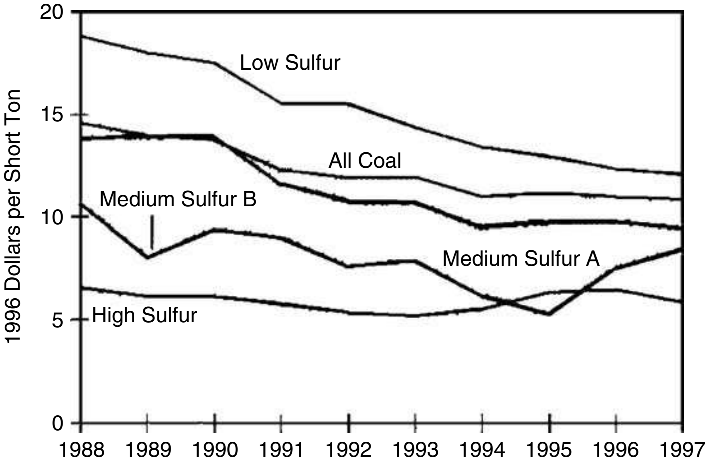

FIGURE 7.3.3 Average rate per ton for contract coal shipments by rail, by sulfur category, 1988 to 1997. Notes: low sulfur = less than or equal to 0.6 lb of sulfur per million Btu; medium sulfur A = 0.61 to 1.25 lb per million Btu; medium sulfur B = 1.26 to 1.67 lb per million Btu; high sulfur = greater than 1.67 lb per million Btu. 1997. (From Energy Information Administration, Coal Transportation Rate Database).

Environmental Aspects

Richard Bajura

Along with coal production and use comes a myriad of potential environmental problems, most of which can be ameliorated or effectively addressed during recovery, processing, conversion, or reclamation. Underground coal reserves are recovered using the two principal methods of room-and-pillar mining (60%) and longwall mining (40%). In room-and-pillar mining, coal is removed from the seam in a checkerboard pattern (the "room") as viewed from above, leaving pillars of coal in an alternate pattern to support the roof of the mine. When using this technology, generally half of the reserves are left underground. Depending upon the depth of the seam and characteristics of the overburden, subsidence due to the removal of the coal may affect the surface many years after the mining operation is completed. Because of the danger of collapse and movement of the surface, undermined lands are not used as building sites for large, heavy structures.

Longwall mining techniques employ the near-continuous removal of coal in rectangular blocks with a vertical cross section equal to the height of the seam multiplied by the horizontal extent (width) of the panel being mined. As the longwall cutting heads advance into the coal seam, the equipment is automatically moved forward. The roof of the mine collapses behind the shields, and most of the effects of subsidence are observed on the surface within several days of mining. If the longwall mining operation proceeds in a continuous fashion, subsidence may occur smoothly so that little damage occurs to surface structures. Once subsidence has occurred, the surface remains stable into the future. Longwall mining operations may influence water supplies as a result of fracturing of water-bearing strata far removed from the panel being mined.

When coal occurs in layers containing quartz dispersed in the seam or in the overburden, miners are at risk of exposure to airborne silica dust, which is inhaled into their lungs. Coal workers' pneumoconiosis, commonly called black lung disease, reduces the ability of a miner to breathe because of the effects of fibrosis in the lungs.

Surface mining of coal seams requires the removal of large amounts of overburden, which must eventually be replaced into the excavated pit after the coal resource is extracted. When the overburden contains large amounts of pyrite, exposure to air and water produces a discharge known as acid mine drainage, which can contaminate streams and waterways. Iron compounds formed as a result of the chemical reactions precipitate in the streams and leave a yellow- or orange-colored coating on rocks and gravel in the streambeds. The acid caused by the sulfur in the pyrite has been responsible for significant destruction of aquatic plants and animals. New technologies have been and continue to be developed to neutralize acid mine drainage through amendments applied to the soil during the reclamation phases of the mining operation. Occasionally, closed underground mines fill with water and sufficient pressure is created to cause "blowouts" where the seams reach the surface. Such discharges have also been responsible for massive fish kills in receiving streams.

The potential for acid rain deposition from sulfur and nitrogen oxides released to the atmosphere during combustion is a significant concern. About 95% of the sulfur oxide compounds can be removed through efficient stack gas cleaning processes such as wet and dry scrubbing. Also, techniques are available for removing much of the sulfur from the coal prior to combustion. Combustion strategies are also being developed that reduce the formation and subsequent release of nitrogen oxides.

The potential for greenhouse warming due to emissions of carbon dioxide during combustion (as well as methane during mining and mine reclamation) has also been raised as a significant concern. Because coal is largely composed of carbon with relatively little hydrogen, its combustion leads to a higher level of carbon dioxide emissions per unit of energy released than for petroleum-based fuels or natural gas.

Defining Terms

Coalification: the physicochemical transformation that coal undergoes after being buried and subjected to elevated temperature and pressure. The classification of a particular coal by rank is a measure of the extent of its coalification. Thus, coalification is a measure of the "age" of a particular coal.

Fixed carbon content: one of the constituents that make up the proximate analysis of a coal. It is normally measured by difference. That is, one measures the volatile matter content and the moisture and ash contents, if the fixed carbon content is reported on a basis containing one or both of those constituents, and subtracts the result(s) from 100% to find the fixed carbon content. One should not confuse the fixed carbon content of a coal with its (elemental) carbon content found in the ultimate analysis. Although carbon is certainly in the material making up the fixed carbon content, it is not all of the carbon present in the original coal, and other elements are also present.

Gross calorific value: calorific value is a measure of the energy content of a material — in this case, a coal sample. Calorific value is measured by ASTM Standard Test Method D 2015M, Gross Calorific Value of Solid Fuel by the Adiabatic Bomb Calorimeter, or by ASTM Standard Test Method D 3286, Gross Calorific Value of Solid Fuel by the Isothermal-Jacket Bomb Calorimeter. The *gross* calorific value takes into account the additional heat gained by condensing any water present in the products of combustion, in contrast to the *net* calorific value, which assumes that all water remains in the vapor state.

Maceral: an organic substance or optically homogeneous aggregate of organic substance in a coal sample that possesses distinctive physical and chemical properties.

Proximate analysis: a method to measure the content of four separately identifiable constituents in a coal: volatile matter content; fixed carbon content; moisture content; and ash content, all of which are reported on a weight percent basis. The standard method for obtaining the proximate analysis of coal or coke is defined by the ASTM in Standard Test Method D 3172.

Rank: a classification scheme for coals that describes the extent of coalification that a particular coal has undergone. The structure, chemical composition, and many other properties of coals vary systematically with rank. The standard method for determining the rank of a coal sample is defined by the ASTM in Standard Test Method D 388.

Type: a classification scheme for coals that references the original plant material from which the coal was derived.

Ultimate analysis: a method to measure the elemental composition of a coal sample. Typical ultimate analyses include carbon, hydrogen, oxygen, sulfur, and nitrogen contents, but other elements can also be reported. These other elements are usually not present to any appreciable extent. However, if they are reported, the sum of all the elements reported (including moisture and ash content) should equal 100%. The standard method for the ultimate analysis of coal or coke is defined by the ASTM in Standard Test Method D 3176.

Volatile matter content: the mass of material released upon heating the coal sample under specific conditions, defined by the ASTM Standard Test Method D 3175.

References

Elliott, M.A. and Yohe, G.R. 1981. The coal industry and coal research and development in perspective, in *Chemistry of Coal Utilization. Second Supplementary Volume,* M.A. Elliott, Ed., John Wiley & Sons, New York, 26.

Habermehl, D., Orywal, F., and Beyer, H.-D. 1981. Plastic properties of coal, in *Chemistry of Coal Utilization. Second Supplementary Volume,* M.A. Elliott, Ed., John Wiley & Sons, New York, 319-328.

Villagran, R.A. 1989. *Acid Rain Legislation: Implications for the Coal Industry,* Shearson, Lehman, Button, New York, 37–39.

Further Information

An excellent resource for understanding coal, its sources, uses, limitations, and potential problems is the book by Elliott referenced under Elliott and Yohe (1981) and Habermehl et al. (1981). A reader wishing an understanding of coal topics could find no better resource. Another comprehensive book, which includes more-recent information but is not quite as weighty as Elliott's (664 pages vs. 2374 pages), is

The Chemistry and Technology of Coal, edited (second edition, revised and expanded) by James G. Speight. For information specific to the environmental problems associated with the use of coal, the reader is referred to Norbert Berkowitz's chapter entitled "Environmental Aspects of Coal Utilization" in *An Introduction to Coal Technology.* For information on the standards for coal analyses and descriptions of the associated procedures, the reader is referred to any recent edition of the ASTM's *Annual Book of ASTM Standards.* Section 5 covers petroleum products, lubricants, and fossil fuels, including coal and coke.

Oil

Philip C. Crouse

Overview

The U.S. Department of Energy's Energy Information Administration (EIA) annually provides a wealth of information concerning most energy forms including fossil fuels. The oil and natural gas sections are extracted summaries for the most germane information concerning oil and natural gas. Fossil fuel energy continues to account for over 85% of all world energy in 2000. The EIA estimates that in 2025, fossil fuels will still dominate energy resources with natural gas having the most growth. The base case of the EIA predicts that world energy consumption will grow by 60% over the next two decades. Figure 7.3.4 shows steady growth in global energy consumption. The projections show that in 2025 the world will consume three times the energy it consumed in 1970.

In the United States, wood served as the preeminent form of energy for about half of the nation's history. Around the 1880s, coal became the primary source of energy. Despite its tremendous and rapid expansion, coal was overtaken by petroleum in the middle of the 1900s. Natural gas, too, experienced rapid development into the second half of the 20th century, and coal began to expand again. Late in the 1900s, nuclear electric power was developed and made significant contributions.

Although the world's energy history is one of large-scale change as new forms of energy have been developed, the outlook for the next couple of decades is for continued growth and reliance on the three major fossil fuels of petroleum, natural gas, and coal. Only modest expansion will take place in renewable resources and relatively flat generation from nuclear electric power, unless major breakthroughs occur in energy technologies. Table 7.3.7 shows EIA's estimate of growth of selected energy types with oil needs dominating the picture over the next 20 years.

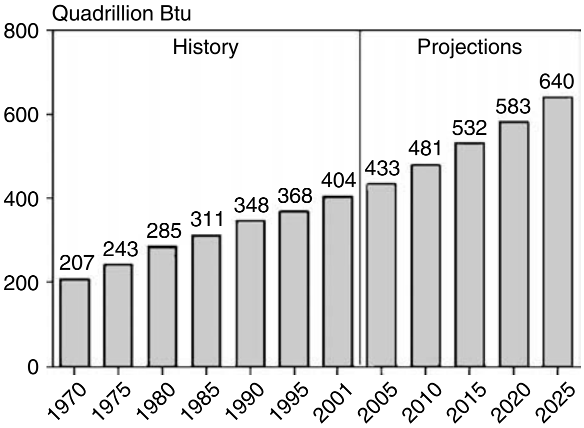

FIGURE 7.3.4 World energy consumption, 1970–2025. (History from EIA, International Energy Annual 2001, DOE/EIA-0219(2001), Washington, D.C., Feb. 2003, www.eia.doe.gov/iea/. Projections from EIA, System for the analysis of Global Energy Markets (2003).)

TABLE 7.3.7 World Total Energy Consumption by Region and Fuel, Reference Case, 1990–2025[a]

	History			Projections					Average Annual Percent Change,
Region/Country	1990	2000	2001	2005	2010	2015	2020	2025	2001–2025
				Industrialized Countries					
North America									
Oil	40.4	46.3	45.9	48.3	54.2	59.7	64.3	69.3	1.7
Natural Gas	23.1	28.8	27.6	30.6	34.0	37.9	42.0	46.9	2.2
Coal	20.7	24.5	23.9	24.9	27.3	28.7	30.0	31.8	1.2
Nuclear	6.9	8.7	8.9	9.4	9.6	9.7	9.7	9.5	0.3
Other	9.5	10.6	9.4	11.3	12.0	12.7	13.4	13.9	1.7
Total	**100.6**	**118.7**	**115.6**	**124.6**	**137.2**	**148.7**	**159.4**	**171.4**	**1.7**
Western Europe									
Oil	25.8	28.5	28.9	29.2	29.7	30.3	30.6	31.6	0.4
Natural gas	9.7	14.9	15.1	15.9	17.5	20.1	23.4	26.4	2.4
Coal	12.4	8.4	8.6	8.3	8.2	7.5	6.8	6.7	-1.0
Nuclear	7.4	8.8	9.1	8.9	9.1	8.8	8.1	6.9	-1.1
Other	4.5	6.0	6.1	6.8	7.5	8.0	8.4	8.8	1.5
Total	**59.9**	**66.8**	**68.2**	**69.1**	**72.1**	**74.7**	**77.3**	**80.5**	**0.7**
Industrialized Asia									
Oil	12.1	13.2	13.0	13.5	14.3	15.1	15.8	16.7	1.1
Natural gas	2.5	4.0	4.1	4.4	4.6	5.0	5.3	5.9	1.5
Coal	4.2	5.7	5.9	5.8	6.3	6.7	7.0	7.4	0.9
Nuclear	2.0	3.0	3.2	3.2	3.6	3.9	4.0	3.9	0.9
Other	1.6	1.6	1.6	1.9	2.0	2.1	2.3	2.4	1.7
Total	**22.3**	**27.5**	**27.7**	**28.8**	**30.8**	**32.8**	**34.4**	**36.4**	**1.1**
Total industrialized									
Oil	78.2	88.1	87.8	90.9	98.2	105.1	110.7	117.6	1.2
Natural Gas	35.4	47.7	46.8	50.9	56.1	63.0	70.7	79.2	2.2
Coal	37.3	38.6	38.5	39.1	41.9	42.9	43.7	45.9	0.7
Nuclear	16.3	20.5	21.2	21.5	22.3	22.3	21.8	20.4	–0.2
Other	15.6	18.2	17.1	20.0	21.6	22.8	24.0	25.2	1.6
Total	**182.8**	**213.0**	**211.5**	**222.5**	**240.1**	**256.2**	**271.1**	**288.3**	**1.3**
EE/FSU									
Oil	21.0	10.9	11.0	12.6	14.2	15.0	16.5	18.3	2.1
Natural gas	28.8	23.3	23.8	27.9	31.9	36.9	42.0	47.0	2.9
Coal	20.8	12.2	12.4	13.7	12.7	12.5	11.2	10.2	–0.8
Nuclear	2.9	3.0	3.1	3.3	3.3	3.3	3.0	2.6	–0.7
Other	2.8	3.0	3.2	3.6	3.7	3.9	4.0	4.1	1.1
Total	**76.3**	**52.2**	**53.3**	**61.1**	**65.9**	**71.6**	**76.7**	**82.3**	**1.8**
				Developing Countries					
Developing Asia									
Oil	16.1	30.2	30.7	33.5	38.9	45.8	53.8	61.9	3.0
Natural gas	3.2	6.9	7.9	9.0	10.9	15.1	18.6	22.7	4.5
Coal	29.1	37.1	39.4	41.3	49.4	56.6	65.0	74.0	2.7
Nuclear	0.9	1.7	1.8	2.6	3.1	4.1	4.5	5.0	4.3
Other	3.2	4.5	5.1	6.1	7.8	8.9	10.0	11.0	3.2
Total	**52.5**	**80.5**	**85.0**	**92.5**	**110.1**	**130.5**	**151.9**	**174.6**	**3.0**

[a] Quadrillion Btu.

Source: International Energy Outlook-2003, U.S. Dept. of Energy, Energy Information Administration.

Crude Oil Classification and World Reserves

Obtaining accurate estimates of world petroleum and natural gas resources and reserves is difficult and uncertain, despite excellent scientific analysis made over the years. Terminology standards used by industry to classify resources and reserves has progressed over the last 10 years with the Society of

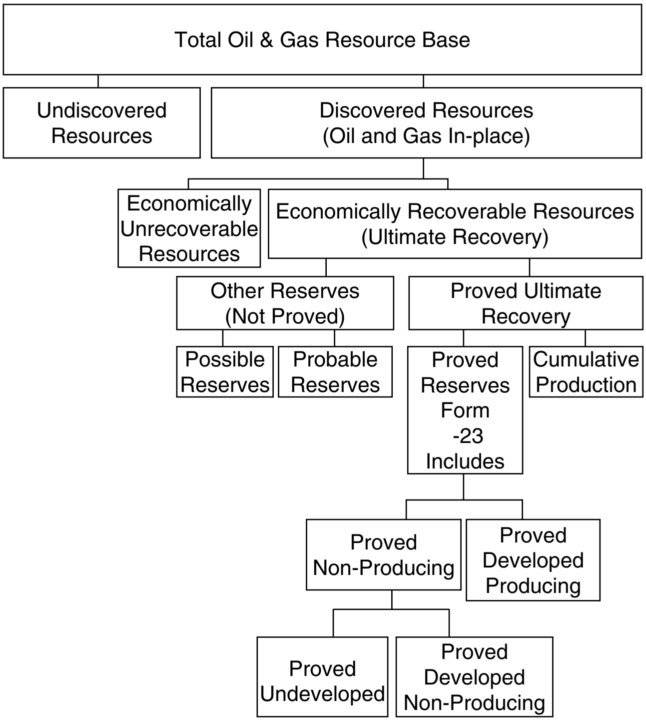

FIGURE 7.3.5 Components of the oil and gas resource base. (From EIA, Office of Gas and Oil.)

Petroleum Evaluation Engineers leading an effort to establish a set of standard definitions that would be used by all countries in reporting reserves. Classifications of reserves, however, continue to be a source of controversy in the international oil and gas community. This subsection uses information provided by the Department of Energy classification system. The next chart shows the relationship of resources to reserves. **Recoverable reserves** include discovered and undiscovered resources. **Discovered resources** are those resources that can be economically recovered. Figure 7.3.5 shows the relationship of petroleum resource and reserves terms.

Discovered resources include all production already out of the ground and reserves. Reserves are further broken down into proved reserves and other reserves. Again, many different groups classify reserves in different ways, such as measured, indicated, internal, probable, and possible. Most groups break reserves into producing and nonproducing categories. Each of the definitions is quite voluminous and the techniques for qualifying reserves vary globally. Table 7.3.8 shows estimates made by the EIA for total world oil resources.

Standard Fuels

Petroleum is refined into petroleum products that are used to meet individual product demands. The general classifications of products are:

1. NATURAL GAS LIQUIDS AND LIQUEFIED REFINERY GASES. This category includes ethane (C_2H_6); ethylene (C_2H_4); propane (C_3H_8); propylene (C_3H_6); butane and isobutane (C_4H_{10}); and butylene and isobutylene (C_4H_8).
2. FINISHED PETROLEUM PRODUCTS. This category includes motor gasoline; aviation gasoline; jet fuel; kerosene; distillate; fuel oil; residual fuel oil; petrochemical feed stock; naphthas; lubricants; waxes; petroleum coke; asphalt and road oil; and still gas.

TABLE 7.3.8 Estimated World Oil Resources, 2000–2025[a]

Region and Country	Proved Reserves	Reserve Growth	Undiscovered
Industrialized			
U.S.	22.45	76.03	83.03
Canada	180.02	12.48	32.59
Mexico	12.62	25.63	45.77
Japan	0.06	0.09	0.31
Australia/New Zealand	3.52	2.65	5.93
Western Europe	18.10	19.32	34.58
Eurasia			
Former Soviet Union	77.83	137.70	170.79
Eastern Europe	1.53	1.46	1.38
China	18.25	19.59	14.62
Developing countries			
Central and South America	98.55	90.75	125.31
India	5.37	3.81	6.78
Other developing Asia	11.35	14.57	23.90
Africa	77.43	73.46	124.72
Middle East	685.64	252.51	269.19
Total	1,212.88	730.05	938.90
OPEC	819.01	395.57	400.51
Non-OPEC	393.87	334.48	538.39

[a] Billion barrels.

Note: Resources include crude oil (including lease condensates) and natural gas plant liquids.

Source: U.S. Geological Survey, *World Petroleum Assessment 2000*, web site http://greenwood.cr.usgs.gov/energy/WorldEnergy/DDS-60.

- *Motor gasoline* includes reformulated gasoline for vehicles and oxygenated gasoline such as gasohol (a mixture of gasoline and alcohol).
- *Jet fuel* is classified by use such as industrial or military and naphtha and kerosene type. Naphtha fuels are used in turbo jet and turbo prop aircraft engines and exclude ram-jet and petroleum rocket fuel.
- *Kerosene* is used for space heaters, cook stoves, wick lamps, and water heaters.
- *Distillate fuel oil* is broken into subcategories: No. 1 distillate, No. 2 distillate, and No. 4 fuel oil, which is used for commercial burners.
- *Petrochemical feedstock* is used in the manufacture of chemicals, synthetic rubber, and plastics.
- *Naphthas* are petroleums with an approximate boiling range of 122 to 400°F.
- *Lubricants* are substances used to reduce friction between bearing surfaces, as process materials, and as carriers of other materials. They are produced from distillates or residues. Lubricants are paraffinic or naphthenic and separated by viscosity measurement.
- *Waxes* are solid or semisolid material derived from petroleum distillates or residues. They are typically a slightly greasy, light colored or translucent, crystallizing mass.
- *Asphalt* is a cement-like material containing bitumens. *Road oil* is any heavy petroleum oil used as a dust pallatine and road surface treatment.
- *Still gas* is any refinery by-product gas. It consists of light gases of methane; ethane; ethylene; butane; propane; and the other associated gases. Still gas is typically used as a refinery fuel.

Table 7.3.9 shows *world refining capacity* as of January 1, 2002. The number of oil refineries continues to grow as demands for petroleum products have continued to grow.

TABLE 7.3.9 World Crude Oil Refining Capacity, January 1, 2002

		Thousand Barrels per Day			
Region/Country	Number of Refineries	Crude Oil Distillation	Catalytic Cracking	Thermal Cracking	Reforming
North America	180	20,254	6,619	2,450	4,140
Central and South America	70	6,547	1,252	435	447
Western Europe	112	15,019	2,212	1,603	2,214
Eastern Europe and Former U.S.S.R.	87	10,165	778	516	1,353
Middle East	46	6,073	312	406	570
Africa	46	3,202	195	88	387
Asia and Oceania	203	20,184	2,673	421	2,008
World Total	744	81,444	14,040	5,918	11,119

Source: Last updated on 3/14/2003 by DOE/EIA.

Natural Gas

Philip C. Crouse

Overview

Natural gas has been called the environmentally friendly fossil fuel because it releases fewer harmful contaminants. World production of dry natural gas was 73.7 trillion ft^3 and accounted for over 20% of world energy production. In 1990 Russia accounted for about one third of world natural gas. With about one quarter of the world's 1990 natural gas production, the second largest producer was the U.S.

According to the U.S. Department of Energy, natural gas is forecast to be the fastest growing primary energy. Consumption of natural gas is projected to nearly double between 2001 and 2025, with the most robust growth in demand expected among the developing nations. The natural gas share of total energy consumption is projected to increase from 23% in 2001 to 28% in 2025.

Natural gas traded across international borders has increased from 19% of the world's consumption in 1995 to 23% in 2001. The EIA notes that pipeline exports grew by 39% and liquefied natural gas (LNG) trade grew by 55% between 1995 and 2001. LNG has become increasingly competitive, suggesting the possibility for strong worldwide LNG growth over the next two decades. Figure 7.3.6 shows projections of natural gas consumption in 2025 to be five times the consumption level in 1970.

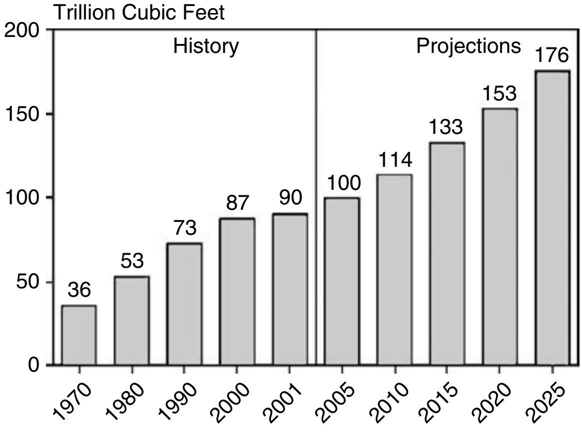

FIGURE 7.3.6 World natural gas consumption, 1970–2025. (History from EIA, International Energy Annual 2001, DOE/EIA-0219(2001), Washington, D.C., Feb. 2003, www.eia.doe.gov/iea/. Projections from EIA, System for the analysis of Global Energy Markets (2003).)

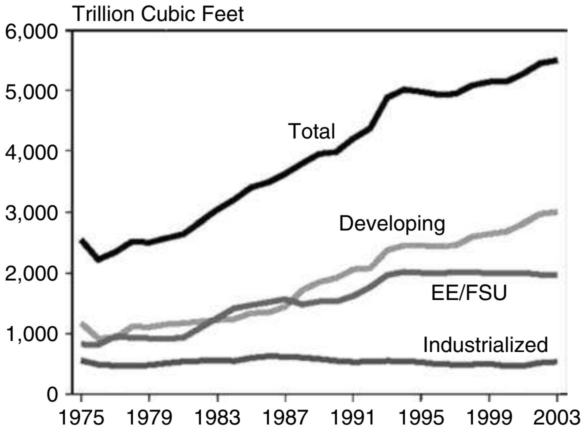

FIGURE 7.37 World natural gas reserves by region, 1975–2003. (Data for 1975–1993 from Worldwide oil and gas at a glance, *International Petroleum Encyclopedia,* Tulsa, OK: PennWell Publishing, various issues. Data for 1994–2003 from *Oil & Gas Journal*, various issues.)

Reserves and Resources

Since the mid-1970s, world natural gas reserves have generally trended upward each year As of January 1, 2003, proved world natural gas reserves, as reported by *Oil & Gas Journal*, were estimated at 5,501 trillion ft^3. Over 70% of the world's natural gas reserves are located in the Middle East and the EE/FSU, with Russia and Iran together accounting for about 45% of the reserves. Reserves in the rest of the world are fairly evenly distributed on a regional basis.

The U.S. Geological Survey (USGS) regularly assesses the long-term production potential of worldwide petroleum resources (oil, natural gas, and natural gas liquids). According to the most recent USGS estimates, released in the *World Petroleum Assessment 2000*, the mean estimate for worldwide undiscovered gas is 4839 trillion ft^3. Outside the U.S. and Canada, the rest of the world reserves have been largely unexploited. Outside the U.S., the world has produced less than 10% of its total estimated natural gas endowment and carries more than 30% as remaining reserves. Figure 7.3.7 shows world natural gas reserves by region from 1975 to 2003. Table 7.3.10 shows natural gas reserves of the top 20 countries compared to world reserves. Russia, Iran, and Qatar account for over half of estimated world gas reserves.

Natural Gas Production Measurement

Natural gas production is generally measured as "dry" natural gas production. It is determined as the volume of natural gas withdrawn from a reservoir less (1) the volume returned for cycling and repressuring reservoirs; (2) the shrinkage resulting from the removal of lease condensate and plant liquids; and (3) the nonhydrocarbon gases. The parameters for measurement are 60°F and 14.73 lb standard per square inch absolute.

World Production of Dry Natural Gas

From 1983 to 1992, dry natural gas production grew from 54.4 to 75 trillion ft^3. The breakdown by region of world is shown in Table 7.3.11.

Compressed Natural Gas

Environmental issues have countries examining and supporting legislation to subsidize the development of cleaner vehicles that use compressed natural gas (CNG). Even with a push toward the use of CNG-burning vehicles, the numbers are quite small when compared with gasoline vehicles. Recent efforts toward car power have been focused on hybrid electric-gasoline cars and fuel cell vehicles.

TABLE 7.3.10 World Natural Gas Reserves by Country as of January 1, 2003

Country	Reserves (trillion ft^3)	Percent of World Total
World	5501	100.0
Top 20 countries	4879	88.7
Russia	1680	30.5
Iran	812	14.8
Qatar	509	9.2
Saudi Arabia	224	4.1
United Arab Emirates	212	3.9
U.S.	183	3.3
Algeria	160	2.9
Venezuela	148	2.7
Nigeria	124	2.3
Iraq	110	2.0
Indonesia	93	1.7
Australia	90	1.6
Norway	77	1.4
Malaysia	75	1.4
Turkmenistan	71	1.3
Uzbekistan	66	1.2
Kazakhstan	65	1.2
Netherlands	62	1.1
Canada	60	1.1
Egypt	59	1.1
Rest of World	622	11.3

Source: *Oil Gas J.*, 100(52) (December 23, 2002), 114–115.

TABLE 7.3.11 World Dry Natural Gas Production[a]

Country/Region	1983	1992	2000
North, Central, and South America	21.20	25.30	30.20
Western Europe	6.20	7.85	10.19
Eastern Europe and former U.S.S.R.	21.09	28.60	26.22
Middle East and Africa	2.95	6.87	12.01
Far East and Oceania	2.96	6.38	9.48
World total	54.40	75.00	88.10

[a] Trillion ft^3.

Source: From EIA, Annual Energy Review 1993, EIA, Washington, D.C., July 1994, 305, and International Energy Outlook-2003.

Liquefied Natural Gas (LNG)

Natural gas can be liquefied by lowering temperature until a liquid state is achieved. It can be transported by refrigerated ships. The process of using ships and providing special-handling facilities adds significantly to the final LNG cost. LNG projects planned by a number of countries may become significant over the next 20 years, with shipments of LNG exports ultimately accounting for up to 25% of all gas exports.

Physical Properties of Hydrocarbons

The most important physical properties from a crude oil classification standpoint are density or specific gravity and the viscosity of liquid petroleum. Crude oil is generally lighter than water. A Baume-type scale is predominantly used by the petroleum industry and is called the API (American Petroleum Institute) gravity scale (see Table 7.3.12). It is related directly to specific gravity by the formula:

$$\varphi = (141.5)/(131.5 + °\mathrm{API})$$

TABLE 7.3.12 Relation of API Gravity, Specific Gravity, and Weight per Gallon of Gasoline

Degree API	Specific Gravity	Weight of Gallon (lb)
8	1.014	8.448
9	1.007	8.388
10	1.000	8.328
15	0.966	8.044
20	0.934	7.778
25	0.904	7.529
30	0.876	7.296
35	0.850	7.076
40	0.825	6.870
45	0.802	6.675
50	0.780	6.490
55	0.759	6.316
58	0.747	6.216

Note: The specific gravity of crude oils ranges from about 0.75 to 1.01.

TABLE 7.3.13 Other Key Physical Properties of Hydrocarbons

Compound	Molecular Weight	Boiling Point at 14.7 psia in °F	Liquid Density at 14.7 psia and 60°F-lb/gal
Methane	16.04	–258.7	2.90
Ethane	30.07	–125.7	4.04
Propane	44.09	–43.7	4.233
Isobutane	58.12	10.9	4.695
n-Butane	58.12	31.1	4.872
Isopentane	72.15	82.1	5.209
n-Pentane	72.15	96.9	5.262
n-Hexane	86.17	155.7	5.536
n-Heptane	100.2	209.2	5.738
n-Octane	114.2	258.2	5.892
n-Nonane	128.3	303.4	6.017
n-Decane	142.3	345.4	6.121

where φ = specific gravity. Temperature and pressure are standardized at 60°F and 1 atm pressure.

Other key physical properties involve the molecular weight of the hydrocarbon compound and the boiling point and liquid density. Table 7.3.13 shows a summation of these properties.

Defining Terms

API gravity: A scale used by the petroleum industry for specific gravity.

Discovered resources: Include all production already out of the ground and reserves.

Proved resources: Resources that geological and engineering data demonstrate with reasonable certainty to be recoverable in future years from known reservoirs under existing economic and operating conditions.

Recoverable resources: Include discovered resources.

Further Information

The Energy Information Agency of the U.S. Department of Energy, Washington, D.C., publishes *International Energy Outlook* and other significant publications periodically.

7.4 Biomass Energy

Ralph P. Overend and Lynn L. Wright

Biomass energy encompasses a wide variety of energy technologies that use renewable plant matter, or phytomass, derived from photosynthesis as a feedstock to produce solid, liquid, and gaseous biofuels or used directly as an energy source producing heat and electricity. Biorefinery concepts are being developed that could result in the production of multiple energy carriers, as well as bioproducts from the same biomass resource.

Biomass Feedstock Technologies

Photosynthesis

Biomass fuels are derived from green plants, which capture solar energy and store it as chemical energy through the **photosynthetic** reduction of atmospheric carbon dioxide. Plant leaves are biological solar collectors while the stems, branches, and roots are the equivalent of batteries storing energy-rich complex carbon compounds. Elemental analysis shows that wood and grasses are about 50% carbon. The average photosynthetic efficiency of converting solar energy into energy stored in organic carbon compounds on an annual basis varies from less than 0.5% in temperate and tropical grasslands to about 1.5% in moist tropical forests (Cralle and Vietor, 1989). Although seemingly quite low, the worldwide annual storage of photosynthetic energy in terrestrial biomass is huge, representing approximately 10 times world annual use of energy (Hall et al., 1993). This annual energy storage reflects the diversity and adaptability of terrestrial plants in many different climate zones, from the polar regions to the tropics.

Biomass Residue Resources

The majority of biomass energy used today is derived from residues associated with the production of timber and food crops in the field and the forest, as well as in their processing into final products. On the average, for each tonne of grain or timber harvested, there is an equivalent amount of stalk, straw, or forest residues such as branch materials. Residues from agricultural crops, such as cereal straws, are already used for bioenergy in many parts of the world and represent a large, immediately accessible resource for bioenergy in the United States. Agriculture residue recovery in the U.S. will have the most potential in high-yield cropland areas, especially those in which no-till management systems are used. Under such conditions, some portion of the crop residue may be sustainably and economically recoverable for bioenergy.

Under conventional management practices, corn stover, wheat straw, and other crop residues often have greater economic value because they are left on the land to restore nutrients, reduce erosion, and stabilize soil structure. Sustainably recoverable agricultural crop residues in the U.S. are estimated to be less than136 Mt (Walsh et al., 2000; Gallagher et al., 2003) (all biomass amounts are on a dry basis). Crop residues worldwide are estimated to have an energy value of 12.5 EJ (Hall et al., 1993).

Recoverable wood residues from all sources in the U.S. are estimated to be approximately 94.3 Mt (McKeever, 2003). This includes 67.6 Mt of logging residues; 16.4 Mt of construction and demolition wastes; and 8.7 Mt of recoverable solid wood from the postconsumer urban residue stream (or municipal solid waste stream). Primary timber mills produce about 73.7 Mt of residues; however, about 97% of this is already utilized.

A potentially large wood residue resource consists of the small-diameter growing trees and woody debris that need to be removed from U.S. forests to reduce hazardous fuel loading in forest fire mitigation. Small-diameter wood is already harvested for fuelwood in many parts of the world. The estimated forest residues, worldwide have an energy value of 13.5 EJ (Hall et al., 1993). Forest industry processing residues (e.g., sawdust or black liquor from pulping processes) are already used for energy in most cases.

Potential Forestry Biomass Resources Worldwide

The amount of harvestable woody biomass produced by natural forests on an annual basis ranges from about 2 to 6 t ha^{-1} y^{-1} (with the higher yields usually in tropical regions); this could be increased to 4 to

12 t ha^{-1} y^{-1} if brought under active management. Such management would include optimizing harvesting strategies for production, fertilization, and replanting natural stands with faster-growing species. As of 1990, 10% of world forests, or 355 Mha, were actively managed. If managed forests were increased to 20%, and if 20% of the harvested material were used for energy, the annual worldwide resource of wood for energy from currently forested land would amount to between 284 to 852 Mt of available wood, or about 5.6 to 17 EJ of primary energy based on potential yield ranges of managed forests. The most optimistic estimates of biomass potential would provide a total primary energy resource of about 30 EJ from managed forests (Sampson et al., 1993).

Potential Energy Crop Production

Significantly increasing the world's biomass energy resources will require the production of high-yield crops dedicated to conversion to bioenergy. The most environmentally beneficial dedicated crop production systems will be the production of perennial plants, using genetically superior materials, established on previously cropped land, and managed as agricultural crops. Perennials such as annually harvested grasses or short rotation trees harvested on a cycle of 3 to 10 years minimize soil disturbance, increase the build-up of soil carbon, provide wildlife habitat, and generally require fewer inputs of chemicals and water for a given level of production.

Energy crop yields will be highest in locations where genetically superior material is planted on land with plenty of access to sunshine and water. In the moist tropics and subtropics, as well as in irrigated desert regions, yields in the range of 20 to 30 t ha^{-1} y^{-1} are achievable with grasses and trees (e.g., eucalypts and tropical grasses, and hybrid poplars in the irrigated Pacific Northwest of the U.S.). Without irrigation, temperate woody crops would be expected to yield 9 to 13 t ha^{-1} y^{-1} of harvestable biomass, though several experimental trials have demonstrated yields of improved genotypes of poplars in the range of 12 to 20 t ha^{-1} y^{-1} and best yields up to 27 t ha^{-1} y^{-1} (Wright, 1994). Unimproved temperate perennial grasses with no irrigation typically yield about 7 to 11 t ha^{-1} y^{-1}; selected grasses in experimental trials have commonly achieved yields of 11 to 22 t ha^{-1} y^{-1} with occasional yields of 16 to 27 t ha^{-1} y^{-1} in some years. Although grass yields vary from year to year, the Alamo variety of switchgrass has averaged around 23 t ha^{-1} y^{-1} (10 dry ton/acre/year) over 12 years in the southeastern U.S., where a long growing season favors warm-season grasses (McLaughlin and Kszos, personal communication).

Temperate shelterbelts and tropical agroforestry plantings could also contribute greatly to biomass energy resources. Assuming a range of possible yields, the primary energy resource potential of converting 10 to 15% of cropland to energy crops has been estimated to range from a low of 18 EJ to a high of 49 EJ. A further 25 to 100 EJ has been estimated to be available from the conversion of grasslands and degraded areas to the production of biomass energy resources worldwide (Sampson et al., 1993).

Terrestrial and Social Limitations

M.J.R. Cannell provides estimates of theoretical, realistic, and conservative/achievable capacity of biofuel plantations of trees or annual crops to produce primary energy and offset global carbon emissions between 2050 to 2100 (Cannell, 2003). The theoretical estimate of biomass energy potential assumes 600 to 800 Mha, or a maximum of 55% of current cropland area (although including large areas of previous crop land that are now degraded) and average yields increasing from 10 to 25 t ha^{-1} y^{-1} providing 150 to 300 EJ. The realistic estimate of biomass energy potential assumes 200 to 400 Mha (14 to 28% of current cropland area) and average yields of 10 t ha^{-1} y^{-1} (37 to 74 EJ); the conservative/achievable estimate assumes 50 to 200 Mha of current cropland and average yields of 10 t ha^{-1} y^{-1} (9 to 37 EJ).

Cannell's conservative estimate recognizes that developing countries continue to face food and water shortages and increasing populations, and that substantial economic and policy obstacles must be overcome. Additionally, the life cycle environmental and social impacts are not always strongly positive, depending on the crop management systems used and the conversion process employed.

Biomass Facility Supply Considerations

The location of large biorefinery facilities will be limited by local biomass supply availability and price considerations. Siting opportunities for facilities in the U.S. that require 500 t d^{-1} or less of biomass

TABLE 7.4.1 Impact of Facility Size and Energy Crop Productivity on Area Required

Yield	Plant Throughput 500 t d^{-1}		Plant Throughput 2000 t d^{-1}		Plant Throughput 10,000 t d^{-1}	
t ha^{-1} y^{-1}	Hectares	% area[a]	Hectares	% area[a]	Hectares	% area[a]
3.3	44,535	2.2	178,141	8.8	890,705	44.3
9.0	16,330	0.8	65,318	3.3	326,592	16.3
18.0	8,165	0.3	32,659	1.6	163,296	8.13

[a] Percent area required within 80-km radius of demand center.

TABLE 7.4.2 Impact of Facility Size and Process Efficiency on Expected Outputs of Fuels and Electricity

	Electricity[a]		Ethanol		Fischer–Tropsch liquids		Hydrogen[b]	
Scale	Capacity MW		Production kL/d		Production Bbl/d		Production t/d	
td^{-1}	Present	Future	Present	Future	Present	Future	Present	Future
500	30.4	45.6	165.9	186.6	453.5	538.5	6.5	7.7
2,000	121.5	182.3	663.5	746.4	1813.8	2,153.9	25.9	30.8
10,000	607.6	911.5	3317.5	3732.2	9069.0	10,769.5	129.7	154.1

[a] Efficiency: present = 30%; future = 45%.
[b] Efficiency: present = 50%; future = 60%.

delivered at prices of 40 \$ t^{-1} or greater will be abundant, especially if dedicated crops are included in the supply mix. U.S. locations with abundant supplies of biomass delivered at 20 \$ t^{-1} or less will be quite limited. As facility size increases to 2000 t d^{-1} (the smallest size being considered for most biorefineries), up to 10,000 dt/day, suitable locations will become increasingly limited and/or prices will be considerably higher (Graham et al., 1995).

Facilities with the capability of processing a wide variety of feedstock types may gain a price benefit from seasonal feedstock switching (such as using corn stover in fall, woody crops in winter, and grasses in summer) and from using opportunity feedstock (such as trees blown down from storms). Facilities with a large demand for feedstocks with specific characteristics will depend upon crops genetically selected and tailored for the specific process. The higher feedstock prices would presumably be offset by the economies of scale leading to reductions in processing costs (Jenkins, 1997).

Acceptance of biomass facility siting will depend in part on the land area changes required to supply a facility. For economic analysis, it is normally assumed that biomass supplies will be available within an 80 km radius (although in many situations worldwide supply is coming from longer distances, with international trading emerging in some areas). An approximate idea of the hectares and percent land area within an 80 km radius required as a function of the biomass yield that can be sustainably harvested/collected from the land is provided in Table 7.4.1. The lower yield is representative of levels of agricultural residues (such as corn stover and wheat straw) that could be collected in some areas.

Dedicated energy crops will vary between 9 and 18 t ha^{-1} y^{-1} in the near future and could rise higher. Facility demands would be expected to decrease in the future as conversion technology efficiencies increase, requiring less land per unit of final product output. Table 7.4.2 shows the expected yield of typical secondary energy products from the same daily biomass inputs. The efficiencies are described as *present*, representing the state of the art today, and *future*, in which there are foreseeable changes in the technology.

Biomass Conversion Technologies

The energy services that can be satisfied by biomass are the supply of heat and combined heat and power, as well as the conversion of biomass into other energy forms such as electricity, liquid, and gaseous fuels identified (see Table 7.4.2). The transformation of the energy in the raw biomass to other forms of energy and fuels requires an acknowledgment of the physical and chemical differences between biomass resources in order to effect the most efficient transformation at the desired scale of operation. Each conversion process must take into account the differences in biomass physical characteristics on receipt at the processing facility and its proximate composition, which can vary widely in terms of moisture and ash content. Many processes require knowledge of the elemental composition and may even need information at the ultra-structural and polymeric level.

Physical Characteristics

Physical properties are important in the design and handling of biomass fuels and feedstocks at processing plants. In the raw state, woody biomass has a relatively low bulk density compared with fossil fuels. Bituminous coal or crude oil, for example, has a volume of 30 $dm^3\ GJ^{-1}$, while solid wood has around 90 $dm^3\ GJ^{-1}$. In chip form, the volume increases to 250 $dm^3\ GJ^{-1}$ for hardwood species and 350 $dm^3\ GJ^{-1}$ for coniferous species. Straw has even less energy density, ranging from 450 $dm^3\ GJ^{-1}$ for large round bales to 1 to 2 $m^3\ GJ^{-1}$ for chopped straw, similar to bagasse. The cell walls of biomass fibers have densities of about 1.5 $g\ cm^{-3}$; however, the large volume of the vascular elements that make up the fibers results in the low energy densities described previously. The fibrous nature also precludes close packing, which is the reason that chips and chopped straw have densities that are so low.

Size reduction of biomass resources is often more difficult than with minerals because the materials are naturally strong fibers, and the production of uniform particle size feedstocks is correspondingly difficult. The size reduction challenge is often mitigated in combustion and gasification on account of the high chemical reactivity of the biomass materials. However, when it is necessary to have penetration of chemicals into the structure of the biomass or to create access for biological agents as in acid and enzymatic hydrolysis of biomass, a higher degree of size reduction will be required. The energy requirements for size reduction are proportional to the surface exposure and rise in inverse proportion to the cube of the average length, so although moderate amounts of energy are required at particle sizes of several millimeters, the energy penalty at the 100-μm size is considerable.

Chemical Characteristics

Proximate Analysis

The value of the proximate analysis is that it identifies the fuel value of the as-received biomass material; provides an estimate of the ash handling and water removal requirements; and describes something of the characteristics in burning (Table 7.4.3). Generally, highly volatile fuels, such as biomass, need to have specialized combustor designs to cope with the rapid evolution of gas. Coals with very high fixed carbon need to be burnt on a grate because they take a long time to burn out if they are not pulverized to a very small size.

The energy content of biomass is always reported for dry material; however, most woody crops are harvested in a green condition with as much as 50% of their mass water. Two different heating value reporting conventions are in use. The term *higher heating value*, or HHV, refers to the energy released in combustion when the water vapor resulting from the combustion is condensed, thus releasing the latent heat of evaporation. Much of the data from North America are reported in this way. The *lower*

TABLE 7.4.3 Proximate Analysis of Solid Fuels

Fuel	Ash Content (%)	Moisture (%)	Volatiles (%)	Heating Value (HHV $GJ\ Mg^{-1}$)[a]
Anthracite coal	7.83	2.80	1.3	30.90
Bituminous coal	2.72	2.18	33.4	34.50
Sub-bituminous	3.71	18.41	44.3	21.24
Softwood	1.00	20.00	85.0	18.60

[a] On a moisture and ash free basis (maf).

TABLE 7.4.4 Ultimate Analysis Data for Biomass and Selected Solid Fuels[a]

Material	C	H	N	S	O	Ash	HHV GJ Mg^{-1}
Bituminous coal	75.5	5.0	1.20	3.10	4.90	10.3	31.67
Sub bituminous coal	77.9	6.0	1.50	0.60	9.90	4.1	32.87
Charcoal	80.3	3.1	0.20	0.00	11.30	3.4	31.02
Douglas fir	52.3	6.3	0.10	0.00	40.50	0.8	21.00
Douglas fir bark	56.2	5.9	0.00	0.00	36.70	1.2	22.00
Eucalyptus grandis	48.3	5.9	0.15	0.01	45.13	0.4	19.35
Beech	51.6	6.3	0.00	0.00	41.50	0.6	20.30
Sugar cane bagasse	44.8	5.4	0.40	0.01	39.60	9.8	17.33
Wheat straw	43.2	5.0	0.60	0.10	39.40	11.4	17.51
Poplar	51.6	6.3	0.00	0.00	41.50	0.6	20.70
Rice hulls	38.5	5.7	0.50	0.00	39.80	15.5	15.30
Rice straw	39.2	5.1	0.60	0.10	35.80	19.2	15.80

[a] Dry basis, weight percent.

heating value, or LHV, reports the energy released when the water vapor remains in a gaseous state. The HHV and LHV are the same for pure carbon, which only produces carbon dioxide when burned. For hydrogen, one molecule of water is produced for each molecule of hydrogen, and the HHV is 18.3% greater than the LHV. The HHV is 11.1% greater than the LHV for the combustion of one molecule of methane (CH_4).

Ultimate Analysis

The elemental composition of the fuel biomass is usually reported on a totally dry basis and includes the ash. Table 7.4.4 gives the ultimate analysis for several different fuels.

Polymeric Composition

Biomass conversion technologies that depend on the action of microorganisms are very sensitive to the ultrastructure and polymeric composition of biomass feedstocks. In ethanol production and in anaerobic digestion, a complex sequence of biochemical events take place in which the polymers are broken down into smaller units and hydrolysed to give simple sugars, alcohols, and acids that can be processed into fuel molecules. Wood, grasses, and straws are collectively called lignocellulosics and consist mainly of fibers composed of lignin, cellulose, and hemicellulose. Cellulose, hemicellulose, and lignin are different carbon–hydrogen–oxygen polymers with differing energy contents and chemical reactivities.

Lignocellulosics typically contain cellulose (40 to 50%) and hemicellulose (25 to 30%) along with lignin (20 to 30%), some extractives, and inorganic materials. Cellulose is depolymerized and hydrolyzed to glucose, a six-carbon sugar (C-6), while hemicellulose is a complex mixture of mainly five-carbon sugar (C-5) precursors with xylose, a major product. Lignin is a complex polymer based on phenyl propane monomeric units. Each C_9 monomer is usually substituted with methoxy groups on the aromatic ring, occurring mainly in syringyl (dimethoxy) and guaiacyl (monomethoxy) forms for which the ratio is a signature characteristic of grasses, hardwoods, and softwoods.

Other major plant components containing polymers of carbon, hydrogen, and oxygen that are also used for energy include:

- Starches that are the major part of the cereal grains, as well as the starch from tubers such as mannioc and potatoes
- Lipids produced by oil seed-bearing plants such as soya, rape, or palms, which are possible diesel fuel substitutes when they are esterified with simple alcohols such as methanol and ethanol
- Simple sugars produced by sugar beet in temperate climates or sugar cane in the tropics, which can be directly fermented to alcohols

In addition to the carbon, hydrogen, and oxygen polymers, there are more complex polymers such as proteins (which can contain sulfur in addition to nitrogen), extractives, and inorganic materials. The inorganic materials range from anions such as chlorine, sulphate, and nitrates, and cations such as potassium, sodium, calcium, and magnesium as major constituents. Many trace elements, including manganese and iron, are the metallic elements in key enzyme pathways involved in cell wall construction.

Combustion Applications

More than 95% of the worldwide use of biomass is through its combustion. The majority is used in developing countries for use in *daily living*, to provide heat for cooking and space heating. In the industrialized countries, a parallel in the cold regions of the northern hemisphere is the *community applications* of district heating. *Industrial applications* — especially of CHP (combined heat and power) — are important in industrialized countries as well as in the agricultural processing sector of developing countries. In several countries, biomass is burned directly to produce electricity without the coproduction of heat; however, like coal and oil-fired steam electricity generation, this is relatively inefficient.

Daily Living

Half of all solid biomass combustion worldwide goes into cooking and space heating at the household level, serving the primary fuel needs of over 2 billion people. The typical final energy demand for cooking is around 12 MJ a day for a household in Southeast Asia. This demand can be met with around 20 MJ d^{-1} of primary energy input using LPG (propane or butane) or kerosene with a typical conversion efficiency of 60 to 75%. Biomass efficiencies are much lower, ranging between 10 and 20%; thus, the required primary energy input is between 60 and 120 MJ d^{-1}. The three-stone stove has been extensively studied and has a peak power rating of 5 kW in the startup and a simmer rate of around 2 kW. The measured efficiency with a skilled operator is 10 to 15%. Daily household biomass consumption is therefore in the region of 2 to 4 kg d^{-1} or about 0.5 to 1.0 t y^{-1}.

The low efficiency of use is mainly due to poor combustion efficiency and inadequate heat transfer to the cooking vessels. The poor combustion results in the loss of fuel as solid particulate (soot), unburnt hydrocarbons and carbon monoxide; these are often referred to as the products of incomplete combustion (PIC). The heat transfer problem is related to the poor contact between the hot gases from the burner and the pot, and its fouling with PIC (Prasad, 1985). The PICs are not only a loss of fuel value, but are also toxic chemicals to which human exposure should be minimized.

Carbon monoxide is a chemical asphyxiant, and the aldehydes, phenols, and other partial combustion products are skin, eye, and lung irritants; some, such as benzopyrenes, are even carcinogens. Because many stoves are used in enclosed spaces and do not have chimneys, the household is exposed to these hazards; eye and lung damage is experienced especially by women and children, who work closely with the stoves while cooking. The epidemiological data on this are extensive (Ezzati and Kammen 2001), and large efforts to improve the efficiency and minimize the emissions in cookstoves are underway. The health impacts are of such a magnitude that subsidized alternative fuels such as LPG could be a significant social benefit while reducing the impacts of biomass harvesting

Space Heating

Space heating with wood in the form of logs is very common in forested areas of the northern hemisphere and Latin America with wood stoves supplying a household heat requirement of 30 to 100 kW. The thermal efficiencies are about 60 to 70%. Log burning is controlled by air starvation to reduce power output and may result in severe emissions of PIC, causing poor air quality in regions with high densities of wood-fueled space heating. Residential wood stoves using advanced combustion system designs or catalysts reduce PIC. Legislation has mandated emissions testing of new appliances before sale to ensure that they meet new source performance standards (NSPS) in the U.S. The use of dry prepared fuels such as pellets (manufactured by drying, grinding, and compression into a pellet about 1 to 2 cm in diameter) allows combustion to be efficiently managed so that PIC are extremely low with 75 to 80% thermal efficiency.

Community Systems

Biomass use in community district heating (DH) systems results in improved thermal efficiency with reduced emissions because of the scale of the equipment. Europe has seen large-scale adoption of biomass-fired district heating. There are over 300 round wood-fired DH schemes in Austria with an average heating effect of 1 MW or less, serving villages of 500 to 3000 inhabitants with minigrids using hot water distribution. Using straw, 54 Danish systems cover larger population centers and range in size from 600 kW to 9MW. Larger scale DH systems can be CHP units producing process steam for industries, heating for households, and electricity for the grid with high-quality emissions control systems. In Finland, even larger units are serving cities, e.g., the Forssa wood-fired CHP–DH plant is rated at 17.2 MW_e and 48 MW_{th} district heating, generating steam at 6.6 MPa and 510°C, with a bubbling fluidized bed boiler. The seasonal efficiency, which includes a condensing steam cycle in the summer, is 78%.

Industrial Applications — Combined Heat and Power (CHP) or Cogeneration

Many industrial processes, such as pulp production or cane sugar manufacture, have large heat requirements that are satisfied by generating low pressure steam at 1.7 MPa and 250° using their own process residues such as hog fuel (a mix of wood and bark); black liquor (the lignin by-product of pulp manufacture in kraft pulp mills); or bagasse (the fibrous residue after the pressing of sugar cane). A proportion of the steam is used in direct drives for the process plant's needs. Often, because the primary goal has been to eliminate residue disposal, the systems have not operated at maximum efficiency.

In industries such a pulp and paper (P&P), the trend is already toward requiring higher power–heat (P/H) ratios because steam demand is trending down due to energy conservation practices and electricity demand is rising to supply the increasing environmental and process needs. The thermal demand reduction is a consequence of improvements in drying and evaporation technologies, which have decreased from 8.6 to only 4 GJ adt^{-1} (adt = air dry tonne of pulp). The average pulp mill energy consumption has gone from 17 GJ adt^{-1} in the 1980s to 7 to 8 GJ adt^{-1} in the 1990s.

The application of advanced power generation cycles in the pulp and paper industry using black liquor and wood residues as feedstocks would give large increases in electricity export from that industry. Similar energy conservation trends in the sugar industry can reduce the requirement of steam to process cane from 58.5% (tonne steam/tonne of cane processed) to less than 35%. If investments in energy conservation and adoption of integrated gasification combined cycle (IGCC) technology were applied worldwide, the annual amount of power that could be produced from the large sugar cane resource would be >650 TWh based on the current >1.0 Gt of cane. Current cane generation is estimated to be 30 to 50 TWh y^{-1} because only sufficient electricity is generated in most instances to power the mill in season.

Electric Power Generation from Biomass

Prime Mover Systems and Fuels

Power generation takes place in *prime movers*, a technical term to describe engines of all kinds attached to alternators to generate electricity. Prime movers include the:

- Steam engine
- Steam turbine engine (the Rankine cycle)
- Internal combustion engine (ICE), which comes in two types: the Otto or gasoline-based spark ignition (SI) engine, and the diesel or compression ignition (CI) engine
- Gas turbine engine (Brayton cycle)
- Stirling engine

Each of these requires that the raw biomass be processed to some level and then used in the prime mover. Eventually fuel cells will replace the prime mover and alternator requirement by generating electricity directly from biomass-derived hydrogen fuels.

The steam cycle (already discussed) uses combustor and boiler combinations to generate steam, requiring that the fuel be reduced in size (perhaps dried to some level) and have physical contaminants removed.

The high-pressure steam is then expanded through a steam engine at small scales or through a turbine at larger scales. The efficiency of conversion technologies for combustion steam boiler systems is very scale dependent — a small steam engine or turbine would not exceed 10%. However, typically sufficient biomass is available over a transportation radius of 10 to 80 km to operate a unit in the range of 10 to 50 MW electricity output. Current Rankine cycles, at that scale, operate in the range of 25 to 30% efficiency and, as a consequence, require approximately 0.75 to 1 t of dry biomass to produce 1 MWh of electricity.

Industrial and power generation boilers range in size from 100 to 300 MW thermal output. The major types of boilers are: pile burners; grate boilers; suspension fired boilers; fluidized beds; and circulating fluid beds. Recent trends in power generation are to use circulating and bubbling fluidized bed combustors, although the majority of units in current service are stoker-fired moving grate units.

Biomass resources can be used in ICEs and gas turbine systems only if they are converted into clean liquid or gaseous fuels. Ethanol, biodiesel from lipids, or Fischer–Tropsch liquids can be used with little alteration to SI or CI engines. Gaseous fuels include the mixture of methane and carbon dioxide (biogas) produced by the action of microorganisms on biomass in anaerobic digestion (AD). AD is conducted at an industrial scale, using sewage or effluent streams containing high levels of soluble sugars, alcohols, and acids, as well as in landfills.

The installed landfill power generation capacity in the U.S. is now in excess of 1 GW (Goldstein, 2002). The energy content of biogas is typically 20 to 25 MJ Nm^{-3} or between 50 and 60% that of natural gas. Fuel gases can also be produced by thermal gasification; when this is carried out at small scales, the gasifying agent is usually air. The product gas, which has a low calorific value (LCV) with a heating value of 12 to 15% that of natural gas, is often called a producer gas. LCV gas at about 5 to 6 MJ Nm^{-3} has carbon monoxide (CO), hydrogen (H_2), and methane (CH_4) as the main fuel components, diluted with a lot of nitrogen and carbon dioxide. Larger scale processes can utilize pure oxygen, enriched air, or an indirect heating method to produce medium calorific value (MCV) gas in the range of 15 to 25 MJ Nm^{-3} heating value with essentially the same fuel gas components but with much less inert diluent. Clean MCV gases can be burnt without much modification of ICEs or gas turbines.

Cofiring Biomass with Coal

In a biomass/coal cofiring operation, a biomass fuel is used to replace a portion of the coal fed to an existing coal-fired boiler. This has been practiced, tested, or evaluated for a variety of boiler technologies. There are four types of coal boilers: pulverized coal (PC); cyclone; stoker; and fluidized bed. PC boilers are the most common type in the U. S., representing about 92% of the U.S. coal-generating capacity, with cyclone boilers as the next most common, with about 7% representation. Demonstrations have been undertaken at coal plants ranging in size from about 30 MW_e through to 700 MW_e. Wood residues, hybrid poplar, and switchgrass have all been tested as supplemental fuels, and several utilities have biomass cofiring plants in commercial operation.

Solid biomass can be fed to coal boilers by blending biomass on the coal pile or separately injecting biomass into the boiler. Introducing blended feeds to PC boilers can cause operational problems with the pulverizer, so the biomass proportion is limited to no more than 2 to 3% by heat input (4 to 5% by mass). Separate injection allows for the introduction of higher biomass percentages to the PC boiler — typically up to 15% on a heat input basis (about 30% by mass).

However, separate injection requires additional fuel handling equipment and increased fuel preparation. Capital costs for the blended feed approach are typically \$50/100 kW^{-1}. For the separate feed approach, capital costs are typically higher, in the range of \$175/200 kW^{-1}. Cofiring can reduce boiler efficiency to some degree. For example, cofiring in a PC boiler with 10% of the heat input from wood may decrease the boiler efficiency by 0.5 to 1.5%; after "tuning" the boiler's combustion output and adjusting for any efficiency losses, the combustion efficiency to electricity would be approximately 33%.

Because coal plants comprise more than half of U.S. power plant capacity currently in operation, cofiring technology has the advantage of improving environmental performance at existing power plants, while providing fuel source flexibility and using proven and familiar equipment. It reduces air pollution

TABLE 7.4.5 Heating Values of Fuel Gases

	HHV[a]	LHV[b]	HHV[a]	LHV[b]
	Btu ft^{-3} [c]		MJ Nm^{-3} [d]	
Hydrogen	325	275	12.75	10.79
Carbon monoxide	322	322	12.63	12.63
Methane	1013	913	39.74	35.81
Ethane	1792	1641	69.63	63.74
Propane	2590	2385	99.02	91.16
Butane	3370	3113	128.39	118.56

Note: Conversion factors for 1 MJ Nm^{-3} at 273.15 K and 101.325 kPa. | 25.45 Btu ft^{-3} at 60°F and 14.73 psia. Inverse 1 Btu ft^{-3} at 60°F and 30 in. Hg. | 0.0393 MJ Nm^{-3}.

[a] Higher heating value.

[b] Lower heating value.

[c] Standard temperatures and pressure of dry gas are 60°F and 14.73 psia (NIST, 2004).

[d] S.I. units

emissions, GHG emissions, and the amount of waste ash generated as a by-product of the combustion. In addition, it requires relatively low up-front capital expenses compared to other renewable energy options; this makes it a straightforward and inexpensive way to diversify the fuel supply and divert biomass from landfill disposal.

Thermal Gasification Technologies

The conversion of biomass into a gaseous fuel opens up modern applications in electric power generation, the manufacture of liquid fuels, and the production of chemicals from biomass. The chemistry of gasification of biomass is best viewed as an extension of the pyrolysis process. Pyrolysis is simply defined as the chemical changes occurring in the solid biomass when heat is applied to a material in the absence of oxygen. The products of biomass pyrolysis include water, charcoal (or more correctly *char*, a carbonaceous solid), oils or tars, and permanent gases including methane, hydrogen, carbon monoxide, and carbon dioxide.

The majority of gasifiers are partial oxidation reactors, in which just sufficient air or oxygen is introduced to burn part of the input biomass to provide the heat for pyrolysis and gasification. If the oxidant is air, the product gas is diluted by the nitrogen present**.** Although air is 79% nitrogen, the stoichiometry of partial oxidation is such that the final LCV product, gas, has about 50% nitrogen as a diluent. The energy content of the typical gases produced in biomass gasification **is** shown in Table 7.4.5. The use of pure oxygen as the gasification agent eliminates the nitrogen diluent and can produce medium calorific value (MCV) gases in the range of 10 to 20 MJ Nm^{-3}.

An alternative strategy is to carry out the gasification process by means of indirect heat the product stream is even higher in calorific value, because neither nitrogen nor the carbon dioxide produced from the combustion in-situ of the partial oxidation processes is present in the product gas stream. The challenges to achieve a clean and useable fuel gas have been addressed through gasifier design and postgasification processing to remove tar and particulate contaminants from the gas stream.

Gasifier Systems

The main challenge in gasification is enabling the pyrolysis and gas-reforming reactions to take place, using the minimum amount of energy, in reactors that are economical to construct. During a history dating back to the late 18th century, an extraordinary number of different designs and process configurations have been proposed. Prior to the development of fluidized bed technologies in the 1920s, the majority of the gasifiers were so-called fixed bed units. The flow of gasifying agents, usually air and steam, could be cocurrent with the biomass feed, or countercurrent; these are often described, respectively, as downdraft and updraft gasifiers.

Downdraft gasification was widely used during the Second World War as an on-board fuel gas generator to offset the lack of gasoline. Millions of units were constructed and then abandoned as soon as petroleum supplies resumed. Units derived from the automotive application are marketed today as stationary generating sets equipped with ICEs, with SI or CI for power production in remote locations and in developing countries without grid systems.

The simplest and oldest gasifier is the counterflow moving bed, which consists of an insulated shaft into which the feedstock (typically pieces larger than 3 cm on a side) are fed. The shaft is filled to a depth of 0.5 to 2 times the vessel diameter, and the mass of material is supported on a grate. The oxidant (air or enriched air/oxygen) and sometimes steam are introduced below the grate. The grate material is ignited and the hot gases flow up through the bed, exchanging heat with the down-flowing biomass material and, at the same time, pyrolyzing and drying it. At steady state, the bed level is maintained by continuous additions of the feed.

The product gases include the desired fuel gases (methane, carbon monoxide, hydrogen, and C_2 hydrocarbons), nitrogen, carbon dioxide, and water vapor, which exit at relatively low temperatures (<250°C). The water arises from the moisture content of the feed and the products of combustion. The gas also contains several percent of condensable tars. Because the temperatures in the combustion zone can be very high, problems with the formation of slags (molten mixtures that can impede the oxidant flow) may occur. Some of the systems are constructed deliberately to form a molten ash or slag, and this is handled by dropping the slag into a receiving tank, where it solidifies and shatters to an easily handled aggregate.

The throughput of air-based systems is relatively low, handling about 150 kg m^{-2} h^{-1} of dry biomass. This operational limitation is due to the need to reduce the rate of heat generation at the grate to avoid slagging in dry systems. The lower throughput rate also helps to manage the problems of maintaining a uniform flow of the descending material to avoid channeling and even greater reductions in throughput. The largest units are typically 3 to to 4 m in diameter and handle between 50 and 100 t d^{-1} of material with a rating of 10 to 20 MW_{th} input. The hot gas efficiency can be as high as 80% conversion of the input energy into a fuel gas and sensible heat. The cold gas efficiency will be about 70%.

If the gas is maintained at temperature and then fired in a kiln or boiler, the presence of tars and particulate are of little consequence because the tars are combusted in the excess air and the particulate is removed in the kiln exhaust or boiler flue gas system. Such close-coupled systems are quite common applications of biomass gasification in several industries and the basis of district heating systems used in Finland. The gas typically has a heating value of 6 MJ Nm^{-3} on a dry basis and is richer in methane, ethene, and ethyne than most other gasifier systems using air. For engine applications the gas must be cleaned up and cooled to ambient temperatures. Typically, this is done with some sort of aqueous quench and scrubbing system (e.g., a wet electrostatic precipitator) to remove tar and particulate matter, and the tar/water removed must be separated and then treated for release to the environment.

Fluidized beds can remove the grate limitation of the moving bed gasifier because, due to their high mixing rates and outstanding heat transfer rates, they can achieve through-puts of over 1500 kg m^{-2} h^{-1} of dry biomass. The two modes of fluidized bed operation involve bubbling (BFB) and circulating (CFB) solids. In a BFB, the inert fluid bed medium (silica sand, dolomite, alumina, and olivine) is retained in the body of the bed, which is expanded and in motion (literally bubbling) due to the flow of the fluidizing gas medium into the bed. The terminal velocity of a particle in the flow is still higher than the linear flow rate of the gas and thus remains in the body of the unit. In the CFB, the gas flow is increased to the point that the terminal velocity of the particle is exceeded and it is transferred out of the expanded bed and captured in a cyclone for return to cycle.

The effective rating of a 3-m diameter unit is over 50 MW_{th} input of biomass. Because the combustion process and the pyrolysis process are now mixed, the exit gas temperatures are typically 700 to 800°C.

Due to cracking processes, the tar production is lower and mainly composed of secondary and tertiary tar components; however, the tolerance of high moisture content feedstocks is much more limited than the countercurrent moving bed unit. The system design is also more complex, requiring blowers to inject the oxidant at the base of the fluidized bed. In addition to the expansion of the gas due to temperature, the gas volume increases due to the formation of the fuel gas. This necessitates careful design of the CFB and the freeboard in a BFB; in a CFB, this is accommodated by the fact that the entire bed is in circulation. The oxidant requirement is typically 0.3 kg O_2 kg^{-1} of dry feedstock.

The highest reactivity gasification systems are entrained flow units in which the feedstock is finely divided and burnt in a substoichometric flame at high temperatures. The postcombustion gases are then allowed to reach chemical equilibrium before being quenched. Such units produce very few higher hydrocarbons and tar materials. The challenge for biomass is to obtain a sufficient rate of fuel injection to the flame. One configuration is the Koppers–Totzek gasifier. For fossil fuels, the Texaco gasifier uses a dense slurry of coal or petroleum coke in water as the feed to a pressurized oxygen flame, producing a hydrogen and carbon monoxide mixture for use as a syngas or as a fuel in gas turbines.

Cocurrent moving bed gasifiers (also known as downdraft and cross-draft units) were widespread during World War II (various estimates put the number at over 1 million). Like the other gasifiers described earlier, the design is a partial oxidation system. The physical arrangement is a shaft reactor into which the biomass is introduced at the top; the material then flows down to an oxidation zone, where the air is admitted. This zone feeds heat back to the incoming biomass to pyrolyze the material into gases, tars, and charcoal. The charcoal is partially combusted in the oxidation zone, and the products of pyrolysis flow through the incandescent combustion zone to be cracked into, primarily, hydrogen and carbon monoxide as the fuel gases, with few or no tars passing through. The combusted gases flow on through the hot charcoal, reacting with it, until the rate of reaction effectively goes to zero because the reactions are very endothermic.

The net result is a gas at about 500°C that is very low in condensible tars; other than carbon dioxide, water vapor, and nitrogen, the fuel gases are mainly hydrogen and carbon monoxide with only a small amount of methane and higher hydrocarbons. The low tar production is the reason this was the favored system for on-road vehicles in the 1940s. Like all moving bed reactors, the operation depends on the presence of an adequate void space between particles. The wood feedstock must produce a char that has sufficient strength to support the column of feedstock without crushing and blocking the flow.

The overall efficiency is lower than the countercurrent system for two reasons. Chemically, it is not possible to convert the charcoal fully; the sensible heat from the combustion zone is not transferred to the incoming feed material, but rather must be heat exchanged with air oxidant prior to being quenched. Because of the need for uniformity of mass and heat transfer in the high-temperature reaction zone, the diameter of such units is generally limited to less than 1.5 m and, with typical throughputs of 300 kg m^{-2} h^{-1} of dry biomass, the size of units ranges from 100 kW_{th} to 2 MW_{th} input. The chemistry of this gasifier has a lot in common with iron blast furnaces and is significantly different from the other gasifiers, which have very high burdens of liquids such as tars in the product gas.

Medium calorific value (MCV) gas can be produced without using oxygen or air in gasification. This requires an independent source of heat to be transferred to the biomass to pyrolize the feedstock under conditions of high severity, i.e., long residence times at high temperatures. To this end, proposals have been made to use concentrated solar energy or high-temperature nuclear reactors as the heat source in the gasification of a wide range of feedstocks. In the case of biomass, the pyrolysis gasification process will provide a char stream with slow or fast pyrolysis to temperatures of 600 to 750°C, in amounts representing between 12 and 25% of the input biomass. This contains sufficient energy to drive the pyrolysis process.

A number of developments in which biomass is pyrolized using a solid heat carrier in an inert atmosphere or steam or product MCV gas to generate the MCV fuel gas and char are already in the demonstration phase. The char and the cooled heat carrier, which can be silica sand, alumina, or a mineral such as olivine, are then transferred to a separate air combustion unit in which the char is combusted to heat up the heat carrier, which is then returned to the pyrolysis gasification unit. Mechanical separation and isolation devices in the heat carrier circulation loops prevent the passage of fuel gas from the gasifier to the oxidation conditions of the combustor. The transportation mechanism is via fluidization of the heat carrier.

To this end, a group in Austria constructed a version with a CFB combustion unit and BFB pyrolysis gasifier; in the U.S., units have been constructed with a CFB pyrolysis reactor and a BFB combustor as well as a dual CFB configuration scaled up to 60 MW_{th} biomass input. Another variant, developed by Manufacturing and Technology Conversion International, Inc. (MTCI), a U.S. company, was a BFB pyrolysis and steam char reaction system with the heat supply from immersed heat exchanger bundles in the bed. The heat exchanger bundles are fueled with part of the product gas, and the char from pyrolysis is consumed, as in the cocurrent gasifier.

Commercialization

Use of gasifiers as precombustors in which the hot gases are passed through a high-temperature duct into a boiler or industrial process kiln has been widespread; cofiring is an example. Foster Wheeler Energia Oy CFB has been supplying a LCV gas for several years to an existing large-scale utility boiler at the Kymijärvi 167 MW_e and 240 MW_{th} fossil-fired plant close to Lahti, Finland. A combination of forestry residues, industrial wood residues, and recycled fuel (a clean fraction of the municipal waste stream composed mainly of wood, paper, and cardboard separated at the source) is the fuel source. This project builds on many years of successful operation of biomass CFBs in thermal applications and substitutes for about 15% of the total fuel used in the boiler.

Applications in which clean gases (free of particulate and tar) are utilized occur mainly in the development and demonstration stages, with the exception of deployment of cocurrent gasifier–ICE generator sets. In 2000, Sydkraft A.B. successfully completed a high-pressure LCV gas biomass integrated gasification and combined cycle (IGCC) operation, which was part of the Värnamo (Sweden) district heating system. This first complete biomass-fueled pressurized CFB IGCC was fueled with about 18 MW_t equivalent of wood residues and produced about 6 MW_e (4 from the gas turbine, 2 from the steam cycle) and 9 MW_{th}. The LCV gas is cooled to 350 to 400°C before it is cleaned in metal filters and then passed to the Typhoon gas turbine, which is manufactured by Alstom. The project demonstrated more than 1500 h of IGCC operation on the product gas prior to its shutdown at the end of the demonstration phase (Stahl et al., 2000).

Small-scale gasifiers for the production of fuel gas for cooking, as well as the demonstration of electricity in ICEs, are already commercial in India and China. Their introduction has been accelerated by the use of moderate government subsidies, especially for communities not served by the electricity grid. In development circles, such systems are often referred to as village power systems. Considerable discussion among the OECD nations concerns the use of distributed energy resources, which would provide local power and heat (e.g., CHP units) while remaining connected to the grid. Many of these units are based on natural gas; however, when the economics and availability of biomass are appropriate, gasification is considered; demonstrations of gasfier–ICEs with CHP applications in district heating have taken place in Denmark.

Biological Process Technologies

The polymers that make up biomass are produced through photosynthetically driven biological reactions at the cellular level in the plant. The resulting phytomass is then fuel and food (or feedstock) for a large number of the fauna on Earth. From simple bacteria to large mammals, the processes to digest and metabolize plant polymers have evolved over billions of years. In a number of instances, the biological degradation processes have been harnessed in industrial conversion processes to produce biofuels and bioproducts to serve humanity. Of the many processes, only two have attained large-scale use: anaerobic digestion and ethanol production.

Anaerobic Digestion

Anaerobic microorganisms convert the biodegradable fraction of organic materials to carbon dioxide and methane in the absence of oxygen. Commercial-scale anaerobic digestion has been used in many parts of the world for many years and is only beginning to be commercial in the U.S. Several utilities are currently producing "green energy" with biogas from landfills. Biogas from anaerobic digesters on dairy and hog farms and cattle feed lots is beginning to contribute to the energy mix in the U.S.

Ethanol Production

Ethanol is currently the most important liquid fuel produced from biomass. It is produced by fermentation of sugars. The fermentable sugars can be obtained directly from sugar cane and sugar beet, or they can be produced by means of the hydrolysis of starches or cellulose and hemicelluloses. Starch crops include cereals, and manioc in tropical countries, while cellulose and hemicellulose are the major polymers of wood, grasses, straws, and stalks. The production from sugar cane in Brazil has been in the range of 11 to 13 GL y^{-1} for the last few years; in the U.S., the annual production has grown rapidly from 5.42 GL in 2000 to 8.08 GL in 2002. This growth is primarily due to legislation banning the use of methyl tertiary–butyl ether as an octane enhancer in several state markets.

Over 90% of the U.S. production is from corn, which is processed in wet or dry mills. Corn kernels have about 70 to 75% starch content; approximately 10% protein (gluten); 4 to 5% germ (the source of corn oil); and 3 to 4% fiber content. Dry milling consists of grinding the whole kernel into a flour and then slurrying this with enzymes to break down the starch to fermentable sugars. The stillage separated from the beer is composed of coarse grain and a wide range of soluble materials. The solubles are concentrated by evaporation into a syrup (condensed distillers solubles), which is then added to the coarse grain to produce dried distillers grain with solubles or DDGS. This is marketed as a feed for animals. Dry milling theoretically produces about 460 L of ethanol per tonne of corn.

Wet milling is an example of a biomass refinery. The corn kernels are steeped in dilute sulfurous acid for 48 h in a mild prehydroylsis process prior to a grinding step to separate the corn germ. Corn oil is recovered from the germ as high-value cooking oil. The starch and the gluten protein are then separated. The gluten is dried and sold as a 60% protein feed to mainly poultry markets. The starch fraction is the source of dried or modified cornstarches and a syrup converted enzymatically into high-fructose corn syrup or passed to a fermentation step producing ethanol and other fermentation-derived chemicals.

Yields of ethanol are somewhat lower than those from dry milling at around 440 L t^{-1} of corn. According to the National Corn Growers Association (www.ncga.com), corn utilization rates of the 246.25 Mt, 2002 harvest (9.695 billion bushel) were: 58% as feed; 19% as export grain; 6% as high-fructose corn syrup; 9% as fuel ethanol; and 8% from all other applications (including breakfast cereal, cornstarches, and seed corn).

Since the inception of the corn-to-ethanol process technology in the 1970s, continuous improvement has occurred in terms of yield, process efficiency, reduced capital investment, and nonfeed operating costs. The industry average yield has gone from 360 L t^{-1} (2.4 USgal/bu) to 410 L t^{-1} (2.75 USgal/bu), while the capital cost has declined from 220 to about 115 \$ L^{-1} d^{-1} capacity (2.5 down to 1.3 USD per annual gallon of capacity), according to the industry.

Liquid Fuels and Bioproducts from Lignocellulosics

Lignocellulosics (such as wood, straw, and grasses) contain cellulose (40 to 50%) and hemicellulose (25 to 30%). There is considerable ethanol potential through fermentation of the sugars derived from these polymers, producing similar theoretical yields per tonne as corn, i.e., 450 L t^{-1} and a price structure, which is more stable relative to the fuel markets than foodstuffs. Alternative processes would include thermochemical routes through the production of synthesis gas and its catalytic synthesis to mixed alcohols, Fischer–Tropsch liquids, or hydrogen — a future transportation fuel (Table 7.4.2).

Current RD&D in the U.S. is focused on the development of two product platforms: a sugar platform that inherits much of the prior research into the production of ethanol from lignocellulosic biomass, and a syngas platform evolved from the development of biomass gasifiers primarily for power production

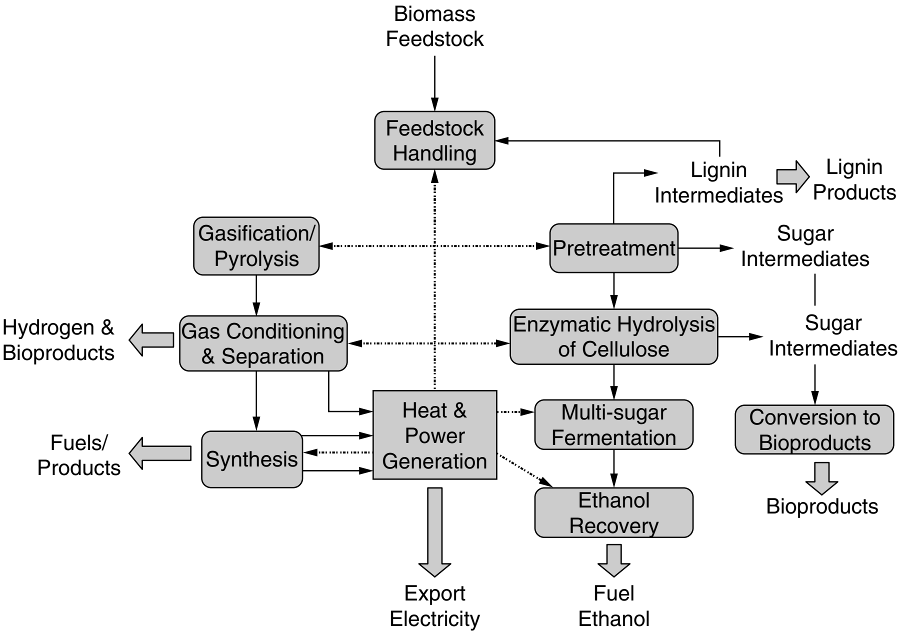

FIGURE 7.4.1 The U.S. RD&D approach to the sugar and syngas platforms.

coupled with the extensive downstream catalysis developments of the petrochemical industry. The syngas platform is also the basis for the combustion units for the utilities component of the platforms, which are shown diagramatically in Figure 7.4.1.

The sugar platform inherits over two decades of work on the ethanol conversion process from lignocellulosics (Wyman, 1994). The polymers involved are much more recalcitrant than starches and, because of the complex nature of lignocellulosics, they require extensive effort to break down the lignin, cellulose, and hemicellulose structure so that the individual polymers become available for hydrolysis. Cellulose is hydrolyzed to glucose, a six-carbon sugar (C-6), while hemicellulose is a complex mixture of mainly five-carbon sugar (C-5) precursors, with xylose as a major product. Although the C-6 sugars are relatively easy to ferment with yeasts, such as *Saccharomyces* spp., the C-5 sugars have not been as easy to ferment to ethanol (Zhang et al., 1995). The pretreatment stages can include steam, acid, and alkali treatments, while the hydrolysis steps can be carried out with acids or enzymes. Because of inhibition of the enzymatic hydrolysis by the sugars produced, the National Renewable Energy Laboratory (NREL) developed a simultaneous saccharification and fermentation process to remove the sugars as they are formed by producing ethanol in the same reactor. Such process integration will be the key to producing low-cost sugars and thus ethanol or other bioproducts in the future (Lynd et al., 1999).

The syngas platform using biomass would enable the production of renewable liquid fuels and chemicals such as ammonia and hydrogen by well-established and proven syngas technologies. Today these processes utilize the syngas produced by the steam reforming of natural gas or use syngas from coal gasification. The production of liquid fuels from syngas has a long history dating from the pioneering work of Fischer and Tropsch to synthesize hydrocarbon fuels in Germany in the 1920s. The process was implemented in Germany in the 1930s where nine plants operated during World War II on syngas from coal gasification; after the war, until the mid 1950s, they operated on syngas from the gasification of heavy oil. In the 1950s, South Africa constructed the first of the South African Synthetic Oil Limited (SASOL) plants, an activity that has continued its development to the present day using syngas produced from coal and natural gas. Both of these developments were initiated during times of petroleum shortages, to fuel the transportation systems of Germany and South Africa.

Continuing research and development is based on the environmental advantages of producing zero sulfur fuels, with combustion properties tailored to specific engine designs to minimize emissions from petroleum-derived fuels. At the time of writing, there are at least six developers of what are known as Fischer–Tropsch liquids (FTL) plants, which are scaled to use remote and difficult-to-get-to-market sources of natural gas as the feedstock for the syngas. FTL processes use catalysts based mainly on iron, cobalt, ruthenium, and potassium and have been extensively characterized. They operate at high pressures between 2.5 and 4.5 MPa, and temperatures between 220 and 450°C. The reactors range from fixed catalyst beds to bubbling as well as circulating fluidized beds. The product distribution depends on the polymerization on the surface of the catalyst. The hydrocarbon chains are built up one carbon atom at a time — a process known as homologation. Polymer growth of this type is now understood to take place via what is known as the Anderson–Shulz–Flory mechanism, and it is not possible to produce a single compound with a fixed number of carbon atoms or even a narrowly defined distribution of molecular weights.

Extensive product recycling and recirculation of unreacted syngas can be used to reduce the number of small hydrocarbon molecules (e.g., C_1 to C_5); however, production of wax-like molecules with as many as 30 to 50 carbon atoms also exists. The conversion per pass of the syngas over the catalysts is often limited, due in part to the fact that the polymerization reaction is exothermic and the equilibrium mixtures obtained are very temperature sensitive, affecting the yield and proportions of the desired products. The recycle processes are very energy intensive and reduce the throughput of the catalyst system.

Recent progress in enhancing the yields of gasoline and diesel products has been made partly by optimization of the catalysts and operating conditions, and also by companies such as Shell with its Shell Middle Distillate Synthesis (SMDS) process in which the higher molecular weight waxes are hydrotreated over selective catalysts to increase the yield of the desired range of hydrocarbons C_8 through C_{20}. The smaller carbon number products, C_1 to C_5, are also reformed to increase the hydrogen to the overall process. Other innovations in the FTL arena include slurry reactors, which use very finely divided catalysts suspended in an oil medium. Such reactors often demonstrate much increased conversion in a single pass and offer economies with respect to recycle energy and investment. However, from the chemical engineering perspective; such three-phase reaction systems have required a lot of R&D and development.

An alternative production process would use a high conversion single-pass catalyst such as a slurry reactor and then utilize the tail gas after the catalyst as fuel for a gas turbine combined cycle. Such a process would then coproduce electricity, heat, and a liquid fuel and offer lower investment costs and higher overall efficiency.

Higher alcohols are produced from syngas over typical Fischer–Tropsch catalysts under conditions of greater severity than those used predominantly in the production of hydrocarbons. Pressures are between 5 and 15 MPa and are generally at temperatures higher than FTL synthesis. The Anderson–Shulz–Flory mechanism does not appear to determine the product distribution, although homologation through the addition of one carbon atom at a time is followed, so that product methanol is recycled over the catalyst to grow into higher alcohols.

Changes in catalyst composition can determine the isomer composition of the higher ($>C_3$) alcohols. Also, mixed thermochemical syngas and biotechnology routes to ethanol are under development. Ethanol can be synthesized from syngas using an anaerobic bacterium, *Clostridium ljungdahlii.* The growth conditions of the bacterium are managed so as to maximize the ethanol yield over the production of acetate (as acetic acid) from the key biological pathway intermediate acetyl-CoA, which is derived from the syngas. Although not yet commercialized, many of the development challenges of producing the bacterium and making effective gas–liquid contactors and bioreactors have been overcome. Yields are similar to those from the inorganic high temperature Fischer–Tropsch catalysts.

References

Anonymous. (1994). Sweden's largest biofuel-fired cfb up and running, Tampere, Finland, 16–17.

Cannell, M.G.R. (2003). Carbon sequestration and biomass energy offset: theoretical, potential and achievable capacities globally, in Europe and the U.K. *Biomass Bioenergy.* 24: 97–116.

Cralle, H. T., and Vietor, D. M. (1989). Productivity: solar energy and biomass, in *Biomass Handbook*, O. Kitani and C. W. Hal, Eds., Gordon and Breach Science Publishers, New York. 11–20.

Ezzati, M. and Kammen, D.M. (2001). Quantifying the effects of exposure to indoor air pollution from biomass combustion on acute respiratory infections in developing countries. *Environ. Health Perspect*. 109(5): 481–488.

Gallagher, P., Dikeman, M., Fritz,J., Wailes, E., Gauther, W., and Shapouri, H. (2003). Biomass from crop residues: cost and supply estimates. U.S. Department of Agriculture, Office of the Chief Economist, Office of energy Policy and New Uses. Agricultural Economic Report No. 819.

Goldstein, J. (2002). Electric utilities hook up to biogas. *Biocycle.* March 2002: 36–37.

Graham, R.L. et al. (1995). The Effect of location and facility demand on the marginal cost of delivered wood chips from energy crops: a case study of the state of Tennessee. In *Proc. 2nd Biomass Conf. Am.: Energy, Environ., Agric., Ind.*, 1324–1333.

Hall, D.O., Rosillo–Calle, F., Williams, R.H., and Woods, J. (1993). Biomass for energy: supply prospects, in *Renewable Energy: Sources for Fuels and Electricity*, T.B. Johansson, H. Kelly, A.K.N. Reddy, and R.H. Williams, Eds., Island Press, Washington, D.C., 593–651.

Jenkins, B.M. (1997). A Comment on the optimal sizing of a biomass utilization facility under constant and variable cost scaling. *Biomass Bioenergy.* 13(1/2): 1–9.

Lynd, L.R., C.E. Wyman, and T.U. Gerngross. (1999). Biocommodity engineering. *Biotechnol. Progress.* 15(5): 777–793.

McKeever, D. (2003). Taking inventory of woody residuals. *Biocycle*. July 2003: 31–35.

McLaughlin, S. and L. Kszos, personal communication. (2003). (These managers of switchgrass research at Oak Ridge National Laboratory have summarized the past 15 years of switchgrass research in a *Biomass and Bioenergy* 2005 paper in press).

NIST (2004). Handbook 44, Specifications, Tolerances, and Other Technical Requirements for Weighing and Measuring Devices. Butcher, T., Crown, L., Suiter, R., and Williams, J., Eds.

Prasad, K. (1985). Stove design for improved dissemination, in *Wood-Stove Dissemination*, Robin Clarke, Ed., Intermediate Technology Publications. London 59–74.

Sampson, R.N. et al. (1993). Biomass management and energy. *Water, Air, Soil Pollut*. 70: 139–159.

Stahl, K., M. Neergard, and J. Nieminen. (2000). Final report: Varnamo demonstration programme. In *Progress in Thermochemical Biomass Conversion*, Ed. A.V. Bridgwater, Blackwell Sciences Ltd., Oxford U.K. 549–563.

Walsh, M.E., R.L. Perlack, A. Turhollow, D.G. de la Torre Ugarte, D.A. Becker, R.L. Graham, S.E. Slinsky, and D.E. Ray. (2000). Biomass feedstock availability in the United States: 1999 state level analysis. Report prepared for the U.S. Department of Energy found at: http://bioenergy.ornl.gov/pubs/resource_data.html.

Wright, L.L. (1994). Production technology status of woody and herbaceous crops. *Biomass Bioenerg*., 6(3): 191–209.

Wyman, C.E. (1994). Ethanol from lignocellulosic biomass: technology, economics, and opportunities, *BioResource Technol*., 50(1): 3–16.

Zhang, M., C. Eddy, K. Deanda, M. Finkelstein, and S. Picataggio. (1995). Metabolic engineering of a pentose metabolism pathway in ethanologenic *Zymomonas mobilis*. *Science*. 267(5195): 13 January 1995. 240–243.

Further information

Combustion is widely described in the literature. The International Energy Agency recently produced an extremely useful reference book on the topic of biomass combustion: van Loo, S. and J. Koppejan, Eds. (2002). *Handbook of Biomass Combustion and Cofiring*. Enschede, Netherlands, Twente University Press (A multiauthor IEA Bioenergy collaboration Task 32 publication).

Power generation is described and analyzed in: EPRI (1997). *Renewable Energy Technology Characterizations*. Washington, D.C., Electric Power Research Institute.

Gasification in general and synthetic liquid fuels are well described in: Probstein, R. F. and R. E. Hicks (1982). *Synthetic Fuels*. New York, McGraw–Hill Inc.

Anaerobic digestion is the subject of a wonderful handbook that is only available in German at present: Schulz, H. and B. Eder (2001). *Bioga Praxis: grundlagen, planung, anlagenbau, beispiele*. Freiburg, Germany, Ökobuch Verlag, Staufen bei Freiburg.

Ethanol from lignocellulosics as well as a useful section on starch ethanol can be obtained in: Wyman, C. E., Ed. (1996). *Handbook on Bioethanol: Production and Utilization*. Applied Energy Technology Series. Washington, D.C., Taylor and Francis.

Additional information on ethanol can be obtained from the Web sites of the National Corn Growers Association (http://www.ncga.com) and the Renewable Fuels Association (http://www.ethanolrfa.org/).

The last three decades of biomass activity in the United States are described in: Chum, H. L. and R. P. Overend (2003). *Biomass and Bioenergy in the United States*. In *Advances in Solar Energy: an Annual Review of Research and Development*. Ed. Y. Goswami. American Solar Energy Society, Boulder, CO. USA. 83–148.

Additional information on energy efficiency and renewable energy technologies can be obtained from the U.S. Energy Efficiency and Renewable Energy Websites http://www.eere.energy.gov/biomass.html, and http://www.eere.energy.gov/RE/bioenergy.html. Also the Website http://bioenergy.ornl.gov/ provides useful resource information and many links to other bioenergy Websites.

7.5 Nuclear Resources

James S. Tulenko

The Nuclear Fuel Cycle

Sources of Nuclear Fuels and World Reserves

Nuclear power can use two naturally occurring elements, uranium and thorium, as the sources of its fissioning energy. Uranium can be a fissionable source (fuel) as mined (Candu Reactors in Canada), while thorium must be converted in a nuclear reactor into a fissionable fuel. Uranium and thorium are relatively plentiful elements ranking about 60th out of 80 naturally occurring elements. All isotopes of uranium and thorium are radioactive. Today, natural uranium contains, in atomic abundance, 99.2175% Uranium-238 (U^{238}); 0.72% Uranium-235 (U^{235}); and 0.0055% Uranium-234 (U^{234}). Uranium has atomic number 92, meaning all uranium atoms contain 92 protons, with the rest of the mass number being composed of neutrons. Uranium-238 has a half-life of 4.5×10^9 years (4.5 billion years), U-235 has a half-life of 7.1×10^8 years (710 million years), and U-234 has a half-life of 2.5×10^5 years (250 thousand years). Since the age of the earth is estimated at 3 billion years, roughly half of the U-238 present at creation has decayed away, while the U-235 has changed by a factor of sixteen. Thus, when the earth was created, the uranium-235 enrichment was on the order of 8%, enough to sustain a natural reactor of (there is evidence of such an occurrence in Africa). The U-234 originally created has long disappeared, and the U-234 currently present occurs as a product of the decay of U-238.

Uranium was isolated and identified in 1789 by a German scientist, Martin Heinrich Klaproth, who was working with pitchblend ores. No one could identify this new material he isolated, so in honor of the planet Uranus which had just been discovered, he called his new material Uranium. It wasn't until 1896, when the French scientist Henri Becquerel accidentally placed some uranium salts near some paper-wrapped photographic plates, that radioactivity was discovered.

Until 1938, when the German scientists Otto Hahn and Fritz Shassroen succeeded in uranium fission by exposure to neutrons, uranium had no economic significance except in coloring ceramics, where it proved valuable in creating various shades of orange, yellow, brown, and dark green. When a uranium atom is fissioned it releases 200 million electron volts of energy; the burning of a carbon (core) atom releases 4 electron volts. This diffenence of 50 million times in energy release shows the tremendous difference in magnitude between chemical and nuclear energy.

Uranium is present in the earth's crust to the extent of four parts per million. This concentration makes uranium about as plentiful as beryllium, hafnium, and arsenic; and greater in abundance than tungsten, molybdenum, and tantalum. Uranium is an order of magnitude more plentiful than silver and a hundred times more plentiful than gold. It has been estimated that the amount of uranium in the earth's crust to a depth of 12 miles is of the order of 100 trillion tons.

Thorium, which is composed of only one isotope, Thorium-232, has a half-life of 14 billion years (1.4×10^{10} yr), is more than three times more abundant than uranium, and is in the range of lead and gallium in abundance. Thorium was discovered by Berjelius in 1828 and named after Thor, the Scandinavian god of war. For reference, copper is approximately five times more abundant than thorium and twenty times more abundant than uranium.

Uranium is chemically a reactive element; therefore, while it is relatively abundant, it is found chemically combined as an oxide (U_3O_8 or UO_2) and never as a pure metal. Uranium is obtained in three ways, either by underground mining, open pit mining, or in situ leaching. An economic average ore grade is normally viewed as .2% (4 pounds per short ton), though recently ore grades as low as .1% have been exploited. A large quantity of uranium exists in sea-water which has an average concentration of 3×10^{-3} ppm, yielding an estimated uranium quantity available in sea-water of 4000 million tons. A pilot operation was successfully developed by Japan to recover uranium from sea-water, but the cost was about $900/lb, and the effort was shut down as uneconomical.

The major countries with reserves of urnaium in order of importance are Australia, United States, Russia, Canada, South Africa, and Nigeria. The countries with major thorium deposits are India, Brazil, and the United States. It is estimated that for a recovery value of $130/kg ($60/lb), the total uranium reserves in these countries are approximately 1.5 million tonnes of uranium in the U.S., 1 million tonnes of uranium in Australia, .7 million tonnes of uranium in Canada, and 1.3 million tonnes of uranium in the former Soviet Union. As mentioned earlier, thorium reserves are approximately four times greater. With the utilization of breeder reactors, there is enough uranium and thorium to provide electrical power for the next thousand years at current rates of usage.

Processing of Nuclear Fuel

Once the uranium ore is mined it is sent to a concentrator (mill) where it is ground, treated, and purified. Since the ore is of a grade of .1 to .2% uranium, a ton of ore contains only between 1 to 2 kilograms of uranium per 1000 kilograms of ore. Thus, thousands to tonnes of ore have to be extracted and sent to a mill to produce a relatively small quantity of uranium. In the concentration process approximately 95% of the ore is recovered as U_3O_8 (yellowcake) to a purity grade of about 80%. Thus, assuming 0.15% uranium ore, the milling and processing of a metric ton (1000 kg) of ore yields a concentrate of 1.781 kg (1.425 kg of uranium and 0.356 kg of impurities). For this reason the mills must be located relatively close to the mine site. The ore tailings (waste) amounts to 998.219 kg and contains quantities of radon and other urnaium decay products and must be disposed of as a radioactive waste.

The U_3O_8 concentrate is then taken to a conversion plant where the concentrate is further purified (the 20% impurities are removed) and the uranium yellowcake is converted to uranium hexafluoried UF_6). The uranium hexafluoride is a gas at fairly low temperature and is an ideal material for the U-235 isotope enriching processes of either gaseous diffusion or gaseous centrifuge. The UF_6 is shipped in steel cylinders in a solid state, and UF_6 is vaporized by putting the cylinder in a steam bath.

If the uranium is to be enriched to 4% U^{235}, then 1 kilogram of 4% U^{235} product will require 7.4 kilograms of natural uranium feed and will produce 6.4 kilograms of waste uranium (tails or depleted uranium) with a U^{235} isotope content of 0.2%. This material is treated as a radioactive waste. Large quantities of tails (depleted uranium) exist as UF_6 in their original shipping containers at the enriching plants. Depleted uranium (a dense material) has been used as shields for radioactive sources, armor piercing shells, balancing of helicopter rotor tips, yacht hold ballast, and balancing of passenger aircraft.

The enriched UF_6 is then sent to a fabrication plant where it is converted to a uranium dioxide (UO_2) powder. The powder is pressed and sintered into cylindrical pellets which are placed in zircaloy tubes (an

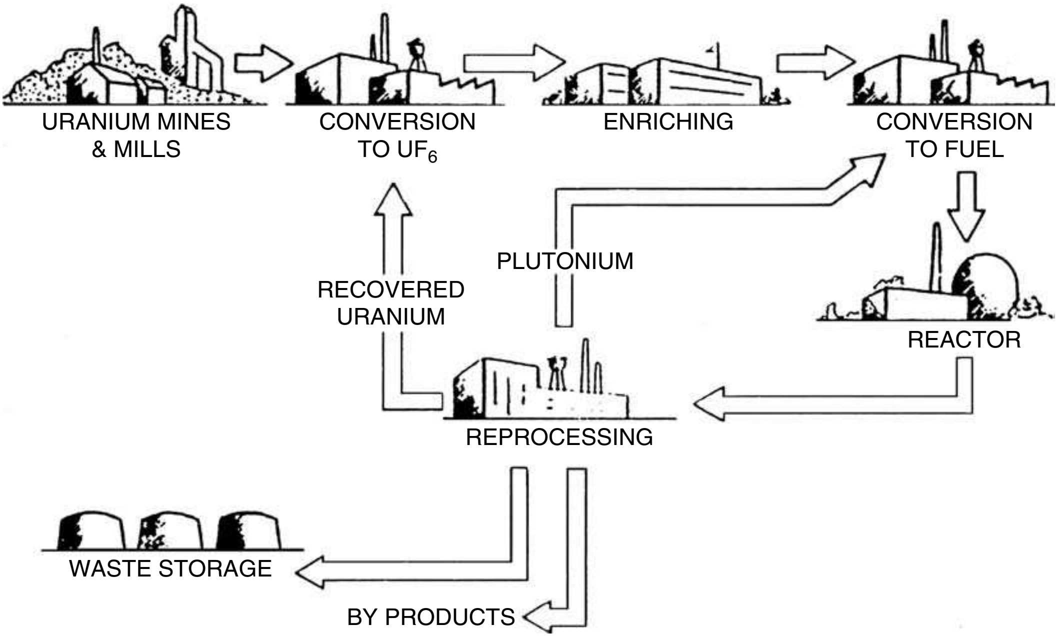

FIGURE 7.5.1 The nuclear fuel cycle.

alloy of zirconium), pressurized with helium, and sealed. The rods are collected in an array (~17 × 17) bound together by spacer grids, with top and bottom end fittings connected by tie rods or guide tubes. Pressurized water reactor fuel assemblies, each containing approximately 500 kilograms of uranium, are placed in a reactor for 3 to 4 years. A single fuel assembly produces 160,000,000 kilowatt hours of electricity and gives 8,000 people their yearly electric needs for its three years of operation. When the fuel assembly is removed from the reactor it must be placed in a storage pond to allow for removal of the decay heat. After approximately five years of wet storage, the fuel assembly can be removed to dry storage in concrete or steel containers. In the United States the current plan is to permanently store the nuclear fuel, with the Department of Energy assuming responsiblility for the "spent" fuel. The money for the government to handle the storage comes from a fee of 1 mill per kilowatt hour paid by consumers of nuclear-generated electricity. A mill is a thousandth of a dollar or a tenth of a penny. Thus, the fuel assembly described above would have collected $160,000 in the waste fund for the Department of Energy to permanently store the fuel. In Europe, when the fuel is taken out of wet storage it is sent to a reprocessing plant where the metal components are collected for waste disposal; and the fuel is chemically recovered as 96% uranium, which is converted to uranium dioxide for recycling to the enrichment plant, 1% plutomium, which is converted to fuel or placed in storage, and 3% fission products which are encased in glass and permanently stored.

The important thing to remenber about the fuel cycle is the small quantitiy of radioactive fission products (1.5 kilograms) which are created as radioactive waste in producing power which can serve the yearly eletricity needs of 8,000 people for the three years that it operates. The schematic of the entire fuel cycle showing both the United States system (once-through) and the European (recycle) system is given in Figure 7.51.

7.6 Solar Energy Resources

D. Yogi Goswami

The sun is a vast nuclear power plant of the fusion variety which generates power in the form of radiant energy at a rate of 3.8×10^{23} kW. An extremely small fraction of this is intercepted by Earth, but even this small fraction amounts to the huge quantity of 1.8 × 10^{14} kW. On the average, about 60% of this energy incident at the outer edge of the atmosphere, reaches the surface. To compare these numbers with our energy needs, consider the present electrical-generating capacity in the United States, which is approximately of 7 × 10^8 kW. This is equivalent to an average solar radiation falling on only 1000 square miles in a cloudless desert area. It must, however, be remembered that solar energy is distributed over the entire surface of Earth facing the sun, and it seldom exceeds 1.0 kW/m^2. Compared to other sources, such as fossil fuels or nuclear power plants, solar energy has a very low energy density. However, solar radiation can be concentrated to achieve very high energy densities. Indeed, temperatures as high as 3000 K have been achieved in solar furnaces.

Solar energy technology has been developed to a point where it can replace most of the fossil fuels or fossil fuel-derived energy. In many applications it is already economical, and it is a matter of time before it becomes economical for other applications as well.

This section deals in the availability of solar radiation, including methods of measurement, calculation, and available data.

Solar Energy Availability

Detailed information about solar radiation availability at any location is essential for the design and economic evaluation of a solar energy system. Long-term measured data of solar radiation are available for a large number of locations in the United States and other parts of the world. Where long-term measured data are not available, various models based on available climatic data can be used to estimate the solar energy availability. The solar energy is in the form of electromagnetic radiation with the wavelengths ranging from about 0.3 μm (10^{-6} m) to over 3 μm, which correspond to ultraviolet (less than 0.4 μm), visible (0.4 and 0.7 μm), and infrared (over 0.7 μm). Most of this energy is concentrated in the visible and the near-infrared wavelength range (see Figure 7.6.1). The incident solar radiation, sometimes called **insolation**, is measured as irradiance, or the energy per unit time per unit area (or power per unit area). The units most often used are watts per square meter (W/m^2), British thermal units per hour per square foot (Btu/hr-ft^2), and Langleys (calories per square centimeter per minute, cal/cm^2-min).

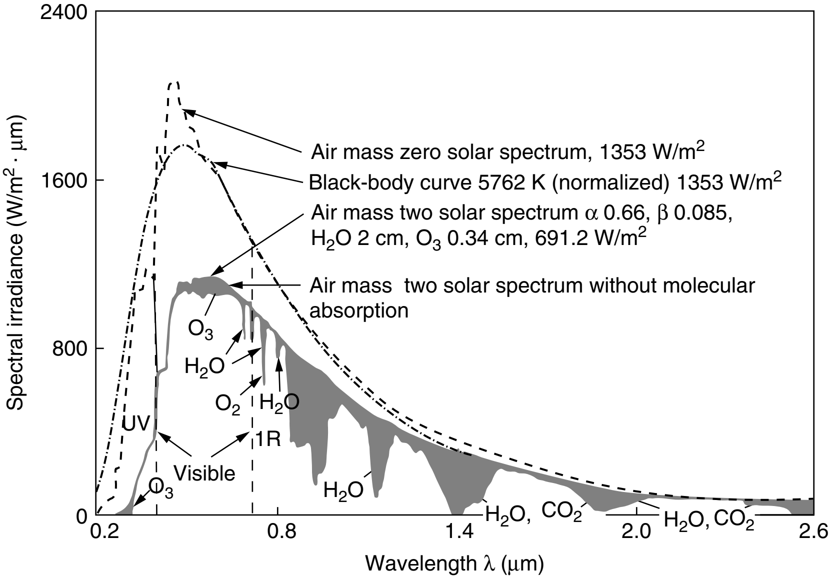

FIGURE 7.6.1 Spectral distribution of solar energy at sea level. (Reprinted by permission from Goswami, D.Y., Kreith, F., and Kreider, J.F., *Principles of Solar Engineering*, Taylor and Francis, Philadelphia, PA, 2000.)

The amount of solar radiation falling on a surface normal to the rays of the sun outside the atmosphere of the earth (extraterrestrial) at mean Earth-sun distance (D) is called the **solar constant**, I_o. Measurements by NASA indicated the value of solar constant to be 1353 W/m^2 (±1.6%). This value was revised upward and the present accepted value of the solar constant is 1377 W/m^2 (Quinlan, 1979) or 437.1 Btu/hr-ft^2 or 1.974 langleys. The variation in seasonal solar radiation availability at the surface of Earth can be understood from the geometry of the relative movement of Earth around the sun.

Earth-Sun Relationships

Figure 7.6.2 shows the annual motion of Earth around the sun. The **extraterrestrial solar radiation** varies throughout the year because of the variation in the Earth-sun distance (D) as:

$$I = I_o \left(D/D_o \right)^2 \tag{7.6.1}$$

which may be approximated as (Spencer, 1971)

$$\left(D/D_o \right)^2 = 1.00011 + 0.034221\cos(x) + 0.00128\sin(x) + 0.000719\cos(2x) + 0.000077\sin(2x) \tag{7.6.2}$$

where

$$x = 360(N-1)/365° \tag{7.6.3}$$

and N = Day number (starting from January 1 as 1). The axis of the Earth is tilted at an angle of 23.45° to the plane of its elliptic path around the sun. This tilt is the major cause of the seasonal variation of solar radiation available at any location on Earth. The angle between the Earth-sun line and a plane through the equator is called **solar declination**, δ. The declination varies between –23.45° to +23.45° in 1 year. It may be estimated by the relation:

$$\delta = 23.45° \sin\left[360(284+N)/365°\right] \tag{7.6.4}$$

The apparent motion of the sun around the earth is shown in Figure 7.6.3. The **solar altitude angle**, β, and the **solar azimuth angle**, Φ, describe the position of the sun at any time.

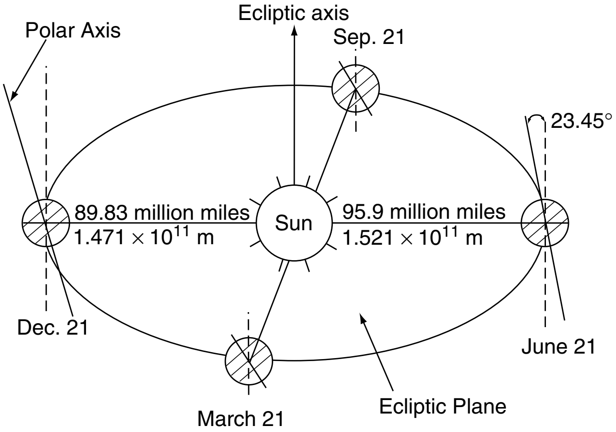

FIGURE 7.6.2 Annual motion of the Earth around the sun. (Adapted from Goswami, D.Y., Kreith, F., and Kreider, J., *Principles of Solar Engineering*, Taylor and Francis, Philadelphia, PA, 2000.)

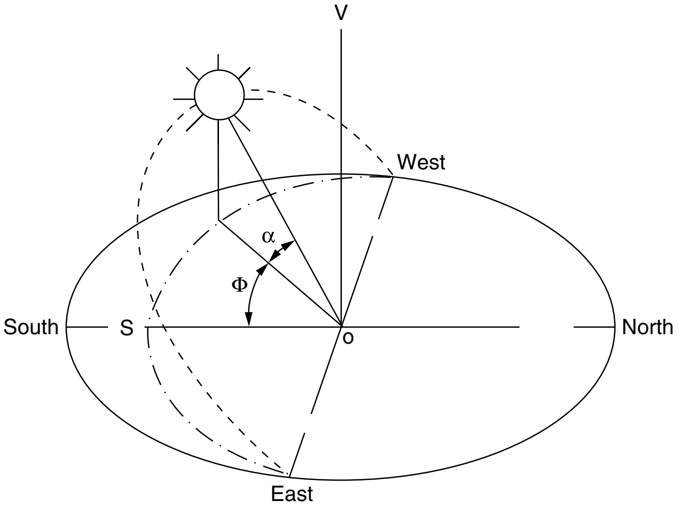

FIGURE 7.6.3 Apparent daily path of the sun across the sky from sunrise to sunset, showing the solar altitude and azimuth angles.

Solar Time

The sun angles are found from the knowledge of solar time, which differs from the local time. The relationship between solar time and local standard time (LST) is given by

$$\text{Solar Time} = \text{LST} + \text{ET} + 4\left(L_{st} - L_{loc}\right) \tag{7.6.5}$$

where ET is the **equation of time**, which is a correction factor in minutes that accounts for the irregularity of the motion of the Earth around the sun. L_{st} is the standard time meridian and L_{loc} is the local longitude. ET can be calculated from the following empirical equation:

$$\text{ET(in minutes)} = 9.87\sin 2B - 7.53\cos B - 1.5\sin B \tag{7.6.6}$$

where $B = 360(N - 81)/365°$.

The sun angles α (altitude) and Φ (azimuth) can be found from the equations:

$$\sin\alpha = \cos\ell\cos\delta\cos H + \sin\ell\sin\delta \tag{7.6.7}$$

where ℓ = latitude angle,

$$\sin\Phi = \cos\delta\sin H/\cos\alpha \tag{7.6.8}$$

and

$$H = \text{Hour angle} = \frac{\text{Number of minutes from local solar noon}}{4\ \text{min/degree}} \tag{7.6.9}$$

(At solar noon, $H = 0$, so $\alpha = 90 - |\ell - \delta|$ and $\Phi = 0$.)

TABLE 7.6.1 Average Values of Atmospheric Optical Depth (τ) and Sky Diffuse Factor (C) for 21st Day of Each Month

Month	1	2	3	4	5	6	7	8	9	10	11	12
τ	0.142	0.144	0.156	0.180	0.196	0.205	0.207	0.201	0.177	0.160	0.149	0.142
C	0.058	0.060	0.071	0.097	0.121	0.134	0.136	0.122	0.092	0.073	0.063	0.057

Source: Threlkeld, J.L. and Jordan, R.C., *ASHRAE Trans.*, 64, 45, 1958.

Solar Radiation on a Surface

As solar radiation, I, passes through the atmosphere, some of it is absorbed by air and water vapor, while some gets scattered by molecules of air, water vapor, aerosols, and dust particles. The part of solar radiation that reaches the surface of the Earth with essentially no change in direction is called **direct or beam normal radiation**, I_{bN}. The scattered radiation reaching the surface from the atmosphere is called **diffuse radiation**, I_d.

I_{bN} can be calculated from the extraterrestrial solar irradiance, I, and the atmospheric optical depth τ as (Goswami et al., 1981; ASHRAE, 1995)

$$I_{\mathrm{bN}} = Ie^{-\tau \sec \theta_z} \tag{7.6.10}$$

where θ_z is the solar zenith angle (angle between the sun rays and the vertical). The atmospheric optical depth determines the attenuation of the solar radiation as it passes through the atmosphere. Threlkeld and Jordan (1958) calculated values of τ for average atmospheric conditions at sea level with a moderately dusty atmosphere and amounts of precipitable water vapor equal to the average value for the United States for each month. These values are given in Table 7.6.1. To account for the differences in local conditions from the average sea level conditions Equation (7.6.10) is modified by a parameter called Clearness Number, Cn, introduced by Threlkeld and Jordan (1958):

$$I_{\mathrm{bN}} = \mathrm{Cn} Ie^{-\tau \sec \theta_z} \tag{7.6.11}$$

values of Cn vary between 0.85 and 1.15.

Solar Radiation on a Horizontal Surface

Total incident solar radiation on a horizontal surface is given by

$$I_{t,\mathrm{Horizontal}} = I_{\mathrm{bN}} \cos \theta_z + CI_{\mathrm{bN}} \tag{7.6.12}$$

$$= I_{\mathrm{bN}} \sin \beta + CI_{\mathrm{bN}} \tag{7.6.13}$$

where θ_z is called the solar zenith angle and C is called the sky diffuse factor, as given in Table 7.6.1.

Solar Radiation on a Tilted Surface

For a surface of any orientation and tilt as shown in Figure 7.6.4, the angle of incidence, θ, of the direct solar radiation is given by

$$\cos \theta = \cos \alpha \cos \gamma \sin \beta + \sin \alpha \cos \beta \tag{7.6.14}$$

where γ is the angle between horizontal projections of the rays of the sun and the normal to the surface. β is the tilt angle of the surface from the horizontal.

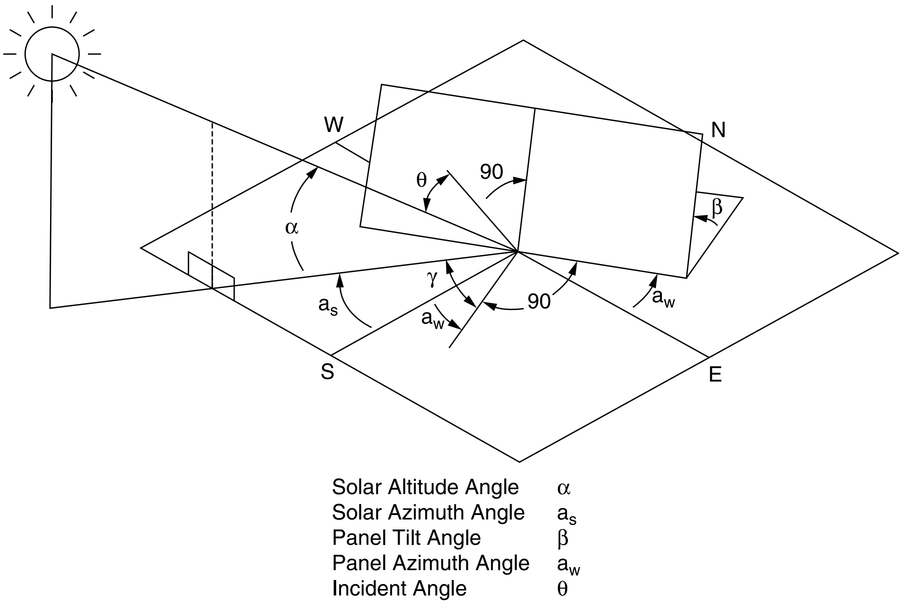

FIGURE 7.6.4 Definitions of solar angles for a tilted surface.

For a tilted surface with angle of incidence θ, the total incident solar radiation is given by

$$I_b = I_{\mathrm{bN}} \cos\theta + I_{\mathrm{diffuse}} + I_{\mathrm{reflected}} \tag{7.6.15}$$

where

$$I_{\mathrm{diffuse}} = CI_{\mathrm{bN}}\left(1+\cos\beta\right)/2 \tag{7.6.16}$$

and

$$I_{\mathrm{reflected}} = \rho I_{\mathrm{bN}}\left(C+\sin\alpha\right)\left(1-\cos\beta\right)/2 \tag{7.6.17}$$

where ρ is the reflectivity of the surroundings. For ordinary ground or grass, ρ is approximately 0.2 while for ground covered with snow it is approximately 0.8.

Solar Radiation Measurements

Two basic types of instruments are used in measurements of solar radiation. These are (see Figure 7.6.5):

1. *Pyranometer:* An instrument used to measure global (direct and diffuse) solar radiation on a surface. This instrument can also be used to measure the diffuse radiation by blocking out the direct radiation with a shadow band.
2. *Pyrheliometer:* This instrument is used to measure only the direct solar radiation on a surface normal to the incident beam. It is generally used with a tracking mount to keep it aligned with the sun.

More-detailed discussions about these and other solar radiation measuring instruments can be found in Zerlaut (1989).

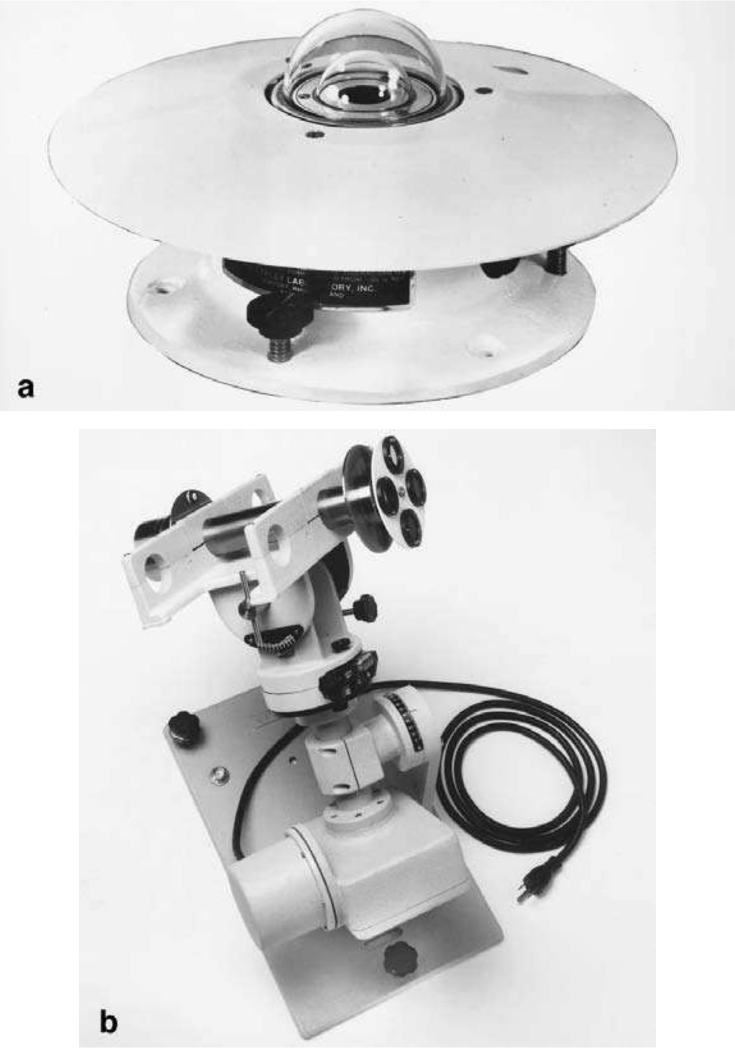

FIGURE 7.6.5 Two basic instruments for solar radiation: (a) pyranometer; (b) pyrheliometer.

Solar Radiation Data

Measured values of solar radiation data for locations in the United States are available from the National Climatic Center in Asheville, NC. A number of states have further presented solar radiation data for locations in those states in readily usable form. Weather services and energy offices in almost all the countries have available some form of solar radiation data or climatic data that can be used to derive solar radiation data for locations in those countries. Table 7.6.2 to Table 7.6.4 give solar radiation data for clear days for south-facing surfaces in the Northern Hemisphere (and northern-facing surfaces in the Southern Hemisphere) tilted at 0°, 15°, 30°, 45°, 60°, 75°, and vertical, for latitudes 0°, 30°, and 60°. The actual average solar radiation data at a location is less than the values given in these tables because of the cloudy and partly cloudy days in addition to the clear days. The actual data can be obtained either from long-term measurements or from modeling based on some climatic parameters, such as percent sunshine.

Worldwide solar radiation data is available from the World Radiation Data Center (WRDC). WRDC has been archiving data from over 500 stations and operates a website in collaboration with NREL (wrdc-mgo.nrel.gov).

TABLE 7.6.2 Average Daily Total Solar Radiation on South-Facing Surfaces in Northern Hemisphere; Latitude = 0°N

Month	Horiz.	15°	30°	45°	60°	75°	90°
1	31.11	34.13	35.13	34.02	30.90	25.96	19.55
2	32.34	33.90	33.45	31.03	26.80	21.05	14.18
3	32.75	32.21	29.79	25.67	20.12	13.53	6.77
4	31.69	29.13	24.93	19.39	12.97	6.59	4.97
5	29.97	26.08	20.81	14.64	8.34	4.92	5.14
6	28.82	24.43	18.81	12.54	6.66	5.07	5.21
7	29.22	25.08	19.66	13.48	7.45	5.17	5.31
8	30.59	27.48	22.87	17.13	10.82	5.58	5.32
9	31.96	30.51	27.34	22.65	16.78	10.18	5.33
10	32.18	32.82	31.54	28.44	23.73	17.72	10.84
11	31.33	33.80	34.28	32.72	29.24	24.08	17.58
12	30.51	33.90	35.27	34.53	31.73	27.05	20.83

TABLE 7.6.3 Average Daily Total Solar Radiation on South-Facing Surfaces in Northern Hemisphere; Latitude = 30°N

Month	Horiz.	15°	30°	45°	60°	75°	90°
1	17.19	22.44	26.34	28.63	29.15	27.86	24.85
2	21.47	26.14	29.25	30.59	30.06	27.70	23.68
3	26.81	30.04	31.50	31.09	28.84	24.90	19.54
4	31.48	32.71	32.06	29.57	25.44	19.96	13.60
5	34.49	33.96	31.56	27.49	22.08	15.82	9.49
6	35.61	34.24	31.03	26.28	20.40	13.97	8.02
7	35.07	34.06	31.21	26.76	21.11	14.77	8.68
8	32.60	33.00	31.54	28.35	23.68	17.89	11.57
9	28.60	30.87	31.35	30.02	26.97	22.42	16.67
10	23.41	27.38	29.74	30.33	29.10	26.14	21.66
11	18.50	23.48	27.05	28.98	29.14	27.51	24.20
12	15.90	21.19	25.21	27.68	28.44	27.43	24.71

TABLE 7.6.4 Average Daily Total Solar Radiation on South-Facing Surfaces in Northern Hemisphere; Latitude = 60°N

Month	Horiz.	15°	30°	45°	60°	75°	90°
1	1.60	3.54	5.26	6.65	7.61	8.08	8.03
2	5.49	9.38	12.71	15.25	16.82	17.32	16.72
3	12.82	17.74	21.60	24.16	25.22	24.73	22.71
4	21.96	26.22	28.97	30.05	29.38	27.00	23.09
5	30.00	32.79	33.86	33.17	30.73	26.72	21.45
6	33.99	35.82	35.93	34.29	31.00	26.26	20.46
7	32.26	34.47	34.97	33.71	30.78	26.36	20.80
8	25.37	28.87	30.80	31.02	29.53	26.42	21.94
9	16.49	21.02	24.34	26.22	26.54	25.27	22.51
10	8.15	12.39	15.90	18.45	19.85	20.01	18.92
11	2.70	5.27	7.53	9.31	10.51	11.03	10.84
12	0.82	2.06	3.16	4.07	4.71	5.05	5.07

Note: Values are in megajoules per square meter. Clearness number = 1.0; ground reflection = 0.2.

Defining Terms

Diffuse radiation: Scattered solar radiation coming from the sky.

Direct or beam normal radiation: Part of solar radiation coming from the direction of the sun on a surface normal to the sun's rays.

Equation of time: Correction factor in minutes, to account for the irregularity of the Earth's motion around the sun.

Extraterrestrial solar radiation: Solar radiation outside Earth's atmosphere.

Insolation: Incident solar radiation measured as W/m^2 or Btu/hr-ft^2.

Solar altitude angle: Angle between the solar rays and the horizontal plane.

Solar azimuth angle: Angle between the true south horizontal line and the horizontal projection of the sun's rays.

Solar constant: Extraterrestrial solar radiation at the mean Earth-sun distance.

Solar declination: Angle between the Earth-sun line and a plane through the equator.

References

ASHRAE. 1995. 1995 *HVAC Applications*, ASHRAE, Atlanta, GA.

Goswami, D.Y. 1986. *Alternative Energy in Agriculture,* Vol. 1, CRC Press, Boca Raton, FL.

Goswami, D.Y., Klett, D.E., Stefanakos, E.K., and Goswami, T.K. 1981. Seasonal variation of atmospheric clearness numbers for use in solar radiation modelling, *AIAA J. Energ.*, 5(3) 185.

Goswami, D.Y., Kreith, F., and Kreider, J. 2000. *Principles of Solar Engineering,* Taylor and Francis, Philadelphia, PA.

Kreith, F. and Kreider, J.F. 1978. *Principles of Solar Engineering,* Hemisphere Publishing, Washington, D.C.

Quinlan, F.T., Ed. 1979. *SOLMET Volume 2: Hourly Solar Radiation — Surface Meteorological Observations*, National Oceanic and Atmospheric Administration, Asheville, NC.

Spencer, J.W. 1971. Fourier series representation of the position of the sun, *Search,* 2, 172.

Threlkeld, J.L. and Jordan, R.C. 1958. Direct radiation available on clear days, *ASHRAE Trans.,* 64, 45.

Zerlaut, G. 1989. Solar Radiation Instrumentation, Chapter 5, *Solar Resources,* R.L. Hulstrom, Ed., The MIT Press, Cambridge, MA.

Further Information

Solar Resources, edited by R.H. Hulstrom, MIT Press, Cambridge, MA, 1989.

World Radiation Data Center (WRDC), St. Petersburg, Russia: WRDC, operating under the auspices of World Meteorological Organization (WMO), has been archiving data over 500 stations and operates a website in collaboration with NREL (wrdc-mgo.nrel.gov).

7.7 Wind Energy Resources[2]

Dale E. Berg

Wind Origins

The primary causes of atmospheric air motion, or wind, are uneven heating of the Earth by solar radiation and the Earth's rotation. Differences in solar radiation absorption at the surface of the Earth and transference back to the atmosphere create differences in atmospheric temperature, density, and pressure,

---

[2] This work was supported by the United States Department of Energy under Contract DE-AC04-94AL85000.

which in turn create forces that move air from one place to another. For example, land and water along a coastline absorb radiation differently, and this is the dominant cause of the light winds or breezes normally found along a coast. The Earth's rotation gives rise to semipermanent global wind patterns such as trade winds, westerlies, easterlies, and subtropical and polar jets.

Wind Power

The available power in the wind with air density ρ, passing through an area A, perpendicular to the wind, at a velocity U, is given by

$$\text{Power} = \tfrac{1}{2}\rho A U^3 \tag{7.7.1}$$

Air density decreases with increasing temperature and increasing altitude above sea level. The effect of temperature on density is relatively weak and is normally ignored because these variations tend to average out over the period of a year. The density difference due to altitude, however, is significant; it does not average out and cannot be ignored. For example, the air density at Denver, Colorado (elevation 1600 m, or 5300 ft, above sea level), is approximately 14% lower than at sea level, so wind at Denver contains 14% less power than wind of the same velocity at sea level.

From Equation (7.7.1), it is obvious that the most important factor in the available wind power is the velocity of the wind — an increase in wind velocity of only 20%, e.g., from 5 to 6 m/s (11.2 to 13.4 mph), yields a 73% increase in available wind power.

Wind Shear

Wind moving across the Earth's surface is slowed by trees, buildings, grass, rocks, and other obstructions in its path. The result is a wind velocity that varies with height above the Earth's surface — a phenomena known as **wind shear**. For most situations, wind shear is positive (wind speed increases with height), but situations in which the wind shear is negative or inverse are not unusual. In the absence of actual data for a specific site, a commonly used approximation for wind shear in an open area is:

$$U/U_o = (h/h_o)^{\alpha} \tag{7.7.2}$$

where

U = the velocity at a height h
U_o = the measured velocity at height h_o
α = the wind shear exponent

The wind shear exponent, α, varies with terrain characteristics, but usually falls between 0.10 and 0.25. Wind over a body of open water is normally well modeled by a value of α of about 0.10; wind over a smooth, level, grass-covered terrain such as the U.S. Great Plains by an α of about 0.14; wind over row crops or low bushes with a few scattered trees by an α of 0.20; and wind over a heavy stand of trees, several buildings, or hilly or mountainous terrain by an α of about 0.25. Short-term shear factors as large as 1.25 have been documented in rare, isolated cases.

The available wind power at a site can vary dramatically with height due to wind shear. For example, for $\alpha = 0.20$, Equation (7.7.1) and Equation (7.7.2) reveal that the available wind power at a height of 50 m is approximately $\{(50/10)^{0.2}\}^3 = 2.63$ times the available wind power at a height of 10 m.

Wind Energy Resource

The amount of energy available in the wind (the **wind energy resource**) is the average amount of power available in the wind over a specified period of time — commonly 1 year. If the wind speed is 20 m/s,

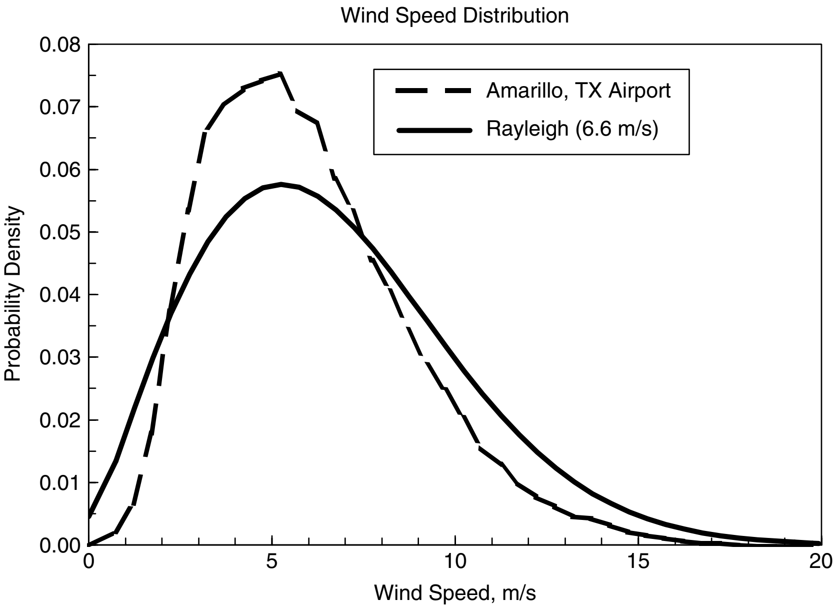

FIGURE 7.7.1 Rayleigh and measured wind speed distributions.

the available power is very large at that instant, but if it only blows at that speed for 10 h per year and the rest of the time the wind speed is near zero, the resource for the year is small. Therefore, the site **wind speed distribution**, or the relative frequency of occurrence for each wind speed, is very important in determining the resource. This distribution is often presented as a probability density function, such as the one shown in Figure 7.7.1. The probability that the wind occurs in any given wind speed range is given by the area under the density function for that wind speed range. If the actual wind speed probability density distribution is not available, it is commonly approximated with the Rayleigh distribution, given by:

$$f(U) = \frac{\pi}{4}\frac{U}{\overline{U}}\exp\left[-\frac{\pi}{4}\frac{U^2}{\overline{U}^2}\right] \tag{7.7.3}$$

where

$f(U)$ = the frequency of occurrence of wind speed U

$\overline{U}$ = the yearly average wind speed

The measured wind speed distribution at the Amarillo, Texas, airport (yearly average wind speed of 6.6 m/s) is plotted in Figure 7.7.1, together with the Rayleigh distribution for that wind speed. It is obvious that the Rayleigh distribution is not a good representation for the Amarillo airport.

How large is the wind energy resource? Even though wind energy is very diffuse, the total resource is very, very large. In the U.S. and many other countries around the world, the resource is large enough to supply the entire current energy consumption of the country, potentially. In 1987, scientists at Batelle Pacific Northwest Laboratory (PNL) in the U.S. carefully analyzed and interpreted the available long-term wind data for the U.S. and summarized their estimate of the wind energy resources in the *Wind Energy Resource Atlas of the United States* (Elliott et al., 1987). Their summary for the entire U.S. is reproduced in Figure 7.7.2. The results are presented in terms of wind power classes based on the annual average power available per square meter of intercepted area (see the legend on Figure 7.7.2).

Scientists at Denmark's Risø National Laboratory have produced a European wind atlas (Troen and Petersen, 1989) that estimates the wind resources of the European Community countries and summarizes the resource available at a 50 m height for five different topographic conditions. A summary of these results is reproduced in Figure 7.7.3. The estimates presented in Figure 7.7.2 and Figure 7.7.3 are quite crude and have been superceded in recent years by much higher resolution maps, made possible by improvements in wind resource computer modeling programs and increases in computer speed.

Many countries around the world have recently embarked on high-resolution mapping efforts to quantify their wind resources and identify those areas of highest resource accurately. The resultant resource maps are frequently available to the public, but in some cases a payment is required to obtain them. High-resolution wind resource maps of the individual states in the U.S. may be found on the Web at www.eere.energy.gov/windpoweringamerica/wind_resources.html. Similar maps for some other countries may be found at www.rsvp.nrel.gov/wind_resources.html, and information on where to find maps and/or data for other countries may be found at www.windatlas.dk/index.htm.

Remember that even the highest resolution resource estimates are just that — estimates. The actual wind resources in any specific area can vary dramatically from those estimates and should be determined with long-term, site-specific measurements.

Wind Characterization

Wind speed, direction, distribution, and shear can vary significantly over fairly short distances in the horizontal or vertical directions, so in order to get the best possible estimate of the wind energy resource at a particular location, it is important to measure the wind resource at the specific site and height of interest. However, a comprehensive site characterization normally requires measuring the wind for at least 12 months, according to meteorologists at PNL (Wegley et al., 1980). This is a very time-consuming and potentially expensive effort. Long-term data from the nearest airport or weather recording station can help determine whether the data obtained at a site are representative of normal winds for the site or of higher or lower than average winds. Wegley et al. (1980) and Gipe (1993) give suggestions on methods of using available data from nearby sites to estimate site wind speed with minimal on-site data.

Sites of wind power class 4 or above (at least 200 W/m^2 at 10 m height or 400 W/m^2 at 50 m height) are often considered economic for utility-scale wind power development with available wind technology. Sites of wind power class 3 (150 to 200 W/m^2 at 10 m height or 300 to 400 W/m^2 at 50 m height) are not considered economic for utility development today but are likely to become economic with near-term wind technology advances. Sites of wind power class 2 or lower (less than 150 W/m^2 at 10 m height or 300 W/m^2 at 50 m height) are usually considered economic only for remote or hybrid wind power systems.

Wind Energy Potential

With a wind speed distribution and a turbine power curve (the electrical power generated by the turbine at each wind speed) properly adjusted for the local air density, the **wind energy potential**, or gross annual wind energy production, for a specific site can be estimated as:

$$\text{Energy} = 0.85\left[8760\sum_{i=1}^{n} f(U_i)\,\Delta U_i\;P(U_i)\right] \tag{7.7.4}$$

where

8760 = the number of hours in a year
n = the number of wind speeds considered
$f(U_i)\Delta U_i$ = the probability of a wind speed occurring in the wind-speed range ΔU_i
$P(U_i)$ = the electrical power produced by the turbine at wind speed U_i, the center of the range ΔU_i

The leading 0.85 factor assumes 15% in losses (10% due to power transfer to the grid, control system losses, and decreased performance due to dirty blades; 5% due to operation within an array of wind turbines). If the turbine is not inside an array, replace 0.85 with 0.90. Wind energy potential is typically 20 to 35% of the wind energy resource.

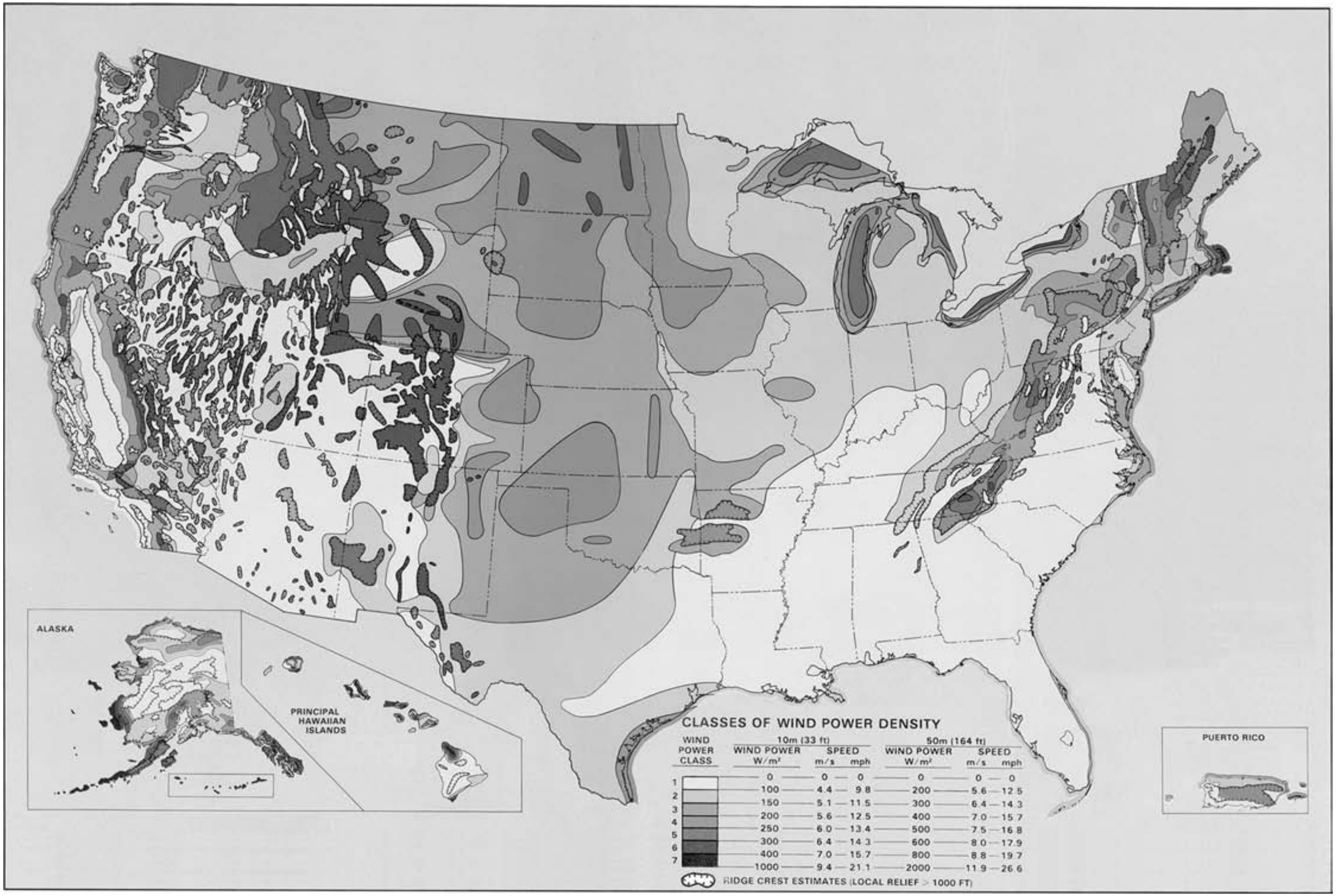

FIGURE 7.7.2 Map of U.S. wind energy resources. Reproduced from Elliott et al. *Wind Energy Resource Atlas of the United States*. (Courtesy of National Renewable Energy Laboratory, Golden, Colorado.)

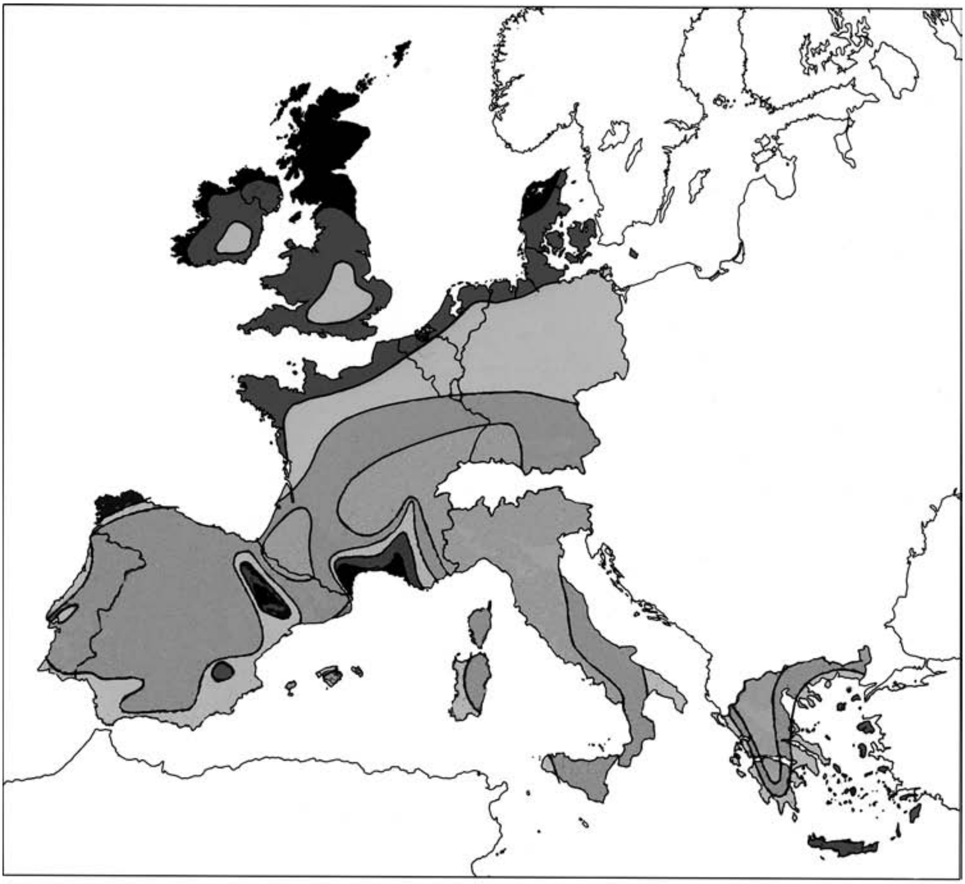

Wind resources[1] at 50 metres above ground level for five different topographic conditions										
	Sheltered terrain[2]		Open plain[3]		At a sea coast[4]		Open sea[5]		Hills and ridges[6]	
	m s^{-1}	Wm^{-2}	m s^{-1}	Wm^{-2}	m s^{-1}	Wm^{-2}	m s^{-1}	Wm^{-2}	m s^{-1}	Wm^{-2}
■	> 6.0	> 250	> 7.5	> 500	> 8.5	> 700	> 9.0	> 800	> 11.5	> 1800
▩	5.0-6.0	150-250	6.5-7.5	300-500	7.0-8.5	400-700	8.0-9.0	600-800	10.0-11.5	1200-1800
□	4.5-5.0	100-150	5.5-6.5	200-300	6.0-7.0	250-400	7.0-8.0	400-600	8.5-10.0	700-1200
▨	3.5-4.5	50-100	4.5-5.5	100-200	5.0-6.0	150-250	5.5-7.0	200-400	7.0- 8.5	400- 700
░	< 3.5	< 50	< 4.5	< 100	< 5.0	< 150	< 5.5	< 200	< 7.0	< 400

1. The resources refer to the power present in the wind. A wind turbine can utilize between 20 and 30% of the available resource. The resources are calculated for an air density of 1.23 kg m^{-3}, corresponding to standard sea level pressure and a temperature of 15°C. Air density decreases with height but up to 1000 m a.s.l. the resulting reduction of the power densities is less than 10%.
2. Urban districts, forest and farm land with many windbreaks (roughness class 3).
3. Open landscapes with few windbreaks (roughness class 1). In general, the most favourable inland sites on level land are found here.
4. The classes pertain to a straight coastline, a uniform wind rose and a land surface with few windbreaks (roughness class 1). Resources will be higher, and closer to open sea values, if winds from the sea occur more frequently, i.e. the wind rose is not uniform and/or the land protrudes into the sea. Conversely, resources will generally be smaller, and closer to land values, if winds from land occur more frequently.
5. More than 10 km offshore (roughness class 0).
6. The classes correspond to 50% overspeeding and were calculated for a site on the summit of a single axisymmetric hill with a height of 400 metres and a base diameter of 4 km. The overspeeding depends on the height, length and specific setting of the hill.

FIGURE 7.7.3 Map of European wind energy resources. Reproduced from Troen and Petersen, 1989. *European Wind Atlas*. (Courtesy of Risø National Laboratory, Roskilde, Denmark.)

Defining Terms

Wind energy potential: total amount of energy that can actually be extracted from the wind, taking into account the efficiency of the wind turbine.

Wind energy resource: total amount of energy present in the wind.

Wind shear: change in wind velocity with increasing height above the ground.

Wind speed distribution: probability density of occurrence of each wind speed over the course of a year for the site in question

References

Elliott, D.L., Holladay, C.G., Barchet, W.R., Foote, H.P., and Sandusky, W.F. 1987. *Wind Energy Resource Atlas of the United States*, DOE/CH10094-4, Solar Energy Research Institute, Golden, Colorado.

Gipe, P. 1993. *Wind Power for Home & Business — Renewable Energy for the 1990s and Beyond*, Chelsea Green Publishing Company, Post Mills, VT.

Troen, I. and Petersen, E.L. 1989. *European Wind Atlas*, Risø National Laboratory, Roskilde, Denmark.

Wegley, H.L., Ramsdell, J.V., Orgill, M.M., and Drake, R.L. 1980. *A Siting Handbook for Small Wind Energy Conversion Systems*, PNL-2521, Pacific Northwest Laboratory, Richland, WA.

Further Information

Wind Characteristics — An Analysis for the Generation of Wind Power, J.S. Rohatgi and V. Nelson, Alternative Energy Institute, West Texas A&M University, is an excellent source for additional information on the wind resource.

Wind Turbine Technology, Fundamental Concepts of Wind Turbine Engineering, D. Spera, Ed., ASME Press, New York, contains a wealth of information on wind energy resources, history, and technology, together with extensive reference lists.

Extensive information on wind energy resources and technology may also be found on the World Wide Web. Excellent sites to start with include those of the U.S. National Renewable Energy Laboratory Wind Energy Technology Center at www.nwtc.nrel.gov; the Danish Risø National Laboratory at www.risoe.dk/vea/index.htm; the American Wind Energy Association at www.awea.org; the British Wind Energy Association at www.britishwindenergy.co.uk; and the European Wind Energy Association at www.ewea.org.

7.8 Geothermal Energy

Joel L. Renner and Marshall J. Reed

The word *Geothermal* comes from the combination of the Greek words *gê*, meaning Earth, and *thérm*, meaning heat. Quite literally, geothermal energy is the heat of the Earth. Geothermal resources are concentrations of the Earth's heat, or geothermal energy, that can be extracted and used economically now or in the reasonable future. Currently, only concentrations of heat associated with water in permeable rocks can be exploited. Heat, fluid, and permeability are the three necessary components of all exploited geothermal fields. This section of Energy Resources will discuss the mechanisms for concentrating heat near the surface, the types of geothermal systems, and the environmental aspects of geothermal production.

Heat Flow

Temperature within the Earth increases with depth at an average of about 25°C/km. Spatial variations of the thermal energy within the deep crust and mantle of the Earth give rise to concentrations of thermal energy near the surface of the Earth that can be used as an energy resource. Heat is transferred from the deeper portions of the Earth by conduction of heat through rocks, by the movement of hot, deep rock toward the surface, and by deep circulation of water. Most high-temperature geothermal resources are associated with concentrations of heat caused by the movement of magma (melted rock) to near-surface positions where the heat is stored.

In older areas of continents, such as much of North America east of the Rocky Mountains, heat flow is generally 40 to 60 mWm^{-2} (milliwatts per square meter). This heat flow coupled with the thermal conductivity of rock in the upper 4 km of the crust yields subsurface temperatures of 90 to 110°C at 4 km depth in the Eastern United States. Heat flow within the Basin and Range (west of the Rocky Mountains) is generally 70 to 90 mWm^{-2}, and temperatures are generally greater than 110°C at 4 km. There are large variations in the Western United States, with areas of heat flow greater than 100 mWm^{-2} and areas which have generally lower heat flow such as the Cascade and Sierra Nevada Mountains and the West Coast. A more detailed discussion of heat flow in the United States is available in Blackwell et al. (1991).

Types of Geothermal Systems

Geothermal resources are hydrothermal systems containing water in pores and fractures. Most hydrothermal resources contain liquid water, but higher temperatures or lower pressures can create conditions where steam and water or only steam are the continuous phases (White et al., 1971; Truesdell and White, 1973). All commercial geothermal production is expected to be restricted to hydrothermal systems for many years because of the cost of artificial addition of water. Successful, sustainable geothermal energy usage depends on reinjection of the maximum quantity of produced fluid to augment natural recharge of hydrothermal systems.

Other geothermal systems that have been investigated for energy production are (1) geopressured-geothermal systems containing water with somewhat elevated temperatures (above normal gradient) and with pressures well above hydrostatic for their depth; (2) magmatic systems, with temperature from 600 to 1400°C; and (3) hot dry rock geothermal systems, with temperatures from 200 to 350°C, that are subsurface zones with low initial permeability and little water. These types of geothermal systems cannot be used for economic production of energy at this time.

Geothermal Energy Potential

The most recent report (Huttrer, 1995) shows that 6800 MW_e (megawatts electric) of geothermal electric generating capacity is on-line in 21 countries (Table 7.8.1). The expected capacity in the year 2000 is 9960 MW_e. Table 7.8.2 lists the electrical capacity of U.S. geothermal fields. Additional details of the U.S. generating capacity are available in DiPippo (1995) and McClarty and Reed (1992). Geothermal resources also provide energy for agricultural uses, heating, industrial uses, and bathing. Freeston (1995) reports that 27 countries had a total of 8228 MW_t (megawatts thermal) of direct use capacity. The total energy used is estimated to be 105,710 TJ/year (terajoules per year). The thermal energy used by the ten countries using the most geothermal resource for direct use is listed in Table 7.8.3.

The U.S. Geological Survey has prepared assessments of the geothermal resources of the U.S. Muffler(1979) estimated that the identified hydrothermal resource, that part of the **identified accessible base** that could be extracted and utilized at some reasonable future time, is 23,000 MW_e for 30 years. This resource would operate power plants with an aggregate capacity of 23,000 MW_e for 30 years. The undiscovered U.S. resource (inferred from knowledge of Earth science) is estimated to be 95,000 to 150,000 MW_e for 30 years.

Geothermal Applications

In 1991, geothermal electrical production in the United States was 15,738 GWh (gigawatt hours), and the largest in the world (McLarty and Reed, 1992).

TABLE 7.8.1 Installed and Projected Geothermal Power Generation Capacity

Country	1995	2000
Argentina	0.67	n/a[b]
Australia	0.17	n/a
China	28.78	81
Costa Rica	55	170
El Salvador	105	165
France	4.2	n/a
Greece[a]	0	n/a
Iceland	49.4	n/a
Indonesia	309.75	1080
Italy	631.7	856
Japan	413.705	600
Kenya	45	n/a
Mexico	753	960
New Zealand	286	440
Nicaragua	35	n/a
Philippines	1227	1978
Portugal (Azores)	5	n/a
Russia	11	110
Thailand	0.3	n/a
Turkey	20.6	125
U.S.	2816.775	3395
Totals	6797.975	9960

[a] Greece has closed its 2.0 MWe Milos pilot plant.

[b] n/a = information not available.

Source: Huttrer, G.W., in *Proceedings of the World Geothermal Congress, 1995*, International Geothermal Association, Auckland, N.Z., 1995, 3–14. With permission.

Most geothermal fields are water dominated, where liquid water at high temperature, but also under high (hydrostatic) pressure, is the pressure-controlling medium filling the fractured and porous rocks of the reservoir. In water-dominated geothermal systems used for electricity, water comes into the wells from the reservoir, and the pressure decreases as the water moves toward the surface, allowing part of the water to boil. Since the wells produce a mixture of flashed steam and water, a separator is installed between the wells and the power plant to separate the two phases. The flashed steam goes into the turbine to drive the generator, and the water is injected back into the reservoir.

Many water-dominated reservoirs below 175°C used for electricity are pumped to prevent the water from boiling as it is circulated through heat exchangers to heat a secondary liquid that then drives a turbine to produce electricity. **Binary geothermal plants** have no emissions because the entire amount of produced geothermal water is injected back into the underground reservoir. The identified reserves of lower-temperature geothermal fluids are many times greater than the reserves of high-temperature fluids, providing an economic incentive to develop more-efficient power plants.

Warm water, at temperatures above 20°C, can be used directly for a host of processes requiring thermal energy. Thermal energy for swimming pools, space heating, and domestic hot water are the most widespread uses, but industrial processes and agricultural drying are growing applications of geothermal use. In 1995, the United States was using over 500 TJ/year of energy from geothermal sources for direct use (Lienau, et al., 1995). The cities of Boise, ID; Elko, NV; Klamath Falls, OR; and San Bernardino and Susanville, CA have geothermal district-heating systems where a number of commercial and residential buildings are connected to distribution pipelines circulating water at 54 to 93°C from the production wells (Rafferty, 1992).

TABLE 7.8.2 U.S. Installed Geothermal Electrical Generating Capacity in MW_e

Rated State/Field	Plant Capacity	Type
California		
Casa Diablo	27	B
Coso	240	2F
East Mesa	37	2F
East Mesa	68.4	B
Honey Lake Valley	2.3	B
Salton Sea	440	2F
The Geysers	1797	S
Hawaii		
Puna	25	H
Nevada		
Beowawe	16	2F
Brady Hot Springs	21	2F
Desert Peak	8.7	2F
Dixie Valley	66	2F
Empire	3.6	B
Soda Lake	16.6	B
Steamboat	35.1	B
Steamboat	14.4	1F
Stillwater	13	B
Wabuska	1.2	B
Utah		
Roosevelt	20	1F
Cove Fort	2	B
Cove Fort	9	S

Note: S = natural dry steam, 1F = single flash, 2F = double flash, B = binary, H = hybrid flash and binary.

TABLE 7.8.3 Geothermal Energy for Direct Use by the Ten Largest Users Worldwide

Country	Flow Rate, kg/sec	Installed Power, MWt	Energy Used, TJ/year
China	8,628	1,915	16,981
France	2,889	599	7,350
Georgia	1,363	245	7,685
Hungary	1,714	340	5,861
Iceland	5,794	1,443	21,158
Italy	1,612	307	3,629
Japan	1,670	319	6,942
New Zealand	353	264	6,614
Russia	1,240	210	2,422
U.S.	3.905	1,874	13.890
Total	37,050	8,664	112,441

Source: Freeston, D.H., in *Proceedings of the World Geothermal Congress, 1995,* International Geothermal Association, Auckland, N.Z., 1995, 15–26. With permission.

The use of geothermal energy through ground-coupled heat pump technology has almost no impact on the environment and has a beneficial effect in reducing the demand for electricity. Geothermal heat pumps use the reservoir of constant temperature, shallow groundwater and moist soil as the heat source during winter heating and as the heat sink during summer cooling. The energy efficiency of geothermal heat pumps is about 30% better than that of air-coupled heat pumps and 50% better than electric-resistance heating. Depending on climate, advanced geothermal heat pump use in the United States reduces energy consumption and, correspondingly, power-plant emissions by 23 to 44% compared to advanced air-coupled heat pumps, and by 63 to 72% compared with electric-resistance heating and standard air conditioners (L'Ecuyer et al., 1993).

Environmental Constraints

Geothermal energy is one of the cleaner forms of energy now available in commercial quantities. Geothermal energy use avoids the problems of acid rain, and it greatly reduces greenhouse gas emissions and other forms of air pollution. Potentially hazardous elements produced in geothermal brines are removed from the fluid and injected back into the producing reservoir. Land use for geothermal wells, pipelines, and power plants is small compared with land use for other extractive energy sources such as oil, gas, coal, and nuclear. Geothermal development projects often coexist with agricultural land uses, including crop production or grazing. The average geothermal plant occupies only 400 m^2 for the production of each gigawatt hour over 30 years (Flavin and Lenssen, 1991). The low life-cycle land use of geothermal energy is many times less than the energy sources based on mining, such as coal and nuclear, which require enormous areas for the ore and processing before fuel reaches the power plant. Low-temperature applications usually are no more intrusive than a normal water well. Geothermal development will serve the growing need for energy sources with low atmospheric emissions and proven environmental safety.

All known geothermal systems contain aqueous carbon dioxide species in solution, and when a steam phase separates from boiling water, CO_2 is the dominant (over 90% by weight) **noncondensible gas.** In most geothermal systems, noncondensible gases make up less than 5% by weight of the steam phase. Thus, for each megawatt-hour of electricity produced in 1991, the average emission of carbon dioxide by plant type in the United States was 990 kg from coal, 839 kg from petroleum, 540 kg from natural gas, and 0.48 kg from geothermal flashed-steam (Colligan, 1993). Hydrogen sulfide can reach moderate concentrations of up to 2% by weight in the separated steam phase from some geothermal fields.

At The Geysers geothermal field in California, either the Stretford process or the incineration and injection process is used in geothermal power plants to keep H_2S emissions below 1 ppb (part per billion). Use of the Stretford process in many of the power plants at The Geysers results in the production and disposal of about 13,600 kg of sulfur per megawatt of electrical generation per year. Figure 7.8.1, shows a typical system used in the Stretford process at The Geysers (Henderson and Dorighi, 1989).

The incineration process burns the gas removed from the steam to convert H_2S to SO_2, the gases are absorbed in water to form SO_3^{-2} and SO_4^{-2} in solution, and iron chelate is used to form $S_2O_3^{-2}$ (Bedell and Hammond, 1987). Figure 7.8.2 shows an incineration abatement system (Bedell and Hammond, 1987). The major product from the incineration process is a soluble thiosulfate which is injected into the reservoir with the condensed water used for the reservoir pressure-maintenance program. Sulfur emissions for each megawatt-hour of electricity produced in 1991, as SO_2 by plant type in the United States was 9.23 kg from coal, 4.95 kg from petroleum, and 0.03 kg from geothermal flashed-steam (Colligan, 1993). Geothermal power plants have none of the nitrogen oxide emissions that are common from fossil fuel plants.

The waters in geothermal reservoirs range in composition from 0.1 to over 25 wt% dissolved solutes. The geochemistry of several representative geothermal fields is listed in Table 7.8.4. Temperatures up to 380°C have been recorded in geothermal reservoirs in the United States, and many chemical species have a significant solubility at high temperature. For example, all of the geothermal waters are saturated in silica with respect to quartz. As the water is produced, silica becomes supersaturated, and, if steam is flashed, the silica becomes highly supersaturated. Upon cooling, amorphous silica precipitates from the supersaturated solution. The high flow rates of steam and water from geothermal wells usually prevent silica from precipitating in the wells, but careful control of fluid conditions and residence time is needed to prevent precipitation in surface equipment. Silica precipitation is delayed in the flow stream until the water reaches a crystallizer or settling pond. There the silica is allowed to settle from the water, and the water is then pumped to an injection well.

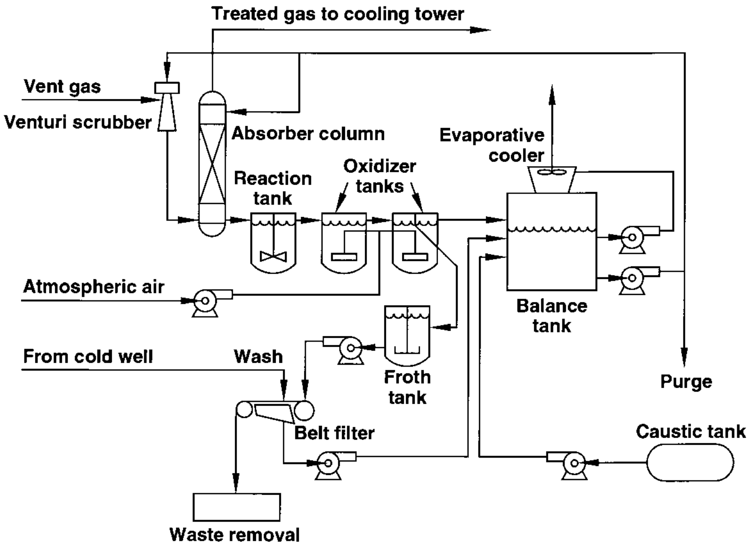

FIGURE 7.8.1 Typical equipment used in the Stretford process for hydrogen sulfide abatement at The Geysers geothermal field. (Based on the diagram of Henderson, J.M. and Dorighi, G.P., *Geotherm. Resour. Counc. Trans.*, 13, 593–595, 1989.)

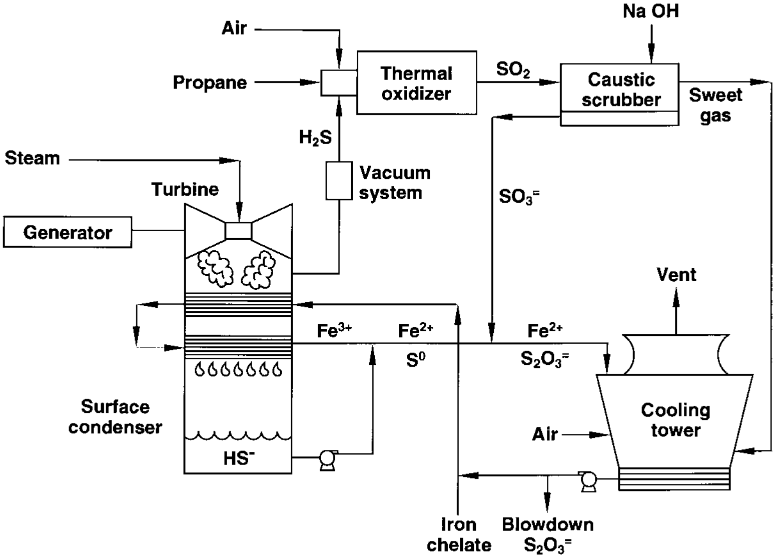

FIGURE 7.8.2 Equipment used in the incineration process for hydrogen sulfide abatement at The Geysers geothermal field. (Based on the diagram of Bedell, S.A. and Hammond, C.A., *Geotherm. Resour. Counc. Bull.*, 16(8), 3–6, 1987.)

Operating Conditions

For electrical generation, typical geothermal wells in the United States have production casing pipe in the reservoir with an inside diameter of 29.5 cm, and flow rates usually range between 150,000 and

TABLE 7.8.4 Major Element Chemistry of Representative Geothermal Wells

Field	T(°C)	Na	K	Li	Ca	Mg	Cl	F	Br	SO_4	Total[a] CO_2	Total[a] SiO_2	Total[a] B	Total[a] H_2S
Reykyavik, Iceland	100	95	1.5	<1	0.5	—	31	—	—	16	58	155	0.03	—
Hveragerdi, Iceland	216	212	27	0.3	1.5	0.0	197	1.9	0.45	61	55	480	0.6	7.3
Broadlands, N. Zealand	260	1050	210	1.7	2.2	0.1	1743	7.3	5.7	8	128	805	48.2	<1
Wairekai, New Zealand	250	1250	210	13.2	12	0.04	2210	8.4	5.5	28	17	670	28.8	1
Cerro Prieto, Mexico	340	5820	1570	19	280	8	10420		14.1	0	1653	740	12.4	700
Salton Sea, California	340	50400	17500	215	28000	54	155000	15	120	5	7100	400	390	16
Roosevelt, Utah[b]	<250	2320	461	25.3	8	<2	3860	6.8	—	72	232	563	—	—

[a] Total CO_2, Sio_2 etc. is the total CO_2 + HCO_2^- + CO_3^{2-} expressed as CO_2, silica + silicate as SIO_2, etc.

[b] From Wright (1991); remainder of data from Ellis and Mahon (1977).

350,000 kg/hr of total fluid (Mefferd, 1991). The geothermal fields contain water, or water and steam, in the reservoir, and production rates depend on the amount of boiling in the reservoir and the well on the way to the surface. The Geysers geothermal field in California has only steam filling fractures in the reservoir, and, in 1987 (approximately 30 years after production began), the average well flow had decreased to 33,000 kg/hr of dry steam (Mefferd, 1991) supplying the maximum field output of 2000 MW_2. Continued pressure decline has decreased the production.

In the Coso geothermal field near Ridgecrest, CA initial reservoir conditions formed a steam cap at 400 to 500 m depth, a two-phase (steam and water) zone at intermediate depth, and a liquid water zone at greater depth. Enthalpy of the fluid produced from individual wells ranges from 840 to 2760 kJ/kg (Hirtz et al., 1993), reservoir temperatures range from 200 to 340°C, and the fluid composition flowing from the reservoir into the different wells ranges from 100% liquid to almost 100% steam. Production wells have a wide range of flow rates, but the average production flow rate is 135,000 kg/hr (Mefferd, 1991). Much of the produced fluid is evaporated to the atmosphere in the cooling towers of the power plant, and only about 65% of the produced mass is available for injection into the reservoir at an average rate of 321,000 kg/hr (Mefferd, 1991).

The Salton Sea geothermal system in the Imperial Valley of southern California has presented some of the most difficult problems in brine handling. Water is produced from the reservoir at temperatures between 300 and 350°C and total dissolved solid concentrations between 20 and 25% by weight at an average rate of 270,000 kg/hr (Mefferd, 1991). When up to 20% of the mass of brine boils during production, the salts are concentrated in the brine causing supersaturation with respect to several solid phases. Crystallizers and clarifier and thickener tanks are needed to remove solids from the injection water. Figure 7.8.3 shows the flow stream for removal of solids from the vapor and brine (Signorotti and Hunter, 1992). Other power plants use the addition of acid to lower the pH and keep the solutes in solution (Signorotti and Hunter, 1992). The output from the crystallizers and clarifiers is a slurry of brine and amorphous silica. The methods used to dewater the salt and silica slurry from operations in the Salton Sea geothermal system are described by Benesi (1992). Approximately 80% of the produced water is injected into the reservoir at an average rate of 310,000 kg/hr.

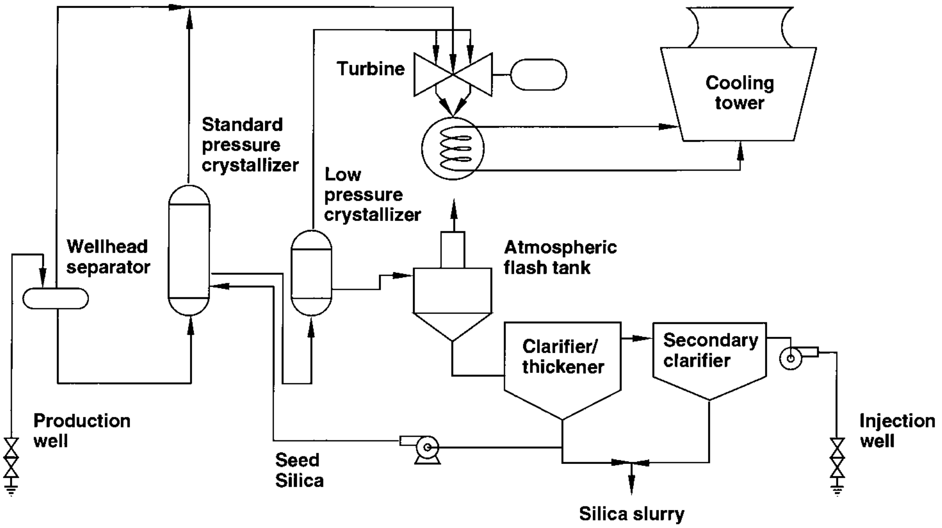

FIGURE 7.8.3 The flow stream for removal of solids from the vapor and brine in typical power plants in the Salton Sea geothermal field. (Modified from the diagram of Signorotti, V. and Hunter, C.C., *Geotherm. Resour. Counc. Bull.*, 21(9), 277–288, 1992).

Acknowledgments

This study was supported in part by the U.S. Department of Energy, Assistant Secretary for Energy Efficiency and Renewable Energy, Geothermal Division, under DOE Idaho Operations Office Contract DE-AC07-941D13223.

Defining Terms

Binary geothermal plant: A geothermal electric generating plant that uses the geothermal fluid to heat a secondary fluid that is then expanded through a turbine.

Identified accessible base: That part of the thermal energy of the Earth that is shallow enough to be reached by production drilling in the foreseeable future. *Identifed* refers to concentrations of heat that have been characterized by drilling or Earth science evidence. Additional discussion of this and other resource terms can be found in Muffler (1979).

Noncondensible gases: Gases exhausted from the turbine into the condenser that do not condense into the liquid phase.

References

Bedell, S.A. and Hammond, C.A. 1987. Chelation chemistry in geothermal H_2S abatement, *Geotherm. Resour. Counc. Bull.,* 16(8), 3–6.

Benesi, S.C. 1992. Dewatering of slurry from geothermal process streams. *Geotherm. Resourc. Counc. Trans.,* 16, 577–581.

Blackwell, D.B., Steele, J.L., and Carter, L.S. 1991. Heat-flow patterns of the North American continent; a discussion of the geothermal map of North America, in *Neotectonics of North America,* D.B. Slemmons, E.R. Engdahl, M.D. Zoback, and D.B. Blackwell, Eds., Geological Society of America, Boulder, CO, 4123–1436.

Colligan, J.G. 1993. U.S. electric utility environmental statistics, in *Electric Power Annual 1991,* U.S Department of Energy, Energy Information Administration, DOE/EIA-0348(91), Washington, D.C.

DiPippo, R. 1995. Geothermal electric power production in the United States: a survey and update for 1990–1994, in *Proceedings of the World Geothermal Congress,* 1995, International Geothermal, Association, Auckland, N.Z., 353–362.

Ellis, A.J. and Mahon, W.A.J. 1977. *Chemistry and Geothermal Systems,* Academic Press, New York.

Flavin, C. and Lenssen, N. 1991. Designing a sustainable energy system, in *State of the World, 1991, A Worldwatch Institute Report on Progress Toward a Sustainable Society,* W.W. Norton and Company, New York.

Freeston, D.H. 1995. Direct uses of geothermal energy 1995 — preliminary review, in *Proceedings of the World Geothermal Congress, 1995,* International Geothermal Association, Auckland, N.Z., 15–26.

Henderson, J.M. and Dorighi, G.P. 1989. Operating experience of converting a Stretford to a Lo-Cat(R) H_2S abatement system at Pacific Gas and Electric Company's Geysers unit 15, *Geotherm. Resour. Counc. Trans.,* 13, 593–595.

Hirtz, P., Lovekin, J., Copp, J., Buck, C., and Adams, M. 1993. Enthalpy and mass flowrate measurements for two-phase geothermal production by tracer dilution techniques, in *Proceedings, 18th Workshop on Geothermal Reservoir Engineering,* Stanford University, Palo Alto, CA, SGPTR-145, 17–27.

Huttrer, G.W. 1995. The status of world geothermal power production 1990–1994, in *Proceedings of the World Geothermal Congress,* 1995, International Geothermal Association, Auckland, N.Z., 3–14.

L'Ecuyer, M., Zoi, C., and Hoffman, J.S. 1993. *Space Conditioning — The Next Frontier,* U.S. Environmental Protection Agency, EPA430-R-93-004, Washington, D.C.

Lienau, P.J., Lund, J.W., and Culver, G.G. 1995. Geothermal direct use in the United States, update 1990–1995, in *Proceedings of the World Geothermal Congress, 1995,* International Geothermal Association, Auckland, N.Z., 363–372.

McLarty, L. and Reed, M.J. 1992. The U.S. geothermal industry: three decades of growth, *Energ. Sources,* 14, 443–455.

Mefferd, M.G. 1991. *76th Annual Report of the State Oil & Gas Supervisor: 1990,* California Division of Oil & Gas, Pub. 06, Sacramento, CA.

Muffler, L.J.P., Ed. 1979. Assessment of geothermal resources of the United States — 1978, U.S. Geological Survey Circular 790, Washington, D.C.

Rafferty, K. 1992. A century of service: the Boise Warm Springs water district system. *Geotherm. Resour. Counc. Bull.,* 21(10), 339–344.

Signorotti, V. and Hunter, C.C. 1992. Imperial Valley's geothermal resource comes of age, *Geotherm. Resour. Counc. Bull.,* 21(9), 277–288.

Truesdell, A.H. and White, D.E. 1973. Production of superheated steam from vapor-dominated reservoirs, *Geothermics,* 2, 145–164.

White, D.E., Muffler, L.T.P., and Truesdell, A.H. 1971. Vapor-dominated hydrothermal systems compared with hot-water systems, *Econ. Geol.,* 66(1), 75–97.

Wright, P.M. 1991. Geochemistry, *Geo-Heat Cent. Bull.,* 13(1), 8–12.

Further Information

Geothermal education materials are available from the Geothermal Education Office, 664 Hilary Drive, Tiburon, CA 94920.

General coverage of geothermal resources can be found in the proceedings of the Geothermal Resources Council's annual technical conference, *Geothermal Resources Council Transactions,* and in the Council's *Geothermal Resources Council Bulletin,* both of which are available from the Geothermal Resources Council, P.O. Box 1350, Davis, CA 95617–1350.

Current information concerning direct use of geothermal resources is available from the Geo-Heat Center, Oregon Institute of Technology, Klamath Falls, OR 97601.

A significant amount of geothermal information is also available on a number of geothermal home pages that can be found by searching on "geothermal" through the Internet.

8

Energy Conversion

John Kern
Siemens Power Generation

Steven I. Freedman
Gas Research Institute

David E. Klett
North Carolina A&T State University

Elsayed M. Afify
North Carolina State University

Roger E. A. Arndt
University of Minnesota

William B. Stine
California State Polytechnic University

Anthony F. Armor
Electric Power Research Institute

Chand K. Jotshi
AT&TL, Inc.

D. Yogi Goswami
Univeristy of Florida

Roberto Pagano (deceased)
University of Florida

James S. Tulenko
University of Florida

Thomas E. Shannon
University of Tennessee

Dale E. Berg*
Sandia National Laboratories

Carl J. Bliem (deceased)
CJB Consulting

Gregory L. Mines
Idaho National Engineering Laboratory

Kitt C. Reinhardt
Air Force Research Laboratory

Mysore L. Ramalingam
UES, Inc.

Jean-Pierre Fleurial
Jet Propulsion Laboratory/California Institute of Technology

William D. Jackson
HMJ Corporation

Alex Lezuo
Siemans Power Generation

---

* Sandia is a multiprogram laboratory operated by Sandia Corporation, a Lockheed Martin Company, for the United States Department of Energy under contract DE-AC04-94AK85000.

Desikan Bharathan
National Renewable Energy Laboratory
Frederica Zangrando
National Renewable Energy Laboratory

8.1 Steam Power Plant

John Kern

Introduction

This section provides an overview of the steam power cycle. There are noteworthy omissions in the section: site selection; fuel handling; activities related to civil engineering (such as foundations); controls; and nuclear power. Thermal power cycles take many forms, but the majority are fossil steam, nuclear, simple-cycle gas turbine, and combined cycle. Of those listed, conventional coal-fired steam is the predominant power producer — especially in developing countries that have indigenous coal or can import coal inexpensively. A typical steam power plant is shown in Figure 8.1.1.

Because the Rankine cycle is the overwhelmingly preferred process for steam power generation, it is discussed first. Topping and bottoming cycles, with one exception, are rare and mentioned only for completeness. The exception is the combined cycle, in which the steam turbine cycle is a bottoming cycle. Developed countries have been moving to the combined cycle because of relatively low capital costs when compared with coal-fired plants; its high thermal efficiency, which approaches 60%, and low emissions.

The core components of a steam power plant are boiler; turbine; condenser and feedwater pump; and generator. These are covered in successive subsections. The final subsection is an example of the layout and contents of a modern steam power plant.

As a frame of reference, the following efficiencies are typical for modern, subcritical, fossil fuel steam power plants. The specific example chosen has steam conditions of 2400 psia; 1000°F main steam temperature; and 1000°F reheat steam temperature: boiler thermal 92; turbine/generator thermal 44; turbine isentropic 89; generator 98.5; boiler feedwater pump and turbine combined isentropic 82; condenser 85; plant overall 34 (Carnot 64). Supercritical steam plants operate with main steam above the "critical" pressure for water where water and steam have the same density and no longer exist as separate phase states. They are generally used when higher efficiency is desired. Modern supercritical coal plants with main steam conditions of 3600 psia at 1050°F and 1050°F for reheat steam can exceed 40% in overall net plant efficiency.

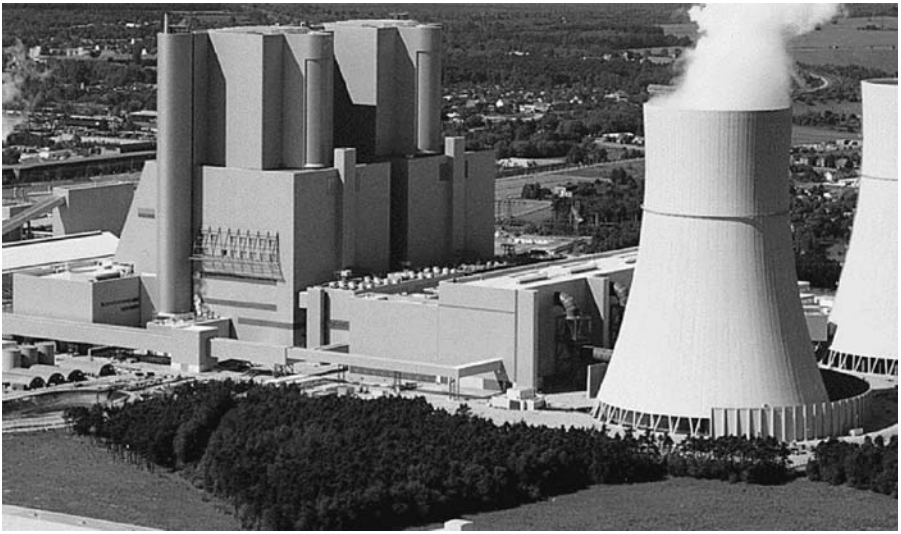

FIGURE 8.1.1 Modern steam power plant.

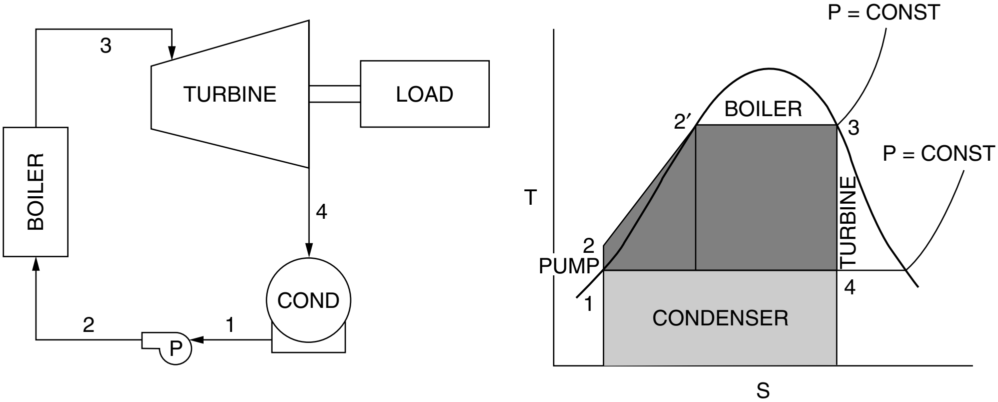

FIGURE 8.1.2 Basic Rankine cycle.

Nuclear power stations are so unique that they are worthy of a few closing comments. Modern stations are all large, varying from 600 to 1500 MW. The steam is low temperature and low pressure (~600°F and ~1000 psia), compared with fossil applications, and hovers around saturation conditions. Therefore, the boilers, superheater equivalent (actually a combined moisture separator and reheater), and turbines are unique to this cycle. The turbine generator thermal efficiency is around 36%.

Rankine Cycle Analysis

Modern steam power generation is based on the Rankine cycle and thermodynamics govern the ultimate performance of the cycle whether used in a coal-fired steam plant or the bottoming cycle of a combined-cycle plant. The basic, ideal Rankine cycle is shown in Figure 8.1.2. The ideal cycle comprises the processes from state 1:

1–2: Saturated liquid from the condenser at state 1 is pumped isentropically (i.e., $S_1 = S_2$) to state 2 and into the boiler.

2–3: Liquid is heated at constant pressure in the boiler to state 3 (saturated steam).

3–4: Steam expands isentropically (i.e., $S_3 = S_4$) through the turbine to state 4, where it enters the condenser as a wet vapor.

4–1: Constant-pressure transfer of heat in the condenser takes place to return the steam to state 1 (saturated liquid).

If changes in kinetic and potential energy are neglected, the total heat added to the Rankine cycle can be represented by the shaded area on the *T–S* diagram in Figure 8.1.2; the work done by this cycle can be represented by the crosshatching within the shaded area. The thermal efficiency of the cycle (η) is defined as the work (W_{NET}) divided by the heat input to the cycle (Q_H).

The Rankine cycle is preferred over the Carnot cycle for the following reasons:

- The heat transfer process in the boiler must be at constant temperature for the Carnot cycle, whereas in the Rankine cycle it is superheated at constant pressure. Superheating the steam can be achieved in the Carnot cycle during heat addition, but the pressure must drop to maintain constant temperature. This means the steam is expanding in the boiler while heat is being added, which is not a practical method.
- The Carnot cycle requires that the working fluid be compressed at constant entropy to boiler pressure. This would require taking wet steam from point 1′ in Figure 8.1.2 and compressing it to saturated liquid condition at 2′. A pump required to compress a mixture of liquid and vapor isentropically is difficult to design and operate. In comparison, the Rankine cycle takes the saturated liquid and compresses it to boiler pressure. This is more practical and requires much less work.

The efficiency of the Rankine cycle can be increased by utilizing a number of variations to the basic cycle. One such variation is superheating the steam in the boiler. The additional work done by the cycle is shown in the crosshatched area in Figure 8.1.3.

The efficiency of the Rankine cycle can also be increased by increasing the pressure in the boiler. However, increasing the steam generator pressure at a constant temperature will result in the excess moisture content of the steam exiting the turbine. To take advantage of higher steam generator pressures and keep turbine exhaust moistures at acceptably low values, the steam is expanded to some intermediate pressure in the turbine and then reheated in the boiler. Following reheat, the steam is expanded to the cycle exhaust pressure. The reheat cycle is shown in Figure 8.1.4.

Another variation of the Rankine cycle is the regenerative cycle, which involves the use of feedwater heaters. The regenerative cycle regains some of the irreversible heat lost when condensed liquid is pumped

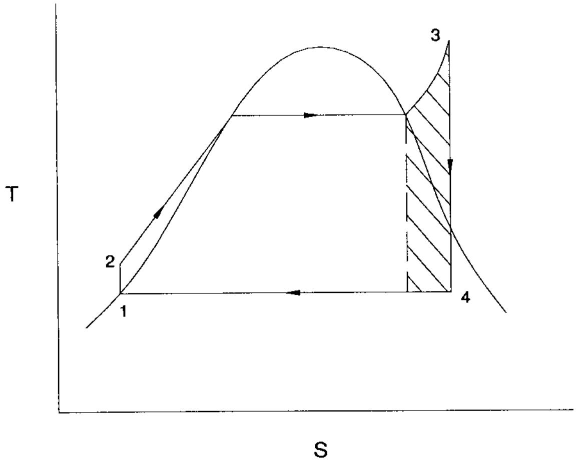

FIGURE 8.1.3 Rankine cycle with superheat.

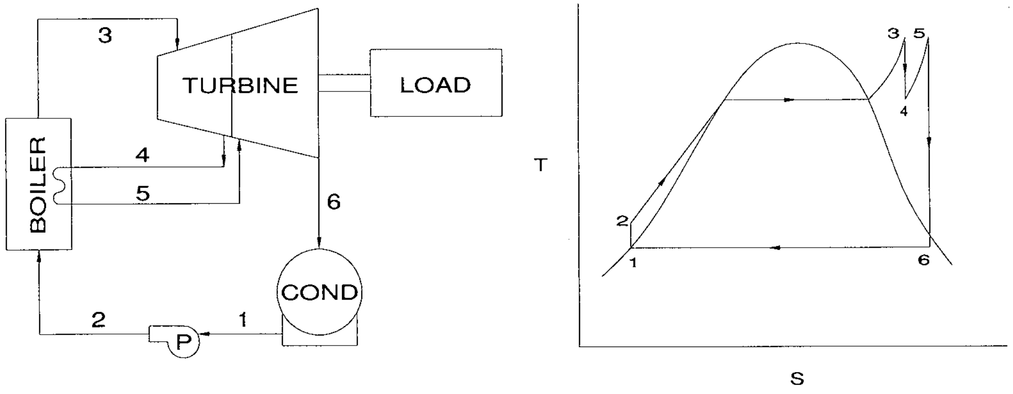

FIGURE 8.1.4 Rankine cycle with reheat.

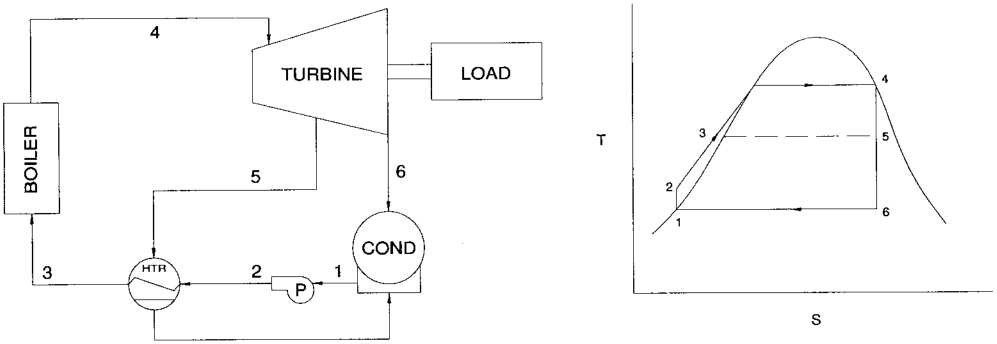

FIGURE 8.1.5 Rankine cycle with regeneration.

directly into the boiler by extracting steam from various points in the turbine and heating the condensed liquid with this steam in feedwater heaters. Figure 8.1.5 shows the Rankine cycle with regeneration.

The actual Rankine cycle is far from ideal because losses are associated with the cycle. They include piping losses due to friction and heat transfer; turbine losses associated with steam flow; pump losses due to friction; and condenser losses when condensate is subcooled. The losses in the compression (pump) and expansion process (turbine) result in an increase in entropy. Also, energy is lost in heat addition (boiler) and rejection (condenser) processes as they occur over a finite temperature difference.

Most modern power plants employ some variation of the basic Rankine cycle in order to improve thermal efficiency. For larger power plants, economies of scale will dictate the use of one or all of these variations to improve thermal efficiency. In most cases, power plants in excess of 200,000 kW will have 300°F superheated steam leaving the boiler reheat and seven to eight stages of feedwater heating.

References

Salisbury, J.K. 1950. *Steam Turbines and Their Cycles*, reprint 1974. Robert K. Krieger Publishing, Malabar, FL.

Van Wylen, G.J. and Sonntag, R.E. 1986. *Fundamentals of Classical Thermodynamics*, 3rd ed., John Wiley & Sons, New York.

Topping and Bottoming Cycles

Steam Rankine cycles can be combined with topping and/or bottoming cycles to form binary thermodynamic cycles. These topping and bottoming cycles use working fluids other than water. Topping cycles change the basic steam Rankine cycle into a binary cycle that better resembles the Carnot cycle and improves efficiency. For conventional steam cycles, state-of-the-art materials allow peak working fluid temperatures higher than the supercritical temperature for water. Much of the energy delivered into the cycle goes into superheating the steam, which is not a constant-temperature process. Therefore, a significant portion of the heat supply to the steam cycle occurs substantially below the peak cycle temperature.

Adding a cycle that uses a working fluid with a boiling point higher than water allows more of the heat supply to the thermodynamic cycle to be near the peak cycle temperature, thus improving efficiency. Heat rejected from the topping cycle is channeled into the lower-temperature steam cycle. Thermal energy not converted to work by the binary cycle is rejected to the ambient-temperature reservoir. Metallic substances are the working fluids for topping cycles. For example, mercury has been used as the topping cycle fluid in a plant that operated for a period of time but has since been dismantled. Significant research and testing has also been performed over the years toward the eventual goal of using other substances, such as potassium, sodium, or cesium, as a topping-cycle fluid, but none has proven to be commercially successful.

Steam power plants in a cold, dry environment cannot take full advantage of the low heat rejection temperature available. The very low pressure to which the steam would be expanded to take advantage of the low heat sink temperature would increase the size of the low-pressure (LP) turbine to such an extent that it is impractical or at least inefficient. A bottoming cycle that uses a working fluid with a vapor pressure higher than water at ambient temperatures (such as ammonia or an organic fluid) would enable smaller LP turbines to function efficiently. Thus, a steam cycle combined with a bottoming cycle may yield better performance and be more cost effective than a stand-alone Rankine steam cycle. However, again, these techniques are not at present commercially viable and are not being broadly pursued.

Further Information

Fraas, A.P. 1982. *Engineering Evaluation of Energy Systems*, McGraw–Hill, New York.

Horlock, J.H. 1992. *Combined Power Plants, Including Combined Cycle Gas Turbine (CCGT) Plants*, Pergamon Press, Oxford.

Lezuo, A. and Taud, R. 2001. Comparative evaluation of power plants with regard to technical, ecological and economical aspects, Proceedings of ASME Turbo Expo 2001, New Orleans.

Steam Boilers

A boiler, also referred to as a steam generator, is a major component in the plant cycle. It is a closed vessel that efficiently uses heat produced from the combustion of fuel to convert water to steam. Efficiency is the most important characteristic of a boiler because it has a direct bearing on electricity production. Boilers are classified as drum-type or once-through (Figure 8.1.6). Major components of boilers include an economizer, superheaters, reheaters, and spray attemperators.

Drum-Type Boilers

Drum-type boilers depend on constant recirculation of water through some of the components of the steam–water circuit to generate steam and keep the components from overheating. These boilers circulate water by natural or controlled circulation.

Natural Circulation Boilers. Natural circulation boilers use the density differential between water in the downcomers and steam in the waterwall tubes for circulation.

Controlled Circulation Boilers. Controlled circulation boilers use boiler-water-circulating pumps to circulate water through the steam–water circuit.

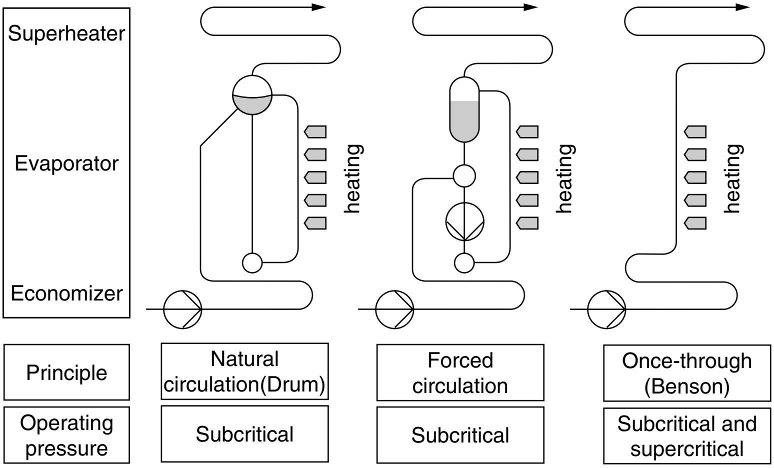

FIGURE 8.1.6 Boiler principles.

Once-Through Boilers

Once-through boilers convert water to steam in one pass through the system rather than re-circulating through the drum. Current designs for once-through boilers use a spiral-wound furnace to assure even heat distribution across the tubes.

Major Boiler Components

- *Economizer.* The economizer is the section of the boiler tubes in which feedwater is first introduced into the boiler and flue gas is used to raise the temperature of the water.
- *Steam drum (drum units only).* The steam drum separates steam from the steam–water mixture and keeps the separated steam dry.
- *Superheaters.* Superheaters are bundles of boiler tubing located in the flow path of the hot gases created by the combustion of fuel in the boiler furnace. Heat is transferred from the combustion gases to the steam in the superheater tubes. Superheaters are classified as primary and secondary. Steam passes first through the primary superheater (located in a relatively cool section of the boiler) after leaving the steam drum. There the steam receives a fraction of its final superheat and then passes through the secondary superheater for the remainder.
- *Reheaters.* Reheaters are bundles of boiler tubes that are exposed to the combustion gases in the same manner as superheaters.
- *Spray attemperators.* Attemperators, also known as desuperheaters, are spray nozzles in the boiler tubes between the two superheaters. These spray nozzles supply a fine mist of pure water into the flow path of the steam to prevent tube damage from overheating. Attemperators are provided for the superheater and the reheater.

Worldwide, the current trend is to use higher temperatures and pressures to improve plant efficiency, which in turn reduces emissions. Improvements in high-temperature materials such as T-91 tubing provide high-temperature strength and improved corrosion resistance permitting reliable operation in advanced steam cycles. In addition, the development of reliable once-through Benson type boilers has resolved most of the operational problems experienced with first- and second-generation supercritical plants.

Steam plant boilers burning coal require advanced exhaust gas clean-up systems to meet today's strict environmental emissions limits. A typical plant burning high-sulfur eastern coal will have an SCR (selective catalytic reduction) for NO_x control, a precipitator for particulate control, and a wet limestone scrubber to reduce SO_x. A typical plant burning low-sulfur western coal might include an SCR, a baghouse filter for particulate control, and a dry scrubber for SO_x reduction.

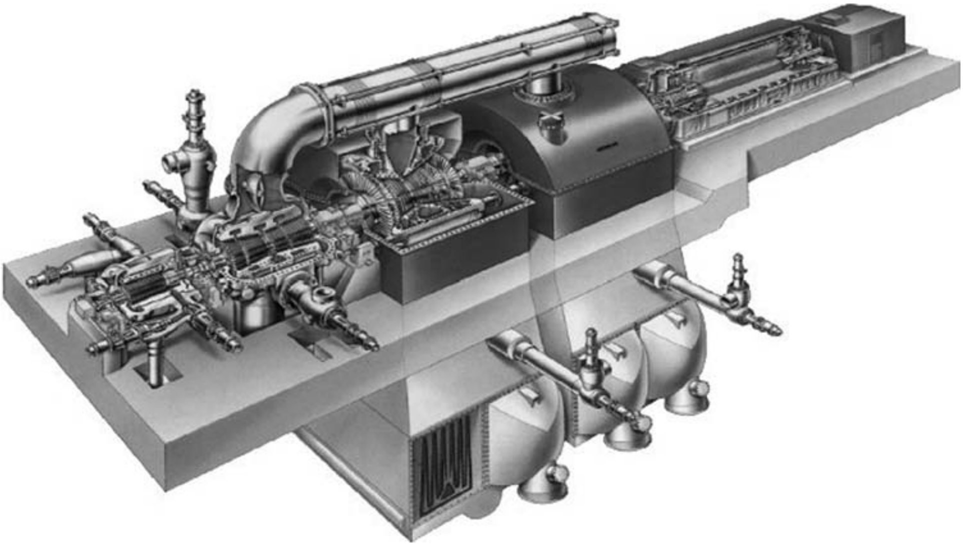

FIGURE 8.1.7 Modern steam turbine generator for a coal-fired steam plant.

Steam Turbines

General

Each turbine manufacturer has unique features in its designs that affect efficiency, reliability, and cost. However, the designs appear similar to a non-steam-turbine engineer. Figure 8.1.7 shows a modern steam turbine generator as used in a coal-fired steam power plant. Steam turbines for power plants differ from most prime movers in at least three ways:

- All are extremely high powered, varying from about 70,000 to 2 million hp, and require a correspondingly large capital investment, which puts a premium on reliability.
- Turbine life is normally between 30 and 40 years with minimal maintenance.
- Turbines spend the bulk of their lives at constant speed, normally 3600 or 1800 rpm for 60-Hz operation.

These three points dominate the design of the entire power station, particularly of the steam turbine arrangement and materials. Figure 8.1.8 shows the dramatic increase of steam turbine power output for one manufacturer over the past 50 years. This is reasonably typical of the industry.

In an earlier subsection it was shown that high steam-supply temperatures make for more efficient turbines. In Europe and Japan, the trend is to use increasingly higher steam-supply temperatures to reduce fuel cost and emissions.

Blading

The most highly stressed component in steam turbines is the blades. Blades are loaded by centrifugal and steam-bending forces and also harmonic excitation (from nonuniform circumferential disturbances in the blade path). All blades are loaded by centrifugal and steam-bending loads, and smaller blades are designed to run when the harmonic excitation is resonant with the natural modes of the blade. If harmonic excitation is permitted on very long blades, however, the blades become impractically large. Fortunately, because the turbine runs at constant speed, the blade modes can be tuned away from resonant conditions so that the harmonic loads are significantly reduced. This forms a split in blade design, commonly referred to as tuned and untuned blading.

Blades guide steam throughout the turbine in as smooth and collision-free a path as possible. Collisions with blades (incidence) and sudden expansions reduce the energy available for doing work. Until recently,

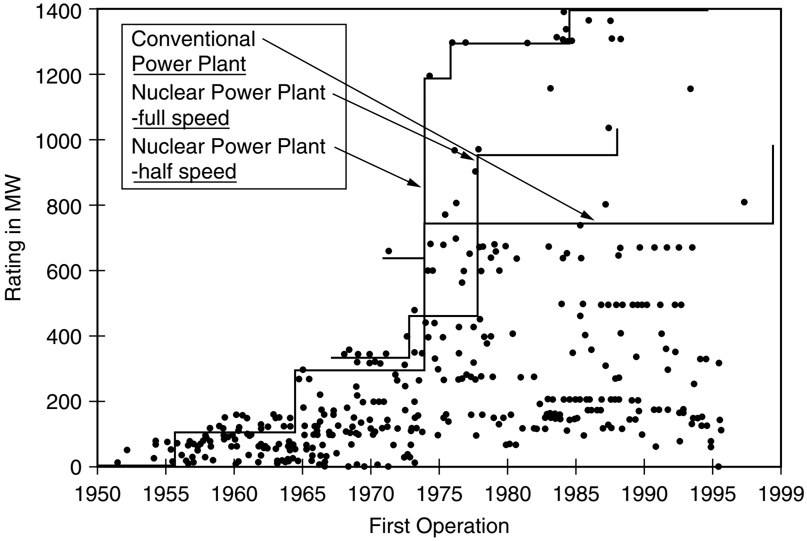

FIGURE 8.1.8 Increase of steam turbine power.

designers would match flow conditions with radially straight blades (called parallel-sided blades). Turbine physics does not recognize this convenience for several reasons. The most visually obvious is the difference in tangential velocity between blade hub and tip. The latest blades address the full three-dimensional nature of the flow by curving in three dimensions (bowed blades). Three dimensional design techniques allow for better matching of the flow (and area) conditions and now, with the use of numerical control machine tools to make it more cost competitive, three-dimensional blading is used extensively in many modern turbines. Examples of three-dimensional and parallel-sided blades are shown in Figure 8.1.9.

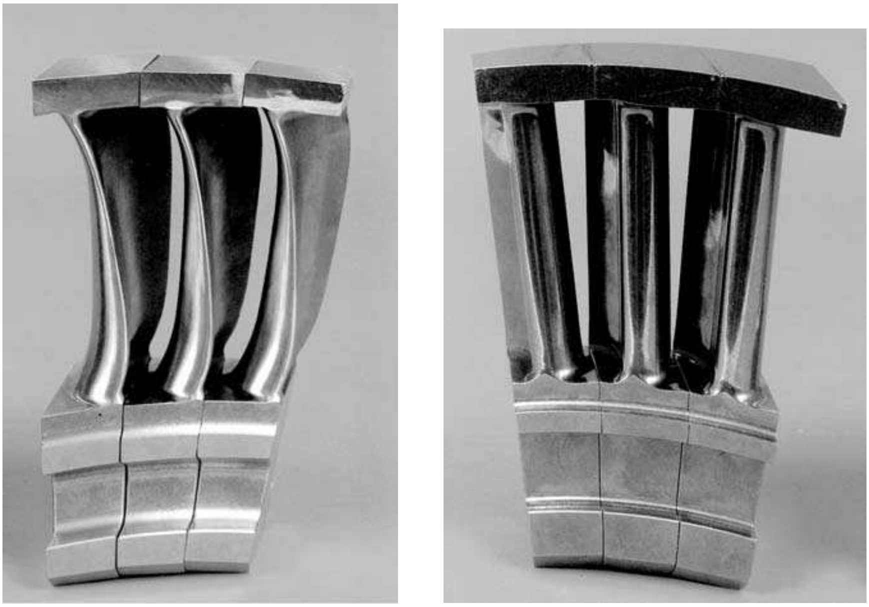

FIGURE 8.1.9 Typical steam turbine blades.

Rotors

After blades, steam turbine rotors are the second most critical component in the machine. Rotor design must take into account

- The large high-strength alloy steel rotor forging that must have uniform chemistry and material properties
- Centrifugal force from the rotor body and the increased centrifugal pull from the attached blades
- The need to have high resistance to brittle fracture, which could occur when the machine is at high speed and the material is still not up to operating temperature
- Creep deformation of the high-pressure (HP) and intermediate-pressure (IP) rotors under steady load while at high temperature

The life cycle is further complicated by transient fatigue loads that occur during power changes and start-up. Two further events are considered in rotor design: torsional and lateral vibrations caused by harmonic steam and electrical loads. As with tuned blades, this is normally addressed by tuning the primary modes away from resonance at full running speed.

Choosing the Turbine Arrangement

Because the turbine shaft would be too long and flexible if it were built in one piece with all the blades in sequence, the rotor is separated into supportable sections. The "cuts" in the shaft result in HP (high pressure), IP (intermediate pressure), and LP (low pressure) cylinders. Manufacturers address the grouping of cylinders in many different ways, depending upon steam conditions. It is common practice to combine HPs and IPs into one cylinder for subcritical units in the power range of about 250 to 600 MW. One manufacturer's grouping, shown in Figure 8.1.10, is fairly representative of the industry.

So far, the text has discussed the steam flow as though it expanded monotonically through the turbine. This is usually not the case for two reasons. First, the most common steam conditions would cause steam exiting the last row of blades to be very wet, creating excessive erosion. Second, thermal efficiency can be raised by removing the steam from the turbine, reheating, and then returning it to the blade path; this increases the "average" heat supply temperature and reduces moisture levels in the turbine exhaust. The turbine position for reheat is normally between the HP and IP turbines.

Type	Basic Configuration	Power
HP-IP-LP (with reheat)	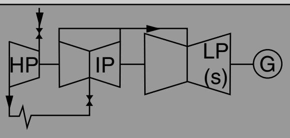	200–1200 MW
HP/IP-LP (with reheat)	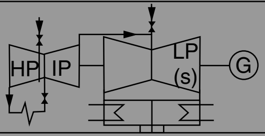	160–700 MW
HP-IP/LP (with reheat)	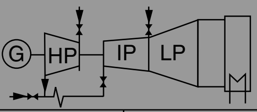	120–260 MW
Single Case (without reheat)	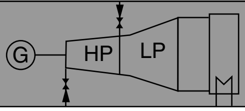	50–300 MW

FIGURE 8.1.10 Steam turbine product combinations.

There is one further geometric arrangement. Cylinders need not be all on one shaft with a single generator at the end. A cross-compound arrangement exists in which the steam path is split into two separate parallel paths with a generator on each path. Commonly, the split will be with paths of HP–LP generator and IP–LP generator. Torsional and lateral vibrations are more easily analyzed with shorter trains, which make the foundation more compact. The primary shortcoming is the need for two generators, two control systems, and a larger power house — all of which increase overall plant cost.

Historically, steam turbines have been split into two classes, reaction and impulse, as explained in Basic Power Cycles. This difference in design makes an observable difference between machines. Impulse turbines have fewer, wider stages than reaction machines. As designs have been refined, the efficiencies and lengths of the machines are now about the same. For a variety of reasons, the longer blades in the LP ends are normally reaction designs. Because each stage may now be designed and fabricated separately, the line between impulse and reaction turbines is diminishing with most manufacturers supplying blading that has characteristics of both technologies. Turbine blading is broadly split between machines as shown in the following table.

	Cylinder			
			LP	
	HP	IP	Short Blades	End Blade(s)
Reaction turbines	Reaction	Reaction	Reaction	Reaction
Impulse turbines	Impulse	Impulse	Impulse	Reaction

Materials

Materials are among the most variable of all turbine parts, with each manufacturer striving to improve performance by using alloying and heat-treatment techniques. It follows that accurate generalizations are difficult. Even so, the following table is reasonably representative for steam turbines with 1000 to 1050°F inlet temperatures:

Item	Common Material Description								
High-temperature HP and IP blades	Moderate- and cold-temperature stator blades	Moderate-temperature rotating blades	Cold LP rotating blades	High-temperature rotors	Low-temperature rotors	Hot	LP	High-temperature bolting	Cold bolting
Mod'd SS403	SS304	SS403	SS403 or 17/4 PH	1CrMoV, occasionally 10Cr	3.5 NiCrMoV	1.25Cr or 2.25Cr	Carbon, steel	SS422	B16

Cylinders and Bolting

These items are relatively straightforward, except for the very large sizes and precision required for the castings and fabrications. In a large HP–IP cylinder, the temperature and pressure loads split between an inner and outer cylinder. In this case, finding space and requisite strength for the bolting presents a challenge for the designer.

Valves

The turbine requires many valves for speed control, emergency control, drains, hydraulics, bypasses, and other functions. Of these, four valves are distinguished by their size and duty: throttle or stop; governor or control; reheat stop; and reheat interceptor. The throttle, reheat stop, and reheat interceptor valves normally operate fully open, except in some control and emergency conditions. Their numbers and design are selected for the appropriate combination of redundancy and rapidity of action. The continuous control of the turbine is accomplished by throttling the steam through the governor valve. This irreversible process detracts from cycle efficiency. In more modern units, the efficiency loss is reduced by reducing the boiler pressure (normally called sliding pressure) rather than throttling across the valves when reducing output.

Further Information

Japikse, D. and Nicholas, C.B. 1994. *Introduction to Turbomachinery*, Concepts ETI, Norwich, VT.

Kutz, M. 1986. *Mechanical Engineers' Handbook*, John Wiley & Sons, New York.

Stodola, A. and Loewenstein, L.C. 1927. *Steam and Gas Turbines*, reprint of 6th ed., 1945, Peter Smith, New York.

Heat Exchangers, Pumps, and Other Cycle Components

Heat Exchangers

Heaters. The two classifications of condensate and feedwater heaters are the open or direct contact heater and the closed or shell-and-tube heater.

Open Heaters. In an open heater, the extraction or heating steam comes in direct contact with the water to be heated. Although open heaters are more efficient than closed heaters, each requires a pump to feed the outlet water ahead in the cycle. This adds cost and maintenance and increases the risk of water induction to the turbine, making the closed heater the preferred heater for power plant applications.

Closed Heaters. These heaters employ tubes within a shell to separate the water from the heating steam (see Figure 8.1.11). They can have three separate sections in which the heating of the feedwater occurs.

First is the drain cooler section where the feedwater is heated by the condensed heating steam before cascading back to the next-lower-pressure heater. The effectiveness of the drain cooler is expressed as the drain cooler approach (DCA), which is the difference between the temperature of the water entering the heater and the temperature of the condensed heating steam draining from the heater shell. In the second section (condensing section), the temperature of the water is increased by the heating steam condensing around the tubes. In the third section (desuperheating section), the feedwater reaches its final exit temperature by desuperheating the extraction steam. Performance of the condensing and superheating sections of a heater is expressed as the terminal temperature difference (TTD). This is the difference between the saturation temperature of the extraction steam and the temperature of the feedwater exiting the heater. Desuperheating and drain cooler sections are optional depending on the location of the heater in the cycle (for example, desuperheating is not necessary in wet extraction zones) and economic considerations.

The one exception is the deaerator (DA), which is an open heater used to remove oxygen and other gases that are insoluble in boiling water. The DA is physically located in the turbine building above all other heaters, and the gravity drain from the DA provides the prime for the boiler feed pump (BFP).

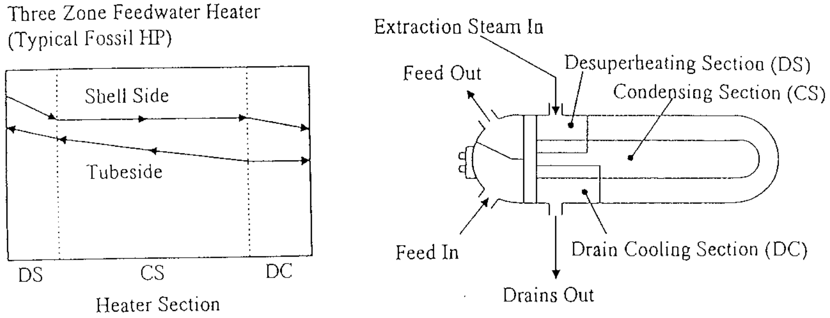

FIGURE 8.1.11 Shell-and-tube feedwater heater.

Two other critical factors considered in heater design and selection are (1) venting the heater shell to remove any noncondensable gases; and (2) the protection of the turbine caused by malfunction of the heater system. Venting the shell is required to avoid air-binding a heater, which reduces its performance. Emergency drains to the condenser open when high water levels are present within the shell to prevent back-flow of water to the turbine, which can cause serious damage. Check valves on the heating steam line are also used with a water-detection monitor to alert operators to take prompt action when water is present.

Condenser. Steam turbines generally employ surface-type condensers comprising large shell-and-tube heat exchangers operating under vacuum. The condenser (1) reduces the exhaust pressure at the last-stage blade exit to extract more work from the turbine; and (2) collects the condensed steam and returns it to the feedwater-heating system. Cooling water circulates from the cooling source to the condenser tubes by large motor-driven pumps. Multiple pumps, each rated less than 100% of required pumping power, operate more efficiently at part load and are often used to allow for operation if one or more pumps are out of service. Cooling water is supplied from a large heat sink water source, such as a river, or from cooling towers. The cooling in the cooling tower is assisted by evaporation of 3 to 6% of the cooling water. Airflow is natural draft (hyperbolic towers) or forced draft. Noncondensable gases are removed from the condenser with a motor-driven vacuum pump or, more frequently, steam jet air ejectors, which have no moving parts.

When adequate cooling water is not available, a dry condenser can be used. This device uses large motor-driven fans to move air across a large radiator-like heat exchanger to condense the steam at ambient temperature. Air condensers are significantly more expensive than wet condensers and generally decrease overall plant efficiency, so they are used only when necessary.

Pumps

Condensate Pump. Condensate is removed from the hot well of the condenser and passed through the LP heater string via the condensate pump. Typically, two or more vertical (larger units) or horizontal (medium and small units) motor-driven centrifugal pumps are located near the condenser hot well outlet. Depending on the size of the cycle, condensate booster pumps may be used to increase the pressure of the condensate on its way to the DA.

Feedwater Booster Pump. The DA outlet supplies the feedwater booster pump, which is typically a motor-driven centrifugal pump. This pump supplies the required suction head for the BFP (boiler feed pump).

Boiler Feed Pump. These pumps are multiple-stage centrifugal pumps that, depending on the cycle, can be turbine or motor driven. BFP turbines (BFPT; Figure 8.1.12), are single-case units that draw extraction steam from the main turbine cycle and exhaust to the main condenser. Typical feed pump turbines require 0.5% of the main unit power at full-load operation. Multiple pumps rated at 50 to 100% each are typically used to allow the plant to operate with one pump out of service.

With the increasing reliability of large electric motors, many plant designers are now using motors to drive the feed pumps for plants up to about 800 MW. Although the cycle is not quite as efficient as using a turbine drive, the overall plant capital cost is significantly less when motor BFP drives are used.

Further Information

British Electricity International. 1992. *Modern Power Station Practice,* 3rd ed., Pergammon Press, Oxford.
Lammer, H.B. and Woodruff. 1967. *Steam Plant Operation,* 3rd ed., McGraw-Hill, New York.
Powell, C. 1955. *Principles of Electric Utility Operation,* John Wiley & Sons, New York.

Generators

The electric generator converts rotating shaft mechanical power of the steam turbine to three-phase electrical power at voltages between 11.5 and 27 kV, depending upon the power rating. The generator

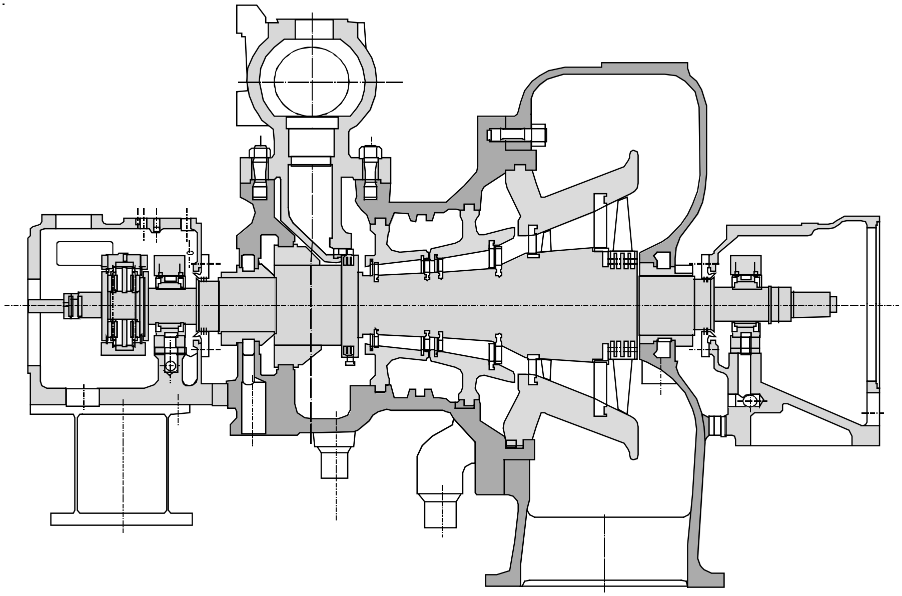

FIGURE 8.1.12 Boiler feed pump turbine.

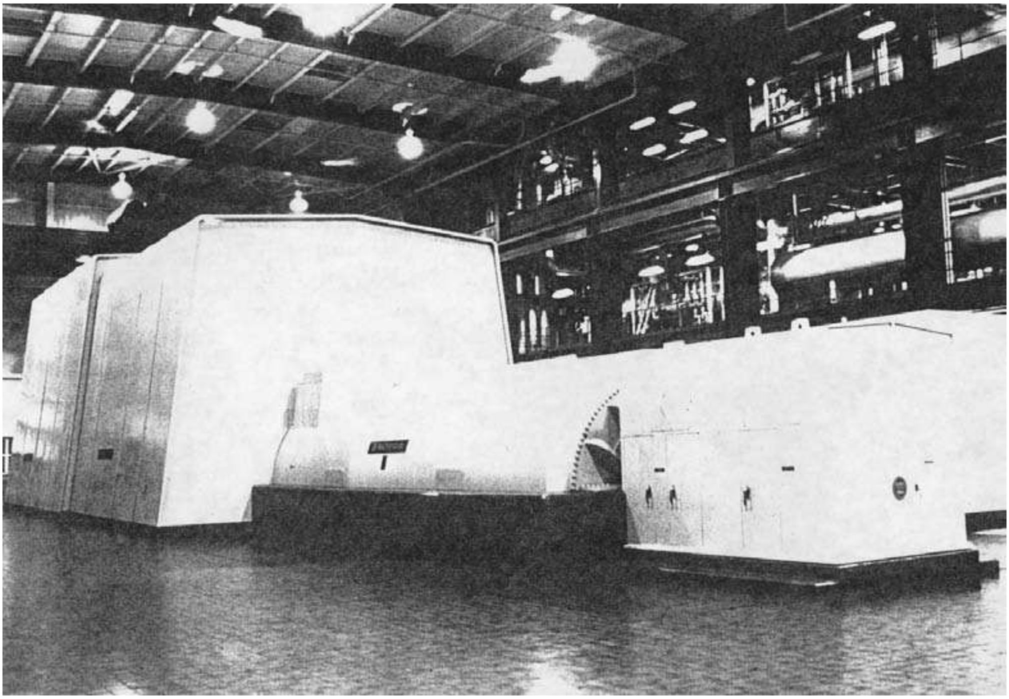

FIGURE 8.1.13 Generator and exciter.

comprises a system of ventilation, auxiliaries, and an exciter. Figure 8.1.13 shows an installed hydrogen-cooled generator and brushless exciter of about 400 MW. Large generators greater than 25 MW usually have a solid, high-strength steel rotor with a DC field winding embedded in radial slots machined into the rotor. The rotor assembly then becomes a rotating electromagnet that induces voltage in stationary conductors embedded in slots in a laminated steel stator core surrounding the rotor (see Figure 8.1.14).

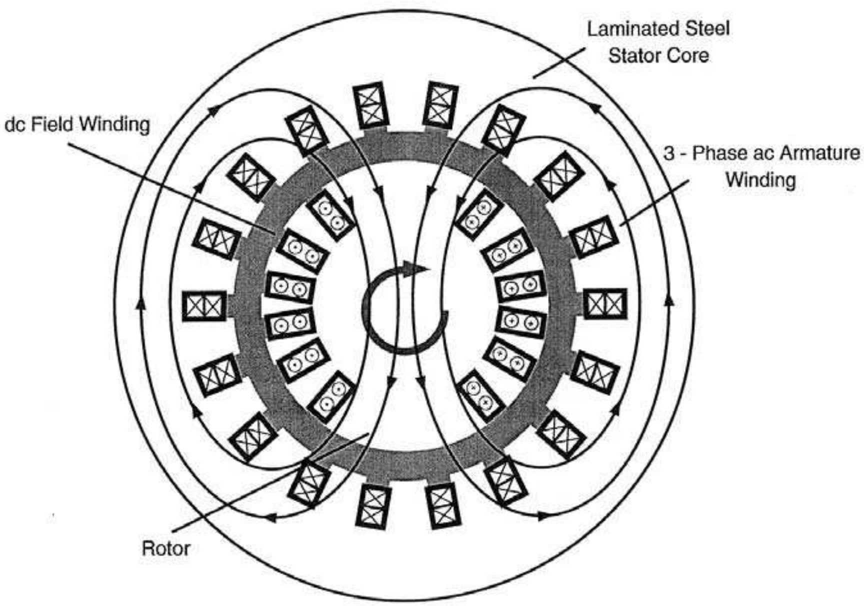

FIGURE 8.1.14 Generator magnetic paths.

The stator conductors are connected to form a three-phase AC armature winding. The winding is connected to the power system, usually through a step-up transformer. Most steam turbines driven by fossil-fired steam use a two-pole generator and rotate at 3600 rpm in 60-Hz countries and 3000 rpm in 50-Hz countries. Most large steam turbines driven by nuclear steam supplies use a four-pole generator and rotate at 1800 or 1500 rpm for 60 and 50 Hz, respectively.

Generator Ventilation

Cooling the active parts of the generator is of such importance that generators are usually classified by the type of ventilation they use. Air-cooled generators are used commonly up to 300 MW. Some use ambient air, drawing air through filters, and others recirculate air through air-to-water heat exchangers. Above 250 MW, most manufacturers offer hydrogen for overall cooling. Hydrogen has 14 times the specific heat of air and is 14 times less dense. This contributes to much better cooling and much lower windage and blower loss. The frame must be designed to withstand the remote circumstance of a hydrogen explosion and requires shaft seals. Hydrogen is noncombustible with purities greater than 70%. Generator purities are usually maintained well above 90%. Depending upon the manufacturer, generators with ratings above 500 MW generally have water-cooled stator winding; the remaining components are cooled with hydrogen.

Generator Auxiliaries

Large generators must have a lubrication oil system for the shaft journal bearings. Major components of this system are pumps, coolers, and a reservoir. In most cases, the turbine and generator use a combined system. For hydrogen-cooled generators, a shaft seal system and hydrogen supply system are needed. The shaft seal system usually uses oil pumped to a journal seal ring at a pressure somewhat higher than the hydrogen pressure. Its major components are pumps, coolers, and reservoir, similar to the lubrication system. The hydrogen supply system consists of a gas supply and regulators. A CO_2 supply is used to purge the generator when going from air to hydrogen or vice versa to avoid a combustible hydrogen–air mixture. The stator winding water supply again uses pumps, coolers, and a reservoir. It requires demineralizers to keep the water nonconducting because the water flow provides a path between the high-voltage conductors and ground. Depending upon the design approach, it may also include chemistry or oxygen content control to avoid corrosion in the winding cooling passages.

Excitation

The rotor field winding must have a DC source. Many generators use rotating "collector" rings with stationary carbon brushes to transfer DC current from a stationary source, such as a thyristor-controlled "static" excitation system, to the rotor winding. A rotating exciter, known as a brushless exciter, is used for many applications. It is essentially a small generator with a rotating rectifier and transfers DC current through the coupling into the rotor winding without the need for collectors and brushes.

Further Information

Fitzgerald, A.E., Kingsley, C.F., and Umans, S.D. 2002. *Electric Machinery*, 6th ed., McGraw–Hill, New York.

IEEE C50.13-2003 Standard for Cylindrical-Rotor 50 and 60 Hz Synchronous Generators Rated 10 MVA and Above.

IEEE 67-1990 (R1995) Guide for Operation and Maintenance of Turbine Generators.

IEEE 37.102-1995 Guide for AC Generator Protection.

Nelson, R.J. et al. 2000. Matching the capabilities of modern large combustion turbines with air- and hydrogen-cooled generators, Proceedings of the American Power Conference, Chicago, April 2000.

Modern Steam Power Plant — an Example

The purpose of a power plant is to generate electric power. It does so by converting chemical energy contained in fuel into thermal energy in steam; thermal energy in steam into mechanical energy in the turbine/generator; and mechanical energy in the turbine/generator into electrical energy. Operating efficiency of a typical modern steam plant is about 35 to 45%. The primary losses result from (1) heat sink losses in the condenser; (2) boiler losses; and (3) electrical losses. Steam plant capacities range from 50 to 1600 MW; however, modern plants are being designed for more than 250 MW due to energy demands, system load requirements, and economies of scale in the larger centralized stations.

Major Steam Plant Components

Steam plants comprise three major components (1) boiler; (2) turbine; and (3) main steam condenser. The boiler and turbine have been covered in earlier subsections and neither will be repeated here. A graphic of the entire fluid or work cycle is shown in Figure 8.1.15.

Condenser. The condenser (also discussed earlier) is a large heat exchanger that takes the LP turbine exhaust steam and converts it back to water. The steam passes over a bundle of tubes located in the condenser and is cooled by the circulating water that passes through the tubes. The steam is condensed into water drops and collected in the condenser hot well. The condensate is delivered from the condenser hot well through the condensate and feedwater systems and back to the boiler, where it becomes steam again.

Fuels. Coal, oil, and gas are used to fuel fossil plants. Although coal possesses the highest carbon content, it also possesses the highest sulfur, nitrogen, and ash content, thereby requiring air pollution-control equipment. Controlling these pollutants requires:

- Installation of scrubbers for sulfur control
- Overfire air or gas recirculation for in-furnace nitrous oxides (NO_x) control
- Selective catalytic reduction (SCR) for postcombustion NO_x control
- Electrostatic precipitators (ESP) or baghouse for fly ash control
- Pneumatic, hydraulic, or mechanical ash-handling systems for bottom ash removal

Fuel oil and natural gas are chiefly composed of compounds of hydrogen and carbon (hydrocarbons) with very low percentages of sulfur, nitrogen, and ash; they do not require pollution-control equipment.

Power Plant System

Power plants comprise the following main systems: fuel handling; air handling; gas handling; main steam; reheat steam; auxiliary steam; extraction steam; condensate; feedwater; circulating water; and air removal.

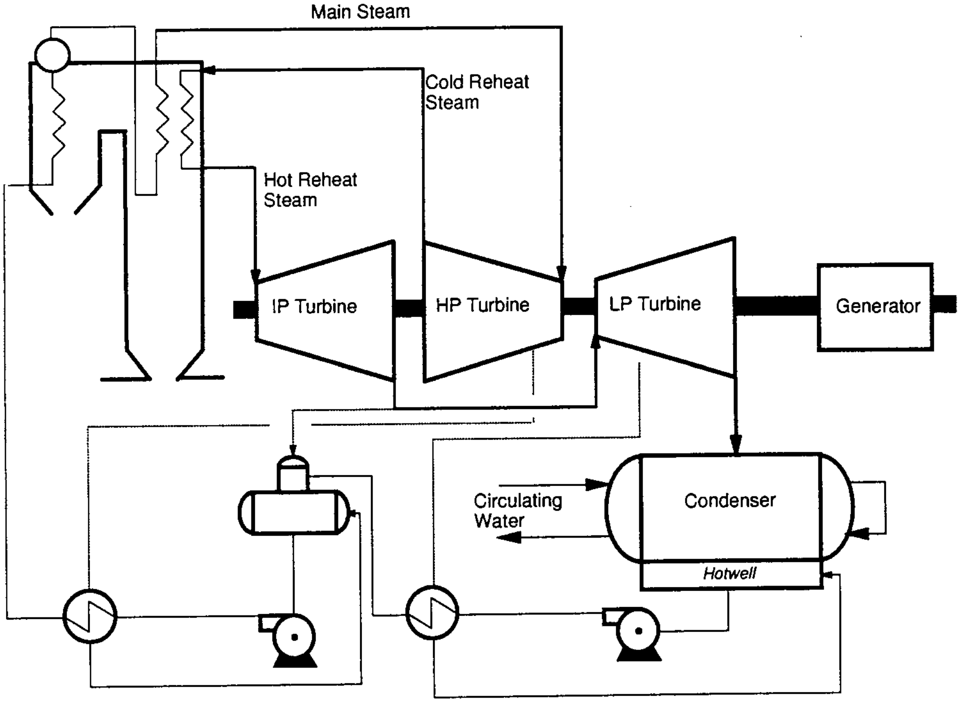

FIGURE 8.1.15 Steam power plant schematic.

Fuel-Handling System. The fuel-handling system consists of delivery, transfer, and processing. Fuel is delivered to the plant from the fuel source by truck, boat, rail (coal and oil), or pipeline (oil and gas). Once delivered, the fuel is transferred from the delivery point to various locations throughout the fuel-handling system. For coal and oil, the fuel is transferred to storage or sent directly to the boiler. For gas, the fuel is directly transferred to the boiler without any storage. Prior to delivery to the boiler for burning, the fuel must be processed so that it will readily mix with air and burn completely. Coal must be broken down into smaller pieces by crushers and then reduced to a fine powder in pulverizers. Oil requires steam, air, or mechanical atomization. Gas requires no processing.

Air/gas-Handling Systems. Steam plants are classified as pressurized or balance draft. Pressurized systems include forced-draft fans to provide the necessary air for fuel; an air heater to transfer heat from the exit gas to the inlet air; and a wind box in which the air is stored and then directed to the individual burner ports. A balanced draft system includes all of the components of the pressurized systems and induced-draft fans to exhaust the combustion products from the boiler, thus maintaining the furnace under slightly negative pressure. Balanced draft is the preferred method because it is better suited to the major exhaust gas clean-up systems now required on all new steam plants.

Main Steam System. The main steam system controls and regulates the flow of high-temperature, HP steam generated in the boiler furnace as it moves from the boiler to the turbine. The components in this system include main steam piping, safety valves, main steam stop valve, and turbine control valve.

Reheat Steam System. The reheat steam system improves overall plant efficiency by increasing the energy of steam that has been exhausted from the HP turbine. Steam from the hot reheat steam system is delivered to the IP turbine. The components of the reheat steam system are cold reheat piping; the reheater section of the boiler; hot reheat piping; safety relief valves; reheat stop valves; reheater desuperheater; and intercept valves.

Auxiliary Steam System. The auxiliary steam system directs and regulates auxiliary steam from the cold reheat line to the auxiliary steam users. The auxiliary steam system users are typically steam/air preheating coils; outdoor freeze protection/heat tracing; turbine seals; and plant heating.

Extraction Steam System. The extraction steam system directs and regulates the flow of the extraction steam from the turbine to the feedwater heaters, turbine driven BFP, and auxiliary steam system. The extraction steam heats the feedwater that flows through the heaters, thus improving overall plant efficiency. In large steam plants, seven or eight stages of feedwater heating are typical.

Condensate System. The condensate system consists of condensate pumps, LP feedwater heaters, and DA. The condensate pumps remove condensate from the main condenser hot well, increase condensate pressure, and deliver it through the LP heaters to the DA. During this process, the condensate is heated, deaerated, and chemically treated.

Feedwater System. The feedwater system consists of BFPs, HP feedwater heaters, piping, and valves. The boiler feedwater pumps deliver water from the DA storage tank, through the HP heaters, and into the boiler. Feedwater is supplied at sufficient quantities and pressure to satisfy unit demands during start-ups, shutdowns, and normal operation. The BFP is also the primary source of spray water for the superheater and reheater desuperheaters for control of the main and reheat steam temperatures. BFPs can be turbine or motor driven. Booster pumps may be required to provide additional net positive suction head (NPSH) to the main and start-up BFPs for plants designed with a low DA setting.

Circulating Water System. The circulating water system pumps cooling water through the condenser tubes at sufficient capacity, temperature, and pressure to absorb the latent heat in the LP exhaust steam. Circulating water systems are classified as once-through systems, when a large water source is available, or recirculating systems employing cooling towers. In once-through systems, circulating water pumps deliver water from the plant water supply (river, lake, or ocean) through the condenser tubes to absorb latent heat in the exhaust steam. Water flows through the system once and is returned to its source. The major parts of this system are screens, pumps, expansion valves, and piping. In recirculating systems, the cooling tower cools the heated circulating water from the main condenser by exposing it to air. The cooled water is stored in a basin located below the tower and is then circulated back through the system by the circulating water pumps.

Air Evacuation System. The air evacuation system removes air and noncondensable gases in the main steam condenser and helps maintain the vacuum created by the volume reduction of the condensing steam during normal operation. The system also establishes a normal vacuum in the condenser prior to turbine start-up.

Further Information

Singer, J.G., Ed. 1991. *Combustion Fossil Power*, 4th ed., Combustion Engineering, Inc., Windsor, CN.

Termühlen, H. and Emsperger W. 2003. *Clean and Efficient Coal-fired Power Plants*. ASME Press, New York.

8.2 Gas Turbines

Steven I. Freedman

Overview

Gas turbines are steady-flow power machines in which a gas (usually air) is compressed, heated, and expanded for the purpose of generating power. The term *turbine* is the component which delivers power from the gas as it expands; it is also called an expander. The term *gas turbine* refers to a complete power machine. The term gas turbine is often shortened to simply turbine, which can lead to confusion with the term for an expander.

The basic thermodynamic cycle on which the gas turbine is based is known as the Brayton cycle. Gas turbines may deliver their power in the form of torque or one of several manifestations of pneumatic power, such as the thrust produced by the high-velocity jet of an aircraft propulsion gas turbine engine.

Gas turbines vary in size from large, 250,000-hp utility machines, to small 5 hp, automobile and motorcycle turbochargers. Microturbines, 25 to 250 kW, recuperated gas turbines are now being sold.

Gas turbines are used in electric power generation, propulsion, and compressor and pump drives. The most efficient power generation systems in commercial service are gas turbine combined cycle plants with power-to-fuel energy efficiencies of more than 54% (higher heating value basis) or 59% (lower heating value basis). Systems five points higher in efficiency are now under development and are being offered commercially, and systems of even higher efficiency are considered feasible.

History

The fourth quarter of the 19th century was one of great innovation in power machinery. Along with the spark-ignited gasoline engine, the compression-ignited diesel engine, and the steam turbine, engineers applied their skills to several hot-air engines. Charles Curtis received the first U.S. patent for a complete gas turbine on June 24, 1895. Aegidius Elling built the first gas turbine in 1903, which produced 11 hp.

The first commercial stationary gas turbine engineered for power generation was a 4000-kW machine built by the Brown Boverei Company in Switzerland in 1939.

Aviation provided the impetus for gas turbine development in the 1930s. In Germany, Hans von Ohain's first engine ran in March 1937. Frank Whittle's first engine ran in England in April 1937. The first airplane flight powered by a gas turbine jet engine was in Germany on August 27, 1939. The first British airplane powered by a gas turbine flew on May 15, 1941.

A Swiss railway locomotive using a gas turbine was first run in 1941. The first automobile powered by a gas turbine was a British Rover, which ran in 1950. And, in 1956, a gas turbine-powered Plymouth car drove over 3000 miles on a coast-to-coast exhibition trip in the United States.

Fuels and Firing

The first heat engines were external combustion steam engines. The combustion products never came in contact with the working fluid, so ash, corrosive impurities, and contaminants in the fuel or exhaust did not affect the internal operation of the engine. Later, internal combustion (piston) engines were developed. In these engines, a mixture of air and fuel burned in the space enclosed by the piston and cylinder walls, thereby heating the air. The air and combustion products formed the working fluid, and contacted internal engine parts.

Most gas turbines in use today are internal combustion engines and consequently require clean fuels to avoid corrosion and erosion of critical turbine components. Efforts were made to develop gas turbines rugged enough to burn residual or crude oil. However, due to the higher efficiencies obtainable by burning extremely clean fuel at higher temperatures, there is little current interest in using fuel other than clean gas and distillate oil in gas turbines. Interest in the use of coal and residual oil is now centered on gasifying and cleaning these fuels prior to use.

A few external combustion gas turbines have been built for use with heavy oil, coal, nuclear reactor, radioisotope, and solar heat sources. However, none of these has become commercial. The added cost and pressure drop in the fired heater make externally fired gas turbines expensive. Because the working fluid temperature cannot be greater than that of the walls of the fired heater, externally fired gas turbines are substantially less efficient than modern internal combustion gas turbines with internally cooled blades.

The only internal combustion coal-fired gas turbine of current interest is the pressurized fluidized bed (PFB) combustion system. In the PFB, air discharged from the compressor of the turbine is used to fluidize a bed of limestone or dolomite in which coal is burned. The bed is maintained at modest temperature so that the ash in the coal does not form sticky agglomerates. Fortuitously, this temperature range also minimizes NO_x formation and allows capture of sulfur dioxide (SO_2) in the bed. Bed temperature is maintained in the desired range by immersed boiler tubes. Carryover fly ash is separated from gaseous combustion products by several stages of cyclone inertial separators and, in some cases, ceramic filters. The power turbine is modified to accommodate the combustion products, which after mechanical cleanup may still contain particles as large as 3 to 5 μm.

The most common gas turbine fuels today are natural gas and distillate oil. To avoid hot corrosion by alkali metal sulfates, the total sodium and potassium content of the fuel is typically limited to less than 5 ppm. Liquid fuels may also contain vanadium, which also causes corrosion. Fuels must be ash-free because particles larger than 3 to 5 μm rapidly erode blades and vanes.

Efficiency

The term *efficiency* is applied not only to complete power generation machines but also to the individual compression, expansion, and combustion processes that make up the gas turbine operating cycle. Different definitions of efficiency apply in each case. In an **expansion process**, the **turbine efficiency** is the ratio of the actual power obtained to the maximum power that could have been obtained by expanding the gas reversibly and adiabatically between the same initial and final pressures.

Gas turbines typically involve high-speed gas flows, so appreciable differences exist between the static pressure and temperature and the total (or stagnation) pressure and temperature. Care must be taken in interpreting data to be sure that the pressure condition — static or stagnation — at each component interface is properly used.

Irreversible losses in one stage of an expansion process show up as heat (increased temperature) in later stages and add to the power delivered by such stages. Hence, a distinction exists between the polytropic efficiency (used to describe the efficiency of a process of differential pressure change) and the adiabatic (complete pressure change) efficiency. The efficiency of compressors and turbines based on their inlet and outlet pressures is called the isentropic or adiabatic efficiency. Unfortunately, both terms are reported in the literature, and confusion can exist regarding the meaning of the term *efficiency.*

Combustion efficiency in well-engineered and well-built internal combustion gas turbines is almost always close to 100%. The combustion losses appear as carbon monoxide, unburned hydrocarbons, and soot, which are typically below 50 ppm, with clean fuels.

The **gas turbine or engine efficiency** is the ratio of the net power produced to the energy in the fuel consumed. The principal gas turbine fuels are liquid and gaseous hydrocarbons (distillate oil and natural gas) which have high hydrogen content. Consequently, the term *engine efficiency* needs to be qualified as to whether it is based on the higher or the lower heat content of the fuel (the difference between the two being the latent heat of condensation of the water vapor in the products of combustion). Utility fuel transactions are traditionally based on higher heating values, and most engine publications presume the lower heating value of the fuel as the efficiency basis. In the case of natural gas fuel, the higher heating value (HHV) efficiency is greater than the lower heating value (LHV) efficiency by 10% of the value of the HHV efficiency.

Engineers analyze gas turbine machines to evaluate improvements in component performance, in higher temperature and pressure ratio designs, and in innovative cycles. Ideal case cycle calculations generally assume the following:

- Air (with either constant or temperature-dependent specific heats) is the working fluid in both turbine and compressor (with equal mass flows);
- Air is the working fluid in both turbine and compressor but with the turbine mass flow greater by the amount of fuel used.

Components are modeled with or without frictional pressure drops, and heat transfer effectiveness may be ideal (unity) or actual, depending on the purpose of the analysis. Use of compressor air for cooling of high-temperature structure, nozzles, and blades are modeled in varying degrees of complexity. Two-dimensional temperature profiles or pattern factors exist. Component inlet and exit total pressure losses should be included in cycle analyses.

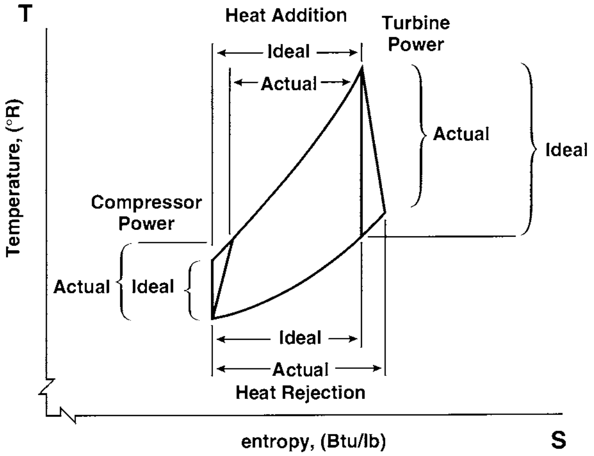

FIGURE 8.2.1 T-S diagram for a simple cycle illustrating the differences in compressor and turbine power for ideal (100% efficient) and actual components.

Gas Turbine Cycles

Gas turbine cycles are usually plotted on temperature-entropy (T-S) coordinates. Readers unfamiliar with entropy are referred to the chapter on thermodynamics. The T-S plot is useful in depicting cycles because in an adiabatic process — as is the case for turbines and compressors — the power produced or consumed is the product of the mass flow and the enthalpy change through the process. Thus, temperature difference, which is found on a T-S plot, is proportional to the power involved. Additionally, the heat exchange in a process involving zero power — such as a combustor or heat exchanger — is the product of the absolute temperature and the entropy change. On a T-S chart, the area under a process line for a combustor or heat exchanger is the heat exchanged.

The slope of a constant-pressure line on a T-S diagram is proportional to the absolute temperature. Consequently, lines of constant pressure become steeper, and diverge as the temperature increases. This illustrates that more work is obtained expanding a gas between fixed pressures at higher temperatures than at lower temperatures. Figure 8.2.1 shows a comparison of the process of an ideal and an actual simple cycle gas turbine on a T-S diagram. The increased compressor power consumption and the decreased turbine power generation in the actual cycle are shown to provide an understanding of the differences that component efficiencies make on machine performance.

The incremental amount of power produced per differential pressure change in the gas is given by

$$d(\text{Power/mass flow}) = -RT\, dp/p$$

Two phenomena are illustrated by this equation. First, power is proportional to the absolute temperature of the gas. Second, power is proportional to the percent change in pressure. This latter point is important in understanding the effect of pressure losses in cycle components. In heat exchangers, the proper measure of power lost is the percent pressure drop.

Cycle Configurations

The basic Brayton cycle consists of a compressor, a combustor or burner, and an expander. This configuration is known as the simple cycle. In idealizing the actual cycle, combustion is replaced by constant-pressure heat addition, and the cycle is completed by the assumption that the exhaust to ambient pressure could be followed by a zero-pressure-loss cooling to inlet conditions.

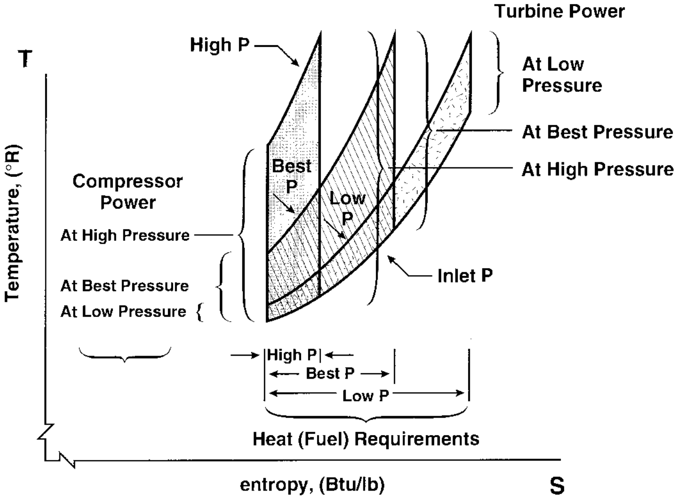

FIGURE 8.2.2 T-S diagram illustrating the power and heat (fuel) requirements at low, best, and high cycle pressures.

A T-S diagram of the simple cycle gas turbine with an upper temperature limit set by metallurgical conditions is illustrated in Figure 8.2.2 for cycles of low, medium, and high pressure ratios. The heat addition is only by fuel combustion, simplified here to be without mass addition or change in specific heat of the working fluid.

It is seen that the low-pressure-ratio cycle requires a large heat addition, which leads to a low efficiency, and the high-pressure-ratio cycle has turbine power output barely greater than the compressor power requirement, thereby leading to low net output and low efficiency. At intermediate pressure ratios, the turbine power output is substantially higher than the compressor power requirement, and the heat addition is modest in comparison with the difference between the turbine and compressor powers. There is an optimum pressure ratio for maximum efficiency, which is a function mainly of the maximum gas temperature in the machine, and to a lesser extent, by the component efficiencies, internal pressure losses, and the isentropic exponent. There is another optimum pressure ratio for maximum specific power (power per unit mass flow).

As the achievable turbine inlet temperature increases, the optimum pressure ratios (for both maximum efficiency and maximum specific power) also increase. The optimum pressure ratio for maximum specific power is at a lower pressure level than that for maximum efficiency for all cycles not employing a recuperator. For cycles with a recuperator, the reverse is true: maximum efficiency occurs at a lower pressure ratio than maximum specific power. Heavy-duty utility and industrial gas turbines are typically designed to operate near the point of maximum specific power, which approximates lowest equipment cost, while aeroderivative gas turbines are designed to operate near the point of maximum efficiency, approximating highest thrust. Figure 8.2.3 shows a performance map (efficiency as a function of power per unit of air flow) for a simple cycle gas turbine for two turbine inlet temperatures. It is seen that at higher temperature, both the efficiency and specific power increase, as well as the optimum pressure ratios for both the maximum efficiency and maximum specific power conditions.

Aircraft gas turbines operate at temperatures above the limit of turbine materials by using blades and vanes with complex internal cooling passages. The added cost is economically justified because these machines can command high prices in the aircraft propulsion marketplace. Aeroderivative engines have higher pressure ratios, higher efficiencies, and lower exhaust temperatures than heavy-duty machines. The stationary power markets served by aeroderlvative gas turbines are principally pipeline compressor stations and oil/gas production wells. Aeroderivative gas turbines also are economically advantageous for intermediate-duty electric power generation applications.

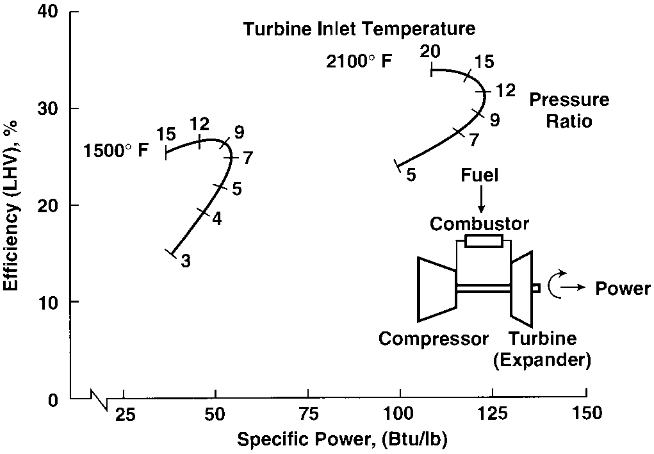

FIGURE 8.2.3 Performance map of a simple cycle gas turbine.

Components Used in Complex Cycles

Recuperators and **regenerators** recover heat from the turbine exhaust and use it to preheat the air from the compressor before it enters the combustor, thereby saving fuel. This heat transfer is shown in Figure 8.2.4. While recuperators and regenerators are quite similar thermodynamically, they are totally different in design. Recuperators are conventional heat exchangers in which hot and cold gases flow steadily on opposite sides of a solid (usually metal) wall.

Regenerators are periodic-flow devices. Fluid streams flow in opposite directions through passages in a wheel with heat storage walls. The wheel rotates, transferring heat from one stream to the other. Regenerators usually use a nest of very small parallel passages oriented axially on a wheel which rotates between hot and cold gas manifolds. Such regenerators are sometimes used in industrial processes for furnace heat recovery, where they are referred to as heat wheels. Because regenerators are usually more compact than recuperators, they were used in experimental automotive gas turbines. The difficulty in

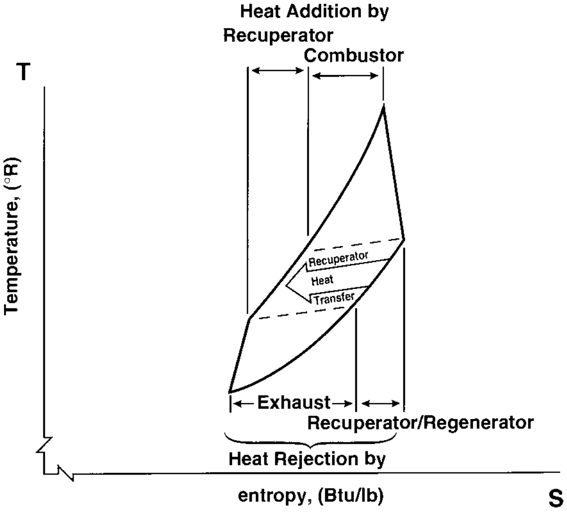

FIGURE 8.2.4 T-S diagram illustrating the heat transfer from the turbine exhaust to the compressor discharge accomplished by a recuperator/regenerator.

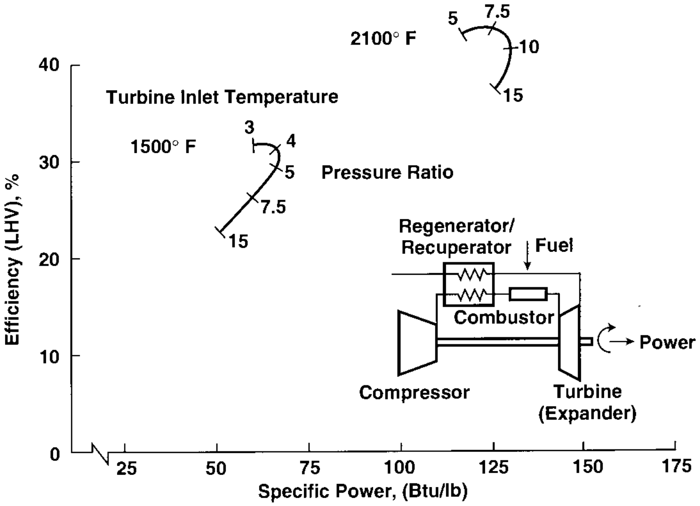

FIGURE 8.2.5 Performance map of a regenerative cycle gas turbine.

using regenerators on gas turbines intended for long life is that the two gas streams are at very different pressures. Consequently, the seals between the manifolds and the wheel must not leak excessively over the maintenance overhaul interval of the engine. If they do, the power loss due to seal leakage will compromise engine power and efficiency. Figure 8.2.5 shows a performance map for the regenerative gas turbine cycle for two temperatures. It is seen that as the temperature increases, the efficiency, specific power, and optimum pressure ratio all increase.

Current research on the recovery of gas turbine exhaust heat includes examination of thermochemical recuperation, where exhaust heat is used to effect a chemical reaction (reforming) of the fuel with steam, thereby increasing the heating value of the fuel. Although this process is feasible, research is underway to determine if it is practical and economic.

Industrial process compressors frequently use **intercoolers** to reduce compressor power when the compressor has a high pressure ratio and operates for a large number of hours per year. When analyzing cycles with intercoolers, the added pressure drops in the compressor interstage entrance and exit diffuser and scroll and the pressure drop in the intercooler itself should be included.

In a similar manner, turbine reheat can be used to increase the power output of a large-pressure-ratio turbine. This is the thermodynamic principle in turbojet afterburner firing. Turbine reheat increases power, but decreases efficiency unless the turbine exhaust heat is used for additional power generation, as is the case with a combined cycle, or is used with a recuperator to preheat combustor inlet air.

Intercoolers and reheat burners increase the temperature difference between the compressor and turbine discharges, thereby increasing the opportunity to use a recuperator to preheat the burner air with exhaust heat. An intercooled recuperated (ICR) machine is at present in development. The efficiency decrease at part load of an ICR gas turbine is much less than of conventional simple cycle machines.

Small gas turbines have uncooled turbine blades as a result of the difficulty in manufacturing extremely small cooling passages in small blades. This results in low efficiencies, making it difficult for such turbines to compete with high-volume production (low-cost) reciprocating (piston) engines. The low-pressure-ratio recuperated cycle has greater efficiency, although at higher cost. The recuperated cycle is finding favor in programs for small (under 300-kW) gas turbines used for stationary power.

Because of their compact size, low emissions, and light weight, gas turbines are also being considered for hybrid engine-battery vehicles. Proponents are pursuing the low-pressure-ratio recuperated gas turbine as the way to obtain high efficiency and low emissions in a compact power plant.

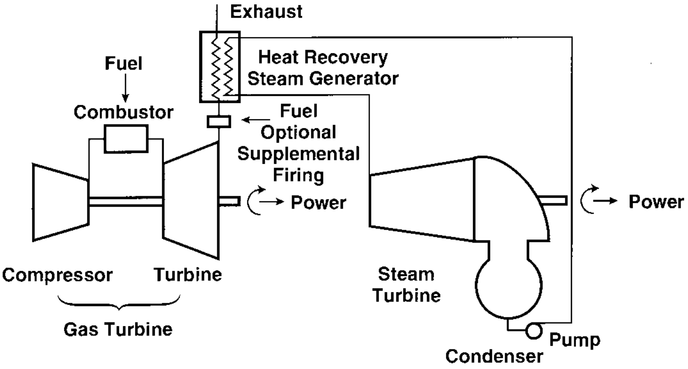

FIGURE 8.2.6 Combined (Brayton-Rankine) cycle.

An ingenious gas turbine cycle is the closed cycle in which the working fluid is sealed in the system. Heat is added to the fluid with an externally fired heater and extracted from the fluid through heat exchangers. The working fluid may be any gas, and the density of the gas may be varied — to vary the power delivered by the machine — by using a gas storage cylinder connected to the compressor discharge and inlet. The gas storage system is at an intermediate pressure so that it can discharge gas into the lowest pressure point in the cycle and receive gas from the highest pressure point in the cycle. About ten such units were built between 1938 and 1968; however, in spite of its sophistication, the added cost and low efficiency inherent in external combustion systems prevented this system from becoming economic.

The exhaust from a gas turbine is quite hot and can be used to raise steam, which can then be used to generate additional power with a steam turbine. Such a compound gas turbine-steam turbine system is referred to as a **combined cycle.** Figure 8.2.6 shows a schematic diagram of the equipment in a combined cycle. Because the exhaust of heavy-duty machines is hotter than that of aeroderivative machines, the gain in combined cycle system efficiency through use of the steam bottoming cycle described above is greater for heavy-duty machines than for aeroderivatives. Indeed, heavy-duty machines are designed with two criteria in mind: achieving lowest cost for peaking (based on the simple cycle configuration) and achieving highest efficiency in combined cycle configuration for baseload use. The optimum pressure ratios for these two system configurations are very close. Steam bottoming cycles used in combined cycles usually use steam at multiple pressure levels to increase efficiency.

Another system in which the power and efficiency of a gas turbine is increased through the use of steam is the **steam-injected gas turbine**. Figure 8.2.7 shows a schematic diagram of a steam-injected gas turbine cycle. Here the turbine exhaust flows into a heat recovery steam generator (HRSG) operating at a pressure somewhat higher than the compressor discharge pressure. The steam is introduced into the gas turbine at the combustor. The steam-air mixture then passes into the turbine, where the augmented mass flow increases the power produced by the turbine. Additional fuel is required by the combustor because the steam must be heated from the HRSG delivery temperature to the combustor discharge temperature. Typical turbines can accommodate only a limited additional mass flow — from 5 to 15%, depending on the design of the original gas turbine. Steam-injected gas turbines enable the host to use the steam for industrial purposes, space heating, or for the generation of additional power.

A group of cycles under consideration for development involve the use of **adiabatic saturators** to provide steam at compressor discharge pressure to augment greatly the mass flow through the turbine, and consequently increase cycle power and efficiency. In the adiabatic saturator, water flows in a counter-current path to the compressor discharge air in a mass transfer tower. Such equipment is often used in the chemical processing industries. The saturated air is preheated in a turbine exhaust heat recuperator. This cycle is called the **humid air turbine**, or HAT, cycle. The HAT cycle is particularly useful in using

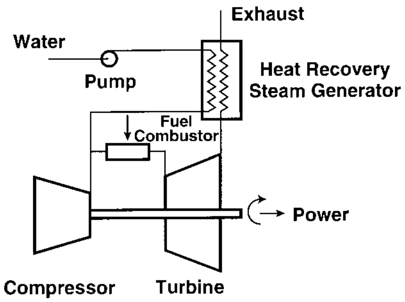

FIGURE 8.2.7 Steam-injected gas turbine.

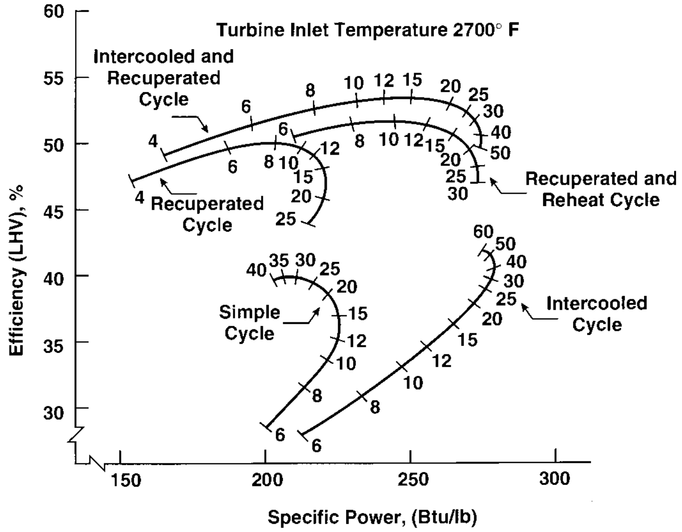

FIGURE 8.2.8 Specific power (Btu/lb).

the low-temperature heat generated in coal-gasification-fueled gas turbine power plants. As the mass flow through the turbine is significantly augmented, engineers can no longer use the expansion turbine which was matched to the compressor in a conventional simple cycle gas turbine.

Figure 8.2.8 shows performance maps for the gas turbine cycles of major interest for a turbine inlet temperature typical of new products. Intercooling increases the specific power appreciably when compared with a simple cycle; however, such improvement requires an increase in pressure ratio. Recuperated cycles have considerably higher efficiency than similar cycles without recuperation. The effect of pressure ratio on the performance of recuperated cycles is opposite to that of similar cycles without recuperation. For recuperated cycles, the pressure ratio for maximum efficiency is considerably lower than for maximum specific power. Performance maps such as these are used in screening cycle alternatives for improved performance. Individual curves are generated for specific component performance values for use as a guide in developing new or improved machines.

Upper Temperature Limit

Classically, gas turbine engineers often spoke of a metallurgical limit in reference to maximum turbine inlet temperature. Later, turbine vane and blade cooling became standard on large machines. This situation creates a temperature difference between the combustion products flowing through the turbine and the turbine blade wall. Thus, because heat can be removed from the blades, the turbine can be operated with a combustion gas temperature higher than the metallurgical limit of the blade material. As a rule, the blades and vanes in new large gas turbines contain complex internal passages, through which up to 20% of compressor discharge air is directed. The cooling air first flows through internal convective cooling passages, then through impingement passages, where the air is directed at the blade and vane walls, and finally through small holes in the blade, where it is used to provide a low-temperature film over the blade surface. This film cooling of the surface reduces heat transfer to the blade.

The design of blade and vane cooling passages is an extremely competitive endeavor because greater cooling enables use of higher combustion temperatures without exceeding the metallurgical limit of the blade material. However, a balance between air flow for cooling and air flow for power must be achieved; the cooling air flowing within a blade drops in pressure without producing any power within that stage (although it is available for power in later stages). In the newest gas turbines, blade cooling, the difference between turbine inlet gas temperature and blade metal temperature, is around 1000°F.

Some of the latest large gas turbines being introduced to the market in the 2005 period are being offered for combined cycle application with closed-circuit **steam cooling** of selected hot section parts. Steam cooling reduces the need for air cooling, so that more of the compressor discharge air can be used for NO_x reduction in the combustor and for power generation. The heat transferred to the steam increases the efficiency of the bottoming cycle. The additional combustion products which flow through the high-pressure portions of the turbine generate substantially more power, thereby increasing both the power output and the efficiency of the machine. With more air for combustion, the fuel can be burned as a leaner mixture, with either less NO_x produced, or, as is preferred, with higher-temperature gases going to the turbine and the same NO_x (or a combination of these benefits).

Materials

The high-technology parts of a gas turbine are its hot section parts: blades, vanes, combustors and transition pieces. Gas turbine power, efficiency, and economics increase with the temperature of the gas flowing through the turbine blade passages. It is in the fabrication of these hot section parts that manufacturers are most competitive. Materials are selected to survive in serviceable condition for over 50,000 hr and associated numbers of thermal cycles. Ceramic coatings protect materials from oxidation and corrosion and provide thermal insulation, permitting higher gas temperatures.

Gas turbine alloys are frequently referred to as superalloys because of their extremely high strength at high temperatures. These superalloys are nickel based (such as IN 738), cobalt based (such as FSX-414), or with a nickel-iron base such as Inconel 718. Nickel resists oxidation and is creep resistant, but is subject to corrosive sulfidation. Alloy and manufacturing advancements have been led by the needs of military aircraft engines. Coating developments for corrosion resistance have been led by the needs of stationary power for overhaul intervals as large as 50,000 hr. The developmental needs of automotive gas turbines have led to significant advances in strength and reliability of high-temperature ceramic components, including radial inflow turbines. Ceramic materials, principally silicon nitride, are of interest to the developer of service soon in small gas turbines.

Combustion

Gas turbine combustors appear to be simple in design, yet they solve several difficult engineering challenges. Until relatively recently, gas turbine combustors employed a (turbulent) diffusion flame design approach, which created the most compact flame. European heavy-duty gas turbine manufacturers — with substantial interest in burning heavy fuel oils — preferred large, off-engine combustors, often called silo combustors because of their appearance, in order to obtain lower flame velocities and longer residence times. American heavy-duty gas turbine manufacturers use compact on-engine combustors and design for gaseous and clean (distillate) liquid fuels. Aeropropulsion gas turbines require the smallest possible frontal area and use only clean liquid fuels; hence, they use on-engine combustors.

Recently, stationary engines have been required to reduce NO_x emissions to the greatest extent possible, and combustors on stationary gas turbines first modified their diffusion flame combustors and employed water and steam injection to quench flame hot spots. Most recently, designs changed to the lean-premixed process. With the improved blade cooling, materials, and coatings now in use, the material limits on turbine inlet temperature and the NO_x emission limits on combustor temperature appear to be converging on a combustion-temperature asymptote around 2700°F (1482°C). This may be increased if catalytic combustors prove practical.

Mechanical Product Features

In view of the need to achieve all the performance features described above, one must keep in mind that a gas turbine is a high-speed dynamic machine with numerous machine design, materials, and fabrication features to consider. Major issues include the following: critical shaft speed considerations, bearing rotational stability, rotor balancing, thrust bearing design, bearing power loss, oil lubrication system, oil selection, air filter design and minimization of inlet and exhaust diffuser pressure drops, instrumentation, controls, diagnostic systems, scheduled service and inspection, overhaul, and repair. All of these topics must be addressed to produce a cost-effective, reliable, long-lived, practical gas turbine product that will satisfy users while also returning to investors sufficient profit for them to continue to offer better power generation products of still higher performance.

Defining Terms

Adiabatic saturator: A combined heat-and-mass-exchanger whereby a hot gas and a volatile liquid pass through a series of passages such that the liquid is heated and evaporates into the gas stream.

Combined cycle: An arrangement of a gas turbine and a stream turbine whereby the heat in the exhaust from the gas turbine is used to generate steam in a heat recovery boiler which then flows through a steam turbine, thereby generating additional power from the gas turbine fuel.

Combustion efficiency: Ratio of rate of heat delivered in a device which burns fuel to the rate of energy supplied in the fuel.

Expansion process: Process of power generation whereby a gas passes through a machine while going from a condition of high pressure to one of low pressure, usually the machine produces power.

Gas turbine or engine efficiency: The ratio of the net power delivered (turboexpander power minus compressor and auxiliary power) to the rate of energy supplied to the gas turbine or engine in the form of fuel, or, in certain cases such as solar power, heat.

Humid air turbine: A gas turbine in which the flow through the expander is augmented by large amounts of steam generated by use of an adiabatic saturator.

Intercooler: A heat exchanger used to cool the flow between sections of a compressor such that the high pressure section acts on a stream of reduced volumetric flow rate, thereby requiring less overall power to compress the stream to the final pressure.

Recuperator: A heat exchanger in which the hot and cold streams pass on opposite sides of a wall through which heat is conducted.

Regenerator: A heat exchanger in which the hot and cold streams alternately heat and cool a wall whose temperature rises and falls, thereby transferring heat between the streams.

Steam cooling: A process in which steam is used as the heat transfer fluid to cool a hot component.

Steam-injected gas turbine: A system in which the gas turbine flow is augmented by steam, thereby generating additional power.

Turbine efficiency: Ratio of the power delivered in an expansion process employing a turbine as the expander to the maximum power which could be produced by expanding the gas in a reversible adiabatic (isentropic) process from its initial pressure and temperature to its final pressure to the actual power.

Further Information

Wilson, D.G. 1984. *The Design of High-Efficiency Turbomachinery and Gas Turbines*, MIT Press, Cambridge, MA.

Kerrebrock, J. 1992. *Aircraft Engines and Gas Turbines*, MIT Press, Cambridge, MA.

Boyce, M.P. 1982. *Gas Turbine Engineering Handbook,* Gulf Publishing, Houston, TX.

Sawyer's Gas Turbine Engineering Handbook, Vol. 1: *Theory and Design,* Vol. 2: *Section and Application*, Vol. 3: *Accessories and Support*, Turbomachinery International Publications, Norwalk, CT, 1985.

Appendix

Equations for gas turine calculations based on the use of a perfect gas as the working fluid.

Perfect gas law	$pv = RT$
Gas constant	$R = \check{R}/\text{molecular weight}$
For air (molecule weight of 28.97)	$R = 286.96\ \text{J/kg} \cdot \text{K}$
	$= 0.06855\ \text{Btu/lb}_m \cdot {}^\circ\text{R}$
	$= 53.32\ \text{ft} \cdot \text{lb}_f/\text{lb}_m \cdot {}^\circ\text{R}$
Universal gas constant	$\check{R} = 8313\ \text{J/kg} \cdot \text{mol} \cdot \text{K}$
	$= 1.986\ \text{Btu/lb} \cdot \text{mol} \cdot {}^\circ\text{R}$
	$= 1545\ \text{ft} \cdot \text{lb}_f/\text{lb} \cdot \text{mol} \cdot {}^\circ\text{R}$
Relationships of properties	$c_p = c_v + \text{R}$
Isentropic exponet	$\gamma = c_p/c_v$ (air, $\gamma = 1.4$)
	$(\gamma - 1)/\gamma = R/c_p$
Isentropic process	$pv^\gamma = \text{constant}$
	$P_2/P_1 = (T_2/T_1)^{\gamma/(\gamma-1)}$
Prolytropic process	$pv^n = \text{constant}$
	$P_2/P_1 = (T_2/T_1)^{n/(n-1)}$
Pressure ratio	$r = P_2/P_1$
Ratio of stagnation T° and p° to static *T* and *p*	$\frac{T^\circ}{T} = 1 + \frac{\gamma - 1}{2} M^2$
	$\frac{p^\circ}{p} = \left(1 + \frac{\gamma - 1}{2} M^2\right)^{\gamma/(\gamma-1)}$
Mach number	$M = V\big/\sqrt{g_c \gamma R T}$
Gravitational constant	$\text{g}_\text{c} = \text{ma/F}$
Subscripts	t = turbine
	c = compressor
	f = fuel
	i = inlet
	e = exit

Cycle efficiency:

$$\eta = \frac{\dot{m}_t \Delta h_t - \dot{m}_c \Delta h_c}{\dot{m}_f HV}$$

where HV = heating value of fuel.

For specific heat independent of temperature and small mass flow of fuel in comparison to air:

$$\eta = \frac{\Delta T_t - \Delta T_c}{\Delta T_b}$$

Isentropic efficiency (finite pressure ratio):

$$\eta_t = \Delta T \text{ actual}/\Delta T \text{ isentropic}$$

$$\eta_t = \frac{1 - T_e/T_i}{1 - r^{(\gamma-1)/\gamma}}$$

or

$$\eta_t = \frac{1 - r^{(n-1)/n}}{1 - r^{(\gamma-1)/\gamma}}$$

and

$$\eta_c = \Delta T \text{ isentropic}/\Delta T \text{ actual}$$

$$\eta_c = \frac{r^{(\gamma-1)/\gamma} - 1}{T_e/T_i - 1}$$

or

$$\eta_c = \frac{r^{(\gamma-1)/\gamma} - 1}{r^{(\eta-1)/\eta} - 1}$$

Polytropic efficiency (differential pressure ratio):

$$\eta_t = \frac{(n-1)/n}{(\gamma-1)/\gamma}$$

and

$$\eta_c = \frac{(\gamma-1)/\gamma}{(n-1)/n}$$

Relationships between isentropic and polytropic efficencies:

$$\eta_{s,c} = \frac{r^{(\gamma-1)/\gamma} - 1}{r^{(\gamma-1)/\gamma\eta_{pc}} - 1}$$

$$\eta_{s,t} = \frac{1 - r^{(\gamma-1)/\gamma\eta_{p,t}}}{1 - r^{(\gamma-1)/\gamma}}$$

$$\eta_{p,c} = \frac{\ln r^{(\gamma-1)/\gamma}}{\ln\left[\dfrac{r^{(\gamma-1)/\gamma} - 1}{\eta_{s,c}} + 1\right]}$$

$$\eta_{p,t} = \frac{\ln\left[1 - \eta_{s,t}\left(1 - r^{(\gamma-1)/\gamma}\right)\right]}{\ln r^{(\gamma-1)/\gamma}}$$

8.3 Internal Combustion Engines

David E. Klett and Elsayed M. Afify

Introduction

This section discusses the two most common reciprocating internal combustion (IC) engine types in current use: the **spark ignition** (SI) and the **compression ignition** (CI or diesel) **engines**. The Stirling engine (technically, an external combustion engine) and the gas turbine engine are covered in other sections of this chapter. Space limitations do not permit detailed coverage of the very broad field of IC engines. For a more detailed treatment of SI and CI engines and for information on variations, such as the Wankel rotary engine and the Miller cycle engine (a variation on the reciprocating four-stroke SI engine introduced in production by Mazda in 1993), several excellent textbooks on the subject, technical papers, and other sources are included in the list of references and the section on further information.

Basic SI and CI engines have not fundamentally changed since the early 1900s with the possible exception of the introduction of the Wankel rotary SI engine in the 1960s (Norbye, 1971). However, major advances in the areas of materials, manufacturing processes, electronic controls, and computer-aided design have led to significant improvements in dependability, longevity, thermal efficiency, and emissions during the past decade. Electronic controls, in particular, have played a major role in efficiency gains in SI automotive engines through improved control of the fuel injection and ignition systems that control the combustion process. Electronic control of diesel fuel injection systems is also now quite common and is producing improvements in diesel emissions and fuel economy.

This section presents the fundamental theoretical background of IC engine function and performance, including **four-stroke** and **two-stroke** SI and CI **engines**. Sections on combustion, emissions, fuels, and intake pressurization (**turbocharging** and **supercharging**) are also included.

Engine Types and Basic Operation

IC engines may be classified by a wide variety of characteristics; the primary ones are SI vs. CI; four stroke vs. two stroke; and reciprocating vs. rotary. Other possible categories of classification include intake type (naturally aspirated vs. turbocharged or supercharged); number of cylinders; cylinder arrangement (in-line, vee, opposed); cooling method (air vs. water); fueling system (injected vs. carbureted); valve gear arrangement (overhead cam vs. pushrod); type of **scavenging** for two-stroke engines (cross, loop, or uniflow); and type of injection for diesel engines (direct vs. indirect).

Four-Stroke SI Engine

Figure 8.3.1 is a cross-section schematic of a four-stroke SI engine. The SI engine relies on a spark plug to ignite a volatile air–fuel mixture as the piston approaches **top dead center** (**TDC**) on the compression stroke. This mixture may be supplied from a carburetor, a single throttle-body fuel injector, or by individual fuel injectors mounted above the intake port of each cylinder. One combustion cycle involves two revolutions of the crankshaft and thus four strokes of the piston, referred to as the intake, compression, power, and exhaust strokes. Intake and exhaust valves control the flow of mixture and exhaust gases into and out of the cylinder, and an ignition system supplies a spark-inducing high voltage to the spark plug at the proper time in the cycle to initiate combustion.

On the intake stroke, the intake valve opens and the descending piston draws a fresh combustible charge into the cylinder. During the compression stroke, the intake valve closes and the fuel–air mixture is compressed by the upward piston movement. The mixture is ignited by the spark plug, typically before TDC. The rapid, **premixed, homogeneous combustion** process causes a sharp increase in cylinder

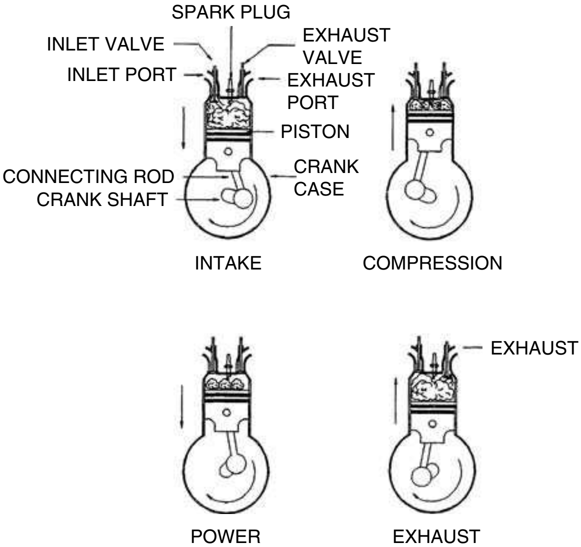

FIGURE 8.3.1 Schematic diagram of four-stroke SI engine.

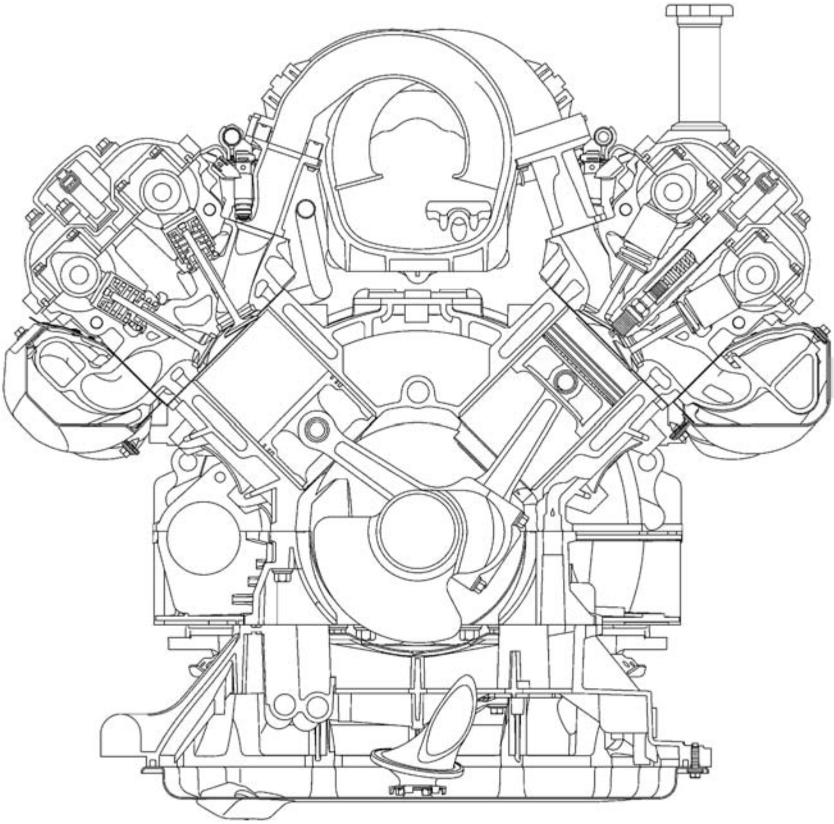

FIGURE 8.3.2 Ford 4.6-L aluminum V-8 SI engine. (Courtesy of Ford Motor Company.)

temperature and pressure that forces the piston down for the power stroke. Near **bottom dead center** (BDC), the exhaust valve opens and the cylinder pressure drops rapidly to near atmospheric. The piston then returns to TDC, expelling the exhaust products. At TDC, the exhaust valve closes and the intake valve opens to repeat the cycle again. Figure 8.3.2 is a cutaway drawing of a modern high-performance automotive SI engine. This is a fuel-injected normally aspirated aluminum alloy V-8 engine of 3.9 L displacement with dual overhead cams for each cylinder bank and four valves per cylinder. Peak power output is 188 kw at 6100 rpm and peak torque is 354 N-m at 4300 rpm.

Two-Stroke SI Engine

The two-stroke SI engine completes a combustion cycle for every revolution of the crankshaft by essentially overlapping the power and exhaust functions in one downward stroke and the intake and compression processes in one upward stroke. A single-cylinder, crankcase-scavenged, two-stroke SI engine is illustrated schematically in Figure 8.3.3. The operation is as follows.

On the upward stroke, the piston first covers the transfer port and then the exhaust port. Beyond this point, the fresh charge is compressed and ignited near TDC. During the upward stroke, the negative pressure created in the crankcase below the piston draws in a fresh charge of fuel–air mixture through a one-way valve. On the downward power stroke, the mixture in the crankcase is pressurized. The piston uncovers the exhaust port and the high-pressure exhaust gases exit. Near BDC, the transfer port is uncovered and the pressurized mixture flows from the crankcase into the cylinder and the cycle repeats. Because the crankcase is part of the induction system, it does not contain oil, and lubrication is accomplished by mixing oil with the fuel. With the cross-flow scavenging configuration illustrated in Figure 8.3.3, there will be a certain degree of mixing of the fresh charge with the combustion products remaining in the cylinder and some loss of fresh charge out the exhaust port.

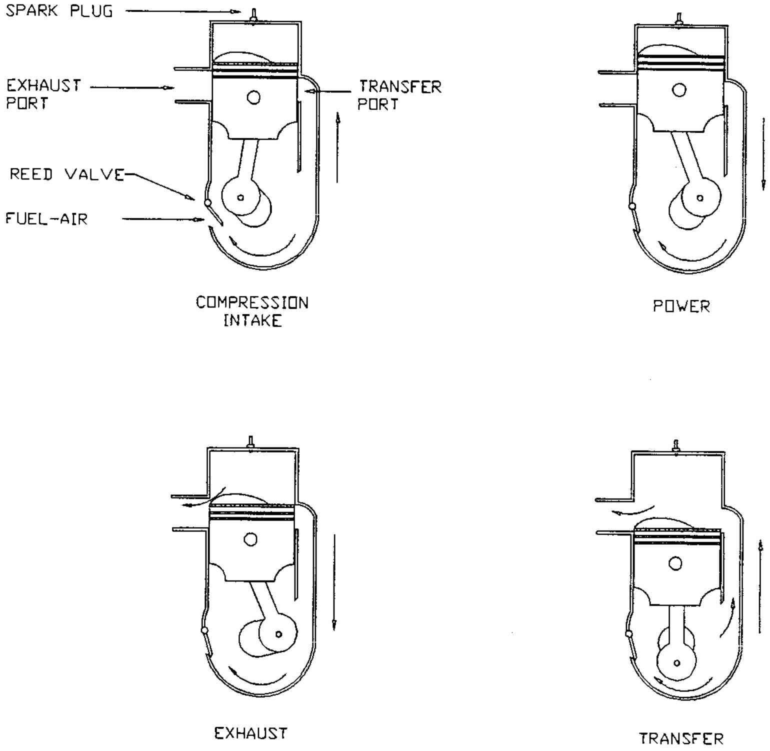

FIGURE 8.3.3 Schematic drawing of two-stroke SI engine.

Because two-stroke engines produce twice the power impulses of four-stroke engines for the same rpm, a two-stroke engine has a higher **power density** and is thus smaller and lighter than a four-stroke engine of equal output. The disadvantages of the two-stroke engine have historically been lower fuel efficiency and higher exhaust emissions because of overlapping intake and exhaust processes and the loss of some fresh intake mixture with the exhaust products. For this reason, two-stroke SI engines have largely been confined to small-displacement applications, such as small motorcycles, outboard marine engines, and small equipment. Several manufacturers have addressed these shortcomings in recent years and have achieved significant improvements in two-stroke engine fuel economy and emissions (Blair, 1988).

The Orbital combustion process (OCP), as illustrated in Figure 8.3.4, applies air-assisted direct injection of the fuel into the cylinder of a two-stroke engine and, in conjunction with a high turbulence combustion chamber design, achieves very favorable fuel economy and significantly reduced levels of hydrocarbon emissions. This system, in use today on single-cylinder scooters and on 2-, 3-, and 6-cylinder marine two-stroke engine applications, is also applicable to four-stroke engines.

Compression Ignition Engine

The basic valve and piston motions are the same for the CI, or diesel, engine as discussed earlier for the SI engine. The CI engine relies on the high temperature and pressure of the cylinder air resulting from the compression process to cause **autoignition** of the fuel, which is injected directly into the combustion chamber of **direct injection** (**DI**) engines or into the prechamber of **indirect injection** (**IDI**) engines, when the piston approaches TDC on the compression stroke. Compression ratios are typically much higher for CI than for SI engines to achieve the high air temperatures required for autoignition, and the fuels used must have favorable autoignition qualities.

The time period between the start of fuel injection and the occurrence of autoignition is called the **ignition delay period**. Long ignition delay periods allow more time for fuel vaporization and fuel–air

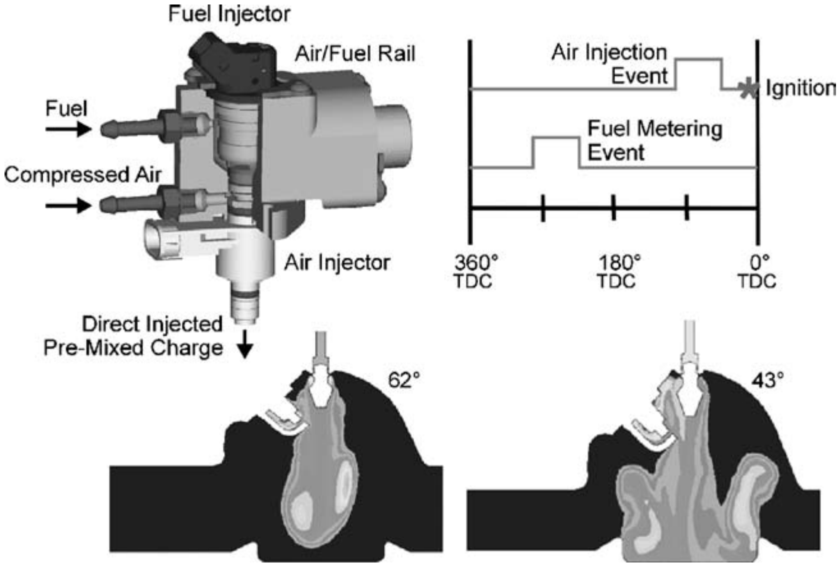

FIGURE 8.3.4 Orbital OCP combustion system. (Courtesy of Orbital Engine Company.)

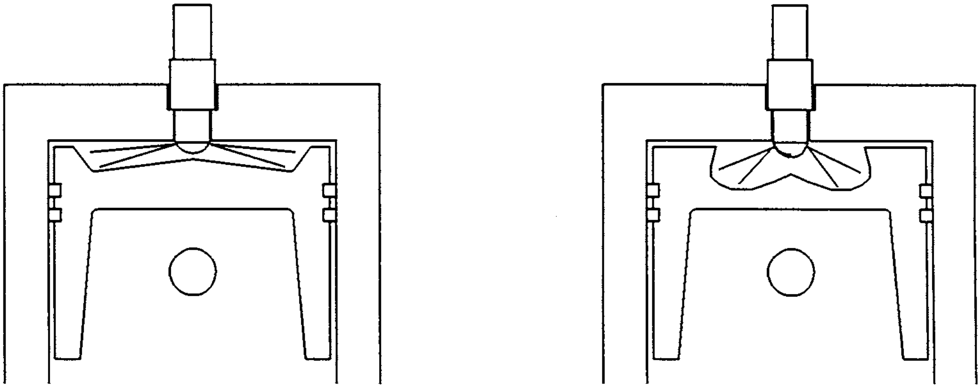

Quiescent Bowl **Toroidal Bowl**

FIGURE 8.3.5 Examples of DI diesel combustion chamber design.

mixing and result in objectionable diesel knock when this larger premixed charge autoignites. Combustion chambers and fuel injection systems must be designed to avoid extended ignition delay periods. Diesel engines may be classified as DI or IDI. In DI engines, the combustion chamber consists of a bowl formed in the top of the piston; the fuel is injected into this volume. The injector tip generally has from four to eight holes to form multiple spray cones.

Two variations are illustrated in Figure 8.3.5. The quiescent chamber engine utilizes a large-diameter shallow bowl shape that produces low **swirl** and low turbulence of the air during compression. Fuel is injected at high pressure through a multihole nozzle; mixing of the fuel and air relies primarily on the energy of the injected fuel to cause air entrainment in the spray cone and diffusion of vaporized fuel into the air. This system is suited to large slow-speed engines that are operated with significant excess air.

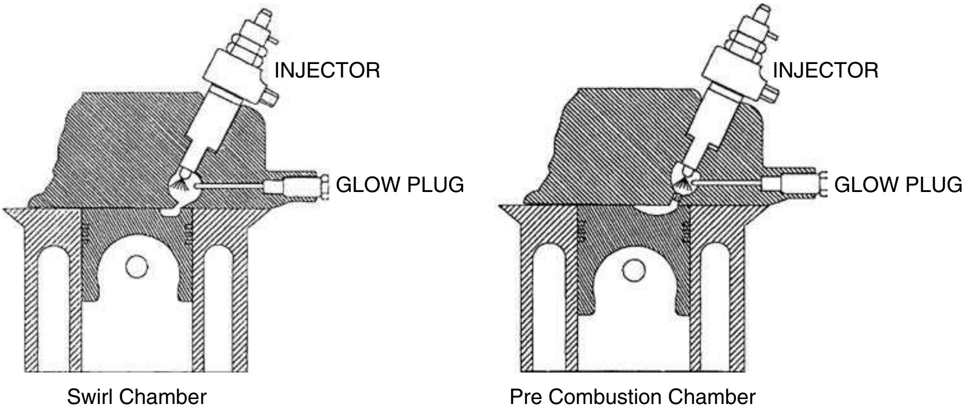

Swirl Chamber

Pre Combustion Chamber

FIGURE 8.3.6 Two examples of IDI combustion chambers.

The toroidal bowl combustion chamber is used in conjunction with intake ports and/or valve shrouds designed to produce air swirl to enhance fuel–air mixing. The **swirl ratio** is defined by swirl ratio = swirl speed (rpm)/engine speed (rpm). The swirl velocity component is normal to the fuel spray direction and tends to promote mixing in the regions between the individual spray cones. This system makes better use of the available air and is utilized extensively in moderate-speed engines such as over-the-road truck engines. DI does not lend well to high-speed operation because less time is available for proper mixing and combustion. Diesel engines for passenger car applications are generally designed for higher speed operation to produce higher specific output. They typically utilize IDI combustion systems, two of which are illustrated in Figure 8.3.6.

IDI systems make use of small prechambers incorporated in the cylinder head to promote rapid mixing of fuel and air and shorten the ignition delay period. Swirl chambers are designed to produce a strong vortex in the prechamber during compression. The fuel is sprayed into the chamber through a single-hole nozzle and the high vorticity promotes rapid mixing and short ignition delay periods. Precombustion chambers do not attempt to generate an orderly vortex motion within the chamber; instead, to promote mixing, they rely on a high level of turbulence created by the rush of air into the chamber during compression. Both types of prechambers generally include a lining of low-conductivity material (ceramic) to increase the surface temperature to promote fuel evaporation. Prechambers can be used in small-displacement diesel engines to achieve operating speeds up to 5000 rpm.

Disadvantages of the IDI system include poor cold-start characteristics due to high heat-transfer rates from the compressed air to the chamber wall that result from the high velocities and turbulence levels in the chamber. **Glow plugs** are often installed in each prechamber to heat the air to improve cold starting. Higher compression ratios are also used for IDI engines to improve cold starting. The compression ratios, typically 18 to 24, are higher than the optimum for fuel efficiency (due to decreased mechanical efficiency resulting from higher friction forces), and IDI engines are typically less efficient than larger, slower, DI engines. The use of IDI is generally restricted to high-speed automotive engines, with displacements in the range of 0.3 to 0.8 l per cylinder, and some degree of fuel economy is sacrificed in the interest of improved driveability.

CI engines are produced in two-stroke and four-stroke versions. Because the fuel is injected directly into the combustion chamber of CI engines just prior to TDC, two-stroke CI engines do not suffer the same emission and efficiency shortcomings as do older crankcase-scavenged two-stroke SI engines. Thus, they are available in much larger displacements for high-power-requirement applications such as locomotive and ship propulsion and electric power generation systems. Two-stroke CI engines are generally of the DI type because the use of IDI in a two-stroke engine would lead to aggravated cold-start problems due to lower compression ratios.

Air Standard Power Cycles

The actual operation of IC engines is idealized at a very basic level by the air standard power cycles (ideal thermodynamic models for converting heat into work on a continuous basis). The following simplifying assumptions are common to the air standard cycles: (1) the working substance is air, (2) the air is assumed to behave as an ideal gas with constant specific heats, (3) heat is added to the cycle from an external source, and (4) expansion and compression processes not involving heat transfer occur isentropically. The air standard cycles, while grossly oversimplified in terms of the complex processes occurring within actual engines, are nevertheless useful in understanding some fundamental principles of SI and CI engines. The simplified models also lend insight into important design parameters, e.g., **compression ratio**, that govern theoretical maximum cycle thermal efficiencies.

Constant-Volume Heat Addition — Ideal Otto Cycle

The theory of operation of the SI engine is idealized by the Otto cycle, which assumes that heat is added to the system at constant volume. Constant-volume heat addition is approximated in the SI engine by virtue of the combustion process taking place rapidly when the piston is near TDC. A P-V diagram for the Otto cycle is illustrated in Figure 8.3.7. The cycle consists of the following processes: 1 → 2 isentropic compression; 2 → 3 constant-volume heat addition; 3 → 4 isentropic expansion; and 4 → 1 constant-volume heat rejection. The constant-volume heat rejection process is approximated in SI engines by the exhaust valve opening near BDC and the rapid blow-down of exhaust gases.

Thermal efficiency for a power cycle is defined as the ratio of work output to heat input per cycle,

$$\eta = \frac{W_{\text{out}}}{Q_{\text{in}}} \tag{8.3.1}$$

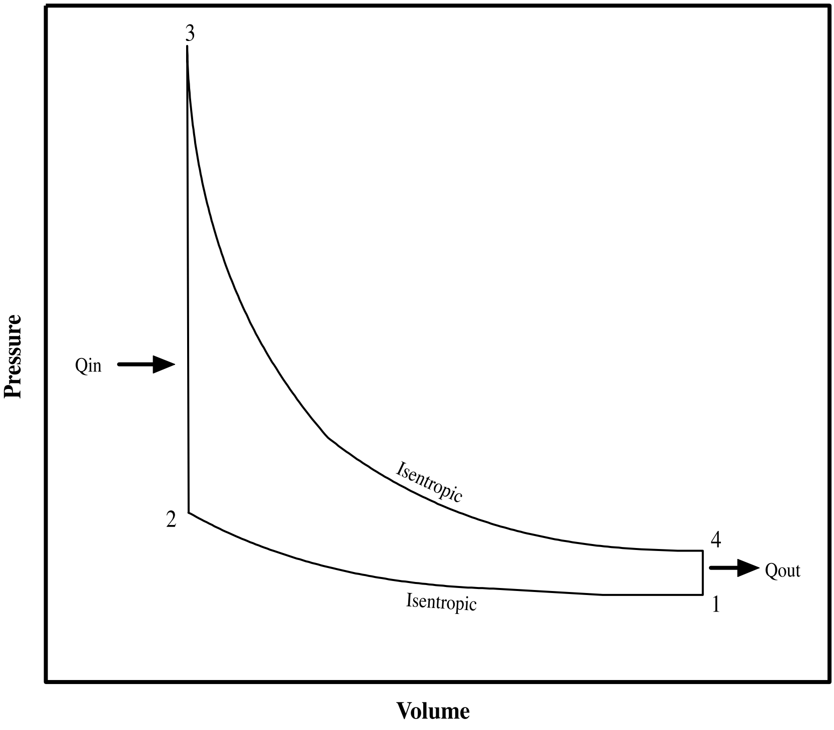

FIGURE 8.3.7 Schematic pressure-volume diagram for the ideal Otto cycle.

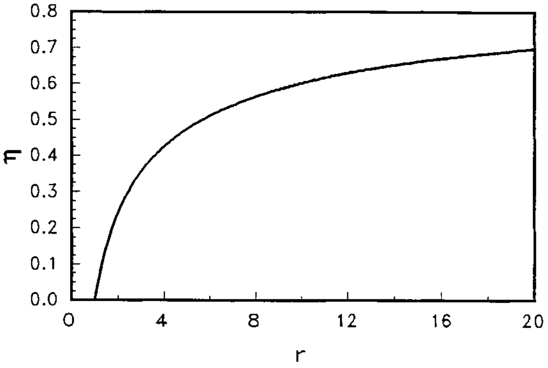

FIGURE 8.3.8 Efficiency of the ideal Otto cycle.

For the Otto cycle, the basic efficiency expression can be manipulated into the form

$$\eta = 1 - \frac{1}{r^{\gamma-1}} \tag{8.3.2}$$

where γ is the ratio of specific heats ($\gamma = C_p/C_v$) and r is the compression ratio, or ratio of the maximum to minimum cycle volumes ($r = V_1/V_2$).

In actual IC engines, the minimum cycle volume is referred to as the **clearance volume** and the maximum cycle volume is the **cylinder volume**. The ideal Otto cycle efficiency for air, with $\gamma = 1.4$, is shown plotted in Figure 8.3.8. The theoretical efficiency of the constant volume heat addition cycle increases rapidly with compression ratio, up to about $r = 8$. Further increases in compression ratio bring moderate gains in efficiency. Compression ratios in practical SI engines are limited because of autoignition (knock) and high NO_x emission problems that accompany high compression ratios. Production SI automotive engines typically have compression ratios in the range of 8 to 10, whereas high-performance normally aspirated racing engines may have compression ratios as high as 14, but require the use of special fuels to avoid autoignition.

Constant-Pressure Heat Addition — Ideal Diesel Cycle

The air standard diesel cycle is the idealized cycle underlying the operation of CI or diesel engines. The diesel cycle, illustrated by the *P-V* diagram in Figure 8.3.9, consists of the following processes: $1 \rightarrow 2$ isentropic compression from the maximum to the minimum cycle volume; $2 \rightarrow 3$ constant-pressure heat addition during an accompanying increase in volume to V_3; $3 \rightarrow 4$ isentropic expansion to the maximum cycle volume; and $4 \rightarrow 1$ constant-volume heat rejection.

Actual diesel engines approximate constant-volume heat addition by injecting fuel for a finite duration that continues to burn and release heat at a rate that tends to maintain the pressure in the cylinder over a period of time during the expansion stroke. The efficiency of the ideal diesel cycle is given by

$$\eta = 1 - \frac{1}{r^{\gamma-1}} \left[\frac{r_c^{\gamma} - 1}{\gamma (r_c - 1)} \right] \tag{8.3.3}$$

The efficiency of the ideal diesel cycle depends not only on the compression ratio, r, but also on the **cut-off ratio**, $r_c = V_3/V_2$, the ratio of the volume when heat addition ends to the volume when it begins. Equation (8.3.3) is shown plotted in Figure 8.3.10 for several values of r_c and for $\gamma = 1.4$. An r_c value of 1 is equivalent to constant-volume heat addition — i.e., the Otto cycle. The efficiency of the ideal Diesel cycle is less than the efficiency of the ideal Otto cycle for any given compression ratio and any value of the cut-off ratio greater than 1. The fact that CI engines, by design, operate at much higher compression

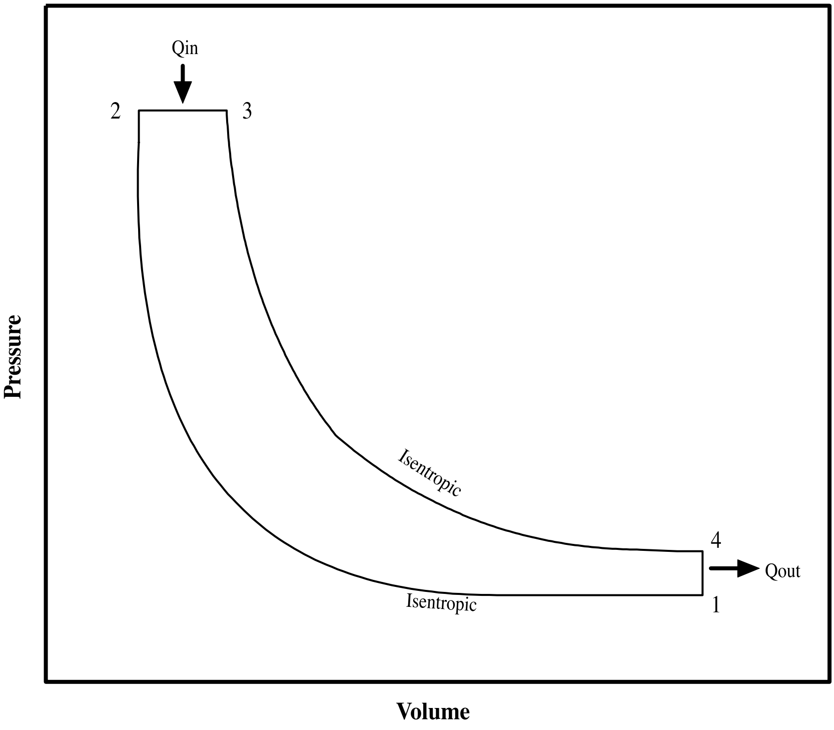

FIGURE 8.3.9 Schematic pressure-volume diagram of ideal diesel cycle.

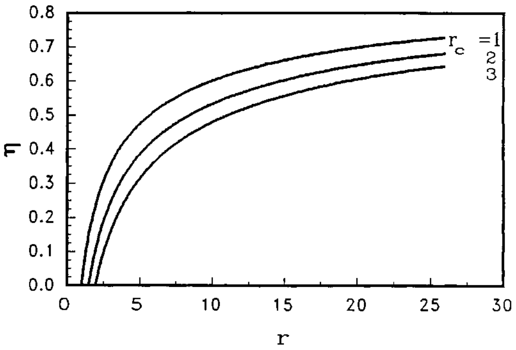

FIGURE 8.3.10 Efficiency of the ideal diesel cycle.

ratios than SI engines (generally between 12 and 24) accounts for their typically higher operating efficiencies relative to SI engines.

Actual Cycles

IC engines do not operate on closed thermodynamic cycles, such as the air standard power cycles, but rather on open mechanical cycles; heat addition occurs neither at constant volume nor at constant pressure. Figure 8.3.11 is a schematic representation of an **indicator diagram** (pressure-volume history) of a four-stroke IC engine; it could be SI or CI. The pressure changes during the intake and exhaust strokes are exaggerated in the diagram. The **indicated work** performed per cycle can be calculated by taking the integral of *PdV* for the complete cycle. The **indicated mean effective pressure, imep**, is defined as the ratio of the net indicated work output to the **displacement volume**:

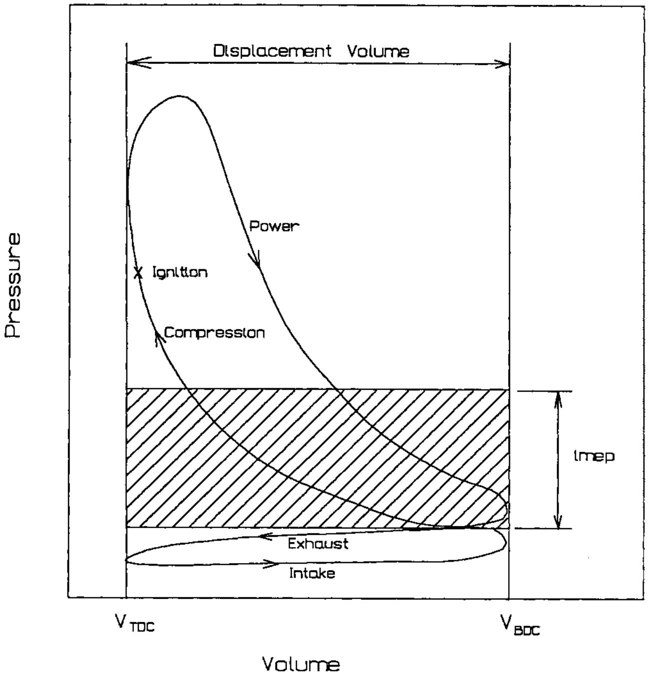

FIGURE 8.3.11 Schematic indicator diagram.

$$\text{imep} = \frac{\text{indicated work output per cycle}}{\text{displacement volume}} \tag{8.3.4}$$

The shaded area in Figure 8.3.11 thus represents the net indicated work output per cycle. During the intake and exhaust processes of a normally aspirated engine, the negative work performed represents pumping losses and acts to decrease the net work output of the engine. The magnitude of the pumping losses depends on the flow characteristics of the intake and exhaust systems, including the valves, ports, manifolds, piping, mufflers, etc. The more restrictive these passages are, the higher the pumping losses will be.

SI engines control power output by throttling the intake air. Thus, under partial-load conditions, the pressure drop resulting from the air throttling represents a significant increase in pumping loss with a corresponding decrease in operating efficiency. SI engines are therefore less efficient at partial-load operation than at full load. The power level of CI engines, on the other hand, is controlled by varying the amount of fuel injected, as opposed to throttling the intake air, making them significantly more efficient than SI engines under partial-load conditions.

Brake work (or power) is the actual work (or power) produced at the output shaft of an engine, as measured by a dynamometer. The brake work will be less than the indicated work due to friction losses and any parasitic power requirements for oil pumps, water pumps, etc. The **brake mean effective pressure, bmep**, is defined as

$$\text{bmep} = \frac{\text{brake work output per cycle}}{\text{displacement volume}} \tag{8.3.5}$$

The mechanical efficiency can then be defined as

$$\eta_m = \frac{\text{brake work (power)}}{\text{indicated work (power)}} = \frac{\text{bmep}}{\text{imep}} \tag{8.3.6}$$

Engine thermal efficiency can be determined from the ratio of power output to rate of fuel energy input, or

$$\eta_t = \frac{\text{Power}}{m_f Q_c} \tag{8.3.7}$$

where m_f is the rate of fuel consumption per unit time and Q_c is the heat of combustion per unit mass of fuel. The thermal efficiency in Equation (8.3.7) could be indicated or brake depending on the nature of the power used in the calculation. Uncertainty associated with variations of energy content of fuels may present a practical difficulty with determining engine thermal efficiency. In lieu of thermal efficiency, **brake-specific fuel consumption (bsfc)** is often used as an efficiency index.

$$\text{bsfc} = \frac{\text{fuel consumption rate } (\text{kg/hr})}{\text{brake power } (\text{kW})} \tag{8.3.8}$$

The efficiency of engines operating on the same fuel may be directly compared by their bsfc.

Volumetric efficiency, η_v, is an important performance parameter for four-stroke engines defined as

$$\eta_v = \frac{m_{\text{actual}}}{m_d} \tag{8.3.9}$$

where m_{actual} is the mass of intake mixture per cycle and m_d is the mass of mixture contained in the displacement volume at inlet conditions (pressure and temperature near the inlet port).

For SI engines, the mixture mass includes air and fuel; for CI engines only air is present during intake. With the intake mixture density determined at inlet conditions, η_v accounts for pressure losses and charge heating associated with the intake ports, valves, and cylinder. Sometimes, for convenience, the mixture density is taken at ambient conditions. In this case, η_v is called the overall volumetric efficiency and includes the flow performance of the entire intake system.

Because a certain minimum amount of air is required for complete combustion of a given amount of fuel, it follows that the maximum power output of an engine is directly proportional to its air-flow capacity. Therefore, although not affecting the thermal efficiency of the engine in any way, the volumetric efficiency directly affects the maximum power output for a given displacement and thus can affect the efficiency of the overall system in which the engine is installed because of the effect on system size and weight. Volumetric efficiency is affected primarily by intake and exhaust valve geometry; valve lift and timing; intake port and manifold design; mixing of intake charge with residual exhaust gases; engine speed; ratio of inlet pressure to exhaust back pressure; and heat transfer to the intake mixture from warmer flow passages and combustion chamber surfaces. For further information on the fundamentals of IC engine design and operation, see Taylor (1985); Ferguson and Kirkpatrick (2001); Heywood (1988); and Stone (1993).

Combustion in IC Engines

Combustion in Spark Ignition Engines

Background. In SI engines, combustion of the fuel–air mixture is initiated by a spark generated between the electrodes of a spark plug. The intake and compression strokes are designed to prepare the mixture for combustion by completely vaporizing the fuel and heating the mixture to just below its autoignition temperature. This is one reason, in addition to controlling emissions, for the current practice of limiting the maximum compression ratio of nonracing SI engines to about 10:1. Near the end of compression, the mixture is well conditioned for combustion and the spark is discharged to initiate the combustion process. For best fuel economy, the combustion process must be completed as close as possible to TDC.

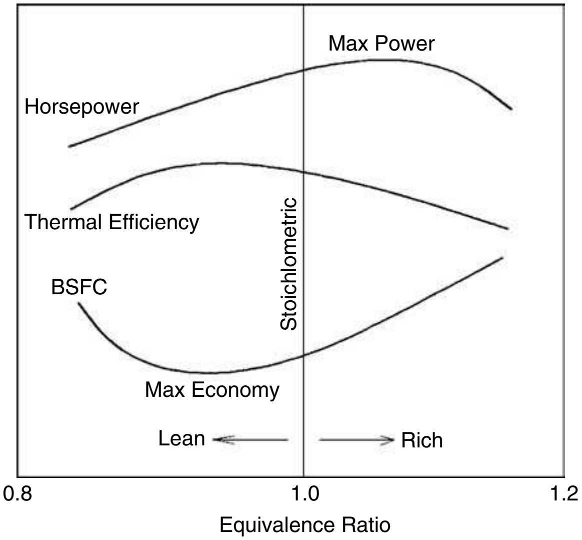

FIGURE 8.3.12 Effect of fuel–air mixture on indicated performance of an SI engine.

This requires that the spark timing be controlled for varying operating speed and load conditions of the engine. Fuel metering and control, according to the engine load requirements and with minimum variation from cylinder to cylinder and cycle to cycle, are essential for good fuel economy, power output, and emission control of the engine.

Carburetors and fuel injection systems are used for fuel-metering control. Because of the superior control capabilities of fuel injection systems, they are nearly universally used today in production automotive applications. Carburetors are used for applications with less-stringent emission requirements, e.g., small engines for lawn and garden equipment.

Figure 8.3.12 illustrates the effect of **fuel–air ratio** on the indicated performance of an SI engine. The **equivalence ratio** (ϕ) is defined by the ratio fuel–air$_{\text{actual}}$/fuel–air$_{\text{stoichiometric}}$. Rich mixtures have fuel–air ratios greater than stoichiometric ($\phi > 1$) and lean mixtures have fuel–air ratios less than stoichiometric ($\phi < 1$). Optimum fuel economy, coinciding with maximum thermal efficiency, is obtained at part throttle with a lean mixture as a result of the fact that the heat release from lean mixtures suffers minimal losses from dissociation and variation of specific heat effects when compared with stoichiometric and rich fuel–air ratios.

Maximum power is obtained at full throttle with a slightly rich mixture — an indication of the full utilization of the air within the cylinders. Idling with a nearly closed throttle requires a rich mixture due to the high percentage of residual exhaust gas that remains in the cylinders. The fuel–air mixture requirement under transient operation, such as acceleration, requires a rich mixture to compensate for the reduced evaporation caused by the sudden opening of the throttle. Cold starting also requires a rich mixture to ensure the vaporization of sufficient amounts of the highly volatile components in the fuel to achieve proper ignition.

Normal Combustion Process. The combustion processes in SI engines can be divided into two categories: normal and abnormal. The normal combustion process occurs in three stages: initiation of combustion; flame propagation; and termination of combustion. Combustion normally starts within the spark plug gap when the spark is discharged. The fuel molecules in and around the spark discharge zone are ignited and a small amount of energy is released. The important criterion for the initial reaction to be self-sustaining is that the rate of heat release from the initial combustion be larger than the rate of heat transfer to the surroundings. The factors that play an important role in making the initial reaction self-sustaining, and thereby establishing a flame kernel, are the ignition energy level; the spark plug gap; the fuel–air ratio; the initial turbulence; and the condition of the spark plug electrodes.

After a flame kernel is established, a thin spherical flame front advances from the spark plug region progressively into the unburned mixture zone. Flame propagation is supported and accelerated by two processes. First, the combined effect of the heat transfer from the high-temperature flame region and the migration of active radicals from the flame front into the adjacent unburned zone raise the temperature and accelerate the reactivity of the unburned mixture region directly ahead of the flame front. This helps to condition and prepare this zone for combustion.

Second, the increase in the temperature and pressure of the burned gases behind the flame front will cause it to expand and progressively create thermal compression of the remaining unburned mixture ahead of the flame front. The flame speed will be slow at the start of combustion, then reach a maximum at about half the flame travel, and finally decrease near the end of combustion. Overall, the flame speed is strongly influenced by the level of turbulence in the combustion chamber; the shape of the combustion chamber; the mixture strength; the type of fuel; and the engine speed.

When the flame front approaches the walls of the combustion chamber, the high rate of heat transfer to the walls slows down the flame propagation and, finally, the combustion process terminates close to the walls because of surface quenching. This leaves a thin layer of unburned fuel close to the combustion chamber walls that shows up in the exhaust as unburned hydrocarbons.

Abnormal Combustion. Abnormal combustion may occur in SI engines associated with two combustion phenomena: **knock** and **surface ignition**. Knock occurs near the end of the combustion process if the end portion of the unburned mixture, which is progressively subjected to thermal compression and seeding by active radicals, autoignites prematurely before the flame front reaches it. As a result of the sudden energy release, a violent pressure wave propagates back and forth across the combustion chamber, causing the walls or other parts of the engine to vibrate, producing a sharp metallic noise called knock. If knock persists for a period of time, the high rate of heat transfer caused by the traveling high pressure and temperature wave may overheat the spark plug electrode or ignite carbon deposits that may be present in the combustion chamber, causing uncontrolled combustion and surface ignition. As a result, loss of power and serious engine damage may occur.

Knock is sensitive to factors that increase the temperature and pressure of the end portion of the unburned mixture, as well as to fuel composition and other time factors. Factors that increase the probability of knock include: (1) increasing the temperature of the mixture by increasing the charge intake temperature, increasing the compression ratio, or turbo/supercharging; (2) increasing the density of the mixture by turbo/supercharging or increasing the load; (3) advancing the spark timing; (4) increasing the time of exposure of the end portion of the unburned mixture to autoignition conditions by increasing the length of flame travel or decreasing the engine speed and turbulence; and (5) using low-octane fuel and/or maximum power fuel–air ratios

Other engine design factors that affect knock in SI engines include the shape of the combustion chamber and the location of the spark plug and inlet and exhaust valves relative to the location of the end portion of the unburned mixture. Modern computerized engine management systems that incorporate a knock sensor can automatically retard the ignition timing at the onset of knock, greatly reducing the possibility of engine damage due to knock.

Surface ignition is the ignition of the unburned mixture by any source in the combustion chamber other than the normal spark. Such sources could include overheated exhaust valves or spark plug electrodes, glowing carbon deposits, or other hot spots. Surface ignition will create secondary flame fronts, which cause high rates of pressure rise resulting in a low-pitched, thudding noise accompanied by engine roughness. Severe surface ignition, especially when it occurs before spark ignition, may cause serious structural and/or component damage to the engine.

Combustion in Compression Ignition Engines

Unlike the SI engine, in which the charge is prepared for combustion as a homogeneous mixture during the intake and compression strokes, fuel preparation for combustion in CI engines occurs in a very short period of time called the ignition delay period, which lasts from the beginning of fuel injection until the

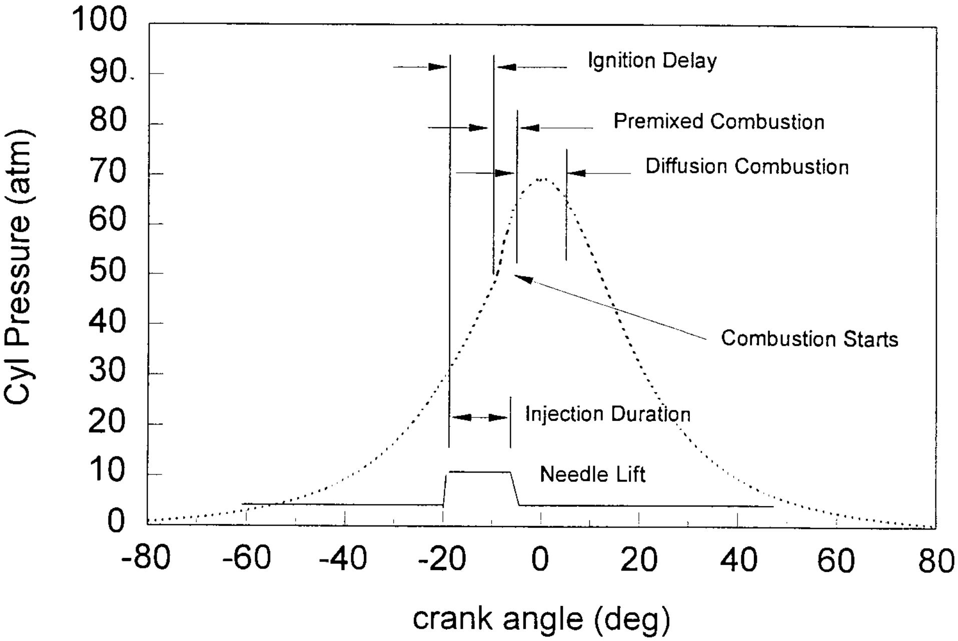

FIGURE 8.3.13 Combustion process in a CI engine.

moment of autoignition. During this period, the fuel injected into the high-temperature air near the end of the compression stroke undergoes two phases of transformation. A physical delay period, during which the fuel is vaporized, mixed with the air, and raised in temperature, is followed by a chemical delay period during which fuel cracking and decomposition occur; this leads to autoignition and combustion of the fuel.

The combustion process is **heterogeneous** and involves two modes, usually identified as premixed combustion and diffusion combustion. Premixed combustion occurs early in the process when the fuel that has evaporated and mixed with air during the ignition delay period autoignites. This mode is characterized by uncontrolled combustion and is the source of combustion noise because it is accompanied by a high rate of heat release, which produces a high rate of pressure rise. When the premixed fuel–air mixture is depleted, diffusion combustion takes over, characterized by a lower rate of heat release and producing controlled combustion during the remainder of the process. Figure 8.3.13 depicts the different stages of the combustion process in CI engines.

The ignition delay period plays a key role in controlling the time duration of the two modes of combustion. Prolonging the ignition delay, through engine design factors or variations in operating conditions, will generate a larger portion of premixed fuel–air mixture and thus tend to increase the premixed combustion mode duration and decrease the diffusion mode duration. This may lead to higher peak cylinder pressure and temperature; this may improve thermal efficiency and reduce CO and **unburned hydrocarbon** (**UHC**) emissions at the expense of increased emissions of oxides of nitrogen (**NO$_x$**).

Large increases in the ignition delay period will cause high rates of pressure rise during premixed combustion and may lead to objectionable diesel knock. Reducing the ignition delay period causes the premixed combustion duration to decrease while increasing the diffusion combustion duration. A large reduction in ignition delay may lead to loss of power, decrease in thermal efficiency, and possible deterioration of exhaust emissions. Several factors related to the fuel–air mixture temperature and density, engine speed, combustion chamber turbulence, injection pressure, rate of injection, and fuel composition influence the duration of the ignition delay period.

Knock in CI Engines. Because the combustion process in CI engines is triggered by autoignition of the fuel injected during the ignition delay period, factors that prolong the ignition delay period will increase the premixed combustion duration, causing very high rates of energy release and thus high rates of pressure rise. As a result, diesel knock may occur. The phenomenon is similar to knock in SI engines except that it occurs at the beginning of the combustion process rather than near the end, as observed in SI combustion. Factors that reduce the ignition delay period will reduce the possibility of knock in diesel engines. Among them are increasing the compression ratio; supercharging; increasing combustion chamber turbulence; increasing injection pressure; and using high-**cetane-number (CN)** fuel. For a more detailed discussion of the combustion process in IC engines, see Henein (1972); Lenz (1992); and Keating (1993).

Exhaust Emissions

Harmful Constituents

The products of combustion from IC engines contain several constituents that are considered hazardous to human health, including CO, UHCs NO_x, and **particulates** (from diesel engines). These emission products are discussed briefly next, followed by a description of the principal schemes for their reduction.

Carbon Monoxide. CO is a colorless, odorless, and tasteless gas that is highly toxic to humans. Breathing air with a small volumetric concentration (0.3%) of CO in an enclosed space can cause death in a short period of time. CO results from the incomplete combustion of hydrocarbon fuels. One of the main sources of CO production in SI engines is the incomplete combustion of the rich fuel mixture that is present during idling and maximum power steady-state conditions and during such transient conditions as cold starting, warm-up, and acceleration. Fuel maldistribution, poor condition of the ignition system, and slow CO reaction kinetics also contribute to increased CO production in SI engines. CO production is not as significant in CI engines because these engines are always operated with significant excess air.

Unburned Hydrocarbons. When UHCs combine with NO_x (see following) in the presence of sunlight, ozone and photochemical oxidants form that can adversely affect human health. Certain UHCs are also considered to be carcinogenic. The principal cause of UHC in SI engines is incomplete combustion of the fuel–air charge, resulting in part from flame quenching of the combustion process at the combustion chamber walls and engine misfiring. Additional sources in four-stroke engines may include fuel mixture trapped in crevices of the top ring land of the piston and outgassed fuel during the expansion (power) stroke that was absorbed into the lubricating oil film during intake. In two-stroke SI engines, the scavenging process often results in a portion of the fresh mixture exiting the exhaust port before it closes, resulting in high UHC emissions.

The presence of UHC in CI engines is related to the heterogeneous nature of the fuel–air mixture. Under certain conditions, fuel–air mixtures that lie outside the flammability limits at the lean and rich extremes can exist in portions of the combustion chamber and escape combustion, thus contributing significantly to UHC in the exhaust. Fuel injected near the end of the combustion process and fuel remaining in the nozzle **sac volume** at the end of injection contribute to UHC emission in CI engines. Engine variables that affect UHC emissions include the fuel–air ratio; intake air temperature; and cooling water temperature.

Oxides of Nitrogen. Nitric oxide (NO) is formed from the combination of nitrogen and oxygen present in the intake air under the high-temperature conditions that result from the combustion process. As the gas temperature drops during the expansion stroke, the reaction is frozen, and levels of NO persist in the exhaust products far in excess of the equilibrium level at the exhaust temperature. In the presence of additional oxygen in the air, some NO transforms to nitrogen dioxide (NO_2), a toxic gas.

The combined NO and NO_2 are referred to as oxides of nitrogen or NO_x. The production of NO_x is in general aggravated by conditions that increase the peak combustion temperature. In SI engines, the most important variables that affect NO_x production are the air/fuel ratio; spark timing; intake air temperature; and amount of residual combustion products remaining in the cylinder after exhaust. In CI engines, ignition delay, which affects the degree of premixed combustion, plays a key role in NO_x formation. A larger premixed combustion fraction will produce higher combustion temperatures and higher levels of NO_x.

Particulates. Particulates are a troublesome constituent in the exhaust from CI engines. They are defined by the U.S. Environmental Protection Agency (EPA) as any exhaust substance (other than water) that can be trapped on a filter at temperatures of 325 K or below. Particulates trapped on a filter may be classified as soot plus an organic fraction of hydrocarbons and their partial oxidation products. Soot consists of agglomerates of solid uncombusted carbon particles. Particulates are of concern because their small size permits inhalation and entrapment in the lung walls, making them potential lung carcinogens.

Soot is formed in CI engines under conditions of heavy load when the gas temperature is high and the concentration of oxygen is low. Smoke production is affected by such parameters as fuel CN; rate of fuel injection; inlet air temperature; and the presence of secondary injection.

Control of Emissions from IC Engines

Figure 8.3.14 depicts the relative concentrations of CO, NO_x, and UHC in the exhaust products of an SI engine as a function of the fuel–air mixture. Lean mixture combustion, which promotes good thermal efficiency, also results in low UHC and CO production but causes high levels of NO_x emission. Increasing the fuel/air ratio to reduce NO_x results in increased CO and UHC emission. Approaches to reduce total emissions fall under two categories: (1) engine design and fuel modifications; and (2) treatment of exhaust gases after they leave the engine.

In SI engines, the first approach focuses on addressing engine variables and design modifications, which improve in-cylinder mixing and combustion in an effort to reduce CO and UHC emissions. To reduce NO_x, attention is focused on factors that reduce peak combustion temperature and reduce the oxygen available in the flame front. Design and operating parameters implemented or modified for decreased emissions include compression ratio reduction, increased coolant temperature, modification of the combustion chamber shape to minimize surface-to-volume ratio and increase turbulence, improvement of intake manifold design for better charge distribution, use of fuel injection instead of carburetors for better mixture control, use of exhaust gas recirculation to reduce NO_x by lowering combustion temperatures, positive crankcase ventilation to reduce UHC, and increased aromatic content in gasoline.

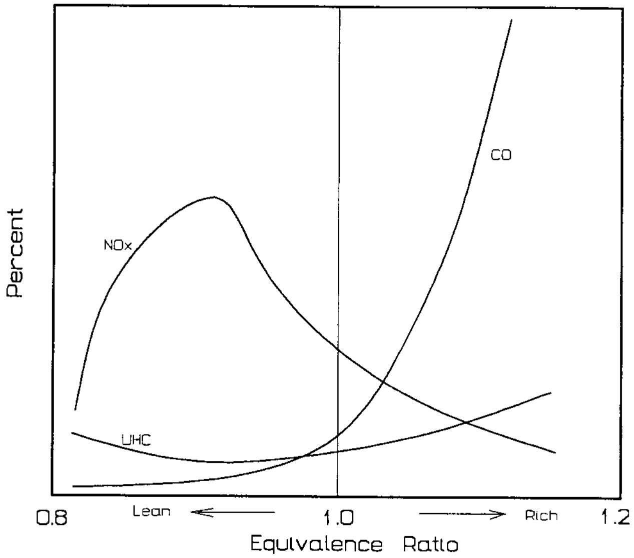

FIGURE 8.3.14 Emission levels from an SI engine vs. fuel–air mixture.

Engine modifications that have been implemented to reduce emissions from CI engines include modifications to the combustion chamber shape to match the air swirl pattern and fuel spray pattern for better mixing and complete combustion; use of exhaust gas recirculation to limit NO_x production; use of higher injection pressure for better atomization to reduce soot and UHC; and the use of precise injection timing with electronic control.

In the second approach, several devices have been developed for after treatment of exhaust products. A thermal reactor may be used to oxidize UHC and CO. These typically consist of a well-insulated volume placed close to the exhaust manifold, with internal baffles to increase the gas residence time and an air pump to supply fresh oxygen for the oxidation reactions. Thermal reactors are ineffective for NO_x reduction and thus have limited application.

Catalytic converters utilize a catalyst, typically a noble metal such as platinum, rhodium, or palladium, deposited on a ceramic substrate to promote reactions at lower temperatures. Two types are in use: oxidation converters and reduction converters. Oxidation catalytic converters use the excess air available in lean mixtures (or supplied from an external air pump) to oxidize CO and UHC emissions. Reduction catalytic converters operate with low levels of oxygen to cause reduction of NO_x. Sometimes, dual catalytic converters are employed to treat all three pollutants with a reducing converter, to reduce NO_x, placed upstream of an oxidation converter for treating CO and UHC. This arrangement requires that the engine be operated with a rich mixture, which decreases fuel economy.

Three-way catalytic converters are a recent development that permits treatment of NO_x, CO, and UHC in a single device, thus reducing size and weight of the exhaust system. Proper operation of a three-way catalyst requires very nearly stoichiometric combustion. If the combustion is too lean, NO_x is not adequately reduced, and if it is too rich, UHC and CO are not adequately oxidized. Within a narrow band for equivalence ratio (from about 0.999 to 1.007), conversion efficiency is 80% or better for all three pollutants (Kummer, 1980). Maintaining engine operation within this narrow mixture band requires a closed-loop fuel-metering system that utilizes an oxygen sensor placed in the exhaust system to monitor excess oxygen and control the fuel injection to maintain near stoichiometric combustion.

Reduction catalytic converters cannot be used with CI engines to reduce NO_x because they normally run lean with significant amounts of excess oxygen in the exhaust. Thus, engine design factors must be relied on to keep NO_x as low as possible. Soot emission may be reduced by after treatment using a device called a trap oxidizer. A trap oxidizer filters particulate matter from the exhaust stream and oxidizes it, usually with the aid of a catalyst for reducing the oxidation temperature. These have been used on small, high-speed automotive diesel engines, but their application to larger, slower speed engines is limited because of the higher level of particulate production and the lower exhaust temperature. For additional information on emissions, see Henein (1972); Obert (1973); and *SAE Surface Vehicle Emissions Standards Manual* (1993).

Fuels for SI and CI Engines

Background

The primary distinguishing factor between SI and CI engines is the fundamental difference in the combustion process. SI engines rely on homogeneous, spark-ignited, premixed combustion, while CI engines are designed for heterogeneous combustion with an autoignited premixed combustion period followed by a diffusion combustion period. The differences in the combustion process call for quite different qualities in the fuels to achieve optimum performance.

By far the most common fuel for SI engines is gasoline, although other fuels can be used in special circumstances, including alcohol, natural gas, and propane. Even such low-grade fuels as wood gas and coal gas have been used to fuel SI engines during wartime when conventional fuels were in short supply. Diesel fuel is the predominant fuel for CI engines, but they too can be designed to operate on a variety of other fuels, such as natural gas, bio-gas, and even coal slurries. This discussion is confined to gasoline and diesel fuel, both of which are distilled from crude oil.

Crude oil is composed of several thousand different hydrocarbon compounds that, upon heating, are vaporized at different temperatures. In the distillation process, different "fractions" of the original crude are separated according to the temperatures at which they vaporize. The more volatile fraction, naphtha, is followed in order of increasing temperature of vaporization by fractions called distillate, gas oil, reduced crude, and residual oil. These fractions may be further subdivided into light, middle, and heavy classifications. Light virgin naphtha can be used directly as gasoline, although it has relatively poor antiknock quality. The heavier fractions can be chemically processed through coking and catalytic cracking to produce additional gasoline. Diesel fuel is derived from the light to heavy virgin gas oil fraction and from further chemical processing of reduced crude.

Gasoline

Gasoline fuels are mixtures of hydrocarbon compounds with boiling points in the range of 32 to 215°C. The two most important properties of gasoline for SI engine performance are volatility and octane rating. Adequate volatility is required to ensure complete vaporization, as required for homogeneous combustion, and to avoid cold-start problems. If the volatility is too high, however, vapor locking in the fuel delivery system may become a problem. Volatility may be specified by the distillation curve (the distillation temperatures at which various percentages of the original sample have evaporated). Higher volatility fuels will be characterized by lower temperatures for given fixed percentages of evaporated sample or, conversely, by higher percentages evaporated at or below a given temperature. Producers generally vary the volatility of gasoline to suit the season, increasing the volatility in winter to improve cold-start characteristics and decreasing it in summer to reduce vapor locking.

The octane rating of a fuel is a measure of its resistance to autoignition or knocking; higher octane fuels are less prone to autoignition. The octane rating system assigns the value of 100 to iso-octane (C_8H_{18}, a fuel that is highly resistant to knock) and the value 0 to *n*-heptane (C_7H_{16}, a fuel that is prone to knock). Two standardized methods are employed to determine the octane rating of fuel test samples: the research method and the motor method; see ASTM Standards Part 47 — Test Methods for Rating Motor, Diesel and Aviation Fuels (ASTM, 1995).

Both methods involve testing the fuel in a special variable compression-ratio engine (cooperative fuels research or CFR engine). The test engine is operated on the fuel sample and the compression ratio is gradually increased to obtain a standard knock intensity reading from a knock meter. The octane rating is obtained from the volumetric percentage of iso-octane in a blend of iso-octane and *n*-heptane that produces the same knock intensity at the same compression ratio.

The principal differences between the research method and the motor method are the higher operating speed, higher mixture temperature, and greater spark advance employed in the motor method. Ratings obtained by the research method are referred to as the **research octane number** (RON); those obtained with the motor method are called the motor octane number (MON). MON ratings are lower than RON ratings because of the more stringent conditions, i.e., higher thermal loading of the fuel. The octane rating commonly advertised on gasoline pumps is the **antiknock index**, $(R + M)/2$, which is the average of the values obtained by the two methods. The typical range of antiknock index for automotive gasolines currently available at the pump is 87 to 93. In general, higher compression SI engines require higher octane fuels to avoid autoignition and to realize full engine performance potential from engines equipped with electronic control systems incorporating a knock sensor.

Straight-run gasoline (naphtha) has a poor octane rating on the order of 40 to 50 RON. Higher octane fuels are created at the refinery by blending with higher octane components produced through alkylation wherein light olefin gases are reacted with isobutane in the presence of a catalyst. Iso-octane, for example, is formed by reacting isobutane with butene. Aromatics with double carbon bonds shared between more than one ring, such as naphthalene and anthracene, serve to increase octane rating because the molecules are particularly difficult to break.

Additives are also used to increase octane ratings. In the past, a common octane booster added to automotive fuels was lead alkyls — tetraethyl or tetramethyl lead. For environmental reasons, lead has been removed from automotive fuels in most countries. It is, however, still used in aviation fuel. Low-lead fuel has a concentration of about 0.5 g/L, which boosts octane rating by about five points. The use of leaded fuel in an engine equipped with a catalytic converter to reduce exhaust emissions will rapidly deactivate the catalyst (typically a noble metal such as platinum or rhodium), quickly destroying the utility of the catalytic converter. Octane-boosting additives in current use include the oxygenators methanol, ethanol, and methyl tertiary butyl ether (MTBE).

RON values of special-purpose, high-octane fuels for racing and aviation purposes can exceed 100 and are arrived at through an extrapolation procedure based on the knock-limited indicated mean effective pressure (klimep). The klimep is determined by increasing the engine intake pressure until knock occurs. The ratio of the klimep of the test fuel to that for iso-octane is used to extrapolate the octane rating above 100.

Diesel Fuels

Diesel fuels are blends of hydrocarbon compounds with boiling points in the range of 180 to 360°C. Properties of primary importance for CI fuels include the density, viscosity, cloud point, and ignition quality (CN). Diesel fuel exhibits a much wider range of variation in properties than does gasoline. The density of diesel fuels tends to vary according to the percentages of various fractions used in the blend. Fractions with higher distillation temperatures tend to increase the density. Variations in density result in variations in volumetric energy content and thus fuel economy, because fuel is sold by volume measure. Higher density fuel will also result in increased soot emission.

Viscosity is important to proper fuel pump lubrication. Low-viscosity fuel will tend to cause premature wear in injection pumps. Too high viscosity, on the other hand, may create flow problems in the fuel delivery system. Cloud point is the temperature at which a cloud of wax crystals begins to form in the fuel. This property is critical for cold-temperature operation because wax crystals will clog the filtration system. ASTM does not specify maximum cloud point temperatures, but rather recommends that cloud points be no more than 6°C above the 10th percentile minimum ambient temperature for the region for which the fuel is intended; see ASTM D 975 (ASTM, 1995).

CN provides a measure of the autoignition quality of the fuel and is the most important property for CI engine fuels. The CN of a fuel sample is obtained through the use of a CI CFR engine in a manner analogous to the determination of octane rating. The test method for CN determination is specified in standard ASTM D 613. *n*-Cetane (same as hexadecane, $C_{16}H_{34}$) has good autoignition characteristics and is assigned the cetane value of 100. The bottom of the cetane scale was originally defined in terms of α-methyl naphthalene ($C_{11}H_{10}$), which has poor autoignition characteristics and was assigned the value 0. In 1962, for reasons of availability and storability, the poor ignition quality standard fuel used to establish the low end of the cetane scale was changed to heptamethylnonane (HMN), with an assigned CN of 15. The CN of a fuel sample is determined from the relative volumetric percentages of cetane and HMN in a mixture that exhibits the same ignition delay characteristics as the test sample using the relation

$$\text{CN} = \%\ n\text{-cetane} + 0.15\left(\%\ \text{HMN}\right) \tag{8.3.10}$$

ASTM standard D 976 (ASTM, 1995) provides the following empirical correlation for calculating the **cetane index** of straight petroleum distillate fuels (no additives) as an approximation to the measured CN:

$$\text{Cetane index} = 454.74 - 1641.416D + 774.74D^2 - 0.554B + 97.803\ (\log B)^2 \tag{8.3.11}$$

where D = density at 15°C (g/mL) and B = mid-boiling temperature (°C).

ASTM standard D 975 (ASTM, 1995) establishes three classification grades for diesel fuels (No. 1-D, No. 2-D, and No. 4-D) and specifies minimum property standards for these grades. No. 1-D is a volatile distillate fuel for engines that must operate with frequent changes in speed and load. No. 2-D is a lower volatility distillate fuel for industrial and heavy mobile service engines. No. 4-D is a heavy fuel oil for low- and medium-speed engines. Nos. 1-D and 2-D are principally transportation fuels, while No. 4-D is for stationary applications. The ASTM minimum CN for No. 1-D and No. 2-D is 40, and for No. 4-D the minimum is 30. Typical CNs for transportation fuels lie in the range of 40 to 55. Use of a low-cetane fuel aggravates diesel knock because of the longer ignition delay period, which creates a higher fraction of premixed combustion.

Antiknock quality (octane number) and ignition quality (CN) are opposing properties of distillate fuels. The CN increases with decreasing octane rating of various fuels. Gasoline, with good antiknock quality, has a CN of approximately 10, while a diesel fuel with a CN of 50 will have an octane number of about 20. Thus, gasoline is not a suitable fuel for CI engines because of its poor autoignition quality, and diesel fuel is inappropriate for use in SI engines as a result of its poor antiknock quality. For additional information on fuels for IC engines see Owen and Coley (1995) and the *SAE Fuels and Lubricants Standards Manual* (1993).

Intake Pressurization — Supercharging and Turbocharging

Backround

Pressurizing the intake air (or mixture) by means of a compressor may be used to boost the specific power output of SI and CI engines. Supercharging generally refers to the use of compressors that are mechanically driven from the engine crankshaft, while turbocharging refers to compressors powered by a turbine, which extracts energy from the exhaust stream. Increasing the intake pressure increases the density and thus the mass flow rate of the intake mixture; this allows an increase in the fueling rate, thereby producing additional power.

The mere process of increasing the cylinder pressure results in increased work output per cycle, as illustrated in the *P-V* diagram in Figure 8.3.15, which compares supercharged and naturally aspirated, air standard Otto cycles having the same compression ratio. The work done for the compressed intake cycle (Area 1,2,3,4,1 and Area 5,6,7,1,5) is greater than that for the naturally aspirated cycle (Area 1′,2′,3′,4′,1′) due to the boost of the intake pressure. Positive-displacement superchargers are capable of producing higher boost pressures than turbochargers, which are nearly always centrifugal-type fans. From a practical standpoint, the maximum useful boost pressure from either system is limited by the onset of autoignition in SI engines and by the permissible mechanical and thermal stresses in CI engines.

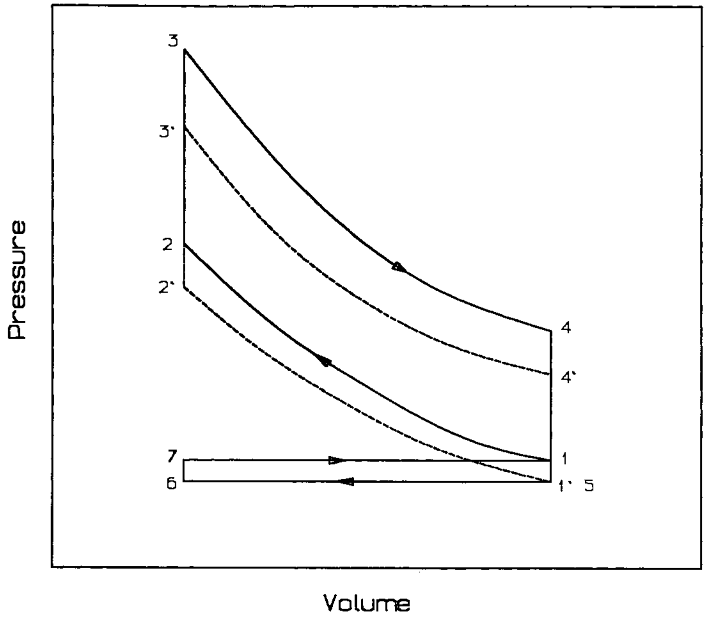

FIGURE 8.3.15 Comparison of supercharged and naturally aspirated Otto cycle.

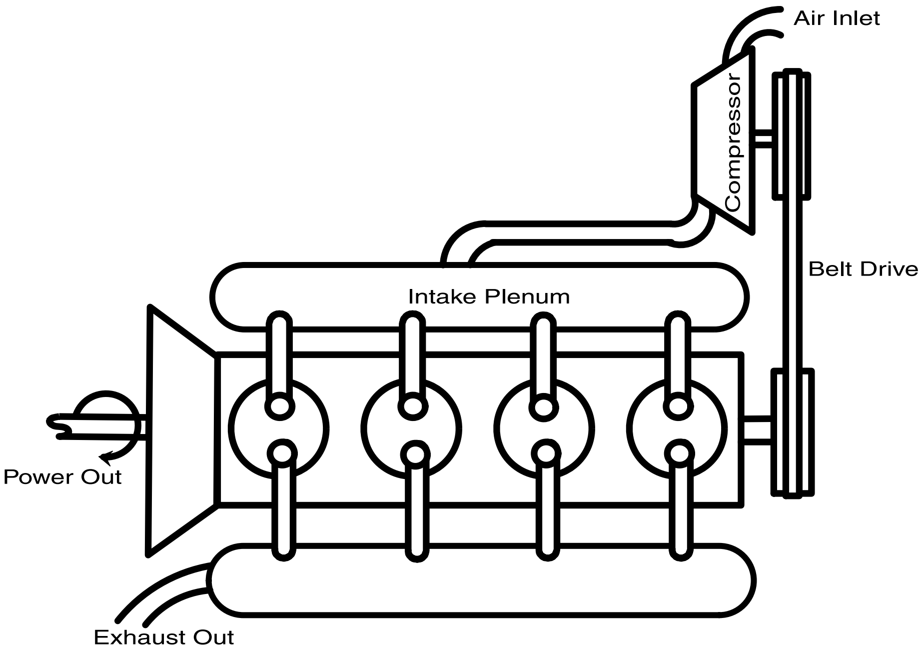

FIGURE 8.3.16 Schematic diagram of supercharged engine.

Supercharging

The principal applications of supercharging SI engines are in high-output drag-racing engines and in large aircraft piston engines to provide high specific output at takeoff and to improve power output at high altitudes. A few high-performance production automobiles also use a supercharger in lieu of the more common turbocharger to achieve their increased performance. For diesel applications, supercharging is used mainly in marine and land-transportation applications. It is common to use supercharging or turbocharging to improve the scavenging process in two-stroke diesel engines. Figure 8.3.16 is a schematic of an engine with a mechanically driven supercharger. Superchargers may be belt, chain, or gear driven from the engine crankshaft.

Two types of superchargers are in use: the positive displacement type (Roots blower) and the centrifugal type. Roots blowers may be classified as: (1) straight double lobe; (2) straight triple lobe; and (3) helix triple lobe (twisted 60%). The helix triple-lobe type runs more quietly than the others and is generally recommended, especially for diesel engines operating under high torque at various speed conditions. Because of its high capacity and small weight and size, the centrifugal type is best suited for applications in which power and volumetric efficiency improvement are required at high engine speed, e.g., with aircraft engines. A centrifugal blower will also survive a backfire more readily than a Roots blower in SI applications. Because superchargers are directly driven from the engine output shaft, no inherent lag in the rate of pressure increase with engine speed is present, as is typically the case with turbochargers.

Turbocharging

Turbochargers utilize a centrifugal compressor directly connected to a turbine that extracts energy from the exhaust gases of the engine and converts it to the shaft work necessary to drive the compressor. Turbocharging is widely used to increase power output in automotive and truck applications of four-stroke SI and CI engines and to improve scavenging of two-stroke CI engines.

There are three methods of turbocharging: the constant pressure; the pulse; and the pulse converter. In the constant-pressure method, as illustrated in Figure 8.3.17, the exhaust pressure is maintained at a nearly constant level above atmospheric. To accomplish this, the exhaust manifold must be large enough to damp out the pressure fluctuations caused by the unsteady flow characteristic of the engine exhaust

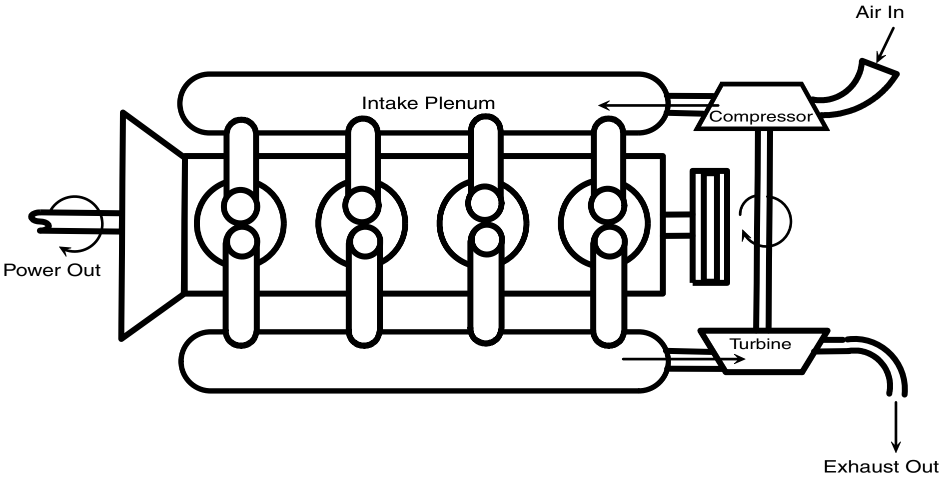

FIGURE 8.3.17 Schematic diagram of a constant-pressure turbocharger.

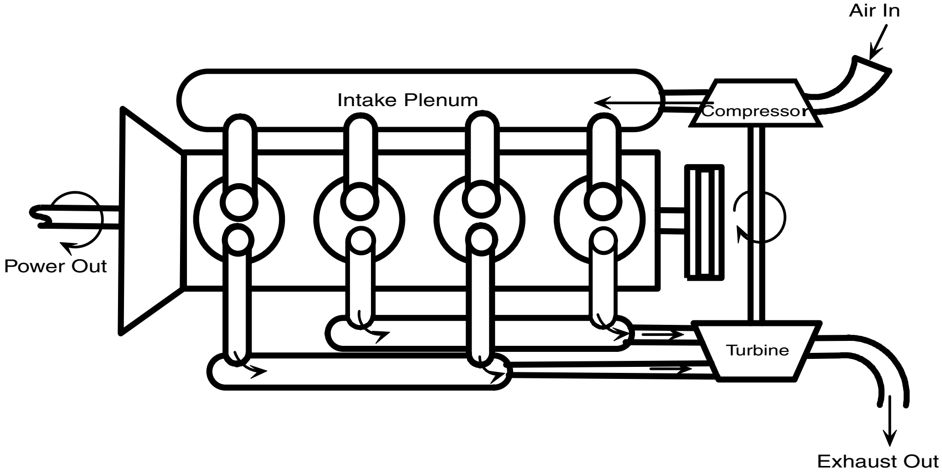

FIGURE 8.3.18 Schematic diagram of a pulse turbocharger.

process. In this method, the turbine operates efficiently under steady-flow conditions; however, some engine power is lost because of the increased backpressure in the exhaust manifold.

The pulse turbocharger, as illustrated in Figure 8.3.18, utilizes the kinetic energy generated by the exhaust blow-down process in each cylinder. This is accomplished by using small exhaust lines grouped together in a common manifold to receive the exhaust from the cylinders, which are blowing down sequentially. In this method, the pressure at the turbine inlet tends to fluctuate; this is not conducive to good turbine efficiency. This is offset to a large degree, however, by improved engine performance as a result of the lower exhaust backpressure relative to the constant-pressure method. The pulse converter method represents a compromise between the previous two techniques. In principle, this is accomplished by converting the kinetic energy in the blow-down process into a pressure rise at the turbine by utilizing one or more diffusers. Details of the different methods of turbocharging may be found in Watson and Janota (1982).

Recent advances in turbocharging technology have focused mainly on (1) improving turbine transient response (turbo-lag); (2) improving torque-speed characteristics of the engine; and (3) increasing the power output by increasing the boost pressure and using charge cooling (intercooling). The use of ceramic materials in fabricating turbine rotors improves the turbine transient response because they are lighter in weight and have less rotational inertia. Ceramic rotors also have greater thermal operating range because of their lower thermal expansion. The use of variable-geometry turbochargers can improve the low-speed torque characteristics of the engine and help reduce the transient response time. This is due to the ability of the variable-geometry turbocharger to change its internal geometry to accommodate low flow rates at low engine speeds and higher volume flow rates at high engine speeds.

However, because the geometry of the turbine rotor remains unchanged while the internal geometry varies, the turbine efficiency will be reduced for all internal geometries other than the optimum design geometry. In response to increased demand for diesel engines with high boost pressure and with size constraints, advances in the aerothermodynamics of axial/radial flow and of two-stage turbochargers, as well as in the design of compressor and turbine blades, have allowed high boost pressure at improved overall turbocharger efficiency.

Charge cooling by means of a heat exchanger (intercooler) between the compressor and the intake ports is effective in reducing NO_x emissions and improving the power output of turbocharged diesel engines and in reducing the probability of knock in SI engines. Two types of charge cooling are in use: air–air and air–water. Air-to-water cooling is used in marine applications, in which a source of cool water is available; air-to-air intercoolers are used for automotive and truck applications.

Defining Terms

Antiknock index: The average of the two octane numbers obtained by the research method and the motor method.

Autoignition: The ability of a fuel–air mixture to ignite spontaneously under conditions of high temperature and pressure.

Bottom dead center (BDC): Piston located at its lowest position in the cylinder. Cylinder volume is maximum at BDC.

Brake mean effective pressure (bmep): Ratio of brake work output per cycle to the displacement volume.

Brake specific fuel consumption (bsfc): The ratio of fuel consumption rate in kilograms per hour to the engine output in kilowatts.

Brake work: Work produced at the output shaft of an IC engine as measured by a dynamometer.

Cetane index: An approximation to the measured cetane number determined from an empirical relationship specified in ASTM D 976.

Cetane number: A measure of the autoignition quality of a fuel important for proper performance of CI engines determined experimentally through use of a CI CFR test engine.

Clearance volume: Combustion chamber volume remaining above the piston at TDC.

Compression ignition (CI) engine: Air alone is compressed in the cylinder and fuel is injected near TDC. Combustion results from autoignition of the fuel–air mixture due to the high temperature of the air.

Compression ratio: The ratio of the cylinder volume at BDC to the volume at TDC.

Cut-off ratio: Ratio of cylinder volume at the end of heat addition to the volume at the start of heat addition in the ideal diesel cycle.

Cylinder volume: Volume above piston at BDC; equals displacement volume plus clearance volume.

Direct injection (DI): Method of fuel injection in low- and medium-speed CI engines wherein fuel is injected into the main combustion chamber formed by a bowl in the top of the piston.

Displacement volume: Difference in cylinder volume between TDC and BDC.

Equivalence ratio: Actual fuel–air ratio divided by stoichiometric fuel–air ratio.

Four-stroke engine: Entire cycle completed in two revolutions of the crankshaft and four strokes of the piston.

Fuel–air ratio: Ratio of mass of fuel to mass of air in the cylinder prior to combustion.

Glow plug: Electric heater installed in prechamber of an IDI diesel engine to aid cold starting.

Heterogeneous combustion: Refers to the mixture of liquid fuel droplets and evaporated fuel vapor and air mixture present in CI engine combustion chambers prior to ignition.

Ignition delay period: Period between start of injection and onset of autoignition in a CI engine.

Indicated mean effective pressure (imep): Ratio of net indicated work output of an IC engine to the displacement volume.

Indicated work: Work output of an IC engine cycle determined by an area calculation from an indicator diagram.

Indicator diagram: Pressure-volume trace for an IC engine cycle; area enclosed by diagram represents work.

Indirect injection (IDI): Method of fuel injection used in high-speed CI engines wherein the fuel is injected into a precombustion chamber to promote fuel–air mixing and reduce ignition delay.

Knock: In SI engines: the noise that accompanies autoignition of the end portion of the uncombusted mixture prior to the arrival of the flame front. In CI engines: The noise that accompanies autoignition of large premixed fractions generated during prolonged ignition delay periods. Knock is detrimental to either type of engine.

NO_x: Harmful oxides of nitrogen (NO and NO_2) appearing in the exhaust products of IC engines.

Octane number: Antiknock rating for fuels important for prevention of autoignition in SI engines.

Particulates: Any exhaust substance, other than water, that can be collected on a filter. Harmful exhaust product from CI engines.

Power density: Power produced per unit of engine mass.

Premixed homogeneous combustion: Fuel and air are mixed in an appropriate combustible ratio prior to ignition process. This is the combustion mode for SI engines and for the initial combustion phase in CI engines.

Sac volume: Volume of nozzles below the needle of a diesel fuel injector that provides a source of UHC emissions in CI engines.

Scavenging: The process of expelling exhaust gases and filling the cylinder with fresh charge in two-stroke engines. This is often accomplished in SI engines by pressurizing the fresh mixture in the crankcase volume beneath the piston and in CI engines by using a supercharger or turbocharger.

Spark ignition (SI) engine: Homogeneous charge of air–fuel mixture is compressed and ignited by a spark.

Stroke: Length of piston movement from TDC to BDC; equal to twice the crankshaft throw.

Supercharging: Pressurizing the intake of an IC engine using a compressor that is mechanically driven from the crankshaft.

Surface ignition: A source of autoignition in SI engines caused by surface hot spots.

Swirl: Circular in-cylinder air motion designed into CI engines to promote fuel–air mixing.

Swirl ratio: Ratio of rotational speed of in-cylinder air (rpm) to engine speed (rpm).

Top dead center (TDC): Piston located at its uppermost position in the cylinder. Cylinder volume (above the piston) is minimum at TDC.

Turbocharging: Pressurizing the intake of an IC engine with a compressor driven by a turbine that extracts energy from the exhaust gas stream.

Two-stroke engine: Entire cycle completed in one revolution of the crankshaft and two strokes of the piston.

Unburned hydrocarbons (UHC): Harmful emission product from IC engines consisting of hydrocarbon compounds that remain uncombusted.

Volumetric efficiency: Ratio of the actual mass of air intake per cycle to the displacement volume mass determined at inlet temperature and pressure.

References

ASTM, 1995. *Annual Book of ASTM Standards*. American Society for Testing and Materials, Philadelphia.

Blair, G.P. Ed. 1988. *Advances in Two-Stroke Cycle Engine Technology*. Society of Automotive Engineers, Inc., Warrendale, PA.

Ferguson, C.R. and Kirkpatrick, A.T., 2001. *Internal Combustion Engines, Applied Thermosciences*. John Wiley & Sons, New York.

Henein, N.A. 1972. *Emissions from Combustion Engines and Their Control*. Ann Arbor Science Publishers, Ann Arbor, MI.

Heywood, J.B. 1988. *Internal Combustion Engine Fundamentals*. McGraw–Hill, New York.

Keating, E.L. 1993. *Applied Combustion*. Marcel Dekker, New York.

Kummer, J.T. 1980. Catalysts for automobile emission control. *Prog. Energy Combust. Sci.* 6:177–199.

Lenz, H.P. 1992. *Mixture Formation in Spark-lgnition Engines*. Springer–Verlag, New York.

Norbye, J.P. 1971. *The Wankel Engine*. Chilton Press, Philadelphia.

Obert, E.F. 1973. *Internal Combustion Engines and Air Pollution*, 3rd ed. Harper & Row, New York.

Owen, K. and Coley, T. 1995. *Automotive Fuels Reference Book*, 2nd ed. Society of Automotive Engineers, Inc., Warrendale, PA.

SAE Fuels and Lubricants Standards Manual. 1993. Society of Automotive Engineers, Inc., Warrendale, PA.

SAE Surface Vehicle Emissions Standards Manual. 1993. Society of Automotive Engineers, Inc., Warrendale, PA.

Stone, R. 1993. *Introduction to Internal Combustion Engines*, 2nd ed. Society of Automotive Engineers, Inc., Warrendale, PA.

Taylor, C.F. 1985. *The Internal Combustion Engine in Theory and Practice*, 2nd ed. Vol. I and II. MIT Press, Cambridge, MA.

Watson, N. and Janota, M.S. 1982. *Turbocharging the Internal Combustion Engine*, John Wiley & Sons, New York.

Further Information

The textbooks on IC engines by Ferguson and Kirkpatrick (2001); Heywood (1988); Obert (1973); Stone (1993); and Taylor (1985) listed under the references provide excellent treatments of this subject. In particular, Stone's book is up to date and informative. The *Handbook of Engineering* (1966) published by CRC Press, Boca Raton, Florida, contains a chapter on IC engines by A. Kornhauser. The Society of Automotive Engineers (SAE) publishes transactions, proceedings, and books related to all aspects of automotive engineering, including IC engines. Two very comprehensive handbooks distributed by SAE are the *Bosch Automotive Handbook* and the *SAE Automotive Handbook*. For more information contact: SAE Publications, 400 Commonwealth Drive, Warrendale, PA, 15096–0001; (412)776-4970.

8.4 Hydraulic Turbines

Roger E.A. Arndt

A hydraulic turbine is a mechanical device that converts the potential energy associated with a difference in water elevation (**head**) into useful work. Modern hydraulic turbines are the result of many years of gradual development. Economic incentives have resulted in the development of very large units (exceeding 800 MW in capacity) with efficiencies that are sometimes in excess of 95%.

The emphasis on the design and manufacture of very large turbines is shifting to the production of smaller units, especially in developed nations, where much of the potential for developing large base-load plants has been realized. At the same time, the escalation in the cost of energy has made many smaller sites economically feasible and has greatly expanded the market for smaller turbines. The increased value of energy also justifies the cost of refurbishment and increasing the capacity of older facilities. Thus, a new market area is developing for updating older turbines with modern replacement runners that have higher efficiency and greater capacity. The introduction of modern computational tools in the last decade has had considerable influence on turbine design.

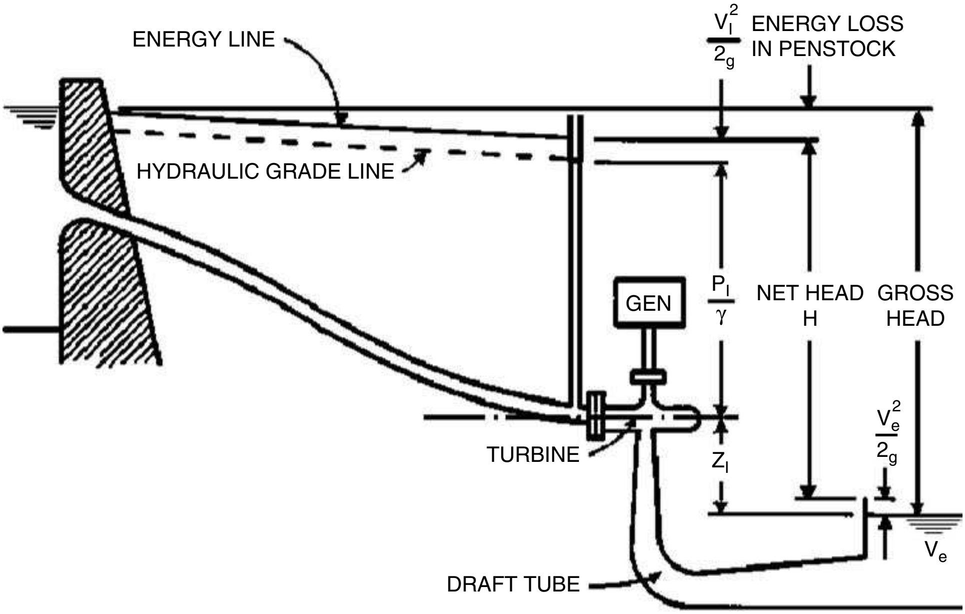

FIGURE 8.4.1 Schematic of a hydropower installation.

General Description

Typical Hydropower Installation

As shown schematically in Figure 8.4.1, the hydraulic components of a hydropower installation consist of an intake, penstock, guide vanes or distributor, turbine, and **draft tube**. Trash racks are commonly provided to prevent ingestion of debris into the turbine. Intakes usually require some type of shape transition to match the passageway to the turbine and also incorporate a gate or some other means of stopping the flow in case of an emergency or turbine maintenance. Some types of turbines are set in an open flume; others are attached to a closed-conduit penstock.

Turbine Classification

The two types of turbines are denoted as impulse and reaction. In an *impulse turbine*, the available head is converted to kinetic energy before entering the **runner**; the power available is extracted from the flow at approximately atmospheric pressure. In a *reaction turbine*, the runner is completely submerged and the pressure and the velocity decrease from inlet to outlet. The velocity head in the inlet to the turbine runner is typically less than 50% of the total head available.

Impulse Turbines. Modern impulse units are generally of the Pelton type and are restricted to relatively high head applications (Figure 8.4.2). One or more jets of water impinge on a wheel containing many curved buckets. The jet stream is directed inwardly, sideways, and outwardly, thereby producing a force on the bucket, which in turn results in a torque on the shaft. All kinetic energy leaving the runner is "lost." A draft tube is generally not used because the runner operates under approximately atmospheric pressure and the head represented by the elevation of the unit above tailwater cannot be utilized. (In principle, a draft tube could be used; this requires the runner to operate in air under reduced pressure. Attempts at operating an impulse turbine with a draft tube have not met with much success.) Because this is a high-head device, this loss in available head is relatively unimportant. As will be shown later, the Pelton wheel is a **low specific speed** device. Specific speed can be increased by the addition of extra nozzles — the specific speed increasing by the square root of the number of nozzles. Specific speed can

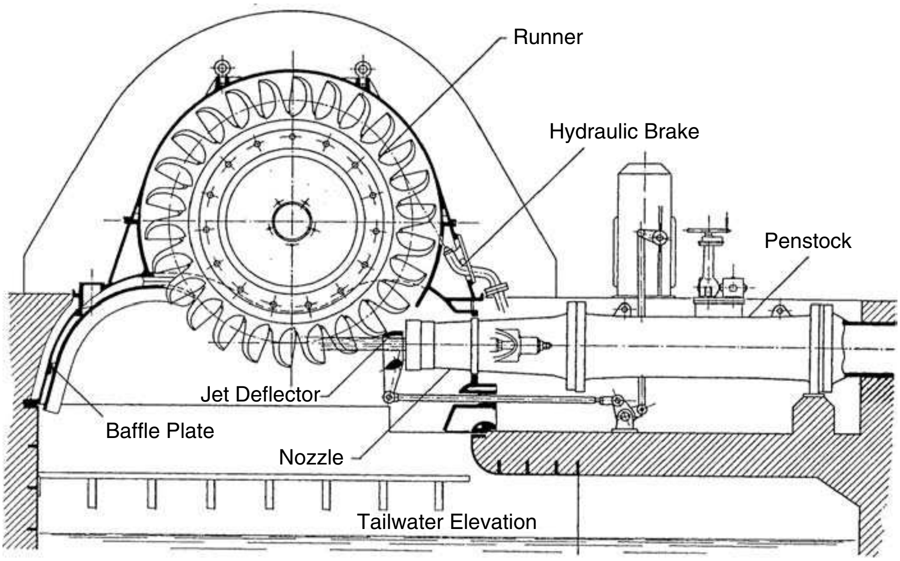

FIGURE 8.4.2 Cross section of a single-wheel, single-jet Pelton turbine. This is the third highest head Pelton turbine in the world, $H = 1447$ m; $n = 500$ rpm; $P = 35.2$ MW; $N_s \sim 0.038$. (Courtesy of Vevey Charmilles Engineering Works. Adapted from Raabe, J. 1985. *Hydro Power: The Design, Use, and Function of Hydromechanical, Hydraulic, and Electrical Equipment.* VDI Verlag, Dusseldorf, Germany.)

also be increased by a change in the manner of inflow and outflow. Special designs such as the Turgo or crossflow turbines are examples of relatively high specific speed impulse units (Arndt, 1991).

Most Pelton wheels are mounted on a horizontal axis, although newer vertical-axis units have been developed. Because of physical constraints on orderly outflow from the unit, the number of nozzles is generally limited to six or less. Whereas **wicket gates** control the power of a reaction turbine, the power of the Pelton wheel is controlled by varying the nozzle discharge by means of an automatically adjusted needle, as illustrated in Figure 8.4.2. Jet deflectors or auxiliary nozzles are provided for emergency unloading of the wheel. Additional power can be obtained by connecting two wheels to a single generator or by using multiple nozzles. Because the needle valve can throttle the flow while maintaining essentially constant jet velocity, the relative velocities at entrance and exit remain unchanged, producing nearly constant efficiency over a wide range of power output.

Reaction Turbines. Reaction turbines are classified according to the variation in flow direction through the runner. In radial- and mixed-flow runners, the flow exits at a radius different from the radius at the inlet. If the flow enters the runner with only radial and tangential components, it is a radial-flow machine. The flow enters a mixed-flow runner with radial as well as axial components. Francis turbines are of the radial- and mixed-flow type, depending on the design specific speed. A Francis turbine is illustrated in Figure 8.4.3.

Axial-flow propeller turbines are generally of the fixed-blade or Kaplan (adjustable-blade) variety. The “classical” propeller turbine, illustrated in Figure 8.4.4, is a vertical-axis machine with a scroll case and a radial wicket gate configuration that is very similar to the flow inlet for a Francis turbine. The flow enters radially inward and makes a right-angle turn before entering the runner in an axial direction. The Kaplan turbine has adjustable runner blades and adjustable wicket gates. The control system is designed so that the variation in blade angle is coupled with the wicket gate setting in a manner that achieves best overall efficiency over a wide range of flow rates.

Some modern designs take full advantage of the axial-flow runner; these include the tube, bulb, and Straflo types illustrated in Figure 8.4.5. The flow enters and exits the turbine with minor changes in direction. A wide variation in civil works design is also permissible. The tubular type can be fixed-

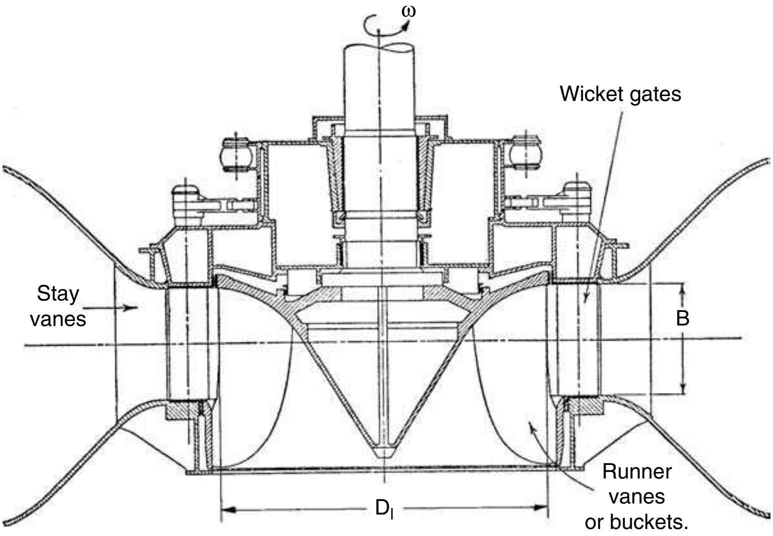

FIGURE 8.4.3 Francis turbine, $N_s \sim 0.66$. (Adapted from Daily, J.W. 1950. In *Engineering Hydraulics,* Ed., H. Rouse. Wiley, New York. Reprinted with permission.)

propeller, semi-Kaplan, or fully adjustable. An externally mounted generator is driven by a shaft that extends through the flow passage upstream or downstream of the runner. The bulb turbine was originally designed as a high-output, low-head unit. In large units, the generator is housed within the bulb and is driven by a variable-pitch propeller at the trailing end of the bulb. Pit turbines are similar in principle to bulb turbines, except that the generator is not enclosed in a fully submerged compartment (the bulb). Instead, the generator is in a compartment that extends above water level. This improves access to the generator for maintenance.

Principles of Operation

Power Available, Efficiency

The power that can be developed by a turbine is a function of the head and flow available:

$$P = \eta \rho g Q H \tag{8.4.1}$$

where η is the turbine efficiency; ρ is the density of water (kg/m^3); g is the acceleration due to gravity (m/s^2); Q is the flow rate (m^3/s); and H is the net head in meters. *Net head* is defined as the difference between the *total head* at the inlet and the tailrace, as illustrated in Figure 8.4.1. Various definitions of net head are used in practice; these depend on the value of the exit velocity head, $V_e^2/2g$, that is used in the calculation. The International Electrotechnical Test Code uses the velocity head at the draft tube exit.

The efficiency depends on the actual head and flow utilized by the turbine runner; flow losses in the draft tube; and the frictional resistance of mechanical components.

Similitude and Scaling Formulae

Under a given head, a turbine can operate at various combinations of speed and flow depending on the inlet settings. For reaction turbines the flow into the turbine is controlled by the wicket gate angle, α. The nozzle opening in impulse units typically controls the flow. Turbine performance can be described in terms of nondimensional variables,

$$\psi = \frac{2gH}{\omega^2 D^2} \tag{8.4.2}$$

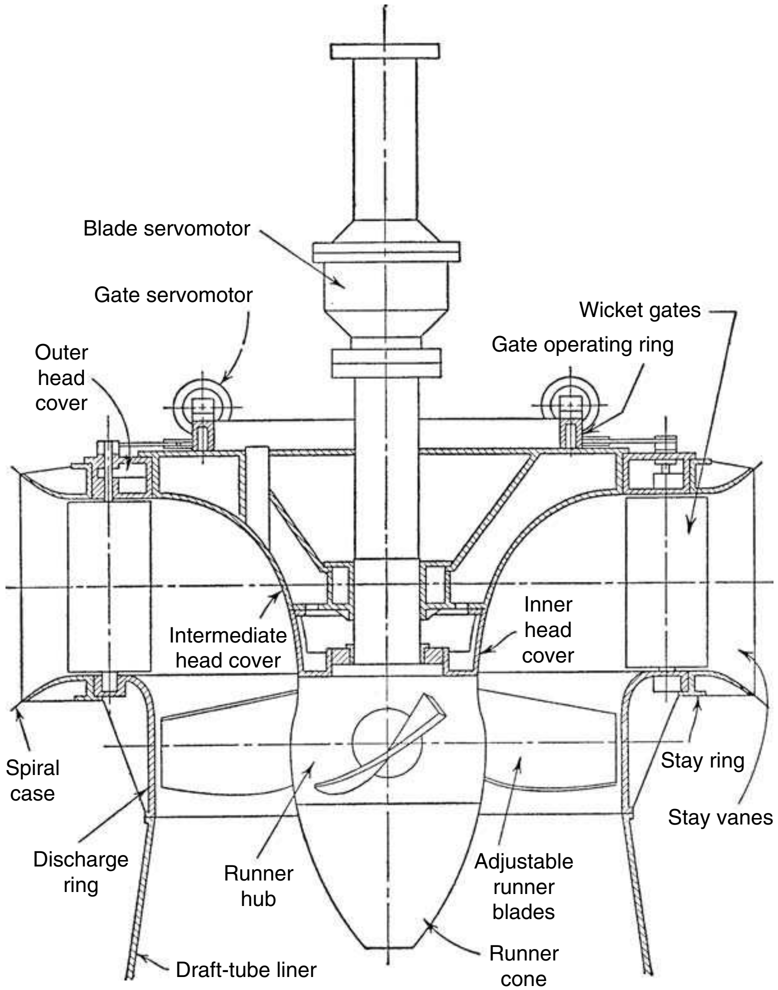

FIGURE 8.4.4 Smith–Kaplan axial-flow turbine with adjustable-pitch runner blades, $N_S \sim 2.0$. (From Daily, J.W. 1950. In *Engineering Hydraulics,* Ed., H. Rouse. Wiley, New York. Reprinted with permission.)

$$\phi = \frac{Q}{\sqrt{2gHD^2}} \tag{8.4.3}$$

where ω is the rotational speed of the turbine in radians per second and D is the diameter of the turbine.

The hydraulic efficiency of the runner alone is given by

$$\eta_h = \frac{\phi}{\sqrt{\psi}}\left(C_1 \cos\alpha_1 - C_2 \cos\alpha_2\right) \tag{8.4.4}$$

where C_1 and C_2 are constants that depend on the specific turbine configuration, and α_1 and α_2 are the inlet and outlet angles that the absolute velocity vectors make with the tangential direction. The value of cos α_2 is approximately zero at peak efficiency. The terms ϕ, ψ_2, α_1, and α_2 are interrelated. Using model test data, isocontours of efficiency can be mapped in the $\phi\psi$ plane. This is typically referred to as a *hill diagram*, as shown in Figure 8.4.6.

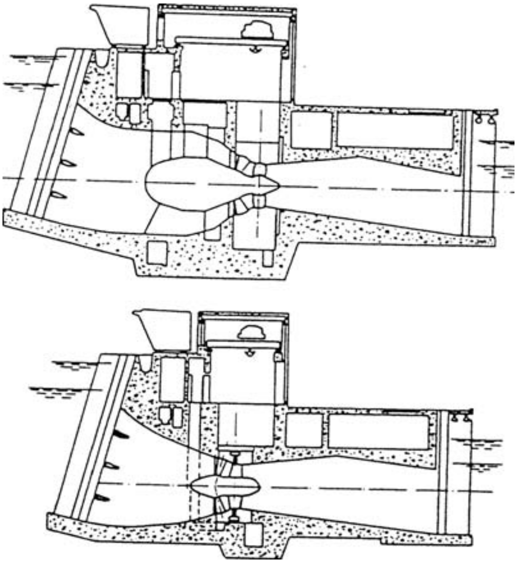

FIGURE 8.4.5 Comparison between bulb (upper) and Straflo (lower) turbines. (Courtesy U.S. Dept. of Energy.)

The **specific speed** is defined as

$$N_s = \frac{\omega\sqrt{Q}}{(2gH)^{3/4}} = \sqrt{\frac{\phi}{\psi}} \tag{8.4.5}$$

A given specific speed describes a specific combination of operating conditions that ensures similar flow patterns and the same efficiency in geometrically similar machines regardless of the size and rotational speed of the machine. It is customary to define the design specific speed in terms of the value at the design head and flow where peak efficiency occurs. The value of specific speed so defined permits a classification of different turbine types.

The specific speed defined here is dimensionless. Many other forms of specific speed exist are dimensional and have distinct numerical values depending on the system of units used (Arndt, 1991). (The literature also contains two other minor variations of the dimensionless form. One differs by a factor of $1/\pi^{1/2}$ and the other by $2^{3/4}$.) The similarity arguments used to arrive at the concept of specific speed indicate that a given machine of diameter D operating under a head H will discharge a flow Q and produce a torque T and power P at a rotational speed ω given by

$$Q = \phi D^2 \sqrt{2gH} \tag{8.4.6}$$

$$T = T_{11}\rho D^3 2gH \tag{8.4.7}$$

$$P = P_{11}\rho D^2 (2gH)^{3/2} \tag{8.4.8}$$

$$\omega = \frac{2u_1}{D} = \omega_{11}\frac{\sqrt{2gH}}{D}, \quad \left[\omega_{11} = \frac{1}{\sqrt{\psi}}\right] \tag{8.4.9}$$

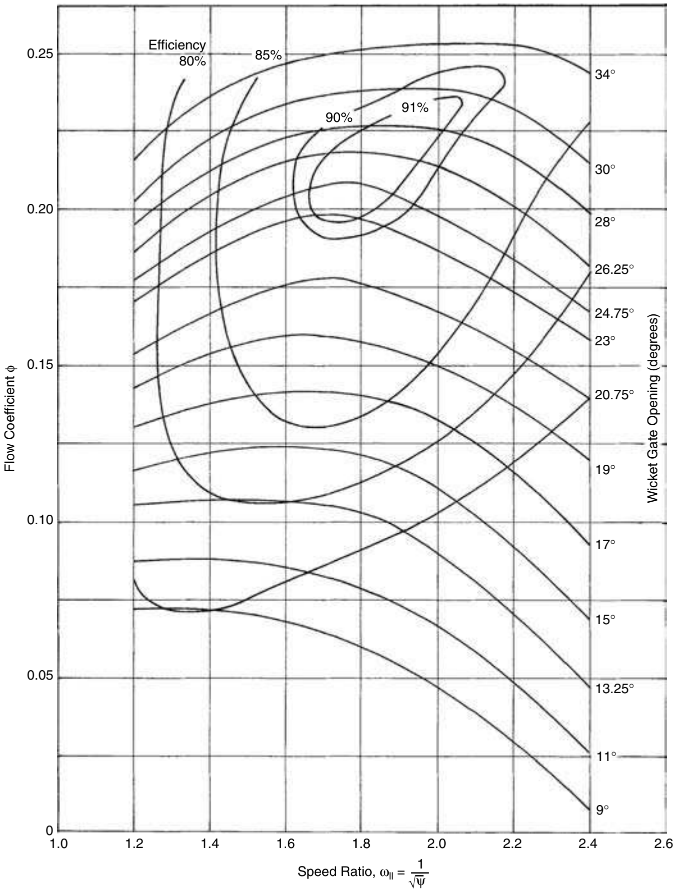

FIGURE 8.4.6 Typical hill diagram. Information of this type is obtained in turbine test stand (see Figure 8.4.9). (Adapted from Wahl, T.L. 1994. Draft tube surging times two: the twin vortex problem. *Hydro Rev.* 13(1):60–69, 1994. With permission.)

with

$$P_{11} = T_{11}\omega_{11} \tag{8.4.10}$$

where T_{11}, P_{11}, and ω_{11} are also nondimensional. (The reader is cautioned that many texts, especially in the American literature, contain dimensional forms of T_{11}, P_{11}, and ω_{11}.) In theory, these coefficients are fixed for a machine operating at a fixed value of specific speed, independent of the size of the machine. Equation (8.4.6) through Equation (8.4.10) can be used to predict the performance of a large machine using the measured characteristics of a smaller machine or model.

Factors Involved in Selecting a Turbine

Performance Characteristics

Impulse and reaction turbines are the two basic types of turbines. They tend to operate at peak efficiency over different ranges of specific speed, due to geometric and operational differences.

Impulse Turbines. Of the head available at the nozzle inlet, a small portion is lost to friction in the nozzle and to friction on the buckets. The rest is available to drive the wheel. The actual utilization of this head depends on the velocity head of the flow leaving the turbine and the setting above tailwater. Optimum conditions, corresponding to maximum utilization of the head available, dictate that the flow leaves at

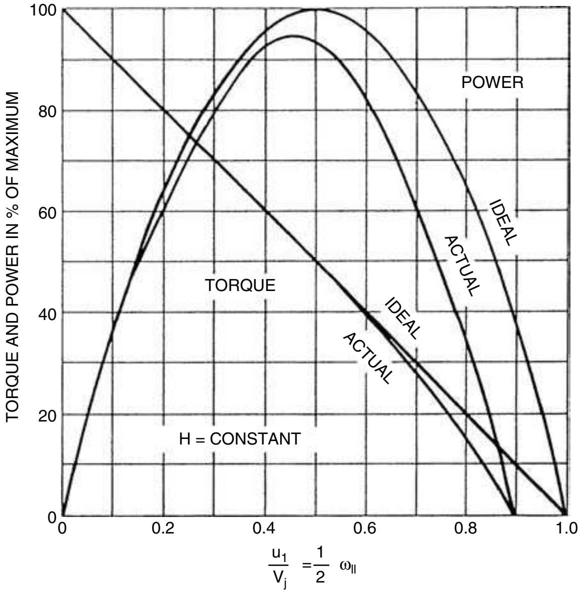

FIGURE 8.4.7 Ideal and actual variable-speed performance for an impulse turbine. (Adapted from Daily, J.W. 1950. In *Engineering Hydraulics*, Ed., H. Rouse. Wiley, New York. With permission.)

essentially zero velocity. Under ideal conditions, this occurs when the peripheral speed of the wheel is one half the jet velocity. In practice, optimum power occurs at a speed coefficient, ω_{11}, somewhat less than 1.0 (illustrated in Figure 8.4.7). Because the maximum efficiency occurs at fixed speed for fixed H, V_j must remain constant under varying flow conditions. Thus, the flow rate Q is regulated with an adjustable nozzle. However, maximum efficiency occurs at slightly lower values of ω_{11} under partial power settings. Present nozzle technology is such that the discharge can be regulated over a wide range at high efficiency.

A given head and penstock configuration establishes the optimum jet velocity and diameter. The size of the wheel determines the speed of the machine. The design specific speed is approximately

$$N_S = 0.77 \frac{d_j}{D} \text{ (Pelton turbines)} \tag{8.4.11}$$

Practical values of d_j/D for Pelton wheels to ensure good efficiency are in the range 0.04 to 0.1, corresponding to N_s values in the range 0.03 to 0.08. Higher specific speeds are possible with multiple nozzle designs. The increase is proportional to the square root of the number of nozzles. In considering an impulse unit, one must remember that efficiency is based on net head; the net head for an impulse unit is generally less than the net head for a reaction turbine at the same gross head because of the lack of a draft tube.

Reaction Turbines. The main difference between impulse units and reaction turbines is that a pressure drop takes place in the rotating passages of the reaction turbine. This implies that the entire flow passage from the turbine inlet to the discharge at the tailwater must be completely filled. A major factor in the overall design of modern reaction turbines is the draft tube. It is usually desirable to reduce the overall equipment and civil construction costs by using high specific speed runners. Under these circumstances, the draft tube is extremely critical for flow stability and efficiency. (This should be kept in mind when retrofitting on older, low specific speed turbine with a new runner of higher capacity.) At higher specific speed, a substantial percentage of the available total energy is in the form of kinetic energy leaving the runner. To recover this efficiently, considerable emphasis should be placed on the draft tube design.

The practical specific speed range for reaction turbines is much broader than for impulse wheels. This is due to the wider range of variables that control the basic operation of the turbine. The pivoted guide vanes allow for control of the magnitude and direction of the inlet flow. Because of a fixed relationship among blade angle, inlet velocity, and peripheral speed for shock-free entry, this requirement cannot be completely satisfied at partial flow without the ability to vary blade angle. This is the distinction between the efficiency of fixed-propeller and Francis types at partial loads and the fully adjustable Kaplan design.

In Equation (8.4.4), optimum hydraulic efficiency of the runner would occur when α_2 is equal to 90°. However, the overall efficiency of the turbine is dependent on the optimum performance of the draft tube as well, which occurs with a little swirl in the flow. Thus, the best overall efficiency occurs with $\alpha_2 \approx 75°$ for high specific speed turbines.

The determination of optimum specific speed in a reaction turbine is more complicated than for an impulse unit because there are more variables. For a radial-flow machine, an approximate expression is

$$N_S = 1.64\left[C_V \sin\alpha_1 \frac{B}{D_1}\right]^{1/2} \omega_{11} \quad \text{(Francis turbines)} \tag{8.4.12}$$

where C_v is the fraction of net head that is in the form of inlet velocity head and B is the height of the inlet flow passage (see Figure 8.4.3). N_s for Francis units is normally found to be in the range 0.3 to 2.5.

Standardized axial-flow machines are available in the smaller size range. These units are made up of standard components, such as shafts and blades. For such cases,

$$N_S \sim \frac{\sqrt{\tan\beta}}{n_B^{3/4}} \quad \text{(Propeller turbines)} \tag{8.4.13}$$

where β is the blade pitch angle and n_B is the number of blades. The advantage of controllable pitch is also obvious from this formula; the best specific speed is simply a function of pitch angle.

It should be further noted that ω_{11} is approximately constant for Francis units and N_S is proportional to $(B/D_1)^{1/2}$. It can also be shown that velocity component based on the peripheral speed at the throat, ω_{11e}, is proportional to N_S. In the case of axial-flow machinery, ω_{11} is also proportional to N_S. For minimum cost, peripheral speed should be as high as possible — consistent with cavitation-free performance. Under these circumstances N_S would vary inversely with the square root of head (H is given in meters):

$$N_S = \frac{C}{\sqrt{H}} \tag{8.4.14}$$

where the range of C is 8 to 11 for fixed-propeller units and Kaplan units and 6 to 9 for Francis units.

Performance Comparison. The physical characteristics of various runner configurations are summarized in Figure 8.4.8. It is obvious that the configuration changes with speed and head. Impulse turbines are efficient over a relatively narrow range of specific speed, whereas Francis and propeller turbines have a wider useful range. An important consideration is whether a turbine is required to operate over a wide range of load. Pelton wheels tend to operate efficiently over a wide range of power loading because of their nozzle design. In the case of reaction machines that have fixed geometry, such as Francis and propeller turbines, efficiency can vary widely with load. However, Kaplan and Deriaz (an adjustable-blade mixed-flow turbine; see Arndt, 1991) turbines can maintain high efficiency over a wide range of operating conditions. The decision of whether to select a simple configuration with a relatively "peaky" efficiency curve or incur the added expense of installing a more complex machine with a broad efficiency curve will depend on the expected operation of the plant and other economic factors.

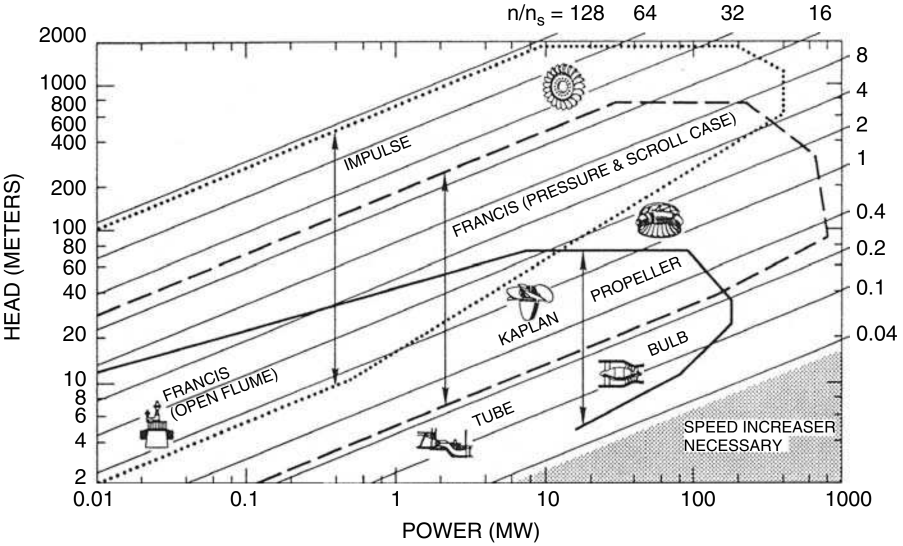

FIGURE 8.4.8 Application chart for various turbine types (n/n_S is the ratio of turbine speed in rpm, n, to specific speed defined in the metric system, $n_S = nP^{1/2}/H^{5/4}$, with P in kilowatts). (From Arndt, R.E.A. 1991. In *Hydropower Engineering Handbook*, Eds., J.S. Gulliver and R.E.A. Arndt, 4.1–4.67. McGraw–Hill, New York. With permission.)

Note that in Figure 8.4.8 an overlap in the range of application of various types of equipment is shown. This means that either type of unit can be designed for good efficiency in this range, but other factors, such as generator speed and cavitation, may dictate the final selection.

Speed Regulation

The speed regulation of a turbine is an important and complicated problem. The magnitude of the problem varies with size; type of machine and installation; type of electrical load; and whether the plant is tied into an electrical grid. It should also be kept in mind that runaway or no-load speed can be higher than the design speed by factors as high as 2.6. This is an important design consideration for all rotating parts, including the generator.

The speed of a turbine must be controlled to a value that matches the generator characteristics and the grid frequency:

$$n = \frac{120f}{N_P} \tag{8.4.15}$$

where n is turbine speed in rpm; f is the required grid frequency in Hertz; and N_P is the number of poles in the generator. Typically, N_p is in multiples of 4. There is a tendency to select higher speed generators to minimize weight and cost. However, consideration must be given to speed regulation.

It is beyond the scope of this section to discuss the question of speed regulation in detail. Regulation of speed is normally accomplished through flow control. Adequate control requires sufficient rotational inertia of the rotating parts. When load is rejected, power is absorbed, accelerating the flywheel; when load is applied, some additional power is available from deceleration of the flywheel. Response time of the governor must be carefully selected, because rapid closing time can lead to excessive pressures in the penstock.

Opening and closing the wicket gates, which vary the flow of water according to the load, control a Francis turbine. The actuator components of a governor are required to overcome the hydraulic and frictional forces and to maintain the wicket gates in fixed position under steady load. For this reason, most governors have hydraulic actuators. On the other hand, impulse turbines are more easily controlled because the jet can be deflected or an auxiliary jet can bypass flow from the power-producing jet without changing the flow rate in the penstock. This permits long delay times for adjusting the flow rate to the new power conditions. The spear on needle valve controlling the flow rate can close quite slowly, e.g., in 30 to 60 seconds, thereby minimizing any pressure rise in the penstock.

Several types of governors are available that vary with the work capacity desired and the degree of sophistication of control. These vary from pure mechanical to mechanical–hydraulic and electrohydraulic. Electrohydraulic units are sophisticated pieces of equipment and would not be suitable for remote regions. The precision of governing necessary will depend on whether the electrical generator is synchronous or asynchronous (induction type). The induction type of generator has its advantages. It is less complex and therefore less expensive, but typically has slightly lower efficiency. Its frequency is controlled by the frequency of the grid into which it feeds, thereby eliminating the need for an expensive conventional governor. It cannot operate independently but can only feed into a network and does so with lagging power factor, which may be a disadvantage, depending on the nature of the load. Long transmission lines, for example, have a high capacitance and, in this case, the lagging power factor may be an advantage.

Speed regulation is a function of the flywheel effect of the rotating components and the inertia of the water column of the system. The start-up time of the rotating system is given by

$$t_s = \frac{I\omega^2}{P} \tag{8.4.16}$$

where I = moment of inertia of the generator and turbine, kg · m^2 (Bureau of Reclamation, 1966).

The start-up time of the water column is given by

$$t_p = \frac{\sum LV}{gH} \tag{8.4.17}$$

where L = the length of water column and V = the velocity in each component of the water column.

For good speed regulation, it is desirable to keep $t_s/tp > 4$. Lower values can also be used, although special precautions are necessary in the control equipment. It can readily be seen that higher ratios of t_s/t_p can be obtained by increasing I or decreasing t_p. Increasing I implies a larger generator, which also results in higher costs. The start-up time of the water column can be reduced by reducing the length of the flow system, using lower velocities, or by adding surge tanks, which essentially reduce the effective length of the conduit. A detailed analysis should be made for each installation because, for a given length, head, and discharge, the flow area must be increased to reduce t_p, which leads to associated higher construction costs.

Cavitation and Turbine Setting

Another factor that must be considered prior to equipment selection is the evaluation of the turbine with respect to tailwater elevations. Hydraulic turbines are subject to pitting, loss in efficiency, and unstable operation due to cavitation (Arndt, 1981, 1991, Arndt et al., 2000). For a given head, a smaller, lower cost, high-speed runner must be set lower (i.e., closer to tailwater or even below tailwater) than a larger, higher cost, low-speed turbine runner. Also, atmospheric pressure or plant elevation above sea level is a factor, as are tailwater elevation variations and operating requirements. This is a complex subject that can only be accurately resolved by model tests. Every runner design will have different cavitation characteristics. Therefore, the anticipated turbine location or setting with respect to tailwater elevations is an important consideration in turbine selection.

Cavitation is not normally a problem with impulse wheels. However, by the very nature of their operation, cavitation is an important factor in reaction turbine installations. The susceptibility for cavitation to occur is a function of the installation and the turbine design. This can be expressed conveniently in terms of Thoma's sigma, defined as

$$\sigma_T = \frac{H_a - H_v - z}{H} \tag{8.4.18}$$

where H_a is the atmospheric pressure head; H is the vapor pressure head (generally negligible); and z is the elevation of a turbine reference plane above the tailwater (see Figure 8.4.1). Draft tube losses and the exit velocity head have been neglected.

The term σ_T must be above a certain value to avoid cavitation problems. The critical value of σ_T is a function of specific speed (Arndt, 1991). The Bureau of Reclamation (1966) suggests that cavitation problems can be avoided when

$$\sigma_T > 0.26 N_s^{1.64} \tag{8.4.19}$$

Equation (8.4.19) does not guarantee total elimination of cavitation, only that cavitation is within acceptable limits. Cavitation can be totally avoided only if the value of σ_T at an installation is much greater than the limiting value given in Equation (8.4.19). The value of σ_T for a given installation is known as the plant sigma, σ_P Equation (8.4.19) should only be considered a guide in selecting σ_P, which is normally determined by a model test in the manufacturer's laboratory. For a turbine operating under a given head, the only variable controlling σ_P is the turbine setting z. The required value of σ_P then controls the allowable setting above tailwater:

$$z_{\text{allow}} = H_a - H_v - \sigma_P H \tag{8.4.20}$$

It must be borne in mind that H_a varies with elevation. As a rule of thumb, H_a decreases from the sea-level value of 10.3 m by 1.1 m for every 1000 m above sea level.

Performance Evaluation

Model Tests

Model testing is an important element in the design and development phases of turbine manufacture. Manufacturers own most laboratories equipped with model turbine test stands. Major hydro projects have traditionally had proof-of-performance tests in model scale (at an independent laboratory or the manufacturer's laboratory) as part of the contract. In addition, it has been shown that competitive model testing at an independent laboratory can lead to large savings at a major project because of improved efficiency.

Recently, turbine design procedures have been dramatically improved through the use of sophisticated numerical analysis of the flow characteristics. These analysis techniques, linked with design programs, provide the turbine designer with powerful tools for achieving highly efficient turbine designs. In spite of this progress, computational methods require fine-tuning with model tests. In addition, model testing is necessary for determining performance over a range of operating conditions and for determining quasitransitory characteristics. Model testing can also be used to eliminate or mitigate problems associated with vibration, cavitation, hydraulic thrust, and pressure pulsation (Fisher and Beyer, 1985).

A typical turbine test loop is shown in Figure 8.4.9. All test loops perform basically the same function. A model turbine is driven by high-pressure water from a head tank and discharges into a tail tank, as shown. The flow is recirculated by a pump, usually positioned well below the elevation of the model to ensure cavitation-free performance of the pump while performing cavitation testing with the turbine model. One important advantage of a recirculating turbine test loop is that cavitation testing can be done over a wide range of cavitation indices at constant head and flow.

The extrapolation of model test data to prototype values has been a subject of considerable debate for many years. Equation 8.4.6 through Equation 8.4.10 can be used to predict prototype values of flow, speed, power, etc. from model tests. Unfortunately, many factors lead to scale effects, i.e., the prototype

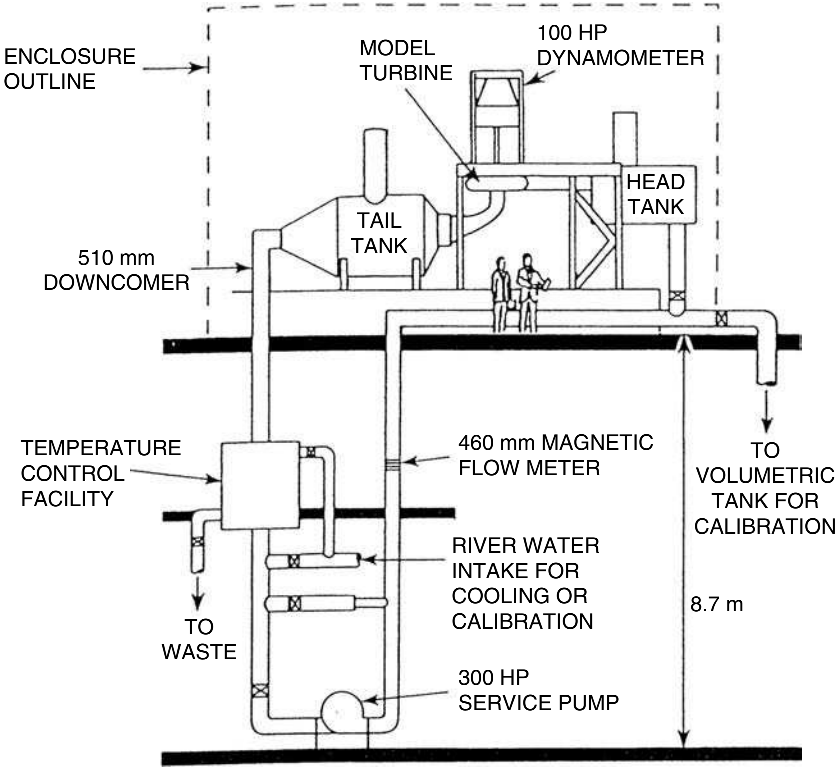

FIGURE 8.4.9 Schematic of the SAFL Independent Turbine Test Facility. *(*Courtesy of the St. Anthony Falls Laboratory, University of Minnesota.)

efficiency and model efficiency are not identical at a fixed value of specific speed. The cited scale-up formulae are based on inviscid flow. Several sources of energy loss lead to an efficiency that is less than ideal. All of these losses follow different scaling laws and, in principle, perfect similitude can only be achieved by testing the prototype. Several attempts at rationalizing the process of scaling up model test data have been made. The International Electrotechnical Test Code and various ASME publications outline in detail the differences in efficiency between model and prototype. It should also be pointed out that other losses, such as those in the draft tube and "shock" losses at the runner inlet, might not be independent of Reynolds number.

Numerical Simulation[1]

Until very recently, the analysis of turbines and other components of hydropower facilities was largely dependent on approximate models such as the Euler equation and Reynolds averaged Navier–Stokes (RANS) models because the complete Navier–Stokes equations were considered to be too difficult to be solved for hydropower components (see Chapter 3). The Euler equation model has been applied with reasonable success for turbine runner simulation, but energy losses and the efficiency could not be calculated. RANS models have been applied for the spiral case and the draft tube simulations with limited success. Goede et al. (1991) contains a good summary of experiences with the application of these computational methods to various hydropower components. Very recently, reliable commercial codes

---

[1] This subsection was prepared by Professor Charles Song of the Saint Anthony Falls Laboratory, University of Minnesota.

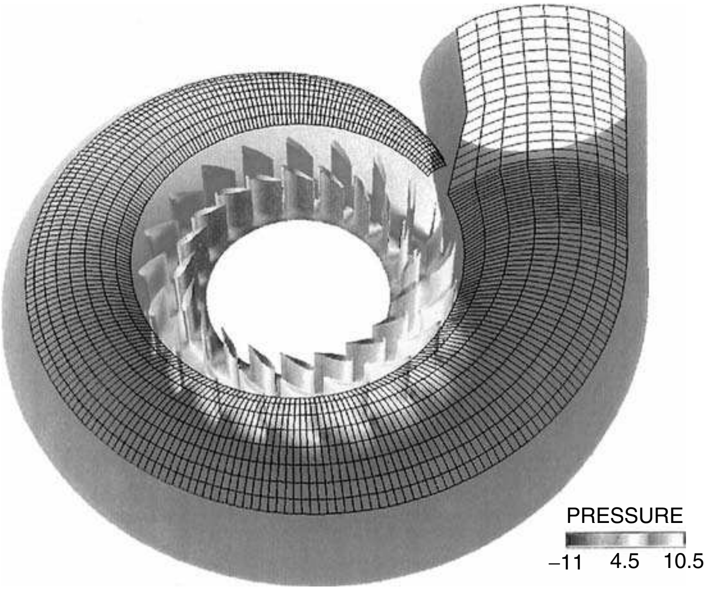

FIGURE 8.4.10 Simulated velocity field in a spiral case showing the pressure distribution on the boundaries of the spiral case, the stay vanes, and wicket gates. (Adapted from Song et al. *Hydro Rev.* XIV(4), 104–111. With permission.)

have become available and are used with increasing frequency. Many of the current commercial codes rely on variants of RANS models although rapid progress is being made in adapting LES.

The large eddy simulation method (LES) is a step forward in the application of CFD Song et al. (1995). This technique is able to capture the effects of turbulent flow in a turbine more accurately than previous techniques. At the present time, it requires a supercomputer to achieve sufficient resolution and good accuracy for final design purposes. Parallel processing with desktop computers shows promise and can presently be used for relatively simple geometry or for preliminary evaluation purposes. However, progress in its application is very rapid and it is anticipated that an entire computation may be carried out on a high-end desktop computer in the near future.

The components that require simulation include the spiral case, wicket gates, the runner, and the draft tube. Often the spiral case, including stay vanes and wicket gates, is modeled as a unit. This is necessary because the stay vanes and wicket gates are so close to each other that their mutual interactions cannot be ignored; each stay vane may be of slightly different shape and orientation and cannot be modeled separately. A typical spiral case contains more than 20 stay vanes and an equal number of wicket gates, requiring extensive computational resources for a complete simulation. A sample calculation is shown in Figure 8.4.10. In this example, the calculated energy loss through this device is 2.62% of the net available energy for this particular case. This is significant and justifies additional computational effort to minimize the losses.

The runner is the most extensively studied component of a turbine. Because all the blades in a runner are of the same geometrical shape, only one- or two-flow passage models are commonly used for runner simulation. A complete model is required if vibration or cavitation due to nonsymmetrical modes of interactions between blades and vortices are to be studied. An important application of computer simulation is in the design of runners for units used for pumped storage.

Pumped-storage schemes are becoming a very popular for smoothing out the difference between energy demand and supply. Special care is required in the design because a runner must be designed to act efficiently as a turbine and a pump. Because of viscous effects, a runner optimized under the turbine mode may have poor efficiency in the pump mode. Flow in the pumping mode can be unstable and more difficult to calculate. An LES-based analysis greatly facilitates the optimum design of this type of

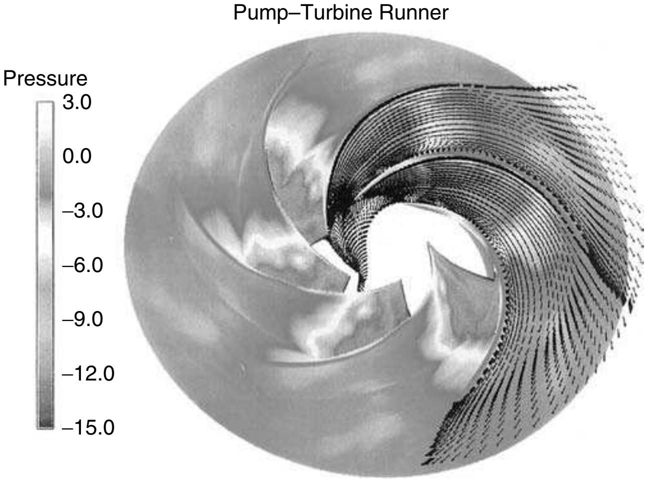

FIGURE 8.4.11 Simulation of the velocity and pressure distribution in a pump turbine runner operating in the pumping mode. (Adapted from Song et al. *Hydro Rev.* XIV(4), 104–111. With permission.)

runner. Figure 8.4.11 is an example of the calculated flow in the pump mode. A small flow separation near the entrance can be observed. This kind of information is very useful to determine how the blade geometry can be modified to improve performance.

Draft tube design is an important factor in the efficiency and stability of operation of a turbine. Although a typical draft tube geometry is somewhat simpler than that of a runner, it takes much more advanced computational techniques to simulate its performance accurately. This is because the diffuser-like flow produces secondary currents, three-dimensional vortex shedding, and horseshoe vortices that are very important contributors to energy loss. Current RANS models are ineffective for this flow; at the present time only the LES model can fulfill the requirements for draft tube simulation.

Figure 8.4.12 illustrates the complexity of the problem. The instantaneous pressure distribution on the walls of an elbow-type draft tube with a divider wall is compared with the same draft tube with the divider wall removed. A dramatic change in the flow pattern and pressure distribution occurs when the divider wall is removed. By removing the wall, the draft tube becomes a diffuser of large angle with very unstable flow. Clearly, the divider wall stabilizes the flow and reduces the energy loss due to vortex shedding. These types of simulations are invaluable in evaluating draft tube performance. This is underscored by the fact that many projects involve refurbishing existing units. Typically, only the runner is replaced, usually with increased design flow. On many occasions, the existing draft tube is unable to operate efficiently at higher flow rates, thus canceling out any improvements that a new runner can provide.

Field Tests

Model tests and numerical simulations are only valid when geometric similitude is adhered to, i.e., the prototype machine is not guaranteed to be an accurate reproduction of the design. In addition, approach flow conditions, intake head losses, the effect of operating other adjacent units, etc. are not simulated in model tests. For these reasons, field performance tests are often performed. The several different types of field tests serve different purposes. The *absolute* efficiency is measured for acceptance or performance tests. *Relative* efficiency is often measured when operating information or fine-tuning of turbine performance is desired. Field tests are also carried out for commissioning a site and for various problem-solving activities. Basic procedures are covered by codes of the American Society of Mechanical Engineering (1992) and the International Electrotechnical Commission (1991).

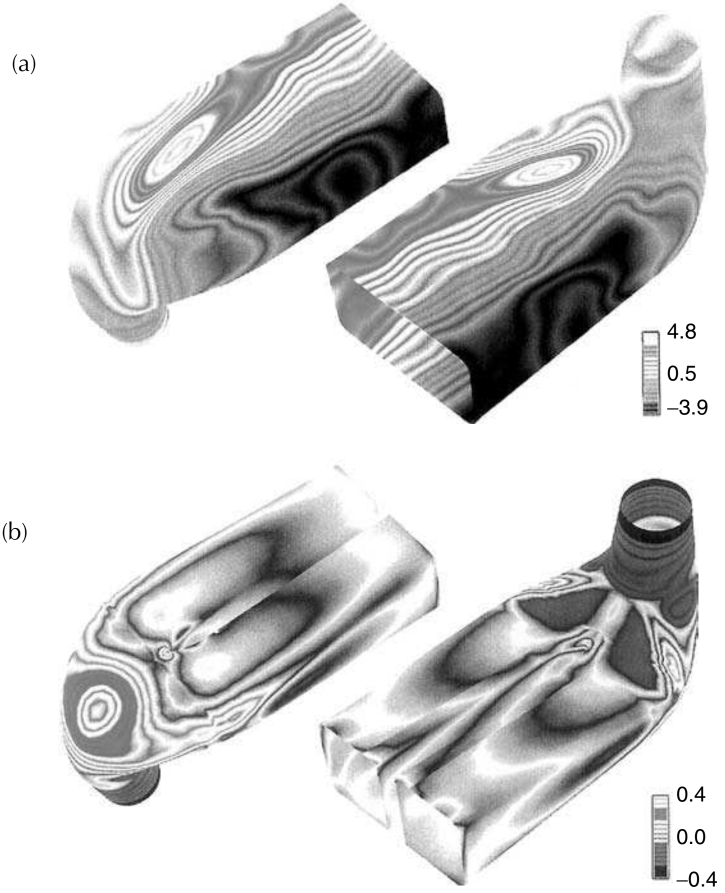

FIGURE 8.4.12 Simulation showing a comparison of the flow in a draft tube with and without a dividing wall. (a) The pressure patterns on the walls indicate a very asymmetrical flow pattern without a divider wall. (b) With a wall in place, a very uniform flow pattern is evident. (Adapted from Song et al. *Hydro Rev.* XIV(4), 104–111. With permission.)

The major difference between an "absolute" and a relative or index test is in the measurement of flow rate. Net head is evaluated in the same manner for each procedure. A variety of methods for measuring flow are code accepted. These include the pressure-time technique; tracer methods (salt velocity, dye dilution); area velocity (Pitot tubes or current meters); volumetric (usually on captive pumped storage sites); Venturi meters; and weirs. The thermodynamic method is actually a direct measure of efficiency. Flow is not measured. In addition to the code-accepted methods, it has been demonstrated that acoustic meters can measure flow in the field with comparable accuracy.

The *pressure-time technique* relies on measuring the change in pressure necessary to decelerate a given mass of fluid in a closed conduit. The method requires the measurement of the piezometric head at two cross sections spaced a distance *L* apart. A downstream valve or gate is necessary for this procedure. This technique requires load rejection for each test point and the need to estimate or measure any leakage. An adequate length of conduit is required and the conduit geometry must be accurately measured (Hecker and Nystrom, 1987).

The *salt velocity method* is based on measuring the transit time, between two sensors, of an injected cloud of concentrated salt solution. Given the volume of the conduit between sensors, the flow rate may be calculated from the average transit time. Electrodes that measure the change in conductivity of the liquid detect the passage of the salt cloud at a given location.

The *dye-dilution method* is based on conservation of a tracer continuously injected into the flow. A sufficient length for complete mixing is necessary for accurate results. The data required are the initial concentration and injection flow rate of the tracer and the measured concentration of the fully mixed tracer at a downstream location. The method is quite simple, but care is necessary to achieve precise results.

In principle, *area-velocity measurements* are also quite simple. Pitot tubes or propeller-type current meters are used to measure point velocities that are integrated over the flow cross section. The method is applicable to closed conduits or open channels. A relatively uniform velocity distribution is necessary for accurate results. A single unit can be traversed across the conduit or a fixed or movable array of instruments can be used to reduce the time for data collection.

The *thermodynamic method* is a direct indication of turbine efficiency. Flow rate is not measured. In its simplest form, the method assumes adiabatic conditions, i.e., no heat transfer from the flow to its surroundings. Under these conditions, the portion of available energy not utilized in the machine to produce useful work results in increased internal energy of the fluid, which is sensed as an increase in temperature.

Acoustic flow meters have been developed that produce results with a precision equal to or greater than the code-accepted methods. Flow velocity is determined by comparing acoustic travel times for paths diagonally upstream and downstream between pairs of transducers. The speed of sound is assumed constant. The difference in travel time is related to the component of flow velocity along the acoustic path (increased travel time upstream, decreased travel time downstream). An extensive evaluation and comparison of this method has been reported (Sullivan, 1983).

Index tests circumvent the problem of accurate flow measurement by measuring relative flow detected by the differential pressure between two points in the water passages leading to the runner. Often the differential pressure is measured with Winter–Kennedy taps positioned at the inner and outer radii of the spiral case of a turbine. Calibration of properly placed Winter–Kennedy taps shows that flow rate is very closely proportional to the square root of the pressure difference. Index testing is useful for calibration of relative power output vs. gate opening and for optimizing the various combinations of gate opening and blade setting in Kaplan units. The use of index testing to optimize cam settings in Kaplan turbines has resulted in substantial increases in weighted efficiency (i.e., a flatter efficiency curve over the full range of operation).

Defining Terms

Draft tube: the outlet conduit from a turbine that normally acts as a diffuser. This is normally considered an integral part of the unit.

Forebay: the hydraulic structure used to withdraw water from a reservoir or river. This can be positioned a considerable distance upstream from the turbine inlet.

Head: the specific energy per unit weight of water. *Gross head* is the difference in water surface elevation between the forebay and tailrace. *Net head* is the difference between *total head* (the sum of velocity head, $V^2/2g$, pressure head, $p/\rho g$, and elevation head, z), at the inlet and outlet of a turbine. Some European texts use specific energy per unit mass, for example, specific kinetic energy is $V^2/2$.

Pumped storage: a scheme in which water is pumped to an upper reservoir during off-peak hours and used to generate electricity during peak hours.

Runner: the rotating component of a turbine in which energy conversion takes place.

Specific speed: a universal number for a given machine design.

Spiral case: the inlet to a reaction turbine.

Surge tank: a hydraulic structure used to diminish overpressures in high-head facilities due to water hammer resulting from the sudden stoppage of a turbine.

Wicket gates: pivoted, streamlined guide vanes that control the flow of water to the turbine.

References

Arndt, R.E.A. 1981. Cavitation in fluid machinery and hydraulic structures. *Ann. Rev. Fluid Mech.* 13:273–328.

Arndt, R.E.A. 1991. Hydraulic turbines. In *Hydropower Engineering Handbook*, Eds., J.S. Gulliver and R.E.A. Arndt, 4.1–4.67. McGraw–Hill, New York.

Arndt, R.E.A., Keller, A. and Kjeldsen, M. 2000. Unsteady operation due to cavitation. *Proc. 20th IAHR Symp. Hydraulic Machinery Syst.*, Charlotte, NC, August.

American Society of Mechanical Engineers. 1992. Power Test Code 18.

Bureau of Reclamation. 1966. *Selecting Hydraulic Reaction Turbines*. Engineering Monograph No. 20.

Daily, J.W. 1950. Hydraulic machinery. In *Engineering Hydraulics*, Ed., H. Rouse. Wiley, New York.

Fisher, R.K. and Beyer, J.R. 1985. The value of model testing for hydraulic turbines. *Proc. Am. Power Conf.*, ASME 47, 1122–1128.

Goede, E., Cuenod, R., Grunder, R., and Pestalozzi, J. 1991. A new computer method to optimize turbine design and runner replacement, *Hydro Review*, X(1), Feb., 76–88.

Hecker, G.E. and Nystrom, J.B. 1991. Which flow measurement technique is best? *Hydro Rev.* 6(3), June.

International Electrotechnical Commission. 1991. International Code for the Field Acceptance Tests of Hydraulic Turbines. Publication 41. International Electrotechnical Commission.

Raabe, J. 1985. Hydro Power: The Design, Use, and Function of Hydromechanical, Hydraulic, and Electrical Equipment. VDI Verlag, Dusseldorf, Germany.

Song, C.C.S., Chen, X., He, J., Chen, C., and Zhou, F. 1995. Using computational tools for hydraulic design of hydropower plants. *Hydro Rev.* XIV(4), 104–111, July.

Sullivan, C.W. 1983. Acoustic flow measurement systems: economical, accurate, but not code accepted *Hydro Rev.* 6(4), August.

Wahl, T.L. 1994. Draft tube surging times two: the twin vortex problem. *Hydro Rev.* 13(1):60–69.

Further Information

J. Fluids Eng. Published quarterly by the ASME.

ASME Symposia Proc. on Fluid Machinery and Cavitation. Published by the Fluids Eng. Div.

Hydro Rev. Published eight times per year by HCI Publications, Kansas City, MO.

Moody, L.F. and Zowski, T. 1992. Hydraulic machinery. In *Handbook of Applied Hydraulics,* Eds. C.V. Davis and K.E. Sorenson. McGraw–Hill, New York.

Waterpower and Dam Construction. Published monthly by Reed Business Publishing, Surrey, U.K.

8.5 Stirling Engines

William B. Stine

Introduction

The Stirling engine was patented in 1816 by Rev. Robert Stirling, a Scottish minister (Figure 8.5.1). Early Stirling engines were coal-burning, low-pressure air engines built to compete with saturated steam engines for providing auxiliary power for manufacturing and mining. In 1987, John Ericsson built an enormous marine Stirling engine with four 4.2-m-diameter pistons. Beginning in the 1930s, the Stirling engine was brought to a high state of technology development by Philips Research Laboratory in Eindhoven, The Netherlands with the goal of producing small, quiet electrical generator sets to be used with high-power-consuming vacuum tube electronic devices. Recently, interest in Stirling engines has resurfaced, with solar electric power generation (Stine and Diver, 1994) and hybrid automotive applications in the forefront.

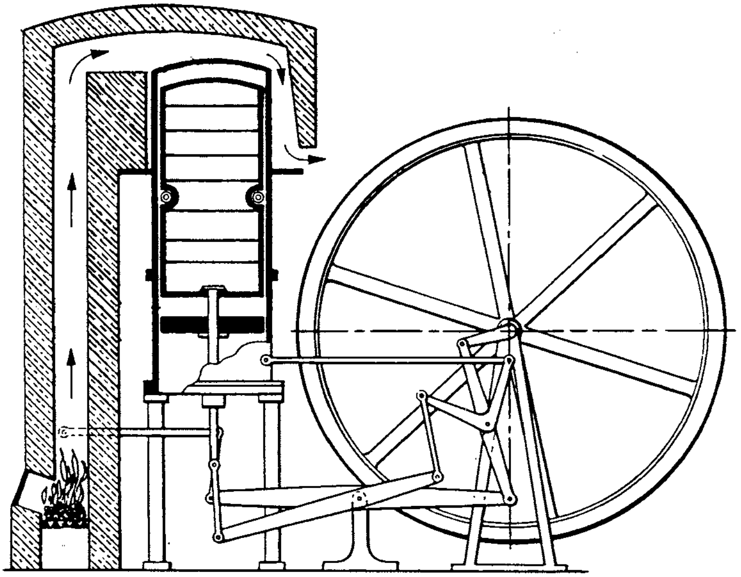

FIGURE 8.5.1 The original patent Stirling engine of Rev. Robert Stirling.

In theory, the **Stirling cycle** engine can be the most efficient device for converting heat into mechanical work with high efficiencies requiring high-temperatures. In fact, with regeneration, the efficiency of the Stirling cycle equals that of the Carnot cycle, the most efficient of all ideal thermodynamic cycles. (See West, 1986 for further discussion of the thermodynamics of Stirling cycle machines.)

Since their invention, prototype Stirling engines have been developed for automotive purposes; they have also been designed and tested for service in trucks, buses, and boats (Walker, 1973). The Stirling engine has been proposed as a propulsion engine in yachts, passenger ships, and road vehicles such as city buses (Meijer, 1992). The Stirling engine has also been developed as an underwater power unit for submarines, and the feasibility of using the Stirling for high-power space-borne systems has been explored by NASA (West, 1986). The Stirling engine is considered ideal for solar heating, and the first solar application of record was by John Ericsson, the famous British-American inventor, in 1872 (Stine and Diver, 1994).

Stirling engines are generally externally heated engines. Therefore, most sources of heat can be used to drive them, including combustion of just about anything, radioisotopes, solar energy, and exothermic chemical reactions. High-performance Stirling engines operate at the thermal limits of the materials used for their construction. Typical temperatures range fiom 650 to 800°C (1200 to 1470°F), resulting in engine conversion efficiencies of around 30 to 40%. Engine speeds of 2000 to 4000 rpm are common

Thermodynamic Implementation of the Stirling Cycle

In the ideal Stirling cycle, a **working gas** is alternately heated and cooled as it is compressed and expanded. Gases such as helium and hydrogen, which permit rapid heat transfer and do not change phase, are typically used in the high-performance Stirling engines. The ideal Stirling cycle combines four processes, two constant-temperature heat-exchange processes and two constant-volume heat-exchange processes. Because more work is done by expanding high-temperature, high-pressure gas than is required to compress low-temperature, low-pressure gas, the Stirling cycle produces net work, which can drive an electric alternator or other mechanical devices.

Working Gases

In the Stirling cycle, the working gas is alternately heated and cooled in constant-temperature and constant-volume processes. The traditional gas for Stirling engines has been air at atmospheric pressure. At this pressure, air has a reasonably high density and therefore can be used directly in the cycle with loss of working gas through seals a minor problem. However, internal component temperatures are limited because of the oxygen in air which can degrade materials rapidly.

Because of their high heat-transfer capabilities, hydrogen and helium are used for high-speed, high-performance Stirling engines. To compensate for the low density of these gases, the mean pressure of the working gas is raised by charging the gas spaces in the engine to high pressures. Compression and expansion vary above and below this **charge pressure**. Hydrogen, thermodynamically a better choice, generally results in more-efficient engines than does helium (Walker, 1980). Helium, on the other hand, has fewer material-compatibility problems and is safer to work with. To maximize power, high-performance engines typically operate at high pressure, in the range of 5 to 20 MPa (725 to 2900 psi). Operation at these high gas pressures makes sealing difficult, and seals between the high-pressure region of the engine and those parts at ambient pressure have been problematic in some engines. New designs to reduce or eliminate this problem are currently being developed.

Heat Exchange

The working gas is heated and cooled by heat exchangers that add heat from an external source, or reject heat to the surroundings. Further, in most engines, an internal heat storage unit stores and rejects heat during each cycle.

The **heater** of a Stirling engine is usually made of many small-bore tubes that are heated externally with the working gas passing through the inside. External heat transfer by direct impingement of combustion products or direct adsorption of solar irradiation is common. A trade-off between high heat-transfer rate using many small-bore tubes with resulting pumping losses, and fewer large-bore tubes and lower pumping losses drives the design. A third criterion is that the volume of gas trapped within these heat exchangers should be minimal to enhance engine performance. In an attempt to provide more uniform and constant-temperature heat transfer to the heater tubes, **reflux** heaters are being developed (Stine and Diver, 1994). Typically, by using sodium as the heat-transfer medium, liquid is evaporated at the heat source and is then condensed on the outside surfaces of the engine heater tubes.

The **cooler** is usually a tube-and-shell heat exchanger. Working gas is passed through the tubes, and cooling water is circulated around the outside. The cooling water is then cooled in an external heat exchanger. Because all of the heat rejected from the power cycle comes from the cooler, the Stirling engine is considered ideal for cogeneration applications.

Most Stirling engines incorporate an efficiency-enhancing **regenerator** that captures heat from the working gas during constant-volume cooling and replaces it when the gas is heated at constant volume. Heating and cooling of the regenerator occurs at over 60 times a second during high-speed engine operation. In the ideal cycle, all of the heat-transferred during the constant volume heating and cooling processes occurs in the regenerator, permitting the external heat addition and rejection to be efficient constant-temperature heat-transfer processes. Regenerators are typically chambers packed with fine-mesh screen wire or porous metal structures. There is enough thermal mass in the packing material to store all of the heat necessary to raise the temperature of the working gas from its low to its high temperature. The amount of heat stored by the regenerator is generally many times greater than the amount added by the heater.

Power Control

Rapid control of the output power of a Stirling engine is highly desirable for some applications such as automotive and solar electric applications. In most Stirling engine designs, rapid power control is implemented by varying the density (i.e., the mean pressure) of the working gas by bleeding gas from the cycle when less power is desired. To return to a higher power level, high-pressure gas must be

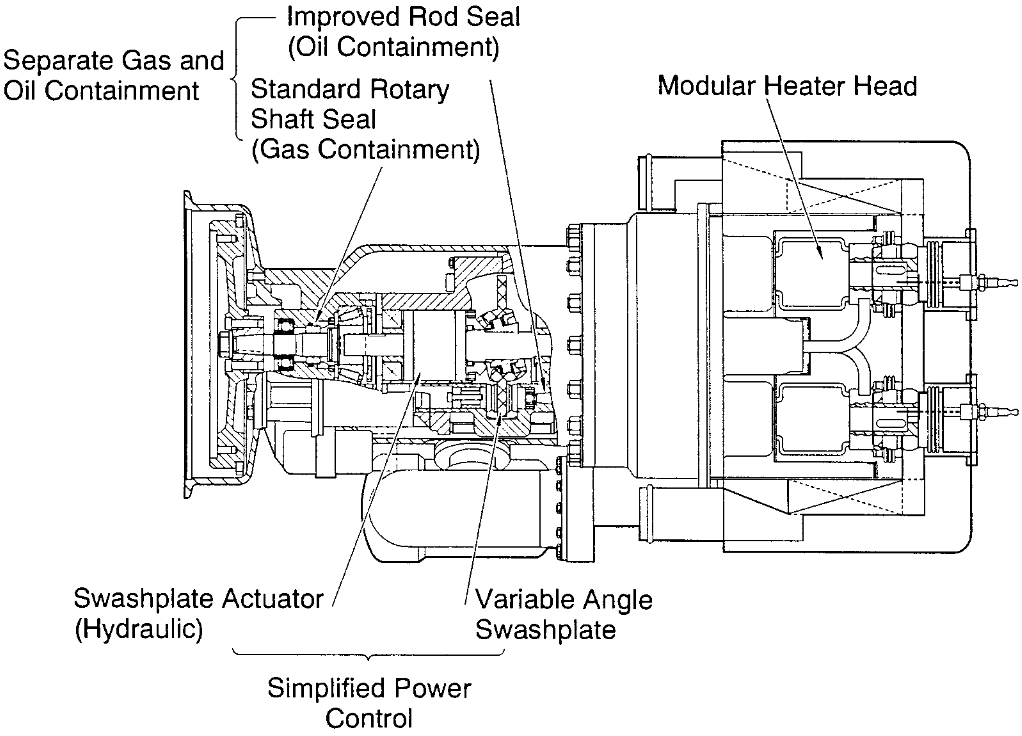

FIGURE 8.5.2 Stirling Thermal Motors 4-120 variable swash plate Rinia configuration engine. (Courtesy Stirling Thermal Motors, Ann Arbor, Michigan.)

reintroduced into the cycle. To accomplish this quickly and without loss of working gas, a complex system of valves, a temporary storage tank, and a compressor are used.

A novel method of controlling the power output is to change the length of stroke of the power piston. This can be accomplished using a variable-angle swash plate drive as described below. Stirling Thermal Motors, Inc., uses this method on their STM 4-120 Stirling engine (Figure 8.5.2).

Mechanical Implementation of the Stirling Cycle

Piston/Displacer Configurations

To implement the Stirling cycle, different combinations of machine components have been designed to provide for the constant-volume movement of the working gas between the high- and low-temperature regions of the engine, and compression and expansion during the constant-temperature heating and cooling. The compression and expansion part of the cycle generally take place in a cylinder with a piston. Movement of the working gas back and forth through the heater, regenerator, and cooler at constant volume is often implemented by a **displacer**. A displacer in this sense is a hollow plug that, when moved to the cold region, displaces the working gas from the cold region causing it to flow to the hot region and vice versa. Only a small pressure difference exists between either end of the displacer, and, therefore, sealing requirements and the force required to move it are minimal.

Three different design configurations are generally used (Figure 8.5.3). Called the alpha-, beta-, and gamma-configurations. Each has its distinct mechanical design characteristics, but the thermodynamic cycle is the same. The **alpha-configuration** uses two pistons on either side of the heater, regenerator, and the cooler. These pistons first move uniformly in the same direction to provide constant-volume processes to heat or cool the gas. When all of the gas has been moved into one cylinder, one piston remains fixed and the other moves to compress or expand the gas. Compression work is done by the **cold piston** and

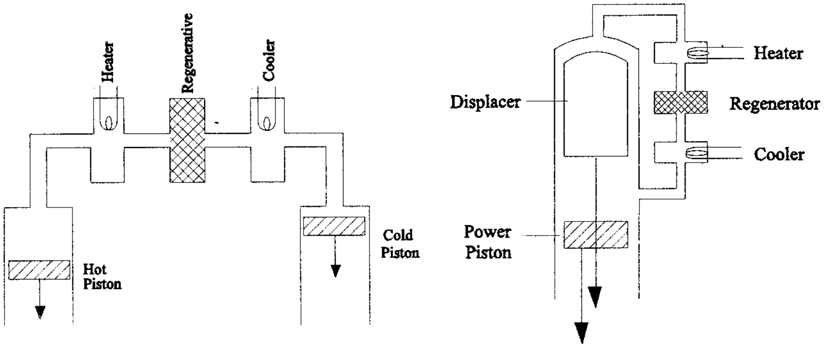

The Alpha-Configuration

The Beta-Configuration

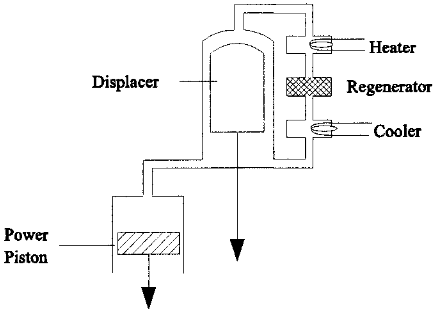

The Gamma-Configuration

FIGURE 8.5.3 Three fundamental mechanical configurations for Stirling Engines.

expansion work done on the **hot piston** The alpha-configuration does not use a displacer. The Stirling Power Systems V-160 engine (Figure 8.5.4) is an example of this configuration.

A variation on using two separate pistons to implement the alpha-configuration is to use the front and back side of a single piston called a **double-acting piston**. The volume at the front side of one piston is connected, through the heater, regenerator, and cooler, to the volume at the back side of another piston. With four such double-acting pistons, each 90° out of phase with the next, the result is a four-cylinder alpha-configuration engine. This design is called the *Rinia* or *Siemens configuration* and the United Stirling 4-95 (Figure 8.5.5) and the Stirling Thermal Motors STM 4-120 (Figure 8.5.2) are current examples.

The **beta-configuration** is a design incorporating a displacer and a power piston in the same cylinder. The displacer shuttles gas between the hot end and the cold end of the cylinder through the heater, regenerator, and cooler. The power piston, usually located at the cool end of the cylinder, compresses the working gas when the gas is in the cool end and expands the working gas when the gas has been moved to the hot end. The original patent engine by Robert Stirling and most free-piston Stirling engines discussed below are of the beta-configuration.

The third configuration, using separate cylinders for the displacer and the power piston, is called the **gamma-configuration.** Here, the displacer shuttles gas between the hot end and the cold end of a cylinder through the heater, regenerator, and cooler, just as with the beta-configuration. However, the power piston is in a separate cylinder, pneumatically connected to the displacer cylinder.

Piston/Displacer Drives

Most Stirling engine designs dynamically approximate the Stirling cycle by moving the piston and displacer with **simple harmonic motion**, either through a crankshaft, or bouncing as a spring/mass

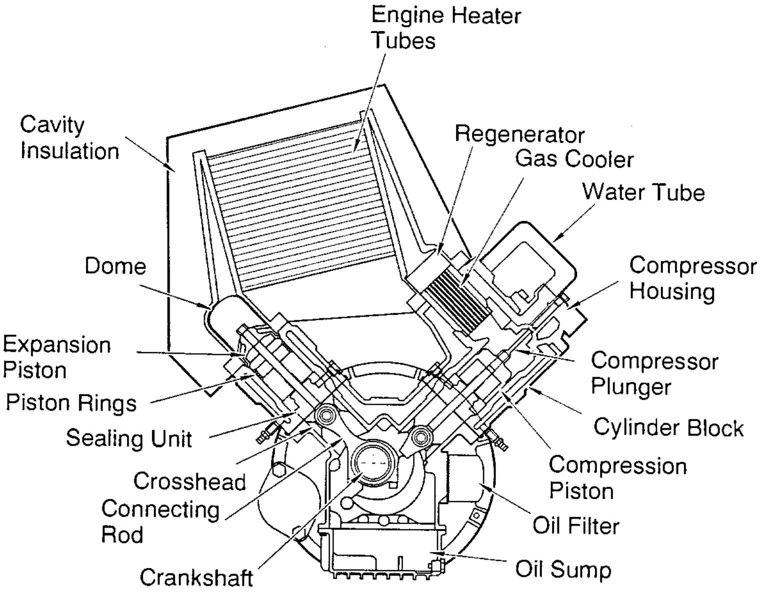

FIGURE 8.5.4 Stirling Power Systems/Solo Kleinmotoren V-160 alpha-configuration Stirling engine.

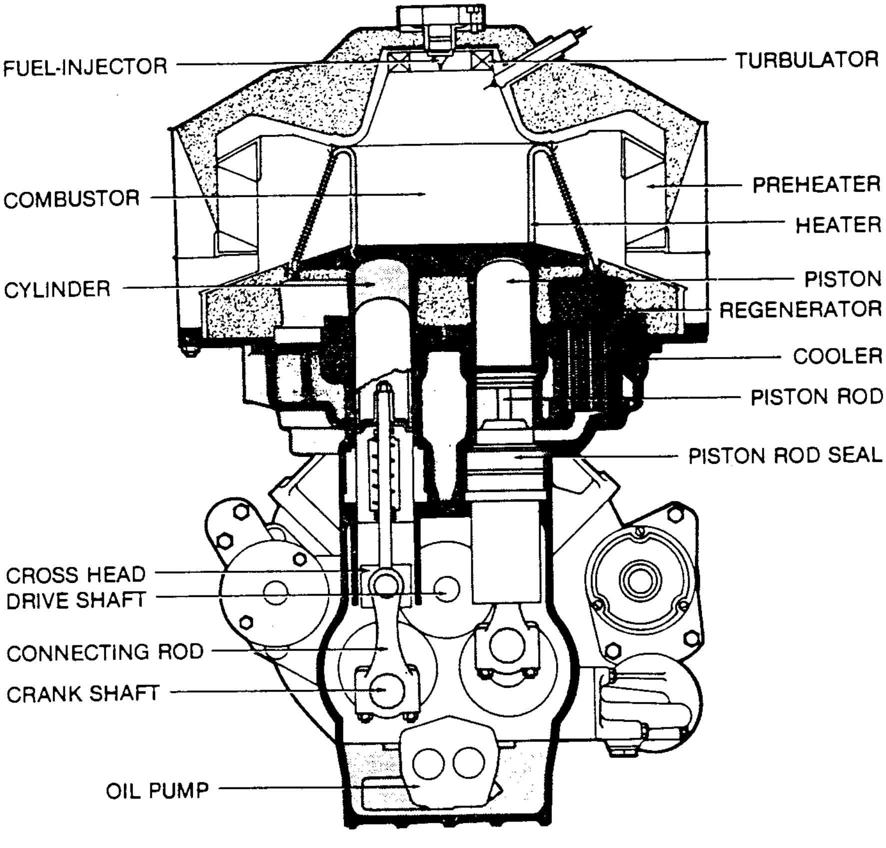

FIGURE 8.5.5 The 4-95 high-performance Siemens configuration Rinia engine by United Stirling (Malmo, Sweden).

second-order mechanical system. For both, a performance penalty comes from the inability of simple harmonic motion to perfectly follow the desired thermodynamic processes. A more desirable dynamic from the cycle point of view, called overdriven or **bang-bang motion**, has been implemented in some designs, most notably the **Ringbom configuration** and engines designed by Ivo Kolin (West, 1986).

Kinematic Engines. Stirling engine designs are usually categorized as either kinematic or free-piston. The power piston of a **kinematic Stirling engine** is mechanically connected to a rotating output shaft. In typical configurations, the power piston is connected to the crankshaft with a connecting rod. In order to eliminate side forces against the cylinder wall, a **cross-head** is often incorporated, where the connecting rod connects to the cross-head, which is laterally restrained so that it can only move linearly in the same direction as the piston. The power piston is connected to the cross-head and therefore experiences no lateral forces. The critical sealing between the high-pressure and low-pressure regions of the engine can now be created using a simple **linear seal** on the shaft between the cross-head and the piston. This design also keeps lubricated bearing surfaces in the low-pressure region of the engine, reducing the possibility of fouling heat-exchange surfaces in the high-pressure region of the engine. If there is a separate displacer piston as in the beta- and gamma configurations, it is also mechanically connected to the output shaft.

A variation on crankshaft/cross-head drives is the **swash plate** or **wobble-plate drive**, used with success in some Stirling engine designs. Here, a drive surface affixed to the drive shaft at an angle, pushes fixed piston **push rods** up and down as the slanted surface rotates beneath. The length of stroke for the piston depends on the angle of the plate relative to the axis of rotation. The STM 4-120 engine (Figure 8.5.2) currently being commercialized by Stirling Thermal Motors incorporates a **variable-angle swash plate drive** that permits variation in the length of stroke of the pistons.

Free-Piston Engine/Converters. An innovative way of accomplishing the Stirling cycle is employed in the free-piston engine. In this configuration, the power piston is not mechanically connected to an output shaft. It bounces alternately between the space containing the working gas and a spring (usually a gas spring). In many designs, the displacer is also free to bounce on **gas springs** or mechanical springs (Figure 8.5.6). This configuration is called the Beale free-piston Stirling engine after its inventor, William Beale. Piston stroke, frequency, and the timing between the two pistons are established by the dynamics of the spring/mass system coupled with the variations in cycle pressure. To extract power, a magnet can be attached to the power piston and electric power generated as it moves past stationary coils. These Stirling engine/alternator units are called **free-piston Stirling converters**. Other schemes for extracting power from free-piston engines, such as driving a hydraulic pump, have also been considered.

Free-piston Stirling engines have only two moving parts, and therefore the potential advantages of simplicity, low cost, and ultra-reliability. Because electricity is generated internally, there are no dynamic seals between the high-pressure region of the engine and ambient, and no oil lubrication is required.

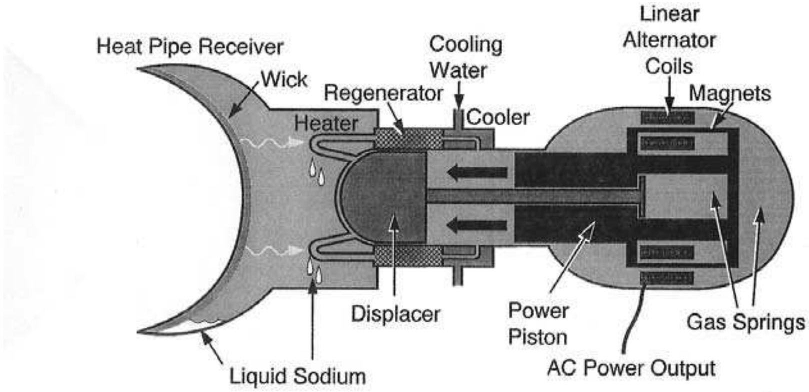

FIGURE 8.5.6 Basic components of a Beale free-piston Stirling converter incorporating a sodium heat pipe receiver for heating with concentrated solar energy.

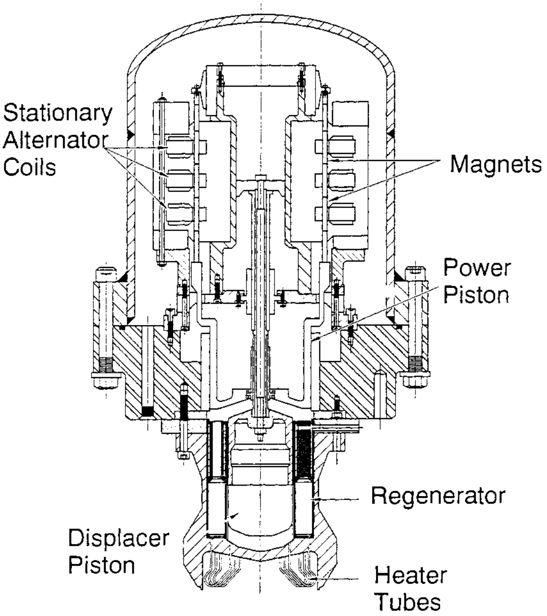

FIGURE 8.5.7 The Sunpower 9-kWe free-piston beta-configuration Stirling engine.

This design promises long lifetimes with minimal maintenance. A number of companies are currently developing free-piston engines including Sunpower, Inc. (Figure 8.5.7), and Stirling Technology Company.

Seals and Bearings

Many proposed applications for Stirling engine systems require long-life designs. To make systems economical, a system lifetime of at least 20 years with minimum maintenance is generally required. Desired engine lifetimes for electric power production are 40,000 to 60,000 hr — approximately ten times longer than that of a typical automotive internal combustion engine. Major overhaul of engines, including replacement of seals and bearings, may be necessary within the 40,000- to 60,000-hr lifetime, which adds to the operating cost. A major challenge, therefore, in the design of Stirling engines is to reduce the potential for wear in critical components or to create novel ways for them to perform their tasks.

Piston seals differ from those used in internal combustion engines in a number of ways. Sealing of the power piston is critical since **blow-by loss** of the hydrogen or helium working gas must be captured and recompressed, or replaced from a high-pressure cylinder. Displacer sealing is less critical and only necessary to force most of the working gas through the heater, regenerator, and cooler. Oil for friction reduction or sealing cannot be used because of the danger of it getting into the working gas and fouling the heat-exchange surfaces. This leads to two choices for sealing of pistons, using **polymer sealing rings** or **gas bearings** (simply close tolerance fitting between piston and wall).

Free-piston engines with gas springs have special internal sealing problems. Small leakage can change the force-position characteristics of the "spring" and rapidly upset the phase and displacement dynamics designed into the engine. In order to prevent this, *centering ports* are used to ensure that the piston stays at a certain location; however, these represent a loss of potential work from the engine.

Materials

Materials used in Stirling engines are generally normal steels with a few exceptions. Materials that can withstand continuous operation at the cycle high temperature are required for the heater, regenerator, and the hot side of the displacement volume. Because most engines operate at high pressure, thick walls are often required. In the hot regions of the engine, this can lead to *thermal creep* due to successive heating and cooling. In the cool regions, large spaces for mechanical linkages can require heavy, thick walls to contain the gas pressure. Use of composite structure technology or reducing the size of the pressurized space can eliminate these problems.

Future of the Stirling Engine

The principal advantages of the Stirling engine, external heating and high efficiency, make this the engine of the future, replacing many applications currently using internal combustion engines and providing access to the sun as an inexpensive source of energy (Figure 8.5.6). For hybrid-electric automotive applications, the Stirling engine is not only almost twice as efficient as modern spark-ignition engines, but because of the continuous combustion process, it burns fuel more cleanly and is not sensitive to the quality or type of fuel. Because of the simplicity of its design, the Stirling engine can be manufactured as an inexpensive power source for electricity generation using biomass and other fuels available in developing nations.

Most importantly, the Stirling engine will provide access to inexpensive solar energy. Because it can receive its heat from a resource 93 million miles away using concentrating solar collectors, and because its manufacture is quite similar to the gasoline or diesel engine, and because economies of scale are certain when producing thousands of units per year, the Stirling engine is considered to be the least expensive alternative for solar energy electric generation applications in the range from 1 kWe to 100 MWe.

Defining Terms

Alpha-configuration: Design of a Stirling engine where two pistons moving out of phase, and cause the working gas between them to go through the four processes of the Stirling cycle.

Beale free-piston Stirling engine: Stirling engine configuration where the power piston and displacer in a single cylinder are free to bounce back and forth along a single axis, causing the enclosed working gas to go through the four processes of the Stirling cycle. Restoration forces are provided by the varying pressure of the working gas, springs (gas or mechanical), and the external load which can be a linear alternator or a fluid pump.

Beta-configuration: Design of a Stirling engine where the displacer and power piston are located in the same cylinder and cause the enclosed working gas to go through the four processes of the Stirling cycle.

Blow-by: The gas that leaks past a seal, especially a piston-to-cylinder seal.

Charge pressure: Initial pressure of the working gas.

Cooler: Heat exchanger that removes heat from the working fluid and transfers it out of the cycle.

Cross-head: A linear sliding bearing surface connected to a crankshaft by a connecting rod. It is purpose is to provide linear reciprocating motion along a single line of action.

Displacer: Closed volume ‘plug’ that forces the working fluid to move from one region of the engine to another by displacing it.

Double-acting piston: A piston in an enclosed cylinder where pressure can be varied on both sides of the piston, resulting a total amount of work being the sum of that done on or by both sides.

Dynamic seals: Seals that permit transfer of motion without permitting gas or oil leakage. These can be either *linear seals* permitting a shaft to move between two regions (i.e., the piston rod seals in a Stirling engine), or *rotating seals* that permit rotating motion to be transmitted from one region to another (i.e., the output shaft of a Stirling engine).

Free-piston Stirling converters: A name given to a hermetically sealed free-piston Stirling engine incorporating an internal alternator or pump.

Gamma-configuration: A design of a Stirling engine where the displacer and power piston are located in separate, connected cylinders and cause the enclosed working gas to go through the four processes of the Stirling cycle.

Gas bearing: A method of implementing the sliding seal between a piston and cylinder as opposed to using piston rings. Uses a precision-fitting piston that depends on the small clearance and long path for sealing and on the viscosity of the gas for lubrication.

Gas spring: A piston that compresses gas in a closed cylinder where the restoration force is linearly proportional to the piston displacement. This is a concept used in the design of free-piston Stirling engines.

Heater: A heat exchanger which adds heat to the working fluid from an external source.

Kinematic stirling engine: Stirling engine design that employ physical connections between the power piston, displacer, and a mechanical output shaft.

Linear seal: see **dynamic seals**.

Overdriven (bang-bang) motion: Linear motion varying with time as a square-wave function. An alternative to simple harmonic motion and considered a better motion for the displacer of a Stirling engine but difficult to implement.

Phase angle: The angle difference between displacer and power piston harmonic motion with a complete cycle representing 360°. In most Stirling engines, the harmonic motion of the power piston follows (lags) the motion of the displacer by approximately 90°.

Push rod: A thin rod connected to the back of the piston that transfers linear motion through a dynamic linear seal, between the low- and high-pressure regions of an engine.

Reflux: A constant-temperature heat-exchange process where a liquid is evaporated by heat addition and then condensed as a result of cooling.

Regenerator: A heat-transfer device that stores heat from the working gas during part of a thermodynamic cycle and returns it during another part of the cycle. In the Stirling cycle the regenerator stores heat from one constant-volume process and returns it in the other constant-volume process.

Ringbom configuration: A Stirling engine configuration where the power piston is kinematically connected to a power shaft, and the displacer is a free piston that is powered by the difference in pressure between the internal gas and atmospheric pressure.

Simple harmonic motion: Linear motion varying with time as a sine function. Approximated by a piston connected to a crankshaft or a bouncing of a spring mass system.

Stirling cycle: A thermodynamic power cycle with two constant-volume heat addition and rejection processes and two constant-temperature heat-addition and rejection processes.

Swash plate drive: A disk on a shaft, where the plane of the disk is tilted away from the axis of rotation of the shaft. Piston push rods that move parallel to the axis of rotation but are displaced from the axis of rotation, slide on the surface of the rotating swash plate and therefore move up and down.

Variable-angle swash plate drive: A swash plate drive where the tilt angle between the drive shaft and the plate can be varied, resulting in a change in the displacement of the push rods.

Wobble plate drive: Another name for a swash plate drive.

Working gas: Gas within the engine that exhibits pressure and temperature change as it is heated or cooled and/or compressed or expanded.

References

Meijer, R.F. 1992. Stirling engine, in *McGraw-Hill Encyclopedia of Science and Technology*, 7th ed., pp. 440–445, McGraw-Hill, New York.

Stine, W.B. and Diver, R.E. 1994. A *Compendium of Solar Dish Stirling Technology,* Report SAND94-7026, Sandia National Laboratories, Albuquerque, NM 87185.

Walker, G. 1973. The Stirling engine, *Sci. Am.,* 229(2):80–87.

Walker, G. 1980. *Stirling Engines,* Clarendon Press, Oxford.

West, C.D. 1986. *Principles and Applications of Stirling Engines,* Van Nostrand Reinhold, New York.

Further Information

Books

Hargraves, C.M. *The Philips Stirling Engine,* Elsevier Press, London, 1991.

Organ, A.J. *Thermodynamics and Gas Dynamics of the Stirling Cycle Machine,* Cambridge University Press, Cambridge, 1992.

Senft, J.R. *Ringbom Stirling Engines,* Oxford University Press, Oxford, 1993.
Stine, W.B. and R.E. Diver, A *Compendium of Solar Dish/Stirling Technology,* SAND93-7026, Sandia National Laboratory, Albuquerque, 1994.
Urieli, I. and D.M. Berchowitz, *Stirling Cycle Engine Analysis,* Adam Hilger, Bristol, 1984
Walker, G. *Stirling Engines,* Clarendon Press, Oxford, 1980.
Walker, G. and J.R. Senft, *Free-Piston Stirling Engines,* Springer-Verlag, New York, 1985.
Walker, G., G. Reader, O.R. Fauvel, E.R. Bingham, *The Stirling Alternative,* Bordon & Breach, New York, 1994.
West, C.D. *Principles and Applications of Stirling Engines,* Van Nostrand Reinhold, New York, 1986.

Periodicals

Proceedings of the Intersociety Energy Conversion Engineering Conference (IECEC), published annually.
Stirling Machine World, a quarterly newsletter devoted to advancements in Stirling engines, edited by Brad Ross, 1823 Hummingbird Court, West Richland, WA 99353-9542.

Stirling Engine Developers

Stirling Technology Company, 4208B W. Clearwater Ave., Kennewick, WA 99336.
Stirling Thermal Motors, 275 Metty Drive, Ann Arbor, MI 48103.
Sunpower Incorporated, 6 Byard Street, Athens, OH 45701.
Clever Fellows Innovation Consortium, 302 Tenth St., Troy, NY 12180.
Mechanical Technologies Inc., 968 Albany-Shaker Rd., Latham, NY 12110.
Solo Kleinmotoren GmbH, Postfach 60 0152; D-71050 Sindelfingen; Germany.
Aisin-Seiki Ltd., 1, Asahi-Mach: 2-chome; Kariya City Aich: Pref 448; Japan.

8.6 Advanced Fossil Fuel Power Systems

Anthony F. Armor

Introduction

The generation of electric power from fossil fuels has seen continuing, and in some cases dramatic, technical advances over the last 20 to 30 years. Technology improvements in fossil fuel combustion have been driven largely by the need to reduce emissions and conserve fossil fuel resources, as well as by the economics of the competitive marketplace. The importance of fossil fuel-fired electric generation to the world is undeniable — more than 70% of all power in the U.S. is fossil fuel-based; worldwide the percentage is higher, and growing. Today, although most large power plants worldwide burn coal, generating companies increasingly are turning to natural gas, particularly when the cost of gas-fired generation and the long-term supply of gas appear favorable. This section reviews the current status and likely future deployment of competing generation technologies based on fossil fuels.

It is likely, particularly in the developed world, that gas turbine-based plants will continue to dominate the new generation market in the immediate future. The most advanced combustion turbines now achieve more than 40% **lower heating value** (LHV) efficiency in simple cycle mode and greater than 50% efficiency in **combined cycle** mode. In addition, combustion turbine/combined cycle (CT/CC) plants offer siting flexibility, swift construction schedules, and capital costs between $400 and $800/kW. These advantages, coupled with adequate natural gas supplies (though new wells and pipelines will be needed in the U.S.) and the assurance, in the longer term, of **coal gasification** back-up, make this technology currently the prime choice for green field and repowered plants in the U.S. and Europe.

However, the developing world, particularly China and India, have good reasons why the coal-fired power plant may still be the primary choice for many generation companies. Fuel is plentiful and inexpensive, and sulfur dioxide scrubbers have proved to be more reliable and effective than early plants indicated. In fact, up to 99% SO_2 removal efficiency is now possible. Removal of nitrogen oxides is also well advanced with over 95% removal possible using selective catalytic reduction (SCR). Ways to remove

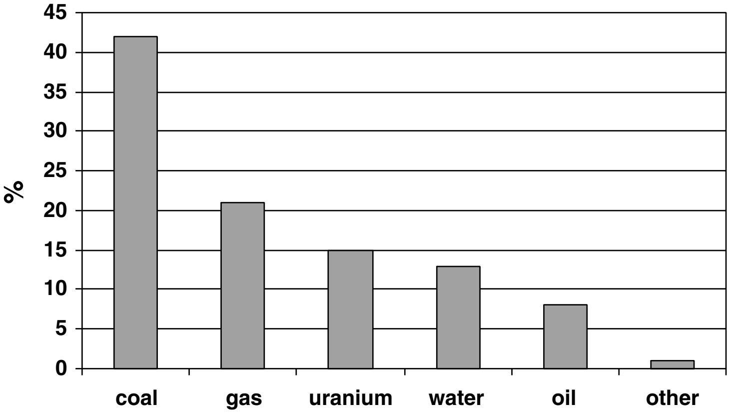

FIGURE 8.6.1 U.S. installed capacity by fuel percentage.

mercury are currently under study, and the issue of carbon dioxide control and sequestration from fossil plants is receiving renewed attention as ways to control global warming are pursued.

Combustion of coal can occur in three basic forms: direct combustion of pulverized coal; combustion of coal in a suspended bed of coal and inert matter; and coal gasification. The pulverized coal (PC) plant, the most common form of coal combustion, has the capability for much improved efficiency even with full **flue gas desulfurization** because ferritic materials technology has now advanced to the point at which higher steam pressures and temperatures are possible. Advanced supercritical PC plants are moving ahead commercially, particularly in Japan and Europe. Even higher steam conditions for PC plants, perhaps using nickel-based superalloys, are under study.

Worldwide, the application of atmospheric fluidized bed combustion (AFBC) plants has increased; these plants offer reductions in SO_2 and NO_x while permitting the efficient combustion of vast deposits of low-rank fuels such as lignites. Since the early 1990s, AFBC boiler technology power — with its advantage of in-furnace SO_2 capture with limestone — has become established worldwide as a mature, reliable technology for the generation of steam and electricity. In fact, the major impetus in the widespread deployment of this relatively new boiler technology since the mid-1980s has been its resemblance to a conventional boiler with the added capability for *in-situ* SO_2 capture, which could eliminate or reduce the need for flue gas desulfurization.

Coal gasification power plants are operating at the 250- to 300-MW level. Much of the impetus came from the U.S. DOE clean coal program where two gasification projects are in successful commercial service. Large gasification plants for power are also in operation in Europe. Gasification with combined cycle operation not only leads to minimum atmospheric (SO_2 and NO_x) and solid emissions, but also provides an opportunity to take advantage of new gas turbine advances. With the rapid advances now being introduced in combustion turbine technology, the coal gasification option is seen as a leading candidate for new plant construction within the first half of the 21st century.

Fuels for Electric Power Generation in the U.S.

The Energy Information Administration listed 498 GW of fossil-steam generating facilities in the U.S. in 1999. This included 407 GW at utilities and 91 GW at nonutilities. Coal-fired units dominated with 1393 units capable of generating 305 GW. All told, fossil-steam plants generate more than 70% of all electric energy in the country (Figure 8.6.1); these aging units (on average more than 30 years old) will remain the foundation of the power industry for the immediate future.

The U.S. electric power industry burns about $30 billion worth of fossil fuels each year, accounting for 70 to 80% of the operating costs of fossil-fired plants. Coal dominates and recent changes to the fuel mixes include:

- A mix of eastern high-sulfur coal with low-sulfur, low-cost western coals, often from Powder River Basin (PRB) deposits in Montana and Wyoming. Compared with eastern bituminous coals, PRB coals have lower heating value, sulfur and ash, but higher moisture content and finer size.
- A mix of 10 to 20% gas with coal in a boiler designed for coal firing.
- Orimulsion, a bitumen-in-water emulsion produced only from the Orinoco Basin in Venezuela. This fuel is relatively high in sulfur and vanadium. Power plants that use it need to add scrubbers.
- A mix of coal with petroleum coke, a by-product of refining, whose cost is currently low but whose sulfur content is high.

Coal as a Fuel for Electric Power (World Coal Institute, 2000)

Coal is the altered remains of prehistoric vegetation that originally accumulated as plant material in swamps and peat bogs. The accumulation of silt and other sediments, together with movements in the Earth's crust (tectonic movements), buried these swamps and peat bogs, often to great depth.

With burial, the plant material was subjected to elevated temperatures and pressures, which caused physical and chemical changes in the vegetation, transforming it into coal. Initially, peat, the precursor of coal, was converted into **lignite** or **brown coal** — coal-types with low organic maturity. Over time, the continuing effects of temperature and pressure produced additional changes in the lignite, progressively increasing its maturity and transforming it into what is known as **sub-bituminous coals**. As this process continued, further chemical and physical changes occurred until these coals became harder and more mature; at this point they are classified as **bituminous** coals. Under the right conditions, the progressive increase in the organic maturity continued, ultimately forming **anthracite**.

The degree of metamorphism or coalification undergone by a coal as it matures from peat to anthracite has an important bearing on its physical and chemical properties, and is referred to as the "rank" of the coal. Low-rank coals, such as lignite and sub-bituminous coals, are typically softer, friable materials with a dull, earthy appearance; they are characterized by high moisture levels and low carbon content, and thus a low energy content. Higher rank coals are typically harder and stronger and often have a black vitreous luster. Increasing rank is accompanied by a rise in the carbon and energy contents and a decrease in the moisture content of the coal. Anthracite is at the top of the rank scale and has a correspondingly higher carbon and energy content and a lower level of moisture.

Large coal deposits only formed after the evolution of land plants in the Devonian period, some 400 million years ago. Significant accumulations of coal occurred during the Carboniferous period (280 to 350 million years ago) in the Northern Hemisphere; the Carboniferous/Permian period (225 to 350 million years ago) in the Southern Hemisphere; and, more recently, the late Cretaceous period to early Tertiary era (approximately 15 to 100 million years ago) in areas as diverse as the U.S., South America, Indonesia, and New Zealand. Of all the fossil fuels, coal is the most plentiful in the world. It is geographically dispersed, spread over 100 countries and all continents (led by Asia with 137 million tons; Eastern Europe and the former Soviet Union with 113 million tons; and North America with 117 million tons).

Current coal reserve/production rations confirm over 200 years of resource availability. The percent of the world reserves categorized by type and use is shown in Figure 8.6.2. Almost one half (48%) of the world's coal reserves are lignite and sub-bituminous coals, which are used primarily for power generation.

Clean Coal Technology Development

At an increasing rate in the last few years, innovations have been developed and tested aimed at reducing emissions through improved combustion and environmental control in the near term, and in the longer term by fundamental changes in the way coal is preprocessed before converting its chemical energy to electricity. Such technologies are referred to as "clean coal technologies" and described by a family of precombustion, combustion–conversion, and postcombustion technologies. They are designed to provide the coal user with added technical capabilities and flexibility and the world with an opportunity to exploit its most abundant fossil source. They can be categorized as:

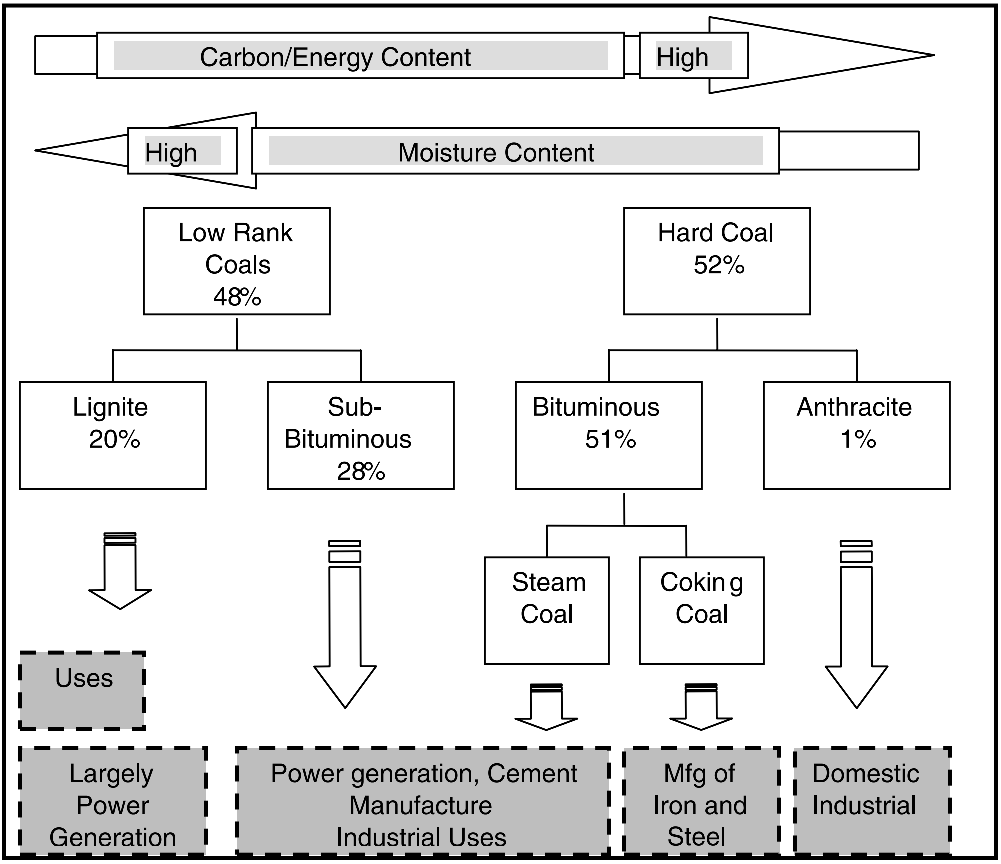

FIGURE 8.6.2 Coals cover a spectrum from lignites (high-moisture, lower-carbon content) to bituminous and anthracite coals (lower moisture, higher carbon content). All the coals can be burned to generate electricity.

- *Precombustion:* sulfur and other impurities are removed from the fuel before it is burned.
- *Combustion:* techniques to prevent pollutant emissions are applied in the boiler while the coal burns.
- *Postcombustion:* the flue gas released from the boiler is treated to reduce its content of pollutants.
- *Conversion:* coal, rather than being burned, is changed into a gas or liquid that can be cleaned and used as a fuel.

Coal Cleaning

Cleaning of coal to remove sulfur and ash is well established in the U.S., with more than 400 operating plants, mostly at mines. Coal cleaning removes primarily pyritic sulfur (up to 70% SO_2 reduction is possible) and in the process increases the heating value of the coal, typically about 10% but occasionally 30% or higher. The removal of organic sulfur, chemically part of the coal matrix, is more difficult, but may be possible using micro-organisms or through chemical methods; research is underway (Couch, 1991). Heavy metal trace elements can be removed also; conventional cleaning can remove (typically) 30 to 80% of arsenic, mercury, lead, nickel, antimony, selenium, and chromium.

Pulverized-Coal Plants

In the late 1950s the first units operating at supercritical pressures were introduced, initially in the U.S. and Germany. American Electric Power put the Philo supercritical unit in service in 1957 and Philadelphia

Electric soon followed with Eddystone 1, a unit still in active service. Today, 159 supercritical units operate in the U.S., and worldwide more than 500 supercritical units are operating with ratings from 200 to 1300 MW. Steam pressures for these units are typically 240 Bar (3500 psi), most of them single reheat designs. Steam temperatures are usually limited to about 594°C (1100°F), in order to utilize all-ferritic materials for thick wall components. A few (for example, Eddystone 1) utilize higher steam temperatures. The increased pressures and temperatures provide significant efficiency improvements over subcritical units, with attendant reductions in environmental emissions: SO_x, NO_x, CO_2, and particulates.

The greatest concentration of installed supercritical units is in the countries of the former USSR where the 232 units in operation provide 40% of all electric power. These units are designed at specific sizes of 300, 500, 800, or 1200 MW, and have steam conditions typically 24 MPa/565°C/565°C. The former USSR has also manufactured 18 supercritical units of 300- and 500-MW output, with shaft speeds of 3000 rpm, for China and Cuba (Oliker and Armor, 1992).

In Japan more than 60 supercritical plants are in operation; 25 are coal fired with another 9 due to start up in the next 2 years. Until the early 1990s, these plants had steam conditions of 24.6 MPa/538°C/566°C but, starting in 1993, the steam temperatures of the newer plants have climbed to the ultrasupercritical range, approaching 600°C.

There are about 60 supercritical units in Western Europe, largely in Germany, Italy (mostly oil fired), and Denmark. In the U.S., it is notable that the original Eddystone 1 unit, constructed in 1960, is still operating with the highest steam pressures and temperatures in the world, 4800 psi, 1150°F (322 Bar, 610°C), more than 35 years after commissioning. After the first supercritical units were installed in the late 1950s, early problems with these first-generation units began to surface. The majority of the problems were related to specific designs, changes in operating conditions, or plant malfunctions unrelated to higher pressure and temperature levels. Nevertheless, a few areas needed improvement, as noted later, to push the envelope of operating conditions as well as to improve the reliability and availability of these plants.

The design and material improvements that have been achieved now offset any deleterious effect of higher steam conditions on the cyclic fatigue life of components. The net result is that current designs do not push design margins on materials beyond the traditional margin of safety used for subcritical units; thus, new units based on their designs should have the same, if not better, availability.

Materials Advances

Higher steam temperatures (to 1150°F) and **supercritical steam pressures** are an important aspect of the modern pulverized coal plant. They are possible now because of advances in ferritic materials technology that extend life, provide greater creep and fatigue strength, and offer resistance to **temper embrittlement** and, in the boiler, to coal ash corrosion (Armor et al., 1999). Of particular note in those units operating today are:

- **Coextruded tubing** or monotubing for superheaters and reheaters, resistant to coal ash corrosion
- Improved 9-chrome steel (P91) for steam piping, valves, headers, and casings
- Improved creep-resistant 12-chrome forgings for HP/IP turbines
- "Superclean" 3.5 NiCrMoV rotors for LP turbines that are resistant to temper embrittlement

Because of the severe temperatures and stresses that exist throughout the boiler and turbine, alloys have been developed that mitigate creep and creep-fatigue problems. Particularly in the headers, steam lines, and HP and IP rotors, the impact of start–stop cycling is a concern as steam temperatures advance. To date, it is reasonable to view 1100°F (593°C) as a steam temperature for which ferritic steels for boilers and turbines are well established using P91 steels. It is likely that 1150°F (620°C) will be possible with improved ferritic steels in the near future, and perhaps even 1200°F (650°C) with the addition of tungsten as an alloying agent of steels such as P92 and P122 (Armor et al., 2003).

Additional long-term creep data may be necessary for these advanced steels. Beyond 1200°F (650°C), it is anticipated that superalloys will replace the traditional ferritic steels for HP and IP rotors. Nickel-based superalloys will be required for turbine forgings, as well as for superheater tubes, boiler outlet headers, steam piping, valve bodies, and turbine casings (Dalton et al., 2001). Because of the increased thermal expansion coefficients of these materials over ferritic steels, forging and casting thermal stresses become an important issue in start-ups and load cycling. For this reason, it is thought that such high temperature designs might be more suitable for base load duty in which thermal stress-caused fatigue damage is limited, rather than for on–off or load-change operation.

Cycle Selection

The selection of a supercritical vs. a subcritical cycle is dependent on many site-specific factors, including fuel cost; emissions regulations; capital cost; load factor; duty; local labor rates; and perceived reliability and availability. As to the reliability and availability of the supercritical cycle, it can match or better the subcritical cycle for base-loaded operation because early problems in first- and second-generation supercritical boilers and steam turbines have been overcome.

In fact, the use of subcritical cycles for the limited number of plants built in the U.S. in the last 20 years has been mainly due to relatively low fuel costs, which eliminated the cost justification for the somewhat higher capital costs of the higher efficiency cycles. However, in some international markets in which fuel cost is a higher fraction of the total cost, the higher efficiency cycles offer a favorable cost-of-electricity comparison and provide lower emissions compared to a subcritical plant. This is true in Europe and Japan.

For future plants though, the issue on cycle selection is likely to be decided based on efficiency considerations. The reduction of CO_2 emissions due to the supercritical cycle could be a deciding factor as ways are sought to reduce global warming concerns.

Supercriticals

Designs in U.S.

A survey of 159 supercritical units operating in the U.S. (EPRI, 1986) showed significant efficiency advantages (up to 3%), compared to typical subcritical units, and outage rates comparable to drum units after an initial learning period. Further studies were carried out in the early 1980s on the optimum steam pressures and temperatures for supercritical cycles (EPRI, 1982) and on the materials of choice for boiler and turbine components. As noted earlier, better materials have now been adopted worldwide for new supercritical units and include the use of P91 (super 9 chrome) for thick wall headers, steam lines, valves, and turbine casings.

The optimum design for a new supercritical cycle was recommended (EPRI, 1985) as a 700-MW double-reheat unit with steam conditions of 309 Bar/594/594/594°C (4500 psi, 1100/1100/1100°F). Such units have been constructed or are in planning in Japan and Denmark. As mentioned, it is notable that the original Eddystone 1 unit, constructed in 1960, is still operating with the highest steam pressures and temperatures in the world (322 Bar, 610°C), more than 35 years after commissioning. Table 8.6.1 notes other double-reheat units operating in the U.S.

Designs in Japan

In Japan more than 60 supercritical plants are in operation; 25 are coal fired with another 9 due to start up by 2004. Until the early 1990s, these plants had steam conditions of 24.6 MPa/538°C/566°C (3500 psi/960°F/1000°F); however, starting in 1993, the steam temperatures of the newer plants have climbed to the ultrasupercritical range, approaching 600°C (1100°F). The more recent of the large-scale, coal-fired supercritical plants to come on line and those planned for commissioning by 2004 are shown in Table 8.6.2 and Table 8.6.3 respectively. It is notable that new USC plants such as Tachibana will use advanced ferritic steels NF616 (P92) and HCM 12A (P122).

With few natural resources, Japan depends on efficient fossil generation plants burning coal, LNG, and heavy oil (as well as nuclear). Efficiency has always been a key issue for resource use minimization as well as environmental control. The Japanese supercriticals have adopted the best in European and U.S. technologies for their plants, including the European spiral-wound boiler and the U.S. partial arc admission turbine. Japanese steel-making is among the best in the world and the original EPRI advanced plant studies involved the leading Japanese steel makers. The first superclean low-pressure turbine steels (an EPRI innovation to avoid temper embrittlement) were first deployed in units at the Chubu Kawagoe station. Material advances for ferritic steels beyond P91 have been stimulated by formulations using tungsten as an alloying element (P92, for example).

TABLE 8.6.1 Advanced Supercritical Cycles at U.S. Locations with Double Reheat

Unit Name and Company	Steam Conditions (MPa/°C/°C/°C)	Design Capacity (MW)
Eddystone 1, PECO	34.3/649/565/565	325
Breed 1, AEP	24/565/565/565	450
Sporn 5, AEP	24/565/565/565	450
Eddystone 2, PECO	24/565/565/565	325
Tanners Creek 4, AEP	24/538/552/565	580
Muskingum River 5, AEP	24/538/552/565	590
Cardinal 1&2, AEP	24/538/552/565	600
Hudson 1, PSEG	24/538/552/565	400
Brayton Point 3, NEP	24/538/552/565	600
Hudson 2, PSEG	24/538/552/565	600
Big Sandy 2, AEP	24/538/552/565	760
Chalk Point 1&2, PEPCO	24/538/552/565	355
Haynes 5&6, LADWP	24/538/552/565	330
Mitchell 1&2, AEP	24/538/552/565	760
Amos 1&2	24/538/552/565	760

Note: More than 150 supercriticals operate in the U.S., although few have been installed in recent years.

TABLE 8.6.2 Recent Coal-Fired Ultrasupercritical Units in Japan

Power Plant	Company	Output (MW)	Steam Conditions (MPa/°C/°C)	Start-Up Date
Hekinann #3	Chubu	700	24.6/538/593	April 93
Noshiro #2	Tohoku	600	24.6/566/593	Dec 94
Nanao-Ohta #1	Hokuriku	500	24.6/566/593	March 95
Reihoku #1	Kyushu	700	24.1/566/566	July 95
Haramachi #1	Tohoku	1000	25/566/593	July 97
Maatsuura #2	EPDC	1000	24.6/593/593	July 97
Misumi #1	Chugoku	1000	25/600/600	June 98
Haramachi #2	Tohoku	1000	25/600/600	July 98
Nanoa-Ohta #2	Hokuriku	700	24.6/593/593	July 98

Note: Several other supercriticals are fired by oil or LNG.

TABLE 8.6.3 New and Upcoming Coal-Fired Ultrasupercritical Units in Japan

Power Plant	Company	Output (MW)	Steam Conditions (MPa/°C/°C)	Start-Up Date
Hekinann #4	Chubu	1000	24.6/566/593	Nov 2001
Hekinann #5	Chubu	1000	24.6/566/593	Nov 2002
Tsuruga #2	Hokuriku	700	24.6/593/593	Oct 2000
Tachibana-wan	Shikoku	700	24.6/566/566	July 2000
Karita #1 (PFBC)	Kyushu	350	24.6/566/593	July 2000
Reihoku #2	Kyushu	700	24.6/593/593	July 2003
Tachibana-wan #1	EPDC	1050	25/600/610	July 2000
Tachibana-wan #2	EPDC	1050	25/600/610	July 2001
Isogo (New #1)	EPDC	600	25.5/600/610	April 2002
Hitachinaka #1	Tokyo	1000	24.5/600/600	2002
Maizuni #1	Kansai	900	24.1/593/593	2003
Maizuni #2	Kansai	900	24.1/593/593	2003

Note: Noticeably, these are all single reheat units; double reheat is reserved for the more expensive oil- and gas-fired units.

TABLE 8.6.4 Recent European Supercritical Units with Advanced Steam Conditions

Power Plant	Fuel	Output (MW)	Steam Conditions (MPa/°C/°C/°C)	Start-Up Date
Skaerbaek 3	Gas	411	29/582/580/580	1997
Nordjyllands 3	Coal	411	29/582/580/580	1998
Avedore	Oil, biomass	530	30/580/600	2000
Schopau A,B	Lignite	450	28.5/545/560	1995–1996
Schwarze Pumpe A,B	Lignite	800	26.8/545/560	1997–1998
Boxberg Q,R	Lignite	818	26.8/545/583	1999–2000
Lippendorf R,S	Lignite	900	26.8/554/583	1999–2000
Bexbach II	Coal	750	25/575/595	1999
Niederaussem K	Lignite	1000	26.5/576/599	2002

Note: The trend in Europe appears to be in the direction of larger unit sizes.

It is noticeable in the tables that the units are of large size — sometimes a deterrent to cycling operation because of the thermal stresses involved. However, careful adaptation of automated start-up systems and the use of turbine by-pass systems have essentially solved today's start-up and cycling problems. The next generation, however, with the likely use of austenitic steels or of nickel-based superalloys will present new design challenges.

Designs in Europe

There are more than 100 supercritical units in Europe, largely in Germany, Italy (mostly oil fired), Holland, and Denmark. The most recent European coal-fired units with advanced supercritical steam conditions are listed in Table 8.6.4. Pioneering work on supercritical machines was carried out in Germany in the late 1950s and early 1960s, parallel with the U.S. advances. Particularly of note was the development of the spiral-wound boiler that permitted the pressure to slide up and down without concerns related to any departure from nucleate boiling, a situation that would severely damage boiler tubing. These boilers are now routinely used in Japan and Europe for full sliding pressure supercritical operation.

It is also significant that supercritical units in Germany, with double reheat, were built in unit sizes down to 220 MW — a size that would have appeal in the U.S., where smaller sizes are often sought by generating companies. Unit sizes are climbing in Germany, particularly as shown by the big lignite units at Schwarze Pumpe, Lippendorf, and Niederaussem. Lignite is a major resource in Germany and in several other European counties, such as Greece, where a lignite-fired, supercritical, district heating plant is in construction at Florina. New advanced plants for steam conditions are seen in Denmark, where the 411-MW, double-reheat supercritical units at Skaerbeck and Nordjyllands have steam temperatures of 580°C (1050°F), and at Avedore, a single-reheat design, 600°C (1110°F).

Emissions Controls for Pulverized Coal Plants (Armor and Wolk, 2002)

Today, worldwide, about 40% of electricity is generated from coal and the total installed coal-fired generating capacity is more than 1000 GW, largely made up of 340 GW in North America; 220 GW in Western Europe, Japan, and Australia; 250 GW in Eastern Europe and the former USSR; and 200 GW in China and India. More than 200 GW of new coal capacity has been added since 1990. Thus, together with the potential impact of carbon dioxide emissions contributing to global warming, the control of particulates, sulfur dioxides and nitrogen oxides from those plants is one of the most pressing needs of today and the future. To combat these concerns, a worldwide move toward environmental retrofitting of older fossil-fired power plants is underway, focused largely on sulfur dioxide scrubbers and combustion or postcombustion optimization for nitrogen oxides. Carbon dioxide control and sequestration options are now under study worldwide.

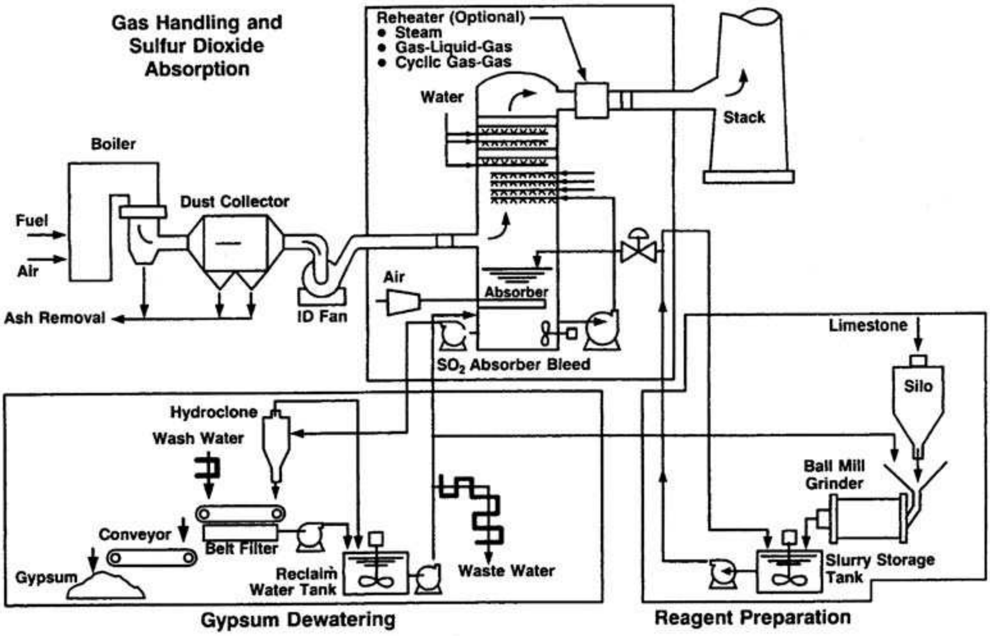

FIGURE 8.6.3 The conventional lime/limestone wet scrubber is the dominant system in operation in the U.S. With recent refinements, this system can be 98-99% effective in removing SO_2.

Conventional Lime/Limestone Wet Scrubber

The dominant SO_2 scrubbing system is the wet limestone design because limestone costs one quarter that of lime as a reagent. In this system (Figure 8.6.3), the limestone is ground and mixed with water in a reagent preparation area. It is then conveyed to a spray tower, called an absorber, as a slurry of 90% water and 10% solids, and sprayed into the flue gas stream. The SO_2 in the flue gas is absorbed in the slurry and collected in a reaction tank where it combines with the limestone to produce water and calcium sulfate or calcium sulfate crystals. A portion of the slurry is then pumped to a thickener where these solids/crystals settle out before going to a filter for final dewatering. Mist eliminators installed in the system ductwork at the spray tower outlet collect slurry/moisture entrained in the flue gas stream. Calcium sulfate is typically mixed with flyash (1:1) and lime (5%) and disposed of in a landfill.

Various improvements can be made to this basic process, including the use of additives for performance enhancement and the use of a hydrocyclone for dewatering, replacing the thickener and leading to a saleable gypsum byproduct. The Chiyoda-121 process (Figure 8.6.4) reverses the classical spray scrubber and bubbles the gas through the liquid. This eliminates the need for spray pumps, nozzle headers, separate oxidation towers, and thickeners. The Chiyoda process was demonstrated in a DOE Clean Coal Technology project on a 100-MW unit at the Yates plant of Georgia Power Company.

Spray Drying

Spray drying (Figure 8.6.5) is the most advanced form of dry SO_2 control technology. Such systems tend to be less expensive than wet FGD but remove typically a smaller percentage of the sulfur (90% compared with 98%). They are usually used when burning low-sulfur coals and utilize fabric filters for particle collection, although recent tests have shown applicability to high-sulfur coals also.

Spray driers use a calcium oxide reagent (quicklime) that, when mixed with water, produces a calcium hydroxide slurry. This slurry is injected into the spray drier where it is dried by the hot flue gas. As the drying occurs, the slurry reacts to collect SO_2. The dry product is collected at the bottom of the spray tower and in the downstream particulate removal device where further SO_2 removal may take place. It may then be recycled to the spray drier to improve SO_2 removal and alkali utilization.

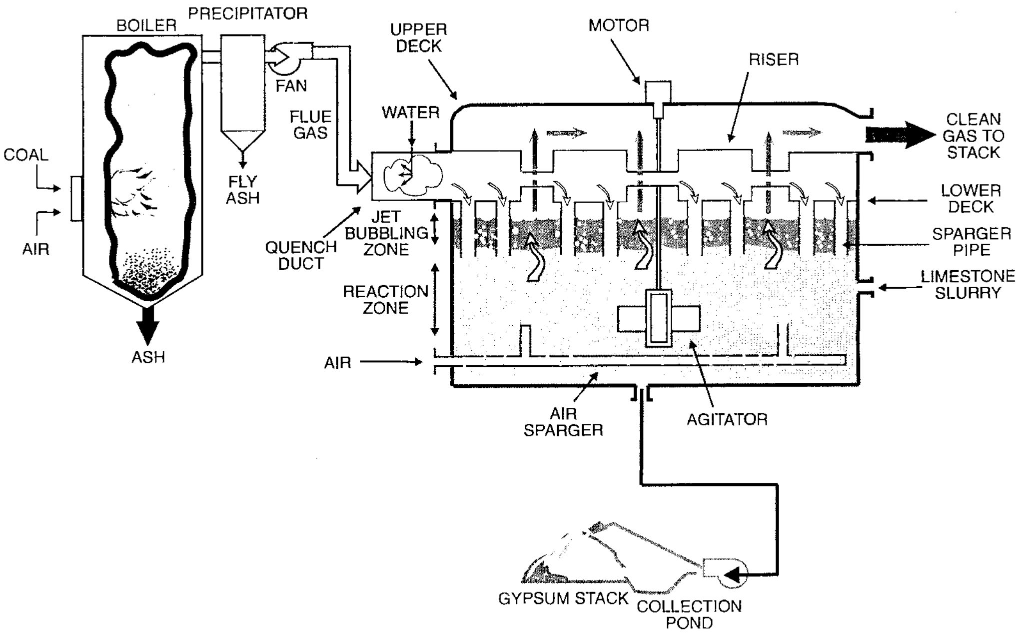

FIGURE 8.6.4 The Chioda-121 scrubber simplifies the process by bubbling the flue gas through the liquid, eliminating some equipment needs.

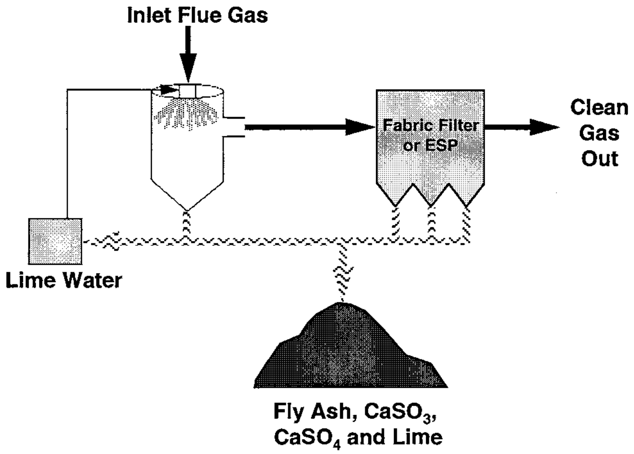

FIGURE 8.6.5 Spray driers use a calcium oxide reagent mixed with water, which is dried by the flue gas. A dry product is collected in a fabric filter.

For small, older power plants with existing **electrostatic precipitators** (ESPs), the most cost effective retrofit spray dry configuration locates the spray dryer and fabric filter downstream of the ESP, separating in this manner the spray dryer and fly ash waste streams. The fly ash can then be sold commercially.

Control of Nitrogen Oxides

Nitrogen oxides can be removed during or after coal combustion. The least expensive option, and the one generating the most attention in the U.S., is combustion control, first through adjustment of the fuel–air mixture, and second through combustion hardware modifications. Postcombustion processes seek to convert NO_x to nitrogen and water vapor through reactions with amines such as ammonia and

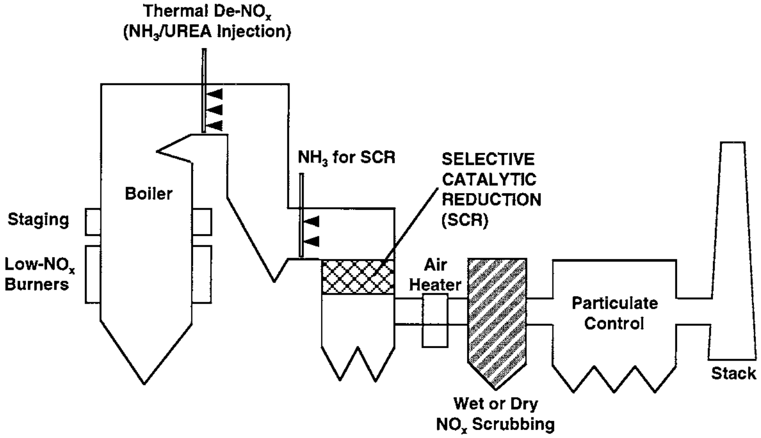

FIGURE 8.6.6 Control options for NO_x include operational, hardware, and postcombustion modifications.

urea. Selective catalytic reduction (SCR) injects ammonia in the presence of a catalyst for greater effectiveness. The options (Figure 8.6.6) can be summarized as:

- *Operational changes:* reduced excess air, and biased firing, including taking burners out of service
- *Hardware combustion modifications:* low NO_x burners, air staging, and fuel staging (reburning)
- *Postcombustion modifications:* injection of ammonia or urea into the convection pass, selective catalytic reduction (SCR), and wet or dry NO_x scrubbing (usually together with SO_2 scrubbing)

Low NO_x burners can reduce NO_x by 50% and SCR by 80%, but the low NO_x burner option is much more cost effective in terms of cost per ton of NO_x removed. Reburning is intermediate in cost per removed ton and can reduce NO_x 50%, or 75% in conjunction with low NO_x burners.

Postcombustion Options

Selective catalytic reduction is used widely in Europe (especially in Germany, where it is installed on more than 30,000 MW of coal-fired boilers) and in Japan, but sparingly to date in the U.S., although applications of SCR are increasing. In an SCR, ammonia is injected into the boiler exhaust gases before the catalyst bank (at about 550 to 750°F). NO_x and NH_3 then react to produce nitrogen and water; the chemical reactions are:

$$4NO + 4NH_3 + O_2 \rightarrow 4N_2 + 6H_2O$$

$$6NO_2 + 8NH_3 \rightarrow 7N_2 + 12H_2O$$

$$2NO_2\ 4NH_3 + O_2 \rightarrow 3N_2 + 6H_2O$$

The reaction can result in a potential NO_x removal capability of more than 90%, though practical limitations include ineffective mixing of NO_x and NH_3; velocity and temperature variations; NH_3 slip; and gradual loss of catalyst activity. Retrofit installation of an SCR system can require considerable space, although the reactor can be placed inside the original ductwork if NO_x reduction levels are modest. This would be difficult for coal-fired systems due to the high gas velocities. A separate reactor allows more flexibility in design.

In general, SCR has been successful in current installations, although impacts on the boiler system have included air heater deposition and plugging due to the formation of ammonium sulfate and bisulfate; ammonia contamination of fly ash; and ammonia slip. SCR systems operate at significantly lower temperatures than SNCR and are much more flexible in achieving the desired degree of NO_x reduction. These systems utilize catalyst coated metal plates to react flue gas. Inlet temperatures to the catalyst panels are controlled by bypassing flue gas around the catalyst zone to meet the required level of NO_x removal. Clearly, an option with relatively high operational cost, it remains an effective proven method for NO_x reductions.

Selective noncatalytic combustion (SNCR) is a promising lower capital cost alternative to SCR ($10/kW vs. more than $50/kW), but with lower performance (20 to 35% reduction compared with 50 to as high as 80% for SCR). In SNCR, the injection of a reagent like urea or ammonia into the upper part of the furnace converts NO_x from combustion into nitrogen; this conversion is a direct function of furnace temperature and reagent injection rate. Usual practice is to inject the reagent into a region of the boiler or convective pass where the temperature is in the range of 1600 to 2100°F (871 to 1149°C). NO_x reductions can range from 20 to as high as 50%, as previously stated, but are typically in the range of 20 to 35%. The level of reduction varies with the amount of nitrogen-containing chemical injected.

One major operating issue is that the system is not very flexible because the temperature of the flue gas at the point of ammonia injection is a function of boiler load. Additional operating issues of concern are the amount of unreacted ammonia (or slip) that exits the reaction zone; air heater fouling by sulfate compounds formed by reaction between SO_3 and excess ammonia; plume formation; and ammonia content of flyash. The operating cost is significant, although reagent consumption can be controlled.

Control of Mercury (EPRI, 2000)

Trace amounts of mercury are present in coal. Consequently, whenever it is combusted, such as in the generation of electricity, some of this mercury is emitted into the air along with exhaust gases. Power plant emissions account for about one third of the mercury emitted to the air from industrial sources in the U.S., but this is only about 2 to 3% of total global mercury emissions. After power plants release mercury, it becomes part of a global cycle.

The behavior of mercury in this cycle depends on its chemical form. Oxidized mercury (also called ionic mercury) may fall or wash out of the air and return to the Earth relatively near its source. Elemental mercury becomes part of the global inventory of mercury in the atmosphere, where it may remain for months to years. Eventually, it too returns to the Earth. This deposited mercury may enter bodies of water, directly or via runoff from surrounding soils, and enter the food chain. The ultimate environmental concern is humans' and animals' ingestion of fish containing elevated levels of mercury. Significant uncertainty and controversy remain about the contribution of individual sources to local or regional water bodies, as well as what constitutes safe levels of mercury in fish.

The removal of mercury from coal-fired units can be accomplished in several ways (Figure 8.6.7). Coal cleaning before combustion can remove some mercury and other heavy metals. After combustion, the injection of a sorbent such as an activated carbon can be very effective. Existing precipitators and SO_2

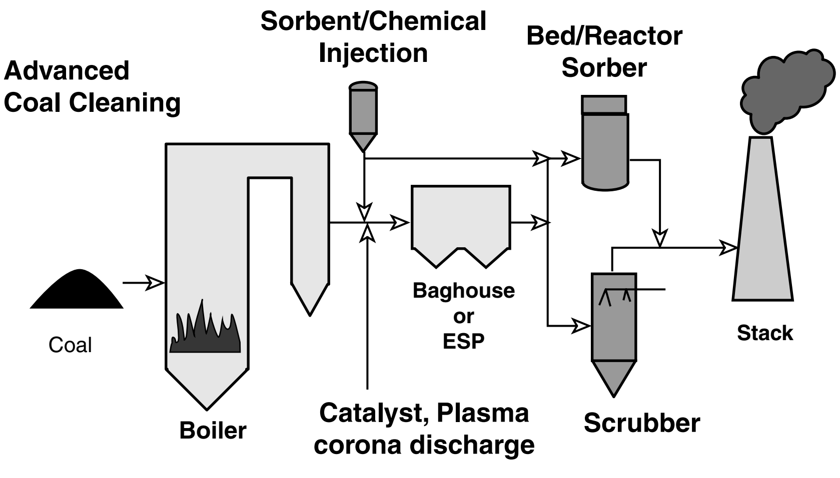

FIGURE 8.6.7 Options for the removal of mercury.

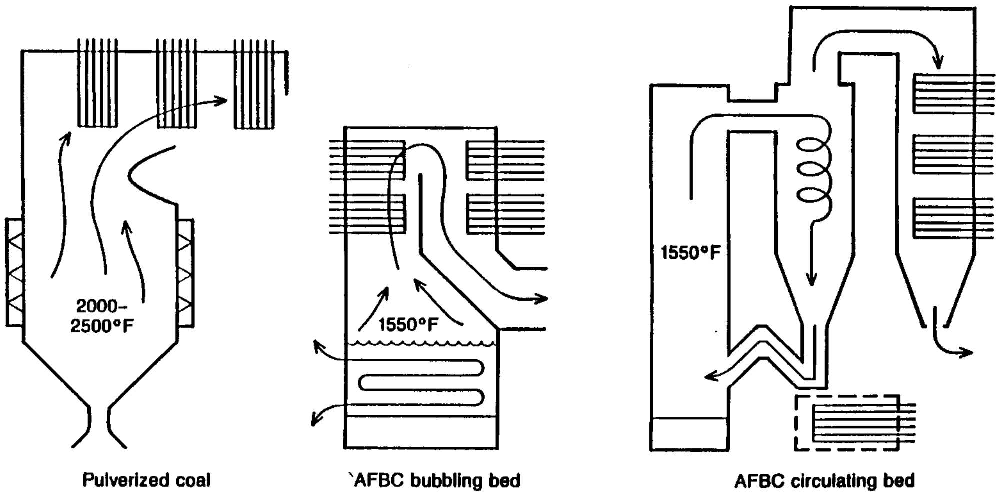

FIGURE 8.6.8 An illustration of the distinguishing features of pulverized coal and fluidized bed boilers. Noticeable in this diagram are the in-bed tubes characteristic of bubbling beds, and the cyclone separator of the circulating bed.

scrubbers can capture from 20 to 60% of mercury. Catalysts and certain chemicals can be injected that oxidize elemental mercury to enhance scrubber capture. Fixed beds, coated with materials such as gold, can form amalgams with mercury.

Fluidized Bed Plants

Introduced nearly 30 years ago, the **fluidized bed combustion** (FBC) boiler has found growing application for power generation. From the first FBC boiler, which generated 5000 lb/h of steam in 1967, the technology has matured to the 350-MW size units available today. In North America, more than 160 units now generate in excess of 9000 MW (EPRI, 2002). Burning coal in a suspended bed with limestone or dolomite permits effective capture of sulfur and fuel flexibility allows a broad range of opportunity fuels. These fuels might include coal wastes (culm from anthracite, gob from bituminous coal), peat, petroleum coke, and a wide range of coals from bituminous to lignite. A low (1500°F) combustion temperature leads to low NO_x formation. The salient features of atmospheric fluidized bed boilers, compared with a pulverized coal boiler, are shown in Figure 8.6.8.

Utility size demonstration projects at the Tennessee Valley Authority in 1989 (Manaker, 1992) (Shawnee, 160 MW) and Northern States Power in 1986 (Hinrichsen, 1989) (Black Dog, 133 MW) are examples of successful atmospheric bubbling-bed units. The Black Dog unit has been dispatched in a daily cycling mode and has successfully fired a blend of coal and petroleum coke. However, the focus of AFBC in the U.S. is now on the circulating fluid bed (CFB). In fact, more than 70% of operating fluid bed boilers in the U.S. are of the circulating type. The CFB unit at Nucla (Tri-State G&T Association) (Blunden, 1989) has been successful in demonstrating the technology at the 110-MW level and commercial CFB plants have now reached 250 MW in size. Most fluidized bed units for electricity generation are installed by independent power producers in the 50- to 100-MW size range; here, the inherent SO_2 and NO_x advantages over the unscrubbed PC plant have encouraged installations even in such traditional noncoal arenas as California (Melvin and Friedman, 1994). Worldwide, the AFBC boiler is employed largely for steam heat; hundreds of them operate in Russia and India, and thousands in China.

Atmospheric Fluidized Bed Combustion (AFBC)

In the bubbling bed version of the AFBC, the fuel and inert matter, together with limestone or dolomite for SO_2 capture, is suspended through the action of fluidizing air, which flows at a velocity of 3 to 8 ft/s in essentially a one-pass system. Circulating fluid beds (CFB) differ from bubbling beds in that much of

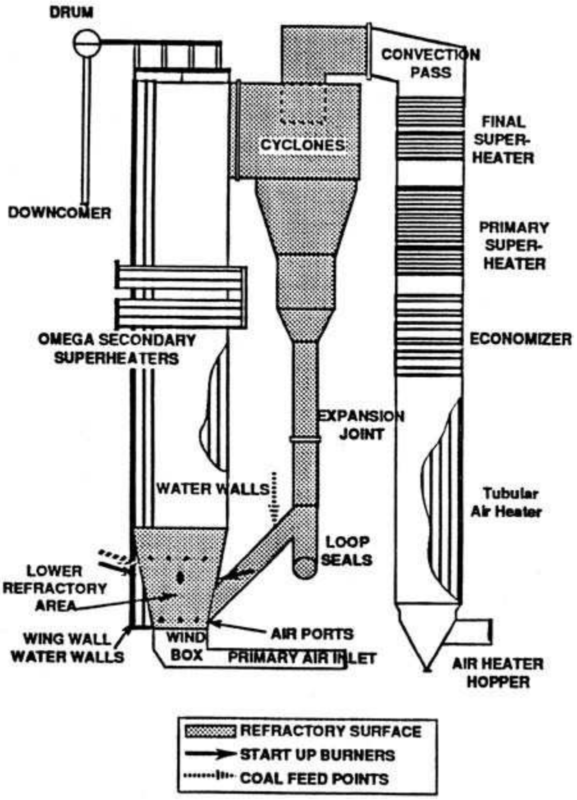

FIGURE 8.6.9 A circulating fluid bed boiler installed at the ACE Cogeneration Company at Trona, California. This 108-MW unit burns low-sulfur, western bituminous coal with limestone in a bed, which circulates back to the boiler after passing through a cyclone separator.

the bed material passes through a cyclone separator before being circulated back to the boiler (Figure 8.6.9). In-bed tubes are generally not used for CFB units permitting a much higher fluidizing velocity of 16 to 26 ft/s. Since the early AFBC designs, attention has been directed toward increasing unit efficiency, and reheat designs are now usual in large units. When SO_2 capture is important, a key parameter is the ratio of calcium in the limestone to sulfur in coal. Typical calcium–sulfur ratios for 90% SO_2 reduction are in the range of 3.0 to 3.5 for bubbling beds and 2.0 to 2.5 for circulating beds. This depends on the fuel, however, and the 200-MW CFB plant at the NISCO cogeneration plant, which burns 100% **petroleum coke** (4.5% S), has a Ca–S ratio of below 1.7 for more than 90% sulfur capture. NO_x levels in AFBCs are inherently low and nominally less than 0.2 lb/MMBtu.

It is important to note that for CFBs, boiler efficiencies can be as high as a pulverized coal unit (Table 8.6.5). In fact, designs now exist for AFBCs with supercritical steam conditions, with prospects for cycles up to 4500 psia, 1100°F with **double reheat** (Skowyra et al., 1995). Large CFB units in the Americas are shown in Table 8.6.6.

Pressurized Fluidized Bed Combustion (PFBC)

In a PFBC combined cycle unit (Figure 8.6.10), coal in a fluid bed is burned with dolomite or limestone in a pressurized steel chamber, raising steam for a steam turbine generator. The pressurized flue gases are expanded through a gas turbine. Commercial plants at about the 80-MW level in Sweden, the U.S., and Spain have demonstrated that bubbling-bed PFBC plants, with a calcium–sulfur molar ratio of about 1.5, offer sulfur capture up to 95%, together with inherently low NO_x emissions due to low combustion temperatures. Cleanup of the flue gas before entry to the gas turbines is a key technical objective, and

TABLE 8.6.5 Typical Boiler Efficiencies, Pulverized Coal (PC), and Fluidized Beds

		Calculated Heat Loss (%)		
Loss/Gain Parameter	PC	Highest Efficiency CFB	Lowest Efficiency CFB	Bubbling Bed
Moisture in limestone	NA	0.06	0.10	0.10
Calcination	NA	1.02	1.69	2.70
Sulfation credit	NA	–1.60	–1.60	–1.60
Unburned carbon	0.25	0.50	2.0	4.0
Heat in dry flue gas	5.28	5.57	5.60	5.75
Moisture in fuel	1.03	1.03	1.03	1.03
Moisture from burning H_2	41.9	4.19	4.19	4.19
Radiation and convection	0.30	0.30	0.80	0.30
Moisture in air	0.13	0.14	0.14	0.14
Sensible heat in boiler ash	0.03	0.09	0.76	0.50
Bottom ash	0.05	NA	NA	NA
Fan-power credit	–0.25	–0.75	–0.40	–0.50
Pulverizer/crusher power gain	–0.20	NA	NA	NA
Total losses/gains	10.81	10.55	14.31	16.51
Overall boiler efficiency,%	89.19	89.45	85.69	83.49

Source: Fluidized Bed Boilers, POWER Magazine, January 1987.

TABLE 8.6.6 U.S., Canadian, and Latin American CFB Units Larger Than 75 MW

Plant/Location (Vendor)	Start-Up	Capacity, MW (Net)	Fuels
Tri-State Generation & Transmission/Colorado	1987	1 × 100	Bit. coal
AES Shady Point/Oklahoma	1989	4 × 75	Bit. coal
AES Thames/Connecticut	1989	2 × 90	Bit. coal
Schuylkill Energy/Pennsylvania	1989	1 × 80	Culm
ACE Cogeneration/California	1990	1 × 97	Low-S bit. coal
Texas-New Mexico Power/Texas	1990	2 × 150	Lignite
AES Barbers Point/Hawaii	1992	2 × 90	Bit. coal
Nelson Industrial Steam Co. (NISCO)/Louisiana	1992	2 × 110	Coke
Cedar Bay Generating Co./Florida	1993	3 × 90	Bit. coal
Nova Scotia Power/Nova Scotia	1993	1 × 165	30% bit. coal and 70% coke
Colver Power/Pennsylvania	1995	1 × 105	Gob
Northampton Generating Co./Pennsylvania	1995	1 × 112	Culm
ADM/Illinois	1996/2000	2 × 132	Bit. coal and up to 5% TDF
ADM/Iowa	2000	1 × 132	Bit. coal
AES Warrior Run/Maryland	1999	1 × 180	Bit. coal
Choctaw Generation – the Red Hills project/Mississippi	2001	2 × 220	Lignite
Bay Shore Power—First Energy/Ohio	2001	1 × 180	Coke
AES Puerto Rico/Puerto Rico	2002	2 × 227	Bit. coal
JEA/Florida	2002	2 × 265	Bit. coal and coke
Southern Illinois Power Cooperative/Illinois	2002	1 × 113	Waste bit. coal
Termoelectrica del Golfo/Mexico	2002	2 × 115	Coke
Termoelectrica de Penoles/Mexico	2003	2 × 115	coke
Reliant Energy Seward Station/Pennsylvania (ALSTOM)	2004	2 x 260	Gob & bit. coal
East Kentucky Power Cooperative/Kentucky	2004	1 × 268	Unwashed high-sulfur bit. coals
Figueira/Brazil	2004	1 × 128	Bit. coal

Source: EPRI, *Atmospheric Fluidized-Bed Combustion Handbook*, EPRI Report 1004493, December 2002.

first-generation units have used cyclones together with gas turbines ruggedized with special blade coatings. For more advanced, higher efficiency PFBC systems, hot-gas cleanup technology, where the gas is directed through large ceramic filter units, will likely be needed.

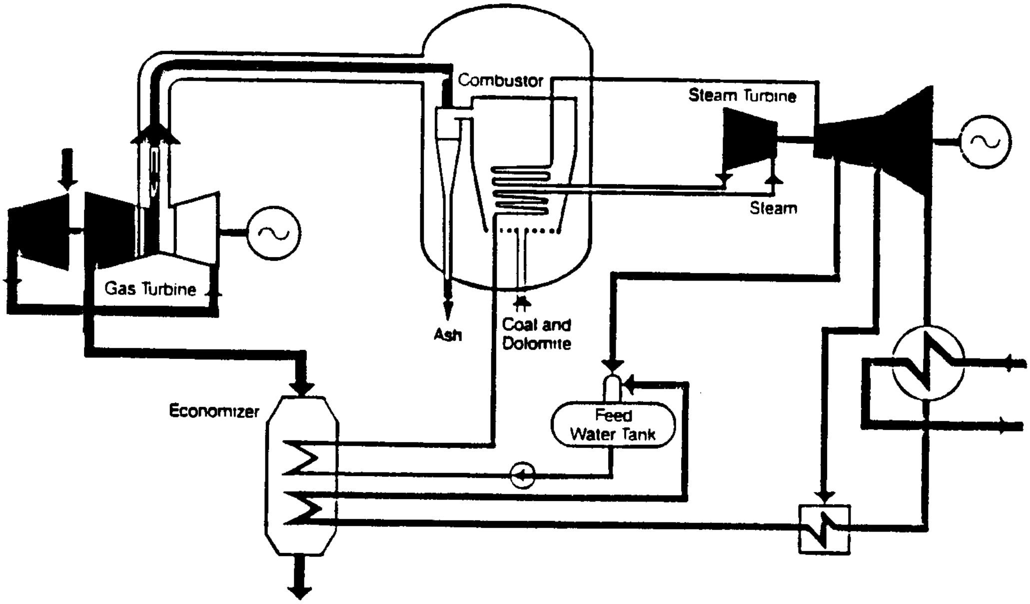

FIGURE 8.6.10 Pressurized, fluidized-bed combustor with combined cycle. This 70-MW system has operated at the Tidd plant of American Electric Power.

Early designs included the 80-MW units at Vaertan (Sweden) and Escatron (Spain) and the 70-MW unit at Tidd (AEP), which operated satisfactorily. The modular aspect of the PFBC unit is a particularly attractive feature, leading to short construction cycles and low-cost power. One promising use for PFBC units is for small, in-city cogeneration plants in which the inherent size advantages, high efficiencies, and effective coal gas cleanup approach permits compact plants to be retrofitted in place of heating boilers; the small steam turbines can be easily be adapted to electricity and hot water supply (Olesen, 1985).

A 250-MW subcritical unit based on the Hitachi bubbling bed technology was built at Osaka for Chugoku Electric and started commercial operation in late 2000. Steam conditions are 16.7 MPa/566°C/593°C (386psig/1050°F/1100°F). A 360-MW supercritical unit based on the ABB technology was constructed in Japan at Karita for Kyushu Electric Power Company. The boiler is designed for steam conditions of 24.1 MPa/565°C/593°C (3500 psig/1050°F/1100°F). The plant started up in late 1999.

In early 2000, ABB decided that it would no longer market PFBC but would confine its role to that of supplying the gas turbine. Alstom subsequently acquired ABB's power business. Thus, it appears that the future of PFBC will depend on the market in Japan However, in the Japanese market, PFBC faces strong competition from the several 800- to 1000-MW ultrasupercritical (USC) PC plants that have entered service. These have been performing very well, so the economies of scale represented by these large USC PC plants will make it very difficult for PFBC to compete. At this time (2003), commercialization of PFBC in the U.S is not currently actively progressing (Courtright et al., 2003).

Gasification Plants

One option of growing interest to coal-burning utilities is that of coal gasification. After the EPRI Cool Water demonstration in 1984 at the 100-MW level, the technology has moved ahead in the U.S. largely through demonstrations under the Clean Coal Technology (CCT) program (U.S. DOE, 2002).

Gasification-based plants have among the lowest emissions of pollutants of any central station fossil technology. Using the efficiency advantages of combined cycles, CO_2 emissions are also low. Fuel flexibility is an additional benefit because the gasifier can accommodate a wide range of coals, plus petroleum coke. Integrated gasification combined cycle (IGCC) plants permit a hedge against long-term increases in

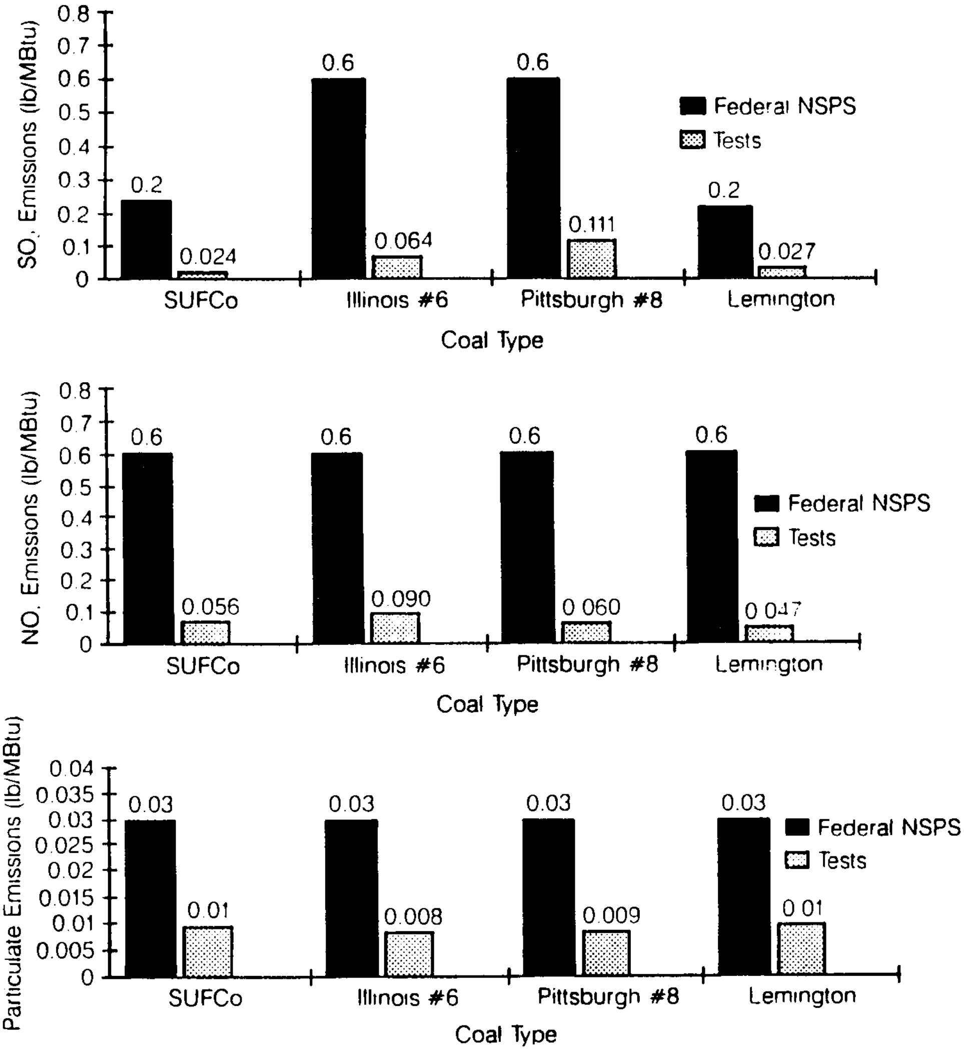

FIGURE 8.6.11 Tests at Cool Water on four coals show emissions of SO_2, NO_X, and particulates substantially below the federal New Source Performance Standards.

natural gas prices because natural gas-fired combustion turbines can be installed initially, and gasifiers at a later time, when a switch to coal becomes prudent (Douglas, 1986).

The pioneering Cool Water plant, the first of its kind in the world, operated for more than 4 years, gasifying 1.1 million tons of coal and producing 2.8 million MWh of electricity. The project was a collaborative effort of the industry involving the utility (Southern California edition); equipment manufacturers (Texaco, General Electric); and consultants/research consortia (Bechtel, EPRI, and others). Particularly notable was the achievement of exceptionally low levels of emissions of SO_2, NO_X, and particulates, as shown in Figure 8.6.11.

Basically, IGCC plants replace the traditional coal combustor with a gasifier and gas turbine. Ultralow emissions are realized; over 99% of the coal's sulfur is removed before the gas is burned in the gas turbine. A gasification cycle can take advantage of all the technology advances made in combustion turbines and steam turbines, so as to enhance overall cycle efficiency

There are currently two coal-based IGCC commercial sized demonstration plants operating in the U.S. and two in Europe (Table 8.6.7). The U.S. projects were all supported under the U.S. Department

TABLE 8.6.7 Coal-Based Commercial Size IGCC Plants

Operating IGCC Plants	Gasification Technology	Plant Size (MW)	Start-Up Date
Wabash River, Indiana	Destec	262	October 1995
Tampa Electric, Florida	Texaco	250	September 1996
SEP/Demkolec, Buggenum, The Netherlands	Shell	253	Early 1994
ELCOGAS, Puertollano, Spain	Krupp–Uhde Prenflo	310	December 1997 on coal

of Energy's (DOE) Clean Coal Technology (CCT) demonstration program. The 262-MW Wabash River IGCC repowering project in Indiana started up in October 1995 and uses the E-GAS™ (formerly Destec) gasification technology. The 250-MW Tampa Electric Company (TEC) IGCC project in Florida started up in September 1996 and is based on the Texaco gasification technology.The first of the European IGCC plants, the SEP/Demkolec project at Buggenum, the Netherlands, uses the Shell gasification technology and started operations in early 1994. The second European project, the ELCOGAS project in Puertollano, Spain, which uses the Prenflo gasification technology, started coal-based operations in December 1997.

Polk County IGCC

Texaco's pressurized, oxygen-blown, entrained-flow gasifier is used at the Tampa Electric Polk County plant to produce a medium-Btu fuel gas (Figure 8.6.12). Coal/water slurry and oxygen are combined at high temperature and pressure to produce a high-temperature syngas. Molten coal ash flows out of the bottom of the vessel and into a water-filled quench tank where it is turned into a solid slag. The syngas from the gasifier moves to a high-temperature heat-recovery unit, which cools the gases.

The cooled gases flow to a particulate-removal section before entering gas-cleanup trains. A portion of the syngas is passed through a moving bed of metal oxide absorbent to remove sulfur. The remaining

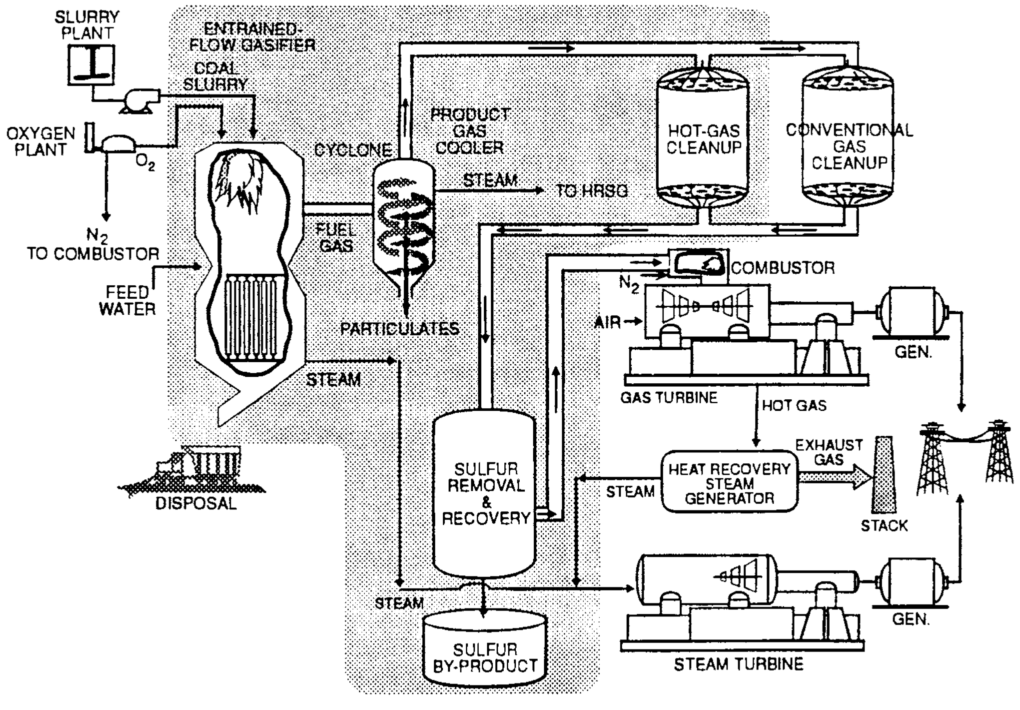

FIGURE 8.6.12 Integrated gasification, combined cycle at Tampa Electric, Polk County plant. A Texaco oxygen-blown gasifier is used. Total net generation is 250 MW.

syngas is further cooled through a series of heat exchangers before entering a conventional gas-cleanup train where sulfur is removed by an acid-gas removal system. These cleanup systems combined are expected to maintain sulfur levels below 0.21 lb/million Btu (96% capture). The cleaned gases are then routed to a combined-cycle system for power generation. A gas turbine generates about 192 MW. Thermally generated NO_x is controlled to below 0.27 lb/MM Btu by injecting nitrogen as a dilutent in the turbine's combustion section. A heat-recovery steam generator uses heat from the gas-turbine exhaust to reduce high-pressure steam. This steam, along with the steam generated in the gasification process, is routed to the steam turbine to generate an additional 120 MW. The IGCC heat rate for this demonstration is approximately 8600 Btu/kWh (40% efficient). Coals used in the demonstration are Illinois 6 and Pittsburgh 8 bituminous coals with sulfur contents ranging from 2.5 to 3.5%.

By-products from the process — sulfuric acid and slag — can be sold commercially, sulfuric acid by-products as a raw material to make agricultural fertilizer and the nonleachable slag for use in roofing shingles and asphalt roads and as a structural fill in construction projects.

Buggenum IGCC

Tests are in progress on the 250-MW IGCC plant in Buggenum, Netherlands. After successful operations running on natural gas, a switch was made to coal gas using Columbia coals. Buggenum comprises a 2000 ton/day single reactor coal gasification unit and an air separation plant able to produce 1700 ton/day of 95% pure oxygen. Syngas drives a Siemens combined cycle power unit, including a 156-MW, V94.2 gas turbine and a 128-MW steam turbine. The gasifier, operating at 28-bar pressure and 2700°F is designed to produce syngas containing 42% nitrogen, 25% carbon monoxide, and 12% hydrogen, with a combustion value of 4.3 MJ/kg. The environmental constraints are defined by permit requirements fixing upper limits of SO_2 at 0.22g/kWh, NO_x at 0.62 g/kWh, and particulates at 0.007 g/kWh.

Key steps for limiting emissions include:

- Removing fly ash with cyclone and candle filters after gas cooling
- Removing halogens and other soluble pollutants with water scrubbing
- Desulfurizing gas by catalytic and chemical processes; sulfur is fixed in sulfinol-*M* solvent, which is further treated to produce elemental sulfur
- Desulfurized gas is mixed with nitrogen from the air separation units and saturated with water vapor to reduce its lower heating value from about 11,000 to 4300 kJ/kg, thus greatly reducing NO_x production

Combustion Turbine Plants

Combustion turbine (CT)-based plants comprise the fastest growing technology in power generation. Almost all of these CT and CC plants will be gas fired, leading to a major expansion of gas for electricity generation. It is likely that combustion turbines and combined cycles will grow steadily more important in all generation regimes — peaking, mid-range and base load. The present 2300°F firing temperature machines operate reliably and durably and CT and CC plants are beginning to replace older steam plants. Combustion turbine plants will be a competitive choice for new fossil generation, and advanced CT cycles, with intercooling, reheat, and possibly chemical recuperation and humidification; they will spear-head the drive to higher efficiencies and lower capital costs. Gasification, which guarantees a secure bridge to coal in the near term, will come into its own as natural gas prices rise under demand pressure.

Modern gas turbines for power generation are mostly heavy-frame machines, with 60 HZ ratings in a simple cycle configuration around 170 to 190 MW for the high firing temperatures (~2300°F) of the **"F-class" machines**. Efficiencies (lower heating value) are 36 to 38% in simple cycles. In combined cycles, the units are 260 to 380 MW in size and 53 to 56% efficient. The next generation of CTs, with efficiencies from 57 to 60% is now emerging (Table 8.6.8). Smaller scale aeroderivative machines have benefited from turbofan engines designed for wide-body aircraft and today are available in ratings of 35 to 65 MW and with efficiencies of 40% or more for turbine inlet temperatures around 2250°F.

TABLE 8.6.8 Modern Gas Turbine Specifications

Turbine		Large Heavy Frame Machines			
		Simple Cycle		Combined Cycle	
		MW	Efficiency % (LVH)	MW	Plant Efficiency % (LHV)
		Current			
GE	GE7FA/9FA	172/256	36.0	262/367	56.0/55.3
MHI	M501F/701F	185/270	38.1	280/—	56.7/—
Siemens/W	W501F	187	38.1	273	55.5
Siemens/W	V94.2A	190	36.2	293	55.2
		New			
Alstom	GT24/26	179/262	—	260/378	56.5/57.0
Siemens/W	V94.3A	265	38.0	385	57.1
MHI	M501G/701G	254/334	38.5	500/—	58.0/—
GE	GE7G/9G	240/282	39.5	350/420	58.0
GE	GE7H/9H	—	—	400/480	60.0/60.0

Source: *Gas Turbine World 2000–2001 Handbook*, Vol. 21, Pequot Publishing Inc.

Advanced Combustion Turbines

Under the Department of Energy Advanced Turbine System (ATS) program (DOE, 2001), development work was carried out with two manufacturers to enhance the efficiency and environmental performance of utility-scale gas turbines. The goals were to achieve 60% efficiency or more in a combined-cycle mode; NO_x emission levels less than 9 ppm; and a 10% reduction in the cost of electricity. To achieve the efficiency objective required significantly higher turbine inlet temperatures. These higher temperatures required advancements in materials, cooling systems, and low-NO_x combustion techniques.

The focus of General Electric work for DOE was the "H" series gas turbine. To accommodate turbine inlet temperatures of 2800°F, General Electric is employing closed loop steam cooling for the first and second stages to reduce the differential between combustion (2800°F) and firing (2600°F) temperatures; the company is also developing new single-crystal (nickel superalloy) turbine blades with better thermal fatigue and creep characteristics. Thermal barrier coatings protect the metal substrate from the combustion gases using a ceramic top coat for thermal resistance and a metal bond coat for oxidation resistance. An MS9001H unit is being deployed in the U.K., and an MS7001H in Scriba, New York, in 2004.

Siemens–Westinghouse used its 501G turbine as a test bed for the ATS design. Computer modeling has allowed design refinements contributing to capital cost reduction and efficiency enhancement. These include a piloted ring combustor, which uses a lean, premixed multistage design to produce ultralow pollutant emissions and stable turbine operation. Siemens–Westinghouse has also developed brush and abradable coating seals to reduce internal leakage and new thermal barrier coatings for turbine blades to permit higher temperatures. These ATS developments will be incorporated into the commercial 501G turbine at the Lakeland Electric McIntosh station in Florida and demonstrated in 2005. A comparison of the "F" and "H" class machines for GE is shown in Table 8.6.9.

Humidified Air Power Plants (Cohn, 1994)

A new class of combustion turbines has been designed based on humidifying the combustion air. In these combustion turbine cycles, the compressor exit air is highly humidified prior to combustion. This reduces the mass of dry air needed and the energy required to compress it, thus raising plant efficiency.

The continuous plant cycle for this concept is termed the **humid air turbine** (HAT). This cycle has been calculated to have a heat rate for natural gas about 5% better than current high-technology combined cycles. The HAT cycle is adaptable to coal gasification — leading to the low-emissions and high-efficiency

TABLE 8.6.9 Comparison of "F" and "H" Class Machines

	GE Advanced Machines			
	7FA	7H	9FA	9H
	Characteristics			
Firing temperature F©	2350 (1300)	2600/1430	2350 (1300)	2600 (1430)
Air flow, lb/sec (kg/sec)	974 (442)	1230/558	1327 (602)	1510 (685)
Pressure ratio	15	23	15	23
Specific work, MW/lb/sec (MW/kg/sec)	0.26 (0.57)	0.33 (0.72)	0.26 (58)	0.32 (70)
	Performance			
Simple cycle output, MW	168	—	227	—
Simple cycle efficiency,%	36	—	36	—
Combined cycle net output, MW	253	400	349	480
Combined cycle net efficiency,%	55	60	55	60
NOx (ppmvd at 15% O2)	9	9	25	25

Source: GE Power Systems, Power system for the 21st century: H gas turbine combined cycle, 1995.

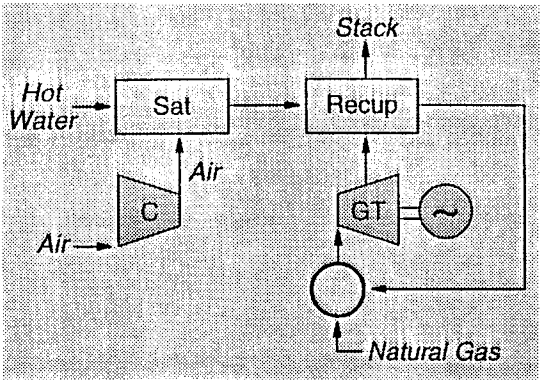

FIGURE 8.6.13 The humid air turbine (HAT) cycle adds moisture to the compressor exit air, reducing the air mass flow needed and increasing cycle efficiency.

characteristics of gasification combined cycle plants — but at a low capital cost because the steam turbine bottoming cycle is eliminated. A simple humidified air turbine cycle is shown in Figure 8.6.13. The addition of moisture means that perhaps 25% more mass flow goes through the turbine than through the compressor. This suggests the use of separate spools for the turbine and compressor. Using today's 2350°F firing temperatures, it is reasonable to expect a HAT heat rate of about 6100 Btu/kWh from this cycle.

The ideal natural-gas-fired HAT plant has been calculated to have higher efficiency (about 2 points higher) than a combined cycle for the same turbine cooling technology. Thus, it would provide the lowest heat rate for a natural-gas-fired thermal plant and would be utilized in baseload or long intermediate dispatch. The capital cost of this power plant has been calculated to be only slightly higher than that of a combined cycle. However, the anticipated development cost for the ideal turbo machinery has been estimated to be very high, in excess of $250 million.

In contrast, the CHAT (cascaded humid air turbine) plant utilizes turbine components, which are now available, with few exceptions, in a cascade arrangement that allows them to match together. The development cost of the CHAT equipment is currently estimated to be only in the $5 to 10 million range, making its development much more practical.

The HAT and CHAT cycles can be integrated with gasification. Because these cycles directly incorporate humidification, they can make direct use of hot water generated in the gasification plant, but cannot readily utilize steam. Thus, they match well with the lower capital cost, but lower-efficiency, quench types of gasifier. This provides an overall power plant with efficiency about the same as an IGCC. Moreover, the capital cost of the IGHAT plant has been calculated to be about $150/kW less than an IGCC plant. These humidification cycles have yet to be offered commercially. The main obstacle is the need to demonstrate low-emission, high-efficiency, full-scale combustors utilizing very humid air experimentally.

Other Combustion Turbine Cycle Enhancements (Lukas, 1986)

Several variants of the combustion turbine-based Brayton cycle increase plant efficiency and capacity. **Regenerative cycles** use storage type heat exchangers, where porous or honeycomb wall structures store energy from the hot gases. This is released later to the cold gases. A **recuperative cycle** uses a heat exchanger where the hot and cold streams are separated by walls through which heat transfer occurs. This is the approach commonly used in combustion turbines, allowing gains in efficiency and reduced fuel consumption, but no specific output increase.

Intercooling between compressor stages increases useful output by about 30% for a given air mass flow, by reducing the volume flow and increasing available energy to the power turbine. It has minimal effect on efficiency because heat removed must be added back in the combustion chamber, but it is commonly used in conjunction with recuperation. In a reheat cycle the fuel is introduced at two locations, increasing the total energy available to produce work. A combination of intercooling, reheat, and recuperation is shown in Figure 8.6.14.

Steam injection, in which the steam is injected directly into the combustion chamber, increases the mass flow through the turbine and results in increased output power. Steam-injected gas turbine (SIGT)

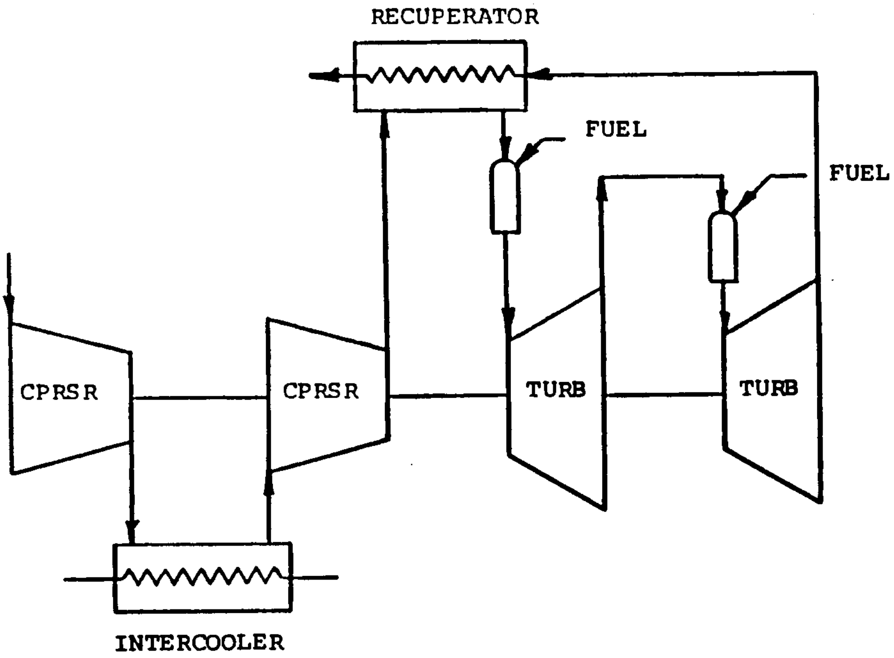

FIGURE 8.6.14 Improvement in combustion turbine performance is illustrated in this schematic, which combines an intercooler for the compressor with a recuperator using combustion turbine exhaust heat, and a reheat cycle for the turbine to improve efficiency.

cycles have been compared from the viewpoints of efficiency, power generation, capital and operating costs, and environmental impacts with combined cycle systems (Esposito, 1989). Above 50-MW size, it was found that combined cycle plants were more economical and achieved significantly better heat rates, although cooling tower fog, visible plumes, and drift deposition favored SIGT plants for a flat site

Central Station Options for New Generation

Coal and gas fuels are expected to continue to dominate U.S. central stations in the next decade, with gas-fired combined cycles supplanting several older fossil steam stations. This process is already underway, and by the end of 1999, 118 gas-fired combined cycles were in planning, totaling 56 GW of new power.

The U.S. central station generation options for fossil fuels may be described as follows:

- *Coal, oil, and gas-fired plants of conventional design with typical plant efficiencies of 35% (coal and oil) and 33% (gas); mostly Rankine cycles.* These represent the majority of plants currently in operation. On average, they are 30 years old, many (more than 70,000 MW) equipped with SO_2 scrubbers; most are facing NO_x control additions and perhaps other environmental upgrades. Yet they provide for the bulk of electricity needs; are extremely reliable; and are increasingly in demand as evidenced by an average capacity factor at an all-time high of nearly 70%.
- *Repowered plants, based on gas-firing and combined cycle operation, with efficiencies up to 45%.* Many of the gas-fired steam plants are now targeted for repowering, i.e., combustion turbines will be added to provide exhaust heat for producing steam for the existing steam turbines. This combination of gas and steam turbine cycles adds megawatts, reduces emissions, and improves efficiencies 5% or more.
- *New combined cycles based on gas-firing (about 45% efficiency with today's gas turbines and 50% with advanced gas turbines), and on coal-firing with gasification, utilizing advanced gas and steam turbine technology (50% efficiency).* Gas-fired combined cycles are currently the new plants of choice. Although relatively few are in operation today, more than 50 GW are planned. The massive deployment of these plants in the future raises questions of gas and gas pipeline availability, gas prices, and a potential retreat from coal that could have serious future energy consequences. Coal plants, whether pulverized or gasified, also lend themselves to combined cycles, although none are planned domestically outside the DOE Clean Coal demonstrations.
- *Coal-fired Rankine cycles with advanced steam conditions and up to 50% plant efficiency.* Advancing steam temperatures and pressures in pulverized coal steam plants greatly improve overall efficiency. Such ultrasupercritical cycles are already in operation outside the U.S. Advancing steam temperatures to 750°C from current levels of about 590°C permits plants to rival the best gas combined cycles. When used in coal combined cycles and with temperatures increased to 850°C or beyond, a coal plant approaching 60% efficiency is attained. Significant challenges still exist in materials technology.
- *Integrated coal gasification fuel cells, perhaps combined with gas turbines with efficiencies of 60% or more.* The fuel cell is an exciting advance that will change the energy picture in the long term. Shorter term, and in small sizes, great advances are being made in mobile as well as stationary applications. If the fuel cell can be used as a combuster for a gas turbine, efficiencies can be raised above 60%. Clearly, this is a power source of great promise for the second half of this century

Overall Plant Performance and Cost Estimates

As shown in Figure 8.6.15, mature versions of IGCC plants are expected to have capital costs slightly higher than the capital costs for PC plants, while the capital costs for PFBC plants are expected to be slightly lower than for PC plants. More advanced coal plants, when they become commercially available, are expected to have capital costs that are 20 to 25% lower than today's PC plants (Booras, 1999). These calculations include all engineering and construction costs. They assume a mature technology in which the plant achieves rated performance as designed. (Figure 8.6.16).

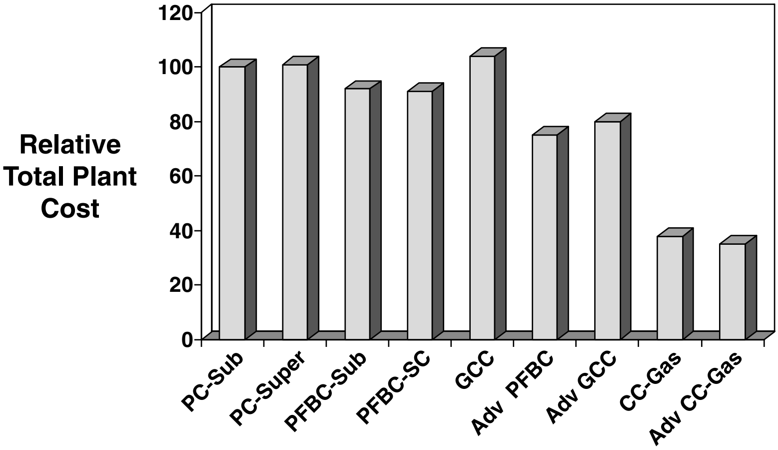

FIGURE 8.6.15 Capital costs for coal and gas-fired central stations. These costs assume mature technologies and fully functional equipment manufacturing lines for the newer technologies.

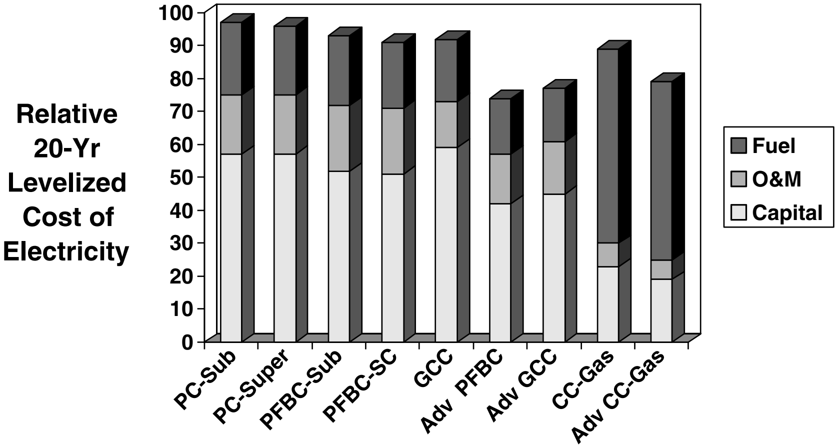

FIGURE 8.6.16 Levelized cost of electricity comparisons based on mean fuel prices for the U.S. and a 2010 start-up date. Coal is assumed at \$1.06/MMBtu and gas at \$3.08/MMBtu, a price differential about 40% greater than in 2000.

Summary

The preceding section has described how the future for electric power generation will increasingly be dominated by environmental control needs, putting an emphasis on the base efficiency of new generation, and on heat rate recovery for existing units. The pulverized coal-fired power plant with flue gas desulfurization will remain a focus of most near-term activity related to upgrades and retrofits. However, new technology, based on coal gasification, is under development and being tested in a growing number of demonstration plants that promise extremely low emissions.

The future for many nations will be based on exploiting the opportunities offered by clean and efficient use of coal. This implies access to the range of new technologies now being tested at large scale in the U.S. and other developed nations. This strategy is timely and prudent on a global basis as the world increasingly voices concerns related to carbon combustion.

New, base-load, central generation plants will largely be focused in the immediate future on the rapidly developing areas of the world: Asia (particularly China and India) and Latin America. In these areas, the fuel of choice will likely be coal, particularly in Asia, and the generating unit most often will be a conventional pulverized coal unit; such units will increasingly deploy supercritical steam at temperatures of 1100°F and above. In North America, Europe, and Japan, gas-fired central plants using combustion turbines, often in a combined cycle, will continue to be built through 2010 due to the short construction time and lower carbon dioxide emissions (compared with conventional PC plants).

As the cost of natural gas, relative to coal, increases, this will then encourage the installation of coal gasification units enabling the enormous world coal reserves to be utilized fully. Then, as the 21st century progresses, smaller distributed generating sources will begin to emerge, based on gas-fired fuel cells, small combustion turbines, or possibly photovoltaics. As the economics for the distributed option become favorable, these smaller generating units will encourage broad electrification of the developing countries of the world, avoiding the immediate need for large high-voltage transmission systems. Such distributed generation plants will also be added at strategic locations in the developed world as ways are sought to relieve the growing congestion on transmission networks.

Defining Terms

Lower heating value: Fuels containing hydrogen produce water vapor as a product of combustion. Fuel heating value is said to be "lower" if the combustion process leaves all products in the gaseous state, but "higher" if the fuel heating value includes the latent heat of vaporization. Practice in the U.S. is to use the higher value.

Combined cycle: Power stations that employ combustion turbines (Brayton cycle) and condensing steam turbines (Rankine cycle) where the waste heat from the CTs generate steam for the STs are called "combined" cycle plants. Overall plant efficiency improves.

Coal gasification: Coal can be converted into a mixture of carbon monoxide and hydrogen by burning it with a controlled deficiency of oxygen. Use of pure oxygen produces a medium calorific value gas, and air a low calorific value gas. This "syngas" can then be used to power a combustion turbine.

Flue gas desulfurization: Removal of sulfur dioxide, SO_2, from combustion gases is accomplished in a number of flue gas desulfurization methods. Most of these involve wet "scrubbing" of the gas using lime or limestone, and result in a calcium sulfate waste product. A 95% removal efficiency, or higher, is possible.

Slagging and fouling: The mineral matter in coal can attach itself following combustion to the boiler walls and heat exchanger surfaces. Oxides of silicon, aluminum, iron, calcium, and magnesium can foul all boiler surfaces, requiring soot blowers for cleaning. Hot ash can melt, becoming sticky and sometimes coalescing in the furnace to cause slagging problems.

On–off cycling capability: Generating units are often not required on a 24-h basis. Some are shut down during low demand times and started up perhaps hours later. This form of "on–off cycling" imposes thermal stresses on the equipment, leading to premature equipment failure unless special measures are taken to deal with this.

Temper embrittlement: Tempering of steel in the manufacturing process removes some of the brittleness and is carried out by a heating and cooling process. During operation, though, it is possible that ductility can worsen close to specific "tempering temperatures." The material is then said to be temper embrittled and premature cracking may follow.

Coextruded tubing: Tubing for superheaters and reheaters must be strong enough to withstand the pressures and temperatures expected, and also corrosion resistant to depositions of fly ash. By making tubing with a strong inner layer and corrosion-resistant outer layer through an extrusion process, both concerns can be dealt with.

Spray drying: Spray dryers, for desulfurization, used typically when burning lower sulfur coals, use a spray of quicklime, which is dried by the hot flue gas and results in a dry solid product. A 90% removal efficiency is typical.

Electrostatic precipitators: Flue gas particles, when electrically charged in an ionized gas flow, collect on electrodes in the presence of a strong electrostatic field. Collected dust is discharged by rapping into hoppers. A collection efficiency above 99% is possible.

Fluidized bed: A process of burning solid fuels, particularly coal, by combustion suspending the fuel within a column of air supplied from below the furnace. This method permits effective combustion of poor-quality fuels; lowers NO_x emissions due to low combustion temperatures; and captures sulfur in the bed by mixing limestone or dolomite in with the fuel.

Petroleum coke: Petroleum coke is a residual product of the oil refining process, and in its fuel grade form is an almost pure carbon by-product. About 19 million tons of fuel grade pet coke is produced each year in the U.S. It is inexpensive, although it may have high sulfur and vanadium content.

Double reheat: Modern designs of fossil steam-generating units remove a portion of the steam before full expansion through the turbine and reheat it in the boiler before returning it to the turbine. This enhances the thermal efficiency of the cycle by up to 5%. For supercritical cycles, two stages of reheat can be justified — double reheat.

Cogeneration: Cogeneration refers to the production of multiple products from a power plant. Typically, process steam, or hot water for heating, are produced in addition to electricity. This approach leads to high plant utilization, the "effective" heat rate being 70% or more.

Ash-softening temperature: The tendency for fly ash to adhere to tube banks is increased as the ash softens and melts. The point at which the ash begins to soften is dependent on the type of coal and is difficult to predict, depending on the many coal constituents. Slagging and fouling of tubes can lead to severe tube corrosion.

Fuel cell: Fuel cells convert gaseous or liquid fuels directly to electricity without any combustion process. Like a continuous battery, the fuel cell has electrodes in a electrolyte medium. Typically, hydrogen and air are supplied and DC electricity, water, and carbon dioxide are produced.They are currently high-cost, low-size devices, but with minimum environmental emissions.

Hot gas cleanup: Cycles that use gas from the combustion of coal, typically pressurized fluidized bed or gasification cycles, need to clean up the ash particles before passing them through a gas turbine. This prevents severe erosion of the turbine blades and other components. Hot gas cleanup can involve the application of hanging particulate traps, using ceramic filters.

F-class machines: Recent designs of combustion turbines have increased efficiencies resulting from increased firing temperatures. The first generation of these machines has firing temperatures of about 2300°F. They have been termed "F class" machines (for example the GE 7F). Even higher temperatures have now been incorporated into "G-class" turbines. Aeroderivative turbine: in the 1960s, gas turbines derived from military jet engines formed a source of utility peaking capacity. Now modern airline fan jets are being converted to utility service. These lighter combustion turbines are highly efficient and can have low NO_x emissions, high pressure ratios, and low capital cost.

Humid air turbine: A new type of combustion turbine uses humidified compressor exit air for the combustor. The mass of dry air needed is thus lessened for a given mass flow, and turbine efficiency increases. Several applications of this "HAT" appear attractive in gasification and compressed air storage cycles.

Regenerative cycles: Combustion turbine cycles using heat exchangers to store and transfer heat from hot gases to cold gases are termed regenerative cycles.

Recuperative cycle: Recuperative cycles for combustion turbines use walls between the hot and cold streams through which heat is transferred. This improves efficiency and reduces fuel consumption.

Intercooling: Increased output from a combustion turbine can be obtained by cooling the air between compressor stages. This reduces volume flow and increases energy to the power turbine.

Steam injection: Injecting steam directly into the combustion chamber of a combustion turbine increases turbine mass flow and thus increases the output power.

References

Armor A.F., Bakker, W.T., Holt, N.H., and Viswanathan, R., Supercritical fossil-fired power plants: designs and materials for the new millennium, Proc. PowerGen International Conf., New Orleans, LA, November 1, 1999.

Armor, A.F. and Wolk, R.H., *Productivity Improvement Handbook for Fossil Steam Plants*: 3rd ed., EPRI Report 1006315, October 2002.

Armor, A.F., Viswanathan, R., and Dalton, S.M., Ultrasupercritical steam turbines: design and materials issues for the next generation, coal utilization and fuel systems, DOE Annu. Conf., Clearwater, FL, March 10–13, 2003.

Blunden, W.E., Colorado-UTE's Nucla circulating AFBC demonstration project, EPRI Report CS-5831, February, 1989.

Booras, G., Overview of the economics of clean coal technologies as compared with alternatives for power generation, Proc. DOE Clean Coal Technol. Conf., Knoxville, TN, May 1999.

Carpenter, L.K. and Dellefield, R.J., The U.S. Department of Energy PFBC perspective, EPRI fluidized bed combustion for power generation conference, Atlanta, May 17–19, 1994.

Cohn, A., Humidified power plant options, AFPS developments, Spring 1994, Electric Power Research Institute.

Couch, G., Advanced coal cleaning technology, IEACR/44, London, IEA Coal Research, December 1991.

Courtright, H.A., Armor, A.F., Holt, N.H., and Dalton, S.M., Clean coal technologies and their commercial development, POWER-GEN International, Conf. Proc., Las Vegas, NV, December 9–11, 2003.

Dalton, S.M., Viswanathan, R., Gehl, S.M., Armor, A.F., and Purgert, R., Ultrasupercritical materials, DOE Clean Coal Conf., Washington, D.C., November 20, 2001

DOE Fossil energy — tomorrow's turbines, April 30, 2001, http://fossil.energy.gov/coal_power/turbines/index.shtml

Douglas, J., IGCC: phased construction for flexible growth, *EPRI J.*, September, 1986.

EPRI, Engineering assessment of an advanced pulverized-coal power plant, EPRI Report CS-2555, August 1982.

EPRI, Development plan for advanced fossil fuel power plants, EPRI Report CS-4029, May 1985.

EPRI, Assessment of supercritical power plant performance, EPRI Report CS-4968, December 1986.

Esposito, N.T., A comparison of steam-injected gas turbine and combined cycle power plants, EPRI Report GS-6415, June 1989.

EPRI, An assessment of mercury emissions from U.S. coal-fired power plants, EPRI Report 1000608, November 2000.

EPRI, Atmospheric fluidized-bed combustion handbook, EPRI Report 1004493, December 2002.

GE Power Systems, Power system for the 21st century: H gas turbine combined cycle, 1995.

Gas Turbine World 2000–2001 Handbook, Vol. 21, Pequot Publishing Inc.

Hinrichsen, D., AFBC conversion at Northern States Power Company, EPRI Report CS-5501, April, 1989.

Lucas, H., Survey of alternative gas turbine engineer and cycle design, EPRI Report AP-4450, February 1986.

Manaker, A.M., TVA 160-MW atmospheric fluidized-bed combustion demonstration project, EPRI Report TR-100544, December 1992.

Melvin, R.H. and Friedman, M.A., Successful coal-fired AFBC cogeneration in California: 108 MW ACE cogeneration facility, EPRI Fluidized Bed Combustion Conf., Atlanta, May 17–19, 1994.

Olesen, C., Pressurized fluidized bed combustion for power generation, in EPRI CS-4028, *Proc. Pressurized Fluidized-Bed Combustion Power Plants*, May, 1985.

Oliker, I. and Armor, A.F., Supercritical power plants in the USSR, EPRI Report TR-100364, February 1992.

Skowyra et al. Design of a supercritical sliding pressure circulating fluidized bed boiler with vertical waterwalls, *Proc. 13th Int. Conf. Fluidized Bed Combustion*, ASME, 1995.

U.S. Department of Energy, Clean Coal Technology Demonstration Program, DOE/FE-0444, July 2002.

Further Information

Annual energy outlook, 2003, Energy Information Administration: www.eia.doe.gov
National Engineering Technology Laboratory: www.netl.doe.gov
EPRI: www.epri.com
Steam, Its Generation and Use, Babcock and Wilcox, New York.
Combustion: Fossil Power Systems, J.G. Singer, Ed., Combustion Engineering, Inc. Windsor, CT.
Tapping global expertise in coal technology, EPRI J., Jan/Feb., 1986.
IGCC: new fuels, new players, EPRI J., July/Aug. 1994.
A brighter future for PFBC, EPRI J., Dec. 1993.
Fuel cells for urban power, EPRI J., Sept. 1991.
Distributed generation, EPRI J., April/May, 1993.
Plant repowering, EPRI J., September/October, 1995
Smart materials, EPRI J., July/August, 1998
Merchant plants, EPRI J., Summer, 1999.
Energy and air emissions, EPRI J., Summer, 2000.
Global coal initiative, EPRI J., Summer 2001.

8.7 Energy Storage

Chand K. Jotshi and D. Yogi Goswami

Introduction

Energy storage is very important for utility load leveling, electrical vehicles, solar energy systems, uninterrupted power supply, and energy systems at remote locations. Two important parameters for energy storage are duration of storage and **specific energy** or **energy density**. Duration of energy storage may vary from many years to a fraction of a second. In a nuclear power plant, nuclear fuel is stored within a reactor for a year. Coal piles, gas and oil storage tanks, or pumped hydro are kept by power utilities for several days use, depending upon the need. Similarly for a solar energy system, requirement of energy storage may be on an hourly, daily, or weekly basis. Specific energy or energy density is a critical factor for the size of a storage system.

Energy can be stored as mechanical, thermal, chemical, electrical, or magnetic energy. In this section, storage of thermal, mechanical, and electrical energy are described.

Thermal Energy Storage (TES)

Thermal energy can be stored as sensible heat, latent heat, or as the heat of chemical reaction (thermochemical).

Sensible heat, Q, is stored in a material of mass m and specific heat C_p by raising the temperature of the storage material and is expressed by Equation (8.7.1):

$$Q = mc_p \Delta T \tag{8.7.1}$$

Most common sensible heat storage materials are water, organic oils, rocks, ceramics, and molten salts. Some of these materials along with their physical properties are listed in Table 8.7.1. Water has the highest specific heat value of 4190 J/kg · C.

Thermal energy, Q, can be stored as latent heat in a material of mass, m, that undergoes phase transformation as given by Equation (8.7.2):

$$Q = m\lambda \tag{8.7.2}$$

where λ = heat of phase transformation.

TABLE 8.7.1 Physical Properties of Some Sensible Heat Storage Materials

Storage Medium	Temperature Range, °C	Density (ρ), kg/m^3	Specific Heat (C), J/kg K	Energy Density(ρC) kWhr/m^3 K	Thermal Conductivity (W/m K)
Water	0–100	1000	4190	1.16	0.63 at 38°C
Water (10 bar)	0–180	881	4190	1.03	—
50-ethylene glycol–50 water	0–100	1075	3480	0.98	—
Dowtherm A® (Dow Chemical, Co.)	12–260	867	2200	0.53	0.112 at 260°C
Therminol 66® (Monsanto Co.)	–9–343	750	2100	0.44	0.106 at 343°C
Draw salt ($50NaNO_3$-$50KNO_3$)[a]	220–540	1733	1550	0.75	0.57
Molten Salt ($53KNO_3/40NaNO_2/7NaNO_3$)[a]	142–540	1680	1560	0.72	0.61
Liquid sodium	100–760	750	1260	0.26	67.5
Cast iron	m.p. (1150–1300)	7200	540	1.08	42.0
Taconite	—	3200	800	0.71	—
Aluminum	m.p. 660	2700	920	0.69	200
Fireclay	—	2100–2600	1000	0.65	1.0–1.5

[a] Composition in percent by weight.
Note: m.p. = melting point.

TABLE 8.7.2 Physical Properties of Latent Heat Storage Materials or PCMs

Storage Medium	Melting Point °C	Latent Heat, kJ/kg	Specific Heat (kJ/kg °C)		Density (kg/m^3)		Energy Density (kWhr/m^3 K)	Thermal Conductivity (W/m K)
			Solid	Liquid	Solid	Liquid		
$LiClO_3 \cdot 3H_2O$	8.1	253	—	—	1720	1530	108	—
$Na_2SO_4 \cdot 10H_2O$	32.4	251	1.76	3.32	1460	1330	92.7	2.25
$Na_2S_2O_3 \cdot 5H_2O$	48	200	1.47	2.39	1730	1665	92.5	0.57
$NaCH_3COO \cdot 3H_2O$	58	180	1.90	2.50	1450	1280	64	0.5
$Ba(OH)_2 \cdot 8H_2O$	78	301	0.67	1.26	2070	1937	162	0.653ℓ
$Mg(NO_3) \cdot 6H_2O$	90	163	1.56	3.68	1636	1550	70	0.611
$LiNO_3$	252	530	2.02	2.041	2310	1776	261	1.35
$LiCO_3/K_2CO_3$, (35:65)[a]	505	345	1.34	1.76	2265	1960	188	—
$LiCO_3/K_2CO_3/Na_2CO_3$ (32:35:33)[a]	397	277	1.68	1 63	2300	2140	165	—
n-Tetradecane	5.5	228	—	—	825	771	48	0.150
n-Octadecane	28	244	2.16	—	814	774	52.5	0.150
HDPE (cross-linked)	126	180	2.88	2.51	960	900	45	0.361
Steric acid	70	203	—	2.35	941	847	48	0.172ℓ

[a] Composition in percent by weight.
Note: ℓ = liquid.

Four types of phase transformations useful for latent heat storage are: solid $\rightleftarrows$ liquid, liquid $\rightleftarrows$ vapor, solid $\rightleftarrows$ vapor, and solid $\rightleftarrows$ solid. Since phase transformation is an isothermal process, thermal energy is stored and retrieved at a fixed temperature known as the transition temperature. Some common phase change materials (PCMs) used for thermal storage are paraffin waxes, nonparaffins, inorganic salts (both anhydrous and hydrated), and eutectics of organic and/or inorganic compounds. Table 8.7.2 lists some PCMs with their physical properties.

Thermochemical energy can be stored as heat of reaction in reversible chemical reactions. In this mode of storage, the reaction in the forward direction is endothermic (storage of heat), while the reverse reaction is exothermic (release of heat). For example,

TABLE 8.7.3 Properties of thermochemical storage media

	Condition of Reaction						
Reaction	Pressure, kPa	Temperature, °C	Component (Phase)	Pressure, kPa	Temperature, °C	Density, kg/m^3	Volumetric Storage Density, kWhr/m^3
$MgCO_3$ (s) + 1200 kJ/kg =	100	427–327	$MgCO_3$(s)	100	20	1500	
MgO (s) + CO_2(g)			$CO_2(\ell)$	7400	31	465	
							187
$Ca(OH)_2$(s) + 1415 kJ/kg =	100	572–402	$Ca(OH)_2$(s)	100	20	1115	
CaO(s) + H_2O(g)			$H_2O(\ell)$	100	20	1000	345
SO_3(g) + 1235 kJ/kg =	100	520–960	$SO_3(\ell)$	100	45	1900	
SO_2(g) + ½O_2(g)			$SO_2(\ell)$	630	40	1320	
			O_2(g)	10000	20	130	280

Note: s = solid, ℓ = liquid, g =gas.

$$A + \Delta H \rightleftarrows B + C \tag{8.7.3}$$

The amount of heat Q stored in a chemical reaction depends on the heat of reaction and the extent of conversion as given by Equation (8.7.4):

$$Q = a_r m \Delta H \tag{8.7.4}$$

where a_r = fraction reacted, ΔH = heat of reaction per unit mass, and m = mass.

Chemical reaction is generally a highly energetic process. Therefore, a large amount of heat can be stored in a small quantity of a material. Another advantage of thermochemical storage is that the products of reaction can be stored at room temperature and need not be insulated. For sensible and latent heat storage materials, insulation is very important. Examples of reactions include decomposition of metal hydrides, oxides, peroxides, ammoniated salts, carbonates, sulfur trioxide, etc. Some useful chemical reactions are reported in Table 8.7.3.

Applications and Examples

Cool Storage has major applications in space cooling of buildings, food and medicine preservation, and transportation of items that need to be stored at low temperatures. A major application of cool storage is in the use of off-peak electricity for air-conditioning during peak hours. During off-peak hours electricity can be used to make ice or chilled water, which can be used later for air-conditioning of buildings during the peak hours. The advantage of using ice as a storage medium over chilled water is that a much larger amount of coolness can be stored in ice; 1 kg of ice stores 335 kJ, whereas 1 kg of water stores only 42 kJ for a temperature swing of 10°C. The disadvantage of ice is its lower thermal conductivity, which is responsible for lower heat-transfer rates.

Cool storage systems have been used in several buildings in the United States and Canada. The Merchandise Mart of Chicago boasts the largest ice storage system in the world: each day more than 1 million kg of ice are made and melted. For long-term cool storage, aquifers have been used for chilled water storage. Examples include cooling of buildings at the University of Alabama and the United States Postal Service in Long Island, NY, using chilled water stored in aquifers (Tomlinson and Kannberg, 1990). Other materials which have been found to have cool storage potential are PCMs like $LiClO_3 \cdot 3H_2O$, a eutectic of Glauber's salt, paraffins and their mixtures, and some gas hydrates or clatherates.

Heat Storage has major applications in space heating, crop drying, cooking, electric power generation, industrial process heat (air and steam), waste heat utilization, and solar energy utilization, etc. Heat storage in water is the most economical and well-developed technology. Epoxy-lined steel, fiberglass-reinforced polymer, concrete with plastic liner, and wood tanks are suitable containment materials for systems using water as the storage material. The storage tanks may be located above or below ground.

In North America and China, aquifers have been used for long-term storage of hot water and chilled water. Pressurized water tanks are used to store heat from off-peak electricity (ASHRAE, 1995). For example, water is heated to maximum temperatures of about 138°C in a tank at a pressure of 50 psig.

Molten nitrate salt (50 wt% $NaNO_3$/50 wt% KNO_3) also known as Draw salt, which has a melting point of 222°C, has been used as a storage and a heat-transfer fluid in an experiment in Sandia National Labs, Albuquerque, NM. It was the first commercial demonstration of generating power from storage (Delameter and Bergen, 1986). Solar Two, a 10-MW solar thermal power demonstration project in Barstow, CA, is also designed to use this molten salt to store solar energy (Chavez et al., 1995). Another molten nitrate salt is 40 wt% $NaNO_2$/7 wt% $NaNO_3$/53 wt% KNO_3, known as HTS (heat-transfer salt) with a melting point of 142°C. This salt has been widely used in the chemical industry.

For applications in heating and cooling of buildings the containment of PCM can become an integral part of the building. It may be part of the ceiling, wall, or floor of the building and may serve a structural or a nonstructural function. Tubes, trays, rods, panels, balls, canisters, and tiles containing PCMs have been studied in the 1970s and 1980s for space-heating applications (Moses and Lane, 1983). The PCMs used were mostly salt hydrates such as Glauber's salt ($Na_2SO_4 \cdot 10H_2O$), Hypo ($Na_2S_2O_3 \cdot 5H_2O$), $NaCH_3COO \cdot 3H_2O$, $Na_2HPO_4 \cdot 12H_2O$, $Ba(OH)_2 \cdot 8H_2O$, $MgCl_2 \cdot 6H_2O$, and $Mg(NO_3)_2 \cdot 6H_2O$. Paraffin mixtures have been used for thermal storage in wall boards. Some PCMs, such as salt hydrates, exhibit supercooling and phase segregation problems during heat removal. Low thermal conductivity and complex mechanism of heat transfer during melting and freezing introduce complexities in the design of their containment systems.

Mechanical Energy Storage

Mechanical energy may be stored as potential or kinetic energy.

Kinetic Energy

Kinetic energy can be stored in the rotating mass of a wheel, commonly known as a flywheel. Kinetic energy of a rotating body is given by Equation (8.7.5):

$$KE = \frac{1}{2} I \omega^2 \tag{8.7.5}$$

where I = moment of inertia, and ω = angular velocity.

The maximum specific energy of a flywheel is expressed by the following equation (Jensen, 1980):

$$\frac{KE_{\max}}{m} = A \frac{\rho_{\max}}{\rho} \tag{8.7.6}$$

where A = shape factor, and its value depends on the geometry of flywheel; A = 1.0 for a constant stress disk and 0.5 for a thin-rimmed flywheel. This equation shows that high tensile strength and low density are the key parameters to store maximum energy. Tensile strength, density, and specific energy of some materials are given in Table 8.7.4.

Storing energy in a flywheel is one of the oldest techniques used in ancient potteries. Present-day flywheels are much more advanced as a result of superstrong/ultralight composite materials and frictionless high-performance magnetic bearings.

Potential Energy

If a body of mass m is elevated against the gravitational force g to a height Δh, the potential energy stored is given by

$$\mathrm{PE} = mg\Delta h \tag{8.7.7}$$

TABLE 8.7.4 Flywheel Rotor Materials

Material	Design Stress, MN/m^2	Density, kg/m^3	Specific Energy, Whr/kg
Composite fiber[a]/epoxy	750	1550	51.5
E-glass fiber[a]/epoxy	250	1990	14.0
S-glass fiber[a]/epoxy	350	1900	19.6
Kevlar fiber[a]/epoxy	1000	1400	76.2
Maraging steel	900	8000	24.2
Titanium alloy	650	4500	30.8

[a] 60% fiber.

From Equation (8.7.7), 1 Wh of energy can be stored in 1 kg mass of a body by raising it to a height of 367 m.

Potential energy is also stored in a spring, either by compressing or expanding. Here, energy stored is given by

$$\mathrm{PE} = (1/2)kx^2 \tag{8.7.8}$$

where k = spring constant and x is the distance to which the spring is compressed or expanded. Springs have been widely used to power toys and watches mainly because of very low values of energy density.

Pumped Hydro

Water may be pumped from a lower reservoir to a higher reservoir using electricity during off-peak hours, which may be used to generate electricity using hydraulic turbines during peak hours. Advantages of pumped hydro units include simple operation, high reliability, low maintenance, long life, quick start from standstill, and economic generation of peaking electrical energy. In the United States a large number of such systems are in operation. Power-generating capacities of these systems vary between 5 and 2000 MW (Makansi, 1994). The overall efficiencies of these power plants vary between 65 and 90%, which includes the efficiencies of pumps, hydraulic turbines, generators, and losses from the upper reservoir. In spite of the technical and economic viability of pumped hydro, the requirement of a specific type of topography and some environmental concerns limit its application.

Electrical Energy Storage

Electrochemical energy storage, more commonly known as battery storage, stores electrical energy as chemical energy. Batteries are classified as primary and secondary batteries. Only secondary batteries are rechargeable and are therefore suitable for energy storage applications. Lead-acid and nickel-cadmium are well-known rechargeable batteries that are most commonly used. Lead-acid batteries have been used for over a century and are still the most popular batteries.

Electrochemical operation of a cell during discharge and charge is shown in Figure 8.7.1a and Figure 8.7.1b. During discharge when a cell is connected to a load, electrons flow from the anode to the cathode. In this operation oxidation, or loss of electrons, takes place at the anode, and reduction, or gain of electrons, occurs at the cathode. The cell chemistry of a lead-acid battery is as follows: the anode is lead (Pb) and the cathode is lead oxide (PbO_2); the electrolyte is H_2SO_4. The cell reaction is

$$2H_2SO_4 \rightarrow 4H^+ + 2SO_4^-$$

$$\text{Anodic reaction:} \quad Pb + SO_4^{2-} = PbSO_4 + 2e^- \tag{8.7.9}$$

$$\text{Cathodic reaction:} \quad PbO_2 + SO_4^{2-} + 4H^+ + 2e^- = PbSO_4 + 2H_2O \tag{8.7.10}$$

Theoretical voltages and capacities of some known batteries are reported in Table 8.7.5.

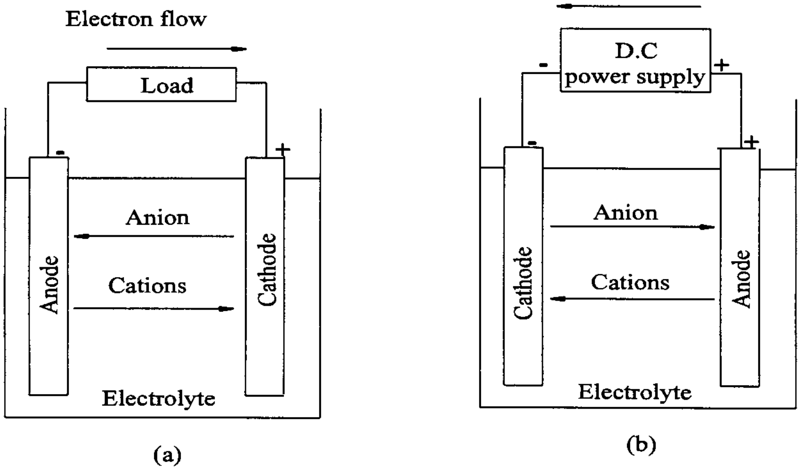

FIGURE 8.7.1 Electrochemical operation of a cell: (a) discharge; (b) charge.

TABLE 8.7.5 Properties of Some Rechargeable Batteries

No.	System	Electrolyte	Temp. °C	O.C.V. (V)	Energy Density (Theoretical), Whr/kg	Energy Density (Achievable), Whr/kg	In/Out Electrical Effciency	Cycle Life
1	Lead-Acid	H_2SO_4	20–30	2.05	171	50	75	1000
2	Nickel-Iron	KOH	20–30	1.37	267	60	55	2000
3	Zinc-Iron	KOH	50–60	1.65	1084	90	45	600
4	Sodium-Sulfur	β-Al_2O_3	300–375	1.76–2.08	664	120	75	2000
5	Lithium-Iron Sulfide	LiCl-KCl (eutectic)	400–450	1.6	869	150	75	1000

Note: O.C.V. = open cell voltage.

Applications

Battery storage is used in a wide range of applications. Currently, the main emphasis of research is on applications in vehicles and load leveling.

Electric Vehicles. For electric vehicles, the specific energy and specific power are two important parameters. The greater the specific energy, the farther a vehicle can travel. If specific power is high, a vehicle can accelerate more quickly and have a higher top speed. Other important requirements are the ability to charge and discharge a large number of times, to retain charge over an extended period of time, and to charge and discharge over a wide range of temperatures. Table 8.7.5 provides information about some rechargeable batteries.

Power Plants. Recent start-up of a commercial unit for the Puerto Rico Electric Power Authority (PREPA) is the latest development in large-scale application of lead-acid batteries. The facility stores 20 MW for 20 min, both for peaking requirement and voltage and frequency control. Maximum discharge is limited to 10 MW (Makansi, 1994).

Defining Terms

Cool storage: The storage of thermal energy at temperatures below the nominal temperature required by the space or process.

Heat storage: The storage of thermal energy at temperatures above the nominal temperature required by the space or process.

Energy density: Amount of energy stored per unit volume, kJ/m^3 or kWh/m^3.
Specific energy: Amount of energy stored per unit mass, kJ/kg or kWh/kg.

References

ASHRAE, 1995. Thermal storage, in *ASHRAE Handbook, HVAC Application*, p. 40.15. American Society of Heating, Refrigerating and Air-Conditioning Engineers, 1791 Tullie Circle, N.E., Atlanta.

Beckman, G. and Gilli, P.V. 1984. *Topics in Energy — Thermal Energy Storage.* Springer-Verlag, New York.

Chavez, J.M. et al. 1995. The Solar Two Power Tower Project: a 10MWe power plant, in *Proceedings of the 1995 IECEC*, Vol. 2, pp. 469–475, ASME, New York.

Delameter, W.R. and Bergen, N.E. 1986. Review of Molten Salt Electric Experiment: Solar Central Receiver Project. SAND 86-8249, Sandia National Laboratory, Albuquerque.

Garg, H.P., Mullick, S.C., and Bhargava, A.K. 1985. *Solar Thermal Energy Storage.* D. Reidel, Boston.

Glendenning, I. 1981. Advanced mechanical energy storage, in *Energy Storage and Transportation,* G. Beghe, Ed., pp. 50–52. D. Reidel, Boston.

Jensen, J. 1980. *Energy Storage.* Newnes-Butterworth, Boston.

Makansi, J. 1994. Energy storage reinforces competitive business practices. *Power.* 138(9):63.

Moses, P.J. and Lane, G.A. 1983. Encapsulation of PCMs, in *Solar Heat Storage: Latent Heat Materials*, Vol. II, pp. 93–152. CRC Press, Boca Raton, FL.

O'Connor, L. 1993. Energizing the batteries for electric cars. *Mech. Eng.* 7:73–75.

Sharma, S.K. and Jotshi, C.K. 1979. Discussion on storage subsystems, in *Proceedings of the First National Workshop on Solar Energy Storage*, pp. 301–308. Panjab University, Chandigarh, India.

Tomlinson, J.J. and Kannberg, L.D. 1990. Thermal energy storage. *Mech. Eng.* 9:68–72.

8.8 Nuclear Power

Roberto Pagano and James S. Tulenko

Nuclear power refers to power generated through reactions involving atomic nuclei (i.e., nuclear reactions). These reactions fall into three broad categories — fusion reactions, fission reactions, and radioisotopes. In fusion, two light nuclei (most commonly isotopes of hydrogen) combine to form a heavier nucleus (usually helium), with energy being released in the process. Nuclear fusion is the source of energy generated in the stars (our sun). In artificial applications, the technology to induce fusion reactions has been available for several decades, but such reactions have been essentially uncontrolled (the hydrogen bomb). Once initiated, fusion reactions generate huge amounts of energy, which is subsequently released explosively. Means to produce and release energy from fusion in a sustained, controlled manner are still being developed. Extensive research is ongoing, both in the United States and abroad, on the development of nuclear fusion as a controlled source of power.

Nuclear fission, in contrast, is the basis of a mature technology applied to the generation of power. Fission is the fragmentation of a heavy nucleus into two, sometimes three, lighter nuclei. Certain nuclides found in nature fission spontaneously, that is, with no external intervention. However, spontaneous fission in naturally occurring nuclides takes place at a very slow rate. Fission can be induced through a nuclear reaction. Of primary interest here is the fissioning of several specific nuclei through interactions with neutrons. Again, the fissioning of a nucleus is accompanied by the release of energy.

At present, the element of primary importance with respect to nuclear fission power is uranium. Naturally occurring uranium consists of three isotopes — ^{238}U, ^{235}U, and ^{234}U. In a mixture of isotopes of an element, the abundance of any one is usually expressed as the number of atoms of that isotope present per 100 atoms of the mixture, abbreviated as atom percent a/o or weight percent w/o. Natural uranium consists of 99.2745 a/o ^{238}U, 0.7200 a/o ^{235}U, and 0.0055 a/o ^{234}U.

Radioisotope power is the third form of nuclear energy. When radioisotopes decay, high-energy electrons (beta particles), helium atoms (alpha particles), and gamma rays (photons) are emitted. When the energy of these radiations is stopped and converted to heat, a power source is created. Radioisotopes decay energies range from 0.01 to 10 MeV. Radioisotopes are generally separated from radioactive wastes produced from nuclear power plants. The most common radioisotopes are polonium-210 (alpha emitter of 5.3 MeV), plutonium-238 (alpha emitter of 5.46 MeV), cesium-144 (beta emitter of 1.25 MeV), and strontium-90 (beta emitter of 1.10 MeV).

The Fission Process

Consider first the fission of a nucleus of ^{235}U caused by an interaction with a neutron. A compound nucleus of ^{236}U is initially formed. If fission occurs, it does so within a very short time. Normally with thermal reaction, 85% of the interaction leads to fission. Alternatively, the compound nucleus dissipates energy by emitting a gamma photon, no fission occurs and the nucleus remains as ^{236}U. This latter process occurs in 20% of the interaction of ^{235}U with a neutron.

The fissioning of a nucleus produces fission fragments called fission products, a number of neutrons and gamma photons. Most frequently, the number of neutrons is 2 or 3, ranging in extreme cases from 0 to 8. In the fissioning of ^{235}U, the average number of neutrons released, designated by υ, has a value of 2.42. This value applies strictly if the fission is induced by a neutron of relatively low kinetic energy, called a thermal neutron.

In a nuclear reactor, which is a special material medium in which ^{235}U is dispersed for the reactor to work, one of the neutrons liberated in the fissioning of a nucleus must go on to induce a fission in another nucleus. This leads to the idea of a self-sustaining chain reaction or, more specifically, a **critical configuration** in which a self-sustaining chain reaction can be maintained indefinitely. To this end, an adequate supply of ^{235}U must be on hand and replenished as needed. Further, the configuration must be such that the likelihood that any particular neutron ultimately induces a fission is adequately high to ensure that on average one neutron will induce a fission.

The energy liberated in fission results from Einstein's equation $E = Mc^2$, which says that mass and energy are equivalent. A summation of the masses of the fission fragments and the neutrons resulting from fission shows that the combined mass of the products of a fission is less than the mass of the compound nucleus before fission occurs. It is found that the energy released is equal to $E = \Delta Mc^2$ when ΔM is the difference in the masses. This nuclear energy is traditionally expressed in units of electron volts (eV), with the equivalence of $1 \text{ eV} = 1.602 \times 10^{-19}$ J. The single fission of a single uranium atom releases approximately 200×10^6 eV, or 200 MeV, of energy. When one realizes that the combusion of a single carbon atom ($C + O_2 \rightarrow CO_2$) releases 4 eV, a quantity 50 million times smaller, one gets a true appreciation of the concentrated power of nuclear energy.

Most of the energy liberated in a fission appears as the kinetic energy of the fission fragments (168 MeV, or 84%) and the kinetic energy of the neutrons (5 MeV, or 2.5%). The remainder is distributed among the gamma photons appearing instantaneously with the fission and the energy associated with the radioactive decay of the fission fragments. These fragments are readily stopped in the reactor. Their range is of the order of 0.01 to 0.001 mm. Thus, the major portion of the energy from a fission is deposited within a very short distance from the site of the fission.

In the largest power reactors in operation in the United States today, heat is generated at the rate of 3800 MW. At 200 MeV per fission, fissioning in such reactors must occur at the rate of 1.2×10^{20} fissions/sec to produce the power. In terms of ^{235}U, this requires the fissioning of all the nuclei contained in 0.047 g of ^{235}U, or the fissioning of approximately 4 kg per day. Thus, as a rule of thumb, the fissioning of all the nuclei present in 1 g of ^{235}U is sufficient to generate 1 MW day of thermal energy. In contrast, the generation of the same amount of energy from coal requires the combustion of 4 tons of coal of typical heating value. With the combustion of coal there is the associated release of a large quantity of carbon dioxide (~14 tons) to the atmosphere with its effects on global warming.

Cross Sections

A measure of the probability of a particular nuclide to interact with a neutron is provided by a quantity known as a **cross section**. Numerical values of cross sections are determined experimentally and are expressed in units of barns (b), with 1 b defined as 10^{-24} cm^2, or 10^{-28} m^2.

As a quantity, a cross section may be interpreted as a target area — the larger the cross section, the more likely the interaction of the nucleus with a neutron in its vicinity. For example, the cross section for fission of ^{235}U, denoted by σ_f^{235}, has a value of 582 b if the interacting neutron is traveling at the velocity associated with thermal energy (2200 m/sec). If the neutron is traveling at high energy, the cross section may drop to a value of approximately 2 b. With respect to the radiative capture of a neutron in ^{235}U leading to the formation of ^{236}U, the cross section is given by $\sigma_c^{235} = 99$ b, if the neutron is thermal. In summary, a cross section is a property specific to a given nuclide, but it is a property whose value depends on the energy of the interacting neutron.

Cross sections are additive. Thus, the cross section for the absorption of a thermal neutron in ^{235}U — whether the absorption gives rise to a fission or a radiative capture — is given by $\alpha_a = \alpha_f + \alpha_{\mathrm{c}} = 582$ b + 99 b = 681 b. Further, the probability of a fission occurring as a result of a thermal neutron being absorbed in ^{235}U is given by α_f/α_a = 582 b/681 b = 0.85. Fission is, therefore, the more likely outcome of an interaction between a ^{235}U nuclide and a thermal neutron.

On average, the neutrons arising from the fissioning of ^{235}U have a kinetic energy of 2 MeV, corresponding to a speed of 2×10^7 m/sec. These neutrons are four orders of magnitude greater than the speed at which a neutron is considered to be thermal (2200 m/sec).

Categories of Nuclear Reactors

A prerequisite for a self-sustaining chain reaction is that sufficient ^{235}U be present in the medium to ensure that the absorption of a neutron in a nucleus of ^{235}U is a likely occurrence. If the population of neutrons present in the medium at any instant consists predominantly of slow neutrons, a far lesser amount of ^{235}U is needed to ensure criticality than would be the case if the population were to consist of fast neutrons. This comes about because of the difference in the values of the cross sections mentioned previously.

There is, from this particular standpoint, an incentive to slow down the neutrons originating in fission in order to reduce the inventory of ^{235}U needed to maintain criticality. In the power reactors operating today, means are provided to slow down the neutrons. The slowing down is effected through multiple elastic scatterings of the neutrons with the nuclei of light elements deliberately present in the medium acting as so-called **moderators**. Notable among such elements are hydrogen present in water, deuterium in heavy water, and carbon in the form of graphite.

All of the reactors in which substantive moderation of the neutrons occurs are categorized as **thermal reactors**. This term stems from the distinguishing feature that the neutron population is in, or near, thermal equilibrium with the nuclei of the moderator. As a consequence, there is no net exchange of energy between the neutron population and its surroundings. The neutrons are then referred to as thermal neturons.

In a population of **thermal neutrons**, the distribution of the speeds of the neutrons is characterized, adequately in many cases, by the Maxwell-Boltzmann distribution, originally formulated to apply to the molecules of an ideal gas. According to this distribution, the most probable speed of the neutrons at the reference temperature of 20°C is 2200 m/sec and the kinetic energy corresponding to the most probable speed is 0.025 eV.

Reactors that are not thermal reactors fall in the category of **fast reactors**. In these reactors, the moderation of neutrons is much reduced for reasons discussed later.

Nuclear Fuel

In light-water reactors (LWR), the type of power reactors most commonly in service today, the nuclear fuel is uranium with a content of 2 to 4% of ^{235}U. This fuel is produced by enriching natural uranium in ^{235}U by one of several technologies, principally gaseous diffusion and gaseous centrifugation (Benedict et al., 1981). Neutrons of all energies, down to and including thermal energies, can induce fission in ^{235}U. For this reason, ^{235}U is said to be fissile.

In contrast, ^{238}U, present to the extent of 96 to 98% in the fuel, can be fissioned to a significant extent by neutrons with energies in excess of a threshold of roughly 2 MeV. Fissions of ^{238}U, referred to as fast fissions, play only a slight role in the chain reaction in an LWR. However, ^{238}U absorbs neutrons radiatively to yield ^{239}U. This nuclide is radioactive and decays to ^{239}Np which, in turn, decays to ^{239}Pu, a **fissile nuclide**. Thus, in LWR fuel ^{239}Pu, produced from ^{238}U, is available for fissioning by neutrons of all energies and contributes to the chain reaction. Because of its ability to form fissile ^{239}Pu, ^{238}U is termed a **fertile nuclide**.

Conversion and Breeding

To characterize the unique capability of nuclear fuel simultaneously to produce and consume fissile material, a figure of merit known as the **conversion ratio** (CR) is informative. It is defined by the relation:

$$\mathrm{CR} = \frac{\text{number of fissile nuclei produced from fertile nuclei}}{\text{number of fissile nuclei consumed}}$$

In fuel irradiated in an LWR, the conversion ratio typically has a value of 0.5. If the appropriate combination of materials, design, and operating parameters could be found to raise the conversion ratio to a value greater than unity, a reactor would become a breeder reactor, that is, one that produces more fissile material than it consumes in its operation.

To illustrate the possibility of breeding, consider a parameter known as the reproduction factor and given by

$$\eta = \nu \frac{\text{number of neutrons causing fission in fuel}}{\text{total number of neutrons absorbed in fuel}} = \nu \frac{\sigma_f^{\text{fuel}}}{\sigma_a^{\text{fuel}}}$$

In the case of ^{235}U and thermal neutrons, the value of η is given by $\eta_{235} = 2.42 \times 582/(589 + 99) = 2.42 \times 0.85 = 2.07$.

If a chain reaction is to be self-sustaining in a reactor, the condition $\eta > 1$ must apply. To achieve breeding requires that $\eta > 2$. In other words, one neutron from fission would be available to sustain the chain reaction and another to produce a fissile nucleus from a fertile nucleus. Practical considerations indicate that the value of η must be substantially greater than 2, since neutrons will be lost by absorption in structural materials, heat removal medium, fission fragments, the moderator, if present, and by escaping from the physical confines of the reactor.

As shown, ^{235}U has a value of η slightly above 2 with neutrons at thermal energies. Breeding or near-breeding conditions could arise, in principle, if very judicious choices of materials and parameters prevail. A more attractive fuel from the standpoint of breeding is ^{233}U. This isotope of uranium is produced artificially by placing the naturally occurring nuclide ^{232}Th in a reactor. A radiative capture of a neutron in ^{232}Th leads to the formation of the radioactive nuclide ^{233}Th. Two successive radioactive decays yield ^{233}U. In a thermal reactor, the value of η with ^{233}U is 2.29, approaching the level where breeding might be contemplated. Intermediate between the two fissile isotopes of uranium is ^{239}Pu, which at thermal energies yields a value of η of 2.15.

Figure 8.8.1 shows the behavior of η as the energy of the neutrons inducing fission increases. A little above thermal energies the value of η for ^{239}Pu and ^{235}U drops below 2, indicating that breeding is impossible at such energies. As energy increases, the values of η for both reache the threshold of 2 and continue to increase steadily, with ^{239}Pu clearly the more attractive fuel from the standpoint of breeding. The value of ^{239}Pu for ^{235}U is relatively insensitive to increases in energy and remains continuously above 2. Again, at higher energies, η is the more attractive fuel.

Research on the development of **breeder reactors** has focused on the ^{239}Pu fuel cycle, both in the U.S. and abroad. Representative of these reactors is the liquid metal fast breeder reactor (LMFBR) in which

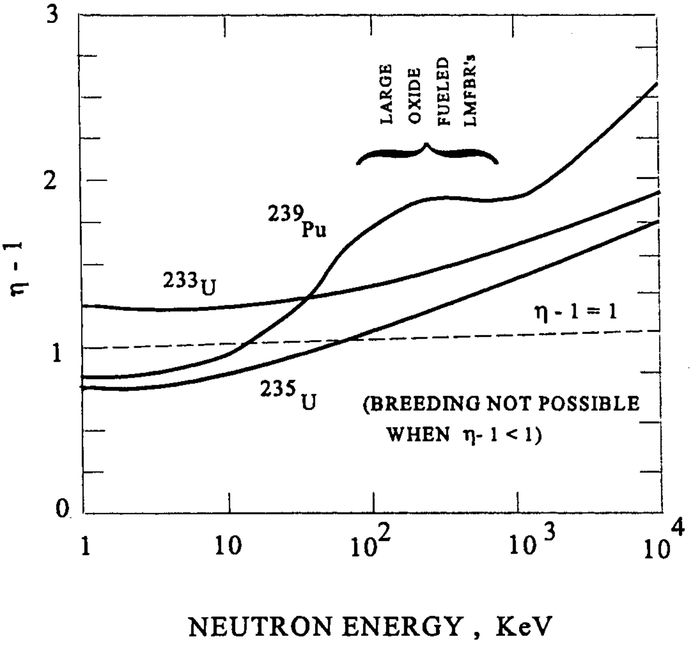

FIGURE 8.8.1 Dependence of reproduction factor of neutron energy.

liquid sodium is the heat-removal fluid and provides the small amount of moderation needed. Breeder reactors with ^{233}U as fuel, represented by an adaptation of the high-temperature gas-cooled reactor (HTGCR), in which the heat-removal fluid is helium and the moderator is graphite, although less attractive, in principle, as breeders, might with further research and development prove to be viable alternatives to the LMFBR.

LWR Fuel

Nuclear fuel in light water is in the form of small cylindrical pellets of the ceramic UO_2, with the uranium enriched to 2 to 4% in ^{235}U, as mentioned previously. These pellets are stacked vertically in tubes and the ends of the tubes are sealed off. The dimensions and further details given here apply strictly to the more common type of LWR, known as the pressurized water reactor (PWR), but may be taken as generally representative of LWRs.

The tubes containing the fuel pellets are referred to as fuel rods. They are 4.3 to 4.7 m in length and 0.0095 m in outside diameter. An array typically of 17 × 17 rods constitutes a fuel assembly, as shown in Figure 8.8.2. Certain fuel rods within the assembly are replaced by guide sheaths in which absorber rods can be moved vertically. These rods absorb neutrons, thus providing one of the means of controlling the chain reaction as the rods are inserted or withdrawn. Within the fuel assembly the fuel rods are placed on a pitch of 0.0127 m, leaving vertical passages through which water can flow. A total of approximately 200 fuel assemblies, juxtaposed to form a roughly cylindrical configuration constitute the core of the reactor. Water is circulated through the core where the water serves both to moderate the neutrons and to remove the heat generated by fissions in the nuclear fuel.

Light-Water Reactors

LWRs currently make up the largest portion of the installed nuclear generating capacity throughout the world. Among these, the PWRs are more numerous. By operating at a sufficiently high pressure, bulk boiling of the reactor coolant is suppressed in a PWR. In contrast, the coolant is allowed to boil in a boiling water reactor (BWR) and a portion of the coolant is converted to steam as it circulates through the core.

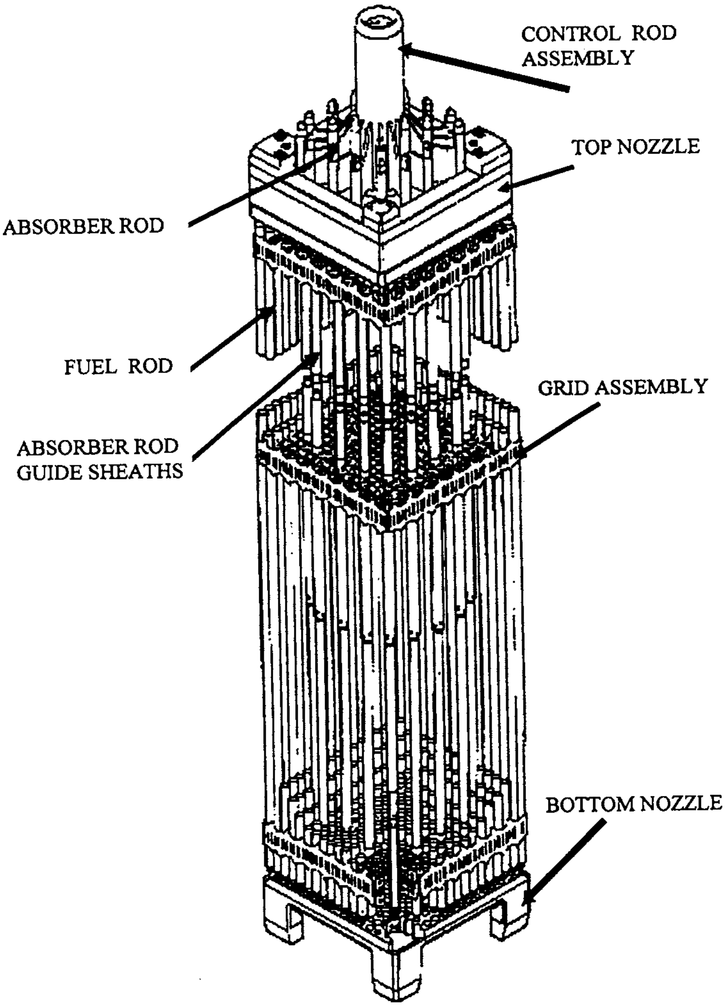

FIGURE 8.8.2 PWR fuel assembly.

Pressurized Water Reactors

A schematic of a PWR system is shown in Figure 8.8.3. At the heart of the system is the core made up of fuel assemblies and associated control rods. The core is contained in a reactor vessel, or pressure vessel, designed to operate at a pressure typically of 15.5 mPa. Water is circulated through the core where it acts as a moderator and also removes the heat generated through fission. Typical operating temperatures at full power are 295°C at the inlet and 330°C at the outlet, an increase of 35°C as a result of the water passing through the core.

From the reactor vessel, the coolant is circulated to steam generators and returned to the reactor vessel to complete the so-called primary loop. This loop constitutes the nuclear steam supply (NSS). Steam emerging from the steam generators is directed toward the secondary loop, or balance of plant, consisting of turbine generator, condenser, and feedwater pumps. Extremely small quantities of radioactive contaminants may be present in the steam generated in PWRs, and all releases to the environment from the secondary side of the plant are carefully monitored and controlled. Otherwise, steam from the NSS differs from steam generated in fossil fueled plants only inasmuch as its grade is inferior.

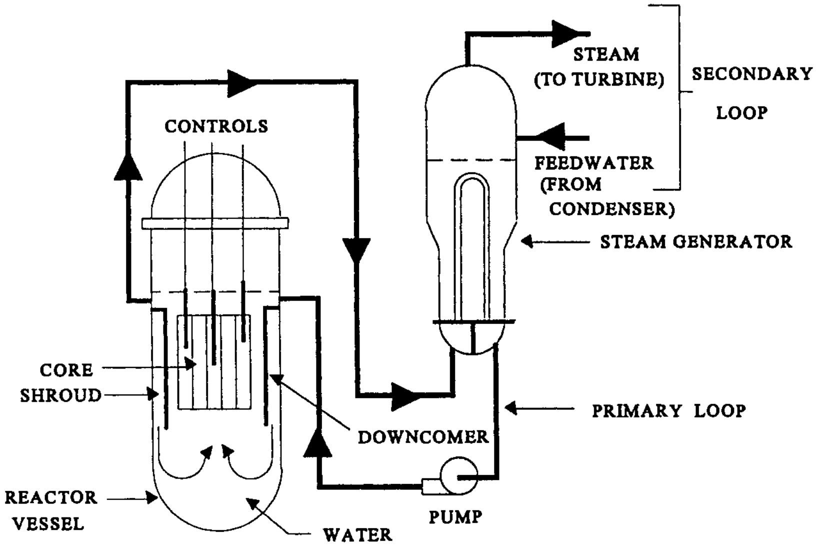

FIGURE 8.8.3 Schematic of a pressurized water reactor.

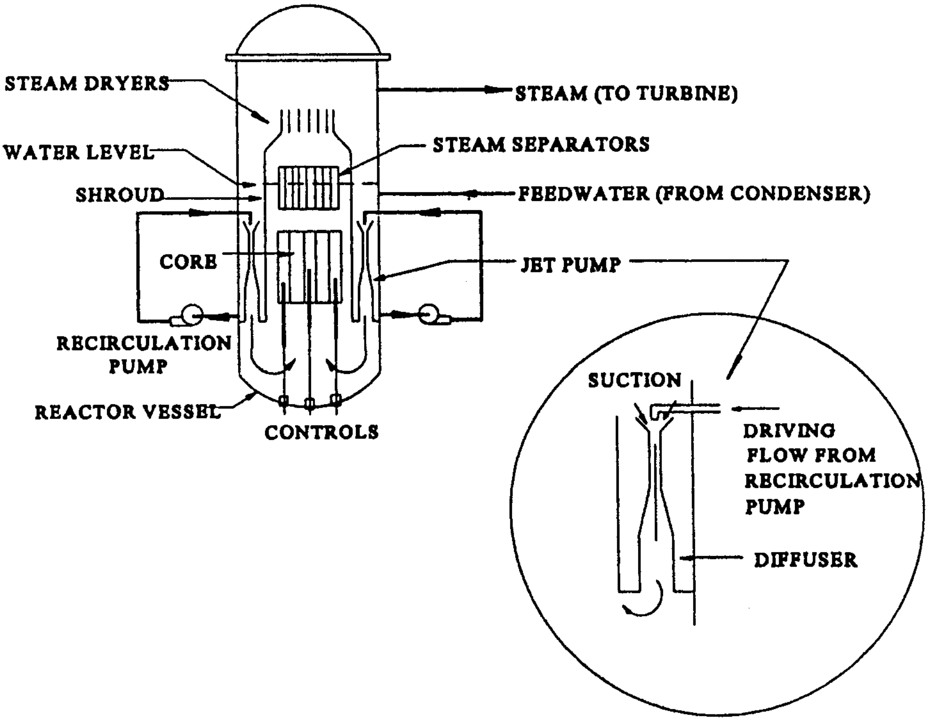

FIGURE 8.8.4 Schematic of a boiling water reactor.

Boiling Water Reactors

Figure 8.8.4 is a schematic of a BWR system. A reduced operating pressure of 7.2 MPa causes a portion of the coolant to flash to steam. Steam separators and driers allow dry steam to emerge from the reactor vessel, thus eliminating the need for separate steam generators and a secondary loop. Steam from the reactor vessel flows through a turbine generator and condenser, from which circulating pumps return the condensate to the reactor. Large quantities of radioactive contamination may be present in the steam produced by a BWR because of the direct cycle, so releases must be carefully monitored. A distinguishing feature of the BWR are the jet pumps, typically 24 in number, placed along the periphery of the core. These pumps augment the flow of coolant through the core.

Defining Terms

Breeder reactors: Reactors in which the conversion ratio is greater than unity.
Conversion ratio: The ratio of the number of fissile nuclei produced in a reactor to the number of fissile of nuclei consumed.
Critical configuration: A medium containing nuclear fuel in which a self-sustaining chain reaction can be maintained.
Cross section: A numerical quantity, determined experimentally, related to the probability that a specific nuclide will undergo a given nuclear reaction.
Fast reactors: Reactors in which little moderation of the neutrons occurs and the neutron populations consist of neutrons of relatively high speeds.
Fertile nuclide: A nuclide that, through the absorption of a neutron and subsequent radioactive decays, can produce a fissile nuclide.
Fissile nuclide: A nuclide that can be fissioned by neutrons of all energies, down to and including thermal energies.
Moderator: A component of a reactor present expressly to slow down neutrons and produce a population of thermal neutrons.
Thermal neutrons: A population of neutrons in, or near, thermal equilibrium with the nuclei of a medium in which the populations exists.
Thermal reactors: Reactors in which the neutron populations consist predominantly of thermal neutrons.

References

Benedict, M., Pigford, T.H., and Levi, H.W. *Nuclear Engineering,* 2nd ed., McGraw-Hill, New York, 1981.

Further Information

Glasstone, S. and Sesonske, A. *Nuclear Reactor Engineering,* 3rd ed., Van Nostrand Reinhold, New York, 1981.

8.9 Nuclear Fusion

Thomas E. Shannon

Introduction

Nuclear fusion holds the promise of providing almost unlimited power for future generations. If the process can be commercialized as envisioned by reactor design studies (Najmabadi et al., 1994), many of the problems associated with central electric power stations could be eliminated. Fusion power plants would not produce the pollution caused by the burning of fossil fuel and would eliminate the concern for meltdown associated with nuclear fission. The amount of radioactive waste material produced by a fusion reactor will be much less than that of a fission reactor since there is essentially no radioactive ash from the fusion reaction. If **low activation advanced materials** such as silicon carbide composites can be developed for the reactor structural material, the problem of disposal of activated components can also be eliminated.

Fusion Fuel

Although a number of different atomic nuclei can combine to release net energy from fusion, the reaction of **deuterium and tritium** (D-T) is the basis of planning for the first generation of fusion reactors. This choice is based on considerations of reactor economy. The D-T reaction occurs at the lowest temperature, has the highest probability for reaction, and provides the greatest output of power per unit of cost (Shannon, 1989). The disadvantages of D-T as a fusion fuel are twofold. Tritium does not occur naturally in nature and must be bred in the fusion reactor or elsewhere. Second, tritium is a radioactive isotope of hydrogen with a relatively long **half-life** of 12.3 years. Since tritium can readily combine with air and water, special safety procedures will be required to handle the inventory necessary for a fusion reactor. There is hope that a less reactive fuel, such as deuterium alone (D-D) will eventually prove to be an economically acceptable alternative (Shannon, 1989).

Confinement Concepts

Magnetic fusion, based on the tokamak concept, has received the majority of research funding for fusion energy development. However, other magnetic fusion concepts, such as the stellarator, the spherical torus, reversed-field pinch, and field-reversed configurations, are being developed as possible alternatives to the tokamak (Sheffield, 1994). It may also be possible to develop fusion power reactors by inertial confinement concepts (Waganer et al., 1992). Research on these concepts has been done primarily in support of weapons development; therefore, the level of scientific understanding for power reactor applications is significantly less than that of magnetic fusion. The remainder of this discussion on reactor development, fusion energy conversion, and transport will consider only the tokamak magnetic fusion concept.

Tokamak Reactor Development

The tokamak device has proved to be the most effective means of producing the conditions necessary for magnetic fusion energy production. In 1994, researchers at the Princeton Plasma Physics Laboratory achieved in excess of 10 MW of D-T fusion power in a research tokamak, the Tokamak Fusion Test Reactor (TFTR). This accomplishment, coupled with worldwide progress in 40 years of magnetic fusion research, has established the scientific feasibility of the tokamak concept. The next major step, the International Thermonuclear Experimental Reactor (ITER) is being carried out under an international agreement among Europe, Japan, Russia, and the United States (Conn et al., 1992). A drawing of the ITER tokamak is shown in Figure 8.9.1. If the project is approved for construction, it will be in operation around 2005. The ITER is being designed to produce a fusion power in excess of 1000 MW. This will be a significant step on the path to commercial fusion power.

The U.S. Department of Energy has proposed a strategy, shown in Figure 8.9.2, which will lead to a demonstration power reactor by the year 2025. Supporting research and development programs necessary to achieve this goal are shown in this figure.

Fusion Energy Conversion and Transport

The energy from fusion is created in the form of charged particles and neutrons. The D-T reaction produces a neutron with an energy of 14.1 MeV and an alpha particle (helium) with an energy of 3.5 MeV in the reaction

$$\mathrm{D} + \mathrm{T} \rightarrow \mathrm{He}^4\ (3.5\ \mathrm{MeV}) + \mathrm{n}(14.1\ \mathrm{MeV})$$

In the tokamak device, the reaction will take place in the toroidal vacuum vessel as previously shown in the ITER drawing, Figure 8.9.1. The D-T fuel, in the form of a **plasma**, will absorb energy from the positively charged alpha particles to sustain the temperature necessary for the reaction to continue. The neutron, having no charge, will escape from the plasma and pass through the wall of the vessel and

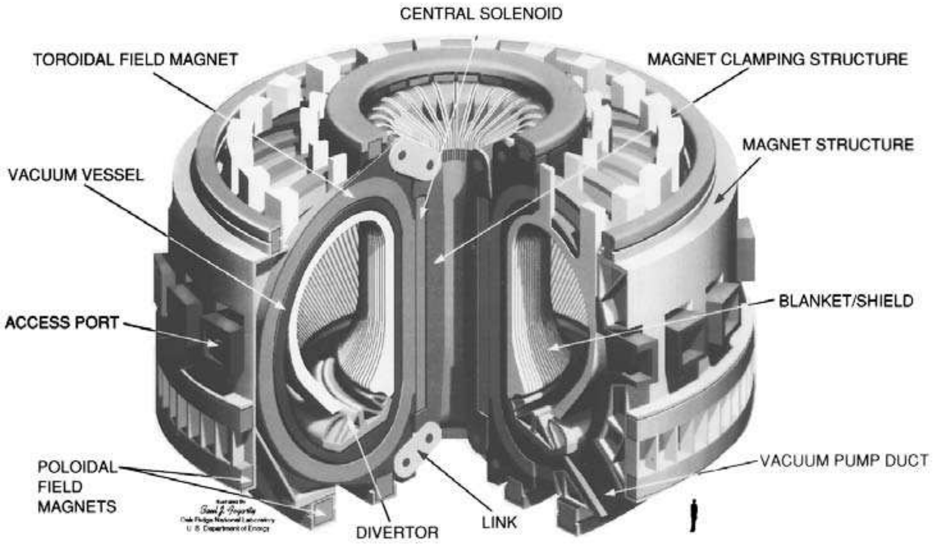

FIGURE 8.9.1 The International Thermonuclear Experimental Reactor (ITER).

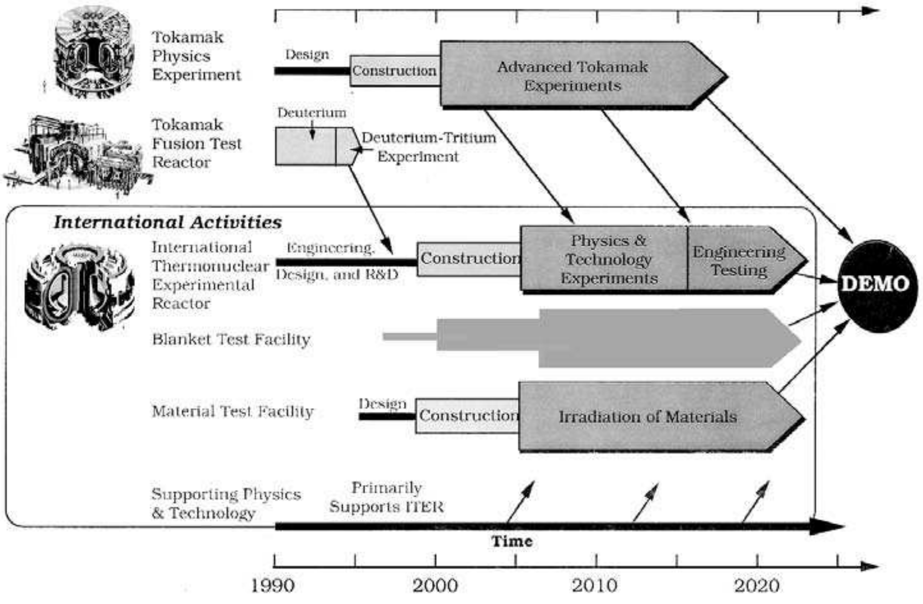

FIGURE 8.9.2 The U.S. Department of Energy magnetic fusion energy strategy.

penetrate into the surrounding blanket/shield structure. The kinetic energy of the alpha particles from the fusion reaction is eventually deposited on the wall of the vacuum vessel by radiation and conduction heat transfer from the plasma while the neutron deposits most of its energy within the cross section of the blanket/shield. The resulting thermal energy is transferred by a coolant such as water to a steam generator where a conventional steam to electric generator system may be used to produce electricity. An overall schematic diagram of the energy conversion and heat-transport system is shown in Figure 8.9.3.

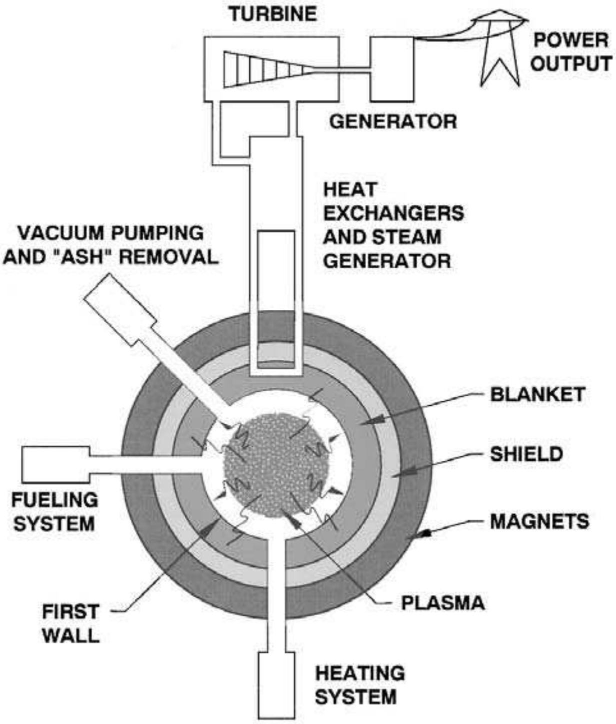

FIGURE 8.9.3 Schematic Diagram of a Magnetic Fusion Reactor Power Plant.

Defining Terms

Deuterium and tritium: Isotopes of hydrogen as the fuel for fusion reactors.

Half-life: The time required for half of the radioactive material to disintegrate.

Low activation advanced materials: Structural materials that significantly reduce the radioactivity induced by exposure to fusion neutrons.

Plasma: A gas such as a mixture of deuterium and tritium raised to a very high temperature at which the electrons and the nuclei of the atoms separate. The plasma, consisting of electrons and ions, can conduct electricity and react to magnetic fields.

References

Conn, R.W., Chuyanov, V.A., Inoue, N., and Sweetman, D.R. 1992. The International Thermonuclear Experimental Reactor, *Sci. Am.* 266(4).

Najmabadi, F. et al. 1994. The ARIES-II and -IV Second Stability Tokamak Reactors, University of California, Los Angeles, report UCLA-PPG-1461.

Shannon, T.E. 1989. Design and cost evaluation of a generic magnetic fusion reactor using the D–D fuel cycle. *Fusion Technol.* 15(2), Part 2B, 1245–1253

Sheffield, J. 1994. The physics of magnetic fusion reactors. *Rev. Mod. Phy.* 66(3).

Waganer, L. et al. 1992. Inertial Fusion Energy Reactor Design Studies. U.S. Department of Energy Report. Vol. I, II, and III, DOE/ER-54101 MDC 92E0008.

Further Information

The U.S. Department of Energy, Office of Fusion Energy maintains a home page on the World Wide Web. The address http://wwwofe.er.doe.gov provides an excellent source of up-to-date information and access to information from most institutions involved in fusion research.

8.10 Solar Thermal Energy Conversion

D. Yogi Goswami

Introduction

Solar thermal energy applications such as space and water heating have been known for a long time. Researchers over the past few decades have developed a number of additional solar thermal applications, such as industrial process heat, refrigeration and air-conditioning, drying and curing of agricultural products, and electric power production by solar thermal conversion. This section will cover solar thermal energy conversion including solar thermal collectors and conversion systems.

Solar Thermal Collectors

A simple **solar thermal collector** consists of (1) an absorber surface (usually a dark, thermally conducting surface), (2) some insulation behind the absorber to reduce heat loss, (3) a trap for thermal reradiation from the surface such as glass, which transmits the shorter-wavelength solar radiation but blocks the longer-wavelength radiation from the absorber, and (4) a heat-transfer medium such as air, water, etc. High-temperature collectors require reflectors of sunlight that concentrate solar radiation on the absorber. The technology of solar collectors is developed to achieve temperatures as high as 1000°C or even higher. The design of a solar collector and the choice of working fluids depend on the desired temperature and the economics of the application. Table 8.10.1 lists the types of solar thermal collectors based on their temperature range.

Flat Plate Collectors

Flat plate collectors may be designed to use liquids (water, oil, etc.) or air as the heat-transfer fluid. Figure 8.10.1 shows a typical liquid-type flat plate collector. The choice of materials for glazing and absorber needs special attention.

Glazing. The purpose of **glazing** is to (1) transmit the shorter-wavelength solar radiation, but block the longer-wavelength reradiation from the absorber plate, and (2) reduce heat loss by convection from the top of the absorber plate. Glass is the most widely used glazing material. Transmittance of low iron glass in the visible and near infrared wavelength range can be as much as 91%, while for the longer-wavelength radiation (>3 μm) its transmittance is almost zero. Other materials that can be used as glazings include certain plastic sheets such as polycarbonates (Lexan® and Tuffac® — transmittance ~75%), acrylics (Plexiglass® and Lucite® — transmittance ~92%), and thin plastic films such as polyethylene. A major advantage of the plastics is that they are shatterproof; however, they scratch easily and lose transparency over time.

Absorbers. Copper is the most common material used for absorber plates and tubes because of its high thermal conductivity and high corrosion resistance. For low-temperature applications such as swimming pool heating, a plastic material called ethylene propylene polymer (trade names EPDM, HCP, etc.) can be used to provide inexpensive absorber material. To compensate for low thermal conductivity of these

TABLE 8.10.1 Types of Solar Collectors and Their Typical Temperature Range

Type of Collector	Concentration Ratio	Typical Working Temperature Range (°C)
Flat plate collector	1	≤70
High-efficiency flat plate collector	1	60–120
Fixed concentrator	2–5	100–150
Parabolic trough collector	10–50	150–350
Parabolic dish collector	200–2000	250–700
Central receiver tower	200–2000	400–1000

Source: Compiled from Goswami, D.Y., *Alternative Energy in Agriculture,* Vol. 1, CRC Press, Boca Raton, FL, 1980.

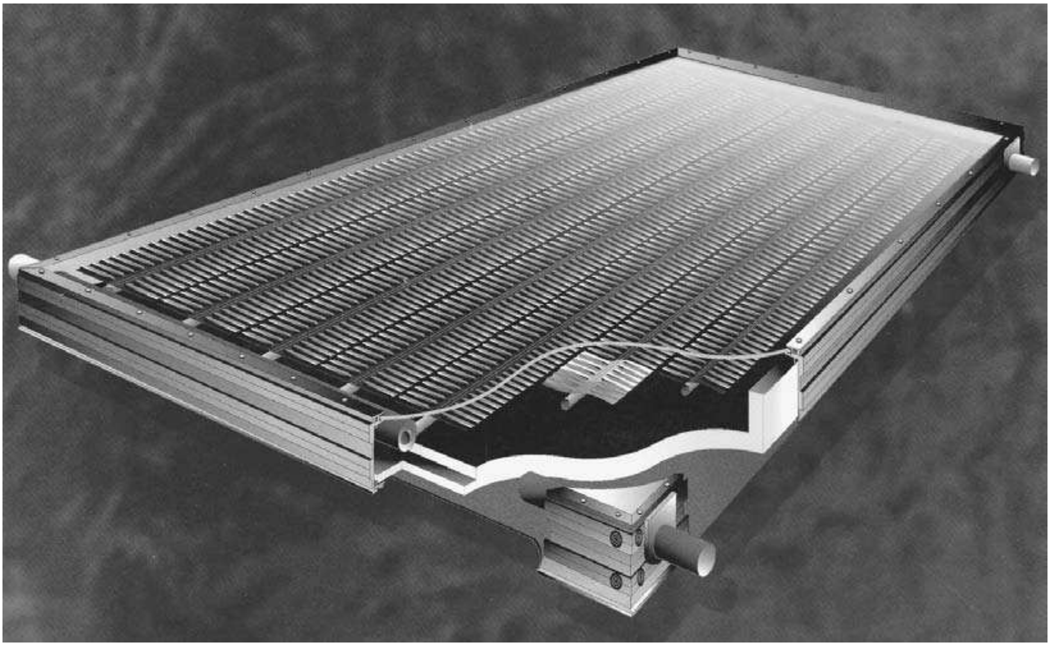

FIGURE 8.10.1 A typical liquid flat plate collector.

TABLE 8.10.2 Absorptivity and Emissivity of Common Selective Surfaces

Surface	Absorbtivity	Emissivity
Black chrome	0.95	0.1
Black nickel	0.9	0.08
Copper oxide	0.9	0.17
Lead sulfide	0.89	0.2
Flat black paint	0.98	0.98

Source: Compiled from Goswami, D.Y., Kreith, F., and Kreider, J., *Principles of Solar Engineering,* Taylor and Francis, Washington, D.C., 2000.

materials, a large surface area is provided for heat transfer. In order to increase the absorption of solar radiation and to reduce the emission from the absorber, the metallic absorber surfaces are painted or coated with flat black paint or some selective coating. Absorptivities and emissivities of some common **selective surfaces** are given in Table 8.10.2.

Evacuated Tube Collectors. Evacuated tube collectors have essentially a vacuum between the absorber and the glazing tube. This eliminates most of the heat loss by conduction and convection. Therefore, these collectors give a very high efficiency at higher temperatures. Evacuated tube collectors are typically used in the temperature range of 80 to 140°C

Concentrating Collectors. Concentrating collectors use reflectors or lenses to focus solar radiation from a large area onto a small area, thereby creating higher temperatures. Such collectors are usually used for temperatures higher than 100°C. Figure 8.10.2 shows schematics of some of the concentrating collectors.

Nontracking Concentrators. The simplest concentrating collector can be made by using flat wall reflectors to concentrate the solar radiation on a flat plate collector. Concentration ratios of two to three can be achieved this way. For slightly higher concentration ratios, a novel design, developed by Roland Winston, called a “compound parabolic concentrator” (CPC) can be used (Winston, 1974).

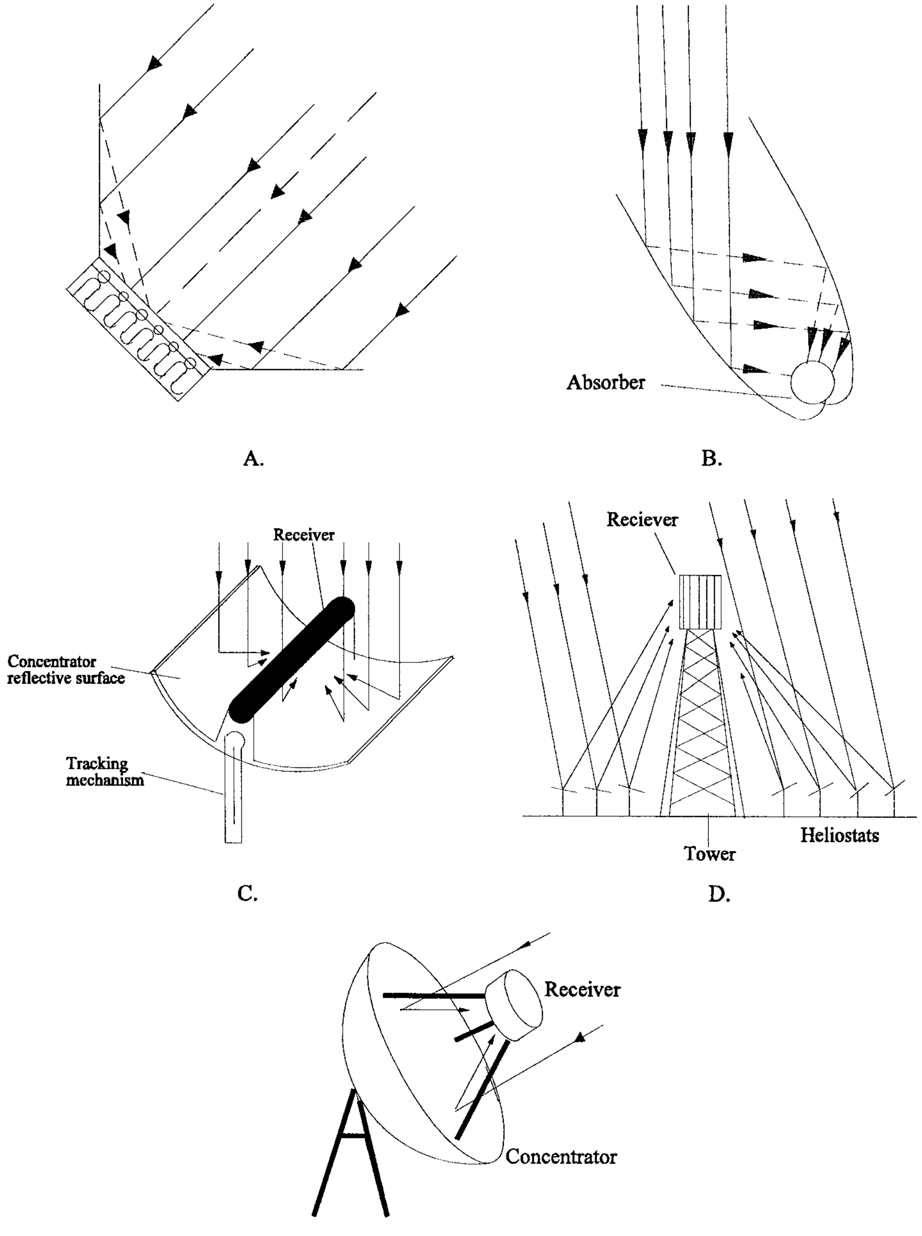

FIGURE 8.10.2 Types of concentrating collectors. (A) Flat plate collector with reflective wings; (B) Compound parabolic concentrator; (C) parabolic trough; (D) central receiver; (E) parabolic dish.

Tracking Concentrators. For temperatures up to 350°C, cylindrical parabolic trough collectors are used. These collectors focus solar radiation on a line focus where the absorber is located. These collectors usually require tracking on one axis only with seasonal adjustment on the other axis. A reflecting spherical or paraboloidal bowl is used when temperatures of the order of 250 to 500°C are needed. These collectors require two-axis tracking. In some cases, the dish is kept stationary while the receiver is moved to track the focus of the reflected solar radiation. Finally, for extremely high temperatures (500 to 1000°C) needed for large-scale thermal power generation, a large field of tracking flat mirrors (called heliostats) is used to concentrate solar radiation on a receiver that is located on top of a central tower.

Collector Thermal Performance

The instantaneous efficiency of a collector is given by

$$\eta = \frac{\text{Useful energy collected}}{\text{Incident solar energy}} = \frac{Q_u/A}{I} \tag{8.10.1}$$

where

$$Q_u = \dot{m}C_p\left(T_o - T_i\right) \tag{8.10.2}$$

and A = area of the collector, I = incident solar energy per unit area, $\dot{m}$, C_p, T_i, and T_o are the mass flow rate, specific heat, and inlet and outlet temperatures of the heat-transfer fluid.

The efficiency of a flat plate solar collector can also be written by the Hottel–Whillier–Bliss equation:

$$\eta = F_R(\tau\alpha)_e - F_R U_L \frac{\left(T_i - T_{\text{amb}}\right)}{I} \tag{8.10.3}$$

where F_R, called the collector heat-removal factor, is a convenient parameter that gives the ratio of the actual useful energy gain of a flat plate collector to the useful gain if the whole collector surface were at the inlet fluid temperature; $(\tau\alpha)_e$ = effective transmittance absorptance product; and U_L = collector heat-loss coefficient.

Equation 8.10.2 suggests that if the efficiency, η, is plotted against $(T_i - T_{\text{amb}})/I$, the resulting curve will have a y intercept equal to F_R $(\tau\alpha)_e$ and a slope of $F_R U_L$. A linear curve usually gives an adequate approximation. Figure 8.10.3 shows an example of a performance curve for a water-heating flat plate collector, which is a linear least square curve fit to the actual test data.

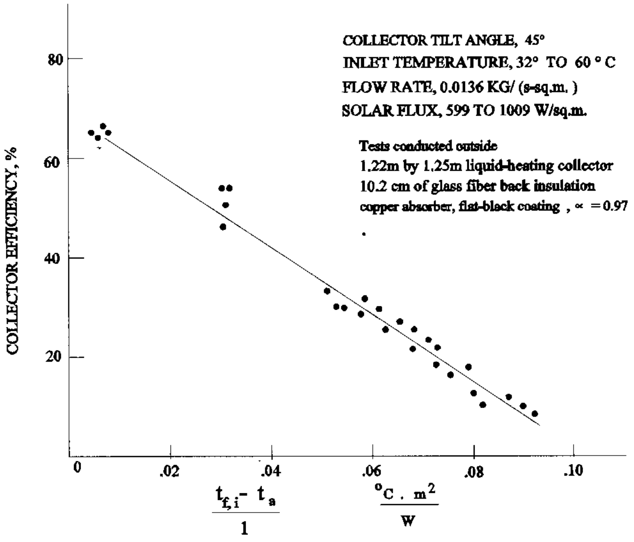

FIGURE 8.10.3 Thermal efficiency curve for a double-glazed flat plate liquid-type of solar collector. (Reprinted by permission of the American Society of Heating, Refrigerating and Air-Conditioning Engineers, Inc., Atlanta, GA, from ASHRAE Standard 93-77, *Methods of Testing to Determine the Thermal Performance of Solar Collectors*, 1977.)

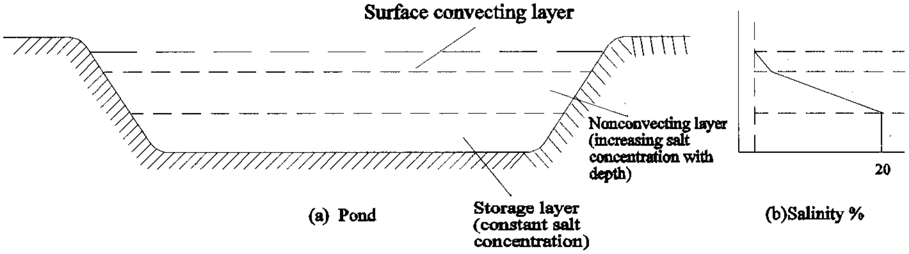

FIGURE 8.10.4 Schematic of a salt gradient solar pond.

Solar Ponds

A solar pond combines collector and energy storage in one unit. Solar radiation that enters the pond travels some distance through the water before being totally absorbed, thus increasing the temperature of the water at that depth. The heat thus collected can be stored in the pond by creating a stagnant, transparent, insulating layer in the top part of the pond. The most common method is by the addition of a salt into the pond to increase the density of water in the lower section of the pond. This type of pond is called a **salt gradient solar pond**. Reid (1987) reviewed the progress in the design and applications of salt gradient solar ponds. Figure 8.10.4 shows a schematic of a salt gradient pond along with a density profile in the pond.

The theory of salt gradient solar ponds has been described by Tabor (1981). The most important aspect of such ponds is the creation and maintenance of the salt gradient. Theory shows that the condition for maintaining stability is

$$\frac{\partial S}{\partial Z} > -1.14 \frac{\partial \rho}{\partial T} \frac{\partial T}{\partial Z} \frac{\partial \rho}{\partial S} \tag{8.10.4}$$

where S is the salt concentration in kilograms per cubic meter, Z is the depth from the surface in meters, ρ is the density in kilograms per cubic meter, and T is the temperature in Kelvin. The two most common salts considered for solar pond applications are NaCl and $MgCl_2$. According to the above criteria, there is no difficulty in obtaining stability with $MgCl_2$ and it is somewhat difficult but possible to get stability with NaCl.

Solar Water-Heating Systems

Solar water-heating systems represent the most common application of solar energy at the present time. Small systems are used for domestic hot water applications while larger systems are used in industrial process heat applications. There are basically two types of water-heating systems: **natural circulation or passive solar system** (thermosyphon) and **forced circulation or active solar system**.

Natural Circulation

Figure 8.10.5 shows a schematic of a natural circulation solar water-heating system. It is also called a thermosyphon or passive solar water heater because it does not require a pump to circulate water. The storage tank is located above the collector. When the water in the collector gets heated, it rises into the tank, because of density change, setting up a circulation loop.

Forced Circulation

Figure 8.10.6 shows three configurations of forced circulation systems: (1) open loop, (2) closed loop, and (3) closed loop with drainback. In an open loop system, the collectors are empty when they are not providing useful heat and the storage tank is at atmospheric pressure. A disadvantage of this system is the high pumping power required to pump the water to the collectors every time the collectors get hot.

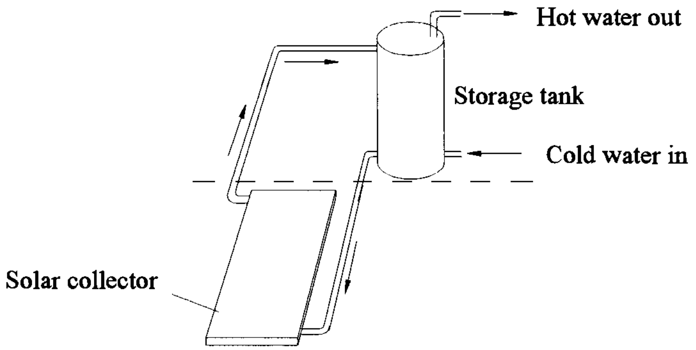

FIGURES 8.10.5 Schematic of a thermosyphon solar water-heating system.

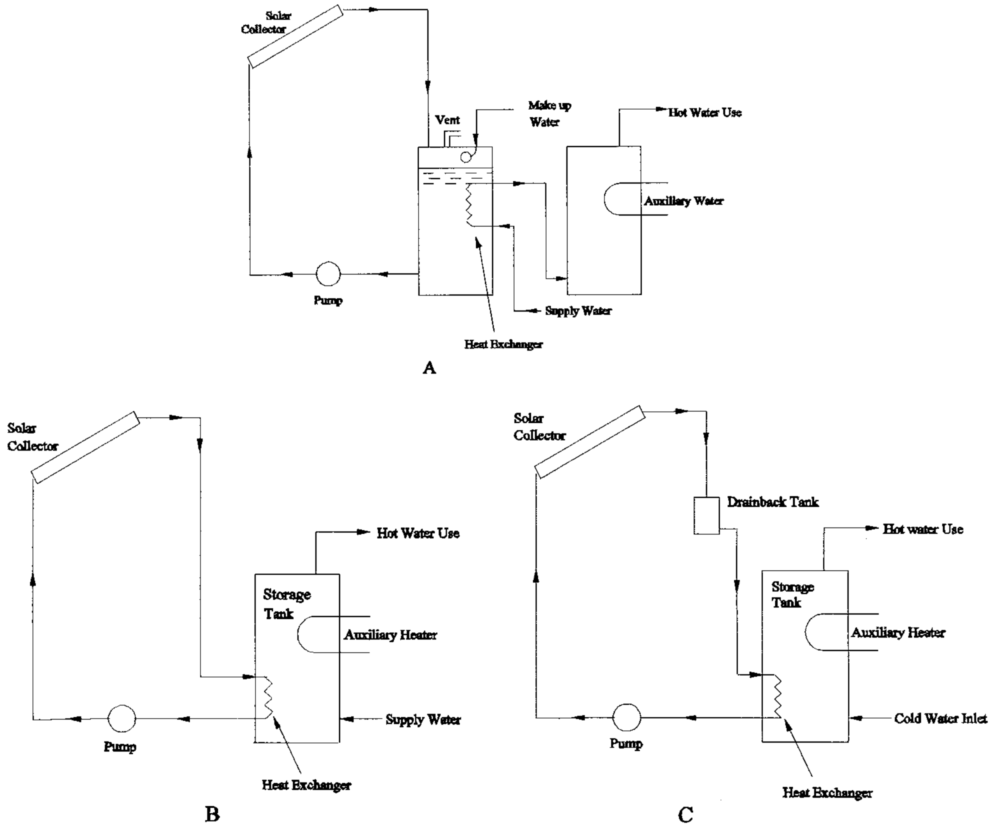

FIGURE 8.10.6 Typical configurations of solar water-heating systems: (A) open loop system, (B) closed loop system, (C) closed loop drainback system. (Adapted from Goswami, D.Y., *Alternative Energy in Agriculture,* Vol. 1, CRC Press, Boca Raton, FL, 1986.)

This disadvantage is overcome in the pressurized closed loop system (Figure 8.10.6B) since the pump has to overcome only the resistance of the pipes. Because water always stays in the collectors of this system, antifreeze (propylene glycol or ethylene glycol) is required for locations where freezing conditions can occur. During stagnation conditions (in summer), the temperature in the collector can become very high, causing the pressure in the loop to increase. This can cause leaks in the loop unless some fluid is allowed to escape through a pressure-relief valve. In both cases, air enters the loop causing the pump to

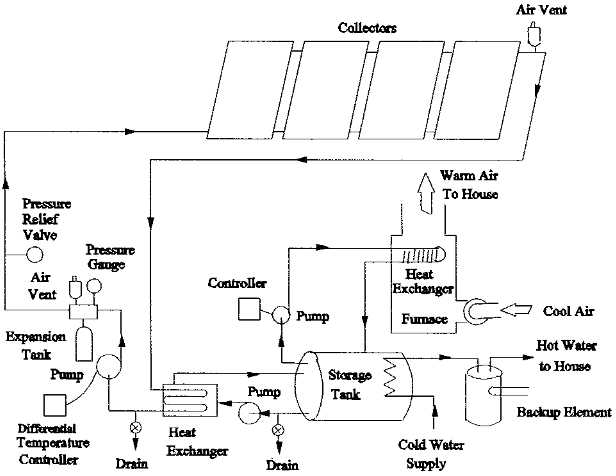

FIGURE 8.10.7 Schematic of an active solar space-heating system.

run dry. This disadvantage can be overcome in a closed loop drainback system (Figure 8.10.6C). In this system, when the pump shuts off, the water in the collectors drains back into a small holding tank, which can be located where freezing does not occur. The holding tank can be located at a high level to reduce pumping power.

Industrial Process Heat Systems

For temperatures of up to about 100°C, required for many industrial process heat applications, forced circulation water-heating systems described above can be used. The systems, however, will require a large collector area, storage and pumps, etc. For higher temperatures, evacuated tube collectors or concentrating collectors must be used.

Space-Heating Systems

Solar space-heating systems can be classified as active or passive depending on the method utilized for heat transfer. A system that uses pumps and/or blowers for fluid flow in order to transfer heat is called an *active system*. On the other hand, a system that utilizes natural phenomena for fluid flow and heat transfer is called a *passive system*. Examples of passive solar space-heating systems include direct gain, attached greenhouse, and storage wall (also called Trombe wall).

Active space-heating systems store solar collected heat in water or rocks. Heat from water storage can be transferred to the space by convertors or by fan-coil units. A system using a fan-coil unit can be integrated with a conventional air system as shown in Figure 8.10.7. Heat from rock storage can be transferred to air by simply blowing air over the rocks.

Solar Thermal Power

Solar thermal energy can be used to produce electrical power using conventional thermodynamic power cycles such as Rankine, Stirling, and Brayton cycles. The choice of power cycle and the working fluids depends on the temperature obtainable in the solar system, which depends on the type of solar collectors used. At present, developed solar thermal power systems include

Parabolic trough systems
Central receiver systems
Parabolic dish-Stirling engine system

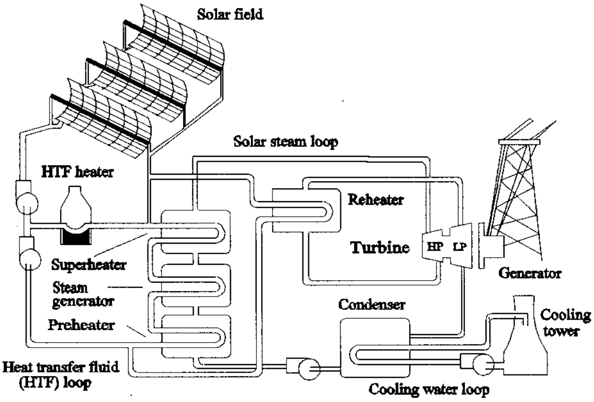

FIGURE 8.10.8 Schematic of SEGS IX power plant.

TABLE 8.10.3 Plant Characteristics — SEG IX

Power Block		Solar Field	
Gross power	88 MWe	Number of collectors	888
Net power	80 MWe	Aperature area	483,960 m^2
Steam inlet pressure	100 bar	Inlet temperature	293°C
Steam inlet temperature	371°C	Outlet temperature	390°C
Reheat pressure	17.2 bar	Annual thermal efficiency	50%
Reheat temperature	371°C	Peak optical efficiency	80%
Conversion efficiency	37.6%	Heat-transfer fluid (HTF)	Oil (VP-1)
Annual gas use	25.2×10^9 m^3	HTF volume	1289 m^3

Source: DeLaquil, P. et al., in *Renewable Energy Sources for Fuel and Electricity*, Island Press, Washington, D.C., 1993.

Parabolic Trough Systems

Parabolic trough systems are simple in concept and, therefore, the most developed commercially. In 1984, Luz Company installed a Solar Electric Generating System (SEGS I) of 14 MW$_e$ capacity in Southern California, utilizing parabolic trough solar collectors and natural gas fuel for superheat and backup. From 1984 to 1991, Luz Company installed eight additional plants, SEGS II to SEGS IX, with the total capacity of the nine plants being 354 MW$_e$. With each successive SEGS plant the technology was improved and the cost reduced. The cost of electricity was reduced from about 30¢/kWhr for the first plant to about 8¢/kWhr for the last plant. A schematic of the SEGS IX is shown in Figure 8.10.8, and some important data for the system are given in Table 8.10.3.

It has been recognized that this design does not utilize the energy of the natural gas efficiently. It has been suggested that energy of natural gas can be better utilized by combining the solar system with a natural gas turbine combined-cycle power plant (DeLaquil et al., 1993; Washom et al., 1994). Such a hybrid system would use the exhaust of a natural gas turbine for superheating and preheating of water, while the solar field would be used for steam generation. Such a hybrid system can achieve conversion efficiency as high as 60%. A schematic of a **solar hybrid combined cycle** is shown in Figure 8.10.9.

Central Receiver System

A central receiver system can potentially operate at very high temperature and therefore can have much higher efficiency than parabolic trough systems. However, the system can be economical only at larger capacities, such as 100 MW and above. The central receiver absorber can heat the working fluid or an intermediate fluid to a temperature as high as 600 to 1000°C which can be used to drive a Rankine cycle or Brayton cycle.

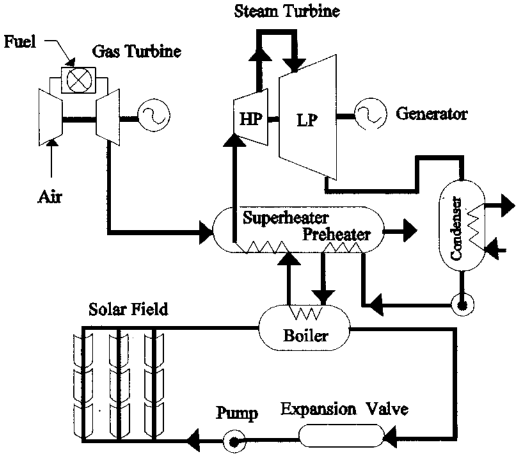

FIGURE 8.10.9 Solar hybrid combined cycle. (Adapted from Washom, B. et al., paper preesnted at the 1994 ASES Annual Conference, San Jose, CA, 1994.)

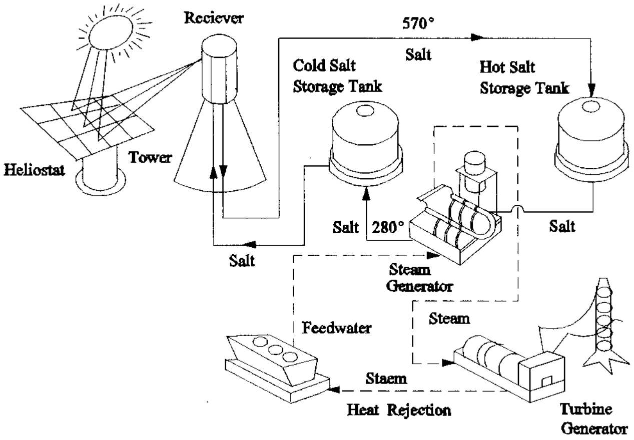

FIGURE 8.10.10 Schematic of Solar Two.

Solar One, a 10-MW$_e$ central receiver power plant started operating in 1982 in Barstow, California. This plant generated superheated steam at 510°C and 10.3 MPa in the receiver absorber, which was used to drive a simple steam Rankine power cycle. The plant operated successfully for 6 years and provided a good learning experience. The plant was redesigned as Solar Two in which molten sodium nitrate is used as the heat-transfer fluid as well as for storage. Use of molten salt allows operation of the receiver absorber at much lower pressures The constraint is that the salt must always be above its melting point (220°C). Figure 8.10.10 shows a schematic of the Solar Two power plant.

Parabolic Dish Systems

Parabolic dish systems can achieve very high temperatures. The high temperatures produced by parabolic dishes can be used to drive Rankine, Stirling, and Brayton power cycles. So far, Rankine and Stirling cycles have been successfully demonstrated with parabolic dishes for electrical power production.

Early versions of parabolic dishes were made from die-stamped aluminum petals made reflective using a metallized polymer film. Later designs used simpler flat mirror facets fixed on a structure in such a way as to approximate a parabolic dish. The latest designs use a polymer film stretched on a circular frame (Mancini, 1994). The film is given a slight concave curvature by providing a vacuum behind it. These stretched polymer films are fixed on a structure to approximate a parabolic dish. Because of the low weight of the polymer film, the dish structure can be made out of light tubular members, thereby reducing the cost of the dish considerably. Parabolic dishes require two-axis tracking.

McDonnell Douglas Corporation successfully demonstrated a 25-KW$_e$ parabolic dish system using a Stirling engine and a generator assembly fixed at the focal point of the dish in 1985 (Gupta, 1987). The concept is very attractive because it provides a modular design of stand-alone power plants for small communities and independent power applications. Present development is based on stretched polymer film facets for a parabolic dish, a heat pipe receiver absorber, a free-piston Stirling engine, and a linear alternator, resulting in a very compact power generation system. A detailed discussion of Stirling engines is given in Section 8.5.

Nomenclature

A = area of collector
C_p = specific heat
m = mass flow rate
T = temperature
I = incident solar radiation
Qn = useful heat collected
F_R = collector heat-removal factor
U_L = collector heat-loss coefficient
S = salt concentration
Z = depth

Greek Symbols

α = absorptance
τ = transmittance
η = efficiency
ρ = density

Subscripts

i = inlet
o = outlet
amb = ambient
e = effective

Defining Terms

Forced circulation or active solar system: A solar thermal system that uses active means, such as pumps, for fluid flow and heat transfer.

Glazing: A material used in a solar collector that transmits short-wavelength solar radiation and blocks longer-wavelength reradiation from the absorber plate.

Natural circulation passive solar system: A solar thermal system that uses natural means, such as the thermosyphon effect, for fluid flow and heat transfer.

Salt gradient solar pond: A solar pond that uses high salt concentration in the lowest layer and a concentration gradient in the middle layer to make those layers nonconvective.

Selective surface: A surface that has high absorptance in short wavelengths and low emittance in longer wavelengths.

Solar hybrid combined cycle: A hybrid of solar and natural gas turbine combined cycle.

Solar thermal collector: A solar collector that absorbs sunlight and converts it to heat.

References

ASHRAE. 1977. ASHRAE Standard 93-77, *Method of Testing to Determine the Thermal Performance of Solar Collectors*, ASHRAE, Atlanta, GA.

DeLaquil, P., Kearney, D., Geyer, M., and Diver, R. 1993. Solar thermal electric technology, Chapter 5 in *Renewable Energy Sources for Fuel and Electricity*, T.B. Johansson, M. Kelly, A.K.N. Reddy, and R.H. Williams, Eds., Island Press, Washington, D.C.

Duffie, J.A. and Beckman, W.A. 1980. *Solar Engineering of Thermal Processes*, John Wiley & Sons, New York.

Goswami, D.Y. 1986. *Alternative Energy in Agriculture,* Vol. I, CRC Press, Boca Raton, FL.

Gupta, B.P. 1987. Status and progress in solar thermal research and technology, in *Progress in Solar Engineering*, Ed. D.Y. Goswami, Hemisphere Publishing, Washington, D.C.

Mancini, T.R. 1994. The DOE solar thermal electric program, in *Proceedings of the 1994 IECEC*, pp. 1790–1975. AIAA, Washington, D.C.

Reid, R.L. 1987. Engineering design of salt gradient solar pond for thermal and electric energy, in *Progress in Solar Engineering*, Ed. D.Y. Goswami, Hemisphere Publishing, Washington, D.C.

Tabor, H. 1981. Solar ponds. *Solar Energy*, 27(3), 181.

Washom, B., Mason, W., Schaefer, J.C., and Kearney, D. 1994. Integrated Solar Combined Cycle Systems (ISCCS) Utilizing Solar Parabolic Trough Technology — Golden Opportunities for the 90s, paper presented at the 1994 ASES Annual Conference, San Jose, CA.

Winston, R. 1974. Principles of solar concentrators of novel design. *Solar Energy*, 16(2), 89.

Further Information

Principles of Solar Engineering, by D.Y. Goswami, F. Kreith, and J.F. Kreider, Taylor and Francis, Washington, D.C., 2000.

Solar Engineering of Thermal Processes, by J.A. Duffie and W.A. Beckman, John Wiley & Sons, New York, 1990.

8.11 Wind Energy Conversion[2]

Dale E. Berg

Introduction

Wind energy is the most rapidly expanding source of energy in the world today. Over the past decade, the world-wide installed capacity of wind energy has grown at an average rate of over 28% per year, leading to an installed nameplate capacity at the end of 2002 of over 31,000 MW — enough to power 7.5 million average American homes or 16 million average European homes. As of January, 2003, Germany was the world leader in wind energy installations, with 12,001 MW installed, followed by Spain (4830); the U.S. (4685); Denmark (2880); India (1702); Italy (785); the Netherlands (688); the U.K. (552); China (468); and Japan (415). Although wind power only supplies about 0.4% of the world's electricity demand today, the size of that contribution is growing rapidly. In Germany, the contribution of wind power to electricity consumption is over 5%, and in Denmark it is approximately 25%. The cost to generate wind energy has decreased dramatically from about $0.38 per kilowatt-hour (kWh) in the early 1980s to the $0.03 to $0.06/kWh range in 2003, and it continues to decrease.

---

[2] This work was supported by the United States Department of Energy under contract DE-AC04-94AL85000.

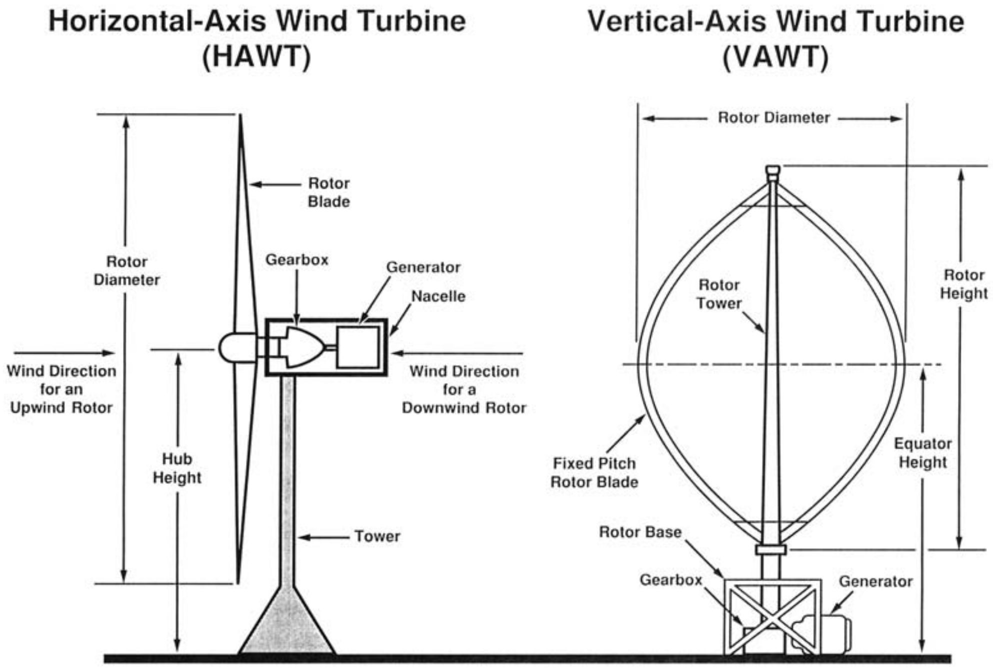

FIGURE 8.11.1 Wind turbine configurations.

The first wind machines were built over 2000 years ago. The wind turbines of today may look much different from those first machines, but the basic idea remains the same: use the power in the wind to generate useful energy. Modern wind machines, called wind turbines, tend to have a small number of airfoil-shaped blades, in contrast to the older windmills that usually had several flat or slightly curved blades. (Dutch windmills, with four blades, obviously do not fit this stereotype.) The reasons for this difference in blade number will be examined a little later.

Although many different configurations of wind turbines exist, most of them can be classified as horizontal-axis wind turbines (HAWTs), which have blades that rotate about a horizontal axis parallel to the wind, or vertical-axis wind turbines (VAWTs), with blades that rotate about a vertical axis. Figure 8.11.1 illustrates the main features of HAWTs and VAWTs.

As shown in Figure 8.11.1, HAWTs and VAWTs have very different configurations, each with its own set of strengths and weaknesses. HAWTs usually have all of their drive train (the transmission, generator, and any shaft brake) equipment located in a nacelle or enclosure mounted on a tower; their blades are subjected to cyclic stresses due to gravity as they rotate and their rotors must be oriented (yawed) so that the blades are properly aligned with respect to the wind. HAWTs may readily be placed on tall towers to access the stronger winds typically found at greater heights. The most common type of modern HAWT is the propeller-type machine; these machines are generally classified according to the rotor orientation (upwind or downwind of the tower); blade attachment to the main shaft (rigid or hinged); maximum power control method (full or partial-span blade pitch or blade stall); and number of blades (generally two or three blades).

VAWTs, on the other hand, usually have most of their drive train on the ground; their blades do not experience cyclic gravitational stresses and do not require orientation with respect to the wind. However, VAWT blades are subject to severe alternating aerodynamic loading due to rotation, and VAWTs cannot readily be placed on tall towers to exploit the stronger winds at greater heights. The most common types of modern VAWTs are the Darrieus turbines, with curved, fixed-pitch blades, and the “H” or “box” turbines with straight fixed-pitch blades. All of these turbines rely on blade stall for maximum power control.

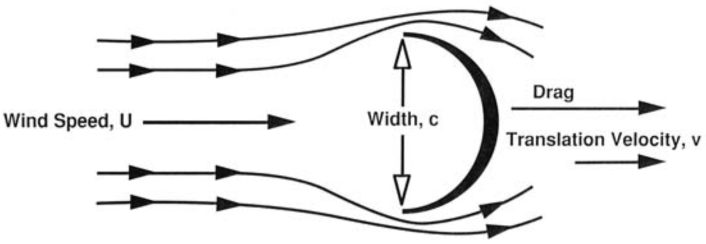

FIGURE 8.11.2 Schematic of translating drag device.

Although there are a few manufacturers of VAWTs in the world today, the overwhelming majority of wind turbine manufacturers have elected to devote their efforts to developing improved (and usually bigger) HAWTs.

Because the fuel for wind turbines is free, the initial cost of a wind turbine is a very large contributor to the cost of energy (COE) for the energy generated by that turbine. In order to minimize that COE, wind turbine designs must be optimized for the particular site or wind environment in which they will operate. Trial and error methods become very expensive and time-consuming when applied to optimizing and/or developing turbines, especially larger ones. An optimized wind turbine can be developed at a reasonable cost only if the designers can accurately predict the performance of conceptual machines and investigate the effects of design alternatives. In the past two decades, numerous techniques have been developed to predict the aerodynamic and structural dynamic performance of wind turbines accurately; these analytical models are not, in general, amenable to simple approximations, but must be solved with the use of computer codes of varying complexity. These models are summarized in the following paragraphs.

Wind Turbine Aerodynamics

Items exposed to the wind are subjected to forces in the drag direction (parallel to the air flow) and the lift direction (perpendicular to the air flow). The earliest wind machines, known as windmills, used the drag on the blades to produce power, but many windmill designs over the last few centuries did make limited use of lift to increase their performance. Because large numbers of blades resulted in higher drag and produced more power, predominantly drag machines tended to have many blades. The Dutch windmills utilized lift, and because lift devices must be widely separated to generate the maximum possible amount of lift, those machines evolved with a small number of blades.

The high-lift, low-drag shapes, referred to as airfoils, developed for airplane wings and propellers in the early part of the 20th century were quickly incorporated into wind machines to produce the first modern wind machines, usually known as wind turbines. Wind turbines use the lift generated by the blades to produce power. As mentioned earlier, the blades must be widely separated to generate the maximum amount of lift, so lift-type machines tend to have a small number of blades. The following paragraphs contrast the characteristics of drag- and lift-type machines.

Figure 8.11.2 illustrates the flow field about a moving drag device. The drag results from the relative velocity between the wind and the device. The power generated by the device (the product of the drag force and the translation velocity) may be expressed as

$$P = Dlv = \left[0.5\rho(U - v)^2\right]C_D clv \tag{8.11.1}$$

where

P = power extracted from the wind
D = drag force per unit length in the span direction (into the page)
l = length of device in the span direction (into the page)
v = translation velocity

ρ = air density
U = steady free-stream wind velocity
C_D = drag coefficient (function of device geometry)
c = device width (perpendicular to the wind, in the plane of the page)

The translation velocity of the device must always be less than the wind velocity or no drag is generated and no power produced. The power extraction efficiency of the device may be expressed as the ratio of the power extracted by the device to the power available in the area occupied by the device ($\frac{1}{2}\rho U^3 A = \frac{1}{2}\rho U^3 cl$), a ratio known as the **power coefficient** or C_p. For a drag machine, this ratio is

$$C_P = \frac{P}{\frac{1}{2}\rho U^3 cl} = \frac{v}{U}\left[1-\frac{v}{U}\right]^2 C_D \tag{8.11.2}$$

Now consider a device that utilizes lift to extract power from the wind, i.e., an airfoil. Figure 8.11.3 illustrates an airfoil moving at some angle relative to the wind that is subject to lift and drag forces. The relative wind across the airfoil is the vector sum of the wind velocity, U, and the blade velocity, v. The angle between the direction of the relative wind and the airfoil chord (the straight line from the leading edge to the trailing edge of the airfoil) is termed the angle of attack, α. The power extracted by this device may be expressed as

$$P = \frac{1}{2}\rho U^3 cl \frac{v}{U}\left[C_L - C_D\frac{v}{U}\right]\sqrt{1+\left(\frac{v}{U}\right)^2} \tag{8.11.3}$$

where

c = chord length
C_L, C_D = lift and drag coefficients, respectively (functions of airfoil shape and α)

The other quantities are as defined for Equation (8.11.1).

The power coefficient then is

$$C_P = \frac{v}{U}\left[C_L - C_D\frac{v}{U}\right]\sqrt{1+\left(\frac{v}{U}\right)^2} \tag{8.11.4}$$

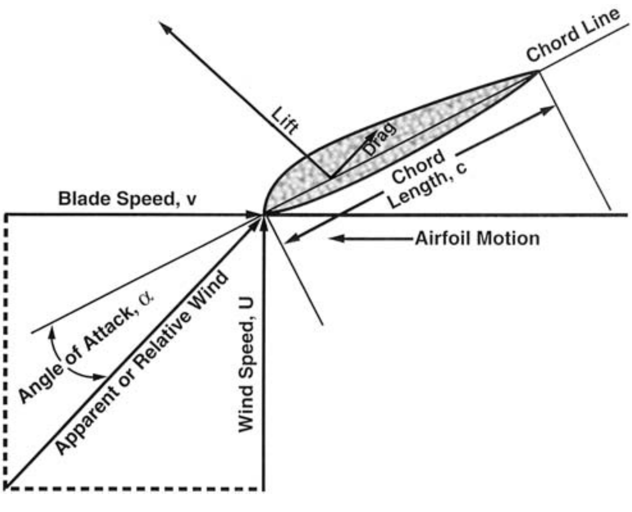

FIGURE 8.11.3 Schematic of translating lift device.

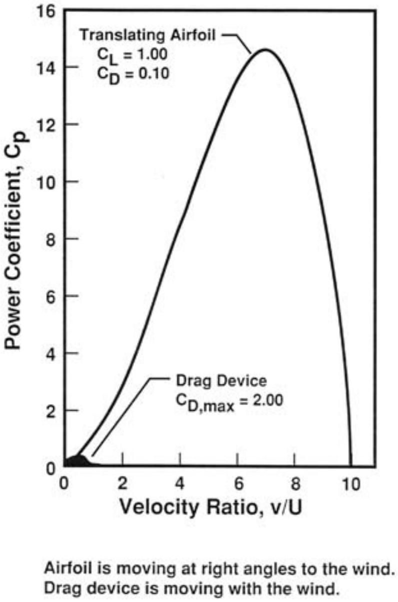

FIGURE 8.11.4 Comparison of power coefficients for a translating airfoil and a translating drag device.

Keep in mind that Equation 8.11.2 and Equation 8.11.4 express the performance coefficients of these devices in terms of the device surface area. Figure 8.11.4 compares Equation 8.11.2 and Equation 8.11.4 using $C_L = 1.0$ and $C_D = 0.10$ for the airfoil (reasonable values for modern airfoils), and a drag coefficient of 2.0 (the maximum possible) for the drag device. The airfoil has a maximum power coefficient of about 15, compared with 0.3 for the drag device; it extracts 50 times more power per unit of device surface area. Of course, the airfoil must be translated across the wind to produce power, but this is easily achieved with rotating machines such as wind turbines.

As mentioned earlier, lift-type machines tend to have only a few blades, while drag-type machines tend to have many. Thus, the difference in performance of actual machines is much less than might be expected from the preceding analysis; a well-designed lift-type machine may achieve a peak power coefficient (based on the area covered by the rotating turbine blades) of 0.5 to 0.59, while a pure drag-type machine will achieve a peak power coefficient of no more than 0.2. Some of the multibladed drag-type windmills actually utilize a blade shape that creates some lift, and they may achieve power coefficients as high as 0.3. However, experience has shown that lift-type machines can produce electricity at a significantly lower COE than can drag-type machines can. Only lift-type machines will be considered in the remainder of this discussion.

Aerodynamic Models

The aerodynamic analysis of a wind turbine has two primary objectives: 1) to predict the aerodynamic performance or power production of the turbine; and 2) to predict the detailed distribution of aerodynamic loads acting on the turbine rotor blades. In general, the same models are used to accomplish both objectives. Accurate prediction of turbine aerodynamic performance does not guarantee accurate prediction of the loading distribution. The performance predictions result from the integration of aerodynamic lift and drag over the entire turbine, and significant errors may be present in the detailed lift and drag predictions but balance out in the performance predictions.

Although a considerable body of data shows good agreement of predicted performance with measured performance, very few data are available against which to compare detailed load-distribution predictions. The aerodynamics of wind turbines are far too complex to model with simple formulas that can be solved with hand-held calculators; computer-based models ranging from very simple to very complex are required. Several commonly used aerodynamic models are described next.

Momentum Models

The simplest aerodynamic model of a wind turbine is the actuator disk or **momentum model** in which the turbine rotor is modeled as a single porous disk. This analysis was originally adapted for wind turbine use by Betz (1920) from the propeller theory developed by Froude (1889) and Lanchester (1915). In this model, the axial force acting on the rotor is equated to the time rate of change of the momentum of the air stream passing through the rotor. Utilizing conservation of mass, conservation of axial momentum, the Bernoulli equation, and the first law of thermodynamics, and assuming isothermal flow, the power produced by the turbine (the product of the axial force and the air velocity at the rotor) may be expressed as

$$P = 2\rho A U^3 a(1-a)^2 \tag{8.11.5}$$

where

$a = (U - v)/U$
v = wind velocity at the disk

The power coefficient for the turbine becomes

$$C_P = 4a(1-a)^2 \tag{8.11.6}$$

This is maximized for $a = 1/3$, yielding $C_{P,\max} = 16/27 = 0.593$ as the maximum possible performance coefficient for a lift-type machine, a maximum often referred to as the **Betz limit**. Expressed in slightly different terms, this result states that no lift-type turbine can extract more than 59.3% of the available energy in the wind passing through the rotor.

The typical performance of various types of wind machines is compared to the Betz limit in Figure 8.11.5, in which the variations of the turbine power coefficients with the **tip-speed ratio** (the ratio of the speed of the blade tip to the free-stream wind speed) are presented. Even though the maximum performance of modern HAWTs and VAWTs is well above that of the older, drag-type machines, it is still well below the Betz limit.

For horizontal-axis wind turbines, the momentum model can be expanded to the widely used **blade element momentum (BEM) model** in which the blades are divided into small radial elements and local flow conditions at each element are used to determine blade forces and loads on those elements. To obtain accurate predictions, this theory typically incorporates numerous modifications to account for blade and turbine wake effects; the three-dimensional flow near blade tips; the thick blade sections near the root; and blade stall at high wind speeds. Additional information on these models may be found in Hansen and Butterfield (1993), Wilson (1994), and Snel (1998).

The momentum model for vertical-axis wind turbines may be expanded into the multiple streamtube and the double-multiple steamtube models that are the VAWT equivalent of the HAWT blade element model. Additional information on these models may be found in Touryan et al. (1987), Wilson (1994), and Paraschivoiu (2002).

Momentum-based models are extremely popular with wind turbine designers because they are simple, fast, and fairly accurate for performance prediction. However, they are approximate because they are based upon the assumptions of steady flow and stream tubes that are fixed in time and space. They cannot predict the effects of yawed flow, unsteady aerodynamics, and other complex flows present on wind turbines — all of which can have large impacts on turbine performance and loads. In some cases, specialized codes based on experimental results are used to model some of these effects, but these codes are limited to specific turbine sizes and geometries. In other cases, more realistic models such as vortex-based models, hybrid models, and full computational fluid dynamics (CFD) models have been used to estimate these effects.

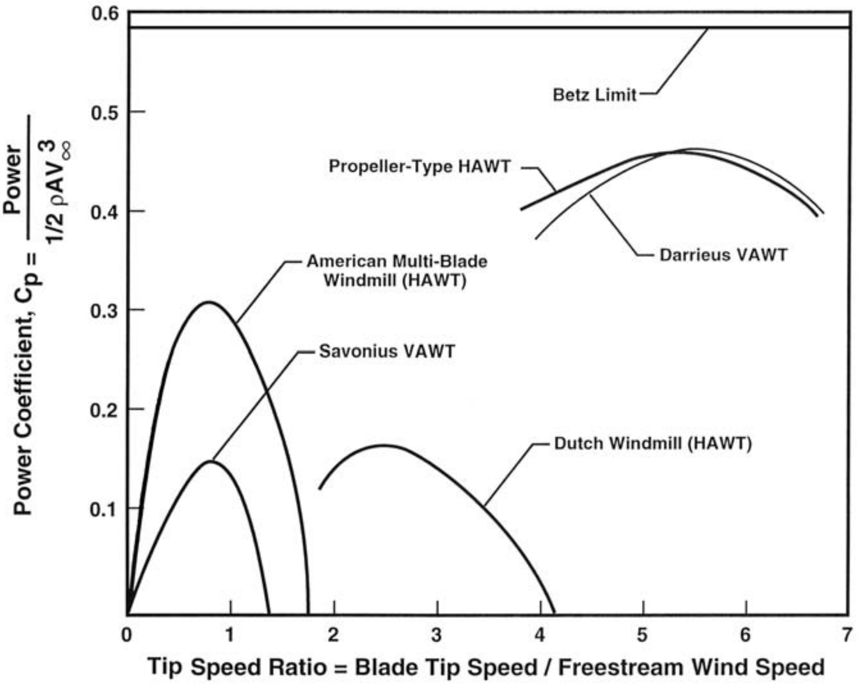

FIGURE 8.11.5 Typical performance of various types of wind turbines.

Vortex Models

Vortex models are usually more properly referred to as lifting line or lifting surface models, depending on whether a lifting line or a lifting surface formulation is used to model the blades. In the lifting line method, each rotor blade is modeled as a segmented "bound vortex line" located at the blade one-quarter chord line. Vortex strengths, defined by the blade lift at each radial location, are associated with the line segments at those radial locations. The lifting surface method represents the blade in more detail, as a distribution of vortex elements over the blade surface.

Either of these models will generate trailing vorticity (perpendicular to the span of the blade), due to the differences in vortex strength along the blade span, and shed vorticity (parallel to the span of the blade), due to time-dependent changes in vortex strength, which is shed into the wake. These vortex methods lend themselves to the modeling of unsteady problems because the shed vorticity models the time-dependent changes in the blade bound vortex strength. Solutions are achieved by placing the rotating turbine into a uniform flow field and allowing the flow field to develop until it reaches a steady state or periodic condition.

The manner in which the transport of the vorticity is modeled in the wake depends on whether a free wake or a fixed (or prescribed) wake model is used. In the free-wake model, the vorticity is allowed to convect, stretch, and rotate as it is transported through the wake. However, the movement of each element of vorticity (whether a line element or particle) is influenced by the presence of all of the other elements of vorticity, including those on the blade. As the computation progresses in time, the number of elements that must be followed, as well as the time required to calculate the element interactions, grow very quickly.

In order to minimize the need for large computer resources, the fixed or prescribed wake models have been developed. In these models, the geometry of the wake is either fixed or described by only a few parameters, and the vortex interactions in the wake are no longer modeled. The result is a much faster execution time, but the accuracy of the predicted power generation and blade loads depends very heavily upon the fidelity with which the specified wake approximates the actual physical wake. The three-dimensional, lifting-surface, free-wake formulation is the most physically realistic of the vortex models, but a computer program implementing such a model will require a large amount of computer resources and time. Experience has shown that the dramatic increase in computer resources required by such a model does not yield significantly more accurate predictions than what can be obtained with a three-dimensional, lifting-line, free-wake model.

A major problem with vortex codes is finding a good balance among model simplification (and the associated limitations on fidelity), computation time, and desired accuracy. Vortex models are not widely used in the wind industry today. Additional information on vortex models may be found in Strickland et al. (1981), Kocurek (1987), and Snel (1998), among others.

Limitations Common to the Momentum and Vortex Models

Momentum-based and vortex models normally utilize airfoil performance characteristic tables (lift and drag coefficients as functions of angle of attack and air velocity) to determine the blade lift and drag. These tables are generated from static two-dimensional wind tunnel test results or two-dimensional static airfoil design code predictions. The table contents are modified with empirical, semiempirical, or analytic methods and used to estimate blade loads under the three-dimensional, dynamic conditions actually experienced by the turbine blades. The greatest difficulty in obtaining accurate load distribution predictions with either type of model is determination of the appropriate airfoil performance characteristics.

Computational Fluid Dynamics Models

In a broad sense, computational fluid dynamics (CFD) is the solution of the partial differential equations describing the flow field by approximating these equations with algebraic expressions (discretizing them), and then solving those expressions numerically with the aid of a computer. Within the wind-energy community, the term CFD normally refers to the numerical solution of the unsteady Navier–Stokes equations, usually restricted to four partial differential equations (one conservation of mass equation and conservation of momentum equations in three orthogonal directions) that describe general ideal, incompressible, nonreacting fluid flow.

Arguably, the most detailed and physically realistic method of modeling the performance of and loads on a wind turbine is to utilize CFD to model the airflow around the turbine and through the rotor. The flow field in the vicinity of the wind turbine is approximated as a computational grid of variable density, and the discretized Navier–Stokes equations are applied to each element of that grid. The computational grid close to the turbine blades must be very, very dense in order to capture the details of the airflow around the blades; it becomes less dense as the distance from the turbine becomes greater and the effect of the blades on the airflow decreases. The resulting set of simultaneous equations must be solved, frequently in a time-marching manner, to determine the time-dependent nature of the entire flow field.

Duque et al. (2003) describe a fairly recent CFD investigation of a wind turbine in which they utilized a complex grid with 11.5 million points to model the flow around a 10-m diameter HAWT rotor and tower combination. A steady-flow solution for that model at a single wind speed, utilizing eight PC processors, each operating at 1.4 GHz in a parallel processor computer configuration, required approximately 26 h. An unsteady-flow solution with the same computing resources required over 48 h for each rotor revolution. Sørensen et al. (2002) and Johansen et al. (2003) report other recent CFD modeling efforts. At this point, CFD is suitable for research use or final design verification only — it is far too slow and requires far too many computer resources to be considered for use as a routine design tool.

Hybrid Models

The hybrid model approach typically approximates the airflow close to the turbine with the descretized Navier–Stokes equations, similar to the procedure used by the CFD models. However, away from the turbine, the model uses nonviscous or potential flow equations that are much less complex and can be solved much faster than the Navier–Stokes equations. The two solutions must be merged at the boundary between the two regions. The result is a code with the accuracy of the CFD model, but one that requires an order of magnitude less computing resources to solve. Xu and Sankar (2002) describe recent work on such a code. Even this model requires a large amount of computer resources and is too slow and expensive to be considered a practical design tool.

None of these models is capable of accurately predicting the performance of and detailed loads on an arbitrary wind turbine operating at a variety of wind speeds. In order to have high confidence in the code predictions for a turbine design, the code must be calibrated against the measured performance and loads obtained from turbines of similar size and shape. Simms et al. (2001) report on the ability of 19 codes based on the preceding models to predict the distributed loads on and performance of an upwind HAWT with a 10-m diameter rotor that was tested in the NASA/Ames 80 ft × 120 ft wind tunnel. Although the rotor was small compared to the 80-m diameter and larger commercial turbines built today, a panel of experts from around the world concluded that it was large enough to yield results representative of what would be observed on the larger turbines.

The comparisons of the code predictions and the experimental results were not especially encouraging: turbine power predictions ranged from 30 to 275% of measured and blade-bending moment predictions ranged from 85 to 150% of measured for what is considered to be the most easy-to-predict conditions of no yaw, steady state, and no stall. Many aerodynamic code developers have spent considerable effort over the past 2 years attempting to identify the sources of the discrepancies and improving the accuracy of their various codes.

Additional information and references on wind turbine aerodynamics models may be found in Hansen and Butterfield (1993), Wilson (1994), and Snel (1998) for HAWTs and in Touryan et al. (1987) and Wilson (1994) for VAWTs.

Wind Turbine Loads

The wind is **stochastic** in nature, with significant short-term variations or turbulence in direction and in velocity. Wind turbine aerodynamic loads may be regarded as falling into one of two broad categories: (1) the deterministic loads occurring in narrow frequency bands resulting from the mean steady atmospheric wind, wind shear, rotor rotation, and other deterministic effects; and (2) the random loads occurring over all frequencies resulting from the wind turbulence. As recently as 10 years ago, the deterministic loads were frequently predicted with an aerodynamics code, such as those described in the previous parts of this section, utilizing a uniform wind input, and the random loads were estimated with empirical relations. However, turbine designers now recognize that this approach may lead to serious underprediction of the maximum blade loads, resulting in costly short-term component failures. Most analysts today utilize an aerodynamics performance code with a wind model that includes a good representation of the turbulence of the wind in all three dimensions to predict long-term wind turbine loads. The appropriate method of determining the wind-induced extreme events that limit the lifetime of a turbine remains the subject of ongoing research.

Wind Turbine Structural Dynamics

Horizontal Axis Turbines

Small horizontal axis turbine designs usually use fairly rigid, high-aspect-ratio blades, cantilevered from a rigid hub and main shaft. As turbine size increases, the flexibility of the components tends to increase, even if the relative scales remain the same; thus, the blades on larger turbines tend to be quite flexible, and the hub and main shaft tend to be far less rigid than the components on the small turbines. The entire drive-train assembly is mounted on and yaws about a tower that may also be flexible.

These structures have many natural vibration modes and some of them may be excited by the wind or the blade rotation frequency to cause a **resonance** condition in which the vibrations are amplified and cause large stresses in one or more components. Operating at a resonance condition would quickly destroy a turbine. Careful structural analysis during the turbine design can ensure that the turbine will not experience a resonance condition, but ignoring the analysis altogether or failing to conduct parts of it properly may result in a turbine that will experience one or more resonance conditions leading to early failure. Although the relatively rigid small turbines are not too likely to experience these resonance problems, the very flexible, highly dynamic larger turbines are quite likely to experience resonance problems unless they are very carefully designed and controlled.

The large relative motion between the rotor and the tower precludes the use of standard commercial finite element analysis codes and requires the use of a model constructed specifically for analysis of wind turbines. Development of such a model can be a rather daunting task because it requires the formulation and solution of the full nonlinear governing equations of motion. The model must incorporate

- Yaw motion of the nacelle
- Pitch control of the blades
- Any motion and control associated with hinged blades
- Interaction between the rotor and the supporting tower
- Starting and braking sequences, etc.

If the full equations of motion are developed with finite-element or multibody dynamics formulations, the resultant models contain moderate numbers of elements and potential motions (or degrees of freedom, DOF), and significant computer resources are required to solve the problem. On the other hand, a modal formulation utilizing limited DOF may yield an accurate representation of the wind turbine, resulting in models that do not require large computing resources. The development of the modal equations of motion does require considerably more effort than do the finite-element or multibody equations.

The modal degrees of freedom must include blade bending in two directions, blade motion relative to the main shaft, drive train torsion, tower bending in two directions, and nacelle yaw. Blade torsional bending is not normally included in current models, but it will become more important as the turbine sizes continue to increase and the blades become more flexible. The accuracy of the modal formulation is typically limited by its inability to model the nonlinear variation of airfoil lift with angle of attack that occurs as a result of aerodynamic stall. The modal formulation is the most widely used analysis tool today; however, as computer resources become more readily available and cheaper, the finite element and multibody dynamic codes will gain in popularity.

The resultant equations of motion, whether finite-element, multibody, or modal, can be solved in the frequency domain or in the time domain. The frequency domain calculations are fast, but they are unable to account for nonlinear structural dynamics due to large component deflections and nonlinear control system dynamics. In spite of these limitations, frequency-domain solutions of the modal formulation are frequently used in the preliminary design of a wind turbine, when quick analysis of many configurations is required. Regardless of the methods used in preliminary design, the state of the art in wind turbine design today is to use finite-element-based equations of motion, coupled with time-accurate solutions to analyze the turbine behavior for the detailed final design calculations.

Malcolm and Wright (1994) provide a list of some of the available HAWT dynamics codes that have been developed, together with their limitations. Buhl et al. (2000) compare some of the HAWT dynamics codes that have been extensively verified and are widely used today, and Quarton (1998) provides a good history of the development of HAWT wind-turbine analysis codes.

Vertical Axis Turbines

Darrieus turbine designs normally use relatively slender, high-aspect-ratio structural elements for the blades and supporting tower. As with large HAWTs, the result is a very flexible, highly dynamic structure, with many natural modes of vibration that, again, must be carefully analyzed to ensure that the turbine will avoid structural resonance conditions under all operating environments. The guy cables and turbine support structure can typically be analyzed with commercial or conventional finite element codes, but the tower and blades require a more refined analysis, usually requiring the use of a finite element code possessing options for analyzing rotating systems. With such a code, the blades and tower of a VAWT are modeled in a rotating coordinate frame resulting in time-independent interaction coefficients. The equations of motion must incorporate the effects of the steady centrifugal and gravitational forces, the aerodynamic forces due to the turbulent wind, and the forces arising from rotating coordinate system effects. Detailed information on finite-element modeling of VAWTs may be found in Lobitz and Sullivan (1983).

Wind Turbine Electrical Generators

Once a wind turbine has converted the kinetic energy in the wind into rotational mechanical energy, it is usually converted into electricity that can be readily transported wherever it is needed. Although some wind turbines utilize permanent magnet alternators to generate electricity, most grid-connected turbines today utilize synchronous or induction generators. Induction generators are cheaper and easier to control than synchronous generators and provide some power-train damping; however, they tend to create adverse effects upon the power carried by the grid to which they are connected. These adverse effects can usually be solved fairly quickly and at low cost with modern power electronics.

Permanent magnet generators tend to achieve higher efficiency at low power ratings than induction or synchronous generators do, leading to increased energy capture, but the technology is less mature than it is for the others and the cost is somewhat higher.

Although most older turbines operate at a single fixed rotational speed, most newer turbines, and especially the larger ones, are variable speed, operating within a fixed range of rotational speeds. Variable-speed turbine operation offers the following major advantages over fixed-speed operation:

- The aerodynamic efficiency of the rotor at low to moderate wind speeds may be improved by changing the rotational speed to keep the turbine operating close to the optimum tip-speed ratio, maximizing the power coefficient. At higher wind speeds, the blades are in stall or are pitched to limit peak power and it is not necessary to operate at the optimum tip-speed ratio.
- System dynamic loads may be attenuated by the inertia of the rotor as it speeds up and slows down in response to wind gusts.
- The turbine may be operated in a variety of modes, including operation at maximum efficiency for lower wind speeds to maximize energy capture or operation to minimize fatigue damage

In variable-speed operation, certain rotational speeds within the operating-speed range will likely excite turbine vibration modes, causing structural resonance and increased rates of fatigue damage. These rotational speeds must be avoided during operation, leading to complex control schemes.

Variable-speed operation, in general, generates variable-frequency power. Most applications include interfacing with power grids, requiring high-quality power at a reference frequency. Several methods have been developed for accomplishing this with sophisticated power electronics (Smith, 1989), but research to develop improved methods with higher efficiencies continues.

In general, generator efficiency drops off rapidly as the generated power falls below the rated generator capacity, and single-generator systems tend to be very inefficient at low wind speeds. Some turbine designs address this deficiency by having multiple smaller generators. At low wind speed, only one generator might be attached to the drive train, with more added as the wind speed increases. The net result is that each generator operates close to its rated power much of the time, increasing the overall generator efficiency. Similar results can be obtained with a single generator utilizing pole switching or multiple windings.

Wind Turbine Controls

All wind turbines include auxiliary systems to control turbine performance and protect the turbine from excessive loads. The more common systems include the following.

Yaw Systems

The rotor of a HAWT must be oriented so that the rotor axis is parallel to the wind direction for peak power production. Most upwind HAWTs and a few downwind HAWTs incorporate active yaw control systems, using a wind direction sensor and a drive motor to orient the rotor with respect to the wind direction. Some downwind HAWTs are designed to utilize the wind to orient the rotor automatically. Active yaw systems tended to be extremely problematical in early turbines, basically because the loads acting on them were not well understood. Because yaw loads are much better understood today, these systems are no longer a major problem area. VAWTs do not require yaw systems.

Peak Power Regulation System

All turbines incorporate some method of regulating or limiting the peak power produced. Because the entire turbine must be sized to handle the loads associated with peak power production, the entire system would be tremendously overdesigned and the generator and transmission would be very inefficient at normal wind speeds if such a capability were absent. Regulating the peak power enables the designer to size the generator so that it will operate near its design power rating, where it is most efficient, at normal operating wind speeds (between the rated wind speed and the shut-down wind speed). The additional energy captured due to the increase in generator efficiency over the lower wind speeds is usually many times greater than that lost due to limiting the peak power at the infrequent high wind speeds. Most large horizontal-axis turbines use blade pitch control, but some use blade stall control. Small turbines frequently incorporate features that turn the rotor so that the axis is at an angle to the wind in order to achieve peak power regulation.

With full-span blade pitch control, the blade is rotated about its longitudinal axis to decrease the effective angle of attack as the wind speed increases, causing decreased blade lift to regulate the peak power. Although pitch control results in decreased drag loads at high winds, a major disadvantage is poor peak-power control during high-wind stochastic conditions; power excursions can exceed twice the rated power levels before the high-inertia blade pitch system can respond. With blade stall control, the blades are designed to encounter **stall** at high wind speeds, resulting in decreased blade lift and increased blade drag to regulate the peak power. Major disadvantages of stall control include increasing blade drag loads as the wind speed increases (even after stall) and possible large dynamic loads due to wind turbulence. A major advantage of stall control is the lower cost compared to that of the active pitch control. Sample power curves for stall- and pitch-regulated 500-kW turbines are shown in Figure 8.11.6.

Partial-span control surfaces typically regulate the peak power by decreasing the lift and increasing the drag of a portion of the blade. These control surfaces are usually much smaller than the full blade, so they can respond to wind changes much faster than can the full-span blade. However, partial span

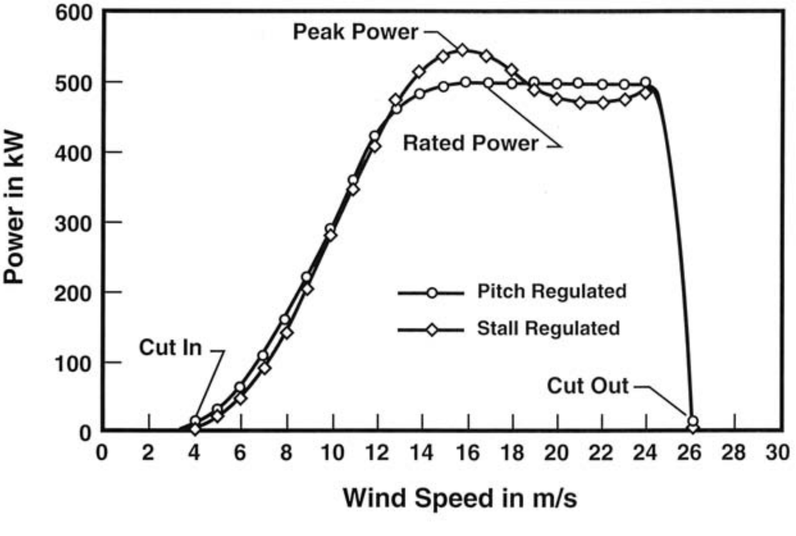

FIGURE 8.11.6 Sample power curves for stall-regulated and pitch-regulated wind turbines.

devices are very difficult to integrate into a blade and they tend to create noise. Recent work has focused on very small load control devices that can generate large changes in lift and drag while experiencing small loads. Dimensions of these devices are typically on the order of 1% of the blade chord and they can therefore be activated very quickly to alleviate excess loads. Their small size helps to limit noise creation.

Several other methods of pitch control have also been used, but on a limited basis. Passive pitch-control techniques automatically adjust the blade pitch angle by using cams activated by centrifugal loads or by using tailored blade materials that permit the blade to twist under high loads. These devices are very carefully tailored to maintain peak performance at lower wind speeds; however, they limit the peak power and blade loads at high wind speed.

Virtually all vertical-axis wind turbines utilize stall regulation with fixed-pitch blades to control peak power.

High Wind Speed Protection System

In general, wind turbines are designed to operate when the incident wind is high enough to generate electricity and to cease operation when the wind speeds exceed 25 to 30 m/s, where high loads threaten to damage the operating wind turbine. In spite of the tremendous amount of power present in high winds, these winds are normally present only for short periods of time, and the additional energy that can be captured is usually more than offset by the increased cost of a turbine that is designed to withstand the attendant high loads.

Controller System

Every wind turbine contains a controller, usually a microprocessor-based system, to control turbine operations. The basic turbine controller will start and stop the machine, connect or disconnect the generator output to the power grid, as needed; control the operation of the yaw and pitch systems (if present); perform diagnostics to monitor the operation of the machine; and perform normal or emergency shutdown of the turbine as required. For older turbines, the controller was frequently a fairly generic device with a minimum of machine-specific features that was simply added to an existing turbine.

For newer turbines, especially large, variable-speed machines, controllers incorporate much more intelligence than the old, generic type; they may be designed to

- Utilize the pitch system to limit peak power and/or torque
- Control the rotor speed
- Maximize energy capture
- Trade off energy capture and loads mitigation
- Reduce power fluctuations
- Control power quality
- Actively control some turbine dynamics

Controllers with any or all of these capabilities should be included in the models of system dynamics and must be designed from scratch as an integral component of the wind turbine.

Wind Turbine Materials

Most of the materials used in the construction of wind turbines are typical of materials used in other rotating machinery and towers — relatively common structural materials such as metal, wood, concrete, and glass-fiber reinforced plastic (GFRP) composites. However, wind turbine blades are fatigue critical structures (their design is driven by consideration of the fatigue loads they must endure), and the number of fatigue cycles they experience in a 30-year design life is three orders of magnitude beyond the 10^6 cycles that are the common limit of fatigue data for these materials. Over the past 15 years, high-cycle fatigue databases for many potential blade materials have been developed specifically for wind turbine applications. The blade material of choice today is GFRP composites due to the high strength and stiffness that can be obtained; the ease of tailoring them to the loads; and their relatively low cost (Sutherland, 2000).

However, the trend to larger and larger turbines, with the resultant increase in blade weight and flexibility, has created intense interest in utilizing some carbon fiber in the blades to decrease weight and add stiffness. Carbon fiber, even in the cheapest form available today, remains relatively expensive, and the challenge to turbine designers is to incorporate it into blades in a cost-effective manner.

Defining Terms

Betz limit: Maximum portion of available wind energy that can be extracted by a wind turbine, according to momentum theory.

Blade element momentum (BEM) model: An enhanced version of the momentum model that is the primary model used to compute aerodynamic performance and structural loading for HAWTs.

Horizontal-axis wind turbine (HAWT): A turbine in which the blades rotate about a horizontal axis.

Momentum model: A method of estimating the performance of a turbine by equating the time rate of change of air momentum through the turbine to the force acting on turbine blades.

Power coefficient: The ratio of captured energy to the energy available in the reference area.

Resonance: A vibration of large amplitude caused by a relatively small excitation at or near a system natural frequency.

Stall: An operating condition in which an airfoil experiences a decrease in lift and a large increase in drag as the angle of attack increases.

Stochastic: Containing variations from a smooth, uniform flow.

Tip-speed ratio: The ratio of the speed of the blade tip to the free-stream wind speed.

Vertical-axis wind turbine (VAWT): A turbine in which the blades rotate about a vertical axis.

References

Buhl, M.L. Jr., Wright, A.D., and Pierce, K.G., 2000, Wind turbine design codes: a comparison of the structural response, *Collection 2000 ASME Wind Energy Symp. Tech. Papers*, Reno Nevada, 10–13 January, 12–22.

Betz, A., 1920, Das Maximum der theoretisch möglichen Ausnützung des Windes durch Windmotoren, *Z. Gesamte Turbinewesen*, 26.

Duque, E.P.N., Burkland, M.D., and Johnson, W., 2003. Navier–Stokes and comprehensive analysis performance predictions of the NREL phase VI experiment, *Collection 2003 ASME Wind Energy Symp. Tech. Papers*, Reno Nevada, 6–9 January, 43–61.

Fingersh, L., Simms, D., Hand, M., Jager, D., Cotrell, J., and Robinson, M., 2001, Wind tunnel testing of NREL's unsteady aerodynamic experiment, *Collection 2001 ASME Wind Energy Symp. Tech. Papers*, Reno Nevada, 11–14 January, 194–200.

Froude, R.E., 1889, On the part played in propulsion by differences of fluid pressure, *Trans. Inst.. Naval Architects*, 30.

Hansen, A.C. and Butterfield, C.P., 1993, Aerodynamics of horizontal-axis wind turbines, *Annu. Rev. Fluid Mech.*, 115–149.

Johansen, J., Sørensen, N., Michelsen, J., and Schreck, S., 2003, Detached-eddy simulation of flow around the NREL phase-VI rotor, *Proc. 2003 Eur. Wind Energy Conf. Exhibition*, Madrid, 16–19 June.

Kocurek, D., 1987, Lifting surface performance analysis for horizontal axis wind turbines. *NREZ/STR*-217-3163, National Renewable Energy Laboratory, Golden, CO.

Lanchester, F.W., 1915, A contribution to the theory of propulsion and the screw propeller, *Trans. Inst. Naval Architects*, 57.

Lobitz, D.W. and Sullivan, W.N., 1983, A comparison of finite element prediction and experimental data for forced response of DOE 100 kW VAWT, *Proc. 6th Biennial Wind Energy Conf. Workshop, Minneapolis, MN*, 843–853.

Malcolm, D.J. and Wright, A.D., 1994, The use of ADAMS to model the AWT-26 prototype, *Proc. 1994 ASME Wind Energy Symp.*, New Orleans, LA., 125–132.

Paraschivoiu, I., 2002, *Wind Turbine Design*, Polytechnic International Press, Montreal, Quebec.

Quarton, D.C., 1998, The evolution of wind turbine design analyses – a twenty year progress review, *Wind Energy*, 1, 5–24.

Simms, D., Schreck, S., Hand, M., and Fingersh, L., 2001, NREL unsteady aerodynamics experiment in the NASA–Ames wind tunnel: a comparison of predictions to measurements, NREL/TP-500-29494, National Renewable Energy Laboratory, Golden, CO.

Smith, G.A., 1989, Electrical control methods for wind turbines, *Wind Eng.*, 13(2), 88–98.

Snel, H., 1998, Review of the present status of rotor aerodynamics, *Wind Energy*, 1, 46–69.

Sørensen, N., Michelsen, J., and Schreck, S., 2002, Navier–Stokes predictions of the NREL phase VI rotor in the NASA Ames 80 ft × 120 ft wind tunnel, *Wind Energy*, 5, 151–169.

Strickland, J.H., Smith, T., and Sun, K., 1981, A vortex model of the Darrieus turbine: an analytical and experimental study, SAND81-7017, Sandia National Laboratories, Albuquerque, NM.

Sutherland, H.J., 2000, A summary of the fatigue properties of wind turbine materials, *Wind Energy*, 3, 1–34.

Touryan, K.J., Strickland, J.H., and Berg, D.E., 1987, Electric power from vertical-axis wind turbines, *J. Propulsion Power*, 3(6), 481–493.

Wilson, R.E., 1994, Aerodynamic behaviour of wind turbines, in *Wind Turbine Technology, Fundamental Concepts of Wind Turbine Engineering*, Ed., D. Spera, 215–282, ASME Press, New York.

Xu, G. and Sankar, L.N., 2002, Application of a viscous flow methodology to the NREL phase VI rotor, *Collection 2002 ASME Wind Energy Symp. Tech. Papers*, Reno Nevada, 14–17 January, 83–93.

Further Information

Excellent summaries of HAWT and VAWT aerodynamics, together with extensive reference lists, are presented by C. Hansen and S. Butterfield in their paper "Aerodynamics of Horizontal-Axis Wind Turbines" in *Annual Review of Fluid Mechanics, 1993*, and by K. Touryan, J. Strickland, and D. Berg, in their paper "Electric Power from Vertical-Axis Wind Turbines" in the *Journal of Propulsion*, 3(6), 1987, respectively. Volume 1 of *Wind Energy, 1998* contains a comprehensive set of review papers covering wind turbine rotor aerodynamics, design analysis, and overall system design. The latest developments in the field of wind energy in the U.S. and Europe may be found in the following annual conference proceedings:

A Collection of the ASME Wind Energy Symposium Technical Papers, American Institute of Aeronautics and Astronautics, 59 John Street, 7th Floor, New York, NY 10038.

Proceedings of Windpower, American Wind Energy Association (AWEA), 122 C St. NW, Suite 380, Washington, D.C. 20001

Proceedings of the European Wind Energy Association, European Wind Energy Association, Rue du Trone 26, B-1040 Brussels. Belgium

Proceedings of the British Wind Energy Association, British Wind Energy Association, Renewable Energy House, 1 Aztec Row, Berners Road, London, N1 0PW, UK.

Extensive information on wind energy technology may also be found on the Worldwide Web. Excellent sites to start with include those of the Danish Wind Energy Association, http://www.windpower.org/en/core.htm; the American Wind Energy Association, www.awea.org; the British Wind Energy Association, www.britishwindenergy.co.uk; the European Wind Energy Association, www.ewea.org; the U.S. National Renewable Energy Laboratory Wind Energy Technology Center, www.nwtc.nrel.gov; Sandia National Laboratories Wind Energy Technology Department, www.sandia.gov/wind; and the Danish Risø National Laboratory, www.risoe.dk/vea/index.htm.

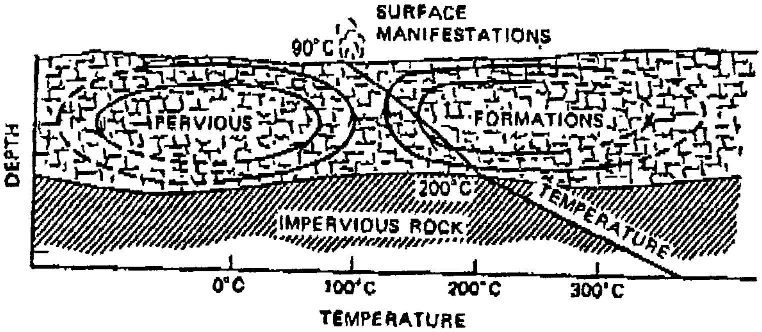

FIGURE 8.12.1 Schematic diagram of the convective cells in a geothermal reservoir. (From Kestin, J., Ed., Sourcebook on the Production of Electricity from Geothermal Energy, U.S. DOE, DOE/RA/4051-1, Washington, D.C., 1980).

8.12 Energy Conversion of the Geothermal Resource

Carl J. Bliem and Gregory L. Mines

This section discusses the uses of the geothermal resource. The primary use of the energy from geothermal resources to date has been in the production of electrical energy. Other applications, such as process heat and space conditioning, have also been made and will be discussed under the topic of direct use. This section begins with a discussion of the geothermal resource as it applies to the use of the energy. Then discussion of the three types of electrical generating facilities presently in use: — the **direct steam system**, the **flashed steam system**, and the **binary system** — is given. Finally, some discussion of direct-use applications is given.

Geothermal Resource Characteristics Applicable to Energy Conversion

Geothermal energy as defined here applies to hot fluids under pressure found at a reasonable depth (1 to 2 km) in the earth's crust. If one disregards the complex geological details relating to the formation of such naturally occurring reservoirs of hot fluids, Figure 8.12.1 and Figure 8.12.2 present schematic representations of these reservoirs. High-temperature fluid (200 to 300°C) is created by the convection of water through the porous rock. As the water circulates, it dissolves various amounts of minerals containing sodium, potassium, calcium, silica, carbonates, and chlorides and gases such as nitrogen and carbon dioxide. In **geopressured resources** of the Gulf of Mexico, high pressures and significant amounts of dissolved methane are seen.

The convective cells operate over large horizontal distances of as much as 30 km. The time in which the transfer of energy from the magma to the water takes place is of the order of 10^5 to 10^6 years. At the present time, it is difficult to say whether or not the resource can be considered "renewable." If natural circulation or the injection of spent geothermal liquid into the reservoir can make up for the liquid extracted during the energy conversion process, the reservoir can be considered at least of a very long life. (Individual wells generally have a life of about 10 years.)

The resources considered in this section are said to be **hydrothermal**. (Work is being done on creating artificial reservoirs by injecting water into hot dry rock, but this development is in its early stages and will not be considered here. The geopressured resource will not be considered either.)

As the geofluid is extracted from a reservoir, it flows to a region of lower static pressure. If this pressure falls below the saturation pressure for the temperature of the geofluid (close to but not equal to the saturation pressure of pure water because of the presence of the dissolved solids and gases), the geofluid will flash into steam. Therefore, the person using this energy source may have a number of different physical forms to consider:

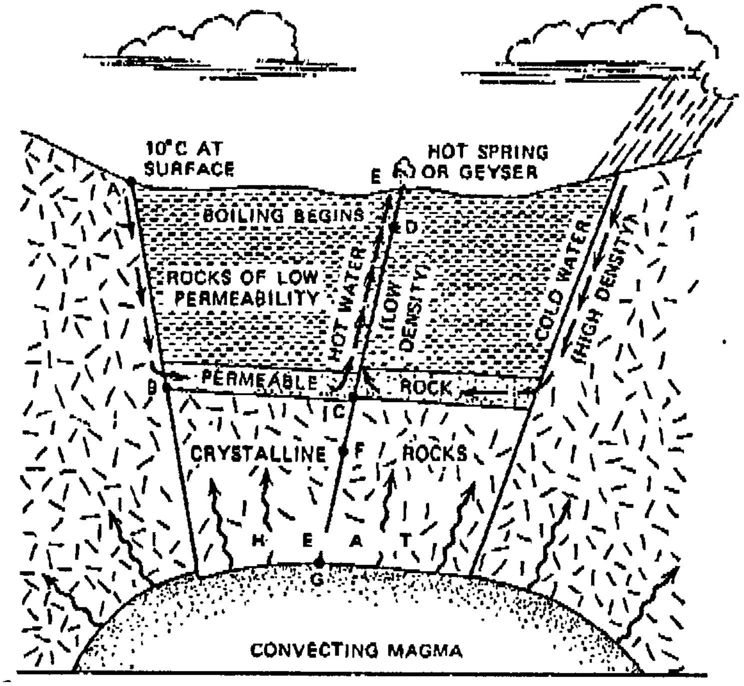

FIGURE 8.12.2 Schematic diagram of a characteristic geothermal reservoir. (From Kestin, J., Ed., Sourcebook on the Production of Electricity from Geothermal Energy, U.S. DOE, DOE/RA/4051-1, Washington, D.C., 1980).

1. Wet steam from a *vapor-dominated resource*;
2. Superheated or saturated steam from a vapor-dominated resource;
3. Liquid at a pressure above the saturation pressure from a *liquid-dominated resource*;
4. A mixture of liquid and vapor at a relatively low quality from a liquid-dominated resource.

Electrical Energy Generation from Geothermal Resources

The type of energy conversion system used to produce electrical power depends on the type and quality (temperature) of the geothermal resource. Vapor-dominated resources use systems where steam is expanded directly through a turbine, similar to conventional fossil fuel steam plants. Liquid-dominated resources use flash steam systems and binary systems, with binary systems predominantly used for the lower-quality resources. The term **binary system** is used to describe a power cycle where the geothermal fluid provides the source of thermal energy for a closed-loop Rankine cycle using a secondary working fluid. In this closed loop, the working fluid is vaporized using the energy in the geofluid, expanded through a turbine, condensed, and pumped back to the heater completing the closed loop.

Hydrothermal resources typically contain varying amounts of numerous dissolved minerals and dissolved gases. In power cycles where steam is extracted from the geothermal resource directly (vapor dominated) or indirectly (flashing liquid dominated) and expanded through a condensing turbine, the design and operation of the power cycle must account for the removal of the noncondensable gases. If the gases are not removed from the condenser, they will accumulate in the condenser, raising the turbine back pressure and decreasing the power output. In systems where the liquid geofluid is handled (binary cycle heat exchangers and piping and flash steam flash tanks and piping), measures must be taken to prevent the precipitation of the dissolved solids and/or to provide a means of removal of the resulting scale.

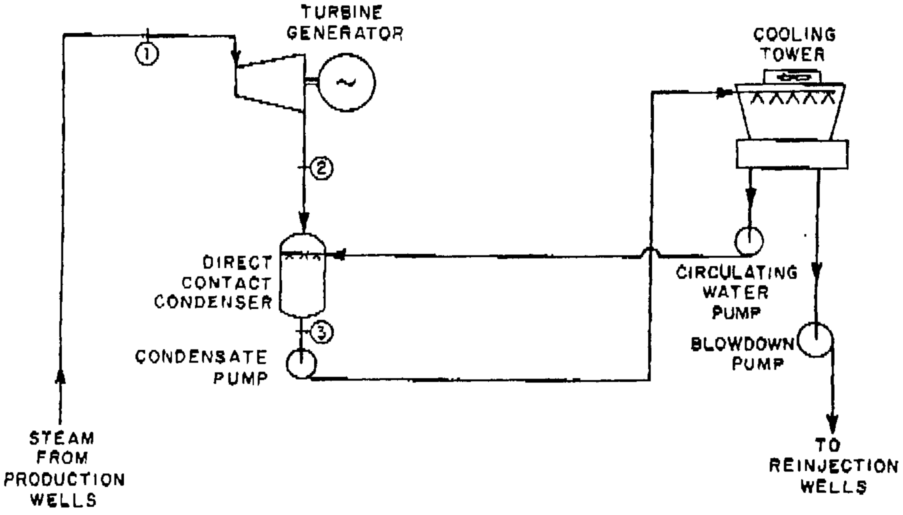

FIGURE 8.12.3 Schematic diagram of a direct dry-steam plant. (From Kestin, J., Ed., Sourcebook on the Production of Electricity from Geothermal Energy, U.S. DOE, DOE/RA/4051-1, Washington, D.C., 1980).

Direct Steam Systems — Vapor-Dominated Resources

For a geothermal resource producing a superheated or saturated vapor steam (Case 2), the vapor from the geothermal production well is sent to a conventional steam turbine as shown in Figure 8.12.3. (This is done after appropriate removal of rocks and debris and possibly after scrubbing with water to remove corrosive substances.) Normally, the turbine is a condensing type, as shown in the figure, although in some applications a back-pressure turbine is used, exhausting the steam to the atmosphere. The back-pressure turbine is typically used for small systems with the possible later addition of another turbine and a condenser to increase the power generated by the geofluid flow from the wells.

Figure 8.12.3 shows a system with a direct-contact condenser and a wet cooling tower. In this type of system, the condensate from the condenser is more than enough to make up the evaporation and blowdown from the cooling tower. Therefore, the figure shows some of the condensate being injected into the reservoir. In many cases, direct-contact condensers are not feasible because of the hydrogen sulfide in the steam which would be released in the cooling tower exhaust. When hydrogen sulfide is in the steam, the majority of it appears as noncondensable and the noncondensable gas from the condensers must be treated. For these systems, surface condensers are normally used in conjunction with wet cooling towers. The actual hardware configuration is dictated by the process for removal of the sulfur. Again, some of the condensate can be used for cooling tower makeup if the sulfur is removed from the process. A number of processes have been developed to remove sulfur from the process.

Figure 8.12.4 depicts a system which is similar to the one described above, but one which receives wet steam (Case 1). Here, the liquid is separated from the vapor prior to the entry of the vapor into the turbine. Otherwise, the system is the same as the one in Figure 8.12.3 and the same comments apply.

Flash Steam Systems — Liquid Dominated Resources

When the geofluid is flashed before it leaves the well, flash steam systems are generally used. This indicates that the resource is at a relatively high temperature. Figure 8.12.5 and Figure 8.12.6 depict single- and dual-flash systems schematically. The single-flash system in Figure 8.12.5 is quite similar to the system in Figure 8.12.4. The only difference is that the geofluid pressure is dropped further before the steam is separated and sent to the turbine. An optimum flash pressure exists because the lower the flash pressure, the more steam which is evolved. However, the work done per unit mass of steam flowing through the turbine will also decrease with the lower flash pressure. For a given set of geofluid conditions entering the plant, a flash pressure exists that will maximize the energy produced per unit mass of geofluid and

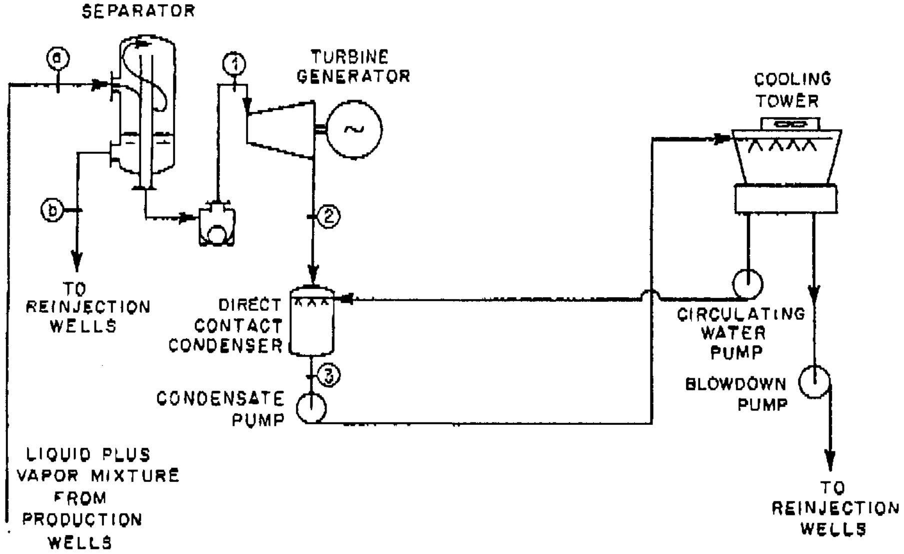

FIGURE 8.12.4 Schematic diagram of a plant using a two-phase resource. (From Kestin, J., Ed., Sourcebook on the Production of Electricity from Geothermal Energy, U.S. DOE, DOE/RA/4051-1, Washington, D.C., 1980).

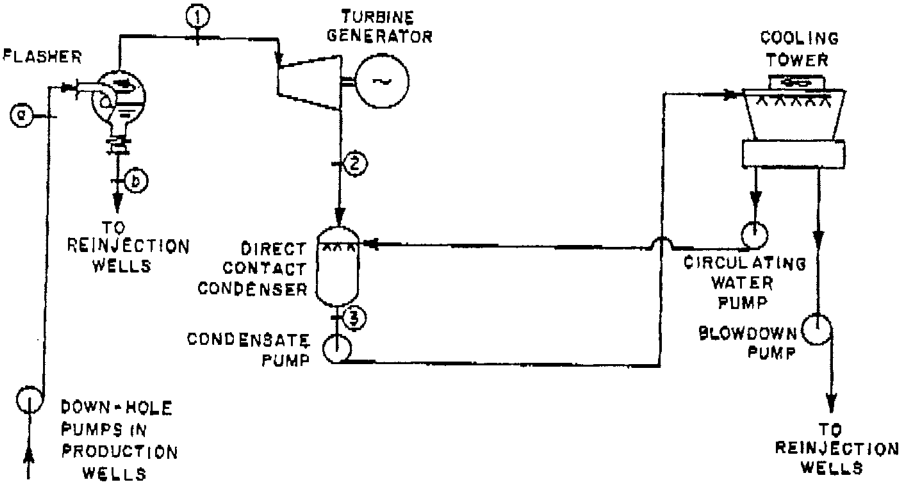

FIGURE 8.12.5 Schematic diagram of a single-flash plant. (From Kestin, J., Ed., Sourcebook on the Production of Electricity from Geothermal Energy, U.S. DOE, DOE/RA/4051-1, Washington, D.C., 1980).

also minimize the levelized energy cost (LEC). The performance and cost optima will be near, but not generally at the same pressure.

The flash steam system can also be utilized in applications where the fluid enters the plant as a liquid (single phase). In these systems, the geothermal fluid is throttled with an expansion valve to the desired flash pressure. This flashing process can be considered adiabatic, where the amount of steam evolved can be determined from energy and mass balances of a simple throttling calculation.

Most successful flash systems are dual flash. The first flash is generally near the well-head pressure and the second flash near atmospheric pressure. The low-pressure flash is normally kept above atmospheric

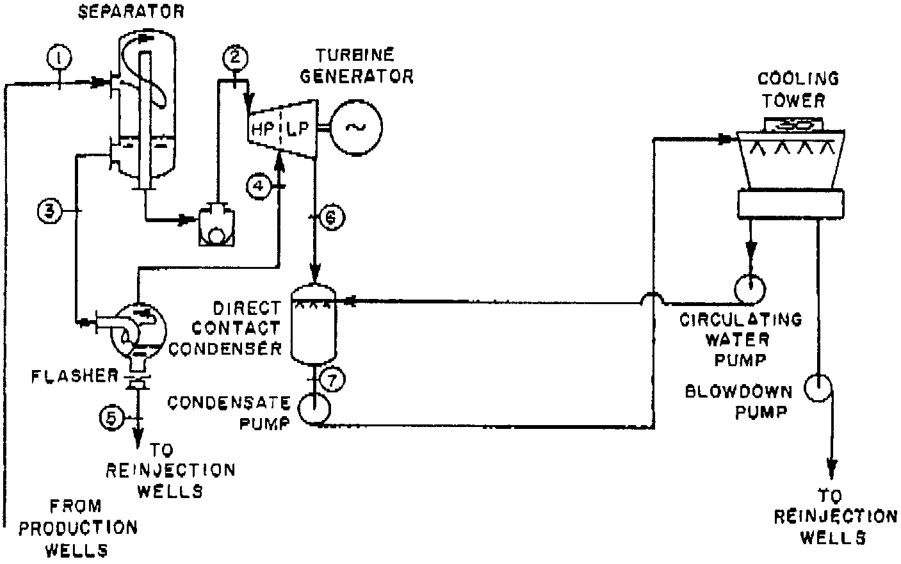

FIGURE 8.12.6 Schematic diagram of a dual-flash plant. (From Kestin, J., Ed., Sourcebook on the Production of Electricity from Geothermal Energy, U.S. DOE, DOE/RA/4051-1, Washington, D.C., 1980).

pressure to prohibit leakage of air into the system in the flasher. Some recent studies have indicated that for low-temperature resources, a subatmospheric second flash would produce a cost-effective system. Again, optimization of the two flash pressures is necessary to minimize the LEC. In cases in which the geofluid has a high dissolved solid content, flash crystallizers are used to remove the precipitated dissolved solids. The flashing process releases carbon dioxide dissolved in lowering the geofluid pH, which causes the precipitation of insoluble carbonates. The solubility of silica is temperature dependent; lowering the geofluid temperature causes the precipitation of silica.

None of the steam cycles depicted provides for the removal of the noncondensable gases from the condenser. This removal is typically accomplished with steam ejectors or compressors which continuously remove the small stream of vapor from the condenser. Some steam is lost in this process of removing the noncondensable gases.

Binary Systems — Liquid-Dominated Resources

Recent studies have shown that for resources below 200°C, current technology binary systems have lower LEC than flash steam plants for liquid-dominated resources. Figure 8.12.7 shows a typical binary system with an evaporative heat-rejection system. This type of heat-rejection system has been replaced by air-cooled condensers in most applications. In the areas where the geothermal resource exists, there is little excess water for makeup in the cooling tower, as shown in Figure 8.12.7. All of the cooled geofluid in a binary system is typically injected back into the reservoir. This provides an environmentally acceptable means of disposal of the fluid and, more important, provides a recharge of the reservoir to maintain the reservoir productivity.

The binary cycle is an attempt to reduce the scaling potential of the geofluid. Carbonates are precipitated when the pressure of the geofluid is reduced and carbon dioxide comes out of solution as the geofluid flashes. With downhole pumps in the wells, this can be eliminated by keeping the fluid pressurized. Some resources do not require pumps to maintain the flow and pressure necessary to eliminate flashing (artesian flow). Similarly, if the exit temperature of the geofluid remains above some minimum value, silica will not be precipitated. These two operational strategies limit the scaling in a binary plant. Any constraint imposed on the geofluid exit temperature will impact the design of the binary plant, affecting the selection of turbine inlet conditions as well as the possible choice of working fluid.

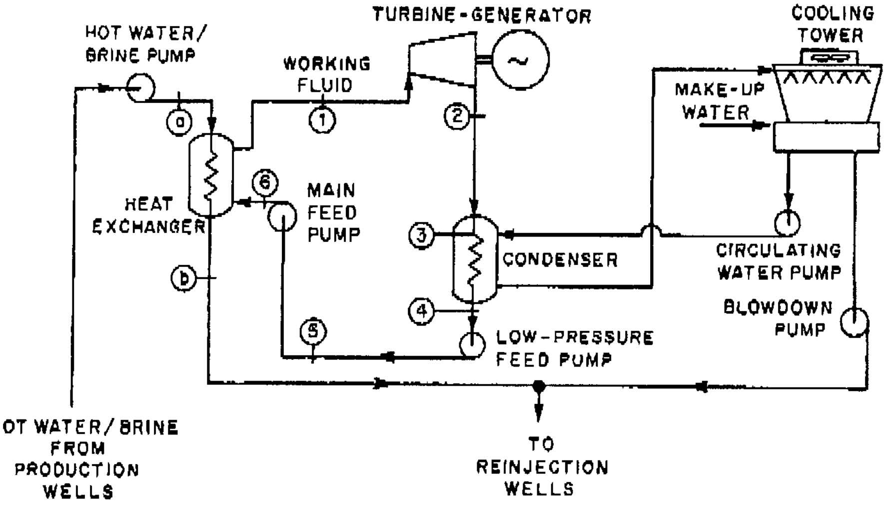

FIGURE 8.12.7 Schematic diagram of a binary plant. (From Kestin, J., Ed., Sourcebook on the Production of Electricity from Geothermal Energy, U.S. DOE, DOE/RA/4051-1, Washington, D.C., 1980).

The binary cycle consists of a closed loop of a working fluid normally performing a Rankine cycle. Most existing binary cycles use isobutane, pentane, or isopentane as working fluids. Studies have indicated that mixtures of hydrocarbons, e.g., 96% isobutane/4% hexane, will produce better utilization of a 180°C resource and in some instances lower LEC.

The performance of the binary system depends on a number of factors. Some plant designs incorporate multiple or staged boiling cycles, where the working fluid flow is split and boiling occurs at multiple pressures. In these cycles, multiple or staged turbines are required. The advantage of these cycles is the fact that the working fluid heat-addition process more closely matches the sensible cooling of the liquid geofluid (as shown on the T-Q or T-h diagram). This lowers temperature differences through the cycle, reducing cycle irreversibilities and increasing performance. The same effect can be achieved by heating the working fluid at supercritical pressures (pressures above the critical pressure). While the supercritical cycle will have higher component, material, and pumping costs because of higher operating pressures, they have fewer components because they are less complex than multiple boiling cycles. (In many cases, the maximum pressure can be kept below 600 psi with hydrocarbons such as isobutane.) Lowering the mean temperature difference in heat exchangers tends to require larger units so that capital costs are increased. In general, the LEC is reduced because the effects of increased performance more than outweigh the increase in capital cost.

The choice of the working fluid for the power cycle will also impact the cycle performance. In general, as resource temperature decreases, the more volatile fluids will produce more power per unit mass of geofluid. Power cycles using the more volatile fluids typically operate at higher pressures and have higher associated material and equipment cost. These higher costs may offset the gains in performance and produce higher LECs in some cases.

Working fluid mixtures have been shown to provide superior performance to the single component or pure working fluids. This performance improvement is due to the nonisothermal phase changes of this type of fluid at constant-pressure (both boiling and condensing), which allows the working fluid to match more closely the sensible cooling of the geofluid. More importantly in the reduction of irreversibilities, the desuperheating and condensing process more closely matches the sensible heating of cooling water or air in the heat-rejection process.

One additional type of binary cycle that has been proposed uses an ammonia-water mixture for the working fluid. A great deal of recuperative preheat of the working fluid is accomplished by splitting the duty of the geofluid, turbine exhaust, and preheated liquid flows through a more complex heat-transfer train than is shown in Figure 8.12.7. These systems are known as **Kalina systems**. In general, these systems do not change the composition of the mixture in the cycle as the Kalina cycle for applications such as is the case for gas turbine bottoming.

There is some consideration of using a binary cycle as a bottoming cycle for a flash steam or direct steam system. Similarly, a binary cycle could be used to bottom another binary system, perhaps with a different working fluid.

Design Considerations

The selection of the working fluid in binary cycles imposes safety considerations to be considered in the design of the power plant. Equipment and facility designs must take into account the flammable characteristic of the hydrocarbon working fluids.

The selection of materials of construction for the piping and components exposed to the geofluid will be resource specific. Typically, carbon steel is used for piping and pressure vessels. Turbines that use the steam directly may have stainless steel components, although the use of stainless may be limited by the presence of chlorides and the potential for stress cracking. The standard design for heat exchangers in binary cycles is for the geofluid to be on the tube side. This facilitates the cleaning of the exchanger if scaling or fouling occurs on the surfaces exposed to the geofluid. If the geofluid has a high scaling potential, components and piping should be designed to allow for periodic cleaning.

Direct Use of the Geothermal Resource

A number of direct-use applications of the heat in a geothermal resource have been successfully implemented. These include

1. Space conditioning (heating with the resource or a secondary fluid and cooling with heat pumps);
2. Heating of greenhouses;
3. Aquaculture;
4. Process heating (drying vegetable products);
5. Ground coupled heat pumps.

Although the United States is one of the world leaders for the production of electrical power from geothermal energy, other nations take the lead for the direct use of this energy source. In Iceland, over 85% of the buildings are supplied with heat and domestic hot water from geothermal systems (Ragnorson, 1995).

Typical direct-use applications are either closed systems with produced fluids being injected back into the geothermal reservoir or systems where the produced water is pure enough for beneficial use or disposal to surface waterways. Experience has shown that it is usually worthwhile to inject as much of the cooled fluid as possible back into the reservoir to maintain pressure and production rates.

Defining Terms

Binary system: A binary system that uses thermal energy from the geofluid to vaporize a secondary working fluid in a Rankine cycle.

Direct steam system: A geothermal energy conversion system that utilizes steam directly from a geothermal well.

Flashed steam system: A geothermal energy conversion system that utilizes steam flashed from the liquid geofluid.

Geopressurized resource: Naturally occurring reservoirs of hot pressurized fluid created by convection of water through hot porous rock.

Hydrothermal resource: Artificial reservoirs created by injecting water into hot dry rock in the earth's core.

Kalina system: A binary system using a mixture of ammonia and water as the working fluid in the power cycle.

Reference

Ragnorson, A. Iceland country update, in *Proceedings of the World Geothermal Congress, 1995*, Florence, Italy, May 1995, 145–161.

Further Information

Kestin, J. Ed., *Sourcebook on the Production of Electricity from Geothermal Energy,* U.S.DOE, DOE/RA/4051-1, Washington, D.C., 1980.
Lienau, Paul J. and Ben C. Lunis, Eds., *Geothermal Direct Use Engineering and Design Guidebook,* USDOE, Idaho Falls, ID, 1991.
Transactions of the Geothermal Resources Council, Vol. 1–19, (1977–1995), Geothermal Resources Council, Davis, CA.

8.13 Direct Energy Conversion

Solar Photovoltaic Cells

Kitt C. Reinhardt

Introduction

Solar photovoltaic cells convert sunlight directly into electrical energy via the collection of solar photon-generated semiconductor charge carriers. The collection of charge carriers within the cell produces a voltage across the terminals of the cell, called the **photovoltaic effect**, that can drive an external electrical circuit or charge a storage battery. Photovoltaic cells are useful in both space and terrestrial power applications. Silicon, Si, photovoltaic cells have provided the main source of electrical power to virtually all Earth-bound satellites since the advent of the space program in the late 1950s. In the early 1970s, photovoltaics generated a significant amount of interest for use in terrestrial power systems when oil supplies to the industrial world were disrupted. Today, while photovoltaic power remains the primary energy source for most communication and surveillance satellites, issues concerning system efficiency, reliability, and cost currently prevent its widespread use in residential and power utility applications. For example, in the United States the average price for conventional utility electricity is 6¢/kWhr, compared with ~35¢/kWhr for terrestrial photovoltaic electricity (Zweibel, 1995). Thus, the cost of photovoltaic power must be reduced by a factor of ~6 for it to become economically viable. At present, photovoltaic power is generally only cost-competitive for use in remotely located systems where conventional power is cost-prohibitive, such as in remote water-pumping and communications stations, signal and emergency lighting, and for village power. Factors that influence photovoltaic system energy costs include cell panel efficiency, total system lifetime, and cost per unit area. The present discussion will focus on issues concerning photovoltaic cells and panels. Detailed literature on power conditioning electronics and energy storage systems can be found elsewhere. A large number of different photovoltaic cell designs have been demonstrated by researchers over the years. However, the most common and practical cell designs are fabricated using single-crystal Si. Consequently, Si will be used to describe basic principles of semiconductors and photovoltaic cell operation.

Introduction to Semiconductors

We begin with a description of the concept of covalent bonding, valence electrons, and energy bands, which relates to conduction in semiconductors (Sze, 1981). The crystalline structure of Si is diamond, where each Si atom in the lattice is covalently bonded to four equidistant nearest neighbors that lie at the corners of a tetrahedron. Each Si atom has four electrons in its outer orbit, called valence electrons, and each atom shares these electrons with its four neighbors to form four covalent bonds. The atomic configuration of the 14 electrons of Si is $1s^2 2s^2 2p^6 3s^2 3p^2$. At practical temperatures, only the $3s^2 3p^2$ valence electrons contribute to the electrical conductivity; the $1s^22s2^2p^6$ core electrons are too tightly bounded to the nucleus to participate. In a simplified model, as N Si atoms are brought together at 0 K to form a crystal, two distinct and nearly continuous bands of electronic energy levels form that are separated by an energy gap called the semiconductor **band gap, E_g**. The resulting upper **conduction band** contains 4N states, as does the lower **valence band**. The 4N electrons that come from the Si $3s^23p^2$ states completely fill the 4N states in the valence band at 0 K, and the conduction band states are completely empty. Since there are no unoccupied states in the valence band for electrons to move and the conduction band is empty, Si is a perfect insulator at 0 K.

As the temperature of the crystal increases, electrons in the valence band gain sufficient thermal energy ($>E_g$) to be excited across the band gap into the conduction band, leaving holes (missing electrons) behind in the valence band. When current conduction in a semiconductor is dominated by thermally generated electrons and holes, it is called intrinsic. In this case, the resulting number of electrons per unit volume in the conduction band, n, equals the number of holes per volume in the valence band, p, that is $n = p = n_i$, where n_i is called the intrinsic carrier concentration. In the presence of an electric field, intrinsic electrons and holes gain kinetic energy and conduct electricity. However, since at room temperature n_i for Si is only 1.45×10^{10} cm^{-3}, compared with a free-electron density of more than 10^{22} cm^{-3} in metals, Si behaves as a very good insulator, i.e., electrical conductivity, σ, is given by $\sigma = q(n\mu_n + p\mu_p)$, where q is the electronic charge and μ is the respective carrier mobility.

In order to increase the conductivity to values useful for solid-state devices, the level of n and p can be increased by purposely adding impurity atoms into the crystal, called doping, that liberate extra electrons or holes. In the case of Si, which is in column IV of the periodic table, and hence has four valence electrons for bonding, doping is achieved using either column III elements (boron, aluminum, gallium, or indium), which have three valence electrons, or column V elements (phosphorus, arsenic, or antimony), which have five valence electrons. When an arsenic atom with five valence electrons replaces (substitutes) an Si atom, four of its electrons are used to form covalent bonds with the four neighboring Si atoms. The fifth electron is loosely bound to the arsenic nucleus, and at room temperature is ionized and "donated" to the conduction band. Arsenic is therefore called a donor, and Si becomes an n-type (mostly electrons) semiconductor. Similarly, when a boron atom with three valence electrons substitutes for an Si atom, one of the boron four covalent bonds becomes deficient of one electron. Boron can then accept one electron from the valence band to satisfy the bond requirement, which creates a positively charged hole in the valence band. Boron is therefore called an acceptor, and Si becomes a p-type (mostly holes) semiconductor. In this way the electrical conductivity of semiconductors can be precisely controlled by varying the concentration of donor and acceptor impurities. In practical solid-state devices, typical values of n and p range between 10^{15} and 10^{19} cm^{-3}.

The p-n Junction Diode

The p-n junction is a basic structure used for solid-state device rectification, amplification, and switching, as well as for photocarrier collection in photovoltaic cells. A p-n junction is formed when a p-type semiconductor is metallurgically joined with an n-type semiconductor (Streetman, 1980). Before they are joined, the p-material has a large concentration of holes and very few electrons, whereas the converse is true for the n-material. Upon joining the two materials, holes instantaneously diffuse from the p-side into the n-side and electrons diffuse from the n-side into the p-side. The transport of these carriers constitutes a "diffusion" current from the p-side to n-side; electron current is opposite in direction to electron flow by convention. As shown in Figure 8.13.1, negative acceptor ions are left behind as holes leave the p-side of the junction, creating a negative space-charge region (SCR), and positive donor ions are left behind as electrons leave the n-side of the junction, creating a positive SCR. Consequently, an electric field directed from the positive SCR to the negative SCR results that opposes the further diffusion of electrons and holes; i.e., the electric field creates a drift component of current from the n-side to p-side that opposes the diffusion component. In the absence of any external fields a condition of equilibrium is established, and the net current flow across the junction is zero. As will be discussed, the p-n junction electric field is also responsible for separating and collecting photon-generated carriers in photovoltaic cells.

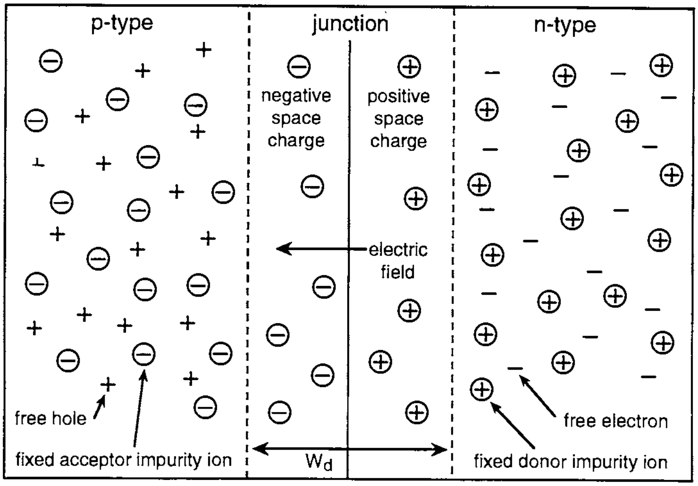

FIGURE 8.13.1 Schematic diagram illustrating an abrupt p-n junction with a uniform concentration of donor impurities in the n-region and acceptor impurities in the p-region.

When a voltage is applied across a p-n junction, the balance between the electron and hole drift and diffusion currents is disturbed and a net current results. Under forward bias, a positive voltage is applied to the p-side relative to the n-side, and the electric field across the junction is reduced; i.e., the electric field associated with the applied voltage subtracts from the zero-bias field. The reduced field enhances hole diffusion from the p-side to the n-side and electron diffusion from the n-side to the p-side, thereby increasing the "positive" current; the transport of current from the p-side to the n-side is positive by convention. Conversely, under reverse bias a negative voltage is applied to the p-side relative to the n-side, and the electric field across the junction increases. Consequently, the diffusion component of current decreases relative to the drift component, and a net "negative" current results across the junction.

The dark current-voltage (I-V) characteristics for an Si p-n junction are generally well described by the ideal Shockley diode equation (Sze, 1981),

$$I_D = I_o\left[\exp\left(qV/nkT\right) - 1\right] \tag{8.13.1}$$

where I_D is the junction dark current, I_o is the reverse saturation current, V is the forward-bias voltage, n is the diode ideality factor, and T is the absolute temperature. The value of n is ~1.0 when the current is dominated by carrier diffusion, but increases and approaches values of ~2 or greater when other current mechanisms become important, such as carrier recombination or tunneling. In high-quality Si p-n junction photovoltaic cells, the value of n is ~1.0 near the relevant operating voltage. The parameter I_o varies with T and E_g according to

$$I_o = qA\left[D_n n_p / L_n + D_p p_n / L_p\right] \propto T^3 \exp\left(-E_g/kT\right) \tag{8.13.2}$$

where A is the junction area and D_n and D_p, n_p and p_n, and L_n and L_p are the diffusion coefficients, minority carrier densities, and diffusion lengths for electrons and holes, respectively. The value of I_o decreases strongly as E_g increases, which, as will be shown, increases the photovoltage obtainable from a photovoltaic cell.

Cell Operation and Efficiency

Cell Operation. Photovoltaic energy conversion in a p-n junction is a two-step process where free electrons and holes (photocarriers) are generated in the semiconductor via the absorption of solar energy and then

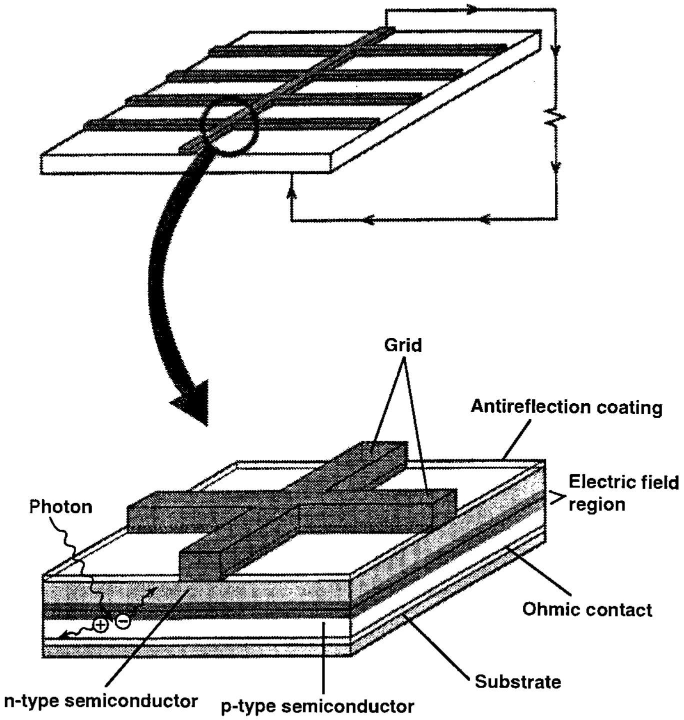

FIGURE 8.13.2 Schematic diagram of a typical p-n junction photovoltaic cell. (From Stone, J.L. *Phys. Today*, September 24, 1993. With permission.)

simultaneously collected across the junction (Fahrenbruch and Bube, 1983). Consider the schematic of a typical photovoltaic cell shown in Figure 8.13.2 which consists of a p-n junction formed very close to the top surface of the cell. Front metal ohmic contact grid fingers allow solar energy to pass into the absorber layers. The entire top surface is covered with an antireflection coating to minimize reflective losses, and the entire back surface is covered with an ohmic contact. The ohmic contacts form n and p region terminals that transfer (conduct) current from the semiconductor to the external circuit with a negligible amount of voltage drop.

When the photovoltaic cell is exposed to solar radiation, photons with energies greater than E_g (super-band-gap photons) are absorbed in the n and p layers, and free electrons and holes are generated via the breaking of covalent bonds. These electron-hole pairs, or **photocarriers**, are shown in Figure 8.13.1. The energy of the free photocarriers is converted directly into a current and voltage via photocarrier collection by the junction. The absorbed photons effectively contribute an energy E_g to the cell output, and energy greater than E_g is lost as heat. Photons with energies less than E_g (sub-band-gap photons) are transmitted through the cell. After generation, minority photocarriers, that is, holes on the n-side and electrons on the p-side, diffuse toward the edges of the junction due to a gradient of carriers that exists there. If the minority carriers are generated within a diffusion length, L, of the junction, they will reach it and be swept across it by the electric field of the junction. Hence, electrons are swept from the p-side to the n-side and holes from the n-side to the p-side, and thus they are separated. The minority carrier gradient present at the edges of the junction is due to the depletion of minority carriers that results from their transfer across the junction. The diffusion flux of minority carriers toward and across the junction constitutes a light-generated current, I_L, or photocurrent, that is directed from the n-side to the p-side of the cell. The build-up of positive holes on the p-side and negative electrons on the n-side gives rise to a **photovoltage** across the junction. The polarity of both the photovoltage and photocurrent is identical to that of a battery, and power is delivered from the junction to the external circuit.

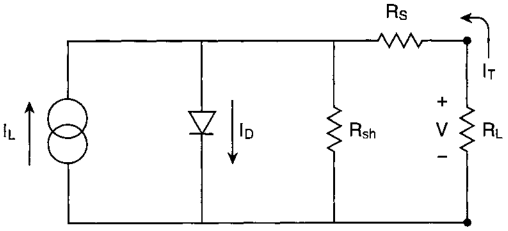

FIGURE 8.13.3 Schematic of equivalent circuit model for a p-n photovoltaic cell.

Cell Efficiency. In order to derive the solar conversion efficiency, it is convenient to model the photovoltaic cell as an ideal p-n diode in parallel with a **light-generated** (constant) **current** source, $\boldsymbol{I_L}$, as shown in the equivalent circuit of Figure 8.13.3. Parasitic series and shunt resistance losses, R_s and R_{sh}, respectively, are also shown, where R_s is due to ohmic contact and semiconductor resistances, and R_{sh} is due to defect-related carrier recombination and/or tunneling phenomena (Stirn, 1972). A qualitative expression for I_L is given by Tada et al. (1982):

$$I_L = qAG\left(L_n + W_d + L_p\right) \tag{8.13.3}$$

where G is the photocarrier generation rate in carriers/cm^3-sec due to solar photon absorption, which depends on E_g and the photon energy (wavelength) and intensity (concentration), and W_d is the sum of the negative and positive SCR widths. As mentioned, I_L is directed from the n-side to the p-side. In contrast, the dark diode current given by Equation (8.13.1) is directed oppositely from the p-side to the n-side. The **dark current** is due to the forward-bias photovoltage that appears across the cell p-n junction when it is illuminated. Thus, the dark current opposes the light current. In the ideal case, that is, when $R_s = 0$ and $R_{\text{sh}} = \infty$, the total forward current, I_T, is given by

$$I_T = I_D - I_L = I_o\left[\exp\left(qV/nkT\right) - 1\right] - I_L \tag{8.13.4}$$

A plot of dark and light current-voltage (I-V) curves resulting from Equation (8.13.1) and Equation (8.13.4), respectively, is shown in Figure 8.13.4 for a typical p-n solar cell. Under illumination, the forward-bias dark I-V curve is displaced downward into the fourth quadrant by the **photocurrent,** $\boldsymbol{I_L}$. It is noted from Figure 8.13.3 that the voltage drop across the load resistance, R_L, is $V = -I_T R_L$. Under short-circuit conditions, that is, when the n and p terminals are tied to each other, R_L is negligible. The resulting voltage drop across the p-n junction will also be negligible, and from Equation (8.13.1), $I_D \approx 0$. As shown in Figure 8.13.4, the resultant current is termed the **short-circuit current,** $\boldsymbol{I_{\text{sc}}}$, or $I_T = -I_{\text{sc}} = -I_L$. As the value of R_L increases, a voltage appears across the junction, $V = -I_T R_L$, called the **photovoltage**, and I_D increases in accordance with Equation 8.13.1. Under this condition the cell is operating in the fourth quadrant of the I-V characteristic (i.e., the junction voltage is positive and the current is negative), and, consequently, the cell delivers power (product of the current and voltage) to R_L. As the value of R_L continues to increase, so too does V and I_D. When the value of R_L approaches infinity, that is, under open-circuit conditions, I_D approaches I_L and I_T goes to zero. The resulting **open-circuit voltage,** $\boldsymbol{V_{\text{oc}}}$, is shown in Figure 8.13.4. V_{oc} can be obtained by setting $I_T = 0$ in Equation (8.13.4) and solving for V. For $V \gg \text{kT/q}$,

$$V_{oc} = nkT/q \ln\left[I_L/I_o\right] \tag{8.13.5}$$

Thus, the operating point on the I-V curve in the fourth quadrant can be swept from (I_{sc}, 0) to (0, V_{oc}) by varying the value of R_L. When the optimum load is chosen (i.e., $R_L \approx V_{\text{oc}}/I_{\text{sc}}$), approximately 80% of the product $I_{\text{sc}}V_{\text{oc}}$ can be extracted as useful power as shown by the shaded maximum-power rectangle

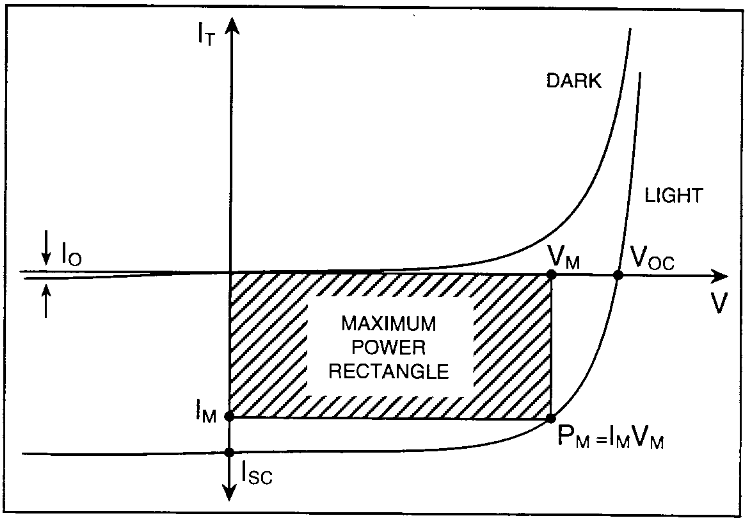

FIGURE 8.13.4 Typical dark and light current-voltage characteristics for a p-n photovoltaic cell.

in Figure 8.13.4. Also shown in Figure 8.13.4 are the parameters I_m and V_m, which correspond to values of current and voltage, respectively, that yield the maximum cell power, P_m, where $P_m = I_m V_m$. The knee that appears at P_m is due to the parasitic effects of R_s and R_{sh}. The curvature of the knee at P_m is described by the **fill factor**, **FF**, where

$$\mathrm{FF} = I_m V_m / I_{sc} V_{oc} \tag{8.13.6}$$

The photovoltaic cell **conversion efficiency**, **η**, is defined as

$$\eta = I_m V_m / P_{\mathrm{in}} A$$

or

$$\eta = FF\, I_{sc} V_{oc} / P_{\mathrm{in}} \tag{8.13.7}$$

where P_{in} is the incident power in W/m^2 equal to the sum in energy of the incident photons per time per area. Values for V_{oc}, I_{sc}, FF, and η can be obtained in the laboratory under various air mass conditions from light *I-V* curves measured using a carefully controlled (calibrated) light source to illuminate the cell.

Cell Material vs. Efficiency

The optimum value of material E_g for solar photovoltaic conversion is ~1.0 to 1.5 eV. To understand how the choice of cell material affects conversion efficiency, an ideal expression can be derived using Equation 8.13.4 for the theoretical conversion efficiency. The output power can be expressed as (Henry, 1980)

$$P = IV = I_o V\left[\exp\left(qV/nkT\right) - 1\right] - I_L V \tag{8.13.8}$$

The maximum output power is obtained when $dP/dV = 0$, and an expression for I_m and V_m can be obtained from Equation (8.13.8) and multiplied to give P_m, where

$$P_m = I_m V_m \approx I_L\left[V_{oc} - kT/q \ln\left(qV_m/kT + 1\right) - kT/q\right] \tag{8.13.9}$$

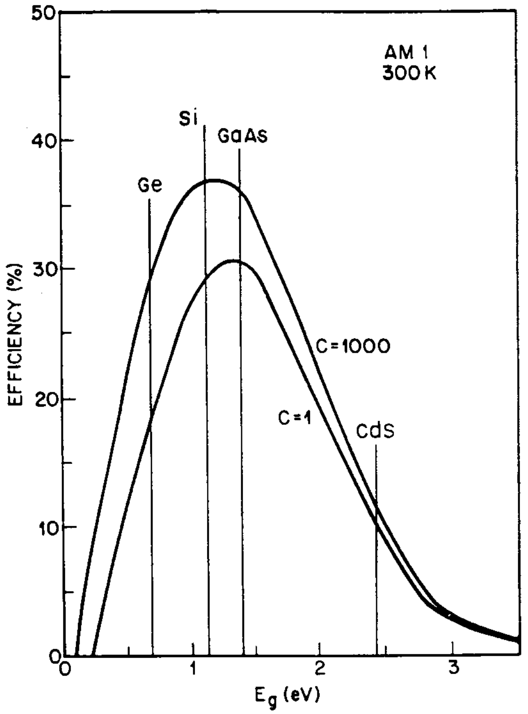

FIGURE 8.13.5 Theoretical AM1 efficiency vs. semiconductor band gap E_g for an ideal photovoltaic cell under 1 sun and 1000 suns concentrations. (From Henry, C.H., *J. Appl. Phys.*, 51, 4494, 1980. With permission.)

In practical cells, values for V_m and V_{oc} are typically $\frac{1}{2}E_g/q$ to $\frac{2}{3}E_g/q$. Thus, for materials with $E_g \sim 1 - 2$ eV, the quantity in the large brackets of Equation (8.13.9) becomes $\sim V_{oc}$, and the factors that determine I_L and V_{oc} also determine P_m. From Equation (8.13.2) and Equation (8.13.5), it is clear that V_{oc} increases with E_g through the reduction in I_o. In contrast, as E_g increases, I_L decreases because a smaller portion of the solar spectrum is energetic enough to be absorbed; i.e., I_L is the product of q and the number of available photons with energy greater than E_g. Hence, for a given solar spectrum there is an optimum value of E_g that maximizes the product of V_{oc} and I_L. A plot of ideal AM1 conversion efficiency vs. E_g is shown in Figure 8.13.5 for "one sun" (925 W/m^2) and "1000 suns" (925 kW/m^2) concentrations (Henry, 1980). The efficiency curves were obtained using Equation (8.13.1) through Equation (8.13.7) at 300 K. A maximum in efficiency occurs for $E_g \sim 1.0 - 1.5$ eV.

Manufacture of Cells and Panels

There are basically five important solar cell design concepts, and each offers a trade-off between efficiency and cost: (1) Large-area single-crystal planar cells, typically 1 × 1 cm^2 to 6 × 6 cm^2, yield high efficiencies under normal light conditions, 2) single-crystal small-area concentrator cells, typically less than 1 × 1 cm^2, are potentially less costly and yield higher efficiencies under concentrated light, i.e., concentration ratios of 20 to 1000 are typical; (3) more-complex single-crystal multijunction cells yield the highest efficiencies measured to date, but are substantially more expensive; (4) cells made from polycrystalline materials are less expensive than single-crystalline cells, but are less efficient; and (5) cells made from thin film amorphous materials provide the lowest-cost approach yet, but are generally less efficient than polycrystalline cells.

A typical 15% 4 × 4 cm^2 photovoltaic cell produces only ~0.25 W under AM1.5 conditions. Therefore, individual cells must be electrically wired together to form larger submodules or panels to increase the total output power. The cells can be connected in series to increase the total voltage or in parallel to increase the current. The modular nature of photovoltaic power allows the design of systems that can deliver electrical power from a few watts to many megawatts. In terrestrial applications the cells are typically supported and held in place with a rigid substrate, i.e., typically aluminum, Plexiglas, fiberglass, or glass, and are encapsulated with glass or a polymeric material; in space applications the support structure may be rigid or flexible, and the cells are protected from the space environment with quartz cover slides. The electrical power generated by the cells is conducted to an electrical load or storage battery. Metal interconnects soldered to the ohmic contacts of the cells conduct electrical current from one cell to the next. Current is then conducted from the network of series- and parallel-connected cells by wires to a distribution terminal "bus" that transfers the power to either the load or battery.

Single-Crystal Cells. The p-n photovoltaic cells made from **single-crystal** Si dominate in space and terrestrial applications because of their high efficiency and reliability. The formation of single-crystal p-type Si results from the selective cooling of pure molten Si to form large cylindrical crystal ingots, called boules, from which thin wafers are sliced and polished. The p-type impurities, usually boron, are added to the melt, to give the desired impurity concentration. A large-area p-n junction is then formed by diffusion of n-type impurity atoms, usually phosphorus. Front and back metal ohmic contacts and an antireflection coating are then formed using standard photolithography thermal evaporation or sputtering techniques (Sze, 1985). The resulting cell structure is shown in Figure 8.13.2, and typical cell areas range from 1 to 36 cm^2. Different semiconductors absorb sunlight more efficiently than others, described by a factor called the absorption coefficient. Si has a relatively small absorption coefficient compared with other materials, such as InP, GaAs, and amorphous-Si, and consequently requires an absorption layer thickness of ~100 μm to maximize conversion efficiency. Conventional Si cells have a thickness on the order of 250 μm, but can be chemically or mechanically polished to a thickness of 100 μm.

Single-crystal III-V photovoltaic cells, such as InP and GaAs, are made from elements in the III and V columns of the periodic table. The band gaps of these cells, 1.35 and 1.42 eV, respectively, are close to the optimum value. These materials involve the growth of single-crystal semiconductor layers upon a single-crystal semiconductor substrate. This technique is called epitaxy and it provides a method to produce both n-type and p-type layers to form the p-n junction. Epitaxial growth of n and p layers is required for InP and GaAs because diffusion of impurities at high temperatures is confounded by the high vapor pressure of the material. The formation of ohmic contacts and antireflection coating employ the same techniques as used for Si cells. The required absorption layer thickness for these cells is only a few microns because of their large absorption coefficients. However, issues concerning yield and mechanical strength limit their minimum thickness to ~100 μm The best reported efficiencies for single-crystal Si, GaAs, and InP cells under AM1.5 conditions are 24, 25, and 22%, respectively (Green et al., 1995).

Polycrystalline Cells. In the case of **polycrystalline** Si cells, molten Si is directly deposited into either cylindrical or rectangular ingots. As the material solidifies, individual crystalline regions form that are separated by grain boundaries which contain large numbers of structural defects. When the cell is illuminated, these defects capture a portion of the light-generated electron-hole pairs through recombination processes before they can reach the junction and be collected. Thus, the grain boundaries diminish the light-generated current and overall efficiency of the cell. However, polycrystalline silicon cells are sufficiently inexpensive to be commercially viable (Stone, 1993). An area that requires improvement is the slicing of polycrystalline ingots, where yields as low as 50% are common. An approach that eliminates the expense of sawing and polishing altogether is the growth of polycrystalline Si directly into the form of thin ribbons using a technique called edge-defined film-fed growth (EFG) (Fahrenbruch and Bube, 1983). In this approach, a carbon die with a slot-shaped aperture is immersed in a crucible of molten Si. The liquid Si wets the die and flows through the slot where it cools and is pulled to form a thin ribbon. This material also has high crystalline defect densities, but has good overall yields. An additional approach involves the growth of films of nearly single-crystal quality, where two parallel supporting dendrites form the boundaries of a web or ribbon pulled from a supercooled melt of Si. The best efficiency for polycrystalline Si cells under AM1.5 conditions is ~18%; that for Si cells grown by the EFG technique is 14%; and that for Si dendritic web cells is 15.5% (Stone, 1993). It is important to note that although these lower-cost films yield lower cell efficiencies compared with single-crystal cells, the cost of cells depends on the cost of the starting material and the cost per watt is more important than efficiency (Zweibel, 1995).

Thin Film Cells. Thin films cells provide an even lower-cost (and lower-efficiency) approach because they require a very small amount of semiconductor. An excellent review on thin film photovoltaic technologies, particularity on present and future cost issues, is given by Zweibel (1995). The general approach involves depositing only a few microns of material on a low-cost substrate using various vacuum deposition techniques, although a multitude of other deposition techniques have also been demonstrated. The top thin film cell candidates are amorphous Si, a-Si, cadmium telluride, CdTe, and copper indium diselenide, CIS (and related alloys). The highest reported thin film AM1.5 efficiencies are 17% for CIS, followed by 15.8% for CdTe, and ~11% for a-Si (Zweibel, 1995). However, the relative level of maturity of each design for commercial application must be put into perspective. While the best CIS cell efficiency is quite high, the best CIS square foot panel efficiency reported back in 1988 was, and still is today, only 11%. Significant manufacturing problems have plagued the CIS cell, and currently it is still not commercially available. CdTe is believed to be the easiest of the thin film cells to fabricate, and probably represents the closest to large-scale commercialization. Two U.S. companies have publicly announced CdTe manufacturing plants, and commercial efficiencies are likely to be in the range of 6 to 8% in the first plants. The future of a-Si cells is currently believed to be limited if it cannot overcome a 10% efficiency at the module level. Development problems include electrochemical instability to light that results in a 20 to 40% degradation. However, it appears that the use of multijunction thin film a-Si layers may solve the problem, and modules of 7 to 9% are expected in the near term.

Concentrator Cells. Photovoltaic modules are typically either of the flat plate or concentrator configuration. Flat plate modules can be fixed with respect to the sun or mounted to track the sun in one or two axis. Concentrator modules use large-area mirrors or lenses to concentrate sunlight onto smaller-area cells. Concentrator cells operate at higher efficiencies. However, concentrator modules require one- or two-axis tracking which adds system complexity and cost that generally offsets the module efficiency and lower area cost benefits. The increase in conversion efficiency with illumination intensity is shown in the 1000-sun concentration curve of Figure 8.13.5. Values for I_L increase linearly with concentration through the factor G in Equation (8.13.3) and V_{oc} increases logarithmically with concentration through I_L in Equation (8.13.5). Under solar concentration of "20 suns" or greater, a significant amount of cell heating can occur. While J_{sc} increases slightly with increasing temperature, values of V_{oc} and FF drop strongly. Thus, on adequate heat sink or active cooling is required at high concentrations. The reported AM1.5 efficiency for Si cells increases from 24 to 26.5% under a concentration of 255; and that for GaAs cells increases from 25 to 27.6% under a concentration of 140 (Green et al., 1995).

Multijunction Cells. Another approach to increase photovoltaic cell efficiency is through the use of multijunction tandem solar cells. A multijunction solar cell consists of a stack of three or four layers of light-sensitive semiconductor material, successively grown atop one another, that optimally converts the sun's light energy into electricity. Each layer in the stack absorbs a different portion of the solar spectrum, which is determined by its electronic bandgap, E_g. Generally, the top layer absorbs the ultraviolet light, the middle layer absorbs the visible, and the bottom layer(s) absorb the infrared. The trick to maximizing multijunction solar cell conversion efficiency is finding the optimum combination of semiconductor layers that have the right bandgap and can be grown atop each other. Current practice multijunction solar cells utilize a three-junction, two-terminal device configuration, where three p-n junctions are epitaxially grown atop each other on an inactive substrate as shown in Figure 8.13.6. The top p-n junction has the highest seminconductor bandgap, E_{g1}, in the stack and absorbs photons with energies $\geq E_{g1}$. The middle p-n junction has a bandgap of E_{g2}, and absorbs photons with energies E, where $E_{g1} < E < E_{g2}$. The bottom p-n junction has a bandgap of E_{g3}, and absorbs photons with energies $E_{g2} < E < E_{g3}$. The values for semiconductor E_{g1}, E_{g2}, and E_{g3} must be chosen to achieve both maximum solar absorption and current mathcing; i.e., the three p-n junctions must generate equal electrical currents when illuminated. The current state-of-practice triple junction solar cell consists of a $GaInP_2/GaAs/Ge$ design, having

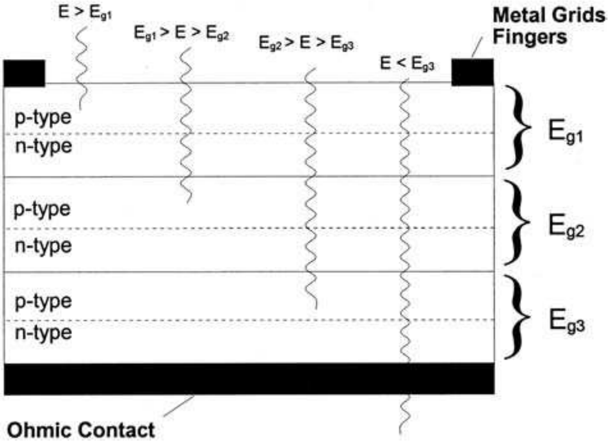

FIGURE 8.13.6 Schematic diagram of a triple junction solar photovoltaic cell under illumination.

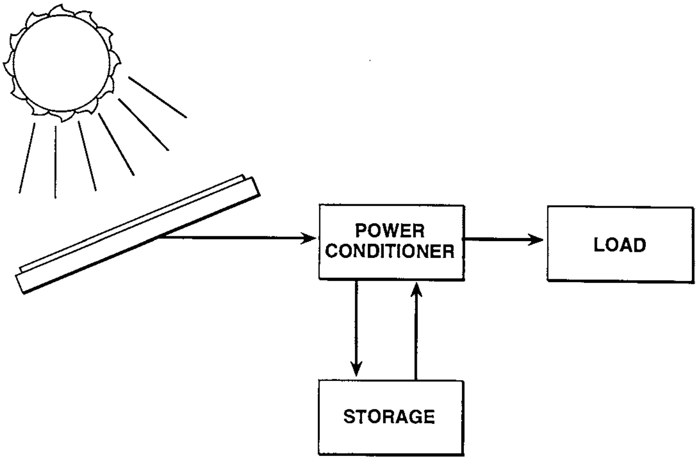

FIGURE 8.13.7 Schematic diagram depicting the basic components of a typical photovoltaic power system.

the bandgap combination of $E_{g1} = 1.9$ eV ($GaInP_2$), $E_{g2} = 1.4$ eV (GaAs) and $E_{g3} = 0.7$ eV (Ge). Large area (30 cm^2) $GaInP_2$/GaAs/Ge solar cell conversion efficiencies range from 26 to 28% in space (AM0 spectrum) and 31% on the ground (AM1.5 spectrum). Today, the primary use for multijunction solar cells is in space power applications, due to their relatively high cost compared to lower cost, lower efficiency silicon solar cells that dominate in terrestrial applications.

Design of a Photovoltaic Generating System

A schematic diagram depicting the basic components of a typical photovoltaic power generation system is shown in Figure 8.13.7 (Pulfrey, 1978). The system includes a photovoltaic array that consists of many smaller submodules, each containing many hundreds or thousands of photovoltaic cells. The DC output power from the array is controlled by a power conditioning unit that contains an inverter for developing AC power and an input power tracking device to maintain the optimal array load to achieve maximum output power. Power is directly fed to the electrical load and/or storage system by the conditioning unit. The storage system is needed to save energy when power is generated in excess of the immediate demand, or when the load demand exceeds the immediate generation level. Total photovoltaic power system efficiency is the product of the efficiencies of the individual components. Typical efficiencies for the power conditioning unit (determined by the inverter) and energy storage system are about 95% and

50-80%, respectively. Thus, an array efficiency of 10% would result in a total system efficiency of about 5 to 8%, and a total system efficiency of 10% would require an array efficiency in excess of 13%.

Defining Terms

Band gap (E_g): The difference in energy between the energy level of the bottom of the conduction band and the energy level of the top of the valence band.

Conduction band: A range of allowable energy states in a solid in which electrons can move freely.

Conversion efficiency (η): The ratio of the available power output photovoltaic cell to the total incident radiant power.

Dark current: Any current that flows through the p-n junction in the absence of external irradiation.

Fill factor (ff): The ratio of the maximum photovoltaic cell output power to the product of the open-circuit voltage and short-circuit current.

Light-generated current (I_L): The electrical current obtained from an illuminated p-n junction resulting from the collection of photocarriers across the junction.

Open-circuit voltage (V_{oc}): The voltage obtained across the terminals of an illuminated p-n photovoltaic cell under open-circuit conditions.

Photocarriers: Electrons and holes generated within a semiconductor via the absorption of photon energy.

Photocurrent: Synonymous with light-generated current.

Photovoltaic effect: The production of a voltage difference across a p-n junction resulting from the absorption of photon energy.

Photovoltage: The voltage resulting from the photovoltaic effect.

Polycrystalline: A material characterized by an array or agglomerate of small single-crystal sections of various crystal orientations separated from one another by grain boundaries, which are localized regions of very severe lattice disruptions and dislocations.

Short-circuit current (I_{sc}): The electrical current measured through the terminals of an illuminated p-n photovoltaic cell under short-circuit conditions.

Single crystal: A material characterized by a perfect periodicity of atomic structure; the basic arrangement of atoms is repeated throughout the entire solid.

Valence band: A range of allowable energy states in a solid crystal in which lie the energies of the valence electrons that bind the crystal together.

References

Fahrenbruch, A.L. and Bube, R.H. 1983. *Fundamentals of Solar Cells — Photovoltaic Solar Energy Conversion,* Academic Press, New York.

Green, M.A., Emery, K., Bucher, K., and King, D.L. 1995. *Short communication: solar cell efficiency tables (version 5), Prog. Photovoltaics Res. Dev.*, 3, 51–55.

Henry, C.H. 1980. Limiting efficiency of ideal single and multiple energy gap terrestrial solar cells, *J. Appl. Phys.,* 51, 4494.

Pulfrey, D.L. 1978. *Photovoltaic Power Generation,* Van Nostrand Reinhold, New York.

Stirn, R.J. 1972. *Junction characteristics of Si solar cells,* in Proceedings of the 9th IEEE Photovoltaics Specialists Conference, p.72.

Stone, J.L. 1993. Photovoltaics: unlimited electrical power from the sun, *Phys. Today,* Sepember, 22–29.

Streetman, B.G. 1980. *Solid State Electronic Devices,* Prentice-Hall, Englewood Cliffs, NJ.

Sze, S.M. 1981. *Physics of Semiconductor Devices,* 2nd ed., John Wiley & Sons, New York.

Sze, S.M. 1985. *Semiconductor Devices: Physics and Technology,* John Wiley & Sons, New York, 341–457.

Tada, H.Y., Carter, J.R., Anspaugh, B.E., and Downing, R.G. 1982. *Solar Radiation Handbook.* JPL Publication 82-69, 2-11

Zweibel, K. 1995. *Thin Films: Past, Present, Future.* NREL/IP-413-7486 Publication (DOE UC Category 1260 DE95004084).

Further Information

An excellent presentation of the basic theory of the various photovoltaic cell designs is given in *Fundamentals of Solar Cells: Photovoltaic Solar Energy Conversion*, by Alan L. Fahrenbruch and Richard H. Bube. This text covers the basics of solar insolation, semiconductors, p-n junctions, and single-crystal, polycrystalline, thin film, and concentrator photovoltaic cells.

An excellent review of the progress achieved in terrestrial and space photovoltaics can be traced in the *Proceedings of the IEEE (Institute of Electrical and Electronics Engineers) Photovoltaics Specialists Conference* (PVSC) that dates back to 1961. These proceedings include thousands of papers that address nearly every aspect of photovoltaic cell development: basic theory, design, fabrication, and application.

The monthly journal *Solar Energy Materials and Solar Cells* covers many aspects of improving device efficiency, reducing costs, and testing and applications.

The monthly journal *Progress in Photovoltaics* documents recent results of research work conducted in photovoltaics worldwide. This journal is an excellent source for currently reported cell conversion efficiencies.

Proceedings of the conference *Space Photovoltaics Research and Technology* is an excellent source for the reader interested in the development of photovoltaics for use in space.

Fuel Cells

D. Yogi Goswami

Introduction

A *fuel cell* is an electrochemical device in which a fuel and an oxidant react in such a controlled manner that the chemical energy of reaction is converted directly into electrical energy. Ordinarily, a fuel reacts violently with an oxidant in a combustion reaction resulting in the release of heat of combustion. The heat of combustion can, then, be converted into electrical energy via mechanical work with the constraint of the second law of thermodynamics. The overall efficiency of the series of conversion processes is of the order of 40%. A fuel cell bypasses these processes resulting in potential efficiencies of the order of 80%. As an example, when hydrogen is burned in an atmosphere of oxygen it results in the following reaction:

$$H_2 + \frac{1}{2}O_2 \rightarrow H_2O + \Delta H \quad \text{(heat of reaction)} \tag{8.13.10}$$

In this reaction, two hydrogen atoms bond with an oxygen atom by sharing their electrons with the outermost orbit of oxygen, which becomes full, resulting in a stable structure.

The reactants H_2 and O_2 may be combined to form the same product (H_2O) by first stripping the electrons away from the hydrogen atoms and allowing the electrons to pass through an external circuit before combining with oxygen.

$$H_2 \rightarrow 2H^+ + 2e^- \quad \text{(electrons)} \tag{8.13.11}$$

$$2H^+ + O + 2e^- \rightarrow H_2O \tag{8.13.12}$$

Figure 8.13.8 shows a schematic of an arrangement that would allow the above reaction to proceed.

In order for the above reactions to occur according to the schematic of Figure 8.13.8:

1. Electrodes must be porous to let the fuel and electrolyte penetrate.
2. The electrolyte must be permeable to H^+ and $(OH)^-$ ions.
3. Electrode materials must be catalysts for the reaction (Pt, Ni, etc.).

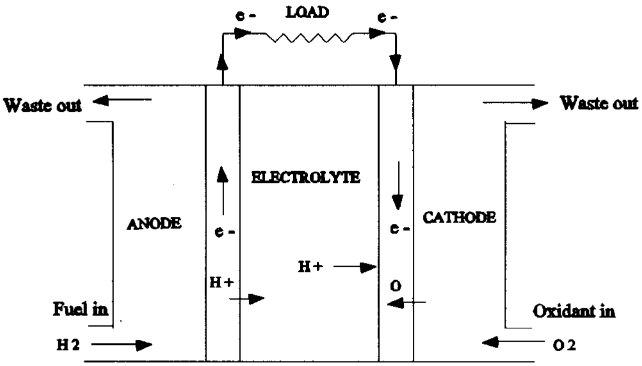

FIGURE 8.13.8 Conceptual schematic of a hydrogen fuel cell.

In 1839, William Grove, an English investigator, constructed a chemical battery in which he noticed that the water-forming reaction of hydrogen and oxygen generated an electrical current. However, it was not until 50 years later that two English chemists, Ludwig Mond and Carl Langer, developed a device they actually called a fuel cell (Angrist, 1982). There has been a strong resurgence in research and development of fuel cells in the last four decades.

Thermodynamic Performance

The energy released or needed in any chemical reaction (ΔH) is equal to the difference between the enthalapy of formation of the products and the reactants.

$$\Delta H = \sum (\Delta H)_{\text{products}} - \sum (\Delta H)_{\text{reactants}} \tag{8.13.13}$$

In an exothermic reaction the change in enthalpy of formation (ΔH) is negative. Table 8.13.1 gives values of ΔH for various compounds at 25°C at 1 atm. All naturally occurring elements have a ΔH value of zero.

In a combustion reaction all of the change in the enthalpy of formation (ΔH) is converted to heat and is, therefore, called the higher heating value (HHV).

$$-(\Delta H)_{\text{reaction}} = \text{HHV of fuel} \tag{8.13.14}$$

For example, for complete combustion of hydrogen according to the following reaction:

$$H_2 + \frac{1}{2}O_2 \rightarrow H_2O \quad (\text{liquid}) \tag{8.13.15}$$

TABLE 8.13.1 Enthalty of Formation ΔH^0 and Gibbs Free Energy ΔG^0 of Compounds at 1 atm and 298 K

Compound or Ion	Enthalpy of Formation, ΔH^0, J/kg · mol	Gibbs Free Energy ΔG^0, J/kg · mol
CO	-110.0×10^6	-137.5×10^6
CO_2	-394.0×10^6	-395.0×10^6
CH_4	-74.9×10^6	-50.8×10^6
Water	-286.0×10^6	-237.0×10^6
Steam	-241.0×10^6	-228.0×10^6
C, H_2, O_2	0	0
O(g)	$+249.2 \times 10^6$	$+231.8 \times 10^6$
H(g)	$+218.0 \times 10^6$	$+203.3 \times 10^6$

Source: Adapted from Wark, K., *Thermodynamics*, McGraw–Hill, New York, 1988. With permission.

Change in the enthalpy of formation is

$$\Delta H = \Delta H_{\mathrm{H_2O}} - \Delta H_{\mathrm{H_2}} - \frac{1}{2}\left(\Delta H_{\mathrm{O_2}}\right) = \left(-286 \times 10^{6}\right) - 0 - 0 = -286 \times 10^{6} \text{ J/kg} \cdot \text{mol H}_2 \quad (8.13.16)$$

In a fuel cell, most of ΔH can be converted to electricity directly. The part that cannot be converted to work directly gets converted into heat. The minimum amount that must be converted to heat is represented by reversible heat transfer $\int T\, dS$. If a fuel cell operates isothermally, the maximum amount of electrical work (W_e) produced is given by

$$W_e, \max = \Delta H - T\Delta S \quad (8.13.17)$$

In an irreversible reaction

$$W_e, \max < \Delta H - T\Delta S \quad (8.13.18)$$

Gibbs free energy, G, is given by:

$$G = H - TS \quad (8.13.19)$$

Therefore, in a reversible isothermal process

$$\Delta G = \Delta H - T\Delta S = W_e, \max \quad (8.13.20)$$

The actual electrical work in a fuel cell is given by

$$W_e \le \Delta G \quad \text{(change in Gibbs free energy for the reaction)} \quad (8.13.21)$$

$$\Delta G_{\text{reaction}} = \sum (\Delta G)_{\text{products}} - \sum (\Delta G)_{\text{reactants}} \quad (8.13.22)$$

The electrical work, W_e, is associated with the work of electrons passing through an external resistance. 1 g · mol of electrons is equal to Avogadro's number (6.022×10^{23}) and the charge of these electrons is equal to 96,439 C which is called a **faraday** (F). If n g · mols of electrons are generated and E is the internal reversible cell voltage, then the maximum electrical work is given by

$$W_e, \max = \Delta G = -nFE \quad (8.13.23)$$

denoting values under standard conditions (25°C, 1 atm) by superscript 0, we have

$$\Delta G^0 = -nFE^0 \quad (8.13.24)$$

Values of G^0 for various compounds are given in Table 8.13.1. For fuel cell reactions as below:

$$aA + bB \rightarrow cC + dD \quad (8.13.25)$$

if the reactants (A and B) and the products (C and D) are assumed to be ideal gases with partial pressures P_A, P_B, P_C, and P_D the change in Gibbs free energy ΔG and the internal reversible cell voltage, E, are given by

$$\Delta G = \Delta G^0 + R_u T \ln \frac{(P_C)^c (P_D)^d}{(P_A)^a (P_B)^b} \tag{8.13.26}$$

$$E = E^0 + \frac{R_u T}{nf} \ln \frac{(P_A)^a (P_B)^b}{(P_C)^c (P_D)^d} \tag{8.13.27}$$

where R_u is the universal gas constant. Equation 8.13.27 is also called the Nernst equation.

Table 8.13.2 gives typical electrochemical reactions in fuel cells.

TABLE 8.13.2 Electrochemical Reactions in Fuel Cells

Fuel Cell	Anode Reaction	Cathode Reaction	Overall Reaction
Proton exchange	$H_2 \rightarrow 2H^+ + 2e^-$	$½O_2 + 2H^+ + 2e^- \rightarrow H_2O$	$H_2 + ½O_2 \rightarrow H_2O$
Alkaline	$H_2 + 2(OH)^- \rightarrow 2H_2O + 2e^-$	$½O_2 + H_2O + 2e^- \rightarrow 2(OH)^-$	$H_2 + ½O_2 \rightarrow H_2O$
Phosphoric acid	$H_2 \rightarrow 2H^+ + 2e^-$	$½O_2 + 2H^+ + 2e^- \rightarrow H_2O$	$H_2 + ½O_2 \rightarrow H_2O$
Molten carbonate	$H_2 + CO_3^= \rightarrow H_2O + CO_2 + 2e^-$	$½O_2 + CO_2 + 2e^- \rightarrow CO_3^=$	$H_2 + ½O_2 + CO_2$ (cathode)
	$CO + CO_3^= \rightarrow 2CO_2 + 2e^-$		$\rightarrow H_2O + CO_2$ (anode)
Solid oxide	$H_2 + O^- \rightarrow H_2O + 2e^-$	$½O_2 + 2e^- \rightarrow O^-$	$H_2 + ½O_2 \rightarrow H_2O$
	$CO + O^- \rightarrow CO_2 + 2e^-$		$CO + ½O_2 \rightarrow CO_2$
	$CH_4 + 4O^- \rightarrow 2H_2O + CO_2 + 8e^-$		$CH_4 + 2O_2 \rightarrow H_2O + CO_2$

Source: Hirschenhofer, J.H. et al., *Fuel Cells, A Handbook*, rev. 3, Gilbert/Commonwealth, Morgantown, WV, 1994. With permission.

Table 8.13.3 gives Nernst equations for the electrochemical reactions listed in Table 8.13.2.

TABLE 8.13.3 Fuel Cell Reactions and the Corresponding Nernst Equations

Cell Reactions	Nernst Equation
$H_2 + ½O_2 \rightarrow H_2O$	$E = E^0 + (RT/2F)\ln[P_{H_2}(P_{O_2})^{1/2}/P_{H_2O}]$
$H_2 + ½O_2 + CO_2(c) \rightarrow H_2O + CO_2(a)$	$E = E^0 + (RT/2F)\ln[P_{H_2}(P_{O_2})^{1/2}(P_{CO_2})_c/(P_{H_2O}(P_{CO_2})_a)]$
$CO + ½O_2 \rightarrow CO_2$	$E = E^0 + (RT/2F)\ln[P_{CO}(P_{O_2})^{1/2}/P_{CO_2}]$
$CH_4 + 2O_2 \rightarrow 2H_2O + CO_2$	$E = E^0 + (RT/8F)\ln[P_{CH_4}(P_{O_2})^2/P^2_{H_2O}P_{CO_2}]$

Note: (a) = anode; (c) = cathode; E = equilibrium potential.

Source: Hirschenhofer, J.H. et al., *Fuel Cells, A Handbook*, Gilbert/Commonwealth, Morgantown, WV, 1994. With permission.

The maximum conversion efficiency of a fuel cell is given by

$$\eta_{\max} = \frac{W_e, \max}{\Delta H} = \frac{\Delta G}{\Delta H} = 1 - \frac{T\Delta S}{\Delta H} = \frac{-nFE}{\Delta H} \tag{8.13.28}$$

As current is drawn through an external circuit, the actual voltage drop (V) will be less than the internal cell voltage (E). Therefore, the actual conversion efficiency of a fuel cell will be lower than above and may be calculated as

$$\eta_{\text{actual}} = \frac{-nFV}{\Delta H} = \frac{ItV}{\Delta H} \tag{8.13.29}$$

where I is the current drawn through an external circuit for a period of time, t.

Types of Fuel Cells

Fuel cells are primarily classified by type of electrolyte, since many characteristics, particularly operating temperatures, are limited by the electrolyte properties (Hirschenhofer et al., 1994). Major fuel cells under active development at this time are the **phosphoric acid fuel cell** (PAFC), the **molten carbonate fuel cell** (MCFC), the **solid oxide fuel cell** (SOFC), the **polymer electrolyte membrane fuel cell** (PEMFC), and the **alkaline fuel cell** (AFC).

Phosphoric Acid Fuel Cell. PAFC uses concentrated phosphoric acid (H_3PO_4) as the electrolyte, hydrogen as the fuel, and oxygen (from air) as the oxidant. Table 8.13.4 provides information on the electrodes and other materials for PAFC as well as other fuel cells.

The reactions take place at the porous electrodes on highly dispersed electrocatalyst Pt particles supported on carbon black and a polymeric binder, usually polytetrafluoroethylene (PTFE) (about 30 to 50% by weight) (Kinoshita et al., 1988; Hirschenhofer et al., 1994). A porous carbon paper substrate provides structural support for the electrocatalyst and serves as the current collector. A typical carbon paper electrode impregnated with the electrocatalyst has a porosity of about 60%, consisting of micropores of about 34 Å diameter and macropores of 3 to 50 μm diameter.

Dipolar plates (usually graphite) are used to separate the individual cells and electrically connect them in series in a fuel cell stack. In PAFC stacks, provisions are included to remove the waste heat, by liquids (usually water) or gases (usually air) which flow through channels provided in the cell stack.

Molten Carbonate Fuel Cells. MCFCs use as electrolytes mixtures of molten carbonates of lithium (Li_2CO_3), potassium (K_2CO_3), and sodium (Na_2CO_3) in proportions as shown in Table 8.13.4. The operating temperature of the cell (~650°C) is higher than the melting temperature of the carbonate electrolytes. Besides H_2 (fuel) and O_2 (oxidant from air), the cell uses CO_2 which transfers from the cathode to the anode according to the reactions in Table 8.13.2.

According to the reactions, 1 g · mol of CO_2 is transferred along with 2 g · mol of electrons ($2F$). The reversible potential for an MCFC, taking into account the transfer of CO_2, is given by the Nernst equation in Table 8.13.3.

It is usual practice to recycle the CO_2 generated at the anode to the cathode where it is consumed. An early process used to fabricate electrolyte structures involved hot processing mixtures of $LiAlO_2$ and alkali carbonates at temperatures slightly below the melting point of carbonates. These electrolyte structures had problems of void spaces, nonuniformity of microstructure, poor mechanical strength, and high iR drop. To overcome these problems, processes have been developed recently that include tape casting (Maru et al., 1984; Hirschenhofer et al., 1994) and electrophoretic deposition (Baumgartner et al., 1985; Hirschenhofer et al., 1994).

Increasing the operating pressures results in enhanced cell voltages. Increasing the operating temperature above 550°C also enhances the cell performance. However, beyond 650°C the gains are diminished and the electrolyte loss and material corrosion are increased. Therefore, 650°C is about the optimum operating temperature.

Solid Oxide Fuel Cell. SOFCs offer a number of advantages over MCFCs for high-temperature operation, since there is no liquid electrolyte. Solid electrolyte allows flexibility in cell shape design based on application. Cells of several shapes, as shown in Figure 8.13.9, are being developed. Because of the high temperature of operation (~1000°C) carbon monoxide (CO) and hydrocarbons such as methane (CH_4) can be used as fuels. At 1000°C, these fuels can easily produce H_2 that is used at the anode by steam reforming and water-gas reactions as

$$CO + H_2O \rightarrow CO_2 + H_2 \quad \text{(water-gas)} \tag{8.13.30}$$

$$CH_4 + H_2O \rightarrow CO + 3H_2 \quad \text{(steam reforming)} \tag{8.13.31}$$

TABLE 8.13.4 Cell Components for Various Fuel Cells

Component	PAFC	MCFC	SOFC[b]	PEMFC	AFC
Anode	• PTFE-bonded Pt/C • Vulcan XC-72[a] • 0.1 mg Pt/cm^2	• Ni-10 wt% Cr • 3–6 µm pore size • 50–70% initial porosity • 0.5–1.5 mm thickness • 0.1–1 m^2/g	• Ni/ZrO$_2$ cermet[c] (30 mol% Ni) • Deposit slurry • 12.5 × 10^{-6} cm/cm °C • ~150 µm thickness • 20–40% porosity	• 10% Pt thin film	• Dual Porosit Ni • 16 µm max pore on electrolyte side • 30 µm pore on gas side
Cathode	• PTFE-bonded Pt/c • Vulcan XC-72[a] • 0.5 mg Pt/cm^2	• Lithiated NiO • 7–15 µm pore size • 60–65% after lithiation and oxidation • 70–80% initial porosity • 0.5–0.75 mm thickness • 0.5 m^{2}g	• Sr-doped lanthanum manganite (10 mol% Sr) • Deposit slurry, sinter • ~1 mm thickness • 12 × 10^{-6} cm/cm °C expansion from room temperature to 1000°C[d] • 20–40% porosity	• 10% Pt thin film	• Porous lithinated NiO
Electrode support	• Carbon paper	—	—	• Carbon paper with Teflon coating on one side	
Electrolyte support	• PTFE-bonded SiC	• γ-LiAlO$_2$ • 0.1–12m^2/g • 0.5 mm thickness	—	—	—
Electrolyte[a]	• 100% H$_3$PO$_4$	• 62 Li-38 K • 50 Li-50 Na • 50 Li-50 K • Tape cast • 0.5 mm thickness	• Yttria-stabilized ZrO$_2$ (8 mol% Y) • EVD[d] • 10.5 × 10^{-6} cm/cm °C expansion from room temperature to 1000°C[d] • ~40 µm thickness	• Proton conducting membrane of perfluoro sulfonic acid polymer	• KOH (45% to 85%)

[a] Conductive oil furnace black, product of Cabot Corp. Typical properties: 002 d-spacing of 3.6 Å by X-ray diffusion, surface area of 220 m^2/g by nitrogen adsorption, and average particle size of 30 µm by electron microscopy.

[b] Specifications for Westinghouse SOFC.

[c] Y$_2$O$_3$ stabilized ZrO$_2$.

[d] EVD = electrochemical vapor deposition.

Source: Hirschenhofer, J.H. et al., *Fuel Cells, Handbook,* Gilbert/Commonwealth, Morgantown, WV, 1994. With permission.

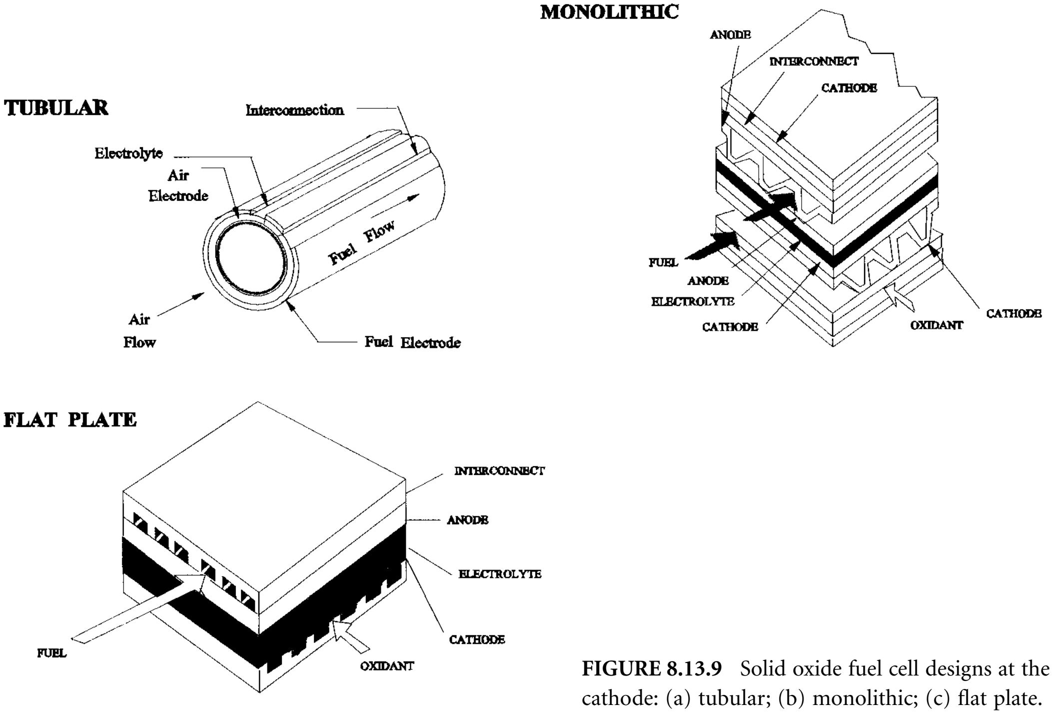

FIGURE 8.13.9 Solid oxide fuel cell designs at the cathode: (a) tubular; (b) monolithic; (c) flat plate.

Because of very high operating temperatures the choice of cell materials is limited by (1) chemical stability in oxidizing and reducing atmosphere; (2) chemical stability of contacting materials; and (3) conductivity and thermomechanical compatibility. A detailed description of the current status is given by Minh (1991; 1993) and Appleby and Foulkes (1989). Present SOFC designs make use of thin film wall concepts where films of electrodes, electrolyte, and interconnect material are deposited on each other and sintered to form cell structure. Electrochemical vapor deposition (EVD) is now used to deposit thin layers.

Increasing pressure and temperature enhances the performance of SOFC.

Polymer Electrolyte Membrane Fuel Cell. The basic cell consists of a proton-conducting membrane such as perfluoro sulfonic acid polymer sandwiched between two Pt-impregnated porous electrodes. The backs of the electrodes are made hydrophobic by coating with Teflon®, which provides a path for gas to diffuse to the catalyst layer.

The electrochemical reactions for PEMFC are similar to PAFC as given in Table 8.13.2.

The protons from the anode diffuse through the membrane with the help of water molecules soaked in the membrane. The cell operates at low temperature (80°C) and can have very high current densities. Therefore, the cell can be made very compact and can have fast start. There are no corrosive fluids (acids or alkalis) in the cell. Because of these attributes the cell is particularly suited for vehicle-power operation. Present research includes investigation of using methanol and natural gas as the fuel for the cell.

Alkaline Fuel Cell. Alkaline electrolytes have faster kinetics, which allows the use of non-noble metal electrocatalysts. However, AFCs suffer a drastic performance loss if CO_2 is present in the fuel or the oxidant, for example, air. Therefore, AFCs are restricted for use where pure H_2 and O_2 can be used. They have been used in the past in the space program.

Fuel Cell Performance

The performance of fuel cells is affected by the operating variables (e.g., temperature, pressure, gas composition, reactant utilization, and current density) and other factors that influence the reversible cell potential (impurities) and the magnitude of the irreversible voltage losses (polarization, contact resistance, exchange current).

The cell voltage (V_{cell}) is given by

$$V_{\text{cell}} = E - iR - \mu_p \tag{8.13.32}$$

where i is the current through the cell, R is the cell resistance, and μ_p is the polarization loss.

Current Density. Current density has a major impact on the cell voltage. Figure 8.13.10 shows how various losses affect the current-voltage characteristics.

Temperature and Pressure. Increase in pressure generally has a beneficial effect on the cell performance. Increased reactant pressure increases gas solubility and mass transfer rates. In addition, electrolyte loss due to evaporation is decreased.

Theoretically, the reversible potential of an H_2/O_2 fuel cell decreases with an increase in temperature. The practical effect of temperature is mixed, as shown in Figure 8.13.11.

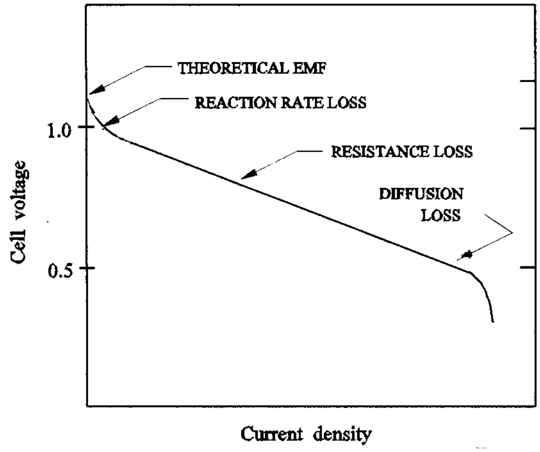

FIGURE 8.13.10 Losses affecting current-voltage characteristics.

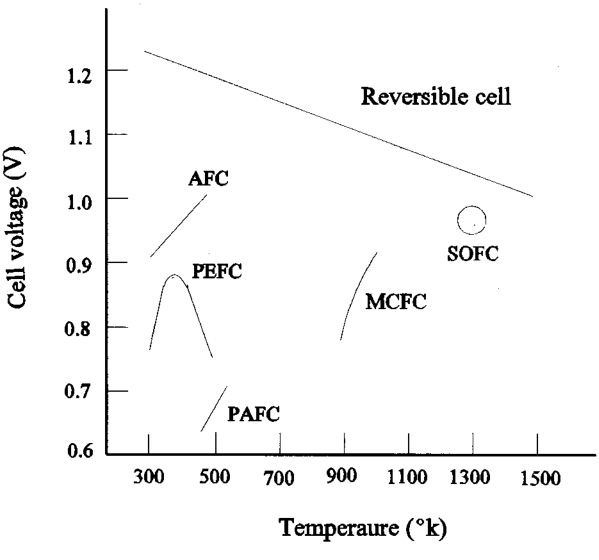

FIGURE 8.13.11 Dependence of the initial operating cell voltage of typical fuel cells on temperature. (From Simons, R.B. et al., in *Symposium Proceedings Fuel Cells Technology Status and Applications,* E.H. Camara, Ed., Institute of Gas Technology, Chicago, 1982. With permission.

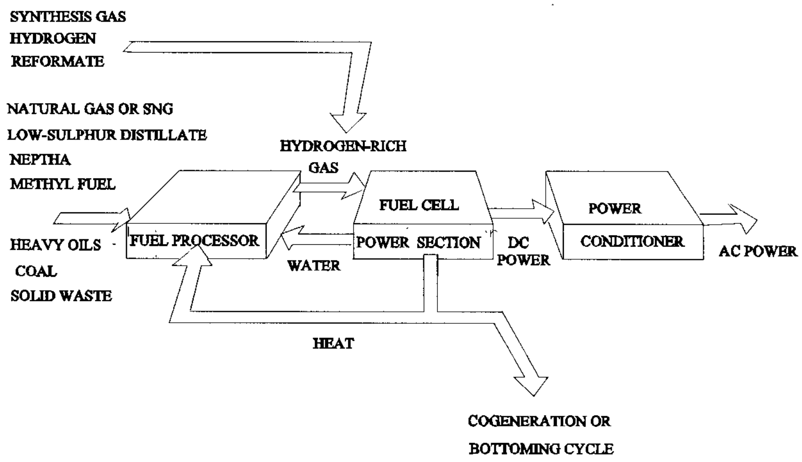

FIGURE 8.13.12 Basic fuel cell power system.

Fuel Cell Power Systems

A general fuel cell power system consists of a fuel processor, fuel cell stack, power conditioner, and possibly a cogeneration or bottoming system to utilize the rejected heat. A schematic of a basic system is shown in Figure 8.13.12.

Fuel Processors. If pure hydrogen is available, no additional fuel processor is needed. However, in most applications hydrogen needs to be generated from other fuels, such as natural gas, methane, methanol, etc.

Natural Gas Processing. Natural gas is mostly methane (CH_4) with small amounts of other hydrocarbons. It can be converted to H_2 and CO in a steam-reforming reactor according to Equation (8.13.31). Fuels are typically steam reformed at temperatures of 760 to 980°C.

Liquid Fuel Processing. Liquid fuels such as distillate, naphtha, diesel oil, and fuel oil can be reformed by noncatalytic partial oxidation of the fuel by oxygen in the presence of steam with flame temperatures of 1300 to 1500°C.

Nomenclature

E = internal cell voltage
F = Faraday, charge of 1 g-mol of electrons
G = Gibbs free energy
H = enthalpy
ΔH = heat of reaction, enthalpy of formation
I = current
n = number of g-mol
P = Pressure
R = gas constant
S = entropy
t = time
T = temperature
V = voltage drop
W_e = electrical work

Superscript

0 = values under standard conditions — 25°C, 1 atm

Defining Terms

Alkaline fuel cell (AFC): A fuel cell using KOH as the electrolyte.
Faraday: Change of 1 g · mol of electrons, which equals 96,439 C.
Molten carbonate fuel cell (MCFC): A fuel cell using molten carbonate as the electrolyte.
Phosphoric acid membrane fuel cell (PAMFC): A fuel cell using phosphoric acid as the electrolyte.
Polymer electrolyte fuel cell (PEFC): A fuel cell using Zerconia as the electrolyte.
Solid oxide fuel cell (SOFC): A fuel cell using potassium as the electrolyte.

References

Angrist, S.W. 1982. Chapter 8, in *Direct Energy Conversion.* Allyn and Bacon, Boston.

Appleby, A.J. and Foulkes, F.R. 1989. *Fuel Cell Handbook,* Van Nostrand Reinhold, New York.

Baumgartner, C.E., DeCarlo, V.J., Glugla, P.G., and Grimaldi, J.J. 1985. *J. Electrochem. Soc,* 132, 57.

Farooque, M. 1990. ERC, Development on Internal Reforming Carbonate Fuel Cell Technology, Final Report, prepared for United States DOE/METC, DOC/MC/23274-2941, pp. 3–19, October.

Hirschenhofer, J.H., Stauffer, D.B., and Engleman, R.R. 1994. *Fuel Cells, A Handbook,* rev. 3. Prepared by Gilbert/Commonwealth, Inc., under U.S. DOE Contract No. DE-AC01-88FE61684, United States Department of Energy, Office of Fossil Energy, Morgantown, WV.

Kinoshita, K., McLarnon, F.R., and Cairns, E.J. 1988. *Fuel Cells, A Handbook.* Prepared by Lawrence Berkeley Laboratory for the United States DOE under contract DE-AC03765F00098.

Maru, H.C., Paetsch, L., and Piegeaud, A. 1984. In *Proceedings of the Symposium on Molten Carbonate Fuel Technology,* R.J. Selman and T.D. Claar, Eds., The Electrochemical Society, Pennington, NJ, p. 20.

Minh, N.Q. 1991. High-temperature fuel cells, Part 2: The solid oxide cell, *Chem. Tech.,* 21, February.

Minh, N.Q. 1993. Ceramic fuel cells, *J. Am. Ceram. Soc.,* 76(3), 563–588.

Pigeaud, A., Skok, A.J., Patel, P.S., and Maru, H.C. 1981. *Thin Solid Films,* 83, 1449.

Wark, K. 1988. *Thermodynamics*, McGraw-Hill, New York, p. 873.

Further Information

Information presented in this section borrows heavily from Hirschenhofer et al. (1994) which lists original references of works published by thousands of researchers across the world. For those references and further information, readers are referred to the *Fuel Cell* handbooks by Hirschenhofer, Stauffer, and Engleman (1994), and Appleby and Foulkes (1989), listed in the References section.

Thermionic Energy Conversion

Mysore L. Ramalingam

Introduction

Thermionic energy conversion (TEC) is the process of converting heat directly to useful electrical work by the phenomenon of thermionic electron emission. This fundamental concept can be applied to a cylindrical version of the planar converter, considered the building block for space nuclear power systems (SNPS) at any power level. Space nuclear reactors based on TEC can produce power in the range of 5 kWe to 5 MWe, a spectrum that serves the needs of current users such as National Aeronautics and Space Administration (NASA), United States Air Force (USAF), United States Department of Energy (USDOE), and Ballistic Missile Defense Organization (BMDO). Electrical power in this range is currently being considered for commercial telecommunication satellites, navigation, propulsion, and planetary exploration missions.

The history of thermionic emission dates back to the mid-1700s when Charles Dufay observed that electricity is conducted in the space near a red-hot body. Although Thomas Edison requested a patent in the late 1800s, indicating that he had observed thermionic electron emission while perfecting his electric light system, it was not until the 1960s that the phenomenon of TEC was adequately described

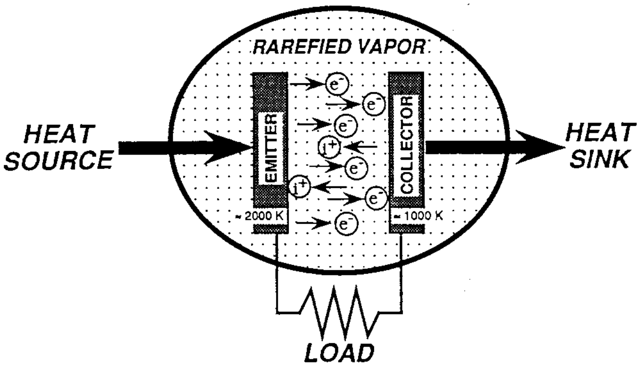

FIGURE 8.13.13 Schematic of an Elementary TEC.

theoretically and experimentally (Hatsopoulos and Gryftopoulos, 1973). These pioneering activities have led to the development of thermionic SNPS that could potentially be augmented by Brayton and Stirling cycle generators to produce additional power from waste heat in NASA manned lunar and martian exploration missions (Ramalingam and Young, 1993).

Principles of Thermionic Energy Conversion

Figure 8.13.13 represents a schematic of the essential components and processes in an elementary thermionic converter (TC). Electrons "boil-off" from the emitter material surface, a refractory metal such as tungsten, when heated to high temperatures (2000 K) by a **heat source**. The electrons then traverse the small interelectrode gap, to a colder (1000 K) collector surface where they condense, producing an output voltage that drives the current through the electrical load and back to the emitter. The flow of electrons through the electrical load is sustained by the temperature difference and the difference in **surface work functions** of the electrodes.

Surface Work Function. In a simple form, the energy required to separate an electron from a metal surface atom and take it to infinity outside the surface is termed the electron work function or the work function of the metal surface. The force experienced by an electron as it crosses an interface between a metal and a rarefied vapor can be represented by the **electron motive, Ψ,** which is defined as a scalar quantity whose negative gradient at any point is a measure of the force exerted on the electron at that point (Langmuir and Kingdon, 1925). At absolute zero the kinetic energy of the **free electrons** would occupy quantum energy levels from zero to some maximum value called the Fermi level. Each energy level contains a limited number of free electrons, similar to the electrons contained in each electron orbit surrounding the nucleus of an atom. Fermi energy, μ, corresponds to the highest energy of all free electrons at absolute zero. At temperatures other than absolute zero some of the free electrons begin to experience energies greater than that at the Fermi level. Thus, the electron work function Φ, would be defined as

$$\Phi = \Psi_T - \mu \tag{8.13.33}$$

where Ψ_T represents the electron motive or energy at some temperature, T, above absolute zero.

Interelectrode Motive Distribution. Figure 8.13.14 provides a schematic representation of the electron motive distribution in the interelectrode space of a thermionic converter. Under ideal conditions of particle transport, the motive varies linearly from Ψ_{EM}, the motive just outside the emitter, to Ψ_{CO}, the motive outside the collector surface. The magnitudes of the Fermi energies of the emitter and collector relative to Ψ_{EM} and Ψ_{CO} are clearly indicated. The internal voltage drop of the converter is defined as;

$$\Delta V = \left(\Psi_{EM} - \Psi_{CO}\right)/e \tag{8.13.34}$$

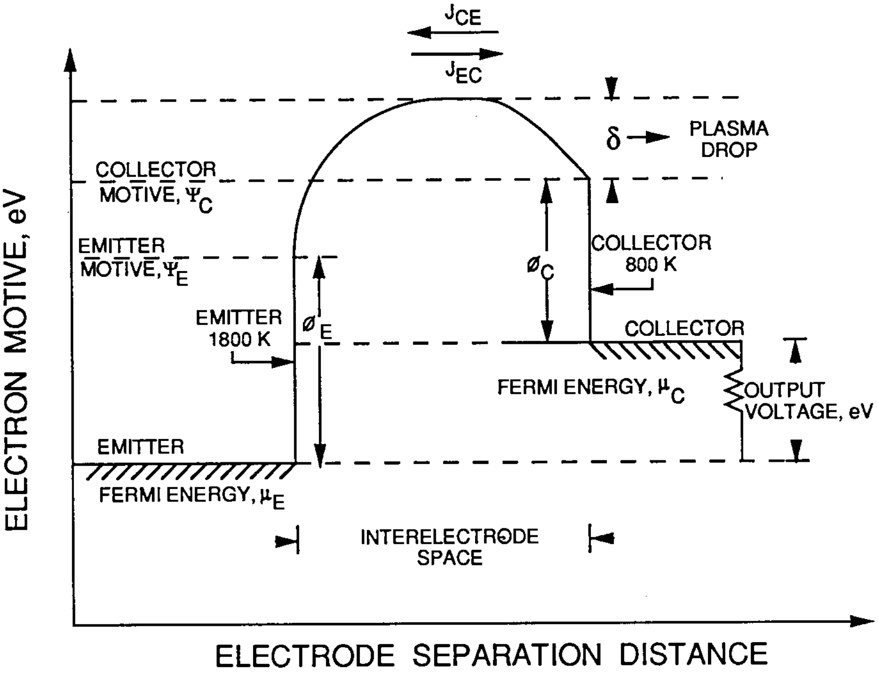

FIGURE 8.13.14 Electron motive distribution in the interelectrode gap.

In a conventional thermionic converter, the emitter and collector are not at the same temperature, but to a good approximation, the output voltage, neglecting **lead losses** and **particle interaction losses**, can be represented by the relationship.

$$V = \left(\mu_{\mathrm{CO}} - \mu_{\mathrm{EM}}\right)/e \tag{8.13.35}$$

Since a real thermionic converter has an ionizing medium to improve its performance, a similar motive distribution can be defined for the ions. It is sufficient to state that the ion interelectrode motive has a slope equal and opposite to the corresponding electron interelectrode motive. The ions are, therefore, decelerated when the electrons are accelerated and vice versa.

Electron Saturation Current. In the absence of a strong influence from an external electrical source, the electron current ejected from a hot metal at the emitter surface into the vacuum ionizing medium is termed the *electron saturation current.* As this quantity depends on the number of free electrons $N(\varepsilon_x)$, Fermi-Dirac statistics provide the means to compute the number of free electrons, $N(\varepsilon_x)\, d\varepsilon_x$, incident on a unit area within the metal in unit time with energies corresponding to the motion normal to the area, between ε_x and $\varepsilon_x + d\varepsilon_x$. For energies greater than the Fermi energy, the functional dependence of $N(\varepsilon_x)$ on ε_x is given by (Fowler, 1955)

$$N\left(\varepsilon_x\right) \approx \left[4\pi m_e kT/h^3\right]\left[\exp\left\{-\varepsilon_x - \mu/kT\right\}\right] \tag{8.13.36}$$

where m_e is the mass of the electron = 9.108×10^{-28} g and h is Planck's constant = 4.140×10^{-15} eV · sec.

The electron saturation current density, J_{sat}, for a uniform surface, is found by integrating $N(\varepsilon_x)$ in the range of ε_x from Ψ_T to infinity for all $\Psi_T - \mu > kT$, which is the case for almost all materials and practical temperatures. The result of the integration yields

$$J_{\mathrm{sat}} = AT^2 \exp\left[-\left(\Psi_T - \mu\right)/kT\right] \tag{8.13.37}$$

or

$$J_{\text{sat}} = AT^2 \exp\left[-(\Phi)/kT\right] \tag{8.13.38}$$

where A is the Richardson constant ≈ 120 A/cm² · K².

Equation (8.13.38), which is the most fundamental and important relationship for the design of a thermionic converter, is called the Richardson-Dushmann equation (Richardson, 1912). On similar lines, the ion saturation current density for a converter with an ionizing medium is given by the relationship (Taylor and Langmuir, 1933):

$$\tilde{J}_{\text{iSat}} = ep_g \Big/ \left[\left(2\pi m_g kT_g\right)^{0.5}\left(1 + 2\exp\left\{\left(V_i - \Phi/kT\right)\right\}\right)\right] \tag{8.13.39}$$

where p_g, T_g, m_g, and V_i are the pressure, temperature, mass, and first ionization energy, respectively, of the ionizing medium.

Types of Thermionic Converters

Thermionic converters can be broadly classified as vacuum thermionic converters and vapor thermionic converters, depending on the presence of an ionizing medium in the interelectrode gap. In vacuum thermionic converters the interelectrode space is evacuated so that the space is free of particles other than electrons and the two electrodes are placed very close together, thereby neutralizing the negative space charge buildup on the electrode surface and reducing the total number of electrons in transit. Due to machining limitations, vacuum converters have been all but completely replaced by vapor-filled thermionic converters. In vapor-filled thermionic converters, the interelectrode space is filled with a rarefied ionizing medium at a vapor pressure generally on the order of 1 to 10 torr. The vapor generally used is cesium as it is the most easily ionized of all stable gases and this can be provided through an external two-phase reservoir or an internal graphite reservoir (Young et al., 1993). The vapor neutralizes the negative space charge effect by producing positive ions at the electrode surfaces and gets adsorbed on the surfaces, thereby altering the work function characteristics.

Converter Output Characteristics

Figure 8.13.15 represents the output current-voltage characteristics for various modes of operation of the vacuum and vapor-filled thermionic converters. Characteristics obtained by not considering particle interactions in the interelectrode gap are generally considered ideal output characteristics. The figure essentially displays three types of converter output current-voltage characteristics, an ideal characteristic, an ignited mode characteristic, and an unignited mode characteristic. For an ideal converter in the interelectrode space the net output current density consists of the electron current density, J_{EMCO} flowing from emitter to collector diminished by the electron current density J_{COEM} flowing from collector to emitter and the ion-current density $\tilde{J}_{i\text{EMCO}}$ flowing from emitter to collector. Thus,

$$J_{\text{net}} = J_{\text{EMCO}} - J_{\text{COEM}} - \tilde{J}_{i\text{EMCO}} \tag{8.13.40}$$

By expressing the individual terms as functions of ϕ, T, and V,

$$\begin{aligned} J_{\text{net}} = {} & AT_{\text{EM}}^2 \exp\left[-\left(\Phi_{\text{EM}}/kT_{\text{EM}}\right)\right] - AT_{\text{CO}}^2 \exp\left[-\left(\Phi_{\text{EM}} - eV\right)/kT_{\text{CO}}\right] \\ & - \tilde{J}_{\text{EMS}} \exp\left[-\left(\Psi_{\text{EM}} - \Psi_{\text{CO}}\right)kT_{\text{EM}}\right] \end{aligned} \tag{8.13.41}$$

$$\text{for} \quad eV < \Phi_{\text{EM}} - \Phi_{\text{CO}}$$

Similar relationships can be generated for various types of thermionic converters.

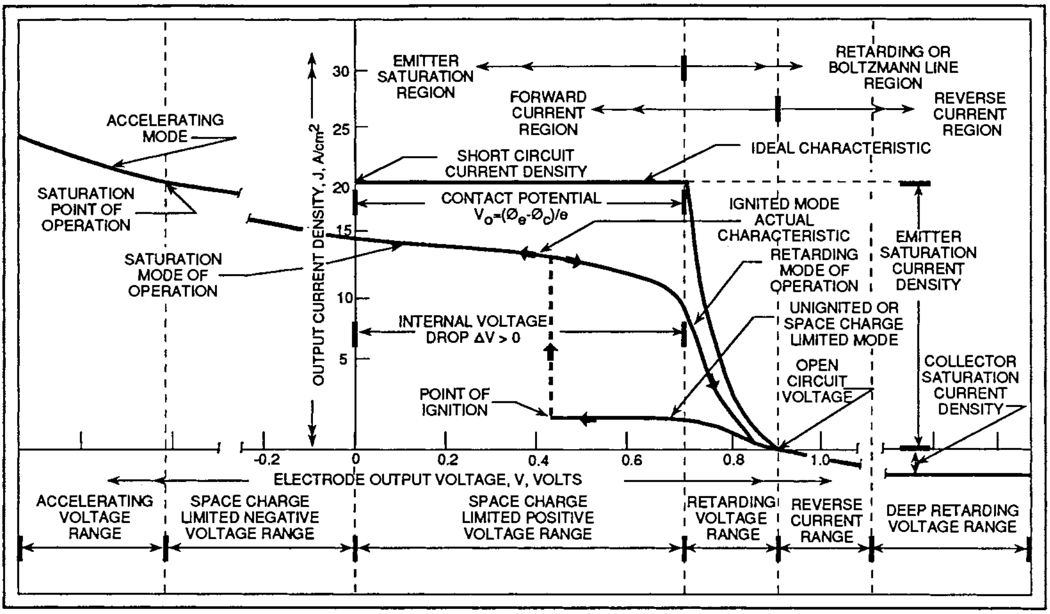

FIGURE 8.13.15 Thermionic diode output current density characteristics and nomenclature.

Thermodynamic Analysis

In thermodynamic terms a thermionic converter is a heat engine that receives heat at high temperature, rejects heat at a lower temperature, and produces useful electrical work while operating in a cycle analogous to a simple vapor cycle engine. Based on the application of the first law of thermodynamics to the control volumes around the emitter (Houston, 1959; Angrist, 1976),

$$\text{Energy In} = \text{Energy Out} \tag{8.13.42}$$

i.e.,

$$q_{\text{CB}} + q_{\text{JH}} + q_{\text{HS}} = q_{\text{EC}} + q_{\text{WB}} + q_{\text{CD}} + q_{\text{RA}} \tag{8.13.43}$$

where, by using the terminology in Figure 8.13.14, each of the terms in Equation (8.13.43) can be elaborated as follows:

(a) Energy supplied by back emission of the collector:

$$q_{\text{CB}} = J_{\text{COEM}}\left[\Phi_{\text{CO}} + \delta + V + \left(2kT_{\text{CO}}/e\right)\right] \tag{8.13.44}$$

(b) Energy supplied by joule heating of lead wires and plasma:

$$q_{\text{JH}} = 0.5\left[J_{\text{EMCO}} - J_{\text{COEM}}\right]^2\left(R_{\text{LW}} + R_{\text{PL}}\right) \tag{8.13.45}$$

(c) Energy dissipated by electron cooling:

$$q_{\text{EC}} = J_{\text{EMCO}}\left[\Phi_{\text{CO}} + \delta + V - \Phi_{\text{EM}} + \left(2kT_{\text{EM}}\right)/e\right] \tag{8.13.46}$$

(d) Energy dissipated due to phase change by electron evaporation:

$$q_{\mathrm{WB}} = J_{\mathrm{EM}}\Phi_{\mathrm{EM}} \tag{8.13.47}$$

(e) Energy dissipated by conduction through the lead wires and plasma:

$$q_{\mathrm{CD}} = \Delta T\left[\left(K_{\mathrm{LW}}A_{\mathrm{LW}}/A_e L_{\mathrm{LW}}\right) + \left(K_{\mathrm{PL}}A_{\mathrm{PL}}/A_e L_{\mathrm{IG}}\right)\right] \tag{8.13.48}$$

Here, K represents thermal conductivity, LW = lead wires, PL = plasma, and IG = interelectrode gap.

(f) Energy dissipated by radiation from emitter to collector:

$$q_{\mathrm{RA}} = 5.67\times 10^{-12}\left(T_{\mathrm{EM}}^{2} - T_{\mathrm{CO}}^{4}\right)\left(\varepsilon_{\mathrm{EM}}^{-1} + \varepsilon_{\mathrm{CO}}^{-1} - 1\right)^{-1} \tag{8.13.49}$$

Substitution for the various terms in Equation (8.13.42) yields q_{Hs}, the energy supplied to the emitter from the heat source.

The thermal efficiency of the thermionic converter is now expressed as

$$\eta_{\mathrm{TH}} = \left[V\left(J_{\mathrm{EMCO}} - J_{\mathrm{COEM}}\right)/q_{\mathrm{HS}}\right] \tag{8.13.50}$$

Design Transition to Space Reactors — Concluding Remarks

All the fundamentals discussed so far for a planar thermionic converter can be applied to a cylindrical version which then becomes the building block for space power systems at any power level. In a thermionic reactor, heat from the nuclear fission process produces the temperatures needed for thermionic emission to occur. The design of a thermionic SNPS is a user-defined compromise between the required output power and the need to operate reliably for a specified lifetime. Based on the type of contact the emitter has with the nuclear fuel, the power systems can be categorized as "in-core" or "out-of-core" power systems. At this stage it suffices to state that the emitter design for in-core systems is extremely complex because of its direct contact with the hot nuclear fuel.

Defining Terms

Electron motive: A scalar quantity whose negative gradient at any point is a measure of the force exerted on an electron at that point.

Free electrons: Electrons available to be extracted from the emitter for thermionic emission.

Heat source: Electron bombardment heating of the emitter.

Lead losses: Voltage drop as a result of the built-in resistance of the leads and joints.

Particle interaction losses: Voltage drop in the interelectrode gap as a result of particle collisions and other interactions.

Surface work function: A measure of the electron-emitting capacity of the surface.

Thermionic energy conversion: Energy conversion from heat energy to useful electrical energy by thermionic electron emission.

References

Angrist, S.W. 1976. *Direct Energy Conversion,* 3rd ed., Allyn and Bacon, Boston.

Fowler, R.H. 1955. *Statistical Mechanics,* 2nd ed., Cambridge University Press, New York.

Hatsopoulos, G.N. and Gyftopoulos, E.P. 1973. *Thermionic Energy Conversion,* Vol. 1, MIT Press, Cambridge, MA.

Houston, J.M. 1959. Theoretical efficiency of the thermionic energy converter, *J. Appl. Phys.*, 30:481–487.

Langmuir, I. and Kingdon, K.H. 1925. Thermionic effects caused by vapors of alkali metals, *Proc. R. Soc. London, Ser. A*, 107:61–79.

Ramalingam, M.L. and Young, T.J. 1993. The power of thermionic energy conversion, *Mech. Eng.*, 115(9):78–83.

Richardson, O.W. 1912. Some applications of the electron theory of matter, *Philos. Mag.*, 23:594–627.

Taylor, J.B. and Langmuir, I. 1933. The evaporation of atoms, ions and electrons from cesium films on tungsten, *Phys. Rev.*, 44:423–458.

Young, T.J., Thayer, K.L., and Ramalingam, M.L. 1993. Performance simulation of an advanced cylindrical thermionic fuel element with a graphite reservoir, presented at 28th AIAA Thermophysics Conference, Orlando, FL.

Further Information

Hatsopoulos, G.N. and Gryftopoulos, E.P. 1979. *Thermionic Energy Conversion*, Vol. 2, MIT Press, Cambridge, MA.

Cayless, M.A. 1961. Thermionic generation of electricity, *Br. J. Appl. Phys.*, 12:433–442.

Hernquist, K.G., Kanefsky, M., and Norman, F.H. 1959. Thermionic energy converter, *RCA Rev.*, 19:244–258.

Rasor, N.S. 1960. Figure of merit for thermionic energy conversion, *J. Appl. Phys.*, 31:163–167.

Ramalingam, M.L. 1993. The Advanced Single Cell Thermionic Converter Program, WL-TR-93-2112, USAF Technical Report, Dayton, OH.

Thermoelectric Power Conversion

Jean-Pierre Fleurial

Introduction

The advances in materials science and solid-state physics during the 1940s and 1950s resulted in intensive studies of thermoelectric effects and related applications in the late 1950s and through the mid-1960s (Rowe and Bhandari, 1983). The development of semiconductors with good thermoelectric properties made possible the fabrication of thermoelectric generators and refrigerators. Being solid-state devices, thermoelectric systems offer some unique advantages, such as high reliability, long life, small-size and no-vibrations refrigerators, and can be used in a wide temperature range, from 200 to 1300 K. However, because of their limited conversion efficiencies, these devices have remained confined to specialized applications. As the following sections will emphasize, the performance of those devices is closely associated with the magnitude of the **dimensionless figure of merit**, *ZT*, of the thermoelectric semiconductor.

ZT represents the relative magnitude of electrical and thermal cross-effect transport in materials. State-of-the-art thermoelectric materials, known since the early 1960s, have been extensively developed. Although significant improvements of the thermoelectric properties of these materials have been achieved, a maximum *ZT* value close to 1 is the current approximate limit over the whole 100 to 1500 K temperature range (Figure 8.13.16). To expand the use of thermoelectric devices to a wide range of applications will require improving *ZT* by a factor of two to three. There is no theoretical limitation on the value of *ZT*, and new promising approaches are now focusing on the investigation of totally different materials and the development of novel thin film heterostructure.

Thermoelectric Effects

Thermoelectric devices are based on two transport phenomena: the Seebeck effect for power generation and the Peltier effect for electronic refrigeration. If a steady temperature gradient is applied along a conducting sample, the initially uniform charge carrier distribution is disturbed as the free carriers located at the high-temperature end diffuse to the low-temperature end. This results in the generation of a back emf which opposes any further diffusion current. The open-circuit voltage when no current flows is the

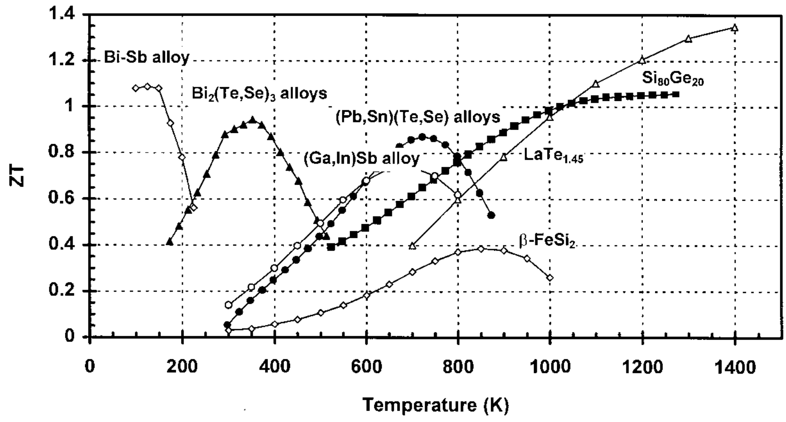

FIGURE 8.13.16 Typical temperature variations of *ZT* of state-of-the-art n-type thermoelectric alloys.

Seebeck voltage. When the junctions of a circuit formed from two dissimilar conductors (n- and p-type semiconductors) connected electrically in series but thermally in parallel are maintained at different temperatures T_1 and T_2, the open-circuit voltage V developed is given by $V = S_{\mathrm{pn}}(T_1 - T_2)$, where S_{pn} is the Seebeck coefficient expressed in $\mu\mathrm{V} \cdot \mathrm{K}^{-1}$.

The complementary Peltier effect arises when an electrical current I passes through the junction. A temperature gradient is then established across the junctions and the corresponding rate of reversible heat absorption $\dot{Q}$ is given by $\dot{Q} = \Pi_{\mathrm{pn}} I$, where Π_{pn} is the Peltier coefficient expressed in $W \cdot A^{-1}$ or V. There is actually a third, less-important phenomenon, the Thomson effect, which is produced when an electrical current passes along a single conducting sample over which a temperature gradient is maintained. The rate of reversible heat absorption is given by $\dot{Q} = \beta I(T_1 - T_2)$, where β is the Thomson coefficient expressed in $\mathrm{V} \cdot \mathrm{K}^{-1}$. The three coefficients are related by the Kelvin relationships:

$$S_{\mathrm{pn}} = \frac{\Pi_{\mathrm{pn}}}{T} \quad \text{and} \quad \frac{dS_{\mathrm{pn}}}{dT} = \frac{\beta_{\mathrm{p}} - \beta_{\mathrm{n}}}{T} \tag{8.13.51}$$

Thermoelectric Applications

The schematic of a thermoelectric device, or module, on Figure 8.13.17, illustrates the three different modes of operation: power generation, cooling, and heating. The *thermoelectric module* is a standardized device consisting of several p- and n-type legs connected electrically in series and thermally in parallel, and bonded to a ceramic plate on each side (typically alumina). The modules are fabricated in a great variety of sizes, shapes, and number of thermoelectric couples and can operate in a wide range of currents, voltages, powers, and efficiencies. Complex, large-scale thermoelectric systems can be easily designed and built by assembling various numbers of these modules connected in series or in parallel depending on the type of applications.

Power Generation. When a temperature gradient is applied across the thermoelectric device, the heat absorbed at the hot junction (Figure 8.13.17, hot side $T_h - T_1$ and cold side, $T_c - T_2$) will generate a current through the circuit and deliver electrical power to the load resistance R_L (Harman and Honig, 1967). The conversion efficiency η of a thermoelectric generator is determined by the ratio of the electrical energy, supplied to the load resistance, to the thermal energy, absorbed at the hot junction, and is given by

$$\eta = \frac{R_L I^2}{S_{\mathrm{pn}} I T_h + K\left(T_h - T_c\right) - \frac{1}{2} R I^2} \tag{8.13.52}$$

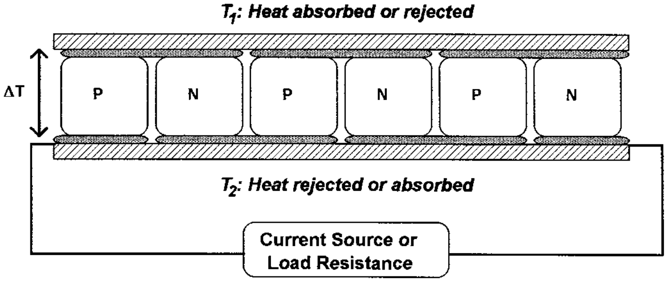

FIGURE 8.13.17 Schematic of a thermoelectric module.

where K is the thermal conductance in parallel and R is the electrical series resistance of one p-n thermoelectric couple. The electrical power P_L generated can be written as

$$P_L = \frac{S_{\mathrm{pn}}\left(T_h - T_c\right)^2 R_L}{\left(R_L + R\right)^2} \tag{8.13.53}$$

The thermoelectric generator can be designed to operate at maximum power output, by matching the load and couple resistances, $R_L = R$. The corresponding conversion efficiency is

$$\eta_P = \frac{T_h - T_c}{\frac{3}{2}T_h + \frac{1}{2}T_c + \frac{1}{4}Z_{\mathrm{pn}}^{-1}} \tag{8.13.54}$$

where Z_{pn} is the figure of merit of the p-n couple given by

$$Z_{\mathrm{pn}} = \frac{S_{\mathrm{pn}}^2}{RK} \tag{8.13.55}$$

The figure of merit can be optimized by adjusting the device geometry and minimizing the RK product. This results in Z_{pn} becoming independent of the dimensions of the **thermoelectric legs**. Moreover, if the p- and n-type legs have similar transport properties, the figure of merit, $Z_{\mathrm{pn}} = Z$, can be directly related to the Seebeck coefficient S, electrical conductivity σ or resistivity ρ, and thermal conductivity λ of the thermoelectric material:

$$Z = \frac{S^2}{\rho\lambda} = \frac{S^2\sigma}{\lambda} \tag{8.13.56}$$

The maximum performance $\eta_{\max}$ of the generator is obtained by optimizing the load-to-couple-resistance ratio, leading to the maximum energy conversion efficiency expressed as

$$\eta_{\max} = \frac{T_h - T_c}{T_h} \frac{\sqrt{1 + Z_{\mathrm{pn}}T_{\mathrm{av}}} - 1}{\sqrt{1 + Z_{\mathrm{pn}}T_{\mathrm{av}}} + \frac{T_c}{T_h}} \tag{8.13.57}$$

It must be noted that the maximum efficiency is thus the product of the Carnot efficiency, less than unity, and of a material-related efficiency, increasing with increasing Z_{pn} values as illustrated in Figure 8.13.18.

Refrigeration. When a current source is used to deliver electrical power to a thermoelectric device, heat can be pumped from T_1 to T_2 and the device thus operates as a refrigerator (Figure 8.13.17, hot side $T_h = T_2$

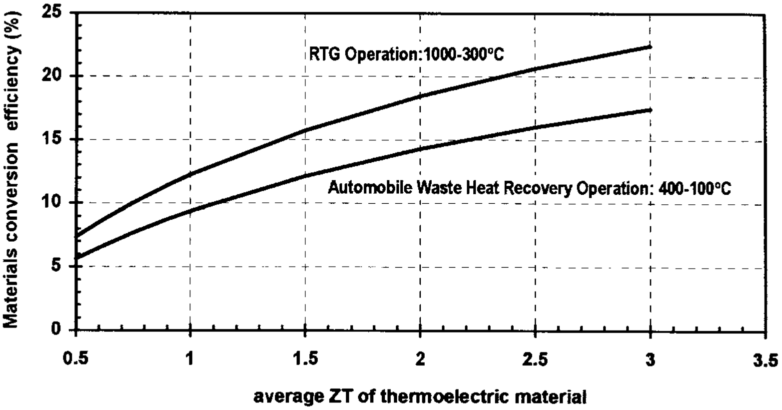

FIGURE 8.13.18 Maximum conversion efficiency $\eta_{\max}$ as a function of the average material figure of merit *ZT*, calculated using Equation (8.13.57) for two systems operating in different temperature ranges: the radioisotope generator (RTG) used for deep space missions and an automobile waste heat recovery generator.

and cold side, $T_c = T_1$). As in the case of a thermoelectric generator the operation of a thermoelectric cooler depends solely upon the properties of the p-n thermocouple materials expressed in terms of the figure of merit Z_{pn} and the two temperatures T_c and T_h (Goldsmid, 1986). The conversion efficiency or coefficient of performance, COP, of a thermoelectric refrigerator is determined by the ratio of the cooling power pumped at the cold junction to the electrical power input from the current source and is given by

$$\text{COP} = \frac{S_{\text{pn}} T_c I - \frac{1}{2} R I^2 - K\left(T_h - T_c\right)}{S_{\text{pn}}\left(T_h - T_c\right) I + R I^2} \tag{8.13.58}$$

There are three different modes of operation which are of interest to thermoelectric coolers. A thermoelectric cooler be designed to operate at maximum cooling power, $Qc_{\max}$, by optimizing the value of the current:

$$I_{Qc_{\max}} = \frac{S_{\text{pn}} T_c}{R} \quad \text{and} \quad Qc_{\max} = \frac{1}{2}\frac{\left(ST_c\right)^2}{R} - K\left(T_h - T_c\right) \tag{8.13.59}$$

Similarly, the conditions required for operating at maximum efficiency, $\text{COP}_{\max}$, across a constant temperature gradient, are determined by differentiating Equation (8.13.58) with respect to *I*, with the solution:

$$I_{\text{COP}_{\max}} = \frac{K\left(T_h - T_c\right)_c}{S_{\text{pn}} T_{\text{av}}}\left(1 + \sqrt{1 + Z_{\text{pn}} T_{\text{av}}}\right) \tag{8.13.60}$$

$$\text{COP}_{\max} = \frac{T_c}{T_h - T_c} \frac{\sqrt{1 + Z_{\text{pn}} T_{\text{av}}} - \frac{T_h}{T_c}}{\sqrt{1 + Z_{\text{pn}} T_{\text{av}}} + 1} \tag{8.13.61}$$

By reversing the input current to the device, the thermoelectric refrigerator can become a heat pump, with T_1 being the hot junction temperature. The expression of the maximum conversion efficiency of the heat pump is very similar to Equation (8.13.61) because of the following relationship:

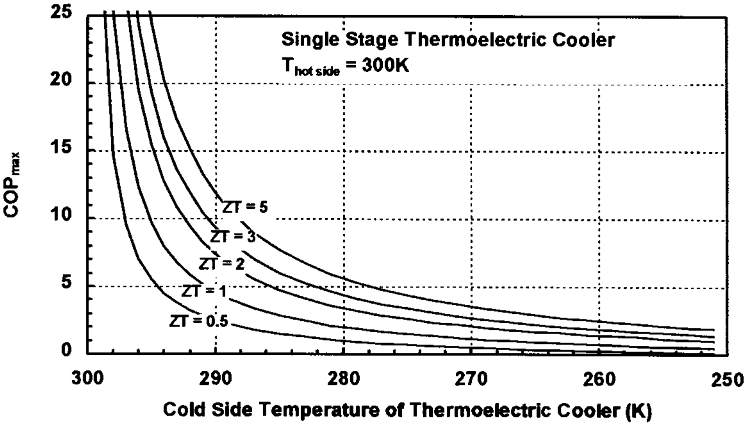

FIGURE 8.13.19 Maximum material coefficient of performance COP$_{\max}$ of a single-stage thermoelectric cooler calculated using Equation (8.13.61) as a function of the cold-side temperature (hot-side temperature of 300 K). Curves corresponding to various values of the average material figure of merit are displayed.

$$\left(\text{COP}_{\max}\right)^{\text{heat pump}} = 1 + \left(\text{COP}_{\max}\right)^{\text{refrigerator}} \tag{8.13.62}$$

The maximum COP expression in Equation (8.13.61) is similar to the one derived for the conversion efficiency η of a thermoelectric generator in Equation (8.13.57). However, there is a major difference between the COP$_{\max}$ and $\eta_{\max}$ parameters. Clearly, $\eta_{\max}$ increases with increasing ΔT values but is limited by the Carnot efficiency (Equation 8.13.54) which is less than 1, while COP$_{\max}$ in Equation (8.13.52) increases with decreasing ΔT values and can reach values much larger than 1. Figure 8.13.19 represents the variations of the COP$_{\max}$ of a thermoelectric cooling device optimized for working voltage and geometry as a function of average ZT values and temperature differences (hot junction temperature at 300 K). The average ZT value for current state-of-the-art commercially available materials (Bi_2Te_3-based alloys) is about 0.8. For example, it can be seen that a COP$_{\max}$ of 4 is obtained for a $(T_h - T_c)$ difference of 10 K, meaning that to pump 8 W of thermal power only 2 W of electrical power needs to be provided to the thermoelectric cooling device. This also means that 10 W of thermal power will be rejected at the hot side of the cooler.

The operation of a thermoelectric refrigerator at maximum cooling power necessitates a substantially higher input current than the operation at maximum efficiency. This is illustrated by calculating the variations of the maximum COP and cooling power with the input current and temperature difference which have been plotted in Figure 8.13.20 and Figure 8.13.21. The calculation was based on the properties of a thermoelectric cooler using state-of-the-art Bi_2Te_3-based alloys, and the arbitrary units are the same for both graphs. It can be seen that $I_{\text{COP}_{\max}}$ increases while $I_{Qc_{\max}}$ decreases with increasing ΔT. Also, it is possible to operate at the same cooling power with two different current values.

Finally, the third problem of interest for thermoelectric coolers is to determine the maximum temperature difference, $\Delta T_{\max}$, that can be achieved across the device. As shown on Figure 8.13.21, by operating at maximum cooling power and extrapolating Equation (8.13.59) to $Qc_{\max} = 0$, $\Delta T_{\max}$ is given by

$$\Delta T_{\max} = \frac{1}{2} Z_{\text{pn}} T_c^2 \quad \text{and} \quad T_{c\,\min} = \frac{\sqrt{1 + 2Z_{\text{pn}} T_h} - 1}{Z_{\text{pn}}} \tag{8.13.63}$$

where $T_{c\,\min}$ corresponds to the lowest cold-side temperature achievable. If the cooler operates at a ΔT close to $\Delta T_{\max}$ or higher, it becomes necessary to consider a cascade arrangement with several **stages.** The

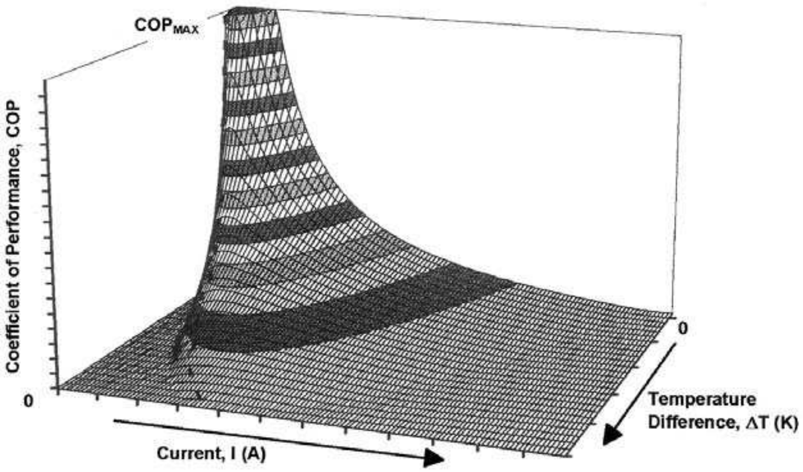

FIGURE 8.13.20 Three-dimensional plot of the variations of the COP of a thermoelectric cooler as a function of the operating current and the temperature difference.

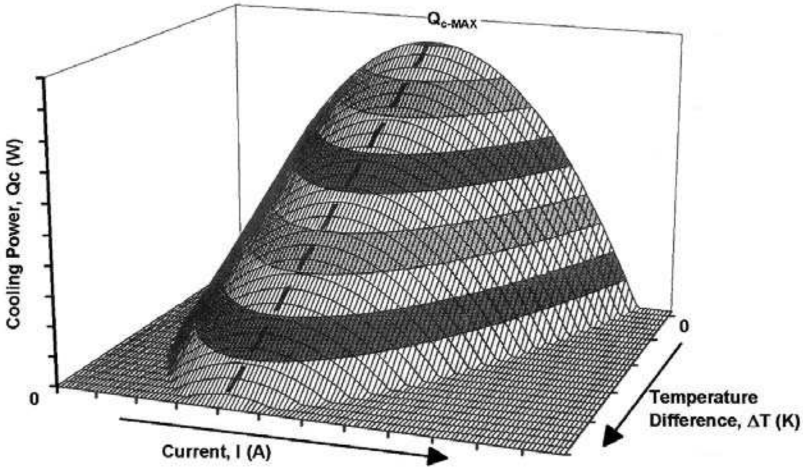

FIGURE 8.13.21 Three-dimensional plot of the variations of the cooling power of a thermoelectric cooler as a function of the operating current and the temperature difference.

COP of an n-stage thermoelectric cooler is optimized if the COP of each stage, COP_i, is the same, which requires $\Delta T_i / T_{i-1}$ to be the same for each stage. The overall maximum COP is then expressed as

$$\mathrm{COP}_{\max} = \frac{1}{\left(\prod_{i=1}^{n}\left(1 + \frac{1}{\mathrm{COP}_i}\right) - 1\right)} \tag{8.13.64}$$

Additional Considerations

When considering the operation of an actual thermoelectric device, several other important parameters must be considered. The thermal and electrical contact resistances can substantially degrade the device performance, in particular for short lengths of the thermoelectric legs. For example, the conversion efficiency of a radioisotope generator system is about 20% lower than the value calculated in Figure 8.13.18

for the thermoelectric materials only. The electrical contact resistance arises from the connection (see Figure 8.13.17) of all the legs in series. Typical values obtained for actual generators and coolers are 10 to 25 $\mu\Omega \cdot \mathrm{cm}^2$. The thermal contact resistance is generated by the heat-transfer characteristics of the ceramic plates and contact layers used to build the thermoelectric module. The heat exchangers and corresponding heat losses should also be taken into account.

In addition, the transport properties of the thermoelectric materials vary with temperature, as illustrated in Figure 8.13.16. When a thermoelectric device is operating across a wide temperature range, these variations should be factored in the calculation of its performance.

Nomenclature

COP	coefficient of performance
$\mathrm{COP}_{\max}$	maximum coefficient of performance
COP_i	coefficient of performance of the *i*th stage of a multistage thermoelectric cooler
I	current intensity
$I_{\mathrm{COP}_{\max}}$	current intensity required to operate a thermoelectric cooler at maximum conversion efficiency
$I_{Qc_{\max}}$	current intensity required to operate a thermoelectric cooler at maximum cooling power
K	thermal conductance
Q	rate of reversible heat absorption
R	electrical resistance
R_L	load resistance
P_L	electrical power delivered to the load resistance
S	Seebeck coefficient
S_{pn}	Seebeck coefficient of a p-n couple of thermoelements
T_1	temperature
T_2	temperature
T_{av}	average temperature across the thermoelectric device
T_c	cold-side temperature of a thermoelectric device
$T_{c\,\min}$	minimum cold-side temperature which can be achieved by a thermoelectric cooler
T_h	hot-side temperature of a thermoelectric device
V	voltage; open-circuit voltage
Z	thermoelectric figure of merit
Z_{pn}	thermoelectric figure of merit of a p-n couple of thermoelements
ZT	dimensionless thermoelectric figure of merit
β	Thomson coefficient
β_p	Thomson coefficient for the p-type thermoelement
β_n	Thomson coefficient for the n-type thermoelement
ΔT	temperature difference across a thermoelectric device
$\Delta T_{\max}$	maximum temperature difference which can be achieved across a thermoelectric cooler
η	thermoelectric conversion efficiency
$\eta_{\max}$	maximum thermoelectric conversion efficiency
λ	thermal conductivity
Π_{pr}	Peltier coefficient
ρ	electrical resistivity

Defining Terms

Coefficient of performance: Electrical to thermal energy conversion efficiency of a thermoelectric refrigerator, determined by the ratio of the cooling power pumped at the cold junction to the electrical power input from the current source.

Dimensionless figure of merit: The performance of a thermoelectric device depends solely upon the properties of the thermoelectric material, expressed in terms of the dimensionless figure of merit

ZT, and the hot-side and cold-side temperatures. *ZT* is calculated as the square of the Seebeck coefficient times the absolute temperature divided by the product of the electrical resistivity to the thermal conductivity. The best *ZT* values are obtained in heavily doped semiconductors, such as Bi_2Te_3 alloys, PbTe alloys, and Si-Ge alloys.

Stage: Multistage thermoelectric coolers are used to achieve larger temperature differences than possible with a single-stage cooler composed of only one module.

Thermoelectric leg: Single thermoelectric element made of n-type or p-type thermoelectric material used in fabricating a thermoelectric couple, the building block of thermoelectric modules. The geometry of the leg (cross-section-to-length ratio) must be optimized to maximize the performance of the device.

Thermoelectric module: Standardized device consisting of several p- and n-type legs connected electrically in series and thermally in parallel, and bonded to a ceramic plate on each. The modules are fabricated in a great variety of sizes, shapes, and number of thermoelectric couples.

References

Goldsmid, H.J. 1986. *Electronic Refrigeration,* Pion Ltd., London.

Hannan, T.C. and Honig, J.M. 1967. *Thermoelectric and Thermomagnetic Effects and Applications,* McGraw-Hill, New York.

Rowe, D.M and Bhandari, C.M. 1983. *Modern Thermoelectrics,* Reston Publishing, Reston, VA.

Further Information

The *Proceedings of the Annual International Conference on Thermoelectrics* are published annually by the International Thermoelectric Society (ITS). These proceedings provide the latest information on thermoelectric materials research and development as well as thermoelectric devices and systems. The ITS also publishes a semiannual newsletter. For ITS membership or questions related to thermoelectrics, you may contact the current ITS secretary: Dr. Jean-Pierre Fleurial, Jet Propulsion Laboratory, MS 277-212, Pasadena, CA 91109. Phone (818)-354-4144. Fax (818) 393-6951. E-mail jean-pierre.fleurial@jpl.nasa.gov.

Also, the *CRC Handbook of Thermoelectrics,* edited by D.M. Rowe was published by CRC Press Inc., Boca Raton, FL, became available in 1996. This handbook covers all current activities in thermoelectrics.

Magnetohydrodynamic Power Generation

William D. Jackson

Introduction

The discipline known as magnetohydrodynamics (MHD) deals with the interactions between electrically conducting fluids and electromagnetic fields. First investigated experimentally by Michael Faraday in 1832 during his efforts to establish the principles of electromagnetic induction, application to energy conversion yields a heat engine which has its output in electrical form and, therefore, qualifies as a direct converter. This is generally referred to as an MHD generator, but could be better described as an electromagnetic turbine as it operates on a thermodynamic cycle similar to that of a gas turbine.

The operating principle is elegantly simple, as shown in Figure 8.13.22. A pressurized, electrically conducting fluid flows through a transverse magnetic field in a channel or duct. Electrodes located on the channel walls parallel to the magnetic field and connected through an external circuit enable the motionally induced "Faraday electromotive force" to drive an electric current through the circuit and thus deliver power to a load connected into it. Taking the fluid velocity as **u** and the magnetic flux density as **B**, the intensity of the motionally induced field is $\mathbf{u} \times \mathbf{B}$. The current density, **J**, in the channel for a scalar conductivity σ is then given by Ohm's law for a moving conductor as

$$\mathbf{J} = \sigma[\mathbf{E} + \mathbf{u} \times \mathbf{B}]$$

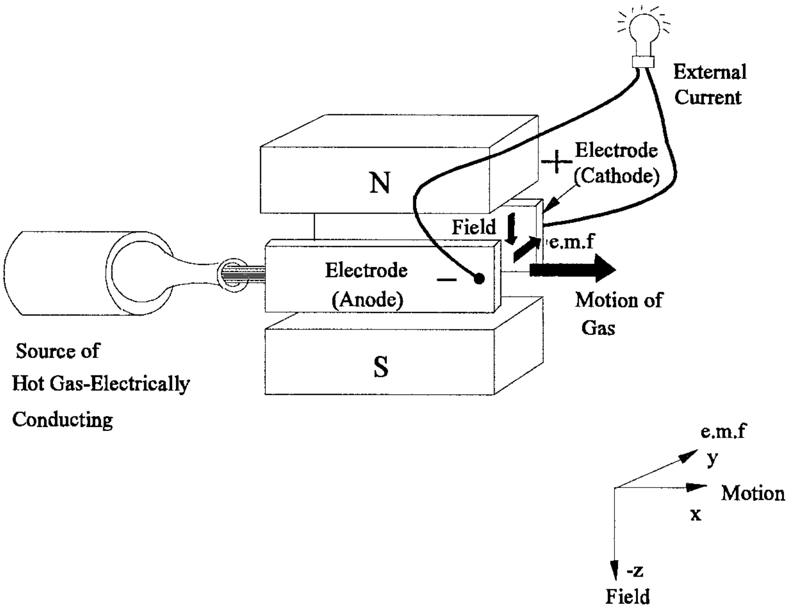

FIGURE 8.13.22 Principle of electromagnetic turbine or MHD generator.

By taking the coordinates of Figure 8.13.22 and assuming that the quantities are constant, the power density flow from the MHD generator is, using **E** · **J**

$$w_e = \sigma u_x^2 B^2 k(1-k)$$

where $k = Ez/u \times B$ is the "loading factor" relating loaded electric field to open circuit induction and is used in the same manner as the regulation of an electrical machine is applied to its terminal voltage.

It is instructive at this point to determine the power density of an MHD generator using values representative of the most commonly considered type of MHD generator. Combustion gas with σ = 10 S/m, a flow velocity of 800 m/sec and an applied field of 5 T for maximum power transfer (k = 0.5) yields w_e as 40 MW/m^3. This value is sufficiently attractive to qualify MHD generators for bulk power applications. An intensive, worldwide development effort to utilize this and other MHD generator properties has been conducted since the late 1950s. However, this has not yet led to any significant application of MHD generators. To understand how this has come about and what still needs to be accomplished to make MHD attractive will now be summarized.

Electrical Conductivity Considerations

Two approaches have been followed to obtain adequate ionization and, therefore, conductivity in the working fluid. What may be termed the mainline approach to achieving electrical conductivity is to add a readily ionizable material to "seed" the working fluid. Alkali metals with ionization potentials around 4 V are obvious candidates, although a lower value would be highly desirable. A potassium salt with an ionization potential of 4.09 eV has been widely used because of low cost but cesium with a 3.89-eV value is the preferred seed material when the running time is short or the working fluid is recycled. There are two methods of ionization:

1. Thermal ionization in which recombination ensures a common temperature for electrons, ions, and neutrals; the mass action law (Saha equation) is followed; and the heat of ionization in electron volts is the ionization potential; and
2. Extrathermal or nonequilibrium ionization where electrons and heavy particles are at different temperatures and the concept of entwined fluids (electron, ion, and neutral gases) is involved.

The former is applicable to diatomic combustion gases while the latter occurs in monatomic (noble) gases but is also observed in hydrogen. Only a small amount of seed material is required and is typically around 1% of the total mass flow for maximum conductivity.

The existence of mutually perpendicular **E** and **B** fields in an MHD generator is of major significance in that the electrons are now subjected to the Hall effect. This causes electrons and, therefore, electric currents to flow at an angle with respect to the **E** field in the collision-dominated environment of the MHD generator. The presence of a significant Hall effect requires that the electrical boundary conditions on the channel be carefully selected and also introduces the possibility of working fluid instabilities driven by force fluctuations of electrical origin. A further source of fluctuations and consequent loss of conductivity occurs when nonequilibrium ionization is employed due to current concentration by Joule heating. This latter effect is controlled by operating only in a regime where, throughout the channel, complete ionization of the seed material is acheived.

Generator Configurations and Loading

The basic consequence of the Hall effect is to set up **E** fields in both transverse and axial directions in the generator channel and these are generally referred to as the Faraday and Hall fields, respectively. The direction of the Faraday field depends on the magnetic field; the Hall field depends on the Hall parameter and is always directed toward the upstream end of the channel. These considerations, in turn, lead to the MHD generator having the characteristics of a gyrator — a two-terminal pair power-producing device in which one terminal pair (Faraday) is a voltage source and the other (Hall) is a current source dependent in this case on the Hall parameter. Electric power can be extracted from either the Faraday or Hall terminals, or both.

This has resulted in several electrical boundary conditions being utilized with the axial flow channel as shown in Figure 8.13.23. These are most readily understood by treating each anode-cathode pair as a generating cell. The segmented Faraday configuration (Figure 8.13.23a) is then simply a parallel operation of cells which leads to the apparently inconvenient requirement of separate loading of individual cells: the Hall connection (Figure 8.13.23b) utilizes a single load by series connection but depends on the Hall parameter for its performance; and the diagonal connection (Figure 8.13.23c) connects the cells in series-parallel and so avoids Hall parameter dependence while retaining the single load feature. In all three linear configurations, the channel walls are electrically segmented to support the Hall field, and experience

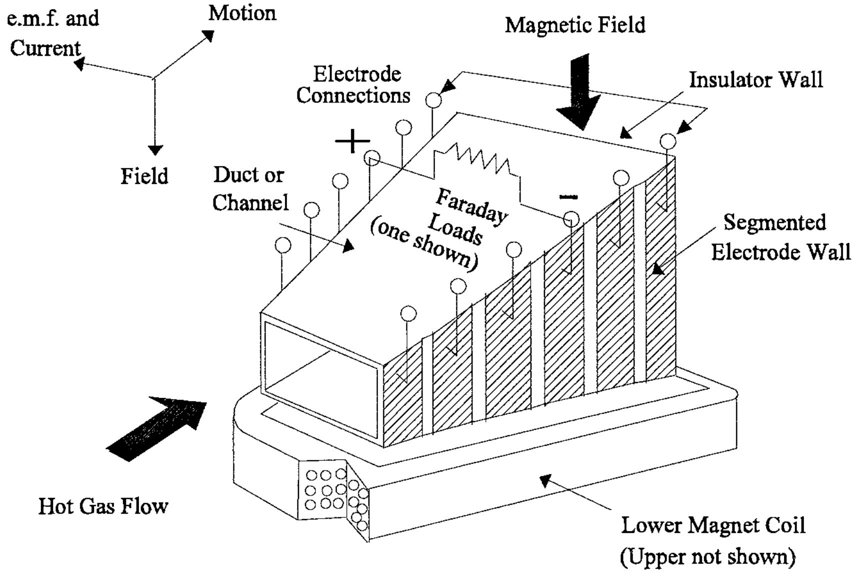

FIGURE 8.13.23 Basic Faraday linear MHD generator.

has shown that this must be sufficiently finely graded so that no more than 50 V is supported by the interelectrode gaps to avoid electrical breakdown.

The MHD generator is a linear version of the homopolar machine originally demonstrated by Faraday and is, as a practical matter, confined to DC generation. Accordingly, some form of DC-AC conversion using power electronics is required for the vast majority of applications. The single load feature loses significance in this situation as the "power conditioning" can readily be arranged to combine (consolidate) the individual cell outputs before conversion to the required AC system conditions. Indeed, to maximize power extraction while limiting interelectrode voltages and controlling electrode currents (to ensure adequate lifetime), the power conditioning is arranged to extract power from both Faraday and Hall terminal pairs.

An alternative geometry is to set up a radial flow (usually but not necessarily outward) with the disk configuration of Figure 8.13.23d. The result is a Hall generator, which is generally favored for nonequilibrium ionization as it avoids the inevitable nonuniformities associated with electrode segmentation with their proclivity for promoting ionization instabilities. A measure of Faraday performance is achievable through the introduction of swirl, and additional ring electrodes enable power conditioning to control (and optimize) the radial electric field.

Components

An MHD generator per se requires several components to make up a complete powertrain. In addition to the power conditioning needed for DC-AC conversion these include a magnet, seed injector, combustor with fuel and oxidizer supply or an input heat exchanger, nozzle, compressor, diffuser, exhaust gas-cleaning system (for once-through systems), and controls. The need to accommodate a channel between the poles of a magnet qualifies the MHD generator as a large-air-gap machine.

Systems

Power systems incorporating MHD generators are either of the once-through (open-cycle) or working fluid recycle (closed-cycle) type, and the complete MHD system described in the previous section can either be stand-alone or incorporated into a more complex configuration such as a binary cycle. In the latter case, the high-temperature operation of the MHD unit makes it a topping cycle candidate and it is in this mode that MHD has received most system consideration. An MHD generator operated directly on ionized combustion gas is usually associated with an open cycle while nonequilibrium ionization with seeded noble gases and LMMHD are invariably considered for closed-cycle operation. An exception is nonequilibrium ionization in cesium-seeded hydrogen which has received some attention for open-cycle operation.

Heat Sources, Applications, and Environmental Considerations

A heat source capable of providing from 1000 K for LMMHD to over 3000 K for open-cycle systems for power production is a candidate. Rocket motor fuels, all fossil fuels, high-temperature nuclear reactors cooled with hydrogen and biomass are suitable for open cycles, while closed cycles can be driven through a heat exchanger by any of these combustion sources. A high-temperature nuclear reactor, probably helium cooled, is also a feasible source for MHD and in the early stages of development of the process received much attention. With the abandonment of efforts to develop commercial reactors to operate at temperatures above 1200 K, attention has focused on high-energy fuels for pulse power (few seconds) operation and coal for utility power generation.

While the debate over the role of fossil energy in the long-term electricity generation scenario continues, it is established that coal is a major resource which must be utilized at maximim efficiency to limit CO_2 production and must be combusted in a manner which reduces SO_2 and NO_x effluents to acceptable levels. The use of MHD generators significantly advances all of these objectives. Briefly, it was first observed that the "electromagnetic turbine" has the major advantage that it cannot only provide the highest efficiency of any known converter from the Carnot viewpoint but that its operation is not adversely affected by coal slag and ash. Indeed, slag provides an excellent renewable coating for the channel walls and increases lifetime.

System calculations have shown that, when coupled as a topping cycle to the best available steam plant technology, a thermal efficiency with coal and full environmental control is 52.5%. When coupled into a ternary cycle with either a gas turbine or fuel cells and a steam turbine, efficiencies upward of 60% are possible.

Technology Status

A pulse-type MHD generator was successfully built and operated by Avco (now Textron Defense Industries) in 1963 and a complete natural gas-fired pilot plant with a nominal 20-MW MHD generator was commissioned in the U.S.S.R. on the northern outskirts of Moscow in 1971. In the decade of the 1980s, development was focused on coal firing as a result of the oil crises of the 1970s and in the U.S. progressed to the point where the technology base was developed for a demonstration plant with a 15-MW MHD generator.

Future Prospects

The two particular attributes of the MHD generator are its rapid start-up to multimegawatt power levels for pulse power applications and its ability to provide a very high overall thermal efficiency for power plants using coal while meeting the most stringent environmental standards. The first has already been utilized in crustal exploration, and the second must surely be utilized when coal is the fuel of choice for electric power production. In the meantime, MHD has been established as a viable technology on which further development work will be conducted for advanced applications such as the conversion system for thermonuclear fusion reactors.

Further Information

The following proceedings series contain a full and complete record of MHD generator and power system development:

1. *Proceedings of the Symposia for the Engineering Aspects of Magnetohydrodynamics*, held annually in the U.S. since 1960 (except for 1971 and 1980).
2. *Proceedings of 11 International Conferences on Magnetohydrodynamic Electrical Power Generation*, held in 1962, 1964, 1966, 1968, 1971 , 1975, 1980, 1983, 1986, 1989, and 1992. The 12th conference will be held in Yokahama, Japan in October 1996.

8.14 Ocean Energy Technology

Desikan Bharathan and Federica Zangrando

The ocean contains a vast renewable energy potential in its waves and tides; in the temperature difference between cold, deep waters and warm surface waters; and in the salinity differences at river mouths (SERI, 1990; WEC, 1993; Cavanagh et al., 1993). Waves offer a power source for which numerous systems have been conceived. Tides are a result of the gravity of the sun, the moon, and the rotation of the Earth working together. The ocean also acts as a gigantic solar collector, capturing the energy of the sun in its surface water as heat. The temperature difference between warm surface waters and cold water from the ocean depths provides a potential source of energy. Other sources of ocean energy include ocean currents, salinity gradients, and ocean-grown biomass.

The following subsections briefly describe the status and potential of the various ocean energy technologies, with emphasis placed on those with a near-term applicability.

Ocean Thermal Energy Conversion

Ocean thermal energy conversion (OTEC) technology is based on the principle that energy can be extracted from two reservoirs at different temperatures (SERI, 1989). A temperature difference of as little as 20°C can yield usable energy. Such temperature differences prevail between ocean waters at the surface and at depths up to 1000 m in tropical and subtropical latitudes between 24° north and south of the equator. Here, surface water temperatures range from 22 to 29°C, while temperatures at a depth of 1000 m range from 4 to 6°C. This constitutes a vast, renewable resource, estimated at 10^{13} W, for potential base load power generation.

Past research has been concentrated on two OTEC power cycles, namely, **closed cycle** and **open cycle**, for converting this thermal energy to electrical energy (Avery and Wu, 1994). Both cycles have been demonstrated, but no commercial system is in operation. In a closed-cycle system, warm seawater is used to vaporize a working fluid such as ammonia flowing through a heat exchanger (evaporator). The vapor expands at moderate pressures and turns a turbine. The vapor is condensed in a condenser using cold seawater pumped from the ocean depths and the condensed fluid is pumped back to the evaporator to repeat the cycle. The working fluid remains in a closed system and is continuously circulated (Figure 8.14.1).

In an open-cycle system, the warm seawater is "flash" evaporated in a vacuum chamber to make steam at an absolute pressure of about 2.4 kPa. This steam expands through a low-pressure turbine coupled to a generator to produce electricity. The steam is then condensed by using cold seawater. If a surface condenser is used, condensed steam is separated as desalinated water (Figure 8.14.2).

Effluent from a closed-cycle or an open-cycle system can be further processed to make more desalinated water through evaporator/condenser systems in subsequent stages. For combined production of power and water, these systems can be competitive with conventional systems in several coastal markets.

Tidal Power

The energy from tides is derived from the kinetic energy of water moving from a higher to a lower elevation, similar to hydroelectric plants. High tide can provide the potential energy for seawater to flow into an enclosed basin or estuary and then be discharged at low tide (Ryan, 1980). Electricity is produced from the gravity-driven inflow or outflow or both through a turbogenerator. The tidal resource is variable but predictable, and there are no technical barriers for deployment of this technology. Because costs are strongly driven by the civil works required to dam the reservoir, only a few sites around the world have the proper conditions of tides and landscape to use this technology. Recent developments in marine and offshore construction have helped reduce construction time and cost; however, the economics of tidal power production remains uncompetitive to conventional energy systems.

The highest tides in the world can reach above 17 m, as in the Bay of Fundy between Maine and Nova Scotia, where it is projected that up to 10,000 MW could be produced by tidal systems in this bay alone. A minimum tidal range (difference between mean high and low tides) of 5 m is required for plants using conventional hydroelectric equipment. More recently, low-head hydroelectric power equipment has proved adaptable to tidal power and new systems for 2-m ranges have been proposed.

A few tidal power stations are operating in France, the former U.S.S.R., China, and Canada. The largest and longest-operating plant is the 240-MW tidal power station on the Rance River estuary in northern France (Banal and Bichon, 1981), which has operated with 95% availability since 1968. The 400-kW tidal plant in Kislaya Bay on the Barents Sea in the former U.S.S.R. has been operating since 1968; at this favorable site, only a 50-m-wide dam was needed to close the reservoir. The 20-MW Canadian plant at Annapolis on the Bay of Fundy has operated reliably since 1984. A number of small turbine generator plants of up to 4 MW are also installed on the China coastline.

Wave Power

Waves contain significant power that can be harnessed by shore-mounted or offshore systems. Offshore installations will have larger incident power on the device but require more costly installations. A myriad of wave-energy converter concepts have been devised, transforming wave energy into other forms of mechanical (rotary, oscillating, or relative motion), potential, or pneumatic energy, and ultimately into electricity; very few have been tested at sea.

The power per unit frontal length of the wave is proportional to wave height squared and to wave period, with their representative values on the order of 2 m and 10 sec. The strong dependence on wave height makes the resource highly variable, even on a seasonal and a yearly average basis. The northeastern Pacific and Atlantic coasts have average yearly incident wave power of about 50 kW/m, while near the tip of South America the average power can reach 100 kW/m. Japan, on the other hand, receives an average of 15 kW/m. Waves during storms can reach 200 kW/m, but large waves are unsafe for operation. Because of their severity, they impose severe constraints and increase system costs. Overall, the amount of power that could be harvested from waves breaking against world coastlines is estimated to be on the order of the current global consumption of energy. However, total installed capacity amounts to less than 1 MW worldwide.

A commonly deployed device is the oscillating water column (OWC), which has so far been mounted on shore but is also proposed for floating plants. It consists of an air chamber in contact with the sea so that the water column in the chamber oscillates with the waves. This motion makes the air flow in and out of the chamber, turning a turbine. A Wells turbine uses symmetrical airfoil blades in a simple rotor to extract power from the airflow in both directions. Flywheels are often used to smooth out fluctuating delivered energy by the waves.

Two of the largest wave-energy power plants were built at Toftestallen, near Bergen, Norway. A Norwegian company, Norwave A.S., built a 350-kW tapered channel (Tapchan) device in 1984, which survived a severe storm in 1989 (the 500 kW multiresonant OWC plant built by Kvaerner Brug A.S. did not). The channel takes advantage of the rocky coastline to funnel waves through a 60-m-wide opening into a coastal reservoir of 5500 m^2, while maintaining civil engineering costs to a minimum. Wave height increases as the channel narrows over its 60-m length, and the rising waves spill over the 3-m-high channel walls, filling the reservoir. Continuous wave action maintains the reservoir level at a relatively constant elevation above sea level, providing potential energy for a low-head hydroelectric Kaplan turbogenerator. Estimates by Norwave to rebuild an identical plant at this site suggested capital costs of $3500/kW installed, and energy costs of 8¢/kWh, at a plant capacity factor of 25% (ASCE, 1992). In recent efforts, the National Institute of Ocean Technology, India, has installed a 150-kW wave-energy conversion device in the southern tip of India.

Concluding Remarks

Among the many ocean energy prospects, OTEC, tides, and tapered channel wave-energy converters offer the most near-term potential and possess applicability for a large variety of sites. To realize their potential, additional research and development is required. Ocean resources can be most suitable to address humanity's future needs for water and hydrogen for fuel cells.

Defining Terms

Ocean thermal energy conversion (OTEC): a system that utilizes the temperature difference between the seawater at the surface and at depths.

Closed-cycle OTEC: uses a working fluid in a closed cycle.

Open-cycle OTEC: uses steam flashed from the warm seawater as the working fluid that is condensed and exhausted.

References

ASCE, 1992, *Ocean Energy Recovery, the State of the Art*, R.J. Seymour, Ed., American Society of Civil Engineers, New York.

Avery, W.H. and Wu, C. 1994, *Renewable Energy from the Ocean, a Guide to OTEC*, Oxford University Press, New York.

Banal, M. and Bichon, A. 1981. Tidal energy in France: the Rance Estuary tidal power station — some results after 15 years of operation, Paper K3, 2nd Symposium on Wave and Tidal Energy, Cambridge, England, September.

Cavanagh, J.E., Clarke, J.H., and Price, R. Ocean energy systems, in *Renewable Energy, Sources for Fuels and Electricity*, T.B. Johansson, H. Kelley, A.K.N. Reddy, and R.H. Williams (Eds.), Island Press, Washington, D.C., 1993, chap 12.

Ryan, P.R. 1979/80. Harnessing power from tides: state of the art, *Oceanus*, 22(4), 64–67.

SERI, 1989. Ocean thermal energy conversion: an overview, Solar Energy Research Institute, SERI/SP-220-3024, Golden, CO.

SERI, 1990. The potential of renewable energy: an interlaboratory white paper, Solar Energy Research Institute, SERI/TP-260-3674, Golden, CO.

WEC, 1993. Renewable energy resources — opportunities and constraints 1990–2020, World Energy Council, London, England.

Further Information

CEC, 1992. Energy technology status report, California Energy Commission, Sacramento, CA, 1992.

Funakoshi, H., Ohno, M., Takahashi, S., and Oikawa, K. Present situation of wave energy conversion systems, *Civil Eng. Jpn.*, 32, 108–134, 1993.

8.15 Combined-Cycle Power Plants

Alex Lezuo

In the decades since the early 1970s, power plant concepts featuring a combination of gas and steam turbines have been successfully commercialized. These combined-cycle power plants make very efficient use of fuel compared with other power plants. The first combined-cycle power plants in the 1970s achieved net efficiencies of about 40%, while the most recent ones attain net plant efficiencies of more than 58%.

Combined-Cycle Concepts

The considerable amount of energy available in the exhaust of a gas turbine also can be used in a secondary system, increasing overall efficiency considerably. Figure 8.15.1 shows three of the most common types of combined-cycle (CC) concepts.

The *natural-gas-fired CC* power plant, which offers the highest efficiency potential, is the most commonly used system today. However, to attain these high efficiencies, only fuels such as natural gas can be burned in the gas turbine. The use of other fuels results in a higher heat rate. The arrangement is relatively simple and therefore has the lowest specific investment costs among all power generation systems.

The *parallel-powered CC* power plant is mainly used for repowering existing coal-fired power plants. This is an efficient way of reducing the heat rate of older coal-fired power plants with a relatively small investment and short implementation schedules. In addition, this concept provides excellent part-load behavior, thus making it suitable for cycling duty. Instead of generating steam with the combustion turbine exhaust gas, it is also possible simply to heat the feedwater of a coal-fired power plant and thus reduce the amount of extraction steam required from the steam turbine for the feedwater heaters. This can increase the output and efficiency of the coal plant.

When no natural gas is available, the CC can also be used in connection with a coal gasification plant. Integrated systems (*integrated gasification combined cycle, IGCC*) increase system complexity and most likely decrease overall plant availability, but permit the use of lower cost fuels such as coal or petcoke in an environmentally acceptable manner. Several industrial-scale demonstration plants have proven the technical feasibility, but wider application is dependent on the price spread between coal and natural gas.

Other CC developments have been proposed but the natural-gas-fired CC has proven to be the most efficient and most economical under present technical and economical boundary conditions. Therefore, this CC will be described in greater detail.

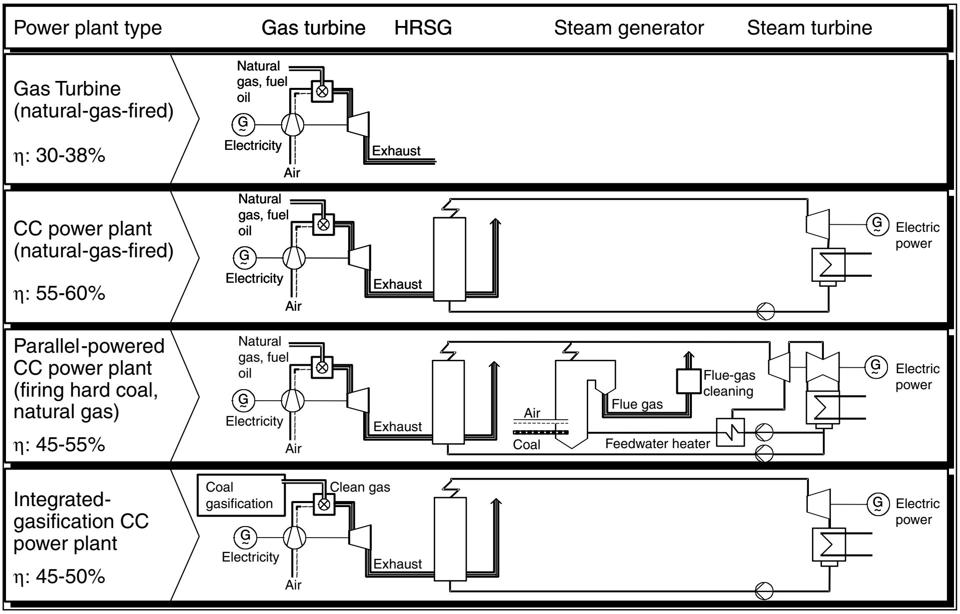

FIGURE 8.15.1 Combined-cycle power plant concepts.

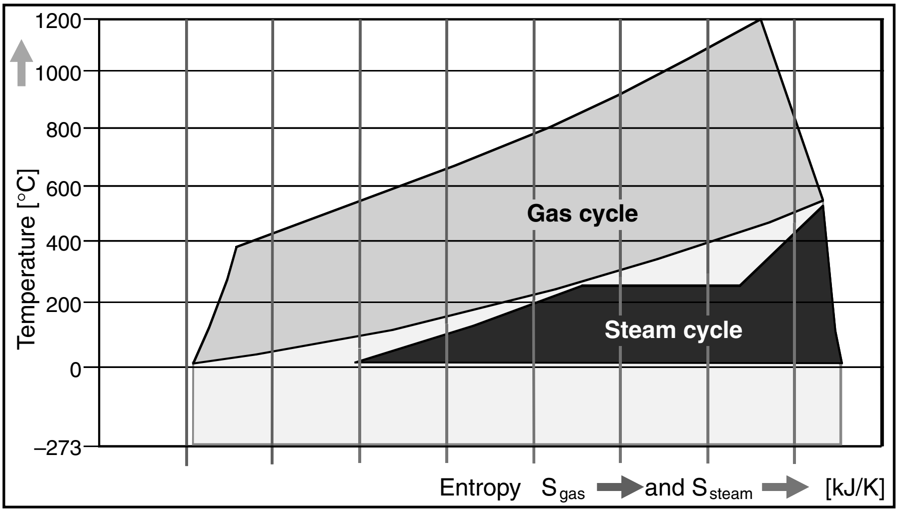

FIGURE 8.15.2 *T–S* diagram of a combined-cycle power plant with single-pressure steam cycle.

Combined-Cycle Thermodynamics

The exhaust gas temperature of today's gas turbines varies between 500°C (932°F) for small and older gas turbines and 600°C (1112°F) for advanced GTs, and the specific exhaust gas stream amounts to 2 to 3 kg/s (4.4 to 6.6 lb/s) per megawatt, where the smaller figure relates to large, advanced gas turbines. By using the heat of this exhaust gas in a water–steam cycle, total cycle efficiency can be raised considerably because a very high total temperature difference can be utilized in the combined cycle (Figure 8.15.2) compared to a simple-cycle gas turbine.

With the improvement of gas turbines and the accompanying increase in exhaust temperature, main steam pressure and temperature of the steam cycle have been raised to as high as 165 bar (2400 psi) and 565°C (1050°F). In addition, multipressure heat-recovery steam generators (HRSGs) with reheat are

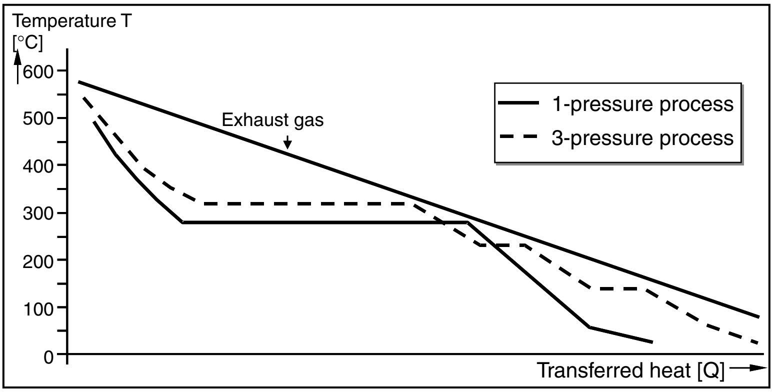

FIGURE 8.15.3 *T*–*Q* diagram for heat-recovery steam generators.

used, which represents another improvement in utilization of the exhaust heat. In this way, the losses can be reduced as shown in Figure 8.15.3, which compares a single-pressure HRSG with a triple-pressure system. The ideal temperature/heat transfer diagram would be one in which the temperature difference in the HRSG between the steam and the exhaust gases is constant.

The exhaust gases leaving the gas turbine enter the HRSG at a temperature between approximately 550 and 600°C (1022 and 1112°F) and leave the HRSG typically between 80 and 100°C (176 and 212°F). The water in the steam cycle portion of the combined cycle enters the HRSG economizer as a subcooled liquid. The temperature of the water is increased in the economizer until the liquid becomes saturated. At this point, the minimum temperature difference between the water in the steam cycle and the exhaust gases occurs and is called the "pinch point." Typical pinch-point values range from 8 to 30°C (46 to 86°F); the smaller the pinch point difference is, the larger the required heat-transfer surface area. After evaporation at constant temperature, the steam is superheated to the final temperature in the superheater section.

Figure 8.15.3 shows the improvement in heat transfer from the single-pressure cycle to the triple-pressure cycle. High-performance plant designs are today equipped with a triple-pressure HRSG with one reheat stage.

Table 8.15.1 lists net plant output and performance values for a selection of CCs from the four main suppliers worldwide. This is just a selection of available gas turbines and possible configurations because manufacturers are developing and improving their engines on a regular basis. Performance data are based on standard designs and configurations at ISO conditions of 15°C (59°F), which provides a normalized basis for comparison.

Combined-Cycle Arrangements

Today, several designs for natural-gas-fired CCs are available. All consist of the following main components (Figure 8.15.4):

- Gas turbine
- Steam turbine
- Generator
- HRSG
- Stack
- Condenser with heat removal system
- Condensate pumps
- Feedwater pumps
- Auxiliary systems for gas and steam turbine
- Main and auxiliary transformers

TABLE 8.15.1 Net Plant Output and Performance Data for Selected Combined Cycles

Supplier Model	Frequency, Hz	Number of GTs	Net Plant Output, MW	Heat Rate, LHV Btu/kWh	Net Plant Efficiency, %	Configuration
Alstom Power (AP)						
KA8C-2	50	2	80.0	6965	49.0	2-P
KA 13E2-2	50	2	480.0	6450	52.9	2-P
KA 24-1	60	1	250.8	6129	55.7	2-P/RH
KA 26-1	50	1	392.5	6061	56.3	3-P/RH
GE Power Systems						
S106B	50/60	1	64.3	7020	49.0	3-P
S206FA	50/60	2	218.7	6930	54.1	3-P/RH
S107EA	60	1	130.2	6380	50.2	3-P
S209EC	50	2	522.6	6415	54.4	3-P/RH
S107FA	60	1	262.6	6170	56.0	3-P/RH
Mitsubishi Heavy Industries (MHI)						
M501F	60	1	279.0	6074	56.2	3-P/RH
M701F	50	1	399.0	5994	56.9	3-P/RH
M501G	60	1	371.0	5879	58.0	3-P/RH
M701G	50	1	484.0	5879	58.0	3-P/RH
Siemens PG//Siemens Westinghouse						
CC 1S.V64.3A	60	1	99.8	6541	52.2	2-P
CC 1.V94.2	50	1	239.4	6533	52.2	2-P
CC 1S.V943A	50	1	392.2	5946	57.4	3-P/RH
CC 2.W501F	60	2	568.5	6060	56.3	3-P/RH
CC 1S.W501G	60	1	365.0	5880	58.0	3-P/RH

Notes: 2-P = double-pressure HRSG; 3-P = triple-pressure HRSG; RH = reheat.
Source: From company Web pages, Aug. 2003. (Alstom.com, GEPower.com, MHI.co.jp, powergeneration.siemens.com)

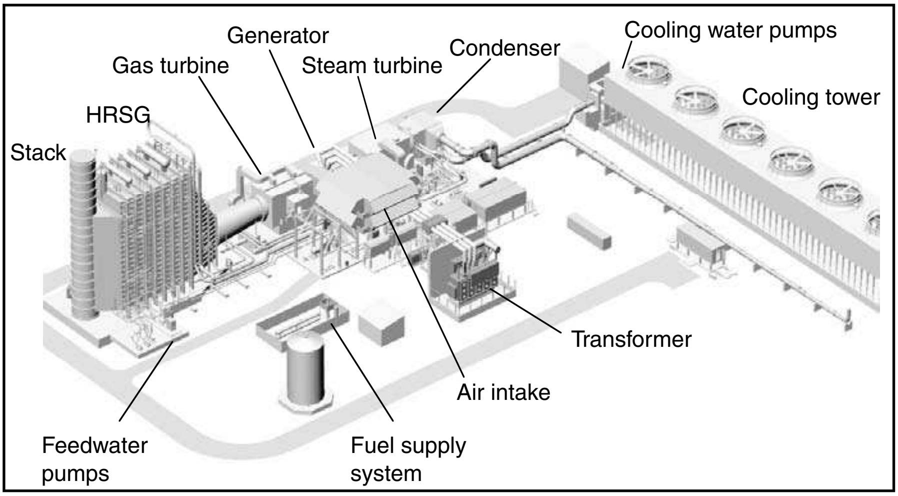

FIGURE 8.15.4 Arrangement and main components of a single-shaft CC plant.

- Fuel supply system
- Electrical equipment
- Instrumentation and control systems

Figure 8.15.5 shows the configuration of a *single-shaft CC* arrangement with the steam turbine at one end, the common generator in the center, and a synchronous self-shifting (SSS) clutch between the

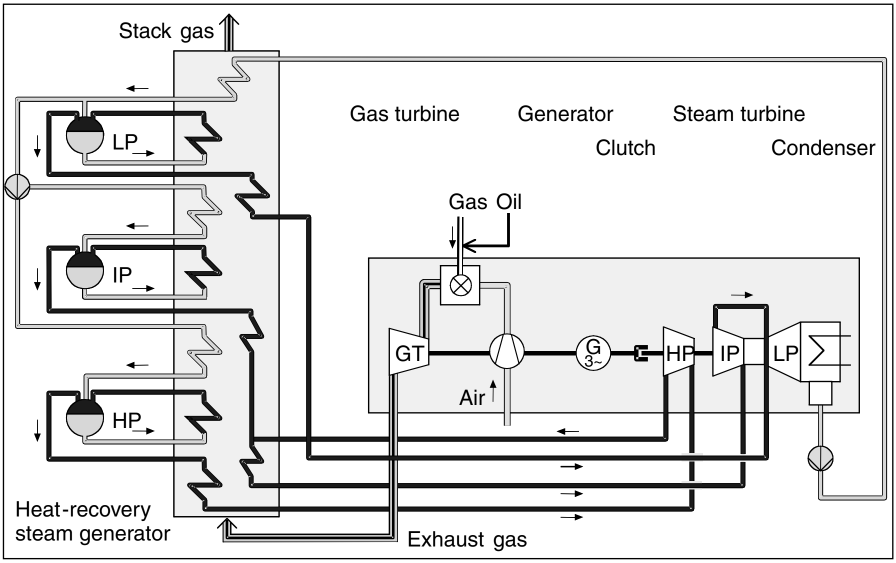

FIGURE 8.15.5 Single-shaft CC plant schematic with triple-pressure reheat.

generator and the steam turbine. The gas turbine can be started independently without any restrictions arising from the actual condition (hot, warm, or cold) of the steam turbine and the cooling system. The clutch acts as a coupling to enable unrestricted axial expansion of the steam turbine shaft relative to the generator. This allows optimized axial clearances for the steam turbine blading, resulting in improved efficiency.

The clutch engages automatically once the steam turbine approaches the operational rotating speed of the generator (3000 or 3600 rpm). It automatically disconnects the steam turbine whenever the steam turbine slows down relative to the generator. The clutch allows the gas turbine to be started and operated independently of the steam turbine. The gas turbine can be started up relatively quickly and the steam turbine can be accelerated at a suitable rate once the gas turbine is loaded. The steam turbine can be shut down at any time, leaving the gas turbine operating in open-cycle mode. In this mode, the steam produced is dumped to the condenser via the bypass station. The single-shaft configuration requires less space and can be built in efficient and independent units.

In the *multishaft CC* arrangement, the gas turbine and the steam turbine are separated; each engine has its own generator and transformer. They are built in 1 + 1 configuration, which means one gas turbine, one HRSG and one steam turbine as the schematic in Figure 8.15.6 shows, or in the very common 2 + 1 configuration (two gas turbines, two HRSGs, and one common steam turbine). Sometimes a 3 + 1 arrangement and even a 4 + 1 arrangement are used.

The multishaft arrangement offers the advantage that the plant can be built in what is known as “phased construction.” The gas turbine with its very fast construction time can be installed first and operated in a simple cycle (of course, with low efficiency); the plant can be extended later by adding an HRSG and steam turbine along with all the other necessary equipment. In this way, the customer gets not only a gradual increase in power output but also a deferment of the necessary investment. In such an unfired configuration, about two thirds of the total power output is generated in the gas turbine and one third in the steam turbine. This is due to the fixed amount of exhaust energy from the gas turbine.

Natural- gas-fired CC plants have relatively small auxiliary systems and do not require major stack gas clean-up systems. Consequently, the parasitic power of CC plants is low compared to steam power plants — amounting to approximately 1.5% of total rated power output.

One way to increase the plant output is to introduce supplementary firing in the exhaust duct between the gas turbine exit and HRSG inlet. This increases temperature and available heat transferred to the steam cycle (Figure 8.15.7).

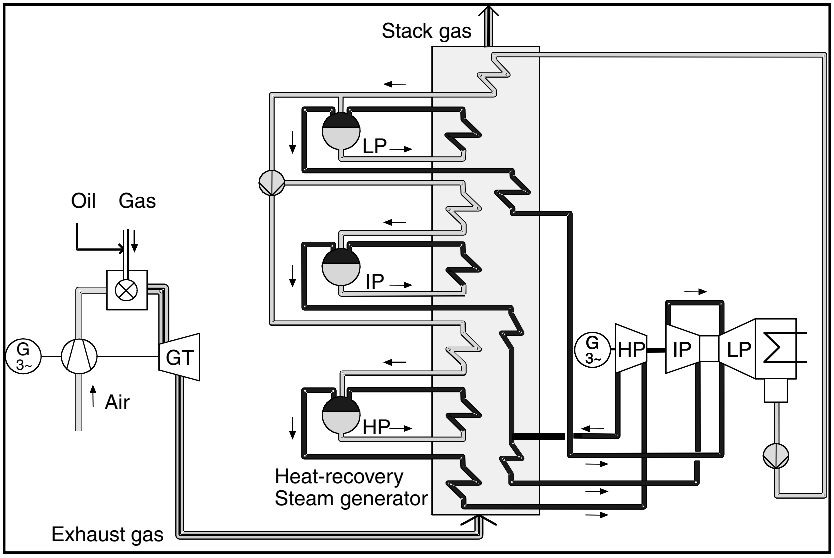

FIGURE 8.15.6 Multishaft CC plant arrangement with triple-pressure reheat.

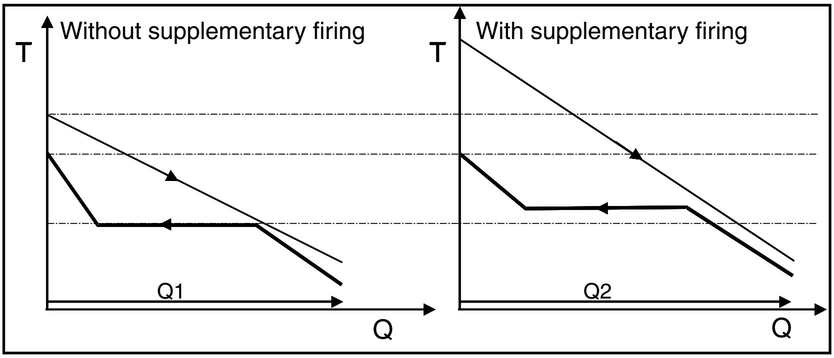

FIGURE 8.15.7 *T*–*Q* diagrams for CC without/with supplementary firing.

The advantages of adding supplementary or duct firing are:

- The total output from the combined cycle will increase with a higher fraction of the output coming from the steam turbine cycle.
- The temperature at the HRSG inlet can be controlled. This is important because the temperature and mass flow rate at the exit from the gas turbine are highly dependent on ambient temperature.
- The implementation of supplementary firing requires relatively low investment.
- Duct firing can be easily turned on or off, making it an excellent choice for peaking capacity.

The disadvantage is that a drop in overall plant efficiency occurs when the duct firing is employed.

Duct firing can be employed in varying amounts, from small firing rates to compensate for high ambient temperature reductions in CT output to firing levels that can double the steam cycle output. For this reason, an economic analysis is recommended before applying this option.

Combined Heat and Power from Combined-Cycle Plants

As in other power plants, not only electricity but also usable heat can be produced in CC plants and thus a fuel utilization factor ($(P_{electricity} + P_{heat})/Q_{fuel}$) up to 90% can be achieved. Depending on specific

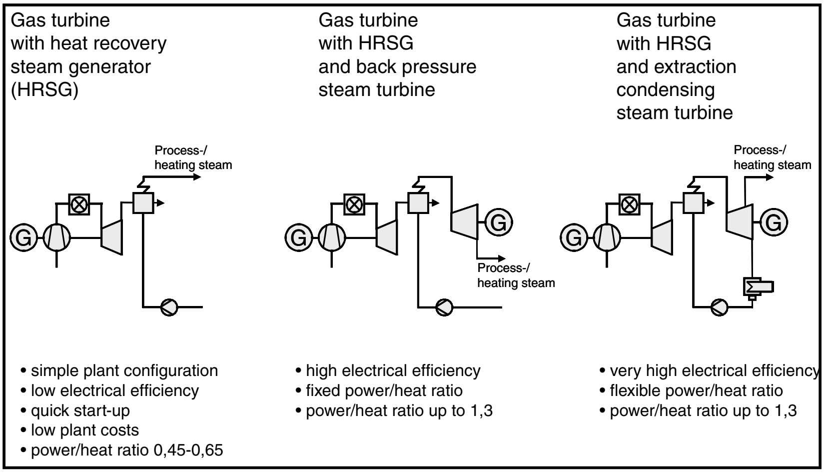

FIGURE 8.15.8 CHP concepts using gas turbines.

requirements, several different gas turbine power plant configurations can be utilized in cogeneration applications (Figure 8.15.8). A plant with a backpressure turbine has a relatively inflexible operation profile, while the use of an extraction condensing turbine makes it possible to vary the electric power-to-heat ratio depending on the demand. The required temperature and amount of heated steam are the primary factors for determining the design concept.

Environmental Aspects

From an environmental perspective, the natural-gas-fired CC is one of the most environmentally benign fossil-fueled power plant designs. As a result of its high efficiency and the use of clean natural gas, emissions of the greenhouse gas carbon dioxide (CO_2) are very low. Depending on plant design, a value of approximately 320 to 380 g/kWh (0.70 and 0.83 lb/kWh) can be obtained. The very high efficiency is also the reason for the relatively small amount of waste heat that must be dumped into the atmosphere.

With the development of dry low-NO_x (DLN) burners, the standard NO_x emissions are today <25 ppmvd with a tendency to even lower values. With the help of selective catalytic reduction (SCR) values of <5 ppmvd can be achieved. CO emissions in the exhaust gas are usually <10 ppmvd in the upper load range. CO catalysts can lower this value to <4 ppmvd.

Further Information

Barclay, F.J., Combined power and process. An exergy approach. *Professional Eng.*, 1998.

Bonzani, G. et al. Technical and economic optimization of a 450-MW combined cycle plant, in *1991 ASME Cogen-Turbo, 5th International Symposium and Exposition on Gas Turbines in Cogeneration, Repowering and Peak-Load Power Generation*, van der Linden, S. et al., Eds., 131–143, ASME, New York, 1991.

Dechamps, P.J. et al. Advanced combined cycle alternatives with advanced gas turbines, in *ASME Cogen-Turbo Power93, 7th Congress and Exposition on Gas Turbines in Cogeneration and Utility*, Holland, H.W. et al., Eds., 387–396, ASME, New York, 1993.

Gyarmathy, G. and Ortmann, P., The off design of single- and dual-pressure steam cycles in CC plants, in *1991 ASME Cogen-Turbo, 5th International Symposium and Exposition on Gas Turbines in Cogeneration, Repowering and Peak-Load Power Generation*, van der Linden, S. et al., Eds., 271–280, ASME, New York, 1991.

Hannemann, F. et al., V94.2 Buggenum experience and improved concepts for syngas application. Gasification Technology Council (GTC), San Francisco, 2002.

Horlock, J.H., *Combined Power Plants Including Combined Cycle Gas Turbine (CCGT) Plants*, Pergamon Press, New York, 1992.

Huettenhofer, K. and Lezuo A., Cogeneration Power Plant Concepts Using Advanced Gas Turbines. VGB PowerTech 6/2001 (50–56).

Kehlhofer, W., *Combined-Cycle Gas & Steam Turbine Power Plants*, Fairmont Press, Englewood Cliffs, NJ, 1991.

Kehlhofer, R., Bachmann, R., Nielson, H., and Warner, J., *Combined Cycle Gas and Steam Turbine Power Plants*, 2nd ed., PennWell Books, Tulsa, OK, 1999.

Kiameh, P. and McCombs, K., *Power Generation Handbook. Selection, Applications, Operation,and Maintenance*, McGraw–Hill, 2002.

Maurer, R., Destec's successes and plans for coal gasification combined cycle (CGCVC) power systems, in *1992 ASME Cogen-Turbo, 6th International Conference in Cogeneration and Utility*, Cooke, D.H. et al., Eds., 75–85, ASME, New York, 1992.

9

Air-Conditioning and Refrigeration

Herbert A. Ingley
University of Florida

Shan K. Wang
Consultant

Ari Rabl
Centre d'Energetique
E-Cole des Mines de Paris

Peter S. Curtiss
Curtiss Engineering

Zalman Lavan
Deceased

9.1 Introduction

Shan K. Wang

Air-Conditioning

Air-conditioning is a process that simultaneously conditions air; distributes it combined with ventilation air to the conditioned space; and at the same time controls and maintains the space's temperature, humidity, air movement, air cleanliness, sound level, and pressure differential within predetermined limits for the health and comfort of the occupants, for product processing, or both.

The acronym HVAC&R stands for heating, ventilating, air-conditioning, and refrigerating. The combination of these processes is equivalent to the functions performed by air-conditioning.

Because I-P units are widely used in the HVAC&R industry in the U.S., I-P units are used in this chapter.

Air-Conditioning Systems

An *air-conditioning* or *HVAC&R system* consists of components and equipment arranged in sequential order to heat or cool, humidify or dehumidify, clean and purify, attenuate objectionable equipment noise, transport the conditioned outdoor air and recirculate air to the conditioned space, and control and maintain an indoor or enclosed environment at optimum energy use.

The types of buildings which the air-conditioning system serves can be classified as:

- Institutional buildings, such as hospitals and nursing homes
- Commercial buildings, such as offices, stores, and shopping centers
- Residential buildings, including single-family and multifamily low-rise buildings of three or fewer stories above grade
- Manufacturing buildings, which manufacture and store products

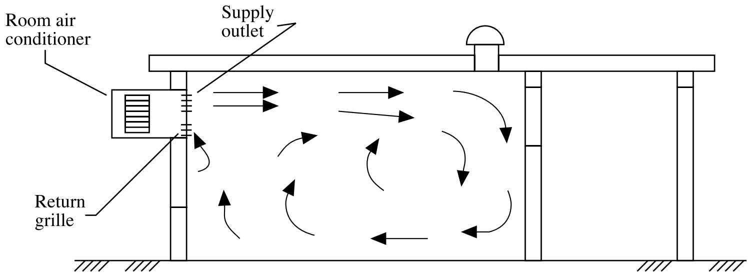

FIGURE 9.1.1 An individual room air-conditioning system.

Types of Air-Conditioning Systems

In institutional, commercial, and residential buildings, air-conditioning systems are mainly for the occupants' health and comfort. They are often called *comfort air-conditioning systems.* In manufacturing buildings, air-conditioning systems are provided for product processing, or for the health and comfort of workers as well as processing, and are called *processing air-conditioning systems.*

Based on their size, construction, and operating characteristics, air-conditioning systems can be classified as the following.

Individual Room or Individual Systems. An individual air-conditioning system normally employs either a single, self-contained, packaged room air conditioner (installed in a window or through a wall) or separate indoor and outdoor units to serve an individual room, as shown in Figure 9.1.1. "Self-contained, packaged" means factory assembled in one package and ready for use.

Space-Conditioning Systems or Space Systems. These systems have their air-conditioning—cooling, heating, and filtration—performed predominantly in or above the conditioned space, as shown in Figure 9.1.2. Outdoor air is supplied by a separate outdoor ventilation system.

Unitary Packaged Systems or Packaged Systems. These systems are installed with either a single self-contained, factory-assembled packaged unit (PU) or two split units: an indoor air handler, normally with ductwork, and an outdoor condensing unit with refrigeration compressor(s) and condenser, as shown in Figure 9.1.3. In a packaged system, air is cooled mainly by direct expansion of refrigerant in coils called DX coils and heated by a gas (or oil) furnace or electric heating. The unit may also function as a reverse cycle and provide heat (heat pump).

Central Hydronic or Central Systems. A central system uses chilled water or heating hot water from a central plant to cool and heat the air at the coils in an air handling unit (AHU) as shown in Figure 9.1.4. For energy transport, the heat capacity of water is about 3400 times greater than that of air. Central systems are built-up systems assembled and installed on the site.

Both central and space-conditioning systems consist of the following.

Air Systems. An air system is also called an air handling system or the air side of an air-conditioning or HVAC&R system. Its function is to condition the air, distribute it, and control the indoor environment according to requirements. The primary equipment in an air system is an AHU or air handling unit; both of these include fan, coils, filters, dampers, humidifiers (optional), supply and return ductwork, supply outlets and return inlets, and controls.

Water Systems. These systems include chilled water, hot water, and condenser water systems. A water system consists of pumps, piping work, and accessories. The water system is sometimes called the water side of a central or space-conditioning system.

Central Plant Refrigeration and Heating Systems. The refrigeration system in the central plant of a central system is usually in the form of a chiller package with an outdoor condensing unit. The refrigeration system is also called the refrigeration side of a central system. A boiler and accessories make up the

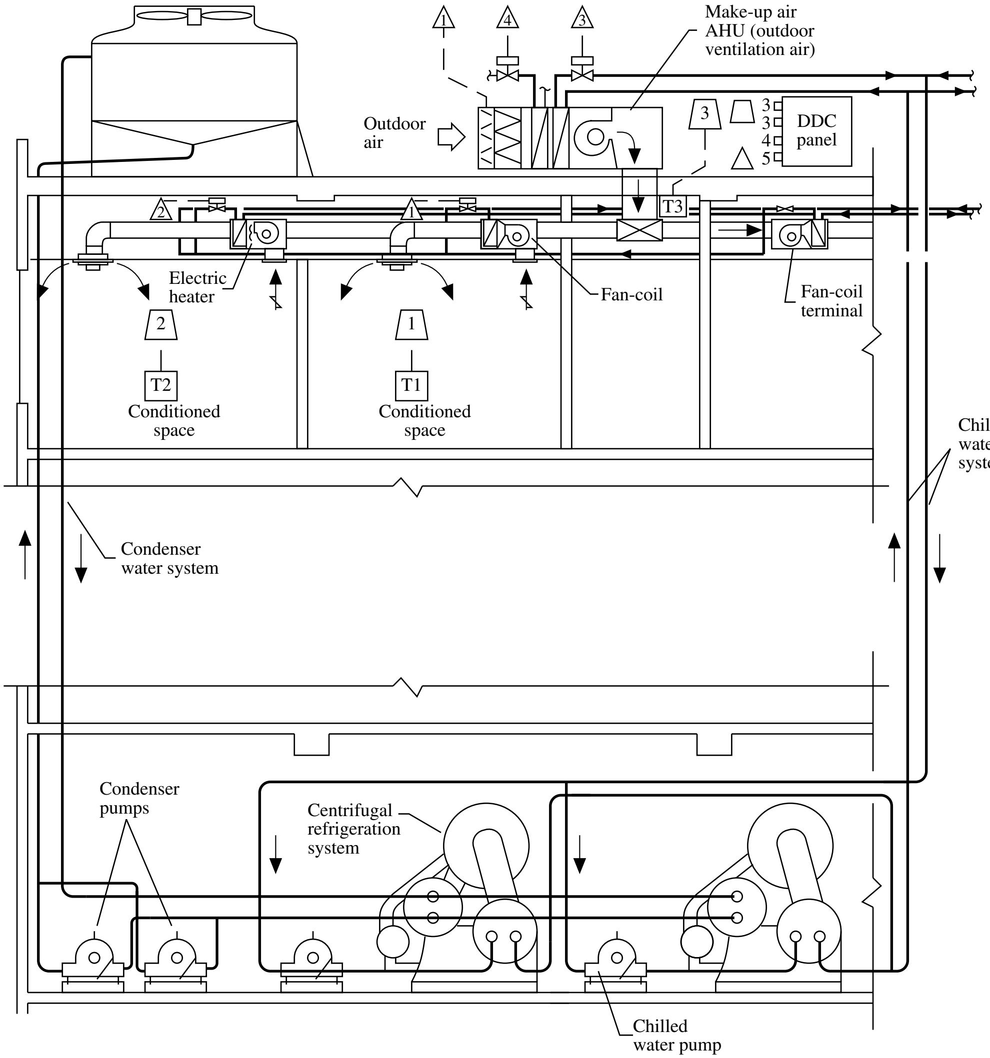

FIGURE 9.1.2 A space-conditioning air-conditioning system (fan-coil system).

heating system in a central plant for a central system, and a direct-fired gas furnace is often the heating system in the air handler of a rooftop packaged system.

Control Systems. Control systems usually consist of sensors, a microprocessor-based direct digital controller (DDC), a control device, control elements, personal computer (PC), and communication network.

Air-Conditioning Project Development and System Design

The goal of an air-conditioning/HVAC&R system is to provide a healthy and comfortable indoor environment with acceptable indoor air quality, while being energy efficient and cost effective.

ASHRAE Standard 62 defines *acceptable indoor air quality* as "air in which there are no known contaminants at harmful concentrations as determined by cognizant authorities and with which a substantial majority (80% or more) of the people exposed do not express dissatisfaction."

The basic steps in the development and use of an air-conditioning project are scope definition design, procurement, installation, commissioning, operation, and maintenance. There are several types of air-conditioning projects: *design-bid, design-build,* and construction management to name a few. A design-bid

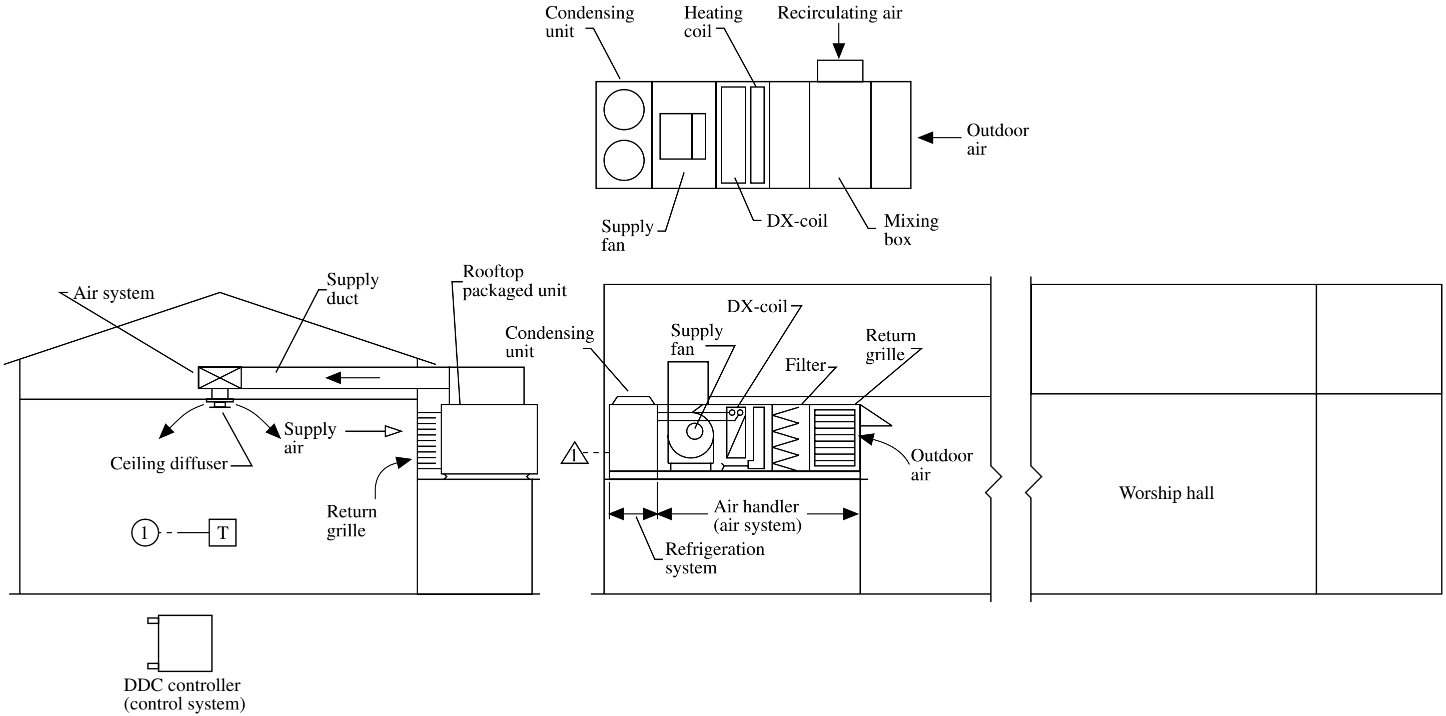

FIGURE 9.1.3 A packaged air-conditioning system.

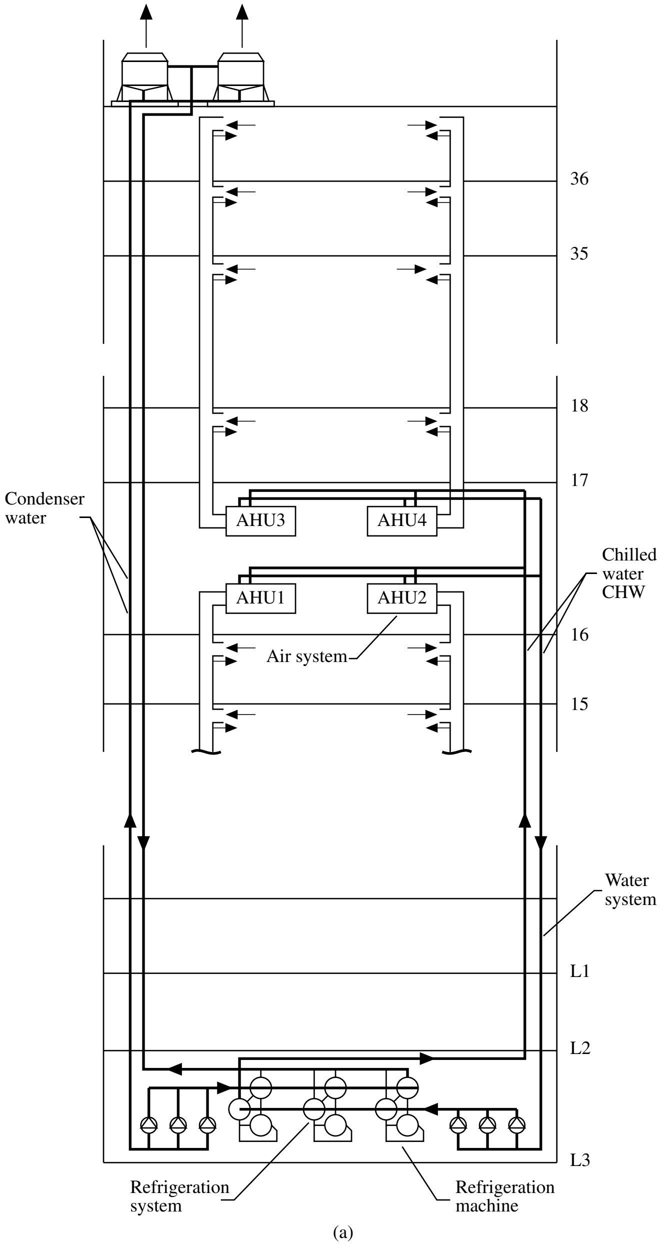

FIGURE 9.1.4a A central air-conditioning system: schematic diagram.

project separates the design (engineering consultant) and installation (contractors) responsibilities. In a design-build project, the design is also done by the installation contractor. A design-build project is usually a small project or a project having insufficient time to go through normal bidding procedures.

In the building construction industry, air-conditioning or HVAC&R is one of the *mechanical services*; these also include plumbing, fire protection, and escalators.

Air-conditioning design is a process of selecting the optimum system, subsystem, equipment, and components from various alternatives and preparing the drawings and specifications. Haines (1994) summarized this process in four phases: gather information, develop alternatives, evaluate alternatives, and sell

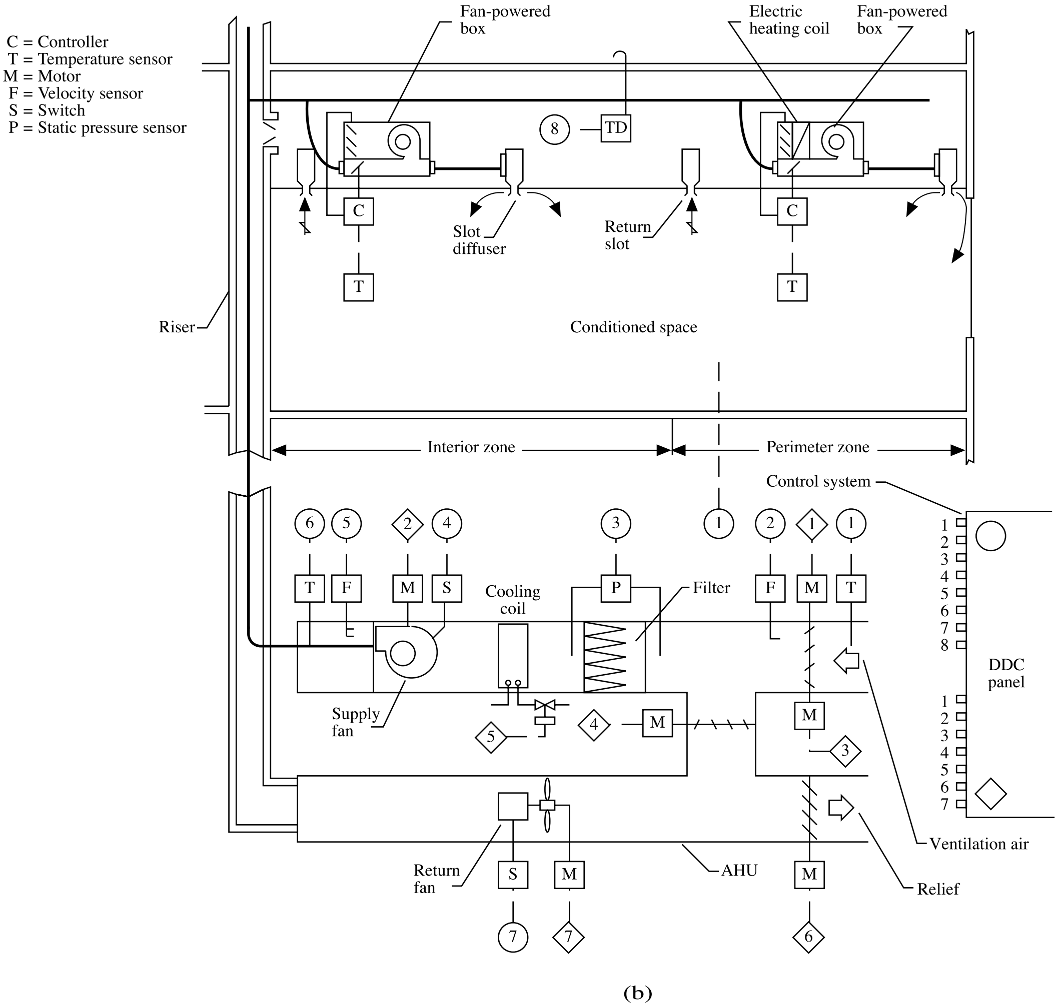

FIGURE 9.1.4b A central air-conditioning system: air and control systems for a typical floor.

the best solution. Design determines the basic operating characteristics of a system. After an air-conditioning system is designed and constructed, it is difficult and expensive to change its basic characteristics.

The foundation of a successful project is teamwork and coordination between designer, contractor, and operator and between mechanical engineer, electrical engineer, facility operator, architect, and structural engineer.

Field experience is helpful to the designer. Before beginning the design process it is advisable to visit similar projects that have operated for more than 2 years and talk with the operator to investigate actual performance.

Mechanical Engineer's Responsibilities

The normal procedure in a design-bid construction project and the mechanical engineer's responsibilities are

1. Initiation of a project by owner or developer
2. Define scope, develop schedule, establish budget
3. Organizing a design team
4. Negotiation of a contract
5. Determining the design criteria and indoor environmental parameters

6. Calculation of cooling and heating loads
7. Selection of systems, subsystems, and their components
8. Preparation of schematic layouts; sizing of piping and ductwork
9. Preparation of contract documents: drawings and specifications
10. Competitive biddings by various contractors; evaluation of bids; negotiations and modifications
11. Advice on awarding of contract
12. Monitoring, supervision, and inspection of installation; reviewing shop drawings
13. Supervision of commissioning
14. Modification of drawings to the as-built condition; preparation of the operation and maintenance manual
15. Handing over to the property management for operation

Design Documents

Drawings and *specifications* are legal documents of a construction contract. The designer conveys the owner's or developer's requirements to the contractor through these documents. Drawings and specifications complement each other.

Drawings should clearly and completely show, define, and present the work. Adequate plan and sectional views should be drawn. More often, isometric drawings are used to show the flow diagrams for water or the supply, return, and exhaust air. Drawings provide information on size, quantity and location and may schedule specific systems by model number and performance.

Specifications include the legal contract between the owner and the contractor, installer, or vendor and the technical specifications, which describe in detail what kind of material and equipment should be used and how they are to be installed.

Most projects now use a format developed by the Construction Specifications Institute (CSI) called the Masterformat for Specifications.

Each section includes general considerations, equipment and material, and field installation. Design criteria and selected indoor environmental parameters that indicate the performance of the HVAC&R system must be clearly specified.

There are two types of specifications: the performance specification, which depends mainly on the required performance criteria, and the or-equal specification, which specifies the wanted vendor. Specifications should be written in simple, direct, and clear language without repetition.

Computer-Aided Design and Drafting

With the wide acceptance of the PC and the availability of numerous types of engineering software, the use of *computer-aided drafting* (CAD) and *computer-aided design and drafting* (CADD) has become common practice in the engineering office.

Drafting software used to reproduce architectural drawings is the foundation of CADD. Automated CAD (AutoCAD) is the leading personal computer-based drafting tool software used in architectural and engineering design firms.

Software for piping system design and analysis can also be integrated with CAD. The software developed at the University of Kentucky, KYCAD/KYPIPE, is intended for the design and diagnosis of large water piping systems, has extensive hydraulic modeling capacities, and is the most widely used. Softdesk AdCADD Piping is relative new software; it is intended for drafting in 2D and 3D, linking to AutoCAD through design information databases.

Currently, software for CADD for air-conditioning and HVAC&R falls into two categories: engineering and product. The engineering category includes CAD (AutoCAD integrated with duct and piping system), load calculations and energy analysis, etc. The most widely used software for load calculations and energy analysis is Department of Energy DOE-2, Trane Company's TRACE 700, and Carrier Corporation's softwares for load calculation, HAP.

Product categories include selection, configuration, performance, price, and maintenance schedule. Product manufacturers provide software including data and CAD drawings for their specific product.

Codes and Standards

Codes are federal, state, or city laws that require the designer to perform the design without violating people's (including occupants and the public) safety and welfare. Federal and local codes must be followed. The designer should be thoroughly familiar with relevant codes. HVAC&R design codes are definitive concerning structural and electrical safety, fire prevention and protection (particularly for gas- or oil-fired systems), environmental concerns, indoor air quality, and energy conservation.

Often standards are referenced by codes and thus become enforceable. Otherwise, conformance with *ASHRAE Standards* is voluntary.

For the purpose of performing an effective, energy-efficient, safe, and cost-effective air-conditioning system design, the following ASHRAE Standards should be referred to from time to time:

- ANSI/ASHRAE/IESNA Standard 90.1-2001, Energy Standard for Buildings Except New Low-Rise Residential Buildings
- ANSI/ASHRAE Standard 62, Ventilation for Acceptable Indoor Air Quality
- ANSI/ASHRAE Standard 55-1992, Thermal Environmental Conditions for Human Occupancy
- ASHRAE Standard 15-2001, Safety Standard for Refrigeration Systems

9.2 Psychrometrics

Shan K. Wang

Moist Air

Above the surface of the earth is a layer of air called the *atmosphere*, or *atmospheric air*. The lower atmosphere, or homosphere, is composed of moist air, that is, a mixture of dry air and water vapor.

Psychrometrics is the science of studying the thermodynamic properties of moist air. It is widely used to illustrate and analyze the change in properties and the thermal characteristics of the air-conditioning process and cycles.

The composition of dry air varies slightly at different geographic locations and from time to time. The approximate composition of dry air by volume is nitrogen, 79.08%; oxygen, 20.95%; argon, 0.93%; carbon dioxide, 0.03%; other gases (e.g., neon, sulfur dioxide), 0.01%.

The amount of water vapor contained in the moist air within the temperature range 0 to 100°F changes from 0.05 to 3% by mass. The variation of water vapor has a critical influence on the characteristics of moist air.

The equation of state for an ideal gas that describes the relationship between its thermodynamic properties covered in Chapter 2 is

$$pv = RT_R \tag{9.2.1}$$

or

$$pV = mRT_R \tag{9.2.2}$$

where

p = pressure of the gas, psf (1 psf = 144 psi)
v = specific volume of the gas, ft^3/lb
R = gas constant, ftlb$_f$/lb$_m$ °R
T_R = absolute temperature of the gas, °R
V = volume of the gas, ft^3
m = mass of the gas, lb

The most exact calculation of the thermodynamic properties of moist air is based on the formulations recommended by Hyland and Wexler (1983) of the U.S. National Bureau of Standards. The psychrometric charts and tables developed by ASHRAE are calculated and plotted from these formulations. According to Nelson et al. (1986), at a temperature between 0 and 100°F, enthalpy and specific volume calculations using ideal gas Equation (9.2.1) and Equation (9.2.2) show a maximum deviation of 0.5% from the results of Hyland and Wexler's exact formulations. Therefore, ideal gas equations are used in the development and calculation of psychrometric formulations in this handbook.

Although air contaminants may seriously affect human health, they have little effect on the thermodynamic properties of moist air. For thermal analysis, moist air may be treated as a binary mixture of dry air and water vapor.

Applying Dalton's law to moist air:

$$p_{\mathrm{at}} = p_{\mathrm{a}} + p_{\mathrm{w}} \tag{9.2.3}$$

where

p_{at} = atmospheric pressure of the moist air, psia
p_{a} = partial pressure of dry air, psia
p_{w} = partial pressure of water vapor, psia

Dalton's law is summarized from the experimental results and is more accurate at low gas pressure. Dalton's law can also be extended, as the Gibbs-Dalton law, to describe the relationship of internal energy, enthalpy, and entropy of the gaseous constituents in a mixture.

Humidity and Enthalpy

The *humidity ratio* of moist air, *w*, in lb/lb is defined as the ratio of the mass of the water vapor, m_{w} to the mass of dry air, m_{a}, or

$$w = m_{\mathrm{w}}/m_{\mathrm{a}} = 0.62198 p_{\mathrm{w}}/\left(p_{\mathrm{at}} - p_{\mathrm{w}}\right) \tag{9.2.4}$$

The *relative humidity* of moist air, φ, or RH, is defined as the ratio of the mole fraction of water vapor, x_{w}, to the mole fraction of saturated moist air at the same temperature and pressure, x_{ws}. Using the ideal gas equations, this relationship can be expressed as:

$$\varphi = x_{\mathrm{w}}/x_{\mathrm{ws}}\big|_{T,p} = p_{\mathrm{w}}/p_{\mathrm{ws}}\big|_{T,p} \tag{9.2.5}$$

and

$$x_{\mathrm{w}} = n_{\mathrm{w}}/\left(n_{\mathrm{a}} + n_{\mathrm{w}}\right); \quad x_{\mathrm{ws}} = n_{\mathrm{ws}}/\left(n_{\mathrm{a}} + n_{\mathrm{ws}}\right)$$

$$x_{\mathrm{a}} + x_{\mathrm{w}} = 1 \tag{9.2.6}$$

where

p_{ws} = pressure of saturated water vapor, psia
T = temperature, °F
n_{a}, n_{w}, n_{ws} = number of moles of dry air, water vapor, and saturated water vapor, mol

Degree of saturation μ is defined as the ratio of the humidity ratio of moist air, *w*, to the humidity ratio of saturated moist air, w_{s}, at the same temperature and pressure:

$$\mu = w/w_{\mathrm{s}}\big|_{T,p} \tag{9.2.7}$$

The difference between φ and μ is small, usually less than 2%.

At constant pressure, the difference in specific enthalpy of an ideal gas, in Btu/lb, is $\Delta h = c_p \Delta T$. Here c_p represents the specific heat at constant pressure, in Btu/lb. For simplicity, the following assumptions are made during the calculation of the *enthalpy* of moist air:

1. At 0°F, the enthalpy of dry air is equal to zero.
2. All water vapor is vaporized at 0°F.
3. The enthalpy of saturated water vapor at 0°F is 1061 Btu/lb.
4. The unit of the enthalpy of the moist air is Btu per pound of dry air and the associated water vapor, or Btu/lb.

Then, within the temperature range 0 to 100°F, the enthalpy of the moist air can be calculated as:

$$\begin{aligned} h &= c_{\text{pd}} T + w\left(h_{\text{g0}} + c_{\text{ps}} T\right) \\ &= 0.240T + w(1061 + 0.444T) \end{aligned} \tag{9.2.8}$$

where

c_{pd}, c_{ps} = specific heat of dry air and water vapor at constant pressure, Btu/lb°F. Their mean values can be taken as 0.240 and 0.444 Btu/lb°F, respectively.

h_{g0} = specific enthalpy of saturated water vapor at 0°F.

Moist Volume, Density, Specific Heat, and Dew Point

The specific *moist volume* v, in ft^3/lb, is defined as the volume of the mixture of dry air and the associated water vapor when the mass of the dry air is exactly 1 lb:

$$v = V/m_{\text{a}} \tag{9.2.9}$$

where V = total volume of the moist air, ft^3. Since moist air, dry air, and water vapor occupy the same volume,

$$v = R_{\text{a}} T_{\text{R}} / p_{\text{at}} (1 + 1.6078w) \tag{9.2.10}$$

where R_{a} = gas constant for dry air.

Moist air density, often called *air density* ρ, in lb/ft^3, is defined as the ratio of the mass of dry air to the total volume of the mixture, or the reciprocal of the moist volume:

$$\rho = m_{\text{a}}/V = 1/v \tag{9.2.11}$$

The *sensible heat of moist air* is the thermal energy associated with the change of air temperature between two state points. In Equation (9.2.8), $(c_{\text{pd}} + wc_{\text{ps}})T$ indicates the sensible heat of moist air, which depends on its temperature T above the datum 0°F. *Latent heat of moist air*, often represented by wh_{fg0}, is the thermal energy associated with the change of state of water vapor. Both of them are in Btu/lb. Within the temperature range 0 to 100°F, if the average humidity ratio w is taken as 0.0075 lb/lb, the *specific heat of moist air* c_{pa} can be calculated as:

$$c_{\text{pa}} = c_{\text{pd}} + wc_{\text{ps}} = 0.240 + 0.0075 \times 0.444 = 0.243 \text{ Btu/lb °F} \tag{9.2.12}$$

The *dew point temperature* T_{dew}, in °F, is the temperature of saturated moist air of the moist air sample having the same humidity ratio at the same atmospheric pressure. Two moist air samples of similar dew points T_{dew} at the same atmospheric pressure have the same humidity ratio w and the same partial pressure of water vapor p_{w}.

Thermodynamic Wet Bulb Temperature and Wet Bulb Temperature

The *thermodynamic wet bulb temperature* of moist air, T^*, is equal to the saturated state of a moist air sample at the end of a constant-pressure, ideal adiabatic saturation process:

$$h_1 + \left(w_s^* - w_1\right)h_w^* = h_s^* \tag{9.2.13}$$

where

h_1, h_s^* = enthalpy of moist air at the initial state and enthalpy of saturated air at the end of the constant-pressure, ideal adiabatic saturation process, Btu/lb

w_1, w_s^* = humidity ratio of moist air at the initial state and humidity ratio of saturated air at the end of the constant-pressure, ideal adiabatic saturation process, lb/lb

h_w^* = enthalpy of water added to the adiabatic saturation process at temperature T^*, Btu/lb

An *ideal adiabatic saturation process* is a hypothetical process in which moist air at initial temperature T_1, humidity ratio w_1, enthalpy h_1, and pressure p flows over a water surface of infinite length through a well-insulated channel. Liquid water is therefore evaporated into water vapor at the expense of the sensible heat of the moist air. The result is an increase of humidity ratio and a drop of temperature until the moist air is saturated at the thermodynamic wet bulb temperature T^* during the end of the ideal adiabatic saturation process.

The thermodynamic wet bulb temperature T^* is a unique fictitious property of moist air that depends only on its initial properties, T_1, w_1, or h_1.

A sling-type *psychrometer*, as shown in Figure 9.2.1, is an instrument that determines the temperature, relative humidity, and thus the state of the moist air by measuring its dry bulb and wet bulb temperatures. It consists of two mercury-in-glass thermometers. The sensing bulb of one of them is dry and is called the dry bulb. Another sensing bulb is wrapped with a piece of cotton wick, one end of which dips into a water tube. This wetted sensing bulb is called the wet bulb and the temperature measured by it is called the *wet bulb temperature* T'.

When unsaturated moist air flows over the surface of the wetted cotton wick, liquid water evaporates from its surface. As it absorbs sensible heat, mainly from the surrounding air, the wet bulb temperature drops. The difference between the dry and wet bulb temperatures is called *wet bulb depression* ($T - T'$). Turning the handle forces the surrounding air to flow over the dry and wet bulbs at an air velocity between 300 to 600 fpm. Distilled water must be used to wet the cotton wick.

At steady state, if heat conduction along the thermometer stems is neglected and the temperature of the wetted cotton wick is equal to the wet bulb temperature of the moist air, as the sensible heat transfer from the surrounding moist air to the cotton wick exactly equals the latent heat required for evaporation, the heat and mass transfer per unit area of the wet bulb surface can be evaluated as:

$$h_c\left(T - T'\right) + h_r\left(T_{ra} - T\right) = h_d\left(w_s' - w_1\right) \tag{9.2.14}$$

where

h_c, h_r = mean conductive and radiative heat transfer coefficient, Btu/hr ft²°F

h_d = mean convective mass transfer coefficient, lb/hr ft²

T = temperature of undisturbed moist air at a distance from the wet bulb, °F

T_{ra} = mean radiant temperature (covered later), °F

w_1, w_s' = humidity ratio of the moist air and the saturated film at the interface of cotton wick and surrounding air, lb/lb

h_{fg}' = latent heat of vaporization at the wet bulb temperature, Btu/lb

The humidity ratio of the moist air is given by:

$$w_1 = w_s' - K'\left(T - T'\right)\left(1 + \left\{h_r\left(T_{ra} - T'\right)/\left[h_c\left(T - T'\right)\right]\right\}\right)$$

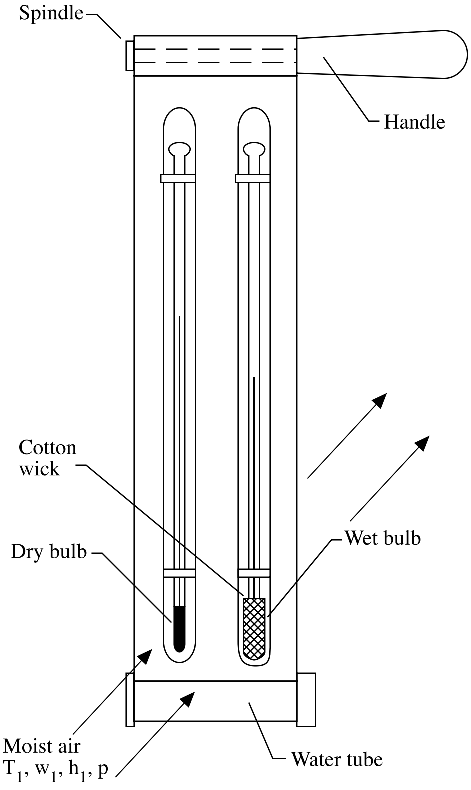

FIGURE 9.2.1 A sling psychrometer.

$$K' = c_{pa} Le^{0.6667} \big/ h'_{fg} \tag{9.2.15}$$

where

K' = wet bulb constant, which for a sling psychrometer = 0.00218 1/°F
Le = Lewis number

The wet bulb temperature T' depends not only on its initial state but also on the rate of heat and mass transfer at the wet bulb. Therefore, the thermodynamic wet bulb temperature is used in ASHRAE psychrometric charts.

Psychrometric Charts

A *psychrometric chart* is a graphical presentation of the thermodynamic properties of moist air and various air-conditioning processes and air-conditioning cycles. A psychrometric chart also helps in calculating and analyzing the work and energy transfer of various air-conditioning processes and cycles.

Psychrometric charts currently use two kinds of basic coordinates:

1. *h-w* charts. In *h-w* charts, enthalpy *h*, representing energy, and humidity ratio *w*, representing mass, are the basic coordinates. Psychrometric charts published by ASHRAE and the Charted Institution of Building Services Engineering (CIBSE) are *h-w* charts.
2. *T-w* charts. In *T-w* charts, temperature *T* and humidity ratio *w* are basic coordinates. Psychrometric charts published by Carrier Corporation, the Trane Company, etc. are *T-w* charts.

Figure 9.2.2 shows an abridged ASHRAE psychrometric chart. In the ASHRAE chart:

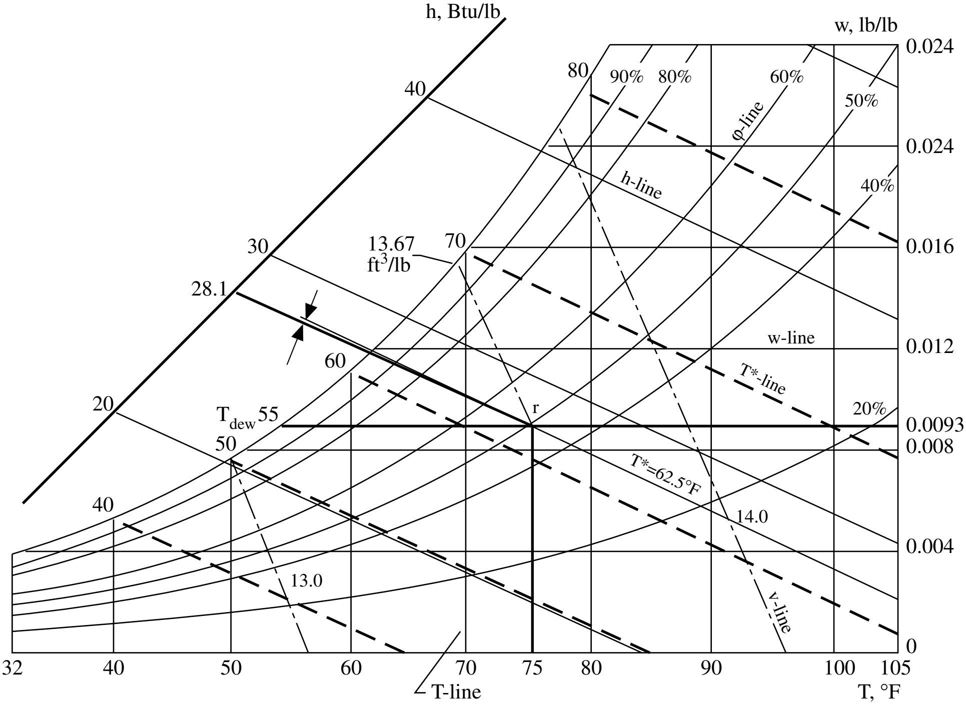

FIGURE 9.2.2 The abridged ASHRAE psychrometric chart and the determination of properties as in Example 9.2.1.

- A normal temperature chart has a temperature range of 32 to 120°F, a high-temperature chart 60 to 250°F, and a low-temperature chart –40 to 50°F. Since enthalpy is the basic coordinate, temperature lines are not parallel to each other. Only the 120°F line is truly vertical.
- Thermodynamic properties of moist air are affected by atmospheric pressure. The standard atmospheric pressure is 29.92 in. Hg at sea level. ASHRAE also published charts for high altitudes of 5000 ft, 24.89 in. Hg, and 7500 ft, 22.65 in. Hg. Both of them are in the normal temperature range.
- Enthalpy h-lines incline downward to the right-hand side (negative slope) at an angle of 23.5° to the horizontal line and have a range of 12 to 54 Btu/lb.
- Humidity ratio w-lines are horizontal lines. They range from 0 to 0.28 lb/lb.
- Relative humidity φ-lines are curves of relative humidity 10%, 20%, … 90% and a saturation curve. A saturation curve is a curve of the locus of state points of saturated moist air, that is, $\varphi = 100\%$. On a saturation curve, temperature T, thermodynamic wet temperature bulb T^*, and dew point temperature T_{dew} have the same value.
- Thermodynamic wet bulb T^*-lines have a negative slope slightly greater than that of the h-lines. A T^*-line meets the T-line of the same magnitude on the saturation curve.
- Moist volume v-lines have a far greater negative slope than h-lines and T^*-lines. The moist volume ranges from 12.5 to 15 ft³/lb.

Moist air has seven independent thermodynamic properties or property groups: h, T, φ, T^*, p_{at}, $\rho - v$, and $w - p_{\text{w}} - T_{\text{dew}}$. When p_{at} is given, any additional two of the independent properties determine the state of moist air on the psychrometric chart and the remaining properties.

Software using AutoCAD to construct the psychrometric chart and calculate the thermodynamic properties of moist air is available. It can also be linked to the load calculation and energy programs to analyze the characteristics of air-conditioning cycles.

Refer to Wang's *Handbook of Air Conditioning and Refrigeration* (1993) and *ASHRAE Handbook, Fundamentals* (2001) for details of psychrometric charts and psychrometric tables that list thermodynamic properties of moist air.

Example 9.2.1

An air-conditioned room at sea level has an indoor design temperature of 75°F and a relative humidity of 50%. Determine the humidity ratio, enthalpy, density, dew point, and thermodynamic wet bulb temperature of the indoor air at design condition.

Solution

1. Since the air-conditioned room is at sea level, a psychrometric chart of standard atmospheric pressure of 14.697 psi should be used to find the required properties.
2. Plot the state point of the room air at design condition r on the psychrometric chart. First, find the room temperature 75°F on the horizontal temperature scale. Draw a line parallel to the 75°F temperature line. This line meets the relative humidity curve of 50% at point r, which denotes the state point of room air as shown in Figure 9.2.2.
3. Draw a horizontal line toward the humidity ratio scale from point r. This line meets the ordinate and thus determines the room air humidity ratio $\varphi_r = 0.0093$ lb/lb.
4. Draw a line from point r parallel to the enthalpy line. This line determines the enthalpy of room air on the enthalpy scale, $h_r = 28.1$ Btu/lb.
5. Draw a line through point r parallel to the moist volume line. The perpendicular scale of this line indicates $v_r = 13.67$ ft^3/lb.
6. Draw a horizontal line to the left from point r. This line meets the saturation curve and determines the dew point temperature, $T_{dew} = 55$°F.
7. Draw a line through point r parallel to the thermodynamic wet bulb line. The perpendicular scale to this line indicates that the thermodynamic wet bulb temperature $T^* = 62.5$°F.

9.3 Air-Conditioning Processes and Cycles

Shan K. Wang

Air-Conditioning Processes

An *air-conditioning process* describes the change in thermodynamic properties of moist air between the initial and final stages of conditioning as well as the corresponding energy and mass transfers between the moist air and a medium, such as water, refrigerant, absorbent or adsorbent, or moist air itself. The energy balance and conservation of mass are the two principles used for the analysis and the calculation of the thermodynamic properties of the moist air.

Generally, for a single air-conditioning process, heat transfer or mass transfer is positive. However, for calculations that involve several air-conditioning processes, heat supplied to the moist air is taken as positive and heat rejected is negative.

The *sensible heat ratio* (SHR) of an air-conditioning process is defined as the ratio of the change in absolute value of sensible heat to the change in absolute value of total heat, both in Btu/hr:

$$\mathrm{SHR} = \left|q_{\mathrm{sen}}\right| / \left|q_{\mathrm{total}}\right| = \left|q_{\mathrm{sen}}\right| / \left(\left|q_{\mathrm{sen}}\right| + \left|q_{1}\right|\right) \tag{9.3.1}$$

For any air-conditioning process, the sensible heat change

$$q_{\mathrm{sen}} = 60 \mathring{V}_{\mathrm{s}} \rho_{\mathrm{s}} c_{\mathrm{pa}} \left(T_2 - T_1\right) = 60 \mathring{m}_{\mathrm{a}} c_{\mathrm{pa}} \left(T_2 - T_1\right) \tag{9.3.2}$$

where

$\overset{\circ}{V}_s$ = volume flow rate of supply air, cfm

ρ_s = density of supply air, lb/ft³

T_2, T_1 = moist air temperature at final and initial states of an air-conditioning process, °F

and the mass flow rate of supply air

$$\overset{\circ}{m}_s = \overset{\circ}{V}_s \rho_s \tag{9.3.3}$$

The latent heat change is

$$q_l \approx 60\overset{\circ}{V}_s \rho_s \left(w_2 - w_1\right) h_{\text{fg.58}} = 1060 \times 60\overset{\circ}{V}_s \rho_s \left(w_2 - w_1\right) \tag{9.3.4}$$

where w_2,w_1 = humidity ratio at final and initial states of an air-conditioning process, lb/lb.

In Equation (9.3.4), $h_{\text{fg58}} \approx 1060$ Btu/lb represents the latent heat of vaporization or condensation of water at an estimated temperature of 58°F, where vaporization or condensation occurs in an air-handling unit or packaged unit. Therefore

$$\text{SHR} = \overset{\circ}{m}_a c_{pa}\left(T_2 - T_1\right) \Big/ \left[\overset{\circ}{m}_a c_{pa}\left(T_2 - T_1\right) + \overset{\circ}{m}_a \left(w_2 - w_1\right) h_{\text{fg.58}}\right] \tag{9.3.5}$$

Space Conditioning, Sensible Cooling, and Sensible Heating Processes

In a *space conditioning process*, heat and moisture are absorbed by the supply air at state *s* and then removed from the conditioned space at the state of space air *r* during summer, as shown by line *sr* in Figure 9.3.1, or heat or moisture is supplied to the space to compensate for the transmission and infiltration losses through the building envelope as shown by line *s′r′*. Both processes are aimed at maintaining a desirable space temperature and relative humidity.

The space cooling load q_{rc}, in Btu/hr, can be calculated as:

$$q_{rc} = 60\overset{\circ}{m}_a\left(h_r - h_s\right) = 60\overset{\circ}{V}_s \rho_s \left(h_r - h_s\right) \tag{9.3.6}$$

where h_r, h_s = enthalpy of space air and supply air, Btu/lb.

The space sensible cooling load q_{rs}, in Btu/hr, can be calculated from Equation (9.3.2) and the space latent load q_{rl}, in Btu/hr, from Equation (9.3.1). In Equation (9.3.4), T_2 should be replaced by T_r and T_1 by T_s. Also in Equation (9.3.1), w_2 should be replaced by w_r and w_1 by w_s. The space heating load q_{rh} is always a sensible load, in Btu/hr, and can be calculated as:

$$q_{rh} = 60\overset{\circ}{m}_a c_{pa}\left(T_s - T_r\right) = 60\overset{\circ}{V}_s \rho_s c_{pa}\left(T_s - T_r\right) \tag{9.3.7}$$

where T_s, T_r = temperature of supply and space air, °F.

A *sensible heating process* adds heat to the moist air in order to increase its temperature; its humidity ratio remains constant, as shown by line 1-2 in Figure 9.3.1. A sensible heating process occurs when moist air flows over a heating coil. Heat is transferred from the hot water inside the tubes to the moist air. The rate of heat transfer from the hot medium to the colder moist air is often called the heating coil load q_{rh}, in Btu/hr, and is calculated from Equation (9.3.2).

A *sensible cooling process* removes heat from the moist air, resulting in a drop of its temperature; its humidity ratio remains constant, as shown by line 1′-2′ in Figure 9.3.1. The sensible cooling process

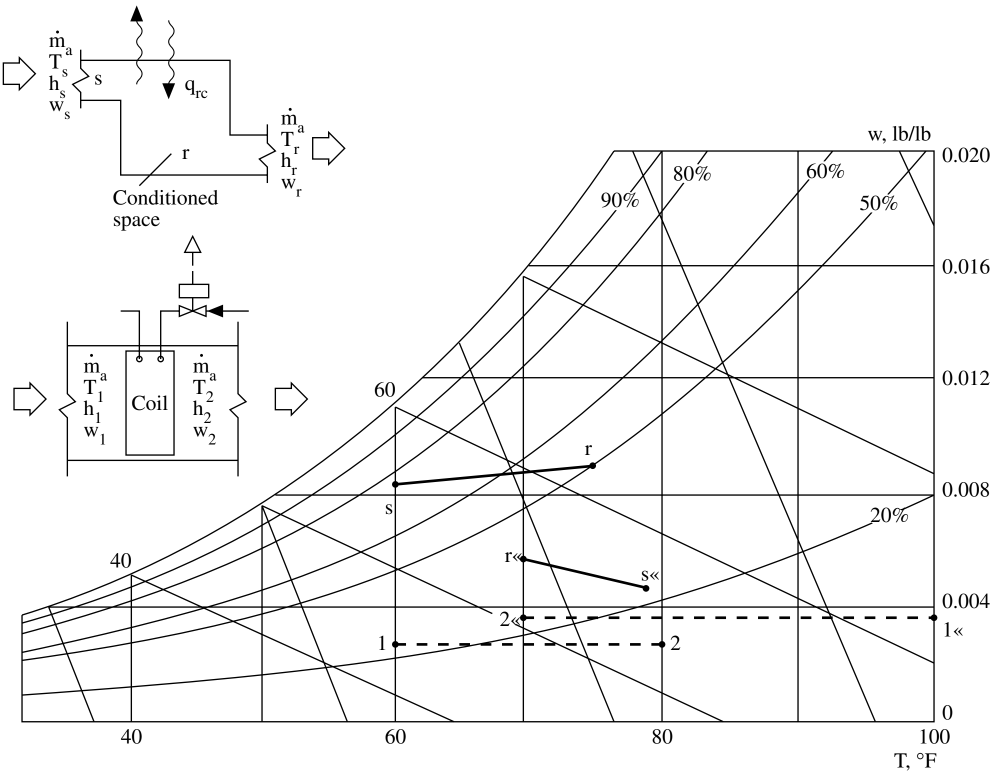

FIGURE 9.3.1 Supply conditioning, sensible heating, and sensible cooling processes.

occurs when moist air flows through a cooling coil containing chilled water at a temperature equal to or greater than the dew point of the entering moist air. The sensible cooling load can also be calculated from Equation (9.3.2). T_2 is replaced by T_1 and T_1 by $T_{2'}$.

Humidifying and Cooling and Dehumidifying Processes

In a *humidifying process*, water vapor is added to moist air and increases the humidity ratio of the moist air leaving the humidifier if the moist air entering is not already saturated. Large-scale humidification of moist air is usually performed by steam injection, evaporation from a water spray, atomizing water, a wetted medium, or by passing a side stream of air over water with submerged heating elements. Dry steam in a steam injection humidifying process is often supplied from the main steam line to a grid-type humidifier and injected into the moist air directly through small holes at a pressure slightly above atmospheric, as shown by line 1-2 in Figure 9.3.2(a) and (b). The humidifying capacity $\mathring{m}_{hu}$, in lb/min, is given by:

$$\mathring{m}_{hu} = \mathring{V}_s \rho_s \left(w_{hl} - w_{he} \right) \tag{9.3.8}$$

where w_{hl}, w_{he} = humidity ratio of moist air leaving and entering the humidifier, lb/lb. The slight inclination at the top of line 1-2 is due to the high temperature of the steam. The increase in temperature of the moist air due to steam injection can be calculated as:

$$\left(T_2 - T_1 \right) = w_{sm} c_{ps} T_s \Big/ \left(c_{pd} + w_{12} c_{ps} \right) \tag{9.3.9}$$

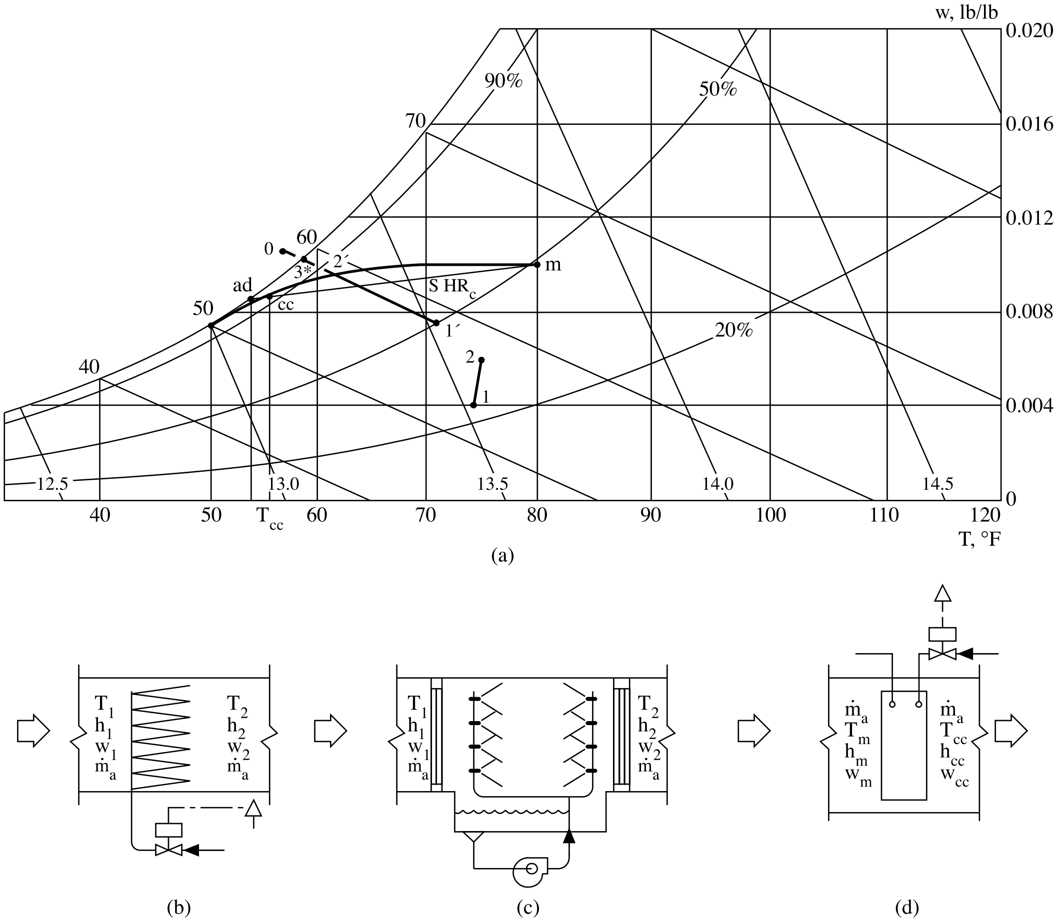

FIGURE 9.3.2 Humidifying and cooling and dehumidifying processes: (a) process on psychrometric chart, (b) steam humidifier, (c) air washer, and (d) chilled water cooling or DX coil.

where

T_2, T_1 = temperature of moist air at initial and final states, °F
w_{sm} = ratio of mass flow rate of injected steam to moist air, $\overset{\circ}{m}_s / \overset{\circ}{m}_a$
T_s = temperature of injected steam, °F
w_{12} = average humidity ratio of moist air, lb/lb

An *air washer* is a device that sprays water into moist air in order to humidify, to cool and dehumidify, and to clean the air, as shown in Figure 9.3.2(c). When moist air flows through an air washer, the moist air is humidified and approaches saturation. This actual adiabatic saturation process approximately follows the thermodynamic wet bulb line on the psychrometric chart as shown by line 1′-2′. The humidity ratio of the moist air is increased while its temperature is reduced. The cooling effect of this adiabatic saturation process is called *evaporative cooling*.

Oversaturation occurs when the amount of water present in the moist air w_{os}, in lb/lb, exceeds the saturated humidity ratio at thermodynamic wet bulb temperature w_s^*, as shown in Figure 9.3.2(a). When moist air leaves the air washer, atomizing humidifier, or centrifugal humidifier after humidification, it often contains unevaporated water droplets at state point 2′, w_w, in lb/lb. Because of the fan power heat gain, duct heat gain, and other heat gains providing the latent heat of vaporization, some evaporation takes place due to the heat transfer to the water drops, and the humidity ratio increases further. Such evaporation of oversaturated drops is often a process with an increase of both humidity ratio and enthalpy of moist air. Oversaturation can be expressed as:

$$w_{os} = w_o - w_s^* = \left(w_{2'} + w_w\right) - w_s^* \tag{9.3.10}$$

where

$w_{2'}$ = humidity ratio at state point 2′, lb/lb
w_o = sum of $w_{2'}$ and w_w, lb/lb

The magnitude of w_w depends mainly on the construction of the humidifier and water eliminator, if any. For an air washer, w_w may vary from 0.0002 to 0.001 lb/lb. For a pulverizing fan without an eliminator, w_w may be up to 0.00135 lb/lb.

Cooling and Dehumidifying Process

In a cooling and dehumidifying process, both the humidity ratio and temperature of moist air decrease. Some water vapor is condensed in the form of liquid water, called *condensate*. This process is shown by curve m-cc on the psychrometric chart in Figure 9.3.2(a). Here m represents the entering mixture of outdoor and recirculating air and cc the conditioned air leaving the cooling coil.

Three types of heat exchangers are used in a cooling and dehumidifying process: (1) chilled water cooling coil as shown in Figure 9.3.2(d); (2) direct expansion DX coil, where refrigerant evaporates directly inside the coil's tubes; and (3) air washer, in which chilled water spraying contacts condition air directly.

The temperature of chilled water entering the cooling coil or air washer T_{we}, in °F, determines whether it is a sensible cooling or a cooling and dehumidifying process. If T_{we} is smaller than the dew point of the entering air T''_{ae} in the air washer, or T_{we} makes the outer surface of the water cooling coil $T_{s.t} < T''_{ae}$, it is a cooling and dehumidifying process. If $T_{we} \geq T''_{ae}$, or $T_{s.t} \geq T''_{ae}$, sensible cooling occurs. The cooling coil's load or the cooling capacity of the air washer q_{cc}, in Btu/hr, is

$$q_{cc} = 60\overset{\circ}{V}_s \rho_s \left(h_{ae} - h_{cc}\right) - 60\overset{\circ}{m}_w h_w \tag{9.3.11a}$$

where

h_{ae}, h_{cc} = enthalpy of moist air entering and leaving the coil or washer, Btu/lb
$\overset{\circ}{m}_w$ = mass flow rate of the condensate, lb/min
h_w = enthalpy of the condensate, Btu/lb

Since the thermal energy of the condensate is small compared with q_{cc}, in practical calculations the term $60\overset{\circ}{m}_w h_w$ is often neglected, and

$$q_{cc} = 60\overset{\circ}{V}_s \rho_s \left(h_{ae} - h_{cc}\right) \tag{9.3.11b}$$

The sensible heat ratio of the cooling and dehumidifying process SHR_c can be calculated from

$$SHR_c = q_{cs}/q_{cc} \tag{9.3.12}$$

where q_{cs} = sensible heat removed during the cooling and dehumidifying process, Btu/hr. SHR_c is shown by the slope of the straight line joining points m and cc.

The relative humidity of moist air leaving the water cooling coil or DX coil depends mainly on the outer surface area of the coil including pipe and fins. For coils with ten or more fins per inch, if the entering moist air is around 80°F dry bulb and 68°F wet bulb, the relative humidity of air leaving the coil (off-coil) may be estimated as:

Four-row coil	90 to 95%
Six-row and eight-row coils	96 to 98%

Two-Stream Mixing Process and Bypass Mixing Process

For a *two-stream adiabatic mixing process*, two moist air streams, 1 and 2, are mixed together adiabatically and a mixture *m* is formed in a mixing chamber as shown by line 1-m1-2 in Figure 9.3.3. Since the AHU or PU is well insulated, the heat transfer between the mixing chamber and ambient air is small and is usually neglected. Based on the principle of heat balance and conservation of mass:

$$\begin{aligned} \mathring{m}_1 h_1 + \mathring{m}_2 h_2 &= \mathring{m}_m h_m \\ \mathring{m}_1 w_1 + \mathring{m}_2 w_2 &= \mathring{m}_m w_m \\ \mathring{m}_1 T_1 + \mathring{m}_2 T_2 &= \mathring{m}_m T_m \end{aligned} \tag{9.3.13}$$

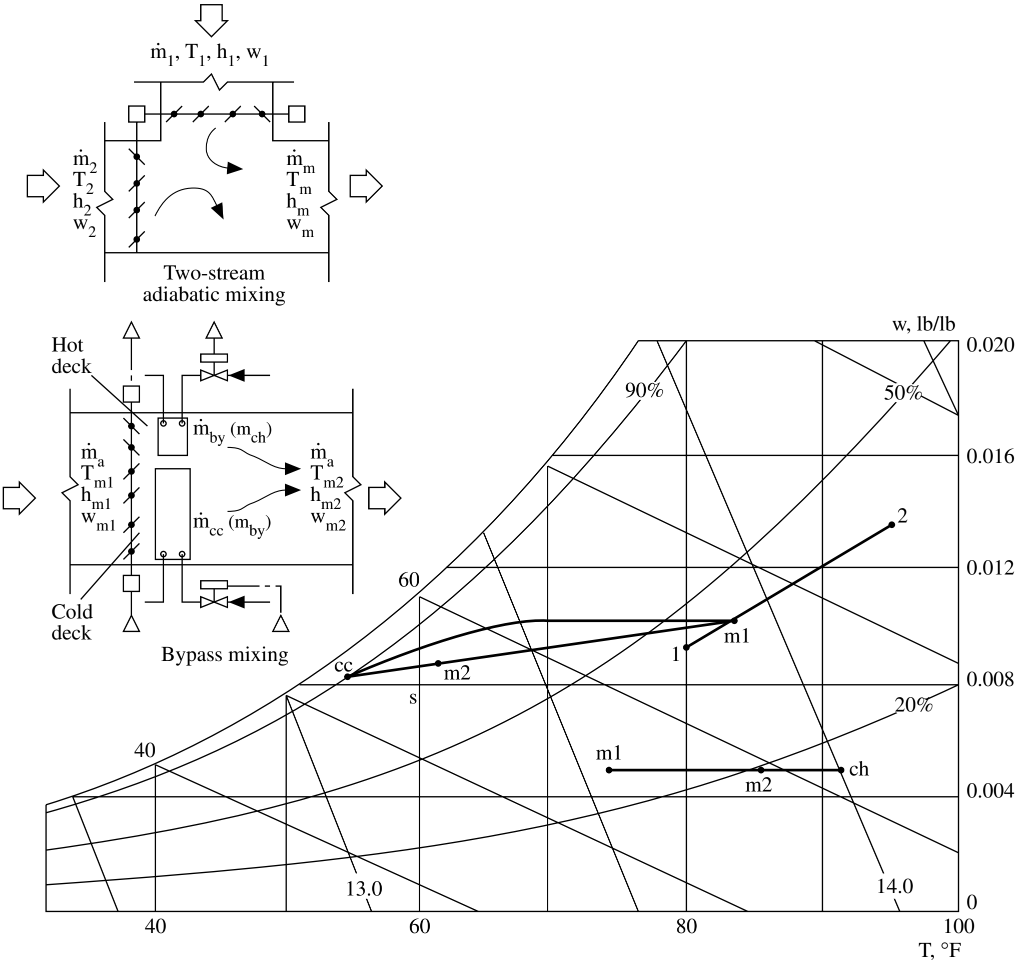

FIGURE 9.3.3 Mixing processes.

In Equation (9.3.13), $\mathring{m}$ represents the mass flow rate of air, lb/min; h the enthalpy, in Btu/lb; w the humidity ratio, in lb/lb; and T the temperature, in °F. Subscripts 1 and 2 indicate air streams 1 and 2 and m the mixture; also,

$$\begin{aligned} \mathring{m}_1/\mathring{m}_{\mathrm{m}} &= \left(h_2 - h_{\mathrm{m}}\right)/\left(h_2 - h_1\right) = \left(w_2 - w_{\mathrm{m}}\right)/\left(w_2 - w_1\right) \\ &= \left(\text{line segment m1 2}\right)/\left(\text{line segment 12}\right) \end{aligned} \tag{9.3.14}$$

Similarly,

$$\begin{aligned} \mathring{m}_2/\mathring{m}_{\mathrm{m}} &= \left(h_{\mathrm{m}} - h_1\right)/\left(h_2 - h_1\right) = \left(w_{\mathrm{m}} - w_1\right)/\left(w_2 - w_1\right) \\ &= \left(\text{line segment 1-ml}\right)/\left(\text{line segment 1-2}\right) \end{aligned} \tag{9.3.15}$$

Mixing point m must lie on the line that joins points 1 and 2 as shown in Figure 9.3.3.

If the differences between the density of air streams 1 and 2 and the density of the mixture are neglected,

$$\begin{aligned} \mathring{V}_1 h_1 + \mathring{V}_2 h_2 &= \mathring{V}_{\mathrm{m}} h_{\mathrm{m}} \\ \mathring{V}_1 w_1 + \mathring{V}_2 w_2 &= \mathring{V}_{\mathrm{m}} w_{\mathrm{m}} \\ \mathring{V}_1 T_1 + \mathring{V}_2 T_2 &= \mathring{V}_{\mathrm{m}} T_{\mathrm{m}} \end{aligned} \tag{9.3.16}$$

$$\mathring{V}_1 + \mathring{V}_2 = \mathring{V}_{\mathrm{m}} \tag{9.3.17}$$

In a *bypass mixing process*, a conditioned air stream is mixed with a bypass air stream that is not conditioned. The cold conditioned air is denoted by subscript "cc", the heated air "ch", and the bypass air "by".

Equation (9.3.14) and Equation (9.3.17) can still be used but subscript 1 should be replaced by cc or ch and subscript 2 by "by" (bypass).

Let $K_{\mathrm{cc}} = \mathring{m}_{\mathrm{cc}}/\mathring{m}_{\mathrm{m}}$ and $K_{\mathrm{ch}} = \mathring{m}_{\mathrm{ch}}/\mathring{m}_{\mathrm{m}}$; then the cooling coil's load q_{cc} and heating coil's load q_{ch}, both in Btu/hr, for a bypass mixing process are

$$\begin{aligned} q_{\mathrm{cc}} &= K_{\mathrm{cc}} \mathring{V}_{\mathrm{s}} \rho_{\mathrm{s}} \left(h_{\mathrm{m}} - h_{\mathrm{cc}}\right) \\ q_{\mathrm{ch}} &= K_{\mathrm{ch}} \mathring{V}_{\mathrm{s}} \rho_{\mathrm{s}} \left(h_2 - h_1\right) \end{aligned} \tag{9.3.18}$$

In Equation (9.3.18), subscript s denotes the supply air and m the mixture air stream.

Air-Conditioning Cycle and Operating Modes

An *air-conditioning cycle* comprises several air-conditioning processes that are connected in a sequential order. An air-conditioning cycle determines the operating performance of the air system in an air-conditioning system. The *working substance* to condition air may be chilled or hot water, refrigerant, desiccant, etc.

Each type of air system has its own air-conditioning cycle. Psychrometric analysis of an air-conditioning cycle is an important tool in determining its operating characteristics and the state of moist air at various system components, including the volume flow rate of supply air, the coil's load, and the humidifying and dehumidifying capacity.

According to the cycle performance, air-conditioning cycles can be grouped into two categories:

- *Open cycle*, in which the moist air at its end state does not resume its original state. An air-conditioning cycle with all outdoor air is an open cycle.
- *Closed cycle*, in which moist air resumes its original state at its end state. An air-conditioning cycle that conditions the mixture of recirculating and outdoor air, supplies it, recirculates part of the return air, and mixes it again with outdoor air is a closed cycle.

Based on the outdoor weather and indoor operating conditions, the operating modes of air-conditioning cycles can be classified as:

- *Summer mode*: when outdoor and indoor operating parameters are in summer conditions.
- *Winter mode*: when outdoor and indoor operating parameters are in winter conditions.
- *Air economizer mode*: when all outdoor air or an amount of outdoor air that exceeds the minimum amount of outdoor air required for the occupants is taken into the AHU or PU for cooling. The air economizer mode saves energy use for refrigeration.

Continuous modes operate 24 hr a day and 7 days a week. Examples are systems that serve hospital wards and refrigerated warehouses. An *intermittently operated mode* usually shuts down once or several times within a 24-hr operating cycle. Such systems serve offices, class rooms, retail stores, etc. The 24-hr day-and-night cycle of an intermittently operated system can again be divided into:

1. *Cool-down or warm-up period.* When the space is not occupied and the space air temperature is higher or lower than the predetermined value, the space air should be cooled down or warmed up before the space is occupied.
2. *Conditioning period.* The air-conditioning system is operated during the occupied period to maintain the required indoor environment.
3. *Nighttime shut-down period.* The air system or terminal is shut down or only partly operating to maintain a set-back temperature.

Summer, winter, air economizer, and continuously operating modes consist of *full-load* (design load) and part-load operations. *Part load* occurs when the system load is less than the design load. The capacity of the equipment is selected to meet summer and winter system design loads as well as system loads in all operating modes.

Basic Air-Conditioning Cycle — Summer Mode

A *basic air-conditioning system* is a packaged system of supply air at a constant volume flow rate, serving a single zone, equipped with only a single supply/return duct. A *single zone* is a conditioned space for which a single controller is used to maintain a unique indoor operating parameter, probably indoor temperature. A *basic air-conditioning cycle* is the operating cycle of a basic air-conditioning system. Figure 9.1.3 shows a basic air-conditioning system. Figure 9.3.4 shows the basic air-conditioning cycle of this system. In summer mode at design load, recirculating air from the conditioned space, a worship hall, enters the packaged unit through the return grill at point ru. It is mixed with the required minimum amount of outdoor air at point o for acceptable indoor air quality and energy saving. The mixture *m* is then cooled and dehumidified to point cc by the DX coil, and the conditioned air is supplied to the hall through the supply fan, supply duct, and ceiling diffuser. Supply air then absorbs the sensible and latent load from the space, becoming the space air r. Recirculating air enters the packaged unit again and forms a closed cycle. *Return air* is the air returned from the space. Part of the return air is exhausted to balance the outdoor air intake and infiltration. The remaining part is the *recirculating air* that enters the PU or AHU.

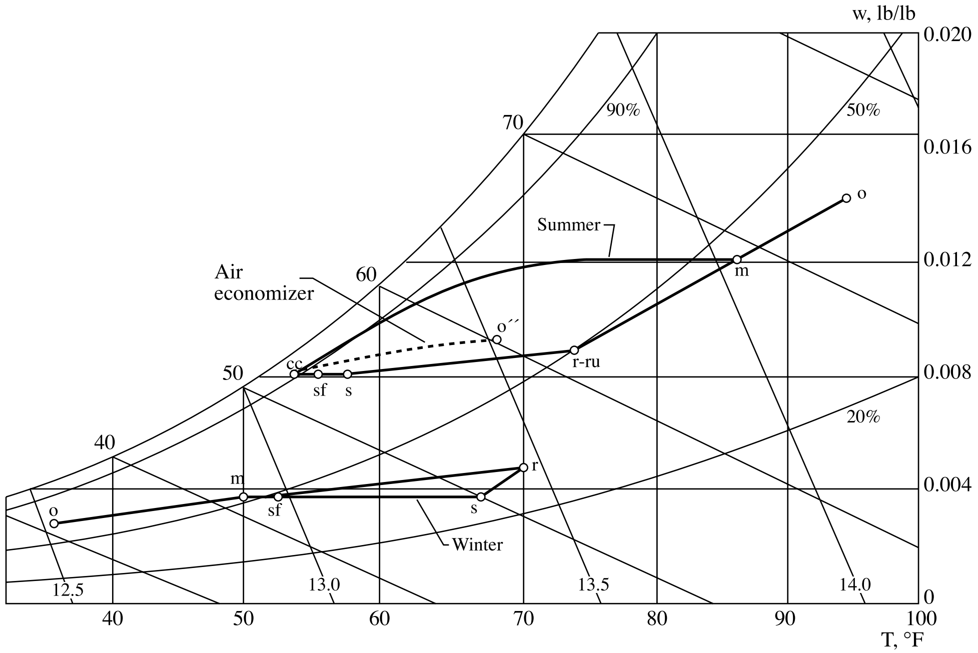

FIGURE 9.3.4 Basic air-conditioning cycle — summer, winter, and air economizer mode.

The summer mode operating cycle consists of the following processes:

1. Sensible heating process, represented by line r-ru, due to the return system gain $q_{r.s}$, in Btu/hr, when recirculating air flows through the return duct, ceiling plenum, and return fan, if any. In this packaged system, the return system heat gain is small and neglected.
2. Adiabatic mixing process of recirculating air at point ru and outdoor air at point o in the mixing box, represented by line ru-m-o.
3. Cooling and dehumidifying process m cc at the DX coil whose coil load determines the cooling capacity of the system calculated from Equation (9.3.11).
4. Sensible heating process related to the supply system heat gain $q_{s.s}$, in Btu/hr, represented by line cc sf s. $q_{s.s}$ consists of the fan power heat gain q_{sf}, line cc sf, and duct heat gain q_{sd}, line sf s, that is:

$$q_{s.s} = q_{sf} + q_{sd} = \mathring{V}_s \rho_s c_{pa} \Delta T_{s.s} \tag{9.3.19}$$

   It is more convenient to use the temperature rise of the supply system $\Delta T_{s.s}$ in psychrometric analysis.
5. Supply conditioning process line s-r.

Design Supply Volume Flow Rate

Design supply volume flow rate and cooling and heating capacities are primary characteristics of an air-conditioning system. Design supply volume flow rate is used to determine the size of fans, grills, outlets, air-handling units, and packaged units. For most comfort systems and many processing air-conditioning systems, *design supply volume flow rate* $\mathring{V}_{s.d}$, in cfm, is calculated on the basis of the capacity to remove the space cooling load at summer design conditions to maintain a required space temperature T_r:

$$\mathring{V}_{s.d} = q_{rc.d} \Big/ \left[60\rho_s \left(h_r - h_s\right)\right] = q_{rs.d} \Big/ \left[60\rho_s c_{pa} \left(T_r - T_s\right)\right] \tag{9.3.20}$$

where $q_{\mathrm{rc.d}}$, $q_{\mathrm{rs.d}}$ = design space cooling load and design sensible cooling load, Btu/hr. In Equation (9.3.20), the greater the $q_{\mathrm{rs.d}}$, the higher $\mathring{V}_{\mathrm{s}}$ will be. Specific heat c_{pa} is usually considered constant. Air density ρ_{s} may vary with the various types of air systems used. A greater ρ_{s} means a smaller $\mathring{V}_{\mathrm{s.d}}$ for a given supply mass flow rate. For a given $q_{\mathrm{rs.d}}$, the supply temperature differential $\Delta T_{\mathrm{s}} = (T_{\mathrm{r}} - T_{\mathrm{s}})$ is an important parameter that affects $\mathring{V}_{\mathrm{s.d}}$. Conventionally, a 15 to 20°F ΔT_{s} is used for comfort air-conditioning systems. Recently, a 28 to 34°F ΔT_{s} has been adopted for cold air distribution in ice-storage central systems. When ΔT_{s} has a nearly twofold increase, there is a considerable reduction in $\mathring{V}_{\mathrm{s}}$ and fan energy use and saving in investment on ducts, terminals, and outlets.

The summer cooling load is often greater than the winter heating load, and this is why q_{rc} or $q_{\mathrm{rs.d}}$ is used to determine $\mathring{V}_{\mathrm{s.d}}$, except in locations where the outdoor climate is very cold.

Sometimes the supply volume flow rate may be determined from the following requirements:

- To dilute the concentration of air contaminants in the conditioned space C_{i}, in mg/m^3, the design supply volume flow rate is

$$\mathring{V}_{\mathrm{s.d}} = 2118\mathring{m}_{\mathrm{par}} \big/ \left(C_1 - C_{\mathrm{s}}\right) \tag{9.3.21}$$

  where
  C_{s} = concentration of air contaminants in supply air, mg/m^3
  $\mathring{m}_{\mathrm{par}}$ = rate of contaminant generation in the space, mg/sec

- To maintain a required space relative humidity φ_{r} and a humidity ratio w_{r} at a specific temperature, the design supply volume flow rate is

$$\mathring{V}_{\mathrm{s.d}} = q_{\mathrm{rl.d}} \Big/ \left[60\rho_{\mathrm{s}}\left(w_{\mathrm{r}} - w_{\mathrm{s}}\right)h_{\mathrm{fg.58}}\right] \tag{9.3.22}$$

  where $q_{\mathrm{rl.d}}$ = design space latent load, Btu/hr.

- To provide a required air velocity v_{r}, in fpm, within the working area of a clean room, the supply volume flow rate is given by

$$\mathring{V}_{\mathrm{s.d}} = A_{\mathrm{r}}v_{\mathrm{r}} \tag{9.3.23a}$$

  where A_{r} = cross-sectional area perpendicular to the air flow in the working area, ft^2.

- To exceed the outdoor air requirement for acceptable air quality for occupants, the supply volume flow rate must be equal to or greater than

$$\mathring{V}_{\mathrm{s}} \ge n\mathring{V}_{\mathrm{oc}} \tag{9.3.23b}$$

  where
  n = number of occupants
  $\mathring{V}_{\mathrm{oc}}$ = outdoor air requirement per person, cfm/person

- To exceed the sum of the volume flow rate of exhaust air $\mathring{V}_{\mathrm{ex}}$ and the exfiltrated or relief air $\mathring{V}_{\mathrm{ef}}$, both in cfm,

$$\mathring{V}_{\mathrm{s}} \ge \mathring{V}_{\mathrm{ex}} + \mathring{V}_{\mathrm{ef}} \tag{9.3.24}$$

The design supply volume flow rate should be the largest of any of the foregoing requirements.

Rated Supply Volume Flow Rate

For an air system at atmospheric pressure, since the required mass flow rate of the supply air is a function of air density and remains constant along the air flow,

$$\begin{aligned}\mathring{m}_{\mathrm{a}} &= \mathring{V}_{\mathrm{cc}}\,\rho_{\mathrm{cc}} = \mathring{V}_{\mathrm{s}}\,\rho_{\mathrm{s}} = \mathring{V}_{\mathrm{sf}}\,\rho_{\mathrm{sf}} \\ \mathring{V}_{\mathrm{sf}} &= \mathring{V}_{\mathrm{s}}\,\rho_{\mathrm{s}}\big/\rho_{\mathrm{sf}}\end{aligned} \tag{9.3.25}$$

where

$\mathring{V}_{\mathrm{sf}}$ = volume flow rate at supply fan outlet, cfm
ρ_{sf} = air density at supply fan outlet, lb/ft^3

A supply fan is rated at *standard air conditions*, that is, dry air at a temperature of 70°F, an atmospheric pressure of 29.92 in. Hg (14.697 psia), and an air density of 0.075 lb/ft^3. However, a fan is a constant-volume machine at a given fan size and speed; that is, $\mathring{V}_{\mathrm{s.f}} = \mathring{V}_{\mathrm{sf.r}}$. Here $\mathring{V}_{\mathrm{sf.r}}$ represents the rated volume flow rate of a fan at standard air conditions. Therefore,

$$\mathring{V}_{\mathrm{sf.r}} = \mathring{V}_{\mathrm{sf}} = q_{\mathrm{rs.d}}\Big/\Big[60\rho_{\mathrm{sf}}c_{\mathrm{pa}}\big(T_{\mathrm{r}} - T_{\mathrm{s}}\big)\Big] \tag{9.3.26}$$

- For conditioned air leaving the cooling coil at T_{cc} = 55°F with a relative humidity of 92% and T_{sf} of 57°F, $\rho_{\mathrm{sf.r}} = 1/v_{\mathrm{sf}} = 1/13.20 = 0.0758$ lb/ft^3. From Equation (9.3.26):

$$\mathring{V}_{\mathrm{sf.r}} = q_{\mathrm{rs.d}}\Big/\Big[60\times 0.0758\times 0.243\big(T_{\mathrm{r}} - T_{\mathrm{s}}\big)\Big] = q_{\mathrm{rs.d}}\Big/\Big[1.1\big(T_{\mathrm{r}} - T_{\mathrm{s}}\big)\Big] \tag{9.3.26a}$$

  Equation (9.3.26a) is widely used in calculating the supply volume flow rate of comfort air-conditioning systems.
- For cold air distribution, T_{cc} = 40°F and φ_{cc} = 98%, if T_{sf} = 42°F, then v_{sf} = 12.80 ft^3/lb, and the rated supply volume flow rate:

$$\mathring{V}_{\mathrm{sf.r}} = 12.80q_{\mathrm{rs.d}}\Big/\Big[60\times 0.243\big(T_{\mathrm{r}} - T_{\mathrm{s}}\big)\Big] = q_{\mathrm{rs.d}}\Big/\Big[1.14\big(T_{\mathrm{r}} - T_{\mathrm{s}}\big)\Big] \tag{9.3.26b}$$

- For a blow-through fan in which the fan is located upstream of the coil, if T_{sf} = 82°F and φ_{sf} = 43%, then v_{sf} = 13.87 ft^3/lb, and the rated supply volume flow rate:

$$\mathring{V}_{\mathrm{sf.r}} = 13.87q_{\mathrm{rs.d}}\Big/\Big[60\times 0.243\big(T_{\mathrm{r}} - T_{\mathrm{s}}\big)\Big] = q_{\mathrm{rs.d}}\Big/\Big[1.05\big(T_{\mathrm{r}} - T_{\mathrm{s}}\big)\Big] \tag{9.3.26c}$$

Effect of the Altitude

The higher the altitude, the lower the atmospheric pressure and the air density. In order to provide the required mass flow rate of supply air, a greater $\mathring{V}_{\mathrm{sf.r}}$ is needed. For an air temperature of 70°F:

$$\mathring{V}_{\mathrm{x.ft}} = \mathring{V}_{\mathrm{sf.r}}\big(p_{\mathrm{sea}}/p_{\mathrm{x.ft}}\big) = \mathring{V}_{\mathrm{sf.r}}\big(\rho_{\mathrm{sea}}/\rho_{\mathrm{x.ft}}\big) \tag{9.3.27}$$

where

$\mathring{V}_{\mathrm{x.ft}}$ = supply volume flow rate at an altitude of *x* ft, cfm
p_{sea}, $p_{\mathrm{x.ft}}$ = atmospheric pressure at sea level and an altitude of *x* ft, psia
ρ_{sea}, $\rho_{\mathrm{x.ft}}$ = air density at sea level and an altitude of *x* ft, psia

Following are the pressure or air density ratios at various altitudes. At 2000 ft above sea level, the rated supply volume flow rate $\mathring{V}_{\mathrm{r.2000}} = \mathring{V}_{\mathrm{sf.r}}\ (p_{\mathrm{sea}}/p_{\mathrm{x.ft}}) = 1.076\ \mathring{V}_{\mathrm{sf.r}}$ cfm instead of $\mathring{V}_{\mathrm{sf.r}}$ cfm at sea level.

Altitude, ft	p_{at}, psia	ρ, lb/ft^3	$(p_{\mathrm{sea}}/p_{\mathrm{x,ft}})$
0	14.697	0.075	1.000
1000	14.19	0.0722	1.039
2000	13.58	0.0697	1.076
3000	13.20	0.0672	1.116
5000	12.23	0.0625	1.200

Off-Coil and Supply Air Temperature

For a given design indoor air temperature T_r, space sensible cooling load q_{rs}, and supply system heat gain $q_{s.s}$, a lower air off-coil temperature T_{cc} as well as supply temperature T_s means a greater supply temperature differential ΔT_s and a lower space relative humidity φ_r and vice versa. A greater ΔT_s decreases the supply volume flow rate $\overset{\circ}{V}_s$ and then the fan and terminal sizes, duct sizes, and fan energy use. The result is a lower investment and energy cost.

A lower T_{cc} and a greater ΔT_s require a lower chilled water temperature entering the coil T_{we}, a lower evaporating temperature T_{ev} in the DX coil or refrigerating plant, and therefore a greater power input to the refrigerating compressors. When an air-conditioning system serves a conditioned space of a single zone, optimum T_{cc}, T_s, and T_{we} can be selected. For a conditioned space of multizones, T_{cc}, T_s, and T_{we} should be selected to satisfy the lowest requirement. In practice, T_s and T_{we} are often determined according to previous experience with similar projects.

In general, the temperature rise due to the supply fan power system heat gain q_{sf} can be taken as 1 to 3°F depending on the fan total pressure. The temperature rise due to the supply duct system heat gain at design flow can be estimated as 1°F/100 ft insulated main duct length based on 1-in. thickness of duct insulation. Note that ANSI/ASHRAE/IESNA Standard 90.1-2001 covers duct insulation energy standards.

Outside Surface Condensation

The outside surface temperature of the ducts, terminals, and supply outlets T_{sur} in the ceiling plenum in contact with the return air should not be lower than the dew point of the space air T_r'', in °F. The temperature rise due to the fan power heat gain is about 2°F. According to Dorgan (1988), the temperature difference between the conditioned air inside the terminal and the outside surface of the terminal with insulation wrap is about 3°F. For a space air temperature of 75°F and a relative humidity of 50%, its dew point temperature is 55°F. If the outside surface temperature $T_s = (T_{cc} + 2 + 3) \leq 55°\text{F}$, condensation may occur on the outside surface of the terminal. Three methods are often used to prevent condensation:

1. Increase the thickness of the insulation layer on the outside surface.
2. Adopt a supply outlet that induces more space air.
3. Equip with a terminal that mixes the supply air with the space air or air from the ceiling plenum.

Example 9.3.1

The worship hall of a church uses a package system with a basic air system. The summer space sensible cooling load is 75,000 Btu/hr with a latent load of 15,000 Btu/hr. Other design data for summer are as follows:

Outdoor summer design temperature: dry bulb 95°F and wet bulb 75°F
Summer indoor temperature: 75°F with a space relative humidity of 50%:
Temperature rise: fan power 2°F
supply duct 2°F
Relative humidity of air leaving cooling coil: 93%
Outdoor air requirement: 1800 cfm

Determine the

1. Temperature of supply air at summer design conditions
2. Rated volume flow rate of the supply fan
3. Cooling coil load
4. Possibility of condensation at the outside surface of the insulated branch duct to the supply outlet

Solution

1. From Equation 9.3.1 the sensible heat ratio of the space conditioning line is

$$\text{SHR}_s = |q_{rs}| / (|q_{rs}| + |q_{rl}|) = 60{,}000/(60{,}000 + 15{,}000) = 0.8$$

On the psychrometric chart, from given $T_r = 75°F$ and $\varphi_r = 50\%$, plot space point r. Draw a space conditioning line sr from point r with $SHR_s = 0.8$.

Since $\Delta T_{s.s} = 2 + 2 = 4°F$, move line segment cc s (4°F) up and down until point s lies on line sr and point cc lies on the $\varphi_{cc} = 93\%$ line. The state points s and cc are then determined as shown in Figure 9.3.4:

$T_s = 57.5°F$, $\varphi_s = 82\%$, and $w_s = 0.0082$ lb/lb

$T_{cc} = 53.5°F$, $\varphi_{cc} = 93\%$, $h_{cc} = 21.8$ Btu/lb, and $w_{cc} = 0.0082$ lb/lb

2. Since $T_{sf} = 53.5 + 2 = 55.5°F$ and $w_{sf} = 0.0082$ lb/lb, $\rho_{sf} = 1/v_{sf} = 1/13.15 = 0.076$ lb/ft^3. From Equation 9.4.2, the required rated supply volume flow rate is

$$\overset{\circ}{V}_{sf.r} = q_{rs.d} \Big/ \left[60 \rho_{sf} c_{pa} \left(T_r - T_s\right)\right]$$

$$= 60{,}000 \big/ \left[60 \times 0.076 \times 0.243 (75 - 57.5)\right] = 3094 \text{ cfm}$$

3. Plot outdoor air state point o on the psychrometric chart from given dry bulb 95°F and wet bulb 75°F. Connect line r-o. Neglect the density differences between points r, m, and o; then

$$\text{r-m/r-o} = 1800/3094 = 0.58$$

From the psychrometric chart, the length of line r-o is 2.438 in. As shown in Figure 9.3.4, point m is then determined as:

$$T_m = 86.7°\text{F}, \qquad h_m = 35 \text{ Btu/lb}$$

From Equation (9.3.11), the cooling coil load is

$$q_{cc} = 60 \overset{\circ}{V}_s \rho_s \left(h_m - h_{cc}\right) = 60 \times 3094 \times 0.076 (35 - 21.8) = 186{,}234 \text{ Btu/lb}$$

4. From the psychrometric chart, since the dew point of the space air $T_r'' = 55°F$ and is equal to that of the plenum air, the outside surface temperature of the branch duct $T_s = 53.5 + 2 + 3 = 58°F$ which is higher than $T_r'' = 55°F$. Condensation will not occur at the outside surface of the branch duct.

Basic Air-Conditioning Cycle — Winter Mode

When the basic air-conditioning systems are operated in winter mode, their air-conditioning cycles can be classified into the following four categories:

Cold Air Supply without Space Humidity Control. In winter, for a fully occupied worship hall, if the heat loss is less than the space sensible cooling load, a cold air supply is required to offset the space sensible cooling load and maintain a desirable indoor environment as shown by the lower cycle in Figure 9.3.4. Usually, a humidifier is not used.

The winter cycle of a cold air supply without humidity control consists of the following air-conditioning processes:

1. Adiabatic mixing process of outdoor air and recirculating air o m r.
2. Sensible heating process due to supply fan power heat gain m sf. Because of the smaller temperature difference between the air in the ceiling plenum and the supply air inside the supply duct, heat transfer through duct wall in winter can be neglected.
3. Supply conditioning line sr.

For a winter-mode basic air-conditioning cycle with a cold air supply without space humidity control, the space relative humidity depends on the space latent load, the humidity ratio of the outdoor air, and the amount of outdoor air intake. In order to determine the space humidity ratio w_r, in lb/lb, and the space relative humidity φ_r, in %, Equation (9.3.15) and Equation (9.3.22) should be used to give the following relationships:

$$\begin{aligned}
&\left(w_r - w_m\right) \big/ \left(w_r - w_o\right) = \mathring{V}_o \big/ \mathring{V}_s \\
&\left(w_r - w_s\right) = q_{rl} \Big/ \left(60 \mathring{V}_s \rho_s h_{fg.58}\right) \\
&w_s = w_m
\end{aligned} \tag{9.3.28}$$

For a cold air supply, if there is a high space sensible cooling load, the amount of outdoor air must be sufficient, and the mixture must be cold enough to satisfy the following relationships:

$$\begin{aligned}
&\left(T_r - T_s\right) = q_{rs} \Big/ \left(60\ \mathring{V}_s \rho_s c_{pa}\right) \\
&\left(T_r - T_s\right) \big/ \left(T_r - T_o\right) = \mathring{V}_o \big/ \mathring{V}_s
\end{aligned} \tag{9.3.29}$$

The heating coil load for heating of the outdoor air can be calculated using Equation (9.3.7).

Example 9.3.2

For the same packaged air-conditioning system using a basic air system to serve the worship hall in a church as in Example 9.3.1, the space heating load at winter design condition is 10,000 Btu/hr and the latent load is 12,000 Btu/hr. Other winter design data are as follows:

Winter outdoor design temperature	35°F
Winter outdoor design humidity ratio	0.00035 lb/lb
Winter indoor design temperature	70°F
Temperature rise due to supply fan heat gain	2°F
Outdoor air requirement	1800 cfm

Determine (1) the space relative humidity at winter design temperature and (2) the heating coil load.

Solution

1. Assume that the supply air density $\rho_{sf} = 1/v_{sf} = 1/13.0 = 0.0769$ lb/ft^3, and the mass flow rate of the supply air is the same as in summer mode. Then from Equation 9.3.28 the humidity ratio difference is

$$\left(w_r - w_s\right) = q_{rl} \Big/ \left(60 \mathring{V}_{sf.r} \rho_{sf} h_{fg.58}\right) = 12{,}000/(60 \times 3094 \times 0.0769 \times 1060) = 0.00079 \text{ lb/lb}$$

From Equation 9.3.29, the supply air temperature differential is

$$\left(T_r - T_s\right) = q_{rs.d} \Big/ \left(60 \mathring{V}_{sf.r} \rho_{sf} c_{pa}\right) = 10{,}000/(60 \times 3094 \times 0.0769 \times 0.243) = 2.88°\text{F}$$

Since $\mathring{V}_o / \mathring{V}_s = 1800/3094 = 0.58$ and $w_s = w_m$,

$$\left(w_r - w_s\right) \big/ \left(w_r - w_o\right) = 0.00079 \big/ \left(w_r - w_o\right) = \mathring{V}_o \big/ \mathring{V}_s = 0.58$$

$$\left(w_r - w_o\right) = 0.00079/0.58 = 0.00136 \text{ lb/lb}$$

And from given information,

$$w_r = 0.00136 + w_o = 0.00136 + 0.0035 = 0.00486 \text{ lb/lb}$$

From the psychrometric chart, for T_r = 70°F and w_r = 0.00486 lb/lb, point r can be plotted, and φ_r is about 32% (see Figure 9.3.4).

2. Since mr/or = 0.58, point m can be determined, and from the psychrometric chart T_m = 50.0°F. As T_s = 70 – 2.88 = 67.12°F and $T_{sf} = T_m + 2 = 50.0 + 2 = 52.0$°F, from Equation 9.3.7 the heating coil's load is

$$q_{ch} = 60 \overset{\circ}{V}_s \rho_s c_{pa} \left(T_s - T_{sf}\right) = 60 \times 3094 \times 0.0769 \times 0.243(67.12 - 52.0) = 52{,}451 \text{ Btu/hr}$$

Warm Air Supply without Space Humidity Control

When the sum of space heat losses is greater than the sum of the internal heat gains in winter, a warm air supply is needed. For many comfort systems such as those in offices and stores, in locations where winter is not very cold, humidification is usually not necessary. The basic air-conditioning cycle for a warm air supply without space humidity control is shown in Figure 9.3.5(a). This cycle is similar to the winter mode cycle of a cold air supply without space humidity control shown in Figure 9.3.4 except that the supply air temperature is higher than space temperature, that is, $T_s > T_r$. To prevent stratification, with the warm supply air staying at a higher level, $(T_s - T_r) > 20$°F is not recommended.

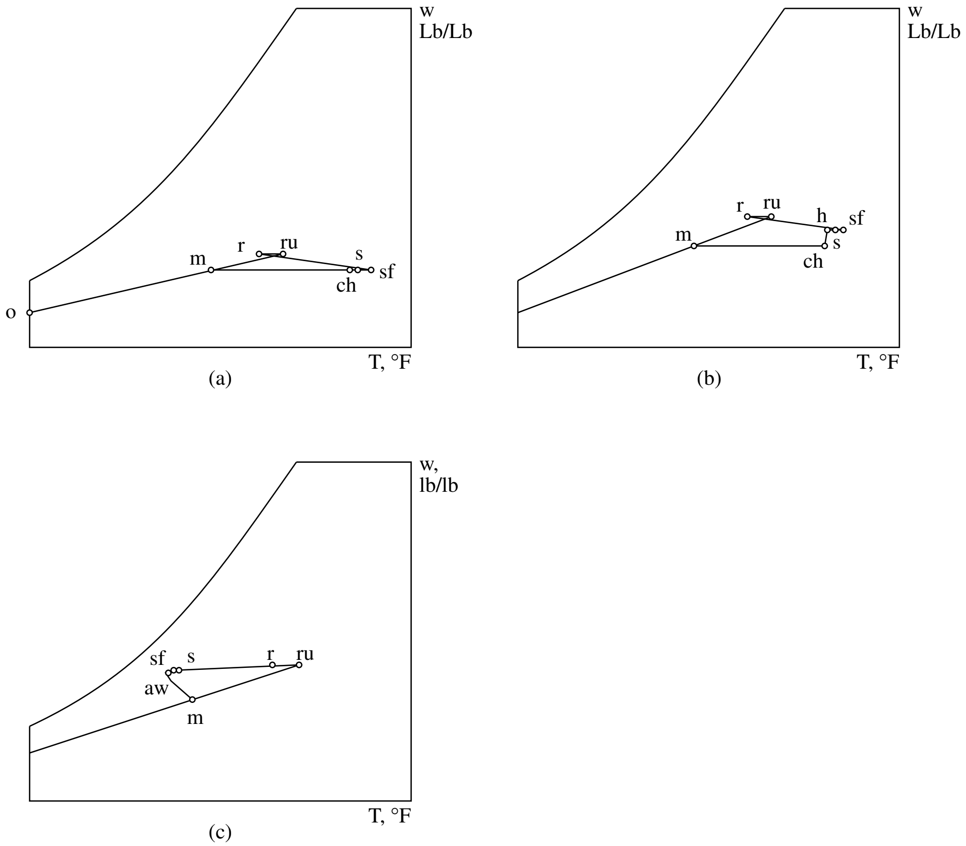

FIGURE 9.3.5 Basic air-conditioning cycle — winter modes: (a) warm air supply without space humidity control, (b) cold air supply without space humidity control, and (c) cold air supply with space humidity control. ch = air leaving heating coil, h = air leaving humidifer, and aw = air leaving air washer.

Warm Air Supply with Space Humidity Control

This operating cycle (see Figure 9.3.5[b]) is often used for hospitals, nurseries, etc. or in locations where winter is very cold. The state point of supply air must be determined first by drawing a space conditioning line with known SHR_s and then from the calculated supply temperature differential ΔT_s. The difference in humidity ratio ($w_s - w_{ch}$) is the water vapor must be added at the humidifier. Humidifying capacity can be calculated from Equation 9.3.8.

Cold Air Supply with Space Humidity Control

This operating cycle (shown in Figure 9.3.5[c]) is widely used in industrial applications such as textile mills where a cold air supply is needed to remove machine load in winter and maintains the space relative humidity required for the manufacturing process. An outdoor air and recirculating air mixture is often used for the required cold air supply. An air washer is adopted for winter humidification.

Air Economizer Mode

In the *air economizer* mode, as shown by the middle dotted line cycle o″-cc-sf-s-r in Figure 9.3.4, all outdoor air or an outdoor air-recirculating air mixture is used to reduce the refrigeration capacity and improve the indoor air quality during spring, fall, or winter.

When all outdoor air is admitted, it is an open cycle. Outdoor air is cooled and often dehumidified to point cc. After absorbing fan and duct heat gains, it is supplied to the conditioned space. Space air is exhausted entirely through openings, relief dampers, or relief/exhaust fans to the outside. An all-outdoor air-operating mode before the space is occupied is often called an *air purge* operation, used to dilute space air contaminants.

Cool-Down and Warm-Up Modes

In summer, when an air system is shut down during an unoccupied period at night, the space temperature and relative humidity often tend to increase because of infiltration of hot and humid air and heat transfer through the building envelope. The air system is usually started before the space is occupied in cool-down mode to cool the space air until the space temperature falls within predetermined limits.

In winter, the air system is also started before the occupied period to warm up the space air to compensate for the nighttime space temperature setback to 55 to 60°F for energy saving or the drop of space temperature due to heat loss and infiltration.

If dilution of indoor air contaminants is not necessary, only recirculating space air is used during cool-down or warm-up periods in order to save energy. Care should be taken in suggesting cool-down or warm-up modes as for some applications after-hour conditions could result in damage to interior surfaces or materials.

9.4 Refrigerants and Refrigeration Cycles

Shan K. Wang

Refrigeration and Refrigeration Systems

Refrigeration is the cooling effect of the process of extracting heat from a lower temperature heat source, a substance or cooling medium, and transferring it to a higher temperature heat sink, probably atmospheric air and surface water, to maintain the temperature of the heat source below that of the surroundings.

A *refrigeration system* is a combination of components, equipment, and piping, connected in a sequential order to produce the refrigeration effect. Refrigeration systems that provide cooling for air-conditioning are classified mainly into the following categories:

1. *Vapor compression systems.* In these systems, a compressor(s) compresses the refrigerant to a higher pressure and temperature from an evaporated vapor at low pressure and temperature. The compressed refrigerant is condensed into liquid form by releasing the latent heat of condensation to the condenser water. Liquid refrigerant is then throttled to a low-pressure, low-temperature vapor,

producing the refrigeration effect during evaporation. Vapor compression is often called *mechanical refrigeration*, that is, refrigeration by mechanical compression.

2. *Absorption systems.* In an absorption system, the refrigeration effect is produced by means of thermal energy input. After liquid refrigerant produces refrigeration during evaporation at very low pressure, the vapor is absorbed by an aqueous absorbent. The solution is heated by a direct-fired gas furnace or waste heat, and the refrigerant is again vaporized and then condensed into liquid form. The liquid refrigerant is throttled to a very low pressure and is ready to produce the refrigeration effect again.
3. *Gas expansion systems.* In an air or other gas expansion system, air or gas is compressed to a high pressure by compressors. It is then cooled by surface water or atmospheric air and expanded to a low pressure. Because the temperature of air or gas decreases during expansion, a refrigeration effect is produced.

Refrigerants, Cooling Mediums, and Absorbents

A *refrigerant* is a primary working fluid used to produce refrigeration in a refrigeration system. All refrigerants extract heat at low temperature and low pressure during evaporation and reject heat at high temperature and pressure during condensation.

A *cooling medium* is a working fluid cooled by the refrigerant during evaporation to transport refrigeration from a central plant to remote cooling equipment and terminals. In a large, centralized air-conditioning system, it is more economical to pump the cooling medium to the remote locations where cooling is required. Chilled water and brine are cooling media. They are often called secondary refrigerants to distinguish them from the primary refrigerants.

A *liquid absorbent* is a working fluid used to absorb the vaporized refrigerant (water) after evaporation in an absorption refrigeration system. The solution that contains the absorbed vapor is then heated. The refrigerant vaporizes, and the solution is restored to its original concentration to absorb water vapor again.

A numbering system for refrigerants was developed for hydrocarbons and halocarbons. According to ANSI/ASHRAE Standard 34-1997, the first digit is the number of unsaturated carbon–carbon bonds in the compound. This digit is omitted if the number is zero. The second digit is the number of carbon atoms minus one. This is also omitted if the number is zero. The third digit denotes the number of hydrogen atoms plus one. The last digit indicates the number of fluorine atoms. For example, the chemical formula for refrigerant R-123 is $CHCl_2CF_3$. In this compound:

No unsaturated carbon–carbon bonds, first digit is	0
There are two carbon atoms, second digit is	$2 - 1 = 1$
There is one hydrogen atom, third digit is	$1 + 1 = 2$
There are three fluorine atoms, last digit is	3

To compare the relative ozone depletion of various refrigerants, an index called the *ozone depletion potential* (ODP) has been introduced. ODP is defined as the ratio of the rate of ozone depletion of 1 lb of any halocarbon to that of 1 lb of refrigerant R-11. For R-11, ODP = 1.

Similar to the ODP, halocarbon global warming potential (HGWP) is an index used to compare the global warming effect of a halocarbon refrigerant with the effect of refrigerant R-11.

Classification of Refrigerants

Nontoxic and nonflammable synthetic chemical compounds called *halogenated hydrocarbons*, or simply *halocarbons*, were used almost exclusively in vapor compression refrigeration systems for comfort air-conditioning until 1986. Because chlorofluorocarbons (CFCs) cause ozone depletion and global warming, they must be replaced. A classification of refrigerants based on ozone depletion follows (see Table 9.4.1):

TABLE 9.4.1 Properties of Commonly Used Refrigerants 40°F Evaporating and 100°F Condensin

		Chemical Formula	Molecular Mass	Ozone Depletion Potential (ODP)	Global Warming Potential (HGWP)	Evaporating Pressure, psia	Condensing Pressure, psia	Compression Ratio	Refrigeration Effect, Btu/lb
Hydrofluorocarbons HFCs									
R-32	Difluoromethane	CH_2F_2	52.02	0.0	0.14	135.6	340.2	2.51	
R-125	Pentafluoroethane	CHF_2CF_3	120.03	0.0	0.84	111.9	276.2	2.47	37.1
R-134a	Tetrafluoroethane	CF_3CH_2F	102.03	0.0	0.26	49.7	138.8	2.79	65.2
R-143a	Trifluoroethane	CH_3CF_3	84.0	0.0					
R-152a	Difluoroethane	CH_3CHF_2	66.05	0.0		44.8	124.3	2.77	
R-245ca	Pentafluoropropane	$CF_3CF_2CH_3$	134.1	0.0					
HFC's azeotropic blends									
R-507	R-125/R-143 (45/55)			0.0	0.98				
HFC's near azeotropic blends									
R-404A	R-125/R-143a (44/52/4)			0.0	0.94				
R-407A	R-32/R-125/R-134a (20/40/40)			0.0	0.49				
R-407C	R-32/R-125/R-134a (23/25/52)			0.0	0.70				
Hydrochlorofluorocarbons HCFCs and their azeotropic blends									
R-22	Chlorodifluoromethane	$CHClF_2$	86.48	0.05	0.40	82.09	201.5	2.46	69.0
R-123	Dichlorotrifluoroethane	$CHCl_2CF_3$	152.93	0.02	0.02	5.8	20.8	3.59	62.9
R-124	Chlorotetrafluoroethane	$CHFClCF_3$	136.47	0.02		27.9	80.92	2.90	5.21
HCFC's near azeotropic blends									
R-402A	R-22/R-125/R-290 (38/60/2)			0.02	0.63				
HCFC's azeotropic blends									
R-401A	R-22/R-124/R-152a (53/34/13)			0.37	0.22				
R-401B	R-22/R-124/R-152a (61/28/11)			0.04	0.24				

TABLE 9.4.1 (continued) Properties of Commonly Used Refrigerants 40°F Evaporating and 100°F Condensin

		Chemical Formula	Molecular Mass	Ozone Depletion Potential (ODP)	Global Warming Potential (HGWP)	Evaporating Pressure, psia	Condensing Pressure, psia	Compression Ratio	Refrigeration Effect, Btu/lb
Inorganic compounds									
R-717	Ammonia	NH_3	17.03	0	0	71.95	206.81	2.87	467.4
R-718	Water	H_2O	18.02	0					
R-729	Air		28.97	0					
Chlorofluorocarbons CFCs, halons BFCs and their azeotropic blends									
R-11	Trichlorofluoromethane	CCl_3F	137.38	1.00	1.00	6.92	23.06	3.33	68.5
R-12	Dichlorodifluoromethane	CCl_2F_2	120.93	1.00	3.20	50.98	129.19	2.53	50.5
R-13B1	Bromotrifluoromethane	$CBrF_3$	148.93	10					
R-113	Trichlorotrifluoroethane	CCl_2FCClF_2	187.39	0.80	1.4	2.64	10.21	3.87	54.1
R-114	Dichlorotetrafluoroethane	CCl_2FCF_3	170.94	1.00	3.9	14.88	45.11	3.03	42.5
R-500	R-12/R-152a (73.8/26.2)		99.31			59.87	152.77	2.55	60.5
R-502	R-22/R-115 (48.8/51.2)		111.63	0.283	4.10				

TABLE 9.4.1 (continued) Properties of Commonly Used Refrigerants 40°F Evaporating and 100°F Condensing

	Replacement of	Trade Name	Specific Volume of Vapor ft³/lb	Compresssor Displacement cfm/ton	Power Consumption hp/ton	Critical Temperature °F	Discharge Temperature °F	Flammability	Safety
Hydrofluorocarbons HFCs									
R-32			0.63			173.1			
R-125			0.33			150.9	103	Nonflammable	A1
R134a	R-12		0.95			213.9		Nonflammable	A1
R143a									
R-152a			1.64			235.9		Lower flammable	A2
R-245ca									
HFC's azeotropic blends									
R-507	R-502	Genetron AZ-50							
HFC's near azeotropic blends									
R-404A	R-22	SUVA HP-62							A1/A1[a]
R-407A	R-22	KLEA 60							A1/A1[a]
R-407C	R-22	KLEA 66							A1/A1[a]
Hydrochlorofluorocarbons HCFC's and their azeotropic blends									
R-22			0.66	1.91	0.696	204.8	127	Nonflammable	A1
R-123	R-11		5.88	18.87	0.663	362.6		Nonflammable	B1
R-124			1.30	5.06	0.698	252.5			
HCFC's near azeotropic blends									
R-402A	R-502	SUVA HP-80							A1/A1[a]
HCFC's azeotropic blends									
R-401A	R-12	MP 39							A1/A1[a]
R-401B	R-12	MP 66							A1/A1[a]
Inorganic compounds									
R-717			3.98	1.70	0.653	271.4	207	Lower flammability	B2
R-718								Nonflammable	
R-729								Nonflammable	

TABLE 9.4.1 (continued) Properties of Commonly Used Refrigerants 40°F Evaporating and 100°F Condensing

	Replacement of	Trade Name	Specific Volume of Vapor ft³/lb	Compresssor Displacement cfm/ton	Power Consumption hp/ton	Critical Temperature °F	Discharge Temperature °F	Flammability	Safety
Chlorofluorocarbons CFCs, halons BFCs, and their azeotropic blends									
R-11			5.43	15.86	0.636	388.4	104	Nonflammable	A1
R-12			5.79	3.08	0.689	233.6	100	Nonflammable	A1
R-13B1			0.21			152.6	103	Nonflammable	A1
R-113			10.71	39.55	0.71	417.4	86	Nonflammable	A1
R-114			2.03	9.57	0.738	294.3	86	Nonflammable	A1
R-500	R-12/R-152a (73.8/26.2)		0.79	3.62	0.692	221.9	105	Nonflammable	A1
R-502	R-22/R-115 (48.8/51.2)						98	Nonflammable	A1

Source: Adapted with permission from *ASHRAE Handbooks 1993 Fundamentals.* Also from refrigerant manufacturers.

[a] First classification is that safety classification of the formulated composition. The second is the worst case of fractionation.

Hydrofluorocarbons (HFCs)

HFCs contain only hydrogen, fluorine, and carbon atoms and cause no ozone depletion. HFCs group include R-134a, R-32, R-125, and R-245ca.

HFC's Azeotropic Blends or Simply HFC's Azeotropes

An azeotrope is a mixture of multiple components of volatilities (refrigerants) that evaporate and condense as a single substance and do not change in volumetric composition or saturation temperature when they evaporate or condense at constant pressure. HFC's azeotropes are blends of refrigerant with HFCs. ASHRAE assigned numbers between 500 and 599 for azeotropes. HFC's azeotrope R-507, a blend of R-125/R-143, is the commonly used refrigerant for low-temperature vapor compression refrigeration systems.

HFC's Near Azeotropic

A near azeotrope is a mixture of refrigerants whose characteristics are near those of an azeotrope. Because the change in volumetric composition or saturation temperature is rather small for a near azeotrope, such as, 1 to 2°F, it is thus named. ASHRAE assigned numbers between 400 and 499 for zeotropic. R-404A (R-125/R-134a/R-143a) and R-407B (R-32/R-125/R134a) are HFC's near azeotrope. R-32 is flammable; therefore, its composition is usually less than 30% in the mixture. HFC's near azeotropes are widely used for vapor compression refrigeration systems.

Zeotropes or nonazeotropes, including near azeotropes, show a change in composition due to the difference between liquid and vapor phases, leaks, and the difference between charge and circulation. A shift in composition causes the change in evaporating and condensing temperature/pressure. The difference in dew point and bubble point during evaporation and condensation is called glide, expressed in °F. Near azeotrope has a smaller glide than zeotropes. The midpoint between the dew point and bubble point is often taken as the evaporating and condensing temperature for refrigerant blends.

Hydrochlorofluorocarbons (HCFCs) and Their Zeotropics

HCFCs contain hydrogen, chlorine, fluorine, and carbon atoms and are not fully halogenated. HCFCs have a much shorter lifetime in the atmosphere (in decades) than CFCs and cause far less ozone depletion (ODP 0.02 to 0.1). R-22, R-123, R-124, etc. are HCFCs. HCFCs are the most widely used refrigerants today.

HCFC's near azeotropes and *HCFC's zeotropes* are blends of HCFCs with HFCs. They are transitional or interim refrigerants and are scheduled for a restriction in production starting in 2004.

Inorganic Compounds

These compounds include refrigerants used before 1931, like ammonia R-717, water R-718, and air R-729. They are still in use because they do not deplete the ozone layer. Because ammonia is toxic and flammable, it is used in industrial applications. Inorganic compounds are assigned numbers between 700 and 799 by ASHRAE.

Chlorofluorocarbons, Halons, and Their Azeotropic Blends

CFCs contain only chlorine, fluorine, and carbon atoms. CFCs have an atmospheric lifetime of centuries and cause ozone depletion (ODP from 0.6 to 1). R-11, R-12, R-113, R-114, R-115… are all CFCs.

Halons or BFCs contain bromide, fluorine, and carbon atoms. R-13B1 and R-12B1 are BFCs. They cause very high ozone depletion (ODP for R-13B1 = 10). Until 1995, R-13B1 was used for very low temperature vapor compression refrigeration systems.

Phaseout of CFCs, BFCs, HCFCs, and Their Blends

On September 16, 1987, the European Economic Community and 24 nations, including the United States, signed a document called the Montreal Protocol. It is an agreement to restrict the production and consumption of CFCs and BFCs in the 1990s because of ozone depletion.

The Clean Air Act amendments, signed into law in the United States on November 15, 1990, concern two important issues: the phaseout of CFCs and the prohibition of deliberate venting of CFCs and HCFCs.

In February 1992, President Bush called for an accelerated ban of CFCs in the United States. In late November 1992, representatives of 93 nations meeting in Copenhagen agreed to phase out CFCs beginning January 1, 1996. Restriction on the use of HCFCs will start in 2004, with a complete phaseout by 2030.

In the earlier 1990s, R-11 was widely used for centrifugal chillers, R-12 for small and medium-size vapor compression systems, R-22 for several other vapor compression systems, and CFC/HCFC blend R-502 for low-temperature vapor compression systems. Because of the phaseout of CFCs and BFCs before 1996 and HCFCs in the early years of the next century, alternative refrigerants have been developed to replace them:

- R-123 (an HCFC of ODP = 0.02) to replace R-11 is a short-term replacement that causes a slight reduction in capacity and efficiency. R-245ca (ODP = 0) may be the long-term alternative to R-11.
- R-134a (an HFC with ODP = 0) to replace R-12 in broad applications. R-134a is not miscible with mineral oil; therefore, a synthetic lubricant of polyolester is used.
- R-404A (R-125/R-134a/143a) and R-407C (R-32/R-125/R-134a) are both HFCs near azeotropic of ODP = 0. They are long-term alternatives to R-22. For R-407C, the composition of R-32 in the mixture is usually less than 30% so that the blend will not be flammable. R-407C has a drop of only 1 to 2% in capacity compared with R-22.
- R-507 (R-125/R-143a), an HFC's azeotropic with ODP = 0, is a long-term alternative to R-502. Synthetic polyolester lubricant oil will be used for R-507. There is no major performance difference between R-507 and R-502. R-402A (R-22/R-125/R-290), an HCFC's near azeotropic, is a short-term immediate replacement, and drop-in of R-502 requires minimum change of existing equipment except for reset of a higher condensing pressure.

Required Properties of Refrigerants

A refrigerant should not cause ozone depletion. A low global warming potential is required. Additional considerations for refrigerant selection are

1. *Safety*, including toxicity and flammability. ANSI/ASHRAE Standard 34-1997 classifies the *toxicity* of refrigerants as Class A and Class B. Class A refrigerants are of low toxicity. No toxicity was identified when their time-weighted average concentration was less than or equal to 400 ppm, to which workers can be exposed for an 8-hr workday and 40-hr work week without adverse effect. Class B refrigerants are of higher toxicity and produce evidence of toxicity.

ANSI/ASHRAE Standard 34-1982 classifies the *flammability* of refrigerants as Class 1, no flame propagation; Class 2, lower flammability; and Class 3, higher flammability.

The safety classification of refrigerants is based on the combination of toxicity and flammability: A1, A2, A3, B1, B2, and B3. R-134a and R-22 are in the A1 group, lower toxicity and nonflammable; R-123 in the B1 group, higher toxicity and nonflammable; and R-717 (ammonia) in the B2 group, higher toxicity and lower flammability.

2. *Effectiveness of refrigeration cycle*. High effectiveness is a desired property. The power consumed per ton of refrigeration produced, hp/ton or kW/ton, is an index for this assessment. Table 9.4.1 gives values for an ideal single-stage vapor compression cycle.
3. *Oil miscibility*. Refrigerant should be miscible with mineral lubricant oil because a mixture of refrigerant and oil helps to lubricate pistons and discharge valves, bearings, and other moving parts of a compressor. Oil should also be returned from the condenser and evaporator for continuous lubrication. R-22 is partially miscible. R-134a is hardly miscible with mineral oil; therefore, synthetic lubricant of polyolester will be used.
4. *Compressor displacement*. Compressor displacement per ton of refrigeration produced, in cfm/ton, directly affects the size of the positive displacement compressor and therefore its compactness. Ammonia R-717 requires the lowest compressor displacement (1.70 cfm/ton) and R-22 the second lowest (1.91 cfm/ton).

5. Desired properties:
   - Evaporating pressure p_{ev} should be higher than atmospheric. Then noncondensable gas will not leak into the system.
   - Lower condensing pressure for lighter construction of compressor, condenser, piping, etc.
   - A high thermal conductivity and therefore a high heat transfer coefficient in the evaporator and condenser.
   - Dielectric constant should be compatible with air when the refrigerant is in direct contact with motor windings in hermetic compressors.
   - An inert refrigerant that does not react chemically with material will avoid corrosion, erosion, or damage to system components. Halocarbons are compatible with all containment materials except magnesium alloys. Ammonia, in the presence of moisture, is corrosive to copper and brass.
   - Refrigerant leakage can be easily detected. Halide torch, electronic detector, and bubble detection are often used.

Ideal Single-Stage Vapor Compression Cycle

Refrigeration Process

A refrigeration process shows the change of the thermodynamic properties of the refrigerant and the energy and work transfer between the refrigerant and surroundings.

Energy and work transfer is expressed in British thermal units per hour, or Btu/hr. Another unit in wide use is ton of refrigeration, or ton. A ton = 12,000 Btu/hr of heat removed; i.e., 1 ton of ice melting in 24 hr = 12,000 Btu/hr.

Refrigeration Cycles

When a refrigerant undergoes a series of processes like evaporation, compression, condensation, throttling, and expansion, absorbing heat from a low-temperature source and rejecting it to a higher temperature sink, it is said to have undergone a refrigeration cycle. If its final state is equal to its initial state, it is a *closed cycle*; if the final state does not equal the initial state, it is an *open cycle*. Vapor compression refrigeration cycles can be classified as single stage, multistage, compound, and cascade cycles.

A *pressure-enthalpy diagram* or *p-h* diagram is often used to calculate the energy transfer and to analyze the performance of a refrigeration cycle, as shown in Figure 9.4.1. In a *p-h* diagram, pressure *p*, in psia or psig logarithmic scale, is the ordinate, and enthalpy *h*, in Btu/lb, is the abscissa. The saturated liquid and saturated vapor line encloses a two-phase region in which vapor and liquid coexist. The two-phase region separates the subcooling liquid and superheated vapor regions. The constant-temperature line is nearly vertical in the subcooling region, horizontal in the two-phase region, and curved down sharply in the superheated region.

In the two-phase region, a given saturated pressure determines the saturated temperature and vice versa. The constant-entropy line is curved upward to the right-hand side in the superheated region. Each kind of refrigerant has its own *p-h* diagram.

Refrigeration Processes in an Ideal Single-Stage Cycle

An *ideal cycle* has isentropic compression, and pressure losses in the pipeline, valves, and other components are neglected. All refrigeration cycles covered in this section are ideal. Single stage means a single stage of compression.

There are four refrigeration processes in an ideal single-stage vapor compression cycle, as shown in Figure 9.4.2(a) and (b):

1. Isothermal evaporation process 4–1 — The refrigerant evaporates completely in the evaporator and produces refrigeration effect q_{rf}, in Btu/lb:

$$q_{rf} = \left(h_1 - h_4\right) \tag{9.4.1}$$

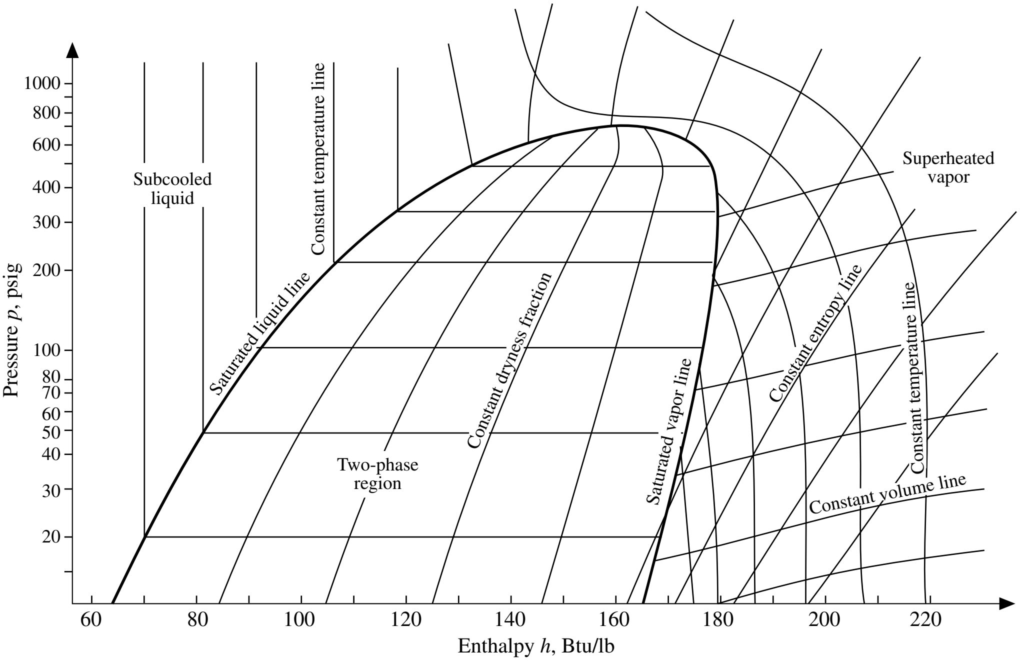

FIGURE 9.4.1 Skeleton of pressure-enthalpy diagram for R-22.

where h_1,h_4 = enthalpy of refrigerant at state points 1 and 4, respectively, Btu/lb.

2. Isentropic compression process 1–2 — Vapor refrigerant is extracted by the compressor and compressed isentropically from point 1 to 2. The work input to the compressor W_{in}, in Btu/lb, is

$$W_{in} = (h_2 - h_1) \tag{9.4.2}$$

where h_2 = enthalpy of refrigerant at state point 2, Btu/lb.

The greater the difference in temperature/pressure between the condensing pressure p_{con} and evaporating pressure p_{ev}, the higher will be the work input to the compressor.

3. Constant pressure condensation process 2–3 — Hot gaseous refrigerant discharged from the compressor is condensed in the condenser into liquid, and the latent heat of condensation is rejected to the condenser water or ambient air. The heat rejection during condensation, q_{2-3}, in Btu/lb, is

$$-q_{2-3} = (h_2 - h_3) \tag{9.4.3}$$

where h_3 = enthalpy of refrigerant at state point 3, Btu/lb.

4. Throttling process 3–4 — Liquid refrigerant flows through a throttling device (e.g., an expansion valve, a capillary tube, or orifices) and its pressure is reduced to the evaporating pressure. A portion of the liquid flashes into vapor and enters the evaporator. This is the only irreversible process in the ideal cycle, usually represented by a dotted line. For a throttling process, assuming that the heat gain from the surroundings is negligible:

$$h_3 = h_4 \tag{9.4.4}$$

The mass flow rate of refrigerant $\overset{\circ}{m}_r$, in lb/min, is

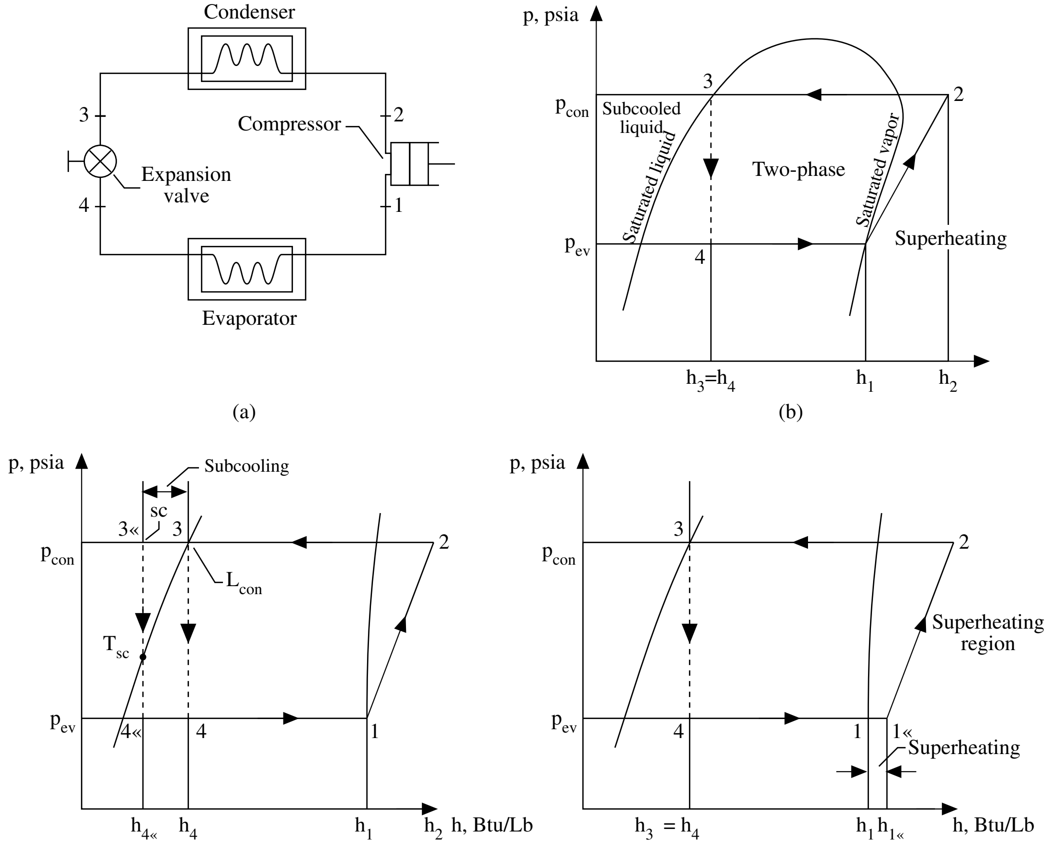

(a) (b) (c) (d)

FIGURE 9.4.2 A single-stage ideal vapor compression refrigeration cycle: (a) schematic diagram, (b) *p-h* diagram, (c) subcooling, and (d) superheating.

$$\overset{\circ}{m}_{r} = q_{rc}/60q_{rf} \tag{9.4.5}$$

where q_{rc} = refrigeration capacity of the system, Btu/hr.

The ideal single-stage vapor compression refrigeration cycle on a *p-h* diagram is divided into two pressure regions: high pressure (p_{con}) and low pressure (p_{ev}).

Coefficient of Performance of Refrigeration Cycle

The *coefficient of performance* (COP) is a dimensionless index used to indicate the performance of a thermodynamic cycle or thermal system. The magnitude of COP can be greater than 1.

- If a *refrigerator* is used to produce a refrigeration effect, COP_{ref} is

$$\text{COP}_{ref} = q_{rf}/W_{in} \tag{9.4.6}$$

- If a *heat pump* is used to produce a useful heating effect, its performance denoted by COP_{hp} is

$$\text{COP}_{hp} = q_{2-3}/W_{in} \tag{9.4.7}$$

- For a heat recovery system when both refrigeration and heating effects are produced, the COP_{hr} is denoted by the ratio of the sum of the absolute values of q_{rf} and $q_{2\text{-}3}$ to the work input, or

$$\text{COP}_{\text{hr}} = \left(\left|q_{\text{rf}}\right| + \left|q_{2-3}\right|\right) / W_{\text{in}} \tag{9.4.8}$$

Subcooling and Superheating

Condensed liquid is often subcooled to a temperature lower than the saturated temperature corresponding to the condensing pressure p_{con}, in psia or psig, as shown in Figure 9.4.2(c). *Subcooling* increases the refrigeration effect to $q_{\text{rf.sc}}$ as shown in Figure 9.4.2(c):

$$q_{\text{rf.sc}} = \left(h_{4'} - h_1\right) > \left(h_4 - h_1\right) \tag{9.4.9}$$

The enthalpy of subcooled liquid refrigerant h_{sc} approximately equals the enthalpy of the saturated liquid refrigerant at subcooled temperature $h_{\text{s.sc}}$, both in Btu/lb:

$$h_{\text{sc}} = h_{3'} = h_{4'} = h_{1.\text{con}} - c_{pr}\left(T_{\text{con}} - T_{\text{sc}}\right) \approx h_{\text{s.sc}} \tag{9.4.10}$$

where

$h_{3'}$, $h_{4'}$ = enthalpy of liquid refrigerant at state points 3′ and 4′ respectively, Btu/lb
$h_{\text{l.con}}$ = enthalpy of saturated liquid at condensing temperature, Btu/lb
c_{pr} = specific heat of liquid refrigerant at constant pressure, Btu/lb °F
T_{con} = condensing temperature or saturated temperature of liquid refrigerant at condensing pressure, °F
T_{sc} = temperature of subcooled liquid refrigerant, °F

The purpose of *superheating* is to prevent liquid refrigerant flooding back into the compressor and causing slugging damage as shown in Figure 9.4.2(d). The degree of superheating depends mainly on the types of refrigerant feed, construction of the suction line, and type of compressor. The state point of vapor refrigerant after superheating of an ideal system must be at the evaporating pressure with a specific degree of superheat and can be plotted on a *p-h* diagram for various refrigerants.

Refrigeration Cycle of Two-Stage Compound Systems with a Flash Cooler

A *multistage system* employs more than one compression stage. Multistage vapor compression systems are classified as compound systems and cascade systems. A *compound system* consists of two or more compression stages connected in series. It may have one high-stage compressor (higher pressure) and one low-stage compressor (lower pressure), several compressors connected in series, or two or more impellers connected internally in series and driven by the same motor.

The *compression ratio* R_{com} is defined as the ratio of discharge pressure p_{dis} to the suction pressure at the compressor inlet p_{suc}:

$$R_{\text{com}} = p_{\text{dis}} / p_{\text{suc}} \tag{9.4.11}$$

Compared to a single-stage system, a multistage has a smaller compression ratio and higher compression efficiency for each stage of compression, greater refrigeration effect, lower discharge temperature at the high-stage compressor, and greater flexibility. At the same time, a multistage system has a higher initial cost and more complicated construction.

The pressure between the discharge pressure of the high-stage compressor and the suction pressure of the low-stage compressor of a multistage system is called *interstage pressure* p_{i}, in psia. Interstage

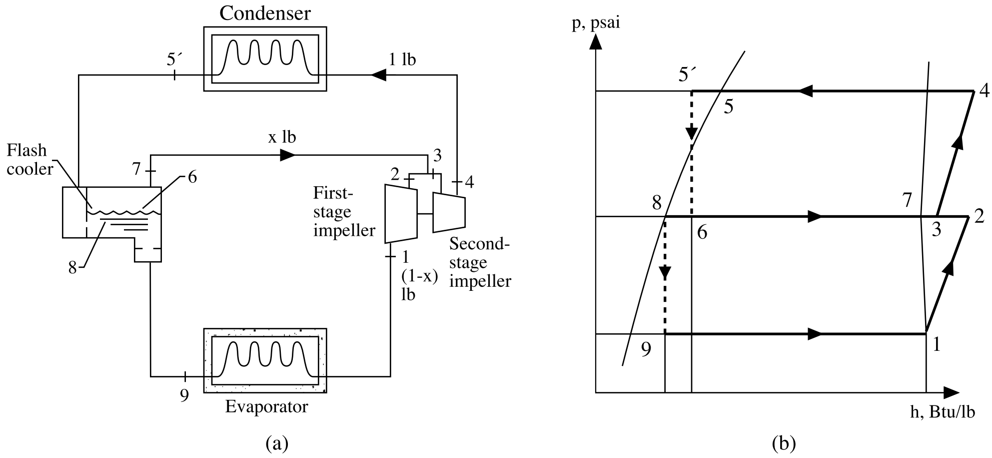

FIGURE 9.4.3 Two-stage compound system with a flash cooler: (a) schematic diagram and (b) refrigeration cycle.

pressure for a two-stage system is usually determined so that the compression ratios are nearly equal between two stages for a higher COP. Then the interstage pressure is

$$p_i = \sqrt{\left(p_{con} p_{ev}\right)} \tag{9.4.12}$$

where p_{con}, p_{ev} = condensing and evaporating pressures, psia.

For a multistage system of *n* stages, then, the compression ratio of each stage is

$$R_{com} = \left(p_{con}/p_{suc}\right)^{1/n} \tag{9.4.13}$$

Figure 9.4.3(a) shows a schematic diagram and Figure 9.4.3(b) the refrigeration cycle of a two-stage compound system with a flash cooler. A *flash cooler*, sometimes called an economizer, is used to subcool the liquid refrigerant to the saturated temperature corresponding to the interstage pressure by vaporizing a portion of the liquid refrigerant in the flash cooler.

Based on the principle of heat balance, the fraction of evaporated refrigerant, *x*, or quality of the mixture in the flash cooler is

$$x = \left(h_{5'} - h_8\right)/\left(h_7 - h_8\right) \tag{9.4.14}$$

where $h_{5'}$, h_7, h_8 = enthalpy of the refrigerant at state points 5′, 7, and 8, respectively, Btu/lb. The coefficient of performance of the refrigeration cycle of a two-stage compound system with a flash cooler, COP_{ref}, is given as

$$\text{COP}_{ref} = q_{rf}/W_{in} = (1-x)\left(h_1 - h_9\right)/\left[(1-x)\left(h_2 - h_1\right) + \left(h_4 - h_3\right)\right] \tag{9.4.15}$$

where h_1, h_2, h_3, h_4, h_9 = enthalpy of refrigerant at state points 1, 2, 3, 4, and 9, respectively, Btu/lb. The mass flow rate of refrigerant flowing through the condenser, $\overset{\circ}{m}_r$, in lb/min, can be calculated as

$$\overset{\circ}{m}_r = q_{rc}/60q_{rf} \tag{9.4.16}$$

Because a portion of liquid refrigerant is flashed into vapor in the flash cooler and goes directly to the second-stage impeller inlet, less refrigerant is compressed in the first-stage impeller. In addition, the

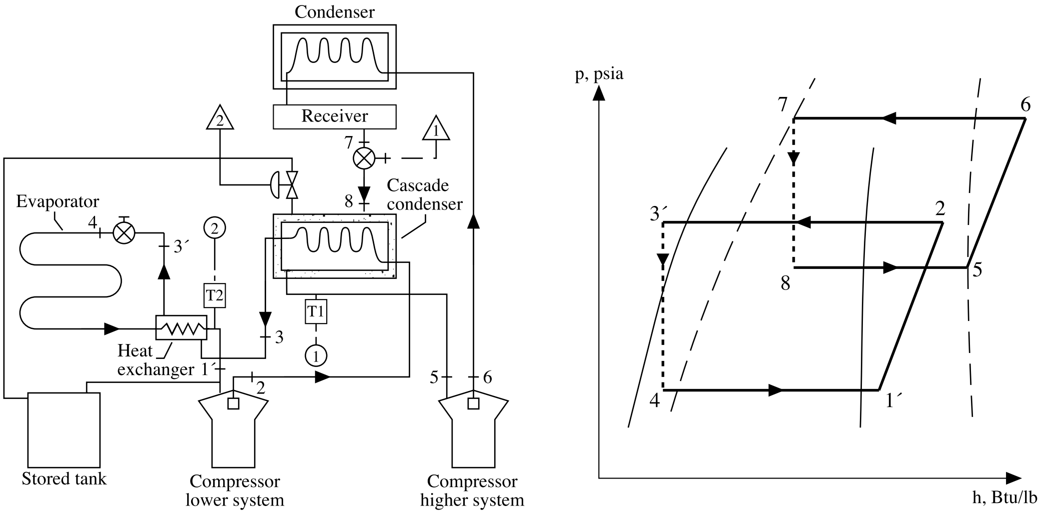

(a)

(b)

FIGURE 9.4.4 Cascade system: (a) schematic diagram and (b) refrigeration cycle.

liquid refrigerant in the flash cooler is cooled to the saturated temperature corresponding to the interstage temperature before entering the evaporator, which significantly increases the refrigeration effect of this compound system. Two-stage compound systems with flash coolers are widely used in large central air-conditioning systems.

Cascade System Characteristics

A *cascade system* consists of two independently operated single-stage refrigeration systems: a lower system that maintains a lower evaporating temperature and produces a refrigeration effect and a higher system that operates at a higher evaporating temperature as shown in Figure 9.4.4(a) and (b). These two separate systems are connected by a *cascade condenser* in which the heat released by the condenser in the lower system is extracted by the evaporator in the higher system.

A heat exchanger is often used between the liquid refrigerant from the condenser and the vapor refrigerant leaving the evaporator of the lower system. When the system is shut down in summer, a relief valve connected to a stored tank should be used to relieve the higher pressure of refrigerant at the higher storage temperature.

The main advantages of a cascade system compared with a compound system are that different refrigerants, oils, and equipment can be used for the lower and higher systems. Disadvantages are the overlap of the condensing temperature of the lower system and the evaporating temperature of the higher system because of the heat transfer in the cascade condenser and a more complicated system.

The refrigeration effect q_{rf} of the cascade system is

$$q_{\mathrm{rf}} = \left(h_1 - h_4\right) \tag{9.4.17}$$

where h_1, h_4 = enthalpy of the refrigerant leaving and entering the evaporator of the lower system, Btu/lb. The total work input to the compressors in both higher and lower systems W_{in}, in Btu/lb, can be calculated as

$$W_{\mathrm{in}} = \left(h_2 - h_{1'}\right) + \mathring{m}_{\mathrm{h}}\left(h_6 - h_5\right)\Big/\mathring{m}_1 \tag{9.4.18}$$

where

h_2 = enthalpy of refrigerant discharged from the compressor of the lower system
$h_{1'}$ = enthalpy of the vapor refrigerant leaving the heat exchanger
h_6, h_5 = enthalpy of the refrigerant leaving and entering the high-stage compressor
$\mathring{m}_h, \mathring{m}_1$ = mass flow rate of the refrigerant of the higher and lower systems, respectively

The coefficient of performance of a cascade system $\mathrm{COP}_{\mathrm{ref}}$ is

$$\mathrm{COP}_{\mathrm{ref}} = q_{\mathrm{rf}}/W_{\mathrm{in}} = \mathring{m}_1\left(h_1 - h_4\right)\Big/\left[\mathring{m}_1\left(h_2 - h_{1'}\right) + \mathring{m}_h\left(h_6 - h_5\right)\right] \qquad (9.4.19)$$

9.5 Outdoor Design Conditions and Indoor Design Criteria

Shan K. Wang

Outdoor Design Conditions

In principle, the capacity of air-conditioning equipment should be selected to offset or compensate for the space load so that indoor design criteria can be maintained if the outdoor weather does not exceed the design values. Outdoor and indoor design conditions are used to calculate the design space loads. In energy use calculations, hour-by-hour outdoor climate data of a design day should be adopted instead of summer and winter design values.

ASHRAE Handbook 2001 Fundamentals (Chapter 27) and *Wang's Handbook of Air Conditioning and Refrigeration* (Chapter 7) both list tables of climate conditions for the U.S. and Canada based on the data from the National Climate Data Center (NCDC), U.S. Air Force, U.S. Navy, and Canadian Atmospheric Environment Service.

Indoor Design Criteria and Thermal Comfort

Indoor design criteria, such as space temperature, humidity, and air cleanliness, specify the requirements for the indoor environment as well as the quality of an air-conditioning or HVAC&R project.

The human body requires energy for physical and mental activity. This energy comes from the oxidation of food. The rate of heat release from the oxidation process is called the *metabolic rate*, expressed in met (1 met = 18.46 Btu/h.ft^2). The metabolic rate depends mainly on the intensity of the physical activity of the human body. Heat is released from the human body by two means: *sensible heat exchange* and *evaporative heat loss*. Experience and experiments all show that there is thermal comfort only under these conditions:

- Heat transfer from the human body to the surrounding environment causes a steady state of thermal equilibrium; that is, there is no heat storage in the body core and skin surface.
- Evaporative loss or regulatory sweating is maintained at a low level.

The physiological and environmental factors that affect the thermal comfort of the occupants in an air-conditioned space are mainly:

1. Metabolic rate M determines the amount of heat that must be released from the human body.
2. *Indoor air temperature* T_r and *mean radiant temperature* T_{rad}, both in °F. The *operating temperature* T_o is the weighted sum of T_r and T_{rad}. T_{rad} is defined as the temperature of a uniform black enclosure in which the surrounded occupant would have the same radiative heat exchange as in an actual indoor environment. T_r affects both the sensible heat exchange and evaporative losses, and T_{rad} affects only sensible heat exchange. In many indoor environments, $T_{\mathrm{rad}} \approx T_r$.
3. Relative humidity of the indoor air φ_r, in %, which is the primary factor that influences evaporative heat loss.
4. Air velocity of the indoor air v_r, in fpm, which affects the heat transfer coefficients and therefore the sensible heat exchange and evaporative loss.
5. *Clothing insulation* R_{cl}, in clo (1 clo = 0.88 h.ft^2.°F/Btu), affects the sensible heat loss. Clothing insulation for occupants is typically 0.6 clo in summer and 0.8 to 1.2 clo in winter.

Indoor Temperature, Relative Humidity, and Air Velocity

For comfort air-conditioning systems, according to ANSI/ASHRAE Standard 55-1992, the following indoor design temperatures and air velocities apply for conditioned spaces where the occupant's activity level is $\leqslant$1.2 met, mean air speed $\leqslant$ 30 fpm, indoor space relative humidity is 50% (in summer only), and $T_r = T_{rad}$:

	Clothing Insulation (clo)	Indoor Temperature (°F)
Winter	0.9	68–75
Summer	0.5	73–79

Regarding the indoor humidity:

1. Many comfort air-conditioning systems are not equipped with humidifiers. Winter indoor relative humidity should not be specified in such circumstances.
2. When comfort air-conditioning systems are installed with humidifiers, ASHRAE/IES Standard 90.1-2001 provides specific requirements for economy of operation.
3. Indoor relative humidity should not exceed 75% to avoid increasing bacterial and viral populations.
4. For air-conditioning systems that use flow rate control in a chilled water cooling coil, space indoor relative humidity may be substantially higher in part load than at full load.

Therefore, for comfort air-conditioning systems, the recommended indoor relative humidities, in %, are

	Tolerable range	Preferred value
Summer	30–65	40–50
Winter		
With humidifier		25–30
Without humidifier		Not specified

In surgical rooms or similar health care facilities, the indoor relative humidity is often maintained at 40 to 60% year round.

Indoor Air Quality and Outdoor Ventilation Air Requirements

According to the National Institute for Occcupational Safety and Health (NIOSH), 1989, the causes of indoor air quality complaints in buildings are inadequate outdoor ventilation air, 53%; indoor contaminants, 15%; outdoor contaminants, 10%; microbial contaminants, 5%; construction and furnishings, 4%; unknown and others, 13%. For space served by air-conditioning systems using low- and medium-efficiency air filters, according to the U.S. Environmental Protection Agency (EPA) and Consumer Product Safety Commission (CPSC) publication "A Guide to Indoor Air Quality" (1988) and the field investigations reported by Bayer and Black (1988), *indoor air contaminants* may include some of the following:

1. *Total particulate concentration*. This concentration comprises particles from building materials, combustion products, mineral fibers, and synthetic fibers. In February 1989, the EPA specified the allowable indoor concentration of particles of 10 μm and less in diameter (which penetrate deeply into lungs) as:

   50 μg/m^3 (0.000022 grain/ft^3), 1 year

   150 μg/m^3 (0.000066 grain/ft^3), 24 hr

   In these specifications, "1 year" means maximum allowable exposure per day over the course of a year.
2. *Formaldehyde and organic gases*. Formaldehyde is a colorless, pungent-smelling gas. It comes from pressed wood products, building materials, and combustion. Formaldehyde causes eye, nose, and

throat irritation as well as coughing, fatigue, and allergic reactions. Formaldehyde may also cause cancer. Other organic gases come from building materials, carpeting, furnishings, cleaning materials, etc.

3. *Radon*. Radon, a colorless and odorless gas, is released by the decay of uranium from the soil and rock beneath buildings, well water, and building materials. Radon and its decay products travel through pores in soil and rock and infiltrate into buildings along the cracks and other openings in the basement slab and walls. Radon at high levels causes lung cancer. The EPA believes that levels in most homes can be reduced to 4 pCi/l (picocuries per liter) of air. The estimated national average is 1.5 pCi/l, and levels as high as 200 pCi/l have been found in houses.
4. *Biologicals*. These include bacteria, fungi, mold and mildew, viruses, and pollen. They may come from wet and moist walls, carpet furnishings, and poorly maintained dirty air-conditioning systems and may be transmitted by people. Some biological contaminants cause allergic reactions, and some transmit infectious diseases.
5. *Combustion products*. These include environmental tobacco smoke, nitrogen dioxide, and carbon monoxide. *Environmental tobacco* smoke from cigarettes is a discomfort factor to other persons who do not smoke, especially children. Nicotine and other tobacco smoke components cause lung cancer, heart disease, and many other diseases. *Nitrogen dioxide* and *carbon monoxide* are both combustion products from unvented kerosene and gas space heaters, woodstoves, and fireplaces. Nitrogen dioxide (NO_2) causes eye, nose, and throat irritation; may impair lung function; and increases respiratory infections. Carbon monoxide (CO) causes fatigue at low concentrations; impaired vision, headache, and confusion at higher concentrations; and is fatal at very high concentrations. Houses without gas heaters and gas stoves may have CO levels varying from 0.5 to 5 parts per million (ppm).
6. *Human bioeffluents*. These include the emissions from breath including carbon dioxide exhaled from the lungs, body odors from sweating, and gases emitted as flatus.

There are three basic means of reducing the concentration of indoor air contaminants and improving indoor air quality: (1) eliminate or reduce the source of air pollution, (2) enhance the efficiency of air filtration, and (3) increase the ventilation (outdoor) air intake. Dilution of the concentrations of indoor contaminants by outdoor ventilation air is often the simple and cheapest way to improve indoor air quality. The amount of outdoor air required for metabolic oxidation is rather small.

Outdoor air requirements listed in ANSI/ASHRAE Standard 62-1999 can be used in the ventilation procedure method to satisfy indoor air quality requirements. The minimum outside air ventilation per person for any type of space is 15 cfm.

This requirement is based on the analysis of dilution of CO_2 as the representative human bioeffluent to an allowable indoor concentration within 0.07% (700 ppm) of the outdoor concentration. Field measurements of daily maximum CO_2 levels in office buildings reported by Persily (1993) show that most of them were within the range 400 to 820 ppm. The quality of outdoor air must meet the EPA's National Primary and Secondary Ambient Air Quality Standards, some of which is listed below:

	Long-Term Concentration			Short-Term Concentration		
Pollutants	µg/m³	ppm	Exposure	µg/m³	ppm	Exposure
Particulate	75		1 year	260		24 hr
SO_2	80	0.03	1 year	365	0.14	24 hr
CO				40,000	35	1 hr
				10,000	9	8 hr
NO_2	100	0.055	1 year			
Lead	1.5		3 months			

Here exposure means average period of exposure.

If unusual contaminants or unusually strong sources of contaminants are introduced into the space, or recirculated air is to replace part of the outdoor air supply for occupants, then acceptable indoor air quality is achieved by controlling known and specific contaminants. This is called an indoor air quality procedure. Refer to ANSI/ASHRAE Standard 62-1999 for details.

Clean Rooms

Electronic, pharmaceutical, and aerospace industries and operating rooms in hospitals all need strict control of air cleanliness during manufacturing and operations. According to ASHRAE Handbook 1991 HVAC Applications, clean rooms can be classified as follows based on the particle count per ft^3:

Class	Particle Size 0.5 µm and Larger	 5 µm and Larger
	Particle Count per ft^3 Not to Exceed	
1	1	0
10	10	0
100	100	
1000	1000	
10,000	10,000	65
100,000	100,000	700

For clean rooms, space temperature is often maintained at 72 ± 2°F and space humidity at 45 ± 5%. Here, ±2°F and ±5% are allowable tolerances. Federal Standard 209B specifies that the ventilation (outdoor air) rate should be 5 to 20% of the supply air.

Space Pressure Differential

Most air-conditioning systems are designed to maintain a slightly higher pressure than the surroundings, a positive pressure, to prevent or reduce infiltration and untreated air entering the space directly. For laboratories, restrooms, or workshops where toxic, hazardous, or objectional gases or contaminants are produced, a slightly lower pressure than the surroundings, a negative pressure, should be maintained to prevent or reduce the diffusion of these contaminants' exfiltrate to the surrounding area.

For comfort air-conditioning systems, the recommended pressure differential between the indoor and outdoor air is 0.02 to 0.05 in in. WG. WG indicates the pressure at the bottom of a top-opened water column of specific inches of height; 1 in. WG = 0.03612 psig.

For clean rooms, Federal Standard No. 209B, Clean Rooms and Work Stations Requirements (1973), specifies that the minimum positive pressure between the clean room and any adjacent area with lower cleanliness requirements should be 0.05 in. WG with all entryways closed. When the entryways are open, an outward flow of air is to be maintained to prevent migration of contaminants into the clean room. In comfort systems, the space pressure differential is usually not specified in the design documents.

Sound Levels

Noise is any unwanted sound. In air-conditioning systems, noise should be attenuated or masked with another less objectionable sound.

Sound power is the capability to radiate power from a sound source exited by an energy input. The intensity of sound power is the output from a sound source expressed in watts (W). Due to the wide variation of sound output at a range of 10^{20} to 1, it is more convenient to use a logarithmic expression to define a *sound power level* L_w, in dB:

$$L_w = 10 \log\left(w/10^{-12}\ \mathrm{W}\right) \text{ re 1 pW} \tag{9.5.2}$$

where w = sound source power output, W.

The human ear and microphones are sound pressure sensitive. Similarly to the sound power level, the *sound pressure level* L_p, in dB, is defined as:

$$L_p = 20\log\left(p/2\times10^{-5}\ \text{Pa}\right)\ \text{re}\ 20\ \mu\text{Pa} \qquad (9.5.3)$$

where p = sound pressure, Pa.

The sound power level of any sound source is a fixed output. It cannot be measured directly; it can only be calculated from the measured sound pressure level. The sound pressure level at any one point is affected by the distance from the source and the characteristics of the surroundings.

Human ears can hear frequencies from 20 Hz to 20 kHz. For convenience in analysis, sound frequencies are often subdivided into eight octave bands. An *octave* is a frequency band in which the frequency of the upper limit of the octave is double the frequency of the lower limit. An octave band is represented by its center frequency, such as 63, 125, 250, 500, 1000, 2000, 4000, and 8000 Hz. On 1000 Hz the octave band has a higher limit of 1400 Hz and a lower limit of 710 Hz. Human ears do not respond in the same way to low frequencies as to high frequencies.

The object of noise control in an air conditioned space is to provide background sound low enough that it does not interfere with the acoustical requirements of the occupants. The distribution of background sound should be balanced over a broad range of frequencies, that is, without whistle, hum, rumble, and beats.

The most widely used criteria for sound control are the noise criteria NC curves. The shape of NC curves is similar to the equal-loudness contour representing the response of the human ear. NC curves also intend to indicate the permissible sound pressure level of broad-band noise at various octave bands rated by a single NC curve. NC curves are practical and widely used.

Other criteria used are room criteria RC curves and A-weighted sound level, dBA. RC curves are similar to NC curves except that the shape of the RC curves is a close approximation to a balanced, bland-sounding spectrum. The A-weighted sound level is a single value and simulates the response of the human ear to sound at low sound pressure levels.

The following are abridged indoor design criteria, NC or RC range, listed in *ASHRAE Handbook 1987 Systems and Applications*:

Type of Area	Recommended NC or RC Range (dB)
Hotel guest rooms	30–35
Office	
Private	30–35
Conference	25–30
Open	30–35
Computer equipment	40–45
Hospital, private	25–30
Churches	25–30
Movie theaters	30–35

For industrial factories, if the machine noise in a period of 8 hr exceeds a prescribed level given in dBA, Occupational Safety and Health Administration Standard Part 1910.95 requires the occupants to use personal protection equipment. If the period is shorter, the dBA level can be slightly higher. Refer to this standard for details.

9.6 Principles of Load Calculations

Ari Rabl and Peter Curtiss

Design Conditions

Loads are the heat that must be supplied or removed by HVAC equipment to maintain a space at the desired conditions. Loads depend on the indoor conditions that one wants to maintain and on the weather. The latter is not known in advance. If the HVAC equipment is to guarantee comfort at all times, it must be designed for peak conditions. What are the extremes? For most buildings it would not be practical to aim for total protection by choosing the most extreme weather on record and adding a safety margin. Such oversizing of the HVAC equipment would be excessive, not just in initial cost but also in operating cost; most of the time, the equipment would run with poor part-load efficiency. Therefore, compromise — reducing the cost of the HVAC equipment significantly while accepting the risk of slight discomfort under rare extremes of weather — is necessary. The greater the extreme is, the more rarely it occurs.

Wind speed is another weather-dependent variable that has a bearing on loads. Traditionally the ASHRAE (2001) value

$$v_{win} = 15 \text{ mi/h } \left(6.7 \text{ m/s}\right) \tag{9.6.1}$$

has been recommended for heating loads, if extreme conditions (such as an exposed hilltop location) are not implied. For cooling loads, a value half as large is recommended:

$$V_{sum} = 7.5 \text{ mi/s } \left(3.4 \text{ m/s}\right) \tag{9.6.2}$$

because wind tends to be less strong in summer than in winter. Of particular interest is the surface heat transfer coefficient (radiation plus convection) h_o for which ASHRAE (2001) recommends the design values:

$$h_{o,win} = 6.0 \text{ Btu}\Big/\left(\text{h}\cdot\text{ft}^2\cdot{}^\circ\text{F}\right) \;\; 34.0 \text{ W}\Big/\left(\text{m}^2\cdot\text{K}\right) \tag{9.6.3}$$

$$h_{o,sum} = 4.0 \text{ Btu}\Big/\left(\text{h}\cdot\text{ft}^2\cdot{}^\circ\text{F}\right) \;\; 22.7 \text{ W}\Big/\left(\text{m}^2\cdot\text{K}\right) \tag{9.6.4}$$

This coefficient is only one of several components of the calculation of thermal loads, and it enters only through the building heat transmission coefficient defined in the next section. The better a building is insulated and tightened, the less its heat transmission coefficient K_{tot} depends on wind. With current practice for new construction in the United States, typical wind speed variations may change the heat transmission coefficient by about 10% relative to the value at design conditions.

Building Heat Transmission Coefficient

One of the most important terms in the heat balance of a building is the heat flow across the envelope. Heat flow can be assumed to be linear in the temperature difference when the range of temperatures is sufficiently small; this is usually a good approximation for heat flow across the envelope. Thus, one can calculate the heat flow through each component of the building envelope as the product of its area A; its conductance U; and the difference $T_i - T_o$ between the interior and outdoor temperatures.

The total conductive heat flow from interior to exterior is

$$\dot{Q}_{cond} = \sum_k U_k A_k (T_i - T_o), \tag{9.6.5}$$

with the sum running over all parts of the envelope that have a different composition. It is convenient to define a total conductive heat transmission coefficient K_{cond}, or UA value, as

$$K_{cond} = \sum_k U_k A_k \tag{9.6.6}$$

so that the conductive heat flow for the typical case of a single interior temperature T_i can be written as

$$\dot{Q}_{cond} = K_{cond}(T_i - T_o) \tag{9.6.7}$$

In most buildings, the envelope consists of a large number of different parts; the greater the desired accuracy is, the greater the amount of detail to be taken into account.

As a simplification, one can consider a few major groups and use effective values for each. The three main groups are glazing, opaque walls, and roof. The reason for distinguishing the wall and the roof lies in the thickness of the insulation: roofs tend to be better insulated because it is easier and less costly to add extra insulation there than in the walls. With these three groups, one can write

$$K_{\mathrm{cond}} = U_{\mathrm{glaz}} A_{\mathrm{glaz}} + U_{\mathrm{wall}} A_{\mathrm{wall}} + U_{\mathrm{roof}} A_{\mathrm{roof}} \tag{9.6.8}$$

if one takes for each the appropriate effective value. Results for aggregate U values for walls and roofs of typical construction can be found in ASHRAE lookup tables.

In the energy balance of a building, one other term is proportional to $T_i - T_o$. It is the flow of sensible heat [W (Btu/h)] due to air exchange:

$$\dot{Q}_{air} = \rho c_p \dot{V}(T_i - T_o) \tag{9.6.9}$$

where

ρ = density of air
c_p = specific heat of air
$\dot{V}$ = air exchange rate ft³/h (m³/s)

At standard conditions, 14.7 psia (101.3 kPa) and 68°F (20°C), the factor ρc_p has the value

$$\rho c_p = 0.018 \text{ Btu/(ft}^3 \cdot {}^\circ\text{F) } [1.2 \text{ kJ/(m}^3 \cdot \text{K)}] \tag{9.6.10}$$

In USCS units, if $\dot{V}$ is in cubic feet per minute, it must be converted to cubic feet per hour by multiplying by 60 (ft³/h)/(ft³/min). It is convenient to combine the terms proportional to $T_i - T_o$ by defining the total heat transmission coefficient K_{tot} of the building as the sum of conductive and air change terms:

$$K_{\mathrm{tot}} = K_{cond} + \rho c_p \dot{V} \tag{9.6.11}$$

Note that $\dot{V}$ increases with the temperature difference for a number of reasons (see Kreider et al., 2001).

Heat Gains

Heat gains affect heating as well as cooling loads. In addition to solar gains, heat gains occur from occupants, lights, and equipment such as appliances, motors, computers, and copiers. Power densities for lights in office buildings are around 20 to 30 W/m². For lights and for resistive heaters, the nominal power rating (i.e., the rating on the label) is usually close to the power drawn in actual use. However, for office equipment, that would be quite misleading; the actual power has been measured to be much lower, often by a factor of two to four (Norford et al., 1989). Some typical values are indicated in Table 9.6.1. In recent decades, the computer revolution has brought a rapid increase in electronic office equipment, and the impact on loads has become quite important, comparable to that of lighting. The energy consumption for office equipment is uncertain: will the occupants turn off the computers between uses or keep them running nights and weekends?

For special equipment such as laboratories or kitchens, it is advisable to estimate the heat gains by taking a close look at the inventory of the equipment to be installed, paying attention to the possibility that much of the heat may be drawn directly to the outside by exhaust fans.

TABLE 9.6.1 Typical Heat Gain Rates for Several Kinds of Equipment

Equipment	Heat Gain Btu/h	Heat Gain W	Comments
Television set	170–340	50–100	
Refrigerator	340–680	100–200	Recent models more efficient
Personal computer (desktop)	170–680	50–200	Almost independent of use while turned on
Impact printer	34–100	10–30 standby	Increases about twofold during printing
Laser printer	500	150 standby	Increases about twofold during printing
Copier	500–1000	150–300 standby	Increases about twofold during printing

Note: Measured values are often less than half of the nameplate rating.

Source: Based on ASHRAE, 1989, *Handbook of Fundamentals*. American Society of Heating, Refrigerating and Air-Conditioning Engineers, Atlanta; Norford, L.K. et al., 1989, in T.B. Johansson et al., Eds. *Electricity: Efficient End Use and New Generation Technologies, and Their Planning Implications*. Lund University Press, Lund, Sweden, 427–460; and updates.

TABLE 9.6.2 Nominal Heat Gain Values from Occupants

	Total		Sensible		Latent	
Activity	Btu/h	W	Btu/h	W	Btu/h	W
Seated at rest	340	100	240	70	100	30
Seated, light office work	410	120	255	75	150	45
Standing or walking slowly	495	145	255	75	240	70
Light physical work	850	250	310	90	545	160
Heavy physical work	1600	470	630	185	970	285

Source: Based on ASHRAE, 1989, *Handbook of Fundamentals*. American Society of Heating, Refrigerating and Air-Conditioning Engineers, Atlanta.

Heat gain from occupants depends on the level of physical activity. Nominal values are listed in Table 9.6.2. It is instructive to reflect on the origin of this heat gain. The total heat gain must be close to the caloric food intake because most of the energy is dissipated from the body as heat. An average of 100 W corresponds to

$$100 \text{ W} = 0.1 \text{ kJ/s} \times \left(\frac{1\,kcal}{4.186\,kJ}\right) \times (24 \times 3600 \text{ s/day}) = 2064 \text{ kcal/day} \tag{9.6.12}$$

indeed, a reasonable value compared to the typical food intake (note that the dietician's calorie is really a kilocalorie).

The latent heat gain must be equal to the heat of vaporization of water that is exhaled or transpired. Dividing 30 W by the heat of vaporization of water, yields a water quantity of 30 W/(2450 kJ/kg) = 12.2×10^{-6} kg/s, or about 1.1 kg/24 h. That also appears quite reasonable.

The latent heat gain due to the air exchange is

$$\dot{Q}_{air,lat} = \dot{V}\rho h_{fg}(W_o - W_i) \tag{9.6.13}$$

where

$\dot{V}$ = volumetric air exchange rate, ft^3/min (m^3/s or L/s)

ρ = density, lb$_m$/ft^3 (kg/m^3)

$\rho\, h_{fg}$ = 4840 Btu/(h · ft^3/min) [3010 W/(L/s)] at standard conditions

W_i, W_o = humidity ratios of indoor and outdoor air

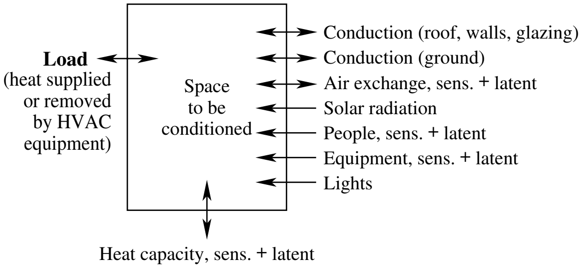

FIGURE 9.6.1 The terms in a load calculation.

Heat Balance

Load calculations are like accounting. One considers all the heat that is generated in the space or flows across the envelope; the total energy, including the thermal energy stored in the space, must be conserved according to the first law of thermodynamics. The principal terms are indicated in Figure 9.6.1. Outdoor air, occupants, and possibly certain kinds of equipment contribute sensible and latent heat terms.

Load calculations are straightforward in the static limit, i.e., if all input is constant. As discussed in the following subsection, that is usually an acceptable approximation for the calculation of peak heating loads. However, for cooling loads, dynamic effects (i.e., heat storage) must be taken into account because some of the heat gains are absorbed by the mass of the building and do not contribute to the loads until several hours later. Dynamic effects are also important whenever the indoor temperature is allowed to float.

Sometimes it is appropriate to distinguish several aspects of the load. If the indoor temperature is not constant, the instantaneous load of the space may differ from the rate at which heat is being supplied or removed by the HVAC equipment. The load for the heating or cooling plant is different from the space load if there are significant losses from the distribution system or if part of the air is exhausted to the outside rather than returned to the heating or cooling coil. It is convenient to classify the terms of the static energy balance according to the following groups. The sensible energy terms are:

- Conduction through building envelope other than ground:

$$\dot{Q}_{cond} = K_{cond}(T_i - T_o) \tag{9.6.14}$$

- Conduction through floor, $\dot{Q}_{floor}$
- Heat due to air exchange (infiltration and/or ventilation), at rate $\dot{V}$:

$$\dot{Q}_{air} = \dot{V}\rho c_p(T_i - T_o) \tag{9.6.15}$$

- Heat gains from solar radiation, lights, equipment (appliances, computers, fans, etc.), and occupants:

$$\dot{Q}_{gain} = \dot{Q}_{sol} + \dot{Q}_{lit} + \dot{Q}_{equ} + \dot{Q}_{occ} \tag{9.6.16}$$

Combining the heat loss terms and subtracting the heat gains, one obtains the total *sensible load*:

$$\dot{Q} = \dot{Q}_{cond} + \dot{Q}_{air} + \dot{Q}_{floor} - \dot{Q}_{gain} \pm \dot{Q}_{stor} \tag{9.6.17}$$

where a term, $\dot{Q}_{stor}$, has been added on the right to account for storage of heat in the heat capacity of the building (the terms *thermal mass* and *thermal inertia* are also used to designate this effect). A dynamic analysis includes this term; a static analysis neglects it.

$\dot{Q}_{floor}$ has been kept as a separate item because it should not be taken proportional to $T_i - T_o$ except in cases like a crawl space, where the floor is in fairly direct contact with outside air. More typical is conduction through massive soil, for which other methods are required. In traditional construction, the floor term has usually been small, and often it has been neglected altogether; however, in superinsulated buildings it can be relatively important.

Using the total heat transmission coefficient K_{tot},

$$K_{tot} = K_{cond} + \dot{V}\rho c_p \tag{9.6.18}$$

one can write the sensible load in the form

$$\dot{Q} = K_{tot}(T_i - T_o) + \dot{Q}_{floor} - \dot{Q}_{gain} \pm \dot{Q}_{stor} \tag{9.6.19}$$

For signs, take the convention that $\dot{Q}$ is positive when there is a heating load and negative when there is a cooling load. Sometimes, however, it will be preferable to have a positive sign for cooling loads. In that case, subscripts c and h will be added with the understanding that

$$\dot{Q}_c = -\dot{Q} \text{ and } \dot{Q}_h = \dot{Q} \tag{9.6.20}$$

The *latent heat gains* are mainly due to air exchange, equipment (such as in the kitchen and bathroom), and occupants. Their sum is

$$\dot{Q}_{lat} = \dot{Q}_{lat,air} + \dot{Q}_{lat,occ} + \dot{Q}_{lat,equ} \tag{9.6.21}$$

The total load is the sum of the sensible and the latent loads.

During the heating season, the latent gain from air exchange is usually negative (with the signs of Equation 9.6.13) because the outdoor air is relatively dry. A negative Q_{lat} implies that the total heating load is greater than the sensible heating load alone, but this is relevant only if humidification can maintain the specified humidity ratio W_i. For buildings without humidification, one has no control over W_i, and it is pointless to calculate the latent contribution to the heating load at a fictitious value of W_i.

Zones

So far the interior has been considered as a single zone at uniform temperature — a fair approximation for simple houses, for certain buildings without windows (such as warehouses), or for buildings dominated by ventilation. In large or complex buildings, however, one must usually calculate the loads separately for a number of different zones, for several reasons. An obvious case is a building in which different rooms are maintained at different temperatures, e.g., a house with an attached sunspace. Here, the heat balance equation is written for each zone, but with an additional term:

$$\dot{Q}_{j-k} = U_{j-k} A_{j-k}(T_j - T_k) \tag{9.6.22}$$

for the heat flow between zones j and k.

However, even when the entire building is kept at the same temperature, multizone analysis becomes necessary if the spatial distribution of heat gains is too nonuniform. Consider, for example, a building with large windows on the north and south sides, during a sunny winter day when the gains just balance the total heat loss. In that case, neither heating nor cooling would be required, according to a one-zone analysis — but how can the heat from the south get to the north?

Heat flow is the product of the heat transfer coefficient and the temperature difference, as in Equation (9.6.22). Temperature differences between occupied zones are small, usually not more than a few Kelvins;

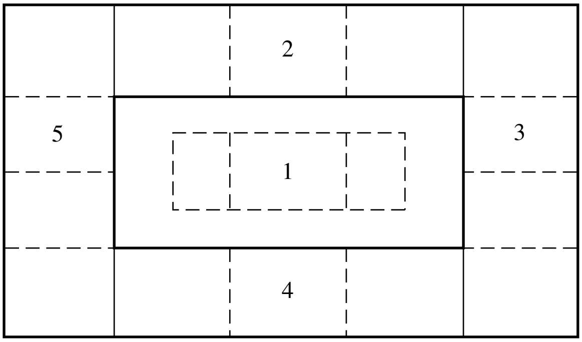

FIGURE 9.6.2 Example of recommended zoning. Thick lines represent zones, labeled 1 through 5. Dashed lines represent subzones.

otherwise there would be complaints about comfort. The heat transfer coefficients between zones are often not sufficiently large for effective redistribution of heat, especially if walls or partitions are part of the space — thus the thermodynamically perverse fact that many large buildings require simultaneous heating and cooling.

The problem of divergent zone loads is one of the prime targets for energy conservation in large buildings. The first step is to reduce the loads through the envelope, by improved insulation and control of solar radiation. The smaller the loads are, the smaller the differences between the loads. Careful attention must be paid to the design of the HVAC system and the choice of its zones. Finally, heat pump may be able to recover and redistribute heat between zones.

The basic criterion for zoning is the ability to control the comfort conditions; the control is limited by the number of zones one is willing to consider. *To guarantee comfort, the HVAC plant and distribution system must be designed with sufficient capacity to meet the load of each zone.* In choosing the zones for a multizone analysis, the designer should try to match the distribution of heat gains and losses. A common and important division is between interior and perimeter zones, because the interior is not exposed to the changing environment. Different facades of the perimeter should be considered separately for cooling load calculations, as suggested in Figure 9.6.2. Corner rooms should be assigned to the facade with which they have the most in common; usually, this will be the facade where a corner room has the largest windows. Corner rooms are often the critical rooms in a zone, requiring more heating or cooling (per unit floor area) than single-facade rooms of the same zone.

Actually, a zoning analysis has different levels, corresponding to different levels of the HVAC system. In an air system, major zones correspond to each air handler. Within each air handler zone, the air ducts, air outlets, and heating or cooling coils must have sufficient capacity and controllability to satisfy the loads of each subzone; the design flow rates for each room are scaled according to the design loads of the room. For best comfort (and if cost were no constraint), each zone should have its own air handler and each room its own thermostat. There is a tradeoff between equipment cost and achievable comfort, and the best choice depends on the circumstances. If temperature control is critical, one installs separate air handlers for each of the five zones in Figure 9.6.2 and separate thermostats for each room. To save equipment cost, one often assigns several zones to one air handler and several rooms to one thermostat; however, the more divergent the loads are, the more problematic the control. For the building of Figure 9.6.2, a single air handler and five thermostats may be adequate if the distribution of heat gains is fairly uniform and if the envelope is well insulated, with good control of solar gains.

Another example is a house in which air distribution system has a single fan (typical of all but the largest houses). Even though there is only one major zone, the detailed design of the distribution system demands some attention to subzones. Within each room, the peak heating capacity should match the peak heat loss. Also, it is advisable to place heat sources close to points with large heat loss, i.e., under windows (unless they are highly insulating).

The choice of zones is not always clear-cut, and the design process may be iterative. Depending on the distribution of gains and losses, one may want to assign several rooms to a zone, one room to a zone, or even several zones to a room (if it is very large). With finer zonal detail, one improves the control of comfort, but at the price of greater calculation effort and higher HVAC system cost. In an open office space, no obvious boundary exists between interior and perimeter; here a good rule is to make the perimeter zone as deep as the penetration depth of direct solar radiation, typically a few meters. Spaces connected by open doors, for example, offices and adjacent hallways, can sometimes be treated as a single zone. Separate zones are advisable for rooms with large computers or energy-intensive equipment. In multistory buildings, one may want to treat the top floor apart from the rest.

The calculation of peak *heating* loads and capacities can often be done without defining different perimeter zones because peak heating loads occur when the sun is not present; with uniform internal gains, the corresponding thermal balance is uniform around the perimeter. Although the calculation can be carried out for a single zone, the operation requires multiple zones because the heating system must allow separate control of different facades to compensate for the variability of solar gains during the day. For *cooling* loads, a multizone analysis is essential, even at the calculation stage, because the loads occur when the sun is shining.

Peak cooling loads require a dynamic analysis whereas peak heating loads can be estimated quite well by static models (at least in the absence of thermostat setback). Compared to heating loads, the calculation of cooling loads of large buildings is thus doubly complicated: It requires multiple zones and dynamic analysis if one wants reasonable accuracy.

A related issue is the coincidence between peak loads of different zones. To determine the capacity of the central plant, one needs to know the peak load of the totality of zones served by the plant. This is usually less than the simple sum of the individual peak loads because of noncoincidence. The term *diversity* is used to designate the ratio of the actual system peak to the sum of the individual peak loads. In practice, one often finds diversity around 0.6 to 0.8 for large buildings or groups of buildings (e.g., university campuses); for better estimates at the design stage, computer simulations are recommended.

Heating Loads

Because the coldest weather is likely to occur during periods without solar radiation, it is advisable not to rely on the benefit of solar heat gains when calculating peak heating loads (unless the building contains long-term storage). If the indoor temperature T_i is constant, a static analysis is sufficient and the calculation of the peak heating load $\dot{Q}_{h,\max}$ is very simple: find the design heat loss coefficient K_{tot}; multiply by the design temperature difference $T_i - T_o$; and subtract the internal heat gains on which one can count during the coldest weather:

$$\dot{Q}_{h,\max} = K_{tot}(T_i - T_o) - \dot{Q}_{gain} \tag{9.6.23}$$

What would happen if the thermostat were set back at night? For a rough indication, consider that a house of lightweight construction typical in the U.S. requires heat input at the rate of 1.2 kW if its temperature is increased by 2 K in 5 h. For setback recovery after winter nights, one might want rates that are several times faster, say, 4 K in 2.5 h. Assuming that the heat input is proportional to the warmup rate,[1] the extra load for setback recovery (also known as the *pickup load*) would be 4 × 1.2 kW = 4.8 kW, comparable to the static design heat load. In this case, the capacity of the heating system would need to be doubled relative to the case without setback.

In a given situation, the required extra capacity depends on the amount of setback $T_i - T_o$, the acceptable recovery time, and building construction. For reasonable accuracy, a dynamic analysis is recommended.

---

[1] Actually, at faster rates the effective heat capacity is smaller (the heat pulse takes longer than 1 h to penetrate the entire mass); thus, the real increment for setback recovery is less. One does not know how much without a detailed dynamic analysis.

Optimizing the capacity of the heating system involves a tradeoff between energy savings and capacity savings, with due attention to part-load efficiency. As a general rule for residences, ASHRAE (1989) recommends oversizing by about 40% for a night setback of 10°F (5.6 K), to be increased to 60% oversizing if additional setback occurs during the day. In any case, some flexibility can be provided by adapting the operation of the building. If the capacity is insufficient, one can reduce the depth and duration of the setback during the coldest periods.

In commercial buildings with mechanical ventilation, the demand for extra capacity during setback recovery is reduced if the outdoor air intake is closed during unoccupied periods. In winter that should always be done for energy conservation (unless air quality problems demand high air exchange at night).

CLTD/SCL/CLF Method for Cooling Loads

Because of thermal inertia, it is advisable to distinguish several heat flow rates. The *heat gain* is the rate at which heat is transferred to or generated in a space. The *cooling load* is the rate at which the cooling equipment would have to remove thermal energy from the air in the space in order to maintain constant temperature and humidity. Finally, the *heat extraction rate* is the rate at which the cooling equipment actually does remove thermal energy from the space.

Conductive heat gains and radiative heat gains do not enter the indoor air directly; rather, they pass through the mass of the building, increasing its temperature relative to the air. Only gradually are they transferred to the air. Thus their contribution to the cooling load is delayed, and there is a difference between heat gain and cooling load. Averaged over time, these rates are, of course, equal, by virtue of the first law of thermodynamics.

The heat extraction rate is equal to the cooling load only if the temperature of the indoor air is constant (as assumed in this section). Otherwise the heat flow to and from the building mass causes the heat extraction rate to differ from the cooling load.

To account for transient effects without resorting to a full-fledged dynamic analysis, a special shorthand method has been developed that uses the *cooling load temperature difference (CLTD)* and *cooling load factor (CLF)*. To explain the principles, note that the cooling load due to conduction across an envelope element of area *A* and conductance *U* would be simply

$$\dot{Q}_{cond} = U\,A\,(T_o - T_i) \tag{9.6.24}$$

under static conditions, i.e., if indoor temperature T_i and outdoor temperature T_o were both constant. When the temperatures vary, this is no longer the case because of thermal inertia. However, if the temperatures follow a periodic pattern, day after day, $\dot{Q}_{c,cond}$ will also follow a periodic pattern. Once $\dot{Q}_{c,cond}$ has been calculated, one can define a CLTD as the temperature difference that gives the same cooling load when multiplied by *UA*. If such temperature differences are tabulated for typical construction and typical temperature patterns, they can be looked up for quick determination of the load. Thus, the conductive cooling load is

$$\dot{Q}_{cond,t} = U\,A\,\mathrm{CLTD}_t \tag{9.6.25}$$

where the subscript *t* indicates the hour *t* of the day.

Likewise, if there is a constant radiative heat gain in a zone, the corresponding cooling load is simply equal to that heat gain. If the heat gain follows a periodic pattern, the cooling load also follows a periodic pattern. The cooling load factor (CLF) is defined such that it yields the cooling load at hour *t* when multiplied by the daily maximum $\dot{Q}_{\max}$ of the heat gain:

$$\dot{Q}_{c,rad,t} = \dot{Q}_{\max}\ \mathrm{CLF}_t \tag{9.6.26}$$

The CLFs account for the fact that radiative gains (solar, lights, etc.) are first absorbed by the mass of the building, becoming a cooling load only as they are transferred to the air. Only convective gains can be counted as cooling load without delay. Some heat gains, for example, from occupants, are partly convective and partly radiative; the corresponding CLFs take care of that.

The CLTDs and CLFs of ASHRAE have been calculated by means of the transfer functions discussed in the next section. To keep the bulk of numerical data within reasonable limits, only a limited set of standard construction types and operating conditions has been considered. Some correction factors are available to extend the applicability, however, without escaping the constraint that the indoor temperature T_i be constant. For a list of these factors, see ASHRAE (2001) or Kreider et al. (2001).

Roof CLTD Value Selection

The CLTD/SCL/CLF method uses 10 types of roofs. The roof types are numbered 1, 2, 3, 4, 5, 8, 9, 10, 13, and 14. The roof type chosen depends on the principal roof material; location of the mass in the roof; overall R value of the roof; and whether the ceiling is suspended.

The tables of new roof CLTD values are calculated based on an indoor temperature of 78°F, maximum and mean outdoor temperatures of 95 and 85°F, respectively, and a daily range of 21°F. Once the 24 CLTD values are selected, they are each adjusted by

$$\text{Corrected CLTD} = \text{CLTD} + (78 - T_i) + (T_{om} - 85) \tag{9.6.27}$$

where T_i is the actual inside design dry bulb temperature and T_{om} is the mean outside design dry bulb temperature,

$$T_{om} = \text{Outside design dry bulb temperature} - \frac{\text{Daily range}}{2} \tag{9.6.28}$$

No adjustments to the CLTD are recommended for color or ventilation. The CLTD charts are usually published for several different latitudes; interpolation between the latitudes for an exact site is acceptable.

Wall CLTD Value Selection

The CLTD/SCL/CLF uses 15 wall types numbered sequentially 1 through 16 with no wall 8. The wall type is chosen based on the principal wall material; secondary wall material; location of the mass in the wall; and overall wall R value. The tables of wall CLTD values are broken down by latitude. The wall CLTDs were calculated using the same conditions as the roof CLTD values and may require adjustments based on the actual inside and ambient conditions. Interpolation between the tables may be necessary to obtain the correct values for a given site.

Once the roof and wall CLTD values have been selected and adjusted as necessary, the conductive heat flow through the roof and walls is calculated for each hour t

$$q(t) = U\,A\,\text{CLTD}(t) \tag{9.6.29}$$

where

U = overall heat transfer coefficient for the surface (Btu/h·ft^2·°F)
A = area of surface
CLTD = cooling load temperature difference

Glass CLTD Value Selection

As with the roof and wall CLTDs, the fenestration CLTD values may need to be corrected. The conductive load calculation from the glass uses the same method as that for the roof and walls.

Solar Cooling Load

The solar cooling load (SCL) is used to calculate the radiative (solar) heat gain through any glass surface in the building. The radiative solar gains are then given by

$$q(t) = A \text{ SC SCL}(t) \tag{9.6.30}$$

where A is the area of the glass surface and SC is the shading coefficient. The shading coefficient is the ratio of the actual solar heat gain to that from the reference window used to calculate the SCL.

Using the SCL value tables requires that one know the number of walls, floor covering, and inside shading, as well as a number of other variables for the zone. The tables are also broken down by building type, with different tables for zones in

- Single-story buildings
- Top floor of multistory buildings
- Middle floors of multistory buildings
- First floor of multistory buildings

The zone types used for determining the SCL are not necessarily the same zone type used for the CLF tables. Once the zone type has been determined, the SCL is found from lookup tables.

Accounting for Adjacent Zones

The CLTD/SCL/CLF method treats the conductive heating load from any adjacent spaces through internal partitions, ceilings, and floors as a simple steady-state energy flow:

$$q(t) = U\,A\,(T_a - T_r) \tag{9.6.31}$$

where T_a is the temperature in the adjacent space and T_r is the temperature of the room in question.

Occupant Loads

People within a space add sensible as well as latent loads to the space. The heating load at any given hour due to the occupants is given as

$$q(t) = N\,F_d\,[q_s \text{ CLF}(t) + q_l] \tag{9.6.32}$$

where

N = the number of people in the space
F_d = the diversity factor
CLF = the cooling load factor for occupants on a given schedule

As implied by Equation (9.6.32), the latent load is assumed to translate immediately into a cooling load on the system while the sensible load is subject to some time delay as dictated by the mass of the room — i.e., its capability to absorb heat and release it at a later time. The diversity factor F_d takes into account the variability of the actual number of occupants in the space.

The CLF values come from tables. To find the CLF, it is first necessary to determine the zone type. This is done in a fashion similar to that for the solar cooling loads. That is, the building type, room location, and floor coverings must be known before the zone type can be found. Note that the zone type for occupants and equipment is not the same as for lighting. The same holds true for the solar cooling load: the zone type for occupants is not the same as the zone type for the SCL.

Once the zone type has been determined, the occupant CLF is found from the lookup tables. Zone type A is for light construction and the zones get progressively more massive for types B, C, and D. Figure 9.6.3 shows the cooling load factors for type A and D zones that are occupied for 12 h. Note that the occupant CLF will be 1.0 for all hours in a building with high occupant density (greater than 1 person per 10 ft^2) such as auditoriums and theaters. The CLF will also be 1.0 in buildings with occupancy 24 h/day.

Lighting Loads

At any given hour the load due to the lighting is approximated as

$$q(t) = \text{watts } F_d\,F_{sa} \text{ CLF}(t) \tag{9.6.33}$$

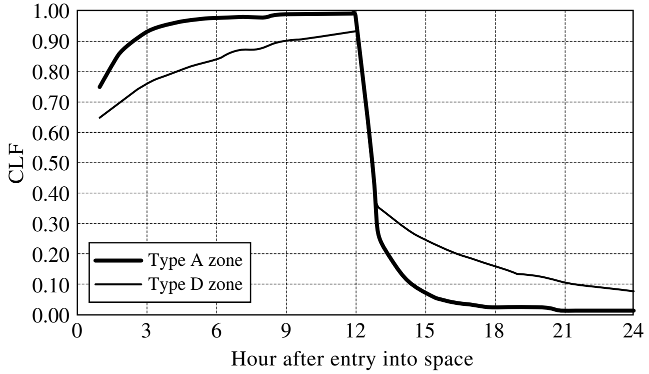

FIGURE 9.6.3 Occupant cooling load factors for type A and type D zones for a space occupied for 12 h.

where

Watts = the total lamp wattage in the space
F_d = the diversity factor
F_{sa} = a ballast special allowance factor
CLF = the cooling load factor for the lights for a given on/off schedule

The diversity factor F_d takes into account the variability of the actual wattage of lights on at any given time.

The lighting CLF values come from tables and are found in a fashion similar to that for the occupants. The zone types for lighting are not necessarily the same zone types for the solar cooling load or the occupants. Note that the lighting CLF will be 1.0 for buildings in which the lights are on 24 h/day or the cooling system is shut off at night or on the weekends. If the calculations are done in inch–pound units, then the result from Equation (9.6.33) is multiplied by 3.41 to convert watts to British thermal units per hour.

Appliance and Equipment Loads

Equipment can add heat through resistive heating or from electrical motors operating in the equipment. The CLTD/SCL/CLF method accounts for both types of equipment heat separately. In addition, the equipment loads are further broken down into sensible or latent components. The latent components are assumed to become immediate loads on the cooling system. The latent loads are found in tables devoted to hospital equipment, restaurant equipment, and office equipment. Latent loads are cited only for the hospital and restaurant equipment. The sensible component of the loads is adjusted by

$$q(t) = q_{sa}\,\mathrm{CLF}(t) \tag{9.6.34}$$

where q_{sa} is the sensible heat gain per appliance as found from the tables. The cooling load factor is found by first determining the zone type and then looking up the CLF in a table appropriate for that zone type, as was done for the occupants and lighting. Although the zone type is similar for occupants and equipment, it may not be the same as that for lighting.

The total cooling load in the space is then found from the sum of the sensible and latent loads. If a cooling load is due to equipment with electrical motors that run equipment in the space, then the space cooling load is incremented by

$$q(t) = 2545\frac{\mathrm{HP}}{\eta}F_l F_u\,\mathrm{CLF}(t) \tag{9.6.35}$$

where

HP = the rated horsepower of the motor
η = the efficiency
F_l = the load factor average (power used divided by rated horsepower, typically around 12)
F_u = the motor use factor (accounting for intermittent use)

The term 2545 converts from horsepower to Britsh thermal units per hour and CLF is the cooling load factor for the equipment on a given schedule. Equation (9.6.32a) assumes that the equipment and the motor are located within the space. If the equipment is in the space but the motor is located outside the space, then this equation is derated by the motor efficiency:

$$q(t) = 2545 \text{ HP } F_l F_u \text{CLF}(t) \tag{9.6.36}$$

Conversely, if the motor is inside the space but it acts on equipment outside the space, the cooling load is incremented by

$$q(t) = 2545 \text{HP} \frac{1-\eta}{\eta} F_l F_u \text{CLF}(t) \tag{9.6.37}$$

As with the lighting, the CLF is always 1.0 when the cooling system does not operate 24 h/day.

Air Infiltration

The infiltrating air is assumed to become a load on the cooling system immediately.

Transfer Functions for Dynamic Load Calculations

Basis of the Method

The *load* $\dot{Q}$ can be considered the response of the building or room to the driving terms $\{T_i, T_o, \dot{Q}_{sol}$, etc.) that act on it. The transfer function method calculates the response of a system by making the following basic assumptions:

- *Discrete time steps*: all functions of time are represented as series of values at regular time steps (hourly in the present case).
- *Linearity*: the response of a system is a linear function of the driving terms and of the state of the system.
- *Causality*: the response at time *t* can depend only on the past, not on the future.

As an example, suppose a single driving term $u(t)$ and the response $y(t)$. To make the expressions more readable, indicate the time dependence as a subscript, in the form $y(t) = y_t$, $u(t) = u_t$, and so on. Then, according to the transfer function model, the relation between the response and the driving term is of the form:

$$y_t = -(a_1 y_{t-1\Delta t} + a_2 y_{t-2\Delta t} + \cdots + a_n y_{t-n\Delta t}) + (b_0 u_t + b_1 u_{t-1\Delta t} + b_2 u_{t-2\Delta t} + \cdots + b_m u_{t-m\Delta t}) \tag{9.6.38}$$

with time step

$$\Delta t = 1 \text{ h} \tag{9.6.39}$$

where a_1 to a_n and b_0 to b_m are coefficients that characterize the system; they are independent of the driving term or response. Equation (9.6.33) is obviously linear. It satisfies causality because y_t depends only on the past values of the response ($y_{t-1\Delta t}$ to $y_{t-n\Delta t}$) and on present and past values of the driving terms (u_t to $u_{t-m\Delta t}$).

The past state of the system enters because of the coefficients a_1 to a_n and b_1 to b_m; this is how thermal inertia is taken into account. The response is instantaneous only if these coefficients are zero. The greater their number and magnitude are, the greater the weight of the past. The accuracy of the model increases as the number of coefficients is enlarged and as the time step is reduced. For most load calculations, hourly time resolution and a handful of coefficients per driving term will suffice. The coefficients are called *transfer function coefficients*.

Incidentally, the relation between *u* and *y* could be written in symmetric form:

$$a_0 y_t + a_1 y_{t-1\Delta t} + a_2 y_{t-2\Delta t} + \cdots + a_n y_{t-n\Delta t} = b_0 u_t + b_1 u_{t-1\Delta t} + b_2 u_{t-2\Delta t} + \cdots + b_m u_{t-m\Delta t} \tag{9.6.40}$$

which is equivalent because one can divide both sides of the equation by a_0. Because the roles of u and y are symmetric, one can use the same model to find, for example, the load (i.e., the heat $\dot{Q}$ to be supplied or removed) as a function of T_i, or T_i as a function of $\dot{Q}$.

Equation (9.6.35) can be readily generalized to the case where there are several driving terms. For instance, if the response T_i is determined by two driving terms, heat input $\dot{Q}$, and outdoor temperature T_o, then one can write the transfer function model in the form

$$\begin{aligned} a_{i,0}T_{i,t} + a_{i,1}T_{i,t-1\Delta t} + \cdots + a_{i,n}T_{i,t-n\Delta t} &= a_{o,0}T_{o,t} + a_{o,1}T_{o,t-1\Delta t} + \cdots + a_{o,m}T_{o,t-m\Delta t} \\ &+ a_{Q,0}\dot{Q}_t + a_{Q,1}\dot{Q}_{t=1\Delta t} + a_{Q,2}\dot{Q}_{t-2\Delta t} + \cdots + a_{Q,r}\dot{Q}_{t-r\Delta t} \end{aligned} \tag{9.6.41}$$

with three sets of transfer function coefficients: $a_{i,0}$ to $a_{i,n}$; $a_{o,0}$ to $a_{o,m}$; and $a_{Q,0}$ to $a_{Q,r}$. This equation can be considered an algorithm for calculating $T_{i,t}$, hour by hour, given the previous values of T_i and the driving terms T_o and $\dot{Q}$. Likewise, if T_i and T_o were given as driving terms, one could calculate $\dot{Q}$ as response.

Any set of response and driving terms can be handled in this manner. Thus, loads can be calculated hour by hour, for any driving terms (meteorological data, building occupancy, heat gain schedules, etc.); in fact, this method is used by the computer simulation program DOE2.1 (Birdsall et al., 1990).

Once the necessary numerical values of the transfer function coefficients have been obtained, the calculation of peak loads is simple enough for a spreadsheet. One specifies the driving terms for the peak day and iterates an equation like Equation (9.6.36) until the result converges to a steady daily pattern. Transfer function coefficients have been calculated and listed for a wide variety of standard construction types (ASHRAE, 1989).

In the remainder of this section, the ASHRAE transfer function method is discussed in detail. The method involves three steps:

- Calculate the conductive heat gain (or loss) for each distinct component of the envelope, by Equation (9.6.37).
- Calculate the load of the room at constant temperature, based on this conductive heat gain (or loss) as well as any other heat source in the room, by Equation (9.6.42).
- Calculate the heat extraction (or addition) rate for the cooling (or heating) device and thermostat setpoints of the room.

Conductive Heat Gain

The conductive heat gain (or loss) $\dot{Q}_{cond,t}$ at time t through the roof and walls is calculated according to the formula:

$$\dot{Q}_{cond,t} = -\sum_{n\geq 1} d_n \dot{Q}_{cond,t-n\Delta t} + A\left(\sum_{n\geq 0} b_n T_{os,t-n\Delta t} - T_i \sum_{n\geq 0} c_n\right) \tag{9.6.42}$$

where

A = area of roof or wall, m^2 (ft^2)
Δt = time step = 1 h
$T_{o,st}$ = sol–air temperature of outside surface at time t
b_n, c_n, d_n = coefficients of conduction transfer function

The indoor temperature T_i is multiplied by the sum of the c_n values, so the individual c_n coefficients are not needed (because T_i is assumed constant at this point). In general, the initial value $\dot{Q}_{\text{cond},t} = O$ is not known; its value does not matter if the calculation is repeated over a sufficient number of time steps until the resulting pattern becomes periodic within the desired accuracy. Usually a few days to a week will be sufficient.

Numerical values of the coefficients of the conduction transfer function are listed in Table 9.6.3: roofs in section (a) of the table and walls in section (b). If the room in question is adjacent to rooms at a different temperature, the heat gain across the partitions is also calculated according to Equation (9.6.37).

TABLE 9.6.3 Coefficients of Conduction Transfer Function

		$n = 0$	$n = 1$	$n = 2$	$n = 3$	$n = 4$	$n = 5$	$n = 6$	Σc_n	U
(a) Roofs[a]										
Layers E0 A3 B25 E3 E2 A0	b_n	0.00487	0.03474	0.01365	0.00036	0.00000	0.00000	0.00000	0.05362	0.080
Steel deck with 3.33 in. insulation	d_n	1.00000	–0.35451	0.02267	–0.00005	0.00000	0.00000	0.00000		
Layers E0 A3 B14 E3 E2 A0	b_n	0.00056	0.01202	0.01282	0.00143	0.00001	0.00000	0.00000	0.02684	0.055
Steel deck with 5 in. insulation	d_n	1.00000	–0.60064	0.08602	–0.00135	0.00000	0.00000	0.00000		
Layers E0 E1 B15 E4 B7 A0	b_n	0.00000	0.00065	0.00339	0.00240	0.00029	0.00000	0.00000	0.00673	0.043
Attic roof with 6 in. insulation	d_n	1.00000	–1.34658	0.59384	–0.09295	0.00296	–0.00001	0.00000		
Layers E0 B22 C12 E3 E2 C12 A0	b_n	0.00059	0.00867	0.00688	0.00037	0.00000	0.00000	0.00000	0.01652	0.138
1.67 in. insulation with 2 in. h.w. concrete RTS	d_n	1.00000	–1.11766	0.23731	–0.00008	0.00000	0.00000	0.00000		
Layers E0 E5 E4 B12 C14 E3 E2 A0	b_n	0.00000	0.00024	0.00217	0.00251	0.00055	0.00002	0.00000	0.00550	0.057
3 in. insul. w/4 in. I.w. conc. deck and susp. clg.	d_n	1.00000	–1.40605	0.58814	–0.09034	0.00444	–0.00006	0.00000		
Layers E0 E5 E4 C5 B6 E3 E2 A0	b_n	0.00001	0.00066	0.00163	0.00049	0.00002	0.00000	0.00000	0.01477	0.090
1 in. insul. w/4 in. h.w. conc. deck and susp. clg.	d_n	1.00000	–1.24348	0.28742	–0.01274	0.00009	0.00000	0.00000		
Layers E0 E5 E4 C13 B20 E3 E2 A0	b_n	0.00001	0.00060	0.00197	0.00086	0.00005	0.00000	0.00000	0.00349	0.140
6 in. h.w. deck w/0.76 in. insul. and Susp. clg.	d_n	1.00000	–1.39181	0.46337	–0.04714	0.00058	0.00000	0.00000		
Layers E0 E5 E4 B15 C15 E3 E2 A0	b_n	0.00000	0.00000	0.00002	0.00014	0.00024	0.00011	0.00002	0.00053	0.034
6 in. insul. w/6 in. I.w. conc. deck and susp. clg.	d_n	1.00000	–2.29459	1.93694	–0.75741	0.14252	–0.01251	0.00046		
Layers E0 C13 B15 E3 E2 C12 A0	b_n	0.00000	0.00000	0.00007	0.00024	0.00016	0.00003	0.00000	0.00050	0.045
6 in. h.w. deck w/6 in. ins. and 2 in. h.w. RTS	d_n	1.00000	–2.27813	1.82162	–0.60696	0.07696	–0.00246	0.00001		

(b) Walls[a]

Layers E0 A3 B1 B13 A3 A0	b_n	0.00768	0.03498	0.00719	0.00006	0.00000	0.00000	0.00000	0.04990	0.066
Steel siding with 4 in. insulation	d_n	1.00000	–0.24072	0.00168	0.00000	0.00000	0.00000	0.00000		
Layers E0 E1 B14 A1 A0 A0	b_n	0.00016	0.00545	0.00961	0.00215	0.00005	0.00000	0.00000	0.01743	0.055
Frame wall with 5 in. insulation	d_n	1.00000	–0.93389	0.27396	–0.02561	0.00014	0.00000	0.00000		
Layers E0 C3 B5 A6 A0 A0	b_n	0.00411	0.03230	0.01474	0.00047	0.00000	0.00000	0.00000	0.05162	0.191
4 in. h.w. concrete block with 1 in. insulation	d_n	1.00000	–0.76963	0.04014	–0.00042	0.00000	0.00000	0.00000		
Layers E0 A6 C5 B3 A3 A0	b_n	0.00099	0.00836	0.00361	0.00007	0.00000	0.00000	0.00000	0.01303	0.122
4 in. h.w. concrete with 2 in. insulation	d_n	1.00000	–0.93970	0.04664	0.00000	0.00000	0.00000	0.00000		
Layers E0 E1 C8 B6 A1 A0	b_n	0.00000	0.00061	0.00289	0.00183	0.00018	0.00000	0.00000	0.00552	0.109
8 in. h.w. concrete block with 2 in. insulation	d_n	1.00000	–1.52480	0.67146	–0.09844	0.00239	0.00000	0.00000		
Layers E0 A2 C2 B15 A0 A0	b_n	0.00000	0.00000	0.00013	0.00044	0.00030	0.00005	0.00000	0.00093	0.043
Face brick and 4 in. I.w. conc. block with 6 in. insul.	d_n	1.00000	–2.00875	1.37120	–0.37897	0.03962	–0.00165	0.00002		
Layers E0 C9 B6 A6 A0 A0	b_n	0.00000	0.00005	0.00064	0.00099	0.00030	0.00002	0.00000	0.00200	0.106
8 in. common brick with 2 in. insulation	d_n	1.00000	–1.78165	0.96017	–0.16904	0.00958	–0.00016	0.00000		
Layers E0 C11 B6 A1 A0 A0	bn	0.00000	0.00001	0.00019	0.00045	0.00022	0.00002	0.00000	0.00089	0.112
12 in. h.w. concrete with 2 in. insulation	dn	1.00000	–2.12812	1.53974	–0.45512	0.05298	–0.00158	0.00002		

Note: U, b_n, and c_n are in Btu/(h · ft^2 · °F); d_n and A are dimensionless.

[a] Layer sequence left to right = inside to outside.

Source: From ASHRAE, 1989, *Handbook of Fundamentals*. American Society of Heating, Refrigerating and Air-Conditioning Engineers, Atlanta. With permission.

It is instructive to establish the connection of the transfer function coefficients with the U value. In the steady-state limit, i.e., when $\dot{Q}_{\text{cond}}$, T_{os}, and T_i are all constant, Equation (9.6.37) becomes

$$\dot{Q}_{cond}\sum_{n\geq 1} d_n = A\left(T_{os}\sum_{n\geq 0} b_n - T_i\sum_{n\geq 0} c_n\right) \tag{9.6.43}$$

where $d_0 = 1$.

Because that limit also contains

$$\dot{Q}_{\text{cond}} = A\ U\ (T_{os} - T_i) \tag{9.6.44}$$

the coefficients of T_{os} and T_i must be equal,

$$\sum_{n\geq 0} b_n = \sum_{n\geq 0} c_n \tag{9.6.45}$$

and the U value is given by

$$U = \frac{\sum\limits_{n\geq 0} c_n}{\sum\limits_{n\geq 0} d_n} \tag{9.6.46}$$

The Load at Constant Temperature

The preceding calculation of the conductive heat gain (or loss) is to be repeated for each portion of the room envelope that has a distinct composition. The relation between these conductive gains and the total load depends on the construction of the entire room. For example, a concrete floor can store a significant fraction of the heat radiated by lights or by a warm ceiling, thus postponing its contribution to the cooling load of the room.

For each heat gain component $\dot{Q}_{\text{gain}}$, the corresponding cooling load $\dot{Q}_c$ (or reduction of the heating load) at constant T_i is calculated by using another set of coefficients: the coefficients v_n and w_n, of the *room transfer function*

$$\begin{aligned}\dot{Q}_{c,t} = v_0\dot{Q}_{\text{gain},t} + v_1\dot{Q}_{\text{gain},t-1\Delta t} + v_2\dot{Q}_{\text{gain},t-2\Delta t} + \cdots \\ -w_1\dot{Q}_{c,t-1\Delta t} - w_2\dot{Q}_{c,t-2\Delta t} - \cdots\end{aligned} \tag{9.6.47}$$

with the subscript t indicating time, as before. The coefficient w_0 of $\dot{Q}_{c,t}$ is not shown because it is set equal to unity.

Equation (9.6.42) must be applied separately to each of the heat gain types and the resulting cooling load components, $\dot{Q}_{c,t}$, are added to obtain the total cooling load of the room at time t. The heat gain types are as follows:

- Solar gain (through glass without interior shade) and the radiative component of heat from occupants and equipment
- Conduction through envelope and solar radiation absorbed by interior shade
- Lights
- Convective gains (from air exchange, occupants, equipment)

For lights the coefficients depend on the arrangement of the lighting fixture and the ventilation system.

Specific numbers vary a great deal with the circumstances; however, the general pattern is common to all peak cooling loads: *thermal inertia attenuates and delays the peak contributions of individual load components*. The total peak is usually less than the result of a steady-state calculation, although it could be more if the time delays act in the sense of making the loads coincide.

In contrast to peak loads, daily average loads can be determined by a static calculation if the average indoor temperature is known; that follows from the first law of thermodynamics. However, if the thermostat allows floating temperatures, the indoor temperature is, in general, not known without a dynamic analysis.

With the transfer functions described so far, one can calculate peak loads when the indoor temperature T_i is constant. That is how the cooling load factors and cooling load temperature differences of the previous section have been determined. Of course, the indoor temperature T_i may vary, not only because of variable thermostat setpoints but also because of limitations of the HVAC equipment (capacity, throttling range, imperfect control). The extension to variable T_i requires one additional transfer function, which is described in ASHRAE (1997) and Kreider et al. (2001).

9.7 Air Handling Units and Packaged Units

Shan K. Wang

Terminals and Air Handling Units

A *terminal unit*, or *terminal*, is a device or equipment installed directly in or above the conditioned space to cool, heat, filter, and mix outdoor air with recirculating air. Fan-coil units, VAV boxes, fan-powered VAV boxes, etc. are all terminals.

An *air handling unit* (AHU) handles and conditions the air, controls it to a required state, and provides motive force to transport it. An AHU is the primary equipment of the air system in a central air-conditioning system. The basic components of an AHU include a supply fan with a fan motor, a water cooling coil, filters, a mixing box except in a makeup AHU unit, dampers, controls, and an outer casing. A return or relief fan, heating coil(s), and humidifier are optional depending on requirements. The supply volume flow rate of AHUs varies from 2000 to about 60,000 cfm.

AHUs are classified into the followings groups according to their structure and location.

Horizontal or Vertical Units

Horizontal AHUs have their fan, coils, and filters installed at the same level as shown in Figure 9.7.1(a). They need more space and are usually for large units. In *vertical units*, as shown in Figure 9.7.1(b), the supply fan is installed at a level higher than coils and filters. They are often comparatively smaller than horizontal units.

Draw-Through or Blow-Through Units

In a *draw-through unit,* as shown in Figure 9.7.1(a), the supply fan is located downstream of the coils. Air is evenly distributed over the coil section, and the fan discharge can easily be connected to a supply duct of nearly the same air velocity. In a *blow-through unit*, as shown in Figure 9.7.1(c), the supply fan is located upstream of the coils. It usually has hot and cold decks with discharge dampers connected to warm and cold ducts, respectively.

Factory-Fabricated and Field Built-Up Units

Factory-fabricated units are standard in construction and layout, low in cost, of higher quality, and fast in installation. *Field built-up units* or *custom-built units* are more flexible in construction, layout, and dimensions than factory-built standardized units.

Rooftop and Indoor Units

A *rooftop AHU*, sometimes called a penthouse unit, is installed on the roof and will be completely weatherproof. An *indoor AHU* is usually located in a fan room or ceiling and hung like small AHU units.

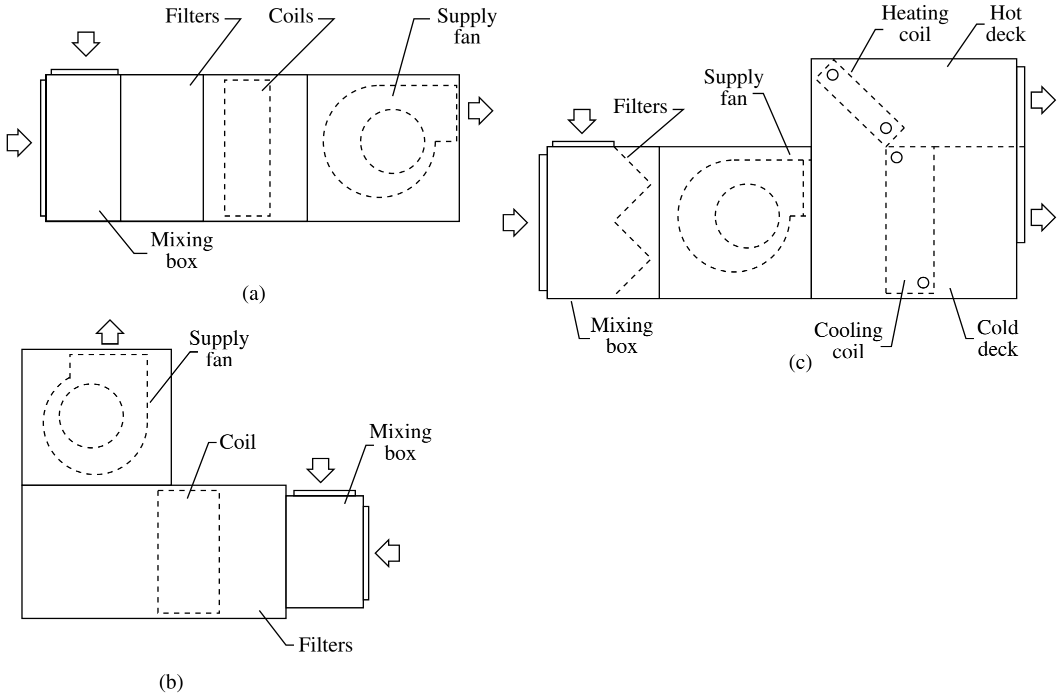

FIGURE 9.7.1 Type of air handling units: (a) horizontal draw-through unit, (b) vertical draw-through unit, and (c) multizone blow-through unit.

Make-Up Air and Recirculating Units

A *make-up AHU*, also called a primary-air unit, is used to condition outdoor air entirely. It is a once-through unit. There is no return air and mixing box. *Recirculating units* can have 100% outdoor air intake or mixing of outdoor air and recirculating air.

Packaged Units

A *packaged unit* (PU) or Packaged Terminal Air Conditioner (PTAC) is a self-contained air conditioner. It conditions the air and provides it with motive force and is equipped with its own heating and cooling sources. The packaged unit is the primary equipment in a packaged air-conditioning system and is always equipped with a DX coil for cooling, unlike an AHU. R-22, R-134a, and others are used as refrigerants in packaged units. The portion that handles air in a packaged unit is called an *air handler* to distinguish it from an AHU. Like an AHU, an indoor air handler has an indoor fan, a DX coil (indoor coil), filters, dampers, and controls. Packaged units can be classified according to their place of installation: rooftop, indoor, and split packaged units.

Rooftop Packaged Units

A *rooftop packaged unit* is mounted on the roof of the conditioned space as shown in Figure 9.7.2. From the types of heating/cooling sources provided, rooftop units can be subdivided into:

- Gas/electric rooftop packaged unit, in which heating is provided by gas furnace and cooling by electric power-driven compressors.
- Electric/electric rooftop packaged unit, in which electric heating and electric power-driven compressors provide heating and cooling.

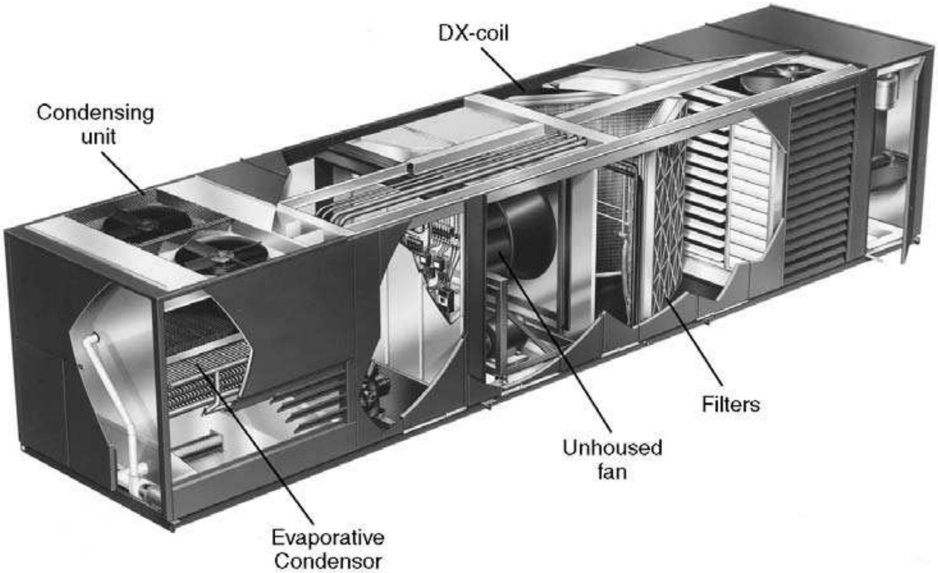

FIGURE 9.7.2 A cut view of a rooftop package unit. (Source: Mammoth, Inc. Reprinted by permission.)

- Rooftop packaged heat pump, in which both heating and cooling are provided by the same refrigeration system using a four-way reversing valve (heat pump) in which the refrigeration flow changes when cooling mode is changed to heating mode and vice versa. Auxiliary electric heating is provided if necessary.

Rooftop packaged units are single packaged units. Their cooling capacity may vary from 3 to 220 tons with a corresponding volume flow rate of 1200 to 80,000 cfm. Rooftop packaged units are the most widely used packaged units.

Indoor Packaged Units

An *indoor packaged unit* is also a single packaged and factory-fabricated unit. It is usually installed in a fan room or a machinery room. A small or medium-sized indoor packaged unit could be floor mounted directly inside the conditioned space with or without ductwork. The cooling capacity of an indoor packaged unit may vary from 3 to 100 tons and volume flow rate from 1200 to 40,000 cfm.

Indoor packaged units are also subdivided into:

- Indoor packaged cooling units
- Indoor packaged cooling/heating units, in which heating may be provided from a hot water heating coil, a steam heating coil, and electric heating
- Indoor packaged heat pumps

Indoor packaged units have either an air-cooled condenser on the rooftop or a shell-and-tube or double-tube water-cooled condenser inside the unit.

Split Packaged Units

A *split packaged unit* consists of two separate pieces of equipment: an indoor air handler and an outdoor condensing unit. The indoor air handler is often installed in the fan room. Small air handlers can be ceiling hung. The condensing unit is usually located outdoors, on a rooftop or podium or on the ground.

A split packaged unit has its compressors and condenser in its outdoor condensing unit, whereas an indoor packaged unit usually has its compressors indoors. The cooling capacity of split packaged units varies from 3 to 75 tons and the volume flow rate from 1200 to 30,000 cfm.

Rating Conditions and Minimum Performance

Air Conditioning and Refrigeration Institute (ARI) Standards and ASHRAE/IES Standard 90.1-2001 specified the following rating indices:

- Energy efficiency ratio (EER) is the ratio of equipment cooling capacity, in Btu/hr, to the electric input, in W, under rating conditions.
- SEER is the seasonal EER, or EER during the normal annual usage period.
- IPLV is the integrated part-load value. It is the summarized single index of part-load efficiency of PUs based on weighted operations at several load conditions.
- HSPF is the heating seasonal performance factor. It is the total heating output of a heat pump during its annual usage period for heating, in Btu, divided by the total electric energy input to the heat pump during the same period, in watt-hours.

For water- and evaporatively cooled packaged units including heat pumps, refer to ASHRAE/IES Standard 90.1-2001 and also ARI Standards.

Coils

Coils, Fins, and Water Circuits

Coils are indirect contact heat exchangers. Heat transfer or heat and mass transfer takes place between conditioned air flowing over the coil and water, refrigerant, steam, or brine inside the coil for cooling, heating, dehumidifying, or cooling/dehumidifying. Chilled water, brine, and refrigerants that are used to cool and dehumidify the air are called *coolants*. Coils consist of tubes and external fins arranged in rows along the air flow to increase the contact surface area. Tubes are usually made of copper; in steam coils they are sometimes made of steel or even stainless steel. Copper tubes are staggered in 2, 3, 4, 6, 8, or up to 10 rows.

Fins are extended surfaces often called *secondary surfaces* to distinguish them from the *primary surfaces*, which are the outer surfaces of the tubes. Fins are often made from aluminum, with a thickness F_t = 0.005 to 0.008 in., typically 0.006 in. Copper, steel, or sometimes stainless steel fins are also used. Fins are often in the form of continuous plate fins, corrugated plate fins to increase heat transfer, crimped spiral or smooth spiral fins that may be extruded from the aluminum tubes, and spine pipes, which are shaved from the parent aluminum tubes. Corrugated plate fins are most widely used.

Fin spacing S_f is the distance between two fins. *Fin density* is often expressed in fins per inch and usually varies from 8 to 18 fins/in.

In a water cooling coil, *water circuits* or *tube feeds* determine the number of water flow passages. The greater the finned width, the higher the number of water circuits and water flow passages.

Direct Expansion (DX) Coil

In a *direct expansion coil*, the refrigerant, R-22, R-134a, or others, is evaporated and expanded directly inside the tubes to cool and dehumidify the air as shown in Figure 9.7.3(a). Refrigerant is fed to a distributor and is then evenly distributed to various copper tube circuits typically 0.375 in. in diameter. Fin density is usually 12 to 18 fins/in. and a four-row DX coil is often used. On the inner surface of the copper tubes, microfins, typically at 60 fins/in. and a height of 0.008 in., are widely used to enhance the boiling heat transfer.

Air and refrigerant flow is often arranged in a combination of counterflow and cross flow and the discharge header is often located on the air-entering side. Refrigerant distribution and loading in various circuits are critical to the coil's performance. Vapor refrigerant cleaning the DX coil is superheated 10 to 20°F in order to prevent any liquid refrigerant from flooding back to the reciprocating compressors and damaging them. Finally, the vapor refrigerant is discharged to the suction line through the header.

For comfort air-conditioning systems, the evaporating temperature of refrigerant T_{ev} inside the tubes of a DX coil is usually between 37 and 50°F. At such a temperature, the surface temperature of the coil is often lower than the dew point of the entering air. Condensation occurs at the coil's outside surface,

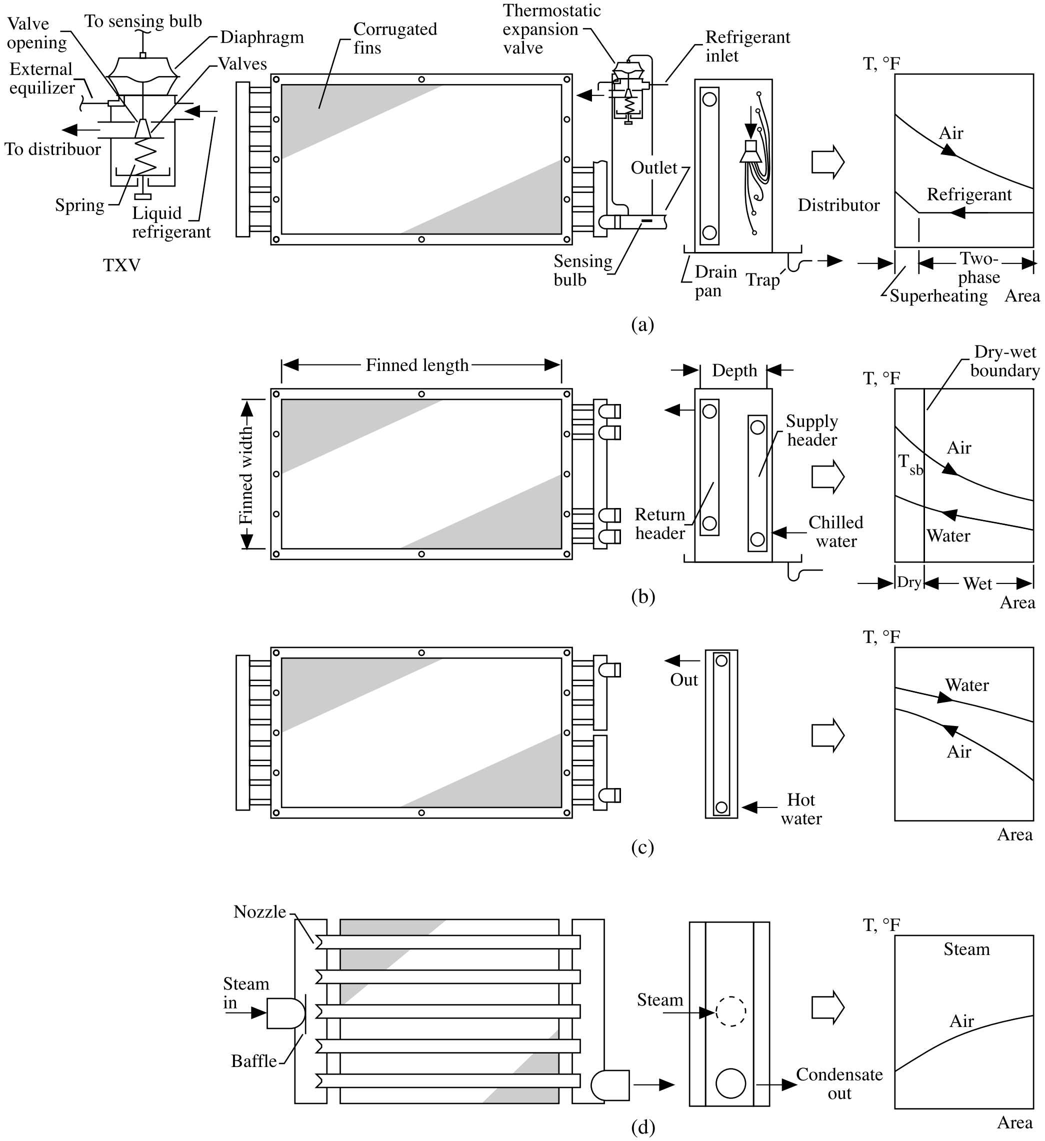

(a)

(b)

(c)

(d)

FIGURE 9.7.3 Types of coils: (a) direct expansion coil, (b) water cooling coil, (c) water heating coil, and (d) steam heating coil.

and the coil becomes a wet coil. A condensate *drain pan* is necessary for each vertically banked DX coil, and a trap should be installed to overcome the negative pressure difference between the air in the coil section and the ambient air. Some units are equipped with IAQ drainpans — drain pans that are sloped to drain connections so that they completely drain.

Face velocity of the DX coil v_a, in fpm, is closely related to the blow-off of the water droplets of the condensate, the heat transfer coefficients, the air-side pressure drop, and the size of the air system. For corrugated fins, the upper limit is 600 fpm, with an air-side pressure drop of 0.20 to 0.30 in. WG/row. A large DX coil is often divided into two refrigerant sections, each with its own expansion valve, distributor, and discharge header.

For a packaged unit of a specific model, size, face velocity and condition of entering air and outdoor air, the DX coil's cooling capacities in nominal tons, number of rows, and fin density are all fixed values.

Water Cooling Coils — Dry–Wet Coils

In a water cooling coil, chilled water at a temperature of 40 to 50°F, brine, or glycol-water at a temperature of 34 to 40°F during cold air distribution enters the coil. The temperature of chilled water, brine, or glycol-water is usually raised 12 to 24°F before it leaves the water cooling coil.

The water tubes are usually copper tubes of 1/2 to 5/8 in. diameter with a tube wall thickness of 0.01 to 0.02 in. They are spaced at a center-to-center distance of 0.75 to 1.25 in. longitudinally and 1 to 1.5 in. transversely. These tubes may be staggered in 2, 3, 4, 6, 8, or 10 rows. Chilled water coils are often operated at a pressure of 175 to 300 psig.

As in a DX coil, the air flow and water flow are in a combination of counterflow and cross flow. The temperature of the outer surface of a chilled water cooling coil at the air entering side T_{se} is often greater than the dew point of the entering air T''_{ae}, or $T_{se} > T''_{ae}$. The outer surface temperature of the coil at the air leaving side T_{sl} may be smaller than T''_{ae}, or $T_{sl} < T''_{ae}$. Then the water cooling coil becomes a dry–wet coil with part of the dry surface on the air entering side and part of the wet surface on the air leaving side. A *dry–wet boundary* divides the dry and wet surfaces. At the boundary, the tube outer surface temperature $T_{sb} = T''_{ae}$ as shown in Figure 9.7.3(b). A condensate drain pan is necessary for a dry–wet coil.

A water cooling coil is selected from the manufacturer's selection program or from its catalog at (1) a dry and wet bulb temperature of entering air, such as 80°F dry bulb and 67°F wet bulb; (2) an entering water temperature, such as 44 or 45°F; (3) a water temperature rise between 10 and 24°F; and (4) a coil face velocity between 400 and 600 fpm. The number of rows and fins per inch is varied to meet the required sensible and cooling coil load, in Btu/hr.

Water Cooling Coil–Dry Coil

When the temperature of chilled water entering the water cooling coil $T_{we} \geq T''_{ae}$, condensation will not occur on the outer surface of the coil. This coil becomes a sensible cooling–dry coil, and the humidity ratio of the conditioned air w_a remains constant during the sensible cooling process.

The construction of a sensible cooling–dry coil, such as material, tube diameter, number of rows, fin density, and fin thickness, is similar to that of a dry–wet coil except that a dry coil always has a poorer surface heat transfer coefficient than a wet coil, and therefore a greater coil surface area is needed; the maximum face velocity of a dry coil can be raised to $v_a \leq 800$ fpm; and the coil's outer surface is less polluted. The effectiveness of a dry coil $\in_{dry}$ is usually 0.55 to 0.7.

Water Heating Coil

The construction of a water heating coil is similar to that of a water cooling coil except that in water heating coils hot water is supplied instead of chilled water and there are usually fewer rows, only 2, 3, and 4 rows, than in water cooling coils. Hot water pressure in water heating coils is often rated at 175 to 300 psig at a temperature up to 250°F. Figure 9.7.3(c) shows a water heating coil.

Steam Heating Coil

In a steam heating coil, latent heat of condensation is released when steam is condensed into liquid to heat the air flowing over the coil, as shown in Figure 9.7.3(d). Steam enters at one end of the coil, and the condensate comes out from the opposite end. For more even distribution, a baffle plate is often installed after the steam inlet. Steam heating coils are usually made of copper, steel, or sometimes stainless steel.

For a steam coil, the coil core inside the casing should expand or contract freely. The coil core is also pitched toward the outlet to facilitate condensate drainage. Steam heating coils are generally rated at 100 to 200 psig at 400°F.

Coil Accessories and Servicing

Coil accessories include air vents, drain valves, isolation valves, pressure relief valves, flow metering valves, balancing valves, thermometers, pressure gauge taps, condensate drain taps, and even distribution baffles. They are employed depending on the size of the system and operating and serving requirements.

Coil cleanliness is important for proper operation. If a medium-efficiency air filter is installed upstream of the coil, dirt accumulation is often not a problem. If a low-efficiency filter is employed, dirt accumulation may block the air passage and significantly increase the pressure drop across the coil. Coils should normally be inspected and cleaned every 3 months in urban areas when low-efficiency filters are used. Drain pans should be cleaned every month to prevent buildup of bacteria and microorganisms. IAQ drain pans can be specified to minimize this cleaning.

Coil Freeze-Up Protection

Improper mixing of outdoor air and recirculating air in the mixing box of an AHU or PU may cause coil freeze-up when the outdoor air temperature is below 32°F. Outdoor air should be guided by a baffle plate and flow in an opposite direction to the recirculating air stream so that they can be thoroughly mixed without stratification. Preheat coils can also be used to temper outside air before it enters the mixing box.

Run the chilled water pump for the idle coil with a water velocity of 2.5 ft/sec, so that the cooling coil will not freeze when the air temperature drops to 32°F. A better method is to drain the water completely. For a hot water coil, it is better to reset the hot water temperature at part-load operation instead of running the system intermittently. A steam heating coil with inner distributor tubes and outer finned heating tubes provides better protection against freeze-up.

Air Filters

Air Cleaning and Filtration

Air cleaning is the process of removing airborne particles from the air. Air cleaning can be classified as air filtration and industrial air cleaning. Industrial air cleaning involves the removal of dust and gaseous contaminants from manufacturing processes as well as from the space air, exhaust air, and flue gas for air pollution control. In this section, only air filtration is covered.

Air filtration involves the removal of airborne particles presented in the conditioned air. Most of the airborne particles removed by air filtration are smaller than 1 μm, and the concentration of these particles in the airstream seldom exceeds 2 mg/m^3. The purpose of air filtration is to benefit the health and comfort of the occupants as well as meet the cleanliness requirements of the working area in industrial buildings.

An *air filter* is a kind of air cleaner that is installed in AHUs, PUs, and other equipment to filter the conditioned air by inertial impaction or interception and to diffuse and settle fine dust particles on the fibrous medium. The filter medium is the fabricated material that performs air filtration.

Operating performance of air filters is indicated by their:

- *Efficiency* or effectiveness of dust removal
- *Dust holding capacity* m_{dust}, which is the amount of dust held in the air filter, in grains/ft^2
- *Initial pressure drop* when the filter is clean Δp_{fi} and *final pressure drop* Δp_{ff} when the filter's m_{dust} is maximum, both in in. WG
- *Service life,* which is the operating period between Δp_{fi} and Δp_{ff}

Air filters in AHUs and PUs can be classified into low-, medium-, and high-efficiency filters and carbon activated filters.

Test Methods

The performance of air filters is usually tested in a test unit that consists of a fan, a test duct, the tested filter, two samplers, a vacuum pump, and other instruments. Three test methods with their own test dusts and procedures are used for the testing of low-, medium-, and high-efficiency air filters.

The *weight arrestance test* is used for low-efficiency air filters to assess their ability to remove coarse dusts. Standard synthetic dusts that are considerably coarser than atmospheric dust are fed to the test unit. By measuring the weight of dust fed and the weight gain due to the dust collected on the membrane of the sampler after the tested filter, the arrestance can be calculated.

The *atmospheric dust spot efficiency test* is used for medium-efficiency air filters to assess their ability to remove atmospheric dusts. *Atmospheric dusts* are dusts contained in the outdoor air, the outdoor atmosphere. Approximately 99% of atmospheric dusts are dust particles <0.3 μm that make up 10% of the total weight; 0.1% of atmospheric dusts is particles >1 μm that make up 70% of the total weight.

Untreated atmospheric dusts are fed to the test unit. Air samples taken before and after the tested filter are drawn through from identical fiber filter-paper targets. By measuring the light transmission of these discolored white filter papers, the efficiency of the filter can be calculated. Similar atmospheric dust spot test procedures have been specified by American Filter Institute (AFI), ASHRAE Standard 52.1, and former National Bureau of Standards (NBS).

The *DOP penetration and efficiency test* or simply *DOP test* is used to assess high-efficiency filters removing dusts particles of 0.18 μm. According to U.S. Military Standard MIL-STD-282 (1956), a smoke cloud of uniform dioctyl phthalate (DOP) droplets 0.18 μm in diameter, generated from the condensation of the DOP vapor, is fed to the test unit. By measuring the concentration of these particles in the air stream upstream and downstream of the tested filter using an electronic particle counter or laser spectrometer, the penetration and efficiency of the air filter can be calculated.

Low-Efficiency Air Filters

ASHRAE weight arrestance for low-efficiency filters is between 60 and 95%, and ASHRAE dust spot efficiency for low-efficiency filters is less than 20%. These filters are usually in panels as shown in Figure 9.7.4(a). Their framework is typically 20 × 20 in. or 24 × 24 in. Their thickness varies from 1 to 4 in.

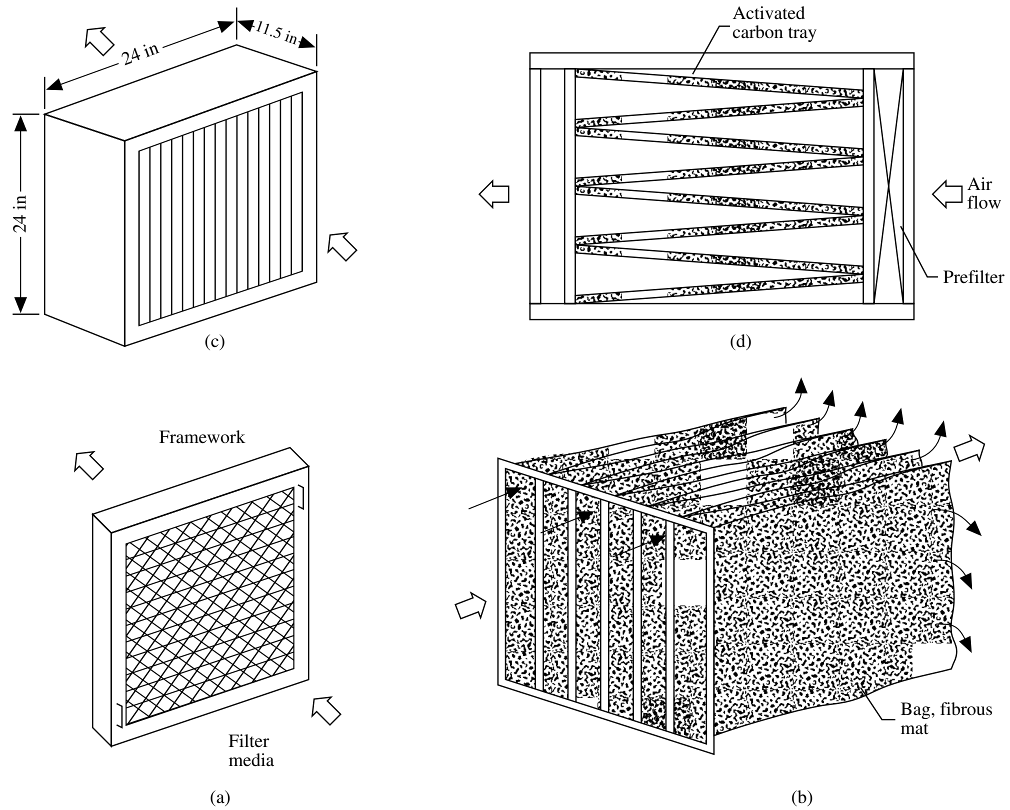

FIGURE 9.7.4 Various types of air filters: (a) low efficiency, (b) medium efficiency, (c) HEPA and ULPA filters, and (d) activated carbon filter.

For low-efficiency filters, the filter media are often made of materials such as

- Corrugated wire mesh and screen strips coated with oil, which act as adhesives to enhance dust removal. Detergents may be used to wash off dusts so that the filter media can be cleaned and reused — they are therefore called *viscous and reusable*.
- Synthetic fibers (nylon, terylene) and polyurethane foam can be washed, cleaned, and reused if required — *dry and reusable*.
- Glass fiber mats with fiber diameter greater than 10 μm. The filter medium is discarded when its final pressure drop is reached — *dry and disposable*. The face velocity of the panel filter is usually between 300 and 600 fpm. The initial pressure drop varies from 0.05 to 0.25 in. WG and the final pressure drop from 0.2 to 0.5 in. WG.

Medium-Efficiency Air Filters

These air filters have an ASHRAE dust spot efficiency usually between 20 and 95%. Filter media of medium-efficiency filters are usually made of glass fiber mat with a fiber diameter of 10 to 1 μm using nylon fibers to join them together. They are usually dry and disposable. In addition:

- As the dust spot efficiency increases, the diameter of glass fibers is reduced, and they are placed closer together.
- Extended surfaces, such as pleated mats or bags, are used to increase the surface area of the medium as shown in Figure 9.7.4(b). Air velocity through the medium is 6 to 90 fpm. Face velocity of the air filter is about 500 fpm to match the face velocity of the coil in AHUs and PUs.
- Initial pressure drop varies from 0.20 to 0.60 in. WG and final pressure drop from 0.50 to 1.20 in. WG.

High-Efficiency Particulate Air (HEPA) Filters and Ultra-Low-Penetration Air (ULPA) Filters

HEPA filters have a DOP test efficiency of 99.97% for dust particles ≥0.3 μm in diameter. *ULPA filters* have a DOP test efficiency of 99.999% for dust particles ≥0.12 μm in diameter.

A typical HEPA filter, shown in Figure 9.7.4(d), has dimensions of 24 × 24 × 11.5 in. Its filter media are made of glass fibers of submicrometer diameter in the form of pleated paper mats. The medium is dry and disposable. The surface area of the HEPA filter may be 50 times its face area, and its rated face velocity varies from 190 to 390 fpm, normally at a pressure drop of 0.50 to 1.35 in. WG for clean filters. The final pressure drop is 0.8 to 2 in. WG. Sealing of the filter pack within its frame and sealing between the frame and the gaskets are critical factors that affect the penetration and efficiency of the HEPA filter.

An ULPA filter is similar to a HEPA filter in construction and filter media. Both its sealing and filter media are more efficient than those of a HEPA filter.

To extend the service life of HEPA filters and ULPA filters, both should be protected by a medium-efficiency filter, or a low-efficiency and a medium-efficiency filter in the sequence low–medium just before the HEPA or ULPA filters. HEPA and ULPA filters are widely used in clean rooms and clean spaces. Often the removal and disposal of HEPA and ULPA filters require special handling due to the concentration of biological species present on the filter.

Activated Carbon Filters

These filters are widely used to remove objectional odors and irritating gaseous airborne particulates, typically 0.003 to 0.006 μm in size, from the air stream by adsorption. *Adsorption* is physical condensation of gas or vapor on the surface of an activated substance like activated carbon. Activated substances are extremely porous. One pound of activated carbon contains 5,000,000 ft^2 of internal surface.

Activated carbon in the form of granules or pellets is made of coal, coconut shells, or petroleum residues and is placed in trays to form activated carbon beds as shown in Figure 9.7.4(d). A typical carbon tray is 23 × 23 × 5/8 in. thick. Low-efficiency prefilters are used for protection. When air flows through the carbon beds at a face velocity of 375 to 500 fpm, the corresponding pressure drop is 0.2 to 0.3 in. WG.

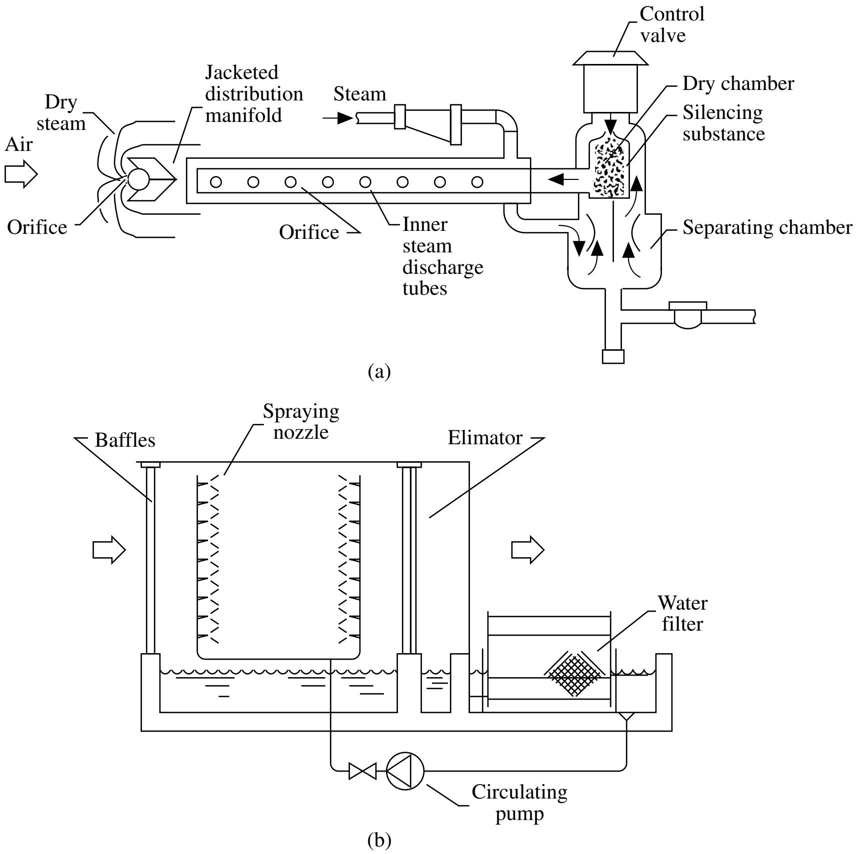

(a)

(b)

FIGURE 9.7.5 Steam grid humidifier (a) and air washer (b).

Humidifiers

A *humidifier* adds moisture to the air. Air is humidified by: (1) heating the liquid to evaporate it; (2) atomizing the liquid water into minute droplets by mechanical means, compressed air, or ultrasonic vibration to create a larger area for evaporation; (3) forcing air to flow through a wetted element in which water evaporates; and (4) injecting steam into air directly before it is supplied to the conditioned space.

For comfort air-conditioning systems, a steam humidifier with a separator as shown in Figure 9.7.5(a) is widely used. Steam is supplied to a jacketed distribution manifold. It enters a separating chamber with its condensate. Steam then flows through a control valve, throttles to a pressure slightly above atmospheric, and enters a dry chamber. Due to the high temperature in the surrounding separating chamber, the steam is superheated. Dry steam is then discharged into the ambient air stream through the orifices on the inner steam discharge tubes.

For an air system of cold air supply with humidity control during winter mode operation, an air washer is economical for large-capacity humidification in many industrial applications.

An air washer is a humidifier, a cooler, a dehumidifier, and an air cleaner. An air washer usually has an outer casing, two banks of spraying nozzles, one bank of guide baffles at the entrance, one bank of eliminators at the exit, a water tank, a circulating pump, a water filter, and other accessories as shown in Figure 9.7.5(b). Outer casing, baffles, and eliminators are often made of plastics or sometimes stainless steel. Spraying nozzles are usually made of brass or nylon, with an orifice diameter of 1/16 to 3/16 in., a smaller orifice for humidification, and a larger orifice for cooling and dehumidification. An eccentric inlet connected to the discharge chamber of the spraying nozzle gives centrifugal force to the water stream and atomizes the spraying water. Water is supplied to the spraying nozzle at a pressure of 15 to 30 psig. The distance between two spraying banks is 3 to 4.5 ft, and the total length of the air water from 4 to 7 ft. The air velocity inside an air washer is usually 500 to 800 fpm.

Selection of AHUs and PUs

- The size of an AHU is usually selected so that the face velocity of its coil is 600 fpm or less in order to prevent entrained condensate droplets. The cooling and heating capacities of an AHU can be varied by using coils of different numbers of rows and fin densities. The size of a PU is determined by its cooling capacity. Normally, the volume flow rate per ton of cooling capacity in PUs is 350 to 400 cfm. In most packaged units whose supply fans have belt drives, the fan speed can be selected so that the volume flow rate is varied and external pressure is met.
- To improve the indoor air quality, save energy, and prevent smudging and discoloring building interiors, a medium-efficiency filter of dust spot efficiency ≥50% and an air economizer are preferable for large AHUs and PUs.
- See ANSI/ASHRAE/IESNA 90.1-2001 for energy standards on equipment selection.

9.8 Refrigeration Components and Evaporative Coolers

Shan K. Wang

Refrigeration Compressors

A refrigeration compressor is the heart of a vapor compression system. It raises the pressure of refrigerant so that it can be condensed into liquid, throttled, and evaporated into vapor to produce the refrigeration effect. It also provides the motive force to circulate the refrigerant through condenser, expansion valve, and evaporator.

According to the compression process, refrigeration compressors can be divided into *positive displacement* and *nonpositive displacement* compressors. A positive displacement compressor increases the pressure of the refrigerant by reducing the internal volume of the compression chamber. Reciprocating, scroll, rotary, and screw compressors are all positive displacement compressors. The centrifugal compressor is the only type of nonpositive displacement refrigeration compressor widely used in refrigeration systems today.

Based on the sealing of the refrigerant, refrigeration compressors can be classified as

- *Hermetic compressors*, in which the motor and the compressor are sealed or welded in the same housing to minimize leakage of refrigerant and to cool the motor windings by using suction vapor
- *Semihermetic compressors*, in which motor and compressor are enclosed in the same housing but are accessible from the cylinder head for repair and maintenance
- *Open compressors*, in which compressor and motor are enclosed in two separate housings

Refrigeration compressors are often driven by a motor directly or by a gear train.

Performance Indices

Volumetric efficiency η_v of a refrigeration compressor is defined as

$$\eta_v = \mathring{V}_{a.v} / \mathring{V}_p \tag{9.8.1}$$

where

$\mathring{V}_{a.v}$ = actual induced volume of the suction vapor at suction pressure, cfm

$\mathring{V}_p$ = calculated displacement of the compressor, cfm

Isentropic efficiency η_{isen}, *compression efficiency* η_{cp}, compressor efficiency η_{com}, and *mechanical efficiency* η_{mec} are defined as

$$\begin{aligned}\eta_{\text{isen}} &= (h_2 - h_1)/(h_2' - h_1) = \eta_{\text{cp}}\eta_{\text{mec}} = \eta_{\text{com}} \\ \eta_{\text{cp}} &= W_{\text{sen}}/W_{\text{v}} \\ \eta_{\text{mec}} &= W_{\text{v}}/W_{\text{com}}\end{aligned} \tag{9.8.2}$$

where

h_1, h_2, h_2' = enthalpy of the suction vapor, ideal discharged hot gas, and actual discharged hot gas, respectively, Btu/lb

W_{isen}, W_{v}, W_{com} = isentropic work = $(h_2 - h_1)$, work delivered to the vapor refrigerant, and work delivered to the compressor shaft, Btu/lb

The actual power input to the compressor P_{com}, in hp, can be calculated as

$$\begin{aligned}P_{\text{com}} &= \mathring{m}_{\text{r}}(h_2 - h_1)/(42.41\eta_{\text{isen}}\eta_{\text{mo}}) \\ \mathring{m}_{\text{r}} &= \mathring{V}_{\text{p}}\,\eta_{\text{v}}\rho_{\text{suc}} \\ \eta_{\text{mo}} &= P_{\text{com}}/P_{\text{mo}}\end{aligned} \tag{9.8.3}$$

where

$\mathring{m}_{\text{r}}$ = mass flow rate of refrigerant, lb/min

ρ_{suc} = density of suction vapor, lb/ft^3

P_{mo} = power input to the compressor motor, hp

Power consumption, kW/ton refrigeration, is an energy index used in the HVAC&R industry in addition to EER and COP.

Currently used refrigeration compressors are reciprocating, scroll, screw, rotary, and centrifugal compressors.

Reciprocating Compressors

In a reciprocating compressor, as shown in Figure 9.8.1(a), a crankshaft connected to the motor shaft drives 2, 3, 4, or 6 single-acting pistons moving reciprocally in the cylinders via a connecting rod.

The refrigeration capacity of a reciprocating compressor is a fraction of a ton to about 200 tons. Refrigerants R-22 and R-134a are widely used in comfort and processing systems and sometimes R-717 in industrial applications. The maximum compression ratio R_{com} for a single-stage reciprocating compressor is about 7. Volumetric efficiency η_{v} drops from 0.92 to 0.65 when R_{com} is raised from 1 to 6. Capacity control of reciprocating compressor including: on-off and cylinder unloader in which discharge gas is in short cut and return to the suction chamber.

Although reciprocating compressors are still widely used today in small and medium-sized refrigeration systems, they have little room for significant improvement and will be gradually replaced by scroll and screw compressors.

Scroll Compressors

A scroll compressor consists of two identical spiral scrolls assembled opposite to each other, as shown in Figure 9.8.1(b). One of the scrolls is fixed, and the other moves in an orbit around the motor shaft whose amplitude equals the radius of the orbit. The two scrolls are in contact at several points and therefore form a series of pockets.

Vapor refrigerant enters the space between two scrolls through lateral openings. The lateral openings are then sealed and the formation of the two trapped vapor pockets indicates the end of the suction process. The vapor is compressed and the discharge process begins when the trapped gaseous pockets open to the discharge port. Compressed hot gas is then discharged through this opening to the discharge

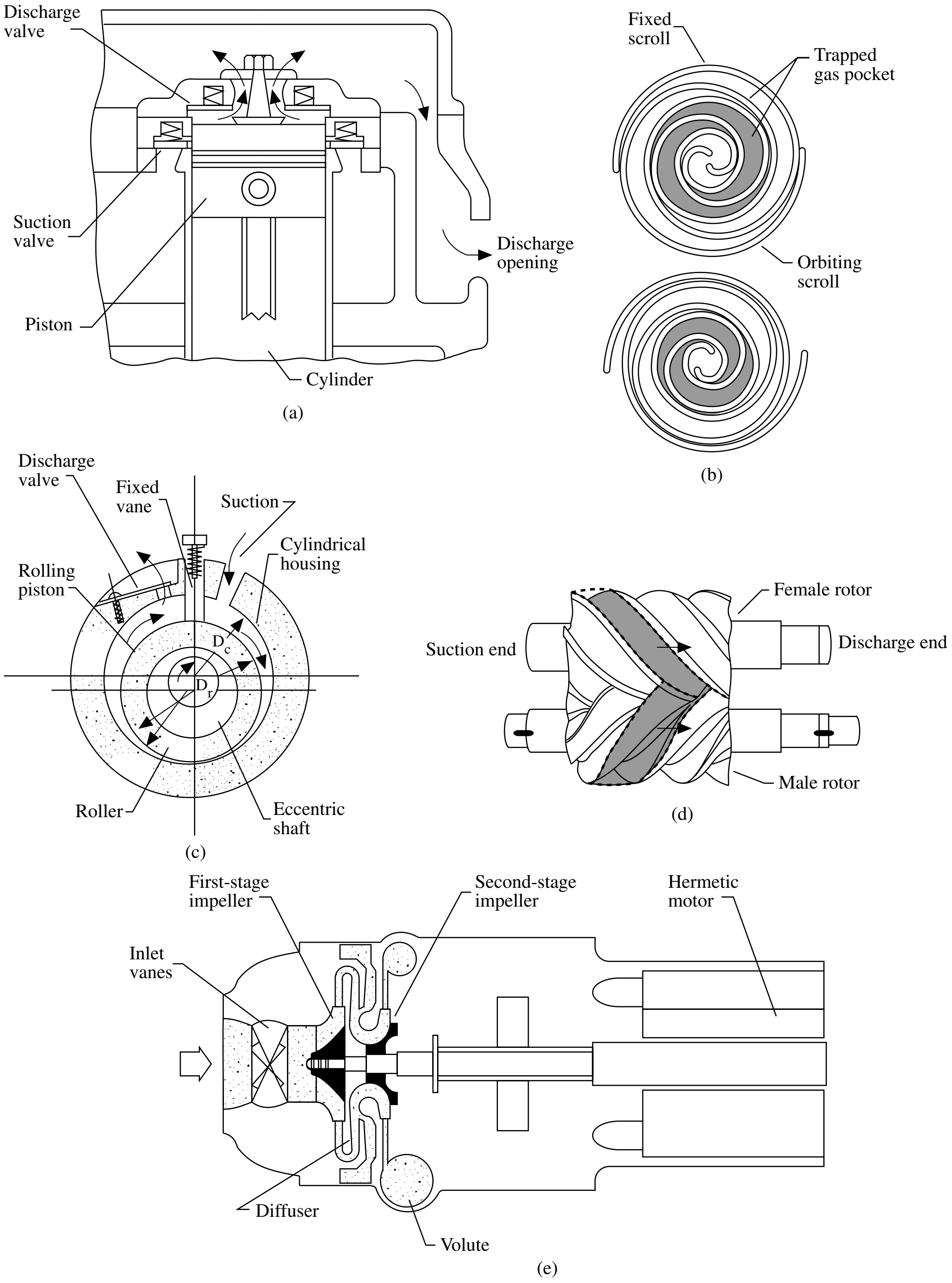

FIGURE 9.8.1 Various types of refrigeration compressors: (a) reciprocating, (b) scroll, (c) rotary, (d) twin-screw, and (e) centrifugal.

line. In a scroll compressor, the scrolls touch each other with sufficient force to form a seal but not enough to cause wear.

The upper limit of the refrigeration capacity of currently manufactured scroll compressors is 60 tons. A scroll compressor has $\eta_v > 95\%$ at $R_{com} = 4$ and $\eta_{isen} = 80\%$. A scroll compressor also has only about half as many parts as a reciprocating compressor at the same refrigeration capacity. Few components result in higher reliability and efficiency. Power input to the scroll compressor is about 5 to 10% less than to the reciprocating compressor. A scroll compressor also operates more smoothly and is quieter.

Rotary Compressors

Small rotary compressors for room air conditioners and refrigerators have a capacity up to 4 tons. There are two types of rotary compressors: rolling piston and rotating vane. A typical rolling piston rotary compressor is shown in Figure 9.8.1(c). A rolling piston mounted on an eccentric shaft is kept in contact with a fixed vane that slides in a slot. Vapor refrigerant enters the compression chamber and is compressed by the eccentric motion of the roller. When the rolling piston contacts the top housing, hot gas is squeezed out from the discharge valve.

Screw Compressors

These are also called *helical rotary compressors*. Screw compressors can be classified into single-screw compressors, in which there is a single helical rotor and two star wheels, and twin-screw compressors. Twin-screw compressors are widely used.

A typical twin-screw compressor, as shown in Figure 9.8.1(d) consists of a four-lobe male rotor and a six-lobe female rotor, a housing with suction and discharge ports, and a sliding valve to adjust the capacity during part load. Normally, the male rotor is the driver. Twin-screw compressors are often direct driven and of hermetic type.

Vapor refrigerant is extracted into the interlobe space when the lobes are separated at the suction port. During the successive rotations of the rotor, the volume of the trapped vapor is compressed. When the interlobe space is in contact with the discharge port, the compressed hot gas discharges through the outlet. Oil injection effectively cools the rotors and results in a lower discharge temperature. Oil also provides a sealing effect and lubrication. A small clearance of 0.0005 in. as well as the oil sealing minimizes leakage of the refrigerant.

The refrigeration capacity of twin-screw compressors is 50 to 1500 tons. The compression ratio of a twin-screw compressor can be up to 20:1. R-22 and R-134a are the most widely used refrigerants in comfort systems. In a typical twin-screw compressor, η_v decreases from 0.92 to 0.87 and η_{isen} drops from 0.82 to 0.67 when R_{com} increases from 2 to 10. Continuous and stepless capacity control is provided by moving a sliding valve toward the discharge port, which opens a shortcut recirculating passage to the suction port.

Twin-screw compressors are more efficient than reciprocating compressors. The low noise and vibration of the twin-screw compressor together with its positive displacement compression results in more applications today.

Centrifugal Compressors

A *centrifugal compressor* is a turbomachine and is similar to a centrifugal fan. A hermetic centrifugal compressor has an outer casing with one, two, or even three impellers internally connected in series and is driven by a motor directly or by a gear train. At the entrance to the first-stage impeller are inlet guide vanes positioned at a specific opening to adjust refrigerant flow and therefore the capacity of the centrifugal compressor.

Figure 9.8.1(e) shows a two-stage hermetic centrifugal compressor. The total pressure rise in a centrifugal compressor, often called head lift, in psi, is due to the conversion of the velocity pressure into static pressure. Although the compression ratio R_{com} of a single-stage centrifugal compressor using R-123 and R-22 seldom exceeds 4, two or three impellers connected in series satisfy most of the requirements in comfort systems.

Because of the high head lift to raise the evaporating pressure to condensing pressure, the discharge velocity at the exit of the second-stage impeller approaches the acoustic velocity of saturated vapor v_{ac} of R-123, 420 ft/sec at atmospheric pressure and a temperature of 80°F. Centrifugal compressors need high peripheral velocity and rotating speeds (up to 50,000 rpm) to produce such a discharge velocity. It is not economical to manufacture small centrifugal compressors. The available refrigeration capacity for centrifugal compressors ranges from 100 to 10,000 tons. Centrifugal compressors have higher volume flow per unit refrigeration capacity output than positive displacement compressors. Centrifugal compressors are efficient and reliable. Their volumetric efficiency almost equals 1. At design conditions, their η_{isen} may reach 0.83, and it drops to 0.6 during part-load operation. They are the most widely used refrigeration compressors in large air-conditioning systems.

Refrigeration Condensers

A *refrigeration condenser* or simply a *condenser* is a heat exchanger in which hot gaseous refrigerant is condensed into liquid and the latent heat of condensation is rejected to the atmospheric air, surface water, or well water. In a condenser, hot gas is first desuperheated, then condensed into liquid, and finally subcooled.

The capacity of a condenser is rated by its *total heat rejection* Q_{rej}, in Btu/hr, which is defined as the total heat removed from the condenser during desuperheating, condensation, and subcooling. For a refrigeration system using a hermetic compressor, Q_{rej} can be calculated as

$$Q_{rej} = U_{con} A_{con} \Delta T_m = 60 \mathring{m}_r \left(h_2 - h_3'\right) = q_{rl} + \left(2545 P_{com}\right) / \eta_{mo} \tag{9.8.4}$$

where

U_{con} = overall heat transfer coefficient across the tube wall in the condenser, Btu/hr.ft^2.°F
A_{con} = condensing area in the condenser, ft^2
ΔT_m = logarithmic temperature difference, °F
$\mathring{m}_r$ = mass flow rate of refrigerant, lb/min
h_2, h_3' = enthalpy of suction vapor refrigerant and hot gas, Btu/lb
q_{rl} = refrigeration load at the evaporator, Btu/hr

A factor that relates Q_{rej} and q_{rl} is the *heat rejection factor* F_{rej}, which is defined as the ratio of total heat rejection to the refrigeration load, or

$$F_{rej} = Q_{rej} / q_{rl} = 1 + \left(2545 P_{com}\right) / \left(q_{rl} \eta_{mo}\right) \tag{9.8.5}$$

Fouling factor R_f, in hr.ft^2.°F/Btu, is defined as the additional resistance caused by a dirty film of scale, rust, or other deposits on the surface of the tube. ARI Standard 550-88 specifies the following for evaporators and condensers:

Field fouling allowance	0.00025 hr.ft^2.°F/Btu
New evaporators and condensers	0

According to the cooling process used during condensation, refrigeration condensers can be classified as air-cooled, water-cooled, and evaporative-cooled condensers.

Air-Cooled Condensers

In an *air-cooled condenser*, air is used to absorb the latent heat of condensation released during desuperheating, condensation, and subcooling.

An air-cooled condenser consists of a condenser coil, a subcooling coil, condenser fans, dampers, and controls as shown in Figure 9.8.2(a). There are refrigeration circuits in the condensing coil. Condensing coils are usually made of copper tubes and aluminum fins. The diameter of the tubes is 1/4 to 3/4 in., typically 3/8 in., and the fin density is 8 to 20 fins/in. On the inner surface of the copper tubes, microfins, typically 60 fins/in. with a height of 0.008 in., are used. A condensing coil usually has only two to three rows due to the low pressure drop of the propeller-type condenser fans. A subcooling coil is located at a lower level and is connected to the condensing coil.

Hot gas from the compressor enters the condensing coil from the top. When the condensate increases, part of the condensing area can be used as a subcooling area. A receiver is necessary only when the liquid refrigerant cannot all be stored in the condensing and subcooling coils during the shut-down period in winter.

Cooling air is drawn through the coils by a condenser fan(s) for even distribution. Condenser fans are often propeller fans for their low pressure and large volume flow rate. A damper(s) may be installed to adjust the volume flow of cooling air.

In air-cooled condensers, the volume flow of cooling air per unit of total heat rejection $\mathring{V}_{ca}/Q_{u.rej}$ is 600 to 1200 cfm/ton of refrigeration capacity at the evaporator, and the optimum value is about 900 cfm/ton. The corresponding cooling air temperature difference — cooling air leaving temperature minus outdoor temperature ($T_{ca.l} - T_o$) — is around 13°F.

The condenser temperature difference (CTD) for an air-cooled condenser is defined as the difference between the saturated condensing temperature corresponding to the pressure at the inlet and the air intake temperature, or ($T_{con.i} - T_o$). Air-cooled condensers are rated at a specific CTD, depending on the evaporating temperature of the refrigeration system T_{ev} in which the air-cooled condenser is installed. For a refrigeration system having a lower T_{ev}, it is more economical to equip a larger condenser with a smaller CTD. For a comfort air-conditioning system having a T_{ev} of 45°F, CTD = 20 to 30°F.

A higher condensing temperature T_{con}, a higher condensing pressure p_{con}, and a higher compressor power input may be due to an undersized air-cooled condenser, lack of cooling air or low $\mathring{V}_{ca}/Q_{u.rej}$ value, a high entering cooling air temperature at the roof, a dirty condensing coil, warm air circulation because of insufficient clearance between the condenser and the wall, or a combination of these. The clearance should not be less than the width of the condensing coil.

If p_{con} drops below a certain value because of a lower outdoor temperature, the expansion valve in a reciprocating vapor compression system may not operate properly. At a low ambient temperature T_o, the following controls are often used:

- Duty cycling, turning the condenser fans on and off until all of them are shut down, to reduce cooling air volume flow
- Modulating the air dampers to reduce the volume flow
- Reducing the fan speed

Some manufacturers' catalogs start low ambient control at T_o = 65°F and some specify a minimum operating temperature at T_o = 0°F.

Water-Cooled Condensers

In a *water-cooled condenser*, latent heat of condensation released from the refrigerant during condensation is extracted by water. This cooling water, often called condenser water, is taken directly from river, lake, sea, underground well water or a cooling tower.

Two types of water-cooled condensers are widely used for air-conditioning and refrigeration: double-tube condensers and horizontal shell-and-tube condensers.

A *double-tube condenser* consists of two tubes, one inside the other. Condenser water is pumped through the inner tube and refrigerant flows within the space between the inner and outer tubes in a counterflow arrangement. Because of its limited condensing area, the double-tube condenser is used only in small refrigeration systems.

A horizontal *shell-and-tube water-cooled condenser* using halocarbon refrigerant usually has an outer shell in which copper tubes typically 5/8 to 3/4 in. in diameter are fixed in position by tube sheets as shown in Figure 9.8.2(b). Integral external fins of 19 to 35 fins/in. and a height of 0.006 in. and spiral internal grooves are used for copper tubes to increase both the external and the inner surface area and their heat transfer coefficients.

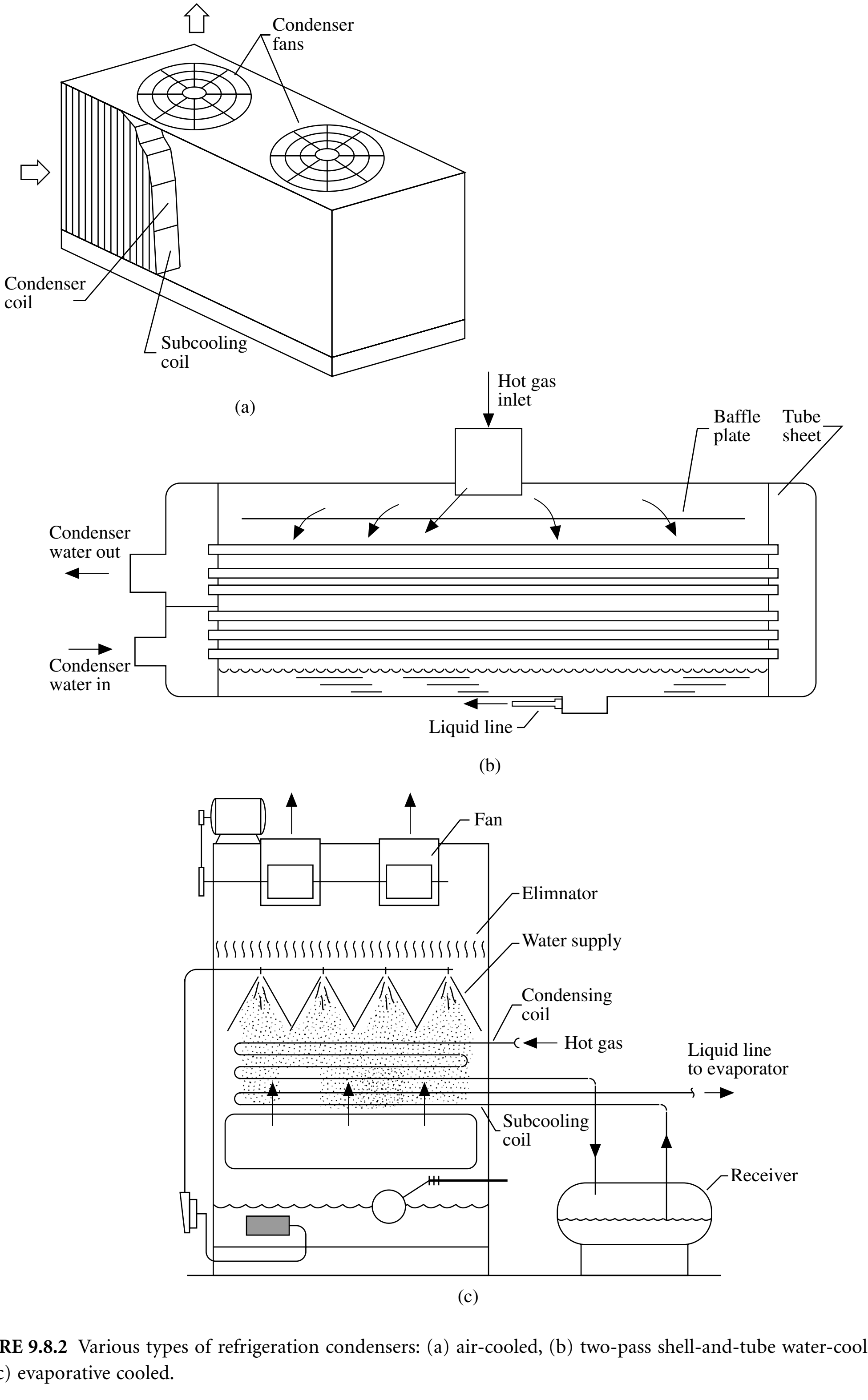

FIGURE 9.8.2 Various types of refrigeration condensers: (a) air-cooled, (b) two-pass shell-and-tube water-cooled, and (c) evaporative cooled.

Hot gas from the compressor enters the top inlet and is distributed along the baffle to fill the shell. Hot gas is then desuperheated, condensed, subcooled into liquid, and discharged into the liquid line at the bottom outlet. Usually one sixth of the volume is filled with subcooled liquid refrigerant. Subcooling depends on the entering temperature of condenser water T_{ce}, in °F, and usually varies between 2 and 8°F.

Condenser water enters the condenser from the bottom for effective subcooling. After extracting heat from the gaseous refrigerant, condenser water is discharged at a higher level. Two-pass or three-pass water flow arrangements are usually used in shell-and-tube water-cooled condensers. The two-pass arrangement means that water flows from one end to the opposite end and returns to the original end. Two-pass is the standard setup. In a shell-and-tube water-cooled condenser, the condensing temperature T_{con} depends mainly on the entering temperature of condenser water T_{ce}, the condenser area, the fouling factor, and the configuration of the copper tube.

Evaporative Condenser

An *evaporative condenser* uses the evaporation of water spray on the outer surface of the condensing tubes to remove the latent heat of condensation of refrigerant during condensation.

An evaporative condenser consists of a condensing coil, a subcooling coil, a water spray, an induced draft or sometimes forced draft fan, a circulating water pump, a water eliminator, a water basin, an outer casing, and controls as shown in Figure 9.8.2(c). The condensing coil is usually made of bare copper, steel, or sometimes stainless steel tubing.

Water is sprayed over the outside surface of the tubing. The evaporation of a fraction of condenser water from the saturated air film removes the sensible and latent heat rejected by the refrigerant. The wetted outer surface heat transfer coefficient h_{wet} is about four or five times greater than the dry surface heat transfer coefficient h_o, in Btu/hr.ft^2.°F. The rest of the spray falls and is collected by the basin. Air enters from the inlet just above the basin. It flows through the condensing coil at a face velocity of 400 to 700 fpm, the water spray bank, and the eliminator. After air absorbs the evaporated water vapor, it is extracted by the fan and discharged at the top outlet. The water circulation rate is about 1.6 to 2 gpm/ton, which is far less than that of the cooling tower.

An evaporative condenser is actually a combination of a water-cooled condenser and a cooling tower. It is usually located on the rooftop and should be as near the compressor as possible. Clean tube surface and good maintenance are critical factors for evaporative condensers. An evaporative condenser also needs low ambient control similar as in an air-cooled condenser.

Comparison of Air-Cooled, Water-Cooled, and Evaporative Condensers

An air-cooled condenser has the highest condensing temperature T_{con} and therefore the highest compressor power input. For an outdoor dry bulb temperature of 90°F and a wet bulb temperature of 78°F, a typical air-cooled condenser has $T_{con} = 110$°F. An evaporative condenser has the lowest T_{con} and is most energy efficient. At the same outdoor dry and wet bulb temperatures, its T_{con} may be equal to 95°F, even lower than that of a water-cooled condenser incorporating with a cooling tower, whose T_{con} may be equal to 100°F. An evaporative condenser also consumes less water and pump power. The drawback of evaporative condensers is that the rejected heat from the interior zone is difficult to recover and use as winter heating for perimeter zones and more maintenance is required.

Evaporators and Refrigerant Flow Control Devices

An *evaporator* is a heat exchanger in which the liquid refrigerant is vaporized and extracts heat from the surrounding air, chilled water, brine, or other substance to produce a refrigeration effect.

Evaporators used in air-conditioning can be classified according to the combination of the medium to be cooled and the type of refrigerant feed, as the following.

Direct expansion DX coils are air coolers, and the refrigerant is fed according to its degree of superheat after vaporization. DX coils were covered earlier.

Direct expansion ice makers or *liquid overfeed ice makers* are such that liquid refrigerant is forced through the copper tubes or the hollow inner part of a plate heat exchanger and vaporized. The refrigeration effect freezes the water in the glycol-water that flows over the outside surface of the tubes or the plate heat exchanger. In direct expansion ice makers, liquid refrigerant completely vaporizes inside the copper tubes, and the superheated vapor is extracted by the compressor. In liquid overfeed ice makers, liquid refrigerant floods and wets the inner surface of the copper tubes or the hollow plate heat exchanger. Only part of the liquid refrigerant is vaporized. The rest is returned to a receiver and pumped to the copper tubes or plate heat exchanger again at a circulation rate two to several times greater than the evaporation rate.

Flooded shell-and-tube liquid coolers, or simply *flooded liquid coolers*, are such that refrigerant floods and wets all the boiling surfaces and results in high heat transfer coefficients. A flooded shell-and-tube liquid cooler is similar in construction to a shell-and-tube water-cooled condenser, except that its liquid refrigeration inlet is at the bottom and the vapor outlet is at the top. Water velocity inside the copper tubes is usually between 4 and 12 ft/sec and the water-side pressure normally drops below 10 psi. Flooded liquid coolers can provide larger evaporating surface area and need minimal space. They are widely used in large central air-conditioning systems.

Currently used refrigerant flow control devices include thermostatic expansion valves, float valves, multiple orifices, and capillary tubes.

A *thermostatic expansion valve* throttles the refrigerant pressure from condensing to evaporating pressure and at the same time regulates the rate of refrigerant feed according to the degree of superheat of the vapor at the evaporator's exit. A thermostatic expansion valve is usually installed just prior to the refrigerant distributor in DX coils and direct-expansion ice makers.

A thermostatic expansion valve consists of a valve body, a valve pin, a spring, a diaphragm, and a sensing bulb near the outlet of the DX coil, as shown in Figure 9.7.3(a). The sensing bulb is connected to the upper part of the diaphragm by a connecting tube.

When the liquid refrigerant passes through the opening of the thermostatic expansion valve, its pressure is reduced to the evaporating pressure. Liquid and a small fraction of vaporized refrigerant then flow through the distributor and enter various refrigerant circuits. If the refrigeration load of the DX coil increases, more liquid refrigerant vaporizers. This increases the degree of superheat of the leaving vapor at the outlet and the temperature of the sensing bulb. A higher bulb temperature exerts a higher saturated pressure on the top of the diaphragm. The valve pin then moves downward and widens the opening. More liquid refrigerant is allowed to enter the DX coil to match the increase of refrigeration load. If the refrigeration load drops, the degree of superheat at the outlet and the temperature of the sensing bulb both drop, and the valve opening is narrower. The refrigeration feed decreases accordingly. The degree of superheat is usually 10 to 20°F. Its value can also be adjusted manually by varying the spring tension. The bulbs of the thermostatic expansion valves can be charged with the same refrigerant as in the system or "cross-charged" by using a different refrigerant to improve response.

A *float valve* is a valve in which a float is used to regulate the valve opening to maintain a specific liquid refrigerant level. A lower liquid level causes a lower valve pin and therefore a wider opening and vice versa.

In a centrifugal refrigeration system, two or more orifice plates, *multiple orifices*, are sometimes installed in the liquid line between the condenser and the flash cooler and between the flash cooler and the flooded liquid cooler to throttle their pressure as well as to regulate the refrigerant feed.

A *capillary tube*, sometimes called a *restrictor tube*, is a fixed length of small-diameter tubing installed between the condenser and the evaporator to throttle the refrigerant pressure from p_{con} to p_{ev} and to meter the refrigerant flow to the evaporator. Capillary tubes are usually made of copper. The inside diameter D_{cap} is 0.05 to 0.06 in. and the length L_{cap} from an inch to several feet. There is a trend to use short capillary tubes of L_{cap}/D_{cap} between 3 and 20. Capillary tubes are especially suitable for a heat pump system in which the refrigerant flow may be reversed.

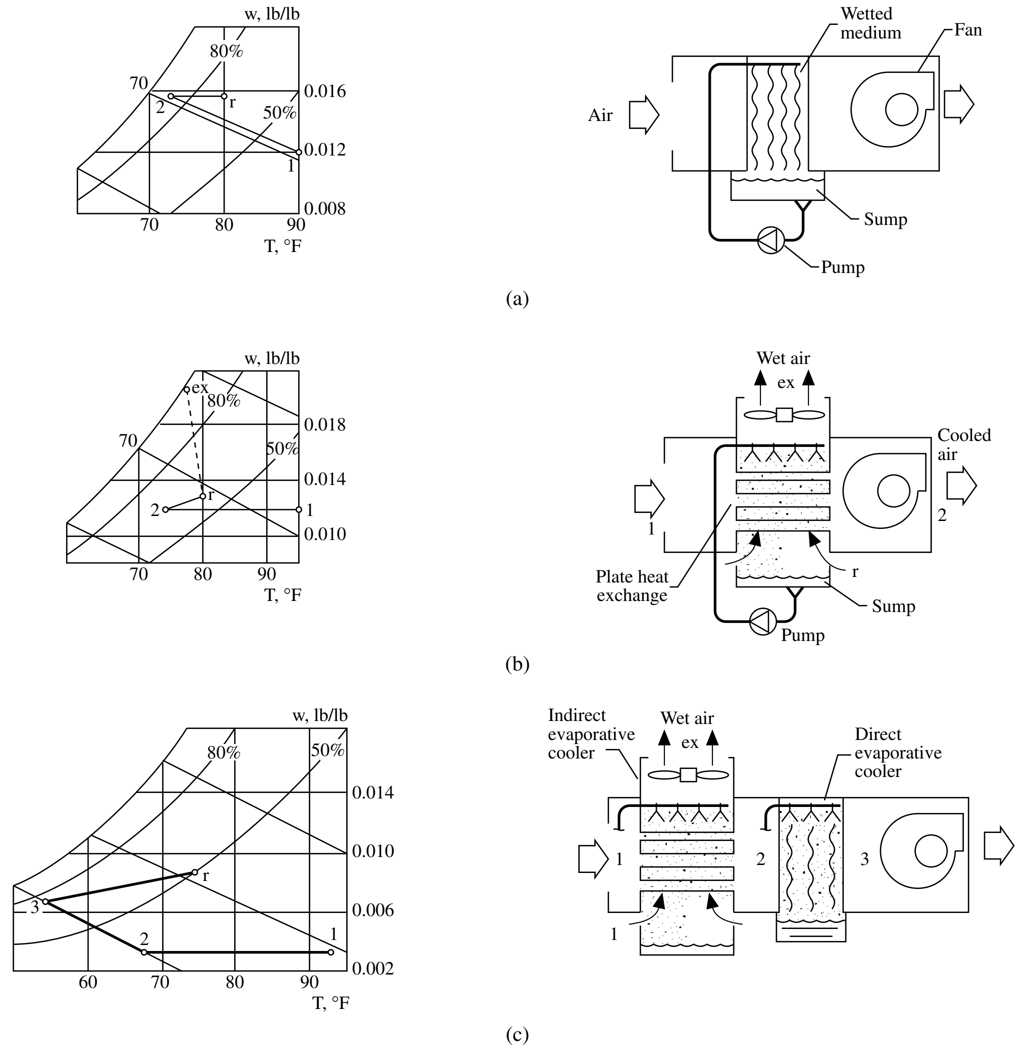

FIGURE 9.8.3 Types of evaporative coolers: (a) direct, (b) indirect, and (c) indirect–direct.

Evaporative Coolers

An evaporative cooling system is an air-conditioning system in which air is cooled evaporatively. It consists of evaporative coolers, fan(s), filters, dampers, controls, and others. A mixing box is optional. An evaporative cooler could be a stand-alone cooler or installed in an air system as a component. There are three types of evaporative coolers: (1) direct evaporative coolers, (2) indirect evaporative coolers, and (3) indirect–direct evaporative coolers.

Direct Evaporative Cooler

In a *direct evaporative cooler*, the air stream to be cooled directly contacts the water spray or wetted medium as shown in Figure 9.8.3(a). Evaporative pads made of wooden fibers with necessary treatment at a thickness of 2 in., rigid and corrugated plastics, impregnated cellulose, or fiber glass all dripping with water are wetted mediums.

The direct evaporation process 12 takes place along the thermodynamic wet bulb line on the psychrometric chart. Saturation effectiveness ε_{sat} is an index that assesses the performance of a direct evaporative cooler:

$$\varepsilon_{\text{sat}} = \left(T_{\text{ae}} - T_{\text{al}}\right) / \left(T_{\text{ae}} - T^{*}_{\text{ae}}\right) \tag{9.8.6}$$

where T, T^{*} = temperature and thermodynamic wet bulb temperature of air stream, °F. Subscript ae indicates the entering air and al the leaving air. ε_{sat} usually varies between 0.75 and 0.95 at a water–air ratio of 0.1 to 0.4.

Indirect Evaporative Coolers

In an *indirect evaporative cooler*, the cooled-air stream to be cooled is separated from a wetted surface by a flat plate or tube wall as shown in Figure 9.8.3(b). A wet-air stream flows over the wetted surface so that liquid water is evaporated and extracts heat from the cooled-air stream through the flat plate or tube wall. The cooled-air stream is in contact with the wetted surface indirectly.

The core part of an indirect evaporative cooler is a plate heat exchanger. It is made of thin polyvinyl chloride plates 0.01 in. thick and spaced from 0.08 to 0.12 in. apart to form horizontal passages for cooled air and vertical passages for wet air and water. As in a direct evaporative cooler, there are also fan(s), water sprays, circulating pump, air intake, dampers, controls, etc.

An indirect evaporative cooling process is represented by a horizontal line on a psychrometric chart, which shows that humidity ratio remains constant. If the space air is extracted and used as the wet air intake, the wet air will be exhausted at point x at nearly saturated state.

The performance of an indirect evaporative cooler can be assessed by its performance factor e_{in}, which is calculated as:

$$e_{\text{in}} = \left(T_{\text{ca.e}} - T_{\text{ca.l}}\right) / \left(T_{\text{ca.e}} - T_{\text{s.a}}\right) \tag{9.8.7}$$

where $T_{\text{ca.e}}$, $T_{\text{ca.l}}$ = temperature of cooled air entering and leaving the indirect evaporative cooler, °F, and $T_{\text{s.a}}$ = temperature of the saturated air film on the wet air side and is about 3°F higher than the wet bulb temperature of the entering air, °F.

An indirect evaporative cooler could be so energy efficient as to provide evaporative cooling with an EER up to 50 instead of 9 to 12 for a reciprocating compression refrigeration system.

Direct–Indirect Evaporative Cooler. A direct–indirect evaporative cooler is a two-stage evaporating cooler, as shown in Figure 9.15.6(c), in which the first-stage indirect evaporative cooler is connected in series with a second-stage direct evaporative cooler for the purpose of increasing the evaporating effect.

Operating Characteristics. The saturation effectiveness ε_{sat} and performance factor e_{in} are both closely related to the air velocity flowing through the air passages. For a direct evaporative cooler, face velocity is usually less than 600 fpm to reduce drift carryover. For an indirect evaporative cooler, face velocity v_s is usually between 400 to 1000 fpm. A higher v_s results at a greater air-side pressure drop.

Scofield et al. (1984) reported the performance of an indirect–direct evaporative cooler in Denver, Colorado. Outdoor air enters the indirect cooler at a dry bulb of 93°F and a wet bulb of 67.5° and was evaporatively cooled to 67.5°F dry bulb and 49.8°F wet bulb with an $e_{\text{in}} = 0.76$ as shown in Figure 9.8.3(c). In the direct cooler, conditioned air was further cooled to a dry bulb of 53.5°F and the wet bulb remained at 49.8°F at a saturation effectiveness $\varepsilon_{\text{sat}} = 0.8$.

In locations where outdoor wet bulb $T'_o \le 60$°F, a direct evaporative can often provide an indoor environment of 78°F and a relative humidity of 60%. In locations $T'_o \le 68$°F, an indirect–direct evaporative cooler can maintain a comfortable indoor environment. In locations $T'_o \ge 72$°F, an evaporative cooler with a supplementary vapor compression refrigeration may be cost effective. Because the installation cost of an indirect–direct cooler is higher than that of refrigeration, cost analysis is required to select the right choice. Evaporative coolers are not suitable for dehumidification except in locations where $T'_o \le 60$°F.

9.9 Water Systems

Herbert A. Ingley and Shan K. Wang

Types of Water Systems

In central and space conditioning air-conditioning systems, water that links the central plant and the air handling units or terminals, that extracts condensing heat, or that provides evaporative cooling may be classified as

- *Chilled water system*, in which chilled water is first cooled in the centrifugal, screw, and reciprocating chillers in a central plant. Chilled water is then used as a cooling medium to cool the air in the cooling coils in AHUs and terminals.
- *Evaporative-cooled water system*, used to cool air directly or indirectly in evaporative coolers.
- *Hot water system*, in which hot water is heated in the boiler and then used to heat the air through heating coils in AHUs, terminals, or space finned-tube heaters.
- *Dual-temperature water system*, in which chilled water and hot water are supplied to and returned from the coils in AHUs and terminals through separate or common main and branch pipes. Using common main and branch pipes requires a lengthy changeover from chilled water to hot water or vice versa for a period of several hours.
- *Condenser water system*, which is a kind of cooling water system used to extract the latent heat of condensation from the condensing refrigerant in a water-cooled condenser and heat of absorption from the absorber.

Water systems can also be classified according to their operating characteristics.

Closed System

In a closed system, water forms a closed loop for water conservation and energy saving when it flows through the coils, chillers, boilers, heaters, or other heat exchangers and water is not exposed to the atmosphere.

Open System

In an open system, water is exposed to the atmosphere. A condenser water system with a cooling tower would be an example of an open system.

Once-Through System

In a once-through system, water flows through a heat exchanger(s) only once without recirculation. A condenser water system using well water that is ultimately rejected to a pond would be an example of a once-through system.

Basics

Volume Flow and Temperature Difference

The rate of heat transfer between water and air or water and refrigerant when water flows through a heat exchanger q_w, in Btu/hr, can be calculated as

$$q_w = 500 \mathring{V}_{gal} \left(T_{wl} - T_{we}\right) = 500 \mathring{V}_{gal} \Delta T_w \tag{9.9.1}$$

where

$\mathring{V}_{gal}$ = volume flow rate of water, gpm
T_{wl}, T_{we} = temperature of water leaving and entering the heat exchanger, °F
ΔT_w = temperature rise or drop of water when it flows through a heat exchanger, °F
$500 \cong 8.34$ lb/gal $*$ 1 Btu/lb°F $*$ 60 min/hr

The temperature of chilled water leaving the water chiller T_{el} should not be lower than 38°F in order to prevent freezing in the evaporator. Otherwise, brine or glycol-water should be used. The T_{el} of chilled water entering the coil T_{we} and the temperature difference of chilled water leaving and entering the coil ΔT_w directly affect the temperature of air leaving the cooling coil T_{cc}. The lower T_{we}, the higher will be the compressor power input. The smaller ΔT_w, the greater will be the water volume flow rate, the pipe size, and the pump power. For chilled water in conventional comfort systems, T_{we} is usually 40 to 45°F and ΔT_w 12 to 24°F. Only in cold air distribution, T_{we} may drop to 34°F. For a cooling capacity of 1 ton refrigeration, a ΔT_w of 12°F requires a $\overset{\circ}{V}_{gal} = 2$ gpm.

For hot water heating systems in buildings, hot water often leaves the boiler and enters the heating coil or heaters at a temperature T_{we} of 180 to 200°F. It returns at 150 to 160°F. For dual-temperature systems, hot water is usually supplied at 100 to 150°F and returns at a ΔT_w of 20 to 40°F.

Pressure Drop

Usually the pressure drop of water in pipes due to friction for HVAC&R systems, H_f, is in the range 1.0 ft/100 ft length of pipe to 4 ft/100 ft. A pressure loss of 2.5 ft/100 ft is most often used. Figure 9.9.1(a), (b), and (c) shows the friction charts for steel, copper, and plastic pipes for closed water systems.

Water Piping

The piping materials of various water systems for HVAC&R are as follows:

Chilled water	Black and galvanized steel
Hot water	Black steel, hard copper
Condenser water	Black steel, galvanized ductile iron, polyvinyl chloride (PVC)

The pipe thickness varies from Schedule 10, a light wall pipe, to Schedule 160, a very heavy wall pipe. Schedule 40 is the standard thickness for a pipe of up to 10 in. diameter. For copper tubing, type K is the heaviest, and type L is generally used as the standard for pressure copper tubes.

Steel pipes of small diameter are often joined by threaded cast-iron fittings. Steel pipes of diameter 2 in. and over, welded joints, and bolted flanges are often used.

In a water system, the maximum allowable working pressure for steel and copper pipes at 250°F varies from 125 to 400 psig, depending on the pipe wall thickness. Not only pipes, but also their joints and fittings should be considered.

During temperature changes, pipes expand and contract. Both operating and shut-down periods should be taken into consideration. Bends like U-, Z-, and L-bends, loops, and sometimes packed expansion joints, bellows, or flexible metal hose mechanical joints are used.

ASHRAE/IES Standard 90.1-2001 specifies minimum thickness of pipe insulation for chilled water and heating hot water piping.

Corrosion, Impurities, and Water Treatments

Corrosion is a destructive process caused by a chemical or electrochemical reaction on metal or alloy. In water systems, dissolved *impurities* cause corrosion and scale and the growth of microbiologicals like algae, bacteria, and fungi. *Scale* is the deposit formed on a metal surface by precipitation of the insoluble constituents. In addition to the dissolved solids, unpurified water may contain suspended solids.

Currently used chemicals include crystal modifiers to change the crystal formation of scale and sequestering chemicals. Growth of bacteria, algae, and fungi is usually treated by biocides to prevent the formation of an insulating layer resulting in lower heat transfer as well as restricted water flow. Chlorine and its compounds are effective and widely used. Blow-down is an effective process in water treatment and should be considered as important as chemical treatments.

Piping Arrangements

Main and Branch Pipes. In a piping circuit as shown in Figure 9.9.2(a), chilled water from a chiller or hot water from a boiler is often supplied to a *main pipe* and then distributed to *branch pipes* that connect

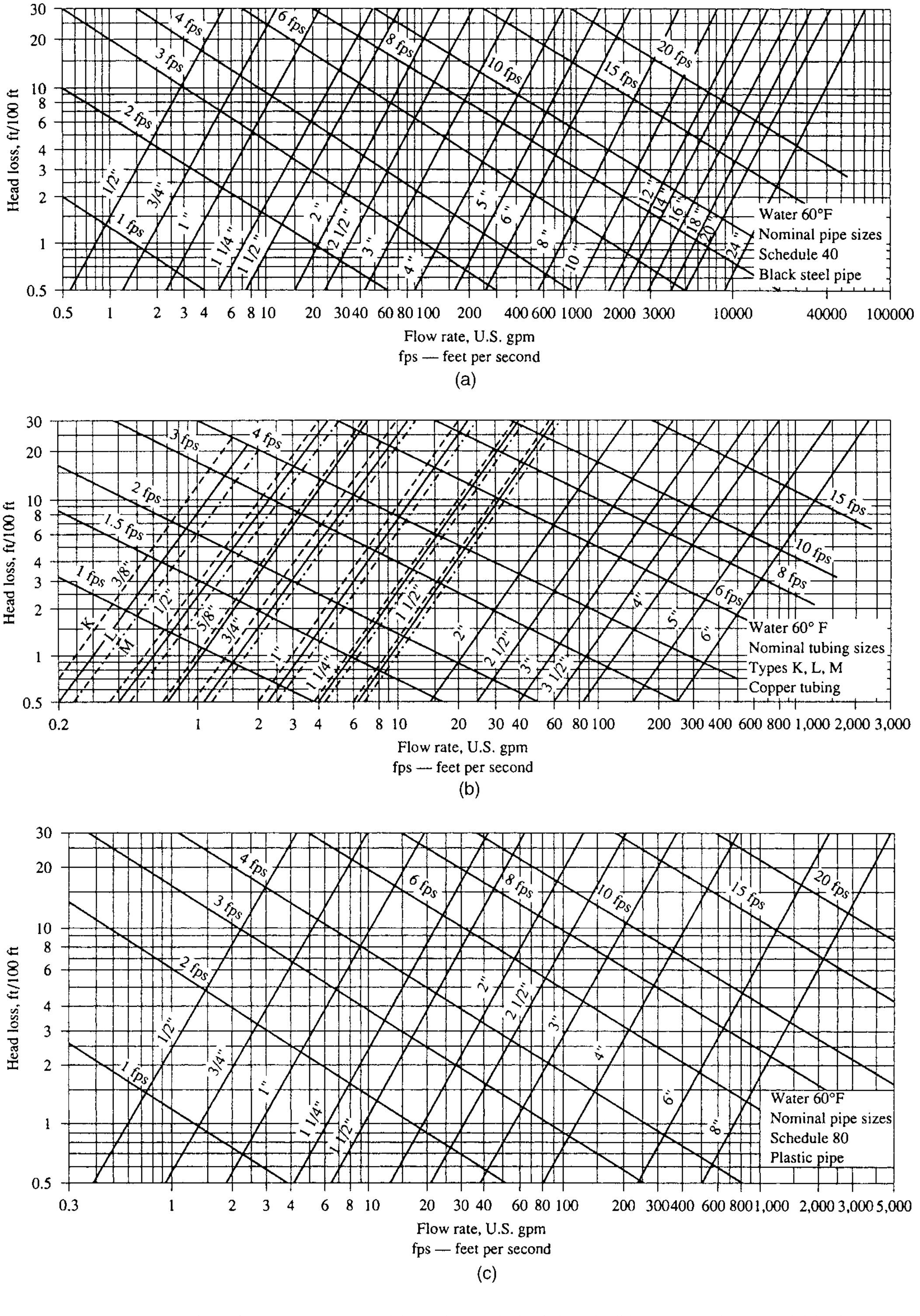

FIGURE 9.9.1 Friction chart for water in pipes: (a) steel pipe (schedule 40), (b) copper tubing, and (c) plastic pipe (schedule 80). (Souce: *ASHRAE Handbook 1993 Fundamentals*. Reprinted with permission.)

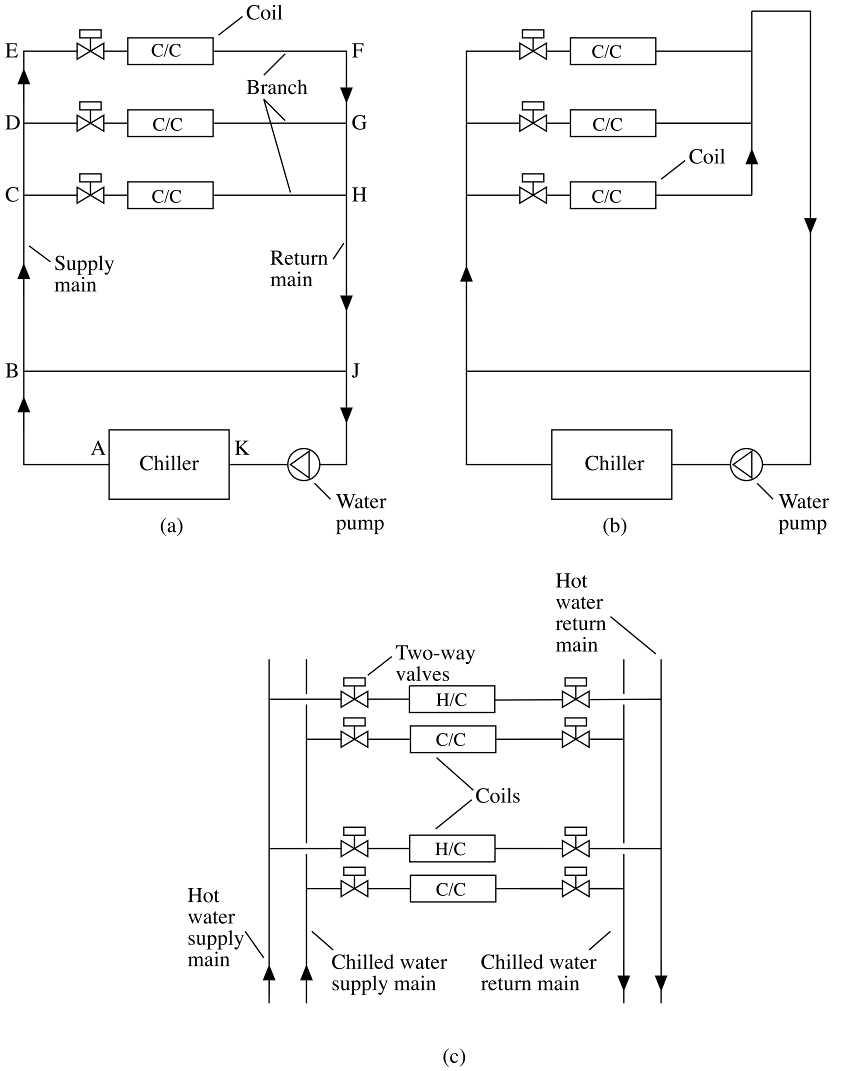

FIGURE 9.9.2 Piping arrangements: (a) two-pipe direct return system, (b) two-pipe reverse system, and (c) four-pipe system.

to coils and heat exchangers. Chilled or hot water from the coils and heat exchangers is accumulated by the return main pipe through return branch pipes and then returned to the chiller or boiler.

Constant Flow and Variable Flow. In a constant-flow water system, the volume flow rate at any cross-sectional plane of the supply and return mains remains constant during the entire operating period. In a variable-flow water system, the volume flow rate varies when the system load changes during the operating period.

Direct Return and Reverse Return. In a *direct return* system, the water supplies to and returns from various coils through various piping circuits. ABCHJKA, … ABCDEFGHJKA are not equal in length, as shown in Figure 9.9.2(a). Water flow must be adjusted and balanced by using balance valves to provide required design flow rates at design conditions. In a *reverse-return* system, as shown in Figure 9.9.2(b), the piping lengths for various piping circuits including the branch and coil are almost equal. Water flow rates to various coils are easier to balance.

Two-Pipe or Four-Pipe. In a dual-temperature water system, the piping from the chiller or boiler to the coils can be either a *two-pipe* system with a supply main and return main as shown in Figure 9.9.2(a) or (b) or a *four-pipe* system with a chilled water supply main, a hot water supply main, a chilled water return main, and a hot water return main as shown in Figure 9.9.2(c). The two-pipe system needs a changeover from chilled to hot water and vice versa. A four-pipe system is more expensive to install.

9.10 Heating Systems

Shan K. Wang

Warm Air Furnaces

A *warm air furnace* is a device in which gaseous or liquid fuel is directly fired or electric resistance heaters are used to heat the warm supply air. Natural gas, liquefied petroleum gas (LPG), oil, electric energy, or occasionally wood may be used as the fuel or energy input. Among these, natural gas is most widely used. In a warm air furnace, the warm air flow could be *upflow*, in which the warm air is discharged at the top, as shown in Figure 9.10.1(a) and (b); downflow, with the warm air discharged at the bottom; or *horizontal flow*, with the warm air discharged horizontally.

Natural Vent Combustion Systems. There are two types of combustion systems in a natural gas-fired warm air furnace: natural vent or power vent combustion systems. In a *natural vent* or *atmospheric vent* combustion system, the buoyancy of the combustion products carries the flue gas flowing through the heat exchanger and draft hood, discharging from the chimney or vent pipe. The gas burner is an *atmospheric burner.* In an atmospheric burner, air is exracted for combustion by the suction effect of the high-velocity discharged gas and the buoyance effect of the combustion air. An atmospheric burner can be either an in-shot or an up-shot burner or multiple ports. Atmospheric burners are simple, require only a minimal draft of air, and need sufficient gas pressure for normal functioning.

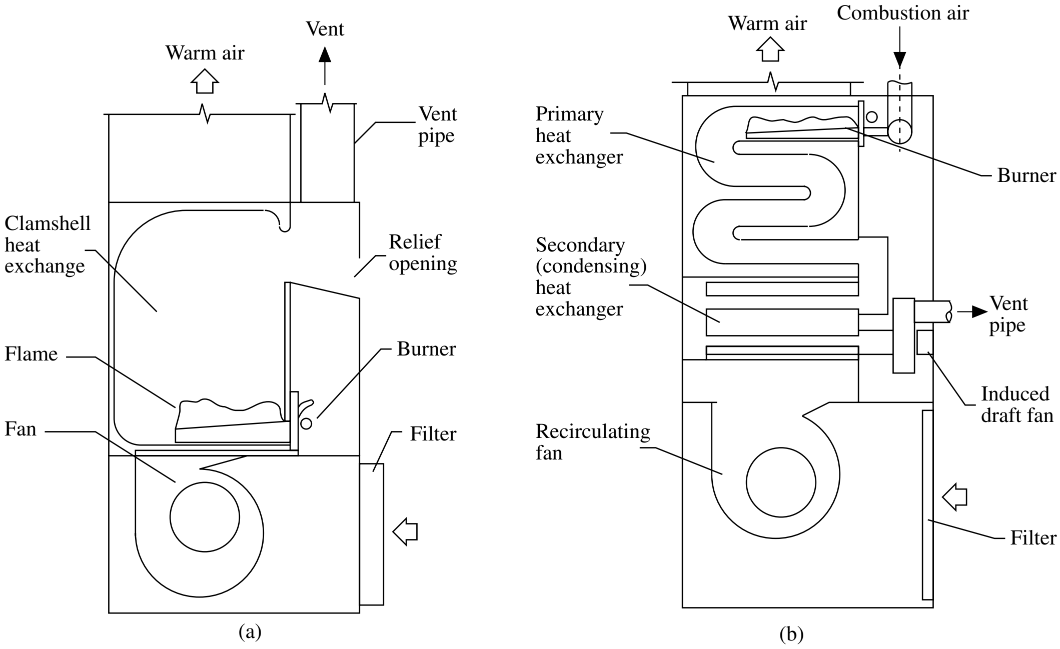

FIGURE 9.10.1 Upflow warm air gas furnace: (a) a natural-vent gas furnace and (b) a power-vent high-efficiency gas furnace.

Two types of ignition have been used in burners: standing pilot and spark ignition. In *standing pilot ignition*, the small pilot flame is monitored by a sensor and the gas supply is shut off if the flame is extinguished. *Spark ignition* fires intermittently only when ignition is required. It saves gas fuel if the furnace is not operating.

In a natural vent combustion system, the heat exchanger is often made from cold-rolled steel or aluminized steel in the shape of a clamshell or S. A fan or blower is always used to force the recirculating air flowing over the heat exchanger and distribute the heated air to the conditioned space. A low-efficiency disposable air filter is often located upstream of the fan to remove dust from the recirculating air. A draft hood is also installed to connect the flue gas exit at the top of the heat exchanger to a vent pipe or chimney. A relief air opening is employed to guarantee that the pressure at the flue gas exit is atmospheric and operates safely even if the chimney is blocked. The outer casing of the furnace is generally made of heavy-gauge steel with access panels.

Power Vent Combustion Systems. In a *power vent* combustion system, either a forced draft fan is used to supply the combustion air or an induced draft fan is used to induce the flue gas to the vent pipe or chimney. A power vent is often used for a large gas furnace or a high-efficiency gas furnace with condensing heat exchangers.

Gas burners in a power vent system are called *power burners*. The gas supply to the power burner is controlled by a pressure regulator and a gas valve to control the firing rate. Intermittent spark ignition and *hot surface ignition* that ignites the main burners directly are often used.

Usually, there are two heat exchangers in a power vent combustion system: a primary heat exchanger and a secondary or condensing heat exchanger. The primary heat exchanger constitutes the heating surface of the combustion chamber. When the water vapor in the flue gas is condensed by indirect contact with the recirculating air, part of the latent heat of condensation released is absorbed by the air. Thus the furnace efficiency is increased in the *secondary* or *condensing heat exchanger*. Both primary and secondary heat exchangers are made from corrosion-resistant steel. A fan is also used to force the recirculating air to flow over the heat exchangers and to distribute the heated air to the conditioned space.

Most natural gas furnaces can use LPG. LPG needs a pressure of 10 in. WG at the manifold, compared with 3 to 4 in. for natural gas. It also needs more primary air for gas burners. Oil furnaces are usually forced draft and installed with pressure-atomizing burners. The oil pressure and the orifice size of the injection nozzle control the firing rate.

Furnace Performance Indices. The performance of a gas-fired furnace is usually assessed by the following indices:

- Thermal efficiency E_t, in percent, is the ratio of the energy output of heated air or water to the fuel energy input during specific test periods using the same units:

$$E_t = 100(\text{fuel energy output})/(\text{fuel energy input}) \tag{9.10.1}$$

- Annual fuel utilization efficiency (AFUE), in percent, is the ratio of the annual output energy from heated air or water to the annual input energy using the same units:

$$\text{AFUE} = (100 \text{ annual output energy})/(\text{annual input energy}) \tag{9.10.2}$$

- Steady-state efficiency (SSE) is the efficiency of a given furnace according to an ANSI test procedure, in percent:

$$\text{SSE} = 100(\text{fuel input} - \text{fuel loss})/(\text{fuel input}) \tag{9.10.3}$$

Jakob et al. (1986) and Locklin et al. (1987), in a report on ASHRAE Special Project SP43, gave the following performance indices based on a nighttime setback period of 8 hr with a setback temperature of 10°F:

Description	AFUE (%)	SSE (%)
Natural vent		
Pilot ignition	64.5	77
Intermittent ignition	69	77
Intermittent ignition plus vent damper	78	77
Power vent		
Noncondensing	81.5	82.5
Condensing	92.5	93

ASHRAE/IES Standard 90.1-2001 specifies AFUEs for both gas-fired and oil-fired furnaces of heating capacity <225,000 Btu/hr.

Operation and Control. Gas is usually brought from the main to the pressure regulator, where its pressure is reduced to 3.5 in. WG. Gas then flows through a valve and mixes with the necessary amount of outside primary air. The mixture mixes again with the ambient secondary air and is burned. The combustion products flow through the heat exchanger(s) due either to natural draft or power vent by a fan. The flue gas is then vented to the outside atmosphere through a vent pipe or chimney.

Recirculating air is pulled from the conditioned space through the return duct where it may be mixed with the ventilation air. The mixture is forced through the heat exchanger(s) by a fan and is then heated and distributed to the conditioned space. The fan is often started 1 min after the burner is fired in order to prevent a cold air supply.

At part-load operation, the reduction of the heating capacity of the warm air furnace is usually controlled by the gas valve and the ignition device. For small furnaces, the gas valve is often operated at on–off control. For large furnaces, a two-stage gas valve operates the furnace at 100, 50, and 0% heating capacity as required.

Low NO_x Emissions. NO_x means nitrogen oxides NO and NO_2. They are combustion products in the flue gas and become air pollutants with other emissions like SO_2, CO and CO_2 when they are discharged to the atmosphere. NO_x cause ozone depletion as well as smog.

Southern California regulations required that NO_x emissions should be 30 ppm or less for gas-fired warm air furnaces and boilers. Many gas burner manufactures use induced flue gas recirculation to cool the burner's flame, a cyclonic-type burner to create a swirling high-velocity flame, and other technologies to reduce NO_x and other emissions while retaining high furnace and boiler efficiencies.

Hot Water Boilers

Types of Hot Water Boilers. A *hot water boiler* is an enclosed pressure vessel used as a heat source for space heating in which water is heated to a required temperature and pressure without evaporation. Hot water boilers are fabricated according to American Society of Mechanical Engineers (ASME) codes for boilers and pressure vessels. Boilers are generally rated on the basis of their gross output delivered at the boiler's outlet. Hot water boilers are available in standard sizes from 50 to 50,000 MBtu/hr (1 MBtu/hr = 1000 Btu/hr).

Hot water boilers can be classified as *low-pressure boilers*, whose working pressure does not exceed 160 psig and working temperature is 250°F or less, and *medium-* and *high-pressure boilers*, whose working pressure is above 160 psig and working temperature above 250°F. Most of the hot water boilers are low-pressure boilers except those in campus-type or district water heating systems.

Based on their construction and material, hot water boilers can be classified as fire tube boilers, water tube boilers, cast iron sectional boilers, and electric boilers. Water tube boilers are used mainly to generate steam. Cast iron sectional boilers consist of many vertical inverted U-shaped cast iron hollow sections. They are lower in efficiency and used mainly for residential and small commercial buildings. Electric boilers are limited in applications because of their higher energy cost in many locations in the United States.

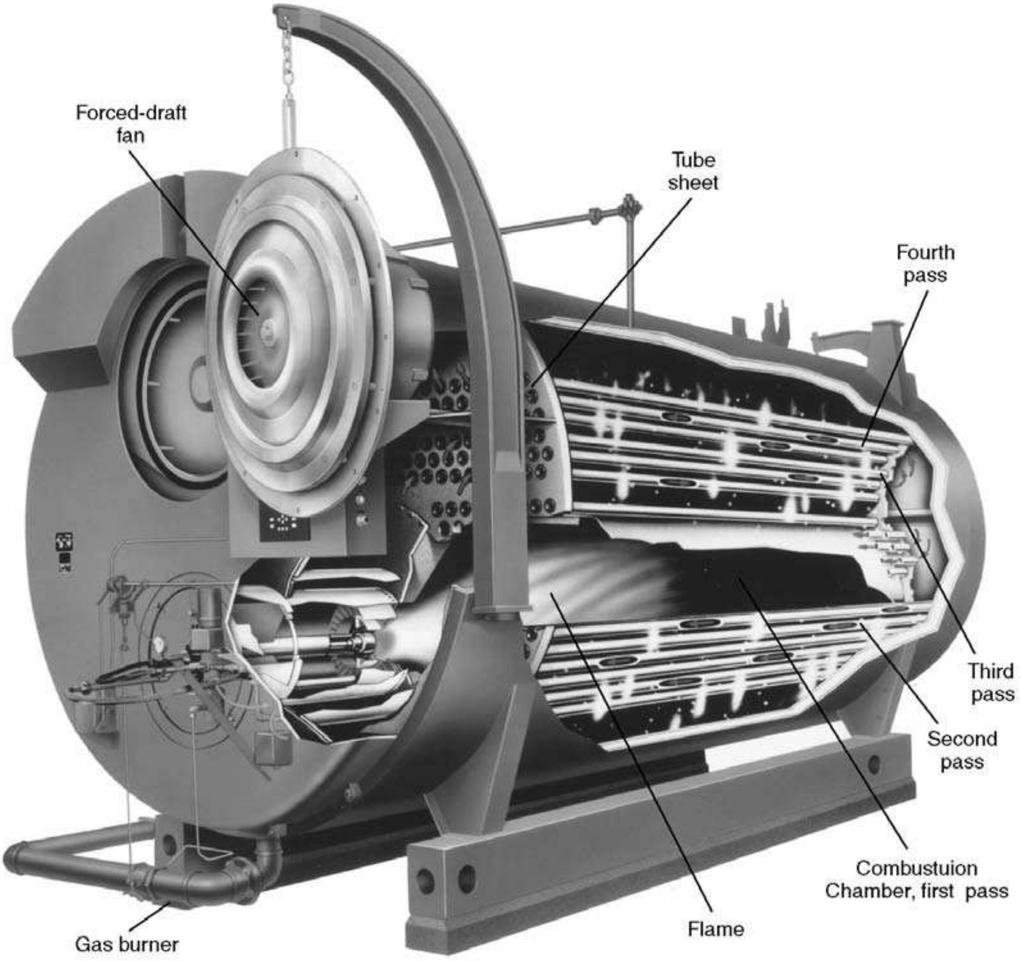

FIGURE 9.10.2 A Scotch Marine packaged boiler. (Source: Cleaver Brooks. Reprinted by permission.)

Scotch Marine Boiler. In a *fire tube* hot water boiler, the combustion chamber and flue gas passages are in tubes. These tubes are enclosed by an outer shell filled with water. A recently developed fire tube model is the modified Scotch Marine packaged boiler, which is a compact, efficient, and popular hot water boiler used today.

A *Scotch Marine* boiler, as shown in Figure 9.10.2, consists of a gas, oil, or gas/oil burner, a mechanical forced-draft fan, a combustion chamber, fire tubes, flue gas vent, outer shell, and corresponding control system. A packaged boiler is a one-piece factory-assembled boiler.

The dew point of the flue gas is often 130°F. If the temperature of the return water in a *condensing boiler* is below 125°F, it can be used as a condensing cooling medium to condense the water vapor contained in the flue gas. Latent heat of condensation of water vapor can then be recovered. Corrosion in the condensing heat exchanger and the flue gas passage should be avoided.

The *chimney*, or *stack*, is the vertical pipe or structure used to discharge flue gas, which usually has a temperature rise of 300 to 400°F above the ambient temperature. The chimney or stack should be extended to a specified height above adjacent buildings according to local codes.

Operation and Safety Controls. During part-load operation, reduction of heating capacity is achieved by sensing the temperature of return water and controlling the firing rate of the gas burners in on–off, high–low–off, or modulating modes.

For gas burners, two pressure sensors are often provided to maintain the gas pressure within a narrow range. For modulating controls, the ratio of maximum to minimum input is called the *turn-down* ratio. The minimum input is usually 5 to 25% of the maximum input, that is, a turn-down ratio of 20:1 to 4:1. The boiler should be shut off if the input is less than the minimum.

Pressure and temperature relief valves should be installed in each boiler. An additional high limit control is often equipped to shut down the boiler in case the sensed water pressure or temperature exceeds the predetermined limits. A flame detector is often used to monitor the flame and an airflow sensor to verify the combustion airflow. As soon as the flame is extinguished or the combustion airflow is not sensed, the fuel valve closes and the boiler is shut down. ASHRAE/IES Standard 90.1-2001 specifies the minimum AFUE for gas-fired boilers.

Low-Pressure Warm Air Heating Systems

A *low-pressure warm air heating system* is often equipped with an upflow gas-fired furnace having a furnace heat capacity Q_f to air flow $\mathring{V}_a$ ratio, $Q_f / \mathring{V}_a$, of 50 to 70 Btu/hr.cfm and a temperature rise immediately after the furnace of 50 to 70°F. The external pressure loss of the supply and return duct system is usually not higher than 0.5 in. WG. The supply temperature differential $(T_s - T_r)$ is often 20 to 35°F. The heating system is often integrated with a cooling system, forming a heating/cooling system.

Low-pressure warm air heating systems usually have a heating capacity not exceeding 100,000 Btu/hr. They are often used in residences and sometimes in small commercial buildings.

System Characteristics. A low-pressure warm air heating system is equipped with either supply and return ducts or a supply duct and a return plenum. Recirculating air is then returned from living, dining, bed, and study rooms to the return plenum through door undercuts in case the doors are closed.

When a low-pressure warm air heating system is operating, the supply duct leakage in the attic or basement raises its pressure to a positive value and promotes exfiltration. Return duct leakage extracts the ambient air, lowers the attic or basement pressure to a negative value, and induces infiltration. Gammage et al. (1986) reported that both types of leakage increase the whole house infiltration to 0.78 ach when the low-pressure warm air heating system is operating. The infiltration rate is only 0.44 ach when the low-pressure warm air heating system is shut off.

If the supply temperature differential $\Delta T_s = (T_s - T_r)$ exceeds 30°F, or if there is a high ceiling, thermal stratification may form in the conditioned space. Greater supply volume flow rates and suitable locations of the supply and return outlets may reduce thermal stratification and vertical temperature difference.

Part-Load Operation and Control. For a low-pressure warm air heating system, a space thermostat is often used to control the gas valve of the furnace operated in on–off or high–low–off mode. The proportion of on and off times in an operating cycle can be varied to meet the change of space heating load. The time period of an on–off operating cycle is usually 5 to 15 min.

A warm-air heating system that has an external pressure higher than 0.5 in. WG is often integrated with a cooling system and becomes a part of an air-conditioning system.

Low-Temperature Hot Water Heating System Using Fin-Tube Heaters

In a *low-temperature hot water heating system*, the operating temperature is 250°F or less with a maximum working pressure not exceeding 150 psig, usually less than 30 psig. Low-temperature hot water heating systems are widely used for space heating in residences and commercial buildings.

Fin-Tube Heaters. A *fin-tube heater* or convector is a device installed directly inside the conditioned space to add heat to the space through radiant and convective heat transfer. A fin-tube heater consists of a finned-tube element and an outer casing as shown in Figure 9.10.3(a). The tubes are often made of copper and steel. Copper tubes are generally 0.75, 1, and 1.25 in. in diameter and steel tubes 1.25 and 2 in. in diameter. The fins are usually made of aluminum for copper tubes and of steel for steel tubes. Fin density may vary from 24 to 60 fins per foot. A fin heater may have a maximum length of 12 ft. The outer casing of a finned-tube heater always has a bottom inlet and top outlet for better convection.

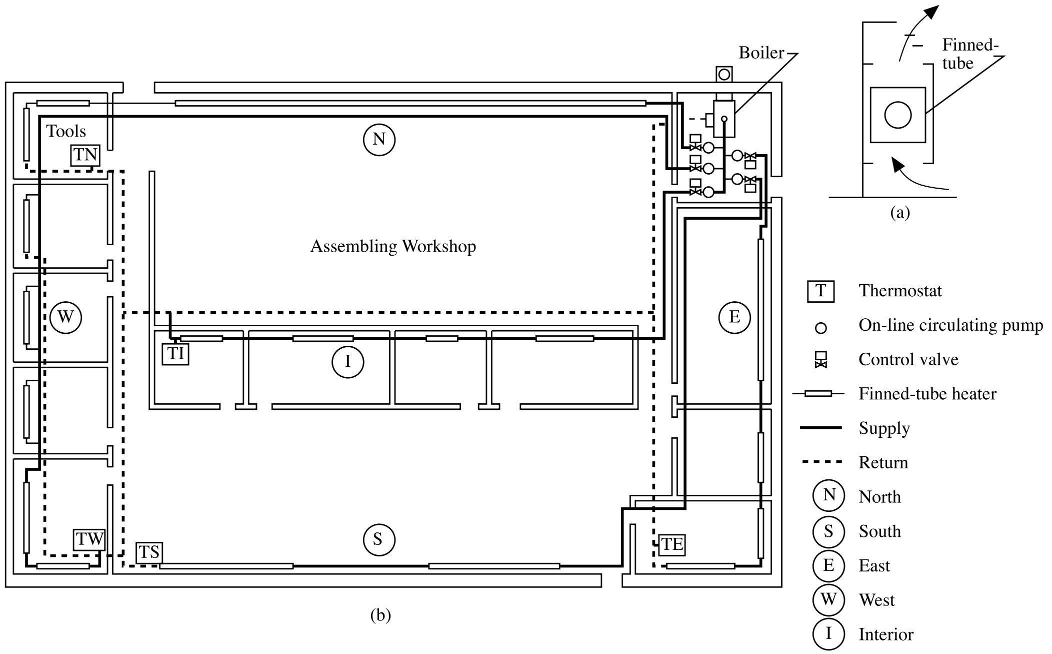

FIGURE 9.10.3 A two-pipe individual-loop low-temperature hot water heating system: (a) finned-tube heater and (b) piping layout.

The most widely used finned-tube heater is the *baseboard heater*, which is often mounted on cold walls at a level 7 to 10 in. from the floor. It is usually 3 in. deep and has one fin-tube row. A wall finned-tube heater has a greater height. A convector has a cabinet-type enclosure and is often installed under the windowsill.

Two-Pipe Individual-Loop Systems. Current low-temperature hot water heating systems using finned-tube heaters are often equipped with zone controls. Zone controls can avoid overheating rooms facing south and underheating rooms facing north because of the effects of solar radiation.

Figure 9.10.3(b) shows the piping layout of a *two-pipe individual-loop system* that is widely used in low-temperature hot water heating systems. Two-pipe means that there are a supply main and a return main pipe instead of one common main for both supply and return. Individual-loop means that there is an individual loop for each control zone. Several finned-tube heaters in a large room can be connected in series, while finned-tube heaters in several small rooms can be connected in reverse return arrangement.

The sizing of low-temperature hot water pipes is usually based on a pressure drop of 1 to 3 ft per 100 ft of pipe length. For a small low-temperature hot water heating system, an open-type expansion tank is often used. A diaphragm tank is often used for a large system. On-line circulating pumps with low head are often used.

Part Load and Control. Usually a hot water sensor located at the exit of the hot water boiler is used to control the firing rate of the boiler at part-load operation. Its set point is usually reset according to the outdoor temperature. Zone control is provided by sensing the return hot water temperature from each individual loop or zone and then varying the water volume flow rate supplied to that zone by modulating the speed of each corresponding on-line circulating pump or its control valve. For hot water heating systems using multiple boilers, on and off for each specific boiler depend not only on the heating demand, but also on minimizing the energy cost.

Infrared Heating

Infrared heating is a process that uses radiant heat transfer from a gas-fired or electrically heated high-temperature device to provide space heating on a localized area for the health and comfort of the occupants or to maintain a suitable indoor environment for a manufacturing process.

An *infrared heater* is a device used to provide infrared heating. Heat radiates from an infrared heater in the form of electromagnetic waves and scatters in all directions. Most infrared heaters have reflectors to focus the radiant beam onto a localized area. Therefore, they are often called *beam radiant heaters.* Infrared heaters are widely used in high-ceiling supermarkets, factories, warehouses, gymnasiums, skating rinks, and outdoor loading docks.

Gas Infrared Heaters. Infrared heaters can be divided into two categories: gas and electric infrared heaters. *Gas infrared heaters* are again divided into porous matrix gas infrared heaters and indirect gas infrared heaters. In a *porous matrix gas infrared heater*, a gas and air mixture is supplied and distributed evenly through a porous ceramic, a stainless steel panel, or a metallic screen, which is exposed to the ambient air and backed by a reflector. Combustion takes place at the exposed surface with a maximum temperature of about 1600°F. An indirect infrared heater consists of a burner, a radiating tube, and a reflector. Combustion takes place inside the radiating tube at a temperature not exceeding 1200°F.

Gas infrared heaters are usually vented and have a small conversion efficiency. Only 10 to 20% of the input energy of an open combustion gas infrared heater is radiated in the form of infrared radiant energy. Usually 4 cfm of combustion air is required for 1000 Btu/hr gas input. A thermostat often controls a gas valve in on–off mode. For standing pilot ignition, a sensor and a controller are used to cut off the gas supply if the flame is extinguished.

Electric Infrared Heaters. An *electric infrared heater* is usually made of nickel–chromium wire or tungsten filaments mounted inside an electrically insulated metal tube or quartz tube with or without inert gas. The heater also contains a reflector that directs the radiant beam to the localized area requiring heating. Nickel–chromium wires often operate at a temperature of 1200 to 1800°F. A thermostat is also used to switch on or cut off the electric current. An electric infrared heater has a far higher conversion efficiency and is cleaner and more easily managed.

Design Considerations. An acceptable radiative temperature increase ($T_{rad} - T_r$) of 20 to 25°F is often adopted for normal clothed occupants using infrared heating. The corresponding required watt density for infrared heaters is 30 to 37 W/ft^2. At a mounting height of 11 ft, two heaters having a spacing of 6.5 ft can provide a watt density of 33 W/ft^2 and cover an area of 12 × 13 ft. The mounting height of the infrared heaters should not be lower than 10 ft. Otherwise the occupants may feel discomfort from the overhead radiant beam. Refer to Grimm and Rosaler (1990), *Handbook of HVAC Design,* for details.

Gas and electric infrared heaters should not be used in places where there is danger of ignitable gas or materials that may decompose into toxic gases.

9.11 Refrigeration Systems

Herbert A. Ingley and Shan K. Wang

Classifications of Refrigeration Systems

Most of the refrigeration systems used for air-conditioning are vapor compression systems. Because of the increase in the energy cost of natural gas in the 1980s, the application of absorption refrigeration systems has dropped sharply. Air expansion refrigeration systems are used mainly in aircraft and cryogenics.

Refrigeration systems used for air-conditioning can be classified mainly in the following categories:

- Direct expansion (DX) systems and heat pumps
- Centrifugal chillers
- Screw chillers
- Absorption systems

Each can be either a single-stage or a multistage system.

Direct Expansion Refrigeration Systems

A *direct expansion refrigeration (DX) system*, or simply *DX system*, is part of the packaged air-conditioning system. The DX coil in the packaged unit is used to cool and dehumidify the air directly as shown in Figure 9.11.1(a).

Refrigerants R-22 and R-134a are widely used. Azeotropes and near azeotropes are the refrigerants often used for low-evaporating-temperature systems like those in supermarkets. Because of the limitation of the size of the air system, the refrigeration capacity of DX systems is usually 3 to 100 tons.

Components and Accessories. In addition to the DX coil, a DX refrigeration system has the following components and accessories:

- *Compressor(s)* — Both reciprocating and scroll compressors are widely used in DX systems. Scroll compressors are gradually replacing reciprocating compressors because they have fewer parts and comparatively higher efficiency. For large DX systems, multiple compressors are adopted.
- *Condensers* — Most DX systems in rooftop packaged units are air cooled. Water-cooled condensers are adopted mainly for DX systems in indoor packaged units due to their compact volume. Evaporative-cooled condensers are also available.
- *Refrigeration feed* — Thermostatic expansion valves are widely used as the throttling and refrigerant flow control devices in medium and large DX systems, whereas capillary tubes are used in small and medium-sized systems.
- *Oil lubrication* — R-22 is partly miscible with mineral oil. Since R-134a is not miscible with mineral oil, synthetic polyolester oil should be used. For medium and large reciprocating compressors, an oil pump of vane, gear, or centrifugal type is used to force the lubricating oil to the bearings and moving surfaces via grooves. For small reciprocating compressors, splash lubrication using the rotation of the crankshaft and the connecting rod to splash oil onto the bearing surface and the cylinder walls is used.

A scroll compressor is often equipped with a centrifugal oil pump to force the oil to lubricate the orbiting scroll journal bearing and motor bearing. For the scroll contact surfaces, lubrication is provided by the small amount of oil entrained in the suction vapor.

- *Refrigerant piping* — Refrigerant piping transports refrigerant through the compressor, condenser, expansion valve, and DX coil to provide the required refrigeration effect. As shown in Figure 9.11.1(a), from the exit of the DX coil to the inlet of the compressor(s) is the *suction line*. From the outlet of the compressor to the inlet of the air-cooled condenser is the *discharge line*. From the exit of the condenser to the inlet of the expansion valve is the *liquid line*.

Halocarbon refrigerant pipes are mainly made of copper tubes of L type. In a packaged unit, refrigerant pipes are usually sized and connected in the factory. However, the refrigerant pipes in field-built and split DX systems for R-22 are sized on the basis of a pressure drop of 2.91 psi corresponding to a change of saturated temperature ΔT_{suc} of 2°F at 40°F for the suction line and a pressure drop of 3.05 psi corresponding to 1°F at 105°F for the discharge and liquid line. The pressure drop includes pressure losses of pipe and fittings. Refrigerant pipes should also be sized to bring back the entrained oil from the DX coil and condenser through the discharge and suction lines.

Accessories include a filter dryer to remove moisture from the refrigerant, strainer to remove foreign matter, and sight glass to observe the condition of refrigerant flow (whether bubbles are seen because of the presence of flash gas in the liquid line).

Capacity Controls. In DX systems, control of the mass flow rate of refrigerant through the compressor(s) is often used as the primary refrigeration capacity control. Row or intertwined face control at the DX coil is also used in conjunction with the capacity control of the compressor(s).

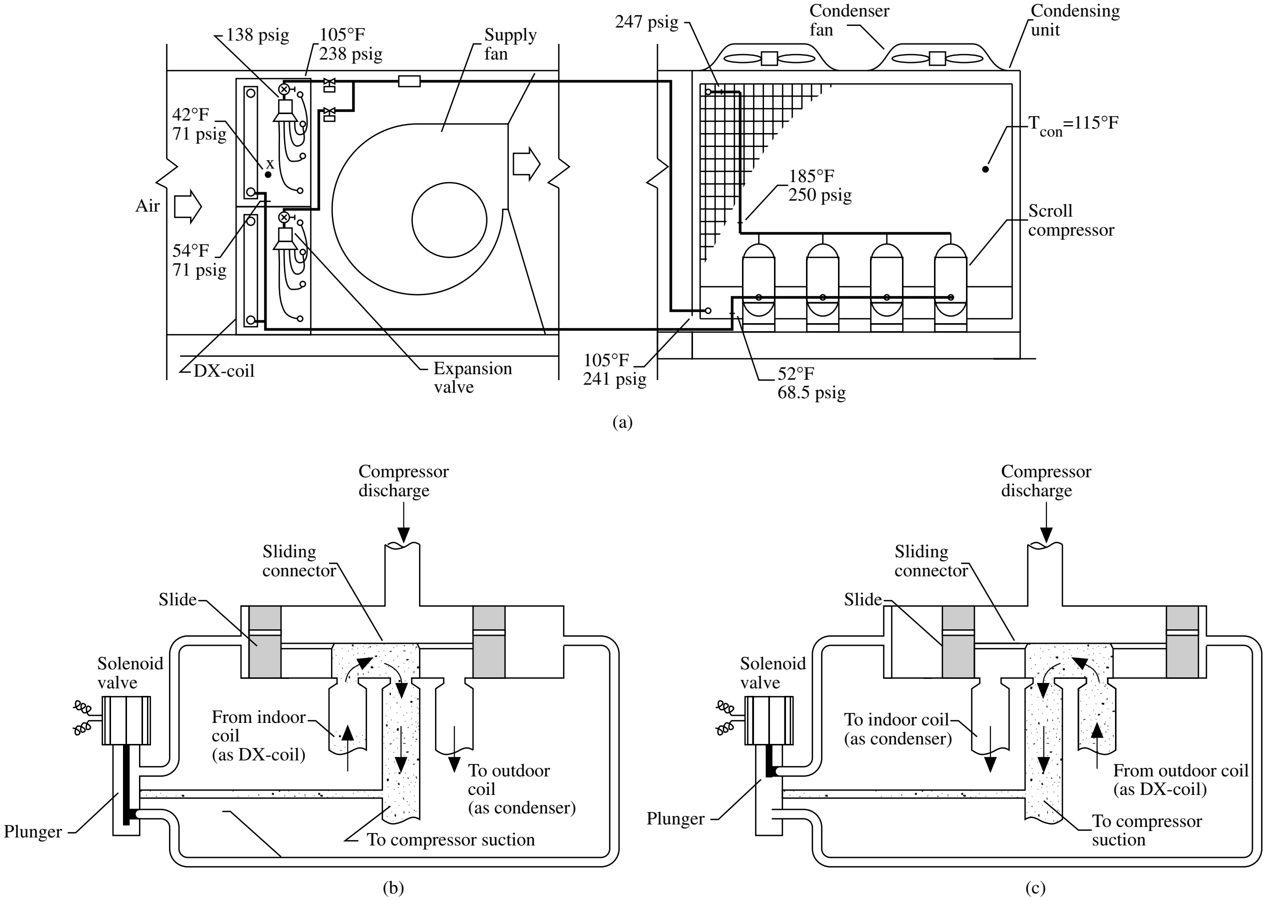

FIGURE 9.11.1 A DX refrigeration system: (a) schematic diagram: (b) four-way reversing valve, cooling mode; and (c) four-way reversing valve, heating mode.

Three methods of capacity controls are widely used for reciprocating and scroll compressors in DX systems:

- *On–off control* — Starting or stopping the compressor is a type of step control of the refrigerant flow to the compressor. It is simple and inexpensive, but there is a 100% variation in capacity for DX systems installed with only a single compressor. On–off control is widely used for small systems or DX systems with multiple compressors.
- *Cylinder unloader* — For a reciprocating compressor having multiple cylinders, a cylinder unloader mechanism bypasses the compressed gas from one, two, or three cylinders to the suction chamber to reduce the refrigeration capacity and compressing energy.
- *Speed modulation* — A two-speed motor is often used to drive scroll or reciprocating compressors so that the capacity can be reduced 50% at lower speed.

Safety Controls. In *low- and high-pressure control*, the compressor is stopped when suction pressure drops below a preset value, the cut-in pressure, or the discharge pressure of the hot gas approaches a dangerous level, the cut-out pressure.

In *low-temperature control*, a sensor is mounted on the outer pipe surface of the DX coil. When the surface temperature drops below 32°F, the controller stops the compressor to prevent frosting.

If the pressure of the oil discharged from the pump does not reach a predetermined level within a certain period, a mechanism in *oil pressure failure control* opens the circuit contact and stops the compressor.

In *motor overload control*, a sensor is used to measure the temperature of the electric winding or the electric current to protect the motor from overheating and overloading.

Pump-down control is an effective means of preventing the migration of the refrigerant from the DX coil (evaporator) to the crankcase of the reciprocating compressor. This prevents mixing of refrigerant and oil to form slugs, which may damage the compressor.

When a rise of suction pressure is sensed by a sensor, a DDC controller opens a solenoid valve and the liquid refrigerant enters the DX coil. As the buildup of vapor pressure exceeds the cut-in pressure, the compressor starts. When the DX system needs to shut down, the solenoid valve is closed first; the compressor still pumps the gaseous refrigerant to the condenser. As the suction pressure drops below the cut-in pressure, the compressor stops.

Full- and Part-Load Operations. Consider a DX system in a rooftop packaged unit using four scroll compressors, each with a refrigeration capacity of 10 tons at full load. Performance curves of the condensing unit and the DX coil of this DX system are shown in Figure 9.11.2(a). A DDC controller actuates on–off for these scroll compressors based on the signal from a discharge air temperature T_{dis} sensor.

On a hot summer day, when the rooftop packaged unit starts with a DX coil load or refrigeration capacity, $q_{rc} \approx 40$ tons, all four scroll compressors are operating. The operating point is at A′ with a suction temperature T_{suc} of about 42°F, and the discharge air temperature T_{dis} is maintained around 53°F. As the space cooling load q_{rc} as well as T_{dis} decreases, the required DX coil load q_{rl} drops to 35 tons. Less evaporation in the DX coil causes a decrease of T_{suc} to about 40°F, and the operating point may move downward to point A with a DX coil refrigeration capacity of 39 tons. Since $q_{rc} > q_{rl}$, T_{dis} drops continually until it reaches 50°F, point A in Figure 9.11.2(b), and the DDC controller shuts down one of the scroll compressors. The operating point immediately shifts to B′ on the three-compressor curve.

Because the refrigeration capacity at point B′ q_{rc} is 29 tons, which is less than the required $q_{rl} = 35$ tons, both T_{dis} and T_{suc} rise. When the operating point moves up to B* and T_{dis} reaches 56°F, the DDC controller starts all four scroll compressors at operating point A″ with a refrigeration capacity of 42 tons. Since $q_{rc} > q_{rl}$, the operating point again moves downward along the four-compressor curve and forms an operating cycle A″AB′ and B*. The timing of the operating period on four- or three-compressor performance curves balances any required q_{rl} between 29 and 42 tons. Less evaporation at part load in the DX coil results in a greater superheating region and therefore less refrigeration capacity to balance the reduction of refrigeration capacity of the compressor(s) as well as the condensing unit. The condition

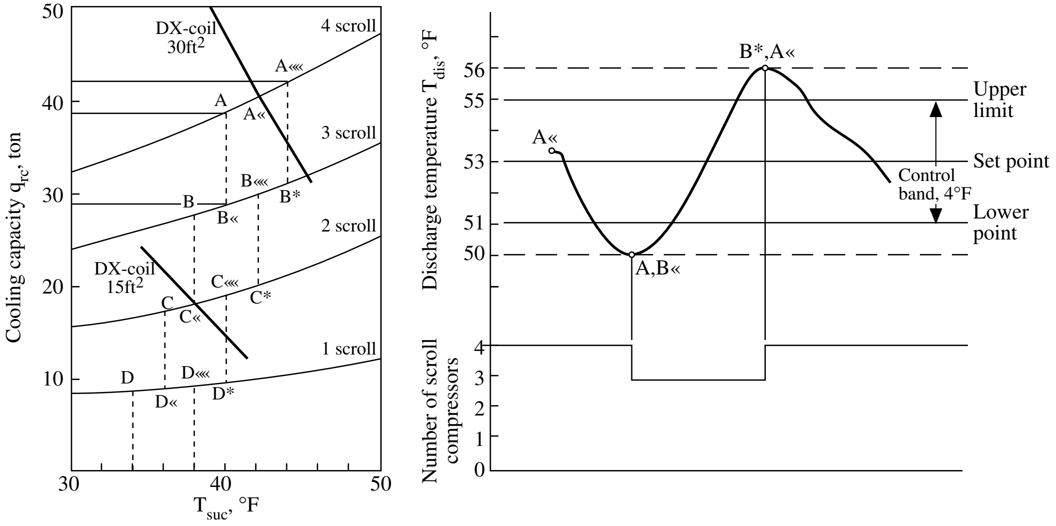

(a)

(b)

FIGURE 9.11.2 Capacity control of a DX refrigeration system: (a) performance curves and operating points and (b) locus of control point.

will be similar when q_{rl} < 30 tons, only three- or two-compressor, or two- or one-compressor, or even on–off of one compressor forms an operating cycle.

Main Problems in DX Systems

- *Liquid slugging* is formed by a mixture of liquid refrigerant and oil. It is formed because of the flooding back of liquid refrigerant from the DX coil to the crankcase of the reciprocating compressor due to insufficient superheating. It also may be caused by migration of liquid refrigerant from the warmer indoor DX coil to the colder outdoor compressor during the shut-down period in a split packaged unit. Liquid slugging dilutes the lubricating oil and causes serious loss of oil in the crankcase of the reciprocating compressor. Liquid slugging is incompressible. When it enters the compression chamber of a reciprocating compressor, it may damage the valve, piston, and other components. Pump-down control and installation of a crankcase heater are effective means of preventing liquid refrigerant migration and flooding back.
- *Compressor short cycling* — For on–off control, too short a cycle, such as less than 3 min, may pump oil away from the compressor or damage system components. It is due mainly to a too close low-pressure control differential or to reduced air flow.
- *Defrosting* — If the surface of a DX coil is 32°F or lower, frost accumulates on it. Frost blocks the air passage and reduces the rate of heat transfer. It should be removed periodically. The process of removing frost is called defrosting.
- Air at a temperature above 36°F, hot gas inside the refrigerant tubes and an installed electric heating element can be used for defrosting. The defrosting cycle is often controlled by sensing the temperature or pressure difference of air entering the DX coil during a fixed time interval.
- *Refrigerant charge* — Insufficient refrigerant charge causes lower refrigeration capacity, lower suction temperature, and short on–off cycles. Overcharging refrigerant may cause a higher condensing pressure because part of the condensing surface becomes flooded with liquid refrigerant.

Heat Pumps

A *heat pump* in the form of a packaged unit is also a *heat pump system*. A heat pump can either extract heat from a heat source and reject heat to air and water at a higher temperature for heating, or provide refrigeration at a lower temperature and reject condensing heat at a higher temperature for cooling. During summer, the heat extraction, or refrigeration effect, is the useful effect for cooling in a heat pump. In winter, the rejected heat and the heat from a supplementary heater provide heating in a heat pump.

There are three types of heat pumps: air-source, water-source, and ground-coupled heat pumps. Ground-coupled heat pumps have limited applications. Water-source heat pump systems are covered in detail in a later section.

Air-Source Heat Pump. An *air-source heat pump*, or *air-to-air heat pump*, is a DX system with an additional four-way reversing valve to change the refrigerant flow from cooling mode in summer to heating mode in winter and vice versa. The variation in connections between four means of refrigerant flow — compressor suction, compressor discharge, DX coil exit, and condenser inlet — causes the function of the indoor and outdoor coils to reverse. In an air-source heat pump, the coil used to cool or to heat the recirculating/outdoor air is called the *indoor coil*. The coil used to reject heat to or absorb heat from the outside atmosphere is called the *outdoor coil*. A short capillary or restrict tube is often used instead of a thermostatic expansion valve. Both reciprocating and scroll compressors are used in air-source heat pumps. R-22 is the refrigerant widely used. Currently available air-source heat pumps usually have a cooling capacity of $1^1/_2$ to 40 tons.

Cooling and Heating Mode Operation. In *cooling mode operation*, as shown in Figure 9.11.1(b), the solenoid valve is deenergized and drops downward. The high-pressure hot gas pushes the sliding connector to the left end. The compressor discharge connects to the outdoor coil, and the indoor coil connects to the compressor inlet.

In *heating mode operation*, as shown in Figure 9.11.1(c), the solenoid plunger moves upward and pushes the slide connector to the right-hand side. The compressor discharge connects to the indoor coil, and the outdoor coil exit connects to the compressor suction.

System Performance. The performance of an air-source heat pump depends on the outdoor air temperature T_o, in °F as well as the required space heating load q_{rh}. During cooling mode operation, both the refrigeration capacity q_{rc}, in Btu/hr, and EER for the heat pump EER_{hp}, in Btu/hr.W, increase as T_o drops. During heating mode operation, the heating capacity q_{hp}, in Btu/hr, and COP_{hp} decrease, and q_{rh} increases as the T_o drops. When $q_{rh} > q_{hp}$, supplementary heating is required. If COP_{hp} drops below 1, electric heating may be more economical than a heat pump.

If on–off is used for compressor capacity control for an air-source heat pump in a split packaged unit, refrigerant tends to migrate from the warmer outdoor coil to the cooler indoor coil in summer and from the warmer indoor coil to the cooler outdoor coil in winter during the off period. When the compressor starts again, 2 to 5 min of reduced capacity is experienced before the heat pump can be operated at full capacity. Such a loss is called a *cycling loss*.

In winter, most air-source heat pumps switch from the heating mode to cooling mode operation and force the hot gas to the outdoor coil to melt frost. After the frost is melted, the heat pump is switched back to heating mode operation. During defrosting, supplementary electric heating is often necessary to prevent a cold air supply from the air-source heat pump.

Minimum Performance. ANSI/ASHRAE/IESNA Standard 90.1-2001 specifies a minimum performance for air-cooled DX systems in packaged units as covered in Section 9.7.

Centrifugal Chillers

A chiller is a refrigeration machine using a liquid cooler as an evaporator to produce chilled water as the cooling medium in a central air-conditioning system. A *centrifugal chiller*, as shown in Figure 9.11.3(a), is a refrigeration machine using a centrifugal compressor to produce chilled water. It is often a factory-assembled unit with an integrated DDC control system and sometimes may separate into pieces for transportation. A centrifugal chiller is also a *centrifugal vapor compression refrigeration system*.

Refrigerants. As mentioned in Section 9.4, production of CFCs, including R-11 and R-12, ceased at the end of 1995 with limited exception for service. R-123 (HCFC) will replace R-11. The chiller's efficiency

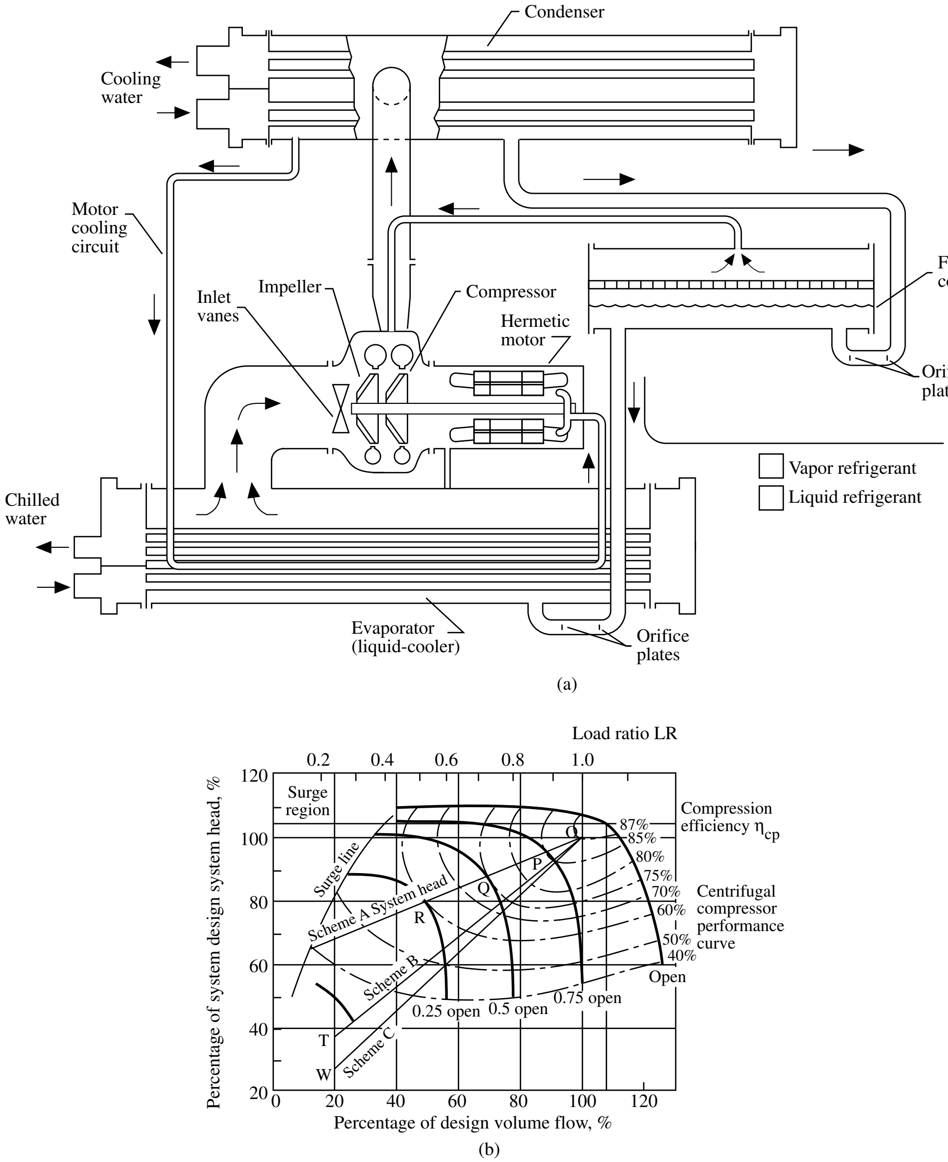

(a)

(b)

FIGURE 9.11.3 A two-stage water-cooled centrifugal chiller: (a) schematic diagram and (b) centrifugal compressor performance map at constant speed.

may drop 2 to 4%, and a capacity reduction of 5% is possible. R-123 has low toxicity. Its allowable exposure limit was raised to 50 ppm in 1997 from 30 ppm in 1993 by its manufacturers. A monitor and alarm device to detect R-123 in air should be installed in plant rooms and places where there may be refrigerant leaks. See ANSI/ASHRAE Standard 15-2001 for other requirements.

R-134a (HFC) will replace R-12. According to Lowe and Ares (1995), as a result of the changeout from R-12 to R-134a for a 5000-hp centrifugal chiller in Sears Tower, Chicago, its speed increased from 4878 to 5300 rpm, its cooling capacity is 12 to 24% less, and its efficiency is 12 to 16% worse.

System Components. A centrifugal chiller consists of a centrifugal compressor, an evaporator or liquid cooler, a condenser, a flash cooler, throttling devices, piping connections, and controls. A purge unit is optional.

- Centrifugal compressor — According to the number of internally connected impellers, the centrifugal compressor could have a single, two, or more than two stages. A two-stage impeller with a flash cooler is most widely used because of its higher system performance and comparatively simple construction. Centrifugal compressors having a refrigeration capacity less than 1200 tons are often hermetic. Very large centrifugal compressors are of open type. A gear train is often required to raise the speed of the impeller except for very large impellers using direct drive.
- Evaporator — Usually a liquid cooler of flooded shell-and-tube type evaporator is adopted because of its compact size and high rate of heat transfer.
- Condenser — Water-cooled, horizontal shell-and-tube condensers are widely used.
- Flash cooler — For a two-stage centrifugal compressor, a single-stage flash cooler is used. For a three-stage compressor, a two-stage flash cooler is used.
- Orifice plates and float valves — Both multiple-orifice plates such as that shown in Figure 9.11.3(a) and float valves are used as throttling devices in centrifugal chillers.
- Purge unit — R-123 has an evaporating pressure p_{ev} = 5.8 psia at 40°F, which is lower than atmospheric pressure. Air and other noncondensable gases may leak into the evaporator through cracks and gaps and usually accumulate in the upper part of the condenser. These noncondensable gases raise the condensing pressure, reduce the refrigerant flow, and lower the rate of heat transfer. A purge unit uses a cooling coil to separate the refrigerant and water from the noncondensable gases and purge the gases by using a vacuum pump.

Performance Ratings. The refrigeration cycle of a typical water-cooled, two-stage centrifugal chiller with a flash cooler was covered in Section 9.4. Centrifugal chillers have the same refrigeration capacity as centrifugal compressors, 100 to 10,000 tons.

The integrated part-load value (IPLV) of a centrifugal chiller or other chillers at standard rating conditions can be calculated as:

$$\text{IPLV} = 0.1(A + B)/2 + 0.5(B + C)/2 + 0.3(C + D)/2 + 0.1D \tag{9.11.1}$$

where A, B, C, and D = kW/ton or COP at 100, 75, 50, and 25% load, respectively. If the operating conditions are different from the standard rating conditions, when T_{el} is 40 to 50°F, for each °F increase or decrease of T_{el}, there is roughly a 1.5% difference in refrigeration capacity and energy use; when T_{ce} is between 80 to 90°F, for each °F of increase or decrease of T_{ce}, there is roughly a 1% increase or decrease in refrigeration capacity and 0.6% in energy use.

ANSI/ASHRAE/IESNA Standard 90.1-2001 and ARI Standard 550 specify the minimum performance for water-cooled water chillers.

Air-cooled centrifugal chillers have COPs from 2.5 to 2.8. Their energy performance is far poorer than that of water-cooled chillers. Their application is limited to locations where city water is not allowed to be used as makeup water for cooling towers.

Capacity Control. The refrigeration capacity of a centrifugal chiller is controlled by modulating the refrigerant flow at the centrifugal compressor. There are mainly two types of capacity controls: varying the opening and angle of the inlet vanes, and using an adjustable-frequency AC inverter to vary the rotating speed of the centrifugal compressor.

When the opening of the inlet vanes has been reduced, the refrigerant flow is throttled and imparted with a rotation. The result is a new performance curve at lower head and flow. If the rotating speed of a centrifugal compressor is reduced, it also has a new performance curve at lower volume flow and head. Inlet vanes are inexpensive, whereas the AC inverter speed modulation is more energy efficient at part-load operation.

Centrifugal Compressor Performance Map. Figure 9.11.3(b) shows a single-stage, water-cooled *centrifugal compressor performance map* for constant speed using inlet vanes for capacity modulation. A performance map consists of the compressor's performance curves at various operating conditions. The *performance* *curve* of a centrifugal compressor shows the relationship of volume flow of refrigerant $\overset{\circ}{V}_r$ and its head lift Δp or compression efficiency η_{cp} at that volume flow. It is assumed that η_{cp} for a two-stage compressor is equal to the average of the two single-stage impellers having a head of their sum.

On the map, the required *system head curve* indicates the required system head lift at that volume flow of refrigerant. The intersection of the performance curve and the required system head curve is called the *operating point* O, P, Q, R, … as shown in Figure 9.11.3(b). One of the important operating characteristics of a centrifugal chiller (a centrifugal vapor compression refrigeration system as well) is that the required system head lift is mainly determined according to the difference in condensing and evaporating pressure $\Delta p_{c\text{-}e} = (p_{con} - p_{ev})$. The pressure losses due to the refrigerant piping, fittings, and components are minor.

In Figure 9.11.3(b), the abscissa is the percentage of design volume flow of refrigerant, % $\overset{\circ}{V}_r$, or load ratio; the ordinate is the percentage of design system head $\Delta H_{s.d}$, or percentage of design temperature lift $(T_{con} - T_{ev})$. Here load ratio LR is defined as the ratio of the refrigeration load to the design refrigeration load $q_{rl}/q_{rl.d}$. There are three schemes of required system head curves:

- Scheme A — T_{ce} = constant and T_{el} = constant
- Scheme B — T_{el} = constant and a drop of 2.5°F of T_{ce} for each 0.1 reduction of load ratio
- Scheme C — A reset of T_{el} of 1°F increase and a drop of 2.5°F of T_{ce} for each 0.1 reduction of load ratio

At design $\overset{\circ}{V}_r$ and system head $H_{s.d}$, $\eta_{cp} = 0.87$. As $\overset{\circ}{V}_r$, load ratio, and required system head Δp decrease, η_{cp} drops accordingly.

Surge is a unstable operation of a centrifugal compressor or fan resulting in vibration and noise. In a centrifugal chiller, surge occurs when the centrifugal compressor is unable to develop a discharge pressure that satisfies the requirement at the condenser. A centrifugal compressor should never be operated in the surge region.

Part-Load Operation. During part-load operation, if T_{el} and T_{ce} remain constant, the evaporating temperature T_{ev} tends to increase from the design load value because there is a greater evaporating surface and a smaller temperature difference $(T_{el} - T_{ev})$. Similarly, T_{con} tends to decrease.

The ratio of actual compressor power input at part load to the power input at design load may be slightly higher or lower than the load ratios, depending on whether the outdoor wet bulb is constant or varying at part load or whether there is a T_{el} reset; it also depends on the degree of drop of η_{cp} at part load.

Specific Controls. In addition to generic controls, specific controls for a centrifugal chiller include:

- Chilled water leaving temperature T_{el} and reset
- Condenser water temperature T_{ce} control
- On and off of multiple chillers based on actual measured coil load
- Air purge control
- Safety controls like oil pressure, low-temperature freezing protection, high condensing pressure control, motor overheating, and time delaying

Centrifugal Chillers Incorporating Heat Recovery. A *HVAC&R heat recovery system* converts waste heat or waste cooling from any HVAC&R process into useful heat and cooling. A heat recovery system is often subordinate to a parent system, such as a heat recovery system to a centrifugal chiller.

A centrifugal chiller incorporating a heat recovery system often uses a double-bundle condenser in which water tubes are classified as tower bundles and heating bundles. Heat rejected in the condenser may be either discharged to the atmosphere through the tower bundle and cooling tower or used for heating through the heating bundle. A temperature sensor is installed to sense the temperature of return hot water from the heating coils in the perimeter zone. A DDC controller is used to modulate a bypass three-way valve which determines the amount of condenser water supplied to the heating bundle. The tower and heating bundles may be enclosed in the same shell, but baffle sheets are required to guide the water flows.

A centrifugal chiller incorporating a heat recovery system provides cooling for the interior zone and heating for the perimeter zone simultaneously in winter with a higher COP_{hr}. However, it needs a higher condenser water-leaving temperature T_{cl} of 105 to 110°F, compared with 95°F or even lower in a cooling-only centrifugal chiller. An increase of 10 to 12°F of the difference ($T_{con} - T_{ev}$) requires an additional 10 to 15% power input to the compressor. For a refrigeration plant equipped with multiple chillers, it is more energy efficient and lower in first cost to have only part of them equipped with double-bundle condensers.

Screw Chillers

A *screw chiller* or a *helical rotary chiller* is a refrigeration machine using a screw compressor to produce chilled water. A factory-fabricated and assembled screw chiller itself is also a screw vapor compression refrigeration system.

Twin-screw chillers are more widely used than single-screw chillers. A twin-screw chiller consists of mainly a twin-screw compressor, a flooded shell-and-tube liquid cooler as evaporator, a water-cooled condenser, throttling devices, an oil separator, an oil cooler, piping, and controls as shown in Figure 9.11.4(a). The construction of twin-screw compressors has already been covered. For evaporator, condenser, and throttling devices, they are similar to those in centrifugal chillers. Most twin-screw chillers have a refrigeration capacity of 100 to 1000 tons.

Following are the systems characteristics of screw chillers.

Variable Volume Ratio. The ratio of vapor refrigerant trapped within the interlobe space during the intake process V_{in} to the volume of trapped hot gas discharged V_{dis} is called the *built-in volume ratio* of the twin-screw compressor $V_i = V_{in}/V_{dis}$, or simply *volume ratio*, all in ft^3.

There are two types of twin-screw chiller: fixed and variable volume ratio. For a twin-screw chiller of *fixed volume ratio*, the isentropic efficiency η_{isen} becomes maximum when the system required compression ratio $R_{s.com} \approx V_i$. Here $R_{s.com} = p_{con}/p_{ev}$. If $p_{dis} > p_{con}$, overcompression occurs, as shown in Figure 9.11.4(b). The discharged hot gas reexpands to match the condensing pressure. If $p_{dis} < p_{con}$, undercompression occurs (Figure 9.11.4[c]). A volume of gas at condensing pressure reenters the trapped volume at the beginning of the discharge process. Both over- and undercompression cause a reduction of η_{isen}.

For a twin-screw chiller of *variable volume ratio*, there are two slides: a sliding valve is used for capacity control and a second slide. By moving the second slide back and forth, the radial discharge port can be relocated. This allows variation of suction and discharge pressure levels and still maintains maximum efficiency.

Economizer. The hermetic motor shell is connected to an intermediate point of the compression process and maintains an intermediate pressure p_i between p_{con} and p_{ev}. Liquid refrigerant at condensing pressure p_{con} is throttled to p_i, and a portion of the liquid is flashed into vapor. This causes a drop in the temperature of the remaining liquid refrigerant down to the saturated temperature corresponding to p_i. Although the compression in a twin-screw compressor is in continuous progression, the mixing of flashed gas with the compressed gas at the intermediate point actually divides the compression process into two stages. The resulting economizing effect is similar to that of a two-stage compound refrigeration system with a flash cooler: an increase of the refrigeration effect and a saving of the compression power from ($p_{con} - p_{ev}$) to ($p_{con} - p_i$).

Oil Separation, Oil Cooling, and Oil Injection. Oil entrained in the discharged hot gas enters an oil separator. In the separator, oil impinges on an internal perforated surface and is collected because of its inertia. Oil drops to an oil sump through perforation. It is then cooled by condenser water in a heat exchanger. A heater is often used to vaporize the liquid refrigerant in the oil sump to prevent dilution of the oil. Since the oil sump is on the high-pressure side of the refrigeration system, oil is forced to the rotor bearings and injected to the rotors for lubrication.

Oil slugging is not a problem for twin-screw compressors. When suction vapor contains a small amount of liquid refrigerant that carries over from the oil separator, often called *wet suction*, it often has the benefit of scavenging the oil from the evaporator.

Twin-screw compressors are positive displacement compressors. They are critical in oil lubrication, sealing, and cooling. They are also more energy efficient than reciprocating compressors. Twin-screw chillers are gaining more applications, especially for ice-storage systems with cold air distribution.

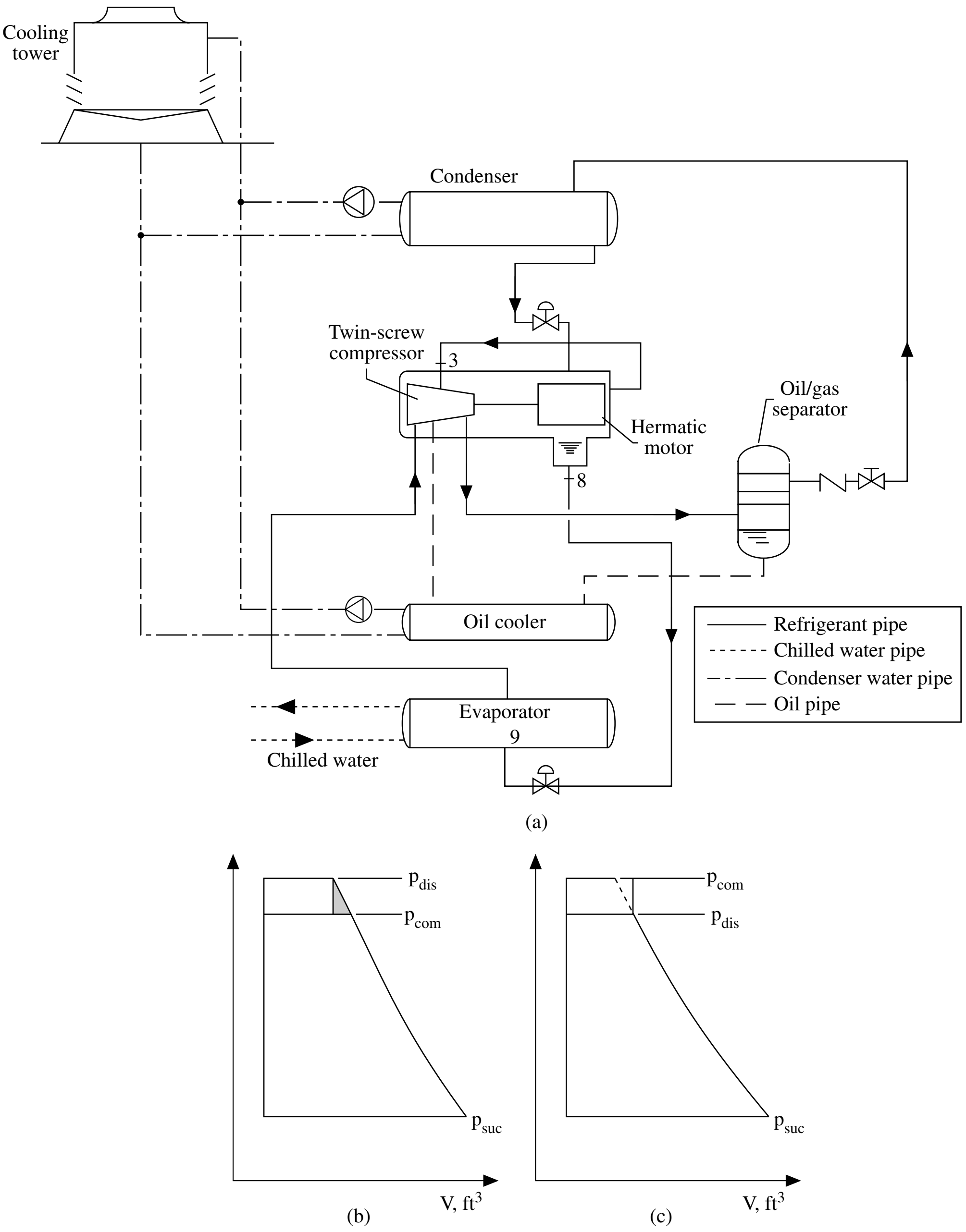

FIGURE 9.11.4 A typical twin-screw chiller: (a) schematic diagram, (b) over-compression, and (c) under-compression.

9.12 Thermal Storage Systems

Shan K. Wang

Thermal Storage Systems and Off-Peak Air-Conditioning Systems

Many electric utilities in the United States have their *on-peak hours* between noon and 8 p.m. during summer weekdays, which include the peak-load hours of air-conditioning. Because the capital cost of a new power plant is so high, electric utilities tend to increase their power output by using customers' thermal energy storage (TES) systems, or simply thermal storage systems, which are much less expensive.

A *thermal storage system* as shown in Figure 9.12.1(a) may have the same refrigeration equipment, like chillers, additional storage tank(s), additional piping, pumps, and controls. The electric-driven compressors are operated during off-peak, partial-peak, and on-peak hours. *Off-peak hours* are often nighttime hours. *Partial-peak hours* are hours between on-peak and off-peak hours in a weekday's 24-hr day-and-night cycle. Chilled water or ice is stored in tanks to provide cooling for buildings during on-peak hours when higher electric demand and electric rates are effective. Although thermal storage systems operate during nighttime when outdoor dry and wet bulbs are lower, they are not necessarily energy saving due to lower evaporating temperature, additional pump power, and energy losses. Thermal storage systems significantly reduce the electric energy cost.

Utilities in the United States often use higher electric demand and rates as well as incentive bonus to encourage the shift of electric load from on-peak to off-peak hours by using thermal storage systems and others. Such a shift not only saves expensive capital cost, but also increases the use of base-load high-efficiency coal and nuclear plants instead of inefficient diesel and gas turbine plants.

The air-conditioning systems that operate during off-peak and partial-peak hours for thermal storage, or those that use mainly natural gas to provide cooling to avoid higher electric demand and rates during on-peak hours, are called *off-peak air-conditioning systems*. These systems include ice-storage and chilled-water storage systems, desiccant cooling systems, absorption systems, and gas engine chillers.

Absorption chillers and desiccant cooling systems are covered in other sections. Gas engine-driven reciprocating chillers are often a cogeneration plant with heat recovery from engine jacket and exhaust gas, and will not be covered here.

Full Storage and Partial Storage

Ice and chilled-water storage systems are the two most common thermal energy storage systems today. Knebel (1995) estimated that more than 4000 cool storage systems are operated in various commercial buildings.

The unit of stored thermal energy for cooling is ton-hour, or ton.hr. One *ton.hr* is the refrigeration capacity of one refrigeration ton during a 1-hr period, or 12,000 Btu.

In order to achieve minimum life-cycle cost, thermal storage systems could be either full storage or partial storage. For a *full-storage*, or *load shift,* thermal storage system, all refrigeration compressors cease to operate during on-peak hours. Building refrigeration loads are entirely offset by the chilled water or brine from the thermal storage system within an on-peak period. In a *partial storage*, or *load-leveling*, thermal storage system as shown in Figure 9.12.1(b) all or some refrigeration compressor(s) are operated during on-peak hours.

Direct cooling is the process in which refrigeration compressors produce refrigeration to cool the building directly. During a specific time interval, if the cost of direct cooling is lower than the stored energy, the operation of a thermal storage system is said to be in *chiller priority.* On the contrary, if the cost of direct cooling is higher than the cost of stored energy, the operation is said to be at *storage priority.*

The optimum size of a thermal storage system is mainly determined according to the utility's electric rate structure, especially a time-of-day structure whose electric rates are different between on-peak, partial-peak, and off-peak hours. Not only the design day's instantaneous building peak cooling load is important, but also an hour-by-hour cooling load profile of the design day is required for thermal storage design. A simple payback or a life-cycle cost analysis is usually necessary.

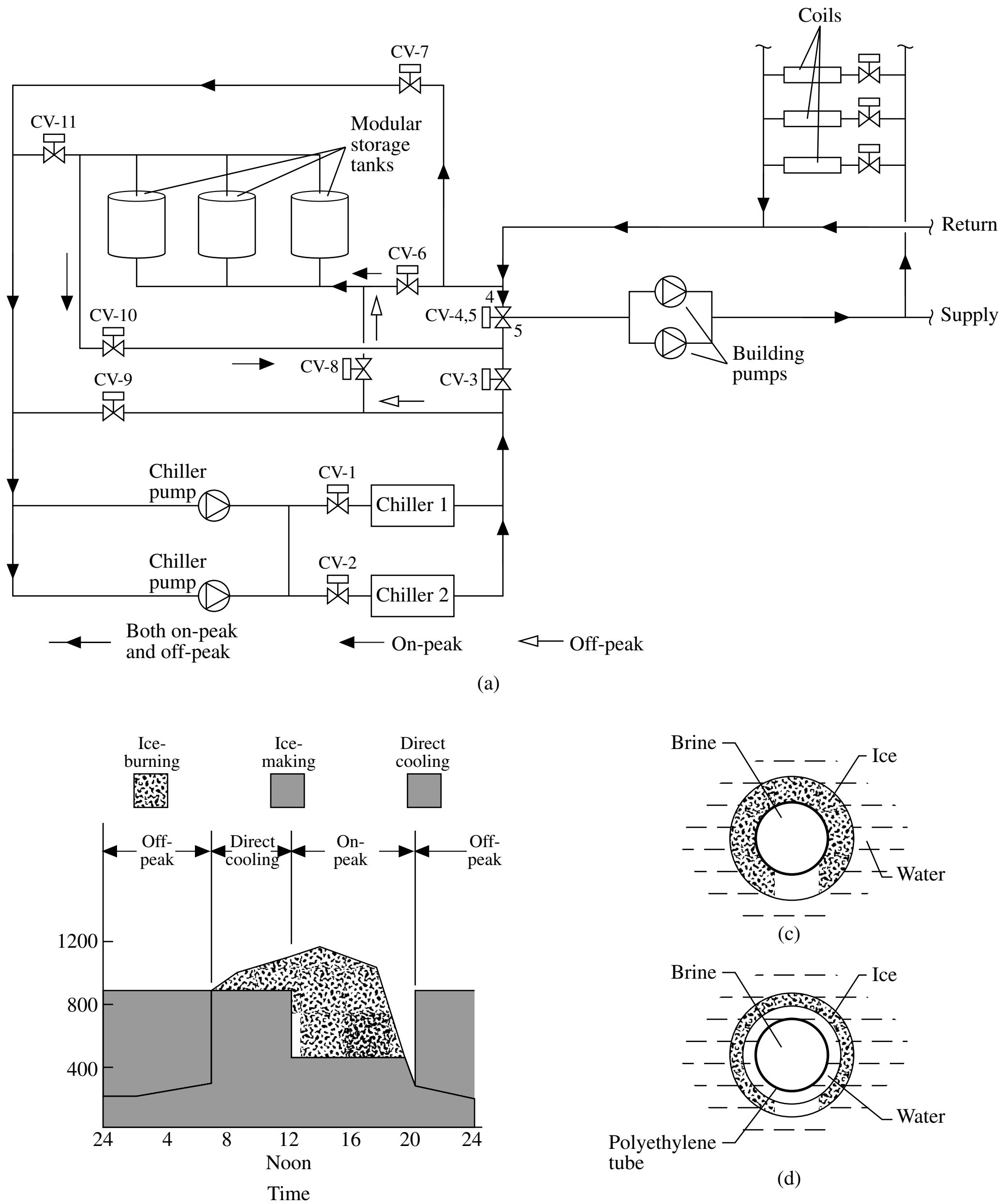

FIGURE 9.12.1 A brine-coil ice-storage system: (a) schematic diagram, (b) partial-storage time schedule, (c) ice making, and (d) ice burning.

Ice-Storage Systems

System Characteristics

In an *ice-thermal-storage* system, or simply an *ice-storage* system, ice is stored in a tank or other containers to provide cooling for buildings in on-peak hours or on- and partial-peak hours. One pound of ice can store [(1 × 144) + (55 – 35)] = 164 Btu instead of (60 – 44) = 16 Btu for chilled water storage. For the same cooling capacity, the storage volume of ice is only about 12% of chilled water. In addition, an air-conditioning system using ice storage often adopts cold air distribution to supply conditioned air at a temperature typically at 44°F. Cold air distribution reduces the size of air-side equipment, ducts, and investment as well as fan energy use. It also improves the indoor air quality of the conditioned space. Since the late 1980s, ice storage has gained more applications than chilled water storage.

Brine is a coolant that does not freeze and flash during normal operation. The freezing point of brine, which has a mass fraction of ethylene glycol of 25%, drops to 10°F, and a mass fraction of a propylene glycol brine of 25% drops to 15°F. Glycol-water, when glycol is dissolved in water, is another coolant widely used in ice-storage systems. Ice crystals are formed in glycol-water when its temperature drops below its freezing point during normal operation.

In an ice-storage system, *ice making* or *charging* is a process in which compressors are operated to produce ice. *Ice burning*, or *discharging*, is a process in which ice is melted to cool the brine or glycol-water to offset a refrigeration load.

Brine-Coil Ice-Storage Systems. Currently used ice-storage systems include brine-coil, ice-harvester, and ice-on-coil systems. According to Knebel (1995), the brine-coil ice-storage system is most widely used today because of its simplicity, flexibility, and reliability as well as using modular ice-storage tanks.

In a typical brine-coil ice-storage system, ice is charged in multiple modular factory-fabricated storage tanks as shown in Figure 9.12.1(a). In each storage tank, closely spaced polyethylene or plastic tubes are surrounded by water. Brine, a mixture of 25 to 30% of ethylene glycol by mass and 70 to 75% water, circulates inside the tubes at an entering temperature of 24°F during the ice-making process. The water surrounding the tubes freezes into ice up to a thickness of about 1/2 in. as shown in Figure 9.12.1(c). Brine leaves the storage tank at about 30°F. Water usually at atmospheric pressure is separated from brine by a plastic tube wall. Plastic tubes occupy about one tenth of the tank volume, and another one tenth remains empty for the expansion of ice. Multiple modular storage tanks are always connected in parallel.

During the ice-melting or -burning process, brine returns from the cooling coils in the air-handling units (AHUs) at a temperature of 46°F or higher. It melts the ice on the outer surface of the tubes and is thus cooled to a temperature of 34 to 36°F, as shown in Figure 9.12.1(d). Brine is then pumped to the AHUs to cool and dehumidify the air again.

Ice-Harvester Ice-Storage Systems. In an *ice-harvester* system, glycol-water flows on the outside surface of the evaporator and forms ice sheets with a thickness of 0.25 to 0.40 in. within 20 to 30 min. Ice is harvested in the form of flakes when hot gas is flowing inside the tubes of the evaporator during a time interval of 20 to 30 sec. Ice flakes fall to the glycol-water in the storage tank below. The glycol-water at a temperature of 34°F is then supplied to the cooling coils in AHUs for conditioning. After cooling and dehumidifying the air, glycol-water returns to the storage tank at a temperature of 50 to 60°F and is again cooled to 34°F again.

Ice harvesting is an intermittent process. It has a cycle loss due to harvesting of about 15%. In addition, because of its operating complexity and maintenance, its applications are more suitable for large ice-storage systems.

Ice-on-Coil Ice-Storage Systems. In an ice-on-coil system, refrigerant is evaporated in the coils submerged in water in a storage tank. Ice of a thickness not exceeding 0.25 in. builds up on the outer surface of the coils. The remaining water in the storage tank is used for cooling in AHUs. Ice-on-coil systems need large amounts of refrigerant charge and are less flexible in operation. They are usually used in industrial applications.

Ice-in-Containers Ice-Storage Systems. Ice-in-containers ice-storage systems store ice in enclosed containers. Brine circulating over the containers produces the ice inside containers. Complexity in control of the ice inventory inside the containers limits the application of the ice-in-containers systems.

Chilled-Water Storage Systems

Basics

Chilled-water storage uses the same water chiller and a similar coolant distribution system, except for additional water storage tanks and corresponding piping, additional storage pumps, and controls. The larger the chilled-water storage system, the lower the installation cost per ton.hr storage capacity.

Various types of storage tanks had been used in chilled-water storage systems during the 1970s. A diaphragm tank uses a rubber diaphragm to separate the colder and warmer water. Baffles divide the tank into cells and compartments. Today, stratified tanks have become the most widely used chilled-water storage systems because of their simplicity, low cost, and negligible difference in loss of cooling capacity between stratified tanks and other types of storage tanks.

During the storage of chilled water, the loss in cooling capacity includes direct mixing, heat transfer between warmer return chilled water and colder stored chilled water, and also heat transfer between warmer ambient air and colder water inside the tank. An enthalpy-based easily measured index called *figure of merit* (*FOM*) is often used to indicate the loss in cooling capacity during chilled-water storage. FOM is defined as:

$$\text{FOM} = q_{\text{dis}}/q_{\text{ch}} \tag{9.12.1}$$

where

q_{dis} = cooling capacity available in the discharge process, Btu/hr
q_{ch} = theoretical cooling capacity available during charging process, Btu/hr

Charging is the process of filling the storage tank with colder chilled water from the chiller. At the same time, warmer return chilled water is extracted from the storage tank and pumped to the chiller for cooling.

Discharging is the process of discharging the colder stored chilled water from the storage tank to AHUs and terminals. Meanwhile, the warmer return chilled water from the AHUs and terminals fills the tank.

Stratified Tanks. Stratified tanks utilize the buoyancy of warmer return chilled water to separate it from the colder stored chilled water during charging and discharging. Colder stored chilled water is always charged and discharged from bottom diffusers, and the warmer return chilled water is introduced to and withdrawn from the top diffusers.

Chilled-water storage tanks are usually vertical cylinders and often have a height-to-diameter ratio of 0.25:0.35. Steel is the most commonly used material for above-grade tanks, with a 2-in.-thick spray-on polyurethane foam, a vapor barrier, and a highly reflective coating. Concrete, sometimes precast, prestressed tanks are widely used for underground tanks.

A key factor to reduce loss in cooling capacity during chilled water storage is to reduce mixing of colder and warmer water streams at the inlet. If the velocity pressure of the inlet stream is less than the buoyancy pressure, the entering colder stored chilled water at the bottom of tank will stratify. Refer to Wang's handbook (1993) and Knebel (1995) for details.

A *thermocline* is a stratified region in a chilled-water storage tank of which there is a steep temperature gradient. Water temperature often varies from 42°F to about 60°F. Thermocline separates the bottom colder stored chilled water from the top warmer return chilled water. The thinner the thermocline, the lower the mixing loss.

Diffusers and symmetrical connected piping are used to evenly distribute the incoming water streams with sufficient low velocity, usually lower than 0.9 ft/sec. Inlet stream from bottom diffusers should be downward and from the top diffusers should be upward or horizontal.

Field measurements indicate that stratified tanks have a FOM between 0.85 to 0.9.

9.13 Air System Basics

Shan K. Wang

Fan-Duct Systems

Flow Resistance

Flow resistance is a property of fluid flow which measures the characteristics of a flow passage resisting the fluid flow with a corresponding total pressure loss Δp, in in. WG, at a specific volume flow rate $\overset{\circ}{V}$, in cfm:

$$\Delta p = R\mathring{V}^2 \tag{9.13.1}$$

where R = flow resistance (in. WG/(cfm)^2).

For a duct system that consists of several duct sections connected in series, its flow resistance R_s, in in. WG/(cfm)^2, can be calculated as

$$R_s = R_1 + R_2 + \ldots + R_n \tag{9.13.2}$$

where R_1, R_2, … R_n = flow resistance of duct section 1, 2, … n in the duct system (in. WG/(cfm)^2).

For a duct system that consists of several duct sections connected in parallel, its flow resistance R_p, in in. WG/(cfm)^2, is:

$$1/\sqrt{R_p} = 1/\sqrt{R_1} + 1/\sqrt{R_2} + \ldots + 1/\sqrt{R_n} \tag{9.13.3}$$

Fan-Duct System

In a *fan-duct system*, a fan or several fans are connected to ductwork or ductwork and equipment. The volume flow and pressure loss characteristics of a duct system can be described by its performance curve, called *system curve*, and is described by $\Delta p = R\,\mathring{V}^2$.

An *air system* or an air handling system is a kind of fan-duct system. In addition, an outdoor ventilation air system to supply outdoor ventilation air, an exhaust system to exhaust contaminated air, and a smoke control system to provide fire protection are all air systems, that is, fan-duct systems.

Primary, Secondary, and Transfer Air

Primary air is the conditioned air or makeup air. Secondary air is often the induced space air, plenum air, or recirculating air. Transfer air is the indoor air that moves to a conditioned space from an adjacent area.

System-Operating Point

A *system-operating point* indicates the operating condition of an air system or fan-duct system. Since the operating point of a fan must lie on the fan performance curve, and the operating point of a duct system on the system curve, the system operating point of an air system must be the intersection point P_s of the fan performance curve and system curve as shown in Figure 9.13.1(a).

Fan-Laws

For the same air system operated at speeds n_1 and n_2, both in rpm, their relationship of $\mathring{V}$ volume flow rate, in cfm, system total pressure loss, in in. WG, and fan power input, in hp, can be expressed as

$$\begin{aligned} \mathring{V}_2/\mathring{V}_1 &= n_2/n_1 \\ \Delta p_{t2}/\Delta p_{t1} &= (n_2/n_1)^2(\rho_2/\rho_1) \\ P_2/P_1 &= (n_2/n_1)^3(\rho_2/\rho_1) \end{aligned} \tag{9.13.4}$$

where ρ = air density (lb/ft^3). Subscripts 1 and 2 indicate the original and the changed operating conditions. For air systems that are geometrically and dynamically similar:

$$\begin{aligned} \mathring{V}_2/\mathring{V}_1 &= (D_2/D_1)^3(n_2/n_1) \\ \Delta p_{t2}/\Delta p_{t1} &= (D_2/D_1)^2(n_2/n_1)^2(\rho_2/\rho_1) \\ P_2/P_1 &= (D_2/D_1)^5(n_2/n_1)^3(\rho_2/\rho_1) \end{aligned} \tag{9.13.5}$$

where D = diameter of the impeller (ft).

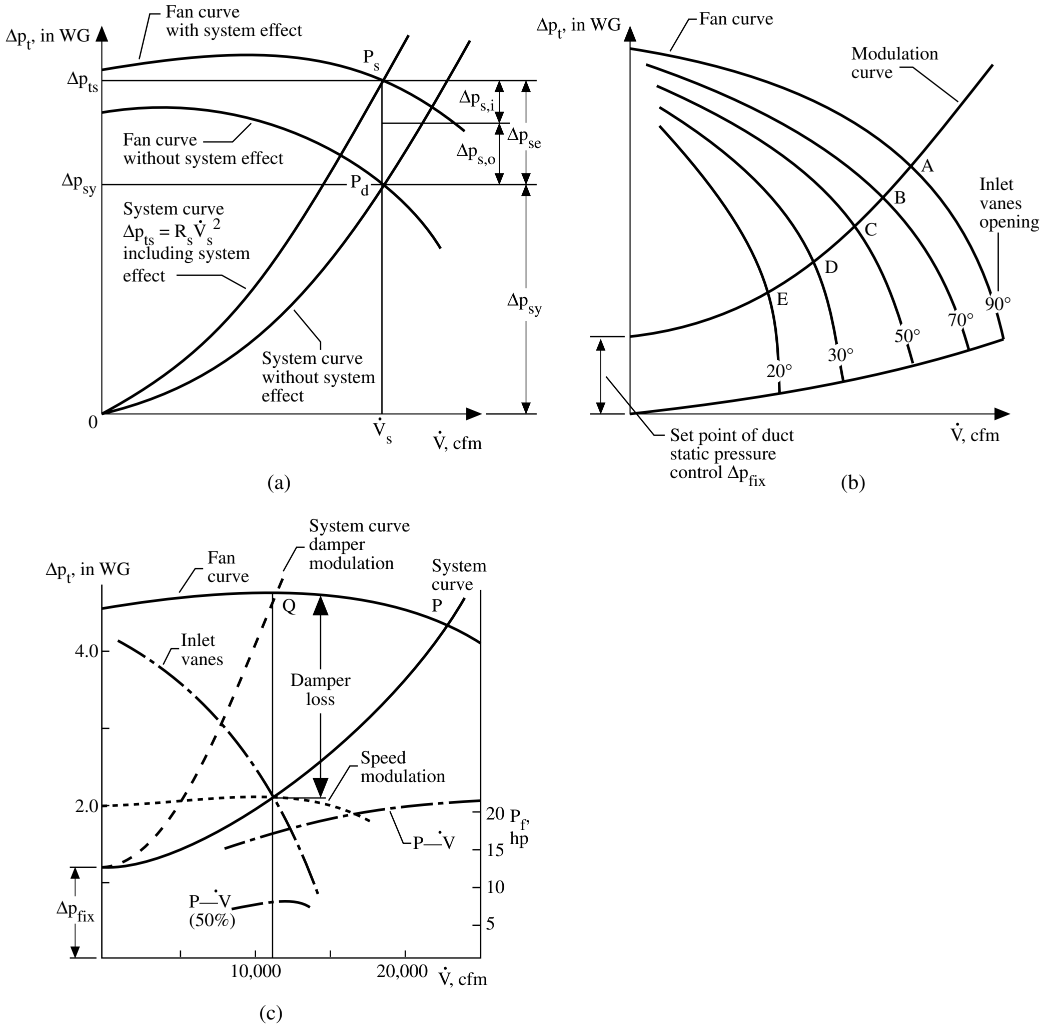

FIGURE 9.13.1 Air system $\mathring{V}$ - Δp_t performance: (a) system operating point and system effect, (b) modulation curve, and (c) damper, inlet vanes, and fan speed modulation.

Geometrically similar means that two systems are similar in shape and construction. For two systems that are dynamically similar, they must be geometrically similar, and in addition, their velocity distribution or profile of fluid flow should also be similar. When fluid flows in the air systems are at high Reynolds number, such as Re > 10,000, their velocity profiles can be considered similar to each other.

System Effect

The system effect Δp_{se}, in in. WG, of an air system is its additional total pressure loss caused by uneven or nonuniform velocity profile at the fan inlet, or at duct fittings after the fan outlet, due to the actual inlet and outlet connections as compared with the total pressure loss of the fan test unit during laboratory ratings. The selected fan total pressure which includes the system effect Δp_{ts}, in in. WG, as shown in Figure 9.13.1(a), can be calculated as

$$\begin{aligned}\Delta p_{ts} &= \Delta p_{sy} + \Delta p_{se} = \Delta p_{sy} + \Delta p_{s.i} + \Delta p_{s.o} \\ &= \Delta p_{sy} + C_{s.i}\left(v_{fi}/4005\right)^2 + C_{s.o}\left(v_{fo}/4005\right)^2\end{aligned} \tag{9.13.6}$$

where

Δp_{sy} = calculated total pressure loss of the air system, in WG
$\Delta p_{s.i}, \Delta p_{s.o}$ = fan inlet and outlet system effect loss, in WG
$C_{s.i}, C_{s.o}$ = local loss coefficient of inlet and outlet system effect, in WG
v_{fi}, v_{fo} = velocity at fan inlet (fan collar) and fan outlet, fpm

Both $C_{s.i}$ and $C_{s.o}$ are mainly affected by the length of connected duct between the duct fitting and fan inlet or outlet, by the configuration of the duct fitting, and by the air velocity at the inlet or outlet. Because v_{fi} and v_{fo} are often the maximum velocity of the air system, system effect should not be overlooked.

Modulation of Air Systems

Air systems can be classified into two categories according to their operating volume flow: constant volume and variable-air-volume systems. The volume flow rate of a *constant volume system* remains constant during all the operating time. Its supply temperature is raised during part load. For a *variable-air-volume* (*VAV*) *system,* its volume flow rate is reduced to match the reduction of space load at part-load operation. The system pressure loss of a VAV system can be divided into two parts: variable part Δp_{var} and fixed part Δp_{fix}, which is the set point of the duct static pressure control as shown in Figure 9.13.1(b) and (c). The *modulation curve* of a VAV air system its its operating curve, or the locus of system operating points when its volume flow rate is modulated at full- and part-load operation.

The volume flow and system pressure loss of an air system can be modulated either by changing its fan characteristics or by varying its flow resistance of the duct system. Currently used types of modulation of volume flow rate of VAV air systems are

1. *Damper modulation* uses an air damper to vary the opening of the air flow passage and therefore its flow resistance.
2. *Inlet vanes modulation* varies the opening and the angle of inlet vanes at the centrifugal fan inlet and then gives different fan performance curves.
3. *Inlet cone modulation* varies the peripheral area of the fan impeller and therefore its performance curve.
4. *Blade pitch modulation* varies the blade angle of the axial fan and its performance curve.
5. *Fan speed modulation* using *adjustable frequency AC drives* varies the fan speed by supplying a variable-frequency and variable-voltage power source. There are three types of AC drives: adjustable voltage, adjustable current, and pulse width modulation (PWM). The PWM is universally applicable.

Damper modulation wastes energy. Inlet vanes are low in cost and are not so energy efficient compared with AC drives and inlet cones. Inlet cones are not expensive and are suitable for backward curved centrifugal fans. Blade pitch modulation is energy efficient and is mainly used for vane and tubular axial fans. AC or variable frequency drives (VFD) are the most energy-efficient type of modulation; however, they are expensive and often considered cost effective for air systems using larger centrifugal fans.

Example 9.13.1

A multizone VAV system equipped with a centrifugal fan has the following characteristics:

$\overset{\circ}{V}$ (cfm)	5,000	10,000	15,000	20,000	25,000
Δp_t, in. WG	4.75	4.85	4.83	4.60	4.20
P, hp		17.0	18.6	20.5	21.2

At design condition, it has a volume flow rate of 22,500 cfm and a fan total pressure of 4.45 in. WG. The set point of duct static pressure control is 1.20 in. WG.

When this VAV system is modulated by inlet vanes to 50% of design flow, its fan performance curves show the following characteristics:

$\overset{\circ}{V}$ (cfm)	5,000	10,000	11,250
Δp_t, in. WG	3.6	2.5	2.1
P, hp		7.5	7.8

Determine the fan power input when damper, inlet vanes, or AC drive fan speed modulation is used. Assume that the fan total efficiency remains the same at design condition when the fan speed is reduced.

Solutions

1. At 50% design flow, the volume flow of this VAV system is 0.5 × 22,500 = 11,250 cfm. The flow resistance of the variable part of this VAV system is

$$R_{\text{var}} = \Delta p_{\text{va}} = R\overset{\circ}{V}^2 = (4.45 - 1.20)/(22{,}500)^2 = 6.42 \times 10^{-9} \text{ in. WG}/(\text{cfm})^2$$

   When damper modulation is used, the system operating point Q must be the intersection of the fan curve and the system curve that has a higher flow resistance and a $\overset{\circ}{V}$ = 11,250 cfm. From Figure 9.13.1(c), at point Q, the fan power input is 17.0 hp.
2. From the given information, when inlet vane modulation is used, the fan power input is 7.8 hp.
3. The total pressure loss of the variable part of the VAV system at 50% volume flow is

$$\Delta p_{\text{var}} = R_{\text{var}}\overset{\circ}{V}^2 = 6.42 \times 10^{-9}(11{,}250)^2 = 0.81 \text{ in. WG}$$

   From Figure 9.13.1(c), since the fan power input at design condition is 21.2 hp, then its fan total efficiency is:

$$\eta_f = \overset{\circ}{V}\Delta p_{\text{tf}}/(6356P_f) = 22{,}500 \times 4.45/(6356 \times 21.2) = 74.3\%$$

   The fan power input at 50% design volume flow is:

$$P = \overset{\circ}{V}\Delta p_{\text{tf}}/(6356\eta_f) = 11{,}250(0.81 + 1.20)/(6356 \times 0.743) = 4.8 \text{ hp}$$

   Damper modulation has a energy waste of (17 – 4.8) = 12.2 hp

Fan Combinations in Air-Handling Units and Packaged Units

Currently used fan combinations in air-handling units (AHUs) and packaged units (PUs) (except dual-duct VAV systems) are shown in Figure 9.13.2(a), (b), and (c):

Supply and Exhaust Fan/Barometric Damper Combination

An air system equipped with a single supply fan and a constant-volume exhaust fan, or a supply fan and a barometric damper combination as shown in Figure 9.13.2(a), is often used in buildings where there is no return duct or the pressure loss of the return duct is low. An all-outdoor air economizer cycle is usually not adopted due to the extremely high space pressure. A barometric relief damper is often installed in or connected to the conditioned space to prevent excessively high space pressure. When the space-positive pressure exerted on the barometric damper is greater than the weight of its damper and/or a spring, the damper is opened and the excessive space pressure is relieved.

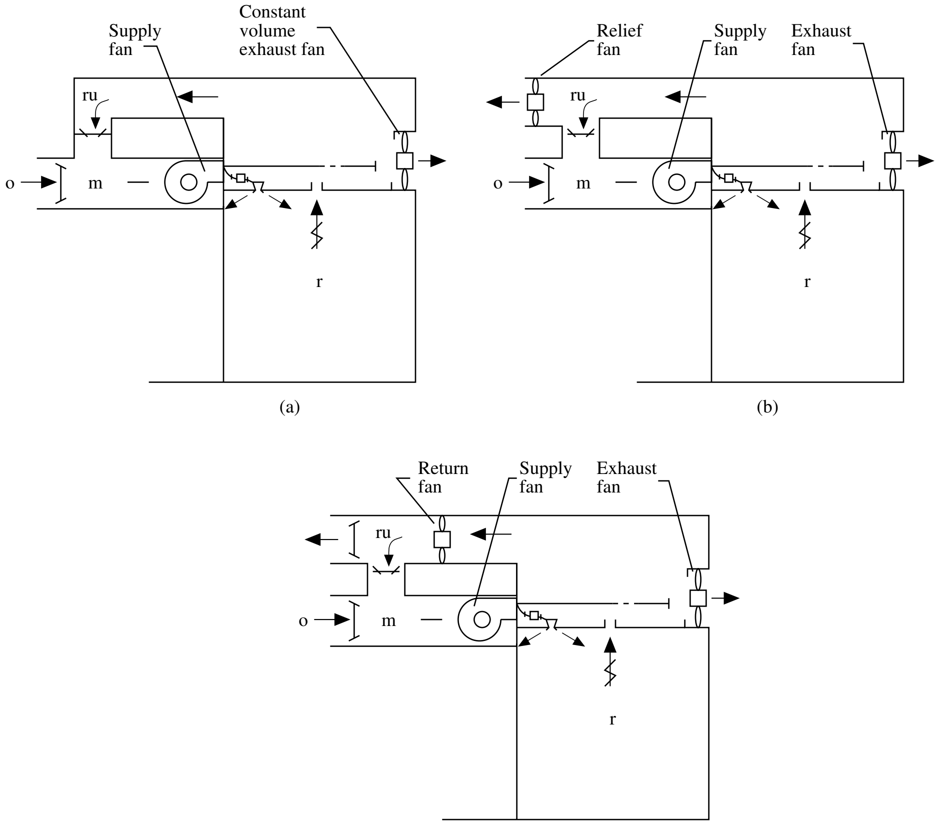

(a)

(b)

(c)

FIGURE 9.13.2 Fan combinations: (a) supply and exhaust fan, (b) supply and relief fan, and (c) supply and return fan.

Supply and Relief Fan Combination

Figure 9.13.2(b) shows the schematic diagrams of an air system of supply fan and relief fan combination. A relief fan is used to relieve undesirable high positive space pressure by extracting space air and relieving it to the outside atmosphere. A relief fan is always installed in the relief flow passage after the junction of return flow, relief flow, and recirculating flow passage, point ru. It is usually energized only when the air system is operated in air economizer mode. A relief fan is often an axial fan. Since the relief fan is not energized during recirculating mode operation, the volume flow and pressure characteristics of a supply fan and relief fan combination are the same as that in a single supply fan and barometric damper combination when they have the same design parameters.

Supply Fan and Return Fan Combination

A *return fan* is always installed at the upstream of the junction of return, recirculating, and exhaust flow passage, point ru as shown in Figure 9.13.2(c). A supply and return fan combination has similar pressure and volume flow characteristics as that of a supply and relief fan combination, except a higher total pressure at point ru. If the return fan is improperly selected and has an excessive fan total pressure, total pressure at point m may be positive. There will be no outdoor intake at the PU or AHU, and at the same time there will also be a negative space pressure and an infiltration to the space.

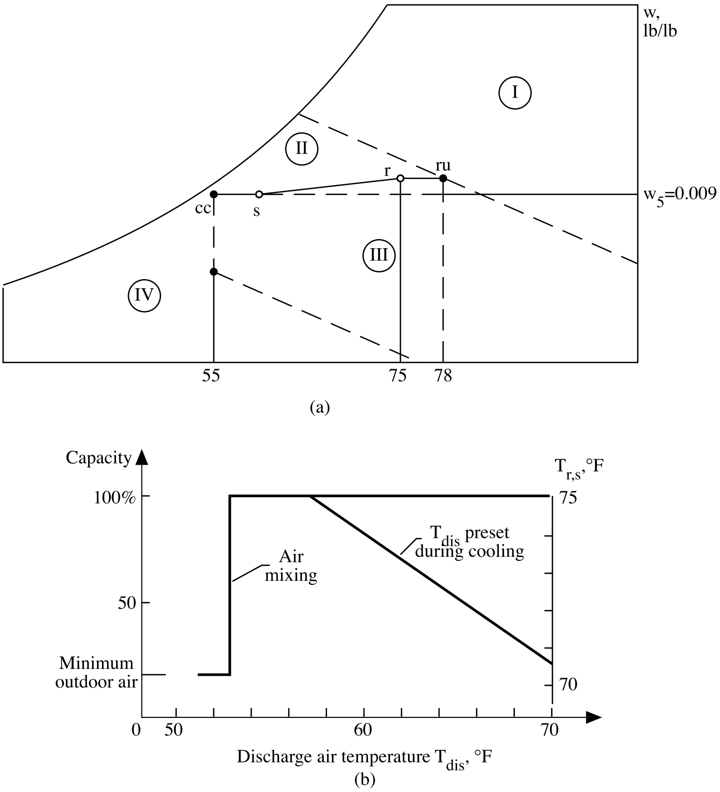

FIGURE 9.13.3 (a) Year-round operation and (b) discharge air temperature for a VAV reheat system.

Comparison of These Three Fan Combination Systems

A supply fan and barometric damper combination is simpler and less expensive. It is suitable for an air system which does not operate in an air economizer mode and has a low pressure drop in the return system.

For those air systems whose pressure drop for the return system does not exceed 0.3 in. WG, or there is a considerable pressure drop in relief or exhaust flow passage, a supply and relief fan combination is recommended. For air systems whose return system has a pressure drop exceeding 0.6 in. WG, or those requiring a negative space pressure, a supply and return fan combination seems more appropriate.

Year-Round Operation and Economizers

Consider a typical single-duct VAV reheat system to serve an occupied space whose indoor temperature is 75°F with a relative humidity of 50%. During summer, the off-coil temperature is 55°F. The year-round operation of this air system can be divided into four regions on the psychrometric chart, as shown in Figure 9.13.3(a):

- *Region I — Refrigeration/evaporative cooling.* In this region, the enthalpy of the outdoor air h_o is higher than the enthalpy of the recirculating air h_{ru}, $h_o > h_{ru}$. It is more energy efficient to condition the mixture of recirculating air and minimum outdoor air.
- *Region II — Free cooling and refrigeration.* In this region, $h_o \le h_{ru}$. It is more energy efficient and also provides better indoor air quality to extract 100% outdoor air.

- *Region III — Free cooling evaporative cooling, and refrigeration.* In this region, extract 100% outdoor air for free cooling because $h_o \le h_{ru}$. Use evaporative cooling and refrigeration to cool and humidify if necessary.
- *Region IV — Winter heating.* Maintain a 55°F supply temperature by mixing the recirculating air with the outdoor air until the outdoor air is reduced to a minimum value. Provide heating if necessary.

An economizer is a device consisting of dampers and control that uses the free cooling capacity of either outdoor air or evaporatively cooled water from the cooling tower instead of mechanical refrigeration. An air economizer uses outdoor air for free cooling. There are two kinds of air economizers: enthalpy-based, in which the enthalpy of outdoor and recirculating air is compared, and temperature-based, in which temperature is compared. Economizers require routine maintenance and calibration in order to realize maximum savings. A water economizer uses evaporatively cooled water.

Fan Energy Use

For an air system, fan energy use for each cfm of conditioned air supplied from the AHUs and PUs to the conditioned space within a certain time period, in W/cfm, can be calculated as

$$\text{W/cfm} = 0.1175\Delta p_{sy} / (\eta_f \eta_m) \tag{9.13.7}$$

where

Δp_{sy} = mean system total pressure loss during a certain time period, in. WG
η_f = fan total efficiency
η_m = combined motor and drive (direct drive or belt drive) efficiency

For an air system using a separate outdoor ventilation system, its fan energy use, in W/cfm, is then calculated as

$$\text{W/cfm} = (1 + R_{o.s}) \left[0.1175\Delta p_{sy} / (\eta_f \eta_m) \right] \tag{9.13.8}$$

where $R_{o.s}$ = ratio of outdoor air volume flow rate to supply volume flow rate.

Outdoor Ventilation Air Supply

Basics

- An adequate amount of outdoor ventilation air supply is the key factor to provide acceptable indoor air quality (IAQ) for a conditioned space. Although an inadequate amount of outdoor ventilation air supply causes poor IAQ, an oversupply of outdoor ventilation air other than in an air economizer cycle is often a waste of energy.
- According to local codes and ANSI/ASHRAE Standard 62, the minimum outdoor ventilation rate for each person must be provided at the outdoor air intake of AHU or PU, or by an outdoor air ventilation system. If the minimum outdoor ventilation air rate is reduced by using higher efficiency filters to remove air contaminants in the recirculating air, then indoor air contaminant concentration must be lower than the specified level in ANSI/ASHRAE Standard 62.
- For a multizone air system, although the ratio of outdoor ventilation air rate to supply air volume flow rate required may be varied from zone to zone, the excessive outdoor air supply to a specified zone will increase the content of unused outdoor air in the recirculating air in AHU or PU. This helps to solve the problem in any zone that needs more outdoor air.
- Since the occupancy in many buildings is often variable and intermittent, a demand-based variable amount of outdoor ventilation air control should be used instead of time-based constant volume outdoor ventilation air control, except during the air economizer cycle.

- Carbon dioxide (CO_2) is a gaseous body effluent. CO_2 is an indicator of representative odor and an indicator of adequate outdoor ventilation rate at specific outdoor and indoor air concentration in a control zone at steady state. For most of the comfort air-conditioning systems, it is suitable to use CO_2 as a key parameter to control the intake volume flow rate of outdoor ventilation air to maintain an indoor CO_2 concentration not exceeding 800 to 1000 ppm in a critical or representative zone. As mentioned in Section 9.5, Persily (1993) showed that the actual measured indoor daily maximum CO_2 concentration levels in five buildings were all within 400 to 820 ppm.

If a field survey finds that a specific indoor air contaminant exceeds a specified indoor concentration, then a gas sensor for this specific contaminant or a mixed gas sensor should be used to control this specific indoor concentration level.

Types of Minimum Outdoor Ventilation Air Control. There are four types of minimum outdoor ventilation air control that are currently used:

- Type I uses a CO_2 sensor or a mixed gas sensor and a DDC controller to control the volume flow rate of outdoor ventilation air for a separate outdoor ventilation air system on the demand-based principle.
- Type II uses a CO_2 or mixed gas sensor and a DDC controller to control the ratio of the openings between outdoor and recirculating dampers and, therefore, the volume flow rates of outdoor air and recirculating air in AHUs or PUs on the demand-based principle.
- Type III uses a flow sensor or a pressure sensor and a DDC controller to control the openings of outdoor and recirculating dampers to provide a nearly constant volume outdoor air intake in VAV AHUs or VAV PUs.
- Type IV adjusts the opening of the outdoor damper manually to provide a constant volume of outdoor air in constant-volume AHUs and PUs. If the outdoor intake is mounted on the external wall without a windshield, the volume flow of outdoor ventilation air intake will be affected by wind force and direction.

Type I is the best minimum outdoor ventilation air control for the air system. For a VAV system, it is expensive. Type II is a better choice. Type III is more complicated and may cause energy waste. Type IV has the same result as Type III and is mainly used in constant-volume systems.

Outdoor intake must be located in a position away from the influence of exhaust outlets. Fans, control dampers, and filters should be properly operated and maintained in order to provide a proper amount of outdoor ventilation air as well as an acceptable IAQ.

9.14 Absorption System

Shan K. Wang

Absorption systems use heat energy to produce refrigeration as well as heating if it is required. Water is the refrigerant and aqueous lithium bromide (LiBr) is widely used as the carrier to absorb the refrigerant and provide a higher coefficient of performance.

The mixture of water and anhydrous LiBr is called *solution*. The composition of a solution is usually expressed by its mass fraction, or percentage of LiBr, often called *concentration*. When the water vapor has boiled off from the solution, it is called *concentrated solution.* If the solution has absorbed the water vapor, it is called *diluted solution.*

Absorption systems can be divided into the following categories:

- *Absorption chillers* use heat energy to produce refrigeration.
- *Absorption chiller/heaters* use direct-fired heat input to provide cooling or heating separately.
- *Absorption heat pumps* extract heat energy from the evaporator, add to the heat input, and release them both to the hot water for heating.
- *Absorption heat transformers* raise the temperature of the waste heat source to a required level.

Most recently installed absorption chillers use direct-fired natural gas as the heat source in many locations in the United States where there are high electric demand and electric rates at on-peak hours. Absorption chillers also are free from CFC and HCFC refrigerants. An energy cost analysis should be done to determine whether an electric chiller or a gas-fired absorption chiller is the suitable choice.

Absorption heat pumps have only limited applications in district heating. Most absorption heat transformers need industrial waste heat. Both of them will not be covered here.

Double-Effect Direct-Fired Absorption Chillers

Figure 9.14.1(a) shows a double-effect direct-fired absorption chiller. *Double effect* means that there are two generators. *Direct fired* means that gas is directly fired at the generator instead of using steam or hot water. A single-effect absorption chiller using steam as the heat input to its single generator has a COP only from 0.7 to 0.8, whereas a double-effect direct-fired absorption chiller has a COP approximately equal to 1 and therefore is the mot widely used absorption chiller in the United States for new and retrofit projects today. The refrigeration capacity of double-effect direct-fired absorption chillers varies from 100 to 1500 tons.

A double-effect direct-fired absorption chiller mainly consists of the following components and controls:

- Evaporator — An *evaporator* is comprised of a tube bundle, spray nozzles, a water trough, a refrigerant pump, and an outer shell. Chilled water flows inside the tubes. A refrigerant pump sprays the liquid refrigerant over the outer surface of the tube bundle for a higher rate of evaporation. A water trough is located at the bottom to maintain a water level for recirculation.
- Absorber — In an *absorber*, there are tube bundles in which cooling water flows inside the tubes. Solution is sprayed over the outer surface of the tube bundle to absorb the water vapor. A solution pump is used to pump the diluted solution to the heat exchanger and low-temperature generator.
- Heat exchangers — There are two heat exchangers: *low-temperature heat exchanger* in which the temperature of hot concentrated solution is lower, and *high-temperature heat exchanger* in which the temperature of hot concentrated solution is higher. In both heat exchangers, heat is transferred from the hot concentrated solution to the cold diluted solution. Shell-and-tube or plate-and-frame heat exchangers are most widely used for their higher effectiveness.
- Generators — *Generators* are also called *desorbers*. In the *direct-fired generator*, there are the fire tube, flue tube, vapor/liquid separator, and flue-gas economizer. Heat is supplied from the gas burner or other waste heat source. The *low-temperature generator* is often of the shell-and-tube type. The water vapor vaporized in the direct-fired generator is condensed inside the tubes. The latent heat of condensation thus released is used to vaporize the dilute solution in the low-temperature generator.
- Condenser — A condenser is usually also of the shell-and-tube type. Cooling water from the absorber flows inside the tubes.
- Throttling devices — Orifices and valves are often used as throttling devices to reduce the pressure of refrigerant and solution to the required values.
- Air purge unit — Since the pressure inside the absorption chiller is below atmospheric pressure, air and other noncondensable gases will leak into it from the ambient air. An *air purge unit* is used to remove these noncondensable gases from the chiller. A typical air purge unit is comprised of a pickup tube, a purge chamber, a solution spray, cooling water tubes, a vacuum pump, a solenoid valve, and a manual shut-off valve.

When noncondensable gases leak into the system, they tend to migrate to the absorber where pressure is lowest. Noncondensable gases and water vapor are picked from the absorber through the pickup tube. Water vapor is absorbed by the solution spray and returned to the absorber through a liquid trap at the bottom of the purge chamber. Heat of absorption is removed by the cooling water inside the tubes. Noncondensable gases are then evacuated from the chamber periodically by a vacuum pump to the outdoor atmosphere.

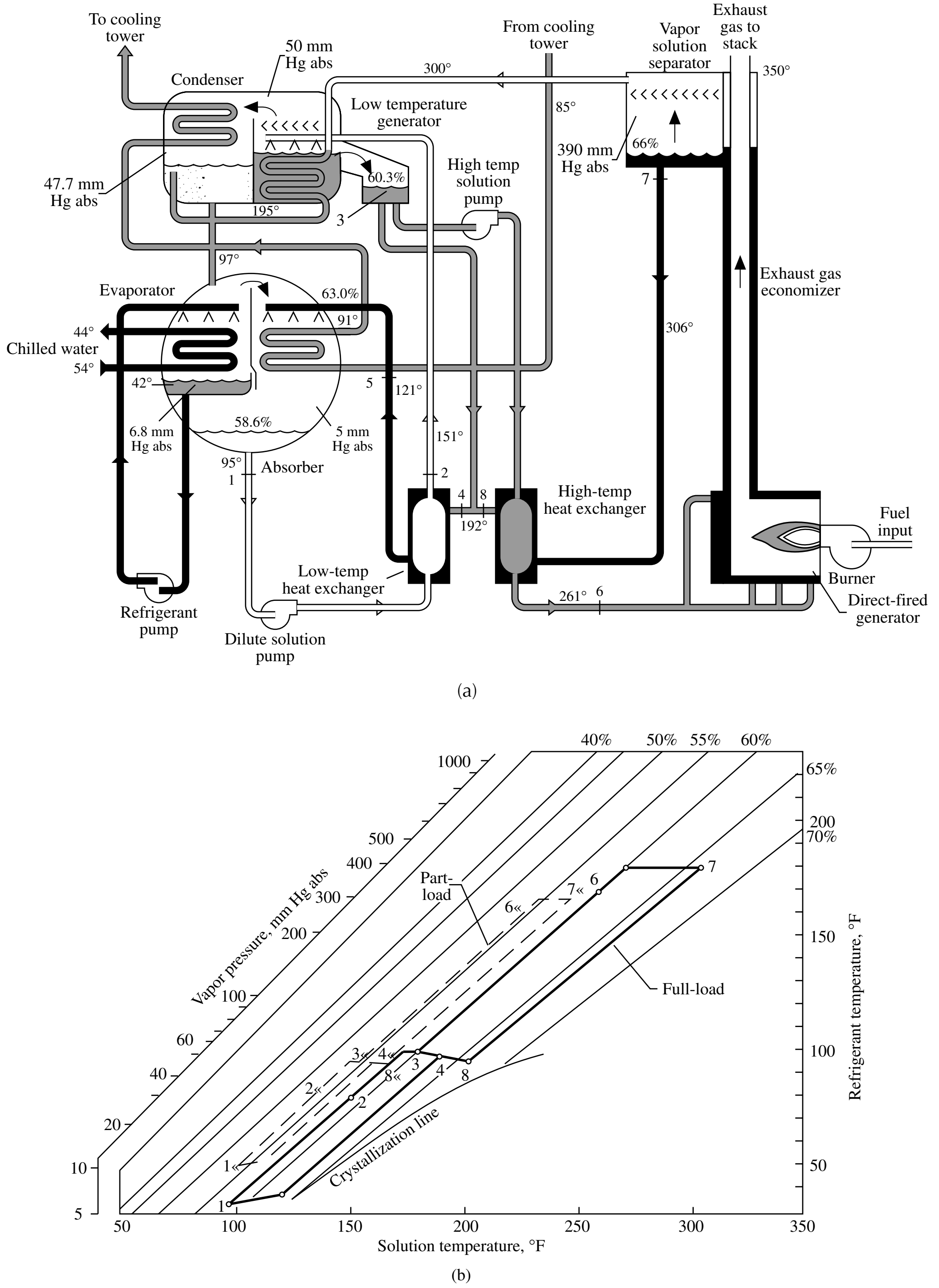

FIGURE 9.14.1 A double-effect direct-fired reverse-parallel-flow absorption chiller: (a) schematic diagram (reprinted by permission from the Trane catalog) and (b) absorption cycle.

Palladium cells are used to continuously remove a small amount of hydrogen that is produced due to corrosion. Corrosion inhibitors like lithium chromate are needed to protect the machine parts from the corrosive effect of the absorbent when air is present.

Absorption Cycles, Parallel-, Series-, and Reverse-Parallel Flow

An *absorption* cycle shows the properties of the solution and its variation in concentrations, temperature, and pressure during absorbing, heat exchanging, and concentration processes on an equilibrium chart as shown in Figure 9.14.1(b). The ordinate of the equilibrium chart is the saturated temperature and pressure of water vapor, in °F and mm Hg abs. The abscissa is the temperature of the solution, in °F. Concentration lines are incline lines. At the bottom of the concentration lines, there is a *crystallization line* or *saturation line*. If the mass of fraction of LiBr in a solution which remains at constant temperature is higher than the saturated condition, that part of LiBr exceeding the saturation condition tends to form solid crystals.

Because there are two generators, the flow of solution from the absorber to generators can be in series flow, parallel flow, or reverse-parallel flow. In a series-flow system, the diluted solution from the absorber is first pumped to the direct-fired generator and then to the low-temperature generator. In a parallel-flow system, diluted solution is pumped to both direct-fired and low-temperature generators in parallel. In a reverse-parallel-flow system as shown in Figure 9.14.1(a), diluted solution is first pumped to the low-temperature generator. After that, the partly concentrated solution is then sent to the direct-fired generator as well as to the intermediate point 4 between high- and low-temperature heat exchangers in parallel. At point 4, partly concentrated solution mixes with concentrated solution from a direct-fired generator. A reverse-parallel-flow system is more energy efficient.

Solution and Refrigerant Flow

In a typical double-effect direct-fired reverse-parallel-flow absorption chiller operated at design full load, water is usually evaporated at a temperature of 42°F and a saturated pressure of 6.8 mm Hg abs in the evaporator. Chilled water returns from the AHUs or fan coils at a temperature typically 54°F, cools, and leaves the evaporator at 44°F. A refrigeration effect is produced due to the vaporization of water vapor and the removal of latent heat of vaporization from the chilled water.

Water vapor in the evaporator is then extracted to the absorber due to its lower vapor pressure. It is absorbed by the concentrated LiBr solution at a pressure of about 5 mm Hg abs. After absorption, the solution is diluted to a concentration of 58.6% and its temperature increases to 95°F (point 1). Most of the heat of absorption and the sensible heat of the solution is removed by the cooling water inside the tube bundle. Diluted solution is then pumped by a solution pump to the low-temperature generator through a low-temperature heat exchanger.

In the low-temperature generator, the dilute solution is partly concentrated to 60.3% at a solution temperature of 180°F (point 3). It then divides into two streams: one of them is pumped to the direct-fired generator through a high-temperature heat exchanger, and the other stream having a slightly greater mass flow rate is sent to the intermediate point 4. In the direct-fired generator, the concentrated solution leaves at a concentration of 66% and a solution temperature of 306°F (point 7).

The mixture of concentrated and partly concentrated solution at point 4 has a concentration of 63% and a temperature of 192°F. It enters the low-temperature heat exchanger. Its temperature drops to 121°F before entering the absorber (point 5).

In the direct-fired generator, water is boiled off at a pressure of about 390 mm Hg abs. The boiled-off water vapor flows through the submerged tube in the low-temperature generator. The release of latent heat of condensation causes the evaporation of water from the dilution solution at a vapor pressure of about 50 mm Hg abs. The boiled-off water vapor in the low-temperature generator flows to the condenser through the top passage and is condensed into liquid water at a temperature of about 99°F and a vapor pressure of 47.7 mm Hg abs. This condensed liquid water is combined with the condensed water from the submerged tube at the trough. Both of them return to the evaporator after its pressure is throttled by an orifice plate.

Part-Load Operation and Capacity Control

During part-load operation, a double-effect direct-fired reverse-parallel-flow absorption chiller adjusts its capacity by reducing the heat input to the direct-fired generator through the burner. Lower heat input results at less water vapor boiled off from the solution in the generators. This causes the drop in solution concentration, the amount of water vapor extracted, the rate of evaporation, and the refrigeration capacity. Due to less water vapor being extracted, both evaporating pressure and temperature will rise. Since the amount of water vapor to be condensed is greater than that boiled off from the generators, both the condensing pressure and condensing temperature decrease.

Coefficient of Performance (COP)

The COP of an absorption chiller can be calculated as

$$\mathrm{COP} = 12{,}000/q_{1g} \tag{9.14.1}$$

where q_{1g} = heat input to the direct-fired generator per ton of refrigeration output (Btu/hr.ton).

9.15 Air-Conditioning Systems and Selection

Shan K. Wang

Basics in Classification

The purpose of classifing air-conditioning or HVAC&R systems is to distinguish one type from another so that an optimum air-conditioning system can be selected according to the requirements. Proper classification of air-conditioning systems also will provide a background for using knowledge-based expert systems to help the designer to select an air-conditioning system and its subsystems.

Since air system characteristics directly affect the space indoor environmental parameters and the indoor air quality, the characteristics of an air system should be clearly designated in the classification.

The system and equipment should be compatible with each other. Each system has its own characteristics which are significantly different from others.

Individual Systems

As described in Section 9.1, air conditoning or HVAC&R systems can be classified as individual, space, packaged, and central systems.

Individual systems usually have no duct and are installed only in rooms that have external walls and external windows. Individual systems can again be subdivided into the following.

Room Air-Conditioner Systems

A room air conditioner is the sole factory-fabricated self-contained equipment used in the room air-conditioning system. It is often mounted on or under the window sill or on a window frame as shown in Figure 9.1.1. A room air-conditioner consists mainly of an indoor coil, a small forward-curved centrifugal fan for indoor coil, a capillary tube, a low-efficiency dry and reusable filter, grilles, a thermostat or other controls located in the indoor compartment, and a rotary, scroll, or reciprocating compressor, an outdoor coil, and a propeller fan for the outdoor coil located in the outdoor compartment. There is an outdoor ventilation air intake opening and a manually operated damper on the casing that divides the indoor and outdoor compartments. Room air-conditioners have a cooling capacity between 1/2 to 2 tons.

The following are system characteristics of a room air-conditioner system:

Room heat pump system is a room air-conditioner plus a four-way reversing valve which provides both the summer cooling and winter heating.

Air system: single supply fan
- Fan, motor, and drive combined efficiency: 25%
- Fan energy use: 0.3 to 0.4 W/cfm
- Fan speed: HI-LO 2-speed or HI-MED-LO 3-speed
- Outdoor ventilation air system: type IV

Cooling system: DX system, air-cooled condenser
    EER 7.5 to 9.5 Btu/hr.W
    Evaporating temperature T_{ev} at design load: typically 45°F
Heating system: electric heating (if any)
Part-load: on–off of refrigeration compressor
Sound level: indoor NC 45 to 50
Maintenance: More maintenance work is required.

Summer and winter mode air-conditioning cycles of a room air-conditioning system are similar to that shown in Figure 9.3.4.

Packaged Terminal Air-Conditioner (PTAC) Systems

A packaged terminal air-conditioner is the primary equipment in a PTAC system. A PTAC system is similar to a room air-conditioner system. Their main differences are

- A PTAC uses a wall sleeve and is intended to be mounted through the wall.
- Heating is available from hot water, steam, heat pump, electric heater, and sometimes even direct-fired gas heaters.

PTACs are available in cooling capacity between 1/2 to 1 1/2 tons and a heating capacity of 2500 to 35,000 Btu/hr. Larger PTAC units have capacities in the range of 5 to 7 1/2 tons and may come equipped with heat recovery options.

Space (Space-Conditioning) Systems

Most space conditioning air-conditioning systems cool, heat, and filtrate their recirculating space air above or in the conditioned space. Space conditioning systems often incorporate heat recovery by transferring the heat rejected from the interior zone to the perimeter zone through the condenser(s). Space systems often have a separate outdoor ventilation air system to supply the required outdoor ventilation air.

Space systems can be subdivided into four-pipe fan-coil systems and water-source heat pump systems.

Four-Pipe Fan-Coil Systems

In a four-pipe fan-coil unit system, space recirculating air is cooled and heated at a fan coil by using four pipes: one chilled water supply, one heating hot water supply, one chilled water return, and one heating hot water return. Outdoor ventilation air is conditioned at a make-up AHU or primary AHU. It is then supplied in a neutral thermal state to the fan coil where it mixes with the recirculating air, as shown in Figure 9.15.1(a), or is supplied to the conditioned space directly.

A *fan-coil unit* or a *fan coil* is a *terminal* as shown in Figure 9.15.1(b). Fan-coil units are available in standard sizes 02, 03, 04, 06, 08, 10, and 12 which correspond to 200 cfm, 400 cfm, and so on in volume flow.

The following are system characteristics of a four-pipe fan-coil system:

A *water-cooling electric heating fan-coil system* uses chilled water for cooling and an electric heater for heating as shown in Figure 9.1.2. This system is often used in a location that has a mild winter.

Air system:
    Fan-coil, space air recirculating
    Fan, motor, and drive combined efficiency: 25%
    Fan speed: HI-LO 2-speed and HI-MED-LO 3-speed
    External pressure for fan coil: 0.06 to 0.2 in. WG
    System fan(s) energy use: 0.45 to 0.5 W/cfm
    No return air and return air duct
    Outdoor ventilation air system: type I
    An exhaust system to exhaust part of the outdoor ventilation air

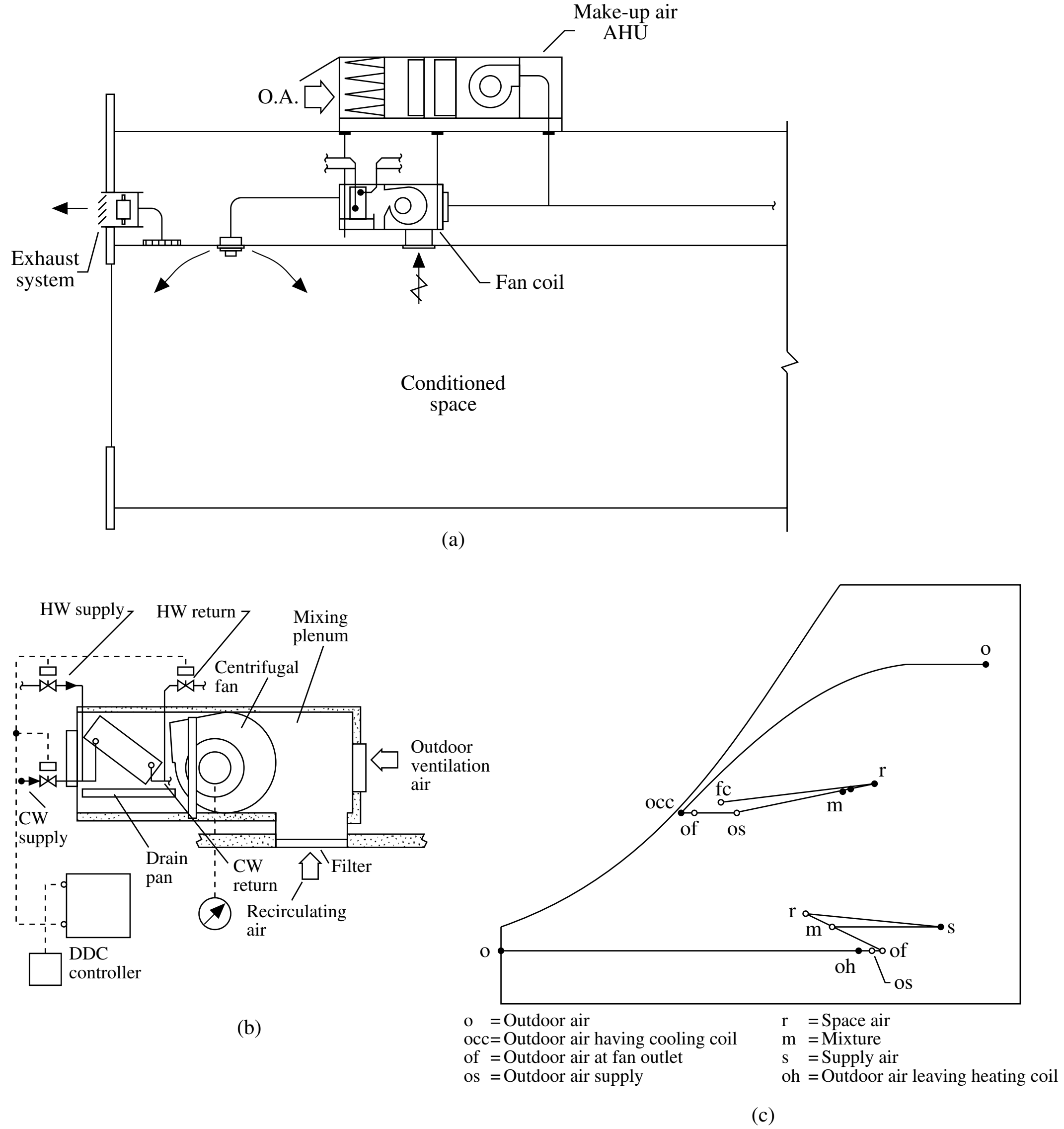

FIGURE 9.15.1 A four-pipe fan-coil system: (a) schematic diagram, (b) fan-coil unit, and (c) air-conditioning cycle.

Cooling system: chilled water from centrifugal or screw chiller
Water-cooled chiller energy use: 0.4 to 0.65 kW/ton
Heating system: hot water from boiler, electric heater
Part load: control the flow rate of chilled and hot water supplied to the coil. Since air leaving coil temperature T_{cc} rises during summer mode part load, space relative humidity will be higher.
Sound level: indoor NC 40 to 45
Maintenance: higher maintenance cost
System fan(s) energy use: 0.45 to 0.55 W/cfm (includes all fans in the four-pipe fan-coil system)

An air-conditioning cycle for a four-pipe fan-coil system with outdoor ventilation air delivered to the suction side of the fan coil is shown in Figure 9.15.1(c). A part of the space cooling and dehumidifying load is usually taken care by the conditioned outdoor ventilation air from the make-up AHU. A double-bundle

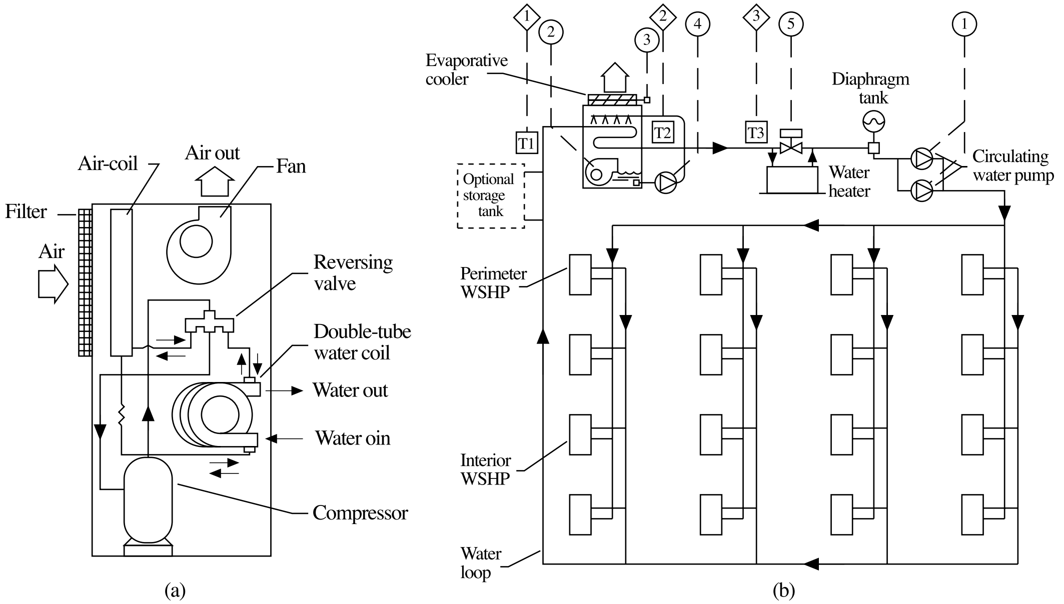

(a) (b)

FIGURE 9.15.2 A water-source heat pump system: (a) vertical system and (b) system schematic diagram.

condenser is often adopted in a centrifugal chiller to incorporate heat recovery for providing winter heating.

Water-Source Heat Pump Systems

Water-source heat pumps (WSHPs) are the primary equipment in a water-source heat pump system as shown in Figure 9.15.2(a). A *water-source heat pump* usually consists of an air coil to cool and heat the air; a water coil to reject and extract heat from the condenser water; a forward-curved centrifugal fan; reciprocating, rotary, or scroll compressor(s); a short capillary tube; a reversing valve; controls; and an outer casing. WSHPs could be either a horizontal or vertical unit. WSHPs usually have cooling capacities between 1/2 to 26 tons. Small-capacity WSHPs of 3 tons or less without ducts are used in perimeter zones, whereas large-capacity WSHPs with ductwork are used only in interior zones.

In addition to the WSHPs, a WSHP system usually is also comprised of an evaporative cooler or cooling tower to cool the condenser water; a boiler to provide the supplementary heat for the condenser water if necessary; two circulating pumps, one of them being standby; and controls, as shown in Figure 9.15.2(b). A separate outdoor ventilation air system is required to supply outdoor air to the WSHP or directly to the space.

During hot humid weather, when the outdoor wet bulb can reach 78°F, all the WSHPs are operated in the cooling mode. Condenser water leaves the evaporative cooler at a temperature typically 92°F and absorbs condensing heat rejected from the condensers — the water coils in WSHPs. Condenser water is then raised to 104°F and enters the evaporative cooler. In an evaporative cooler, condenser water is evaporatively cooled indirectly by atmospheric air, so that it would not foul the inner surface of water coils in WSHPs.

During moderate weather, the WSHPs serving the shady side of a building may be in heating mode, and while serving the sunny side of the building and the interior space in cooling mode. During cold weather, most of the WSHPs serving perimeter zones are in heating mode, while serving interior spaces are in cooling mode except morning warm-up. Cooling WSHPs reject heat to the condenser water loop; meanwhile heating WSHPs absorb heat from the condenser water loop. The condenser water is usually maintained at 60 to 90°F. If its temperature rises above 90°F, the evaporative cooler is energized. If it drops below 60°F, the boiler or electric heater is energized. A WSHP system itself is a combination of

WSHP and a heat recovery system to transfer the heat from the interior space and sunny side of the building to the perimeter zone and shady side of building for heating in winter, spring, and fall.

System characteristics of air, cooling, and heating in a WSHP system are similar to a room conditioner heat pump system. In addition:

Outdoor ventilating air system: type I and IV
Water system: two-pipe, close circuit
Centrifugal water circulating pump
Water storage tank is optional

To prevent freezing in locations where outdoor temperature may drop below 32°F, isolate the outdoor portion of the water loop, outdoor evaporative cooler, and the pipe work from the indoor portion by using a plate-and-frame heat exchanger. Add ethylene or propylene glycol to the outdoor water loop for freezing protection.

There is another space system called a panel heating and cooling system. Because of its higher installation cost and dehumidification must be performed in the separate ventilation systems, its applications are very limited.

A space conditioning system has the benefit of a separate demand-based outdoor ventilation air system. A WSHP system incorporates heat recovery automatically. However, its indoor sound level is higher; only a low-efficiency air filter is used for recirculating air, and more space maintenance is required than central and packaged systems. Because of the increase of the minimum outdoor ventilation air rate, it may gain more applications in the future.

Packaged Systems

In packaged systems, air is cooled directly by a DX coil and heated by direct-fired gas furnace or electric heater in a packaged unit (PU) instead of chilled and hot water from a central plant in a central system. Packaged systems are different from space conditioning systems since variable-air-volume supply and air economizer could be features in a packaged system. Packaged systems are often used to serve two or more rooms with supply and return ducts instead of serving individual rooms only in an individual system.

As mentioned in Section 9.7, packaged units are divided according to their locations into rooftop, split, or indoor units. Based on their operating characteristics, packaged systems can be subdivided into the following systems:

Single-Zone Constant-Volume (CV) Packaged Systems

Although a single-zone CV packaged system may have duct supplies to and returns from two or more rooms, there is only a single zone sensor located in the representative room or space. A CV system has a constant supply volume flow rate during operation except the undesirable reduction of volume flow due to the increase of pressure drop across the filter.

A single-zone CV packaged system consists mainly of a centrifugal fan, a DX coil, a direct-fired gas furnace or an electric heater, a low or medium efficiency filter, mixing box, dampers, DDC controls, and an outer casing. A relief or a return fan is equipped for larger systems.

A single-zone CV packaged system serving a church is shown in Figure 9.1.3. This system operates on basic air-conditioning cycles as shown in Figure 9.3.4 during cooling and heating modes.

The system characteristics of a single-zone CV packaged system are

Air system: single supply fan, a relief or return fan for a large system
    Fan, motor, and drive combined efficiency: 40 to 45%
    Fan total pressure: 1.5 to 3 in. WG
    Fan(s) energy use: 0.45 to 0.8 W/cfm
    Outdoor ventilation air system: type IV and II
    Enthalpy or temperature air economizer

Cooling systems: DX system, air cooled
    Compressor: reciprocating or scroll
    EER: 8.9 to 10.0 Btu/hr.W
Heating system: direct-fired gas furnace, air-source heat pump, or electric heating
Part load: on–off or step control of the compressor capacity, DX-coil effective area, and the gas flow to the burner
Sound level: indoor NC 35 to 45
Maintenance: higher maintenance cost than central systems

Single-zone, CV packaged systems are widely used in residences, small retail stores, and other commercial buildings.

Constant-Volume Zone-Reheat Packaged Systems

System construction and system characteristics of a CV zone-reheat system are similar to the single-zone CV packaged systems except:

1. It serves multizones and has a sensor and a DDC controller for each zone.
2. There is a reheating coil or electric heater in the branch duct for each zone.

A CV zone-reheat packaged system cools and heats simultaneously and therefore wastes energy. It is usually used for the manufacturing process and space needs control of temperature and humidity simultaneously.

Variable-Air-Volume Packaged Systems

A variable-air-volume (VAV) system varies its volume flow rate to match the reduction of space load at part load. A VAV packaged system, also called a *VAV cooling packaged system*, is a multizone system and uses a VAV box in each zone to control the zone temperature at part load during summer cooling mode operation, as shown in Figure 9.15.3(a).

A *VAV box* is a terminal in which the supply volume flow rate of the conditioned supply air is modulated by varying the opening of the air passage by means of a single blade damper, as shown in Figure 9.15.3(b), or a moving disc against a cone-shaped casing.

The following are the system characteristics of a VAV packaged system:

Single-zone VAV packaged system which serves a single zone without VAV boxes. A DDC controller modulates the position of the inlet vanes or the fan speed according to the signal of the space temperature sensor.

Air system: a supply/relief fan or supply/return fan combination. Space pressurization control by a relief/return fan
    Fan, motor, and drive combined efficiency: 45%
    Supply fan total pressure: 3.75 to 4.5 in. WG
    Fan(s) energy use at design condition: 1 to 1.25 W/cfm
    VAV box minimum setting: 30% of peak supply volume flow
    Outdoor ventilation air system: type II and III
Economizer: enthalpy air economizer or water economizer
Cooling system: DX coil, air-, water-, or evaporative-cooled condenser
    Compressor: reciprocating, scroll, and screw
    EER: 8.9 to 12 Btu/hr.W
Capacity: 20 to 100 tons
Part load: zone volume flow modulation by VAV box; step control of compressor capacity; modulation of gas flow to burner; and discharge air temperature reset
Smoke control: exhausts smoke on the fire floor, and supplies air and pressurizes the floors immediately above or below the fire floor
Diagnostics: a diagnostic module displays the status and readings of various switches, dampers, sensors, etc. and the operative problems by means of expert system

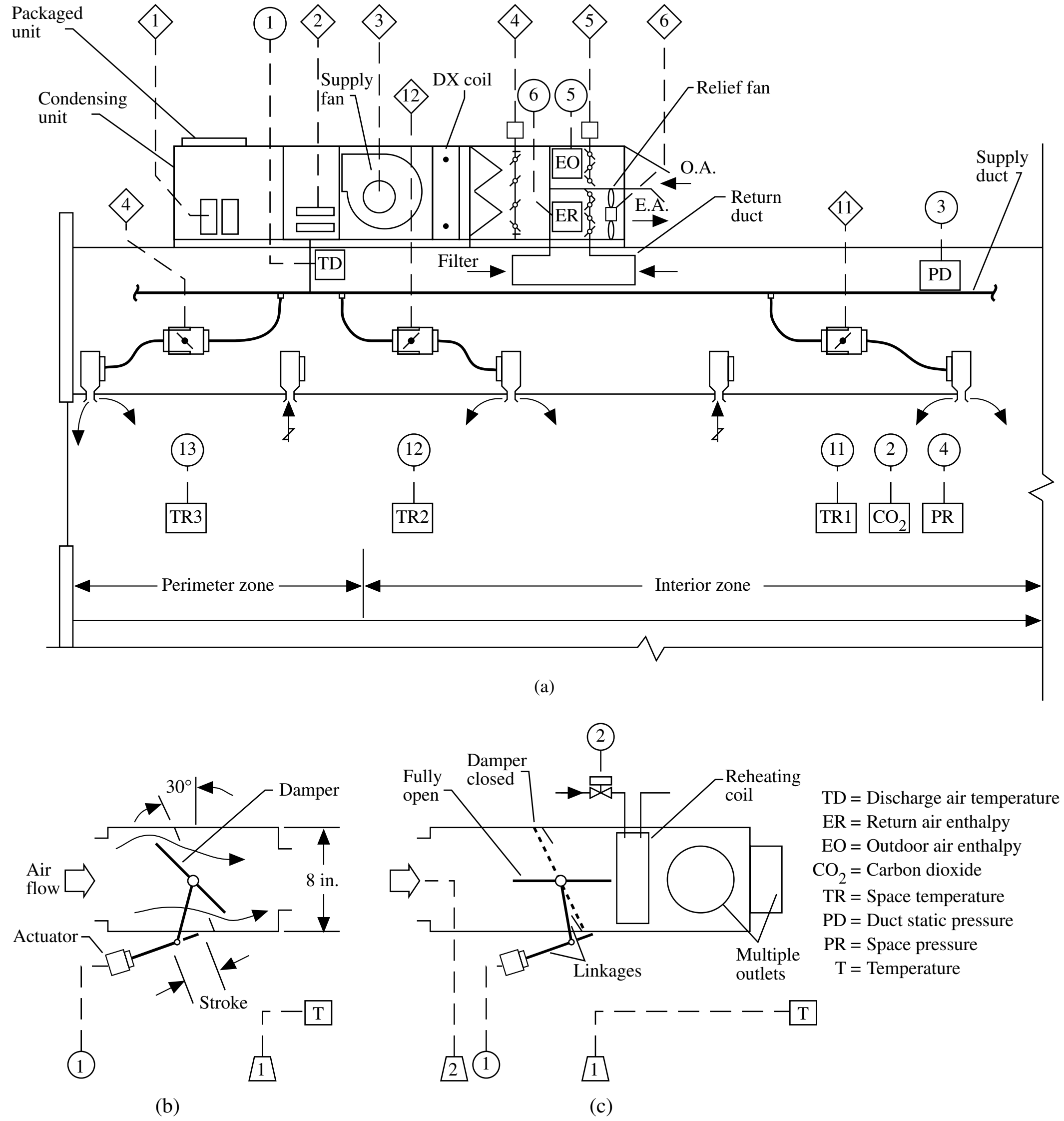

FIGURE 9.15.3 A variable-air-volume (VAV) package system: (a) schematic diagram, (b) VAV box, (c) reheating box, (d) parallel-flow fan-powered VAV box.

Maintenance: higher than central system
Sound level: indoor NC 30 to 45

Heating system characteristics as well as the air-conditioning cycles are similar as that in a single-zone CV packaged system.

VAV Reheat Packaged Systems

A VAV reheat packaged system has its system construction and characteristics similar to that in a VAV packaged system except in each VAV box there is an additional reheating coil. Such a VAV box is called a *reheating VAV box*, as shown in Figure 9.15.2(a) and 9.15.3(c). VAV reheat packaged systems are used to serve perimeter zones where winter heating is required.

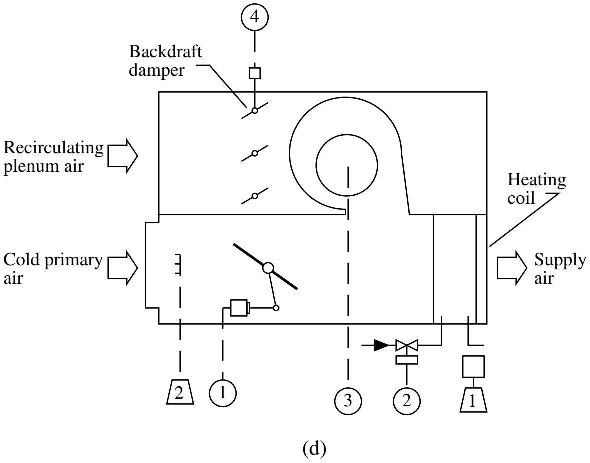

FIGURE 9.15.3d

Fan-Powered VAV Packaged Systems

A fan-powered VAV packaged system is similar to that of a VAV packaged system except *fan-powered VAV boxes* as shown in Figure 9.15.3(d) are used instead of VAV boxes.

There are two types of fan-powered VAV boxes: parallel-flow and series-flow boxes. In a *parallel-flow* fan-powered box, the plenum air flow induced by the fan is parallel with the cold primary air flow through the VAV box. These two air streams are then combined and mixed together. In a *series-flow* box, cold primarily from the VAV box is mixed with the induced plenum air and then flows through the small fan. The parallel-flow fan-powered VAV box is more widely used.

In a fan-powered VAV box, volume flow dropping to minimum setting, extracting of ceiling plenum air, and energizing of reheating coil will actuate in sequence to maintain the space temperature during part-load/heating mode operation. A fan-powered VAV box can also mix the cold primary air from cold air distribution with the ceiling plenum air and provides greater space air movements during minimum space load.

Packaged systems are lower in installation cost and occupy less space than central systems. During the past two decades, DDC-controlled packaged systems have evolved into sophisticated equipment and provide many features that only a built-up central system could provide before.

Central Systems

Central systems use chilled and hot water that comes from a central plant to cool and heat the air in the air-handling units (AHUs). Central systems are built-up systems. The most clean, most quiet thermal-storage systems, and the systems which offer the most sophisticated features, are always central systems. Central systems can be subdivided into the following.

Single-Zone Constant-Volume Central Systems

A single-zone CV central system uses a single controller to control the flow of chilled water, hot water, or the opening of dampers to maintain a predetermined indoor temperature, relative humidity, or air contaminants. They are often used in manufacturing factories. The system characteristics of a single-zone CV central system are

Single-zone CV air washer central system uses an air washer to control both space relative humidity and temperature. This system is widely used in textile mills. The reason to use constant volume is to dilute the fiber dusts produced during manufacturing. A rotary filter is often used for high dust-collecting capacity.

Air system: supply and return fan combination
    Fan, motor, and drive combined efficiency: 45 to 50%
    Outdoor ventilation air system: type II and IV
Economizer: air or water economizer
Smoke control: exhaust smoke on the fire floor, and pressurize adjacent floor(s) or area
Cooling system: centrifugal or screw chiller, water-cooled condenser
    Cooling energy use: 0.4 to 0.65 kW/ton
Heating system: hot water from boiler or from heat recovery system
Part load: modulate the water mass flow to cooling and heating coils in AHUs, and discharge air temperature reset
Sound level: indoor NC 30 to 45. Silencers are used both in supply and return air systems if they are required
Maintenance: in central plant and fan rooms, lower maintenance cost

Single-Zone CV Clean Room Systems

This is the central system which controls the air cleanliness, temperature, and relative humidity in Class 1, 10, 100, 1000, and 10,000 clean rooms for electronic, pharmaceutical, and precision manufacturing and other industries. Figure 9.15.4(a) shows a schematic diagram of this system. The recirculating air unit (RAU) uses prefilter, HEPA filters, and a water cooling coil to control the space air cleanliness and required space temperature, whereas a make-up air unit (MAU) supplies conditioned outdoor air, always within narrow dew point limits to the RAU at any outside climate, as shown in Figure 9.15.4(b). A unidirectional air flow of 90 fpm is maintained at the working area. For details, refer to *ASHRAE Handbook 1991 HVAC Applications* and Wang's *Handbook of Air Conditioning and Refrigeration*.

CV Zone-Reheat Central Systems

These systems have their system construction and characteristics similar to that for a single-zone CV central system, except they serve multizone spaces and there is a reheating coil, hot water, or electric heating in each zone. CV zone-reheat central systems are often used for health care facilities and in industrial applications.

VAV Central Systems

A VAV central system is used to serve multizone space and is also called *VAV cooling central system*. Its schematic diagram is similar to that of a VAV packaged system (Figure 9.15.3) except air will be cooled or heated by water cooling or heating coils in the AHUs. The same VAV box shown in Figure 9.15.3(b) will be used in a VAV central system. The system characteristics of VAV central systems are as follows:

Single-zone VAV central system differs from a VAV central system only because it serves a single zone, and therefore there is no VAV box in the branch ducts. Supply volume flow is modulated by inlet vanes and AC inverter.

Air system: supply and relief/return fan combination
    Fan, motor, and drive combined efficiency for airfoil centrifugal fan with AC inverter fan speed modulation: 55%
    Fan(s) energy use: 0.9 to 1.2 W/cfm
    VAV box: minimum setting 30% of peak supply volume flow
    Outdoor ventilation air system: type I, II, and III
Cooling system: centrifugal, screw, and reciprocating chillers, water-cooled condenser, with energy use 0.4 to 0.65 kW/ton; or sometimes absorption chiller
Heating system: hot water from boiler or electric heating at the terminals
Economizer: air and water economizer
Part load: zone volume flow modulation, discharge air temperature reset, and chilled water temperature reset
Smoke control: exhausts smoke from the fire floor and pressurizes the immediate floors above and below

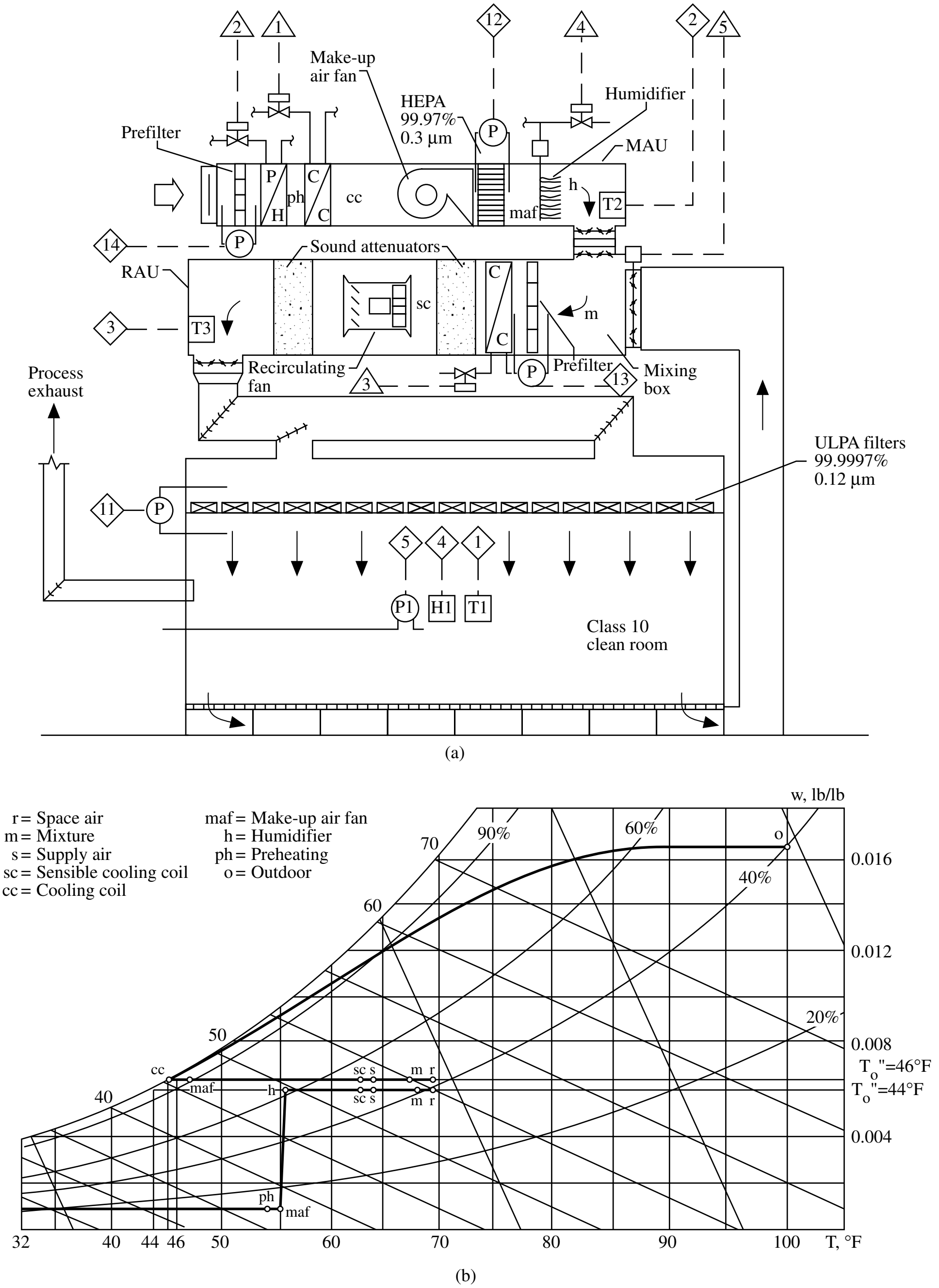

FIGURE 9.15.4 A single-zone CV clean room system: (a) schematic diagram and (b) air-conditioning cycle. (Source: Wang, S. K., *Handbook of Air Conditioning and Refrigeration*, McGraw-Hill, 1993. Reprinted by permission.)

Sound level: indoor NC 20 to 40. Silencers are often used both in supply and return systems.
Maintenance: less space maintenance

VAV central systems are widely used for interior zone in buildings.

VAV Reheat Central Systems

A VAV reheat system is similar in system construction and characteristics to that in a VAV central system except that reheating boxes are used instead of VAV boxes in a VAV central system.

Fan-Powered VAV Central Systems

A fan-powered VAV central system is similar in system construction and characteristics to that in a VAV central system except that fan-powered VAV boxes are used instead of VAV boxes.

Dual-Duct VAV Central Systems

A dual-duct VAV system uses a warm air duct and a cold air duct to supply both warm and cold air to each zone in a multizone space. Warm and cold air are first mixed in a mixing VAV box, and are then supplied to the conditioned space. The warm air duct is only used for perimeter zones.

A *mixing VAV box* consists of two equal air passages, one for warm air and one for cold air, arranged in parallel. Each of them has a single blade damper and its volume flow rate is modulated. Warm and cold air are then combined, mixed, and supplied to the space.

A dual-duct VAV system is usually either a single supply fan and a relief/return fan combination, or a warm air supply fan, a cold air supply fan, and a relief/return fan. A separate warm air fan and cold air supply fan are beneficial in discharge air temperature reset and fan energy use.

During summer cooling mode operation, the mixture of recirculating air and outdoor air is used as the warm air supply. The heating coil is not energized. During winter heating mode operation, the mixture of outdoor and recirculating air or 100% outdoor air is used as the cold air supply; the cooling coil is not energized.

Because there is often air leakage at the dampers in the mixing VAV box, more cold air supply is needed to compensate for the leaked warm air or leaked cold air.

Other system characteristics of a dual-duct VAV central system are similar to a VAV central system.

Dual-Duct CV Central System

This is another version of a dual-duct VAV central system and is similar in construction to a dual-duct VAV system, except that a mixing box is used instead of a mixing VAV box. The supply volume flow rate from a mixing box is nearly constant. Dual-duct CV central systems have only limited applications, like health care facilities, etc.

Some of the air-conditioning systems are not listed because they are not effective or are a waste of energy, and therefore rarely used in new and retrofit projects such as:

- High-velocity induction space conditioning systems which need a higher pressure drop primary air to induce recirculating air in the induction unit and use more energy than fan-coil systems
- Multizone central systems which mix warm and cool air at the fan room and use a supply duct from fan room to each control zone
- Air skin central systems which use a warm air heating system to offset transmission loss in the perimeter zone and overlook the effect of the solar radiation from variation building orientations

In the future, there will be newly developed systems added to this classification list.

Air-Conditioning System Selection

As described in Section 9.1, the goal of an air-conditioning or HVAC&R system is to provide a healthy, comfortable, manufacturable indoor environment at acceptable indoor air quality, keeping the system energy efficient. Various occupancies have their own requirements for their indoor environment. The basic considerations to select an air-conditioning system include:

1. The selection of an air-conditioning system must satisfy the required space temperature, relative humidity, air cleanliness, sound level, and pressurization. For a Class 100 clean room, a single-zone CV clean room system is always selected. A four-pipe fan-coil space conditioning system is

usually considered suitable for guest rooms in hotels for operative convenience, better privacy, and a guaranteed outdoor ventilation air system. A concert hall needs a very quiet single-zone VAV central system for its main hall and balcony.

2. The size of the project has a considerable influence on the selection. For a small-size residential air-conditioning system, a single-zone constant-volume packaged system is often the first choice.
3. Energy-efficient measures are specified by local codes. Comparison of alternatives by annual energy-use computer programs for medium and large projects is often necessary. Selection of energy source includes electricity or gas, and also using electrical energy at off-peak hours, like thermal storage systems is important to achieve minimum energy cost.

   For a building whose sound level requirement is not critical and conditioned space is comprised of both perimeter and interior zones, a WSHP system incorporating heat recovery is especially suitable for energy saving.
4. First cost or investment is another critical factor that often determines the selection.
5. Selection of an air-conditioning system is the result of synthetical assessment. It is difficult to combine the effect of comfort, reliability, safety, and cost. Experience and detailed computer program comparisons are both important.

The selection procedure usually begins whether an individual, space conditioning, packaged, central system, or CV, VAV, VAV reheat, fan-powered VAV, dual-duct VAV, or thermal storage system is selected. Then the air, refrigeration, heating, and control subsystems will be determined. After that, choose the option, the feature, the construction, etc. in each subsystem.

Comparison of Various Systems

The sequential order of system performance — excellent, very good, good, satisfactory — regarding temperature and relative humidity control (T&HC), outdoor ventilation air (OA), sound level, energy use, first cost, and maintenance for individual, space conditioning (SC), packaged, and central systems is as follows:

	Excellent (low or less)	Very Good	Good	Satisfactory
T&HC	Central	Packaged	Space	Individual
IAQ	Space	Central	Packaged	Individual
Sound	Central	Packaged	Space	Individual
Energy use	Individual	Space	Packaged	Central
First cost	Individual	Packaged	Space	Central
Maintenance	Central	Packaged	Space	Individual

Among the packaged and central systems, VAV cooling systems are used only for interior zones. VAV reheat, fan-powered VAV, and dual-duct VAV central systems are all for perimeter zones. VAV reheat systems are simple and effective, but have a certain degree of simultaneous cooling and heating when their volume flow has been reduced to minimum setting required for proper ventilation. Fan-powered VAV systems have the function of mixing cold primary air with ceiling plenum air. They are widely used in ice-storage systems with cold air distribution. Fan-powered VAV is also helpful to create a greater air movement at minimum cold primary air flow. Dual-duct VAV systems are effective and more flexible in operation. They are also more complicated and expensive.

Subsystems

Air Systems

The economical size of an air system is often 10,000 to 25,000 cfm. A very large air system always has higher duct pressure loss and is more difficult to balance. For highrise buildings of four stories and higher, floor-by-floor AHU(s) or PU(s) (one or more AHU or PU per floor) are often adopted. Such an arrangement is beneficial for the balance of supply and return volume flow in VAV systems and also for fire protection. A fan-powered VAV system using a riser to supply less cold primary to the fan-powered VAV box at various floors may have a larger air system. Its risers can be used as supply and exhaust ducts for a smoke-control system during a building fire.

In air systems, constant-volume systems are widely used in small systems or to dilute air contaminants in health care facilities and manufacturing applications. VAV systems save fan energy and have better operating characteristics. They are widely used in commercial buildings and in many factories.

Refrigeration Systems

For comfort air-conditioning systems, the amounts of required cooling capacity and energy saving are dominant factors in the selection of the refrigeration system. For packaged systems having cooling capacity less than 100 tons, reciprocating and scroll vapor compression systems with air-cooled condensers are most widely used. Evaporative-cooled condensers are available in many packaged units manufactured for their lower energy use. Scroll compressors are gradually replacing the reciprocating compressors for their simple construction and energy saving. For chillers of cooling capacity of 100 tons and greater, centrifugal chillers are still most widely used for effective operation, reliability, and energy efficiency. Screw chillers have become more popular in many applications, especially for ice-storage systems.

Heating Systems

For locations where there is a cold and long winter, a perimeter baseboard hot water heating system or dual-duct VAV systems are often a suitable choice. For perimeter zones in locations where winter is mild, winter heating is often provided by using warm air supply from AHU or PU from terminals with electric or hot water heaters. Direct-fired furnace warm air supply may be used for morning warm-up. For interior or conditioned zones, a cold air supply during occupied periods in winter and a warm air supply from the PUs or AHUs during morning warm-up period is often used.

Control Systems

Today, DDC microprocessor-based control with open data communication protocol is often the choice for medium- and large-size HVAC&R projects. For each of the air, cooling, and heating systems, carefully select the required generic and specific control systems. If a simple control system and a more complicated control system can provide the same required results, the simple one is always the choice.

Energy Conservation Recommendations

1. Turn off electric lights, personal computers, and office appliances when they are not needed. Shut down AHUs, PUs, fan coils, VAV boxes, compressors, fans, and pumps when the space or zone they serve is not occupied or working.
2. Provide optimum start and stop for the AHUs and PUs and terminals daily.
3. Temperature set point should be at its optimum value. For comfort systems, provide a dead band between summer and winter mode operation. Temperature of discharged air from the AHU or PU and chilled water leaving the chiller should be reset according to space or outdoor temperature or the system load.
4. Reduce air leakages from ducts and dampers. Reduce the number of duct fittings and pipe fittings and their pressure loss along the design path if this does not affect the effectiveness of the duct system. The maximum design velocity in ducts for comfort systems should not exceed 3000 fpm.
5. Adopt first the energy-efficient cooling methods: air and water economizer, evaporative cooler, or ground water instead of refrigeration.
6. Use cost-effective high-efficiency compressors, fans, pumps, and motors as well as evaporative-cooled condensers in PUs. Use adjustable-frequency fan speed modulation for large centrifugal fans. Equipment should be properly sized. Over-sized equipment will not be energy efficient.

7. Use heat recovery systems and waste heat for winter heating or reheating. Use a heat-pump system whenever its COP_{hp} is greater than 1.
8. For medium- and large-size air-conditioning systems, use VAV systems instead of CV systems except for health care or applications where dilution of air contaminant is needed. Use variable flow for building-loop and distribution-loop water systems.
9. Use double- and triple-pane windows with low emissive coatings. Construct low U-value roofs and external walls.

9.16 Desiccant Dehumidification and Air-Conditioning

Zalman Lavan

Introduction

Desiccant air-conditioning is a promising emerging technology to supplement electrically driven vapor compression systems that rely almost exclusively on R22 refrigerant that causes depletion of the ozone layer. To date, this technology has only a limited market, e.g., in supermarkets where the latent heat loads are very high, in specialized manufacturing facilities that require very dry air, and in hospitals where maximum clean air is required. However, recent emphasis on increased air change requirements (see ASHRAE standards, ANSI 62), improved indoor air quality, and restriction on use of CFC refrigerants (see The Montreal Protocol Agreement, as amended in Copenhagen in 1992, United Nations Environmental Programme, 1992) may stimulate wider penetration of desiccant-based air-conditioning which can be used as stand-alone systems or in combination with conventional systems. (See Table 9.4.1 for properties of some refrigerants.)

Sorbents and Desiccants

Sorbents are materials which attract and hold certain vapor or liquid substances. The process is referred to **absorption** if a chemical change takes place and as **adsorption** if no chemical change occurs. **Desiccants**, in both liquid and solid forms, are a subset of sorbents that have a high affinity to water molecules. Liquid desiccants *absorb* water molecules, while solid desiccants *adsorb* water molecules and hold them on their vast surfaces (specific surface areas are typically hundreds of square meters per gram).

While desiccants can sorb water in both liquid and vapor forms, the present discussion is limited to **sorption** of water vapor from adjacent air streams. The sorption driving force for both liquid and solid desiccants is a vapor pressure gradient. Adsorption (in solid desiccants) and absorption (in liquid desiccants) occur when the water vapor partial pressure of the surrounding air is larger than that at the desiccant surface. When an air stream is brought in contact with a desiccant, water vapor from the air is attracted by the desiccant, the air is **dehumidified**, and the water content of the desiccant rises. As the water sorbed by the desiccant increases, the sorption rate decreases and finally stops when *sorption equilibrium* is reached. For dehumidification to be resumed, water must be removed from the desiccant by heating. This process is referred to as **desorption**, **reactivation**, or **regeneration**. The heat of sorption (or desorption) is generally higher than the latent heat of vaporization of water; it approaches the latter as sorption equilibrium is reached.

Some typical *liquid desiccants* are water solutions of calcium chloride (CaCl), lithium chloride (LiCl), lithium bromide (LiBr), and triethylene glycol. The equilibrium water vapor pressure at the solution surface as a function of temperature and water content is shown in Figure 9.16.1 for water-lithium chloride solution. The surface vapor pressure (and dew point) increases with increasing solution temperature and decreases with increasing moisture content.

Common *solid desiccants* are silica gel, molecular sieves (zeolites), activated alumina, and activated carbon. The equilibrium sorption capacity (or moisture content) at a constant temperature, referred to

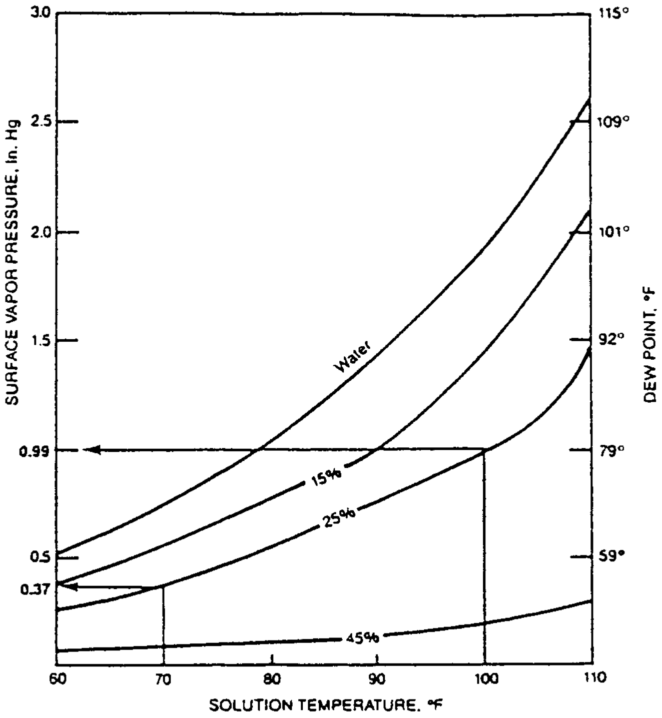

FIGURE 9.16.1 Surface vapor pressure of water-lithium chloride solutions. (Source: ASHRAE 1993, *Fundamentals Handbook*, chap. 19. With permission.)

as an **isotherm**, is usually presented as percent water (mass of water divided by mass of dry desiccant) vs. percent relative humidity (vapor pressure divided by saturation vapor pressure). Sorption capacity decreases with increasing temperature, but the spread of isotherms is relatively small (especially for concave down isotherms). Figure 9.16.2 shows normalized loading (sorption capacity divided by sorption capacity at 100% relative humidity) vs. relative humidity for silica gel, molecular sieve, and a generic desiccant, type 1 (modified) or simply 1-M (Collier et al., 1986).

Dehumidification

Dehumidification by vapor compression systems is accomplished by cooling the air below the dew point and then reheating it. The performance is greatly hindered when the desired outlet dew point is below 40°F due to frost formation on the cooling coils (*ASHRAE, Systems and Equipment Handbook,* 1992).

Desiccant dehumidification is accomplished by direct exchange of water vapor between an air stream and a desiccant material due to water vapor pressure difference. Figure 9.16.3 shows the cyclic operation of a desiccant dehumidification system.

In *sorption (1–2),* dry and cold desiccant (point 1) sorbs moisture since the vapor pressure at the surface is lower than that of the air stream. During this process the moisture content (loading or uptake) increases, the surface vapor pressure increases, and the liberated heat of sorption raises the desiccant temperature. During *desorption (2–3)*, the desiccant is subjected to a hot air stream, and moisture is removed and transferred to the surrounding air. The surface vapor pressure is increased and the desiccant temperature rises due to the added heat. The cycle is closed by *cooling (3–1)*. The desiccant is cooled while its moisture content is constant and the surface vapor pressure is lowered. The above cycle of sorption, desorption, and cooling can be modified by combining the sorption process with cooling to approach isothermal rather than adiabatic sorption.

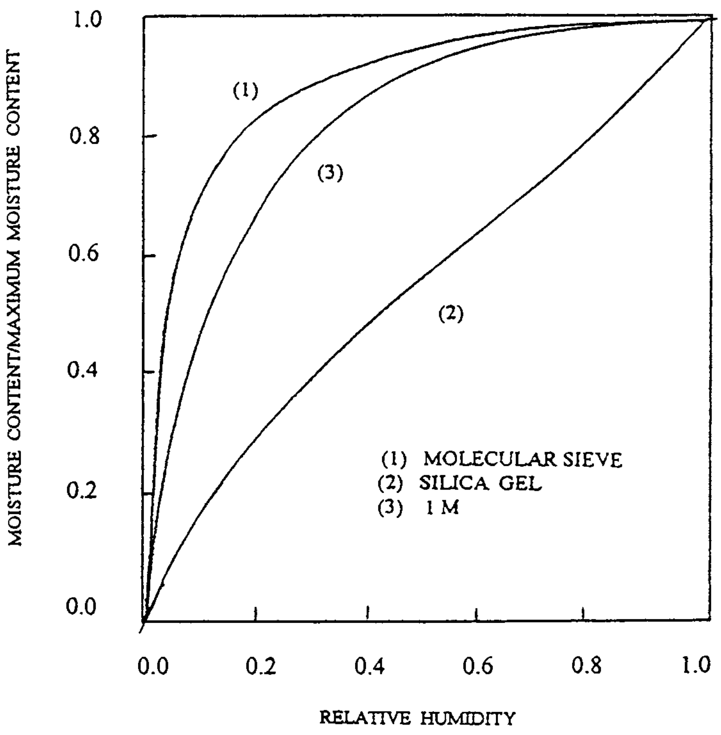

FIGURE 9.16.2 Normalized solid desiccant isotherms.

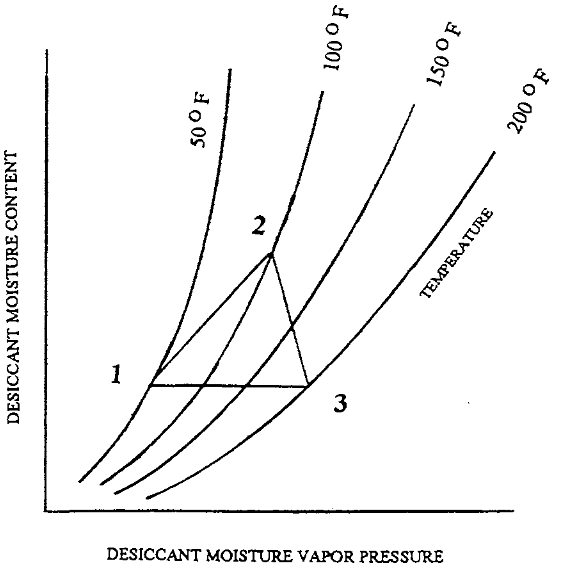

FIGURE 9.16.3 Cyclic dehumidification processes.

Desirable Characteristics for High-Performance Liquid and Solid Desiccant Dehumidifiers

High equilibrium moisture sorption capacity
High heat and mass transfer rates
Low heat input for regeneration
Low pressure drop

Large contact transfer surface area per unit volume
Compatible desiccant/contact materials
Inexpensive materials and manufacturing techniques
Minimum deterioration and maintenance

Additional Requirements for Liquid Desiccant Dehumidifiers

Small liquid side resistance to moisture diffusion
Minimum crystallization

Additional Requirements for Solid Desiccant Dehumidifiers

The desiccant should not deliquesce even at 100% relative humidity.
The airflow channels should be uniform.
The desiccant should be bonded well to the matrix.
The material should not be carciogenic or combustible.

Liquid Spray Tower

Figure 9.16.4 is a schematic of a liquid spray tower. A desiccant solution from the sump is continuously sprayed downward in the absorber, while air, the process stream, moves upward. The air is dehumidified and the desiccant solution absorbs moisture and is weakened. In order to maintain the desired solution concentration, a fraction of the solution from the sump is passed through the regenerator, where it is heated by the heating coil and gives up moisture to the desorbing air stream. The strong, concentrated solution is then returned to the sump. The heat liberated in the absorber during dehumidification is removed by the cooling coil to facilitate continuous absorption (see Figure 9.16.1 and Figure 9.16.3). The process air stream exits at a relatively low temperature. If sufficiently low water temperature is available (an underground well, for example), the process stream could provide both sensible and latent cooling.

The heating and cooling coils, shown in Figure 9.16.4, are often eliminated and the liquid solutions are passed through heating and cooling heat exchangers before entering the spray towers.

Advantages

The system is controlled to deliver the desired level of dry air by adjusting the solution concentration.

Uniform exit process stream conditions can be maintained.
A concentrated solution can be economically stored for subsequent drying use.
The system can serve as a humidifier when required by simply weakening the solution.
When used in conjunction with conventional A/C systems, humidity control is improved and energy is conserved.

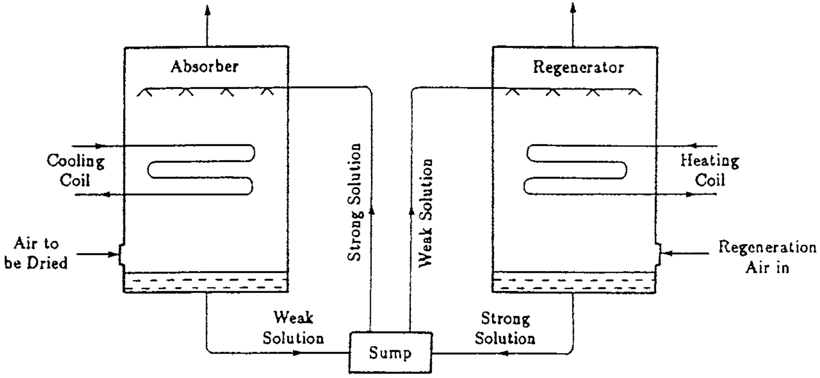

FIGURE 9.16.4 Liquid desiccant dehumidifier with heating and cooling coils.

Disadvantages

Some desiccants are corrosive.
Response time is relatively large.
Maintenance can be extensive.
Crystallization may be a problem.

Solid Packed Tower

The dehumidification system, shown in Figure 9.16.5, consists of two side-by-side cylindrical containers filled with solid desiccant and a heat exchanger acting as a desiccant cooler. The air stream to be processed is passed through dry desiccant in one of the containers, while a heated air stream is passed over the moist desiccant in the other. Adsorption (1–2) takes place in the first container, desorption (2–3) in the other container, and cooling (3–1) occurs in the desiccant cooler. The function of the two containers is periodically switched by redirecting the two air streams.

Advantages

No corrosion or crystallization
Low maintenance
Very low dew point can be achieved

Disadvantages

The air flow velocity must be low in order to maintain uniform velocity through the containers and to avoid dusting.
Uniform exit process stream dew point cannot be maintained due to changing moisture content in the adsorbing desiccant.

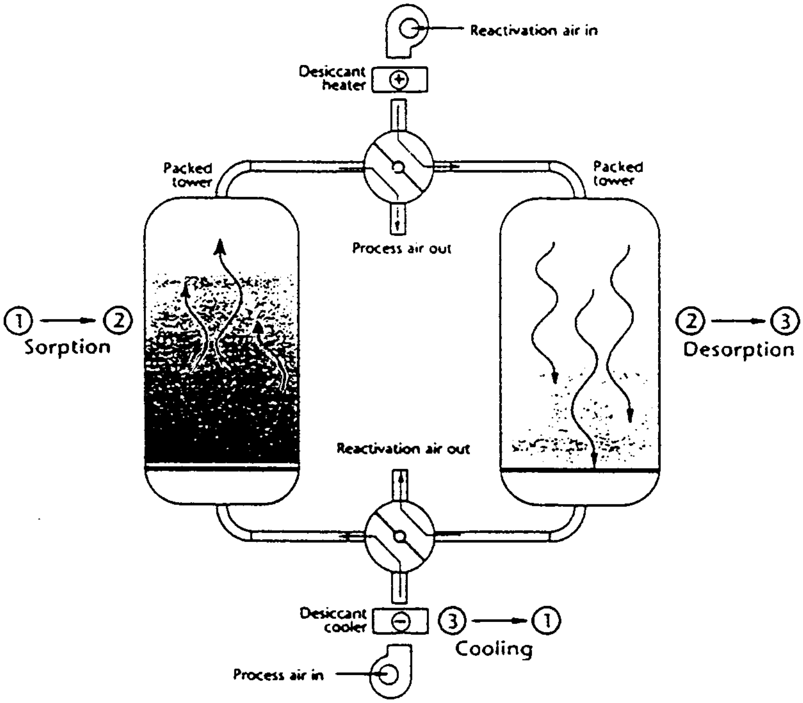

FIGURE 9.16.5 Solid packed tower dehumidification. (From Harriman, L. G., III. 1990. *The Dehumidification Handbook*, 2nd ed. Munters Cargocaire. With permission.)

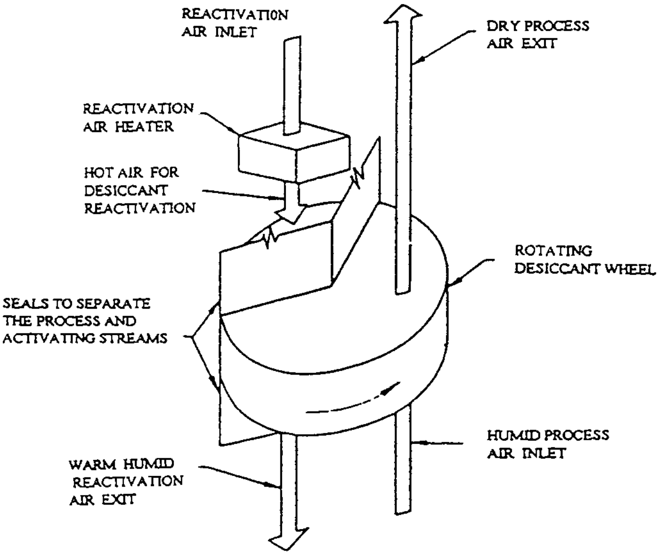

FIGURE 9.16.6 Rotary desiccant dehumidification wheel. (Source: ASHRAE 1992, *Systems and Equipment Handbook*, chap. 22. With permission.)

Rotary Desiccant Dehumidifiers

A typical rotary solid desiccant dehumidifier is shown in Figure 9.16.6. Unlike the intermittent operation of packed towers, rotary desiccant dehumidifiers use a wheel (or drum) that rotates continuously and delivers air at constant humidity levels.

Desiccant wheels typically consist of very fine desiccant particles dispersed and impregnated with a fibrous or ceramic medium shaped like a honeycomb or fluted corrugated paper. The wheel is divided into two segments. The process stream flows through the channels in one segment, while the regenerating (or reactivating) stream flows through the other segment.

Desiccant Material

The desired desiccant properties for optimum dehumidification performance are a suitable isotherm shape and a large moisture sorption capacity. The isotherms of silica gel are almost linear. The moisture sorption capacity is high; the desiccant is reactivated at relatively low temperatures and is suitable for moderate dehumidification. Molecular sieves have very steep isotherms at low relative humidity. The desiccant is reactivated at relatively high temperatures and is used for deep dehumidification. The isotherm of the type 1-M yields optimum dehumidification performance (Collier et al., 1986), especially when used in conjunction with high regeneration temperatures.

The Desiccant Wheel

Some considerations for selection of desiccant wheels are:

Appropriate desiccant materials
Large desiccant content
Wheel depth and flute size (for large contact surface area and low pressure drop)
Size and cost

The actual performance depends on several additional factors that must be addressed. These include:

Inlet process air temperature and humidity
Desired exit process air humidity
Inlet reactivating air temperature and humidity

Face velocity of the two air streams
Size of reactivation segment

It should be noted that:

Higher inlet process air humidity results in higher exit humidity and temperature (more heat of sorption is released).
Lower face velocity of the process stream results in lower exit humidity and higher temperature.
Higher regeneration temperatures result in deeper drying, hence lower exit process air humidity and higher temperature.
When lower exit air temperature is required, the exit process air should be cooled by a heat exchanger.
Final cooling of the exit process air can be achieved by partial humidification (this counteracts in part previous dehumidification).

The following is a range of typical parameters for rotary desiccant wheels:

Rotation speed: 4 to 10 rpm
Desiccant fraction: 70 to 80%
Flute size: 1 to 2 mm
Reactivation segment: 25 to 30% of wheel
Face velocity: 300 to 700 fpm
Reactivating temperature: 100 to 300°F

Hybrid Cycles

A limited number of hybrid systems consisting of desiccant dehumidifiers and electrically driven vapor compression air-conditioners are presently in use in supermarkets. This application is uniquely suited for this purpose since the latent heat loads are high due to the large number of people and frequent traffic through doors. Also, low relative humidity air is advantageous for open-case displays.

Vapor compression systems are inefficient below a dew point of 45 to 50°F. When used in supermarkets, they require high airflow rates, the air must be reheated for comfort, and the evaporator coils must be defrosted frequently. Hybrid systems offer improved performance and lower energy cost in these cases.

Figure 9.16.7 shows a typical hybrid air-conditioning system for supermarkets. A mixture of outdoor and recirculated air is first passed through the desiccant and sensible heat exchanger wheels, where it is dehumidified and precooled. It then enters the conventional chiller before it is introduced to the interior of the supermarket. The sensible heat exchanger wheel is cooled by outdoor air and the desiccant wheel is regenerated by air heated with natural gas. Energy cost can be further reduced by preheating the reactivating air stream with waste heat rejected from the condenser of the refrigeration and/or air-conditioning systems.

The advantages of these hybrid systems are

Air-conditioning requirement is reduced by up to 20%.
The vapor compression system operates at a higher coefficient of performance (COP) since the evaporator coils are at a higher temperature.
Airflow requirements are reduced; electric fan energy is saved and duct sizes are reduced.
The refrigeration cases run more efficiently since the frequency of defrost cycles is greatly reduced.

Solid Desiccant Air-Conditioning

Several stand-alone desiccant air-conditioning systems were suggested and extensively studied. These systems consist of a desiccant wheel, a sensible heat exchanger wheel, and evaporating pads. Sorption can be adiabatic or cooled (if cooling is combined with sorption). When room air is dehumidified and recirculated, the system is said to operate in the **recirculating** mode. When 100% outside air is used as the process stream, the system operates in the **ventilating mode**.

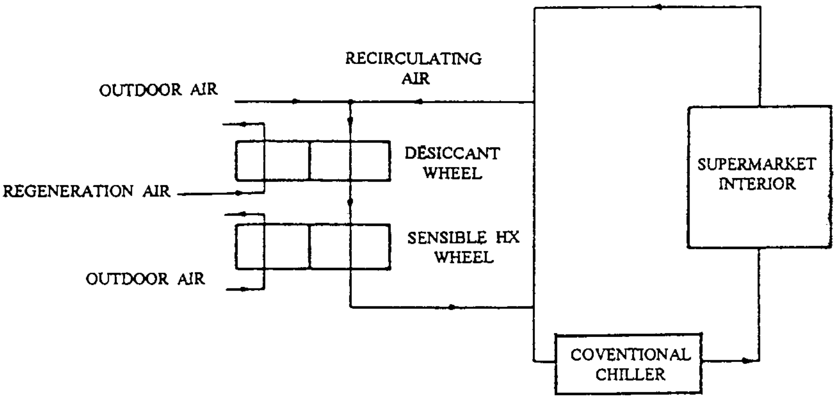

FIGURE 9.16.7 Hybrid air-conditioning system for supermarkets.

Ventilation Mode

In the *adsorption path* the process air stream drawn from the outdoors is passed through the dry section of the desiccant wheel where it is dehumidified and heated by the liberated heat of sorption. It then passes through the sensible heat exchanger wheel and exits as dry but slightly warm air. The hot and dry air leaving the dehumidifier enters the heat exchanger, where it is sensibly cooled down to near room temperature. It is then passed through the evaporative cooler, where it is further cooled and slightly humidified as it enters the conditioned space.

In the *desorption path,* air is drawn from the conditioned space; it is humidified (and thus cooled) in the evaporative cooler. The air stream enters the sensible heat exchanger, where it is preheated, and it is then heated to the desired regeneration temperature by a suitable heat source (natural gas, waste heat, or solar energy), passed through the desiccant wheel (regenerating the desiccant material), and discharged out of doors.

Performance. In order to achieve high performance, the maximum moisture content of the desiccant should be high and the isotherm should have the optimum shape (1 M). In addition, Zheng et al. (1993) showed that the optimum performance is very sensitive to the rotational speed of the desiccant wheel. Glav (1966) introduced stage regeneration. He showed that performance is improved when the reactivation segment of the wheel is at a temperature which increases in the direction of rotation. Collier (Collier et al., 1986) showed that well-designed open-cycle desiccant cooling systems can have a thermal COP of 1.3. This, however, would require the use of high-effectiveness sensible heat exchangers, which would be large and expensive. Smaller and more affordable heat exchangers should yield system COPs in the order of unity. An extensive review of the state-of-the-art assessment of desiccant cooling is given by Pesaran et al. (1992).

Conclusions

Desiccant-based air-conditioning offers significant advantages over conventional systems. Desiccant systems are already successfully used in some supermarkets. It is expected that these systems will gradually attain wider market penetration due to environmental requirements and potential energy savings.

The advantages of desiccant air-conditioning are summarized below:

No CFC refrigerants are used.
Indoor air quality is improved.
Large latent heat loads and dry air requirements are conveniently handled.
Individual control of temperature and humidity is possible.
The energy source may be natural gas and/or waste heat.
Less circulated air is required.
Summer electric peak is reduced.

Defining Terms

Absorb, absorption: When a chemical change takes place during sorption.
Adsorb, adsorption: When no chemical change occurs during sorption.
Dehumidification: Process of removing water vapor from air.
Desiccant: A subset of sorbents that has a particular affinity to water.
Desorb, desorption: Process of removing the sorbed material from the sorbent.
Isotherm: Sorbed material vs. relative humidity at a constant temperature.
Reactivation: Process of removing the sorbed material from the sorbent.
Recirculation: Indoor air only is continuously processed.
Regeneration: Process of removing the sorbed material from the sorbent.
Sorbent: A material that attracts and holds other gases or liquids.
Sorption: Binding of one substance to another.
Staged regeneration: When the temperature of the regeneration segment of the desiccant wheel is not uniform.
Ventilation mode: 100% of outdoor air is processed.

References

AMCA. 1973. Fan and Systems Publication 201. AMCA, Arlington Heights, IL.

Amistadi, H. 1993. Design and drawing software review, *Eng. Syst.* 6:18–29.

ANSI/ASHRAE. 1992. ANSI/ASHRAE Standard 34-1992, *Numbering Designation and Safety Classification of Refrigerants.* ASHRAE, Atlanta, GA.

ASHRAE. 1989. *Handbook of Fundamentals.* American Society of Heating, Refrigerating and Air-Conditioning Engineers, Atlanta.

ASHRAE. 1991. *ASHRAE Handbook, HVAC Applications.* ASHRAE, Atlanta, GA.

ASHRAE. 1992. *ASHRAE Handbook, HVAC Systems and Equipment.* ASHRAE, Atlanta, GA.

ASHRAE. 1994. *ASHRAE Handbook, Refrigeration.* ASHRAE, Atlanta, GA.

ASHRAE. 1997. *Handbook of Fundamentals.* American Society of Heating, Refrigerating and Air-Conditioning Engineers, Atlanta.

ASHRAE. 2001. *ASHRAE Handbook, Fundamentals.* ASHRAE, Atlanta, GA.

Bayer, C.W. and Black, M.S. 1988. IAQ evaluations of three office buildings. *ASHRAE J.* 7:48–52.

Birdsall, B., W.F. Buhl, K.L. Ellington, A.E. Erdem, and F.C. Winkelmann. 1990. Overview of the DOE2.1 building energy analysis program. Report LBL-19735, rev. 1. Lawrence Berkeley Laboratory, Berkeley, CA.

Bushby, S.T. and Newman, H.M. 1994. BACnet: a technical update, *ASHRAE J.* 1:S72–84.

Carlson, G.F. 1968. Hydronic systems: analysis and evaluation, I. *ASHRAE J.* 10:2–11.

Collier, R.K. 1989. Desiccant properties and their effect on cooling system performance. *ASHRAE Trans.* 95(1):823–827.

Collier, R.K, Cale, T.S., and Lavan, Z. 1986. *Advanced Desiccant Materials Assessment,* pb-87-172805/XAB. Gas Research Institute, Chicago, IL.

DOE. 1981. DOE-2 Reference Material (Version 2.1A). National Technical Information Service, Springfield, VA.

Dorgan, C.E. and Elleson, J.S. 1988. Cold air distribution. *ASHRAE Trans.* I:2008–2025.

Durkin, J. 1994. *Expert Systems Design and Development.* Macmillan, New York.

EIA. 1994. Commercial Buildings Characteristics 1992. U.S. Government Printing Office, Washington, D.C.

Elyashiv, T. 1994. Beneath the surface: BACnet™ data link and physical layer options. *ASHRAE J.* 11:32–36.

EPA/CPSC. 1988. The Inside Story: A Guide to Indoor Air Quality. Environmental Protection Agency, Washington, D.C.

Fanger, P.O., Melikow, A.K., Hanzawa, H., and Ring, J. 1989. Turbulence and draft. *ASHRAE J.* 4:18–25.

Fiorino, D.P. 1991. Case study of a large, naturally stratified, chilled-water thermal storage system. *ASHRAE Trans.* II:1161–1169.

Gammage, R.B., Hawthorne, A.R., and White, D.A. 1986. Parameters Affecting Air Infiltration and Air Tightness in Thirty-One East Tennessee Homes, Measured Air Leakage in Buildings, ASIM STP 904. American Society of Testing Materials, Philadelphia.

Glav, B.O. 1966. Air Conditioning Apparatus, U.S. Patent No. 3251402.

Goldschmidt, I.G. 1994. A data communucations introduction to BACnet™. *ASHRAE J.* 11:22–29.

Gorton, R.L. and Sassi, M.M. 1982. Determination of temperature profiles and loads in a thermally stratified air-conditioning system. I. Model studies. *ASHRAE Trans.* II:14–32.

Grimm, N.R. and Rosaler, R.C. 1990. *Handbook of HVAC Design.* McGraw-Hill, New York.

Harriman, L.G. III. 1990. *The Dehumidification Handbook Second Edition.* Munters Cargocaire, Amesbury, MA.

Hartman, T.B. 1989. TRAV — a new HVAC concept. *Heating/Piping/Air Conditioning.* 7:69–73.

Hayner, A.M. 1994. Engineering in quality. *Eng. Syst.* 1:28–33.

Heyt, H.W. and Diaz, M.J. 1975. Pressure drop in spiral air duct. *ASHRAE Trans.* II:221–232.

Huebscher, R.G. 1948. Friction equivalents for round, square, and rectangular ducts. *ASHRAE Trans.* 101–144.

Hummel, K.E., Nelson, T.P., and Tompson, P.A. 1991. Survey of the use and emissions of chlorofluorocarbons from large chillers. *ASHRAE Trans.* II:416–421.

Jakob, F.E., Locklin, D.W., Fisher, R.D., Flanigan, L.G., and Cudnik, L.A. 1986. SP43 evaluation of system options for residential forced-air heating. *ASHRAE Trans.* IIB:644–673.

Kimura, K. 1977. *Scientific Basis of Air Conditioning.* Applied Science Publishers, London.

Knebel, D.E. 1995. Current trends in thermal storage. *Eng. Syst.* 1:42–58.

Korte, B. 1994. The health of the industry. *Heating/Piping/Air Conditioning.* 1:111–112.

Kreider, J.F., P. Curtiss, and A. Rabl (2001). *Heating and Cooling of Buildings: Design for Efficiency*, McGraw–Hill, New York.

Locklin, D.W., Herold, K.E., Fisher, R.D., Jakob, F.E., and Cudnik, R.A. 1987. Supplemental information from SP43 evaluation of system options for residential forced-air heating. *ASHRA Trans.* II:1934–1958.

Lowe, R. and Ares, R. 1995. From CFC-12 to HFC-134a: an analysis of a refrigerant retrofit project. *Heating/Piping/Air Conditioning.* 1:81–89.

McQuiston, F.C. and Spitler, J.D. 1992. *Cooling and Heating Load Calculating Manual,* 2nd ed. ASHRAE, Atlanta, GA.

Mitalas, G.P. 1972. Transfer function method of calculating cooling loads, heat extraction rate and space temperature, *ASHRAE J.* 12:52–56.

Mitalas, G.P. and Stephenson, D.G. 1967. Room thermal response factors. *ASHRAE Trans.* 2, III.2.1.

Modera, M.P. 1989. Residential duct system leakage: magnitude, impact, and potential for reduction. *ASHRAE Trans.* II:561–569.

Molina, M.J. and Rowland, S. 1974. Stratospheric sink for chloromethanes: chlorine atom catalyzed destruction of ozone. *Nature.* 249:810–812.

NIOSH. 1989. Congressional Testimony of J. Donald Miller, M.D., before the Subcommittee of Superfund, Ocean, and Water Protection, May 26, 1989. NIOSH, Cincinnati, Cleveland.

Norford, L.K., A. Rabl, J.P. Harris, and J. Roturier (1989). Electronic office equipment: the impact of market trends and technology on end use demand. In T.B. Johansson et al., Eds. *Electricity: Efficient End Use and New Generation Technologies, and Their Planning Implications*. Lund University Press, Lund, Sweden, 427–460.

Parsons, B.K., Pesaran, A.A., Bharathan, D., and Shelpuk, B. 1989. Improving gas-fired heat pump capacity and performance by adding a desiccant dehumidification subsystem. *ASHRAE Trans.* I:835–844.

Persily, A.K. 1993. Ventilation, carbon dioxide, and ASHRAE Standard 62-1989. *ASHRAE J.* 7:40–44.

Pesaran, A.A., Penny, T.R., and Czanderna. 1992. *Desiccant Cooling: State-of-the-Art Assessment.* National Renewable Energy Laboratory, Golden, CO.

Reynolds, S. 1994. CFD modeling optimizes contaminant elimination. *Eng. Syst.* 2:35–37.

Rowland, S. 1992. The CFC controversy: issues and answers. *ASHRAE J.* 12:20–27.

Rudoy, W. and Duran, F. 1975. Development of an improved cooling load calculation method. *ASHRAE Trans.* II:19–69.

Scofield, C.M. and DesChamps, N.H. 1984. Indirect evaporative cooling using plate-type heat exchangers. *ASHRAE Trans.* I B:148–153.

Shinn, K.E. 1994. A specifier's guide to BACnet™. *ASHRAE J.* 4:54–58.

Sowell, E.F. 1988. Classification of 200,640 parametric zones for cooling load calculations. *ASHRAE Trans.* II:754–777.

Spitler, J.D., McQuiston, F.C., and Lindsey, K.L. 1993. The CLTD/SCL/CLF Cooling Calculation Method. *ASHRAE Trans.* I:183–192.

Straub, H.E. and Cooper, J.G. 1991. Space heating with ceiling diffusers. *Heating/Piping/Air Conditioning.* May:49–55.

Tackett, R.K. 1989. Case study: office building use ice storage, heat recovery, and cold air distribution. *ASHRAE Trans.* I:1113–1121.

Threlkeld, J.L. 1970. *Thermal Environmental Engineering.* Prentice-Hall, Englewood Cliffs, NJ.

The Trane Company. 1992. TRANE TRACE 600, Engineering Manual. The Trane Co., Lacrosse, WI.

Tinsley, W.E., Swindler, B., and Huggins, D.R. 1992. Rooftop HVAC system offers optimum energy efficiency. *ASHRAE J.* 3:24–28.

Tsal, R.J., Behls, H.F., and Mangel, R. 1988. T-method duct design. I. Optimizing theory. *ASHRAE Trans.* II:90–111.

Tsal, R.J., Behls, H.F., and Mangel, R. 1988. T-method duct design. II. Calculation procedure and economic analysis. *ASHRAE Trans.* II:112–150.

United Nations Environmental Programme. 1992. Report of the fourth meeting of the parties to the Montreal protocol on substances that deplete the ozone layer, November 23–25, 1992, Copenhagen.

Vaculik, F. and Plett, E.G. 1993. Carbon dioxide concentration-based ventilation control. *ASHRAE Trans.* I:1536–1547.

Van Horn, M. 1986. *Understanding Expert Systems.* Bantam Books, Toronto.

Wang, S.K. 1993. *Handbook of Air Conditioning and Refrigeration.* McGraw-Hill, New York.

Wang, S.K., Leung, K.L., and Wong, W.K. 1984. Sizing a rectangular supply duct with transversal slots by using optimum cost and balanced total pressure principle. *ASHRAE Trans.* II A:414–429.

Williams, P.T., Baker, A.J., and Kelso, R.M. 1994. Numerical calculation of room air motion. III. Three-dimensional CFD simulation of a full scale experiment. *ASHRAE Trans.* I:549–564.

Wong, S.P.W. and Wang, S.K. 1990. Fundamentals of simultaneous heat and moisture transfer between the building envelope and the conditioned space air. *ASHRAE Trans.* II:73–83.

Wright, D.K. 1945. A new friction chart for round ducts. *ASHRA Trans.* 303–316.

Zheng, W., Worek, W.M., and Novosel, D. 1993. Control and optimization of rotational speeds for rotary dehumidifiers. *ASHRAE Trans.* 99(1).

10

Transportation

Frank Kreith
University of Colorado

Michael D. Meyer
Georgia Institute of Technology

John Leonard II
Georgia Institute of Technology

Paul W. Shuldiner
University of Massachusetts

Kenneth B. Black
University of Massachusetts

Paul Schonfeld
University of Maryland

Paul Norton
National Renewable Energy Laboratory

Wendy Clark
National Renewable Energy Laboratory

Iqbal Husain
University of Akron

Sumit Ghosh
Stevens Institute of Technology

Introduction

Frank Kreith

An efficient and economically viable transportation system is an essential part of a modern industrial society. This is particularly true in the U.S., where growth of suburbia requires the average American worker to commute a considerable distance daily between home and work. The situation is exacerbated in many locations by a lack of adequate public transportation, which requires commuters to travel by private automobiles. The use of single occupancy vehicles not only causes congestion, delays, and air pollution, but also imposes a severe economic penalty on many Americans. A recent consumer expenditure survey showed that transportation for most Americans is an expense second only to housing. The vast majority of the transportation spending (98%) is for the purchase, operation, and maintenance of automobiles.

From a national perspective, the transportation sector presents enormous challenges for the future. At present, more than 97% of the fuel used for ground transportation in the U.S. is petroleum-based and over 50% is imported. The transportation sector accounts for approximately 20% of the gross domestic product, and the cost of gas and oil has become a growing concern to the government. In 1999, the U.S. Department of Energy presented three oil price scenarios with predictions through the year

2020. In the reference case, prices were predicted to rise slowly to $23 per barrel by 2020, and in the high price scenario, an increase to about $30 per barrel was predicted. Today, the price of oil already exceeds $40 per barrel, and barring a worldwide recession, there is no reason to expect a long-term drop in crude oil prices in the future. The transportation sector is also the nation's largest single source of air pollution, with personal vehicles producing 26% of volatile organic compounds, 32% of nitrous oxide, and 62% of carbon monoxide. Thus, ways to promote transportation efficiency are one of the most important facets of reducing fossil fuel consumption and improving environmental quality.

Transportation engineering is a highly intradisciplinary field, dealing with the planning, design, construction, maintenance, and operation of various transportation modes. This section presents an overview of transportation engineering, emphasizing planning, design, operation, environmental impact, system analysis, and emerging issues, such as alternative fuels, electric and hybrid vehicles, and intelligent highway systems. Emphasis is placed on those facets of transportation that impact the mechanical engineering profession, but the area also needs social, political, and management inputs to arrive at appropriate engineering solutions of specific problems.

10.1 Transportation Planning

Michael D. Meyer

Transportation planning is undertaken for a variety of reasons. With the provision of much of the world's transportation infrastructure the responsibility of governments, transportation planning is undertaken primarily to support public officials in their choice of most cost-effective investments. Because transportation investment has a strong influence on how a community evolves, transportation planning must necessarily consider a variety of factors when assessing the cost effectiveness of alternative investment options. For example, transportation investment can strongly influence land use patterns, the attractiveness of different parts of a region for economic development, the equitable distribution of mobility benefits among different population groups, and the environmental consequences of both the construction and operation of transportation facilities. Transportation planning must therefore be forward-looking, as well as give attention to current problems in the transportation system.

Basic Framework of Transportation Planning

The basic framework for transportation planning that could be applied at any scale of application is shown in Figure 10.1.1. The steps shown in this framework are discussed in the following sections.

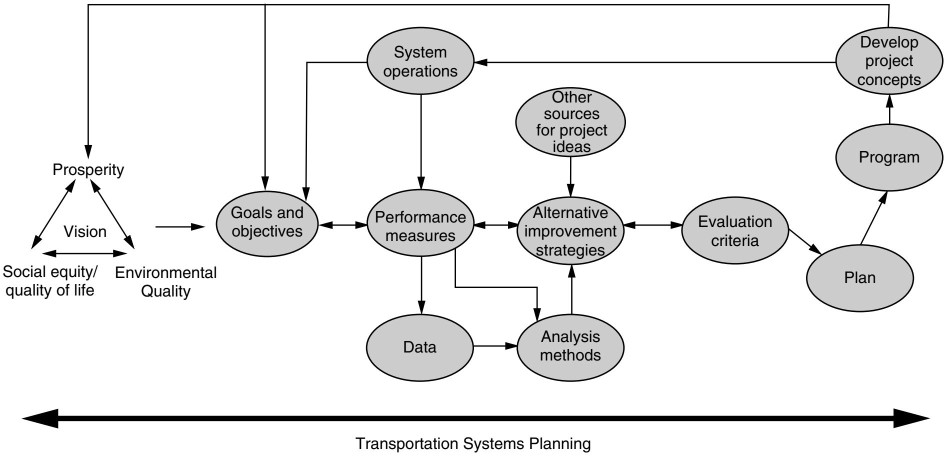

FIGURE 10.1.1 Transportation planning process.

Define a Vision

The transportation system can impact society in a variety of ways — providing mobility and accessibility, promoting economic development, contributing to quality of life, as well as negatively affecting the natural environment. The first step in transportation planning thus usually consists of defining what it is that the nation, state or region desires in terms of its future characteristics.

Identify Goals and Objectives

Once a desired vision is articulated, *goals* can be identified that relate the vision to the ultimate achievement of a transportation plan. *Objectives* are more specific statements that indicate the means by which these goals will be achieved. Goals and objectives not only provide overall direction to the transportation planning process, but they also help define the criteria, known as *measures of effectiveness,* that are used later in the process for evaluating alternative courses of action.

Identify Performance Measures

An important aspect of a continuing transportation planning process is the monitoring of system performance. This monitoring systematically identifies areas where improvements might occur, and, in addition, helps transportation officials assess the effectiveness of previously implemented actions. Performance measures can focus explicitly on transportation system operations, e.g., the level of freeway delay during the morning peak travel hours, or on other issues of importance to transportation officials, e.g., the level of transportation-related air pollutants emitted during specified periods of time.

Collect Data

Given that transportation investment is usually aimed at upgrading the *physical condition* of a facility (e.g., repaving a road or building a new bridge) or at improving its *performance* (e.g., providing new person-carrying capacity by setting aside highway lanes for multi-occupant vehicles or by building a new road), engineers are continually collecting data on the many different components of the transportation system. The base condition or performance of all the different facilities or services that make up a transportation system is called an *inventory.*

Forecasting future demand for transportation requires engineers and planners to characterize the current and likely future states of the factors that influence this demand. Thus, for example, the type of data that is collected includes such things as current land use and socioeconomic characteristics of the traveling population. Current land use is readily attained through land use inventories. The methods of estimating future land use range from trends analysis to large-scale land use models that predict household and employment sites decades into the future. Important socioeconomic characteristics include level of household income, number of members of the household, number of autos in the household, number of children, age of the head of household, and highest level of education achieved. Each of these factors has been shown through research to influence the amount and type of travel associated with a typical household.

Use Analysis Tools to Identify System Deficiencies or Opportunities

The analysis tools and methods used to identify transportation deficiencies and improvement opportunities can vary widely. In some cases, computer-based transportation network models are used to estimate future traffic volumes and transit ridership, with the results then compared to existing system capacity to handle such volumes. This comparison relies on one of the more popular performance measures used in transportation planning today, the volume-to-capacity (V/C) ratio. However, given the many different goals and objectives that can characterize a transportation planning process, a wide variety of measures are often used for determining system deficiencies. Other types of analysis tools include time–distance diagrams, queuing models, fluid-flow approximation methods, macro- and micro-simulation models, and mathematical programming techniques.

Develop and Analyze Alternatives

Various types of strategies can result from the planning process:

1. Improving the *physical infrastructure* of the transportation system — for example, adding new highway lanes or extending an existing subway line
2. Improving *system operations* — for example, coordinating traffic signals, improving traffic flow through improved geometric design of intersections, or making transit operations more efficient through schedule coordination
3. Reducing *travel demand* so that the transportation system can handle peak loads more effectively — for example, flexible working hours, increasing average vehicle occupancy through such measures as carpools or transit use, or raising the "price" of travel through the use of tolls

In the past 10 years, the application of advanced transportation technologies to the operation of the transportation system, known *as intelligent transportation systems* (ITS), has become an important type of strategy in many cities. Thus, it is not uncommon for major cities to now have a centralized traffic management center, with a regional surveillance and traveler communication system that permits transportation system managers to communicate to travelers the best times for travel and which routes are least congested.

Evaluate Alternatives

Evaluation brings together all of the information gathered on individual alternatives/plans and provides a systematic framework to compare the relative worth of each. This evaluation process most often relies on the various measures of effectiveness that link to the goals and objectives defined at the beginning of the process. Different types of evaluation methods include use of benefit/cost ratios, cost-effectiveness indices, goals matrix analysis, and subjective assessment of the merits of individual alternatives.

Develop Transportation Plan

One of the most important products of the transportation planning process is the *transportation plan.* The plan outlines the many different strategies and projects that are necessary to meet the challenges and opportunities facing a state or region. In the U.S., federal law requires that every state and every metropolitan area over 50,000 population have a transportation plan. The state department of transportation (DOT) is responsible for preparing the state transportation plan; an agency called the metropolitan planning organization (MPO) is responsible for preparing the metropolitan transportation plan.

Implement Plan

Another major product of the transportation planning process is a strategy for implementing all of the actions identified in the plan. In the U.S., federal law requires each state and every metropolitan area over 50,000 population to produce a *transportation improvement program* that lists the projects that will be implemented over the next 3 to 5 years, identifies which agency is responsible for each project, and describes the source of project funding.

The implemented projects will affect the performance of the transportation system. Through a continuing monitoring process, linked directly to important performance measures, the performance of individual projects or of the entire transportation system can be fed back into the planning process as a means of identifying new problems.

Transportation Modeling

The level of transportation analysis can vary according to the level of complexity and scale of application of potential solution strategies. Thus, for example, the consideration of a new subway system would necessarily have to be examined from a metropolitan level, while the transportation impacts of a new development site would likely be analyzed at a subregional level. In most cases, however, the modeling process consists of four major steps — trip generation, trip distribution, mode split, and trip assignment. Even though recent models combine some of these steps together during the analysis process, the concept of the "trip" consisting of these four stages still holds. Each study area (whether a nation, state, metropolitan

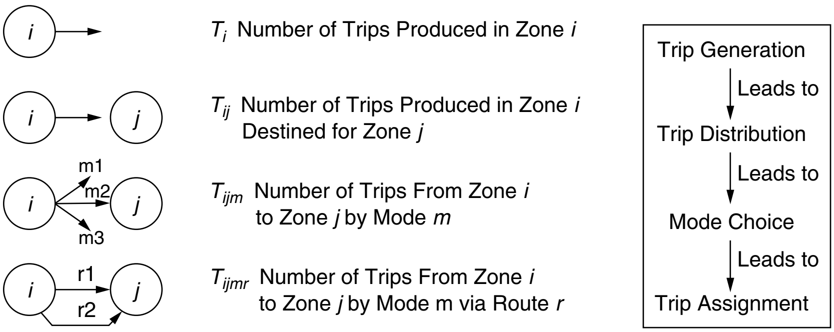

FIGURE 10.1.2 Transportation modeling framework.

area, or community) is divided into *zones* of homogeneous characteristics (e.g., similar household incomes) that can then be used as the basic foundation for estimating trips from or attracted to that zone. Most planning studies define these zones to be similar to those used in other data collection activities (e.g., the U.S. census tracts) so that data useful to the transportation study collected by others can be readily linked to the transportation analysis. The transportation system is represented in models as a network of links and nodes. Links represent line-haul facilities, such as roads or transit lines, and nodes represent points of connection, such as an intersection or transit terminal. Given the complex nature of transportation systems, the typical transportation network consists of links representing only highly used facilities or other facilities that are critical to the overall performance of the transportation system.

The steps in a typical modeling exercise are shown in Figure 10.1.2. Basic to this approach is the concept of *derived demand*. Derived demand means that a trip is taken to accomplish some activity at a destination, and that the trip itself is simply a means of reaching this activity. There is no intrinsic value of the trip itself. Thus, modeling trip-making requires linking travel behavior to the characteristics of the trip-maker and to the activities at the origin and destination ends of the trip that will influence the way the trips are made.

Trip generation is the process of analytically deriving the number of trips that will be generated from a location or zone based on socioeconomic characteristics of the household, or in the case of freight movement, the zonal economic characteristics. Trip generation also includes predicting the number of trips that will be attracted to each zone in the study area.

$$\text{Number of trips produced in a zone} = f\,(\text{Population socio-economic characteristics, land use, transportation mode availability})$$

$$\text{Number of trips attracted to a zone} = f\,(\text{Attractiveness of the zone})$$

Two approaches are often used to estimate the number of trips generated. The first uses trip rate models that are based on trip-making behavior as compared to important variables. For example, see Table 10.1.1. The other approach is to use regression models that are estimated either from survey data

TABLE 10.1.1 Cross-Classification Analysis, Trips per Day, by Household Size and Income

	Number of People in Households		
	1	2	3+
Low income	2.4	3.3	4.5
Medium income	3.5	3.8	4.8
High income	3.9	4.2	5.4

collected throughout the study area or from some other data source, such as the U.S. Census. The following regression equations illustrate this approach.

Zone Trip Productions: $T_i = 184.2 + 120.6\ (\text{Workers}_i) + 34.5\ (\text{Autos}_i)$

Household Trip Productions: $T_{ih} = 0.64 + 2.3 + (\text{Employee}_i) + 1.5\ (\text{HHAuto}_i)$

Zonal Attractions: $T_j = 54.2 + 0.23\ (\text{Office}_j) + 0.43\ (\text{Retail}_j)$

where T_i = total number of trips generated in zone *i*; T_{ih} = total trips generated per household in zone *i*; T_j = total trips attracted to zone *j*; Workers_i = number of workers in zone *i*; Autos_i = number of autos in zone *i*; Employee_i = number of employees per household in zone *i*; HHAuto_i = number of autos per household in zone *i*; Office_j = number of office employees in zone *j*; and Retail_j = number of retail employees in zone *j*.

Trip distribution is the process of estimating the number of trips that travel from each zone to every other zone in the study area. The results of the trip distribution process is a matrix called the *trip table,* which shows the number of trips traveling between each origin–destination (O-D) pair for the time period being examined. A common method for distributing trips in a zonal system is the gravity model, which is of the following form:

$$T_{ij} = P_i \times \frac{A_i \times F_{ij} \times K_{ij}}{\sum (A_j \times F_{ij} \times K_{ij})}$$

where T_{ij} = total trips originating in zone *i* and destined to zone *j*; P_i = number of trips produced in zone *i*; A_j = level of attractiveness of zone *j* (e.g., number of retail employees); F_{ij} = friction or impedance factor between zones *i* and *j* (a value usually a function of travel time); and K_{ij} = socioeconomic adjustment factors for trips between zones *i* and *j* (a value that represents variables that influence trip making not accounted for by other variables).

Mode choice is the process of estimating the percentage of travelers who will use one mode of transportation vs. the others available for a given trip. The basic approach in making this estimation is that each mode has associated with it some empirically known characteristics that, when combined with characteristics of the traveler in a mathematical equation, can define that mode's *utility.* Variables such as travel time, travel cost, modal reliability, and so on are often incorporated into a mode's *utility function*, along with socioeconomic characteristics of the traveler. Freight models use a similar concept in estimating commodity flows by mode. One of the most familiar forms of mode choice models, based on the concept of consumer choice, is the logit model, which predicts mode shares based on the following equation:

$$P_{ik} = \frac{e_k^U}{\sum e_m^U} \quad \text{for all modes } n$$

where P_{ik} = probability of individual *i* choosing mode *k*; U_k = utility of mode *k*; U_m = utility of mode *m*; *n* = number of modes available for trip.

The utility of each mode is often represented as a linear function of those variables found to influence an individual's choice of mode. For example, a utility function for the automobile mode might be of the form,

$$U_a = 6.3 - 0.21\ (X_1) - 0.43\ (X_2) - 0.005\ (X_3)$$

where U_a = utility of automobile; X_1 = access and egress time when automobile is chosen; X_2 = line-haul travel time; and X_3 = cost of travel.

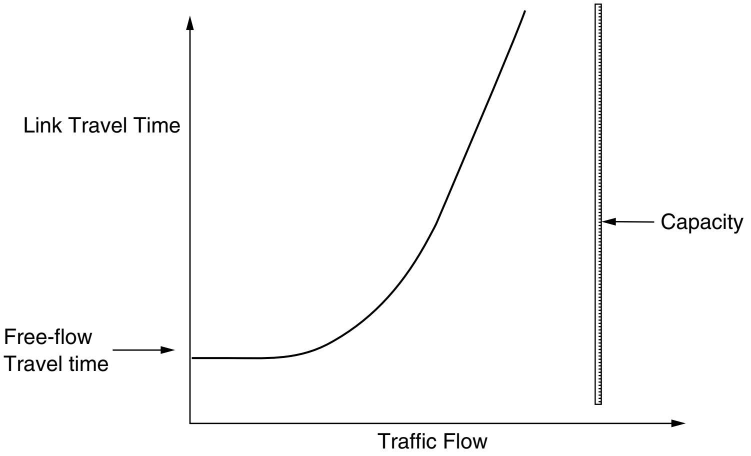

FIGURE 10.1.3 Link performance function.

The utility functions of other modes available for a specific trip would be similarly specified. The respective probabilities would then be multiplied by the total number of trips between an origin and destination to obtain the number of trips made by mode.

Trip assignment is the process of estimating the trip paths through a transportation network based on a trip table (which is produced in trip distribution). The basic concept found in all trip assignment methods is that travelers choose modes that will minimize travel time, that is, they will choose the shortest path through a network (once again, the assumption of derived demand influencing the analysis approach). Link performance functions that relate travel time to the number of vehicles or riders on that link are used to iteratively update estimated link travel times so that minimum path travel times reflect the effect of congestion (see Figure 10.1.3). A portion of the total O-D travel demand is assigned to the network, with travel times then updated based on the link performance function, given the volume on each link. An additional portion of the O-D travel is next assigned given the updated travel times, still following the minimum travel time path through the network. This process continues until all estimated trips have been assigned to a link path in the network. Stochastic assignment is also used in many planning studies. This assignment recognizes that, in certain cases, some subset of trip routes will have associated with them some characteristics that attract specific types of travelers, even if the travel time is longer. A probabilistic approach takes these characteristics into account.

In order to develop more behaviorally based travel models, researchers in recent years have focused on the fact that travel arises out of the need to participate in out-of-home activities (work, shopping, school, etc.). This directly leads to the conclusion that what one should study in the first instance is not travel per se, but rather the participation in the *activities* that ultimately generate travel. This approach has been referred to as “activity-based modeling.” Figure 10.1.4 shows the difference in the traditional approach toward modeling and the activity-based approach. Many activity-based models are being implemented within a *micro-simulation* framework, within which the behavior of each individual is dynamically simulated over time.

Defining Terms

Demand management: Reducing the demand for travel during specific time periods by shifting trips to other times, diverting trips to other routes or modes, or reducing the need for trip-making to begin with.

Derived demand: An assumption that travelers make a trip to accomplish some objective at the destination and that the trip itself is simply a means of reaching that activity.

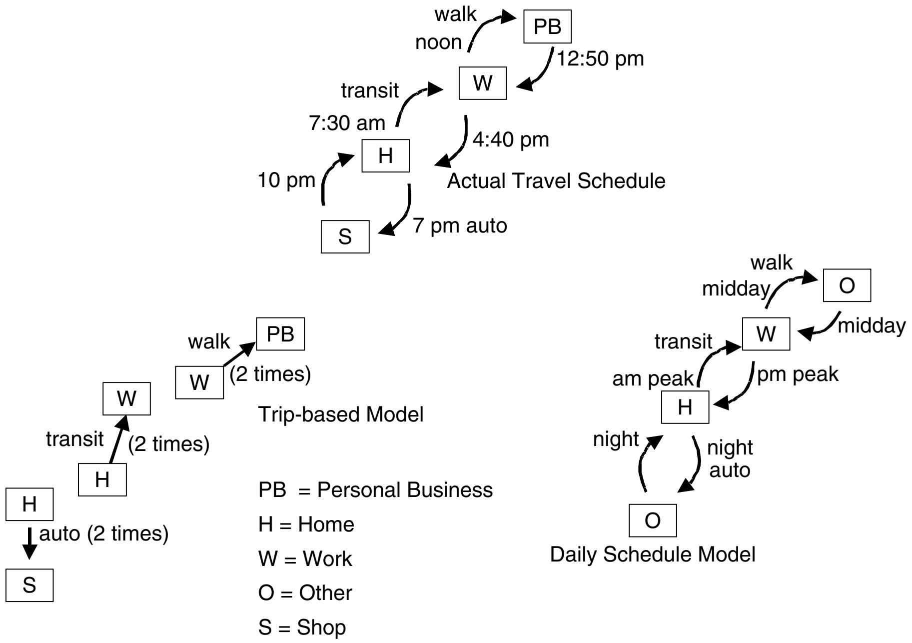

FIGURE 10.1.4 Difference between trip-based modeling and activity-based modeling.

Intelligent transportation systems: Application of surveillance, communication, and control technologies to the management of the transportation system, and in some cases, to the control of individual vehicles.

Transportation network: A transportation system is represented in models as a network of links and nodes. Links represent line-haul facilities, such as roads and transit lines, and nodes represent points of connection.

Utility function: A mathematical formulation that assigns a numerical value to the attractiveness of individual modes of transportation based primarily on that mode's characteristics.

Zonal system: Each study area (whether nation, state, metropolitan region, or community) is divided into zones of homogeneous characteristics that can then be used as the basic foundation for estimating trips from, or attracted to, that zone.

References

Goulias, K. (Ed). 2003. *Transportation Systems Planning,* CRC Press, Boca Raton, FL.

Grava, S. 2003. *Urban Transportation Systems,* McGraw-Hill, New York.

Hall, R. (Ed). 2003. *Handbook of Transportation Science,* 2nd ed. Kluwer, Boston.

Institute of Transportation Engineers. 1997. *Trip Generation Handbook,* 6th ed. ITE, Washington, DC.

Meyer, M. and Miller, E. 2001. *Urban Transportation Planning: A Decision-Oriented Approach,* 2nd ed. McGraw-Hill, New York.

Ortuzar, J. and Willumsen. L.G. 1994. *Modelling Transport,* 2nd ed. John Wiley & Sons, New York.

Taylor, M. A. P., Young, W. and Bonsall, P. W. 1996. *Understanding Traffic Systems: Data, Analysis and Presentation,* Ashgate, Brookfield, VT.

Vuchic, V. 1999. *Transportation for Livable Cities,* Center for Urban Policy Research, Rutgers, The State University of New Jersey, New Brunswick, NJ.

Further Information

American Association of State Highway and Transportation Officials
444 N. Capitol St. NW
Suite 225
Washington, DC 20001

Institute of Transportation Engineers
1099 14th St. NW
Suite 300W
Washington, DC 20005

Transportation Research Board, National Research Council
500 Fifth Street, NW
Washington, DC 20001

10.2 Design of Transportation Facilities

John Leonard II and Michael D. Meyer

The efficient movement of people and goods requires transportation systems and facilities that are designed to provide sufficient capacity for the demands they face in as safe a manner as possible. In addition, in most modern societies, the design of transportation facilities must explicitly minimize harm to the natural and human-made environment while providing for mitigation measures that relate to those impacts that are unavoidable. In many ways the critical challenge to today's designers of transportation projects is successfully designing a facility that minimally harms the environment.

The design of a transportation facility almost always takes place within the context of a much broader **project development process.** This process can vary in complexity with the type of project under design and with the scale of implementation. The importance of the project development process to the designer is that it:

- Establishes the key characteristics of the project that must be considered in the design
- Indicates the time frame that will be followed for project design
- Establishes which agencies and groups will be involved in the process and when this involvement will likely occur
- Links the specific elements of the project design with other tasks that must be accomplished for the project to be constructed
- Satisfies legal requirements for a design process that is open for public review and comment
- Indicates the specific products that must be produced by the designers to complete the project design process

In most cases the project development process consists of a well-defined set of tasks that must be accomplished before the next task can occur. These tasks include both technical activities and public involvement efforts that are necessary for successful project development.

Components of the Project Development Process

Identify Project Need

A project need can be identified through a formal planning process or from a variety of other sources, including suggestions from elected officials, agency managers, transportation system users, and citizens. Important in this early portion of project development is an indication of what type of improvement is likely to be initiated. For example, a project could relate to one or more of the following types of improvement strategies:

- *New construction.* A transportation facility constructed at a new location
- *Major reconstruction.* Addition of new capacity or significant changes to the existing design of a facility, but usually occurring within the area where the current facility is located
- *Rehabilitation/restoration.* Improvements to a facility usually as it is currently designed and focusing on improving the physical condition of the facility or making minor improvements to enhance safety
- *Resurfacing.* Providing new pavement surface to a transportation facility that prolongs its useful life
- *Spot improvements.* Correction of a problem or hazard at an isolated or specific location

Establish Project Limits and Context

One of the very first steps in the design process is to define the boundaries or limits of the project. This implies establishing how far the project will extend beyond the area being targeted for improvement and the necessary steps to ensure smooth connections to the existing transportation system. Project boundaries also have important influence on the amount of right-of-way that might have to be purchased by an agency to construct a project.

Establish Environmental Impact Requirements

The design of a project will most likely be influenced by environmental laws or regulations that require design compliance with environmental mandates. These mandates could relate to such things as wetland protection, preservation of historic properties, use of public park lands, maintaining or enhancing water quality, preserving navigable waterways, protecting fish and wildlife, reducing air pollutants and noise levels, and protecting archaeological resources. One of the first steps in project development is to determine whether the likely project impacts are significant enough to require a detailed environmental study.

Develop Strategy for Interagency Coordination and Public Involvement

Depending on the complexity and potential impact of a project, the project designer could spend a great deal of time interacting with agencies having some role in or jurisdictional control over areas directly related to the project. These agencies could have jurisdiction by law (e.g., wetlands) or have special expertise that is important to project design (e.g., historic preservation). In addition to interagency coordination, transportation project development is often subject to requirements for public outreach and/or public hearings. An important aspect of recent project development efforts is to develop very early in the process a consensus among involved agencies on what environmental impacts will have to be carefully studied and on the definition of the project purpose and need.

Initiate Project Design and Preliminary Engineering

Topographic data of the study area and forecasted vehicular volumes expected to use the facility in the design year are used as input into the preliminary design of the horizontal and vertical alignment of the facility, that is, the physical space the facility will occupy once finished. This preliminary engineering step also includes the preparation of initial right-of-way (ROW) plans, which indicate the amount of land that must be available to construct the facility. Preliminary engineering is a critical step for environmental analysis in that it provides the first detailed examination of the scope and extent of potential environmental impacts.

Project Engineering

Once preliminary engineering has provided the basic engineering information for the project, the more detailed project design begins. This entails specific layouts of horizontal and vertical geometry, soils/subsurface examination and design, design of utility location, drainage design, more detailed ROW plans, and initial construction drawings. Concurrent with this design process, the environmental process continues with updated information on project changes that might cause additional environmental harm, the initiation of any permitting process that might be needed to construct the project (e.g., environmental agency permission to affect wetlands), and public hearings/meetings to keep the public involved with project development.

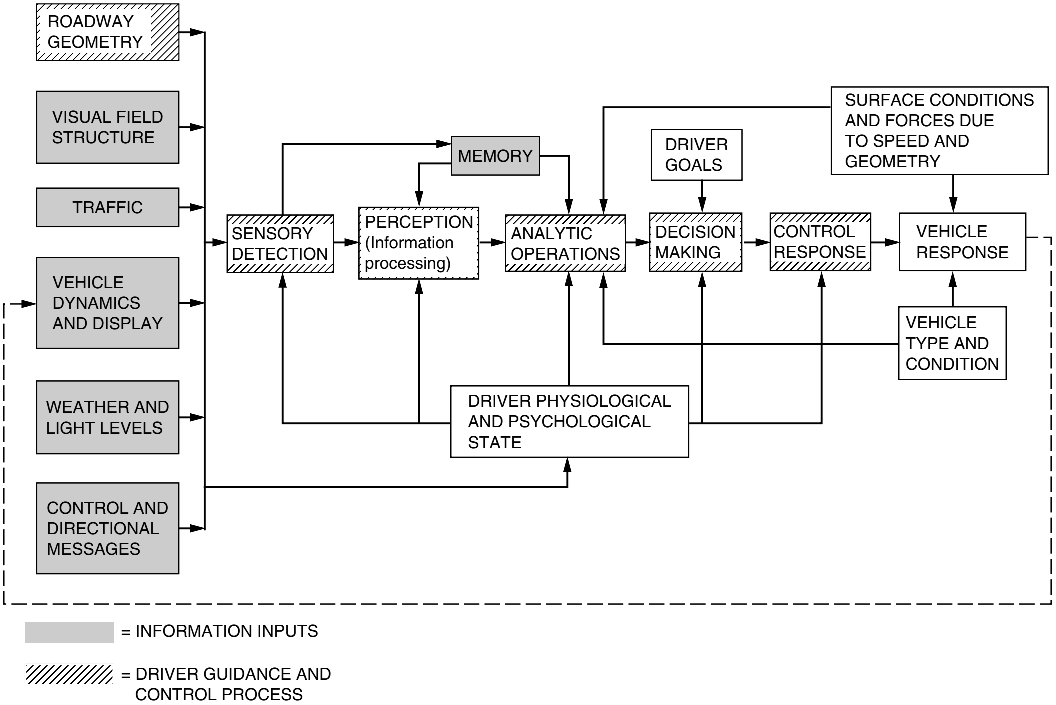

FIGURE 10.2.1 Driver-vehicle-roadway interface.

Final Engineering

The final engineering step is the culmination of the design process, which completes the previous design plans to the greatest level of detail. This step includes finalizing ROW plans, cost estimates, construction plans, utility relocation plans, and any agreements with other agencies or jurisdictions that might be necessary to complete the project. Environmental permits are received and final project review for environmental impacts is completed.

Context-Sensitive Design

One of the important characteristics of transportation facility design is the potentially negative impact that new facilities could have on the surrounding community and natural environment. Engineers and planners have begun to consider such impacts earlier in the project development process so that the context within which a facility is constructed is incorporated into the design itself. This process is called **context-sensitive design.**

Basic Concepts of Project Design

Human Factors

Human factors have a great deal of influence on the design of transportation facilities in such things as width of facility, length and location of access/egress points, vehicle braking distance, location of information/guidance aids such as signs, and geometric characteristics of the facility's alignment. The driver-vehicle-roadway interface is shown in Figure 10.2.1.

Vehicle or User Performance Factors

The dynamics of vehicle motion play an important role in determining effective and safe design. The key vehicle characteristics that relate to facility design criteria include:

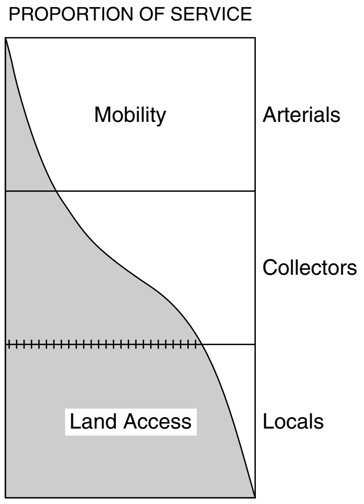

FIGURE 10.2.2 Relationship of functionally classified systems in relation to traffic mobility and land access. (*Source:* American Association of State Highway and Transportation Officials. 2001. *A Policy on the Geometric Design of Highways and Streets,* AASHTO, Washington, DC. Figure 1 through Figure 5.)

- *Vehicle size.* Influences vertical and horizontal clearances, turning radii, alignment width, and width of vehicle storage berths.
- *Vehicle weight.* Influences strength of material needed to support vehicle operations.
- *Vehicle or user performance.* Influences specifications for horizontal and vertical geometry, braking distances, operational performance and needed capacity to allow passing and successful maneuvering (e.g., assumed walking speed of pedestrians crossing a road that dictates how long a traffic signal must remain red).

Classification Schemes

The transportation system serves many functions, ranging from providing access to specific locations to providing high-speed, high-capacity movement over longer distances. Classification schemes are used to represent these various roles and influence the design criteria that are associated with the facilities in each classification category. A common **functional classification** scheme for highways is shown in Figure 10.2.2.

Capacity and Level of Service

Every design usually begins with some estimation of the demand for the transportation facility that will likely occur if the facility is built. The key design question then becomes, what facility capacity (e.g., number of road lanes, runways, transit lines, or vehicle departures) is necessary if a certain level of performance is desired? These different levels of performance are referred to as **level of service (LOS).** Level of service is a critical element in establishing important design factors (see Figure 10.2.3).

Design Standards

Design standards dictate minimum or maximum values of project characteristics that are associated with a particular facility type. Design standards usually result from extensive study of the relationship between various facility characteristics, vehicle performance, and the safe handling of the vehicles by human operators. Design standards often vary by the "design speed" of the facility (and thus the importance of the facility classification) and by the "design vehicle." Design standards are often the basis for developing typical cross-sections (see Figure 10.2.4 and Figure 10.2.5).

FREEWAYS

Level of Service	Maximum Density (pc/mi/ln)	Minimum Speed (mph)	Max Service Flow Rate (pcphpl)	Maximum *v/c* Ratio
Free-Flow Speed = 70 mph				
A	10.0	70.0	700	0.318/0.304
B	16.0	70.0	1120	0.509/0.487
C	24.0	68.5	1644	0.747/0.715
D	32.0	63.0	2015	0.916/0.876
E	36.7/39.7	60.0/58.0	2200/2300	1.000
F	var	var	var	var
Free-Flow Speed = 65 mph				
A	10.0	65.0	650	0.295/0.283
B	16.0	65.0	1040	0.473/0.452
C	24.0	64.5	1548	0.704/0.673
D	32.0	61.0	1952	0.887/0.849
E	39.3/43.4	56.0/53.0	2200/2300	1.000
F	var	var	var	var
Free-Flow Speed = 60 mph				
A	10.0	60.0	600	0.272/0.261
B	16.0	60.0	960	0.436/0.417
C	24.0	60.0	1440	0.655/0.626
D	32.0	57.0	1824	0.829/0.793
E	41.5/46.0	53.0/50.0	2200/2300	1.000
F	var	var	var	var
Free-Flow Speed = 55 mph				
A	10.0	55.0	550	0.250/0.239
B	16.0	55.0	880	0.400/0.383
C	24.0	55.0	1320	0.600/0.574
D	32.0	54.8	1760	0.800/0.765
E	44.0/47.9	50.0/48.0	2200/2300	1.000
F	var	var	var	var

Note: In table entries with split values, the first value is for four-lane freeways, and the second is for six- and eight-lane freeways.

PEDESTRIAN WALKWAYS

		Expected flows and Speeds		
Level of Service	Space (sq ft/ped)	Ave. Speed, *S* (ft/min)	Flow Rate, *v* (ped/min/ft)	Vol/Cap Ratio, *v/c*
A	≥130	≥260	≤ 2	≤0.08
B	≥ 40	≥250	≤ 7	≤0.28
C	≥ 24	≥240	≤10	≤0.40
D	≥ 15	≥225	≤15	≤0.60
E	≥ 6	≥150	≤25	≤1.000
F	< 6	<150	—Variable—	

*Average conditions for 15 min.

FIGURE 10.2.3 Example level of service characteristics (*Source:* Transportation Research Board, 2000. *Highway Capacity Manual,* National Academy Press, Washington, DC.) *Continued.*

SIGNALIZED INTERSECTIONS

Level of Service	Stopped Delay per Vehicle (sec)
A	≤5.0
B	5.1 to 15.0
C	15.1 to 25.0
D	25.1 to 40.0
E	40.1 to 60.0
F	>60.0

ARTERIAL ROADS

Arterial Class	I	II	III
Range of Free Flow Speeds (mph)	45 to 35	35 to 30	35 to 25
Typical Free Flow Speed (mph)	40 mph	33 mph	27 mph
Level of Service	Average Travel Speed (mph)		
A	≥35	≥30	≥25
B	≥28	≥24	≥19
C	≥22	≥18	≥13
D	≥17	≥14	≥ 9
E	≥13	≥10	≥ 7
F	<13	<10	< 7

FIGURE 10.2.3 *Continued.*

Intermodal Transportation Terminals or Transfer Facilities

Terminals or transfer facilities are locations where users of the transportation system change from one mode of travel to another. The effective design of such facilities is a critical element of successful transportation system performance, given the potential bottlenecks they represent if not designed appropriately. The design of terminals and transfer facilities must pay special attention to the needs of the users of the facility, in that they serve to establish the effective capacity of the facility, for example:

1. Internal pedestrian movement facilities and areas (stairs, ramps, escalators, elevators, corridors, etc.)
2. Line-haul transit access area (entry control, fare collection, loading, and unloading)
3. Components that facilitate movements between access modes and the station (ramps or electric doors)
4. Communications (public address systems and signage)
5. Special provisions for disabled patrons (elevators and ramps)

The criteria that could relate to the design of such a facility include threshold values for pedestrian level of service, delay at access points, connectivity from one area of the facility to another, and low-cost maintenance. For the vehicle side of such terminals, special consideration must be given to the performance of the design vehicle (e.g., turning radii of buses or semitrailer trucks) and the vehicle storage requirements (e.g., the number, size, and orientation of loading/unloading berths).

RECOMMENDED ROADWAY SECTION WIDTHS

Functional Class	U/R	Number of Lanes	Travel Lane	Shoulder	
				Right	Left[1]
Freeway	Urban	4–8	12	10	4[2]
	Rural	4–8	12	10	4[2]
Arterial	Urban	Multilane with median	12	10	4
	Urban	Multilane without median	11–12	8–10*	N/A
	Rural	2 lane	12	See Table 5.2	N/A
	Rural	Multilane with median	12	8–10	4

WIDTH OF USABLE SHOULDER—EACH SIDE OF TRAVEL WAY
RURAL TWO-LANE ARTERIAL

	Design Traffic Volume				
	Current ADT Under 400	Current ADT Over 400	DHV 100–200	DHV 200–400	DHV Over 400
All design speeds	4 ft	6 ft	6 ft	8 ft	10 ft

RECOMMENDED WIDTH OF TRAVEL WAY AND GRADED SHOULDER
RURAL COLLECTOR

	Design Traffic Volume				
Design Speed (mph)	Current ADT Under 400	Cuurent ADT Over 400	DHV 100–200	DHV 200–400	DHV Over 400
30	20 ft	20 ft	20 ft	22 ft	24 ft
40	20 ft	22 ft	22 ft	22 ft	24 ft
50	20 ft	22 ft	22 ft	24 ft	24 ft
60	22 ft	22 ft	22 ft	24 ft	24 ft
Graded Shoulder (Each Side)*					
All speeds	2 ft	4 ft	6 ft	8 ft	8 ft

*If right-of-way permits

FIGURE 10.2.4 Example design criteria. (*Source:* Massachusetts Department of Public Works. 1988. *Highway Design Manual,* Boston, MA.)

Advanced Technology Projects

One of the characteristics of transportation system development in recent years has been the increased application of advanced (usually electronic) technologies to improve system performance. Known as **intelligent transportation systems (ITS),** the following steps apply in their design.

Define Problems and Needs

Typical problems or needs might relate to congestion, excessively high accident rates, or improving current system capabilities and levels of service.

Define System

A system definition should include a mission statement, listing of physical components (e.g., roads, travelers, buses, rolling stock, existing rail lines, control centers, and communication links), and the physical relationship between those components.

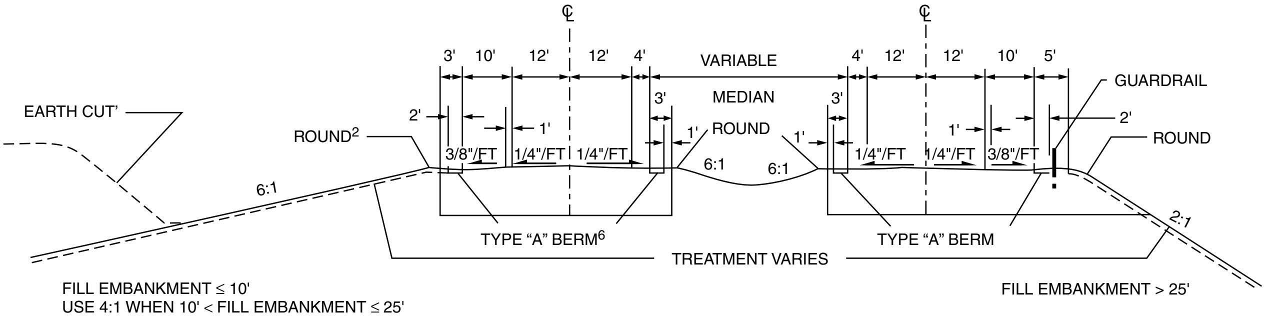

Typical Freeway/Expressway Section

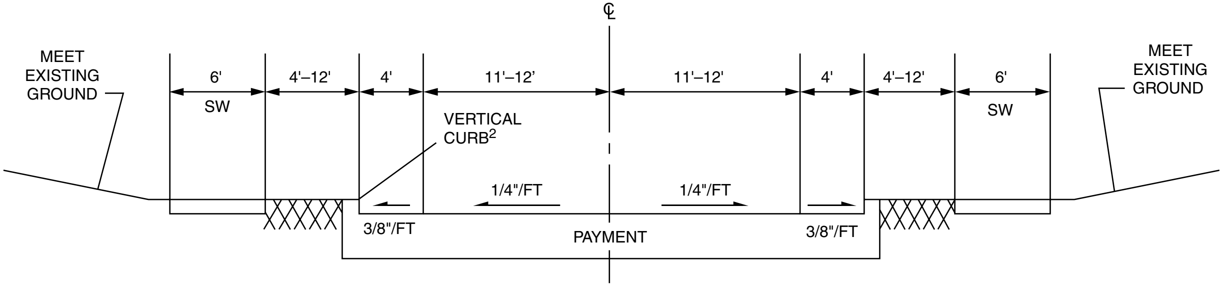

Typical Urban Collector and Local Road

FIGURE 10.2.5 Example cross-sections.

Define Users

System users is a rather broad description of all individuals, organizations, and other systems that might interact or have a stake in the fully implemented transportation system under study.

Establish Institutional Framework and Partnerships

Various organizations possess differing missions, priorities, and policies — sometimes in conflict. Strong emphasis on coalition building during the early stages of project planning and engineering can help diffuse potential project-stopping disagreements later in the process.

Develop User Service Plan

The development of a user service plan consists of the following steps: (1) establish user services, (2) identify technology areas, and (3) map user services to technology areas. User services might include:

- Traveler information services
- Freight and fleet management services
- Emergency vehicle management services
- Traffic management services
- Public transport services

Available technologies fall within one of the following functional areas: (1) surveillance, (2) communications, (3) traveler interface, (4) control strategies, (5) navigation/guidance, (6) data processing, and (7) in-vehicle sensors.

Define System Architecture

A logical architecture consists of a *block diagram* identifying the major systems and subsystems, the participating agencies, and users. Through the use of arrows, the flow of information between these elements is identified. A logical architecture also shows the allocation of responsibilities throughout the transportation system.

Evaluate Alternative Technologies

Some of the factors to be considered in this evaluation include (1) cost, (2) performance, (3) reliability, (4) compatibility, (5) environmental impacts, and (6) compliance to standards.

Defining Terms

Context-sensitive design: A design process in which the community and environmental context is considered very early in the project development process. Mitigation and avoidance of significant impacts are proposed at this stage.

Design standard: Physical characteristics of a proposed facility that are professionally accepted and often based on safety considerations.

Functional classification: Classifying a transportation facility based on the function it serves in the transportation system. Such classification becomes important in that design standards are often directly related to the functional classification of a facility.

Intelligent transportation systems: Use of information and surveillance technologies to monitor and control the operation of the transportation system. Many of these systems are targeted at specific travel markets.

Level of service: An assessment of the performance of a transportation facility based on measurable physical characteristics (e.g., vehicular speed, average delay, density, flow rate). Level of service is usually subjectively defined as ranging from level of service A (good performance) to level of service F (bad or heavily congested performance).

Project development process: The steps that are followed to take a project from initial concept to final engineering. This process includes not only the detailed engineering associated with a project design but also the interaction with the general public and with agencies having jurisdiction over some aspect of project design.

References

American Association of State Highway and Transportation Officials. 2001. *A Policy on the Geometric Design of Highways and Streets,* AASHTO, Washington, DC.

Federal Highway Administration, 1997. *Flexibility in Highway Design*, Report FHWA-PD-97-062, FHWA, Washington, DC.

Transportation Research Board, 1999. Transit Capacity and Quality of Service Manual, Transit Cooperative Research Web Document 6, National Academy Press, Washington, D.C., www.gulliver.trb.org/publications/tcrp/tcrp_webdoc_6-a.pdf.

Transportation Research Board. 2000. *Highway Capacity Manual,* National Academy Press, Washington, D.C.

Further Information

Transportation Research Board, National Academy of Sciences, 2101 Constitution Ave., N.W., Washington, D.C. 20418

American Association of State Highway and Transportation Officials, 444 N. Capitol St., N.W., Suite 225, Washington, D.C. 20001

Institute of Transportation Engineers, 525 School St., S.W., Suite 410, Washington, D.C. 20024

Federal Highway Administration, 400 7th St. S.W., Washington, D.C. 20590

10.3 Operations and Environmental Impacts

Michael D. Meyer, Paul W. Shuldiner, and Kenneth B. Black

The safe and efficient movement of vehicles and people are the two most important goals of highway design. This is accomplished through careful geometric design of the layout and physical features of the roads, and through operational procedures and devices designed to guide, advise, and regulate vehicle operators in their use of the road. Proper design is based on a thorough understanding of the complex interactions among driver, vehicle, and roadway characteristics. For example, the design of a highway passing lane reflects the performance characteristics of the vehicle, the reaction time of the driver, and the ability of the road itself to provide sufficient distance that allows safe vehicle passing.

The following sections present the fundamental equations of vehicle flow and engineering principles upon which good highway design is based.

Fundamental Equations

Flow, q, is given by the following formula:

$$q = \frac{n \times 3600}{T} \quad \text{vehicles per hour} \tag{10.3.1}$$

where n = number of vehicles passing a point in T seconds.

Density, k, is given by

$$k = \frac{n}{L} \times 5280 \quad \text{vehicles per mile} \tag{10.3.2}$$

where n = number of vehicles occupying a length of road, L, and L is in feet, or by

$$k = \frac{n}{L} \times 1000 \quad \text{vehicles per kilometer} \tag{10.3.3}$$

where n = number of vehicles occupying a length of road, L, and L is in meters.

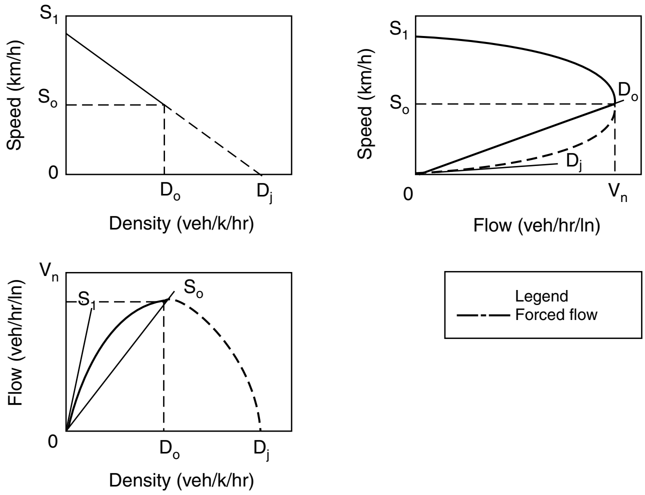

FIGURE 10.3.1 Relationships among flow, density, and speed.

Average speed, $\bar{u}$, is given by

$$\bar{u}_t = \frac{1}{n}\sum_{i=1}^{n} u_i \tag{10.3.4}$$

where u_i = speed of the *i*th vehicle, termed the *time mean speed*, and by

$$\bar{u}_s = \frac{n \cdot s}{\sum_{i=1}^{n} t_i} \tag{10.3.5}$$

where t_i = time for the *i*th vehicle to traverse distance *s*, termed the *space mean speed.* The values $\bar{u}_s$ and $\bar{u}_t$ usually differ very slightly from one another unless there are wide variations among the speeds of individual vehicles.

Flow, Speed, and Density Relationships

The fundamental equation relating flow, density, and speed can be formulated as follows:

$$q = k \times \bar{u}_s \tag{10.3.6}$$

For simplicity, it is often assumed that average speed, *u*, decreases linearly as density, *k*, increases. Given this assumption and the dimensional identity expressed in Equation (10.3.6), it follows that flow, density, and speed are related as shown in Figure 10.3.1. It may be seen from Figure 10.3.1 that

1. When density on the highway is zero, there are no vehicles on the highway and the flow is zero.
2. As density goes to its maximum, flow goes to zero as vehicles line up — essentially bumper to bumper.
3. As density increases, flow also increases — up to the point where $k = kj/2$ — and then decreases as density increases.
4. As flow increases from zero to a maximum (the capacity of the roadway), speed also decreases. Once the flow approaches capacity, any impediment to the steady movement of traffic will reduce both flow and speed abruptly, with a concomitant rapid increase in density.

Level of Service (LOS)

Level of service is a measure of how freely a given transportation system is operating. It is affected primarily by traffic **volume**, but other factors such as proportion of heavy vehicles, roadway geometrics, and incidents also affect the level of service. LOS is designated by letters A through F. LOS A is characterized as *free flow* and is applied to conditions of very low traffic volume in which there is little or no restriction to traffic flow. LOS F is characterized as *forced flow* with congested, stop-and-go movement. LOS C involves some restriction to free movement of traffic and is the level of service commonly used as the target for road design. The maximum flow along a facility occurs at LOS E.

Different elements of the road system emphasize different LOS measures. For example, the following measures are the key determinants in the LOS for the identified element of the road network.

Urban street:	Average travel speed for through vehicles
Freeway:	Average speed, freedom to maneuver, and proximity of other vehicles
Freeway ramp:	Vehicle density
Signalized intersection:	Average traffic control delay per vehicle
Two-lane highways:	Percent time spent following other vehicles, and average speed
Pedestrian walkways:	Space per pedestrian, flow rate, and average speed

The calculation of road level of service varies by type of road. For example, the *Highway Capacity Manual,* the manual that defines how level of service should be calculated, describes different methodologies for the following transportation facilities: urban streets, signalized intersections, unsignalized intersections, pedestrian walkways, bicycle facilities, two-lane highways, multi-lane highways, freeway facilities, basic freeway segments, freeway weaving sections, ramps, interchange ramp terminals, and transit services.

As an example, the LOS for a freeway segment is calculated with the following two equations:

$$\mathrm{FFS} = \mathrm{BFFS} - f_{LW} - f_{LC} - f_N - f_{ID} \tag{10.3.7}$$

where FFS = free flow speed (mi/h); BFFS = base free flow speed (70 mi/h for urban and 75 mi/h for rural); f_{LW} = adjustment for lane width; f_{LC} = adjustment for right-shoulder lateral clearance; f_N = adjustment for number of lanes; and f_{ID} = adjustment for interchange density.

$$D = \frac{V}{S \times (\mathrm{PHF} \times N \times f_{HV} \times f_P)} \tag{10.3.8}$$

where D = density (pc/mi/ln); S = average passenger car speed (mi/h); V = hourly volume (veh/h); PHF = peak hour factor (variation in traffic low within hour); N = number of lanes; f_{HV} = heavy vehicle adjustment factor; and f_P = driver population factor.

The results of these two equations for the circumstances of a specific freeway segment are then entered into a table that defines a corresponding level of service.

Highway Capacity

The **capacity** of a highway, that is the maximum flow of vehicles or passengers, depends on many geometric and traffic characteristics. The capacity of a road occurs at LOS E. Equation 10.3.7 and Equation 10.3.8 indicate that the most important of these factors include number of lanes, width of lanes, lateral clearance to obstructions, percentage of the traffic stream made up of trucks and buses, characteristics of the driver population and percent grade of the roadway (incorporated into the heavy vehicle adjustment factor). Lane widths will vary according to the type of road; however, for high-capacity, high-speed roads such as freeways, the lane width should be at least 12 ft. Obstructions should be a minimum of 6 ft from the edge of pavement. Vertical grades of 3% or more that are one-half mile long or longer will reduce the capacity of a highway, especially where commercial vehicles are present. For freeways, maximum lane capacity under ideal conditions is generally assumed to be 2400 vehicles/hr per lane. Ideal conditions, however, are seldom achieved.

Intersection Capacity

The *Highway Capacity Manual* provides a detailed method for estimating the capacity of a signalized intersection. This method examines the geometric, traffic and signalization conditions for each lane approach to the intersection. Similar to Equation 10.3.7 and Equation 10.3.8, the following equation is used to determine the saturation flow rate for each group of lanes entering an intersection.

$$S = s_0 \times N \times f_W \times f_{HV} \times f_g \times f_p \times f_{bb} \times f_a \times f_{LU} \times f_{LT} \times f_{RT} \times f_{Lpb} \times f_{Rpb} \qquad (10.3.9)$$

where S = saturation flow rate for each group of lanes (veh/h); s_0 = base saturation flow rate per lane (pc/h/ln); N = number of lanes in lane group; f_W = adjustment for lane width; f_{HV} = adjustment for heavy vehicles (trucks and buses); f_g = adjustment for approach grade; f_p = adjustment for existence of parking lane and parking activity adjacent to lane group; f_{bb} = adjustment for blocking effect of local buses that stop within intersection area; f_a = adjustment for area type; f_{LU} = adjustment for lane utilization; f_{LT} = adjustment for left turns in lane group; f_{RT} = adjustment for right turns in lane group; f_{Lpb} = pedestrian–bicycle adjustment factor for left-turn movements; and f_{Rpb} = pedestrian–bicycle adjustment factor for right-turn movements.

The result of Equation 10.3.9 is then multiplied by the amount of green time per total signal cycle time for the lane group being analyzed to obtain the capacity of the lane group. As shown, Equation 10.3.9 illustrates the basic concept of first starting with an "ideal" capacity or saturation flow and then modifying this value with adjustments that reflect physical characteristics of the existing facility and area.

Traffic Control Devices

Traffic signs, signals, and pavement markings (**traffic control devices**) are used to regulate, warn, and guide the users of the road. The effectiveness of such devices is greatly enhanced through the uniformity of their design — including shape, color, and message — and through their use and placement on the roadway. Uniformity is ensured by adherence to the standards promulgated in the *Manual of Uniform Traffic Control Devices* [U.S. DOT and FHWA, 2000] or an equivalent manual adopted by each state highway agency. As stated in the **Manual**, to be effective, a traffic control device should meet five basic requirements: fulfill a need, command attention, convey a simple and clear meaning, command respect from road users, and give adequate time for proper response.

One of the ways that traffic control devices gain respect from road users is by using them in situations where such devices are clearly warranted. Experience over many decades and engineering judgement have become the basis for "warrants," guidelines that are used by engineers to justify the use of particular traffic control devices. Two examples of how this principle is used by engineers are provided below for STOP signs and traffic signals.

STOP signs should be used only where one or more of the following conditions or warrants hold:

1. At an intersection of a less important road with a main road where application of the normal right-of-way rule would not be expected to provide reasonably safe operation
2. Where a street enters a through highway or street
3. At an unsignalized intersection in a signalized area
4. At other intersections where a combination of high speed, restricted view, and crash records indicate a need for control by a STOP sign

Traffic control signals should not be installed unless at least one of several signal warrants is met (the *Manual* defines eight warrants). Eleven signal warrants are used to account for such factors as traffic volume, crash experience, school crossings, and pedestrian volumes. In addition to a review of these warrants, an engineering study should be conducted to show that the installation of such a signal would improve the overall safety and operation of the intersection.

Consideration should be given to other, less restrictive measures before these warrants are applied.

Coordinated System Operations

The efficient operation of a road network requires more than simply placing traffic control devices at warranted locations. A regional road network for a modern metropolitan area consists of many different road types, whose jurisdiction is shared by numerous different organizations. One of the key challenges facing many metropolitan areas today is coordinating the many different responsibilities for operating a regional road network. This can be accomplished through ad hoc working groups focusing on specific operations strategies (e.g., coordinating traffic signals across jurisdictions) or by the creation of a regional entity with a legislative mandate to operate all transportation services in a region (much more common in countries other than the U.S.). In the U.S., some of the strategies used to coordinate system operations include:

1. Standardized strategies to be implemented in response to expected incidents or events
2. Shared databases and information retrieval
3. Corridor teams that focus on network operations
4. Regional programs, e.g., incident management efforts or traffic signal coordination, which target key determinants of system performance
5. Regional traffic management centers that collect data on system performance and provide information and guidance to road network users
6. Formal information and technological systems architecture that specifies protocols and processes for computer-supported approaches to system operations

With the advent of more powerful computers and improved sensors, it seems likely that future developments in coordinated system operations will to a large extent rely on the application of advanced technology.

Environmental Impacts

One of the most important characteristics of transportation system performance is the corresponding impact on the natural and human environment. This impact occurs not only during the construction of transportation facilities themselves but also from the resulting operations. For example, automobile travel in many urban areas is a primary source of many air pollutants. In terms of energy consumption, total auto travel accounts for approximately 25% of U.S. oil consumption, with about two-thirds of this consumption occurring in urban areas. Table 10.3.1 shows the environmental impacts that are of concern to transportation officials. Of those shown, the impacts that are directly linked to the operations of a facility or transportation system include air quality, noise, vibration, stormwater, energy consumption, and ecological effects.

It is often difficult to determine the best operations strategy for minimizing these impacts. For example, the air quality impacts of motor vehicles are a function of the number, type, and condition of vehicles on the highway and of the speed and efficiency with which these vehicles operate. Carbon monoxide, hydrocarbons, and oxides of nitrogen are the primary pollutants emitted by vehicular traffic. The level of emission of each pollutant is complicated and difficult to predict. In general, the emission of carbon monoxide and hydrocarbons is minimized at speeds between 35 and 45 mi/h, whereas the emission of oxides of nitrogen increases over this speed range. Therefore, there is no ideal speed at which the level of emission of all three pollutants will be minimized. Nevertheless, smoothly flowing traffic will tend to produce less pollution, and, therefore, whatever can be done to reduce delay and congestion — especially when combined with a reduction in total vehicle miles traveled — will result in an improvement in air quality.

TABLE 10.3.1 Transportation System Impacts of Concern to Transportation Officials

Natural System Impacts	Social and Cultural Impacts
Terrestrial ecology (habitats and animals)	Historic and archaeological
Aquatic ecology (habitats and animals)	Displacement of people
	Community cohesion
Physical Impacts	Resource consumption
Air quality	Land use
Noise	Aesthetics
Vibration	Infrastructure effects
Water quality	Accessibility of facilities, services, and jobs
Hazardous wastes	Environmental justice
Stormwater	Employment, income, and business activity
Energy consumption	
Erosion and sedimentation	
Farmland conversion	

The reader is referred to the following site for information on the many environmental impacts that are of concern to transportation officials: http://www.fhwa.dot.gov/environment/index.htm

Defining Terms

Capacity: A maximum flow of vehicles or persons at a specific location, given the characteristics of the facility.

Density (*k*): Number of vehicles or persons occupying a given length of a facility at an instant in time; usually expressed as veh/mi or veh/km for vehicles and persons/ft^2 or persons/m^2 for individuals.

Flow (*q*): Time rate of flow of facility users; usually expressed as veh/h or passenger/h.

Level of service (LOS): The quality of movement experienced by the users of a facility in a traffic stream; usually expressed in terms of the freedom of movement of facility users, ranging from little or no restriction (LOS A) to stopped flow (LOS F).

Speed (*u*): Average speed of vehicles in a traffic stream; usually expressed as miles per hour (mph) or kilometers per hour (kph).

Traffic control devices: Signs, signals, and pavement markings placed on streets or highways to guide, inform, or regulate the movement of vehicles on those facilities.

References

Garber, N. and L. Hoel. 1997. *Traffic and Highway Engineering,* 2nd ed., PWS Publishing, Boston.

Institute of Transportation Engineers. 2001. *Traffic Control Devices Handbook,* Washington, DC.

Khisty, C.J. and B. K. Lall. 2003. *Transportation Engineering, An Introduction,* 3rd ed., Prentice Hall, New York.

Meyer, M. and E. Miller. 2001. *Urban Transportation Planning: A Decision-Oriented Approach,* 2nd ed., McGraw-Hill, New York.

TRB. 2000. *Highway Capacity Manual,* Transportation Research Board, Washington, DC.

U.S. DOT and FHWA. 2001. *Manual on Uniform Traffic Control Devices,* U.S. Department of Transportation, Federal Highway Administration, Washington, DC.

Further Information

American Society of Civil Engineers
1801 Alexander Bell Drive
Reston, VA 20191
(800) 548-2723

Federal Highway Administration
U.S. Department of Transportation
400 7th Street, S.W.
Washington D.C. 20590
http://www.ops.fhwa.dot.gov/traffic/

Institute of Transportation Engineers
1099 14th Street, NW
Suite 300 West
Washington, D.C. 20005-3438
202-289-0222
Fax 202-289-7722

Transportation Research Board
Keck Center of the National Academies
500 Fifth Street, NW
Washington, D.C. 20001
202-334-2934
Fax 202-334-2003

10.4 Transportation Systems

Paul Schonfeld

The various forms of transportation that have been developed over time are called **modes**. The classification of modes may be very broad (e.g., highway transportation or air transportation) or more restrictive (e.g., chartered helicopter service). The major distinctions among transportation modes that help to classify them include:

1. Medium (e.g., air, space, surface, underground, water, underwater)
2. Users (e.g., passengers vs. cargo, general-purpose vs. special trips or commodities, common vs. private carrier)
3. Service type (scheduled vs. **demand responsive**, fixed vs. variable route, nonstop vs. express or local, mass vs. personal)
4. Right-of-way type (exclusive, semi-exclusive, shared)
5. Technology:
   a. Propulsion (e.g., electric motors, diesel engines, gas turbines, linear induction motors, powered cables)
   b. Energy sources (e.g., petroleum fuels, natural gas, electric batteries, electric power from conducting cables)
   c. Support (e.g., aerodynamic lift, flotation on water, steel wheels on two steel rails, monorails, air cushions, magnetic levitation, suspension from cables)
   d. Local control (e.g., lateral control by steering wheels, wheel flanges on railroad vehicles, rudders, longitudinal control by humans or automatic devices)
   e. Network guidance and control systems (with various degrees of automation and optimization)

A mode may be defined by its combination of such features. The number of conceivable combinations greatly exceeds the number of modes that have been actually tried, which, in turn, exceeds the number of successful modes. Success may be limited to relatively narrow markets and applications (e.g., for helicopters or aerial cablecars) or may be quite general. Thus, automobiles are successful in a very broad range of applications and have become the basis for distinct transportation modes such as taxis, carpools, or ambulances.

The relative success of various transportation modes depends on available technology and socioeconomic conditions at any particular time, as well as on geographic factors. As technology or socioeconomic conditions change, new transportation modes appear, develop, and may later decline as more effective competitors appear. For many centuries water transportation was considerably cheaper than overland transportation. Access to waterways was quite influential in the location of economic activities and cities. Access to good transportation is still very important to industries and communities. Technological developments have so drastically improved the relative effectiveness of air transportation that within a short period (approximately 1950 to 1965) aircraft almost totally replaced ships for transporting passengers across oceans. It is also notable that as economic prosperity grows, personal transportation tends to shift from the walking mode to bicycles, motorcycles, and then automobiles. Geography can significantly affect the relative attractiveness of transportation modes. Thus, natural waterways are highly valuable where they exist. Hilly terrain decreases the economic competitiveness of artificial waterways or conventional railroads while favoring highway modes. In very mountainous terrain even highways may become uncompetitive compared to alternatives such as helicopters, pipelines, and aerial cablecars.

The relative shares of U.S. intercity passenger and freight traffic are shown in Table 10.4.1. The table shows the relative growth since 1929 of airlines, private automobiles, and trucks and the relative decline of railroad traffic.

Transportation System Components

The major components of transportation systems are:

1. Links
2. Terminals
3. Vehicles
4. Control systems

Certain "continuous-flow" transportation systems such as pipelines, conveyor belts, and escalators have no discrete vehicles and, in effect, combine the vehicles with the link.

Transportation systems may be developed into extensive networks. The networks may have a hierarchical structure. Thus, highway networks may include freeways, arterials, collector streets, local streets, and driveways. Links and networks may be shared by several transportation modes (e.g., cars, buses, trucks, taxis, bicycles, and pedestrians on local streets). Exclusive lanes may be provided for particular modes (e.g., pedestrian or bicycles) or groups of modes (e.g., buses and carpools).

Transportation terminals provide interfaces among modes or among vehicles of the same mode. They may range from marked bus stops or truck loading zones on local streets to huge airports or ports.

Evaluation Measures

Transportation systems are evaluated in terms of their effects on their suppliers, users, and environment. Both their costs and benefits may be classified into supplier, user, and external components. Private transportation companies normally seek to maximize their profits (i.e., total revenues minus total supplier costs). Publicly owned transportation agencies should normally maximize net benefits to their jurisdictions, possibly subject to financial constraints.

From the supplier's perspective, the major indicators of performance include measures of **capacity** (maximum throughput), speed, **utilization rate** (i.e., fraction of time in use), **load factor** (i.e., fraction of maximum payload actually used), energy efficiency (e.g., Btu per ton-mile or per passenger mile), and labor productivity (e.g., worker hours per passenger mile or per ton-mile). Measures of environmental impact (e.g., noise decibels or parts of pollutant per million) are also increasingly relevant. To users, price and service quality measure, including travel time, wait time, access time, reliability, safety, comfort (ride quality, roominess), simplicity of use, and privacy are relevant in selecting modes, routes, travel times, and suppliers.

TABLE 10.4.1 Volume of U.S. Intercity Freight and Passenger Traffic

Millions of Revenue Freight Ton-Miles and Percentage of Total

Year	Railroads	%	Trucks	%	Great Lakes	%	Rivers and Canals	%	Oil Pipelines	%	Air	%	Total
1929	454,800	74.9	19,689	3.2	97,322	16.0	8,661	1.4	26,900	4.4	3	0.0	607,375
1939	338,850	62.3	52,821	9.7	76,312	14.0	19,937	3.7	55,602	10.2	12	0.0	543,534
1944	746,912	68.6	58,264	5.4	118,769	10.9	31,386	2.9	132,864	12.2	71	0.0	1,088,266
1950	596,940	56.2	172,860	16.3	111,687	10.5	51,657	4.9	129,175	12.2	318	0.0	1,062,637
1960	579,130	44.1	285,483	21.7	99,468	7.6	120,785	9.2	228,626	17.4	0.1	0.0	1,314,270
1970	771,168	39.8	412,000	21.3	114,475	5.9	204,085	10.5	431,000	22.3	3,295	0.2	1,936,023
1980	932,000	37.5	555,000	22.3	96,000	3.9	311,000	12.5	588,000	23.6	4,840	0.2	2,486,840
1986	889,000	35.5	634,000	25.3	68,000	2.7	325,000	13.0	578,000	23.1	7,340	0.3	2,501,340
1987	968,000	36.3	668,000	25.1	78,000	2.9	358,000	13.4	585,000	22.0	8,720	0.3	2,665,720

Millions of Revenue Passenger-Miles and Percentage of Total (Except Private)

Year	Railroads	%	Buses	%	Air Carriers	%	Inland Waterways	%	Total (except private)	Private Automobiles	Private Airplanes	Total (including private)
1929	33,965	77.1	6,800	15.4	—	—	3,300	7.5	44,065	175,000	—	219,065
1939	23,669	67.7	9,100	26.0	683	2.0	1,486	4.3	34,938	275,000	—	309,938
1944	97,705	75.7	26,920	20.9	2,177	1.7	2,187	1.78	128,989	181,000	1	309,990
1950	32,481	47.2	26,436	38.4	8,773	12.7	1,190	1.7	68,880	438,293	1,299	508,472
1960	21,574	28.6	19,327	25.7	31,730	42.1	2,688	3.6	75,319	706,079	2,228	783,626
1970	10,903	7.3	25,300	16.9	109,499	73.1	4,000	2.7	149,702	1,026,000	9,101	1,184,803
1980	11,000	4.5	27,400	11.3	204,400	84.2	NA	—	242,800	1,300,400	14,700	1,557,900
1986	11,800	3.4	23,700	6.9	307,900	89.7	NA	—	343,400	1,450,100	12,400	1,805,900
1987	12,300	3.4	22,800	6.2	329,100	90.4	NA	—	364,200	1,494,900	12,400	1,871,500

Note: Railroads includes all classes, including electric railways, Amtrak and Auto-Train.
Source: Transportation Policy Associates.
Source: Railroad facts, 1988 Edition, Association of American Railroads.

Air Transportation

Air transportation is relatively recent, having become practical for transporting mail and passengers in the early 1920s. Until the 1970s its growth was paced primarily by technological developments in propulsion, aerodynamics, materials, structures, and control systems. These developments have improved its speed, load capacity, energy efficiency, labor productivity, reliability, and safety, to the point where it now dominates long-distance mass transportation of passengers overland and practically monopolizes it over oceans. Airliners have put ocean passenger liners out of business because they are much faster and also, remarkably, more fuel and labor efficient. However, despite this fast growth, the cargo share of air transportation is still small.

For cargoes that are perishable, high in value, or urgently needed, air transportation is preferred over long distances. For other cargo types, ships, trucks, and railroads provide more economical alternatives. In the 1990s, the nearest competitors to air cargo are containerships over oceans and trucks over land. For passengers, air transportation competes with private cars, trains, and intercity buses over land, with practically no competitors over oceans. The growth of air transportation has been restricted to some extent by the availability of adequate airports, by environmental concerns (especially noise), and by the fear of flying of some passengers.

There are approximately 10,000 commercial jet airliners in the world, of which the largest (as of 1997) are Boeing B-747 types, of approximately 800,000 lb gross takeoff weight, with a capacity of 550 passengers. The economical cruising speed of these and smaller "conventional" (i.e., **subsonic**) airliners has stayed at around 560 mph since the late 1950s. A few supersonic transports (SSTs) capable of cruising at approximately 1300 mph were built in the 1970s (the Anglo-French Concorde and the Soviet Tu-144) but, due to high capital and fuel costs, were not economically successful. About eight Concorde SSTs are still operating, with government subsidies.

The distance that an aircraft can fly depends on its payload, according to the following equation:

$$R = \frac{V}{c'}\left(\frac{L}{D}\right)\ln\left(W_{\mathrm{TO}}/W_L\right) \tag{10.4.1}$$

where

R = range (mi)
c' = specific fuel consumption (lb fuel/lb thrust × h)
(L/D) = lift-to-drag ratio (dimensionless)
W_{TO} = aircraft takeoff weight (lb) = $W_L + W_F$
W_L = aircraft landing weight (lb) = $W_E + W_R + P$
W_E = aircraft empty weight (lb)
W_R = reserve fuel weight (lb)
W_F = consumed fuel weight (lb)
P = payload (lb)

This equation assumes that the difference between the takeoff weight and landing weight is the fuel consumed. For example, suppose that for a Boeing B-747 the maximum payload carried (based on internal fuselage volume and structural limits) is 260,000 lb, maximum W_{TO} is 800,000 lb, $W_R = 15{,}000$ lb, $W_E = 370{,}000$, $L/D = 17$, $V = 580$ mph, and $c' = 0.65$ lb/lb thrust × h. The resulting weight ratio [$W_{\mathrm{TO}}/W_L = 800/(370 + 15 + 260)$] is 1.24 and the range R is 3267 mi. Payloads below 260,000 lb allow greater ranges.

Most airline companies fly scheduled routes, although charter services are common. U.S. airlines are largely free to fly whatever routes (i.e., origin–destination pairs) they prefer in the United States. In most of the rest of the world, authority to serve particular routes is regulated to negotiated by international agreements. The major components of airline costs are direct operating costs (e.g., aircraft depreciation or rentals, aircrews, fuel, and aircraft maintenance) and indirect operating costs (e.g., reservations, advertising and other marketing costs, in-flight service, ground processing of passengers and bags, and administration).

The efficiency and competitiveness of airline service is heavily dependent on efficient operational planning. Airline scheduling is a complex problem in which demand at various times and places, route authority, aircraft availability and maintenance schedules, crew availability and flying restrictions, availability of airport gates and other facilities, and various other factors must all be considered. Airline management problems are discussed in (Wells, 1984).

Airports range from small unmarked grass strips to major facilities requiring many thousands of acres and billions of dollars. Strictly speaking, an airport consists of an airfield (or "airside") and terminal (or "landside"). Airports are designed to accommodate specified traffic loads carried by aircraft up to a "design aircraft," which is the most demanding aircraft to be accommodated. The design aircraft might determine such features as runway lengths, pavement strengths, or terminal gate dimensions at an airport. Detailed guidelines for most aspects of airport design (e.g., runway lengths and other airfield dimensions, pavement characteristics, drainage requirements, allowable noise and other environmental impacts, allowable obstruction heights, lighting, markings, and signing) are specified by the U.S. Federal Aviation Administration (FAA) in a series of circulars.

Airport master plans are prepared to guide airport growth, usually in stages, toward ultimate development. These master plans:

1. Specify the airport's requirements.
2. Indicate a site if a new airport is considered.
3. Provide detailed plans for airport layout, land use around the airport, terminal areas, and access facilities.
4. Provide financial plans, including economic and financial feasibility analysis.

Major new airports tend to be very expensive and very difficult to locate. Desirable airport sites must be reasonably close to the urban areas they serve yet far enough away to ensure affordable land and acceptable noise impacts. Many other factors—including airspace interference with other airports, obstructions (e.g., hills, buildings), topography, soil, winds, visibility, and utilities—must be reconciled. Hence, few major new airports are being built, and most airport engineering and planning work in the United States is devoted to improving existing airports. Governments sometimes develop multi-airport system plans for entire regions or countries.

National agencies (such as the FAA in the United States) are responsible for traffic control and airspace management. Experienced traffic controllers, computers, and specialized sensors and communication systems are required for this function. Increasingly sophisticated equipment has been developed to maintain safe operations even for crowded airspace and poor visibility conditions. For the future we can expect increasing automation in air traffic control, relying on precise aircraft location with global positioning satellite (GPS) systems and fully automated landings. Improvements in the precision and reliability of control systems are increasing (slowly) the capacity of individual runways as well as the required separation among parallel runways, allowing capacity increases in restricted airport sites.

Railroad Tranportation

The main advantages of railroad technology are low frictional resistance and automatic lateral guidance. The low friction reduces energy and power requirements but limits braking and hill-climbing abilities. The lateral guidance provided by wheel flanges allows railroad vehicles to be grouped into very long trains, yielding economies of scale and, with adequate control systems, high capacities per track. The potential energy efficiency and labor productivity of railroads is considerably higher than for highway modes, but is not necessarily realized, due to regulations, managerial decisions, demand characteristics, or terrain.

The main competition of railroads include automobiles, aircraft, and buses for passenger transportation, and trucks, ships, and pipelines for freight transportation. To take advantage of their scale economies, railroad operators usually seek to combine many shipments into large trains. Service frequency is thus necessarily reduced. Moreover, to concentrate many shipments, rail cars are frequently re-sorted into different trains, rather than moving directly from origin to destination, which results in long periods spent waiting in classification yards, long delivery times, and poor vehicle utilization. An alternative operational concept relying on direct nonstop “unit trains” is feasible only when demand is sufficiently large between an origin–destination pair.

Substantial traffic is required to cover the relatively high fixed costs of railroad track. Moreover, U.S. railroads, which are privately owned, must pay property taxes on their tracks, unlike their highway competitors. By 1920 highway developments had rendered low-traffic railroad branch lines noncompetitive in the United States. Abandonment of such lines has greatly reduced the U.S. railroad network, even though the process was retarded by political regulation.

The alignment of railroad track is based on a compromise between initial costs and operating costs. The latter are reduced by a more straight and level alignment, which requires more expensive earthwork, bridges, or tunnels. Hay (1982) provides design guidelines for railroads.

In general, trains are especially sensitive to gradients. Thus, compared to highways, railroad tracks are more likely to go around rather than over terrain obstacles, which increases the **circuity factors** for railroad transportation.

The resistance for railroad vehicles may be computed using the Davis equation (Hay, 1982):

$$r = 1.3 + 29/w + bV + CAV^2/wn + 20G + 0.8D \tag{10.4.2}$$

where

G = gradient (%)
D = degree of curvature
r = unit resistance (lb of force per ton of vehicle weight)
w = weight (tons per axle of car or locomotive)
n = number of axles
b = coefficient of flange friction, swaying, and concussion (0.045 for freight cars and motor cars in trains, 0.03 for locomotives and passenger cars, and 0.09 for single-rail cars)
C = drag coefficient of air [0.0025 for locomotives (0.0017 for streamlined locomotives) and single- or head-end-rail cars, 0.0005 for freight cars, and 0.00034 for trailing passenger cars, including rapid transit]
A = cross-sectional area of locomotives and cars (usually 105 to 120 ft^2 for locomotives, 85 to 90 ft^2 for freight cars, 110-120 ft^2 for multiple-unit and passenger cars, and 70 to 110 ft^2 for single- or head-end-rail cars)
V = speed (mph)

The coefficients shown for this equation reflect relatively old railroad technology and can be significantly reduced for modern equipment (Hay, 1982). The equation provides the unit resistance in pounds of force per ton of vehicle weight. The total resistance of a railroad vehicle (in lb) is

$$R_v = rwn \tag{10.4.3}$$

The total resistance of a train R is the sum of resistances for individual cars and locomotives. The rated horsepower (hp) required for a train is:

$$\text{hp} = \frac{RV}{375\eta} \tag{10.4.4}$$

where η = transmission efficiency (typically about 0.83 for a diesel electric locomotive).

The hourly fuel consumption for a train may be computed by multiplying hp by a specific fuel consumption rate (approximately 0.32 lb/hp × h for a diesel electric locomotive).

Diesel electric locomotives with powers up to 5000 hp haul most trains in the United States. Electric locomotion is widespread in other countries, especially those with low petroleum reserves. It is especially competitive on high-traffic routes (needed to amortize electrification costs) and for high-speed passenger trains. Steam engines have almost disappeared.

The main types of freight rail cars are box cars, flat cars (often used to carry truck trailers or intermodal containers), open-top gondola cars, and tank cars. Passenger trains may include restaurant cars and sleeping cars. Rail cars have tended toward increasing specialization for different commodities carried, a trend that reduces opportunities for back hauls. Recently, many "double-stack" container cars have been built to carry two tiers of containers. Such cars require a vertical clearance of nearly 20 ft, as well as reduced superelevation (banking) on horizontal curves. In the United States standard freight rail cars with gross weights up to 315,000 lb are used.

High-speed passenger trains have been developed intensively in Japan, France, Great Britain, Italy, Germany, and Sweden. The most advanced (in 1995) appear to be the latest French TGV versions, with cruising speeds of 186 mph and double-deck cars. At such high speeds, trains can climb long, steep grades (e.g., 3.5%) without slowing down much. Construction costs in hilly terrain can thus be significantly reduced. Even higher speeds are being tested in experimental railroad and magnetic levitation (MAGLEV) trains.

Highway Transportation

Highways provide very flexible and ubiquitous transportation for people and freight. A great variety of transportation modes, including automobiles, buses, trucks, motorcycles, bicycles, pedestrians, animal-drawn vehicles, taxis, and carpools, can share the same roads. From unpaved roads to multilane freeways, roads can vary enormously in their cost and performance. Some highway vehicles may even travel off the roads in some circumstances. The vehicles also range widely in cost and performance, and at their lower range (e.g., bicycles) are affordable for private use even in poor societies.

Flexibility, ubiquity, and affordability account for the great success of highway modes. Personal vehicles from bicycles to private automobiles offer their users great freedom and access to many economic and social opportunities. Trucks increase the freedom and opportunities available to farmers and small businesses. Motor vehicles are so desirable and affordable that in the United States the number of registered cars and trucks approximates the number of people of driving age. Other developed countries are approaching the same state despite strenuous efforts to discourage motor vehicle use.

The use of motor vehicles brings significant problems and costs. These include:

1. Road capacity and congestion. Motor vehicles require considerable road space, which is scarce in urban areas and costly elsewhere. Shortage of road capacity results in severe congestion and delays.
2. Parking availability and cost.
3. Fuel consumption. Motor vehicles consume vast amounts of petroleum fuels. Most countries have to import such fuels and are vulnerable to price increases and supply interruptions.
4. Safety. The numbers of people killed and injured and the property damages in motor vehicle accidents are very significant.
5. Air quality. Motor vehicles are major contributors to air pollution.
6. Regional development patterns. Many planners consider the low-density "sprawl" resulting from motor vehicle dominance to be inefficient and inferior to the more concentrated development produced by mass transportation and railroads.

In the United States trucks have steadily increased their share of the freight transportation market, mostly at the expense of railroads, as shown in Table 10.4.1. They can usually provide more flexible, direct, and responsive service than railroads, but at higher unit cost. They are intermediate between rail and air transportation in both cost and service quality. With one driver required per truck, the labor productivity is much lower than for railroads, and there are strong economic incentives to maximize the load capacity for each driver. Hence, the tendency has been to increase the number, dimensions, and weights allowed for trailers in truck-trailer combinations, which requires increased vertical clearances (e.g., bridge overpasses), geometric standards for roads, and pavement costs.

The main reference for highway design is the AASHTO manual [AASHTO, 1990]. For capacity, the main reference is the Transportation Research Board *Highway Capacity Manual* (TRB, 1985). Extensive software packages have been developed for planning, capacity analysis, geometric design, and traffic control.

Water Transportation

Water transportation may be classified into (1) marine transportation across seas and (2) inland waterway transportation; their characteristics differ very significantly. Inland waterways consist mostly of rivers, which may be substantially altered to aid transportation. Lakes and artificial canals may also be part of inland waterways. Rivers in their natural states are often too shallow, too fast, or too variable in their flows. All these problems may be alleviated by impounding water behind dams at various intervals. (This also helps generate electric power.) Boats can climb or descend across dams by using **locks** or other elevating systems (Hochstein, 1981). In the U.S. inland waterway network there are well over 100 major lock structures, with chambers up to 1200 ft long and 110 ft wide. Such chambers allow up to 18 large barges (35 × 195 ft) to be raised or lowered simultaneously.

In typical inland waterway operations, large diesel-powered “towboats” (which actually push barges) handle a rigidly tied group of barges (a “tow”). Tows with up to 48 barges (35 × 195 ft, or about 1300 tons per barge) are operated on the lower Mississippi, where there are no locks or dams. On other rivers, where locks are encountered at frequent intervals, tow sizes are adjusted to fit through locks. The locks constitute significant bottlenecks in the network, restricting capacity and causing significant delays.

Table 10.4.1 indicates that the waterway share of U.S. freight transportation has increased substantially in recent years. This is largely attributable to extensive improvements to the inland waterway system undertaken by the responsible agency, the U.S. Army Corps of Engineers.

The main advantage of both inland waterway and marine transportation is low cost. The main disadvantage is relatively low speed. Provided that sufficiently deep water is available, ships and barges can be built in much larger sizes than ground vehicles. Ship costs increase less than proportionally with ship size, for ship construction, crew, and fuel. Energy efficiency is very good at low speeds [e.g., 10–20 knots (nautical mi/h)]. However, at higher speeds the wave resistance of a conventional ship increases with the fourth power of speed (V^4). Hence, the fuel consumption increases with V^4 and the power required increases with V^5. Therefore, conventional-displacement ships almost never exceed 30 knots in commercial operation. Higher practical speed may be obtained by lifting ships out of the water on hyrdrofoils or air cushions. However, such unconventional marine vehicles have relatively high costs and limited markets at this time, ships have increased in size and specialization. Crude oil tankers of up to 550,000 tons (of payload) have been built. Tankers carrying fluids are less restricted in size than other ships because they can pump their cargo from deep water offshore without entering harbors. Bulk carriers (e.g., for coal, minerals, or grains) have also been built in sizes exceeding 300,000 tons. They may also be loaded through conveyor belts built over long pier structures to reach deep water. General cargo ships and containerships are practically always handled at shoreline berths and require much storage space nearby.

The use of intermodal containers has revolutionized the transportation of many cargoes. Such containers greatly reduce the time and cost required to load and unload ships. Up to 4500 standard 20-ft containers (20 × 8 × 8 ft) can be carried at a speed of about 24 knots on recently built containerships.

Port facilities for ships should provide shelter from waves and sufficiently deep water, including approach channels to the ports. In addition, ports should provide adequate terminal facilities, including loading and unloading equipment, storage capacity, and suitable connections to other transportation networks. Ports often compete strenuously with other ports and strive to have facilities that are at least equal to those of competitors. Since ports generate substantial employment and economic activities, they often receive financial and other support from governments.

Geography limits the availability of inland waterways and the directness of ship paths across oceans. Major expensive canals (e.g., Suez, Panama, Kiel) have been built to provide shortcuts in shipping routes. These canals may be so valuable that ship dimensions are sometimes compromised (i.e., reduced) to fit through these canals. In some parts of the world (e.g., Baltic Sea, North Sea, most U.S. coasts) the waters are too shallow for the largest ships in existence. Less efficient, smaller ships must be used there. The dredging of deeper access channels and ports can increase the allowable ship size, if the costs and environmental impacts are considered acceptable.

Public Transportation

Public transportation is the term for ground passenger transportation modes available to the general public. It connotes public availability rather than ownership. "Conventional" public transportation modes have fixed routes *and* fixed schedules and include most bus and rail transit services. "Unconventional" modes (also labeled "paratransit") include taxis, carpools and van pools, rented cars, dial-a-ride services, and subscription services.

The main purposes of public transportation services, especially conventional mass transportation services in developed countries, are to provide mobility for persons without automobiles (e.g., children, poor, nondrivers); to improve the efficiency of transportation in urban areas; to reduce congestion effects, pollution, accidents, and other negative impacts of automobiles; and to foster preferred urban development patterns (e.g., strong downtowns and concentrated rather than sprawled development).

Conventional services (i.e., bus and rail transit networks) are quite sensitive to demand density. Higher densities support higher service frequencies and higher network densities, which decrease user wait times and access times, respectively. Compared to automobile users, bus or rail transit users must spend extra time in access to and from stations and in waiting at stations (including transfer stations). Direct routes are much less likely to be available, and one or more transfers (with possible reliability problems) may be required. Thus, mass transit services tend to be slower than automobiles unless exclusive rights-of-way (e.g., bus lanes, rail tunnels) can favor them. Such exclusive rights-of-way can be quite expensive if placed on elevated structures or in tunnels. Even when unhindered by traffic, average speeds may be limited by frequent stops and allowable acceleration limits for standing passengers. Prices usually favor mass transit, especially if parking for automobiles is scarce and expensive.

The capacity of a transit route can be expressed as:

$$C = FLP \tag{10.4.5}$$

where

C = one-way capacity (passengers/hour) past a certain point
F = service frequently (e.g., trains/hour)
L = train length (cars/train)
P = passenger capacity of cars (spaces/car)

For rail transit lines where high capacity is needed in peak periods, C can reach 100,000 passengers/hour (i.e., 40 trains/hour × 10 cars/train × 250 passenger spaces/car). There are few places in the world where such capacities are required. For a bus line the train length L would usually be 1.0. If no on-line stops are allowed, an exclusive bus lane also has a large capacity (e.g., 1000 buses/hour × 90 passenger spaces/bus), but such demand levels for bus lanes have not been observed.

The average wait time of passengers on a rail or bus line depends on the headways, which is the interval between successive buses or trains. This can be approximated by:

$$\overline{W} = \overline{H}/2 + \mathrm{var}(H)/2\overline{H} \tag{10.4.6}$$

where

$\overline{W}$ = average wait time (e.g., minutes)
$\overline{H}$ = average headway (e.g., minutes)
$\mathrm{var}(H)$ = variance of headway (e.g., minutes^2)

It should be noted that the headway is the inverse of the service frequency.

The number of vehicles N required to serve a route is:

$$N = RFL \tag{10.4.7}$$

where R = vehicle round trip time on route (e.g., hours).

The effectiveness of a public transportation system depends on many factors, including demand distribution and density, network configuration, routing and scheduling of vehicles, fleet management, personnel management, pricing policies, and service reliability. Demand and economic viability of services also depend on how good and uncongested the road system is for automobile users.

Engineers can choose from a great variety of options for propulsion, support, guidance and control, vehicle configurations, facility designs, construction methods, and operating concepts. New information and control technology can significantly improve public transportation systems. It will probably foster increased automation and a trend toward more personalized (i.e., taxilike) service rather than mass transportation.

Defining Terms

Capacity: The maximum flow rate that can be expected on a transportation facility. “Practical” capacity is sometimes limited by “acceptable:” delay levels, utilization rates, and load factors.

Circuity factor: Ratio of actual distance on network to shortest airline distance.

Delay: Increase in service time due to congestion or service interruptions.

Demand-responsive: A mode whose schedule or route is adjusted in the short term as demand varies, such as taxis, charter airlines, and “TRAMP” ships.

Load factor: Fraction of available space or weight-carrying capability that is used.

Lock: A structure with gates at both ends which is used to lift or lower ships or other vessels.

Modes: Distinct forms of transportation.

Subsonic: Flying below the speed of sound (Mach 1), which is approximately 700 mph at cruising altitudes of approximately 33,000 ft.

Utilization rate: Fraction of time that a vehicle, facility, or equipment unit is in productive use.

References

AASHTO (American Society of State Highway and Transportation Officials). 1990. *A Policy on Geometric Design of Highways and Streets.* Washington, DC.

Brun, E. 1981. *Port Engineering*. Gulf Publishing, Houston.

Hay, W.W. 1982. *Railroad Engineering*. John Wiley & Sons, New York.

Hochstein, A. 1981. *Waterways Science and Technology.* Final Report DACW 72-79-C-003. U.S. Army Corps of Engineers, August.

Homburger, W.S. 1982. *Transportation and Traffic Engineering Handbook*. Prentice-Hall, Englewood Cliffs, NJ.

Horonjeff, R. and McKelvey, F. 1994. *Planning and Design of Airports*. McGraw-Hill, New York.

Morlok, E.K. 1976. *Introduction to Transportation Engineering and Planning*. McGraw-Hill, New York.

TRB (Transportation Research Board). 1985. *Highway Capacity Manual*. Special Report 209. TRB, Washington, DC.

Vuchic, V. 1981. *Urban Public Transportation*. Prentice-Hall, Englewood Cliffs, NJ.

Wells, A.T. 1984. *Air Transportation*. Wadsworth Publishing Co., Belmont, CA.

Wright, P.H. and Paquette, R.J. 1987. *Highway Engineering*. John Wiley & Sons, New York.

Further Information

The ITE Handbook (Homburger, 1992) and Morlok (1978) cover most transportation modes. Horonjeff and McKelvey (1994), Hay (1982). Wright and Paquette (1987), Brun (1981), and Vuchic (1981) are more specialized textbooks covering airports, railroads, highways, ports, and urban public transportation systems, respectively. Periodicals such as *Aviation Week & Space Technology, Railway Age, Motor Ship, and Mass Transit* cover recent developments in their subject areas.

10.5 Alternative Fuels for Motor Vehicles

Paul Norton and Wendy Clark

Overview

Motor vehicle fuels that provide an alternative to conventional gasoline or diesel include ethanol, methanol, natural gas, propane, electricity, and biodiesel. Legislation such as the Clean Air Act Amendments of 1990 (CAAA) and the Energy Policy Act of 1992 (EPACT) has increased interest in alternative fuels. This legislation promotes alternative fuels for their potential to decrease emissions from cars and trucks and lessen the dependence of the United States on imported petroleum. These fuels may also have benefits in terms of reduced emissions of global warming gases.

Modifications must be made to conventional vehicles to use many of these alternative fuels. However, all are burned in internal combustion engines similar to those used for conventional gasoline or diesel fuel. Notable exceptions are 10% ethanol/gasoline blends and 20% biodiesel/diesel blends that require no engine or fuel system modifications. The engine and fuel system must be modified to account for the properties of the alternative fuel. The components that are typically added or changed to transform a gasoline vehicle into a compressed natural gas vehicle are shown in Figure 10.5.1. A major challenge is finding space on the vehicles for enough gas cylinders to give the vehicle an acceptable range between refuelings. These cylinders store the natural gas at pressures of 3000 to 3600 psi and must be protected from road debris and corrosive substances such as battery acid.

In light-duty "flexible-fueled" or "variable-fueled" vehicles, ethanol and methanol is blended with gasoline in the vehicle's fuel tank. The car can be fueled on any mix of the specified alcohol and gasoline

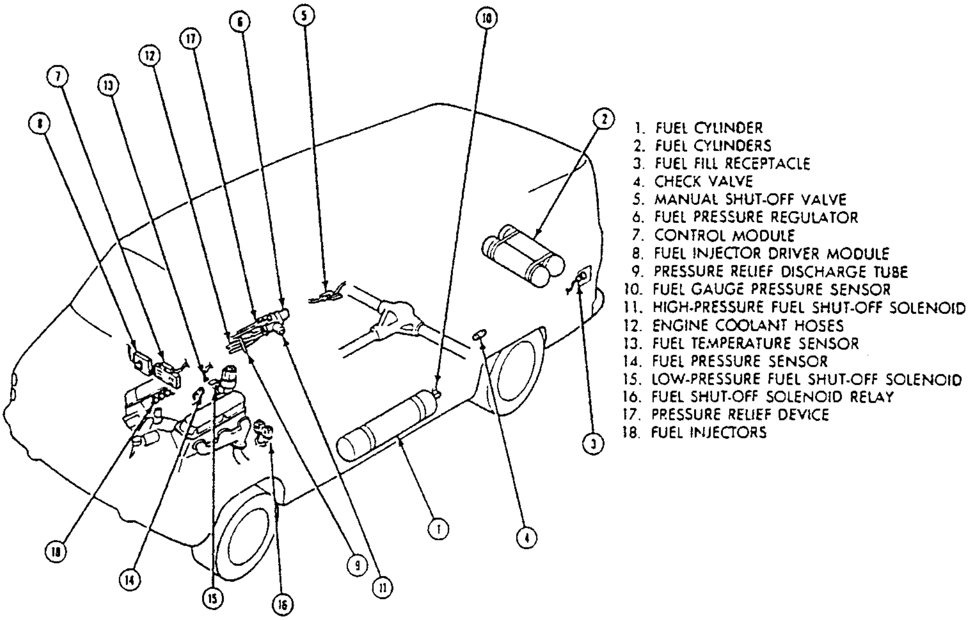

FIGURE 10.5.1 Typical Components of a compressed natural gas vehicle.

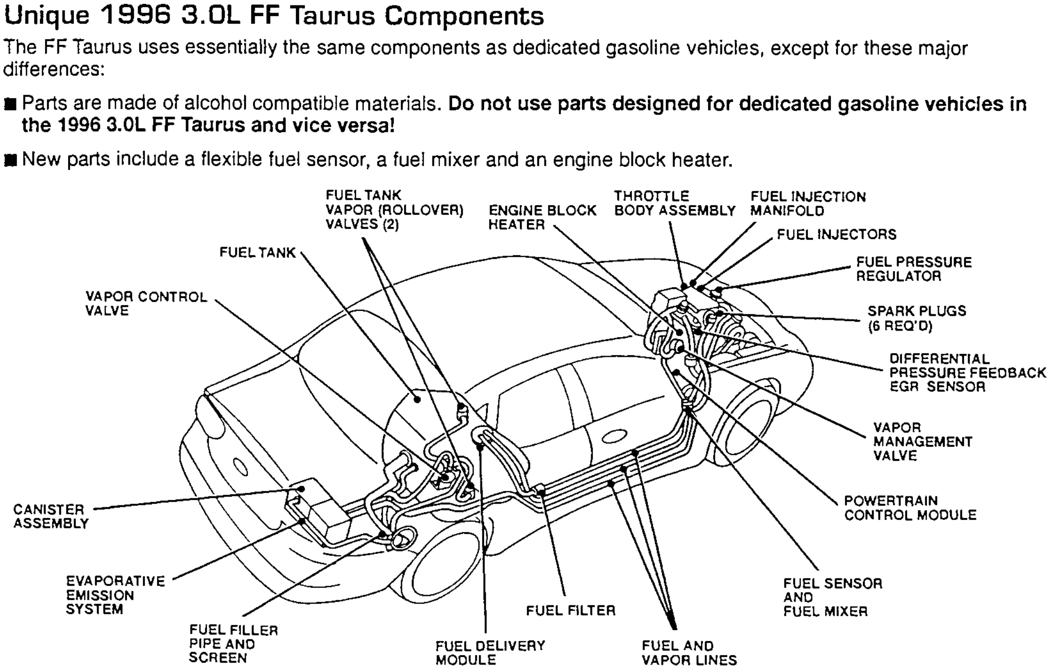

Unique 1996 3.0L FF Taurus Components

The FF Taurus uses essentially the same components as dedicated gasoline vehicles, except for these major differences:

- Parts are made of alcohol compatible materials. **Do not use parts designed for dedicated gasoline vehicles in the 1996 3.0L FF Taurus and vice versa!**
- New parts include a flexible fuel sensor, a fuel mixer and an engine block heater.

FIGURE 10.5.2 Components of a flexible fuel vehicle.

up to 85% alcohol. Therefore an ethanol flexible-fueled vehicle (FFV) could be fueled on 85% ethanol (E85) at one refueling, and pure gasoline at the next. A sensor in the fuel line constantly measures the percentage of ethanol in the fuel and the engine control system adjusts the air/fuel ratio accordingly. The typical unique components in an FFV are shown in Figure 10.5.2. All components in the fuel system must be compatible with ethanol or methanol. The fuel injectors must have a higher flow capacity to account for the lower heating value of ethanol and methanol compared to gasoline.

Vehicles can be modified to run on an alternative fuel by the original manufacturer (OEM) or they can be modified by an aftermarket conversion shop. In general, alternative fuel vehicles produced by an OEM go through a much more rigorous development and testing process than an aftermarket conversion. The alternative fuel system for the OEM vehicle is designed for one specific model of vehicle or engine, whereas the aftermarket conversion is designed to fit on a wide variety of vehicles. Therefore the OEM system can be optimized for the one vehicle it was designed for, but the aftermarket conversion kit must be a compromise that will work with many different vehicles. Today's cars and trucks are highly developed and difficult to improve upon. Recent studies have found that compressed natural gas and propane aftermarket conversions had higher emissions in some regulated properties than they did on gasoline before the conversions (Motta et al., 1996). The same study points out that tests on OEM compressed natural gas cars showed substantially lower levels of all four regulated emissions than their gasoline powered counterparts.

Advantages and Disadvantages of Alternative Fuels

Each alternative fuel has unique physical properties that lead to advantages and disadvantages compared to conventional fuels and to each other. All the alternative fuels contain less energy per unit volume than gasoline or diesel fuel. This leads to the need to store more fuel on the vehicle to achieve the same operating range between refuelings. In many cases, this disadvantage is balanced by lower fuel cost and/or lower emissions than a gasoline or diesel vehicle. A summary of some of the properties of the most popular alternative fuels is shown in Table 10.5.1. Some of the advantages and disadvantages of using these fuels are outlined in Table 10.5.2.

TABLE 10.5.1 Properties of Conventional and Alternative Fuels

Fuel	Cetane Number	Research Octane Number	Motor Octane Number	Density (lb/gal)	LHV[a] (Btu/gal)	LHV[a] Btu/lb)	DEE[b] Gallons	DEE[b] Pounds
Liquids at atm. Pressure								
100% Ethanol		109	90	6.6	75600	11500	0.59	0.66
85% Ethanol (E85)	—	105	89	6.5	83600	12855	0.64	0.72
10% Ethanol/gasoline	—	96.5	86	6.1	111000	18000	0.86	1.39
10% Ethanol/diesel	45	—	—	7.0	123000	17500	0.95	1.01
100% Methanol	approx. 5	109	89	6.7	56200	8400	0.44	0.48
100% (Soy methyl-ester) 20% Biodiesel (B20)	49			7.3	120200	16500	0.93	0.95
#2 Diesel	45			7.4	129000	17400	1.00	1.00
#1 Diesel	45			7.6	125800	16600	0.98	0.95
Gasoline		90–100	80–90	6.0	115400	19200	0.89	1.10
Gases at atm. Pressure								
Compressed natural gas (CNG)[c]	<0	>127	122	n/a	n/a	20400	n/a	1.17
Liquified natural gas (LNG)[d]	<0	>127	122	3.5	78000	22300	0.60	1.28
Propane (LPG)		109	96	4.2	83600	19900	0.65	1.14
Dimethyl ether (DME)	55–60			5.6	74800	13600	0.58	0.78

[a] Lower heating value.

[b] Diesel energy equivalent = the LHV of the alternative fuel divided by the LHV of #2 Diesel = the number of gallons (or pounds) of diesel fuel that has the same energy content as one gallon (or pound) of the alternative fuel.

[c] Average values for natural gas in the United States.

[d] 100% Methane at –263°F.

TABLE 10.5.2 Advantages and Disadvantages of Alternative Fuels

Fuel	Advantages	Disadvantages
Liquefied Petroleum Gas (LPG) Liquefied petroleum gas is the most widely used alternative fuel. In the U.S., LPG is mostly propane with small amounts of butane and ethane. In 1993, an estimated 350,000 vehicles powered by propane (mostly conversions) were plying the nation's highways.	• Most widely available alternative fuel with an estimated 11,000 refueling sites nationwide • LPG is nontoxic • Liquefies at relatively low pressures • One gallon of liquefied propane has about 70% energy content of gasoline • Can reduce carbon monoxide and ozone forming hydrocarbon emissions • Refueling stations are relatively inexpensive	• 45% of LPG in the U.S. is derived from oil • Proper detection and ventilation are required for indoor storage and maintenance of vehicles • Starting problems may occur at very low temperatures due to low vapor pressure • Perception of a safety problem
Compressed Natural Gas (CNG) Natural gas is composed primarily of methane. It is stored on the vehicle under 3000 to 4000 psi of pressure. There are currently (2001) an estimated 110,000 vehicles operating on compressed natural gas in U.S. fleets.	• High North American resource base • Natural gas reserves are more globally distributed than oil reserves • Can reduce all regulated emissions • Is especially effective in reducing particulate emissions from large trucks • Less expensive than gasoline in some areas • Eliminates evaporative emissions because the fuel system is sealed • Can be produced from renewable resources at high cost	• Requires bulky pressure cylinders and high pressure fuel lines • Fuel system costs as much as $2500 more than gasoline for cars • Refueling infrastructure is expensive • Energy storage density is low, making it difficult to achieve equivalent range • Composition of natural gas varies regionally

TABLE 10.5.2 Advantages and Disadvantages of Alternative Fuels (continued)

Fuel	Advantages	Disadvantages
Methanol Methanol is an alcohol which can be produced from coal, wood, methane, or natural gas. It is often blended with gasoline; e.g., "M85" contains 85 percent methanol and 15 percent gasoline to overcome cold start and poor flame visibility problems.	• Can be produced domestically but near-term sources are likely to be imports • Can be produced from renewable resources, but is currently produced predominantly from natural gas • Can reduce ozone-forming hydrocarbon emissions and particulate emissions • Eliminates toxic benzene emissions • A liquid fuel at ambient temperatures	• May increase formaldehyde emissions • Corrosive and toxic • Requires the use of special methanol-compatible materials in fuel system • Poor flame visibility • Has a lower energy content than gasoline, therefore requires larger fuel tanks • Currently significantly more expensive than gasoline • Lack of refueling infrastructure • Difficult to start in cold temperatures
Ethanol (E85) Ethanol is an alcohol derived from biomass-corn and other agricultural products such as sugar cane. Ethanol is denatured by blending with natural gasoline to avoid taxation as an alcoholic beverage.	• Is produced domestically from renewable resources • Can reduce carbon dioxide and ozone-forming hydrocarbon emissions • Eliminates toxic benzene emissions • A liquid fuel at ambient temperatures • May increase acetaldehyde emissions • Has higher energy content than methanol	• Currently significantly more expensive than gasoline • Has a lower energy content than gasoline; therefore reduces vehicle range • Lack of significant refueling infrastructure although this is growing in corn-growing states • Requires the use of special ethanol-compatible materials in fuel system
Ethanol (E10)	• Domestic, renewable • Reduces vehicle CO (especially in older vehicles), CO_2, and benzene tailpipe emissions • All vehicle fuel system materials produced since the early 1980s are compatible	
Liquefied Natural Gas (LNG) Natural gas can be stored on the vehicle as a cryogenic liquid at about –260F. LNG is used primarily for heavy-duty vehicles.	Same advantages as CNG plus: • Has higher storage density than CNG so a higher range can be achieved • Usually higher methane content than CNG • Does not require high pressure cylinders for storage	• Is a cryogenic liquid with special handling requirements • Requires vacuum-insulated storage tank • Refueling infrastructure is expensive • Lack of refueling infrastructure • Poor compression-ignition quality
Biodiesel Biodiesel is a methyl ester that can be made from a variety of products. Most biodiesel used in the U.S. is made from soybean oil or waste grease. Biodiesel is usually blended with diesel. The most common blend is 20% biodiesel, 80% conventional diesel.	• Is made from a renewable resource • Is produced domestically • Can reduce carbon monoxide, hydrocarbon, and particulate matter emissions • Is used in existing diesel engines without modifications • Is nontoxic • Has energy content comparable to diesel • Can reduce global warming	• Is more expensive than conventional diesel • Can increase emissions of oxides of nitrogen • Needs to be blended with conventional diesel to reduce gelling effect at low temperatures • Currently only limited engine warranty coverage is available for the use of B20
Dimethyl Ether (DME) DME can be made from natural gas and is a liquid at relatively low pressures (similar to LPG). It appears to be a good candidate for heavy-duty trucks. Prototype engines are currently being produced.	• Can reduce emissions significantly • Has a high cetane number so it can be used in a diesel engine • Can be produced from domestic renewable sources	• No commercially available engines at this time • Limited fuel supply • No refueling infrastructure • Uncertain production cost

* Reformulated gasoline is considered a "clean fuel" in the Clean Air Act Amendments, but is not considered an alternative fuel in the Energy Policy Act of 1992.

References

Motta, R. et al. April 1996. *Compressed Natural Gas and Liquefied Petroleum Gas Conversions: The National Renewable Energy Laboratory's Experience*, National Renewable Energy Laboratory. NREL/SP-425-20514.

Owen, K. and Coley, T. 1995. *Automotive Fuels Reference Book*, 2nd ed. Society of Automotive Engineers.

Reda Moh. Beta, ed. 1995. *Alternative Fuels, A Decade of Success and Promise,* Society of Automotive Engineers, SAE No. PT-48.

Whalen, P. et al. *19th Alternative Fuel Light-Duty Vehicles: Summary of Results from the National Renewable Energy Laboratory's Vehicle Evaluation Data Collection Efforts,* NREL/SP-425-20821, May.

Federal Alternative Motor Fuels Programs; Fourth Annual Report to Congress, United States Department of Energy, DOE/GO-10095-150, July, 1995.

10.6 Electric and Hybrid Vehicles

Iqbal Husain

Electric and hybrid electric vehicles (EV), enabled by high efficiency electric motors and controllers, provide the means for an environmentally friendly urban transportation system. The interest in electric vehicles soared in recent years with intense drive from the government, environmental activists, and associated industries to advance the technology. The legislative mandates are for zero emission vehicles (ZEVs). Electric vehicles, powered by alternative renewable energy sources, is the only solution for a true zero emission vehicle. The California Air Resources Board mandate requires that 4% of vehicles sold by a company selling more than 35,000 vehicles in California must be ZEVs by 2003 and an additional 6% of the sales must be made up of either more ZEVs and partial ZEVs.[1–3] However, this mandate was not enforced.

The electric vehicles paved their way into public use as early as in the middle of the 19th century, even before the introduction of gasoline powered vehicles.[4,5] In 1900, 4200 automobiles were sold out of which 40% were steam powered, 38% were electric powered and 22% were gasoline powered. The invention of the starter motor, improvements in mass production technology of gas-powered vehicles and inconvenience in battery charging led to the disappearance of electric vehicles in the early 1900s. The interest in EVs resurged in the 1960s due to environmental pollution concerns and the unpleasant dependence on foreign oil. The growth in the enabling technologies, added to the environmental and economic concerns over the next several decades, increased the demand for investing in research and development for electric vehicles.

The significant R&D efforts focused on developing ZEV technologies have been hindered by unsuitable battery technologies. In addition, the battery charging requirements place increased demand on the power grid, and ultimatley the generating sources, thus only shifting the pollution location. A near term solution for minimizing the environmental pollution problem due to the absence of a suitable, high energy density energy store or source for electric vehicles is perceived in the hybrid electric vehicles. The hybrid vehicles use both an electric motor and an internal combustion engine and thus do not solve the pollution problem. The current research interest is focused on developing the fuel cell technology that will lead to affordable and competitive electric vehicles for public use. The fuel cell electric vehicles (FCEV) can be a viable alternative to battery electric vehicles to serve as zero emission vehicles without the range problem.

EV System

An electric vehicle (EV) is a transportation unit having the two features: (1) The energy source is portable and electromechanical or electromechanical in nature, and (2) traction effort is supplied only by an electric motor. The primary components of an electric vehicle system are the motor, controller, power source, and transmission. The structure of an electric vehicle system along with the available choice of various components is shown in Figure 10.6.1.[1]

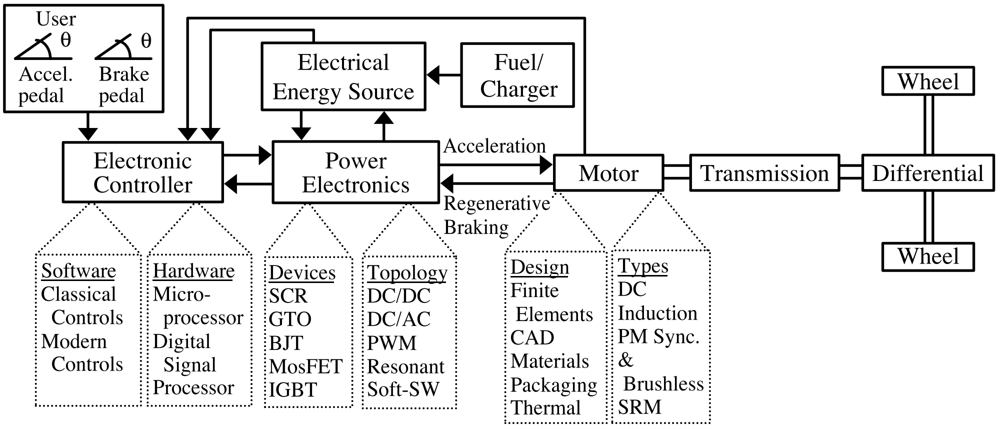

FIGURE 10.6.1 Major components and available choices for an electric vehicle system

Energy Sources and Stores

The electrical energy required in electric vehicles for vehicle propulsion is typically obtained through conversion of chemical energy stored in devices such as batteries and fuel cells. The issue of portability of the energy source is the biggest challenge for mass production of electric vehicles. Electrochemical batteries have been the traditional choice of portable energy source, but the low-power density problem, slow recharge time, and high replacement cost are the biggest obstacles for commercialization of battery-powered road vehicles. The fuel cells, which have been used by NASA successfully in space missions since the Apollo programs in the early 1960s, are a possible candidate for portable energy source. The fuel cell converts chemical energy directly into electrical energy, and the by-product is simply water when hydrogen is used as the fuel. The flywheel is an alternative portable source, in which energy is stored in mechanical form to be converted into electrical energy on demand for vehicle propulsion. The ultracapacitor technology has also advanced tremendously in the recent years, although it is unlikely to achieve specific energy levels high enough to serve as the sole energy source of a vehicle. However, the ultracapacitors in conjunction with a battery or fuel cell have the possibility of providing an excellent portable energy source with sufficient specific energy and specific power for the next generation vehicles.

Ragone Plots

The two important parameters for energy sources are specific energy *(SE)* and specific power *(SP)*. Specific energy defines the amount of energy that can be stored in an energy source and is represented by discharge energy per unit mass. Specific power is related to how rapidly energy can be released from a source and is given in terms of power delivered per unit mass. The plot of *SP* vs. *SE* on a log-log scale is known as a Ragone plot. The Ragone plots of some common batteries, along with those of ultracapacitors, fuel cells, and heat engines, are shown in Figure 10.6.2.

Batteries

The desirable features of batteries for EV and hybrid EV (HEV) applications are high-specific power, high-specific energy, high-charge acceptance rate for both recharging and regenerative braking, and long calendar and cycle life. Additional technical issues include methods and designs to balance the battery segments or packs electrically and thermally, accurate techniques to determine a battery's state of charge, and recycling facilities of battery components. Above all, the cost of batteries must be reasonable for EVs and HEVs to be commercially viable. The batteries need a charger to restore the stored energy level once its available energy is near depletion due to usage. The specific power of a battery energy source is low, leading to the limited range problem of battery-powered vehicles.

Lead/acid batteries have been the primary choice because of their well-developed technology and low cost, although promising new battery technologies are being tested in many prototype vehicles. The

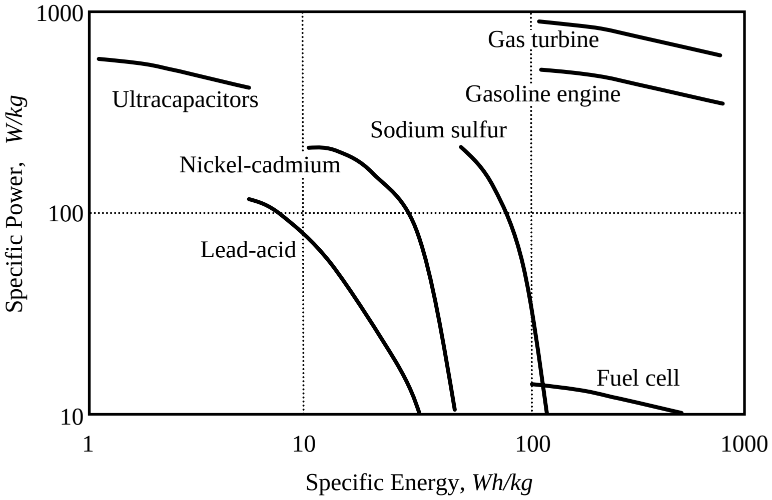

FIGURE 10.6.2 Specific power vs. specific energy (Ragone plots) of batteries, gasoline engine, and fuel cell. (From Husain, I., 2003, *Electric and Hybrid Vehicles: Design Fundamentals*, CRC Press, Boca Raton, FL.)

recently introduced hybrid vehicles, Toyota Prius and Honda Civic, use NiMH, which is an alkaline battery where electrical energy is derived from the chemical reaction of a metal with oxygen in an alkaline electrolyte medium. The NiMH is likely to survive as the leading rechargeable battery in the future for traction applications, with strong challenges coming from lithium-ion and lithium-polymer batteries. The lithium-metal has high electrochemical reduction potential (3.045V) and the lowest atomic mass (6.94). The lithium-ion batteries have high-specific energy, high-specific power, high-energy efficiency, good high-temperature performance, and low self-discharge. The components of Li-ion batteries are also recyclable. The Li-polymer batteries, using solid electrolytes, have potential for the highest specific energy and power.[2,3]

Batteries can be configured in series or in parallel, or in a combination thereof. The design depends on the output voltage and the discharge requirements. The series connection yields the required voltage, whereas the parallel connection delivers the desired capacity for the battery pack for minimum runtime before recharging. The battery pack also includes electronics, which are typically located outside the battery pack. The electronic circuit of a multilevel battery pack controls charging and ensures reliability and protection against overcharge, overdischarge, short circuits, and thermal abuse.

Fuel Cells

A fuel cell is an electrochemical device that produces electricity by means of a chemical reaction, much like a battery.[4] The major difference between batteries and fuel cells is that the latter can produce electricity as long as fuel is supplied, whereas batteries produce electricity from stored chemical energy and hence require frequent recharging. The basic structure of a fuel cell is shown in Figure 10.6.3. The fuels supplied to the cell are hydrogen and oxygen. The concept of the fuel cell is the opposite of electrolysis of water, where hydrogen and oxygen are combined to form electricity and water.

The alkaline fuel cells with their high efficiencies were first considered for mobile applications.[5,6] They require pure hydrogen as fuel, and operate at low temperatures (80°C). The current choice of fuel cells for electric vehicles is the proton exchange membrance (PEM) fuel cells. These fuel cells also operate at low temperatures (around 80°C), and use a perfluorinated sulphonated polymer membrane (e.g., Nafion) as the electrolyte. While having lower electrical efficiency than the alkaline cells (about 40%), these fuel cells are rugged, and stacks of cells can be easily constructed. Many automotive companies have decided to explore the use of methanol as a fuel by onboard reforming it into hydrogen because of the higher energy density and ease of handling of this hydrocarbon fuel when compared to hydrogen gas. A direct methanol fuel cell (DMFC) works on the same premise as the PEM except that the temperature is

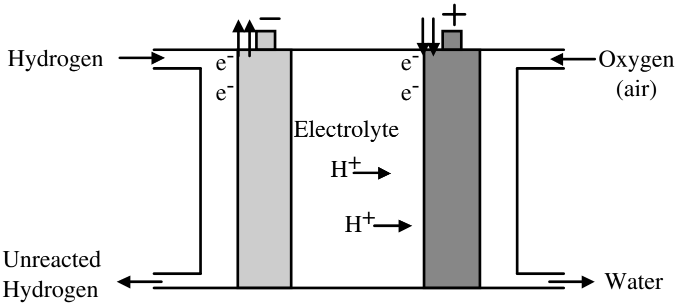

FIGURE 10.6.3 Basic fuel cell structure. (From Husain, I. 2003. *Electric and Hybrid Vehicles: Design Fundamentals*, CRC Press, Boca Raton, FL.)

increased (to the range of 90 to 120°C) such that internal reformation of methanol into hydrogen is possible. This type of fuel cell is still in the design stages since the search for a good electro-catalyst to both reform the methanol efficiently and to reduce oxygen in the presence of methanol is still ongoing. This type of cell has low electrical efficiency, at about 30%.

Electric Motors

The electric machine converts the available onboard electrical energy into mechanical energy for vehicle propulsion.[7,8] The desirable features in an electric motor for EV/HEV applications are ruggedness, high torque-to-inertia ratio, high power-to-weight ratio, extended constant power region, flexible drive control, fault tolerance, high efficiency, and low acoustic noise.

The electric machine also processes regenerative energy during vehicle braking, which can be used to recharge the batteries of EVs or HEVs. The energy available during braking is the kinetic energy that was acquired by the vehicle during acceleration, and part of this energy can be recovered through an appropriate motor controller. Regenerative braking can increase the range of EVs by about 10 to 15%.

The strength of electric motors and integrated circuit (IC) engines are typically described with horsepower (HP) ratings, although a comparison between electric motors and IC engines in terms of HP only is not fair. The power that an electric motor can continuously deliver without overheating is its rated HP, which is typically a derated figure. For short periods of time the motor can deliver 2 to 3 times the rated HP. Therefore, at starting a high power is available from an electric motor for acceleration, and the motor torque can be the maximum under stall conditions, that is, at zero speed. On the contrary, an IC engine is rated at a specific r/min level for maximum torque and maximum HP. The torque characteristics of motors are shown in Figure 10.6.4 along with torque characteristics of IC engines. The electric motor has constant power characteristics over a wide speed range. Therefore, the electric motor can be attached directly to the drive wheels and accelerate the vehicle from zero all the way up to the top speed. The motor and hence the vehicle speed can be controlled directly through the power electronic converter feeding the current into the motor. There is essentially no requirement for a transmission with an electric motor, other than a fixed gear for appropriately sizing the motor and matching the vehicle and motor speeds.

AC motors are preferred over DC motors for electric propulsion applications because of their ruggedness, simplicity in construction, and higher torque and power densities. Although the controls are complex for AC motors, the recent developments in IC technology enable complex control implementations in microprocessor and digital signal processors with high degrees of accuracy and excellent performance. The choice of AC motors suitable for propulsion applications are induction motors, permanent magnet (PM) motors, and switched reluctance motors (SRMs).[9] The well-established technology and ruggedness of induction motors make it a very good choice for traction applications, and it has been used in vehicles like Saturn EV1 from GM. Although the costs of permanent magnet motors are relatively higher compared to its competitors, the high-power density and excellent performance make it the first

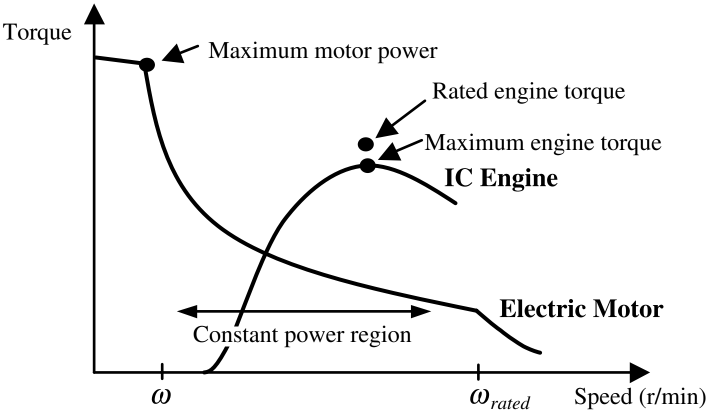

FIGURE 10.6.4 Electric motor and IC engine torque characteristics. (From Husain, I. 2003. *Electric and Hybrid Vehicles: Design Fundamentals*, CRC Press, Boca Raton, FL.)

choice for many automotive manufacturers of electric vehicles. The SRM can be an ideal motor for traction applications, with its simplicity and fault-tolerance characteristics. However, the technology of SRM is not mature, and the acoustic noise problems need to be overcome before it can find widespread applications for electric vehicle propulsion.

Electric Motor Drive

The electric motor is driven by a power electronics–based power processing unit that converts the fixed dc voltage available from the source into a variable-voltage, variable-frequency source controlled to maintain the desired operation of the vehicle. The power electronic converter segment of the motor drive is made of solid-state devices and handles the flow of bulk power from the source to the motor input terminals.[10,11] The controller processes the command input and the feedback information to generate the switching signals for the power converter solid-state switches. The coordination of the components of the motor drive with the source and the motor is shown in Figure 10.6.5.

A power converter is made of high-power, fast-acting semiconductor devices, such as bipolar junction transistor (BJT), metal oxide semiconductor field effect transistor (MOSFET), insulated gate bipolar transistor (IGBT), silicon controlled rectifier or thyristor (SCR), gate turn-off SCR (GTO), and MOS-controlled thyristor (MCT). These solid-state devices, configured in a certain circuit topology, function as an on-off electronic switch to convert the fixed-supply voltage into a variable-voltage and variable-frequency supply. All these devices have a control input gate or base through which the devices are turned on and off according to the command generated by the controller. The tremendous advances in the power semiconductor technology over the past two decades have enabled the development of compact, efficient, and reliable dc-dc and dc-ac power electronic converter topologies.

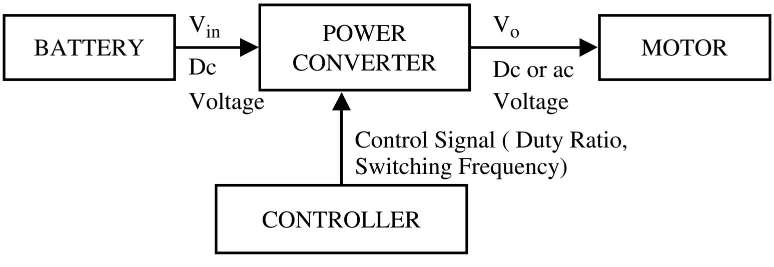

FIGURE 10.6.5 Block diagram of a motor drive. (From Husain, I., 2003. *Electric and Hybrid Vehicles: Design Fundamentals*, CRC Press, Boca Raton, FL.)

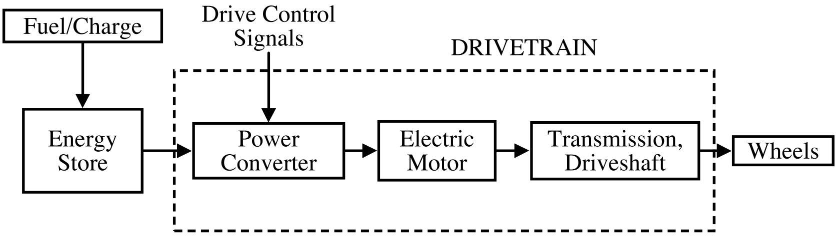

FIGURE 10.6.6 Drivetrain of an electric vehicle

EV Drivetrain

The *drivetrain* of the vehicle is the electromechanical energy conversion linkage system between the vehicle energy store and the wheels. The drivetrain of an EV is shown in Figure 10.6.6. The drivetrain has electrical as well as mechanical components. The electric vehicles can be either a front-wheel drive or a rear-wheel drive. In the case of front-wheel drive, the electric motor drives the gearbox mounted on the front axle. A single motor can drive the transaxle on a common axis, delivering power to the two wheels differentially through a hollow motor shaft. Altenatively, two motors mounted on the chassis or on the half-shafts can be used to drive the front two wheels in order to simplify the transmission and to eliminate the differential. In-wheel motor arrangement is also a possibility, but the cost associated with high-power, high-torque motors is the primary impediment for such arrangement. The transmission is more complex in the case of a rear-wheel drive, which requires a differential to accommodate unequal speeds of the inside and outside wheels of the rear axle during vehicle cornering.

Hybrid Electric Vehicles

The hybrid electric vehicles evolved out of two basic configurations: series and parallel. A *series* hybrid is one in which only one energy converter can provide propulsion power. The heat engine or IC engine acts as a prime mover in this configuration to drive an electric generator that delivers power to the battery or energy storage link and the propulsion motor. The component arrangement of a series HEV is shown in Figure 10.6.7. In series HEVs, the power required to propel the vehicle is provided solely by the electric motor. Beyond the heat engine and the generator, the propulsion system is exactly the same as in an EV, making the electric motor power requirements exactly the same as in the EV. The series hybrid has a simpler drivetrain, but all three drivetrain components — namely, IC engine, generator, and motor — need to be sized for maximum power for long distance–sustained, high-speed driving. This is required since the batteries will exhaust fairly quickly, leaving the IC engine to supply all the power through the generator.

A *parallel* hybrid is one in which more than one source can provide propulsion power. The heat engine and the eletric motor are configured in parallel with a mechanical coupling that blends the torque coming from the two sources. The component arrangements of a parallel hybrid are shown in Figure 10.6.8. In

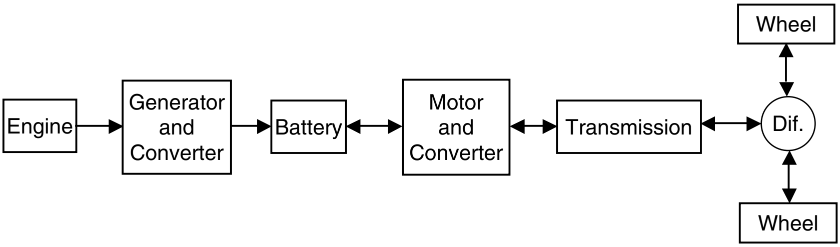

FIGURE 10.6.7 Series hybrid electric vehicle drivetrain. (From Husain, I., 2003. *Electric and Hybrid Vehicles: Design Fundamentals*, CRC Press, Boca Raton, FL.)

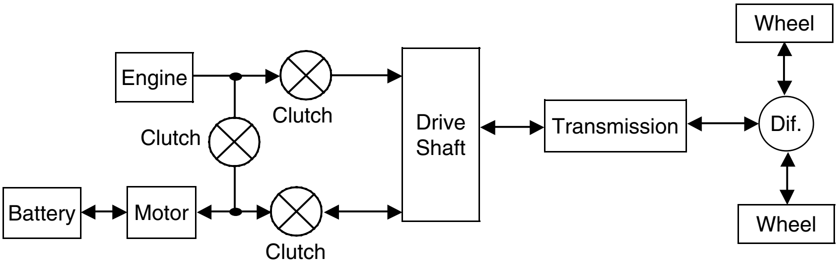

FIGURE 10.6.8 Parallel hybrid electric vehicle drivetrain. (From Husain, I., 2003. *Electric and Hybrid Vehicles: Design Fundamentals*, CRC Press, Boca Raton, FL.)

a parallel HEV, both the heat engine and the electric motor are connected to the driveshaft through separate clutches. The parallel hybrid needs two propulsion components: an ICE and an electric machine, with the latter functioning both as a motor and a generator. The control complexity increases significantly, since power flow needs to be regulated and blended from two parallel sources.

Both series and parallel hybrids come in a variety of types. The mission of the vehicle and the optimum design for that mission dictates the choice. Although HEVs initially evolved as either series or parallel, manufacturers later realized the advantages of a combination of the series and parallel configuration for practical road vehicles. In these combination hybrids, the heat engine is also used to charge the battery. The recently available Toyota Prius is an example of such a hybrid, where a small series element is added to the primarily parallel HEV. The small series element ensures that the battery remains charged in prolonged wait periods, such as at traffic lights or in a traffic jam.

Internal Combustion Engines

The heat engines of interest for the EV/HEV applications are the internal combustion engine and the gas turbine. The internal combustion engines used in automobiles, trucks, and buses use the reciprocating piston-cylinder arrangement. The two types of reciprocating IC engines are the spark-ignition engine (SI) and the compression-ignition (CI) engine.[12] The two engines are commonly known as gasoline/petrol engine and diesel engine. The gas turbines used in power plants are also internal combustion engines, where the processes occur in an interconnected series of different components. The Brayton cycle gas-turbine engine has been adapted to the automotive propulsion engine; it has the advantage of burning fuel that requires little refining and the fuel burns completely. The gas turbines have fewer moving parts because there is no need to convert the rotary motion of the turbine. The disadvantages of gas-turbines are their complex construction and lower efficiency. Nevertheless, gas turbines are being considered for hybrid electric vehicles, and prototype vehicles have been developed.

Fuel Cell EVs

A fuel cell EV consists of a fuel storage system that is likely to include a fuel processor to reform raw fuel to hydrogen, the fuel cell stack and its control unit, the power processing unit and its controller, and the propulsion unit consisting of the electric machine and drivetrain. The fuel cell has current source type characteristics, and the output voltage of a cell is low. Several fuel cells have to be stacked in series to obtain a higher voltage level, and then the output voltage needs to be boosted in order to interface with the dc/ac inverter driving an ac propulsion motor, assuming that an ac motor is used for higher power density. The block diagram of a fuel cell EV system is shown in Figure 10.6.9. The power electronic interface circuit between the fuel cell and electric motor includes the dc/dc converter for voltage boost, the dc/ac inverter to supply an ac motor, the microprocessor/digital signal processor for controls, and battery/capacitors for energy storage. The time constant of the fuel cell stack is much slower than that of the electrical load dynamics. A battery storage system is necessary to supply the power during transient and overload conditions and also to absorb the reverse flow of energy due to regenerative braking.

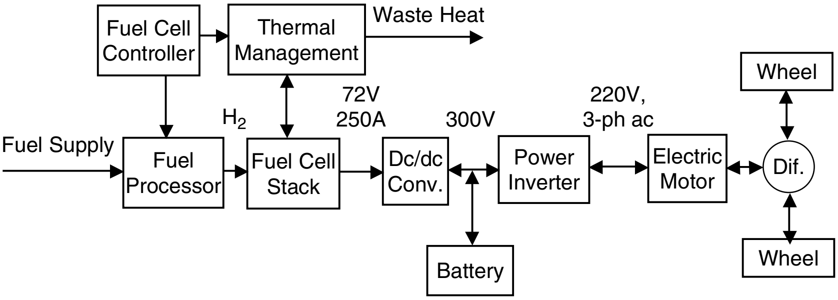

FIGURE 10.6.9 A fuel cell electric vehicle. (From Husain, I., 2003. *Electric and Hybrid Vehicles: Design Fundamentals*, CRC Press, Boca Raton, FL.)

EV Advantages and Disadvantages

The relative advantages and disadvantages of electric vehicles and IC engine vehicles can be better appreciated from a comparison of the two on the basis of efficiency, pollution, cost, and dependence on oil. In order to evaluate the efficiencies of IC engine vehicle (ICEV), battery EV, hybrid EV, and fuel cell EV (FCEV) on a level ground, we must consider the complete process in all systems, starting with crude oil in the wells to power available at the wheels. The ICEV energy conversion starts with the conversion of crude oil to fuel oil in the refinery. The ICEV process includes the transmission of fuel oil from refinery to gas stations, power conversion in the internal combustion engine of the vehicle, and power transfer from the engine to the wheels through the transmission before it is available at the wheels. The EV process starts not at the vehicles but at the source of raw power, whose conversion efficiency must be considered to calculate the overall efficiency of electric vehicles. For battery EVs, the efficiencies of electricity generation and transmission to the outlets need to be considered, since batteries must be recharged regularly. For FCEVs, the fuel production and fuel cell efficiencies must be evaluated in addition to the efficiencies of the electrical and mechanical components of the drivetrain. The well-to-wheel efficiencies for conventional ICEVs, battery EVs, and FCEVs using various types of fuels are presented in Table 10.6.1. The table has been compiled using experimental data from various sources and was originally published in reference 13. The numbers will obviously vary for experiments conducted for vehicles or engines with

TABLE 10.6.1 Comparison of Well-to-Wheel Efficiencies of Different Types of Vehicles

Propulsion System	Fuel	Fuel Production Efficiency[1] (%)	Peak Brake Engine Efficiency/ Stack Efficiency (%)	Part Load Efficiency Factor	Transmission Efficiency (%)	Weight Factor × Idle Factor[2]	Total Cycle Efficiency (%)
Conventional SI	NG	87.5	38	0.68	85	1.0	19
	H_2	59					13[3]
Conventional Diesel	F-T Diesel	70	45	0.77	85	1.9	21
	Dual Fuel	86	40	0.77	85	1.0	22.5
Hybrid SI	NG	87.5	38	0.85	85	1.3	31
Hybrid Diesel	F-T Diesel	70	45	0.9	85	1.3	31
	Dual-Fuel	86	40	0.85	85	1.3	32
Battery EV	Electricity	37	49	1.0	90	1.0	16
Fuel Cell EV	Methanol	57.5	28	1.1	90	1.0	16
	H_2	59	44.5	1.1	90	1.0	26

From Kreith, F., West, R.E. and Isler, B.E., "Efficiency of Advanced Ground Transportation Technologies," in *J. of Energy Resour. Technol.*, p. 177, September 2002.

1. See reference 13.
2. Idle factor is the product of the engine idle-off and regeneration factor and vehicle weight factor.
3. Experimental data provided vehicle tank-to-wheel efficiency.

a different design, but one can get a representative figure from this table. The table shows that the efficiencies of IC engine vehicles and electric vehicles are of the same order of magnitude, with all of them around 20% when the overall process is considered. The most promising technology, as far as efficiency is concerned, are the HEVs, with efficiencies exceeding 30% for those powered by natural gas (NG), Fisher-Tropsch (F-T) diesel, or dual-fuel. The Fisher-Tropsch refers to the chemical process of producing liquid fuel from natural gas or coal. The fuel obtained by combining approximately 10% diesel fuel with natural gas is known as *dual-fuel*. Experiments showed that auto-ignition can be achieved at a higher compression ratio than in a spark ignition (SI) engine with dual-fuel, resulting in greater efficiency.[13]

Transportation accounts for one third of all energy usage, making it the leading cause of environmental pollution through carbon emissions.[14] The U.S. Department of Energy has projected that if 10% of automobiles nationwide were zero-emission vehicles, regulated air pollutants would be cut by one million tons per year and 60 million tons of greenhouse carbon dioxide gas would be eliminated. On the other hand, thermal pollution by large power plants would increase with increased EV usage. With stricter sulfur-dioxide (SO_2) power-plant emission standards, EVs would have little impact on SO_2 levels. Emissions due to power generation at localized plants are much easier to regulate than those emanating from IC engine vehicles that are individually maintained and scattered all over. The people dwelling in cities are not exposed to power plant–related emissions, since these facilities are mostly located outside urban areas. The environmental benefits of battery and fuel cell electric vehicles can be better appreciated when electricity or fuel is produced for the respective propulsion units from renewable sources such as wind or solar.

The initial EV capital costs are higher than ICEV capital cost primarily due to the lack of mass production opportunities. However, EV capital costs are expected to decrease as volume increases. Capital costs of EVs easily exceed capital costs of ICEVs due to the cost of the battery. The total life-cycle cost of an EV is projected to be less than that of a comparable ICEV.

The transportation industry depends heavily on oil, with more than half of the oil used for ground transportation in the U.S. being imported. An average ICEV in its lifetime uses 94 barrels of oil based on 28 mi/gal fuel consumption. On the other hand, an average EV uses two barrels of oil in its lifetime based on 4mi/kWh. The oil is used in the EV process during electricity generation, although only 4% of electricity generated is from oil.

The appropriate infrastructure must also be in place for battery or fuel cell EVs to become more popular. The infrastructure-related issues for battery electric vehicles are battery charging facilities, standardization of EV components, sales and distribution, service and technical support ,and parts supply. For fuel cell EVs powered by hydrogen only, it will be necessary to build a hydrogen distribution infrastructure. The alternative is to use methanol as the fuel with a reformer and utilize the current gasoline infrastructure with certain modifications to address the corrosivity of methanol.[6] The issues of standardization of electrical components, sales and distribution, service and technical support, and parts supply for fuel cell EVs are similar to those of battery EVs.

References

1. Husain, I. 2003. *Electric and Hybrid Vehicles: Design Fundamentals*. CRC Press, Boca Raton, FL.
2. Rand, D.A.J., Woods, R., and Dell, R.M. 1998. *Batteries for Electric Vehicles*, John Wiley & Sons Inc., New York.
3. Dell, R.M. and Rand, D.A.J. 2001. *Understanding Batteries*, Royal Society of Chemistry, UK.
4. Appleby, A.J., and Foulkes, F.R. 1989. *Fuel Cell Handbook*, Van Nostrand Reinhold, New York.
5. Andrews, N. Poised for growth: DG and Ride through Power. In *Power Quality*, January/February 2002, pp. 10–15.
6. Laughton, M.A. Fuel cells. *Power Eng. J.*, February 2002, pp. 37–47.
7. Krause, P.C. and Wasynchuk, O. 1986. *Analysis of Electric Machinery*, McGraw Hill, New York.

8. Novotny, D.W. and Lipo, T.A. 1996. *Vector Control and Dynamics of AC Drives*, Oxford University Press, Inc., New York.
9. Miller, T.J.E. 1989. *Brushless Permanent Magnet and Switched Reluctance Motor Drives*, Oxford University Press, Oxford.
10. Mohan, N., Undeland, T.M., and Robins, W.P. 2003. *Power Electronics: Converters, Applications and Design,* John Wiley & Sons Inc., New York.
11. Trzynadlowski, A.M. 1998. *Introduction to Modern Power Electronics*, John Wiley & Sons Inc., New York.
12. Moran, M.J. and Shapiro, H.N. 1992. *Fundamentals of Engineeing Thermodynamcis*, 2nd edition, John Wiley & Sons, Inc., New York.
13. Kreith, F., West, R.E., and Isler, B.E., Efficiency of advanced ground transportation technologies *Trans. of the ASME, J. of Energy Resour. Technol.*, pp. 173–79, September 2002.
14. The Energy Foundation, 2001 Annual Report, San Francisco, CA.

10.7 Intelligent Transportation Systems

Sumit Ghosh

Origin of ITS

As ITS America[1] noted in 1994, surface transportation in the U.S. is at a crossroads. While the nation's 4 million miles of paved roads are badly clogged with 200 million vehicles and congestion continuing to rise, the conventional wisdom of building more roads is not working for financial and environmental reasons. Since that time, the situation has only continued to worsen.[2] Today, at the beginning of the twenty-first century there is little money for repairing existing highways, let alone for building new highways; the cost of adding lanes is escalating quickly, especially in the suburbs and urban areas where congestion is severe and land availability is low; and many pavements are in poor repair. With the push for increasing productivity, the average driver's impatience is on the rise, further aggravating an already stressful situation. In the surface transportation industry, even veteran professional drivers are quitting in large numbers, citing increased stress from requirements to conform to limited time windows for just-in-time delivery and pickup in highly congested areas.[3] In 2000, congestion costs were estimated at $100 billion[4] annually in lost productivity, energy wastage, vehicle deterioration, road rage, and increased emissions from vehicle idling. Traffic accidents in 1993 alone caused 40,000 deaths and 5 million injuries.

In response to the growing problems, the U.S. Congress passed the Intermodal Surface Transportation Efficiency Act (ISTEA) of 1991, whose basic goal is to develop a national transportation system that is economically efficient and environmentally sound, and that can move people and goods in an energy-efficient manner. Following the passage of ISTEA, the U.S. Department of Transportation, led by the Federal Highway Administration, immediately launched the Intelligent Vehicle Highway System (IVHS) program. IVHS did not aim to address the capacity problem. Its goal was to steering drivers away from bottlenecks and to introduce and manage reasonable enforcement measures such as congestion pricing. Surface transportation related problems are not unique to the U.S. In fact, in countries with higher population densities, such as Japan and European countries, the problem is far more acute. The Programme for a European Traffic with Highest Efficiency and Unprecedented Safety (PROMETHEUS)[5] project in Europe and the Advanced Mobile Traffic Information and Communication System (AMTICS) program[6] in Japan closely paralleled the IVHS program in the U.S.

A careful analysis reveals that the problem of efficiently moving people and goods is not just confined to surface transportation, that is, vehicles and roadways, but that it involves trains, passenger planes, air cargo, ferries, ships, and every available and currently utilized mode of transportation. This thinking helped foster the broader notion of the intelligent transportation system (ITS), superseding IVHS. Clearly, to synthesize a genuine and practical solution at the national level, possibly international level, one must adopt a holistic approach that takes into consideration complex interdependencies between the many transportation modes and that is guided by a fundamental goal, namely, minimizing the transit time for every traveler and merchandise in transit, subject to fair distribution of available resources.

Underlying ISTEA and the ITS America movement is the general belief that the solution to this complex problem rests on two key scientific and engineering advances. The first is the increased availability of computing power in the form of powerful desktop workstations and mobile laptops, palmtops, and handheld PDAs. The second is the increasing availability of networking, both wire-line and wireless, for communications and control. However, the mere availability of computing power and networking does not automatically guarantee a solution. For instance, Carley[7] from the General Electric locomotive-building unit reports that locomotives sit idle as much as 40% due to bottlenecks in the rail corridors stemming from poor information, coordination, and control. With annual fuel budgets for many of the railroad companies running in excess of $800 million, and the need to leave diesel locomotive engines running even when idle, the extent of fuel wastage is staggering. The key to successful solutions to complex transportation problems, according to reference 8, lies in the comprehensive understanding of the control and coordination algorithms that, while abstract, serve to unify the computing and networking resources in a synergistic, nontangible manner. Analysis of historical evidence reveals the critical role played by these algorithms in different forms in the past two revolutions[8] in transportation. Analysis also shows that we are poised to experience the third major revolution and possibly the most complex — the transformation from the centralized paradigm to the asynchronous, distributed paradigm.

Current Status of ITS

Despite the ISTEA of 1991, to virtually every driver today the current interstate and state highway system continues to be a source of great frustration, the principal reason being congestion. The problem is not new; congestion has been around for a very long time. In London, the average vehicular speed in 2003 was 17 mph, unchanged from 100 years ago when horse-drawn carriages were around.[9] In Manhattan, pedestrians today average a speed of 3.3 mph that, ironically, is higher than that of vehicular traffic, at 3.1 mph. In 1986, King[10] observed that driver navigational waste was equal to 6.4% of all distance and 12% of all time spent in travel by noncommercial motorists, amounting to millions of dollars. In 1992, the Rhode Island Department of Transportation (RIDOT)[11,12] estimated that 60% of all vehicle-hours lost was due to accidents, stalled vehicles, and other road mishaps that are dynamic and unpredictable a priori. Similar findings were reported by other state DOT agencies. In 1997, Peters, McGurrin, Shank, and Cheslow[13] estimated that the ITS infrastructure must improve vehicle-handling capacity by 30% in order to keep congestion from growing beyond the current level. In 2000, congestion costs were estimated at $100 billion[4] annually in lost productivity, energy wastage, vehicle deterioration, road rage, and increased emissions from vehicle idling. Based on a ten-year study of the five most congested areas (Los Angeles; Washington, DC; San Francisco-Oakland; Miami; and Chicago), Lomax[2] reported in 2002 that the average travel delay, in the form of idle waiting, equates to one workweek per year per driver and that the cost of wasted fuel from idling totals $8.6 billion annually in Los Angeles alone. The worst travel delay equals 75 hours per year in the San Bernardino-Riverside area, and the highest per capita fuel wastage of $860 occurs in Washington, DC.

This section presents the current status of ITS from two distinct perspectives. The first perspective consists of a review of the scientific literature on ITS research. It addresses a number of areas, including assessing overall ITS approach, system planning, vehicular traffic modeling, system evaluation, vehicle tracking, autonomous driving and Global Positioning System (GPS)-based guidance, signal control, braking, lane detection and steering control, intelligent cruise control, disseminating road work information to drivers, noise pollution, platooning, simulators for evaluating ITS systems, and training ITS personnel. White[3] observes that the surface transportation problem is complicated by increased congestion, decreased use of public transportation, and shifting demographics coupled with escalating cost of adding lanes. Nitz and Chung[14] stress that in the spirit of ITS, copper cables must be replaced with optical fibers to improve communications in rapid transit systems. Horioka[15] presents an architecture for a universal traffic management system (UTMS) for the city of Kochi, where all traffic signals are managed at centralized traffic control. In support of the UTMS architecture, Hayashi and Sugimoto[16] recompute and adjust the length of the red signals in increments of 1% at intervals of 5 minutes to improve efficiency. Fu, Hellinga, and Zhu[17] recognize the challenge of modeling congested arterials and present flow conservation-based traffic models to predict congestion. Widodo and Hasegawa[18] propose utilizing intervehicle communications to enhance traffic flow and pack vehicles more closely on the roadway. In evaluating the Rockwell-developed "National System Architecture Program," Weissenberger, Lo, and Hickman[19] reflect on the challenge of assessing the architecture stemming from the uncertainty associated with technology performance and cost. Chen, Shyu, and Zhang[20] utilize video indexing to identify and track vehicles and, in turn, measure congestion. Their effort is largely theoretical and fails to address clutter, presence of large numbers of cars, and real-world scenarios.

Laugier, Paromtchik, and Parent[21] report on the use of experimental electric cars for autonomous maneuvering studies under lane-following and lane-changing scenarios. Their test results reveal that linear cameras at 1000 Hz provide relative distance accurate down to 1 mm at a distance of 10 m and a speed of 60 km/hr, with a deceleration of 2 m/sec^2. While Goh and Wang[22] describe the navigation of a two-wheel steerable vehicle using sensor data from a differential GPS, Kim and Lee[23] describe a route-guidance approach in which cars in transit upload their positions and travel times to a centralized operations center, which then predicts the traffic between any two points in the system, statistically, and downloads the information to in-car navigation systems. In the spirit of assisting drivers, Kase, Hattori, Ohsuga, and Honide[24] propose automatic downloading of parking vacancies to cars while in transit. A key component of autonomous maneuvering consists of intelligent braking. Goodrich, Boer, and Inoue[25] report on an effort to model human braking behavior under emergency that has been incorporated in an adaptive cruise control (ACC). While the driver reveals unique skills in some areas, they note that the ACC exhibits superior abilities elsewhere. Yoshizawa[26] argues that road repair information is critical in route selection and recommends that the police consolidate and disseminate the information. Building on this idea, Onoue[27] recommends that the consolidated information be analyzed and employed to control traffic signals. Focusing on the environmental aspect of ITS, Araya, Shingaki, and Oota[28] investigate the relationship between traffic noise and traffic volume along National Route 43 in Japan and report that significant noise is generated in acceleration zones, especially where cars speed from 30 to 52 km/hr. To increase transport efficiency, Lee, Kim, Yim, Jung, Oh, and Kim[29] propose platooning of vehicles subject to longitudinal and lateral control. Headway controllers employing millimeter wave (MMW) radar are placed on each car to monitor the distance from the preceding vehicle. Mayr and Bauer[30] propose an intelligent cruise control that is characterized by two separate control systems. The first control system engages when the vehicles are proceeding smoothly and is responsible for ensuring safe distance between cars. However, in the event the car ahead brakes due to an emergency, a second control system takes over and ensures adequate deceleration in a timely manner. Handmann, Leefken, Tzomakas, and von Seelen[31] stress the difficulty in obtaining reliable and accurate data from real-world scenarios that is critical for designing practical ITS systems. Yim and Oh[32] present an image-processing algorithm that is capable of automatically extracting lane information without any a priori information about the lanes or even requiring manual intervention. However, the authors neglect to address the issue of performance, especially where the lane markings may have faded with age. To reduce costly rear-end collisions and improve safety, Ikeda and Matano[33] propose equipping every vehicle with display boards that inform drivers how far ahead the tail of the congestion is located.

There is general agreement in the ITS community that modeling and simulation constitute a key to testing complex ideas prior to developing expensive prototypes or even deploying them in the real world that may inadvertently cause irreversible damage. Yamashita and Muramatsu[34] present a simulator that models every vehicle and traffic signal. For each vehicle, its speed, direction, and acceleration or deceleration are modeled. Assuming a traffic insertion rate of 2000 vehicles/hr, they report limiting the wall clock time to 1 hour for a simulation of 120 sec of actual traffic. Uno, Sakaguchi, and Tsugawa[35] report developing a simulator to study how to integrate a merging control algorithm with intervehicle communication under the platoon concept. Dahlgren[36] acknowledges the critical role of simulation but warns that the cost of a simulation and the accuracy that it may yield must be weighed against the benefit to the project. Adler, Wallace, and Yavuz[37] report on a professional capacity-building program utilized by the Federal Highway Administration in 1996. It employed an interactive multimedia educational tool that featured a computer game for electronic design, a toll-collection system, and experiments in wireless communications.

The second perspective consists of a critical examination of the products and services that have been introduced into the market by the ITS industry since 1991. For example, in many of the U.S. cities, there are toll-free phone numbers (e.g., Boston) and public web sites (e.g., Seattle, WA) where one can obtain up-to-date information on the congestion states of the roadways. These services are immensely valuable, but there are three key problems. First, the information is limited to the major roadways, which are generally few in number, and is missing or outdated for the many more secondary roads. Second, the time necessary to broadcast complete information on all of the highways is usually so long that its usefulness to any given driver is severely limiting. Third, the information is not dynamic in that it may change substantially due to accidents or incidents while the driver is in transit. Today, a number of trucks, airport shuttle service vans, and luxury automobiles are equipped with GPS-based navigation aids. The principal difficulty again is the lack of accurate congestion information in a timely manner. A number of highway authorities have turned to AM radio to broadcast ramp closures, lane constrictions due to construction, and other relevant highway conditions. This effort, while of great value, has run into unique problems that originate from the lack of comprehensive thinking. Consider the following actual anecdote. On a weekday in March 2003, at 9:00 AM, the New Jersey Turnpike authority broadcasts on radio station 1680 on the AM dial, that, due to heavy congestion, the high-occupancy vehicle (HOV) lane has been opened to all traffic regardless of the number of passengers per car. Yet, the HOV lane is virtually empty from exit 11 all the way to exit 14 while vehicles on all other lanes are at a standstill. AM station 1680 is silent except for an annoying buzz and sporadic crosstalk from an adjacent station. After an hour delay, one approaches the tollbooth near Holland Tunnel, only to hear the broadcast that the HOV lane had been open all the time.

Among the state departments of transportation, there is a strong drive to mount cameras along highways and freeways, feed the signals back to a centralized traffic control center, and monitor congestion. The Minneapolis traffic control center has been a pioneer in this effort, and a similar center was recently installed in Phoenix, AZ. While installation and maintenance costs are high, the cameras can be immensely valuable in zooming onto accident sites and guiding en-route police and paramedics or reading license plates of vehicles under suspicion. However, relative to the issue of congestion monitoring and control, the impact of the cameras is minimal.[18] In fact, other devices, including optical fibers embedded underneath the pavements as in the case of Interstate 10 in Phoenix, are relatively inexpensive and highly reliable.

Electronic toll-collection systems, such as the E-ZPass in the Eastern U.S. and along the Interstate 95 corridor, have been viewed by many in the ITS community as a major achievement. The thinking is that cars can whiz by at speeds of up to 15 mph, avoiding the need to come to a complete stop to conduct cash transactions. In reality, however, E-ZPass's performance has been, at best, mixed, especially because many drivers have chosen not to sign up, concerned by E-ZPass's technical and administrative problems. On any given weekday during rush hour, thousands of cars hurl toward the tollbooths, dangerously zigzagging their way from their current lanes toward the appropriate toll lanes, with some slowing down and others coming to a dead stop, in effect creating a highly stressful and unsafe environment. While the queues at the cash tollbooths are significantly long, E-ZPass toll lanes barely register average vehicle speeds of more than 2 or 3 mph. Beyond the tollbooths, the combination of the abrupt reduction of ten toll lanes down to three or four highway lanes, along with drivers accelerating trying to make up for lost time, creates an even more dangerous environment. The concept of electronic toll collection, as currently deployed, is inefficient in that it slows down traffic unnecessarily, unsafe in that it fosters a dangerous driving environment, and environmentally unsound, all of which fundamentally contradicts the basic goals of ISTEA and the objectives of ITS.

Careful analysis of ITS products and services to date reveals that the slow progress may be attributed to two factors: (1) failure to recognize fundamental principles underlying ITS, and (2) lack of a holistic, comprehensive approach to solving ITS problems. Both factors are addressed in greater detail in the next section. For insight into the need for a comprehensive approach to ITS, consider the issue of improving air travel in the future. The first thought that is likely to arise in one's mind is the need to design commercial jets that can fly faster than the current limit of 600 mph. However, upon deeper thinking, one quickly realizes that the real cause of delay in air travel emanates from waiting for flight connections and layovers in the current hub-and-spoke air transport system, not to mention the lengthy airport security checks and travel to and from the airport. According to Boeing Corp., even if faster and consequently less-fuel-efficient jetliners were to be developed, the reduction of uncertainties and air travel delays will be minimal to none.

Key Principles Underlying ITS

Here are some important points underlying ITS:

- The single biggest cause of driver impatience that leads to reckless driving, incidents, road rage, and accidents is ignorance. When a driver encounters an obstacle and does not know what lies ahead, a rational or irrational fear may arise in that he or she might not succeed in reaching the destination on time, which, in turn, may have untold consequences. The ITS architecture's greatest contribution may consist in providing logically relevant and accurate information in a timely manner to needy drivers in a form that they can utilize to determine alternatives and recompute their plans. For example, consider that Joe, a busy executive in some city, scheduled to be on a flight, say XYZ, from a nearby airport, is late in leaving the office. Joe panics and drives recklessly, nearly running over a pedestrian, and barely makes into the airport in time to catch the flight, only to find out that XYZ has been delayed for 2 hours since the incoming aircraft had developed an unexpected mechanical problem. If under ITS the flight delay information, as soon as it becomes available, is automatically transmitted to every passenger scheduled for XYZ, in this case Joe's cell phone, most if not all of Joe's driving-related problems may disappear immediately.
- Except under truly emergency conditions, the ITS architecture should neither attempt to control nor dictate drivers' behavior, for two reasons. First, no centralized authority[8] can know with certainty the goals, objectives, and thinking of every driver, and therefore, any attempt to control will invariably be based on erroneous assumptions. Second, in the long run, drivers will resent the intrusion on their freedom to make their own decisions and ultimately abandon ITS. The key principle is to provide drivers with as much relevant information as possible and equip them with appropriate networking and computing resources so that they can determine and freely choose the right course of action under the given circumstances.
- Information must be accurate, timely, relevant, and consistent. Otherwise, drivers will begin to question the value of the ITS technology and abandon it prematurely. Any out-of-date piece of data can quickly assume the form of misinformation with severe unintended consequences. Consider two recent occurrences, intended to serve as examples of what must not be permitted under ITS. In June 2002, a programmable overhead electronic information board on Interstate 10 warns drivers that the air quality between Phoenix and Tucson is poor. The driver reading the sign finds the information interesting but irrelevant since he or she is driving west toward Los Angeles and is just about to leave behind the Phoenix city line. The information should have been displayed on the opposite side of the interstate between Phoenix and Tucson. In July 2003, a similar highway sign near exit 6 on the New Jersey Turnpike flashes an urgent bulletin that there is congestion up ahead. The problem is that it is late Sunday night at 11 PM and there seems to be no sign of congestion. In reality, the sign had been turned on in the afternoon during severe congestion stemming from lane constriction but someone neglected to turn it off.
- The ITS architecture must be fundamentally centered around each individual driver or traveler, subject to safety and fair resource availability for all. That is, while gross metrics such as pavement

utilization, average travel time, network bandwidth usage, and compute horsepower are important to the planners and operational managers, the individual driver's parameters must remain at the forefront.

- ITS architectures must acquire, process, and disseminate accurate, that is, precise and up-to-date, information to the drivers. Automated decision-making computer systems may greatly facilitate this function. In the traditional approach, data is first collected at a centralized unit and then processed, and the resulting information is disseminated to the geographically dispersed customers. Given the geographical distance and the finite speed of propagation of electromagnetic radiation, when a customer intercepts information relative to the transport of a unit in transit, a finite time interval has elapsed since the information was originally generated. For dynamic systems, this delay implies that the information received by the customer has incurred latency and is, in essence, inaccurate and imprecise. The degree of the error due to latency is a function of the length of the delay, relative to the dynamic nature of the system, and the resolution of accuracy. Thus, latency is fundamental to every transportation system. ITS architectures must focus on distributed schemes that aim at eliminating all unnecessary sources of latency, where possible, and realizing efficient, accurate, and timely decisions.
- A fundamental, enabling characteristic of transportation networks is as follows. Although it is an obvious fact that matter in the form of goods and people is transported in a transportation network, the implication is profound. The material units being transported may carry with them their own computing engines, which, at the present time, are necessarily matter. In contrast, in a communications network, the units of information constitute pure electromagnetic energy and they cannot carry with them their own computing engines while in transit. While carried along with the goods and people, the computers, in turn, may facilitate dynamic, travel-related computations and decision making. Also, since the constituent units of a transportation system may communicate with one another while in motion, utilizing wireless or infrared techniques, there is hope that the need for centralizing the information gathering and decision-making functions may be eliminated. The trend of decreasing physical size and cost, increasing capability, and lower power consumption in computer designs is encouraging and will likely render their use in transportation networks increasingly practical.
- ITS architectures must develop innovative computational and networking techniques to offer flexibility, personalized services, accurate estimates, efficiency, and freedom of choice. To achieve precise control and coordination, new distributed control techniques[8,38] must be utilized. Because the constituent units and the resources of any transportation system are geographically dispersed, the use of distributed algorithms is a logical choice. The units to be transported across a network are likely to request service, independent of one another and at irregular intervals of time. Thus, the interactions in the system, in essence, will be asynchronous, requiring the design of asynchronous, distributed algorithms for control, coordination, and resource allocation. Although challenging, these techniques underlie most processes in nature and are exceptionally effective and reliable.

  By design, an asynchronous, distributed algorithm for a transportation system must necessarily reflect the highest, meta-level purpose or intent of the system. The algorithm manifests itself in the behavior of every constituent unit. It will hold the potential of exploiting the maximal parallelism inherent in the system. Furthermore, local computations must be maximized while minimizing the communications between the entities, thereby implying high throughput, robustness, and scalability.
- For many of today's transportation systems, given the increasing size and complexity (which implies a large number of variables and parameters that characterize a system), the wide variation in their values, and the great diversity in the behaviors, the results of the analytical efforts have been restrictive. ITS systems are likely to be complex, implying that modeling and large-scale asynchronous distributed simulation may be the most logical and, often, the only mechanism to study them objectively. Key benefits of modeling and simulation are many. First, they enable one to detect design errors, prior to developing a prototype, in a cost-effective manner. Second,

simulation of system operations may identify potential problems, including rare and otherwise elusive ones, during operations. Third, analysis of simulation results may yield performance estimates of the target system architecture.

- By their very nature, complex systems may contain design errors that manifest rarely and are elusive. To address this weakness, ITS architectures must incorporate automatic mechanisms to continually accept any errors reported by users and bubble them up to the system-architect level so that corrections and refinement may be effected. For example, as of August 2002, the Internet Mapquest program provided erroneous directions to a retail store located in Saddlebrook, NJ, misdirecting drivers to a neighborhood, say X. The neighbors reported that hundreds of other drivers have made the same error over the past 2 years and complained that calls to the store have been in vain since Mapquest provides no mechanism to accept user-reported errors.
- Any ITS architecture must be based on sound logical principles, and where established norms pose inconsistencies, they must be carefully analyzed. For example, virtually everywhere in the U.S., HOV lanes, where present, are located at the extreme left. Since pavements to the left are designated fast lanes, the immediate connotation is that the HOV is a fast lane. This is reinforced by the fact that, often, fast non-HOV cars use the HOV lane to overtake and pass slower cars in the left lane. Furthermore, to get to this lane, an HOV entering the highway from a ramp typically located on the right must maneuver through fast-moving cars in the left lanes, if at all possible on a congested day, leading one to an underlying assumption that HOV drivers intend to drive fast. The assumption may be seriously wrong since many of the HOV vehicles may represent families traveling together who would prefer to drive at the speed limit and avoid accidents. As a second example, consider the nature of many of the highways whose origins date back to the 1700s before the union was formed. To drive from town S to T, one is advised to follow highway H, which will lead straight to a major interstate freeway. Although H appears as a straight-line road on the map with no major intersecting highways until the interstate freeway, a driver unexpectedly encounters forks at three different locations. The peculiarity of these forks is that if one follows the most obvious branch of the fork, which has the same make and feel of the road that he or she was on, that would be a mistake. To continue on H, one would have to make a sharp turn, left or right, on the less obvious branch of the fork. There are signs posted at the forks, but they are worn out and obscured by years of overgrown vegetation. Presumably, pieces of the road date back hundreds of years, and when these pieces were consolidated into highway H, the sharp jogs were left in place to avoid running through people's homes, places of worship, and so forth. Clearly, thousands of drivers following H must have gotten lost, frustrated, and angry. The cumulative delay over the past 50 decades must run into hundreds of thousands of hours, and clearly, such waste is very difficult to justify today. If unabated, this will continue for the next hundred years and the future generation may not view us kindly. For ITS to make a real difference, these problems must be addressed scientifically yet compassionately.

For a true revolution in the transportation scene, across the U.S. and throughout the world, the cultivation of an entirely new breed of ITS engineers is an absolute necessity. In addition to the teaching them pavement design, these engineers must be trained in key aspects of automobile technology, optical-fiber behavior under stress, networking, algorithm design, computing structures, programming, and large-scale distributed software, from an entirely new way of precision thinking.

Promises for the Future

In our vision, the future will witness remarkable progress in ITS in two key fronts. First, in the near future, the key ideas underlying the intelligent transportation of matter will extend beyond vehicular traffic and trains to other modes of transportation, including cargo air transport, passenger air transport, marine ferries, and personalized rapid transport (PRT) systems. The distant future may even witness its extension into interplanetary travel. The need for intelligent transportation will be felt most acutely under three scenarios — increased travel speeds, significant increase in the number of travelers, and increased demand for precise and timely information by travelers, all of which are highly likely in the future. From the scientific and engineering perspective, the advances in intelligent transportation will occur in the theoretical plane and in the form of technological innovations. From the ordinary traveler's point of view, however, the real advance and the direct benefit will occur in the seamless and natural integration of the various modes of transportation. As a result of the integration, the traveler will (1) gain access to fairly accurate status information of any transportation mode, anywhere in the world, from any point in the system, and (2) be permitted to effect reservations, dynamically, even while en route, on any transportation mode in the world. Precision and timeliness of information are crucial to developing faith and trust in the system among travelers. In general, this is best achieved through asynchronous distributed systems. Utilizing intelligent personalized decision aids, the traveler may process the available information to compute the most efficient route or re-route across all different transportation modes, including air, railways, automobiles, and ferries. The most frequent causes for replanning include changes in the traveler's intention and needs and unscheduled delays in a currently reserved transportation system.

Second, ITS systems are complex and very expensive, and once they are deployed, it is logical to expect them to remain in service for a reasonably long period of time. It is, therefore, absolutely essential to develop a sound and comprehensive understanding since such systems must be amenable to enhancements as societal needs evolve with time. For this as well as for efficiency and economy, the exact details of the system architecture and design trade-offs must be studied thoroughly, utilizing the most practical scientific tool available to us today — behavior modeling and asynchronous distributed simulation. Under asynchronous distributed simulation, a single simulation run for a highly complex system may be executed in a matter of days, whereas the current uniprocessor simulators may require up to months. Given that a study may require up to hundreds of simulation runs, behavior modeling and asynchronous distributed simulation may yield insights into the behaviors of such complex systems, thereby constituting an indispensable tool for developing future ITS systems. As an example, consider the need to interconnect a number of traffic-management centers in a given geographical region of the U.S. A behavior modeling and simulation effort may provide meaningful and valuable insights into the topology of the interconnection and the nature of the information exchange between the centers, for a given set of long-term, high-level objectives. It would not be logical to invest millions of dollars and deploy a system that, after completion, reveals an inability to meet the objectives and sustain growth.

References

1. Intelligent Transportation System America and U.S. Department of Transportation. ITS architecture development program phase I. *ITS America*, Washington, DC, 1994.
2. Lomax, T. Five most congested urban areas: LA, DC, SFO-Oakland, Miami, Chicago. Texas Transportation Institute, June 24, 2002.
3. White, C.C III. Intelligent transportation systems: integrating information technology and the surface transportation system. *Proc. of the IEEE Int. Conf. on Syst., Man and Cybernetics*, Vancouver, BC, October 22–25, 1995.
4. Private Communication with Dr. Frank Kreith, Fellow, ASME & National Conference of State Legislatures, Denver, CO, May 16, 2000.
5. Catling, I. and McQueen, B. Road transport informatics in Europe — major programs and demonstrations. *IEEE Trans. on Vehicular Technol.*, 40(1):132–40, February 1991.
6. Kawashima, H. Two major programs and demonstrations in Japan. *IEEE Trans. on Vehicular. Technol.*, 40(1):141–46, February 1991.
7. Carley, W.A. Railroads test satellite positioning in effort to improve safety, efficiency. *The Wall Street Journal Interactive Edition*, June 29, 1998.
8. Ghosh, S. and Lee, T. 2002. *Intelligent Transportation Systems: New Principles and Architectures.* CRC Press, Boca Raton, FL.
9. Peter Jennings, ABC News broadcast, February 20, 2003.

10. King, G. Driver performance in highway navigation tasks. Transportation Research Record, National Research Council, Washington, DC, (1093):1–11, 1986.
11. Rhode Island Department of Transportation. State of Rhode Island Incident Management Plan, Providence, RI, September 1992.
12. Levesque, C. Rhode to the future. *Traffic Technol. Int.*, 0:38–42, June/July 1998.
13. Peters, J., McGurrin, M., Shank, D., and Cheslow, M. Estimate of transportation cost savings from using intelligent transportation system (ITS) infrastructure. *ITE J.*, 67(11):42–47, November 1997.
14. Nitz, H. and Chung, T. Evolution of a systems plan for advanced communications within a rapid transit system. *Proc. of the 1996 ASME/IEEE Joint Railroad Conf.*, pp. 217–24, Oakbrook, IL, April 30–May 2, 1996.
15. Horioka, T. The advancement on Kochi-ITS. *Proc. of the 1999 IEEE Int. Conf. on Intelligent Transp. Syst.*, pp. 856–58, Tokyo, October 5–8, 1999.
16. Hayashi, K. and Sugimoto, M. Signal control system (MODERATO) in Japan. *Proc. of the 1999 IEEE Int. Conf. on Intelligent Transp. Syst.*, pp. 988–992, Tokyo, October 5–8, 1999.
17. Fu, L., Hellinga, B., and Zhu, Y. An adaptive model for real-time estimation of overflow queues on congested arterials. *Proc. of the 2001 IEEE Intelligent Transp. Syst. Conf.*, pp. 219–26, Oakland, CA, August 25–29, 2001.
18. Widodo, A. and Hasegawa, T. A study on the effective road capacity and the modified road capacity: new evaluation parameters for traffic flow evaluation. *Proc. of the 1999 IEEE Intelligent Transp. Syst. Conf.*, pp. 617–21, Tokyo, October 5–8, 1999.
19. Weissenberger, S., Lo, H., and Hickman, M. A methodology for evaluating systems architectures. *Proc. of the 1995 Vehicle Navigation and Inf. Syst. Conf.*, pp. 397–403, Seattle, WA, July 30–August 2, 1995.
20. Chen, S., Shyu, M., and Zhang, C. An intelligent framework for spatio-temporal vehicle tracking. *Proc. of the 2001 IEEE Intelligent Transp. Syst. Conf.*, pp. 213–18, Oakland, CA, August 25–29, 2001.
21. Laugier, C., Paromtchik, I., and Parent, M. Developing autonomous maneuvering capabilities for future cars. *Proc. of the 1999 IEEE International Conf. on Intelligent Transp. Syst.*, pp. 68–73, Tokyo, October 5–8, 1999.
22. Goh, C.T. and Wang, H. State estimation for a golf buggy via Differential Global Positioning System. *Proc. of the 1999 IEEE International Conf. on Intelligent Transp. Syst.*, pp. 649–54, Tokyo, October 5–8, 1999.
23. Kim, S. and Lee, J. A study on design of dynamic route guidance system using forecasted travel time based on GPS data and modified shortest path algorithm. *Proc. of the 1999 IEEE Int. Conf. on Intelligent Transp. Syst.*, pp. 44–48, Tokyo, October 5–8, 1999.
24. Kase, N., Hattori, M., Ohsuga, A., and Honide, S. InfoMirror-agent-based information assistance to drivers. *Proc. of the 1999 IEEE International Conf. on Intelligent 'I'ransp. Syst.*, pp. 734–39, Tokyo, October 5–8, 1999.
25. Goodrich, M.A., Boer, E.R., and Inoue, H. A model of human brake initiation behavior with implications for ACC design. *Proc. of the 1999 IEEE Int. Conf. on Intelligent 'I'ransp. Syst.*, pp. 86–91, Tokyo, October 5–8, 1999.
26. Yoshizawa, H. Grasp of road work information and its best use. *Proc. of the 1999 IEEE Int. Conf. on Intelligent 'I'ransp. Syst.*, pp. 811–15, Tokyo, October 5–8, 1999.
27. Onoue, K. Trip analysis with uplinked information in Kyoto City. *Proc. of the IEEE Int. Conf. on Intelligent 'I'ransp. Syst.*, pp. 398–403, Tokyo, October 5–8, 1999.
28. Araya, K., Shingaki, H., and Oota, T. Environmental measures implemented on national route 43 results of noise study and measures against traffic pollution. *Proc. of the 1999 IEEE Int. Conf. on Intelligent 'I'ransp. Syst.*, pp. 880–84, Tokyo, October 5–8, 1999.
29. Lee, G.D., Kim, S.W., Vim, Y.U., Jung, J.H., Oh, S.Y., and Kim, B.S. Longitudinal and lateral control system development for a platoon of vehicles. *Proc. of the 1999 IEEE International Conf. on Intelligent Transp. Syst.*, pp. 605–10, Tokyo, October 5-8, 1999.

30. Mayr, R. and Bauer, O. Safety issues in intelligent cruise control. *Proc. of the 1999 IEEE Int. Conf. on Intelligent 'I'ransp. Syst.*, pp. 970–75, Tokyo, October 5-8, 1999.
31. Handmann, U., Leefken, I., Tzomakas, C., and von Seelen, W. A flexible architecture for intelligent cruise control. *Proc. of the 1999 IEEE Int. Conf. on Intelligent 'I'ransp. Syst.*, pp. 958–63, Tokyo, October 5–8, 1999.
32. Yim, Y. and Oh, S. Three-feature based automatic lane detection algorithm (TFALDA) for autonomous driving. *Proc. of the 1999 IEEE Int.Conf. on Intelligent 'I'ransp. Syst.*, pp. 929–32, Tokyo, October 5-8, 1999.
33. Ikeda, H. and Matano, M. Introduction of congestion tail display system into Metropolitan Expressway. *Proc. of the IEEE Int. Conf. on Intelligent 'I'ransp. Syst.*, pp. 266–71, Tokyo, October 5-8, 1999.
34. Yamashita, H. and Muramatsu, N. Simulator for evaluating traffic management system. *Proc. of the IEEE International Conf. on Intelligent Transp. Syst.,* pp. 506–11, Tokyo, October 5-8, 1999.
35. Uno, A., Sakaguchi, T., and Tsugawa, S. A merging control algorithm based on inter-vehicle communication. *Proc. of the IEEE International Conf. on Intelligent 'I'ransp. Syst.*, pp. 783–87, Tokyo, October 5–8, 1999.
36. Dahlgren, J. To simulate or not to simulate. *Proc. of the IEEE Int. Conf. on Intelligent Transp. Syst.*, pp. 559–62, Oakland, CA, August 25–28, 2001.
37. Adler, J.L., Wallace, W.A., and Yavuz, V.A. Advanced educational tools for Intelligent Transportation Systems training. *Proc. of the 2000 IEEE Eng. Manage. Society Conf.*, pp. 431–38, Albuquerque, NM, August 13–15, 2000.
38. Ghosh, S. 2003. *Algorithm Design for Networked Information Technology Systems: Principles and Applications.* Springer-Verlag Inc., New York.

11

Engineering Design

Ashok V. Kumar
University of Florida

Nam P. Suh
Massachusetts Institute of Technology

Nagaraj K. Arakere
University of Florida

Nam Ho Kim
University of Florida

11.1 Introduction

Ashok V. Kumar

Engineering design practice has evolved over the years and has undergone significant changes in the last few decades as a result of advances in technology. It has been strongly influenced by technological tools that became available to assist in the design, as well as by design philosophies and methodologies that have evolved in academia and in various industries. Often some of the tools and methodologies vary from industry to industry due to specialized needs. However, over the years a few design tools and methods have become invaluable and are widely used across many industries. In particular, geometry design and engineering analyses are required in all industries. Therefore, it is not surprising that the tools developed to assist in these areas are used across a wide variety of industries. The focus of this chapter is on design methodology, tools, and theories that are widely applicable irrespective of industry or application area.

The section on design theories (11.2) focuses primarily on design methodologies, theories, algorithms, and strategies that are general in nature and that are particularly valuable in generating design concepts and formulating the problem. The next section (11.3) deals with two design tools that are not only widely used but have contributed to significant improvement in the productivity of design engineers and also in quality of the designed products. These tools are the solid modeling technology for designing geometry and the finite element method, which helps in engineering analysis and simulation. Significant advances have occurred in the last two decades in the geometric and solid modeling technologies, available to engineers via computer-aided design (CAD) software. These advances have enhanced the ability of engineers to design an entire product or system on a computer, starting often with the conceptual stages of design. The finite element method is a numerical technique that is used for a wide variety of engineering analysis. It has become the preferred method for analyzing the performance of structures and machine components during design. An important aspect of structural design is failure analysis. Criteria for failure under static and dynamic loading conditions are presented in the section following design tools (11.4).

The final section of this chapter (11.5) deals with design-optimization techniques. Optimization algorithms can be used to automate some aspects of the design process, enabling design engineers to compute optimal parameters and dimensions of the design that would maximize or minimize some design objective. The application of these techniques for structural optimization and sensitivity analysis is described, followed by a brief listing of the important optimization algorithms.

11.2 Elements of the Design Process

Nam P. Suh

All design activities must do the following:

1. *Know* the "*customers' needs.*"
2. *Define the essential problems* that must be solved to satisfy the needs.
3. *Conceptualize the solution through synthesis,* which involves the task of satisfying several different functional requirements using a set of inputs such as product design parameters within given constraints.
4. *Analyze* the proposed solution to establish its optimum conditions and parameter settings.
5. *Check the resulting design solution* to see if it meets the original customer needs.

Design proceeds from abstract and qualitative ideas to quantitative descriptions. It is an iterative process by nature: new information is generated with each step, and it is necessary to evaluate the results in terms of the preceding step. Thus, design involves a continuous interplay between *the requirements the designer wants to achieve* and *how the designer wants to achieve these requirements*.

Designers often find that a clear description of the design requirements is a difficult task. Therefore, some designers deliberately leave them implicit rather than explicit. Then they spend a great deal of time trying to improve and iterate the design, which is time consuming at best. To be efficient and generate the design that meets the perceived needs, the designer must specifically state the users' requirements before the synthesis of solution concepts can begin.

Solution alternatives are generated after the requirements are established. Many problems in mechanical engineering can be solved by applying practical knowledge of engineering, manufacturing, and economics. Other problems require far more imaginative ideas and inventions for their solution. The word "creativity" has been used to describe the human activity that results in ingenious or unpredictable or unforeseen results (e.g., new products, processes, and systems). In this context, creative solutions are discovered or derived by inspiration and/or perspiration, without ever defining specifically what one sets out to create. This creative "spark" or "revelation" may occur, since our brain is a huge information storage and processing device that can store data and synthesize solutions through the use of associative memory, pattern recognition, digestion and recombination of diverse facts, and permutations of events. Design will always benefit when "inspiration" or "creativity," and/or "imagination" plays a role, but this process must be augmented by amplifying human capability systematically through fundamental understanding of cognitive behavior and by the development of scientific foundations for design methods.

11.3 Design Tools

Ashok V. Kumar

Geometry Design

For mechanical and structural systems, geometry design is an important and necessary aspect of the overall design process. For structural components, the geometry is clearly important because it determines the overall stiffness and strength of the component. But for both structural and nonstructural components, the geometry is significant for many other reasons as well, including aesthetics, ergonomics, ease of manufacturing, assembly, and disassembly. Geometry design of a component or structure is often an iterative process because the geometry is designed to satisfy multiple purposes. Traditionally, the final detailed geometry is recorded as an engineering drawing after the design process is over. Creating such a drawing is not usually part of the design iterations because it is an expensive process. Drafting software made engineering drawings easier to create and edit but were not quite useful as a design tool. However, over the last two decades, many new geometry design tools have evolved that have had a profound impact on the design process.

CAD software evolved as design tools from simple geometry and solid modeling software that were originally difficult to use and were often thought of as visualization tools rather than design tools. With the evolution of dimension-driven solid modeling technology, it became easier to create and edit complex three-dimensional geometry, allowing even major design changes to be made with minimal effort. Dimension-driven solid models, also referred to as parametric models, can be automatically regenerated or updated in response to dimension (or parameter) changes. In order to ensure that the model updates in accordance to the designer's intent, the history of the solid creation as well as a variety of geometric constraints are recorded as the geometry is being created. This enables the software to update the solid model automatically to reflect dimension changes while maintaining the design intent.

Another capability available in modern solid modeling software that enhances design engineers' productivity is feature-based modeling. Design features can be thought of as geometric primitives that are building blocks to be used to create more complex geometry. These features are driven by a set of rules and definitions, and can be controlled by finite number of dimensions or parameters. User-defined features can be created by combining simple features already available. This capability significantly improves the productivity of engineers by allowing commonly occurring design features to be defined once and reused in many different designs. In addition to feature-based and dimension-driven solid modeling, CAD software available today includes a variety of other applications, such as drawing generation from solid models, engineering analysis tools, manufacturing planning, and tool path generation capabilities.

This section summarizes important concepts and results from geometric modeling theory that forms the basis of the geometry design tools built into CAD software. Geometric models are mathematical and computational models used to represent the geometry of curves, surfaces, and solids. Very broadly, geometric models can be classified as wireframe models, surface models, and solid models. Most CAD software supports all three types of models.

Wireframe models were the earliest and simplest geometric models, where a shape is represented as a collection of characteristic points (vertices), lines, and curves (edges). Although it has some advantages, such as simple user inputs and ease of implementation, there are many disadvantages that make this representation unsuitable for modeling solids. First, the shapes represented by only curves and points are very ambiguous since it is not always possible to determine whether a given point is inside or outside the solid. Second, there is no information about bounding surfaces of the object. Therefore, it cannot be used for mass property computation, tool path generation, or finite element analysis.

Surface models have bounding surface information in addition to the information contained in wireframe models. Therefore, it is possible to generate realistic graphical displays as well as to generate tool paths for the numerically controlled (NC) machining. However, surface models are also ambiguous because they do not have information to distinguish between the inside and outside of the object, which makes it difficult or impossible to construct algorithms for automatically computing mass properties or to construct Boolean combinations of such models. However, surface models are sufficient for many applications, including computer graphics, visualization, and imaging.

For engineering applications, a precise, unambiguous, and editable model of a solid is essential. *Solid modeling* was introduced to overcome some of the limitations of wireframe and surface models. The two popular solid modeling schemes are *boundary representation* (or B-Rep) and *constructive solid geometry* (CSG).[1–4] These two representation schemes are described in the following section.

Constructive Solid Geometry (CSG)

Constructive solid geometry (CSG) representation is based on set theory, and therefore in this approach, solids are modeled as a set of points in space. Complex solids are constructed as Boolean combinations

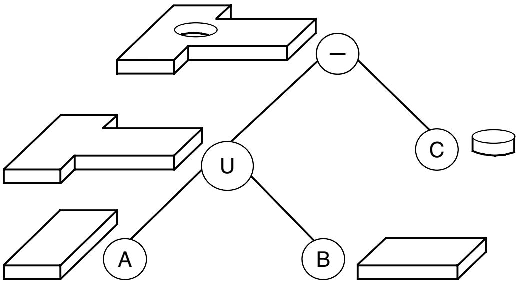

FIGURE 11.3.1 Example of CSG binary tree structure.

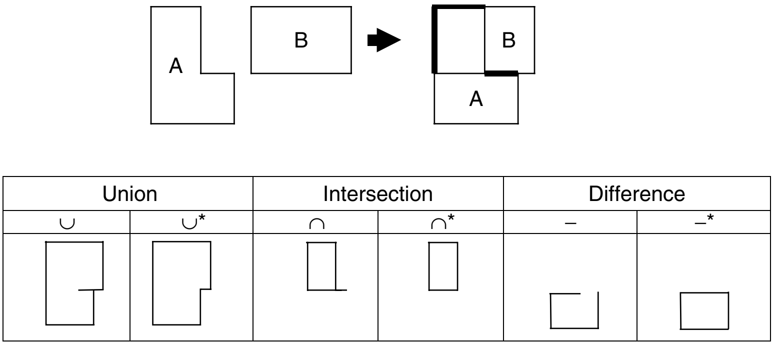

FIGURE 11.3.2 Comparison between the ordinary Boolean and regularized Boolean operation.

of simpler solids called *primitives*. A binary tree data structure is used to represent the Boolean operations between primitives. Figure 11.3.1 shows an example of a CSG tree data structure, where the final solid is generated by the union of the primitives A and B, followed by subtraction of the primitive C. In this tree structure, leaf nodes represent primitive solids and branch nodes represent Boolean types, such as union, difference, and intersection. Boolean operations as defined in set theory are not suited for direct application to solid modeling because they often produce results that are not valid solids and may have dangling edges or faces. For a solid modeling scheme to be unambiguous, it is necessary that any given point be classified as a point inside, outside, or on the boundary of the solid. Such a classification is referred to as *point membership classification*. For a solid to be valid, it should be dimensionally homogeneous. In particular, it is essential that if a point is classified as being on the boundary of the solid based on the Boolean definition, then there should be some points in its neighborhood that are inside the solid and some that are outside. All the points in the neighborhood of a point should be inside the solid if it is classified as an internal point, and vice versa. To ensure these properties, a modified set of Boolean operations have been defined for solid modeling that are referred to as *regularized Boolean* operations, where the Boolean combination of primitives are valid and dimensionally homogeneous solids that do not have dangling edges or faces.

Figure 11.3.2 shows the difference between ordinary and regularized Boolean operations. Regularized Boolean operations are denoted by $\cup^*$, $\cap^*$, and $-^*$ respectively, whereas the ordinary Boolean operations are denoted by $\cup$, $\cap$, and $-$.

As shown in Figure 11.3.2, an ordinary Boolean operation may result in a solid that has dangling edges because a point that is on the boundary of both primitives is classified as a point on the boundary of the union (or intersection) of the two primitives, even though with respect to the Boolean result, every point in its neighborhood may be entirely inside or outside the solid. The problems always occur when the boundaries of the primitives overlap. At such boundaries it is necessary to use additional information to determine whether points are on, in, or outside the regularized Boolean result. One way to make this

	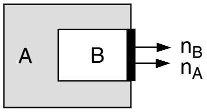	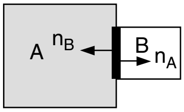
$\cup^*$	ON	IN
$\cap^*$	ON	OUT
$-^*$	OUT	ON

FIGURE 11.3.3 Point membership classification for overlapping boundaries.

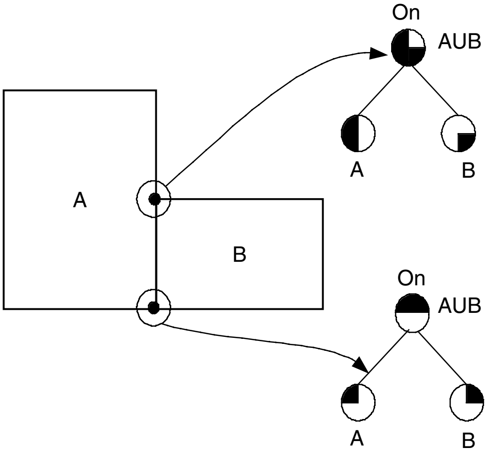

FIGURE 11.3.4 Examples of neighborhood models on the vertices in 2D.

determination is by comparing the directions of the normal vectors of both the boundaries. For example, for the regularized intersection, if both normal vectors have same directions, then the point is also on the boundary of the regularized Boolean combination; otherwise, this point is an external point. Figure 11.3.3 shows the classification of points on the overlapping boundary of primitive A and B based on the direction of the boundary normal vectors of A and B.

The method just described for classifying points for regularized Boolean combination cannot be used when multiple normal vectors are involved. For instance, vertices and points on edges cannot be classified using this approach because a unique normal cannot be defined for these points. In such cases, it is necessary to inspect the neighborhood of the point to correctly classify it. Figure 11.3.4 shows a two-dimensional example where small disks are used to symbolize the neighborhood of a point with respect to a solid and the shaded area of the disk represents the region that is inside the solid. The neighborhood of a point with respect to the Boolean combination of two primitives can be obtained as the Boolean combination of the neighborhoods of the point with respect to the primitives, as shown in Figure 11.3.4. If the neighborhood thus obtained is fully shaded, it implies that every point in the neighborhood is inside the solid and therefore the point is internal. Similarly, if all points in the neighborhood are external, then the point is an external point. If the disk is partially shaded, then it implies that some points in the neighborhood are internal while others are external; therefore, this point must be on the boundary of the solid. This approach can be extended to three dimensions by using spheres to represent the neighborhood of points.

Primitives are simple shapes, such as a block, cylinder, sphere, or cone, and are defined as the intersection of a set of half-spaces expressed as $f(x,y,z) \geq 0$. A half-space divides the space into two regions; for instance, the *x-y* plane ($z = 0$) divides the space into a region where $z \geq 0$ and a region where $z < 0$ as shown in Figure 11.3.5(a). Figure 11.3.5(b) and Figure 11.3.5(c) show a block and cylinder defined using half-spaces. The block is represented as the intersection of six planar half-spaces and the

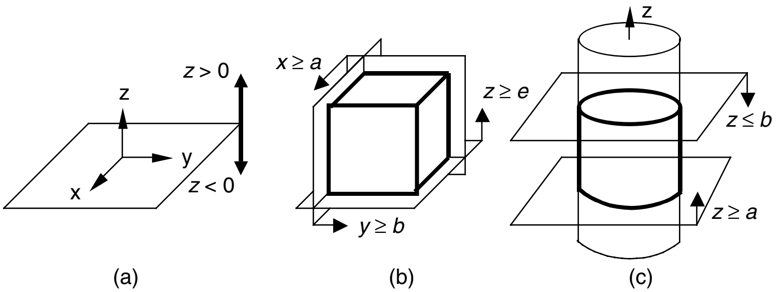

FIGURE 11.3.5 Mathematical description of the primitives by half-spaces: (a) half-space by x-y plane, (b) block by half-spaces, (c) cylinder by half-spaces.

cylinder is represented as the intersection of a cylindrical half-space and two planar half-spaces. The arrows indicate the direction of the material.

The equations of half-spaces used to create the block and cylinder can be stated compactly as follows:

$$\text{Block: } a \le x \le b\,,\ c \le y \le d\,,\ e \le z \le f$$

$$\text{Cylinder: } r^2 - x^2 + y^2 \ge 0\,,\ a \le z \le b$$

The boundaries of the primitives defined in this manner are implicit equations of curves and surfaces in the form $f(x,y,z)=0$. Implicit equations simplify point membership classification because the sign of the implicit function indicates which side of the function the point is on. Despite this advantage, implicit equations are not favorable for application to solid modeling because these equations are axes dependent so that any change in the coordinate system can change the form of the equation. Furthermore, graphical display is difficult and computationally expensive to generate when the boundaries of the solid are represented by implicit equations. CSG representation does not explicitly store information about the connectivity between boundary entities, such as which two bounding surfaces intersect to create an edge. Such connectivity information is needed for many reasons, including interactive solid editing, mesh generation, and tool path generation for machining. For these reasons, in more modern CAD software the solid is stored using the B-Rep scheme described in the next section, even though the concepts of primitives and Boolean trees are often used in conjunction.

Boundary Representation (B-Rep)

The B-Rep model of a solid describes the boundaries of a solid using both geometric information and connectivity information.[5–6] The geometry information in a B-Rep model is composed of surface equations, curve equations, and point coordinates that together define the boundaries of the solid. The connectivity information, also referred to as the *topology* or *combinatorial structure*, records how these geometrical entities are connected together.

B-Rep models are based on the idea that the boundary of a solid consists of *faces* (surfaces) bounded by *edges* (curves), which in turn are bounded by *vertices* (points). A face is a subset or limited region of some more extensive surface. For example, planar faces are subsets of infinite planes that are bounded by one or more boundaries. These boundaries can be defined using edges. The geometry of the edges themselves are curves represented using parametric equations bounded by vertices. Figure 11.3.6 shows a cube whose six faces have been named F1–F6 in the figure. The geometries associated with these faces are planes. Each face has only one boundary, and the boundaries are defined using edges that have lines as their geometry.

To define the solid precisely and unambiguously, we must formally define the topological entities and strictly follow the definition and conventions when building a data structure to represent the solid. The

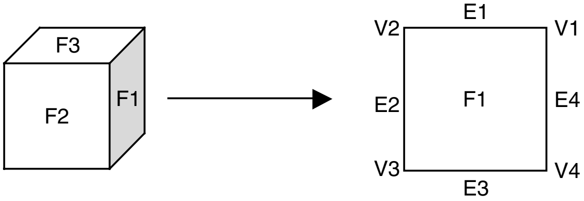

FIGURE 11.3.6 Basic concept of the B-Rep model.

topological entities used to define B-Rep solid model using half-edge data structure are vertices, edges, co-edges/half-edges, loops, faces, shells, lumps, and the body.

A solid model is represented in B-Rep as a collection of lumps. A *lump* can be defined as a simply connected region in space whose boundaries are defined by closed shells. A *shell* is a collection of faces; it is *closed* if it divides space into two disconnected regions, one of which is finite and the other infinite. A closed shell is a *peripheral shell* if the finite region created by the shell is defined as the inside of the shell, whereas it is a *void* if its infinite region is considered the inside of the shell.

A *face* is a finite, simply connected region of a surface that is non-self-intersecting and has a direction. The geometry of a face is represented using a parametric equation of a surface in the form $\mathbf{R}(u, v)$, where $\mathbf{R}$ is the position vector of points on the surface expressed as a function of two parameters, u and v. The boundaries of a face are defined using loops, and its direction is specified by a normal vector. A face can have multiple boundaries, each defined by a separate loop.

A *loop* is a piecewise, non-self-intersecting, closed space curve that defines the boundary of a face. It lies on the surface representing the face and is defined as an ordered sequence of half-edges.

A *half-edge* (also referred to as a *co-edge*) is used to record the occurrence of an edge in a loop, and it defines the direction of the loop with respect to the direction of the edge. Half-edge directions are defined such that when connected together they form a loop whose direction satisfies the right-hand rule with the normal to the face. Another way to define this orientation is that the loop direction is such that as one travels along the loop in its specified direction, points on the left are inside the face and points on the right are outside (assuming that you are on the outside surface of the face). This convention is used so that simple algorithms can be constructed to perform point membership classification to determine whether a given point is inside, outside, or on the boundary of a face.

An *edge* is defined as a bounded, directed, finite, non-self-intersecting space curve. The geometry is represented by a parametric equation of a curve, $\mathbf{R}(u)$, where $\mathbf{R}$ is the position vector of a point on the curve expressed as a function of a parameter u. Since this curve may not be bounded (and can be infinite), the start and end points of an edge are defined using vertices. The vertices defined as the beginning and the end of an edge need not be distinct if the edge is a closed curve. The direction of the edge can be defined by the sequence of its bounding vertices or by the direction of curve corresponding to the increasing parameter value. Finally, vertices are topological entities that are used to bound edges. The geometry of a vertex is defined by the position vector of a point.

Hybrid Systems

Creating B-Rep models manually by defining each vertex, edge, and surface is extremely cumbersome. Therefore, hybrid systems are used in most modern CAD systems, where the solid is represented procedurally using a CSG tree but the primitives are represented using B-Rep instead of defining them as intersections of half-spaces. The B-Rep model of the solid represented by the CSG tree is evaluated automatically using *boundary evaluator* algorithms.[7] For each regularized Boolean operation, the boundary evaluator algorithm detects intersections between participating solids, computes intersection geometries (intersection points and curves as well as subdivided faces), and classifies them using set membership classification algorithms to determine whether the geometry is in, on, or outside the final solid defined by the Boolean operation. While set membership classification is easy when the solid is represented as a combination of half-spaces (where the surfaces are implicit equations, $f(x,y,z) = 0$), it is more difficult to do for B-Reps. Furthermore, constructing the topology of the resultant solid automatically is also difficult. As a result, it is very expensive to build robust and reliable software that can handle every special case. However, over the years many commercial systems have been developed that have reliable boundary evaluator algorithms that are robust and that can handle almost all special and degenerate cases.

Sweep Features

A sweep feature is defined by sweeping a planar shape along an arbitrary space curve referred to as a sweep trajectory, where the cross section of the sweep solid can be either constant or varying. This is a popular and useful method due to the fact that the solid represented by sweeping is simple to understand and execute. If the sweep trajectory is a straight line, it is called as a *translational sweep* (or extruded solid). When the sweep trajectory is a circular arc, it is termed a *rotational sweep* (or revolved solid). When the sweep trajectory is an arbitrary parametric curve, it is referred to as a *general sweep*. In modern CAD systems, it has now become common practice to use a feature-based approach for constructing a solid model. Each sweep feature can be thought as a user-defined primitive; it is a sweep solid that is created interactively by defining one or more two-dimensional geometries (or profiles) and a trajectory for sweep. Upon defining the sweep using its profile and trajectory, the software automatically constructs the B-Rep model of this primitive so that the user does not have to define the topological and geometric entities of this B-Rep manually.

The profile for the sweep can be sketched on a face of a previously created feature or a reference plane, thus positioning the sweep with respect to previously created geometry. Boolean operations are performed automatically between the newly created feature and the previously defined solid to construct the B-Rep model of the solid with the feature applied.

Parametric Equation of a Curve

The equations of curves in B-Rep models are expressed as parametric equations[8] because it is convenient to generate points on the curve for graphics and most properties of the curve can be easily evaluated. Curves commonly used in solid models include simple analytic curves such as lines, circles, and ellipses, as well as freeform (or synthetic) curves that can only be created interactively. Equations of commonly used analytic curves as well as freeform curves are listed next.

Lines

A line passing through the points $\mathbf{P}_1$ and $\mathbf{P}_2$ is

$$\mathbf{R}(u) = \mathbf{P}_1 + (\mathbf{P}_2 - \mathbf{P}_1)u \tag{11.3.1}$$

Circles and Ellipses

An ellipse with center at the point $\mathbf{P}_c$ and whose major and minor axes are along the unit vectors $\hat{\mathbf{m}}$ and $\hat{\mathbf{n}}$ and whose major radius = A and minor radius = B can be stated as

$$\mathbf{R}(u) = \mathbf{P}_c + A\cos(u)\hat{\mathbf{m}} + B\sin(u)\hat{\mathbf{n}} \tag{11.3.2}$$

A circle is a special case of an ellipse when $A = B$ = radius of the circle. Any two mutually perpendicular vectors in the plane of the circle can be used as $\hat{\mathbf{m}}$ and $\hat{\mathbf{n}}$.

Parabolas

The equation of a parabola on a plane defined by two mutually perpendicular unit vectors, $\hat{\mathbf{m}}$ and $\hat{\mathbf{n}}$ (where $\hat{\mathbf{m}}$ is the axis of symmetry), can be stated as

$$\mathbf{R}(u) = \mathbf{P}_v + Au^2\hat{\mathbf{m}} + Bu\hat{\mathbf{n}} \tag{11.3.3}$$

$\mathbf{P}_v$ is the vertex of the parabola where it intersects with its line of symmetry.

Hermite Curves

The equation of a cubic polynomial curve between points $\mathbf{P}_1$ and $\mathbf{P}_2$ whose tangents at these points are $\dot{\mathbf{P}}_1$ and $\dot{\mathbf{P}}_2$ can be expressed using Hermite polynomials as basis functions and is therefore called a Hermite curve:

$$\mathbf{R}(u)=\mathbf{P}_1H_1(u)+\mathbf{P}_2H_2(u)+\dot{\mathbf{P}}_1H_3(u)+\dot{\mathbf{P}}_2H_4(u) \tag{11.3.4}$$

where $H_i(u)$ are Hermite polynomials defined as

$$\begin{aligned} H_1(u)&=2u^3-3u^2+1\\ H_2(u)&=-2u^3+3u^2\\ H_3(u)&=u^3-2u^2+u\\ H_4(u)&=u^3-u^2 \end{aligned} \tag{11.3.5}$$

Alternatively, the Hermite curve can be expressed using matrix notation as

$$\mathbf{R}(u)=\{\mathbf{U}\}^T[\mathbf{H}]\{\mathbf{P}\} \tag{11.3.6}$$

where $\{\mathbf{U}\}^T=\left\{u^3 \quad u^2 \quad u \quad 1\right\}$

$$[\mathbf{H}]=\begin{bmatrix} 2 & -2 & 1 & 1\\ -3 & 3 & -2 & -1\\ 0 & 0 & 1 & 0\\ 1 & 0 & 0 & 0 \end{bmatrix} \text{ and } \{\mathbf{P}\}=\begin{Bmatrix} \mathbf{P}_1\\ \mathbf{P}_2\\ \dot{\mathbf{P}}_1\\ \dot{\mathbf{P}}_2 \end{Bmatrix} \tag{11.3.7}$$

Bezier Curves

A Bezier curve is a polynomial of degree n that is controlled by n+1 control points, $\mathbf{P}_i$, i = 1, …, n+1:

$$\mathbf{R}(u)=\sum_{i=0}^{n}\mathbf{P}_iB_{i,n}(u), \quad u\in[0,1] \tag{11.3.8}$$

where the basis functions $B_{i,n}(u)$ are Bernstein polynomials defined as

$$B_{i,n}(u)=\frac{n!}{i!(n-i)!}u^i(1-u)^{n-i} \tag{11.3.9}$$

The curve can be interactively edited by moving the control points. The curve passes through the first and last control points, and its tangents at the beginning and end are parallel to the first and last segments of the control polygon (obtained by joining the control points by lines):

$$\dot{\mathbf{R}}(0)=n(\mathbf{P}_1-\mathbf{P}_0) \text{ and } \dot{\mathbf{R}}(1)=n(\mathbf{P}_n-\mathbf{P}_{n-1}) \tag{11.3.10}$$

B-Spline Curves

A polynomial of degree (K-1), controlled by n control points $\mathbf{P}_i$, i = 1, …, n, is given by

$$\mathbf{R}(u)=\sum_{i=0}^{n}\mathbf{P}_iN_{i,K}(u) \tag{11.3.11}$$

where the basis functions can be recursively defined as

$$N_{i,k}(u)=\frac{(u-t_i)N_{i,k-1}(u)}{t_{i+k-1}-t_i}+\frac{(t_{i+k}-u)N_{i+1,k-1}(u)}{t_{i+k}-t_{i+1}} \quad \text{for } k = 2, \ldots, \mathrm{K} \tag{11.3.12}$$

$$\begin{aligned} N_{i,1}(u)&=1 \quad \text{if } t_i \le u < t_{i+1} \\ &=0 \quad \text{Otherwise} \end{aligned} \tag{11.3.13}$$

The t_j are knot values defined for $j = 0, \ldots, n + \mathrm{K}$ as

$$\begin{aligned} t_j &= 0 && \text{if } j < \mathrm{K} \\ t_j &= j-K+1 && \text{if } \mathrm{K} \le j \le n \\ t_j &= n-K+2 && \text{if } j < n \end{aligned} \tag{11.3.14}$$

The degree of the B-spline curve, K, is independent of the number of control points n. The curve passes through the first and last control points, and can be edited interactively by moving control points. Each control point affects only four spans of the curve, thus allowing local control of the curve during interactive editing. A cubic B-spline curve is C^2 continuous so that at every point its tangent and normal are defined and the curvature varies continuously.

Properties of the Parametric Curves

Let $\mathbf{R}(u)$ be the parametric equation of a curve defined over a domain $a \le u \le b$. A vector tangent to this curve at any point can be computed as

$$\text{Tangent vector} = \mathbf{T} = \mathbf{R}_u = \frac{d\mathbf{R}}{du} \quad \text{and Unit tangent vector} = \hat{\mathbf{T}} = \frac{\mathbf{T}}{|\mathbf{T}|} \tag{11.3.15}$$

The magnitude of the derivative of $\mathbf{R}(u)$ is called the speed of the curve, and it is often denoted as

$$\dot{s} = \left|\frac{d\mathbf{R}}{du}\right| \tag{11.3.16}$$

The curvature of a curve is defined as the rate of turning angle of a curve with respect to arc length:

$$\text{Curvature} = \kappa = \frac{1}{\rho} = \frac{d\phi}{ds} \tag{11.3.17}$$

where ρ = radius of curvature, ϕ = turning angle, and s = arc length. The second derivative of $\mathbf{R}(u)$ is a vector on the plane of the curve defined by the tangent and normal of the curve at any point:

$$\ddot{\mathbf{R}} = \mathbf{R}_{uu} = \frac{d^2\mathbf{R}}{du^2} = \ddot{s}\hat{\mathbf{T}} + \dot{s}^2\kappa\hat{\mathbf{N}} \tag{11.3.18}$$

where κ = curvature and $\hat{\mathbf{N}}$ = unit normal vector. The vector normal to the plane of the curve at any point on the curve is called its binormal. It can be conveniently computed as the cross-product of the first and second derivatives of $\mathbf{R}(u)$:

$$\text{Binormal vector} = \mathbf{B} = \dot{\mathbf{R}} \times \ddot{\mathbf{R}} = \dot{s}^3 k\hat{\mathbf{B}} \tag{11.3.19}$$

$\hat{\mathbf{B}}$ = Unit Binormal vector

The curvature of a curve at any point can be computed as follows:

$$\text{Curvature} = \kappa = \frac{\left|\dot{\mathbf{R}} \times \ddot{\mathbf{R}}\right|}{\left|\dot{\mathbf{R}}\right|^3} \tag{11.3.20}$$

Parametric Equations of Surfaces

Parametric equations of the form $\mathbf{R}(u, v)$ are the preferred method for representing surfaces for B-Rep models.[8] It is easy to generate points on the surface by computing the equation for various values of the parameter within its domain, $(u, v) \in [a,b] \times [c,d]$. The common method for defining simple analytical surfaces is by sweeping a curve over another curve. Surfaces defined in this fashion are used for defining the boundaries of sweep solids. Freeform surfaces are most often defined using Hermite, Bezier, and B-spline patches. Some of the most commonly used surfaces are defined next.

Planar Surfaces

Let $\mathbf{P}_1$ be a point on the plane and $\mathbf{m}$ and $\mathbf{n}$ be two nonparallel vectors (preferably perpendicular unit vectors) on the plane. Its equation can be written as

$$\mathrm{R}(u, v) = \mathbf{P}_1 + u\mathbf{m} + v\mathbf{n} \tag{11.3.21}$$

A plane can also be defined by specifying three noncollinear points on the plane: $\mathbf{P}_1$, $\mathbf{P}_2$, and $\mathbf{P}_3$. The equation for this plane can be written as

$$\mathrm{R}(u, v) = \mathbf{P}_1 + u(\mathbf{P}_2 - \mathbf{P}_1) + v(\mathbf{P}_3 - \mathbf{P}_1) \tag{11.3.22}$$

Extruded Surfaces (or Tabulated Surfaces)

Let $\mathrm{R}_1(u)$ be the equation of a curve that is extruded in the direction $\mathbf{n}$. The equation of the extruded surface can be written as

$$\mathrm{R}(u, v) = \mathrm{R}_1(u) + v\mathbf{n} \tag{11.3.23}$$

Revolved Surfaces

Let $\mathbf{n}_1$, $\mathbf{n}_2$, and $\mathbf{n}_3$ be three mutually perpendicular vectors and let $\mathbf{G}(u)$ be the parametric equation of a curve on the $\mathbf{n}_1 - \mathbf{n}_3$ plane. The equation of the surface obtained by revolving $\mathbf{G}(u)$ around $\mathbf{n}_3$ is given by

$$\mathrm{R}(u, v) = g_1(u)\cos(2\pi v)\mathbf{n}_1 + g_1(u)\sin(2\pi v)\mathbf{n}_2 + g_3(u)\mathbf{n}_3, \quad (u, v) \in [0,1] \times [0,1] \tag{11.3.24}$$

where $\mathrm{G}(u) = \begin{Bmatrix} g_1(u) \\ g_3(u) \end{Bmatrix}$ is the planar curve revolved around $\mathbf{n}_3$.

Blended or Ruled Surfaces

Let $\mathrm{R}_1(u)$ and $\mathrm{R}_2(u)$, $u \in [0,1]$ be the parametric equations of two curves. The blended or ruled surface (also known as lofted surface) between these two curves can be defined as

$$\mathrm{R}(u, v) = v\mathbf{R}_1(u) + (1 - v)\mathbf{R}_2(u), \quad v \in [0,1] \tag{11.3.25}$$

General Sweep Surfaces

Let $\mathbf{C}(u)$, $u \in [0,1]$ be the parametric equation of the curve representing the sweep trajectory, and let $\mathbf{G}(v)$ be the planar profile curve being swept along this trajectory. The equation of the sweep surface is

$$\mathbf{R}(u,v) = \mathbf{C}(u) + g_1(v)\hat{\mathbf{N}} + g_2(v)\hat{\mathbf{B}} \tag{11.3.26}$$

where the planar profile curve is $\mathbf{G}(v) = \begin{Bmatrix} g_1(v) \\ g_2(v) \end{Bmatrix}$, $v \in [0,1]$

and $$\hat{\mathbf{B}} = \text{unit binormal} = \frac{\dot{\mathbf{C}}(u) \times \ddot{\mathbf{C}}(u)}{\left|\dot{\mathbf{C}}(u) \times \ddot{\mathbf{C}}(u)\right|}, \quad \hat{\mathbf{N}} = \text{unit normal vector} = \hat{\mathbf{B}} \times \hat{\mathbf{T}}, \quad \hat{\mathbf{T}} = \frac{\dot{\mathbf{C}}(u)}{\left|\dot{\mathbf{C}}(u)\right|} \tag{11.3.27}$$

Hermite Patches

The equation of a Hermite bicubic surface patch can be written in terms of its four corner points, two tangents in the parametric directions, and the twist vector at these points as

$$\mathbf{R}(u,v) = \{\mathbf{U}\}^T [\mathbf{H}][\mathbf{B}][\mathbf{H}]\{\mathbf{V}\} \tag{11.3.28}$$

where $\{\mathbf{U}\}^T = \{u^3 \;\; u^2 \;\; u \;\; 1\}$ and $\{\mathbf{V}\}^T = \{v^3 \;\; v^2 \;\; v \;\; 1\}$

$$[\mathbf{H}] = \begin{bmatrix} 2 & -2 & 1 & 1 \\ -3 & 3 & -2 & -1 \\ 0 & 0 & 1 & 0 \\ 1 & 0 & 0 & 0 \end{bmatrix} \tag{11.3.29}$$

$$[\mathbf{B}] = \begin{bmatrix} \mathbf{P}_0 & \mathbf{P}_1 & \mathbf{P}_{v0} & \mathbf{P}_{v1} \\ \mathbf{P}_2 & \mathbf{P}_3 & \mathbf{P}_{v2} & \mathbf{P}_{v3} \\ \mathbf{P}_{u0} & \mathbf{P}_{u1} & \mathbf{P}_{uv0} & \mathbf{P}_{uv1} \\ \mathbf{P}_{u2} & \mathbf{P}_{u3} & \mathbf{P}_{uv2} & \mathbf{P}_{uv3} \end{bmatrix} \tag{11.3.30}$$

The four corner points of the patch are $\{\mathbf{P}_0 \;\; \mathbf{P}_1 \;\; \mathbf{P}_2 \;\; \mathbf{P}_3\}$.
Tangents at the corner points in the u direction are $\{\mathbf{P}_{u0} \;\; \mathbf{P}_{u1} \;\; \mathbf{P}_{u2} \;\; \mathbf{P}_{u3}\}$.
Tangents at the corner points in the v direction are $\{\mathbf{P}_{v0} \;\; \mathbf{P}_{v1} \;\; \mathbf{P}_{v2} \;\; \mathbf{P}_{v3}\}$.
Twist vectors at the corner points are $\{\mathbf{P}_{uv0} \;\; \mathbf{P}_{uv1} \;\; \mathbf{P}_{uv2} \;\; \mathbf{P}_{uv3}\}$.

Bezier Patches

A Bezier surface patch is an extension of the Bezier curve and has two parameter directions, u and v. Its shape is controlled by $(n+1)\times(m+1)$ control points $\mathbf{P}_{ij}$ that form a control polyhedron:

$$\mathbf{R}(u,v) = \sum_{i=0}^{n}\sum_{j=0}^{m} \mathbf{P}_{ij} B_{i,n}(u) B_{j,m}(v), \quad (u,v) \in [0,1]\times[0,1] \tag{11.3.31}$$

where the basis functions are the Bernstein polynomials

$$B_{i,n}(u) = \frac{n!}{i!(n-i)!} u^i (1-u)^{n-i} \tag{11.3.32}$$

The Bezier surface interpolates the four corner points, and the surface is tangent to the corner segments of the control polyhedron.

B-Spline Patches

A B-spline surface can be created by extending the B-spline curve to a surface defined by an array of $(n + 1) \times (m + 1)$ control points:

$$\mathbf{R}(u,v) = \sum_{i=0}^{n} \sum_{j=0}^{m} \mathbf{P}_{ij} N_{i,k}(u) N_{j,l}(v) \ , \ \ (u,v) \in [0,u_{\max}] \times [0,v_{\max}] \tag{11.3.33}$$

The basis functions of the B-spline surface are the same as for the curve (defined earlier in (Equation 11.3.12, Equation 11.3.13, and Equation 11.3.14). B-spline surfaces provide local control over the patch. The degree of the patch is independent of the number of control points. The surface is C^2 continuous.

Properties of Parametric Surfaces

Tangents

For a parametric surface $\mathbf{R}(u,v)$, a series of isoparametric curves can be defined on it for various fixed values of u and v. Two isoparametric curves, $\mathbf{R}(u,v_0)$ and $\mathbf{R}(u_0,v)$, on this surface intersect at the point $\mathbf{R}(u_0,v_0)$, and one can compute the tangent vectors for these two curves as

$$\text{Tangent to surface in the u-direction} = \mathbf{R}_u = \frac{\partial \mathbf{R}(u,v_0)}{\partial u} \tag{11.3.34}$$

$$\text{Tangent to surface in the v-direction} = \mathbf{R}_v = \frac{\partial \mathbf{R}(u_0,v)}{\partial v} \tag{11.3.35}$$

Since these two curves lie on the surface, these vectors are also tangents to the surface. Using these two vectors, we can express the tangent plane to the surface at the point $\mathbf{R}(u_0,v_0)$ as

$$\mathbf{T}(r,s) = \mathbf{R}(u_0,v_0) + r\mathbf{R}_u(u_0,v_0) + s\mathbf{R}_v(u_0,v_0) \tag{11.3.36}$$

Let $\mathbf{P}(t) = \begin{Bmatrix} u(t) \\ v(t) \end{Bmatrix}$ be an arbitrary curve in the parametric space of the surface. The equation of the corresponding curve in real space is $\mathbf{R}(t) = \mathbf{R}(u(t),v(t))$.

The tangent vector along this curve is

$$\mathbf{R}_t = \frac{d\mathbf{R}}{dt} = \frac{\partial \mathbf{R}}{\partial u}\frac{\partial u}{\partial t} + \frac{\partial \mathbf{R}}{\partial v}\frac{\partial v}{\partial t} = \mathbf{R}_u \dot{u} + \mathbf{R}_v \dot{v} \tag{11.3.37}$$

The speed of this curve is the magnitude of this tangent vector:

$$\dot{s} = \left|\mathbf{R}_t\right| = \sqrt{\mathbf{R}_u \cdot \mathbf{R}_u \dot{u}^2 + 2\mathbf{R}_u \cdot \mathbf{R}_v \dot{u}\dot{v} + \mathbf{R}_v \cdot \mathbf{R}_v \dot{v}^2} \tag{11.3.38}$$

The length of this curve from t = a to t = b is:

$$S = \int_a^b \sqrt{\mathbf{R}_u \cdot \mathbf{R}_u \dot{u}^2 + 2\mathbf{R}_u \cdot \mathbf{R}_v \dot{u}\dot{v} + \mathbf{R}_v \cdot \mathbf{R}_v \dot{v}^2}\, dt \tag{11.3.39}$$

Equation 11.3.39 is often written in the following form, which is referred to as the *First Fundamental Quadratic Form* of a surface:

$$ds^2 = E(u,v)du^2 + 2F(u,v)dudv + G(u,v)dv^2 \tag{11.3.40}$$

where

$$E = \mathbf{R}_u \cdot \mathbf{R}_u, F = \mathbf{R}_u \cdot \mathbf{R}_v, G = \mathbf{R}_v \cdot \mathbf{R}_v \tag{11.3.41}$$

The Curvature of a Curve on a Surface

The curvature of the curve $\mathbf{P}(t)$ can be computed by taking the dot product between the second derivative of the curve with the unit normal to the curve:

$$\hat{\mathbf{n}}.\ddot{\mathbf{R}} = \hat{\mathbf{n}}.\mathbf{R}_{uu}\left(\frac{du}{dt}\right)^2 + 2\hat{\mathbf{n}}.\mathbf{R}_{uv}\frac{du}{dt}\frac{dv}{dt} + \hat{\mathbf{n}}.\mathbf{R}_{vv}\left(\frac{dv}{dt}\right)^2 = \dot{s}^2\kappa \tag{11.3.42}$$

Therefore, the curvature of the curve $\mathbf{P}(t)$ on the surface is

$$\kappa = \frac{\hat{\mathbf{n}}.\mathbf{R}_{uu}\dot{u}^2 + 2\hat{\mathbf{n}}.\mathbf{R}_{uv}\dot{u}\dot{v} + \hat{\mathbf{n}}.\mathbf{R}_{vv}\dot{v}^2}{\mathbf{R}_u \cdot \mathbf{R}_u\dot{u}^2 + 2\mathbf{R}_u \cdot \mathbf{R}_v\dot{u}\dot{v} + \mathbf{R}_v \cdot \mathbf{R}_v\dot{v}^2} = \frac{L\dot{u}^2 + 2M\dot{u}\dot{v} + N\dot{v}^2}{E\dot{u}^2 + 2F\dot{u}\dot{v} + G\dot{v}^2} \tag{11.3.43}$$

Equation 11.3.43, written in the following form, is referred to as the *Second Fundamental Quadratic Form* of a surface:

$$ds^2\kappa = Ldu^2 + 2Mdudv + Ndv^2 \tag{11.3.44}$$

where

$$L = \hat{\mathbf{n}}.\mathbf{R}_{uu}, M = \hat{\mathbf{n}}.\mathbf{R}_{uv}, N = \hat{\mathbf{n}}.\mathbf{R}_{vv} \tag{11.3.45}$$

The Curvature of a Surface

At any given point, the curvature of an arbitrary curve through the point is given by Equation 11.3.43. This equation can be rewritten as follows:

$$\begin{Bmatrix} du & dv \end{Bmatrix}\begin{bmatrix} E & F \\ F & G \end{bmatrix}\begin{Bmatrix} du \\ dv \end{Bmatrix}k = \begin{Bmatrix} du & dv \end{Bmatrix}\begin{bmatrix} L & M \\ M & N \end{bmatrix}\begin{Bmatrix} du \\ dv \end{Bmatrix} \tag{11.3.46}$$

This is a generalized eigenvalue problem, and the eigenvalues represent the maximum ($k_{\max}$) and minimum ($k_{\min}$) curvature of the surface at the point. The eigen vectors represent the direction in which the surface has the maximum and minimum curvature. Because the curvature is different in every direction, the following measures of curvature are commonly used to define the curvature of a surface at a point:

$$\text{Gaussian curvature} = K = k_{\max}k_{\min} = \frac{LN - M^2}{EG - F^2} \tag{11.3.47}$$

$$\text{Mean curvature} = H = \frac{1}{2}(k_{\max} + k_{\min}) = \frac{EN + GL - 2FM}{2(EG - F^2)} \tag{11.3.48}$$

$$\text{Maximum curvature} = k_{\max} = H + \sqrt{H^2 - K} \tag{11.3.49}$$

$$\text{Minimum curvature} = k_{\min} = H - \sqrt{H^2 - K} \tag{11.3.50}$$

Engineering Analysis Tools: Finite Element Analysis

The finite element method (FEM) is a numerical method that can be used for solving boundary value problems that occur frequently in engineering analysis.[9–11] Structural analysis has been the most popular application of FEM, but it is now routinely used for solving a variety of linear and nonlinear engineering analysis problems that arise during the design of structures and machines. These include problems in solid mechanics, heat conduction, fluid flow, dynamics and vibrations, electrostatics, and electromagnetism. Commercial finite element analysis (FEA) programs provide all these capabilities and therefore have now become an indispensable tool for engineering design. FEA software is now routinely used to simulate the performance of engineering components that have been designed but not yet manufactured. The design of mechanical components is often an iterative process involving design, analysis, modification of design, and repeated analysis. Alternatively, FEA has also been used in conjunction with optimization software to automate these iterations to synthesize mechanical components and assemblies that satisfy functional requirements.

A summary of the major concepts and results related to application of FEM for solving linear static problems most commonly encountered in engineering design, including static structural and heat conduction problems, is presented here. The governing equations for these problems are partial differential equations that must be satisfied for equilibrium. These equations must be satisfied over a domain that is the geometry of the structure/component being analyzed while also satisfying some constraints (referred to as boundary conditions) along the boundaries of the domain. Such problems are commonly referred to as *boundary value problems*. FEM solves the weak form of these boundary value problems derived using Galerkin's method.[10] The solutions to these problems are field variables, such as the displacement field (a vector field) for structural problems or temperature field (a scalar field) for heat-conduction problems. FEM divides the domain of analysis (or the geometry) into simple elements to create a mesh. The field variable is "discretized" by defining it as a piecewise interpolation so that within each element the field variables are interpolated using the values at the nodes of the elements. This allows the values at the nodes to be used as the discrete variables to be solved for, instead of solving for the original scalar or vector field, which are continuous functions. The weak form of boundary value problems is an integral equation that involves integration over the volume of the geometry. FEM carries out this integration piecewise over each element to derive the equilibrium equations for each element and then assembles them to form the global equations for the entire domain.

In this section, the various elements commonly available in FEA software are first listed and categorized as one-, two-, and three-dimensional elements. The basis functions (also known as shape functions) used for interpolating the field variables within each element and the common applications of each type of element are listed. Then, a variety of engineering analysis problems and the elements used for the analysis are described. For each analysis type, the boundary value problem (or governing equations) and the corresponding weak forms are given. The element type used for the analysis, the formulation of the element equations, and typical boundary conditions are also described.

Element Types

One-Dimensional Elements

A problem where the field variable can be expressed as a function of a single spatial coordinate is a one-dimensional problem and can be solved using a one-dimensional element whose geometry is a line or a curve. The real geometry of all structures is three-dimensional, of course, so this is an idealization that is used to simplify problems where the field variable varies in only one direction.

Two-Node Linear Elements. A one-dimensional two-node element assumes that the field variable varies linearly within the element. If $u(r)$ is the field variable expressed in terms of a local (or parametric) coordinate system r and the values of this variable at the nodes of the element are u_1 and u_2, then the variable is interpolated within the element as

$$u(r) = u_1 N_1(r) + u_2 N_2(r) \tag{11.3.51}$$

where $N_i(r)$ are the shape functions (or the basis functions):

$$N_1(r) = \frac{1}{2}(1-r)\,,\quad N_2(r) = \frac{1}{2}(1+r) \tag{11.3.52}$$

Since the variable is interpolated as a function of $r \in [-1,1]$, a mapping between this parameter space and the real space is necessary. In the isoparametric elements the interpolation functions defined above are also used to define the mapping between the local coordinates and the global coordinate x as follows:

$$x(r) = x_1 N_1(r) + x_2 N_2(r) \tag{11.3.53}$$

Three-Node Quadratic Elements. The field variable within a three-node isoparametric element is interpolated using quadratic polynomial basis functions as

$$u(r) = u_1 N_1(r) + u_2 N_2(r) + u_3 N_3(r) \tag{11.3.54}$$

where $r \in [-1,1]$, u_i are the nodal values at the three nodes of the element and

$$N_1(r) = -\frac{1}{2}r(1-r),\quad N_2(r) = \frac{1}{2}r(1+r) \text{ and } N_3(r) = (1-r^2) \tag{11.3.55}$$

The mapping between local coordinates and the global coordinate x is

$$x(r) = x_1 N_1(r) + x_2 N_2(r) + x_3 N_3(r) \tag{11.3.56}$$

Two-Node Hermite Elements. The Hermite element provides a tangent continuous cubic polynomial interpolation of the field variable by using both the value of the variable and its derivative at each node for the interpolation:

$$u(r) = u_1 N_1(r) + u_2 N_2(r) + \dot{u}_1 N_3(r) + \dot{u}_2 N_4(r) \tag{11.3.57}$$

where u_i are the values of the variable, $\dot{u}_i$ are the derivates of the variable at the nodes, and the shape functions $N_i(r)$ are

$$\begin{aligned} N_1(r) &= 2r^3 - 3r^2 + 1 \\ N_2(r) &= -2r^3 + 3r^2 \\ N_3(r) &= L_e(r^3 - 2r^2 + r) \\ N_4(r) &= L_e(r^3 - r^2) \end{aligned}\quad,\quad r = \frac{x}{L_e} \tag{11.3.58}$$

where x is the local coordinate (distance along the element) and L_e is the length of the element.

Two-Dimensional Elements

A problem can be modeled as two-dimensional when the field variable varies within a plane and is constant in the direction normal to the plane. Therefore, the field variables can be expressed as a function of two spatial coordinates, and geometry of the element is a two-dimensional planar region of constant thickness. Some of the most commonly used two-dimensional elements and their shape functions are listed next.

Three-Node Triangular Elements. The three-node triangular element interpolates a field variable, $u(x, y)$, linearly within a triangle. If u_i are the nodal values of this variable, then the interpolation within the element can be written as

$$u(x,y) = u_1 L_1(x,y) + u_2 L_2(x,y) + u_3 L_3(x,y) \tag{11.3.59}$$

where L_i the shape functions for this element, also known as area coordinates and barycentric coordinates, satisfy the following relations:

$$\begin{Bmatrix} 1 \\ x \\ y \end{Bmatrix} = \begin{bmatrix} 1 & 1 & 1 \\ x_1 & x_2 & x_3 \\ y_1 & y_2 & y_3 \end{bmatrix} \begin{Bmatrix} L_1 \\ L_2 \\ L_3 \end{Bmatrix} \tag{11.3.60}$$

$$L_i = a_i + b_i x + c_i y \qquad i = 1,2,3 \tag{11.3.61}$$

$$\begin{Bmatrix} a_1 \\ a_2 \\ a_3 \end{Bmatrix} = \frac{1}{2A} \begin{Bmatrix} x_2 y_3 - x_3 y_2 \\ x_3 y_1 - x_1 y_3 \\ x_1 y_2 - x_2 y_1 \end{Bmatrix}, \quad \begin{Bmatrix} b_1 \\ b_2 \\ b_3 \end{Bmatrix} = \frac{1}{2A} \begin{Bmatrix} y_2 - y_3 \\ y_3 - y_1 \\ y_1 - y_2 \end{Bmatrix}, \quad \begin{Bmatrix} c_1 \\ c_2 \\ c_3 \end{Bmatrix} = \frac{1}{2A} \begin{Bmatrix} x_3 - x_2 \\ x_1 - x_3 \\ x_2 - x_1 \end{Bmatrix} \tag{11.3.62}$$

where A is the area of the triangle.

In the above equations, (x_i, y_i) are the coordinates of the nodes of the triangular element. The interpolation is linear, and therefore the derivatives of the field variable are constant for this element.

Four-Node Quadrilateral Elements. The four-node quadrilateral element is formulated as an isoparametric element where the interpolations are with respect to a local (or parametric) coordinate system. This element provides a bilinear interpolation of the nodal values of the field variable, $u(r, s)$, as follows:

$$u(r,s) = \sum_{i=1}^{4} u_i N_i(r,s) \tag{11.3.63}$$

where the shape functions are

$$\begin{aligned} N_1(r,s) &= \frac{1}{4}(1+r)(1+s) \\ N_2(r,s) &= \frac{1}{4}(1+r)(1-s) \\ N_3(r,s) &= \frac{1}{4}(1-r)(1-s) \\ N_4(r,s) &= \frac{1}{4}(1-r)(1+s) \end{aligned} \tag{11.3.64}$$

The mapping between the parametric coordinates (*r, s*) and the global coordinates (*x, y*) is expressed as

$$x(r,s)=\sum_{i=1}^{4}x_iN_i(r,s)$$
$$y(r,s)=\sum_{i=1}^{4}y_iN_i(r,s) \tag{11.3.65}$$

Three-Dimensional Elements

Problems that cannot be modeled as one- or two-dimensional, because the field variable varies in all the spatial directions, have to be modeled using three-dimensional elements. The commonly used elements and their shape functions are discussed next.

Four-Node Tetrahedral Elements. The four-node tetrahedral element is the three-dimensional analog of the triangular element. It interpolates the field variable, $u(x,y,z)$, linearly within a tetrahedral region. As for the triangular element, barycentric coordinates (or volume coordinates) can be used as shape functions that satisfy the relations

$$\begin{Bmatrix}1\\x\\y\\z\end{Bmatrix}=\begin{bmatrix}1&1&1&1\\x_1&x_2&x_3&x_4\\y_1&y_2&y_3&y_4\\z_1&z_2&z_3&z_4\end{bmatrix}\begin{Bmatrix}L_1\\L_2\\L_3\\L_4\end{Bmatrix} \tag{11.3.66}$$

where (x_i,y_i,z_i) are the coordinates of the four nodes of the tetrahedron. The inverse of the above equation gives relations for barycentric coordinates with respect to (x,y,z). The field variable, $u(x,y,z)$, is interpolated as

$$u(x,y,z)=\sum_{i=1}^{4}u_iL_i(x,y,z)\ . \tag{11.3.67}$$

As for the triangular element, the derivatives of the field variable are constant within this element because the field variable is linearly interpolated.

Eight-Node Hexahedral Elements. The eight-node hexahedral element is formulated as an isoparametric element and is the three-dimensional analog of the four-node quadrilateral element. The field variable is interpolated using trilinear shape functions that are expressed in terms of a local (or parametric) coordinate system (r,s,t) as

$$u(r,s,t)=\sum_{i=1}^{8}u_iN_i(r,s,t) \tag{11.3.68}$$

where N_i are the shape functions that are defined as

$$N_i=\frac{1}{8}(1+r_ir)(1+s_is)(1+t_it) \tag{11.3.69}$$

where (r_i,s_i,t_i) are the coordinates of the ith node of the element in the parametric coordinate system. In this coordinate system, the element is a perfect cube of size 2 × 2 × 2 centered at the origin. The mapping between the parametric coordinates and the global (x,y,z) coordinates is given as

$$x=\sum_{i=1}^{8}x_iN_i(r,s,t)\ ,\quad y=\sum_{i=1}^{8}y_iN_i(r,s,t)\ ,\quad z=\sum_{i=1}^{8}z_iN_i(r,s,t) \tag{11.3.70}$$

Engineering Analysis Problems

The interpolation schemes defined in the previous section are used to solve various engineering analysis problems. The type of element and interpolation used depends on whether the physical problem involved can be idealized as one-, two-, or three-dimensional. It also depends on the boundary value problem that needs to be solved. In this section, we examine a few engineering analysis problems frequently encountered in engineering design and the corresponding elements.

Rods and Trusses

Rod-like structures that are subjected to purely axial load (tension or compression) can be modeled using rod/truss elements. The term "truss" is used to refer to a structure constructed by connecting together many rods by frictionless pin joints and are loaded and supported only at these joints. Under these conditions, each rod in the structure will be subjected only to pure axial load and therefore can be modeled using rod (or truss) elements. The field variable for this element is the axial displacement of points on the element $u(s)$, where s is a local coordinate along the axis of the rod. The displacement in this element can be modeled using the two-node linear element described earlier. Since the displacement varies linearly within an axially loaded rod (within elastic limit) as assumed in the two-node linear element, the analysis using this element gives an exact solution of the mathematical model. The governing equation for this element can be written as

$$\frac{d}{ds}\left(EA\frac{du}{ds}\right)=0 \tag{11.3.71}$$

where E = Young's modulus of elasticity and A = area of cross section of the element. The weak form of this differential equation can be stated as

$$\int_0^L \frac{d\delta u}{ds}EA\frac{du}{ds}ds = F_1\delta u_1 + F_2\delta u_2 \tag{11.3.72}$$

In the previous equation, L is the length of the element, δu is the virtual displacement, and F_i and δu_i are the forces and virtual displacements at the two nodes of the element. The boundary conditions that can be applied on this element are

Essential boundary condition: $u_i = a_i$, where a_i = prescribed displacement at node i

Natural boundary condition: $EA\dfrac{du}{ds} = F_i$

The equilibrium equation for an element can be expressed as $[\mathbf{K}_e]\{\mathbf{X}_e\} = \{\mathbf{F}_e\}$, where

$$\left[\mathbf{K}_\mathbf{e}\right]=\frac{EA}{Le}\begin{bmatrix}1 & -1\\ -1 & 1\end{bmatrix},\ \left\{\mathbf{X}_e\right\}=\begin{Bmatrix}u_1\\ u_2\end{Bmatrix} \text{ and } \left\{\mathbf{F}_e\right\}=\begin{Bmatrix}F_1\\ F_2\end{Bmatrix} \tag{11.3.73}$$

The field variables just described are with respect to a local coordinate system, s, that is attached to the truss element. However, a truss-like structure is constructed using many such elements, and therefore it is convenient to express the displacement at each node with respect to a global coordinate system, as shown in Figure 11.3.7. The three components of the displacement along the global coordinate axes correspond to three degrees of freedom at each node. Thus a general "3D truss" element available in FEA software can be used for constructing a three-dimensional truss structure with each element arbitrarily oriented in space. At each node, three components of displacement or forces can be specified.

Beams and Frames

A slender rod-like structure subjected to bending and transverse loads can be modeled using a beam element. As in the case of truss elements, this is a one-dimensional element because its field variables

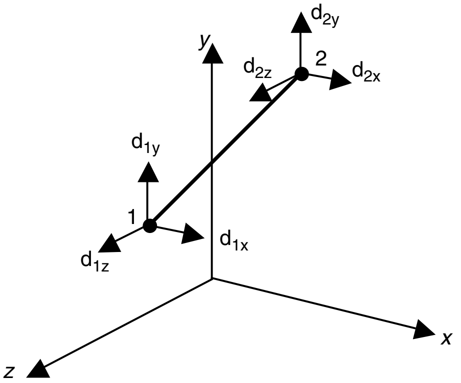

FIGURE 11.3.7 Truss element.

can be expressed as a function of one spatial dimension, *s*, which is a local coordinate system that measures distance along the axis of the beam. It is possible to formulate the beam equations with respect to this local coordinate system to get a simple equilibrium equation for a beam element that has only two degrees of freedom per node and is subjected only to bending and transverse load as described next. This simple beam element would have only two degrees for freedom per node (transverse deflection and rotation). However, the beam element implemented in most FEA software is more general, and it is expressed in terms of a global coordinate system and can be subjected to axial loads and torsion as well.

The governing equation of the beam expresses the condition for static equilibrium as follows:

$$\frac{d^2}{ds^2}\left(EI\frac{d^2w}{ds^2}\right)=f \tag{11.3.74}$$

where $w(s)$ is the transverse displacement field, f is the distributed transverse load acting on the structure, E = Young's modulus of elasticity, and I is the moment of inertia of the cross-section. The weak form of this equation can be stated as

$$\int_0^L \frac{d^2\delta w}{\mathrm{ds}^2}EI\frac{d^2w}{ds^2}ds=\delta w_1V_1+\delta\theta_1M_1+\delta w_2V_2+\delta\theta_2M_2+\int_0^L f\delta w ds \tag{11.3.75}$$

where L is the length of the element, δw is the virtual transverse deflection, V_i and M_i are the shear force and bending moment, respectively, at node *i*, while δw_i and $\delta\theta_i$ are the virtual deflection and rotation at node *i*.

Since the weak form involves the second derivatives of the transverse deflection, it is necessary that the interpolation of this field is tangent (or C^1) continuous. Therefore, for this element the Hermite interpolation described earlier is used. This interpolation requires two nodal degrees of freedom: the transverse deflection and its derivative, which is the slope. For small deflections, the slope is the same as angular displacement or rotation. The boundary conditions that can be specified for this element are

Essential boundary conditions:

(i) Deflection at a node: $w_i = d_i$ = specified deflection at node *i*

(ii) Slope at a node: $\left.\frac{dw}{ds}\right|_i = \theta_i$ = specified rotation at node *i*

Natural boundary conditions:

(i) Bending moment at node: $\left.EI\frac{d^2w}{ds^2}\right|_i = M_i$ = specified bending moment at node *i*

(ii) Shear force at node: $\left.EI\frac{d^3w}{ds^3}\right|_i = V_i$ = specified shear force at node *i*

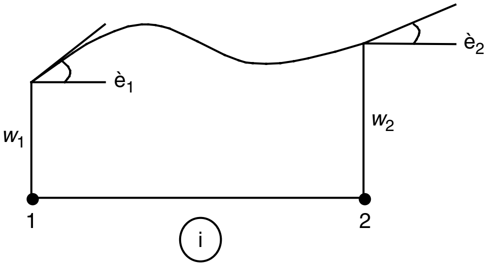

FIGURE 11.3.8 Hermite element.

The displacement field within the element is interpolated as shown next using Hermite polynomials N_i defined earlier in Equation 11.3.58.

$$w(s) = w_1N_1 + \theta_1N_1 + w_2N_3 + \theta_2N_4 \tag{11.3.76}$$

The equilibrium equations for one beam element can be derived using this interpolation in the weak form as $[\mathbf{K}_e]\{\mathbf{X}_e\} = \{\mathbf{F}_e\}$, where

$$\text{Stiffness matrix} = [\mathbf{K}_e] = \frac{EI}{L^3}\begin{bmatrix} 12 & 6L & -12 & 6L \\ 6L & 4L^2 & -6L & 2L^2 \\ -12 & -6L & 12 & -6L \\ 6L & 2L^2 & -6L & 4L^2 \end{bmatrix}, \tag{11.3.77}$$

$$\text{Displacement vector} = \{\mathbf{X}_e\} = \begin{Bmatrix} w_1 \\ \theta_1 \\ w_2 \\ \theta_2 \end{Bmatrix}, \tag{11.3.78}$$

$$\text{Force vector} = \{\mathbf{F}_e\} = \begin{Bmatrix} V_1 \\ M_1 \\ V_2 \\ M_2 \end{Bmatrix} + \int_0^L f \begin{Bmatrix} N_1 \\ N_2 \\ N_3 \\ N_4 \end{Bmatrix} ds \tag{11.3.79}$$

If the distributed load f is a uniform load across the beam, then the nodal values of the load that is equivalent to the distributed load can be computed as

$$\{\mathbf{F}_d\} = \frac{fL}{12}\begin{Bmatrix} -6 \\ -L \\ -6 \\ L \end{Bmatrix} \tag{11.3.80}$$

Most FEA software provides multiple beam elements, including sometimes the simple beam formulation with two degrees of freedom as described above. However, to construct frame-like structures by assembling multiple beam elements, it is necessary to use appropriate transformation so that the nodal variables are expressed as displacement components along a global coordinate system. In the most general case, the beam can be oriented arbitrarily in space as shown in Figure 11.3.9. Therefore, at each node there are six degrees of freedom corresponding to translations (d_{ix}, d_{iy}, d_{iz}) and rotations (θ_{ix}, θ_{iy}, θ_{iz}) along the x, y, and z axes.

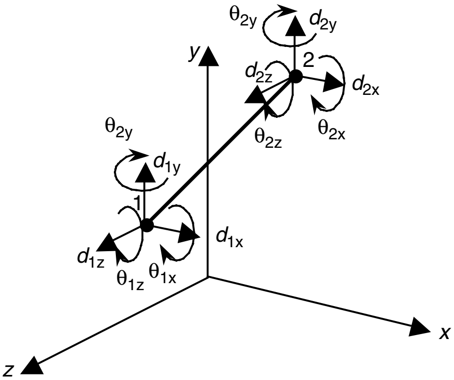

FIGURE 11.3.9 Beam element.

The element shown in Figure 11.3.9 is the general "3D beam" element for which one can specify up to three components of displacement and three components of angular displacement as boundary conditions. Similarly, at any node one can specify three components of force and moments about the three axes. The general 3D beam includes not only the bending stiffness described earlier, but also axial stiffness (similar to the truss element) and torsional stiffness. Furthermore, since the applied moments need not be about the axes of symmetry of the beam cross section, it is necessary to specify all components of the moments of inertia of the cross section. The geometric constants that need to be specified for the general 3D beam include, A = area of cross section, I_{yy}, I_{zz}, and I_{yz} the three components of moment of inertia, J = Polar moment of inertia, d_{sc} = distance from the centroid of the cross section to its shear center, as well as the (y,z) coordinates of the points at which stress needs to be computed.

Since the common node between two elements share the angle of rotation at that node, the deformed shape of the beam is guaranteed to be C^1 or tangent continuous if the elements are collinear before deforming. Similarly, if the two beam elements meet at an angle, they behave as if they are welded together. In other words, during the deformation any change in angle between the elements requires a bending moment transmission from one element to the other. Therefore, frame-like structures constructed by welding together slender beams can be modeled using these beam elements. Beam element formulation ignores shear strain energy; therefore, beam elements give accurate answers only if the beam length is much larger (at least ten times) than the beam cross-sectional dimensions.

Plane Stress Problems

Structural problems where the displacement vector can be expressed as a function of just two spatial coordinates can be modeled using two-dimensional finite elements. The field variable is the displacement vector and can be expressed as $\mathbf{u}(x,y) \in \mathbf{R}^2$. A plane stress problem is one such example where the stress in the structure is limited to a plane so that all stress components normal to this plane are zero.

The most common example is a plate-like structure that is only subjected to in-plane loads such as the plate shown in Figure 11.3.10. There are no loads acting on this plate that have a component perpendicular to the plate, and there are no bending moments, either. Therefore, the structure does not deflect in the direction perpendicular to the plane of the plate, and the displacement vector is two-dimensional and can be expressed as

$$\mathbf{u}(x,y) = \{\mathbf{u}\} = \begin{Bmatrix} u_x(x,y) \\ u_y(x,y) \end{Bmatrix} \tag{11.3.81}$$

Assuming that the stress components are restricted to the x-y plane, the stress and strain components for a plane stress problem can be expressed as the following column matrix:

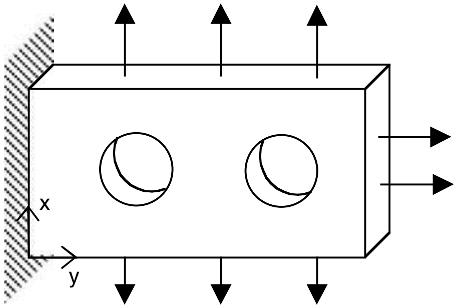

FIGURE 11.3.10 Plane stress problem.

$$\text{Stress} = \{\sigma\} = \begin{Bmatrix} \sigma_{xx} \\ \sigma_{yy} \\ \tau_{xy} \end{Bmatrix} \text{ and Strain} = \{\varepsilon\} = \begin{Bmatrix} \varepsilon_{xx} \\ \varepsilon_{yy} \\ \gamma_{xy} \end{Bmatrix} \tag{11.3.82}$$

Even though the stress components normal to the *x-y* plane are zero, the strain component is not necessarily zero. In fact, the normal stress in the *z* direction can be shown to be equal to

$$\varepsilon_{zz} = \frac{\nu}{E}\left(\sigma_{xx} + \sigma_{yy}\right) \tag{11.3.83}$$

The stress-strain relation for isotropic linear elastic materials is *Hooke's law*, which can be stated as follows for the plane stress problem:

$$\{\sigma\} = \left[C_{pstress}\right]\{\varepsilon\} \tag{11.3.84}$$

$$\text{where } [C_{pstress}] = \begin{bmatrix} \hat{\lambda}+2\mu & \hat{\lambda} & 0 \\ \hat{\lambda} & \hat{\lambda}+2\mu & 0 \\ 0 & 0 & \mu \end{bmatrix}, \ \hat{\lambda} = \frac{E\nu}{1-\nu^2} \text{, and } \mu = \frac{E}{2(1+\nu)} \tag{11.3.85}$$

The weak form for two- and three-dimensional problems is the *principle of virtual work*, which can be stated as follows for the plane stress problem:

$$\int_V \{\delta\varepsilon\}^T \left[C_{pstress}\right]\{\varepsilon\} dV = \int_S \{\delta u\}^T \{T\} dS + \int_V \{\delta u\}^T \{B\} dV \tag{11.3.86}$$

In the Equation 11.3.86, {**δu**} and {δε} are the virtual displacement and virtual strain, respectively. {**T**} is the traction acting on the boundary of the solid *S*, and {**B**} is the body force (or force per unit volume) acting on the structure. In order to carry out the integration over the volume and surface of the structure, a mesh needs to be generated over the volume using any of the two-dimensional elements described earlier. The material properties that need to be specified for plane stress problems for isotropic linear elastic material are *E* = Young's modulus and ν = Poisson's ratio. The only geometric property that needs to be specified is the thickness, because plane stress problems are plate-like structures with uniform thickness that are subjected only to in-plane forces.

Plane Strain Problems

If the deformation of a structure is planar so that the displacement at all points is restricted to a plane and all components of strain and displacement normal to this plane are zero, then the structure can be modeled using plane strain elements. If the plane of deformation is assumed to be the *x-y* plane, then the displacement component and the strain components in the *z*-direction are zero. Using the same notation for stress and strain vectors as in the plane stress case, the stress-strain relation (Hooke's law) can be stated as follows for the plane strain problem:

$$\{\sigma\} = [\mathbf{C}_{pstrain}]\{\varepsilon\} \tag{11.3.87}$$

where

$$[\mathbf{C}_{pstrain}] = \begin{bmatrix} \lambda+2\mu & \lambda & 0 \\ \lambda & \lambda+2\mu & 0 \\ 0 & 0 & \mu \end{bmatrix}, \ \lambda = \frac{E\nu}{(1+\nu)(1-2\nu)}, \ \mu = \frac{E}{2(1+\nu)} = G = \text{shear modulus} \tag{11.3.88}$$

Even though the strain components in the *z*-direction are zero, the stress component in the *z*-direction is non-zero for the plane strain problem. It can be shown using the generalized Hooke's law that the normal stress in the *z*-direction is

$$\sigma_{zz} = \nu(\sigma_{xx} + \sigma_{yy}) \tag{11.3.89}$$

The weak form (or the principle of virtual work) may be stated as follows for the plane strain problem:

$$\int_V \{\delta\varepsilon\}^{\mathrm{T}} [\mathbf{C}_{pstrain}]\{\varepsilon\} dV = \int_S \{\delta\mathbf{u}\}^{\mathrm{T}} \{\mathrm{T}\} dS + \int_V \{\delta\mathbf{u}\}^{\mathrm{T}} \{\mathrm{B}\} dV \tag{11.3.90}$$

The only difference between the plane strain element and the plane stress element is in the elasticity matrix $[\mathbf{C}_{pstrain}]$. Plane strain elements can also use any of the two-dimensional interpolation schemes including three-node triangles and four-node quadrilaterals that are described earlier. Again two elastic moduli (E and ν) are sufficient to specify the material properties if the material is isotropic and linear elastic. There is no need to specify the thickness of the structure since plane strain problems usually correspond to structures that are very thick in the *z*-direction compared to its dimensions in the *x-y* plane. Therefore, unit thickness is assumed for plane strain elements. When applying loads on plane strain models, we must take care to ensure that the applied loads are calculated as load per unit depth.

Three-Dimensional Structural Problems

Structures that cannot be modeled using one- and two-dimensional idealization have to be modeled using three-dimensional elements. These elements assume that the displacement at any point in the structure can be in any arbitrary direction in space; therefore, the displacement vector is

$$\{\mathbf{u}(x,y,z\} = \begin{Bmatrix} u_x(x,y,z) \\ u_y(x,y,z) \\ u_z(x,y,z) \end{Bmatrix} \tag{11.3.91}$$

The stress and strain components for the general three-dimensional problem can be expressed as tensors using 3 × 3 matrices. However, for expressing the stress strain relation, it is easier to represent stress and strains using column matrices. The generalized Hooke's law can be written in the following form:

$$\{\sigma\} = [C]\{\varepsilon\} \tag{11.3.92}$$

where [**C**] is a 6 × 6 square matrix and {σ}, {ε} are 6 × 1 column matrices

$$\{\sigma\} = \begin{Bmatrix} \sigma_{xx} \\ \sigma_{yy} \\ \sigma_{zz} \\ \tau_{xy} \\ \tau_{yz} \\ \tau_{zx} \end{Bmatrix}, \quad \{\varepsilon\} = \begin{Bmatrix} \varepsilon_{xx} \\ \varepsilon_{yy} \\ \varepsilon_{zz} \\ \gamma_{xy} \\ \gamma_{yz} \\ \gamma_{zx} \end{Bmatrix} \quad [C] = \begin{bmatrix} \lambda+2\mu & \lambda & \lambda & 0 & 0 & 0 \\ \lambda & \lambda+2\mu & \lambda & 0 & 0 & 0 \\ \lambda & \lambda & \lambda+2\mu & 0 & 0 & 0 \\ 0 & 0 & 0 & \mu & 0 & 0 \\ 0 & 0 & 0 & 0 & \mu & 0 \\ 0 & 0 & 0 & 0 & 0 & \mu \end{bmatrix} \tag{11.3.93}$$

$$\lambda = \frac{E\nu}{(1+\nu)(1-2\nu)}, \quad \mu = \frac{E}{2(1+\nu)} = G = \text{shear modulus} \tag{11.3.94}$$

The weak form for the three-dimensional static structural boundary value problem is the three-dimensional principle of virtual work, which looks similar to two-dimensional versions except that the stress and strain vectors are now 6 × 1 vectors. The displacements, virtual displacements {**δu**}, surface traction {**T**}, and body force {**B**} are all now three-dimensional vectors:

$$\int_V \{\delta\varepsilon\}^T [C]\{\varepsilon\} dV = \int_S \{\delta u\}^T \{T\} dS + \int_V \{\delta u\}^T \{B\} dV \tag{11.3.95}$$

The field variable is the three-dimensional displacement vector {**u**}, which can be interpolated within any three-dimensional elements, including the four-node tetrahedral elements and eight-node hexahederal elements described earlier. The material properties that are required are the elastic moduli (E and ν) for isotropic linear elastic materials.

Heat Transfer

Heat-conduction problems in one, two and three dimensions can be solved using linear static heat-conduction elements available in most FEA software. The field variable is the temperature field $T(x, y, z)$ within a solid that is conducting heat. The general three-dimensional governing equations and the weak form are described next. These can be easily simplified into one- and two-dimensional equations.

The governing equation for heat conduction is the following partial differential equation, which is derived from the condition of equilibrium in heat flow and Fourier's law relating heat flow to temperature gradient:

$$\nabla \cdot (k\nabla T) + f = 0 \tag{11.3.96}$$

Here f is the heat generation per unit volume of the solid and k is the thermal conductivity of the material assuming that the material is isotropic. The gradient of temperature ∇T is a two- or three-dimensional vector depending on the dimension of the problem. Three different types of boundary conditions that may be applied for heat conduction problems:

1. Temperature specified on part of the boundary S_1
2. Heat flux specified on part of the boundary S_2: $q_n = -q_0$ (if q_0 is flowing out), where q_n = heat flux normal to boundary, $q_n = \mathbf{q} \cdot \hat{\mathbf{n}} = -(k\nabla T) \cdot \hat{\mathbf{n}}$, where $\hat{\mathbf{n}}$ is the unit vector normal to the surface
3. Heat transfer by convection along S_3: $q_n = -(k\nabla T) \cdot \hat{\mathbf{n}} = h(T - T_a)$, where h = convection coefficient and T_a = ambient temperature

The weak form of the heat-conduction problem can be stated as

$$\int_V \nabla\delta T k \nabla T dV = \int_S (k\nabla T)\cdot\hat{\mathbf{n}}\delta T dS + \int_V f\delta T dV \tag{11.3.97}$$

The surface integral on the right-hand side of the equation can be split into integration over regions of the surface on which the various different boundary conditions have been applied. This yields the following modified weak form:

$$\int_V \nabla\delta T k \nabla T dV + \int_{S_3} hT\delta T ds = \int_{S_2} q_0\delta T ds + \int_{S_3} hT_a\delta T ds + \int_V f\delta T dV \tag{11.3.98}$$

Heat-conduction elements can be used to compute temperature distribution in solids. The material property to be specified is k, the thermal conductivity of the material. If convective heat transfer is occurring along part of the boundary, then the convection coefficient also needs to be specified along with the ambient temperature or the temperature of the surrounding to which heat transfer due to convection is occurring. Heat generation per unit volume, f, can also be specified if heat is being generated within the material, for example, due to electrical current flow.

References

1. Hoffmann, C. 1989, *Geometric and Solid Modeling: An Introduction*, Morgan Kaufmann, San Francisco, CA.
2. Mäntylä, M. 1988. *An Introduction to Solid Modeling*, Computer Science Press, Rockville, MD.
3. Mortenson, M.E. 1997. Geometric Modeling, 2nd ed., Wiley Computer Publishing, John Wiley & Sons, New York.
4. Requicha, A.A.G. 1980. Representation of rigid solids: theory, methods, and systems., *Computing Surveys*, 12 (4), pp. 437–64.
5. Zied I. 1991. *CAD/CAM Theory and Practice*, McGraw-Hill, New York.
6. Lee, K. 1999. *Principles of CAD/CAM/CAE Systems*, Addison-Wesley, New York.
7. Requicha, A.A.G. and Voelcker, H.B. 1985. Boolean operations in solid modeling: boundary evaluation and merging algorithms. *Proc. of the IEEE*, 73(2), pp. 30–44.
8. Farin, G. 1997, *Curves and Surfaces for Computed Aided Geometric Design*, 4th ed., Academic Press, New York.
9. Bathe, K.J. 1996. *Finite Element Procedures*, Prentice Hall, Englewood Cliffs, NJ.
10. Chandrupatla, T.R. and Belegundu, A.D. 1997. *Introduction to Finite Elements in Engineering*, 2nd ed., Prentice Hall, NJ.
11. Logan, D.L. 2002. *A First Course in Finite Element Method*, Brooks/Cole, CA.

11.4 Structural Design Criteria

Nagaraj K. Arakere

Mechanical failure is generally referred to as any change in the size, shape, or material properties of a structure, machine, or machine part that renders it incapable of satisfactorily performing its intended function.[1] This is an extremely broad definition of mechanical failure, and in the context of this book we will cover only specific types of failure. We will examine what kind of stress causes failure: Is it tensile, compressive, or shear stress? To answer these questions, we need to know the type of material and its relative strengths in compression, tension, and shear; whether the loading was static or dynamic; and whether there are cracks in the material.[1-4] The failure criteria are restricted to metallic isotropic structural materials and, for the most part, to ductile materials. Materials that exhibit a ductility of 5% or more elongation in a 2-in. gage length are classified as nominally ductile materials, whereas materials that exhibit a ductility of less than 5% elongation in a 2-in. gage length are classified as nominally brittle materials.[1] Metallic materials used in engineering applications are largely isotropic polycrystalline ductile metallic alloys. Specialized topics such as static and fatigue failure due to contact mechanics and high-temperature effects such as creep and thermomechanical fatigue are not addressed.

Static Failure Criteria

In general, ductile materials subjected to static tensile loading are limited by their shear strengths, whereas brittle materials are limited by their tensile strengths, although there can be exceptions to this rule.[1,4] This requires that we have different failure criteria for ductile and brittle materials. Failure is defined by the onset of yield that can result in the significant distortion of the part. A part may also fail by fracturing or separating. The mechanisms that cause fractures can be very different. In general, only ductile materials yield significantly before fracturing. Static loads are slowly applied and remain essentially constant with time. Dynamic loads are suddenly applied (impact loads) or are cyclic loads that vary with time (fatigue loads), or they can be both. There are significant differences in failure mechanisms under static and dynamic loading, and hence we will address them separately.

Failure of Ductile Materials Under Static Loading

We will establish yield criteria for ductile materials subjected to static loading. Ductile materials will fracture if statically stressed beyond their ultimate tensile strength. However, failure is generally defined by the onset of yield under static loading. The yield strength of a ductile material is less than its ultimate strength.[4]

The state of stress and strain at a point in a body can be described by six stress components (σ_x, σ_y, σ_z, τ_{xy}, τ_{xz}, τ_{yz}) and six strain components (ε_x, ε_y, ε_z, γ_{xy}, γ_{xz}, γ_{yz}) acting on orthogonal planes x, y, and z. Stresses and strains acting in any other direction or plane can be found by using appropriate transformation equations or graphically by using Mohr's circle. Of special significance to both static and fatigue analysis are the magnitudes and directions of the maximum normal principal stress, σ_1; the maximum shearing stress, τ_{max}; the maximum normal principal strain, ε_1; and the maximum shearing strain, γ_{max}, acting at the critical location in the part. Even though only a few planes experience the maximum principal normal stress (or strain) and the maximum shearing stress (or strain), many other planes can experience a large percentage of these quantities.[3] Consider the case of simple uniaxial tension where, even though only the loading plane experiences the maximum normal stress σ_1, all planes oriented between ±13 degrees from the loading plane experience at least 95% of σ_1. Also, a shearing stress is present on every stressed plane, except for the loading plane.

For any three-dimensional stress state in a body in mechanical equilibrium, the principal normal stresses, which act on orthogonal planes that are free of shear stresses, can be found by solving the stress cubic equation given by

$$\sigma^3 - I_1\sigma^2 - I_2\sigma - I_3 = 0 \tag{11.4.1}$$

where I_1, I_2 and I_3, are called the stress invariants, and they are independent of the orientation of the coordinate system chosen to describe the stress components. They are given by

$$\begin{aligned} I_1 &= \sigma_{ii} = \sigma_{11} + \sigma_{22} + \sigma_{33} \\ I_2 &= \frac{1}{2}(\sigma_{ij}\sigma_{ij} - I_1^2) = \frac{1}{2}(\sigma_{11}^2 + \sigma_{22}^2 + \sigma_{33}^2 + 2\sigma_{12}^2 + 2\sigma_{23}^2 + 2\sigma_{31}^2 - I_1^2) \\ I_3 &= \det\left[\sigma_{ij}\right] \end{aligned} \tag{11.4.2}$$

The principal stresses are denoted by σ_1, σ_2, and σ_3 with $\sigma_1 \geq \sigma_2 \geq \sigma_3$. The normal mean stress or the hydrostatic stress, σ_H, is defined as

$$\sigma_H = \sigma_{mean} = \frac{1}{3}(\sigma_1 + \sigma_2 + \sigma_3) = \frac{1}{3}\sigma_{kk} = \frac{I_1}{3} \tag{11.4.3}$$

The hydrostatic stress σ_H causes a change in volume only and does not distort or change the shape of an isotropic body. The deviatoric stress components are defined as

$$s_{ij} = \sigma_{ij} - \frac{\delta_{ij} I_1}{3} = \sigma_{ij} - \delta_{ij}\sigma_H \tag{11.4.4}$$

These deviatoric stress components bring about a change of shape or distortion in the body and influence plastic deformation. A new set of scalar invariants, J_1, J_2 and J_3, based on the deviatoric stresses, can be defined as

$$\begin{aligned} J_1 &= \sigma_{ii} - I_1 = 0 \\ J_2 &= \frac{1}{2}(s_{ij}s_{ij} - J_1^2) = \frac{1}{2}s_{ij}s_{ij} = -(s_{11}s_{22} + s_{22}s_{33} + s_{33}s_{11}) \\ J_3 &= \frac{1}{3}(s_{ij}s_{jk}s_{ki}) = s_{11}s_{22}s_{33} \end{aligned} \tag{11.4.5}$$

The shear stresses and strains on the octahedral planes are of importance in yielding prediction and fatigue analysis.[3] There are eight octahedral planes making equal angles with the three principal stress directions. The shearing stress on these planes is given by

$$\tau_{oct} = \frac{1}{3}\sqrt{(\sigma_1 - \sigma_2)^2 + (\sigma_2 - \sigma_3)^2 + (\sigma_3 - \sigma_1)^2} \tag{11.4.6}$$

The normal stress on an octahedral plane is the hydrostatic stress σ_H given by

$$\sigma_{oct} = \sigma_H = \sigma_{mean} = \frac{1}{3}(\sigma_1 + \sigma_2 + \sigma_3) \tag{11.4.7}$$

The shear strain on an octahedral plane is given by

$$\gamma_{oct} = \frac{2}{3}\sqrt{(\varepsilon_1 - \varepsilon_2)^2 + (\varepsilon_2 - \varepsilon_3)^2 + (\varepsilon_3 - \varepsilon_1)^2} \tag{11.4.8}$$

When a ductile material is loaded beyond the elastic limit, it undergoes permanent plastic deformation. The total strain imposed on the elastic-plastic solid ε_{ij} can be written as a sum of the elastic and plastic strain components ε_{ij}^e and ε_{ij}^P, respectively. Plastic flow in metals can be assumed to be incompressible ($\varepsilon_{ii}^P = 0$).[1,2] The basic elements of plasticity theory consist of a yield function to determine when plastic flow begins, a flow rule that relates the applied stress increments to the resulting plastic strain increments once the plastic flow has begun, and a hardening rule that describes the change in yield criterion as a function of plastic strains.[2,3] Thus, yielding depends on the instantaneous increments of stress or strain and on the prior history of the material.

The yield criterion is a function $f(\sigma_{ij})$ of the current state of stress. Rate-independent plasticity theories postulate that material response is elastic for $f(\sigma_{ij}) < 0$. Elastic unloading occurs from a plastic state when $f(\sigma_{ij}) = 0$ and $(\partial f / \partial \sigma_{ij}) d\sigma_{ij} < 0$, where $d\sigma_{ij}$ is the stress increment. Plastic deformation occurs when $f(\sigma_{ij}) = 0$ and $(\partial f / \partial \sigma_{ij}) d\sigma_{ij} \geq 0$. The deformation of metals is insensitive to moderate levels of hydrostatic stress σ_H and hence the yield function depends only on the deviatoric stress s_{ij}.[2]

The yield criterion can be visualized in a stress space in which each of the coordinate axes represents one principal stress. The von Mises and Tresca yield criteria are two of the most widely used flow criteria for metal plasticity. The von Mises condition states that

$$f \equiv J_2 - k^2 \equiv \frac{1}{2} s_{ij} s_{ij} - k^2 = 0 \tag{11.4.9}$$

In terms of principal stresses, the von Mises yield function can be written as

$$f = \frac{1}{6}\left[(\sigma_1 - \sigma_2)^2 + (\sigma_2 - \sigma_3)^2 + (\sigma_3 - \sigma_1)^2\right] - k^2 = 0 \tag{11.4.10}$$

The von Mises yield criterion can be visualized as a right circular cylinder in the stress space. The axis of the cylinder passes through the origin of the coordinates, and is inclined at equal angles to the three coordinate axes and represents pure hydrostatic stress. For an elastic, perfectly plastic solid k is a constant, and it is influenced by prior strain history in a work-hardening material. The von Mises yield condition implies that plastic flow occurs when the distortional energy reaches a critical value. For uniaxial tension, $\sigma_1 = \sigma_y$, $\sigma_1 = \sigma_3 = 0$, and $k = \sigma_y/\sqrt{3}$, where σ_y is the tensile yield stress. For pure shear $\sigma_1 = -\sigma_3 = \tau_y$, $\sigma_2 = 0$, and $k = \tau_y$, where τ_y is the shear yield stress.[2] The multiaxial stress state can be written in terms of an equivalent stress, σ_e, given by

$$\sigma_e = \frac{1}{\sqrt{2}} \sqrt{\left[(\sigma_1 - \sigma_2)^2 + (\sigma_2 - \sigma_3)^2 + (\sigma_3 - \sigma_1)^2\right]} = \sqrt{3 J_2} \tag{11.4.11}$$

or

$$\sigma_e = \frac{1}{\sqrt{2}} \sqrt{\left[(\sigma_x - \sigma_y)^2 + (\sigma_y - \sigma_z)^2 + (\sigma_z - \sigma_x)^2 + 6(\tau_{xy}^2 + \tau_{yz}^2 + \tau_{zx}^2\right]} \tag{11.4.12}$$

Yielding occurs when $\sigma_e = \sigma_y$. The equivalent stress σ_e is also related to the octahedral shear stress τ_{oct}, and hence the von Mises yield theory is sometimes also called the octahedral shear stress theory.

The Tresca yield condition (maximum shear stress theory) states that the material will yield when the maximum shear stress reaches a critical value:

$$\frac{1}{2}\left|\sigma_1 - \sigma_3\right| = k \tag{11.4.13}$$

where the principal stresses have been arranged in the order $\sigma_1 \geq \sigma_2 \geq \sigma_3$. For uniaxial tension, the Tresca condition predicts that $k = \sigma_y/2$. The yield surface represented by the Tresca condition is a regular hexagonal prism. Figure 11.4.1 shows experimental data from tensile tests superposed on three failure theories.

Once plastic deformation has begun, we need to establish a flow rule to relate stresses and plastic strains. Equations that relate stresses and plastic strains are also called *constitutive* equations and are generally based on the normality condition. This condition states that the increment of plastic strain caused by an increment of stress is such that the vector representing the plastic strain increment is normal to the yield surface during plastic deformation. A hardening rule is needed to describe the behavior of the material once it is plastically deformed or yielded. The isotropic hardening rule assumes that the

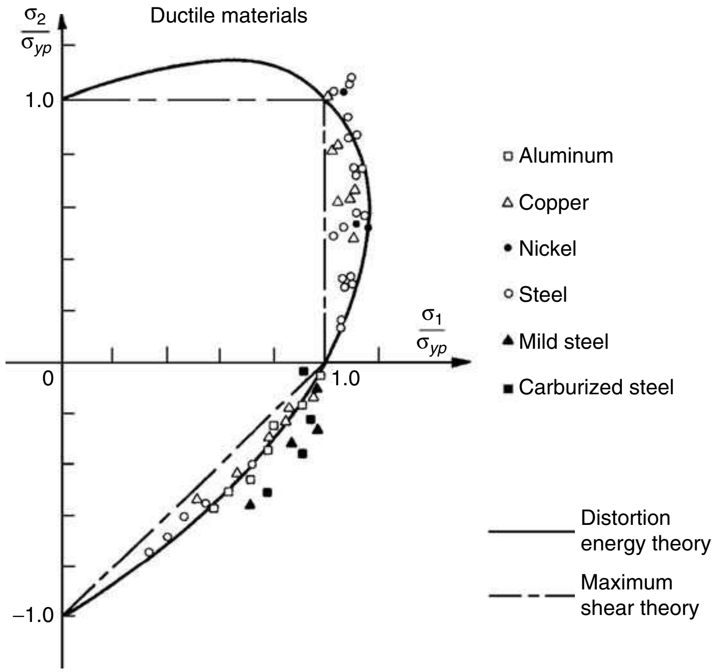

FIGURE 11.4.1 Comparison of yield theories for ductile materials under biaxial state of stress. [From Figure 6.8, p. 158, in reference 1.]

yield surface enlarges (i.e., an increase in σ_y) without a change in shape or position of the stress space. The kinematic rule assumes that strain hardening shifts the yield surface without changing its shape or size.[2,3,5]

Failure of Brittle Materials Under Static Loading

Brittle materials fracture rather than yield. The normal tensile stress is the determining factor for failure by brittle fracture in tension, and hence the maximum normal-stress theory is applicable to this case. The maximum normal stress theory states that failure will occur when the normal stress in the specimen reaches the tensile yield strength or ultimate tensile strength. Brittle fracture in compression is due to some combination of normal compressive stress and shear stress and requires a different theory of failure.[4]

Some brittle materials such as hardened tool steel have compressive strengths equal to their tensile strengths and are called *even materials*. Many cast materials, such as gray cast iron, are brittle but have compressive strengths much greater than their tensile strengths. These are called *uneven materials*.[4] For some cast brittle materials, the shear strength can be greater than their tensile strength. This is very different from ductile materials, where the shear strength is about one-half of the tensile strength. For uneven brittle materials, the preferred failure theory under static loading is the modified Mohr theory envelope, shown in Figure 11.4.2.[4]] For us to use this theory, it is convenient to have expressions for an effective stress that would account for all the applied stresses and allow direct comparison to a material strength property, as was done for ductile materials with von Mises effective stress, σ_e. Dowling[6] develops a set of expressions for this effective stress involving the three principal stresses:

$$C_1 = \frac{1}{2}\left[\left|\sigma_1 - \sigma_2\right| + \frac{S_{uc} + 2S_{ut}}{S_{uc}}(\sigma_1 + \sigma_2)\right]$$
$$C_2 = \frac{1}{2}\left[\left|\sigma_2 - \sigma_3\right| + \frac{S_{uc} + 2S_{ut}}{S_{uc}}(\sigma_2 + \sigma_3)\right] \qquad (11.4.14)$$

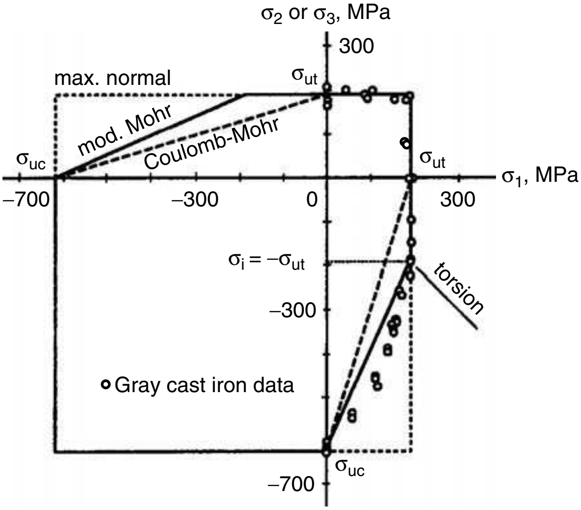

FIGURE 11.4.2 The modified Coulomb-Mohr theory for failure prediction of uneven brittle materials. [From Figure 7.13, p. 255, in reference 6.]

$$C_3 = \frac{1}{2}\left[\left|\sigma_3 - \sigma_1\right| + \frac{S_{uc} + 2S_{ut}}{S_{uc}}(\sigma_3 + \sigma_1)\right]$$

where S_{ut} and S_{uc} are the material strengths in tension and compression. The largest of the set of six values (C_1, C_2, C_3, σ_1, σ_2, σ_3) is the effective stress suggested by Dowling.[6]

$$\tilde{\sigma}_e = \mathrm{Max}(C_1, C_2, C_3, \sigma_1, \sigma_2, \sigma_3) \tag{11.4.15}$$

If all the arguments are negative, then the effective stress is zero. The effective stress, $\tilde{\sigma}_e$, is compared to either the yield stress or the ultimate tensile strength, to predict failure.

The Linear Elastic Fracture Mechanics (LEFM) Approach

The static failure theories discussed so far have all assumed that the material is perfectly homogeneous and isotropic, and free of any defects such as cracks, voids, or inclusions, which could act as stress raisers. This is rarely true for real materials, and typically all materials are considered to contain small flaws, whose size and distribution are dependent on the material and its processing. These may include nonmetallic inclusions, microstructural defects, microvoids, weld defects, quench marks, and so forth.[4] Development of predictive models of fracture in engineering structures and machines at the macroscopic level is well known as the area of *fracture mechanics*. Dislocation theory has been successful in explaining the mechanisms of deformation and fracture of engineering materials at the atomic level. However, it has not provided engineers with quantitative tools necessary to estimate potentially critical combinations of loading, geometry, and material properties.[1] The field of fracture mechanics was given impetus by numerous failures of engineering structures since the 1940s. Some examples are the 1289 failures out of 4694 Liberty Ships constructed during the 1940s, the Comet aircraft failures of the early 1950s, missile tank failures and large steam turbine failures of the mid-1950s, the Bomark helium tank failure in 1960, the large solid rocket motor case failures and Apollo tank failures of the mid-1960s, and many others to this day.[1] The reasons behind these failures involve the development of new higher strength materials, a thrust toward higher efficiency in design, the use of welding, reduction in the capacity of structural members to accommodate local plastic strain without fracture, residual stresses due to machining, fluctuating service loads of greater severity, and more aggressive environments. To prevent or minimize

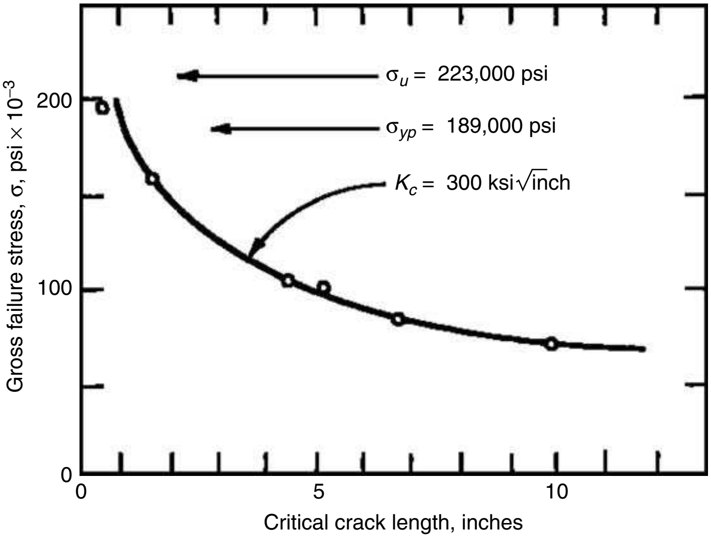

FIGURE 11.4.3 Influence of crack length on gross failure stress for center-cracked steel plate, 36 in. wide, 0.14 in. thick, room temperature, 4330 M steel. [From Figure 3.26, p. 51, in reference 1.]

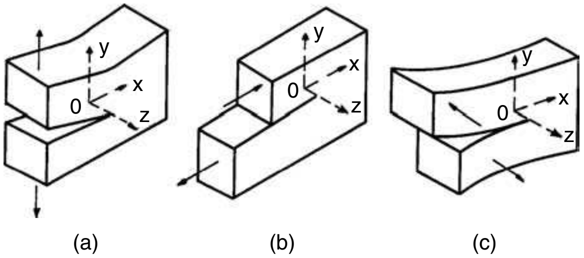

FIGURE 11.4.4 Basic modes of crack displacement [1]. (a) Mode I; (b) Mode II; (c) Mode III. [From Figure 5.3, p. 146, in reference 2.]

failure due to fracture, concepts of fracture control have evolved, which consist of controlling the combination of nominal stress and existing crack size so that they are always below a critical level for the material being used in a given structure/machine.[1]

The magnitude of nominal applied stress, which causes fracture, is related to the size of the crack or crack-like flaw within the structure. For example, Figure 11.4.3 shows the tensile stress required to cause unstable crack growth leading to failure, as a function of crack length, for central through-the-thickness cracks in a steel plate oriented normal to the applied tensile stress.[7] The figure indicates that for longer initial crack lengths the fracture stress, that is, the stress corresponding to rapid crack extension, was lower.[1]

The abrupt change from slow crack propagation to rapid crack propagation establishes an important material property called *fracture toughness*. It may be used as a design criterion in fracture prevention, just as the yield strength is used as a design criterion in prevention of yielding of a ductile material under static loading.[1]

The crack surface displacements in the three basic modes of separation are shown schematically in Figure 11.4.4. Mode I is the *tensile opening mode*, in which the crack faces separately in a direction normal to the plane of the crack and the corresponding displacements of the crack walls are symmetric with respect to the x-z and x-y planes. Mode II is the *in-plane sliding mode*, in which the crack faces are mutually sheared in a direction normal to the crack front. Here the displacements of the crack walls are

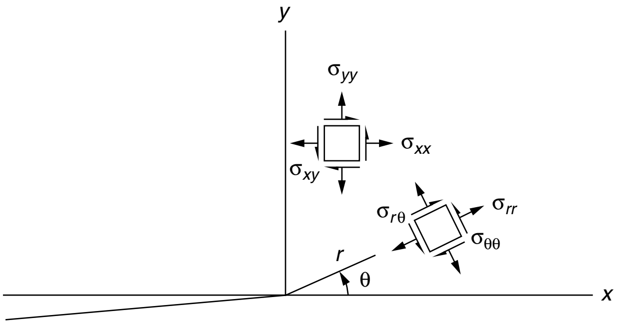

FIGURE 11.4.5 Stress field in the near-tip region of a crack in a plate. [From Figure 5.4, p. 147, in reference 2.]

symmetric with respect to the x-y plane and antisymmetric with respect to the x-z plane. Mode III is the *tearing or antiplane shear mode,* in which the crack faces are sheared parallel to the crack front. The displacements of the crack walls in this case are antisymmetric with respect to the x-z and x-y planes.[2]

The stress and displacement field in the near-tip region of a semi-infinite crack in an infinite plate (the plane problem, shown in Figure 11.4.5), for Mode I can be obtained as (an asymptotic solution with higher order terms neglected)[1–3]

$$\begin{Bmatrix} \sigma_{xx} \\ \sigma_{yy} \\ \sigma_{xy} \end{Bmatrix} = \frac{K_I}{\sqrt{2\pi r}} \cos\frac{\theta}{2} \begin{Bmatrix} 1 - \sin\frac{\theta}{2}\sin\frac{3\theta}{2} \\ 1 + \sin\frac{\theta}{2}\sin\frac{3\theta}{2} \\ \sin\frac{\theta}{2}\cos\frac{3\theta}{2} \end{Bmatrix} + [O]r^{1/2} \tag{11.4.16}$$

$$\sigma_{zz} = \nu_1(\sigma_{xx} + \sigma_{yy}), \qquad \sigma_{xz} = \sigma_{yz} = 0$$

$$\begin{Bmatrix} u_x \\ u_y \end{Bmatrix} = \frac{K_I}{2E}\sqrt{\frac{r}{2\pi}} \begin{Bmatrix} (1+\nu)\left[(2\kappa - 1)\cos\frac{\theta}{2} - \cos\frac{3\theta}{2}\right] \\ (1+\nu)\left[(2\kappa - 1)\sin\frac{\theta}{2} - \sin\frac{3\theta}{2}\right] \end{Bmatrix}, \; u_z = -\left(\frac{\nu_2 z}{E}\right)(\sigma_{xx} + \sigma_{yy}) \tag{11.4.17}$$

In Equation 11.4.16 and Equation 11.4.17, *E* is the Young's modulus and *n* is the Poisson's ratio. For plane stress,

$$\kappa = \frac{(3-\nu)}{(1+\nu)}, \quad \nu_1 = 0, \quad \nu_2 = \nu \tag{11.4.18}$$

and, for plane strain,

$$\kappa = (3 - 4\nu), \quad \nu_1 = \nu, \quad \nu_2 = 0 \tag{11.4.19}$$

The stress and displacement fields for Modes II and III are similar and can be found in references 1–3. The term K_{I} in Equation 11.4.16 and Equation 11.4.17 is the Mode I stress intensity factor (SIF), which incorporates the boundary conditions of the cracked body and is a function of loading, crack length, and geometry. For plane problems, it is independent of elastic constants. The stress intensity factors for Modes II and III are denoted by K_{II} and K_{III}. Under LEFM assumptions, stress fields for combined loadings can be obtained by linear superposition.

The SIFs are a measure of the intensity of the near-tip fields under elastic conditions. The $1/\sqrt{r}$ singularity in the asymptotic stress solution indicates that a plastic zone will form near the crack tip. Metals and their alloys, except for a few intermetallics, are inherently ductile, that is, plastic deformation precedes fracture in these materials. Therefore, resistance to fracture is directly related to the development of the plastic zone at the crack tip. The plastic zone can be very small or even nonexistent in the case of brittle ceramics. The annular region ahead of the crack tip is known as the *K-dominant* region, within which the SIF provides a unique measure of the intensity of the stress, strain, or deformation. The outer radius of the annular zone is determined by the radial distance at which the approximate, asymptotic singular solutions, Equation 11.4.16 and Equation 11.4.17, deviate significantly from the full elasticity solutions, which include the higher-order terms. The asymptotic results in Equation 11.4.16 and Equation 11.4.17 provide a reasonable solution with the assumption of "small-scale yielding." This condition requires that the crack tip zone of inelastic deformation be confined well inside the region of K-dominance. An understanding of the conditions of K-dominance is essential for the characterization of fatigue fracture involving crystallographic crack growth, mixed-mode loading, or small fatigue flaws. These issues are discussed in great detail in reference 2.

Based on dimensional considerations[1] in Equation 11.4.16, the SIF K must have the form

$$K = C_I \sigma \sqrt{a} \tag{11.4.20}$$

For an infinite plate containing a through the thickness crack of length $2a$, the elasticity solution gives $C_I = \sqrt{\pi}$. For remote loadings, in general, the SIF are of the form

$$K = C\sigma\sqrt{\pi a} \tag{11.4.21}$$

where C is dependent on the type of loading and the geometry away from the crack. There is a large body of literature that exists for determining values of C for a wide variety of conditions; a good example is reference 8.

The SIF K increases proportionately with far-field nominal stress and is also a function of the instantaneous crack length a. The value of K associated with the onset of rapid crack extension is designated as the *critical stress intensity*, K_c, and provides a single-parameter fracture criterion based on the condition $K = C\sigma\sqrt{\pi a} \geq K_c$.

A simple correction factor to account for small-scale plasticity at the crack tip is to estimate the plastic zone radius, shown in Figure 11.4.6. The plastic zone correction factors for monotonic loading, plane stress, and plane strain conditions are given by reference 1:

$$\begin{aligned} r_{Y\sigma} &= \frac{1}{2\pi}\left(\frac{K}{\sigma_y}\right)^2 \quad \text{(planestress)} \\ r_{Y\varepsilon} &= \frac{1}{6\pi}\left(\frac{K}{\sigma_y}\right)^2 \quad \text{(planestrain)} \end{aligned} \tag{11.4.22}$$

Because of the crack-tip plastic deformation, the crack is blunted, as shown in Figure 11.4.6. An effective crack length $a' = a + r_Y$ is used, leading to

$$K = C\sigma\sqrt{\pi(a + r_Y)} \tag{11.4.23}$$

Evaluating Equation 11.4.23 requires an iterative solution since K and C depend on r_Y, and r_Y depends on the magnitude of K.

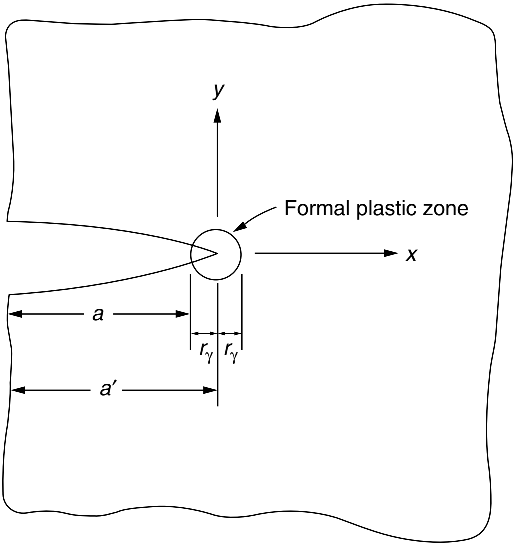

FIGURE 11.4.6 Definition of plastic zone at the crack tip. [From Figure 3.30, p. 59, in reference 1.]

The critical stress intensity K_c decreases to a lower limiting value as plane strain conditions are approached at the crack tip. This lower limiting value defines a basic material property K_{Ic}, the *plane strain fracture toughness* for the material. The minimum material thickness B required for plane strain conditions to exist at the crack tip can be estimated by the empirical relation:[1]

$$B \geq 2.5\left(\frac{K_{Ic}}{\sigma_y}\right)^2 \tag{11.4.24}$$

If plane strain conditions are not met, then the state of stress conditions prevail at the crack tip. The critical SIF for failure prediction under plane stress conditions K_c can be estimated using the semiempirical relation shown here:[1]

$$K_c = K_{Ic}\left(1 + \frac{1.4}{B^2}\left\{\frac{K_{Ic}}{\sigma_y}\right\}^4\right)^{1/2} \tag{11.4.25}$$

The strain energy release rate G, is related to and the SIF K as follows:

$$G = \frac{1}{E}\left(K_I^2 + K_{II}^2\right) \text{ (planestress)}; \quad G = \frac{(1-\nu^2)}{E}\left(K_I^2 + K_{II}^2\right) + \frac{(1+\nu)}{E}K_{III}^2 \text{ (planestrain)} \tag{11.4.26}$$

For self-similar, coplanar crack growth (crack advances in its own plane), the strain energy release rates for the different modes of fracture are simply additive.[2]

If the conditions of small-scale yielding are not satisfied at the crack tip, a better design approach would be to employ an appropriate elastic-plastic fracture mechanics procedure, such as the path-independent J-integral.[1–3]

Fatigue Failure Criteria

A majority of engineering structures and machine elements are subjected to fluctuating or cyclic loads. Such loading induces fluctuating or cyclic stresses that can result in failure by fatigue. Fatigue loading

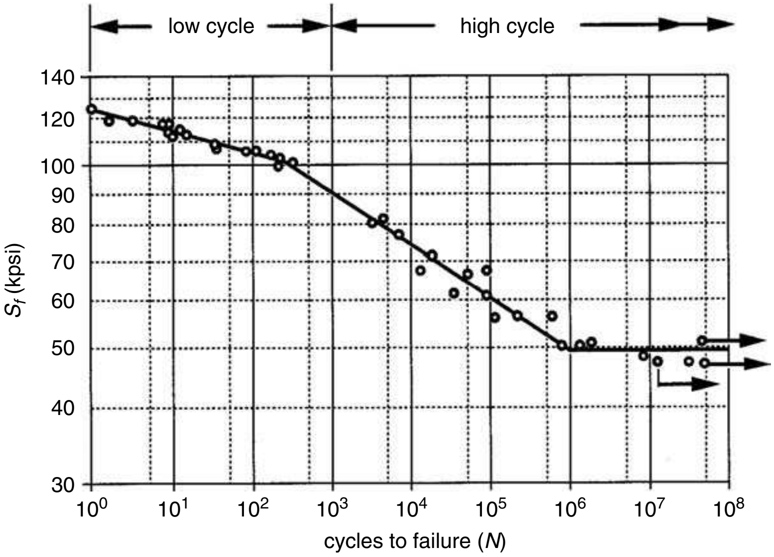

FIGURE 11.4.7 Fully reversed axial S-N diagram for AISI 4130 steel. [From Figure 6-13, p. 364, in reference 4.]

results in changes in properties of materials from the application of cyclic loads. Study of cyclic deformation and fracture of materials by fatigue dates back to the nineteenth century.[2] Characterizing fatigue life of machine components is generally done using phenomenological continuum approaches. The variables used are applied stress range, strain range, mean stress, and environmental conditions. These stress- or strain-based approaches attempt to evaluate the damage evolution, crack nucleation, and crack growth stages of fatigue using continuum formulations and experimental data. The fatigue life of a component is defined as the total number of cycles to induce fatigue damage and to initiate a dominant fatigue flaw that is propagated to failure.[2]

Stress-Life Approach

This approach is stress based and seeks to determine a fatigue strength and/or an endurance limit for the material so that the cyclic stresses can be kept below that level and avoid failure for the required number of cycles. This approach emerged from the work of Wöhler in 1860,[9] who characterized fatigue life in terms of nominal stress amplitudes using experimental data obtained from rotating bend tests on smooth specimens. The crack-initiation phase requires that localized plastic yielding occur in regions of stress concentration, leading to slip band formation. The stress cycling results in the formation of additional slip bands, which coalesce into microscopic cracks. Designing a part so that the stress amplitude never exceeds the material’s fatigue strength (or endurance limit) is an attempt to keep local stresses in notches so low that the crack-initiation phase never begins. The design goal in the stress-life approach is to ensure that the stresses and strains remain in the elastic region so that no yielding occurs to initiate a crack. This approach is generally used for high-cycle fatigue (HCF) applications where the life is expected to be greater than about 10^3 cycles and the stresses are likely to be in the elastic range. This approach is relatively easy to implement, although it is empirical and not accurate in terms of defining local stress/strain states in the part.

The basis for this method is the S-N diagram, an example of which is shown in Figure 11.4.7. The cycles to failure and the alternating stress amplitude are plotted on the x- and the y-axis, respectively, on a log-log scale. Note the slope change at around 10^3 cycles, which corresponds roughly to the transition from the LCF to the HCF regime. The endurance limit is reached at about 10^6 cycles. The data shown is for zero mean stress or fully reversed loading. Figure 11.4.8 shows the nomenclature for fatigue loading and the variation of stress with time.

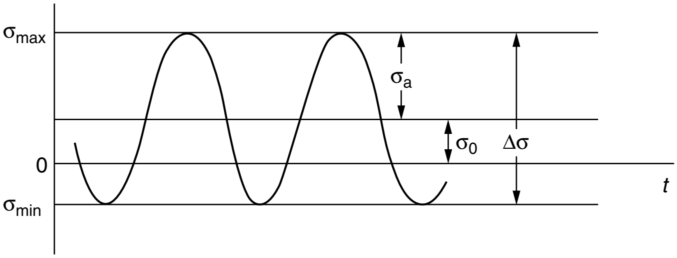

FIGURE 11.4.8 Nomenclature for fatigue loading. [From Figure 4.3, p. 131, in reference 2.]

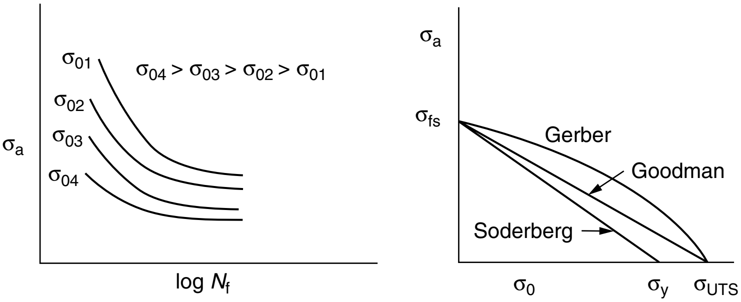

FIGURE 11.4.9 Effect of nonzero mean stress on fatigue life. [From Figure 4.4, p. 132, in reference 2.]

$$\begin{aligned}
&\Delta\sigma = \sigma_{\max} - \sigma_{\min} = \text{Stress range} \\
&\sigma_a = (\sigma_{\max} - \sigma_{\min})/2 = \text{ Stress amplitude} \\
&\sigma_0 = \sigma_m = (\sigma_{\max} + \sigma_{\min})/2 = \text{ Mean stress} \\
&R = \frac{\sigma_{\min}}{\sigma_{\max}}
\end{aligned} \tag{11.4.27}$$

The linear relationship seen in Figure. 11.4.7 on a log-log scale can be given in terms of a power law fit as

$$\frac{\Delta\sigma}{2} = \sigma_a = \sigma'_f\left(2N_f\right)^b \tag{11.4.28}$$

where σ'_f is the fatigue strength coefficient (which approximately equals the true fracture strength σ_f, corrected for necking, in a monotonic tension test for most metals), and b is the fatigue strength exponent or Basquin exponent, which for most metals, is in the range of –0.05 to –0.12.[2]

The presence of a tensile mean stress has a pronounced effect on fatigue life. The allowable alternating stress to achieve the same life is reduced with increasing tensile mean stress. Effects of mean stress on fatigue can be represented in terms of constant-life diagrams, as shown in Figure 11.4.9.[2] Different combinations of the stress amplitude and mean stress are plotted to provide a constant fatigue life in these models. The most commonly used model is that of Goodman:

$$\begin{aligned}
&\sigma_a = \sigma_{fs}\left(1 - \frac{\sigma_m}{\sigma_y}\right)\text{: Soderberg relation} \\
&\sigma_a = \sigma_{fs}\left(1 - \frac{\sigma_m}{\sigma_{UT}}\right)\text{: Goodman relation}
\end{aligned} \tag{11.4.29}$$

$$\sigma_a = \sigma_{fs}\left(1 - \left\{\frac{\sigma_m}{\sigma_{UT}}\right\}^2\right)\text{: Gerber relation}$$

where σ_a is the allowable stress amplitude in the presence of a nonzero mean stress σ_m, σ_{fs} is the fatigue strength for a fixed life for fully reversed loading ($\sigma_m = 0$), and σ_y and σ_{UT} are the yield strength and ultimate tensile strength of the material, respectively.

The stress-life approach discussed thus far applies for uniaxial fatigue loading. It can be extended for the case of multiaxial loading by using equivalent stress approaches, which are extensions of static yield criteria to fatigue. Equivalent mean and alternating stresses are calculated using the von Mises or the Tresca theories, thus reducing the problem to an equivalent uniaxial case. The appropriate S-N diagram along with a mean stress correction factor is used to evaluate fatigue life.

$$\begin{aligned}\sigma'_a &= \frac{1}{\sqrt{2}}\sqrt{\left[(\sigma_{1a}-\sigma_{2a})^2 + (\sigma_{2a}-\sigma_{3a})^2 + (\sigma_{3a}-\sigma_{1a})^2\right]} = \text{Equiv.alt.stress}\\ \sigma'_m &= \frac{1}{\sqrt{2}}\sqrt{\left[(\sigma_{1m}-\sigma_{2m})^2 + (\sigma_{2m}-\sigma_{3m})^2 + (\sigma_{3m}-\sigma_{1m})^2\right]} = \text{Equiv.mean stress}\end{aligned} \tag{11.4.30}$$

Cumulative Damage

Service load histories for engineering applications are usually variable amplitude, whereas the stress-life approach outlined is only applicable for constant amplitude loading. It is important to have a theory, verified by experimental observations, that will permit good design estimates to be made for operation under spectrum loading using the standard constant amplitude S-N curves that are available. Cumulative damage under spectrum loading is evaluated by taking into account the cyclic stress amplitude, the number of cycles of operationat that stress amplitude, and also the total number of cycles of life of an undamaged specimen at that stress amplitude. The damage incurred is considered permanent, and operation at several different stress amplitudes in sequence will result in an accumulation of total damage equal to the sum of the damage increments accrued at each individual stress level. When the total accumulated damage reaches a critical value, fatigue failure is predicted to occur.[1]

The linear damage rule by Palmgren and Miner is widely used because of its simplicity and is illustrated in Figure 11.4.10. At a given stress amplitude S_1 with total life N_1, the *damage fraction* for n_1 cycles (less than N_1) is defined as

$$D_1 = \frac{n_1}{N_1}.$$

For spectrum loading, failure is predicted to occur if the sum of the damage fractions is greater than or equal to unity, that is, $D_1 + D_2 + \ldots D_{i-1} + D_i \geq 1$. The assumption here is that the damage accumulation is linear and that the order of application of loads is not important. By the Palmgren-Miner rule, failure is predicted to occur if

$$\frac{n_1}{N_1} + \frac{n_2}{N_2} + \ldots + \frac{n_{i-1}}{N_{i-1}} + \frac{n_i}{N_i} \geq 1 \tag{11.4.31}$$

There is experimental evidence that the order of application of loads has a significant influence and also that damage rate at a given stress level is likely a function of prior stress history. For instance, a large stress cycle will produce a large plastic zone at a crack tip, inducing a residual compressive stress. For subsequent loading cycles, crack growth rate is retarded while the crack is propagating through the

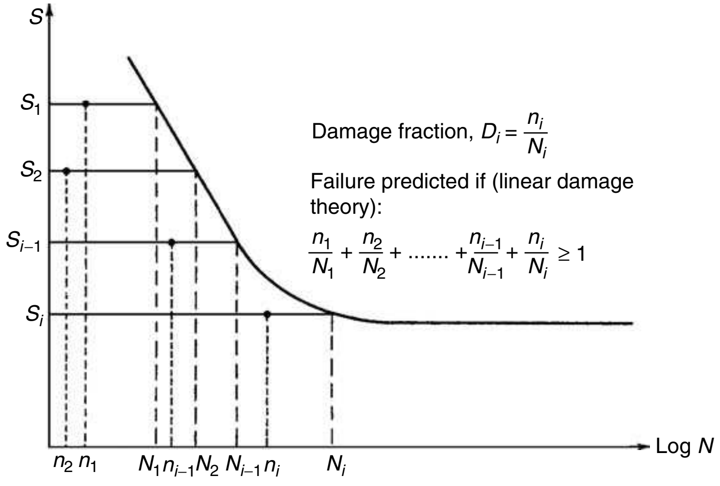

FIGURE 11.4.10 Palmgren-Miner linear damage hypothesis for spectrum loading. [From Figure 8.1, p. 256, in reference 1.]

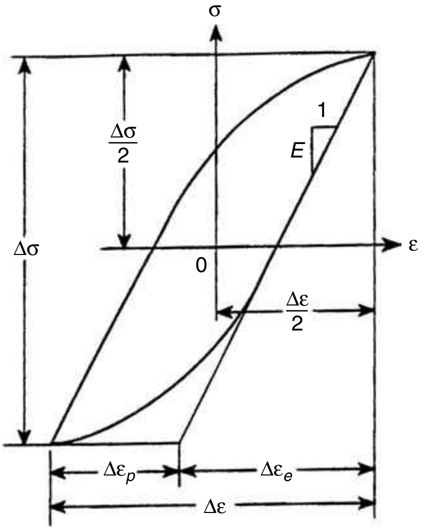

FIGURE 11.4.11 Representation of cyclic stress and strain amplitudes in a stabilized hysteresis loop.

residual compressive stress field. Many other cumulative damage theories account for such nonlinear effects, these are discussed in detail in references 1–3.

Strain-Life Approach

The strain-life method predicts the life expectancy based on the magnitude of strain amplitude. This method is appropriate when components have regions of high-stress concentration with constrained loading conditions, where the fatigue loading induces alternating plastic stresses and strains. In these situations, it is more appropriate to consider the life of a component under a strain-controlled condition that represents a constrained loading situation.[2]

The cyclic stress-strain relations in a stable hysteresis loop, shown in Figure 11.4.11, can be expressed as

$$\frac{\Delta\varepsilon}{2} = \frac{\Delta\varepsilon_e}{2} + \frac{\Delta\varepsilon_p}{2} = \frac{\Delta\sigma}{2E} + \left(\frac{\Delta\sigma}{2K'}\right)^{1/n'} \qquad (11.4.32)$$

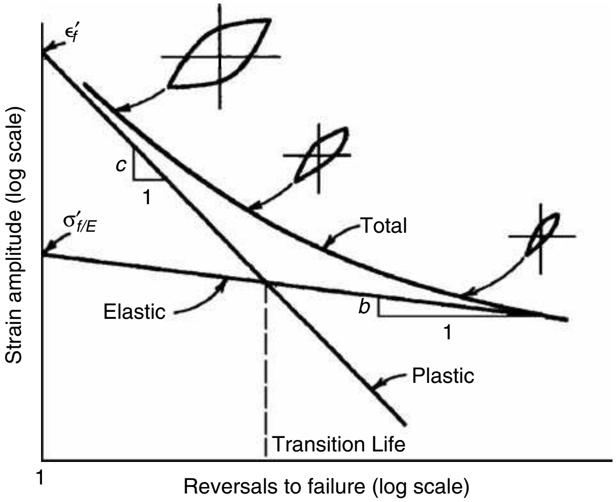

FIGURE 11.4.12 Representation of elastic, plastic, and total strain amplitude vs. fatigue life. [From Figure 11.7, p. 399, in reference 1.]

where $\Delta\varepsilon_e/2$ and $\Delta\varepsilon_p/2$ are the elastic and plastic strain amplitudes, respectively, K' is the cyclic strength coefficient, and n' is the cyclic strain hardening exponent.

The empirical Coffin-Manson equation, Equation 11.4.33, relates strain amplitude with numbers of fatigue cycles to nucleate a crack:

$$\frac{\Delta\varepsilon}{2} = \frac{\Delta\varepsilon_e}{2} + \frac{\Delta\varepsilon_p}{2} = \frac{\sigma_f'}{E}\left(2N_f\right)^b + \varepsilon_f'\left(2N_f\right)^c \tag{11.4.33}$$

where ε_f' is the fatigue ductility coefficient (which is experimentally found to be approximately equal to the true fracture ductility ε_f in monotonic tension) and c is the fatigue ductility exponent (which is in the range of –0.5 to –0.7 for most metals).[2]

This characterization is based on the observation that the logarithm of elastic and plastic strain amplitudes, $\Delta\varepsilon_e/2$ and $\Delta\varepsilon_p/2$, plotted against the logarithm of the number of load reversals to failure, $2N_f$, follows a linear relationship for metallic materials, as shown in Figure 11.4.12. The transition life, $(2N_f)_t$, which is the life at which the elastic and plastic strain amplitudes are equal, is given by

$$\left(2N_f\right)_t = \left(\frac{\varepsilon_f' E}{\sigma_f'}\right)^{1/(b-c)} \tag{11.4.34}$$

At short fatigue lives, that is, when $2N_f << (2N_f)_t$, plastic strain amplitudes are more dominant than the elastic strain amplitude and the fatigue life of the material is controlled by *ductility*. At long fatigue lives, that is, when $2N_f >> (2N_f)_t$, the elastic strain amplitude is more significant than the plastic strain amplitude and the fatigue life is dictated by *fracture strength*. Optimizing overall fatigue properties requires a judicious balance between strength and ductility.[2]

Mean stress effects can be incorporated into the strain-life method by using Manson's rule:

$$\frac{\Delta\varepsilon}{2} = \left(\frac{\sigma_f' - \sigma_m}{E}\right)\left(2N_f\right)^b + \varepsilon_f'\left(\frac{\sigma_f' - \sigma_m}{\sigma_f'}\right)^{1/n'}\left(2N_f\right)^c \tag{11.4.35}$$

Manson's rule does not account for stress relaxation at high plastic strains. Descriptions of other relations that account for effects of nonzero mean stress can be found in references 2 and 3.

Evaluating stress and strain amplitudes in regions of stress concentration such as notches requires the complex task of implementing three-dimensional elastic-plastic finite element modeling procedures with appropriate constitutive relations. To estimate the local stresses and strains in notches, Neuber's rule[10] is often used in conjunction with cyclic stress-strain properties and the fatigue stress concentration factor. If loads are such that the overall structural member is nominally elastic, then Neuber's rule can be adapted as shown here:

$$\Delta\sigma\,\Delta\varepsilon = \frac{(K_f\,\Delta S)^2}{E} \tag{11.4.36}$$

where K_f is the fatigue stress concentration factor and ΔS the nominal stress range. This relation is used in conjunction with Equation 11.4.32 to obtain the cyclic stress amplitude, using the nonlinear algebraic relation shown in Equation 11.4.37:

$$(\Delta\varepsilon)^2 - 2\Delta\varepsilon\left(\frac{(K_f\Delta S)^2}{2K'E\Delta\varepsilon}\right)^{1/n'} = \frac{(K_f\Delta S)^2}{E^2} \tag{11.4.37}$$

Once the cyclic strain amplitude, $\Delta\varepsilon/2$, is evaluated using Equation 11.4.37, fatigue life can be computed using Equation 11.4.33. If nonzero mean stress effects are present, Equation 11.4.35 can be used. Neuber's rule treats the stresses and strains in a notch from a uniaxial perspective, even though the state of stress is triaxial. The strain amplitude evaluated by Equation 11.4.37 can be viewed as von Mises or Tresca equivalent strain amplitude.

Critical Plane Methods and Nonproportional Loading

Cracks have been experimentally observed to nucleate and grow on specific planes, termed "critical planes." These critical planes can be planes of maximum shear stress or maximum tensile stress, depending on the material and loading conditions. *Critical plane models* are multiaxial fatigue models relating the fatigue damage process to stresses and/or strains on these planes. These models can predict not only the fatigue life but also the orientation of the crack or failure plane.[3] A detailed discussion of several critical plane models in use can be found in reference 3. The critical plane model by Fatemi and Socie[11] is presented here in Equation 11.4.38:

$$\frac{\Delta\gamma_{\max}}{2}\left(1 + k\frac{\sigma_{n,\max}}{\sigma_y}\right) = \frac{\tau'_f}{G}\left(2N_f\right)^{b_o} + \gamma'_f\left(2N_f\right)^{c_o} \tag{11.4.38}$$

The left-hand side of Equation 11.4.38 represents the fatigue damage parameter based on the critical plane model, where $\Delta\gamma_{\max}/2$ represents the maximum shear strain amplitude and $\sigma_{n,\max}$ is the maximum normal stress acting on the maximum shear strain amplitude plane. The damage parameter is an attempt to model the crack-tip driving forces using the shear strain along a crack face and the normal stress perpendicular to the crack that tends to separate the crack surfaces. At the microscopic level, cracks are shaped irregularly because the crack grows through the material grain structure. During cyclic shear loading, this causes friction forces and interlocking between the crack surfaces (i.e., crack closure). A tensile stress perpendicular to the crack plane tends to separate crack surfaces and reduce the interlocking and frictional forces, which in turn increases the crack-tip driving force. The material constant, k, can be found by fitting fatigue data from simple uniaxial tests to fatigue data from simple torsion tests. If test data are not available, $k \approx 1$ serves as a first approximation

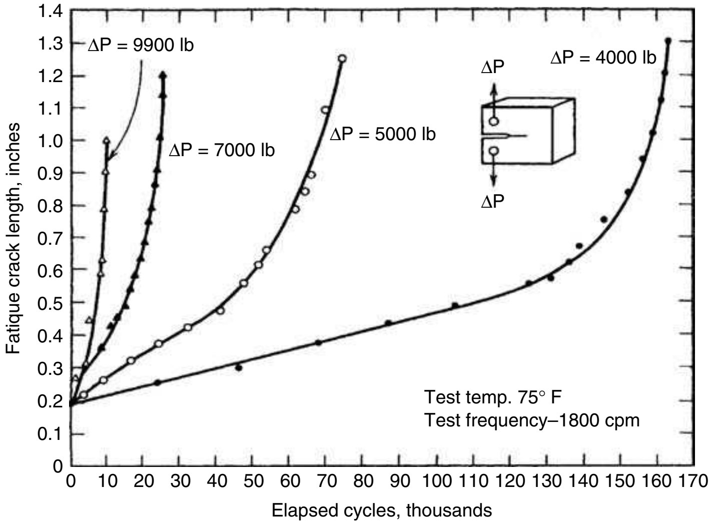

FIGURE 11.4.13 Effect of cyclic load range on crack growth in Ni-Mo-V steel for released tension loading (R=0). [From Figure 8.21, p. 295, in reference 1.]

Mean or residual stress effects on fatigue life in this model are accounted for by the maximum normal stress term:

$$\sigma_{n,\max} = \sigma_{n,a} + \sigma_{n,m} \tag{11.4.39}$$

where $\sigma_{n,a}$ and $\sigma_{n,m}$ are the alternating normal and mean or residual normal stresses, respectively.[3,11]

The right-hand side of Equation 11.4.38 represents the shear-strain life model, similar to Equation 11.4.33, where G is the shear modulus, τ'_f is the shear fatigue strength coefficient, γ'_f is the shear ductility coefficient, and b_0 and c_0 are shear fatigue strength and shear fatigue ductility exponents, respectively. These properties can be estimated from uniaxial strain-life properties as $\tau_f' \approx \sigma_f'/\sqrt{3}$, $b_o \approx b$, $\gamma_f' \approx \sqrt{3}\varepsilon_f'$ and $c_o \approx c$.[3]

The Fatemi and Socie model is applicable for *nonproportional* loading conditions. This can occur if the axial and torsional cyclic loading are out of phase, for example, leading to principal directions of the alternating stresses varying with respect to the loading axes, as a periodic function of time. The additional hardening that can result from nonproportional loading is incorporated by the maximum normal stress term since additional hardening results in an increase in the alternating normal stress, $\sigma_{n,a}$.

Linear Elastic Fracture Mechanics (LEFM) Approach for Fatigue Crack Growth

The fatigue crack growth rate under conditions of constant amplitude stress reversals is characterized in terms of the crack length increment per cycle, da/dN. Values of da/dN for different loading conditions are determined from experimentally measured changes in crack length over a certain number of elapsed fatigue cycles. When the applied stress range is held constant, the rate of growth of a fatigue crack generally climbs with an increasing number of fatigue cycles, although there can be exceptions to this trend. Figure 11.4.13 shows a typical fatigue crack growth curve. The mechanisms of crack propagation described in this section apply to those of “long” through-the-thickness fatigue cracks, typically several millimeters or more in all directions. Detailed discussions on small crack growth and what constitutes a “small” crack can be found in reference 2. It is assumed that conditions of LEFM are met, that is, the zone of plastic deformation ahead of the advancing fatigue crack is a minor perturbation in an otherwise elastic field.

Paris, Gomez, and Anderson[12] suggest that for a cyclic variation of imposed stress field, under LEFM assumptions, the rate of fatigue crack growth should be based on the stress intensity factor range:

$$\Delta K = K_{\max} - K_{\min} \tag{11.4.40}$$

where $K_{\max}$ and $K_{\min}$ are the maximum and minimum values, respectively of the SIF during a fatigue stress cycle, and, following Equation 11.4.21, are given by

$$\begin{aligned} K_{\max} &= C\sigma_{\max}\sqrt{\pi a}, \quad K_{\min} = C\sigma_{\min}\sqrt{\pi a} \\ \Delta K &= C\Delta\sigma\sqrt{\pi a}, \quad \Delta\sigma = \sigma_{\max} - \sigma_{\min} \end{aligned} \tag{11.4.41}$$

The fatigue crack growth rate is related to the SIF range by the power law relationship:[12]

$$\frac{da}{dN} = C_m\left(\Delta K\right)^m \tag{11.4.42}$$

where C_m and m are scaling constants and are influenced by variables such as environment, material microstructure, cyclic load frequency, waveform, test temperature, and load ratio R. The exponent m is typically between two and four for ductile alloys.[2] Equation Equation 11.4.42 is widely known as the "Paris law," and is applicable for single-mode far-field loading. This power law relationship was based on the observation that the log-log plot of da/dN. vs. ΔK was a straight line fit over the "Region II" phase, as seen in Figure 11.4.14(b). Figure 11.4.14(a) shows the experimentally measured fatigue crack growth

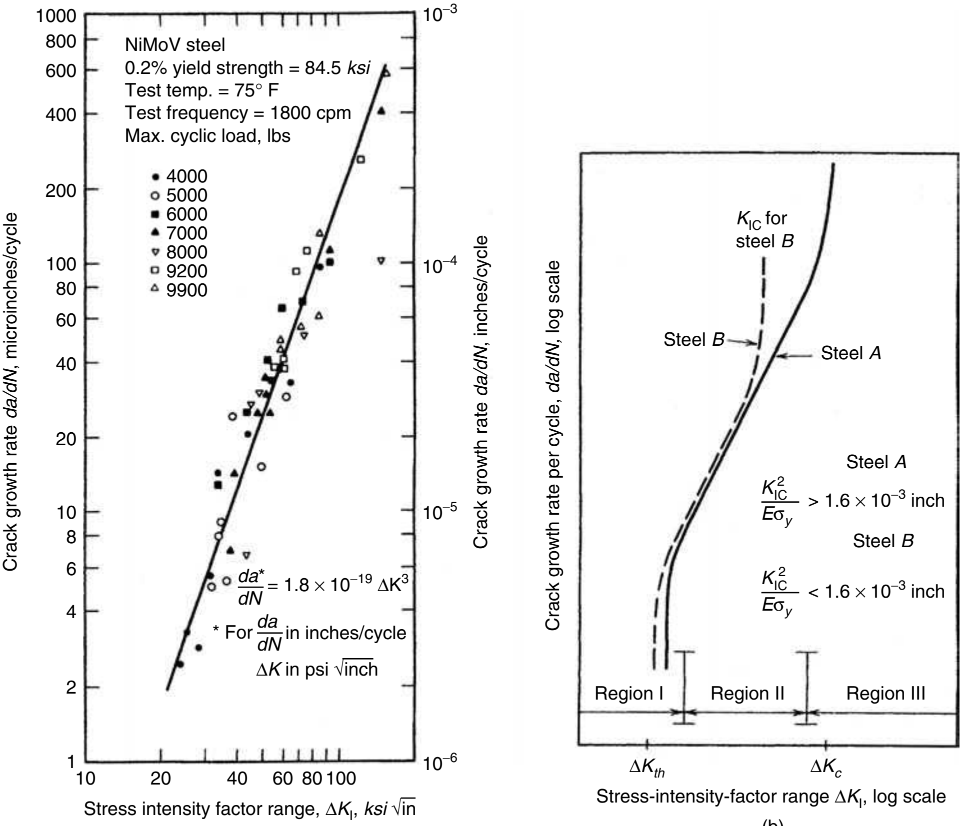

(a) (b)

FIGURE 11.4.14 Crack growth rate as a function of stress intensity factor range (a) Experimental data for Ni-Mo-V steel [From Figure 8.22, p. 296, in reference 1]; (b) Fatigue crack growth rate in steel for regions I, II and III. [From Figure 8.23, p. 297, in reference 1.]

curve for Ni-Mo-V steel along with the curve fit parameters. Region I in Figure 11.4.13(b) corresponds to the crack nucleation region, and Region III corresponds to the transition into the unstable regime of rapid crack extension. The Paris law given by Equation 11.4.42 is applicable only to Region II, also called the Paris regime, which represents the stable crack growth phase. At extreme values of ΔK, both below and above that of the Paris regime, there is a steep rise in crack growth rates with increasing ΔK. The threshold SIF range, ΔK_{th}, shown in Figure 11.4.14(b), represents a lower limit below which cracks are either dormant or grow at undetectable rates. Region III corresponds to the transition into unstable regime of rapid crack growth where ΔK values are high.

The microscopic mode of fatigue crack growth in Region I is strongly affected by the slip characteristics of the material, characteristic microstructural dimensions, applied stress level, and the extent of near tip plasticity. When the crack and the zone of plastic deformation surrounding the crack tip are confined to within a few grain diameters, crack growth occurs predominantly by single shear, in the direction of primary slip system. This single slip mechanism leading to a zig-zag crack path is termed Region I or Stage I crack growth.[2] A detailed discussion of Region I crack growth is given in reference 2.

Paris and Erdogan[13] present crack growth experiments on aluminum alloys with different combinations of stress range and crack length with different specimen geometries that unambiguously established the validity of such a characterization. Although Equation 11.4.42 is empirical, it has remained one of the most useful expressions in the analysis of fatigue crack for a vast spectrum of materials and test conditions.[2]

Fatigue life calculations in the Paris regime are done by combining Equation 11.4.41 and Equation 11.4.42 to obtain

$$\frac{da}{dN} = C_m \left(C \, \Delta\sigma \sqrt{\pi a} \right)^m \tag{11.4.43}$$

and integrating from an assumed initial crack size a_o to a critical crack size a_f. The resulting fatigue life is[2]

$$\begin{aligned} N_f &= \frac{2}{(m-2) C_m C^m (\Delta\sigma)^m \pi^{m/2}} \left\{ \frac{1}{(a_o)^{(m-2)/2}} - \frac{1}{(a_f)^{(m-2)/2}} \right\}, \quad \text{for } m \neq 2 \\ N_f &= \frac{1}{C_m C^2 (\Delta\sigma)^2 \pi} \ln \frac{a_f}{a_o}, \quad \text{for } m = 2 \end{aligned} \tag{11.4.44}$$

In general, C varies with a and hence the integration is performed numerically. Note that when $a_o << a_f$ (which is usually the case for ductile alloys), N_f is not very sensitive to a_f, but is strongly influenced by the choice of a_o.[2]

Mixed-Mode Loading Conditions

Fatigue crack growth under the influence of multiaxial far-field stress states results in mixed-mode loading conditions at the crack tip. Even when a fatigue crack is subjected to purely tensile far-field loading, mixed-mode conditions may prevail ahead of the crack tip if it is inclined to the tensile axis, or microstructural and environmental factors promote a nonplanar fatigue crack growth. A characteristic of mixed-mode fatigue cracks is that they can grow in a nonplanar non-self similar manner, that is, the crack changes its direction of growth.[2,3] Different combinations of mixed-mode loading can exist from multiaxial loads. For instance, in simple torsion of smooth shafts, surface cracks can form and grow in longitudinal and/or transverse directions along the maximum shear planes, where mixed-mode II and III exists along the crack front. Cracks can also form and grow along the ±45-degree angle to the axis of the shaft along planes of maximum principal stress where they grow in Mode I. In plate components with edge or central cracks under in-plane biaxial tension mixed-mode I and II, crack growth prevails. However, the Mode I contribution often becomes dominant after a short period of crack growth.[3]

Several parameters have been used to correlate fatigue crack growth rates under mixed-mode conditions such as equivalent stress intensity factors, equivalent strain intensity factors, strain energy density, and the *J*-integral. Fatigue cracks can also deflect in new directions and branch into multiple cracks under mixed-mode loading conditions. References 2 and 3 discuss these complex fatigue crack growth issues in detail.

References

1. Collins, J. 1991. *Failure of Materials in Mechanical Design*, 2nd ed., Wiley Interscience.
2. Suresh, S. 1991. *Fatigue of Materials*. Cambridge University Press, Cambridge, U.K.
3. Stephens, R.I., Fatemi, A., Stephens, R.R., and Fuchs, H.O. 2001. *Metal Fatigue in Engineering*, 2nd ed., Wiley Interscience, New York.
4. Norton, R.L. 1996. *Machine Design*. Prentice Hall, Englewood Cliffs, NJ.
5. Stouffer, D.C. and Dame, L.T. 1995. *Inelastic Deformation of Metals: Models, Mechanical Properties, and Metallurgy.* Wiley Interscience, New York.
6. Dowling, N.E. 1993. *Mechanical Behavior of Materials*. Prentice-Hall, Englewood Cliffs, NJ.
7. Progress in Measuring Fracture Toughness and Using Fracture Mechanics, *Materials Research Standards*, ASTM (March 1964): 103–19.
8. Tada, H., Paris, P.C., and Irwin, G.E. 1985 *The Stress Analysis of Cracks Handbook*, 2nd ed. Paris Productions, Inc., St. Louis, MO.
9. Wöhler, A. Versuche über die Festigkeit der Eisenbahnwagenachsen, *Zeitschrift für Bauwesen*, Vol. 10, 1860; English summary (1867), *Engineering*, Vol. 4, 160-1.
10. Neuber, H., Theory of stress concentration for shear-strained prismatical bodies with arbitrary nonlinear stress-strain law. *J. of Appl. Mech.*, ASME Transactions, Vol. 8, pp. 544–50, 1961.
11. Fatemi, A. and Socie, D.F., A critical plane approach to multiaxial fatigue damage including out-of-phase loading, *Fatigue Fract. Eng. Mater. Struct.*, Vol. 11, No. 3, 1988, p. 149.
12. Paris, P.C., Gomez, M.P., and Anderson, W.P., A rational analytic theory of fatigue, *The Trend in Engineering*, Vol. 13, pp. 9–14, 1961.
13. Paris, P.C. and Erdogan, F., A critical analysis of crack propagation laws, *J. of Basic Eng.*, Vol. 85, pp. 528–34, 1963.

11.5 Design Optimization

Nam Ho Kim

Introduction

The design of a structural system has two categories: designing a new structure and improving the existing structure to perform better. The design engineer's experience and creative ideas are required in the development of a new structure, since it is difficult to quantify a new design using mathematical measures. Recently, limited inroads have been made in the creative work of the structural design using mathematical tools.[1] However, the latter evolutionary process is encountered much more frequently in engineering designs. For example, how many times does an automotive company design a new car using a completely different concept? The majority of a design engineer's work concentrates on improving the existing vehicle so that the new car can be more comfortable, more durable, and safer. In this section, we will focus on a design's evolutionary process by using mathematical models and computational tools.

Structural design is a procedure for improving or enhancing the performance of a structure by changing its parameters. A *performance measure,* which can be quite general in engineering fields, can include the following: the weight, stiffness, and compliance of a structure; the fatigue life of a mechanical component; the noise in the passenger compartment; the vibration level; the safety of a vehicle in a crash, and so forth. However, this does not address such aesthetic measures as whether a car or a structural design is attractive to customers. All performance measures are presumed to be measurable quantities. System parameters are variables that a design engineer can change during the design process. For example, the thickness of a vehicle body panel can be changed to improve vehicle performance. The cross section of a beam can be changed in designing bridge structures. System parameters that can be changed during the design process are called *design variables*, even including the geometry of the structure.

Great strides have been made during the past decade in computer-aided design (CAD) and computer-aided engineering (CAE) tools for mechanical system development. Discipline-oriented simulation capabilities in structures, mechanical system dynamics, aerodynamics, control systems, and numerous related fields are now being used to support a broad range of mechanical system design applications. Integration of these tools to create a robust simulation-based design capability, however, remains a challenge. Based on their extensive survey of the automotive industry in the mid-1980s, Clark and Fujimoto[2] concluded that simulation tools in support of vehicle development were on the horizon but not yet ready for pervasive application. The explosion in computer, software, and modeling and simulation technology that has occurred since the mid-1980s suggests that high-fidelity tools for simulation-based design are now at hand. Properly integrated, they can resolve uncertainties and significantly affect mechanical system design.

Modern developments of structural design are closely related to concurrent engineering environments by which multidisciplinary simulation, design, and manufacturing are possible. Even though concurrent engineering is not the focus of this section, we want to emphasize structural design as a component of concurrent engineering. An important feature of the concurrent engineering is database management using the CAD tool. Structural modeling and most interfaces are achieved using the CAD tool. Thus, design parameterization and structural model updates have to be carried out within the CAD model. Through the design parameterization, CAD, CAE, and CAM procedures are interrelated to form a concurrent engineering environment.

The structural engineering design in the simulation-based process consists of structural modeling, design parameterization, structural analysis, design problem definition, design sensitivity analysis, and design optimization. Figure 11.5.1 is a flowchart of the structural design process in which computational analysis and mathematical programming play essential roles in the design. The success of the system-level, simulation-based design process strongly depends on a consistent design parameterization, an accurate structural and design sensitivity analysis, and an efficient mathematical programming algorithm.

A design engineer simplifies the physical engineering problem into a mathematical model that can represent the physical problem up to the desired level of accuracy. A mathematical model has parameters that are related to the system parameters of the physical problem. A design engineer identifies those design variables to be used during the design process. *Design parameterization*, which allows the design engineer to define the geometric properties for each design component of the structural system being designed, is one of the most important steps in the structural design process. The principal role of design parameterization is to define the geometric parameters that characterize the structural model and to collect a subset of the geometric parameters as design variables. Design parameterization forces engineering teams in design, analysis, and manufacturing to interact at an early design stage, and supports a unified design variable set to be used as the common ground to carry out all analysis, design, and manufacturing processes. Only proper design parameterization will yield a good optimum design, since the optimization algorithm will search within a design space that is defined for the design problem. The design space is defined by the type, number, and range of design variables. Depending on whether it is a concept or detailed design, selected design variables could be non-CAD based parameters. An example of such a design variable is a tire's stiffness characteristic in vehicle dynamics during an early vehicle design stage.

Structural analysis can be carried out using experiments in actual or reduced scale, which is a straightforward and still prevalent method for industrial applications. However, the expense and inefficiency involved in fabricating prototypes make this approach difficult to apply. The analytical method may resolve these difficulties, since it approximates the structural problem as a mathematical model and solves

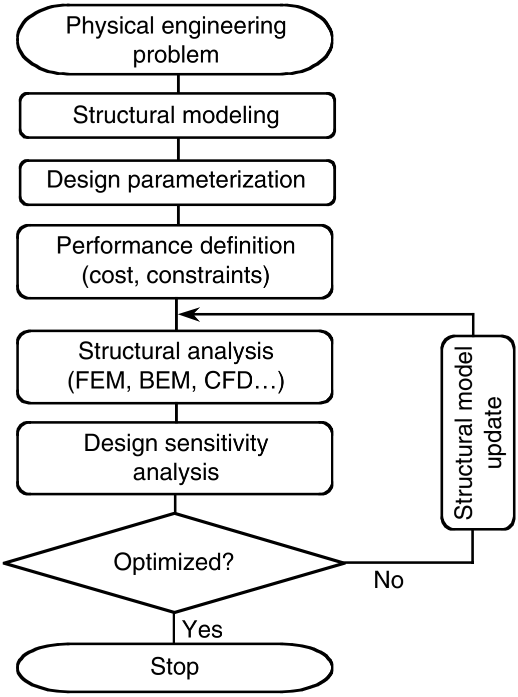

FIGURE 11.5.1 Structural design process.

it in a simplified form. The mathematical model can be used to evaluate the performance measures of a structural problem. However, the analytical method has limitations even for simple structural problems.

With the emergence of various computational capabilities, most analytical approaches to mathematical problems have been converted to numerical approaches, which are able to solve very complicated, real engineering applications. Finite element analysis (FEA), boundary element analysis (BEA), and meshfree analysis are a short list of mathematical tools used in structural analysis. The development of FEA is one of the most remarkable successes in structural analysis. The governing differential equation of the structural problem is converted to its integral form and then solved using FEA. Vast amounts of literature are published regarding FEA; for example, refer to Reference 3 and the references therein. The complex structural domain is discretized by a set of nonoverlapping, simple-shaped finite elements, and an equilibrium condition is imposed on each element. By solving a linear system of matrix equations, we can compute the performance measures of a structure in the approximated domain. The accuracy of the approximated solution can be improved by reducing the size of finite elements and/or increasing the order of approximation within an element.

Selection of a design space and an analysis method must be carefully determined since the analysis, both in terms of accuracy and efficiency, must be able to handle all possible designs in the chosen design space. That is, the larger the design space, the more sophisticated the analysis capability must be. For example, if larger shape design changes are expected during design optimization, mesh distortion in FEA could be a serious problem and a finite element model that can handle large shape design changes must be used.

A *performance measure* in a simulation-based design is the result of structural analysis. Based on the evaluation of analysis results, such engineering concerns as high stress, clearance, natural frequency, or mass can be identified as performance measures for design improvement. Typical examples of performance measures are mass, volume, displacement, stress, compliance, buckling, natural frequency, noise, fatigue life, and crashworthiness. A definition of performance measures permits the design engineer to specify the structural performance from which the sensitivity information can be computed.

Cost and constraints can be defined by combining certain performance measures with appropriate constraint bounds for interactive design optimization. The *cost function*, sometimes called the *objective function*, is minimized (or maximized) during optimization. Selection of a proper cost function is an important decision in the design process. A valid cost function has to be influenced by the design variables of the problem; otherwise, it is not possible to reduce the cost by changing the design. In many situations, an obvious cost function can be identified. In other situations, the cost function is a combination of different structural performance measures. This is called a *multiobjective* cost function.

Constraint functions are the criteria that the system has to satisfy for each feasible design. Among all design ranges, those that satisfy the constraint functions are candidates for the optimum design. For example, a design engineer may want to design a bridge whose weight is minimized and whose maximum stress is less than the yield stress. In this case, the cost function, or weight, is the most important criterion to be minimized. However, as long as stress, or constraint, is less than the yield stress, the stress level is not important.

Design sensitivity analysis is used to compute the sensitivity of performance measures with respect to design variables. This is one of the most expensive and complicated procedures in the structural optimization process. Structural design sensitivity analysis is concerned with the relationship between design variables available to the engineer and the structural response determined by the laws of mechanics. Design sensitivity information provides a quantitative estimate of desirable design change, even if a systematic design optimization method is not used. Based on the design sensitivity results, a design engineer can decide on the direction and amount of design change needed to improve the performance measures. In addition, design sensitivity information can provide answers to "what if" questions by predicting performance measure perturbations when the perturbations of design variables are provided.

Substantial literature has emerged in the field of structural design sensitivity analysis.[4] Design sensitivity analysis of structural systems and machine components has emerged as a much-needed design tool, not only because of its role in optimization algorithms but also because design sensitivity information can be used in a computer-aided engineering environment for early product trade-off in a concurrent design process.

Recently, the advent of powerful graphics-based engineering workstations with increasing computational power has created an ideal environment for making interactive design optimization a viable alternative to more monolithic batch-based design optimization. This environment integrates design processes by letting the design engineer create a geometrical model, build a finite element model, parameterize the geometric model, perform FEA, visualize FEA results, characterize performance measures, and carry out design sensitivity analysis and optimization.

Design sensitivity information can be used during a postprocessing of the interactive design process. The principal objective of the postprocessing design stage is to utilize the design sensitivity information to improve the design. Figure 11.5.2 shows the four-step interactive design process: (1) to visually display design sensitivity information, (2) to carry out what-if studies, (3) to make trade-off determinations, and (4) to execute interactive design optimization. The first three design steps, which are interactive modes of the design process, help the design engineer improve the design by providing structural behavior information at the current design stage. The last design step, which could be either interactive or a batch mode of the design process, launches a mathematical programming algorithm to perform design optimization. Depending on the design problem, the design engineer could use some or all of the four design steps to improve the design at each iterative step. As a result, new designs could be obtained from what-if, trade-off, or interactive optimization design steps.

For the purposes of design optimization, a mathematical programming technique is often used to find an optimum design that can best improve the cost function within a feasible region. Mathematical programming generates a set of design variables that require performance values from structural analysis and sensitivity information from design sensitivity analysis to find an optimum design. Thus, the structural model has to be updated for a different set of design variables supplied by mathematical programming. If the cost function reaches a minimum with all constraint requirements satisfied, then an optimum design is obtained.

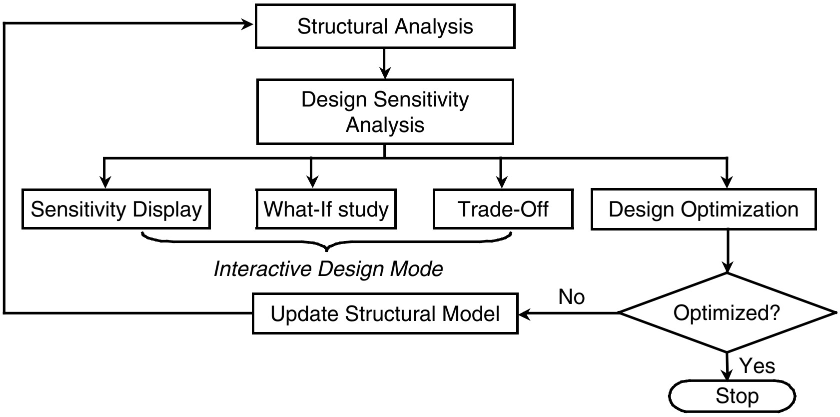

FIGURE 11.5.2 Postprocessing design stage.

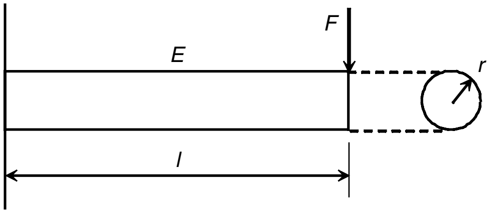

FIGURE 11.5.3 Parameters defining circular cross-sectional cantilever beam.

Structural Design Parameterization

In structural modeling, the physical problem is represented by mathematical expressions, which contain parameters for defining that problem. For example, the cantilever beam in Figure 11.5.3 has parameters that include the length l, the radius of cross section r, and Young's modulus E. These parameters, which define the system, are called *design variables*. If design variables are determined, then the structural problem can be analyzed. Obviously, different design variable values usually yield different analysis results. The aim of the structural design process is to find the values of design variables that satisfy all requirements.

All design variables must satisfy the physical requirements of the problem. For example, length l of the cantilever beam in Figure 11.5.3 cannot have a negative value. Physical requirements define the design variable bounds. Valid design variables may have to take into account various manufacturing requirements. For example, the radius of a cantilever beam satisfies its physical requirement if r is a positive number. However, in real applications, the circular cross-sectional beam may not be manufactured if its radius is bigger than r^0. Thus, the range of feasible design can be stated as $0 < r \leq r^0$.[1] In addition, the design engineer may want to impose certain design constraints on the problem. For example, the maximum stress of the beam may not exceed σ^0 and the maximum tip displacement of the beam must not be greater than z^0. A set of design variables that satisfy the constraints is called a *feasible design*, whereas a set that does not satisfy constraints is called an *infeasible design*. It is difficult to determine whether a current design is feasible unless the structural problem is analyzed. For complicated structural problems, it may not be simple to choose the appropriate design constraints so that the feasible region is not empty.

There are two types of design variables: continuous and discrete. Many design optimization algorithms consider design variables to be continuous. In this section, we presume that all design variables are

---

[1] In general, the bounds of design variables are denoted as $r^L \leq r \leq r^U$ where r^L is called the lower bound and r^U is called the upper bound, respectively.

continuous within their lower- and upper-bound limits. However, discrete design problems often appear in real engineering problems. For example, due to manufacturing limitations, the structural components of many engineering systems are only available in fixed shapes and sizes. Discrete design variables can be thought of as continuous design variables with constraints. As a result, it is more expensive to obtain an optimum design for a problem with discrete design variables. It is possible, however, to solve the problem assuming continuous design variables. After obtaining an optimum solution for the design problem, the nearest discrete values of the optimum design variables can be tested for feasibility. If the nearest discrete design variables are not feasible, then several iterations can be carried out to find the nearest feasible design.

It is convenient to classify design variables according to their characteristics. In the design of structural systems made of truss, beam, membrane, shell, and elastic solid members, there are five kinds of design variables: material property design variables such as Young's modulus; sizing design variables such as thickness and cross-sectional area; shape design variables such as length and geometric shape; configuration design variables such as orientation and location of structural components; and topological design variables.

The Material Property Design Variable

In structural modeling, the material property is used as a parameter of the structural problem. Young's modulus and Poisson's ratio, for example, are required in the linear elastic problem. If these material properties are subject to change, then they are called *material property design variables*. These kinds of design variables do not appear in regular design problems, since in most cases material properties are presumed to be constant. Analysis using such a constant material property is called the deterministic approach. Another approach uses probability and assumes that material properties are not constant but distributed within certain ranges. This is called the probabilistic approach and is more practical, since a number of experiments will usually yield a number of different test results. In this case, material properties are no longer considered to be constant and can therefore be used as design variables.

The Sizing Design Variable

The *sizing design variable* is related to the geometric parameter of the structure, and it is often called a parametric design variable. For example, most automotive and airplane parts are made from plate/shell components. It is natural that a design engineer wants to change the thickness (or gauge) of the plate/shell structure in order to reduce the weight of the vehicle. For a structural model, plate thickness is considered a parameter. However, the global geometry of the structure does not change. Plate thickness can be considered a sizing design variable. The sizing design variable is similar to the material property design variable in the sense that both variables change the parameters of the structural problem.

Another important type of sizing design variable is the cross-sectional geometry of the beam and truss. Figure 11.5.4 provides some examples of the shapes and parameters that define these cross sections. In the structural analysis of truss, for example, the cross-sectional area is required as a parameter of the problem. If a rectangular cross section is used, then the area would be defined as $A = b \times h$. Thus, without any loss of generality, b and h can be considered design variables of the design problem.

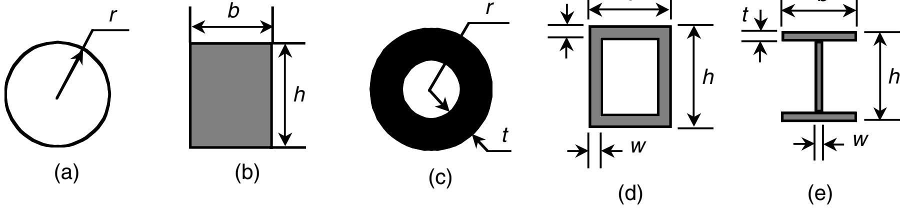

FIGURE 11.5.4 Sizing design variables for cross-sectional areas of truss and beam. (a) solid circular; (b) rectangular; (c) circular tube; (d) rectangular tube; (e) I-section.

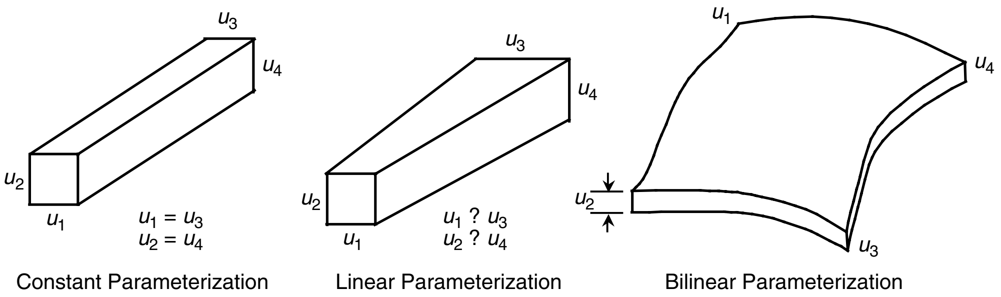

(a) Line Design Component (b) Surface Design Component

FIGURE 11.5.5 Line and surface design parameterization.

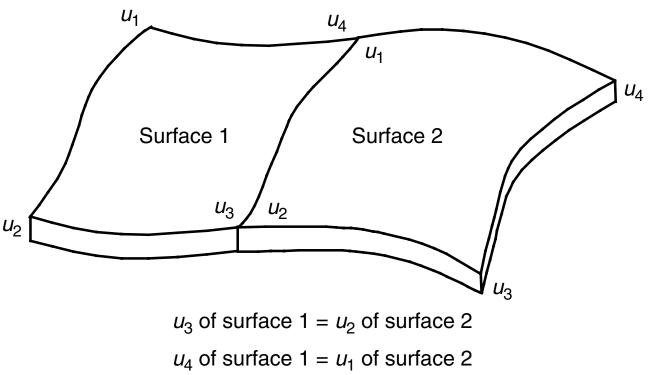

FIGURE 11.5.6 Design variable linking.

In this section, several possible design parameterizations, such as constant and linear designs as described in Figure 11.5.5, are introduced for the line and surface design components. These are not at all the only possible design parameters, and other more complicated design parameterizations can be used. However, the method presented in this section can be extended to other complicated design parameterizations. One important thing to consider when more complicated design parameterizations are used is that the finite element model must be sophisticated enough to support the design parameterization method used. Geometric parameters can be defined at the end grid points of a line, or at the corner points of a surface. A bilinear thickness distribution can be used to characterize a surface design component, as shown in Figure 11.5.5(b). Note that each dimension that defines the cross-sectional shape, such as width and height in Figure 11.5.5(a), can be treated as a design variable, and be allowed to vary to the same degree as the corresponding variable at the other end (constant parameterization), or to a different degree (linear parameterization). Moreover, in order to maintain design continuity for a symmetric design, or to reduce the number of design variables, design variables can change either independently of, or proportionally to, certain variables across design components through design variable linking, as shown in Figure 11.5.6.

Line Design Components

A three-dimensional line component can be used for truss or beam design components. A truss design component can handle tensile and compressive load and may be composed of several truss finite elements. A beam design component can handle tensile, compressive, and bending load. A linearly tapered cross-sectional shape can be considered within the design component. There are three cross-section types for this design component: symmetric, un-symmetric, and general. Figure 11.5.7 illustrates the geometry of a line design component.

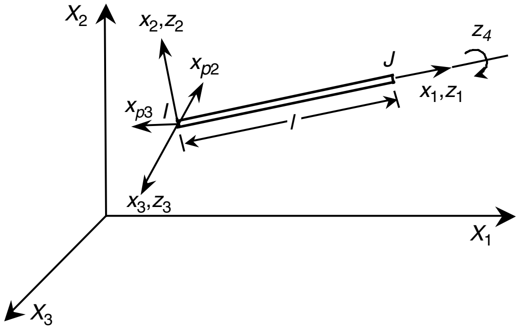

FIGURE 11.5.7 Line design component.

Material properties, such as mass density and Young's modulus, and geometric parameters that define the cross-sectional shape can be taken as design variables along the axial axis x_1. All material property design variables are assumed to be constant along the design component's axial axis.

The geometric design variables that can linearly vary along the axis of the design component are the dimensions of each cross-section, that is, r for a solid and hollow circular cross section, and b and h for other cross sections, as shown in Table 11.5.1 and Table 11.5.2.

TABLE 11.5.1 Symmetric Cross Sections

		Design Variable[a]					
Cross-Sectional Shape		1	2	3	4	5	6
Solid circular	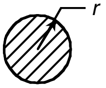	r	E	ρ	—	—	—
Solid rectangular	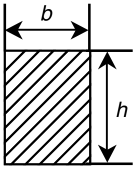	h	b	E	ρ	—	—
Hollow circular	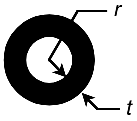	r	t	E	ρ	—	—
Hollow rectangular	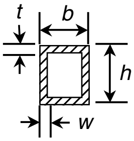	h	b	t	w	E	ρ
I-section	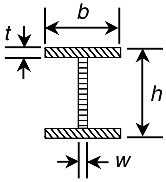	h	b	t	w	E	ρ

[a] E is Young's modulus and ρ is the mass density.

TABLE 11.5.2 Unsymmetric Cross Sections

Cross-Sectional Shape		Design Variable						
		1	2	3	4	5	6	7
Channel	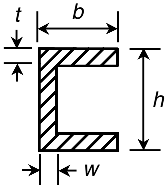	*h*	*b*	*t*	*w*	*E*	ρ	—
Angle	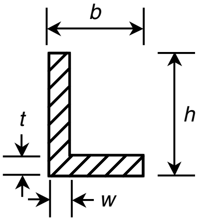	*h*	*b*	*t*	*w*	*E*	ρ	—
T-section	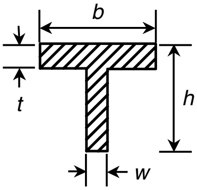	*h*	*b*	*t*	*w*	*E*	ρ	—
Unsymmetric I-section	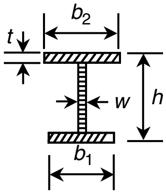	*h*	b_1	b_2	*t*	*w*	*E*	ρ

Proportionality can be used between two geometric design variables within a design component through design variable linking. Such proportional design variables are used to meet local buckling requirements for a structural design specification, to maintain geometric proportionality, or to reduce the number of design variables. The pairs of geometric design variables that may be considered for proportionality purposes are (t,b) and (w,h) for a hollow rectangle, an I-section, (b,h) for a solid rectangle, and (t,r) for a hollow circle.

The symmetric cross section has two perpendicular axes of symmetry, as shown in Table 11.5.1. These two axes are the principal axes of the cross section, and are usually taken as two component coordinates. The component's axial axis is assumed to be the same as the centroidal axis. Solid and hollow circles, solid and hollow rectangles, and the I-section are all placed in this category.

The unsymmetric cross section has either only one axis of symmetry, or no symmetry with some shape regularity, as shown in Table 11.5.2. The channel, angle, T-section, and unsymmetric I-section all fit into this category. The component coordinates x_2 and x_3 may be different from the principal axes x_{p2} and x_{p3}, respectively. The centroidal axis is assumed to coincide with the axial axis x_1 of the truss design component.

The general cross section has no regular shape and may be composed of several thin-walled segments, as shown in Table 11.5.3.

TABLE 11.5.3 General Cross Sections

	Design Variable					
General Cross-Sectional Shape	1	2	3	…	$2n+1$	$2n+2$
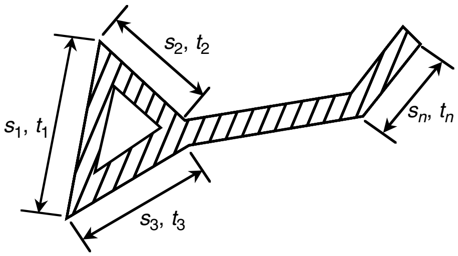	s_1	t_1	s_1	…	E	ρ

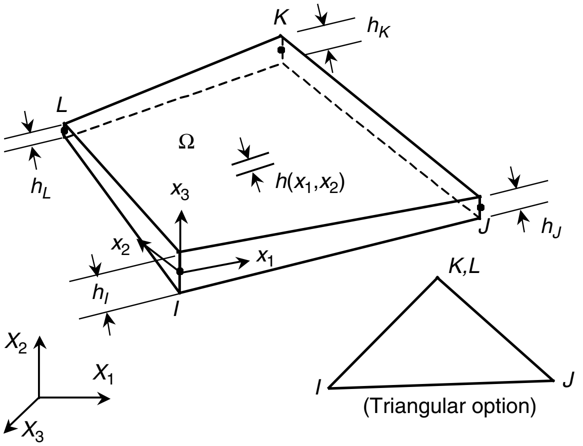

FIGURE 11.5.8 Surface design component.

Surface Design Components

A plane stress component can handle both an in-plane tensile and a compressive load. A shell component can handle an in-plane tensile, compressive, and bending load. The design component may be composed of several plane stress/shell finite elements. Figure 11.5.8 illustrates the geometry of a plane stress/shell design component.

Surface component design variables include thickness, mass density, and Young's modulus. Surface thickness is parameterized using a bilinear shape function. Four geometric design variables are defined for each surface design component: thickness h_I, h_J, h_K, and h_L at grid points I, J, K, and L, respectively, as shown in Figure 11.5.8 and Table 11.5.4.

The four-node quadrilateral surface component can be reduced to a triangular surface component by defining duplicate node numbers for the third and fourth (K and L) node locations. If node L is not defined, then it defaults to node K. The design component thickness is assumed to vary bi-linearly inside the design component.

TABLE 11.5.4 Design Variables of Surface Design Component

Design Variables					
1	2	3	4	5	6
E	ρ	h_I	h_J	h_K	h_L

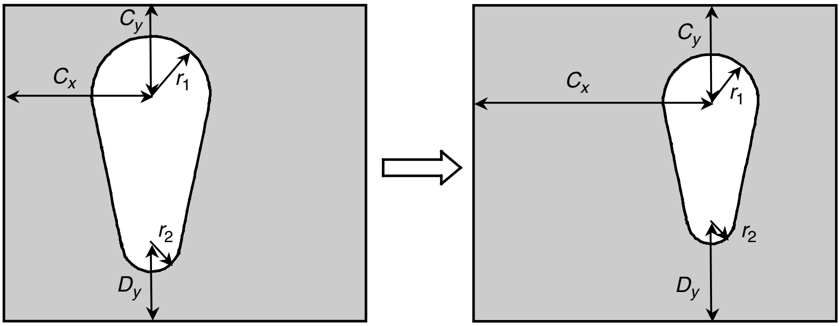

FIGURE 11.5.9 Shape design variables.

The Shape Design Variable

While material property and the sizing design variables are related to the parameters of the structural problem, the shape design variable is related to the structure's geometry. The shape of the structure does not explicitly appear as a parameter in the structural formulation. Although the design variables in Figure 11.5.4 determine the cross-sectional shape, they are not shape design variables, since these cross-sectional shapes are considered parameters in the structural problem. However, the length of the truss or beam should be treated as a shape design variable. Usually, the shape design variable defines the domain of integration in structural analysis. Thus, it is not possible to extract shape design variables from a structural model and to use them as sizing design variables.

Consider a rectangular block with a slot, as presented in Figure 11.5.9. The location and size of the slot is determined by the geometric values of C_x, C_y, D_y, r_1, and r_2, which are shape design variables. Different values of shape design variables yield different structural shapes. However, these shape design variables do not explicitly appear in the structural problem. If the finite element method is used to perform structural analysis, then integration is carried out over the structural domain (the gray area), which is the shape design variable. Since shape design variables do not explicitly appear in the structural problem, the shape design problem is more difficult to solve than the sizing design problem.

Shape design parameterization, which describes the boundary shape of a structure as a function of the design variables, is an essential step in the shape design process. Inappropriate parameterization can lead to unacceptable shapes.[5,6] To parameterize the structural boundaries and to achieve optimum shape design, boundary shape can be described in three ways: (1) by using boundary nodal coordinates, (2) by using polynomials, or (3) by using spline blending functions. However, it is important to point out that there are many methods of parameterization and that the methods presented in this section are only a few of them, including complicated parameterization methods developed in commercial CAD tools. One important aspect of shape design parameterization is the connection of the design parameterization to the computation of the design velocity field.

In the first method, boundary nodal coordinates of the finite element model are used as shape design variables. Although the method is simple and easy to use, it has the following drawbacks: (1) the number of design variables tends to become very large, which may lead to high computational costs and optimization problems that are difficult to solve; (2) the first derivative of the design boundary is not continuous across boundary nodes, which may lead to an unacceptable or impractical design; and (3) computational accuracy is not ensured, since it is difficult to maintain an adequate finite element mesh during the optimization process. One can use coordinates of selected master nodes as shape design variables and employ an isoparametric mapping to generate a finite element mesh.

Several methods have been developed to parameterize the design boundary with polynomials. Bhavikatti and Ramakrishnan[7] used a 5th-degree polynomial, with the coefficients taken as design variables, to parameterize the boundary shape of a rotating disk. Prasad and Emerson[8] used a similar approach to optimize an engine connecting rod. In a more general approach, such as that used by Kristensen and Madsen[9] and Pedersen and Laursen,[10] the boundary is parameterized using a linear combination of shape functions, with the coefficients as design variables. The total number of shape design variables can be reduced using polynomials for shape representation. However, using high-order polynomials to represent the boundary shape may result in oscillating boundaries.

Splines eliminate the problem of oscillating boundaries since they are composed of low-order polynomial segments that are combined to maximize the smoothness of the boundaries. Yang and Choi,[11] Luchi et al.,[12] and Weck and Steinke[13] used a cubic spline to define the boundary geometry. The spline representation was shown to yield better sensitivity accuracy than a piecewise linear representation of the boundary.[11] Braibant et al.[14] used Bezier and B-spline blending functions to describe the design boundary. Blending functions provide great flexibility for geometrical description. Using B-splines, Braibant and Fleury[15] optimized a beam in bending, a fillet, and a hole in a plate. Finally, Yao and Choi[16–18] used a Bezier surface to optimize an engine bearing cap and an arch dam.

The shape design parameterization method presented in this section deals with geometric features. A geometric feature is a subset of the geometric boundaries of a structural component. For example, a fillet or a circular hole is a geometric feature that contains characteristics associated with it and is likely to be chosen as a design variable. A geometric feature whose design variables are defined is known as a parameterized geometric feature, and is treated as a single entity in the shape design process. For example, a circular hole with its radius and center location defined as design variables is a parameterized geometric feature. Such a parameterized circular hole can be moved around in the structure with a varied size due to design changes. However, the shape of the circular hole itself remains constant.

Two steps are involved in the design parameterization process: geometric modeling and defining the design variables. A geometric model is first generated in the modeling process, with all its dimensions defined. Geometric features that can be varied in the design process need to be identified by both design and manufacturing engineers at the beginning of the design process. The design engineer then parameterizes the geometric model, using the geometric feature that is consistent with both engineering requirements and manufacturing limitations. The design parameterization developed in this section is based on the assumption that the geometric model has already been created and its dimensions defined.

In general, structural shape design problems can be classified into four types, in terms of the characteristics of the design boundary. In the first type, the shape of an arbitrary open or closed boundary is determined, such as a fillet[4] or a dam surface.[16] In the second type, the dimensions of predefined shapes are determined, such as the radius of a circular hole, the major and minor axes of an elliptic hole, the dimensions of a slot, the length of a rectangular membrane, or the radius of a rounded corner. In the third type, the design boundary location is determined, such as the center location of a circular hole, an elliptic hole, an arbitrarily shaped hole, or a slot. In the final type, a rotation angle of the design boundary, either arbitrary or predefined, is treated as the design variable. In this section, shape design parameterization of the first three types of design problems is considered.

In general, geometric entities can be represented using parametric cubic (PC) lines, patches (surfaces), and hyperpatches (solids). A parametric cubic line is represented by three functions:

$$\left.\begin{aligned} x &= x(u) \\ y &= y(u) \\ z &= z(u) \end{aligned}\right\} \tag{11.5.1}$$

where u is the parametric direction of the line with domain [0,1]. Each of these functions is, at most, a cubic polynomial of the form

$$z(u) = s_3 u^3 + s_2 u^2 + s_1 u + s_0 \tag{11.5.2}$$

The first and second derivatives of Equation 11.5.2 can be written as

$$z_{,u}(u) = 3s_3u^2 + 2s_2u + s_1 \tag{11.5.3}$$

$$z_{,uu}(u) = 6s_3u + 2s_2 \tag{11.5.4}$$

From Equation 11.5.3 and Equation 11.5.4, note that the slope of the cubic line can change its sign only twice, and that the curve can have only one inflection point. Thus, PC entities such as PC lines and PC patches minimize the possibility of yielding oscillating boundaries during the design process.[6] However, geometric entities with predefined or sophisticated shapes, such as a circular hole, cannot be represented by a single cubic curve. To minimize modeling errors, such a boundary can be broken into small pieces. These pieces are then "glued" together in the design process as one geometric feature by appropriately linking design variables. For shape design, planar parametric cubic lines and spatial parametric bicubic patches are utilized to represent the design boundaries of two-dimensional and three-dimensional structural components, respectively.

There are a number of methods for creating geometric entities, for example, defining four control points to create a Bezier curve, or constructing four edge curves to create a surface. Although geometric entities have different characteristics depending on the way they are created, they are nevertheless always represented by polynomials with the same order regardless of the way they are created. Consequently, a single geometric entity can be created using a variety of methods. For example, the planar curve shown in Figure 11.5.10(a) is created by defining four distinct points in the plane, and is thus called a four-point curve.

The mathematical expression of the four-point curve is given as

$$\left.\begin{aligned} x(u) &= 3u \\ y(u) &= 9u^3 - 13.5u^2 + 6.5u \end{aligned}\right\} \tag{11.5.5}$$

The same curve shown in Figure 11.5.10(b) can also be created by giving the position and slope at the endpoints, referred to as geometric coefficients:

$$\left.\begin{aligned} \mathbf{p}_0 &= [0,0] \\ \mathbf{p}_1 &= [3,2] \\ \mathbf{p}_0^u &= [3,6.5] \\ \mathbf{p}_1^u &= [3,6.5] \end{aligned}\right\} \tag{11.5.6}$$

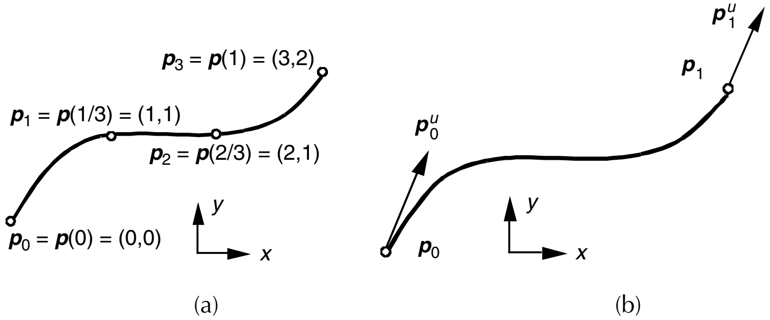

FIGURE 11.5.10 Planar parametric cubic curves (a) curve created by four points; (b) curve created by geometric coefficients.

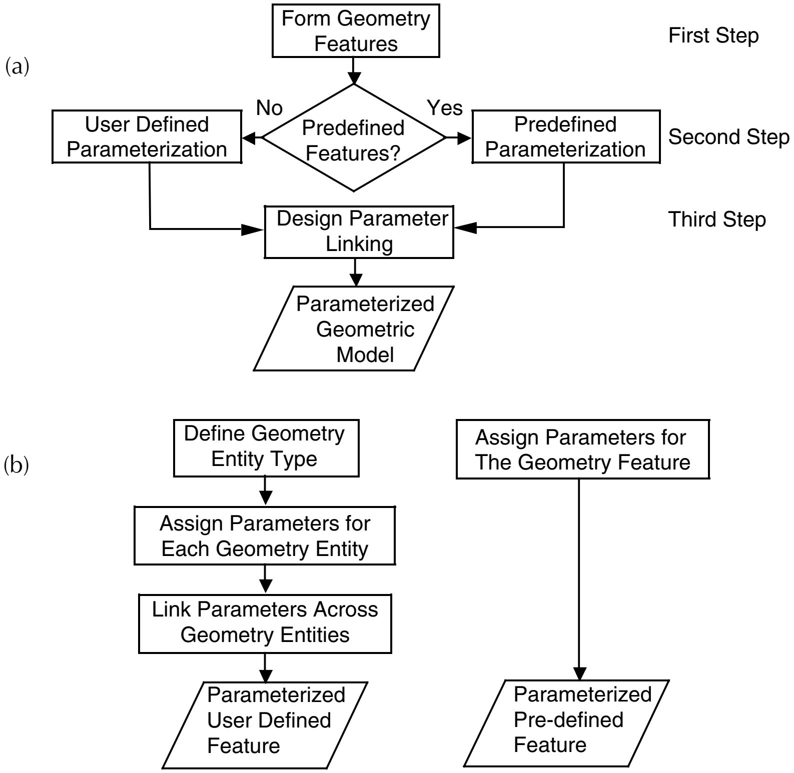

FIGURE 11.5.11 Shape design parameterization of features (a) overall design parameterization process; (b) parameterization for a user-defined feature; (c) parameterization for a predefined feature.

Therefore, one curve can be represented using different methods. However, these representations of curves and patches are mathematically equivalent, and one can be transformed into another by using certain linear transformations. For example, the geometric coefficients of a curve can be transformed into a four-point format, so the shape of the curve can be controlled according to the position of the four points. In fact, geometric coefficients are selected as unified geometric data, independent of the methods used to create geometric entities. Because design parameterization has the versatility of representing the same geometric entity in different ways, it can be systematically developed to provide the design engineer with sufficient resources for solving a wide variety of shape design problems.

The design parameterization method presented in this section is a three-step process, as illustrated in Figure 11.5.11. The first step is to create a geometric feature by grouping a number of interconnected geometric entities together, and by defining the type of geometric feature. The design engineer identifies the geometric entities that form the geometric features.

The second step is to define the design variables within each geometric feature. Geometric features that are frequently used in the construction of structural components can be put in the library of predefined geometric features. The design engineer can then parameterize these predefined features simply by selecting associated predefined shape design variables. To demonstrate the use of the library, two predefined geometric features have been defined, a circular hole and a tapered slot, as shown in Figure 11.5.12. For the circular hole, which is formed by connecting a number of circular arcs end to end with the same center point and radius, both the radius and center point of the circle can be defined as shape design variables. For the tapered slot, which is formed by connecting a number of straight lines and circular arcs, length dp3, radii dp4 and dp5, and center point dp1 and dp2 can all be defined as shape design variables. The design parameterization flow for the predefined geometric feature is illustrated in Figure 11.5.11(c).

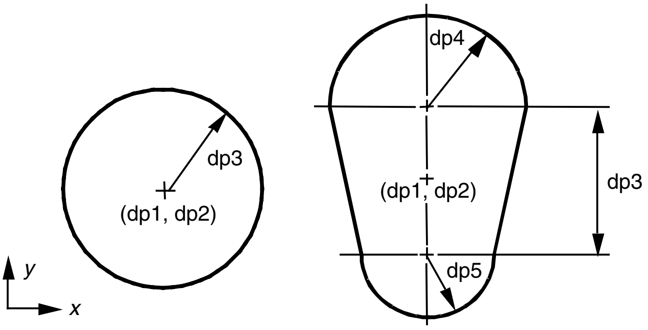

(a) (b)

FIGURE 11.5.12 Predefined geometric features (a) circular hole; (b) tapered slot.

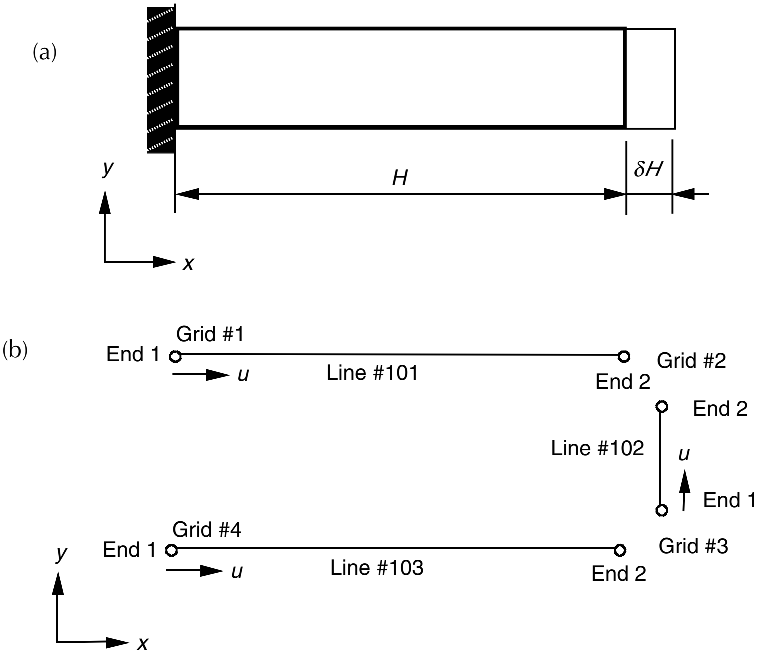

FIGURE 11.5.13 Parameterization of a cantilever beam (a) cantilever beam; (b) geometric feature of the beam.

A geometric feature that is not included in the library can be seen as a user-defined feature. To generate the latter, the design engineer can define the design variable by using geometric entities, and can then link these variables across the entities. For example, suppose a cantilever beam is to be parameterized such that its length *H* can be varied, as shown in Figure 11.5.13(a). To parameterize the beam, the following procedure can be used:

1. Identify lines #101, #102, and #103 to form the geometric feature, that is, the edges of the beam, as shown in Figure 11.5.13(b).
2. Define line #102 as a straight line and define the *x*-coordinate at end 1 of line 102, that is, grid #3, as the free design variable dp1, and the *x*-coordinate at end 2 of line #102, i.e., grid #2, to be proportional to dp1 with a proportionality of 1.0.
3. Define lines #101 and #103 as straight lines, and define the *x*-coordinate at end 2 of lines #101 and #103, that is, grids #2 and #3, as the free design variables dp2 and dp3, respectively.
4. Link dp2 and dp3 to dp1, with a proportionality of 1.0.

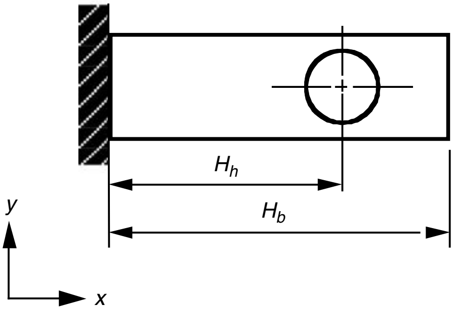

FIGURE 11.5.14 Design variable linking across parameterized geometric features.

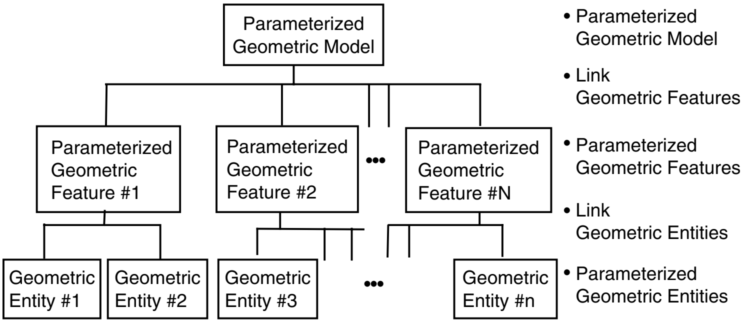

FIGURE 11.5.15 Hierarchy of shape design parameterization.

After design variable linking, only one design variable, dp1, the beam length represented by the *x*-coordinate of grid #3 in line #102, is allowed to vary independently. The parameterization flow for the user-defined feature is shown in Figure 11.5.11(b).

The shape design parameterization procedure for a user-defined geometric feature, as illustrated above, is summarized as follows:

1. Identify the types of geometric entities that are to be used to construct the user-defined geometric feature.
2. Parameterize the geometric entities by defining free and proportional design variables in each geometric entity.
3. Generate the parameterized geometric feature by linking free design variables across geometric entities.

Each predefined geometric feature that can be included in the feature library, such as the circular hole and tapered slot, is preconstructed by using this procedure.

If necessary, the third step is designed to link design variables across geometric features. For example, a cantilever beam with a circular hole, as shown in Figure 11.5.14, is to be parameterized so that the position of the hole is proportional to the beam length. The *x*-coordinate of the circular hole H_h can be parameterized by using the predefined parameterization process, as described in Figure 11.5.11(a). The length of beam H_b can be parameterized as a user-defined feature, as illustrated in Figure 11.5.13. With the two parameterized features, the *x*-coordinate of the hole can be linked to the beam length.

As described here, fundamental shape design parameterization is defined within geometric entities, and the parameterized features are created by using geometric entities. A hierarchy of the design parameterization method to build a parameterized geometric model is shown in Figure 11.5.15.

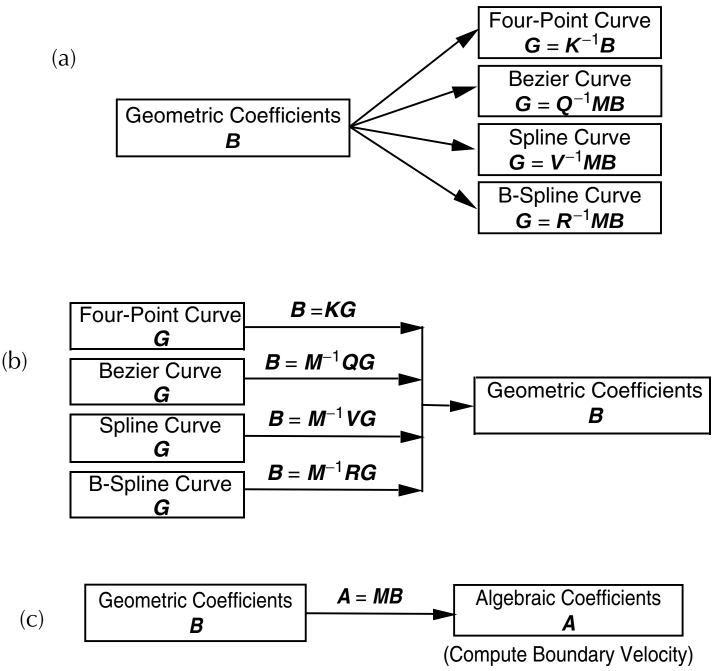

FIGURE 11.5.16 Curve format transformations for two-dimensional shape design (a) transformations from **B** to **G**; (b) transformations from **G** to **B**; (c) transformations from **B** to **A**.

Curve Design Parameterization

For a two-dimensional shape design, the boundaries are planar curves. In general, there are eight degrees of freedom for a planar cubic curve, as expressed in Equation 11.5.1 and Equation 11.5.2, with $z(u)$ serving as the constant. Planar curves with eight degrees of freedom are designated as basic curves, while predefined curves that are constrained, such as a circular arc, are designated as specialized curves. A specialized curve has fewer degrees of freedom since some of the basic degrees of freedom are linked (constrained) in order to define the required characteristics of the curve.

From a computational point of view, algebraic and geometric curves are the most interesting among the six basic types of curves. All parametric cubic entities can be transformed into various other formats by using certain linear transformations. For shape design, three major transformations are necessary: (1) from the geometric coefficient matrix **B** to the design variable matrix **G** to compute design variable values; (2) from matrix **G** to matrix **B** to update geometric entities for a perturbed design shape; and (3) from matrix **G** to the algebraic coefficient matrix **A** to compute the boundary velocity field. For the basic curves, the transformation from matrix **G** to matrix **B** for each curve format can be described by their corresponding 4×4 constant matrices. The curve format transformations are summarized in Figure 11.5.16.

Surface Design Parameterization

For three-dimensional shape design, design boundaries are surfaces in space. In general, there are 48 degrees of freedom for a parametric bicubic surface. For a parametric bicubic surface, the x-, y-, and z-components can be expressed using the three functions, as

$$\left.\begin{aligned} x &= x(u,w) \\ y &= y(u,w) \\ z &= z(u,w) \end{aligned}\right\} \tag{11.5.7}$$

where *u* and *w* are the parametric directions of the geometric entity, and $(u, w) \in [0,1] \times [0,1]$. Each of these functions is, at most, a bicubic function of the form

$$\begin{aligned} z(u,w) = {} & a_{33}u^3w^3 + a_{32}u^3w^2 + a_{31}u^3w + a_{30}u^3 \\ & + a_{23}u^2w^3 + a_{22}u^2w^2 + a_{21}u^2w + a_{20}u^2 \\ & + a_{13}u^1w^3 + a_{12}u^1w^2 + a_{11}u^1w^1 + a_{10}u \\ & + a_{03}w^3 + a_{02}w^2 + a_{01}w + a_{00} \\ = {} & \sum_{i,j=0}^{3} a_{ij}u^iw^j \end{aligned} \tag{11.5.8}$$

Surfaces with 48 degrees of freedom are defined as basic surfaces, whereas specialized surfaces are constrained to represent predefined conditions. As with the specialized curve, the specialized surface has fewer degrees of freedom. There are four basic surfaces — algebraic, geometric, 16-point, and Bezier — and there are also four specialized surfaces — plane, cylindrical, ruled, and surface of revolution, which have been developed to handle three-dimensional shape design problems. The B-spline surface is not recommended for three-dimensional shape design since, in contrast to the B-spline curve, the control points at the edges of the polyhedron are not on the B-spline surface. Therefore, the physical surface boundary does not closely resemble the characteristic polyhedron, and consequently, it is difficult to use in geometric modeling and design.

Similar to the basic types of curves, transformations between matrices **G**, **A**, and **B** of the basic surface can be used to obtain shape design variables, to update geometric entities, and to compute the boundary velocity field. The various surface format transformations are categorized in Figure 11.5.17.

The Configuration Design Variable

For those built-up structures made of truss, beam, and shell components, there is another type of design variable in addition to shape design; it's called the configuration design variable, and it is related to the structural component's orientation. These components have local coordinate systems fixed on the body of the structure, and state variables of the problem are described in local coordinate systems. If several components are connected together for the built-up structure, the state variables described in the local coordinate system are transformed to the global coordinate system. If the structural components change

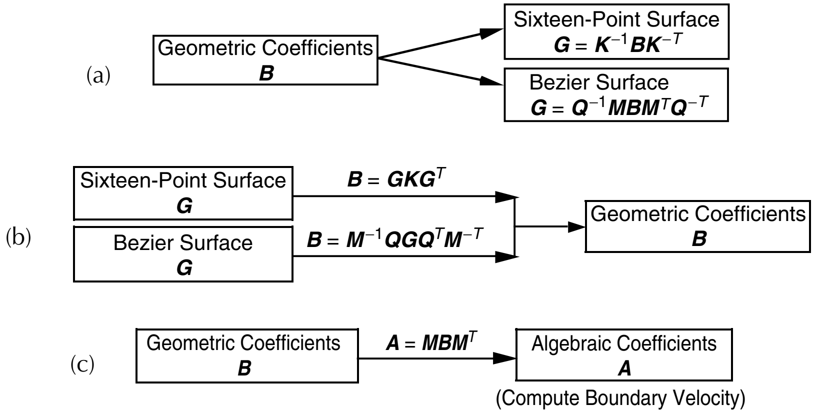

FIGURE 11.5.17 Surface format transformations for three-dimensional shape design (a) transformations from **B** to **G**; (b) transformations from **G** to **B**; (c) transformations from **B** to **A**.

their orientation in space, the transformation between the local and global coordinates also changes. Thus, this transformation can be considered the configuration design variable. Since configuration design variables are defined for built-up structures, they are inherently coupled with shape design variables. That is, in order to allow one member of the built-up structure to rotate, another member's shape needs to be changed. The configuration design variable is not applicable to solid components in which all rotations can be expressed in terms of shape changes.

The Topology Design Variable

If shape and configuration design variables represent changes in structural geometry and orientation, then topology design determines the structure's layout. For example, in Figure 11.5.9, shape design can change the size and location of the slot within the block. However, shape design cannot completely remove the slot from the block, or introduce a new slot. Topology design determines whether the slot can be removed or an additional slot is required.

The choice of the topology design variable is nontrivial compared to other design variables. Which parameter is capable of representing the birth or death of the structural layout? Early developments in topology design focused on truss structures. For a given set of points in space, design engineers tried to connect these points using truss structures, in order to find the best layout to support the largest load. Thus, the on-off types of topology design variables are used. These kinds of designs, however, could turn out to be discontinuous and unstable.

Recent developments in topology design are strongly related to FEA. The candidate design domain is modeled using finite elements, and then the material property of each element is controlled. If it is necessary to remove a certain region, then the material property value (e.g., Young's modulus) will approach zero, such that there will be no structural contribution from the removed region. Thus, material property design variables could be used for the purpose of topology design variables. The on-off type of design variable can be approximated by using continuous polynomials in order to remove the difficulties associated with discrete design variables.

In many applications, topology design is used at the concept design stage such that the layout of the structure is determined. After the layout is determined, sizing and shape designs are used to determine the detailed geometry of the structure.

A final comment on design parameterization: it is desirable to have a linearly independent set of design variables. If one does not, then relations between design variables must be imposed as constraints, which may make the design optimization process expensive, as the number of design variables and constraints increase. Furthermore, if design variable constraints are not properly established, meaningless design results will be obtained after an extensive amount of computational effort. As mentioned before, this problem is strongly related to structural modeling, since a well-defined structural model should have an independent set of parameters to define the entire system. Even if defining a good model is not an easy task for a complicated design problem, the design engineer nevertheless has to define a proper and independent set of parameters as much as possible in the structural modeling stage.

Design Variable Linking across Geometric Entities

There are three methods for categorizing the shape design problem: (1) identifying the arbitrary boundary shape, (2) determining the dimensions of the predefined shape, and (3) finding the locations of the boundaries. A design variable linking process is discussed in this section in order to support and ensure continuity between boundaries, as well as to retain predefined boundary shapes. For a geometric feature that is formed by a set of B-spline curves, C^2-continuity across curves is naturally retained.

As described in the previous sections, for the first type of shape design boundary any basic curve or surface can be utilized for parameterization. If constrained boundary shapes are required for two-dimensional structures, such as a straight edge or circular arc, then that specific type of curve must be used. For three-dimensional structures, the constrained boundaries can be predefined, such as a plane, cylinder, ball, or surface of revolution. If the geometric feature is composed of more than one curve or surface, continuity across curves or surfaces must be retained by linking shape design variables at the joint

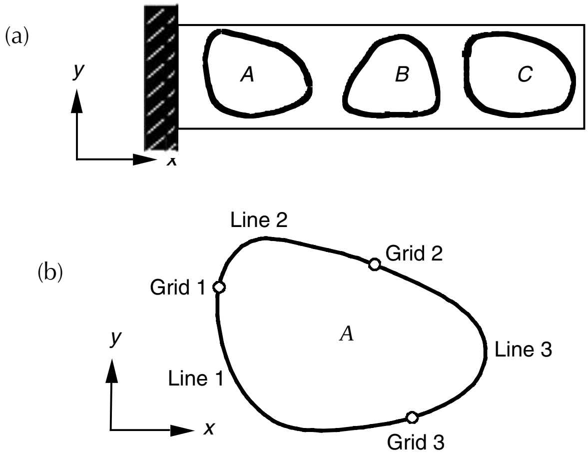

FIGURE 11.5.18 Parameterization of arbitrarily shaped holes (a) beam with arbitrarily shaped holes; (b) Hole *A* formed by three curves.

point or curve. As mentioned before, C^0-, C^1-, and C^2-continuities can be retained for two-dimensional structures by using the appropriate curve type and design variable linking. For three-dimensional problems, C^2-continuity is difficult to maintain. The following three examples illustrate how the design variable linking process can be used to support the three types of shape design problems.

Type One Problems — Identifying the Arbitrary Boundary Shape

A two-dimensional beam with arbitrarily shaped holes, shown in Figure 11.5.18(a), illustrates a design variable linking process that supports the first type of shape design problem.

Figure 11.5.18(b) shows that hole *A* is formed by three curves. To parameterize this hole, the curves are defined as geometric curves. The endpoints and tangent vectors at the endpoints of these connected curves are linked to retain C^0- and C^1-continuities, respectively.

The shape of the hole can be changed due to endpoint movement, length, or the direction of the tangent vector, as shown in Figure 11.5.19. Hole shape change due to movement δdp_1 of grid 3 in the negative *y*-direction is shown in Figure 11.5.19(a), such that the tangent vectors of lines 1 and 3 at grid 3 are kept the same. Moreover, hole shape change due to scaling the tangent vector of line 3 at grid 3 by δdp_2, shown in Figure 11.5.19(b), is such that the location of grid 3 and the direction of the tangent vector are kept the same. Finally, hole shape change due to change δdp_3 in the tangent vector direction of lines 1 and 3 is shown in Figure 11.5.19(c).

To avoid meaningless designs, for example, a hole that penetrates the boundary edges of a beam, the geometric boundaries can be displayed after the design change. Furthermore, numerical limits can be defined for design variables in order to restrict the degree of design perturbation.

Type Two Problems — Determining the Dimensions of a Predefined Shape

For the second type of shape design problem, specialized curves and surfaces are used to parameterize geometric entities. In addition, design variable linking may be carried out in the design process to group curves and surfaces that define the geometric feature.

The design variable linking method for parameterizing the second type of shape design boundary can be described using an elliptic hole formed by four conic curves, as shown in Figure 11.5.20. Each conic curve has three points to control its shape; however, relative altitude ρ is kept constant.

To vary the major axis, the *x*-coordinate of point $\mathbf{p}_7$ is defined as the independent design variable dp1. Points $\mathbf{p}_6$ and $\mathbf{p}_8$ are linked to dp1, with a proportionality of 1.0. In addition, the *x*-coordinates of points 1, 2, and 3 are linked to dp1 with a proportionality of –1.0. The elliptic hole varies in shape when the major axis is perturbed by δdp1, as shown in Figure 11.5.21(a). Similarly, for a design change in the minor axis, the *y*-coordinate of point $\mathbf{p}_4$ is defined as the independent design variable dp2. Points $\mathbf{p}_1$ and

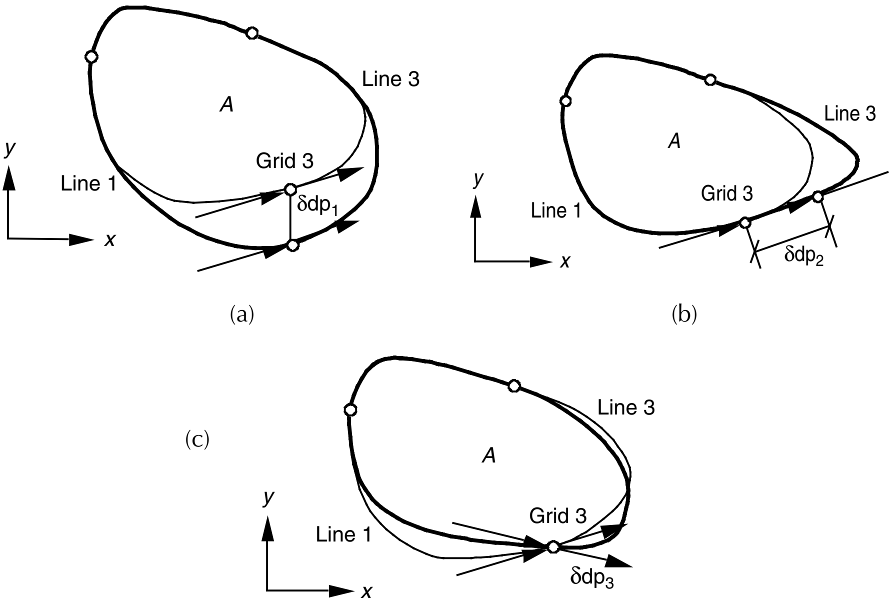

(a) (b)

FIGURE 11.5.19 Shape variation of Hole A (a) grid point movement; (b) length of tangent vector change; (c) y-component of tangent vector change.

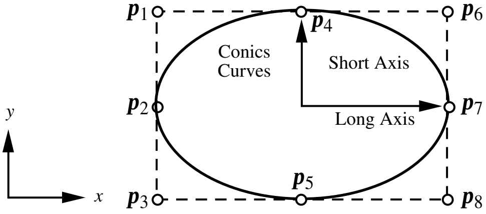

FIGURE 11.5.20 Parameterization of an elliptic hole.

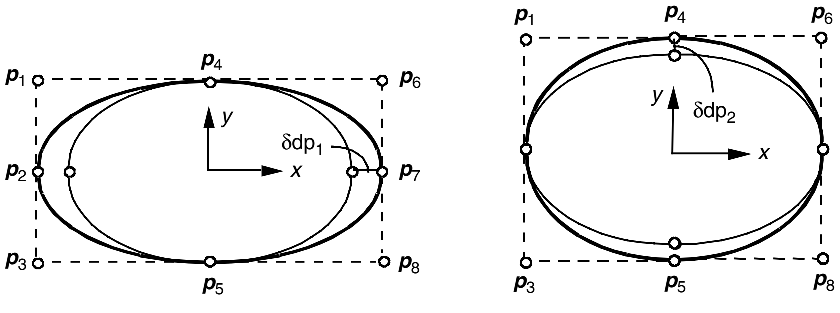

(a) (b)

FIGURE 11.5.21 Shape variation of an elliptic hole (a) variation of major axis; (b) variation of minor axis.

$\mathbf{p}_6$ are linked to dp2, with a proportionality of 1.0. Also, the y-coordinates of points $\mathbf{p}_3$, $\mathbf{p}_5$, and $\mathbf{p}_8$ are linked to dp2, with a proportionality of –1.0. Shape change due to the perturbation δdp2 of the minor axis is shown in Figure 11.5.21(b).

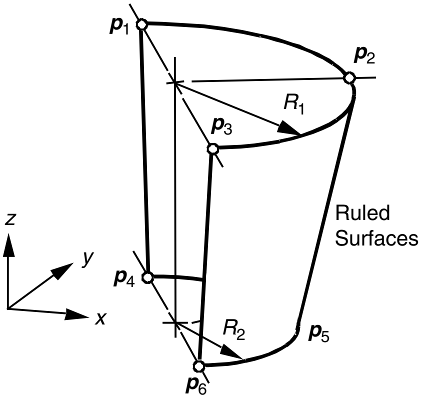

FIGURE 11.5.22 A semitapered cylinder formed by two ruled surfaces.

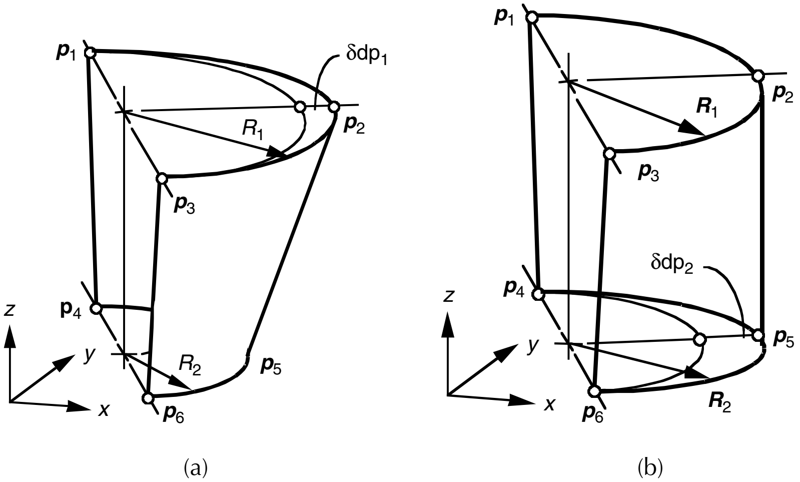

(a)

(b)

FIGURE 11.5.23 Shape variation of a tapered semicylindrical surface (a) shape variation due to δdp1; (b) shape variation due to δdp2.

For three-dimensional problems, this type of shape design can be the radius of a ball, a shell, or a cylindrical hole. For example, the tapered semicylindrical surface shown in Figure 11.5.22 can be parameterized by linking the design variables defined in the two ruled surfaces that form the tapered semicylindrical surface. The first ruled surface $\mathbf{p}_1\mathbf{p}_2\mathbf{p}_4\mathbf{p}_5$ is created using circular arcs $\mathbf{p}_1\mathbf{p}_2$ and $\mathbf{p}_4\mathbf{p}_5$. The other ruled surface $\mathbf{p}_2\mathbf{p}_3\mathbf{p}_5\mathbf{p}_6$ is created using circular arcs $\mathbf{p}_2\mathbf{p}_3$ and $\mathbf{p}_5\mathbf{p}_6$.

To vary the radius R_1, the radius of arc $\mathbf{p}_1\mathbf{p}_2$ is defined as the independent design variable dp1, and the radius of arc $\mathbf{p}_2\mathbf{p}_3$ is linked to dp1 with a proportionality of 1.0. Similarly, the design variable dp2 can be defined for radius R_2. The shape of the tapered semicylindrical surface is defined by the shape design variables dp1 and dp2, as shown in Figure 11.5.23(a) and Figure 11.5.23(b), respectively.

Type Three Problems — Finding the Locations of the Boundaries

To support the third type of shape design problem, such geometric entities as curves or surfaces that form the geometric feature are linked together so that only *x*-, *y*-, and *z*-movements of the parameterized geometric feature are allowed. For example, the *x*-coordinate of points $\mathbf{p}_1$ to $\mathbf{p}_8$ of the elliptic hole shown in Figure 11.5.22 can be linked, with a proportionality of 1.0, so that the four conic curves can be moved together to form an elliptic hole.

Design Sensitivity Analysis

Design sensitivity analysis computes the rate of performance measure change with respect to design variable changes. With the structural analysis, the design sensitivity analysis generates a critical information, gradient, for design optimization. Obviously, the performance measure is presumed to be a differentiable function of the design, at least in the neighborhood of the current design point. For complex engineering applications, it is not simple to prove a performance measure's differentiability with respect to the design. For most problems in this section, one can assume that the performance measure is continuously differentiable with respect to the design.

In general, a structural performance measure depends on the design. For example, a change in the cross-sectional area of a beam would affect the structural weight. This type of dependence is simple if the expression of weight in terms of the design variables is known. For example, the volume of a straight beam with a circular cross-section can be expressed as

$$W(r) = \pi r^2 l$$

where $u = r$ is the radius and l is the length of the beam. If the radius is a design variable, then the design sensitivity of W with respect to r would be

$$\frac{dW}{dr} = 2\pi r l$$

This type of function is *explicitly dependent* on the design, since the function can be explicitly written in terms of that design. Consequently, only algebraic manipulation is involved, and no FEA is required to obtain the design sensitivity of an explicitly dependent performance measure.

However, in most cases, a structural performance measure does not explicitly depend on the design. For example, when the stress of a beam is considered as a performance measure, there is no simple way to express the design sensitivity of stress explicitly in terms of the design variable r. In the linear elastic problem, the stress of the structure is determined from the displacement, which is a solution to the FEA. Thus, the sensitivity of stress $\sigma(\mathbf{z})$ can be written as

$$\frac{d\sigma}{dr} = \frac{d\sigma}{d\mathbf{z}}^{\mathrm{T}} \frac{d\mathbf{z}}{dr} \tag{11.5.9}$$

where $\mathbf{z}$ is the displacement of the beam. Since the expression of stress as a function of displacement is known, $d\sigma/d\mathbf{z}$ can be easily obtained. The only difficulty is the computation of $d\mathbf{z}/dr$, which is the state variable (displacement) sensitivity with respect to the design variable r.

When a design engineer wants to compute the design sensitivity of performance measures such as stress $\sigma(\mathbf{z})$ in Equation 11.5.9, structural analysis (FEA, for example) has presumably already been carried out. Assume that the structural problem is governed by the following linear algebraic equation:

$$\mathbf{K}(u)\mathbf{z} = \mathbf{f}(u) \tag{11.5.10}$$

Equation 11.5.10 is a matrix equation of finite elements if $\mathbf{K}$ and $\mathbf{f}$ are understood to be the stiffness matrix and load vector, respectively. Suppose the explicit expressions of $\mathbf{K}(u)$ and $\mathbf{f}(u)$ are known and differentiable with respect to u. Since the stiffness matrix $\mathbf{K}(u)$ and load vector $\mathbf{f}(u)$ depend on the design u, solution $\mathbf{z}$ also depends on the design u. However, it is important to note that this dependency is implicit, which is why we need to develop a design sensitivity analysis methodology. As shown in Equation 11.5.9, $d\mathbf{z}/du$ must be computed using the governing equation of Equation 11.5.10. This can be achieved by differentiating Equation 11.5.10 with respect to u, as

$$\mathrm{K}(u)\frac{d\mathrm{z}}{du} = \frac{d\mathrm{f}}{du} - \frac{d\mathrm{K}}{du}\mathrm{z} \tag{11.5.11}$$

Assuming that the explicit expressions of $\mathbf{K}(u)$ and $\mathbf{f}(u)$ are known, $d\mathbf{K}/du$ and $d\mathbf{f}/du$ can be evaluated. Thus, if solution $\mathbf{z}$ in Equation 11.5.10 is known, then $d\mathbf{z}/du$ can be computed from Equation 11.5.11, which can then be substituted into Equation 11.5.9 to compute $d\sigma/du$. Note that the stress performance measure is *implicitly dependent* on the design through state variable $\mathbf{z}$.

In this text, it is assumed that the general performance measure ψ depends on the design explicitly and implicitly. That is, the performance measure ψ is presumed to be a function of design u, and state variable $\mathbf{z}(u)$, as

$$\psi = \psi\big(\mathbf{z}(u), u\big) \tag{11.5.12}$$

The sensitivity of ψ can thus be expressed as

$$\frac{d\psi(\mathbf{z}(u),u)}{du} = \left.\frac{\partial\psi}{\partial u}\right|_{\mathbf{z}=\text{const}} + \left.\frac{\partial\psi}{\partial \mathbf{z}}\right|^{T}_{u=\text{const}} \frac{d\mathbf{z}}{du} \tag{11.5.13}$$

The only unknown term in Equation 11.5.13 is $d\mathbf{z}/du$. Various computational methods to obtain $d\mathbf{z}/du$ are introduced in the following subsections.

Methods of Structural Design Sensitivity Analysis

Various methods employed in design sensitivity analysis are listed in Figure 11.5.24. Four approaches are used to obtain the design sensitivity: the finite difference, discrete, continuum, and computational derivatives. In the finite difference approach, design sensitivity is obtained by either the *forward finite difference* or the *central finite difference method*. In the discrete method, design sensitivity is obtained by taking design derivatives of the discrete governing equation. For this process, it is necessary to take the design derivative of the stiffness matrix. If this derivative is obtained analytically using the explicit expression of the stiffness matrix with respect to the design variable, it is an *analytical method*, since the analytical expressions of $\mathbf{K}(u)$ and $\mathbf{f}(u)$ are used. However, if the derivative is obtained using a finite difference method, the method is called a *semianalytical method*. In the continuum approach, the design derivative of the variational equation is taken before it is discretized. If the structural problem and sensitivity equations are solved as a continuum problem, then it is called the *continuum-continuum method*. However, only very simple, classical problems can be solved analytically. Thus, the continuum sensitivity equation is solved by discretization in the same way that structural problems are solved. Since differentiation is taken at the continuum domain and is then followed by discretization, this method is

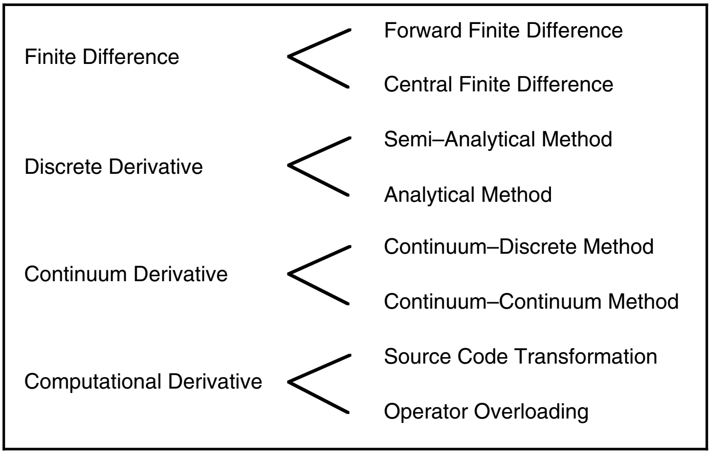

FIGURE 11.5.24 Approaches to design sensitivity analysis.

called the *continuum-discrete method*. Finally, computational, algorithmic or automatic differentiation refers to a differentiation of the computer code itself.

Except for the finite differences option, the other three come in direct and adjoint methods (called the reverse mode for computational derivative). In the direct method, one obtains the derivatives of the entire structural response, and often of intermediate quantities as well. The sensitivities of performance measures can then be obtained from the chain rule of differentiation. In the adjoint method, one defines an adjoint problem, which depends on the performance measure. The sensitivities of performance measures can then be obtained using the structural and adjoint responses. Thus, all of the system response sensitivities are not required, which is particularly an advantage in cases with many design variables, though few performance measures of interest.

The Global Finite Difference Method

The easiest way to compute sensitivity information of the performance measure is by using the finite difference method. Different designs yield different analysis results and, thus, different performance values. The finite difference method actually computes design sensitivity of performance by evaluating performance measures at different stages in the design process. If u is the current design, then the analysis results provide the value of performance measure $\psi(u)$. In addition, if the design is perturbed to $u+\Delta u$, where Δu represents a small change in the design, then the sensitivity of $\psi(u)$ can be approximated as

$$\frac{d\psi}{du} \approx \frac{\psi(u+\Delta u)-\psi(u)}{\Delta u} \tag{11.5.14}$$

Equation 11.5.14 is called the *forward difference method* since the design is perturbed in the direction of $+\Delta u$. If $-\Delta u$ is substituted in Equation 11.5.14 for Δu, then the equation is defined as the *backward difference method*. Additionally, if the design is perturbed in both directions, such that the design sensitivity is approximated by

$$\frac{d\psi}{du} \approx \frac{\psi(u+\Delta u)-\psi(u-\Delta u)}{2\Delta u} \tag{11.5.15}$$

then the equation is defined as the *central difference method*.

The advantage of the finite difference method is obvious. If structural analysis can be performed and the performance measure can be obtained as a result of structural analysis, then the expressions in Equation 11.5.14 and Equation 11.5.15 are virtually independent of the problem types considered. Consequently, this method is still popular in engineering design.

However, sensitivity computation costs become the dominant concern in the design process. If n represents the number of designs, then $n+1$ number of analyses have to be carried out for either forward or backward difference method, and $2n+1$ analyses are required for the central difference method. For modern, practical engineering applications, the cost of structural analysis is rather expensive. Thus, this method is not feasible for large-scale problems containing many design variables.

Another major disadvantage of the finite difference method is the accuracy of its sensitivity results. In Equation 11.5.14, accurate results can be expected when Δu approaches zero. Figure 11.5.25 shows some sensitivity results using the finite difference method. The tangential slope of the curve at u_0 is the exact sensitivity value. Depending on perturbation size, we can see that sensitivity results are quite different. For a mildly nonlinear performance measure, relatively large perturbation provides a reasonable estimation of sensitivity results. However, for highly nonlinear performances, a large perturbation yields completely inaccurate results. Thus, the determination of perturbation size greatly affects the sensitivity result. And even though it may be necessary to choose a very small perturbation, numerical noise becomes dominant for a too small perturbation size. That is, with a too small perturbation, no reliable difference can be found in the analysis results. The most obvious source of this type of errors is computational errors associated with arithmetic with finite number of digits and possibly ill-conditioning in the problem.

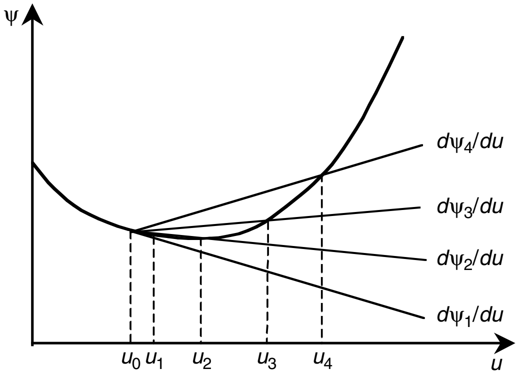

FIGURE 11.5.25 Influence of step-size in forward finite difference method.

For example, if up to five digits of significant numbers are valid in a structural analysis, then any design perturbation in the finite difference that is smaller than the first five significant digits cannot provide meaningful results. As a result, it is difficult to determine design perturbation sizes that work for all problems. Other potential sources are the discretization of both the spatial and the temporal domain. A typical example could be numerical noise induced by re-meshing.

Computational efficiency, accuracy and consistency, and implementation effort for global finite differences depend to a large extent on the type of solvers used for the linear system of Equation 11.5.10. The main issue is whether computational investments associated with solving the equations for the nominal structure can help reduce the effort associated with solving these equations for a perturbed structure.

When direct solvers are used for the solution, so that the matrix **K** has been factored, there is an array of methods that provide fast re-analysis of the perturbed structure. A disadvantage of many of these techniques is that accuracy is generally compromised, that is, certain inaccuracies will be introduced. When the perturbation leads to a low-rank modification of **K** — for example, because only a single finite element is modified — then an exact analysis of the perturbed structure can be performed using the Sherman-Morrison-Woodbury formulas.[19] The main computational cost of this approach is the solution of Equation 11.5.10 for a number of right-hand sides equal to the rank of the perturbation in **K**. Akgün et al.[19] discuss several variants of this approach, including the method of virtual distortions. When the perturbation in the matrix is more extensive, as in shape variation, it is still possible to use a binomial series solution[20,21] or a similar approximation of the inverse of **K** using a Neuman series.[22,23]

The Discrete Method

A structural problem is often discretized in finite dimensional space in order to solve complex problems. The discrete method computes the performance design sensitivity of the discretized problem, where the governing equation is a system of linear equations, as in Equation 11.5.10. If the explicit form of the stiffness matrix $\mathbf{K}(u)$ and the load vector $\mathbf{f}(u)$ are known, and if solution $\mathbf{z}$ of matrix equation $\mathbf{K}(u)\mathbf{z} = \mathbf{f}(u)$ is obtained, then the design sensitivity of the displacement vector can also be obtained, from Equation 11.5.11, as

$$\mathrm{K}(u)\frac{d\mathrm{z}}{du} = \mathrm{p} \tag{11.5.16}$$

where the pseudo-load vector **p** is defined as

$$\mathrm{p} = \frac{d\mathrm{f}}{du} - \frac{d\mathrm{K}}{du}\mathrm{z} \tag{11.5.17}$$

It is clear from Equation 11.5.16 that the design sensitivities require the solution of the same set of equations as solved for the response functions, but for another right-hand side (compare with Equation 11.5.10), the latter being the pseudo-load vector (see Equation 11.5.17).

In calculating the pseudo-load vector, it is not necessary to differentiate the global load vector and stiffness matrix, but to differentiate only those elements that are affected by the design variable. The evaluation of the pseudo-load vector is then carried out by an assembly of all individual nodal points and finite element contributions. These contributions are obtained by differentiating the finite element stiffness matrices with respect to the design variables and following a similar procedure for all load contributions. The fact that the pseudo-load vector only depends on elements that are affected may be exploited to make the computation of the pseudo-load vector more efficient. For shape design variables, this requires some additional attention. For that purpose, one often tries to link the design variables only to boundary elements, which means that only a boundary layer of elements is affected by the shape design variables.

The analytical differentiation process may become tedious. This especially holds true for shape design variables. Additional procedures must be implemented for each element used within the sensitivity analysis. The procedure must account for all possible design variables and particularly for shape design variables, as they are usually more complex than the original finite element routines. This type of discrete design sensitivity is referred to as *analytical* discrete design sensitivity.

It is not difficult to compute $d\mathbf{f}/du$, since the applied force is usually either independent of the design, or it has a simple expression. However, the computation of $d\mathbf{K}/du$ in Equation 11.5.16 depends on the type of problem. In addition, modern advances in the finite element method use numerical integration in the computation of $\mathbf{K}$. In this case, the explicit expression of $\mathbf{K}$ in terms of u may not be available. Moreover, in the case of the shape design variable, computation of the analytical derivative of the stiffness matrix is quite costly. Because of this, frequently approximations are accepted for the pseudo-load vector that reduces this effort. These approximations particularly involve finite difference schemes for evaluation of the pseudo-load vector. Forward and central finite difference schemes are the most popular. This type of design sensitivity is commonly denoted *semianalytical* discrete design sensitivity. However, Barthelemy and Haftka[24] show that the semianalytical method can have serious accuracy problems for shape design variables in structures modeled by beam, plate, truss, frame, and solid elements. They found that accuracy problems occur even for a simple cantilever beam. Moreover, errors in the early stage of approximation multiply during the matrix equation solution phase. As a remedy, Olhoff et al.[25] proposed an exact numerical differentiation method when the analytical form of the element stiffness matrix is available.

For shape design variables, design perturbation involves both the size of the perturbation and its distribution over the domain. For the choice of perturbation size, similar considerations as discussed for global finite differences play a role. Unfortunately, the semianalytical formulation may be extremely sensitive with respect to this choice. We will come back to this aspect extensively, and we only note here that this drawback may negate all advantages of a semianalytical formulation and motivates modifications to the semianalytical method.

The Continuum Method

In the continuum method, the design derivative of the variational equation (the continuum model of the structure) is taken before discretization. Since differentiation is taken before any discretization takes place, this method provides more accurate results than the discrete approach. In addition, profound mathematical proofs are available regarding the existence and uniqueness of the design sensitivity.

Sizing design variables are distributed parameters of the continuum equation. For shape design variables, the material derivative concept of continuum mechanics is used to relate variations in structural shape to the structural performance measures.[4] Using the continuum approach, we can obtain design sensitivity expressions in the form of integrals, with integrands written in terms of such physical quantities as displacement, stress, strain, and domain shape change. If exact solutions to the continuum equations are used to evaluate these design sensitivity expressions, then this procedure is referred to as the continuum-continuum method. On the other hand, if approximation methods such as the finite element, boundary element, or mesh-free method are used to evaluate these terms, then this procedure is called the continuum-discrete method. The continuum-continuum method provides the exact design sensitivity of the exact model, whereas the continuum-discrete method provides an approximate design sensitivity of the exact model. When FEA is used to evaluate the structural response, then the same discretization method as structural analysis has to be used to compute the design sensitivity of performance measures in the continuum-discrete method.

In the continuum approach, the design variables may be considered as fields that are functions of the spatial coordinates. As a consequence, sensitivity is to be understood as a variation of a function. Let us consider that the design variable s is perturbed to $s + \tau\eta$ in which τ is the scalar that measures the perturbation size and η is the direction of design change. For simplicity, it is assumed that the structural design variable s does not affect the domain. The variation of field response **u** with respect to s can then be defined as

$$\mathbf{u}' \equiv \lim_{\tau \to 0} \left\{ \frac{\mathbf{u}(s+\tau\eta) - \mathbf{u}(s)}{\tau} \right\} = \left. \frac{\partial \mathbf{u}}{\partial \tau} \right|_{\tau=0} \eta \tag{11.5.18}$$

Since the direction of design change η can be arbitrary, Equation 11.5.18 must be linear with respect to η and the coefficient of η is called the sensitivity of field response **u**, which is equivalent to the derivative in the context of other approaches.

The continuum method of design sensitivity analysis starts from the principle of virtual work, which is convenient for formulating the equations of equilibrium, as

$$\iint_V \delta\boldsymbol{\epsilon}^T \mathbf{C} \boldsymbol{\epsilon}\, dV = \iint_{\delta\mathbf{u}^T \mathbf{b} dV} \delta\mathbf{u}^T \mathbf{b}\, dV + \int_A \delta\mathbf{u}^T \mathbf{h}\, dA \tag{11.5.19}$$

for all $\delta\mathbf{u}$ that belong to the space of kinematically admissible displacements. In Equation 11.5.19, $\delta\boldsymbol{\epsilon}$ is the virtual strain; **C** is the elasticity matrix; $\boldsymbol{\epsilon}$ is the strain vector; **b** denotes the external load per unit volume; and **h** reflects tractions acting on the outer surface A of the structure.

Using Equation 11.5.18, the equations of equilibrium, Equation 11.5.19, can be differentiated to obtain the following continuum sensitivity equation:

$$\iint_V \delta\boldsymbol{\epsilon}^T \mathbf{C} \boldsymbol{\epsilon}'\, dV = \iint_V \delta\mathbf{u}^T \mathbf{b}'\, dV + \int_A \delta\mathbf{u}^T \mathbf{h}'\, dA - \iint_V \delta\varepsilon^T \mathbf{C}' \varepsilon\, dV \tag{11.5.20}$$

for all $\delta\mathbf{u}$ that belong to the space of kinematically admissible displacements. The left side of Equation 11.5.20 is the same as the left side of Equation 11.5.19 if **u** is replaced by $\mathbf{u}'$. The right side of Equation 11.5.20 defines a pseudo-load (or fictitious load), which explicitly depends on the design. Thus, solving the sensitivity equation is the same as solving original structural equilibrium equation with different load terms. The major advantage of the continuum approach is that the sensitivity formulation is independent of discrete model and numerical schemes. Once the continuum sensitivity equation is obtained, it can be discretized in the same manner as the original analysis equations in order to obtain a system of matrix equations similar to Equation 11.5.10.

When the design variables affect the shape of the domain, the differentiation of the equations of equilibrium is much more complicated because the integral domain depends on the design. Interested readers are referred to Haug et al.[4] for the material derivative approach and Arora[26] or Phelan and Haber[27] for the control volume approach.

One frequently asked question is "Are the discrete and continuum-discrete methods equivalent?" To answer this question, we have to give four conditions. First, the same discretization (shape function) used in the FEA method must be used for continuum design sensitivity analysis. Second, an exact integration (instead of a numerical integration) must be used in the generation of the stiffness matrix and in the evaluation of continuum-based design sensitivity expressions. Third, the exact solution (and not a numerical solution) of the finite element matrix equation and the adjoint equation should be used to compare these two methods. Fourth, the movement of discrete grid points must be consistent with the design parameterization method used in the continuum method. For the sizing design variable, it is shown in reference 4 that the discrete and continuum-discrete methods are equivalent under the conditions given above, using a beam as the structural component. It has also been argued that the discrete and continuum-discrete methods are equivalent in shape design problems under the conditions given above.[28] One point to note is that these four conditions are not easy to satisfy; in many cases, numerical integration is used and exact solutions of the FE matrix equation cannot be obtained.

Computational Derivative

Even if the finite element programs are composed of many complicated subroutines and functions, they are basically a collection of elementary functions. Computational (or automatic) differentiation method defines the partial derivatives of these elementary functions, and then the derivatives of complicated subroutines and functions are computed using propagation and the chain rule of differentiation. The arguments of elementary functions can be either one or two. Without loss of generality, let us assume that an elementary function has two arguments, defined as

$$a = f_{\text{elem}}(z_i, z_j) \tag{11.5.21}$$

where $f_{\text{elem}}(\gg,\gg)$ represents $(++, \sin(\gg), \ldots)$ operators for the single argument and (+, –, *, /, …) operators for the double arguments.

In the direct differentiation method, the derivative of Equation 11.5.21 can be defined as

$$\frac{\partial a}{\partial s} = \frac{\partial f_{\text{elem}}}{\partial z_i}\frac{\partial z_i}{\partial s} + \frac{\partial f_{\text{elem}}}{\partial z_j}\frac{\partial z_j}{\partial s} \tag{11.5.22}$$

This derivative can propagate through complicated functions and subroutines using the chain rule of differentiation. This propagation eventually produces the derivative of the structural response.

In the reverse mode, which corresponds to the adjoint method in the previous sections, the derivatives are computed backward through the computation. Due to the reverse procedure, this approach requires saving the entire function evaluation, which also requires a significant amount of memory.

Software that creates a computer program that calculates the derivatives of output of other computer programs is now available, and is applicable for small to medium-size programs.[24] The largest program that we found mentioned had about 140,000 lines.[30] Both first- and higher-order derivatives can be obtained. This approach was initially called automatic differentiation, but after a while it was realized that human intervention in the process is required in many cases to obtain a reasonably efficient code. So the name was generalized to computational differentiation.

There are several automatic differentiation tools widely available today, notably ADIFOR (Automatic Differentiation of Fortran[31] and ADOL-C for C/C++ programs.[32] In terms of implementation, there are two basic approaches to automatic differentiation — source code transformation and operator overloading. Source code transformation can be viewed as a precompiler that adds code for computing the derivatives. Operator overloading is available in modern computer languages, such as C++ and Fortran 90, that provide the ability to redefine the meaning of elementary operators (such as multiplication) for various classes of variables. By defining new variable types that have gradient objects associated with them, and overloading the elementary operators to produce gradients as well, we can transform the code without increasing its size substantially. ADOL-C and ADOL-F are examples of operator-overloading tools for automatic differentiation.

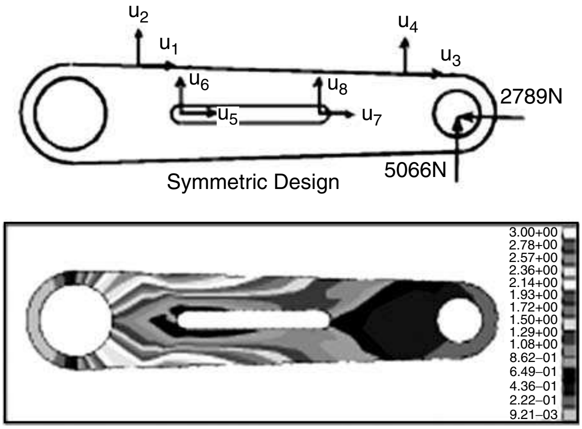

FIGURE 11.5.26 Design parameterization and mesh-free analysis results of a torque arm.

Examples

Torque Arm Model[33]

In order to show the accuracy of sensitivity calculation, a torque arm design problem, presented by Bennett and Botkin,[34] is used as a numerical example. The geometry of the torque arm (see Figure 11.5.26) is modeled using MSC/PATRAN,[35] and is represented by parametric coordinates. The displacement on the left hole is fixed, while the horizontal and vertical forces are applied at the center of the right hole. Design parameterization was performed by selecting the control points of the parametric curves such that the boundary curves move according to the design change. The design parameter was linked in order to obtain a symmetric design change. Design velocity vectors that represent the movement of particles in the direction of a given design parameter were computed by perturbing the parametric coordinates. This process is referred to as the isoparametric mapping method. Design parameterization and design velocity vector computation were also carried out by using a design sensitivity and optimization tool (DSO).[36] In all, eight design parameters were chosen in order to perturb the outer/inner boundary curves of the torque arm.

An automatic discretization procedure was used to discretize the torque arm structure. The domain of the torque arm was discretized by 478 degrees of freedom. The plane stress formulation is used with a thickness of 0.3 cm. The torque arm is made of steel with $E = 207$ GPa, and $\nu = 0.3$.

The structural analysis required 5.19 seconds, whereas by using one processor of HP Exemplar s-class workstation the sensitivity analysis required $4.55 \div 8 = 0.57$ seconds per each design parameter. The efficiency of the sensitivity computation derives from the fact that sensitivity analysis uses the same constitutive matrix, already factorized from the response analysis stage.

The sensitivity coefficients of the performance measures, including the structural area and stresses, were computed based on the continuum approach. The highest stress values at 19 locations are selected as the performance measure, which will be served as constraints during optimization. Using a very small perturbation size, the accuracy of the sensitivity coefficients is compared with the finite difference results, as shown in Table 11.5.5. Very accurate sensitivity results are observed. In Table 11.5.5, the first column represents design parameters, the second column represents performance measures, that is, structural area and von Mises stress at eight integration zones. The third column $\Delta\psi$ denotes the first-order sensitivity results obtained from the forward finite difference method with a perturbation of $\tau = 10^{-6}$. The fourth column represents the sensitivity computation results from the method employed. As has been shown in the fifth column, the ratio between the third and the fourth columns are very close to 100%, which means the calculated sensitivity information is very accurate.

Figure 11.5.27 shows the design sensitivity plot of the von Mises stress performance with respect to design u_3. Such a sensitivity plot graphically illustrates the effect of design change to the performance

TABLE 11.5.5 Design Sensitivity Results and Comparison with Finite Difference Results

u	ψ	$\Delta\psi$	ψ'	$\Delta\psi/\psi' \times 100$
u_1	Area	.10361E-5	.10362E-5	100.00
	σ_{82}	-.62892E-7	-.62891E-7	100.00
	σ_{85}	-.17736E-8	-.17722E-8	100.08
	σ_{88}	-.88829E-7	-.88828E-7	100.00
	σ_{91}	-.11245E-6	-.11245E-6	100.00
	σ_{97}	-.77783E-7	-.77781E-7	100.00
	σ_{136}	-.15990E-6	-.15991E-6	100.00
	σ_{133}	.33665E-7	.33667E-7	100.00
	σ_{100}	-.67624E-7	-.67623E-7	100.00
u_3	Area	.10118E-5	.10119E-5	100.00
	σ_{82}	-.78084E-9	-.78177E-9	99.88
	σ_{85}	.14674E-9	.14678E-9	99.97
	σ_{88}	-.58752E-8	-.58748E-8	100.01
	σ_{91}	-.19387E-7	-.19387E-7	100.00
	σ_{97}	-.39358E-7	-.39357E-7	100.00
	σ_{136}	-.38821E-9	-.38886E-9	99.83
	σ_{133}	.41596E-9	.41525E-9	100.17
	σ_{100}	-.59788E-7	-.59787E-7	100.00
u_7	Area	-.20000E-5	-.20000E-5	100.00
	σ_{82}	.20682E-8	.20709E-8	99.87
	σ_{85}	.47302E-8	.47324E-8	99.95
	σ_{88}	.60386E-8	.60409E-8	99.96
	σ_{91}	.81475E-8	.81496E-8	99.98
	σ_{97}	.16225E-7	.16227E-7	99.99
	σ_{136}	-.78753E-9	-.78694E-9	100.08
	σ_{133}	.26136E-9	.26181E-9	99.83
	σ_{100}	.25006E-7	.25008E-7	99.99

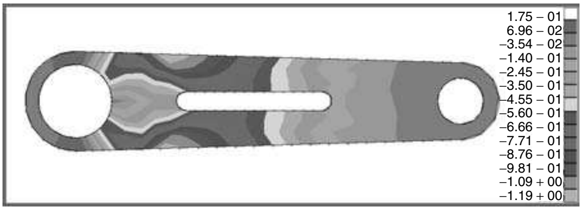

FIGURE 11.5.27 Von Mises stress sensitivity plot with respect to design u_3.

change, which provides very useful information in the interactive design process without invoking the automated design optimization procedure.

The Road Arm Model[33]

A road arm structure, as shown in Figure 11.5.28, transfers a force and torque from a road wheel to a suspension unit for a combat vehicle. The road arm model is discretized with 4365 degrees of freedom. The road arm is made of steel with E = 206 GPa, and ν = 0.3. At the center of the right hole, a vertical force of 3736 N and a torque of 44,516 N-m are applied, whereas the displacement on the left hole is fixed. As was illustrated in Figure 11.5.28, the stress concentration appears in the left corner of the road arm. If the highest stress level in the left corner is considered as a reference value, then the dimension of the right corner cross section can be reduced, because this region has a large amount of safety margin.

Since two holes are connected to the road wheel and torsion bar, the dimension and the geometry of the holes are fixed. The design goal is to determine the dimension of the cross sections of the arm. The

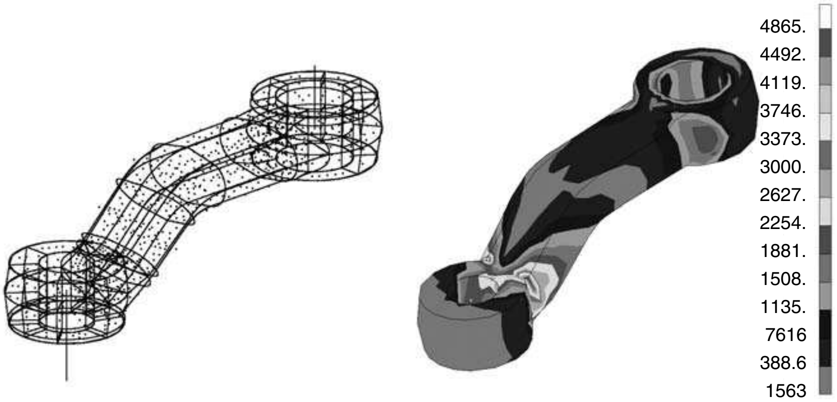

FIGURE 11.5.28 Discrete road arm model and simulation results (stress).

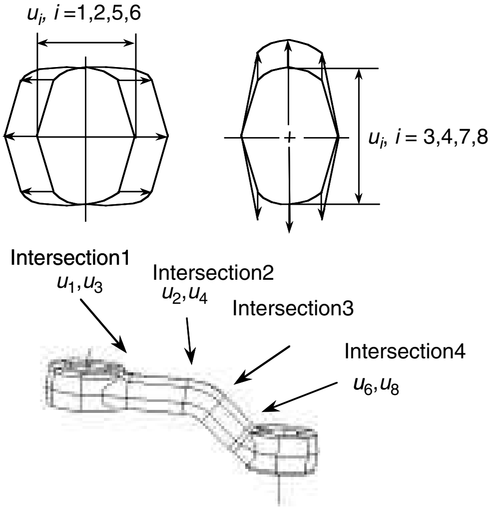

FIGURE 11.5.29 Design parameters for the rod arm model.

heights and widths of four sections are selected as design parameters (see Figure 11.5.29). Thus, a total of eight design parameters are considered in this example.

As the design variable changes, the boundary surface of the structure changes. At the same time, the discrete model also needs to be moved according to the design variable's change. Even if the design variable changes the boundary surface, it is recommended that the interior nodes be moved too. Otherwise, the accuracy of the perturbed model may deteriorate. The relation between a design variable and the motion of each node is denoted by the *design velocity field*. Figure 11.5.30 shows the design velocity field for two different design variables, u_2 and u_4, respectively. The arrows denote the magnitude and direction of nodal movement according to the corresponding design variable's change.

For a given design variable, the design sensitivity coefficients of various performance measures can be calculated using the design velocity field. Table 11.5.6 shows the design sensitivity coefficients, compared with the finite difference results. Displacement, stress, and volume of the structure are considered as performance measures. For example, zx4 represents the x-directional displacement at node 4, and sx10 is the x-directional normal stress at element 10. Very accurate sensitivity results are observed. This sensitivity information will be provided to the design optimization algorithm, to obtain the optimum design for given constraints.

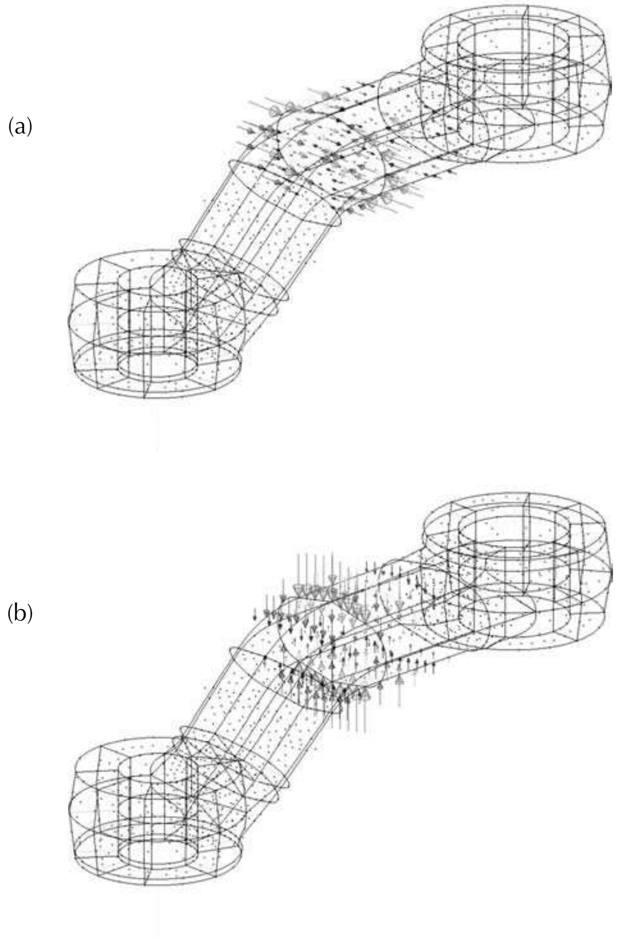

FIGURE 11.5.30 Design velocity field vectors: (a) design u_2; (b) design u_4.

TABLE 11.5.6 Design Sensitivity Results Compared with Finite Difference Method

Design	Perform.	ψ	$\Delta\psi$	$\psi'\Delta\tau$	$\Delta\psi/\psi'\Delta\tau \times 100$
u1	zx4	7.98472E–04	6.64019E–11	6.64028E–11	100.00
	zy8	–1.74039E–04	–1.50522E–11	–1.50526E–11	100.00
	sx10	1.38382E+01	–3.25110E–06	–3.26009E–06	99.72
	sy14	1.25479E+01	–1.40765E–05	–1.40762E–05	100.00
	sz18	–3.11292E+00	–1.79759E–06	–1.80037E–06	99.85
	Volume	4.68909E+02	–4.53781E–05	–4.53781E–05	100.00
u5	zx4	7.98472E–04	2.13594E–10	2.13594E–10	100.00
	zy8	–1.74039E–04	–7.76925E–11	–7.76924E–11	100.00
	sx10	1.38382E+01	4.83484E–07	4.83908E–07	99.91
	sy14	1.25479E+01	–4.81065E–06	–4.81087E–06	100.00
	sz18	–3.11292E+00	–4.00414E–06	–4.00603E–06	99.95
	Volume	4.68909E+02	–7.24906E–06	–7.24905E–06	100.00

Structural-Acoustic Design of a Vehicle[37]

As a last example, the design sensitivity analysis of a structural-acoustic problem is demonstrated. The goal is to estimate the sensitivity of a structure-borne noise caused by vibration of a vehicle. In order to calculate the noise level at the driver's ear position, sequential analysis procedure is employed. First, the

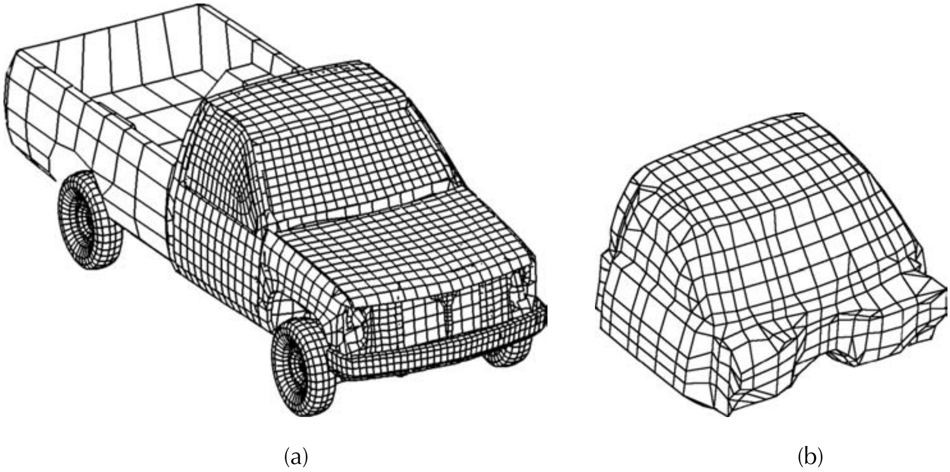

FIGURE 11.5.31 Computational model for structural-acoustic problem (a) finite element model of the vehicle; (b) boundary element model of the cabin compartment.

structural vibration problem is solved using the frequency response analysis. The vehicle structure is modeled using the finite element method, as shown in Figure 11.5.31(a). The sources of excitation are power-train vibration, wheel/terrain interaction, and a hydraulic pump load. Because of this additional source of excitation, vibration and noise is more significant than with a conventional power train. The frequency response analysis calculates the vibration velocity of vehicle's panels. Second, after solving for the panel velocity, the boundary element method is employed to calculate the pressure level in the cabin compartment using the panel velocity as a boundary condition. Figure 11.5.31(b) shows the boundary element model of the cabin compartment. In this example, the noise level of the passenger compartment is chosen as the performance measure, and vehicle-panel thicknesses are chosen as design variables. From the power-train analysis and rigid-body dynamic analysis, the harmonic excitations at 12 locations are obtained. The following frequency response analysis is carried out using MSC/NASTRAN to obtain the velocity response at eight frequencies, which correspond to the peak values of structure's velocity below 100 Hz:

$$[j\omega\mathbf{M} + \kappa\mathbf{K}]\{\mathbf{v}(\omega)\} = \{\mathbf{f}(\omega)\} \tag{11.5.23}$$

where $j = \sqrt{-1}$, ω is the excitation frequency, [**M**] is the structural mass matrix, $\kappa = (1 + j\phi)/j\omega$, ϕ is the structural damping coefficient, [**K**] is the stiffness matrix, {**v**} is the panel velocity vector, and {**f**} is the harmonic excitation force.

After solving the structure's velocity response, acoustic BEA is carried out using the cabin acoustic boundary element model, as shown in Figure 11.5.31(b). First, the emanating pressure from the panel is calculated using all panels' vibration velocity, as

$$[\mathbf{A}]\{\mathbf{p}_s\} = [\mathbf{B}]\{\mathbf{v}\} \tag{11.5.24}$$

where the matrices [**A**] and [**B**] are functions of geometry and {$\mathbf{p}_s$} is the surface pressure of the panel. After calculating the surface pressure distribution, the sound pressure at the interior of the cabin can be calculated from

$$p = \{\mathbf{b}\}^T\{\mathbf{v}\} + \{\mathbf{e}\}^T\{\mathbf{p}_s\} \tag{11.5.25}$$

where the vectors {**b**} and {**e**} are functions of geometry.

TABLE 11.5.7 Acoustic Pressures at the Driver's Ear Position

Frequency (Hz)	Pressure (kg/mm·sec^2)	Phase Angle (Degree)
47.3	0.64275E–04	66.915
59.5	0.35889E–03	328.99
75.9	0.66052E–04	193.91
81.8	0.41081E–03	264.21
86.0	0.21629E–03	176.18
90.5	0.43862E–03	171.44
93.6	0.75627E–02	178.30
98.7	0.22676E–03	226.07

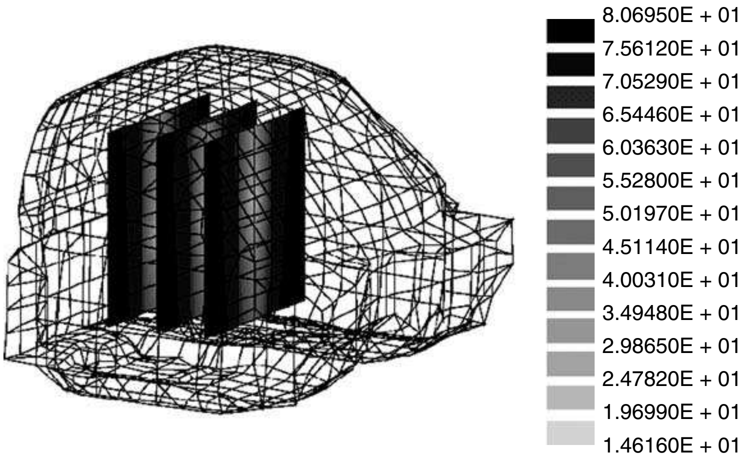

FIGURE 11.5.32 Acoustic pressure distribution inside the cabin compartment at 93.6 Hz.

Table 11.5.7 shows sound pressure levels at the driver's ear position. Since the sound pressure level at 93.6 Hz is significantly higher than at other frequencies, design modification is carried out at that frequency. In fact, this frequency corresponds to the fundamental frequency of the acoustic domain. Figure 11.5.32 shows the sound-pressure level inside the cabin compartment. The maximum sound pressure level at the driver's ear is 77.8 dB when the reference pressure of 2×10^{-8} kg/mm·s^2 is used.

In order to identify which panel thickness affects the sound pressure, the design sensitivity analysis has been performed. Forty design variables are selected in this example, which are grouped based on the manufacturing constraints. The adjoint method is employed in calculating the design sensitivity information because the number of performance measure (pressure at driver's ear position) is much smaller than the number of design variables. Table 11.5.8 shows the normalized sensitivity information for the 12 design variables whose effects are the most significant. The results show that a thickness change in the chassis component has the greatest potential for achieving a reduction in sound-pressure levels. Since the numerical integration process is carried out on each finite element, the element sensitivity information

TABLE 11.5.8 Normalized Sensitivity Values for Various Design Variables

Component	Sensitivity	Component	Sensitivity
Chassis	–1.0	Chassis MTG	–0.11
Left wheelhouse	–0.82	Chassis connectors	–0.10
Right door	0.73	Right fender	–0.07
Cabin	–0.35	Left door	–0.06
Right wheelhouse	–0.25	Bumper	–0.03
Bed	–0.19	Rear glass	0.03

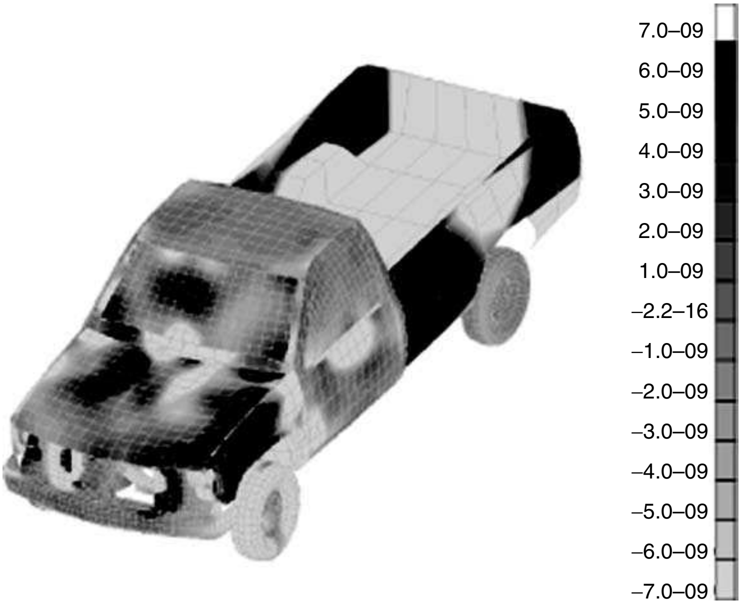

FIGURE 11.5.33 Design sensitivity contribution of each element to the sound pressure level.

can be calculated without any additional effort. Figure 11.5.33 plots the sensitivity contribution of the each element to the sound-pressure level. Such graphic-based sensitivity information is very helpful for the design engineer in determining the direction of the design modification.

As was shown in Table 11.5.8, the chassis component has the highest sensitivity for the sound-pressure level, which means that a change in the thickness of the chassis component is the most effective way to reduce the sound-pressure level. To see the effect of the chassis component, the thickness of the chassis is increased by 1.0 mm and the whole analysis process is repeated for the modified design. It turns out that the maximum value of the sound pressure is reduced from 77.8 dB to 75.0 dB.

Gradient-Based Design Optimization

When the design parameters are continuous, various numerical techniques have been developed to find the local optimum design systematically. Unfortunately, no mathematical theory exists that can find the global optimum design for general nonlinear functions. To find the optimum design, at least a possible candidate must exist within a feasible design region to satisfy problem constraints. Every design in the feasible region is an acceptable design, even if it is not the best one. The best design is usually the one that minimizes (or maximizes) the cost function of the design problem. Thus, the goal of the design optimization problem is to find a design that minimizes the cost function among all feasible designs. In this section, design optimization algorithms are briefly introduced. However, this brief discussion is by no means a complete treatment of optimization methods. For a more detailed treatment, see references 38, 39, and 40.

Most gradient-based optimization algorithms are based on the mathematical programming method, which requires the function values and sensitivity information at given design variables. Each algorithm has its own advantages and disadvantages. The performance of an optimization algorithm critically depends on the characteristics of the design problem and the types of cost and constraint functions.

The Linear Programming Method

The linear programming method can be used when cost and constraints are linear functions of the design variables.[41] Most structural design problems, however, are nonlinear with respect to their design variables. Thus, the linear programming method is not of much use for structural problems. However, a nonlinear problem can be solved by approximating a sequence of linear problems. The standard form of a linear programming problem is

$$\begin{aligned} &\text{minimize} \quad f = \mathbf{c}^T\mathbf{u} \\ &\text{subject to} \quad \mathbf{Au} = \mathbf{b} \\ &\qquad\qquad\quad \mathbf{u} \geq \mathbf{0} \end{aligned} \tag{11.5.26}$$

where $\mathbf{c} = [c_1, c_2, \ldots, c_n]^T$ is the coefficient of the cost function, **A** is the $m \times n$ matrix, and **b** is the $m \times 1$ vector. Inequality constraints can be treated as equality constraints by introducing slack variables. Since all functions are linear, the feasible regions defined by linear equalities are convex, along with the cost function. Thus, if any optimum solution of Equation 11.5.26 exists, then it is a global minimum solution of the problem. The reason for introducing the linear problem here is that a very efficient method exists for solving linear programming problems, namely *the simplex method*. A positive feature of a linear programming problem is that the solution always lies on the boundary of the feasible region. Thus, the simplex method finds a solution by moving each corner point of the convex boundary.

Unconstrained Optimization Problems

When cost and/or constraints are nonlinear functions of the design, the design problem is called a *nonlinear programming method*, as contrasted to the linear programming method discussed in the previous section. Most engineering problems fall into the former category. Because the properties of nonlinear programming are nonlinear, this method is frequently solved using the numerical, rather than the analytical, method.

When there are no constraints on the design problem, it is referred to as an *unconstrained optimization problem*. Even if most engineering problems have constraints, these problems can be transformed into unconstrained ones by using the penalty method, or the Lagrange multiplier method. The unconstrained optimization problem sometimes contains the lower and upper limits of a design variable, since this type of constraint can be treated in simple way. The standard form of an unconstrained optimization problem can be written as

$$\begin{aligned} &\text{minimize} \quad f(\mathbf{u}) \\ &\text{subject to} \quad u_k^L \leq u_k \leq u_k^U, \qquad k = 1, \cdots, n \end{aligned} . \tag{11.5.27}$$

In the following subsections, numerical methods for solving Equation 11.5.27 are discussed.

The Steepest Descent Method

The numerical procedure for solving Equation 11.5.26 is an iterative update of design **u**. If $\mathbf{u}^k$ is the value of the design at the k-th iteration, then the new design at the $(k+1)$-th iteration can be obtained by

$$\mathbf{u}^{k+1} = \mathbf{u}^k + \alpha \mathbf{d}^{k+1} \tag{11.5.28}$$

where $\mathbf{d}^{k+1}$ is called the descent direction and α is a step size, used to determine the amount of movement in the direction of $\mathbf{d}^{k+1}$. If the descent direction is given, then parameter α is determined by using the line search procedure to find the minimum value of a cost function in the descent direction. The steepest descent method uses the gradient of the cost function as the descent direction, such that

$$\mathbf{d}^{k+1} = -\frac{\partial f(\mathbf{u}^k)}{\partial \mathbf{u}^k} = -\nabla f(\mathbf{u}^k) \tag{11.5.29}$$

which is the design sensitivity of the cost function. This method suffers from a slow convergence near the optimum design, since it does not use any information from the previous design, and only first-order information of the function is used. Note that $\mathbf{d}^k$ and $\mathbf{d}^{k+1}$ are always orthogonal, such that a zigzagging pattern appears in the optimization process.

The Conjugate Gradient Method

The conjugate gradient method developed by Fletcher and Reeves[42] improves the rate of slow convergence in the steepest descent method by using gradient information from the previous iteration. The difference in this method is the computation of $\mathbf{d}^{k+1}$ in Equation 11.5.28. The new descent direction is computed by

$$\mathbf{d}^{k+1} = -\nabla f(\mathbf{u}^k) + \beta_k^2 \mathbf{d}^k \tag{11.5.30}$$

where

$$\beta_k = \frac{\left\| \nabla f(\mathbf{u}^k) \right\|}{\left\| \nabla f(\mathbf{u}^{k-1}) \right\|} \tag{11.5.31}$$

and where the first iteration is the same as Equation 11.5.28. This method tends to select the descent direction as a diagonal of two orthogonal steepest descent directions, such that a zigzagging pattern can be eliminated. This method always has better convergence than the steepest descent method.

The Newton Method

The previous methods we have examined use first-order information (first-order design sensitivity) of the cost function to find the optimum design, which is called linear approximation. The Newton method uses second-order information (second-order design sensitivity) to approximate the cost function as a quadratic function of the design. The major concern is how to compute the second-order design sensitivity (or Hessian) matrix. Let us define the Hessian matrix as second-order design sensitivity, as

$$\mathbf{H}(\mathbf{u}^k) \equiv \left[\frac{\partial f(\mathbf{u}^k)}{\partial u_i^k \partial u_j^k} \right], \quad i, j = 1, \cdots, n \tag{11.5.32}$$

The new design can then be determined, as

$$\mathbf{u}^{k+1} = \mathbf{u}^k + \Delta\mathbf{u}^{k+1} \tag{11.5.33}$$

where

$$\Delta\mathbf{u}^{k+1} = -\mathbf{H}(\mathbf{u}^k)^{-1} \nabla f(\mathbf{u}^k) \tag{11.5.34}$$

If the current estimated design $\mathbf{u}^k$ is sufficiently close to the optimum design, then Newton's method will show a quadratic convergence. However, the greater the number of design variables, the greater the cost of computing $\mathbf{H}(\mathbf{u}^k)$ in Equation 11.5.32. In addition, Newton's method does not guarantee a convergence. Thus, several modifications are available. For example, the design update algorithm in Equation 11.5.33 can be modified to include a step size by using a line search, as in Equation 11.5.28.

The Quasi-Newton Method

Although Newton's method has a quadratic convergence, the cost of computing the Hessian matrix, and the lack of a guaranteed convergence, are drawbacks to this method. The quasi-Newton method has an advantage over the steepest descent method and Newton's method: it only requires first-order sensitivity information, and it approximates the Hessian matrix to speed up the convergence.

The DFP (Davidon-Fletcher-Powell)[42] method approximates the inverse of the Hessian matrix using first-order sensitivity information. By initially assuming that the inverse of the Hessian is the identity matrix, this method updates the inverse of the Hessian matrix during design iteration. A nice feature of this method is that the positive definiteness of the Hessian matrix is preserved.

The BFGS (Broydon-Fletcher-Goldfarb-Shanno)[43] method updates the Hessian matrix directly, rather than updating its inverse as with the DFP method. Starting from the identity matrix, the Hessian matrix remains positive definite if exact line search is used.

Constrained Optimization Problems

Most engineering problems have constraints that must be satisfied during the design optimization process. These two types of constraints are handled separately: equality and inequality constraints. The standard form of the design optimization problem in constrained optimization can be written as

$$\begin{aligned} &\text{minimize} \quad f(\mathbf{u}) \\ &\text{subject to} \quad h_i(\mathbf{u}) = 0, \qquad i = 1,\cdots,p \\ &\qquad\qquad\quad g_j(\mathbf{u}) \le 0, \qquad j = 1,\cdots,m \\ &\qquad\qquad\quad u_l^L \le u_l \le u_l^U,\ l = 1,\cdots,n \end{aligned} \tag{11.5.35}$$

The computational method to find a solution to Equation 11.5.35 has two phases: first, to find a direction **d** that can reduce the cost $f(\mathbf{u})$ while correcting for any constraint violations that are violated; and second, to determine the step size of movement α in the direction of **d**.

Sequential Linear Programming (SLP)

The SLP method approximates the nonlinear problem as a sequence of linear programming problems such that the simplex method described earlier may be used to find the solution to each iteration. By using function values and sensitivity information, the nonlinear problem in Equation 11.5.35 is linearized in a similar way as Taylor's expansion method in the first order, as

$$\begin{aligned} &\text{minimize} \quad f(\mathbf{u}^k) + \nabla f^T \Delta\mathbf{u}^k \\ &\text{subject to} \quad h_i(\mathbf{u}^k) + \nabla h_i{}^T \Delta\mathbf{u}^k = 0, \quad i = 1,\cdots,p \\ &\qquad\qquad\quad g_i(\mathbf{u}^k) + \nabla g_i{}^T \Delta\mathbf{u}^k \le 0, \quad j = 1,\cdots,m \\ &\qquad\qquad\quad u_l^L \le u_l \le u_l^U, \qquad\qquad l = 1,\cdots,n \end{aligned} \tag{11.5.36}$$

Since all functions and their sensitivities at $\mathbf{u}^k$ are known, the linear programming problem in Equation 11.5.36 can be solved using the simplex method for $\Delta\mathbf{u}^k$. Even if the sensitivity information is not used to solve a linear programming problem, design sensitivity information is required in order to approximate the nonlinear problem as a linear one with SLP. In solving Equation 11.5.36 for $\Delta\mathbf{u}^k$, the move limit $\Delta\mathbf{u}_L^k \le \Delta\mathbf{u}^k \le \Delta\mathbf{u}_U^k$ is critically important for convergence.

Sequential Quadratic Programming (SQP)

Compared to previous methods, which use first-order sensitivity information to determine the search direction **d**, SQP solves a quadratic subproblem to find that search direction, which has both quadratic cost and linear constraints:

$$\begin{aligned} &\text{minimize} \quad f(\mathbf{u}^k) + \nabla f^T \mathbf{d} + \frac{1}{2}\mathbf{d}^T \mathbf{H}\mathbf{d} \\ &\text{subject to} \quad h_i(\mathbf{u}^k) + \nabla h_i{}^T \mathbf{d} = 0, \quad i = 1,\cdots,p \\ &\qquad\qquad\quad g_j(\mathbf{u}^k) + \nabla g_j{}^T \mathbf{d} \le 0, \quad j = 1,\cdots,m \end{aligned} \tag{11.5.37}$$

This special form of the quadratic problem can be effectively solved, for example, by using the Kuhn-Tucker condition and the simplex method. Starting from the identity matrix, the Hessian matrix **H** is updated at each iteration by using the aforementioned methods in unconstrained optimization algorithms. The advantage of solving Equation 11.5.37 in this way is that for positive definite **H** the problem is convex and the solution is unique. Moreover, this method does not require the move limit as in SLP.

The Constrained Steepest Descent Method

In the unconstrained optimization process described earlier, the descent direction **d** is obtained from the cost function sensitivity. When constraints exist, this descent direction has to be modified in order to include their effects. If constraints are violated, then these constraints are added to the cost function using a penalty method. Design sensitivity of the penalized cost function combines the effects of the original cost function and the violated constraint functions.

The Constrained Quasi-Newton Method

If the linear approximation of constraints in SQP is substituted for a quadratic approximation, then the convergence rate of Equation 11.5.37 will be improved. However, solving the optimization problem for quadratic cost and constraints is not an easy process. The constrained quasi-Newton method combines the Hessian information of constraints with the cost function by using the Lagrange multiplier method. Nevertheless, it is still necessary to compute the constraint function Hessian. The main purpose of the constrained quasi-Newton method is to approximate the Hessian matrix by using first-order sensitivity information. The extended cost function is

$$L(\mathbf{u},\mathbf{v},\mathbf{w}) = f(\mathbf{u}) + \sum_{i=1}^{p} v_i h_i(\mathbf{u}) + \sum_{j=1}^{m} w_i g_i(\mathbf{u}) \tag{11.5.38}$$

where both $\mathbf{v} = [v_1, v_2, \ldots, v_p]^T$ and $\mathbf{w} = [w_1, w_2, \ldots, w_m]^T$ are the Lagrange multipliers for equality and inequality constraints, respectively. Note that $\mathbf{w} > \mathbf{0}$. Let the second-order design sensitivity of L be $\nabla^2 L$. The extended quadratic programming problem of Equation 11.5.37 thus becomes

$$\begin{aligned}
\text{minimize} \quad & f(\mathbf{u}^k) + \nabla f^T \mathbf{d} + \frac{1}{2}\mathbf{d}^T \nabla^2 L \mathbf{d} \\
\text{subject to} \quad & h_i(\mathbf{u}^k) + \nabla h_i^T \mathbf{d} = 0, \quad i = 1,\cdots,p \\
& g_j(\mathbf{u}^k) + \nabla g_j^T \mathbf{d} \le 0, \quad j = 1,\cdots,m \\
& w_l \ge 0, \qquad\qquad l = 1,\cdots,m
\end{aligned} \tag{11.5.39}$$

The Feasible Direction Method

The feasible direction method is designed to allow design movement within the feasible region in each iteration. Based on the previous design, the updated design reduces the cost function and remains in the feasible region. Since all designs are feasible, a design at any iteration can be used, even if it is not an optimum design. Because this method uses the linearization of functions as in SLP, it is difficult to maintain nonlinear equality constraints. Thus, this approach is used exclusively for inequality constraints. Search direction **d** can be found by solving the following linear subproblem:

$$\begin{aligned}
\text{minimize} \quad & \beta \\
\text{subject to} \quad & \nabla f^T \mathbf{d} \le \beta \\
& \nabla g_i^T \mathbf{d} \le \beta, \quad i = 1,\cdots,m_{active} \\
& -1 \le d_j \le 1, \quad j = 1,\cdots,n
\end{aligned} \tag{11.5.40}$$

where m_{active} is the number of active inequality constraints. After finding a direction **d** that can reduce cost function and maintain feasibility, a line search is used to determine step size α.

The Gradient Projection Method

The feasible direction method solves the linear programming problem to find the direction of the design change. The gradient projection method, however, uses a simpler method for computing this direction. The direction obtained by the steepest descent method is projected on the constraint boundary, such that the new design can move along the constraint boundary. Thus, the direction of the design change reduces the cost function while maintaining the constraint along its boundary. For a general nonlinear constraint, however, a small movement along the tangent line of the boundary will violate this constraint. Thus, in actual implementation, a correction algorithm has to be followed. The gradient projection method behaves well when the constraint boundary is moderately nonlinear.

Examples

The Torque Arm Model

The torque arm model is used here to demonstrate the design optimization. The design optimization problem is formulated in such a way that the total area of the structure is minimized with respect to its shape design parameters, with design constraints defined as the second invariant of the stress tensors (von Mises stress), as

$$\begin{array}{ll} \text{minimize} & \text{mass} \\ \text{subject to} & \sigma_{\text{MAX}} \le 800\ \text{MPa} \end{array} \tag{11.5.41}$$

As has been shown in Figure 11.5.26, the maximum stress at the initial design was 305 MPa. Thus, the design that meets the constrained boundary in Equation 11.5.41 is far away from the initial design, which means the amount of shape change during design optimization is significantly large.

For design optimization, the sequential quadratic programming method described earlier has been used employing a commercially available optimization program.[39] The structural analysis provides the function values (i.e., mass and stress), whereas the sensitivity analysis provides the gradient information to the optimization algorithm. The design optimization problem converges after 20 numbers of iteration. Figure 11.5.34 shows the structural analysis results at optimum design where the stress constraints along the upper side of torque arm became active. The left diameter of the interior slot significantly increases to reduce the structural mass, whereas the right diameter is slightly decreased. The vertical position of the right boundary (u_4) is significantly reduced so that the thickness of the torque arm becomes constant.

Table 11.5.9 shows the values of design variables at the initial and optimum designs. The lower and upper bounds are selected such that the structure maintains its topology during design optimization. All design variables start from zero, which means the values of design variables are relative change of its coordinates. Four design variables are changed up to their lower or upper bounds.

Figure 11.5.35 provides an optimization history of the mass function. Through optimization, the structural mass was reduced from 0.878 kg to 0.421 kg (47.9%). The highest stress value initially, 305 MPa around the left hole, shifts to 800 MPa around the upper frame at optimum design. A total of 41 response analyses and 20 sensitivity analyses were carried out during 20 optimization iterations. When

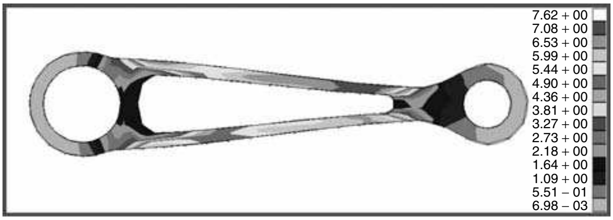

FIGURE 11.5.34 Analysis result at optimum design.

TABLE 11.5.9 Design Variables at the Initial and Optimum Designs

Design	Lower Bound	Initial Design	Optimum Design	Upper Bound
u_1	−3.000	0.0	−3.000	2.000
u_2	−0.500	0.0	−0.500	2.000
u_3	−2.000	0.0	−0.589	2.000
u_4	−3.000	0.0	−2.700	2.000
u_5	−4.500	0.0	−4.490	2.000
u_6	−0.500	0.0	2.000	2.000
u_7	−2.000	0.0	4.460	5.000
u_8	−0.500	0.0	−0.00714	2.000

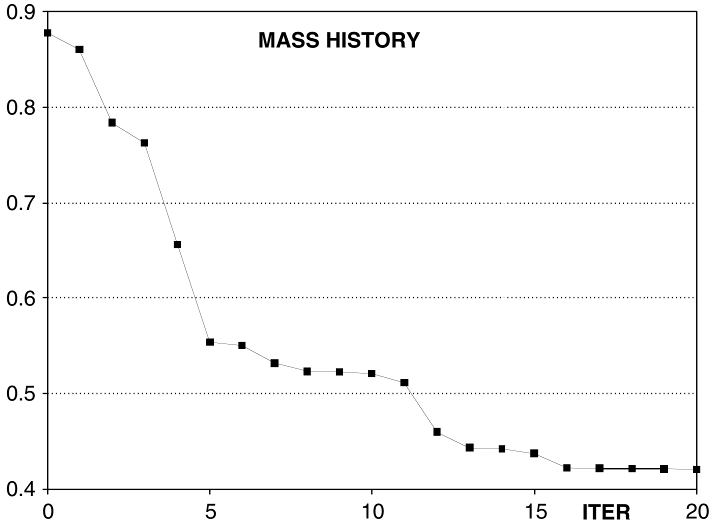

FIGURE 11.5.35 Histories of design optimization.

the finite difference methods are used with a re-meshing process,[34] the optimization process converged at 45 iterations with eight re-meshing processes. Thus, this approach reduces the cost of design more than 50%, without even mentioning the cost related to the re-meshing process.

The Road Arm Model

As a second example, the design optimization is carried out to minimize the structural weight of the road arm, while maintaining the maximum stress level. The same algorithm as with the torque arm model is used. Design optimization problem converges after eight iterations. Figure 11.5.36 compares the structural analysis result at the initial and optimum designs. The structural weight at the optimum design is reduced by 23% compared to the initial weight. Since the stress concentration appears in the left corner at the initial design, the optimization algorithm tried to reduce the cross section of the right corner so that both parts may have the same level of stress values. Figure 11.5.37 shows the optimization history of cost function and design variables. Due to the accurate sensitivity information, the optimization algorithm converges rather quickly. Also, the small design change can be another explanation of the fast convergence.

Gradient-Free Design Optimization

Genetic Algorithms

Genetic algorithms (GA) are inspired by Darwin's principle of evolution, which states that a population of individuals is capable of adapting to its environment because individuals who possess traits that make them less vulnerable than others are more likely to have descendents and therefore to pass on their desirable

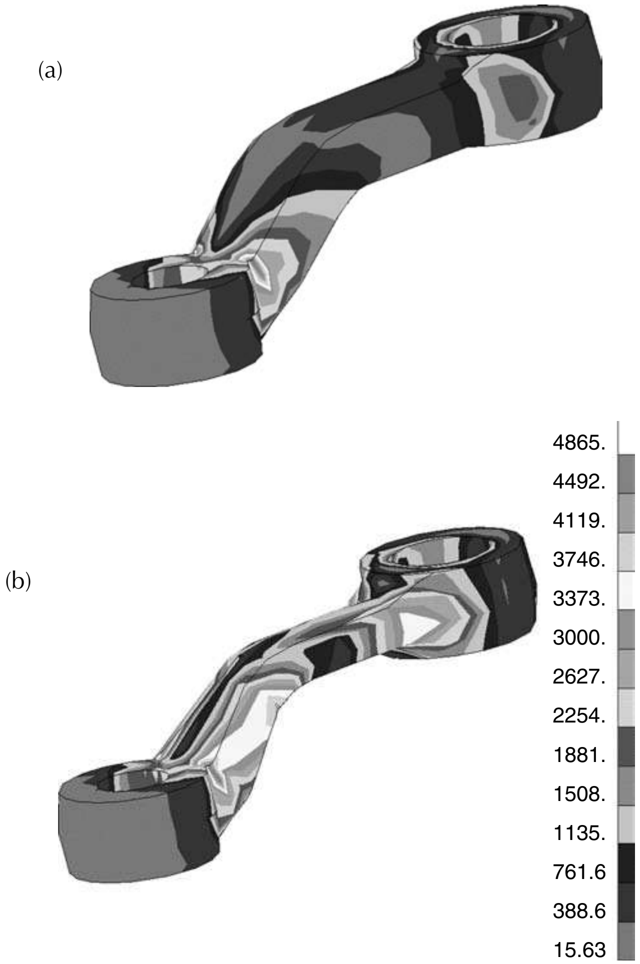

FIGURE 11.5.36 Structural analysis results (a) initial design; (b) optimum design.

traits to the next generation. One can think of this process of adaptation as an optimization process that probabilistically creates fitter individuals through selection and recombination of good characters. Genetic algorithms are simplified computer models of evolution, where the environment is emulated by the objective function to maximize, and the structure to optimize plays the role of the individuals.

A flowchart of a genetic algorithm is presented in Figure 11.5.38. GAs start by initializing a population of individuals at random. Each individual encode of a particular candidate structure in the form of one or several chromosomes, which are strings of finite length. Then the objective function of each individual, called the fitness function in the context of evolutionary computation, is computed. The fitness of each individual determines its probability of being selected for reproduction. Instead of moving from one design point to another, the search is based on a population of design points that evolve from one generation to another. Recombination and mutation operators are then applied to the selected individuals (the parents) to create a population of children. Finally a survival rule determines the individuals among the parent and child population that will be kept to form the new population.

When to Use Genetic Algorithms?

Genetic algorithms are computationally expensive compared to deterministic algorithms. Consequently, their domain of application consists of problems that would be difficult to solve by gradient-based algorithms, or problems that would be out of range for these algorithms. Some of the main advantages of GAs are the following:

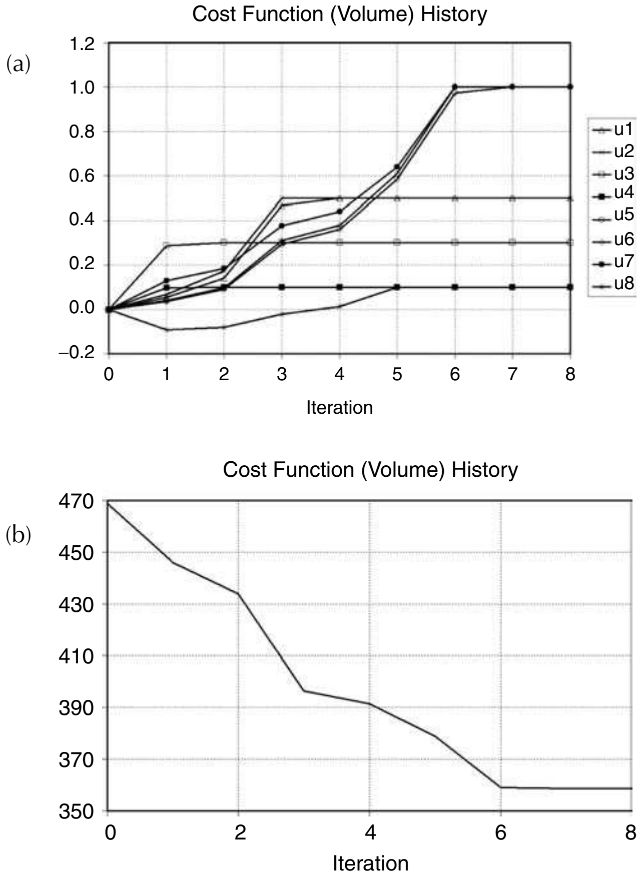

FIGURE 11.5.37 Design optimization history (a) cost function history; (b) design variable history.

- GAs do not require continuity or differentiability of the objective function. They do not need gradients.
- They are robust: they are very insensitive to noise.
- They are modular and therefore portable; because the evolutionary mechanism is separate from the problem representation, they can be transferred from problem to problem.
- They are particularly efficient on discrete and combinatorial problems, which are typically difficult to solve by conventional algorithms; they can be used for problems involving both discrete and continuous variables.
- Because they explore the design space with populations, GAs are “naturally” amenable to parallelization.

Examples of Applications

GAs have been used to solve a wide variety of engineering problems that would be difficult to tackle with other methods, such as scheduling problems, distribution network optimization, plant or product design, and real-time control of industrial processes and communications networks. A practical example of application is the optimization of the lay-up of composite laminate, where the goal is to determine the optimal fiber orientation of each of the layers of the laminate. This problem is difficult to solve by gradient-based algorithms because the objective function is often multimodal, and the fiber orientations have to be chosen from a set of discrete values to meet manufacturability requirements. On these problems, GAs prove to be very effective design tools.

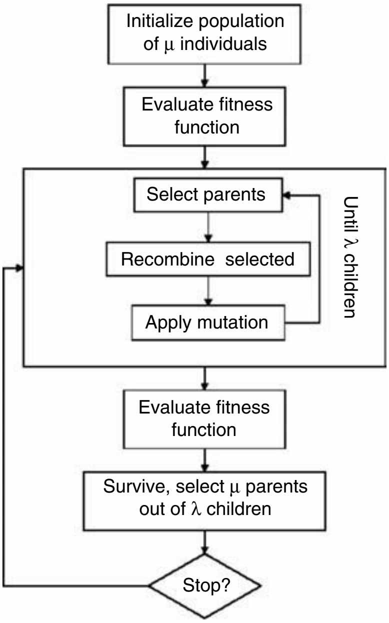

FIGURE 11.5.38 Genetic algorithm.

Simulated Annealing

Simulated annealing (SA) is based on a simple algorithm introduced by Metropolis et al.[44] to efficiently predict the behavior of a collection of atoms in equilibrium at a given temperature. The Metropolis approach simulates the cooling process by means of an iterative algorithm, in which each atom is given a small random displacement and the resulting change of energy ΔE is computed. If $\Delta E \leq 0$ the displacement is accepted and the resulting configuration is used as the initial point for the next iteration. If $\Delta E > 0$ a probability of acceptance is calculated with the Boltzmann factor:

$$P(\Delta E) = e^{-\left(\frac{\Delta E}{k_b T}\right)}$$

If ΔE is less than $P(\Delta E)$ the new configuration is accepted and used in the next iteration. This criterion ensures that the system will eventually evolve into a Boltzmann equilibrium distribution.

By using the Metropolis procedure with a cost function in place of system energy, the simulated annealing algorithm is obtained.[45] The configuration of atoms will then be a combination of design parameters, which are evaluated in the same manner.

The temperature T becomes a control parameter with the same units as the cost function, and is used to first “melt” the system at a high temperature, with a population of possible parameter configurations being generated. The iterative simulation is then run at this temperature until the system is considered to be in equilibrium, and only then is the temperature reduced by a small fraction. This cooling and equilibrium process continues until no further improvement becomes possible and the system is considered “frozen” or crystallized, with the design parameters at this condition optimal. The temperature reduction sequence and number of iterations allowed for the system to reach equilibrium are considered analogues to an annealing schedule.

An important difference from iterative improvement procedures such as gradient-based methods is that the Metropolis method need not get stuck since transitions out of a local optimum are always possible at a nonzero temperature.

Applications of this algorithm include the well-known traveling salesman problem,[46] and routing and layout of electrical connections on computers,[44] among others. Like genetic algorithms, this population-based method is relatively insensitive to noise, and doesn't require gradient information. A major drawback to this method, however, is the problem dependency of algorithm parameters, for example, it is important to use an annealing schedule that is tailored to the type of optimization problem being solved; otherwise, the optimizer will perform poorly. Various statistical methods have been proposed, all with limited success, to obtain optimum cooling rates to avoid entrapment in local optima.

References

1. Bendsoe, M.P. 1995. *Optimization of Structural Topology, Shape, and Materials*. Springer-Verlag, Berlin.
2. Clark, K.B. and Fujimoto, T. 1991. *Product Development Performance*. Harvard Business School Press, Boston.
3. Zienkiewicz, O.C. 1977. *The Finite Element Method*. McGraw-Hill, New York.
4. Haug, E.J., Choi, K.K., and Komkov, V. 1986. *Design Sensitivity Analysis of Structural Systems*. Academic Press, London.
5. Haftka, R.T. and Grandhi, R.V., Structural shape optimization — a survey. *Computer Methods in Appl. Mech. and Eng.*, 57, 91–106, 1986.
6. Ding, Y., Shape optimization of structures — a literature survey. *Comput. and Structures*, 24, 6, 985–1004, 1986.
7. Bhavikatti, S.S. and Ramakrishnan, C.V., Optimum shape design of rotating disks. *Comput. and Structures*, 11, 397–401, 1980.
8. Prasad, B. and Emerson, J.F., Optimal structural remodeling of multi-objective systems. *Comput. and Structures*, 18, 4, 619–28, 1984.
9. Kristensen, E.S. and Madsen, N.F., On the optimum shape of fillets in plates subjected to multiple in-plane loading cases. *Int. J. for Numerical Methods in Eng.*, 10, 1007–19, 1976.
10. Pedersen, P. and Laursen, C.L., Design for minimum stress concentration by finite elements and linear programming. *J. of Structural Mech.*, 10, 375–91, 1982.
11. Yang, R.J. and Choi, K.K., Accuracy of finite element based shape design sensitivity analysis. *J. of Structural Mech.*, 13, 223–39, 1985.
12. Luchi, M.L., Poggialini, A., and Persiani, F., An interactive optimization procedure applied to the design of gas turbine discs. *Comput. and Structures*, 11, 629–37, 1980.
13. Weck, M. and Steinke, P., An efficient technique in shape optimization. *J. of Structural Mech.*, 11, 433–49. 1983–84.
14. Braibant, V., Fleury, C., and Beckers, P. 1983. *Shape Optimal Design: An Approach Matching CAD and Optimization Concepts*, Aerospace Laboratory of the University of Liege, Belgium.
15. Braibant, V. and Fleury, C., S*hape optimal design using B-spline. Computer Methods in Appli. Mech. and Eng.*, 44, 247–67, 1984.
16. Yao, T.M. and Choi, K.K., 3-D shape optimal design and automatic finite element regridding. Int. *J. for Numerical Methods in Eng.*, 28, 369–84, 1989.
17. Yao, T.M. and Choi, K.K., Shape optimal design of an arch dam. *ASME J. of Structural Eng.*, 115, 9, 2401–5, 1989.
18. Choi, K.K. and Yao, T.M., 3-D shape modeling and automatic regridding in shape design sensitivity analysis. *Sensitivity Analysis in Engineering*, NASA Conference Publication 2457, pp. 329–45, 1987.
19. Akgün, M.A., Garcelon, J.H., and Haftka, R.T., Fast exact linear and nonlinear structural reanalysis and the Sherman-Morrison-Woodbury formulas. *Int. J. Numerical Methods in Eng.*, 50, 7, 1587–1606, 2001.
20. Yoon, B.G. and Belegundu, A.D., Iterative methods for design sensitivity analysis. *AIAA J.*, 26, 11, 1413–15, 1988.

21. Kirsch, U. and Lui, S., Structural reanalysis for general layout modifications. *AIAA J.,* 35, 382–88, 1997.
22. Oral, S., An improved semianalytical method for sensitivity analysis. *Structural Optimization*, 11, 67–69, 1996.
23. Hörnlein, H.R.E.M., Effiziente semi-analytische gradientenberechnung in der strukturoptimierung. Z. Angew. *Math. Mech.*, 81, s669–s670, 2000.
24. Barthelemy, B.M. and Haftka, R.T., Accuracy Analysis of the Semi-analytical Method for Shape Sensitivity Calculation. 29th AIAA/ASME/ASCE/AHS Structures, Structural Dynamics and Materials Conference, 1988.
25. Olhoff, N., Rasmussen, J., and Lund, E., A method of exact numerical differentiation for error elimination in finite-element-based semianalytical shape sensitivity analyses. *Mech. of Structures and Machines*, 21, 1, 1–66, 1993.
26. Arora, J.S., An exposition of the material derivative approach for structural shape sensitivity analysis. *Computer Methods in Appl. Mech. and Eng.*, 105 ,41–62, 1993.
27. Phelan, D.G. and Haber, R.B., Sensitivity analysis of linear elastic systems using domain parameterization and a mixed mutual energy principle. *Computer Methods in Appl. Mech. and Eng.*, 77, 31–59, 1989.
28. Yang, R.J. and Botkin, M.E., Accuracy of the domain method for the material derivative approach to shape design sensitivities, in *Sensitivity Analysis in Engineering*, 1987, NASA Conference Publication 2457, pp. 347–53.
29. Ozaki, I. and Terano, T., Applying an automatic differentiation technique to sensitivity analysis in design optimization problems. *Finite Elements in Analysis and Design*, 14, 143–151, 1993.
30. Walsh, J.L., Young, K.C., Tarzanin, F.J., Hirsh, J.E., and Young, D.E., Optimization issues with complex rotorcraft comprehensive analysis. 7th AIAA/USAF/NASA/ISSMO Symposium on Multidisciplinary Analysis and Optimization (September 2–4, 1998), Volume Part 2, AIAA 98-4889.
31. Bischof, C., Carle, A., Khademi, P., and Mauer, A., The adifor 2.0 system for the automatic differentiation of fortran 77 programs. *IEEE Computational Science & Eng.*, 3, 18–32, 1996.
32. Griewank, A., Juedes, D., and Utke, J., Adol-c, a package for the automatic differentiation of algorithms written in C/C++. *TOMS*, 22, 2, 131–67, 1996.
33. Kim, N.H., Choi, K.K., and Botkin, M.E., Numerical method of shape optimization using meshfree method. *Structural and Multidisciplinary Optimization*, 24, 6, 418–29, 2003.
34. Bennett, J. A. and Botkin, M.E., Structural shape optimization adaptive mesh refinement. *AIAA J.*, 23, 458–64, 1985.
35. *MSC/PATRAN User's Guide*. The MacNeal–Schwendler Corp., Los Angeles, CA, 1999.
36. Chang, K.H., Choi, K.K., Tsai, C.S., Chen, C.J., Choi, B.S., and Yu, X.,. Design sensitivity analysis and optimization tool (DSO) for shape design applications. *Computing Syst. in Eng*. 6, 151–175, 1995.
37. Kim, N.H., Dong, J., Choi, K.K., Vlahopoulos, N., Ma, Z.D., Castanier, M.P., and Pierre, C., Design sensitivity analysis for a sequential structural-acoustic problem. *J. Sound and Vibration*, 263, 3, 569–91, 2003.
38. Arora, J.S. 1999. *Introduction to Optimum Design*. McGraw-Hill, New York.
39. Vanderplaats, G.N. 1999. *Numerical Optimization Techniques for Engineering Design with Applications*. Vanderplaats Research & Development Inc., Colorado Springs, CO.
40. Haftka, R.T. and Karmat, M.P. 1985. *Elements of Structural Optimization*. Nijhoff Publishers, Netherlands.
41. Luenberger, D.G. 1984. *Linear and Nonlinear Programming*. Addison-Wesley, Boston.
42. Fletcher, R. and Reeves, R.M., Function minimization by conjugate gradients. *Computer J.*, 7, 149–60, 1964.
43. Fletcher, R. and Powell, M.J.D., A rapidly convergent descent method for minimization. *Computer J.*, 6, 163–80, 1963.

44. Metropolis,N., Rosenbluth, A., Rosenbluth, M., Teller, A., and Teller, E., Equation of state calculations by fast computing machines. *J. Chem. Phys.*, 21, 6, 1087–92, 1953.
45. Kirkpatrick, S., Gelatt C.D. Jr., and Vecchi, M.P., Optimization by simulated annealing. In *Science*, 220, 4598, 671–80, 1983.
46. Cerny, V., Thermodynamical approach to the traveling salesman problem: an efficient simulation algorithm, *J. Opt. Theory Appl.*, 45, 1, 41–51, 1985.

12
Materials

Victor A. Greenhut
Rutgers University

James D. Idol
Rutgers University

Richard L. Lehman
Rutgers University

Daniel J. Strange
Alfred University

Steven H. Kosmatka
Portland Cement Institute

Bhuvenesh C. Goswami
Clemson University

Weiping Wang
General Electric Corporate R&D

R. Alan Ridilla
General Electric Plastics

Matthew B. Buczek
General Electric Aircraft Engines

William F. Fischer, III
Lanxide Corporation

12.1 Metals

Victor A. Greenhut

Introduction — Nature and Properties of Pure Metals

Metals achieve engineering importance because of their abundance, variety, and unique properties as conferred by metallic bonding. Twenty-four of the 26 most abundant elements in the Earth's crust are metals, with only two nonmetallic elements, oxygen and silicon, exceeding metals in frequency. The two

---

most abundant metallic elements, iron (5.0%) and aluminum (8.1%), are also the most commonly used structural metals. Iron is the most-used metal, in part because it can be extracted from its frequently occurring, enriched ores with considerably less energy penalty than aluminum, but also because of the very wide range of mechanical properties its alloys can provide (as will be seen below). The next 15 elements in frequency, found at least in parts per thousand, include most common engineering metals and alloys: calcium (3.6%), magnesium (2.1%), titanium (0.63%), manganese (0.10), chromium (0.037%), zirconium (0.026%), nickel (0.020%), vanadium (0.017%), copper (0.010%), uranium (0.008%), tungsten (0.005%), zinc (0.004%), lead (0.002%), cobalt (0.001%), and beryllium (0.001%). The cost of metals is strongly affected by strategic abundance as well as secondary factors such as extraction/processing cost and perceived value. Plain carbon steels and cast irons, iron alloys with carbon, are usually most cost-effective for ordinary mechanical applications. These alloys increase in cost with alloying additions.

A variety of metal properties are unique among materials and of importance technologically. These properties are conferred by metallic bonding, in which the “extra” outer valence electrons are “shared” among all metal ion cores. This bonding is different from other types of solids in that the electrons are free to acquire energy, and the metallic ions are relatively mobile, and quite interchangeable with regard to their positions in the crystal lattice, the three-dimensional repeating arrangement of atoms in a solid. This section of the chapter will concentrate on the mechanical properties of metals, for which metallic bonding provides ductile deformation, i.e., shows substantial permanent shape change under mechanical load prior to fracture. The ductility of metals at low and moderate temperature makes them formable as solids and also confers safety (fracture toughness) in mechanical applications, in that under impact loading the metal will absorb energy rather than break catastrophically.

Metals are good conductors of heat and electricity because thermal and electrical energy can be transferred by the free electrons. These two properties tend to parallel each other. For example, the pure noble metals (e.g., copper, silver, gold, platinum) are among the best electrical and thermal conductors. As a broad generalization, metallic elements with an odd number of valence electrons tend to be better conductors than those with an even number. These behaviors can be seen in Table C.6A of the Appendix. Thermal conductivity and electrical resistivity (inverse conductivity) have a reciprocal relationship and follow the indicted trends. As metals are alloyed with other elements, are deformed, contain multiple phases, and contain crystalline imperfections, their electrical and thermal conductivity usually decreases significantly from that of the pure, perfect, unalloyed metal. The specific values of thermal conductivity and electrical resistivity for several common engineering alloys is given in Table C.6B of the Appendix. Electrical and thermal conductivities tend to decrease proportionately to each other with increasing temperature for a specific metal. These conductivities may be altered if heating introduces metallurgical change during annealing (see subsection on mechanical forming).

Metals are opaque to and reflective of light and most of the electromagnetic spectrum, because electromagnetic energy is transferred to the free electrons and immediately retransmitted. This gives most metals a characteristic reflective “metallic color” or sheen, which if the metal is very smooth yields a mirror surface. At very short wavelengths (high energies) of the electromagnetic spectrum, such as X rays, the radiant energy will penetrate the material. This is applied in radiographic analysis of metals for flaws such as cracks, casting porosity, and inclusions.

Metals are almost always crystalline solids with a regular repeating pattern of ions. A number of atomic-level defects occur in this periodic array. A large number of atomic sites are “vacancies” (point defects) not occupied by atoms (Figure 12.1.1). The number and mobility of vacant sites increase rapidly with temperature. The number and mobility of vacancies in metals are quite high compared with other materials because there are no charge balance or local electron bond considerations. This means that solid metal can undergo significant changes with only moderate thermal excitation as vacancy motion (diffusion) provides atom-by-atom reconstruction of the material. Vacancies allow solid metals to homogenize in a “soaking pit” after casting and permit dissimilar metals to diffusion bond at moderate temperatures and within short times. In the process, substitutional metallic atoms (ions) shown in Figure 12.1.1 move via vacancy jumps while small interstitial atoms such as carbon (Figure 12.1.1) move from

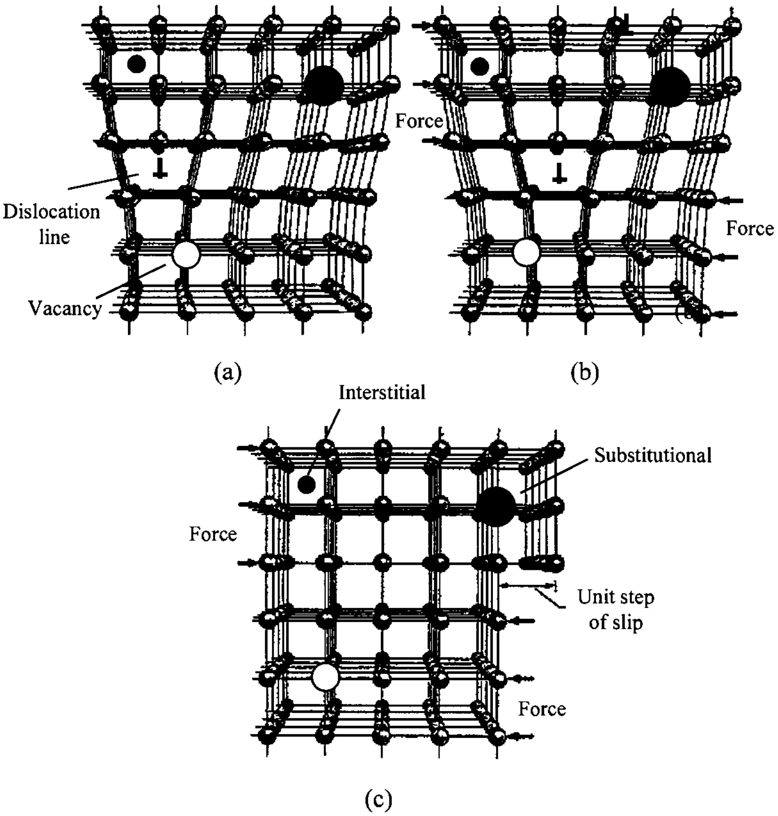

FIGURE 12.1.1 Point defects exist in the metal crystal structure: vacancies, substitutional atoms (ions), ions, and interstitial atoms (ions). A dislocation (⊥) line moves under an applied shear force until a surface step of plastic deformation is produced on the surface.

interstice to interstice. Vacancy mobility gives rise to major changes in mechanical properties during annealing (see subsection on mechanical forming) and is an important mechanism in creep deformation under load at elevated temperature (see subsection on corrosion and environmental effects).

At a slightly larger level, linear atomic packing defects known as dislocations, give rise to the ability of metallic materials to deform substantially under load. When a plane of atoms in the lattice ends, it gives rise to an edge "dislocation" such as that shown in Figure 12.1.1a. Such a dislocation can break and remake bonds relatively easily in a metal and thereby shift an atomic distance (Figure 12.1.1b). The process can continue until a surface step results. Many dislocations moving in this fashion can give rise to significant shape change in the material at moderate stresses. The onset of such massive dislocation motion in a metal is termed *yield* and occurs at the "yield stress" or "elastic limit" (see subsection on strength and deformation). Dislocations explain why the yield stress can be as low as about 100 Pa (10 psi) in a pure, pristine, single crystal of metal. Dislocations also explain how a fine-grained polycrystalline metal containing many microstructural features which interfere with dislocation motion may have a yield stress as great as 10 gPa (1000 ksi). Dislocations interact with each other in three dimensions and multiply. Therefore, dislocation motion can cause a major increase in dislocation density and yield stress, termed *cold work*. Vacancies can rearrange these dislocation tangles, restoring the metal to a condition closer to its original state, thereby lowering the yield stress. This can occur at moderate annealing temperatures (see subsection on mechanical forming).

The interaction of deformation, alloying elements, temperature, and time can cause a wide variety of microstructures in a solid metal down to near atomic levels with mechanical (and other) properties which can vary over a very wide range. It is possible to manipulate the properties of a single metal composition over a very wide range in the solid state — a behavior which can be used to mechanically form a particular metal and then use it in a demanding load-bearing application. The use of minor alloying additions can provide a yet wider range of properties with appropriate thermal and mechanical treatment.

Casting

One of the important technological advantages of metals is their ability to incorporate a wide variety of secondary elements in a particular metal and thereby create alloys of the metal. Alloying can increase the strength of a metal by several orders of magnitude and permit the strength and ductility to be varied over a wide range by thermal and/or mechanical treatment, resulting in ease of mechanical forming or resistance to deformation.

Several metal phases may exist together in the solid as grains (crystals), or secondary phases may occur as smaller entities on grain (intercrystal) boundaries or within grains. Often the strengthening phase is submicroscopic and cannot be detected by optical metallography (reflection optical microscopy). The size and distribution of secondary phases is manipulated by thermomechanical (thermal and/or mechanical) treatment of the solid metal as well as the original casting procedure.

Casting methods include expendable mold casting (investment/precision, plaster mold, dry sand, and wet sand casting), permanent mold casting (ingot, permanent mold, centrifugal, and die casting), and continuous casting (direct chill and "splat" casting). These are listed in approximate order of cooling rate in Figure 12.1.2. As cooling rate increases, the grain (crystal) size tends to be smaller and the strength increases while compositional segregation decreases, providing more uniform properties. At the extremely high casting rates (10^5 to 10^6/sec) of continuous splat casting, it is possible to produce homogeneous metals not possible in terms of phase diagrams, and many metals have been produced in the amorphous state, yielding unusual metallic glasses. Ingot casting and continuous direct chill casting are primarily used to produce solid metal which will be extensively mechanically formed to final shape. The other casting methods are used to produce shapes near final dimensions, but to varying extends may receive extensive machining, forming, or finishing prior to use. For the latter group, grain refiners are frequently added to reduce solidification grain size. Metal tends to solidify directionally, with grains elongated in the direction of heat flow. This gives rise to directional mechanical properties which should be accounted for in design.

To obtain optimum properties and prevent flaws which may cause failure, the casting procedure must avoid or control compositional segregation, shrinkage cavities, porosity, improper texture (grain directionality), residual (internal) stresses, and flux/slag inclusions. This can be accomplished with good

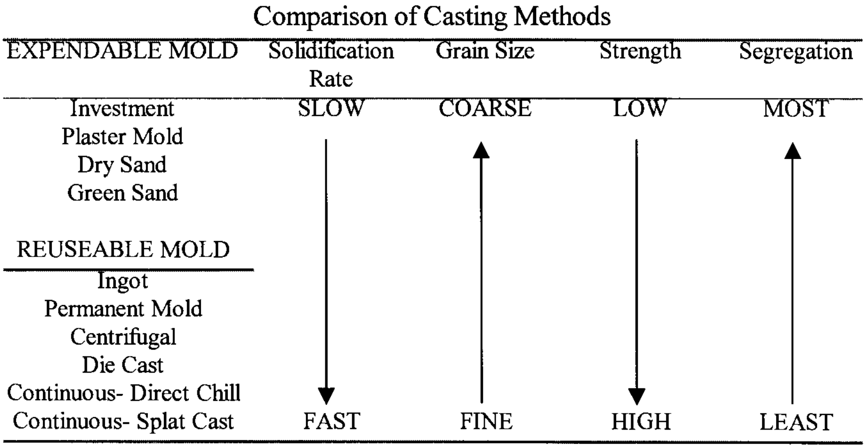

FIGURE 12.1.2 The effects of casting speed (solidification rate) are compared.

casting practice. With the exception of investment (lost wax, precision) casting and to a lesser extent die casting, it is difficult to achieve very exacting tolerances and fine surface finish without postfinishing or forming of a casting.

Strength and Deformation, Fracture Toughness

Figure 12.1.3 shows a typical stress–strain diagram for a metal. The first portion is a linear, spring-type behavior, termed *elastic*, and attributable to stretching of atomic bonds. The slope of the curve is the "stiffness" (given for various metals in Table C.3 of the Appendix). The relative stiffness is low for metals as contrasted with ceramics because atomic bonding is less strong. Similarly, high-melting-point metals tend to be stiffer than those with weaker atomic bonds and lower melting behavior. The stiffness behavior is frequently given quantitatively for uniaxial loading by the simplified expressions of Hooke's law:

$$\varepsilon_x = \sigma_x / E \qquad \varepsilon_y = \varepsilon_z = -\upsilon\sigma_x / E \tag{12.1.1}$$

where σ_x is the stress (force per unit area, psi or Pa) in the x direction of applied unidirectional tensile load, ε_x is the strain (length per unit length or percent) in the same direction ε_y and ε_z are the contracting strains in the lateral directions, E is Young's modulus (the modulus of elasticity), and υ is Poisson's ratio. Values of the modulus of elasticity and Poisson's ratio are given in Table C.6A of the Appendix for pure metals and in C.6B for common engineering alloys. It may be noted that another property which depends on atomic bond strength is thermal expansion. As the elastic modulus (stiffness) increases with atomic bond strength, the coefficient of linear expansion tends to decrease, as seen in Table C.6.

The relationship of Equation (12.1.1) is for an isotropic material, but most engineering metals have some directionality of elastic properties and other structure-insensitive properties such as thermal expansion coefficient. The directionality results from directional elongation or preferred crystal orientation, which result from both directional solidification and mechanical forming of metals. In most cases two

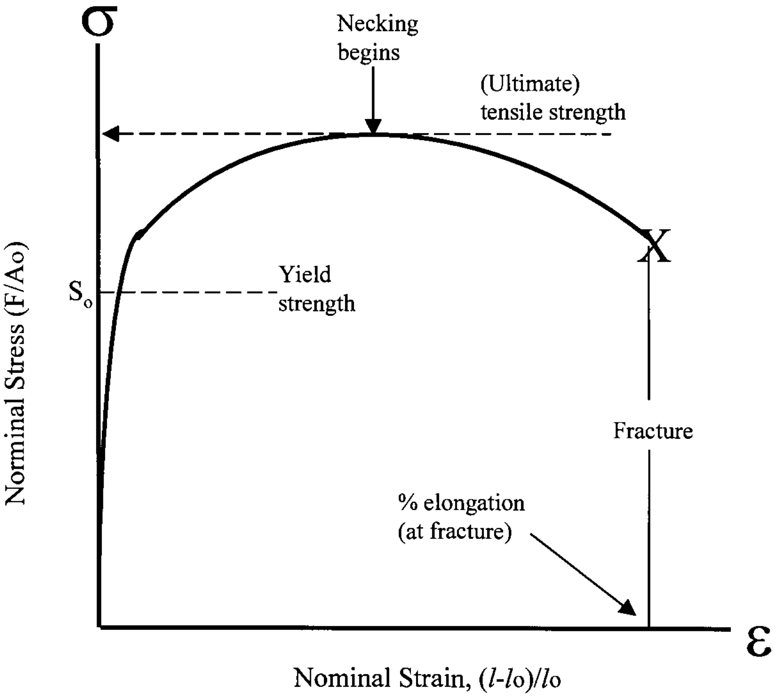

FIGURE 12.1.3 Typical engineering stress–strain curve for a metal.

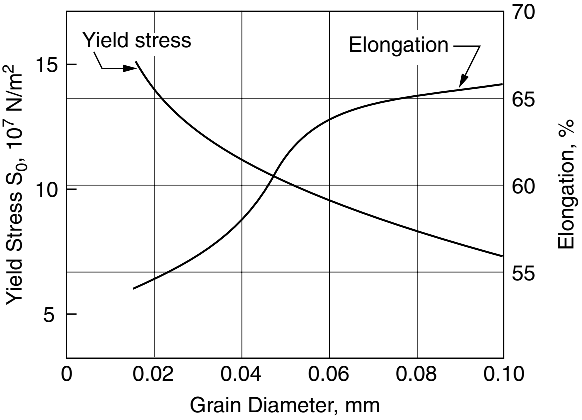

FIGURE 12.1.4 The effect of grain (crystal) size on yield stress and elongation to failure (ductility) for cartridge brass (Cu–30 Zn) in tension.

elastic moduli and a Poisson's ratio are required to fully specify behavior. A principal modulus might be given in the rolling direction of sheet or plate with a secondary modulus in the transverse direction. A difference of 2 to 5% should ordinarily be expected, but some metals can show an elastic modulus difference as great as a factor of 2 in the principal directions of heavily formed material. Such directional differences should be accounted for when spring force or dimensional tolerance under load (or change of temperature) is critical in a design.

At a critical stress the metal begins to deform permanently, as seen as a break in the straight-line behavior in the stress-strain diagram of Figure 12.1.3. The stress for this onset is termed the yield stress or elastic limit. For engineering purposes it is usually taken at 0.2% plastic strain in order to provide a predictable, identifiable value. An extensive table of yield values and usual applications for commercial metals and alloys is given in Appendix C.5. In the case of steel a small yield drop allows for clear identification of the yield stress and this value is used. The onset of yield is a structure-sensitive property. It can vary over many orders of magnitude and depends on such factors as grain size and structure, phases present, degree of cold work, and secondary phases in grains or on grain boundaries as affected by the thermal and mechanical treatment of the alloy. The extension to failure, the ductility, and maximum in the stress–strain curve, the "ultimate stress" or "tensile strength" (see Appendix C.5) are also structure-sensitive properties. The strength and specific strength (strength-to-weight ratio) generally decrease with temperature.

The ductility usually decreases as the strength (yield or ultimate) increases for a particular metal. Reduction in the grain size of the metal will usually increase yield stress while decreasing ductility (Figure 12.1.4). Either yield or ultimate strength are used for engineering design with an appropriate safety factor, although the former may be more objective because it measures the onset of permanent deformation. Ductility after yield provides safety, in that, rather than abrupt, catastrophic failure, the metal deforms.

A different, independent measure is needed for impact loads — "toughness." This is often treated in design, materials selection, and flaw evaluation by extending Griffith's theory of critical flaw size in a brittle material:

$$\sigma_f = K_{1c} / \gamma c^{1/2} \tag{12.1.2}$$

where σ_f is the failure stress, K_{1c} is a structure-sensitive materials property, the "fracture toughness" or "stress intensity factor" for a normal load, γ is a constant depending on orientation, and c is the depth of a long, narrow surface flaw or crack (or half that of an internal flaw). This is a separate design issue from that of strength. It is of particular importance when a metal shows limited ductility and catastrophic failure must be avoided. In some applications the growth of cracks, c is monitored to prevent catastrophic failure. Alternatively, as a performance test sufficient energy absorption as characteristic of a metal is determined when it is fractured in a Charpy or Izod impact test. Many metals will show a rapid decline in such energy absorption below a nil ductility temperature (NDT), which may establish a lowest use temperature for a particular metal in a particular state and for a particular application. Welds are often qualified by impact tests as well as strength testing. Care must be taken to apply the impact test appropriate to an application.

Hardness, the resistance of the near surface of a metal to penetration by an indentor, is also employed as a mechanical test. Increased hardness can often be correlated with an increase in yield and ultimate strengths. Typical hardness values for a large number of commercial metals and alloys are provided in Appendix C.5. A hardness indent is frequently done to "determine" the strength of a steel, using "equivalency" tables. Great caution must be taken in applying such tables because while hardness is an easy test to perform, it measures a complex and interactive set of properties, increasing with strength, elastic modulus, and work hardening rate. It is also an observation of surface properties which may not be characteristic of the bulk metal — particularly thick-gauge steel used in tension. Surface-hardening treatments can make the simplistic use of an "equivalency" table particularly dangerous. Application to nonferrous metals is also problematic. If a hardness tested part is to be put into service, the placement of hardness indents (surface flaws) can cause permanent failure.

A summary of important engineering metals can be found in Appendix C.5. This extensive table provides strength, hardness, and applications information for many commercial metals in varied heat treatments.

Mechanical Forming

Hot working is used when major shape change, cross-section reduction, or texture (directional) properties are desired. Cold working is preferred when close tolerances and fine surface finish are needed. The cold-worked form of a metal typically shows higher yield and tensile strength, as can be seen for several alloys listed in Appendix C.5. Rolling, forging, and extrusion are primarily done hot, while shape drawing, extrusion, deep drawing, stretching, spinning, bending, and high-velocity forming are more commonly performed cold. Hot rolling between parallel rollers is used to reduce ingots to plates, sheets, strips, and skelp, as well as structural shapes, rail, bar, round stock (including thick-walled pipe), and wire. Sheet metal and threads on round or wire stock may be rolled to shape cold. Closed die hot forging employs dies with the final part shape, while open die forging (including swaging and roll forging) uses less-shaped dies. Coining, embossing, and hobbing are cold-forging operations used to obtain precision, detailed surface relief or dimensions. Generally, extrusion and die drawing require careful control of die configuration and forming rate and, in the latter case, lubricant system. Impact extrusion, hydrostatic extrusion, and deep drawing (thin-walled aluminum cans) permit very large precise dimensional and cross-section changes to be made cold in a single pass. Stretching, spinning, bending are usually used to shape sheet or plate metal and the spring-back of the metal due to elastic modulus must be accounted for to obtain a precise shape.

Solute, Dispersion, and Precipitation Strengthening and Heat Treatment

Alloying additions can have profound consequences on the strength of metals. Major alloying additions can lead to multiphase materials which are stronger than single-phase materials. Such metal alloys may also give very fine grain size with further strengthening of material. Small alloying additions may also substantially increase strength by solute strengthening as solid solution substitutional or interstitial atoms and or by particle strengthening as dispersion or precipitation hardening alloys.

Substitutional solute strengthening of copper by various atoms is shown in Figure 12.1.5. As the amount of an alloying element in solution increases, the strength increases as dislocations are held in place by the "foreign" atoms. The greater the ionic misfit (difference in size — Sn is a much larger ion than Ni), the greater the strengthening effect. The strength increase can be quite dramatic — as much as a 20-fold

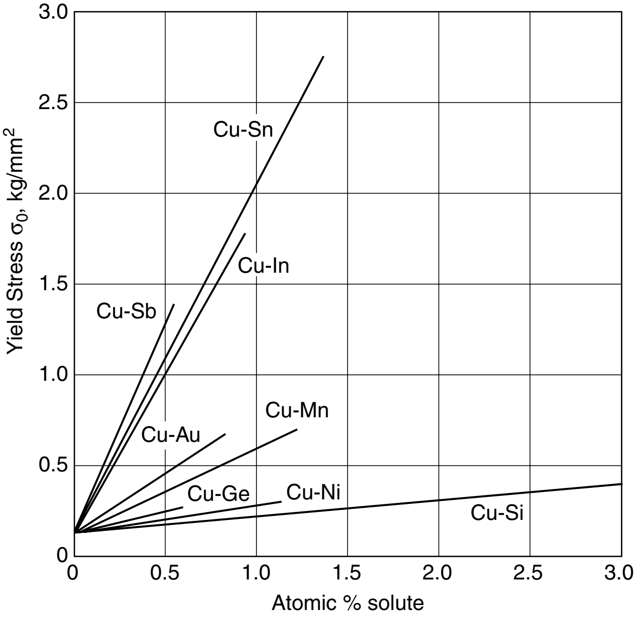

FIGURE 12.1.5 Effect of various substitutional atoms on the strength of copper. Note that as the ionic size of the substitutional atom becomes larger the strengthening effect becomes greater.

increase with a 1.5% addition to copper. Alternatively, a large addition of a very soluble element such as nickel can give major strengthening — monel, the Cu–70Ni alloy is more than four times stronger than pure copper (Figure 12.1.6). Interstitial solid solution carbon contributes to the strength of iron and is one contributor to strength in steels and cast irons. Solute strengthening can become ineffective in strengthening at elevated temperature relative to the absolute melting point of a metal as a result of rapid diffusion of substitutional and interstitial elements. The addition of more than one solute element can lead to synergistic strengthening effects, as this and other strengthening mechanisms can all contribute to the resistance of a metal to deformation.

Ultrafine particles can also provide strengthening. A second phase is introduced at submicroscopic levels within each crystal grain of the metal. This may be done by a variety of phase-diagram reactions, the most common being precipitation. In this case the solid alloy is heated to a temperature at which the secondary elements used to produce fine second-phase particles dissolve in the solid metal — this is termed *solution heat treatment*. Then the metal is usually quenched (cooled rapidly) to an appropriate temperature (e.g., room temperature or ice brine temperature) and subsequently held at an elevated temperature for a specified "aging" time during which particles precipitate and grow in size at near atomic levels throughout the solid metal. Temperature, time, alloy composition, and prior cold work affect the size and distribution of second-phase particles. The combination of treatments can be quite complex, and recently "thermomechanical treatments" combining temperature, time, and dynamic working have resulted in substantial property improvements. Heat treatment can be performed by the user, but it is difficult to achieve the optimum properties obtained by a sophisticated metallurgical mill. The heat treatment can manipulate structure and properties to obtain maximum strength or impact resistance. When metal is to be cold worked, a "softening treatment" can be employed which provides low yield stress and high ductility. The difference between the "dead soft" and maximum strength conditions can be over an order of magnitude — a useful engineering property change.

Alternative surface diffusion methods such as nitriding and carburizing, which introduce particles for fracture and wear resistance, are presented in the subsection on metal surface treatments.

In the case of dispersion strengthening (hardening), the fine strengthening particles are a discontinuous second phase without atomic continuity with the matrix. The behavior of such particles is shown

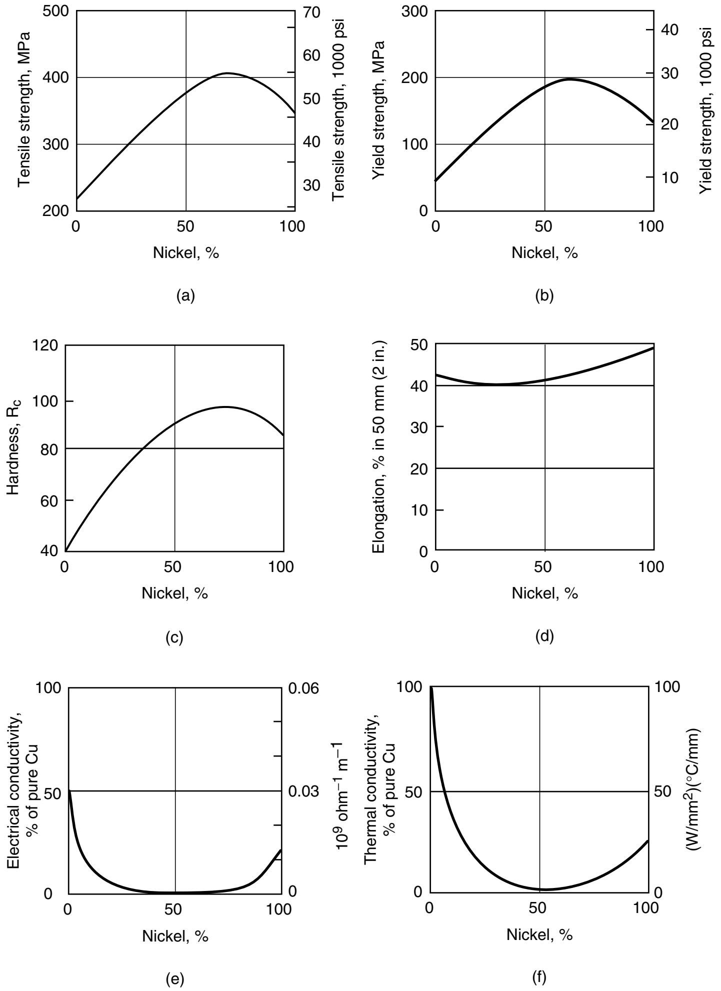

FIGURE 12.1.6 Variation in properties for copper–nickel random solid solution alloys. Note that over time at low temperature alloys (monel) may become nonrandom with significant strength increases.

schematically in Figure 12.1.7a as a function of increasing aging time or aging temperature (fixed time) which result in larger, more widely spaced dispersed-phase particles. Under stress, dislocations must move around (bypass) such particles, so that yield strength decreases with increased aging. Long aging times may be used to decrease yield strength ("soften") of the metal for fabrication. A short aging time, would be used for maximum strength. The dispersed phase can also provide some enhancement of ductility. A dispersion-strengthened metal for which the dispersed phase is stable at elevated temperatures can provide both high-temperature strength and creep resistance (subsection on high-temperature effects). Surface diffusion treatments usually produce dispersion hardening.

Precipitation strengthening (hardening) employs particles which have at least some atomic continuity with the matrix metal. Thus, when the metal is deformed, dislocations can either bypass or pass through (cut) the particles. The resulting behavior is shown in Figure 12.1.7b. As aging time or temperature increases (particles grow larger and more widely spaced), the yield stress increases to a maximum and then decreases. The maximum is termed *critically aged*, and when this designation is part of an alloy treatment, precipitation strengthening may be assumed. For fabrication by cold working, the lower-strength, higher-ductility *underaged* condition is usually employed. There are different possible combinations of thermal and mechanical treatment which will provide a maximum critical aging treatment.

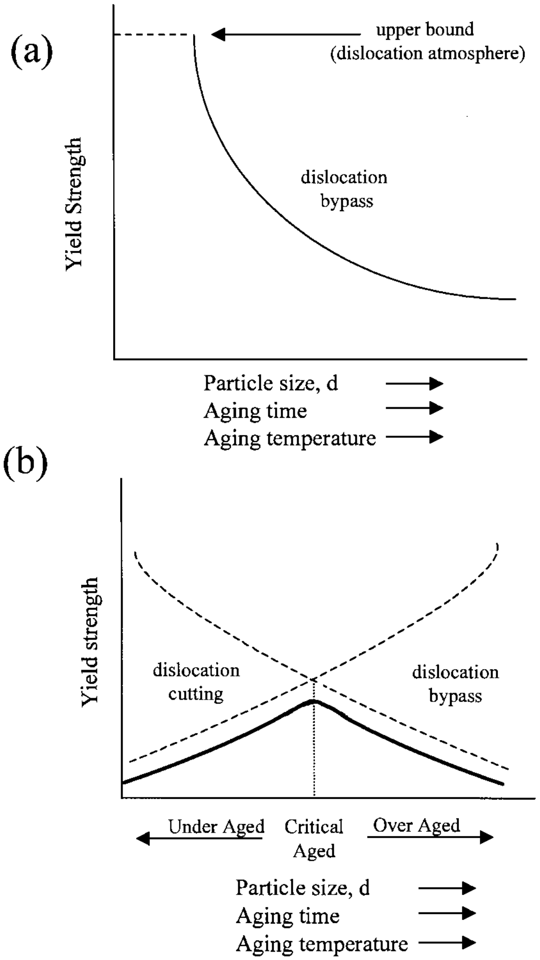

FIGURE 12.1.7 Effect of aging on dispersion- and precipitation-strengthened alloys for a fixed second–phase addition. (a) Dispersion strengthening: as aging time or temperature increases (dispersed phase particles larger and more separated), yield strength increases. A lower bound exists for near atomic size particles. (b) Precipitation hardening: two behaviors can occur giving a composite curve with a maximum at the critical aging time or temperature (optimum size and spacing of particles).

Usually the best optimum for strength is given in handbooks and data sheets. However, improved treatments may be available, particularly of the combined thermomechanical type.

Strengthening of Steels and Steel Heat Treatment

Steels, perhaps the most important of all engineering metals, are alloys of iron and carbon usually containing about 0.02 to 1.0 $^w/_o$ carbon. The binary Fe–C phase diagram is important in describing this behavior and is shown in Figure 12.1.8. This diagram shows what phases and structures will occur in quasi equilibrium at various carbon contents and temperatures (under atmospheric pressure). Steel forming and heat treatment center on the transformation from austenite, γ phase, at elevated temperature to ferrite (α phase) plus cementite (iron carbide, Fe_3C) below 727°C (1340°F), the Ac_1 temperature, a eutectoid transformation. If there are no other intentional alloying elements, the steel is a "plain carbon" steel and has an AISI (American Iron and Steel Institute) designation 1002 to 10100. The first two characters indicate that it is a plain carbon steel, while the latter characters indicate the "points" of

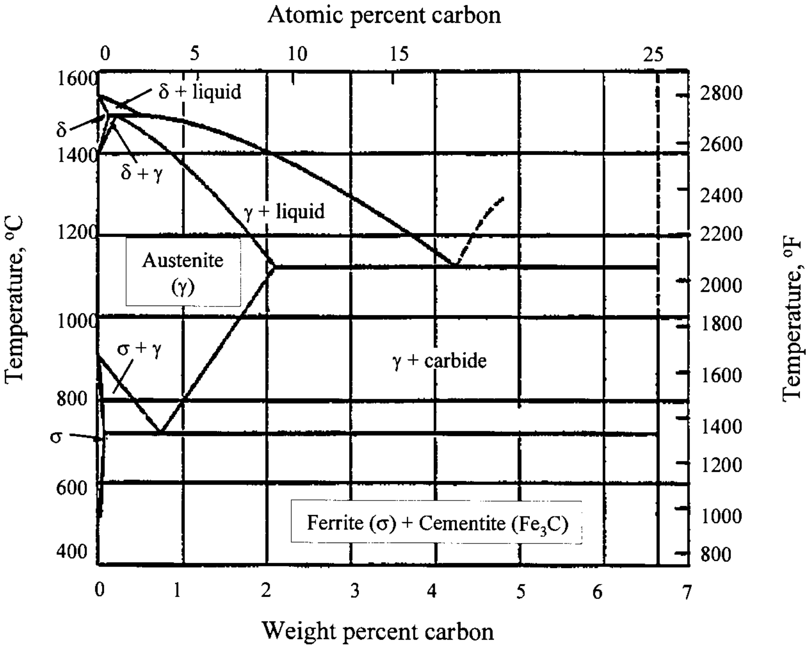

FIGURE 12.1.8 Iron–carbon phase diagram relevant for steel. The steel composition range is from about 0.02 to 1.00 $^{w}/_{o}$ carbon. Steel strengthening treatments require heating into the austenite region (above the Ac_3) and then quenching.

carbon.[1] Alloy steels, containing intentional alloying additions, also indicate the points of carbon by the last digits and together with the first digits provide a unique designation of alloy content. In the phase diagram (Figure 12.1.8) iron carbide (Fe_3C, cementite) is shown as the phase on the right. This is for all practical purposes correct, but the true thermodynamically stable phase is graphite (C) — relevant when the eutectic at 1148°C (2048°F) is used to produce cast irons (alloys greater than 2 $^{w}/_{o}$ C).

The solid-state eutectoid transformation is promoted by the magnetic effect in iron as nonmagnetic austenite transforms below the eutectoid (Ac_1) temperature to the two magnetic solid phases ferrite (iron with solid solution carbon) and cementite solid phase.[2] At the eutectoid composition, 0.77 $^{w}/_{o}$ carbon, the two phases form as a fine alternating set of plates (lamellae) termed *pearlite* because of their pearllike appearance in a metallographic microscope. This two-phase structure of metal (ferrite) and carbide (cementite) provides strength (very slowly cooled — about 65 ksi, 14% tensile elongation), which increases as a more-rapid quenching yields a finer pearlite microstructure (to about 120 ksi). As strength increases, ductility and fracture toughness decrease. With yet more rapid quenching and more local atomic diffusion, the austenite transforms to bainite, a phase of alternating carbon and iron-rich atomic planes. This has yet higher strength (to about 140 ksi) and lower ductility. When the metal is quenched so rapidly that carbon diffusion is prevented, the austenite becomes unstable. Below a critical temperature, the martensitic start temperature (M_s), the metal transforms spontaneously by shear to martensite. Full transformation occurs below the martensite finish temperature (M_f). The formation of this hard phase

---

[1] Plain carbon steels contain about 0.2 $^{w}/_{o}$ Si, 0.5 $^{w}/_{o}$ Mn, 0.02 $^{w}/_{o}$ P, and 0.02 $^{w}/_{o}$ S.

[2] It should be noted that austenitic stainless steels (300 and precipitation hardening, PH, series designations), nonmagnetic alloys with considerable chromium and nickel content to provide corrosion resistance, do not ordinarily transform from austenite to the lower-temperature phases. They are not intentionally alloyed with carbon, are not magnetic, and do not show the phase transformation strengthening mechanisms of steels. The term *steel* is something of a misnomer for these alloys.

introduces enormous microscopic deformation and residual stress. The strength is very much higher (about 300 ksi) but there is almost no ductility. This rapidly cooled material can spontaneously fail from "quench cracking," which results from residual stresses and the martensite acting as an internal flaw. To relieve stresses and provide some fracture toughness, martensitic steel is "tempered" at an intermediate temperature such as 500°C for about an hour to provide some ductility (about 7%) while sacrificing some strength (about 140 ksi). Tempering for shorter times or at lower temperatures can give intermediate properties. High-carbon steels are often used for cutting tools and forming dies because of their surface hardness and wear resistance. When a high-carbon steel (>0.7 $^w/_o$ C) requires fabrication at lower temperature, it may be held at a temperature just under the eutectoid for an extended time (e.g., for 1080 steel: 700°C, 1300°F — 100 hr) either after or without quenching to provide a soft condition (<60 ksi, 20% extension). A variety of different quenching temperatures, media, and procedures can be used to vary required combinations of the microstructures above and mechanical properties. The discussion above centered on eutectoid steel and holds for other high-carbon steels. Increasing carbon content favors the formation of martensite in steels, thereby providing increased strength, hardness, and wear resistance. However, such steels can be quite brittle.

At lower carbon content, "primary ferrite" forms (Figure 12.1.8) as the steel is quenched from above the boundary of austenitic (γ) region, the Ac_3. Subsequently, pearlite (ferrite and cementite), bainite, and/or martensite can form. Lower carbon content increases the amount of primary ferrite, a weaker/ductile phase, and decreases the tendency to form martensite, a stronger/brittle phase. The result is a more fracture tough, ductile ("safer") steel, but strength is lower. Such steels are also mechanically more forgiving if welded. Thus, a 1010 steel (0.10 $^w/_o$ C) might be used for applications where extreme "formability" and "weldability" are required, such as for car bodies and cans, while a 1020 steel (0.20 $^w/_o$ C) might be used for construction materials for which some increased strength is desired while maintaining safety. A medium-carbon steel such as a 1040 would be used when a balance of strength and toughness (and ease of welding) is needed.

In order to quench (and temper) steels continuous cooling transformation (CCT) diagrams are used such as that in Figure 12.1.9 for a 1040, medium-carbon steel. The steel is quenched from above the Ac_3. Vertical lines indicate quenching rates as shown in the lower left inset of the diagram. The cooling rate for the center of a round bar of given diameter quenched in air, oil, and water is given below the diagram. Solid lines on the diagram indicate percent transformation (start, 10%, 50%, 90%, finish of transformation), and a dotted line separates the region where primary ferrite forms from that of transformation to pearlite. The lower diagram shows the indentation hardness to be expected, as this and other mechanical behavior can be predicted from the CCT curve. As an example, the center of a 15 mm ($\sim ^1/_2$ in.) diameter bar quenched in air would be about 25% primary ferrite and 75% fine pearlite, with a Rockwell C hardness (HRC) of about 15. If quenched in oil, the bar center would be chiefly bainite with a small amount of martensite (HRC $\cong$ 25). The same bar quenched in water would be all martensite (HRC $\cong$ 55) before tempering. The transformation at other positions in the bar and for other engineering shapes (sheet, pipe, square rod, etc.) can be obtained from conversion curves.

It should be noted that layers in the steel closer to the quenched surface cool more quickly and are therefore displaced toward the left of the CCT diagram. There is a variation in structure and mechanical properties from the quenched surface to the center. One result is that the surface of the steel tends to be stronger, harder, and more wear resistant than the center. A steel beam undergoing bending has maximum strength at the near surface which undergoes the greatest stresses, while the center provides safety because of its relative fracture toughness and ductility. A thin knife edge cools quickly and can be resistant to deformation and wear, while the thick back prevents the blade from snapping in half when bent.

Many elements may be incorporated in steels to promote specific properties. Almost all common additions (other than cobalt) tend to promote strengthening by the formation of martensite (or bainite) instead of pearlite. When alloying additions tend to promote martensite throughout a thick section independent of cooling rate, the alloy is said to have *high hardenability.* Some elements such as chromium, molybdenum, and nickel also may help to provide high-temperature strength and environmental resistance. One class of alloys with relatively small alloying additions are termed *HSLA* steels (high strength,

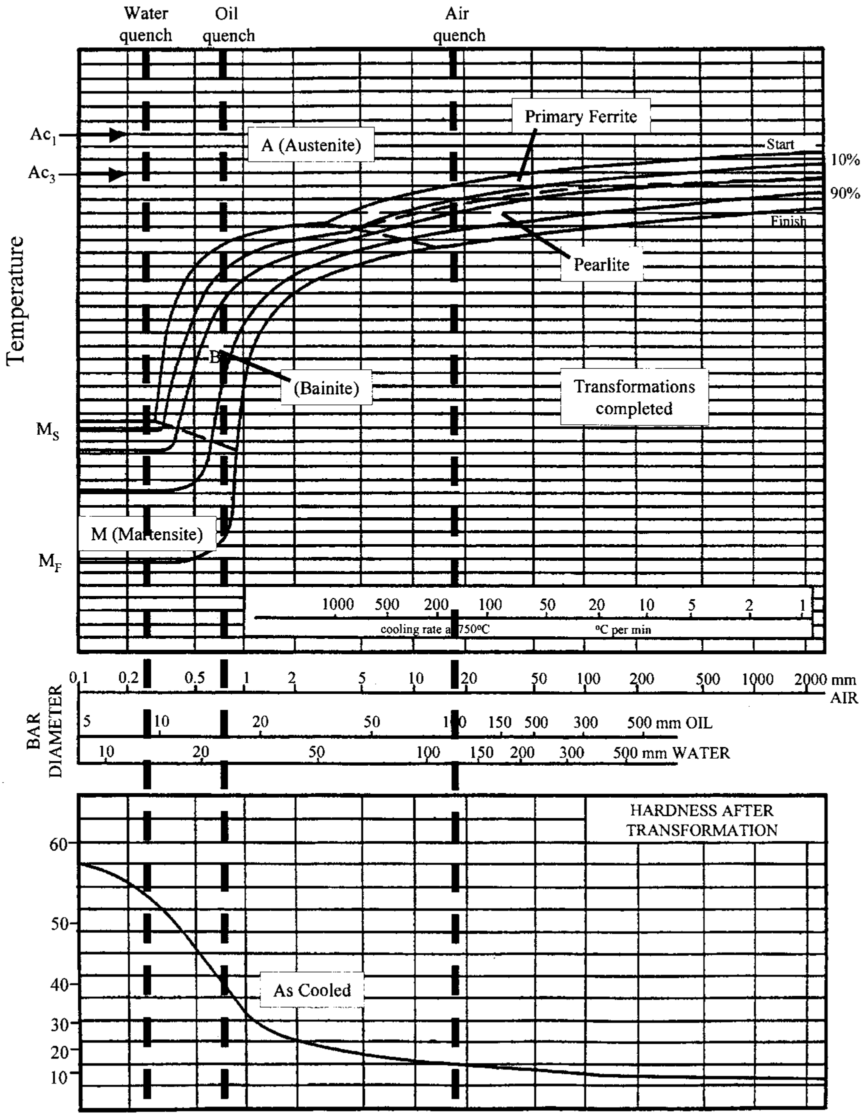

FIGURE 12.1.9 CCT diagram for 1040 steel. A 15-mm round bar air quenched from above the Ac_3 will be chiefly fine pearlite (ferrite and iron carbide, cementite) with about a quarter of the structure primary ferrite at the center. Quenching in oil will yield bainite with about 10% martensite. Water quenching will produce wholly martensite at the center. (After Atkins, M., *Atlas of Continuous Cooling Transformation Diagrams for Engineering Steels*, ASM International, Materials Park, OH, 1980.)

low alloy) and usually show somewhat superior mechanical properties to their plain carbon steel equivalents. As steel is alloyed, the relative cost increases substantially. A useful strategy in steel selection (and steels are usually the first engineering candidate on a cost basis) is to start by determining if a medium-carbon steel will do. If greater safety and formability are needed, a lower carbon content may be used (with slightly lower cost); alternatively, a higher-carbon steel would be chosen for greater strength and wear resistance. Heat treatment would be used to manipulate the properties. If plain carbon steels prove unsatisfactory, the HSLA steels would be the next candidate. For very demanding applications, environments, and long-term operations, specialty alloy steels would be selected insofar as they are cost-effective.

Fatigue

Fatigue is the repeated loading and unloading of metal due to direct load variation, eccentricity in a rotating shaft, or differential thermal expansion of a structure. Even substantially below the yield point (elastic limit) of a metal or alloy this repeated loading can lead to failure, usually measured in terms of the number of cycles (repeated load applications) to failure. Some studies have suggested that well over 80% of all mechanical failures of metal are attributable to fatigue.

High-stress, low-cycle fatigue usually occurs at stresses above the yield point and lifetimes are tens or hundreds of cycles (to about a thousand cycles). Failure occurs as a result of the accumulation of plastic deformation, that is, the area (energy) under the stress–strain curve (Figure 12.1.3). A simple lifetime predictive equation can be used to predict lifetime:

$$N \approx \left[\varepsilon_u / 2\varepsilon_{\mathrm{pf}}\right]^2 \tag{12.1.3}$$

where N is the number of cycles to failure, ε_u is total strain from the stress–strain curve, and $\varepsilon_{\mathrm{pf}}$ is the plastic strain amplitude in each fatigue cycle.

More commonly, metals are used well below their yield point and fail after many, many cycles of repeated loading in low-stress, high-cycle fatigue. There is microscopic, local plastic deformation (cold working) and vacancy generation (recovery effects) during such cyclic loading which result in "fatigue hardening" (strengthening) of unworked metal and "fatigue softening" of unworked metal. Some have even found success relieving residual stressed with a vibratory anneal. Early in the fatigue process surface flaws or in some cases severe internal flaws begin to propagate. The fatigue crack propagates in areas of high stress a small, usually submicroscopic, distance with each tensile loading. The propagation on each cycle frequently leaves identifiable marking on the failure surface termed *fatigue striations* which mark the progress of the subcritical crack. When the crack becomes so large that the fracture toughness criterion is exceeded (Equation 12.1.2), catastrophic overload failure occurs. When the future fatigue loading can be predicted and the cyclic crack propagation rate is known, fatigue cracks can be inspected or monitored in different applications such as aircraft structures and pressure vessels to decommission or replace parts before fatigue failure. This must be done cautiously because a change to a more aggressive (corrosive, oxidative, elevated temperature) environment can increase the crack propagation rate. If a harmonic resonance occurs in the metal part, vibratory maxima can cause premature fatigue failure. Harmonics can change as fatigue cracks propagate. Harmonic vibration can be prevented with vibratory (dynamic) design concepts and/or direct monitoring.

Figure 12.1.10 shows typical metal *S–N* curves (stress vs. number of cycles to failure) for a high-strength aluminum and for a titanium alloy. Note that the convention is to make stress the vertical axis and to plot the number of cycles to failure on a logarithmic scale. For high-stress, low-cycle fatigue ($<10^3$ cycles) the curve is flat and linear, consistent with the model of Equation12.1.3. For high cycle fatigue the lifetime is a rapidly varying function of stress until very low stresses (long lifetimes occur). The actual fatigue life varies statistically about the mean value shown in approximate proportion to the number of cycles to failure. These curves are for testing in ambient air. Fatigue life would be longer in an inert environment and may be shortened drastically in an aggressive environment. Iron- and titanium-based alloys, such as the example shown, usually have an "endurance limit," a stress below which lifetime is ostensibly infinite. In air, at room temperature, the endurance limit is about half the tensile strength for most iron and titanium alloys. Other metals appear to show no stress below which they last indefinitely. Therefore, a "fatigue limit" is designated — usually the stress at which the fatigue life is 10^8 cycles. This may be a long lifetime or not depending on the frequency of loading and engineering lifetime. The fatigue limit is generally about 0.3 times the tensile strength for metals with strengths below about 100 ksi (700 MPa). The factor is somewhat poorer for higher-strength metals. It is apparent that on a relative strength basis, iron- and titanium-based alloys are fatigue-resistant metals when compared with others. Dispersion-strengthened alloys have been seen to provide some lifetime advantage in fatigue.

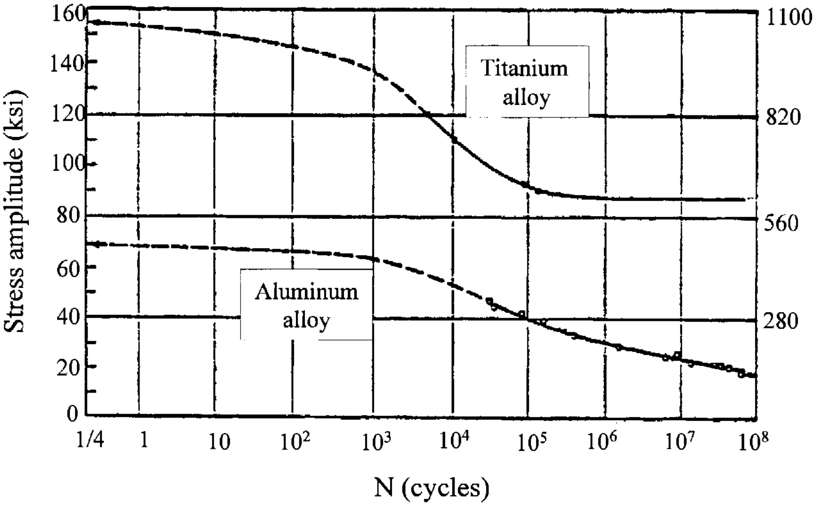

FIGURE 12.1.10 *S–N* (fatigue) curves for high-strength titanium (upper curve) and aluminum alloys. Note that titanium (and iron) alloys show an endurance limit, a stress below which the metal lasts indefinitely.

A number of mathematical relationships have been proposed to predict fatigue life, but none works with complete success and all require experimental data. Perhaps the most successful of the so-called fatigue "laws" are the "cumulative damage" laws. The simplest is Miner's law:

$$\sum i\left[n_i/N_i\right]=1 \tag{12.1.4}$$

where n_i is the number of cycles applied and N_i is the number of cycles for failure at a particular stress level, σ_i. The conceptual basis is that the number of fatigue cycles at a stress level uses up its relative fraction of total fatigue lifetime and may be correlated to fatigue crack propagation (striation spacing). Modifications of this model account for the order and relative magnitude of loads. Several techniques have met with partial success in increasing fatigue lifetime beyond that predicted by the cumulative damage models:

1. Coaxing — intermittent or continuous, superimposed vibration at very low stress,
2. Overstressing — intermittent or superimposed compressive loading,
3. Surface compression — intermittent shot peening or surface rolling,
4. Surface removal — chemical or mechanical surface polishing.

All but 1 are thought to close or eliminate fatigue cracks and surface damage. Coaxing has been said to introduce more of the vacancy-related recovery effects associated with fatigue.

High-Temperature Effects — Creep and Stress Rupture

Elevated temperature can cause a significant loss of strength and elastic modulus, so that a metal part may fail as a result of overheat even at loads which appear small at room temperature. High temperature is a relative matter and is usually judged as a fraction of the melting point measured on the absolute temperature scale. Thus, even moderate temperature excursions can be important for low-melting-point metals and alloys. As indicated in several sections above, many alloying and cold work strengthening methods depend upon heat treatment; an alloy can undergo metallurgical change due to overheat or to long-term holds at moderate temperatures and thereby alter properties significantly. Thus, the thermal

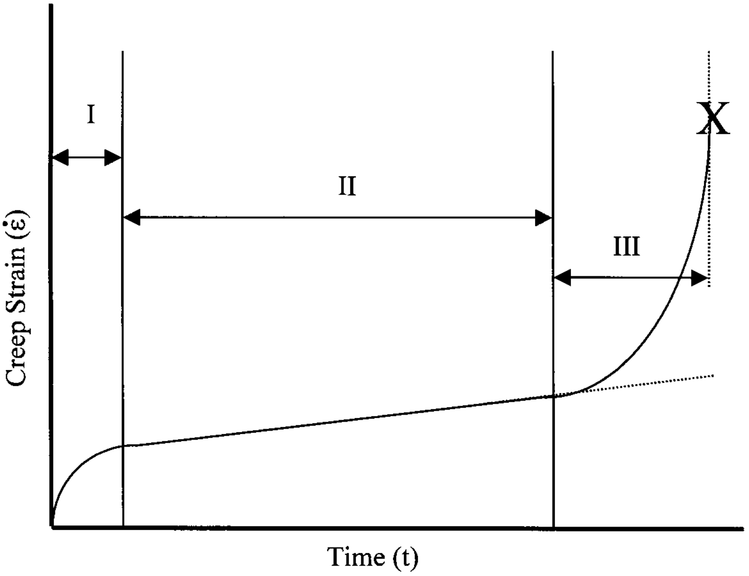

FIGURE 12.1.11 Schematic creep curve showing transient creep (I), steady-state creep (II), and tertiary creep (III). Note that the slope of the straight-line portion is the steady-state creep rate (minimum creep rate).

stability of the microstructure should be determined. For example, metallographic replica techniques have been developed for determining in the field if microstructure has coarsened, making the metal weak.

Creep deformation is the continued deformation of a metal under load at elevated temperature, usually at a design stress well below the yield point. While measurable creep can occur at low temperatures over very long times or at very high (compressive) loads, creep usually becomes of engineering importance above about two thirds the melting point (absolute) of an alloy. Thus, both lead, which creeps at room temperature, and tungsten, which creeps in an incandescent light bulb at white heat, require a mechanical support or creep-resistant alloying additions. Figure 12.1.11 shows a schematic creep curve plotting creep strain[3] vs. time, t, at a particular tensile load and temperature. After the immediate elastic strain ($t = 0$), "transient creep" occurs in Region I. At elevated temperature this usually follows a $t^{1/3}$ behavior (Andrade creep). The majority of the curve has a straight-line behavior (Region II) in which the extension with time is constant. The slope of this part of the curve is termed the *steady-state strain rate* or *minimum creep rate*. It is used to calculate the creep extension which could cause functional failure when dimensional tolerances are exceeded. A simplified predictive model is

$$\varepsilon' = A\sigma^m e^{-h/kT} \tag{12.1.5}$$

where ε' is the minimum creep rate, A is a constant, σ is the applied stress, m is the stress dependence exponent (often 4 to 8), h is the activation enthalpy for creep, and T the absolute temperature.

In Region III the creep rate accelerates as the metal necks down severely in a local area, thereby increasing the local stress. The steady-state rate would continue (dotted line) if the load were adjusted to give constant load at the minimum cross section. Since loads do not readjust to compensate for necking in real applications, a final accelerated stage can be experienced. For example, a blowout can occur in late creep of a pressurized high-temperature piping system. The time to failure is termed the *stress rupture lifetime*. Predictive models are developed from Equation (12.1.5) to provide lifetime information.

---

[3] If a constant extension is applied to an object, the force it generates will decline over time due to creep. This is called *stress relaxation* and can be treated in a similar way.

Lowering use temperature or applied stress decreases susceptibility to creep deformation and increases stress rupture lifetime. Frequently, a moderate temperature decrease is most effective in this regard. Higher-melting-point metals are more creep resistant, so that the refractory metals tungsten and molybdenum can be used but require an inert atmosphere or protective coating to prevent rapid oxidation. In air or other active atmosphere, niobium-, nickel-, titanium-, and iron-based alloys may be used for creep resistance. Dispersion hardening, particularly with a high-temperature stable phase, such as an oxide, nitride, or carbide, can confer a degree of creep resistance.

Corrosion and Environmental Effects

Corrosion usually involves the slow removal of metal due to chemical and/or electrochemical reaction with an environment. Most metallic corrosion involves a galvanic, that is, electrochemical, component and localized attack in the form of pitting, attack in crevices, grain boundary attack, selective leaching of one phase, and exfoliation (attack parallel to the surface causing layers to peel away). Uniform corrosion is less common and also less of a concern as long as the rate of material removal is gradual and predictable.

Galvanic corrosion requires a medium, usually liquid (water), often containing a specific agent which promotes corrosion, a potential difference, and a complete electrical circuit, as well as an anode and a cathode. The anode will be the attacked, corroded, portion of the system. One cause for potential corrosion is dissimilar metals. For example, the galvanic series in seawater shows magnesium alloys as most anodic followed by zinc, aluminum, iron, nickel, brass, and copper alloys which are progressively more cathodic. When coupled electrically, the more-anodic metal would be corroded and the more cathodic would promote corrosion. One way of preventing corrosion is to isolate with insulator material the metal parts electrically so that a circuit is interrupted. The surfaces can be isolated from the corroding medium with paint, protective metal, conversion coatings, or a corrosion inhibitor additive to the liquid. In this situation it is more important to coat the cathode (noncorroding metal) since it impresses corrosion on the anodic metal dependent on exposed area. When in doubt, all parts should be painted repeatedly to prevent pinholes. Other possibilities include cathodic protection with an impressed electrical counterpotential or use of a sacrificial anode which is attacked instead of the metal components. Some metals such as stainless steels and aluminum alloys provide protection via an oxide coating, a *passive film*, which will form under specific, controlled electrochemical conditions providing *anodic protection.*

Another source for an anode and cathode can be the solution itself. Differences in temperature, ion concentration, oxygen content, and pH can all lead to a potential difference which results in corrosion. Often corrosion occurs far more rapidly for a specific range of solution concentration — indeed, sometimes dilution may accelerate corrosive attack. An oxygen deficiency cell under dirt or in a crevice frequently causes attack at the resulting anode. Potential differences can also exist in the metal itself: between different phases, inclusions, or grain chemistries; between grains and grain boundaries; between surface films and metal; and between different grain orientations. Selective leaching such as dezincification of high-zinc brasses (Cu–Zn) is an example for composition differences, while exfoliation corrosion of aluminum alloys and sensitized stainless steel are examples of grain boundary attack. Cold-worked metal tends to be anodic to annealed material so that a heavily formed part of a metal part may corrode preferentially.

Another important environmental cause of failure is stress corrosion cracking (SCC). A combination of applied or residual tensile stress and environmental attack results in progressive slow crack propagation over a period of time. Eventually, the crack becomes critical in size (Equation 12.1.2) and catastrophic failure occurs. There need be no evidence of corrosion for SCC to occur. When the loading is of a cyclic nature the effect is termed *corrosion fatigue.* To prevent these long-term crack propagation effects the environment and/or the source of tensile load may be removed. Considerable effort has been made to identify an ion concentration below which stress corrosion cracking will not occur (e.g., Cl for austenitic stainless steels), but there may be no level for complete immunity, merely a practical maximum permissible level.

Hydrogen embrittlement and hydrogen cracking can occur in the presence of stress and a hydrogen source. Embrittlement results when hydrogen diffuses into the metal and/or acts on the crack tip altering the fracture toughness. Hydrogen cracking may be regarded as a special case of stress corrosion cracking. Either environmental effect can lead to catastrophic failure. The source of hydrogen can be an acid solution, hydrogen evolved during corrosion, electrochemical treatment (plating, electropolishing), or hydrocarbons. Often isolation from the hydrogen source is difficult because hydrogen diffuses quickly through most materials and barrier coatings. Glass coating has met with some success.

Metal Surface Treatments

A number of treatments are employed to strengthen the surface of steels and make them more resistant to failure or wear. Some of the techniques may also be applied to selected nonferrous alloys. Flame, induction, and laser hardening provide intense heat to the outer surface of a medium- or high-carbon (hardenable) steel bringing it into the austenitic region, above Ac_3 (see subsection on fatigue). The bulk of the metal is not heated so that the surface can then be quenched rapidly forming hardening phases and a compressive surface stress. This provides strength and wear resistance. Another surface-hardening technique is carburizing. This can also be used on steels with lower carbon content. The metal is exposed to a controlled balance of carbon monoxide and carbon dioxide or is packed in graphite. At elevated temperature (usually above the Ac_3) carbon diffuses into the surface, converting it to a high-carbon steel. The steel is then either quenched directly from the carburizing temperature or reaustenitized and quenched. The result is similar to flame hardening, but higher hardness and surface compression can be accomplished compared with flame hardening. The center of the piece, with much lower carbon content, can provide fracture toughness, ductility, and safety. Nitriding exposes steel containing appropriate alloying elements (chromium, aluminum, vanadium, …) to monatomic nitrogen in the form of cracked ammonia, cyanide, or high-energy dissociated nitrogen gas. This is done below the eutectoid (lower transformation) temperature. Dispersed-phase nitrides are formed as nitrogen diffuses into the surface which harden the surface without a need for further heat treatment. The effects of both carburizing and nitriding can be introduced by carbonitriding above the transformation temperature and quenching or nitrocarburizing below the transformation to austenite.

Suggested Reading

ASM International, 1985, *Metals Handbook Desk Edition,* ASM International, Materials Park, OH.
ASM International, *Metals Handbook, 8th–10th ed.,* ASM International, Materials Park, OH.

12.2 Polymers

James D. Idol and Richard L. Lehman

Introduction

Polymers constitute a wide range of materials which are derived at least in part from organic, usually petroleum-based, raw materials; they consist of repeating molecular units and have special properties obtained by engineering the form of the molecular structures. The term *polymer* is derived from Greek roots and means "having many parts," a term which aptly describes the infinite number of compounds which can be synthesized from a relatively limited number of monomer units. The term *plastic* is often used in describing polymers, although this term is not in current usage since it is a general descriptive which refers to the forming rheology of many polymers but is too general to accurately describe this group of materials.

Polymers are used as engineering materials in the neat form, i.e., as the pure material, or in combination with a large diversity of additives, both organic and inorganic. These additives may be, among others,

TABLE 12.2.1 Physical Properties of Polymers

Properties of Plastics	ρ (kg m^{-3})	Tensile Strength (N mm^{-2})	Elongation (%)	E (GN m^{-2})	BHN	Machinability
Thermoplastics						
PVC rigid	1330	48	200	3.4	20	Excellent
Polystyrene	1300	48	3	3.4	25	Fair
PTFE	2100	13	100	0.3	—	Excellent
Polypropylene	1200	27	200–700	1.3	10	Excellent
Nylon	1160	60	90	2.4	10	Excellent
Cellulose nitrate	1350	48	40	1.4	10	Excellent
Cellulose acetate	1300	40	10–60	1.4	12	Excellent
Acrylic (methacrylate)	1190	74	6	3.0	34	Excellent
Polyethylene (high density)	1450	20–30	20–100	0.7	2	Excellent
Thermosetting plastics						
Epoxy resin (glass filled)	1600–2000	68–200	4	20	38	Good
Melamine formaldehyde (fabric filled)	1800–2000	60–90	—	7	38	Fair
Urea formaldehyde (cellulose filled)	1500	38–90	1	7–10	51	Fair
Phenol formaldehyde (mica filled)	1600–1900	38–50	0.5	17–35	36	Good
Acetals (glass filled)	1600	58–75	2–7	7	27	Good

Note: BHN = Brinell hardness number, ρ = density, E = Young's modulus.

plasticizers which reduce the rigidity or brittleness of the material, fillers which increase strength and load deflection behavior under load, or stabilizers which protect the polymer against ultraviolet radiation.

The following discussion will separate polymers into two groups, thermoplastic and thermosetting, based on the distinctly different thermal processing behavior of these two broad classes of polymers. Thermoplastic polymers soften when heated and can be reshaped, the new shape being retained on cooling. The process can be repeated many times by alternate heating and cooling with minimal degradation of the polymer structure. Thermosetting polymers (or thermosets) cannot be softened and reshaped by heating. They are plastic and moldable at some state of processing, but finally set to a rigid solid and cannot be resoftened. Thermosets are generally stronger and stiffer than thermoplastic.

Table 12.2.1 of this section gives an overview of the physical properties of the most commonly used industrial polymers. Table 12.2.2 provides an overview of properties such as chemical resistance, ease of machining, and compressive strength for thermoplastic and thermosetting plastics, while Table 12.2.3 is a selection guide for polymers by application. A detailed summary of polymer properties, including electrical properties, thermal properties, optical properties, and fabrication, is presented in Table 12.2.4.

Thermoplastic Polymers

Acetal and Polyacetal

These combine very high strength, good temperature and abrasion resistance, exceptional dimensional stability, and low coefficient of thermal expansion. They compete with nylon (but with many better properties) and with metal die castings (but are lighter). Chemical resistance is good except for strong acids. Typical applications are water-pump parts, pipe fittings, washing machines, car instrument housings, bearings, and gears.

Acrylics (Methylmethacrylate, PMMA)

These are noted for their optical clarity and are available as sheet, rod, tubings, etc., as Perspex (U.K.) and Plexiglas (U.S., Germany, etc.). They are hard and brittle and quite resistant to discoloring and, especially, weathering. Applications include outdoor display signs, optical lenses and prisms, transparent

TABLE 12.2.2 Relative Properties of Polymers

Material	Tensile Strength[a]	Compressive Strength[b]	Machining Properties	Chemical Resistance
Thermoplastics				
Nylon	E	G	E	G
PTFE	F	G	E	O
Polypropylene	F	F	E	E
Polystyrene	E	G	F	F
Rigid PVC	E	G	E	G
Flexible PVC	F	P	P	G
Thermosetting plastics				
Epoxy resin (glass-fiber filled)	O	E	G	E
Formaldehyde (asbestos filled)	G	G	F	G
Phenol formaldehye (Bakelite)	G	G	F	F
Polyester (glass-fiber filled)	E	G	G	F
Silicone (asbestos filled)	O	G	F	F

Note: O = outstanding, E = excellent, G = good, F = fair, P = poor.

[a] Tensile strength (typical): E = 55 $\mathrm{Nmm^{-2}}$; P = 21 $\mathrm{Nmm^{-2}}$.

[b] Compressive strength (typical): E = 210 $\mathrm{Nmm^{-2}}$; P = $\mathrm{Nmm^{-2}}$.

TABLE 12.2.3 Selection Guide for Polymers by Application

Application or Service	Properties Required	Suitable Plastics
Chemical and thermal equipment	Resistance to temperature extremes and to wide range of chemicals; minimum moisture absorption; fair to good strength	Fluorocarbons, chlorinated polyether, polyvinylidene fluoride, polypropylene, high-density polyethylene, and epoxy glass
Heavily stressed mechanical components	High-tensile plus high-impact strength; good fatigue resistance and stability at elevated temperatures; machinable or moldable to close tolerance	Nylons, TFE-filled acetals, polycarbonates, and fabric-filled phenolics
Electrostructural parts	Excellent electrical resistance in low to medium frequencies; high-strength and -impact properties; good fatigue and heat resistance; good dimensional stability at elevated temperatures	Allylics, alkyds, aminos, epoxies, phenolics, polycarbonates, polyesters, polyphenylene oxides, and silicones
Low-friction applications	Low coefficient of friction, even when nonlubricated; high resistance to abrasion, fair to good form stability and heat and corrosion resistance	Fluorocarbons (TFE and FEP), filled fluorocarbons (TFE), TFE fabrics, nylons, acetals, TFE-filled acetals, and high-density polyethylenes
Light-transmission components, glazing	Good light transmission in transparent or translucent colors; good to excellent formability and moldability; shatter resistance; fair to good tensile strength	Acrylics, polystyrenes, cellulose acetates, cellulose butyrates, ionomers, rigid vinyls, polycarbonates, and medium-impact styrenes
Housings, containers, ducts	Good to excellent impact strength and stiffness; good formability and moldability; moderate cost; good environmental resistance; fair to good tensile strength and dimensional stability	ABS, high-impact styrene, polypropylene, high-density polyethylene, cellulose acetate butyrate, modified acrylics, polyester–glass and epoxy–glass combinations

coverings, drafting instruments, reflectors, control knobs, baths, and washbasins. They are available in a wide range of transparent and opaque colors.

Acrylonitrile-Butadiene-Styrene (ABS)

This combination of three monomers gives a family of materials which are strong, stiff, and abrasion resistant with notable impact-resistance properties and ease of processing. The many applications include

TABLE 12.2.4 Properties of Polymers

Chemical class	Cellulose acetate	Cellulose acetate	Cellulose acetate butyrate	Cellulose acetate butyrate	Nylon	Polycarbonates	Polyethylene	Polyethylene
	Thermoplastic	Thermoplastic	Thermoplastic	Thermoplastic	Thermoplastic	Thermoplastic	Thermoplastic	Thermoplastic
	Soft	Hard	Soft	Hard	6/6	Unfilled	Low Density	Medium Density
ELECTRICAL PROPERTIES								
D.C. resistivity, ohm-cm	10^{10}-10^{13}	10^{10}-10^{13}	10^{10}-10^{12}	10^{10}-10^{12}		2×10^{16}	$>10^{15}$	$>10^{15}$
Dielectric constant, 60 cps	3.5-7.5	3.5-7.5	3.5-6.4	3.5-6.4	4.0-4.6	3.17	2.3-2.35	2.3
Dielectric constant, 10^6 cps	3.2-7.0	3.2-7.0	3.2-6.2	3.2-6.2	3.4-3.6	2.96	2.3-2.35	2.3
Dissipation factor, 60 cps	0.01-0.06	0.01-0.06	0.01-0.04	0.01-0.04	0.014-0.04	0.0009	<0.0005	<0.0005
Dissipation factor, 10^6 cps	0.01-0.10	0.01-0.10	0.01-0.04	0.01-0.04	0.04	0.01	<0.0005	<0.0005
MECHANICAL PROPERTIES								
Modulus of elasticity, 10^3 psi	86-250	190-400	74-126	150-200		290-325	14-38	35-90
Tensile strength, psi	1,900-4,700	4,600-8,500	1,900-3,800	5,6800	9,000-12,000	8,000-9,500	1,000-1,400	1,200-3,500
Ultimate elongation, %	32-50	6-40	60-74	38-54	60-300	20-100	400-700	50-600
Yield stress, psi	2,200-4,200	4,100-7,600	1,200-2,600	3,600-6,100		8,000-10,000	1,100-1,700	1,500-2,600
Yield strain, %							20-40	10-20
Rockwell hardness	R 49-R 103	R 101-R 123	R 59-R 95	R 108-R 117	R 108-R 120	M 70-M 180		
Notched Izod impact strength, ft lb/in.	2.0-5.2	0.4-2.7	2.5-5.4	0.7-2.4	1.0-2.0	8-16	No break	0.5->16
Specific gravity	1.27-1.34	1.27-1.34	1.15-1.22	1.19-1.25	1.13-1.15	1.2	0.91-0.925	0.926-0.941
THERMAL PROPERTIES								
Burning rate	Medium	Medium	Medium	Medium	Self-extinguishing	Self-extinguishing	Very slow	Slow
Heat distortion, 264 psi. C	44-57	60-113	49-58	70-99		135-145		
Specific heat, cal/g	0.3-0.42	0.3-0.42	0.3-0.4	0.3-0.4	0.4	0.3	0.55	0.55
Linear thermal expansion coefficient, 10^{-5}, C	8-16	8-16	11-17	11-17	8.0	6.6	10-20	14-16
Maximum continuous service temperature, C					80-150	138-143	60-77	71-93
CHEMICAL RESISTANCE								
Mineral acids, weak	Fair to good	Fair to good	Good	Good	Very good	Excellent	Good	Excellent
Mineral acids, strong	Poor	Poor	Fair to good	Fair to good	Poor	Fair	Good	Excellent
Oxidizing acids, concentrated	Very poor	Very poor			Poor		Good to poor	Good to poor
Alkalies, weak	Poor	Poor	Good	Good	No effect	Poor	Good	Excellent
Alkalies, strong	Very poor	Very poor	Poor	Poor	No effect	Poor	Good	Excellent
Alcohols	Poor	Poor	Poor	Poor	Good	Poor	Excellent to poor	Excellent to poor
Ketones	Poor	Poor	Poor	Poor	Good	Poor	Excellent to poor	Excellent to poor
Esters	Poor	Poor	Poor	Poor	Good	Poor	Excellent to poor	Excellent to poor
Hydrocarbons, aliphatic	Fair to good	Fair to good	Fair to good	Fair to good	Very good	Poor	Fair	Fair
Hydrocarbons, aromatic	Poor to fair	Poor to fair	Poor	Poor	Fair to good	Poor	Fair	Good
Oils: vegetable, animal, mineral	Fair to good	Fair to good	Good	Good	Good	Poor	Good	Excellent
MISCELLANEOUS PROPERTIES								
Clarity	Excellent	Excellent	Good to excellent	Good to excellent	Clear	Clear	Translucent	Translucent
Color	Pale to colorless	Pale to colorless	Pale to colorless	Pale to colorless	Pale amber to colorless	Colorless	Colorless	Colorless
Refractive index, n_D	1.46-1.50	1.46-1.50	1.46-1.49	1.46-1.49	1.53	1.60	1.50-1.54	1.52-1.54
FABRICATION								
Cl—calendering, Cs—casting, E—extrusion, F—hot forming or drawing, I—impregnation, MC—blow molding, MC—compression molding, MI—injection molding, S—spreading	Cs, E, F, MB, MC, MI, S	Cs, E, F, MB, MC, MI, S	Cs, E, F, MB, MC, MI, S	Cs, E, F, MB, MC, MI, S	E, F, MB, MC, MI	Cs, E, F, MB, MC, MI	Cl, E, F, MB, MC, MI	Cl, E, F, MB, MC, MI

TABLE 12.2.4 (continued) Properties of Polymers

Polyethylene	Polymethylmethacrylate	Polypropylene	Polypropylene	Polystyrene	Polystyrene-acrylonitrile	Polytetrafluoroethylene	Polytrifluorochloroethylene	Polyvinylchloride and vinylchloride acetate	Polyvinylchloride and vinylchloride acetate	Epoxy
Thermoplastic	Thermoplastic	Thermoplastic	Thermoplastic	Thermoplastic	Thermoplastic	Thermoplastic	Thermoplastic	Thermoplastic	Thermoplastic	Thermosetting
High Density	Unmodified	Unmodified	Copolymer	Unmodified	Unmodified	Unmodified	Unmodified	Unmodified, rigid	Plasticized, non-rigid	Unfilled
$>10^{15}$	$>10^{14}$	$>10^{15}$	$>10^{17}$	$>10^{16}$	10^{13}-10^{17}	10^{18}	10^{18}	10^{12}-10^{16}	10^{11}-10^{14}	10^{12}-10^{14}
2.3-2.35	3.5-4.5	2.2-2.6	2.3	2.5-2.65	2.6-3.4	2.	2.2-2.8	3.2-4.0	5.0-9.0	3.5-5.0
2.3-2.35	3.0-3.5	2.2-2.6	2.3	2.5-2.65	2.5-3.1	2.	2.3-2.5	3.0-4.0	3.0-4.0	3.4-4.4
<0.0005	0.04-0.06	<0.0005	0.0001-0.0005	0.0001-0.0003	0.006-0.008	0.0002	0.001	0.01-0.02	0.03-0.05	0.001-0.005
<0.0005	0.02-0.03	0.0005-0.002	0.0001-0.002	0.0001-0.0004	0.008-0.01	0.0002	0.005	0.006-0.02	0.06-0.1	0.03-0.05
85-160	350-500	1.4-1.7		400-600	$>10^{16}$	33-65	150	200-600		>300
3,100-5,500	7,000-11,000	4,300-5,500	2,900-4,500	5,000-10,000	9,000-12,000	2,000-4,500	4,500-6,000	5,000-9,000	1,500-3,000	4,000-13,000
15-100	2.0-10	>220	200-700	1.0-2.5	1.0-2.5	200-400	250	2.0-40	200-400	2.0-6.0
2,400-5,000		4,900				1,600-2,000	4,200			
5-10		15				50-75	10	1.0-5.0		
R 30-R 50	M 80-M 105	93	R 50-R 96	M 65-M 85	M 75-M 90	D 50-D 65	J 75-J 95	R 110-R 120		M 75-M 110
1.5-20	0.3-0.6	1.0	1.1-12	0.25-0.60	0.3-0.6	2.5-4.0	2.5-4.0	0.4-2.0		0.2-1.0
0.941-0.965	1.18-1.20	0.90	0.90	1.04-1.08	1.05-1.1	2.1-2.3	2.1-2.3	1.36-1.4	1.15-1.35	1.115
Slow	Slow	Medium	Medium	Medium to slow	Slow	Self-extinguishing	Self-extinguishing	Self-extinguishing	Slow to self-extinguishing	Slow
	66-99				91-104	60		60-80		Up to 120
0.55	0.35	0.5	0.5	0.32-0.35	0.32-0.35	0.25	0.22	0.2-0.28	0.36-0.5	0.25-0.4
11-13	5.0-9.0	5.8-10	8-10	6.0-8.0	3.6-3.8	10	7.0	5.0-18	7.0-25	4.5-9.0
92-200	60-93		190-240	66-82	77-88	260	200	70-74	80-105	80
Excellent	Good	Excellent	Excellent	Excellent	Excellent	Excellent	Excellent	Excellent	Fair to good	Excellent
Excellent	Fair to poor	Excellent	Excellent	Excellent	Good to excellent	Excellent	Excellent	Good to excellent	Fair to good	Fair to good
Good to poor	Attacked	Good to poor	Poor	Poor	Poor	Excellent	Excellent	Fair to good	Poor to fair	Excellent
Excellent	Good	Excellent to good	Excellent	Excellent	Excellent	Excellent	Excellent	Excellent	Fair to good	Excellent
Excellent	Poor	Excellent to good	Good	Excellent	Good to excellent	Excellent	Excellent	Good	Fair to good	Excellent
Excellent to poor		Excellent to good	Good below 80 C	Excellent	Good to excellent	Excellent	Excellent	Excellent	Fair	Poor
Excellent to poor	Dissolves	Excellent to good	Good below 80 C	Dissolves	Dissolves	Excellent	Excellent	Poor	Poor	
Excellent to poor	Dissolves	Excellent to good	Good below 80 C	Poor	Dissolves	Excellent	Excellent	Poor	Poor	Excellent
Fair	Good	Good to fair	Good below 80 C	Poor	Good	Excellent	Excellent	Excellent	Poor	Excellent
Fair	Softens	Good to fair	Good below 80 C	Dissolves	Fair to good	Excellent	Excellent	Poor	Poor	Excellent
Good	Good	Good		Fair to poor	Good to excellent	Excellent	Excellent	Excellent	Poor	
Translucent		Transparent	Transparent	Transparent	Transparent	Translucent	Transparent	Transparent	Transparent	Transparent
Colorless	Colorless	Colorless to sl. yellow	Colorless to sl. yellow	Colorless	Colorless to amber	Colorless to gray	Colorless to pale	Colorless to amber	Colorless to amber	Colorless
1.54	1.48-1.50	1.49		1.59-1.60	1.56-1.57	1.30-1.40	1.43	1.54	1.50-1.55	1.58
Cl, E, F, MB, MC, MI	Cs, E, F, Lq, MB, MC, MI		Cl, E, F, MB, MC, MI	E, F, MB, MC, MI	Cl, E, F, MB, MC, MI	E, F, MC, MI	Cs, E, F, I, MC, MI, S	Cl, Cs, E, F, I, MB, MC, MI, S	Cl, Cs, E, MB, MC, MI, S	Cs, I, S

TABLE 12.2.4 (continued) Properties of Polymers

Properties of Polymers [continued]

Melamine-formaldehyde	Melamine-formaldehyde	Phenol-formaldehyde	Phenol-formaldehyde	Phenol-formaldehyde	Polyester (styrene-alkyd)	Silicones	Urea Formaldehyde	Acrylonitrile-butadiene-styrene (ABS)	Acetal	Alkyd resins
Thermosetting	Thermosetting	Thermosetting	Thermosetting	Thermosetting	Thermosetting	Thermosetting	Thermoplastic	Thermoplastic	Thermoplastic	Thermosetting
-Cellulose filled	Mineral filled (electrical	Cord filled	Cellulose filled	Unfilled cast phenolic, mechanical and chemical grade	Glassfiber mat reinforced	Mineral filled	-Cellulose filled	High-heat resistant	Homopolymer	Synthetic-fiber filled
10^{12}-10^{14}	10^{13}-10^{14}	10^{11}-10^{12}	10^{11}-10^{13}	1.0-7.0 × 10^{12}	10^{11}	>10^{12}	0.5-5.0	2.4-5.0		3.8-5.0
7.9-9.4	10.2	7.0-10.0	5.0-9.0	6.5-7.5	4.0-5.5	3.5-3.6	7.7-9.5	2.4-3.8	3.7	3.6-4.7
7.2-8.4	6.1	5.0-6.0	4.0-7.0	4.0-5.5	4.0-5.5	3.4-3.6	6.7-8.0	0.003-0.008		0.012-0.026
0.03-0.08	0.10	0.1-0.3	0.04-0.3	0.10-0.15	0.01-0.04	0.004	0.036-0.043	0.007-0.015	0.004	0.01-0.016
0.03-0.043	0.051	0.04-0.09	0.03-0.07	0.04-0.05	0.01-0.06	0.005-0.007	0.025-0.035			
1,300	1,950	900-1,300	800-1,200	4.0-5.0	500-1,500		1,300-1,400	7,000-8,000	10,000-12,000	4,500-6,500
7,000-13,000	5,500-6,500	6,000-9,000	6,500-8,500	6,000-9,000	30,000-50,000	3,000-4,000	5,500-13,000	1.0-20	15-75	
0.6-0.9		0.5-1.0	0.6-1.0	1.5-2.0	0.5-1.5		0.6	4,000-9,000		10,000-13,000
M 110-M 124	E 90		M 110-M 120	M 93-M 120	M 80-M 120	M 85-M 95	E 94-E 97	R 110-R 115	M 94, R 120	E 76
0.24-0.35	0.3-0.4	4.0-8.0	0.24-0.34	0.25-0.4	7.0-30	0.25-0.35	0.24-0.40	2.0-4.0	1.4-2.3	0.50-4.5
1.47-1.52	1.78	1.36-1.43	1.32-1.55	1.307-1.318	1.5-2.1	1.8-2.8	1.47-1.52	1.06-1.08	1.43	1.24-2.6
Self-extinguishing	Self-extinguishing	Self-extinguishing	Self-extinguishing	Self-extinguishing	Self-extinguishing	Self-extinguishing	Self-extinguishing	Slow	Slow	Self-extinguishing
204	130	121-127	143-171	74-80	93-288	>260	130	115-118		
0.4			0.35-0.40		0.2-0.4	0.2-0.3	0.6	0.3-0.4	0.35	
2.0-5.7	2.1-4.3		3.0-4.5	6.0-8.0	1.8-3.0	2.0-4.0	2.2-3.6	6.0-6.5	8.1	4.0-5.5
99.0	149	121	149-177		121-204	288	77	88-110	84	149-220
Good	Fair	Variable	Variable	Fair to good	Good	Fair to good	Poor	Good	Fair	Good
Poor	Poor	Poor	Poor	Poor to good	Poor	Poor to good	Poor	Good	Poor	Fair
Poor	Poor	Poor	Poor	Poor	Poor		Poor	Poor	Poor	
Good	Fair	Variable	Variable	Poor to good	Good	Fair	Fair	Good	Poor	Good
Poor	Poor	Poor	Poor	Poor	Poor	Poor	Poor	Good	Poor	Fair
Good	Good	Good	Good to excellent	Good to excellent	Good	Poor	Good	Good	Good	Fair to good
Good	Good	Poor to fair	Fair	Fair	Poor	Poor	Good	Poor	Good	Fair to good
Good	Good	Fair to good	Fair to good	Fair to good	Good		Good	Poor	Good	Fair to good
Good	Good	Fair to good	Excellent	Good to excellent	Good	Fair to good	Good	Fair	Good	Fair to good
Good	Good	Fair to good	Excellent	Good	Poor to fair	Poor	Good	Fair	Good	Fair to good
Good	Good	Good	Excellent	Excellent	Good	Good	Good	Good	Good	
Translucent	Opaque	Opaque	Opaque	Clear	Translucent	Opaque	Translucent	Translucent to opaque	Translucent to opaque	Opaque
Colorless	Dark			Colorless to amber	Colorless	Pale to dark	Colorless	Colorless	Colorless	Colorless
							1.54-1.56		1.48	
MC	MC	MC	MC	Cs, F	I	MC	MC	CI, E, MB, MI	MI, E	Cs MC, MI

Properties of Polymers [continued]

Chemical class	Polyketone							
	aliphatic thermoplastic							
	neat resin							
ELECTRICAL PROPERTIES								
D.C. resistivity, ohm-cm	103							
Dielectric constant, 60 cps	5-6							
Dielectric constant, 10^6 cps								
Dissipation factor, 60 cps								
Dissipation factor, 10^6 cps	0.04							
MECHANICAL PROPERTIES								
Modulus of elasticity, 10^3 psi	250							
Tensile strength, psi	>9000							
Ultimate elongation, %	300							
Yield stress, psi	9000							
Yield strain, %	2.2							
Rockwell hardness								
Notched Izod impact strength, ft lb/in.	4							
Specific gravity	1.24							
THERMAL PROPERTIES								
Burning rate								
Heat distortion, 264 psi. C	105-110							
Specific heat, cal/g								
Linear thermal expansion coefficient, 10^{-5}, C	9-11							
Maximum continuous service temperature, C								
CHEMICAL RESISTANCE								
Mineral acids, weak	Good							
Mineral acids, strong	Fair							
Oxidizing acids, concentrated	Fair							
Alkalies, weak	Good							
Alkalies, strong	Good							
Alcohols	Excellent							
Ketones	Excellent							
Esters	Excellent							
Hydrocarbons, aliphatic	Excellent							
Hydrocarbons, aromatic	Excellent							
Oils: vegetable, animal, mineral								
MISCELLANEOUS PROPERTIES								
Clarity	translucent							
Color	white crystals							
Refractive index, n_D								
FABRICATION								
Cl—calendering, Cs—casting, E—extrusion, F—hot forming or drawing, I—impregnation, MC—blow molding, MC—compression molding, MI—injection molding, S—spreading	E, MI							

pipes, refrigerator liners, car-instrument surrounds, radiator grills, telephones, boat shells, and radio and television parts. Available in medium, high, and very high impact grades.

Cellulosics

"Cellulose nitrate" is inflammable and has poor performance in heat and sunlight. Its uses are therefore limited. Cellulose acetate has good strength, stiffness, and hardness and can be made self-extinguishing. Glass-filled grades are made. Cellulose acetate-butyrate (CAB) has superior impact strength, dimensional stability, and service temperature range and can be weather stabilized. Cellulose proprionate (CP) is similar to CAB, but has better dimensional stability and can have higher strength and stiffness. Ethyl cellulose has better low-temperature strength and lower density than the others. Processing of cellulose plastics is by injection molding and vacuum forming. Applications include all types of moldings, electrical insulation, and toys.

Ethylene-Vinyl Acetate (EVA)

This material gives tough flexible moldings and extrusions suitable for a wide temperature range. The material may be stiffened by the use of fillers and is also specially formulated for adhesives. Applications include all types of moldings, disposable liners, shower curtains, gloves, inflatables, gaskets, and medical tubing. The material is competitive with polyvinyl chloride (PVC), polyethene, and synthetic rubbers, and is also used for adhesives and wax blends.

Fluorocarbons

This class of polymers, characterized by fluorine substitution, has outstanding chemical, thermal, and electrical properties and is characterized by the following four main classes of structures.

Polytetrafluoroethylene (PTFE), known commercially as Teflon or Fluon, is the best-known material and resists all known chemicals, weather, and heat, has an extremely low coefficient of friction, and is "non-stick." These materials are inert with good electrical properties. They are nontoxic, nonflammable, and have a working temperature range of –270 to 260°C. They may be glass filled for increased strength and rigidity. They do not melt and they must be formed by sintering of powders. Applications include chemical, mechanical, and electrical components, bearings (plain or filled with glass and/or bronze), tubing, and vessels for "aggressive" chemicals.

Fluoroethylenepropylene (FEP), unlike PTFE, can be processed on conventional molding machines and extruded, but thermal and chemical resistance properties are not quite as good.

Ethylenetetrafluoroethylene (ETFE) possess properties similar to but not as good as those of PTFE. However, the material exhibits a thermoplastic character similar to that of polyethylene which gives it a very desirable molding behavior.

Perfluoroalkoxy (PFA) is the fourth group of fluorinated polymers. These materials have the same excellent properties as PTFE, but the compound is melt processible and, therefore, suitable for linings for pumps, valves, pipes, and pipe fittings.

Ionomers

These thermoplastics are based on ethylene and have high melt strength, which makes them suitable for deep forming, blowing, and other similar forming processes. They are used for packaging, bottles, moldings for small components, tool handles, and trim. They have a high acceptance of fillers.

Polymethylpentene

Polymethylpentene (TPX) is a high-clarity resin with excellent chemical and electrical properties and the lowest density of all thermoplastics. It has the best resistance of all transparent plastics to distortion at high temperature — it compares well with acrylic for optical use, but has only 70% of its density. It is used for light covers, medical and chemical ware, high-frequency electrical insulation, cables, microwave oven parts, and radar components. It can withstand soft soldering temperatures.

Polyethylene Terephthalate

Polyethylene terephthalate (PETP) and modified versions thereof have high strength, rigidity, chemical and abrasion resistance, impact resistance in oriented form, and a low coefficient of friction. It is attacked by acetic acid and concentrated nitric and sulfuric acids. It is used for bearings, tire reinforcement, bottles, automotive parts, gears, and cams.

Polyamides (Nylons)

The polyamides are a family of thermoplastics, e.g., Nylon 6, Nylon 66, and Nylon 610, which are among the toughest engineering plastics with high vibration-damping capacity, abrasion resistance, inherent lubricity, and high load capacity for high-speed bearings. They have a low coefficient of friction and good flexibility. Pigment-stabilized types are not affected by ultraviolet radiation and chemical resistance is good. Unfilled nylon is prone to swelling due to moisture absorption. Nylon bearings may be filled with powdered molybdenum disulfide or graphite. Applications include bearings, electrical insulators, gears, wheels, screw fasteners, cams, latches, fuel lines, and rotary seals.

Polyethylene

Low-density polyethylene (orinally called *polythene*) is used for films, coatings, pipes, domestic moldings, cable sheathing, and electrical insulation. High-density polyethylene is used for larger moldings and is available in the form of sheet, tube, etc. Polyethylene is limited as an engineering material because of its low strength and hardness. It is attacked by many oxidizing chemical agents and some hydrocarbon solvents.

Polyketone, Aliphatic

Aliphatic polyketones are relatively strong, tough, ductile polymeric resins derived from equal proportions of ethylene and carbon monoxide with an additional few percent of higher olefin for property and processibility adjustment. Their physical, thermal, and mechanical properties are similar to polyamides and polyacetals. Mechanical properties are characterized by preservation of high levels of stiffness, toughness, and strength over a broad temperature range. Resistance to hydrolysis, swelling, and permeation provides broad chemical resistance. Relatively new in commercial supply, they find application in gears, machine components, and similar engineering applications. Tribological performance is very good, and in particular they have a low coefficient of friction and a low wear factor against steel. The electrical properties of the neat polyketone are typical of those of polar, semicrystalline thermoplastics.

Polyethersulfone

Polyethersulfone is a high-temperature engineering plastic — useful up to 180°C in general and some grades have continuous operating ratings as high as 200°C. It is resistant to most chemicals and may be extruded or injection molded to close tolerances. The properties are similar to those of nylons. Applications are as a replacement for glass for medical needs and food handling, circuit boards, general electrical components, and car parts requiring good mechanical properties and dimensional stability.

Polystyrene

This polymer is not very useful as an engineering material because of brittleness in unmodified forms, but it is well known for its use in toys, electrical insulation, refrigerator linings, packaging, and numerous commercial articles. It is available in unmodified form as a clear transparent resin and also in clear and opaque colors. High-impact forms are achieved by compounding with butadiene or other rubbery resins and heat-resistant forms are achieved by the use of fillers. Polystyrene can be stabilized against ultraviolet radiation and also can be made in expanded form for thermal insulation and filler products. It is attacked by many chemicals, notably aromatic hydrocarbon solvents, and by ultraviolet light.

Polysulfone

Polysulfone has properties similar to nylon, but these properties are retained up to 180°C compared with 120°C for nylon, which greatly expands the range of applications. Its optical clarity is good and its moisture absorption lower than that of nylon. Applications are as a replacement for glass for medical needs and chemistry equipment, circuit boards, and many electrical components.

Polyvinyl Chloride

This is one of the most widely used of all plastics. With the resin mixed with stabilizers, lubricants, fillers, pigments, and plasticizers, a wide range of properties is possible from flexible to hard types, in transparent, opaque, and colored forms. It is tough, strong, with good resistance to chemicals, good low-temperature characteristics and flame-retardant properties. PVC does not retain good mechanical performance above 80°C. It is used for electrical conduit and trunking, junction boxes, rainwater pipes and gutters, decorative profile extrusions, tanks, guards, ducts, etc.

Polycarbonate

Polycarbonate is an extremely tough thermoplastic with outstanding strength, dimensional stability, and electrical properties, high heat distortion temperature and low-temperature resistance (down to –100°C). It is available in transparent optical, translucent, and opaque grades (many colors). Polycarbonates have only fair resistance to chemicals as evidenced by the stress cracking caused by many solvents. The weathering tendencies can be stabilized against ultraviolet radiation by the use of proper additives. Polycarbonate compounds are used for injection moldings and extrusions for glazing panels, helmets, face shields, dashboards, window cranks, and gears. Polycarbonate is an important engineering plastic.

Polypropylene

Polypropylene is a low-density, hard, stiff, creep-resistant plastic with good resistance to chemicals, good wear resistance, low water absorption, and is relatively low cost. Polypropylene can be spun into filaments, converted into weaves, injection molded, and is commonly produced in a large variety of forms. Glass-filled polypropylene is widely used for its enhanced mechanical properties. It is used for food and chemical containers, domestic appliances, furniture, car parts, twine, toys, tubing, cable sheath, and bristles.

Polyphenylene Sulfide

Polyphenylene sulfide is a high-temperature plastic useful up to 260°C. Ambient temperature properties are similar or superior to those of nylon. It has good chemical resistance and is suitable for structural components subject to heat. Glass filler improves strength and enables very high heat resistance to 300°C. Uses are similar to those of nylon, but for higher temperatures.

Polyphenylene Oxide

This is a rigid engineering plastic similar to polysulfone in uses. It can be injection molded and has mechanical properties similar to those for nylon. It is used for automotive parts, domestic appliances, and parts requiring good dimensional stability. Frequently, the commercially available product is blended (or “alloyed”) with polystyrene which acts as a cost-effective extender.

Thermosetting Polymers

Alkyds

There are two main groups of alkyds: diallyphthalate (DAP) and diallylisopthalate (DIAP). These have good dimensional stability and heat resistance (service temperature 170°C; intermittent use 260°C), excellent electrical properties, good resistance to oils, fats, and most solvents, but limited resistance to strong acids and alkalis. The mechanical properties are improved by filling with glass or minerals. The main uses are for electrical components and encapsulation. A wide range of colors and fast-curing grades are available.

Amino Resins

These are based on formaldehyde reacted with urea or melamine and are formulated as coatings and adhesives for laminates, impregnated paper textiles, and molding powders. The resins are usually compounded with fillers of cellulose, wood flour, and/or other extenders. As composites with open-weave fabric, they are used for building panels. Uses also include domestic electrical appliances and electric light fittings; the melamine type is used for tableware. The strength is high enough for use in stressed components, but the material is brittle. Electrical, thermal, and self-extinguishing properties are good.

Epoxies

Epoxy resins are used extensively across industry as engineering polymers and as adhesives. They can be cold cured without pressure using a "hardener" or may be heat cured. Inert fillers, plasticizers, flexibilizers, and extenders give a wide range of properties from soft flexible to rigid solid materials. Bonding to nearly all materials, e.g., wood, metal, glass, is excellent as are the mechanical, electrical, and chemical properties. Epoxies are used in all branches of engineering, including large castings, electrical parts, circuit boards, potting, glass and carbon fiber structures, flooring, protective coatings, and adhesives. Importantly, they exhibit little or no shrinkage on cure.

Phenolics (Phenol Formaldehyde, PF)

PF, the original "Bakelite," is usually filled with 50 to 70% wood flour for molded nonstressed or lightly stressed parts. Other fillers are mica for electrical parts, asbestos for heat resistance, glass fiber for strength and electrical properties, nylon, and graphite. Phenolics represent one of the best polymers for low-creep applications. Moldings have good strength, good gloss, and good temperature range (150°C wood filled; intermittent use 220°C), but are rather brittle. Applications include electrical circuit board, gears, cams, and car brake linings (when filled with asbestos, glass, metal powder, etc.). The cost is low and the compressive strength very high.

Polyester

Polyester resins can be cured at room temperature with a hardener or alone at 70 to 150°C. It is used unfilled as a coating, for potting, encapsulation, linings, thread locking, castings, and industrial moldings. It is used mostly for glass-reinforced-plastic (GRP) moldings.

Polyimides

Polyimides are noted for their unusually high resistance to oxidation and service temperatures up to 250°C (400°C for intermittent use). The low coefficient of friction and high resistance to abrasion make them ideal for nonlubricated hearings. Graphite or molybdenum disulfide filling improves these properties. They are used for high-density insulating tape. Polyimides have high strength, low moisture absorption, and resist most chemicals, except strong alkalis and ammonia solutions.

Silicones

These may be cold or heat cured and are used for high-temperature laminates and electrical parts resistant to heat (heat distortion temperature 450°C). Unfilled and filled types are used for special-duty moldings. Organosilicones are used for surface coatings and as a superior adhesive between organic and nonorganic materials.

Laminated Polymer Structures

A wide range of composite structures are prepared from polymer resins combined with fibers. The reader is referred to Section 12.6 for a more extensive discussion of polymer composites. Laminated polymer structures consist of layers of fibrous material impregnated with and bonded together usually by a thermosetting resin to produce sheets, bars, rods, tubes, etc. The laminate may be "decorative" or "industrial," the latter being of load-bearing mechanical or electrical grade.

Phenolics

Phenolic plastics can be reinforced with paper, cotton fabric, asbestos paper fabric or felt, synthetic fabric, or wood flour. They are used for general-purpose mechanical and electrical parts. They have good mechanical and electrical properties.

Epoxies

These are used for high-performance mechanical and electrical duties. Fillers used are paper, cotton fabric, and glass fiber.

Tufnol

"Tufnol" is the trade name for a large range of sheet, rod, and tube materials using phenolic resin with paper and asbestos fabric and epoxy resin with glass or fabric.

Polyester

This is normally used with glass fabric (the cheapest) filler. The mechanical and electrical properties are inferior to those of epoxy. It can be rendered in self-colors.

Melamine

Fillers used for melamine are paper, cotton fabric, asbestos paper fabric, and glass fabric. Melamines have a hard, nonscratch surface, superior electrical properties, and can be rendered in self-colors. They are used for insulators, especially in wet and dirty conditions, and for decorative and industrial laminates.

Silicone

Silicone is used with asbestos paper and fabric and glass fabric fillers for high-temperature applications (250°C; intermittent use 300°C). It has excellent electrical but inferior mechanical properties.

Polyimide

Polyimide is most often used with glass fabric as filler. Polyimides have superior thermal and electrical properties with a service temperature similar to that for silicones but with two to three times the strength and flexibility.

Foam and Cellular Polymers

Thermoplastics

Polyurethane Foams. The "flexible" type is the one most used. It is "open cell" and used for upholstery, underlays, thermal and vibration insulation, and buoyancy. It can be generated *in situ*. The rigid type has "closed cells" and is used for sandwich construction, insulation, etc. Molded components may be made from rigid and semirigid types.

Expanded Polystyrene. This material is produced only in rigid form with closed cells. It can be formed *in situ*. The density is extremely low, as is the cost. Chemical resistance is low and the service temperature is only 70°C. It is used for packaging, thermal and acoustic insulation, and buoyancy applications.

Cellular Polyvinyl Chlorides. The low-density type is closed cell and flexible. It is used for sandwich structures, thermal insulation, gaskets, trim, to provide buoyancy, and for insulating clothing. The moderate- to high-density open-cell type is similar to latex rubber and is used as synthetic leather cloth. The rigid closed-cell type is used for structural parts, sandwich construction, thermal insulation, and buoyancy. Rigid open-cell PVC (microporous PVC) is used for filters and battery separators. In general, cellular PVC has high strength, good flame resistance, and is easy to work.

Polyethylene Foams. The flexible type is closed cell and has low density with good chemical resistance and color availability, but is a poor heat insulator and is costly. The flexible foams are used for vibration damping, packaging, and gaskets. The rigid type has high density and is used for filters and cable insulation. A structural type has a solid skin and a foam core.

Ethylene Vinyl Acetates. These are microcellular foams similar to microcellular rubber foam, but are much lighter with better chemical resistance and color possibilities.

Other Types. Other types of thermoplastics include cellular acetate, which is used as a core material in constructions; expanded acrylics, which have good physical properties, thermal insulation, and chemical resistance; expanded nylon (and expanded ABS), which are low-density, solid-skin constructions; expanded PVA, which has similar properties to expanded polystyrene; and expanded polypropylene, which gives high-density foams.

Thermosets

Phenolics. These can be formed *in situ*. They have good rigidity, thermal insulation, and high service temperature, but are brittle.

Urea Formaldehyde (UF) Foam. This is readily formed *in situ* and has good thermal insulation. It has open pores and is used for cavity-wall filling.

Expanded Epoxies. These have limited use because of their high cost. They give a uniform texture and good dimensional stability and are used for composite forms, e.g., with polystyrene beads.

Silicon Foams. These are rigid and brittle with a high service temperature (300°C; 400°C intermittent use). Their use is limited to high-temperature-resistant sandwich constructions. The flexible closed-cell type is costly but will operate up to 200°C and is used for high-temperature seals and gaskets.

Elastomers

Cellular Rubbers. There are three types: *sponge*, solid rubber blown to give an open-cell structure, *foam*, a liquid rubber expanded to form open or closed cells which is stiffer than sponge; and *expanded*, a solid rubber blown with mainly closed cells, also it is stiffer than sponge. Uses include gaskets, seals, thermal insulation, cushioning, shock absorption, sound and vibration damping, buoyancy, and sandwich constructions.

Elastomers

Elastomers, or rubbers, are essentially amorphous polymers with linear chain molecules with some cross-linking, which ensures elasticity and the return of the material to its original shape when a load is removed. They are characterized by large strains (typically 100%) under stress. The synthetic rubber styrene butadiene is the most-used elastomer, with natural rubber a close second. The following describes the commonly used elastomers and gives some applications and properties.

Natural Rubbers (Polyisoprene, NR)

These elastomers have high strength, flexibility, and resilience, but have poor resistance to fuels, oils, flame, and sunlight aging. They are more costly than synthetic rubbers, which often replace them. "Soft-rubber" contains 1 to 4% sulfur as a vulcanizer. Wear resistance is increased by inclusion of fillers such as carbon black, silicon dioxide, clay, and wood flour. "Hard rubber" may contain up to 25% sulfur. Applications include vehicle tires and tubes, seals, antivibration mountings, hoses, and belts. Full vulcanization of 45% produces ebonite. Shore hardness: 30 to 90. Temperature range: –55 to 82°C.

Synthetic Rubbers

Styrene Butadiene Rubbers (SBR, GRS, BUNAS). These are similar to natural rubbers in application, but are usually inferior in mechanical properties, although cheaper. They are used in car brake hydraulic systems and for hoses, belts, gaskets, and antivibration mountings. Shore hardness: 40 to 80. Temperature range: –50 to 82°C.

Butadiene Rubbers (Polynutadiene, BR). These are used as substitutes for natural rubber, but are generally inferior. They have similar applications as natural rubber. Shore hardness: 40 to 90. Temperature range: –100 to 93°C.

Butyl Rubbers (Isobutylene Isoprene, GR 1). These are extremely resistant to water, silicon fluids and grease, and gas permeation. They are used for puncture-proof tires, inner tubes, and vacuum seals. Shore hardness: 40 to 90. Temperature range: –45 to 150°C.

Nitrile Rubbers (Butadiene Acrylonitrile, BUNA, N.NBR). These have good physical properties and good resistance to fuels, oils, solvents, water, silicon fluids, and abrasion. They are used for O rings and other seals, petrol hoses, fuel-pump diaphragms, gaskets, and oil-resistant shoe soles. Shore hardness: 40 to 95. Temperature range: –55 to 82°C.

Neoprene Rubbers (Polychloroprene, Chloroprene). These are some of the best general-purpose synthetic rubbers. They have excellent resistance to weather aging, moderate resistance to oils, and good resistance to refrigerants and mild acids. Shore hardness: 40 to 95. Temperature range: –40 to 115°C.

Chlorosulfonated Polyethylene Rubbers (CSM). These have poor mechanical properties but good resistance to acids and heat with complete resistance to ozone. They are used in chemical plants, tank linings, and high-voltage insulation. Shore hardness: 45 to 100. Temperature range: –100 to 93°C.

Ethylene Propylene Rubbers (EP, FPM). These specialized rubbers are especially resistant to weather aging heat, many solvents, steam, hot water, dilute acids and alkalis, and ketones, but not petrol or mineral oils. They are used for conveyor belts, limited automotive applications, silicone fluid systems, and electrical insulation. Shore hardness: 40 to 90. Temperature hardness: –50 to 177°C.

Fluorocarbon Rubbers. These comprise a wide range of rubbers with excellent resistance to chemical attack, heat, acids, fuels, oils, aromatic compounds, etc. They have a high service temperature. They are particularly suitable for vacuum applications. Shore hardness: 60 to 90. Temperature hardness: –23 to 260°C.

Isoprenes (Polyisoprene, IR). These are chemically the same as natural rubber but are more costly. The properties and applications are similar to those of natural rubber. Shore hardness: 40 to 80. Temperature hardness: –50 to 82°C.

Polyacrylic Rubbers (ACM, ABR). This is a group of rubbers with properties midway between nitrile and fluorocarbon rubbers with excellent resistance to mineral oils, hypoid oils, and greases and good resistance to hot air and aging. The mechanical strength is low. They are often used for spark plug seals and transmission seals. Shore hardness: 40 to 90. Temperature hardness: –30 to 177°C.

Polysulfide Rubbers. These have poor physical properties and heat resistance, but good resistance to oils, solvents, and weathering and are impermeable to gases and moisture. They are used for caulking and sealing compounds and as a casting material. Shore hardness: 40 to 85. Temperature hardness: –50 to 121°C.

Polyurethane Rubbers. These have exceptional strength and tear and abrasion resistance (the best of all rubbers), low-temperature flexibility, and good resistance to fuels, hydrocarbons, ozone, and weather. Resistance to solutions of acids and alkalis, hot water, steam, glycol, and ketones is poor. They are used for wear-resistant applications such as floor coverings. Shore hardness: 35 to 100. Temperature hardness: –53 to 115°C.

Silicone Rubbers (SI). These have exceptionally high service-temperature ranges, but the mechanical properties and chemical resistance are poor. They cannot be used in applications which expose them to fuels, light mineral oils, or high-pressure steam. They are used for high- and low-temperature seals, high-temperature rotary seals, cable insulation, hydraulic seals, and aircraft door and canopy seals. Shore hardness: 30 to 90. Temperature hardness: –116 to 315°C (380°C for intermittent use).

Fluorosilicone Rubbers. These are similar to silicone rubbers but have better oil resistance and a lower temperature range. Shore hardness: 40 to 80. Temperature hardness: –64 to 204°C.

12.3 Adhesives

Richard L. Lehman

Introduction

Adhesives are substances capable of holding materials together in a useful manner by surface attachment. The principal attribute of adhesives is their ability to form strong bonds with surfaces of a wide range of materials and to retain bond strength under expected use conditions. Although most adhesives do not have excellent bulk properties and it is therefore important to keep adhesive films thin, some materials such as epoxies have bulk properties which qualify them as engineering materials and thus can be used in multifunctional applications.

Advantages and Limitations of Use

The principal advantages of adhesives are their ability to bond similar to dissimilar materials of different thickness; to enable the fabrication of complex shapes not feasible by other fastening means; to smooth external joint surfaces; to permit economic and rapid assembly; to distribute stresses uniformly over joined interfaces, to provide weight reduction in critical structures via the elimination of fasteners; to dampen vibrations; to prevent or reduce galvanic corrosion; and to provide thermal and electrical insulation.

The limitations of adhesives depend on the specific adhesive and application and may include the necessity of surface preparation, long curing times, service-temperature limitations, loss of properties during service, toxicity of flammability during assembly or use, and the tendency of many adhesives to creep under sustained load.

Classes of Adhesives

Thermoplastic adhesives are a general class of adhesives based upon long-chained polymeric structure, and are capable of being softened by the application of heat with subsequent hardening upon cooling (hot-melt adhesives). The softening process if reversible for numerous cycles, which facilitates assembly and disassembly of structures. Thermosetting adhesives are a general class of adhesives based upon cross-linked polymeric structures which develop strong bonds that cannot be reversibly broken once they are formed. Thus, the thermoset adhesives are incapable of being softened once solidified.

Thermoplastic and thermosetting adhesives are cured, a process often referred to as setting, by polymerization or solidification, by heat, catalysis, chemical reaction, free-radical activity, radiation, evaporation of solvent, or another process as governed by the chemical nature of the particular adhesive.

Elastomers are a special class of thermoplastic adhesive possessing the common quality of substantial flexibility or elasticity. Refer to Section 12.2 on polymers.

Anaerobic adhesives are a special class of thermoplastic adhesive, the polyacrylates, that set only in the absence of air (oxygen). The two basic types are (1) machinery — possessing shear strength only and (2) structural — possessing both tensile and shear strength.

Pressure-sensitive adhesives are permanently and aggressively tacky solids which form immediate bonds when two parts are brought together under pressure. They are available as films and tapes as well as hot-melt systems.

Performance of Adhesives

To obtain optimum mechanical performance of an adhesive, it is critical to select the proper compound for the target application. Table 12.3.1 illustrates compatibility of adhesives and five broad classes of common materials. Generally, for good adhesive bonds the chemistry of the adhesive must match or be similar to the surface energy, polarity, and/or chemistry of the material being bonded. The elastic modulus of the adhesive should not be greater than the bonded material.

Adhesives are used in two classes of application, those requiring only shear strength and those requiring structural properties, often tensile and shear strength. Table 12.3.2 provides a quick reference for some typical applications. A much more detailed summary and classification of adhesives is given in Table 12.3.3.

Table 12.3.3 presents a sample of a number of adhesives (with practical information) that are available from various sources. The table is adapted from the rather extensive one found in J. Shields, *Adhesives Handbook*, CRC Press, Boca Raton, FL, 1970. For other extensive lists of trade sources, the reader is referred to Charles V. Cagle, Ed., *Handbook of Adhesive Bonding*, McGraw-Hill, New York, 1972, and Lerner et al., *Adhesives Red Book*, Palmerton Publishing Co., New York, 1968.

TABLE 12.3.1 Relative Performance of Adhesive Resins

	Adherence To:					Resistance			
Adhesive Resin	Paper	Wood	Metal	Ceramics	Rubbers	Water	Solvents	Alkali	Acids
Alkyd	6	7	5	6	7	7	2	2	5
Cellulose acetate	4	3	1	3	5	2	3	1	3
Cellulose acetate butyrate	3	1	4	5	2	3	1	3	3
Cellulose nitrate	5	1	5	5	3	2	2	4	4
Ethyl cellulose	3	1	3	5	2	3	3	3	3
Methyl cellulose	1	1	3	3	1	6	3	3	3
Carboxy methyl cellulose	1	2	3	2	1	6	1	4	4
Epoxy resin	10	8	8	8	8	7	8	8	8
Furane resin	7	2	8	7	8	9	7	8	8
Melamine resin	10	5	2	5	4	9	5	5	5
Phenolic resins	8	5	5	7	6	10	7	8	8
Polyeseter, unsaturated	8	4	5	7	7	6	2	5	7
Polyethylacrylate	4	3	5	6	8	4	6	7	7
Polymethylmethacrylate	4	4	3	6	6	5	6	7	7
Polystyrene	3	2	2	5	8	5	5	8	8
Polyvinylacetate	7	7	7	3	3	3	4	6	6
Polyvinyl alcohol	2	2	4	6	1	7	1	3	3
Polyvinyl acetyl	7	8	7	7	8	5	3	5	5
Polyvinyl chloride	7	6	7	6	8	6	10	9	9
Polyvinyl acetate chloride	8	6	7	5	8	5	8	8	5
Polyvinylidene copolymer	7	6	7	7	8	7	10	9	9
Silicone T.S.	6	7	7	8	10	7	6	6	6
Urethane T.S.	10	10	9	10	7	8	4	4	4
Acrylonitrile rubber	6	8	6	9	7	5	8	8	8
Polybutene rubber	3	6	2	8	8	3	10	9	9
Chlorinated rubber	5	7	4	7	6	3	10	9	9
Styrene rubber	7	6	5	8	7	3	8	9	9

Note: 1 = low performance; 10 = high performance.

Source: Adapted from Simonds, H.R. and Church, J.M., *A Concise Guide to Plastics*, 2nd ed., Reinhold, New York, 1963. With permission.

TABLE 12.3.2 High-Performance Engineering and Machine Part Adhesives

Thread locking	• Anaerobic acrylic
Hub mounting	• Anaerobic acrylic — compatible materials or flow migration unimportant • Modified acrylic — large gaps or migration must be avoided • Epoxy — maximum strength at high temperatures
Bearing mounting	• Anaerobic acrylic — compatible materials necessary and flow into bearing area to be prevented • Modified acrylic — for lowest cost
Structural joining	• Epoxies and modified epoxies — for maximum strength (highest cost) • Acrylics — anaerobic or modified cyanacrylates
Gasketing	• Silicones — primarily anaerobic

TABLE 12.3.3 Properties and Applications of Adhesive Materials

Basic Type	Curing Cycle, Time at Temperature	Service Temperature Range, C	Adherends	Main Uses	Remarks
			Animal		
Animal (hide)	Melted at 70–75°C; sets on cooling	<70	Paper, wood, textiles	Woodworking, carpet materials, paper, bookbinding	May be thinned with water
Animal (hide) + plasticizers	Applied as a melt at 60°C	<60	Paper, cellulosic materials	Bookbinding, stationery applications	Cures to permanent flexible film
Fish glue	1 hr at 20°C	<60	Wood, chipboard, paper	General-purpose for porous materials	Rapid setting; good flexibility, moderate resistance to water; high tack
Casein	Cold setting after 20 min standing period on mixing	<50	Timber with moisture content	Laminated timber arches and beams, plybox beams, and engineering timber work	Full bond strength developed after seasoning period of 48 hr
Casein + 60% latex	Cold setting after 20 min standing period on mixing	<60	Aluminum, wood, phenolic formaldehyde (rigid, leather, rubber)	Bonding of dissimilar materials to give flexible, water-resistant bond	Flexible
			Vegetable		
Dextrine	Air drying		Paper, cardboard, leather, wood, pottery	General-purpose glue for absorbent materials	Medium drying period of 2–3 hr
Dextrine–starch blend	Applied above 15°C air drying	<48	Cellulosic materials, cardboard, paper	Labeling, carton sealing, spiral-tube winding	Fast setting; may be diluted with water
Gum arabic	Cold setting	<50	Paper, cardboard	Stationery uses	Fast drying
			Mineral		
Silicate	8 hr at 20°C	10–430	Asbestos, magnesia	Lagging asbestos cloth on high-temperature insulation	Unsuitable where moisture; not recommended for glass or painted surfaces

TABLE 12.3.3 (continued) Properties and Applications of Adhesive Materials

Basic Type	Curing Cycle, Time at Temperature	Service Temperature Range, C	Adherends	Main Uses	Remarks
Silicate with china-clay filler	Dried at 80°C before exposure to heat	–180–1500	Asbestos, ceramics, brickwork, glass, silver, aluminum, steel (mild)–steel	General purpose cement for bonding refractory materials and metals; furnace repairs and gastight jointing of pipe work; heat-insulating materials	Resistant to oil, gasoline, and weak acids
Sodium silicate	Dried at 20–80°C before exposure to heat	0–850	Aluminum (foil), paper, wood–wood	Fabrication of corrugated fiber board; wood bonding, metal foil to paper lamination	Suitable for glass-to-stone bonding
Aluminum phosphate + silica filler	Dried $^{1}/_{2}$ hr at 20°C, then $^{1}/_{2}$ hr at 70°C + $^{1}/_{2}$ hr at 100°C + 1 hr at 200°C + 1 hr at 250°C; repeat for two overcoatings and finally cure at 1 hr at 350°C	<750	Steels (low-alloy), iron, brass, titanium, copper, aluminum	Strain-gauge attachment to heat-resistant metals; heater-element bonding	Particularly suited to heat-resistant steels where surface oxidation of metal at high temperatures is less detrimental to adhesion
Bitumen/latex emulsion	Dried in air to a tacky state	0–66	Cork, polystyrene (foam), polyvinyl chloride, concrete, asbestos	Lightweight thermal-insulation boards, and preformed sections to porous and nonporous surfaces; building applications	Not recommended for constructions operated below 0°C
			Elastomers		
Natural rubber	Air dried 20 min at 20°C and heat-cured 5 min at 140°C	<60	Rubber (styrene butadiene), rubber (latex), aluminum, cardboard, leather, cotton	Vulcanizing cement for rubber bonding to textiles and rubbers	May be thinned with toluene
Natural rubber in hydrocarbon solvent	Air dried 10 min at 20°C and heat-cured for 20 min at 150°C	<100	Hair (keratin), bristle, polyamide fiber	Brush-setting cement for natural- and synthetic-fiber materials	Resistant to solvents employed in oil, paint and varnish industries, can be nailed without splitting
Rubber latex	Air drying within 15 min	<60	Canvas, paper, fabrics, cellulosic materials	Bonding textiles, papers packaging materials; carpet bonding	Resistant to heat; should be protected from frosts, oils

TABLE 12.3.3 (continued) Properties and Applications of Adhesive Materials

Basic Type	Curing Cycle, Time at Temperature	Service Temperature Range, C	Adherends	Main Uses	Remarks
Chlorinated rubber in hydrocarbon solvents	Air dried 10 min at 20°C and contact bonded	–20–60	Polyvinyl chloride, acrylonitrile butadiene styrene, polystyrene, rubber, wood	General-purpose contact adhesive	Resistant to aging, water, oils, petroleum
Styrene–butadene rubber lattices	Air drying	–20–60	Polystyrene (foam), wood, hardboard, asbestos, brickwood	Bonding polystyrene foams to porous surface	—
Neoprene/nitrile rubbers in (?)	Dried 30 min in air and bonded under pressure; tacky	–20–60	Wood, linoleum, leather, paper, metals, nitrile rubbers, glass, fabrics	Cement for bonding synthetic rubbers to metals, woods, fabrics	May be thinned with ketones
Acrylonitrile rubber + phenolic resin	Primer air dried 60 min at 20°C, film cured 60 min at 175°C under pressure; pressure released on cooling at 50°C	–40–130	Aluminum (alloy)–aluminum to DTD 746	Metal bonding for structural applications at elevated temperatures	Subject to creep at 150°C for sustained loading
Polysulfide rubber in ketone solvent and catalyst	3 days at 25°C	–50–130, withstands higher temperatures for short periods	Metals	Sealant for fuel tanks and pressurized cabins in aircraft, where good weatherproof and waterproof properties are required	Resistant to gasoline, oil, hydraulic fluids, ester lubricants; moderate resistance to acids and alkalis
Silicone rubber	24 hr at 20°C (20% R.H.); full cure in 5 days	–65–260	Aluminum, titanium, steel (stainless), glass, cork, silicone rubber, cured rubber–aluminum, cured rubber–titanium, cured rubber–steel (stainless), aluminum–aluminum (2024 Alclad), cork–cork (phenolic bonded)	General-purpose bonding and scaling applications; adhesive/sealant for situations where material is expected to support considerable suspended weight; high-pressure exposure conditions	Resistant to weathering and moisture
Reclaim rubber	Contact bonded when tacky	<50	Fabric, leather, wood, glass, metals (primed)	General industrial adhesive for rubber, fabric, leather, porous materials	May be thinned with toluene
Polychloroprene	Air dried 10–20 min at 20°C	<60	Rubber, steel, wood, concrete	Bonding all types of rubber flooring to metals, woods, and masonry	Good heat resistance

TABLE 12.3.3 (continued) Properties and Applications of Adhesive Materials

Basic Type	Curing Cycle, Time at Temperature	Service Temperature Range, C	Adherends	Main Uses	Remarks
Modified polyurethane	3 hr at 18°C to 16 hr at –15°C	–80–110	Concrete, plaster, ceramics, glass, hardboards, wood, polyurethane (foam), phenol formaldehyde (foam), polystyrene (foam), copper, lead, steel, aluminum	Bonding to rigid and semirigid panels to irregular wall surfaces, wall cladding and floor laying; building industry applications	Foam remains flexible on aging even at elevated temperatures; will withstand a 12% movement
			Thermoplastic		
Nitrocellulose in ester solvent	Heat set 1 hr at 60°C after wet bonding	60	Paper, leather, textiles, silicon carbide, metals	Labeling, general bonding of inorganic materials including metals	Good resistance to mineral oils
Modified methyl cellulose	Dries in air	<50	Vinyl-coated paper, polystyrene foam	Heavy-duty adhesive; decorating paper and plastics	Contains fungicide to prevent biodeterioration
Ethylene vinyl acetate copolymer + resins	Film transfer at 70–80°C followed by bonding at 150–160°C	60, or 1 hr at 90	Cotton (duck)–cotton, resin rubber–leather, melamine laminate–plywood, steel (mild)–steel, acrylic (sheet) acrylic	Metals, laminated plastics, and textiles; fabrication of leather goods; lamination work	Good electrical insulation
Polyvinyl acetate	Rapid setting	<60	Paper, cardboard	Carton sealing in packaging industry	Resistant to water
Synthetic polymer blend	Applied as a melt at 177°C	<70	Paper, cardboard, polythene (coated materials)	Carton and paperbag sealing; packaging	—
Polychloroprene/resin blend in solvent	Air dried 10 min at 20°C and cured 4 days at 20°C to 7 hr at 75°C	<70	Chlorosulfonated polythene, polychloroprene fabrics, polyamide fabrics, leather, wood, textiles	Bonding synthetic rubbers and porous materials; primer for polyamide-coated fabrics such as nylon, terylene	—
Polychloroprene	Air dried 10–20 min at 20°C	—	Rubber, steel, wood, concrete	Bonding all types of rubber flooring to metals, woods, and masonry	Good heat resistance
Saturated polyester + isocyanate catalyst in ethyl acetate	Solvent evaporation and press cured at 40–80°C when tacky	—	Cellulose, cellulose acetate, polyolefins (treated film), polyvinyl chloride (rigid), paper, aluminum (foil), copper (foil)	Lamination of plastic films to themselves and metal foils for packaging industry, printed circuits	Resistant to heat, moisture, and many solvents

TABLE 12.3.3 (continued) Properties and Applications of Adhesive Materials

Basic Type	Curing Cycle, Time at Temperature	Service Temperature Range, C	Adherends	Main Uses	Remarks
Cyanoacrylate (anaerobic)	15 sec to 10 min at 20°C substrate dependent	Melts at 165	Steel–steel, steel–aluminum, aluminum–aluminum, butyl rubber–phenolic	Rapid assembly of metal, glass, plastics, rubber components	Anaerobic adhesive. Curing action is based on the rapid polymerization of the monomer under the influence of basic catalysts; absorbed outer layer on most surfaces suffices to initiate polymerization and brings about bonding
Polyacrylate resin (anaerobic)	3 min at 120°C to 45 min at 65°C or 7 days at 20°C	–55–95	Aluminum–aluminum	Assembly requirements requiring high resistance to impact or shock loading; metals, glass and thermosetting plastics	Anaerobic adhesive
			Thermosetting		
Urea formaldehyde	9 hr at 10°C to 1 hr at 21°C after mixing powder with water (22%)	<90	Wood, phenolic laminate	Wood gluing and bonding on plastic laminates to wood; plywood, chipboard manufacture; boat building and timber engineering	Excess glue may be removed with soapy water
Phenolic formaldehyde + catalyst PX-12	Cold acting	<100	Wood	Timber and similar porous materials for outdoor-exposure conditions; shop fascia panels	Good resistance to weathering and biodeterioration
Resorcinol formaldehyde + catalyst RXS-8	Cured at 16–80°C under pressure	<100	Wood, asbestos, aluminum, phenolic laminate, polystyrene (foam), polyvinyl chloride, polyamide (rigid)	Constructional laminates for marine craft; building and timber applications; aluminum–plywood bonding; laminated plastics	Recommended for severe outdoor-exposure conditions
Epoxy resin + catalyst	24–48 hr at 20°C to 20 min at 120°C	100	Steel, glass, polyester–glass fiber composite, aluminum–aluminum	General-purpose structural adhesive	—

TABLE 12.3.3 (continued) Properties and Applications of Adhesive Materials

Basic Type	Curing Cycle, Time at Temperature	Service Temperature Range, C	Adherends	Main Uses	Remarks
Epoxy resin + catalyst	8 hr at 24°C to 2 hr at 66°C to 45 min at 121°C	65	Steel, copper, zinc, silicon carbide, wood, masonry, polyester–glass fiber composite, aluminum–aluminum	Bonding of metals, glass, ceramics, and plastic composites	Cures to strong, durable bond
Epoxy + steel filler (80% w/w)	1–2 hr at 21°C	120	Iron, steel, aluminum, wood, concrete, ceramics, aluminum–aluminum	Industrial maintenance repairs; metallic tanks, pipes, valves, engine castings, castings	Good resistance to chemicals, oils, water
Epoxy + amine catalyst (ancamine LT)	2–7 days at 20°C for 33% w/w catalyst content	–5–60	Concrete stonework	Repair of concrete roads and stone surfaces	Excellent pigment-wetting properties; effective underwater and suited to applications under adverse wet or cold conditions
Epoxy resin (modified)	4–5 hr at 149°C to 20 min at 230°C to 7 min at 280°C	150	Aluminum, steel, ceramics	One-part structural adhesive for high-temperature applications	Good gap-filling properties for poorly fitting joints; resistant to weather, galvanic action
Epoxy	45 sec at 20°C	—	Gem stones, glass, steel, aluminum–aluminum	Rapid assembly of electronic components, instrument parts, printed circuits; stone setting in jewelry and as an alternative to soldering	—
Epoxy resin in solvent + catalyst	8 hr at 52°C to $^1/_2$ hr at 121°C	–270–371	Aluminum and magnesium alloys for elevated-temperature service	Strain gauges for cryogenic and elevated-temperature use; micromeasurement strain gauges	Cured material resists outgassing in high vacuum
Epoxy polyamide	8 hr at 20°C to 15 min at 100°C	100	Copper, lead, concrete, glass, wood, fiberglass, steel–steel aluminum–aluminum	Metals, ceramics, and plastics bonding; building and civil engineering applications	Resists water, acids, oils, greases

TABLE 12.3.3 (continued) Properties and Applications of Adhesive Materials

Basic Type	Curing Cycle, Time at Temperature	Service Temperature Range, C	Adherends	Main Uses	Remarks
Epoxy/polysulfide	24 hr at 20°C to 3 hr at 60°C to 20 min at 100°C	<120	Asbestos (rigid), ceramics, glass–fiber composites, carbon, polytetrafluoroethylene (treated), polyester (film), polystyrene (treated), rubber (treated), copper (treated), tungsten carbide, magnesium alloys, aluminum–aluminum, steel (stainless)–steel	Cold-setting adhesive especially suitable for bonding materials with differing expansion properties	Cures to flexible material; resistant to water, petroleum, alkalis, and mild acids
Phenol furfural + acid catalyst	2 days at 21°C	90–140	Alumina, carbon (graphite)	Formulation of chemically resistant cements; bedding and joining chemically resistant ceramic tiles	Extremely resistant to abrasion and heat
			Pressure-sensitive		
	Heated by air drying for several hours or 15–30 min at 210°F	—	Teflon–Teflon, Teflon–metal	—	Good resistance to acids and alkalis; excellent electrical properties
			Miscellaneous		
Ceramic-based	Dried for 1/2 hr at 77°C and cured 1/2 hr at 200°C + 1 hr at 250°C; postcured, 1 hr at 350°C	816	Metals	Strain gauges, temperature sensors for elevated-temperature work	—

References

ANSI/ASTM Standards D896-D3808, 1996 Annual Book of Standards, ASTM, Conshohocken, PA.

Avallone, Ed., *Mark's Standard Handbook for Mechanical Engineers,* 9th ed., McGraw-Hill, New York, 6-141–6-148.

Bikerman, 1968. *The Science of Adhesive Joints,* Academic Press, New York.

Cagle, C.V., Ed., 1972. *Handbook of Adhesive Bonding*, McGraw-Hill, New York.

Cook, 1970. *Construction Sealants and Adhesives,* John Wiley & Sons, New York.

Lerner, Kotsher, and Sheckman, 1968. *Adhesive Red Book*, Palmerton Publishing Co., New York.

NASA SP-5961 (01) Technology Utilization, *Chemistry Technology: Adhesives and Plastics,* National Technical Information Services, VA.

Patrick, 1973. *Treatise on Adhesives,* Marcel Dekker, New York.

Shields, J. 1970. *Adhesives Handbook*, CRC Press, Boca Raton, FL.

Simonds, H.R. and Church, J.M. 1963. *A Concise Guide to Plastics,* Reinhold, New York.

12.4 Wood

Daniel J. Strange

Definition

Wood is the structural component of a tree. It is composed of dead cells which were originally formed near the cambium (just beneath the bark). As the tree grows, the cambium moves outward, leaving the dead cells behind to serve as structure.

The two broad classifications for types of wood and softwoods and hardwoods. Softwoods come from conifers while hardwoods come from deciduous trees, and as the name implies softwoods are generally softer and hence weaker and with lower elastic modulus than hardwoods, although this generalization is not universally true.

The wood closest to the bark is called sapwood, and this layer extends about an inch into the tree. Although most of the cells in this layer are dead, this is the layer which transports moisture to the rest of the tree by capillary action. Beneath the sapwood layer is the heartwood, which is almost totally inactive except to provide structural support.

Composition

Wood is a fibrous cellular material with the cell walls composed primarily of cellulose, hemicellulose, and lignin. Cellulose is a linear polymer of glucose units and is the single most common organic chemical in nature. It accounts for roughly 40 to 50% of the wood by weight. Hemicellulose is a modified form of cellulose comprising approximately 30% of the cell wall whose structure can vary depending upon the exact type of wood. Lignin is a complex three-dimensional phenolic polymer which composes 20 to 30% of the structure of the wood. The rest of the weight of the wood is composed primarily of extraneous extractive substances which reside within the cellular structure and affect properties such as specific gravity, moisture absorption, and durability.

Variations in the compositions, structures, and volumes of these four components can have dramatic effects on the properties of the wood. These properties are relatively constant within a species, although growing conditions can have a significant influence.

Mechanical Properties

The properties of wood can vary substantially depending upon moisture content. "Green" wood, wood taken directly from a living tree with associated high moisture level, is significantly weaker (lower Young's modulus, tensile strength, and compressive strength) than oven-dried wood. Typical ratios of dry to green wood strength properties vary from 1.2 to 1.8.

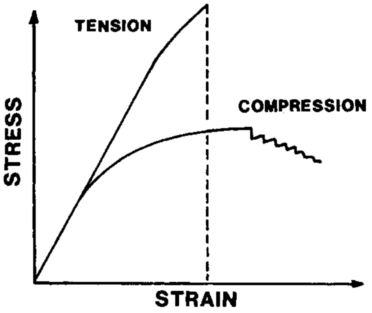

FIGURE 12.4.1 Stress–strain behavior of wood in tension and compression. Stress–strain curves for wood in tension and compression parallel to grain. Signs of stress and strain have been ignored so that both may be plotted together. Note particularly the difference in strength and in the extent of the nonlinear deformation prior to maximum stress. (From Wangaard, F.F., Ed., *Wood: Its Structure and Properties,* The Pennsylvania State University, University Park, 1981, 250.)

The failure modes of wood are more complex than one might expect. Because wood is essentially a composite material, it does not follow Hooke's law at high stresses but instead exhibits viscoelastic behavior. Figure 12.4.1 shows typical stress–strain curves for wood in tension and compression. At very high stresses, creep can occur. Wood is strongest in tension parallel to the grain, on the order of 100 MPa for a typical softwood. Perpendicular to the grain this value drops to about 4 MPa. In compression the strength values are approximately half the tension values, due to the collapse of the cellular structure and buckling of the wood fibers.

There are three principal shear failure modes in wood, six if one distinguishes between the radial and tangential directions. These modes are shear perpendicular to grain, shear parallel to grain, and rolling shear. Rolling shear occurs when the failure plane is parallel to the grain but the sliding direction is perpendicular to the grain, hence the fibers "roll" over each other. Wood is strongest when the shear is perpendicular to the grain, and weakest in rolling shear.

Decay Resistance

Totally dry wood does not decay. Furthermore, wood kept completely submerged will not decay significantly. Wood decays most rapidly in warm, humid, low-altitude areas. Some species of wood are more decay resistant than others as a result of the presence of extractives. White oak, walnut, cherry, cedar, and yew are examples of highly decay-resistant woods. Pines, willows, elms, beeches, and spruces are examples of low decay-resistant woods.

Composites

By gluing wood plies, chips, fibers, or pulp together a composite material can be formed which has more isotropic and homogenous properties than regular timber. In addition, this technique creates a strong and durable product out of wood unsuitable for timber. In general, wood composites homogenize the extreme anisotropy of timber into a nearly isotropic material whose properties are an average of the properties in each direction of the original timber. Table 12.4.1 classifies the various wood composites based upon the constitutive particle and the binder.

The most common wood composite is paper. Paper is made from pulped and chemically treated cellulose fibers, which is then rolled into sheets, pressed, and dried. There is no glue involved, as the microfibrils of the cellulose interlock and form hydrogen bonds. Fiberboard is similar to paper, only thicker (by an arbitrary value, typically 0.012 in.) and with larger fiber bundles. *Hardboard* simply refers to a high-density fiberboard.

TABLE 12.4.1 Allowable Stresses for Plywood (Stresses in MPa)

Type of Stress	Species Group of Face Ply	Grade Stress Level S-1 Wet	S-1 Dry	S-2 Wet	S-2 Dry	S-3 Dry Only
Tension in plane of plies (at 45° to face use 1/6 value)	1	9.86	13.79	8.20	11.38	11.38
	2,3	6.76	9.65	5.65	8.27	8.27
	4	6.48	9.17	5.38	7.65	7.65
Compression in plane of plies (at 45° to face use 1/3 value)	1	6.69	11.31	6.21	10.62	10.62
	2	5.03	8.27	4.69	7.58	7.58
	3	4.21	7.31	4.00	6.83	6.83
	4	4.21	6.89	4.00	6.55	6.55
Shear in plane perpendicular to plies (45° use 2 × value)	1	1.41	1.72	1.41	1.72	1.45
	2,3	1.10	1.28	1.10	1.28	1.10
	4	1.00	1.21	1.00	1.21	1.07
Shear, rolling, in the plane of plies (at 45° to face grain use $1\frac{1}{3}$ value)	Marine and Structural I	0.43	0.52	0.43	0.52	—
	Structural II and 2.4.1	0.34	0.39	0.34	0.39	0.38
	All Other	0.30	0.37	0.30	0.37	0.33
Modulus of rigidity (shear in plane perpendicular to plies)	1	480	620	480	620	570
	2	410	520	410	520	470
	3	350	410	350	410	380
	4	310	350	310	350	310
Bearing (on face) (perpendicular to plane of plies)	1	1.45	2.34	1.45	2.34	2.34
	2,3	0.93	1.45	0.93	1.45	1.45
	4	0.72	1.10	0.72	1.10	1.10
Modulus of elasticity in bending in plane of plies (face grain parallel or ⊥ to span)	1	10,300	12,400	10,300	12,400	12,400
	2	9,000	10,300	9,000	10,300	10,300
	3	7,600	8,300	7,600	8,300	8,300
	4	6,200	6,900	6,200	6,900	6,900

Adapted from American Plywood Association, Plywood Design Specifications, 1976.

Wood chips and/or sawdust pressed and glued together is referred to as *particleboard*. Typically, the chips range in size from 10 to 300 mm long and are in the form of flakes or fibers. Particleboard is effectively isotropic, easily machineable, and inexpensive. It is often used in furniture and for floor underlayment. When larger wood chips are used the product is referred to as *flakeboard*.

Plywood is created by layering plies of radial-cut wood. Typically, the plies are oriented at 90° to each other, which results in a strong material when the stress in parallel or perpendicular to the grain of the face plies, but a lesser strength at any other angle. Some design strength specifications of plywood are given in Table 12.4.2. Plywood makes efficient use of timber due to its radial cut, minimizes the effects of imperfections, resists warping, and can be formed into large sheets. Plywood is also less expensive than clear lumber.

TABLE 12.4.2 Classification of Wood Composites

Material	Constitutive Particle	Binder
Wood flour molding	Wood flour	Plastic; synthetic resin
Fiber-reinforced plastic	Fiber	Plastic
Paper	Fiber segment; fiber	Cellulose; hemicellulose; synthetic resin
Fiberboard	Fiber segment; fiber; fiber bundle	Lignin; synthetic resin
Particleboard	Splinter; chip; flake; planer shaving	Synthetic resin
Plywood	Veneer	Synthetic resin; natural glue
Laminated wood	Lumber	Synthetic resin; natural glue; mechanical connector
Solid wood	Single fiber or earlywood–latewood and wood ray, etc.	Lignin; hemicellulose

The reader is referred to Table C.14 in the Appendix for an overview of the physical properties and uses of American woods. The table also contains recommendations for appropriate applications. Table E.1 in the Appendix gives nominal sizes for lumber and timber, as well as allowable stresses in tension and compression and moduli of elasticity of various kinds of woods.

Selected Reference and Bibliography

Bodig, J. and Jayne, B. 1982. *Mechanics of Wood and Wood Composites*, Van Nostrand Reinhold, New York.

Forest Products Laboratory. 1974. *Wood Handbook: Wood as an Engineering Material*, U.S. Government Printing Office, Washington, D.C.

Perkins, R., Ed. 1990. *Mechanics of Wood and Paper Materials*, American Society of Mechanical Engineers, New York.

Shirasishi, N., Hiromu, K., and Norimoto, M., Eds. 1993. *Recent Research on Wood and Wood-Based Materials*, Elsevier Science Publishers, Barking, Essex, U.K.

Wangaard, F.F., Ed. 1981. *Wood: Its Structure and Properties,* The Pennsylvania State University, University Park.

12.5 Portland Cement Concrete

Steven H. Kosmatka

Introduction

Portland cement concrete is a simple material in appearance with a very complex internal nature. In contrast to its internal complexity, versatility, durability, and economy of concrete have made it the most-used construction material in the world. This can be seen in the variety of structures it is used in, from highways and bridges to buildings and dams.

Concrete is a mixture of portland cement, water, and aggregates, with or without admixtures. The portland cement and water form a paste that hardens as a result of a chemical reaction between the cement and water. The paste acts as a glue, binding the aggregates (sand and gravel or crushed stone) into a solid rocklike mass. The quality of the paste and the aggregates dictate the engineering properties of this construction material. Paste qualities are directly related to the amount of water used in relation to the amount of cement. The less water that is used, the better the quality of the concrete. Reduced water content results in improved strength and durability and in reduced permeability and shrinkage. As the fine and coarse aggregates make up 60 to 75% of the total volume of the concrete (Figure 12.5.1), their selection is important. The aggregates must have adequate strength and resistance to exposure conditions and must be durable.

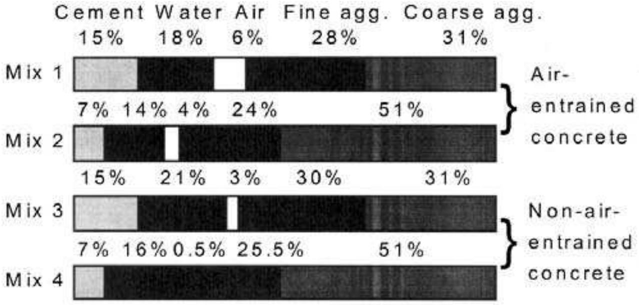

FIGURE 12.5.1 Range of proportions of materials used in concrete. (From *Design and Control of Concrete Mixtures,* EB001, Portland Cement Association, Skokie, IL, 1992. With permission.)

Fresh Concrete Properties

Freshly mixed concrete should be in a semifluid state capable of being molded by hand or mechanical means. All the particles of sand and coarse aggregate are encased and held in suspension. The ingredients should not segregate or separate during transport or handling. After the concrete hardens, it becomes a homogeneous mixture of all the components. Concrete of plastic consistency should not crumble, but flow sluggishly without segregation.

Concrete must be consolidated to form a homogeneous mass without the presence of large voids to achieve the desired strength and durability of the construction material. Internal and external vibration of concrete using vibrators allows stiff, slow-slump mixtures to be properly densified. The use of mechanical vibration provides an economical, practical method to quickly consolidate concrete without detrimentally affecting its properties.

Hardened Concrete Properties

Strength

Concrete gains strength by the reaction between cement and water — called hydration. Portland cement is primarily a calcium silicate cement. The calcium silicate combines with water and forms calcium silicate hydrate, which is responsible for the primary engineering properties of concrete, such as setting, hardening, strength, and dimensional stability. The compressive strength of concrete increases with age as long as an appropriate moisture content and temperature are available. This is illustrated in Figure 12.5.2. Compressive strength is usually specified at the age of 28 days; however, depending on the project, ages of 3 and 7 days can also be specified. For general-use concrete, a 28-day compressive strength between 20 and 40 MPa (3000 and 6000 psi) is used. 28 MPa (4000 psi) is most common. Higher-strength concrete, 50 to 140 MPa (7000 to 20,000 psi), is used in special applications to minimize structural dimensions, increase abrasion resistance and durability, and minimize creep (long-term deformation).

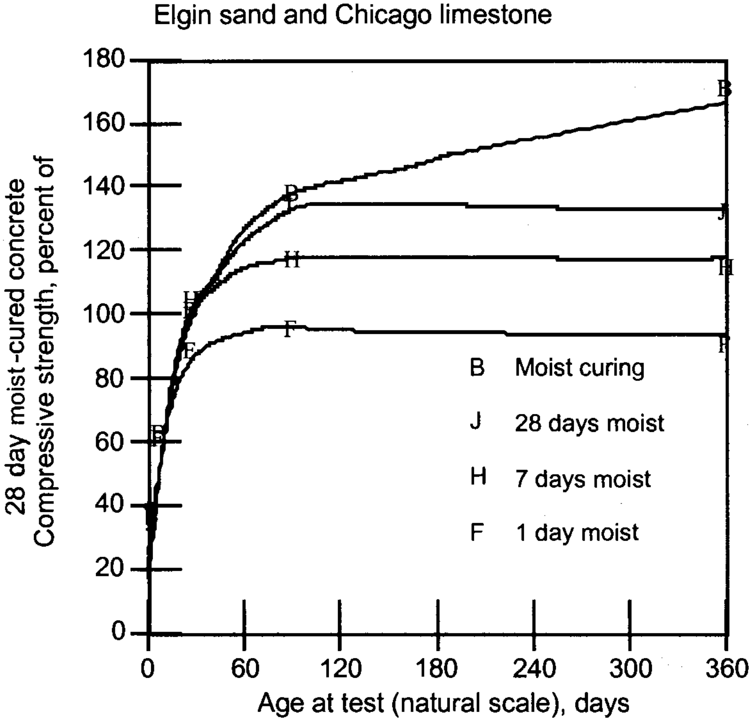

FIGURE 12.5.2 Concrete strength increases with age as long as moisture and a favorable temperature are present.

TABLE 12.5.1 Typical Properties of Normal-Strength Portland Cement Concrete

Compressive strength	20–40 MPa (3000–6000 psi)
Flexural strength	3–5 MPa (400–700 psi)
Tensile strength	2–5 MPa (300–700 psi)
Modulus of elasticity	14,000–41,000 MPa (2–6 million psi)
Permeability	1×10^{-10} cm/sec
Coefficient of thermal expansion	10^{-5}/°C (5.5×10^{-6}/°F)
Drying shrinkage	$4–8 \times 10^{-4}$
Drying shrinkage of reinforced concrete	$2–3 \times 10^{-4}$
Poisson's ratio	0.20–0.21
Shear strain	6000–17,000 MPa (1–3 million psi)
Density	2240–2400 kg/m^3 (140–150 lb/ft^3)

Increase in strength with age continues as long as any unhydrated cement is still present, the relative humidity in the concrete is approximately 80% or higher, and the concrete temperature is favorable. In order to maintain this increase in strength, concrete must be properly cured. Curing means that not only will a favorable temperature be present, but also moisture loss will not be permitted or extra water will be provided at the surface.

The compressive strength of concrete is directly related to the water/cement ratio. A decrease in water/cement ratio results in higher strength. Concrete achieves about 70 to 75% of its 28-day strength in 7 days. Although concrete is very strong in compression, it is weak in tensile strength. Tensile strength is about 8 to 12% of the compressive strength. Flexural strength is 0.7 to 0.8 times (for English units 5 to 7.5 times) the square root of the compressive strength. Shear strength is about 20% of the compressive strength. Modulus of elasticity ranges from 14,000 to 41,000 MPa and can be estimated as 5000 times the square root of the compressive strength (2 to 6 million psi or 57,000 times the square root of the compressive strength in English units). Refer to Table 12.5.1 to Table 12.5.3.

Density

Normal-weight concrete has a density of 2240 to 2400 kg/m^3 (140 to 150 lb/ft^3). The density of concrete varies with the relative density of the aggregate, the amount of air present in the paste, and the amount of water and cement in the mixture.

Permeability

Concrete permeability is a function of the permeability of the paste and aggregate and the interface between them. Decreased permeability improves the resistance of concrete to saturation, sulfate attack, chemical attack, and chloride penetration. Paste permeability has the greatest influence on concrete permeability. Paste permeability is directly related to the water/cement ratio and the degree of hydration or length of moist curing. A low water cement ratio and an adequate moist-curing period result in concrete with low permeability (Figure 12.5.3). The water permeability of mature, good-quality concrete, is approximately 1×10^{-10} cm/sec.

Abrasion Resistance

Abrasion resistance is directly related to the compressive strength of the concrete. The type of aggregate and the surface finish also have a strong influence on abrasion resistance. A hard aggregate, such as a granite, would provide more abrasion resistance than a soft limestone aggregate.

Volume Change and Crack Control

Concrete changes slightly in volume for various reasons. Understanding the nature of these changes is useful in planning concrete work and preventing cracks from forming. If concrete is free to move, normal volume changes would have very little consequence; but since concrete in service is usually restrained by foundations, subgrades, reinforcement, or connecting elements, significant stresses can develop. As the concrete shrinks, tensile stresses develop that can exceed the tensile strength of the concrete, resulting in crack formation.

TABLE 12.5.2 Compressive Strength of Concrete Made from Type I Cement, psi[a]

Series	Mix Id.	w/c by Weight	1 Day	3 Days	7 Days	28 Days	3 Months	1 Year	3 Years	5 Years	10 Years	20+ Years
						Moist Curing						
308	1	0.37	2160	4430	5930	7080	8260	8410		10400		
308	2	0.51	1040	2690	4200	5890	6410		8520			
308	3	0.65	610	1770	2780	4320	5030	5020		6050		
308	4	0.82	330	990	1580	2700	3180	3290		3680		
308	5	0.36	2060	4300	5820	7010	7750	8930		10330		
308	6	0.50	990	2780	4110	5950	6440	7280		8180		
308	7	0.64	550	1710	2700	4420	5190	5390		6180		
308	8	0.83	500	1000	1690	2850	3330	3490		3790		
308	9	0.36	2010	4330	5770	6940	7940	8550		10170		
308	10	0.50	900	2600	4250	6210	6490	7280		8670		
308	11	0.64	530	1720	2810	4510	5130	5770		6470		
308	12	0.82	250	920	1670	2880	3570	3540		3750		
356	AV1	0.40		5650	7140	9020	9460	8870	10760	10070	11020	12700
356	AV2	0.53		3390	4760	6510	7480	6890	7780	7720	8900	9680
356	AV3	0.71		1770	2540	4160	4540	4540	4960	5030	5840	6130
356	DV1	0.40		5000	6710	7980	8530	8660	10240	10340	10540	12300
356	DV2	0.53		3070	4810	6720	7400	7840	8780	8720	9330	9980
356	DV3	0.71		1580	2610	4380	5060	5360	5680	5700	6470	6710
356	EV1	0.40		4670	6650	8530	9790	10090	9940	11330	10900	12460
356	EV2	0.53		2700	4580	6730	7690	7860	8240	8960	8580	10290
356	EV3	0.71		1470	2500	4290	5010	5070	5110	5770	6200	6420
356	XL1	0.40		4780	6300	8090		9470		10780	10740	11730
356	XL2	0.53		3170	4470	6040		7740		8070	8370	8060
356	XL3	0.71		1800	2650	4060		4990		5220	5280	5260
356	XV1	0.40		5220	6950	8520		9720		10550	10850	13100
356	XV2	0.53		3350	4870	6700		7950		8710	8760	9800
356	XV3	0.71		1680	2810	4120		5060		5610	6280	6590
356	XW1	0.40		4680	6200	7780		9840		10100	10310	11480
356	XW2	0.53		3100	4520	6270		7420		8180	8150	8760
356	XW3	0.71		1770	2680	4140		5290		5560	5630	5460
374	11	0.41	1550		5680	7390	7610	9160	9810		10070	10460
374	11	0.56	780		4210	5870	6390	7020	6910		6740	7410
374	12	0.41	1120		5920	7490	8770	9170	9710		9710	10900
374	12	0.55	580		3800	5710	6650	7010	7380		7010	7300
374	13	0.42	1520		4320	6280	7560	8280	8620		9100	9940
374	13	0.57	890		2740	4730	5760	6400	6750		6340	7360
374	14	0.41	1490		5020	6460	7160	8730	9280		9400	10140
374	14	0.55	800		3480	5190	5700	6540	7030		6560	7410
374	15	0.45	2230		6080	7180	7820	8530	9290		9520	10770
374	15	0.59	1260		4730	5830	6280	6440	6360		5980	
374	16	0.41	1820		6040	7230	8080	9540	10160		10400	
374	16	0.56	1020		4000	5820	6520	7060	7640		7230	6840
374	17	0.46	1340		5220	7040	7560	8700	9310		9280	
374	17	0.61	740		3480	5770	6410	6560	6890		6700	7190
374	18	0.49	1220		5290	7000	7600	8360	9110		10290	10630
374	18	0.58	670		3600	5600	6230	6540	6810		6660	
374	19A	0.45	770		3090	4810	6600	7350	7930		8610	9240
374	19A	0.54	410		1710	3100	4280	5060	5940		5950	6480
374	19B	0.45	1110		4350	6560	7450	7740	8850		9550	10550
374	19B	0.60	560		2640	4260	5140	5420	6000		6360	6730
374	19C	0.45	1540		5370	6860	7390	7960	9000		9520	
374	19C	0.59	890		3910	5520	6200	6580	6970		6640	7220
436	1	0.36	2640	4780	6460	8070	8890	9670	9840		11030	10710
436	2	0.49	1320	2780	4200	6110	7210	7920	7990		8990	8940

TABLE 12.5.2 (continued) Compressive Strength of Concrete Made from Type I Cement, psi[a]

Series	Mix Id.	w/c by Weight	1 Day	3 Days	7 Days	28 Days	3 Months	1 Year	3 Years	5 Years	10 Years	20+ Years
436	3	0.62	700	1620	2550	4170	5210	5840	5850		6010	5390
436	4	0.42	1760	3500	5080	7200	8100	8720	9640		10540	10820

[a] To convert to MPa, multiply by 0.00689476.

Source: From Wood, S.L., *Research and Development Bulletin RD102T,* Portland Cement Association, Skokie, IL, 1992. With permission.

The primary factors affecting volume change are temperature and moisture changes. Concrete expands slightly as temperature rises and contracts as temperature falls. The average value for the coefficient of thermal expansion of concrete is about 1.0×10^{-5}/°C (5.5×10^{-6}/°F). This amounts to a length change of 5 mm for a 10-m length (0.66 in. for 100 ft) of concrete subjected to a rise or fall of 50°C (100°F). The thermal coefficient of expansion for steel is about 1.2×10^{-5} per degree Celsius (6.5×10^{-6}/°F), comparable to that of concrete. The coefficient for reinforced concrete can be assumed as 1.1×10^{-5}/°C (6×10^{-6}/°F).

Concrete expands slightly with a gain in moisture and contracts with a loss in moisture. The drying-shrinkage of concrete specimens ranges from 4 to 8×10^{-4} when exposed to air at a 50% relative humidity. Concrete with a unit shrinkage of 5.5×10^{-4} shortens about the same amount as a thermal contraction caused by a decrease in temperature of 55°C (100°F). The shrinkage of reinforced concrete is less than that for plain concrete because of restraint offered by the reinforcement. Reinforced concrete structures with normal amounts of reinforcement have a drying-shrinkage in the range of 2 to 3×10^{-4}. The amount of shrinkage is directly related to the amount of water in the concrete. Higher water content results in higher shrinkage. Specimen size also has an effect. Larger specimens shrink less than small specimens.

Drying-shrinkage is an inherent and unavoidable property of concrete; therefore, properly positioned reinforcing steel is used to reduce crack widths or joints are used to predetermine or control the location of cracks. Shrinkage control joints should be spaced about 25 to 30 times the thickness of a concrete slab on ground.

Deformation and Creep

Concrete will deform a small amount when a load is placed on it. When concrete is loaded, the deformation caused by the load can be divided into two parts: a deformation that occurs immediately, such as elastic strain, and a time-dependent deformation that begins immediately but continues at a decreasing rate for as long as the concrete is loaded (Figure 12.5.4). This latter deformation is called creep. The amount of creep is dependent on the magnitude of the stress, the age and strength of the concrete when the stress is applied, and the length of time the concrete is stressed. Creep is of little concern for normal concrete pavements, bridges, and small buildings; however, creep should be considered in design for very tall buildings or very long bridges.

Concrete Ingredients

Portland Cements

Portland cements are hydraulic cements; that is, they set and harden by reacting with water. This reaction, called hydration, combines water and cement to form a stonelike mass. Portland cement was invented in 1824 by an English mason, Joseph Aspdin, who named his product portland cement because it produced a concrete that was of the same color as natural stone on the Isle of Portland in the English Channel.

Portland cement is produced by combining appropriate proportions of lime, iron, silica, and alumina and heating them. These raw ingredients are fed into a kiln that heats the ingredients to temperatures of 1450 to 1650°C (2600 to 3000°F) and changes the raw materials chemically into cement clinker. The

TABLE 12.5.3 Flexural Strength of Concrete Made from Type I Cement, psi[a] (Third-Point Loading)

Series	Mix Id.	w/c by Weight	1 Day	3 Days	7 Days	28 Days	3 Months	1 Year	3 Years	5 Years	10 Years	20 Years
						Moist Curing						
308	1	0.37	295	540	625	855	975	925		960		
308	2	0.51	160	415	570	765	805	845		780		
308	3	0.65	80	290	425	595	675	680		645		
380	4	0.82	40	155	285	450	505	485		480		
308	5	0.36	285	510	680	825	890	940		930		
308	6	0.50	165	445	545	720	810	760		815		
308	7	0.64	95	290	465	605	695	655		690		
308	8	0.83	45	180	310	450	530	525		470		
308	9	0.36	310	535	655	820	905	970		915		
308	10	0.50	175	410	570	710	860	815		830		
308	11	0.64	90	320	440	675	715	715		690		
308	12	0.82	40	180	330	490	575	555		495		
356	XL1	0.40			705	880						
356	XL2	0.53			555	720						
356	XL3	0.71			420	555						
356	XV1	0.40			625	725						
356	XV2	0.53			555	655						
356	XV3	0.71			385	490						
356	XW1	0.40			620	750						
356	XW2	0.53			515	665						
356	XW3	0.71			395	515						
374	11	0.41	240		640	765	840	905	855		945	1070
374	11	0.56	135		520	625	710	690	730		730	830
374	12	0.41	180		640	790	910	925	965		970	1030
374	12	0.55	100		530	705	785	755	770		795	850
374	13	0.42	260		525	690	845	885	915		995	1140
374	13	0.57	165		420	595	705	765	765		800	880
374	14	0.41	250		620	725	800	915	890		965	
374	14	0.55	150		490	630	740	765	745		780	890
374	15	0.45	320		660	755	865	865	870		945	970
374	15	0.59	215		580	650	710	710	665		735	830
374	16	0.41	265		675	755	890	920	935		1035	1110
374	16	0.56	165		535	655	760	770	775		820	930
374	17	0.46	210		600	685	855	870	935		905	
374	17	0.61	120		490	650	735	760	720		695	
374	18	0.49	220		585	720	830	915	895		965	1090
374	18	0.58	130		510	650	750	740	730		725	
374	19A	0.45	145		450	605	745	840	870		950	1000
374	19A	0.54	75		300	470	610	655	700		735	850
374	19B	0.45	195		555	670	810	835	875		955	1060
374	19B	0.60	105		415	580	680	725	715		785	840
374	19C	0.45	275		605	750	890	920	890		950	1050
374	19C	0.59	170		510	665	775	810	765		790	890
436	1	0.36	370	555	655	770	925	1980	955		960	1030
436	2	0.49	225	435	565	745	825	860	905		900	960
436	3	0.62	135	300	420	620	690	720	730		730	800
436	4	0.42	320	505	655	755	875	890	1005		1010	1060

[a] To convert to MPa, multiply by 0.00689476.

Source: From Wood, S.L., *Research and Development Bulletin RD102T,* Portland Cement Association, Skokie, IL, 1992. With permission.

clinker is cooled and then pulverized. During this operation a small amount of gypsum is added to control the setting of the cement. The finished pulverized product is portland cement. Portland cement is essentially a calcium silicate cement.

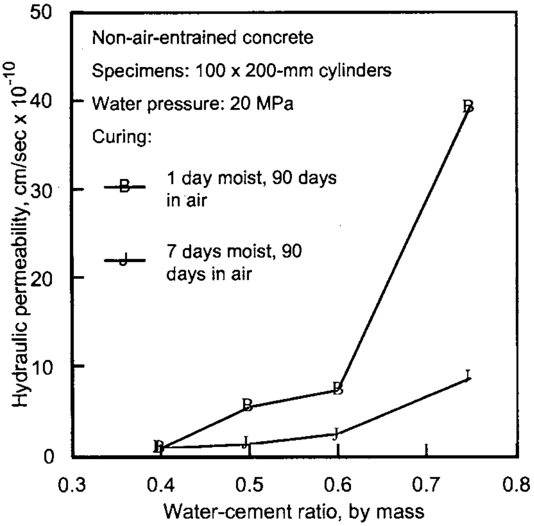

FIGURE 12.5.3 Water permeability of concrete as affected by water/cement ratio and curing. (From *Design and Control of Concrete Mixtures,* EB001, Portland Cement Association, Skokie, IL, 1992. With permission.)

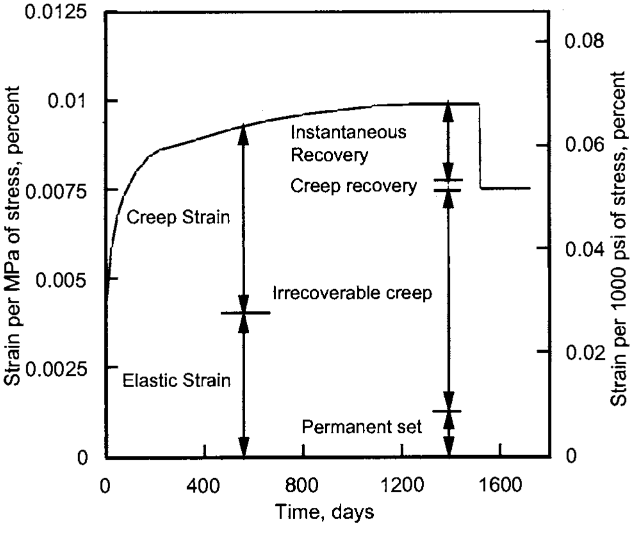

FIGURE 12.5.4 Combined curve of elastic and creep strains showing amount of recovery. (From *Design and Control of Concrete Mixtures,* EB001, Portland Cement Association, Skokie, IL, 1992. With permission.)

The American Society for Testing and Materials (ASTM) Standard C 150, Specification for Portland Cement, provides for the following types of portland cement:

Type I	General portland cement
Type II	Moderate-sulfate-resistant cement
Type III	High-early-strength cement
Type IV	Low–heat-of-hydration cement
Type V	High-sulfate-resistant cement

Types I, II, and III may also be designated as being air entraining. Type I portland cement is a general cement suitable for all uses where special properties of other cements are not required. It is commonly used in pavements, building, bridges, and precast concrete products.

Type II portland cement is used where precaution against moderate sulfate attack is important where sulfate concentrations in groundwater or soil are higher than normal, but not severe. Type II cement can also be specified to generate less heat than Type I cement. This moderate heat of hydration requirement is helpful when placing massive structures, such as piers, heavy abutments, and retaining walls. Type II cement may be specified when water-soluble sulfate in soil is between 0.1 and 0.2%, or when the sulfate content in water is between 150 and 1500 ppm. Types I and II are the most common cements available.

Type III portland cement provides strength at an early age. It is chemically similar to Type I cement except that the particles have been ground finer to increase the rate of hydration. It is commonly used in fast-track paving or when the concrete structure must be put into service as soon as possible, such as in bridge deck repair.

Type IV portland cement is used where the rate and amount of heat generated from hydration must be minimized. This low heat of hydration cement is intended for large, massive structures, such as gravity dams. Type IV cement is rarely available.

Type V portland cement is used in concrete exposed to very severe sulfate exposures. Type V cement would be used when concrete is exposed to soil with a water-soluble sulfate content of 0.2% and higher or to water with over 1500 ppm of sulfate. The high sulfate resistance of Type V cement is attributed to its low tricalcium aluminate content.

Blended Hydraulic Cements

Blended hydraulic cements are produced by intimately blending two or more types of cementitious material. Primary blending materials are portland cement, ground granulated blast-furnace slag, fly ash, natural pozzolans, and silica fume. These cements are commonly used in the same manner as portland cements. Blended hydraulic cements conform to the requirements of ASTM C 595 or C 1157. ASTM C 5195 cements are as follows: Type IS — portland blast-furnace slag cement, Type IP and Type P — portland–pozzolan cement, Type S — slag cement, Type I (PM) — pozzolan-modified portland cement, and Type I (SM) — slag-modified portland cement. The most common blended cements available are Types IP and IS.

ASTM C 1157 blended hydraulic cements include the following: Type GU — blended hydraulic cement for general construction, Type HE — high-early-strength cement, Type MS — moderate-sulfate-resistant cement, Type HS — high-sulfate-resistant cement, Type MH — moderate-heat-of-hydration cement, and Type LH — low-heat-of-hydration cement.

Supplementary Cementing Materials (Mineral Admixtures)

Supplementary cementing materials, also called mineral admixtures, are sometimes added to concrete mixtures. They contribute to the properties of hardened concrete through hydraulic or pozzolanic activity. Typical examples are natural pozzolans, fly ash, ground granulated blast-furnace slag, and silica fume. These materials react chemically with calcium hydroxide released from the hydration of portland cement to form cement compounds.

Below is a summary of the specifications and classes of supplementary cementing materials:

1. Ground granulated iron blast-furnace slag—ASTM C 989
   - Grade 80 — Slags with a low activity index
   - Grade 100 — Slags with a moderate activity index
   - Grade 120 — Slags with a high activity index
2. Fly ash and natural pozzolans — ASTM C 618
3. Class N — Raw or calcined natural pozzolans including diatomaceous earth, opaline cherts, shales, tuffs, volcanic ashes, and some calcined clays and shales
4. Class F — Fly ash with pozzolanic properties
5. Class C — Fly ash with pozzolanic and cementitious properties
6. Silica fume — ASTM C 1240

Mixing Water for Concrete

Almost any natural water that is drinkable can be used as mixing water for making concrete. However, some waters that are not fit for drinking may be suitable for concrete. Reference 1 provides guidance concerning the use of waters containing alkali carbonates, chlorides, sulfates, acids, oils, and other materials, and provides guidance as to allowable levels of contamination.

Aggregates for Concrete

The importance of using the right type and quality of aggregates cannot be overemphasized since the fine coarse aggregates occupy between 60 to 75% of the concrete volume and strongly influence the freshly mixed and hardened properties, mix proportions, and economy of the concrete. Fine aggregates consist of natural sand or crushed rock with particles smaller than 5 mm (0.2 in). Coarse aggregates consist of a combination of gravel or crushed aggregate with particles predominately larger than 5 mm (0.2 in.) and generally between 10 and 13 mm ($^3/_8$ and $^1/_2$ in.). The most common coarse aggregate size is 19 and 25 mm ($^3/_4$ and 1 in.) aggregate.

Normal weight aggregates should meet the requirements of ASTM C 33. This specification limits the amounts of harmful substances and states the requirements for aggregate characteristics, such as grading. The grading and maximum size of the aggregate affect the relative aggregate proportions as well as cement and water requirements, workability, pumpability, economy, shrinkage, and durability of the concrete.

Chemical Admixtures for Concrete

Admixtures are ingredients in concrete other than portland cement, water, and aggregates that are added to the mixture immediately before or during mixing. Common chemical admixtures include air-entraining, water-reducing, retarding, accelerating, and superplasticizing admixtures. The major reasons for using admixtures are to reduce the cost of concrete construction, achieve certain properties in concrete more effectively than by other means, or to ensure the quality of concrete during the states of mixing, transporting, placing, or curing in adverse weather conditions. Refer to Table 12.5.4.

Air-entraining admixtures are used purposely to entrain microscopic air bubbles in concrete. Air entrainment will dramatically improve the durability of concrete exposed to moisture during freezing and thawing. Air-entraining admixtures are commonly used to provide between 5 and 8% air content in concrete.

Water-reducing admixtures are used to reduce the quantity of mixing water required to produce concrete of a certain slump, reduce water/cement ratio, reduce cement content, or increase slump. Typical water-reducing admixtures reduce the water content by approximately 5 to 10%. High-range water reducers (superplasticizers) reduce the water content by approximately 12 to 30% and they can produce a highly fluid concrete.

Retarding admixtures are used to retard the rate of setting of concrete. An accelerating admixture is used to accelerate strength development of concrete at an early age.

Proportioning Normal Concrete Mixtures

The objective in proportioning concrete mixtures is to determine the most economical and practical combination of readily available materials to produce a concrete that will satisfy the performance requirements under particular conditions of use. To fulfill these objectives a properly proportioned concrete mix should possess these qualities: (1) acceptable workability of freshly mixed concrete, (2) durability, strength, and uniform appearance of hardened concrete, and (3) economy. Only with proper selection of materials and mixture characteristics can the above qualities be obtained in concrete production.

The key to designing a concrete mixture is to be fully aware of the relationship between the water/cement ratio and its effect on strength and durability. The specified compressive strength at 28 days and durability concerns dictate the water/cement ratio established for a concrete mixture. The water/cement ratio is simply the weight of water divided by the weight of cement. If pozzolans or slags are used, it would include their weights and would be referred to as the water/cementitious material

TABLE 12.5.4 Concrete Admixtures by Classification

Type of Admixture	Desired Effect	Material
Accelerators (ASTM C 494, Type C)	Accelerate setting and early-strength development	Calcium chloride (ASTM D 98) Triethanolamine, sodium thiocyanate, calcium formate, calcium nitrite, calcium nitrate
Air detrainers	Decrease air content	Tributyl phosphate, dibutyl phthalate, octyl alcohol, water-insoluble esters of carbonic and boric acid, silicones
Air-entrained admixtures (ASTM C 260)	Improve durability in environments of freeze-thaw, deicers, sulfate, and alkali reactivity Improve workability	Salts of wood resins (Vinsol resin) Some synethic detergents Salts of sulfonated lignin Salts of petroleum acids Salts of proteinaceous material Fatty and resinous acids and their salts Alkylbenzene sulfonates Salts of sulfonated hydrocarbons
Alkali-reactivity reducers	Reduce alkali-reactivity expansion	Natural pozzolans, fly ash, silica fume, blast-furnace slag, salts of lithium and barium
Bonding admixtures	Increase bond strength	Rubber, polyvinyl chloride, polyvinyl acetate, acrylics, butadiene-styrene copolymers
Coloring agents	Colored concrete	Modified carbon black, iron oxide, phthalocyanine, umber, chromium oxide, titanium oxide, cobalt blue (ASTM C 979)
Corrosion inhibitors	Reduce steel corrosion activity in a chloride environment	Calcium nitrite, sodium nitrite, sodium benzoate, certain phosphates or fluorosilicates, fluoroaluminates
Dampproofing admixtures	Retard moisture penetration into dry concrete	Soaps of calcium or ammonium stearate or eleate Butyl stearate Petroleum products
Finely divided mineral admixtures		
Cementitious	Hydraulic properties Partial cement replacement	Ground granulated blast-furnace slag (ASTM C 989) Natural cement Hydraulic hydrated lime (ASTM C 141)
Pozzolans	Pozzolanic activity Improve workability, plasticity, sulfate resistance; reduce alkali reactivity, permeability, heat of hydration Partial cement replacement Filler	Diatomaceous earth, opaline cherts, clays, shales, volcanic tufts, pumicites (ASTM C 618, Class N); fly ash (ASTM C 618, Classes F and C), silica fume
Pozzolanic and cementitious	Same as cementitious and pozzolan categories	High calcium fly ash (ASTM C 618, Class C) Ground granulated blast-furnace slag (ASTM C 989)
Nominally inert	Improve workability Filler	Marble, dolomite, quartz, granite
Fungicides, germicides, and insecticides	Inhibit or control bacterial and fungal growth	Polyhalogenated phenols Dieldrin emulsions Copper compounds
Gas formers	Cause expansion before setting	Aluminum powder Resin soap and vegetables or animal glue Saponin Hydrolized protein
Grouting agents	Adjust grout properties for specific applications	See Air-entraining admixtures, Accelerators, Retarders, Workability agents
Permeability reducers	Decrease permeability	Silica fume (ASTM C 1240) Fly ash (ASTM C 618) Ground slag (ASTM C 989) Natural pozzolans (ASTM C 618) Water reducers Latex

TABLE 12.5.4 (continued) Concrete Admixtures by Classification

Type of Admixture	Desired Effect	Material
Pumping aids	Imnprove pumpability	Organic and synthetic polymers Organic flocculents Organic emulsions of paraffin, coal tar, asphalt, acrylics Bentonite and pyrogenic silicas Natural pozzolans (ASTM C 618, Class N) Fly ash (ASTM C 618, Classes F and C) Hydrated lime (ASTM C 141)
Retarders (ASTM C 494, Type B)	Retard setting time	Lignin Borax Sugars Tartaric acid and salts
Superplasticizers[a] (ASTM C 1017, Type 1)	Flowing concrete Reduce water/cement ratio	Sulfonated melamine formaldehyde condensates Sulfonated napthalene formaldehyde condensates Ligonsulfonates
Superplasticizer[a] and retarder (ASTM C 1017, Type 2)	Flowing concrete with retarded set Reduce water	See Superplasticizers and also Water reducers
Water reducer (ASTM C 494, Type A)	Reduce water demand at least 5%	Lignosulfonates Hydroxylated carboxylic acids Carbohydrates (Also tend to retard set so accelerator is often added)
Water reducer and accelerator (ASTM C 494, Type E)	Reduce water (minimum 5%) and accelerate set	See Water reducer, Type A (Accelerator is added)
Water reducer and retarder (ASTM C 494, Type D)	Reduce water (minimum 5%) and retard	See Water reducer, Type A
Water reducer — high range (ASTM C 494, Type F)	Reduce water demand (miniumum 12%)	See Superplasticizers
Water reducer — high range — and retarder (ASTM C 494, Type G)	Reduce water demand (miniumum 12%) and retard set	See Superplasticizers and also Water reducers
Workability agents	Improve workability	Air-entraining admixtures Finely divided admixtures, except silica fume Water reducers

[a] Superplasticizers are also referred to as high-range water reducers or plasticizers. These admixtures often meet both ASTM C 494 and C 1017 specifications simultaneously.

Source: From *Design and Control of Concrete Mixtures,* EB001, Portland Cement Association, Skokie, IL, 1992. With permission.

ratio. The water/cement ratio can be established by a known relationship to strength or by durability requirements. For example, a concrete structure may require only 20 MPa (3000 psi) compressive strength, which would relate to a water/cement ratio of about 0.6; however, if the concrete is exposed to deicers, the maximum water/cement ratio should be 0.45 (Table 12.5.5). For corrosion protection or reinforced concrete exposed to deicers, the maximum water/cement ratio should be 0.40. When designing concrete mixtures, remember that where durability is concerned, water/cement ratio should be as low as practical. Entrained air must be used in all concrete that will be exposed to freezing and thawing and the presence of deicing chemicals. A typical air content for concrete would range from 5 to 8%. Reference 1 provides step-by-step procedures for proportioning concrete. Refer to Table 12.5.6 to Table 12.5.8.

Mixing, Transporting, and Placing Concrete

All concrete should be mixed thoroughly until it is uniform in appearance with all ingredients evenly distributed. If concrete has been adequately mixed, samples taken from different portions of a batch will

TABLE 12.5.5 Relationships Between Water Cement Ratio and Compressive Strength of Concrete

Compressive Strength at 28 days, MPa (psi)	Water-Portland Cement Ratio, by Mass: Non-Air-Entrained Concrete	Air-Entrained Concrete
40 (5800)	0.42	—
35 (5100)	0.47	0.39
30 (4400)	0.54	0.45
25 (3600)	0.61	0.52
20 (2900)	0.69	0.60
15 (2200)	0.79	0.70

Note: Strength is based on 150 × 300-mm cylinders moist cured 28 days at 23 ± 2°C. Relationship assumes maximum size of aggregate about 25 mm.

Adapted from *Design and Control of Concrete Mixtures,* EBDD1, Portland Cement Association, Skokie, IL, 1992. With permission.

have essentially the same unit weight, air content, slump, and strength. Concrete is sometimes mixed at a job site at a stationary mixer or paving mixer, and other times it is mixed in central mixers at ready-mix plants (ASTM C 94). Once concrete is transported to a job site it is then conveyed by a variety of methods including belt conveyors, buckets, shoots, cranes, pumps, wheelbarrows, and other equipment. Concrete should be conveyed in a manner in which the concrete is not allowed to dry out, be delayed, or allowed to segregate before it is placed.

Curing

All concrete must be properly cured. Curing is the maintenance of a satisfactory moisture content and temperature in concrete during some definite time period immediately following placing and finishing so that the desired properties of strength and durability may develop. Concrete should be moist cured for 7 days at a temperature between 10 and 27°C (50 and 80°F). Common methods of curing include ponding, spraying, or fogging; use of wet covers, impervious paper, plastic sheets, and membrane-forming curing compounds; or a combination of these.

Durability

Freeze-Thaw and Deicer Scaling Resistance

As water freezes in wet concrete, it expands 9%, producing hydraulic pressures in the cement paste and aggregate. Accumulated effects of successive freeze-thaw cycles and disruption of the paste and aggregate eventually cause significant expansion and extensive deterioration of the concrete. The deterioration is visible in the form of cracking, scaling, and crumbling.

The resistance of hardened concrete to freezing and thawing in a moist condition, with or without the presence of deicers, is significantly improved by the use of entrained air. Air entrainment prevents frost damage and scaling and is required for all concretes exposed to freezing and thawing or deicer chemicals. An air content of between 5 and 8% should be specified. Air-entrained concrete should be composed of durable materials and have a low water/cement ratio (maximum 0.45), a minimum cement content of 335 kg/m^3 (564 lb/yd^3) or move, proper finishing after bleed water has evaporated from the surface, adequate drainage, a minimum of 7-days moist curing at or above 10°C (50°F), a minimum compressive strength of 28 MPa (4000 psi), and a minimum 30-day drying period after moist curing. Sealers may also be applied to provide additional protection against the effects of freezing and thawing and deicers. However, a sealer should not be necessary for properly proportioned and placed concrete.

Sulfate-Resistant Concrete

Excessive amounts of sulfates in soil or water can, over 5 to 30 years, attack and destroy concrete that is not properly designed. Sulfates attack concrete by reacting with hydrated compounds in the hardened

TABLE 12.5.6A (Metric Units) Example Trial Mixtures for Air-Entrained Concrete of Medium Consistency, 80 to 100 mm Slump

					With Fine Sand, Fineness Modulus = 2.50			With Coarse Sand, Fineness Modulus = 2.90		
Water/Cement Ratio, kg/kg	Nominal Maximum Size of Aggregate, mm	Air Content, %	Water, kg/m^3 of Concrete	Cement kg/m^3 of Concrete	Fine Aggregate % of Total Aggregate	Fine Aggregate, kg/m^3 of Concrete	Coarse Aggregate, kg/m^3 of Concrete	Fine Aggregate % of Total Aggregate	Fine Aggregate, kg/m^3 of Concrete	Coarse Aggregate, kg/m^3 of Concrete
0.40	10	7.5	202	505	50	744	750	54	809	684
	14	7.5	194	485	41	630	904	46	702	833
	20	6	178	446	35	577	1071	39	648	1000
	40	5	158	395	29	518	1255	33	589	1184
0.45	10	7.5	202	450	51	791	750	56	858	684
	14	7.5	194	428	43	678	904	47	750	833
	20	6	178	395	37	619	1071	41	690	1000
	40	5	158	351	31	553	1255	35	625	1184
0.50	10	7.5	202	406	53	833	750	57	898	684
	14	7.5	194	387	44	714	904	49	785	833
	20	6	178	357	38	654	1071	42	726	1000
	40	5	158	315	32	583	1225	36	654	1184
0.55	10	7.5	202	369	54	862	750	58	928	684
	14	7.5	194	351	45	744	904	49	815	833
	20	6	178	324	39	678	1071	43	750	1000
	40	5	158	286	33	613	1225	37	684	1184
0.60	10	7.5	202	336	54	886	750	58	952	684
	14	7.5	194	321	46	768	904	50	839	833
	20	6	178	298	40	702	1071	44	773	1000
	40	5	158	262	33	631	1225	37	702	1184
0.65	10	7.5	202	312	55	910	750	59	976	684
	14	7.5	194	298	47	791	904	51	863	823
	20	6	178	274	40	720	1071	44	791	1000
	40	5	158	244	34	649	1225	38	720	1184
0.70	10	7.5	202	288	55	928	750	59	994	684
	14	7.5	194	277	47	809	904	51	880	833
	20	6	178	256	41	738	1071	45	809	1000
	40	5	158	226	34	660	1225	38	732	1184

From *Design and Control of Concrete Mixtures,* EB001, Portland Cement Association, Skokie, IL, 1992. With permission.

TABLE 12.5.6B (English Units) Example Trial Mixtures for Air-Entrained Concrete of Medium Consistency, 3- to 4-in. Slump

					With Fine Sand, Fineness Modulus = 2.50			With Coarse Sand, Fineness Modulus = 2.90		
Water/ Cement Ratio, lb per lb	Maximum Size of Aggregate, in,	Air Content, %	Water, lb per cu yd of Concrete	Cement lb per cu yd of Concrete	Fine Aggregate % of Total Aggregate	Fine Aggregate, lb per cu yd of Concrete	Coarse Aggregate, lb per cu yd of Concrete	Fine Aggregate % of Total Aggregate	Fine Aggregate, lb per cu yd of Concrete	Coarse Aggregate, lb per cu yd of Concrete
0.40	$^3/_8$	7.5	340	850	50	1250	1260	54	1360	1150
	$^1/_2$	7.5	325	815	41	1060	1520	46	1180	1400
	$^3/_4$	6	300	750	35	970	1800	39	1090	1680
	1	6	285	715	32	900	1940	38	1010	1830
	$1^1/_2$	5	265	665	29	870	2110	33	990	1990
0.45	$^3/_8$	7.5	340	755	51	1330	1260	56	1440	1150
	$^1/_2$	7.5	325	720	43	1140	1520	47	1260	1400
	$^3/_4$	6	300	665	37	1040	1800	41	1160	1680
	1	6	285	635	33	970	1940	37	1080	1830
	$1^1/_2$	5	265	590	31	930	2110	35	1050	1990
0.50	$^3/_8$	7.5	340	680	53	1400	1260	57	1510	1150
	$^1/_2$	7.5	325	650	44	1200	1520	49	1320	1400
	$^3/_4$	6	300	600	38	1100	1800	42	1220	1680
	1	6	285	570	34	1020	1940	38	1130	1830
	$1^1/_2$	5	265	530	32	980	2110	36	1100	1990
0.55	$^3/_8$	7.5	340	620	54	1450	1260	58	1550	1150
	$^1/_2$	7.5	325	590	45	1250	1520	49	1370	1400
	$^3/_4$	6	300	545	39	1140	1800	43	1260	1680
	1	6	285	520	35	1060	1940	39	1170	1830
	$1^1/_2$	5	265	480	33	1030	2110	37	1150	1990
0.60	$^3/_8$	7.5	340	565	54	1490	1260	58	1600	1150
	$^1/_2$	7.5	325	540	46	1290	1520	50	1410	1400
	$^3/_4$	6	300	500	40	1180	1800	44	1300	1680
	1	6	285	475	36	1100	1940	40	1210	1830
	$1^1/_2$	5	265	440	33	1060	2110	37	1180	1990
0.65	$^3/_8$	7.5	340	525	55	1530	1260	59	1640	1150
	$^1/_2$	7.5	325	500	47	1330	1520	51	1450	1400
	$^3/_4$	6	300	460	40	1210	1800	44	1330	1680
	1	6	285	440	37	1130	1940	40	1240	1830
	$1^1/_2$	5	265	410	34	1090	2110	38	1210	1990

TABLE 12.5.6B (continued) (English Units) Example Trial Mixtures for Air-Entrained Concrete of Medium Consistency, 3- to 4-in. Slump

					With Fine Sand, Fineness Modulus = 2.50			With Coarse Sand, Fineness Modulus = 2.90		
Water/ Cement Ratio, lb per lb	Maximum Size of Aggregate, in,	Air Content, %	Water, lb per cu yd of Concrete	Cement lb per cu yd of Concrete	Fine Aggregate % of Total Aggregate	Fine Aggregate, lb per cu yd of Concrete	Coarse Aggregate, lb per cu yd of Concrete	Fine Aggregate % of Total Aggregate	Fine Aggregate, lb per cu yd of Concrete	Coarse Aggregate, lb per cu yd of Concrete
0.70	$^3/_8$	7.5	340	485	55	1560	1260	59	1670	1150
	$^1/_2$	7.5	325	465	47	1360	1520	51	1480	1400
	$^3/_4$	6	300	430	41	1240	1800	45	1360	1680
	1	6	285	405	37	1160	1940	41	1270	1830
	$1^1/_2$	5	265	380	34	1110	2110	38	1230	1990

TABLE 12.5.7 Proportions by Mass to Make $^1/_{10}$ m^3 of Concrete for Small Jobs

Maximum-Size Coarse Aggregate, mm	Air-Entrained Concrete				Non-Air-Entrained Concrete			
	Cement, kg	Wet Fine Aggregate, kg	Wet Coarse Aggregate, kg	Water, kg	Cement, kg	Wet Fine Aggregate, kg	Wet Coarse Aggregate, kg[a]	Water, kg
10	46	85	74	16	46	94	74	18
14	43	74	88	16	43	85	88	18
20	40	67	104	16	40	75	104	16
40	37	61	120	14	37	69	120	14

[a] If crushed stone is used, decrease coarse aggregate by 5 kg and increase fine aggregate by 5 kg.

Source: From *Design and Control of Concrete Mixtures*, EB001, Portland Cement Associate, Skokie, IL, 1992. With permission.

TABLE 12.5.8 Proportions by Volume[a] of Concrete for Small Jobs

Maximum-Size Coarse Aggregate, mm	Air-Entrained Concrete				Non-Air-Entrained Concrete			
	Cement	Wet Fine Aggregate	Wet Coarse Aggregate	Water	Cement	Wet Fine Aggregate	Wet Coarse Aggregate	Water
10	1	$2^1/_4$	$1^1/_2$	$^1/_2$	1	$2^1/_2$	$1^1/_2$	$^1/_2$
14	1	$2^1/_4$	2	$^1/_2$	1	$2^1/_2$	2	$^1/_2$
20	1	$2^1/_4$	$2^1/_2$	$^1/_2$	1	$2^1/_2$	$2^1/_2$	$^1/_2$
40	1	$2^1/_4$	3	$^1/_2$	1	$2^1/_2$	3	$^1/_2$

[a] The combined volume is approximately $^2/_3$ of the sum of the original bulk volumes.

Source: From *Design and Control of Concrete Mixtures*, EB001, Portland Cement Associate, Skokie, IL, 1992. With permission.

cement paste. Due to crystallization growth, these expansive reactions can induce sufficient pressure to disrupt the cement paste, resulting in cracking and disintegration of the concrete. The first defense against sulfate attack is to use a low water/cement ratio (0.45 or preferably less), and to select a Type II or V cement (see the section on cement).

Corrosion Protection

Concrete protects embedded steel from corrosion through its highly alkaline nature. The high-pH environment (usually greater than 12.5) causes a passive and noncorroding protective oxide film to form on steel. However, carbonation or the presence of chloride ions from deicers or seawater can destroy or penetrate the film, causing rusting of the reinforcing steel. In addition to using a water/cement ratio of 0.40 or less, the following protective strategies can be used individually or in combination to reduce the risk of corrosion:

1. Cover thickness of 90 mm (3.5 in.) or more of concrete over top, reinforcing steel of compression zones. [*Note:* Excessive cover in tension zones exacerbates surface crack width.]
2. Low-slump dense concrete overlay
3. Latex-modified concrete overlay
4. Interlayer membrane/asphaltic concrete systems
5. Epoxy-coated reinforcing steel
6. Corrosion-inhibiting admixtures in concrete
7. Sealers with or without overlay
8. Silica-fume or other pozzolans that significantly reduce concrete permeability
9. Low water/cement ratio (<0.35) superplasticized concrete
10. Cathodic protection
11. Polymer concrete overlay
12. Galvanized reinforcing steel

13. Polymer impregnation
14. Lateral and longitudinal prestressing for crack control
15. Blended cements containing silica fume or other pozzolans to reduce permeability

Alkali–Silica Reaction

Most aggregates are chemically stable in hydraulic cement concrete, without deleterious interaction with other concrete ingredients. However, this is not the case for aggregates containing certain siliceous substances that react with soluble alkalis in concrete. Alkali–silica reactivity (ASR) is an expansive reaction between reactive forms of silica in aggregate and alkali hydroxides in concrete. Very reactive aggregates can induce cracks within a year, whereas slowly reactive aggregates can take over 20 years to induce noticeable cracks. ASR is best controlled through the use of fly ash, slag, silica fume, natural pozzolans, or blended hydraulic cement. With proper care in analyzing aggregates and selecting appropriate concrete ingredients, ASR can be effectively minimized using available materials. Reference 2 provides guidance on ASR.

Related Standards and Specifications

American Society for Testing and Materials (ASTM)

C 33	Specification for Concrete Aggregates
C 150	Specification for Portland Cement
C 595	Specification for Blended Hydraulic Cements
C 618	Specification for Fly Ash and Raw and Calcined Natural Pozzolans for Use as a Mineral Admixture in Portland Cement Concrete
C 989	Specification for Ground Granulated Blast-Furnace Slag for Use in Concrete and Mortars
C 1157	Performance Specification for Blended Hydraulic Cement
C 1240	Specification for Silica Fume for Use in Hydraulic-Cement Concrete and Mortar

References

1. *Design and Control of Concrete Mixtures,* EB001, Portland Cement Association, Skokie, IL, 1992, 214 pages.
2. *Guide Specification for Concrete Subject to Alkali-Silica Reactions*, IS415, Portland Cement Association, Skokie, IL, 1995, 8 pages.
3. *Specifications for Structural Concrete for Buildings*, ACI 301, American Concrete Institute, Farmington Hills, MI, 1996, 43 pages.
4. *Guide to Durable Concrete,* ACI 201.2R-92, American Concrete Institute, Farmington Hills, MI, 1992, 39 pages.
5. Wood, S.L., Evaluation of the Long-Term Properties of Concrete. Research and Development Bulletin RD102T, Portland Cement Association, Skokie, IL, 1992.

12.6 Composites

Bhuvenesh C. Goswami

Introduction

A *composite material* is defined as a combination of two or more components that yields unique characteristics in the final material. The selection of the materials and processes in developing and manufacturing composite structures depends on the end-use application. The development of new processes for making fibrous structures from polymers, metals, ceramics, and other precursors and the combination of those materials in various forms have allowed these materials to be used in a variety of applications. In other words, composites have been developed to satisfy the desired properties where no single quasi-continuous material would satisfy the need. Composites are usually made by combining a one-phase continuous material called a *matrix* with a second discontinuous component, usually termed *reinforcement*. The second component can be in the particulate form, that is, as *filler*, chopped fibers, continuous filaments or bundles of filaments, or continuous sheet materials in a two- or three-dimensional textile architecture. The nature of the architecture and the type of filler material will determine whether it will yield a high-, medium-, or low-performance end product. One method of configuration of composites may be based on the matrix-filler concept. Based on this concept, the composites can be divided into major categories, such as *ceramic matrix* (CMC) *metal matrix* and *polymer (plastics) matrix* (PMC) composites. Composites are further subdivided according to the shape and configuration of the reinforcing material. Table 12.6.1 shows the various forms (architecture) of reinforcements. When the reinforcing material is either ceramic or glass in the form of particulate, similar in all dimensions, it is called *particulate-reinforced* composite; and if it consists of short, needle-shaped single crystals, it is called *whisker-reinforced*. If fibers are of the order of a few millimeters in length, the reinforcing material is called *chopped fiber-reinforced*; and if it is a bundle of continuous filaments, it is called *fiber-reinforced composite*. Fiber-reinforced composites are further subdivided according to the configuration or the architecture of the reinforcement. Filaments aligned in one direction are classified as *uniaxial fiber composites*, and if the filaments are arranged in layers, such as filament-wound net shape or layered fabrics, then they are called *laminar composites*. Filaments that can be knitted or woven in a three-dimensional near-net shape form or deposited on a mandrel during extrusion are called *three-dimensional knitted* or *three-dimensional woven*, or *three-dimensional nonwoven composites*, respectively. Combination and lamination of knitted, woven, and braided structures to form three-dimensional forms can be further divided by the structure.

Wood, a natural composite of cellulose fibers bonded together with a matrix of lignin, has been used as an engineering material since time immemorial. But the first known important engineering material, dating back thousands of years, was husk or straw, employed as a reinforcement in clay or mud to make sun-dried bricks for use in adobe structures. Sawdust mixed with clay is an example of particulate composite. Lamination of wood has been used to make bows since prehistorical times. The earlier techniques used were very sophisticated. For example, the Mongols constructed the bows from composite of bull's tendon, wood and silk bonded together with adhesive derived from animal by products. Laminated wood has been found at Thebes dating back to 1500 B.C., and similar laminates based on shellac resin have been known and used in India for over 3000 years. Phoenicians used glass fibers as fillers in the making of bottles, but it was not until 1713 that it was rediscovered. The use of polymers as a doping agent started only after the development of synthetic chemistry, when the first polyester resin was prepared by Swedish chemist Jöns Jacob Berzelius. But the commercial use of doped fabrics, for aircraft wings, was seen in the early 1900s. Bakelite resin, a composite of phenol-formaldehyde, though discovered years earlier, was first marketed in 1909, with paper or cloth.

Glass fabric–reinforced/polymer (plastics) were first developed in the 1940s. Since then, with the development of various polymers, much attention has been paid to the making of reinforced structures from carbon and ceramic-based fibers, such as boron, developed in the 1960s. With the development of very high tenacity aramid polymeric fibers, for example, Kevlar® in the 1970s, and hydrocarbon-based fibers, for example, an ultrahigh molecular weight polyethylene, Spectra®, in the 1980s, the field of high-performance polymer-based composites has exploded.

In the last three decades of the twentieth century, there were phenomenal advances in both fiber and matrices, especially in the growth of lightweight aerospace metal matrix composites (MMCs), carbon-carbon composites, and high-temperature ceramic fiber matrix composites (CMCs). The properties of some of the engineering composites are shown in Table 12.6.2. Ceramic fiber polymer matrix composites have also been developed for personal protection, in addition to the damage protection of equipment from projectiles. In addition to the major advances in the development of lightweight and high-temperature composite for aerospace applications, the use of glass-reinforced polymer composites has achieved phenomenal growth in the past two decades.

The use of chopped-glass fibers and *tows* (large bundles of filaments) of glass fibers — in such applications as automobiles, pleasure boats, blades for windmills, and the frame structure for an entire cooling tower for power plants — accounts for increased use of polymer matrix composites (PMCs) in terms of volume and value. Glass fiber, both chopped and in tow forms, offers the low-cost composites made with polymer or plastic as a matrix. However, most of the polymer fiber matrices have low thermal

TABLE 12.6.1 Textile Architecture for Reinforced Composites

Classification	Figure	Manufacturing of the Textile			Fiber Arrangement		
			Degree of Automation	Production Costs	Fiber Angle	Fiber Crimpg	Thread Distance
1. 3D-woven fabrics 1.1 Various weft insertion systems 1.1.1 Rectangular/ orthogonal	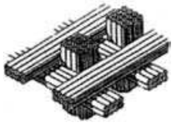	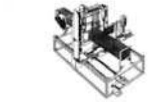 Insertion of two rectangular weft threads by double shed opening	→	↗	only 0°, 90°, z-direction	warp and weft without crimping of fibers	constant
1.2 Profiled woven fabric 1.2.1 Spherical woven fabric	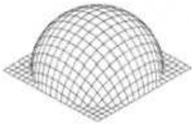	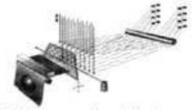 Weaving process with a device to vary the distance between single weaving point in the fabric: 1. compacting and spreading of warp threads; 2. withdrawal of warp threads with different lengths	↘	→	variable	low	irregular
1.2.2 Unfoldable woven fabric	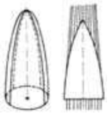	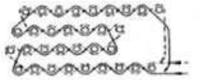 Fabric with "pockets" inside, separation of warp threads, expanding of the cone; only on shuttle loom	→	↗	variable, but approx. 0° and 90°	low	irregular
1.2.3 Circular woven fabric		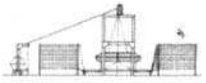 Circular moving shuttles with local shedding	↑	↓	warp and weft, 0° and 90°	low	constant
1.3 Multilayer woven fabric 1.3.1 Several connected warp threads	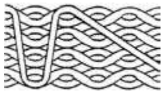	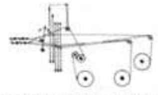 Connection of several layers without spacing by interlocking or linking warp threads	↗	↓	0°, 90°, in z-direction variable	low up to medium	constant

Characteristics of the Textile Structure									Special Characteristics of Composites		Structures and Applications	Availability on the Market
Isotropic Property	Shear Strength	Tensile Strength	Compressive Strength	Sheaning Strength	Flexural/Bending Strength	Strain	Drapeability	Special Characteristics	Peeling Properties/ Delamination Behavior	Impact Strength/ Impact Behavior/ Damage Tolerance		
✓	↘	↑	↗	↗	↗	↓	↓	Only block structures, no contour	↗	↑	<u>FRP:</u> Small carbon fiber ceramics for high thermic stress; rocket noses, aerofoil chords, engine mount <u>Medicine:</u> Prosthesis for lower leg; human implants	+
X	↘	↗	↓	↘	↓	↘	↗	Fiber fraction not constant, local adjustable orientation	↗	↗	<u>FRP:</u> Helmets, bumpers, seat shells, elements of car bodies, sails <u>Building/concrete:</u> Filter technique, geotextiles, fiber reinforced pillar and props <u>Medicine:</u> Safety helmets and protection for chins	+
X	↘	↗	↓	↘	↓	↘	↗	2 lines of intersection in circumference; characteristics comparable with 2D-woven fabric, distance of warp threads not constant	↗	→	Conical shells, cylinder, cones	+
X	↘	↗	↓	↘	↓	↘	→		↗	→	<u>Medicine:</u> Vascular grafts with low porosity <u>Miscellaneous:</u> Packaging, sacks	+
X	↗	↗	↗	↗	↗	↑	↗	Risk of fiber damage	↑	↗	<u>FRP:</u> Multilayer structure sensitive to impact, e.g., underbodies for automobiles <u>Concrete/building:</u> Conveyor belts	+

TABLE 12.6.1 (continued) Textile Architecture for Reinforced Composites

Classification	Figure	Manufacturing of the Textile			Fiber Arrangement		
			Degree of Automation	Production Costs	Fiber Angle	Fiber Crimpg	Thread Distance
1.3.2 Double-velour fabric	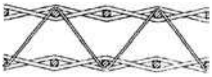	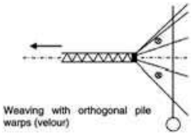	↑	↓	variable	low up to medium	constant
1.4 Multilayer circular woven fabric		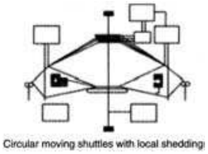	→	→	0°, 90°, radial	high crimping of fibers bad mechanical properties	constant
1.5 Profiled woven fabric 1.5.1 Integrally woven fabric		Conventional multilayer fabric with spacing to be cut open and unfolded	↘	→	irregular	low up to medium	irregular
1.5.2 Profiled woven layer fabric	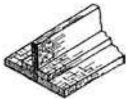		↘	→	0°, 90° and in z-direction	gering bis mittel	constant
2. Warp knitted fabrics, knitted fabrics 2.1 3D-knitted spacer fabrics	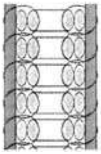	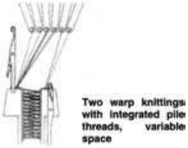	↑	↘	variable	very high, low mechanical properties	constant

Characteristics of the Textile Structure									Special Characteristics of Composites		Structures and Applications	Availability on the Market
Isotropic Property	Shear Strength	Tensile Strength	Compressive Strength	Sheaning Strength	Flexural/Bending Strength	Strain	Drapeability	Special Characteristics	Peeling Properties/ Delamination Behavior	Impact Strength/ Impact Behavior/ Damage Tolerance		
X	↘	↗	↗	↓	↗	↘	→	Adjustable distance, high impact resistance	↑	↗	FRP: Sandwich laminates for lightweight building board, shell component parts, machines cases; cable entries, double skin tanks Concrete/building: Lightweight construction, fillable double-skin fabric, pipes, insulation walls/sound insulation walls Medicine: decubitus prophylaxis	+
X	↗	↗	↗	↗	↗	↘	↘		↗	↗	FRP: Rocket nose, wing edges elements for loudspeakers	+
X	↗	↗	→	↗	↗	→	↓		↗	↗	FRP: Rocket fin, leading edge of wings	+
X	→	↗	↗	→	→	↘	↓		↗	↗	FRP: Reinforced shell structures with no or very little curvature; ribs	+
X	↘	↘	↘	↓	→	↗	↗	Can be deep drawn, inlay of straight fibers, less straightened fibers within loops; layers of different materials; tailored three-dimensional fabrics	↗	↗	FRP: Very light and less stressed sandwich panels; high spherically shaped components Concrete/building: Filter, drainage and separation layers Medicine: Decubitus prophylaxis, diving suit with less exposure Miscellaneous: Padding, isolation	+

TABLE 12.6.1 (continued) Textile Architecture for Reinforced Composites

Classification	Figure	Manufacturing of the Textile			Fiber Arrangement		
			Degree of Automation	Production Costs	Fiber Angle	Fiber Crimpg	Thread Distance
2.2 Profiled warp knitted fabrics/warp knitted tubes/circular warp knitted fabrics	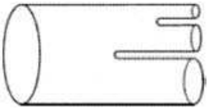	Double needle bar raschel warp knitting machine; production of two warp knited fabrics, closing of the hose with edge threads, production of branches by guide bars; production of hoses by circular warp knitting machines	↗	↓	variable	dependent on number of loops in warp knitted fabric	irregular
2.3 Multilayer circular warp knitted fabric	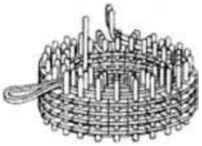	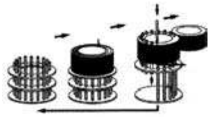 1. Flexible bars, warp knitting and filling the space with threads 2. Replacement of the bars	→	↑		high fiber curvature low mechanical properties	constant
2.4 Knitted fabrics 2.4.1 Circular knitted fabrics	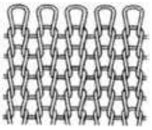	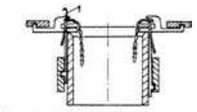 Circular knitting machine	↑	↓	loop form	with loops high, within wefts none	irregular
2.4.2 Biaxial reinforced multilayer knitted fabric	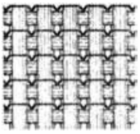	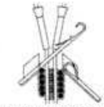 Knitted fabric with additional 3 weft and 2 warp thread systems	↗	→	variable	none in direction of the reinforcement, in the knitted fabric high	constant
3. Layer fabric/nonwovens 3.1 D-layer fabrics 3.1.1 Multilayer layer fabrics/ stitch bonded fabrics 3.1.1.1 Multilayer layer fabrics/ multiaxial warp knitted fabrics	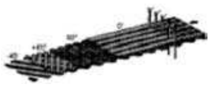	 Layers from weft threads combined by warp knitting process	↗	↘	variable	none	constant

Characteristics of the Textile Structure									Special Characteristics of Composites		Structures and Applications	Availability on the Market
Isotropic Property	Shear Strength	Tensile Strength	Compressive Strength	Sheaning Strength	Flexural/Bending Strength	Strain	Drapeability	Special Characteristics	Peeling Properties/ Delamination Behavior	Impact Strength/ Impact Behavior/ Damage Tolerance		
X	↘	↘	↓	↓	↘	↗	↑	High fiber damage, integration of stationary threads; brittle fibers cause problems during manufacturing	↗	↗	Concrete/building: Thin-walled tubes Medicine: Decubitus prophylaxis, diving suits with less exposure; vascular grafts	+
X	↗	↗	→	↘	↗	↘	↘	Brittle fibers cause problems during manufacturing	↗	↑	FRP: Randomes, nozzles for solid fuel rockets	+
X	↘	↘	↓	↘	↓	↗	↑	Partial reinforcement; brittle fibers cause problems during manufacturing; easy change of patterning	→	↑	FRP: Reinforcement of hoses	+
X	→	↗	→	→	↘	↘	↗	High component density, minimum damage of the reinforced fibers; partial reinforcement possible; can be deep drawn	↗	↗		–
X	↘	↑	↗	→	→	↘	↗	Orientation of fibers according to the stress direction	↗	↗	FRP: Rotor blade of wind generators, surfboards, components for aeronautics and aerospace Miscellaneous: Bulletproof clothing	+

TABLE 12.6.1 (continued) Textile Architecture for Reinforced Composites

Classification	Figure	Manufacturing of the Textile			Fiber Arrangement		
			Degree of Automation	Production Costs	Fiber Angle	Fiber Crimpg	Thread Distance
3.1.1.2 Locally reinforced multiaxial fabrics	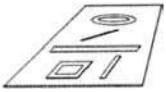	Adding of 2D-textiles for reinforcement	↘	→	0°, 90° and in z-direction	low up to medium	constant
3.1.2 Unidirectional layers	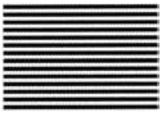	Arrangement of prepregs, single filaments or threads in one single orientation	↑	↘	variable	none	constant
3.2 3D-nonwovens 3.2.1 Oriented nonwovens		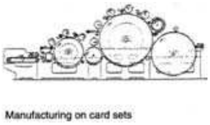	↑	↓		none	variable
3.2.2 Non-oriented nonwovens		Manufacturing: card, aerodynamic web formation, spunbonding or wet process	↑	↓		low up to medium	variable
3.2.3 3D-shaped nonwovens	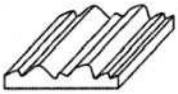	Accumulation of material at defined patches (aerodynamic web formation)	→	→		low up to medium	variable
4. 3D-braid 4.1 Packing braids 4.1.1 Compact 3D, constant cross section	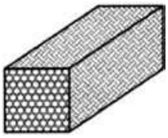	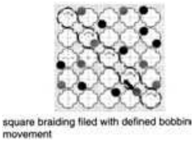	↗	→	variable	low up to medium	constant

Characteristics of the Textile Structure									Special Characteristics of Composites		Structures and Applications	Availability on the Market
Isotropic Property	Shear Strength	Tensile Strength	Compressive Strength	Sheaning Strength	Flexural/Bending Strength	Strain	Drapeability	Special Characteristics	Peeling Properties/ Delamination Behavior	Impact Strength/ Impact Behavior/ Damage Tolerance		
X	→	↗	↗	→	→	↘	↓	Pin-loaded holes	↗	→	FRP: Manholes in aerofoil chord, windows in fuselages	+
X	↘	↑	↘	↘	↘	↓	↗	Extraordinary characteristics only in direction of fiber	↗	↗		+
X	↘	→	→	↘	↘	↗	↗	Good characteristics in fiber direction; bonding necessary	→	↗		+
X	↘	↘	→	↘	↘	↗	↗	Bonding necessary	→	↗	Concrete/building: Barrier layer, filter	+
X	↘	↘	→	↘	↘	↗	↗	Bonding necessary	→	↗	Miscellaneous: Automobile interior	–
Possible	↑	↑	↗	↗	↗	↘	→	Optimized load bearing behavior	↗	↑	FRP: Seals Concrete/building: Seals	+

TABLE 12.6.1 (continued) Textile Architecture for Reinforced Composites

Classification		Figure	Manufacturing of the Textile			Fiber Arrangement		
				Degree of Automation	Production Costs	Fiber Angle	Fiber Crimpg	Thread Distance
4.1.2	Profile, variable cross section	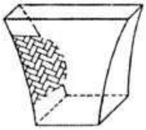	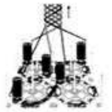 Braiding with individual control of the bobbin movement	↗	→	variable	low up to medium	irregular
4.2	Circular braids	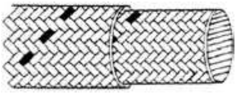	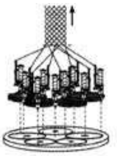 Braiding with bobbin movement on a defined path	↗	↘	variable	low up to medium	constant
4.3	Overbraiding	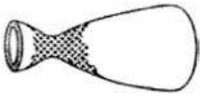	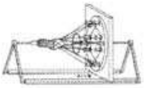 Circular braiding over a core	↗	↘	dependent on braiding outline	low up to medium	irregular
5. 5.1	Joining techniques Sewing	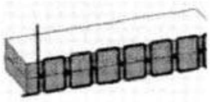	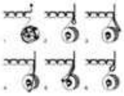 Joining of different textiles by sewing	↑	↘	variable	variable, depending on settings	constant
5.2	Bonding		Joining of two surfaces by applying adhesive	↘	↘			
5.3	Welding	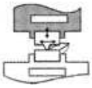	Softening of thermoplastic textiles, partially melding in joining zone and pressing together	↗	↘			

Characteristics of the Textile Structure									Special Characteristics of Composites		Structures and Applications	Availability on the Market
Isotropic Property	Shear Strength	Tensile Strength	Compressive Strength	Sheaning Strength	Flexural/Bending Strength	Strain	Drapeability	Special Characteristics	Peeling Properties/ Delamination Behavior	Impact Strength/ Impact Behavior/ Damage Tolerance		
X	↗	↗	↗	↗	↗	↘	→	High flexibility of possible outlines, low production rates, optimized load adjusted fiber orientation	↑	↗	FRP: Semifinished product with a profile, for lightweight constructions, ribs for reinforcement; marine propellers; crash elements; force including components, seals Medicine: Artificial ligaments	+
X	↘	↗	→	→	→	→	↗		→	→	FRP: Reinforcement of hoses, sport devices (tennis racket, paddels, …), torsion rollers in paper machines Medicine: Artificial grafts and ligaments	+
X	↘	↗	→	→	→	→	↗	Core often takes over functions, e.g., to bear compressive force	↗	↗	FRP: Cover for rocket propulsion, bent scaffold pole, reinforcement of hose, paddels, pressure vessels	+
X	↗	↗	↗	↗	↗	↘	↗	Local reinforcement possible, damaging of threads by the needle; mechanical characteristics depend on sewed material	↗	↗	FRP: Stringer reinforced moldings Medicine: OP-garments Miscellaneous: Clothing, joining of textile structures	+
X	↘	→	↗	↘	↘	↗	↘	Mechanical characteristics depend on bonded materials, characteristics temperature-dependent	↓			+
X	↗	↗	↗	↗	↘	↘	↘	Quality of weld joint decreases with time, only thermoplasts can be welded, the welding of heterogene combinations of materials is limited	→			–

TABLE 12.6.1 (continued) Textile Architecture for Reinforced Composites

Classification	Figure	Manufacturing of the Textile			Fiber Arrangement		
			Degree of Automation	Production Costs	Fiber Angle	Fiber Crimpg	Thread Distance
5.4 Embroidery	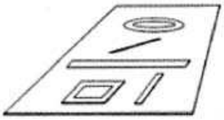	Embroidering of load carrying fibers	↓	↘	variable	high in the sewing yarn	irregular
6. Miscellaneous 6.1 3D-winding	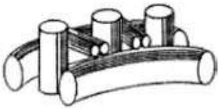	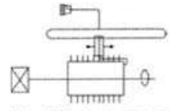 Hardend radial threads on a core are winded with axial and circumferential threads	↗	↘	variable	stretched orientation of fibers	irregular
6.2 Kemafil		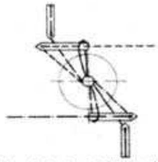 Spiral mesh structure is knitted on a hose by grippers	↗	↘	constant	in the loops high, in the laps low	constant
6.3 Hybride yarns		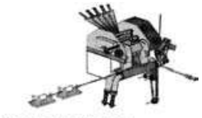 Wrapping of covering yarns	↗	→			

Signs and symbols:

↑	mentioned property is fulfilled very well or in a very high extent
↗	mentioned property is fulfilled well or in a high extent
→	mentioned property is fulfilled
↘	mentioned property is fulfilled badly
↓	mentioned propeerty is not fulfilled
X	non-isotropic properties
✓	isotropic properties
+	available
–	non or rarely available

Source: Berndt, E., Guer, M., and Wulfhorst, B., Three-dimensional textile structures for the production of technical textiles (2000).

Characteristics of the Textile Structure									Special Characteristics of Composites		Structures and Applications	Availability on the Market
Isotropic Property	Shear Strength	Tensile Strength	Compressive Strength	Sheaning Strength	Flexural/Bending Strength	Strain	Drapeability	Special Characteristics	Peeling Properties/ Delamination Behavior	Impact Strength/ Impact Behavior/ Damage Tolerance		
X	↗	↗	↗	→	↗	→	↗	Changing of amount and orientation of different kinds of fibers in every layer possible; local reinforcement possible; pattern can easily be changed	↗	↗	FRP: Linking of rotor blades, protection for manholes	+
X	↘	↗	→	↗	→	→	→	High efficiency of tenacity of the yarn, suitable in case of internal pressure, risk of slipping of layers on the pole caps	↗	→	FRP: components for aeronautics and aerospace; reinforcement of hoses; hybrid rods made from carbon reinforces composites and titan; tanks	–
X	→	↗	↗	→	↘	→	↗	Square end structure in case of thin or not exisiting core material	↗	→	Miscellaneous: Sheating of hoses and pressure vessels	+
								Mechanical properties depend highly on the 3D-structure	→	↗	Miscellaneous: Flat textile structures, formed by deep drawing	+

TABLE 12.6.2 Typical Properties of Some Engineering Materials

Material	Density (ρ) (g/cc)	Tensile Modulus (E) (Gpa)	Tensile Strength (σ) (Gpa)	Specific Modulus (E/ρ)	Specific Strength (σ/ρ)	Max Service Temp. (C)
Metal						
Cast iron, grade 20	7.0	100	0.14	14.3	0.02	230–300
Steel, AISI 1045 hot-rolled	7.8	205	0.57	26.3	0.073	500–650
Aluminium 2024-T4	2.7	73	0.45	27	0.17	150–250
Aluminium 6061-T6	2.7	69	0.27	25.5	0.10	150–250
Plastics						
Nylon 6/6	1.15	2.9	0.082	2.52	0.071	75–100
Polypropylene	0.9	1.4	0.033	1.55	0.037	50–80
Epoxy	1.25	3.5	0.069	2.8	0.055	80–215
Phenolic	1.35	3.0	0.006	2.22	0.004	70–120
Ceramics						
Alumina	3.8	350	0.17	92.1	0.045	1425–1540
MgO	3.6	205	0.06	56.9	0.017	900–1000
Short-fiber composites						
Glass-filled epoxy (35%)	1.90	25	0.30	8.26	0.16	80–200
Glass-filled polyester (35%)	2.00	15.7	0.13	7.25	0.065	80–125
Glass-filled nylon (35%)	1.62	14.5	0.20	8.95	0.12	75–110
Glass-filled nylon (60%)						
Unidirectional composites						
S-glass/epoxy (45%)	1.81	39.5	0.87	21.8	0.48	80–215
Carbon/epoxy (61%)	1.59	142	1.73	89.3	1.08	80–215
Kevlar/epoxy (53%)	1.35	63.6	1.1	47.1	0.81	80–215

Source: Sanjay K. Mazumdar, *Composites Manufacturing, Materials, Product, and Process Engineering*, CRC Press, 2002. Reproduced with permission.

stability with operating temperatures of less than 100°C. Some polymers, such as polyetheretherketone (PEEK) and epoxy, can withstand temperatures of up to ~200°C before losing some mechanical properties. However, the PMCs do show improved strength (resistance to failure), higher stiffness (resistance to bending), and better structural integrity. Although metals inherently have high stiffness, strength, thermal stability, and thermal and electrical conductivity, the incorporation of metal or ceramic fibers (MMCs) offer high hardness, maintenance of hardness at elevated temperatures, and precise tolerance in the final product. The metal matrix imparts some ductility to the material, thus avoiding the catastrophic failure in solely ceramic material. The incorporation of ceramic fibers in CMCs allows better reliable failure predictability, though it may or may not increase the strength of the composite.

Reinforcement with carbon or graphite and other high-technology fibers such as aramids (Kevlar®) with epoxy have become the composite materials of choice in the aerospace industry. Carbon epoxy composite laminates can be designed to give a zero coefficient of thermal expansion. In 2002 the aerospace industry consumed nearly 25 million pounds of composite materials. Composites made from carbon and other advanced technology fibers are also being used with increased frequency in biomedical, automotive, and high-performance/high-cost consumer products such as sporting goods and civil engineering applications.

The mechanical behavior of a composite is a reflection of the interaction between the interface of the matrix and the reinforcement. In short, if there is no binding between the two, for small strain at least, there will be failure in mutual stress transfer. At higher strain the deforming matrix may impose itself on the more rigid filler, thereby producing mechanical friction, which will make the filler to determine the response of the material. If there is adhesion between the matrix and the reinforcement, then even at low strains the stress transfer will take place across the interface and the two phases will share the stress. The quality of the bond between the matrix and the reinforcement is an important consideration in the production of composites. The mechanical properties of MMCs and PMCs are decided and

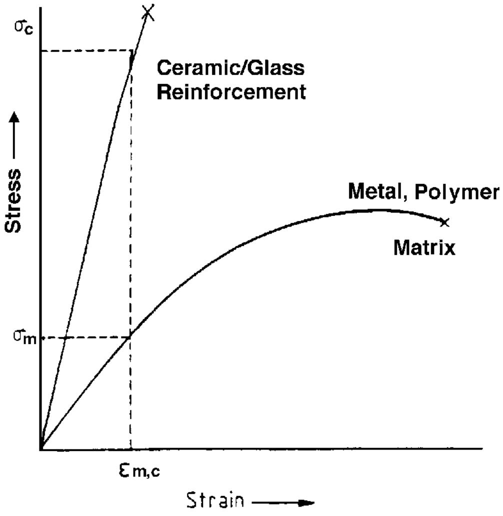

FIGURE 12.6.1 In a composite with good bonding between high-modulus ceramic and low-modulus metal or polymer matrix, the interfacial strain must be the same. Thus, the high-strength ceramic fiber bears most of the load (stress).

maximized by the efficient load transfer from the matrix (Figure 12.6.1) to the relatively high-strength, high-elastic modulus ceramic, carbon, or glass.

In light of the considerable importance of the interfacial bonding between the matrix and reinforcement, it is not surprising that a lot of research effort has gone into practical and theoretical understanding of the interface. But it is by no means an easy problem to study experimentally as it is a two-dimensional domain rather than a three-dimensional bulk phase, which is much easier to study. For best results there must be no relative sliding or interface failure, so the strain at the matrix-to-reinforcement area can be maximum and equal ($\varepsilon_{\text{matrix}} = \varepsilon_{\text{reinforcement}} = \varepsilon_{m,c}$). In other words, the reinforcements bear the major portion of the road, σ_c, while the weaker matrix bears a lower load, σ_m, because it has lower modulus. There are two aspects of relevance — wetting and adhesion on the one hand, and polymer adsorption on the other — in achieving the load transfer. The bond interface must be engineered because metals and polymers do not show intrinsic binding to ceramic reinforcement. This is accomplished by using a *coupling agent*, often xylene, which is applied to the ceramic or glass to promote bonding to a polymer; for metals, a metal matrix often has to be selected because it will bond to metals and some selected ceramics when molten or sintering during fabrication. To achieve a strong metal-to-ceramic bond, a controlled "forming gas" atmosphere must be used in the manufacture of MMC composites. Ceramics bond to ceramics easily, and materials form strong bonds during fabrication of CMCs. The implication of the nature and the quality of bonds in CMCs, MMCs, and PMCs for high-performance applications and the mechanics of these structures are discussed in the subsequent sections. Some recent publications for further readings on the manufacturing processes and properties of three-dimensional fiber-reinforced composites are listed at the end of the section on composites.

Polymer Matrix Composites

Weiping Wang, R. Allan Ridilla, and Mathew B. Buczek

Introduction

PMCs are used extensively as commodity and specialty engineering materials and constitute the largest class of composite materials on a dollar basis. The enormous success of PMCs arises from the wide range of properties that can be obtained and the low cost of low-end materials, such as fiberglass-reinforced

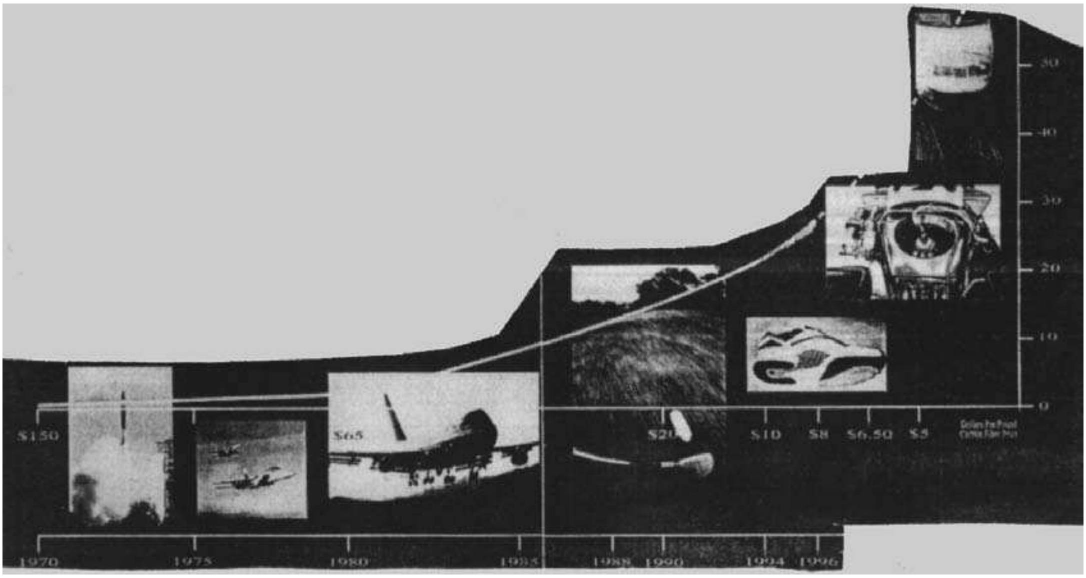

FIGURE 12.6.2 The evolution of carbon fiber composite applications since 1970, with fiber price and industry volume illustrated. (Source: Zoltek Co. Inc.)

polyester. Furthermore, the combination of high-strength/high-stiffness fibers in commodity polymer matrices offers an outstanding example of the composite principle — taking the best properties of both materials. The result is a strong, tough, stiff material, which, depending on the matrix and reinforcement type, provides value in applications as diverse as consumer products, construction, and aerospace.

A distinction must be made between reinforced plastics and advanced composites. The term *reinforced plastics* generally refers to plastic materials fabricated with a relatively low percentage of discontinuous, randomly oriented fibers, with rather moderate properties, and used in commodity applications. *Advanced composites*, on the other hand, refers to a class of materials where a high percentage of continuous, highly oriented fibers are combined with a suitable polymeric matrix to produce articles of high specific strength and specific stiffness. At present, composites are widely used in the aerospace and sporting goods industries for their superior performance. Figure 12.6.2 illustrates the evolution of applications for carbon fibers.

Polymers are also often "filled" with particulate reinforcements to increase certain properties, such as deflection temperature under load (DTUL). Although these materials are formally composites, they are usually regarded as filled polymers and not composites and thus will not be discussed explicitly in this section. Refer to Section 12.2.

Architecture

Each of the constituent materials in advanced composites must act synergistically to provide aggregate properties that are superior to the materials individually. The functional effectiveness of composites is principally due to the anisotropy of the materials and the laminate concept, where materials are bonded together in multiple layers. This allows the properties to be tailored to the applied load so that the structure can be theoretically more efficient than if isotropic materials were used. The reinforcements come in a variety of forms. Unidirectional tapes with all fibers along a common axis, woven fabrics constructed with fibers along both axes in the x–y plane, and three-dimensional architectures with reinforcements in more than two axial directions are just a few of the building blocks of composite structures.

The concept of laminate is illustrated in Figure 12.6.3. On the left is the unidirectional composite, where all reinforcements are aligned in one direction. This construction provides excellent properties in

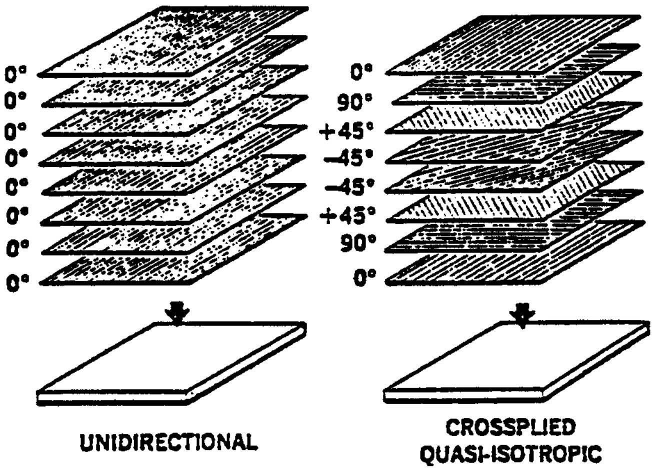

FIGURE 12.6.3 The basic concept of composite laminate (From Brandt, A.M. and Marshall, I.H., Eds., *Brittle Matrix Composites I*, Elsevier Applied Science, New York, 1986. With permission.)

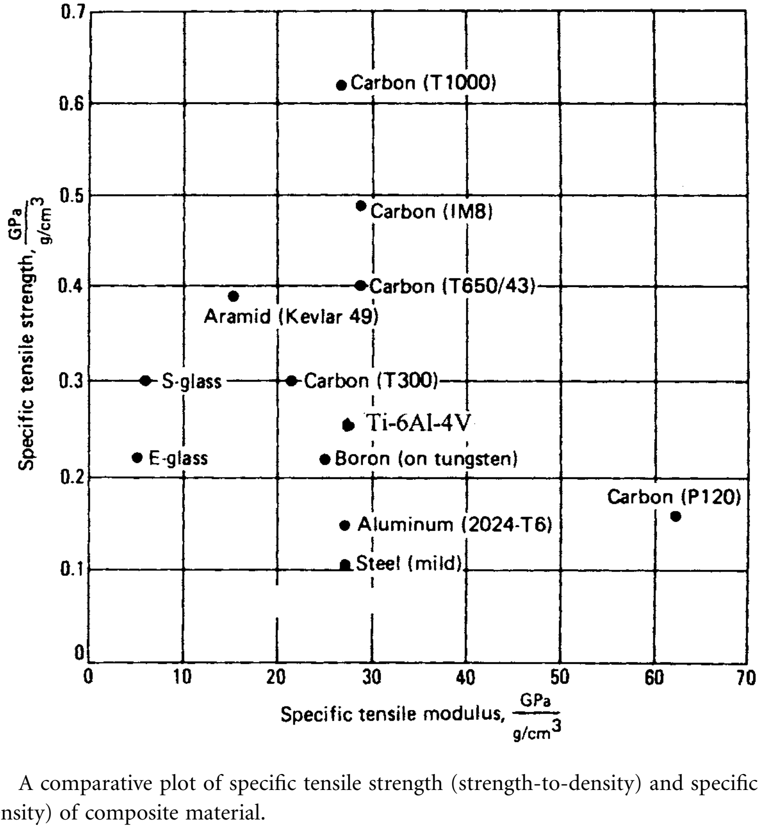

FIGURE 12.6.4 A comparative plot of specific tensile strength (strength-to-density) and specific tensile modulus (modulus-to-density) of composite material.

the fiber direction but is limited to the properties of the resin in the transverse direction. The cross-plied construction on the right creates a structure that has common properties in the x- and y-direction but is limited to the characteristics of the resin in the z-direction. A large number of variations exist, allowing the designer to tailor the properties of the structure by varying the type of fibers and fiber orientations. Shown in Figure 12.6.4 are typical values of specific tensile strength (strength-to-density ratio) and specific

TABLE 12.6.3 Advantages and Limitations of Polymer Matrix Composites

Potential Advantages	Potential Limitations
High strength-to-density ratio	Low–volume production methods
High stiffness-to-density ratio	High raw material cost
Excellent corrosion resistance	Poor impact resistance
Good fatigue resistance	Poor high-temperature performance
Low thermal expansion	Delamination/out-of-plane loading

tensile modulus (modulus-to-density ratio) for 65% volume fraction, cross-plied quasi-isotropic composites. Also included in the plot for comparison are properties of mild steel, titanium (Ti-6A1-4V), and aluminum (2024-T6). The actual properties of a composite will vary significantly due to flaws created during processing.

In selecting polymer composite materials for design, one should consider both the potential advantages and concerns typical to composites, as illustrated in Table 12.6.3. Clearly, the advantages of materials should be put into use to achieve higher levels of performance in many kinds of products. On the other hand, potential issues in higher raw material cost and lower production volume and yield should also be weighed.

Fiber

Introduction. The most common reinforcement in polymer composites are fibers. Fibrous reinforcements come from compounds of light elements, (e.g., B, C, Si, O). These compounds typically contain stable covalent bonds, which impart greater strength and stiffness compared with metallic or ionic bonds. The compounds are processed to the final usable form of a fiber or filament with a highly aligned and directional microstructure so that the strength and stiffness properties are optimized along the fiber axis. Glass, graphite/carbon, aramid, and boron are among most notable fibers currently used in polymer composites.

Glass Fiber. Glass-fiber reinforcements represent the largest volume used in the composites industry. These fibers are characterized by their low cost, clear to white color, good mechanical and electrical properties, high moisture and chemical resistance, and excellent dimensional stability with operational service to 550°C. Manufacturing of the fibers begins with molten glass, which is drawn through a furnace into a fibrous form of final diameter of about 10 mm and then quenched to secure the final amorphous microstructure prior to applying final coatings or sizing. Common types of commercially available glass fiber are E-glass and S-glass, both of which are low-alkali boro-alumino-silicate glasses. E-glass fiber, the workhorse of glass-fiber applications, is the lower-cost fiber and is used in both structural and electrical applications. S-glass provides higher tensile properties and increased temperature resistance needed for aerospace and aircraft applications with a price premium. Representative properties for the glass fibers are shown in Table 12.6.4.

TABLE 12.6.4 Fibers Used in Polymer Composites — Mechanical Properties

	E-Glass	S-Glass	AS4 PAN-Based Carbon	IM7 PAN-Based Carbon	P120 Pitch-Based Graphite	Kevlar-49	Boron
Tensile strength (ksi)	510	670	578	710	325	530	525
Tensile modulus (MSI)	10.5	12.8	35.5	46	120	18	58
Elongation (%)	4.9	5.5	1.6	1.7	0.27	2.5	1
Density (lb/in3)	0.095	0.09	0.065	0.063	0.079	0.052	0.093
Axial coefficient of expansion (10–6 in./in. F)	2.8	3.1	0 to –0.4	0 to –0.6	0 to –0.7	–1.1	2.5

Carbon Fiber. Graphite/carbon fibers are the reinforcement of industrial choice for advanced composite applications where stiffness and performance are critical. Typical attributes of these fibers are excellent tensile strength and elastic modulus, ease of handling, black color, and a wide range of properties and cost. Graphite fibers are initially formed from polymer precursor compounds such as polyacrylonitrile (PAN) or rayon and pitch, an amorphous, aromatic by-product of petroleum distillation. PAN-based graphite fiber, the predominant commercial fiber, starts with the liquid PAN polymer, which is spun into a fiber and stretched to align the microstructure. It is then stabilized and the microstructure is aligned at 400 to 500°F in an oxidizing atmosphere under tension. Next, carbonization occurs in an inert atmosphere at 1800 to 2300°F to remove most noncarbon elements. Finally, the graphitization step is performed on the carbon fiber by applying tension to the fiber in an inert atmosphere at 3600 to 6500°F. The result is a highly aligned, highly graphitic fiber with preferred graphite orientation along the fiber axis. The temperature and tension fabrication parameters of the graphitization step, along with the purity of the initial PAN polymer, are the variables that are modified to differentiate "low-end" (low strength, modulus, cost) from the "high-end" fiber (high strength, modulus, cost) and all of the grades in between. Typical properties of several commercial grades of carbon/graphite fiber are listed in Table 12.6.2.

Aramid Fibers. The aramid fiber derives its properties from long, rodlike aromatic polyamides. These fibers are characterized by low density, white yellow color, extremely high tensile properties, poor compressive strength, and high toughness, and they are difficult to cut mechanically. The manufacturing process for these fibers involves complex polymerization steps as the liquid polymer in acid is extruded or spun into a fiber form, water-washed, dried, and finally heat-treated under tension. The result is a highly aligned radial system of axially pleated lamellae in the microstructure. Aramid fibers have proved extremely useful in tension-critical applications where the intrinsic compressive weaknesses of the fiber cannot be exploited. Commercially known as Kevlar, the most notable applications for aramid fibers are bulletproof vests (without matrix) and various high-pressure composite vessels. Typical properties for Kevlar 49 are listed in Table 12.6.2.

Boron Fibers. Boron reinforcements are referred to as filaments rather than fibers since they are made by the chemical vapor deposition of boron onto a fine tungsten wire. This fabrication process produces a large-diameter, stiff, and expensive reinforcement that is somewhat difficult to handle and produce into subsequent product forms such as fabrics and contoured structures. Although boron filaments possess the combination of high strength and high specific modulus that glass could not achieve, their use has been reduced to a minuscule level. Carbon/graphite fiber varieties have supplanted boron where high specific modulus is a requirement. A small volume of boron filaments still remain in a handful of military aircraft as well as in some recreational products, such as golf club shafts. Typical properties of boron filaments are shown in Table 12.6.2.

Polymer Matrix Materials

Introduction. While fibers provide much of the strength and stiffness in advanced composites, equally important is the matrix resin. The matrix holds the fiber network together, to protect the structure from environmental attack and to support the fibers so that loads can be transferred throughout the structure through a shear mechanism. Polymeric matrices can either be thermoset or thermoplastic resins.

Thermosets cannot be reformed or thermally reworked after polymerization (curing). They are subdivided into categories based on their chemical reactions. The first are addition-type polymers, generally considered easier to process, where two (or more) reactants combine to form the final cured product. The second is the condensation type, in which the reactants combine to form products in addition to water and other volatile constituents. These systems are more difficult to process due to the required management of the volatile to minimize process defects such as porosity.

Thermoplastic materials, on the other hand, are polymers that can be softened and melted with the application of heat. Although they can be recycled, thermoplastic matrices have found more-limited applications in the advanced composite applications since they are particularly susceptible to attack by fluids and to creep at high stresses, and are relatively difficult to handle in laminate or structural form prior to final consolidation. The remainder of this discussion will focus on thermoset matrices, which account for more than 90% of present-day advanced composite applications. Three principal organic matrix materials will be discussed: polyesters, epoxies, and polyimides.

Polyester Matrix. Low-cost polyester resins constitute the highest volume usage for the general composite industry. There are many resins, formulations, curatives, and other additive constituents that provide a wide array of properties and performance characteristics, such as mechanical strength, toughness, and heat resistance. The vast majority of applications utilize glass since its interfacial adhesion to these resins has been optimized by the development of silane surface treatments. These resins when combined with glass have found wide application in chemical processing construction and in marine industries where cured properties and low cost are tailor-made for design requirements. Applications with carbon/graphite and aramid fibers are far less frequent since adhesion to these fibers is generally poor and cure shrinkage on these resins is quite high. Additionally, structures requiring the high performance of carbon/graphite can often justify the use of more-expensive epoxy resins.

Epoxy Matrix. Epoxy resins are the prevalent polymer used with advanced composites. Their extensive use is primarily due to their superior mechanical properties, excellent adhesion, good processibility utilizing addition-type reactions, low cure shrinkage, and low cost. When choosing epoxy resins, two elements are crucial: the base resin and the curing agent or hardener. Since there are many base resins and curing agents, we present the following general relationships to provide a practical framework when utilizing epoxy compounds:

- *Chemistry*: Aromatic compounds are more thermally stable, stronger, and more resistant to fluids than are aliphatics.
- *Cross-link density*: Higher-temperature cures and longer cure times will increase cross-link density and therefore strength/modulus, service temperature, and chemical resistance.
- *Curing agents*: Amine-cured systems have better chemical resistance and superior thermal stability but are more brittle than anhydride-cured systems.

Epoxies are categorized by the cure temperature. The “250 F epoxies” are those that cure at 250°F and are suitable for service up to 250°F. The “350 F epoxies” are those with higher processing and service temperatures. One of the design concerns with epoxies is moisture absorption. The effects of moisture often require design stresses to be reduced in applications where moisture is a concern. Modern epoxy formulations include lower cost, higher toughness, and other properties, which continue to make epoxies attractive to the end user.

Polyimide resins span the temperature spectrum from 350 to 600°F. There are three general types of polyimides:

1. *Addition-reaction* polyimides, such as bismaleimides (BMIs)
2. *Condensation-reaction* polyimides, such as commercial Monsanto Skybond resin
3. *Combination* condensation/addition-reaction polyimides, such as PMR-15

BMIs are similar to epoxies in that they undergo addition reactions, are easy to process, and share many of the handling characteristics that make epoxies desirable. These materials are the composite resins of choice for temperatures in the range of 350 to 450°F to bridge the temperature gap between epoxies and other polyimides. They are more expensive and tend to be more brittle than epoxies. Condensation polyimides are used for composite applications from 450 to 520°F. These materials are difficult to process and tend to be quite brittle so their application is limited to adhesive bonding with some structural composite hardware. Combination-reaction polyimides have the highest thermal and oxidative stability and are used at service temperatures to 600°F. These resins are considerably more complicated because of their reaction mechanisms and the handling difficulties of the chemicals. Their application is principally restricted to aerospace composite structures where the performance needs to justify the difficult processing and high cost.

Processing

Continuous-fiber composites are manufactured in two steps: preform fabrication and consolidation/curing. The material comes in either the dry-fiber (without resin) form or with resin included called *prepreg*. Dry fibers are used in filament winding, pultrusion, weaving, and braiding. In the case of filament winding and pultrusion, resin is introduced at the same time fibers are during the time of winding and pultrusion. Resin can also be introduced to the fiber later by resin-transfer molding (RTM). Prepreg, at a higher material cost, eliminates the step of resin addition and provides the adhesion to hold the material together. Lay-up of prepreg, a time-consuming process, is a common method used in the aerospace industry where complex contoured surfaces are present.

Consolidation and curing consist of compacting the material to remove entrapped air, volatile, and excess resins while developing the structural properties by increasing the polymer chain length and cross-linking. Thermosetting polymer matrices must be cured *in situ* with the fibers to form composites. The goals of a successful cure are good consolidation with low porosity and high conversion of initial monomeric constituents to polymer (degree of cure).

The cure cycle of an epoxy resin composite is shown in Figure 12.6.5. At the start of the cure cycle, the material is normally under vacuum to remove residual volatile. The temperature is then ramped to the point where the polymer is melted. The ramp rates on heating must be slow enough as not to cause unnecessary thermal gradients and to avoid dangerous exotherm (runaway reactions) but not so slow as to cause excessive process time or premature cross-linking. Normal ramp rates are generally in the 1 to

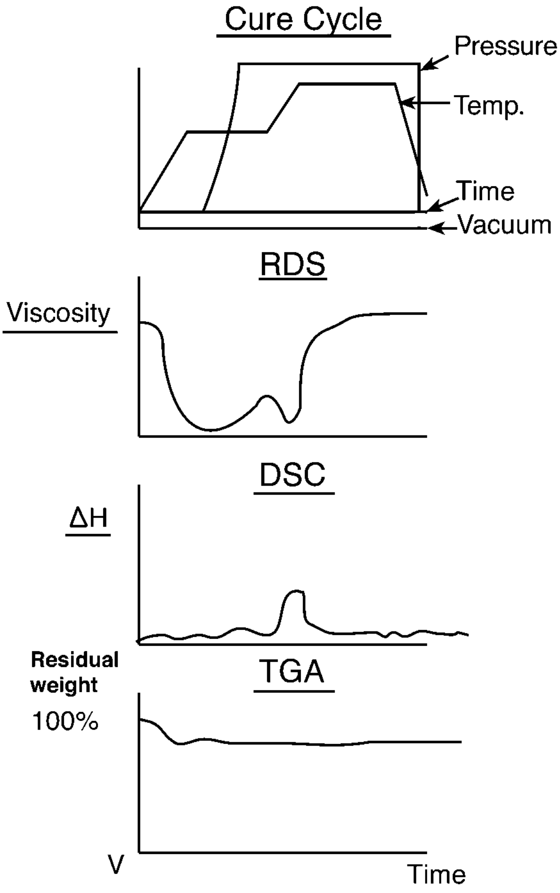

FIGURE 12.6.5 A typical curing cycle of epoxy composite with corresponding Rheometric Dynamic Spectroscopy (RDS), Differential Scanning Calorimetry (DSC), and Thermogravimetric Analysis (TGA) curves

5°F/min range. An isothermal hold of about 30 to 60 min is performed at the point where the resin reaches its minimum in viscosity, during which pressure is applied and the polymer is allowed to flow, thus consolidating the laminate. Following consolidation, the temperature is increased to the point where cross-linking occurs (350°F for this example). An additional hold of about 30 to 90 min is performed at this temperature to allow for the material to complete cross-linking. This event is shown as the end of the exothermic peak in the DSC curve as well as the asymptotic high-viscosity region.

Epoxies cure via additional reactions, where no volatile is generated during the cross-linking process. However, many other matrix materials (e.g., phenolics and many polyimides) cure via condensation reactions.

Mechanical Properties

Mechanical properties of polymer composites depend substantially on the processing and fabrication methods used, as well as on the fiber orientation. Thus, standard materials do not exist and it is difficult to generalize regarding properties. The three most significant factors in determining properties are the type of fiber, the volume fraction of fiber, and the orientation of the fiber. High-strength high-modulus graphitic carbon fibers will, of course, produce stronger, stiffer composites than those produced from fiberglass. Similarly, 60 vol% fiber composites will be stronger and stiffer than 30 vol%, and uniaxially aligned fiber composites will have maximum properties along the alignment axis, but will be highly anisotropic and will have poor properties in off-axis orientations. Cross-ply and laminated structures were standard approaches to reducing anisotropy during the early developments of composites, especially for aerospace applications. Since the early developments in cross-plying and lamination of two-dimensional woven, knitted, or stitched fabrics, composite structures made from three-dimensional woven, three-dimensional knits, and three-dimensional braided are being deployed in the field. Although tensile properties and failure mechanisms have been investigated since the 1980s, it is only recently that an understanding and modeling of the tensile behavior of such structures has become available. The reason for the slow progress has been the complexity of the geometry of the structure and the failure mechanism of fibers in these structures. The deformation behavior of two-dimensional laminates differs from that of the three-dimensional woven fabrics, as shown in Figure 12.6.6. Some structural features of a three-dimensional orthogonal woven fabric are shown in Figure 12.6.7. On the other hand, three-dimensional woven fabrics perform better in impact damage, as shown in Figure 12.6.6. Braid angle influences the mechanical properties, and some mechanical properties of carbon/epoxy, multilayer interlock three-dimensional braids are shown in Table 12.6.8.

Cross-ply and laminated structures are standard approaches to reducing anisotropy. Composite stiffness, E_c, can be approximated for polymer composites by application of the rule of mixtures:

$$E_c = E_f V_f + E_m(1 - V_f)$$

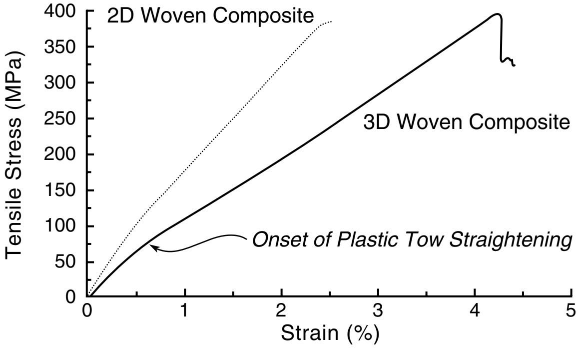

FIGURE 12.6.6 Tensile stress-strain curves for a two-dimensional and three-dimensional woven composite (From: Tong, L., Mourtiz, A.P, and Bannister, M.K, *3D Fibre Reinforced Polymer Composites*, Elsevier, New York, 2002. Reproduced with permission.)

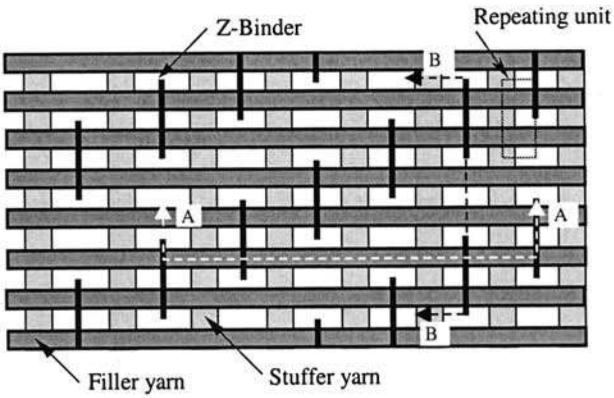

(a) A schematic of the top view for the 3D orthogonal woven CFRP composite

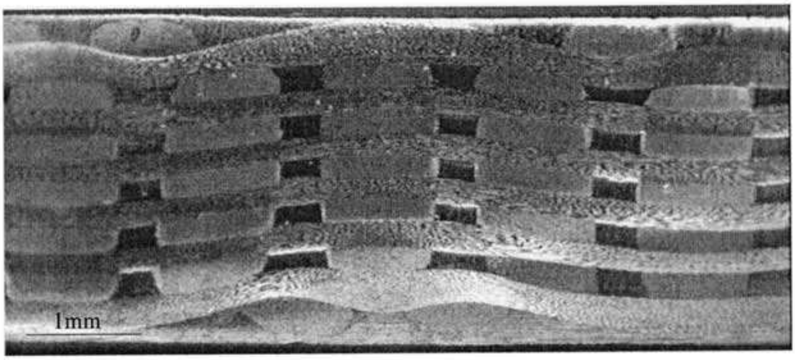

(b) Micrograph of cross section A-A showing misalignment of filler yarns

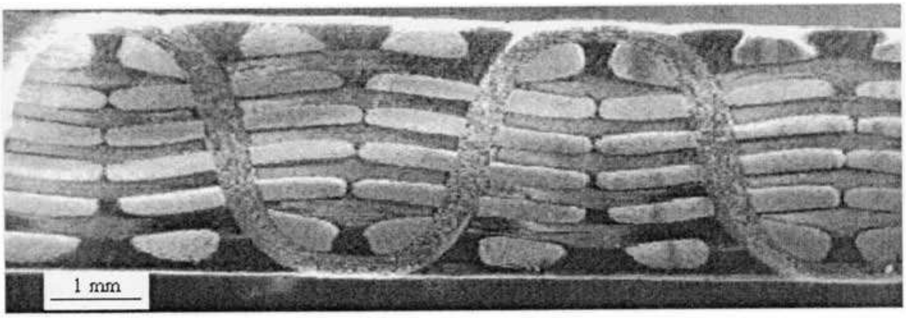

(c) Micrograph of cross section B-B showing true path of the z-binder and distorted filler yarns

FIGURE 12.6.7 Architectural features of a three-dimensional orthogonal woven CFRP composite (From: Tan, P., Tong, L., Steven, G.P., and Ishikawa, T. 2000a. Behavior of 3D orthogonal woven CFRP composites. I Experimental Investigation, *Composites*, 31A: 255–71; Tan, P., Tong, L., and Steven, G.P, 200b, II: Theoretical and FEA modeling, *Composites*, 31A: 273–81. Reproduced with permission.)

where E is the modulus of elasticity and V is the volume fraction fibers. Subscripts c, f, and m refer to composite, fiber, and matrix, respectively. Similar expressions approximate other properties. Properties of commonly used commodity composite materials are given in Table 12.6.5 to Table 12.6.7. Advanced engineering polymer composites have specialized properties that depend on the parameters discussed

TABLE 12.6.5 Typical Properties of Glass Fiber–Reinforced Polymers

	Base Resin				
Property	Polyester	Phenolic	Epoxy	Melamine	Polyurethane
Molding quality	Excellent	Good	Excellent	Good	Good
Compression molding					
Temperature, °F	170–320	280–350	300–330	280–340	300–400
Pressure, psi	250–2000	2000–4000	300–5000	2000–8000	100–5000
Mold shrinkage, in./in.	0.0–0.002	0.0001–0.001	0.001–0.002	0.001–0.004	0.009–0.03
Specific gravity	1.35–2.3	1.75–1.95	1.8–2.0	1.8–2.0	1.11–1.25
Tensile strength, 1000 psi	25–30	5–10	14–30	5–10	4.5–8
Elongation,%	0.5–5.0	0.02	4	—	10–650
Modulus of elasticity, 10^{-5} psi	8–20	33	30.4	24	—
Compression strength, 1000 psi	15–30	17–26	30–38	20–35	20
Flexural strength, 1000 psi	10–40	10–60	20–26	15–23	7–9
Impact. Izod, ft-lb/in. or notch	2–10	10–50	8–15	4–6	No break
Hardness, Rockwell	M70–M120	M95–M100	M100–M108	—	M28–R60
Thermal expansion, per °C	$2–5 \times 10^{-5}$	1.6×10^{-5}	$1.1–3.0 \times 10^{-5}$	1.5×10^{-5}	$10–20 \times 10^{-5}$
Volume resistivity at 50% RH, 23°C, Ω-cm	1×10^{14}	7×10^{12}	3.8×10^{15}	2×10^{11}	$2 \times 10^{11}–10^{14}$
Dielectric strength 1/8 in. thickness, v/mil	350–500	140–370	360	170–300	330–900
Dielectric constant					
At 60 Hz	3.8–6.0	7.1	5.5	9.7–11.1	5.4–7.6
At 1 kHz	4.0–6.0	6.9	—	—	5.6–7.6
Dissipation factor					
At 60 Hz	0.01–0.04	0.05	0.087	0.14–0.23	0.015–0.048
At 1 kHz	0.01–0.05	0.02	—	—	0.043–0.060
Water absorption, %	0.01–1.0	0.1–1.2	0.05–0.095	0.09–0.21	0.7–0.9
Sunlight (change)	Slight	Darkens	Slight	Slight	None to slight
Chemical resistance	Fair[a]	Fair[a]	Excellent	Very good[b]	Fair
Machining qualities	Good	—	Good	Good	Good

Note: Filament-wound components with high glass content, highly oriented, have higher strengths. The decreasing order of tensile strength is: roving, glass cloth, continuous mat, and chopped-strand mat.

[a] Attacked by strong acids or alkalies

[b] Attacked by strong acids

From Spang, C.A. and Davis, G.J., *Machine Design*, 40(29); 32, December 12, 1968. With permission.

previously. Expected properties of such advanced polymer composites can only be approximated once the component and material variables are determined during the design stage. The recommended approach is to work with a composite fabricator during the design phase to establish the expected mechanical properties.

Metal Matrix Composites

Introduction

The term *metal matrix composites* is usually reserved for fiber-reinforced materials, although technically it applies to particulate-reinforced systems as well. The general term for particulate-, whisker-, and chopped-fiber-reinforced systems is *cermet*. A majority of commonly used systems are based on particulate reinforcements.

Cermets and Cemented Carbides — Particulate-Reinforced MMCs

The term *cemented carbide* is applied to particulate composites based on tungsten carbide in a cobalt matrix. This distinction is largely historical, not technical. The tungsten carbide–cobalt-based materials were first developed in Germany, while development of other cermets (including noncarbide-, oxide-, and nitride-based systems) occurred in the U.S. during and immediately after World War II. Thus, a

TABLE 12.6.6 Properties of Reinforced Nylon Polymer

Property	Type 6/6	Type 6	Type 6/10	Type 11	Glass-Reinforced Type 6/6, 40%	MoS2-filled, 21/2%	Direct Polymerized, Castable
Mechanical							
Tensile strength, psi	11,800	11,800	8200	8500	30,000	10,000–14,000	11,000–14,000
Elongation,%	60	200	240	120	1.9	5–150	10–50
Tensile yield stress, psi	11,800	11,800	8500	—	30,000	—	—
Flexural modulus, psi	410,000	395,000	280,000	151,000	1,800,000	450,000	—
Tensile modulus, psi	420,000	380,000	280,000	178,000	—	450,000–600,000	350,000–450,000
Hardness, Rockwell	118R	119R	111R	55A	75E–80E	110R–125R	112R–120R
Impact strength, tensile, ft-lb/sq in.	76	—	160	—	—	50–180	80–100
Impact strength, Izod. ft-lb/in. of notch	0.9	1.0	1.2	3.3	3.7a	0.6	0.9
Deformation under load, 2000 psi, 122°F,%	1.4	1.8	4.2	2.02b	0.4c	0.5–2.5	0.5–1
Thermal							
Heat deflection temp, °F							
At 66 psi	360	365	300	154	509	400–490	400–425
At 264 psi	150	152	135	118	502	200–470	300–425
Coefficient of thermal expansion per °F	4.5 × 10–5	4.6 × 10–5	5 × 10–5	10 × 10–5	0.9 × 10–5	3.5 × 10–5	5.0 × 10–5
Coefficient of thermal conductivity, Btu in./hr ft3 °F	1.7	1.7	1.5	—	—	—	—
Specific heat	0.3–0.5	0.4	0.3–0.5	0.58	—	—	—
Brittleness temp, °F	–112	—	–166	—	—	—	—
Electrical							
Dielectric strength, short time, v/mil	385	420	470	425	480	300–400	500–600d
Dielectric constant							
At 60 Hz	4.0	3.8	3.9	—	4.45	—	3.7
At 103 Hz	3.9	3.7	3.6	3.3	4.40	—	3.7
At 106 Hz	3.6	3.4	3.5	—	4.10	—	3.7
Power factor							
At 60 Hz	0.014	0.010	0.04	0.03	0.009	—	0.02
At 103 Hz	0.02	0.016	0.04	0.03	0.011	—	0.02
At 106 Hz	0.04	0.020	0.03	0.02	0.018	—	0.02
Volume resistivity, W-cm	1014–1015	3 × 1015	1014–1015	2 × 1013	2.6 × 1015	2.5 × 1013	—
General							
Water absorption, 24 hr,%	1.5	1.6	0.4	0.4	0.6	0.5–1.4	0.9

TABLE 12.6.6 (continued) Properties of Reinforced Nylon Polymer

Property	Type 6/6	Type 6	Type 6/10	Type 11	Glass-Reinforced Type 6/6, 40%	MoS2-filled, 21/2%	Direct Polymerized, Castable
Specific gravity	1.13–1.15	1.13	1.07–1.09	1.04	1.52	1.14–1.18	1.15–1.17
Melting point, °F	482–500	420–435	405–430	367	480–490	496 ± 9	430 ± 10
Flammability	Self-extinguishing	Self-extinguishing	Self-extinguishing	Self-extinguishing	Self-extinguishing	Self-extinguishing	Self-extinguishing
Chemical resistance to							
Strong acids	Poor	Poor	Poor	Poor	Poor	Poor	Poor
Strong bases	Good	Good	Good	Fair	Good	Good	Good
Hydrocarbons	Excellent	Excellent	Excellent	Good	Excellent	Excellent	Excellent
Chlorinated hydrocarbons	Good	Good	Good	Fair	Good	Good	Good
Aromatic alcohols	Good	Good	Good	Good	Good	Good	Good
Aliphatic alcohols	Good	Good	Good	Fair	Good	Good	Good

Notes: Most nylon resins listed in this table are used for injection molding, and test values are determined from standard injection-molded specimens. In these cases a single typical value is listed. Exceptions are MoS2-filled nylon and direct-polymerized (castable) nylon, which are sold principally in semifinished stock shapes. Ranges of values listed are based on tests on various forms and sizes produced under varying processing conditions.

Because single values apply only to standard molded specimens, and properties vary in finished parts of different sizes and forms produced by various processes, these values should be used for comparison and preliminary design considerations only. For final design purposes the manufacturer should be consulted for test experience with the form being considered. Listed values should not be used for specification purposes.

[a] 1/2 × 1/4-in. bar

[b] 2000 psi, 73°F

[c] 4000 psi, 122°F

[d] 0.040-in. thick

From Carswell, D.D., *Machine Design*, 40(29), 62, December 12, 1968. With permission.

TABLE 12.6.7 Comparative Properties of Reinforced Plastics

	Polyamide		Polystyrenea		Polycarbonate		Styrene Acrylonitrileb		Polypropylene		Acetal		Linear Polyethylene	
Property	U	R	U	R	U	R	U	R	U	R	U	R	U	R
Tensile strength, 1000 psi	11.8	30.0	8.5	14.0	9.0	20.0	11.0	18.0	5.0	6.6	10.0	12.5	3.3	11.0
Impact strength, notched, ft-lb/in.														
At 73°F	0.9	3.8	0.3	2.5	2.0[c]	4.0[c]	0.45	3.0	1.3–2.1	2.4	60.0	3.0	—	4.5
At –40°F	0.6	4.2	0.2	3.2	1.5[c]	4.08[c]	—	4.0	—	2.2	—	3.0	—	5.0
Tensile modulus, 10^5 psi	4.0	—	4.0	12.1	3.2	17.0	5.2	15.0	2.0	4.5	4.0	8.1	1.2	9.0
Shear strength, 1000 psi	9.6	14.0	—	9.0	9.2	12.0	—	12.5	4.6	4.7	9.5	9.1	—	5.5
Flexural strength, 1000 psi	11.5	37.0	11.0	20.0	12.0	26.0	17.0	26.0	6–8	7.0	14.0	16.0	—	12.0
Compressive strength, 1000 psi	4.9d	24.0	14.0	17.0	11.0	19	17.0	22.0	8.5	6.0	5.2	13.0	2.7–3.6	6.0
Deformation, 4000-psi load, %	2.5	0.4	1.6	0.6	0.3	0.1	—	0.3	—	6.0	—	1.0	—	0.4[e]
Elongation, %	60.0	2.2	2.0	1.1	60–100	1.7	3.2	1.4	>200	3.6	9–15	1.5	60.0	3.5
Water absorption, in 24 hr, %	1.5	0.6	0.03	0.07	0.3	0.09	0.2	1.15	0.01	0.05	0.20	1.1	0.01	0.04
Hardness, Rockwell	M79	E75–80	M70	E53	M70	E57	M83	E65	R101	M50	M94	M90	R64	R60
Specific gravity	1.14	1.52	1.05	1.28	1.2	1.52	1.07	1.36	0.90	1.05	1.43	1.7	0.96	1.30
Heat distortion temperature, at 264 psi, °F	150	502	190	220	280	300	200	225	155	280	212	335	126	260
Coefficient of thermal expansion, per F × 10^{-5}	5.5	0.9	4.0	2.2	3.9	0.9	4.0	1.9	4.7	2.7	4.5	1.9	9.0	1.7
Dielectric strength, short time, v/mil	385	480	500	396	400	482	450	515	750	—	500	—	—	600
Volume resistivity Ω-cm × 10^{15}	450	2.6	10.0	36.0	20.0	1.4	10^{16}	43.5	17.0	15.0	0.6	38.0	10^{15}	29.0
Dielectric constant, at 60 Hz	4.1	4.5	2.6	3.1	3.1	3.8	3.0	3.6	2.3	—	—	—	2.3	2.9
Power factor, at 60 Hz	0.0140	0.009	0.0030	0.0048	0.0009	0.0030	0.0085	0.005	—	—	—	—	—	0.001
Approximate cost, ¢/in.^{3}	3.0	8.0	0.5	2.5	3.6	6.5	0.9	3.5	0.6	2.1	3.3	7.8	0.7	3.1

Note: U = reinforced; R = reinforced. Multiply tabular values in psi by 6895 to obtain N/m^2.

[a] Medium-flow, general-purpose grade

[b] Heat-resistant grade

[c] Impact values for polycarbonates are a function of thickness

[d] At 1% deformation

[e] 1000-psi load

From Lachowecki, W., *Machine Design*, 40(29), 34, December 12, 1968. With permission.

TABLE 12.6.8 Effect of Braid Angle on the Mechanical Properties of Carbon/Epoxy, Multilayer Interlock 3D Braids

Materials	3D Braids		2D Triaxial Braids	
Lay-Ups	#45°/0°/±45°	±60°/0°/±60°	±45°/0°/±45°	±60°/0°/±60°
Longitudinal tensile strength (MPa)	316	192	367	133
Transverse tensile srength (MPa)	156	338	250	309
Longitudinal tensile modulus (GPa)	32.6	26.7	33.7	26.6
Transverse tensile modulus (GPa)	19.8	45.5	16.3	34.4
Longitudinal compressive strength (MPa)	320	218	280	267
Transverse compressive strength (MPa)	183	207	201	248
Longitudinal compressive modulus (GPa)	25.6	25.5	31.4	26.7
Transverse compressive modulus (GPa)	22.1	24.4	20.9	22.2
CAI strength 0.1/mm	320	218	280	267
CAI strength 3.1/mm	203	214	202	190
CAI strength 7.1/mm	195	182	177	183

CAI = Compresson-after-impact.

From Brookstein. D., Preller, T., and Brandt, J. Jr., 1993. On the mechanical properties of three dimensional multilayer interlock braided composites, *Proc. of the TechTextil Symposium 93 for Technical Textiles and Textile – Reinforced Materials*, Frankfurtam Mein, Germany, June 7–9, Vol. 3.2, paper 3.28. Reproduced with permission.

distinguishing nomenclature was developed both because "carbide" was no longer completely appropriate with oxide systems available and for geopolitical reasons. This nomenclature confusion between the most common cermets, the cemented carbides, and other materials still survives. The structure consists of a continuous metal alloy functioning as cement, which holds together particles of carbide, oxide, or nitride ceramic. These materials provide strength, high hardness, wear (abrasion) resistance, low sliding friction, and precise tolerance even at quite high temperatures. Cermets and cemented carbides derive their usefulness when the compressive strength, hardness, and thermal resistance of the ceramic reinforcement is coupled with the ductility, toughness, adhesion, and lubricity provided by the metal. Common applications include metal and rock cutting and grinding tools, high-temperature containers, and pouring spouts, rocket nozzles, turbine parts, flame nozzles, friction and glide parts, seals, magnetron tube cathodes, flame nozzles, and ballpoint pen tips.

A cermet is usually fabricated by mixing the ceramic and metal powders together with a binder. This often requires high-energy mixing because of density differences with tooling made of the same cermet to avoid contamination. Subsequently, the part is formed, commonly by unidirectional or isostatic pressing, to final shape (accounting for shrinkage) with a wear-resistant die and with the formed object, then in the liquid phase is sintered in a controlled-atmosphere furnace. The chemistry is often quite complex in order to control the structure and the interfacial bond between metal and ceramic. Molybdenum promotes wetting of titanium carbide by molten nickel. Tantalum and titanium carbides are usually added to tungsten carbide-cobalt cemented carbides. Some cermets are prepared by slip casting, liquid metal infiltration, hot pressing, or solid-state sintering of parts. In some cases the material is "deficient" in metal to provide porosity for the passage of ink (pen tips) or incorporation of lubricant.

As indicated in the introduction to this section, a good bond between ceramic grain and metal "cement" is required for proper load transfer and to provide a homogeneous structure for good load bearing and uniform deformation. This normally requires a good wetting between liquid metal and ceramic grains. This is affected by minor alloying additions to the metal and the firing atmosphere.

The distribution, stability, and composition of phases have profound effects on properties. The production of WC–6 w/o Co is a good example of the need for strict compositional control. The tertiary-phase diagram shows that the composition range from 6.00 to 6.12 w/o must be adhered to in order to prevent formation of phases other than WC and Co — a composition range of less than 0.12 w/o! Embrittlement by graphite occurs at higher carbon content and by eta phase (h–WCl-x) at lower carbon levels. Precise formulation and furnace atmosphere control is required, usually assisted by using a

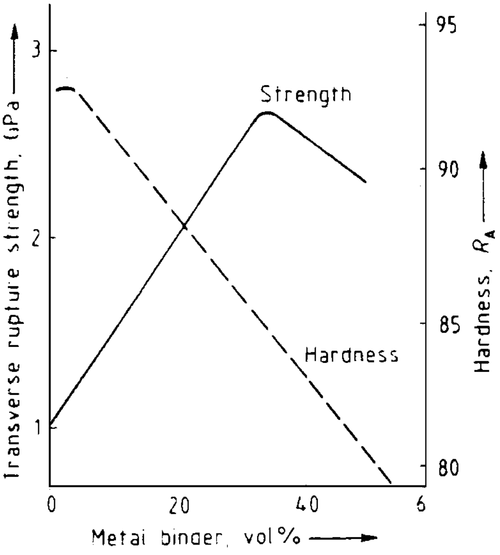

FIGURE 12.6.8 Effect of increased binder on strength and hardness of a TiC-Ni-Mo cermet with a 1 µm average carbide particle size

graphite-lined furnace. About 0.1% outside the acceptable composition range there is a drop of about 25% from the optimum strength.

It is important to engineer the microstructure of cermets in order to optimize properties. A uniform dispersion of round oxide, carbide, or nitride grains in the matrix of metal binder is desired. Inhomogeneity and sharp grain corners can act as failure origins. Round grains result from powder preparation and/or partial dissolution of sharp contours in the molten metal. As the amount of binder increases (Figure 12.6.8), the indentation hardness of the composite decreases, because metal, compared with ceramic, has a lower elastic modulus and will deform more easily. Fracture strength increases with binder because the metal phase confers fracture toughness. Generally, as ceramic grain size decreases, hardness and resistance to deformation increase for a fixed relative amount of ceramic. However, if the surface area increases sufficiently because of small grain size, there may not be enough metal to wet all the grain.

With these diverse factors a simplified way of looking at microstructural features and adjusting them for optimum performance is the mean free path, the average distance between neighboring ceramic grains (the average thickness of the binder phase). The mean free path depends on the size and shape of the grains and the amount of metal matrix available. Hardness, elevated-temperature hardness, strength, and toughness depend on the mean free path because it is the zone for absorption of crack energy and the medium for load transfer from grain-to-grain. Figure 12.6.9 shows that hardness varies with mean free path for a variety of cobalt contents and tungsten carbide grain sizes in cemented carbide. The curve does not continue below 0.1 mm because the metal binder becomes discontinuous.

Table 12.6.9 presents data for selected metal matrix systems with particulate reinforcement, including strength values at elevated temperatures. A section of Table 12.6.10 provides stiffness values for cobalt and nickel strengthened with sintered carbides.

Fiber-Reinforced MMCs

Fiber-reinforced MMCs may still be classed as an emerging materials area. A number of applications have been practiced, driven by the need for a lightweight, high-stiffness material and/or for elevated-temperature resistance in structures. These applications are typically for aerospace and similar advanced applications, which can use a premium material. The limited scope of current practical application and the limitations placed on technology disclosure by the Export Control Act and International Traffic-in-Arms Regulations make this section brief.

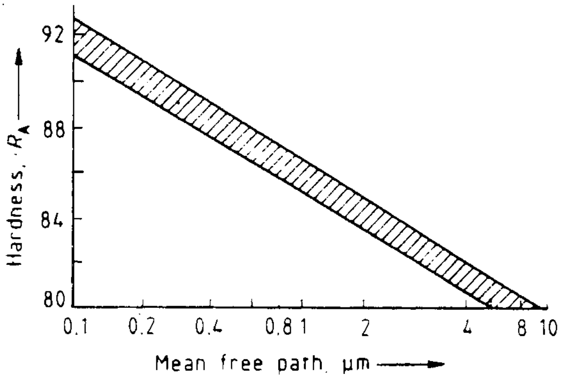

FIGURE 12.6.9 Effect of mean free path on hardness for a cemented carbide

TABLE 12.6.9 Particle-Reinforced Metals

A. Metals Strengthened by Dispersed Powders

	Strengthener		Stress, kpsi	
Matrix Metals	Component	% vol	Matrix Only, No Reinforcement	Composite Material
Pure iron	Al_2O_3	4	2.2[a]	10[a]
Pure iron	Al_2O_3	10	2.2[a]	21[a]
Pure copper	Al_2O_3	10	2.2[b]	20[b]
Platinum	ThO_2	12.5	0.6[c]	6.1[c]
Uranium	Al_2O_3	3.5	6[d]	14[d]
Uranium	Al_2O_3	7.5	6[d]	20[d]
Copper	W (powder)	60	(E = 18)[e]	(E = 34)[e]

[a] Stress for 100-hr rupture life, 650°C.

[b] Stress for 100-hr rupture life, 450°C.

[c] Stress for 100-hr rupture life, 1100°C.

[d] Stress for 10–4 in./in./hr creep rate.

[e] Modulus of elasticity, E = stress/strain.

B. Strength Ratios at High Temperatures

	Dispersed Particles		Strength by Test	
Matrix Metal	Material	% by Volume (Range)	Range of Test Temperatures, °F	Strength Ratio, (Referred to Matrix at Same Temperature)
Aluminum	Al^2O^3	10–15	400–800	2–4a
Copper	Al^2O^3	3–10	800–1100	5–10
Iron	Al^2O^3	8–10	1100–1300	5–10
Nickel	ThO^2	3	1600–2100	Strength higher than that of many super alloys
Platinum	ThO^2	12	2000–2400	8–11
Uranium	Al^2O^3	4–7	900–1100	2–3

[a] The tensile strength of the final product is two to four times the strength of the aluminum.

High-strength/high-elastic-modulus fibers such as boron, silicon carbide, graphite, aluminum oxide, and tungsten metal are typically incorporated in light metal matrices such as aluminum, magnesium, and titanium. The specific modulus (elastic modulus divided by density) has been shown to be two to

TABLE 12.6.10 Fiber- and Particle-Reinforced Metals — Test Results on Composite Metals

	Strengthener		Stress, kpsi	
Matrix Metals	Components	% Vol	Matrix Only, No Reinforcement	Composite Material
Metals Strengthened by Fibers				
Copper	W fibers	60	20	200[a]
Silver	Al_2O_3 whiskers	35	10[b]	75[b]
Aluminum	Glass fibers	50	(23%)[c]	(94%)[c]
Aluminum	Al_2O_3	35	25[d]	161[d]
Aluminum	Steel	25	25[d]	173[d]
Nickel	B	8	70[d]	384[d]
Iron	Al_2O_3	36	40[d]	237[d]
Titanium	Mo	20	80[d]	96[d]
Metals Strengthened by Sintered Carbides				
Cobalt	WC	90	($E = 30$)[e]	($E = 85$)[e]
Nickel	TiC	75	($E = 31$)[f]	($E = 55$)[f]

[a] Tensile strength with continuous fibers

[b] Tensile strength at 350°C; modulus of elasticity: Cu = 17, composite 42 (millions of psi)

[c] Percentage of tensile strength at room temperature retained when tested at 300°C

[d] Tensile strength, room temperature

[e] Modulus of elasticity, E, measured in compression; hardness, 90 R-A; compressive strength, about 600,000 psi

[f] Modulus of elasticity, E measured in compression; hardness about 85 R-A

Compiled from various sources.

four times that of high-strength structural metals. The specific strength may be substantially higher than the metal. These properties are maintained to many hundreds of degrees above ambient, whereas those of many advanced structural metals deteriorate both in immediate heating and long-term creep. Some systems have been shown to have considerable fatigue resistance, showing several times the stress for equivalent cycle lifetimes. These properties are important for structural shapes in which lightweight and elevated-temperature resistance can afford a premium. Some applications have been struts and tubes for space structures, bicycle frames, turbine parts, propellers, and engine components. The fiber may be incorporated unidirectionally, as a woven two-dimensional laminate or a three-dimensional structure. Fabrication methods include diffusion bonding, pultrusion (hot isostatic drawing), hot rolling, molten metal infiltration, and casting.

Table 12.6.10 gives metal matrix strengthening values for fiber reinforcements added in volume percentages from 8 to 60%.

Ceramic Matrix Composites

Richard L. Lehman and Daniel J. Strange

CMCs are ceramic matrix materials, either oxide, carbide, nitride, boride, or similar material, reinforced with particulates, whiskers, or continuous fibers. The reinforcing phase may be of any material, but most interest is directed toward ceramic reinforcement media. The following sections address fiber- and whisker-reinforced ceramic composites, the materials that offer the greatest potential for ameliorating the brittleness of ceramics and for developing exceptional mechanical and structural properties.

TABLE 12.6.11 Ceramic Matrix Composites: Fiber and Matrix Properties

Material	E	a	R	UTS	e^*	$g(Kc)$	T	r
Nicalon	180–200	3.1–4.0	7.5	2.5–3.0	1.4	(2.3)	1300	2.55
HM-carbon	345–414	–8–0.8	4	1.7–2.8	0.7	—	400, 3500	1.91
SCS-6 (SiC)	350–415	3.6	70	3.45	0.83	—	1300	3.3
FP-Al2O3	380	5.7	10	1.4	0.37	—	1316	3.9
Nextel 440	180	3.5	6	2.7	1.2	—	1426	3.1
Tyranno	193	3.1	5	2.76	1.5	—	1300	2.5
Ca-aluminosilicate	88–89	4.5–5.0	—	0.08–0.17	0.15	25 (2.2)	1350	2.8
Borosilicate glass	63–68	3.2–3.5	—	0.1	0.16	4.7, 40	600	2.2
Li aluminosilicate	74–88	0.9–1.5	—	0.17	0.21	10–40	1000–1200	2.1–2.4
Mg aluminosilicate	110	2.6	—	0.14	0.13	—	1200	2.6–2.8
Ba Mg aluminosilicate	106	2.7	—	—	—	40	1250	2.6
AS-1723	70–88	5.2	—	—	—	7–9, 40	700	—
7761	63	2.6	—	—	—	—	—	—
9741	50	4.9	—	—	—	—	—	—
7052	57	5.2	—	—	—	—	—	—
Reaction-bonded Si_3N_4	110	3.6	—	0.084	0.08	—	1900	3.2
SiC	340–380	4.3	—	0.35–0.92	0.1	(1.5–4.2)	1500	3.2
SiO_2	70–80	1.0	—	—	—	7–9	1150	—
ZrO_2	195	4.2	—	0.216	0.11	(2.5)	1500	6.0
Mullite	145	5.7	—	0.185	—	(2.2)	—	2.8

Note: E = Young's modulus (GPa), a = coefficient of thermal expansion (×106/°C), R = fiber radius (mm), UTS = ultimate tensile strength (GPa), e^* = failure strain (%), g = surface energy (J/m2), Kc = fracture toughness (MPa $m^{1/2}$), T = maximum-use temperature (°C), r = density (g/cm^3).

Source: Karandikar, P.G. and Chou, T.-W., in *Handbook on Continuous Fiber-Reinforced Ceramic Matrix Composites*, Lehman, R.L. et al. Eds., Purdue Research Foundation, 1995, West Lafayette, IN. With permission.

Ceramic Matrix Fiber Composites

Introduction. Ceramic matrix fiber composites (CMFCs) are the focus of substantial research but of limited commercial application as of this writing. The research enthusiasm is stimulated by the potential of high strength and toughness, mechanical and chemical durability, hardness, and oxidation resistance, all at elevated temperatures in the range 1000 to 1400°C. The limited commercialization, which is principally in military and aerospace applications, stems from the substantial cost of the fabricated materials, often in the range of thousands of dollars per kilogram. Fiber and matrix materials and properties used in CMFCs are presented in Table 12.6.11.

Mechanical Behavior. The primary goal of reinforcing a ceramic material with ceramic fibers is to increase the fracture toughness of otherwise brittle ceramic materials. In a monolithic ceramic, a flaw will propagate through the material under tension due to stress concentration at the crack tip. CMCs are designed with $E_f/E_m > 1$ so that the reinforcing fiber absorbs stresses, which tend to open and propagate cracks. Thus, the stress at the crack tip is reduced. Fiber debonding at the crack front, sliding, crack deflection, and other mechanisms also contribute to toughness. Often this is referred to as "rising R-curve" behavior, indicating that the strength of the ceramic at a crack tip increases with increasing crack length, stopping or slowing further crack growth. The most significant feature of CMFCs is the extensive fiber pullout, which occurs during failure. The fiber pullout results from low interfacial shear strengths, τ, which is designed into the composite by modifying interfacial properties and by using fibers with a *low* Weibull modulus. Loading is characterized by an initial elastic region followed by progressive failure of the matrix. The behavior is illustrated in Figure 12.6.10. During this matrix failure region, monotonically increasing loads are supported by the fibers. Ultimately, the fibers begin to fail according to bundle theory, and the remaining load support is provided by the frictional resistance to fiber pullout, a highly significant effect that absorbs large amounts of energy and contributes a high strain-to-failure performance previously unknown in ceramics. This "graceful" failure allows for a less catastrophic failure than normally

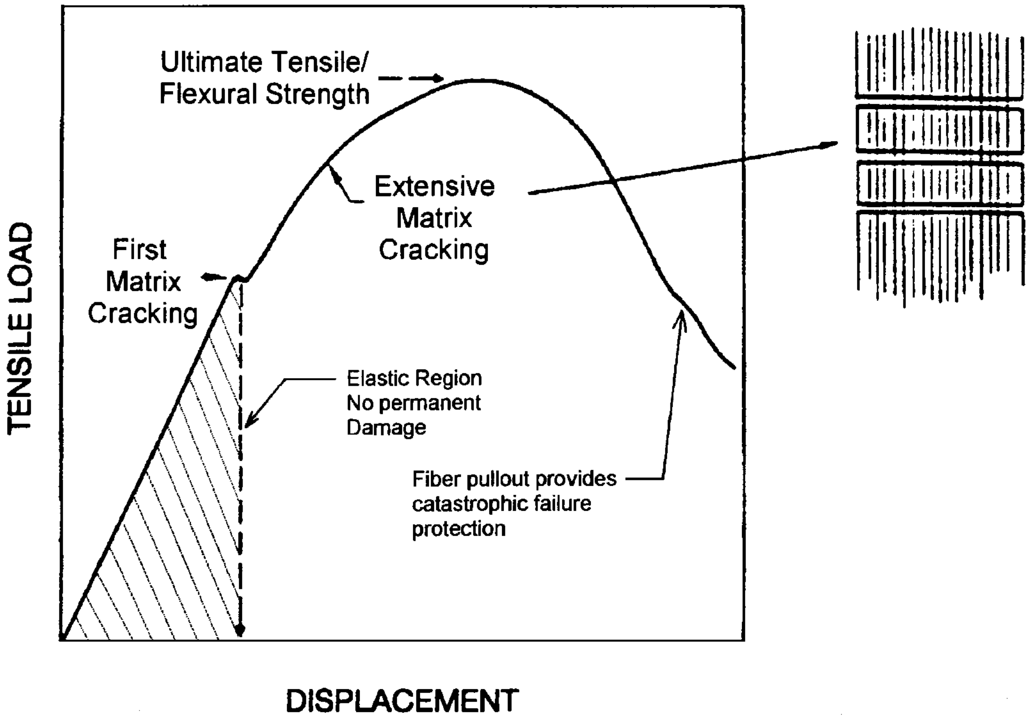

FIGURE 12.6.10 Load deflection behavior of CMFCs illustrating regions of fracture behavior

encountered in ceramics and is of great significance in the design of such materials as turbine blades, where the consequences of catastrophic failure are severe.

Continuous and Chopped Fiber Composites. The use of a continuous fiber reinforcement can have several advantages over the use of chopped fibers. There is a larger strain to pullout due to the increased fiber length, and the continuous fibers do not have stress-concentrating "flaws," as do the exposed ends of chopped fibers. Also, the prearrangement of the fibers allows very careful control of the properties in each direction, and the properties parallel to the fiber orientation will more closely mirror those of the fibers themselves than of the matrix. However, this type of composite is much more difficult to fabricate because of the problems of fiber weaving and forming, resistance to matrix infiltration, and resistance to densification, which necessitates expensive densification techniques, such as hot pressing, chemical vapor infiltration, polymer pyrolysis, directed metal oxidation, or sol-gel infiltration.

Glass Matrix CMFCs. A broad class of CMFCs has been developed and commercialized based on glassy matrix materials. The incentive for using a glassy matrix is the ease with which the matrix can be densified at low temperatures by vitreous sintering as opposed to the high-temperature solid-state sintering required for crystalline matrices. The low-temperature processing, in addition to being lower cost, preserves the high-strength properties of the fibers, which can easily be degraded at high temperatures. Unfortunately, the useful temperature of a glass-based CMC is limited to the Tg of the matrix, or slightly above, which prohibits traditional glass matrix CMCs from being used in extreme temperature applications (above approximately 1000°C). Newer glass and glass-ceramic compositions in the $CaO\text{-}Al_2O_3\text{-}SiO_2$ system are pushing this limit to the region of 1300°C. Two commercial glass matrix composites are Compglas™ and Blackglas™, both glass and glass/ceramic matrix materials reinforced with SiC fibers.

Polycrystalline matrix CMCs achieve higher temperature stability than the glass matrix composites, allow a wider choice of matrix materials, and generally have fewer problems with matrix reactivity. Typical

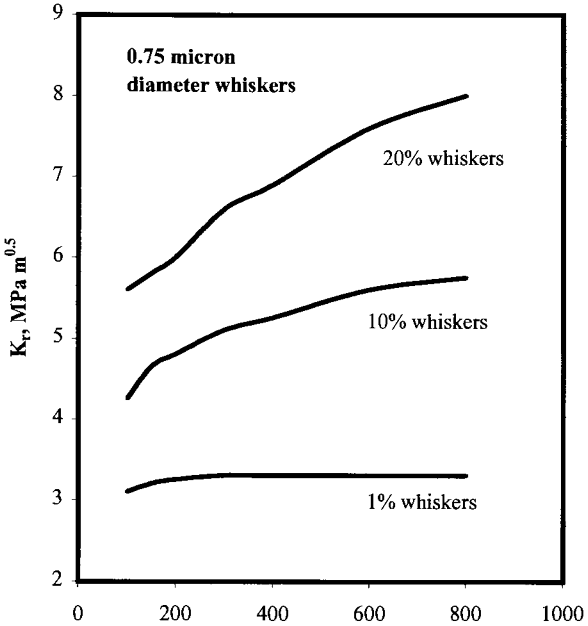

FIGURE 12.6.11 Fracture toughness and R-curve behavior of ceramic matrix whisker composites

crystalline matrix materials are the SiC, Si_3N_4, Al_2O_3, ZrO_2, and mixed silicates. Unfortunately, it is extremely difficult to sinter a CMC with a polycrystalline matrix to full density because of the interference of the fibers. This is particularly true with the nonoxide matrix materials. Pressureless sintering is ineffective for these materials, which necessitates the use of hot pressing or other exotic forming processes, which raise material costs considerably.

Ceramic Matrix Whisker Composites (CMWCs)

Whisker reinforcement of ceramic matrices, while not as exotic, can dramatically increase toughness while preserving relatively inexpensive forming techniques. Figure 12.6.11 illustrates the "rising R-curve" behavior of alumina with the addition of SiC whiskers, while Figure 12.6.12 shows the increase in fracture strength. The composites can generally be fully densified with hot pressing or hot isostatic pressing (HIP). Unfortunately, the toughness values achieved to date with whisker reinforcement are not as high as those for continuous-fiber reinforcement, although the lower cost of whisker composites has stimulated industrial applications. Cutting tool inserts, which must withstand high stresses at elevated temperatures (1200°C), are fabricated commercially from SiC-whisker-reinforced Al_2O_3 (SiC/Al_2O_3). These composite inserts have been a commercial product for a decade and are an excellent example of cost-effective CMCs, that is, high-value-added material applied to a small part exposed to extreme conditions. Health concerns regarding highly durable ceramic whiskers produced from SiC or Si_3N_4 have severely limited development and commercialization of these composites in the U.S. and Europe.

Carbon–Carbon Composites

Introduction

Carbon–carbon composites were originally developed for rocket nose cones in the 1960s because of their high specific strength, fracture toughness, thermal shock, and erosion resistance. Today, carbon–carbon composites are used in a broader range of applications, including brake components, fasteners, heaters, crucibles, and other assorted high-strength/high-temperature products.

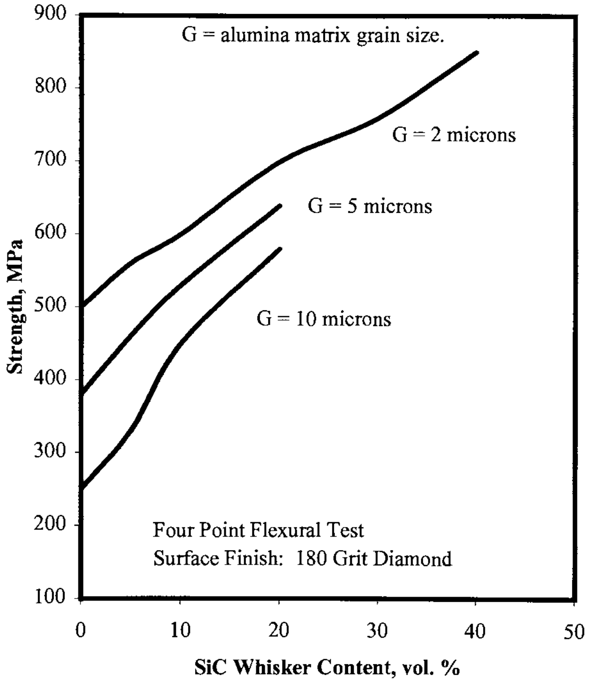

FIGURE 12.6.12 Strength behavior of SiC whisker-reinforced alumina matrix ceramic composite

High-Temperature Oxidation

Perhaps the greatest obstacle to the use of carbon–carbon composites as an engineering material, aside from high cost, is low oxidation resistance above 500°C. Although carbon–carbon maintains its mechanical properties to very high temperatures (>2000°C), it must be protected from oxidizing atmospheres at these temperatures or it will quickly degrade. Generally this is accomplished with SiC coatings with varying degrees of success. For most high-temperature oxidizing applications, carbon–carbon composite components are simply replaced when erosion reaches specified limits.

Fabrication

Most carbon–carbon composites are fabricated by polymer pyrolysis, the process of soaking carbon fiber yarns in a solution of a suitable polymer, then winding or laminating the fibers into the desired shape. Coal tar–based pitches, phenolics, and polyimides are also used as precursors.

The resulting green composite is then pressed, cured, and heated to 800 to 1200°C in an inert atmosphere, carbonizing the precursor. Some structures are heated to 2500°C to graphitize the matrix. The matrix after carbonization will contain a high porosity, typically 30%. This porosity is reduced by infiltrating the matrix with the precursor again and repeating the carbonization cycle. The densification cycle is repeated until the desired density is reached.

Carbon–carbon composites can be formed in random, unidirectional, two-dimensional, two-and-a-half-dimensional, and three-dimensional weaves. Unidirectional weaves provide the highest strength along the fiber axis but much lower strength in other directions. Unidirectional weaves are generally only used in laboratory investigations, as they have little technical value. Two-dimensional weaves (fabrics) are by far the most common due to the relative ease of manufacture and good mechanical properties in the plane of the fabric. Two-and-a-half-dimensional and three-dimensional weaves allow the weaving of very complex structures with good properties in any desired direction, yet the weaving costs can be prohibitive and unnecessary for most industrial applications.

TABLE 12.6.12 Properties of Selected Carbon–Carbon Composites

		Structural Grade[a]			Fastener Grade[b]		
Property	Units	Warp Direction	Fill Direction	Across Ply	Warp Direction	Fill Direction	Across Ply
Tensile strength	MPa	112	115	N/A	139	128	N/A
Tensile modulus	Gpa	89.6	91	N/A	71	717	N/A
Tensile strain to fail	%	0.126	0.126	N/A	0.271	0.242	N/A
Compressive strength	MPa	57	67	122 (min)	68	60	122 (min)
Flexural strength	MPa	86.2	N/A	N/A	106	106	N/A
Interlaminar shear	MPa	3.92	N/A	N/A	8.62	N/A	N/A
Thermal conductivity	J m^{-1} s^{-1} $°C^{-1}$	5.82	4.22	1.44	6.73	10.1	3.43
Coefficient of thermal expansion	10^{-7}°C^{-1} at 371°C	–0.94	–0.94	23.4	–1.2	–1.0	20.4
Density	g/cc		1.52			1.7	
Izod impact value	J cm–1		3.52			5.95	
Hardness (Shore) "D" method			69.8			79.8	
Porosity	%			<20			<8.5
Resistivity, in plane, room-temperature	Ω-cm			24×10^{-4}			21×10^{-4}
Resistivity, in plane, 1750°C	Ω-cm			24×10^{-4}			—

[a] Fiber materials C3 16 PC — 2 × 2 twill, 1780 denier continuous PAN fibers

[b] Fiber materials C3 40 PS — 8 harness satin, 600 denier, staple PAN fibers

Source: Fiber Materials Inc., Biddeford, Maine

Mechanical Properties

Properties of some carbon–carbon composite materials are given in Table 12.6.12. The properties can vary considerably, however, depending on factors such as the weave, tow diameter, precursor, pressing pressure, heat-treatment temperature, and number of densification cycles.

Under cyclical loading, carbon–carbon withstands 70 to 80% of its ultimate tensile strength. Carbon–carbon composites also have large strains to failure, exhibiting pseudoplastic behavior. This is unusual for a high-temperature ceramic material and is one of its prime attractions. The responsibility for this behavior lies with the low fiber–matrix interfacial bond strength and matrix microcracking. Unlike most high-temperature materials, the mechanical properties of carbon–carbon do not degrade at high temperatures. In fact, in inert atmospheres the strength of carbon–carbon composites increases by 40 to 50% up to a temperature of 1600°C.

Thermal conduction, electrical conduction, and thermal expansion are all much greater along the direction of the weave than perpendicular to it. Interestingly, thermal expansion is negative in two-dimensional weaves perpendicular to the fibers. It is therefore possible to use the fiber architecture to achieve near-zero thermal expansion in some directions.

Selected References and Bibliography

ASM International. 1987. Composites, *Engineered Materials Handbook*, Vol. 1, ASM, Materials Park, OH.

Brandt, A.M. and Marshall, I.H., Eds. 1986. *Brittle Matrix Composites 1*, Elsevier Applied Science, New York.

Chou, T.W. 1989. *Textile Structure Composites*, Elsevier, New York.

Lehman, R.L., El-Rahaiby, S.K., and Wachtman, J.B., Eds. 1995. *Handbook on Continuous Fiber-Reinforced Ceramic Matrix Composites*, CIAC/CINDAS, Purdue University, West Lafayette, IN.

Mazumdar, Sanjay K., 2002. *Composites Manufacturing: Materials, Product, and Process Engineering*, CRC Press, New York.

Schwartz, M.M. 1984. *Composites Materials Handbook*, McGraw-Hill, New York.

Singh, J.P. and Bansal, N.P., Eds. 1994. *Advances in Ceramic Matrix Composites II,* American Ceramic Society, Westerville, OH.

Summerscales, J., Ed. 1987. *Non-Destructive Testing of Fiber-Reinforced Plastics Composites*, Vols. 1 and 2, Elsevier, New York.

Tong, L, Mouritz A.P., and Bannister, M.K. 2002. *3D Fiber Reinforced Polymer Composites*, Elsevier, New York.

Ziegler, G. and Huttner, W. 1991. Engineering properties of carbon–carbon and ceramic matrix composites. In *ASM Engineered Materials Handbook*, Vol. 4, ASM International, Materials Park, OH.

12.7 Ceramics and Glass

Richard L. Lehman, Daniel J. Strange, and William F. Fischer, III

Traditional Ceramics

Traditional ceramics encompass many materials, not simply pottery, dinnerware, tile, and sanitaryware, but also technical whitewares, structural clay products, refractories, glazes, and enamels. The product and processing technology of these materials has advanced substantially in recent years which has improved products, reduced costs, and expanded application. Refer to Table 12.7.1 for properties of selected ceramics in this group.

Whitewares

Whitewares are principally comprised of traditional ceramic bodies that are white, cream, ivory, or light gray in appearance. Most whiteware materials are formulated from clay, flint, and feldspar (triaxial compositions) although other additives may be incorporated. The engineering properties of whitewares are strongly affected by porosity, a characteristic that reduces frost resistance and cleanability but is essential for certain aesthetic effects.

Vitreous. Vitreous whiteware bodies are translucent and have no open porosity, while earthenware and wall tile, for example, have substantial porosity, and semivitreous bodies bridge the gap in both porosity and translucency. The firing temperature is largely responsible for the differences in properties of the bodies by affecting the degree of vitrification. The general categories of products within the whiteware group are given in Table 12.7.2.

TABLE 12.7.1 (PART I) Physical Properties of Selected Ceramics

Material	Porcelain	Cordierite Refractory	Alumina, Alumina Silicate Refractories	Magnesium Silicate
Specific gravity	2.2–2.4	1.6–2.1	2.2–2.4	2.3–2.8
Coefficient of linear thermal expansion, ppm/°C, 20–700°	5.0–6.5 × 10^6	2.5–3.0 × 10^6	5.0–7.0 × 10^6	11.5 × 10^6
Safe operating temperature, °C	~400	1,250	1,300–1,700	1,200
Thermal conductivity (cal/cm^2/cm/sec/°C)	0.004–0.005	0.003–0.004	0.004–0.005	0.003–0.005
Tensile strength (psi)	1,500–2,500	1,000–3,500	700–3,000	2,500
Compressive strength (psi)	25,000–50,000	20,000–45,000	13,000–60,000	20,000–30,000
Flexural strength (psi)	3,500–6,000	1,500–7,000	1,500–6,000	7,000–9,000
Impact strength (ft-lb; $^1/_2$″ rod)	0.2–0.3	0.2–0.25	0.17–0.25	0.2–0.3
Modulus of elasticity (psi)	7–10 × 10^6	2–5 × 10^6	2–5 × 10^6	4–5 × 10^6
Thermal shock resistance	Moderate	Excellent	Excellent	Good
Dielectric strength, (V/mil; 0.25″ specimen)	40–100	40–100	40–100	80–100
Resistivity (Ω/cm^2, 22°C)	10^2–10^4	10^2–10^4	10^2–10^4	10^2–10^5
Power factor at 10^6 Hz	0.010–0.020	0.004–0.010	0.002–0.010	0.008–0.010
Dielectric constant	6.0–7.0	4.5–5.5	4.5–6.5	5.0–6.0

TABLE 12.7.1 (PART II) Physical Properties of Selected Ceramics

Material	High-Voltage Porcelain	Alumina Porcelain	Steatite	Forsterite	Zirconia Porcelain	Lithia Porcelain	Titania/Titanate Ceramics
Specific gravity	2.3–2.5	3.1–3.9	2.5–2.7	2.7–2.9	3.5–3.8	2.34	3.5–5.5
Coefficient of linear thermal expansion, ppm/°C, 20–700°	5.0–6.8 × 10^6	5.5–8.1 × 10^6	8.6–10.5 × 10^6	11 × 10^6	3.5–5.5 × 10^6	1 × 10^6	7.0–10.0 × 10^6
Safe operating temperature, °C	1,000	1,350–1,500	1,000–1,100	1,000–1,100	1,000–1,200	1,000	—
Thermal conductivity (cal/cm^2/cm/sec/°C)	0.002–0.005	0.007–0.05	0.005–0.006	0.005–0.010	0.010–0.015	—	0.008–0.01
Tensile strength (psi)	3,000–8,000	8,000–30,000	8,000–10,000	8,000–10,000	10,000–15,000	—	4,000–10,000
Compressive strength (psi)	25,000–50,000	80,000–25,000	65,000–130,000	60,000–100,000	80,000–150,000	60,000	40,000–120,000
Flexural strength (psi)	9,000–15,000	20,000–45,000	16,000–24,000	18,000–20,000	20,000–35,000	8,000	10,000–22,000
Impact strength (ft-lb; $^{1}/_{2}$″ rod)	0.2–0.3	0.5–0.7	0.3–0.4	0.3–0.4	0.4–0.5	0.3	0.3–0.5
Modulus of elasticity (psi)	7–14 × 10^6	15–52 × 10^6	13–15 × 10^6	13–15 × 10^6	20–30 × 10^6	—	0.3–0.5 × 10^6
Thermal shock resistance	Moderate–good	Good	Moderate	Poor	Good	Excellent	Poor
Dielectric strength, (V/mil; 0.25″ specimen)	250–400	250–400	200–350	200–300	250–350	200–300	50–300
Resistivity (Ω/cm^2, 22°C)	10^{12}–10^{14}	10^{14}–10^{15}	10^{13}–10^{15}	10^{13}–10^{15}	10^{13}–10^{15}	—	10^{8}–10^{15}
Power factor at 10^6 Hz	0.006–0.010	0.001–0.002	0.008–0.035	0.0003	0.0006–0.0020	0.05	0.0002–0.050
Dielectric constant	6.0–7.0	8–9	5.5–7.5	6.2	8.0–9.0	5.6	15–10,000

TABLE 12.7.2 Whiteware Materials

Class and Subclass	Percent Water Absorption	Example Product Type
Earthenware		
Natural clay	>15	Artware and tableware
Fine earthenware	10–15	Tableware, kitchenware, and artware
Semivitreous Earthenware	4–9	Tableware and artware
Talc earthenware	10–20	Ovenware and artware
Stoneware		
Natural stoneware	<5	Kitchware, artware, and drainage pipes
Fine stoneware	<5	Cookware, tableware and artware
Jasper stoneware	<1	Artware
Basalt stoneware	<1	Artware
Technical vitreous stoneware	<0.2	Chemicalware
China		
Vitreous china	0.1–0.3	Sanitaryware
Hotel china	0.1–0.3	Tableware
Cookware	1–5	Ovenware and stoveware
Technical china	<0.5	Chemicalware and ball mill jars and media
Fine china	<0.5	Tableware and artware
Porcelains		
Technical porcelains	<0.2	Chemicalware
Triaxial electrical porcelains	<0.2	Low-frequency insulators
High-strength electrical porcelains	<0.2	Low-frequency insulators
Dental porcelains	<0.1	Dental fixtures

Earthenware. Earthenware materials are defined as a nonvitreous clay-based ceramic ware of medium porosity (4 to 20%). They can be glazed or unglazed in their finished form. There are four primary subclasses of earthenware, natural clay, fine, semivitreous, and talc earthenware. Natural clay earthenware is derived from a single, unbeneficiated clay, whereas fine earthenware possesses beneficiated clays, as well as nonplastic materials, to comprise a triaxial body. Semivitreous earthenware is also a triaxial body, but it is fired to a higher temperature to form a more glassy phase, thereby creating a body with the lowest porosity of the earthenware group, usually between 4 and 9%. The final earthenware body is talc earthenware, produced principally from raw talc, with porosity ranging up to 20%. Earthenware bodies range in color from white for the talc and triaxial bodies, to tan and brown for many artware bodies, to a rusty red for terra-cotta.

Stoneware. Stoneware bodies can be either vitreous or semivitreous. They are primarily composed of nonrefractory fireclays or a combination of triaxial materials that matches the forming, firing, and finished properties of a natural stoneware body, bodies made from a single, naturally occurring, largely unbeneficiated clay-bearing material. Fine stonewares incorporate beneficiated clays, as well as nonplastics. Jasper stonewares are composed primarily from barium-containing compounds, while basalt stonewares contain large amounts of iron oxide.

Vitreous stoneware bodies are made from blends of a variety of beneficiated materials that are fired to higher temperatures to achieve low porosity levels (0 to 5%) necessary for many applications. Stoneware bodies are usually quite durable and resistant to chipping. However, translucency is less than that of china and the colors are not as white because of the presence of iron and other impurities.

China and Porcelain. China and porcelain are nearly synonymous terms which refer to fully vitreous (no porosity) clay, flint, feldspar compositions which are typically glazed, fired to high temperatures, and exhibit strength, hardness, and chemical durability. The term *china* is used to describe exceptionally fine materials prepared from low-impurity raw materials and used in artware and dinnerware. In modern times there has been a trend toward highly vitreous and highly translucent china compositions. Porcelain is used to describe mostly technical ceramics of the triaxial composition which are used as electrical insulators, sanitaryware, and chemical ware.

Subclassifications of china exist, such as vitreous china, hotel china, cookware, technical ceramics, fine chinas, and porcelains. Body formulations are usually based on the triaxial body, clays, flint/silica and fluxing agents, most usually feldspathic materials. However, there are a large number of bodies that are composed of a large fraction of other materials. Inclusive of these are alumina, bone ash, cordierite, other fluxes, and/or lithium compounds. Vitreous china is a category of traditional ceramics referring to the various sanitaryware plumbing fixtures and accompaniments. Hotel chinas, as the name implies, are generally used in commercial food establishments. Both bodies are glazed in a single firing operation in which both the body and glaze mature at the same time.

Technical whitewares account for a wide variety of vitreous ceramics used in the chemical, dental, refractory, mechanical, electrical, and structural areas. The compositions of most of these materials are similar to that used in the hotel chinas, with the possible substitution of alumina and zircon for some or all of the silica. These materials can be either glazed or unglazed with water absorption less than 0.5%.

Fine china bodies, including bone china, are highly vitrified and translucent materials that are usually fired in two or more separate operations. The first, higher-temperature firing matures the body and a second, lower-temperature firing matures the newly applied glaze. The separate firing conditions allow for the use of high-gloss glazes. Subsequent firings are used to apply decals and metallic decorations.

Porcelain ceramics are mostly used in technical applications. The typical body is triaxial (Table 12.7.2), although some or all of the silica can be replaced with alumina to increase the mechanical properties. Aside from triaxial porcelains, compositions in the $MgO \cdot Al_2O_3 \cdot SiO_2$ composition range are popular for electronic applications due to the absence of mobile alkali ions.

Refractories

Introduction. Refractory ceramic materials are by nature inert, high-melting-point compounds that are resistant to corrosion throughout the temperature range of use. Refractories must also withstand thermal cycling, thermal shock, mechanical fatigue, and a range of chemical attack from the elevated-temperature environments typical of most applications. Refractory materials are used in the processing of metals (75% of all refractories), glass, cement, and in the processing of nearly all ceramics.

Temperature Tolerance. A quality refractory must be stable at the intended use temperature. Refractoriness is a measure of the highest use temperature the material can withstand and is limited by the softening or melting point of the constituent oxides. Most refractories are a mixture of phases, and, as such, do not display a distinct melting point, but have a range of temperatures where the material starts to soften or melt. Most frequently, a refractory is categorized by an upper use temperature, but sometimes the refractoriness is quantified by the PCE or pyrometric cone equivalent. The PCE is a measure of the heat content that the refractory can withstand before beginning to soften, which is determined by the slumping of pyrometric cones during thermal cycle testing. This value may correspond to different temperatures under different environments or atmospheres and is thus a good indicator of maximum-use conditions. Refractory suppliers can provide PCEs for specific products. Another measure of a refractory quality is the failure under load temperature. The temperature where a refractory sags or deforms is part of all refractory specifications and is related to the amount and composition of the glassy phase within the material.

Dimensional Stability and Spalling. Dimensional stability and resistance to spalling are important performance criteria for most refractories. Spalling is the cracking or flaking of the refractory which usually results from thermal cycling, thermal gradients within the refractory, or compression effects due to differing thermal expansion of the different system materials. Spalling reduces the effectiveness and lifetime of the refractory. The dimensional stability of the refractory is also important. Since the refractory is subjected to both heating and cooling cycles, as well as thermal gradients in use, the expansion of the material is very important when choosing a refractory. Large changes in the size of a refractory set up stresses that can reduce the effectiveness of the refractory and may result in its failure..

Porosity. Refractory porosity is closely controlled in manufacturing since it leads to a reduction in the mechanical strength of the material and allows for the penetration and chemical attack of liquids or gases to the internal surface of the refractory. However, on the positive side, the presence of internal pores reduces the thermal conductivity of the material and increases fracture toughness, K_{IC}.

Fireclay Refractories. Fireclay refractories are composed of hydrated aluminosilicates with silica content of up to 75% or more with alumina and other minor contents of less than 40%, although alumina-fortified fireclay refractories are made with considerably higher alumina contents. Properties vary greatly over this wide range of compositions — generally, the higher the alumina content, the higher the performance. Fireclay refractories based on kaolin have a high refractoriness and high load resistance. Resistance to chemical attack and thermal conductivity decrease with increasing porosity, whereas spalling resistance increases. Increased alumina content raises the resistance of the material to attack in molten environments. Fireclay refractories are the most widely used refractory and find application in many industries.

Alumina Refractories. High-alumina refractories contain 80 to 99% or more aluminum oxide. As with fireclay materials, the higher the alumina content, the higher the refractoriness and the higher the load-bearing capacity. The chemical resistance of alumina refractories is greater than that of the fireclay refractories. Alumina brick is used to replace fireclay brick in more severe applications in the steel industry. Alumina bricks with phosphate bonding are used in the production of aluminum because of their refractoriness and the resistance of the phosphate bonding to chemical attack by the molten aluminum. Mullite ($3Al_2O_3 \cdot 2SiO_2$) refractories are similar to alumuna refractories in performance, but are cheaper and more resistant to thermal shock at the expense of some temperature capability.

Silica. Silica brick refractories, used in the glassmaking industry, range in composition from almost pure silica to mixtures containing lime, iron oxide, and alumina, depending on the degree of beneficiation of the raw materials. These refractories show a high degree of volume stability below 650°C (1200°F) and a lower degree of spalling than the fireclay bricks, largely because of the low thermal expansion of the silica.

Basic Refractories. Basic refractories are constituted from magnesite (MgO), calcia (CaO), and chrome (Cr_2O_3) and are used widely in metallurgical industries where basic slags predominate. They are not suitable in acid, or high-silica, environments. Refractories in this group, such as pure magnesite, dolomite (CaO-MgO), and chrome magnesite materials, have high refractoriness, volume stability, and are very resistant to chemical attack. Magnesite refractories have between 80 and 95% MgO content, a level at which the refractoriness and resistance to chemical attack is extremely high. Chromite refractories also have excellent chemical resistance in basic environments, with moderate resistance in acidic environments. The chrome content in these refractories ranges between 30 and 45%. Chrome–magnesite refractories are composed of over 60% MgO. Compositions and properties of selected basic and high-duty refractories are given in Table 12.7.3.

Glazes and Enamels

A glaze is a continuous glassy layer that is bonded to the surface of a ceramic. The glaze is typically hard, impervious to moisture, and easily cleaned. An enamel is similar in properties to a glaze, but the substrate is metallic. The surface finish of either can be altered from glossy to matte by varying the composition or the firing conditions. A glaze is usually composed of an aqueous suspension of ceramic particles that is applied to the surface of a material, dried, and fired. During firing, the materials within the glaze react and melt, forming a thin glassy layer on the surface of the ceramic material. Some materials are prefired and then the glaze is applied, or, as is becoming more common, the glaze can be fired along with the body. The maturing temperature of most glazes is on the order of 500 to 1500°C, or 930 to 2730°F. Glazes

TABLE 12.7.3 Compositions and Properties of Selected Basic and High-Duty Refractories

		Maximum Use Temperature in O_2		Thermal Conductivity		
Refractory	Composition	(°C)	(°F)	100°C/212°F	500°C/930°F	100°C/1830°F
Basic Refractories						
Silica	93–96% SiO_2	1700	3090	0.8–1.0	1.2–1.4	1.5–1.7
Fireclay	55–80% SiO_2 and 15–45% Al_2O_3	1300–1450	1370–2640	0.8–0.9	0.9–1.1	2.4–2.6
Magnesite	80–95% MgO Fe_2O_3 Al_2O_3	1800	3270	3.8–9.7	2.7–4.7	2.2–2.6
Chromite	30–45% Cr_2O_3, 14–19% MgO, 10–17% Fe_2O_3, 15–33% Al_2O_3	1700	3090	1.3	1.5	1.7
Chromite–magnesite	60+% Fe_2O_3 Al_2O_3	1800	3270	1.9–3.5	1.2–2.3	1.6
High-Duty Refractory						
Alumina	100% Al_2O_3	1950	3540	26	9.4	5.3
Magnesia	100% MgO	2400	4350	31	12	6
Silica	100% SiO_2	1200	2190	0.8	1.4	1.8
Mullite	72% Al_2O_3, 28% SiO_2	1850	3360	5.3	3.8	3.4

can be either clear, transparent, or opaque. Some glazes are formulated to form crystals within the glaze for a variety of optical effects, such as opalescence.

There are three main types of glazes used. The first of these are the raw glazes. Raw glazes can be further broken down into leaded, leadless, zinc-containing, slip, and porcelain glazes. Lead promotes the processing of the glaze via low viscosity and surface tension and imparts a high refractive index to the finished glaze. However, due to the health hazards associated with free lead, there has been a movement toward lead-free glazes in certain applications. Lead-free glazes require an increase in the firing temperature of approximately 150°C, from 1030 to around 1190°C. Porcelain glazes mature at temperatures in the same regime as the underlying body from which they get their name. Zinc-containing glazes are similar to porcelain glazes except that they mature at lower temperatures. Slip glazes are used in artware glazing and high-tension electrical insulators. Fritted glazes are in the form of prereacted glass which has been ground to form a powder. Special glazes offer special optical properties in the finished surface. Salt glazes are formed by injecting salts into the firing kiln, with the resulting glaze having a complex pattern of crystalline and glassy phases. Crystalline glazes are often zinc based and produce crystals within the glaze, again for artistic value. Luster glazes form a metallic coating on the glaze.

Structural Clay Products

Ceramic materials are used in a wide variety of applications in the construction industry, ranging from concrete and cement for buildings and highways, to structural clay materials for use in piping and roofing. For a discussion of concrete materials refer to Section 12.5.

Structural clay products have been used for millennia. Original uses included tile and clay brick for building construction, as well as pipes in water supply and sewer applications. These materials are still used today because of their high compressive strength and imperviousness to water. Structural ceramics are coarse-grained materials with the one exception of ceramic tile. Typical raw material compositions for these bodies are 35 to 55% clay, 25 to 45% filler, usually silica, and 25 to 55% fluxing material. Colors range from white for the kaolinitic clay products, to a buff for the fireclay materials, to red for the illitic materials. Properties vary widely between the different materials. Most concern is placed on the water absorption, which relates to freeze/thaw durability and compressive strength.

TABLE 12.7.4 Selected Properties of Crystalline Phases Used in Engineered Ceramics

Crystalline Phases	Formula	Melting Temperature (C)	Thermal Expansion α (ppm/°C)	Dielectric Constant κ
Magnesia	MgO	2852	14	5.5
Magnesia spinel	$MgO \cdot Al_2O_3$	2135	8	8.0
Alumina	Al_2O_3	2072	9	10.0
Mullite	$3Al_2O_3 \cdot 2SiO_2$	1920	5.5	4.5
Silica	SiO_2	1723	—	3.8
Protoenstatite	$MgO \cdot SiO_2$	1557	8.0	6.0
Forsterite	$2MgO \cdot SiO_2$	1910	12.0	6.0
Cordierite	$2MgO \cdot 2Al_2O_3 \cdot 5SiO_2$	1450	2.0	5.0
Carbon	C	3652	4.4	—
Silicon carbide	SiC	2700	4.4	—
Silicon nitride	Si_3N_4	1900	—	—
Zirconium oxide	ZrO_2	5000	—	—
Zircon	$ZrO_2 \cdot SiO_2$	2550	4.5	6.5
Wollastonite	$CaO \cdot SiO_2$	1540	5.5	6.0
Titania	TiO_2	1830	—	90
Calcium titanate	$CaO \cdot TiO_2$	1975	—	180
Strontium titanate	$SrO \cdot TiO_2$	—	—	360
Magnesium titanate	$MgO \cdot TiO_2$	—	—	14
Barium titanate	$BaO \cdot TiO_2$	—	—	2000
Magnesium ferrite	$MgO \cdot Fe_2O_3$	—	—	—
Zinc ferrite	$ZnO \cdot Fe_2O_3$	—	—	—

Advanced Ceramics

Classes of Advanced Ceramics

Advanced ceramic materials are materials which have been engineered to possess exceptional levels of mechanical, optical, thermal, or other property. Most often the materials possess high strength, high stiffness, or are chemically inert. Typical materials contain oxides, nitrides, or carbides which may be monolithic structures or reinforced with various particulate and/or fibrous materials. Refer to Section 12.6 for a detailed discussion of composites. The reinforcement phase usually, but not necessarily, differs from the matrix material. Phases used in designing engineered ceramics are listed in Table 12.7.4 with specific property characteristics as indicated. Advanced ceramic materials are currently much more varied and less standardized than metals, and materials from different manufacturers, or even from different production lots, will have varied properties.

Structural Ceramics

Required Properties. Structural applications involve the use of ceramic materials in load-bearing situations. Material properties required for these conditions include strength over a wide temperature range, often as high as 1400°C, stiffness, creep resistance, resistance to corrosion and oxidation, and, ideally, damage tolerance or toughness. The major difficulty in the use of ceramics for structural applications is their low fracture toughness compared with metals. Conversely, ceramics excel at high-temperature behavior, have low density/weight ratios, high stiffness, and chemical inertness. At the present level of technology, there is a trade-off between high strength and high toughness. To get a high-strength material usually requires a fine-grain-sized ceramic, while a tough ceramic material often has elongated grains or reinforcement phases that are usually quite large.

Applications. Existing and potential applications include automotive, biomedical, power generation, heat exchangers, wear materials, aerospace and military applications, cutting tools, and various other technologies. Table 12.7.5 provides the mechanical properties of selected advanced ceramics. The property

TABLE 12.7.5 Mechanical Properties of Selected Advanced Ceramic Materials

Material	Composition	Density (g/cc)	Elastic Modulus (GPa)	Fracture Strength (MPa)	Fracture Toughness K_{IC} (MPa · $m^{0.5}$)	Hardness (Vickers)
Alumina	Al_2O_3	3.9	380	Up to 400	4–9	2000
Beryllia	BeO	2.8–2.9	340	125	5	1100–1400
Chromic oxide	Cr_2O_3	4.2–4.4	—	—	4–9	—
Magnesia	MgO	3.5	300	—	3–5	500–600
Spinel	$MgAl_2O_4$	3.2	260	50–100	2–5	1200–1500
Zircon	ZrO_2 SiO_2	4.25	160	50–100	2–4	—
Zirconia	ZrO_2 stabilized with CaO	5.5	200	500	Up to 13	1200–1500
Zirconia	ZrO_2 stabilized with MgO	5.5	200	500	Up to 13	1200–1500
Zirconia	ZrO_2 stabilized with Y_2O_3	5.6	200	500–600	Up to 13	1200–1500
Zirconia (tetragonal)	ZrO_2	6.0	200	750	Up to 13	—
Zirconia (monoclinic)	ZrO_2	5.5	200	450	Up to 10	—
Reaction-bonded silicon nitride (RBSN)	Si_3N_4	1.9–2.8	150–250	300–400	Up to 12	750
Silicon nitride (hot pressed)	Si_3N_4	3.1–3.2	310	400–700	5–9	1600–2800
Silicon carbide (sintered)	SiC	3.0–3.2	400	400–500	6–9	2400–2800
Silicon carbide (hot pressed)	SiC	3.0–3.2	440	550–650	7–9	2500
Silicon carbide (RBSC)	SiC	3.0–3.15	350–400	300–400	4–8	2000
Boron carbide	B_4C	2.3–2.5	450	400–600	—	2800–3200
Boron nitride	BN	2.0–2.1	20–100[a]	—	—	Soft anisotropic
Graphite	C	1.9	3–15[a]	<50	—	Soft
Tungsten carbide	WC	15	600	450–750	Up to 20[b]	1300–1600
Titanium nitride	TiN	4.9	—	—	—	—
Titanium carbide	TiC	4.9	—	—	—	2800–3700

[a] Anisotropic.

[b] With Co additions.

values listed are guidelines; exact properties are difficult to specify since the exact properties depend largely on processing. Material selection is governed by the environmental conditions of each application.

Electronic and Magnetic Ceramics

Electronic and magnetic ceramic materials have a variety of useful functions. Alumina, alumina titanate, and aluminum nitride are used as substrate materials, zirconia is used in oxygen sensors, lead zirconate titanate (PZT) and lead magnesium niobate are common actuator and transducer materials, and barium titanate and related materials are used in capacitors. Ceramic materials are used not only in military and aerospace applications, but also in consumer electronics, computers, automotive and transportation systems, and power generation systems. Electronic/magnetic ceramics are useful as a result of a variety of properties. Refer to Table 12.7.1 for dielectric property data of selected compositions.

Optical Ceramics

Zirconia and transparent alumina, or sapphire, are often used as high-temperature windows, due to their high melting points, chemical inertness, and high transparency. They are also used as watch crystals, due to their high scratch resistance. Mirrors made from silicon carbide are being evaluated because of the higher strength-to-weight ratio compared with glass materials and the relatively low coefficient of thermal expansion of SiC. Laser crystals are a group of materials which are often based on doped crystals — yttrium aluminum garnet (YAG) is representative, Infrared (IR) transparent windows and shields are used principally in military and aerospace applications to protect IR sensors from damage. Missile nose cones, or randomes, must possess high mechanical strength and be resistant to mechanical erosion and thermal shock. Typical materials include aluminum oxynitride, spinel, zinc sulfide, calcium fluoride, yttria, and sapphire. Refer to Table 12.7.6 for IR absorption ranges of important ceramic materials.

Effect of Finishing and Machining on Properties

Final finishing of many advanced ceramics is required to obtain the optimum mechanical properties or to meet design tolerances. Since sharp corners act as stress concentrators and are not associated with good design, they are usually machined to a several-millimeter radius if they occur in the as-manufactured product. Other operations include surface grinding, polishing, or lapping operations. Ceramics are very hard materials, which makes final matching machining extremely time-consuming and expensive. Every effort should be made to fabricate components to close to net shape tolerances, or to machine the piece as much as possible prior to final firing.

Traditional Glasses

Definition and Introduction

Traditionally, glass is defined as an inorganic product of fusion which has cooled to a rigid state without crystallizing. This broad definition says nothing about the chemistry of the glass but rather refers to the traditional concept of cooling liquid melts below the melting point to form substances which are rigid elastic mechanical solids but which have not crystallized. The historical model for this process is the melting of soda–lime silicate glass by fusing the raw materials at high temperature and cooling quickly to form the well-known window and container glass still in wide use today. Although this definition is still generally valid, processes exist today in which glass is made without fusion. Chemical and physical vapor deposition, and sol–gel processes are examples. Many organic and metallic materials form glasses and are in commercial use today, thus rendering the “inorganic” part of the historical definition inappropriate.

A more applicable definition of glass is an X-ray diffraction amorphous material which exhibits a glass transition. A glass transition is the temperature point at which the amorphous solid exhibits a continuous change in thermodynamic quantities such as heat capacity and expansion coefficient. Because the structure of the glass is frozen before it reaches equilibrium, a glass is metastable with respect to its corresponding

TABLE 12.7.6 IR Transmission Limits for Selected Materials

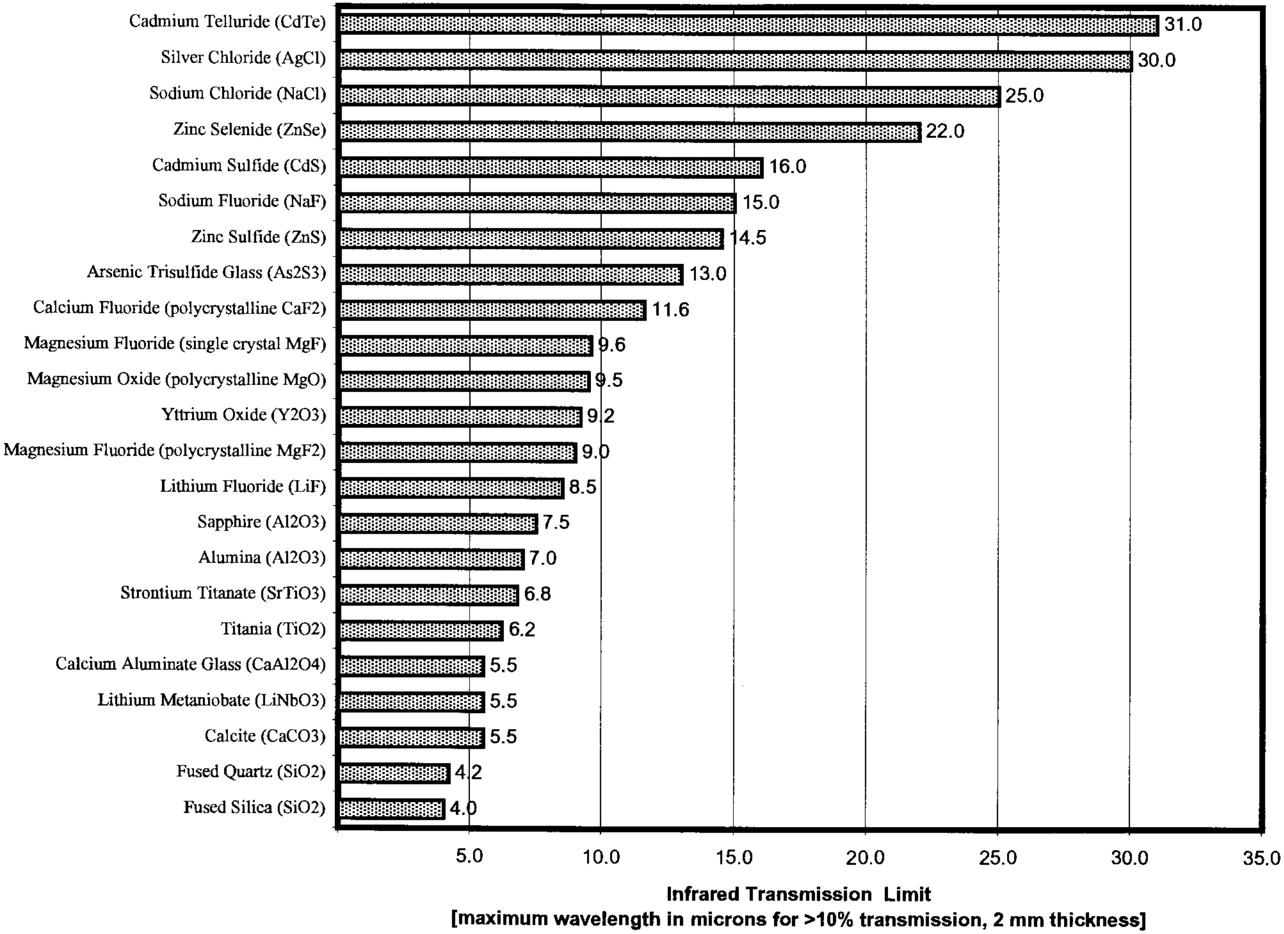

crystalline phase. Unlike the crystalline phase, the glass can have a range of physical properties depending upon the rate of cooling (thermal history) and these properties are universally isotropic.

Although glass can be made from an enormous range of polymers, oxides, metals, and inorganic and organic salts, the principle glasses of interest to a mechanical engineer will be glasses with oxide network formers such as SiO_2, B_2O_3, P_2O_5. These oxides, among others, are known as glass formers. They are capable of forming the three-dimensional network essential to the existence of the glassy state. Other oxides, such as alkalis, alkaline earths, and various transition elements simply serve to modify the basic network to produce varying properties.

The most common glass in use today is the very old soda–lime–silicate glass composition based on the weight composition: 74% SiO_2, 16% Na_2O, and 10% CaO. In this composition the silica is the network former, the sodium breaks up the silicate network to permit melting and fabrication at reasonable temperatures, and the calcia provides ionic bonding within the network to provide chemical durability. This composition is used today, with minor variations, for early all container, window, and tableware glass articles.

Composition/Properties

Traditional glasses are silicate glasses, i.e., glass which contain SiO_2 as the principal network-forming oxide. Table 12.7.7 give compositions for a representative range of commercial glasses, and Table 12.7.8 lists properties for flat glass. All glasses in Table 12.7.7 contain at least 50% SiO_2 and many are quite close to the traditional 74/16/10 composition mentioned above. The types and amount of modifier oxides are determined by the properties required in use. A more specific list of technical glass compositions from Corning, Inc., and identified by Corning glass codes, is given in Table 12.7.9. Principal glass types are discussed in the following sections.

Pure Silica Glass. Pure silica glass (fused silica) has excellent thermal, mechanical, chemical, and optical properties. Thermal expansion is 5.5×10^{-7}°C^{-1}, use temperature is above 1000°C, and it has excellent visible and ultraviolet (UV) transmission. However, the melting point is greater than 2000°C, which makes manufacture extremely difficult and expensive. Therefore, fused silica is used primarily for such demanding applications as optical fibers, semiconductor process equipment, UV lamps, optics, and space shuttle windows. If 7 wt% titanium dioxide (TiO_2) is added, the thermal expansion coefficient is reduced to zero in normal temperature ranges. This glass (ULE, or ultra low expansion) is used in applications which require exceptional dimensional stability. Telescope mirrors are an example.

High-Silica Glass. The high melting temperatures needed to produce pure SiO_2 glass can be avoided by first melting a special sodium borosilicate glass which can be formed into the desired shape. This glass (Vycor®) phase separates and after acid leaching results in a high (>96%) silica glass with nearly the same properties as pure vitreous silica.

Soda Silica. In order to lower the melting point, a flux is added. The most common flux is sodium oxide (Na_2O), which makes a low-melting glass that is soluble in water and is called water glass. Dissolved glass is used to seal or bond materials such as low-speed grinding wheels.

Soda–Lime–Silica. This is the most common glass and accounts for more than 90% of all the glasses made today. In this glass, lime (CaO) has been added to improve the durability of simple soda–silica glass. Small amounts of other oxides such as alumina (Al_2O_3), magnesium oxide (MgO), and potassium oxide (K_2O) are also added to further enhance the desired properties. The lime is usually obtained from limestone, and the sodium monoxide is obtained from any number of sodium compounds, notably sodium bicarbonate or common baking soda.

Aluminosilicate Glass. Aluminosilicate glass is produced by adding up to 20% Al_2O_3 to soda–lime glass. Aluminosilicate glasses are resistant to thermal shock and high temperatures, and they are not as difficult to produce as silica glass. They find wide use in electronics and in high-temperature laboratory equipment.

TABLE 12.7.7 Commercial Glass Compositions by Application (Wt% oxide)

Oxide	(Optical)V itreous silica	(High silica) Vycor	Plate	Window	Con-tainer	Light bulb	Tubing	Lime table-ware	Low-expansion boro-silicate	Thermo-meter	Boro-silicate Crown	Lead table-ware	Halogen lamp	(Textile fiber) E glass	S glass	Optical flint
SiO_2	100.0	94.0	72.7	72.0	74.0	73.6	72.1	74.0	81.0	72.9	69.6	67.0	60.0	52.9	65.0	49.8
Al_2O_3			0.5	0.6	1.0	1.0	1.6	0.5	2.0	6.2		0.4	14.3	14.5	25.0	0.1
B_2O_3		5.0							12.0	10.4	9.9			9.2		
SO_3			0.5	0.7	tr	5.2							0.3			
CaO			13.0	10.0	5.4	3.6	5.6	7.5		0.4			6.5	17.4		
MgO				2.5	3.7		3.4			0.2				4.4	10.0	
BaO					tr						2.5		18.3			13.4
PbO												17.0				18.7
Na_2O		1.0	13.2	14.2	15.3	16.0	16.3	18.0	4.5	9.8	8.4	6.0	0.01			1.2
K_2O					0.6	0.6	1.0			0.1	8.4	9.6	tr	1.0		8.2
ZnO																8.0
As_2O_3			tr	tr	tr	tr		tr		tr	0.3	tr				0.4

Source: Varshneya, A.K., *Fundamentals of Inorganic Glasses,* Academic Press, New York, 1994. With permission.

TABLE 12.7.8 Properties of Clear and Tinted Flat Glass (Applicable Federal Specification Standard DD-G-451c)

Property	Value
Specific gravity	2.5
Specific heat	0.21
Hardness (Moh's)	5–6
Softening point, °C	729
Refractive index, sodium D-line	1.52
Modulus of elasticity, GPa	70
Tensile strength, MPa	45
Poisson's ratio	0.23
Coefficient of linear expansion, ppm/°C	8.8
Dielectric constant, 1 Mhz	7.1

Borosilicate Glass. In borosilicate glass much of the soda and lime of ordinary glass is replaced by boric oxide. The result is a glass that has a low thermal expansion and is thus resistant to heat and to sudden changes in temperature. The first borosilicate glass was developed by the Corning Glass Works under the trade name Pyrex. Borosilicate glasses are used in laboratory glassware, as well as in home ovenware. Because of their low thermal expansion they are suitable for applications requiring dimensional stability.

Lead Silicates. Lead silicate glass has a higher index of refraction and also a higher dispersion than soda–lime–silicate glass and thus finds use in optical applications. The high gloss resulting from high Fresnel reflection makes lead glasses of 24 to 35% PbO popular for consumer products in the form of artware and lead crystal glass. Lead glasses of different compositions are used widely in electronic applications since low-melting sealing glasses can be formed with little or no alkali, a constituent which promotes high electrical loss.

Strength of Glass

Theoretical Strength. Glass below the glass transition temperature (T_g) is a brittle solid, with failure originating at flaws (scratches, defects, minute compositional differences) which act as stress concentrators. Without flaws of any kind the strength of glass approaches theoretical levels of about 17 GPa (2.5×10^6 psi). Unfortunately, unless glass is processed under the utmost pristine conditions and then immediately coated to prevent surface abrasion by dust or other environmental agents, the glass will contain flaws which decrease the strength by several orders of magnitude from theoretical levels. Synthetic silica glass optical fibers, prepared under meticulous conditions and tested at 77 K, are among the few glass materials which exhibit nearly theoretical strength.

Nominal and Design Strength. The exact failure stress for a specific piece of glass will depend upon the configuration and size of the defect at the crack origin. Since these defects vary in size over a wide range, the standard deviation in the strength of glass will also be large. The glass design engineer must allow large safety factors, often 20 to 50%, to account for the statistical variation. For most types of glass a nominal strength of 70 MPa and a design stress of 7 MPa are typical. Table 12.7.10 summarizes strength and variability in the strength of glasses.

Strengthening and Tempering. Glass can be substantially strengthened, or tempered, either by rapid cooling or by ion-exchange of the surface to develop compressive stresses. Fast, uniform cooling of glass plates heated to the softening point will introduce surface compressive stresses on the glass (with corresponding tensile stress in the center) which become permanently frozen into place upon cooling to room temperature. These compressive stresses, typically 70 to 200 MPa, will resist externally applied tensile stresses and help to prevent crack propagation. Tempering will increase the strength of glass by as much as three to six times. Tempered glass will shatter violently when it fails as a result of the sudden release of stored elastic energy, although the broken pieces will not be sharp. Generally, only simple shapes can safely be thermally tempered.

TABLE 12.7.9 Compositions of Silicate Glasses — Corning Glass Types by Number (approximate wt%)

Glass No.[a]	SiO_2, Silica	Na_2O, Soda	K_2O, Potash	PbO, Lead	CaO, Lime	B_2O_3, Boric Oxide	Al_2O_3, Aluminum Oxide	Other
0010	63	7	7	22	—	—	1	—
0080	73	17	—	—	5	—	1	4% MgO
0120	56	4	9	29	—	—	2	—
1720	62	1	—	—	8	5	17	7% MgO
1723	57	—	—	—	10	5	15	6% BaO, 7 MgO
1990	41	5	12	40	—	—	—	2% Li_2O
2405	70	5	—	—	—	12	1	11% ZnO + CdS, Se
2475	67	10	7	—	—	—	—	12% ZnO, 2% CdO + F^-
3320	76	4	2	—	—	14	3	1% U_3O_8
6720	60	9	2	—	5	1	10	9% ZnO + 4% F^-
6750	61	15	—	—	—	1	11	9% BaO + 3% F^-
6810	56	7	1	3	4	1	10	12% ZnO + 6% F^-
7040	67	4	3	—	—	23	3	—
7050	67	7	—	—	—	24	2	—
7052	65	2	3	—	—	18	7	3% BaO + F^-, 1% Li_2O
7056	70	1	8	—	—	17	3	1% Li_2O
7070	71	0.5	1	—	—	26	1	0.5% Li_2O
7250	78	5	—	—	—	15	2	—
7570	3	—	—	75	—	11	11	—
7720	73	4	—	6	—	15	2	—
7740	81	4	—	—	—	13	2	—
7760	79	2	2	—	—	15	2	—
7900	96	—	—	—	—	3	0.3	—
7913	96.5	—	—	—	—	3	0.5	—
7940	99.9	—	—	—	—	—	—	0.1% H_2O
8160	56	3	10	23	1	—	2	5% BaO + F^-
8161	40	—	5	51	—	—	—	2% BaO + 2% Rb_2O
8363	5	—	—	82	—	10	3	—
8871	42	2	6	49	—	—	—	1% Li_2O
9010	67	7	7	2	—	—	4	12% BaO + Co_3O_4 + NiO + F^-, 1% Li_2O
9606	56	—	—	—	—	—	20	9% TiO_2, 15% MgO
9700	80	5	—	—	—	13	2	—
9741	66	2	—	—	—	24	6	1% F^-, 1% Li_2O

[a] See Table C.12 in Appendix.

Source: Hutchins, J.R., III and Harrington, R.V., *Kirk-Othmer Encyclopedia of Chemical Technology,* Vol. 10, p. 542. Copyright © 1966 by John Wiley & Sons, Inc. Reprinted by permission.

Ion-exchange tempering also improves the strength of the glass by introducing surface compression. In the ion-exchange process large ions are “stuffed” into the interstices in the glass structure previously occupied by smaller ions. This is done by immersing the glass in a molten bath of the alkali salt (typically KNO_3 for a sodium-containing glass) at an elevated temperature. The larger ions will introduce a compressive strain as they force their way into the glass network. The strains obtainable are much higher than those from thermal tempering, generating stresses as high as 700 MPa, although the surface compressive layer is quite shallow and subject to penetration. Ion-exchanged glasses can be more than 10 to 20 times as strong as normal glass and are used, for example, in aircraft windshields to resist bird impacts.

TABLE 12.7.10 Ideal and Practical Strengths of Glass, Glass Fibers, and Glass–Ceramics

Type of Glass	Tensile Strength, psi	Strength/Weight Ratio, psi/lb per cu. in.
Untreated Glass		
Theoretical strength	1,000,000–4,000,000	45,000,000
Fibers, protected in vacuum	Up to 2,000,000	—
Fibers, in air, commercially available	250,000 average	6,000,000 average
Fibers, effective strength in plastic	150,000 average	1,800,000–4,500,000
Bulk glass, protected in vacuum	Up to 500,000	—
Blown ware, unabraded	Up to 100,000	90,000
Pressed ware, unabraded	8,000 average	55,000
Bulk glass, abraded	4,000–8,000 average	30,000
Bulk glass, abraded, 1000-hr stress	2,000 minimum	—
Bulk glass, abraded, design strength	500–1,500	—
Tempered Glass		
Bulk glass, abraded	15,000–35,000	—
Normal design strength	1,500–6,000	—
Chemically Strengthened Glass		
Bulk glass, abraded	100,000 and more	—
Glass–Ceramics		
Bulk material, unabraded	20,000–35,000	27,000
Bulk material, abraded	10,000–24,000	—
Design strength	3,000–6,000	—
Chemically Strengthened Glass–Ceramics		
Bulk material, abraded	200,000 and more	—

Compiled from several sources.

Behavior at Elevated Temperatures

Glasses do not have a clearly defined melting temperature. Instead, there is a temperature range where the viscosity of the glass changes smoothly from solid (greater than 10^{14} Pa · sec) to liquid (less than 10 Pa · sec). It is useful to define some points on the viscosity–temperature curve to create a clearer picture of the viscosity behavior of a glass. The strain point is defined as the temperature at which a glass will release 95% of its stresses within a period of 6 hr. This occurs at a viscosity of approximately $10^{13.5}$ Pa · sec. The annealing point occurs at 10^{12} Pa · sec a viscosity at which 95% of stresses will be released in 15 min. At $10^{6.6}$ Pa · sec, the softening point, the glass will deform under its own weight. The working point is defined as 10^3 Pa · sec, and is a typical minimum viscosity for machine working during forming. Refer to Table C.12 in the Appendix, Properties of Silicate Glasses. Many properties of glasses are presented in this comprehensive table, including maximum application temperatures (upper working temperature) and viscosity data for most common glasses. Generally, the extreme upper working temperature corresponds to the strain point of the glass. Normal service conditions are typically 50 to 60% of the strain point on the Kelvin temperature scale. Under normal service conditions glass is a brittle, mechanical solid, it possesses no mechanical characteristics of a liquid, and it will not flow. Specific heat and thermal conductivity data are presented in Table 12.7.11. Below the glass transition, glass is not a supercooled liquid, it is a glass. Old windows are not thicker at the bottom because of viscous flow.

Chemical Durability

Although glass is often considered an extraordinarily inert material, even the most durable glasses undergo some environmental degradation and many glasses are rapidly attacked by strong acid or basic solutions. Corrosive aqueous environments can cause the ions in the glass to be extracted by a leaching process. Chemical durability behavior is difficult to generalize and trial-and-error testing is usually required for each application. The most severe attack is experienced at extreme high and low pH values; neutral pH solutions rarely attack glass at significant rates. Glasses high in SiO_2, Al_2O_3, and CaO are generally most durable. Glasses high in alkali, such as Na_2O or K_2O, are less durable. B_2O_3 and PbO are intermediate.

TABLE 12.7.11 Thermal Properties of Several Glass Types

	Specific Heat			Thermal Conductivity, cal/cm sec°C × 10^{4a}			
Material	25°C	500°C	1000°C	–100°C	0°C	100°C	400°C
Fused silica	0.173	0.268	0.292	25.0	31.5	35.4	—
7900	0.18	0.24	0.29	24	30	34	—
7740	0.17	0.28	—	21	26	30	—
1723	0.18	0.26	—	—	29	33	—
0311 (chemically strengthened)	0.21	0.28	—	—	27	29	35
Soda–lime window glass	0.190	0.300	0.333	19	24	27	—
Heavy flint, 80% PbO, 20% SiO_2	—	—	—	10	12	14	—
Foamglass insulation	0.20	—	—	(0.97)	1.3	1.73	(2.81)
Fibrous glass	—	—	—	—	(0.8)	—	—
9606 glass–ceramic	0.185	0.267	0.311	—	90	86	75
9608 low-expansion glass–ceramic	0.195	0.286	—	—	48	51	55

Notes: Parentheses indicate extrapolated values. Specific heat increases with temperature and approaches zero at 0° K. There are no critical temperatures or phase changes. Thermal conductivity increases with temperature and is very high for glass ceramics.

[a] To convert to SI units, 1 cal/cm sec °C = 418.6 w/mk.

Source: Hutchins, J.R. III and Harrington, R.V., *Kirk-Othmer Encyclopedia of Chemical Technology*, Vol. 10, p. 598. Copyright © 1966 by John Wiley & Sons, Inc. Reprinted by permission.

A notable form of chemical degradation which occurs under simple, apparently benign, conditions is weathering. Standard soda–lime–silicate window glass can be permanently damaged in a short time (~30 days) if held under high humidity with a means to retain adsorbed moisture on the surface. Such a means can be a dirt film or perhaps a sheet of newspaper. The moisture ion-exchanges with sodium ions in the glass, which form a high-pH surface film which accelerates the attack on the glass. Pitting and adherent surface deposits can quickly form, making the glass unusable.

For container applications requiring extremely high purity, it is common to use a durable glass such as a borosilicate or to increase the chemical resistance of the glass using surface treatments of SO_2, SnO_2, or TiO_2.

Optical Properties

Traditional glasses are principally used because they are transparent in the visible region of the spectrum; windows, containers, and precision optics are examples. Although pure silica is highly transmissive overt the entire visible spectrum, impurities impart coloration which detract from the performance of some glasses but which can also be used to produce beautiful and useful colored glasses. Table 12.7.12 lists impurity ions and their resulting colors. Iron is the most common impurity, imparting a blue-green-yellow tint depending on the oxidation state. It is possible to neutralize but not bleach impurity colors by "decolorization," the addition of complementary coloring oxides to produce an overall neutral gray absorption. Traditional glasses do not transmit well in the UV or IR range, with the exception of certain specialty glasses. Pure silica is the best example, enabling high transmission levels (>10%, 2 mm thickness) from 160 nm to 4 μm.

The refractive index of common silicate glasses are in the range of 1.5 to 1.7 and specific values are given in Table C.12 in the Appendix, *Properties of Silicate Glasses.*

Specialty Glasses

Non-Silica-Oxide Glasses

Glasses made from B_2O_3 and P_2O_3 glass formers rather than SiO_2 possess some special thermal, optical, and chemical properties which make them of interest in certain narrow engineering fields. Borate glasses, often in combination with PbO, are useful solder and sealing glasses for electronic applications; phosphate glasses have special optical properties and are also used as water-soluble chemicals in industry. Tellurite

TABLE 12.7.12 Coloring Additives to Glass

Color	Additive
Red	Colloidal Au or Cu, Cd-Se (S, Te)
Pink	$MnO_2 \cdot CeO_2$, Se^{2-}
Orange	CdS (Se)
Amber	FeS_x, $Fe_2O_3 \cdot TiO_2$
Yellow	UO_2, $CeO_2 \cdot TiO_2$, CdS
Green	Cr_2O_3, Fe_2O_3, CuO, U_2O_3
Blue	CoO, FeO, CuO
Violet	NiO, Mn_2O_3
Gray	$Co_3O_4 \cdot NiO$
Black	$Mn_2O_3 \cdot Cr_2O_3$, PbS, FeS, $CoSe_x$
UV absorption	CeO_2, TiO_2, Fe_2O_3, V_2O_5, CrO_3
IR absorption	FeO, CuO
Decolorization, i.e., mask Fe_2O_3 color	MnO, Se^{2-}, NiO, Co_3O_4
Opacification, i.e., white opals	CaF_2, NaF, ZnS, $Ca_2(PO_4)_3$
Solarization	Cerium, arsenic

glasses have high refractive indexes and, hence, are used in some demanding refractive optic applications. Glasses based on Bi_2O_3, Sb_2O_3, TeO_2, or V_2O_5 have very low melting points, suggesting their use as low-temperature electrical seals. Boro-aluminates have very high electrical resistivities. Alkaline earth aluminates have excellent IR transmitting properties and make excellent high-temperature lamp seals. Despite their unique properties, non-silica-oxide glasses are costly and make up only a very small percentage of the glass produced annually.

Chalcogenide Glasses

A class of excellent IR-transmitting glasses, the chalcogenides, are obtained by combining group VI elements with group V and IV elements. Glasses in this group also exhibit photoconductivity and semiconductivity. Applications for these glasses consist of IR-transmitting optical waveguides (to 20 μm), high-performance IR optical applications, and specialty applications which utilize their photoconductivity properties. Most notable of these applications is the photosensitive coating applied to photocopy drums. Purity issues have limited applications in optical fibers as of this writing.

Heavy Metal Fluoride Glasses

Heavy metal fluoride glasses (HMFG) are an important new (1975) composition group because of their extremely low theoretical optical attenuation (10^{-3} dB/km at 3.5 μm), which makes them candidates for repeaterless transoceanic communication links. Unfortunately, this magnitude of transmission has not been obtained in practice because of problems with high oxygen impurities and crystallization. Furthermore, HMFGs are readily attacked by water, and current development efforts are aimed at improving chemical durability. At present, HMFGs are limited to short transmission distance IR optical applications.

Amorphous Metals

Certain metal compositions can be fabricated as glasses by subjecting streams of the molten metal to extremely rapid quenching rates (10^5 to 10^8°C/sec). The resulting glasses possess intriguing properties. Strengths approach theoretical limits, and electrical resistivities are greater than their crystalline counterparts yet decrease with temperature. Most importantly, they have extremely low B–H hysteresis curves. For this reason they are used commercially as power transformer core laminations.

Amorphous Semiconductors

Many elements and compounds which exhibit semiconducting properties in the crystalline state are also semiconductors in the amorphous state. Si, Ge, P, As, $CdGe_xAs_2$ ($x = 0$ to 1.2), $Si_{1-x}H_x$ ($x = 0.1$ to 0.2) are important examples. These materials are use in fabrication of inexpensive vapor deposition fabrication of photovoltaic cells.

Glass Ceramics

A useful group of materials is made by batching, melting, and forming a product as a glass followed by heat treatment to nucleate and grow crystalline phases from the glass to produce a ceramic with up to 99% crystalline phase content. The microstructure contains crystals of about 1 μm size, a glassy matrix, and no porosity. The processing route is a principal advantage since high-speed glass-forming methods can be used, no porosity exists, the formed shape can be inspected as a transparent glass, and rejects at the forming stage can be recycled.

Glass ceramics are typically stronger than most ceramics as a result of zero porosity, and they are tougher than glass because of the deflection of crack fronts around the crystals. High-temperature properties are generally not good due to the glassy phase and the nature of the process, thus limiting most glass ceramics to low- and intermediate-temperature applications (<1000°C). A wide range of products has been made from glass ceramics, from home cookware to industrial bearings and aerospace radomes.

Selected References and Bibliography

1. Doremus, R.H. 1994. *Glass Science.* 2nd ed. John Wiley & Sons, New York.
2. Fanderlik, I. 1983. *Optical Properties of Glass.* Elsevier, New York.
3. Henkes, V.E., Onoda, G.Y., and Carty, W.M. 1996. *Science of Whitewares.* American Ceramic Society, Westerville, OH.
4. Jones, J.T. and Berard, M.F. 1972. *Ceramics — Industrial Processing and Testing.* Iowa State University Press, Ames.
5. Kingery, W.D., Bowen, H.K., and Uhlmann, D.R. 1976. *Introduction to Ceramics.* 2nd ed. John Wiley & Sons, New York.
6. Reed, J. 1988. *Introduction to the Principles of Ceramic Processing.* John Wiley & Sons, New York.
7. Richerson, D.W. 1982. *Modern Ceramic Engineering.* Marcel Dekker, New York.
8. Schneider, S.J., Ed. 1991. *Engineered Materials Handbook, Vol. 4: Ceramics and Glasses.* ASM International, Materials Park, OH.
9. Shand, E.B. 1982. *Glass Engineering Handbook,* 2nd ed. McGraw-Hill, New York.
10. Tooley, F.V. 1974. The *Handbook of Glass Manufacture,* Vol. I and II. Ashlee Publishing Company, New York.
11. Tooley, F.V. 1988. *Handbook on Glass Manufacturing.* Ashlee Publishing Company, New York.
12. Varshneya, A.K. 1994. *Fundamentals of Inorganic Glasses.* Academic Press, New York.

Scott Smith
University of North Carolina

Robert E. Schafrik
National Research Council

Steven Y. Liang
Georgia Institute of Technology

Trevor D. Howes
University of Connecticut

John Webster
University of Connecticut

Ioan Marinescu
Kansas State University

K. P. Rajurkar
University of Nebraska-Lincoln

W. M. Wang
University of Nebraska-Lincoln

Talyan Altan
Ohio State University

Weiping Wang
General Electric R & D Center

Alan Ridilla
General Electric R & D Center

Matthew Buczek
General Electric R&D Center

Ira Pence
Georgia Institute of Technology

Toskiaki Yamaguchi
NSK Ltd.

Yashitsuga Taketomi
NSK Ltd.

Carl J. Kempf
NSK Ltd.

John Fildes
Northwestern University

Yoram Koren
University of Michigan

M. Tomizuka
University of California-Berkeley

Kam Lau
Automated Precision, Inc.

David C. Anderson
Purdue University

Tien-Chien Chang
Purdue University

Hank Grant
University of Oklahoma

(continued on next page)

13
Modern Manufacturing

Tien-I. Liu
California State University at Sacramento

J. M. A. Tanchoco
Purdue University

Andrew C. Lee
Purdue University

Su-Hsia Yang
Purdue University

Takeo Nakagawa
Fine Tech Corporation

H. E. Cook
University of Illinois at Urbana-Champaign

Chris Wang
IBM

Roop L. Mahajan
University of Colorado

13.1 Introduction

Scott Smith

The dictionary entry for the word "manufacture" indicates that it comes from the Latin words *manu factus*, which literally mean "hand made." Manufacturing is an activity that has been with humankind from the beginning, and which has been present throughout recorded history. Indeed, the one activity that clearly distinguishes early human beings in the archeological record is their creation of handmade artifacts, such as tools, weapons, artworks, and jewelry, from the raw materials found in nature.

It is interesting then to look at the title of this chapter and find the word "Modern," meaning "involving recent techniques, methods, or ideas," next to "Manufacturing," one of the oldest known human endeavors. From the earliest arrows (created of wood, flint, feathers, and sinew) to aircraft (created of aluminum, titanium, steel, nickel, and their alloys, polymers, ceramics, composites, cloth, and many other materials), human minds have struggled to efficiently create products that meet the demands of consumers and improve the quality of life. Surely all of that effort must have long since explored and exhausted the entire spectrum of possible manufacturing techniques and processes. Nothing could be further from the truth! In fact, even though many manufacturing processes are thousands of years old, the pace of process improvement, and the pace of development of new manufacturing processes, continues to rapidly increase. Many examples of the latest developments and technologies of manufacturing are presented here.

Wealth and prosperity in human society is created by mining and agricultural activities (the means by which natural resources are extracted from the environment), and by manufacturing (the means by which those natural resources are transformed into products that meet the needs and wants of consumers). In 2001, approximately 14% of the U.S. gross domestic product resulted from production of durable and nondurable goods. Approximately 71% of total U.S. exports were manufactured goods. The manufacturing sector accounted for 95% of industrial research and development spending, and manufacturing industries employed a workforce of over 16 million people in over 300,000 companies. In the modern economy, manufacturing success requires the development and application of manufacturing processes capable of economically producing high-quality products in an environmentally acceptable manner.

In the broadest sense, manufacturing refers to the entire range of activities that together transform those natural resources into products. The scope of activities and infrastructure required to manufacture even the simplest products in everyday life is staggering. The industrial capability of a nation and of the world is an intricately woven interaction of the best efforts of millions of creative individuals. The process begins with the recognition of a need or want, and the development of a design to fulfill that need or want. During the design phase, alternative solutions are considered and judgments are made concerning component geometry, tolerances, material choices, and so on. Then the resources required to produce the part are acquired. Among these are financial resources, capital equipment, skilled workers, raw materials, energy, and distribution means. Increasingly, the manufacturing function extends throughout the life cycle of the product, including its use, service, and recycling or safe disposal.

Product quality and reliability, responsiveness to customer demands, increased labor productivity, and efficient use of capital continue to be areas that manufacturing companies must emphasize to respond to the challenge of global competitiveness. Leading manufacturing organizations must be able to adapt management and labor practices to the changing competitive climate, must develop and produce virtually defect-free products quickly in response to opportunities, must employ smaller adaptive workforces, and must provide worldwide service and support. Manufacturing practices must be continually evaluated and improved. New materials, new processes, creative use of existing resources, and the pervasive deployment of information technology play an indispensable role maintaining a competitive edge in the face of lower-wage competition from developing economies. A skilled, educated workforce can adapt and improve, and it is a critical component of a state-of-the-art manufacturing capability. Training and education are essential, not only as preparation before the start of a career, but continually throughout an entire career.

The practice of manufacturing has artisan-craftsman roots. Many manufacturing trades were learned in the past by trial and error or apprenticeship. This process is no longer sufficient. Modern manufacturing is rapidly evolving from an art into a science. Scientific and technical understanding of the individual manufacturing processes and of the manufacturing enterprise as a whole is needed to most effectively apply existing capabilities, quickly incorporate new developments, and identify the best available solutions to solve problems.

13.2 Unit Manufacturing and Assembly Processes

Robert E. Schafrik

There are a tremendous number of manufacturing processes able to impart physical shape and structure to a workpiece. However, if these processes are broken down into their basic elements and then examined for commonality, only a few fundamental processes remain. These are the building blocks, or unit processes, from which even the most complicated manufacturing system is constructed. This section describes these unit processes in sufficient detail that a technically trained person, such as a design engineer serving as a member of an integrated product and process design team consisting of members from other specialties, could become generally knowledgeable regarding the essential aspects of manufacturing processes. Also, the information presented in this section will aid such an individual in pursuing further information from more specialized manufacturing handbooks, publications, and equipment/tool catalogs.

Considering the effect that a manufacturing process has on workpiece configuration and structure, the following five general types of unit manufacturing process can be identified (Altan et al. 1983; NRC 1995):

Material removal processes — Geometry is generated by changing the mass of the incoming material in a controlled and well-defined manner, e.g., milling, turning, electrodischarge machining, and polishing.

Deformation processes — The shape of a solid workpiece is altered by plastic deformation without changing its mass or composition, e.g., rolling, forging, and stamping.

Primary shaping processes — A well-defined geometry is established by bulk forming material that initially had no shape, e.g., casting, injection molding, die casting, and consolidation of powders.

Structure-change processes — The microstructure, properties, or appearance of the workpiece are altered without changing the original shape of the workpiece, e.g., heat treatment and surface hardening.

Joining and assembly processes — Smaller objects are put together to achieve a desired geometry, structure, and/or property. There are two general types: (1) consolidation processes that use mechanical, chemical, or thermal energy to bond the objects (e.g., welding and diffusion bonding), and (2) strictly mechanical joining (e.g., riveting, shrink fitting, and conventional assembly).

Each component being manufactured has a well-defined geometry and a set of requirements that it must meet. These typically include

- Shape and size
- Bill-of-material
- Accuracy and tolerances
- Appearance and surface finish
- Physical (including mechanical) properties
- Production quantity
- Cost of manufacture

In order to satisfy these criteria, more than one solution is usually possible and trade-off analyses should be conducted to compare the different approaches that could be used to produce a particular part.

Every unit process must be controlled or directed in some way. The need for improved accuracy, speed, and manufacturing productivity has spurred the incorporation of automation into unit processes regarding both the translation of part design details into machine instructions, and the operation of the unit process itself and as a subsystem of the overall production environment. The section of this chapter on computer-aided design/computer-aided manufacturing (CAD/CAM) discusses the technology involved in creating and storing CAD files and their use in CAM. The expectations of precision are continuing to change, as indicated in Figure 13.2.1. This drive for ever-tighter tolerances is helping spur interest in continual improvements in design and manufacturing processes.

Modern machine tool controls are emphasizing two areas: adaptive control and communication. For *adaptive control* the controller must adapt its control gains so that the overall system remains at or near the optimal condition in spite of varying process dynamics. Expanded *communication* links the data collected by a unit process controller to other segments of the manufacturing operation. Data regarding production time and quantity of parts produced can be stored in an accessible database for use by inventory control and quality monitoring. This same database can then be used by production schedulers to avoid problems and costs associated with redundant databases.

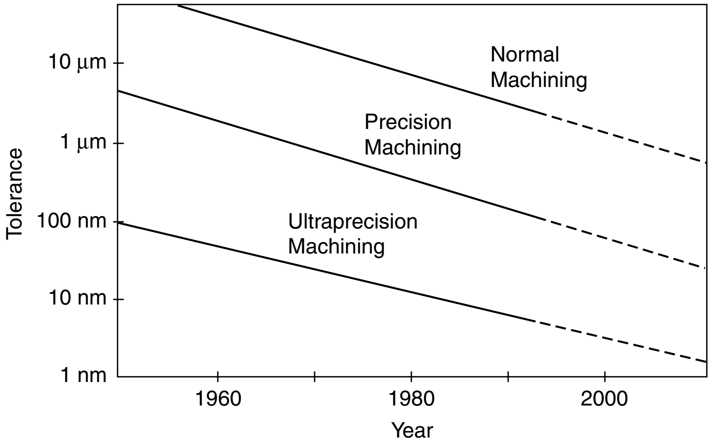

FIGURE 13.2.1 Precision machining domains. (From NRC, *Unit Manufacturing Processes*, National Academy Press, Washington, DC, 1995, 169. With permission.)

At the factory level, machining operations employing two or more numerically controlled (NC) machine tools may use a separate mainframe computer that controls several machine tools or an entire shop. The system is often referred to as *distributed numerical control* (DNC).

Today many factories are implementing *flexible manufacturing systems* (FMS), an evolution of DNC. An FMS consists of several NC unit processes (not necessarily only machine tools) that are interconnected by an automated materials-handling system and that employ industrial robots for a variety of tasks requiring flexibility, such as loading/unloading the unit process queues. A single computer serves as master controller for the system, and each process may utilize a computer to direct the lower-order tasks. Advantages of FMS include

- A wide range of parts can be produced with a high degree of automation.
- Overall production lead times are shortened and inventory levels reduced.
- Productivity of production employees is increased.
- Production cost is reduced.
- The system can easily adapt to changes in products and production levels.

In the following discussion, a number of unit processes are discussed, organized by the effect that they have on workpiece configuration and structure. Many of the examples deal with processing of metals, since that is the most likely material that users of this handbook will encounter. However, other materials are readily processed with the unit processes described in this chapter, albeit with suitable modifications or variations.

Mechanical assembly and material handling are also discussed in this section. On average, mechanical assembly accounts for half of the manufacturing time, and processes have been developed to improve the automation and flexibility of this very difficult task. Material handling provides the integrating link between the different processes — material-handling systems ensure that the required material arrives at the proper place at the right time for the various unit processes and assembly operations.

The section ends with a case study that demonstrates how understanding of the different unit processes can be used to make engineering decisions.

- Material removal (machining) processes
  - Traditional machining
    - Drill and reaming
    - Turning and boring
    - Planing and shaping
    - Milling
    - Broaching
    - Grinding
  - Nontraditional machining
    - Electrical discharge machining
    - Electrical chemical machining
    - Laser beam machining
    - Jet machining (water and abrasive)
    - Ultrasonic machining
- Phase-change processes
  - Green sand casting
  - Investment casting
- Structure-change processes
  - Normalizing steel
  - Laser surface hardening
- Deformation processes
  - Die forging
  - Press-brake forming

- Consolidation processes
  - Polymer composite consolidation
  - Shielded metal-arc welding
  - Mechanical assembly
- Material handling
  - Case study: Manufacturing and inspection of precision recirculating ballscrews

References

Altan, T., Oh, S.I., and Gegel, H. 1983. *Metal Forming — Fundamentals and Applications*, ASM International, Metals Park, OH.

ASM Handbook Series, 10th ed., 1996. ASM International, Metals Park, OH.

Bakerjian, R., ed. 1992. *Design for Manufacturability*, vol. VI, *Tool and Manufacturing Engineers Handbook*, 4th ed., Society of Manufacturing Engineers, Dearborn, MI.

DeVries, W.R. 1991. *Analysis of Material Removal Processes*, Springer-Verlag, New York.

Kalpakjian, S. 1992. *Manufacturing Engineering and Technology*, Addison-Wesley, Reading, MA.

National Research Council (NRC) 1995. *Unit Manufacturing Processes — Issues and Opportunities in Research*, National Academy Press, Washington, DC.

Material Removal Processes

These processes, also known as machining, remove material by mechanical, electrical, laser, or chemical means to generate the desired shape and/or surface characteristic. Workpiece materials span the spectrum of metals, ceramics, polymers, and composites, but metals, and particularly iron and steel alloys, are by far the most common. Machining can also improve the tolerances and finish of workpieces previously shaped by other processes, such as forging. Machining is an essential element of many manufacturing systems (ASM 1989b; Bakerjian 1992).

Machining is important in manufacturing because

- It is precise. Machining is capable of creating geometric configurations, tolerances, and surface finishes that are often unobtainable by other methods. For example, generally achievable surface roughness for sand casting is 400 to 800 μin. (10 to 20 μm), for forging 200 to 400 μin. (5 to 10 μm), and for die casting 80 to 200 μin. (2 to 5 μm). Ultraprecision machining (i.e., super-finishing, lapping, diamond turning) can produce a surface finish of 0.4 μin (0.01 μm) or better. The achievable dimensional accuracy in casting is 1 to 3% (ratio of tolerance to dimension) depending on the thermal expansion coefficient, and in metal forming it is 0.05 to 0.30% depending on the elastic stiffness, but in machining the achievable tolerance can be 0.001%.
- It is flexible. The shape of the final machined product is programmed and therefore many different parts can be made on the same machine tool and just about any arbitrary shape can be machined. In machining, the product contour is created by the path, rather than the shape, of the cutter. By contrast, casting, molding, and forming processes require dedicated tools for each product geometry, thus restricting their flexibility.
- It can be economical. Small lots and large quantities of parts can be relatively inexpensively produced if matched to the proper machining process.

The dominating physical mechanism at the tool/workpiece interface in conventional machining is either plastic deformation or controlled fracture of the workpiece. Mechanical forces are imposed on the workpiece by the application of a tool with sharp edges and higher hardness than the workpiece. However, many new materials are either harder than conventional cutting tools or cannot withstand the high cutting forces involved in traditional machining. Nontraditional manufacturing (NTM) processes can produce precision components of these hard and high-strength materials. NTM processes remove material through thermal, chemical, electrochemical, and mechanical (with high-impact velocity) interactions.

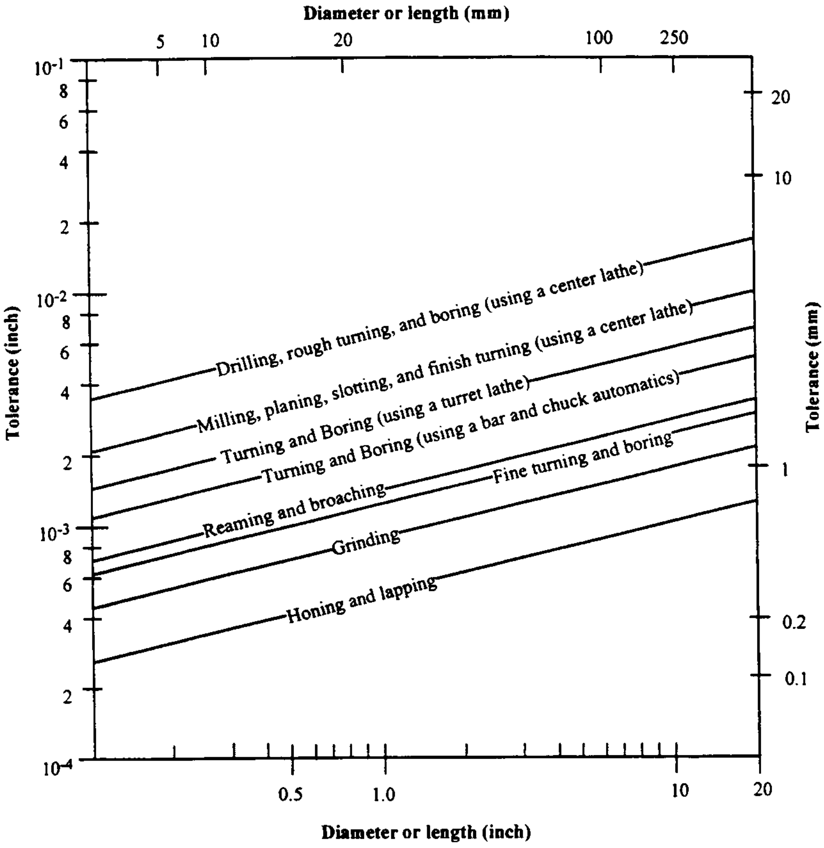

FIGURE 13.2.2 Tolerance vs. dimensional data for machining processes. (From NRC, *Unit Manufacturing Processes*, National Academy Press, Washington, DC, 1995, 168. With permission.)

Machinability is defined in terms of total tool life, power requirements, and resultant workpiece surface finish. To date, no fundamental relationship incorporates these three factors and thus machinability must be empirically determined by testing.

Machine tools can be grouped into two broad categories:

- Those that generate surfaces of rotation
- Those that generate flat or contoured surfaces by linear motion

Selection of equipment and machining procedures depends largely on these considerations:

- Size of workpiece
- Configuration of workpiece
- Equipment capacity (speed, feed, horsepower range)
- Dimensional accuracy
- Number of operations
- Required surface condition and product quality

For example, Figure 13.2.2 graphically indicates the various tolerance levels that can be typically achieved for common machining unit processes as a function of the size of the workpiece. Such data can help in identifying candidate unit processes that are capable of meeting product requirements.

Traditional Machining

Steven Y. Liang

Traditional machining processes remove material from a workpiece through plastic deformation. The process requires direct mechanical contact between the tool and workpiece, and it uses relative motion between the tool and the workpiece to develop the shear forces necessary to form machining chips. The tool must be harder than the workpiece to avoid excessive tool wear. The unit processes described here are a representative sample of the types most likely to be encountered. The reference list at the end of the section should be consulted for more detailed information on the unit processes discussed below, plus those that are not included here.

Process Kinematics in Traditional Machining. In all traditional machining processes, the surface is created by providing suitable relative motion between the cutting tool and the workpiece. There are two basic components of relative motion: primary motion and feed motion. Primary motion is the main motion provided by a machine tool to cause relative motion between the tool and workpiece. The feed motion, or the secondary motion, is a motion that, when added to the primary motion, leads to a repeated or continuous chip removal. It usually absorbs a small proportion of the total power required to perform a machining operation. The two motion components often take place simultaneously in orthogonal directions.

The functional definitions of turning, milling, drilling, and grinding are not distinctively different, but machining process specialists have developed terminology peculiar to a given combination of functions or machine configurations. Commonly used metal-cutting machine tools, however, can be divided into three groups, depending on the basic type of cutter used: single-point tools, multipoint tools, or abrasive grits.

Basic Machine Tool Components. Advances in machine-tool design and fabrication philosophy are quickly eliminating the differences between machine types. Fifty years ago, most machine tools performed a single function such as drilling or turning, and operated strictly stand-alone. The addition of automatic turrets, tool-changers, and computerized numerical control (CNC) systems allowed lathes to become *turning centers* and milling machines to become *machining centers*. These multiprocess centers can perform a range of standard machining functions: turning, milling, boring, drilling, and grinding (Green 1992).

The machine tool *frame* supports all the active and passive components of the tool: spindles, table, and controls. Factors governing the choice of frame materials are resistance to deformation (hardness), resistance to impact and fracture (toughness), limited expansion under heat (coefficient of thermal expansion), high absorption of vibrations (damping), resistance to shop floor environment (corrosion resistance), and low cost.

Guide ways carry the workpiece table or spindles. Each type of way consists of a *slide* moving along a track in the frame. The slide carries the workpiece table or a spindle. The oldest and simplest way is the *box way*. As a result of its large contact area, it has high stiffness, good damping characteristics, and high resistance to cutting forces and shock loads. Box slides can experience stick-slip motion as a result of the difference between dynamic and static friction coefficients in the ways. This condition introduces positioning and feed motion errors. A *linear way* also consists of a rail and a slide, but it uses a rolling-element bearing, eliminating stick-slip. Linear ways are lighter in weight and operate with less friction, so they can be positioned faster with less energy. However, they are less robust because of the limited surface contact area.

Slides are moved by hydraulics, rack-and-pinion systems, or screws. *Hydraulic pistons* are the least costly, most powerful, most difficult to maintain, and the least accurate option. Heat buildup often significantly reduces accuracy in these systems. Motor-driven *rack-and-pinion* actuators are easy to maintain and are used for large motion ranges, but they are not very accurate and require a lot of power to operate. Motor-driven screws are the most common actuation method. The screws can either be leadscrews or ballscrews, with the former being less expensive and the latter more accurate. The *recirculating ballscrew* has very tight backlash; thus, it is ideal for CNC machine tools since their tool trajectories are essentially continuous. A disadvantage of the ball-screw systems is the effective stiffness due to limited contact area between the balls and the thread. (*Note:* a case study at the end of this section discusses the manufacture of precision ballscrews.)

Electric motors are the prime movers for most machine tool functions. They are made in a variety of types to serve three general machine tool needs: spindle power, slide drives, and auxiliary power. Most of them use three-phase AC power supplied at 220 or 440 V. The design challenge with machine tools and motors has been achieving high torque throughout a range of speed settings. In recent years, the operational speed of the spindle has risen significantly. For example, conventional speeds 5 years ago were approximately 1600 rpm. Today, electric motors can turn at 12,000 rpm and higher. Higher speeds cause vibration, which makes use of a mechanical transmission difficult. By virtue of improvement in motor design and control technology, it is now possible to quickly adjust motor speed and torque. Spindle motors are rated by horsepower, which generally ranges from 5 to 150 hp (3.7 to 112 kW) with the average approximately 50 hp (37 kW). Positioning motors are usually designated by torque, which generally ranges from 0.5 to 85 lb-ft (0.2 to 115 Nm).

The *spindle* delivers torque to the cutting tool, so its precision is essential to machine tool operation. The key factors influencing precision are bearing type and placement, lubrication, and cooling.

Cutting-Tool Materials. The selection of cutting tool materials is one of the key factors in determining the effectiveness of the machining process (ASM 1989b). During cutting, the tool usually experiences high temperatures, high stresses, rubbing friction, sudden impact, and vibrations. Therefore, the two important issues in the selection of cutting-tool materials are hardness and toughness. *Hardness* is defined as the endurance to plastic deformation and wear; hardness at elevated temperatures is especially important. *Toughness* is a measure of resistance to impact and vibrations, which occur frequently in interrupted cutting operations such as milling and boring. Hardness and toughness do not generally increase together, and thus the selection of cutting tool often involves a trade-off between these two characteristics.

Cutting-tool materials are continuously being improved. Carbon steels of 0.9 to 1.3% carbon and tool steels with alloying elements such as molybdenum and chromium lose hardness at temperatures above 400°F (200°C) and have largely been replaced by *high-speed steels* (HSS). HSS typically contains 18% tungsten or 8% molybdenum and smaller amounts of cobalt and chromium. HSSs retain hardness up to 1100°F (600°C) and can operate at approximately double the cutting speed with equal life. Both tool steels and HSS are tough and resistive to fracture; therefore, they are ideal for processes involving interrupted engagements and machine tools with low stiffness that are subject to vibration and chatter.

Powder metallurgy (P/M) high-speed tool steels are a recent improvement over the conventionally cast HSS. Powder metallurgy processing produces a very fine microstructure that has a uniform distribution of hard particles. These steels are tougher and have better cutting performance than HSS. Milling cutters are becoming a significant application for these cutting-tool materials.

Cast cobalt alloys, popularly known as Stellite tools, were introduced in 1915. These alloys have 38 to 53% cobalt, 30 to 33% chromium, and 10 to 20% tungsten. Though comparable in room temperature hardness to HSS tools, cast cobalt alloy tools retain their hardness to a much higher temperature, and they can be used at 25% higher cutting speeds than HSS tools.

Cemented carbides offered a four- or fivefold increase in cutting speeds over conventional HSS. They are much harder, but more brittle and less tough. The first widely used cemented carbide was tungsten carbide (WC) cemented in a ductile cobalt binder. Most carbide tools in use now are a variation of the basic WC-Co material. For instance, WC may be present as single crystals or a solid solution mixture of WC-TiC or WC-TiC-TaC. These solid solution mixtures have a greater chemical stability in the cutting of steel. In general, cemented carbides are good for continuous roughing on rigid machines, but should avoid shallow cuts, interrupted cuts, and less rigid machines because of likely chipping.

A thin layer of TiC, TiN, or Al_2O_3 can be applied to HSS or carbide substrate to improve resistance to abrasion, temperature, friction, and chemical attacks. The *coated tools* were introduced in the early

1970s and have gained wide acceptance since. Coated tools have two or three times the wear resistance of the best uncoated tools and offer a 50 to 100% increase in speed for equivalent tool life.

Ceramic tools used for machining are based on alumina (Al_2O_3) or silicon nitride (Si_3N_4). They can be used for high-speed finishing operations and for machining of difficult-to-machine advanced materials, such as superalloys (Komanduri and Samanta 1989). The alumina-based materials contain particles of titanium carbide, zirconia, or silicon carbide whiskers to improve hardness and/or toughness. These materials are a major improvement over the older ceramic tools. Silicon nitride–based materials have excellent high-temperature mechanical properties and resistance to oxidation. These materials also have high thermal shock resistance, and thus can be used with cutting fluids to produce better surface finishes than the alumina tools.

These tools can be operated at two to three times the cutting speeds of tungsten carbide, usually require no coolant, and have about the same tool life at higher speeds as tungsten carbide does at lower speeds. However, ceramics lack toughness; therefore, interrupted cuts and intermittent application of coolants can lead to premature tool failure due to poor mechanical and thermal shock resistance.

Cermets are titanium carbide (TiC) or titanium carbonitride particles embedded in a nickel or nickel/molybdenum binder. These materials, produced by the powder metallurgy process, can be considered as a type of cemented carbide. They are somewhat more wear resistant, and thus can be used for higher cutting speeds. They also can be used for machining of ferrous materials without requiring a protective coating.

Cubic boron nitride (CBN) is the hardest material at present available except for diamond. Its cost is somewhat higher than either carbide or ceramic tools, but it can cut about five times as fast as carbide and can hold hardness up to 200°C. It is chemically very stable and can be used to machine ferrous materials.

Industrial *diamonds* are now available in the form of polycrystalline compacts for the machining of metals and plastics with greatly reduced cutting force, high hardness, good thermal conductivity, small cutting-edge radius, and low friction. Recently, diamond-coated tools are becoming available that promise longer-life cutting edges. Shortcomings with diamond tools are brittleness, cost, and the tendency to interact chemically with workpiece materials that form carbides, such as carbon steel, titanium, and nickel.

Wear of Cutting-Tool Materials. Cutting tools are subjected to large forces under conditions of high temperature and stress. There are many mechanisms that cause wear:

- Adhesion: The tool and chip can weld together; wear occurs as the welded joint fractures and removes part of the tool material, such as along a tool cutting edge.
- Abrasion: Small particles on the wear surface can be deformed and broken away by mechanical action due to the high localized contact stresses; these particles then abrade the cutting tool. Typically, this is the most common wear mode.
- Brittle fracture: Catastrophic failure of the tool can occur if the tool is overloaded by an excessive depth of cut and/or feed rate.
- Diffusion: Solid-state diffusion can occur between the tool and the workpiece at high temperatures and contact pressures, typically at an area on the tool tip that corresponds to the location of maximum temperature, e.g., cemented carbide tools used to machine steel. High-speed machining results in higher chip temperatures, making this an increasingly important wear mode.
- Edge chipping.
- Electrochemical: In the presence of a cutting fluid, an electrochemical reaction can occur between the tool and the workpiece, resulting in the loss of a small amount of tool material in every chip.
- Fatigue.
- Plastic deformation.

Single-Point Cutting-Tool Geometry. Figure 13.2.3 depicts the location of various angles of interest on a single-point cutting tool. The most significant angle is the cutting-edge angle, which directly affects the

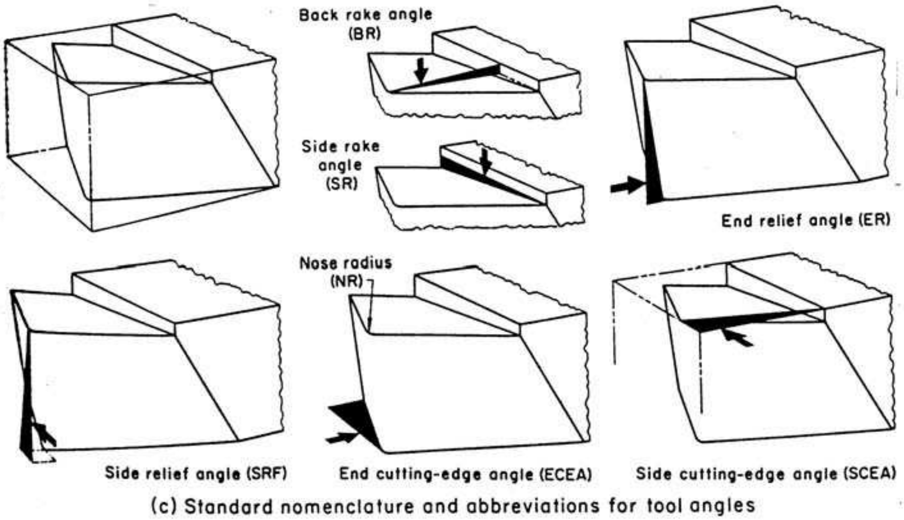

FIGURE 13.2.3 Standard nomenclature for single-point cutting-tool angles. (From *ASM Handbook*, *Machining*, vol. 16, 9th ed., ASM International, Metals Park, OH, 1989, 141. With permission.)

shear angle in the chip formation process, and therefore greatly influences tool force, power requirements, and temperature of the tool/workpiece interface (ASM 1989a). The larger the positive value of the cutting-edge angle, the lower the force, but the greater the load on the cutting tool. For machining higher-strength materials, negative rake angles are used. *Back rake* usually controls the direction of chip flow and is of less importance than the side rake. Zero back rake makes the tool spiral more tightly, whereas a positive back rake stretches the spiral into a longer helix. *Side rake* angle controls the thickness of the tool behind the cutting edge. A thick tool associated with a small rake angle provides maximum strength, but the small angle produces higher cutting forces than a larger angle; the large angle requires less motor horsepower.

The *end relief angle* provides clearance between the tool and the finished surface of the work. Wear reduces the angle. If the angle is too small, the tool rubs on the surface of the workpiece and mars the finish. If the angle is too large, the tool may dig into the workpiece and chatter, or show weakness and fail through chipping. The *side relief angle* provides clearance between the cut surface of the work and the flank of the tool. Tool wear reduces the effective portion of the angle closest to the workpiece. If this angle is too small, the cutter rubs and heats. If the angle is too large, the cutting edge is weak and the tool may dig into the workpiece. The *end cutting-edge angle* provides clearance between the cutter and the finished surface of the work. An angle too close to zero may cause chatter with heavy feeds, but for a smooth finish the angle on light finishing cuts should be small.

Machinability. Optimum speed and feed for machining depend on workpiece material, tool material, characteristics of the cut, cutting-tool configuration, rigidity of setup, tolerance, and cutting fluid. Consequently, it is not possible to recommend universally applicable speeds and feeds.

Drilling and Reaming. Drilling is the most widely used process for making circular holes of moderate accuracy. It is often a preliminary step to other processes such as tapping, boring, or reaming. *Reaming* is used to improve the accuracy of a hole while increasing its diameter. Holes to be reamed are drilled undersize.

Drills are classified by the material from which they are made, method of manufacture, length, shape, number and type of helix or flute, shank, point characteristics, and size series (Table 13.2.1). Selection of drill depends on several factors (ASM 1989b):

TABLE 13.2.1 Common Drill Types

Drill Type	Description	Application
Core	Has large clearance for chips	Roughing cuts; enlarging holes
General-purpose (jobber)	Conventional two-flute design; right-hand (standard) or left-hand helix. Available with flute modification to break up long chips	General-purpose use, wide range of sizes
Gun	Drill body has a tube for cutting fluid; drill has two cutting edges on one side and counter-balancing wear pads on the other side	Drill high-production quantities of holes without a subsequent finishing operation
High helix	Wide flutes and narrow lands to provide a large bearing surface	Soft materials, deep holes, high feed rates
Low helix	Deep flutes facilitate chip removal	Soft materials, shallow holes
Oil hole	Has holes through the drill body for pressurized fluid	Hard materials, deep holes, high feed rate
Screw-machine	Short length, short flutes, extremely rigid	Hard materials; nonflat surfaces
Step	Two or more drill diameters along the drill axis	Produce multiple-diameter holes, such as for drilling/countersinking
Straight flute	Flutes parallel to the drill axis minimize torquing of the workpiece	Soft materials; thin sheets

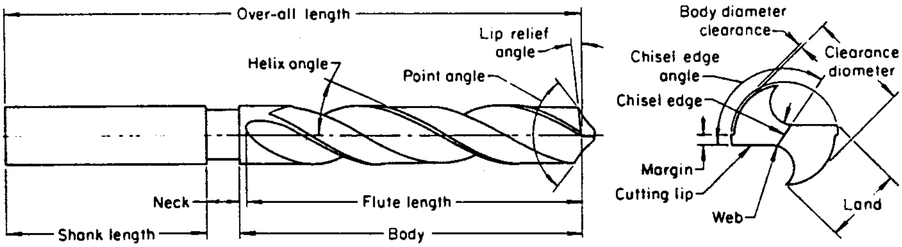

FIGURE 13.2.4 Design features of a typical straight-shank twist drill. (From *ASM Handbook*, *Machining*, vol. 16, 9th ed., ASM International, Metals Park, OH, 1989, 218. With permission.)

- Hardness and composition of the workpiece, with hardness being more important
- Rigidity of the tooling
- Hole dimensions
- Type of drilling machine
- Drill application — originating or enlarging holes
- Tolerances
- Cost

The most widely used drill is the general-purpose twist drill, which has many variations. The flutes on a twist drill are helical and are not designed for cutting but for removing chips from the hole. Typical twist drills are shown in Figure 13.2.4.

Machining forces during *reaming* operations are less than those of drilling, and hence reamers require less toughness than drills and often are more fragile. The reaming operation requires maximum rigidity in the machine, reamer, and workpiece.

Most *reamers* have two or more flutes, either parallel to the tool axis or in a helix, which provide teeth for cutting and grooves for chip removal. The selection of the number of flutes is critical: a reamer with too many flutes may become clogged with chips, while a reamer with too few flutes is likely to chatter (Table 13.2.2).

The optimal speed and feed for drilling depend on workpiece material, tool material, depth of hole, design of drill, rigidity of setup, tolerance, and cutting fluid. For *reaming* operations, hardness of the workpiece has the greatest effect on machinability. Other significant factors include hole diameter, hole

TABLE 13.2.2 Common Reamer Types

Reamer Type	Description	Application
Adjustable	Tool holder allows adjustment of the reamer diameter to compensate for tool wear, etc.	High-rate production
End-cutting	Cutting edges are at right angles to the tool axis	Finish blind holes, correct deviations in through-holes
Floating blade	Replaceable and adjustable cutting edges to maintain tight tolerances	High-speed production (workpiece rotated, tool stationary)
Gun	Hollow shank with a cutting edge (e.g., carbide) fastened to the end and cutting fluid fed through the stem	High-speed production (workpiece rotated, tool stationary)
Shell	Two-piece assemblies, mounted on arbors, can be adjusted to compensate for wear	Used for finishing operations (workpiece rotated, tool stationary)
Spiral flute	Flutes in a helix pattern, otherwise same as straight-flute reamer	Difficult to ream materials, and holes with irregularities
Straight flute	Flutes parallel to the tool axis, typically pointed with a 45° chamfer	General-purpose, solid reamer

configuration (e.g., hole having keyways or other irregularities), hole length, amount of stack removed, type of fixturing, accuracy and finish requirements, size of production run, and cost. Most reamers are more easily damaged than drills; therefore, the practice is to ream a hole at no more than two thirds of the speed at which it was drilled.

Most drilled holes are 1/8 to 1 in. (3.2 to 40 mm) in diameter. However, drills are available for holes as small as 0.001 in. (0.03 mm) (microdrilling), and special drills are available as large as 6 in. (150 mm) in diameter. The range of length-to-diameter (L/D) of holes that can be successfully drilled depends on the method of driving the drill and the straightness requirements. In the simplest form of drilling in which a rotating twist drill is fed into a fixed workpiece, best results are obtained when L/D is <3. But by using special tools, equipment, and techniques, straight holes can be drilled with L/D = 8 or somewhat greater. Nonconventional machining processes can also generate high-aspect-ratio holes in a wide variety of materials.

Reaming and boring are related operations. Hole diameter and length, amount of material to be removed, and required tolerance all influence which process would be most efficient for a given application (ASM 1989b). Most holes reamed are within the size range of 1/8 to 1 inch (3.2 to 40 mm), although larger and smaller holes have been successfully reamed. For most applications with standard reamers, the length of a hole that can be reamed to required accuracy ranges from slightly longer to much shorter than the cutting edges of the reamer, but there are many exceptions to this general rule of thumb. Tolerances of 0.001 to 0.003 in. (0.03 to 0.08 mm) with respect to the diameter are readily achievable in production reaming operations. Surface finish for annealed steels can be held within the range of 100 to 125 µin. (2.50 to 3.20 µm), but a surface as smooth as 40 µin. (1 µm) can be obtained under appropriate processing conditions (ASM 1989b).

Turning and Boring. Turning produces external cylindrical surfaces by removing material from a rotating workpiece, usually with a single-point cutting tool in a lathe. *Boring* is this same process applied for enlarging or finishing internal surfaces of revolution.

The basic equipment for turning is an *engine lathe* that consists of a bed, a headstock, a carriage slide, a cross slide, a tool holder mounted on the cross slide, and a source of power for rotating the workpiece (Table 13.2.3). Engine lathes are often modified to perform additional types of machining operations through the use of attachments. Most turning machines can also perform boring operations, but boring machines may not be able to perform turning operations. Sizes of lathes range from fractional horsepower to greater than 200 hp.

Machines used for boring are noted for their rigidity, adaptability, and ability to maintain a high degree of accuracy (Table 13.2.4). For extremely large workpieces, weighing thousands of pounds, the boring cutting tool is rotated and the workpiece is fixed.

TABLE 13.2.3 Typical Lathes Used for Turning

Lathe	Description	Applications
Bench lathe	An engine lathe that can be placed on a workbench	Small workpieces and prototype parts
Engine lathe	Has a leadscrew that moves the slide uniformly along the bed; available with chucking or centering headstock	Chucking type allows centering and clamping for rotation, e.g., holding castings or forgings Centering type secures workpiece between pointed centers, e.g., for turning long workpieces, such as shafts
Gap-frame lathe	Modified engine lathe for turning larger diameter parts	Workpieces requiring off-center mounting or irregular protuberances
Numerically controlled lathe	Uses a computer program to control the lathe to generate the desired shape	Produces consistent parts in a CAD/CAM environment
Tracer-controlled lathe	A duplicating lathe that uses a stylus moving over a template to control the cutting tool	Manufacture of prototype parts and low-rate production

TABLE 13.2.4 Typical Machines Used for Boring

Boring Machine	Description	Applications
Bar (screw) machine	Modified turret lathe to handle bars and tubes	Parts made from bars or tubes
Engine lathe	Versatile machine; essentially same machine as used for turning	Bores one hole at a time in a single part; limitations regarding workpiece size and configuration
Horizontal boring mill	Workpiece remains stationary and tool rotates	Wide variety of parts; cost-effective for a relatively high production volume
Precision boring machine	Vertical and horizontal models	Parts requiring extreme tolerances
Special-purpose machines	Boring machine modified for specialized application	Single-purpose applications with high production rates
Turret lathe	Has rotating turret on a lathe, tooled for multiple machining operations	More versatile than engine lathe; supports high production rates
Vertical boring mill	Same basic components as a lathe	Very large, heavy, or eccentric workpieces
Vertical turret lathe	Same features as vertical boring mill; may also have a second vertical head	Flexible machine, useful in CAD/CAM environment; simultaneous multiple machining operations possible

Machine Tool and Machining Parameters. In turning and boring operations, a single-point tool is traversed longitudinally along the axisymmetric workpiece axis parallel to the spindle. A tangential force is generated when the cutting tool engages the rotating work. This force is generally independent of the cutting speed and directly proportional to the depth of cut for a particular material, tool shape (particularly side rake angle), and feed rate. That force, when multiplied by the surface speed of the workpiece, estimates the net horsepower required to remove material. The extent to which workpiece material affects required machining power is illustrated in Figure 13.2.5. Moving the tool longitudinally requires much less power (ASM 1989b).

To minimize the number of cuts required, the depth of cut should be as great as possible, which is limited by the strength of the part and the fixturing, and the power output of the machine tool. The feed rate is a function of the finish desired and the strength and rigidity of the part and machine tool.

Components that range in size from those used in watches up to large steel propeller shafts more than 80 ft (24 m) long are regularly turned. Aluminum parts over 10 ft (3 m) in diameter have been turned. In practice, the weight of the workpiece per unit of volume determines the size of the workpiece that is practical to turn. Large, heavy parts can be turned in a vertical boring machine. Irregular-shaped parts,

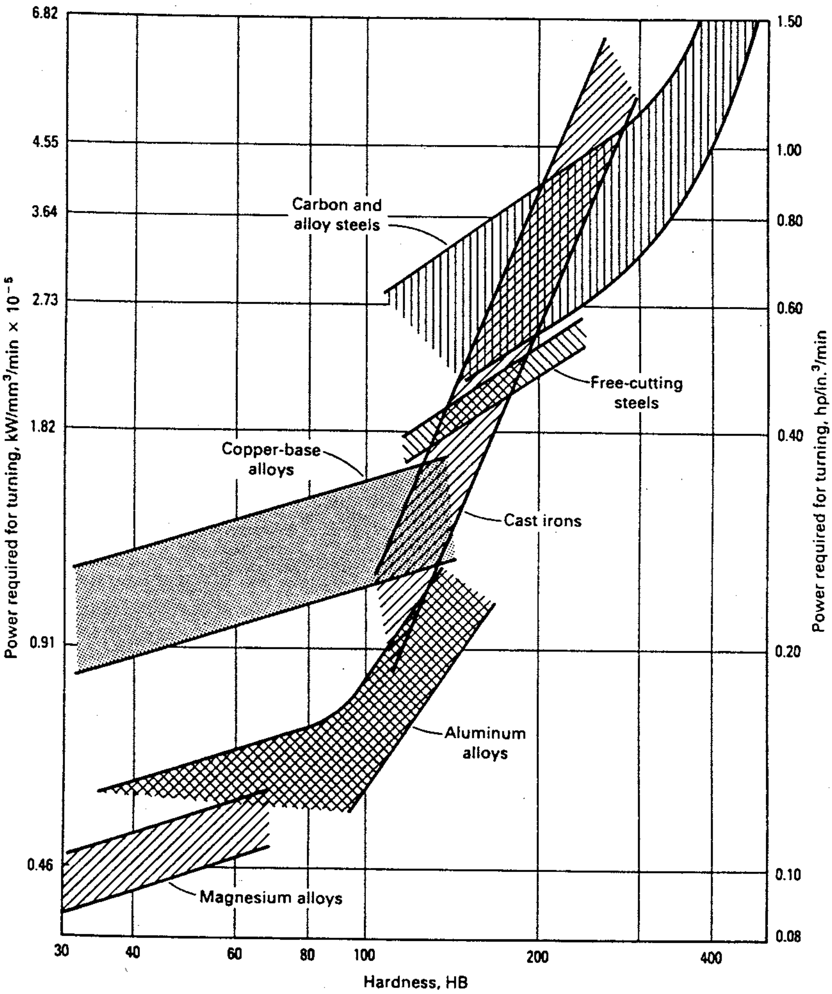

FIGURE 13.2.5 Effect of workpiece composition and hardness on power required for turning. (From *ASM Handbook*, *Machining*, vol. 16, 9th ed., ASM International, Metals Park, OH, 1989, 136. With permission.)

such as crankshafts, may require the use of counter-weighting to achieve dynamic balance for vibration-free turning.

For both turning and boring, the rotation speed, feed, and depth of cut determine the rate of material removal and resulting surface quality. Feed rate for most applications falls between 0.005 and 0.020 in./rev (0.13 and 0.51 mm/rev). Finishing cuts have a significantly lower feed rate (e.g., 0.001 in./rev, 0.03 mm/rev), and roughing cuts are made at a significantly higher feed rate (e.g., 0.25 in./rev, 6.35 mm/rev). Boring is not limited by the L/D ratio of a hole — this ratio can be as great as 50 if the tool bar and workpiece are adequately supported.

There are many potential sources of tolerance error in turning and boring operations. The more common errors are summarized in Table 13.2.5 and Table 13.2.6.

Planing and Shaping. Planing is a widely used process for producing flat, straight surfaces on large workpieces. A variety of contour operations and slots can be generated by use of special attachments. It is often possible to machine a few parts quicker by planing than by any other method. *Shaping* is a process for machining flat and contour surfaces, including grooves and slots.

TABLE 13.2.5 Factors Affecting Dimensional Accuracy in Turning

Quantity	Basic Cause of Inaccuracy	Corrective Actions
Diametrical roundness	Lathe spindle runout	Preload angular bearings to eliminate side and end movement
Diameter variation (taper)	Parallelism of spindle to longitudinal travel	Establish true parallelism between the axis of rotation of the workpiece and the longitudinal travel of the cutting tool
Face flatness	Lack of true normality of cross slide to axis of rotation	Precision align cross slide to axis of rotation
Length dimensions parallel to the axis of rotation	Improper positioning of longitudinal slide	Adjust positioning of longitudinal slide
Diameter accuracy	Inadequate gauging	Employ proper measurement technique

TABLE 13.2.6 Factors Affecting Dimensional Accuracy in Boring

Quantity	Basic Cause of Inaccuracy	Corrective Actions
Diameter accuracy	Inadequate gauging, or heat generated by the machining action	Employ proper measurement techniques; use cutting fluid to control temperature
Taper of the cylindrical bore	Deflection of the boring bar	Reduce the boring bar unsupported length; use a higher-stiffness material for the boring bar
Roundness, as determined by the variation in radius about a fixed axis	Finish cut is not concentric with the previous cut; or out-of-balance workpiece or holder	Begin with a semifinish cut, followed by a finish cut; carefully balance the initial setup
Concentricity of one surface with another	Too great a clamping force on the workpiece	Redesign clamping fixture, or use a precision boring machine
Squareness and parallelism of holes in relation to other features of the work	Dimensional changes in machine components	Maintain constant ambient temperature; maintain cutting fluid at constant temperature; or stabilize oil temperature

Planers develop cutting action from straight-line reciprocating motion between one or more single-point tools and the workpiece; the work is reciprocated longitudinally while the tools are fed sideways into the work. Planer tables are reciprocated by either mechanical or hydraulic drives, with mechanical drives predominating.

Shapers use a single-point tool that is supported by a ram, which reciprocates the tool in a linear motion against the workpiece. The workpiece rests on a flat bed and the cutting tool is driven toward it in small increments by ram strokes. Shapers are available with mechanical and hydraulic drives, with mechanical drives predominating.

Planing and shaping are rugged machining operations during which the workpiece is subjected to significant cutting forces. These operations require high clamping forces to secure the workpiece to the machine bed.

In general, it is advisable to plane steel with as heavy a feed and as high a speed as possible to promote good chip-formation conditions so that chip breakers are not needed. Carbide cutters allow cutting speed to be increased from 225 to 300 surface feet per minute (sfm) (70 to 90 m/min). For best results, uniform cutting speed and feed are maintained throughout the entire stoke (ASM 1989b).

In general, speeds are related to workpiece material characteristics and associated machinability. Feeds are influenced by the workpiece machinability, but also by ram speed, depth of cut, and required dimensional accuracy and surface finish. Common practice in shaping is to make roughing cuts at as high a feed and slow a speed as practical, and make finishing cuts at a low feed rate and high speed (ASM 1989b). For low carbon steel, a typical speed for a roughing cut is 50 sfm (15 m/min), while for a finishing cut it is 80 sfm (25 m/min) using a conventional cutting tool. Similarly for aluminum, a roughing cut of 150 sfm (45 m/min) is typically followed by a finishing cut of 200 sfm (60 m/min).

TABLE 13.2.7 Types of Planers

Planer Type	Description	Application
Double housing	Two vertical uprights support the crossrail which in turn supports the tools	Rigid machine; restricts the width of workpiece
Open side	A single upright column supports a cantilevered crossrail; less rigid than the double-housing type	Accommodates wide workpieces which can overhang one side of the table without interfering with the planer operation

TABLE 13.2.8 Types of Shapers

Shaper Type	Description	Application
Horizontal	The ram drives the tool in the horizontal direction; uses plane or universal table (rotates on three axes)	Gears, splined shafts, racks, and so on; not used for rate production
Vertical	The ram operates vertically, cutting on the downstroke	Slots, grooves, keyways; matching die sets, molds, fixtures; not used for rate production

There is a practical lower bound on minimum feed rate. Feed rates that are too low will cause the tool to chatter; feed rates less than 0.005 in. (0.125 mm) are seldom used in shaping. Similarly, shallow cuts (less than 0.015 in., 0.38 mm) will cause chatter during shaping.

Planers are available in a wide range of sizes (Table 13.2.7). Tools are available in a variety of configurations for undercutting, slotting, and straight planing of either horizontal or vertical surfaces (ASM 1989b).

Shapers are available in a large variety of sizes (Table 13.2.8), ranging from small models with a maximum stroke length of less than 6 in. (150 mm) to large machines with a maximum stroke of 36 in. (914 mm). On each machine, the length of stroke can be varied from its maximum to slightly less than 1 in. (25 mm) for the largest machine, and to 1/8 in. (3.2 mm) for the smallest machine.

Planing is a precision process in which flatness can be held within 0.0005 in. (0.013 mm) total indicated run out (TIR) on workpieces up to 4 ft^2 (0.4 m^2). Although planing is most widely used for machining large areas, it is also used for machining smaller parts, although 12 in. is about the minimum distance for a planing stoke. Size of the workpiece that can be planed is limited by the capacity of the planing equipment.

Shaping is a versatile process in which setup time is short and relatively inexpensive tools can be used. Under good conditions, a shaper can machine a square surface of 18 in. on a side (0.2 m^2) to a flatness within 0.001 in. (0.025 mm); under optimum conditions this can be improved to 0.0005 in. (0.013 mm). The size of the workpiece that can be shaped is limited by the length of the stoke, which is usually about 36 in. (914 mm). Shaping should be considered for machining flat surfaces in these instances:

- Required flatness cannot be achieved by another method.
- Production quantity is insufficient to justify the tooling costs of milling or broaching.

Planing and shaping are interrupted cutting processes, and are comparatively inefficient means of metal removal; for example, shaping costs five times that of milling, exclusive of the tooling and setup costs.

Milling. Milling is a versatile, efficient process for metal removal. It is used to generate planar and contour surfaces through the action of rotating multiple-tooth cutters. Surfaces having almost any orientation can be machined because both the workpiece and cutter can move in more than one direction at the same time.

Cutters with multiple cutting edges rotate in a spindle. The machining process is interrupted as the teeth of the milling cutter alternately engage and disengage from the workpiece.

TABLE 13.2.9 Types of Milling Machines

Milling Machine	Description	Application
Knee-and-column	Six basic components: • Base — the primary support • Column — houses spindle and drive • Overarm — provides support for the arbor-mounted cutting tools • Knee — supports the table, saddle, and workpiece; provides vertical movement • Saddle — provides 1° of horizontal motion • Table — directly supports the workpiece and provides a second degree of horizontal motion	Widely used for low production milling; provides three-axis movement; primary drawback is lack of rigidity due to the number of joints
Bed-type	Table and saddle mounted on a bed in fixed vertical position; vertical motion obtained by movement of the spindle carrier; available with horizontal or vertical spindle	Very rigid machine; permits deep machining cuts and close dimensional control
Planar-type (adjustable rail)	Can accommodate almost any type of spindle for driving cutters and boring bars; utilizes several milling heads	Use for mass-production milling; can perform simultaneous milling and boring operations
Special purpose	Many possible configurations involving major modifications or combinations of the basic types of milling machines; adapted for automated control	Optimized for high-volume production; includes profilers and machining centers; these machines are capable of performing multiple simultaneous machining operations

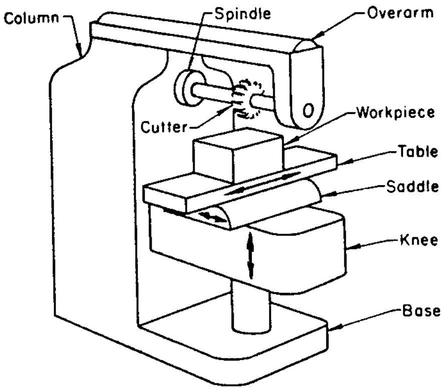

FIGURE 13.2.6 Principal components of a plain knee-and-column milling machine with a horizontal spindle. (From *ASM Handbook*, *Machining*, vol. 16, 9th ed., ASM International, Metals Park, OH, 1989, 304. With permission.)

Most milling is done in machines designed for milling (Table 13.2.9). Milling can also be done by any machine tool that can rigidly hold and rotate a cutter while feeding a workpiece into the cutter. Milling machines are usually classified in terms of their appearance: knee-and-column, bed-type, planar-type, and special purpose. The knee-and-column configuration is the simplest milling machine design. The workpiece is fixed to a bed on the knee and the tool spindle is mounted on a column, as depicted in Figure 13.2.6. For very large workpieces, gantry or bridge-type milling machines are used. Machines having two columns can provide greater stability to the cutting spindle(s). Special-purpose machines are modifications of the three basic models.

The usual power range for knee-and-column machines is 1 to 50 hp (0.75 to 37 kW). Bed-type machines are available in a wide range of sizes, up to 300 hp (225 kW). Planar-type machines are available from 30 to 100 hp (22 to 75 kW).

TABLE 13.2.10 Types of Milling Cutters

Milling Cutters	Description	Application
Peripheral mills	Cutting is primarily done by teeth on the periphery of the cutting tool; mounted on an arbor having its axis parallel to the machined surface	Removing metal from simple flat surfaces; milling contoured surfaces and surfaces having two or more angles or complex forms
Face mills	Machining action is accomplished by the bevel cutting edge located along the circumference of the mill; driven by a spindle on an axis perpendicular to the surfaced being milled	Can be more efficient at removing material than peripheral milling; very rigid tool setup possible; can achieve tight tolerances
End mills	Incorporate cutting edges on both the face and the periphery; can be used for face cuts and periphery cuts	Allow multiple operations without changing cutters; cutters can have difficulty in maintaining dimensional accuracy due to long unsupported length
Special mills	Can be almost any design	Optimized for a particular task

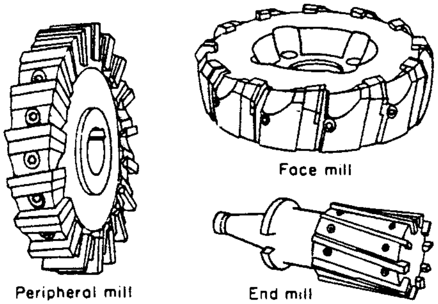

FIGURE 13.2.7 Three typical milling cutters. (From *ASM Handbook*, *Machining*, vol. 16, 9th ed., ASM International, Metals Park, OH, 1989, 311. With permission.)

A wide variety of milling cutters are available, using the full range of cutting-tool materials; there are three basic constructions (ASM 1989b):

Solid — Made from a single piece of HSS or carbide. Cutters can be tipped with a harder material; teeth can be designed for specific cutting conditions; the initial cost is low.

Inserted blade — Usually made from HSS, carbide, or cast alloy. Individual blades can be replaced as they wear out, saving replacement cost; they are ideal for close-tolerance finishing.

Indexable insert — Cutter inserts are made from carbide, coated carbide, ceramic, or ultrahard material such as diamond; each insert has one or more cutting edges; as inserts wear, they are repositioned to expose new cutting surface or indexed to bring another cutting insert on line. These inserts, widely used in computer-controlled machines due to their performance and flexibility, can produce a rougher surface than the other tool constructions and require somewhat higher cutting forces to remove metal.

Milling cutters are also described by the location of the cutting edges, as described in Table 13.2.10. Several cutters are depicted in Figure 13.2.7.

The angular relationships of the cutting edge greatly influence cutting efficiency, analogous to single-point cutting tools. A milling cutter should have enough teeth to ensure uninterrupted contact with the workpiece, yet not so many so as to provide too little space between the teeth to make chip removal difficult.

Milling speed varies greatly depending on workpiece material composition, speed, feed, tool material, tool design, and cutting fluid. Speeds as low as 20 sfm (6.1 m/min) are employed for milling low machinability alloys, while speeds as high as 20,000 sfm (6100 m/min) have been reported for milling aluminum (ASM 1989b). If the setup is sufficiently rigid, carbide or carbide-tipped cutters can be operated three to ten times faster than HSS cutters; top speed is usually constrained by onset of tool chatter.

For highest efficiency in removing metal while minimizing chatter conditions, the feed per tooth should be as high as possible. The optimum feed rate is influenced by a number of factors (ASM 1989b): type of cutter, number of teeth on the cutter, cutter material, workpiece machinability, depth of cut, width of cut, speed, rigidity of the setup, and machine power. The surface finish obtainable by milling can be quite good. A finish of 125 μin. (3.2 μm) can be readily achieved under normal circumstances with HSS mills, and finishes of 63 μin. (1.6 μm) are common if carbide tools are used. With careful selection of cutters and stringent control of process conditions, a finish of 10 min (0.25 mm) can be produced.

The initial cost of a milling machine is considerably greater than that of a planar or a shaper that can machine workpieces of similar size to similar finishes. Milling tools usually cost up to 50 times as much as tools for planers and shapers, and the setup time is usually longer. However, milling is far more efficient in removing material, and milling machines are commonly highly automated. Therefore, milling is preferred for production operations.

Grinding is often preferred to milling when the amount of metal to be removed is small and the dimensional accuracy and surface finish are critical. Milling and grinding are frequently used in combination.

Broaching. Broaching is a precision machining process. It is very efficient since both roughing cuts and finishing cuts are made during a single pass of the broach tool to produce a smooth surface, and further finishing is usually not necessary. Consequently, close tolerances can be readily achieved at a reasonable cost for high rates of production.

Broaches are expensive multi-toothed cutting tools. Thus, the process is usually employed for low or high production when broaching is the only practical method to produce the required dimensional tolerance and surface quality. An example of the latter case is the dovetail slots in jet engine turbine disks.

Broaching is a machining process similar to planing. A broach is essentially a tapered bar into which teeth are cut, with the finishing teeth engaging last on the end with the larger diameter. A single broach has teeth for rough cutting, semifinishing, and finishing. Broaching involves pushing or pulling a broach in a single pass through a hole or across a surface. As the broach moves along the workpiece, cutting is gradual as each successive tooth engages the workpiece, removing a small amount of material. Overall machining forces are much greater than that of other machining methods, and consequently broaching is considered to be the most severe of all machining operations.

Broaching machines are categorized as horizontal or vertical, depending on the direction of broach travel. Industry usage is almost evenly divided between these two categories. The selection of machine type depends heavily on the configuration of the workpiece and available space in the factory, considering both floor space and vertical clearance requirements.

Broaches can be categorized by the method through which they are actuated (push or pull), by type of cut (internal or external), and by the construction of the broach body. Figure 13.2.8 depicts typical internal and external broaching operations. Table 13.2.11 describes broaches according to their construction.

Length and depth of cut have the most influence on determining the required broaching tool length. For internal cutting operations, as the cut length increases, more chip storage capacity must be provided between the cutting edges for the same amount of tooth advance. Cutting fluids are useful in preventing the work metal from adhering to the broach, and thus result in higher-quality surface finishes and increased broach life.

The primary consideration in the selection of optimum broaching speed is the trade-off between speed and wear rate. In general, steels are broached at 10 to 30 sfm (3 to 9 m/min); the harder the steel, the slower the broach speed (ASM 1989b).

Broaching can maintain tight tolerances during long production runs since metal-cutting operations are distributed among the different roughing and finishing teeth. Also, broach teeth can be repeatedly sharpened, allowing cutting efficiency and accuracy to be maintained.

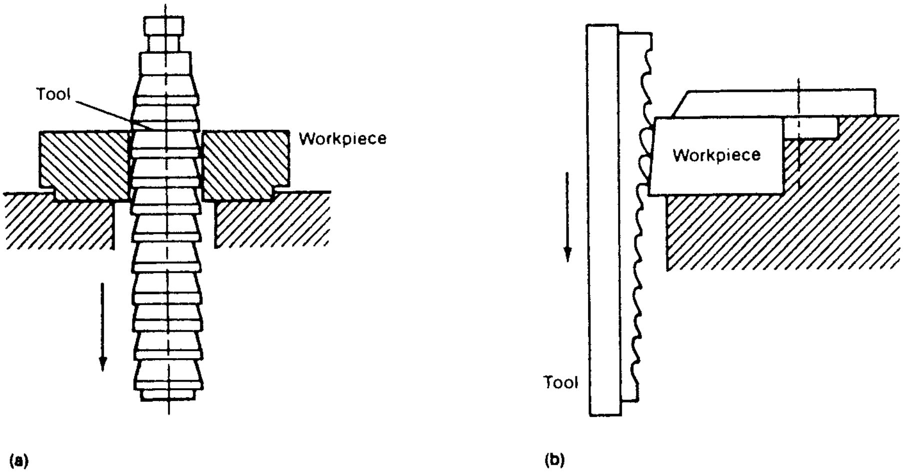

FIGURE 13.2.8 Internal (a) and external (b) broaching. (From *ASM Handbook*, *Machining*, vol. 16, 9th ed., ASM International, Metals Park, OH, 1989, 195. With permission.)

TABLE 13.2.11 Types of Broaches

Broaches	Description	Application
Solid	One-piece broach produced from tapered bar stock; repair of broken teeth is difficult	Parts which require high dimensional accuracy and concentricity
Shell	Multipiece broach consisting of a main body, an arbor section over which a removable shell fits, and a removable shell containing the cutting edges; worn or damaged sections can be replaced	Internal and selected external broaching; sacrifices some accuracy and concentricity as the tool is not as stiff as a solid broach
Insert-type	Effectively a tool holder with inserts to perform the actual cutting; inserts are typically made from HSS or carbides; worn or damaged inserts can be readily replaced	Broaching large, flat surfaces

Broaching is an extremely fast, precise machining operation. It is applicable to many workpiece materials over a wide range of machinability, can be accomplished in seconds, is readily automated, and can easily be done manually. For example, for low-carbon steels, tolerances of 0.002 in. (0.05 mm) can be readily attained with a surface finish of 60 μin. (1.55 μm); if desired, tighter tolerances and surface finishes of 30 μin. (0.8 μm) are possible without much additional effort. For difficult-to-machine superalloys, tolerances of 0.001 in. (0.025 mm) and surface finishes of 30 μin. (0.8 μm) are commonly achieved in production (ASM 1989b).

Broaching is rarely used for removing large amounts of material since the power required would be excessive. It is almost always more effective to use another machining method to remove the bulk of material and use broaching for finishing.

Since a broach moves forward in a straight line, all surface elements along the broach line must be parallel to the direction of travel. Consequently, the entire surface of a tapered hole cannot be broached. Also, cutting is done sequentially with the finishing teeth engaging last. Therefore, a blind hole can be broached only if a sufficiently long recess is provided to permit full travel of the broach.

The direction of travel of the broach cannot realistically be changed during a broaching stroke, except for rotating the tool. Thus, surfaces having compound curves cannot be broached in a single operation. On external surfaces, it is impossible to broach to a shoulder that is perpendicular to the direction of broach movement.

Grinding

Trevor D. Howes, John Webster, and Ioan Marinescu

Grinding, or abrasive machining, refers to processes for removing material in the form of small chips by the mechanical action of irregularly shaped abrasive grains that are held in place by a bonding material on a moving wheel or abrasive belt (Green 1992). In surface-finishing operations (e.g., lapping and honing) these grains are suspended in a slurry and then are embedded in a roll-on or reference surface to form the cutting tool. Although the methods of abrasion may vary, grinding and surface-finishing processes are used in manufacturing when the accuracy of workpiece dimensions and surface requirements are stringent and the material is too hard for conventional machining.

Grinding is also used in cutoff work and cleaning of rough surfaces, and some methods offer high material-removal rates suitable for shaping, an area in which milling traditionally has been used.

Grinding is applied mainly in metalworking because abrasive grains are harder than any metal and can shape the toughest of alloys. In addition, grinding wheels are available for machining plastics, glass, ceramics, and stone. Conventional precision metal and ceramic components and ultraprecision electronic and optical components are produced using grinding.

Three types of energy are involved in grinding (Andrew et al. 1985). Rubbing energy is expended when the grains (cutting edges) of the grinding wheel wear down. As they wear, they cut less and produce increasing friction, which consumes power but removes less material. Plowing energy is used when the abrasive does not remove all of the material but instead plows some of it aside plastically, leaving a groove behind. *Chip-formation energy* is consumed in removing material from the workpiece as the sharp abrasive grain cuts away the material (or chip) and pushes it ahead until the chip leaves the wheel.

The grinding wheel experiences *attritious wear* as the abrasive grains develop wear flats from rubbing on the workpiece, or when grains break free from the bond material. Attritious wear gives rise to rubbing energy resulting from friction, and thus can lead to thermal damage as power consumption increases without an increase in material removal rate. The wheel can wear through *fracture*, predominating at relatively high in-feed rates. In this case, pieces of the abrasive grain break free and expose a new, sharp surface.

Materials can be classified as either easy to grind or difficult to grind. For easy-to-grind materials, most of the power consumption becomes invested in chip formation; thus, rubbing and plowing energy are minimal. *Difficult-to-grind materials* involve considerable rubbing and plowing energy since the force required to remove chips is comparatively high.

In *surface grinding*, the grinding wheel traverses back and forth across the workpiece. Grinding can take place by using either the periphery or side face of the wheel. The table holding the part may also reciprocate. Surface grinding is done most commonly on flat surfaces and surfaces with shapes formed of parallel lines, e.g., slots.

Creep-feed grinding is a form of surface grinding in which the wheel feeds into the workpiece at a low rate (0.4 to 40 in./min, 10 to 1000 mm/min) while grinding at a large depth of cut (0.04 to 0.4 in., 1 to 10 mm, or deeper). A large amount of material can be removed with one pass of the wheel, compared with conventional surface grinding in which the wheel makes many quick passes over the workpiece at slight depths of cut. This process is limited by the large amount of heat generated at the grinding arc, which can result in thermal damage (grinding "burn"). Application of coolant is critical in creep-feed operations. CBN wheels, with their good heat transfer property, can also reduce the severity of burn (King and Hahn 1986).

Cylindrical grinding produces round workpieces, such as bearing rings, although some machines can also grind tapered parts. The workpiece is mounted to a spindle and rotates as the wheel grinds it. The workpiece spindle has it own drive motor so that the speed of rotation can be selected. Both inner surfaces (internal cylindrical grinding) and outer (external cylindrical grinding) can be worked, although usually the same machine cannot do both.

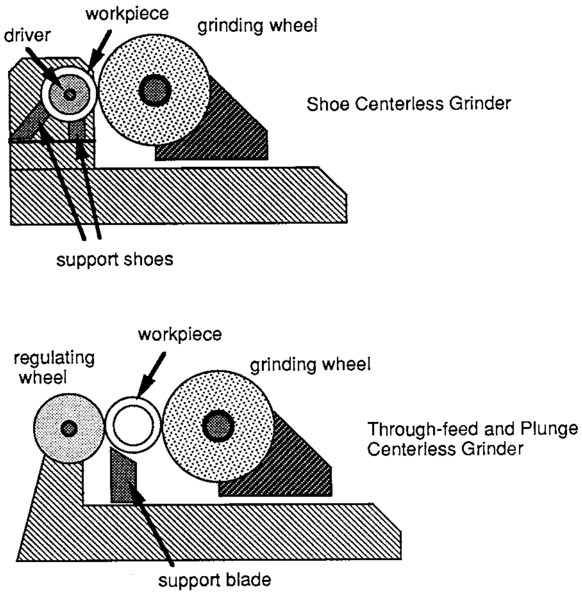

FIGURE 13.2.9 Through-feed and plunge centerless grinding. (Courtesy of T.D. Howes, J. Webster, and I. Marinescu.)

There are three variants for *external grinding*:

Plain grinding — The wheel carriage is brought to the workpiece on its spindle and in-feeds until the desired dimensions are reached.
Traverse grinding — The rotating workpiece is mounted on a table that reciprocates under the wheel; the grinding wheel is stationary except for its downward feed into the workpiece.
Plunge grinding — The table with the rotating workpiece is locked while the wheel moves into the workpiece until the desired dimensions are attained.

Centerless grinding is a form of cylindrical grinding. In this method workpieces are not held in a centering chuck but instead rotate freely between a support, regulating wheel, and the grinding wheel. The force of the rotating grinding wheel holds the workpiece against the support. The supports are usually stationary and so a flow of lubricant is required to reduce friction between workpiece and support. An example of centerless grinding is shown in Figure 13.2.9.

Abrasive belt machines use a flexible fabric coated with an abrasive stretched between two rollers, one of which is driven by a motor. Usually, the abrasive coating is aluminum oxide for steels and bronzes and silicon carbide for hard or brittle materials. In the metal industries, common use of such machines is for dry grinding of metal burrs and flash and polishing of surfaces. However, some fabrics permit use of grinding fluids to enhance chip removal and provide cooling and lubrication, which results in better cutting action and longer belt life.

Honing, lapping, and polishing use abrasives to improve the accuracy of the form of a workpiece or the surface finish beyond the capabilities of grinding.

- *Honing* is a low-surface-speed operation, usually performed on an internal, cylindrical surface but possible also on external ones. Stock is removed by the shearing action of abrasive grains: a simultaneous rotary and reciprocating motion of fixed abrasive in the form of a stone or stick. Finishes range from under 1 to 50 μin. (0.025 to 1.3 μm). The development of CBN has revolutionized the honing process because this material easily outperforms conventional abrasives such as aluminum oxide, lasting up to 100 times longer.

TABLE 13.2.12 Common Grinding Wheel Abrasives

Abrasive	Characteristic	Grinding Application
Aluminum oxide	Friable	Steel: soft or hardened, plain or alloyed
Seeded gel aluminum oxide	More friable and expensive than aluminum oxide	Steel: soft or hardened, plain or alloyed; use at higher stock removal rates
CBN	Tough; increased life at higher speeds; high accuracy and finish	Hardened steels; tough superalloys
Synthetic diamond	Hardest of all abrasives; can be friable; seldom need dressing/truing	Grinding hardened tool steels, cemented carbides, ceramics, and glass; cutting and slicing of silicon and germanium wafers
Silicon carbide	Friable	Cast iron; nonferrous metals; nonmetallics

- *Superfinishing*, like honing, uses fixed abrasives in the form of a stone. Unlike honing, which has a helical motion inside a bore, superfinishing uses high-speed, axial reciprocation combined with slow rotation of the outside diameter of the cylindrical component being processed. The geometry produced by a previous operation generally is not improved.
- *Lapping* is a fine-finishing, abrasive machining process used to obtain superior finish and dimensional accuracy. Lapping is unlike other finishing processes because some of the abrasive is loose rather than bonded. In general, lapping occurs when abrasive grains in a liquid vehicle (called a slurry) are guided across a workpiece by means of a rotating plate.
- *Polishing* uses free abrasive, as in lapping, but requires a soft support unlike the relatively hard support used in lapping. The total depth of cut during polishing can be as little as nanometers where chemical interactions will play a stronger role than mechanical or physical interactions. When the depth of cut is greater than 1 μin. (0.025 μm), the interactions are usually of a mechanical nature. Many industrial components, especially electronic and optical, required highly polished surfaces.

A *grinding wheel* consists of thousands of small, hard grains of abrasive material held on the surface in a matrix of bond material (Table 13.2.12). The bond material is matched to the characteristics of the grain to retain the grain sufficiently to maximize its use before shedding it. The structure of the wheel formed by specific types of grains and bonds determines its characteristics. The grains are spaced apart depending on the cutting required. Widely spaced grains (open structure) cut aggressively, which is useful for hard materials or high rates of material removal, but which tends to produce coarse finishes. Closely packed grains (dense structure) make fine and precise cuts for finish grinding.

Grain spacing is also important for temporary storage of chips of material removed from the workpiece. An open structure is best for storing chips between the grains, which are then released after wheel rotation moves the grains away from the workpiece. An open structure also permits more coolant to enter the spaces to dissipate heat.

The bonding material is important to grinding performance. This material is weaker than the cutting grains so that ideally, during grinding, the grain is shed from the wheel surface when it becomes dull, exposing new sharp grains. For instance, wheels with friable abrasives that fracture to expose new, sharp grains must retain the grains longer to maximize the use of the abrasive; these wheels use stronger bonding materials. The four types of bond material are vitrified, resinoid, rubber, and metal. Table 13.2.13 shows their properties and uses.

Grinding wheels must be resharpened on occasion. *Dressing*, not always required, sharpens the grains before grinding. *Truing* operations ensure the wheel conforms to the required cutting shape and will rotate concentrically to its spindle.

Because grinding wheels have relatively high mass and high operating speed, they must be *precisely balanced*. Imbalance causes vibrations that reduce the quality of the workpiece, hasten the wear of the spindle and bearings of the machine, affect other devices mounted on the grinder, and possibly transmit vibration from the grinder through the shop floor to other machines. Mounting of the wheel on the

TABLE 13.2.13 Characteristics of Grinding Wheel Bonds

Bond Type	Characteristic	Application
Rubber	Relatively flexible	Wet cut-off wheels; high-finish work; regulating wheels for centerless grinding
Resinoid (thermoplastic)	Relatively flexible	Rough grinding; portable grinders
Vitrified (glasslike)	Endure high temperatures; resist chemical effects of coolants; sensitive to impacts	Most widely used of all bonding materials
Metal	Electrodeposited nickel or sintered metal powder often used to bond CBN and diamond abrasives; has long wheel life; electrically conductive	Aggressive cutting operations such as creep-feed and deep grinding; electrically conductive grinding (e.g., electrochemical methods)

spindle and subsequent wheel wear can degrade the balance of the rotating system. Wheels are balanced by moving counterweights on balancing flanges. Some machines have an automatic balancer that shifts internal counterbalance masses.

Coolants are usually sprayed on the grinding zone to cool the wheel and workpiece, lubricate the surface to reduce grinding power, and flush away the chips. Excessive heat can damage both the wheel and workpiece by inducing undesirable physical changes in materials, such as metallurgical phase changes or residual stresses, or softening of the bond material in the grinding wheel. Coolant application is especially important in creep-feed grinding where the wheel-to-workpiece contact arc is long, heat generation is high, and the chips produced and abrasive lost from the wheel must be flushed away.

Selecting the type of *coolant system* depends on many factors, including the grinding wheel speed, material removal rate, depth of cut, and wheel/workpiece materials. The type of fluids used in this system requires consideration of both physical and environmental issues. Use of oil fluids can favor the formation of preferred residual stress patterns and better surface finish, and these oils can be recycled for long periods. However, oils present health risks, potential for groundwater contamination, and fire risks (especially with high-sparking superalloys). Water-based fluids offer far fewer environmental problems. Disadvantages of water-based fluids lie in their limited life expectancy of 3 to 12 months. Also, the relatively low viscosity of a water-based fluid at high velocity promotes a dispersed jet, which reduces cooling capacity.

Surface grinding can be a cheaper, faster, and more precise method than milling and planing operations. For profiled shapes, the grinding wheel can be dressed with less cost and inconvenience than changing milling setups for different parts. Grinding can be used as a high-stock-removal process; for example, creep-feed grinding has a depth of cut more typical of milling operations (0.1 in., 2.54 mm, and deeper). Creep-feed grinding is used for machining materials that are too difficult to work by other machining methods.

High-speed grinding can be extremely efficient. CBN abrasive allows high rates of material removal because CBN transfers heat away from the grinding zone due to its relatively high thermal conductivity, and CBN does not react with steel.

Considerable effort has been expended on modeling and testing the thermal limitations of grinding (Malkin 1989). Nearly all models depend on a fundamental model that relies on sliding contact theory. All models confirm the following guidelines for grinding with conventional abrasives when burn is a limitation: decrease wheel speed, increase workpiece speed, use softer-grade wheels.

Dynamic Stability and Chatter

Scott Smith

In all of the material removal processes just described, the achievable material removal rate may be limited by dynamic interactions between the cutting process and the structure of the machine-tool-workpiece system (Tlusty 1985).The resulting vibrations between the tool and workpiece cause excessive variations of the cutting force, resulting in poor surface quality and reduced life of the cutting tool (Welboum 1970). The vibrations encountered can be classified in three broad categories:

- *Free vibrations.* There is an initial input of energy, which results in a vibration at a damped natural frequency of the system. In a machine tool, such a vibration might occur at the start or end of an axis motion. The decay rate of the vibration is directly related to the amount of damping present. Solutions to free vibration problems typically include elimination of the source or an increase in the damping.
- *Forced vibrations.* These vibrations occur as the result of a period force. They have the frequency of the exciting force, and they persist as long as the excitation force persists. They are particularly problematic if the excitation force is near a natural frequency of the system (the case of "resonance"), in which case the amplitude of the vibration may become quite large. Forced vibrations in material removal might result, for example, from an unbalanced grinding wheel or milling cutter. Solutions to forced vibration problems typically include lowering the excitation force (for example, by balancing the tool) or moving it away from a resonance frequency.
- *Self-excited vibrations.* These vibrations result from an instable feedback mechanism between the cutting process and the structure. Any small vibration causes a wavy surface, which then leads to a variable cutting force, which leaves a wavy surface. If the vibration decreases, then the machining is stable. If it grows, this is the condition referred to as *chatter.* The resulting vibration can easily be large enough to cause the tool to lose contact with the workpiece, damage the workpiece, or break the cutter. Figure 13.2.10 illustrates the surface that may result.

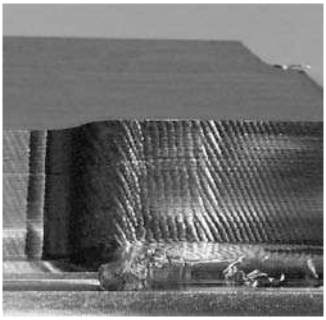

FIGURE 13.2.10 Surface resulting from chatter during milling. (Courtesy of S. Smith.)

Whether or not chatter occurs depends on a complex interaction between the dynamic characteristics of the structure (as represented by a *Frequency Response Function*, or *FRF*), the workpiece material, the cutting depths, and the spindle speed. Some speeds are favorable for stable material removal, while others are not. This chatter relationship is often expressed as a *stability lobe diagram*, as shown in Figure 13.2.11.

In this figure, the horizontal axis shows spindle speed, and the vertical axis shows axial depth of cut for a given radial depth of cut. Conditions above the line indicate chatter, and those below the line result in stable milling. It is clear from the figure that in milling, it is particularly important to exploit a

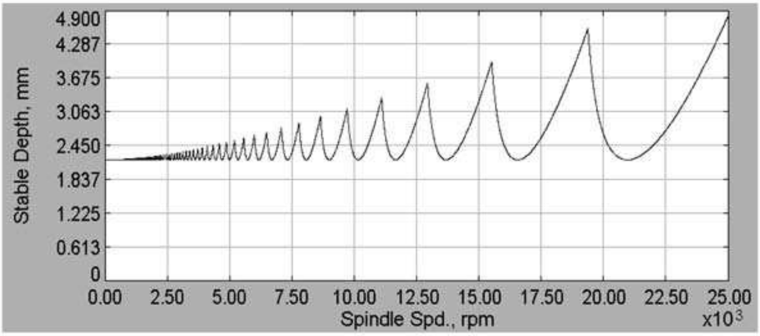

FIGURE 13.2.11 Typical stability lobe diagram for milling in aluminum. (Courtesy of Manufacturing Laboratories Inc.)

knowledge of the stability lobes as the spindle speed becomes high. In this case, milling at 25,000 rpm is substantially more advantageous than milling at 21,000 rpm. It is particularly important to respect the dynamic limitations during NC programming, so that first articles will be chatter-free. Software and hardware tools are continuing to be rapidly developed and deployed to help machine tool users make the required measurements (Delio et al. 1992).

References

Altan, T., Oh, S.I., and Gegel, H. 1983. *Metal Forming — Fundamentals and Applications*, ASM International, Metals Park, OH.

Andrew, C., Howes, T.D., and Pearce, T.R.A. 1985. *Creep Feed Grinding*, Holt, Rinehart, and Winston, London.

ASM 1989a. *Turning*, in *Machining, ASM Handbook*, vol. 16, 9th ed., ASM International, Metals Park, OH, 142–49.

ASM 1989b. *Machining, ASM Handbook*, vol. 16, 9th ed., ASM International, Metals Park, OH.

Bakerjian, R., Ed. 1992. Design for Manufacturability, vol. VI, Tool and Manufacturing Engineers Handbook, 4th ed., Society of Manufacturing Engineers, Dearborn, MI.

DeVries, W.R. 1991. *Analysis of Material Removal Processes*, Springer-Verlag, New York.

Delio, T., Smith, S., Tlusty, J., *ASME J. of Eng. for Industry*, vol. 114, May 1992, 146-57.

Green, R.E., ed. 1992. *Machinery's Handbook*, 24th ed., Industrial Press, New York.

Kalpakjian, S. 1991. *Manufacturing Processes for Engineering Materials*, Addison-Wesley, Reading, MA.

Kalpakjian, S. 1992. *Manufacturing Engineering and Technology*, Addison-Wesley, Reading, MA.

King, R.I. and Hahn, R.S., eds. 1986. *Handbook of Modern Grinding Technology*, Chapman & Hall, New York.

Komanduri, R. and Samanta, S.K. 1989. *Ceramics*, in Machining, *ASM Handbook*, vol. 16, 9th ed., ASM International, Metals Park, OH, 98–104.

Malkin, S. 1989. *Grinding Technology — Theory and Applications of Machining with Abrasives*, John Wiley & Sons, New York.

Shaw, M.C. 1984. *Metal Cutting Principles*, Oxford Science Publications. New York.

Tlusty, J., *Handbook of High Speed Machining Technology*, King, R.I., ed., Chapman & Hall, 1985.

Welboum, D. 1970. *Machine-Tool Dynamics*, Cambridge University Press, New York.

Nontraditional Machining

K. P. Rajurkar and W. M. Wang

The processes described in this section are representative of the types most likely to be encountered. The references listed at the end of the section contain detailed information on these processes, plus those that are not described here.

Electrical Discharge Machining (EDM)

The electrical discharge machining (EDM) process machines hard materials into complicated shapes with accurate dimensions. EDM requires an electrically conductive workpiece. Process performance is unaffected by the hardness, toughness, and strength of the material. However, process performance is a function of the melting temperature and thermal conductivity. EDM is currently widely used in aerospace, machinery, and die and mold industries.

There are two types of EDM processes:

- Die-sinking EDM uses a preshaped tool electrode to generate an inverted image of the tool on the workpiece; commonly used to generate complex-shaped cavities and to drill holes in different geometric shapes and sizes on hard and high-strength materials.
- Wire EDM (WEDM) uses a metal wire as the tool electrode; it can generate two- or three-dimensional shapes on the workpiece for making punch dies and other mechanical parts.

EDM removes workpiece materials by harnessing thermal energy produced by pulsed spark discharges across a gap between tool and workpiece. A spark discharge generates a very small plasma channel having a high energy density and a very high temperature (up to 10,000°C) that melts and evaporates a small amount of workpiece material. The spark discharges always occur at the highest electrical potential point that moves randomly over the machining gap during machining. With continuous discrete spark discharges, the workpiece material is uniformly removed around the tool electrode. The gap size in EDM is in the range of 400 μin. to 0.02 in. (0.01 to 0.5 mm), and is determined by the pulse peak voltage, the peak discharge current, and the type of dielectric fluid.

The discharge energy during EDM is provided by a direct current pulse power generator. The EDM power system can be classified into RC, LC, RLC, and transistorized types. The transistorized EDM power systems provide square waveform pulses with the pulse on-time usually ranging from 1 to 2000 msec, peak voltage ranging from 40 to 400V, and peak discharge current ranging from 0.5 to 500 A. With the RC, LC, or RLC type power system, the discharge energy comes from a capacitor that is connected in parallel with the machining gap. As a result of the low impedance of plasma channel, the discharge duration is very short (less than 5 msec), and the discharge current is very high, up to 1000 A. The peak voltage is in the same range of transistorized power systems.

The transistorized power systems are usually used in die-sinking EDM operations because of their lower tool wear. Capacitive power systems are used for small hole drilling, machining of advanced materials, and micro-EDM because of higher material removal rate and better process stability. The WEDM power generator usually is a transistor-controlled capacitive power system that reduces the wire rupture risk. In this power system, the discharge frequency can be controlled by adjusting the on-time and off-time of the transistors that control the charging pulse for the capacitor connected in parallel with the machining gap.

The machining gap between tool and workpiece during EDM must be submerged in an electrically nonconductive *dielectric fluid*. In die-sinking EDM, kerosene is often used as a dielectric fluid because it provides lower tool wear, higher accuracy, and better surface quality. Deionized water is always used as a dielectric fluid in WEDM to provide a larger gap size and lower wire temperature in order to reduce the wire rupture risk. This fluid also serves to flush debris from the gap and thus helps maintain surface quality.

Copper and graphite are commonly used as die-sinking *EDM tool materials* because of the high electrical conductivity and high melting temperature and the ease of being fabricated into complicated shapes. The wire electrode for WEDM is usually made of copper, brass, or molybdenum in a diameter ranging from 0.01 to 0.5 mm. Stratified copper wire coated with zinc brass with diameter of 0.25 mm is often used.

In the traditional *die-sinking EDM process*, the tool is fabricated into a required shape and mounted on a ram that moves vertically. The spark discharges can only occur under a particular gap size that determines the strength of electric field to break down the dielectric. A servo control mechanism is equipped to monitor the gap voltage and to drive the machine ram moving up or down to obtain a dischargeable gap size and maintain continuous sparking. Because the average gap voltage is approximately proportional to the gap size, the servo system controls the ram position to keep the average gap voltage as close as possible to a preset voltage, known as the *servo reference voltage.*

In a WED machine, the wire electrode is held vertically by two wire guides located separately above and beneath the workpiece, with the wire traveling longitudinally during machining. The workpiece is usually mounted on an *x-y* table. The trajectory of the relative movement between wire and workpiece in the *x-y* coordinate space is controlled by a CNC servo system according to a preprogrammed cutting passage. The CNC servo system also adjusts the machining gap size in real time, similar to the die-sinking EDM operation. The dielectric fluid is sprayed from above and beneath the workpiece into the machining gap with two nozzles.

The power generators in WED machines usually are transistor-controlled RC or RLC systems that provide higher machining rate and larger gap size to reduce wire rupture risks. In some WED machines, the machining gap is submerged into the dielectric fluid to avoid wire vibration to obtain a better accuracy.

The upper wire guide is also controlled by the CNC system in many WED machines. During machining, the upper wire guide and the *x-y* table simultaneously move along their own preprogrammed trajectories to produce a taper and/or twist surface on the workpiece.

The polarity of tool and workpiece in EDM is determined in accordance with the machining parameters. When the discharge duration is less than 20 μsec, more material is removed on the anode than that on the cathode. However, if the discharge duration is longer than 30 μsec, the material-removal rate on the cathode is higher than that on the anode. Therefore, with a transistorized power system, if the pulse on-time is longer than 30 μsec, the tool is connected as anode and the workpiece is connected as cathode. When the on-time is less than about 20 μsec, the polarity must be reversed. With an RC, LC, or RLC power system, since the discharge duration is always shorter than 20 μsec, the reversed polarity is used.

With transistorized EDM power systems, the machining rate and surface finish are primarily influenced by the peak current. The machining rate increases with the peak current. The relationship between the machining rate and pulse on-time is nonlinear, and an optimal pulse on-time exists. Reducing peak current improves the surface finish but decreases the machining rate.

Die-sinking ED machines with transistorized power systems under good gap-flushing conditions can attain a material-removal rate as high as 12 mm^3/min/amp (for a steel workpiece). The wire cut EDM process can cut ferrous materials at a rate over 100 mm^2/min. A surface roughness value of 0.01 in. (0.2 mm) can be obtained with a very low discharge current. The tool wear ratio can be controlled within 1% during rough machining and semifinishing with the transistorized power generator. Dimensional tolerance of ±118 μin. (3 μm) and taper accuracy of 20 to 40 μin. (0.5 to 1 μm/mm) with both die-sinking and WEDM can be obtained.

EDM can machine materials having electrical conductivity of 10^{-2} W^{-1} cm^{-1} or higher. An average current density more than 4 A/cm^2 tends to cause substantial tool wear and unstable machining, and may lead to dielectric fire. This factor largely limits the productivity of EDM. During machining a deep cavity using die-sinking EDM under difficult flush condition, arc discharges occur, and the resultant thermal damage on workpiece substantially limits the productivity and the machined surface quality. Dielectric properties also impose additional constraints.

Electrical Chemical Machining (ECM)

The ECM process uses the electrochemical anodic dissolution effect to remove workpiece material. Like die-sinking EDM, the tool electrode of ECM is preshaped according to the requirements of the workpiece. During machining, the inverted shape of the tool is gradually generated on the workpiece. ECM machines complex contours, irregular shapes, slots, and small, deep, and/or noncircular holes. Typical applications of ECM include machining nickel-based superalloy turbine blade dovetails, slots in superalloy turbine disks, engine castings, gun barrel rifles, and forging dies. ECM is also used for deburring, surface etching, and marking.

Electrolyte fluid is forced through the gap between tool and workpiece during ECM. A low-voltage and high-current DC power system supplies the machining energy to the gap. The tool electrode of ECM must be connected as cathode and the workpiece must be connected as anode. The electrochemical anodic dissolution phenomenon dissolves workpiece surface material into metal ions. The electrolyte fluid flushes the metal ions and removes heat energy generated by the deplating actions. The gap size in ECM is in the range of 0.004 to 0.04 in. (0.1 to 1 mm). ECM process performance is independent of the strength, hardness, and thermal behavior of workpiece and tool materials.

Copper, brass, stainless steel, and titanium are commonly used as *ECM tool electrode materials* due to their good electrical conductivity, resistance to chemical erosion, and ease of being machined into desired shapes. The geometric dimensions of the machined surface generated by ECM depend on the shape of tool and the gap size distribution.

The structure of an EC machine varies with the specific applications. An ECM must have a tool feed system to maintain the machining gap, a power system to supply the power energy, and a fluid-circulating system to supply the electrolyte and to flush the machining gap. The power system used in ECM is a DC power source with the voltage ranging from 8 to 30 V and a high current in the range of 50 to 50,000 A, depending on the specific design of the power system.

The *electrolyte* is the medium enabling the reaction of electrochemical dissolution occurring on the anode. The electrolyte can be classified into categories of aqueous and nonaqueous, organic and nonorganic, alkaline and neutral, mixed and nonmixed, and passivating and nonpassivating, and acidic. The electrolyte is selected according to the type of workpiece material, the desired accuracy, surface finish requirements, and the machining rate. Neutral salts are used in most cases. Acid electrolytes are used only for small hole drilling when the reaction products must be dissolved in the electrolyte.

ECM performance is mainly influenced by electrical parameters, electrolyte, and geometry of tool and workpiece. The electrical parameters include machining current, current density, and voltage. ECM systems with 50 to 50,000 A and 5 to 30 V DC are available, and the current density can be in the range of 10 to 500 A/cm^2. Key electrolyte parameters consist of flow rate, pressure, temperature, and concentration. Important parameters of tool and workpiece geometry are contour gradient, radii, flow path, and flow cross section. When the tool feed rate equals the machining rate, an equilibrium gap size is obtained; this is critical to maintaining shaping accuracy.

The electrolyte selection also plays an important role in ECM dimension control. In this regard, the sodium nitrate solution is preferable because the metal-removal rate at smaller gap size locations is higher than at other places. Therefore, the characteristics of current efficiency in ECM influence the uniformity of the gap size distribution. ECM accuracy has recently been shown to improve with pulsed voltage (instead of continuous voltage) and an appropriate set of pulse parameters (on-time, off-time, etc.).

ECM is capable of machining any electrically conductive metallic material, and the process is generally unaffected by the hardness, strength, and thermal behaviors of materials. This process can be used to machine parts with low rigidity such as parts with thin walls. Machining rates of 2 to 2.5 cm^3/min/1000 A current, surface roughness of 4 to 50 μin. (0.1 to 1.2 μm), and accuracy of 400 μin. to 0.01 in. (10 to 300 μm) can be achieved with ECM. The available ECM equipment can machine a 0.04 to 80 in. (1 to 2000 mm) long workpiece. The typical energy consumption is 300 to 600 J/mm^3.

The machining rate and surface finish with ECM are much higher than that with EDM due to higher allowable current density and the molecular level of material removal. The machining accuracy, however, is substantially lower than EDM and is much more difficult to control.

The gap size distribution is influenced by many factors including the type of electrolyte, electrolyte flow rate and flow pattern, electrolyte temperature, current density of machining, and so forth. Therefore, the gap size distribution is not uniform in most cases and is difficult to determine analytically. The shape of machined surface by ECM will not be a perfect mirror image of the tool electrode. In order to achieve an acceptable accuracy, the tool shape must be modified by using trial-and-error method in test machining before machining of actual workpieces.

ECM cannot machine materials with electrical conductivity less than 103 W^{-1} cm^{-1}. ECM cannot produce very sharp corners (less than 800 μin., 0.02 mm, radius). The machining rate is limited by the electrolytic pressure (less than 5 MPa) and boiling point as well as the applied current (less than 50,000 A). The gap size that determines the final shape and accuracy is limited to 800 μin. to 0.004 in. (0.02 to 0.1 mm).

ECM generates a large amount of sludge and spent electrolyte. This waste requires significant processing before it can be safely disposed of.

Water and Abrasive Jet Machining

Water-jet machining (WJM) and *abrasive water-jet machining* (AWJM) are used in many applications. In the WJM process, relatively soft workpiece materials are cut by a high-velocity water jet; for example, food, wood, paper, plastic, cloth, rubber, and so forth. The AWJM process uses the fine abrasive particles mixed in the water jet to machine harder workpiece materials. The AWJM is used for drilling, contour cutting, milling, and deburring operations on metal workpieces, as well as for producing cavities with controlled depths using multipass and non-through-cutting methods. The cutting path of the WJM and AWJM can be controlled by a CNC system according to a preprogrammed program.

During WJM, the workpiece material is removed by the mechanical energy generated by the impact of a high-velocity water jet. In a water-jet machine, a high-pressure pumping system increases the pressure of water in the pipe system, and the pressurized water is sprayed from a nozzle with a small diameter to generate a high-velocity water jet.

In the AWJM process, pressurized water is sprayed from an orifice in the nozzle body into a mixing chamber to generate a negative pressure that absorbs the abrasive particles (supplied by an abrasive feed hose) into the water jet. The water jet/abrasive grain mixture is then sprayed through a tungsten carbide nozzle. The abrasive grains in the high-velocity water jet provide small cutting edges that remove material. The relative distance between water jet nozzle and workpiece is controlled by a two- or three-dimensional CNC system. This process can be used to generate a complicated shape.

The key parameters are the water and/or abrasive flow velocity, abrasive grain size, and mixing tube (nozzle) length and diameter. The typical water flow velocity is in the range of 2000 to 3000 ft/sec (600 to 900 m/sec) as determined by the water pressure. The water pressure in WJM and AWJM is very high, up to 2.7×10^6 psi (400 MPa), and the nozzle diameter is in the range of 0.003 to 0.08 in. (0.8 to 2 mm). The abrasive flow rate is governed by the water flow rate and the mixing density, and can be controlled up to 10 g/sec. Abrasive particles are usually in the range of 60 to 150 mesh size. Increasing water-jet flow velocity increases cutting depth. The taper error of cutting is determined by the traverse rate that describes the ratio between the material removal and the cutting depth and width. This parameter is influenced by the water and abrasive velocity and cutting speed. Proper selection of AWJ parameters is essential for the elimination of burrs, delaminations, and cracks.

Limitations of the process include stray cutting and surface waviness, high equipment costs, hazard from the rebounding abrasive, high noise levels, and short nozzle lifetimes due to wear and abrasion.

Ultrasonic Machining

Ultrasonic machining (USM) is a process that uses the high velocity and alternating impact of abrasive particles on the workpiece to remove material. The abrasive particles are mixed in a slurry that fills the machining gap between the tool and workpiece. The alternating movement of abrasive particles is driven by the vibration of the frontal surface of the tool at an ultrasonic frequency. The ultrasonic machining process can machine hard and brittle materials.

USM is often used for machining of cavities and drilling of holes on hard and brittle materials including hardened steels, glasses, and ceramics. Rotary ultrasonic machining (RUM) is a new application that uses a diamond grinding wheel as the tool for drilling, milling, and threading operations. During RUM, the tool is rotating at a high speed up to 5000 rpm and vibrating axially at ultrasonic frequency. This process is able to drill holes with diameters from 0.02 to 1.6 in. (0.5 to 40 mm) at depths up to 12 in. (300 mm). The material removal rate of 6 mm^3/sec can be obtained with the RUM process. The tolerance of ±300 µin. (±0.007 mm) can be easily achieved with both conventional and rotary ultrasonic processes.

In the USM process, the machining gap between tool and workpiece is filled with an abrasive slurry composed of an oil mixed with abrasive particles, with the frontal surface of the tool vibrating at ultrasonic frequency to provide the machining energy. The inverted shape of the tool is gradually generated on the workpiece. Material removal by the USM process is very complex. When the machining gap is small, the material may be removed as the frontal surface of the tool moves toward the workpiece, hitting an abrasive particle that impacts the workpiece surface. Material can also be removed by the impact of the abrasive particles when the machining gap is relatively large. In this case, the abrasive particles are accelerated by the pressure of slurry due to the ultrasonic vibration of the frontal surface of the tool. Also, ultrasonic-induced alternating pressure and cavitation in the slurry assist material removal.

The ultrasonic vibration in USM is generated by an *ultrasonic generator*. The ultrasonic generator consists of a signal generator, a transducer, and a concentrator. The signal generator produces an electrical signal whose voltage and/or current is changing at an ultrasonic frequency to drive the transducer. The frequency of the electrical signal can be adjusted in the range of 10 to 40 kHz.

The transducer converts the electrical voltage or current into the mechanical vibration. Two types of transducers are commonly used in USM:

- The *magnetostrictive transducer* was extensively used prior to 1970. This transducer is constructed by surrounding a number of sheets of magnetostrictive material with a coil. When the strength of the electric current in the coil changes at an ultrasonic frequency, a mechanical ultrasonic vibration is generated in the magnetostrictive material. This transducer has a low energy conversion efficiency, usually less than 30%.
- The *piezoelectric ultrasonic transducer* is commonly used today. The geometrical dimensions of this transducer vary with the change in the applied electric field. A mechanical ultrasonic vibration is generated when the strength of the electric voltage applied across the transducer material changes at an ultrasonic frequency. This transducer has an extremely high energy conversion efficiency, up to 95%. The amplitude of the ultrasonic vibration generated directly by the transducer is very small, about 400 μin. (0.01 mm). A concentrator is used for amplifying the amplitude into a level that is acceptable for USM. The transducer is mounted on the larger end of the concentrator; the tool is mounted on the smaller end.

In the ultrasonic machine, the ultrasonic generator is held vertically on the ram that moves vertically, and the workpiece is mounted on an *x-y* table that determines the relative position between tool and workpiece. During machining, a force providing pressure between the tool and workpiece is added through the ram mechanism.

The material-removal rate during USM increases with an increase in the amplitude of ultrasonic vibration, grain size of the abrasive particles, and pressure between the tool and workpiece. The surface finish is essentially determined by the grain size for a given workpiece material; that is, the smaller the grain size, the better surface finish. The abrasive grains used in USM are usually in the range of 100 to 900 mesh number.

The USM process is limited by the softness of the material. Workpiece materials softer than Rockwell C40 result in prohibitively long cycles. The best machining rate can be obtained on materials harder than Rockwell C60.

References

Benedict, G.F. 1987. *Nontraditional Manufacturing Processes*, Marcel Dekker, New York.

McGeough, J.A. 1988. *Advanced Methods of Machining*, Chapman & Hall, London.

Rajurakar, K.P. 1994. Nontraditional manufacturing processes, in *Handbook of Design, Manufacturing and Automation*, Dorf, R.C. and Kusiak, A., eds., John Wiley & Sons, New York, 211–41.

Steen, W.M., 1991. *Laser Material Processing*, Springer-Verlag, New York.

Phase-Change Processes

Phase-change processes produce parts from materials originally in the liquid or vapor phase. These include processes such as metal casting and injection molding of polymers. The two most commonly used metal-casting processes are described in this section. The references listed at the end of the section contain detailed information on all phase-change unit processes.

Metal casting is one of the primary methods of producing bulk shapes. Very complex shapes can be cast from nearly every metal, making casting an extremely versatile process. Castings are made in sizes that range from fractions of an ounce to hundreds of tons.

The selection of the best molding and casting process for an application can be complex, and is governed by many factors, which include casting size, variation in thickness of the casting sections, required mold strength, required surface finish and dimensional accuracy, production rates, environmental factors (e.g., reclamation of the sand and type of sand binder), and cost. Casting processes fall into five categories (Kanicki 1988):

Conventional molding processes — Green sand, shell, flaskless
Precision molding and casting processes — Investment, permanent mold, die casting

Special molding and casting processes — Vacuum molding, evaporative pattern casting, centrifugal casting
Chemically bonded self-setting sand molding — No-bake, sodium silicate
Innovative molding and casting processes — Unbonded sand molding (Patz and Piwonka 1988), rheocasting, squeeze casting, electroslag casting

This section discusses the most widely used conventional molding process, green sand, and the most widely used precision molding and casting process, investment casting. The reference list at the end of the section should be consulted for detailed information on all casting processes.

Properly designed and manufactured castings provide many advantages, and are competitive with other unit process methods. Success with casting processes, as with every process, requires design and process engineers knowledgeable regarding the advantages and limitations of casting processes so that appropriate design and process choices can be made that avoid or minimize the occurrence of defects.

Table 13.2.14 summarizes the most common defects that occur during casting and suggests design and process changes that can avoid or reduce the effect of the defects. However, the suggested mitigation strategies may introduce different casting defects or the evolution of other problems, so each change should be carefully evaluated with regard to the system as a whole.

Green Sand Casting Processes

Sand-mold casting is adaptable to a very wide range of alloys, shapes, sizes, and production quantities. Hollow shapes can be produced in these castings through the use of cores. Sand-mold casting is by far the most common casting process used in industry; some estimates are that as many as 90% of industrial castings use the sand-mold casting process (O'Meara et al. 1988). Green sand molding is currently the most widely used of all sand casting methods, although dry sand methods are preferred for very large castings. "Green" sand refers to the fact that water is added to activate the clay binder. In dry sand molding, the moisture is removed prior to casting.

Green sand-mold casting involves mixing sand with a suitable clay binder (usually a bentonite clay) and other additives, and packing the sand mixture tightly around a pattern that is constructed from the part design. However, the pattern is not an exact replica of the part since various dimensional allowances must be made to accommodate certain physical effects. After extracting the pattern from the sand mold, a cavity is left behind that corresponds to the shape of the pattern. Next, molten metal is poured into this cavity and solidifies into a cast replica of the desired part. After the casting cools, the sand is readily removed from the casting and may be reclaimed for further use.

A *mold pattern* is constructed from the casting design with suitable modifications. Depending on the complexity of the part, CAD/CAM programs are able to design patterns that require very little adjustment to achieve desired solidification control and dimensional accuracy in the resulting casting (Berry and Pehlke 1988). The computation is complex and cannot be easily done for complex shapes. The principal adjustments that must be made to translate a part design to a mold design result from many considerations (ASM 1988). One needs to

- Compensate for shrinkage of the sand during the drying/curing operations.
- Compensate for expansion of the sand caused by the rapid introduction of the molten metal into the mold.
- Compensate for contraction of the liquid metal during freezing.
- Allow easy extraction of the pattern from the packed sand through a taper on the vertical sides of the pattern.
- Add a gating network to allow molten metal to smoothly flow into the cavity.
- Add risers (including size), as required in key locations to continue feeding molten metal into the solidifying casting.
- Add provisions for core prints, as required, to anchor cores that produce internal cavities that could not be directly molded from the pattern.

There are basically three types of molding methods, which are categorized by the resulting hardness or density of the sand mold (O'Meara et al. 1988; Brown 1988):

TABLE 13.2.14 Typical Casting Defects and Mitigation Strategy

Casting Defect	Description and Cause	Mitigation Strategy
Cold shuts	Appear as folds in the metal — occurs when two streams of cold molten metal meet and do not completely weld Possible causes: • Interruption in the pouring operation • Too slow a pouring rate • Improperly design gating	Pour as quickly as possible Design gating system to fill entire mold quickly without an interruption Preheat the mold Modify part design Avoid excessively long thin sections
Hot tears and cracks	Hot tears are cracklike defects that occur during solidification due to overstressing of the solidifying metal as thermal gradients develop Cracks occur during the cooldown of the casting after solidification is complete due to uneven contraction	Fill mold as quickly as possible Change gating system; e.g., use several smaller gates in place of one large gate Apply thermal management techniques within the mold (e.g., chills or exothermic material) to control solidification direction and rate Insulate the mold to reduce its cooling rate Modify casting design: • Avoid sharp transitions between thin and thick sections • Taper thin sections to facilitate establishment of appropriate solidification gradients • Strengthen the weak section with additional material, ribs, etc.
Inclusions	Presence of foreign material in the microstructure of the casting Typical sources: • Furnace slag • Mold and core material	Modify gating system to include a strainer core to filter out slag Avoid metal flow turbulence in the gating system that could cause erosion of the mold Improve hardness of the mold and core
Misruns	Incomplete filling of the mold cavity Causes: • Too low a pouring temperature • Too slow a pouring rate • Too low a mold temperature • High backpressure from gases combined with low mold permeability • Inadequate gating	Control mold and metal temperature Increase the pouring rate Increase the pouring pressure Modify gating system to direct metal to thinner and difficult-to-feed sections quicker
Porosity	Holes in the cast material Causes: • Dissolved or entrained gases in the liquid metal • Gas generation resulting from a reaction between molten metal and the mold material	Pour metal at lowest possible temperature Design gating system for rapid but uniform filling of the mold, providing an escape path for any gas that is generated Select a mold material with higher gas permeability
Microshrinkage	Liquid metal does not fill all the dendritic interstices, causing the appearance of solidification micro-shrinkage	Control direction of solidification • Design gating system to fill mold cavity so that solidification begins at the extremities and progresses toward the feed gate • Lower the mold temperature and increase the pouring temperature • Add risers, use exothermic toppings to maintain temperature longer • Control cooling rate using chills, insulators, etc. in selected portions of the mold

Low-density molding

- *Hand-ramming* is the oldest, slowest, and most variable method for packing sand around the pattern. It is rarely used for production, but it can be employed for prototypes or very limited production runs.
- *Jolt* machines operate with the pattern mounted on a table, which is attached to the top of an air piston. Typically, a flask is placed on the table with the pattern centered in the flask cavity. The flask is filled with sand. Compressed air lifts the piston, and then the air is released, allowing the entire assembly to fall with a sharp jolt. The sequence can be repeated. The sand is compacted by its own weight and is densest at the pattern plate.
- *Jolt-squeeze* molding machines employ the same pattern equipment as the jolt machines, but after the jolting operation, the sand is squeezed by hydraulic pressure to improve the packing uniformity in the mold.

Medium-density molding

- *Rap-jolt machines* are improved versions of the low-pressure machines, capable of exerting higher pressure to compact the sand.
- *Sand slingers* direct sand into a mold from a rotating impeller. Sand-packing density is a function of the centrifugal velocity of the impeller. This method is particularly useful for large molds.

High-pressure molding

- *Pressure wave* methods allow the sand to gravity fill the mold. Then, the top of the mold is sealed and a high-pressure wave is created by a controlled explosion of a combustible gas or by the rapid release of air pressure.
- *Horizontal flaskless molding* utilizes a pattern carrier to support the top half (cope) and bottom half (drag) of the mold pattern. The cope and drag are spaced apart in the carrier, and the space is evacuated. The molding setup is depicted in Figure 13.2.12. Vents in the pattern cause sand to be drawn into the mold. When the mold is filled, it is tightly squeezed.

The details of the *metal pouring* operation vary quite a bit depending on the metal, the material specification, the furnace type, and the foundry layout. A ladling method using gravity pressure is commonly used to transfer the molten metal, which may be alloyed, degassed, and so forth immediately before it is discharged into the poring basin that feeds the gating system of the castings.

A *gating system* must allow complete fill of a mold cavity without causing flow turbulence that can entrap loose sand or slag and feed shrinkage as the liquid metal within the mold cools. The gating system

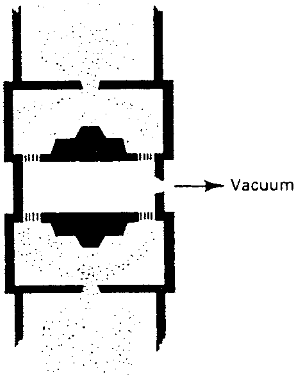

FIGURE 13.2.12 High-pressure vacuum-fill squeeze machine. (From *ASM Handbook*, *Machining*, vol. 15, 9th ed., ASM International, Metals Park, OH, 1989, 343. With permission.)

should be designed to promote progressive solidification from the point most distant from the gate toward the gate.

A *riser* is a reservoir of molten metal that is attached to the casting. It feeds the voids that develop within the casting as the liquid metal cools and begins to solidify. A thin skin of frozen metal first forms in a shell around the outer part of the mold cavity immediately after the metal is poured. This rigid shell serves as a mold for the remainder of the casting. The volume lost by the shrinkage of the metal as it solidifies within this shell must be replaced from a liquid metal source, such as a riser or a feeding gate, to prevent internal porosity. Risers are subsequently removed from the casting.

Management of thermal gradients within the solidifying casting is essential to minimize shrinkage. The solidification of risers can be slowed by the use of an *exothermic material* placed on top of a riser. The heat generated by this material can allow the riser to continue to feed the casting until it is solidified. *Chills* can be used to reduce the local temperature at the mold-casting interface, and thus accelerate freezing in selected locations, thereby establishing the solidification direction. Chills are usually metal inserts strategically placed in the mold. The mold can also be *insulated* to reduce the overall cooling rate of the casting if necessary to reduce residual stresses, but the metallurgical effect must be carefully considered.

In most cases, *electric furnaces* are used for melting, and pouring is nonpressurized.

Properly designed gating systems and risers should produce completely solid castings. A number of design rules for the gating and risering system have been developed for casting various metals to achieve continuous feeding of the solidifying casting. These rules are embedded in computer programs that aid design of casting molds and layouts.

It may be less expensive and easier to change the design than to develop a complex thermal management system within the mold. Typical design changes to evaluate include

- Thickening thin sections that feed heavier, more remote sections
- Reducing the mass of the remote thick section
- Adding a riser to feed separately the remote thick section

Each production step contributes to *dimensional variations* in a sand casting. For instance, dimensions are affected by the sand-packing density, by the process of withdrawing the pattern from the sand, by the moisture content of the sand, and by both the temperature of the molten metal and the speed with which it enters the mold cavity. The result is that sand casting is not inherently a precision process.

The surface finishes of sand castings are controllable only within rather wide limits (ASM 1988). Normally, the maximum allowable surface roughness is specified, and any smoother surface is acceptable. For instance, casting steel in green sand can have a surface roughness varying from 500 to 2000 μin. (12 to 50 μm), and aluminum from 125 to 750 μin. (3 to 20 μm). These values can be improved in certain instances through the application of coatings on the sand mold.

Porosity cannot be prevented in all cases. Changes to the part design and postcasting processing, such as hot isostatic pressing (HIP), should be considered.

Investment Casting

Investment castings are noted for their ability to reproduce extremely fine details and conform to very tight tolerances. As a result, these castings are used in critical, demanding structural applications, such as superalloy turbine airfoils and works of art.

The investment casting process employs a mold produced by enclosing an expendable pattern with a refractory slurry that is then hardened. The pattern, usually made from wax or plastic, is subsequently removed (e.g., by melting, dissolving, or burning), creating the desired mold cavity. The expendable patterns are themselves cast in a permanent pattern die. Ceramic cores can create internal passages within the casting.

Shell investment and solid investment processes are used in the production of investment castings (Horton 1988). The two processes differ in the method of mold preparation, not in pattern preparation or pattern assembly. In the shell investment process, the pattern assembly is precoated, dipped in a coating slurry, and covered with granulated refractory until the shell is built up to desired thickness, usually less than 0.5 in. (20 μmm); the thickness depends on the casting size and weight, cluster size, and type of ceramic and binder. As thin a shell as possible is specified to maximize mold permeability. Ceramic shell molds are used for the investment casting of carbon and alloy steels, stainless steels, heat-resistant alloys, and other alloys with melting points above 1100°C (2000°F).

The *ceramic material* used in shell investments is often silica, zircon (zirconium orthosilicate), an aluminum silicate, or alumina (Horton 1988). *Silica glass* (fused silica) is desirable because it is readily available, but it has a high coefficient of thermal expansion and an abrupt phase transition, and it cannot be used in vacuum casting because the silica decomposes at low vapor pressures, leading to severe metal-mold reaction. *Zircon* is readily available, is resistant to wetting by molten metal, and has a high refractoriness. Its use is limited to prime coats, though, because it is not available in large grain sizes. *Aluminum silicates*, such as mullite, can be manufactured to a range of pellet sizes and over a range of compositions. *Alumina* is more refractory than silica or mullite and is not very reactive with many metals.

The *binders* most often employed in shell investments are colloidal silica, ethyl silicate, and sodium silicate. *Colloidal silica* is an excellent general-purpose binder, and is the most widely used binder. Its primary disadvantage is that it is slow to dry. *Ethyl silicate* produces a bond between the refractory material that is very similar to that of colloidal silica. It dries much faster, but it poses a fire hazard and is more expensive. Liquid *sodium silicate* forms a strong, glassy bond. The material is inexpensive but its refractoriness is poor, and the bond deteriorates in the presence of steam used to remove the wax pattern.

In the *solid investment process*, the pattern assembly is placed in a flask, which is filled with a refractory mold slurry. This slurry hardens in air, forming a solid mass in which the pattern assembly is encased. The types of bonding materials and refractories differ depending on the pouring temperature of the metal. For nonferrous alloys, pouring temperature is usually below 2000°F (1100°C). In these cases, *alpha gypsum* is commonly used as both the refractory and the binder, with other refractories such as silica added to improve mold permeability. The process is primarily used for making dental and jewelry castings.

For extremely limited production and for the development of production process parameters, investment mold patterns can be directly machined from an expendable material, such as plastic. For production-level investment casting, however, the patterns are produced by injecting wax or plastic into *permanent pattern molding dies*. The dimensional tolerance of these permanent dies must be closely controlled.

A mixture of paraffin and microcrystalline wax is widely used for making investment casting patterns (Horton 1988). Waxes are strong, stiff, and provide adequate dimensional control during pattern making. They are easy to remove with pressurized saturated steam or elevated temperatures. *Plastic* patterns have several advantages compared with wax: higher strength, less subject to handling damage, can withstand automatic ejection from the pattern mold, and can reproduce thinner sections, finer definition, sharper corners, and better surface finish. But a major disadvantage is that certain plastics, such as polystyrene, expand during burnout and can crack ceramic shell molds.

Some investment castings require complex internal cavities (e.g., holes and air passages). For complicated shapes, the pattern-die *cores* are used to form portions of the pattern that cannot be withdrawn after the pattern is made. The cores must subsequently be dissolved or etched out from the casting.

As much *gating* as possible is included in the wax patterns. This allows use of standard methods of joining patterns together so that a number of investment castings can be produced during one pouring operation.

Investment casting is done in air and in vacuum. *Gravity pouring* fills the pouring basin from a ladle or directly from a furnace. This method requires low equipment investment but highly skilled operators. In pressure pouring the molds are filled from the furnace with an assist from a pressurized gas to fill rapidly thin sections. With *vacuum-assisted pouring*, a vacuum pump evacuates air from a mold ahead of the stream of molten metal to minimize flow resistance. *Centrifugal casting* uses a spinning mold assembly to develop added pressure to fill the mold.

Investment castings do the following:

- Produce complex shapes that are difficult to make by other means.
- Reproduce fine detail, high dimensional accuracy, and smooth surfaces requiring only minimal finishing.
- Adapt to most metal alloys.
- Allow control of metallurgical properties, such as grain size and grain orientation.

A tolerance of ±0.002 in. (0.05 mm) can be held on investment castings for each inch in its maximum dimension; however, a tolerance of ±0.005 in. (0.13 mm) is more typical (Horton 1988). A surface finish of 125 min. (3 mm) can be readily achieved, and surface finishes as smooth as 30 to 40 min. (0.8 to 1.0 mm) can be produced with suitable process control.

The size and weight of castings that can be investment cast are usually limited by physical and economic considerations. Generally, the process can be applied cost-effectively to casting weighing up to 10 lb (4.5 kg); investment castings weighing 50 lb (22.5 kg) are not unusual, and castings as large as 1000 lb (450 kg) are feasible. The initial tooling costs of investment casting can be high.

References

ASM. 1988. In *Casting*, vol. 15, *ASM Handbook*, 9th ed., ASM International, Metals Park, OH.

Berry, J.T. and Pehlke, R.D. 1988. Modeling of solidification heat transfer. In *Casting*, vol. 15, *ASM Handbook*, 9th ed., ASM International, Metals Park, OH, 860ff.

Brown, R.B. 1988. Sand processing. In *Casting*, vol. 15, *ASM Handbook*, 9th ed., ASM International, Metals Park, OH, 341–51.

Horton, R.A. 1988. Investment casting. In *Casting*, vol. 15, *ASM Handbook*, 9th ed., ASM International, Metals Park, OH, 253–69.

Isayev, A.I. Ed., 1987. *Injection and Compressive Molding Fundamentals*, Marcel Dekker, New York.

Kanicki, D.P. 1988. Casting advantages, applications, and market size. In *Casting*, vol. 15, *ASM Handbook*, 9th ed., ASM International, Metals Park, OH, 37–45.

O’Meara, P., Wile, L.E., Archibald, J.J., Smith, R.L., and Piwanka, T.S. 1988. Bonded sand molds. In *Casting*, vol. 15, *ASM Handbook*, 9th ed., ASM International, Metals Park, OH, 222–30.

Patz, M. and Piwonka, T.S. 1988. Unbonded sand molds. In *Casting*, vol. 15, *ASM Handbook*, 9th ed., ASM International, Metals Park, OH, 230–37.

Structure-Change Processes

Structure-change processes alter the microstructure of a workpiece. These changes can be achieved through thermal treatment involving heating and cooling (quenching) under controlled conditions, sometimes in combination with mechanical forces, in order to effect desired solid-state phase transformations. These processes include those that diffuse selected species into a surface layer to modify its composition or to create a thin layer of material that does not increase the dimensions of the workpiece.

The two structure-change processes described here are representative examples. *Normalization of steel* is a process that changes bulk properties of a workpiece. *Laser surface hardening* of steel only changes its surface properties; it does not affect the bulk properties. Even though both examples relate to ferrous materials, structure-change processes are used to impart desired properties to many material systems; for example, age hardening of aluminum alloys. The references listed at the end of this section contain detailed information on structure-change processes.

Normalizing Steel

Normalizing is a heat-treating process that results in a relatively uniform steel microstructure. Essentially all the standard carbon steels can be normalized. The resulting phases and their size/distribution depend heavily on the carbon content of the steel. Normalization treatments are performed for a variety of reasons (Ruglic 1991):

- Refines the dendritic grain structure remaining from casting
- Eliminates severe texture (and hence anisotropic properties) that results from forging and rolling operations
- Reduces residual stresses
- Improves the response of a steel to further processing, such as machining or surface hardening
- Improves mechanical properties by precipitating desirable phases

The steel workpiece must be heated sufficiently high to transform the entire structure to austenite, a face-centered cubic phase that essentially solutionizes all the carbon (at room temperature iron exists as ferrite, a body-centered cubic phase that has a very low carbon solubility). Diffusion-controlled solid-state phase transformations require time at temperature to occur. Therefore, the workpiece must be held at temperature long enough for austenite to dissolve the carbon.

The workpiece is then cooled slowly enough to avoid trapping the carbon in a supersaturated solution as the iron transforms back from austenite to ferrite. A time–temperature-transformation curve depicts which phase transformations will occur for different cooling gradients. A typical T-T-T curve is shown in Figure 13.2.13, which depicts the difference between a normalizing cool rate and that for annealing. For the normalization treatment to be successful, the regions in the microstructure with a carbon content of 0.8% carbon precipitate fine lamellae of ferrite and iron carbide (Fe_3C) on cooling, known as pearlite. Those areas low in carbon content should precipitate ferrite grains during the initial phase of the cooling cycle, followed by pearlite precipitation. The regions high in carbon should precipitate iron carbide in the austenite grain boundaries, followed by pearlite precipitation (Ruglic 1991).

The end result of normalization is a microstructure, and hence the mechanical properties characteristic of the composition of the steel (primarily governed by carbon content) as opposed to a microstructure that was principally shaped by its previous thermomechanical processing.

Conventional heat-treating furnaces are used for normalization, such as batch or continuous furnaces (Ruglic 1991). The rate of heating is not critical. The furnaces must be able to heat the component to about 100°F (55°C) into the austenitizing region — this temperature depends on the composition of the steel.

Control of the cooling rate is critical. In the usual case, a workpiece can be removed from the furnace and allowed to air cool uniformly until the diffusion-controlled phase transformations are completed.

The ability to normalize the microstructure of steel is governed by thermodynamics. Phase stability and kinetics of the phase transformations are crucial. But heat transfer considerations also play a major role. For instance, it may not be possible to achieve the desired cooling gradient in the center of a thick section, and hence the properties of such sections will not be uniform.

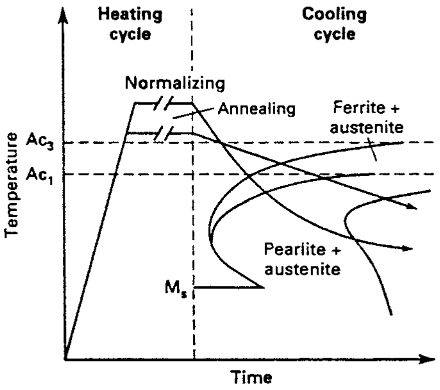

FIGURE 13.2.13 Time–temperature-transformation curve for normalizing compared to annealing. (From *ASM Handbook*, *Heat Treating*, vol. 4, 10th ed., ASM International, Metals Park, OH, 1991, 35. With permission.)

For complex shapes or for those workpieces having a high degree of residual stresses, some distortion will occur during the normalization process. The extent of distortion can be reduced by appropriate fixturing, but it cannot be eliminated. Hence, some tolerance allowance must be made.

Laser Surface Hardening

Laser surface hardening is used as an alternative to flame hardening and induction hardening ferrous materials. The rapid heating rate achievable by the laser minimizes part distortion and can impart surface hardness to low-carbon steels. The ability to locate the laser some distance from the workpiece can also be advantageous. The entire operation can be performed in air. This process is used to harden selected areas of machine components, such as gears, cylinders, bearings, and shafts.

Laser surface hardening imparts wear resistance and strength to the surface of a component without affecting its overall dimensions or changing its bulk properties. It is applied to selected areas that can be accessed by a laser beam. The process relies on rapid laser heating, followed by rapid quenching, to effect the necessary degree of hardening through phase transformation. The result is a very fine grain structure that is extremely hard. Typical case depth is a function of the composition of the ferrous material, but it will usually not exceed 0.1 in. (0.25 cm). For low- and medium-carbon steels, the case depth will range from 0.01 to 0.05 in. (0.03 to 0.13 cm), with the case depth increasing as the carbon content increases (Sandven 1991).

An industrial laser rapidly heats a thin surface layer into the austenite phase region (austenite is a face-centered cubic allotropic phase of iron that has a high solubility for carbon). The interior of the workpiece is unaffected. When the laser beam is moved, the heated surface quickly cools. Consequently, the carbon does not have time to diffuse as the iron attempts to transform back to its ferrite (body-centered cubic) structure. The resulting microstructure is extremely hard since the trapped carbon atoms distort the iron crystal structure into a highly strained body-centered tetragonal form, known as martensite.

The majority of *industrial metalworking lasers* are either solid-state Nd:YAG or carbon dioxide type. Either pulsed or continuous mode can be used for surface treatment. The power output range for YAG lasers is 50 to 500 W. Carbon dioxide lasers are available in much higher power levels, up to 25 kW.

The surface to be hardened is usually *coated* to improve its ability to absorb laser radiation. A typical coating is manganese phosphate. *Paints* containing graphite, silicon, and carbon are also used. These coatings/paints can increase the absorption of laser energy to 80% to 90% (Sandven 1991).

The output beam of the laser must be shaped and directed by an *optical system* to generate a laser spot of desired shape and size at the correct location on the workpiece surface. Reflective optical components are used since they are sturdy and easily adapted to an industrial environment.

Many factors affect the end result of laser surface hardening. Important is the hardenability of the workpiece material, which is affected by its composition and prior thermomechanical history. For the laser process, the key parameters are beam power density, uniformity of the beam, and processing speed. Following are some general processing guidelines (Sandven 1991):

- The range of usable power densities for laser surface hardening is 3200 W/in.^{2} (500 W/cm^2) to 32,000 W/in.^{2} (5000 W/cm^2) with beam dwell times ranging from 0.1 to 10 sec; higher power levels would melt the surface.
- Alloys with high hardenability can be processed at low speed with low power density to produce relatively thick cases.
- Alloys with low hardenability should be processed at high speed with high power density; the result is a shallow case.
- Beam configuration can be rectangular, square, or round; uniform energy density within the beam is very important.
- Maximum achievable surface temperature is proportional to the square root of the processing speed; thus, doubling the beam power density requires the processing speed to be increased by a factor of four to maintain the equivalent maximum surface temperature.
- Smaller workpieces are not as effective a heat sink as larger workpieces, and hence self-quenching may have to be assisted by quenching media.

The depth of hardness that can be practically achieved is limited by the surface melting point. Because of the high beam energy density, heat flow on complex-shaped surfaces, particularly those involving sharp corners or edges, can cause unexpected surface melting. Therefore, power density and process conditions must be carefully controlled.

It may be necessary to overlap passes of the laser beam, such as at the end of a complete pass around a cylinder. As a result, some tempering of the area already hardened occurs. The slower the processing speed, the greater the degree of tempering.

References

ASM. 1995. *Heat Treater's Guide: Practices and Procedures for Irons and Steels*, 2nd ed., ASM International, Metals Park, OH.

Boyer, H.E. 1982. *Practical Heat Treating*, ASM International, Metals Park, OH.

Brooks, C.R. 1982. *Heat Treatment, Structure and Properties of Nonferrous Alloys*, ASM International, Metals Park, OH.

Ruglic, T. 1991. Normalizing of steel. In *Heat Treating, ASM Handbook*, vol. 4, 10th ed., ASM International, Metals Park, OH, 35–42.

Sandven, O.A. 1991. Laser surface hardening. In *Heat Treating, ASM Handbook*, vol. 4, 10th ed., ASM International, Metals Park, OH, 286–96.

Sudarshan, T.S., ed. 1989. *Surface Modification Technologies*, Marcel Dekker, New York.

Deformation Processes

Deformation processes change the shape of an object by forcing material to flow plastically from one shape into another shape without changing mass or composition (Table 13.2.15). The initial shape is usually simple. This shape is plastically deformed between tools or dies to obtain the final desired geometry, properties, and tolerances. A sequence of such processes is generally used to progressively form material. Deformation processes, along with casting and machining, have been the backbone of modern mass production.

In addition to shape change, forming processes alter the microstructure of the workpiece and can improve material properties. Deformation processes are normally considered when (Semiatin 1988)

- Part geometry is moderately complex.
- Component properties and structural integrity are important.
- Sufficient production volume can amortize tooling costs.

Deformation processes can be classified (Semiatin 1988) as bulk forming processes and sheet forming processes.

Bulk forming processes (e.g., rolling, extrusion, and forging) are characterized by

- Input material form is a billet, rod, or slab.
- Workpiece undergoes a significant change in cross section during forming.

TABLE 13.2.15 Significant Factors in Modeling a Deformation Process

Process Component	Characteristics
Input material	Flow stress; workability; surface condition
Output material	Geometry; mechanical properties; dimensional accuracy and tolerances; surface finish
Deformation zone	Deformation mechanics; stress state; temperature
Tooling	Material and geometry; surface conditions; temperature
Tool/material interface	Friction and lubrication; heat transfer
Process equipment	Speed and production rate; power range; precision

Sheet metal forming processes (e.g., stretching, flanging, and drawing) are characterized by

- Input material is a sheet blank.
- Workpiece is deformed into a complex three-dimensional form without appreciably changing the cross section.

The key to attaining desired shape and properties is controlling metal deformation (Altan et al. 1983). The direction of the metal flow, the magnitude of the deformation, the rate of deformation, and the processing temperatures greatly affect the properties of the formed part. Design of the end product and the required deformation process consists of these steps:

- Predicting metal flow by analyzing kinematic relationships (e.g., shape, velocities, strain rates, and strains) between the deformed and undeformed part configurations
- Establishing producibility limits
- Selecting the process equipment and tooling capable of operating within the producibility limits

A bulk forming process (forging) and a sheet forming process (bending) are described next as representative examples of deformation processes. The references listed at the end of the section should be consulted for further information on these unit processes.

Die Forging

Talyan Altan

Forging involves the controlled plastic deformation of metals into useful shapes (ASM 1988c). Deformation may be accomplished by means of pressure, impact blows, or a combination. To reduce the flow stress, forging is usually accomplished at an elevated temperature. Forging refines the microstructure of a metal and can improve its mechanical properties, especially in preferred directions. Forging can also be used for other purposes, such as to consolidate powder preforms by welding grains, eliminate porosity in castings, break up long inclusions in forgings, and demolish the dendritic structure resulting from casting (Altan 1988a).

Forgings are generally considered when strength, reliability, fracture toughness, and fatigue resistance are important. Forgings are used in critical, high-load applications, such as connecting rods, crankshafts, transmission shafts and gears, wheel spindles, and axles. Military and commercial aircraft are major users of forgings for numerous critical items, such as bulkheads, beams, shafts, landing gear cylinders and struts, wheels, wing spars, and engine mounts. Similarly, jet engines depend on forgings for disks, blades, manifolds, and rings.

There are two broad categories of forging processes: closed-die forging and open-die forging. *Closed-die forging*, also known as *impression die forging*, employs precision-machined, matching die blocks to forge material to close dimensional tolerances. Large production runs are generally required to justify these expensive dies. During forging, the die cavity must be completely filled. To ensure this, a slight excess of material is forged. Consequently, as the dies close, the excess metal squirts out of the cavity in a thin ribbon of metal, called flashing, which must be trimmed.

Isothermal forging in heated superalloy dies minimizes the die quenching effect, preventing the rapid cooling of the workpiece in cold dies. This allows complete die fill and the achievement of close dimensional tolerances for difficult to process materials, such as superalloys.

Open-die forgings are the least refined in shape, being made with little or no tooling (Klare 1988). These forgings are large, relatively simple shapes that are formed between simple dies in a large hydraulic press or power hammer. Examples are ship propeller shafts, rings, gun tubes, and pressure vessels. Since the workpiece is always larger than the tool, deformation is confined to a small portion of the workpiece at any point in time. The chief deformation mode is compression, accompanied by considerable spreading in the lateral directions.

There are two major classes of forging equipment as determined by their principle of operation: forging hammer, or drop hammer, which delivers rapid impact blows to the surface of the metal, and forging press, which subjects the metal to controlled compressive force. Each of these classes of forging equipment needs to be examined with respect to load and energy characteristics, its time-dependent characteristics, and its capability for producing parts to dimension with high accuracy.

Forging hammers generate force through a falling weight or ram (Altan 1988b). These machines are energy restricted since the deformation results from dissipating the kinetic energy of the ram. The forging hammer is an inexpensive way to generate high forging loads. It also provides the shortest contact time under pressure, ranging from 1 to 10 msec. Hammers generally do not provide the forging accuracy obtainable in presses.

Forging presses are either mechanical or hydraulic (Altan 1988c). *Mechanical forging presses* are stroke-restricted machines since the length of the press stroke and the available load at various positions of the stroke represent their capacity. Most mechanical presses utilize an eccentric crank to translate rotary motion into reciprocating linear motion of the press slide. The blow of the press is more like a squeeze than an impact of a hammer. Because of this, dies can be less massive and die life is longer than with a hammer. *Hydraulic presses* are load-restricted machines in which hydraulic pressure actuates a piston that squeezes the die blocks together. Full press load is available at any point during the stroke of the ram. A hydraulic press is relatively slow, resulting in longer process time; this may cause undesirable heat loss and die deterioration.

Preform design is the most difficult and critical step in forging design. Proper preform design assures defect-free flow, complete die fill, and minimum flash loss. Although metal flow consists only of two basic types, extrusion (flow parallel to die motion) and upsetting (flow perpendicular to the direction of die motion), in most forgings both types of flow occur simultaneously, leading to a very complex flow field. An important step in understanding metal flow is to identify the neutral surfaces. Metal flows away from the neutral surface in a direction perpendicular to the die motion. Ideally, flow in the finishing step should be lateral toward the die cavity without additional shear at the die-workpiece interface. This type of flow minimizes forging load and die wear. A milestone in metalworking is the use of CAD in establishing the proper design for preforming and finishing dies in closed-die forging (Gegel and Malas 1988). Figure 13.2.14 illustrates the relationships between forging process variables and those of a forging press that must be understood in order to estimate process performance for a hot-forging operation.

Designing a mechanical component that is to be made by forging together with the optimum geometry for the forging dies requires analysis of many factors (Altan 1988a), including

- Design rules
- Workpiece material specification and its critical temperatures
- Flow stress of the material at the process conditions (e.g., temperature, temperature gradient, strain rate, total strain)
- Workpiece volume and weight
- Frictional conditions in the die
- Flash dimensions
- Number of preforming steps and their configuration (flow field for the material)
- Load and energy requirements for each forging operation
- Equipment capability

In closed-die forging, it is particularly difficult to produce parts with sharp fillets, wide thin webs, and high ribs. Moreover, dies must be tapered to facilitate removal of the finished piece; draft allowance is approximately 5° for steel forgings (see Table 13.2.16).

Press-Brake Forming

Press-brake forming is a process used for bending sheet metal; the workpiece is placed over an open die and then pressed into the die by a punch that is actuated by a ram known as a press brake (ASM 1988b). The main advantages of press brakes are versatility, ease and speed with which new setups can be made, and low tooling costs.

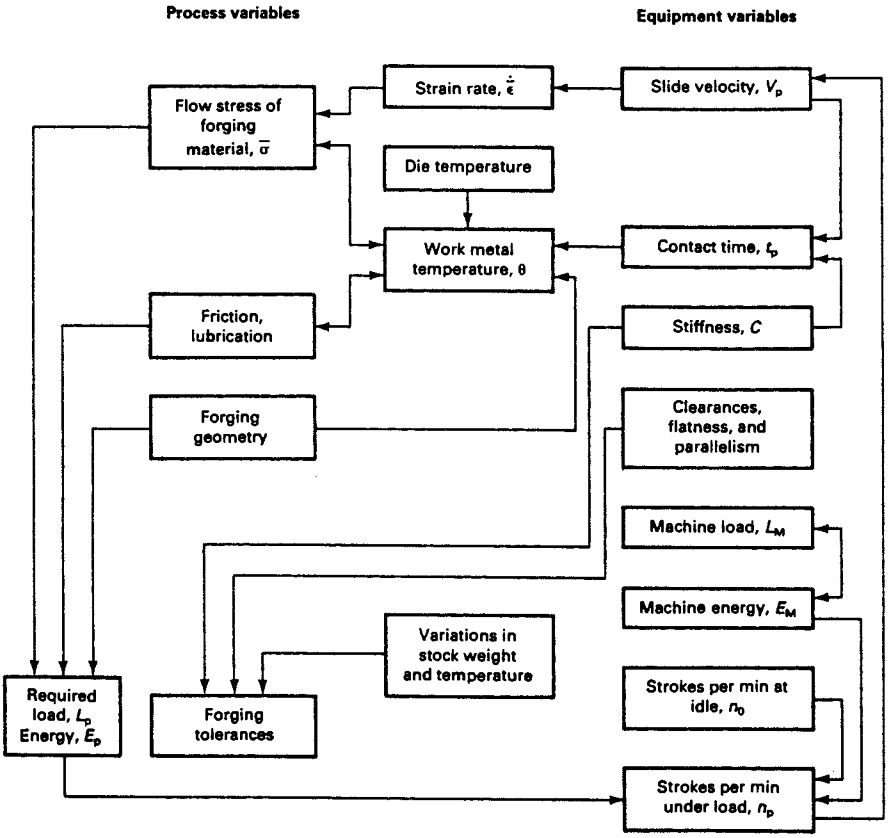

FIGURE 13.2.14 Relationships between process and machine variables in hot-forging processes conducted in presses. (From *ASM Handbook*, *Forming and Forging*, vol. 14, 9th ed., ASM International, Metals Park, OH, 1988, 36. With permission.)

Press-brake forming is widely used for producing shapes from ferrous and nonferrous metal sheet and plate. Although sheet or plate 0.250 in. (10 mm) thick or less is commonly formed, metals up to 1 in. (25 mm) thick are regularly formed in a press brake. The length of a sheet is limited only by the size of the press brake. Forming can be done at room or elevated temperature. Low-carbon steels, high-strength low-alloy steels, stainless steels, aluminum alloys, and copper alloys are commonly formed in a press brake. Press-brake forming is applicable to any metal that can be formed by other methods, such as press forming and roll forming.

Press-brake forming is considered for bending sheet metal parts when the production quantities are small, dimensional control is not critical, or the parts are relatively long. In contrast, press forming would be considered when production quantities are large, tolerances are tight, or parts are relatively small. Contour roll forming would be another option for high-rate production applications (ASM 1988c).

Bending is a method of forming sheet metal by stressing a material beyond its yield strength while remaining below its ultimate strength so that cracking is avoided. In press-brake forming the tooling and setup are relatively simple. A workpiece is placed over a die, typically having a V-shape. The bend angle is determined by the distance the workpiece is pressed into the die by the punch. The width of the die opening (the top of the V) affects the force needed to bend the workpiece. The minimum width is determined by the thickness of the workpiece and the radius of the punch nose.

A *press brake* is basically a slow-speed punch press that has a long, relatively narrow bed and a ram mounted between end housings. Rams are mechanically or hydraulically actuated. Figure 13.2.15 depicts a typical setup for press-brake forming.

TABLE 13.2.16 Typical Forging Defects and Mitigation Strategies

Defect	Description and Cause	Mitigation Strategy
Surface cracking	Fine cracks in the surface of the forging Possible causes: • Excessive working of the surface at too low a temperature • Brittle or low melting phases in the grain boundaries • Cracking at the die parting line	Increase the amount of preheating of the forging billet and forging die Change material specification Change furnace atmosphere to avoid diffusion of unwanted elements Increase the flash thickness Relocate the die parting line to a less critical location Stress relieve the forging prior to flash removal
Cold shut	Appears as a fold; occurs when two surfaces of metal fold against each other without welding Possible causes: • Poor metal flow in the die • Excessive chilling during forging • Poor die lubrication	Redesign forging die and/or forging preform to improve plastic flow of the metal during the forging operation Redesign the forging to avoid areas which are difficult to fill Increase the amount of preheating of the forging billet and forging die Improve die lubrication
Underfill	Incomplete forging in which all details are not produced Possible causes: • Debris residue in die • Scale on forging billet • Billet too small to completely fill die	Clean die thoroughly Completely descale the billet Redesign preform
Internal cracks	Cracks not visible from the surface, but detected during inspection and/or exposed during metal removal Possible causes: • Scale embedded in the internal structure of the forging • High residual tensile stresses	Completely descale the billet For open-die forgings, use concave dies Redesign for closed-die forging Use a hydraulic press and heated dies to avoid formation of excessive tensile stresses during forging

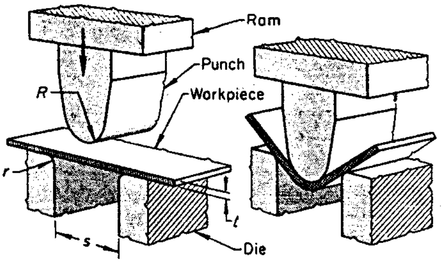

FIGURE 13.2.15 Typical setup for press-brake forming. (From *ASM Handbook*, *Forming and Forging*, vol. 14, 9th ed., ASM International, Metals Park, OH, 1988, 533. With permission.)

V-bending dies and their corresponding punches are the tools most commonly used in press-brake forming. The width of the die opening is usually a minimum of eight times the sheet thickness.

Capacities of commercial press brakes range from 8 to 2500 tons. Required capacity is governed by the size and bending characteristics of the work metal and by the type of bend to be made (ASM 1988b).

The nose radius of the punch should not be less than the work-metal thickness for bending low-carbon steel, and must be increased as the formability of the workpiece material decreases. The radius of the V-bending die must be greater than the nose radius of the punch by an amount at least equal to the workpiece thickness to allow for the bottoming of the punch in the V.

It is preferable to orient a bend so that it is made across the rolling direction rather than parallel to it. Sharper bends can be made across the rolling direction without increasing the probability of cracking the material. If bends must be made in two or more directions, the workpiece should be oriented on the sheet layout such that none of the bends will be parallel to the rolling direction.

Springback after press-brake bending is considered only when close dimensional control is needed. It can be readily compensated for by overbending. Factors that affect springback include the mechanical properties of the work material, the ratio of the bend radius to stock thickness, the angle of bend, the method of bending, and the amount of compression in the bend zone. A greater amount of overbending is needed to correct for springback on small bend angles than on large bend angles.

The generally accepted tolerance for dimensions resulting from bending of metal sheet in the press brake is ±0.016 in. (±0.4 mm) up to and including 0.125 in. (3 mm) thickness (ASM 1988b). For heavier gauges, the tolerance must be increased accordingly. Achievable tolerances are influenced by the part design, stock tolerances, sheet metal blank preparation, the condition of the machine and its tooling, and operator skill.

In press-brake forming, as in other forming processes, the metal on the inside portion of the bend is compressed or shrunk, and the metal on the outside portion is stretched. This results in a strain gradient across the thickness of the workpiece in the area of the bend with tensile strain on the outside and compressive strain inside. These residual strains (and resulting stresses) can lead to distortion of the part under loading conditions, heating, or cooling.

The formability of metals decreases as the yield strength approaches the ultimate strength. In press-brake forming, as the yield strength of the work metal increases, power requirements and springback problems also increase, and the degree of bending that is practical decreases.

There are several factors that will make it difficult to establish or maintain accurate placement of a bend line in a press brake. Corrective action may require a design change or change in processing sequence:

- Bends or holes that are located in close proximity to the required bend line can cause the position of the bend line to wander.
- Notches and cutouts located directly on the bend line make it difficult to maintain an accurate bend location.
- Offset bends will shift location unless the distance between bends in the offset is at least six times the thickness of the workpiece material.

If multiple bends must be made on a workpiece, it may not be possible to avoid a bend that is parallel to the rolling direction. Depending on the degree of texture in the sheet and the anisotropy of the material, a change to a higher-strength material may be necessary to achieve the desired geometry.

References

Altan, T. 1988a. Selection of forging equipment. In *Forming and Forging*, *ASM Handbook*, vol. 14, 9th ed., ASM International, Metals Park, OH, 36–42.

Altan, T. 1988b. Hammers and presses for forging. In *Forming and Forging*, *ASM Handbook*, vol. 14, 9th ed., ASM International, Metals Park, OH, 25–35.

Altan, T., Oh, S.I., and Gegel, H.L. 1983. *Metal Forming: Fundamentals and Applications*, ASM International, Metals Park, OH.

ASM. 1988a. Closed-die forging in hammers and presses. In *Forming and Forging*, *ASM Handbook*, vol. 14, 9th ed., ASM International, Metals Park, OH, 75–80.

ASM. 1988b. Press-brake forming. In *Forming and Forging*, *ASM Handbook*, vol. 14, 9th ed., ASM International, Metals Park, OH, 533–545.

ASM. 1988c. *Forming and Forging*, *ASM Handbook*, vol. 14, 9th ed., ASM International, Metals Park, OH.

Gegel, H.L. and Malas, J.C. 1988. Introduction to computer-aided process design for bulk forming. In *Forming and Forging*, *ASM Handbook*, vol. 14, 9th ed., ASM International, Metals Park, OH, 407ff.

Klare, A.K. 1988. Open-die forging. In *Forming and Forging, ASM Handbook*, vol. 14, 9th ed., ASM International, Metals Park, OH, 61–74.

Kobayashi, S., Oh, S., and Altan, T. 1989. *Metalforming and Finite Element Methods*, Oxford Press, New York.

Lascoe, O.D. 1988. *Handbook of Fabrication Processes*, ASM International, Metals Park, OH.

Muccio, E.A. 1991. *Plastic Part Technology*, ASM International, Metals Park, OH.

Semiatin, S.L. 1988. Introduction to forming and forging processes. In *Forming and Forging, ASM Handbook*, vol. 14, 9th ed., ASM International, Metals Park, OH, 17–21.

Consolidation Processes

Consolidation processes fuse smaller objects such as particles, filaments, or solid sections into a single solid part or component to achieve desired geometry, structure, and/or property. These processes use either mechanical, chemical, or thermal energy to bond the objects. Interaction between the material and the energy that produces the consolidation is a key feature of the process.

Consolidation processes are employed throughout manufacturing, from the initial production of the raw materials to final assembly. One group of processes involves the production of parts from powders of metals, ceramics, or composite mixtures. The resultant consolidated products are typically semifinished and require further processing. For instance, the consolidation of powders produces bar, rod, wire, plate, or sheet for upstream processes.

The consolidation of net shape composite structures (i.e., require minimal finishing work) is an increasingly important area. The design of the structural geometry, selection of material, and choice of consolidation processes all act together to provide the required level of performance. There are two types of matrix materials used: themosetting and thermoplastic. The consolidation process of each of these types of resins is different. A unit process described in this section addresses the consolidation of composites using polymeric thermosetting resins.

An important family of consolidation processes includes welding and joining processes used to permanently assemble subcomponents. Historically, welding and joining processes are developed empirically and quickly evaluated for benefit in manufacturing applications, driven by the promise of significant potential benefits. The need for welding and joining is substantial since only monolithic parts can be made without joining. The ideal joint would be indistinguishable from the base material and inexpensive to produce (Eagar 1993). However, experience indicates that no universal joining process exists that can entirely satisfy the wide range of application needs, and thus design engineers must select the most appropriate joining methods that meet requirements. Shielded metal-arc welding, the most widely used welding process, is described in this section.

The unit processes described here are a representative sample of the types most likely to be encountered. The references listed at the end of the section should be consulted for detailed information on these unit processes.

Polymer Composite Consolidation

Weiping Wang, Alan Ridilla, and Matthew Buczek

A composite material consists of two or more discrete materials whose combination results in enhanced properties. In its simplest form, it consists of a reinforcement phase, usually of high modulus and strength, surrounded by a matrix phase. The properties of the reinforcement, its arrangement, and volume fraction typically define the principal mechanical properties of a composite material. The matrix keeps the fibers in the correct orientation and transfers loads to the fibers.

Continuous-fiber-reinforced materials offer the highest specific strengths and moduli among engineering materials. For example, a carbon fiber/epoxy structural part in tensile loading has only about 20% of the weight of a steel structure of equal stiffness. Composite parts can integrate component piece parts, such as molded-in rib stiffeners, without the need for subsequent assembly operations and fasteners.

Many types of polymer composites are in use. Composities are usually identified by their fiber material and matrix material. Fiber materials are necessarily strong, stable materials that can be processed into fiber formats. Typcial fibers are glass, graphite/carbon, aramid, and boron. *Glass* fibers represent the largest volume usage since they have excellent properties and are low cost. *Graphite/carbon* fibers are widely used for advanced composite applications in which stiffness and high performance are critical. These fibers are also expensive. *Aramid* fibers, a type of polyamide, have proved useful in applications where its performance in axial tension can be exploited without incurring too severe a penalty by the material's poor performance under compressive loading. *Boron* filaments have high strength and high modulus, but most applications requiring high performance, such as military aircraft structures, are now using carbon fibers.

Low-cost *polyester* resins are the most widely used matrix material for the general composite industry; the majority of these applications use glass as the fiber. Many applications are found in the chemical process, construction, and marine industry. The most widely used polymers are *epoxy* resins, which are used with carbon, aramid, and boron fibers for many advanced applications, such as in aircraft structure and rocket motor fuel tanks. *Polyimides* are polymer resins that provide more temperature performance than is possible from the epoxy-based material, and they are used in advanced aircraft structures and jet engine components where heating of the structure will occur.

Each of the constituent materials in advanced composites acts synergistically to provide aggregate properties that are superior to the materials individually. The functional effectiveness of composites is principally due to the anisotropy of the materials and the laminate concept, where materials are bonded together in multiple layers. This allows the properties to be tailored to the applied load so that the structure can be theoretically more efficient than if isotropic materials were used. The reinforcements come in a variety of formats. Unidirectional tapes with all fibers along a common axis, woven fabrics constructed with fibers along both axes in the *x-y* plane, and multidimensional architectures with reinforcements in more than one axial direction are just a few of the available formats.

Consolidation in composites can be considered to occur at two levels: the fibers are infiltrated with the matrix to form a lamina or ply, and the individual laminae are consolidated together to form the final structure. In the prepreg process, these two levels are distinctly separated, since the fiber/matrix consolidation process forms the prepreg, which is then laid up to form the laminate or final component. In other processes, such as resin transfer molding, fiber/matrix infiltration and the consolidation of the final part are done in a single stage. Single-stage consolidation processes are attractive because they eliminate the additional cost associated with prepreg production; however, two-stage consolidation processes have major advantages that often outweigh the benefits of single-stage consolidation. These include flexibility in part geometry, high fiber content, excellent fiber wet-out, and better control of fiber volume fraction distribution. Because of these advantages, prepreg processing is firmly entrenched in high-value products, such as aerospace applications, in spite of its high cost.

Typical steps in manufacturing continuous-fiber composites involve *preform fabrication* and consolidation/curing (Advani 1994). Preform fabrication creates the structure by positioning material close to the final part shape (Table 13.2.17). The material comes in either the *dry fiber* (without resin) form or with resin included, called prepreg. Dry fibers are used in filament winding, weaving, braiding, and pultrusion. The resin can be introduced in the operation or downstream molding. *Prepreg*, at a higher material cost, eliminates the step of resin addition and provides the adhesion to hold the material together. Consolidation/curing involves compacting the preform to remove entrapped air, volatiles, and excess resins while developing the structural properties by increasing the polymer chain length and cross-linking.

Thermosetting polymeric materials will not soften and flow upon reheating after polymerization because of the formation of a cross-linked polymer network. Therefore, thermosetting polymer matrices must be cured *in situ* with the fibers to form the composite structure. The goals of a successful cure are good consolidation with low porosity and high conversion of initial monomeric constituents to polymer.

The challenge of the cure process is to manage the interactions of temperature distribution, degree of cure, laminate thickness, and void content by manipulating the applied temperature, pressure (or displacement), and vacuum. Temperature must be controlled so that resin temperature stays within limits.

TABLE 13.2.17 Methods of Composite Preform Fabrication

Method	Description	Application
Weaving	Process of interlacing yarns to form a stable fabric construction that is flexible Less frequent interlacing results in better composite strength	Closely conforms to surfaces with compound curvature
Braiding	Intertwines parallel strands of fiber A tubular braid consists of two sets of yarn which are intertwined in "maypole dance" fashion; produced with varying diameter or circumferential size	Sporting equipment Good torsional stability for composite shafts and couplings Geometric versatility and manufacturing simplicity
Pultrusion	Reinforcing fibers pulled from a series of creels through a resin impregnating tank; preformed to the shape of the profile to be produced; enters a heated die and is cured to final shape	Produce constant cross-section pieces at high production rates
Filament winding	Pulling roving (unlisted bundles of fibers) over a mandrel by rotating the mandrel about a spindle axis; can cure on the mandrel	Cylindrical parts Can be low cost
Tube rolling	Material cut from prepreg tapes and laid on a flat surface; plies of different orientations joined together; a cylindrical mandrel is rolled on the material; curing is typically done on the mandrel	Low-cost method for making tubular structures or tapered tubes, e.g., golf shafts
Manual layup	Plies of different fiber orientations are cut from flat sheets of the prepreg material and laid up on a tool; bagging materials are applied and sealed to the tool for subsequent consolidation Flexible in producing complicated features at low start-up/tooling cost; building a curved, variable-thickness part can be complicated	Most common method used in the aerospace industry
Automatic tape layup	Computer-controlled machine tools or robots with a material delivery system • Automated tape layup machine uses prepreg tape, typically 3 to 12 in. wide, suitable for large surface of gentle contours • Fiber placement employs multiple tows for more complex surfaces	Provides lower cost and variability over manual layup, but requires higher capital investment

Both the duration and the magnitude of pressure application are important as excessive resin flow results in a resin-starved laminate. Similarly, pressure application too soon in the process can entrap volatiles in the material. Materials can also exhibit lot-to-lot variability. The problem is further complicated when processing a complex-shaped part or multiple parts of different geometry.

Composite cure processes are typically performed in an autoclave or in a heated press. An *autoclave* is essentially a heated pressure vessel. Nitrogen gas is normally used for pressurization. The temperature, pressure, and vacuum are controlled vs. time to effect the cure. Recent advancements in *intelligent processing* use sensors to determine the state of cure in real time, and make appropriate control adjustments to optimize the cure cycle (NRC 1995). Figure 13.2.16, which plots data from an actual implementation, depicts the potential that intelligent processing has in reducing autoclave processing time and cost.

Press molding uses a high-pressure press and matched metal tools to form a part. The main components of a press-molding system include the tools, the ram, and the heated platens. Again, release materials must be applied to the tools to avoid laminate adhesion. Advantages of press molding include improved surface finish (since both sides are tooled) and the elimination of the vacuum bagging systems. However, the pressure inside the mold is not necessarily uniform and volatiles are not easily removed. Consequently, press molding is generally suitable for composite systems that do not generate a significant amount of volatiles.

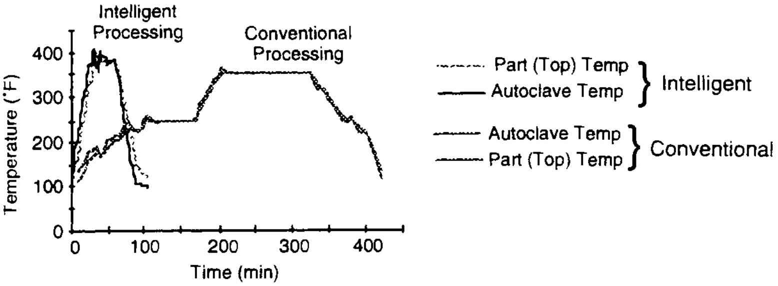

FIGURE 13.2.16 Intelligent processing of composites. (From NRC, *Expanding the Vision of Sensor Materials*, NMAB-470, National Academy Press, Washington, DC, 1995, 39. With permission.)

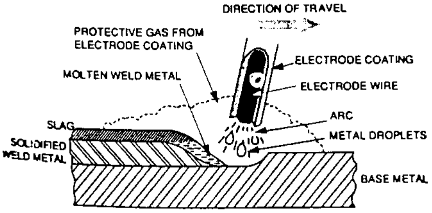

FIGURE 13.2.17 Shielded-metal arc-welding process. (From *ASM Handbook*, *Welding, Brazing, and Soldering*, vol. 6, 10th ed., ASM International, Metals Park, OH, 1993, 175. With permission.)

Shielded-Metal Arc Welding

Bonding is achieved in fusion welding by interposing a liquid of substantially similar composition as the base metal between the surfaces to be joined (Eagar 1993). The need for welding and joining is substantial since only monolithic parts can be made without joining. Traditional welding processes have unique advantages, which make them the processes of choice for a large number of applications. For example, in the fabrication of heavy structures, arc welding will dominate other assembly processes because of the inherent flexibility and economy of welding.

In the majority of arc-welding methods, the workpiece is made part of the electric welding circuit, which has as its power source a welding generator or transformer. To start a weld, an arc is struck by touching the workpiece with the tip of the electrode. The welder guides the electrode by hand in welding a joint, and controls its direction and traveling speed. The welder maintains arc voltage by controlling arc length (the distance between the end of the electrode and the work surface). Because an electric arc is one of the hottest sources of heat, melting occurs instantaneously as the arc touches the metal. Arc welding is a highly popular process because of its flexibility and relatively low cost (ASM 1993).

In shielded-metal arc welding, an arc is struck between the workpiece and a covered (or coated) metal electrode. Filler metal is provided by the consumable electrode. Combustion and decomposition of the electrode covering from the heat of the welding arc produce a gaseous shield that excludes the oxygen and nitrogen in the atmosphere from the weld area; these gases would otherwise cause excessive porosity and poor ductility in the weld. Welds by this method are of very high quality (Juers 1993). Figure 13.2.17 depicts the components of the shielded-metal arc welding process.

For shielded-metal arc welding, the metallurgical properties of a weld depend greatly on the type of electrode and its covering. The *electrode coverings* contain shielding gas formers that exclude atmospheric gases from the weld area. Electrode coverings offer additional capabilities (Juers 1993):

- Deoxidizers and nitrogen absorbers to purify the depositing metal
- Slag formers to protect the weld from oxidation
- Ionizing elements to stabilize the arc

- Alloying elements to produce higher-strength welds
- Iron powder to increase metal deposition rate

Selection of the proper electrode is based on many considerations (Juers 1993):

- Base metal strength
- Base metal composition
- Welding attitude (position)
- Welding current
- Joint design and fit
- Base metal thickness and shape
- Service conditions
- Production efficiency and conditions

Many types and sizes of *power supplies* are used. Supplies can be either direct current (DC) or alternating current (AC) types; combination AC/DC power supplies are widely used. In general, power supplies are required that produce controllable levels of constant-current output. The rate of metal deposition is determined by the output current from the power supply.

Shielded-metal arc welding is the most widely used welding process for joining metal parts, principally because of its versatility. Also, the welding equipment is less complex, more portable, and less costly than for other arc-welding processes.

Shielded-metal arc welding is generally very useful in joining components of complex structural assemblies. Joints in virtually any position that can be reached with an electrode can be welded, even if directly overhead. Joints in blind areas can be welded using bent electrodes. Welding in positions other than flat require the use of manipulative techniques and electrodes that cause faster freezing of the molten metal to counteract gravity. Shielded-metal arc welding can be done indoors or outdoors.

Metals welded most easily by the shielded-metal arc process are carbon and low-alloy steels, stainless steels, and heat-resistant alloys. Cast iron and high-strength steels can also be welded, but preheating and postheating may be required. Shielded-metal arc-welding electrode materials are available for matching the properties of most base metals; thus, the properties of a joint can match those of the metals joined.

Joint design (shape and dimension) is determined by the design of the workpiece, metallurgical considerations, and established codes or specifications.

Welds should preferably be located away from areas of maximum stress. Poorly placed welds can result in undesirable, and unplanned, stress concentrations that can cause early failure of the joint.

Poor joint fit-up increases welding time and is often the cause of poor welds. Metals with a low melting point, such as zinc, lead, and tin, cannot be welded by electric arc methods.

Limitations of shielded-metal arc welding compared with other arc-welding methods are related to metal deposition rate and deposition efficiency. Consumable electrodes have a fixed length, usually 18 in. (460 mm), and hence welding must be stopped periodically to replace the electrode. Another limitation is the requirement to remove the slag covering that forms on the weld after each welding pass.

There is a minimum gauge of sheet that can be successfully welded without burn-through. Generally 0.060 in. (1.5 mm) is the minimum practical sheet thickness for low-carbon steel sheet that can be welded by a welder possessing average skill (Juers 1993).

Special techniques are required when welding pieces of unequal thickness because of their different heat dissipation characteristics. Solutions include

- Placing a copper backing plate against the thinner section to match the heat dissipation from the thick section
- Redesigning the component so that the thick and thin sections taper at the joint to approximately the same size

Distortion is unavoidable in welding because of residual stresses that arise from nonuniform heating and cooling. Various procedures can be used to minimize distortion, such as clamping the workpieces. But straightening of the workpiece may be required to achieve the required dimensional accuracy.

References

Advani, S.G., ed. 1994. *Flow and Rheology in Polymer Composites Manufacturing, Composite Metals Series*, vol. 10, Elsevier, New York.

ASM. 1984. *Powder Metallurgy*, 1984. *ASM Handbook*, vol. 7, 9th ed., ASM International, Metals Park, OH.

ASM. 1993. *Welding, Brazing, and Soldering, ASM Handbook*, vol. 6, 10th ed., ASM International, Metals Park, OH.

David, S.A. and Vitek, J.M., eds. 1993. *International Trends in Welding Science and Technology*, ASM International, Metals Park, OH.

Eagar, T.W. 1993. Energy sources used for fusion welding. In *Welding, Brazing, and Soldering, ASM Handbook*, vol. 6, 10th ed., ASM International, Metals Park, OH, 2–6.

Froes, F. 1996, *Hot Isostatic Pressing*, ASM International, Metals Park, OH.

Humpston, G. and Jacobson, D.M. 1993. *Principles of Soldering and Brazing*, ASM International, Metals Park, OH.

Jenkins, I. and Wood, J. V., eds. 1991. *Powder Metallurgy: An Overview*. Institute of Metals, London.

Juers, R.H. 1993. Shielded metal arc welding. In *Welding, Brazing, and Soldering*, *ASM Handbook*, vol. 6, 10th ed., ASM International, Metals Park, OH, 175–80.

Linnert, G., 1994. *Fundamentals*. In *Welding Metallurgy: Carbon and Alloy Steels*, vol. 1, 14th ed., American Welding Society, Miami, FL.

MPIF. 1995. *Powder Metallurgy Design Manual*, 2nd ed., Metal Powder Industries Federation, Princeton, NJ.

National Research Council (NRC). 1995. Intelligent processing of advanced materials. In *Expanding the Vision of Sensor Materials*, NMAB-470, National Academy Press, Washington, DC, 34–40.

Schwartz, M.M. 1994. *Joining of Composite Matrix Materials*, ASM International, Metals Park, OH.

Woishnis, W.A. 1993. *Engineering Plastics and Composites*, 2nd ed., ASM International, Metals Park, OH.

Mechanical Assembly

S. H. Cho

Total labor involved in the assembly processes in the U.S. varies from 20% (farm machinery) to almost 60% (telecommunications equipment). On average, assembly tasks occupy 53% of manufacturing time, and 10% to 30% of total production cost of most industrial products. Use of improved assembly methods and technologies is essential to reduce overall manufacturing costs.

Assembly Methods and Systems

Assembly systems are classified in several different ways (Table 3.2.18). Figure 13.2.18 indicates the types of automated systems that could be cost-effective based on assembly part count and production volume.

Generally, *automatic assembly systems* consist of three major components:

- *Transfer system* to move work carriers with in-process subassemblies between workstations
- *Parts feeding device* to supply parts to be assembled into the appropriate position, where the parts are loaded by the handling/placing mechanism
- *Parts handling/placing mechanisms* to pick parts and perform assigned assembly tasks such as placing, inserting, and screwing

The *transfer system* can be continuous or intermittent according to the transfer method. In the *intermittent transfer system*, assembly tasks in a workstation are performed during a stationary period of the work carriers, which are transferred to the subsequent workstation after completion of the assembly tasks. *Continuous transfer systems* have a problem of not being able to assure positioning accuracy between an in-process subassembly and the tools of a workstation; thus, the intermittent type is usually used (Boothroyd 1992).

There are two modes of *intermittent transfer*: in-line and rotary. For the *in-line* mechanisms, the walking beam, the shunting work carrier, and the chain-driven work carrier are commonly used. The *rotary* type

TABLE 13.2.18 Classification of Assembly Systems

Type of Assembly System	Classification Basis	Description
Manual	Level of automation	Assembly tasks completed manually
Automatic	Level of automation	Adopts mechanized devices or industrial robots with supplementary equipment for handling and assembling parts
Semiautomatic system	Level of automation	Manual workers and mechanized devices cooperate to complete assembly tasks
Cell-type system	Configuration	Very flexible integrated assembly workstation; assembly completed by various equipment, such as robots or pick-and-place units, parts feeders, parts tray, magazines, automatic tool changer, and auxiliary jig/fixtures
Line-type system	Configuration	Assembly tasks divided into subtasks which are completed at workstations connected by transfer systems; handles large parts, cycle-time variation, and gripper change
Dedicated system	Degree of flexibility	Not flexible — can assemble only one product of a single model; generally economical for large production volumes
Flexible system	Degree of flexibility	Accommodates different products; economical for medium-size and mixed-model production

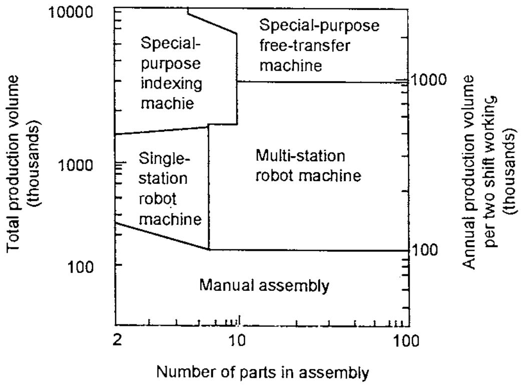

FIGURE 13.2.18 Conditions for economic application of various assemby systems (Courtesy of S. H. Cho)

employs mechanisms such as rack and pinion, ratchet and pawl, Geneva mechanism, and mechanical cam drives. Currently, free-transfer conveyors with stopping and positioning mechanisms are widely used in flexible assembly lines.

Most *feeding systems* have devices to orient parts supplied by the following means (Yeong and Vries 1994):

- *Bulk supply*, for parts that are easily separated, fed, and oriented automatically. Bulk supply usually adopts various part feeders, e.g., vibratory bowl feeders and various nonvibratory mechanical feeders for small parts. These feeders usually only handle one type of part and cannot be applied to assembly systems that require flexible part-feeding devices.
- *Organized supply*, which uses special pallets such as a kit or a magazine for parts that cannot easily be separated, fed, and oriented.

Parts-handling/placing mechanisms include pick-and-place units and various types of industrial robots. To load and assemble parts, the mechanism usually employs various assembly wrists: jaw-type gripper, vacuum suction pad, magnetic chuck, screwdriver, nut runner, and others. A number of different wrists are required when automatically assembling different parts in a workstation. To accommodate this assembly situation, a multifunctional gripper, a tool-changing system, and a universal gripper have been developed and widely used in robotic assembly systems.

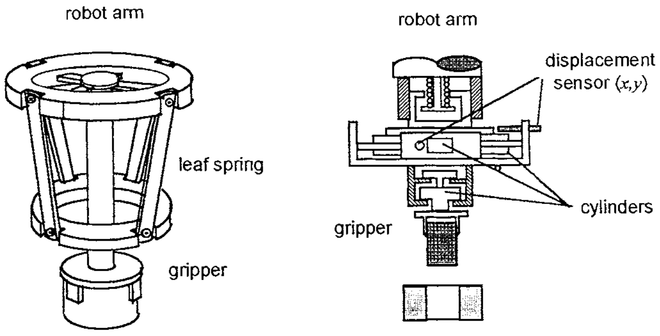

(a) a remote center compliant (RCC) wrist (b) a vibratory wrist

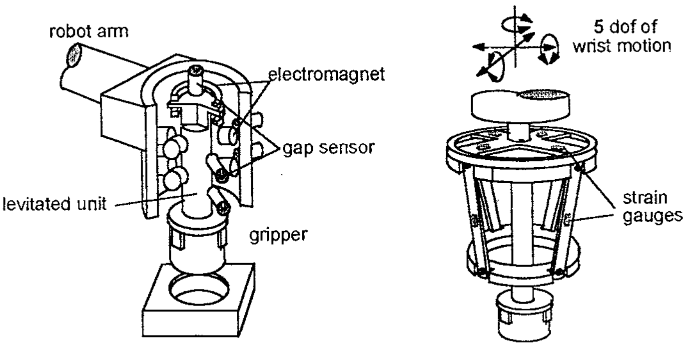

(c) a magnetically levitated hand [9] (d) an active wrist

FIGURE 13.2.19 Various assembly wrists. (Courtesy of S. H. Cho.)

Selection of Assembly Systems

The placement of a part in its assembled position and part mating impose tight constraints on the positioning mechanism and on part properties such as clearances and geometry. These constraints are more severe for assembly systems mating a variety of precision products that must adapt to frequent design changes. The assembly systems of this type must possess the adaptability to changing assembly environments, thus requiring *flexible automatic assembly* (Boothroyd 1984).

A typical *flexible robotic assembly* system uses an industrial robot for part handling, part positioning, and part mating. These systems are limited by positioning and orientation misalignment caused by the low positioning accuracy of robots, uncertainty in part handling, and variation in the location of parts.

Various approaches are available that take into consideration uncertainty in orientation and parts properties variation. Figure 13.2.19 depicts various types of assembly wrists that are in use. In general, wrists can be classified into three basic configurations:

- Passive accommodation
- Active accommodation
- Passive-active accommodation

There are two types of *passive wrist methods*:

- The wrist accommodates misalignments by deforming its structure elastically under the influence of the contact forces generated during the assembly of the misaligned parts. A *mechanically compliant structure* is needed for either the robot wrist or the assembly worktable, which can be deformable according to the reaction force acting on the mating parts. Remote center compliant wrist is one of such typical wrists; this method usually requires part chamfering (Cho et al. 1987).
- The wrist corrects misalignment by *applying external forces* or torques to the misaligned parts in a prescribed manner or a random way. For instance, a vibratory wrist utilizes pneumatic actuators controlled by a pulse width modulation controller to generate desirable vibration; this method does not require part chamfering.

Active wrist methods employ sensor-controlled wrists and compensate misalignments by controlling the fine motion of the assembly wrist or the work table based on sensory feedback. Advances have been made in the area of sensing technique, gripper and actuating mechanism design, and the related control algorithms. Sensors for these wrists are needed prior to contact (vision, range, displacement, proximity), during contact (touch, slip), and after contact (force, moment). Based on the force sensor signals and the associated algorithms, the wrist motion can be corrected to reduce misalignment.

The *passive-active accommodation method* is achieved by combination of the "passive and active" techniques. The basic strategy is that the part mating is continued within some allowable forced moments, while beyond this the insertion method is switched from the passive to active to reduce the mating force by using sensors with compliant structures.

The *sensor-based assembly* is similar to the method employing the active wrist. Both rely on sensory information for fine-motion control. The principal difference is that the former utilizes robot motion, while the latter relies on wrist motion.

Reaction forces (*force/torque information*) that occur during part mating can represent the status of the contact between mating parts. Among the approaches are pattern classifiers that determine the contact state at which the assembly parts are contacting each other, position error recovery via fuzzy logic, heuristic search with fuzzy pattern matching, and learning of nonlinear compliance using neural network.

Visual/optical information is critical to compensate for positioning and orientation error occurring due to misalignment. Visual information is often combined with other data, such as force/torque, pressure, and displacement, because a rather longer time is required for image processing, object recognition, and error calculation and because visual information is sensitive to external environmental conditions such as illumination.

Assembly Line

An assembly line usually consists of a set of workstations that perform distinct tasks linked together by a transfer mechanism. Each task is an assembly operation, and each workstation represents a location along the line where the tasks are processed. A buffer storage is placed between workstations for reducing the effect of a workstation failure on the throughput.

Line balancing is essential for designing a cost-effective assembly system (Groover 1980). The time required for the completion of a task is known as the *process time*, and the sum of the process times of the tasks assigned to a station is the *station time*. The total task processing times for assembling all the parts is the *work content*. When *assembly sequences* are generated without considering line balancing, the sequences may not guarantee the minimum number of workstations. Therefore, line balancing must be concurrently considered in defining the assembly sequences.

Design for Assembly

Approximately 80% of manufacturing cost is determined at the conceptual design stage. Design for assembly (DFA) is crucial during early design. The objective of the DFA is to facilitate the manufacturing and assembly of a product. DFA applies to all the assembly operations, such as parts feeding, separating, orienting, handling, and insertion for automatic or manual assembly (Ghosh and Gagnon 1989).

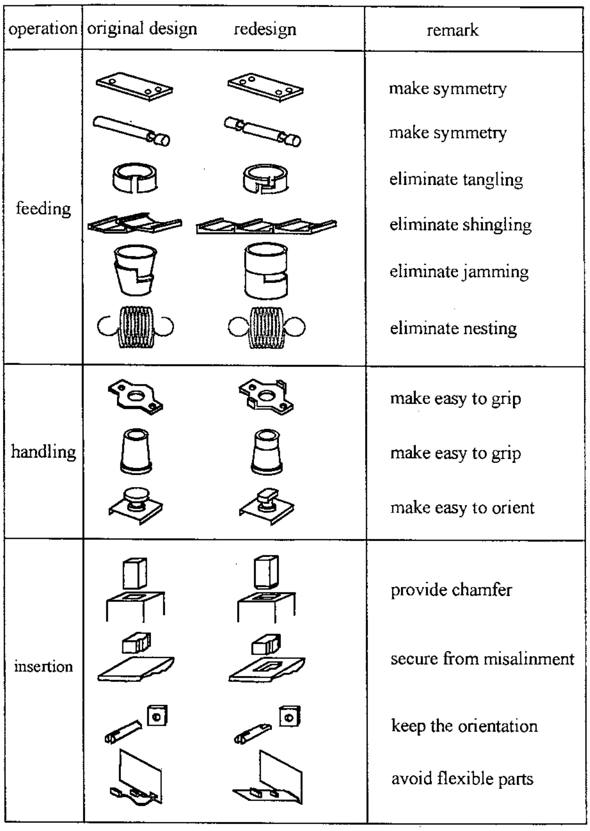

FIGURE 13.2.20 Results of DFA analysis. (Courtesy of S. H. Cho.)

DFA is directed toward

- Reducing the number of parts by modularization
- Easing feeding and minimizing reorientation
- Easing insertion by self-aligning, self-locating, elimination of part interference, and efficient fastening

Axiomatic DFA uses design guidelines based on experience of product designs and assembly operations. *Procedural DFA* evaluates the design efficiency based on the production cost.

Figure 13.2.20 shows results that were obtained using DFA rules to evaluate part designs in consideration of feeding and insertion. Such analysis has great potential in improving assembly operations.

References

Boothroyd, G. 1984. *Economics of General-Purpose Assembly Robots*, CIRP General Assembly, Madison, WI.

Boothroyd, G. 1992. *Assembly Automation and Product Design*, Marcel Dekker, New York.

Cho, H.S., Warnecke, H.J., and Gweon, D.G. 1987. Robotic assembly: a synthesizing overview. *Robotica*, 5, 153–65.

Ghosh, S. and Gagnon, R.J. 1989. A comprehensive literature review and analysis of the design, balancing and scheduling of assembly systems. *Int. J. Prod. Res.*, 27(4), 637–70.

Groover, M.P. 1980. *Automation, Production Systems, and Computer-Aided Manufacturing*, Prentice-Hall, Englewood Cliffs, NJ.

Yeong, M.Y. and Vries, W.R. 1994. A methodology for part feeder design. *Ann. CIRP*, 43(1), 19–22.

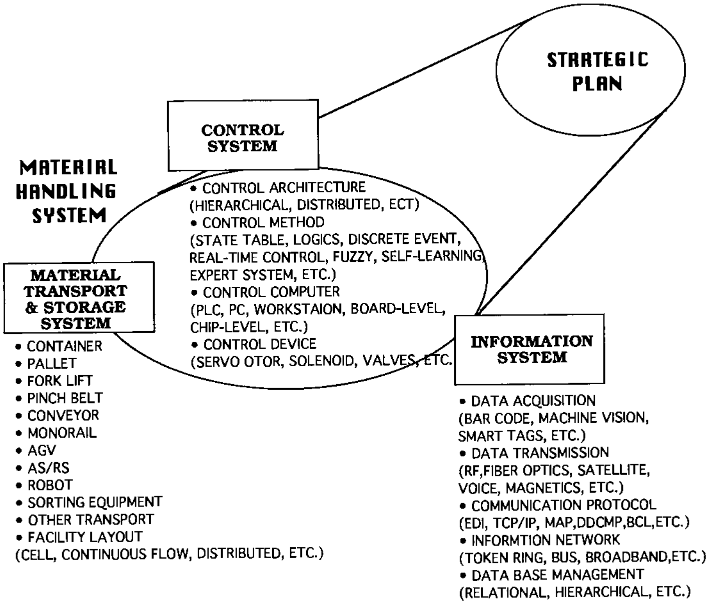

FIGURE 13.2.21 Modern material-handling system. (Courtesy of J. Lee.)

Material Handling

Ira Pence

Material handling provides the right amount of all the required materials at the right place and time to support manufacturing. Properly designed, the material-handling system provides for the acquisition, transportation, and delivery of material so that the minimum cost is incurred considering capital, labor, and expenses. It focuses on obtaining material and supplies, moving them between process steps, and delivering the finished product to the customer. Figure 13.2.21 depicts the elements of a modern materials-handling system, which reaches beyond the factory floor, serving as an integrating force for production operations.

The material-handling system should be analyzed as a single entity so trade-offs in expense in various elements can be made to minimize the total cost. Often, however, the activities are broken into purchasing, transportation, warehousing, and distribution functions, which operate independently. Such divisions are arbitrary because the material-handling system is an unbroken chain of activities that start when the suppliers complete their last value-added operation and extend until the product is delivered. Minimum-cost material handling will not be achieved if the partitioning of material flow into subelements leads to optimization of each subelement at the expense of the entire system.

Planning is crucial to the design of a smoothly functioning materials operation. Planning should be consistent with the strategic plan for the entire manufacturing operation. In formulating the plan, a realistic assessment of the problems and opportunities associated with arranging, controlling, and implementing the material flow must be used. Specific tactics, such as just-in-time delivery, should support the strategic plan. Expensive automation should not be used unless the volume and stability of the product justify its use.

Logistics

The movement of material in a manufacturing enterprise is usually broken into two broad categories, inside the plant and external to it. External movement is generally referred to as "logistics," while the internal flow is known by many different names. Material movement considered logistics is generally marked by a wide geographic scope, diversity of equipment and technology, and some uncertainty in delivery time. But the basic goals are identical to in-plant movement, and most of the analysis tools are applicable to both categories.

For large manufacturing enterprises the number of individual components involved in the production of the product, often referred to as SKUs (stock-keeping units), can be very large. In the past, it was helpful to treat items of similar size, weight, storage requirements, and delivery times as a single commodity. This simplified manual analysis and was sometimes done by computer programs that analyze logistical information. However, current computer systems make it practical to treat each item individually.

Basic Elements

The basic activities associated with material handling are *moving*, *storing*, and *controlling* material. These activities are interrelated with production scheduling and information must flow both ways.

Movement may be over short distances, as from one machining center to another, or long, from one plant to another. In all cases the basic information that must accompany the move includes the part identity, timing, quantity, source, and destination. Each move should be planned and scheduled, taking into account the speed of the basic mechanism as well as allowance for loading, unloading, logging, counting, and so forth.

Movement can be continuous or in batches, synchronous or asynchronous, horizontal or vertical. Each move should be examined for the characteristics of urgency, safety, size, weight, and similar factors before selecting the technology to be used to perform the move. Singular instances should be accommodated in the most expeditious manner, and repetitive moves must be made in the most efficient and effective manner.

One of the basic tenets of material handling is to retain *control* of the material. Inventory control generally maintains up-to-date records on the quantity and location of material on hand. However, in a *virtual warehouse*, it is important to know what material has been ordered and the status. Control includes procedures and equipment to properly handle the material.

The *storage* of material should be minimized. Materials are typically stored to compensate for uncertainty in delivery systems and to allow ordering of economic quantities.

Occasionally unexpected changes in production will result in delaying the release of material to the factory floor and that material must be stored until needed. *Just-in-time delivery*, where parts are delivered directly from local suppliers to the assembly line several times a day, has been proved in several industries. Thus, the need for storage due to uncertainty of delivery has been reduced. At the same time, global sourcing has increased. As supply lines lengthen, the uncertainty of delivery increases. The more complex the supply system, the more likely the occurrence of an unexpected delay. In designing a storage system, the trade-off of higher transportation cost but less inventory vs. volume discounts on purchases and transportation, but with storage costs, must be evaluated.

Further Information

The Material Handling Industry (MHI) produces two catalogs each year. One provides information on the publications available from the MHI, including all the educational material; standards and specifications; operating, maintenance, and safety manuals; and reference works. The other provides a directory of member companies and the products they manufacture. Both are available from the MHI Literature Department.

Case Study: Manufacturing and Inspection of Precision Recirculating Ballscrews

Toskiaki Yamaguchi, Yashitsugu Taketomi, and Carl J. Kempf

The precision and quality of the components of mechanical devices used in both industrial and consumer products must meet high performance and durability requirements. The manufacturing challenges that apply to ballscrews, in general, are representative of other components such as gears, shafts, and bearings.

This case study on precision ballscrews illustrates how the different unit manufacturing processes presented in this chapter apply to a particular application, and how design and manufacturing engineering decisions are affected by quality and cost considerations.

Many of the processing steps and fundamental techniques discussed in this case apply to the manufacture of many other precision components. The case study also illustrates the rationale for continuously improving production processes and discusses strategies for improvement that benefit from past experience.

Overview of Ballscrew Design and Manufacturing Considerations

Ballscrews convert rotary motion into linear motion. Ballscrews have low friction compared with standard leadscrews, and have enabled precise control of mechanical systems at a relatively low cost. They are used extensively in production machinery, such as milling machines, and are being applied in other fields, such as robotics, inspection equipment, and office automation equipment.

The key components of a ball-screw system consist of a screw shaft with a spiral groove, a nut with a corresponding spiral groove that rides along the shaft, and balls that are captured between the shaft and the nut. A recircultation tube provides a return path for the balls from the end of the nut. Components in this assembly are typically made from steel alloys, chosen to provide a good combination of toughness, surface hardness, and ease of manufacture.

Ballscrews are applied in a variety of ways, but the most common configuration is one in which a rotational input of the shaft imparts a translational motion to the nut. The shaft is normally supported by rotating bearings at both ends, and the translating element attached to the nut is supported by linear guide bearings. Ballscrews range in size from very small units with a shaft diameter on the order of 0.08 in. (2 mm) and a length of about 4 in. (100 mm) to very large units with a shaft diameter on the order of 12 in. (300 mm) and a length of up to 50 ft (16 m). Key dimensional features that are controlled to a high degree of precision for an assembled ball-screw system are shown in Figure 13.2.22.

The main factors in ballscrew performance are accuracy and lifetime. *Accuracy* is determined primarily by the precision of the screw lead, that is, the linear displacement of the nut that is produced by rotary displacement of the shaft. The measurements used to assess the *precision* of the lead are discussed later. To obtain a long *lifetime*, the shaft must have high surface hardness in order to withstand loads at the shaft/ball and nut/ball interfaces. Since ballscrews may be subject to a variety of loading conditions, the ballscrew must possess good impact strength and toughness.

Secondary design factors include low audible noise, low static and dynamic friction, low friction variation, minimal backlash, high mechanical stiffness, and resistance to dirt and contaminants. Ballscrews are often used in specialized applications, such as operation in vacuum or ultraclean environments, in corrosive or dirty environments, in a thermally controlled environment, and in environments where vibrations must be minimized. To meet these demands, basic ballscrew designs are adapted to use

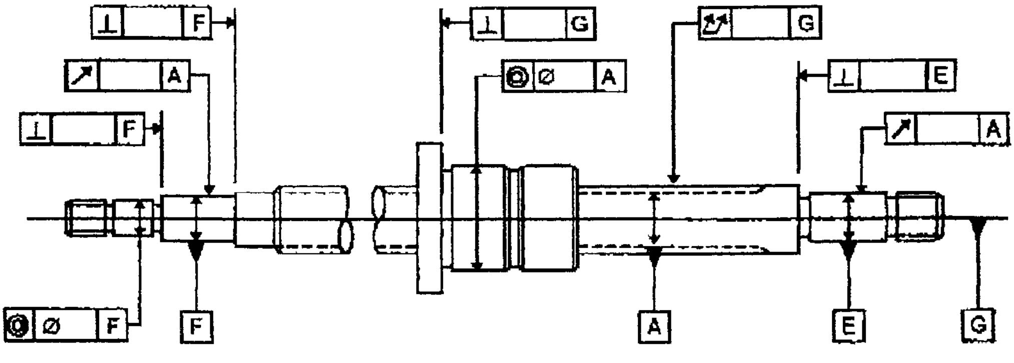

FIGURE 13.2.22 Key ballscrew dimensions. (Courtesy of T. Yamaguchi, Y. Taketomi, and C. J. Kempf.)

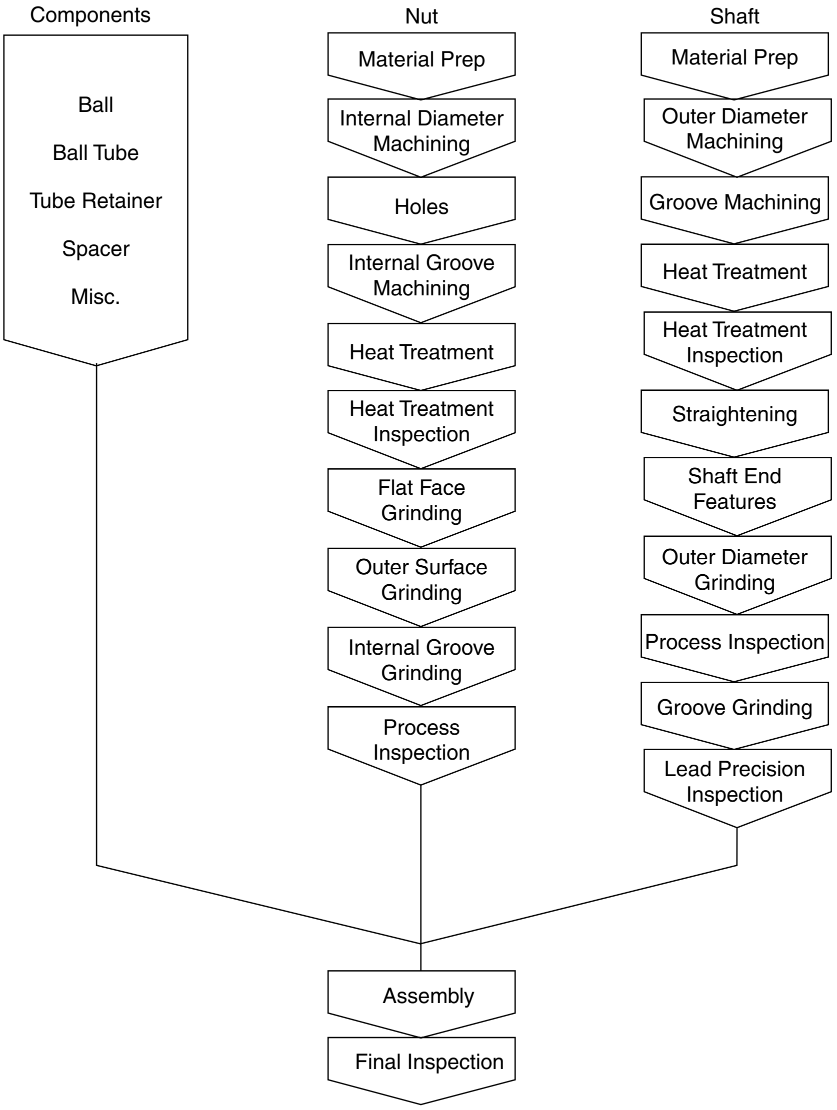

FIGURE 13.2.23 Ballscrew processing flowchart. (Courtesy of T. Yamaguchi, Y. Taketomi, and C. J. Kempf.)

special materials, surface treatments, and to provide features such as hollow shafts for coolant flow or damping materials.

The major steps in production and assembly of traditional ground ballscrews are summarized as a flowchart in Figure 13.2.23.

Initial Machining Operations

A lathe is used to establish the outer diameter of the shaft and cut the groove. In both operations, an allowance is made for material that will be removed in the final grinding operations. For short shafts, the support is provided from the shaft centers and a single cutting tool can be used with multiple passes to produce the desired outside diameter and groove. For long ballscrews, the lateral deflection of the shaft during cutting operations is significant and workpiece supports are necessary to prevent deflection of the shaft.

For long ballscrews, the total processing time can become extremely long using multiple passes with a single-point cutting tool. In such cases, a multiple-point tool that can remove more material on a single cutting pass is more efficient to use. But a multipoint cutter requires more time for setup and adjustment. Thus, there is an economic trade-off between single-point and multipoint cutting techniques.

Because of subsequent heat-treat operations, the shaft will undergo dimensional changes. The design must allow for these dimensional changes. This is an area in which production experience is critical. Statistical analysis of previous manufacturing results, together with modeling of material behavior, is critical to continued design and process improvement.

Surface Treatments

In order to withstand the loads at contact points, a very high surface hardness is necessary. A surface hardness of Rockwell C 58-62 with a depth on the order of 0.8 to 1.2 mm is required. For short ballscrews, *carburization* is used to develop the necessary surface hardness. For longer shafts, carburization is impractical because of the size of carburizing furnaces. In this case, an induction hardening process is used.

Electrically heated gas furnaces are used in the carburizing process. The immersion in the carburizing furnace is followed by quenching and tempering. During carburizing, key parameters such as temperature and gas concentrations are continuously monitored and adjusted by a process control system. Because high hardness is needed only in the ball groove, areas of the shaft and nut that will be subject to subsequent machining operations are coated before carburizing. This coating, which is applied like paint, prevents the diffusion of carbon into the material surface.

For longer shafts, a different steel is chosen and an induction hardening process is used. The general trend within the industry is toward induction hardening since it has the advantage of being a continuous process. When using induction hardening, single shafts can be processed immediately after machining. Induction hardening machines require less initial capital than for a carburizing system.

The shaft undergoes dimensional changes as a result of the surface heating, and a *straightening* operation is necessary. Prior to straightening, the shaft is chilled in a carefully controlled manner to subzero temperatures to ensure that the solid-state transformations are completed; the result is a more stable microstructure. For straightening, a *specialized press* is used to measure automatically the deviation from perfect straightness; it automatically applies loads along the shaft as necessary to restore the shaft to near-perfect straightness.

Grinding and Finishing Operations

After surface treatment, chilling, and straightening, the outside diameter of the shaft is ground to the final dimensions. Except for very short ballscrews, the grinding cutting forces will cause lateral deflection of the shaft, and thus the centers in the shaft ends cannot be used as datums for final machining operations. Consequently, the outside diameter of the shaft is ground to precise tolerances. Although the outer diameter of the shaft is not a functional part of the finished ballscrew, it is used as a datum surface when the final grinding of the shaft groove is performed.

Grinding of the shaft can be done on either centerless grinders or cylindrical grinders. Since centerless grinders take a long time to set up, they are generally used for large production runs of shafts having the same diameter. For the case of cylindrical grinders, the shaft is supported at the centers in the shaft ends as well as at workpiece supports along the length of the shaft. By adjusting the work rests, minor variations in taper and bending of the shafts can be corrected. This processing step requires considerable operator skill and experience in order to minimize variations in the outer diameter and residual bending of the shaft.

To maintain precision and finish of the outer diameter, automatic balancing of the grinding wheel is necessary. CBN grinding wheels are used although they are more expensive than traditional abrasive wheels; their long life and low wear rates make them economical.

After turning the external diameter to final size, shaft end features are produced. These features include bearing seats, keyways, flats, and locknut threads. The final finishing operation for the ballscrew generates the ball groove. This is the key processing step in assuring that the ballscrew possesses the required lead accuracy. If this process is not carefully controlled, there will be variation in the lead, depth of the groove, and smoothness of the groove, causing subsequent problems with accuracy, stiffness, running force and noise, and lifetime.

Removal of the outer layer of hardened material during outer diameter grinding can cause minor bending of the shaft as the net residual stresses in the material change. Prior to final cutting of the ball groove, the straightness of the shafts is checked and minor corrections made.

To maintain very high lead precision, the final groove grinding is done in a specially temperature-controlled environment of 68 ± 2°F (20 ± 1°C). Cutting oil is applied liberally to the shaft to minimize thermal effects due to cutting and deviations between the grinding machine and shaft temperature. As in the case of external diameter grinding, automatic balancing is used to minimize vibrations. To further reduce vibrations, each grinding machine is mounted on an individual base to minimize vibration coupling between various machines. The isolation properties of the machine bases are adjusted when a new machine is placed in service and undergo periodic inspection and adjustment during operation.

Because the size and lead of the groove varies from ballscrew to ballscrew, the grinding wheel must be matched to the groove shape. Thus, an inventory of several types of wheels is necessary; traditional abrasives are used since the costs of CBN wheels would quickly become prohibitive.

In general, accuracy in the groove-grinding process requires a combination of modeling and statistical analysis. As in the case of surface treatment, the collection and analysis of past production data allows continuous refinement of the manufacturing process.

Assembly and Inspection

The main factor in ballscrew accuracy is the lead. To facilitate a quantitative measurement of the lead, four fundamental parameters are used. To measure the lead error, precision measurements over a long travel range are made using computer-controlled laser interferometry.

Unacceptable variations in friction, increased running noise, and a reduction in life result from poorly formed grooves. Thus, the depth and cross-sectional profile of the groove must fall within allowable tolerances. Direct measurement of the groove cross section is quickly performed on an optical profile projector. Precise measurement of groove depth can be made on selected samples. The screw shaft is supported between two centers and rotated at a fixed speed. A table carrying a contact probe moves along the screw shaft in the axial direction synchronously with the screw rotation. The probe is placed in contact with the groove to measure variations in the groove depth over the entire length of the shaft. By performing a frequency analysis on the groove depth errors and accounting for the rotational speed of the ballscrew during the measurement process, frequencies of unwanted vibrations occurring in the production machinery can be detected and the source of the anomaly eliminated to improve the production process.

Even with good control of the screw shaft and nut groove diameters during production, additional steps are necessary to obtain the desired amount of axial play or preload in the assembled ballscrew. By selecting slightly different ball sizes, required axial play or preload can be achieved. For a given nominal ball diameter, balls usually are grouped in steps of 20 to 40 μin. (0.5 or 1.0 μm). To increase production efficiency, assembly jigs are used.

The majority of precision ballscrews are preloaded in order to remove backlash and achieve the desired axial stiffness. Two methods of achieving the desired preload are used. The first preloading method increases the ball size until the desired preload is achieved. The second method uses double-nut preloading in which a spacer is inserted between the two nuts to take up the axial play and achieve the desired preload.

The preloaded ballscrew has some running torque when the screw is rotated. The relation between this running torque and the preload has been determined based on both theoretical and experimental studies. Since preload cannot be measured directly, it is estimated based on measurements of the running torque in a specialized torque-measuring machine.

A special machine is used for direct measurement of axial stiffness. In this process, the screw shaft is clamped and an axial load is applied to the nut. A displacement sensor is fixed to the shaft close to the nut and the relative displacement of the nut can be measured when force is applied. The measurements of force and displacement can be plotted on an X-Y recorder to depict the stiffness characteristics of the ballscrew assembly.

References for Case Study

Oberg, E., Ed. 1971. *Machinery's Handbook*, 19th ed., Industrial Press, New York, 2044–68.
Yamaguchi, T., 1983. Ballscrew manufacturing, and inspection. *Tool Eng. Mag.*, June, 92–99 (in Japanese).

13.3 Essential Elements in Manufacturing Processes and Equipment

Sensors for Manufacturing

John Fildes

Introduction

A good modern definition for a sensor must capture the diversity of these devices. A sensor is a device that detects or measures the state or value of a physical or chemical variable and provides the result in a useful way. At the minimum, a sensor contains a transducer that converts the detected or measured quantity to another form of representation. For example, a very simple sensor is an indicator whose color changes upon reaction with a minimum amount of a chemical species. Nonetheless, the sensors that are normally encountered are more complex, containing a transducer, an output display, and possibly supporting electronics for signal conditioning, communications, and logic functions.

Sensor technology is undergoing rapid change because of three developments. One development is the emergence of integrated and smart sensors, wherein transducers have been miniaturized, usually through the use of silicon micromachining, and integrated with electronics for signal conditioning, communications, and logic functions. The second development is the ongoing adaptation of nondestructive evaluation (NDE) measurements and laboratory measurements for online use in supervisory and intelligent process control systems. These NDE and laboratory-type measurements require rather complex systems, with extensive signal conditioning and data analysis. The third development is also related to the emergence of supervisory control systems. The data from multiple sensors are comparatively analyzed in a process called data fusion to better identify the state of the system and the occurrence of process faults. Thus, the topic of sensors and sensory systems now encompasses transducers, integration with supporting electronics for communications and logic functions, data-analysis techniques, and data-fusion methods.

Classification of Sensors

A good taxonomy for sensors is provided by the requirements for different degrees of process control, which is shown in Figure 13.3.1. This taxonomy contains three classes: sensors used in regulatory feedback control loops, process analyzers, and product quality analyzers. In Figure 13.3.2, the basic element of control is the regulatory feedback loop that maintains controllable processing parameters at the desired values. These types of sensors, which usually provide a single value and are relatively generic in their applicability, are used for monitoring variables such as temperature, pressure, flow, level, displacement, proximity, and velocity. For use of sensors in regulatory control, sensitivity, selectivity, simplicity, speed, reliability, and low cost are the critical attributes. Historically, sensors were almost solely used in this function, but this is no longer the case. Sensors, or more properly sensory systems, are now also used as process analyzers and product quality monitors. Sensors of this type, which are used for feedback in supervisory control, are more complex and application specific, and their output tends to be a matrix of values (e.g., a video image or a spectrum). Sensors of this type provide a representation of the process

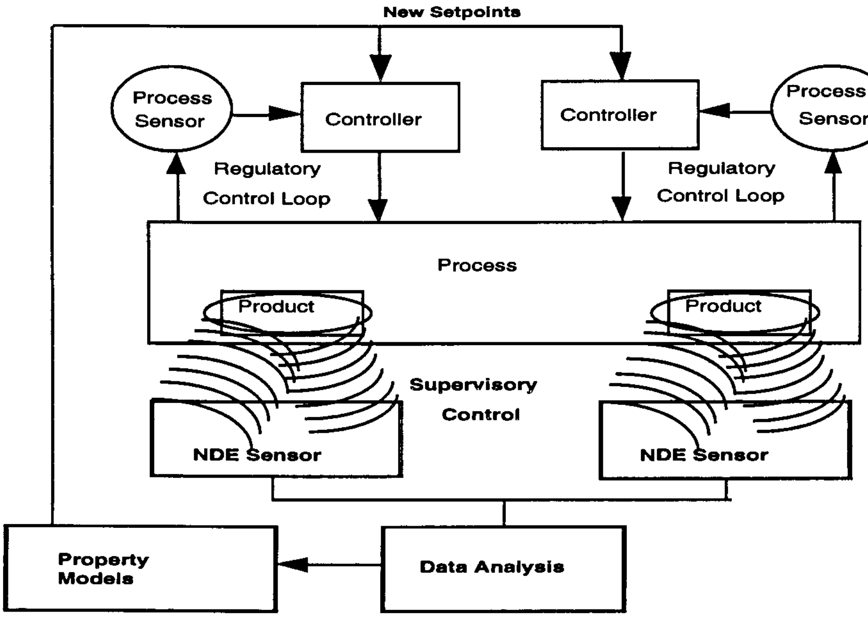

FIGURE 13.3.1 Regulatory and intelligent control.

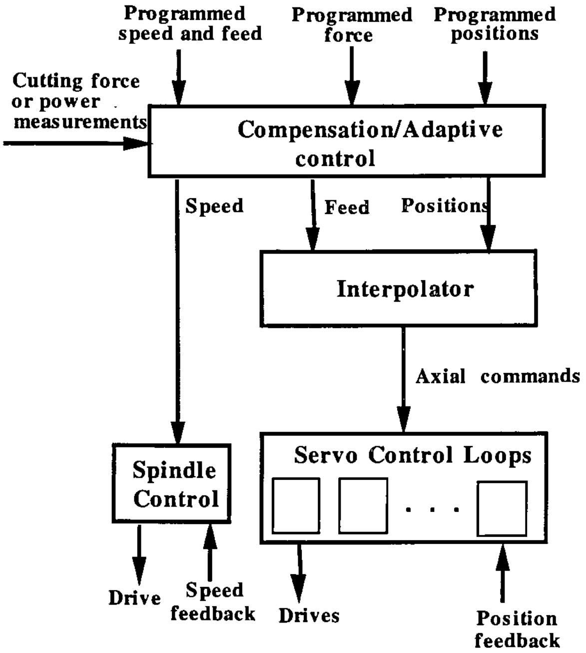

FIGURE 13.3.2 Typical CNC architecture.

or product that has greater information content but that is more abstract than the representation provided by sensors used in regulatory control. Thus, extensive computations and modeling are needed for process analyzers and product quality sensors, but there is also more ability to correct for deficiencies in sensitivity and selectivity through computational means. In this case, measurement speed is usually less demanding. These differences in the three types of sensors are summarized in Table 13.3.1.

TABLE 13.3.1 Characteristics of Regulatory and Intelligent Process Control Sensors

Characteristic	Regulatory Feedback Sensors	Process and Product Sensors
Speed of response	Very fast	Slow
Type of output	Single value	Matrix of values
Relationship of output to system parameter	Simple and direct	Abstract representation
Amount of computation	Little or none	Extensive
Sensitivity	Inherently high	Can be improved by computation and modeling
Selectivity	Inherently high	Can be improved by computation and modeling
Cost	Very low to moderate	High
Size	Small	Large
Applicability	Broad	Application specific

TABLE 13.3.2 Regulatory Processing Variables

Controllable Variable	Influenced Processing Factors
Temperature	Rates of chemical reactions; degree of cure of polymers; degree of softening and viscosity; cooking times; drying times; annealing times; degree of carborization
Pressure	Consolidation density; porosity; concentration of gaseous chemical reactants; forging; bending; injection times in molding
Flow	Mix ratios; quenching time; concentration of chemical reactants; color; pH; humidity
Level	Capacity; mix ratio; concentration of chemical reagents
Humidity	Drying of paper and grains; cooking
Position	Parts handling and placement; machining accuracy
Motion	Assembly; machining accuracy

TABLE 13.3.3 Sensor Technologies for Regulatory Control

Variable	Major Sensor Technologies
Temperature	Thermocouples, thermistors, resistance thermometers, infrared pyrometers, acoustic pyrometers
Pressure	Manometers, bellows and diaphragms, strain gauges, piezoresistive, piezoelectric, capacitive, thermocouple, ionization
Flow	Differential pressure (orifice plate, Venturi, pitot tube); velocity (turbine, vortex, electromagnetic, Doppler ultrasonic, time-of-flight ultrasonic); positive displacement (rotary sliding vane, gear, impeller); mass flow (thermal, coriolis); variable area (rotameters)
Level	Floats, pressure, radio frequency, ultrasonic, microwave, resistance tape, optical
Humidity	Dew point, length of hair, conductivity, capacitive, resonate
Position	Rotary encoder, linear variable differential transformer, potentiometers, magnetostrictive, magnetic, inductive proximity, magnetic, ultrasonic
Motion	Tachometers, pitot tube, anemometers

The typical regulatory variables are temperature, pressure, flow, level, humidity, position, and motion. These variables form the basis for many process factors as summarized in Table 13.3.2; the major sensor technologies for these variables are summarized in Table 13.3.3.

Integration refers to inclusion of signal conditioning on the same substrate as the transducer. One of the major advantages of integration is that the integrated sensor can operate with a very small transducer output, which results in significantly smaller sensors. With the advent in telecommunications and the microelectrical-mechanical systems (MEMS) technologies, we can integrate software, hardware, power source, and communications on the same chip. Table 13.3.4 lists the advantages and disadvantages of integrated sensors.

Smart sensors are defined as those that also include logic functions, rather than just signal-conditioning electronics. Smart sensors may also include communications circuitry, diagnostics, and sometimes control outputs so that they can be directly connected to actuators, and documentation and trending functions.

TABLE 13.3.4 Characteristics of Integrated Microsensors

Characteristic	Advantage/Disadvantage
Batch fabrication	Excellent control, low cost, sensor arrays
Loss of modularity	Difficult to package and limitations on materials
On-chip amplification	Better signal-to-noise ratio
On-chip compensation	Better accuracy through compensation for interferences
On-chip feedback	Better linearity
On-chip scaling and conversion	Standardized output
On-chip multiplexing	Sensor arrays, bus addressable

Conventional pressure sensors have rather broad accuracy limits, such as 0.25% of span. High-end smart pressure sensors have an accuracy of less than 0.1% of span, and midrange smart pressure sensors approach this accuracy. Smart pressure transmitters are already available with built-in proportional-integral-derivative control functions, and fuzzy logic capabilities will soon be available. Multivariate measurement is not yet available but will become so soon. Most likely, pressure and temperature will be the two measurements. Smart sensors are also available for presence detection, positioning, infrared photodetection with triangulation, and flow meters, specifically magnetic meters, Coriolis mass flow meters, and ultrasonic flow meters. Integrated and smart sensor technology is also improving accelerometers, proximity detectors, and tactile sensors. The use of integrated and smart sensors will increase because of the overloading of shared resources and the use of distributed control schemes to solve this problem.

Use of Sensors in Supervisory and Intelligent Control Systems

As shown in Figure 13.3.1, supervisory control augments regulatory control by using process analyzers to better characterize the state of the process and sensors of product characteristics to assess the outcome of the process and to determine corrections for unacceptable deviations. These corrections are then implemented by the regulatory controllers. There are many ways in which supervisory control can be implemented. A common way is to measure important aspects of the process and the product performance, and to use a model to relate variations in processing parameters to variations in product performance.

Process analyzers are central to enabling supervisory control because they allow a more accurate, but abstract, representation of the state of the process. These devices augment regulatory control by monitoring other important variables in the process, but ones that are generally not directly controllable. The use of process analyzers provides improved reliability, flexibility, predictive diagnostics, ease of use, and central data collection with process documentation; trending; recipe handling; and statistical quality assurance. Process analyzers are now used for monitoring important process gases such as oxygen, carbon monoxide and dioxide, oxides of nitrogen and sulfur, and hydrocarbons. For liquids, process analyzers are available for pH, conductivity, redox potential, dissolved oxygen, ozone, turbidity, specific ions, and many organic compounds. The measurement techniques are summarized in Table 13.3.5.

TABLE 13.3.5 Process Analyzers

Process Analyzer Technology	Typical Uses
Electrochemical (potentiometric, amperometric)	Gases such as carbon monoxide and dioxide, oxides of nitrogen and sulfur, and hydrocarbons; species in liquids such as dissolved oxygen, pH, redox potential, specific ions, organic compounds, inorganic compounds
Chromatography (gas and liquid)	Gases such as CO and CO_2; species in liquids such as alcohols, flavors, lipids, polymers, and other organic compounds
Infrared spectroscopy	Near infrared — web processes for thickness, composition, solvent, coating Mid-infrared — chemical and petrochemical processes, polymers, food processes
Ultraviolet/visible	Gases and liquids including all elemental halogens, other inorganics, aromatics, carbonyls, many salts of transition metals

TABLE 13.3.6 Product Quality Sensors

Sensor	Applications
Time-of-flight ultrasound	Either thickness or elastic constants, if the other is known
Electromagnetic acoustic transducer (EMAT)	Either temperature or elastic constants, if the other is known
Eddy currents	Electrical conductivity, magnetic permeability, thickness, temperature, presence of flaws
NMR (high resolution for liquids, low resolution for solids)	Composition of chemicals, petroleum, foods, polymers, fibers
Infrared and Raman spectroscopy	Degree of cure of polymers

Traditionally, process analyzers have been stand-alone devices with a single sensor and a dedicated operator interface. The trend is toward modularity, multiple sensors, and digital communications so that process analyzers can be incorporated into distributed control systems in an open architecture control environment. Smart sensor technology is also turning conventional sensors into process analyzers. A good example is provided by smart infrared temperature sensors. These sensors provide sample and hold, correction for reflected radiation when the emissivity of the target is less than one and its temperature is lower than ambient, analog outputs for control, digital outputs, trend analysis, and area sampling with line scanners. This functionality has made temperature mapping of surfaces in furnaces practical and is used in annealing of aluminum, steel reheating, and oven drying of webs such as paper.

Another trend is the use of sensor fusion, where information from multiple sensors is combined to improve the representation of the process. Sensor-fusion techniques can use mechanistic models, statistical models, or artificial intelligence techniques, such as neural networks, fuzzy logic, and expert systems. Sensor fusion provides more reliability because the validity of the data of each sensor can be assessed from the other sensors, and if a sensor is faulty, its value can be predicted from the other sensors. Sensor fusion provides a better representation of the process because it captures the interrelationships that often exist between processing variables, which are treated independently without sensor fusion.

As shown in Figure 13.3.1, intelligent control involves the use of product quality sensors. Of the three classes of sensors discussed in this section, these sensors tend to be the most complex and provide the most complete, but abstract, representation of the state of the product. In some cases, the same technologies are used for product quality sensors as for process analyzers. An obvious example would be where chemicals undergo reaction without a change of state. In other cases, specialized product quality sensors have emerged. Table 13.3.6 lists some of the product quality sensors that are either being used or evaluated experimentally.

Computer Control and Motion Control in Manufacturing

Yoram Koren and M. Tomizuka

Computerized Numerical Control Architecture

A typical architecture of a CNC system consists of three levels, as shown in Figure 13.3.2. At the lowest level are the axial servocontrol loops and the spindle controller. These servoloops are closed at a high sampling rate. The interpolator that supplies the axial position commands to the control loops is at the intermediate level of this architecture. At the highest level are the compensation algorithms for the errors of mechanical hardware deficiencies, such as machine geometry errors and thermal deformation of the machine structure. This level also includes adaptive control algorithms that adapt the machine feed and speed to the cutting tool and workpiece material to maximize machine productivity at rough cutting and maintain precision at fine cutting.

CNC Part Programs

The CNC software consists of a control program and part programs. The numerical data that are required for producing a specific part by a CNC machine make up the part program. The *part program* is arranged

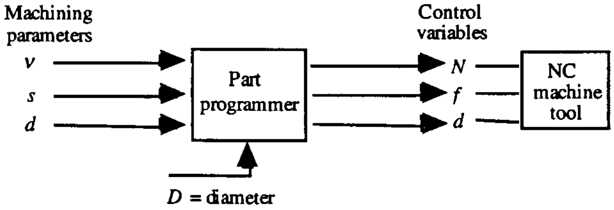

FIGURE 13.3.3 Conversion of machining parameters to control variables.

in the form of *blocks* of information, where each block contains the numerical data required to produce one segment of the workpiece. Each block contains, in coded form, all the information needed for processing a segment of the workpiece: the segment shape and length, its cutting speed, feed, and so forth. Dimensional information (length, width, and radii of circles) and the contour shape (linear, circular, or other) are taken from an engineering drawing. In NC, dimensions are given separately for each axis of motion (X, Y, etc.). Cutting conditions such as cutting speed, feed rate, and auxiliary functions (coolant on and off, spindle direction, clamp, gear changes, etc.) are programmed according to surface finish and tolerance requirements.

The part program contains the required positions of each axis, its direction of motion and velocity, and auxiliary control signals to relays. The controller generates an internal signal indicating that the previous segment is completed and that the new block of the part program should be read. The controller also operates the drives attached to the machine leadscrews and receives feedback signals on the actual position and velocity of each one of the axes.

In CNC systems the part dimensions are expressed in the part programs by integers. Each unit corresponds to the position resolution of the axes of motion and is referred to as the *basic length-unit* (BLU). The BLU is also known as the "increment size" or "bit-weight," and in practice it corresponds approximately to the accuracy of the system. To calculate the position command that the computer sends to the CNC machine, the actual length is divided by the BLU value. For example, in order to move 0.7 in. in the positive X direction in a system with BLU = 0.001 in., the position command is $X + 700$.

In the first generations of CNC systems, dimensions were given in part programs by BLUs, as in NC. In new CNCs, however, dimensions, or desired cutter positions, are given in a normal way, as to a regular computer. The command $X – 0.705$, for example, will move the X-axis in the negative direction by 0.705 in. The resolution by which the dimension commands are given depends on the system BLU.

In addition to cutter positions, the part programmer must program the machining parameters such as tool diameter, cutting speed (n), feed (s), and depth of cut (d). The task of the part programmer is to convert the machining parameters n and s to NC control variables — spindle speed (N) and feed rate (f), as shown in Figure 13.3.3.

Point-to-Point and Contouring Axes of Motion

CNC systems consist of two functional types: point to point (e.g., drilling machine) and contouring, or continuous path (e.g., milling machine).

Point-to-Point Systems. The simplest example of a point-to-point (PTP) CNC machine tool is a drilling machine. In a drilling machine the workpiece is moved along the axes of motion until the center of the hole to be drilled is exactly beneath the drill. Then the drill is automatically moved toward the workpiece (with a spindle speed and feed that can be controlled or fixed), the hole is drilled, and the drill moves out in a rapid traverse feed. The workpiece moves to a new point, and the above sequence of actions is repeated.

In a PTP system, this system requires only position counters for controlling the final position of the tool upon reaching the point to be drilled. The path from the starting point to the final position is not controlled. The data for each desired position are given by coordinate values. However, in high-speed drilling applications, such as the task of single-spindle drilling of an engine block, a control loop is needed to control the acceleration and deceleration of the motion. The digital signal processing technique has been used to control the settling time of the motion system for very fast PTP motion profile (1 to 4 g) so that the spindle could perform drilling operations without breaking the drill. A linear motor-based machine tool has been built and demonstrated by Anorad Corp. (Hauppauge, New York) for Ford Motor's engine machining line.

Contouring Systems. In contouring, or continuous-path, systems, the tool is cutting while the axes of motion are moving, as, for example, in a milling machine. All axes of motion might move simultaneously, each at a different velocity. When a nonlinear path is required, the axial velocity changes, even within the segment. For example, cutting a circular contour requires a sine-rate velocity change in one axis, while the velocity of the other axis is changed at a cosine rate.

In contouring machines, the position of the cutting tool at the end of each segment together with the ratio between the axial velocities determines the desired contour of the part, and at the same time the resultant feed also affects the surface finish. Since, in this case, a velocity error in one axis causes a cutter path position error, the system has to contain continuous-position control loops in addition to the endpoint position counters. Consequently, each axis of motion is equipped with both a position loop and a position counter. Dimensional information is given in the part program separately for each axis and is fed to the appropriate position counter. Then, an *interpolator*, in the controller, determines the proper velocity commands for each axis in order to obtain the desired tool feed rate.

Interpolators. In contouring systems the machining path is usually constructed from a combination of linear and circular segments. It is only necessary to specify in the part program the coordinates of the initial and final points of each segment and the feed rate. The operation of producing the required shape based on this information is termed *interpolation*, and the corresponding software algorithm in CNC is the *interpolator.* The interpolator coordinates the motion along the machine axes, which are separately driven, to generate the required machining path. The two most common types of interpolators are linear and circular. Parabolic interpolators are also available in a few CNC systems that are used in the aircraft industry.

Linear interpolator: The ability to control the movement along a straight line between given initial and final coordinates is termed *linear interpolation*. Linear interpolation can be performed in a plane (two dimensional), using two axes of motion, or in space (three dimensional), where the combined motion of three axes is required. In this chapter only two-dimensional linear interpolators are discussed. To illustrate the interpolator function, consider a two-axis system, where a straight cut is to be made. Assume that the X axis must move p units at the same time that the Y axis moves q units. The contour formed by the axis movement has to be cut with a feed rate of V length-units per second (e.g., mm/sec). The numerical data of p, q, and V are contained in the part program and are fed into the interpolator. The interpolator then generates two velocity signals V_x and V_y, where

$$V_x = \frac{pV}{\sqrt{p^2 + q^2}} \tag{13.3.1}$$

and

$$V_y = \frac{qV}{\sqrt{p^2 + q^2}} \tag{13.3.2}$$

The position reference inputs to the axial control loops are

$$R_x = V_x t \tag{13.3.3}$$

and

$$R_y = V_y t \tag{13.3.4}$$

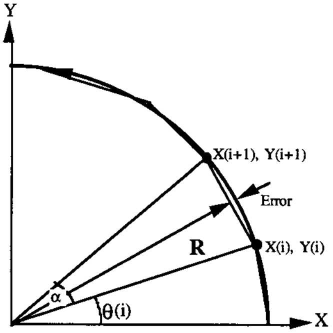

FIGURE 13.3.4 A circular interpolator divides the arc into straight lines.

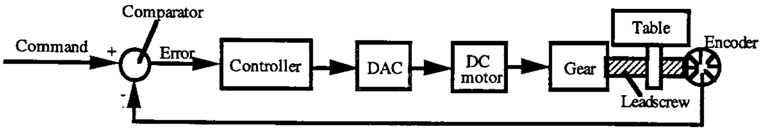

FIGURE 13.3.5 Closed loop of CNC.

As seen, the two-dimensional linear interpolator supplies velocity commands simultaneously to the two machine axes and maintains the ratio between the required incremental distances.

Circular Interpolator: The two most common interpolators in CNC systems are linear and circular. The *circular interpolator* eliminates the need to define many points along a circular arc. Only the initial and final points and the radius are required to generate the arc. The circular interpolator divides the arc into straight lines with a contour error smaller than one BLU. It operates on an iterative basis, where for a given point, $x(i),Y(i)$, a small incremental angle is added to calculate the next point, as shown in Figure 13.3.4.

Both the linear and circular interpolators are based on generating incremental positions every T seconds, where T is the sampling period of the CNC system. Typically, CNC systems operate on one common sampling period for both the interpolator and the control loops. In these systems a typical T may be between 1 and 10 msec. Some other CNC systems utilize a separate computer for the interpolation and another one or several microprocessors for closing the control loops.

Motion Control Systems

A typical closed loop of a CNC machine is shown in Figure 13.3.5. The computer compares the command and the feedback signals and gives, by means of a digital-to-analog converter, a signal representing the position error of the system, which is used to drive the DC servomotor. The feedback device, which is an incremental encoder in Figure 13.3.5, is mounted on the leadscrew and supplies a pulsating output. The incremental encoder consists of a rotating disk divided into segments, which are alternately opaque and transparent. A photocell and a lamp are placed on both sides of the disk. When the disk rotates, each change in light intensity falling on the photocell provides an output pulse. The rate of pulses per minute provided by the encoder is proportional to the revolutions per minute of the leadscrew.

Normally, the motor is mechanically coupled to the load via a drive mechanism. For example, robot links and positioning tables are loads. It is usually a good assumption to ignore the dynamics in the current feedback loop and regard the command current as the actual current, which sets the torque input to the mechanical portion of the system. Notice that the inertia and bearing friction of the motor must be considered as a part of the mechanical portion of the motion control system, which strongly influences the design of the velocity and position loop feedback controllers. These controllers can be implemented in either analog or digital form. In recent years, digital implementation on microprocessors and/or DSPs has become popular, and digital velocity and position controls are often referred to as *digital servo.* The current feedback is usually built into the "drive" (power amplification system). While feedback signals for the velocity and position controllers are usually obtained from the motor, the velocity and position of the load, for example, a positioning table, at the opposite end of the drive mechanism are the quantities of our ultimate concern. Closed-loop control schemes based on the motor velocity and position are sometimes called semi-closed-loop control schemes. The velocity and position of the load must be fed back for full closed-loop control. Typical drive mechanisms are ballscrews and various types of gears. Several manufacturers provide so-called direct drive (DD) motors, which are capable of delivering large torques but with a significantly reduced maximum speed. DD motors may eliminate drive mechanisms. However, they are heavy and may not always be the best solution depending on applications. Common sensors for positions are potentiometers and shaft encoders, and those for velocities are tachogenerators and frequency-to-voltage convertors (FVC), the input to which is encoder pulses. In digital servos, encoders are popular for measuring positions, and velocities are either estimated from encoder pulses or are obtained from FVCs.

Traditional velocity and position loop feedback controllers are of PID (proportional plus integral plus derivative) type. The output of a PID controller is

$$u(t) = k_p e(t) + k_i \int_0^t e(\tau)\, d\tau + k_d \frac{de(t)}{dt} \tag{13.3.5}$$

where $e(t)$ is the error, $u(t)$ is the controlling input, and k_p, k_i, and k_d are, respectively, proportional, integral, and derivative control gains. Equation 13.3.5 represents the PID control law in the continuous-time (analog) form. In digital control, the PID control law

$$u(k) = k_p e(k) + k_i T \sum_{j=0}^{k} e(j) + \left(\frac{k_d}{T}\right)\left[e(k) - e(k-1)\right] \tag{13.3.6}$$

where k denotes the kth sampling instance and T is the sampling period. In position loop feedback control, e and u correspond to the positioning error and the velocity command, respectively. For the velocity loop controller, they are the velocity error and the current command. Another popular linear controller is the lead/lag compensator. Input-output (I/O) interfaces include analog-to-digital convertors (A/D), decoders for processing encoder pulses, and digital-to-analog convertors (D/A). Motion control systems can be built from components and programmed with custom software, they can be purchased as plug-in boards for various buses, or they can be purchased as packaged systems.

PID and lead/lag compensators are simple and utilized in many applications. However, they alone might not be adequate for problems where the performance requirements are stringent. Extreme care must be taken during the design of a closed-loop control system. By increasing the magnitude of the feedback signal (e.g., more pulses per one revolution of the leadscrew), the loop is made more sensitive. That is known as increasing the open-loop gain. Increasing the open-loop gain excessively may cause the closed-loop system to become unstable, which obviously should be avoided.

The basic nature of "feedback" control is that the control action is based on the error. When the reference input for the position loop is fixed, the integral action may assure zero errors at the steady state. In tracking control, however, the position command is continuously varying, which combined with the dynamics of the closed-loop system makes tracking errors always occur. For example, in contouring of a circular arc in machining, the command position signal for each motion control axis is sinusoidal. Such an operation is essentially a test of the frequency response of the motion control axis. The controller is normally tuned so that the frequency response gain is close to but not exactly 1 in the operating range. In high-speed contouring operations, corresponding frequencies are high, and the gain is normally below unity. Then, the actual diameter is slightly smaller than the desired diameter. This consequence is often called the radial reduction error. Such errors may be reduced by applying the disturbance observer scheme to the position loop. However, the disturbance observer is still a feedback controller, and one sampling time delay in digital implementation further diminishes its effectiveness.

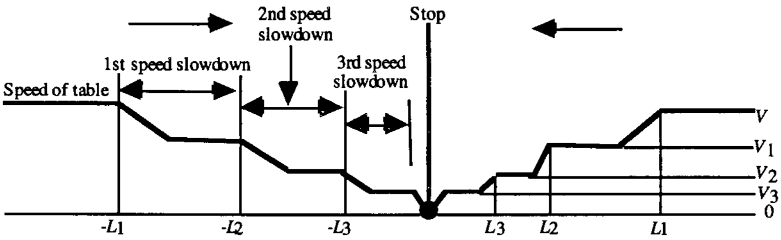

FIGURE 13.3.6 Deceleration procedure in a PTP system.

The following discussion describes some principles of motion control systems for PTP machines and contouring machines.

The control loops of PTP systems are designed to control the position of the machine tool axes. Each axis is *separately* driven and should follow the command signal. The system design starts by selecting the type of control: open loop or closed loop, a decision that depends on the required specifications of the NC system and economy. Open-loop controls use stepping motors as the drive devices of the machine table. The drive units of the stepping motors are directly fed by the controller output pulses. The selection of the appropriate motor depends on the maximum torque, required velocity, and step size in the system. Stepping motors can be implemented on small-sized PTP systems in which the load torque is small and constant. Larger PTP machines and contouring systems utilize closed-loop control systems.

In PTP systems each axis is driven separately at the maximum allowable velocity. This velocity depends on the drive type and on the mechanical structure of the particular machined or manufacturing system. In order to avoid large overshoots, the velocity is decelerated before the target point in which the tool starts to operate (e.g., to drill). Since the path between the points is insignificant, *the deceleration is accomplished in each axis separately.*

In practical systems the deceleration is accomplished by three stages. A typical three-stage deceleration diagram of one axis of the table is given in Figure 13.3.6. The table moves at rapid velocity V until reaching a distance L_1 from the target point, where the table is instructed to move at smaller velocity V_1. After a time delay, which depends on the system inertia, the table moves at a new velocity V_1 until reaching a distance of L_2 units from the target point, where again the velocity is reduced to V_2. When the table is at a distance of L_3 units before the target point, the velocity is reduced once more and the table "creeps" toward the final point at very low velocity V_3, and subsequently stops.

The control in CNC contouring systems operates in closed loops, which compare the command pulses from the interpolator with the feedback signal from the encoder or the resolver. The most sophisticated design applies to the closed-loop control of contouring systems. In the design of these loops, the transfer function of each element must first be determined; the system is then set up in block diagram form, and finally the loop gain is established based on performance analysis. The transfer function of each element is based on its mathematical model. In establishing the mathematical model the engineer is faced with a compromise between *accuracy* and *complexity*, on one hand, and *approximation* and *simplicity*, on the other. In this section we discuss simple models, in which the principles of design can be readily illustrated.

The control loops of contouring systems are usually of the closed-loop type, as shown in Figure 13.3.7. They use two feedback devices: a tachometer that measures the motor speed and is included in the drive unit, and a position feedback transducer, which is capable of also measuring the axis velocity (such as an encoder, resolver, or inductosyn). In encoder-based systems the encoder is mounted on the leadscrew and emits pulses; each pulse indicates a motion of 1 BLU of axis travel. Therefore, the number of pulses represents position and the encoder pulse frequency is proportional to the axis velocity.

Error Sources in CNC Systems

Despite the high precision of CNC equipment, it still has position and contour errors. Error sources in CNC machines are classified into three categories:

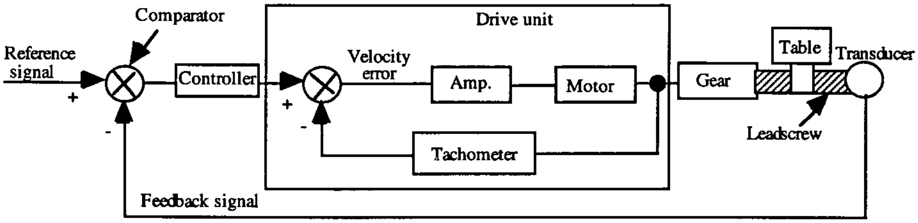

FIGURE 13.3.7 Control loop of contouring system.

1. Mechanical hardware deficiencies
    - Orthogonality of machine axes
    - Straightness of the machine axes
    - Thermal deformation of the machine structure
    - Backlash in the gears and leadscrew nuts
    - Uneven leadscrew pitch
    - Friction in moving components (leadscrews, guideways, etc.)
2. Cutting process effects
    - Tool deflection due to cutting forces
    - Large vibrations and chatter
    - Tool wear
    - Workpiece thermal deformations
    - Workpiece deformations due to cutting forces
3. Controller and drive dynamics
    - Disturbances due to cutting forces
    - Disturbance due to friction forces in the machine guideways
    - Contour errors caused by tracking errors of nonlinear contours (e.g., circles)
    - Contour errors caused by mismatch of equivalent parameters in the axial controllers
    - Corner errors in contouring operations

In general, errors of the first type, such as machine geometry errors and thermal deformation of the machine structure, can be compensated for by the machine controller. To further understand the measurement of errors, the next section will examine the metrology for precision engineering.

References

Ohnishi, K., Matsu, N., and Hori, Y. 1994. Estimation, identification, and sensorless control in motion control system. *Proc. IEEE*, 82(8), 1253–65.

Tomizuka, M. 1993. On the design of digital tracking controllers. *ASME J. Dyn. Syst. Meas. Control*, 115(2), 412–18.

Metrology and Precision Engineering

Kam Lau

Introduction

Precision engineering in manufacturing generally refers to the engineering processes of achieving tighter tolerances or dimensional accuracy of a design. The process of precision engineering consists of the part *design*, part fabrication, and, finally, part *inspection*. This section addresses some of today's precision engineering considerations in fabrication and inspection.

Factors in Precision Engineering

The fabrication process is a material transformation process that determines the final part dimensions through material forming, removal, or insertion. Precision in the fabrication generally refers to the dimensional "repeatability and accuracy" of a part transformed under such a process. The factors to be considered to ensure good "precision" are (1) errors of the *machine* system(s), (2) the *environment* in which the machining is being performed, (3) the *manufacturing process*, and (4) the *instrumentation* to verify the performance of the factors.

Machine Errors. Machine errors can be classified into geometric, thermal-induced, dynamic, and structural errors. Geometric errors are errors related to the undesirable machine geometry caused by nonorthogonality (squareness error) of axes, linear positioning (or scale) error, reversal (or backlash) error, straightness error, pitch, yaw, and roll errors of a machine axis during a linear move. If the machine is equipped with a rotary table, geometric error would include axis wobble, rotational positioning error, eccentricity, and parallelism errors.

Geometric Errors: Geometric errors are much better understood in the machine industry than the thermal, dynamic, and structural errors. The techniques and instruments to check for the geometric error are very well established and are commonly applied in the machine tool industry. However, for small to medium-size machines, geometric errors constitute only about 25% or less of the total manufacturing error. For larger machines, the percentage can go as high as 50%. As such, just knowing the geometric errors of a machine system may not be adequate in the realization of the total manufacturing error.

Traditional devices for measuring different types of geometric errors are the mechanical square, straightedge, autocollimator, electronic level, step gauge, optical polygon, and dial indicator. In some instances, a combination of these devices is needed. Newer instruments that can offer faster and more precise measurements are the laser interferometer system, the 5-D laser interferometer system, and the telescopic ball bar.

Thermal Errors: Thermally induced machine error is considered one of the key factors affecting the accuracy of a machine tool. Thermally induced errors arise as a result of nonuniform heat generation within the machine such as in motors, bearings, and guideways; heat generated during the cutting process; and the coolant effect as well as the environmental effect resulting in the uneven growth of the machine structure. Thermal error can contribute as much as 50% of the total manufacturing error in small to medium-size machines. However, this effect has been largely unrecognized or often ignored by the machine tool industry until recently.

There are basically two alternatives to monitor the thermally induced errors — intermittent and continuous monitorings. Intermittent monitoring generally involves the use of a touch probe or dial indicator(s) to periodically measure against one or multiple fixed positions as the machine is going through a thermal exercise. In the case of the dynamic spindle thermal study, an artifact such as a sphere or a rod can be mounted on the spindle while it is running at a certain speed. At some elapsed time (e.g., 1-min intervals), the spindle will stop momentarily and the machine will reposition the artifact to the dial indicator(s) to check for the repeatability. Any deviations from the initial position (i.e., cold-start position) are considered as thermal growth due to the spindle warm-up. A typical spindle thermal test takes about 4 to 8 hr to complete. A similar procedure can be applied for the environmental and servomotion-related thermal growth measurements.

The continuous thermal growth monitoring generally involves the use of some noncontact sensors such as capacitance gauges, optical sensors, or inductance sensors arranged in the similar fashion as above. The benefits of continuous monitoring are that there is no interruption of the spindle dynamic and that the machine positioning repeatability does not necessarily interfere with the results. Furthermore, the noncontact nature generally allows the spindle to operate at any speeds, thus giving a much broader range of thermal assessment.

Laser interferometer systems are also used occasionally to monitor thermal growth effects. Because of its ability to identify the growth along the entire axis, the laser measurement is better suited for monitoring the growth of a linear-scale system caused by internal or external heat sources. Linear-scale error caused by axis movement is about one fifth that of the spindle thermal in medium to small machines. It is even less in larger machines since the heat dissipation effect in larger machines is much more effective.

Dynamic Errors: Dynamic errors here refer to those caused by the motions of a CNC machining center. These include the servo-gain mismatch, servo-stick-slip, servo-oscillation, and controller error. Errors pertaining to tool chattering, structural deformation (caused by machine carriage acceleration and deceleration), machine/part deadweight, and so forth are considered structural errors and are discussed later in this chapter.

Servo-gain mismatch is often caused by the electrical (or computer) gain setting of one axis not matching the other. The problem is not severe when the machine is primarily used for static positioning purposes, such as drill, boring; however, it can be a problem in precision contour milling when two or more axes are to be used in synchronization with each other. The magnified elliptical error is caused by one axis responding faster than the other in reaching the commanded positions. Servo-gain mismatch can easily be corrected in a routine machine maintenance.

Structural Errors: Structural errors include tool-chattering error and structural deformation error (due to acceleration and deceleration of the machine carriage, the deadweight distribution, and the cutting force, among other factors).

Tool chattering generally affects the machinability and surface finish of the workpiece, not the dimensional accuracy. Structural deformation caused by the acceleration and deceleration of the machine carriage and workpiece is rather insignificant for quasi-static positioning and slow-speed contouring. However, the error can be significant if the contouring speed is high. Another major contributor to the structural error is the cutting force. An excessive amount of cutting force can cause the spindle axis, the tool, the fixture, and the part to deform.

A good device to gauge the potential structural error is a compliance system. A basic compliance system consists of a load cell and a dial indicator, which are set up between the machine table and the spindle. The table is programmed to move in small increments (e.g., 5 mm) in either directions of the load cell. The readings from the load cell (force) and the indicator (actual displacement of the table) are then recorded at every increment. A compliance chart can then be obtained by plotting the forces (F) against the differences between the actual and commanded displacements (DD) of the table (i.e., F vs. DD).

Another type of structural error for large machines is from the machine foundation error. Most large machine bases are built in sections. These sections are then aligned, assembled, and anchored together to a common reinforced concrete foundation. As such, the foundation becomes part of the machine structure and the accuracy and repeatability of the machine are therefore heavily dependent on the stability of the foundation. It is not unusual to find the performance of the machine degraded as a result of floods and earthquakes, and loosening of anchor supports due to prolonged use or lack of maintenance.

Errors Introduced by Environmental Effects. For manufacturing plants that have little or no control of the plant environment, environmental effects can be very significant sources of errors. Two of the most dominant environmental effects are thermal and vibration effects.

Thermal Errors: For many nontemperature-controlled manufacturing plants, it is not unusual to observe a total temperature swing of 20°F throughout a day of operation. This wide fluctuation of environmental temperature can cause significant accuracy and repeatability problems to the machining systems as well as the workpieces. Even in a somewhat controlled environment, thermal errors can still be a major problem. For instance, if the machine is located in the vicinity of a frequently operated bay door, where there is a substantial temperature difference between the plant temperature and the outdoor temperature, or if it is placed next to a heat source such as a welder, an electric blower or exhaust, or a hydraulic pump, or under direct sunlight, the heat source can still cause tremendous localized thermal distortion of the machining system.

In most cases, one can reduce the localized environmental thermal effect by isolating the heat sources with simple panel shielding or by relocating the machines. If an overall plant temperature control is unachievable or impractical for economic reasons, one may consider (1) applying localized thermal control of certain key machining systems, or (2) implementing computer thermal compensation techniques.

Vibration Errors: Environmental vibration error is a result of one or more external vibration sources affecting the structural stability of the machine system. This type of error can be significant if the machining system is located next to a heavy punch press operation or where frequent forklifting operation is present. Using a spindle analyzer or a laser interferometer system to access the amount of the environmental vibration error is common.

Other Errors: Other types of environmental errors are the interference or instability of the electric power source, the factory-supplied pneumatic and hydraulic pressures, air pressure, and humidity. These types of errors may be of lesser magnitude than the ones mentioned earlier; however, it is always good practice not to underestimate their potential effects in any precision manufacturing considerations.

Errors Introduced by the Manufacturing Process. The magnitude of these types of errors depends heavily on the process control and manufacturing practices implemented by each individual plant. In general, the concerns in this area are the effects of the coolant on the workpiece and the machine structure, the pallet and the fixture, the repeatability of the pallet and tool changer, and the tool deflection in manufacturing.

Coolant Effects: Eighty percent of machining uses coolant, sometimes referred to as *wet machining*. In most cases, the coolant temperature is not controlled. For smaller machining systems, a small coolant tank can be found next to the machine. For larger machines, a large coolant tank can be found underneath the ground. The main purposes of the coolant in machining are (1) for lowering the cutting temperature, and (2) for chip removal. As the coolant is being recycled during the machining process, its temperature gradually warms up. This significant increase in temperature affects the workpiece dimensions since the workpiece temperature before machining is generally room temperature. Similarly, the pallet dimensions are also affected.

Tool and Fixture: The conditions of the pallets, tools, and fixtures often govern the repeatability of a manufacturing system. These components should be checked routinely for wear and chipping. Fixtures and clamping devices should be routinely checked to ensure that proper clamping forces can be applied and that contact surfaces are in good condition. Many of these checks can be accomplished visually or by performing dial indicator repeatability checks.

When excessive cutting force is expected, it is necessary to consider the maximum possible amount of the tool, workpiece, and fixture deflections resulting from the force. The amount, if it exceeds the manufacturing tolerance, should be reduced by either decreasing the depth of cut or the feed rate or by strengthening the tool and fixture. A compliance system is a good qualifier to measure the tool deflection under load.

Instrumentation and Inspection in Precision Engineering

The American National Standards Institute developed *ANSI B5.54 Standards for CNC Machining Center Performance Evaluation* for the purpose of providing detailed guidelines for machine tool users and developers to evaluate and compare the performances of CNC machining systems. The *standards* delineate procedures for the measurements of the machine and environmental errors as stated earlier, as well as choices of conventional and state-of-the-art instruments used in doing the measurements. Experience indicates that these measurements are useful not only for performance evaluation but also for better understanding of the sources of errors. This information is crucial for preventive maintenance and for accuracy enhancement of CNC machine systems.

Some of the key techniques introduced by the *B5.54 Standards* are the telescopic ball-bar measurement, spindle dynamic and thermal drift measurement, laser diagonal measurement, and the one-day test.

Instrumentation and Metrology

Telescopic Ball Bar. The telescopic ball-bar test is gradually becoming one of the most powerful and convenient tests for CNC machining center evaluations. As is shown in Figure 13.3.8, a telescopic ball bar consists of a spring-suspended reed having two spheres attached to both ends. The spheres are allowed

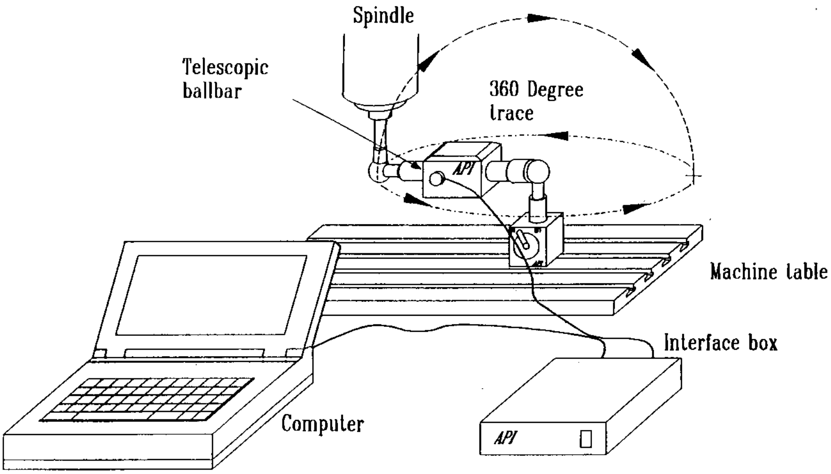

FIGURE 13.3.8 The telescopic ball bar.

to move relative to each other with a limited travel, for example, 3 to 4 mm. Inside the reed is a displacement sensor, known as a linearly variable displacement transducer (LVDT), that measures the relative move of the spheres. The output of the LVDT is connected to a computer.

To use the telescopic ball bar, one of spheres is magnetically attached to the magnetic socket that is installed on the machine spindle; the other is magnetically attached to a second magnetic socket mounted on the table. The machine is then programmed to contour in a circle in the *X-Y*, *X-Z*, or *Y-Z* plane, as shown in Figure 13.3.8. As the contouring proceeds, any errors of the machine in contouring will be translated into relative moves picked up by the LVDT and instantaneously recorded by the computer. After the machine has stopped, the computer then plots the errors on a chart for analysis. Errors such as backlash, axes nonsquareness, scale mismatch, servo-gain mismatch, cyclic motion, stick-slip, and certain straightness errors can be readily detected by using a telescopic ball bar.

Laser Interferometer. A laser interferometer system can produce measurements pertaining to the linear, angular, straightness, and squareness errors of a machine system. To many in the manufacturing industry, laser interferometer measurements are considered as the primary calibration standards. However, it is important that when using a laser interferometer, the proper procedures are followed. Precautions should be taken when using a laser interferometer system: avoid setting up the laser in areas where large air turbulence is present; set up the laser to minimize the cosine error and Abbe error; beware of the environmental effects (i.e., temperature, pressure, and humidity) to the laser accuracy; and understand the material parameters (i.e., material temperature, coefficient of expansion, etc.) to the measuring accuracy. In the event that these effects are significant, it is necessary to compensate for them in the final results.

Setting up a laser interferometer system for machine measurement can be very tedious and sometimes frustrating. It is not unusual to take 2 to 3 days to measure all linear, straightness, angular, and squareness of a mid-size 3-axis CNC machine (referred to as 21 parameters measurement). A new laser system known as the 5-D laser interferometer system, developed by Automated Precision Inc. (Gaithersburg, Maryland), has the capability of measuring 5 degrees of freedom (i.e., *X*-, *dY*, *dZ*, pitch, and yaw) simultaneously in one single setup. In contrast, the 5-D system is able to cut down the measuring time to 3 to 4 hr.

A laser interferometer system should not be confused with an alignment laser system. A laser interferometer system works on the polarized light interference principle and can produce precision to within a tenth (or better) of a wavelength of light (i.e., 630 nm for an HeNe laser). By using the same measuring principle, a laser interferometer system can also generate angle measurements to within 0.1 arc-sec. An alignment laser works on beam-pointing effects and combines the measurements with a photodetector for straightness and angle measurements (not linear measurement). In this case, the laser beam is used as a straightedge. Unless the electro-optics elements are used carefully, the accuracy is much lower than that of a laser interferometer system. Although alignment lasers are commonly used in machine alignment, it should not be construed as a precision calibration standard.

Spindle Analyzer. A spindle analyzer can be used to measure several important parameters of a machining system. These include thermal growth of a machine resulting from environmental variations (i.e., temperature, vibration) and internal heat sources (i.e., motors, spindle bearings, hydraulic systems), spindle dynamic errors resulting from a worn or contaminated bearing, and machine axis repeatability.

For advanced applications, it is recommended that the sensors be of noncontact nature since contact sensors can create problems when measuring a high-speed spindle in motion. The noncontact sensors can be optical, capacitive, or inductive. They all have their advantages and disadvantages dependent on their applications. Users should consult with the manufacturers before making their selections.

Other Metrology Instruments. The above-mentioned metrology instruments represent some of the latest and most commonly used instruments in the manufacturing industry. Other instruments that are also used frequently are electronic autocollimators, electronic levels, force gauges, temperature sensors, vibration sensors, dial indicators, proximity sensors, mechanical straightedges, step gauges, and precision-indexing tables. One should not, however, overlook the benefits offered by some of the latest data acquisition and data analysis software packages such as statistical process control (SPC). Of course, the proper selection and use of any instrument are key to a better understanding of the factors in precision manufacturing.

Inspection System and Metrology

The direct-computer-controlled coordinate measuring machine (DCC-CMM) has been the dominating means for final workpiece dimensional inspection in the manufacturing industry since the early 1980s. Since then, several advanced dimensional measuring devices have also been developed and are gaining wide acceptance in industry. These are the high-speed laser tracking systems and the manually operated measuring robots. There is also a growing interest in the manufacturing industry to reduce the off-line inspection process (i.e., CMM-type applications) by performing some of the inspections on the CNC machining system. This is referred to as on-machine gauging. This section will discuss some of the key considerations related to the use of these advanced inspection systems.

Laser Tracking Interferometer Systems. The laser tracking interferometer system (LTS) was developed at the National Institute of Standards and Technology (NIST) in the mid-1980s for medium- to large-dimensional inspections. It was then commercialized and introduced to the industry in late 1989. Since then, the LTS has been gaining popularity and is becoming one of the dimensional measuring standards.

Through the combination of a precision dual-axis gimbal, a laser interferometer system and an optical target (i.e., a retroreflector), the laser beam is precisely directed to the target through the manipulation of the gimballed mirror via the control computer. As the beam is sent back to the laser by the target, it is partially deflected to a dual-axis photodetector. The beam position is then interpreted by the computer. As the target moves, the photodetector immediately generates an error signal to the computer that drives the mirror to ensure the beam stays locked onto the target. While it is tracking, the computer acquires the laser measurement and the two angle measurements (a and b angles) of the mirror and computes for the three-dimensional position of the target.

The advantages of the LTS are that (1) it is considered one of the most accurate large-dimensional coordinate measuring devices with an accuracy of better than 10 ppm (i.e., 100 mm at 10 m); (2) it has a very measurable envelope — 25 m × 360°; (3) it can track a target moving at a speed of 4 m/sec; (4) it can sample up to 1000 samples/sec; and (5) it is compact, portable, and fully automatic. It is well suited for rapid surface scanning, jigs and fixture alignment, replacement of conventional CMMs for large structural measurements, and large CMMs, robotic devices, or CNC machining center calibrations.

The disadvantages are that (1) when used in areas where significant air turbulence is present, the system becomes less reliable; (2) the accuracy may be reduced when used in areas where heavy forklifting activities are present (since the floor foundation is part of the measuring frame); and (3) the system needs zero referencing if the interferometer beam is interrupted during measurement.

On-Machine Gauging. On-machine gauging (or in-process gauging) refers to the dimensional inspection process implemented during or after a machining cycle right on the machining system. In other words, the machining system, retrofitted with a sensor (i.e., a touch probe), is used to serve as a coordinate measuring machine while the workpiece is still on the machine. This concept certainly has merit since most CNC machining systems have control, scale, and structural integrity equal to or better than many DCC-CMMs.

The advantages of performing dimensional inspections on the same machining system are obvious: (1) it eliminates the need of moving the workpiece to a CMM; (2) it reduces the inspection cycle time; and (3) it eliminates realignment error should reworking the workpiece become necessary. The disadvantages, however, are (1) since the same machine frame is used for machining and inspection, if the machining system has any inherent errors (such as geometric errors) that affect the workpiece accuracy, it is incapable of detecting those errors in the inspection, and (2) the machine will experience a large degree of thermal distortion caused by the internal heats.

In order to implement on-machine inspection, it is therefore necessary to first perform geometric accuracy evaluation of the machining system according to B5.54 Standards. All effort should be made to ensure that the accuracy is maintained. Second, a machine thermal growth analysis should be performed to ascertain the limitation of the thermal distortion in inspection. In either case, a minimum rule of thumb of four times the accuracy tolerance should be applied. New techniques of thermal and geometric modeling and compensation of the machining system can be considered in order to achieve the inspection goals.

Other Inspection Systems. Other emerging inspection machines, such as the manually operated robotic measuring device, stereotriangulation measuring systems, and photogrammetry systems, are also gaining popularity in manufacturing. Although they may not offer the same types of accuracy and versatility as the previously mentioned system, they feature a new trend of inspection requirements — portability, agility, shop-floor hardiness, high-speed data acquisition, low cost, and powerful software capability.

References

ANSI. 1992a. *Performance Evaluation of Computer Numerically Controlled Machining Centers*, ANSI/ASME B5.54-1992, ASME, New York.

ANSI. 1992b. *Axes of Rotation, Methods for Specifying and Testing*, ANSI/ASME B89.3.4M-1985 (R1995), ASME, New York.

ANSI. 1995. *Temperature and Humidity Environment for Dimensional Measurement*, ANSI/ASME B89.6.2-1973 (R1995), ASME, New York.

ANSI. 1997. *Methods for Performance Evaluation of Coordinate Measuring Machines*, ANSI/ASME B89.4.1-1997, ASME, New York.

Slocum, A. 1992. *Precision Machine Design*, Prentice-Hall, Englewood Cliffs, NJ.

Technical Manual, Automated Precision Inc. (API), Gaithersburg, MD.

13.4 Design and Analysis Tools in Manufacturing

Computer-Aided Design Tools for Manufacturing

David C. Anderson

Introduction

Computer-aided design (CAD) tools for manufacturing are computer programs that evaluate producibility of a product under development using computer models of the product and simulation models for manufacturing processes. Examples of such processes are assembly, casting, molding, stamping, forming, and inspection. The early stages of design are critical to the success of the final product since most of the final cost of a product is committed through decisions about the product's geometry and the materials that lead to the selection and planning of manufacturing processes and production facilities.

Concurrent engineering (CE) is a methodology for product development processes in which the tasks are performed simultaneously based on "what if" decision-making processes. CE is a driving force behind the development of CAD tools for manufacturing.

CAD System and Manufacturing

One of the first and most prominent manufacturing applications of the CAD system was the automated programming of numerically controlled (NC) machine tools. NC machines were developed in the 1950s, but their widespread use was hindered by the difficulty in writing the requisite NC programs, lists of coded cutting tool motions that directed the machine to cut the desired part. Computer programs that facilitated the generation of NC programs were among the first CAD tools for manufacturing. Early systems focused on profile cutting, generating cutter location data that described the two-dimensional coordinates of the paths of cutting tools that would remove the material to create the final part. Three-dimensional NC programming capabilities are available in most CAD systems today. The user guides the generation of NC data by interactively selecting each surface to be machined and answering questions about tools, approach directions, and machining preferences.

Solid Models and Manufacturing

A key element of virtually all CAD tools for manufacturing is the need to interpret the CAD data according to manufacturing capabilities, requirements, and constraints. Generally, this interpretation involves determining the characteristic shapes in the CAD data related to the manufacturing process of interest and applying knowledge about the process to determine the manufacturing operations and parameters. Solid models are rigorous computer data structures that contain a complete, unambiguous representation of the nominal geometry of an object. Solid models and solid modeling operations, like the Boolean union, difference, and intersection of solids, enabled geometric computations about the design that were not possible with earlier CAD data. With solid modeling, the emphasis in CAD shifted from data for visual communication to product data models that could be used for more sophisticated computer analyses with more automation.

In solid models, geometric features can be described in a form more suitable for engineering and manufacturing applications. As a result, feature-recognition algorithms have become an important element of many CAD tools for manufacturing for translating CAD models into usable geometric data for design evaluations.

However, feature recognition has limitations because it is not possible to translate every solid model into a given set of features. Also, some applications of feature recognition require additional, nongeometric information. This information must be added to the CAD data before, during, or after the feature-recognition process. For example, part tolerance data are required for machining process planning but are not available in current CAD data. Feature-based design (FBD) was developed to overcome some of the limitations of feature recognition. Instead of deriving a features model from a solid model, FBD systems create the product model with features during the design process. Many FBD applications have been demonstrated in the area of machining, and some commercial CAD vendors have incorporated these features into their systems.

FBD also has limitations. The features that are useful for one manufacturing process may not be useful for another. For example, a model made with cavity features, such as holes, slots, and pockets, provides ready-to-use data for machining planning. However, this model is inappropriate for sheet metal bending or welding processes that require an understanding of the bends and protrusions on a part, not its cavities.

Product Data Standards and Manufacturing

The International Standards Organization (ISO) has developed the Standard for the Exchange of Product (STEP) model data. In the U.S., the Integrated Graphics Exchange Specification (IGES)/PDES Organization

(IPO) developed the Product Data Exchange Specification (PDES). These efforts merged and PDES was renamed Product Data Exchange using STEP, which is now the American National Standard for STEP. STEP became the international standard (ISO 10303) in March 1994.

STEP is organized as a series of "parts" that are developed and published separately. The parts are organized into numerical series: description methods (parts 11 to 20), integrated resources (parts 41 to 200), application protocols (parts 201 to 1200), abstract test suites (parts 1201 to 2200), implementation methods (parts 21 to 30), and conformance testing (parts 31 to 40). The product information is specified in a formal specification language, EXPRESS, which is documented in Part 11. Part 1 is an overview of the entire standard.

The STEP application protocols (APs) are important to CAD tools for manufacturing. These are the implementable portion of the STEP standard. Each AP draws on integrated resources and adds specific constraints, relationships, and attributes to meet the information requirements of a particular application. It is expected that several hundred APs may be developed for many different industrial applications.

Design for "X" Tools

Many CAD tools for manufacturing belong to a class of programs described as "design for x," where "x" signifies an application area, such as design for assembly or design for castability. The phrase *design for manufacturability (DFM)* can be considered as a specialization of design for x in which all the applications are manufacturing. Generally, DFM applications are computer programs that perform computations to analyze the producibility of a product with respect to a specific manufacturing process or set of processes. The format of the design data representing the product required by the program varies greatly. The program then provides an evaluation of the suitability of the design according to this domain. The form of this evaluation also varies with each program.

DFM programs act as "manufacturing experts" that provide qualitative, and perhaps quantitative, information about potential problems in a design based on predefined knowledge about a manufacturing process. The programs emulate the process done by human experts, examining the design data and reporting any problems based on experience. Many efforts are based on expert systems technology from the field of artificial intelligence (AI). The searching is performed through the facilities of an AI language, such as PROLOG or LISP, or using an expert system "shell," a preprogrammed generic expert system. Design data are first translated into a knowledge base, the AI version of a database, containing facts and rules. In a sense, the detailed design data are made into logical data that can be processed using AI methods. The program computationally searches the design data for data patterns that match problem conditions represented in the knowledge base of the program. The problem conditions are computer representations of design data that are known to cause manufacturing difficulties for a given process. For example, a "design for injection molding" program may report that an internal corner radius in a geometric model of a part is too small and may cause problems in the mold. In some cases, the program provides a quantitative evaluation of the design, or producibility index. This provides a convenient numerical comparison between two competing designs.

References

Amirouche, F.M.L., 1993. *Computer-Aided Design and Manufacturing*, Prentice-Hall, Englewood Cliffs, NJ.

Boothroyd, G. 1994. Product design for manufacture and assembly. *Comput. Aided Des.*, 26(7), 505–20.

Laurance, N. 1994. A high-level view of STEP. *Manuf. Rev.*, 7(1), 39–46.

The National Product Data Exchange Resource Center, U.S. Product Data Association (US PRO) National Institute of Standards and Technology, http://elib.cme.nist.gov/nipde/ (Internet document), 1995.

Whitney, D.E., Nevins, J.L., and De Fazio, T.L. 1989. *Concurrent Design of Products and Processes: A Strategy for the Next Generation in Manufacturing*, McGraw-Hill, New York.

Zeid, I. 1991. *CAD/CAM Theory and Practice*, McGraw-Hill, New York.

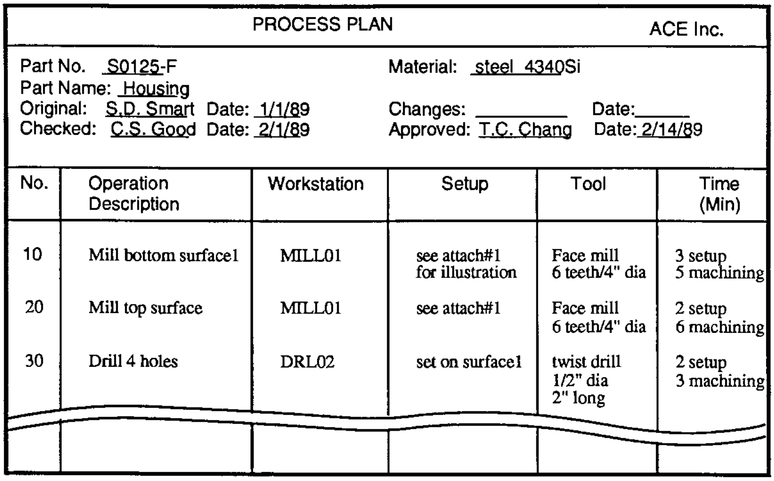

PROCESS PLAN ACE Inc.

Part No. S0125-F
Part Name: Housing
Original: S.D. Smart Date: 1/1/89
Checked: C.S. Good Date: 2/1/89
Material: steel 4340Si
Changes: ________ Date:_____
Approved: T.C. Chang Date: 2/14/89

No.	Operation Description	Workstation	Setup	Tool	Time (Min)
10	Mill bottom surface1	MILL01	see attach#1 for illustration	Face mill 6 teeth/4" dia	3 setup 5 machining
20	Mill top surface	MILL01	see attach#1	Face mill 6 teeth/4" dia	2 setup 6 machining
30	Drill 4 holes	DRL02	set on surface1	twist drill 1/2" dia 2" long	2 setup 3 machining

FIGURE 13.4.1 A process plan.

Tools for Manufacturing Process Planning

Tien-Chien Chang

Introduction

Process planning prepares a production documentation that specifies the operations and operation sequence necessary to manufacture a product. Process planning is defined as an act that determines the manufacturing operations, operation sequence, and resources required to make a product. The process domain includes machining process planning, welding process planning, EDM process planning, forming process planning, and so forth. The product domain includes mechanical part process planning, mechanical assembly process planning, and electronics assembly process planning. The input to a process planning system (or a human process planner) can be an engineering drawing, a CAD model, or a three-dimensional solid model. While most human planners prefer an engineering drawing on paper or in electronic form, process planning systems usually use CAD models.

The result of the process-planning activity is a "process plan" (see Figure 13.4.1), also called route sheet, operation sheet, or operation planning summary. It can be as aggregate as a list of work center identification numbers or as elaborate as a 50-page document with setup drawings, tool specifications, and operation time estimates.

Since the information on the process plan is used in scheduling the production and controlling the machine, the production efficiency and the product quality are affected.

Manual Process Planning

Process planning involves several or all of the following activities:

- Selection of machining operations
- Sequencing of machining operations
- Selection of cutting tools
- Selection of machine tools
- Determination of setup requirements
- Calculations of cutting parameters
- Planning tool path and generation of NC part programs
- Design of jigs and fixtures

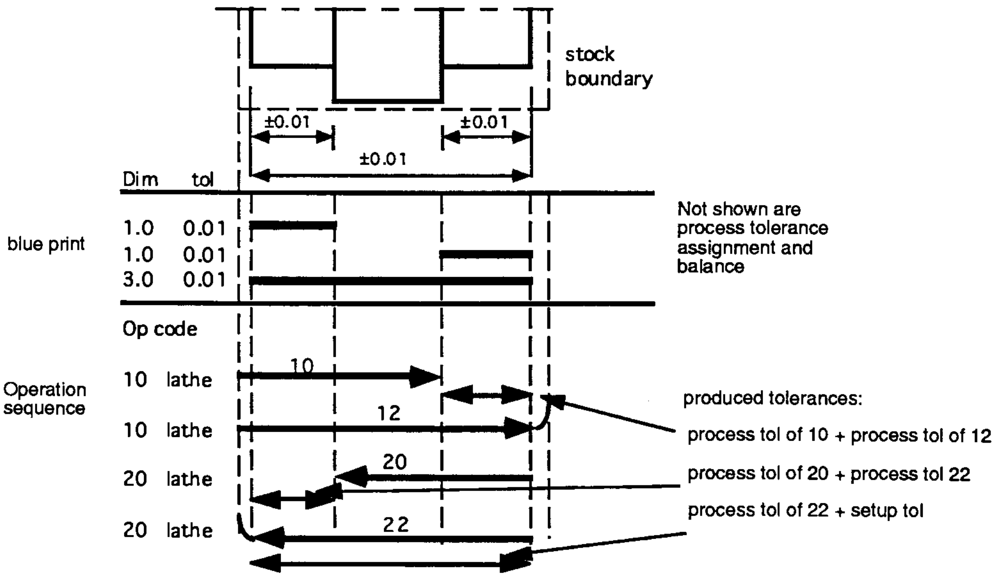

FIGURE 13.4.2 A tolerance chart.

The details incorporated in a typical process plan usually vary from industry to industry. It depends on the type of parts, production methods, and documentation needs. A process plan for a tool room–type manufacturing environment typically relies on the experience of the machinist and does not have to be written in any great detail. In fact, the instruction "make as per part print" may suffice. In typical mass-production-type industries, the process-planning activity is embodied in the transfer and flow lines used for manufacturing component parts and assembly. For metal-forming-type manufacturing activities, such as forging, stamping, die casting, sand casting, or injection molding, the process-planning requirements are embedded directly into the design of the die/mold used, where most process-planning activity is fairly simple. A process planner must

- Be able to understand and analyze part requirements
- Have extensive knowledge of machine tools, cutting tools, and their capabilities
- Understand the interactions between the part, manufacturing, quality, and cost
- Possess analytical capabilities

Tolerance Charting

During process planning it is important to ensure that the setup and operation sequence will yield a satisfactory part. Tolerancing charting (Figure 13.4.2) has been used to help in allocating process tolerances and verifying the operation sequence. A tolerance chart analyzes one dimension at a time. In a tolerance chart, the top is the part drawing. Dimensions and tolerances are presented with the geometry. Dashed lines show the stock boundary. From the features of the part and the stock, extension lines are drawn to the body of the chart. The section below the drawing shows the critical dimensions and tolerances. These dimensions and tolerances must be satisfied after the processes are complete. Following the process sequence, each operation is listed in the third section of the chart. A line is drawn from the reference surface of a setup to the cut surface. For example, in operation 10, the raw stock boundary at the left is the reference surface. The second surface from the right-hand side is created by this operation. From the chart, one can calculate the resultant tolerances. The results are compared with the blueprint tolerance.

Although traditionally a tolerance chart is implemented on paper and through a fixed procedure, it can also be implemented in a computer. The process tolerance stack-up may be used to verify the design specification and select the appropriate processes and sequences.

Computer-Aided Process Planning

There are two basic approaches to computer-aided process planning — variant and generative. The *variant* approach is signified by the terminology used by the computer to retrieve plans for similar components using table lookup procedures. The human process planner then edits the plan to create a "variant" to suit the specific requirements of the component being planned. Creation and modification of standard plans are the process planner's responsibility. The *generative* approach generates a plan for each component without referring to existing plans. Generative-type systems can perform many functions in a generative manner, while the remaining functions are performed with the use of humans in the planning loop.

Variant Process Planning

The variant approach to process planning was the first approach used to computerize the planning techniques. It is based on the concept that similar parts will have similar process plans. The computer can be used as a tool to assist in the identification of similar plans, retrieving them and editing the plans to suit the requirements for specific parts.

In order to implement such a concept, part coding and classification based on group technology is used as a foundation. Individual parts are coded based on several characteristics and attributes. Part families are created of like parts having sufficiently common attributes to group them into a family. This family formation is determined by analyzing the codes of the part spectrum. A "standard" plan consisting of a process plan to manufacture the entire family is created and stored for each part family. The development of a variant-process-planning system has two stages: the preparatory stage and the production stage (Figure 13.4.3).

During the preparatory stage, existing components are coded, classified, and later grouped into families. The part family formation can be performed in several ways. Families can be formed based on geometric shapes or process similarities. Several methods can be used to form these groupings. A simple approach would be to compare the similarity of the part code with other part codes. Since similar parts will have similar code characteristics, a logic that compares part of the code or the entire code can be used to determine similarity between parts.

Families can often be described by a set of family matrices. Each family has a binary matrix with a column for each digit in the code and a row for each value a code digit can have. A nonzero entry in the matrix indicates that the particular digit can have the value of that row, for example, entry (3,2) equals one implies that a code x3xxx can be a member of the family. Because the processes of all family members are similar, a standard plan can be assigned to the family. The standard plan is structured and stored in a coded manner using operation codes (OP-codes). An OP-code represents a series of operations on one machine/workstation. For example, an OP-code DRL10 may represent the sequence center drill, change drill, drill hole, change to reamer, and ream hole. A series of OP-codes constitute the representation of the standard process plan.

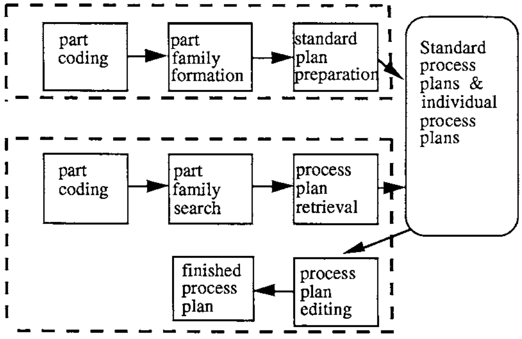

FIGURE 13.4.3 Variant-process-planning approach.

Before the system can be of any use, coding, classification, family formation, and standard plan preparation must be completed. The effectiveness and performance of the variant-process-planning system depend to a large extent on the effort put forth at this stage. The preparatory stage is a time-consuming process.

The production stage occurs when the system is ready for production. New components can be planned in this stage. An incoming component is first coded. The code is then sent to a part family search routine to find the family to which it belongs. Since the standard plan is indexed by family number, the standard plan can be easily retrieved from the database. The standard plan is designed for the entire family rather than for a specific component; thus, editing the plan is unavoidable.

Variant-process-planning systems are relatively easy to build. However, several problems are associated with them:

- The components to be planned are limited to previously planned similar components.
- Experienced process planners are still required to modify the standard plan for the specific component.
- Details of the plan cannot be generated.
- Variant planning cannot be used in an entirely automated manufacturing system, without additional process planning.

Despite these problems, the variant approach is an effective method, especially when the primary objective is to improve the current practice of process planning. In most batch-manufacturing industries, where similar components are produced repetitively, a variant system can improve the planning efficiency dramatically. Some other advantages of variant process planning are

- Once a standard plan has been written, a variety of components can be planned.
- Programming and installation are comparatively simple.
- The system is understandable, and the planner has control of the final plan.
- It is easy to learn and easy to use.

The Generative Approach

Generative process planning is the second type of computer-aided process planning. It can be concisely defined as a system that automatically synthesizes a process plan for a new component. The generative approach envisions the creation of a process plan from information available in a manufacturing database without human intervention. Upon receiving the design model, the system is able to generate the required operations and operation sequence for the component.

Knowledge of manufacturing has to be captured and encoded into computer programs. By applying decision logic, a process planner's decision-making process can be imitated. Other planning functions, such as machine selection, tool selection, and process optimization, can also be automated using generative planning techniques.

A generative-process-planning system consists of three main components:

- Part description
- Manufacturing databases
- Decision-making logic and algorithms

The definition of generative process planning used in industry today is somewhat relaxed. Thus, systems that contain some decision-making capability on process selection are called generative systems. Some of the so-called generative systems use a decision tree to retrieve a standard plan. Generative process planning is regarded as more advanced than variant process planning. Ideally, a generative-process-planning system is a turnkey system with all the decision logic built in. However, due to the differences among manufacturing shops, decision logics have to be customized for each shop.

The generative-process-planning approach has the following advantages:

- Consistent process plans can be generated rapidly.
- New components can be planned as easily as existing components.
- It has potential for integrating with an automated manufacturing facility to provide detailed control information.

There is no fixed representation or procedure that can be identified with generative process planning. The general trend is to use a solid model CAD-based input and expert system or an object-oriented planner construct. Most of the research systems are of this type. A few commercial products can also be classified as generative.

Process Plan Standardization

In the past two decades CAD has became the primary tool for engineering design. CAD data became the driving information for all downstream applications. The international standard. STEP, which began as an electronic product model information standard, has grown to be the information model standard for industrial automation and integration. Process planning model is part of this standard (ISO 10303 Part 224). The standards allow software vendors and machine tool builders to seamlessly interface their products. A computer-aided process planning system can read product definition information through a standard front end, and output process plans in a standard format as well. Presently this feature is still being implemented in CAD/CAM systems.

Conclusions

Process planning is a critical function in design and manufacturing. The quality of the product and the cost of production are affected by the process plan. A process plan incorporates information on the shop capability, resource requirement, and best routing. In order to produce a good process plan, a planner must be knowledgeable in both the manufacturing practices and the current shop status and capabilities. At this moment most computerized planners are still based on data retrieval and database lookup. As the information technology is further developed and we have a better understanding of process capabilities, integrated planning systems will evolve.

References

Chang, T.C. and Wysk, R.A. 1995. *An Introduction to Computer-Aided Process Planning Systems*, Prentice-Hall, Englewood Cliffs, NJ.

Curtis, M.A. 1988. *Process Planning*, John Wiley & Sons, New York.

Halevi, G. and Weill, R.D. 1995. *Principles of Process Planning*, Chapman & Hall, New York.

ISO 10303, Industrial automation system and integration: product data representation and exchange. Part 224, Application protocol; mechanical product definition for process planning using machining features, International Organization for Standardization, Geneva, Switzerland, 1997.

Nelson, D H, Schneider, G. 2001. *Applied Manufacturing Process Planning: With Emphasis on Metal Forming and Machining*, Prentice Hall, Upper Saddle River, NJ.

Palady, P. 1998. The design development and process planning reference guide, *Practical Applications*, Ann Arbor, Michigan.

Scallan, P. 2003. *Process Planning: The Design/Manufacture Interface*, Butterworth-Heinemann, Boston, MA.

van Houten, F.J.A.M. 1991. PART: A Computer Aided Process Planning System, Ph.D. Thesis, Department of Mechanical Engineering, University of Twente.

Wang, H.-P. and Li, J.K. 1991. *Computer-Aided Process Planning*, Elsevier, New York.

Zhang, H.-C. and Alting, L. 1994. *Computerized Manufacturing Process Planning Systems*, Chapman & Hall, New York.

Simulation Tools for Manufacturing

Hank Grant

Introduction

Digital simulation uses a mathematical model to represent a real or hypothetical physical system. A computer simulation model of a physical system provides a laboratory in which alternative designs can be explored and analyzed. The model, executed on the computer, is a software replica of the manufacturing system and is controlled so that the behavior of the system can be studied and analyzed. Decisions can be made concerning production alternatives. For example, adding a new lathe can be considered without disrupting the actual physical system.

Simulation depends on describing a system in terms acceptable to the computer language used. To do this, it is necessary to have a *system-state description*, which is typically characterized by a set of state variables included in the computer program that make up the simulation model.

Types of Simulation Models

Simulation models are typically classified into three types: discrete event, continuous, and combined. Simulation software has been designed to address each of these types of models.

Discrete Event. Discrete event simulation is used to model systems when there are specific events in time when the variables of the system may change in values. The mechanics of those changes must be well known and easily characterized. The behavior of the system is represented by the behavior of individual objects of interest called *entities*. The simulation model characterizes the behavior of these entities as they move through the system in simulated time.

Discrete events are points in time where the characteristics of an entity may change and where the state variables of the system may change. For example, when a customer arrives for service, the state of the system may change (number in the system, status of the server, etc.). The modeling of systems using this approach consists of developing descriptions of the events and how they cause the state variables to change and the entities to be manipulated.

The individual events may not always be predictable, and stochastic elements may be present in the operation of the system. For example, the time between arrivals of customers to the system may be a random variable. Simulation languages have many tools to support random variation in models.

A special kind of discrete event model is a *network model*. Network models use a standard set of symbols to represent the flow of entities in the system. They are graphical in nature, and are useful communication vehicles as well as powerful in building simulation models quickly and easily. Several languages are available that include network modeling capabilities, and they are described later.

Continuous. Continuous simulation is an approach that is popular among engineers and economists. The main building blocks of this approach are as follows (Pidd 1994).

Aggregated variables: Instead of a concern with individual entities, the main concern is with the aggregated behavior of populations (e.g., the changing sales of a product through time).

Smooth changes in continuous time rather than focusing on individual events, where the stress is on the gradual changes that happen as time progresses: Thus, just as the graph of a variable might be smooth, the aim is to model the smooth changes of the variable by developing the suitable continuous equations.

Differential or difference equations: The model consists mainly of a set of equations that define how behavior varies through time; thus, these tend to be differential equations or, in simpler cases such as system dynamics, difference equations.

Nature does not present itself labeled neatly as discrete or continuous; both elements occur in reality. Modeling, however, as mentioned earlier, involves approximation, and the modeler must decide which of these approaches is most useful in achieving the desired aim of the simulation.

Combined Discrete Event/Continuous. In some cases, both approaches are needed and the result is a mixed discrete-continuous simulation. An example of this might be a factory in which there is a cooking process controlled by known physics that is modeled by continuous equations. Also in the factory is a packing line from which discrete pallets of products emerge. To model the factory will require a mixed ap3proach.

Modeling Languages

Specifically designed computer simulation languages provide many features for managing the updating of the state variables and advancing time. They also provide features for recording system performance statistics and for generating random numbers to introduce system randomness.

The lowest level of computer language typically used is FORTRAN or BASIC. This requires that the entire simulation model be coded, which is labor intensive. High-level languages, such as SLAM, SIMSCRIPT, and GPSS, facilitate simulation because they provide subroutines for time advancement, entity maintenance, and statistic collections. Higher-level simulation languages are designed for special purposes; MAP/1, SPEED, and MAST are three designed for the simulation of manufacturing systems.

Some simulation languages can produce animations. This permits the simulation to be illustrated graphically on a computer terminal so that the analyst can see the system in action and observe its interactions and behavior, a visual function beyond the scope of standard reporting technique. For example, TESS (a software program) provides animation, as well as model-building and output analysis capabilities, for the SLAM simulation language.

The following discussion by Banks (1994) provides an overview of the primary languages available.

Applications of simulation exist in many arenas such as manufacturing, material handling, health services, military decision support, natural resources, public services, transportation, and communications, to mention a few.

These simulation applications are usually accomplished with the use of specially developed simulation software. This tutorial describes the software in two categories. The first of these is software for general purposes. This type of software can solve almost any discrete simulation problem. In this section, five products, GPSS/H™, GPSS/World™, SIMSCRIPT II.5©, SIMAN V©, and SLAMSYSTEM©, will be discussed to provide a feel for this type of software.

GPSS/H. GPSS/H is a product of Wolverine Software Corp., Annandale, VA (Smith and Crain 1993). It is a flexible yet powerful tool for simulation. It provides improvements over GPSS V that had been released by IBM many years earlier. These enhancements include built-in file and screen input/output (I/O), use of an arithmetic expression as a block operand, interactive debugger, faster execution, expanded control statement availability, and ampervariables that allow the arithmetic combinations of values used in the simulation. The latest release of GPSS/H is version 2.0. It added a floating-point clock, built-in math functions, and built-in random variate generators. Options available include Student GPSS/H, Personal GPSS/H within the 640K memory limit, and GPSS/H 386, providing unlimited model size.

GPSS World. GPSS World, from Minuteman Software, is a complete redesign of GPSS/PC™ (Cox 1992). It is designed as a high-power environment for simulation professionals. It provides both discrete and continuous simulation. Its features include interactivity, visualizability, and configuration flexibility. It utilizes 32-bit computing, virtual memory, preemptive multitasking, symmetric multiprocessing, and distributed simulation. Highlights include drag-and-drop model building, 512 MB of virtual memory for models, point-and-shoot debugging, an embedded programming language, built-in probability distributions, multiple data types, and many other improvements to GPSS/PC.

The GPSS World family is a set of three software products, including

- GPSS World is the center of the family. This self-contained modeling environment includes local Simulation Server™ capabilities.
- Simulation Server provides simulation services on a remote networked computer. It does not include a model-building user network.
- Simulation Studio provides hierarchical modeling and user-drawn simulation capabilities.

An enhanced memory version of GPSS/PC is also available. It allows access of up to 32 MB of memory.

SIMSCRIPT II.5. SIMSCRIPT II.5 from CACI Products Company is a language that allows models to be constructed that are either process oriented or event oriented (Russell 1993). The microcomputer and workstation version include the SIMGRAPHICS animation and graphics package. SIMSCRIPT can be used to produce both dynamic and static presentation-quality graphics such as histograms, pie charts, bar charts, levels of meters and dials, and time plots of variables. Animation of the simulation output is also constructed using SIMGRAPHICS. SIMGRAPHICS can be used also to produce interactive graphical front ends or forms for entering model input data. An input form may include such graphical elements as menu bars with pull-down menus, text or data boxes, and buttons that can be clicked to select an alternative. The graphical model front end allows for a certain set of modifications to the model to be made without programming, facilitating model use by those who are not programmers.

SIMAN V. SIMAN V from Systems Modeling Corporation is a general-purpose program for modeling discrete and/or continuous systems (Glavach and Sturrock 1993; Banks et al. 1995). The program distinguishes between the system model and the experiment frame. The system model defines components of the environment such as machines, queues, and transporters and their interrelationships. The experiment frame describes the conditions under which the simulation is conducted, including machine capacities and speeds and types of statistics to be collected. What-if questions can usually be asked through changing the experiment frame rather than by changing the model definition. Some important aspects of SIMAN V are as follows:

- Special features that are useful in modeling manufacturing systems, including the ability to describe environments as work centers (stations) and the ability to define a sequence for moving entities through the system.
- Constructs that enable the modeling of material-handling systems including accumulating and nonaccumulating conveyors, transporters, and guided vehicles.
- An interactive run controller that permits break points, watches, and other execution control procedures.
- The ARENA environment, which includes menu-driven point-and-click procedures for constructing the SIMAN V model and experiment; animation of the model using Cinema, the input processor that assists in fitting distributions to data; and the output processor that can be used to obtain confidence intervals, histograms, correlograms, and so on. (More aspects of the ARENA environment are discussed later.)
- Portability of the model to all types of computers.

SLAMSYSTEM. SLAMSYSTEM, from Pritsker Corp., is an integrated simulation system for PCs based on Microsoft® Windows® (Pritsker 1986; O'Reilly 1993). All features are accessible through pull-down menus and dialog boxes and are selected from the SLAMSYSTEM Executive Window. A SLAMSYSTEM project consists of one or more scenarios, each of which represents an alternative system configuration. A project maintainer examines the components of the current scenario to determine if any of them have been modified, indicates whether or not tasks such as model translation should be performed, and allows the user to accomplish these tasks before the next function is requested. SLAMSYSTEM allows multiple tasks to be performed in parallel while the simulation is operating in the background.

Some of the features of SLAMSYSTEM are as follows:

- Models may be built using a graphical network builder and a forms-oriented control builder, or text editor. When using the first method, a network symbol is selected with the mouse, then a form is completed specifying the parameters for that symbol. The clipboard allows many other operations, such as grouping one or more symbols and placing them elsewhere on the network.
- Output analysis includes a "report browser" that allows alternative text outputs to be compared side by side. Output may be viewed in the form of bar charts, histograms, pie charts, and plots. Output from multiple scenarios can be displayed at the same time in bar-chart form. By using the Windows environment, multiple output windows can be opened simultaneously.

- Animations are created under Windows using the facility builder to design the static background and the script builder to specify which animation actions should occur when a particular simulation event occurs. Animations can be performed either concurrently or in a postprocessing mode. Two screens can be updated simultaneously, and up to 225 screens can be swapped into memory during an animation.
- SLAMSYSTEM was designed to be used in an integrated manner. For example, historic data may be read to drive the simulation. CAD drawings may be loaded. Output charts and plots created by SLAMSYSTEM can be exported via the clipboard to other applications.

The newest release of SLAMSYSTEM is version 4.0. Some of its unique features include the following:

- Multiple networks in a single scenario: Networks can be constructed in sections and combined at runtime. The sections can be reused in future models.
- New output graphics: These graphics support three-dimensional X-Y grids and display of point plot data.
- Direct interface to SimStat (product of MC^2 Analysis Systems): These files may be loaded for advanced statistical analysis.
- OS/2 metafiles for graphics: The OS/2 metafile format can be read for animation backgrounds or icons.

Conclusion

Simulation is a powerful approach to modeling manufacturing systems in that many complex and diverse systems can be represented. Simulation can predict system performance measures that are difficult to assess without a model. It is a proven, successful tool and has been in use since the 1950s. The current languages take advantage of the capabilities of today's microprocessors and provide the user with the needed online support for model development, management, and analysis.

References

Banks, J. 1994. Simulation software, paper presented at 1994 Winter Simulation Conference, Atlanta.

Banks, J., Burnette, B., Rose, J.D., and H. Kozloski. 1995. *SIMAN V and CINEMA V*, John Wiley & Sons, New York.

Cox, S.W. 1992. Simulation Studio™. *Proc. of the 1992 Winter Simulation Conference*, J. J. Swain, D. Goldman, R.C. Crain, and J.R. Wilson, eds., Association for Computing Machinery, New York, 347–51.

Glavach, M.A. and Sturrock, D.T. 1993. Introduction to SIMAN/Cinema. *Proc. of the 1993 Winter Simulation Conference*, G.W. Evans, M. Mollaghasemi, E.C. Russell, and W.E. Biles, eds., Association for Computing Machinery, New York, 190–92.

O'Reilly, J.J. 1993. Introduction to SLAM II and SLAMSYSTEM. Proc. of the 1993 Winter Simulation Conference, G.W. Evans, M. Mollaghasemi, E.C. Russell, and W.E. Biles, eds., Association for Computing Machinery, New York, 179–83.

Pidd, M. 1994. An introduction to computer simulation, 1994 Winter Simulative Conference, The Management School, Lancaster University, U.K.

Pritsker, A.B. 1986. *Introduction to Simulation and SLAM II*, 3rd ed., John Wiley & Sons, New York.

Russell, E.C. 1993. SIMSCRIPT II.5 and SIMGRAPHICS tutorial. *Proc. of the 1993 Winter Simulation Conference*, G.W. Evans, M. Mollaghasemi, E.C. Russell, and W.E. Biles, eds., Association for Computing Machinery, New York, 223–27.

Smith, D.S. and Crain, R.C. 1993. Industrial strength simulation using GPSS/H. *Proc. of the 1993 Winter Simulation Conference*, G.W. Evans, M. Mollaghasemi, E.C. Russell, and W.E. Biles, eds., Association for Computing Machinery, New York, 218–22.

Tools for Intelligent Manufacturing Processes and Systems: Neural Networks, Fuzzy Logic, and Expert Systems

Tien-I. Liu

Introduction

Starting in the 1980s, researchers and practitioners became increasingly interested in intelligent machines and intelligent manufacturing. The goal of these systems and processes is to model the skills and expertise of professionals so that machines and manufacturing systems can possess some of the characteristics of human intelligence. Three techniques — neural networks, fuzzy logic, and expert systems — have been widely used in manufacturing. This section describes the principles and functions of these tools. Examples in applying these tools to manufacturing applications are highlighted as well.

Neural Networks

Neural networks consist of a set of nodes that are nonlinear computational elements. The pattern of connectivity between nodes, known as *weights*, can be modified according to some preset learning rule. The knowledge of the networks is stored in their interconnections (Kohonen 1986).

Since neural networks are parallel distributed processing, they have the following advantages:

- They are adaptive and can learn from experience.
- The network can be refined at any time with the addition of new training data.
- Various model architectures can be used.
- They can compute very quickly and thus are very suitable for real-time applications.
- They can be used for analyzing large amounts of data to determine patterns that may predict certain types of behavior.
- They can capture the complexities of the process, including nonlinearities, even if the dynamics of the process is unknown.
- They can make decisions based on incomplete and noisy information.
- They degrade gracefully even when parts of the structure have been destroyed.

Neural networks are best at performing the types of tasks which need human perception. These tasks do not have exact answers, for example, classification and trend analysis. A typical example of such problems is machine diagnosis. An experienced mechanic can point out what is wrong with an automobile by standing beside the car and listening to the sound of the running engine. Another example is character recognition. Any person who is familiar with alphabets can easily identify the letter “A” in any of various typefaces or handwritten scripts. In both cases it is practically impossible to develop a set of if-then rules to let a computer to do the job. These tasks are also difficult to program using standard computer techniques.

Many electronics and computer companies have put considerable effort into neural-network development. IBM has announced a neural-network development package for its computer; Intel Corp. has developed a microchip that supports this technology. Japanese companies such as Fujitsu, Hitachi, Mitsubishi, and Sumitomo Heavy Industries are also working in this field.

A bomb-detection machine that uses neural-network technology to detect plastic explosives hidden in baggage has been developed and installed in several airports. Neural networks have also been applied to ensure the operation of an industrial power distribution substation. It has replaced a conventional mechanical system and improved the performance by greater than an order of magnitude.

Integrating sensors with neural networks for monitoring and diagnostic purposes can enhance production reliability, prevent potential problems caused by abnormal conditions, and maintain high product quality in the factory (Liu and Iyer 1993). The applications of neural networks for monitoring and diagnostic purposes have been used with ball-and-roller bearings, turning processes, milling processes, drilling processes, tapping processes, and glass furnaces. The results are very successful (Liu and Anatharaman 1994).

Neural networks have also been used in the image processing for computer vision and speech-recognition systems (Badal 1993). They also are used for the control of machines and processes. The neural-network controller is capable of online learning of the system dynamics and then taking adequate action to achieve the predetermined goal. They also can be used to tune the gain of control systems.

Fuzzy Logic

The theory of fuzzy sets has been developed as a methodology for the formulation and solution of problems that are too complex or too ill defined to be solved by traditional techniques. In fuzzy logic, the membership in a set is not either 0 or 1; instead it is a value between 0 and 1. Membership functions span some problem domain, such as length or weight, and show the membership for each value of the problem domain. Membership functions are subjective evaluations and can be represented by many kinds of curves. However, the membership function cannot be assigned arbitrarily. The formulation of the membership function should be based on the professional feeling and physical understanding of the problem. Let $S = \{s\}$ represent a space of objects. Then a fuzzy set X in S is a set of ordered pairs

$$X = \left\{s, f_x(s)\right\}, \quad s \_ S(1)$$

where $f_x\ (s)$ is the grade of membership of s in X and $f_x\ (s)$ is a number in the interval (0,1).

Fuzzy mathematics, which consists of precise rules to combine vague expressions, such as "very high" and "somewhat heavy," has been developed (Kandel 1986). Generally speaking, fuzzy logic systems have the following advantages:

- They are inherently flexible.
- They are robust to noisy or missing data, unexpected disturbances, and errors in problem modeling.
- They are suitable to deal with problems for which knowledge is approximate or problems that are so complex that it is difficult to develop an adequate mathematical model.
- They usually are energy efficient.

Fuzzy mathematical techniques are very suitable for the control of machine tools, robots, and electronic systems (Mamdani 1993). They are also applicable to image understanding for computer vision and pattern classification for the monitoring and diagnosis of manufacturing processes (Du et al. 1992).

The very first application of fuzzy logic was the control of the fuel-intake rate and gas flow of a rotating kiln used to produce cement. Since then, it has been used to control many automated manufacturing processes. Fuzzy logic has resulted in significant improvements to many commercial products, such as cameras and air conditioners. Although fuzzy logic was developed in the U.S., most of the installed applications are still in Japan. The most impressive application is a subway system operated by a fuzzy computer. It was installed in the 1980s by Hitachi at Sendai, about 200 mi north of Tokyo. This system is more than 10% more energy efficient than the previous system, and it is so smooth that passengers do not need to hang onto straps.

At AT&T Bell Laboratories, Dr. M. Togai and Dr. H. Watanabe developed the very first fuzzy logic processing chip in 1985. NASA is developing fuzzy controllers to help astronauts pilot the space shuttle in earth orbit. In the U.S. the interest in applying fuzzy logic is growing continuously.

Expert Systems

An expert system is a computer system that possesses the capability of a human expert. An expert system has the following five essential parts (Figure 13.4.4):

1. *User interface:* This module is the interface between the user and other parts of the expert system.
2. *Knowledge base:* The knowledge about solving specific problems is stored in the knowledge base of an expert system. The process of building the knowledge base is called *knowledge engineering* and is done by a knowledge engineer (Figure 13.4.5). Knowledge engineering refers to the acquisition of knowledge from a human expert or other source and the coding of it into the expert

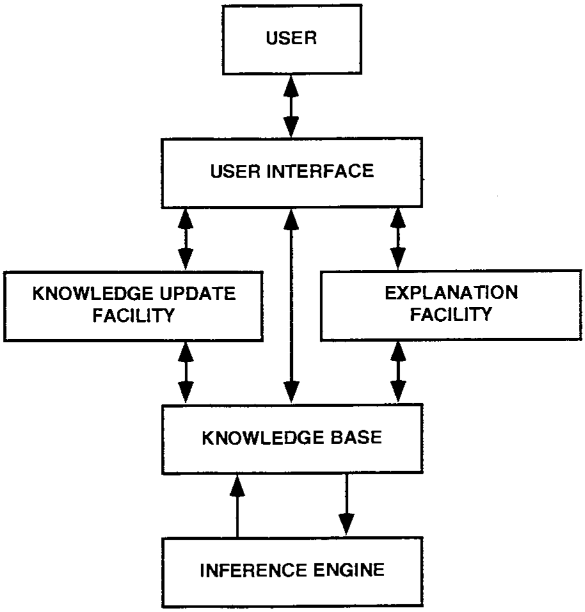

FIGURE 13.4.4 Typical expert system architecture.

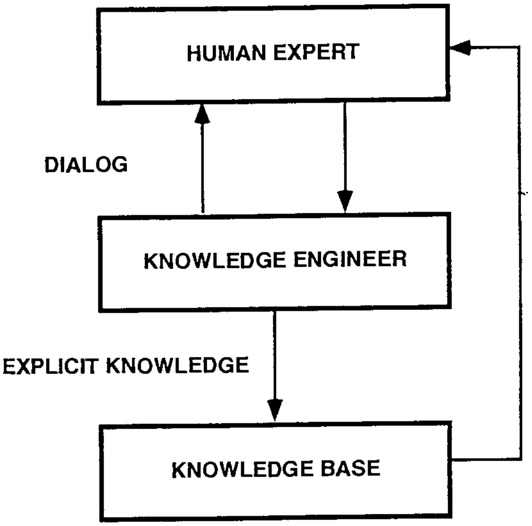

FIGURE 13.4.5 Knowledge engineering.

system. The knowledge base usually consists of rules and facts. Rules are made up of English-like sentences or clauses. Rules are often defined using an if-then syntax that logically connects one or more antecedent clauses with one or more consequent clauses as follows:

IF antecedent THEN consequent

A rule says that if the antecedent is true, then the consequent is also true. The antecedent and consequent of rules refer to a specific fact that describes the state of the world. On the other hand, each fact is a single sentence that describes some aspect of the state of the world.

3. *Inference engine:* The inference engine can infer new knowledge from existing knowledge stored in the knowledge base. Two general inference approaches are commonly used: forward chaining and backward chaining. Forward chaining is the reasoning from facts to conclusions resulting from those facts. Backward chaining involves reasoning in reverse from a hypothesis to the facts that support the hypothesis.
4. *Knowledge update facility:* The knowledge in many fields, including engineering and manufacturing, changes with time. The expert system can be updated through this facility.
5. *Explanation facility:* Just as a human expert can explain how a specific conclusion has been drawn, the explanation facility can explain its reasoning to enhance the credibility of an expert system.

Expert systems are quite different from conventional programs because the problems usually have no algorithmic solution and rely on inferences to achieve a reasonable solution. In other words, the expert system is very suitable to solve problems that require heuristic rules. These heuristic rules can be stored in the knowledge base.

Expert systems have the following advantages as compared with the human expert:

- They are steady and unemotional and have high reliability. Therefore, errors are reduced.
- They have high availability. Users can get answers at any time.
- The expert system can be installed and used at multiple sites.
- They can explain how a conclusion has been reached. Thus, the users feel comfortable working with expert systems.

Expert systems can help people solve problems. They can free the human expert from the routine job to do other work. Hence, they can increase efficiency and reduce cost.

Expert systems have been used in many fields. There are many commercialized expert systems running on different computer platforms that help professionals in various fields, enhancing efficiency and productivity greatly.

Manufacturing, assembly, quality, reliability, and cost need to be taken into consideration in the early stage of product design. Expert systems have been developed for DFM, design for assembly (DFA), design for quality and reliability, product cost estimation, and so forth. These expert systems can be integrated with the existing CAD/CAM systems (Liu et al. 1995). Many expert systems have also been built and used in the areas of facility design, production planning and control, computer-aided process planning, material handling, quality control, equipment maintenance and repair, and real-time control (Alto et al. 1994). Simply put, design and manufacturing work can be upgraded from an experience-based to a science-based function by using expert systems.

Conclusion

Neural networks, fuzzy logic, and expert systems are the trend of the future. They can make machines and manufacturing processes much smarter. Applying these techniques can lead to the realization of a fully automated factory in the future.

References

Alto, A., Dassisti, M., and Galantucci, L.M. 1994. An expert system for reliable tool-replacement policies in metal cutting. *ASME J. Eng. Ind.*, 116(3), 405–6.

Badal, D.Z. 1993. Neural network based object recognition in images. P*roc. IEEE Int. Conf. Neural Networks*, San Francisco, CA, 1283–88.

Du, R.X., Elbestawi, M.A., and Li, S. 1992. Tool condition monitoring in turning using fuzzy set theory. *Int. J. Mach. Tools Manuf.*, 32(6), 781–96.

Kandel, A. 1986. *Fuzzy Mathematical Techniques with Applications*, Addison-Wesley, Reading, MA.

Kohonen, T. 1986. An introduction to neural computing. *Neural Networks*, 1, 3–16.

Liu, T.I. and Anatharaman, K.S. 1994. Intelligent classification and measurement of drill wear. *ASME J. Eng. Ind.,* 116(3), 392–97.

Liu, T.I. and Iyer, N.R. 1993. Diagnosis of roller bearings using neural networks. *Int. J. Adv. Manuf. Technol.*, 8(2), 210–15.

Liu, T.I., Yang, X.M., and Kalambur, G.J. 1995. Design for machining using expert system and fuzzy logic approach. *ASME J. Mater. Eng. Performance*, 4(5), 599–609.

Mamdani, E.H. 1993. Twenty years of fuzzy control: experiences gained and lessons learnt. *Proc. IEEE 2nd Int. Conf. Fuzzy Systems*, San Francisco, CA, 339–44.

Tools for Manufacturing Facilities Planning

J. M. A. Tanchoco, Andrew C. Lee, and Su-Hsia Yang

Introduction

The main function of facility planning is the design of efficient flow of products from raw material to finished goods. It is one of the most important determinants of operating efficiency and production cost. Traditionally, the facility-planning problem is divided into three areas: group technology (GT), material handling, and facility layout (see Figure 13.4.6). GT, which is closely related to cellular manufacturing, is usually defined as the grouping of dissimilar machines in close vicinity. Each group or cell is dedicated to the production of one or more parts families. The parts in the family are similar in their processing requirements (Wemmerlov and Hyer 1989). Two of the most fundamental elements in facility planning are the facility layout and the material-handling system.

Facility layout positions the workstations around the fixed product based on the processing sequence. In a product layout, machines are arranged according to the processing sequence of the product, for example, the assembly of automobiles and certain electronic products. The machines are located so as to provide smooth and logical flow of material. In a group layout, also referred to as a cellular layout, products are grouped into logical product families. All machines that perform similar operations are grouped together in the process layout. A process layout is characterized by a high degree of flexibility and machine utilization. Regardless of the type of facility, a detailed layout should not be designed without giving serious consideration to material-handling requirements. The choice of material-handling methods and equipment is an integral part of the layout design. The facility layout design component performs two basic functions. The first function is to decide how to locate cells with respect to one another. The objective is to minimize either the total material flow distance or transportation time. The second function is to resolve the machine location and orientation relative to each other within the cell. The constraints in layout design or facility structure could prohibit the placement of the cells or machines in some locations, thus changing the machine compositions of the cells. The resolution from this design problem has a significant impact on the distance that material has to be moved.

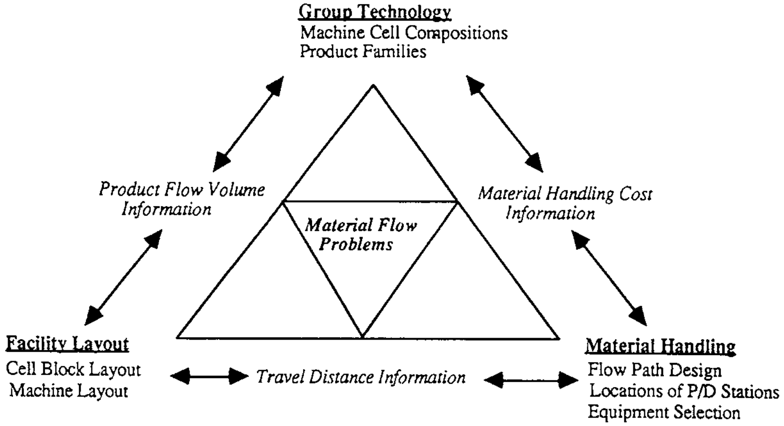

FIGURE 13.4.6 Facilities-planning framework components.

Material handling performs a critical function in modern dynamic manufacturing systems. The transportation of materials within a production system is often accomplished with limited resources, for example, conveyors, forklift trucks, or automated guided vehicles (AGVs). Such transfer mechanisms not only deliver material in a timely fashion but also provide temporary storage capacity. These limited resources require a capital investment, which increases the overall production costs. Excess transportation capability represents expenditures that are not accompanied by increased value. Insufficient capacity, on the other hand, can adversely affect production by delaying the delivery of material, thus reducing the total production volume. Material handling is generally considered as a non-value-adding activitiy. However, one can argue that material handling adds time and space value by making the material available and ready for processing.

The material handling has three functions. First, the flow path design selects the route that material transfers from cell to cell or from machine to machine. Limited by the cost of remodeling, the existing plant configuration (such as the aisle width) might not be able to accommodate the traffic flow. Therefore, considerations must be given to the overall facility layout and building structure. The second function is to locate the pickup and delivery stations along the flow path. Along with the facility layout and flow path design, it is one of the most important determinants of the operating cost of material handling. Finally, the best combination of material-handling equipment is determined. Because of the complex, ill-structured, and experience-based nature of the problem, the decisions for choosing material-handling equipment tend not to be based on rigorous criteria. However, the designers must recognize that there is an appropriate level of technology for every application that will meet the combined need for maximum handling efficiency and acceptable cost.

Decision Factors for Facilities Planning

The effectiveness of a facility-planning system depends on the careful integration of GT, facility layout, and the material-handling system.

Group Technology. Mitrofanov (1959) is recognized as the first person to introduce the concept of GT and machine grouping. Since then, a number of researchers have developed techniques for machine grouping and part family formation. In general, these techniques can be categorized as follows:

1. *Machine-Component Matrix* (McAuley 1972; King 1980; McCormick et al. 1972): The main idea behind this approach is to delineate cells by grouping binary entries of a machine-component incidence matrix into fuzzy blocks along the matrix diagonal.
2. *Mathematical Programming Formulation* (Kusiak et al. 1986; Askin and Standridge 1993): In this approach, a large, combinatorial mixed integer programming formulation is usually required to model the problem.
3. *Graph-Based Formulation/Partitioning* (Rajagopalan and Batra 1975; Faber and Carter 1986): In this approach, the machine-part matrix is represented by a bipartite, transition, or boundary graph. Then, it is solved using graph theoretic clustering methodology.

Facility Layout. The facility layout problem has been formulated as a quadratic assignment problem (QAP). The objective function for this type of formulation is to minimize the total material-handling cost. Given the complexity of the QAP formulation, the size of problems that could be solved by optimal methods is very limited. Thus, heuristic algorithms are more suitable. These heuristics can be classified into two major groups. The first group is called construction algorithms (Seehof and Evans 1967; Lee and Moore 1967; Foulds and Giffin 1985; Hassan and Hogg 1991). The main idea behind these methods is to build the layout by adding one more block (a cell or a department) to a partial block layout until all blocks have been located. The methodology requires two steps: a selection step and a placement step. The selection step determines the order by which the blocks enter the layout, while the placement step selects the location of the new block to enter the layout relative to the blocks that are already in the layout. The objective is to maximize some kinds of performance criteria, for example, total closeness rating. Graph theoretic methods have been applied as a solution methodology for this approach.

The second group of the layout heuristics is called improvement algorithms. This approach starts from an initial layout, and improvements are made by successive pairwise interchanges of blocks. The general form of an improvement algorithm consists of the following steps: (1) select a pair of activities, (2) estimate the cost of interchange, (3) exchange if the total cost is reduced, and (4) repeat until no more improvement can be made. This category of heuristics includes the computerized relative allocation of facilities technique (CRAFT) of Armour and Buffa (1963) and Buffa et al. (1964) and the methods of Hillier (1963), Fortenberry and Cox (1985), and Co et al. (1989).

Recognizing the weaknesses of both construction and improvement algorithms when applied separately, Golany and Rosenblatt (1989) proposed a hybrid method that takes advantages of both construction and improvement algorithms. They use the layout resulting from the construction algorithm as the initial layout and improve upon it using an improvement algorithm. Since most of the heuristics for facility layout are based on the "greedy approach," the solution is very sensitive to the initial layout. The final layout given by the algorithm may not be the best.

Material Handling. Material handling involves moving, storing, and controlling the flow of materials. Several components, such as the flow path design, the locations of pickup and delivery stations, and the material-handling equipment selected, have significant effects on the overall effectiveness of the material-handling system. The objective of flow path design is to determine the best "street network" that transporters pass through when parts are moved from one machine to the next. It is one of the major determinants in the calculations of travel times, operating expenses, and installation costs of the material-handling system. There are numerous types of flow path network configurations. The most widely adopted flow path design is the conventional flow network. It is usually a unidirectional flow network where any cell boundary is used as part of the flow path. In a unidirectional network, one has to determine the flow direction for each aisle. Its flexibility, reliability, and efficiency have made this type of network a popular choice especially when AGVs are used. In comparison, the potential of using a bidirectional flow network could make the system more efficient (Egbelu and Tanchoco 1986). The same authors also developed guidelines for the use of a single-lane bidirectional flow network. However, the advanced hardware requirements and complicated system controllers are viewed negatively.

A single-loop flow path network can be found in many flexible manufacturing systems. The entire flow path design is made up of a single loop. This type of network can potentially minimize some of the problems associated with a conventional flow network. Congestion is inherently low and the operating rules are simple. It also has relatively low initial investment and maintenance costs.

Recently, a new flow path network configuration, a segmented flow topology (SFT), was developed by Sinriech and Tanchoco (1994). It consists of one or more zones, each of which is separated into nonoverlapping segments. Each segment is serviced by a single bidirectional material-handling device. Transfer buffers are located at both ends of each segment. The flow structure in each zone is determined by the logical flow requirements and by the existing aisle network. The SFT provides a simple flow structure and control system. The research also suggested that it can achieve a higher throughput capability compared to other material flow path network configurations.

The locations of pickup and delivery stations have generally been considered as a secondary issue in the design phase of facility layout and a material-handling system. Yet it can have detrimental effects on the costs of material handling and the machine layout configuration. In a study by Warnecke et al. (1985), they confirmed that the actual pickup and delivery station flow distance is much more representative than taking the rectilinear distance between the centers of machine blocks. Since then, several design procedures have been proposed to find the optimal location of material-transfer stations. Montreuil and Ratliff (1988) suggested a systematic methodology for locating pickup and delivery stations within a facility layout using multifacility location theory. The objective function is to minimize the sum of the rectilinear distance traveled by all intercellular flows, given the boundary regions on station location. Luxhoj (1991) developed a two-phase design procedure that is suitable for the spine layout where the active flow lines are well defined.

In terms of material-handling equipment selection, a large variety of equipment types available are with their own special functions and characteristics. Each equipment type has its own capability and limitations. Some of these characteristics are difficult to quantify. The integrated nature of the manufacturing systems complicates the material-handling selection problem. The problem was first addressed by Webster and Reed (1971). The procedure they suggested initially assigns material-handling equipment to departmental moves based on cost alone. Then, move assignments are interchanged to seek improvement in equipment utilization and total cost. Hassan et al. (1985) reformulated Webster and Reed's model as an integer programming model with the objective of minimizing the total operating and capital costs of the selected equipment. Due to the combinatorial nature of the problem, it is solved using a construction heuristic that exploits some similarities to both knapsack and the loading problems. Material Handling Equipment Selection System (MATHES) was developed by Fisher et al. (1988). MATHES is a rule-based system for the selection from 24 different types of material-handling equipment.

Conclusion

The framework discussed in this section provides an alternative perspective from the material flow viewpoint. It integrates all of the important design factors associated with facilities planning. It incorporates most of the desired properties with respect to the overall plant operations. At the same time, the framework also summarizes the difficulties and complexities that confront the facility designer. The description of the framework is intended as a general exposition of the fundamental concepts and a direction for future research in facilities planning.

References

Armour, G.C. and Buffa, E.S., 1963. A heuristic algorithm and similation approach to relative location of facilities. *Manage. Sci.*, 9(2), 294–300.

Askin, G. and Standridge, R. 1993. *Modeling and Analysis of Manufacturing Systems*, John Wiley, New York.

Buffa, E.S., Armour, G.C., and Vollman, T.E. 1964, Allocating facilities with CRAFT. *Harvard Business Rev.*, 42(2), 136–59.

Co, H., Wu, A., and Reisman, A., 1989. A throughput-maximizing facility planning and layout model. In *Int. J. Prod. Res.,* 27(1), 1–12.

Egbelu, P. and Tanchoco, J.M.A. 1986. Potentials for bi-directional guide path for automated guided vehicle base systems. In *Int. J. Prod. Res.*, 24(5), 1075–97.

Faber, Z. and Carter, M.W. 1986. A new graph theory approach to forming machine cells in cellular production systems. In *Flexible Manufacturing Systems: Methods and Studies*, North-Holland, Amsterdam, 301–18.

Fisher, E.L., Farber, J.B., and Kay, M.G. 1988. MATHES: an expert system for material handling equipment selection. In *Eng. Costs Prod. Econ.*, 14(4), 297–310.

Fortenberry, J.C. and Cox, J.F. 1985. Multiple criteria approach to the facilities layout problem. In *Int. J. Prod. Res.*, 23(4), 773–82.

Foulds, L.R. and Giffin, J.W. 1985. A graph-theoretic heuristic for minimzing total transport cost in facility layout. In *Int. J. Prod. Res.*, 23(6), 1247–57.

Golany, B. and Rosenblatt, M.J. 1989. A heuristic algorithm for the quadratic assignment formulation to the plant layout problem. In *Int. J. Prod. Res.*, 27(2), 293–308.

Hassan, M.M.D. and Hogg, G.L. 1991. On constructing a block layout by graph theory. In *Int. J. Prod. Res.*, 29(6). 1263–78.

Hassan, M.M.D., Hogg, G., and Simth, D. 1985. Construction algorithm for the selection and assignment of materials handling equipment. *Int. J. Prod. Res.*, (23(2), 381–92.

Hillier, F.S. 1963. Quantitative tools for plant layout analysis. In *J. Ind. Eng.*, 14(1), 33–40.

Irani, S.A., Cavalier, T.M., and Cohen, P.H. 1993. Virtual manufacturing cells: exploring layout design and intercell flows for the machine sharing problem. In *Int. J. Prod. Res.*, 31(4), 791–810.

King, J.R. 1980. Machine-component grouping in production flow analysis: an approach using rank order clustering algorithm. In *Int. J. Prod. Res.*, 18(2), 213–32.

Kumar, K.R., Kisiak, A., and Vanelli, A. 1986. Grouping of parts and components in flexible manufacturing systems. In *Eur. J. Operat. Res.*, 24, 387–97.

Kusiak, A., Vannelli, A., and Kummar, K.R. 1986. Clustering analysis: models and algorithms. In *Control Cybernetics*, 15(2), 139–54.

Lee, R.C. and Moore, J.M. 1967. CORELAP: COmputerized RElationship LAyout Planning. In *J. Ind. Eng.,* 18(1), 195–200.

Luxhoj, J.T. 1991. A methodology for the location of facility ingress/engress points. In Int. J. Oper. Prod. Manage., 11(5), 6–21.

McAuley, 1972. Machine grouping for efficient production. In *The Prod. Eng.*, pp. 53–57.

McCormick, W.T., Schweitzer, P.J., and White, T.E. 1972. Problem decomposition and data reorganization by a clustering technique. In *Operations Res.*, 20, 993–1009.

Mitrofanov, S.P. 1959. Nauchniye Osnovi Grouppovoi Technologi, Lenizdaz, Leningrad; translated into English, 1966, Scientific Principle of Group Technology, National Lending Library, England.

Rajagopalan R. and Batra, J.L. 1975. Design of cellular production system — a graph theoretic approach. In *Int. J. Prod. Res.*, 13, 567–79.

Seehof, J.M. and Evans, W.O. 1967. ALDEP: Automated Layout DEsign Program. In *J. Ind. Eng.*, 18(2), 690–95.

Sinriech, D. and Tanchoco, J.M.A. 1994. SFT — Segmented flow topology. In *Material Flow Systems in Manufacturing*, J.M.A. Tanchoco, Ed., Chapman & Hall, London, 200–35.

Tompkins, J.A. 1993. *World Class Manufacturing*, IEEE, New York.

Warnecke, H.J., Dangelmier, W., and Kuhnle, H. 1985. Computer-aided layout planning. In *Material Flow,* 1, 35–48.

Webster, D.B. and Reed, R. Jr. 1971. A material handling system selection model. In *AIIE Trans.,* 3(1), 13–21.

Wemmerlov, U. and Hyer, N.L. 1989. Cellular manufacturing in the US industry: a survey of users. In *Int. J. Prod. Res.*, 27(9), 1511–30.

13.5 Rapid Prototyping

Takeo Nakagawa

Manufacturing Processes in Parts Production

The rapid progress of CAD technology for the design of machine parts has now made it easy to store three-dimensional shape data on computers. The application of these three-dimensional data has realized NC programming by CAM system, resulting in the remarkable advance of automated production. The increase in highly functional machine parts and advanced designs has led to the design of more and more complicated surfaces using CAD. To reduce the lead time and costs for the development of new industrial products, "rapid prototyping" has been recognized as a unique, layered manufacturing technique for making prototypes.

With this rapid prototyping, shapes of machine parts are created by building up layers and layers of materials, unlike the material-removal technique which shapes by gradual machining using a cutting tool. In this sense, rapid prototyping resembles the joining technique of small particles or thin layers. Various types of rapid prototyping methods have been born over the last couple of years. A common feature of these methods is that parts are directly shaped fully automatically according to CAD data. Specifically, in all of these methods, the three-dimensional CAD data are taken as composed of thin layers of two-dimensional data. The thin layers are formed using the two-dimensional data and built up to form an actual three-dimensional solid product. With the nature of the processing steps, this rapid prototyping technique is called *layered manufacturing*. Since the method can also be used in other applications than prototyping, it is also referred to as *free-form fabrication*. Because three-dimensional objects can be made from three-dimensional CAD data, this new rapid-prototyping method is also called three-dimensional plotting. At the present time, laser stereolithography is the most widespread rapid-prototyping method.

Rapid Prototyping by Laser Stereolithography

Laser stereolithography involves the use of a liquid photocurable resin, which cures instantaneously when scanned with a laser as a result of polymerization. As shown in Figure 13.5.1, the laser is scanned over this resin repeatedly to form thin layers of cured resin, which eventually build up to form a three-dimensional solid product. Specifically, the process involves first slicing a model based on three-dimensional CAD data stored on computer horizontally into equal thickness. Based on these slice data, the laser scans the thin liquid resin layer to form the first solid layer. Liquid resin is then poured over this cured layer of resin and again scanned by laser to form the next layer according to the next slice data. To ensure that the liquid resin on the cured resin is even, its surface is often swept by a blade. So, by repeating this process and forming layer over layer of cured resin, a solid object is formed.

Although the surface accuracy problems are resolved by making each layer extremely thin, a small amount of roughness of the surface eventually remains and subsequent polishing is often performed to achieve a smooth finish. For shapes that cannot be formed by building the layers upward, the resin is cured on a support. This support is also made of the same photocurable resin and is removed after the product has been formed. For some types of resins that do not cure completely with a laser alone, the whole product is cured by exposure to an ultraviolet lamp after it has been formed.

The photocurable resin is composed of photopolymerizing oligomer, reactive diluent, and photoinitiator. When a laser is irradiated onto this resin, the monomer undergoes a series of reactions to form a solid polymer that has a three-dimensional network structure. The resins used for laser stereolithography are the radical polymerization type, the cation polymerization type, or the hybrid type, which is a combination of the first two types. The curing properties and mechanical properties of the cured resin are important, because these affect the applications of the cured product formed by laser stereolithography. These resins are prepared minutely by adjusting the mixture rate of the resin components and the additives to suit laser stereolithography.

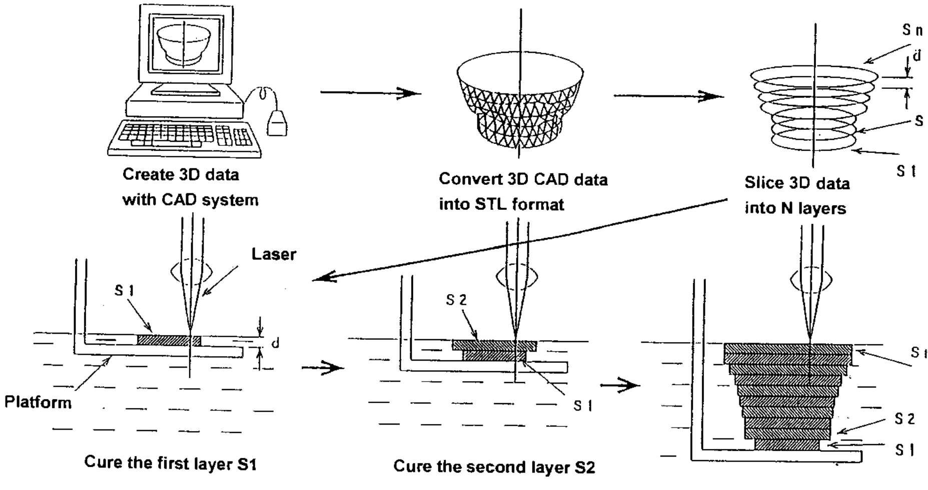

FIGURE 13.5.1 Principle of photocurable resin process.

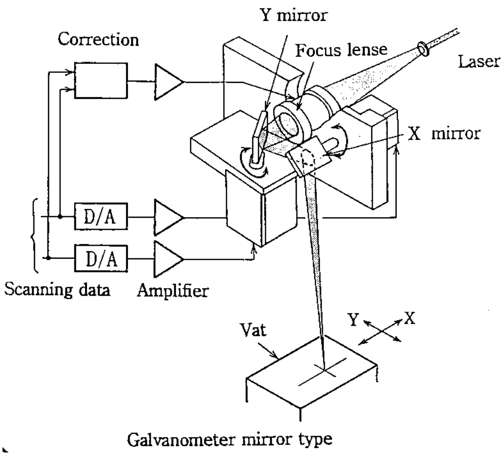

FIGURE 13.5.2 Scanning system of UV laser beam.

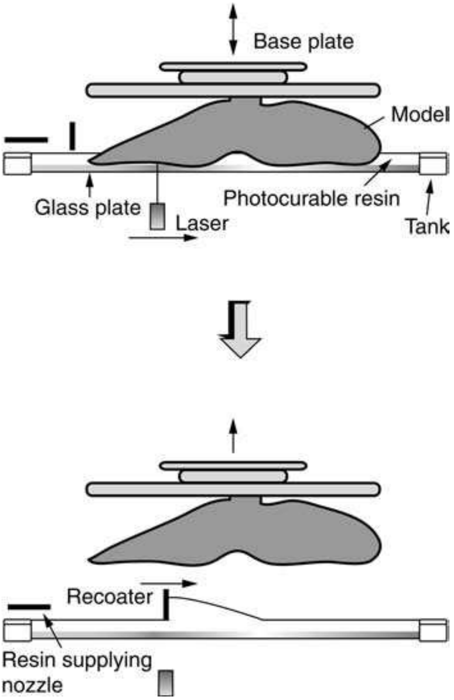

FIGURE 13.5.3 Laser beam radiation from below (Denken).

In most cases, the He-Cd laser with 325-mm wavelength or Ar laser with 364-mm wavelength is used as the light source. Higher-power lasers like Ar perform higher-speed beam scanning, resulting in the increase of modeling speed. As shown in Figure 13.5.2, these lasers scan at very high speed in the same way as the laser printer by rotating galvanomirrors. In some special machines, the laser beam is exposed from the bottom, as shown in Figure 13.5.3, by an *XY* plotter.

Laser stereolithography requires three-dimensional CAD data composed of surface or solid data in order to create solid models. Many types of CAD systems are now available on the market, and most of the CAD data they provide can be transmitted to laser stereolithography systems. At the same time, the

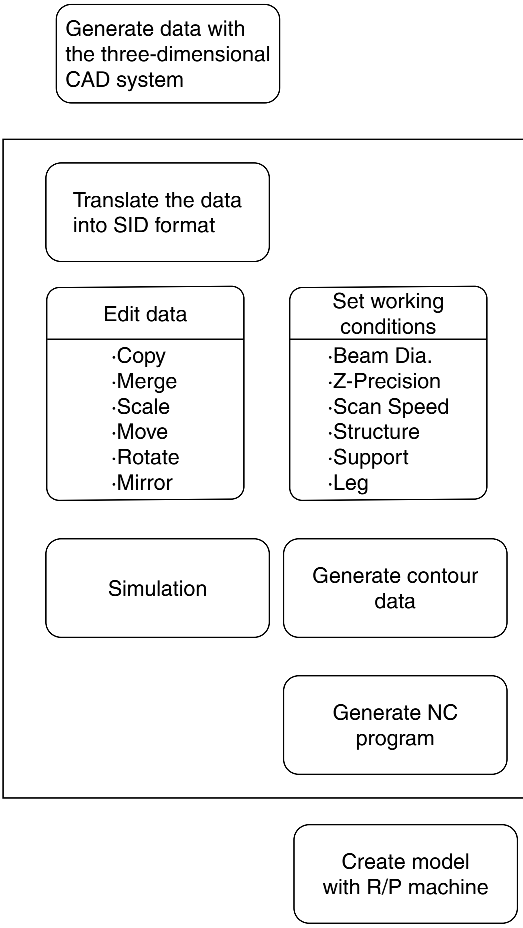

FIGURE 13.5.4 Software for R/P system (CMET).

laser stereolithography system is equipped with a scanning program, support and reinforcing rib design software, magnification/contraction functions, functions to determine the scanning and operating conditions, and simulation functions. Figure 13.5.4 shows a software flowchart in laser stereolithography.

The following shows the advantages of rapid prototyping over material-removing processes such as machining:

1. Deep holes and structures with complicated internal shapes that cannot be machined simply by cutting tools can be formed in a single process. Moreover, one rapid-prototyping machine is usually capable of fabricating any type of shape.
2. Rapid prototyping requires no complicated control programs such as tool path and repositioning of the workpiece. With the three-dimensional CAD data, there is no need for special knowledge of the cutting process, and operations from data input to actual fabrication are simple and short.
3. The rapid-prototyping systems produce no machining wastes. Because they do not vibrate and are silent, they can be used in offices like office business machines. They can also be operated fully automatically even at night since there is no need for the management of tooling.

The major shortcomings of laser stereolithography are that only photocurable resins can be used and the material strength of these materials is slightly worse than the common polymer. In addition, metal products cannot be manufactured directly by laser stereolithography.

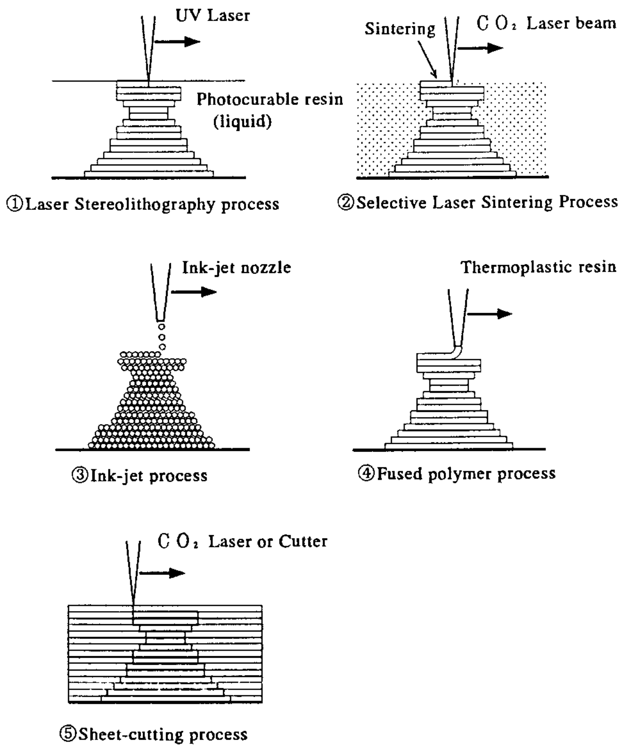

FIGURE 13.5.5 Schematic of various layer-additive fabrication processes.

Other Rapid-Prototyping Methods

The laser stereolithography method was developed in an early stage and is currently applied extensively. Besides laser stereolithography, many types of new rapid-prototyping methods have also emerged. As shown in Figure 13.5.5, rapid prototyping can broadly be classified into photopolymer, powder sintering, ink jetting, fused deposition, and sheet cutting. Figure 13.5.6 shows the history of these rapid-prototyping systems. Most of the methods were developed in the U.S., but the photopolymer process and sheet lamination were first proposed in Japan.

Another photopolymer process is the mask pattern-curing method shown in Figure 13.5.7. Similar to the photocopying process, a master pattern based on slice data is created, the pattern on the glass sheet is placed over a photocurable resin layer, and this layer is exposed to ultraviolet light. Although the machine is large, the exposing speed is faster than the laser beam method mentioned earlier, and the thickness of the product is very precise because each surface formed is cut by milling to obtain precise thin layers.

Three-dimensional objects can also be formed by powder sintering. In the process shown in Figure 13.5.8, powder is used instead of liquid photocurable resin. The powder is evened out using a roller, a CO_2 laser is beamed, and the powder is bonded by heat fusion. In this case, powder is heated up beforehand to the temperature just below the melting point in the antioxidation environment using N_2 gas. It is possible to create high-density polymer solid models as well as porous models.

Porous polycarbonate models are quite suitable for the investment casting model. With this method, metal and ceramic powders can also be used. Metal and ceramic powders used are coated by resin and each metal or ceramic powder is bonded by the coated resin. Sintered porous ceramic molds can be used for casting molds. Powder binding can be performed by spraying binding material on the loose powder layer through the ink jet nozzle, as shown in Figure 13.5.9. This is also used for making the sand mold

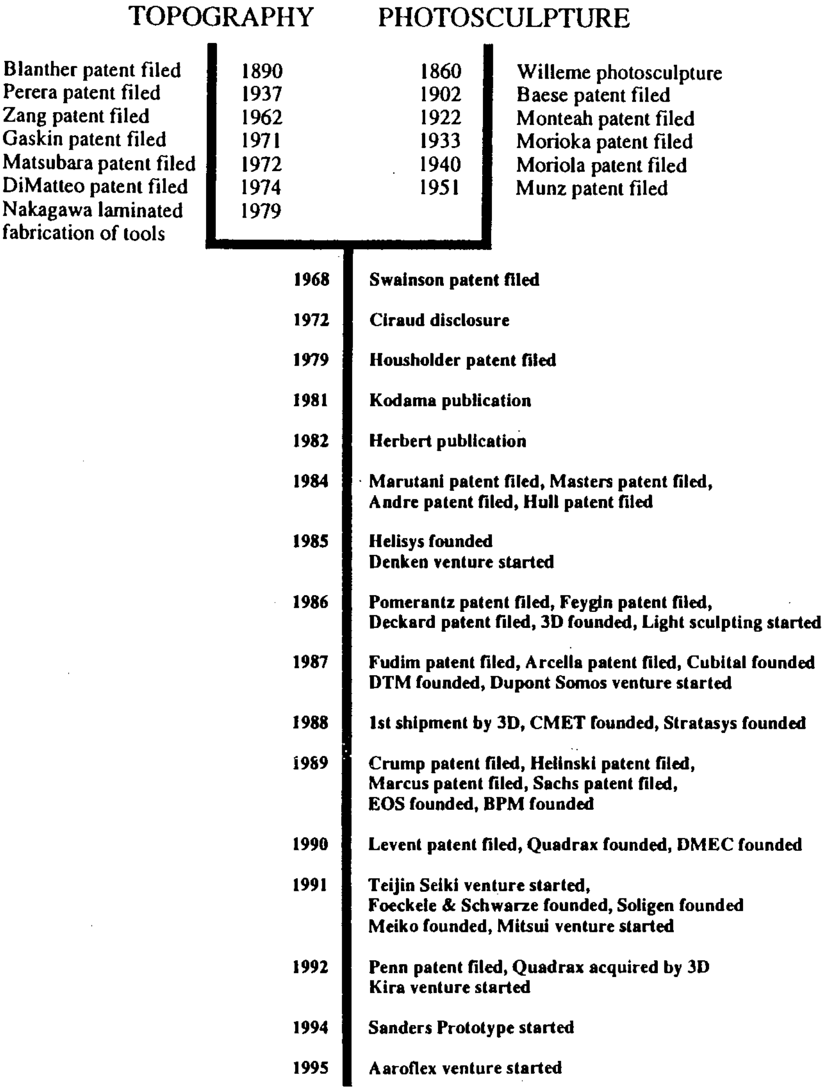

TOPOGRAPHY	
Blanther patent filed	1890
Perera patent filed	1937
Zang patent filed	1962
Gaskin patent filed	1971
Matsubara patent filed	1972
DiMatteo patent filed	1974
Nakagawa laminated fabrication of tools	1979

	PHOTOSCULPTURE
1860	Willeme photosculpture
1902	Baese patent filed
1922	Monteah patent filed
1933	Morioka patent filed
1940	Moriola patent filed
1951	Munz patent filed

1968	Swainson patent filed
1972	Ciraud disclosure
1979	Housholder patent filed
1981	Kodama publication
1982	Herbert publication
1984	Marutani patent filed, Masters patent filed, Andre patent filed, Hull patent filed
1985	Helisys founded Denken venture started
1986	Pomerantz patent filed, Feygin patent filed, Deckard patent filed, 3D founded, Light sculpting started
1987	Fudim patent filed, Arcella patent filed, Cubital founded DTM founded, Dupont Somos venture started
1988	1st shipment by 3D, CMET founded, Stratasys founded
1989	Crump patent filed, Helinski patent filed, Marcus patent filed, Sachs patent filed, EOS founded, BPM founded
1990	Levent patent filed, Quadrax founded, DMEC founded
1991	Teijin Seiki venture started, Foeckele & Schwarze founded, Soligen founded Meiko founded, Mitsui venture started
1992	Penn patent filed, Quadrax acquired by 3D Kira venture started
1994	Sanders Prototype started
1995	Aaroflex venture started

FIGURE 13.5.6 History of R/P (Joseph Beaman).

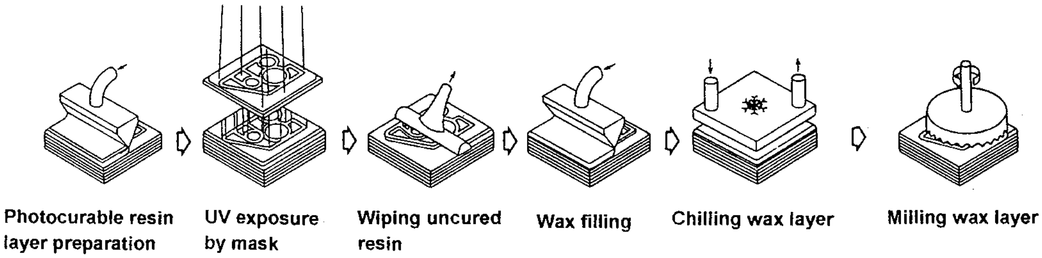

FIGURE 13.5.7 UV stereolithography (Cubital).

for casting. When wax or resin is sprayed from the jet nozzle, wax or resin models can be fabricated, as shown in Figure 13.5.10. In this case, the surface of the sprayed thin layer should be machined smoothly and flatly in order to obtain vertical accuracy.

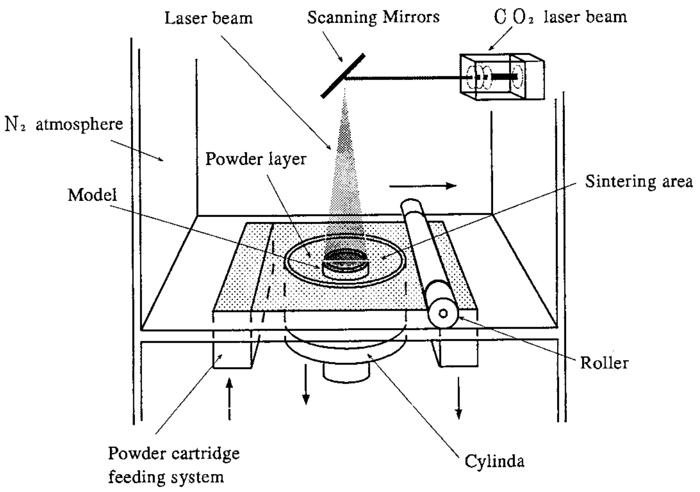

FIGURE 13.5.8 Selective laser sintering process (DTM, EOS).

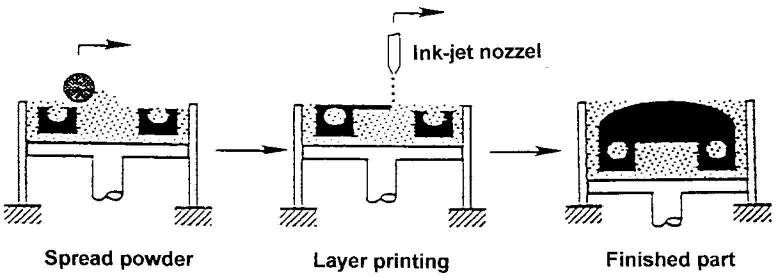

FIGURE 13.5.9 Ink-jet binding process (MIT, 3D printing).

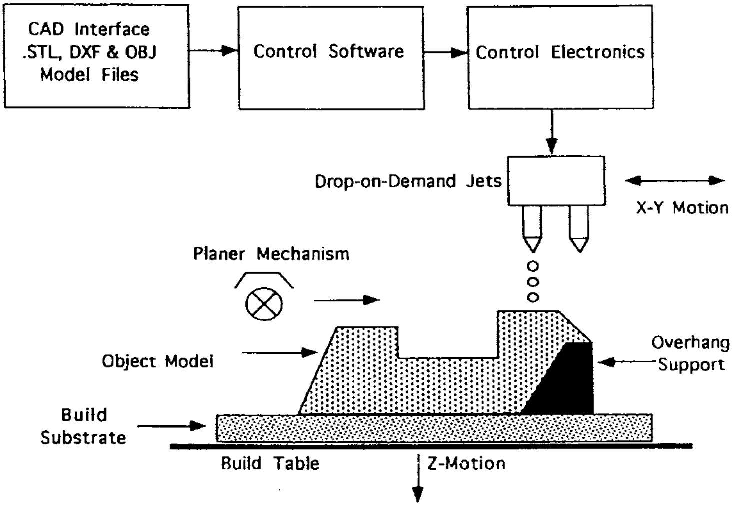

FIGURE 13.5.10 Ink-jet process (Sanders prototype).

Figure 13.5.11 shows the fused-deposition method. In this method, a fine nozzle deposits a layer of resin or wax. Wax is normally used to form lost wax models. Fused deposition systems, in which material is supplied by the pellet or wire, enable materials to be formed very similarly to general injection mold

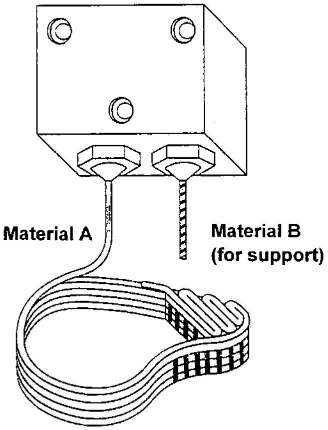

FIGURE 13.5.11 Fused deposition process (Stratasys).

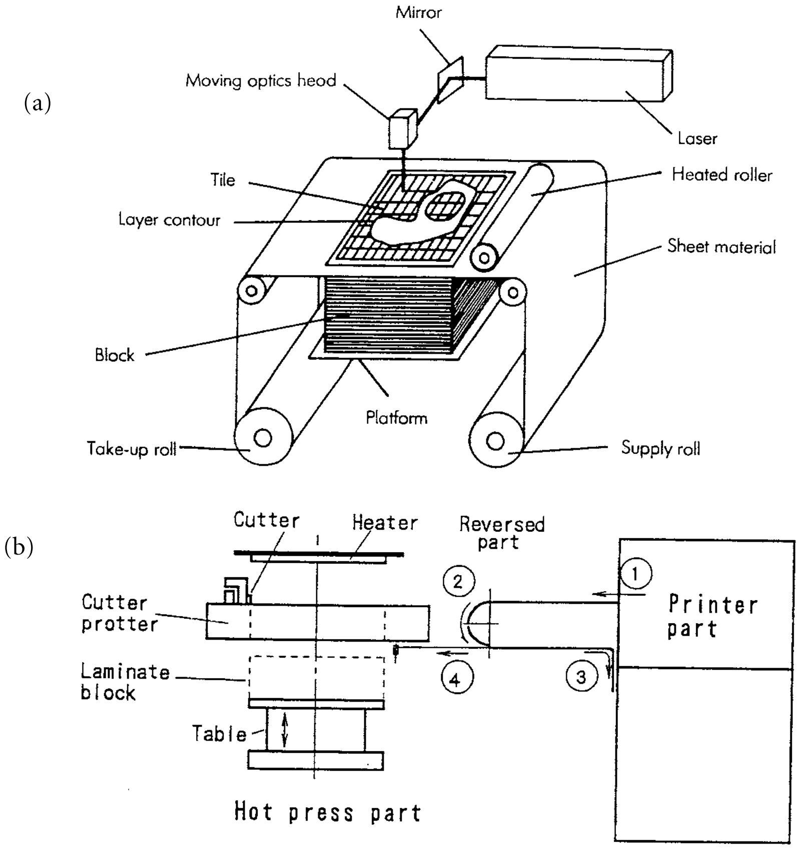

FIGURE 13.5.12 Sheet cutting process: (a) Laser (LOM), (b) Cutter (Kira).

materials like ABS and nylon. One of the two nozzles is used for making the support, where the support material is usually wax with lower melting points.

Figure 13.5.12 shows two methods that cut thin sheets according to slice data and laminate them to form three-dimensional objects. One method uses a laser to cut sheets applied with adhesive, which are then laminated by hot toll pressing, while the other uses a knife to cut the sheets. In the latter case, adhesive is applied to sheets of paper according to the desired shape by spraying the toner using a dry Xerox-type copy machine. Due to the use of paper in these sheet-lamination methods, the model formed should be immediately coated to prevent the absorption of moisture. Although there is a limit to the shapes that can be made, the method is nevertheless used for making wood models for casting, because it is inexpensive and enables large-sized models to be made and the model material is similar to wood.

The common feature of all of these methods is that slice data is obtained from three-dimensional CAD data and these slice data are used to laminate thin layers of material, which means that the same software can be used for all of these methods. Another feature is that all rapid-prototyping machines use the modified printing technology.

Although many of these rapid-prototyping machines tend to be costly, inexpensive models are also now available. Machine cost reduction has been achieved by proper utilization of key parts, which are used for the printer. New and improved methods should continue to be developed with the introduction of printing technology.

Application of Rapid Prototyping

Figure 13.5.13 shows the applications of three-dimensional models made by rapid prototyping. They are mainly intended for verifying CAD data, checking the designs, functional checks of prototypes, wax models for investment casting, master models for die and model making, mold making for prototype manufacturing, casting models, and medical use CT and MRI data. Although dimensional accuracy was given little importance in the verification stage of CAD data and design, high dimensional accuracy is now demanded of the functional check of prototypes. Because photocurable resins contract in the solidification process, slight distortions are generated in the fabricated product. Among the various rapid-prototyping machines, the photocurable resin process is most suitable for making complicated shapes and obtaining the highest accuracy.

Even in laser stereolithography, accuracy has improved to a considerable extent with the enhancement of the resin and scanning method and the accumulation of know-how for positioning the reinforcing rib. It should also be possible to attain the same accuracy as injection molds by measuring formed products, correcting the data, or predicting errors.

In general, photocurable resins are generally weak and brittle as compared with conventional polymer parts produced by injection molds. Urethane resin, which is typically used for vacuum casting with a silicon rubber mold reversely copied from a rapid-prototyping model, also lacks the required strength. In order to carry out the functional check of the prototypes created, other processes that can use normal thermoplastic should be used.

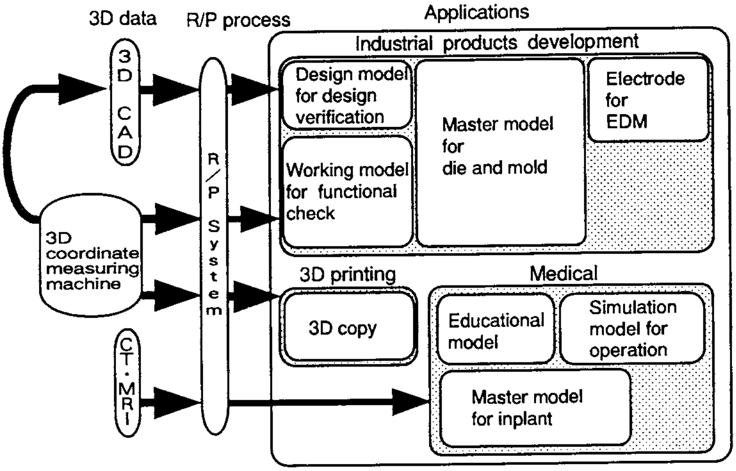

FIGURE 13.5.13 Application of rapid prototyping (Source: CMET).

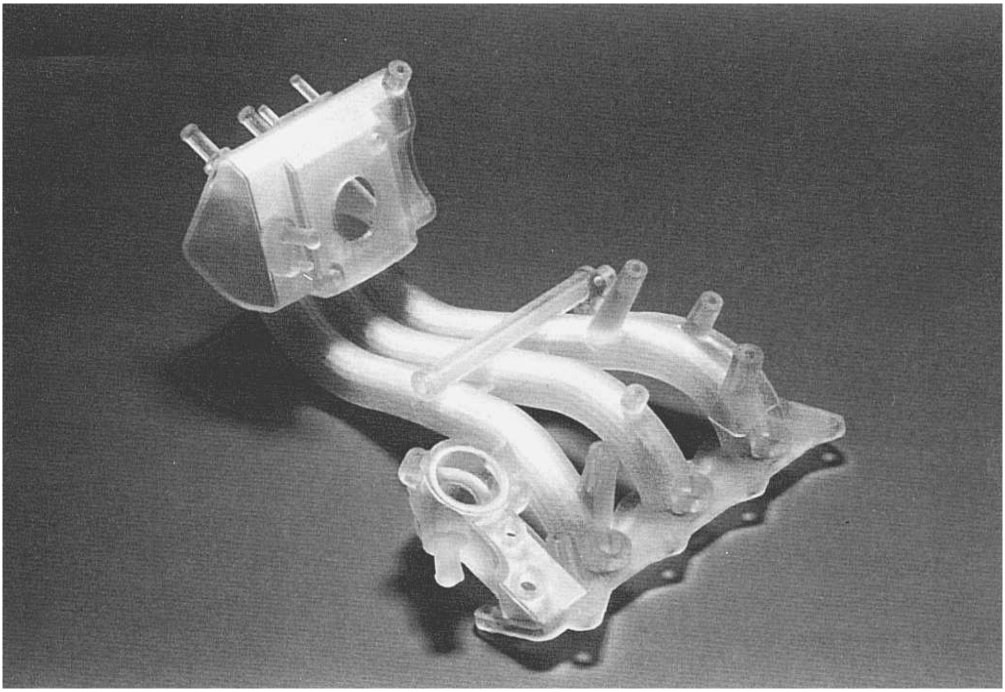

FIGURE 13.5.14 Sample for fluid dynamic analysis.

Figure 13.5.14 shows an intake manifold for car engines made by laser stereolithography. This serves as a test model for checking fluid performance of air. For such purposes, current photocurable resins available prove relatively satisfactory.

Although the powder sintering process can apply some metals, there is no suitable rapid-prototyping technique that can directly form products from metal materials at the moment. Research activities are under way to study the feasibility of producing molds from metal materials directly using a three-dimensional printing technique. In a general application, the lost wax models are first made by rapid prototyping and then used for creating metal prototypes by investment casting.

Rapid prototyping is still a relatively new technology, and therefore considerable opportunities for technical improvements exist.

General Rapid Prototyping in Production

For rapid prototyping to be carried out, three-dimensional CAD data must be available. Creating the CAD data takes far more time than creating the three-dimensional models based on the CAD data. By realizing efficient concurrent engineering, rapid prototyping will no doubt become a very important tool. In general, many other types of production systems can be included in the list of systems currently termed general rapid prototyping (casting and machining, etc.).

Casting methods that are able to produce green sand molds satisfy the conditions of rapid prototyping. Expendable pattern casting is also suitable for rapid manufacturing. In this case, a three-dimensional polystyrene foam model is made by machining or binding. Most of the industrial products around us are produced with dies and molds. Because they are expensive to manufacture, dies and molds are unsuitable for making prototypes and for small-lot production. This may be a reason why rapid prototyping was developed; however, some prototype production methods do involve the use of dies and molds. Flexible prototype production has been carried out in sheet metal forming with the use of the turret punch press, laser beam cutting machine, and NC press brakes. Producing dies and molds rapidly and manufacturing using such dies and molds also fit into the category of general rapid prototyping in the broad sense. Examples include what is known as the low-cost blanking dies using steel rule, deep drawing die made of zinc alloy, and bismuth alloy.

Among the many general rapid-prototyping systems that exist, the newly developed rapid-prototyping methods we discussed are gradually becoming methods for creating complicated products accurately with the use of three-dimensional CAD data. In terms of the total cost, applications of these new methods are still limited, but the spread of three-dimensional CAD data and technological progress of rapid prototyping should make them one of the common manufacturing techniques in the near future.

References

Ashley, S. 1992. Rapid prototyping systems. In *Mech. Eng.*, April, 34–43.

Jacobs, P.F. 1992. *Rapid Prototyping and Manufacturing*, Society of Manufacturing Engineers, Dearborn, MI.

Rapid Prototyping in Europe and Japan, Japan and World Technology Evaluation Centers CJTEC/WTECS Report, September 1996, Loyola College, Baltimore, MD.

Sachs, E. et al. 1990. Three dimensional printing: rapid tooling and prototypes directly from a CAD model. *CIRP Ann.*, 39(1), 201–4.

Solid Freeform Fabrication Symposium, University of Texas, Austin, TX 1991–1993.

13.6 Underlying Paradigms in Manufacturing Systems and Enterprise Management for the 21st Century

Quality Systems

H. E. Cook

Introduction

Quality engineering has been described as the process of minimizing the sum of the total costs and the functional losses of manufactured products. Total costs include variable costs, investment, maintenance/repair costs, environmental losses, and costs of disposal or recycling. Functional losses arise from deviations from ideal performance. A subset of total quality management, quality engineering, focuses on parameter and tolerance design after the target specifications for the product have been developed as part of system design.

In contrast to quality engineering, *total quality management* embraces the entire product realization process. Its objective should be to maximize the net value of the product to society, which includes buyer, seller, and the rest of society. Product value is determined solely by the customer and can be set equal to the maximum amount the customer would be willing to pay for the product. For a product to be purchased, its price must be less than its perceived value to the customer at the time of purchase. Consumer surplus is the difference between value and price.

The true value of a product is formed by the customer after assessing the product's performance over the complete time period that he or she used it. Functional quality loss is also known as the cost of inferior quality that is equal to the loss of value incurred by a product as a result of its attributes being off their ideal specification points (Figure 13.6.1). When manufacturing costs are added to value, the resulting sum (equal to total quality less environmental losses) is maximized when the attribute is off its ideal specification because of the impossibly high costs required to make a product perfect.

Requirements Flow

The systems viewpoint, as expressed by the flow of requirements shown in Figure 13.6.2, is helpful in considering the full ramifications of total quality management. Every system can be divided into subsystems, and every system is but a subsystem of a larger system. Each task receives input requirements from its customer (either internal or external) and sends output requirements to its suppliers.

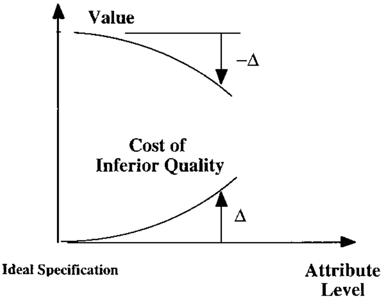

FIGURE 13.6.1 The relation of product value to the cost of inferior quality.

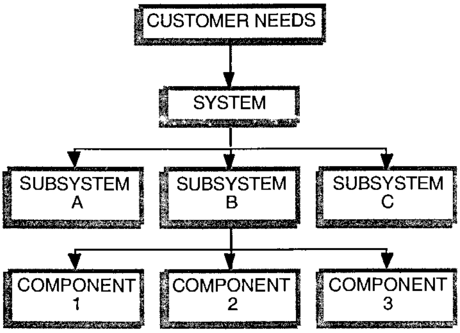

FIGURE 13.6.2 Flow of requirements from the customer through the enterprise.

Task Objectives

A major objective of the system task is to assess customer needs, to translate those needs into a complete set of system-level specifications for the product, and to send a key (but partial) set of subsystem requirements to those responsible for the subsystem tasks. The system specifications and subsystem requirements developed by the system task should be such that (1) customers will want to purchase the product in a competitive marketplace and, with use, find that the product meets or exceeds their expectations, (2) the product will meet the profitability objectives of the enterprise, and (3) all environmental rules and regulations are met. The system task also has the responsibility of resolving conflicts that arise between subsystem tasks.

The subsystem task receives the key requirements from its internal customer, translates them into a complete set of subsystem requirements, and sends a key (but partial) set of component requirements to those responsible for the component tasks. In turn, those responsible for each component task translate the requirements received into a complete set of component requirements and a partial (but key) set of raw material requirements. Requirements set at each level include controls on variable costs, investment, performance, reliability, durability, service, disposal, environmental quality, package, assembly, and timing for both production and prototype parts. Synchronization is very important to total quality management since parts should be received exactly when needed with minimal inventory.

Parts Flow

The response to the requirements flow is a parts flow in the opposite direction that begins with the conversion of raw materials into components. This is followed by the assembly of components into subsystems, which are shipped to the system task for final assembly. The process is completed by shipping the finished product to the customer. Thus, each task shown in Figure 13.6.1 has both a planning or design function as well as other functions, including manufacturing, assembly, purchasing, marketing,

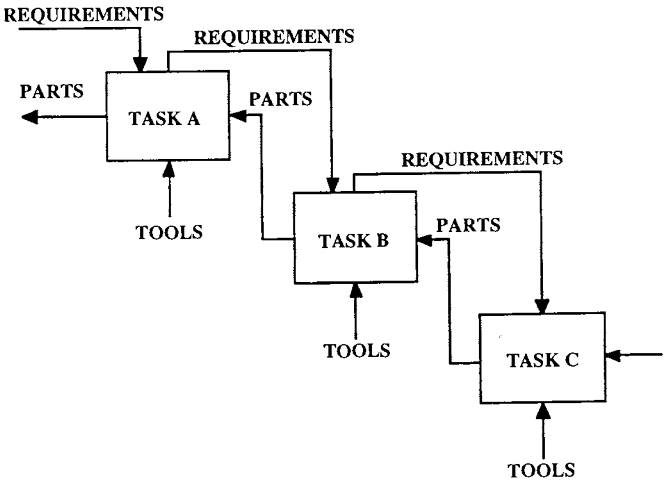

FIGURE 13.6.3 The flow of requirements and parts in a modified IDEF0 (function model) representation.

service, accounting, and finance. The actions taken to meet customer needs should be traceable as the requirements flow through the enterprise. With the systems viewpoint, all parameters are measured or computed at the full system level, including value, costs, and investment.

Task Management

Within each task shown in Figure 13.6.2 are subtasks. The combined flow of requirements and parts between several subtasks is shown in Figure 13.6.3 using a modified IDEF representation. Requirements are shown as controls that flow from left to right, and parts, in response, are shown as flowing from right to left.

Each task is accomplished by exercising its authority, responsibility, and capability. Authority to set requirements on parts should rest fully and undiluted with the task receiving the parts. The task that ships the parts should possess the full authority, responsibility, and capability to manufacture the parts for its customer. Before sourcing of parts, demonstration of capability by the manufacturer is a vital element of sound quality engineering. Capability is ultimately determined by the set of tools that the task has at its disposal and includes the skills and experience of the people as well as the hardware and software used by them.

Because a broad range of skills is needed, the required expertise is generated by forming a team to carry out the task. Quality tools used by the teams include structured methodologies such as Taguchi methods (design of experiments), quality function deployment, failure mode effects and criticality analysis, statistical process control, cost analysis, and value analysis. It is highly recommended that final authority and responsibility for each task rest with one person.

Fundamental and Bottom-Line Metrics

A variety of parameters can be used to measure the progress of quality improvements. These include such factors as the degree of customer satisfaction expressed for the product, the frequency of repair, and the variance found in product dimensions and performance levels that directly affect value to the customer. Repair and operating costs borne by the customer subtract from value if they are greater than what was anticipated by the customer. Likewise, resale price subtracts form value if it is below what the customer expected. Performance degradation of the product over its lifetime of use diminishes its value. Noise and atmospheric pollution caused by the manufacture and use of the product lower the net value of the product to society. The costs to manufacture and develop the product subtract from the net value received by the manufacturer. Moreover, products that are not improved in value and reduced in costs at the pace of competing products will likely be eliminated from the market in time.

These metrics can be grouped into one of three categories — value, cost, and the pace of innovation. They represent the fundamental metrics for the product because they determine what the bottom-line metrics of profitability and market share will be. Management of the fundamental metrics is the management of total quality and, likewise, the management of the total enterprise. The level of sustained profitability is the best measure of how well total quality is being managed in competitive markets.

Electronic Data Interchange

Chris Wang

Introduction

Electronic data interchange (EDI) is a method for exchanging business information between computer systems. In a traditional purchasing environment, buyers, when placing computer-generated orders, will mail them to suppliers, and it could take days before the suppliers receive them and then rekey the orders into their computer systems. Using EDI, the buyer's computer system can generate an EDI standard order transaction and transmit it directly to the supplier's inventory system for material pickup. It happens instantly. The benefit of EDI is quite obvious in this case since it reduces material lead time dramatically. Consequently, the objectives of EDI implementation should not be limited to just reducing paperwork and clerical work; instead, it should be used as a methodology to streamline company processes and allow the company to become competitive in the marketplace.

EDI Elements

EDI consists of the following elements:

- Trading partners — The parties, such as a manufacturer and a supplier, who agree to exchange information.
- Standards — The industry-supplied national or international formats to which information is converted, allowing disparate computer systems and applications to interchange it. This will be discussed in more detail later.
- Applications — The programs that process business information. For example, an orders application can communicate with an order-entry application of the trading partner.
- Translation — The process of converting business information, usually from a format used by an application, to a standard format, and vice versa.
- Electronic transmission — The means by which the information is delivered, such as a public network. Some companies may choose to build their own transmission facilities. For others, a value-added network (VAN) seems to be a good choice since companies do not have to invest heavily in communication equipment and personnel to support it. The VAN provider can handle disparate communication hardware and software and provide wide-area network access at a reasonable cost.

EDI in Manufacturing

In the present-day business environment, many companies are turning to just-in-time (JIT) and other techniques to compete as effectively as possible. EDI can make an important contribution to the success of JIT by ensuring that information exchanged between business partners is also just in time.

In traditional manufacturing, material is stored in quantities much larger than required because of faulty components and possible waste in the production process. To solve problems of carrying safety stock and still producing high-quality product, JIT seems to be an effective technology.

JIT systems are designed to pull raw materials and subassemblies through the manufacturing process only when they are needed and exactly when they are needed. Also, with rapidly changing production needs, orders are getting smaller and are issued more frequently. The traditional paperwork environment simply cannot effectively cope with this change. This is why EDI comes in to play a key role to provide fast, accurate information to achieve these JIT goals. In other words, EDI can provide JIT information in manufacturing processes.

- EDI cuts order delivery and lead time — The more control points you have in a process, the greater the number of potential problems. EDI eliminates "control points" for the order process. It eliminates the need to mail orders and rekey order information at the receiving end. It reduces the material lead time for production use.
- Connect applications and processes — With EDI capability, information, such as scheduling, orders, advance delivery notice, statistical process control data, and material safety data sheets can pass quickly and accurately from the supplier's computer application to the customer's computer application, so that arriving material can be put to production use with confidence. This meets one of the important goals of JIT, that is, to turn the supplier's entire production line into a vast stockroom so a company does not have to maintain a huge warehouse and the working capital tied to excess inventory.
- Improve relationship with customers and suppliers — In the supply chain environment, the quicker the chain moves, the better the customers' needs can be met. With quicker orders, acknowledgments, order changes, and invoices, EDI can satisfy customers' needs more quickly. Also, the time spent on order tracking and error recovery can now be used in a more productive way and can improve customer/supplier relationships. Companies deeply involved in EDI may see the number of suppliers reduced. This is because through the EDI process, a company can weed out many suppliers who are not efficient and reliable.

EDI Standards

When two organizations exchange business forms electronically, information is encoded and decoded by the computer software of both parties. Therefore, the information must be unambiguous, in order to avoid different interpretations. This relates to the meaning of the terms used, the representation of data used, the codes to be used for data, and the sequence in which data are to be transmitted. All these parameters must be arranged between the two parties on a detailed level.

There are many standard types of exchange — it can be based on bilateral agreement, imposed by a dominating party in a certain marketplace, or jointly developed by an industrial group. Some standards have been ratified by international organizations.

The pioneer of EDI standard development was the transportation industry. The Transportation Data Coordinating Committee (TDCC) developed sets of standards for transportation mode — air, ocean, motor, and rail. Later, the U.S. grocery industry developed a set of standards, the Uniform Communication Standard (UCS), based on the TDCC structure.

The TDCC and UCS are more geared toward the business forms exchanged by shipper/carrier, for example, bills of lading. Not until the American National Standards Institute (ANSI) got involved did a general-use standard for all industries start to develop, leading to the birth of ANSI X12 standards.

The ANSI X12 is popular in the U.S. Although ANSI X12 is intended for all industries, different user groups still come up with their own conventions to address their specific needs but remain under the X12 umbrella. To name a few, there are the Automotive Industry Action Group (AIAG) for the auto industry, CIDX for the chemical industry, and EIDC for the electronic industry.

In Europe, at approximately the same time period, under the leadership of the U.K., the Trade Data Interchange (TDI) was developed. The TDI syntax and structure are quite different from the ANSI X12. To resolve the incompatibility, the U.N. organization UNJEDI was formed to develop an EDI international standard containing features from both TDI and ANSI X12. The result was the EDI for Administrative, Commerce, and Transport (EDIFACT). This is the standard to which the world is trying to convert.

EDI Implementation

Before implementation of EDI, planning is critical to success. First, get all the right people involved in planning and implementation of EDI. Ensure that every employee gets EDI education on how to use EDI as a business tool to manage his or her job. Prepare a strategic plan to get approval and support from top management. Managers should be aware of the significant benefits of EDI and should appreciate the potential of EDI as a business methodology to improve the bottom line.

As part of a strategic plan, it is crucial to perform an operational evaluation. This evaluation details how the internal departments of the company function. For each paper document under evaluation, information flow is tracked, processing procedures are scrutinized, time is measured, and costs are calculated. This will provide top management with valuable information as important as industry trends and competition information. The operational evaluation provides the company with detailed documentation about how it does business in a paper-based environment. This information then serves as a benchmark against which to measure projected costs and benefits of the EDI model.

Once the strategic plan is in place, available resources must be allocated to the departments that will generate the most benefits for the company. Once EDI is implemented in the company, the next step is to sell it to trading partners to maximize the EDI investment.

Summary

EDI is on a fast-growing path. EDI software and communication services are available and not expensive. It will not be too long before EDI becomes mandatory as a business practice. If a company is determined to implement EDI, it should look beyond just connecting two computer systems. To achieve the best return on the EDI investment, one should try to use EDI to improve the existing processes within the organization and the relationship with customers and suppliers.

References

Gerf, V.G. 1991. Prospects for electronic data interchange. In *Telecommunications*, January, 57–60.

Mandell, M. 1991. EDI speeds Caterpillar's global march. *Computerworld*, 25(32), 58.

13.7 Electronics Manufacturing: Processes, Optimization, and Control

Roop L. Mahajan

Introduction

We live in the information age, and electronics technology is an important part of it. Since the invention of the transistor in 1947, and the introduction of integrated circuits (ICs) in 1958, the electronics industry has grown rapidly as evidenced by the intrinsic pervasiveness of electronic products in our lives. The sale of these products has been steadily on the rise over the last seven decades, as shown in Figure 13.7.1. In the U.S., starting from an industry-wide sales volume of approximately $210 billion in 1986, electronic sales in the year 2000 were close to $1 trillion.[1] A similar trend is seen in the sale of electronics worldwide. Figure 13.7.2 gives a snapshot view of total global sales in 1980, 1990, and 2000.[2] A breakdown of market share for several product groupings is also shown to indicate the increasing role played by electronic products in business, retail, and the computer industry. This impressive growth in the electronics industry has resulted in a significant change in the composition of the workforce in the U.S., as shown in Figure 13.7.3. About half of the workforce is now employed in the information industry that deals with gathering, creating, processing, disseminating, and using information. As we move into the next century, this fraction is expected to get even larger. It is needless to say that a healthy, competitive electronics industry is vital to the economic health of a nation.

As with other segments of the market, manufacturing is critical to the electronics industry. A classical definition of manufacturing is *an assemblage of all processes required to convert raw material into a finished product*. The raw material in electronics manufacturing is typically an IC, although in some subassembly operations, the starting material may be electronic components, modules, or subsystems. An IC is a collection of electronic circuits made by simultaneous formation of individual transistors, diodes, and resistors on a small chip of semiconductor material. These devices are interconnected to one another with a metal, such as aluminum, deposited on the chip surface. The semiconductor material is typically silicon (≈90% of the applications). For very high speed, high frequency, and optical applications, compound

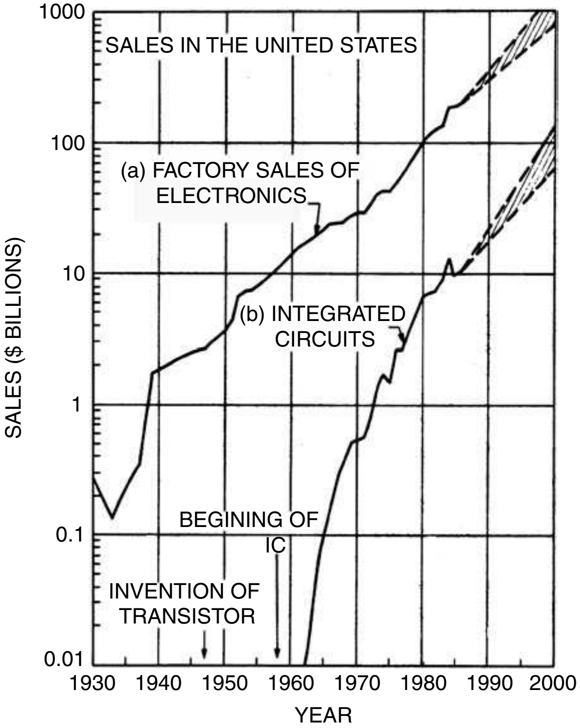

FIGURE 13.7.1 Factory sale of electronics and ICs in the U.S. (Source: Sze, S.M. 1988. *VLSI Technology*, McGraw-Hill, New York, 2.)

semiconductors gallium arsenide (GaAs) and indium phosphide (InP) are the materials of choice. In this chapter, our focus is on silicon ICs only.

IC fabrication is an extraordinary example of mass production and involves many complex manufacturing processes. Some of these are discussed to provide the reader an appreciation of the complexity of the tasks involved in modeling, optimizing, and controlling these processes.

The final products cover an extremely wide range, from consumer electronics to supercomputers. The Semiconductor Industry Association (SIA) Technology Roadmap[3] categorizes these products by the following six market applications:

- *Commodity:* Consumer products, microcontrollers, disk drives, displays, costing less than $300
- *Handheld*: Battery-powered products, mobile products, handheld cellular telecommunications, other handheld products, costing less than $1000
- Cost performance: Notebooks, desktop personal computers, telecommunications, costing less than $3000
- High performance: High-end workstations, servers, avionics, supercomputers, costing $3000 and up
- Auto*motive:* Under-the-hood and other hostile requirements
- *Memory:* Dynamic random access memory (DRAM), standard RAM (SRAM)

A number of assembly processes are involved in converting an IC to any of the listed electronic products; see, for example, Figure 13.7.4, which shows the major stages in manufacturing of a desktop computer. Many of the manufacturing processes required in the production of desktop computers are common to most of the electronic products. These are introduced later in this chapter to give readers a feel for the complexity and diversity of the processes used.

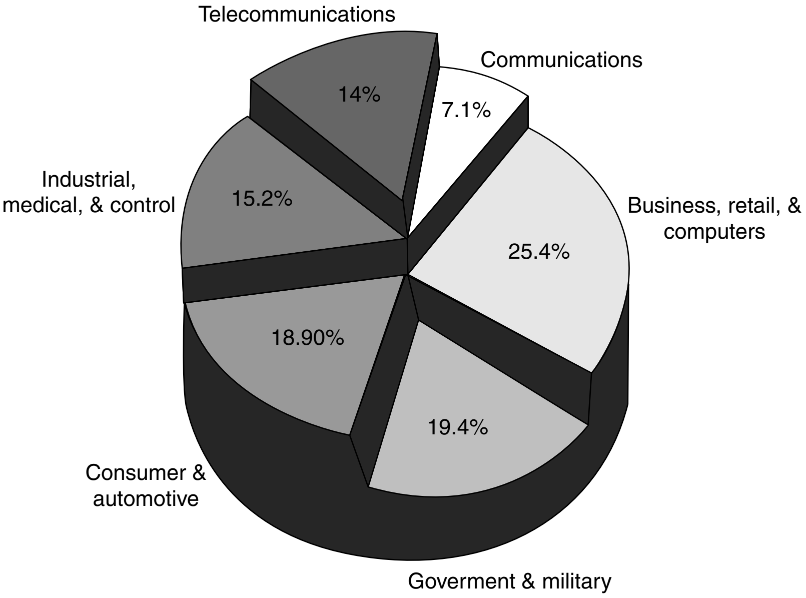

1980 $220 billion

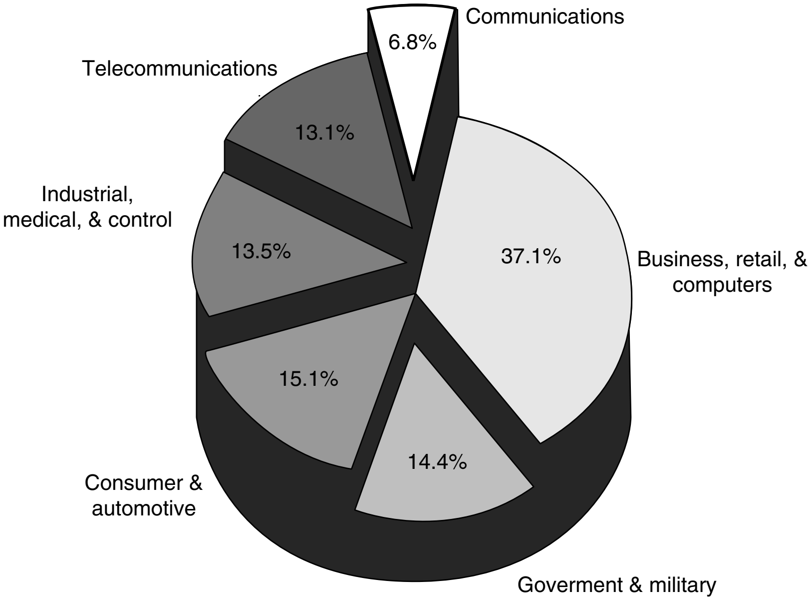

1990 $654 billion

FIGURE 13.7.2 Global electronics markets by product groups. (Source: Landers, T.L., Brown, W.D., Fant, E.N., Malstrom, E.M., and Schmitt, N.M. 1994. *Electronics Manufacturing Processes*, Prentice Hall, Englewood Cliffs, NJ, 8.)

The electronics market is extremely dynamic, highly competitive, and global in nature. There is a continuously increasing demand for higher performance at reduced costs. The industry has responded remarkably well by placing a larger number of devices (transistors, capacitors, resistors, and diodes) on a chip. This strategy has been made possible through a continuous shrinkage in minimum device

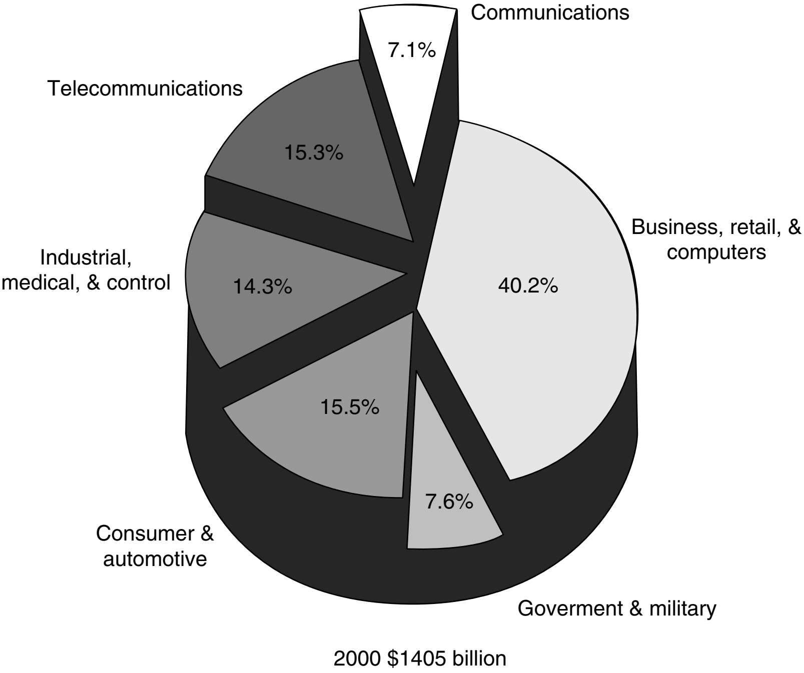

FIGURE 13.7.2 (continued)

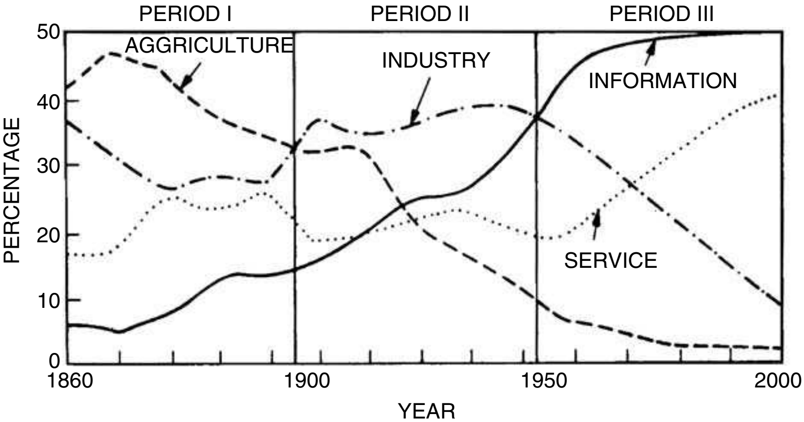

FIGURE 13.7.3 Changing composition of workforce in the U.S. (Source: Sze, S.M. 1988. *VLSI Technology*, McGraw-Hill, New York, 2.)

dimensions, as shown in Figure 13.7.5. Concomitantly, the cost per function has decreased by an average of 25%–30% per year. In 1999, the affordable packaged unit cost/bit for DRAM and microprocessors was 60 and 1735 microcents, respectively. These costs are expected to go down at an average of 29% for DRAM and 24% for microprocessors.[3]

To meet these aggressive goals and the fierce global competitive pressures, an electronic manufacturer has to ensure that each of the many processing steps involved is in control. The processes must be optimized for higher yields. Different strategies required for process optimization and control are the main focus of this chapter. Emphasis is on artificial neural networks that have evolved as a technique with considerable promise.

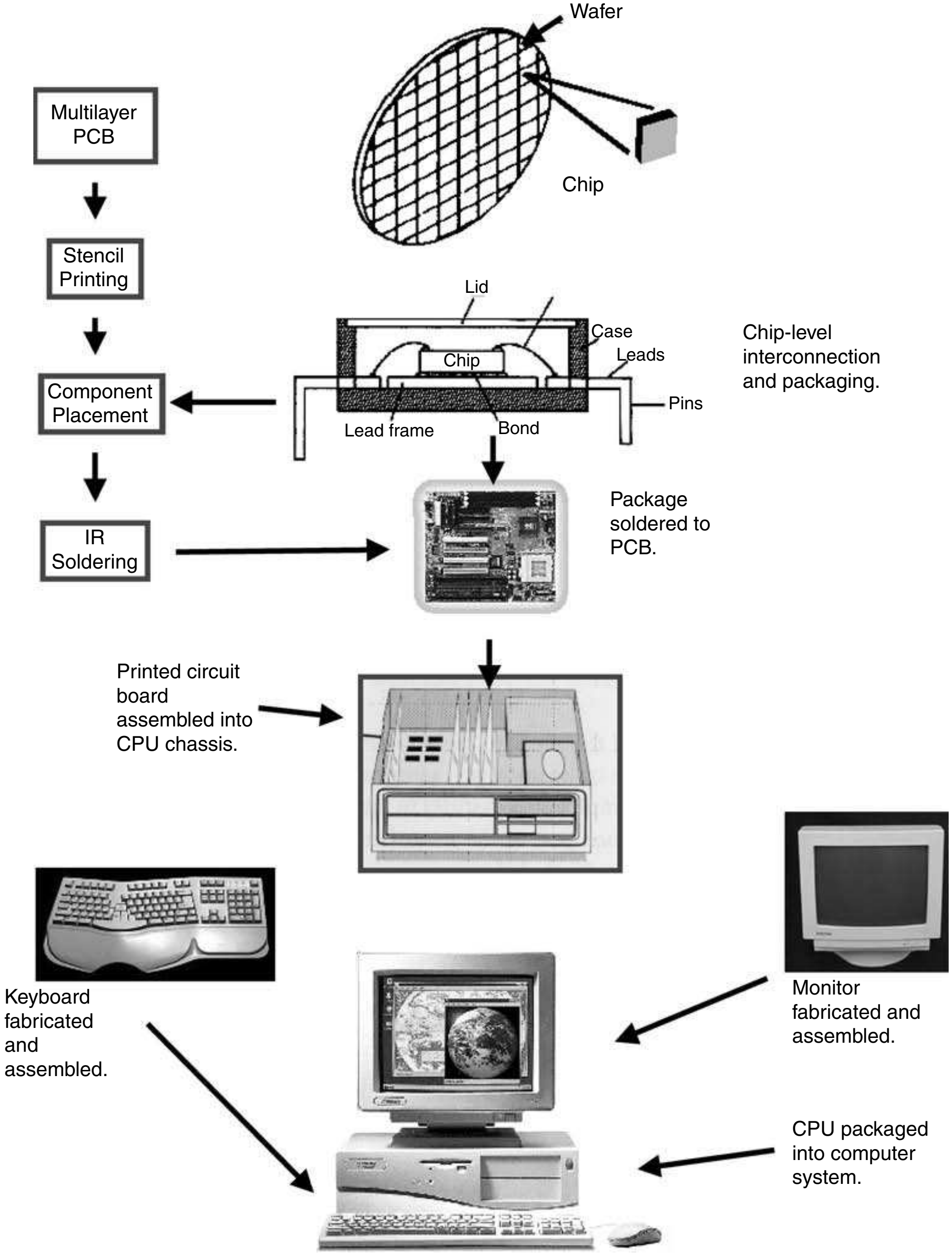

FIGURE 13.7.4 Sequence of steps in the manufacture of a desktop computer. (Source: Landers, T.L., Brown, W.D., Fant, E.N., Malstrom, E.M., and Schmitt, N.M. 1994. *Electronics Manufacturing Processes*, Prentice Hall, Englewood Cliffs, NJ, 8.)

IC Fabrication

The structure of an IC is complex both in topography of its surface and its internal composition. The structure is made up of many layers, each of which is a detailed pattern. Some of the layers lie within the semiconductor wafer, and others are stacked on the top. The manufacturing process consists of forming this sequence of layers precisely to the design specifications.

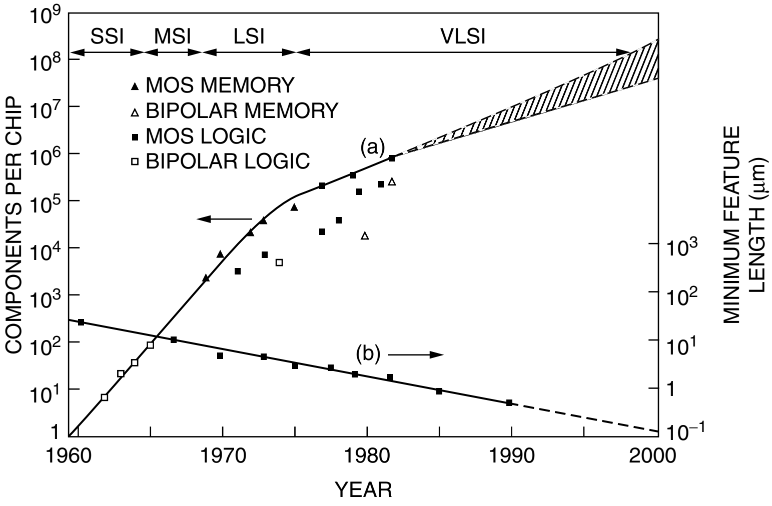

FIGURE 13.7.5 Evolution of minimum device dimension and number of components per IC chip. (Source: Sze, S.M. 1988. *VLSI Technology*, McGraw-Hill, New York, 2.)

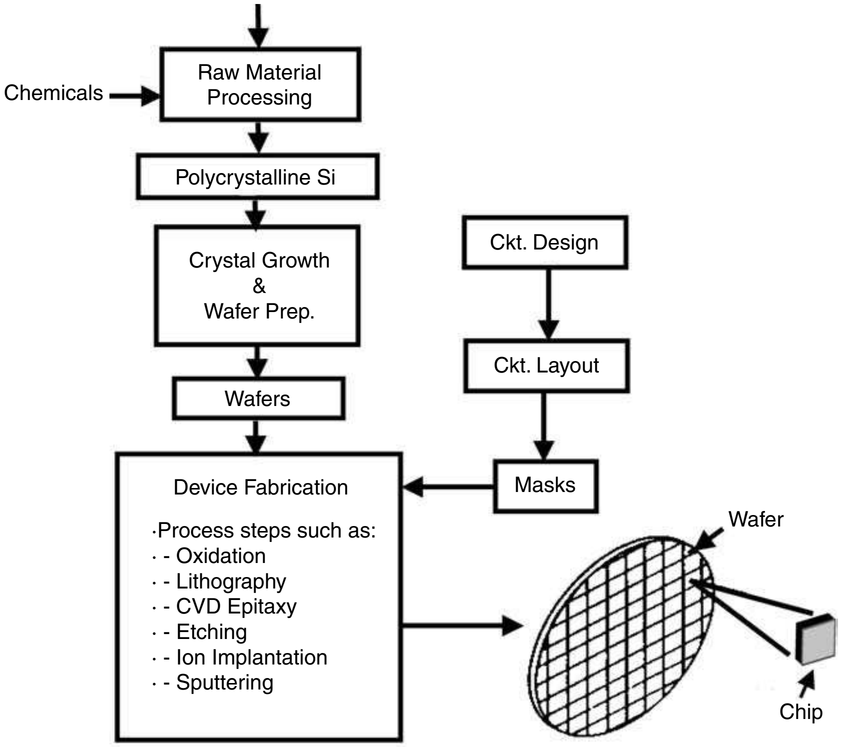

FIGURE 13.7.6 Fabrication sequence from raw material to chip.

A schematic of the device fabrication sequence is shown in Figure 13.7.6. The starting material for the device fabrication is a thin wafer of single crystal silicon doped with an appropriate impurity. The commonly used method to grow pure silicon crystals is the Czochralski method, in which polycrystalline silicon is melted in a quartz crucible (see Figure 13.7.7 for a schematic of this process). A small seed of monocrystalline silicon is dipped into the molten polycrystalline silicon to start the growth process. By

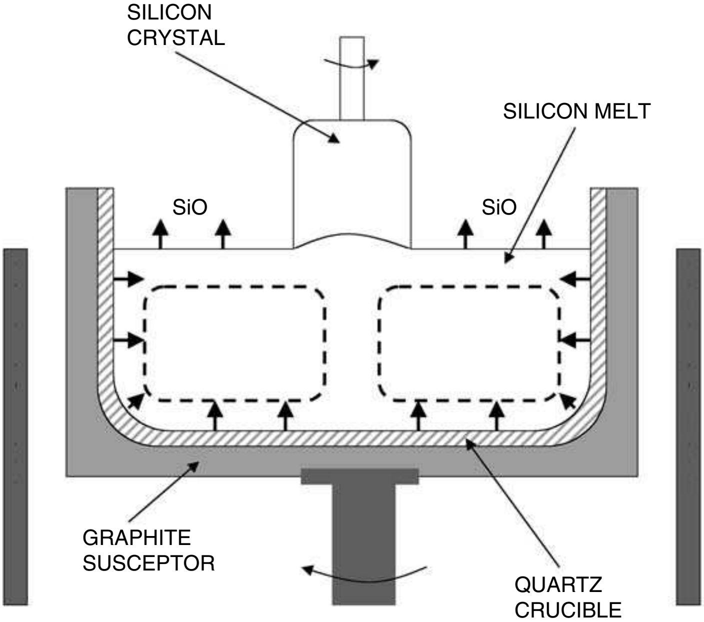

FIGURE 13.7.7 Schematic of Czochralski bulk growth of silicon.

a proper adjustment of the pull rate of the seed crystal and the amount of heat pumped into the crucible, a single crystal ingot of the desired diameter can be grown. As large as 300-mm diameter crystals are now grown, although 200-mm diameter crystals are still popular. The ingots are then sliced to thin wafers (to a thickness on the order of 0.5 mm), which are then polished and stacked in boxes.

It is noted that the polycrystalline material itself is produced using a number of complex manufacturing processes. The starting raw material there is either sand or metallurgical grade silicon. The latter may be available from ore processing, for example, iron refining. These processes include (1) melting silicon in an arc furnace, (2) generating silicon-containing gases (silanes and dichlorosilanes) in a fluidized bed reactor, (3) separation and purification, and (4) using a fluidized bed reactor or deposition chamber to produce polycrystalline silicon. All of these processes are lumped under "Raw Material Processing" in Figure 13.7.6. For more details on these, the reader is referred to Lee.[4]

Before the wafers can be processed in an IC fabrication facility, the circuit has to be designed to the given requirements and specifications, as shown in Figure 13.7.6. The design is generally carried out with the aid of a computer to arrive at the most space-conserving layout of the circuit's elements. The resulting layout is then converted into a set of oversized (generally tenfold) drawings with a schematic for each layer. After checking and correcting, a photographically reduced image of each layer is reproduced in a number of steps to yield a set of final-sized masks for different fabrication steps. Masks are made from emulsion-coated glass plates or glass covered with a hard surface material, such as silicon, iron oxide, chromium oxide, or chromium. A large number of working plates are copied from the final masks.

With the working copies ready, manufacturing can start to fabricate structures according to the design specifications. For illustration, consider the fabrication of a diode, shown in Figure 13.7.8. A diode is the simplest semiconductor device. In operation, it is similar to a one-way valve for fluid flow in that it conducts in one direction (forward) and blocks the flow of current in the opposite direction (reverse). Its role in IC fabrication is the electrical isolation of many different types of active components. The diode can be fabricated by forming a p-n junction either by forming a p-type region in an n-type semiconductor or vice versa, where an n-type semiconductor is formed by adding Group V elements (e.g., phosphorus) as an impurity (dopant) to silicon. A p-type semiconductor, on the other hand, is formed by adding Group III elements (e.g., aluminum) as dopant to silicon. The various steps involved

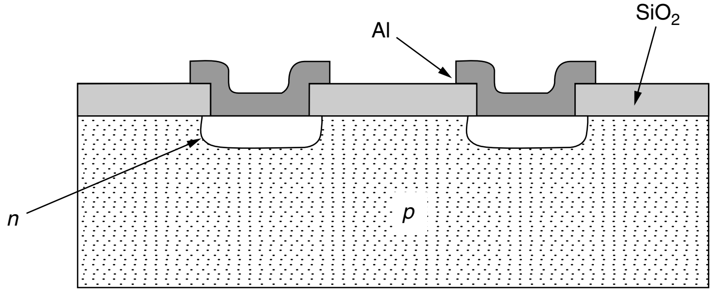

FIGURE 13.7.8 The p-n diode. (Source: Lee, H.H. 1990. *Fundamentals of Microelectronics Processing*, McGraw-Hill, New York, 42.)

in the fabrication of a p-n junction are shown in Figure 13.7.9. A brief description of the various fabrication processes involved is given next.

Oxidation (step 1 in Figure 13.7.9): Oxidation is a low-cost and accurately controlled process that is generally used to grow thin layers of silicon dioxide on silicon wafers. To accomplish this, silicon wafers are heated in an atmosphere of oxygen or water vapor at temperatures in the range between 900 and 1200°C. Oxygen arriving on the surface wafer surface combines with silicon to form silicon dioxide.

$$\mathrm{Si} + \mathrm{O_2} \Rightarrow \mathrm{SiO_2} \tag{13.7.1}$$

$$\mathrm{Si} + 2\mathrm{H_2O} \Rightarrow \mathrm{SiO_2} + 2\ \mathrm{H_2} \tag{13.7.2}$$

Selecting the appropriate time and temperature of oxidation can accurately control the exact thickness. The oxidation process is generally carried out in a high temperature furnace tube made of quartz, polycrystalline silicon, or silicon carbide. Up to several hundred wafers, separated by only a few millimeters, are loaded into slots in a quartz boat. Three zone resistance heated furnaces are used for precise temperature control.

Photolithography (steps 2 to 5 in Figure 13.7.9): This is a method for accurately forming patterns on the wafer and is probably the most important step in wafer fabrication. In operation, the oxidized surface is first coated with photoresist (PR) material that is generally a light-sensitive polymeric material. To accomplish this, a small amount of PR in a solvent is placed on the wafer. The wafer is held on a vacuum check and then spun rapidly at 1000 to 5000 rpm. The solvent evaporates, leaving behind a uniform layer of the polymeric film. A mild heat treatment dries the film thoroughly and enhances its adhesion to the silicon dioxide layer under it. Times range from 10 to 30 min in an oven at 80 to 90°C in an air or nitrogen atmosphere.

A photomask, a square glass plate with a patterned emulsion or metal film on one side, is placed over the wafer. The wafer is now exposed to ultraviolet radiation through the photomask. The photomask allows UV radiation to pass selectively on the wafer according to the preset pattern. The exposed PR material polymerizes and hardens. Following this, the PR is baked in an oven for 20 to 30 min. at 120 to 180°C to further harden the PR. Subsequent washing of the wafer in the selective solvent results in the removal of the unexposed PR film where the mask was opaque. The wafer, with its PR pattern, is now placed in a solution of buffered hydrofluoric acid that dissolves the oxide layer wherever it is unprotected. It is to be noted that the acid does not attack either the photoresist or the silicon wafer itself. After rinsing and drying, wafers are further exposed to another chemical treatment to strip the hardened PR material.

A net result of the steps described is the opening of windows in the wafer according to a preset pattern. These windows are now ready for the next fabrication step, which might be doping or deposition of a desired film.

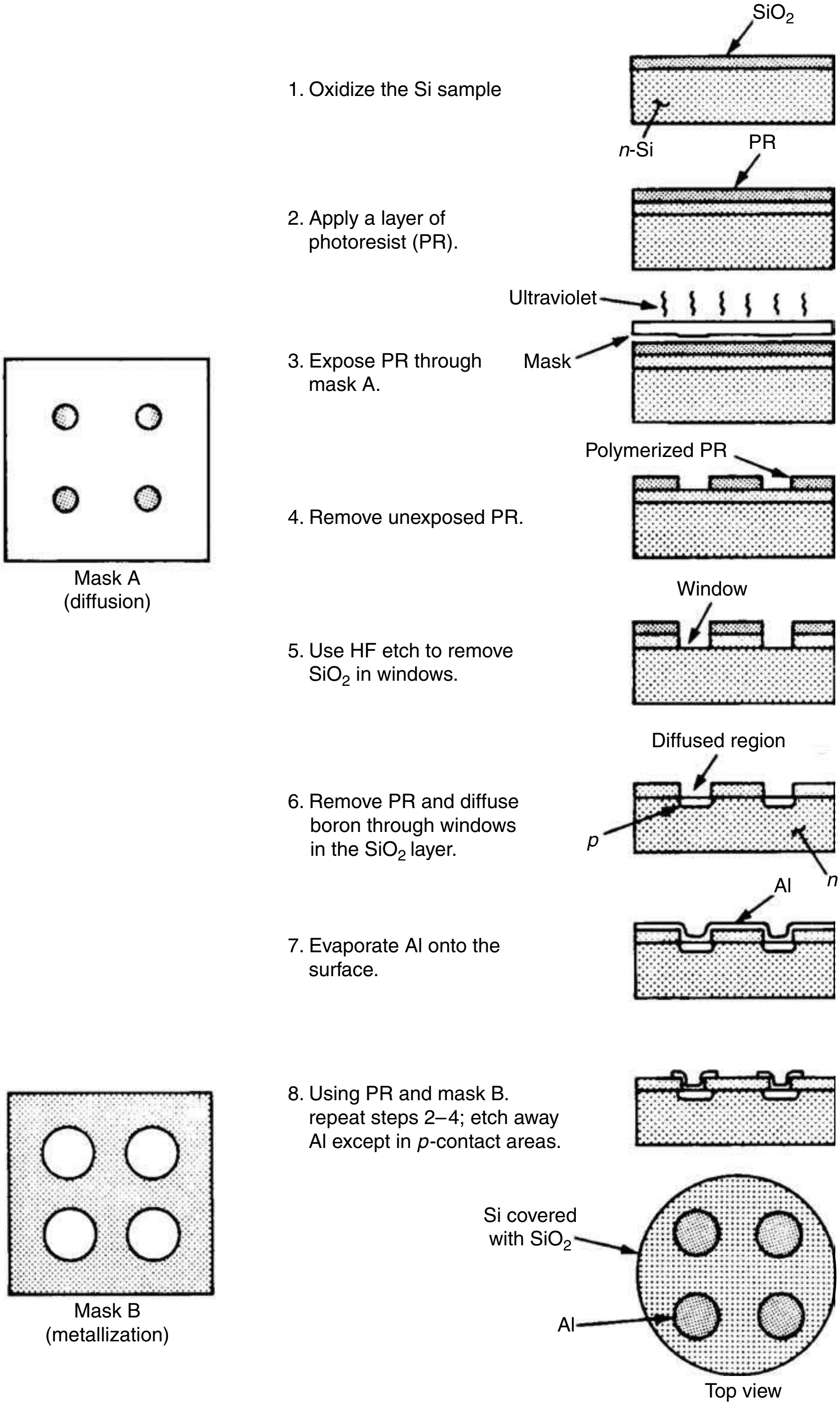

1. Oxidize the Si sample
2. Apply a layer of photoresist (PR).
3. Expose PR through mask A.
4. Remove unexposed PR.
5. Use HF etch to remove SiO_2 in windows.
6. Remove PR and diffuse boron through windows in the SiO_2 layer.
7. Evaporate Al onto the surface.
8. Using PR and mask B. repeat steps 2–4; etch away Al except in *p*-contact areas.

FIGURE 13.7.9 Outline of steps in the fabrication of diodes. (Source: Lee, H.H. 1990. *Fundamentals of Microelectronics Processing*, McGraw-Hill, New York, 42.)

Doping (step 6 in Figure 13.7.9): To make a desired device, it is necessary to selectively induce impurities to create localized n-type or p-type regions. This can be accomplished either through diffusion or ion implantation. The former is similar to the oxidation process described earlier. Silicon wafers are heated to ~1000°C and dopants (boron, phosphorus, etc.) from a vapor or dopant-oxide source are introduced into the quartz tube carrying the wafers. Dopants diffuse through the exposed window in the silicon to form the desired n- or p-type regions.

In ion implantation, the dopant atoms are ionized and accelerated. The ion source operates at ≈25 kV and produces a plasma containing the dopant ions and some other undesired species. An analyzer magnet bends the ion beam through a right angle to select the desired dopant, which then passes through an aperture slit into the main accelerator column. Energy up to 175 KeV is added to the ions to accelerate them to their final velocity. These excited atoms strike the wafers and are embedded at various depths according to their mass and energy. The whole process takes place at room temperature.

The process provides more accurate control than diffusion. However, the wafers have to be annealed to minimize damage due to implantation.

Chemical Vapor Deposition (CVD): Chemical vapor deposition refers to the formation of a crystalline material on a substrate by the reactions of the chemicals from the vapor phase using an activation energy. CVD-deposited films are widely used in IC fabrication. These films provide conducting regions within the device, electrical insulation between metals, or protection from the environment. The material to be deposited is brought in a carrier gas in a reactor housing the heated wafers. The film material diffuses to the substrate wafer, where a chemical reaction takes place, resulting in deposition of the film over the wafers. For example, in epitaxial CVD deposition of silicon on silicon, silane (SiH_4) carried by hydrogen is brought over silicon wafers heated to ~1350°K. Silane decomposes to silicon, and hydrogen and silicon deposit on the wafers. Plasma or laser assisted CVD processes are also used when deposition is required at lower temperatures.

Three common CVD reactor configurations are shown in Figure 13.7.10. While the horizontal and vertical barrel reactors (Figure 13.10a and Figure 13.10b) are commonly used for silicon epitaxy, the tubular hot wall reactor (Figure 13.7.10c) is used for deposition of polysilicon and other dielectric films. Of these, the horizontal reactor (Figure 13.7.10a) is perhaps the oldest configuration. A silicon-coated graphite susceptor is housed in a quartz chamber, and is generally tilted by ≈3° to the horizontal. It has been shown, for example, by Ristorcelli and Mahajan[5] and Eversteyn et al.[6] that this tilt is necessary to ensure uniformity of deposition along the length of the susceptor. The wafers are heated through direct contact with the inductively heated graphite susceptor. The quartz chamber walls, in comparison, are cold. These reactors offer high throughput, but uniformity in deposition is difficult to achieve.

The IR (infrared) heated vertical barrel reactor is the workhorse of the industry for large-volume production of silicon epitaxial wafers. In a reactor of this design, silicon wafers rest in shallow pockets in a multifaceted, slightly tapered susceptor that is rotated inside a quartz bell jar. The most common mode of heating is through an array of IR lamps backed by reflectors. The mixture of appropriate gases enters through two nozzles at the top of the reactor and is exhausted through a central hole at the bottom. The ambient working pressure may be either atmospheric or about 0.1 atm.

In hot wall tubular reactors, Figure 13.7.10c, the quartz tube is heated from outside, and both reactor and wafers are assumed to be isothermal. Fifty to 200 wafers are stacked side by side with a constant small separation between them. The wafers are generally placed back to back, concentric to the tube x-sectional area so that the center of the wafer coincides with the axis of the tube. The total pressure in the heated zone varies from 0.1 to 10 torr, and the temperature ranges from 300 to 900°C.[4] The fluid distributes equally in the annular region between the periphery of the wafers and the inner wall of the reactor and provides the source gas to the inter-wafer region. The deposition is kinetically controlled and is affected mostly by the temperature distribution in the reactor.

Sputtering and evaporation (step 7 in Figure 13.7.9): In sputtering, the target material is bombarded by energetic ions to release (sputter) some atoms. These atoms are then condensed on the substrate to form a film. Evaporation is generally used to lay down the metallic conducting layers. The metallic charge

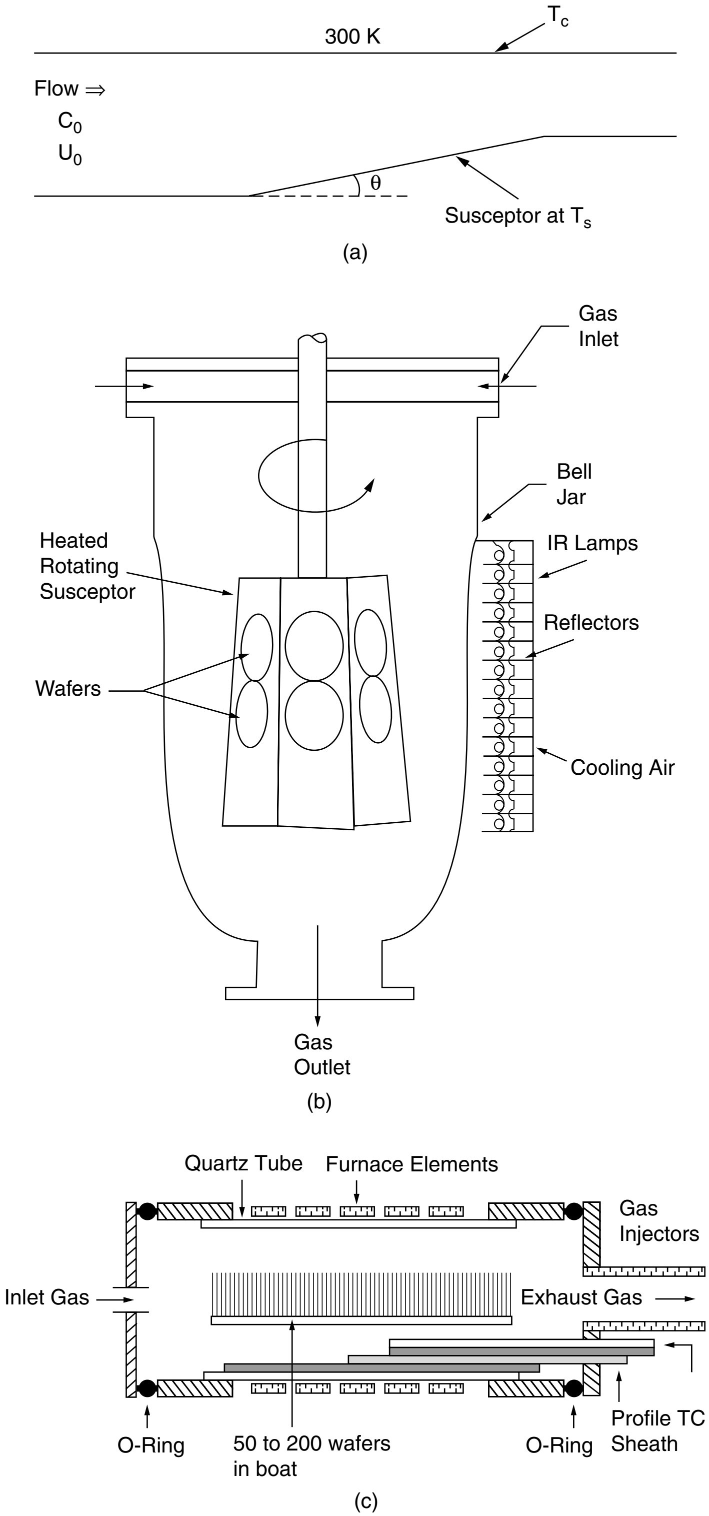

FIGURE 13.7.10 Three common CVD reactor configurations: (a) horizontal reactor; (b) vertical barrel reactor; (c) hot wall tubular reactor. (Source: Mahajan, R.L., Transport phenomena in chemical vapor deposition systems. *Advances in Heat Transfer*, 28, 339, 1996.)

(generally Al) is placed in a crucible, and the wafers are positioned above the charge in a movable fixture (planetary). A jar is lowered over the planetary and high vacuum is generated. Direct bombardment with high-energy electrons heats the metal charge. The charge evaporates and deposits on the wafers. Other forms of heating, for example, induction, resistance, or laser beam heating, can also be deployed.

Reactive plasma etching: The wet chemical etching described under photolithography can be replaced by dry etching, such as reactive plasma etching. In this technique, ionization and fragmentation of gases generated in plasma creates reactive species. These species bombard the substrate surface and remove or etch material from the surface regions not masked by lithographic patterns. Typical gases used are halogen compounds such as CF_4 and Cl_2. Additional gases such as H_2 or O_2 are included to provide desired selectivity and edge profile. For example, CF_4 in O_2 plasma gives rise to atomic fluorine, which then reacts with the surface and causes its removal.

It is noted that step 8 in Figure 13.7.9 is a repetition of steps 2 to 4. The fabrication steps for other semiconductor elements, such as transistors, are more numerous than those for the diode described here but essentially follow the same sequence. The structure is built layer by layer using photolithography to generate patterns according to the specified design for the next step, which could be doping or deposition. For more details on IC fabrication, the reader is referred to Sze,[1] Lee,[4] and Jaeger.[7]

From Chip to Final Product

The end product of the IC fabrication is a wafer with multiple chips on it (see Figure 13.7.6). Each IC (or die) on the wafer is probed to determine whether it functions properly. After testing, the wafer is sectioned to separate the individual chips. This is usually accomplished by scribing between the chips. Generally, a diamond-tipped scribe is used and scribing borders of 75 to 250 μm are formed around the periphery of the dice. Following scribing, the wafer is placed on a soft support and pressure is applied on the wafer using a roller. The wafer breaks along the scribe lines to give individual chips. As mentioned earlier, this good IC serves as the starting material for the final electronic product. Several subassembly processes, along with other feeder components, are encountered before the final finished product is out of the factory.

For example, consider the steps involved in the manufacture of a desktop computer. Referring to Figure 13.7.4, the first step in the assembly is housing the IC in a package called a chip carrier. The chip carriers protect the chips from the environment and provide connections from the chip pads to the circuit board. These are described next to facilitate an understanding of the various assembly steps involved.

Chip Carriers

Two types of chip carriers, through-hole and surface-mount components, are available. In the former (see Figure 13.7.11a), the components have leads that are connected to the pads on the chip. These leads are intended for pin in-hole mounting on the circuit board. The latter come in two categories: the leaded and the leadless. In the leaded surface-mount chip carriers, the leads are intended for attachment to the surface of the board (see Figure 13.7.11b). In the leadless, on the other hand, metallized pads are provided on the chip carrier to provide soldering surfaces for connection to the board (see Figure 13.7.11c). A brief description follows.

Through-Hole Chip Carriers

These come in a variety of configurations, as shown in Table 13.7.1. Of these, the plastic dual-inline package (DIP) is among the most commonly used. The manufacturing steps involved in its assembly are shown in Figure 13.7.12. Shown at the bottom of the figure is a lead frame, which is typically made of a copper alloy. It has a pad in the center to receive the IC and has leads that extend out of the package. As a first step in housing the IC, the dice bearing the finished circuits is first bonded to the central pad. Bonding methods vary depending on the quality of the chip carrier. For the metal lead frame, bonding can be performed using epoxies or polyimide adhesives with a metallic filler. The latter is needed to enhance the thermal conductivity of the epoxy and thus reduce the thermal resistance between the die and the package.

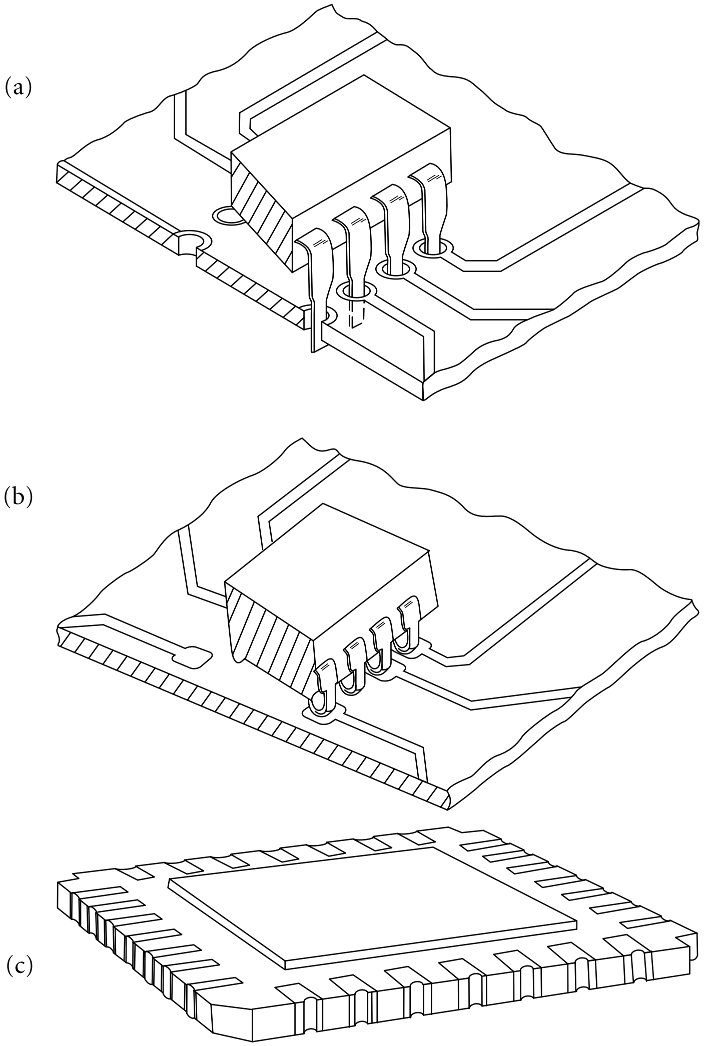

FIGURE 13.7.11 Through-hole and surface-mount chip carriers: (a) through-hole; (b) leaded surface-mount; (c) leadless surface-mount. (Sources: Landers, T.L., Brown, W.D., Fant, E.N., Malstrom, E.M., and Schmitt, N.M. 1994. *Electronics Manufacturing Processes*, Prentice Hall, Englewood Cliffs, NJ, 8. and Dally, J.W., *Packaging of Electronic Systems*, McGraw-Hill, New York, 1990.)

Fine wire leads are then connected from the aluminum bonding pads of the chip to the lead wires on the chip carrier using automatic wire bonding techniques. The protective housing is provided by injection molding of plastic over the frame. After separating individual packages, the leads are bent to produce the package.

Three commonly used automated wire bonding techniques are (1) thermocompression bonding, (2) ultrasonic bonding, and (3) thermosonic bonding. In the thermocompression bonding, a combination of pressure and temperature is used to weld fine gold wires (15 to 75 μm in diameter) to the chip pads and the package leads. Different steps used are shown schematically in Figure 13.7.13. The gold wire is fed from a spool through a heated capillary and a gold ball is formed using a hydrogen torch or electric spark (step a). The ball is positioned over the bonding pad, the capillary is lowered, and the ball deforms into a “nail head” as a result of the pressure and heat from the capillary (step b). Next, the capillary is raised and moved into position over the package (step c). A wedge bond is produced by deforming the wire with the edge of the capillary (step d). Finally, the capillary is raised and the wire is broken near

TABLE 13.7.1 Examples of Through-Hole Packages

PACKAGE NAME	OUTLINE	LEAD SPACING
S-DIP (SHRINK DIP)	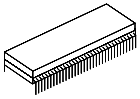	1.78 mm
SKINNY DIP (OR SLIM DIP)	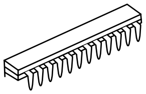	2.54 mm CERAMIC WIDTH 2/3 OR 1/2
SIP (SINGLE INLINE)	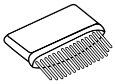	2.54 mm
ZIP (ZIGZAG INLINE)	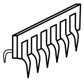	2.54 mm
QUIP (QUAD INLINE)	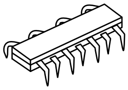	1.27 mm

Source: Sze[1]

the edge of the bond (step e). During this operation, the substrate is typically maintained at a temperature between 150 and 200°C, while the temperature of the bonding interface ranges from 280 to 350°C.

In ultrasonic bonding, aluminum wire is used instead of gold wire and the bond is made through a combination of pressure and ultrasonic vibration in the range of 20 to 60 KHz. The vibration causes the metal to deform and flow easily under pressure at room temperature. Thermosonic bonding combines the features of thermocompression and ultrasonic bonding in that the substrate is maintained at ~150°C, and ultrasonic vibration is also deployed. Excellent bonds result.

The DIPs just described are low-cost packages and are available with as few as four leads to more than 80 leads. For higher pin densities, pin grid array carriers are used (see Table 13.7.1). The body of the package provides a cavity for the chip and the pins are placed in a regular x-y array in the space around the cavity. Wire bonding is still used to connect the die to the gold interconnection lines, which fan out to the array of pins. Other popular through-hole packages are listed in Table 13.7.1.

Most of the through-hole packages are also available in ceramic casings. In the ceramic DIP, for example, the die is mounted in a cavity on a gold-plated ceramic substrate and wire-bonded to gold-plate Kovar leads. A ceramic or metal lid is then used to seal the top of the cavity. Typically, these packages are also hermetically sealed. Compared to plastic packages, ceramic packages are designed for use over a wider range of temperatures but are also more expensive. They are generally used in military and high-end commercial products.

Surface-Mount Packages

These packages offer higher densities than the counterpart through-hole packages. Holes are not necessary in the printed wiring boards (PWBs) to receive the lead wires from the through-hole components. As a result, the leads can be placed on lower pitches. For comparison, the lead pitch for DIPs is 100 mils, while for the surface-mount packages, the lead pitch is 50 mils or less. The packages with pitches of less than 50 mils are referred to as fine-pitch packages and are available in pitches of 33, 25, and 20 mils. Ultra fine pitch (< 20 mils) are also available. Further, both sides of the board can be used to accommodate components. These advantages have made surface-mount the packages of choice, although many of the boards even today deploy both surface-mount and through-hole packages. Note that as in through-hole components, surface-mount packages are also available both in plastic and ceramic bodies.

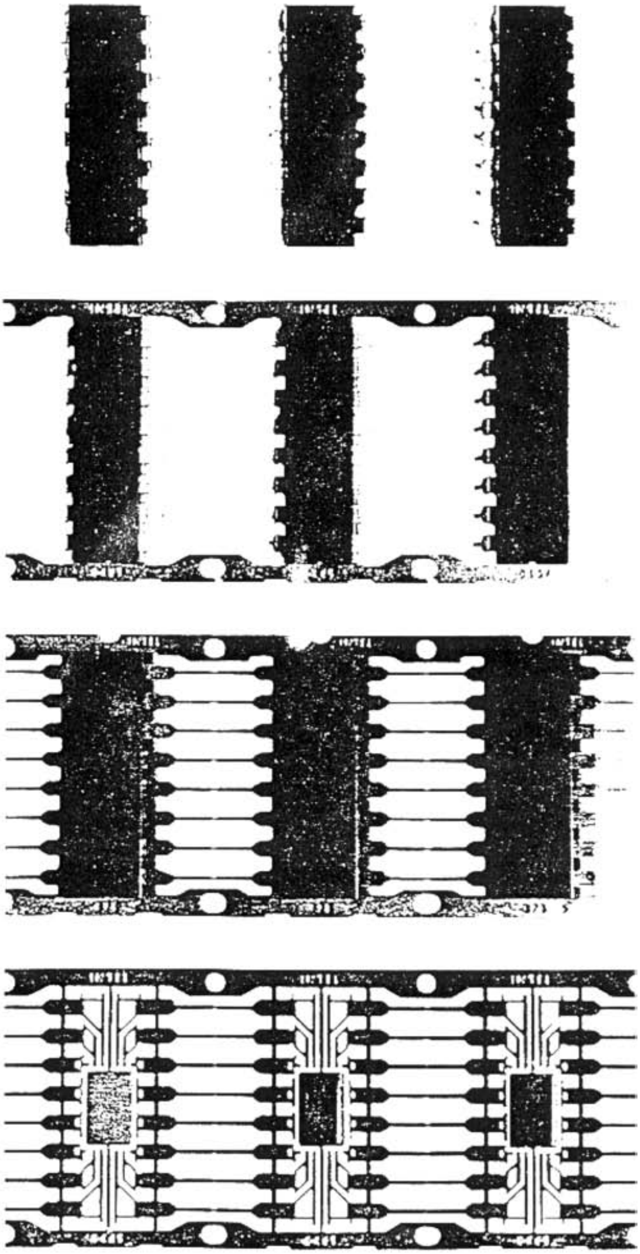

FIGURE 13.7.12 Steps involved in the manufacture of a DIP.

As mentioned earlier, the surface-mount components are available both in leaded and leadless configurations, as shown in Table 13.7.2. The types of leads used in the former are shown in Figure 13.7.14. All the styles permit soldering of the package directly to the board. Of the three, the gull-wing offers the advantage of visual inspection of the solder joint, but it takes more room on the PWB than the others. Also, the leads are more susceptible to damage during handling. The J-leads provide better protection against damage in handling, provide more clearance between the package and the PWB for easier cleaning, but are more expensive to make and inspect. The I-leads are simpler to manufacture than the J-leads, but care must be exercised to ensure coplanarity of the leads during shearing.

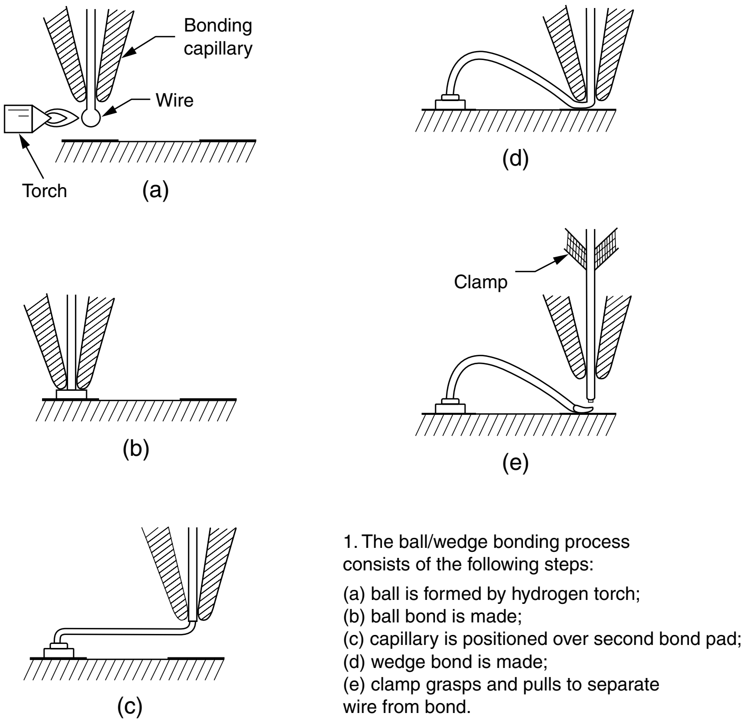

1. The ball/wedge bonding process consists of the following steps:
(a) ball is formed by hydrogen torch;
(b) ball bond is made;
(c) capillary is positioned over second bond pad;
(d) wedge bond is made;
(e) clamp grasps and pulls to separate wire from bond.

FIGURE 13.7.13 Thermosonic ball-wedge bonding of a gold wire. (Source: Dally, J.W., *Packaging of Electronic Systems*, McGraw-Hill, New York, 1990.)

In leadless chip carriers, the die is mounted in a cavity in the middle of the package and connections are made between the package and die using wire bonding. The cavity is then sealed with a cap of metal, ceramic or epoxy. All the leadless chip carriers have metallized pads around the perimeter of the package that allow the package to be soldered to a PWB.

Ball Grid Arrays

The surface-mount packages have progressively evolved toward finer pitches due to the continued demand for higher-density packages. However, at reduced pitches, the process window tightens, and the fine-pitch packages with their fragile leads pose serious handling problems. As a result, new packages called *ball grid arrays* have become very popular in recent years.

A ball grid array is an area array package like a pin grid array except that the leads are now replaced by solder balls. Two types of commonly used BGAs, ceramic ball grid arrays (CBGAs) and plastic ball grid arrays (PBGAs), are shown in Figure 13.7.15. The PBGA, also known as OMPAC (over molded plastic pad array) by Motorola, has a high-temperature laminate consisting of BT (bismaleimide triazene) resin. Other types of BGAs used in practice are ceramic column grid array and tape ball grid array. For more details, see Prasad.[9]

BGAs do not have the limitations of fine-pitch surface-mount packages since instead of fragile leads, they have robust solder balls at much higher pitches that permit higher density and their electrical performance is enhanced due to reduced inducatance and the resulting propagation delay. The additional price is in the increased layer count requirement on the board.

Attaching the Package to the Printed Wiring Board

The PWB is a type of substrate consisting of one or more layers of laminates and metal conductors that provide a mounting surface for electronic packages to be electrically connected and mechanically supported. Three common types of PWBs are the single-sided, double-sided, and multilayer boards. Their

TABLE 13.7.2 Examples of Surface-Mount Packages

Surface Mount	Shape	Material	Typical Features Lead Pitch	# of I/O Pins
Small Outline Package (SOP)	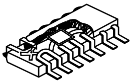	Plastic	• 1.27 mm (50 mil) • 2-direction lead	8–40
Quad Flat Package (QFP)	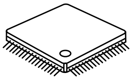	Plastic	• 1.0 mm • 0.8 mm • 0.65 mm • 4-direction lead	88–200
Flat Package of Glass (FPG)	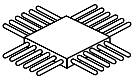	Plastic	• 1.27 mm (50 mil) •.762 mm (30 mil) • 2-direction lead • 4-direction lead	20–80
Leadless Chip Carrier (LCC)	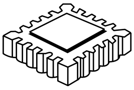	Plastic	• 1.27 mm (50 mil) • 1.016 mm (40 mil) •.762 mm (30 mil)	20–40
Plastic Leaded Chip Carrier (PLCC)	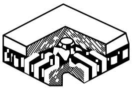	Plastic	• 1.27 mm (50 mil) • J-shaped bend • 4-direction lead	18–124
Very Small Quad Flat Package (VSQF)	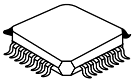	Plastic	• 0.5 mm	32–100

fabrication involves a number of steps, including laminating, pressing, punching/drilling, image transfer, and soldering.

In the single-sided boards, base materials such as laminated layers of woven glass cloth impregnated with epoxy resin are joined together, treated, and cured to form "prepregs." A number of such prepregs are stacked to give the desired board thickness. The stack of prepregs is placed on top of copper foil, and the whole assembly is inserted into a press, which, through application of heat and pressure, binds the laminates together. The boards are then sized to the final dimensions. Following this, the circuit image is applied to the foil using photoresist and then etched so that all the wiring for the electronic components and attachment pods are aligned to match the corresponding leads or pads from the components. Holes are drilled or punched into these laminates for accommodating the through-hole components. Double-sided boards have circuit lines on both the top and bottom surfaces of the laminate. To accommodate any through-hole components, the circuits on the top and bottom sides are connected by drilling holes through the board whose inner surfaces are plated.

Multilayer boards, shown in Figure 13.7.16, are fabricated from several layers of laminates with pre-etched copper foils stacked together in a sandwich with pre-impregnated epoxy-glass sheets positioned between each layer. The assembly is then placed in a hot platen press to produce the finished product. As before, plated through-holes are incorporated in the board to provide connections to the interior planes. In some cases, the plated through-holes are filled with solder to act as thermal vias, which provide an additional thermal path for the heat to be dissipated away from the chip.

Different techniques are deployed for attaching through-hole and surface-mount packages to the board. For surface-mount components, stencil printing, followed by reflow soldering, is the common procedure. Simply stated, the stencil printing process, as shown schematically in Figure 13.7.17, is a process of pushing solder paste through the apertures in a thin metal stencil onto pads of a PWB. The

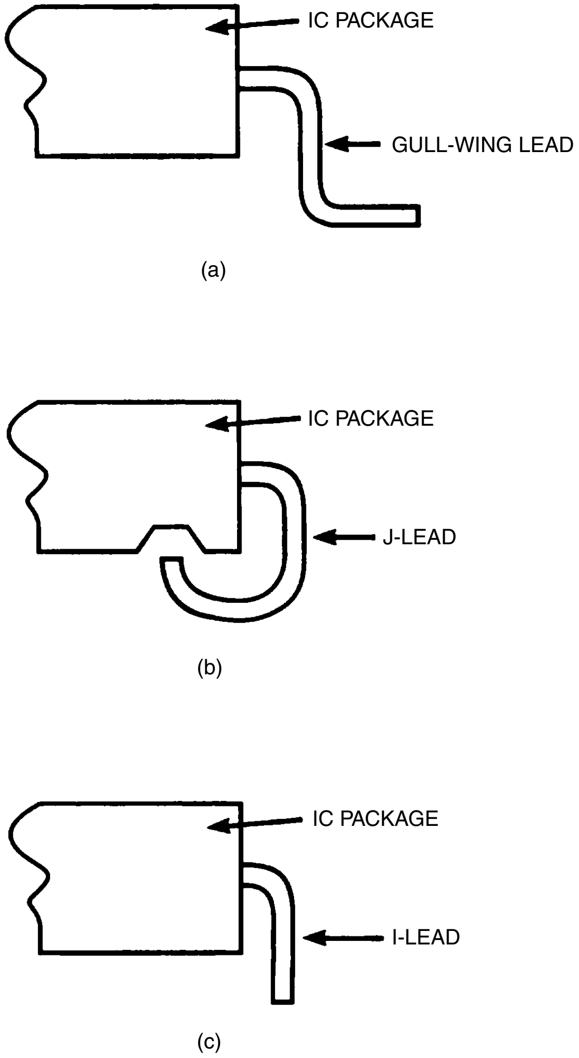

FIGURE 13.7.14 Lead configurations in leaded surface-mount packages.

stencil has openings that correspond to the solder pads on the board. The solder paste is first spread over the stencil, and the squeegee, during its travel over the stencil, forces the requisite amount of paste. The process is quite complex, and involves a large number of variables relating to solder paste, flux, stencil, squeegee, and environmental conditions. An empirical artificial neural network model relating these variables to the process output (the thickness of the solder paste dispensed) is developed later in this section and the optimum settings based on such a model are described.

With the solder paste in place, the surface-mount components are now positioned at the designated locations on the PWB using "pick and place" equipment. The pick and place machine, accompanied by part feeders, is an important part of a surface-mount assembly line. The line's throughput is primarily determined by the pick and place machine, and the majority of manufacturing defects that require rework arise from placement problems. As a result, careful selection of the equipment is important for quality production. For more details, the reader is referred to Prasad.[9]

The next step is reflow soldering using infrared (IR), vapor phase condensation, or convective air heating. Schematic diagrams of an IR oven, a vapor phase facility, and wave soldering machine are shown in Figure 13.7.18. The infrared oven, Figure 13.7.18a, consists of a series of IR panel heaters placed on

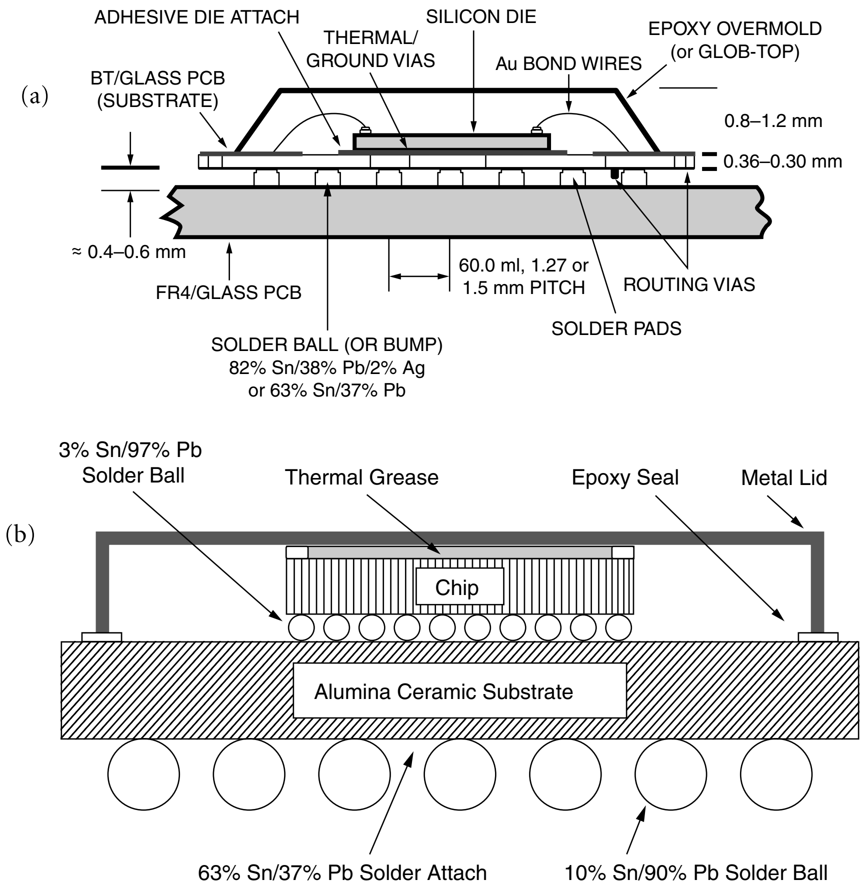

FIGURE 13.7.15 Schematics of (a) plastic and (b) ceramic ball grid arrays. (Source: Prasad, R.P. 1997. *Surface Mount Technology*, Chapman & Hall, New York.)

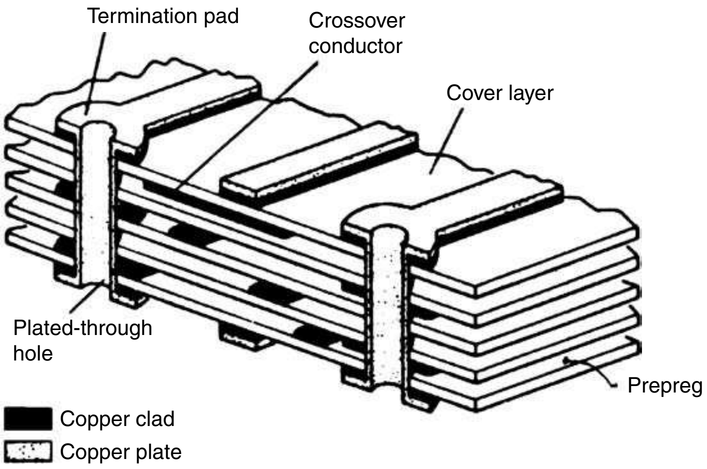

FIGURE 13.7.16 A schematic of a printed wiring board. (Source: Dally, J.W., *Packaging of Electronic Systems*, McGraw-Hill, New York, 1990.)

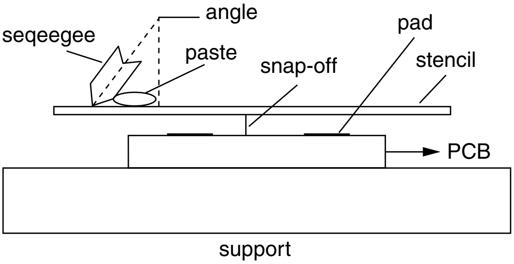

FIGURE 13.7.17 A schematic of the stencil printing process. (Source: Li, Y., Mahajan, R.L., and Nikmanesh, N. 1996. Fine pitch stencil printing process modeling and optimization. *ASME J. Electronic Packag.*, 118, 1, 1.)

the top and bottom of the channel. Each of these heaters is maintained at a unique temperature. A conveyor carries the unsoldered PWB assemblies into the oven where the heaters provide the necessary thermal energy to remove volatiles from the solder paste, liquefy flux, and melt solder paste. In the cooler exit section of the oven, the solder solidifies to form the necessary bond between the modules and PWB. For more details on IR reflow soldering and modeling of the transport phenomena see Prasad,[9] Mahajan,[10] and Fernandes et al.[11]

Wave soldering (Figure 13.7.18b) deploys a pot of molten solder in which a pump produces a solder wave. The solder wave is adjusted to produce a flow of liquid solder that impinges on the underside of the circuit board that is traversed over the wave at an appropriate speed. As the board comes into contact with the wave, molten solder is supplied to all of the solder joints on the board. Several parameters, including wave temperature, the conveyor speed, the preheating temperature, and type of flux used, come into play in determining the assembly yield. The interactions between the various parameters are complex, and extensive experimentation is generally required to achieve optimum performance.[12]

Vapor phase condensation reflow-soldering, Figure 13.7.18c, is an attractive alternative to infrared reflow soldering, especially in those circumstances where accurate temperature control is desired. In principle, a body of hot saturated vapor at a temperature about 30°C above the melting temperature of the solder is generated in a container. As shown in Figure 13.7.18c, this is achieved by boiling the fluid in the container using immersion heaters and condensing them at the cooling coils placed at the top of the container. The fluid used is generally a Fluorinert fluid with a boiling temperature of ~215°C. The vapor is about 25 times heavier than air and is thus easy to confine. The PWB assembly, with the solder paste and components in place, is brought into the hot vapor zone by a conveyor. There, the vapors condense on the cooler part and transfer heat to the solder to reflow it. After the required residence time (typically on the order of one minute), the assembly is brought to rest in the exit region, where the solder solidifies. The maximum temperature attainable in this process is the boiling temperature of the fluid and the temperature everywhere in the assembly is uniform. For more details on this process, the reader is referred to Wenger and Mahajan[13–15] and Prasad.[9]

For attaching through-hole components to the PWB, the component leads are inserted into the plated through-holes in the PWB using automatic insertion tools. The PWB assembly is then passed over a wave soldering facility, as shown in Figure 13.7.18b, where molten solder wicks through the space between the component leads and the inner walls of the plated through-hole and forms a solder joint attaching the component to the board.

PWBs to Enclosure

The next stage in our journey to the finished product is the housing of the PWBs in an enclosure. (In Figure 13.7.4, the enclosure is the CPU chassis, which may be supplied by a contract manufacturer.) The enclosure supports the boards, provides a cooling medium (a small muffin fan in the CPU chassis), and provides protection from the environment. The PWBs are connected together with edge connectors that allow the boards to plug into a back panel, a wire wrap board, or cables.

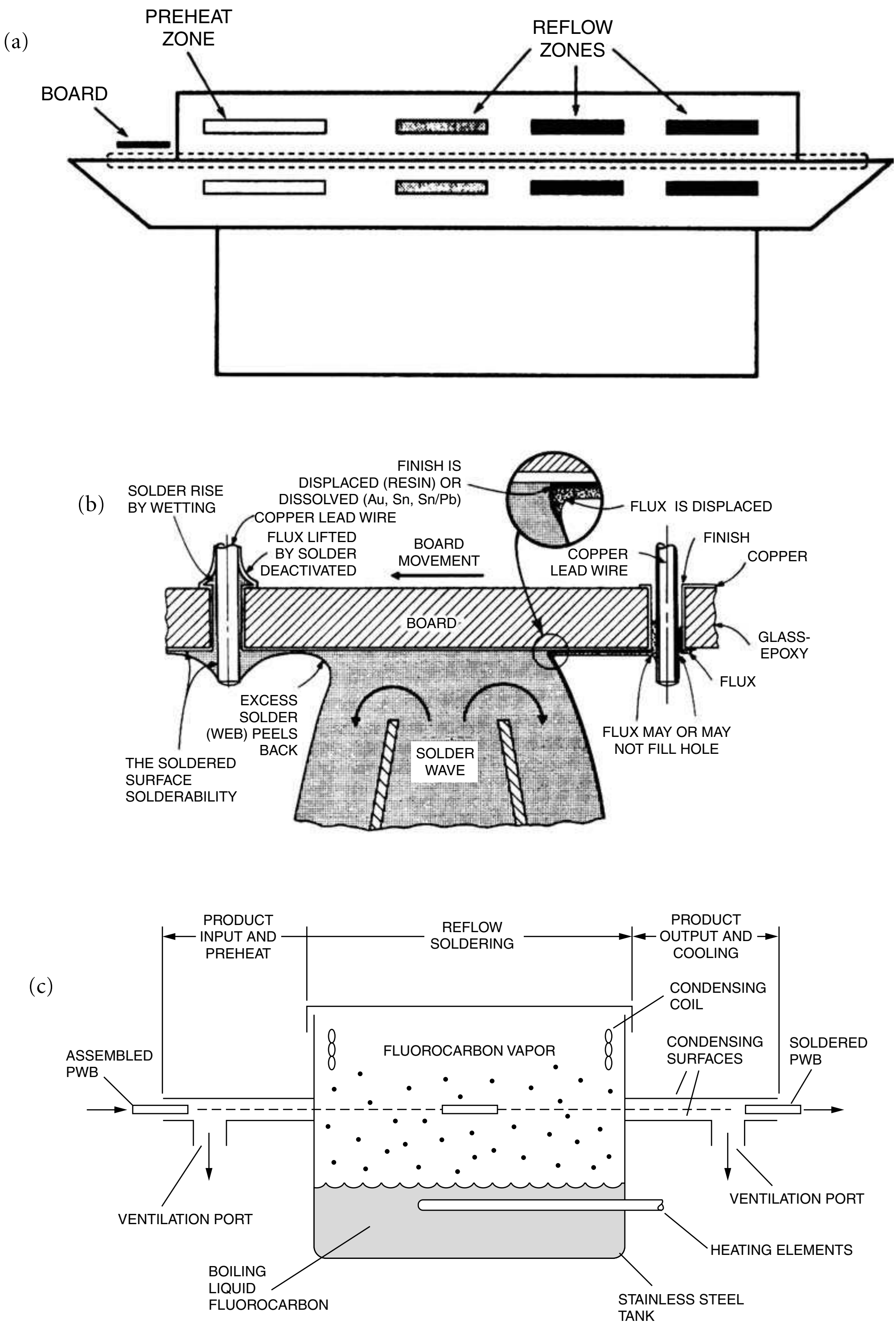

FIGURE 13.7.18 Three commonly used soldering (or reflow soldering) facilities. (a) an IR oven, (b) wave soldering, (c) vapor phase condensation soldering. (Sources: Dally, J.W., *Packaging of Electronic Systems*, McGraw-Hill, New York, 1990. and Prasad, R.P. 1997. *Surface Mount Technology*, Chapman & Hall, New York.)

The Finished Product

Finally, all the back panels, the circuit board, power supplies, and other accessories are housed in a cabinet. The other subassemblies, if any, are integrated to produce the complete electronic system. In Figure 13.7.4, the keyboard and monitor are fabricated and assembled separately and incorporated with the CPU chassis.

For further discussion of the different levels of packaging discussed, the reader is referred to Dally[8] and Landers et al.[2]

The Road to Process Optimization and Control

The goal of the first part of this section was to provide the reader with a feel for the basic nature of the electronics industry and the various processes involved in the manufacture of electronic products. The remainder of this section focuses on process modeling, optimization, and control.

The electronic markets are highly competitive and dynamic, and the processes are complex and diverse. As a result, attainment of higher yield at each manufacturing step is imperative and is the goal of every manufacturing organization. To achieve this, all the variables controlling the desired output in a given process need to be understood, optimized, and controlled to minimize variability and the attendant costs. In addition, the process controller must be quick to detect and correct any departures in the manufacturing process output from the optimum.

To meet these challenges, several tools and methodologies for control of electronic manufacturing processes have been developed over the years. These include conventional and multivariable response surface methodologies and artificial intelligence (artificial neural networks, fuzzy logic, expert system) based optimization and control algorithms. In most general terms, these are designed to address one of the following functions: (1) identifying robust settings for optimum performance, (2) determining whether a process has shifted from its desired settings suggesting equipment and process problems, (3) run-to-run control based on postprocess measurements, and (4) real-time control based on *in-situ* measurements (see Mahajan[16]). We discuss each of these functions and methodologies in some detail. Definitions of a "process," a process "in control," the causes of process variation, and statistical process control are introduced to set the stage for our discussion.

Process

Following the AT&T Statistical Quality Control Handbook,[17] a process is defined as "… any set of conditions, or set of causes, which work together to produce a given result." When applied to manufacturing, this generic definition of the term process may be defined as "a combination of labor, machines, tools, and methods used in a specific environment to manufacture a given product."

Process Variation

The ingredients comprising a manufacturing process — labor, machines, tools, methods — contribute to its variation. These, following Shehwart,[18] can be divided into two major components: (1) assignable causes of variation, and (2) inherent or random variation. While the former can be generally discovered and removed from the process, the latter, an aggregate of causes such as the routine variation of the incoming material, floor vibration, environmental changes, and operator influences, cannot be economically discovered and removed from the process without basic changes in the process. In general, random causes are the reasons behind the run-to-run variability of a process.

To understand quantitatively the structure or underlying patterns, if any, of these variations probability distributions are used. A probability distribution is a mathematical tool that gives the probability of occurrence of the value of a variable in the population. When the variable being measured is expressed on a continuous scale, the distribution is called a continuous distribution. On the other hand, when the variable takes on only discrete values, the probability distribution is called a discrete distribution. The commonly used discrete distributions are the hypergeometric distribution, the Binomial distribution, the Poisson distribution, and the Pascal distributions. For more details, the reader is referred to Montgomery.[42]

Examples of the continuous probability distributions include perhaps the most commonly used normal distribution, the exponential distribution, the gamma distribution, and the Weibull distribution.[42] A brief description of the characteristics of the normal distribution is given below. For the other distributions, the reader is referred to Montgomery.[42]

For a normal random variable, x, the probability distribution is mathematically given by

$$f(x) = \frac{1}{\sigma\sqrt{2\pi}} e^{-\frac{1}{2}\left(\frac{x-\mu}{\sigma}\right)^2} \quad -\infty < x < \infty \tag{13.7.3}$$

where μ is the mean, σ is the standard deviation, and σ^2 is the variance. A normal distribution is shown graphically in Figure 13.7.19(a). The areas under the curves for the variable lying between $\mu \pm \sigma$, $\mu \pm 2\sigma$, and $\mu \pm 3\sigma$ are shown. For example, for a 3σ process, 99.73% of the values fall between the limits defined by the mean plus or minus three standard deviations.

The normal distribution is often assumed as the appropriate probability model for a random variable. The basis for this assumption is the central limit theorem which states that the sum of n independently distributed random variables is approximately normal, regardless of the distributions of the individual variables.[42] Mathematically, if $x_1, x_2 \ldots x_n$ are independent random variables with mean μ, and variance σ_i, and $y = x_1 + x_2 + x_3 + \ldots x_n$, then the distribution of

$$\frac{y - \sum_{i=1}^{n} \mu_i}{\sqrt{\sum_{i=1}^{n} \sigma_i^2}} \tag{13.7.4}$$

approaches the standard normal distribution N(0,1) distribution as $n \to \infty$ where 0 and 1 refer to the mean and standard deviation, respectively. The value of n for which the approximation may hold varies depending on the distribution of each x_i. If the distribution of each x_i does not depart radically from the normal, $n \geq 4$ may be sufficient for the applicability of the central limit theorem.[42]

These variations lead to deviation of the quality characteristic of the product to be manufactured from the target value, which in turn leads to degradation of quality and higher losses. Taguchi's[19] loss function is a recognized way of quantifying these losses and provides a strong motivation for tighter process control. Some of the commonly used measures of variation around the target are the process capability indices, C_p, C_{pu}, C_{pl}, and C_{pk}, where

$$C_p = \frac{USL - LSL}{6\sigma} \tag{13.7.5}$$

$$C_{pu} = \frac{USL - \bar{x}}{3\sigma} \tag{13.7.6}$$

$$C_{pl} = \frac{\bar{x} - LSL}{3\sigma} \tag{13.7.7}$$

$$C_{pk} = \min\left(C_{pu}, C_{pl}\right) \tag{13.7.8}$$

where USL, LSL, $\bar{x}$ and σ refer to the upper specifications limit, the lower specification limit, the process average, and the standard deviation, respectively. C_p is a measure of the potential process performance that can be obtained if the process average is on the nominal of the specification limits for such a normally

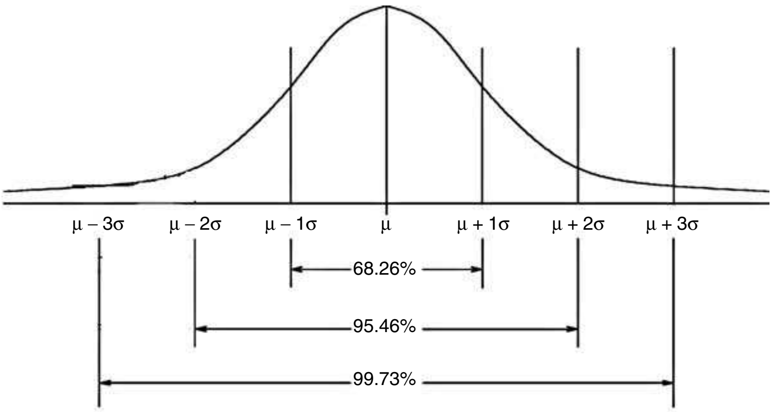

(a) Normal distribution

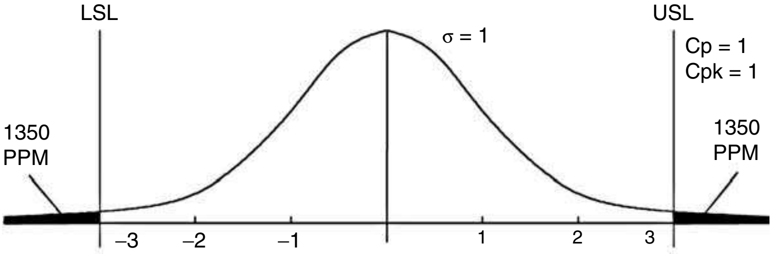

(b) 3σ Process, process mean centered around the nominal

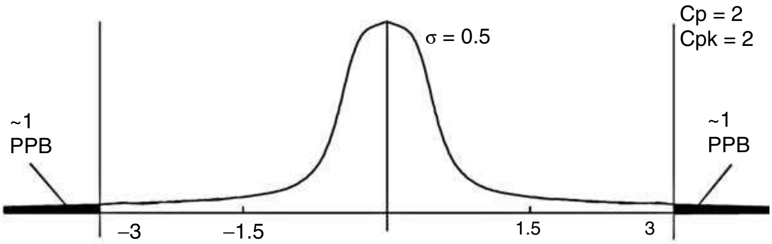

(c) 6σ Process, process mean centered around the nominal

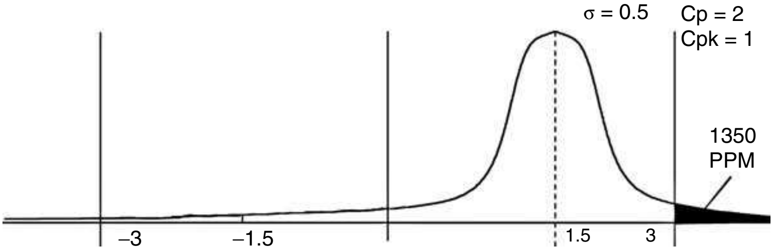

(d) 3σ Process, process mean shifted off the nominal by 3σ.

FIGURE 13.7.19 Normal probability distributions with different values of C_p, C_{pk}.

distributed, ±3σ process, $C_p = 1$ (Figure 13.7.19b) and the associated defect rate is 2700 PPM. For $C_p = 2$ (Figure 13.7.19c), the process is much tighter and the fall out rate drops to 1.7 PPB. Since in actual practice it is common for the process average to shift from its nominal value, C_p does not truly reflect the process performance. C_{pk}, on the other hand, takes this shift into account and is probably a truer measure of the process performance. For example, consider Figure 13.7.19d. The process has $C_p = 2$, but its mean has shifted from its nominal value by 1/2 (USB-LSL). Its $C_{pk} = 1.0$. It is clear from the figure that the defect rate is 1350 PPM, which corresponds to one half of that for $C_p = 1$. Thus, both C_p and C_{pk}, used together, provide a good gage in measuring success of the process control efforts.

Statistical Process Control (SPC)

Introduced by Shehwart around 1930, SPC is a well-established tool used in production for process capability studies, process monitoring, and process improvement. Briefly, a process is in statistical control when it displays only random variations, as discussed earlier, and it is out of statistical control if there are unnatural patterns associated with assignable causes. Classical Shehwart control charts ($\overline{X} - R$, $\overline{X} - S$ and $X - R$) are tools that indicate whether the process is operating as consistently as possible. Here, $\overline{X}$, R, S and X are the sample average, the range, the sample standard deviation, and the individual sample value, respectively. Any unnatural variation suggests an assignable cause and the need for an alarm to take corrective action to bring the process under control. Some other control charts used in practice include the cumulative sum (CUSUM) control charts,[20] control charts with modified control limits,[21] and the moving average control charts, and multivariate charts.[22]

There are several electronic manufacturing processes where the simultaneous control of two or more related quality characteristics is necessary. Use of conventional SPC requires that these parameters be identically, independently, and normally distributed (IIND). However, typically these parameters are statistically correlated with each other, and controlling them using conventional SPC methodology can lead to error. This error increases with an increase in the number of quality characteristics. To allow SPC to be applied to such processes, several multivariate control schemes have been developed. Notable among these is a multivariable SPC scheme developed by Spanos et al.[23] and Spanos.[24] Under this scheme, using time series filters and multivariate statistics based on Hotelling's T^2 statistic, raw measurement signals are filtered to produce independent and normally distributed signals. These signals are combined into a single statistic that can be used to trigger an alarm. The scheme can be used both in a run-to-run and real-time mode. Note that the alarm generated is not based on product measurement but on process parameters that have no specified target value yet are related to how the equipment is functioning. A schematic of their real-time SPC scheme is shown in Figure 13.7.20.

Statistical process control tools allow us to monitor a process and raise a flag when the process exhibits "unnatural" shift due to assignable causes. The next logical step is to have the ability to make the process behave the way we want it to. The goal is to optimize the process and bring it back to the target value of its desired output characteristic. The first step to accomplish this task is to develop a model that captures the underlying relationship between input(s) and output(s). To this end, two kinds of models, physical and empirical, are generally used. These are described next.

Physical Models

These models are developed on the physical and chemical laws underlying a process. The governing equations based on these laws, along with the appropriate boundary conditions, are developed, which

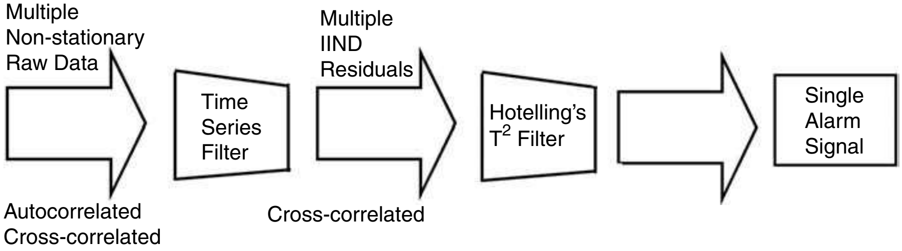

FIGURE 13.7.20 Schematic of the real-time SPC scheme. (Source: Spanos, C.J., Guo, H.F., Miller, A.,and Levine-Parrill, J., Real-time statistical process control using tool data. *IEEE Transactions on Semiconductor Manufacturing*, 5, 4, 308, 1992.)

are then solved analytically or numerically to provide the relationship between the governing parameters and the desired outputs. Consider, for example, the epitaxial growth of silicon by chemical vapor deposition in a horizontal reactor (see Figure 13.7.10a). The reactor consists of an entrance region, a deposition region, and an exit region. A carrier gas, typically H_2 with a small amount of silicon-bearing species, such as $SiCl_4$, SiH_4, $SiHCl_3$, or SiH_2Cl_2, and trace quantities of the desired dopant is passed over the hot wafers maintained at ~1350 K. As mentioned earlier, the silicon-bearing species diffuse from the bulk flow to the silicon substrate, where silicon is deposited by chemical reaction(s).

An important consideration in the epitaxial growth is the uniformity of layer thickness. To achieve this, a basic understanding of the various input parameters — (the inlet reactant concentration C_0, the flow rate U_0, the susceptor temperature Ts, and the downstream distance xy to the growth rate, $\dot{m}$ — is critical. Several analytical and experimental studies[5,6,25–28] on this subject have been reported. For a comprehensive review, see Mahajan.[29] A brief description of the analysis by Mahajan and Wei[28] is provided to give the readers a feel for the power of physical models.

The silicon deposition in the horizontal CVD reactor is diffusion controlled. That is, all the reactants that diffuse to the substrate are instantly consumed, leading to the deposition of a thin layer of silicon. Under these circumstances, the deposition is affected by the flow field in the reactor. Coupled equations of momentum, energy, and mass transport need to be solved to arrive at the deposition rate as a function of the input parameters. These equations for a two-dimensional, laminar flow were numerically solved by Mahajan and Wei.[28] Results were presented for both horizontal ($\theta = 0$), and tilted susceptors for different values of θ. A comparison with the experimental data of Eversteyn et al.[6] showed excellent agreement. It was also shown that the tilted susceptor, by increasing the flow velocity downstream, compensates for the depletion effect of the silicon-bearing species, and hence results in uniform deposition. The analysis suggested a value of $\theta = 2.5$ for optimum results. In actual practice, $\theta = 2.9°$. This agreement is excellent and indeed does point out the power of physical models.

The physical models are attractive since they provide a fundamental understanding of the relationships between the various input and output parameters. They are generally valid over a wide range of input parameters and can provide guidelines for the equipment design and process recipes. However, many a time, simplifying assumptions are made in developing these models to make the solutions tractable. The solutions then are approximate. As a result, their applicability for optimization and control is limited. Further, many of the electronics packaging and manufacturing processes tend to be complex, and hence, may not be amenable to accurate analytical or computational analysis. This difficulty in simulating complex assembly processes is one of the reasons for a general lack of enthusiasm for using physical models in real-life manufacturing.

Empirical Models

As opposed to physical models, empirical models, such as statistical regression, artificial neural networks (ANNs), and fuzzy logic (FL) models, are built from experimental data. Of these, statistical regression models are among those commonly deployed. Such models are accurate over the range in which they are developed. However, they do have their own limitations. They may require a large number of experimental points and may have poor predictive capabilities, especially when the number of input/output (I/O) variables is large. An attractive alternative is to use ANNs and FL techniques for building empirical models. These models can then form the basis for process optimization and control. In this chapter, our focus is on ANNs. However, the strategies discussed for process optimization and control also apply to FL modeling.[10]

Artificial Neural Networks

An artificial neural network is a parallel processing system of interconnected processing elements, *neurons*, which are connected together by weighted, directed interconnections. These interconnection weights are flexible parameters that are adjusted during the training procedure.

In a feed-forward neural network, such as the one shown in Figure 13.7.21, the neurons are organized in layers. There is an *input layer,* comprising input neurons that receive the input into the network; an

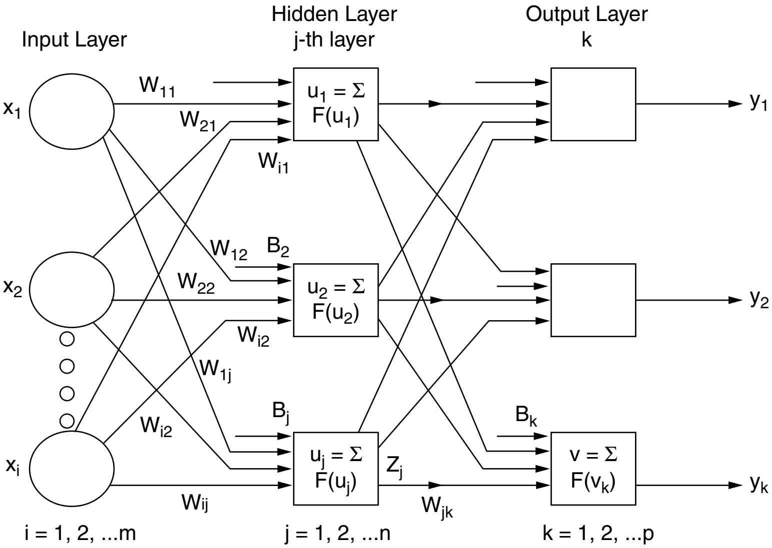

FIGURE 13.7.21 A typical artificial neural network structure. (Source: Marwah, M., Li, Y., and Mahajan, R.L., Integrated neural network modeling for electronic manufacturing. *J. Electronic Manufacturing*, 6, 2, 79, 1996.)

output layer, comprising output neurons that deliver the network's output; and one or several *hidden layers* sandwiched between the input and output layers. It is the neurons in the hidden layers that provide the processing. All interconnections are directed in the forward direction, which is defined as the direction from the input layer to the output layer. Thus, for example, a feed-forward neural network with a single hidden layer may be represented as

$$y_j^\ell = F\left(\sum_{i=1}^{N_{\ell-1}} W_{ij}^\ell y_i^{\ell-1} + B_j^\ell\right) \tag{13.7.9}$$

where y_j^ℓ is the output of the j-th neuron in the ℓ-th layer, W_{ij}^ℓ is the weight on the connection from the i-th neuron in the (ℓ -1)-th layer to the j-th neuron in the ℓ-th layer, B_j^ℓ is the bias connected to the j-th neuron in the ℓ-th neuron, and $N_{\ell-1}$ is the number of neurons in the $(\ell - 1)$-th layer. Note that $y_j^0 = x_i$, where x_i is the input and N_0 is the number of inputs, and F is an activation function that may be thought of as providing a nonlinear gain for the artificial neuron. Typically, F is the sigmoid function

$$F(u) = 1\big/(1 + e^{-u}) \tag{13.7.10}$$

It serves to bound the output from any neuron in the network and allows the network to handle both small and large signals.

Note that the weights (W_{ij} and B_j) are the adjustable variables in the above equation. The power of ANNs lies in the theorem that says that given sufficient hidden neurons the function represented by an ANN can approximate any function, however nonlinear, to arbitrary accuracy in a finite domain.[31] A neural network starts out with random weights, and the weights are adjusted until the required degree of accuracy is obtained. In the context of a neural network, this is *learning*. A powerful algorithm is available for training a neural network. This algorithm, called *back-propagation*, guarantees that a neural network will converge to the mapping underlying its training data. In fact, this algorithm is so relentless that care has to be taken to prevent overfitting of data when those training data are noisy. For a detailed description of neural networks and the back-propagation algorithm, refer to Werbos,[32] Haykin,[33] Smith,[34] and Wasserman.[35]

TABLE 13.7.3 Stencil Printing Factors and Their Levels

	Levels		
Factors	1	2	3
Control Factor			
Squeegee material	Metal	Polyurethane	
Pad material	HASL	Bare copper	
Snap-off distance (mil)	0	5	10
Squeegee pressure (turn)	1/8	1/4	3/8
Squeegee angle (deg)	18	22	26
Squeegee speed (mm/s)	20	25	30
Noise factor			
Printing direction	L-R	R-L	

Source: Li et al.[39]

Recently, Marwah et al.[30] presented an integrated methodology to develop economical and predictive neural network models. The methodology includes data preprocessing, the simple-to-complex network structure approach, and simultaneous training and testing, where training and testing data are identified according to a statistical design of experiments (DOE) to capture the underlying I/O relationship. For some other approaches to determining the optimal neural network configuration, see references 36–38.

Some of the distinguishing features of neural networks are their learning and generalization abilities and nonlinearity. They are thus excellent candidates for modeling the nonlinear, complex, and noisy processes, such as those encountered in electronics manufacturing. A representative application to stencil printing, described earlier, is examined next.

Application to Stencil Printing

As mentioned earlier, the factors affecting solder paste printing are many (see Li et al.[39]). As many as 32 parameters relating to solder paste, stencil design, and machine process parameters were identified. Clearly, building reliable physical models for such a complex process is an extremely difficult task. Li et al. fixed the stencil design and solder paste parameters and built an ANN model relating the machine process parameters to the height of the solder paste dispensed. The six machine parameters listed in Table 13.7.3 were selected as the main effects requiring investigation.

To generate the training and testing data for an ANN model for the stencil printing process, a Taguchi array L27 was selected to set up the experiment. The experiments were conducted on a FUJI-GSP-II printer on one of the assembly lines. The stencil used was of stainless steel with the thickness stepped down to 8, 6, and 4 mils. The board material was FR-4. The solder paste's composition was 63 Sn/37 Pb with powered mesh –325/+500, and the metal load was 90% (w/w). The paste viscosity was 1000 ± 10% kpcs, and the pads on the board were of 20 mil, 25 mil, and 50 mil pitch. A total of 54 experimental runs, 27 for each direction of the printer, were made. The solder paste height on the three 20-mil pitch pads, four 25-mil pitch pads, and seven 50-mil pitch pads was measured on each board using a laser section microscope.

The experimental trials were randomized. The solder paste height on the three 20-mil pitch pads, four 25-mil pitch pads, and seven 50-mil pitch pads was measured on each board. The mean, $\bar{h}$, and the standard deviation (σ) were computed for each pattern for all the 27 trials using Equation 13.7.11 and Equation 13.7.12:

$$\bar{h} = \frac{1}{N} \sum_{i=1}^{1} h_i \tag{13.7.11}$$

$$\sigma = \sqrt{\frac{\sum_{i=1}^{N} \left(h_i - \bar{h}\right)^2}{N-1}} \tag{13.7.12}$$

where h_i is the solder paste height at site i and N is the number of sites measured for each pattern. Thus, a total of 27 data points were obtained. These were then used to develop the neural network models.

Following the neural network modeling approach described by Marwah et al.,[30] the optimum network structure for the mean paste height was found to be 6-4-3, where the three numbers represented the six input neurons corresponding to the six design parameters, four hidden neurons, and the three output neurons corresponding to the mean height for 20-, 25-, and 50-mil pitch pads. The testing relative error, ε_{rel}, for the 20-, 25-, and 50-mil pitch pads was found to be 4%, 4%, and 5%, respectively, where

$$\varepsilon_{rel} = \frac{1}{N}\sum_{i=1}^{N}\frac{\hat{y}_i - y_i}{y_i} \tag{13.7.13}$$

where $\hat{y}_i$ = the predicted output; y_i = the actual output and N is the total number of data points.

A neural network for the standard deviation σ was built to capture the relationship between the inputs and σ. The optimum network structure, in this case, was found to be 6-3-1. The testing relative error was 18%. Considering the relatively small values of σ and data points involved, this kind of relative error was considered to be reasonably good. The variation model formed the basis for determining the optimum settings for minimum variation.

ANN Models as Real-Time Process Analysis Tools

Once an ANN process model has been built to learn the input(s)-output(s) relationship, it can then be used in a predictive mode for providing very fast response to "what if" scenarios. In a reliability simulation study of solder joints, Subbarayan et al.[40] investigated the influence of manufacturing process-induced variations in four design parameters on the fatigue life of solder joints in the 72 I/O OMPAC BGA Package (Figure 13.7.15a). The four parameters were PWB pad size, solder volume, solder joint height, and substrate pad size. The finite element solutions were used to train an ANN. The CPU time taken by the ANN model on a DEC Alphastation 200 4/233 workstation was less than one second. In comparison, an average finite element simulation of the equations took a total of 175 minutes of CPU time. This significant advantage in the speed of analysis is due to the parallel computing process in the neural network. This capability is particularly important in complex electronic manufacturing processes where the process output tends to drift and shift with time. To bring the process back under control, the process technician/engineer, based on his or her past experience, may want to change the input parameters. Instead of conducting a test run and possibly incurring production losses, the technician/engineer can run the simulation on the ANN model that has been trained on the process, and obtain in almost real time an answer to whether the stipulated changes will occur.

Process Optimization

Process optimization may be viewed as an example of off-line process control, where the objective is to estimate the optimal operating point.[41] After fine-tuning, the initial settings provided by optimization may serve to provide guidelines for the local domain in which the process controller ensures that a product is produced to its targeted characteristics.

The most commonly used approach in process optimization is response surface methodology (RSM). RSM is a collection of mathematical and statistical techniques.[42] It uses a low-order polynomial in a local region constructed on the data obtained from the DOE. The gradient descent method is then used to search for the optimum.

Statistical RSM has proven to be effective in many applications. However, as mentioned earlier, when the process is influenced by a large number of variables, is highly nonlinear, and has multiple outputs, the conventional statistical RSM has some limitations. For example, the low-order polynomial cannot fit discrete data well.[43] As an improvement, Guo and Sachs[44] have proposed a "multiple response surfaces" methodology. They use multiple, low-order polynomials to model the output characteristics at each of

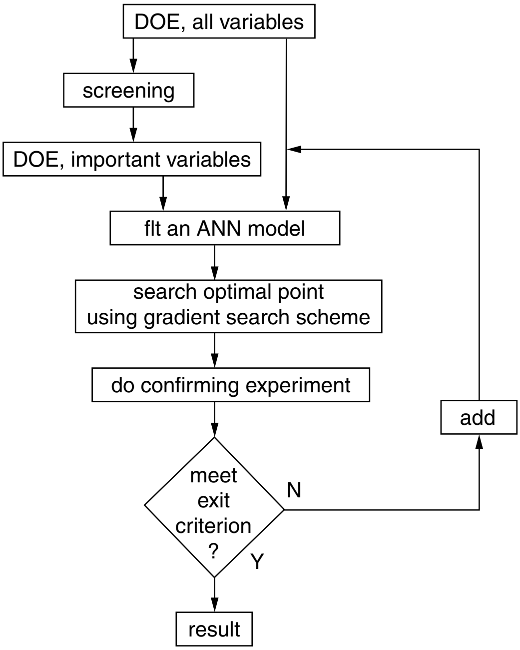

FIGURE 13.7.22 Process optimization using neural network model. (Source: Wang, X.A., and Mahajan, R.L., Artificial neural network model-based run-to-run process controller. *IEEE Transactions on CPMT — Part C*, 19, 19, 1996.)

the measurement sites within a batch of products. The general model is then obtained by manipulating these multiple models.

Since neural nets have excellent correlating capabilities, it is reasonable to expect that the replacement of statistical polynomial regression models by neural network models can lead to economy of experiments in locating the optimum. The methodology for arriving at the optimum settings is shown schematically in Figure 13.7.22. The neural network model, in conjunction with a search algorithm, such as steepest gradient, is used to determine the optimum settings for the desired output. If the predicted output is not satisfactorily confirmed by the experimental data, the indication is that the ANN model may not be that accurate in the region near the optimum. The strategy then is to add the new experimental data to retrain the model. The new model predicts the optimum settings, the accuracy of which is verified again. The process is iterated until the desired accuracy is achieved.

Li et al.[39] used this approach to identify the optimum settings for the stencil printing process described earlier. Based on the ANN model for σ, the optimum settings for the six factors given in Table 13.7.3 for minimum variation were determined, where σ is the standard deviation in the height of paste dispensed. These settings and results are given in Table 13.7.4, where m and c denote metal and bare copper for squeege and pad, respectively.

TABLE 13.7.4 Optimum Settings and Confirmation Results for Stencil Printing

A	B	C	D	E	F	Network Predicted σ	Confirmation Results (trial no.) σ
m	c	7	0.375	22	30	0.28	0.28 (1) 0.26 (2) 0.26 (3)

Source: Li et al.[39]

The actual values of the standard deviation, σ, for three production runs made at these optimum settings are also given in the table. The match between the prediction and the experiments is excellent.

Wang and Mahajan[43] used the algorithm shown in Figure 13.7.22 to demonstrate that ANN RSM outperformed the conventional statistical RSM in arriving at the optimum with fewer experimental data points. The test vehicle used was a production CVD silicon epitaxial barrel reactor (see Figure 13.7.10b). The conclusions were that both for the noise-free and noisy data, the ANN RSM outperformed the statistical RSM in providing more accurate settings with fewer data points. The difference was more significant for noisy data.

Fault Diagnosis

In manufacturing, a common experience is that a process drifts or shifts from its normal performance due to assignable or nonassignable causes. The first step in bringing the process back in control is to detect any significant deviation in the output from the target or norm. Artificial neural networks have traditionally been deployed in pattern recognition and have been shown to provide excellent performance.[46] This strength of ANNs can be exploited in fault diagnosis in manufacturing. The behavior of some characteristic output quantities associated with normal operation as well as certain events can be used to train a neural network to distinguish between normal and off-normal operation and to classify event signatures.

The concept of a spatial and temporal classifier is outlined in Mahajan et al.[47] The former relies on relations between spatially distributed data. These relations define the normality of the process, and sufficient deviation from them is used as a basis for alarms. This approach is useful when consecutive run data are not available. When enough run-by-run data are available, a time series (temporal) event classifier can be designed. Then, time variations in the data over consecutive runs are indicators of shifts and drifts.

Specific events cause characteristic variations in the data. For both spatial and temporal classifiers, neural network models can be trained for the spatial/temporal relations that exist for normal runs and for events.[48] When the operation data are fed into the classifier, the classifier matches the variation to the pre-learned patterns of the different neural networks for events and the normal operation of the process. This discrimination triggers the appropriate control action.

Run-by-Run and Real-Time Process Control

With the fault diagnosis completed, we now need to consider strategies to control a process. Two strategies, run-by-run and real-time control, are available. In the run-by-run controller, diagnosis and adjustment are achieved between runs based on the results of postprocess and *in-situ* measurements (if available) from the current process step and postprocess measurements from the previous steps.[41] In the real-time control, *in-situ* measurements form the basis for process adjustments during a run to bring a process as close to the target as possible.

A multitude of strategies have been developed over the years to achieve manufacturing process control. One way to describe these is to categorize them into two different paradigms: (a) analytical control theory paradigm, and (b) nonanalytical control paradigm. A spirited discussion of these two paradigms is given in Mamdani.[50]

The analytic control theory paradigm, based on the dynamic system theory, assumes that many dynamical systems can be mathematically modeled. System controllers using well-established mathematical techniques can then be analyzed and designed to achieve control. However, as mentioned earlier, there are many processes that may not be amenable to mathematical analysis. This is especially true for the more complex electronic manufacturing processes. This difficulty has led to nonanalytic controls that do away with the mathematical modeling requirement.

The nonanalytic control paradigm control strategy depends on the techniques in the fields of artificial intelligence and pattern recognition to develop diagnostic and control tools. The information about the process is obtained from the experimental data, which may be used in raw form or from I/O models based on the experimental data. The AI techniques used include, among others, rule-based systems, machine learning methods, protocol analysis, neural networks, and FL.

In conventional expert systems, rules to determine corrective actions are developed using a knowledge base (the knowledge gleaned from experts) and inference procedures. For complex manufacturing systems, however, one needs a large amount of knowledge and some means of accurately capturing the many years of experience of an expert or a team of experts.[51] As a result, conventional expert systems have not found a wider acceptance in the control of electronic manufacturing processes.

In one approach to overcome this difficulty, Irani et al.[52] utilize machine learning in extracting knowledge from data. Using their machine learning algorithm (GID3), a modified version of Quinlan's ID3 (1986), a decision tree can be induced from a given set of training data, which (the tree) can then be translated into a set of rules for use in expert systems.

In another approach, control is achieved through automatic process control (APC). In this strategy, variation is minimized not by removing its root cause but rather by transferring the variation into another variable, the manipulated variable.[53] Based on the feedback, the manipulated variable is adjusted to compensate for the process variation.

In integrated automatic-statistical process control (IASPC), the features of both SPC and APC are integrated to gain process control. Vander Weil et al.[54] used this approach (they termed it algorithmic statistical process control) to achieve quality improvement through appropriate process adjustment and elimination of root causes of variability signaled by statistical monitors. They used an autoregressive moving average function (ARMA) model to map the relationship between the off-normal deviation in the output for the current run and that in the input for the previous run. This model provided the compensatory adjustments from run to run. Simultaneously, a cumulative sum (CUSUM) chart was used to detect and provide statistical monitoring of any deviation of the closed-loop process from the estimated model and control algorithm. Application of this methodology to control and monitoring of viscosity in a polymerization process demonstrated success.

Mozumder and Barna[55] proposed applying Western Electric rules to determine an "out-of-control" or "out-of-specification" signal followed by adjustment of the process/equipment models to match the new state of the equipment.

Hu et al.[56] proposed a run-by-run controller that combined SPC and model-based feedback APC. This controller operates in three modes: gradual, rapid, and generalized SPC mode. In the gradual mode, the exponential weighted moving average (EWMA) is used to update a linear controller so that it can catch up with the changing process. Consider, for example, a simple process $y = a + bx$. Assuming that b is constant and only a shifts, a can be estimated at time t as follows:

$$a_t = y_t - bx_t \tag{13.7.14}$$

Applying the EWMA to at

$$a_{et} = wa_t + \left(1 - w\right) a_{e(t-1)} \tag{13.7.15}$$

where w is a weight factor of the EWMA and subscripts t and e_t refer to the time and the EWMA value at time t, respectively. Based on Equation 13.7.14 and Equation 13.7.15, the new setting for the next run is simply

$$x_t = \frac{y_t - a_{et}}{b} \tag{13.7.16}$$

The control adjustment is made every run.

In the rapid mode, the controller approximates the magnitude of the shift and assesses the probability of the shift. Based on this information, the control action is determined. For example, for a given estimated

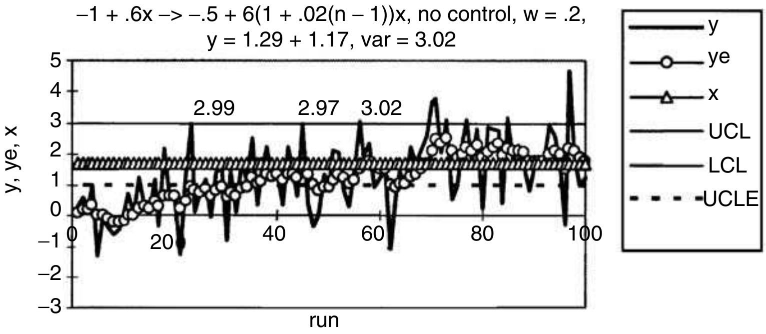

FIGURE 13.7.23 A shifting and drifting process without control (Source: Wang, X.A., and Mahajan, R.L., Artificial neural network model-based run-to-run process controller. *IEEE Transactions on CPMT — Part C*, 19, 19, 1996.)

magnitude, the controller action is smaller for small values of the estimated shift probability, and vice versa. The choice between the gradual and rapid mode is dictated by generalized SPC. For details, see Hu et al.[56]

Note that the EWMA acts as a filter for the process output noise. The smaller the w, the stronger the filter. As a limiting case of $w = 0$, the EWMA ignores the current Δy_t; then $\Delta y_{et} = \Delta y_{e(t-1)} = \Delta y_{e0} = 0$. It thus completely filters out all the noise and the signal changes. For $w = 1$, the EWMA does not filter out any noise, and the EWMA chart becomes the Shewhart chart. In addition to acting as a filter, the EWMA serves to detect process drift and small shifts.[42,57] Drift is generally associated with a slow change in the quality characteristic on the order of 1σ over a period of 100 to 1000 runs.[56] Shift, on the other hand, describes a sudden change in the output characteristic. It can occur, for example, after maintenance operations or specification changes and may be large, on the order of 2σ or larger. It occurs over a few runs. However, as pointed out in Montgomery,[42] the EWMA is not very effective in detecting large shifts. Further, the optimum value of w is a function of the magnitude of the shift. For small shifts, w = 0.2 is a typical value, and for a large shift of 4σ, for example, a value between 0.82 and 0.95 may be more appropriate.[57]

To understand the operation of EWMA, consider a one input-one output process $y = -1 + 0.6x + N(0,1)$ that shifts and drifts to $y = -0.5 + 0.6\ (1 + 0.02\ (n - 10))x + N(0,1)$ at run $n = 10$ (see Figure 13.7.23). Here $N(0,1)$ represents a normal distributed noise with zero mean and unit deviation. The process output mean shifts 0.5σ and the sensitivity drifts 2% per run. The target is zero, hence $\Delta y = y - T = y$. In the absence of any active control, the initial input x = 1.6667 does not change. For the 100 runs, the output mean then is 1.29 with a standard deviation of 1.17. As a result, the overall variance with respect to the original target is 3.02.

In Figure 13.7.23, *ye* is the EWMA of *y*. A nice feature of EWMA is that the standard deviation of the filtered signal, $\sigma_{\Delta ye}$, is less than that of the unfiltered signal, $\sigma_{\Delta y}$. As shown in Mongtomery,[42] if the sample number is moderately large, the standard deviation of Δ_{ye} converges to its asymptotic value as

$$\sigma_{\Delta ye} = \sqrt{\frac{w}{2-w}}\sigma_{\Delta y} \tag{13.7.17}$$

Taking the control limit for Δy as three for the process shown in Figure 13.7.23, and selecting $w = 0.2$, we have $\sigma_{\Delta ye} = \sigma_{\Delta y}/3 = 1$. The control limit for Δye is represented by a short horizontal dotted line legend as UCLE. From Figure 13.7.23, the first out-of-control signal given by the Shewhart chart is at run 56 when $\Delta y = 3.02$. However, examination of filtered data indicates an out-of-control at run 35, where Δye reaches 1.24. Recalling that the process deviation took place at run #10, the Shewhart chart thus gives an out-of-control signal at run 56, which is 46 runs after shift/drift. The EWMA chart, on the other

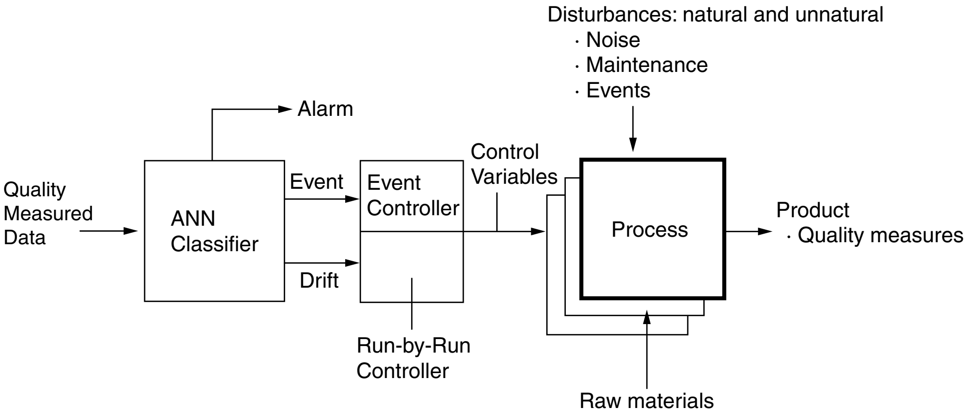

FIGURE 13.7.24 An ANN-based diagnostic/control strategy (Source: Mahajan, R.L., Hopper, P., and Atkins, W., Neural nets and fuzzy logic for semiconductor manufacturing: Part II: Process optimization and control. *Semiconductor Int.*, 111, 1995b and Mahajan, R.L., Hopper, P., and Atkins, W., Neural nets and fuzzy logic for semiconductor manufacturing: Part I: Basic concepts. *Semiconductor International*, 217, 1995a.)

hand, gives out-of-control signal at run 35, only 25 runs after shift/drift. This early detection is attractive since it allows the control action to be taken in advance of potentially bad runs.

Butler and Stefani[59] proposed a double exponential filter to forecast the error in the succeeding run, where one filter is used to estimate the true output and a second filter estimates the trend. The filter equations are as follows:

$$\Delta y_{et} = w_1 \Delta y_t + \left(1 - w_1\right) \Delta y_{e(t-1)} \tag{13.7.18}$$

$$(PE)_t = \Delta y_t - \Delta y_{e(t-1)} \tag{13.7.19}$$

$$(FPE)_t = w_2 (PE)_t + (1 - w_2)(FPE)_{(t-1)} \tag{13.7.20}$$

$$(\Delta y_t)_{\mathrm{Pr}\,ed} = \Delta y_{et} + (FPE)_t \tag{13.7.21}$$

where Δy_t is the current error (deviation from the target), Δy_{et} is the current smoothed error, $(PE)_t$ is the estimated trend at t, $(FPE)_t$ is the current smoothed trend, and $(\Delta y_t)_{\mathrm{Pr}\,ed}$ is greater than 1σ where σ, as usual, is the standard deviation of the process.

Mahajan et al.[42,60] proposed an ANN model-based classifier/controller strategy, shown schematically in Figure 13.7.24. According to this strategy, the product quality data are fed to a classifier that serves the following three functions: (1) to detect in the output data any significant deviation from the normal behavior, (2) to identify the significant deviation with an assignable event to trigger the corresponding control action, and (3) to initiate the appropriate run-by-run controller if the deviation is due to a nonassignable cause.

There are two subcontrollers in the controller module in Figure 13.7.24: an event controller and a run-by-run process controller. An event controller issues a control action specific to that event, whereas a run-by-run controller serves the function of modifying the settings to bring the process output back to the target between the runs. It takes care of the drifts and shifts that are not associated with any particular event.

Run-by-run controllers using neural networks have been used in a number of manufacturing processes.[61–64] A schematic of one such controller is shown in Figure 13.7.25. At the heart of the controller

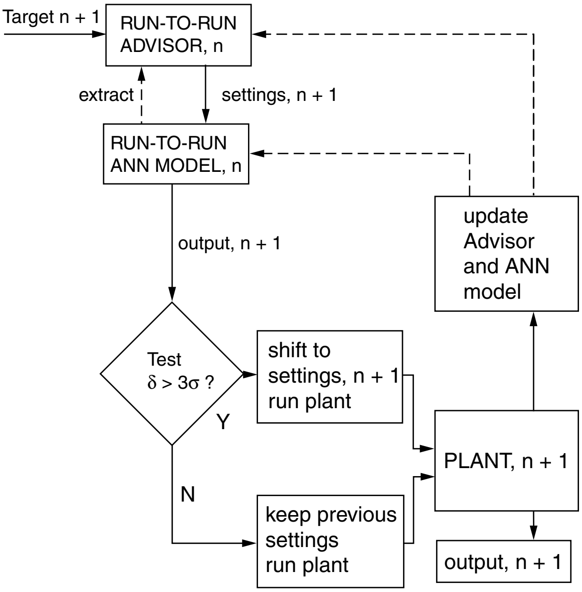

FIGURE 13.7.25 A schematic of a run-by-run controller (Source: Mahajan, R.L., Hopper, P., and Atkins, W., Neural nets and fuzzy logic for semiconductor manufacturing: Part II: Process optimization and control. *Semiconductor Int.*, 111, 1995b and Mahajan, R.L., Hopper, P., and Atkins, W., Neural nets and fuzzy logic for semiconductor manufacturing: Part I: Basic concepts. *Semiconductor International*, 217, 1995a.)

is a dynamic neural network model of the plant which is used to predict the output for a given run before the run is actually made. If the predicted plant output is within the desired specifications, the signal is passed on to the plant to continue the run. Otherwise, the difference between the predicted and the target outputs is fed to the controller, which then provides new input settings for the plant. Both the plant model and controller are updated after each run.

Several variations to the run-by-run process control strategy are possible; see, for example, references 41, 58, and 65–66. In reference 58, the authors proposed a neural network model–based IASPC controller. As a first step, the exponential weighted moving average is used to detect the process shift or drift. The control action is provided by an ANN-model based controller, which is extracted from the process model simply by Taylor expansion and inversion, as follows.

The Taylor expansion of the ANN process model, 17.7.7, $y = f(x_i)$, gives the sensitivities of the output change with respect to the input changes. That is,

$$y - T = \Delta y = \sum_{i=1}^{n} \frac{\partial f}{\partial x_i} \Delta x_i \tag{13.7.22}$$

where T is the control target, and $\partial f/\partial x_i$ is the process sensitivity of output deviation, Δy, to input deviation Δx_i. Note that Equation 13.7.22 is a plane in the n-dimensional space and $\sum_{i=1}^{n}(\partial f/\partial x_i)^2 > 0$. To minimize Δx_i, these were calculated based on the distance from the origin to the plane[67] as ΔS, given in

$$\Delta S = \frac{\Delta y}{\sqrt{\sum_{i=1}^{n} \left(\frac{\partial f}{\partial x_i} \right)^2}} \tag{13.7.23}$$

and Δx_i is the projection of ΔS in the direction of x_i, that is

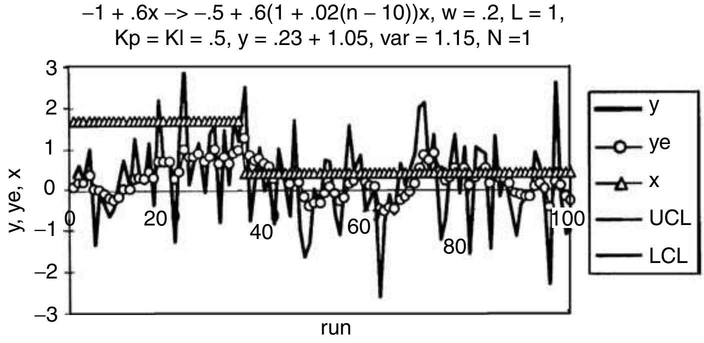

FIGURE 13.7.26 A shifting and drifting process controlled by a run-by-run controller (Source: Wang, X.A., and Mahajan, R.L., Artificial neural network model-based run-to-run process controller. *IEEE Transactions on CPMT — Part C*, 19, 19, 1996.)

$$\Delta x_i = \frac{\dfrac{\partial f}{\partial x_i}}{\displaystyle\sum_{i=1}^{n}\left(\frac{\partial f}{\partial x_i}\right)^2}\Delta y = c_i \Delta y \tag{13.7.24}$$

where c_i is the process sensitivity of input adjustments, Δx_i, to output deviation, Δy. Equation 13.7.24 is thus the controller model that provides the relationship between the controller's outputs Δx_i and its input Δy.

Wang and Mahajan[58] used this strategy and proposed a triple-mode operation for the controller; no action, gradual mode, and rapid mode. If the filtered output deviation is below a threshold limit, no control action is recommended. That is, if $|\Delta y_{et}| < L\sigma_{\Delta y}$ and $|\Delta y_t| < 3\sigma y$, then $|\Delta x_{it}| = 0$ where $L\sigma_{\Delta y}$ is the control action limit for Δy_e. For $w = 0.2$, nominal value of $L = 1$. The argument was that it is generally advisable to leave the process unattended rather than fine-tune it after every run. Generally, the cost of adjusting the input settings is high, and sometimes run-by-run adjustment may even deteriorate the overall performance of the process. This is particularly true for noisy processes. In the gradual mode, if

$$\left|\Delta y_{et}\right| \geq L\sigma_{\Delta y} \ and \left|\Delta y_{et}\right| \leq 3\sigma_{\Delta y} \tag{13.7.25}$$

then the controller issues gradual control action defined by

$$\Delta x_{it} = k_c c_i \Delta y_{et} + \frac{k_p}{M}\sum_{N=1}^{M} c_i \Delta y_{et(1-N)} \tag{13.7.26}$$

where k_c and k_p are weights for the current control action and the previous M runs' average control, respectively. Typically, $k_p = 1 - k_c$.

They used this approach for a simple one input-one output process shown in Figure 13.7.23. Using $k_c = k_p = 0.5$, $w = 0.2$, $L = 1$, and $M = 30$, they showed that only one control action was needed for this simple process at run number 35 (see Figure 13.7.26). The overall variance with respect to target was reduced to less than half of that in Figure 13.7.23.

When the output deviation is large, the controller works in a rapid control mode. Then, the control action is solely based on the current output deviation. The objective is to bring the output to the target rapidly. In other words, if

$$\left|\Delta y_t\right| > 3\sigma_{\Delta t} \tag{13.7.27}$$

then

$$\Delta x_{it} = c_i\,\Delta y_y \tag{13.7.28}$$

Figure 13.7.27 shows an uncontrolled process $y = -1 + 0.6x + N(0,1)$ which at run 10 undergoes a large shift of 6σ and becomes $y = 5 + 0.6x + N(0,1)$. For the 100 runs, the output mean is $y = 5.48$, and the overall variances is 34. Figure 13.7.28 shows the process behavior when it is controlled by a dual controller. At run 10, the output is beyond the upper control limit of three. This activates the rapid mode controller to issue a quick control action at run 11, in accordance with Equation 13.7.25, with $c_i = 1.667$, $\Delta x_i = 9.5$. The new x is 7.83 and the output is brought close to the target. This causes a takeover by the gradual mode controller. At run 71, the EWMA detects the output to be outside the control action limit of one σ, and the controller then issues a gradual correction action. Over 100 runs, the output mean is 0.163 and the overall variance is 1.43, which is much lower than that in Figure 13.7.28. The accompanying control actions are only two and the number of alarms is one.

Wang and Mahajan[58] also reported application of their control strategy to an experimental CVD barrel reactor and demonstrated its effectiveness.

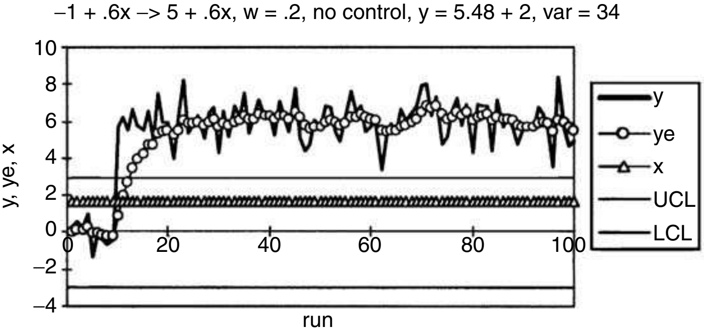

FIGURE 13.7.27 A process with a 6σ shift (Source: Wang, X.A., and Mahajan, R.L., Artificial neural network model-based run-to-run process controller. *IEEE Transactions on CPMT — Part C*, 19, 19, 1996.)

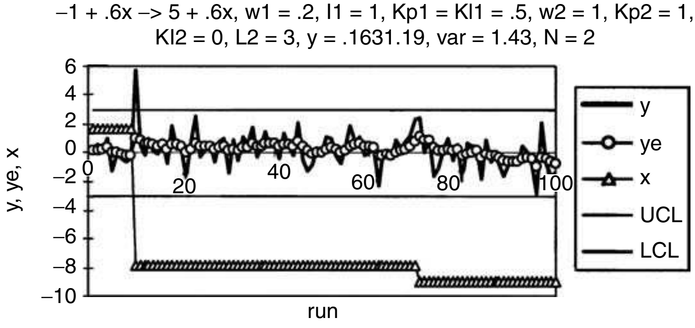

FIGURE 13.7.28 A 6σ shift process controlled by a dual controller (Source: Wang, X.A., and Mahajan, R.L., Artificial neural network model-based run-to-run process controller. *IEEE Transactions on CPMT — Part C*, 19, 19, 1996.)

Concluding Remarks

Electronics manufacturing is perhaps the best example of mass production. The manufacturing processes involved are diverse and complex. In this chapter, an attempt has been made to familiarize the reader with a majority of the manufacturing processes that are involved in fabricating an IC (the central element in electronics manufacturing), packaging an IC, and assembling the package on a printed wiring board that goes into the final product. It has been emphasized that process optimization and control are critical to the success of the electronics manufacturing industry.

The development of strategies to achieve optimum process operations, with minimum scrap, is an active area of research. Multidisciplinary solutions building on the existing techniques in classical control theory, advanced SPC tools, intelligent control techniques based on neural network and FL models, and integrated knowledge-based systems are being developed. In this chapter, some recent research in the use of ANNs for process modeling, optimization, fault diagnosis, and control was described in detail.

Given the complexity and variety of the electronic manufacturing process, it is the belief of this author that in the near future, research in process optimization and control will continue to build on several of the existing technology platforms discussed in this chapter. Integration of different approaches to arrive at elegant, self-adaptive, and comprehensive control solutions will remain an active area of research. Development of real-time controllers needs accelerated research. To this end, integration of *in-situ* sensors, including microelectromechanical systems (MEMS), needs to be explored.

References

1. Sze, S.M. 1988. *VLSI Technology*, McGraw-Hill, New York, 2.
2. Landers, T.L., Brown, W.D., Fant, E.N., Malstrom, E.M., and Schmitt, N.M. 1994. *Electronics Manufacturing Processes*, Prentice Hall, Englewood Cliffs, NJ, 8.
3. The National Technology Roadmap for Semiconductors: Technology Needs, Semiconductor Industry Association, 1997, 135, 19.
4. Lee, H.H. 1990. *Fundamentals of Microelectronics Processing*, McGraw-Hill, New York, 42.
5. Ristorcelli, J.R. Jr. and Mahajan, R.L., Silicon deposition and dopant incorporation in epitaxial processes. *Proc. ASME/JSME Thermal Eng. Conf. 2nd,* Hawaii, 1987.
6. Eversteyn, F.C., Severin, P.J.W., Brekel, C.H.J.U.D., and Peck, H.L. A stagnation layer model for the epitaxial growth of silicon from silane in a horizontal reactor, *J. Electrochem. Soc.*, 1970, 117, 925.
7. Jaeger, R.C. 1988. *Introduction to Microelectronic Fabrication*, Addison-Wesley, Reading, PA.
8. Dally, J.W., *Packaging of Electronic Systems*, McGraw-Hill, New York, 1990.
9. Prasad, R.P. 1997. *Surface Mount Technology*, Chapman & Hall, New York.
10. Mahajan, R.L., Process modeling, optimization and control in electronics manufacturing. *Manufacturing Challenges in Electronics Packaging*, Lee, Y.C. and Chen, W.T., eds., Chapman & Hall, New York,1998.
11. Fernandes, N.J., Bergman, T.L. and Masada, G.Y., Thermal effects during infrared solder reflow — Part I: Heat transfer mechanism, *ASME J. Electronic Packag.*, 114, 41, 1992.
12. Mahajan, R.L., Wang, X.A. and Lin, K.M., Process optimization through neural network modeling: Wave soldering case study. *ASME Winter Annual Meeting*, Anaheim, CA, 1992.
13. Wenger, G.M. and Mahajan, R.L., Condensation soldering technology — Part I: Condensation soldering fluids and heat transfer. *Insulation/Circuits*, 131, 1979.
14. Wenger, G.M. and Mahajan, R.L., Condensation soldering technology — Part II: Equipment and production. *Insulation/Circuits*, 15, 1979.
15. Wenger, G.M. and Mahajan, R.L., Condensation soldering technology — Part III: Installation and application *Insulation/Circuits*, 13, 1979.
16. Mahajan, R.L., Process optimization and control in semiconductor manufacturing (invited paper). *Proc. ASME Winter Annual Meeting*, New Orleans, 1993.
17. *AT&T Statistical Quality Handbook*, AT&T Technologies Inc., 1984.

18. Shewhart, W.A. 1931. *Economic Control of Quality Manufactured Products*, Van Nostrand Reinhold, New York.
19. Taguchi, G. 1986. *Introduction to Quality Engineering*, Asian Productivity Organization, UNIPUB, White Plains, NY, 181.
20. Page, E.S., Continuous inspection schemes. *Biometrica*, 41,100, 1954.
21. Hill, D., Modified control limits. *Applied Statistics*, 5, 1,12, 1956.
22. Hotelling, H., Multivariate quality control. *Technique of Statistical Analysis*, Eisenhart, Hastay and Wallis, eds., McGraw-Hill, New York, 1947.
23. Spanos, C.J., Guo, H.F., Miller, A.,and Levine-Parrill, J., Real-time statistical process control using tool data. *IEEE Transactions on Semiconductor Manufacturing*, 5, 4, 308, 1992.
24. Spanos, C.J., Statistical process control in semiconductor manufacturing. *Proc. of the IEEE*, 80, 819, 1992.
25. Coltrin, M.E., Kee, R.J., and Miller, J.A., A mathematical model of the coupled fluid mechanics and chemical kinetics in a chemical vapor deposition reactor. *J. Electrochemical Society*, 131, 2, 425, 1984.
26. Coltrin, M.E., Kee, R.J. and Miller, J.A., A mathematical model of silicon chemical vapor deposition: Further refinements and effects of thermal diffusion. *J. Electrochemical Society*, 133, 6,1206, 1986.
27. Moffat, H., and Jensen, K.F., Three-dimensional flow effects in silicon CVD in horizontal reactors. *J. Electrochemical Society*, 135, 459, 1988.
28. Mahajan, R.L. and Wei, C., Buoyancy, Soret, Dufour and variable property effects in silicon epitaxy. *ASME J. of Heat Transfer*, 113, 688, 1991.
29. Mahajan, R.L., Transport phenomena in chemical vapor deposition systems. *Advances in Heat Transfer*, 28, 339, 1996.
30. Marwah, M., Li, Y., and Mahajan, R.L., Integrated neural network modeling for electronic manufacturing. *J. Electronic Manufacturing*, 6, 2, 79, 1996.
31. Hornik, M., Stinchcombe, M., and White, H., Multilayer feed forward networks are universal approximators. *Neural Networks*, 2, 359, 1989.
32. Werbos, P.J., Beyond Regression: New Tools for Prediction and Analysis in the Behavioral Sciences, PhD thesis, Harvard University, Boston, 1974.
33. Haykin, S. 1993. *Neural Networks: A Comprehensive Foundation*, Macmillan, New York.
34. Smith, M. 1989. *Neural Networks for Statistical Modeling*, Van Nostrand Reinhold, New York.
35. Wasserman, P.D. 1989. *Neural Computing: Theory and Practice*, Van Nostrand Reinhold, New York.
36. Bhat, N.V. and McAvoy, T.J., Determining model structure for neural models by network stripping. *Computers and Chemical Engineering*, 16, 4, 271, 1992.
37. Kim, B. and May, G.S., An optimal neural network process model for plasma etching. *IEEE Transactions on Semiconductor Manufacturing*, 7, 1, 1994.
38. Han, S.S., Ceiler, M., Bidstrup, S.A., Kohl, P. ,and May, G., Modeling the properties of PECVD silicon dioxide films using optimized back-propagation neural networks. *IEEE Transactions CPMT — Part A*, 17, 2, 174, 1994.
39. Li, Y., Mahajan, R.L., and Nikmanesh, N. 1996. Fine pitch stencil printing process modeling and optimization. *ASME J. Electronic Packag.*, 118, 1, 1.
40. Subbarayan, G., Li, Y., and Mahajan, R.L., Reliability simulations for solder joint using Stochastic Finite Element and Artificial Neural Network Models. *ASME J. Electronic Packaging*, 118, 148, 1996.
41. Sachs, E., Guo, R.S., Ha, S. and Hu, A., Process control system for VLSI fabrication. *IEEE Transactions on Semiconductor Manufacturing*, 4, 2, 134, 1991.
42. Montgomery, D.C. 1991. *Introduction to Statistical Quality Control*, John Wiley & Sons, New York.
43. Wang, W.A., and Mahajan, R.L., Artificial neural network model-based run-to-run process controller. *IEEE Transactions on CPMT — Part C*, 19, 19, 1996.
44. Guo, R-S., and Sachs, E., Modeling, optimization and control of spatial uniformity in manufacturing processes. *IEEE Transactions on Semiconductor Manufacturing*, 6, 1, 41, 1993.

45. Bose, C.B. and Lord, H.A., Neural network models in wafer fabrication. *SPIE Conf. on Applications of Artificial Neural Networks*, Orlando, FL, 1993.
46. Pollard, J.F., Broussard, M.R., Garrison, D.B., and San K.Y., Process identification using neural networks. In *Comput. and Chemical Eng.*, 16, 4, 253, 1992.
47. Mahajan, R.L., Hopper, P., and Atkins, W., Neural nets and fuzzy logic for semiconductor manufacturing: Part II: Process optimization and control. *Semiconductor Int.*, 111, 1995b.
48. Bhatikar, S.R., and Mahajan, R.L., Neural network based diagnosis of CVD barrel reactor. *Advances in Electronic Packaging*, ASME-EEP, 26–1, 621, 1999.
49. Mahajan, R.L., Schichtel, B.E., and Wang, X. A., Liquid crystal thermographic measurements of transport in a CVD-barrel reactor. *Proc. ASME National Heat Transfer Conference*, Atlanta, 1993.
50. Mamdani, E.H., Advances in the linguistic synthesis of fuzzy control. *Int. J. of Man-Machine Studies*, 8,119, 1976.
51. Kalpakjian, S. 1992. *Manufacturing Engineering and Technology*, Addison-Wesley, Reading, PA.
52. Irani, K.B., Cheng, J., Fayyad, U.M., and Qian, Z., Application of machine learning techniques to semiconductor manufacturing. *Proc. of the 8th SPIE Conference on Application of Artificial Intelligence*, Orlando, FL, 1990.
53. Dorf, R.C. 1986. *Modern Control Systems*, Addison-Wesley, Reading, PA.
54. Vander Wiel, S.A., Tucker, W.T., Faltin, F.W., and Duganaksoy, N., Algorithmic statistical process control: Concepts and an application. *Technometrics*, 34, 3, 286, 1992.
55. Mozumder, P.K., and Barna, G.D., Statistical feedback control of a plasma etch process. *IEEE Transactions on Semiconductor Manufacturing*, 7, 1, 1, 1994.
56. Hu, A., Zhang, X., Sachs, E., and Renteln, P., Application of run-by-run controller to the chemical-mechanical planerization process, Part I. *1993 IEEE/CHMT Int. Electron. Manufacturing Symp.*, 235, 1993.
57. Lucas, J., and Saccucci, M.S., Exponentially weighted moving average control schemes: Properties and enhancements. *Technometrics*, 32, 1, 1, 1990.
58. Wang, X.A., and Mahajan, R.L., Artificial neural network model-based run-to-run process controller. *IEEE Transactions on CPMT — Part C*, 19, 19, 1996.
59. Butler, S.W., and Stefani, J.A., Supervisory run-to-run control of polysilicon gate etch using *in-situ* ellipsometry. *IEEE Trans. Semiconductor Manufacturing*, 7, 2, 193, 1994.
60. Mahajan, R.L., Hopper, P., and Atkins, W., Neural nets and fuzzy logic for semiconductor manufacturing: Part I: Basic concepts. *Semiconductor International*, 217, 1995a.
61. Lan, M.S., Lin, P., and Bain, L.J., Modeling and control of the lithographic offset color printing process using artificial neural networks. *ASME Winter Annual Meeting*, November 8–13, Anaheim, CA, 1992.
62. Huang, H.H., and Wang, H.P., Tandem artmap neural networks for feedback process control: A welding case. *ASME Winter Annual Meeting*, November 8–13, Anaheim, CA, 1992.
63. Elanayar, V. T. S., and Shin, Y.C., Robust tool wear monitoring via radial basis function neural network. *ASME Winter Annual Meeting*, November 8-13, Anaheim, CA, 1992.
64. Fan, H.T. and Wu, S.M., Case studies on modeling manufacturing processes using artificial neural networks. *ASME Winter Annual Meeting*, November 8–13, Anaheim, CA, 1992.
65. Hu, A., Sachs, E., Ingolfsson, A., and Langer, P., Run by run process control: Performance benchmarks. *1992 IEEE/SEMI Int. Semiconductor Manufacturing Sci. Symp.*, 73, 1992.
66. Rangwala, S.S. and Dornfield, D.A., Learning and optimization of machining operations using computing abilities of neural networks. *IEEE Transactions on Systems, Man and Cybernetics*, 19, 2, 299, 1989.
67. Spiegel, M.R. 1968. *Mathematical Handbook*, McGraw-Hill, New York.

15

MEMS Technology

Mohamed Gad-el-Hak
Virginia Commonwealth University

Marc J. Madou
University of California, Irvine

Hong Zhou
University of California, Irvine

Liang-Yu Chen
Ohio Aerospace Institute/NASA Glenn Research Center

Phillip J. Zulueta
NASA Jet Propulsion Laboratory/ California Institute of Technology

Srihari Rajgopal
Case Western Reserve University

Christian A. Zorman
Case Western Reserve University

Darrin J. Young
Case Western Reserve University

Mehran Mehregany
Case Western Reserve University

C. Channy Wong
Sandia National Laboratories

Andrew D. Oliver
Sandia National Laboratories

David W. Plummer
Sandia National Laboratories

15.1 Introduction

Mohamed Gad-el-Hak

The length-scale of man, at slightly more than 10^0 m, amazingly fits right in the middle of the smallest subatomic particle, which is approximately 10^{-26} m, and the extent of the observable universe, which is of the order of 10^{26} m. Toolmaking has always differentiated our species from all others on Earth. Aerodynamically correct wooden spears were carved by *archaic Homo sapiens* close to 400,000 years ago. Man builds things consistent with his size, typically in the range of two orders of magnitude larger or smaller than himself. But humans have always striven to explore, build, and control the extremes of length and time scales. In the voyages to Lilliput and Brobdingnag of *Gulliver's Travels*, Jonathan Swift speculates on the remarkable possibilities that diminution or magnification of physical dimensions provides. The Great Pyramid of Khufu was originally 147 m high when completed around 2600 B.C., while the Empire State Building constructed in 1931 is presently 449 m high. At the other end of the spectrum of man-made artifacts, a dime is slightly less than 2 cm in diameter. Watchmakers have practiced the art of miniaturization since the thirteenth century. The invention of the microscope in the seventeenth century opened the way for direct observation of microbes and plant and animal cells. Smaller things were man-made in the latter half of the twentieth century. The transistor in today's integrated circuits has a size of 0.18 micron in production and approaches 10 nanometers in research laboratories.

Microelectromechanical systems (MEMS) refer to devices that have characteristic length of less than 1 mm but more than 1 micron, that combine electrical and mechanical components, and that are fabricated using integrated circuit batch-processing technologies. Current manufacturing techniques for MEMS include surface silicon micromachining; bulk silicon micromachining; lithography, electrodeposition, and plastic molding; and electrodischarge machining. The multidisciplinary field has witnessed explosive growth during the last decade, and the technology is progressing at a rate that far exceeds that of our understanding of the physics involved. Electrostatic, magnetic, electromagnetic, pneumatic and thermal actuators, motors, valves, gears, cantilevers, diaphragms, and tweezers of less than 100-micron size have been fabricated. These have been used as sensors for pressure, temperature, mass flow, velocity, sound, and chemical composition; as actuators for linear and angular motions; and as simple components for complex systems such as robots, micro-heat-engines, and micro-heat-pumps. Worldwide market projections for MEMS devices tend to be optimistic, reaching $30 billion by the year 2006.

In this chapter, we breifly introduce MEMS technology. Readers are referred to more specialized books such as those by Kovacs (1998), Gad-el-Hak (2002), Karniadakis and Beskok (2002), and Madou (2002) for more detailed treatment of the subject. The present chapter consists of seven sections. Following these introductory remarks, MEMS technology and its applications are broadly introduced in the second section. The third section describes the various techniques used to fabricate microelectromechanical systems. Packaging and reliability issues are outlined in the following two sections. The physical modeling of fluid flows and solid mechanics of microdevices are discussed in Sections 6 and 7, respectively.

References

Gad-el-Hak, M., ed. (2002) *The MEMS Handbook*, CRC Press, Boca Raton, FL.

Karniadakis, G.E., and Beskok, A. (2002) *Micro Flows: Fundamentals and Simulation*, Springer-Verlag, New York.

Kovacs, G.T.A. (1998) *Micromachined Transducers Source Book*, McGraw-Hill, Boston.

Madou, M. (2002) *Fundamentals of Microfabrication*, 2nd ed., CRC Press, Boca Raton, FL.

15.2 MEMS Technology and Its Applications

Mohamed Gad-el-Hak

Tool making has always differentiated our species from all others on Earth. Aerodynamically correct wooden spears were carved by archaic Homo sapiens close to 400,000 years ago. Man builds things consistent with his size, typically in the range of two orders of magnitude larger or smaller than himself, as indicated in Figure 15.2.1. Although the extremes of length-scale are outside the range of this figure, man, at slightly more than 10^0 m, amazingly fits right in the middle of the smallest subatomic particle, which is approximately 10^{-26} m, and the extent of the observable universe, which is of the order of 10^{26} m (15 billion light years); neither geocentric nor heliocentric but rather egocentric universe! But humans have always striven to explore, build, and control the extremes of length and time scales. In the voyages to Lilliput and Brobdingnag of *Gulliver's Travels*, Jonathan Swift (1726) speculates on the remarkable possibilities that diminution or magnification of physical dimensions provides. The Great Pyramid of Khufu was originally 147 m high when completed around 2600 B.C., while the Empire State Building constructed in 1931 is presently — after the addition of a television antenna mast in 1950 — 449 m high. At the other end of the spectrum of man-made artifacts, a dime is slightly less than 2 cm in diameter. Watchmakers have practiced the art of miniaturization since the thirteenth century. The invention of the microscope in the seventeenth century opened the way for direct observation of microbes and plant and animal cells. Smaller things were man-made in the latter half of the twentieth century. The transistor —

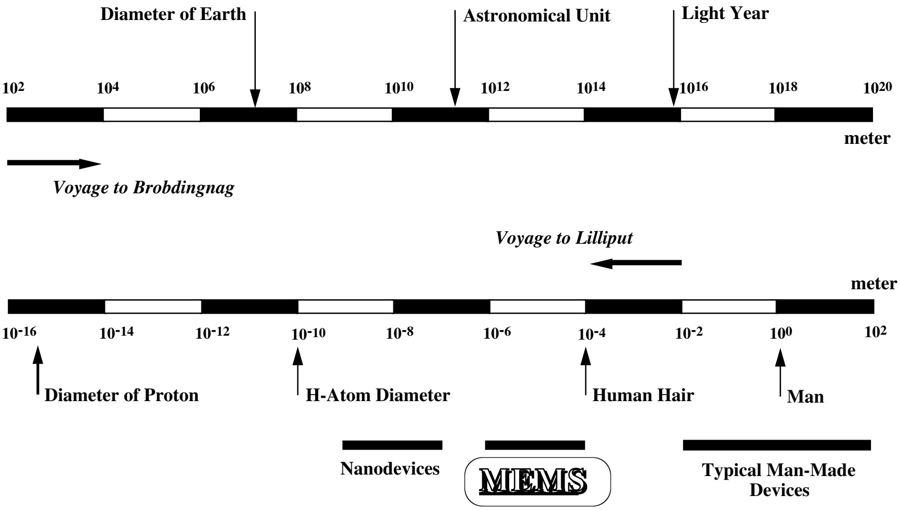

FIGURE 15.2.1 Scale of things, in meters. Lower scale continues in the upper bar from left to right. One meter is 10^6 microns, 10^9 nanometers, or 10^{10} Angstroms.

invented in 1947 — in today's integrated circuits has a size of 0.18 micron (180 nanometers) in production and approaches 10 nm in research laboratories using electron beams. But what about the miniaturization of mechanical parts — machines — envisioned by Feynman (1961) in a legendary speech?

Manufacturing processes that can create extremely small machines have been developed in recent years (Angell et al. 1983; Gabriel et al. 1988; 1992; O'Connor 1992; Gravesen et al. 1993; Bryzek et al. 1994; Gabriel 1995; Ashley 1996; Ho and Tai 1996, 1998; Hogan 1996; Ouellette 1996; Paula 1996; Robinson et al. 1996a, 1996b; Tien 1997; Amato 1998; Busch-Vishniac 1998; Kovacs 1998; Knight 1999; Epstein 2000; O'Connor and Hutchinson 2000; Goldin et al. 2000; Chalmers 2001; Tang and Lee 2001; Gad-el-Hak 2002; Karniadakis and Beskok 2002; Madou 2002). Electrostatic, magnetic, electromagnetic, pneumatic and thermal actuators, motors, valves, gears, cantilevers, diaphragms, and tweezers of less than 100-μm size have been fabricated. These have been used as sensors for pressure, temperature, mass flow, velocity, sound and chemical composition; as actuators for linear and angular motions; and as simple components for complex systems such as robots, micro-heat-engines and micro-heat-pumps (Lipkin 1993; Garcia and Sniegowski 1993, 1995; Sniegowski and Garcia 1996; Epstein and Senturia 1997; Epstein et al. 1997).

Microelectromechanical systems (MEMS) refer to devices that have characteristic length of less than 1 mm but more than 1 micron, that combine electrical and mechanical components, and that are fabricated using integrated circuit batch-processing technologies. The books by and Kovacs (1998), Gad-el-Hak (2002), and Madou (2002) provide excellent sources for microfabrication technology. Current manufacturing techniques for MEMS include surface silicon micromachining; bulk silicon micromachining; lithography, electrodeposition, and plastic molding (or, in its original German, Lithographie Galvanoformung Abformung, LIGA); and electrodischarge machining (EDM). As indicated in Figure 1, MEMS are more than four orders of magnitude larger than the diameter of the hydrogen atom, but about four orders of magnitude smaller than the traditional man-made artifacts. Microdevices can have characteristics length smaller than the diameter of a human hair. Nanodevices (some say NEMS) further push the envelope of electromechanical miniaturization (Roco 2001).

The famed physicist Richard P. Feynman delivered a mere two but profound lectures[†] on electromechanical miniaturization: "There's Plenty of Room at the Bottom," presented at the annual meeting of

---

[†] Both talks have been reprinted in the *Journal of Microelectromechanical Systems,* vol. 1, no. 1, pp. 60–66, 1992, and vol. 2, no. 1, pp. 414, 1993.

the American Physical Society, Pasadena, California, December 29, 1959, and “Infinitesimal Machinery,” presented at the Jet Propulsion Laboratory on February 23, 1983. He could not see a lot of use for micromachines, lamenting in 1959 “[Small but movable machines] may or may not be useful, but they surely would be fun to make,” and 24 years later “There is no use for these machines, so I still don’t understand why I’m fascinated by the question of making small machines with movable and controllable parts.” Despite Feynman’s demurring regarding the usefulness of small machines, MEMS are finding increased applications in a variety of industrial and medical fields, with a potential worldwide market in the billions of dollars ($30 billion by 2006). Accelerometers for automobile airbags, keyless entry systems, dense arrays of micromirrors for high-definition optical displays, scanning electron microscope tips to image single atoms, micro-heat-exchangers for cooling of electronic circuits, reactors for separating biological cells, blood analyzers, and pressure sensors for catheter tips are but a few examples of current usage. Microducts are used in infrared detectors, diode lasers, miniature gas chromatographs, and high-frequency fluidic control systems. Micropumps are used for ink-jet printing, environmental testing, and electronic cooling. Potential medical applications for small pumps include controlled delivery and monitoring of minute amounts of medication, manufacturing of nanoliters of chemicals, and development of an artificial pancreas.

The multidisciplinary field has witnessed explosive growth during the last decade. Several new journals are dedicated to the science and technology of MEMS, such as *Journal of Microelectromechanical Systems*, *Journal of Micromechanics and Microengineering*, and *Microscale Thermophysical Engineering*. Numerous professional meetings are devoted to micromachines, for example, *Solid-State Sensor and Actuator Workshop, International Conference on Solid-State Sensors and Actuators (Transducers), Micro Electro Mechanical Systems Workshop, Micro Total Analysis Systems, Eurosensors,* among others.

In this chapter, we briefly introduce MEMS technology. Readers are referred to more specialized books such as those by Kovacs (1998), Gad-el-Hak (2002), Karniadakis and Beskok (2002), and Madou (2002) for more detailed treatment of the subject. The present chapter contains sections on fabrication, packaging, and reliability of microelectromechanical systems. The physical modeling of fluid flows and solid mechanics of microdevices are also discussed.

References

Amato, I. (1998) Formenting a revolution, in miniature, *Science* 282, no. 5388, 16 October, 402–5.

Angell, J.B., Terry, S.C., and Barth, P.W. (1983) Silicon micromechanical devices, *Faraday Transactions I* 68, 744–48.

Ashley, S. (1996) Getting a microgrip in the operating room, *Mechanical Engineering* 118, September, 91–93.

Bryzek, J., Peterson, K., and McCulley, W. (1994) Micromachines on the march, *IEEE Spectrum* 31, May, 20–31.

Busch-Vishniac, I.J. (1998) Trends in electromechanical transduction, *Physics Today* 51, July, 28–34.

Chalmers, P. (2001) Relay races, *Mechanical Engineering* 123, January, 66–68.

Epstein, A.H. (2000) The inevitability of small, *Aerospace America* 38, March, 30–37.

Epstein, A.H., and Senturia, S.D. (1997) Macro power from micro machinery, *Science* 276, 23 May, 1211.

Epstein, A.H., Senturia, S.D., Al-Midani, O., Anathasuresh, G., Ayon, A., Breuer, K., Chen, K.-S., Ehrich, F.F., Esteve, E., Frechette, L., Gauba, G., Ghodssi, R., Groshenry, C., Jacobson, S.A., Kerrebrock, J.L., Lang, J.H., Lin, C.-C., London, A., Lopata, J., Mehra, A., Mur Miranda, J.O., Nagle, S., Orr, D.J., Piekos, E., Schmidt, M.A., Shirley, G., Spearing, S.M., Tan, C.S., Tzeng, Y.-S., and Waitz, I.A. (1997) Micro-Heat Engines, Gas Turbines, and Rocket Engines — The MIT Microengine Project, AIAA Paper No. 97-1773, AIAA, Reston, VA.

Feynman, R.P. (1961) There’s plenty of room at the bottom, in *Miniaturization*, ed. H.D. Gilbert, 282–96, Reinhold Publishing, New York.

Gabriel, K.J. (1995) Engineering microscopic machines, *Scientific American* 260, September, pp. 150–153.

Gabriel, K.J., Jarvis, J., and Trimmer, W., eds. (1988*) Small Machines, Large Opportunities: A Report on the Emerging Field of Microdynamics, National Science Foundation*, AT&T Bell Laboratories, Murray Hill, New Jersey.

Gabriel, K.J., Tabata, O., Shimaoka, K., Sugiyama, S., and Fujita, H. (1992) Surface-normal electrostatic/pneumatic actuator, *in Proc. IEEE Micro Electro Mechanical Systems '92*, 128–31, 4–7 February, Travemünde, Germany.

Gad-el-Hak, M., ed. (2002) *The MEMS Handbook*, CRC Press, Boca Raton, FL.

Garcia, E.J., and Sniegowski, J.J. (1993) The design and modelling of a comb-drive-based microengine for mechanism drive applications, in *Proc. Seventh International Conference on Solid-State Sensors and Actuators (Transducers'93)*, 763–66, Yokohama, Japan, 7–10 June.

Garcia, E.J., and Sniegowski, J.J. (1995) Surface micromachined microengine, *Sensors & Actuators A* 48, 203–14.

Goldin, D.S., Venneri, S.L., and Noor, A.K. (2000) The Great out of the small, *Mechanical Engineering* 122, November, 70–79.

Gravesen, P., Branebjerg, J. and Jensen, O.S. (1993) Microfluidics — A Review, *J. Micromech. Microeng.* 3, 168–82.

Ho, C.-M., and Tai, Y.-C. (1996) Review: MEMS and its applications for flow control, *J. Fluids Eng.* 118, 437–47.

Ho, C.-M., and Tai, Y.-C. (1998) Micro-Electro-Mechanical Systems (MEMS) and fluid flows, *Annu. Rev. Fluid Mech.* 30, 579–612.

Hogan, H. (1996) Invasion of the micromachines, *New Scientist* 29, June, 28–33.

Karniadakis, G.E., and Beskok, A. (2002) *Micro Flows: Fundamentals and Simulation*, Springer-Verlag, New York.

Knight, J. (1999) Dust mite's dilemma, *New Scientist* 162, no. 2180, 29 May, 40–43.

Kovacs, G.T.A. (1998) *Micromachined Transducers Sourcebook*, McGraw-Hill, New York.

Lipkin, R. (1993) Micro steam engine makes forceful debut, *Science News* 144, September, 197.

Madou, M. (2002) *Fundamentals of Microfabrication*, 2nd ed., CRC Press, Boca Raton, FL.

O'Connor, L. (1992) MEMS: micromechanical systems, *Mechanical Engineering* 114, February, 40–47.

O'Connor, L., and Hutchinson, H. (2000) Skyscrapers in a microworld, *Mechanical Engineering* 122, March, 64–67.

Ouellette, J. (1996) MEMS: mega promise for micro devices, *Mechanical Engineering* 118, October, 64–68.

Paula, G. (1996) MEMS sensors branch out, *Aerospace America* 34, September, 26–32.

Robinson, E.Y., Helvajian, H., and Jansen, S.W. (1996a) Small and smaller: the world of MNT, *Aerospace America* 34, September, 26–32.

Robinson, E.Y., Helvajian, H., and Jansen, S.W. (1996b) Big benefits from tiny technologies, *Aerospace America* 34, October, 38–43.

Roco, M.C. (2001) A frontier for engineering, *Mechanical Engineering* 123, January, 52–55.

Sniegowski, J.J., and Garcia, E.J. (1996) Surface micromachined gear trains driven by an on-chip electrostatic microengine, *IEEE Electron Device Letters* 17, July, 366.

Swift, J. (1726) *Gulliver's Travels*, 1840 reprinting of *Lemuel Gulliver's Travels into Several Remote Nations of the World*, Hayward & Moore, London.

Tang, W.C., and Lee, A.P. (2001) Military applications of microsystems, *The Industrial Physicist* 7, February, 26–29.

Tien, N.C. (1997) Silicon micromachined thermal sensors and actuators, *Microscale Thermophys. Eng.* 1, 275–92.

15.3 Microscale Manufacturing Processes

A Comparison of Miniaturization Techniques: Top-Down and Bottom-Up Manufacturing

Marc J. Madou and Hong Zhou

Introduction

> Progress in science depends on new techniques, new discoveries and new ideas, probably in that order.
>
> **Sydney Brenner, 1980**

> A happy man is too satisfied with the present to dwell too much on the future.
>
> **Albert Einstein, "My Future Plans," September 18, 1896**

In manufacturing, forming and removing are the two primary processes. Forming creates an original shape from a molten mass, a gaseous state, or solid particles. During such processes, cohesion is created among individual particles; examples include plastic molding, thin film metal deposition by evaporation or sputtering, and electroforming. Removing processes destroy cohesion among particles as exemplified in wet chemical etching, electrodischarge machining (EDM), traditional mechanical turning, and laser drilling.[1] In this section, we are interested in those forming and removing processes enabling the manufacture of precision miniature machines.

"Precision machining," when used by mechanical engineers, has typically been reserved for removal processes only, whereas "micromachining," as used to describe integrated circuit (IC)-based fabrication technology, covers both removal and forming processes. Precision machining and Si micromachining are complementary; both strive to improve absolute and relative manufacturing tolerances, with Si-based technology better at obtaining smaller features (absolute tolerance) and traditional methods better at obtaining tighter relative tolerances. In this section, precision machining encompasses removal and forming processes, with micromachining as one of its newest disciplines.

Humans are still best at building structures they can grasp with their hands and see with their eyes, and have only relatively recently started to craft objects at the micro- and nanoscale level. The manufacture of miniature devices is still principally based on top-down manufacturing methods; starting from bigger building blocks, say a whole Si wafer, and reducing them into smaller and smaller pieces by cutting, etching, and slicing. Also, chunks of materials are bolted, riveted, glued, or welded onto the workpiece, or thin layers are deposited onto the substrate. Bottom-up manufacturing methods, in which small particles such as atoms, molecules, and atom clusters are added or removed for the construction of bigger functional structures, are seen by many as the next natural step in human manufacture (e.g., Drexler[2] and Whitesides[3]). Bottom-up methods are nature's way of growing things, and in biomimetics we study how, building bottom-up — that is, atom by atom — nature, through eons of time, developed manufacturing methods, materials, structures, and intelligence. An example of bottom-up manufacturing, or "nanochemistry," is the self-assembly of a monolayer from individual molecules on a gold surface.

Miniaturization science today is still predominantly practiced by electrical and mechanical engineers, but as applications are becoming more and more biological in nature, biologists, materials scientists, chemists, and physicists must work together with electrical and mechanical engineers to develop new miniaturization solutions. We hope that this contribution will further stimulate such collaborations and help bridge the gap between "dry" engineering, in air and with rigid materials, and "wet" engineering, with flexible materials in watery solutions.

Top-Down Manufacturing Methods

Shaping device contours in top-down manufacturing is either lithography based, for example in the fabrication of ICs, or non-lithography based, as in mechanical grinding. Accordingly, the method used results either in truly three-dimensional machines or in projected two-dimensional shapes. The methods may also be characterized according to the energy source involved in removal or addition of materials to the workpiece. The energy sources are chemical (including photochemical), thermal, electrochemical, electrothermal, and mechanical. Here, to illustrate top-down manufacturing, we will review IC processes (which encompass mostly chemical, electrochemical, and thermal processes), LIGA and replication techniques, femto-second laser machining (thermal), and ultraprecision computer numerical controlled (CNC) machining (mechanical) — four techniques most suitable for MEMS fabrication

IC Manufacturing Techniques Suitable for MEMS

Suitable IC techniques for batch manufacturing are applied today to a wide variety of non-IC products, and are also combined with traditional precision manufacturing methods. Undoubtedly, the merging of traditional precision engineering and IC manufacturing methodology will lead to many more interesting, new manufacturing processes. The IC processes of primary interest are lithography, wet and dry etching, and deposition techniques. In each short section we emphasize those features that distinguishes those processes in MEMS from those in IC fabrication.

Lithography

Lithography is a technique used to transfer copies of a master pattern onto the surface of a solid material, such as a silicon wafer. Here we review different forms of lithography, detailing those aspects that differ most from the miniaturization processes used to fashion ICs.

The most widely used form of lithography is photolithography. In photolithography, wavelengths of the light source used for exposure of the resist-coated wafer through a mask featuring the desired pattern, range from the very short wavelengths of extreme ultraviolet (EUV) — 10 to 14 nm, to deep ultraviolet (DUV) — 150 to 300 nm, to near ultraviolet (UV) — 350 to 500 nm. In near UV, one typically uses the g-line (435 nm) or i-line (365 nm) of a mercury lamp. Accurate registration and exposure of a series of successive patterns in a mask aligner lead to complex multilayered ICs. This essentially two-dimensional process has a limited tolerance for nonplanar topography, creating a major constraint for building non-IC miniaturized MEMS systems, which often exhibit extreme topographies. Photolithography has matured rapidly and constantly improved at resolving ever-smaller features. Research in high-aspect-ratio resists features, to satisfy needs of both IC and non-IC miniaturization (e.g., MEMS), is finally also improving photolithography's capacity to cover wide ranges of topography.

Photolithography and pattern transfer involves a set of process steps summarized in Figure 15.3.1. As an example we use an oxidized Si wafer and a negative photoresist system. An oxidized wafer (A) is coated with a 1-μm-thick negative photoresist layer (B). After exposure (C), the wafer is rinsed in a developing solution or sprayed with a spray developer, which removes the unexposed areas of photoresist and leaves a pattern of bare and photoresist-coated oxide on the wafer surface (D). The photoresist pattern is the negative image of the pattern on the photomask. In a typical next step after development, the wafer is placed in a solution of HF or HF + NH_4F, meant to attack the oxide but not the photoresist or the underlying silicon (E). The photoresist protects the oxide areas it covers. Once the exposed oxide has been etched away, the remaining photoresist can be stripped off with a strong acid such as H_2SO_4 or an acid-oxidant combination such as $H_2SO_4 - Cr_2O_3$, attacking the photoresist but not the oxide or the silicon (F). Other liquid strippers include organic solvent strippers and alkaline strippers (with or without oxidants). The oxidized Si wafer with the etched windows in the oxide (F) now awaits further processing. This might entail a wet anisotropic etch of the Si in the oxide windows with SiO_2 as the etch mask.

After near UV lithography has run its course, extreme ultraviolet lithography is one of the most promising next-generation lithography (NGL) options. Extreme ultraviolet lithography (EUVL), using wavelengths in the 10- to 14-nanometer (nm) range to carry out projection imaging, is perhaps the most natural extension of optical projection lithography as in principle it only differs in terms of the wavelength. This type of radiation is also referred to as soft-X-ray radiation and vacuum UV. Sources for this type of radiation are laser-produced plasmas and synchrotrons. The technique is capable of printing sub-100-nm features while maintaining a DOF (depth of focus) of 0.5 μm or larger. Unfortunately things are not that

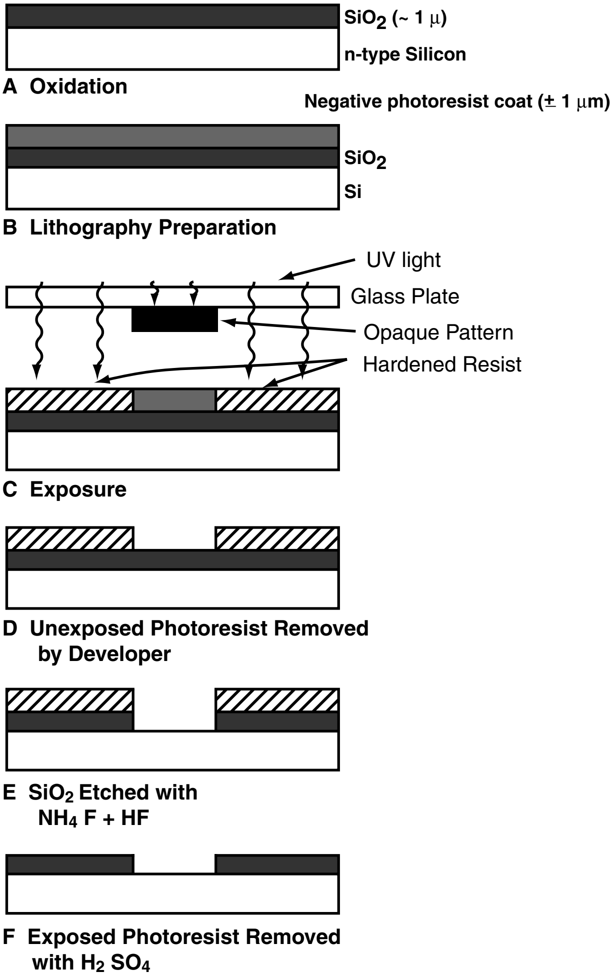

FIGURE 15.3.1 Basic photolithography and pattern transfer. Example uses an oxidized Si wafer and a negative photoresist system. Process steps include exposure, development, oxide etching, and resist stripping. Steps A to F are explained in the text.

simple — EUV is strongly absorbed in virtually all materials and consequently imaging must be carried out in vacuum; also, all camera optics as well as masks used must be reflective rather than refractive. New resists and processing techniques must be developed as well.

In Figure 15.3.2 we compare UV lithography, direct write electron- and ion-beam lithography, and X-ray lithography. Electron-beam and ion-beam lithography are slow, serial direct write techniques, and, since charged particles are involved, they must be held in a vacuum.[4] X-rays do not need to be kept in a vacuum, and another advantage is that one can use flood exposure of resist-coated wafers, ensuring higher throughput than when writing with a thin electron or ion beam. The method is also referred to as deep X-ray lithography (DXRL).

X-ray lithography is superior to optical lithography because of the use of shorter wavelengths and a very large DOF and because exposure time and development conditions are not as stringent. Reproducibility is high as results are independent of substrate type, surface reflections, and wafer topography. Another important benefit is that X-ray lithography is immune to low-atomic-number (Z) particle contamination (dust). With an X-ray wavelength on the order of 10 Å or less, diffraction effects generally are negligible and proximity masking can be used, increasing the lifetime of the mask. With a standard 50 μm proximity gap and using synchrotron X-rays, 0.25 μm patterns can be printed; by decreasing the

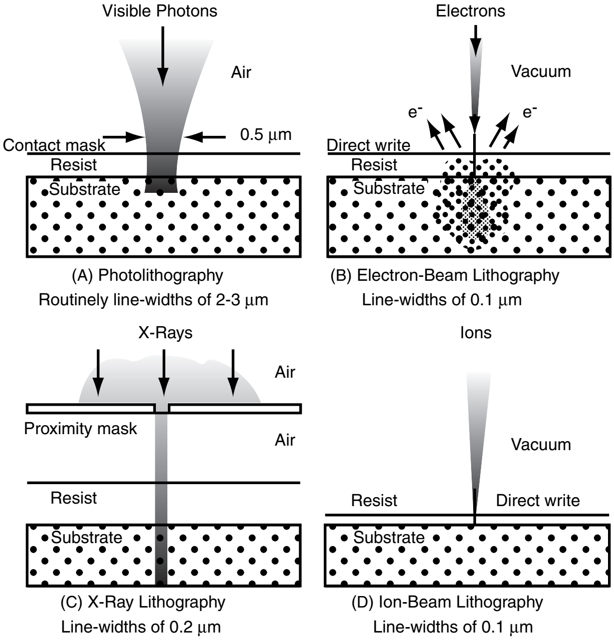

FIGURE 15.3.2 A comparison of photolithography, electron-beam, ion-beam, and X-ray lithography.

proximity gap to 25 µm, patterns of 0.15 µm can be resolved.[5] The obtainable aspect ratio, defined as the structural height or depth to the minimum lateral dimension, reaches more than 100. (With UV photolithography, under special conditions, an aspect ratio of about 25 is possible at most; e.g., by using SU-8 photoresist.) An aspect ratio of 100 corresponds to the aspect ratio attainable by wet chemical anisotropic etching of monocrystalline Si.

In X-ray lithography there are essentially no optics involved, and although this sounds like an advantage, it also presents one major disadvantage — one can only work with 1:1 shadow printing. No image reduction is possible so the mask fabrication process is very complicated.

IC and miniaturization science do have different preferred lithography strategies. The required very high throughput and finer geometries with ICs makes EUVL a good choice. In miniaturization science, modularity, large depth of focus, extending the z-direction, that is, the height of features (skyscraper-type structures), incorporating nontraditional materials (e.g., gas-sensitive ceramic layers, polymers) and replication methods catch the spotlight and very large batch fabrication is not always a prerequisite, making DXRL a better option here.

Wet and Dry Etching

Lithography steps are followed by a number of subtractive and additive processes. Materials are either removed from or added to a device, usually in a selective manner, transferring the lithography patterns onto ICs or three-dimensional micro- or nano-machines. Table 15.3.1 lists the most important subtractive processes encountered in miniaturization science, including wet and dry etching, focused ion-beam (FIB) milling, laser machining, ultrasonic drilling, electro discharge machining (EDM), and traditional precision machining. Applications, which mostly involve Si, typical material removal rates, relevant reference(s), and some remarks on the techniques supplement the list. Two of the most widely used subtractive techniques for micromachining listed in Table 15.3.1 are wet and dry etching. These two most popular techniques are detailed a bit more in what follows.

Wet etching is used for cleaning, shaping three-dimensional structures, removing surface damage, polishing, and characterizing structural and compositional features.[20] The materials etched include semiconductors, conductors, and insulators. The most important parameters in chemical etching are bias

TABLE 15.3.1 Partial List of Subtractive Processes Important in Micromachining

Subtractive Technique	Applications	Typical Etch Rate	Remark	References
Wet chem. etch.: iso.	Si spheres, domes, grooves	Si polishing at 50 μm/min with stirring (RT, acid)	Little control, simple	6
Wet chem. etch.: anis.	Si angled mesas, nozzles, diaphragms, cantilevers, bridges	etching at 1 μm/min on a (100) plane (90°C, alkaline)	With etch-stop more control, simple	6
Electrochem. etch.	Etches p-Si and stops at n-Si (in n-p junction), etches n-Si of highest doping (in n/n+)	p-Si etching 1.25–1.75 μm/min (100) plane, 105–115°C (alkaline)	Complex, requires electrodes	7, 8
Wet photoetch.	Etches p-type layers in p-n junctions	Etches p-Si up to 5 μm/min (acid)	No electrodes required	9
Photo-electrochem. etch.	Etches n-Si in p-n junctions, production of porous Si	Typical Si etch rate: 5 μm/min (acid)	Complex, requires electrodes and light	10
Dry chem. etch.	Resist stripping, isotropic features	Typical Si etch rate: 0.1μm/min (but with more recent methods up to 6 μm/min)	Resolution better than 0.1 μm, loading effects.	11, 12
Physical/chem. etch.	Very precise pattern transfer	Si etch rate: 0.1 to 1 μm/min (but with more recent methods up to 6μm/min)	Most important dry etching technique	12, 13
Physical dry etching, sputter etching, and ion milling	Si surface cleaning, unselective thin film removal	Typical Si etch rate: 300 Å/min.	Unselective and slow, plasma damage	13
Vapor phase etching with XeF$_2$ (and other interhalogens)	Isotropic Si etching in presence of Al and SiO$_2$	Typical Si etch rate: 1–3 μm/min	Very selective, fast, and very simple	14
Focused ion-beam (FIB) milling	Microholes, circuit repair, microstructures in arbitrary materials	Typical Si etch rate: 1 μm/min	Long fabrication time: >2 h including setup	15
Laser machining (with and without reactive gases)	Circuit repair, resistor trimming, hole drilling, labeling of Si wafers	Typical rate for drilling a hole in Si with a Nd:YAG (400W laser): 1 mm/sec (3.5 mm deep and 0.25 mm dia.)	Laser beams can focus to a 1 μm spot, etch with a resolution of 1 μm^3	16
Ultrasonic drilling	Holes in quartz, silicon nitride bearing rings	Typical removal rate of Si: 1.77 mm/min	Especially useful for hard, brittle materials	17
Electrostatic discharge machining (EDM)	Drilling holes and channels in hard brittle metals	Typical removal rate for metals: 0.3 cm^3/min	Poor resolution (>50 μm), only conductors, simple, wire discharge machining resolution much better	18
Mechanical turning, drilling and milling, grinding, honing, lapping, polishing, and sawing	Almost all machined objects surrounding us	Removal rates of turning and milling of most metals: 1 to 50 cm^3/min, for drilling: 0.001 to 0.01 cm^3/min	Prevalent machining technique	19

RT = room temperature, chem. etch. = chemical etching, iso. = isotropic, anis. = anistropic

(undercut), tolerance, etch rate, anisotropy and selectivity, over etch, feature size control, and loading effects. The emphasis in what follows is on Si, but the application is generic. Isotropic etchants, also polishing etchants, etch in all crystallographic directions at the same rate; they usually are acidic, such as HF/HNO$_3$/CH$_3$COOH (HNA), and lead to rounded isotropic features in single crystalline Si. The

HNA etch is also known as the "poly-etch" because in the early days of the integrated circuit industry it was used as an etchant for polysilicon.[21] Isotropic etchants are used at room temperature or slightly above (<50°C). Historically they were the first Si etchants introduced.[20,22–29] [Later it was discovered that some alkaline chemicals will etch anisotropically, that is, they etch away crystalline silicon at different rates depending on the orientation of the exposed crystal plane. Typically the pH stays above 12, while more elevated temperatures are used for these slower type etchants (>50°C). The latter type of etchants surged in importance in the late 1960s for the fabrication of dielectrically isolated structures in silicon.[30–44] These anisotropic etching procedures heralded the emergence of what is now called bulk micromachining. Anisotropic etching of Si also heralded the beginning of MEMS. Isotropic etchants typically show diffusion limitation, whereas anisotropic etchants are reaction rate limited. In both cases the two principal reactions are oxidation of the silicon followed by dissolution of the hydrated silicate.

Wet chemical etching of Si provides a higher degree of selectivity than dry-etching techniques (as we discuss in a moment). Wet etching usually is also faster; a few microns to tens of microns per minute for isotropic etchants and about 1 µm/min for anisotropic wet etchants vs. 0.1 µm/min or less in typical dry etching. More recently, though, with inductively coupled plasma (ICP) dry etching of Si, rates of up to 6 µm/min are achieved. Modification of wet etchant and/or temperature can alter the selectivity to silicon dopant concentration and type and, especially when using alkaline etchants, to crystallographic orientation.

A typical set of examples of wet etched isotropic and anistropic Si pieces is shown in Figure 15.3.3.

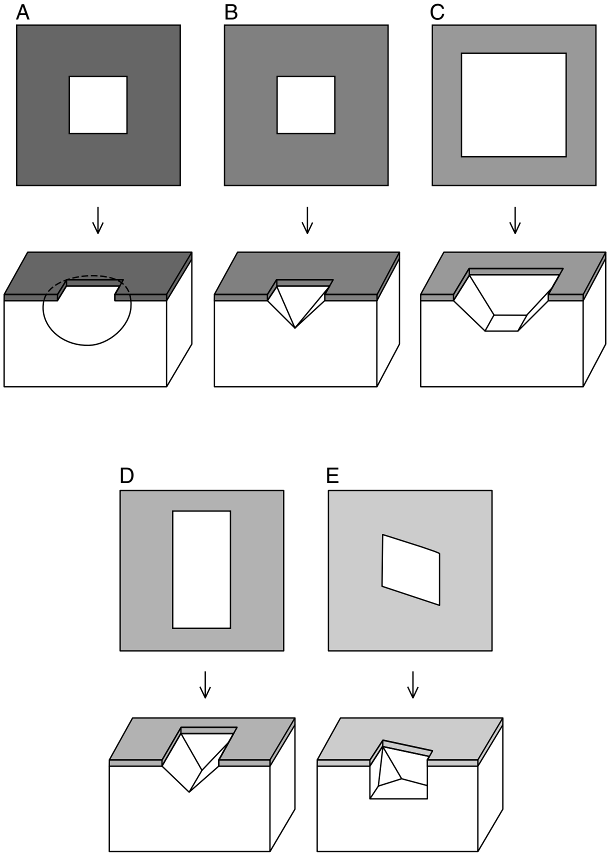

FIGURE 15.3.3 Isotropic and anisotropic wet etched features in [100] and [110] Si wafers. (A) isotropic etch; (B) through (E) anisotropic etch. (A) through (D): [100]-oriented wafers and [E]:[110]-oriented wafer.

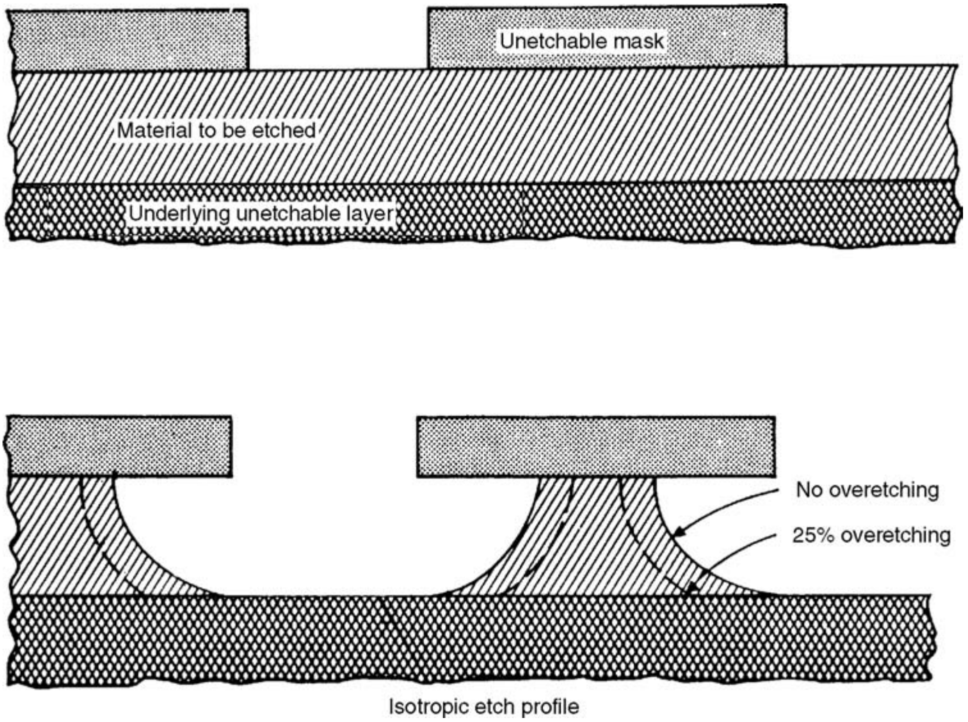

FIGURE 15.3.4 Example of various etch profiles obtained with dry etching in Si.

Dry etching covers a family of methods by which a solid surface is etched in the gas or vapor phase, physically by ion bombardment, chemically by a chemical reaction through a reactive species at the surface, or by combined physical and chemical mechanisms. Plasma-assisted dry etching is categorized according to the specific setup as either *glow discharge* (diode setup) or *ion beam* (triode setup). Using glow discharge techniques, plasma is generated in the same vacuum chamber where the substrate is located; when using ion-beam techniques, plasma is generated in a separate chamber from which ions are extracted and directed in a beam toward the substrate by a number of grids. It is also common to differentiate between (1) chemical plasma etching (PE), (2) synergetic reactive ion etching (RIE), and (3) physical ion-beam etching (IBE).[45] In sputter/ion etching and ion-beam milling, or IBE, etching occurs as a consequence of a physical effect, namely momentum transfer between energetic Ar^+ ions and the substrate surface. Some type of chemical reaction takes place in all the other dry-etching methods. In the case of physical/chemical RIE, impacting ions, electrons, or photons either induce chemical reactions or, in sidewall-protected ion-assisted etching, a passivating layer is cleared by the particle bombardment from horizontal surfaces only. As a result, in the latter case etching occurs almost exclusively on the cleared planar surfaces. In reactive PE, neutral chemical species such as chlorine or fluorine atoms generated in the plasma diffuse to the substrate where they react to form volatile products with the layer to be removed. The only role of the plasma is to supply gaseous, reactive etchant species.

In selecting a dry-etching process, the desired shape of the etch profile and the selectivity of the etching process require careful consideration. Figure 15.3.4 shows different possible etch profiles,[11] where, depending on the mechanism employed, isotropic, directional, or vertical etch profiles are obtained. In dry etching anisotropic etch profiles — directional or vertical — can be generated in single crystalline, polycrystalline, and amorphous materials. The anisotropy is not a result of anisotropy in the etching rate of single crystals as in the case of anisotropic wet chemical etching; rather, the degree of anisotropy is controlled by the plasma conditions. Selectivity of a dry etch refers to the difference in etch rate between the mask and the film to be etched, again controllable by plasma conditions.

TABLE 15.3.2 Comparison of Dry and Wet Thin Film Etching Processes

	Dry Etching		Wet Etching	
Etching Factors	Ion Etching	RIE	Chemical	Electrochemical
Driving force	Plasma	Reactive gases	Etching solution	External current
Environment	Vacuum	Vacuum	Acidic/Alkaline	Mostly neutral Salt solutions
Rate	~100 Å/min	~1000 Å/min	~1 μ/min	10 μ/min
Selectivity	Poor	High	Very High	Very high
Wall slope control	Directional	Anisotropic (flexible)	Isotropic	Better than chemical
Safety and environmental concerns	Low	Moderate/high	High	Low
Monitoring and control issues	Some	Some	Many	Few
Cost	High	High	Low	Moderate

Source: Based on Dr. M. Datta (http://www.research.ibm.com/journal/rd/425/datta.html)

The preference of dry stripping over wet stripping methods is based on a variety of advantages: fewer disposal problems; less corrosion of metal features in the structure, and less undercutting and broadening of photoresist features, that is, better CD control (nanometer dimensions); and, under the right circumstances, a cleaner resulting surface. Also, with the new generations of ICs, all with sub-quarter-micron geometries, surface tension might preclude a wet etchant from reaching down between photoresist features, whereas dry etching precludes any such problem. As in IC manufacture, dry etching has evolved into an indispensable technique in miniaturization science. After the success of wet etched Si micromachined products in the 1980s and early 1990s the maturation of flexible, generic, and fast anisotropic deep reactive ion etching (DRIE) techniques in the late 1990s spawned a second wave of Si miniaturized commercial products.

Different dry and wet thin film etching processes that are applicable in microfabrication are compared in Table 15.3.2 (based on http://www.research.ibm.com/journal/rd/425/datta.html). Dry-etching processes are particularly suitable for patterning very fine dimensions. Relatively low etching rates (at the very best 6 μm/min in DRIE) and high equipment cost restrict their application to precision etching of thin films involving very small amounts of material removal. Wet chemical etching methods, on the other hand, are used in microfabrication because of their selectivity and high etch rates. They are predominantly used in large-scale production of metallic parts involving bulk metal removal. Treatment and disposal of hazardous waste contribute significantly to the product cost in chemical wet-etching manufacturing processes but much less so in electrochemical machining.

Deposition Techniques

Solids can be deposited onto a substrate from a liquid, a plasma, a gas, or a solid state. These additive techniques are often accompanied or followed by thermal processing to obtain desired materials properties and substrate adhesion. Although deposition methods, especially in the thin film arena, are generally the same as in ICs, additive processes in miniaturization science span a much wider range from inorganic to organic materials. Besides the typical microelectronic elements — Si, Al, Au, Ti, W, Cu, Cr, O, N, and Ni-Fe alloys — miniaturization science involves deposition of several nontypical elements such as Zr, Ta, Ir, C, Pt, Pd, Ag, Zn, In, Nb, and Sn. Moreover a plethora of exotic compounds ranging from enzymes to shape memory alloys and from hydrogels to piezoelectrics are used. The number of materials and compounds involved in IC fabrication, in comparison, is very limited. In miniaturization science, particularly in chemical sensors and biomedical devices, modular, thick film technologies are more prevalent.

Table 15.3.3 presents additive processes; Table 15.3.4 lists MEMS materials, typical deposition techniques, and an example application for the deposit. The references in Table 15.3.3 are meant as a basis for further study of additive processes.

In the deposition methods from the gas phase listed in Table 15.3.3, two major categories can be distinguished: direct line-of-sight impingement deposition techniques called *physical vapor deposition*

TABLE 15.3.3 Additive Processes

Additive	Application Example	Reference
Bonding techniques	7740 glass to silicon	46
Casting	Thick resist (10-1000 μm)	
Chemical vapor deposition	Tungsten on metal	47
Dip coating	Wire type ion selective electrodes	
Droplet delivery systems	Epoxy, chemical sensor membranes	
Electrochemical deposition	Copper on steel	48
Electroless deposition	Vias	49
Electrophoresis	Coating of insulation on heater wires	
Electrostatic toning	Xerography	
Ion cluster deposition		50
Ion implantation and diffusion of dopants	Boron into silicon	51
Ion plating	Metal on insulators	50
Laser deposition	Superconductor compounds	52
Liquid phase epitaxy (CVD)	GaAs	53
Material transformation (oxidation, nitridation, etc.)	Growth of SiO_2 on silicon	54
Molecular beam epitaxy (PVD)	GaAs	55
Plastic coatings	Electronics packages	56
Screen printing	Planar ion selective electrodes (ISEs)	57
Silicon crystal growth	Primary process	58
Spin-on	Thin resist (0.1–2 μm)	58
Spray pyrolysis (CVD)	CdS on metal	59
Sputter deposition (PVD)	Gold on silicon	60
Thermal evaporation (PVD)	Aluminum on glass	60
Thermal spray deposition from plasmas or flames	Coatings for aircraft engine parts and ZrO_2 sensors	61
Thermomigration	Aluminum contacts through silicon	62

(PVD) and diffusive-convective mass transfer techniques, that is, *chemical vapor deposition* (CVD). See Figure 15.3.5 for an example of a PVD and a CVD reactor.

Evaporation, sputtering, molecular beam epitaxy (MBE), laser ablation deposition, ion plating, and cluster deposition represent PVD techniques. CVD techniques include plasma-enhanced (PECVD), atmospheric pressure (APCVD), low-pressure (LPCVD), very low pressure (VLPCVD), electron cyclotron resonance (ECRCVD), metallorganic (MOCVD), and spray pyrolysis. Epitaxial techniques have gained importance in ICs and mechanical sensor fabrication. A particulate deposition technique, such as plasma spraying, has potential for chemical sensor applications. Like spray-pyrolysis, plasma spraying does not have IC industry applications but might propel planar thick film chemical sensors into the realm of "batch" manufacturability.

With the growth of the BIOMEMS field, techniques for depositing organic materials for chemical and biological sensors, often arranged in some type of an array configuration, are gaining importance. Techniques with special merit for chemical and biological sensor manufacture include spin coating, dip coating, plastic spraying, casting, Doctors' blade or tape casting, silk-screening, plasma polymerization, and Langmuir-Blodgett deposition. For sensor array manufacture, lithography, ink jetting, mechanical microspotting, digital mirror deposition, and electrochemical deposition of functional chemistries are important.

Electrochemical and electroless metal deposition and micromolding are gaining renewed interest because of the emerging importance of replication methodologies in MEMS.

Surface micromachining constitutes a combination of CVD deposition of structural materials (e.g., poly-Si), dry etching to pattern the structural material and wet etching of sacrificial layers (e.g., SiO_2). A surface micromachining process sequence for the creation of a simple freestanding poly-Si bridge is illustrated in Figure 15.3.6.[64,65] A sacrificial layer, also called a spacer layer or base, is deposited on a silicon substrate coated with a dielectric layer as the buffer/isolation layer (Figure 15.3.6A). Phosphosilicate glass

TABLE 15.3.4 IC and MEMS Materials, Deposition Method, and Typical Application

Material	Deposition Technique	Function
Organic Thin Films		
Hydrogel	Silk screen	Internal electrolyte in chemical sensors
Photoresist	Spin-on	Masking, planarization
Polyimide	Spin-on	Electrical isolation, planarization, microstructures
Metal Oxides		
Aluminum oxide	CVD, sputtering, anodization	Electrical isolation
Indium oxide	Sputtering	Semiconductor
Tantalum oxide	CVD, sputtering, anodization	Electrical isolation
Tin oxide(SnO_2)	Sputtering	Semiconductor in gas sensors
Zinc oxide	Sputtering	Electrical isolation, piezoelectric
Non-Crystalline Silicon Compounds		
α-Si-H	CVD, sputtering, plasma CVD	Semiconductors
Polysilicon	CVD, sputtering, plasma CVD	Conductor, microstructures
Silicides	CVD, sputtering, plasma CVD, alloying of metal and silicon	Conductors
Metals (thin films) with ρ in $\mu\Omega\cdot$cm in ()		
Silver (Ag) (1.58)	Evaporation; sputtering	Electrochemistry electrode
Aluminum (Al) (2.7)	Evaporation, sputtering, plasma CVD	Electrical interconnects, limited to operations below 300°C
Chromium (Cr) (12.9)	Evaporation, sputtering, electroplating	Electrical conduction, adhesion layer (10–100 nm)
Gold (Au) (2.4)	Evaporation, sputtering, electroplating	Electrical interconnects for higher temperatures than Al, optical reflection in the IR
Iridium (Ir) (5.1)	Sputtering	Electrochemistry electrode, biopotential measurements
Molybdenum	Sputtering	Electrical conduction
Platinum(Pt) (10.6)	Sputtering	Electrochemistry electrode, biopotential measurements
Palladium (Pd) (10.8)	Sputtering	Electrical conduction, adhesion layer, electrochemistry electrode, solder wetting layer
Tungsten (W) (5.5)	Sputtering	Electrical interconnects at higher temperatures
Titanium(Ti) (42)	Sputtering	Adhesion layer
Copper(Cu) (1.7)	Sputtering	Low resistivity interconnects
Alloys		
Al-Si-Cu	Evaporation, sputtering	Electrical conduction
Nichrome(NiCr) (200–500)	Evaporation, sputtering	Thin film laser-trimmed resistor
Permalloy™ (Ni_xFe_y)	Sputtering	Magnetoresistor, thermistor
TiNi (80)	Sputtering	Shape memory alloy
Chemically/Physically Modified Silicon		
n/p type silicon	Implantation, diffusion, incorporation in the melt	Conduction modulation, etch stop
Porous silicon	Anodization	Electrical isolation, light-emitting structures, porous junctions
Silicon dioxide	Thermal oxidation, sputtering, anodization, implantation, CVD	Electrical and thermal isolation, masking, encapsulation
Silicon nitride	Plasma enhanced CVD (PECVD)	Electrical and thermal isolation, masking, encapsulation

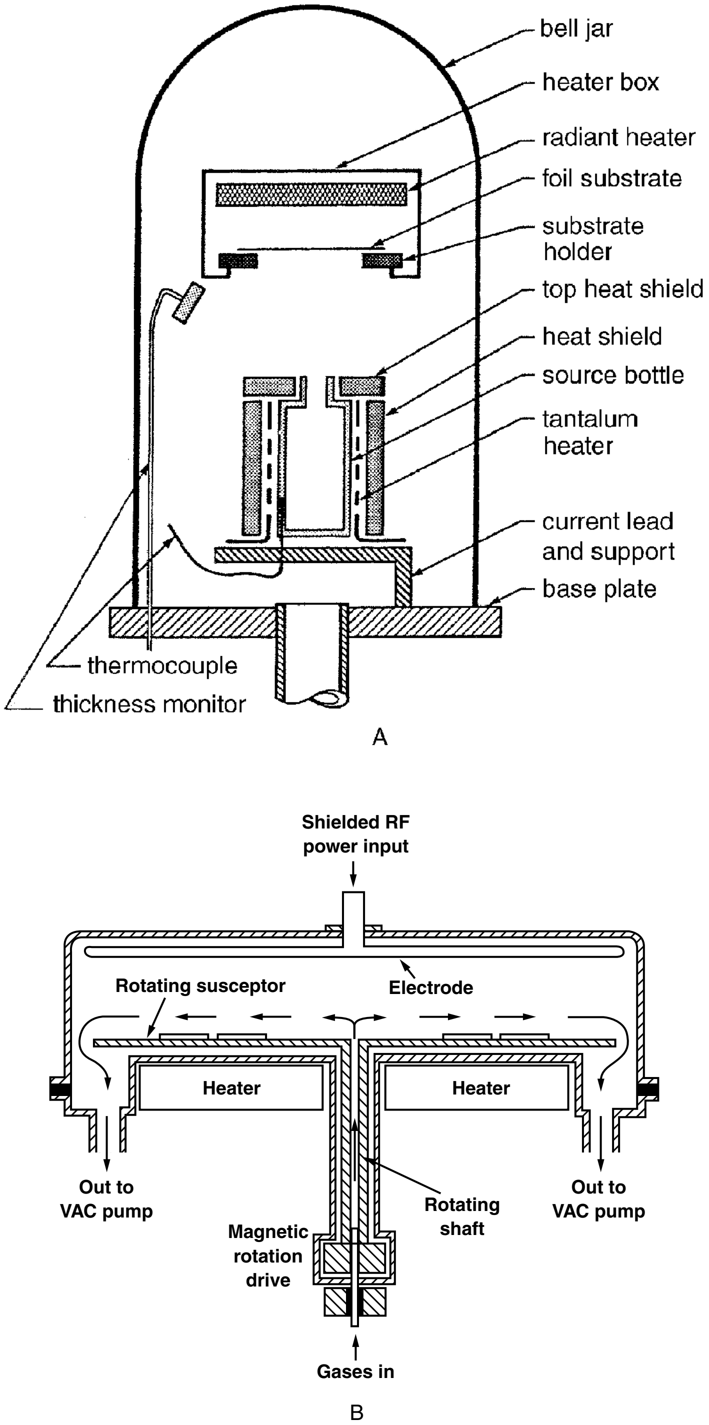

FIGURE 15.3.5 Example setup for PVD: (A) typical thin film deposition by evaporation setup; and (B) for CVD, cross section of a PECVD reactor from Applied Materials.

(PSG) deposited by LPCVD stands out as the best material for the sacrificial layer because it etches even more rapidly in HF than SiO_2. In order to obtain a uniform etch rate, the PSG film must be densified by heating the wafer to 950–1100°C in a furnace or a rapid thermal annealer (RTA).[65] With a first mask,

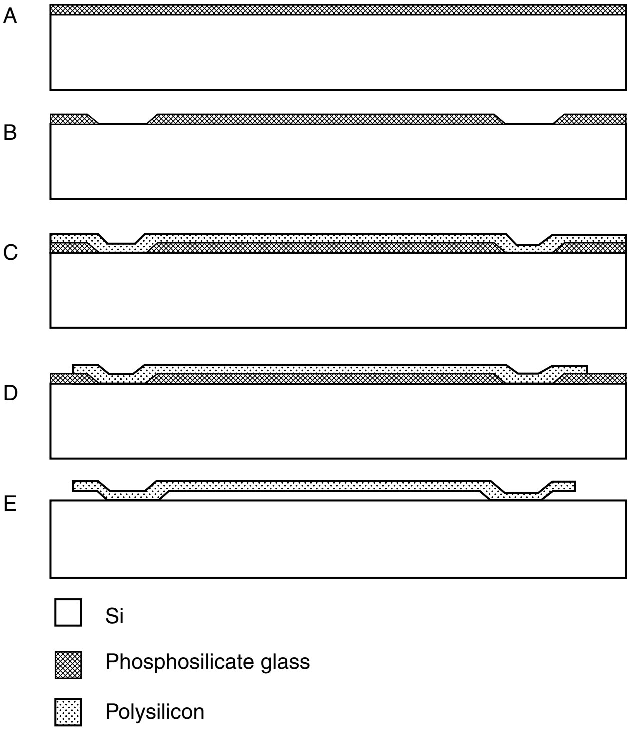

FIGURE 15.3.6 Basic surface micromachining process sequence. (A) Spacer layer deposition (the thin dielectric insulator layer is not shown). (B) Base patterning with mask 1. (C) Microstructure layer deposition. (D) Pattern microstructure with mask 2. (E) Selective etching of spacer layer.

the base is patterned as shown in Figure 15.3.6B. Windows are opened up in the sacrificial layer and a microstructural thin film, whether consisting of polysilicon, metal, alloy, or a dielectric material, is conformably deposited over the patterned sacrificial layer (Figure 15.3.6C). Furnace annealing, in the case of polysilicon at 1050°C in nitrogen for one hour, reduces stress stemming from thermal expansion coefficient mismatch and nucleation and growth of the film. Rapid thermal annealing has been found effective for reducing stress in polysilicon as well.[63] With a second mask, the microstructure layer is patterned, usually by dry etching in a CF_4 + O_2 or a CF_3Cl + Cl_2 plasma (Figure 15.2.6D).[66] Finally, selective wet etching of the sacrificial layer, say in 49% HF, leaves a freestanding micromechanical structure (Figure 15.3.6E). The surface micromachining technique is applicable to combinations of thin films and lateral dimensions where the sacrificial layer can be etched without significant etching or attack of the microstructure, the dielectric, or the substrate. Typically a surface micromachining stack may contain a total of four to five structural and sacrificial layers but more are possible; the poly-Si surface machining process at Sandia's SUMMIT, for example, stacks up to five polysilicon and five oxide layers.

LIGA and Replication Techniques

LIGA is the German acronym for X-ray lithography (X-ray *lithographie*), electrodeposition (*galvanoformung*), and molding (*abformtechnik*). The process involves a thick layer of X-ray resist — from microns to centimeters — high-energy X-ray radiation exposure, and development to arrive at a three-dimensional resist structure. Subsequent metal deposition fills the resist mold with a metal and, after resist removal, a freestanding metal structure results.[67] The metal shape may be a final product or serve as a mold insert for precision plastic molding. Molded plastic parts may in turn be final products or lost molds (see Figure 15.3.7). The plastic mold retains the same shape, size, and form as the original resist structure but is produced quickly and inexpensively as part of an infinite loop. The plastic lost mold may generate metal parts in a second electroforming process or generate ceramic parts in a slip casting process.

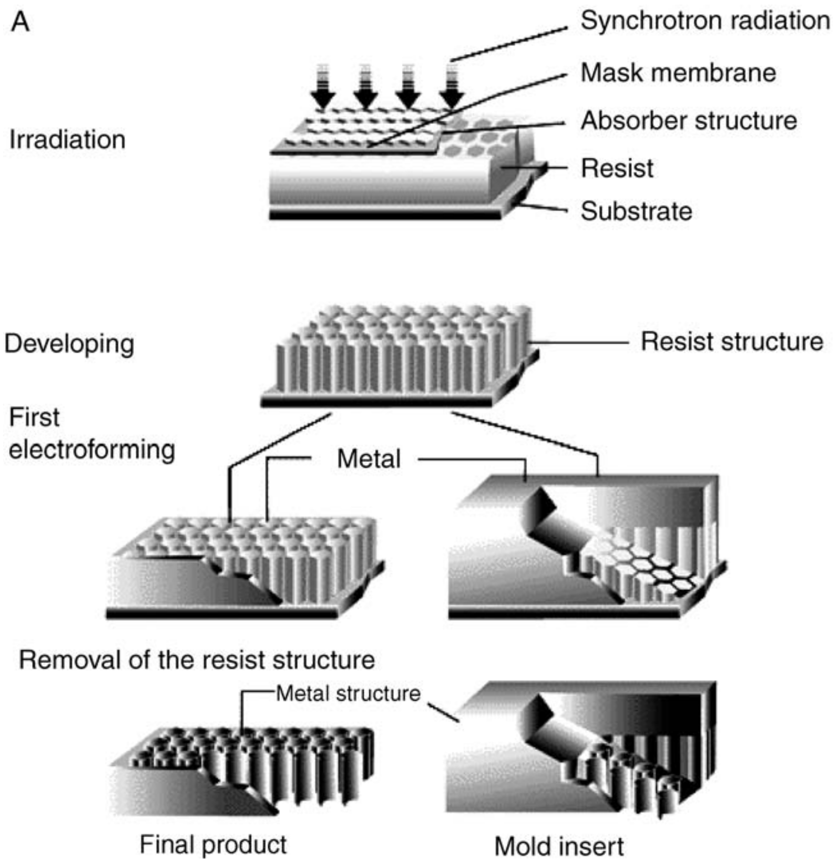

FIGURE 15.3.7 (A) The basic LIGA process steps X-ray deep-etch lithography and first electroforming. (B) Plastic molding and second electroforming/slip casting. (After H. Lehr and M. Schmidt, *The LIGA Technique*, commercial brochure, IMM GmbH, Mainz-Hechtsheim, 1995. With permission.)

The bandwidth of possible sizes in all three dimensions renders LIGA useful for manufacture of microstructures (micron and submicron dimensions), of packages for these microstructures (millimeter and centimeter dimensions), and even for the connectors from those packages to the "macro world" (electrical, e.g., through-vias or physical, e.g., gas in- and outlets).

Once LIGA was established in the research community, interest in other micro- and nano-replication methods became more pronounced. Given the cost of the LIGA equipment, various LIGA-like processes took center stage. These pseudo-LIGA methods involve replication of masters created by alternate means such as deep reactive ion etching (DRIE) and novel ultraviolet thick photoresists. This more generalized lithography and replication procedure is illustrated in Figure 15.3.8.

Micromachining techniques are reshaping manufacturing approaches for a wide variety of small parts. Frequently, IC-based batch microfabrication methods are considered together with more traditional, serial machining methods. In this evolution, LIGA and pseudo-LIGA processes constitute "handshake-technologies," bridging IC and classical manufacturing technologies. The capacity of LIGA and pseudo-LIGA for creating a wide variety of shapes from different materials makes these methods akin to classical machining with the added benefit of unprecedented aspect ratios and absolute tolerances rendered possible by lithography or other high-precision mold-fabrication techniques. The high cost of X-ray lithography caused many miniaturization engineers to search for alternate means for fabricating high-aspect-ratio metal or polymer micro-masters. Micromold inserts (or micro-masters) can be fabricated by a variety of alternate techniques, such as CNC machining, silicon wet bulk micromachining, precision

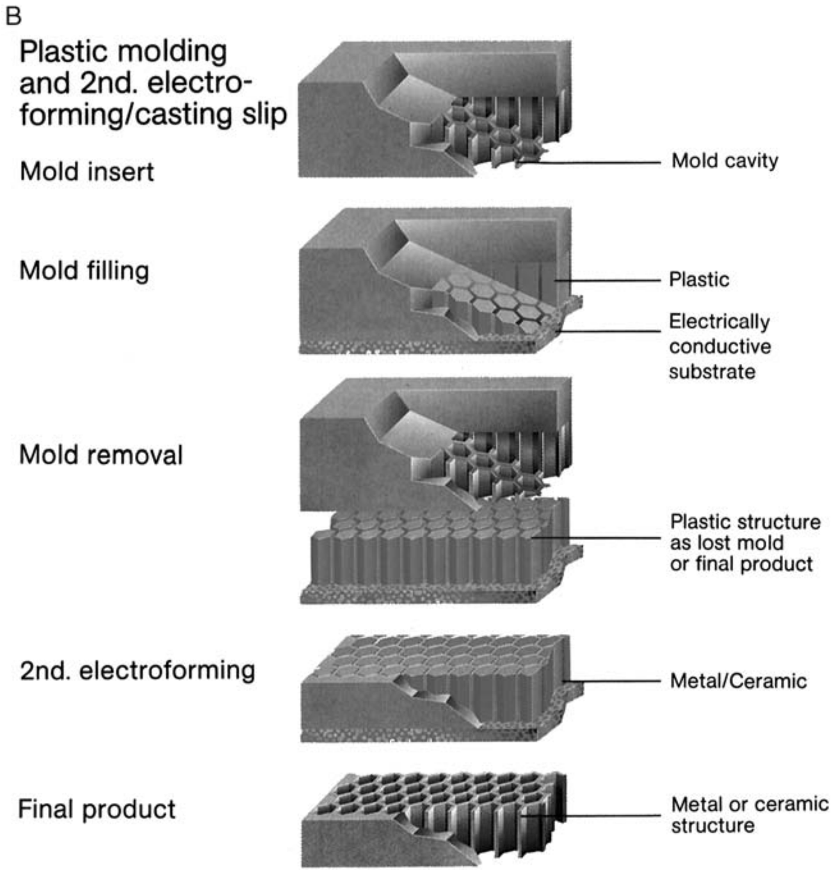

FIGURE 15.3.7 (continued).

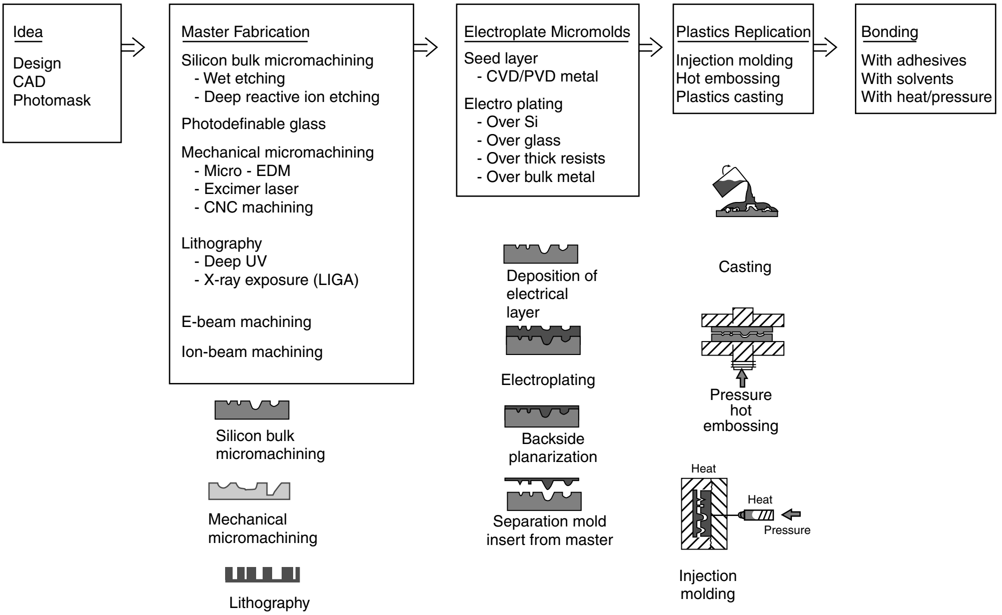

FIGURE 15.3.8 Process flow for plastic microfabrication.

TABLE 15.3.5 Comparison of Micromolds

Parameters	LIGA	DUV	DRIE	LASER	CNC	EDM
Aspect ratio	100	22		<10	14:1 holes (drilling)	Up to 100
Wall roughness	<50 nm		Problematic	100 nm	0.1 μm	0.3–1 μm
Accuracy	<1 μm			A few microns		Some microns
Mask needed?	Yes	Yes	Yes	No	No	No
Maximum height	A few 100 μm	A few 100 μm	A few 100 μm	A few 100 μm	Unlimited	Microns to millimeters

Source: L. Weber, W. Ehrfeld, H. Freimuth, M. Lacher, H. Lehr, and P. Pech, in *SPIE, Macromachining and Microfabrication Process Technology II*, Austin, Texas, 1996, 156–167. With permission.

EDM, thick deep UV resists, DRIE, excimer layer ablation, and e-beam writing. In Table 15.3.5 LIGA metal molds are compared with metal masters fabricated by other means. For example, comparing metal mold inserts made by spark erosive cutting and X-ray lithography, the latter proves far superior.[69] LIGA PMMA features as small as 0.1 μm are replicated in the metal shape with almost no defects. The electroformed structures have a superior surface quality with a surface roughness, R_{max}, of less than 0.02 μm.[70]

Deep reactive-ion etching (DRIE) and thick deep UV-sensitive resists (DUV) such as polyimides, AZ-4000, and SU-8 are recent contenders for micro-master mold fabrication. With respect to dry etching, higher and higher aspect ratio features are being achieved; especially when using highly anisotropic etching conditions as in cryogenic DRIE and in the Bosch process, remarkable results are obtained. Wall roughness, causing form locking, remains a problem with DRIE; the dry-etching process was optimized for speed, not for demolding. For small-quantity production, where the lifetime of mold inserts is not crucial, a silicon wafer etched by DRIE can be utilized directly as a mold insert for anywhere from 5 to 30 molding cycles.[72,73] Figure 15.3.9A shows such a Si mold for building a two-point calibration fluidic device on a compact disc. Wet etching of Si leads to much smoother surfaces than DRIE and is therefore the preferred method for making mastermolds out of Si. For much longer-lasting molds, metallizing the Si structure and using the metal as mold is preferred. Photoresist structures on a silicon substrate have also been tested as mold inserts in plastic molding because of the simplicity and low cost of the process. Figure 15.3.9B shows a SU-8 photoresist mold for the same lab CD platform shown in Figure 15.3.9A. In low-pressure molding processes, such mold inserts do work for a limited number of runs (applying a thin metal layer over the top of the resist may further extend the lifetime of the mold), but their applicability in high-pressure processes needs to be further verified. A better approach is to use deep UV-photosensitive resists for electroplating to yield a metal tool, usually nickel or nickel-cobalt. Figure 15.3.9C shows a nickel mold insert made using SU-8 in our lab for the two-point calibration microfluidic platform. Both DUV and DRIE are more accessible than LIGA and will continue to improve, taking more opportunities away from LIGA. Like LIGA, both alternative techniques can be coupled with plating, but neither technique can yet achieve the extreme low surface roughness and vertical walls of LIGA.

Other competing technologies for making metal masters are laser ablation methods and ultraprecision CNC machining. The latter methods are serial processes and rather slow, but since we are considering the production of a master only these technologies might well be competitive for certain applications.

Laser microablation produces minimum features of about 10 μm width and aspect ratios of 1:10. Challenges include taper and surface finish control. Recast layers around the laser drilled features cause form locking and infidelity in the replication. Femtosecond pulse lasers promise thinner or even the absence of recast layers and excellent resolution, and should be investigated further (see also below).[74]

For large features (>50 μm) with tolerances and repeatability in the range of about 10 μm, traditional CNC machining of materials like tool steel and stainless steel is often accurate enough for making metal mold inserts. The advantage of this technique is that the tool materials used are the same as those in conventional polymer molding, so their design, strength, and service life are well established. Complicated three-dimensional structures can also be machined easily. The main drawbacks are that it is difficult to

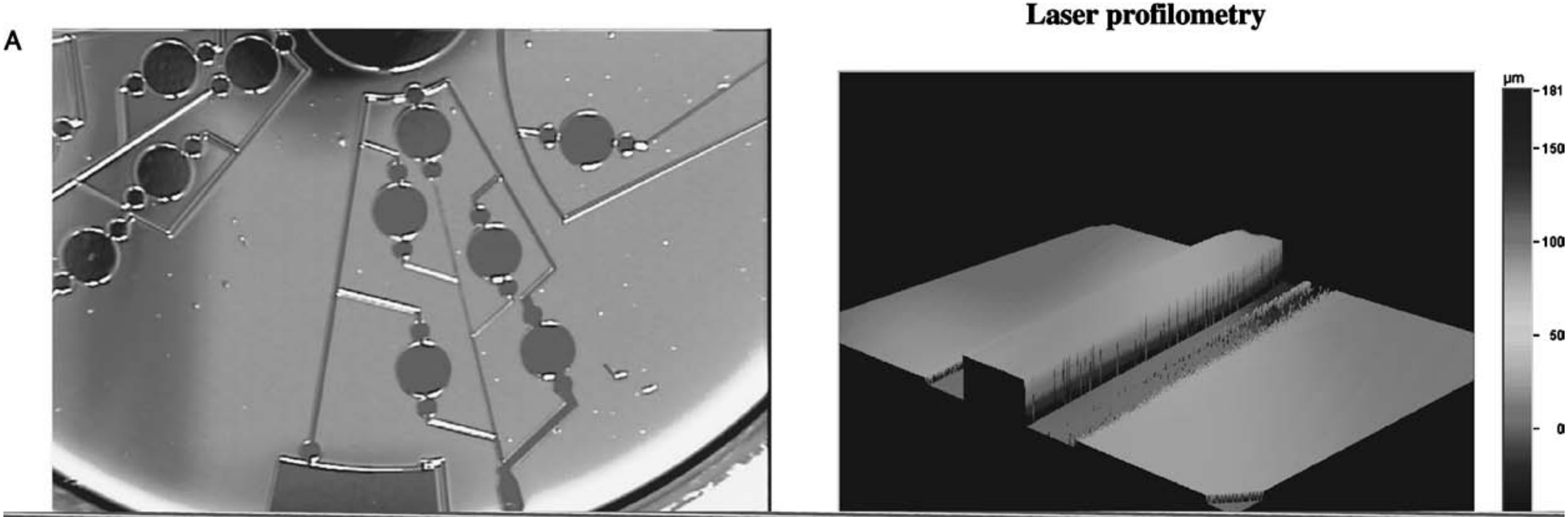

FIGURE 15.3.9A Silicon mold insert made by UV photolithography and deep reactive-ion etching (DRIE) at Burstein Technologies/UCLA/OSU.

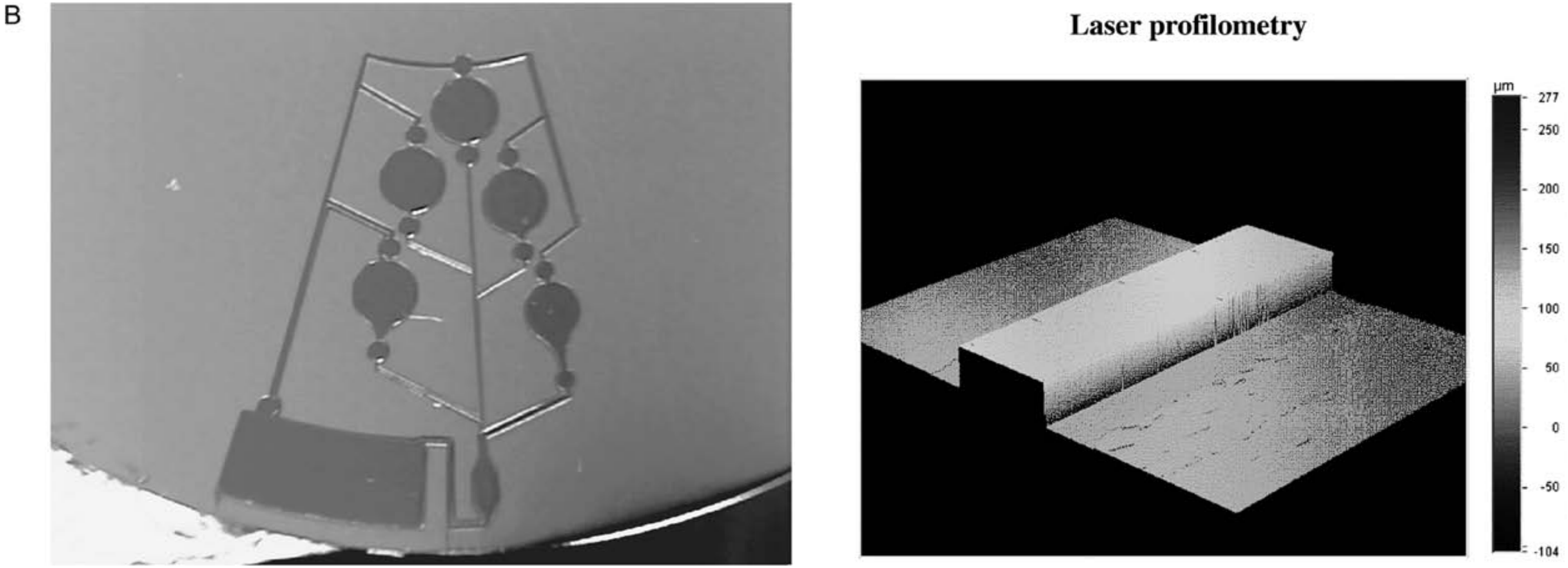

FIGURE 15.3.9B Photoresist (SU-8) mold insert made by UV lithography at OSU.

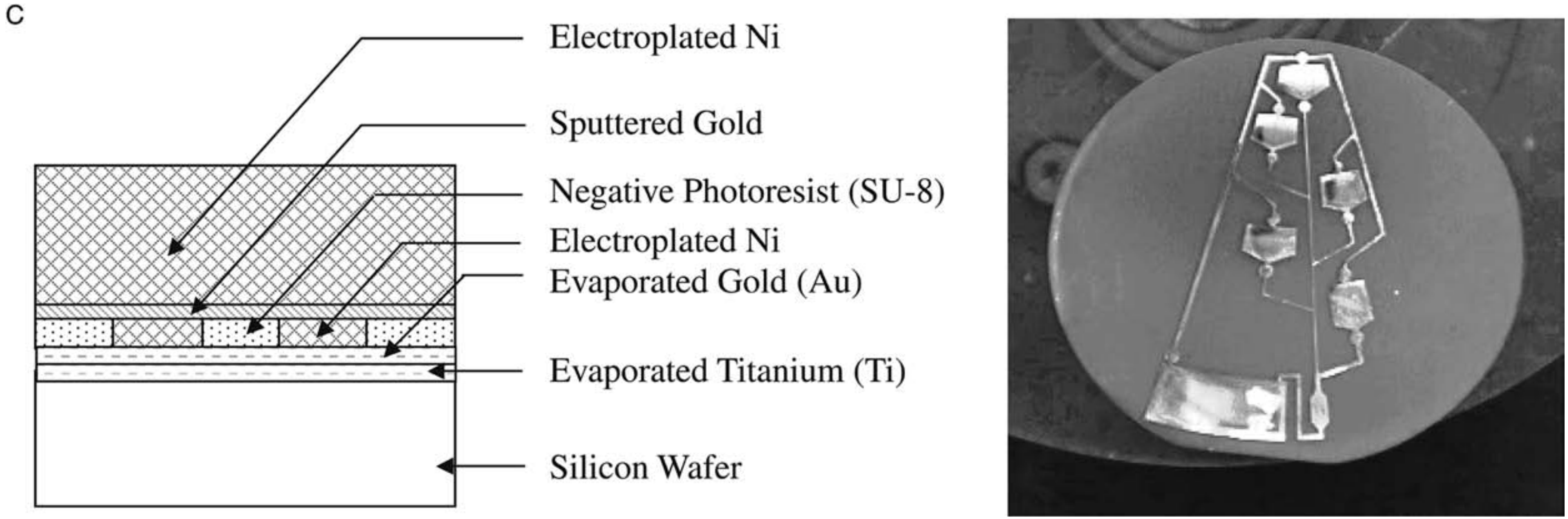

FIGURE 15.3.9C Nickel mold insert made by UV photolithography and electroplating (OSU). The depth of the etched channel is measured by a laser profilometer.

make sharp corners or right angles, and the surface quality is usually poor (surface roughness is around several μm).[75] In contrast, lithographic methods can produce molds with excellent surface quality (surface quality < 0.1 μm), and sharp corners or right angles. However, they cannot be used on conventional tool materials like steel. Diamond-based micromilling and microdrilling[76] reduce the surface roughness to 1 μm or less.[77] While diamond-based methods can achieve features smaller than 10 μm, they are only applicable to "soft" metals such as nickel, aluminum, and copper.

From Table 15.3.5 a significant potential application of LIGA remains the fabrication of those metal molds that cannot be accomplished with other techniques because of the tight wall roughness tolerances, small size, and high-aspect-ratios. From the table it is obvious that LIGA micromolds excel in both very low surface roughness and excellent accuracy.

Summarizing, the requirements for an optimal mold insert fabrication technique are[78]

1. The master has to be removed from the molded structure, so the ease of release through wall inclination control is crucial (undercuts, for example, cannot be tolerated as they cause form locking).
2. The most important parameter, including master lifetime and achievable aspect ratios, depend strongly on the surface quality of the master.
3. The interface chemistry between master and polymer is a critical factor and must be controlled.

Laser Machining

Conventional lithographic techniques for making three-dimensional shapes are limited to unidirectional extensions of two-dimensional patterns. By using laser-beam removal processes, truly three-dimensional structures can be made without the need of masks. Three-dimensional structures are first constructed using a commercial solid-modeling software package. Then these structures are digitized into a stack of planar software masks, each comprising an array of pixels. In a laser machining setup, depth contouring is accomplished by dynamically refocusing the laser beam. Numerous different profiles (masks) can be stored in the laser positioning system and recalled as required. Laser machining is not always narrow beam based. In the case of excimer lasers, a quite broad beam of UV is produced and the shape of the micromachined structures may be controlled by using a chrome on quartz mask, like the masks produced for photolithography. In the simplest system, the mask is placed in contact with the material being machined, and the laser light is shone through it.

Like other thermal removing techniques, laser machining does leave a heat affected zone (HAZ) on the workpiece where molten material resolidified *in situ* or where material was sufficiently heated and cooled rapidly enough to result in embrittlement. This change in material properties can alter subsequent laser ablation and material performance.

Micromachining with laser ablation was first reported by R. Srinivasan and V. Mayne-Banton of IBM Research in 1982.[79] Initial studies by Srinivasan and co-workers showed that pulsed ultraviolet laser radiation at 193 nm can be used to etch organic polymers several micrometers in depth. To illustrate how fast things have been moving since but how little yet is known of the fundamental underlying processes in this field, consider that it was only recently recognized that femtosecond laser pulses interact with matter in a manner that is totally different from traditional lasers with longer pulses. During machining with femtosecond lasers, much less heat dissipates in the substrate, and as a consequence, ultrafast lasers present the potential for micromachined products of superior quality.

Based on pulse length there are three major laser machining operation modes; short, ultrashort, and long (or continuous wave [CW]). *Short* means that the pulse is longer than 10 picoseconds. *Ultrafast* or *ultrashort* means that the laser pulse has a duration that is somewhat less than 10 picoseconds — usually some fraction of a picosecond. *Long* or *CW* lasers are lasers that are operated in a continuous wave (pulse duration > 0.25s) rather than a pulsed mode. Each operation mode has its own micromachining applications. Short pulses of coherent light replace electrons from the electron beam vacuum technology as the cutting tool by vaporizing the substrate (subtractive process). No vacuum is required, but the removal rate is much slower than in electron-beam machining. With ultrashort pulses, so much energy is deposited

TABLE 15.3.6 Laser Parameter and Related Processing Parameters

Laser Parameter	Influence on Material Processing
Power (average)	Temperature (steady state) Process throughput
Wavelength (μm)	Optical absorption, reflection, transmission, resolution, and photochemical effects
Spectral linewidth (nm)	Temporal coherence Chromatic aberration
Beam size (mm)	Focal spot size Depth of focus Intensity
Lasing modes	Intensity distribution Spatial uniformity Speckle Spatial coherence Modulation transfer function
Peak power (W)	Peak temperature Damage/induced stress Nonlinear effects
Pulsewidth (sec)	Interaction time Transient processes
Stability (%)	Process latitude
Efficiency (%)	Cost
Reliability	Cost

Source: Y. S. Liu in *Laser Microfabrication: Thin Film Processes and Lithography*, J.Y. Tsao and D.J. Ehrlich, eds., Academic Press, 1989, p. 3. With permission.

in the material at such a fast rate that the material is forced into a plasma state; the material goes from a solid to a gas phase without first going through a melt phase. This plasma then expands away from the material as a highly energetic gas, taking almost all the heat away with it. This newest operation mode promises to open up a new universe of very accurate micromachined parts unavailable with short laser pulsing. Long pulse or CW lasers can be used to melt the metal for welding (additive process).

Table 15.3.6 summarizes all the different laser parameters that can be controlled and their effect on materials processing.[80] For micromachining purposes, the wavelength, spot size (i.e., the minimum diameter of the focused laser beam), average laser beam intensity, depth of focus, and laser pulse length are the five most important parameters to control.

The most fundamental feature of laser/material interaction in the long pulse regime (e.g., pulse duration 8 ns, energy 0.5 mJ) is that the heat deposited by the laser in the material diffuses away during the pulse duration, that is, the laser pulse duration is longer than the heat diffusion time. This may be desirable for laser welding, but for most micromachining jobs heat diffusion into the surrounding material is undesirable and detrimental to the quality of the machining.

The various undesirable effects associated with long laser pulse etching are illustrated in Figure 15.3.10.

From this discussion it is obvious why we are interested in laser micromachining with short pulses, particularly femtosecond lasers with pulses more than a million times shorter than the several nanosecond duration pulses used in traditional industrial laser micromachining systems. The laser intensity easily reaches the hundreds of terawatts per square centimeter at the work spot itself. No material can withstand the ablation forces at work at these power densities. This means that with ultrafast laser pulses very hard materials (such as diamond) as well as materials with extremely high melting points (such as Molybdenum and Rhenium) can be machined. The most fundamental feature of laser-matter interaction in the very fast pulse regime is that the heat deposited by the laser into the material does not have time to move away from the work spot during the time of the laser pulse. The duration of the laser pulse is shorter than the heat diffusion time. This regime has numerous advantages:

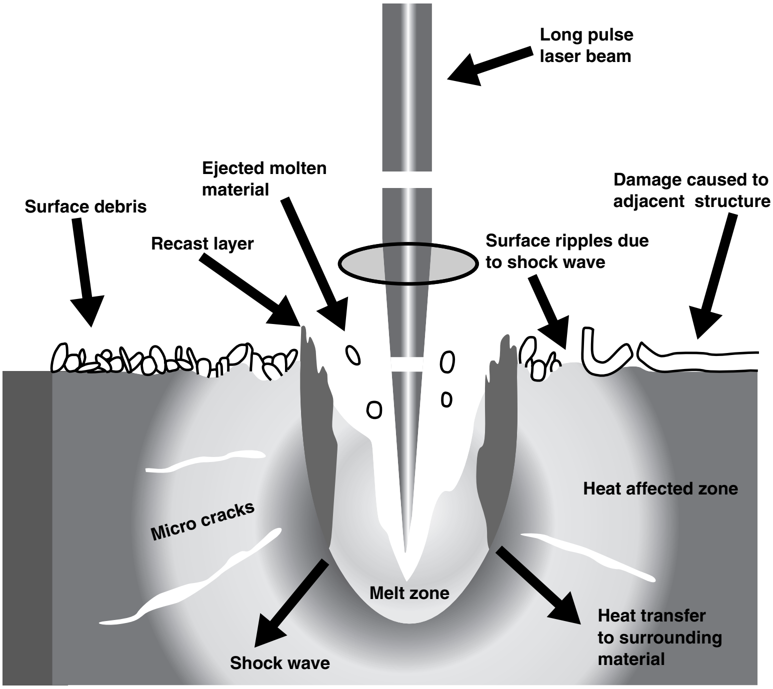

FIGURE 15.3.10 Various undesirable effects associated with laser pulses that are too long, for example, pulse duration 8 ns, energy 0.5 mJ.

- Because the energy does not have the time to diffuse away, the efficiency of the machining process is high. Laser energy piles up at the level of the working spot, whose temperature rises instantly past the melting point of the material and keeps on climbing into what is called the *plasma* regime.
- After the ultrafast laser pulse creates the plasma at the surface of the workpiece, the pressures created by the forces within it cause the material to expand outward from the surface in a highly energetic plume or gas. The internal forces that previously held the material together are vastly insufficient to contain this expansion of highly ionized atoms and electrons from the surface. Consequently, there are no droplets that condense onto the surrounding material. Additionally, since there is no melt phase, there is no splattering of material onto the surrounding surface.
- Heating of the surrounding area is significantly reduced and consequently all the negatives associated with a HAZ are no longer present — which means no melt zone, no micro cracks, no shock wave that can delaminate multilayer materials, no stress that can damage adjacent structures, and no recast layer.

The many advantages associated with working in the femtosecond pulse range are illustrated in Figure 15.3.11.

Mechanical Processes

Introduction

In mechanical precision machining, mechanical energy is the *modus operandi* behind every operation, from grinding and drilling to broaching (removing very thin slices) and milling.[†] In mechanical removing

---

[†] A useful glossary for terms used in metal removal and manufacturing processes in general can be found at http://instruct1.cit.cornell.edu/courses/orie310/mfgproc/mfgprocsummary.html and an introduction to machine tools can be found at http://me.mit.edu/2.70/machine/outline.html and at http://engide.bizland.com/mfg-5-machine.htm.

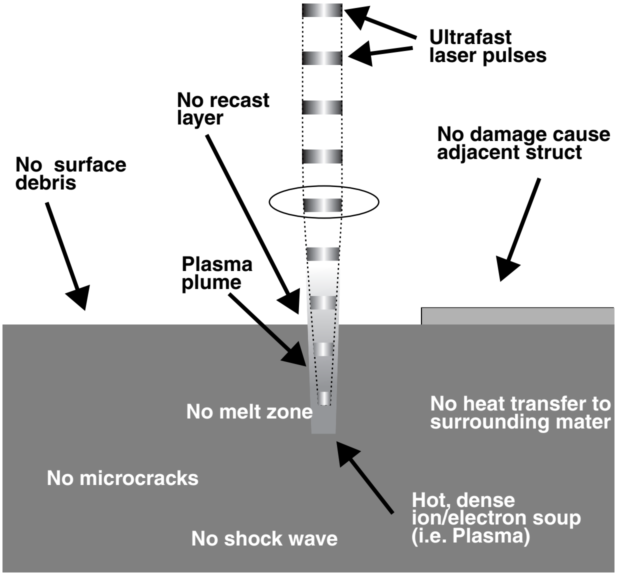

FIGURE 15.3.11 Advantages associated with working with very short laser pulses (<10 picoseconds).

(machining), stresses induced by a tool overcome the strength of the material. How well a part made from a given material holds its shape with time and stress is referred to as the *dimensional stability* of the part and the material. In order to maximize dimensional stability, the machine design engineer tries to minimize the ratios of applied and residual stress to yield strength of the material. A good rule of thumb is to keep the static stress below 10% to 20% of yield. Thermal errors are often the dominant type of error in a precision machine, and thermal characteristics such as thermal expansion coefficient and thermal conductivity deserve special attention.[81]

Precision Mechanical Machining vs. Si Micromachining

For over a hundred years, precise macromachines have been designed and built with mechanical removal techniques achieving part-per-million relative tolerances; recently macromechanical machines have entered the realm of 0.1 ppm relative tolerances.[82] In comparing Si micromachines with mechanically machined macrostructures, Slocum makes some important observations.[82] He notes that, while micromachines are impressive for their small size, their relative accuracy is two orders of magnitude worse than is typically achieved in macromachines, which, moreover, are much more complex. Typical micromachines today, Slocum points out, are comparable with the macromachines of the early 1700s with respect to complexity and accuracy. The surface roughness of micromachines looks high compared to the specular finishes of bearing surfaces. In reality, the absolute roughness is about the same, but in micromachines surface forces such as friction are relatively more important. Thermal errors in a micromachine are generally more relaxed; the small scale and fast thermal equilibrium of the smaller structures is their saving grace. Another key issue Slocum brings up is that of position measurement systems; verification of fabricated geometry and tolerances are much more difficult for micromachines since measurement of a displacement of one part in ten thousand will typically get one down to the nanometer level.

Higher-accuracy machining is needed to provide computer memory disks and optical mirrors and lenses with accuracies to a fraction of the wavelength of light. A better understanding of the limits of traditional and nontraditional machining methods would help the mechanical engineer make the best choice in machining tools. At the same time, as micromachine mechanical complexity increases, it seems appropriate for the designers of micromachines, who are typically electrical engineers, to study macromachine design.

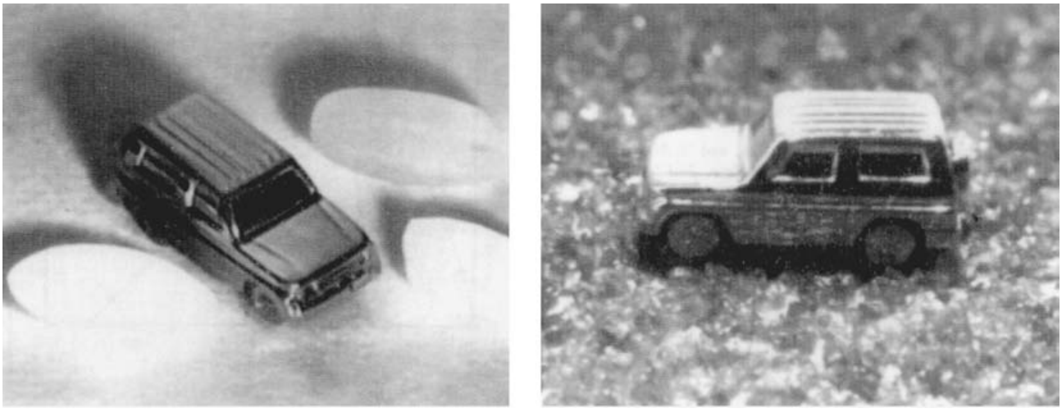

FIGURE 15.3.12 Micro car and rice grains (*left)* and micro-car on sandpaper (grain size = 200 mm) (*right*). The car is 7 mm long, 2.3 mm wide, and 3 mm high. (*Source*: A. Teshigahara, M. Watanabe, N. Kawahara, Y. Ohtsuka, and T. Hattori, *J. Microelectromech. Syst*., 4, 76–80, 1995. With permission.)

Ultra-High Precision Mechanical Machining

In mechanical machining, various factors such as deformation of the workpiece and tool, vibration, thermal deformation, and inaccuracies of machine tools affect the machining accuracy. Ultra-high precision machines with sharp single-crystal diamond tools have made submicrometer precision machining possible. The first CNC machines became available in 1977. The smallest movement the machines could reproducibly make was 0.5 μm. By 1993, 0.05 μm became possible, and today there is equipment available featuring 0.01 μm and even nanometer step resolution.[83] The resolution of the steps a machine can make, of course, is a determining factor for the manufacturing accuracy of the workpiece. Ultraprecision manufacturing is still the commercially preferred technique for the production of computer hard disks, mirrors for X-ray applications, photocopier drums, commercial optics such as polygon mirrors for laser-beam printers, consumer electronics such as mold inserts for the production of CD reader heads and camcorder viewfinders, in addition to high-definition television (HDTV) projection lenses and VCR scanning heads.

Using a diamond tip and numerical control (NC), rice-grain-sized cars were machined at Nippondenso (one car was 4.5 mm long and another was 7.5 mm long) (Figure 15.2.12).[84] The shell of the car was made by the sacrificial mold technique.

The single-crystal diamond tool refinements are not the only reason for the high precision achieved today; submicron precision is also being achieved through high-stiffness machine beds, air bearings (air bearings with a rotational precision of 0.01 μm and better are available now), and measurement systems such as laser interferometry. Furthermore, highly precise instruments such as servomotors, feedback devices, and computers have been implemented, and many types of machine tools are now equipped for CNC, further improving precision and reproducibility of the manufactured parts.

The latest trend is toward flexible manufacturing. In response to the need for automation and the demands created by frequent design changes over a broad variety of products, flexible manufacturing systems (FMS) were developed. FMS is a combination of several technologies such as computers, CNC workstations, robots, transport bands, computer-aided design (CAD), and automatic storage. The technique was developed to produce many varieties of a certain product in smaller quantities rather than many devices of one type. CNC workstations are linked by automatic workpiece transfer and handling, with flexible routing and automatic workpiece loading and unloading.[85]

Fanuc's ROBOnano U_i is an ultraprecision micromachining station capable of making such high precision parts as the mold for diffraction gratings or aspheric lenses. This superprecision micromachining equipment consists of a diamond milling tool rotating at high speed on a superprecision positioning table with nanometer resolution. Using this setup, Fanuc succeeded in relief engraving a minute,

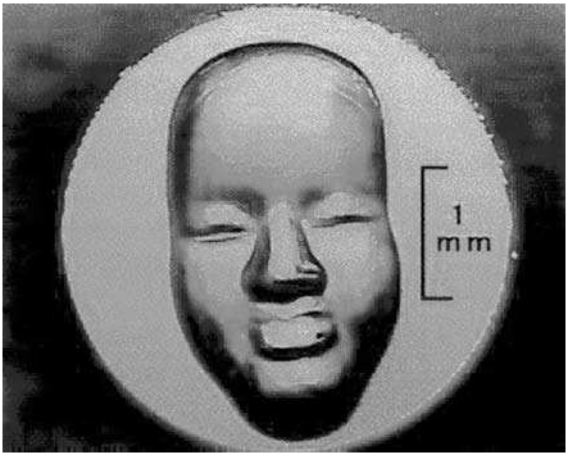

FIGURE 15.3.13 Japanese NOH mask. (*Source:* Fanuc).

mirror-surfaced Noh-mask in copper with a "diamond end mill," which results in a surface smoother than a mirror (see Figure 15.3.13). The roughness of the forehead (R_{max}) of the mask is 60 nm. Thus, Fanuc has realized a superprecision micromachining technique that allows mirror finishing in any direction except in a narrow groove.

Despite all of this progress, the fact that it often takes a 2-ton machine tool to fabricate micro parts where cutting forces are in the milli- to micro-Newton range is a clear indication that a complete machine tool redesign is required for the fabrication of micromachines.[86] Along this line, in Japan the concept for desktop flexible manufacturing systems (DFMS) for building micromachines was proposed in the early 1990s.[87] The manufacturing units would be tabletop size and include universal chuck modules to which workpieces would be continuously clamped through most of the manufacturing process. The miniature die press from Aoki and Takahashi is one of the first examples of progress in that direction.[88]

Bottom-Up Manufacturing

Introduction

At the beginning of the twenty-first century, the performance criteria for top-down manufacturing techniques, that is, Moore's law, which projects the progress in achievable transistor density on a chip, and Taniguchi's curves, which predicts improvements in accuracy for mechanical machining, have started to exhibit signs of a slowdown. Further miniaturization progress will most likely be based on methods originating in nanochemistry, that is, bottom-up methodologies as well as combinations of top-down nanofabrication using "traditional" IC methods and nanochemistry.

A Path to Bottom-Up Manufacturing

Over the next ten years, the size overlap of objects fabricated with either approach will become more significant. Consequently, molecular engineers and supramolecular chemists who are manipulating, with rapidly improving dexterity, nature's building blocks, such as atoms, molecules, proteins, and DNA, will, jointly with MEMS specialists who are now reaching the 0.1 μm lithography limits, find new ways to combine top-down nanofabricated components with bottom-up "natural" products. Previous manufacturing methods discussed in this section are all top-down technologies. In this decade, bottom-up manufacturing methods, in which small particles such as atoms, proteins, and atom clusters are added or removed for the construction of bigger functional structures, will become the most important research domain for the future of manufacturing. Bottom-up methods draw from work in supramolecular chemistry, protein engineering, molecular self-assembly, proximal probes such as STM, photon manipulation of individual atoms, carbon nanotubes, and so forth. For the next two decades, we expect the size of objects that can be built with top-down and bottom-up approaches to overlap more and more as we learn new ways to combine ever smaller components manufactured through nanofabrication with the products of molecular engineers and supramolecular chemists who manipulate nature's building blocks such as atoms, molecules, proteins, and DNA with increasing dexterity.

Guidance from Nature

Nature provides excellent examples in the design of efficient microsystems as it optimizes scaling laws in the micro-domain and even exploits the quantum-size effects of its components. In biological systems, the energy efficiency is approximately proportional to the 2/3 power of the linear dimension. This is because metabolism is proportional to the second power of the linear dimension (surface of the organism, 1^2), and energy uptake (feeding) is proportional to the body volume (1^3), so the smaller organism is, the higher its efficiency. As a consequence, smallness is the ancestral condition of life. Large organisms are built bottom-up from cells rather than divided into cells. Cells are, in turn, fabricated from yet smaller entities. A single *E. coli* bacterium, for example, is shaped like a cylinder about 1 μm across and 3 μm long. It contains at least 3000 different molecular parts and will divide every 20 minutes when nutrients are available. Human manufacturing technology works in the opposite direction; it builds top-down. Humans tend to start with larger building blocks and use stiff materials (e.g., Si or stainless steel), whereas nature prefers small building blocks and mostly soft, low Young's modulus materials (e.g., materials in muscle or skin). As an example of recent human engineering ingenuity, consider Si micromachining or MEMS. Si micromachining involves Si wafer slabs as thick as 500 μm, insulating layers up to a μm thick, Al and Au metal layers between a few hundred and few thousand Ås thick, and, in general, three-dimensional structures with dimensions anywhere between 1 and 500 μm. Although MEMS has led to major advances, the method still presents a limited choice of materials and works with building blocks that are large and crude compared to nature's arsenal.

Biomimetics is the study of how nature, building atom by atom, through eons of time, developed manufacturing methods, materials, structures, and intelligence. These studies are inspiring engineering and design of man-made miniature objects. As nanochemistry is currently inspiring a new wave of biomimetic efforts, caution is in order since, as the legend of Icarus so pointedly reminds us, most previous attempts at biomimetics have resulted in failure. However, we believe that past failures mostly pertain to macroengineering and will not hold true in nanoengineering. In macroengineering, as S. Vogel points out in *Cats' Paws and Catapults,*[89] human and natural technologies form a separate, well-integrated entity, operating in an internally coherent context. Nature, for example, does not use steel, nor does it favor the production of flat surfaces and sharp corners — all very useful in human manufacturing. Nature builds with proteins and produces mostly curved surfaces and rounded corners, resulting in such masterfully engineered objects as biological cells. In large-scale engineering projects, both natural and human manufacturing approaches have their merits within their own proper frame of reference. It is in the nano world that nature is way ahead of human engineering as it has learned to work with much smaller, more versatile building blocks and master the self-assembly of those building blocks. As humankind learns to build with the same construction set, we are bound to challenge nature in nano engineering. Because it uses relatively large building blocks, human manufacturing is rapid and the expectation is that nature, because it uses much smaller building blocks, for example, atoms with a diameter of 0.3 nm, must be very slow. To offset the time it takes to work with small, basic building blocks, nature, in growing an organism, relies on an additive process featuring massive parallelism and self-assembly.

A few of the guiding principles involved in the construction of living organisms are[90]

- The use of composites (rather than monolithic materials in human engineering)
- Several successive levels of organization (hierarchy)
- Soft flexible materials
- Self-assembly, self-organization, and self-replication all through weak bonds
- The use of templates (e.g., the reading of genes by messenger RNA [m-RNA] to build proteins in the cells' ribosomes)
- Compartmentalization

These principles provide inspiration for the implementation of human nanotechnology.

Nanocomposite materials, for example, are widespread in biological systems as in bone, cell walls, soft body tissue, and so forth. The nacre (mother-of-pearl) of abalone shell, an oriented coating composed of alternating layers of aragonite ($CaCO_3$) and a biopolymer, is an often studied example. The laminated structure provides strength, hardness, and toughness. Nacre is twice as hard and 1000 times as tough as its constituent phases. Humankind has accumulated plenty of experience with composite materials, but attempts to make "biomimetic" nanocomposite assemblies are quite recent. Along this line, Sellinger et al. reported on an efficient self-assembly process for preparing nanolaminated organic-inorganic coatings that mimic nacre.[91] New biomimetic materials, such as scaffolds for regrowth of tendons, tend to be composites too, although not on the nanoscale; in the case of tendon scaffolds, composites are made from carbon fibers and polylactic acid.[90]

Proteins, bone, and tissue fibers have a hierarchical organization much more complex than materials of the nonliving world (e.g., crystals). This organization bestows many benefits on living organisms, such as a high strength-to-density ratio and the ability to serve several functions simultaneously. The ability of humans to mimic this feat is still limited and will only improve if we become more adept at manipulating a wider variety of materials at the nanoscale, use smaller building blocks, and build in three dimensions with more dexterity. Traditional lithography is mostly limited to two-dimensional structures and is impractical for printing feature sizes below 0.1 μm.

Self-assembly is the lock-and-key[†][92] assembly of complex molecules, such as in the case of neurotransmitters assembling with molecular recognition sites on proteins that elicit chemical responses — for example, acetylcholine recognition at nerve-muscle junctions resulting in muscle contractions.[3] Self-assembly is taken advantage of, for example, in DNA probes and immunosensors but is not used much yet in human manufacturing. Some early attempts at self-assembly of larger components (e.g., GaAs diodes), include DNA mediated self-assembly.[93–95]

Self-organization leads to large supramolecular architectures such as molecular crystals, liquid crystals, colloids, micelles, spherical bilayer structures of cell walls, phase-separated polymers, and self-organized monolayers, which, to confuse students, are called self-assembled monolayers (SAMs). No chemist needs to specify the individual atom or molecule positions in these systems.[96] For example, after disintegration of ribosomes into their protein and RNA building blocks the molecules will reorganize into functional units in a test tube given the right conditions. Humankind is using self-organization in building SAMs, and in colloid chemistry, one can precipitate inorganic solids such as silver halide crystals with astonishing regularity in size and properties, comparable to what can be accomplished with microlithography. The latter has become one of several routes to build quantum structures.

In self-replication, molecules such as DNA encode the genetic information for cells and the resulting organisms, thus allowing the information to be passed on from cell to cell and from generation to generation.[97]

The use of templates in micromachining has become very extensive, but our templates are at the microscale, not at the nanoscale. Finally, compartmentalization corresponds to the principle of most biological events, and many chemical changes are presided over by nonequivalent bonding interactions in, between, and beyond molecules. Chemistry beyond the molecule has given rise to supramolecular chemistry — a new field of chemistry pioneered by researchers such as Nobel laureate Jean-Marie Lehn from the University of Strasbourg.[98,99] The fundamental concepts underpinning supramolecular science are processes in which atoms, molecules, aggregates of molecules, and components arrange themselves into ordered, functioning entities without human intervention.[100] The weak interactions typically involved are

---

[†] The "lock-and-key" concept of biochemical interactions has over the years been modified in favor of a "hand-in-a-glove" concept because there is some reorganization (conformational change) required to make two biomolecules complementary to each other.[91]

- Hydrogen bonds
- Electrostatic attractions
- van der Waals' forces
- Hydrophobic interactions
- Weak covalent bonds

Through supramolecular chemistry with weak ionic and hydrogen bonds and van der Waals interactions (0.1 to 5 kcal/mol), structures with dimensions of 1 to 100 nm are possible. For chemical synthesis, the largest of these dimensions is often too large and for microfabrication it is often too small. The different fundamental processes at work in supramolecular chemistry can be illustrated by examples from nature.

The Future

Most miniaturization, especially in ICs, over the next 10 to 15 years will be based on nanofabrication, and Moore's law will continue to run its course. In parallel, we will continue to adapt nanochemistry principles and combine them with nanofabrication. There is a significant gap between the scale of individual molecular structures of nanochemistry and the submicrometer structures of nanofabrication. It is exactly in that gap, from about one nanometer to several hundred nanometers, where fundamental materials properties are defined. It is also on the nanometer scale that quantum effects become significant.

There is little doubt that biotechnology analysis tools will keep on improving at an increasingly faster rate. Desktop DNA sequencers and three-dimensional protein readers will be a reality in the not-so-distant future. Genetic engineering will have the most profound impact, though, on how humankind looks at manufacturing. Since it is already possible to synthesize a virus bottom-up, given the sequence of the bases in its genes, it seems quite likely that we will be able to manufacture synthetic viruses designed to enter a cell and carry out diagnostic and therapeutic tasks. Venter has proposed building bottom-up a minimal gene setup required to sustain life in a test tube. Photovoltaic solar cells today have a high conversion efficiency of about 10% to 15% but are expensive to deploy and maintain. Crops grown for energy are also expensive, involve harvesting and are only 1% efficient. It is conceivable that genetic engineering will enable the production of energy crops that convert sunlight into fuel at a 10% efficiency.[101] Through nanochemistry, the current digital information technology (IT) revolution might well be followed by a new analog manufacturing revolution. Today, computers let us shape our digital environment, but by giving computers the means to manipulate the analog world of atoms as easily as they manipulate bits, the same kind of personalization may be brought to our physical three-dimensional environment. In this context Gershenfeld from the MIT Media Laboratory envisions a personal fabricator (PF) akin to the PC.[102]

A human society based on nanomachining will be a much more balanced one with a manufacturing approach based on how the species itself is made. Products will be based on a fundamental understanding of the assembly of their ultimate components, atoms, molecules and proteins, and on how to induce self-assembly into useful objects. Materials will be degradable, flexible, and fully reusable. The smaller building blocks used in manufacture will enable products of more variety and intelligence. There will be less emphasis on the traditional engineering materials such as steel, wood, stone, composites and carbon, and proteins will become much more important.

The transition toward a nano-society will require a major shift in workforce skill level as manipulating data and applying knowledge of bioengineering will be part of a manufacturing worker's daily duties. In academia, less hyper-specialization and better grounding in all the sciences and engineering will become a must as the traditional "dry engineering and sciences," such as electrical engineering and mechanical engineering, merge with the "wet sciences and engineering," such as biology and bioengineering.

References

1. Chryssolouris, G. 1991. *Laser Machining*. Springer Verlag, New York.
2. Drexler, K.E. 1992. *Nanosystems: Molecular Machinery, Manufacturing, and Computation*. John Wiley & Sons, New York.

3. Whitesides, G.M., Mathias, J.P., and Seto, C.T. 1991. Molecular self-assembly and nanochemistry: a chemical strategy for the synthesis of nanostructures, *Science*, vol. 254, 1312–18.
4. Brodie, I. and Muray, J.J. 1982. *The Physics of Microfabrication*. Plenum Press, New York.
5. Arden, W. and Muller, K.H. 1989. Light vs. X-rays: how fine can we get?, *Semicond. Int.*, vol. 12, 128–31.
6. Kern, W. and Deckert, C.A. 1978. Chemical Etching, in *Thin Film Processes*, J.L. Vossen and W. Kern, eds. Academic Press, Orlando, FL.
7. Jackson, T.N., Tischler, M.A., and Wise, K.D. 1981. An electrochemical P-N junction etch-stop for the formation of silicon microstructures, *IEEE Electron Device Lett.*, vol. EDL-2, 44–45.
8. Meek, R.L. 1971. Electrochemically thinned N/N+ epitaxial silicon-method and applications, *J. Electrochem. Soc.*, vol. 118.
9. Yoshida, T., Kudo, T., and Ikeda, K. 1992. Photo-induced preferential anodization for fabrication of monocrystalline micromechanical structures, in *Proceedings: IEEE Micro Electro Mechanical Systems (MEMS '92)*. Travemunde, Germany, 56–61.
10. Watanabe, Y., Arita, Y., Yokoyama, T., and Igarashi, Y. 1975. Formation and properties of porous silicon and its applications, *J. Electrochem. Soc.*, vol. 122, 1351–55.
11. Flamm, D.L. 1983. Feed gas purity and environmental concerns in plasma etching: part I, *Solid State Technol.*, October, 49–54.
12. Pandhumsoporn, T., Feldbaum, M., Gadgil, P., Puech, M., and Maquin, P. 1996. High etch rate anisotropic deep silicon plasma etching for the fabrication of microsensors, in *Micromachining and Microfabrication Process Technology II*. Austin, TX, 94–102.
13. Manos, D.M. and Flamm, D.L., eds. 1989. *Plasma Etching: An Introduction*. Academic Press, Boston.
14. Chang, F.I., Yeh, R., Lin, G., Chu, P.B., Hoffman, E., Kruglick, E.J., Pister, K.S.J., and Hecht, M.H. 1995. Gas-phase silicon micromachining with xenon difluoride, in *Proceedings: SPIE Microelectronic Structures and Microelectromechanical Devices for Optical Processing and Multimedia Applications*, vol. 2641, 117–28.
15. Vasile, M.J., Biddick, C., and Schwalm, S. 1994. Microfabriction by ion milling: the lathe technique, *J. Vac. Sci. Technol.*, vol. B12, 2388–93.
16. Chryssolouris, G. 1991. *Laser Machining*. Springer Verlag, New York.
17. Moreland, M.A. 1992. Ultrasonic Machining, in *Engineered Materials Handbook*, S.J. Schneider, ed., ASM International, Metals Park, OH, 359–62.
18. Kalpajian, S. 1984. *Manufacturing Processes for Engineering Materials*. Addison-Wesley, Reading, MA.
19. DeVries, W.R. 1992. *Analysis of Material Removal Processes*. Springer Verlag, New York.
20. Uhlir, A. 1956. Electrolytic shaping of germanium and silicon, *Bell Syst. Tech. J.*, vol. 35, 333–47.
21. Maluf, N. 2000. *An Introduction to Microelectromechanical Systems Engineering*. Artech House, Boston.
22. Robbins H. and Schwartz, B. 1959. Chemical etching of Silicon-I: the system, HF, HNO3, and H2O, *J. Electrochem. Soc.*, vol. 106, 505–8.
23. Robbins, H. and Schwartz, B. 1960. Chemical etching of Silicon-II: the system HF, HNO3, H2O, and $HC_2C_3O_2$, *J. Electrochem. Soc.*, vol. 107, 108–11.
24. Schwartz, B. and Robbins, H. 1961. Chemical etching of Silicon–III: a temperature study in the acid system, *J. Electrochem. Soc.*, vol. 108, 365–72.
25. Schwartz. B. and Robbins, H. 1976. Chemical etching of Silicon-IV: etching technology, *J. Electrochem. Soc.*, vol. 123, 1903–9.
26. Hallas, C.E. 1971. Electropolishing silicon, *Solid State Technol.*, vol. 14, 30–32.
27. Turner, D.R. 1958. Electropolishing silicon in hydrofluoric acid solutions, *J. Electrochem. Soc.*, vol. 105, 402–8.
28. Kern, W. 1978. Chemical etching of silicon, germanium, gallium arsenide, and gallium phosphide, *RCA Rev.*, vol. 39, 278–308.
29. Klein, D.L. and D'Stefan, D.J. 1962. Controlled etching of silicon in the HF-HNO3 system, *J. Electrochem. Soc.*, vol. 109, 37-42.

30. Stoller, A.I. and Wolff, N.E. 1966. Isolation techniques for integrated circuits, in *Proceedings: Second International Symposium on Microelectronics*, Munich, Germany.
31. Stoller, A.I. 1970. The etching of deep vertical-walled patterns in silicon, *RCA Rev.*, vol. 31, 271–75.
32. Forster, J.H. and Singleton, J.B. 1966. Beam-lead sealed junction integrated circuits, *Bell Laboratories Record*, vol. 44, 313–17.
33. Kenney, D.M. 1967. Methods of isolating chips of a wafer of semiconductor material, U.S. Patent 3,332,137.
34. Lepselter, M.P. 1966. Beam lead technology, *Bell. Sys. Tech. J.*, vol. 45, 233–54.
35. Lepselter, M.P. 1967. Integrated circuit device and method, U.S. Patent 3,335,338.
36. Waggener, H.A. 1970. Electrochemically controlled thinning of silicon, *Bell. Sys. Tech. J.*, vol. 49, 473–75.
37. Kragness, R.C. and Waggener, H.A. 1973. Precision etching of semiconductors, U.S. Patent 3,765,969.
38. Waggener, H.A., Kragness, R.C., and Tyler, A.L. 1967. Anisotropic etching for forming isolation slots in silicon beam leaded integrated circuits, in *Technical Digest: IEEE International Electron Devices Meeting*, Washington, DC, 68.
39. Waggener, H.A., Krageness, R.C., and Tyler, A.L. 1967. Two-Way etch, *Electronics*, vol. 40, 274.
40. Bean, K.E. and Runyan, W.R. 1977. Dielectric isolation: comprehensive, current and future, *J. Electrochem. Soc.*, vol. 124, 5C–12C.
41. Rodgers, T.J., Hiltpold, W.R., Frederick, B., Barnes, J.J., Jenné, F.B., and Trotter, J.D. 1977. VMOS memory technology, *IEEE J. Solid-State Circuits*, vol. SC–12, 515–23.
42. Rodgers, T.J., Hiltpold, W.R., Zimmer, J.W., Marr, G., and Trotter, J.D. 1976. VMOS ROM, *IEEE J. Solid-State Circuits*, vol. SC-11, 614–22.
43. Ammar, E.S. and Rodgers, T.J. 1980. UMOS Transistors on (110) silicon, *IEEE Trans. Electron Devices*, vol. ED-27, 907–14.
44. Schnable, G.L. and Schmidt, P.F. 1976. Applications of electrochemistry to fabrication of semiconductor devices, *J. Electrochem. Soc.*, vol. 123, 310C–315C.
45. Jansen, H., Gardeniers, H., de Boer, M., Elwenspoek, M., and Fluitman, J. 1996. A survey on the reactive ion etching of silicon in microtechnology, *J. Micromech. Microeng.*, vol. 6, 14–28.
46. Ko, W.H., Suminto, J.T., and Yeh, G.J. 1985. Bonding Techniques for Microsensors, in *Micromachining and Micropackaging of Transducers*, C.D. Fung, P.W. Cheung, W.H. Ko, and D.G. Fleming, eds. Elsevier, Amsterdam, Netherlands, 41–61.
47. Sze, S. M., ed. 1988. *VLSI Technology.* McGraw-Hill, New York..
48. Bockris, J.O.M. and Reddy, A.K.N. 1977. *Modern Electrochemistry.* Plenum Press, New York.
49. Mallory, G.O. and Hadju, J.B. eds. 1990. *Electroless Plating: Fundamentals and Applications*. American Electroplaters and Surface Finishers Society (AESF), Orlando, FL.
50. Menz, W. and Bley, P. 1993. *Mikrosystemtechnik fur Ingenieure.* VCH Publishers, Weinheim, Germany.
51. Jaeger, R.C. 1988. *Introduction to Microelectronic Fabrication*. Addison-Wesley, Reading, MA.
52. Cotell, C.M. 1992. Pulsed laser deposition and processing of biocompatible hydroxylapatite thin films, *A Surf. Sci.*, vol. 69, 140–48.
53. Pearce, C.W. 1988. Crystal Growth and Wafer Preparation, in *VLSI Technology,* S.M. Sze, ed. McGraw-Hill, New York.
54. Hess, D.W. and Jensen, K.F., eds. 1989. *Microelectronics Processing: Chemical Engineering Aspects*. American Chemical Society, Washington, DC.
55. Parker, E.H.C. 1985. *The Technology and Physics of Molecular Beam Epitaxy.* Plenum Press, New York.
56. Licari, J.J. 1970.*Plastic Coatings for Electronics*. McGraw-Hill, New York.
57. Harper, C.A., ed. 1982. *Handbook of Thick Film Hybrid Microelectronics*. McGraw-Hill, New York.
58. Colclaser, R.A. 1980. *Microelectronics: Processing and Device Design*. John Wiley& Sons, New York.

59. Mooney, J.B. and Radding, S.B. 1982. Spray pyrolysis processing, *Ann. Rev. Mater. Sci.*, vol. 12, 81–101.
60. Vossen, J.L. and Kern, W., eds. 1978. *Thin Film Processes*. Academic Press, Orlando, FL.
61. Pfender, E. 1988. Fundamental studies associated with the plasma spray process, *Surf. Coat. Technol.*, vol. 34, 1–14.
62. Lischner, D.J., Basseches, H., and D'Altroy, F.A. 1985. Observations of the temperature gradient zone melting process for isolating small devices, *J. Electrochem. Soc.*, vol. 132, 2991–96.
63. Burggraaf, P. 1993. The status of MOCVD technology, *Semicond. Int.*, vol. 16, 80–83.
64. Tomar, M.S. and Garcia, F.J. 1988. Spray pyrolysis in solar cells and gas sensors, *Prog. Cryst. Growth Charact.*, vol. 4, 221–48.
65. Peters, L. SOI takes over where silicon leaves off, *Semicond. Int.*, March, 48–51.
66. Anderson, T.J. 1989. Liquid-phase epitaxy and phase diagrams of compound semiconductors, in *Microelectronics Processing: Chemical Engineering Aspects*, D.W. Hess and K.F. Jensen, eds. American Chemical Society, Washington, DC.
67. IMM, The LIGA Technique, commercial brochure, IMM, 1995.
68. Lehr, H. and Schmidt, M. 1995. The LIGA Technique: Commercial brochure, IMM Institut fur Mikrotechnnik GmbH, Mainz-Hechtsheim.
69. Hagmann, P. and Ehrfeld, W. 1988. Fabrication of microstructures of extreme structural heights by reaction injection molding, *Journal of the Polymer Processing Society*, vol. 4, 188–95.
70. Hagmann, P., Ehrfeld, W., and Vollmer, H. 1987. Fabrication of microstructures with extreme structural heights by reaction injection molding, in *First Meeting of the European Polymer Federation, European Symposium on Polymeric Materials*. Lyon, France, 241–51.
71. Weber, L., Ehrfeld, W., Freimuth, H., Lacher, M., Lehr, H., and Pech, B. 1996. Micro-molding: a powerful tool for the large scale production of precise microstructures, in *SPIE: Micromachining and Microfabrication Process Technology II*. Austin, TX, 156–67.
72. Madou, M. 1997. *Fundamentals of Microfabrication*. CRC Press, Boca Raton, FL.
73. Wimberger-Friedl, R. 1999. Injection molding of sub-μm grating optical elements, *Proc. SPE ANTEC*, 476–80.
74. Momma, C., Nolte, S., Chichkov, N., Alvensleben, B.V., and Tunermann, F.A. 1997. Precise laser ablation with ultrashort pulses, *Applied Surface Science*, vol. 109/110, 15–19.
75. Madou, M.J., Lu, Y., Lai, S., Juang, Y.-J., Lee, L.J., and Daunert, S. 2000. A novel design on a CD disc for 2-point calibration measurement, in *Proceedings: Solid-State Sensor and Actuator Workshop*. Hilton Head Island, SC, 2000, 191–94.
76. Warrington, R.O. 1999. An overview of micromechanical machining processes for BioMEMS, in *Novel Microfabrication Options for BioMEMS Conference (Proceedings)*. The Knowledge Foundation, San Francisco.
77. Roberts, M.A., Rossier, J.S., Bercier, P., and Girault, H. 1997. UV Laser machined polymer substrates for the development of microdiagnostic systems, *Anal. Chem.*, vol. 69, 2035–42.
78. Becker, H. and Gärtner, C. 2000. Polymer microfabrication methods for microfluidic analytical applications, *Electrophoresis*, vol. 21, 12–26.
79. Srinivasan, R. and Mayne-Banton, V. 1982. Self-developing photoetching of poly(ethylene terephthalate) films by far-ultraviolet excimer laser radiation, *Appl. Phys. Lett.*, vol. 41, 576–78.
80. Liu, Y.S. 1989. Sources, Optics and Laser Microfabrication Systems for Direct Write and Projection Lithography, in *Laser Microfabrication: Thin Film Processes and Lithography*, J.Y. Tsao and D.J. Ehrlich, eds. Academic Press, New York, 3.
81. Slocum, A.H. 1992. *Precision Machine Design*. Prentice Hall, Englewood Cliffs, NJ.
82. Slocum, A.H. 1992. Precision machine design: macromachine design philosophy and its applicability to the design of micromachines, in *Proceedings: IEEE Micro Electro Mechanical Systems (MEMS '92)*. Travemunde, Germany, 37–42.

83. Szepesi, D. 1993. Sensoren en Actuatoren in Ultraprecisie Draaibanken, in *Sensoren en Actuatoren in de Werktuigbouw/Machinebouw, Centrum voor Micro-Electronica*. The Hague, Netherlands, 99–107.
84. Teshigahara, A., Watanabe, M., Kawahara, N., Ohtsuka, Y., and Hattori, T. 1995. Performance of a 7-mm micro-fabricated car, *J. Microelectromech. Syst.*, vol. 4, 76–80.
85. Boothroyd, G. and Knight, W.A. 1989. *Fundamentals of Machining and Machine Tools*. Marcel Dekker, New York.
86. Friedrich, C. 1994. Complementary micromachining processes, notes from handouts, Banff, Canada.
87. Higuchi, T. and Yamagata, Y. 1993. Micro machining by machine tools, in *Proceedings: IEEE Micro Electro Mechanical Systems (MEMS '93)*. Fort Lauderdale, FL.
88. Bellows, G. and Kohls, J.B. 1982. Drilling without drills, *Am. Mach. Special Report*, vol. 743, 187.
89. Vogel, S. 1998. *Cats' Paws and Catapults*. W. W. Norton, New York.
90. Ball, P. 1997. *Made to Measure*. Princeton University Press, Princeton, NJ.
91. Sellinger, A., Weiss, P.M., Nguygen, A., Lu, Y., Assink, R.A., Gong, W., and Brinker, C.J. 1998. Continuous self-assembly of organic-inorganic nanocomposite coatings that mimic nacre, *Nature*, vol. 394, 256–59.
92. Bachas, L. 2001. Hand-in-a-glove, personal communication.
93. Yeh, H.-J. and Smith, J.S. 1994. Fluidic Self-assembly for the integration of GaAs light-emitting diodes on Si substrates, *IEEE Photonics Technology Letters*, vol. 6, 706–8.
94. Yeh, H.-J. and Smith, J.S., 1994. Fluidic self-assembly of microstructures and its application to the integration of GaAs on Si, in *Proc. IEEE International Workshop on Micro Electro Mechanical Systems (MEMS '94)*. Oiso, Japan, 279–84.
95. Yeh, H.-J. and Smith, J.S. 1994. Integration of GaAs vertical-cavity surface-emitting laser on Si by substrate removal, *Appl. Phys. Lett.*, vol. 64, 1466–68.
96. Ringsdorf, H., Schlarb, B., and Venzmer, J. 1988. Molecular architecture and function of polymeric oriented systems: models for the study of organization, surface recognition, and dynamics, *Angewandte Chemie, International Edition in English*, vol. 27, 113–58.
97. Achilles, T. and Von Kiedrowski, G. 1993. A self-replicating system from three starting materials, *Angewandte Chemie, International Edition in English*, vol. 32, 1198–201.
98. Lehn, J.M. 1988. Supramolecular chemistry: scope and perspectives (Nobel lecture), *Angewandte Chemie, International Edition in English*, vol. 27, 89–112.
99. Lehn, J.-M. 1993. Supramolecular chemistry, *Nature*, vol. 260, 1762–63.
100. Whitesides, G.M. 1995. Self-assembling materials, *Sci. Am.*, 146–49.
101. Dyson, F.J., 1999. *The Sun, the Genome , and the Internet-Tools of Scientific Revolutions*. Oxford University Press, Oxford.
102. Gershenfeld, N. 1999. *When Things Start to Think*. Henry Holt and Co., New York.

15.4 MEMS Packaging

Liang-Yu Chen and Phillip J. Zulueta

Introduction

The functionality and capability of micro-devices (circuits) have been dramatically complemented and expanded by the emergence of microelectromechanical systems (MEMS). The basic function of conventional microelectronic circuits is to process and exchange electromagnetic signal/power. Thus, the interaction between conventional electronics and their environments is very much limited to electromagnetic exchanges. However, since microsystems composed of electronics and MEMS may have the capabilities to accept nonelectromagnetic signals and provide nonelectromagnetic actuation, the interactions between microsystems and their environments can be electromagnetic, mechanical, optical, thermal, chemical, and biological. Figure 15.4.1 shows the two-way interactions between a generalized MEMS and its

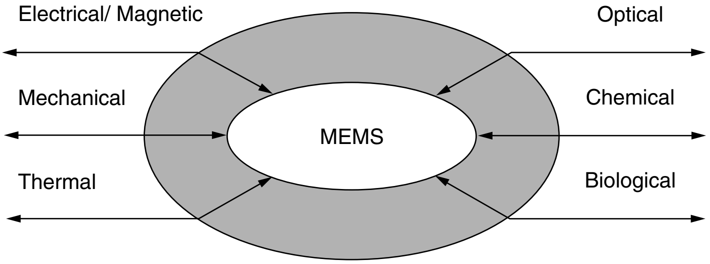

FIGURE 15.4.1 The function of MEMS chip-level packaging as an electrical/magnetic, mechanical, thermal, optical, chemical, and biological interface between a microsystem and its environment.

environment in various physical and chemical formats. Each intake arrow represents a type of possible signal that MEMS can accept, and each outgoing arrow represents a type of possible actuation that MEMS can provide. As the passive interfaces between the microsystems and the outside world, the packaging systems of microsystems may have to be capable of mediating electromagnetic, mechanical, optical, thermal, chemical, and biological interactions. These microsystem packaging functions can be far more complicated than those of conventional electronic packaging, and therefore generate new requirements and challenges to the device packaging field. Packaging requirements for MEMS devices can be device/system dependent; thus a microsystem package very likely must be specifically designed for a designated MEMS system. This is a significant difference between MEMS packaging and conventional electronics packaging, where one type of chip level package can be used for packaging many types of electronic devices/circuits.

Generally speaking, both functions and requirements of a microsystem package may need to be specified electromagnetically, mechanically, thermally, optically, chemically, and biologically. This section will discuss the thermomechanical aspects of microsystem packaging. The basic thermomechanical issues concerned in microsystem packaging include mechanical alignment, mechanical integrity, mechanical testing, stress/strain effects, and thermal mechanical environment durability. The last two issues are interrelated and are the major interest of this section, while other topics are briefly discussed next.

Mechanical alignment. Microsystems with optical MEMS are often connected to optical fibers. For example, MEMS mirror based multi-channel optical switches are connected to over dozens of optical fibers through chip level packaging. The light beams are usually focused down to a few microns diameter (Takshara et al. 2000) at both the fiber tip and chip mirror/photo diode sides. Therefore, mechanical alignment of the relative position of the chip with respect to the fiber(s) becomes one of the critical factors to overall system performance and reliability. Usually, passive alignment uses a relatively expensive expanded mode region of laser diodes. In recent years, passive alignment methods using a single-mode laser source have been reported. These methods provide low-cost, quick, and automated alignment (Owen 2000). The requirement of high-precision mechanical alignment also raises the compatibility issue of the materials used in packaging. The mismatch of thermal expansion of packaging materials can cause significant mechanical misalignment introducing thermal effects on the optical operation of the system when the environmental temperature changes (Takshara et al. 2000). Both mechanical alignment and calibration must be considered in chip-level packaging design.

Mechanical integrity. The MEMS accelerometer used in automobile safety airbag control is one of the first commercialized MEMS devices. Most of these MEMS accelerometers are silicon based. The mechanical environment for the MEMS accelerometer can be harsh. For example, the accelerometer and packaging systems used for many aerospace and military applications, such as spacecraft landing control, missile targeting, and ammunition triggering, can experience acceleration as high as ~10^3 g. Therefore, mechanical strength, mechanical rigidity, and resonant frequencies associated with the sensor package all become critical in packaging design and test.

Mechanical testing and qualification criteria. The core operation of a MEMS device is at least partially mechanical whether or not it is designed for direct mechanical function. Therefore, MEMS devices also need mechanical testing and mechanical qualification criteria in addition to the electrical test and qualification specifications. A MEMS resonator-based RF filter is a typical example: it is a device providing electronic functions with mechanical operations inside the device. Therefore, a complete performance and environment durability spec of this type of device also includes mechanical parameters, such as maximum environmental acceleration and vibration frequency. Mechanical testing of MEMS devices can be complicated and cost prohibitive.

Stress effects and thermal environment durability. The major wafer-level packaging processes include wafer bonding, wafer encapsulating, and solder/eutectics bumping. As discussed in the next section, most of these wafer-level processes are performed at elevated temperatures. The assembly is thermomechanically relaxed at an elevated processing temperature, so the processed (such as bonded) wafers are likely under significant stress because of material Coefficient of Thermal Expansion (CTE) mismatches when being operated or stored at lower temperatures. The material property mismatch at MEMS wafer-level packaging is a unique mechanical concern of MEMS packaging. Chip-level packaging (such as die-attach assembly) has a similar material property mismatch caused by thermal stress issues. Die-attach assembly is composed of a device die, packaging substrate, and a die-attaching layer. Thermomechanical stresses due to mismatch of CTE of packaging materials, such as the substrate, with the wafer material of MEMS devices (such as Si or SiC) is a common mechanical issue. CTE mismatch at the chip-level packaging can cause misalignment of optical MEMS upon environmental temperature change (Takshara et al. 2000). The CTE mismatch can also generate unwanted device thermal response to environmental temperature changes (Beranek 2000). In the extreme case, CTE mismatch can cause permanent mechanical damage, such as cracking of dies.

Piezoresistive MEMS sensors have been extensively used for both static and dynamic pressure measurements. The operation of these sensors depends on the mechanical deformation of a diaphragm on which piezoresistive strain sensors are built. Therefore, these sensors are sensitive to external forces applied on the devices. The most common but unwanted external force on the sensor diaphragm is the die-attach thermomechanical stress generated by mismatch of thermal expansions of die, attach, and substrate materials. The thermal stress may significantly change the thermomechanical configuration of the diaphragm. These stress effects are often neither reversible nor reproducible. Thus, packaging technology is one of the critical factors determining the reliability of packaged MEMS devices.

Packaging stress is especially important to MEMS for high-temperature applications. NASA is developing next-generation aerospace engines with self-monitoring and self-control capabilities. A microsystem that is capable of operation in a high-temperature combustion environment is essential to characterization and control of engine combustion processes in real time (Hunter 2003). Surface and atmospheric temperatures of Venus are about 500°C with a corrosive (acidic) atmosphere. Sensors and electronics for a diving or landing probe to Venus must be able to withstand high temperature and reactive chemical environments. For these high-temperature microsystems for aerospace applications, packaging thermal stress becomes a great concern because these devices may experience wide environmental temperature variation.

In order to discuss the basic MEMS packaging technology and analyze the mechanical stress sources in MEMS packaging at various levels, we will introduce some basic packaging concepts.

Fundamental Packaging Concepts

Four packaging levels. The wafer-level packaging provides micromechanical structures and electronic device structures (on a chip) with micro-level insulation and on-wafer electrical interconnection. It is realized prior to wafer dicing and usually considered as level-zero packaging. Chip-level packaging provides single- or multidevice chip(s) with macro-level insulation and electrical interconnections, so after packaging the device chips are ready to be handled in a macro way; it is considered as level-one packaging. Printed circuit board (PCB)–level packaging provides interconnections between (packaged) chips and passives; it is considered as level-two packaging. The instrument-level packaging provides

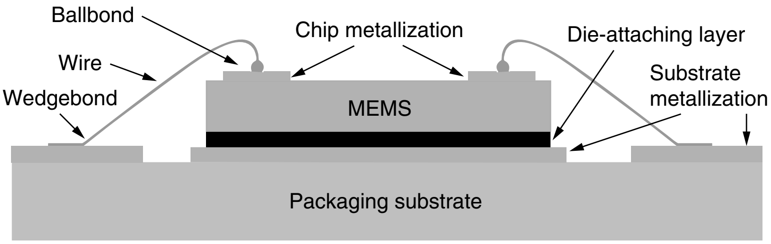

FIGURE 15.4.2 A schematic diagram of conventional chip-level packaging with wire-bond and die-attach.

interconnections between PCBs and other units; it is considered as level-three packaging. This section only addresses mechanical topics of level-0 and -1 packaging.

Substrate. Substrate is the packaging base on which a device die (chip) is mechanically attached and electrical interconnections are built. Substrate also refers to the base of a PCB. Very often, insulating materials such as ceramics and plastics are used for substrate. Coated metals can also be used as substrates. The important material properties of a substrate include electrical resistivity, dielectric constants, thermal expansion coefficient, thermal conductivity, mechanical and electrical strength, and chemical stability. Commonly used substrate materials are aluminum nitride, aluminum oxide, quartz, Kovar, molybdenum, and plastics.

Wire-bond. Wire-bond is one of the common methods for electrical interconnection between the microchip and the chip-level package. A complete wire-bond loop includes a metallization pad on the chip, a metallization pad or input/output (I/O) of the chip-level packaging substrate, and a thin metal wire bonded to both chip and packaging substrate. The wire materials include Au, Cu, Al, and Pd. The bonding methods used for wire-bond include ultrasonic, thermal ultrasonic, thermal compression, and parallel gap welding. The thermal ultrasonic bond is the most popular one for Au and Al wires. During the bonding process, wire and pad surfaces are brought into intimate contact. Heat and ultrasonic energies excite interfacial (atoms) inter-diffusion and electron sharing, resulting in bonding. There are two types of ultrasonic wire-bonds: ball-bond and wedge-bond. Ball-bond is more often used to bond wires onto metallization pads on chips. Ball-bond does not apply to Al wire because Al wire may oxidize during the process of ball formation. Au wire ball-bond is usually performed at elevated temperatures. Compared with wedge-bond the ball-bond provides a smaller footprint and therefore higher bonding density. Wedge-bond can apply to both Au and Al wires. Al wire wedge-bond is performed at room temperature. The disadvantage of wire-bond technology is that it can only apply to low-density interconnections because the pads on the chip have to be at the chip's edges; otherwise, wires may easily cause short circuits. Figure 15.4.2 shows a schematic diagram of the wire-bond-based packaging scheme.

Die-attach. Die-attach is basically the mechanical attachment of a device die to a packaging substrate providing mechanical and possibly electrical interconnection between the die and the packaging substrate. The common materials used for attaching dies include epoxy, solder, low-temperature eutectics, and glass. The physical processes of die attachment include polymerization, melting/condensation, and inter-diffusion (ultrasonic bonding). Traditionally, the active side of a die faces up and the die attachment is made to the backside of the die. Wire-bond is then used to electrically interconnect the chip to the packaging substrate.

Flip-chip. Flip-chip is a die-attach structure where the die active side faces (down) toward the packaging substrate, as shown in Figure 15.4.3. The die is both mechanically and electrically interconnected to a packaging substrate using low-temperature eutectics, solder, or Au(Al) bumps. The physical processes of flip-chip die attachment include melting/condensation and interdiffusion (ultrasonic bonding). Very often, an under-fill material is used to fill the space between the die and the substrate to reinforce the structure for better thermomechanical reliability. The flip-chip scheme provides much higher chip packaging density. Flip-chip technology has been further developed to chip-scale packages (CSP), three-dimensional stacks, three-dimensional hybrid, direct chip attach (DCA), and so forth.

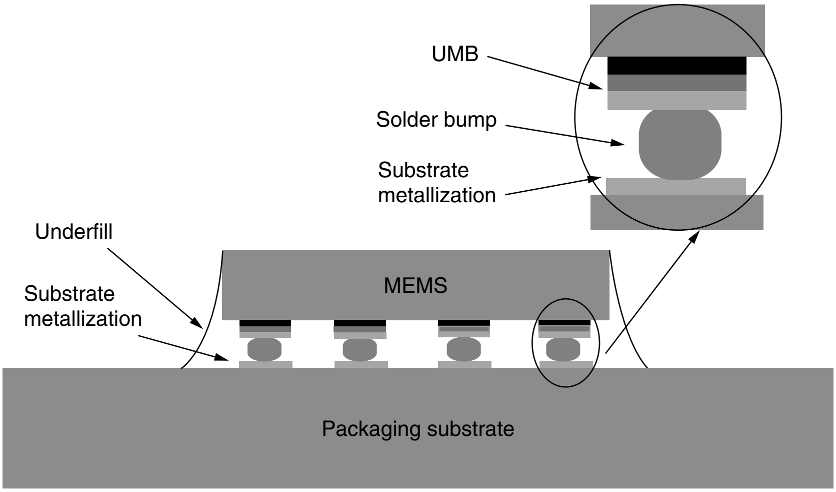

FIGURE 15.4.3 A schematic diagram of flip-chip packaging.

Sealing and Encapsulate. Usually an inert chemical environment is preferred for many MEMS and most electronic devices, so these devices are hermetically sealed into packages by glass, solder, brazing/metallization, and plastics/epoxy to reduce direct exposure to moisture and other reactive chemicals. Usually, sealing directly with glass or plastics without a package lid is considered an "encapsulate."

Harsh Environments. Harsh environments are the environments beyond those suitable for conventional silicon microelectronics and compatible packaging technology. High and extremely low temperatures, high radiation, very high acceleration, very high and dynamic pressure, chemically reactive and corrosive, and bio and medical *in vivo* environments are typical harsh environments for microsystems. Very often harsh environments generate significant challenges and additional requirements to both microsystems and packaging systems.

Wafer. Wafer is the base material on which MEMS devices and electronics are directly built. Single-crystal silicon (and other semiconductive materials such as III-V materials, silicon carbide, germanium, and SOI), poly-crystal silicon, silicon nitride, quartz, and alumina are examples of wafer materials used for fabrication of microsystems.

MEMS Packaging and Thermal Stress

Thermally induced stresses can cause undesired thermal response of MEMS device, irreproducibility of device operation and configuration, and drift of the device output. The thermal stress generated at both wafer bonding and die-attach levels must be suppressed in order to achieve precise and reliable device/system operation. To fully understand the sources of packaging stresses and resolve the issue of stresses generated at both wafer and die-attach levels, we will first discuss various wafer bonding and die-attach assembly methods. Following that, both analytical and numerical methods for packaging stress analysis will be examined.

Wafer-Level Packaging and Thermal Stress

Complicated wafer-level processes are extensively used in both MEMS device fabrication and wafer-level packaging. These wafer-level processes include wafer oxidizing, etching, thin-film deposition (metal, silicon, oxide, nitride, etc.), wafer bonding, sealing, and dicing. The materials used in wafer-level processes include oxides/nitrides, ceramics, metals/alloys, and plastics. Because of the limited space in this section, we concentrate on wafer bonding. Wafer bonding is one of the most important wafer-level packaging steps, and also the major thermal stress source of wafer-level packaging.

Si/Si and SiC/SiC Wafer Bonding

Si to Si wafer bonding is used with deep etching to create cavity-based MEMS devices such as Si capacitive pressure sensors (Ko and Wang 1999; Wang and Ko 1999; Young 2004). Wafer-level cavities are also used for packaging mechanical active components on MEMS chips. In the recent decade, wafer-bonding techniques have developed rapidly to satisfy MEMS fabrication and packaging needs. Si-Si or Si-SiO_2-Si bonding can be realized by fusion bonding at high temperatures. Generally, the process temperature required for Si wafer (without surface oxide) fusion bonding is above 1000°C, and the bonding can be conducted in vacuum to avoid wafer oxidation. The fusion bonding provides very good mechanical strength, but the disadvantage of using this method is the exposure of the wafer to high temperatures during the bonding process. Global high temperature exposure may damage prefabricated device structures and metallization. Chemical vapor deposition (CVD) and plasma-enhanced CVD (PECVD) are also often used to bond Si to Si without the surface oxide layer. These bonding methods are based on growing a thin material layer, such as poly Si, between Si wafers, to join them. Besides the exposure to high temperatures, the wafers are exposed to the CVD chemical environment. In parallel with CVD methods, sputter deposition is another choice for growth of a layer of bonding material. Special spatial geometry is necessary using this method, but the advantages gained over CVD are the control of the growth zone and less exposure to high temperature.

For bonding of Si wafers with a surface oxide layer (SiO_2/Si), usually the wafers are processed in acid first to form surface Si-O-H bonds. These hydrated wafer surfaces can be bonded directly to one another by intimate contact in a wide temperature range, from room temperature to ~1000°C. The bonding strength depends on the bonding temperature. The fact that higher bonding temperature provides better mechanical strength indicates different interfacial chemical reactions at different bonding temperatures (Madou 1997).

Low-temperature eutectics have been widely used to bond Si wafers in microfabrications. The most frequently used eutectics is $Au_{97}Si_3$ alloy, which has a low melting temperature of 363°C (Pecht et al. 1998). This eutectic bonding provides good mechanical strength. The bonding procedure is as follows: A thin SiO_2 layer is first grown on a Si wafer as an insulation layer. A chromium (Cr) thin-film layer with a thickness of 0.05 μm is deposited as an adhesion layer followed by a 0.5 μm Au layer. The second Si wafer is pressed onto the first Si wafer with an Au-coated surface, with ~MPa pressure. Heating the assembly slowly up to 410°C for 10 min provides a good $Au_{97}Si_3$ eutectic bonding.

It has been reported that Si-face 6H-SiC wafers on axis (0001) orientation and $3 \cdot 10^{18}/cm^3$ n-type doping have been fusion bonded at temperatures above 800°C (Yushin 2003). The wafer surface roughness was 1.5 nm (RMS). The samples were cleaned in JTB-111 solution, then 10% hydrofluoric acid and deionized water. Surface oxides were desorbed in ultra-high vacuum (UHV) at 1100°C for 30 min prior to fusion. The fusion bonding was performed in UHV at temperatures between 800 and 1100°C under a uniaxial stress of 20 MPa for 15 hrs. Examination by Transmission Electron Microscope (TEM) showed a 3 nm carbon interlayer at the bonding interface. The interface carbon might have resulted from high-temperature annealing (Bryant et al. 1999). The bonded SiC retained its crystalline quality. Electrical measurements showed that azimuthal orientation misalignment between the wafers had significant effects on interface states. It is important to note that many single-crystal structures of SiC, such as the hexagonal structures (6H and 4H), present polar characteristics, that is, Si terminates one side of a wafer and C terminates the other side of the wafer. The effects of polarity on SiC/SiC direct fusion bonding have not been reported. Except for the difference of the fabrication process for the surface silicon dioxide layer, the bonding process/mechanisms of SiC-SiO_2/SiO_2-SiC may be similar to that of the Si-SiO_2/SiO_2-Si system. However, it is of interest to know the effects of residual interfacial carbon, which usually accumulate at SiO_2/SiC interfaces, on the bonding quality.

Glass/Si and Glass/Metal Bonding

Glass can be bonded to many electrically conductive materials such as Si and metals at temperatures well below the glass-melting temperature with the assistance of a high electrical field (Go et al. 1998 and Madou 1997). The common experimental setup is as follows: The conductive component, such Si or

TABLE 15.4.1 Thermal and Mechanical Properties of Various Materials for MEMS Fabrication

Material	CTE (E-6/°C)	Elastic Modulus (GPa)	Poisson's Ratio	Processing Temperature (°C)
Si	2.49-4.44 (25–1027°C)	112.4	0.28	1000
SiO_2 fused quartz	0.4–0.7	70–78	0.17	1580–1730
SiC	4.5–4.7	459–476	0.14	>1250
Pyrex glass	3.25	62.75	0.2	1252
Al	24–27.4 (20–500°C)	68	0.33	<660.37
Ni	13.1 (20°C)	207	0.31	<1455 (melting)

metal, is connected to the anode, and a sharp cathode is placed on the glass side to generate a high electric field at the material interface. Usually, the anodic bonding is conducted between 200 and 450°C, and the voltage depends on the bonding materials and the thicknesses of the two materials, especially the glass. The bonding process typically starts from the area contacted by the sharp cathodes and proceeds toward the wafer edges. A typical process lasts less than 5 min. Pyrex glass (Dow Corning 7740) is one of the most commonly used glass materials for anodic bonding. The detailed mechanism of this relatively old technology has not yet been completely understood, but some works/literature on this aspect can be found. In order to use this bonding method, very smooth bonding surfaces are required. The advantage of anodic bonding is the relatively low temperature required for bonding. However, the disadvantage is that a high electrical field is used in the bonding process that might be harmful to some prefabricated device structures. The alkali metals in the glass may also migrate under high electrical potential, causing damage to the devices. Apparently, anodic bonding is limited to alkali metal rich glasses.

Thin-metal layers, such as 4 μm thick aluminum (Al), have been used as the bonding layer between Pyrex glass and a Si wafer with a silicon nitride surface layer. First, a 0.5 μm low-pressure CVD silicon nitride is grown on the Si wafer. A thin-film aluminum sealing layer is then deposited on the Pyrex glass. A rapid heating of the assembly to temperatures around 750°C provides a stable bond at the Al/silicon nitride interface. This type of bonding provides hermetic sealing to water.

Stress Issue in Wafer Bonding

Except for (same material) wafer-wafer fusion bonding, most other types of wafer-level bonding involve hetero-material(s) such as oxides/glass and eutectics, as the bonding layer. All these bonds are processed at elevated temperatures. Because of the CTE mismatch between the wafers and the bonding layer, significant thermal stress can be generated after the assembly cools down to room temperature. Table 15.4.1 shows the basic thermal and mechanical properties for some commonly used construction materials for MEMS. These residual thermal stresses generated at wafer-level bonding may have a significant impact on both the operation and performance of the device. In recent years various new/modified wafer bonding methods have been developed with reduced global temperature exposure to the wafer or assembly. These wafer-bonding techniques may have the potential to reduce the wafer-level stresses.

New Wafer Bonding Methods

Lin successfully demonstrated a local heating method to heat only the active/effective bonding areas of the wafer(s) (Lin 2000). Microfabricated polysilicon heaters were used for local heating. The heat spread area of a 1 μm line heater was typically about 1 μm, according to numerical modeling (Lin 2000). This local resistive heating method has been demonstrated for Si-Au eutectic bonding, Si-glass fusion bonding, solder bonding, and local plasma bonding/sealing. Mechanical tests of various wafer bonds using this local heating method showed that the results were comparable to wafer-wide heating methods. The disadvantage of local heating is the limited wafer-bonding area.

Microwave heating was proposed to perform wafer-level eutectic bonding (Budraa et al. 1999): A thin Au layer was first directly deposited on a Si wafer. The second Si wafer was pressed onto the Au coated Si wafer. The Au layer was used as the Au source, forming $Au_{97}Si_3$ eutectics as well as an effective energy-receiving antenna absorbing most of the microwave energy to heat the bonding assembly locally. The effectiveness of microwave heating made the necessary heating process as short as one min. Since the bonding/heating areas defined by Au thin-film were limited, the rest of the wafer could be kept at relatively lower temperatures. But if the bonding area is large, this method loses part of its advantage. Another disadvantage is that this method can only be used before device fabrication because the microwave radiation may also heat the metallization areas on the wafer and damage/change the device behavior.

Ultrasound bonding technology has been widely used for thin-wire bonding of electrical interconnection. Recently, an ultrasound wafer bonding method was developed to bond indium (In)-coated Si wafer to Au- or Al-coated Si wafer at room temperature under 10 ~ 40 MPa pressure. The ultrasound power needed to bond 1.6 ~ 2.1 mm^2 die ranged from 20 ~ 40 Watts. This bonding method turns ultrasound frequency mechanical vibration energy to localized thermal energy. Thus, it enables relatively low-temperature bonding between similar or dissimilar metal-coated wafers. Even though the local surface may be heated up to 200 ~ 300°C due to the friction of two contacting surfaces, the rest of the wafer is still at low temperature because of the rapid bonding process and limited bonding power. This technology was also demonstrated to join ceramic and metal plates (Kim et al. 2002). The disadvantage of this method is that the size of one of the "wafers" is likely limited, so it is suitable for bonding a small die to a wafer/die rather than a whole wafer to another. The ultrasound frequency must be away from the mechanical resonant frequencies of MEMS structures; otherwise the bonding process may damage the microfabricated mechanical structures on the wafer.

Continuous (Wild et al. 2001) and pulsed (Luo and Lin 2002) laser-beam methods have been demonstrated to bond glass to Si wafers. The continuous laser beam is transmitted through the transparent glass wafer to excite the Si/glass interface locally. The locally heated spot or line width is around 300μm or less with a laser beam power of 12 ~ 30-watts and a scanning rate of 50 ~ 500 mm/min. A nanosecond-pulsed YAG laser with a pulse duration of 4 ~ 6 ns and a wavelength of 355 nm has been used to demonstrate bonding glass to a Si wafer. The focal spot size of the laser beam is 1 mm, and a regular white paper with predefined patterns is used as the mask to select bonding areas. The temperature at the bonding spot drops from 2500 to 43°C in 2 ms. A thin indium layer is used as the bonding material. The mechanical strength of the bonded assemblies resulting from the pulsed mode method is limited by the mechanical strength of indium, 2.6 MPa, while the bond strength resulting from the continuous mode method can be as high as 5 ~ 10 MPa. The advantage of laser wafer bonding is localized heating and high selectivity of bonding area. The disadvantage of laser beam bonding is time consumption for large area bonding.

Room temperature wafer bonding between Si and ceramic wafers by means of surface activation using Ar ion-beam etching was reported recently (Takagi et al. 2001). Four-inch Si wafers with mesa structure have been bonded to 3- or 4-inch ceramic wafers in vacuum by intimately mating two wafer surfaces after removing wafer surface oxides and surface adsorbates (contaminations). Before Ar beam etching, the wafer surfaces must be polished. The bonding strength measured between Si wafers with 9 × 9 mm^2 mesas and ceramics materials such as single-crystal a-Al_2O_3, 128°Y-cut $LiNbO_3$, Z-cut $LiNbO_3$, 36°X-cut $LiTaO_3$, and Gd_3GaO_{12} were better than those resulting from conventional wafer bonding methods (Takagi et al. 2001). This is perhaps the "cleanest" wafer-joining method because Ar normally does not react to most elements/materials. But this method is likely only suitable for bonding wafers with a limited effective bonding area. Another disadvantage of this bonding method is that the wafer surfaces have to be exposed to an Ar ion beam, which may destroy any prefabricated MEMS or circuits on the surfaces.

Die Bonding

After wafer-level fabrication, including wafer bonding a die/chip bonding process will usually follow to interconnect the die/chip to the next level packages, such as chip-level packages or directly to the PCB. As discussed in Fundamental Packaging Concepts, there are two basic chip-level packaging schemes: one is die-attach/wire-bond and the other is the flip-chip scheme. The mechanical and electrical interconnections of the die are separated in the die-attach/wire-bond scheme while the mechanical and electrical interconnections are combined in the flip-chip scheme. The die-attach/wire-bond scheme is suitable to a chip-and-board packaging infrastructure. This packaging infrastructure provides a unique flexibility of chip-level packages — in other words, one of these types of chip packages can fit many device chips.

In the era when device yield was a significant concern, this type of single-chip-package and board infrastructure also provided flexibility of component selection and replacement. The wire-bond-based electrical interconnection system provides excellent thermomechanical reliability (Tummala 2001). The wire-bond scheme is the most frequently used electrical interconnection technology in chip-level packaging today. It is predicted that it will remain so in the foreseeable future. The flip-chip scheme is a relatively newer packaging scheme. It was introduced by IBM in 1962. The flip-chip scheme eliminates the space needed for wire-bonds, significantly reducing the package size, that is, increasing the packaging density (the number of packaged chips per unit area). Flip-chip is a favored assembly for high-frequency applications because the short bump interconnection reduces parasitic effects. Flip-chip has been successfully used for high-performance optoelectronics packaging using self-alignment. The flip-chip structure also allows three-dimensional stacking for multichip module and high-density memory chip packaging. The disadvantage of the flip-chip structure is the compromised reliability of the die bonding resulting from the merging of the mechanical and electrical interconnections between the chip and the packaging substrate. Usually the thermal reliability of flip-chip assembly can be improved by suitable underfill. The flip-chip packaging scheme has been further developed. Besides the initial chip-on-board infrastructure, new technologies have been generated based on the flip-chip technology for various applications.

Die-Attach and Wire-bond Scheme

Wire-bond and die-attach packaging is the most popular chip-level packaging scheme. In this approach, the chip/die is mounted to the package with the active die side facing up. The electrical interconnections between the chip/die and the package are then realized through thin-wire bonding, as discussed earlier. Both die-attaching materials and die-attaching processes will be discussed in this section.

Materials. The materials used to attach/bond the die include epoxy, glass, solder, and low-temperature eutectics. Recently, thick-film materials have been tested for high-temperature operable conductive die attachment. Besides the function of mechanical mounting, die-attach sometimes also provides electrical interconnection through the backside contact of the die/chip. Metallic particles are added to nonconductive die-attach materials, such as epoxy and glass, to make the materials electrically conductive.

- *Epoxy and polyimides:* These are two of the most popular low cost die-attach materials. These materials (either one component or two components) polymerize at either room temperature or elevated temperatures, ~125°C, in a few hours. Usually, metal particles such as silver are added to improve the electrical and thermal conductivities. The thermal stability of these materials is an issue for applications with high-reliability requirements. The CTE of epoxy materials ranges from 50 to 80 ppm/°C, which is significantly higher than the CTEs of chip materials (Si and SiC) and ceramic substrate materials. These materials are cured at temperatures up to 180°C. The maximum operating temperature is limited to the glass transition temperature of the epoxy or polyimide.
- *Solder/eutectics:* The melting temperatures of alloys composed of tin (Sn), lead (Pb), indium (In), cadmium (Cd), bismuth (Bi), gallium (Ga), silver (Ag), gold (Au), silicon (Si), and germanium (Ge) cover a wide temperature range from room temperature to 420°C (Tummala 2001, p. 374). The selection of solder materials depends on the processing temperature, temperature of operation, and the metallization materials on both the chip and substrate. AuSi and AuGe eutectics provide high melting temperatures and excellent fatigue/creep resistance. The disadvantage of this type of eutectic is a lack of plastic flow resulting in high-thermal stress due to mismatch of CTEs between the solder and chip/board materials. PbSnInAg-based alloy provides low melting temperatures and better plasticity. Solder/eutectics provide excellent thermal and electrical conductivities. The bonding process using solder and low-temperature eutectics is usually a melting solidification cycle. The maximum operating temperature of solder/eutectics is limited by material softening/melting temperature.
- *Glass:* Silver and other precious metal filled glasses are also used for die bonding. Glass bonding is basically a melting-solidification process so it usually requires high processing temperatures (>400°C). However, glasses provide excellent thermal and chemical stability. Glasses have very low

porosity and adhere/wet well to a large variety of materials. Melting (and solidifying) temperatures of glasses, which are determined by the glass components and additives, cover a broad temperature range; so do thermal expansions coefficients of glasses. In order to select an appropriate glass material for a specific die/substrate bond, we should consider both CTE match and processing temperature. Unlike solder and eutectics, the maximum operating temperature of glass-bonded die-attach can sometimes exceed the die-bonding temperature, the initial melting temperature of the glass, because the glass crystallizes during the solidification process (McCluskey et al. 1996).

- *Thick-Film:* Thick-film materials have been tested for high-temperature operable conductive die attaching/bonding in recent years. Thick-film metallization materials are usually composed of fine metal (for metal/alloy thick-films) or glass (encapsulate) powders, inorganic binder (such as metal oxides), and organic vehicle. Screen-printing techniques are used to provide patterned thick-film coatings with thickness control. During the initial drying process (at 100 ~150°C) the organic vehicle evaporates and the paste becomes a semisolid phase mixture of metal powder and binder. In the final curing process (~850°C recommended for most thick-film products), the inorganic binder molecules migrate to the metal film/substrate (e.g., Au/ceramic) interface and form reactive binding chains. Au thin wires can be bonded directly to Au thick-film metallization pads using commercialized wire-bond equipments to provide electrical interconnection in packaging. Some new thick-film materials may be applicable to various ceramic substrates such as alumina (Al_2O_3) (Keusseyan et al. 1996) and aluminum nitride (AlN) (Wang et al. 2002; Keusseyan et al. 1996; Chitale et al. 1994; Shaikh 1994). Compared with direct thin-film metallization on ceramic substrate, thick-film metallization provides lower cost, simpler processing, lower electrical resistance, and better adhesion, which is provided by the reactive binders at the metal/substrate interface.

  Both the electrical and mechanical properties of Au thick-film materials for applications in hybrid-packaging conventional ICs have been extensively validated at $T < 150°C$. An electrically conductive die-attach scheme using Au thick-film as die-attaching material for Ni metallized SiC devices has been tested for operation at temperatures up to 500°C (Chen et al. 2000). Au has a low elastic modulus and yield strength, and a very wide plastic deformation range. The excellent thermal and mechanical properties of Au make it a feasible die attaching/bonding material, especially for high-temperature and harsh-environment applications.

  A SiC test die with a Ni contact on the back was attached to a ceramic substrate using an optimized two-step Au thick-film process (Chen et al. 2000). A thick-film layer was first screen-printed on the substrate and cured at 850°C using a standard process (DuPont 1999). The SiC die was then attached to the cured thick-film pattern with a second layer of thick film. A sufficient drying process (120 to 350°C) was critical to keep the thick-film bonding layer uniform and the die parallel to the substrate after the curing process. Following the drying process, the attached die was cured at ~600°C. Curing at 600°C or above allowed sufficient diffusion to occur at the Au/Ni and Au/Au interfaces, and consequently established bonding (Chen et al. 2000).

Bonding Processes. A phase transition process from liquid or semiliquid to solid is typically involved in most die-bonding processes except for diffusion bonding. For example, the bonding process is a polymerization process for epoxy and a solidification process for solder, eutectics, and glass. This type of solidification often is enabled at elevated temperatures with a corresponding material volume change during the phase transition. Therefore, significant thermal stress can be generated because of the mismatch of thermochemical properties of materials. The basic structure of the die-attach/bond assembly for thermomechanical study is similar to that of the wafer bond, that is, a sandwich composed of two thicker layers (die and substrate) and a thin bonding layer.

Flip-Chip

In the flip-chip die-attach scheme, the die is interconnected to the packaging substrate both electrically and mechanically using the active side of the device/chip, so the die faces down. Flip-chip technology has been successfully used for MEMS packaging (Boustedt et al. 2002).

General Structure. As illustrated in Figure 15.4.3, the chip is first coated using electroplating and electroless deposition to form a multilayer under bump metallization (UBM) system on the electrical contact area of the chip. Before the deposition of UBM the electrical contact area(s) on the chip are often capped by an Al or Au thin film (Oppermann et al. 2000). The selection of UBM materials is made to match the bump material and bonding method. The bumps are usually deposited using electroplating or electroless deposition directly on UBM. Mature die attaching/bonding methods include thermal compression, low-temperature soldering, and adhesive paste joining. The metallization on the board (substrate) is also selected to be compatible to the bump material and die attaching/bonding method.

Material Systems. The UMB is generally composed of four layers: adhesion, diffusion barrier, wetting, and anti-oxidation/soldering layers. The function of the adhesion layer is to provide sufficient adhesion to the chip metallization surface. Chromium (Cr), titanium (Ti), zinc (Zn), and nickel (Ni) are often used as adhesion-layer materials. The function of the diffusion-barrier layer is to protect the metallization on the chip from the materials/elements of UBM and bump material. The candidate materials for the barrier layer include W, TiW, and Ni. A wetting layer is needed if the bump material does not sufficiently wet the barrier layer. Copper (Cu), Pd, and Ni are often used for this purpose. The anti-oxidation/soldering layer protects the UBM from oxidation, and a gold (Au) thin-film is usually used. For example, Ti/W/Ni/Au, Cr/CrCu/Cu/Au have been used for commercialized solder bumping. In many cases, some of these four layers can be combined to a certain extent so that the UBM is composed of fewer than four layers. For example, Ti/W/Cu UBM is coated on Cu/SnPb electroplated chips for PbSn solder bumps, while the metallization on the substrate/board is Cu/Ni/Au. Ti/W/Au is coated on Au electroplated (an additional Sn layer on top of the Au is needed for AuSn bumps) chips for Au or AuSn solder bumps, and Cu/Sn is used for substrate/board metallization. Ti/W/Au UBM is coated on Au electroplated chips for isotropic conductive adhesive (ICA) paste bonding, and Cu/Au or Cu/Ni/Au is used for substrate/board metallization. ICA paste is usually stencil printed.

Bonding Process. The electrical contacts on the chip are usually fabricated by thin-film deposition and plasma-etch (or lift-off) patterning technologies. In order to reduce the fabrication costs, the UBM layers are usually deposited by electroplating and electroless deposition onto the electrical contacts on the chip. The bumps are deposited by electroplating with a photoresist mask. After the deposition, the mask is etched off and the wafer undergoes a reflow procedure to shape the bumps using the surface tension of the liquefied bump material. There are two categories of die-bonding methods: soldering and thermal compression bonding. During the soldering process the solder bumps melt and wet the metallization pads of the substrate/board. During the thermal compression bonding process, the substrate/board is heated up and the solder/eutectic bumps are compressed and bonded to the metallization pads on the substrate/board. The bonding mechanism of this method is similar to that of thermal compression wire-bonding.

Stress Issues. Thermal compression and solder/eutectics die bonding are both processed at elevated temperatures, so local (the adjacent area surrounding a bump) thermal stress is generated after the assembly cools down because of the CTE mismatches of chip/metallization/UBM/bump/metallization/substrate. Further, global thermal stress is generated because of the mismatch of CTEs of the chip and substrate materials. Thermomechanically, if we consider the UBM, solder/eutectics bump, and the substrate metallization as one metallic layer possessing higher CTE in comparison to the die and substrate materials, a single bump flip-chip die bond presents a die/bonding layer/substrate sandwich structure. This sandwich structure is similar to those of wafer bonding and conventional die-attach. The thermomechanical stress/strain analysis of this sandwich structure, die/adhesive/substrate, is particularly important to MEMS packaging because the thermal stress/strain effects on the packaged devices have been expanded from permanent mechanical damages of package and packaged die(s) to the thermal stress effects on device operation/performance.

Boundary Value Problem and Analytical Methods

In this section a boundary value problem of thermal stress/strain of a generic square-shaped die-attach, as shown in Figure 15.4.4, is established. The major purpose of establishing the boundary value problem

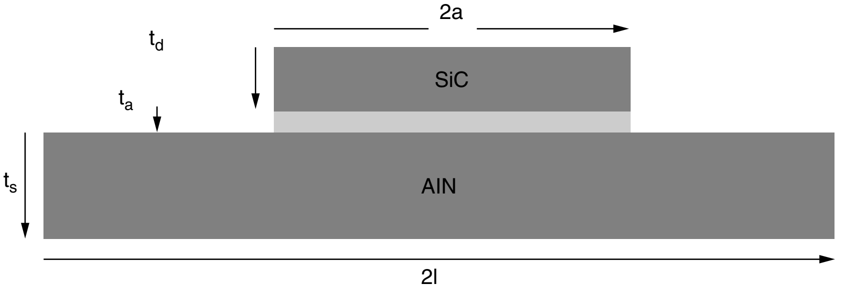

FIGURE 15.4.4 A schematic diagram of a generic SiC die-attach.

is not to directly lead readers to exact analytical solutions of the die-attach stress problem because of the mathematical complexity of the problem. Instead it helps us to understand: (1) the relations between thermomechanical variables, (2) constraints of stress/strain tensors, and (3) the dependences of the thermal configuration of a die-attach assembly on the physical properties of the die-attach materials, the geometric symmetry of the die-attach, the process temperature, and the boundary (and interface) conditions. All these form a base for discussion of approximate analytical methods and numerical solutions later.

Governing Equations of Displacements

Assuming that the temperature distribution in the die-attach is static ($\partial T/\partial t = 0$) and uniform ($\partial T/\partial x = \partial T/\partial y = \partial T/\partial z = 0$), and the external force on the die-attach structure is zero, the general thermal mechanical governing equations for the die-attach system are listed as

$$\frac{\partial^2 u}{\partial x^2} + \frac{\partial^2 v}{\partial x \partial y} + \frac{\partial^2 w}{\partial x \partial z} + (1-2\upsilon)\nabla^2 u = 0 \tag{15.4.1a}$$

$$\frac{\partial^2 v}{\partial y^2} + \frac{\partial^2 u}{\partial x \partial y} + \frac{\partial^2 w}{\partial y \partial z} + (1-2\upsilon)\nabla^2 v = 0 \tag{15.4.1b}$$

$$\frac{\partial^2 w}{\partial z^2} + \frac{\partial^2 u}{\partial x \partial z} + \frac{\partial^2 v}{\partial y \partial z} + (1-2\upsilon)\nabla^2 w = 0 \tag{15.4.1c}$$

where

$$\nabla^2 = \frac{\partial^2}{\partial x^2} + \frac{\partial^2}{\partial y^2} + \frac{\partial^2}{\partial z^2}$$

u, v, and w = the displacements in x-, y-, and z-directions, respectively

υ = Poisson's ratio of the material

The normal stress distributions are determined by the displacements, material properties, and the temperature (Lau et al. 1998):

$$\tau_{xx} = \frac{\lambda}{\upsilon}\left[(1-\upsilon)\frac{\partial u}{\partial x} + \left(\frac{\partial v}{\partial y} + \frac{\partial w}{\partial z}\right)\right] - \beta(T - T_o) \tag{15.4.2a}$$

$$\tau_{yy} = \frac{\lambda}{\upsilon}\left[(1-\upsilon)\frac{\partial v}{\partial y} + \left(\frac{\partial w}{\partial z} + \frac{\partial u}{\partial x}\right)\right] - \beta(T - T_o) \tag{15.4.2b}$$

$$\tau_{zz} = \frac{\lambda}{\upsilon}\left[(1-\upsilon)\frac{\partial w}{\partial z} + \left(\frac{\partial u}{\partial x} + \frac{\partial v}{\partial y}\right)\right] - \beta(T - T_o) \tag{15.4.2c}$$

Shear stresses are reduced from u, v, and w as

$$\tau_{xy} = \frac{E}{2+2\upsilon}\left(\frac{\partial u}{\partial y} + \frac{\partial v}{\partial x}\right) \tag{15.4.3a}$$

$$\tau_{yz} = \frac{E}{2+2\upsilon}\left(\frac{\partial v}{\partial z} + \frac{\partial w}{\partial y}\right) \tag{15.4.3b}$$

$$\tau_{zx} = \frac{E}{2+2\upsilon}\left(\frac{\partial w}{\partial x} + \frac{\partial u}{\partial z}\right) \tag{15.4.3c}$$

where

$\lambda = \dfrac{\upsilon E}{(1+\upsilon)(1-2\upsilon)}$
$\beta = \dfrac{\alpha E}{1-2\upsilon}$
E = Young's modulus
α = the coefficient of linear thermal expansion (CTE)

Material properties α, E, and υ generally are different for the die, attaching layer, and the substrate materials. The strain tensor components are also reduced directly from the displacements:

$$\varepsilon_{XX} = \frac{\partial u}{\partial x} \tag{15.4.4a}$$

$$\varepsilon_{YY} = \frac{\partial v}{\partial y} \tag{15.4.4b}$$

$$\varepsilon_{ZZ} = \frac{\partial w}{\partial z} \tag{15.4.4c}$$

$$\varepsilon_{xy} = \frac{\partial u}{\partial y} + \frac{\partial v}{\partial x} \tag{15.4.4d}$$

$$\varepsilon_{yz} = \frac{\partial v}{\partial z} + \frac{\partial w}{\partial y} \tag{15.4.4e}$$

$$\varepsilon_{zx} = \frac{\partial w}{\partial x} + \frac{\partial u}{\partial z} \tag{15.4.4f}$$

where ε_{XX}, ε_{YY}, and ε_{ZZ} are the three normal strains, which are the diagonal elements of a nine-element strain tensor in the *X-Y-Z* coordinate system. The physical interpretation of a normal strain is one of relative longitudinal elongations under normal stresses. ε_{xy}, ε_{yz}, and ε_{zx} are shear strain components, which are nondiagonal tensor elements. They are usually diagonally (only with respect to the diagonal line along ε_{XX}, ε_{YY}, and ε_{ZZ}) commutable. The physical interpretation of a shear strain is a tangent of deformation of a right angle under the corresponding shear stress. Within the elastic deformation region of an isotropic media the stress and strain tensors have the following linear relations:

$$\varepsilon_{XX} = \frac{1}{E}\left[\tau_{XX} - \upsilon\left(\tau_{YY} + \tau_{ZZ}\right)\right] + \alpha\left(T - T_o\right) \tag{15.4.5a}$$

$$\varepsilon_{YY} = \frac{1}{E}\left[\tau_{YY} - \upsilon\left(\tau_{XX} + \tau_{ZZ}\right)\right] + \alpha\left(T - T_o\right) \tag{15.4.5b}$$

$$\varepsilon_{ZZ} = \frac{1}{E}\left[\tau_{ZZ} - \upsilon\left(\tau_{XX} + \tau_{YY}\right)\right] + \alpha\left(T - T_o\right) \tag{15.4.5c}$$

$$\varepsilon_{XY} = \frac{1}{G}\tau_{XY} \tag{15.4.5d}$$

$$\varepsilon_{YZ} = \frac{1}{G}\tau_{YZ} \tag{15.4.5e}$$

$$\varepsilon_{ZX} = \frac{1}{G}\tau_{ZX} \tag{15.4.5f}$$

G is shear modulus of the material. For an object of uniform and isotropic medium, in a uniform static temperature field, without external mechanical load, all stress components vanish. Consequently, all shear strain components vanish and the thermal strains contribute to three normal strain components only. If a stress is so high that it generates plastic (permanent) strain, then the stress and strain relations are no longer linear functions.

If there is no residual stress at a certain temperature, such as the die-attaching temperature, then the mismatch of CTEs of the die-attach assembly and the temperature deviation from the stress-free temperature (relaxing temperature) are the major sources of thermal mechanical stresses. This would become more apparent if the boundary value problem were listed for the die, the attaching layer, and the substrate separately. There would be an external force term at the boundaries, that is, the interface between the die and the attaching layer and the interface between the attaching layer and the substrate. These external force terms are generated by the mismatch of material CTEs or the residual stresses. In case there is neither residual stress nor CTE mismatch, these external force terms vanish and the solutions for the equations are trivial.

Constraints on Stress and Strain Tensors

For any static configuration, all stresses must meet the equilibrium conditions. We take an infinitesimal volume and consider a local static condition. A force equilibrium between the surface forces (stresses) and body force F must be reached (Sokolnikoff 1956). If the external body force is zero, the constraining conditions for the stress components are established:

$$\frac{\partial \tau_{xx}}{\partial x} + \frac{\partial \tau_{yx}}{\partial y} + \frac{\partial \tau_{zx}}{\partial z} = -F_x = 0 \tag{15.4.6a}$$

$$\frac{\partial \tau_{xy}}{\partial x} + \frac{\partial \tau_{yy}}{\partial y} + \frac{\partial \tau_{zy}}{\partial z} = -F_y = 0 \tag{15.4.6b}$$

$$\frac{\partial \tau_{xz}}{\partial x} + \frac{\partial \tau_{yz}}{\partial y} + \frac{\partial \tau_{zz}}{\partial z} = -F_z = 0 \tag{15.4.6c}$$

Besides the constraints of these partial derivatives of stress tensor components, these equations also indicate the continuity of τ_{ii} in i-direction ($i = x, y, z$) and τ_{ij} in i- and j-directions ($i, j = x, y, z$ but $i \neq j$), where body force density is not unlimited, regardless of the media uniformity.

The equilibrium of moments in various directions leads to very important constraints on the nine element stress tensor (Sokolnikoff 1956, p. 42):

$$\tau_{ij} = \tau_{ji} \tag{15.4.7}$$

This indicates that the stress tensor is diagonally symmetric, so only six out of nine elements of the stress tensor are independent regardless of material properties.

The existence of single-valued continuous solutions of displacements would place the following derivative constraints on the strain tensor components (Sokolnikoff 1956):

$$\frac{\partial^2 \varepsilon_{xx}}{\partial y \partial z} = \frac{\partial}{\partial x}\left(-\frac{\partial \varepsilon_{yz}}{\partial x} + \frac{\partial \varepsilon_{zx}}{\partial y} + \frac{\partial \varepsilon_{xy}}{\partial z}\right) \tag{15.4.8a}$$

$$\frac{\partial^2 \varepsilon_{yy}}{\partial z \partial x} = \frac{\partial}{\partial y}\left(-\frac{\partial \varepsilon_{zx}}{\partial y} + \frac{\partial \varepsilon_{xy}}{\partial z} + \frac{\partial \varepsilon_{yz}}{\partial x}\right) \tag{15.4.8b}$$

$$\frac{\partial^2 \varepsilon_{zz}}{\partial x \partial y} = \frac{\partial}{\partial z}\left(-\frac{\partial \varepsilon_{xy}}{\partial z} + \frac{\partial \varepsilon_{yz}}{\partial x} + \frac{\partial \varepsilon_{zx}}{\partial y}\right) \tag{15.4.8c}$$

$$2\frac{\partial^2 \varepsilon_{xy}}{\partial x \partial y} = \frac{\partial^2 \varepsilon_{xx}}{\partial y^2} + \frac{\partial^2 \varepsilon_{yy}}{\partial x^2} \tag{15.4.8d}$$

$$2\frac{\partial^2 \varepsilon_{yz}}{\partial y \partial z} = \frac{\partial^2 \varepsilon_{yy}}{\partial z^2} + \frac{\partial^2 \varepsilon_{zz}}{\partial y^2} \tag{15.4.8e}$$

$$2\frac{\partial^2 \varepsilon_{zx}}{\partial z \partial x} = \frac{\partial^2 \varepsilon_{zz}}{\partial x^2} + \frac{\partial^2 \varepsilon_{xx}}{\partial z^2} \tag{15.4.8f}$$

Besides the constraints of partial derivatives of strain tensor elements, these equations also indicate continuity of ε_{ii} in j and k ($j, k \neq i$) directions and ε_{ij} ($i \neq j$) in all three directions. However, these equations do not directly apply any constraints on $\partial\varepsilon_{xx}/\partial x$, $\partial\varepsilon_{yy}/\partial y$, and $\partial\varepsilon_{zz}/\partial z$, indicating the possibility of discontinuity of normal strains in the strain orientation. These observations are useful, and it is important to analyze and understand normal and shear strain distributions in an inhomogeneous medium, such as interface areas of a die-attach assembly composed of die, die-attach, and substrate materials.

Boundary, Symmetry, and Interfacial Conditions

The dimensions of a square shaped die attached to a square shaped substrate with a thin die attaching layer are shown in Figure 15.4.4. Assuming there are no external mechanical loads applied on the die-attach (gravity is ignored), the boundary conditions of the die-attach assembly are basically natural boundary conditions: the assembly is free to expand such that all (both normal and shear) stress components on the assembly surfaces vanish at any temperature. Assuming that the distortions of the die-attach assembly are negligible compared with the dimensions of the die-attach, these boundary conditions are: at $x = \pm a$ and $z > t_s$, or $x = \pm l$ and $z < t_s$: $\tau_{xx} = 0$ and $\tau_{xy} = 0$ and $\tau_{xz} = 0$, at $y = \pm a$ and $z > t_s$, or $y = \pm l$ and $z < t_s$: $\tau_{yy} = 0$ and $\tau_{yx} = 0$ and $\tau_{yz} = 0$, at $z = 0$, $z = t_s$ and $|x| > a$ or $|y| > a$, or $z = t_s + t_a + t_d$: $\tau_{zz} = 0$, $\tau_{zx} = 0$, and $\tau_{zy} = 0$.

The symmetry conditions are: at $x = 0$: $u = 0$, $\tau_{yx} = 0$, and $\tau_{zx} = 0$, at $y = 0$: $v = 0$, $\tau_{xy} = 0$, and $\tau_{zy} = 0$. The symmetry conditions basically indicate that the transverse shear stress u and the displacements in the x- and y-directions vanish at the transverse central planes of the x- and y-directions correspondingly.

At the interfaces between the die and the die-attaching layer and between the die-attaching layer and the substrate, the bonding conditions are usually assumed to be ideal. This means all displacements are continuous at the interfaces: $u|_{S_s+} = u|_{S_s-}$, $v|_{S_s+} = v|_{S_s-}$, $w|_{S_s+} = w|_{S_s-}$, $u|_{S_a+} = u|_{S_a-}$, $v|_{S_a+} = v|_{S_a-}$, and $w|_{S_a+} = w|_{S_a-}$. S_s is the interface between the die and the attaching layer, and S_a is the interface between the attaching layer and the substrate, respectively.

The Relaxation Condition

At the die-attaching or wafer-bonding temperature, the attaching or bonding material usually either melts or becomes highly diffusive. So at this temperature, the assembly is thermomechanically relaxed, that is, the stress level of the assembly reaches zero or a minimum. This temperature is usually defined as the relaxation temperature in the following thermal stress/strain discussion. This minimum stress level depends on the physical properties of the assembly materials and the physical/chemical process of the attaching or bonding. For thermal compression of thermal-sonic-compression bonding, relaxation conditions (temperature) may not exist.

Analytical Methods

The thermomechanical boundary value problem of a die-attach with simple geometry is still complicated enough that a closed exact analytical solution has never been derived after decades of efforts. The thermal mechanical boundary value problem of a sandwich type structure is really not new. It has been identified and studied for decades for thermal expansion of bimetal thermostats and electronic packaging. No closed exact analytical solutions have been derived, even in a narrow temperature range in which the material properties, such as thermal expansion and Young's modulus, can be approximately treated as constants. Therefore, various approximations and assumptions have been used to obtain approximate analytical solutions.

Tomoshenko first established a two-dimensional analytic method for the bimetal thermostat using elastic theory. Assuming that the materials are uniform and isotropic, the temperature field is uniform, $t_{d,a,s}/a = \varepsilon \ll 1$, $t_d/t_s = O(1)$ (the thickness of die is at least an order lower than that of the substrate), and $t_a/t_{d,s} = O(\varepsilon)$, an asymptotic solution was derived based on the following assumptions: in the die and substrate, horizontal displacements are linear functions of z, the vertical displacements are a second-order function of z, and the displacements in the die-attaching layer are linear functions of z (Tomoshenko 1925).

Extending Tomoshenko's elastic theory of bi-metal thermostats, Suhir developed a practical one-dimensional model for horizontal distributions of lateral normal (tensile) stress, τ_N, shear stress, τ_S, and peeling (transverse normal) stress, τ_P, at the die/attaching layer interface using the condition of horizontal displacement compatibility at the interface (Suhir 1987):

$$\tau_S = \left[\frac{1-\upsilon_s^2}{E_s t_s} + \frac{1-\upsilon_d^2}{E_d t_d} + \frac{\left(t_d + t_s\right)^2}{4D}\right]^{-1/2} \left[\frac{t_d}{3D_d} + \frac{2t_a}{3G_a}\frac{t_s}{3D_S}\right]^{-1/2} \left(\alpha_s - \alpha_d\right)\left(T - T_R\right)\frac{\mathrm{Sinh}\left(Ax\right)}{\mathrm{Cosh}\left(Al\right)} \tag{15.4.9a}$$

$$\tau_N = \left[\frac{1-\upsilon_s^2}{E_s t_s} + \frac{1-\upsilon_d^2}{E_d t_d} + \frac{\left(t_d + t_s\right)^2}{4D}\right]^{-1} \left[\frac{1}{t_d} + \left(t_d + t_s\right)\frac{E_d t_d}{4D\left(1-\upsilon_d^2\right)}\right]\left(\alpha_s - \alpha_d\right)\left(T - T_R\right)\left(1 - \frac{\mathrm{Cosh}\left(Ax\right)}{\mathrm{Cosh}\left(Al\right)}\right) \tag{15.4.9b}$$

$$\tau_P = 6\left[\frac{t_s t_d^3 E_d}{12\left(1-\upsilon_d^2\right)} - \frac{t_d t_s^3 E_s}{12\left(1-\upsilon_s^2\right)}\right]\left[\frac{2t_a}{3G_a} + \frac{t_d}{3G_d} + \frac{2t_s}{3G_s}\right]^{-1}\left[\frac{E_d t_d^3}{\left(1-\upsilon_d^2\right)} + \frac{E_a t_a^3}{\left(1-\upsilon_a^2\right)} + \frac{E_s t_s^3}{\left(1-\upsilon_s^2\right)}\right]^{-1}$$
$$\frac{\left(\alpha_s - \alpha_d\right)\left(T - T_R\right)\mathrm{Cosh}(Ax)}{\mathrm{Cosh}(Al)} \tag{15.4.9c}$$

where $G_{d,a,s}$, $E_{d,a,s}$, $\upsilon_{d,a,s}$, and $\alpha_{d,a,s}$ are shear moduli, and tensile elastic moduli, Poisson's ratios, and coefficients of thermal expansions (CTE) of the die (*d*), attaching layer (*a*), and substrate (*s*) materials, respectively. Also

$$A=\left[\frac{1-\upsilon_s^2}{E_s t_s}+\frac{1-\upsilon_d^2}{E_d t_d}+\frac{\left(t_d+t_s\right)^2}{4D}\right]^{1/2}\left[\frac{t_d}{3G_d}+\frac{2t_a}{3G_a}+\frac{t_s}{3G_s}\right]^{-1/2} \tag{15.4.9d}$$

and

$$D=D_1+D_2+D_3=\frac{1}{12}\left[\frac{E_d t_d^3}{\left(1-\upsilon_d^2\right)}+\frac{E_a t_a^3}{\left(1-\upsilon_a^2\right)}+\frac{E_s t_s^3}{\left(1-\upsilon_s^2\right)}\right] \tag{15.4.9e}$$

These results indicate that the normal stress in the die is high at the central area and sharply decreases to zero in a narrow area at the die edges. Both shear and peeling stresses are high at die edge areas and decrease rapidly approaching the die central area. These formulae have been suggested for direct reliability assessment of die-attach for conventional electronic packaging through calculation of maximum normal stress in the die, the maximum shear stress at the interface, and the maximum peeling stress at the die/attaching layer interface to predict the failures of die material, attaching layer material, and the adhesion of die/attaching layer interface (Hu and Pecht 1993).

This engineering theory of thermally induced stresses in bimaterial assemblies was extended to a trimaterial assembly for interfacial thermal shear stresses based on the following assumptions: stresses and strains are in the materials' elastic regions, no singular stresses exist at the assembly edges, and the deflections of the assembly are small. The interfacial shear stresses and assembly deflection are determined without considering the effects of peeling stress (Suhir 2001):

$$\tau_{s1}=-kT_1^o\frac{\sinh(kx)}{\cosh(kl)} \tag{15.4.10a}$$

$$\tau_{s2}=-kT_3^o\frac{\sinh(kx)}{\cosh(kl)} \tag{15.4.10b}$$

τ_{s1} and τ_{s2} are shear stresses at the first-layer/second-layer (such as die/die-attaching layer) interface and the second-layer/third-layer (such as attaching layer/substrate) interface, respectively, where

$$k=\left\{\frac{k_1^{\,2}+k_2^{\,2}}{2}\left[1+\left(1-\gamma\left(\frac{2k_1k_2}{k_1^{\,2}+k_1^{\,2}}\right)^{1/2}\right)^2\right]\right\}^{1/2},\quad T_1^o=-\frac{\left(\alpha_3-\alpha_2\right)\lambda_{13}+\left(\alpha_1-\alpha_2\right)\lambda_{33}}{\gamma\lambda_{11}\lambda_{33}}\Delta T\ ,$$

$$T_3^o=-\frac{\left(\alpha_3-\alpha_2\right)\lambda_{11}+\left(\alpha_1-\alpha_2\right)\lambda_{13}}{\gamma\lambda_{11}\lambda_{33}}\Delta T\ ,\ k_1=\left(\lambda_{11}/k_{12}\right)^{1/2}\ ,\ k_2=\left(\lambda_{33}/k_{23}\right)^{1/2}\ ,\ \gamma=1-\frac{\lambda_{13}^{\,2}}{\lambda_{11}\lambda_{13}}\ ,$$

$$k_i=\frac{t_i}{3G_i}\quad (i=1,2,3)\ ,\ \lambda_{11}=\frac{\left(t_1+t_2\right)^2}{4D}+\lambda_1+\lambda_2\ ,\ \lambda_{33}=\frac{\left(t_2+t_3\right)^2}{4D}+\lambda_2+\lambda_3\ ,$$

$$\lambda_{13}=\frac{\left(t_1+t_2\right)\left(t_2+t_3\right)}{4D}-\lambda_2\ ,\ \lambda_i=\frac{1}{E_it_i}\quad (i=1,2,3)$$

E_i is the elastic modulus of the ith component, t_i is the thickness of ith component, and $\Delta T = T - T_o$ is the temperature deviation from the relaxing temperature at which the stresses and strains vanish.

The corresponding peeling stresses at the interfaces are

$$\tau_{Pj} = m_j\left[\chi_0(s,k)V_0(sx) + \chi_2(s,k)V_2(sx)\right] + C_j\frac{\cosh kx}{\cosh kl}\ ,\quad j = 1,2 \tag{15.4.11}$$

where

$$\chi_0(s,k) = \frac{s\sqrt{2}}{k}\frac{\left[V_0(sl)-1\right]\tanh kl + \frac{s\sqrt{2}}{k}V_3(sl)\left(1-1/\cosh kl\right)}{\left[V_0(sl)-1\right]V_1(sl) + V_2(sl)V_3(sl)}\ ,$$

$$\chi_2(s,k) = \frac{s\sqrt{2}}{k}\frac{[V_2(sl)-1]\tanh kl + \frac{s\sqrt{2}}{k}V_1(sl)(1-1/\cosh kl)}{[V_0(sl)-1]V_1(sl) + V_2(sl)V_3(sl)}\ ,\quad V_0(sx) = \cosh sx\cos sx\ ,$$

$$V_2 = \sinh sx\sin sx\ ,\quad s^4 = \frac{s_1^4 + s_2^4}{2}\left[1 + \sqrt{1 - \frac{\delta}{4\left(s_1^4 + s_s^4\right)}}\right],\quad s_1^4 = \frac{D_1 + D_2}{4D_1D_2\delta_{12}}\ ,\quad s_2^4 = \frac{D_2 + D_3}{4D_2D_3\delta_{23}}\ ,$$

$$\delta_{12} = \frac{t_1}{E_1^*} + \frac{t_2}{2E_2^*}\ ,\quad \delta_{23} = \frac{t_3}{E_3^*} + \frac{t_2}{E_2^*}\ ,\text{ and }\ \delta = \frac{D}{\delta_{12}\delta_{23}D_1D_2D_3}$$

where $j = 1$ refers the first-layer/second-layer interface and $j = 2$ refers to the second-layer/third-layer interface.

It is worthwhile to indicate that these interfacial shear, peeling, and normal stresses are derived from engineering theory. They were not mathematically solved from the displacement governing equations; they were derived from interfacial mechanical equilibrium equations of the die-attach assembly (Suhir 2001).

Recently, Ru (2002) developed a nonlocal model assuming that the longitudinal displacement at a bimaterial elastic beam interface also depends on both the shear stress and the second gradient of the interfacial shear stress. Ru's results satisfy both of the requirements of the zero-longitudinal force and zero shear stress at the free edges. The peeling stress calculated from this model is equilibrated at the interface (Ru 2002).

$$\tau_S = \alpha\Delta T\frac{\cosh\left(\rho_1 l\right)\sinh\left(\rho_2 l\right)\sinh\left(\rho_1 x\right)\cos\left(\rho_2 x\right) - \sinh\left(\rho_1 l\right)\cos\left(\rho_2 l\right)\cosh\left(\rho_1 x\right)\sin\left(\rho_2 x\right)}{\Sigma} \tag{15.4.12}$$

$$\begin{aligned}\tau_P = \alpha\Delta T\frac{t_1D_2 - D_1t_2}{2\left(D_1 + D_2\right)}\Bigg\{&\frac{\left[\rho_1\cosh\left(\rho_1 l\right)\sin\left(\rho_2 l\right) - \rho_2\sinh\left(\rho_1 l\right)\cos\left(\rho_2 l\right)\right]\cosh\left(\rho_1 x\right)\cos\left(\rho_2 x\right)}{\Sigma} - \\ &\frac{\left[\rho_1\sinh\left(\rho_1 l\right)\cos\left(\rho_2 l\right) + \rho_2\cosh\left(\rho_1 l\right)\sin\left(\rho_2 l\right)\right]\sinh\left(\rho_1 x\right)\sin\left(\rho_2 x\right)}{\Sigma}\Bigg\}\end{aligned} \tag{15.4.13}$$

where

$$\rho_1 = \left(\frac{\bar{A}}{4\bar{B}} + \frac{1}{2\bar{B}^{-1/2}} \right)^{1/2},$$

$$\rho_2 = \left(\frac{2\bar{B}^{1/2} - \bar{A}}{4\bar{B}} \right)^{1/2},$$

$$\bar{A} = \frac{t_1 K_1 / G_1 + t_2 K_2 / G_2}{\lambda_1 + \lambda_2 + \dfrac{\left(t_1/2 + t_2/2\right)^2}{D_1 + D_2}},$$

$$\bar{B} = \frac{t_1^3 d_1 K_1 / G_1 + t_2^3 d_2 K_2 / G_2}{\lambda_1 + \lambda_2 + \dfrac{\left(t_1/2 + t_2/2\right)^2}{D_1 + D_2}},$$

K_1, K_2, d_1, and d_2 material property related constants (Ru, 2002). The numerical results derived from these formulas are reasonably consistent with those of finite element analysis.

Approximate analytical solutions can provide quick and global stress/strains assessment. In the elastic region, limited parametric studies of the effects of materials, sizes, and process condition on stress/strain distributions can be analyzed using analytical results. However, as it has been noted, the analytical method has limitations as indicated in the following paragraph.

For conventional electronic packaging, material-level permanent damages are a critical concern for die-attach thermomechanical reliability. However, for MEMS packaging, especially high-temperature MEMS, we are interested in precise and quantitative three-dimensional stress/strain distributions in order to examine the mechanical effects of packaging stress/strain on device mechanical operation, before the stress/strain reaches the level causing permanent material damage. As indicated in the introduction of this section, various MEMS sensors for aerospace engine monitoring and combustion control operate in a wide range of high temperatures and pressures. Therefore, the stress formulae derived using constant material properties and zero external load may no longer be suitable. The temperature dependence of material properties makes the die-attach boundary value problem much more complicated, and elastic/plastic nonlinear material properties make the derivation of a closed analytical solution to this boundary value problem almost impossible.

In addition to the complexity caused by temperature dependent nonlinear material properties, the boundary geometry of the MEMS die may generate another obstacle to analytical solutions. As a simple example, a diaphragm-based piezoresistive MEMS sensor may have a round-shaped diaphragm at the center of a square die. Neither Cartesian nor cylindrical coordinates would fit the boundary geometry of this problem. Boundary geometries of MEMS devices can be much more complicated than those of the diaphragm-based sensor. Therefore, it becomes very difficult to derive an analytical solution of a boundary value problem for a high-temperature MEMS die-attach assembly.

Numerical analysis is a powerful method for solving thermomechanical boundary value problems, such as the stress/strain distribution of a die-attach assembly. Finite element analysis (FEA) is the most sophisticated numerical method that can deal with all the previously stated complexities, including the external mechanical load. Chang (2002) successfully used FEA to calculate deflection angles of a nickel-coated microplatform in static magnetic fields generated by a microfabricated DC coil (Chang 2002). Another advantage of FEA is its ability to solve coupled thermal and mechanical loads. The next subsection provides an example in which FEA is used to model stress/strain distributions of an Au thick-film based SiC die-attach over a wide temperature range. This example illustrates the application of FEA in MEMS packaging. In order to avoid possible redundancy the fundamentals of FEA are not covered in

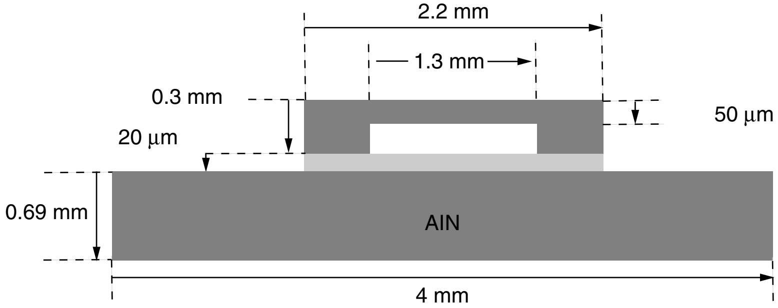

FIGURE 15.4.5 A schematic diagram of SiC pressure sensor die-attach using Au as attaching material for FEA simulation.

detail in this section. Readers can refer to other chapters of this handbook for both FEA fundamentals and practice.

Numerical Analysis of Die-attach Thermal Stresses and Strains

In this section, FEA simulation of stress/strain distributions of a SiC die-attach assembly over a wide temperature range is used to illustrate the application of numerical analysis for thermal stress/strain analysis in MEMS packaging. The SiC die includes a diaphragm structure. Diaphragm structures are used often in MEMS sensors and packaging, such as piezoresistive and capacitive acoustic (Chen et al. 2004) and pressure sensors (Beheim et al. 2001; Okojie et al. 2001).

As shown in Figure 15.4.5, a SiC die (2.2 mm × 2.2 mm × 0.30 mm) is attached to an AlN substrate (4 mm × 4 mm × 0.69 mm) with an Au thick-film layer (20 µm). The round diaphragm of the SiC die has a radius of 0.65 mm and a thickness of 50 microns. The die-attach is processed (cured) at 600°C and then cooled down to room temperature. It is assumed that the die-attach assembly is relaxed at 600°C before it is cooled down to room temperature, and that the cooling process is rapid enough such that the stress/strains caused by temperature deviation from the relaxing temperature are accumulated without relaxation/creeping. Because of the symmetry of the die-attach assembly, the stress/strain distributions of only a quarter of the assembly are simulated at room temperature. Within the ANSYS FEA software tool, the Geometric Non-linearity Option was enabled and Automatic Time-step Process was employed with 10% of the full temperature loading (temperature drops from 600 to 25°C) as the initial time-step. A line search was used with the Newton-Raphson iterative algorithm to improve and accelerate convergence.

The basic mechanical properties of materials included in the die-attach (Au, SiC, and AlN) and the temperature dependences of these material properties that were used in FEA simulation are listed in Table 15.4.2. The temperature dependence of the Young's modulus of AlN in a wide temperature range has not been reported, so it is extrapolated as a constant from the room temperature value. The Poisson's ratios of single-crystal 6H-SiC and AlN have not been published, so they are estimated from those of other carbides and nitrides, respectively. The thermal and mechanical properties of 6H-SiC are assumed to be isotropic. Material CTEs (mismatches) have the most significant effects on the die-attach assembly thermal stresses/strains. Temperature-dependent CTE data of both substrate and die materials (AlN and SiC), as listed in Table 15.4.2, were used for the FEA simulation.

The yield strength data of Au reported in the literature covers a wide range due to different heat-treatments applied to the materials used for these experimental tests. In this simulation, a low Au yield strength (250 psi) and temperature-dependent plasticity of Au are used. These simulation results should be close to stress/strain configurations of an Au thick-film based die-attach assembly sufficiently annealed (stored and operated) at 600°C. Plasticity of gold thick-film is a primary factor responsible for thermally induced stresses in a die-attach assembly. Only limited data of Au plasticity are available in published literature. Temperature dependent ultimate tensile strength of Au have been reported (King et al. 1988).

TABLE 15.4.2 Materials Properties of Au, AlN, Al_2O_3, and SiC Used for FEA

Temperature (°C)	CTE (xE–6/C)	E (xE6 psi)	υ
Au material properties			
15	14.04	11.09	0.44
20	14.24	10.99	0.44
105	14.71	10.83	0.44
205	15.23	10.59	0.44
305	15.75	10.28	0.44
405	16.29	9.92	0.44
505	16.89	9.51	0.44
605	17.58	9.03	0.44
705	18.38	8.50	0.44
SiC material properties			
–15	1.78	66.72	0.3
20	2.07	66.72	0.3
105	2.78	66.42	0.3
205		66.08	0.3
305	4.44	65.74	0.3
505	6.11	65.05	0.3
605		64.71	0.3
705	7.78	64.36	0.3
AlN material properties			
–15	2.89	50.00	0.25
20	3.15	50.00	0.25
105	3.79	50.00	0.25
205		50.00	0.25
305	5.29	50.00	0.25
405		50.00	0.25
505	6.79	50.00	0.25
605		50.00	0.25
705	8.29	50.00	0.25

Sources: H.K. Charles and G.V. Clatterbaugh 1994; F.P. McCluskey, R.R. Grzybowski, and T. Podlesak 1996.

An elongation of 65% was reported for annealed gold (Suhir 1987). The yield strength of gold is 250 psi (King et al. 1988) at room temperature, and it is assumed to be independent of temperature in the calculation. Based on these material properties, approximations, and assumptions, temperature-dependent plasticity behavior of gold was constructed as shown in Figure 15.4.6 (Lin and Chen 2002).

Figure 15.4.7a and Figure 15.4.7b show the von-Mises stress (the second deviatoric stress invariant) contours for the SiC die from an SiC/Au/AlN die-attach assembly at room temperature with an assumed stress relaxing temperature of 600°C. Von-Mises stress is often used to determine if yielding or damage occurs. Since the maximum von-Mises stress of the die is much lower than the yield strength of SiC material, it is anticipated that there is no material level damage to the SiC die. The level of stress around the inner circle (etching wall) of the bottom of the die is high, whereas the stress level is lower towards the die edges and corners of the bottom of the die. The stress level also significantly decreases toward the top of the die. The level of stress in the diaphragm area is significantly higher than those in the areas surrounding the diaphragm. The stress level of the diaphragm area can be used to estimate the effects of die-attach thermal stress on operation and configuration of diaphragm-based MEMS devices. Figure 15.4.7(c) and Figure 15.4.7(d) show the distribution of peeling stress, which is the normal stress perpendicular to the die/attaching-layer interface, at the die/attaching layer interface. Positive peeling stress indicates that the stress is in tension, and the negative stress indicates the stress is compressive. The tension is relatively high around the inner circle of the bottom of the die. At the corner and edge areas, the peeling stress is negative, so it is compressive. Usually, tensile stress causes material damage/cracks.

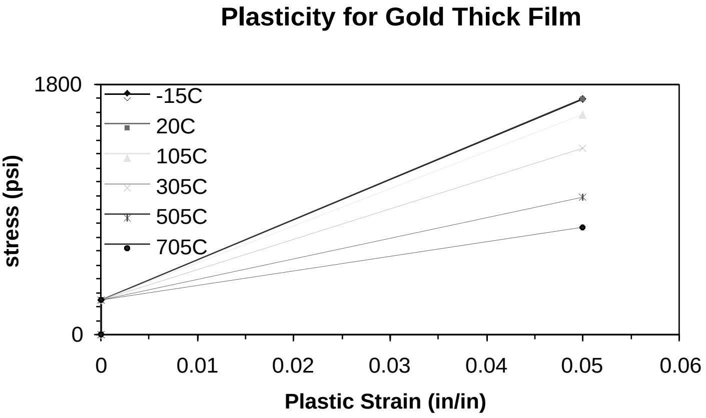

FIGURE 15.4.6 Temperature-dependent plasticity of gold thick film; –15°C and 20°C data overlap each other in the figure.

Compared with the mechanical strength of SiC material, the maximum tensile stress of the SiC die is still low, so no die material damage is anticipated. Figure 15.4.7(e) and Figure 15.4.7(f) show the die shear stress (τ_{zx}) distribution contour. The shear stress of the bottom of the die is high at the area close to the edge. Both peeling and shear stresses decrease rapidly toward the top of the die. The peeling and shear stresses in the diaphragm area are also higher than those outside the diaphragm. The peeling (tensile) stress at the die/attaching interface can be directly compared with the die-attach adhesion tensile strength data for reliability analysis and failure mode prediction. The shear stress at the die/attaching-layer interface can be directly compared to the shear strength of the die-attach material and the shear adhesion strength of the die/attaching layer interface for failure/reliability analysis.

Figure 15.4.7(g) and Figure 15.4.7(h) show von Mises stress contours on the top and bottom of the Au attaching layer. Von Mises stress is high at the corner region, illustrating that the shear component may dominate the von Mises stress at the die/attaching layer interface area. Figure 15.4.7(i–l) show peeling and shear stresses on the top and bottom of the die-attach layer. The peeling and shear stresses on the top of the attaching layer are exactly the same as those on the bottom of the die (the stress scale bars are in different scales). The peeling and shear stress contours on the bottom of the attaching layer are the same as those on the substrate. The strap structure of the shear stress indicates that τ_{zx} increases with the distance from the $x = 0$ neutral point. Because the die-attach assembly has 90° symmetry in the horizontal plane, the shear contour of τ_{zy} can be obtained with 90° rotation of that of τ_{zx}. Peeling and shear stresses at the attach layer/substrate interface can be compared with the experimental measurements of the adhesion strength of the attach layer/substrate interface for reliability assessment and failure-mechanism prediction. Figure 15.4.7(m) and Figure 15.4.7(n) show the equivalent plastic strain (EPS) distributions of the die-attaching layer after cooling to room temperature and heating back to 500°C (one thermal cycle).

The thermal stresses/strains on the diaphragm may cause changes in device configuration and operation. For example, thermal stress can directly generate thermal shift of the piezoresistance of diaphragm-based piezoresistive MEMS sensors such as pressure and acoustic sensors. A thermal shift of the capacitance of a diaphragm-based capacitive sensor due to the deformation of the diaphragm under thermal stress may also occur. These die-attach-related thermal stresses may have significant thermal effects on the packaged devices. In addition to the predications of packaging-related reliability and failure analysis, FEA results may also help MEMS packaging designers to simulate/predict packaging effects on devices. Using the FEA results may allow designers to reduce the parasitic packaging effects through materials selection and structure optimization. In order to study the effects of die-attach materials and die-attach geometries, single-parametric dependence of stress/strain on substrate material, die size, die-attaching layer thickness, and environment/processing temperature can be simulated using FEA (Lin and Chen 2002).

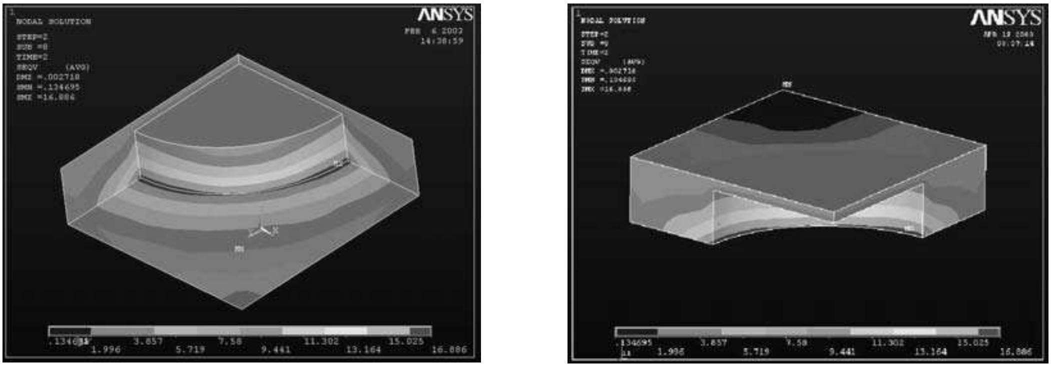

(a) von Mises stresses of SiC with AIN substrate. (b) von Mises stresses of SiC with AIN substrate.

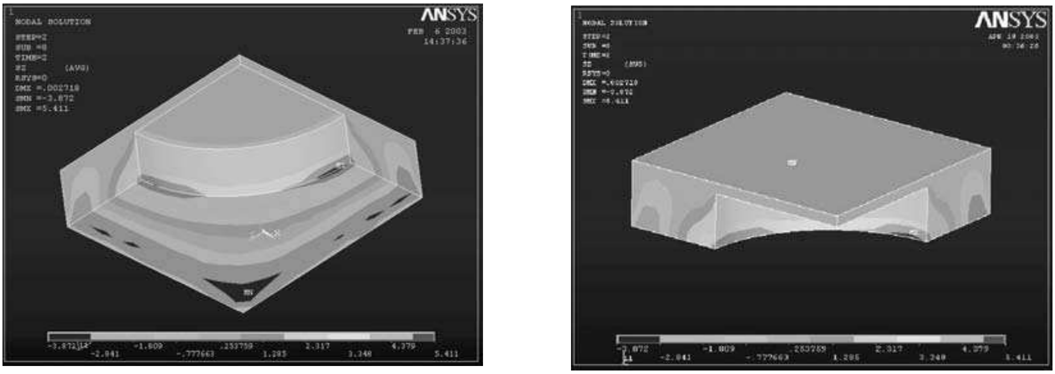

(c) Peeling stresses of SiC die with AIN substrate. (d) Peeling stresses of SiC with AIN substrate.

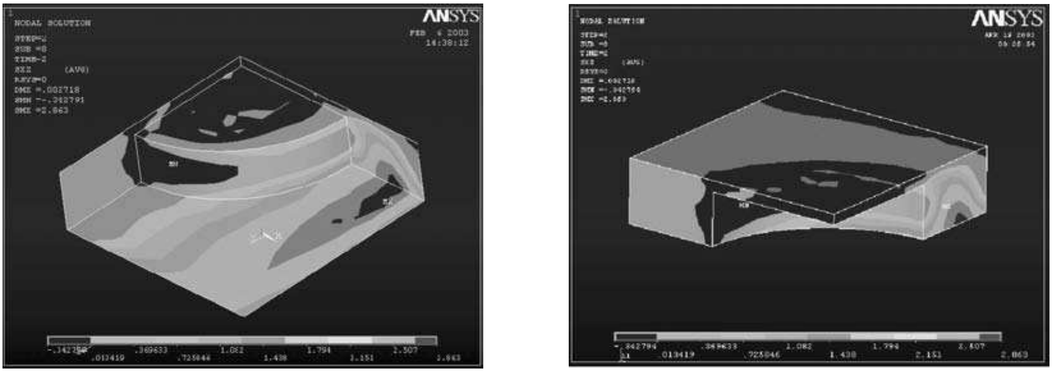

(e) Shear stresses of SiC die with AIN substrate. (f) Shear stresses of SiC with AIN substrate.

FIGURE 15.4.7 Stress and strain contours of SiC diaphragm attached to AlN substrate with Au thick-film. The unit for stresses is MPa. (From P. McCluskey, K. Meyyappan, and L-Y. Chen, Proceedings of 2004 IEEE Aerospace Conferences. With permission.)

In these FEA simulations, the boundary conditions at both SiC/Au-thick-film and Au-thick-film/substrate interfaces are assumed to be ideal. This means that there is no slip at either interface under shear stress. Mathematically, this assumption implies that all three displacement components are continuous at the two interfaces. We made this assumption since limited interfacial thermomechanical properties of this material system are available. Further, it is difficult to either numerically model or experimentally measure the thermal and mechanical properties of interfaces, especially the temperature dependencies of these interfacial thermomechanical properties. This assumption may have limited applicability for those relatively “loosely” bonded interfaces, especially at elevated temperatures.

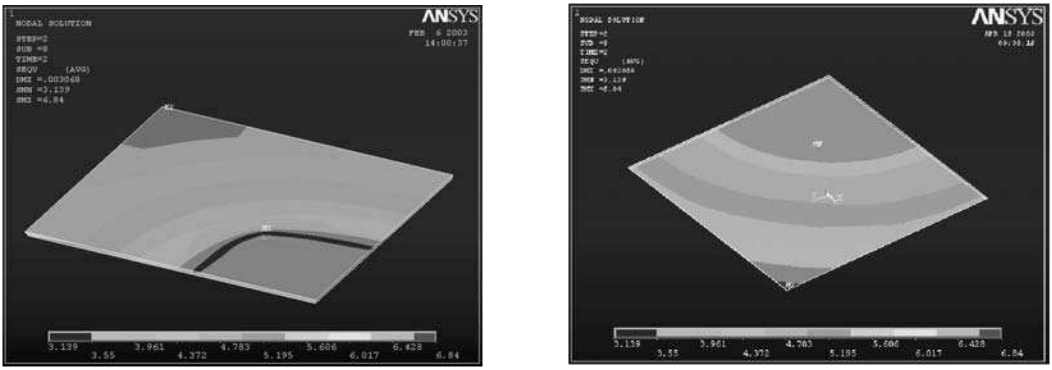

(g) von Mises stresses of top of die attaching layer.

(h) von Mises stresses of bottom of die attaching layer.

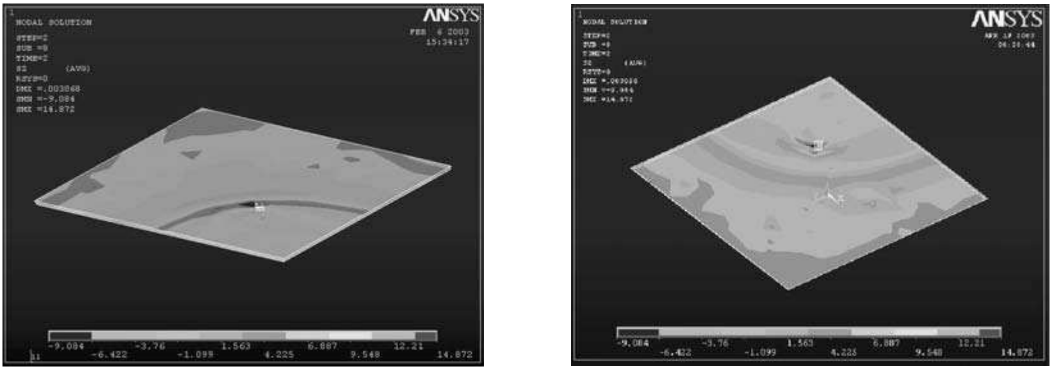

(i) Peeling stresses of top of die attaching layer.

(j) Peeling stresses of bottom of die attaching layer.

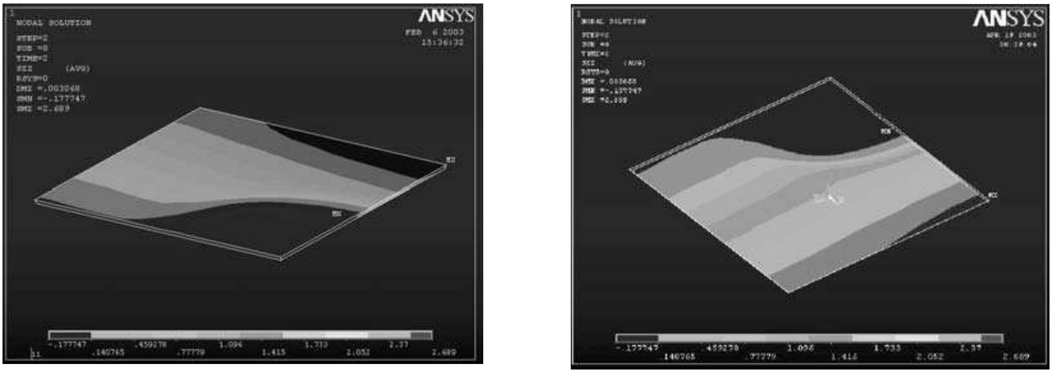

(k) Shear stresses of top of die attaching layer.

(l) Shear stresses of bottom of die attaching layer.

FIGURE 15.4.7 (continued).

The experimental measurement of three-dimensional die-attach stress/strain distributions and detection of the thermal mechanical failure of the Au attaching layer sandwiched between an SiC die and a ceramic substrate can be challenging, especially at elevated temperatures. Therefore, it is important and helpful to numerically validate the FEA results. First, the effect of mesh design/density on the numerical results can be examined by changing the three-dimensional FEA mesh. The convergence of the numerical results with increasing mesh density usually is a good indication of valid results. Second, the stability of the stress/strain dependence on the material properties, such as the CTE of the substrate, can also be used to examine the numerical stability with a small virtual perturbation (upward and downward shifts) of the CTE-temperature curve of the substrate material. Third, the numerical results should (approximately)

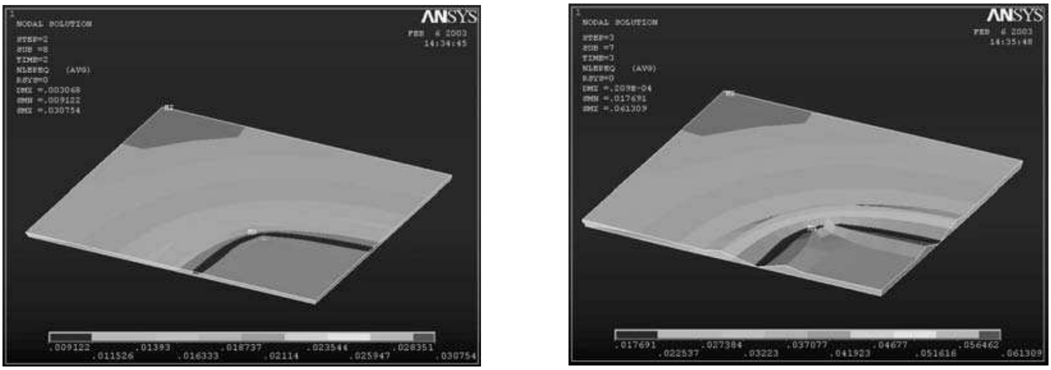

(m) Equivalent Plastic Strain (AIN based substrate) of the top of the die attaching layer at room temperature.

(n) Equivalent Plastic Strain (AIN based substrate) of the top of the die attaching layer at 500°C.

FIGURE 15.4.7 (continued).

satisfy all the boundary/interface and symmetry conditions. This is a simple and quick way to physically validate the numerical results. Fourth, the trends of stress/strain can be compared with those predicted by approximate analytical results if they are available.

Low-Stress Die-Attach

Advanced low-stress die attach methods for MEMS packaging will be discussed in this section.

Low-Stress Die-Attach Materials

As discussed earlier, the die-attach stress/strain increases rapidly with the temperature deviation from T_R. T_R is the temperature at which the die-attach is thermomechanically relaxed (no stress or almost no stress). Usually, the physical/chemical process of die attaching determines T_R such that it is close to the die-attach process/curing temperature. Therefore, the die-attach process temperature is an important process parameter determining die-attach stress/strain and thermal reliability. The ideal situation is that T_R is at the center of the operating temperature range (Lin and Chen 2002). A process called low-temperature transient liquid phase (LTTLP) bonding allows die to be bonded at a relatively low temperature, from 60 to 160°C, yet the bonding layer will remelt only at a much higher temperature. The principle of this bonding process is that the metal(s) of the metallization on the substrate and/or the die dissolve into the melted alloy and form a new alloy that isothermally solidifies (Roman and Eagar 1992). In the mid-1960s it was demonstrated that indium, which melts at 156.7°C, forms In_xAu_y alloy with a melting temperature of ~300°C (Bernstein 1966). The research on LTTLP has been active again since the early 1990s because of the need for low-processing-temperature die-attach materials for reliable large-size high-power devices packaging. Various low-melting-temperature solders of indium, tin, bismuth, and cadmium have been tested for applications with base metals of gold, silver, and copper (Roman and Eagar 1992). Table 15.4.3 shows a recompiled table of melting temperature and tensile strength of these material systems. Low stress die-attach materials are attracting more attention because of the emerging needs of MEMS packaging.

Mechanically, most LTTLP bonds are as strong as an equivalent conventional solder bond (Roman and Eagar 1992). Typically, the remelting temperature and the mechanical strength of LTTLP bonds depend on the processing temperature and temperature profile (temperature vs. time).

Low-Stress Die-Attach Structures

Li and Tseng suggested a "four-dot" low stress die-attach approach for packaging of MEMS accelerometers that reduced die surface strains caused by CTE mismatches (Li 2001). FEA simulation results indicated that a significant stress reduction could be achieved when the area of die-bonding "dots" located at four die corners were small. This die-attach structure can dramatically reduce or eliminate the transverse

TABLE 15.4.3 Melting Temperatures and Mechanical Strength of Various Solder Materials and Remelting Temperatures of New Alloys Formed with Base materials of Ag, Au, and Cu, Listed with Process Temperatures and Times

Solder	Melting Point (°C)	Tensile Strength (psi)	Base Metal	Curing Temp (°C)	Curing Time (hrs)	Remelting Point (°C)
In	156.7	575	Ag	165	3	450
In	156.7	575	Au	165	1	500
In	156.7	575	Cu	165	3	500
$In_{97}Ag_3$	146	800	Ag	155	18	550
$In_{97}Ag_3$	146	800	Au	155	1	500
$In_{97}Ag_3$	146	800	Cu	155	3	500
$In_{80}Pb_{15}Ag_5$	149	2550	Ag	155	24	500
$In_{80}Pb_{15}Ag_5$	149	2550	Au	155	1	400
$In_{80}Pb_{15}Ag_5$	149	2550	Cu	155	24	500
$In_{52}Sn_{48}$	118	1720	Ag	130	60	130
$In_{52}Sn_{48}$	118	1720	Au	130	2	400
$In_{52}Sn_{48}$	118	1720	Cu	130	1	500
$In_{44}Sn_{42}Cd_{14}$	93	2632	Ag	110	20	500
$In_{44}Sn_{42}Cd_{14}$	93	2632	Au	110	18	250
				110	72	400
$In_{44}Sn_{42}Cd_{14}$	93	2632	Cu	110	1	500
$Bi_{58}Sn_{42}$	138	8000	Ag	150	2	500
$Bi_{58}Sn_{42}$	138	8000	Au	150	11	200
				150	96	200
$Bi_{58}Sn_{42}$	138	8000	Cu	150	1	500
$Bi_{46}Sn_{34}Pb_{20}$	100		Ag	110	26	500
$Bi_{46}Sn_{34}Pb_{20}$	100		Au	110	72	250
$Bi_{46}Sn_{34}Pb_{20}$	100		Cu	110	26	500
$Bi_{55.5}Pb_{44.5}$	124	6400	Ag	135	25	500
$Bi_{55.5}Pb_{44.5}$	124	6400	Au	130	26	165
$Bi_{55.5}Pb_{44.5}$	124	6400	Cu			
$Bi_{50}Pb_{26.7}Sn_{13.3}Cd_{10}$	70	5990	Ag	80	72	500
$Bi_{50}Pb_{26.7}Sn_{13.3}Cd_{10}$	70	5990	Au	110	26	<100
$Bi_{50}Pb_{26.7}Sn_{13.3}Cd_{10}$	70	5990	Cu	110	26	<100
$Bi_{49}In_{21}Pb_{18}Sn_{12}$	58	6300	Ag	80	72	500
				110	48	500
$Bi_{49}In_{21}Pb_{18}Sn_{12}$	58	6300	Au	110	26	370
$Bi_{49}In_{21}Pb_{18}Sn_{12}$	58	6300	Cu	110	26	500
$Bi_{44.7}Pb_{22.6}In_{19.1}Sn_{8.3}Cd_{5.3}$	47	5400	Ag	110	26	400
				110	48	500
$Bi_{44.7}Pb_{22.6}In_{19.1}Sn_{8.3}Cd_{5.3}$	47	5400	Au	110	26	<100
$Bi_{44.7}Pb_{22.6}In_{19.1}Sn_{8.3}Cd_{5.3}$	47	5400	Cu	110	10	300
$Bi_{67}In_{33}$	109		Ag	120	13	300
$Bi_{67}In_{33}$	109		Au			
$Bi_{67}In_{33}$	109		Cu			
$In_{66.3}Bi_{33.7}$	72		Ag	110	24	580
$In_{66.3}Bi_{33.7}$	72		Au			
$In_{66.3}Bi_{33.7}$	72		Cu			
$Bi_{60}Cd_{40}$	144		Ag	155	4	240
$Bi_{60}Cd_{40}$	144		Au	155	4	340
$Bi_{60}Cd_{40}$	144		Cu	155	4	580
$In_{74}Cd_{26}$	123		Ag	155	11	540
$In_{74}Cd_{26}$	123		Au			
$In_{74}Cd_{26}$	123		Cu			
Ga	29.8		Ag	150	2	
Ga	29.8		Au	150	25	
Ga	29.8		Cu	150	16	

Source: The data in this table are compiled from Roman and Eagar 1992.

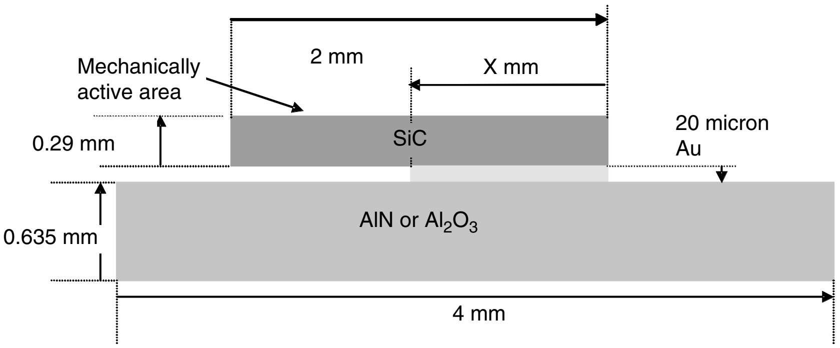

FIGURE 15.4.8 Partial die-attach structure.

normal stress in the central die area. However, it may not be optimized to reduce lateral normal stresses in the die, which is important to diaphragm-based piezoresistive MEMS sensors.

The thermal mechanical stress in the SiC die of the die-attach assembly shown in Figure 15.4.4 has been numerically simulated using FEA. The results show that the stress attenuates rapidly with increasing vertical distance to the interface of SiC and Au thick-film layer. Horizontally, the maximum thermal stress increases rapidly with the die size or die-attaching area (Chen and Lei 2002). Based on these results, an effective thermal stress attenuation method is suggested: lateral stress attenuation die attach (Chen and Lei 2002). This stress reduction die-attach structure requires that the die be partially attached to the substrate through the backside area of the nonmechanically active portion of the die, rather than fully attaching the die to the substrate. A side view of a partially bottom attached die-attach is illustrated in Figure 15.4.8. This die-attach structure allows a lateral distance on the device chip between the mechanically active area(s) and the direct attaching area. This die-attach structure allows the stress generated by thermal expansion mismatch at the die/attach/substrate bonding area to effectively attenuate along this lateral distance. The advantage of using this die-attach structure is the reduction of stress at mechanically active (unattached) areas of MEMS chips. Therefore, the requirement of matching the thermal expansion coefficients of die, attaching, and substrate materials is lessened. This low-stress die-attach technology is especially suitable for applications in high-temperature MEMS packaging for which thermal stress is a critical concern for both (packaged) device performance and reliability. Figure 15.4.9(a) through Figure 15.4.9(d) show various thermal stresses of die-attaches with attaching areas of 1 mm × 1 mm (Chen, 2003). The SiC die is 1 mm wide, 2 mm long, and 0.29 mm thick. The die is attached to an AlN substrate using 20 μm thick Au thick-film material. The substrate is 4 mm × 4 mm and 0.639 mm thick. Apparently, the stress levels in the majority area where the bottom of the chip is not directly attached to the substrate are very low.

Figure 15.4.10(a) and Figure 15.4.10(b) show two-dimensional FEA simulated stresses of a square die attached to a package wall through one of the die sides using Au thick-film material. The area near the far end of the die has low stresses.

Example of a MEMS Package

As discussed in the introduction, because of the nature of nonelectrical interactions between MEMS devices and their environment, the design of a MEMS package is much more complicated compared to a package for conventional electronics. Among the design considerations for MEMS packaging, mechanical design is one of the most important and critical factors for both functionality and reliability of packaged MEMS devices. The design of a multipurpose screw-in type high-temperature sensors package is used to illustrate the mechanical design that minimizes packaging thermal stress effects on MEMS device performance and reliability.

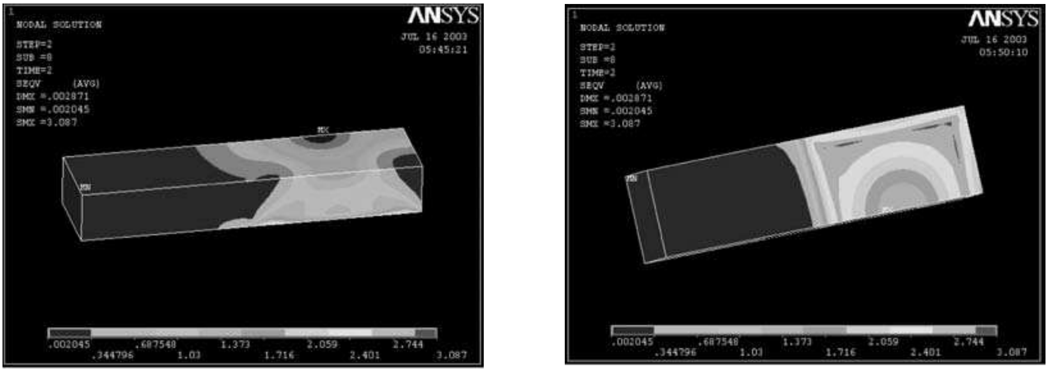

(a) Von Mises Stress contour of top of 1/2 SiC die of the partially attached die. Attaching length is 1.00 mm.

(b) Von Mises Stress contour of bottom of 1/2 SiC die of the partially attached die. Attaching length is 1.00 mm.

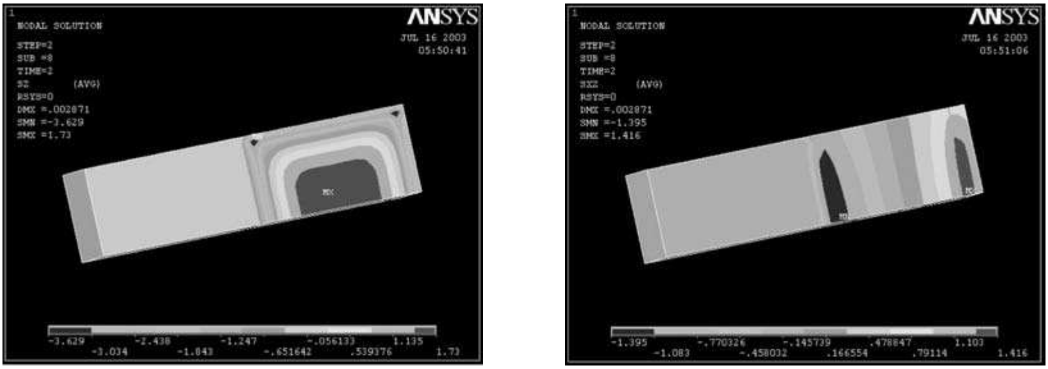

(c) Peeling Stress contour of bottom of 1/2 SiC die of the partially attached die. Attaching length is 1.00 mm.

(d) Sheer Stress contour of bottom of 1/2 SiC die of the partially attached die. Attaching length is 1.00 mm.

FIGURE 15.4.9 FEA simulation of thermal stress of the partial attached SiC die on AlN substrate using 20 μm Au. The attached area of 1 mm × 1 mm. All units are MPa. (From L.-Y. Chen, F.P. McCluskey, K. Meyyappan, and S.-T. Tien, Proceedings of IMAPS 5th Topical Technology Workshop on MEMS, Related Micro-Systems and Nanopackaging, 2003.)

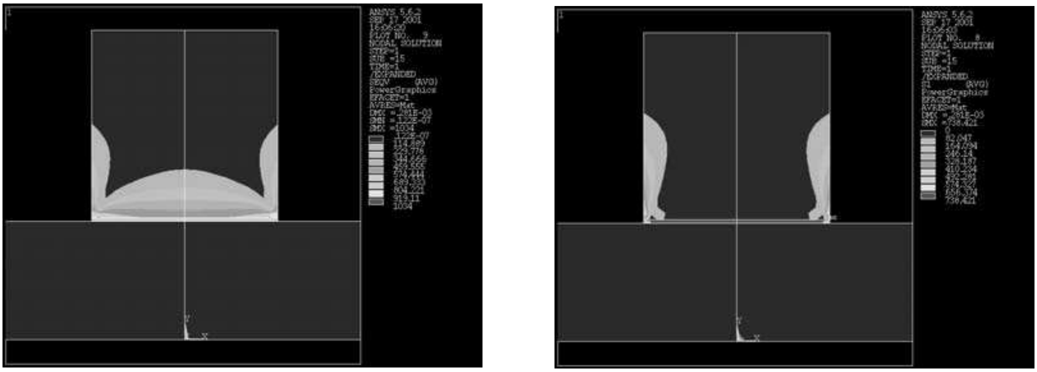

(a)

(b)

FIGURE 15.4.10 Two-dimensional stress contour of side-attached SiC die-attach assembly. (a) Maximum principal stress. (b) von Mises stress. All units are psi.

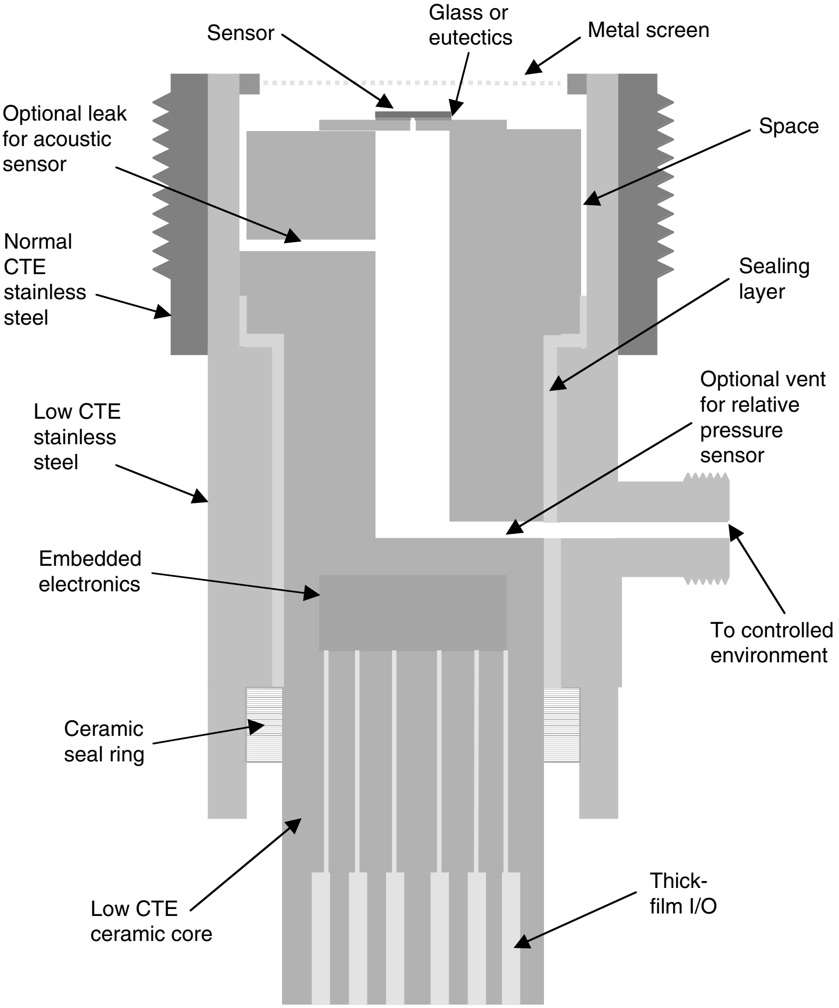

FIGURE 15.4.11 A multipurpose high-temperature MEMS package module for *in situ* characterization of aerospace engine combustion process (500°C). (Chen 2004.)

This multipurpose package is designed for real time *in situ* (500°C) characterization of combustion processes of aerospace engines (Chen 2004). As shown in Figure 15.4.11, the package base is made of a stainless steel material that has the same CTE as that of the engine body. The core of the package is made of a low CTE ceramic such as AlN. A glass material with a low curing temperature and low CTE is used to seal the ceramic core into the stainless steel base. Since the CTEs of stainless steels are usually higher than those of ceramics, the normal stresses at SS/glass and glass/ceramics interfaces are compressive at temperatures below the glass sealing/curing temperature. The upper part of the ceramic core is not directly sealed to the stainless steel base wall, so the compressive stress in the ceramic core attenuates rapidly toward the top of the ceramic core. Meanwhile the mounting stress generated at the thread area is also isolated from the top of the ceramic core where the sensor is mounted. The sensor is directly mounted on a piece of ceramic substrate, which is sealed onto the ceramic core. In order to minimize the die-attach thermal stress, a ceramic substrate with low CTE should be selected.

The static and dynamic pressures (Rossi 1988) in the chamber underneath the sensor are determined by the configuration of the package. The chamber pressure can be used as the reference point for differential measurements: The chamber can be sealed at vacuum so the chamber pressure is low with respect to the pressure in the measurement chamber. This configuration is suitable for absolute pressure measurement using a differential pressure sensor. The chamber can also be vented to atmosphere so the chamber pressure is a constant. This configuration is good for relative pressure measurement. The chamber can also be vented to the measuring chamber through a small leaking channel. Under this configuration the static pressure in the chamber is equal to that of the measuring chamber, but dynamically (above a certain frequency) the chamber can be isolated to the measuring chamber. This configuration is suitable for dynamic/acoustic pressure measurement. The dimensions of the chamber and vent affect both dynamic sensitivity and frequency response (the resonant frequency) of a diaphragm-based sensor through damping effects of the air in the chamber.

Electronics can be integrated into the ceramic core for signal conditioning and power management. For example, for a capacitive pressure sensor, the output signal very often is AC. Therefore, parasitic effects of electrical interconnections become an issue if the measuring electronics are far away from the sensor. The integrated electronics can also be used for *in situ* temperature compensation and output signal modulation and coding.

Discussion

MEMS devices operate mechanically (partially) so these devices can be sensitive to their mechanical environment. The mechanical functions of a MEMS packaging system become important to both device performance and reliability. These mechanical functions and requirements on the packaging system can be far beyond those developed for conventional electronics. Therefore, new research and development in packaging materials and processing are required. Currently, MEMS packaging is still in its initial development stage. Often a significant percentage of the cost of a MEMS product is from packaging, and packaging technology dominates product performance and reliability. The demands of a mature and systematic MEMS packaging technology opened another vivid area in device packaging.

Because of the limited space of this section, many mechanical issues other than thermal stress in MEMS packaging have not been addressed. One of these important issues is pre- and postpackaging mechanical testing and qualification criteria. Both the nature and function of MEMS devices determine that mechanical testing of MEMS can be much more complicated and expensive compared with those for conventional electronics. Establishing mechanical qualification criteria for a MEMS device is essential for a MEMS product.

Traditionally, device packaging is typically a macrofabrication process that has more material cost and less mechanical consistency and accuracy compared with the microfabrication process used for MEMS device fabrication. Because of these reasons and other technical requirements, there is a trend toward realizing more packaging functions at the wafer level, using microfabrication process, to replace chip-level and board-level packaging functions. This trend will likely push one-chip-system or one-module-system technology ahead. However, selection of a packaging scheme is not solely determined by technology suitability but also by cost and market demands.

Acknowledgments

The authors want to thank Drs. Lawrence G. Matus, Glenn M. Beheim, Gary W. Hunter, and Jih-Fen Lei at the NASA Glenn Research Center for their contributions. One of the authors (LC) would like to thank Dr. Carl W. Chang for his proofreading and helpful discussions on finite element analysis (FEA). The authors also would like to thank Dr. Robert S. Okojei for providing his design of SiC pressure sensor for FEA simulation. The FEA simulations were conducted by Dr. F. Patrick McCluskey and Mr. Karumbu Meyyappan at the University of Maryland at College Park, and by Dr. Shun-Tien Lin at United Technology Research Center, with the support of the NASA Electronic Parts and Packaging Program (NEPP) through the NASA Glenn Research Center. Part of this work was supported by Glennan Microsystems Initiatives (GMI).

References

Beheim, G., Ned, A.A., Masheeb, F., Kurtz, A.D., and Wolff, J.M. 2001. Dynamic pressure measurements using silicon carbide transducers, *19th Int. Congress on Instrumentation in Aerospace Simulation Facilities (ICIASF '01)*, Cleveland, OH, August 27–30.

Beranek, M.W., Chan, E.Y., Chen, C.-C., et al. 2000. Passive alignment optical subassemblies for military/aerospace fiber-optic transmitter/receiver modules, *IEEE Transactions on Advanced Packaging*, vol. 23, no. 3, August.

Bernstein, L. 1966. Semiconductor joining by the solid-liquid-interdiffusion (SLID) process, *J. Electrochemical Soc.,* December, 1282–1288.

Boustedt K., Person, K., and Stranneby, D. 2002. Flip-chip as an enabler for MEMS packaging, *52nd Electronic Components and Technology Conf. 2002 (Cat. No.02CH37345)*, 124–28.

Bryant, K.W. and Bozack, M.J. 1999. Surface composition of 4H-SiC as a function of temperature, *8th Int. Silicon Carbide and Related Materials* IOP Publishing, 569.

Budraa, K.N., William, T.P., and Mai, J.D. 1999. Low pressure and low temperature hermatic wafer bonding using microwave heating, in *IEEE Electro Mechanical Systems Technical Digest*, IEEE Catalog No. 99CH36291C.

Chang, C.W. 2002. *Magnetically Actuated Scanning Microplatforms for Intravascular Ultrasound Imaging*, Electrical Engineering Department, University of California at Berkeley, May.

Charles, H.K., and Clatterbaugh, G.V. 1994. Packaging considerations for high temperature operation, *Proc. of 2nd Int. High Temperature Electronics Conf.*, Charlotte, NC, ix–3.

Chen, L.-Y., Hunter, G.W., and Neudeck, P.G. 2000. Silicon carbide die attach scheme for 500°C operation, wide-bandgap electronics devices, *Proc. of Symposium T of MRS 2000 Spring Meeting*, San Francisco, CA, April 10–14.

Chen, L.-Y, and Lei, J.-F. 2002. Packaging of Harsh-Environment MEMS Devices, in *CRC MEMS Handbook*, M. Gad-el-Hak ed., CRC Press, Boca Raton, FL.

Chen, L.-Y., McCluskey, F.P., Meyyappan, K., Lin, S.-T. 2003. Low stress die-attach technology for MEMS packaging, *IMAPS 5th Topical Workshop on MEMS, Related Microsystems Nanopackaging*, Boston, November 20–22.

Chen, L.-Y., Fralick, G.C., Hunter, G.W., et al. A Multi-Function High Temperature Packaging Module for Aerospace Engines Applications, to be published, 2004.

Chitale, S.M., Huang, C., and Sten, S.J. 1987. ELS thick-film materials for AlN, *Advanced Microelectronics* 21(1), 22–23.

DuPont Electronic Materials, DuPont Processing and Performance Data of Thick Film Materials, DuPont Electronic Materials, Research Triangle Park, NC, 1999.

Go, J. S. and Cho, Y.-H. 1998. Design and Strength Evaluation of an Anodically Bonded Pressurized Cavity Array for Wafer-Level MEMS Packaging, Micro-Electro-Mechanical Systems (MEMS), DSC-vol. 66, ASME.

Hu, J.M. and Pecht, M. 1993. Design of reliable die attach, *Int. J. of Microcircuits and Electronic Packaging*, vol. 16, no. 1, First Quarter.

Hunter, G.W. 2003. Morphing, Self-Repairing Engines: A Vision for the Intelligent Engine of the Future, *AIAA/ICAS Int. Aero and Space Symp.*, Dayton, OH, July 14–17. AIAA Paper 2003-3045.

Keusseyan, R.L., Parr, R., Speck, B.S., Crunpton, J.C., Chaplinsky, J.T., Roach, C.J., Valena, K., and Horne, G.S. 1996. New Gold Thick Film Compositions for fine line Printing on Various Substrate Surfaces, *ISHM Symp.*, 1996.

Kim, J., Chiao, M., and Lin, L. 2002. Ultrasonic bonding of In/Au and Al/Al for hermetic sealing of MEMS packaging, 15th *IEEE Int. Conf. on Micro Electro Mechanical Syst.*, Las Vegas, NV, January 20–24, 415–18.

King, J.A., Freer, J., Woodard, R. 1998. *Materials Handbook for Hybrid Microelectronics*, Artech House, Norwood, MA.

Ko, W.H. and Wang, Q. 1999. Touch mode capacitive pressure sensors, *Sensors and Actuators,* 2303.

Li, G. and Tseng, A.A. 2001. Low stress packaging of a micromachined accelerometer, *IEEE Trans. on Electronics Packaging Manufacturing,* vol. 24, no. 1, January.

Lau, J., Wong, C.P., Prince, J.L., and Nakayama, W. 1998. *Electronic Packaging — Design, Materials, Process, and Reliability,* McGraw-Hill, New York.

Lin, L. 2000. MEMS post-packaging by localized heating and bonding, *IEEE Transactions on Advanced Packaging*, vol. 23, no. 4, November.

Lin, S.-T. and Chen, L.-Y. 2002. Thermo-mechanical optimization of a gold thick-film based SiC die-attach assembly using finite element analysis, *Proc. of the 6th Int. High Temperature Electron. Conf.,* Albuquerque, NM, June 2–5.

Luo, C., and Lin, L. 2002. Application of nanosecond-pulsed laser welding technology in MEMS packaging with a shadow mask, *Sensors and Actuators*, A 97–98, 398–404.

Madou, M. 1997 *Fundamentals of Microfabrication*, CRC Press, Boca Raton, FL, 309–91.

McCluskey, F.P., Grzybowski, R., and Podlesak, T. 1996. *High Temperature Electronics*, CRC Press, Boca Raton, FL.

Meyyappan, K., McCluskey, P., and Chen, L.-Y. 2004. Thermo-mechanical analysis of MEMS pressure sensors used in high temperature applications. *Proc. 2004 IEEE Aerospace Conf.,* Big Sky, Montana, March 6–13, 2004.

Okojie, R.S., Beheim, G.M., Saad, G.J., and Savrun, E. 2001. Characteristics of hermetic 6H-SiC pressure sensor at 600°C, *AIAA Space 2001 Conf. and Exposition*, Albuquerque, NM, August 28–30 (AIAA Paper No. 2001-4652).

Oppermann, H.H., Kallmayer, C., Klein, M., Aschenbrener, R., and Reichl, H. 2000. Advanced flip chip technologies in RF, microwave and MEMS applications, *Proc. of Design, Test, Integration, and Packaging of MEMS/MOEMS*, *Proc. of SPIE* vol. 4019, Bernard Coutois et al eds.

Owen, M. 2000. Agilent Technology's singlemode small form factor (SFF) module incorporates micromachined silicon, automated passive alignment, and non-hermetic packaging to enable the next generation of low-cost fiber optic transceiver, *IEEE Transactions on Advanced Packaging*, vol. 23, no. 2, May.

Pecht, M.G., Agarwal, R., McCluskey, F.P. et al. 1998. *High Temperature Electronics*, CRC Press, Boca Raton, FL.

Roman, J.W. and Eagar, T.W., Low stress die attach by low temperature transient liquid phase bonding, *ISHM '92 Proc*, 52–57.

Rossi, M. 1998. *Acoustics and Electroacoustics*, Artech House Publishers, Norwood, MA.

Ru, C.Q. 2000. Interfacial thermal stresses in bimaterial elastic beams: modified beam models revisited, *J. of Electronic Packaging*, vol. 124, no. 3, September, 141–46.

Shaikh, A. 1994. Thick-film pastes for AlN substrates, *Advanced Microelectronics* 21(1), 18–221.

Sokolnikoff, I.S. 1956. *Mathematical Theory of Elasticity*, 2th edition, McGraw-Hill, New York, 41.

Suhir, E. 1987. Die attachment design and its influence on thermal stress in the die and the attachment, *Proc. of IEEE 37th Electronic Components Conf.*, 508–17.

Suhir, E. 2001. Analysis of interfacial thermal stresses in a trimaterial assembly, J. *of Applied Physics*, vol. 89, no. 7, 3685–94.

Takagi, H., Maeda, R., and Suga, T. 2001. Wafer-scale room-temperature bonding between silicon and ceramic wafers by means of argon-beam surface activation, *Proc. of the 14th IEEE Int. Conf. on Micro Electro Mechanical Syst.*, Interlaken, Switzerland, January 21–25,60–63.

Takshara, H., Tanaka, N., and Arai, Y. 2000. Passively aligned LD/PD array submodules by using micro-capillaries, *IEEE Transactions on Advanced Packaging*, vol. 23, no. 2, May.

Tomoshenko, S.P. 1925. Analysis of bi-metal thermalstats, *J. of the Optical Society of America,* vol. 11, September.

Tummala, R.R. 2001. *Fundamentals of Microsystems Packaging*, McGraw-Hill, New York.

Young, D., Du, J., Zorman, C.A., and Ko, W.H. 2004. High-temperature single crystal 3C-SiC capacitive pressure sensor, *IEEE Sensors J.,* Special Issue on Micro Sensors and Activators, August 2004.

Yushin, G.N., Kvit, A.V., Collazo, R. et al. 2003. SiC to SiC wafer bonding, *Silicon Carbide 2002 Materials, Processing and Devices*, S.E. Saddow, D.J. Larkin et al., eds., *Mat. Res. Soc. Symp*. vol. 742.

Wang, Q. and Ko, W.H. 1999. Modeling of touch mode capacitive sensors and diaphragms, *Sensors and Actuators*, 75, 230–41.

Wang, Y.L., Carroll, A.F., Smith, J.D., Cho, Y., Bacher, R.J., Anderson, D.K., Crumpton, J.C., Needes, C.R.S. 2002. Advanced thick film system for AlN substrates, *IMAPS*.

Wild, M.J., Gillner, A., and Poprawe, R. 2001. Advances in silicon to glass bonding with laser, *MEMS Design, Fabrication, Characterization, and Packaging, Proceedings of SPIE*, vol. 4407, U.F. Behringer and D.G. Uttamchandani, eds.

15.5 Reliability and MEMS

Srihari Rajgopal, Christian A. Zorman, Darrin J. Young, and Mehran Mehregany

Introduction

Microelectromechanical Systems (MEMS) is an enabling technology with the potential to revolutionize a wide range of applications that could benefit from the insertion of highly functional, miniaturized electromechanical devices that can independently sense and act on the environments into which they are deployed. From a commercial perspective, MEMS is a particularly attractive technology because a wide range of MEMS devices can be fabricated using the batch-processing methods, techniques, and tools employed by the integrated circuit (IC) industry, thus creating at least the potential for low-cost manufacturing. Without question, research and development in MEMS have yielded devices with a level of complexity and functionality that could only have been imagined just a few years ago. Unfortunately, the pace of commercialization has lagged behind the advancement of the technology, in part because the reliability science of these micro-scale electromechanical devices has not matured. The penetration of MEMS technology into safety, navigation, health-care, and other mission-critical applications is further pushing the need to study, understand, and develop the subject of reliability as it pertains to MEMS.

The purpose of this chapter is to present a short overview of the concepts governing reliability science, and at the same time, to provide insight into the reliability issues pertinent to MEMS. Given the great diversity that exists in MEMS devices in terms of dimensions, materials, and operating environments, along with the fact that reliability is, in many respects, device and application specific, this chapter does not attempt to provide a comprehensive overview of reliability and MEMS. Instead, we present a review of the methods that were used by Texas Instruments to characterize and improve the reliability of the Digital Micromirror Device (DMD).[1] The DMD is one of the most recognizable MEMS-based products in the market today, due in part to the exhaustive reliability studies performed by Texas Instruments to field this product successfully. It is an excellent example for illustrating the importance of reliability analysis in MEMS product development.

Reliability as It Relates to MEMS

Reliability can be defined as the *probability* of a product to meet its design specifications without *failure* for a given period of *time* in a particular operating *environment*. Thus, statistical techniques are applied to analyze the data obtained from failure tests in order to estimate the average lifetime of a product. *Failure* refers to a predefined condition of nonoperation, and the *environment* refers to the operating conditions under which the failure tests were conducted. Operating conditions may replicate or exceed design specifications so as to accelerate product failure. For example, failure rates typically increase with increasing temperatures; therefore, accelerated failure tests are often performed at temperatures well above the specified operating temperature.

With respect to MEMS, the utilization of IC-based fabrication techniques and device interface electronics result in certain reliability issues that are similar to those encountered in the IC industry. However, reliability-related characteristics that are unique to MEMS include

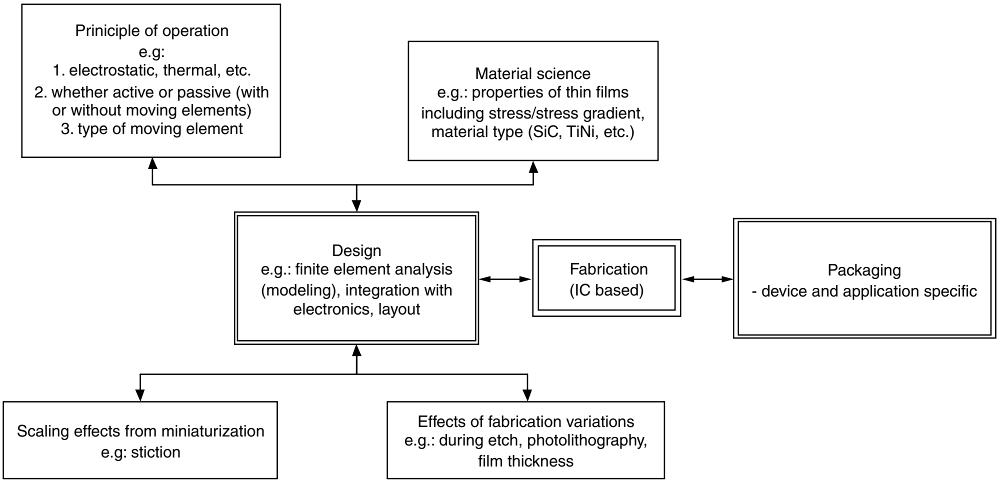

FIGURE 15.5.1 Factors defining the lifetime of a MEMS device.

- The presence of movable mechanical elements such as membranes, cantilevers, and rotating elements and the consequent effects from friction, wear, fatigue, and creep.
- Material characteristics such as
  - Thin film properties that may differ from bulk properties.
  - Thermal or crystallographic mismatch issues between different materials.
  - Film stress and its variation across film thickness (stress gradient).
- Surface interaction effects in mechanical contacts such as stiction and wear.
- Contradictions in packaging whereby the package is to protect the device from environmental factors while providing access to the environment for the desired sensing or actuation.
- Packaging considerations that are unique to a device and application. For example, the packaging requirements of a microvalve operating in a high-temperature environment differ substantially from that of a micromachined oscillator for wireless applications operating in a reduced pressure environment.

Reliability issues related to MEMS are illustrated schematically in Figure 15.5.1. In addition to device specifications and operating conditions, reliability considerations must take into account such factors as desired lifetime, safety concerns, cost, and manufacturability. These are represented schematically in Figure 15.5.2.

The schematic presented in Figure 15.5.1 suggests an integrated approach toward reliability with factors considered from the outset of device development. One such approach is known as the Failure Mode and Effect Analysis (FMEA) method.[1] The procedure begins with any new design and fabrication process, and involves a team of experts with backgrounds covering materials science, modeling, layout, interface electronics design, process technology, and packaging. The goals are to

1. Analyze design constraints, process issues, packaging limitations, and test methods.
2. Anticipate and identify potential failure modes (identifiable symptoms of failure), failure mechanisms, causes of failure, and potential means of acceleration.
3. Estimate the effects of these factors on lifetime.
4. Define appropriate verification tests.

A benefit of this approach is that device development time can be significantly shortened. Where new device technologies limit such analyses due to a lack of prior test data, a series of methodical characterization tests are usually conducted to create a knowledge database.

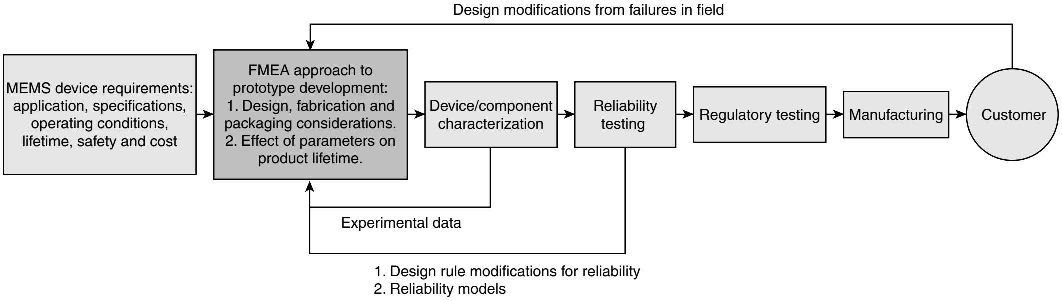

FIGURE 15.5.2 Typical sequence of events enabling final product reliability. (Adapted from Hnatek, E. 2003. Practical Reliability of Electronic Equipment and Products, Marcel Dekker, New York.)

Failure

Device failure is the primary focus of interest in reliability tests, the idea being to eliminate or postpone failure, thereby increasing useful life. This "useful life" is represented by region II in the life characteristic curve (Figure 15.5.3) that displays the failure (or hazard) rate as a function of time for an identical sample of devices under identical stress conditions. The life characteristic curve, otherwise known as the "bathtub curve"[2] is the combination of the other curves depicted, namely quality failures, stress-related failures, and wear-out failures.

The bathtub curve can be subdivided into three distinct regions that are largely based on the age of the device in question. Region I is known as the infant mortality region and encompasses the earliest stage of device life. Failures in this region are primarily related to issues in quality or manufacturing. In the case of microfabricated devices, these include processing defects, particles, and defective packaging. Failure mitigation is achieved primarily through increased quality control measures and improvements to manufacturing processes. To overcome high failure rates early in the lifetime, a "burn-in" procedure is typically used to screen out defective devices prior to product shipment. Depending on the device and application, this may include testing at increased stresses such as exposing devices to elevated or rapid fluctuations in temperature. Wear-out or application-oriented stress failures are usually minimized through design changes.

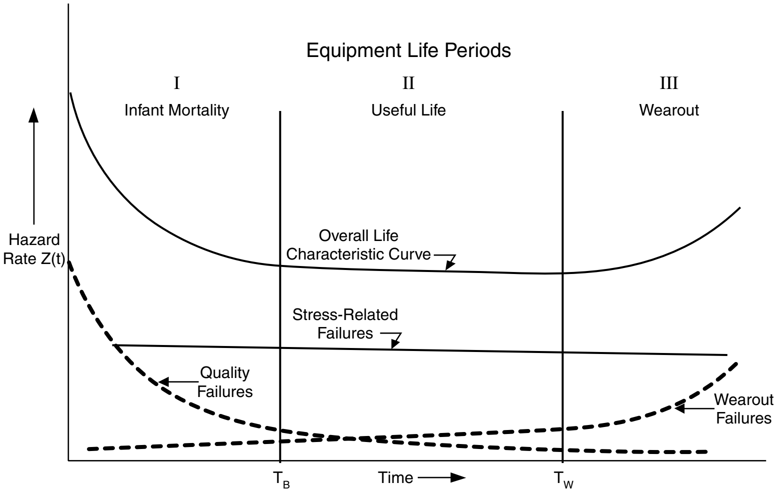

FIGURE 15.5.3 The bathtub curve. (*Source:* Hnatek, E. 2003. *Practical Reliability of Electronic Equipment and Products,* Marcel Dekker, New York.)

TABLE 15.5.1 Failure Regions in the Bathtub Curve and Mitigating Factors

Failure Region in the Bathtub Curve	Mitigation
Region I: Infant mortality	Quality control, improved manufacturing process, and design modification
Region II: Useful life/random failure	Design for reliability
Region III: Wear-out phase	Design for reliability (can only be delayed)

TABLE 15.5.2 Failure Mechanisms in MEMS and Potential Mitigation Methods

Failure Issues	Mitigation
Stiction	Fabrication (coatings), device design, packaging (hermetic)
Friction and wear	Material selection, device design (choice of motion, i.e., rotational, sliding), packaging (corrosive applications)
Creep	Material selection, packaging (such as improving thermal dissipation)
Fatigue/Fracture	Device design (in case of fracture caused by overstress effects), fabrication, and packaging
Shock/vibration	Device design
Dielectric breakdown (including ionizing radiation effects from space applications)	Design and/or packaging
Open/short circuits	Fabrication

Region II encompasses the useful life of the device. During this phase, the failure rate is reduced to an acceptable value and generally remains steady. Few failures are related to quality concerns. Wider device operating margins through design improvements mitigate stress-related failures.

Region III is known as the wear-out phase. Failure rates increase in this region as the device ages and latent defects develop over time. Proper design and adoption of robust technologies and materials help delay the onset of this phase. Table 15.5.1 presents a summary of the mitigation procedures used to minimize the effects of failure in each of the three regions of the bathtub curve.

Failure issues in MEMS that involve quality, stress, and wear-out failure profiles are listed in Table 15.5.2. Of these, stiction, friction/wear, creep and fatigue[3] are particularly important to MEMS owing to the incorporation of moving components in a large percentage of MEMS devices.

Stiction refers to the adhesion of adjacent microstructures and is particularly relevant to devices that rely on the mechanical contact of very smooth surfaces. It often occurs during the drying process (one of the final stages of device manufacturing) that follows a "wet" release step (which involves removal of the sacrificial layer beneath movable elements of the device to enable motion); however, it can also occur during field operation. Several strong adhesive forces, including capillary, electrostatic and van der Waals, result in "stuck" devices incapable of motion. Stiction is particularly troublesome for surface micromachined devices where the vertical distance between the substrate and a released component is often only a few micrometers and the contacting surfaces are very smooth.

Friction and wear are of interest in MEMS devices that incorporate sliding, rotational, or rubbing elements. With respect to silicon, adhesive wear has been found to be one of the most significant wear mechanisms.[3] In this case, the highest points of contact between the rubbing surfaces adhere. Break-off eventually occurs from one of the surfaces, resulting in particle generation. Some of these particles stick to one of the surfaces, forming sites for further particle accumulation. When reaching a certain size, these asperities break off, causing wear and also an accumulation of debris between the rubbing parts.

Humidity has been shown to be a key factor in wear of sliding micromachined polysilicon surfaces when operated in an air environment.[4] It has been observed that the volume of wear debris increases as the relative humidity decreases. Other forms of wear include abrasive wear observed in the presence of higher contacting and corrosive wear brought about by chemical reactions.

Creep has been observed in micromachined metal elements.[5] Creep is the slow change in the dimensions of a mechanical structure when it is exposed to prolonged loads that are below the yield stress of the material. The result is the degradation in performance of structural elements and ultimately a reduction in device lifetime. To better understand the effects of creep, consider the macro world where there is no evidence of creep at temperatures less than $0.3T_m$, where T_m is the melting temperature of the metal. At temperatures greater than $0.3T_m$ and/or high mechanical stress, creep may rapidly lead to fracture. While a corresponding quantitative relation has yet to be established for micro-scale devices, a similar qualitative behavior as a function of temperature may be expected.

Fatigue (progressive fracture under cyclic loading conditions) and fracture have both been explored in silicon and polysilicon, the primary structural materials in MEMS. Contrary to expectations, experimental results have shown that thin films of these "brittle" materials undergo time-dependent cracking (crack extension or crack initiation and growth) under monotonic and cyclic loading. Muhlstein et al.[6] suggested the cause was stress corrosion cracking (SCC) of the surface oxide on silicon and termed it "reaction-layer fatigue." (Stress corrosion cracking, or "static fatigue" in brittle materials like ceramics refers to the propogation of a small crack when subjected to stresses in a corrosive [e.g., humid] environment. Silicon reacts with the ambient to form the initial "native" oxide layer about 2 nm thick.[7]) In this study, micromechanical structures were subjected to environmentally assisted crack initiation, followed by sequential thickening (from continued chemical reactions with the ambient) and crack propagation until the structures suffered from final catastrophic failure. Kahn et al. showed that polysilicon is not susceptible to static SCC.[7] Low-cycle fatigue behavior was found to be dependent on the compressive stresses experienced during loading. It was postulated that microcracks originated from surface asperities created during processing. Fracture occurred from crack propagation during cyclic loading. The results were found to be independent of ambient conditions. In the case of high-cycle fatigue, additional "wedging" and crack extension were theorized from the growth of surface oxide in crack surfaces due to exposure to ambient air. Thus, a corrosive environment was found to exacerbate high-cycle fatigue.

Fatigue predictions based on bulk models have been found to be inconsistent with observations from micromechanical structures made from thin metal films. For instance, it has been reported that the aluminum hinges in the DMD do not experience fatigue.[8] Macroscopic fatigue models are based on the accumulation of dislocations that move to the metal surface, causing fatigue cracks, further accumulation of dislocations, increased mechanical stresses, and eventual breakage. In the case of a thin film, the material is only one or a few grains thick. As a result, a dislocation density sufficient to form fatigue cracks does not accumulate.

Failure resolution at the device level requires that the manifestation, mode, mechanism, and cause of each failure be addressed. *Failure manifestation* is the identification and definition of failure including, but not limited to, such aspects as whether the failure can be reversed, is permanent, or requires customer intervention. *Failure mode* is the measurable characteristic or symptom of failure. *Failure mechanism* is the actual effect observed in the device, and the *cause* is the actual source or initiator of the failure. The analysis process concerns itself with aspects such as whether the failure was random or preordained, catastrophic or gradual, and its time of occurrence. As shown schematically in Figure 15.5.4, every failure characteristic is represented at the infant stage and is consistent with quality, manufacturing, and design issues. Failures in the midlife region are predominantly random catastrophic failures as a result of such events as electrostatic discharge, particles, and processing defects. These failures correspond to the flat midlife region of the bathtub curve. In the wear-out phase, gradual and preordained failures reappear as a function of design, materials, and technology.

Mathematics of Reliability

The previous discussion centered on failure from a cause-and-effect perspective. The current topic focuses on the mathematical methods employed to quantify reliability and is based on detailed discussions presented in References 2, 9, and 10.

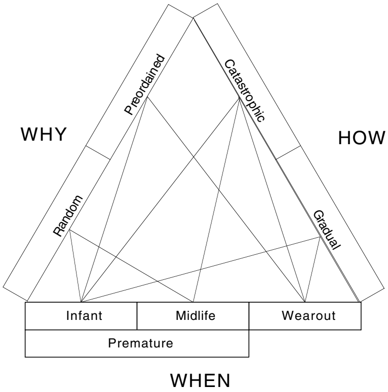

FIGURE 15.5.4 Failure analysis concepts as related to the three regions of the bathtub curve. (*Source:* Ohring, M. 1998. *Reliability and Failure of Electronic Materials and Devices*, Academic Press, San Diego, CA..)

Reliability essentially deals with assessing the failure rate and the service life of products. Thus failure data obtained from laboratory tests and field observations are analyzed using statistics and probability theory to obtain failure rates and project lifetimes of devices. Typical reliability metrics include failures in time (FIT) typically expressed as failures per one billion device hours, mean time between failure (MTBF) for repairable systems, mean time to failure (MTTF) for nonrepairable items, and percent failure per thousand hours.

If the probability density function (PDF) of failure is denoted by $f(t)$, then the cumulative distribution function (CDF), $F(t)$, representing the fraction of devices that fail up to time t can be written as

$$F(t) = \int_{-\infty}^{t} f(v)dv \tag{15.5.1}$$

Thus, the PDF can alternatively be written as

$$f(t) = \frac{d}{dt}F(t) \tag{15.5.2}$$

$F(t)$ may also be referred to as the *unreliability* probability.

The reliability function, $R(t)$, or the probability that the remaining fraction has survived for length of time t, is given by

$$R(t) = 1 - F(t) \tag{15.5.3}$$

therefore

$$f(t) = -\frac{d}{dt}R(t) \tag{15.5.4}$$

The failure rate (also known as the hazard or mortality rate), $\lambda(t)$, is defined as the ratio of the number of devices failing in the next time interval Δt to those that survived up to time t. Mathematically, the failure rate can be written as

$$\lambda(t) = \frac{F(t+\Delta t) - F(t)}{\Delta t\big(1 - F(t)\big)} = \frac{f(t)}{1 - F(t)} = \frac{f(t)}{R(t)} \tag{15.5.5}$$

The mean-time-to-failure (MTTF), the most frequently used reliability unit, is

$$MTTF = \frac{\sum_{j=1}^{n} t_j}{n} \tag{15.5.6}$$

where t_n represents the sum of the failure time of the nth device.

Consider $nf(t)$ as the number of devices that fail in the short interval between t and $t + \Delta t$. Given $nf(t)$ devices with lifetime t, the MTTF can be written as

$$MTTF = \frac{1}{n}\int_0^\infty t\left[nf(t)\right]dt = \int_0^\infty tf(t)dt \tag{15.5.7}$$

Substituting for $f(t)$ from Equation 15.5.4 and simplifying results in

$$MTTF = \int_0^\infty R(t)dt \tag{15.5.8}$$

Table 15.5.3 summarizes these basic reliability parameters.

Various models or life distributions exist to characterize failure rate and reliability, and to facilitate lifetime predictions beyond the range of data obtained through experiment and field observations. The choice of distribution type is based on the properties of these models, an understanding of the failure physics, and prior experience. Table 15.5.4 lists a few of the life distributions. The exponential life

TABLE 15.5.3 Basic Reliability Parameters

	Parameter	Expression	Meaning
1	Probability density function (PDF) $f(t)$	$f(t)\Delta t = P\{t \le T \le t + \Delta t\}$	Probability that failure occurs at time T between t and $t + \Delta t$
2	Cumulative distribution function (CDF) $F(t)$	$F(t) = P\{T \le t\}$	Probability that failure occurs at time T less than or equal to t
3	Reliability $R(t)$	$R(t) = P\{T > t\}$	Probability that failure does not occur by time t
4	Failure rate $\lambda(t)$	$\lambda(t)\Delta t = P\{T < t + \Delta t \mid T > t\}$	Probability that failure occurs at time $T < t + \Delta t$ provided that no failure has occurred at $T = t$
5	Mean time to failure (MTTF)	$MTTF = \int_0^\infty R(t)dt$	

Adapted from Hnatek, E. 2003. *Practical Reliability of Electronic Equipment and Products,* Marcel Dekker, New York.

TABLE 15.5.4 Commonly Used Reliability Distributions

	Distribution Type	Properties	Application	Examples
1	Exponential	Constant failure rate	For devices with minimal infant mortality failures	Random failures such as those caused by external shocks, i.e., failure processes independent of past history
2	Lognormal	time dependent failure rate	For wear-out failures	Failures caused by gradual degradation such as fatigue, and diffusion effects, i.e., failures that are the result of numerous small effects
3	Weibull	time dependent failure rate	Used to describe all three regions of the bathtub curve, i.e., decreasing and increasing failure rates.	Time to failure of individual system components, corrosion effects

distribution is used to model random failures and the lognormal distribution for wear-out failures. The Weibull distribution,[2,9,10] on the other hand, is flexible enough to model all three regions of the bathtub curve (as will become apparent later), and thus is the most commonly used model. We, therefore, will limit our discussion to the Weibull distribution.

For the two-parameter Weibull distribution, the CDF is given by

$$F(t) = 1 - e^{-\left(t/\tau\right)^{\gamma}} \tag{15.5.9}$$

Then, the PDF, failure rate, and reliability become

$$f(t) = \frac{\gamma}{\tau}\left(\frac{t}{\tau}\right)^{\gamma-1} e^{-\left(t/\tau\right)^{\gamma}}, \tag{15.5.10}$$

$$\lambda(t) = \frac{\gamma}{\tau}\left(\frac{t}{\tau}\right)^{\gamma-1}, \tag{15.5.11}$$

$$R(t) = e^{-\left(t/\tau\right)^{\gamma}} \tag{15.5.12}$$

where γ is the shape function and τ is the characteristic time or the scale parameter. The characteristic time occurs when 63.2% of the population fails and is defined to be when $t = \tau$ in Equation 15.5.9. Depending on the shape function, γ, the distribution can represent each of the region of the bathtub curve. Thus, $\gamma < 1$ represents decreasing failure rates in the infant mortality region, $\gamma = 1$ represents constant failure rate in the useful life region, and $\gamma > 1$ represents increasing failure rates in the wear-out region. By appropriately varying the two parameters, the model can be made to fit a wide range of experimental data.

It is common to come across linear plots of data based on the appropriate distribution. Such a plot allows easy derivation of reliability parameters from the slopes and intercepts as well as well a quantitative estimate of the fit. In the case of the Weibull distribution, from Equation 15.5.9,

$$F(t) = 1 - e^{-\left(t/\tau\right)^{\gamma}}$$

Rearranging and performing successive logarithmic operations yields

$$\ln\left[-\ln\left\{1 - F(t)\right\}\right] = \gamma \ln(t) - \gamma \ln(\tau) \tag{15.5.13}$$

Comparing this to the equation $y = mx + c$ results in

$$y = \ln\left[-\ln\left\{1 - F(t)\right\}\right], \quad m = \gamma \quad \text{and} \quad c = -\gamma \ln(\tau)$$

The Weibull probability plot is obtained by plotting $\ln[-\ln\{1 - F(t)\}]$ vs. $\ln(t)$, where F values may be obtained from sample failure data using the following equation:

$$F(t_i) = \frac{i - 0.3}{n + 0.4} \tag{15.5.14}$$

where γ and τ are obtained from the line fitted to the data.[9]

Accelerated Stress Testing

To reduce the development and test time facilitating a rapid deployment to market, accelerated life testing is commonly used to force products to fail more quickly than they would under normal operating conditions, the assumption being that the failure mechanism remains the same and failures in time under normal and accelerated conditions scale only by time. Thus, for true acceleration

$$F_a(t) = F(AF.t)$$

where $F_a(t)$ and $F(t)$ are the failure CDF's under accelerated stress and normal operating conditions, respectively, and $AF > 1$ is the acceleration factor.[10]

Where an empirical relationship cannot be defined directly from the tests, existing mathematical models governing similar stress acceleration modes or reactions are made to determine the acceleration factor. For example, the Arrhenius model based on the well-known reaction rate equation is used when stress testing involves raising the temperature to hasten the aging process. The Arrhenius rate reaction equation is given by

$$R = Ae^{-\frac{E_a}{K_b T}} \tag{15.5.15}$$

where R is the reaction rate, A is a constant, E_a is the activation energy, K_b is Boltzmann's constant, and T is the absolute temperature.[11] To formulate the stress model, from Equation 15.5.12 we define

$$L = Be^{\frac{E_a}{K_b T}} \tag{15.5.16}$$

where L is a life measure such as characteristic time, mean time, median life, etc., B is a model parameter, and T is the temperature (stress) in Kelvin.[11]

Thus the acceleration factor AF, defined as the ratio of the life during use to that at an increased stress, may be given as[11]

$$AF = \frac{L_{use}}{L_{accl}} = \frac{Be^{\frac{E_a}{T_{use}}}}{Be^{\frac{E_a}{T_{accl}}}} = e^{\left[\frac{E_a}{K_b}\left(\frac{1}{T_{use}} - \frac{1}{T_{accl}}\right)\right]} \tag{15.5.17}$$

Models also exist that represent other stress acceleration modes.

Accelerated tests also help define the operational and destruct limits of a device and clarify the effects of prolonged operating and nonoperating times on devices. Figure 15.5.5 shows a schematic plot of stress vs. the number of failures for an arbitrary device.[1] The stress limits for a device are also denoted. The operational limits represent the stress needed to cause the device to malfunction. The device, however, must be able to return to its normal mode on the removal of this stress. The destruct limits represent irreversible failure. The curves about each of these limits represent the failure distributions caused by the specific stresses.

The Digital Micromirror Device (DMD)

The DMD is one of the first commercialized MEMS devices and possesses "typical" microsystem characteristics, namely, moving parts, contact-type motion, and integrated electronics. It is used to digitally redirect light for visual display applications. In comparison to other display technologies, the DMD is more efficient in providing increased brightness, higher contrast ratio, and better reliability in conjunction with simpler optics in a compact form factor.[12]

The device consists of an array of square, aluminum alloy reflective mirrors with each square mirror being ~14 micron on a side.[1] Each mirror is mounted on an aluminum hinge and is capable of tilting

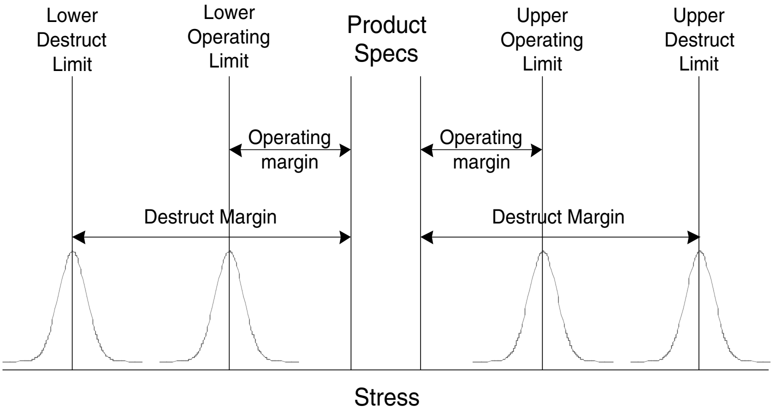

FIGURE 15.5.5 Accelerated test-to-failure methodology to determine operational and destruct parameters. (*Source:* Douglass, M.R. 2003. DMD reliability: a MEMS success story, *Proc. of Int. Society for Optical Eng. (SPIE)*, 4980,1–11.)

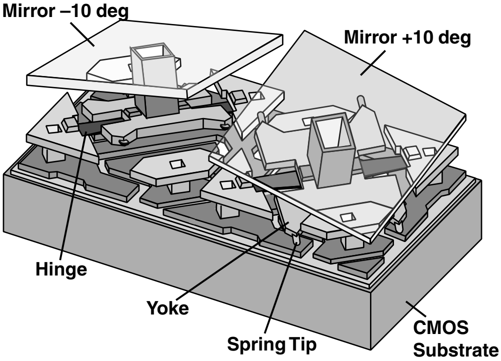

FIGURE 15.5.6 Schematic diagram of two DMD pixels with the mirrors made transparent in order to highlight the underlying device architecture. (*Source:* Sontheimer, A.B. 2002. Digital micromirror device (DMD) hinge memory lifetime reliability modeling, *IEEE Int. Reliability Physics Symposium Proc.*, Dallas, TX, April 7–11, 118–121.)

back and forth from +10° to –10° corresponding to the "on" and "off" positions of the mirror.[5] Mirror rotation is accomplished by tilting the yoke (Figure 15.5.6) using electrostatic attraction. The "on-mirrors" reflect light toward a projection lens to create an on-screen image, and the "off-mirrors" reflect light toward an absorber. The frequency of operation of each mirror during each video frame determines the light intensity. Color images are obtained using either a color wheel or a three-chip setup. Each mechanical structure rests on top of a standard static random access memory (SRAM) cell and is thus individually addressable. Integration with electronics is achieved using CMOS-compatible surface micromachining technology. The close packing density obtained by positioning the electronics and mechanical support structures under the mirrors avoids light diffraction and improves the contrast ratio. Highlights of the technology are shown in Table 15.5.5.[5]

Reliability testing of the DMD technology followed the approach shown schematically in Figure 15.5.7.[1] Failure mechanisms were investigated based on the Failure Modes and Effects Analysis method, as well as characterization tests performed on the fabricated devices. Table 15.5.6 summarizes the failure mechanisms investigated specific to the DMD MEMS superstructure and the methods adopted where necessary to mitigate such failures.

The primary lifetime-limiting parameter in the DMD was found to be hinge memory. What follows is a review of the still ongoing reliability modeling approach to characterize this failure mechanism.[13] Characterization methods and lifetime estimates are also summarized.

TABLE 15.5.5 DMD Technology Details

Device Highlights	Moving Parts: >0.5 Million
Motion	Discrete, contact type; ~ $900*10^9$ contacts/moving part
Process	Low temperature; dry-etched wafer level removal of sacrificial layer
Packaging	Die separation after sacrificial layer removal; hermetic welded lid package
Testing	Electro-optical, prior to die separation

Source: Van Kessel, P.F., Hornbeck, L.J., Meier, R.E., and Douglass, M.R. 1998. A MEMS-based projection display, *Proc. of the IEEE*, 86(8), August, 1687–1704.

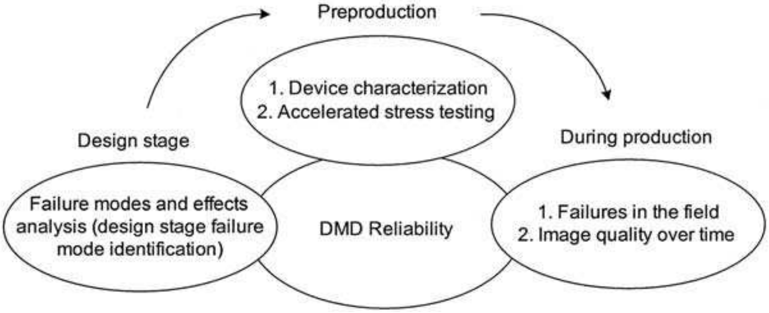

FIGURE 15.5.7 Approach to DMD reliability testing. (Based on References 1, 5, and 8.)

TABLE 15.5.6 DMD Failure Mechanisms Investigated During Reliability Testing

Failure Mechanism Investigated	Failure Cause	Effects on Lifetime	Mitigation
Hinge fatigue	Material	No	N/A
Hinge memory[a]	High temperature; metal creep; high-duty cycle (on-side to off-side ratio)	Yes	Improved hinge material; reversed duty cycle actuation
Stuck mirrors	Particles; stiction; UV light exposure	Yes	Improved packaging and fabrication methods; spring tip design innovation, dry etch release, passivation layer, hermetic sealing UV filter (<400 nm)
Damage from environment	Shock, vibration, acceleration, temperature shock, cycling, and storage	No	N/A

[a] The inability of the mirror to return to its null (or flat) position after the removal of the applied bias voltage (shown in Figure 15.5.8). This occurs when the mirror is continually operated in the same state over a long period.

Based on References 1, 5, 8, and 13.

Hinge Memory

Hinge memory is the residual twist in the torsional hinge that supports a mirror. The twist is expressed as a residual tilt in the mirror following the removal of the actuation (bias) voltage. The tilt is caused from prolonged actuation of a mirror to one side compared to the other. Thus, the tilt is directed toward the side experiencing the greater number of landings. Failure is stated to occur when, beyond a residual tilt angle, the mirror is unable to overcome the electrostatic force of the applied bias voltage and land on the opposite side, causing it to be nonfunctional. A series of DMD micromirrors suffering from the hinge memory effect is shown in the SEM micrograph in Figure 15.5.8.

Parameters to Characterize Hinge Memory Failure — The parameters needed to characterize the hinge memory effect are[13,14]

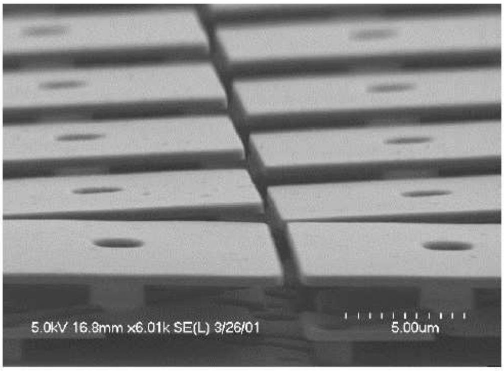

FIGURE 15.5.8 Scanning electron micrograph highlighting the flat mirrors in an unbiased condition (front row) and tilted mirrors after extended operation. (*Source:* Sontheimer, A.B. 2002. Digital micromirror device (DMD) hinge memory lifetime reliability modeling, *IEEE Int. Reliability Physics Symposium Proc.*, Dallas, TX, April 7–11, 118–121.)

Vb50 ±: The difference in DC voltage required to land (half the mirrors) on the plus side vs. the minus side

Vb50 shift%: The change between the voltage required to land a mirror in the direction of tilt and the initial value

To obtain the Vb50±, a DC voltage was applied to the mirrors and stepped up from 11 to 22 V. At each voltage step, the number of landed mirrors was measured using optical techniques for a 5/95 duty cycle, that is, 5 landings on the plus side followed by 95 landings on the minus side. The 5/95 duty cycle was chosen as an extreme scenario representing a less common mode of operation. The decreasing DC voltages required to land the mirrors on the minus side with increasing test time and increasing voltages on the plus side are shown in Figure 15.5.9 and Figure 15.5.10, respectively. The difference in the voltages required to land half of the mirrors on either side was termed Vb50± as derived from Figure 15.5.11. A change in this value is a direct indication of hinge memory.

Accelerated Testing — Figure 15.5.12 shows the results of tests conducted at temperatures of 85°C and 95°C to accelerate hinge memory failure. At these temperatures, nonfunctional mirrors were observed to begin to occur at a Vb50± of –14V. Thus, –14V was considered the conservative limit of device operation. Note the lack of failures at 65°C at the end of 2700 hrs.

Lifetime Estimates — Lifetime estimates were based on two approaches. In the first case, the curve fit to the Vb50± data at 65°C in Figure 15.5.13 was linearly extrapolated to –14V. This corresponded to a

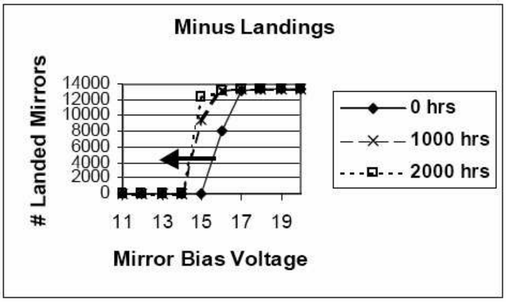

FIGURE 15.5.9 Reduction of bias voltage for minus-side landings as a function of time. (*Source:* Sontheimer, A.B. 2002. Digital micromirror device (DMD) hinge memory lifetime reliability modeling, *IEEE Int. Reliability Physics Symposium Proc.*, Dallas, TX, April 7–11, 118–121.)

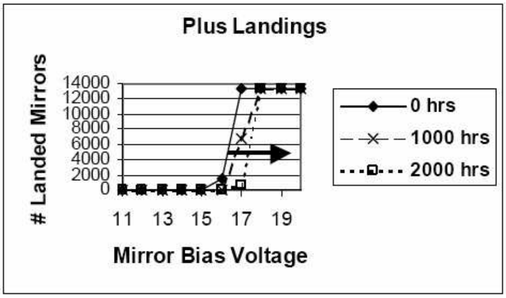

FIGURE 15.5.10 Increase in bias voltage for plus-side landings as a function of time. (*Source:* Sontheimer, A.B. 2002. Digital micromirror device (DMD) hinge memory lifetime reliability modeling, *IEEE Int. Reliability Physics Symposium Proc.*, Dallas, TX, April 7–11, 118–121.)

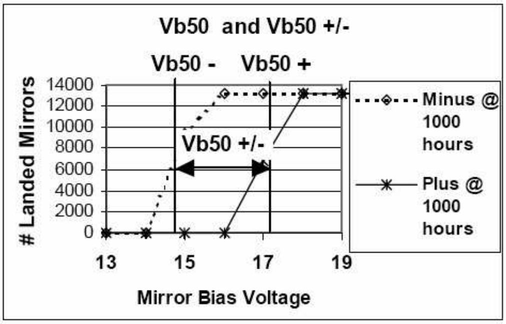

FIGURE 15.5.11 Graphic illustrating the definition of Vb50± . (*Source:* Sontheimer, A.B. 2002. Digital micromirror device (DMD) hinge memory lifetime reliability modeling, *IEEE Int. Reliability Physics Symposium Proc.*, Dallas, TX, April 7–11, 118–121.)

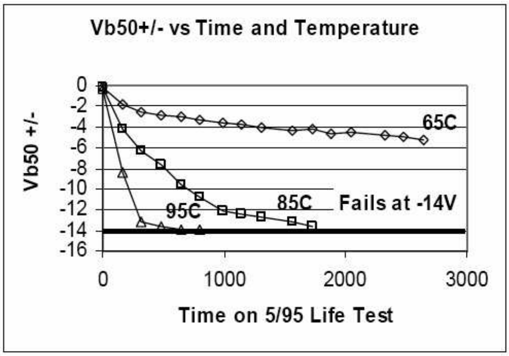

FIGURE 15.5.12 Testing at high temperatures to accelerate failure. (*Source:* Sontheimer, A.B. 2002. Digital micromirror device (DMD) hinge memory lifetime reliability modeling, *IEEE Int. Reliability Physics Symposium Proc.*, Dallas, TX, April 7–11, 118–121.)

pessimistic lifetime estimate of 11,000 hours. In the second case, the linear Weibull plot shown in Figure 15.5.14 was constructed following tests conducted at temperatures of 85°C and 95°C with the same sampling size and otherwise identical conditions. Nonfunctional mirrors were set as a metric for measuring lifetimes. To obtain lifetime estimates at in-use operating temperatures, an acceleration factor based on the Arrhenius model was used to model the temperature-stress acceleration.

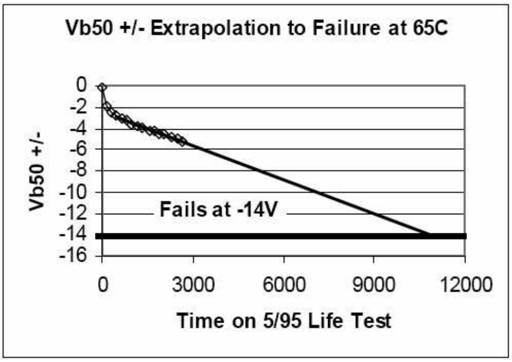

FIGURE 15.5.13 Average lifetime determination at 65°C. (*Source:* Sontheimer, A.B. 2002. Digital micromirror device (DMD) hinge memory lifetime reliability modeling, *IEEE Int. Reliability Physics Symposium Proc.*, Dallas, TX, April 7–11, 118–121.)

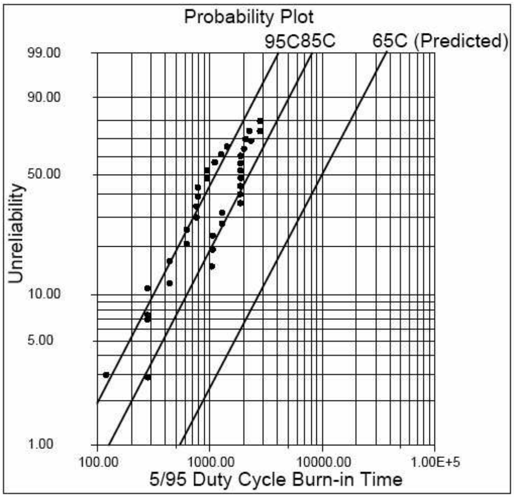

FIGURE 15.5.14 A Weibull distribution charting device failure data at temperatures of 85°C and 95°C. (*Source:* Sontheimer, A.B. 2002. Digital micromirror device (DMD) hinge memory lifetime reliability modeling, *IEEE Int. Reliability Physics Symposium Proc.*, Dallas, TX, April 7–11, 118–121.)

Using these models, conservative estimates assuming a normal operating temperature range of 25°C to 45°C and continuous operation at an aggressive 5/95 duty cycle indicated lifetimes in excess of 100,000 hours (Figure 15.5.15), which corresponds to 100 years of operation at 1000 hours/year. Estimates based on the most recent field data from third-generation DMDs (1999–2001) have indicated failure rates of less than 1000 FIT (failures per 10^9 operating hours), which correspond to a mean time between failures (MTBF) of 1,000,000 hours!

Conclusions

Without question, reliability science and testing are critical to the development of commercially viable MEMS devices. From the MEMS perspective, reliability analysis is multidisciplinary, ranging from fundamental material science on individual device layers to statistical analysis of performance data from system-level device testing under operating conditions. For the successful development of highly complex MEMS devices, reliability analysis needs to be an integral part of the entire effort involving all aspects of device manufacturing, from design and layout to packaging. As the successful commercialization of

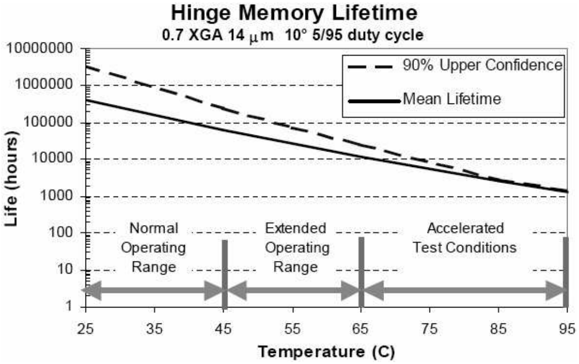

FIGURE 15.5.15 Predicted hinge memory lifetime as a function of temperature. (*Source:* Sontheimer, A.B. 2002. Digital micromirror device (DMD) hinge memory lifetime reliability modeling, *IEEE Int. Reliability Physics Symposium Proc.*, Dallas, TX, April 7–11, 118–121.)

the DMD has shown, proper use of reliability analysis techniques can greatly aid the development of highly sophisticated microchip arrays that integrate micro-scale electrical and mechanical components.

References

1. Douglass, M.R. 2003. DMD reliability: a MEMS success story, *Proc. of Int. Society for Optical Eng. (SPIE)*, 4980,1–11.
2. Hnatek, E. 2003. Practical Reliability of Electronic Equipment and Products, Marcel Dekker, New York.
3. Merlijn van Spengen, W. 2003. MEMS reliability from a failure mechanisms perspective, *Microelectronics Reliability* 43,1049–1060.
4. Tanner, D.M. 2000. Reliability of surface micromachined microelectromechanical actuators, *Proc. of Int. Conf. on Microelectronics (MIEL),* 1, 97–104.
5. Van Kessel, P.F., Hornbeck, L.J., Meier, R.E., and Douglass, M.R. 1998. A MEMS-based projection display, *Proc. of the IEEE*, 86(8), August, 1687–1704.
6. Muhlstein, C.L., Stach, E.A., and Ritchie, R.O. 2002. Mechanism of fatigue in micro-scale films of polycrystalline silicon for microelectromechanical systems, *Applied Physics Letters*, 80(9), 1532–1534.
7. Kahn, H., Ballarini, R., Bellante, J.J., Heuer, A.H. 2002. Fatigue failure in polysilicon not due to simple stress corrosion cracking, *Science*, 298, November, 1215–1218.
8. Douglass, M.R. 1998. Lifetime estimates and unique failure mechanisms of the digital micromirror device (DMD™), *1998 Int. Reliability Proc.*, 36th Annual International Reliability Physics Symposium, Reno, NV, March 31, April 1–2, 9–16.
9. Ohring, M. 1998. *Reliability and Failure of Electronic Materials and Devices*, Academic Press, San Diego, CA.
10. Lewis, E.E. 1996. *Introduction to Reliability Engineering*, John Wiley & Sons, New York.
11. See http://www.weibull.com/AccelTestWeb/arrhenius_relationship_introduction.htm.
12. Gove, R.J. 1994. DMD display systems: the impact of an all-digital display, *Society for Information Display Int. Symposium*, June.
13. Sontheimer, A.B. 2002. Digital micromirror device (DMD) hinge memory lifetime reliability modeling, *IEEE Int. Reliability Physics Symposium Proc.*, Dallas, TX, April 7–11, 118–121.
14. Sontheimer, A.B., Mehrl, D.J. 2003. Effects of operating conditions on DMD Hinge Memory Lifetime, *IEEE Int. Reliability Physics Symposium Proc.*, Dallas, TX, March 30–April 3, 473–477.

Further Information

DLP Technology, white paper, http://www.dlp.com/dlp_technology/dlp_technology_white_papers.asp.

Muller-Fiedler, R. 2003. Reliability, in *Sensors for Automotive Applications*, Marek, J., Trah, H.-P., Suzuki, Y., and Yokomori, I., Eds., Wiley-VCH, New York, 204–223.

15.6 Fluid Flow in Microdevices

Mohamed Gad-el-Hak

Introduction

In this section, we review the status of our understanding of fluid flow physics particular to microdevices. The section is excerpted from an earlier publication by the same author (Gad-el-Hak 1999). Not all MEMS devices involve fluid flows, of course, but the present section will focus on the ones that do. Microducts, micronozzles, micropumps, microturbines, and microvalves are examples of small devices involving the flow of liquids and gases. MEMS can also be related to fluid flows in an indirect way. The availability of inexpensive, batch-processing-produced microsensors and microactuators provides opportunities for targeting small-scale coherent structures in macroscopic turbulent shear flows. Flow control using MEMS promises a quantum leap in control system performance (Gad-el-Hak 2000). Additionally, the extremely small sensors made possible by microfabrication technology allow measurements with spatial and temporal resolutions not achievable before. For example, high-Reynolds-number turbulent flow diagnoses are now feasible down to the Kolmogorov scales (Löfdahl and Gad-el-Hak 1999).

Flow Physics

The rapid progress in fabricating and utilizing microelectromechanical systems during the last decade has not been matched by corresponding advances in our understanding of the unconventional physics involved in the manufacture and operation of small devices (Kovacs 1998; Knight 1999; Gad-el-Hak 1999, 2002; Karniadakis and Beskok 2002; Madou 2002). Providing such understanding is crucial to designing, optimizing, fabricating, and utilizing improved MEMS devices. This section focuses on the physics of fluid flows in microdevices.

Fluid flows in small devices differ from those in macroscopic machines. The operation of MEMS-based ducts, nozzles, valves, bearings, turbomachines, and so forth cannot always be predicted from conventional flow models such as the Navier-Stokes equations with no-slip boundary condition at a fluid-solid interface, as routinely and successfully applied for larger flow devices. Many questions have been raised when the results of experiments with microdevices could not be explained via traditional flow modeling. The pressure gradient in a long microduct was observed to be nonconstant and the measured flow rate was higher than that predicted from the conventional continuum flow model. Load capacities of microbearings were diminished, and electric currents needed to move micromotors were extraordinarily high. The dynamic response of micromachined accelerometers operating at atmospheric conditions was observed to be overdamped.

In the early stages of development of this exciting new field, the objective was to build MEMS devices as productively as possible. Microsensors were reading something, but not many researchers seemed to know exactly what. Microactuators were moving, but conventional modeling could not precisely predict their motion. After a decade of unprecedented progress in MEMS technology, perhaps the time is now ripe to take stock, slow down a bit, and answer the many questions that arose. The ultimate aim of this long-term exercise is to achieve rational-design capability for useful microdevices and to be able to characterize definitively and with as little empiricism as possible the operations of microsensors and microactuators.

In dealing with fluid flow through microdevices, one is faced with the question of which model to use, which boundary condition to apply, and how to proceed to obtain solutions to the problem at hand. Obviously surface effects dominate in small devices. The surface-to-volume ratio for a machine with a characteristic length of 1 m is 1 m^{-1}, while that for a MEMS device having a size of 1 μm is 10^6 m^{-1}. The million-fold increase in surface area relative to the mass of the minute device substantially affects the transport of mass, momentum, and energy through the surface. The small length-scale of microdevices may invalidate the continuum approximation altogether. Slip flow, thermal creep, rarefaction, viscous dissipation, compressibility, intermolecular forces, and other unconventional effects may have to be taken into account, preferably using only first principles such as conservation of mass, Newton's second law, and conservation of energy.

In this section, we discuss continuum as well as molecular-based flow models, and the choices to be made. Computing typical Reynolds, Mach, and Knudsen numbers for the flow through a particular device is a good start to characterize the flow. For gases, microfluid mechanics has been studied by incorporating slip boundary conditions, thermal creep, and viscous dissipation, as well as compressibility effects, into the continuum equations of motion. Molecular-based models have also been attempted for certain ranges of the operating parameters. Use is made of the well-developed kinetic theory of gases, embodied in the Boltzmann equation, and direct simulation methods such as Monte Carlo. Microfluid mechanics of liquids is more complicated. The molecules are much more closely packed at normal pressures and temperatures, and the attractive or cohesive potential between the liquid molecules as well as between the liquid and solid ones plays a dominant role if the characteristic length of the flow is sufficiently small. In cases when the traditional continuum model fails to provide accurate predictions or postdictions, expensive molecular dynamics simulations seem to be the only first-principle approach available to rationally characterize liquid flows in microdevices. Such simulations are not yet feasible for realistic flow extent or number of molecules. As a consequence, the microfluid mechanics of liquids is much less developed than that for gases.

Fluid Modeling

There are basically two ways of modeling a flow field: either as the fluid really is — a collection of molecules — or as a continuum where the matter is assumed continuous and indefinitely divisible. The former modeling is subdivided into deterministic methods and probabilistic ones, while in the latter approach the velocity, density, pressure, and other factors are defined at every point in space and time, and conservation of mass, energy, and momentum leads to a set of nonlinear partial differential equations (Euler, Navier-Stokes, Burnett, among others). Fluid modeling classification is depicted schematically in Figure 15.6.1.

The continuum model, embodied in the Navier-Stokes equations, is applicable to numerous flow situations. The model ignores the molecular nature of gases and liquids and regards the fluid as a continuous medium describable in terms of the spatial and temporal variations of density, velocity, pressure, temperature, and other macroscopic flow quantities. For dilute gas flows near equilibrium, the

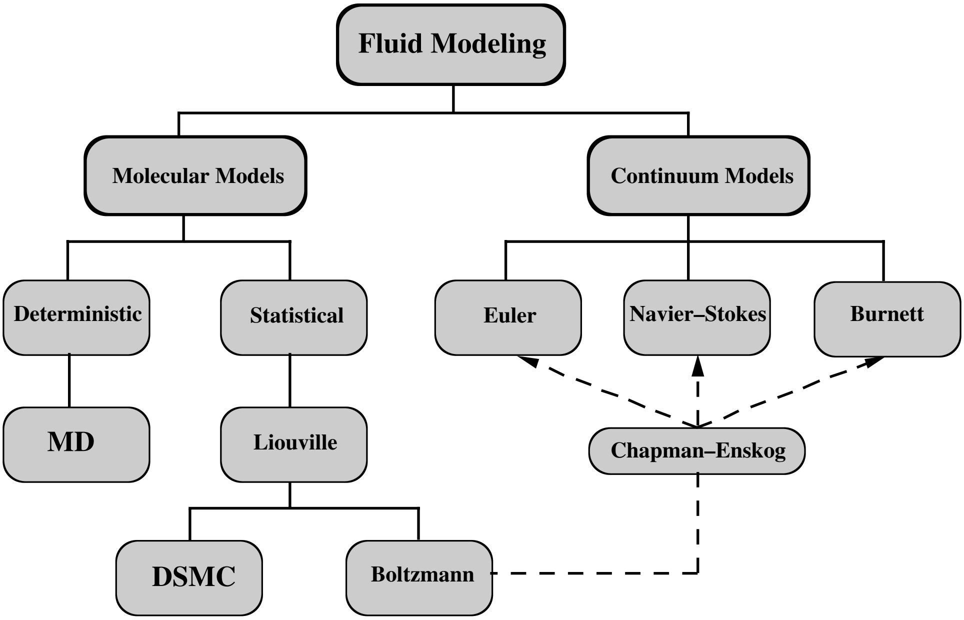

FIGURE 15.6.1 Molecular and continuum flow models.

Navier-Stokes equations are derivable from the molecularly based Boltzmann equation, but can also be derived independently of that for both liquids and gases. In the case of direct derivation, some empiricism is necessary to close the resulting indeterminate set of equations. The continuum model is easier to handle mathematically (and is also more familiar to most fluid dynamicists) than the alternative molecular models. Continuum models should therefore be used as long as they are applicable. Thus, careful considerations of the validity of the Navier-Stokes equations and the like are in order.

Basically, the continuum model leads to fairly accurate predictions as long as local properties such as density and velocity can be defined as averages over elements large compared with the microscopic structure of the fluid but small enough in comparison with the scale of the macroscopic phenomena to permit the use of differential calculus to describe them. Additionally, the flow must not be too far from thermodynamic equilibrium. The former condition is almost always satisfied, but it is the latter that usually restricts the validity of the continuum equations. As will be seen in the following subsection, the continuum flow equations do not form a determinate set. The shear stress and heat flux must be expressed in terms of lower-order macroscopic quantities such as velocity and temperature, and the simplest (i.e., linear) relations are valid only when the flow is near thermodynamic equilibrium. Worse yet, the traditional no-slip boundary condition at a solid-fluid interface breaks down even before the linear stress-strain relation becomes invalid.

To be more specific, we temporarily restrict the discussion to gases where the concept of mean free path is well defined. Liquids are more problematic, and we defer their discussion to a later subsection. For gases, the mean free path L is the average distance traveled by molecules between collisions. For an ideal gas modeled as rigid spheres, the mean free path is related to temperature T and pressure p as follows:

$$L = \frac{1}{\sqrt{2}\,\pi\, n\, \sigma^2} = \frac{k\,T}{\sqrt{2}\,\pi\, p\, \sigma^2} \tag{15.6.1}$$

where n is the number density (number of molecules per unit volume), σ is the molecular diameter, and k is the Boltzmann constant (1.38×10^{-23} J/K.molecule).

The continuum model is valid when L is much smaller than a characteristic flow dimension L. As this condition is violated, the flow is no longer near equilibrium, and the linear relation between stress and rate of strain and the no-slip velocity condition are no longer valid. Similarly, the linear relation between heat flux and temperature gradient and the no-jump temperature condition at a solid-fluid interface are no longer accurate when L is not much smaller than L.

The length-scale L can be some overall dimension of the flow, but a more precise choice is the scale of the gradient of a macroscopic quantity, as, for example, the density ρ:

$$L = \frac{\rho}{\left|\dfrac{\partial \rho}{\partial y}\right|} \tag{15.6.2}$$

The ratio between the mean free path and the characteristic length is known as the Knudsen number:

$$Kn = \frac{L}{L} \tag{15.6.3}$$

and generally the traditional continuum approach is valid, albeit with modified boundary conditions, as long as $Kn < 0.1$.

There are two more important dimensionless parameters in fluid mechanics, and the Knudsen number can be expressed in terms of those two. The Reynolds number is the ratio of inertial forces to viscous ones:

$$\mathrm{Re} = \frac{v_o\ L}{\nu} \tag{15.6.4}$$

where v_o is a characteristic velocity, and ν is the kinematic viscosity of the fluid. The Mach number is the ratio of flow velocity to the speed of sound:

$$Ma = \frac{v_o}{a_o} \tag{15.6.5}$$

The Mach number is a dynamic measure of fluid compressibility and may be considered as the ratio of inertial forces to elastic ones. From the kinetic theory of gases, the mean free path is related to the viscosity as follows:

$$\nu = \frac{\mu}{\rho} = \tfrac{1}{2} L \, \bar{v}_m \tag{15.6.6}$$

where μ is the dynamic viscosity, and $\bar{v}_m$ is the mean molecular speed, which is somewhat higher than the sound speed a_o:

$$\bar{v}_m = \sqrt{\frac{8}{\pi \gamma}} \, a_o \tag{15.6.7}$$

where γ is the specific heat ratio (i.e., the isentropic exponent). Combining Equation 15.6.3 through Equation 15.6.7, we reach the required relation:

$$Kn = \sqrt{\frac{\pi \gamma}{2}} \, \frac{Ma}{\mathrm{Re}} \tag{15.6.8}$$

In boundary layers, the relevant length-scale is the shear-layer thickness δ, and for laminar flows

$$\frac{\delta}{L} \sim \frac{1}{\sqrt{\mathrm{Re}}} \tag{15.6.9}$$

$$Kn \sim \frac{Ma}{\mathrm{Re}_\delta} \sim \frac{Ma}{\sqrt{\mathrm{Re}}} \tag{15.6.10}$$

where Re_δ is the Reynolds number based on the freestream velocity v_o and the boundary layer thickness δ, and Re is based on v_o and the streamwise length-scale L.

Rarefied gas flows are in general encountered in flows in small geometries such as MEMS devices and in low-pressure applications such as high-altitude flying and high-vacuum gadgets. The local value of Knudsen number in a particular flow determines the degree of rarefaction and the degree of validity of the continuum model. The different Knudsen number regimes are determined empirically and are therefore only approximate for a particular flow geometry. The pioneering experiments in rarefied gas dynamics were conducted by Knudsen in 1909. In the limit of zero Knudsen number, the transport terms in the continuum momentum and energy equations are negligible, and the Navier-Stokes equations then reduce to the inviscid Euler equations. Both heat conduction and viscous diffusion and dissipation are negligible, and the flow is then approximately isentropic (i.e., adiabatic and reversible) from the continuum viewpoint, while the equivalent molecular viewpoint is that the velocity distribution function is everywhere of the local equilibrium or Maxwellian form. As Kn increases, rarefaction effects become more important, and eventually the continuum approach breaks down altogether. The different Knudsen number regimes are depicted in Figure 15.6.2, and can be summarized as follows.

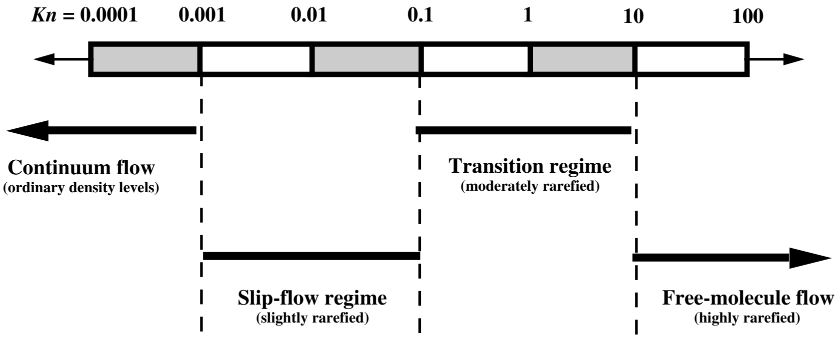

FIGURE 15.6.2 Knudsen number regimes.

Euler equations (neglect molecular diffusion):

$$Kn \to 0 \ (\mathrm{Re} \to \infty)$$

Navier-Stokes equations with no-slip boundary conditions:

$$Kn < 10^{-3}$$

Navier-Stokes equations with slip boundary conditions:

$$10^{-3} \le Kn < 10^{-1}$$

Transition regime:

$$10^{-1} \le Kn < 10$$

Free-molecule flow:

$$Kn \ge 10$$

As an example, consider air at standard temperature ($T = 288$ K) and pressure ($p = 1.01 \times 10^5$ N/m^2). A cube one micron on a side contains 2.54×10^7 molecules separated by an average distance of 0.0034 micron. The gas is considered dilute if the ratio of this distance to the molecular diameter exceeds 7, and in the present example this ratio is 9, barely satisfying the dilute gas assumption. The mean free path computed from Equation 15.6.1 is L =0.065 μm. A microdevice with characteristic length of 1 μm would have $Kn = 0.065$, which is in the slip-flow regime. At lower pressures, the Knudsen number increases. For example, if the pressure is 0.1 atm and the temperature remains the same, $Kn = 0.65$ for the same 1 μm device, and the flow is then in the transition regime. There would still be over 2 million molecules in the same one-micron cube, and the average distance between them would be 0.0074 μm. The same device at 100 km altitude would have $Kn = 3 \times 10^4$, well into the free-molecule flow regime. The Knudsen number for the flow of a light gas like helium is about three times larger than that for airflow at otherwise the same conditions.

Consider a long microchannel where the entrance pressure is atmospheric and the exit conditions are near vacuum. As air goes down the duct, the pressure and density decrease while the velocity, Mach number, and Knudsen number increase. The pressure drops to overcome viscous forces in the channel. If isothermal conditions prevail,[†] density also drops, and conservation of mass requires the flow to

---

[†] More likely the flow will be somewhere in between isothermal and adiabatic, Fanno flow. In that case both density and temperature decrease downstream, the former not as fast as in the isothermal case. None of that changes the qualitative arguments made in the example.

accelerate down the constant-area tube. The fluid acceleration in turn affects the pressure gradient, resulting in a nonlinear pressure drop along the channel. The Mach number increases down the tube, limited only by choked-flow condition $Ma = 1$. Additionally, the normal component of velocity is no longer zero. With lower density, the mean free path increases and Kn correspondingly increases. All flow regimes depicted in Figure 15.6.2 may occur in the same tube: continuum with no-slip boundary conditions, slip-flow regime, transition regime, and free-molecule flow. The airflow may also change from incompressible to compressible as it moves down the microduct. A similar scenario may take place if the entrance pressure is, say, 5 atm, while the exit is atmospheric. This deceivingly simple duct flow may in fact manifest every single complexity discussed in this subsection. In the following six subsections, we discuss in turn the Navier-Stokes equations, compressibility effects, boundary conditions, molecular-based models, liquid flows, and surface phenomena.

The Continuum Model

We recall in this subsection the traditional conservation relations in fluid mechanics. A concise derivation of these equations can be found in Gad-el-Hak (2000). Here, we reemphasize the precise assumptions needed to obtain a particular form of the equations. A continuum fluid implies that the derivatives of all the dependent variables exist in some reasonable sense. In other words, local properties such as density and velocity are defined as averages over elements large compared with the microscopic structure of the fluid but small enough in comparison with the scale of the macroscopic phenomena to permit the use of differential calculus to describe them. As mentioned earlier, such conditions are almost always met. For such fluids, and assuming the laws of nonrelativistic mechanics hold, the conservation of mass, momentum, and energy can be expressed at every point in space and time as a set of partial differential equations as follows:

$$\frac{\partial \rho}{\partial t} + \frac{\partial}{\partial x_k}\left(\rho\, u_k\right) = 0 \tag{15.6.11}$$

$$\rho\left(\frac{\partial u_i}{\partial t} + u_k \frac{\partial u_i}{\partial x_k}\right) = \frac{\partial \Sigma_{ki}}{\partial x_k} + \rho\, g_i \tag{15.6.12}$$

$$\rho\left(\frac{\partial e}{\partial t} + u_k \frac{\partial e}{\partial x_k}\right) = -\frac{\partial q_k}{\partial x_k} + \Sigma_{ki}\frac{\partial u_i}{\partial x_k} \tag{15.6.13}$$

where ρ is the fluid density, u_k is an instantaneous velocity component (u,v,w), Σ_{ki} is the second-order stress tensor (surface force per unit area), g_i is the body force per unit mass, e is the internal energy, and q_k is the sum of heat flux vectors due to conduction and radiation. The independent variables are time t and the three spatial coordinates x_1, x_2, and x_3 or (x,y,z).

Equation 15.6.11, Equation 15.6.12, and Equation 15.6.13 constitute five differential equations for the 17 unknowns ρ, u_i, Σ_{ki}, e, and q_k. Absent any body couples, the stress tensor is symmetric having only six independent components, which reduces the number of unknowns to 14. Obviously, the continuum flow equations do not form a determinate set. To close the conservation equations, the relation between the stress tensor and deformation rate, the relation between the heat flux vector and the temperature field, and appropriate equations of state relating the different thermodynamic properties are needed. The stress-rate of strain relation and the heat flux-temperature gradient relation are approximately linear if the flow is not too far from thermodynamic equilibrium. This is a phenomenological result but can be rigorously derived from the Boltzmann equation for a dilute gas assuming the flow is near equilibrium. For a Newtonian, isotropic, Fourier, ideal gas, for example, those relations read

$$\Sigma_{ki} = -p\,\delta_{ki} + \mu\left(\frac{\partial u_i}{\partial x_k} + \frac{\partial u_k}{\partial x_i}\right) + \lambda\left(\frac{\partial u_j}{\partial x_j}\right)\delta_{ki} \tag{15.6.14}$$

$$q_i = -\kappa\,\frac{\partial T}{\partial x_i} + \text{Heat flux due to radiation} \tag{15.6.15}$$

$$de = c_v\,dT \quad \text{and} \quad p = \rho R T \tag{15.6.16}$$

where p is the thermodynamic pressure; μ and λ are the first and second coefficients of viscosity, respectively; δ_{ki} is the unit second-order tensor (Kronecker delta); κ is the thermal conductivity; T is the temperature field; c_v is the specific heat at constant volume; and R is the gas constant, which is given by the Boltzmann constant divided by the mass of an individual molecule $k = mR$. The Stokes' hypothesis relates the first and second coefficients of viscosity, thus $\lambda + \frac{2}{3}\mu = 0$, although the validity of this assumption for other than dilute, monatomic gases has occasionally been questioned (Gad-el-Hak 1995). With the above constitutive relations and neglecting radiative heat transfer, Equation 15.6.11, Equation 15.6.12, and Equation 15.6.13, respectively, read

$$\frac{\partial\rho}{\partial t} + \frac{\partial}{\partial x_k}(\rho\,u_k) = 0 \tag{15.6.17}$$

$$\rho\left(\frac{\partial u_i}{\partial t} + u_k\,\frac{\partial u_i}{\partial x_k}\right) = -\,\frac{\partial p}{\partial x_i} + \rho\,g_i + \frac{\partial}{\partial x_k}\left[\mu\left(\frac{\partial u_i}{\partial x_k} + \frac{\partial u_k}{\partial x_i}\right) + \delta_{ki}\,\lambda\,\frac{\partial u_j}{\partial x_j}\right] \tag{15.6.18}$$

$$\rho\left(\frac{\partial e}{\partial t} + u_k\frac{\partial e}{\partial x_k}\right) = \frac{\partial}{\partial x_k}\left(\kappa\,\frac{\partial T}{\partial x_k}\right) - p\,\frac{\partial u_k}{\partial x_k} + \phi \tag{15.6.19}$$

The three components of the vector equation (Equation 15.6.18) are the Navier-Stokes equations expressing the conservation of momentum for a Newtonian fluid. In the thermal energy equation (Equation 15.6.198), ϕ is the always positive dissipation function expressing the irreversible conversion of mechanical energy to internal energy as a result of the deformation of a fluid element. The second term on the right-hand side of Equation 15.6.19 is the reversible work done (per unit time) by the pressure as the volume of a fluid material element changes. For a Newtonian, isotropic fluid, the viscous dissipation rate is given by

$$\phi = \tfrac{1}{2}\,\mu\left(\frac{\partial u_i}{\partial x_k} + \frac{\partial u_k}{\partial x_i}\right)^2 + \lambda\left(\frac{\partial u_j}{\partial x_j}\right)^2 \tag{15.6.20}$$

There are now six unknowns, ρ, u_i, p, and T, and the five coupled equations (Equation 15.6.17, Equation 15.6.18, and Equation 15.6.19) plus the equation of state relating pressure, density, and temperature. These six equations together with sufficient number of initial and boundary conditions constitute a well-posed, albeit formidable, problem. The system of Equation 15.6.17, Equation 15.6.18, and Equation 15.6.19 is an excellent model for the laminar or turbulent flow of most fluids such as air and water under many circumstances, including high-speed gas flows for which the shock waves are thick relative to the mean free path of the molecules.

Considerable simplification is achieved if the flow is assumed incompressible, usually a reasonable assumption provided that the characteristic flow speed is less than 0.3 of the speed of sound. The incompressibility assumption is readily satisfied for almost all liquid flows and many gas flows. In such cases, the density is assumed either a constant or a given function of temperature (or species concentration). The governing equations for such flow are

$$\frac{\partial u_k}{\partial x_k} = 0 \tag{15.6.21}$$

$$\rho\left(\frac{\partial u_i}{\partial t} + u_k\,\frac{\partial u_i}{\partial x_k}\right) = -\frac{\partial p}{\partial x_i} + \frac{\partial}{\partial x_k}\left[\mu\left(\frac{\partial u_i}{\partial x_k} + \frac{\partial u_k}{\partial x_i}\right)\right] + \rho g_i \tag{15.6.22}$$

$$\rho\, c_p\left(\frac{\partial T}{\partial t} + u_k\,\frac{\partial T}{\partial x_k}\right) = \frac{\partial}{\partial x_k}\left(\kappa\,\frac{\partial T}{\partial x_k}\right) + \phi_{\text{incomp}} \tag{15.6.23}$$

where ϕ_{incomp} is the incompressible limit of Equation 15.6.20. These are now five equations for the five dependent variables u_i, p and T. Note that the left-hand side of Equation 15.6.23 has the specific heat at constant pressure c_p and not c_v. It is the convection of enthalpy — and not internal energy — that is balanced by heat conduction and viscous dissipation. This is the correct incompressible-flow limit — of a compressible fluid — as discussed in detail in Section 10.9 of Panton (1996); a subtle point perhaps but one that is frequently missed in textbooks.

For both the compressible and the incompressible equations of motion, the transport terms are neglected away from solid walls in the limit of infinite Reynolds number ($Kn \rightarrow 0$). The fluid is then approximated as inviscid and nonconducting, and the corresponding equations read (for the compressible case)

$$\frac{\partial \rho}{\partial t} + \frac{\partial}{\partial x_k}\left(\rho\, u_k\right) = 0 \tag{15.6.24}$$

$$\rho\left(\frac{\partial u_i}{\partial t} + u_k\,\frac{\partial u_i}{\partial x_k}\right) = -\frac{\partial p}{\partial x_i} + \rho\, g_i \tag{15.6.25}$$

$$\rho\, c_v\left(\frac{\partial T}{\partial t} + u_k\,\frac{\partial T}{\partial x_k}\right) = -p\,\frac{\partial u_k}{\partial x_k} \tag{15.6.26}$$

The Euler equation (Equation 15.6.25) can be integrated along a streamline, and the resulting Bernoulli's equation provides a direct relation between the velocity and pressure.

Compressibility

The issue of whether to consider the continuum flow compressible or incompressible seems to be rather straightforward, but is in fact full of potential pitfalls. If the local Mach number is less than 0.3, then the flow of a compressible fluid like air can — according to the conventional wisdom — be treated as incompressible. But the well-known $Ma < 0.3$ criterion is only a necessary and not a sufficient one to allow a treatment of the flow as approximately incompressible. In other words, there are situations where the Mach number can be exceedingly small while the flow is compressible. As is well documented in heat transfer textbooks, strong wall heating or cooling may cause the density to change sufficiently and the incompressible approximation to break down, even at low speeds. Less known is the situation encountered in some microdevices where the pressure may strongly change due to viscous effects even though the speeds may not be high enough for the Mach number to go above the traditional threshold of 0.3. Corresponding to the pressure changes would be strong density changes that must be taken into account when writing the continuum equations of motion. In this subsection, we systematically explain all situations where compressibility effects must be considered. Let us rewrite the full continuity equation (Equation 15.6.11) as follows

$$\frac{D\rho}{Dt}+\rho\,\frac{\partial u_k}{\partial x_k}=0 \tag{15.6.27}$$

where $\frac{D\rho}{Dt}$ is the substantial derivative $\left(\frac{\partial}{\partial t}+u_k\frac{\partial}{\partial x_k}\right)$, expressing changes following a fluid element. The proper criterion for the Incompressible approximation to hold is that $\left(\frac{1}{\rho}\frac{D\rho}{Dt}\right)$ is vanishingly small. In other words, if density changes following a fluid particle are small, the flow is approximately incompressible. Density may change arbitrarily from one particle to another without violating the incompressible flow assumption. This is the case for example in the stratified atmosphere and ocean, where the variable-density/temperature/salinity flow is often treated as incompressible.

From the state principle of thermodynamics, we can express the density changes of a simple system in terms of changes in pressure and temperature:

$$\rho = \rho(p,T) \tag{15.6.28}$$

Using the chain rule of calculus:

$$\tfrac{1}{\rho}\,\frac{D\rho}{Dt} = \alpha\,\frac{Dp}{Dt} - \beta\,\frac{DT}{Dt} \tag{15.6.29}$$

where α and β are, respectively, the isothermal compressibility coefficient and the bulk expansion coefficient — two thermodynamic variables that characterize the fluid susceptibility to change of volume — which are defined by the following relations

$$\alpha(p,T)\equiv\frac{1}{\rho}\left.\frac{\partial\rho}{\partial p}\right|_T \tag{15.6.30}$$

$$\beta(p,T)\equiv-\frac{1}{\rho}\left.\frac{\partial\rho}{\partial T}\right|_p \tag{15.6.31}$$

For ideal gases, $\alpha = 1/p$ and $\beta = 1/T$. Note, however, that in the following arguments it will not be necessary to invoke the ideal gas assumption. The flow must be treated as compressible if pressure and/or temperature changes — following a fluid element — are sufficiently strong. Equation 15.6.29 must of course be properly nondimensionalized before deciding whether a term is large or small. In here, we follow closely the procedure detailed in Panton (1996).

Consider first the case of adiabatic walls. Density is normalized with a reference value ρ_o; velocities with a reference speed v_o; spatial coordinates and time with L and L/v_o, respectively; and the isothermal compressibility coefficient and bulk expansion coefficient with reference values α_o and β_o. The pressure is nondimensionalized with the inertial pressure-scale $\rho_o\, v_o^2$. This scale is twice the dynamic pressure, that is, the pressure change as an inviscid fluid moving at the reference speed is brought to rest.

Temperature changes for the case of adiabatic walls can only result from the irreversible conversion of mechanical energy into internal energy via viscous dissipation. Temperature is therefore nondimensionalized as follows:

$$T^* = \frac{T - T_o}{\left(\dfrac{\mu_o\, v_o^2}{\kappa_o}\right)} = \frac{T - T_o}{\mathrm{Pr}\left(\dfrac{v_o^2}{c_{p_o}}\right)} \tag{15.6.32}$$

where T_o is a reference temperature; μ_o, κ_o, and c_{p_o} are, respectively, reference viscosity, thermal conductivity, and specific heat at constant pressure; and Pr is the reference Prandtl number, $(\mu_o\, c_{p_o})/\kappa_o$.

In the present formulation, the scaling used for pressure is based on the Bernoulli's equation and therefore neglects viscous effects. This particular scaling guarantees that the pressure term in the momentum equation will be of the same order as the inertia term. The temperature scaling assumes that the conduction, convection, and dissipation terms in the energy equation have the same order of magnitude. The resulting dimensionless form of Equation 15.6.29 reads

$$\frac{1}{\rho^*}\,\frac{D\rho^*}{Dt^*} = \gamma_o\, Ma^2 \left\{\alpha^*\,\frac{Dp^*}{Dt^*} - \frac{\mathrm{Pr}\, B\, \beta^*}{A}\,\frac{DT^*}{Dt^*}\right\} \tag{15.6.33}$$

where the superscript * indicates a nondimensional quantity, Ma is the reference Mach number (v_o/a_o, where a_o is the reference speed of sound), and A and B are dimensionless constants defined by $A \equiv \alpha_o \rho_o c_{p_o} T_o$ and $B \equiv \beta_o\, T_o$. If the scaling is properly chosen, the terms having the * superscript in the right-hand side should be of order one, and the relative importance of such terms in the equations of motion is determined by the magnitude of the dimensionless parameter(s) appearing to their left, for example, Ma, Pr, and so forth. Therefore, as $Ma^2 \to 0$, temperature changes due to viscous dissipation are neglected (unless Pr is very large, as for example in the case of highly viscous polymers and oils). Within the same order of approximation, all thermodynamic properties of the fluid are assumed constant.

Pressure changes are also neglected in the limit of zero Mach number. Hence, for $Ma < 0.3$ (i.e., $Ma^2 < 0.09$), density changes following a fluid particle can be neglected and the flow can then be approximated as incompressible.[†] However, there is a caveat in this argument. Pressure changes due to inertia can indeed be neglected at small Mach numbers, and this is consistent with the way we nondimensionalized the pressure term above. If on the other hand pressure changes are mostly due to viscous effects, as is the case for example in a long microduct or a micro-gas-bearing, pressure changes may be significant even at low speeds (low Ma). In that case the term Dp^*/dt in Equation 15.6.33 is no longer of order one, and may be large regardless of the value of Ma. Density then may change significantly and the flow must be treated as compressible. Had pressure been nondimensionalized using the viscous scale ($\mu_o v_o/L$) instead of the inertial one ($\rho_o\, v_o^2$), the revised Equation 15.6.33 would have Re^{-1} appearing explicitly in the first term in the right-hand side, accentuating the importance of this term when viscous forces dominate.

A similar result can be gleaned when the Mach number is interpreted as follows:

$$Ma^2 = \frac{v_o^2}{a_o^2} = v_o^2\, \left.\frac{\partial\rho}{\partial p}\right|_s = \frac{\rho_o\, v_o^2}{\rho_o}\, \left.\frac{\partial\rho}{\partial p}\right|_s \sim \frac{\Delta p}{\rho_o}\,\frac{\Delta\rho}{\Delta p} = \frac{\Delta\rho}{\rho_o} \tag{15.6.34}$$

where s is the entropy. Again, the above equation assumes that pressure changes are inviscid, and therefore a small Mach number means negligible pressure and density changes. In a flow dominated by viscous

---

[†] With an error of about 10% at $Ma = 0.3$, 4% at $Ma = 0.2$, 1% at $Ma = 0.1$, and so on.

effects — such as that inside a microduct — density changes may be significant even in the limit of zero Mach number.

Identical arguments can be made in the case of isothermal walls. Here strong temperature changes may be the result of wall heating or cooling, even if viscous dissipation is negligible. The proper temperature scale in this case is given in terms of the wall temperature T_w and the reference temperature T_o as follows:

$$\widehat{T} = \frac{T - T_o}{T_w - T_o} \tag{15.6.35}$$

where $\widehat{T}$ is the new dimensionless temperature. The nondimensional form of Equation 15.6.29 now reads

$$\frac{1}{\rho^*}\frac{D\rho^*}{Dt^*} = \gamma_o\, Ma^2\, \alpha^*\, \frac{Dp^*}{Dt^*} - \beta^*\, B\left(\frac{T_w - T_o}{T_o}\right)\frac{D\widehat{T}}{Dt^*} \tag{15.6.36}$$

Here we notice that the temperature term is different from that in Equation 15.6.33. *Ma* is no longer appearing in this term, and strong temperature changes, that is, large $(T_w - T_o)/T_o$, may cause strong density changes regardless of the value of the Mach number. Additionally, the thermodynamic properties of the fluid are not constant but depend on temperature, and as a result the continuity, momentum and energy equations all couple. The pressure term in Equation 15.6.36, on the other hand, is exactly as it was in the adiabatic case and the same arguments made before apply: the flow should be considered compressible if $Ma > 0.3$, or if pressure changes due to viscous forces are sufficiently large.

Experiments in gaseous microducts confirm the above arguments. For both low- and high-Mach-number flows, pressure gradients in long microchannels are nonconstant, consistent with the compressible flow equations. Such experiments were conducted by, among others, Prud'homme et al. (1986), Pfahler et al. (1991), van den Berg et al. (1993), Liu et al. (1993; 1995), Pong et al. (1994), Harley et al. (1995), Piekos and Breuer (1996), Arkilic (1997), and Arkilic et al. (1995; 1997a; 1997b). Sample results will be presented in the following subsection.

There are three additional scenarios in which significant pressure and density changes may take place without inertial, viscous, or thermal effects. First is the case of quasi-static compression/expansion of a gas in, for example, a piston-cylinder arrangement. The resulting compressibility effects are, however, compressibility of the fluid and not of the flow. Two other situations where compressibility effects must also be considered are problems with length-scales comparable to the scale height of the atmosphere and rapidly varying flows as in sound propagation (Lighthill 1963).

Boundary Conditions

The continuum equations of motion described earlier require a certain number of initial and boundary conditions for proper mathematical formulation of flow problems. In this subsection, we describe the boundary conditions at a fluid-solid interface. Boundary conditions in the inviscid flow theory pertain only to the velocity component normal to a solid surface. The highest spatial derivative of velocity in the inviscid equations of motion is first-order, and only one velocity boundary condition at the surface is admissible. The normal velocity component at a fluid-solid interface is specified, and no statement can be made regarding the tangential velocity component. The normal-velocity condition simply states that a fluid-particle path cannot go through an impermeable wall. Real fluids are of course viscous, and the corresponding momentum equation has second-order derivatives of velocity, thus requiring an additional boundary condition on the velocity component tangential to a solid surface.

Traditionally, the no-slip condition at a fluid-solid interface is enforced in the momentum equation and an analogous no-temperature-jump condition is applied in the energy equation. The notion underlying the no-slip/no-jump condition is that within the fluid there cannot be any finite discontinuities of velocity/temperature. Those would involve infinite velocity/temperature gradients and so produce infinite viscous stress/heat flux that would destroy the discontinuity in infinitesimal time. The interaction between a fluid particle and a wall is similar to that between neighboring fluid particles, and therefore no discontinuities are allowed at the fluid-solid interface either. In other words, the fluid velocity must be zero relative to the surface and the fluid temperature must equal to that of the surface. But strictly speaking, those two boundary conditions are valid only if the fluid flow adjacent to the surface is in thermodynamic equilibrium. This requires an infinitely high frequency of collisions between the fluid and the solid surface. In practice, the no-slip/no-jump condition leads to fairly accurate predictions as long as $Kn < 0.001$ (for gases). Beyond that, the collision frequency is simply not high enough to ensure equilibrium and a certain degree of tangential-velocity slip and temperature jump must be allowed. This is a case frequently encountered in MEMS flows, and we develop the appropriate relations in this subsection.

For both liquids and gases, the linear Navier boundary condition empirically relates the tangential velocity slip at the wall $\Delta u\big|_w$ to the local shear:

$$\Delta u\Big|_w = u_{fluid} - u_{wall} = L_s \left.\frac{\partial u}{\partial y}\right|_w \tag{15.6.37}$$

where L_s is the constant slip length, and $\left.\frac{\partial u}{\partial y}\right|_w$ is the strain rate computed at the wall. In most practical situations, the slip length is so small that the no-slip condition holds. In MEMS applications, however, that may not be the case. Once again we defer the discussion of liquids to a later section and focus for now on gases.

Assuming isothermal conditions prevail, the above slip relation has been rigorously derived by Maxwell (1879) from considerations of the kinetic theory of dilute, monatomic gases. Gas molecules, modeled as rigid spheres, continuously strike and reflect from a solid surface, just as they continuously collide with each other. For an idealized perfectly smooth wall (at the molecular scale), the incident angle exactly equals the reflected angle and the molecules conserve their tangential momentum and thus exert no shear on the wall. This is termed *specular reflection* and results in perfect slip at the wall. For an extremely rough wall, on the other hand, the molecules reflect at some random angle uncorrelated with their entry angle. This perfectly diffuse reflection results in zero tangential-momentum for the reflected fluid molecules to be balanced by a finite slip velocity in order to account for the shear stress transmitted to the wall. A force balance near the wall leads to the following expression for the slip velocity:

$$u_{gas} - u_{wall} = L \left.\frac{\partial u}{\partial y}\right|_w \tag{15.6.38}$$

where L is the mean free path. The right-hand side can be considered as the first term in an infinite Taylor series, sufficient if the mean free path is relatively small enough. Equation 15.6.38 states that significant slip occurs only if the mean velocity of the molecules varies appreciably over a distance of one mean free path. This is the case, for example, in vacuum applications and/or flow in microdevices. The number of collisions between the fluid molecules and the solid in those cases is not large enough for even an approximate flow equilibrium to be established. Furthermore, additional (nonlinear) terms in the Taylor series would be needed as L increases and the flow is further removed from the equilibrium state.

For real walls some molecules reflect diffusively and some reflect specularly. In other words, a portion of the momentum of the incident molecules is lost to the wall and a (typically smaller) portion is retained by the reflected molecules. The tangential-momentum-accommodation coefficient σ_v is defined as the fraction of molecules reflected diffusively. This coefficient depends on the fluid, the solid and the surface finish, and has been determined experimentally to be between 0.2 and 0.8 (Thomas and Lord 1974; Seidl and Steiheil 1974; Porodnov et al. 1974; Arkilic et al. 1997b; Arkilic 1997), the lower limit being for exceptionally smooth surfaces while the upper limit is typical of most practical surfaces. The final expression derived by Maxwell for an isothermal wall reads

$$u_{gas} - u_{wall} = \frac{2-\sigma_v}{\sigma_v} L \left.\frac{\partial u}{\partial y}\right|_w \tag{15.6.39}$$

For $\sigma_v = 0$, the slip velocity is unbounded, while for $\sigma_v = 1$, Equation 15.6.39 reverts to 15.6.38.

Similar arguments were made for the temperature-jump boundary condition by von Smoluchowski (1898). For an ideal gas flow in the presence of wall-normal and tangential temperature gradients, the complete (first-order) slip-flow and temperature-jump boundary conditions read

$$\begin{aligned} u_{gas} - u_{wall} &= \frac{2-\sigma_v}{\sigma_v} \frac{1}{\rho\sqrt{\frac{2\,R\,T_{gas}}{\pi}}} \tau_w + \tfrac{3}{4} \frac{\Pr\left(\gamma-1\right)}{\gamma\,\rho R\,T_{gas}} \left(-q_x\right)_w \\ &= \frac{2-\sigma_v}{\sigma_v} L \left(\frac{\partial u}{\partial y}\right)_w + \tfrac{3}{4} \frac{\mu}{\rho\,T_{gas}} \left(\frac{\partial T}{\partial x}\right)_w \end{aligned} \tag{15.6.40}$$

$$\begin{aligned} T_{gas} - T_{wall} &= \frac{2-\sigma_T}{\sigma_T} \left[\frac{2\left(\gamma-1\right)}{\left(\gamma+1\right)}\right] \frac{1}{\rho\,R\sqrt{\frac{2\,R\,T_{gas}}{\pi}}} \left(-q_y\right)_w \\ &= \frac{2-\sigma_T}{\sigma_T} \left[\frac{2\,\gamma}{\left(\gamma+1\right)}\right] \frac{L}{\Pr} \left(\frac{\partial T}{\partial y}\right)_w \end{aligned} \tag{15.6.41}$$

where x and y are the streamwise and normal coordinates, ρ and μ, are the fluid density and viscosity, respectively; R is the gas constant; T_{gas} is the temperature of the gas adjacent to the wall; T_{wall} is the wall temperature; τ_w is the shear stress at the wall; Pr is the Prandtl number; γ is the specific heat ratio; and q_x and q_y are the tangential and normal heat flux at the wall, respectively.

The tangential-momentum-accommodation coefficient σ_v and the thermal-accommodation coefficient σ_T are given by, respectively

$$\sigma_v = \frac{\tau_i - \tau_r}{\tau_i - \tau_w} \tag{15.6.42}$$

$$\sigma_T = \frac{dE_i - dE_r}{dE_i - dE_w} \tag{15.6.43}$$

where the subscripts i, r, and w stand for, respectively, incident, reflected, and solid wall conditions; τ is a tangential momentum flux; and dE is an energy flux.

The second term in the right-hand side of Equation 15.6.40 is the *thermal creep*, which generates slip velocity in the fluid opposite to the direction of the tangential heat flux, that is, flow in the direction of increasing temperature. At sufficiently high Knudsen numbers, a streamwise temperature gradient in a conduit leads to a measurable pressure gradient along the tube. This may be the case in vacuum applications and MEMS devices. Thermal creep is the basis for the so-called Knudsen pump — a device with no moving parts — in which rarefied gas is hauled from one cold chamber to a hot one.[†] Clearly, such a pump performs best at high Knudsen numbers, and is typically designed to operate in the free-molecule flow regime.

In dimensionless form, Equation 15.6.40 and Equation 15.6.41 read, respectively

$$u^*_{gas} - u^*_{wall} = \frac{2-\sigma_v}{\sigma_v} Kn \left(\frac{\partial u^*}{\partial y^*} \right)_w + \tfrac{3}{2\pi} \frac{(\gamma - 1)}{\gamma} \frac{Kn^2 \, \mathrm{Re}}{Ec} \left(\frac{\partial T^*}{\partial x^*} \right)_w \tag{15.6.44}$$

$$T^*_{gas} - T^*_{wall} = \frac{2 - \sigma_T}{\sigma_T} \left[\frac{2\gamma}{(\gamma + 1)} \right] \frac{Kn}{\mathrm{Pr}} \left(\frac{\partial T^*}{\partial y^*} \right)_w \tag{15.6.45}$$

where the superscript * indicates dimensionless quantity, *Kn* is the Knudsen number, Re is the Reynolds number, and *Ec* is the Eckert number defined by

$$Ec = \frac{v_o^2}{c_p \, \Delta T} = (\gamma - 1) \frac{T_o}{\Delta T} Ma^2 \tag{15.6.46}$$

where v_o is a reference velocity, $\Delta T = (T_{gas} - T_o)$, and T_o is a reference temperature. Note that very low values of σ_v and σ_T lead to substantial velocity slip and temperature jump even for flows with small Knudsen number.

The first term in the right-hand side of Equation 15.6.44 is first-order in Knudsen number, while the thermal creep term is second-order, meaning that the creep phenomenon is potentially significant at large values of the Knudsen number. Equation 15.6.45 is first-order in *Kn*. Using Equation 15.6.8 and Equation 15.6.46, the thermal creep term in Equation 15.6.44 can be rewritten in terms of ΔT and the Reynolds number. Thus,

$$u^*_{gas} - u^*_{wall} = \frac{2-\sigma_v}{\sigma_v} Kn \left(\frac{\partial u^*}{\partial y^*} \right)_w + \tfrac{3}{4} \frac{\Delta T}{T_o} \frac{1}{\mathrm{Re}} \left(\frac{\partial T^*}{\partial x^*} \right)_w \tag{15.6.47}$$

It is clear that large temperature changes along the surface or low Reynolds numbers lead to significant thermal creep.

The continuum Navier-Stokes equations with no-slip/no-temperature jump boundary conditions are valid as long as the Knudsen number does not exceed 0.001. First-order slip/temperature-jump boundary conditions should be applied to the Navier-Stokes equations in the range of $0.001 < Kn < 0.1$. The transition regime spans the range of $0.1 < Kn < 10$, and second-order or higher slip/temperature-jump boundary conditions are applicable there. Note, however, that the Navier-Stokes equations are first-order accurate in *Kn*, as will be shown later, and are themselves not valid in the transition regime. Either higher-order continuum equations, for example, Burnett equations, should be used there or molecular modeling should be invoked, abandoning the continuum approach altogether.

For isothermal walls, Beskok (1994) derived a higher-order slip-velocity condition as follows:

$$u_{gas} - u_{wall} = \frac{2-\sigma_v}{\sigma_v} \left[L \left(\frac{\partial u}{\partial y} \right)_w + \frac{L^2}{2!} \left(\frac{\partial^2 u}{\partial y^2} \right)_w + \frac{L^3}{3!} \left(\frac{\partial^3 u}{\partial y^3} \right)_w + \cdots \right] \tag{15.6.48}$$

[†] The terminology Knudsen pump has been used by, for example, Vargo and Muntz (1996), but according to Loeb (1961), the original experiments demonstrating such pump were carried out by Osborne Reynolds.

Attempts to implement the previous slip condition in numerical simulations are rather difficult. Second-order and higher derivatives of velocity cannot be computed accurately near the wall. Based on asymptotic analysis, Beskok (1996) and Beskok and Karniadakis (1994; 1999) proposed the following alternative higher-order boundary condition for the tangential velocity, including the thermal creep term:

$$u^*_{gas} - u^*_{wall} = \frac{2-\sigma_v}{\sigma_v}\,\frac{Kn}{1-b\,Kn}\left(\frac{\partial u^*}{\partial y^*}\right)_w + \tfrac{3}{2\pi}\,\frac{(\gamma-1)}{\gamma}\,\frac{Kn^2\,\mathrm{Re}}{Ec}\left(\frac{\partial T^*}{\partial x^*}\right)_w \tag{15.6.49}$$

where b is a high-order slip coefficient determined from the presumably known no-slip solution, thus avoiding the computational difficulties mentioned earlier. If this high-order slip coefficient is chosen as $b = u''_w/u'_w$, where the prime denotes derivative with respect to y and the velocity is computed from the no-slip Navier-Stokes equations, Equation 15.6.49 becomes second-order accurate in Knudsen number. Beskok's procedure can be extended to third- and higher-orders for both the slip-velocity and thermal creep terms.

Similar arguments can be applied to the temperature-jump boundary condition, and the resulting Taylor series reads in dimensionless form (Beskok 1996)

$$T^*_{gas} - T^*_{wall} = \frac{2-\sigma_T}{\sigma_T}\left[\frac{2\gamma}{(\gamma+1)}\right]\frac{1}{\mathrm{Pr}}\left[Kn\left(\frac{\partial T^*}{\partial y^*}\right)_w + \frac{Kn^2}{2!}\left(\frac{\partial^2 T^*}{\partial y^{*2}}\right)_w + \ldots\right] \tag{15.6.50}$$

Again, the difficulties associated with computing second- and higher-order derivatives of temperature are alleviated using an identical procedure to that utilized for the tangential velocity boundary condition.

Several experiments in low-pressure macroducts or in microducts confirm the necessity of applying slip boundary condition at sufficiently large Knudsen numbers. Among them are those conducted by Knudsen (1909), Pfahler at al. (1991), Tison (1993), Liu et al. (1993, 1995), Pong et al. (1994), Arkilic et al. (1995), Harley et al. (1995), and Shih et al. (1995, 1996). The experiments are complemented by the numerical simulations carried out by Beskok (1994, 1996), Beskok and Karniadakis (1994, 1999), and Beskok et al. (1996). Here we present selected examples of the experimental and numerical results.

Tison (1993) conducted pipe flow experiments at very low pressures. His pipe has a diameter of 2 mm and a length-to-diameter ratio of 200. Both inlet and outlet pressures were varied to yield Knudsen number in the range of Kn = 0–200. Figure 15.6.3 shows the variation of mass flow rate as a function of $(p_i^2 - p_o^2)$, where p_i is the inlet pressure and p_o is the outlet pressure.[†] The pressure drop in this rarefied pipe flow is nonlinear, characteristic of low-Reynolds-number, compressible flows. Three distinct flow regimes are identified: (1) slip flow regime, $0 < Kn < 0.6$, (2) transition regime, $0.6 < Kn < 17$, where the mass flow rate is almost constant as the pressure changes, and (3) free-molecule flow, $Kn > 17$. Note that the demarcation between these three regimes is slightly different from that mentioned earlier. As stated, the different Knudsen number regimes are determined empirically and are therefore only approximate for a particular flow geometry.

Shih et al. (1995) conducted their experiments in a microchannel using helium as a fluid. The inlet pressure varied but the duct exit was atmospheric. Microsensors where fabricated in-situ along their MEMS channel to measure the pressure. Figure 15.6.4 shows their measured mass flow rate vs. the inlet pressure. The data are compared to the no-slip solution and the slip solution using three different values of the tangential-momentum-accommodation coefficient, 0.8, 0.9, and 1.0. The agreement is reasonable with the case $\sigma_v = 1$, indicating perhaps that the channel used by Shih et al. was quite rough on the molecular scale. In a second experiment (Shih et al. 1996), nitrous oxide was used as the fluid. The square of the pressure distribution along the channel is plotted in Figure 15.6.5 for five different inlet pressures.

[†] The original data in this figure were acquired by S.A. Tison and plotted by Beskok et al. (1996).

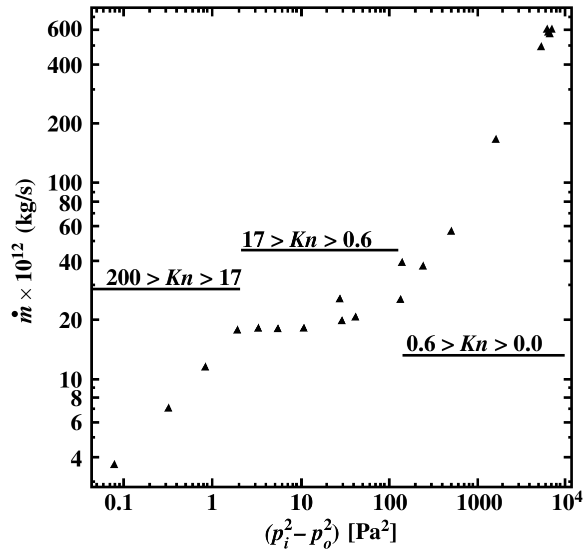

FIGURE 15.6.3 Variation of mass flow rate as a function of $(p_i^2 - p_o^2)$. Original data acquired by S.A. Tison and plotted by Beskok et al. (1996).

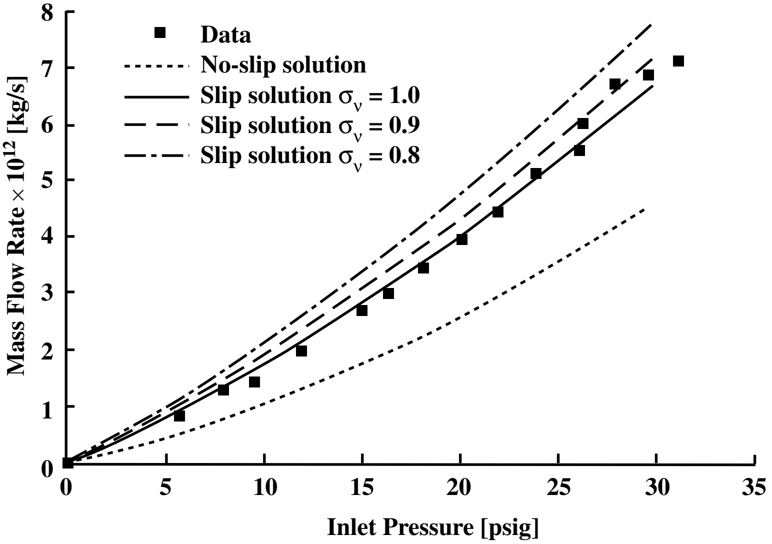

FIGURE 15.6.4 Mass flow rate vs. inlet pressure in a microchannel. From Shih et al. (1995).

The experimental data (symbols) compare well with the theoretical predictions (solid lines). Again, the nonlinear pressure drop shown indicates that the gas flow is compressible.

Arkilic (1997) provided an elegant analysis of the compressible, rarefied flow in a microchannel. The results of his theory are compared to the experiments of Pong et al. (1994) in Figure 15.6.6. The dotted line is the incompressible flow solution, where the pressure is predicted to drop linearly with streamwise distance. The dashed line is the compressible flow solution that neglects rarefaction effects (assumes $Kn = 0$). Finally, the solid line is the theoretical result that takes into account both compressibility and rarefaction via slip-flow boundary condition computed at the exit Knudsen number of $Kn = 0.06$. That theory compares most favorably with the experimental data. In the compressible flow through the

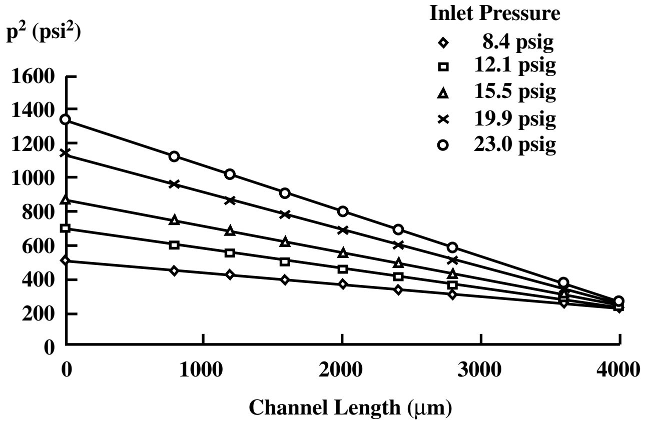

FIGURE 15.6.5 Pressure distribution of nitrous oxide in a microduct. Solid lines are theoretical predictions. From Shih et al. (1996).

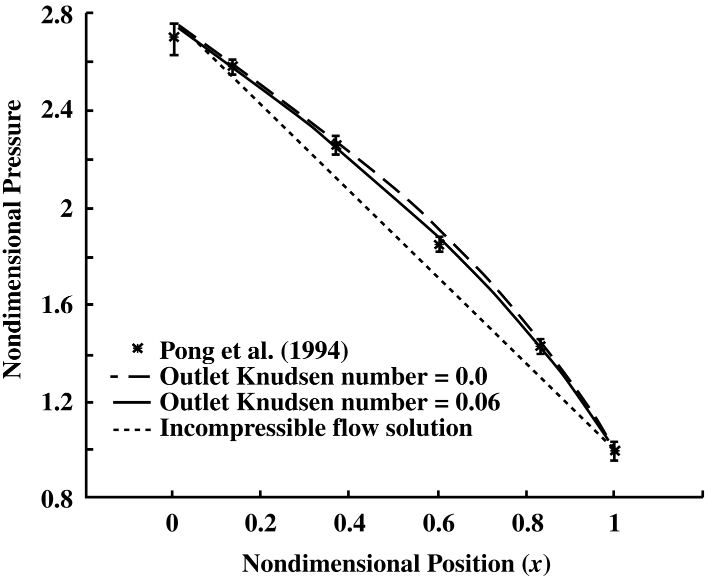

FIGURE 15.6.6 Pressure distribution in a long microchannel. The symbols are experimental data while the lines are different theoretical predictions. From Arkilic (1997).

constant-area duct, density decreases and thus velocity increases in the streamwise direction. As a result, the pressure distribution is nonlinear with negative curvature. A moderate Knudsen number (i.e., moderate slip) actually diminishes, albeit rather weakly, this curvature. Thus, compressibility and rarefaction effects lead to opposing trends, as pointed out by Beskok et al. (1996).

Molecular-Based Models

In the continuum models discussed thus far, the macroscopic fluid properties are the dependent variables while the independent variables are the three spatial coordinates and time. The molecular models recognize the fluid as a myriad of discrete particles: molecules, atoms, ions, and electrons. The goal here is to determine the position, velocity, and state of all particles at all times. The molecular approach is either deterministic or probabilistic (refer to Figure 15.6.1). Provided that there is a sufficient number of microscopic particles within the smallest significant volume of a flow, the macroscopic properties at any location in the flow can then be computed from the discrete-particle information by a suitable averaging or weighted averaging process. This subsection discusses molecular-based models and their relation to the continuum models previously considered.

The most fundamental of the molecular models is a deterministic one. The motion of the molecules are governed by the laws of classical mechanics, although, at the expense of greatly complicating the problem, the laws of quantum mechanics can also be considered in special circumstances. The modern molecular dynamics computer simulations (MD) have been pioneered by Alder and Wainwright (1957, 1958, 1970) and reviewed by Ciccotti and Hoover (1986), Allen and Tildesley (1987), Haile (1993), and Koplik and Banavar (1995). The simulation begins with a set of N molecules in a region of space, each assigned a random velocity corresponding to a Boltzmann distribution at the temperature of interest. The interaction between the particles is prescribed typically in the form of a two-body potential energy and the time evolution of the molecular positions is determined by integrating Newton's equations of motion. Because MD is based on the most basic set of equations, it is valid in principle for any flow extent and any range of parameters. The method is straightforward in principle but there are two hurdles: choosing a proper and convenient potential for particular fluid and solid combinations, and gathering the colossal computer resources required to simulate a reasonable flow-field extent.

For purists, the former difficulty is a sticky one. There is no totally rational methodology by which a convenient potential can be chosen. Part of the art of MD is to pick an appropriate potential and validate the simulation results with experiments or other analytical/computational results. A commonly used potential between two molecules is the generalized Lennard-Jones 6–12 potential, to be used in the following subsection and further discussed in the subsection following that.

The second difficulty, and by far the most serious limitation of molecular dynamics simulations, is the number of molecules N that can realistically be modeled on a digital computer. Since the computation of an element of trajectory for any particular molecule requires consideration of *all* other molecules as potential collision partners, the amount of computation required by the MD method is proportional to N^2. Some saving in computer time can be achieved by cutting off the weak tail of the potential (see Figure 15.6.11) at, say, $r_c = 2.5\sigma$, and shifting the potential by a linear term in r so that the force goes smoothly to zero at the cutoff. As a result, only nearby molecules are treated as potential collision partners, and the computation time for N molecules no longer scales with N^2.

The state of the art of molecular dynamics simulations in the early 2000s is such that with a few hours of CPU time, general-purpose supercomputers can handle around 100,000 molecules. At enormous expense, the fastest parallel machine available can simulate around 10 million particles. Because of the extreme diminution of molecular scales, the above translates into regions of liquid flow of about 0.02 μm (200 Angstroms) in linear size, over time intervals of around 0.001 μs, enough for continuum behavior to set in for simple molecules. To simulate 1 s of real time for complex molecular interactions, for example, including vibration modes, reorientation of polymer molecules, and collision of colloidal particles, requires unrealistic CPU time measured in hundreds of years.

MD simulations are highly inefficient for dilute gases where the molecular interactions are infrequent. The simulations are more suited for dense gases and liquids. Clearly, molecular dynamics simulations are reserved for situations where the continuum approach or the statistical methods are inadequate to compute from first principles important flow quantities. Slip boundary conditions for liquid flows in extremely small devices is such a case, as will be discussed in the following subsection.

An alternative to the deterministic molecular dynamics is the statistical approach where the goal is to compute the probability of finding a molecule at a particular position and state. If the appropriate conservation equation can be solved for the probability distribution, important statistical properties such as the mean number, momentum, or energy of the molecules within an element of volume can be computed from a simple weighted averaging. In a practical problem, it is such average quantities that concern us rather than the detail for every single molecule. Clearly, however, the accuracy of computing average quantities, via the statistical approach, improves as the number of molecules in the sampled volume increases. The kinetic theory of dilute gases is well advanced, but that for dense gases and liquids is much less so due to the extreme complexity of having to include multiple collisions and intermolecular forces in the theoretical formulation. The statistical approach is well covered in books such as those by Kennard (1938), Hirschfelder et al. (1954), Schaaf and Chambré (1961), Vincenti and Kruger (1965), Kogan (1969), Chapman and Cowling (1970), Cercignani (1988, 2000), and Bird (1994), and review articles such as those by Kogan (1973), Muntz (1989), and Oran et al. (1998).

In the statistical approach, the fraction of molecules in a given location and state is the sole dependent variable. The independent variables for monatomic molecules are time, the three spatial coordinates, and the three components of molecular velocity. Those describe a six-dimensional phase space.[†] For diatomic or polyatomic molecules, the dimension of phase space is increased by the number of internal degrees of freedom. Orientation adds an extra dimension for molecules that are not spherically symmetric. Finally, for mixtures of gases, separate probability distribution functions are required for each species. Clearly, the complexity of the approach increases dramatically as the dimension of phase space increases. The simplest problems are, for example, those for steady, one-dimensional flow of a simple monatomic gas.

To simplify the problem we restrict the discussion here to monatomic gases having no internal degrees of freedom. Furthermore, the fluid is restricted to dilute gases and molecular chaos is assumed. The former restriction requires the average distance between molecules δ to be an order of magnitude larger than their diameter σ. That will almost guarantee that all collisions between molecules are binary collisions, avoiding the complexity of modeling multiple encounters.[††] The molecular chaos restriction improves the accuracy of computing the macroscopic quantities from the microscopic information. In essence, the volume over which averages are computed has to have sufficient number of molecules to reduce statistical errors. It can be shown that computing macroscopic flow properties by averaging over a number of molecules will result in statistical fluctuations with a standard deviation of approximately 0.1% if one million molecules are used and around 3% if 1000 molecules are used. The molecular chaos limit requires the length-scale L for the averaging process to be at least 100 times the average distance between molecules (i.e., typical averaging over at least one million molecules).

Figure 15.6.7, adapted from Bird (1994), shows the limits of validity of the dilute gas approximation ($\delta/\sigma > 7$), the continuum approach ($Kn < 0.1$, as discussed previously), and the neglect of statistical fluctuations ($L/\delta > 100$). Using a molecular diameter of $\sigma = 4 \times 10^{-10}$ m as an example, the three limits are conveniently expressed as functions of the normalized gas density ρ/ρ_o or number density n/n_o, where the reference densities ρ_o and n_o are computed at standard conditions. All three limits are straight lines in the log-log plot of L vs. ρ/ρ_o, as depicted in Figure 15.6.7. Note the shaded triangular wedge inside which both the Boltzmann and Navier-Stokes equations are valid. Additionally, the lines describing the three limits very nearly intersect at a single point. As a consequence, the continuum breakdown limit always lies between the dilute gas limit and the limit for molecular chaos. As density or characteristic dimension is reduced in a dilute gas, the Navier-Stokes model breaks down before the level of statistical fluctuations becomes significant. In a dense gas, on the other hand, significant fluctuations may be present even when the Navier-Stokes model is still valid.

The starting point in statistical mechanics is the Liouville equation that expresses the conservation of the N-particle distribution function in $6N$-dimensional phase space,[†††] where N is the number of particles under consideration. Considering only external forces that do not depend on the velocity of the molecules,[††††] the Liouville equation for a system of N mass points reads

$$\frac{\partial F}{\partial t} + \sum_{k=1}^{N} \vec{\xi}_k \cdot \frac{\partial F}{\partial \vec{x}_k} + \sum_{k=1}^{N} \vec{F}_k \cdot \frac{\partial F}{\partial \vec{\xi}_k} = 0 \tag{15.6.51}$$

[†] The evolution equation of the probability distribution is considered; hence time is the seventh independent variable.

[††] Dissociation and ionization phenomena involve triple collisions and therefore require separate treatment.

[†††] Three positions and three velocities for *each* molecule of a monatomic gas with no internal degrees of freedom.

[††††] This excludes Lorentz forces, for example.

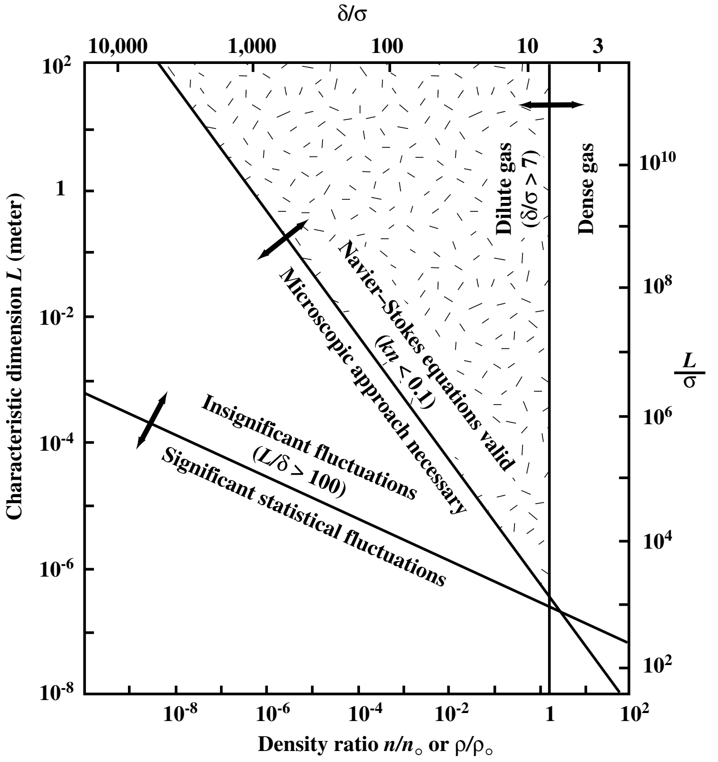

FIGURE 15.6.7 Effective limits of different flow models. From Bird (1994).

where F is the probability of finding a molecule at a particular point in phase space, t is time, $\vec{\xi}_k$ is the three-dimensional velocity vector for the kth molecule, $\vec{x}_k$ is the three-dimensional position vector for the kth molecule, and $\vec{F}$ is the external force vector. Note that the dot product in the previous equation is carried out over each of the three components of the vectors $\vec{\xi}$, $\vec{x}$, and $\vec{F}$, and that the summation is over all molecules. Obviously such an equation is not tractable for realistic number of particles.

A hierarchy of reduced distribution functions may be obtained by repeated integration of the previous Liouville equation. The final equation in the hierarchy is for the single particle distribution that also involves the two-particle distribution function. Assuming molecular chaos, that final equation becomes a closed one (i.e., one equation in one unknown), and is known as the Boltzmann equation, the fundamental relation of the kinetic theory of gases. That final equation in the hierarchy is the only one that carries any hope of obtaining analytical solutions.

A simpler direct derivation of the Boltzmann equation is provided by Bird (1994). For monatomic gas molecules in binary collisions, the integro-differential Boltzmann equation reads

$$\frac{\partial(nf)}{\partial t} + \xi_j \frac{\partial(nf)}{\partial x_j} + F_j \frac{\partial(nf)}{\partial \xi_j} = J\left(f,f^*\right), j = 1,2,3 \tag{15.6.52}$$

where $n\,f$ is the product of the number density and the normalized velocity distribution function ($dn/n = f\, d\vec{\xi}$); x_j and ξ_j are the coordinates and speeds of a molecule, respectively;[†] F_j is a known external force; and $J(f,f^*)$ is the nonlinear collision integral that describes the net effect of populating and

---

[†] Constituting, together with time, the seven independent variables of the single-dependent-variable equation.

depopulating collisions on the distribution function. The collision integral is the source of difficulty in obtaining analytical solutions to the Boltzmann equation, and is given by

$$J\left(f,f^*\right)=\int_{-\infty}^{\infty}\int_{0}^{4\pi} n^2\,\left(f^* f_1^* - f\,f_1\right)\vec{\xi}_r\;\sigma\;d\Omega\,\left(d\vec{\xi}\right)_1 \tag{15.6.53}$$

where the superscript * indicates postcollision values, f and f_1 represent two different molecules, $\vec{\xi}_r$ is the relative speed between two molecules, σ is the molecular cross section, Ω is the solid angle, and $d\vec{\xi} = d\xi_1\,d\xi_2\,d\xi_3$.

Once a solution for f is obtained, macroscopic quantities such as density, velocity, and temperature can be computed from the appropriate weighted integral of the distribution function. For example:

$$\rho = m\,n = m\int\left(n\,f\right)d\vec{\xi} \tag{15.6.54}$$

$$u_i = \int \xi_i\,f\,d\vec{\xi} \tag{15.6.55}$$

$$\tfrac{3}{2}\,k\,T = \int \tfrac{1}{2}\,m\,\xi_i\,\xi_i\,f\,d\vec{\xi} \tag{15.6.56}$$

If the Boltzmann equation is nondimensionalized with a characteristic length L and characteristic speed $[2(k/m)T]^{1/2}$, where k is the Boltzmann constant, m, is the molecular mass, and T is temperature, the inverse Knudsen number appears explicitly in the right-hand side of the equation as follows:

$$\frac{\partial\hat{f}}{\partial\hat{t}} + \hat{\xi}_j\,\frac{\partial\hat{f}}{\partial\hat{x}_j} + \hat{F}_j\,\frac{\partial\hat{f}}{\partial\hat{\xi}_j} = \frac{1}{Kn}\,\hat{J}\left(\hat{f},\hat{f}^*\right),\; j = 1,2,3 \tag{15.6.57}$$

where the topping symbol ^ represents a dimensionless variable, and $\hat{f}$ is nondimensionalized using a reference number density n_o.

The five conservation equations for the transport of mass, momentum, and energy can be derived by multiplying the previous Boltzmann equation by, respectively, the molecular mass, momentum, and energy, and then integrating over all possible molecular velocities. Subject to the restrictions of dilute gas and molecular chaos stated earlier, the Boltzmann equation is valid for all ranges of Knudsen number from 0 to ∞. Analytical solutions to this equation for arbitrary geometries are difficult mostly because of the nonlinearity of the collision integral. Simple models of this integral have been proposed to facilitate analytical solutions; see, for example, Bhatnagar et al. (1954).

There are two important asymptotes to Equation 15.6.57. First, as $Kn \to \infty$, molecular collisions become unimportant. This is the free-molecule flow regime depicted in Figure 15.6.2 for $Kn > 10$, where the only important collision is that between a gas molecule and the solid surface of an obstacle or a conduit. Analytical solutions are then possible for simple geometries, and numerical simulations for complicated geometries are straightforward once the surface-reflection characteristics are accurately modeled. Second, as $Kn \to 0$, collisions become important and the flow approaches the continuum regime of conventional fluid dynamics. The Second Law specifies a tendency for thermodynamic systems to revert to equilibrium state, smoothing out any discontinuities in macroscopic flow quantities. The number of molecular collisions in the limit $Kn \to 0$ is so large that the flow approaches the equilibrium state in a time short compared to the macroscopic time-scale. For example, for air at standard conditions (T = 288 K; p = 1 atm), each molecule experiences, on the average, 10 collisions per nanosecond and travels 1 micron in the same time period. Such a molecule has already *forgotten* its previous state after 1 ns. In a particular flowfield, if the macroscopic quantities vary little over a distance of 1 µm or over a time interval of 1 ns, the flow of STP air is near equilibrium.

At $Kn = 0$, the velocity distribution function is everywhere of the local equilibrium or Maxwellian form:

$$\hat{f}^{(0)} = \frac{n}{n_o}\,\pi^{-3/2}\,\exp\left[-\left(\hat{\xi} - \hat{u}\right)^2\right] \tag{15.6.58}$$

where $\hat{\xi}$ and $\hat{u}$ are, respectively, the dimensionless speeds of a molecule and of the flow. In this Knudsen number limit, the velocity distribution of each element of the fluid instantaneously adjusts to the equilibrium thermodynamic state appropriate to the local macroscopic properties as this molecule moves through the flow field. From the continuum viewpoint, the flow is isentropic, and heat conduction and viscous diffusion and dissipation vanish from the continuum conservation relations.

The Chapman-Enskog theory attempts to solve the Boltzmann equation by considering a small perturbation of $\hat{f}$ from the equilibrium Maxwellian form. For small Knudsen numbers, the distribution function can be expanded in terms of Kn in the form of a power series:

$$\hat{f} = \hat{f}^{(0)} + Kn\,\hat{f}^{(1)} + Kn^2\,\hat{f}^{(2)} + \cdots \tag{15.6.59}$$

By substituting the above series in the Boltzmann equation (Equation 15.6.57) and equating terms of equal order, the following recurrent set of integral equations result:

$$\begin{aligned} \hat{J}\left(\hat{f}^{(0)},\hat{f}^{(0)}\right) &= 0\,, \\ \hat{J}\left(\hat{f}^{(0)},\hat{f}^{(1)}\right) &= \frac{\partial \hat{f}}{\partial \hat{t}} + \hat{\xi}_j\,\frac{\partial \hat{f}^{(0)}}{\partial \hat{x}_j} + \hat{F}_j\,\frac{\partial \hat{f}^{(0)}}{\partial \hat{\xi}_j}\,, \cdots \end{aligned} \tag{15.6.60}$$

The first integral is nonlinear and its solution is the local Maxwellian distribution, Equation 15.6.58. The distribution functions $\hat{f}^{(1)}$, $\hat{f}^{(2)}$, etc., each satisfies an inhomogeneous linear equation whose solution leads to the transport terms needed to close the continuum equations appropriate to the particular level of approximation. The continuum stress tensor and heat flux vector can be written in terms of the distribution function, which in turn can be specified in terms of the macroscopic velocity and temperature and their derivatives (Kogan 1973). The zeroth-order equation yields the Euler equations, the first-order equation results in the linear transport terms of the Navier-Stokes equations, the second-order equation gives the nonlinear transport terms of the Burnett equations, and so on. Keep in mind, however, that the Boltzmann equation as developed in this subsection is for a monatomic gas. This excludes the all-important air that is composed largely of diatomic nitrogen and oxygen.

As discussed earlier, the Navier-Stokes equations can and should be used up to a Knudsen number of 0.1. Beyond that, the transition flow regime commences ($0.1 < Kn < 10$). In this flow regime, the molecular mean free path for a gas becomes significant relative to a characteristic distance for important flow-property changes to take place. The Burnett equations can be used to obtain analytical/numerical solutions for at least a portion of the transition regime for a monatomic gas, although their complexity have precluded much results for realistic geometries (Agarwal et al. 1999). There is also a certain degree of uncertainty about the proper boundary conditions to use with the continuum Burnett equations, and experimental validation of the results have been very scarce. Additionally, as the gas flow further departs from equilibrium, the bulk viscosity ($= \lambda + \frac{2}{3}\mu$, where λ is the second coefficient of viscosity) is no longer zero, and the Stokes' hypothesis no longer holds (see Gad-el-Hak [1995] for an interesting summary of the issue of bulk viscosity).

In the transition regime, the molecularly based Boltzmann equation cannot easily be solved either, unless the nonlinear collision integral is simplified. So, clearly the transition regime is one of dire need of alternative methods of solution. MD simulations as mentioned earlier are not suited for dilute gases. The best approach for the transition regime right now is the direct simulation Monte Carlo (DSMC) method developed by Bird (1963, 1965, 1976, 1978, 1994) and briefly described below. Some recent reviews of DSMC include those by Muntz (1989), Cheng (1993), Cheng and Emmanuel (1995) and Oran et al. (1998). The mechanics as well as the history of the DSMC approach and its ancestors are well described in the book by Bird (1994).

Unlike molecular dynamics simulations, DSMC is a statistical computational approach to solving rarefied gas problems. Both approaches treat the gas as discrete particles. Subject to the dilute gas and molecular chaos assumptions, the direct simulation Monte Carlo method is valid for all ranges of Knudsen number, although it becomes quite expensive for $Kn < 0.1$. Fortunately, this is the continuum regime where the Navier-Stokes equations can be used analytically or computationally. DSMC is therefore ideal for the transition regime ($0.1 < Kn < 10$), where the Boltzmann equation is difficult to solve. The Monte Carlo method is, like its namesake, a random number strategy based directly on the physics of the individual molecular interactions. The idea is to track a large number of randomly selected, statistically representative particles, and to use their motions and interactions to modify their positions and states. The primary approximation of the direct simulation Monte Carlo method is to uncouple the molecular motions and the intermolecular collisions over small time intervals. A significant advantage of this approximation is that the amount of computation required is proportional to N, in contrast to N^2 for molecular dynamics simulations. In essence, particle motions are modeled deterministically while collisions are treated probabilistically, each simulated molecule representing a large number of actual molecules. Typical computer runs of DSMC in the 1990s involve tens of millions of intermolecular collisions and fluid-solid interactions.

The DSMC computation is started from some initial condition and followed in small time steps that can be related to physical time. Colliding pairs of molecules in a small geometric cell in physical space are randomly selected after each computational time step. Complex physics such as radiation, chemical reactions, and species concentrations can be included in the simulations without the necessity of nonequilibrium thermodynamic assumptions that commonly afflict nonequilibrium continuum-flow calculations. DSMC is more computationally intensive than classical continuum simulations, and should therefore be used only when the continuum approach is not feasible.

The DSMC technique is explicit and time marching, and therefore always produces unsteady flow simulations. For macroscopically steady flows, Monte Carlo simulation proceeds until a steady flow is established, within a desired accuracy, at sufficiently large time. The macroscopic flow quantities are then the time average of all values calculated after reaching the steady state. For macroscopically unsteady flows, ensemble averaging of many independent Monte Carlo simulations is carried out to obtain the final results within a prescribed statistical accuracy.

Liquid Flows

From the continuum point of view, liquids and gases are both fluids obeying the same equations of motion. For incompressible flows, for example, the Reynolds number is the primary dimensionless parameter that determines the nature of the flow field. True, water, for example, has density and viscosity that are, respectively, three and two orders of magnitude higher than those for air, but if the Reynolds number and geometry are matched, liquid and gas flows should be identical.[†] For MEMS applications, however, we anticipate the possibility of nonequilibrium flow conditions and the consequent invalidity of the Navier-Stokes equations and the no-slip boundary conditions. Such circumstances can best be researched using the molecular approach. This was discussed for gases earlier, and the corresponding arguments for liquids will be given in this subsection. The literature on non-Newtonian fluids in general and polymers in particular is vast (for example, the bibliographic survey by Nadolink and Haigh [1995]

[†] Barring phenomena unique to liquids such as cavitation, free surface flows, etc.

cites over 4900 references on polymer drag reduction alone) and provides a rich source of information on the molecular approach for liquid flows.

Solids, liquids, and gases are distinguished merely by the degree of proximity and the intensity of motions of their constituent molecules. In solids, the molecules are packed closely and confined, each hemmed in by its neighbors (Chapman and Cowling 1970). Only rarely would one solid molecule slip from its neighbors to join a new set. As the solid is heated, molecular motion becomes more violent and a slight thermal expansion takes place. At a certain temperature that depends on ambient pressure, sufficiently intense motion of the molecules enables them to pass freely from one set of neighbors to another. The molecules are no longer confined but are nevertheless still closely packed, and the substance is now considered a liquid. Further heating of the matter eventually releases the molecules altogether, allowing them to break the bonds of their mutual attractions. Unlike solids and liquids, the resulting gas expands to fill any volume available to it.

Unlike solids, both liquids and gases cannot resist finite shear force without continuous deformation; that is the definition of a fluid medium. In contrast to the reversible, elastic, static deformation of a solid, the continuous deformation of a fluid resulting from the application of a shear stress results in an irreversible work that eventually becomes random thermal motion of the molecules; that is viscous dissipation. There are around 25-million molecules of STP air in a one-micron cube. The same cube would contain around 34-billion molecules of water. So, liquid flows are continuum even in extremely small devices through which gas flows would not be continuum. The average distance between molecules in the gas example is one order of magnitude higher than the diameter of its molecules, while that for the liquid phase approaches the molecular diameter. As a result, liquids are almost incompressible. Their isothermal compressibility coefficient α and bulk expansion coefficient β are much smaller compared to those for gases. For water, for example, a hundred-fold increase in pressure leads to less than 0.5% decrease in volume. Sound speeds through liquids are also high relative to those for gases, and as a result most liquid flows are incompressible.[†] The exception is the propagation of ultra-high-frequency sound waves and cavitation phenomena.

The mechanism by which liquids transport mass, momentum, and energy must be very different from that for gases. In dilute gases, intermolecular forces play no role and the molecules spend most of their time in free flight between brief collisions, at which instances the molecules' direction and speed abruptly change. The random molecular motions are responsible for gaseous transport processes. In liquids, on the other hand, the molecules are closely packed though not fixed in one position. In essence, the liquid molecules are always in a collision state. Applying a shear force must create a velocity gradient so that the molecules move relative to one another, *ad infinitum* as long as the stress is applied. For liquids, momentum transport due to the random molecular motion is negligible compared to that due to the intermolecular forces. The straining between liquid molecules causes some to separate from their original neighbors, bringing them into the force field of new molecules. Across the plane of the shear stress, the sum of all intermolecular forces must, on the average, balance the imposed shear. Liquids at rest transmit only normal force, but when a velocity gradient occurs, the net intermolecular force would have a tangential component.

The incompressible Navier-Stokes equations describe liquid flows under most circumstances. Liquids, however, do not have a well-advanced molecular-based theory as that for dilute gases. The concept of mean free path is not useful for liquids, and the conditions under which a liquid flow fails to be in quasi-equilibrium state are not well defined. There is no Knudsen number for liquid flows to guide us through the maze. We do not know, from first principles, the conditions under which the no-slip boundary condition becomes inaccurate, or the point at which the stress–rate of strain relation or the heat flux–temperature gradient relation fails to be linear. Certain empirical observations indicate that those simple

---

[†] Note that we distinguish between a fluid and a flow being compressible/incompressible. For example, the *flow* of the highly compressible air can be either compressible or incompressible.

relations that we take for granted occasionally fail to accurately model liquid flows. For example, it has been shown in rheological studies (Loose and Hess, 1989) that non-Newtonian behavior commences when the strain rate approximately exceeds twice the molecular frequency-scale:

$$\dot{\gamma} = \frac{\partial u}{\partial y} \geq 2\,T^{-1} \qquad (15.6.61)$$

where the molecular time-scale T is given by

$$T = \left[\frac{m\,\sigma^2}{\varepsilon}\right]^{\frac{1}{2}} \qquad (15.6.62)$$

where m is the molecular mass, and σ and ε are the characteristic length- and energy-scale for the molecules, respectively. For ordinary liquids such as water, this time-scale is extremely small, and the threshold shear rate for the onset of non-Newtonian behavior is therefore extraordinarily high. For high-molecular-weight polymers, on the other hand, m and σ are both many orders of magnitude higher than their respective values for water, and the linear stress-strain relation breaks down at realistic values of the shear rate.

The moving contact line when a liquid spreads on a solid substrate is an example where slip flow must be allowed to avoid singular or unrealistic behavior in the Navier-Stokes solutions (Dussan and Davis 1974; Dussan 1976, 1979; Thompson and Robbins 1989). Other examples where slip-flow must be admitted include corner flows (Moffatt 1964; Koplik and Banavar 1995) and extrusion of polymer melts from capillary tubes (Pearson and Petrie 1968; Richardson 1973; Den 1990).

Existing experimental results of liquid flow in microdevices are contradictory. This is not surprising given the difficulty of such experiments and the lack of a guiding rational theory. Pfahler et al. (1990; 1991), Pfahler (1992), and Bau (1994) summarize the relevant literature. For small-length-scale flows, a phenomenological approach for analyzing the data is to define an *apparent* viscosity μ_a calculated so that if it were used in the traditional no-slip Navier-Stokes equations instead of the fluid viscosity μ, the results would be in agreement with experimental observations. Israelachvili (1986) and Gee et al. (1990) found that $\mu_a = \mu$ for thin-film flows as long as the film thickness exceeds 10 molecular layers (≈5 nm). For thinner films, μ_a depends on the number of molecular layers and can be as much as 10^5 times larger than μ. Chan and Horn's (1985) results are somewhat different: the apparent viscosity deviates from the fluid viscosity for films thinner than 50 nm.

In polar-liquid flows through capillaries, Migun and Prokhorenko (1987) report that μ_a increases for tubes smaller than 1 micron in diameter. In contrast, Debye and Cleland (1959) report μ_a smaller than μ for paraffin flow in porous glass with average pore size several times larger than the molecular length-scale. Experimenting with microchannels ranging in depths from 0.5 micron to 50 microns, Pfahler et al. (1991) found that μ_a is consistently smaller than μ for both liquid (isopropyl alcohol; silicone oil) and gas (nitrogen; helium) flows in microchannels. For liquids, the apparent viscosity decreases with decreasing channel depth. Other researchers using small capillaries report that μ_a is about the same as μ (Anderson and Quinn 1972; Tuckermann and Pease 1981, 1982; Tuckermann 1984; Guvenc 1985; Nakagawa et al. 1990).

Very recently, Sharp (2001) and Sharp et al. (2002) asserted that, despite the significant inconsistencies in the literature regarding liquid flows in microchannels, such flows are well predicted by macroscale continuum theory. A case can be made to the contrary, however, as will be seen at the end of this subsection, and the final verdict on this controversy is yet to come.

The above contradictory results point to the need for replacing phenomenological models by first-principles ones. The lack of molecular-based theory of liquids — despite extensive research by the rheology and polymer communities — leaves molecular dynamics simulations as the nearest weapon to first-principles arsenal. MD simulations offer a unique approach to checking the validity of the traditional continuum assumptions. However, as was pointed out earlier, such simulations are limited to exceedingly minute flow extent.

Thompson and Troian (1997) provide molecular dynamics simulations to quantify the slip-flow boundary condition dependence on shear rate. Recall the linear Navier boundary condition introduced earlier:

$$\Delta u\Big|_w = u_{fluid} - u_{wall} = L_s \frac{\partial u}{\partial y}\Big|_w \tag{15.6.63}$$

where

L_s = the constant slip length

$\frac{\partial u}{\partial y}\Big|_w$ = the strain rate computed at the wall.

The goal of Thompson and Troian's simulations was to determine the degree of slip at a solid-liquid interface as the interfacial parameters and the shear rate change. In their simulations, a simple liquid underwent planar shear in a Couette cell as shown in Figure 15.6.8. The typical cell measured 12.51 × 7.22 × h, in units of molecular length-scale σ, where the channel depth h varied in the range of 16.71σ to 24.57σ, and the corresponding number of molecules simulated ranged from 1152 to 1728. The liquid is treated as an isothermal ensemble of spherical molecules. A shifted Lennard-Jones 6–12 potential is

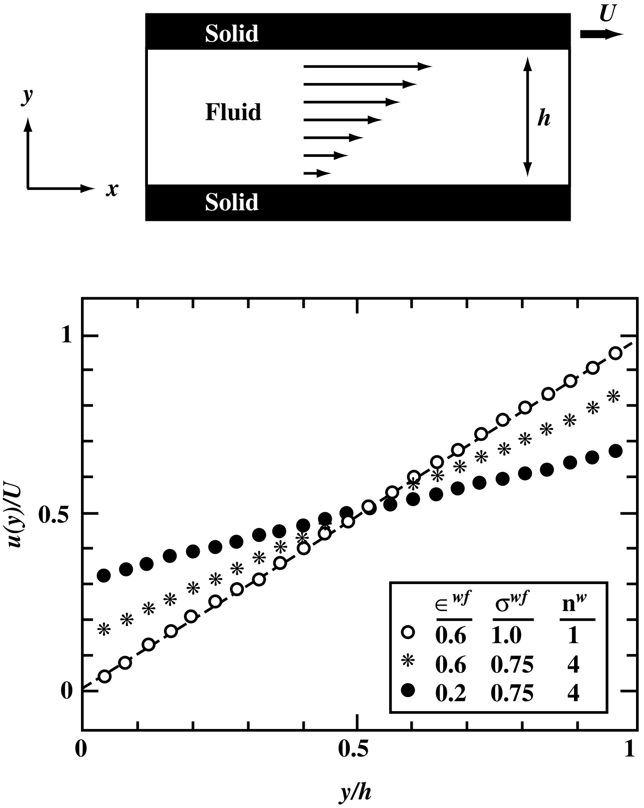

FIGURE 15.6.8 Velocity profiles in a Couette flow geometry at different interfacial parameters. All three profiles are for $U = \sigma T^{-1}$, and $h = 24.57\ \sigma$. The dashed line is the no-slip Couette-flow solution. From Thompson and Troian (1997).

used to model intermolecular interactions, with energy- and length-scales ε and σ, and cutoff distance $r_c = 2.2\sigma$:

$$V(r) = 4\,\varepsilon\left[\left(\frac{r}{\sigma}\right)^{-12} - \left(\frac{r}{\sigma}\right)^{-6} - \left(\frac{r_c}{\sigma}\right)^{-12} + \left(\frac{r_c}{\sigma}\right)^{-6}\right] \tag{15.6.64}$$

The truncated potential is set to zero for $r > r_c$.

The fluid-solid interaction is also modeled with a truncated Lennard-Jones potential, with energy- and length-scales ε^{wf} and σ^{wf}, and cutoff distance r_c. The equilibrium state of the fluid is a well-defined liquid phase characterized by number density $n = 0.81\sigma^{-3}$ and temperature $T = 1.1\ \varepsilon/k$, where k is the Boltzmann constant.

The steady state velocity profiles resulting from Thompson and Troian's (1997) MD simulations are depicted in Figure 15.6.8 for different values of the interfacial parameters ε^{wf}, σ^{wf} and n^w. Those parameters, shown in units of the corresponding fluid parameters ε, σ, and n, characterize, respectively, the strength of the liquid-solid coupling, the thermal roughness of the interface, and the commensurability of wall and liquid densities. The macroscopic velocity profiles recover the expected flow behavior from continuum hydrodynamics with boundary conditions involving varying degrees of slip. Note that when slip exists, the shear rate $\dot{\gamma}$ no longer equals U/h. The degree of slip increases (i.e., the amount of momentum transfer at the wall-fluid interface decreases) as the relative wall density n^w increases or the strength of the wall-fluid coupling σ^{wf} decreases; in other words when the relative surface energy corrugation of the wall decreases. Conversely, the corrugation is maximized when the wall and fluid densities are commensurate and the strength of the wall-fluid coupling is large. In this case, the liquid *feels* the corrugations in the surface energy of the solid owing to the atomic close-packing. Consequently, there is efficient momentum transfer and the no-slip condition applies, or in extreme cases, a "stick" boundary condition takes hold.

Variations of the slip length L_s and viscosity μ as functions of shear rate $\dot{\gamma}$ are shown in parts (a) and (b) of Figure 15.6.9, for five different sets of interfacial parameters. For Couette flow, the slip length is computed from its definition, $\Delta u|_w / \dot{\gamma} = (U/\dot{\gamma} - h)/2$. The slip length, viscosity, and shear rate are normalized in the figure using the respective molecular scales for length σ, viscosity $\varepsilon\ T\ \sigma^{-3}$, and inverse time T^{-1}. The viscosity of the fluid is constant over the entire range of shear rates (Figure 15.6.9b), indicating Newtonian behavior. As indicated earlier, non-Newtonian behavior is expected for $\dot{\gamma} \geq 2\,T^{-1}$, well above the shear rates used in Thompson and Troian's simulations.

At low shear rates, the slip length behavior is consistent with the Navier model, in other words, is independent of the shear rate. Its limiting value L_s^o ranges from 0 to ~17σ for the range of interfacial parameters chosen (Figure 15.6.9a). In general, the amount of slip increases with decreasing surface energy corrugation. Most interestingly, at high shear rates the Navier condition breaks down as the slip length increases rapidly with $\dot{\gamma}$. The critical shear-rate value for the slip length to diverge, $\dot{\gamma}_c$, decreases as the surface energy corrugation decreases. Surprisingly, the boundary condition is nonlinear even though the liquid is still Newtonian. In dilute gases, the linear slip condition and the Navier-Stokes equations, with their linear stress-strain relation, are both valid to the same order of approximation in Knudsen number. In other words, deviation from linearity is expected to take place at the same value of $Kn = 0.1$. In liquids, in contrast, the slip length appears to become nonlinear and to diverge at a critical value of shear rate well below the shear rate at which the linear stress-strain relation fails. Moreover, the boundary condition deviation from linearity is not gradual but is rather catastrophic. The critical value of shear rate $\dot{\gamma}_c$ signals the point at which the solid can no longer impart momentum to the liquid. This means that the same liquid molecules sheared against different substrates will experience varying amounts of slip, and vice versa.

Based on the above results, Thompson and Troian (1997) suggest a universal boundary condition at a solid-liquid interface. Scaling the slip length L_s by its asymptotic limiting value L_s^o and the shear rate $\dot{\gamma}$ by its critical value $\dot{\gamma}_c$, collapses the data in the single curve shown in Figure 15.6.10. The data points are well described by the relation

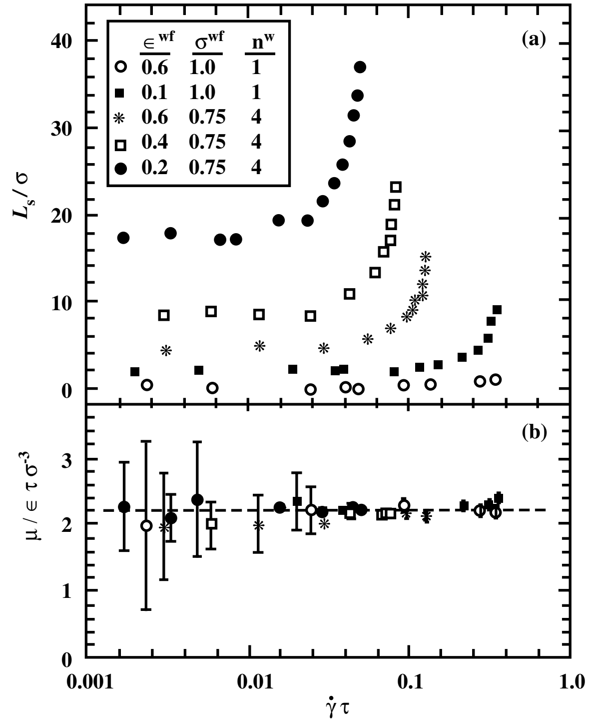

FIGURE 15.6.9 Variation of slip length and viscosity as functions of shear rate. From Thompson and Troian (1997).

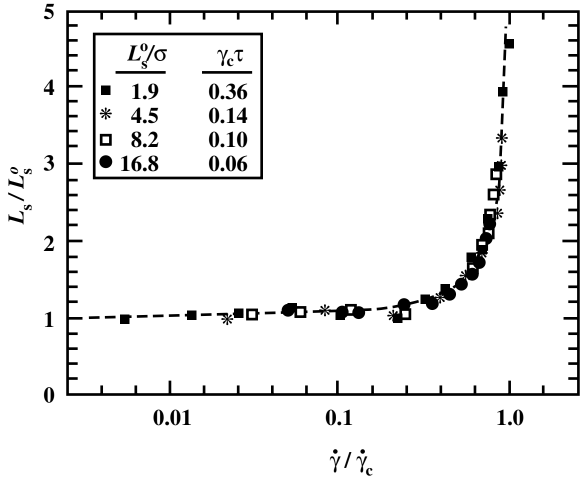

FIGURE 15.6.10 Universal relation of slip length as a function of shear rate. From Thompson and Troian (1997).

$$L_s = L_s^o\left[1 - \frac{\dot\gamma}{\dot\gamma_c}\right]^{-\frac{1}{2}} \tag{15.6.65}$$

The nonlinear behavior close to a critical shear rate suggests that the boundary condition can significantly affect flow behavior at macroscopic distances from the wall. Experiments with polymers confirm this observation (Atwood and Schowalter 1989). The rapid change in the slip length suggests that for flows in the vicinity of $\dot{\gamma}_c$, small changes in surface properties can lead to large fluctuations in the apparent boundary condition. Thompson and Troian (1997) conclude that the Navier slip condition is but the low-shear-rate limit of a more generalized universal relationship that is nonlinear and divergent. Their relation provides a mechanism for relieving the stress singularity in spreading contact lines and corner flows, as it naturally allows for varying degrees of slip on approach to regions of higher rate of strain.

To place the above results in physical terms, consider water[†] at a temperature of $T = 288$ K. The energy-scale in the Lennard-Jones potential is then $\varepsilon = 3.62 \times 10^{-21}$ J. For water, $m = 2.99 \times 10^{-26}$ kg, $\sigma = 2.89 \times 10^{-10}$ m, and at standard temperature $n = 3.35 \times 10^{28}$ molecules/m^3. The molecular time-scale can thus be computed, $T = [m\sigma^2/\varepsilon]^{1/2} = 8.31 \times 10^{-13}$ s. For the third case depicted in Figure 15.6.10 (the open squares), $\dot{\gamma}_c\, T = 0.1$, and the critical shear rate at which the slip condition diverges is thus $\dot{\gamma}_c = 1.2 \times 10^{11}\,\mathrm{s}^{-1}$. Such an enormous rate of strain[††] may be found in extremely small devices having extremely high speeds. On the other hand, the conditions to achieve a measurable slip of 17σ (the solid circles in Figure 15.6.9) are not difficult to encounter in microdevices: density of solid four times that of liquid, and the energy-scale for wall-fluid interaction that is one fifth of the energy-scale for liquid.

The limiting value of slip length is independent of the shear rate and can be computed for water as $L_s^o = 17\sigma = 4.91 \times 10^{-9}$ m. Consider a water microbearing having a shaft diameter of 100 μm and rotation rate of 20,000 rpm and a minimum gap of $h = 1$ μm. In this case, $U = 0.1$ m/s and the no-slip shear rate is $U/h = 10^5\,\mathrm{s}^{-1}$. When slip occurs at the limiting value just computed, the shear rate and the wall slip-velocity are computed as follows:

$$\dot{\gamma} = \frac{U}{h + 2\,L_s^o} = 9.90 \times 10^4\ \mathrm{s}^{-1} \tag{15.6.66}$$

$$\Delta u\big|_w = \dot{\gamma}\, L_s = 4.87 \times 10^{-4}\ \mathrm{m/s} \tag{15.6.67}$$

As a result of the Navier slip, the shear rate is reduced by 1% from its no-slip value, and the slip velocity at the wall is about 0.5% of U, small but not insignificant.

Surface Phenomena

The surface-to-volume ratio for a machine with a characteristic length of 1 m is 1 m^{-1}, while that for a MEMS device having a size of 1 μm is 10^6 m^{-1}. The million-fold increase in surface area relative to the mass of the minute device substantially affects the transport of mass, momentum, and energy through the surface. Obviously surface effects dominate in small devices. The surface boundary conditions in MEMS flows have already been discussed earlier. In microdevices, it has been shown that it is possible to have measurable slip-velocity and temperature jump at a solid-fluid interface. In this subsection, we illustrate other ramifications of the large surface-to-volume ratio unique to MEMS, and provide a molecular viewpoint to surface forces.

In microdevices, both radiative and convective heat loss/gain are enhanced by the huge surface-to-volume ratio. Consider a device having a characteristic length L_s. Use of the lumped capacitance method to compute the rate of convective heat transfer, for example, is justified if the Biot number ($\equiv hL_s/\kappa_s$, where h is the convective heat transfer coefficient of the fluid and κ_s is the thermal conductivity of the solid) is less than 0.1. Small L_s implies a small Biot number and a nearly uniform temperature within the solid. Within this approximation, the rate at which heat is lost to the surrounding fluid is given by

---

[†] Water molecules are complex ones, forming directional, short-range covalent bonds, thus requiring a more complex potential than the Lennard-Jones to describe the intermolecular interactions. For the purpose of the qualitative example described here, however, we use the computational results of Thompson and Troian (1997), who employed the L-J potential.

[††] Note however that $\dot{\gamma}_c$ for high-molecular-weight polymers would be many orders of magnitude smaller than the value developed here for water.

$$\rho_s\, L_s^3\, c_s\, \frac{dT}{dt} = -h\, L_s^2\, \left(T_s - T_\infty\right) \qquad (15.6.68)$$

where ρ_s and c_s are respectively the density and specific heat of the solid, T_s is its (uniform) temperature, and T_∞ is the ambient fluid temperature. Solution of the above equation is trivial, and the temperature of a hot surface drops exponentially with time from an initial temperature T_i:

$$\frac{T_s(t) - T_\infty}{T_i - T_\infty} = \exp\left[-\frac{t}{T}\right] \qquad (15.6.69)$$

where the time constant T is given by

$$T = \frac{\rho_s\, L_s^3\, c_s}{h\, L_s^2} \qquad (15.6.70)$$

For small devices, the time it takes the solid to cool down is proportionally small. Clearly, the million-fold increase in surface-to-volume ratio implies a proportional increase in the rate at which heat escapes. Identical scaling arguments can be made regarding mass transfer.

Another effect of the diminished scale is the increased importance of surface forces and the waning importance of body forces. Based on biological studies, Went (1968) concludes that the demarcation length-scale is around 1 mm. Below that, surface forces dominate over gravitational forces. A 10-mm piece of paper will fall down when gently placed on a smooth, vertical wall, while a 0.1-mm piece will stick. Try it! *Stiction* is a major problem in MEMS applications. Certain structures such as long, thin polysilicon beams and large, thin comb drives have a propensity to stick to their substrates and thus fail to perform as designed (Mastrangelo and Hsu 1992; Tang et al. 1989).

Conventional dry friction between two solids in relative motion is proportional to the normal force, which is usually a component of the moving device weight. The friction is independent of the contact-surface area because the van der Waals cohesive forces are negligible relative to the weight of the macroscopic device. In MEMS applications, the cohesive intermolecular forces between two surfaces are significant and the stiction is independent of the device mass but is proportional to its surface area. The first micromotor did not move — despite large electric current through it — until the contact area between the 100-micron rotor and the substrate was reduced significantly by placing dimples on the rotor's surface (Fan et al. 1988, 1989; Tai and Muller 1989).

One last example of surface effects that to my knowledge has not been investigated for microflows is the adsorbed layer in gaseous wall-bounded flows. It is well known (Brunauer 1944; Lighthill 1963) that when a gas flows in a duct, the gas molecules are attracted to the solid surface by the van der Waals and other forces of cohesion. The potential energy of the gas molecules drops on reaching the surface. The adsorbed layer partakes the thermal vibrations of the solid, and the gas molecules can only escape when their energy exceeds the potential energy minimum. In equilibrium, at least part of the solid would be covered by a monomolecular layer of adsorbed gas molecules. Molecular species with significant partial pressure — relative to their vapor pressure — may locally form layers two or more molecules thick. Consider, for example, the flow of a mixture of dry air and water vapor at STP. The energy of adsorption of water is much larger than that for nitrogen and oxygen, making it more difficult for water molecules to escape the potential energy trap. It follows that the lifetime of water molecules in the adsorbed layer significantly exceeds that for the air molecules (by 60,000 folds, in fact), and as a result, the thin surface layer would be mostly water. For example, if the proportion of water vapor in the ambient air is 1:1000 (i.e., very low humidity level), the ratio of water to air in the adsorbed layer would be 60:1. Microscopic roughness of the solid surface causes partial condensation of the water along portions having sufficiently strong concave curvature. So, surfaces exposed to nondry airflows are mainly liquid water surfaces. In most applications, this thin adsorbed layer has little effect on the flow dynamics, despite the fact that the density and viscosity of liquid water are far greater than those for air. In MEMS applications, however, the layer thickness may not be an insignificant portion of the characteristic flow dimension and the water layer may have a measurable effect on the gas flow. A hybrid approach of molecular dynamics and continuum flow simulations or MD-Monte Carlo simulations may be used to investigate this issue.

It should be noted that recently, Majumdar and Mezic (1998, 1999) have studied the stability and rupture into droplets of thin liquid films on solid surfaces. They point out that the free energy of a liquid film consists of a surface tension component as well as highly nonlinear volumetric intermolecular forces resulting from van der Waals, electrostatic, hydration, and elastic strain interactions. For water films on hydrophilic surfaces such as silica and mica, Majumdar and Mezic (1998) estimate the equilibrium film thickness to be about 0.5 nm (2 monolayers) for a wide range of ambient-air relative humidities. The equilibrium thickness grows very sharply, however, as the relative humidity approaches 100%.

Majumdar and Mezic's (1998, 1999) results open many questions. What are the stability characteristics of their water film in the presence of airflow above it? Would this water film affect the accommodation coefficient for microduct air flow? In a modern Winchester-type hard disk, the drive mechanism has a read/write head that floats 50 nm above the surface of the spinning platter. The head and platter together with the air layer in between form a slider bearing. Would the computer performance be affected adversely by the high relative humidity on a particular day when the adsorbed water film is no longer "thin"? If a microduct hauls liquid water, would the water film adsorbed by the solid walls influence the effective viscosity of the water flow? Electrostatic forces can extend to almost 1 micron (the Debye length), and that length is known to be highly pH-dependent. Would the water flow be influenced by the surface and liquid chemistry? Would this explain the contradictory experimental results of liquid flows in microducts discussed earlier?

The few examples above illustrate the importance of surface effects in small devices. From the continuum viewpoint, forces at a solid-fluid interface are the limit of pressure and viscous forces acting on a parallel elementary area displaced into the fluid, when the displacement distance is allowed to tend to zero. From the molecular point of view, all macroscopic surface forces are ultimately traced to intermolecular forces, which subject is extensively covered in the book by Israelachvilli (1991) and references therein. Here we provide a very brief introduction to the molecular viewpoint. The four forces in nature are (1) the strong and (2) weak forces describing the interactions between neutrons, protons, electrons, etc.; (3) the electromagnetic forces between atoms and molecules; and (4) gravitational forces between masses. The range of action of the first two forces is around 10^{-5} nm, and hence neither concerns us overly in MEMS applications. The electromagnetic forces are effective over a much larger though still small distance on the order of the interatomic separations (0.1–0.2 nm). Effects over longer range — several orders of magnitude longer — can and do arise from the short-range intermolecular forces. For example, the rise of liquid column in capillaries and the action of detergent molecules in removing oily dirt from fabric are the result of intermolecular interactions. Gravitational forces decay with the distance to second power, whereas intermolecular forces decay much quicker, typically with the seventh power. Cohesive forces are therefore negligible once the distance between molecules exceeds few molecular diameters, while massive bodies like stars and planets are still strongly interacting, via gravity, over astronomical distances.

Electromagnetic forces are the source of all intermolecular interactions and the cohesive forces holding atoms and molecules together in solids and liquids. They can be classified into (1) purely electrostatic arising from the Coulomb force between charges, interactions between charges, permanent dipoles, quadrupoles, etc.; (2) polarization forces arising from the dipole moments induced in atoms and molecules by the electric field of nearby charges and permanent dipoles; and (3) quantum mechanical forces that give rise to covalent or chemical bonding and to repulsive steric or exchange interactions that balance the attractive forces at very short distances. The Hellman-Feynman theorem of quantum mechanics states that once the spatial distribution of the electron clouds has been determined by solving the appropriate Schrödinger equation, intermolecular forces may be calculated on the basis of classical electrostatics, in effect reducing all intermolecular forces to Coulombic forces. Note, however, that intermolecular forces exist even when the molecules are totally neutral. Solutions of the Schrödinger equation for general atoms and molecules are not easy, of course, and alternative modeling are sought to represent intermolecular forces. The van der Waals attractive forces are usually represented with a potential that varies as the inverse-sixth power of distance, whereas the repulsive forces are represented with either a power or an exponential potential.

A commonly used potential between two molecules is the generalized Lennard-Jones (L-J 6–12) pair potential given by

$$V_{ij}(r) = 4\,\varepsilon \left[c_{ij} \left(\frac{r}{\sigma} \right)^{-12} - d_{ij} \left(\frac{r}{\sigma} \right)^{-6} \right] \tag{15.6.71}$$

where V_{ij} is the potential energy between two particles i and j, r is the distance between the two molecules; ε and σ are characteristic energy- and length-scales, respectively; and c_{ij} and d_{ij} are parameters to be chosen for the particular fluid and solid combinations under consideration. The first term in the right-hand side is the strong repulsive force that is felt when two molecules are at extremely close range comparable to the molecular length-scale. That short-range repulsion prevents overlap of the molecules in physical space. The second term is the weaker, van der Waals attractive force that commences when the molecules are sufficiently close (several times σ). That negative part of the potential represents the attractive polarization interaction of neutral, spherically symmetric particles. The power of 6 associated with this term is derivable from quantum mechanics considerations, while the power of the repulsive part of the potential is found empirically. The Lennard-Jones potential is zero at very large distances, has a weak negative peak at r slightly larger than σ, is zero at $r = \sigma$, and is infinite as $r \to 0$.

The force field resulting from this potential is given by

$$F_{ij}(r) = -\frac{\partial V_{ij}}{\partial r} = \frac{48\,\varepsilon}{\sigma} \left[c_{ij} \left(\frac{r}{\sigma} \right)^{-13} - \frac{d_{ij}}{2} \left(\frac{r}{\sigma} \right)^{-7} \right] \tag{15.6.72}$$

A typical L-J 6–12 potential and force field are shown in Figure 15.6.11, for $c = d = 1$. The minimum potential $V_{\min} = -\varepsilon$, corresponds to the equilibrium position (zero force) and occurs at $r = 1.12\,\sigma$. The attractive van der Waals contribution to the minimum potential is -2ε, while the repulsive energy contribution is $+\varepsilon$. Thus the inverse 12th-power repulsive force term decreases the strength of the binding energy at equilibrium by 50%.

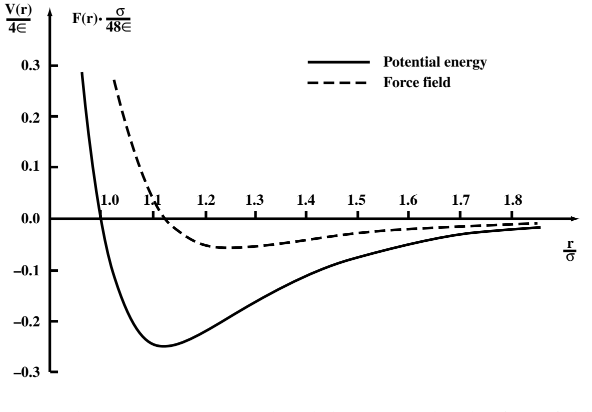

FIGURE 15.6.11 Typical Lennard-Jones 6–12 potential and the intermolecular force field resulting from it. Only a small portion of the potential function is shown for clarity.

The L-J potential is commonly used in molecular dynamics simulations to model intermolecular interactions between dense gas or liquid molecules and between fluid and solid molecules. As mentioned earlier, such potential is not accurate for complex substances, such as water, whose molecules form directional covalent bonds. As a result, MD simulations for water are much more involved.

Parting Remarks

The 40-year-old vision of Richard Feynman of building minute machines is now a reality. Microelectromechanical systems have witnessed explosive growth during the last decade and are finding increased applications in a variety of industrial and medical fields. The physics of fluid flows in microdevices has been explored in this subsection. While we now know considerably more than we did just few years ago, much physics remains to be explored so that rational tools can be developed for the design, fabrication, and operation of MEMS devices.

The traditional Navier-Stokes model of fluid flows with no-slip boundary conditions works only for a certain range of the governing parameters. This model basically demands two conditions:

1. The fluid is a continuum, which is almost always satisfied as there are usually more than 1 million molecules in the smallest volume in which appreciable macroscopic changes take place. This is the molecular chaos restriction.
2. The flow is not too far from thermodynamic equilibrium, which is satisfied if there is sufficient number of molecular encounters during a time period small compared to the smallest time-scale for flow changes. During this time period the average molecule would have moved a small distance compared to the smallest flow length-scale.

For gases, the Knudsen number determines the degree of rarefaction and the applicability of traditional flow models. As $Kn \to 0$, the time- and length-scales of molecular encounters are small compared to those for the flow, and the velocity distribution of each element of the fluid instantaneously adjusts to the equilibrium thermodynamic state appropriate to the local macroscopic properties as this molecule moves through the flow field. From the continuum viewpoint, the flow is isentropic, and heat conduction and viscous diffusion and dissipation vanish from the continuum conservation relations, leading to the Euler equations of motion. At small but finite Kn, the Navier-Stokes equations describe near-equilibrium, continuum flows.

Slip flow must be taken into account for $Kn > 0.001$. The slip boundary condition is at first linear in Knudsen number, then nonlinear effects take over beyond a Knudsen number of 0.1. At the same transition regime, that is, $0.1 < Kn < 10$, the linear stress-rate of strain and heat flux–temperature gradient relations — needed to close the Navier-Stokes equations — also break down, and alternative continuum equations (e.g., Burnett or higher-order equations) or molecular-based models must be invoked. In the transition regime, provided that the dilute gas and molecular chaos assumptions hold, solutions to the difficult Boltzmann equation are sought, but physical simulations such as Monte Carlo methods are more readily executed in this range of Knudsen number. In the free-molecule flow regime, that is, $Kn > 10$, the nonlinear collision integral is negligible and the Boltzmann equation is drastically simplified. Analytical solutions are possible in this case for simple geometries, and numerical integration of the Boltzmann equation is straightforward for arbitrary geometries, provided that the surface-reflection characteristics are accurately modeled.

Gaseous flows are often compressible in microdevices even at low Mach numbers. Viscous effects can cause sufficient pressure drop and density changes for the flow to be treated as compressible. In a long, constant-area microduct, all Knudsen number regimes may be encountered and the degree of rarefaction increases along the tube. The pressure drop is nonlinear, and the Mach number increases downstream, limited only by choked-flow condition.

Similar deviation and breakdown of the traditional Navier-Stokes equations occur for liquids as well, but there the situation is more murky. Existing experiments are contradictory. There is no kinetic theory of liquids, and first-principles prediction methods are scarce. Molecular dynamics simulations can be used, but they are limited to extremely small flow extents. Nevertheless, measurable slip is predicted from MD simulations at realistic shear rates in microdevices.

Much nontraditional physics is still to be learned and many exciting applications of microdevices are yet to be discovered. The future is bright for this emerging field of science and technology. Richard Feynman was right about the possibility of building mite-size machines, but was somewhat cautious in forecasting that such machines, while they "would be fun to make," may or may not be useful.

References

Agarwal, R., Yun, K., and Balakrishnan, R. (1999) Beyond Navier Stokes: Burnett Equations for Flow Simulations in Continuum–Transition Regime, AIAA Paper No. 99-3580, Reston, VA.

Alder, B.J., and Wainwright, T.E. (1957) Studies in molecular dynamics, *J. Chemical Phys.* 27, 1208–1209.

Alder, B.J., and Wainwright, T.E. (1958) Molecular Dynamics by Electronic Computers, in *Transport Processes in Statistical Mechanics*, I. Prigogine, Ed., 97–131, Interscience, New York.

Alder, B.J., and Wainwright, T.E. (1970) Decay of the velocity auto-correlation function, *Phy. Rev. A* 1, 18–21.

Allen, M.P., and Tildesley, D.J. (1987) *Computer Simulation of Liquids*, Clarendon Press, Oxford.

Anderson, J.L., and Quinn, J.A. (1972) Ionic mobility in microcapillaries, *J. Chemical Phys.* 27, 1208–1209.

Arkilic, E.B. (1997) Measurement of the Mass Flow and Tangential Momentum Accommodation Coefficient in Silicon Micromachined Channels, PhD thesis, Massachusetts Institute of Technology, Cambridge, MA.

Arkilic, E.B., Schmidt, M.A., and Breuer, K.S. (1995) Slip Flow in Microchannels, in *Rarefied Gas Dynamics* 19, ed. J. Harvey and G. Lord, Oxford University Press, Oxford.

Arkilic, E.B., Schmidt, M.A., and Breuer, K.S. (1997a) Gaseous slip flow in long microchannels, *J. MEMS* 6, 167–178.

Arkilic, E.B., Schmidt, M.A., and Breuer, K.S. (1997b) TMAC Measurement in Silicon Micromachined Channels, in *Rarefied Gas Dynamics* 20, C. Shen, Ed., 6 pages, Beijing University Press, Beijing, China.

Atwood, B.T., and Schowalter, W.R. (1989) Measurements of slip at the wall during flow of high-density polyethylene through a rectangular conduit, *Rheologica Acta* 28, 134–146.

Bau, H.H. (1994) Transport processes associated with micro-devices, *Thermal Sci. Eng.* 2, 172–178.

Beskok, A. (1994) Simulation of Heat and Momentum Transfer in Complex Micro-Geometries, MSc Thesis, Princeton University, Princeton, NJ.

Beskok, A. (1996) Simulations and Models of Gas Flows in Microgeometries, PhD thesis, Princeton University, Princeton, NJ.

Beskok, A., and Karniadakis, G.E. (1994) Simulation of heat and momentum transfer in complex microgeometries, *J. Thermophys. & Heat Transfer* 8, 355–370.

Beskok, A., and Karniadakis, G.E. (1999) A model for flows in channels, pipes and ducts at micro and nano scales, *Microscale Thermophys. Eng.* 3, 43–77.

Beskok, A., Karniadakis, G.E., and Trimmer, W. (1996) Rarefaction and compressibility effects in gas microflows, *J. Fluids Eng.* 118, 448–456.

Bhatnagar, P.L., Gross, E.P., and Krook, M. (1954) A model for collision processes in gases. I. Small amplitude processes in charged and neutral one-component systems, *Phys. Rev.* 94, 511–524.

Bird, G.A. (1963) Approach to translational equilibrium in a rigid sphere gas, *Phys. Fluids* 6, 1518–1519.

Bird, G.A. (1965) The velocity distribution function within a shock wave, *J. Fluid Mech.* 30, 479–487.

Bird, G.A. (1976) *Molecular Gas Dynamics*, Clarendon Press, Oxford.

Bird, G.A. (1978) Monte Carlo simulation of gas flows, *Annu. Rev. Fluid Mech.* 10, 11–31.

Bird, G.A. (1994) *Molecular Gas Dynamics and the Direct Simulation of Gas Flows*, Clarendon Press, Oxford.

Brunauer, S. (1944) *Physical Adsorption of Gases and Vapours*, Oxford University Press, Oxford.

Cercignani, C. (1988) *The Boltzmann Equation and Its Applications*, Springer-Verlag, Berlin.

Cercignani, C. (2000) *Rarefied Gas Dynamics: From Basic Concepts to Actual Calculations*, Cambridge University Press, London.

Chan, D.Y.C., and Horn, R.G. (1985) Drainage of thin liquid films, *J. Chemical Phys.* 83, 5311–5324.

Chapman, S., and Cowling, T.G. (1970) *The Mathematical Theory of Non-Uniform Gases*, 3rd ed., Cambridge University Press, Cambridge, Great Britain.

Cheng, H.K. (1993) Perspectives on hypersonic viscous flow research, *Annu. Rev. Fluid Mech.* 25, 455–484.

Cheng, H.K., and Emmanuel, G. (1995) Perspectives on hypersonic nonequilibrium flow, *AIAA J.* 33, 385–400.

Ciccotti, G., and Hoover, W.G., eds. (1986) *Molecular Dynamics Simulation of Statistical Mechanics Systems*, North Holland, Amsterdam, the Netherlands.

Debye, P., and Cleland, R.L. (1959) Flow of liquid hydrocarbons in porous vycor, *J. Appl. Phys.* 30, 843–849.

Den, L.M. (1990) Issues in viscoelastic fluid mechanics, *Annu. Rev. Fluid Mech.* 22, 13–34.

Dussan, E.B. (1976) The moving contact line: the slip boundary condition, *J. Fluid Mech.* 77, 665–684.

Dussan, E.B. (1979) On the spreading of liquids on solid surfaces: static and dynamic contact lines, *Annu. Rev. Fluid Mech.* 11, 371–400.

Dussan, E.B., and Davis, S.H. (1974) On the motion of fluid-fluid interface along a solid surface, *J. Fluid Mech.* 65, 71–95.

Fan, L.-S., Tai, Y.-C., and Muller, R.S. (1988) Integrated movable micromechanical structures for sensors and actuators, in *IEEE Transactions on Electronic Devices*, vol. 35, 724–730.

Fan, L.-S., Tai, Y.-C., and Muller, R.S. (1989) IC-processed electrostatic micromotors, *Sensors & Actuators* 20, 41–47.

Gad-el-Hak, M. (1995) Questions in fluid mechanics: Stokes' hypothesis for a Newtonian, isotropic fluid, *J. Fluids Eng.* 117, 3–5.

Gad-el-Hak, M. (1999) The fluid mechanics of microdevices — the Freeman Scholar lecture, *J. Fluids Eng.* 121, 5–33.

Gad-el-Hak, M. (2000) *Flow Control: Passive, Active, and Reactive Flow Management*, Cambridge University Press, London.

Gad-el-Hak, M., ed. (2002) *The MEMS Handbook,* CRC Press, Boca Raton, FL.

Gee, M.L., McGuiggan, P.M., Israelachvili, J.N., and Homola, A.M. (1990) Liquid to solidlike transitions of molecularly thin films under shear, *J. Chemical Phys.* 93, 1895–1906.

Guvenc, M.G. (1985) V-Groove Capillary for Low Flow Control and Measurement, in *Micromachining and Micropackaging of Transducers*, C.D. Fung, P.W. Cheung, W.H. Ko, and D.G. Fleming, Eds., 215–223, Elsevier, Amsterdam, the Netherlands.

Haile, J.M. (1993) *Molecular Dynamics Simulation: Elementary Methods*, John Wiley & Sons, New York.

Harley, J.C., Huang, Y., Bau, H.H., and Zemel, J.N. (1995) Gas flow in micro-channels, *J. Fluid Mech.* 284, 257–274.

Hirschfelder, J.O., Curtiss, C.F., and Bird, R.B. (1954) *Molecular Theory of Gases and Liquids*, John Wiley & Sons, New York.

Israelachvili, J.N. (1986) Measurement of the viscosity of liquids in very thin films, *J. Colloid Interface Sci.* 110, 263–271.

Israelachvili, J.N. (1991) *Intermolecular and Surface Forces*, 2nd ed., Academic Press, New York.

Karniadakis, G.Em, and Beskok, A. (2002) *Micro Flows: Fundamentals and Simulation,* Springer-Verlag, New York.

Kennard, E.H. (1938) *Kinetic Theory of Gases*, McGraw-Hill, New York.

Knight, J. (1999) Dust mite's dilemma, *New Scientist* 162, no. 2180, 29 May, 40–43.

Knudsen, M. (1909) Die Gesetze der Molekularströmung und der inneren Reibungsströmung der Gase durch Röhren, *Annalen der Physik* 28, 75–130.

Kogan, M.N. (1969) *Rarefied Gas Dynamics*, Nauka, Moscow. Translated from Russian, L. Trilling, Ed., Plenum, New York.

Kogan, M.N. (1973) Molecular Gas Dynamics, *Annu. Rev. Fluid Mech.* 5, 383–404.

Koplik, J., and Banavar, J.R. (1995) Continuum deductions from molecular hydroynamics, *Annu. Rev. Fluid Mech.* 27, 257–292.

Kovacs, G.T.A. (1998) *Micromachined Transducers Sourcebook*, McGraw-Hill, New York.

Lighthill, M.J. (1963) Introduction. Real and Ideal Fluids, in *Laminar Boundary Layers*, ed. L. Rosenhead, 1–45, Clarendon Press, Oxford.

Liu, J., Tai, Y.C., Lee, J., Pong, K.C., Zohar, Y., and Ho, C.M. (1993) In-situ monitoring and universal modeling of sacrificial psg etching using hydrofluoric acid, in *Proc. IEEE Micro Electro Mechanical Systems '93*, 71–76, IEEE, New York.

Liu, J., Tai, Y.C., Pong, K., and Ho, C.M. (1995) MEMS for pressure distribution studies of gaseous flows in microchannels, in *Proc. IEEE Micro Electro Mechanical Systems '95*, 209–215, IEEE, New York.

Loeb, L.B. (1961) *The Kinetic Theory of Gases*, 3rd ed., Dover, New York.

Löfdahl, L., and Gad-el-Hak, M. (1999) MEMS applications in turbulence and flow control, *Prog. Aero. Sciences* 35, 101–203.

Loose, W., and Hess, S. (1989) Rheology of dense fluids via nonequilibrium molecular hydrodynamics: shear thinning and ordering transition, *Rheologica Acta* 28, 91–101.

Madou, M. (2002) *Fundamentals of Microfabrication*, 2nd ed., CRC Press, Boca Raton, FL.

Majumdar, A., and Mezic, I. (1998) Stability regimes of thin liquid films, *Microscale Thermophys. Eng.* 2, 203–213.

Majumdar, A., and Mezic, I. (1999) Instability of ultra-thin water films and the mechanism of droplet formation on hydrophilic surfaces, in *Proc. ASME–JSME Thermal Engineering and Solar Energy Joint Conference*, San Diego, CA, 15–19 March. Also to appear in *J. Heat Transfer.*

Mastrangelo, C., and Hsu, C.H. (1992) A simple experimental technique for the measurement of the work of adhesion of microstructures, in *Technical Digest IEEE Solid-State Sensors and Actuators Workshop*, 208–212, IE, New York.

Maxwell, J.C. (1879) On stresses in rarefied gases arising from inequalities of temperature, *Phil. Trans. R. Soc. Part 1* 170, 231–256.

Migun, N.P., and Prokhorenko, P.P. (1987) Measurement of the viscosity of polar liquids in microcapillaries, *Colloid J. of the USSR* 49, 894–897.

Moffatt, H.K. (1964) Viscous and resistive eddies near a sharp corner, *J. Fluid Mech.* 18, 1–18.

Muntz, E.P. (1989) Rarefied gas dynamics, *Annu. Rev. Fluid Mech.* 21, 387–417.

Nadolink, R.H., and Haigh, W.W. (1995) Bibliography on skin friction reduction with polymers and other boundary-layer additives, *Appl. Mech. Rev.* 48, 351–459.

Nakagawa, S., Shoji, S., and Esashi, M. (1990) A micro-chemical analyzing system integrated on silicon chip, in *Proc. IEEE: Micro Electro Mechanical Systems*, Napa Valley, CA, IEEE 90CH2832-4, IEEE, New York.

Oran, E.S., Oh, C.K., and Cybyk, B.Z. (1998) Direct simulation Monte Carlo: recent advances and applications, *Annu. Rev. Fluid Mech.* 30, 403–441.

Panton, R.L. (1996) *Incompressible Flow*, 2nd ed., Wiley-Interscience, New York.

Pearson, J.R.A., and Petrie, C.J.S. (1968) On melt flow instability of extruded polymers, in *Polymer Systems: Deformation and Flow*, R.E. Wetton and R.W. Whorlow, Eds., 163–187, Macmillian, London.

Pfahler, J. (1992) Liquid Transport in Micron and Submicron Size Channels, PhD thesis, University of Pennsylvania, Philadelphia.

Pfahler, J., Harley, J., Bau, H., and Zemel, J.N. (1990) Liquid transport in micron and submicron channels, *Sensors & Actuators A* 21–23, 431–434.

Pfahler, J., Harley, J., Bau, H., and Zemel, J.N. (1991) Gas and Liquid Flow in Small Channels, in *Symp. on Micromechanical Sensors, Actuators, and Systems*, D. Cho et al., Eds., ASME DSC-Vol. 32, 49–60, ASME, New York.

Piekos, E.S., and Breuer, K.S. (1996) Numerical modeling of micromechanical devices using the direct simulation Monte Carlo method, *J. Fluids Eng.* 118, 464–469.

Pong, K.-C., Ho, C.-M., Liu, J., and Tai, Y.-C. (1994) Non-Linear Pressure Distribution in Uniform Microchannels, in *Application of Microfabrication to Fluid Mechanics*, P.R. Bandyopadhyay, K.S. Breuer and C.J. Belchinger, Eds., ASME FED-Vol. 197, 47–52, ASME, New York.

Porodnov, B.T., Suetin, P.E., Borisov, S.F., and Akinshin, V.D. (1974) Experimental investigation of rarefied gas flow in different channels, *J. Fluid Mech.* 64, 417–437.

Prud'homme, R.K., Chapman, T.W., and Bowen, J.R. (1986) Laminar compressible flow in a tube, *Appl. Scientific Res.* 43, 67–74.

Richardson, S. (1973) On the no-slip boundary condition, *J. Fluid Mech.* 59, 707–719.

Schaaf, S.A., and Chambré, P.L. (1961) *Flow of Rarefied Gases*, Princeton University Press, Princeton, NJ.

Seidl, M., and Steinheil, E. (1974) Measurement of Momentum Accommodation Coefficients on Surfaces Characterized by Auger Spectroscopy, SIMS and LEED, in *Rarefied Gas Dynamics* 9, M. Becker and M. Fiebig, Eds., E9.1–E9.2, DFVLR-Press, Porz-Wahn, Germany.

Sharp, K.V. (2001) Experimental Investigation of Liquid and Particle-Laden Flows in Microtubes, Ph.D. thesis, University of Illinois at Urbana–Champaign, Illinois.

Sharp, K.V., Adrian, R.J., Santiago, J.G., and Molho, J.I. (2002) Liquid Flow in Microchannels, in *The Handbook of MEMS*, M. Gad-el-Hak, Ed., CRC Press, Boca Raton, FL.

Shih, J.C., Ho, C.-M., Liu, J., and Tai, Y.-C. (1995) Non-linear pressure distribution in uniform microchannels, ASME AMD-MD-Vol. 238, New York.

Shih, J.C., Ho, C.-M., Liu, J., and Tai, Y-.C. (1996) Monatomic and Polyatomic Gas Flow through Uniform Microchannels, in *Applications of Microfabrication to Fluid Mechanics*, K. Breuer, P. Bandyopadhyay and M. Gad-el-Hak, Eds., ASME DSC-Vol. 59, 197–203, New York.

Tai, Y.-C., and Muller, R.S. (1989) IC-processed electrostatic synchronous micromotors, *Sensors & Actuators* 20, 49–55.

Tang, W.C., Nguyen, T.-C., and Howe, R.T. (1989) Laterally driven polysilicon resonant microstructures, *Sensors & Actuators* 20, 25–32.

Thomas, L.B., and Lord, R.G. (1974) Comparative Measurements of Tangential Momentum and Thermal Accommodations on Polished and on Roughened Steel Spheres, in *Rarefied Gas Dynamics* 8, eds. K. Karamcheti, Academic Press, New York.

Thompson, P.A., and Robbins, M.O. (1989) Simulations of contact line motion: slip and the dynamic contact line, *Nature* 389, 25 September, 360–362.

Thompson, P.A., and Troian, S.M. (1997) A general boundary condition for liquid flow at solid surfaces, *Phys. Rev. Lett.* 63, 766–769.

Tison, S.A. (1993) Experimental data and theoretical modeling of gas flows through metal capillary leaks, *Vacuum* 44, 1171–1175.

Tuckermann, D.B. (1984) Heat Transfer Microstructures for Integrated Circuits, PhD thesis, Stanford University, Stanford, CA.

Tuckermann, D.B., and Pease, R.F.W. (1981) High-performance heat sinking for VLSI, *IEEE Electron Device Lett. EDL-2*, no. 5, May.

Tuckermann, D.B., and Pease, R.F.W. (1982) Optimized convective cooling using micromachined structures, *J. Electrochemical Soc.* 129, no. 3, C98, March.

Van den Berg, H.R., Seldam, C.A., and Gulik, P.S. (1993) Compressible laminar flow in a capillary, *J. Fluid Mech.* 246, 1–20.

Vargo, S.E., and Muntz, E.P. (1996) A Simple Micromechanical Compressor and Vacuum Pump for Flow Control and Other Distributed Applications, AIAA Paper No. 96-0310, AIAA, Washington, DC.

Vincenti, W.G., and Kruger, C.H. Jr. (1965) *Introduction to Physical Gas Dynamics*, John Wiley & Sons, New York.

Von Smoluchowski, M. (1898) Ueber Wärmeleitung in verdünnten Gasen, *Annalen der Physik und Chemie* 64, 101–30.

Went, F.W. (1968) The size of man, *American Scientist* 56, 400–413.

15.7 Solid Mechanics of Microdevices

C. Channy Wong, Andrew D. Oliver, and David W. Plummer

Characteristics of Surface Micromachined Devices

Advances in micromachining technology allow many engineering systems and components to be built smaller and more compact, and having less weight. A system with less weight will have a smaller inertia; thus this system can start running and stop quickly. A smaller system can also be more resistant to shock and vibration, because the strength of a system decreases as the square of its dimensions while the mass and inertia decreases as the cube of its dimensions.

Another difference at the microscale is that other forces, such as van der Waal forces, electrostatic attraction, and surface tension, can be dominant. Hence, the cause of failure can be very different, for example, (1) large frictional forces leading to more rubbing between surfaces and wearing out faster, (2) stiction an unwanted adhesion between two structural layers, and (3) excessive stress and stress gradient in the thin-film layers.

Among existing micromachining processes, surface micromachining (SMM) is very popular because micromachines built by SMM processes can be created and assembled at the same time that the constituent components are being fabricated. This batch fabrication process can minimize the assembly labor costs. However, SMM does have a disadvantage in that there is a limit on the number and types of layers available to designers. In the following discussion, our focus will be on the surface micromachined devices.

Wear

Similar to conventional machines, micromachines quite often have surfaces touching, rubbing, or impacting on each other. These generate friction and wear (see Figure 15.7.1). However, unlike convention machines, which use dissimilar materials to reduce friction and wear, thin-film layers of micromachines are usually made of the same material. Hence friction and wear become an important issue when addressing reliability of microsystems (Dugger 1999, Tanner 2000). Different lubrication methods have been investigated. Because of the extremely small gap size, liquid lubricants are difficult to apply. This leaves gas films and self-assembly monolayer films as the choices for lubrication.

Stiction

Stiction is an unintended adhesion between thin-film layers in the surface micromachined devices (see Figure 15.7.2). Two major categories of stiction have been observed: (1) stiction in the final-release process, and (2) in-use stiction. In surface micromachining, a popular final processing step is to apply aqueous chemical solution (e.g., hydrofluoric acid) to remove the sacrificial layers so that the designed

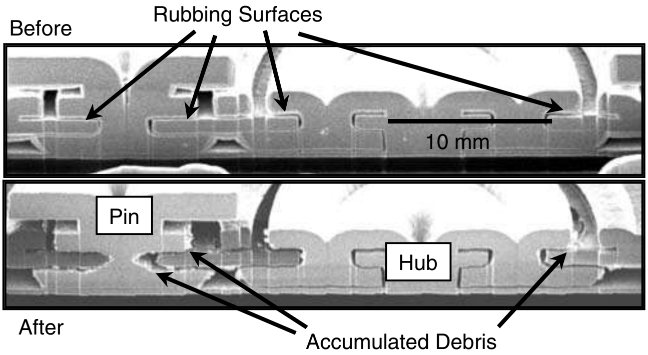

FIGURE 15.7.1 A pin joint and hub joint before and after accelerated wear. (Photograph courtesy of D. Tanner, Sandia National Laboratories.)

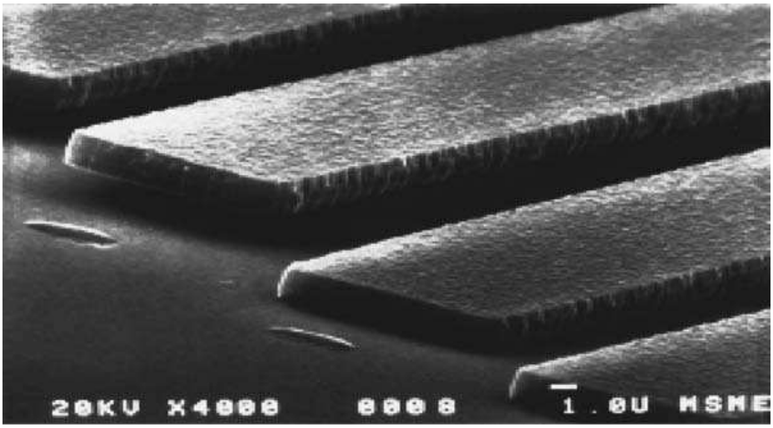

FIGURE 15.7.2 SEM picture of cantilever beams with different lengths. Sticting occurs at those beams on the left. (Photograph courtesy of Sandia National Laboratories.)

parts can move freely and perform work. However, during the release and drying process, capillary forces can pull and hold thin-film layers together and prevent them to move freely and functioning as desired.

The in-use stiction occurs when two thin-film layers unexpectedly adhere together during the normal operation. This can be caused by many factors. One explanation is that electrostatic charges are trapped and built up in the insulating materials, such as silicon nitride, after a long usage. Other factors, such as electrostatics discharge (ESD), can cause stiction as well. Stiction failure is one of the major concerns when addressing the reliability of the surface micromachined devices.

To minimize stiction and wear and to improve performance and reliability of surface micromachined devices, one popular approach is to treat surfaces by applying a hydrophobic coating. Surface treatment is an efficient and effective approach, though it is equally important to incorporate good judgments when developing and designing a microsystem. A few good engineering practices are: (1) to reduce surface area, (2) to add dimples (a small protrusion on the bottom of a structure that act to reduce the area in contact with the structure below), and (3) to increase the stiffness of structure in the out-of-plane direction. In packaging, it is essential to enclose the parts silicon dies in an environment with a dew point well below the minimum storage or operating temperature of the mechanism.

Microsystems Design Considerations

General Guidelines

In addition to the design considerations listed earlier — reducing surface areas, adding dimples, and increasing stiffness — another good practice is to always ground thin-film layers to prevent any electrostatic charge being trapped and built up in the insulating materials, such as silicon nitride, after a long usage. One approach of grounding is to use a conductive ground plane to cover any exposed insulating layers and to connect every object to ground.

Stress in Films and Stress Gradient

Stress can be developed in the thin films for many reasons. A typical source of stress is the differences in the thermal expansion coefficient between various thin films or between thin film and substrate, especially with the thin film is deposited at an elevated temperature (see Figure 15.7.3). Another source is from the doping of semiconductor films if the size of the dopant atoms is quite different from the host atoms. A significant stress buildup or a large stress gradient will lead to cracking, delamination, and/or buckling.

To relieve stresses in microstructures, a sound design practice is to use folded flexures (see Figure 15.7.4). A folded flexure helps because each flexure is free to expand or contract in the axial direction. This can minimize the stress caused by the fabrication process and by thermal expansion mismatches

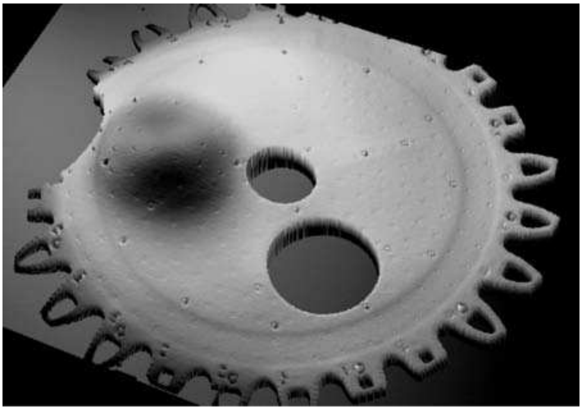

FIGURE 15.7.3 Picture showing the surface profile of a micro-optical shutter as a result of the thermal stress generated from laser spot heating. (Photograph courtesy of O.B. Spahn, Sandia National Laboratories.)

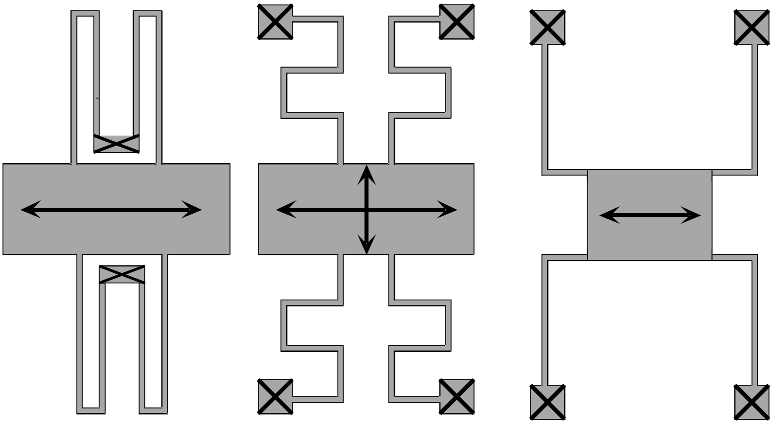

FIGURE 15.7.4 Three flexure designs. From left to right they are folded, meandering flexures, and crab leg flexures.

between the flexures and the substrate. Crab leg flexure and meandering flexure (Figure 15.7.4) can also help to relieve the residual stress in flexures.

Unavoidable stress concentration can still exist even though if we apply the design practice described earlier to help manage stress. Most unavoidable stress concentration is created by the microfabrication process. For example, etch release holes may serve as stress concentrations in plates. Sharp corners in Manhattan (right-angle) geometries can also create stress concentrations. Hence, the design engineer needs to adjust the stress calculated from the standard equations as follows:

$$\sigma_{CONCENTRATION} = K_t \sigma_{NOMINAL} \tag{15.7.1}$$

where K_t is the stress concentration factor.

Next, we will examine three typical component structures: cantilever beam springs, fixed-beam springs, and flexures, which are commonly found in the microsystems, and evaluate their mechanical responses.

Cantilever Beam Springs

For a cantilever beam with a fixed anchor on one end (Figure 15.7.5), the deformation (y) at any arbitrary point (x) is

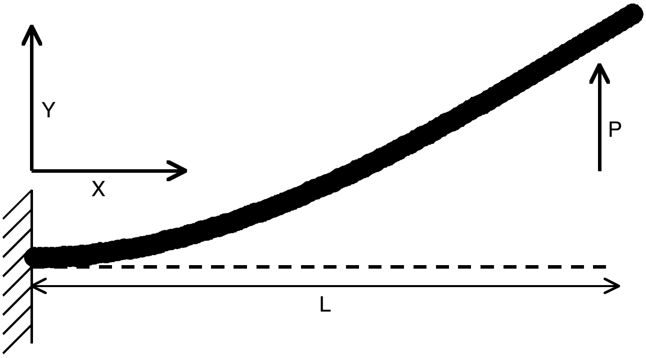

FIGURE 15.7.5 Cantilever beam spring. The deformation of the beam is due to the load "P."

$$y = \frac{P}{6EI}\left(3Lx^2 - x^3\right) \tag{15.7.2}$$

where *L* is the length of the beam, *E* is Young's modulus of the beam material, and *P* is the applied load. The maximum deflection will occur at the end of the beam:

$$y_{MAX} = \frac{PL^3}{3EI} \tag{15.7.3}$$

The maximum stress is at the fixed end where the internal bending moment is *PL*. For a rectangular cross section of thickness *h* and width *w*, the maximum stress is

$$\sigma_{MAX} = \frac{6PL}{h \cdot w^2} \tag{15.7.4}$$

The fundamental resonant frequency in Hertz (Bathe 1982) becomes

$$f_1 = \frac{3.52}{2\pi}\sqrt{\frac{EI}{\rho AL^4}} \tag{15.7.5}$$

where *E* is Young's modulus, *A* is the cross-sectional area (*h·w*), and ρ is the density.

For a microfabricated cantilever beam made of polycrystalline silicon with dimensions of 50 μm wide, 6 μm thick, and 200 μm long, the electrostatic force required to pull down the beam and touch the electrode 2 μm below is as follows:

$$P = \frac{3EIy}{L^3} = \frac{3\left(0.155\mathrm{N}/\mu\mathrm{m}^2\right)\left(900\ \mu\mathrm{m}^4\right)(2\ \mu\mathrm{m})}{(200\ \mu\mathrm{m})^3} = 105\ \mu\mathrm{N}$$

assuming that the Young's modulus for polycrystalline silicon is 155 GPa or 0.155 N/μm^2 and the density of solid polycrystalline silicon is 2.33×10^{-18} kg/μm^3. The area moment of inertia for a rectangular cross section is $I = wt^3/12 = (50\ \mu\mathrm{m})(6\ \mu\mathrm{m})^3/12 = 900\ \mu\mathrm{m}^4$.

If the beam is suddenly released, it will vibrate at the following frequency:

$$f = \frac{3.52}{2\pi}\sqrt{\frac{EI}{\rho AL^4}} = \frac{3.52}{2\pi}\sqrt{\frac{\left(0.155N/\mu\mathrm{m}^2\right)\left(900\ \mu\mathrm{m}^4\right)\left(1000\ \mu\mathrm{m}/\mathrm{m}\right)}{[2.33\left(10^{-18}\right)\mathrm{kg}/\mu\mathrm{m}^3]\left(50\ \mu\mathrm{m}\times 6\ \mu\mathrm{m}\right)\left(200\ \mu\mathrm{m}\right)^4}} = 198\ \mathrm{kHz}$$

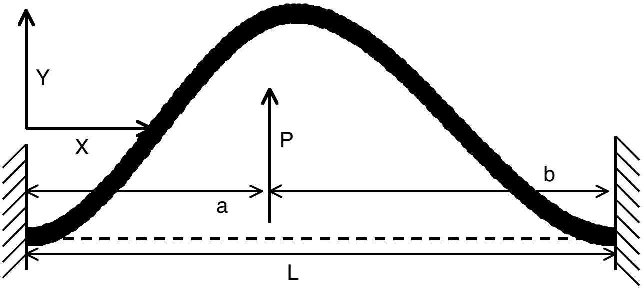

FIGURE 15.7.6 Deflection of a fixed-beam spring due to a point load. The applied load is "P," the load's location is shown by "a" and "b" on the x-axis, and the spring deflects in the direction of the y-axis.

Fixed-Fixed Beam Springs

The deflection of a fixed beam (Figure 15.7.6) at any point, $0 < x <$ a, with a point-applied load (Timoshenko 1959) is

$$y = \frac{Pb^2x^2\left[3aL-(3a+b)x\right]}{6L^3EI} \tag{15.7.6}$$

The fundamental frequency for a fixed beam (Bathe 1982) is

$$f_1 = \frac{22.4}{2\pi}\sqrt{\frac{EI}{\rho AL^4}} \tag{15.7.7}$$

The form of this equation is similar Equation 15.7.5 for cantilever beams. Note that fixing the other end of the beam increases the fundamental frequency by more than a factor of six, with the fixed-fixed beam having the same dimension as the cantilever beam.

For a beam anchored on both ends with dimensions of 50 μm wide, 6 μm thick, and 200 μm long, the force applied at the center needed to pull it down to the substrate 2 μm below is

$$P = \frac{192EIy}{L^3} = \frac{192\left(0.155\text{N}/\mu\text{m}^2\right)\left(900\ \mu\text{m}^4\right)\left(2\ \mu\text{m}\right)}{\left(200\ \mu\text{m}\right)^3} = 6700\ \mu\text{N}$$

and the resulting frequency of vibration when released is

$$f = \frac{22.4}{2\pi}\sqrt{\frac{\left(0.155\text{N}/\mu\text{m}^2\right)\left(900\ \mu\text{m}^4\right)\left(1000\ \mu\text{m}/\text{m}\right)}{\left[2.33\left(10^{-18}\right)\text{kg}/\mu\text{m}^3\right]\left(6\ \mu\text{m}\times 50\ \mu\text{m}\right)\left(200\ \mu\text{m}\right)^4}} = 1.26\ \text{MHz}$$

This illustrates that the fundamental frequency for the beam anchored at both ends is much higher than for the cantilever beam.

Flexures

Flexures can be found in many microsystems. For instance, they can be used for rotation. When a torque is applied to a flexure, it causes twisting, which creates shear stress in the element. The shear stress in a circular bar arising from an applied torque is

$$\tau = \frac{Tc}{J} \tag{15.7.8}$$

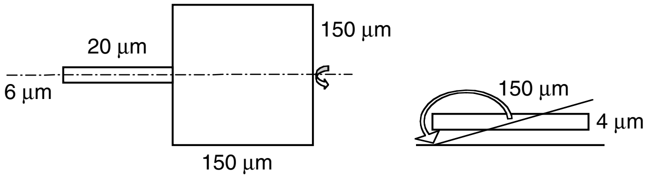

FIGURE 15.7.7 Dimensions of a polysilicon plate supported by torsional flexures.

where τ is the shear stress, T is the applied torque, c is the distance from the central axis to the point where the stress is desired, and J is the polar area moment of inertia.

For a rectangular bar, the resulting shear stress can be found as follows:

$$\tau = \frac{9T}{2wt^2} \tag{15.7.9}$$

where w is the width (larger dimension) of the flexure and t is the thickness (smaller dimension). The deflection created by the applied torque is

$$\theta = \frac{TL}{JG} \tag{15.7.10}$$

where L is the length of the flexure, G is the shear modulus, and J is polar moment of inertia. The polar moment of inertia is defined as

$$J = I_x + I_Y \tag{15.7.11}$$

Consider a 150-μm square, polysilicon plate (Figure 15.7.7), which is supported by 6 μm wide torsional flexures; the axis of rotation is through the plate's midpoint. The plate is 4 μm thick and the flexures are 20 μm long. If one edge is pulled down to the substrate 3 μm from the bottom of the plate, neglecting the deformation of the plate, the flexures are required to rotate through an angle of 2.3° for the plate to touch the substrate:

$$\theta = \tan^{-1}\left(3\ \mu\text{m} \Big/ (150\ \mu\text{m}/2) \right) = 2.3° = 0.040\ \text{rad}$$

The resulting shear stress in the flexure can be found using Equation 15.7.9, which requires us to determine J and T first.

Assuming that the shear modulus of rigidity is 0.0772 N/μm², the polar area moment of inertia for a rectangular section is

$$J = \frac{wt}{12}\left(w^2 + t^2\right) = \frac{(6\ \mu\text{m})(4\ \mu\text{m})}{12}\left[(6\ \mu\text{m})^2 + (4\ \mu\text{m})^2\right] = 104\ \mu\text{m}^4$$

The torque required to rotate one flexure through the angle θ is

$$T = \frac{JG\theta}{L} = \frac{\left(104\ \mu\text{m}^4\right)\left(0.0772\text{N}/\mu\text{m}^2\right)\left(0.04\ \text{rad}\right)}{20\ \mu\text{m}} = 1.6\times10^{-2}\ \mu\text{Nm}$$

The resulting shear stress in each flexure is

$$\tau = \frac{9T}{2wt^2} = \frac{9\times1.6\times10^{-2}\ \text{N}\cdot\mu\text{m}}{2(6\ \mu\text{m})(4\ \mu\text{m})^2} = 7.5\times10^{-4}\text{N}/\mu\text{m}^2 = 0.75\ \ \text{GPa}$$

To predict the vibration frequency, the plate-flexure system can be treated as a rigid body vibrating about a spring. The differential equation of motion for a simple mass-spring system and the associated natural frequency are as follows:

$$i\ddot{\varphi} + K\varphi = 0 \tag{15.7.12}$$

$$f_n = \frac{1}{2\pi}\sqrt{\frac{K}{i}} \tag{15.7.13}$$

where i is the mass moment of inertia (different from the area moment of inertia used to calculate stress) and K is the torsional spring rate.

The spring rate of the flexures is

$$K = \frac{T}{\theta} = \frac{JG}{L} = \frac{\left(104\ \mu\text{m}^4\right)\left(0.0772\text{N}/\mu\text{m}^2\right)}{20\ \mu\text{m}} = 0.40\ \mu\text{Nm}/\text{rad}$$

The mass moment of inertia for a thin rectangular plate vibrating about its center is

$$i = \frac{1}{12}mw^2 = \frac{\left[2.1\times10^{-13}\text{kg}\right]\left(150\ \mu\text{m}\right)^2}{12} = 3.93\times10^{-10}\text{kg}\cdot\mu\text{m}^2$$

The natural frequency is

$$f_n = \frac{1}{2\pi}\sqrt{\frac{(0.40\text{N}\cdot\mu\text{m})(10^6)\mu\text{m}/\text{m}}{3.93\times10^{-10}\text{kg}\cdot\mu\text{m}^2}} = 5.1\text{MHz}$$

Application

This section will apply the material covered in the previous section and show how to design a microsystem. A microflex mirror is used as an example.

Microflex Mirrors

The microflex mirror is a device that deforms out of plane (Garcia 1998). It can be configured as a mirror, an optical shutter, a valve, or any structure that requires a plate or beam to move out of the plane of the base substrate. Figure 15.7.8 shows an SEM photograph of the device. The design consists of a long flexible beam connected to a mirror plate that in turn is connected to two anchors via two additional flexible beams. When a force is placed on the long flexible beam in direction of the anchors, the structure is placed under a compressive force. When the force exceeds the critical value, $F_{CR} = (\pi^2 EI)/(4L^2)$, the structure buckles. Because the long flexible beam is larger in the direction parallel to the plane of the substrate than it is in the direction away from the substrate, it preferentially buckles out of the plane of the substrate. Since the plate and the two anchor beams are wider than the long flexible beam, the majority of the bending occurs in the long flexible beam and not in the plate or the anchor beams.

Consider a main beam with dimensions of 300 μm long, 4 μm wide, and 1 μm thick and that has a Young's modulus of 155 GPa, its moment of inertia will be

$$I = \frac{wt^3}{12} = 3.3\times10^{-25}\text{m}^4$$

By treating it as a cantilever beam and neglecting the buckling of the anchors and the mirror, the axial force required for a micromachined polysilicon mirror to buckle is as follows:

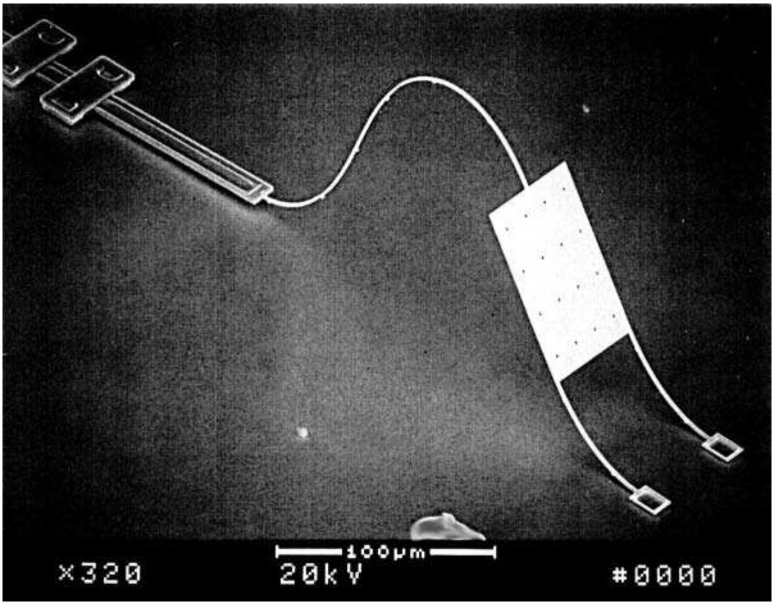

FIGURE 15.7.8 A flexible pop-up mirror that operates via buckling. (Photograph courtesy of E. Garcia, Sandia National Laboratories.)

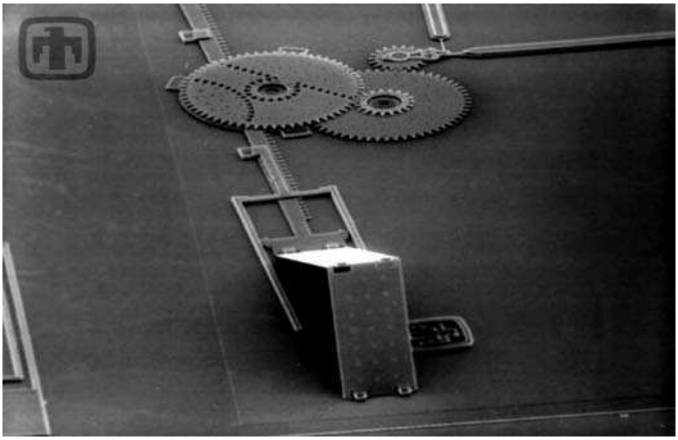

FIGURE 15.7.9 Hinged polysilicon micromirror fabricated in the Sandia National Laboratories SUMMiT process. (Photograph courtesy of Sandia National Laboratories.)

$$F_{cr} = \frac{\pi^2 EI}{4L^2} = \frac{\pi^2 \times 155\times10^9\,\mathrm{N/m^2} \times 3.3\times10^{-25}\,\mathrm{m^4}}{4\times\left(300\times10^{-6}\,\mathrm{m}\right)^2} = 1.4\ \mu\mathrm{N}$$

This analysis shows that it is necessary to have a great deal of force in order to buckle the flexible mirror. To achieve and exceed this buckling force, a transmission developed by Garcia was used to increase the force on the mirror (Garcia 1998), as shown in Figure 15.7.9. The transmission is used to trade displacement for force to ensure that the mirror buckled. The magnitude of deflection after buckling is highly nonlinear and is difficult to predict.

An interesting point about buckling is that it is hard to determine if the beam will initially buckle toward or away from the substrate. If the beam buckles away from the substrate, it will continue to deflect away from the substrate. If it initially buckles toward the substrate, it will contact the substrate and further compression of the beam will result in the structure buckling away from the substrate.

Acknowledgments

We would like to thank many of our colleagues in Microsystems Engineering Science Applications–Technology and Operation Prototype (MESA-TOP) facility at Sandia National Laboratories for their help and efforts. Many of the devices and concepts discussed in this section are due to their efforts. Sandia National Laboratories is a multi-program laboratory operated by the Sandia Corporation, a Lockheed Martin Company, for the United States Department of Energy under contract DE-AC04-94AL8500.

References

Bathe, K-J. 1982. *Finite Element Procedures in Engineering Analysis*, Prentice Hall, Englewood Cliffs, NJ.

Dugger, M.T., Poulter, G.A., and Ohlhausen, J.A. 1991. Surface passivation for reduced friction and wear in surface micromachined devices," *Proceedings of the Fall MRS Symposium*, Boston, December.

Garcia, E.J. 1998. Micro-flex mirror and instability actuation technique, *Proceedings of the 1998 IEEE Conference on Micro Electro Mechanical Systems, MEMS98*, 470–474.

Tanner, D.M. 2000. *Proceedings of the 22nd International Conference on Microelectronics*, invited keynote, Nis, Yugoslavia, 97–104.

Timoshenko, S.P., and Woinowsky-Krieger, S. 1959. *Theory of Plates and Shells*, McGraw-Hill, New York.

Further Information

Gardner, J.W., Varadan, V.K., Awadelkarium, O.O. 2002. *Microsensors, MEMS, and Smart Devices*, John Wiley & Sons, Ltd., Chichester, UK.

Hsu, T.-R. 2002. *MEMS and Microsystems, Design and Manufacture*, McGraw-Hill, New York.

Kovacs, G.T.A. 1998. *Micromachined Transducers — Source Book*, McGraw-Hill, New York.

Senturia, S.D. 2001. *Microsystem Design*, Kluwer Academic Publishers, Boston.

16

Environmental Engineering

Jan F. Kreider
Kreider & Associates

Ari Rabl
Ecole des Mines de Paris

Nevis E. Cook, Jr.
Colorado School of Mines

Ronald R. Hewitt Cohen
Colorado School of Mines

Tissa Illangasekare
Colorado School of Mines

Paolo Zannetti
The EnviroComp Institute

Peter S. Curtiss
Curtiss Engineering

John Firor
National Center for Atmospheric Research

16.1 Introduction

Ari Rabl and Jan F. Kreider

Environmental Engineering and the Role of Mechanical Engineers

The subject of environmental science and management is vast and interdisciplinary, ranging from highly technical matters, such as the design of emission control equipment, to socioeconomic matters, such as the valuation of the impacts of pollution. The goal is to prevent or reduce undesirable impacts of human activities on the environment. Within this endeavor are several areas where mechanical engineers can make important contributions. One type of contribution concerns the design of equipment, in particular for the control of emissions; an example is an electrostatic precipitator to reduce emissions of particulates from the flue gas of a boiler or furnace. Another type of contribution concerns the modeling of the dispersion of pollutants in the environment. This chapter covers air pollution, surface water pollution, and groundwater pollution. Since space is limited and mechanical engineers are most likely to be involved in air pollution analysis and abatement projects, our emphasis is on air pollution problems.

			Impacts				
	Extent				Environment		
Burdens	**Space**	**Time**	**Climate**	**Health**	**Natural**	**Agricultural**	**Man-Made**
Greenhouse gases (CO2, CH4, N2O, ...)	G	P,F	X				
Primary air-pollutants							
Particulates	R	P		X			X
SO2	R	P		X	x	x	x
NOx	R	P		x			x
CO	R	P		x			
Toxic metals (As, Cd, Pb, Hg, ...)	R	P, F		X	X		
Toxic organic compounds (e.g., dioxins)	R	P, F		X	X		
VOC	R	P					
Secondary air pollutants							
O3 (from NO + VOC)	R	P	X	X	X	X	x
Acid rain (from NOx, SOx)	R	P			X	X	X
Nitrates (from NOx)	R	P	x	X	x	x	x
Sulfates (from SOx)			x	X	x	x	x
Liquid residues							
Toxic metals (Pb, Hg, Cd, ...)	L, R	P, F		X	X		
Toxic organic compounds (e.g., dioxins)	L, R	P, F		X	X		
COD	L, R	P, F		x	X	x	
BOD	L, R	P, F		x	X	x	
Solid residues	L	P, F		x	x	x	
Other							
Thermal	L	P			x		
Noise, odor	L	P		x			x

VOC = volatile organic compounds, COD = chemical oxygen demand, BOD = biological oxygen demand;

Impacts: X = important; x = may be important; blank = usually not important;

Extent: L = local (up to tens of kilometers); P = present generation; R = regional (hundreds to thousands of kilometers); G = global; F = future generations.

FIGURE 16.1.1 Overview of environmental burdens and major impact categories, with approximate indication of typical geographic extent and typical importance of impact.

Environmental Burdens and Impacts

Ari Rabl

As general guidance to the field of environmental engineering, it may be helpful to present the most important environmental burdens and impacts in the form of a matrix, as shown in Figure 16.1.1. Burdens, for example, the emission of a pollutant, are listed in the column on the left; impact categories are listed as a row at the top. Each element in this matrix corresponds to a specific impact of a specific burden. An X indicates that the impact from the corresponding burden is likely to be significant. Particulate air pollution, for instance, has been shown to cause a significant increase in mortality.

As an added feature we have indicated the spatial and temporal extent to the burdens. The classic air pollutants (particulates, NO_x, and SO_x) are dispersed over distances on the order of a thousand kilometers, and they affect essentially only the present generation; thus, the second and third columns show the letters R (for regional) and P (for present generation). Global warming from greenhouse gases, on the other hand, affects the entire globe and will persist over decades or centuries, hence the letters G (for global) and P, F (for present and future generations).

The classification in Figure 16.1.1 is not without ambiguities or problems. For example, we have indicated the impact of greenhouse gases as "climate change" only, even though this category includes such effects as deaths from flooding. The relative importance of impacts may change with improved scientific understanding and with the evolution of societal preferences. One should also note that the assignment of effects to causes is in many cases quite uncertain; for instance, the observed mortality from air pollution could be due to particulates or due to SO_2.

Some impacts, especially thermal pollution and noise, can be highly site dependent. The cooling water from a power plant, for instance, could damage the ecosystem of a river, or it could be used to improve the output of a fishery.

Each of the categories in Figure 16.1.1 could be broken down into subcategories:

- Health
  - Mortality
  - Injury
  - Cancer
  - Respiratory illness
- Natural environment
  - Recreational value of land (including forests)
  - Recreational value of water (including fishing)
  - Biodiversity
- Agricultural environment
  - Crops
  - Cattle (milk, meat, fur, …)
  - Wood production by forests
  - Commercial fishing
- Man-made environment
  - Functional buildings
  - Historical buildings
  - Other objects (bridges, cars, …)
  - Noise

16.2 Benchmarks and Reference Conditions

Ari Rabl, Nevis Cook, Ronald R. Hewitt Cohen, and Tissa Illangasekare

Natural Environment

Air Basins

Unpolluted air is an idealization, but its composition has been defined as indicated in Table 16.2.1. Unfortunately, measurements of truly unpolluted air were not, and can never be, made because measurement techniques and even the interest in measurements did not exist when air was unpolluted. Now even the most remote sites have mildly polluted air.

Although measurements of the undisturbed atmosphere were not made, we can gain some insight into trends of air pollutant burden growth by examining emissions. Figure 16.2.1 shows the emissions of the classical air pollutant species in the U.S. since 1940. The emissions of SO_2, PM, and VOC have been decreasing since 1970, but not those of NO_x. Note that Table 16.2.1 uses two sets of units for gaseous pollutants, one volumetric, the other mass based. To convert from one to the other, the ideal gas law is used with the result (at 1 atm and 25°C):

$$1 \text{ ppm} = \text{MW} * 40.9 \ \mu\text{g/m}^3$$

where MW is the molecular weight.

TABLE 16.2.1 Gaseous Composition of Unpolluted Air (Dry Basis)

	ppm (vol)	µg/m^3
Nitrogen	780,000	8.95×10^8
Oxygen	209,400	2.74×10^8
Water	—	—
Argon	9,300	1.52×10^7
Carbon dioxide	315	5.67×10^5
Neon	18	1.49×10^4
Helium	5.2	8.50×10^2
Methane	1.0–1.2	$6.56–7.87 \times 10^2$
Krypton	1.0	3.43×10^3
Nitrous oxide	0.5	9.00×10^2
Hydrogen	0.5	4.13×10^1
Xenon	0.08	4.29×10^2
Organic vapors	~0.02	—

Surface Water Basins

Human activity has also dramatically altered the distribution, quantity, and quality of Earth's water, especially since the industrial revolution. Accurate measurement of many water impurities, particularly trace impurities, has only become possible in the latter part of the twentieth century. Given the quantities and wide distribution of human-generated wastes delivered directly or indirectly (via atmospheric deposition or surface runoff and erosion) to water bodies, recent water quality surveys might not be representative of truly "natural" conditions. As an example, a "pristine," undeveloped alpine lake may show traces of plutonium that are residuals of 1950s through 1960s atmospheric testing of nuclear weapons. Lead from automobile emissions can be detected in the bottom sediments of the Atlantic Ocean, more than 1500 km from the nearest landmass. A tabulation of the averages and ranges of concentrations of many naturally occurring substances detected in minimally impacted waters can serve as a benchmark, admittedly imperfect, against which to compare "polluted" waters, water-quality criteria, and regulatory standards.

Choice of Reference Conditions. The authors propose, as reference conditions, the concentrations of measured impurities in the oceans, "average" rainwaters, and "average" river waters. This choice of reference waters was based on one of two distinct criteria:

1. The volume of water was so large (such as the open oceans) that human activity has had little detectable effect on average water quality conditions.
2. The waste input is small and the water body is rapidly and continuously renewed by unpolluted sources (such as a tributary to a major river).

The major and minor constituents of water and their quantities are easily presented in tables. The use of the word "major" indicates materials present or required in large quantities. Table 16.2.2 summarizes data on the constituents of selected natural waters. Note that the concentration data for major constituents (Table 16.2.2) is given in milligrams per liter and the concentration data for the minor constituents (Table 16.2.3) is given in micrograms per liter. Inclusion of boron and fluoride as major constituents is somewhat arbitrary and was based on their occurrence at greater than 1 mg/L in seawater. In these tables, individual entries are *average values* reported by U.S. regional or national surveys. *Ranges* are derived from the majority of the data from similar surveys, excluding data obtained from waters apparently contaminated by pollution. Some surveys presented results by stating that "very few" samples exceeded certain concentration values or simply reported measurements as "less than" due to analytical detection limits. These results are preceded by the symbol < in the tables. Although the data given are believed to be representative of water found in natural settings, keep in mind that, especially for industrially important trace constituents, the upper limits of the concentration ranges may include some small level of **anthropogenic** inputs.

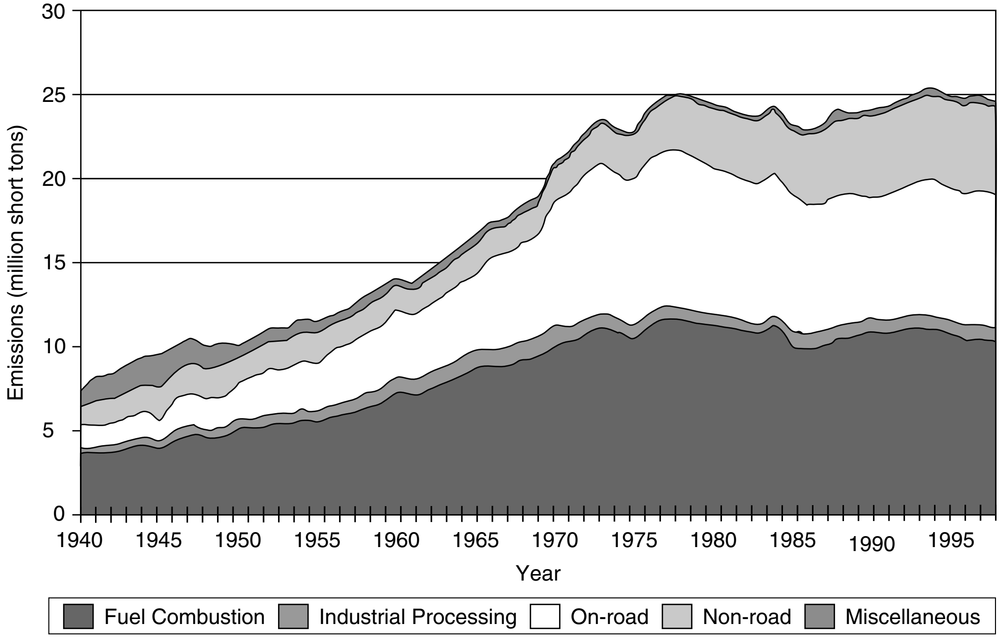

(a)

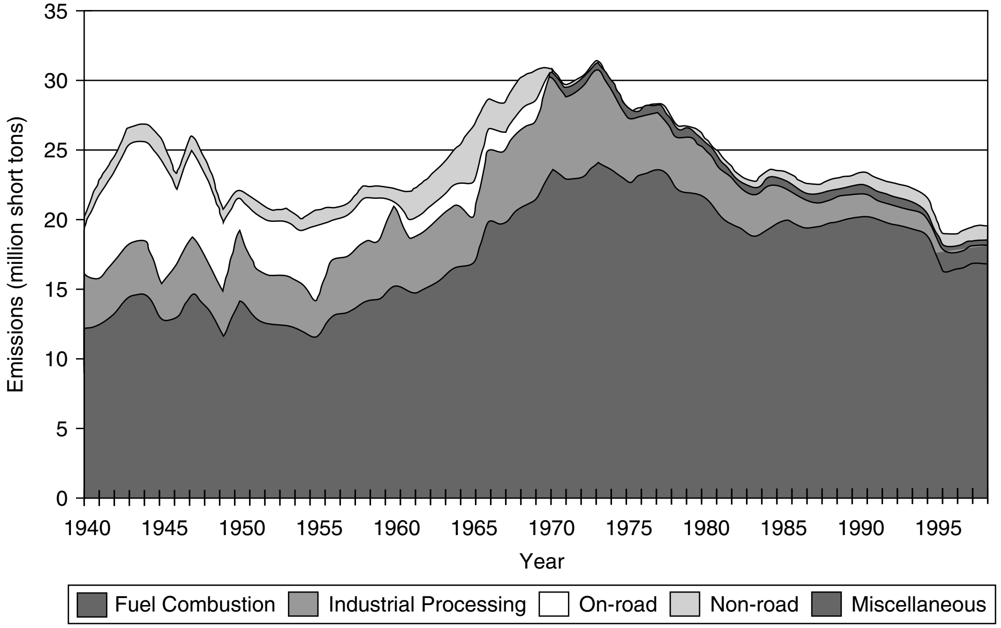

(b)

FIGURE 16.2.1 Trends in U.S. national emissions of air pollutants, 1940–1995. (a) NO_x, (b) SO_2, (c) PM_{10}, (d) VOC. (From EPA, 2000.)

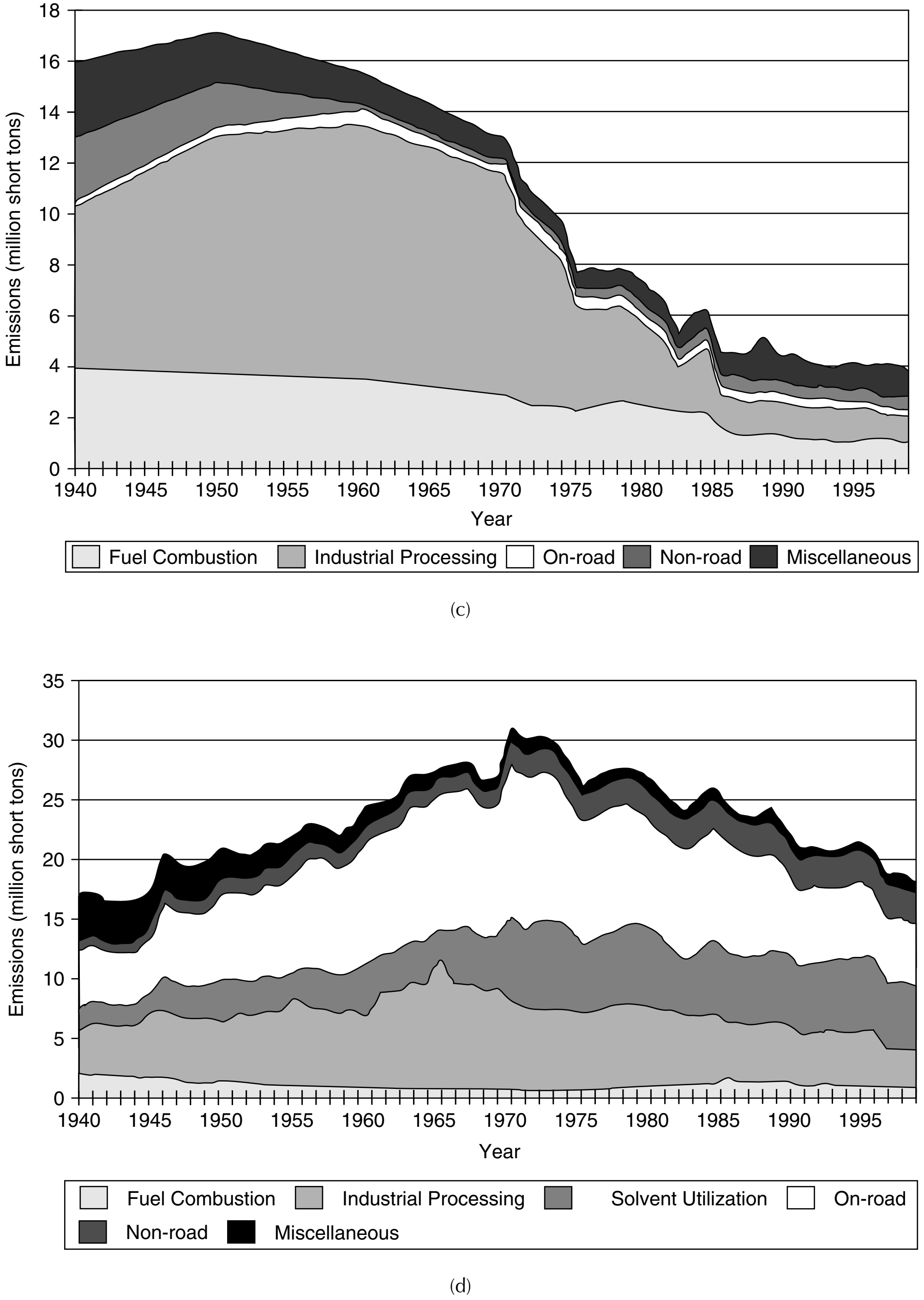

FIGURE 16.2.1 (continued).

Additional categories of natural and contaminant components of water exist. There are complex, difficult-to-characterize, organic humic materials in natural water bodies that represent the endpoint of decay of formerly living organic matter. There are synthetic chemicals by the thousands, produced currently and in the past, by the chemical industry. Some of these compounds and polymers are completely

TABLE 16.2.2 Major Constituents and Characteristics of Natural Waters (constituent concentrations in mg/L, unless otherwise noted)

Constituent	Oceans	Rivers	Rain
Cl^-	19,000	5.8, 7.8	0.2–0.6
Na^+	10,500	5.3, 6.3	0.2–0.6
	2,700	8.3, 11	1.1, 2.2
Mg^{++}	1,350	3.4, 4.1	0.3–1.5
Ca^{++}	410	13.4, 15	0.05–1.5
K^+	390	1.3, 2.3	0.07–0.11
	142	52, 58	1–10
Br^-	0.67	<20	<0.15
Sr^{++}	8	0.06–0.11	—
SiO_2	6.4	10.4, 13	0.1
$B3^-$	4.5	0.3	—
F^-	1.3	<1	—
pH (units)	8.2	6, 7.2, 7.5	5.7
Hardness (total)	—	10–200	—
Ammonia, as N	—	0.05–0.5	—
Nitrate, as N	—	0.1–2.0	—
BOD	—	2–4	—

Note: BOD is biochemical oxygen demand, in mg/L oxygen.

TABLE 16.2.3 Minor Constituents of Natural Waters (constituent concentrations in μg/L)

Constituent	Oceans	Rivers	Rain
N	670	0–1000	0–620
C (organic)	100	3, 6, 19	—
P	90	10–30	—
Ba	20	43, 45	—
Zn	10	5–45, 10, 20	3.6
Ni	7	0.3, 10	—
As	3	0.15–0.45	0.45
Cu	3	10	2.5
Fe	3	10	—
Mn	2	—	—
Sb	0.3	0.54	—
Ag	0.3	0.3	0.001–0.1
Hg	0.2	<0.3	0.2
Cd	0.11	1, <10	—
Se	0.09	0.1, 0.2	—
Cr	0.05	0.43, 1.4, 5.8, <10	0.1–.02
Pb	0.03	<1	<1

new to the natural environment. Many are considered toxic to aquatic organisms and/or humans. For lists of contaminants considered toxic and their effluent limitations, see the many documents available from the U.S. Environmental Protection Agency (USEPA) and other sources.

Soils and Water Basin Definitions

The unconsolidated sediment that covers a comparatively thin mantle of the land surface in general is referred to as soil. Soils are complex mixtures of solid, liquid, and gases. The solid phase consists of a mineral inorganic fraction that is produced by weathering of rocks or transported material. The predominant inorganic elements are silicon, aluminum, and iron. The organic fraction consists of partially or fully decomposed products of flora and fauna. The liquid phase is the water that occupies the pore spaces between and within grains of the solid material. In its natural form, this water, which is referred to as *soil water*, contains dissolved substances introduced from the solids or transported from the ground surface. The pore spaces that are not occupied by water will be filled by water vapor, gases, and air. The complexity of soil systems derives from the fact that the mixture of the solid, liquid, and gases is very heterogeneous and that the composition of the individual phases and the mixture changes in space and with time.

The soils in their natural environment can be subjected to drastic changes not only as a result of the interaction among the solid, liquid, and gas phases but also by external factors that are controlled by pressure, temperature, and light. The physical and chemical characteristics of the changing solid phase have a significant influence on the thermal behavior, water retention and flow, adsorption and entrapment of chemicals and wastes, and transport of dissolved substances. All of these processes are important to the study, understanding, and solution of problems in environmental sciences and engineering associated with soil contamination.

The physical characteristics of soils as a porous medium are affected by the shape, size and size distribution, and arrangement of the solid phase or the soil grains. The *shapes* and *sizes* of the soil grains vary widely, from small colloids to large sand and gravel. Particles that are less than the arbitrary size of 2 μm are the clay fraction that is formed as a secondary product of weathering of rocks or derived from the transported deposits. These particles are platelike or disk shaped. The non-clay fraction formed from inert minerals and fragments of rock consists of silt, sand, and gravel. In a particle size classification used by agricultural scientists that was developed by the U.S. Department of Agriculture (USDA), non-clay particles that are in the size range 2 to 50 μm are classified as silts, in the range 50 to 2000 μm as sands, and above 2000 μm as gravel. In this classification system the sands are further divided into subgroups of very fine, fine, medium, coarse, and very coarse sands. A second system, by the International Society of Soil Science (ISSS) that is also used by agricultural scientists, classifies silts to be in the range 2 to 20 μm, fine sands 20 to 200 μm, and coarse sands 200 to 2000 μm. The American Society of Testing and Materials (ASTM) classifies colloids as particles that are less than 0.1 μm in size.

The surface area of the solid particles contained in a known volume of the soil has a significant influence on the physical and chemical processes that occur on the surfaces of the soil grains. The ratio of the internal solid surface area to the total volume is referred to as the *specific surface*. This parameter is also sometimes expressed as the ratio of the surface area to the mass of the soil grains. This parameter of the soil is affected by the size and shape of the individual soil grains. Because of the platelike or disk-shaped nature of small clay particles, clays in general have very large specific surface compared with the non-clay particles (silts, sand, and gravel). For example, the three common clay minerals kaolinite, illite, and montmorillonite have specific surfaces of 45, 175, and 800 m^2/gm, respectively (Corey, 1994). Because of these enormously large surface areas, the clay fraction in soils has a significant influence on the chemical reactive processes that are controlled by the surface area of the soil grains. The silt and sand fraction will not have a significant influence on the chemical processes, and also the smaller surface areas result in small water retention capacities as compared with clay.

The spaces between the grains that are referred to as intergranular pore spaces control the flow behavior and capacity to hold water by a soil. A physical parameter that is known as the *average porosity* or *porosity* characterizes the secondary pore space enclosed between the aggregates. The porosity of a soil sample is defined as the ratio of the volume of interconnected pores to the total volume of the sample. Soil porosity depends on many factors that include its structure, shape of soil grains, size distribution of the grains, the degree of mixing of the various-sized particles, and the way the soil grains are packed. Under conditions of normal packing, the porosities of unconsolidated sand vary in the range 0.39 to 0.41 and soil with structure in the range 0.45 to 0.55. The organic matter in soil binds the inorganic fraction to form larger aggregates. The primary pore spaces within the soil aggregate play a significant role in retardation and attenuation of dissolved chemicals that are contained in the aqueous phase.

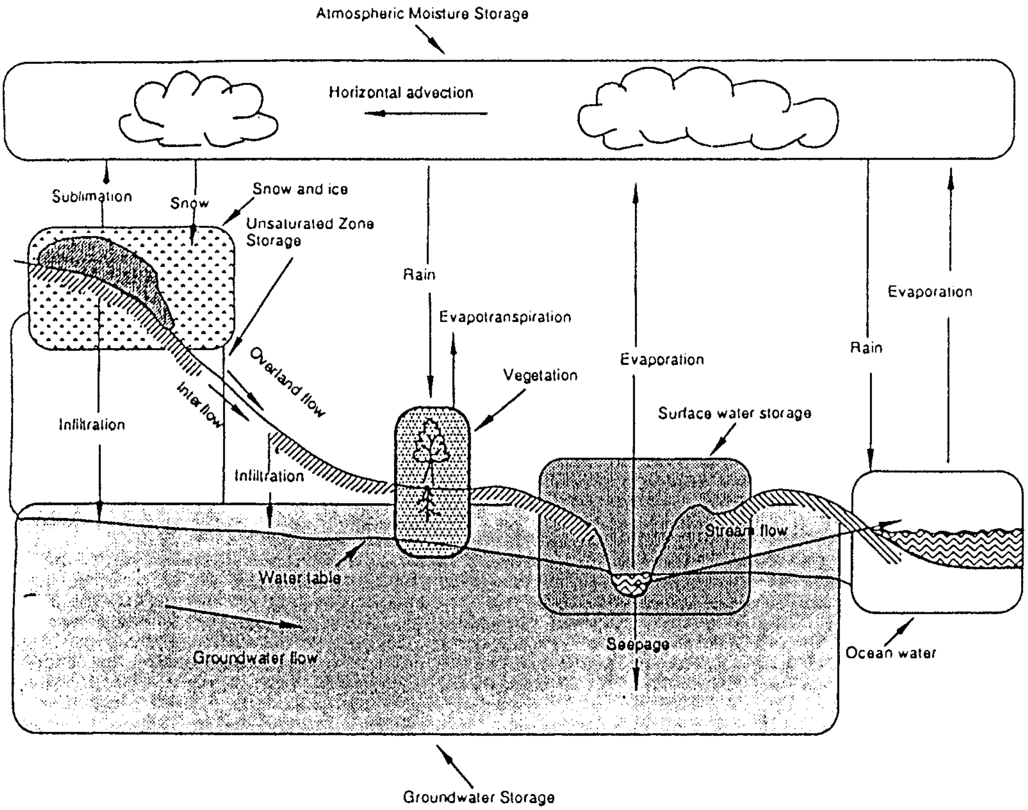

FIGURE 16.2.2 A column of Lagrangian boxes simulating atmospheric dynamics.

The subsurface soil–water environment that exists below the ground surface is divided into two zones, namely, the *unsaturated* or *vadose zone* and the *saturated zone*. In the unsaturated zone pore spaces contain both water and air. The capillary forces created by the surface tension in the water-air interfaces produce water pressures that are less than atmospheric (suction). The water flowing through the unsaturated zone is subjected to capillary driving forces in addition to the gravitational forces. In the saturated zone, the water pores are fully saturated with water and the water pressures are greater than atmospheric. The water in the saturated zone is driven by gravitational forces. The surface that separates the unsaturated and saturated zones is referred to as the *water table*. By definition, the water pressure at the water table is atmospheric. The location of the water table below the ground surface at waste and spill sites becomes critical in determination of the fate and transport of pollutants in the subsurface soil–water environment as described later. Figure 16.2.2 shows the essentials of the situation schematically.

Acceptable Levels of Pollutants

Water

Criteria vs. Standards. The *objective* of water quality control programs, for example, is to protect current or potential *beneficial uses* of water. Criteria define the specific characteristics necessary to protect such uses. Criteria are not absolute but are based on a combination of experience, current scientific knowledge, and the judgment of experts. Toxicological data for many of the water components often are limited. There may be results of tests for acute, or immediate, impact to organisms (including humans), but little

TABLE 16.2.4 Water Quality Criteria and Standards (inorganic contaminants in µg/L)

	Beneficial Use or Protection Category		
Constituent	Aquatic Life	Irrigation	Drinking Water
B	—	750, 500–3,000	—
F	—	1,000	4,000[a]
Ammonia-N	20[b]	—	—
Nitrite-N	—	—	1,000
Nitrate-N	—	5,000–30,000	10,000
Ba	—	—	2,000
Zn	110	2,000	5,000[c]
Ni	160	200	—
As	190	100	50
Cu	12	200, 100–1,000	1,300[c]
Fe	1,000	5,000	300[c]
Mn	—	200	50[c]
Sb	—	—	6
Ag	3[d]	—	—
Hg	0.012, 0.05[e]	—	2
Cd	1.1	10	5
Se	5	20	50
Cr	11	100	100
Pb	3.2	—	15
pH, units	No vertebrates below 4–4.5	—	6.5–8.5

[a] Considered beneficial in drinking water at somewhat lower concentrations.
[b] Temperature and pH dependent; only unionized form (NH_3) is toxic to aquatic life.
[c] Secondary standards based on use impacts (tastes, staining); not health related.
[d] Controversial, based on toxicity of Ag+; rarely present in natural waters.
[e] Extremely low levels partly due to food chain bioaccumulation potential.

information on impact on reproduction, long-term health or tolerance at low concentrations, organism adaptability, acclimatization, or interaction with other substances. General criteria are intended to protect sensitive species subjected to long-term exposure and may be overly conservative in specific situations. The aquatic life column of Table 16.2.4 presents typical, continuous, maximum concentration criteria for freshwaters intended to support a variety of aquatic life. Surface water quality criteria and their relationship to permitted discharges are further discussed later in this chapter. The irrigation criteria given in Table 16.2.4 are intended to protect the yields of agricultural crops.

Due to resource limitations (time, money, data, or a shortage of knowledgeable experts), conservative criteria are often adopted as *standards*. Standards development should, however, include considerations of actual local needs and conditions, economics, technical feasibility, and the defined objectives of environmental policy. In contrast to criteria, standards are usually incorporated into laws and regulations and are often absolute. Either standards are violated or they are not.

Summarized as simple, USEPA (1979) definitions follow:

1. *Water Quality Criterion:* That concentration of a water quality measure that will meet a specific water use.
2. *Water Quality Standard:* The translation of a water quality criterion into a legally enforceable mass discharge of effluent limitation.

The drinking water column of Table 16.2.4 presents a subset of the current U.S. National Standards for drinking water supplied to the public. The health-based standards are enforceable. It should be noted that the drinking water standards list in Table 16.2.2 is not comprehensive. Maximum concentration levels (MCLs) for some inorganics, microbial contaminants, and the many regulated toxic organics have been omitted. Many drinking water MCLs are controversial because they rely on dose-response models that cannot be directly verified at the low levels of exposure that are typical.

Air

Table 16.2.5 to Table 16.2.9 summarize the current U.S. ambient air quality criteria and standards for carbon monoxide, sulfur dioxide, nitrogen dioxide, ozone, and particulate matter. These criteria represent myriad effects depending on the receptor, species of pollutant, and duration and severity of impact. These criteria are descriptive and are used for emission and air quality standards that are summarized briefly. As better data become available, these tables may change.

TABLE 16.2.5 U.S. Ambient Air Quality Criteria for Carbon Monoxide

CoHb in Blood,%	Associated Human Symptoms
80	Death
60	Loss of consciousness; death if exposure is continued
40	Collapse on exercise; confusion
30	Headache, fatigue; judgment disturbed
20	Cardiovascular damage; electrocardiographic abnormalities
5	Decline (linear with increasing CoHb level) in maximal oxygen uptake of healthy young men undergoing strenuous exercise; decrements in visual perception, manual dexterity, and performance of complex sensorimotor tasks
4	Decrements in vigilance (i.e., ability to detect small changes in one's environment that occur at unpredictable times); decreased exercise performance in both healthy persons and those with chronic obstructive pulmonary disease
3–6	Aggravation of cardiovascular disease (i.e., decreased exercise capacity in patients with angina pectoris, intermittent claudication, or peripheral arteriosclerosis)

CoHb = carboxy hemoglobin

Source: Henderson, Y. and Haggard, H.W., *Noxious Gases*, Chemical Catalog Co., New York, 1927; and USEPA, *Air Quality Criteria for Carbon Monoxide*, EPA/600/8-90/045F, Research Triangle Park, NC, December 1991.

TABLE 16.2.6 U.S. Ambient Air Quality Criteria for Sulfur Dioxide

Concentration of SO_2 in Air (ppm)	Exposure Time	Human Symptoms and Effects on Vegetation
400	—	Lung edema; bronchial inflammation
20	—	Eye irritation; coughing in healthy adults
15	1 hr	Decreased mucociliary activity
10	10 min	Bronchospasm
10	2 hr	Visible foliar injury to vegetation in arid regions
8	—	Throat irritation in healthy adults
5	10 min	Increased airway resistance in healthy adults at rest
1	10 min	Increased airway resistance in people with asthma at rest and in healthy adults at exercise
1	5 min	Visible injury to sensitive vegetation in humid regions
0.5	10 min	Increased airway resistance in people with asthma at exercise
0.5	—	Odor threshold
0.5	1 hr	Visible injury to sensitive vegetation in humid regions
0.2	3 hr	Visible injury to sensitive vegetation in humid regions
0.19	24 hr[a]	Aggravation of chronic respiratory disease in adults
0.07	Annual[a]	Aggravation of chronic respiratory disease in children

[a] In the presence of high concentrations of particulate matter

Sources: Air Quality Criteria for Particulate Matter and Sulfur Oxides, final draft, USEPA, Research Triangle Park, NC, December 1981; *Review of the National Ambient Air Quality Standards for Sulfur Oxides: Assessment of Scientific and Technical Information*, Draft OAQPS Staff Paper, USEPA, Research Triangle Park, NC, April 1982; *EPA Green Book*, Part 50, July 2001 (http://www.epa.gov/air/oaqps/greenbk/40CFR50.html)

TABLE 16.2.7 U.S. Air Quality Criteria for Nitrogen Dioxide

Concentration of NO_2 in Air (ppm)	Exposure Time	Human Symptoms and Effects on Vegetation, Materials, and Visibility
300	—	Rapid death
150	—	Death after 2 or 3 weeks by bronchiolitis fibrosa obliterans
50	—	Reversible, nonfatal bronchiolitis
10	—	Impairment of ability to detect odor of NO_2
5	15 min	Impairment of normal transport of gases between the blood and lungs in healthy adults
2.5	2 hr	Increased airway resistance in healthy adults
2	4 hr	Foliar injury to vegetation
1.0	15 min	Increased airway resistance in individuals with bronchitis
1.0	48 hr	Slight leaf spotting of pinto bean, endive, and cotton
0.3	—	Brownish color of target 1 km distant
0.25	Growing season	Decrease of growth and yield of tomatoes and oranges
0.2	8 hr	Yellowing of white fabrics
0.12	—	Odor perception threshold of NO_2
0.1	12 weeks	Fading of dyes on nylon
0.1	20 weeks	Reduction in growth of Kentucky bluegrass
0.05	12 weeks	Fading of dyes on cotton and rayon
0.03	—	Brownish color of target 10 km distant
0.003	—	Brownish color of target 100 km distant

Source: EPA Green Book, Part 50, July 2001 (http://www.epa.gov/air/oaqps/greenbk/40CFR50.html)

TABLE 16.2.8 U.S. Ambient Air Quality Criteria for Ozone

Concentration of O_3 in Air (ppm)	Human Symptoms and Vegetation Injury Threshold
10.0	Severe pulmonary edema; possible acute bronchiolitis; decreased blood pressure; rapid weak pulse.
1.0	Coughing; extreme fatigue; lack of coordination; increased airway resistance; decreased forced expiratory volume.
0.5	Chest constriction; impaired carbon monoxide diffusion capacity; decrease in lung function without exercise.
0.3	Headache; chest discomfort sufficient to prevent completion of exercise; decrease in lung function in exercising subjects.
0.25	Increase in incidence and severity of asthma attacks; moderate eye irritation.
0.15	For sensitive individuals, reduction in pulmonary lung function; chest discomfort; irritation of the respiratory tract, coughing, and wheezing. Threshold for injury to vegetation.

Source: EPA Green Book, Part 50, July 2001 (http://www.epa.gov/air/oaqps/greenbk/40CFR50.html)

TABLE 16.2.9 U.S. Ambient Air Quality Criteria for Particulate Matter

Concentration of Particulate Matter in Air (µg/m³)				
PM_{25}	PM_{10}	$PM_{2.5}$	Exposure Time	Human Symptoms and Effects on Visibility
2000	—	—	2 hr	Personal discomfort
1000	—	—	10 min	Direct respiratory mechanical changes
—	350	—		Aggravation of bronchitis
180	90	—		Increased respiratory disease symptoms
110	55	—	24 hr	Increased respiratory disease risk
—	—	22	13 weeks	Usual summer visibility in eastern U.S., nonurban sites

PM_x = particulates with diameter less than x µm; TP = thoracic particulates
Source: EPA Green Book, Part 50, July 2001 (http://www.epa.gov/air/oaqps/greenbk/40CFR50.html)

16.3 Sources of Pollution and Regulations

Sources

Jan F. Kreider, Nevis Cook, Tissa Illangasekare, and Ronald R. Hewitt Cohen

Air

Air pollutants are found in the form of gases (e.g., SO_2) and particulate matter (e.g., fine dust). They are emitted into the atmosphere from natural sources (e.g., volcanoes) and *anthropogenic* sources (e.g., industrial activities). These pollutants are called "primary" because they are harmful in the form in which they are emitted. Primary pollutants may undergo chemical reactions that result in the subsequent formation of other species called "secondary" pollutants (e.g., O_3).

Air pollution is found at all spatial scales, ranging from a few meters (e.g., indoor pollution) to local, urban, regional, and global scales (Milford and Russell, 1993). *Indoor pollution* is of great concern because a large fraction of our time is spent indoors. Indoor sources of pollutants include combustion processes, aging materials (e.g., formaldehyde emitted from particleboard and plywood), and radon — a natural indoor pollutant that migrates through the soil and may penetrate and accumulate inside buildings. The *local scale* ranges from 100 m to a few kilometers. At this scale, pollution dynamics are dominated by atmospheric diffusion and the role of primary pollutants. The local scale is the one where we experience major exposure to toxic substances and flammable compounds during catastrophic and emergency releases.

The *urban scale* ranges from 10 to 100 km and is characterized by both primary and secondary pollutants. In fact, characteristic residence times are on the order of one or a few days, thus, allowing enough time for chemical transformation to play a role. Two types of urban smog are well known: the "London" smog and the "Los Angeles" smog. The former is characterized by stagnant, foggy meteorological conditions in winter that allow a buildup, over a few days, of SO_2 and particulate matter. The latter, which has become the most common type of atmospheric pollution throughout the cities of the world, is a **photochemical** smog associated with clear, sunny days. Photochemical smog is a mixture of many gaseous compounds and particulate matter, among which the two most important constituents are ozone (a colorless secondary pollutant) and fine secondary particulate matter (such as sulfates, nitrates, and organic particles), which are responsible for most of the visual haze.

The *regional scale* ranges from hundreds to thousands of kilometers (the upper regional scale is also called *continental scale*). Characteristic residence times are on the order of one week. At this scale, pollution dynamics are dominated by chemical transformation and ground deposition phenomena. Acidic deposition, often referred to as *acid rain*, is a phenomenon in which acid substances, such as sulfuric and nitric acid, are brought to Earth by dry and wet deposition. Some lakes are very sensitive to acidic deposition because of their limited buffering capacity. *Global air pollution* is characterized by relatively unreactive compounds, such as CO_2, methane (CH_4), and chlorofluorocarbons (CFCs). The long lifetime of these pollutants allows their global dispersion and accumulation.

Air pollution at any scale creates several adverse effects. Air pollution can just be a nuisance (e.g., odors) or be aesthetically offensive (e.g., visibility impairment). Some adverse effects, however, are of fundamental importance to the welfare of the population and public health. For example, many pollutants cause respiratory effects; some pollutants have mutagenic effects; others have shown carcinogenic effects; some pollutants also have synergistic effects (e.g., the damage of SO_2 to the human respiratory system can be greatly enhanced by the presence of fine particles).

In the rest of this chapter, an overview is presented of analytical and numerical techniques for simulating air pollution phenomena. Air quality modeling is an essential tool for most air pollution studies today. Models can be divided into **deterministic** models, based on fundamental mathematical descriptions of atmospheric processes, and statistical models, based on semiempirical relationships extracted from data and measurements. Deterministic models, in particular, have become a major tool in providing

TABLE 16.3.1 Sources of Water Pollution vs. Contaminant Emission Categories

	General Emissions Type or Category									
Pollution Source	BOD	Pathogens	TSS	Turbidity	TDS	Nutrients N, P	Synthetic Organics	Volatile Organics	Metals	pH
Sewage	X	X	X	—	—	X	—	—	—	—
Mining operation	—	—	X	X	X	—	—	—	X	X
Timber operation	—	—	X	X	—	—	—	—	—	—
Agriculture	—	X	—	X	X	—	—	—	—	—
Food processing	X	—	X	—	X	—	—	—	—	X
Chemical manufacturing	X	—	—	—	—	—	X	X	X	X
Textiles manufacturing	X	—	X	X	X	—	—	—	—	X
Primary metals	—	—	—	—	—	—	—	—	X	X
Pulp and paper	—	—	X	X	X	—	—	—	—	X
Petroleum refining	X	—	X	—	—	X	—	X	X	X
Rubber/plastics	X	—	X	—	X	—	—	—	—	X
Septic systems	—	X	—	—	—	X	—	—	—	—
Injection wells	—	—	—	—	X	—	X	X	X	X
Sewage sludge	—	X	—	—	—	X	—	—	X	—
Urban runoff	—	X	—	X	X	—	X	X	X	—
Landfill leachate	X	—	—	—	X	X	—	—	—	—

Notation: BOD = biochemical oxygen demand; TSS = total suspended solids; TDS = total dissolved solids; synthetic organics = synthetic organic compounds; volatile organics = volatile organic compounds; metals = industrial metals; pH = high (alkaline) or low (acid) pH

objective assessment of air pollution scenarios and evaluating the effectiveness of different air pollution control measures. In fact, only deterministic models provide an unambiguous assessment of the fraction of responsibility of each pollution source in each receptor area, thus allowing the definition and implementation of the most cost-effective cleanup strategy. Statistical models, instead, are useful in situations where deterministic models do not perform well, for example, for real-time forecasting of air pollution episodes.

Waterborne

Table 16.3.1 summarizes important sources of surface water pollution species by economic or technical sectors of the U.S. economy. An X indicates a key source, and no entry indicates a second-order effect at most. Table 16.3.2 lists groundwater pollution sources by cause, extent, and waste type.

Soil and Groundwater

Various waste products and chemicals are generated from industrial, agricultural, commercial, and domestics activities. Unmonitored and uncontrolled long-term application on the land, accidental spillage, and improper storage and disposal result in these chemicals and wastes acting as potential sources of soil and groundwater contamination. LaGrega et al. (1994) use an engineering classification system in which hazardous wastes are grouped under six categories, namely, inorganic aqueous waste, organic aqueous waste, organic liquids, oils, inorganic sludges/solids, and organic sludges/solids. In addition to these, pathogens and nuclear wastes act as sources of contamination. As most of these materials are fully or partially soluble in water, they ultimately will contaminate the water phase contained within the soil pores and the water passing through the soil both in the unsaturated and saturated zones of the subsurface. Figure 16.3.1 shows in schematic form how groundwater pollution occurs.

Inorganic aqueous wastes generated from manufacturing activities involving galvanizing, metal finishing, electroplating, and so forth mostly contain acids, alkalis, or concentrated solutions of inorganic wastes such as heavy metals. Organic aqueous wastes are liquids that primarily contain mixtures of dilute concentrations of organic substances such as pesticides. Organic liquid wastes are complex mixtures or concentrated solutions of **organic compounds**. A common example of organic liquid wastes is halogenated solvents that are used in metal degreasing. Most of the oily wastes are derived from petroleum.

TABLE 16.3.2 Groundwater Pollution Sources in the U.S.

Source	Cause	Extent	Chemical/Wastes
Underground storage tanks	Hole due to internal and external corrosion leaks chemical into soil and groundwater	2.5 million 47 states, 35% of 800,000 fuel tanks leaked	Gasoline, oil, hazardous chemicals, waste products
Landfills	Rainwater leaching chemicals to groundwater	2,395 open dumps 24,000–36,000 closed or abandoned landfills 75,000 on-site industrial landfills 12,000–18,000 municipal landfills containing hazardous wastes	Garbage and trash, sludge, incinerator ash, foundry waste, hazardous substances
Surface impoundments	Direct infiltration to the saturated zone of aquifer	180,000 waste impoundments (1982) 37,000 municipal, 19,400 agricultural 27,912 industrial 25,000 mining 65,688 brine pits for oil and gas Industrial sites evaluated 95% within 1 mile of drinking wells, 70% unlined, 50% on top of aquifers	Settling ponds from municipal wastewater and sewage treatment, animal feed lots and farms, oil and gas industries, mining, paper, chemical operation
Waste-disposal injection wells	Direct dumping through wells to aquifers	Groundwater contamination in 20 states Millions of tons through thousands of wells	Toxic, hazardous, radioactive, metals, wood preservatives, petroleum
Septic systems	Surfacing and flooding due to failure; leaching into aquifers	22 million in U.S. 0.5 million installed every year 30% of population served	Variety of organic and inorganic compounds, fecal coliform, nitrates and nitrites, trichloroethylene, benzene, and methylene chloride
Agricultural waste	Leaching through unsaturated zone to groundwater	50,000 pesticides with 600 active ingredients 10 million t of nitrogen	Nitrates, salts, dissolved solids
Land application	Leachates reaching groundwater	Major threat to groundwater in 20 states 40% of hazardous wastes in California treated by land farming	Heavy metals, toxic chemical, nitrogen, pathogens
Radioactive contaminants	Potential migration to groundwater	Massive production of radioactive isotopes after World War II	Uranium, plutonium

Source: Bedient, P.B., Rifai, H.S., and Newell, C.J. 1994. *Ground Water Contamination: Transport and Remediation*, Prentice Hall, Englewood Cliffs, NJ, 541.

Oils are used as fuels, lubricating oils in engines, and cutting oils in manufacturing. Inorganic sludges/solids wastes are produced from wastewater treatment, smelters, coking, and metal fabrication. Tars and sludges that are produced from manufacturing activities are some examples of wastes that are in the form of organic sludges.

Waste materials and chemicals are released to the soil and groundwater from various sources. The most common sources are leaking underground chemical storage tanks, septic tanks, municipal landfills, industrial landfills, surface impoundments, and abandoned hazardous waste sites. In addition, injection wells, regulated hazardous waste sites, land application, road salting, saltwater intrusion, and oil and gas brine pits contribute to soil and groundwater contamination.

The most frequent use of underground tanks is for storage of gasoline in service stations. Hazardous wastes and chemicals and oils are also stored in buried tanks at industrial sites, farms, and homes. The potential for leakage exists when these tanks corrode internally or externally. In addition, chemicals can leak from pipe joints or holes in the pipes that are connected to the tanks.

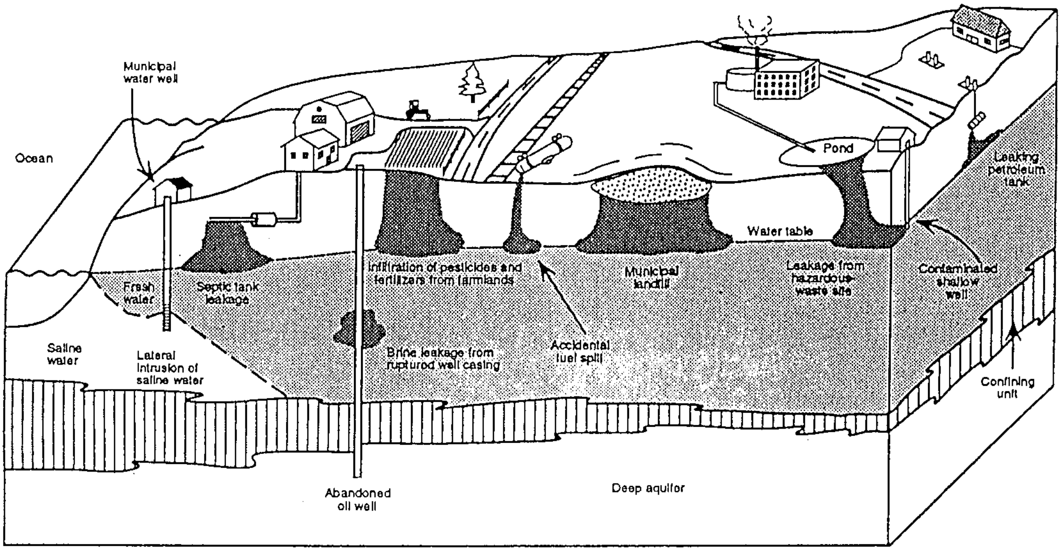

FIGURE 16.3.1 Mechanisms of groundwater contamination. (From Fetter, 1993.)

Older landfills that were not properly designed for containment of liquids or leachates were used to dispose of garbage, sludges from wastewater treatment plants, construction wastes and debris, incinerator ash, waste from foundries, and many other industrial and domestic hazardous and nonhazardous waste products. The chemicals in the landfill become a source of contamination when rain or surface water infiltrating through the landfill produces leachate. These leachates containing the dissolved constituents of the waste eventually contaminate the underlying soil and groundwater. Modern well-designed landfills have synthetic liners and leachate-collection systems.

Surface impoundments in the form of open pits, lagoons, or ponds are designed to accept liquid wastes or mixed solids and liquids. The chemical wastes in these temporary storage sites are treated and discharged or allowed to evaporate or infiltrate into the ground. In addition, to store and dispose of wastewater and products from sewage treatment, surface impoundments are used in paper, mining, and oil and gas industries. They are also used in farms and large feed lots. In unlined impoundments, the liquids leak, and when undetected, can result in soil and groundwater contamination in large zones of the subsurface.

Because of the large number of septic tanks that are in operation in homes, small businesses, service stations, laundries, and industry, septic tanks have become a major source of soil and groundwater contamination. When these systems fail, the sludges or septage floods the drainage field and leachates that are generated act as a source of contamination. The discharges from septic tanks contain many organic and inorganic chemical products, suspended solids, fecal coliform, pathogenic bacteria and viruses, nitrates, and nitrites. Industrial septic systems used in commercial operations discharge hazardous waste chemicals that include synthetic organics (e.g., trichloroethylene, tetrachloroethylene, toluene, etc.) and heavy metals (e.g., lead, copper, and zinc).

Injection wells that are drilled into deep aquifers or aquifers that are not used for water supply are used to discharge liquid wastes into the subsurface. Large volumes of toxic, hazardous, and radioactive wastes that are generated in chemical, petroleum, metals, mining, and wood-treatment industries are disposed of using this method. The contamination of aquifers that are used for drinking water can occur when the injection wells are not designed properly and are placed in formations where the hydrogeolgic conditions are not well known or understood.

Many types of agriculture-related activities use chemicals and produce wastes that contaminate soil and groundwater. Among these products are pesticides, fertilizer, and feed lot waste. Various types of pesticides are used in farming, golf courses, gardens, and parks to control insects and weeds. Many of the modern-day pesticides are biodegradable, but some of the stable ones are carried by rain and irrigation water through the soil to the groundwater. Fertilizers primarily contain nitrogen, potassium, and phosphorus. Because of comparatively high mobility in soil, nitrogen leachates are the primary contaminant of concern that is associated with application of fertilizers. Waste generated at large feed lots can introduce nitrogen, bacteria, and salts to the underlying aquifers. In addition to these sources, the salts that are accumulated in soils from long-term application of irrigation water act as a source of soil and groundwater degradation.

In a treatment and disposal method known as land treatment, the wastewater and sludges that are generated from treatment plants and industrial operations are directly applied on the ground surface. Contamination of the soil and groundwater occurs when heavy metals, toxic chemicals, nitrogen, and pathogens leach through the unsaturated zone.

Another source of soil contamination is the radioactive wastes that are produced in the weapons and nuclear industries. These wastes are primarily associated with the elements uranium and plutonium. The ionizing radiation in the form of alpha and beta particles and gamma rays are damaging to human and animal life. As these contaminants follow a first-order exponential decay law, they remain hazardous for very long time periods, on the order of hundreds to thousands of years. Table 16.3.2 summarizes several of the key sources of groundwater pollution, their extent, and the major associated pollutants.

Pollutant Monitoring

Jan F. Kreider and Tissa Illangasekare

Groundwater

Contaminants that are released to the aqueous phase from the soil or external sources move with the flowing groundwater creating a solute plume. Monitoring the groundwater flow velocity and the propagation of the solute plume is necessary to design schemes and strategies to protect the quality of groundwater that is used for drinking.

Monitoring wells are installed in aquifers to measure water pressure and to sample groundwater water quality. Wells in general consist of a standpipe with a screened interval. The screened interval allows for the aquifer water to flow into the well pipe. The water pressures are used to determine the head gradients, which in turn can be used to estimate the magnitude and direction of groundwater flow. Water samples that are collected at monitoring wells can be used to obtain information on the quality of groundwater.

Piezometric head is the sum of pressure and the elevation heads. The pressure head at any point in the aquifer intercepted by the screen is the height of the water surface in the well bore (or standpipe) above the point on the screen. The elevation head at a point is the elevation of the point above or below a datum. The gradient of the piezometric head determines the magnitude and direction of groundwater flow. By measuring the piezometric heads at many monitoring wells, it is possible to draw the contour lines of equal piezometric head or potential. A flow net is obtained by constructing a set of flow lines that are orthogonal to the equipotential lines. The groundwater flow direction at a point is determined by drawing a tangent to the flow line passing through the point. By constructing the flow net so that the intersection of equipotential lines and the flow lines form curvilinear squares, it is possible to estimate the groundwater flow velocities and discharge in an aquifer. The monitoring well data can also be used to calibrate a groundwater model that then can be used to estimate and monitor groundwater flow.

Groundwater samples collected from monitoring wells can be analyzed in the laboratory to determine the chemical contents. Probes can be inserted into the monitoring wells for the in situ measurement of conductivity and pH.

Process Emissions Monitoring. Methods and instrumentation for the monitoring of industrial waste discharge streams are discussed in detail in the *USEPA Handbook for Sampling and Sample Preservation of Water and Wastewater.* ASTM publishes a frequently updated *Annual Book of ASTM Standards* that extensively details recommended sampling techniques.

The topic of sampling is complex and includes sampling timing and frequency; sample preservation (until analyses can be done); sample preprocessing (i.e., filtering to separate particulate and dissolved components); questions of whether waste streams are continuously monitored for particular environmental variables or whether discrete samples are taken; whether a single "grab" sample is taken or a series of samples in time or space are retrieved and combined into a single "representative" sample; whether there is a single, worker-sampled, grab sample of an automated, continuous sampling apparatus; and whether there is retention of volatile compounds for later analysis. Additionally, there are issues of laboratory analytical techniques, quality control, and quality assurance from the moment of sampling through the reporting of the data, acceptable detection limits, sample contamination, and materials used to sample particular chemicals. The only way to account for all these variables is to know thoroughly the data-reporting requirements of the industrial discharge permits or agreements. Also, the objectives of the sampling and the compounds of concern will dictate the entire structure of the sampling regime. The authors will discuss, briefly, some of these topics.

The ideal characteristics of a process waste discharge stream for monitoring are steady, uniform flow that is chemically homogeneous throughout the cross section. Under such conditions, several grab samples over the day may yield representative results. In many industries, the waste streams vary due to process switching, change of shifts of workers, and cleaning and preparation of process equipment and machinery. Several specified times a day a local beer brewery flushes process wastes from the floor using high-pressure hoses. Occasional grab sampling might miss completely this pulse of waste load to the treatment system. There are continuous sampling devices that take a grab sample at specified time periods, and then rotate to another sample bottle in preparation for the next sample. There are more sophisticated samplers that draw in a sample at timed intervals proportional to stream discharge. Often, the type and frequency of discharge sampling is specified in the discharge permit. For best results, the sampling planner or coordinator should know the plant operation cycles in order to be able to characterize the time variation of discharges.

The material of which a sampling device and storage vessel is constructed must be matched to the materials sampled. Some organics require the use of tetrafluoroethylene (Teflon) tubing and glass storage vials that have been washed with an organic-free cleanser. Using the wrong tubing may result in the leaching of plasticizers into the sample. It is recommended that metal sampling devices *not* be used for collection of metal-laden discharge samples that require later analysis for metal ions. Samplers must be washed between samplings to avoid sample cross-contamination.

Environmental Quality Monitoring. Most of the mechanics and issues of sampling we just discussed for monitoring discharges hold true for environmental sampling, that is, after the discharge has entered a stream or lake. Detailed sampling plans must be prepared. Existing data is gathered (from company files; land-use maps; USEPA; U.S. Geological Survey gauging and water quality station results; state departments of environment, resources, and health; and other federal and local agencies). It helps to have site characteristics prior to the inception of the waste discharge.

The data collection for environmental monitoring often is governed by legal considerations concerning the validity and admissibility of the data. To this end, a quality assurance/quality control (QA/QC) plan must be prepared according to USEPA or state guidelines. These plans will specify the frequency of taking duplicate samples (taken at approximately the same time and place), split samples (one sample is split into two, separate containers), spiked samples (an additional injection of chemicals anticipated to be in the environmental sample are added to a duplicate sample, and the recovery of that known amount of spike is reported). A good QA/QC operation will ensure that the best effort is being made to

1. Obtain representative samples.
2. Use appropriate sampling methods.
3. Use appropriate analytical methods.
4. Ensure adequate records of chain of custody of samples.
5. Develop a sound and acceptable database.

The USEPA can be contacted to send *Interim Guidelines and Specifications for Preparing Quality Assurance Project Plans* (or QAPPS — pronounced "kwaps").

Other documents that may be required include

1. Sampling plans.
2. Site background information.
3. Planned sampling locations.
4. Planned sampling methodology and sample preservation. (Some chemicals decay on exposure to light, microbes may induce decomposition of organic compounds at ambient temperatures, chemically reduced compounds may oxidize on exposure to a head space of air, volatile compounds may escape from an insufficiently sealed vial, solid materials may dissolve, or dissolved materials may precipitate.)
5. Health and safety plans.
6. Plans for sample-handling procedures and chain of custody of samples.
7. Request forms for sample analyses.
8. Frequency and format of data reports.

Air Quality Monitoring

Air quality monitoring has many of the same goals and general techniques as water quality monitoring. A stationary monitoring network should yield the following information:

1. Background concentration
2. Highest concentration levels
3. Representative levels in populated areas
4. Impact of local sources
5. Impact of remote sources
6. Relative impact of natural and anthropogenic sources

Spatial scales range from micro- (up to 100 m) to regional scales (tens to hundreds of kilometers). Site selection is a key part of network design because microclimates can affect readings and cause them to be nonrepresentative of the region.

Mobile monitoring is useful when sites not monitored with the fixed network need assessment. The key drawback of such systems is the scarcity of equipment suitable for reliable and durable mobile monitoring. Remote sensing offers a second alternative to stationary networks.

Quality assurance is a continuous concern of monitoring systems. Good instrumentation installation and maintenance practice along with careful record keeping is essential.

Space precludes presentation of further details on air quality monitoring, but Boubel et al. (1994) has a thorough overview.

16.4 Regulations and Emission Standards

Water

Nevis Cook and Ronald R. Hewitt Cohen

The Clean Water Act (CWA) of 1972 and its amendments establish the framework of current U.S. water pollution control. This act is sometimes referred to as the Federal Water Pollution Control Act Amendments after the original 1965 act, which the CWA amended. The objective of the CWA is to "restore and maintain the chemical, physical, and biological integrity of the nation's waters." The CWA regulates both nonpoint (runoff from farmlands, roads, and city streets) and point sources (discharges from pipes conveying pollutants to surface waters) of water pollution. The discussions in this chapter are limited to regulation of point sources of pollution to *surface* waters. Discharges to groundwaters are regulated under the Safe Drinking Water Act (SDWA) underground injection control (UIC) program and are beyond the scope of this chapter. The discussion is still quite broad, since all domestic and industrial wastewater discharges are considered point sources under the CWA.

Discharge Permits. The CWA prohibits point source discharges to surface waters unless a *discharge permit* is obtained. Permits typically are issued at the state level and are known as state pollution discharge elimination standards (SPDES) permits. If the state has not taken over this responsibility, national (NPDES) permits are issued by the USEPA. The permit for each point source prescribes allowable discharges in terms of amount and concentration of flows and pollutants. In some cases, an industrial facility may avoid obtaining its own permit by discharging into the local public sewer system. Control of these *indirect discharges* is accomplished by requiring publicly owned treatment works (POTWs) receiving such discharges to enter into formal *pretreatment agreements* with industrial users of the sewer. Such pretreatment agreements are intended to prevent industrial discharges to POTWs, which would represent a hazard to the sewer system or its workers, interfere with treatment operations or sewage sludge disposal, or pass through the treatment process, causing a violation of the POTW discharge permit.

Permitted Discharges. Prior to the CWA of 1972, point source water pollution control laws were established at the state level and permitted discharge of pollutants on a discharger-by-discharger and water body-by-water body basis. This approach worked poorly in most states, demonstrating the need for enforceable *federal minimum effluent standards*. For this reason, the CWA and subsequent amendments have established *technology-based* national minimum pretreatment and discharge standards. Technology-based standards reflect the current state of the art with respect to controlling specific pollutant discharges from specific pollution sources. Since technology-based standards represent the capabilities of typical "well-operated" facilities and are not issued on the basis of in-stream water quality, it is not surprising that in some cases compliance with national minimum standards does not adequately protect all potential uses of a water body. In such cases the uses of the receiving water body are said to be *water quality limited*, and *local discharge limits*, more stringent than national limits, may be imposed. In addition, pretreatment agreements reflect the capabilities of local treatment works with respect to pass through, destruction, or partitioning of nondegradable toxic metal pollutants into POTW sludges. Following the development of local water quality–based limits, these are compared with national minimum technology-based standards and the more restrictive criteria are imposed as discharge permit or pretreatment limitations. Further considerations with respect to setting permit values are presented next.

Industrial dischargers may obtain an industrial NPDES permit and directly discharge wastewater to a receiving water body. Alternatively, where municipal sewer service is available, industries may choose to negotiate a pretreatment agreement with the local sewer authority permitting discharge of industrial wastewater to the sewer system. Most industrial facilities employing either discharge option (direct or indirect) are subject to national technology-based minimum effluent standards. In addition, more stringent standards may be imposed at the state or local level.

State permits containing discharge constraints more stringent than the national minimum standards are commonly derived from local water quality considerations. Ideally, local water quality–based standards are developed from science-based use protection criteria, wastewater flow data, and actual receiving water characteristics (such as low-flow conditions for streams). Rational direct discharge permits to streams or rivers can be developed by application of the following procedure: convert use-based, in-stream quality criteria to standards according to local policy; obtain data on upstream water quality and low-flow conditions (conditions at which the waste assimilative capacity of a stream is at a minimum) and determine potential for dilution of the wastewater flow by the receiving water body; compute the allowable water quality–based industrial discharge on a pollutant-by-pollutant basis and compare with national minimum standards; and finally, impose permit restrictions according to the most stringent of the two types of standards developed.

Development of water quality–based permits for direct discharges to lakes, estuaries, bays, or oceans follows a procedure similar to that just outlined. However, estimates of mixing patterns and the dilution

TABLE 16.4.1 U.S. Federal Primary and Secondary Ambient Air Quality Standards

				Concentration	
Pollutant	Type of Standard	Averaging Time	Frequency Parameter	$\mu g/m^3$	ppm
Sulfur oxides (as sulfur dioxide)	Primary	24 hr	Annual maximum	365	0.14
		1 year	Arithmetic mean	80	0.03
	Secondary	3 hr	Annual maximum	1,300	0.5
Particulate matter <10 µm	Primary and Secondary	24 hr	Annual 99th percentile	150	—
		24 hr	Annual arithmetic mean	50	—
Particulate matter <2.5 µm	Primary and Secondary	24 hr	Annual 98th percentile	65	—
		24 hr	Annual arithmetic mean	15	—
Carbon monoxide	Primary and secondary	1 hr	Annual maximum	40,000	35.0
		8 hr	Annual maximum	10,000	9.0
Ozone	Primary and secondary	1 hr[1]	Annual maximum	235	0.12
	Primary and secondary	8 hr[2]	Three-year average of 4th highest daily maximum	15	0.08
Nitrogen dioxide	Primary and secondary	1 year	Annual arithmetic mean	100	0.053
Lead	Primary and secondary	3 months	Quarterly arithmetic mean	1.5	—

[1] Will be phased out in favor of eight-hour standard after three years of compliance with one-hour standard.

[2] Will be phased in after three years of compliance with one-hour standard.

Source: *EPA Green Book*, Part 50, July 2001 (http://www.epa.gov/air/oaqps/greenbk/40CFR50.html)

potential of these water bodies are likely to be more difficult because of the complex flow patterns involved. Water quality–based pretreatment standards for discharges to sewers also follow the same general procedure. However, in this case, the application of use criteria, policy, and potential for in-stream dilution lead to a pollutant-by-pollutant permit for the *local* POTW. Based on this permit and the removal capabilities of the treatment facility, maximum allowable (usually daily) loading of pollutants arriving at the plant is determined on a pollutant-by-pollutant basis. Allowable loads are then allocated to the various municipal and industrial users of the sewer. Setting water quality–based pretreatment standards is obviously complicated by the presence of multiple sewer uses and users. Thus, POTWs receiving significant industrial discharges are required to set up formal programs to negotiate industrial pretreatment agreements and monitor compliance.

Air

Jan F. Kreider

The U.S. Clean Air Act Amendments of 1977 set forth two air quality standard types:

- Primary (to protect health)
- Secondary (to protect health and prevent other adverse impacts)

Table 16.4.1 summarizes the present primary and secondary standards in the U.S. The amendments also specified for certain geographical areas further standards to prevent significant deterioration (PSD areas). These are standards that are to be considered increments over baseline air quality but are more stringent than secondary or primary standards in most cases. Table 16.4.2 lists these PSD standards.

16.5 Mitigation of Water and Air Pollution

This section discusses the methods for abating or mitigating air and water pollution burdens on the environment. Because mechanical engineers are most concerned with air pollution control systems and civil engineers deal with water treatment systems, this section emphasizes the air pollution mitigation side.

TABLE 16.4.2 U.S. Federal PSD Concentration Increments

Pollutant	Increment ($\mu g/m^3$) Class I areas	Class II areas	Class III areas
Particulate matter			
TSP, annual geometric mean	5	19	37
TSP, 24-hr maximum	10	37	75
Sulfur dioxide			
Annual arithmetic mean	2	20	40
24-hr maximum	5	91	182
3-hr maximum	25	512	700
Nitrogen dioxide			
Annual arithmetic mean	2.5	25	50

Overview

Jan F. Kreider

There are several methods for controlling air- or waterborne pollution:

- Process change
- Fuel change
- Pollution removal and disposal
- Pollution prevention

Process change includes everything from modifications that reduce emissions to substitution of a less polluting one for a more polluting one. The latter could be classified as pollution prevention, described shortly. In many cases, for example, in the steel industry, it has proved most economical to replace completely old plants with totally new ones. Likewise, complete substitution has been widely adopted in the pulp and paper industry.

Fuel change as a control strategy is based on the fact that airborne pollutants often are related to the combustion aspects of a process. For example, coal-fired power plants emit SO_2 because coal contains sulfur. Substitution of natural gas for coal eliminates any sulfur in the fuel and, therefore, any oxides of sulfur in the stack gases.

Fuel changes must consider fuel supply, capital cost, and competition for clean fuels among many industries before an engineering design decision can be made. Life-cycle methods that consider all parts of the life of a plant are necessary. For example, a nuclear power plant may produce very low emission electricity but after decommissioning may cause long-term waste disposal problems.

Pollution removal is necessary when process or fuel changes cannot provide adequate emission control. A physical, chemical, or electrical feature of the pollutant to be removed must differ from those types of characteristics of the carrying gas or liquid stream. An example is a baghouse or electrostatic precipitator for particulate emissions. Not only collection of pollutants but also disposal of the collected pollutant must be considered by the design engineer. A whole systems viewpoint is necessary for a successful pollution removal design.

Pollutant disposal is governed by different criteria depending on whether it is hazardous. Hazardous waste disposal is covered by the Resource Conservation and Recovery Act of 1976, which established the Office of Solid Waste with the USEPA. On the other hand, nonhazardous waste disposal is governed by the states. Table 16.5.1 categorizes the ultimate disposal methods for classes of hazardous wastes. Many of the methods apply for nonhazardous wastes as well.

Pollution prevention is the ultimate solution to abatement. This can be accomplished at the source by various technical means, depending on process specifics. This approach is currently the most commonly used term by the USEPA. The Pollution Prevention Act of 1990 provides these policies:

- Prevent or reduce pollution at the source whenever possible.
- Recycle to the environment pollution that cannot be prevented in a safe manner whenever possible.

TABLE 16.5.1 Ultimate Waste Disposal Methods

Process	Purpose	Wastes	Problems (Remarks)
Cementation and vitrification	Fixation Immobilization Solidification	Sludges Liquids	Expensive
Centrifugation	Dewatering Consolidation	Sludges Liquids	—
Filtration	Dewatering Volume reduction	Sludges Liquids	Expensive
Thickening (various methods)	Dewatering Volume reduction	Sludges Liquids	—
Chemical addition (polyelectrolytes)	Precipitation	Sludges	Can be used in conjunction with other processes
	Fixation		
	Coagulation	Liquids	
Submerged combustion	Dewatering	Liquids	Acceptable for aqueous organics
	Major Ultimate Disposal Methods		
Deep well injection	Partial removal from biosphere Storage	Oil field brines; low toxicity, low-persistence wastes; refinery wastes	Monitoring difficulty; need for special geological formations; groundwater contamination
Incineration	Volume reduction Toxicity destruction	Most organics	If poor process control, unwanted emissions produced Can produce NO_x, SO_x, halogen acids
Recovery	Reuse	Metals Solvents	Sometimes energy prohibitive
Landfill	Storage	Inert to radioactive	Volatilization
	Major Waste Disposal Methods		
Land application	Dispersal		Access to biota
Land burial	Isolation		Leaching to groundwater
Ocean disposal	Dispersal	Acids, bases	Contact with ocean ecosystem; containers unstable
	Dilution	Explosives	
	Neutralization	Chemical war agents	
	Isolation(?)	Radioactive wastes	
	Minor Disposal Methods		
Biological degradation	Reduction of concentration Oxidation	Biodegradable organics	Most hazardous wastes do not now qualify.
Chemical degradation (chlorination)	Conversion Oxidation	Some persistent pesticides	—
Electrolytic processes	Oxidation	Organics	—
Long-term sealed storage	Isolation Storage	Radioactive	How good are containers?
Salt deposit disposal	Isolation Storage	radioactive	Are salt deposits stable in terms of waste lifetimes?

- Pollution that can neither be prevented nor recycled should be treated in as environmentally safe a manner as possible.
- Disposal or other release into the environment should be used as only a last resort.

TABLE 16.5.2 Key Characteristics of Pollution Control Devices and/or Systems

Factor Considered	Characteristic of Concern
General	Collection efficiency
	Legal limitations such as best available technology
	Initial cost
	Lifetime and salvage value
	Operation and maintenance costs
	Power requirement
	Space requirements and weight
	Materials of construction
	Reliability
	Reputation of manufacturer and guarantees
	Ultimate disposal/use of pollutants
Carrier gas	Temperature
	Pressure
	Humidity
	Density
	Viscosity
	Dewpoint of all condensables
	Corrosiveness
	Inflammability
	Toxicity
Process	Gas flow rate and velocity
	Pollutant concentration
	Variability of gas and pollutant flow rates, temperature, etc.
	Allowable pressure drop
Pollutant (if gaseous)	Corrosiveness
	Inflammability
	Toxicity
	Reactivity
Pollutant (if particulate)	Size range and distribution
	Particle shape
	Agglomeration tendencies
	Corrosiveness
	Abrasiveness
	Hygroscopic tendencies
	Stickiness
	Inflammability
	Toxicity
	Electrical resistivity
	Reactivity

Air Pollution Control

Jan F. Kreider

The most common method of meeting emission standards in industries that must control air pollution is by *pollution removal*. This section describes the most widely used approaches. Table 16.5.2 lists the important characteristics of control systems for airborne pollutants.

Dry particulate matter is removed by

- Filters — baghouse, fixed beds, or mats
- Electrostatic precipitators — plate-type, tube-type; see Figure 16.5.1
- Inertial collectors — cyclones and baffles; see Figure 16.5.2
- Scrubbers — wet or dry

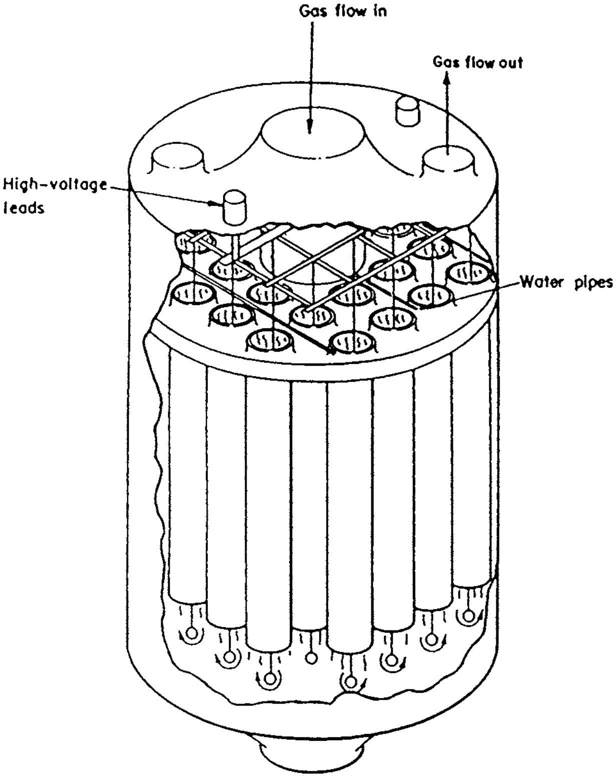

FIGURE 16.5.1 Wet-wall eledtrostatic precipitator with tubular collection electrodes. (From Oglesby, S. Jr., and Nichols, G.B., in *Air Pollution*, 3rd ed., Vol. IV, Stern, A.C., ed., p.238, Academic Press, New York, 1977. With permission.)

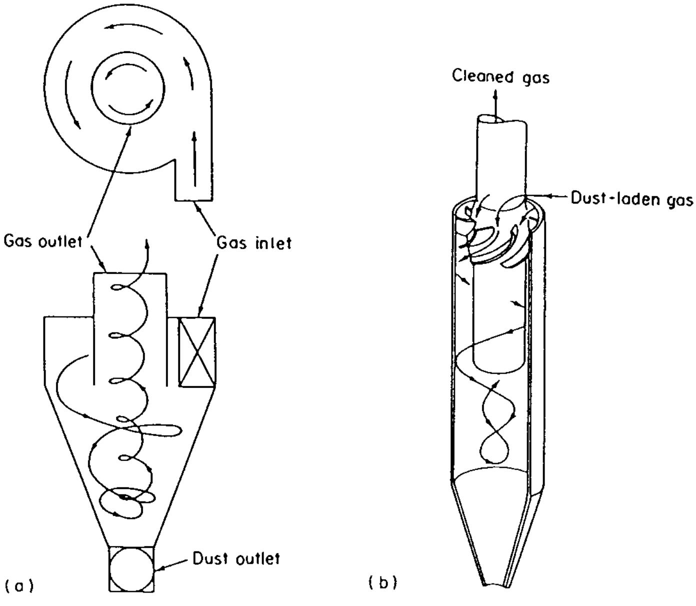

FIGURE 16.5.2 (a) Tangential inlet cyclone (b) Axial inlet cyclone.

TABLE 16.5.3 Comparison of Particulate Removal Systems

Type of Collector	Particle Size Range (µm)	Removal Efficiency	Space Required	Max.Temp. (°C)	Pressure Drop (cm H_2O)
Baghouse	0.1–0.1	Fair	Large	80	10
(cotton bags)	1.0–10.0	Good	Large	80	10
	10.0–50.0	Excellent	Large	80	10
Baghouse (Dacron, nylon,	0.1–1.0	Fair	Large	120	12
Orlon)	1.0–10.0	Good	Large	120	12
	10.0–50.0	Excellent	Large	120	12
Baghouse (glass fiber)	0.1–1.0	Fair	Large	290	10
	1.0–10.0	Good	Large	290	10
	10.0–50.0	Good	Large	290	10
Baghouse (Teflon)	0.1–1.0	Fair	Large	260	20
	1.0–10.0	Good	Large	260	20
	10.0–50.0	Excellent	Large	260	20
Electrostatic precipitator	0.1–1.0	Excellent	Large	400	1
	1.0–10.0	Excellent	Large	400	1
	10.0–50.0	Good	Large	400	1
Standard cyclone	0.1–1.0	Poor	Large	400	5
	1.0–10.0	Poor	Large	400	5
	10.0–50.0	Good	Large	400	5
High-efficiency cyclone	0.1–1.0	Poor	Moderate	400	12
	1.0–10.0	Fair	Moderate	400	12
	10.0–50.0	Good	Moderate	400	12
Spray tower	0.1–1.0	Fair	Large	540	5
	1.0–10.0	Good	Large	540	5
	10.0–50.0	Good	Large	540	5
Impingement scrubber	0.1–1.0	Fair	Moderate	540	10
	1.0–10.0	Good	Moderate	540	10
	10.0–50.0	Good	Moderate	540	10
Venturi scrubber	0.1–1.0	Good	Small	540	88
	1.0–10.0	Excellent	Small	540	88
	10.0–50.0	Excellent	Small	540	88
Dry scrubber	0.1–1.0	Fair	Large	500	10
	1.0–10.0	Good	Large	500	10
	10.0–50.0	Good	Large	500	10

TABLE 16.5.4 Comparison of Gaseous Pollutant Removal Systems

Type of Equipment	Pressure Drop (cm H_2O)	Installed Cost (U.S. $/m3)
Scrubber	10	9.80
Absorber	10	10.40
Condenser	2.5	28.00
Direct flame afterburner	1.2	8.20
Catalytic afterburner	2.5	11.60

Source: Boubel et al. (1994)

Table 16.5.3 lists the key characteristics of these technologies and where they are best applied. Of course, a design is needed upon which a quotation for final cost studies can be based. Table 16.5.4 compares gaseous pollutant removal systems.

Table 16.5.4 compares gaseous pollutant removal systems.

Cataloging of industry-specific designs is beyond the scope of this handbook because of space limitations. The reader is referred to Boubel et al. (1994) for details. One must make an inventory of emissions and then identify the most appropriate control methods based on operating and capital costs considerations.

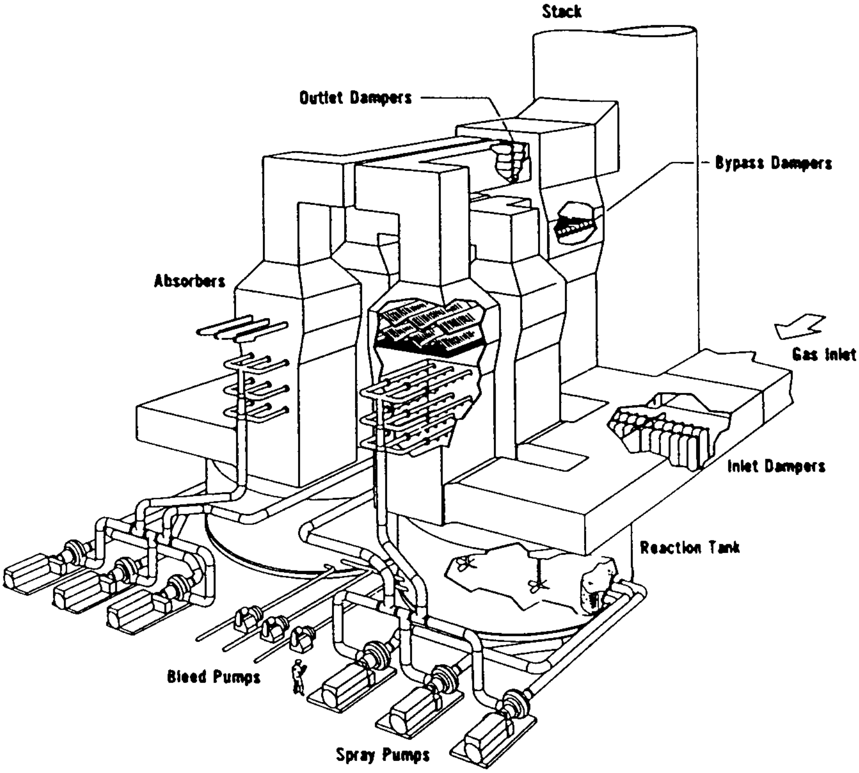

FIGURE 16.5.3 Cutaway drawing of a flue gas desulfurization spray tower absorber. (Courtesy of CE Power Systems, Combustion Engineering Inc.)

For example, Table 16.5.5 shows common emissions and control methods for the petrochemical industry. The energy, power generation, incineration, ferrous and nonferrous metallurgical, agricultural, and mineral/mining industries produce considerable emissions that must be controlled in accordance with federal regulations.

Water Pollution Control

Nevis Cook and Ronald R. Hewitt Cohen

Control of waterborne pollutants is at present undertaken by nine distinct techniques:

- Biological oxidation
- Chemical oxidation
- Chemical reduction
- Conventional treatment
- Precipitation
- Air stripping
- Activated carbon
- Ion exchange
- Reverse osmosis

Table 16.5.6 summarizes these approaches and their applications by contaminant type. The letter A in the table indicates the best available technology, whereas a B indicates an alternative that may apply to a subclass of industries. The reader is referred to the notes for the table to learn further details.

TABLE 16.5.5 Air Pollution Emissions and Controls: Petrochemical Processes

Petrochemical Process	Air Pollutant Emissions	Control Methods in Use
Ethylene oxide (most emissions from purge vents)	Ethane, ethylene, ethylene oxide	Catalytic afterburner
Formaldehyde (most emissions from exit gas stream of scrubber)	Formaldehyde, methanol, carbon monoxide, dimethyl ether	Wet scrubber for formaldehyde and methanol only; afterburner for organic vent gases
Phthalic anhydride (most emissions from off-gas from switch condensers)	Organic acids and anhydrides, sulfur dioxide, carbon monoxide, particulate matter	Venturi scrubber followed by cyclone separator and packed countercurrent scrubber
Acrylonitrile (most emissions from exit gas stream from product absorber)	Carbon monoxide, propylene, propane, hydrogen cyanide, acrylonitrile, acetonitrile NO_x from by-product incinerator	Thermal incinerators (gas-fired afterburners or catalytic afterburners)
		None
Carbon black (most emissions from exit gas stream from baghouse, some fugitive particulate)	Hydrogen, carbon monoxide, hydrogen sulfide, sulfur dioxide, methane, acetylene	Waste heat boiler or flare (no control for SO_2)
	Particulate matter (carbon black)	Baghouse
Ethylene dichloride (most emissions from exit gas stream of solvent scrubber)	Carbon monoxide, methane, ethylene, ethane, ethylene dichloride, aromatic solvent	None at present, but could use a waste heat boiler or afterburner, followed by a caustic scrubber for hydrochloric acid generated by combustion

TABLE 16.5.6 General Effectiveness of Treatment Technology vs. Contaminant Type

Constituent	Biological Oxidation	Chemical Oxidation	Chemical Reduction	Conventional Treatment	Precipitation	Air Stripping	Activated Carbon	Ion-Exchange	Reverse Osmosis
BOD	A	—	—	—	—	—	—	—	—
COD	B	B	—	—	—	—	B	—	—
Mos[a]	—	A	—	A	A	—	—	—	I
Turb.[b]	—	—	—	A	B	—	—	I	I
TDS[c]	—	—	—	—	—	—	—	A	A
Ca, Mg	—	—	—	—	A	I	—	A	A
Fe, Mg	—	P	I	B	A	I	—	I	I
NH_3	A	B	—	—	—	B	—	B	B
	—	—	A	—	—	—	—	B	B
Me++[d]	—	—	—	B	A	—	—	A	A
Cr	—	I	P	B	A	—	—	A	A
As, Se	—	P	I	B	A	—	—	A	A
CN	—	A	—	—	—	I	—	—	B
Phenols	B	A	—	—	—	—	B	—	—
SOC[e]	B	B	—	—	—	—	A	—	A
VOC[f]	B	B	—	—	—	A	B	—	B

A = treatment technology commonly applied to reduce contaminant to acceptable levels; perhaps best conventional technology.

B = treatment technology that has been used to remove a particular contaminant, but might not be fully effective under all conditions.

I = substance could interfere with efficient removal of other contaminants.

P = pretreatment required if technology is to be used.

[a] MO = microbiological contaminants including pathogenic bacteria, protozoa, and viruses.

[b] Turb. includes fine colloidal matter and suspended solids, for true suspended solids use sedimentation.

[c] Total dissolved solids (TDS) includes removal of the highly soluble ions: Na+, K+, Cl–,

[d] Includes the valence +2 transition metals: Cu++, Ni++, Pb++, Zn++.

[e] SOC = synthetic organic compounds, including pesticides.

[f] VOC = volatile organic compounds, including solvents.

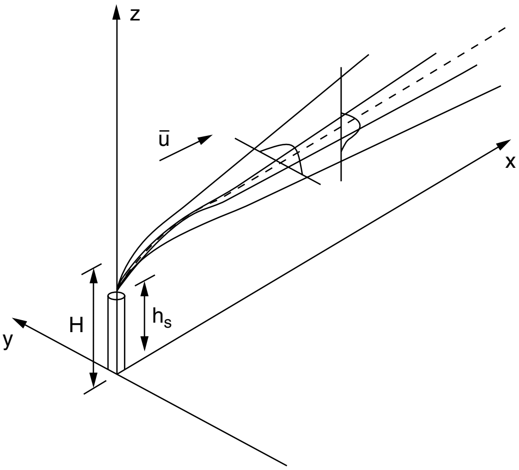

FIGURE 16.6.1 The Gaussian plume in a wind-oriented coordinate system (i.e., the wind is blowing toward the *x* axis). The plume is released from a source located at (0, 0, h_s) and possesses an initial buoyancy. Therefore, the plume behaves as if it were originated from (0, 0, *H*), where *H* is the effective emission height and $\delta h = H - h_s$ is the plume rise. The plume is advected by the average wind speed $\bar{\mathbf{u}}$ and expands in the horizontal and the vertical direction while maintaining a Gaussian distribution along both.

16.6 Environmental Modeling

Air Pollution Dispersion Modeling

Paolo Zannetti

To understand air pollution, it is mandatory, at any scale, to simulate correctly the dispersion characteristics of the emitted chemicals. Therefore, the role of meteorology is essential. Pollutants are typically transported by two types of flows: an "ordered" flow, which is characterized by average wind speed and direction, and a semi-random, turbulent flow, which is characterized by wind fluctuations. All dispersion models aim at simulating these two components. As further discussed next, dispersion modeling techniques can be categorized into four general classes: (1) Gaussian models; (2) Eulerian grid models; (3) Lagrangian box models; and (4) Lagrangian particle models.

Gaussian Models

All Gaussian models assume that the concentration of pollutants maintains a Gaussian distribution in space. The Gaussian distribution, as illustrated in Figure 16.6.1, is a symmetrical bell-shaped distribution, which is described at any given point *x*,*y*,*z* by two parameters: the location of the peak (in this case, the centerline of the plume indicated by the segmented line) and the standard deviation (in this case, the spread of the plume mass about its center). Therefore, the dilution rate of the plume is fully characterized by the two standard deviations, σ_y and σ_z, expressed as a function of the downwind distance, *x*.

In mathematical notation, the Gaussian plume formula in Figure 16.6.1 can be written as

$$c = \frac{Q}{2\pi\sigma_y\sigma_z\bar{u}}\exp\left[-\frac{1}{2}\left(\frac{y}{\sigma_y}\right)^2\right]\exp\left[-\frac{1}{2}\left(\frac{H-z}{\sigma_z}\right)^2\right] \tag{16.6.1}$$

where *c* is the concentration computed at the receptor (*x*, *y*, *z*) [mass/volume], *Q* is the emission rate [mass/time], $\bar{u}$ is the average horizontal wind speed [length/time], *H* is the effective emission height [length], and σ_y and σ_z [length] are functions of the downwind distance, *x*, with parameters that vary with the meteorological conditions (in fact, the stronger the turbulence intensity of the atmosphere, the larger the growth rate of σ_y and σ_z with x).

As can easily be seen, Equation 16.6.1 refers to a stationary state (i.e., c is not a function of time), uses meteorological parameters that must be considered homogeneous and stationary in the modeled area (i.e., between the source and the receptors at which concentrations are computed), and cannot work in calm conditions where the wind speed approaches zero (in general, the wind speed cannot be less than 1 m/sec when Equation 16.6.1 is applied). In spite of these limitations, the simplicity of the Gaussian approach, its relative ease of use, and especially the elevation of this methodology to the quantitative decision-controlling level in the U.S. (USEPA, 1978) have stimulated research aimed at removing some of the limitations of the Gaussian theory in modeling the real-world situations.

Equation 16.6.1 has been modified and expanded to incorporate, among others, the following factors: ground reflection, multiple reflections, hourly simulations as a sequence of steady-state conditions, deposition and decay, chemical transformation, fumigation, complex terrain, gravitational settling, calm conditions, nonstationary and nonhomogenous conditions, and long-term simulations. We next summarize some of these improvements.

Reflection terms can be added to Equation 16.6.1 to account for partial or total reflection of concentration at the ground. Similarly, reflection can be added at the top of **the planetary boundary layer**, or **PBL** (typically, about 500 to 1000 m above the ground). If both reflections are implemented, the plume is trapped inside the PBL. Equation 16.6.1 is generally applied for periods of 1 hr. This allows the incorporation of time-varying emission and meteorological parameters. Chemistry and decay can be incorporated by introducing exponential decay terms (e.g., it can be assumed that an emission of primary gaseous SO_2 is transformed into particulate sulfate at a rate of 1% per hour). Gravitational settling will affect a plume of primary particulate matter. In this case, the plume centerline can be tilted to account for the settling velocity of the particles, which is a function of both particle size and density.

In addition to the Gaussian plume model, Gaussian segment and puff models can be used (Zannetti, 1986a). These models break up the plume into independent elements (plume segments or puffs) whose initial features and time dynamics are a function of time-varying emission and meteorological conditions encountered by the plume elements. These techniques allow us to account properly for nonhomogeneous, nonstationary conditions. Gaussian puff models, in particular, have the additional advantage of being able to simulate calm or low-wind conditions.

Complex terrain conditions affect the plume dynamics — both the motion of the centerline trajectory and the growth of σ_y and σ_z. Finally, the Gaussian plume model equation can be rewritten in a way to simulate long-term concentration averages (e.g., annual averages) by incorporating the joint frequency of occurrence of a predetermined set of emission and meteorological conditions.

Many Gaussian models have been developed and are available for free downloading or purchase. For example, the ISC3 model is one of the most used computer packages and can be found at http://www.epa.gov/scram001/tt22.htm#isc.

Also, a new state-of-the-art Gaussian model (AERMOD) has been recently developed by the US EPA; learn more at http://www.epa.gov/scram001/tt26.htm#aermod.

Among puff models, the CALPUFF modeling system is probably the most comprehensive and can be found at http://www.src.com/calpuff/calpuff1.htm.

Other Models

Eulerian grid models (Lamb [from Longhetto], 1980) simulate pollutant diffusion by superimposing a grid over the computational domain and numerically solving a mass-balance equation (typically, a partial differential equation, PDE, or a set of PDEs) in each grid cell at each time step. This is also called numerical integration. In general, the smaller the grid and time intervals, the more accurate the numerical solution.

Difficulties may be encountered with Eulerian grid models in simulating atmospheric diffusion with the K-theory. In particular, the application of the K-theory to simulate vertical dispersion during daytime, unstable meteorological conditions is highly questionable. To improve the simulation ability of Eulerian grid models, equations of high-order moments of concentration, wind, and temperature fluctuations

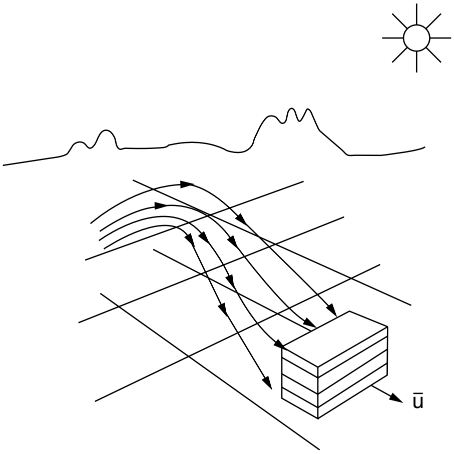

FIGURE 16.6.2 Lagrangian box modeling.

can be solved simultaneously. This approach, called high-order closure, requires the definition of more complex, nonlinear relationships between the turbulent fluxes and the concentration fields.

Lagrangian box models are mostly used to perform fast simulations of photochemical smog. These models define a set of "boxes" (e.g., a column of boxes, as illustrated in Figure 16.6.2), which are advected horizontally according to the local wind speed and direction. Each box encounters emissions along its trajectory. These emissions inject new pollutants inside the box. A full set of chemical reactions inside each box allows the simulation of the photochemical smog and the formation of secondary pollutants, such as ozone.

Lagrangian particle models provide a very interesting alternative method for simulating atmospheric diffusion. Particle motion can be produced by both deterministic velocities and semi-random pseudo-velocities generated using Monte Carlo techniques. In the latter case, the trajectory of a single particle represents a realization from an infinite set of possible solutions, and if enough particles are used, important characteristics can be inferred from the computation of particle **ensemble average** properties.

When using Lagrangian particle models to simulate air pollution, pollutant emissions (both gases and particulate matter) are represented by the injection of fictitious particles into the computational domain. Each particle represents a specified amount of pollution and is moved at each time step by a pseudo-velocity that is time and space dependent. Zannetti (1990) discusses alternative modeling approaches in more detail than is possible here.

Atmospheric Chemistry

Atmospheric chemistry deals essentially with four major issues (Seigneur 1987): (1) photochemical smog in sunny, urban areas; (2) **aerosol** chemistry; (3) acidic deposition; and (4) air toxics. Chemical reactions can be simulated in two ways: (1) with simple first-order terms (e.g., a decay term), and (2) with a full chemical reaction scheme.

First-order terms for simulating atmospheric chemistry can be easily incorporated into any of the models previously discussed. For example, a radioactive pollutant with a specified decay rate (or half-life) can be simulated by introducing the following multiplicative term in any concentration equation

$$\exp\left(-t/T\right) \tag{16.6.2}$$

where t is the travel time and T is the time scale of the decay (easily related to the half-life of the chemical species). Similarly, chemical transformation from a primary to a secondary pollutant (e.g., from gaseous SO_2 to sulfate particulate matter SO_4^{2-}), can be accomplished by introducing two exponential terms — $[\exp(-t/T)]$ and $[1 - \exp(-t/T)]$ — having the effect of simultaneously decreasing the SO_2 concentration and increasing the SO_4^{2-} concentration as time increases. First-order schemes, though relatively simple, may use parameters that are space and time dependent; for example, the SO_2-to-SO_4^{2-} conversion rate may vary as a function of relative humidity and solar radiation.

Photochemical smog, which in the past only affected large cities at low latitudes, such as Los Angeles, has become today the most important and common air pollution problem in urban areas throughout the world. Overall, the photochemical smog reactions can be summarized as

$$\text{ROG} + \text{NO}_x + \text{sunlight} \rightarrow \text{O}_3, \text{PAN}, \text{HCHO}, \text{HNO}_3, \text{PM}, \ldots \tag{16.6.3}$$

where ROG are primary reactive organic gases and NO_x include primary NO and mostly secondary NO_2. This smog includes carbon monoxide (CO), ozone (O_3) formaldehyde (HCHO), peroxyacetyl nitrate (PAN), nitric acid (HNO_3), secondary particles, such as nitrates and organic particles, and other products.

A full chemical reaction scheme is required to simulate complex phenomena, such as the photochemical smog just described, and can be incorporated today only inside Eulerian grids or Lagrangian box models. A typical reaction set, applied in each grid cell at each time step, can be written in terms of linear combinations:

$$\sum_{m=1}^{M} r_{nm} c_m \rightarrow \sum_{m=1}^{M} p_{nm} c_m \qquad n = 1, 2, \ldots, N \tag{16.6.4}$$

where M species participate in N reaction steps, c_m is the concentration of the mth species, and r_{nm} and p_{nm} are numerical constants. Each reaction rate is generally expressed as a product of the concentrations of the species involved, with a temperature-dependent rate constant.

The main difficulty in using Equation 16.6.4 to simulate the photochemical smog is the treatment of **organic compounds**. In fact, due to their very large number, organic species cannot all be included explicitly. Three different types of gas-phase chemical mechanisms are generally used: (1) surrogate mechanisms, which use the chemistry of one or two compounds in each class of organics to represent the chemistry of all species in that class; (2) lumped mechanisms, in which the grouping of chemical compounds is done on the bases of their similar structure and reactivity; and (3) the carbon bond approach, which splits each organic molecule into functional groups using the assumption that the reactivity of the molecule is dominated by the chemistry of each functional group. Each classification technique necessarily introduces a simplification and, therefore, a potential simulation error.

Some key reactions involve the **photolysis** of such species as NO_2, HCHO, and nitrous acid (HONO). These one-species reactions require the calculation of the photolysis rate constant, which is a function, among other things, of solar elevation and temperature.

A few models are available for simulating urban photochemical smog, for example:

- UAM-V (http://uamv.saintl.com/)
- CAMx (http://www.camx.com/overview.html)
- CALGRID (http://www.arb.ca.gov/eos/soft.html)

Aerosol chemistry is particularly difficult to simulate and computationally expensive. However, inclusion of aerosol dynamics within air quality models is of primary importance because of the health effects associated with fine particles in the atmosphere, visibility impairment, and the acid deposition problem. Simple first-order reaction terms can be used to simulate the transformation of SO_2 into sulfates and NO_x into nitrates. These terms can be included in any model. However, a comprehensive simulation of aerosol processes can only be performed within an Eulerian grid or a Lagrangian box model and must include the following fundamental equation of aerosol dynamics (Milford and Russell 1993) which describes aerosol transport, growth, coagulation, and sedimentation:

$$\frac{\delta n}{\delta t} + \nabla \cdot un + \frac{\delta l}{\delta \nu} = \frac{1}{2}\int_0^{\nu} \beta(\bar{\nu}, \nu - \bar{\nu})\, n(\bar{\nu})\, n(\nu - \bar{\nu})\, d\bar{\nu} - \int_0^{\infty} \beta(\bar{\nu}, \nu)\, n(\bar{\nu})\, n(\nu)\, d\bar{\nu} - \nabla \cdot \mathrm{C}n \tag{16.6.5}$$

where n is the particle size distribution function, $\bar{\mathbf{u}}$ is the wind velocity, I is the droplet current that describes particle growth and nucleation due to gas-to-particle conversion, ν is the particle volume, β is the rate of particle coagulation, and $\mathbf{C}$ is the sedimentation velocity.

The simulation of heterogeneous and aqueous-phase chemistry is of key importance for regional-scale acid deposition and **stratospheric** ozone models, but is usually neglected in urban photochemical applications where the main goal is the simulation of tropospheric ozone.

Deposition

Chemical species are removed from the atmosphere by two mechanisms: reaction and deposition. While chemical reactions may produce new pollutants, deposition is the real process in which the atmosphere cleans itself. Some pollutants are highly reactive and, consequently, have short lifetimes. For example, ozone has a typical lifetime of 1–2 days (but it may be much lower in a polluted urban atmosphere). Therefore, ozone concentration will drop unless it is continuously regenerated. Other pollutants have longer lifetimes. For example, SO_2 has a typical lifetime of 5–10 days (however, in a clean atmosphere, the lifetime of SO_2 can be a few weeks). Therefore, under certain circumstances, SO_2 can easily accumulate during multiday episodes (e.g., the "London" smog of the 1950s). Finally, there are pollutants, such as methane and carbon dioxide, with very large lifetimes (years or decades). Because of their low reactivity, they do not cause adverse effects on human health but, nevertheless, can diffuse on a global scale and affect the thermal balance of the Earth. Deposition terms can be introduced in any model discussed above. For example, *dry deposition* can be described by the following formula:

$$F_i = V_d \, c_i \tag{16.6.6}$$

where F_i is the flux of a species i to the ground, c_i is the concentration of the species i at some reference height (e.g., 1 m), and V_d is the deposition velocity. The term V_d has been measured under various meteorological conditions and for a number of surface types (Wesley et al. 1985). Therefore, the calculation of F_i is straightforward.

Wet deposition (i.e., precipitation scavenging) depends on the intensity and size of raindrops. Fog and cloud droplets can also absorb gases, capture particles, and accelerate chemical reactions. Wet deposition is quantified by computing the wet flux of pollution to the surface. This calculation requires the estimate of the washout coefficient, which can be inferred (Scott 1982) as a function of storm type and precipitation amounts.

Because of dry and wet deposition, acidic components such as sulfuric acid particles, particulate nitrate, and nitric acid gas are transferred from the atmosphere to the earth. Areas that are tens and hundreds of kilometers downwind of large SO_2 and NO_x sources (e.g., power plants and smelters) often suffer the greatest deposition impact.

Statistical Models

Statistical models are often used in air pollution studies. They include frequency distribution studies, time series analysis, Kalman filters, receptor-modeling techniques, and others. A general distinction between statistical and deterministic approaches is that air pollution deterministic models initiate their calculations at the pollution sources and aim at the establishment of cause/effect relationships, while statistical models are characterized by their direct use of air quality measurements to infer semi-empirical relationships. Although very useful, especially for real-time short-term forecasting, statistical models are generally unable to quantify cause/effect relationships, with the exception of *receptor modeling*.

The basic concept of the receptor-modeling approach is the apportionment of the contribution of each source, or group of sources, to the measured concentrations without reconstructing the dispersion pattern and trajectory of the pollutants. Typically, receptor models start with *observed* ambient aerosol concentrations measured on filters of particle detectors at different receptor points and seek to apportion the concentrations among several source types (e.g., industrial, transportation, soil, etc.), based on the known chemical composition (i.e., the chemical fractions) of source and receptor materials. In other words, receptor models analyze aerosol data to search and quantify the "fingerprints" of several emission groups.

In mathematical notation, the concentration c_{ik} of the species i in the kth aerosol sample at a certain monitoring station can be written as

$$c_{ik} = \sum_{j=1}^{p} a_{ij} D_{jk} E_{jk} \tag{16.6.7}$$

where p sources (or groups of sources) are assumed to contribute to c_{ik}, a_{ij} is the fractional amount of the component i in the emission from the jth source, D_{jk} is the atmospheric dispersion term, and E_{jk} is the emission rate (i.e., $D_{jk}E_{jk} = S_{jk}$ is the total contribution of the source j to the kth sample at the receptor location). Dispersion models assume a_{ij}, D_{jk}, and E_{jk} to be known (or obtainable from emission and meteorological data) and calculate the output c_{ik}. For receptor models instead, the concentrations c_{ik} and source "profiles" a_{ij} are known, and the $D_{jk}E_{jk}$ products are computed as a model result.

Groundwater Pollution Modeling

Tissa Illangasekare

Saturated Groundwater Flow

The description of the exact movement of fluid particles in a porous medium is difficult (or impossible) because it is not practical to define exactly the boundaries of the flow domain that is described by the geometry of the internal solid surfaces of the grains. The problem of water flow in a porous medium can be treated at the molecular, microscopic, or macroscopic level.

The treatment of the behavior of a system of molecules using theories of classical fluid mechanics is extremely difficult because of the large number of molecules involved and the difficulties in identifying all forces and defining the exact pore geometry. Instead of treating individual molecules, the statistical properties of a very large number of molecules may be inferred from laws governing the motion of individual molecules. Still, this approach will also have similar limitations with respect to the need to define exact pore geometries. A coarser treatment at the microscopic level where fluid is treated as a continuum is feasible, but most applications in groundwater flow may not require this level of refinement. This approach will also require the accurate definition of the pore geometry.

A coarse level of averaging at the macroscopic level that is referred to as the *representative elementary volume (REV)* is used in most practical applications in porous media flow analysis. Porous medium is defined as a portion of a space occupied partly by a solid phase (solid matrix) and partly by voids. The voids in general are occupied by one (single phase) or more fluid phases (multiphase). This level of treatment assumes that the solid phase is distributed throughout the problem domain, and it should be possible to define an REV so that no matter where we place it within the porous media domain, it will contain both solids and voids.

At the macroscopic scale, the rate at which water flows in a soil is quantified using a variable that is referred to as the *Darcy velocity*, or *specific discharge*. This variable, which has the dimensions of velocity, is defined as the discharge per unit gross area of soil that includes both void spaces and the grains in a flow section. For incompressible fluids, a relationship that is referred to as *Darcy's law* expresses the Darcy velocity in terms of a parameter referred to as hydraulic conductivity, K, and the gradient of the piezometric head, h. Darcy's law for saturated flow (a single fluid filling the pore space) in soils in a three-dimensional domain is given by

$$\mathbf{q} = -\mathbf{K}\nabla h \tag{16.6.8}$$

where $\mathbf{q}$ is the vector of specific discharge or Darcy velocity (L/T), h is the piezometric head (L), and $\mathbf{K}$ is a second-rank tensor of hydraulic conductivity.

In groundwater flow, since the velocities are generally very small, the velocity head is neglected and the driving head becomes the sum of the elevation and the pressure heads. The piezometric head is defined as

$$h = h_z + h_p = z + \frac{p}{g} \tag{16.6.9}$$

where ρ is the density of water, z is the elevation, and p is the water pressure.

In anisotropic aquifers where the hydraulic conductivity changes with flow direction, the second-rank tensor **K** is given as

$$\left[\mathbf{K}\right] = \begin{bmatrix} K_{xx} & K_{xy} & K_{xz} \\ K_{yx} & K_{yy} & K_{yz} \\ K_{zx} & K_{zy} & K_{zz} \end{bmatrix} \tag{16.6.10}$$

It can be shown that it is possible to find three mutually orthogonal directions in space so that

$$K_{ij} \neq 0 \; \textit{for all } i = j$$

$$K_{ij} = 0 \; \textit{for all } i \neq j$$

where $i, j = x, y$ and z.

These directions in space are called the principal directions of the anisotropic geologic medium. When principal directions are parallel to the axes of the coordinate system, the tensor reduces to a hydraulic conductivity vector given as

$$\left[\mathbf{K}\right] = \begin{bmatrix} K_{xx} & 0 & 0 \\ 0 & K_{yy} & 0 \\ 0 & 0 & K_{zz} \end{bmatrix} \tag{16.6.11}$$

Under transient conditions, for conservation of mass, the rate of change of mass flux of water should be balanced by the change in storage within a control volume. This gives

$$-\nabla.\rho\mathbf{q} = \frac{\partial(n\rho)}{\partial t} \tag{16.6.12}$$

For homogeneous, incompressible fluid and a nondeformable porous medium

$$\nabla.\mathbf{q} = \mathbf{0} \tag{16.6.13}$$

Noting that the change in head produces a change in storage, we can write the mass conservation equation as

$$\nabla.\mathbf{q} + \mathbf{S}_s \frac{\partial h}{\partial t} = 0 \tag{16.6.14}$$

where $\mathbf{S}_s$ is the specific storage, defined as the volume of water added to storage, per unit volume of porous medium, per unit rise in piezometric head. This is given as

$$S_s = \rho g(\alpha + n\beta) \tag{16.6.15}$$

where β is the compressibility of water and α is the compressibility of the soil matrix.

Combining Darcy's law and the equation of mass conservation, the general equation of saturated groundwater flow is obtained as

$$\nabla.\mathbf{K}\nabla h = S_s \frac{\partial h}{\partial t} \tag{16.6.16}$$

The initial and boundary value problem obtained by combining this second-order partial differential equation with the initial head in the aquifer and the head or flux conditions at the aquifer boundary is solved to obtain the unknown head in the aquifer. The head distribution can then be used with Darcy's law to obtain the groundwater flow velocity in the aquifer.

Solute Transport in Groundwater

Transport of dissolved chemicals in porous material is generally considered to be the result of two processes, namely, advection and dispersion. Advection is the process by which the solute is transported as a result of the movement of water through the intergranular pore spaces of the soil. In the mathematical representation of this process at the REV scale, a macroscopically average velocity that is referred to as the *average linear pore velocity* is used. An approximate value for this average pore water velocity for granular material based on macroscopic variables is given as

$$\bar{\mathbf{v}} = \frac{\mathbf{q}}{n} \tag{16.6.17}$$

where n is the effective porosity. The average liner pore water velocity is also referred to as the *average solution velocity.*

The flux due to advective transport is given by

$$\mathbf{J_a} = C\mathbf{q} \tag{16.6.18}$$

where $\mathbf{J_a}$ is the vector of solute mass flux (mass per unit time per unit area, [MT^{-1} L^{-2}]), and C is the mass concentration of solute per unit volume of the solution (ML^{-3}).

Dispersion is the result of two processes that occur at the pore scale: molecular diffusion and mechanical (or hydrodynamic) mixing. Due to molecular diffusion, the solute will move from the high-concentration to low-concentration regions in the fluid phase. Fick's first law modified to account for the presence of the solid phase is used to represent the solute flux as a function of the concentration gradient given by

$$\mathbf{J_d} = -n\mathbf{D}_d\nabla C \tag{16.6.19}$$

where $\mathbf{J_d}$ is diffusive mass flux, [MT^{-1} L^{-2}]; n is the porosity, $\mathbf{D}_d$ [L^{2}T^{-1}]; a second-rank tensor is the effective diffusion coefficient of the solute in the porous medium; and C is the solute concentration, [M/L^{-3}]. In sandy aquifers, under normal flow conditions, the contribution by molecular diffusion is neglected compared to hydrodynamic mixing. Molecular diffusion becomes dominant when the flow velocities are very small, as in clays where hydraulic conductivities are much smaller compared to that of sandy soils.

The component of dispersion due to mechanical mixing is the result of velocity variation at the microscopic pore-scale. These velocity variations are the result of three basic mechanisms that occur within the pores: (1) viscous shear forces that produce velocity gradients across flow channels, (2) pores size variations that produce pore channels with different sizes transmitting water at different pore velocities, and (3) the changing flow directions due to the tortuosity of the flow channels. The combined effect of these variations results in the solute being mixed at the macroscopic scale and producing mass flux along decreasing concentration gradients. As this process is analogous to the diffusion in the microscopic scale, an equation similar to the Fick's first law is used to describe mass flux due to mechanical mixing. This analogous equation is given as

$$\mathbf{J}_m = -n\mathbf{D}_m \nabla C \tag{16.6.20}$$

where $\mathbf{J}_m$ is the flux due to mechanical mixing, [MT^{-1} L^{-2}], and $\mathbf{D}_m$ is the coefficient of hydrodynamic (mechanical) dispersion.

The total flux due to molecular diffusion and hydrodynamic dispersion is given as

$$\mathbf{J} = \mathbf{J}_d + \mathbf{J}_m \tag{16.6.21}$$

Substituting for $\mathbf{J}_m$ and $\mathbf{J}_d$, we have

$$\mathbf{J} = -n(\mathbf{D}_d + \mathbf{D}_m).\nabla C \tag{16.6.22}$$

Define the dispersion coefficient **D** as

$$\mathbf{D} = \mathbf{D}_d + \mathbf{D}_m \tag{16.6.23}$$

Equation 16.6.24 reduces to

$$\mathbf{J} = -n\mathbf{D}\nabla C \tag{16.6.24}$$

In a three-dimensional system the dispersion coefficient is a second-order tensor that takes the form

$$\left[\mathbf{D}\right] = \begin{bmatrix} D_{xx} & D_{xy} & D_{xz} \\ D_{yx} & D_{yy} & D_{yz} \\ D_{zx} & D_{zy} & D_{zz} \end{bmatrix} \tag{16.6.25}$$

By orienting the x′ axis of the local coordinates at the aquifer point along the direction of groundwater flow (longitudinal direction), the dispersion coefficient tensor can be reduced to

$$\left[\mathbf{D}\right] = \begin{bmatrix} D_{x'x'} & 0 & 0 \\ 0 & D_{y'y'} & 0 \\ 0 & 0 & D_{z'z'} \end{bmatrix} \tag{16.6.26}$$

The local axes x', y', and z' are the principal axes of dispersion, and $D_{x'x'}$, $D_{y'y'}$, and $D_{z'z'}$ are the principal values of the coefficient of dispersion. These coefficients can be expressed in terms of the longitudinal average linear pore velocity as

$$\begin{aligned} D_{x'x'} &= D_d + \alpha_L \bar{v}_{x'} \\ D_{y'y'} &= D_d + \alpha_T \bar{v}_{x'} \\ D_{z'z'} &= D_d + \alpha_T \bar{v}_{x'} \end{aligned} \tag{16.6.27}$$

where α_L and α_T are longitudinal and lateral dispersion coefficients, respectively. The dispersion coefficients that have dimensions of length can be viewed as characteristic lengths of the porous medium at the pore scale. However, in real applications these values are much larger and have been found to depend on the size of the plume (scale dependent).

Combining advective flux given by Equation 16.6.18 and dispersive flux given by Equation 16.6.24 and applying the principal of mass conservation for the solute, one obtains

$$(n\mathbf{D}\nabla C - C\mathbf{q}) \tag{16.6.28}$$

By substituting the approximation for Darcy's velocity in Equation 16.6.28, we can obtain the governing equation for solute transport in saturated porous media as

$$(\mathbf{D}\nabla C - C\overline{\mathbf{v}}) \tag{16.6.29}$$

Equation 16.6.29 is referred to as the *advection-dispersion equation*. The initial and boundary value problem obtained by combining the above second-order PDE with the initial concentration distribution in the aquifer and the concentration and mass flux at the aquifer boundary is solved to obtain the time and space distribution of the solute concentration in contaminant plumes. It should be noted that to solve the advection-dispersion equation it is necessary to first solve for the groundwater velocities using the groundwater flow equation.

Surface Water Pollution Transport Modeling

Ronald R. Hewitt Cohen and Nevis Cook

The study of water quality modeling bloomed in the late 1960s and through the 1970s. Administrators and bureaucrats with minimal mathematical and science backgrounds were greatly impressed by presentations of pages of PDEs, and model outputs were often treated as absolute truth. As the field and model users matured, it was recognized that a model is just a group of hypotheses about the way the modeler believes the world works, all put in mathematical terms. The limitations, shortcomings, and difficulties with environmental models are well recognized and accepted. Models are now used as *tools* for decision making and planning.

An industrial facility may want to assess how reducing or increasing the mass or concentration of some pollutant in a discharge will affect the receiving waters. It may be that a dramatic, negative impact might be predicted. Reducing the level of pollutant in the discharge may result in little to no improvement to water quality. Obviously, the results of the modeling effort will dictate the level of effort and cost going toward the treatment of the pollutant.

The same facility may be instructed by the USEPA or the state to control discharges such that water quality criteria in the receiving waters are met. Good models can be used to address the question "What are the implications to the receiving waters if various facility process modifications are applied?" Thus, a decision could be made as to the process modifications to be focused on to match the criteria or standards.

It is not anticipated that every industrial facility has an individual with the capabilities to construct a water quality transport model. Many models are available to run on microcomputers and can be obtained through the USEPA.

Impact Pathway Methodology

Ari Rabl and Peter S. Curtiss

A step beyond conventional dispersion modeling includes the physical and economic impacts of air pollution. Rational management of the environment requires an assessment of the damage caused by pollution. The logically correct way to analyze environmental impacts is the *impact pathway methodology*, whose principal steps are as follows:

- Specification of the relevant technologies and the environmental burdens they impose (e.g., kilograms per second of particulates emitted by a power plant).
- Calculation of increased pollutant concentration in all affected regions (e.g., micrograms per cubic meter of particulates, using models of atmospheric dispersion and chemistry).
- Calculation of physical impacts (e.g., number of cases of asthma due to these particulates, using a dose-response function).
- In some cases a fourth step may be called for: the monetary valuation of these impacts (e.g., multiplication by the cost of a case of asthma).

The numbers are summed over all receptors (population, crops, buildings, etc.) that are affected by this pollutant. Formally, the procedure can be represented as an equation for the incremental impact I due to an incremental quantity Q of a pollutant emitted by the plant

$$I(Q) = \sum_i \left[f_{DR,i}\left(c_i + \Delta c_i(Q)\right) - f_{DR,i}(c_i) \right] \tag{16.6.30}$$

where c_i = background pollutant concentration for receptor i and Δc_i = incremental pollutant concentration due to Q for receptor i; $f_{DR,i}(c)$ = dose-response function for receptor i (the magnitude of this impact that receptor i will suffer at concentration c). The summation index i runs over all receptors (people, crops, buildings, etc.) of concern.

Which receptors are of concern depends on the purpose of the calculation. One can distinguish three kinds of situation:

1. Episodic values (typically for litigation after pollution episodes)
2. Peak values (typically for obtaining a permit for a new plant, by showing that impacts are below a damage threshold or regulatory limit)
3. Expectation values (typically for policy applications such as setting of regulations, by showing that average impacts are acceptable)

For the first two, the summation will typically be over a limited set of receptors, for instance, the residents in a town. For the third application, one will usually want to know the total damage, and the sum should cover all receptors that make a significant contribution to the total. For most air pollutants the impact region has to cover a range of at least 1000 km. For globally dispersing gases, for example, CO_2, the impact region is the entire globe.

Equation 16.6.30 expresses the damage in functional form; hence, this methodology is also known under the name *damage function*. Of course, while this methodology is logically correct, the practical implementation may not always be feasible for lack of appropriate data or models.

In general a dose-response function $f_{DR,i}(c)$

$$Y = f_{DR,i}(X) \tag{16.6.31}$$

relates the dose X of a pollutant that affects a receptor (e.g., population) to the magnitude Y of the impact on this receptor (e.g., incremental number of deaths). In the narrow sense of the term, X should be the dose actually absorbed by a receptor. But often one uses, as we do in the present section, the term dose-response function in the sense of a concentration-response function (also called the exposure-response function), where X represents the concentration of a pollutant in the ambient air; in that case $f_{DR}(X)$ accounts implicitly for the absorption of the pollutant from the air into the body. Dose-response functions for the classic air pollutants (NO_x, SO_x, O_3, and particulates) are typically of that kind. In the next sections we take a closer look at the major steps of the impact pathway analysis.

The Source Term

The first step of the impact pathway analysis is relatively straightforward. One identifies the site and circumstances of a pollution source, e.g., the tons of PM per kWh emitted by particular power plant. For the major air pollutants (CO_2, CO, NO, SO_2, VOCs, particulate matter PM) the emission rates for a given technology are quite well known. For the example of power plants the rate of CO_2 emission is especially well determined. Emissions of CO, NO, SO_2, VOCs, and particulate matter are somewhat less certain, and they can vary with operating conditions. NO emissions, for instance, are likely to increase above the manufacturer's specifications if a selective catalytic reduction unit is not well maintained. There are different grades of oil and coal, and their sulfur content can vary by an order of magnitude; obviously, the emissions of SO_2 depend on the quality of the fuel that will be used. Usually, there are strict regulations that enforce an upper limit on the emissions; due to cost constraints power plants are unlikely to operate significantly below these limits.

The situation is less clear with regard to trace pollutants such as lead and mercury, since their content in different grades of coal can vary by much more than an order of magnitude. Furthermore, some of these pollutants are emitted in such small concentrations that their measurement is difficult. The dirtier the fuel, the greater the uncertainty of emissions. Especially with waste incineration, there has been concern over toxic metals and dioxins that are emitted into the air.

Probably the most uncertain emissions are emissions from the disposal and storage of wastes, because they depend on events in the future. Solid waste from coal-fired boilers could be dumped into a simple hole in the ground, or it could be placed into an engineered landfill with watertight liners; the possible impacts will be totally different. There may or may not be a breach of containment, depending on the quality of construction and management and on natural events such as floods or earthquakes. The main risk from a landfill is the leaching of toxic minerals into groundwater; such risk can be kept negligible by proper construction and management.

Dispersion of Pollutants

Pollutants can be emitted to air, water, or soil. The majority of pollutants are first emitted into the air, even if they later pass into the water or the soil. Therefore, most of this section focuses on atmospheric dispersion. Dispersion in soil is difficult to model because it can involve complex processes that depend on the physical and chemical properties of the soil at each site.

Transport by surface water, that is, rivers, lakes, and the sea, is relatively simple to analyze if fine geographical resolution is not required. Thus, one can divide these bodies of water into a reasonably small number of compartments that are treated as uniformly mixed. For example, a river may be divided into ten sections. A differential equation with empirical coefficients relates the concentration in a section under consideration to the concentration in the section immediately upstream and to the emission into this section. Sedimentation, removal, and decay processes are included.

Similarly, for the dispersion into marine waters one uses a compartment model where each compartment communicates with one or several neighbors, and the volumes and flow rates are known. For instance, in a model used for the analysis of nuclear power plants (EC 1995c), the European seas have been divided into 34 compartments.

For dispersion in the atmosphere, in general both physical and chemical processes need to be considered (Seinfeld and Pandis 1998; Zannetti 1990), see the beginning of Section 16.6. Some pollutants, for example, CO_2, CH_4, and ^{133}Xe, are sufficiently inert chemically that only the physical transport needs to be analyzed. Some are moderately reactive, and their chemical transformation needs to be taken into account. SO_2, for instance, leads to the formation of SO_3, H_2SO_4, and other sulfates (especially from the interaction with NH_3, emitted mostly by agricultural activities); this can have significant implications for impact analysis on a regional and global scale. For example, sulfate aerosols can reduce the impact of global warming. Ozone is a secondary pollutant, formed by the interaction of NO_x, VOC, and light, and the chemistry is extremely complex.

Even though the modeling of the physical transport of pollutants is difficult, it is far simpler than weather modeling. The reason is that pollutants can be considered a small admixture, passively transported by the currents of the surrounding medium. Such transport is linear: the incremental concentration at a receptor site is proportional to the incremental emission (the only exception arises from secondary pollutants such as ozone whose formation depends on other variables, coupled through nonlinear phenomena).

Furthermore, for most policy applications one needs only expectation values of environmental impacts. While it is well known that chaotic phenomena in the atmosphere render the prediction of the weather impossible beyond a short time, this does not prevent the prediction of expectation values. The climate is much more certain than the weather. For expectation values of air pollution damage, it suffices to know the average motion of the surrounding medium from past observations, by contrast to weather modeling where that very motion needs to be predicted in real time.

Dispersion in Air

A simple model for atmospheric dispersion is the Gaussian plume, discussed earlier. According to this model the concentration of a pollutant is described by the product of two Gaussian distributions, one for the spread in the vertical direction and one for the spread in the horizontal direction perpendicular to the prevailing wind direction. The plume width parameters are based on empirical correlations and take into account the relevant meteorological conditions.

The Gaussian plume is considered adequate for the short range, up to tens of kilometers from the source, even for episodic events (Zannetti 1990). The use of this model at distances beyond 100 km is generally not recommended, although it is acceptable for the prediction of the average values if correction terms are included for reflection at the surface and at the PBL of the earth, and if the depletion mechanisms (deposition, chemical transformation, radioactive decay) are correctly accounted for. As an example of dispersion software based on a Gaussian plume, one can cite the ISC model of the USEPA (Brode and Wang 1992).

For regional modeling most analysts prefer to rely on more-detailed computer simulations, for example the Harwell Trajectory Model (1993) or the EMEP model of the Norwegian Meteorological Service (Barrett 1992; Sandnes 1993; Iversen 1993). The latter model is used for the official allocation of acid rain budgets among the countries of Europe.

A crucial question concerns the geographic range over which the analysis needs to be extended in order to capture most of the impacts. This involves a balance among the rates of emission, of dispersion, and of removal of a pollutant. A look at the results of long-range transport models for SO_2 and NO, for instance, those calculated by EMEP (Sandnes 1993), shows that these pollutants are transported over hundreds, even thousands of kilometers. This is illustrated in Figure 16.6.3 using the EMEP data for a source at Nantes, assuming uniform receptor density and a linear dose-response function. The range of the analysis must be extended to over 1000 km if one wants to capture 80 to 90% of the total impact. The same holds for any air pollutants with comparable removal rate.

Secondary Pollutants

Many pollutants are transformed into secondary pollutants by chemical reactions in the atmosphere. For example, the reactions shown in Figure 16.6.4 create acid rain (wet deposition of H_2SO_4) and ammonium sulfate particulates from SO_2.

Another important secondary pollutant is ozone. It is formed when several chemical reactions take place in sequence. The only reaction that forms ozone directly is

$$O + O_2 + M \rightarrow O_3 + M$$

where M is a molecule such as N_2 or O_2 whose participation is necessary to conserve energy and momentum. The oxygen atom involved in the formation of ozone is derived from photolysis of NO_2 under the action of sunlight (indicated by $h\nu$)

$$NO_2 + h\nu \rightarrow O + NO$$

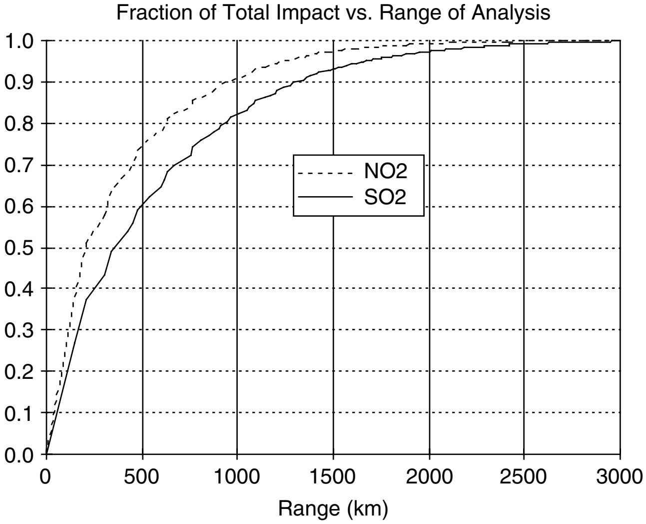

FIGURE 16.6.3 Fraction of total impact vs. range of analysis, for uniform receptor density and linear dose-response function, based on EMEP data (Barrett 1994). Wiggles are due to discretization.

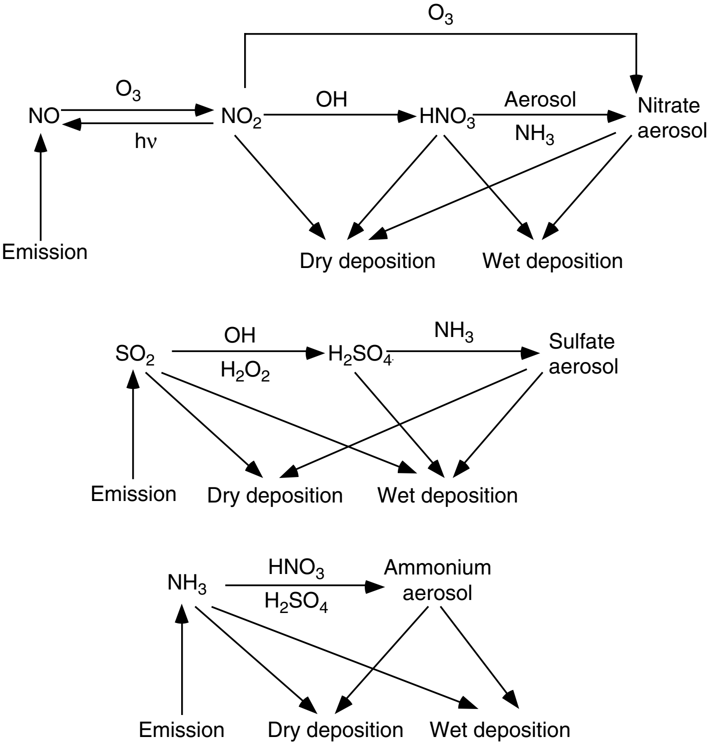

FIGURE 16.6.4 Chemical reactions included in Harwell Trajectory Model. (From EC, 1995c.)

The presence of volatile organic compounds (VOCs) is necessary to prevent the ozone formed from being immediately consumed by NO to produce NO_2 in the following reaction:

$$NO + O_3 \rightarrow O_2 + NO_2$$

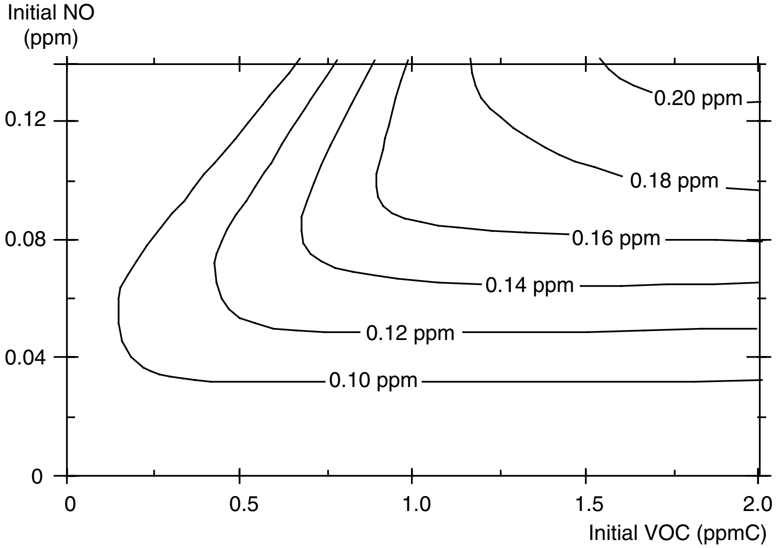

FIGURE 16.6.5 Isopleth plot for the maximum ozone concentration reached during a fixed length of time as a function of initial NO and VOC concentrations. Details of such a plot depend on site and on weather. (From EPRI, 1992.)

VOCs enable the transformation of NO into NO_2 without consuming ozone. Finally, note also that NO_2 plays a double role, since, while being necessary to form ozone, it consumes the radicals needed by VOCs to transform NO into NO_2. In fact, an equilibrium is created between these reactions. The concentration of ozone therefore is very dependent on changes in the concentrations of other products, and, due to the complexity of the phenomena, it is observed, for example, that if VOCs are low (as in the case of an electricity power plant plume), the increase in NO may reduce O_3. Figure 16.6.5 shows the influence of the concentrations of nitrogen oxides and VOCs on the concentration of ozone. In particular, we observe the phenomenon mentioned above: the consequence of an increase in NO on atmospheric ozone depends on the concentration of the organic compounds. The ozone content is also strongly dependent on the $[NO_2]$:[NO] ratio. If this ratio is low, the $[O_3]$ content will remain low.

Dose-Response Functions

Form of the Dose-Response Function. By definition, a dose-response function starts at the origin, and in most cases it increases monotonically with dose X, as sketched schematically in Figure 16.6.6. At very high doses the function may level off in S-shaped fashion, implying saturation. Dose-response functions are determined from epidemiological studies or from laboratory studies. Since the latter are mostly limited to animals, the extrapolation to humans introduces large uncertainties. Another major difficulty is that one needs relatively high doses in order to obtain observable nonzero responses in a sample of realistic size; such doses are usually far in excess of the levels one is concerned with in environmental impact studies. Thus, there is a serious problem of how to extrapolate from the observed data toward low doses. Figure 16.6.6 indicates several possibilities. The simplest is the linear model, that is, a straight line from the origin through the observed data point(s). Cancer from radioactivity is an example. Linearity also seems to be observed for mortality from fine particulates (Dockery et al. 1993; Dockery and Pope 1994; Lipfert 1994).

Another possibility is a straight line down to some threshold, and zero effect below that threshold. Thresholds occur when an organism has a natural repair mechanism that can prevent or counteract damage up to a certain limit. Many dose-response functions for noncancer toxicity are of this type.

There is even the possibility of a "fertilizer effect" at low doses, as indicated by the dashed line in Figure 16.6.6. This can be observed, for example, in the dose-response functions for the impact of NO_x

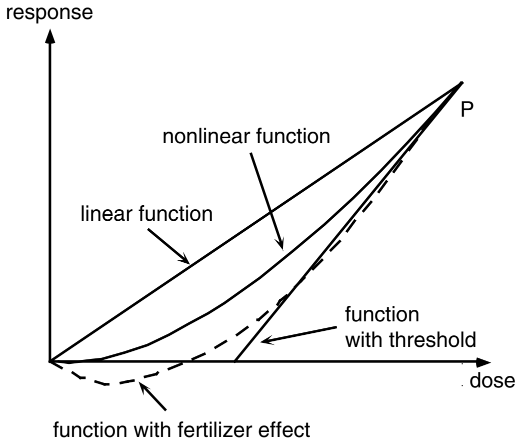

FIGURE 16.6.6 Possible behavior of dose-response functions at low doses: the four functions shown have the same value at P. For the function with threshold, the discontinuity in slope at the threshold is a simplification; in reality there is a smooth transition.

and SO_x on crops: a low dose of these pollutants can increase the crop yield; in other words, the damage is negative. Such a fertilizer effect can occur with pollutants that provide trace elements needed by an organism. It depends on local conditions, in particular the overall balance of nutrients. The fertilizer effect illustrates the link between the understanding of the underlying processes and the choice of the appropriate form for the dose-response function: since N and S are known to be important nutrients for plants, a functional form like the dashed line in Figure 16.6.6 is the most plausible.

If nothing is known about a threshold and a fertilizer effect can be ruled out, the dose-response function could be anywhere between zero and the straight line through the origin, for instance, the curved solid line shown in Figure 16.6.6. *A priori* there is no general rule about the extrapolation to low doses, other than there being apparently no cases of a dose-response function above the straight line. There is even a case where the same substance causes different cancers according to different dose-response functions, one with and one without threshold. This was established in an important experiment where some 24,000 mice were exposed to the carcinogen 2-acetyl-amino-fluorene at several different dose levels (Frith et al. 1981). The response for liver tumor is linear, whereas the one for bladder tumor has a threshold.

Site Dependence of Impacts

Site dependence is illustrated in Figure 16.6.7. This figure shows two variations at once: with stack height, and with source location for five specific sites in France (the nearest big city, 25 to 50 km away, is indicated in parentheses). Plume rise is included for typical conditions of large combustion installations. As an example, we consider a specific impact: the increase in mortality (YOLL = years of life lost) due to an emission of $Q = 10^6$ kg/yr of SO_2 with the dose-response function of Sunyer et al. (1996). The damage is shown on two scales, as number of YOLL per year on the right-hand scale, and in units of D_{uni} (to be explained in a moment) on the left. At a stack height of 100 m the impact for the site near Paris is about 3 times larger than D_{uni} and for Cordemais (a relatively rural site on the Atlantic Ocean) it is about 0.4 times D_{uni}. The impact for Martigues is rather small, despite the proximity of a large city, because the prevailing wind carries the pollutants out to sea.

Site dependence is particularly strong for primary pollutants (i.e., pollutants emitted by a source); this is shown by the examples in Figure 16.6.7. For secondary pollutants (created by chemical reactions of primary pollutants) such as sulfates, nitrates and ozone, the sensitivity to local detail is much lower because these pollutants are not created until some distance from the source. For nitrates and sulfates this occurs over tens to hundreds of km from the source, and so the site dependence is relatively weak;

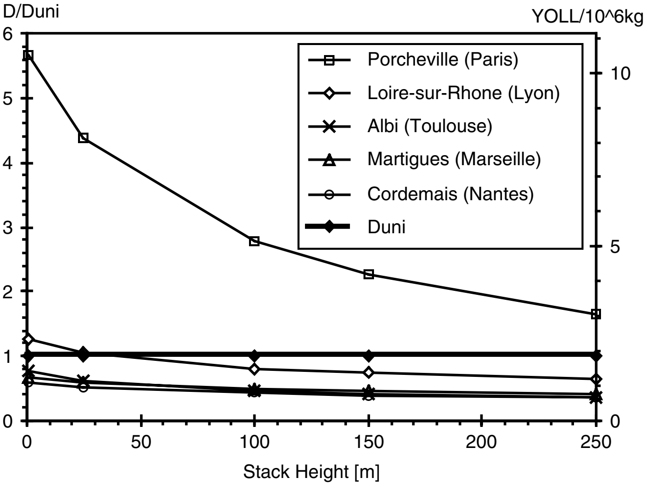

FIGURE 16.6.7 An example of dependence on site and on height of source for a primary pollutant with linear dose-response function: damage D from SO_2 emissions, for five sites in France, in units of D_{uni} for uniform world model Equation 16.6.6 (the nearest big city, 25 to 50 km away, is indicated in parentheses). Scale on right indicates YOLL/yr (acute mortality) from a plant with emission 10^6 kg/yr.

based on EcoSense results, we estimate that variations of sulfate or nitrate damage, per kg of SO_2 or NO_2, with site are around 50%. The creation of ozone is more rapid, within several km to tens of km from the source; based on EMEP data we estimate that ozone damage per kg of precursor could vary with site by about a factor of four in Europe.

To explain D_{uni} (Curtiss and Rabl 1966b) let us write the damage D due to an emission Q as an integral over land area:

$$D = f_{CR} \int dx \int dy \;\; \rho(\mathbf{x}) c(\mathbf{x}) \,. \tag{16.6.32}$$

where

$\rho(\mathbf{x})$ = density of receptors at point $\mathbf{x} = (x,y)$
$c(\mathbf{x})$ = concentration increase at $\mathbf{x}$ due to Q
f_{CR} = slope of dose-response or concentration-response (CR) function

The slope of the CR function states the incremental number of cases (e.g., hospitalizations) per concentration increment. Here we assume that f_{CR} has a constant value independent of $\mathbf{x}$.

It is instructive to relate the concentration $c(\mathbf{x})$ to the depletion rate of the pollutant. There are essentially three mechanisms by which an air pollutant can disappear from the atmosphere (Seinfeld and Pandis 1998):

a. Dry deposition (uptake at the earth's surface by soil, water, or vegetation)
b. Wet deposition (absorption into droplets, removed by precipitation)
c. Decay or transformation (e.g., transformation of SO_2 to $(NH_4)_2SO_4$)

When evaluating the damage of a primary pollutant, this pollutant is no longer counted in the equation once it has been transformed; rather from that point on, a different CR function comes into play for the secondary pollutant.

The dry deposition rate is proportional to the concentration $c(\mathbf{x})$ at the earth's surface, and it is customarily written in the form

$$F_{\text{dry}}(\mathbf{x}) = k_{\text{dry}}\, c(\mathbf{x}) \tag{16.6.33}$$

where

$F_{\text{dry}}(\mathbf{x})$ = deposition flux [in kg/(m²·s)]

k_{dry} = dry deposition velocity [m/s]

Wet deposition and decay or transformation can likewise be characterized in terms of fluxes $F_{\text{wet}}(\mathbf{x})$ and $F_{\text{trans}}(\mathbf{x})$, defined as the rate at which the pollutant is removed by these mechanisms per m^2 (horizontal surface area) and per second. Now let us define a "depletion velocity" $k(\mathbf{x})$, in units m/s, as ratio of the total depletion flux:

$$F(\mathbf{x}) = F_{\text{dry}}(\mathbf{x}) + F_{\text{wet}}(\mathbf{x}) + F_{\text{trans}}(\mathbf{x}) \tag{16.6.34}$$

and the surface concentration $c(\mathbf{x})$ as

$$k(\mathbf{x}) = F(\mathbf{x})/c(\mathbf{x}) = k_{\text{dry}}(\mathbf{x}) + k_{\text{wet}}(\mathbf{x}) + k_{\text{trans}}(\mathbf{x}). \tag{16.6.35}$$

Using $F(\mathbf{x})$ and $k(\mathbf{x})$ we can write the damage in the form

$$D = f_{CR} \int dx \int dy\, \rho(\mathbf{x})\, F(\mathbf{x})/k(\mathbf{x}) \tag{16.6.36}$$

Let us now consider a situation where $k(\mathbf{x})$ are $\rho(\mathbf{x})$ are independent of $\mathbf{x}$. With uniform receptor density $\rho(\mathbf{x}) = \rho_{\text{uni}}$ and uniform depletion velocity $k(\mathbf{x}) = k_{\text{uni}}$, the integral in Equation 16.6.35 is simply

$$D = D_{\text{uni}} = \frac{f_{CR}\rho_{\text{uni}}}{k_{\text{uni}}} Q \tag{16.6.37}$$

because, averaged over time, the surface integral of the depletion flux equals the emission

$$Q = \int dx \int dy\, F(\mathbf{x}) \tag{16.6.38}$$

by conservation of matter. This equation can readily be generalized to secondary pollutants. We shall refer to Equation 16.6.37 as the *uniform world model (UWM)*.

As an illustration we calculate D_{uni} for mortality due to SO_2, with f_{CR} = 5.34E-06 YOLL/(pers·yr·µg/m³) (Sunyer et al. 1996). By fitting EcoSense dispersion data we have found a depletion velocity $k = 0.0073$ m/s for SO_2. Inserting these numbers into Equation 16.6.37 with the regional average population density ρ = 8.0E-5 person/m² we obtain for $Q = 10^6$ kg/yr = 3.17E07 µg/s

$$D_{\text{uni}} = \frac{5.34\times10^{-6}\ \text{YOLL}/\left(\text{person}\cdot\text{yr}\cdot\mu\text{g}/\text{m}^3\right)\times 8.0\times10^{-5}\ \text{person}/\text{m}^3}{0.0073\ \text{m/s}} \times 3.17\times10^{7}\ \mu\text{g/s} = 1.86\ \text{YOLL/yr}$$

This is shown as the horizontal line in Figure 16.6.7. It lies right in the middle of the curves for the five sites.

Even though the assumption $k(\mathbf{x}) = k_{\text{uni}}$ may not appear very realistic, especially near a point source, the sensitivity to deviations from uniformity is surprisingly small. The reason is that with tall stacks much of the total impact occurs in regions sufficiently far from the source where the pollutant is fairly well mixed vertically in the PBL, and variations of $k(\mathbf{x})$ are not too large. Emission height dependence and deviations from uniformity are most pronounced when the receptors are concentrated near the source. A source near Paris seems like a fairly extreme example because France is highly centralized, with some 20% of its population in Greater Paris. Cordemais, in a semi-rural zone on the Atlantic cost, is an opposite extreme.

Thus it is plausible that these results are fairly representative and that the UWM can be a useful first estimate, good to an order of magnitude. If one wants typical results for public policy, without being able to evaluate each and every site, D_{uni} seems as good a choice as any — and it has the advantage of being simple and transparent. Spadaro (1999 and additional calculations) and Spadaro and Rabl (2002) have compared the UWM with the results of detailed site-specific calculations for about 100 installations in many countries of Europe, as well as China, Thailand, and Brazil; the detailed calculations were done with the EcoSense software (Krewitt et al. 1995) of the ExternE Project series (1998). They found UWM to be so close to the average that it can be recommended for the calculation of typical values for emissions from tall stacks, more than about 50 m; for specific sites the agreement is usually within a factor of two to three. For ground-level emissions in cities, the impact can be much larger than UWM because of the combination of high receptor densities with the high concentrations near ground-level sources, but simple estimates can still be obtained by applying correction factors to UWM (Spadaro and Rabl 2002).

Analysis of Uncertainties

An analysis of uncertainties begins with a detailed examination of the uncertainties of each of the steps of the impact pathway analysis. However, by contrast to the relatively small uncertainties and normal (Gaussian) frequency distributions typically encountered in science and engineering, the uncertainties in this field are so large that a conventional error analysis is not appropriate. To obtain the uncertainty of the damage cost, the classic approach is a Monte Carlo calculation. One chooses a specific set of values for each of the uncertain input parameters of the impact pathway analysis and calculates the corresponding damage cost. This process is repeated many times, each time choosing the input parameters according to their respective probability distributions. Thus one obtains the distribution of the damage cost estimates. Obviously this procedure requires an extremely large number of computations.

As much simpler alternative an approximate method has been developed by Rabl and Spadaro (1999). It is an analytic approach based on the fact that the UWM of Equation 16.6.37 is a product of the input parameters, and therefore the logarithm of the damage cost is the sum of the logarithms of the input parameters. The standard deviation of a sum is the square root of the sum of the standard deviations of summands, for any distribution of the individual uncertainties, no matter how wide. Thus it is straightforward for the UWM to obtain the standard deviation of the logarithm of the damage cost; it is called the *geometric standard deviation*. Furthermore, the central limit theorem says that the distribution of a sum approaches a Gaussian in the limit where the number of terms becomes large, regardless of the distributions of the individual summands. In practice the distribution of the sum is close to normal even for a small number of terms, except when the widest distributions are far from normal.

A variable x is said to have a lognormal distribution if the variable $\ln(x)$ has a Gaussian distribution, in other words, if it is normal on a logarithmic scale. Thus one can conclude that the distribution of damage costs is approximately lognormal, unless the widest distributions of the input parameters are far from normal. A closer look at the uncertainties of the input parameters (Rabl and Spadaro 1999) shows that the conditions for lognormality of the damage cost are fairly well satisfied. Thus one can obtain a very simple approximate estimate of the uncertainties.

Analogous to the ordinary normal distribution, which is characterized by two parameters, the mean and the standard deviation, the lognormal distribution can be characterized by the geometric mean and the geometric standard deviation s_G. For this distribution the geometric mean is equal to the median: half of the distribution is above, the other half below the median. The geometric standard deviation has a simple interpretation in terms of multiplicative confidence intervals: for a lognormal distribution 68% of the values are within the interval $(1/s_G, s_G)$; likewise, 95% are within the interval $[(1/s_G)^2, (s_G)^2]$. Note, however, that these values are centered around the median rather than the mean; the lognormal distribution is not symmetric. For impacts of primary air pollutants with relatively well-determined dose-response functions, for example, mortality due to particulates, s_G may be as small as 3. For other impacts, such as cancers due to dioxins, the uncertainties could be an order of a magnitude or even more.

When we compare these two methods for uncertainty analysis, the Monte Carlo method has the advantage of being able to take into account arbitrary distributions of the component uncertainties, but it is computationally intensive and the result is "black box": one does not learn how important each of the component uncertainties is or how the result would change if a component uncertainty changes, unless one performs such a large number of simulations that it becomes difficult to "see the forest for the trees." The lognormal method with the UWM is approximate, but simple and fully transparent; its validity can be improved by calibrating it with the Monte Carlo results. Thus one can combine the best features of the two approaches.

One should note that technical or scientific uncertainties (e.g., uncertainties of emitted quantities or of dose-response functions) are not the only ones. For long-term impacts, such as cancers caused by radioactive waste, one needs to make assumptions about scenarios for the future: what quantities of radionuclides will leak into the environment and how many people will be affected by them. For the estimation of damage costs, there is also the matter of policy/ethical choice, e.g., about discount rate and value of human life.

Results

The impact pathway analysis yields the damage costs per kg of pollutant. Results for pollutants emitted by power plants under typical European conditions are shown in Table 16.6.1. Some indication of the variability with site and stack conditions is given in the notes under the table.

Multiplying the cost per kg by the emission rates in gm/kWh, one readily finds the cost per kWh. Results are plotted in Figure 16.6.8.

TABLE 16.6.1 Typical Damage Costs per kg of Pollutant Emitted by Power Plants in Europe

Pollutant	Impact	Cost [a], ∈/kg
PM10 (primary)	Mortality and morbidity	15.4
SO_2 (primary)	Crops, materials	0.3
SO_2 (primary)	Mortality and morbidity	0.3
SO_2 (via sulfates)	Mortality and morbidity	9.95
NO_2 (primary)	Mortality and morbidity	Small
NO_2 (via nitrates)	Mortality and morbidity	14.5
NO_2 (via O_3)	Crops	0.35
NO_2 (via O_3)	Mortality and morbidity	1.15
VOC (via O_3)	Crops	0.2
VOC (via O_3)	Mortality and morbidity	0.7
CO (primary)	Morbidity	0.002
As (primary)	Cancer	171
Cd (primary)	Cancer	20.9
Cr (primary)	Cancer	140
Ni (primary)	Cancer	2.870
Dioxins, TEQ	Cancer	1.85×10^7
CO_2	Global warming	0.029

[a] Variation with site and stack conditions (stack height, exhaust temperature, exhaust velocity):

- No variation for CO_2;
- Weak variation for dioxin (non-inhalation pathways): factor of 0.7 to 1.5;
- Weak variation for secondary pollutants: factor of 0.5 to 2.0;
- Strong variation for primary pollutants: factor of 0.5 to 5 for site, 0.6 to 3 for stack conditions (up to 15 for ground-level emissions in big city).

Source: [Spadaro and Rabl 1999, Spadaro 1999]

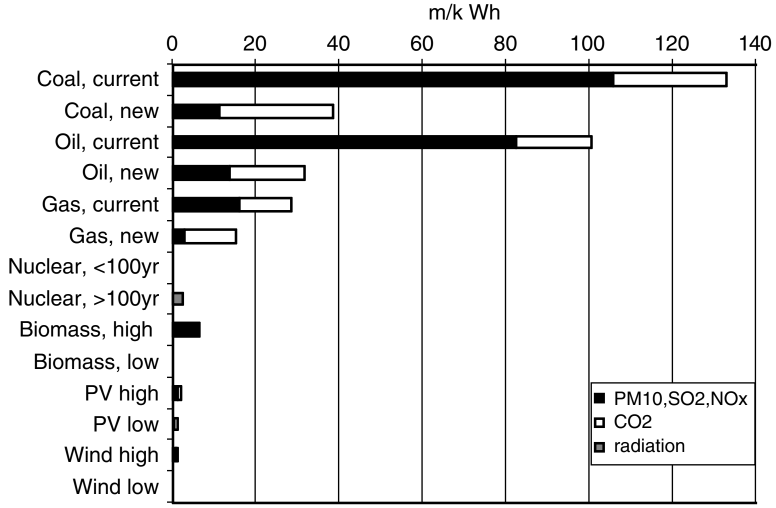

FIGURE16.6.8 Comparison of damage costs, for fuel chains in the European Union (EU), with ∈/kg of Table 16.6.1. For fossil fuel chains "current" corresponds to emissions in the EU and the U.S. during the mid-1990s, "new" to emission limits imposed by the new EU Directive effective after 2000. For renewables "high" and "low" indicate typical range of estimates of ExternE (1998). For nuclear only a single technology is shown (French, with reprocessing), but costs are separated into near (before 100 yr) and far (after 100 yr) future. For comparison production costs of base load electricity in the EU and U.S. are in the range of 25 to 50 m∈/kWh.

Defining Terms

Aerosol: Small solid particle or liquid droplet suspended in the air.

Anthropogenic: Man-made.

Deterministic: Dealing with cause and effect.

Ensemble average: Theoretical average, that is, the value that could be expected as the average from an infinite number of realizations.

Global warming: The warming of the earth as a result of the atmosphere, which traps solar radiation. Currently, the term *global warming* is used to denote the temperature increase due to carbon dioxide, methane, and other greenhouse gases.

Greenhouse gases: Carbon dioxide, methane, and other gases resulting from human activities that increase the amount of solar radiation trapped by the atmosphere.

Numerical advection errors: Numerical errors generated by finite-difference solutions of transport terms using a Eulerian grid model.

Organic compounds: Chemical species containing one or more carbon atoms.

Photochemical: Chemical reactions influenced by light.

Photolysis: Chemical decomposition by the action of light.

Planetary boundary layer (PBL): The atmospheric layer that is affected by the momentum and heat fluxes generated by the earth's surface (typically, the first 500–1000 m of the atmosphere).

PM_d: Particulate matter with a diameter smaller than d μm.

Stratospheric: Related to the stratosphere, the portion of the atmosphere approximately between 10 and 50 km above the ground.

Tropospheric: Related to the troposphere, the lower level of the atmosphere approximately from the surface to 10 km above.

VOC: Volatile organic compounds.

Wind shear: The change in wind speed and direction as a function of height.

References

APHA, AWWA, and WPCF. 1992. *Standard Methods for the Examination of Water and Wastewater*, 18th ed., American Public Health Association, American Water Works Association, Water Pollution Control Federation, Washington, DC.

AWWA. 1996, *National Primary Drinking Water Contaminant Standards, Opflow*, Vol. 22, No. 3, March 1996, American Water Works Association, Denver, CO.

Barrett, K. 1992. *Dispersion of Nitrogen and Sulfur across Europe from Individual Grid Elements: Marine and Terrestrial Deposition*, EMEP/MSC-W Note 3/92. August 1992. Norwegian Meteorological Institute, Oslo.

Boubel, R.W., Fox, D.L., Turner, D.B., and Stern, A.C. 1994. *Fundamentals of Air Pollution*, Academic Press, San Diego, CA.

Brode R.W. and Wang, J. 1992. *User's Guide for the Industrial Source Complex (ISC2) Dispersion Model.* Vols.1–3, EPA 450/4-92-008a, EPA 450/4-92-008b, and EPA 450/4-92-008c. U.S. Environmental Protection Agency, Research Triangle Park, NC 27711.

Cohrssen, J.J. and Covello, V.T. 1989. *Risk Analysis: A Guide to Principles and Methods for Analyzing Health and Environmental Risks, United States Environmental Protection Agency.* Report EPA PB89-137772. Washington, DC.

Corey, A.T. 1994. *Mechanics of Immiscible Fluids in Porous Media*, Water Resources Publications, Littleton, CO.

Curtiss, P.S. and Rabl, A. 1995. *The PATHWAYS2.0 Impact Analysis Program*. Ecole des Mines de Paris.

Curtiss, P.S. and Rabl, A. 1996a. *PATHWAYS: A Software Package for Calculating Impacts and Costs of Environmental Burdens due to Electricity Production by Nuclear or Fossil Fuels.* Program Manual, Ecole des Mines de Paris, Paris.

Curtiss, P.S. and Rabl., A., 1996b. Impacts of air pollution: general relationships and site dependence. Submitted to *Atmos. Environ.*, 30, 3331–3347.

Curtiss, P.S. and Rabl, A. 1996c. Impact Analysis for Air and Water Pollution: Methodology and Software Implementation. In *Environmental Modeling*. Zannetti, P., ed. Vol. 3, chap. 13.

Curtiss, P.S., Hernandez, B., Pons, A., Rabl, A., Dreicer, M., Tort, V., Margerie, H., Landrieu, G., Desaigues, B., and Proult, D. 1995. *Environmental Impacts and Their Costs: the Nuclear and the Fossil Fuel Cycles*, ARMINES (Ecole des Mines), 60 boul. St.-Michel, 75272 Paris CEDEX 06.

de Vera, L. et al. 1980. *Samplers and Sampling Procedures for Hazardous Waste Streams*, EPA-600/2-80-018, USEPA, Washington, DC.

Dockery, D.W. and Pope, C.A. III 1994. Acute respiratory effects of particulate air pollution. *Annu. Rev. Public Health*, 15, 107–132.

Dockery, D.W., Pope, C.A. III, Xu, X., Spengler, J.D., Ware, J.H., Fay, M.E., Ferris, B.G., and Speizer, F.E. 1993. An association between air pollution and mortality in six U.S. cities. *New Eng. J. Med.*, 329, 1753–1759.

EC, 1995a. Externalities of Fuel Cycles, "ExternE" Project: Summary Report, Report No. 1. European Commission, Directorate-General XII, Science Research and Development. JOULE programme.

EC, 1995b. Externalities of Fuel Cycles, "ExternE" Project: Coal Fuel Cycle, Report No. 2. European Commission, Directorate-General XII, Science Research and Development. JOULE programme.

EPRI. 1992. *The use of photochemical air quality models for evaluating emission control strategies. A synthesis report*. Prepared for EPRI (Electric Power Research Institute) by ENVAIR, Albany, CA.

Frith, C.H., Littlefield, N.A., and Umholtz, R. 1981. Incidence of pulmonary metastases for various neoplasms in BALB/cStCrlfC3H/Nctr female mice fed N-2-fluorenylacetamide, JNCI, 703–712.

Heijungs, R. et al. 1992. *Environmental Life Cycle Assessment of Products*, Part 1. Guide. Part 2. Backgrounds, Centre of Environmental Science, Leiden, Netherlands.

Hem, J.D. 1989. *Study and Interpretation of the Chemical Characteristics of Natural Water*, U.S. Geological Survey Water Supply Paper 2254, U.S. Government Printing Office, Washington, DC.

Hohmeyer, O. 1988. *Social Costs of Energy Consumption*. Springer-Verlag, New York.

Houghton, J.T., Jenkins, G.J., and Ephrams, J.J. 1990. *Climate Change, the IPCC Scientific Assessment.* Cambridge University Press, Cambridge, MA.

Iversen, T., 1993. Modeled and measured transboundary acidifying pollution in Europe — verification and trends. *Atmos. Environ.*, 27A, 889–920.

Jones and Henderson-Sellers 1990. History of the greenhouse effect. *Progress in Physical Geography* 14, 1-18, 1990.

Koomey, J., 1990. *Comparative Analysis of Monetary Estimates of External Environmental Costs Associated with Combustion of Fossil Fuels*, Report LBL-28313. Lawrence Berkeley Laboratory, Berkeley, CA 94720.

LaGrega, M.D., Buckingham, P.L., and Evans, J.C. 1994. *Hazardous Waste Management*, McGraw-Hill, New York .

Lange, R. 1978, ADPIC — a three-dimensional particle-in-cell model for the dispersal of atmospheric pollutants and its comparison to regional tracer studies. *J. Appl. Meteor.*, 17, 320.

Leeden, F., Troise, F.L., and Todd, D.K. 1990. *The Water Encyclopedia*, Lewis Publishers, Chelsea, MI.

Lipfert, F.W., 1994. *Air Pollution and Community Health: A Critical Review and Data Sourcebook*, Van Nostrand Reinhold, New York.

Longhetto, A., Ed. 1980. *Atmospheric Planetary Boundary Layer Physics*, Elsevier, New York.

Milford, J.B. and Russell, A.G., 1993. Atmospheric models: atmospheric pollutant dynamics, meteorology and climate. *Environmental Modeling*, Vol. I, Computational Mechanics Publications, chap. 2.

Morandi, L., 1992. *Global Climate Change*, NCSL, Denver, CO, November.

Morrison, R.E. 1989. *Global Climate Change, Congressional Research Service*, Library of Congress 1B8905; Washington, DC.

Nemerow, N.L. 1991. *Industrial and Hazardous Waste Treatment*, Van Nostrand Reinhold, New York.

Nieuwstadt, F.T. and van Dop, H., eds., 1982. *Atmospheric Turbulence and Air Pollution Modeling*, D. Reidel, Dordrecht, Holland.

ORNL/RFF. 1994a. *Fuel Cycle Externalities: Analytical Methods and Issues, Report on the External Costs and Benefits of Fuel Cycles.* July 1994. Prepared by Oak Ridge National Laboratory and Resources for the Future, Oak Ridge National Laboratory, Oak Ridge, TN.

ORNL/RFF. 1994b. *Estimating Externalities of Coal Fuel Cycles, Report on the External Costs and Benefits of Fuel Cycles.* September 1994. Prepared by Oak Ridge National Laboratory and Resources for the Future, Oak Ridge National Laboratory, Oak Ridge, TN.

Ottinger, R.L. et al. 1991. *Environmental Costs of Electricity*, Oceana Publications, New York.

Pescod, M.B. 1992. *Wastewater Treatment and Use in Agriculture*, FAO Irrigation and Drainage Paper 47, Food and Agriculture Organization of the United Nations, Rome.

Rabl, A., P.S. Curtiss, J.V. Spadaro, B. Hernandez, A. Pons, M. Dreicer, V. Tort, H. Margerie, G. Landrieu, B. Desaigues, and D. Proult 1996. *Environmental Impacts and Costs: the Nuclear and the Fossil Fuel Cycles*. Report to EC, DG XII, Version 3.0 June 1996. ARMINES (Ecole des Mines), 60 boul. St.-Michel, 75272 Paris CEDEX 06.

Rodricks, J.V. 1992. *Calculated Risks: The Toxicity and Human Health Risks of Chemicals in Our Environment*, Cambridge University Press, Cambridge, U.K.

Rodriguez, D.J., Greenly, G.D., Gresho, P.M., Lange, R., Lawver, B.S., Lawson, L.A., and Walker, H. 1982. *User's Guide to the MATHEW/ADPIC Models*, Lawrence Livermore National Laboratory Document UASG 82-16, University of California Atmospheric and Geophysical Sciences Division, Livermore, CA.

Ruben, E.S. et al. 1992. Realistic mitigation options for global warming. *Science*, 257, July, 148–149, 261–266.

Sandnes, H. 1993. *Calculated Budgets for Airborne Acidifying Components in Europe*, EMEP/MSC-W Report 1/93. July 1993. Norwegian Meteorological Institute, P.O. Box 43, Blindern, N-0313 Oslo 3.

Schimel, D., et al. 1996. in *Climate Change 1995,* Houghton, J.T. et al. eds., Cambridge University Press, Cambridge, UK, 1996

Schneider, S.H. 1989. The greenhouse effect: science and policy. *Science*, 243, February, 771–779.

Schwartz J. 1993. Air pollution and daily mortality in Birmingham, Alabama, Am. J. Epidemiol., 137, 1136–1147.

Scientific Perspectives on the Greenhouse Problem, 1989. George C. Marshall Institute, Washington, DC.

Scott, B.C. 1982. Theoretical estimates for scavenging coefficient for soluble aerosol as function of precipitation type, rate, and altitude. *Atmos. Environ.,* 16, 1735–1762.

Seigneur, C. 1987, Computer simulation of air pollution chemistry, Environ. Software, 2, 116.

Seinfeld J.H. and Pandis, S.N. 1998. *Atmospheric Chemistry And Physics: From Air Pollution to Climate Change*, John Wiley & Sons, New York.

SETAC. 1992. *Code Practice of Life Cycle Assessment*, Society of Environmental Toxicology and Chemistry, Pensacola, FL.

Sunyer J., Castellsague J., Saez, M., Tobias, A., Anto, J.M. 1996. Air pollution and mortality in Barcelona. *J Epidem. Comm. Health*,. 50 (suppl 1): S76–S80.

U.S. Geological Survey can supply long-term, baseline monitoring of water resources in terms of quantity, flow, and quality, and special short-term, regional studies.

USEPA. 1976. *Quality Criteria for Water*, U.S. Government Printing Office, Washington, DC.

USEPA. 1978, *Guideline on Air Quality Models*, EPA-450/2-78-027, USEPA, Research Triangle Park, NC.

USEPA. 1979 *Handbook for Sampling and Sample Preservation of Water and Wastewater*, U.S. Environmental Protection Agency, U.S. Government Printing Office, Washington, DC. EPA-600/4-82-029 (with addendum).

USEPA. 1983. *Guidelines for Performing Regulatory Impact Analysis*, U.S. Environmental Protection Agency, Office of Policy Analysis. Report EPA-230-01-84-003, reprinted March 1991. Washington, DC

USEPA. 1991. *Technical Support Documents for Water Quality-Based Toxics Control.* EPA 505/2-90-001. Office of Water, USEPA, Washington, DC. Gives access to models such as EXAMS-II (lake, river, estuary for organics); WASP4 or WASP5.x (lake, river, estuary for organics and metals); HSPF (rivers, organics and metals); SARAH-2 (rivers, treatment plant, organic); DYNTOX (river, organics, metals).

USEPA. 1992. *National Water Quality Inventory — Report to Congress*, EPA 503/9-92/006. Office of Water, USEPA, Washington, DC.

USEPA. 2001. *Environmental Protection Agency, Green Book*, Part 50, July 2001. (www.epa.gov/air/oaqps/greenbk/40CFR50.html) or U.S. Government Printing Office.

Watson, R.T., Zinyowera, M., and Moss, R.H., eds. 1995. C*limate Change, the Second Assessment Report of the Intergovernmental Panel on Climate Change*, Vol. 2, *Impacts, Adaptations, and Mitigations — Scientific/Technical Analysis*, Cambridge University Press, Cambridge, MA.

Wesley, M.L., Cook, D.R., Hart, R.L., and Speer, R.E. 1985. Measurements and parameterization of particulate sulfur dry deposition over grass. *J. Geophys. Res.*, 90, 2131–2143.

Zannetti, P. 1986a. A new mixed segment-puff approach for dispersion modeling. *Atmos. Environ.*, 20, 1121–30.

Zannetti, P. 1986b, Monte-Carlo simulation of auto- and cross-correlated turbulent velocity fluctuations (MC-LAGPAR II Model). *Environ. Software*, 1, 26–30.

Zannetti, P. 1990. *Air Pollution Modeling: Theories, Computational Methods and Available Software*, Van Nostrand Reinhold, New York.

Further Information

For a comprehensive textbook on air pollution modeling, see Zannetti, 1990, above. Shorter reviews of air pollution modeling topics can be found in Zannetti 1989, below, and Milford and Russell 1993, above. For a comprehensive review of air pollution issues, see Seinfeld 1986. For a complete discussion on atmospheric chemistry, see Finlayson-Pitts and Pitts 1986, below.

Finlayson-Pitts, B.J. and Pitts, J.N. Jr. 1986. *Atmospheric Chemistry: Fundamental and Experimental Techniques*, John Wiley & Sons, New York.

Zannetti, P. 1989. Simulating short-term, short-range air quality dispersion phenomena. In *Library of Environmental Control Technology*, Vol. 2, *Air Pollution Control*, P.N. Cheremisinoff, ed., Gulf Publishing, Houston, TX, chap. 5.

EPA 2000. *National Air Pollutant Emission Trends, 1900–1998*. United States Office of Air Quality EPA-454/R-00-002. Environmental Protection Planning and Standards. March 2000. Agency Research Triangle Park, NC.

16.7 Global Climate Change

John Firor

It has now been convincingly demonstrated that the average temperature of Earth's surface air has increased substantially in the past hundred years. The cause of this warming is frequently attributed to the release of heat-trapping gases by human activities resulting in heat that would have escaped back to space being retained near the surface of Earth. This process is called the "Greenhouse effect" and the gases are referred to as "Greenhouse gases."

The original warming conclusions were based on records from widely distributed thermometers that had been read daily for many years. These conclusions were subsequently confirmed by a number of independent measurements, including measured warming of the sea surface and land areas far from cities; melting of many glaciers worldwide; and temperatures measured at various depths in abandoned oil wells and other deep holes. For earlier periods, proxies of temperature are available, such as data from isotopic ratios in ice recovered from various depths in Greenland and Antarctic ice; pollen grains recovered from depths of sediments on lake bottoms indicating what plants grew nearby; dates of wine grape harvests; and letters and diaries reporting dates of lake or river freezing or melting and other relevant events.

Long before society began to add greenhouse gases to the air, appreciable amounts of some greenhouse gases were naturally appearing in the air. Also in the late eighteenth century the infrared absorption of carbon dioxide was measured and Jean-Baptiste Fourier — a name familiar to all math students — postulated in 1847 that if carbon dioxide in the atmosphere could absorb energy in the form of infrared light, it would keep the lower atmosphere and the surface of Earth warmer than it would otherwise be (Jones and Henderson-Sellers 1990). Fourier did not include in his speculation an important greenhouse gas that had not yet been recognized as such: water vapor. On average there is so much of this gas in the air, supplied daily by evaporation from oceans, lakes, and rivers, that the total effect of this ancient, natural greenhouse effect is very large. Without it Earth's surface would have been about 33°C colder, and it seems unlikely that the current set of plants and animals would have evolved. This well-established fact leads naturally to the idea that adding more greenhouse gases to the air will make the climate even warmer. Figure 16.7.1 shows that additional amounts of two important greenhouse gases are indeed being added to the atmosphere at the same time that global population is growing, increasing pressure for the emission of greenhouse gases. Both of these increases began with the Industrial Revolution in the 1800s when coal, from which methane is known to emerge as coal is mined, began to be widely used as a fuel.

Figure 16.7.2 shows the increase in global average surface temperature for the period 1860 to 1995, resulting from these additions, a change that gives support to the idea that adding more greenhouse gases will lead to warming. Figure 16.7.3 shows the surface temperature of the Northern Hemisphere during the past millennium deduced from proxy evidence. This graph indicates that, except for a small cooling from 1500 to about 1850, the temperature was fairly stable, until the time of the Industrial Revolution and the start of major coal burning, when it began to rise sharply.

In recent times the theory of the greenhouse effect, including the effect of the additional heat trapping gases released by human activity, has been explored with the use of complex numerical models using super computers. These models trace energy from the sun, in the form of visible light that penetrates the atmosphere and warms the surface. The warmed surface then tries to release this extra heat to space.

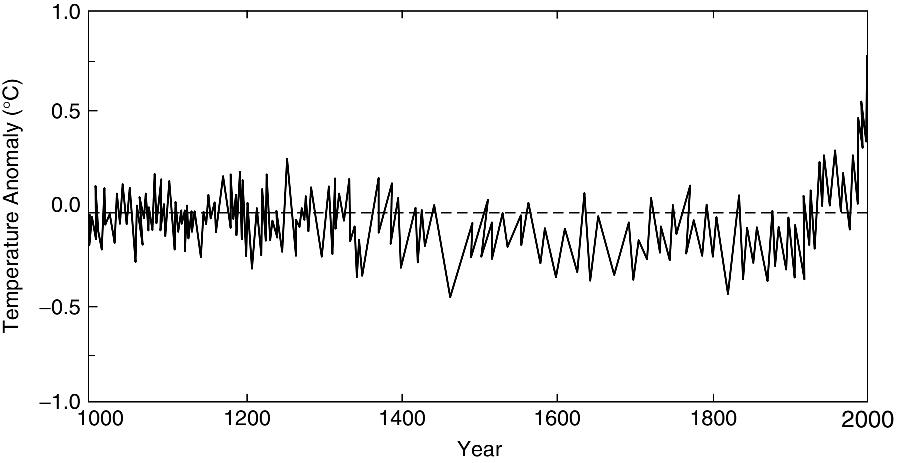

FIGURE 16.7.1 Increases in the atmospheric concentrations of two important greenhouse gases released by human activity and global population increase for 11,000-1993. Drawn from various published data.

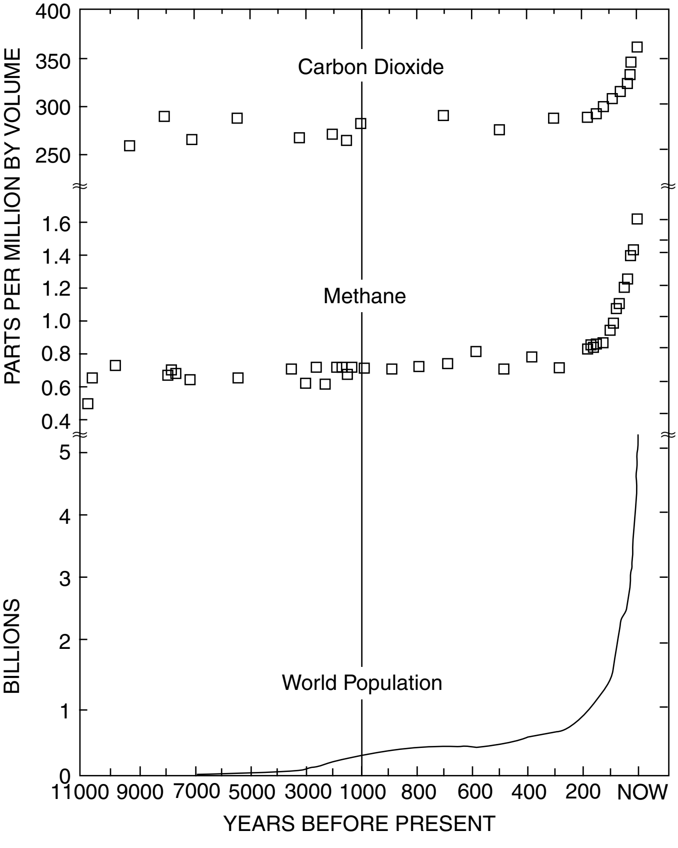

FIGURE 16.7.2 Global average near surface temperature 1860–1995. The black dots are annual average temperatures; the solid line is the running average to smooth out year-to-year variations. fluctuations. Plotted from data assembled and corrected by Phil Jones, Climate Research Unit, University of East Anglia, in the UK. Original numbers available at http://www.cru.uea.ac.uk.

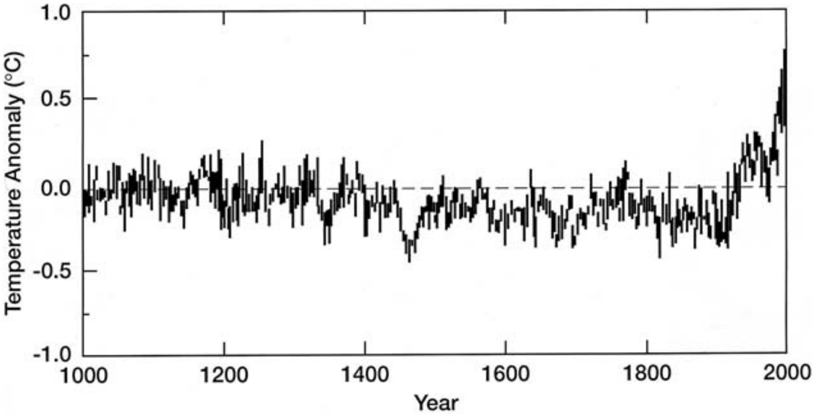

FIGURE 16.7.3 Northern Hemisphere surface temperature during the last millennium deduced from proxy data. The dashed line is along the average temperature 1902–1980. Data after 1990 represent thermometer measurements, as shown in Figure 16.7.1. Chart redrawn from Mann, M.E., Bradley, R.S., and Hughes, M.K., *Geophys. Res. Lets*, 26:729-62, 1999.

Earth's surface is too cool to emit visible light that would easily escape; the emission is of longer wavelength infrared radiation that is absorbed by water vapor, carbon dioxide, methane, and nitrous oxide, ozone, CFCs, and other, less important, species. The calculation concerning the total effect of this process must also include the effect of particles such as soot, sulfates, and others that can either absorb radiation or reflect it. Finally, allowance must be made for the small changes in the intensity of sunlight reaching the top of Earth's atmosphere, changes that in recent times have been measured by instruments carried above the atmosphere on satellites. Correctly simulating all of these interactions, as well as the complex motions of the atmosphere and oceans, forces the vast complexity of the climate change models (Washington and Parkinson 1986). Progress in climate change science is most comprehensibly described by the Intergovernmental Panel on Climate Change (IPCC), created by the World Meteorological Organization and the United Nations Environment Program in 1998, which has issued reviews at five-year internals: 1990, 1995, 2001, each titled Climate Change (*year*), for example, Climate Change 2001 for the most recent one.

These models rather successfully predict the observed average warming of Earth in the past century. This agreement supports the hope that the models will be useful, if not exactly precise, in projecting future climates under a variety of assumptions about future changes in atmospheric composition. Such projections are needed since a major change in climate would have many impacts on society for which we would wish to be prepared.

Water vapor in the air, except locally, is not controlled by human activity. Other gases — carbon dioxide, for example — are tightly coupled to human activity and hence possibly under control of national governments. Good projections of future climate conditions are also needed to guide attempts to ameliorate the most harmful changes.

It should be noted that if all human-induced emissions ceased tomorrow, the climate would continue to warm for decades and sea levels would continue to rise for two thousand years or more, both responding to the fact that some greenhouse gases remain in the air for a hundred or a thousand years or more, continuing to warm Earth's surface. So reductions in emissions cannot prevent all warming but can prevent us from having to deal with a much larger set of climate changes than we are already committed to.

The extra greenhouse gases have, by 2001, increased the average temperature of the global surface air by about .06°C and increased total precipitation and more intense heavy precipitation events in Northern Hemisphere countries. The climate change has also warmed, and thereby expanded, ocean water and melted some glacial and polar ice, the two effects leading to a rise of sea levels by 10 to 25 cm. Assuming "business as usual" emissions of greenhouse gases, models project an additional increase in sea level in the range of 20 to 86 cm by 2100, and a further temperature increase of about 2.5°C (IPCC 2001).

The greenhouse gases capable of being controlled by human action arise from various activities. Carbon dioxide is emitted from the use of fossil fuel — especially coal, with smaller contributions from deforestation and cement manufacturing. Globally, emissions of CO_2 are approximately 25,000 million metric tons a year (MMT/yr). Methane emerges from any wet place in which organic matter decays without enough oxygen present, such as rice cultivation, enteric fermentation in cattle and termites, and landfills. Deforestation, oil wells, coal mining, and leaking natural gas installations also contribute to methane emissions. Global methane emissions are estimated to be around 540, MMT/yr. CFCs and related compounds are entirely human produced, and the Vienna Convention for the Protection of the Ozone Layer and the subsequent Montreal Protocol and its revisions already control the production of these chemicals. Nitrous oxide comes largely from the use of fertilizer containing nitrogen, and the manufacturing of certain industrial acids. These sources provide N_2O emissions of about 5 MMT/yr. Ozone is not normally emitted but is created when sunlight acts on methane, non-methane hydrocarbons, and carbon monoxide in the air, triggering reactions with oxides of nitrogen to produce ozone. Ozone concentrations average about 35ppb (Schimel et al 1996, and IPCC 1995).

Atmospheric concentrations of these gases are measured in parts per million ppm, parts per billion ppb, or parts per trillion ppt. In 1998 the concentrations were CO_2 367 ppm and CH_4 1693 ppb. A number of CFC-related compounds contribute their heat-trapping ability, and, as mentioned earlier, they are all being controlled so that the concentrations are steady or decreasing. The largest CFC concentration in 1998 was that of CFC-12 at 530 ppt. Even with such small concentrations, these chemicals add to the greenhouse effect because each molecule of CFC-12 absorbs several thousand times as much infrared radiation as each molecule of CO_2. Sulfur dioxide emissions are also an important contributor to climate calculations. In the air, sulfur reacts to create sulfate particles that reflect sunlight and decrease the rate of climate warming. These particles only remain in the air for a week or two, but they are rapidly replaced by emissions from coal-burning power plants and the smelting of sulfur containing ores. Global emissions of sulfur dioxide are less well known than carbon dioxide emissions, but may range above 40,000 MMT/yr (WRI 2000).

A major international agreement — the Framework Convention on Climate Change — was negotiated at the United Nations meeting in Rio in 1992 and was ratified by 186 countries by 1995, including the United States. The ultimate objective of the agreement was described as

> …stabilization of the greenhouse concentrations in the atmosphere at a level that would prevent dangerous anthropogenic interference with the climate system. Such a level should be achieved within a time-frame sufficient to allow ecosystems to adapt naturally to climate change, to ensure that food production is not threatened and to enable economic development to proceed in a sustainable manner.

Developed countries additionally agreed to attempt to reduce their carbon dioxide emissions back to 1990 levels by the year 2000, but only England, Germany, and Russia succeeded. The U.S., the largest emitter of greenhouse gases, made little attempt to reduce its emissions, and later, when a protocol was adopted specifying the amount each developed country would be expected to reduce, the U.S. withdrew entirely from the agreement and pronounced that doing anything to make reductions would ruin the economy. Many other countries, however, continued to move toward making this treaty and protocol effective, and some have instituted steps to reduce their emissions even before the protocol is finally ratified. But the extent to which countries will succeed in reducing emissions before the climate changes being induced become very serious is still unknown.

The various claims that the costs of reducing emissions would be excessive have been somewhat softened by a survey of 50 large businesses that had reduced their energy use voluntarily using existing technologies. These companies found that the savings from lower energy bills and incidental improvements usually repaid their investment in one year and continued to produce increased profits indefinitely. Also, a review of the models showing large costs revealed that these calculations assumed “worst case” conditions, omitting considerations that would have reduced the costs (Repetto, D. and Austin, N. 1997).

References

Durning A.T. and Bauman Y. 1998. *Tax Shift*, Northwest Environment Watch, Seattle, WA.

IPCC, *Climate Change* (year), Cambridge University Press, New York 1990, 1995, 2001, WRI, World Resources 2000–2001, WRI, Washington, DC, 2000.

Jones, P., and Henderson-Sellers, A. 1990. History of the Greenhouse effect. *Progress in Physical Geography*, 14, 1, 1990.

Repetto, R. and Austin, D. 1997. *The Cost of Climate Protection*, World Resources Institute, Washington, D.C.

Romm, J. 1999. *Cool Companies: How the Best Businesses Boost Profits and Productivity by Cutting Greenhouse Gas Emissions*. Island Press, Washington, DC, 1999.

Schimel, D., et al. Radiative forcing of climate change. In *Climate Change 1995*, Houghton, J.T. et al., Eds., Cambridge University Press, Cambridge, U.K., 1996, chap 2.

Washington, W.M. and Parkinson, C.L. 1986. *An Introduction to Three-Dimensional Climate Modeling*, University Science Books, Sausalito, CA.

17

Engineering Economics and Project Management

Chan S. Park*
Auburn University

Donald D. Tippett
University of Alabama in Huntsville

17.1 Engineering Economic Decisions

Decisions made during the engineering design phase of product development determine the majority (some say 85%) of the costs of manufacturing that product. Thus, a competent engineer in the 21st century must have an understanding of the principles of economics as well as engineering. This chapter examines the most important economic concepts that should be understood by engineers.

---

[*] Department of Industrial & Systems Engineering, Auburn University, Auburn, AL 36849. Sections 17.1 through 17.6 based on *Contemporary Engineering Economics,* 2nd edition, by Chan S. Park, Addison-Wesley Publishing Company, Reading, MA, 1997.

Engineers participate in a variety of decision-making processes, ranging from manufacturing to marketing to financing decisions. They must make decisions involving materials, plant facilities, the in-house capabilities of company personnel, and the effective use of capital assets such as buildings and machinery. One of the engineer's primary tasks is to plan for the acquisition of equipment (fixed asset) that will enable the firm to design and produce products economically. These decisions are called *engineering economic decisions.*

17.2 Establishing Economic Equivalence

A typical engineering economic decision involves two dissimilar types of dollar amounts. First, there is the investment, which is usually made in a lump sum at the beginning of the project, a time that for analytical purposes is called today, or time 0. Second, there is a stream of cash benefits that are expected to result from this investment over a period of future years.

In such a fixed asset investment funds are committed today in the expectation of earning a return in the future. In the case of a bank loan, the future return takes the form of interest plus repayment of the principal. This is known as the *loan cash flow.* In the case of the fixed asset, the future return takes the form of cash generated by productive use of the asset. The representation of these future earnings along with the capital expenditures and annual expenses (such as wages, raw materials, operating costs, maintenance costs, and income taxes) is the *project cash flow.* This similarity between the loan cash flow and the project cash flow brings us an important conclusion—that is, first we need to find a way to evaluate a money series occurring at different points in time. Second, if we understand how to evaluate a loan cash flow series, we can use the same concept to evaluate the project cash flow series.

Interest: The Cost of Money

Money left in a savings account earns interest so that the balance over time is greater than the sum of the deposits. In the financial world, money itself is a commodity, and like other goods that are bought and sold, money costs money. The cost of money is established and measured by an *interest rate,* a percentage that is periodically applied and added to an amount (or varying amounts) of money over a specified length of time. When money is borrowed, the interest paid is the charge to the brrower for the use of the lender's property; when money is loaned or invested, the interest earned is the lender's gain from providing a good to another. *Interest*, then, may be defined as the cost of having money available for use.

The operation of interest reflects the fact that money has a time value. This is why amounts of interest depend on lengths of time; interest rates, for example, are typically given in terms of a percentage per year. This principle of the time value of money can be formally defined as follows: the economic value of a sum depends on when it is received. Because money has earning power over time (it can be put to work, earning more money for its owner), a dollar received today has a greater value than a dollar received at some future time.

The changes in the value of a sum of money over time can become extremely significant when we deal with large amounts of money, long periods of time, or high interest rates. For example, at a current annual interest rate of 10%, $1 million will earn $100,000 in interest in a year; thus, waiting a year to receive $1 million clearly involves a significant sacrifice. In deciding among alternative proposals, we must take into account the operation of interest and the time value of money to make valid comparisons of different amounts at various times.

The Elements of Transactions Involving Interest

Many types of transactions involve interest — for example, borrowing or investing money, purchasing machinery on credit — but certain elements are common to all of them:

1. Some initial amount of money, called the *principal* (*P*) in transactions of debt or investment
2. The *interest rate* (*i*), which measures the cost or price of money, expressed as a percentage per period of time
3. A period of time, called the *interest period* (or *compounding period*), that determines how frequently interest is calculated
4. The specified length of time that marks the duration of the transaction and thereby establishes a certain *number of interest periods* (*N*)
5. A *plan for receipts or disbursements* (A_n) that yields a particular cash flow pattern over the length of time (for example, we might have a series of equal monthly payments [A] that repay a loan)
6. A *future amount of money* (F) that results from the cumulative effects of the interest rate over a number of interest periods

Cash Flow Diagrams

It is convenient to represent problems involving the time value of money in graphic form with a cash flow diagram (see Figure 17.2.1), which represents time by a horizontal line marked off with the number of interest periods specified. The cash flows over time are represented by arrows at the relevant periods: upward arrows for positive flows (receipts) and downward arrows for negative flows (disbursements).

End-of-Period Convention

In practice, cash flows can occur at the beginning or in the middle of an interest period, or at practically any point in time. One of the simplifying assumptions we make in engineering economic analysis is the *end-of-period convention*, which is the practice of placing all cash flow transactions at the end of an interest period. This assumption relieves us of the responsibility of dealing with the effects of interest within an interest period, which would greatly complicate our calculations.

Compound Interest

Under the compound interest scheme, the interest in each period is based on the total amount owed at the end of the previous period. This total amount includes the original principal plus the accumulated interest that has been left in the account. In this case, you are in effect increasing the deposit amount by

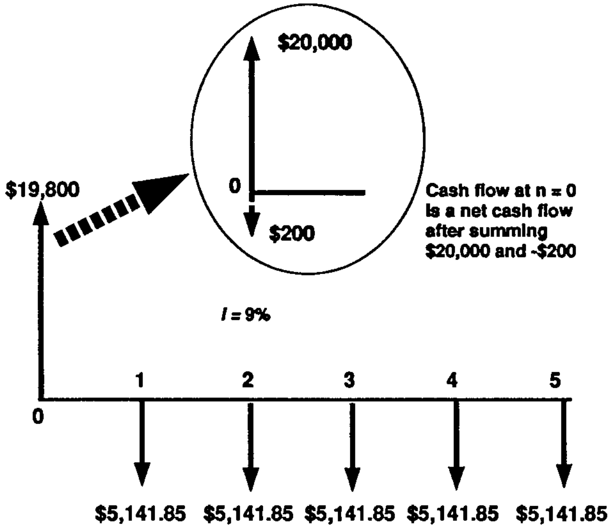

FIGURE 17.2.1 A cash flow diagram for a loan transaction — borrow $20,000 now and pay off the loan with five equal annual installments of $5,141.85. After paying $200 for the loan origination fee, the net amount of financing is $19,800. The borrowing interest rate is 9%.

the amount of interest earned. In general, if you deposited (invested) P dollars at interest rate i, you would have P + iP = P(1 + i) dollars at the end of one period. With the entire amount (principal and interest) reinvested at the same rate i for another period, you would have, at the end of the second period,

$$
\begin{aligned}
P(1+i)+i\left[P(1+i)\right] &= P(1+i)(1+i) \\
&= P(1+i)^2
\end{aligned}
$$

This interest-earning process repeats, and after N periods, the total accumulated value (balance) F will grow to

$$F = P(1+i)^N \tag{17.2.1}$$

Equivalence Calculations

Economic equivalence refers to the fact that a cash flow — whether it is a single payment or a series of payments — can be said to be converted to an *equivalent* cash flow at any point in time; thus, for any sequence of cash flows, we can find an equivalent single cash flow at a given interest rate and a given time.

Equivalence calculations can be viewed as an application of the compound interest relationships developed in Equation 17.2.1. The formula developed for calculating compound interest, $F = P(1 + i)^N$, expresses the equivalence between some present amount, P, and a future amount, F, for a given interest rate, i, and a number of interest periods, N. Therefore, at the end of a 3-year investment period at 8%, $1000 will grow to

$$\$1000(1+0.08)^3 = \$1259.71$$

Thus at 8% interest, $1000 received now is equivalent to $1,25l9.71 received in 3 years and we could trade $1000 now for the promise of receiving $1259.71 in 3 years. Example 17.2.1 demonstrates the application of this basic technique.

Example 17.2.1 — Equivalence

Suppose you are offered the alternative of receiving either $3000 at the end of 5 years or P dollars today. There is no question that the $3000 will be paid in full (no risk). Having no current need for the money, you would deposit the P dollars in an account that pays 8% interest. What value of P would make you indifferent in your choice between P dollars today and the promise of $3000 at the end of 5 years from now?

Discussion

Our job is to determine the present amount that is economically equivalent to $3000 in 5 years, given the investment potential of 8% per year. Note that the problem statement assumes that you would exercise your option of using the earning power of your money by depositing it. The "indifference" ascribed to you refers to economic indifference; that is, within a marketplace where 8% is the applicable interest rate, you could trade one cash flow for the other.

Solution

From Equation (17.2.1), we establish

$$\$3000 = P(1+0.08)^5$$

Rearranging to solve for P,

$$P = \$3000/(1+0.08)^5 = \$2042$$

Comments

In this example, it is clear that if P is anything less than \$2042, you would prefer the promise of \$3000 in 5 years to P dollars today; if P were greater than \$2042, you would prefer P. It is less obvious that at a lower interest rate, P must be higher to be equivalent to the future amount. For example, at $i = 4\%$, $P = \$2466$.

Interest Formulas

In this section is developed a series of interest formulas for use in more complex comparisons of cash flows. It classifies four major categories of cash flow transactions, develops interest formulas for them, and presents working examples of each type.

Single Cash Flow Formulas

We begin our coverage of interest formulas by considering the simplest cash flows: single cash flows. Given a present sum P invested for N interest periods at interest rate i, what sum will have accumulated at the end of the N periods? You probably noticed quickly that this description matches the case we first encountered in describing compound interest. To solve for F (the future sum) we use Equation (17.2.1):

$$F = P(1+i)^N = P(F/P,i,N)$$

Because of its origin in compound interest calculation, the factor (F/P, i, N), which is read as "find F, given P, i, and N" is known as the *single payment compound amount factor*. Like the concept of equivalence, this factor is one of the foundations of engineering economic analysis. Given this factor, all the other important interest formulas can be derived. This process of finding F is often called the compounding process. (Note the time-scale convention. The first period begins at $n = 0$ and ends at $n = 1$.) Thus, in the preceding example, where we had $F = \$1000(1.08)^3$, we can write $F = \$1000(F/P, 8\%, 3)$. We can directly evaluate the equation or locate the factor value by using the 8% interest table* and finding the factor of 1.2597 in the F/P column for $N = 3$.

Finding present worth of a future sum is simply the reverse of compounding and is known as *discounting process*. In Equation (17.2.1), we can see that if we were to find a present sum P, given a future sum F, we simply solve for P.

$$P = F\left[\frac{1}{(1+i)^N}\right] = F(P/F,i,N) \tag{17.2.2}$$

The factor $1/(1 + i)^N$ is known as the *single payment present worth factor* and is designated (P/F, i, N). Tables* have been constructed for the P/F factors for various values of i and N. The interest rate i and the P/F factor are also referred to as *discount rate* and *discounting factor*, respectively. Because using the interest tables is often the easiest way to solve an equation, this factor notation is included for each of the formulas derived in the following sections.

A Stream of Cash Flow Series

A common cash flow transaction involves a series of disbursements or receipts. Familiar situations such as car loans and insurance payments are examples of series payments. Payments of car loans and insurance bills typically involve identical sums paid at regular intervals. However, when there is no clear pattern of payment amounts over a series, one calls the transaction an *uneven cash-flow series*.

---

* All standard engineering economy textbooks (such as *Contemporary Engineering Economics* by C. S. Park, Addison Wesley, 1997) provide extensive sets of interest tables. Or you can obtain such interest tables on a World Wide Web site at http://www.eng.auburn.edu/-park/cee.html, which is a textbook web site for *Contemporary Engineering Economics.*

The present worth of any stream of payments can be found by calculating the present value of each individual payment and summing the results. Once the present worth is found, one can make other equivalence calculations, such as calculating the future worth by using the interest factors developed in the previous section.

Example 17.2.2 — Present Value of an Uneven Series by Decomposition into Single Payments

Wilson Technology, a growing machine shop, wishes to set aside money now to invest over the next 4 years in automating their customer service department. They now earn 10% on a lump sum deposited, and they wish to withdraw the money in the following increments:

Year 1: $25,000 to purchase a computer and data base software designed for customer service use
Year 2: $3000 to purchase additional hardware to accommodate anticipated growth in use of the system
Year 3: No expenses
Year 4: $5000 to purchase software upgrades

How much money must be deposited now to cover the anticipated payments over the next 4 years?

Discussion

This problem is equivalent to asking what value of P would make you indifferent in your choice between P dollars today and the future expense stream of ($25,000, $3000, $0, $5000). One way to deal with an uneven series of cash flows is to calculate the equivalent present value of each single cash flow and sum the present values to find P. In other words, the cash flow is broken into three parts as shown in Figure 17.2.2.

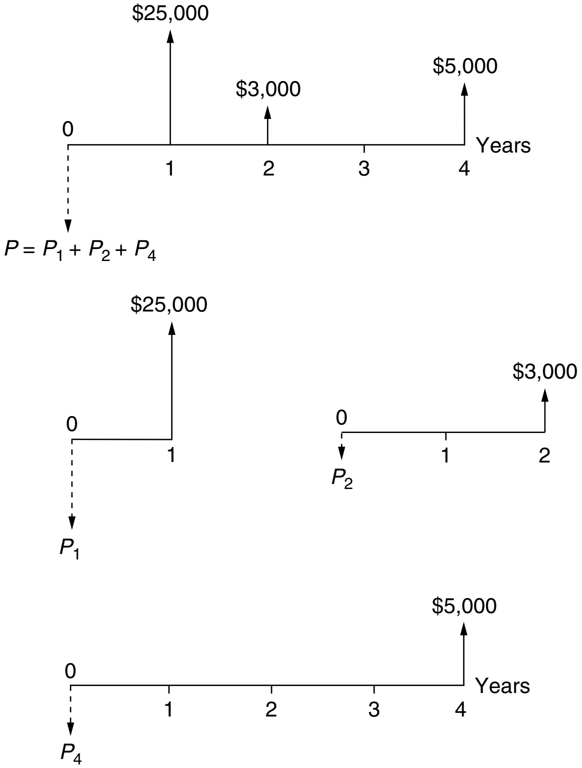

FIGURE 17.2.2 Decomposition of uneven cash flow series into three single-payment transactions. This decomposition allows us to use the single-payment present worth factor.

Solution

$$
\begin{aligned}
P &= \$25{,}000(P/F,10\%,1) + \$3000(P/F,10\%,2) + \$5000(P/F,10\%,4) \\
&= \$28{,}622
\end{aligned}
$$

Cash Flow Series with a Special Pattern

Whenever one can identify patterns in cash flow transactions, one may use them in developing concise expressions for computing either the present or future worth of the series. For this purpose, we will classify cash flow transactions into three categories: (1) equal cash flow series, (2) linear gradient series, and (3) geometric gradient series. To simplify the description of various interest formulas, we will use the following notation:

1. Uniform Series: Probably the most familiar category includes transactions arranged as a series of equal cash flows at regular intervals, known as an *equal-payment series* (or *uniform series*) (Figure 17.2.3a). This describes the cash flows, for example, of the common installment loan contract, which arranges for the repayment of a loan in equal periodic installments. The equal cash flow formulas deal with the equivalence relations of P, F, and A, the constant amount of the cash flows in the series.
2. Linear Gradient Series: While many transactions involve series of cash flows, the amounts are not always uniform: yet they may vary in some regular way. One common pattern of variation occurs when each cash flow in a series increases (or decreases) by a fixed amount (Figure 17.2.3b). A 5-year loan repayment plan might specify, for example, a series of annual payments that increased by $50 each year. We call such a cash flow pattern a *linear gradient series* because its cash flow diagram produces an ascending (or descending) straight line. In addition to P, F, and A, the formulas used in such problems involve the constant amount, G, of the change in each cash flow.
3. Geometric Gradient Series: Another kind of gradient series is formed when the series in cash flow is determined, not by some fixed amount like $50, but by some fixed *rate*, expressed as a percentage. For example, in a 5-year financial plan for a project, the cost of a particular raw material might be budgeted to increase at a rate of 4% per year. The curving gradient in the diagram of such a series suggests its name: a *geometric gradient series* (Figure 17.2.3c). In the formulas dealing with such series, the rate of change is represented by a lowercase g.

Table 17.2.1 summarizes the interest formulas and the cash flow situations in which they should be used. For example, the factor notation (F/A, i, N) represents the situation where you want to calculate the equivalent lump-sum future worth (F) for a given uniform payment series (A) over N period at interest rate i. Note that these interest formulas are applicable only when the interest (compounding) period is the same as the payment period. Also in this table we present some useful interest factor relationships. The next two examples illustrate how one might use these interest factors to determine the equivalent cash flow.

Example 17.2.3 — Uniform Series: Find F, Given i, A, N

Suppose you make an annual contribution of $3000 to your savings account at the end of each year for 10 years. If your savings account earns 7% interest annually, how much can be withdrawn at the end of 10 years? (See Figure 17.2.4.)

Solution

$$
\begin{aligned}
F &= \$3000(F/A,7\%,10) \\
&= \$3000(13.8164) \\
&= \$41{,}449.20
\end{aligned}
$$

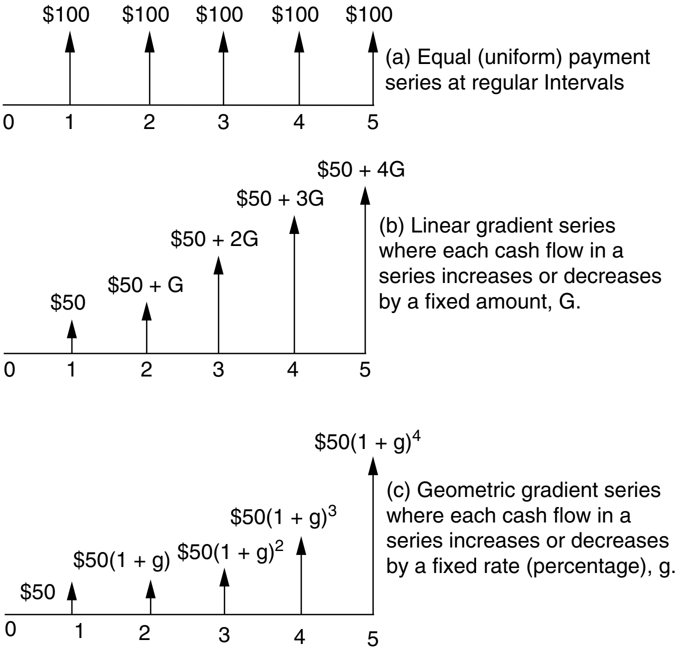

FIGURE 17.2.3 Five types of cash flows: (a) equal (uniform) payment series; (b) linear gradient series; and (c) geometric gradient series.

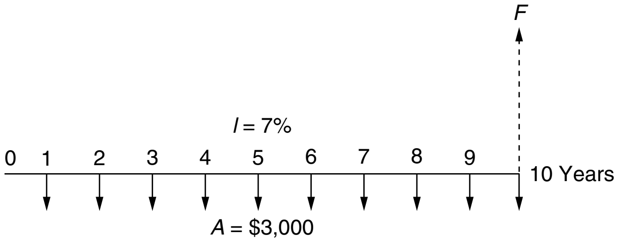

FIGURE 17.2.4 Cash flow diagram (Example 17.2.3).

Example 17.2.4 — Geometric Gradient: Find P, Given A_1, g, i, N

Ansell Inc., a medical device manufacturer, uses compressed air in solenoids and pressure switches in the machines to control the various mechanical movements. Over the years the manufacturing floor has changed layouts numerous times. With each new layout more piping was added to the compressed air delivery system to accommodate the new locations of the manufacturing machines. None of the extra, unused old pipe was capped or removed; thus the current compressed air delivery system is inefficient and fraught with leaks. Because of the leaks in the current system, the compressor is expected to run 70% of the time that the plant is in operation during the upcoming year, which will require 260 kW/hr of electricity at a rate of $0.05/kW-hr. (The plant runs 250 days a year for 24 hr a day.) If Ansell continues to operate the current air delivery system, the compressor run time will increase by 7% per year for the next 5 years due to ever-deteriorating leaks. (After 5 years, the current system cannot meet the plant's compressed air requirement, so it has to be replaced.) If Ansell decides to replace all of the old piping now, it will cost $28,570. The compressor will still run the same number of days; however, it will run 23% less (or 70% (1 – 0.23) = 53.9% usage during the day) because of the reduced air pressure loss. If Ansell's interest rate is 12%, is it worth fixing now?

TABLE 17.2.1 Summary of Discrete Compounding Formulas with Discrete Payments

Flow Type	Factor Notation	Formula	Cash Flow Diagram	Factor Relationship
Single	Compound amount (*F/P, i, N*) Present worth (*P/F, i, N*)	$F = P(1 + i)^N$ $P = F(1 + i)^{-N}$	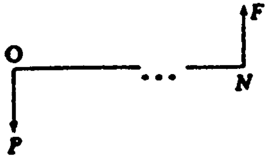	(*F/P, i, N*) = *i*(*F/A, i, N*) + 1 (*P/F, i, N*) = 1 – (*P/A, i N*)*i*
Equal Payment Series	Compound amount (*F/A, i, N*)	$F = A\left[\frac{(1+i)^N - 1}{i}\right]$	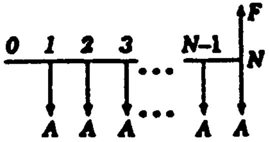	(*A/F, i, N*) = (*A/P, i, N*) – i
	Sinking fund (*A/F, i, N*)	$A = F\left[\frac{i}{(1+i)^N - 1}\right]$		
	Present worth (*P/A, i, N*)	$P = A\left[\frac{(1+i)^N - 1}{i(1+i)^N}\right]$	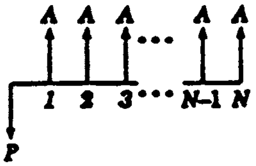	$(A/P,i,N) = \frac{i}{1-(P/F,i,N)}$
	Capital recovery (*A/P, i, N*)	$A = P\left[\frac{i(1+i)^N}{(1+i)^N - 1}\right]$		
Gradient Series	Uniform gradient Present worth (*P/G, i, N*)	$P = C\left[\frac{(1+i)^N - iN - 1}{i^2(1+i)^N}\right]$	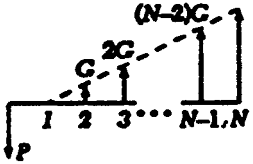	(*F/G, i, N*) = (*P/G, i, N*)(*F/P, i, N*) (*A/G, i, N*) = (*P/G, i, N*)(*A/P, i, N*)
	Geometric gradient Present worth (*P/A*$_1$*, g, i, N*)	$P = \begin{bmatrix} A_1\left[\frac{1-(1+g)^N(1+i)^{-N}}{i-g}\right] \\ \frac{NA_1}{1+i}\ (\text{if}\ i = g) \end{bmatrix}$	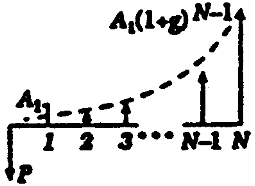	(*F/A*$_1$*, g, i, N*) = (*P/A*$_1$*, g, i, N*)(*F/P, i N*)

Adapted from Park, C.S. 1997. *Contemporary Engineering Economics.* Addison-Wesley, Reading, MA. Tables are constructed for various interest factors and you can obtain such interest tables on a World Wide Web site at http://www.eng.auburn.edu/~park/cee.html, which is a textbook web site for *Contemporary Engineering Economics.*

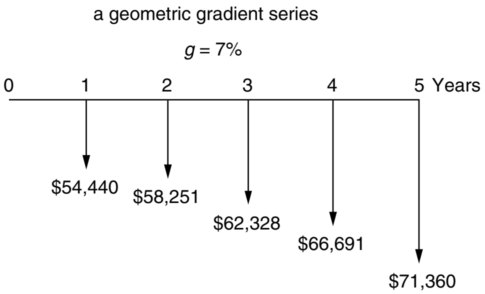

FIGURE 17.2.5 Expected power expenditure over the next 5 years due to deteriorating leaks if no repair is performed (Example 17.2.4).

Solution

- Step 1. Calculate the cost of power consumption of the current piping system during the first year. The power consumption is equal to:

$$\begin{aligned}\text{power cost} &= \%\text{ of day operating} \times \text{days operating per year} \times \text{hours per day}\\ &\quad \times \text{kW/hr} \times \$/\text{kW-hr}\\ &= (70\%) \times (250\ \text{days/year}) \times (24\ \text{hr/day}) \times (260\ \text{kW/hr}) \times (\$0.05/\text{kW-hr})\\ &= \$54{,}440\end{aligned}$$

- Step 2. Each year the annual power cost will increase at the rate of 7% over the previous year's power cost. Then the anticipated power cost over the 5-year period is summarized in Figure 17.2.5. The equivalent present lump-sum cost at 12% for this geometric gradient series is

$$\begin{aligned}P_{Old} &= \$54{,}440\left(P/A_1, 7\%, 12\%, 5\right)\\ &= \$54{,}440\left[\frac{1-(1+0.07)^5(1+0.12)^{-5}}{0.12-0.07}\right]\\ &= \$222{,}283\end{aligned}$$

- Step 3. If Ansell replaces the current compressed air system with the new one, the annual power cost will be 23% less during the first year and will remain at that level over the next 5 years. The equivalent present lump-sum cost at 12% is

$$\begin{aligned}P_{New} &= \$54{,}440(1-0.23)\left(P/A, 12\%, 5\right)\\ &= \$41{,}918.80(3.6048)\\ &= \$151{,}108\end{aligned}$$

- Step 4. The net cost for not replacing the old system now is $71,175 (= $222,283 – $151,108). Since the new system costs only $28,570, the replacement should be made now.

Nominal and Effective Interest Rates

In all our examples in the previous section, we implicitly assumed that payments are received once a year, or annually. However, some of the most familiar financial transactions in both personal financial matters and engineering economic analysis involve nonannual payments; for example, monthly mortgage payments and daily earnings on savings accounts. Thus, if we are to compare different cash flows with different compounding periods, we need to address them on a common basis. The need to do this has led to the development of the concepts of *nominal interest rate* and *effective interest rate.*

Nominal Interest Rate

Even if a financial institution uses a unit of time other than a year — a month or quarter, for instance — in calculating interest payments, it usually quotes the interest rate on an annual basis. Many banks, for example, state the interest arrangement for credit cards in this way: "18% compounded monthly." We say 18% is the *nominal interest rate* or *annual percentage rate* (APR), and the compounding frequency is monthly (12). To obtain the interest rate per compounding period, we divide 18% by 12 to obtain 1.5% per month. Therefore, the credit card statement above means that the bank will charge 1.5% interest on unpaid balance for each month.

Although the annual percentage rate, or APR, is commonly used by financial institutions and is familiar to customers, when compounding takes place more frequently than annually, the APR does not explain precisely the amount of interest that will accumulate in a year. To explain the true effect of more frequent compounding on annual interest amounts, we need to introduce the term effective interest rate.

Effective Annual Interest Rate

The *effective interest rate* is the only one that truly represents the interest earned in a year or some other time period. For instance, in our credit card example, the bank will charge 1.5% interest on unpaid balance at the end of each month. Therefore, the 1.5% rate represents an effective interest rate — on a monthly basis, it is the rate that predicts the actual interest payment on your outstanding credit card balance.

Suppose you purchase an appliance on credit at 18% compounded monthly. Unless you pay off the entire amount within a grace period (let's say, a month), any unpaid balance (P) left for a year period would grow to

$$\begin{aligned} F &= P(1+i)^N \\ &= P(1+0.015)^{12} \\ &= 1.1956P \end{aligned}$$

This implies that for each dollar borrowed for 1 year, you owe \$1.1956 at the end of the year, including the principal and interest. For each dollar borrowed, you pay an equivalent annual interest of 19.56 cents. In terms of an effective annual interest rate (i_a), we can rewrite the interest payment as a percentage of the principal amount

$$i_a = (1+0.015)^{12} - 1 = 0.1956, \text{ or } 19.56\%$$

Thus, the effective annual interest rate is 19.56%.

Clearly, compounding more frequently increases the amount of interest paid for the year at the same nominal interest rate. We can generalize the result to compute the effective interest rate for *any time duration*. As you will see later, we normally compute the effective interest rate based on payment (transaction) period. For example, cash flow transactions occur quarterly but interest rate is compounded monthly. This quarterly conversion allows us to use the interest formulas in Table 17.2.1. To consider this, we may define the effective interest rate for a given payment period as

$$\begin{aligned} i &= (1 + r/M)^C - 1 \\ &= (1 + r/CK)^C - 1 \end{aligned} \tag{17.2.3}$$

where

M = the number of interest periods per year
C = the number of interest periods per payment period
K = the number of payment periods per year

When M = 1, we have the special case of annual compounding. Substituting M = 1 into Equation (17.2.3), we find it reduces to $i_a = r$. That is, when compounding takes place once annually,* effective interest is equal to nominal interest. Thus, in all our earlier examples, where we considered only annual interest, we were by definition using effective interest rates.

Example 17.2.5 — Calculating Auto Loan Payments

Suppose you want to buy a car priced $22,678.95. The car dealer is willing to offer a financing package with 8.5% annual percentage rate over 48 months. You can afford to make a down payment of $2678.95, so the net amount to be financed is $20,000. What would be the monthly payment?

Solution

The ad does not specify a compounding period, but in automobile financing the interest and the payment periods are almost always both monthly. Thus, the 8.5% APR means 8.5% compounded monthly. In this situation, we can easily compute the monthly payment using the *capital recovery factor* in Table 17.2.1:

$$i = 8.5\%/12 = 0.7083\% \text{ per month}$$

$$N = (12)(4) = 48 \text{ months}$$

$$A = \$20{,}000(A/P, 0.7083\%, 48) = \$492.97$$

Example 17.2.6 — Compounding More Frequent Than Payments

Suppose you make equal quarterly deposits of $1000 into a fund that pays interest at a rate of 12% compounded monthly. Find the balance at the end of year 2 (Figure 17.2.6).

Solution

We follow the procedure for noncomparable compounding and payment periods described above.

1. Identify the parameter values for M, K, and C:

$$M = 12 \text{ compounding periods per year}$$

$$K = 4 \text{ payment periods per year}$$

$$C = 3 \text{ interest periods per payment period}$$

---

* For an extreme case, we could consider a continuous compounding. As the number of compounding periods (M) becomes very large, the interest rate per compounding period (r/M) becomes very small. As M approaches infinity and r/M approaches zero, we approximate the situation of *continuous compounding*.

$$i = e^{r/K} - 1$$

To calculate the effective annual interest rate for continuous compounding, we set K equal to 1, resulting in:

$$i_a = e^r - 1$$

As an example, the effective annual interest rate for a nominal interest rate of 12% compounded continuously is $i_a = e^{0.12} - 1 = 12.7497\%$.

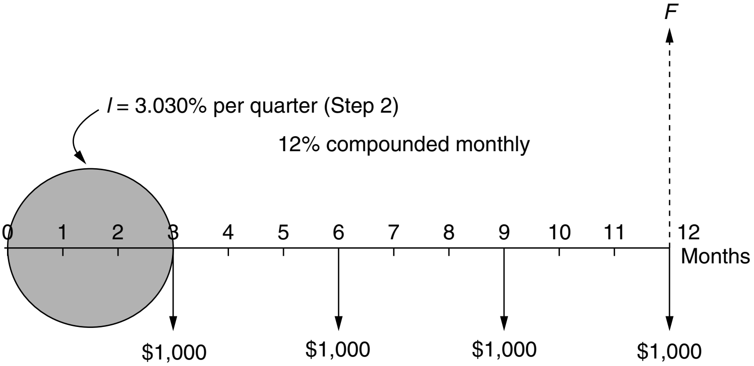

FIGURE 17.2.6 Quarterly deposits with monthly compounding (Example 17.2.6).

2. Use Equation (17.2.3) to compute effective interest per quarter.

$$\begin{aligned} i &= (1+0.12/12)^3 - 1 \\ &= 3.030\% \text{ per quarter} \end{aligned}$$

3. Find the total number of payment periods, N.

$$N = K(\text{number of years}) = 4(2) = 8 \text{ quarters}$$

4. Use i and N in the (F/A, i, N) factor from Table 17.2.1:

$$F = \$1000(F/A, 3.030\%, 8) = \$8901.81$$

Loss of Purchasing Power

It is important to differentiate between the time value of money as we used it in the previous section and the effects of inflation. The notion that a sum is worth more the earlier it is received can refer to its earning potential over time, to decreases in its value due to inflation over time, or to both. Historically, the general economy has usually fluctuated in such a way that it experiences *inflation*, a loss in the purchasing power of money over time. Inflation means that the cost of an item tends to increase over time or, to put it another way, the same dollar amount buys less of an item over time. *Deflation* is the opposite of inflation (negative inflation), in that prices decrease over time and hence a specified dollar amount gains in purchasing power. In economic equivalence calculations, we need to consider the change of purchasing power along with the earning power.

The Average Inflation Rate

To account for the effect of varying yearly inflation rates over a period of several years, we can compute a single rate that represents an *average inflation rate.* Since each individual year's inflation rate is based on the pervious year's rate, they have a compounding effect. As an example, suppose we want to calculate the average inflation rate for a 2-year period for a typical item. The first year's inflation rate is 4% and the second year's is 8%, using a base price index of 100.

- Step 1. We find the price at the end of the second year by the process of compounding:

$$\underbrace{\underbrace{100(1+0.04)}_{}(1+0.08)}_{} = 112.32$$

- Step 2. To find the average inflation rate f over a 2-year period, we establish the following equivalence equation:

$$100(1+f)^2 = 112.32 \leftarrow 100(F/P, f, 2) = 112.32$$

  Solving for f yields

$$f = 5.98\%$$

We can say that the price increases in the last 2 years are equivalent to an average annual percentage rate of 5.98% per year. In other words, our purchasing power decreases at the annual rate of 5.98% over the previous year's dollars. If the average inflation rate is calculated based on the *consumer price index* (CPI), it is known as a *general inflation rate* $(\bar{f})$.

Actual vs. Constant Dollars

To introduce the effect of inflation into our economic analysis, we need to define several inflation-related terms.*

- Actual (current) dollars (A_n): Estimates of future cash flows for year n which take into account any anticipated changes in amount due to inflationary or deflationary effects. Usually these amounts are determined by applying an inflation rate to base year dollar estimates.
- Constant (real) dollars (A'_n): Dollars of constant purchasing power independent of the passage of time. In situations where inflationary effects have been assumed when cash flows were estimated, those estimates can be converted to constant dollars (base year dollars) by adjustment using some readily accepted *general inflation rate*. We will assume that the base year is always time 0 unless we specify otherwise.

Equivalence Calculation under Inflation

In previous sections, our equivalence analyses have taken into consideration changes in the *earning power* of money — that is, interest effects. To factor in changes in *purchasing power* as well — that is, inflation — we may use either (1) constant dollar analysis or (2) actual dollar analysis. Either method will produce the same solution; however, each uses a different interest rate and procedure.

There are two types of interest rate for equivalence calculation: (1) the market interest rate and (2) the inflation-free interest rate. The interest rate that is applicable depends on the assumptions used in estimating the cash flow.

- Market interest rate (i): This interest rate takes into account the combined effects of the earning value of capital (earning power) and any anticipated inflation or deflation (purchasing power). Virtually all interest rates stated by financial institutions for loans and savings accounts are market interest rates. Most firms use a market interest rate (also known as *inflation-adjusted rate of return* [*discount rate*]) in evaluating their investment projects.
- Inflation-free interest rate (i′): An estimate of the true earning power of money when inflation effects have been removed. This rate is commonly known as *real interest rate* and can be computed if the market interest rate and inflation rate are known.

In calculating any cash flow equivalence, we need to identify the nature of project cash flows. There are three common cases:

Case 1. All cash flow elements are estimated in constant dollars. Then, to find the equivalent present value of a cash flow series in constant dollars, use the inflation-free interest rate.

---

* Based on the ANSI Z94 Standards Committee on Industrial Engineering Terminology. 1988. *The Engineering Economist.* Vol. 33(2): 145–171.

Case 2. All cash flow elements are estimated in actual dollars. Then, use the market interest rate to find the equivalent worth of the cash flow series in actual dollars.

Case 3. Some of the cash flow elements are estimated in constant dollars and others are estimated in actual dollars. In this situation, we simply convert all cash flow elements into one type — either constant or actual dollars. Then we proceed with either constant-dollar analysis for case 1 or actual-dollar analysis for case 2.

Removing the effect of inflation by deflating the actual dollars with $\bar{f}$ and finding the equivalent worth of these constant dollars by using the inflation-free interest rate can be greatly streamlined by the efficiency of the *adjusted-discount method*, which performs deflation and discounting in one step. Mathematically we can combine this two-step procedure into one by

$$i = i' + \bar{f} + i'\bar{f} \tag{17.2.4}$$

This implies that the market interest rate is a function of two terms, i', $\bar{f}$. Note that if there is no inflationary effect, the two interest rates are the same ($\bar{f} = 0 \rightarrow i = i'$). As either i' or $\bar{f}$ increases, i also increases. For example, we can easily observe that when prices are increasing due to inflation, bond rates climb, because lenders (that is anyone who invests in a money-market fund, bond, or certificate of deposit) demand higher rates to protect themselves against the eroding value of their dollars. If inflation were at 3%, you might be satisfied with an interest rate of 7% on a bond because your return would more than beat inflation. If inflation were running at 10%, however, you would not buy a 7% bond; you might insist instead on a return of at least 14%. On the other hand, when prices are coming down, or at least are stable, lenders do not fear the loss of purchasing power with the loans they make, so they are satisfied to lend at lower interest rates.

17.3 Measures of Project Worth

This section shows how to compare alternatives on equal basis and select the wisest alternative from an economic standpoint. The three common measures based on cash flow equivalence are (1) equivalent present worth, (2) equivalent annual worth, and (3) rate of return. The present worth represents a measure of future cash flow relative to the time point "now" with provisions that account for earning opportunities. Annual worth is a measure of the cash flow in terms of the equivalent equal payments on an annual basis. The third measure is based on *yield* or percentage.

Describing Project Cash Flows

When a company purchases a fixed asset such as equipment, it makes an investment. The company commits funds today in the expectation of earning a return on those funds in the future. Such an investment is similar to that made by a bank when it lends money. For the bank loan, the future cash flow consists of interest plus repayment of the principal. For the fixed asset, the future return is in the form of cash flows from the profitable use of the asset. In evaluating a capital investment, we are concerned only with those cash flows that result directly from the investment. These cash flows, called *differential* or *incremental cash flows*, represent the change in the firm's total cash flow that occurs as a direct result of the investment.

We must also recognize that one of the most important parts of the capital budgeting process is the estimation of the relevant cash flows. For all examples in this section, however, net cash flows can be viewed as before-tax values or after-tax values for which tax effects have been recalculated. Since some organizations (e.g., governments and nonprofit organizations) are not taxable, the before-tax situation can be a valid base for that type of economic evaluation. This view will allow us to focus on our main area of concern, the economic evaluation of an investment project. The procedures for determining after-tax net cash flows in taxable situations are developed in Section 17.4.

Example 17.3.1 — Identifying Project Cash Flows

Merco Inc., a machinery builder in Louisville, KY, is considering making an investment of $1,250,000 in a complete structural-beam-fabrication system. The increased productivity resulting from the installation of the drilling system is central to the justification. Merco estimates the following figures as a basis for calculating productivity:

- Increased fabricated steel production: 2000 tons/year
- Average sales price/ton fabricated steel: $2566.50/ton
- Labor rate: $10.50/hr
- Tons of steel produced in a year: 15,000 tons
- Cost of steel per ton (2205 lb): $1950/ton
- Number of workers on layout, holemaking, sawing, and material handling: 17
- Additional maintenance cost: $128,500 per year

With the cost of steel at $1950/ton and the direct labor cost of fabricating 1 lb at 10 cents, the cost of producing a ton of fabricated steel is about $2170.50. With a selling price of $2566.50/ton, the resulting contribution to overhead and profit becomes $396/ton. Assuming that Merco will be able to sustain an increased production of 2000 tons per year by purchasing the system, the projected additional contribution has been estimated to be 2000 tons × $396 = $792,000.

Since the drilling system has the capacity to fabricate the full range of structural steel, two workers can run the system, one on the saw and the other on the drill. A third operator is required as a crane operator for loading and unloading materials. Merco estimates that to do the equivalent work of these three workers with conventional manufacture requires, on the average, an additional 14 people for centerpunching, holemaking with radial or magnetic drill, and material handling. This translates into a labor savings in the amount of $294,000 per year ($10.50 × 40 hr/week × 50 weeks/year × 14). The system can last for 15 years with an estimated after-tax salvage value of $80,000. The expected annual corporate income taxes would amount to $226,000. Determine the net cash flow from undertaking the investment. Determine the net cash flows from the project over the service life.

Solution

The net investment cost as well as savings are as follows:

- Cash inflows:
  Increased annual revenue: $792,000
  Projected annual net savings in labor: $294,000
  Projected after-tax salvage value at the end of year 15: $80,000
- Cash outflows:
  Project investment cost: $1,250,000
  Projected increase in annual maintenance cost: $128,500
  Projected increase in corporate income taxes: $226,000

Now we are ready to summarize a cash flow table as follows:

Year	Cash Inflows	Cash Outflows	Net Cash Flows
0	0	$1,250,000	–$1,250,000
1	1,086,000	354,500	731,500
2	1,086,000	354,500	731,500
⋮	⋮	⋮	⋮
15	1,086,000 + 80,000	354,500	811,500

The project's cash flow diagram is shown in Figure 17.3.1.

Assuming these cost savings and cash flow estimates are correct, should management give the go-ahead for installation of the system? If management has decided not to install the fabrication system,

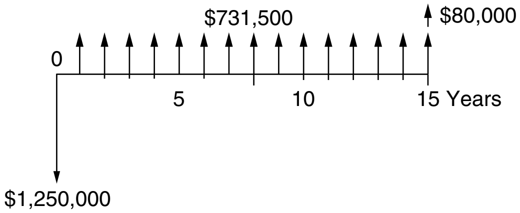

FIGURE 17.3.1 Cash flow diagram (Example 17.3.1).

what do they do with the $1,250,000 (assuming they have it in the first place)? The company could buy $1,250,000 of Treasury bonds. Or it could invest the amount in other cost-saving projects. How would the company compare cash flows that differ both in timing and amount for the alternatives it is considering? This is an extremely important question because virtually every engineering investment decision involves a comparison of alternatives. These are the types of questions this section is designed to help you answer.

Present Worth Analysis

Until the 1950s, the payback method* was widely used as a means of making investment decisions. As flows in this method were recognized, however, business people began to search for methods to improve project evaluations. This led to the development of discounted cash flow techniques (DCF), which take into account the time value of money. One of the DCFs is the net present worth method (NPW). A capital investment problem is essentially one of determining whether the anticipated cash inflows from a proposed project are sufficiently attractive to invest funds in the project. In developing the NPW criterion, we will use the concept of cash flow equivalence discussed in Section 17.2. Usually, the most convenient point at which to calculate the equivalent values is often time 0. Under the NPW criterion, the present worth of all cash inflows is compared against the present worth of all cash outflows that are associated with an investment project. The difference between the present worth of these cash flows, called the *net present worth* (NPW), determines whether or not the project is an acceptable investment. When two or more projects are under consideration. NPW analysis further allows us to select the best project by comparing their NPW figures.

We will first summarize the basic procedure for applying the present worth criterion to a typical investment project.

- Determine the interest rate that the firm wishes to earn on its investments. This represents an interest rate at which the firm can always invest the money in its *investment pool*. We often refer to this interest rate as either a *required rate of return* or a *minimum attractive rate of return* (MARR). Usually this selection will be a policy decision by top management. It is possible for the MARR to change over the life of a project, but for now we will use a single rate of interest in calculating NPW.

---

* One of the primary concerns of most business people is whether and when the money invested in a project can be recovered. The *payback method* screens projects on the basis of how long it takes for net receipts to equal investment outlays. A common standard used in determining whether or not to pursue a project is that no project may be considered unless its payback period is shorter than some specified period of time. If the payback period is within the acceptable range, a formal project evaluation (such as the present worth analysis) may begin. It is important to remember that payback screening is not an *end* itself, but rather a method of screening out certain obvious unacceptable investment alternatives before progressing to an analysis of potentially acceptable ones. But the much-used payback method of equipment screening has a number of serious drawbacks. The principal objection to the payback method is its failure to measure profitability; that is, there is no "profit" made during the payback period. Simply measuring how long it will take to recover the initial investment outlay contributes little to gauging the earning power of a project.

- Estimate the service life of the project.*
- Determine the net cash flows (net cash flow = cash inflow – cash outflow).
- Find the present worth of each net cash flow at the MARR. Add up these present worth figures; their sum is defined as the project's NPW.
- Here, a positive NPW means the equivalent worth of inflows are greater than the equivalent worth of outflows, so project makes a profit. Therefore, if the PW(i) is positive for a single project, the project should be accepted; if negative, it should be rejected. The decision rule is

$$\text{If } PW(i) > 0, \text{ accept the investment}$$

$$\text{If } PW(i) = 0, \text{ remain indifferent}$$

$$\text{If } PW(i) < 0, \text{ reject the investment}$$

Note that the decision rule is for a single project evaluation where you can estimate the revenues as well as costs associated with the project. As you will find later, when you are comparing alternatives with the same revenues, you can compare them based on the cost only. In this situation (because you are minimizing costs, rather than maximizing profits), you should accept the project that results in smallest, or least negative, NPW.

Example 17.3.2 — Net Present Worth

Consider the investment cash flows associated with the metal fabrication project in Example 17.3.1. If the firm's MARR is 15%, compute the NPW of this project. Is this project acceptable?

Solution

Since the fabrication project requires an initial investment of \$1,250,000 at n = 0 followed by the 15 equal annual savings of \$731,500, and \$80,000 salvage value at the end of 15 years, we can easily determine the NPW as follows:

$$PW(15\%)_{outflow} = \$1,250,000$$

$$\begin{aligned} PW(15\%)_{inflow} &= \$731,500(P/A,15\%,15) + \$80,000(P/F,15\%,15) \\ &= \$4,284,259 \end{aligned}$$

---

* Another special case of the PW criterion is useful when the life of a proposed project is *perpetual* or the planning horizon is extremely long. The process of computing the PW cost for this infinite series is referred to as the *capitalization* of project cost. The cost is known as the *capitalized cost.* It represents the amount of money that must be invested today to yield a certain return A at the end of each and every period forever, assuming an interest rate of i. Observe the limit of the uniform series present worth factor as N approaches infinity:

$$\lim_{N\to\infty}(P/A,i,N) = \lim_{N\to\infty}\left[\frac{(1+i)^N - 1}{i(1+i)^N}\right] = \frac{1}{i}$$

Thus, it follows that

$$PW(i) = A(P/A,i,N \to \infty) = \frac{A}{i} \tag{17.5}$$

Another way of looking at this, PW(i) dollars today, is to ask what constant income stream could be generated by this in perpetuity. Clearly, the answer is A = iPW(i). If withdrawals were greater than A, they could be eating into the principal, which would eventually reduce to 0.

Then, the NPW of the project is

$$\begin{aligned} PW(15\%) &= PW(15\%)_{in\ flow} - PW(15\%)_{out\ flow} \\ &= \$4,284,259 - \$1,250,000 \\ &= \$3,034,259 \end{aligned}$$

Since PW (15%) > 0, the project would be acceptable.

Annual Equivalent Method

The annual equivalent worth (AE) criterion is a basis for measuring investment worth by determining equal payments on an annual basis. Knowing that we can convert any lump-sum cash amount into a series of equal annual payments, we may first find the NPW for the original series and then multiply the NPW by the capital recovery factor:

$$AE(i) = PW(i)(A/P,i,N) \tag{17.3.1}$$

The accept-reject decision rule for a single *revenue* project is

$$\begin{aligned} &\text{If } AE(i) > 0, \text{ accept the investment} \\ &\text{If } AE(i) = 0, \text{ remain indifferent} \\ &\text{If } AE(i) < 0, \text{ reject the investment} \end{aligned}$$

Notice that the factor (A/P, i, N) in Table 17.2.1 is positive for $-1 < i < \infty$. This indicates that the AE(i) value will be positive if and only if PW(i) is positive. In other words, accepting a project that has a positive AE(i) value is equivalent to accepting a project that has a positive PW(i) value. Therefore, the AE criterion should provide a basis for evaluating a project that is consistent with the NPW criterion.

As with the present worth analysis, when you are comparing mutually exclusive *service* projects whose revenues are the same, you may compare them based on *cost* only. In this situation, you will select the alternative with the minimum annual equivalent cost (or least negative annual equivalent worth).

Unit Profit/Cost Calculation

There are many situations in which we want to know the unit profit (or cost) of operating an asset. A general procedure to obtain such a unit profit or cost figure involves the following two steps:

- Determine the number of units to be produced (or serviced) each year over the life of the asset.
- Identify the cash flow series associated with the production or service over the life of the asset.
- Calculate the net present worth of the project cash flow series at a given interest rate and then determine the equivalent annual worth.
- Divide the equivalent annual worth by the number of units to be produced or serviced during each year. When you have the number of units varying each year, you may need to convert them into equivalent annual units.

To illustrate the procedure, we will consider Example 17.3.3, where the annual equivalent concept can be useful in estimating the savings per machine hour for a proposed machine acquisition.

Example 17.3.3 — Unit Profit per Machine Hour

Tiger Machine Tool Company is considering the proposed acquisition of a new metal-cutting machine. The required initial investment of $75,000 and the projected cash benefits and annual operating hours over the 3-year project life are as follows.
Compute the equivalent savings per machine hour at i = 15%.

End of Year	Net Cash Flow	Operating Hours
0	–$75,000	
1	24,400	2,000
2	27,340	2,000
3	55,760	2,000

Solution
Bringing each flow to its equivalent at time zero, we find

$$\begin{aligned} PW(15\%) &= -\$75{,}000 + \$24{,}400(P/F,15\%,1) + \$27{,}340(P/F,15\%,2) + \$55{,}760(P/F,15\%,3) \\ &= \$3553 \end{aligned}$$

Since the project results in a surplus of $3553, the project would be acceptable. We first compute the annual equivalent savings from the use of the machine. Since we already know the NPW of the project, we obtain the AE by

$$AE(15\%) = \$3553(A/P,15\%,3) = \$1556$$

With an annual usage of 2000 hr, the equivalent savings per machine hour would be

$$\text{Savings per machine hour} = \$1556/\$2000\text{ hr} = \$0.78/\text{hr}$$

Comments
Note that we cannot simply divide the NPW amount ($3553) by the total number of machine hours over the 3-year period (6000 hr), or $0.59/hr. This $0.59 figure represents the *instant savings* in present worth for each hourly use of the equipment, but does not consider the time over which the savings occur. Once we have the annual equivalent worth, we can divide by the desired time unit if the compounding period is 1 year. If the compounding period is shorter, then the equivalent worth should be calculated for the compounding period.

Rate of Return Analysis

Along with the NPW and AE, the third primary measure of investment worth is based on yield, known as *rate of return*. The NPW measure is easy to calculate and apply. Nevertheless, many engineers and financial managers prefer rate of return analysis to the NPW method because they find it intuitively more appealing to analyze investments in terms of percentage rates of return than in dollars of NPW.

Internal Rate of Return

Many different terms refer to rate of return, including yield (that is, the yield to maturity, commonly used in bond valuation), internal rate of return, and marginal efficiency of capital. In this section, we will define *internal rate of return* as the break-even interest rate, i^*, which equates the present worth of a project's cash outflows to the present worth of its cash inflows, or

$$\begin{aligned} PW(i^*) &= PW_{\text{cash inflows}} - PW_{\text{cash outflows}} \\ &= 0 \end{aligned}$$

Note that the NPW expression is equivalent to

$$PW(i^*) = \frac{A_0}{(1+i^*)^0} + \frac{A_1}{(1+i^*)^1} + \cdots + \frac{A_N}{(1+i^*)^N} = 0 \qquad (17.3.2)$$

Here we know the value of A_n for all n, but not the value of i^*. Since it is the only unknown, we can solve for i^*. There will inevitably be N values of i^* that satisfy this equation. In most project cash flows you would be able to find a unique positive i^* that satisfies Equation (17.3.2). However, you may encounter some cash flow that cannot be solved for a single rate of return greater than –100%. By the nature of the NPW function in Equation (17.3.2), it is certainly possible to have more than one rate of return for a certain type of cash flow.* (For some cash flows, we may not find any rate of return at all.)

Finding the IRR

We don't need laborious manual calculations to find i^*. Many financial calculators have built-in functions for calculating i^*. It is also worth noting here that many spreadsheet packages have i^* functions, which solve Equation (17.3.2) very rapidly. This is normally done by entering the cash flows through a computer keyboard or by reading a cash flow data file. As an alternative, you could try the trial-and-error method to locate the break-even interest that makes the net present worth equal to zero.

Accept/Reject Decision Rules

Why are we interested in finding the particular interest rate that equates a project's cost with the present worth of its receipts? Again, we may easily answer this by examining Figure 17.3.2. In this figure, we notice two important characteristics of the NPW profile. First, as we compute the project's PW(i) at a varying interest rate (i), we see that the NPW becomes positive for $i < i^*$, indicating that the project would be acceptable under the PW analysis for those values of i. Second, the NPW becomes negative for $i > i^*$, indicating that the project is unacceptable for those values of i. Therefore, the i^* serves as a *break-even* interest rate. By knowing this break-even rate, we will be able to make an accept/reject decision that is consistent with the NPW analysis.

At the MARR the company will more than break even. Thus, the IRR becomes a useful gauge against which to judge project acceptability, and the decision rule for a simple project is

$$\begin{aligned} &\text{If IRR} > \text{MARR}, \text{ accept the project} \\ &\text{If IRR} = \text{MARR}, \text{ remain indifferent} \\ &\text{If IRR} < \text{MARR}, \text{ reject the project} \end{aligned}$$

Note that this decision rule is designed to be applied for a single project evaluation. When we have to compare mutually exclusive investment projects, we need to apply the incremental analysis, as we shall see in a later section.

Example 17.3.4 — Rate of Return Analysis

Reconsider the fabrication investment project in Example 17.3.1. (a) What is the projected IRR on this fabrication investment? (b) If Merco's MARR is known to be 15%, is this investment justifiable?

---

* When applied to projects that require investments at the outset followed by a series of cash inflows (or a simple project), the i^* provides an unambiguous criterion for measuring profitability. However, when multiple rates of return occur, none of them is an accurate portrayal of project acceptability or profitability. Clearly, then, we should place a high priority on discovering this situation early in our analysis of a project's cash flows. The quickest way to predict multiple i^*s is to generate a NPW profile and check to see if it crosses the horizontal axis more than once.

In addition to the NPW profile, there are good — although somewhat more complex — analytical methods for predicting multiple i^*s. Perhaps more importantly, there is a good method, which uses a *cost of capital*, of refining our analysis when we do discover multiple i^*s. Use of a cost of capital allows us to calculate a single accurate rate of return (also known as *return on invested capital*); it is covered in *Contemporary Engineering Economics*, C.S. Park, Addison-Wesley, 1997. If you choose to avoid these more complex applications of rate-of-return techniques, you must at a minimum be able to predict multiple i^*s via the NPW profile and, when they occur, select an alternative method such as NPW or AE analysis for determining project acceptability.

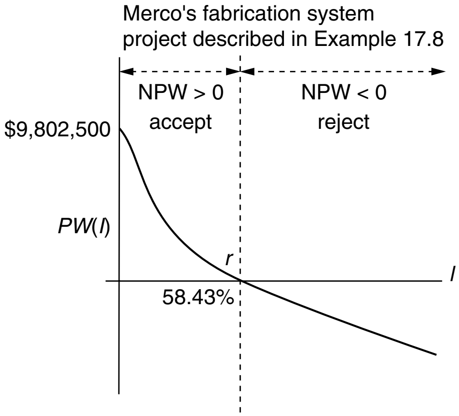

FIGURE 17.3.2 A net present worth profile for the cash flow series given in Figure 17.3.1 at varying interest rates. The project breaks even at 58.43% so that the NPW will be positive as long as the discount rate is less than 58.43%.

Solution

- (a) The net present worth expression as a function of interest rate (i) is

$$\begin{aligned} PW(i) &= -\$1{,}250{,}000 + \$731{,}500(P/A,i,15) + \$80{,}000(P/F,i,15) \\ &= 0 \end{aligned}$$

  Using Excel's financial function (IRR), we find the IRR to be 58.43%. (See Figure 17.3.2.) Merco will recover the initial investment fully and also earn 58.43% interest on its invested capital.
- (b) If Merco does not undertake the project, the $1,250,000 would remain in the firm's investment pool and continue to earn only 15% interest. The IRR figure far exceeds the Merco's MARR, indicating that the fabrication system project is an economically attractive one. Merco's management believes that, over a broad base of structural products, there is no doubt that the installation of its fabricating system would result in a significant savings, even after considering some potential deviations from the estimates used in the analysis.

Mutually Exclusive Alternatives

Until now, we have considered situations in which only one project was under consideration, and we were determining whether to pursue it, based on whether its present worth or rate of return met our MARR requirements. We were making an accept or reject decision about a *single* project.

In the real world of engineering practice, however, it is more typical for us to have two or more choices of projects for accomplishing a business objective. *Mutually exclusive* means that any one of several alternatives will fulfill the same need and that selecting one alternative means that the others will be excluded.

Analysis Period

The *analysis period* is the time span over which the economic effects of an investment will be evaluated. The analysis period may also be called the *study period* or *planning horizon*. The length of the analysis period may be determined in several ways: it may be a predetermined amount of time set by company policy, or it may be either implied or explicit in the need the company is trying to fulfill. In either of these situations, we consider the analysis period to be a *required service period*. When no required service period is stated at the outset, the analyst must choose an appropriate analysis period over which to study the alternative investment projects. In such a case, one convenient choice of analysis period is the period of useful life of the investment project.

When useful life of the investment project does not match the analysis or required service period, we must make adjustments in our analysis. A further complication, when we are considering two or more mutually exclusive projects, is that the investments themselves may have differing useful lives. We must compare projects with different useful lives over an *equal time span*, which may require further adjustments in our analysis.

Analysis Period Equals Project Lives

Let's begin our analysis with the simplest situation where the project lives equal the analysis period. In this case, we compute the NPW for each project and select the one with highest NPW for revenue projects or least negative NPW for service projects. Example 17.3.5 will illustrate this point.

Example 17.3.5 — Two Mutually Exclusive Alternatives

A pilot wants to start her own company to airlift goods to the Commonwealth of Independent States (formerly the U.S.S.R.) during their transition to a free-market economy. To economize the start-up business, she decides to purchase only one plane and fly it herself. She has two mutually exclusive options: an old aircraft (A1) or a new jet (A2) with which she expects to have higher purchase costs, but higher revenues as well because of its larger payload. In either case, she expects to fold up business in 3 years because of competition from larger companies. The cash flows for the two mutually exclusive alternatives are given in thousand dollars:

n	A1	A2
0	–3,000	–$12,000
1	1,350	4,200
2	1,800	6,225
3	1,500	6,330

Assuming that there is no do-nothing alternative, which project would she select at MARR = 10%?

Solution

Since the required service period is 3 years, we should select the analysis period of 3 years. Since the analysis period coincides with the project lives, we simply compute the NPW value for each option. The equivalent NPW figures at $i = 10\%$ would be as follows:

- For A1:

$$
\begin{aligned}
PW(15\%)_{A1} &= -\$3000 + \$1350(P/F,10\%,1) + \$1800(P/F,10\%,2) + \$1500(P/F,10\%,3) \\
&= \$842
\end{aligned}
$$

- For A2:

$$
\begin{aligned}
PW(15\%)_{A2} &= -\$12{,}000 + \$4200(P/F,10\%,1) + \$6225(P/F,10\%,2) + \$6330(P/F,10\%,3) \\
&= \$1719
\end{aligned}
$$

Clearly, A2 is the most economical option.

Project Lives Differ from a Specified Analysis Period

Often project lives do not match the required analysis period and/or do not match each other. For example, two machines may perform exactly the same function, but one lasts longer than the other and both of them last longer than the analysis period for which they are being considered. We are then left with some unused portion of the equipment, which we include as salvage value in our analysis. Salvage value is the amount of money for which the equipment could be sold after its service or the dollar measure of its remaining usefulness.

When project lives are shorter than the required service period, we must consider how, at the end of the project lives, we will satisfy the rest of the required service period. Replacement projects — additional projects to be implemented when the initial project has reached the limits of its useful life — are needed in such a case. Sufficient replacement projects must be analyzed to match or exceed the required service period.

To simplify our analysis, we sometimes assume that the replacement project will be exactly the same as the initial project, with the same corresponding costs and benefits. However, this assumption is not necessary. For example, depending on our forecasting skills, we may decide that a different kind of technology — in the form of equipment, materials, or processes — is a preferable replacement. Whether we select exactly the same alternative or a new technology as the replacement project, we are ultimately likely to have some unused portion of the equipment to consider as salvage value at the end of the required service period. On the other hand, if a required service period is relatively short, we may decide to lease the necessary equipment or subcontract the remaining work for the duration of the analysis period. In this case, we can probably exactly match our analysis period and not worry about salvage values.

Example 17.3.6 — Present Worth Comparison — Project Lives Shorter Than Analysis Period

The Smith Novelty Company, a mail-order firm, wants to install an automatic mailing system to handle product announcements and invoices. The firm has a choice between two different types of machines. The two machines are designed differently but have identical capacities and do exactly the same job. The $12,500 semiautomatic model A will last 3 years with a salvage value of $2000, while the fully automatic model B will cost $15,000 and last 4 years with a salvage value of $1500. The expected cash flows for the two machines including maintenance, salvage value, and tax effects are as follows:

n	Model A	Model B
0	–12,500	–$15,000
1	–5,000	–4,000
2	–5,000	–4,000
3	–5,000 + 2,000	–4,000
4		–4,000 + 1,500
5		

As business grows to a certain level, neither of the models can handle the expanded volume at the end of year 5. If that happens, a fully computerized mail-order system will need to be installed to handle the increased business volume. With this scenario, which model should the firm select at MARR = 15%?

Solution

Since both models have a shorter life than the required service period (5 years), we need to make an explicit assumption of how the service requirement is to be met. Suppose that the company considers leasing comparable equipment that has an annual lease payment of $6000 (after taxes) for the remaining required service period. In this case, the cash flow would look like Figure 17.3.3.

n	*Model A*	*Model B*
0	–12,500	–$15,000
1	–5,000	–4,000
2	–5,000	–4,000
3	–3,000	–4,000
4	**–6,000** –5,000	–2,500
5	**–6,000** –5,000	**–6,000** –5,000

Here the bold figures represent the annual lease payments. (It costs $6000 to lease the equipment and $5000 to operate anually. Other maintenance will be paid by the leasing company.) Note that both alternatives now have the same required service period of 5 years. Therefore, we can use NPW analysis.

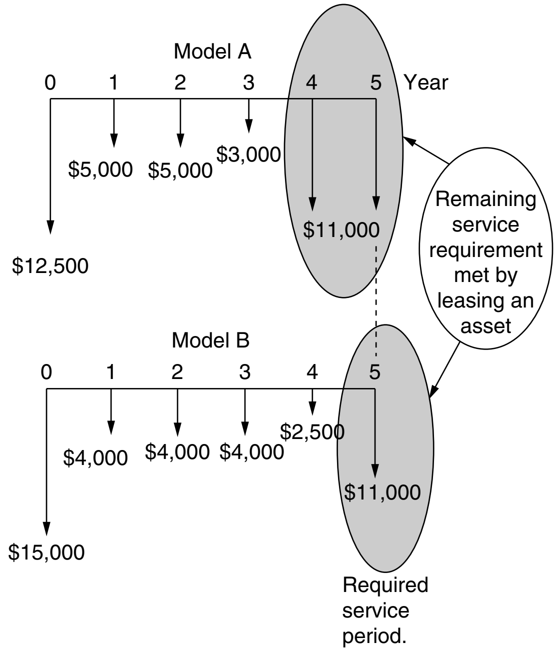

FIGURE 17.3.3 Comparison for unequal-lived projects when the required service period is longer then the individual project life (Example 17.3.6.)

$$
\begin{aligned}
PW(15\%)_A &= -\$12{,}500 - \$5000(P/A,15\%,2) + \$3000(P/F,15\%,3) \\
&\quad - \$11{,}000(P/A,15\%,2)(P/F,15\%,3) \\
&= -\$34{,}359
\end{aligned}
$$

$$
\begin{aligned}
PW(15\%)_B &= -\$15{,}000 - \$4000(P/A,15\%,3) - \$2500(P/F,15\%,4) - \$11{,}000(P/F,15\%,5) \\
&= -\$32{,}747
\end{aligned}
$$

Since these are service projects, model B is the better choice.

Flaws in Project Ranking by IRR

Under NPW, the mutually exclusive project with the highest worth figure was preferred. Unfortunately, the analogy does not carry over to IRR analysis. The project with the highest IRR may *not* be the preferred alternative. To illustrate the flaws of comparing IRRs to choose from mutually exclusive projects, suppose you have two mutually exclusive alternatives, each with a 1-year service life; one requires an investment of $1000 with a return of $2000 and the other requires $5000 with a return of $7000. You already obtained the IRRs and NPWs at MARR = 10% as follows:

n	A1	A2
0	–$1000	–$5000
1	222000	7000
IRR	100%	40%
PW(10%)	$818	$1364

Would you prefer the first project simply because you expect a higher rate of return?

We can see that A2 is preferred over A1 by the NPW measure. On the other hand, the IRR measure gives a *numerically* higher rating for A1. This inconsistency in ranking is due to the fact that the NPW is an *absolute (dollar)* measure of investment worth, while the IRR is a *relative (percentage)* measure and cannot be applied in the same way. That is, the IRR measure ignores the *scale* of the investment. Therefore, the answer is no; instead, you would prefer the second project with the lower rate of return, but higher NPW. The NPW measure would lead to that choice, but comparison of IRRs would rank the smaller project higher. Another approach, called *incremental analysis*, is needed.

Rate of Return on Incremental Investment

In our previous ranking example, the more costly option requires an incremental investment of $4000 at an incremental return of $5000. If you decide to take the more costly option, certainly you would be interested in knowing that this additional investment can be justified at the MARR. The 10% of MARR value implies that you can always earn that rate from other investment sources — $4400 at the end of 1 year for $4000 investment. However, by investing the additional $4000 in the second option, you would make an additional $5000, which is equivalent to earning at the rate of 25%. Therefore, the incremental investment can be justified.

Now we can generalize the decision rule for comparing mutually exclusive projects. For a pair of mutually exclusive projects (A, B), rate of return analysis is done by computing the *internal rate of return on incremental investment* (IRR_Δ) between the projects. Since we want to consider increments of investment, we compute the cash flow for the difference between the projects by subtracting the cash flow for the lower investment-cost project (A) from that of the higher investment-cost project (B). Then, the decision rule is select B, if $\text{IRR}_{\text{B-A}} > \text{MARR}$. Otherwise select A.

Example 17.3.7 — IRR on Incremental Investment: Two Alternatives

Reconsider the two mutually exclusive projects in Example 17.3.5.

n	B1	B2	B2–B1
0	–$3,000	–$12,000	–$9,000
1	1,350	4,200	2,850
2	1,800	6,225	4,425
3	1,500	6,330	4,830
IRR	25%	17.43%	

Since B1 is the lower cost investment project, we compute the incremental cash flow for B2–B1. Then we compute the IRR on this increment of investment by solving

$$-\$9000 + \$2850(P/F,i,1) + \$4425(P/F,i,2) + \$4830(P/F,i,3) = 0$$

We obtain $i^*_{\text{B2-B1}} = 15\%$. Since $\text{IRR}_{\text{B2-B1}} > \text{MARR}$, we select B2, which is consistent with the NPW analysis.

Comments

Why did we choose to look at the increment B2-B1 instead of B1-B2? We want the increment to have investment during at least some part of the time span so that we can calculate an IRR. Subtracting the lower initial investment project from the higher guarantees that the first increment will be investment flow. Ignoring the investment ranking, we might end up with an increment which involves borrowing cash flow and has no internal rate of return. This is the case for B1-B2. ($i^*_{\text{B1-B2}}$ is also 15%, not –15%.) If we erroneously compare this i^* with MARR, we might have accepted project B1 over B2.

17.4 Cash Flow Projections

With the purchase of any fixed asset such as equipment, we need to estimate the profits (more precisely, cash flows) that the asset will generate during its service period. An inaccurate estimate of asset needs can have serious consequences. If you invest too much in assets, you incur unnecessarily heavy expenses. Spending too little on fixed assets also is harmful, for then the firm's equipment may be too obsolete to produce products competitively and without an adequate capacity you may lose a portion of your market share to rival firms. Regaining lost customers involves heavy marketing expenses and may even require price reductions and/or product improvements, all of which are costly. We will begin this section by giving an overview on how a company determines its operating profit.

Operating Profit — Net Income

Firms invest in a project because they expect it to increase their wealth. If the project does this — if project revenues exceed project costs — we say it has generated a *profit*, or *income*. If the project reduces the owner's wealth, we say that the project has resulted in a *loss*. One of the most important roles of the accounting function within an organization is to measure the amount of profit or loss a project generates each year or in any other relevant time period. Any profit generated will be taxed. The accounting measure of a project's after-tax profit during a particular time period is known as *net income.*

Accountants measure the net income of a specified operating period by subtracting expenses from revenues for that period. These terms can be defined as follows:

1. The *project revenue* is the income earned by a business as a result of providing products or services to outsiders. Revenue comes from sales of merchandise to customers and from fees earned by services performed for clients or others.
2. The *project expenses* incurred are the cost of doing business to generate the revenues of that period. Some common expenses are the cost of the goods sold (labor, material, inventory, and supplies), depreciation, the cost of employees' salaries, the operating cost (such as the cost of renting a building and the cost of insurance coverage), and income taxes.

The business expenses listed above are all accounted for in a straightforward fashion on the income statement and balance sheet: the amount paid by the organization for each item would translate dollar for dollar into expenses in financial reports for the period. One additional category of expenses, the purchase of new assets, is treated by depreciating the total cost gradually over time. Because it plays a role in reducing taxable income, depreciation accounting is of special concern to a company.

Accounting Depreciation

The acquisition of fixed assets is an important activity for a business organization, whether the organization is starting up or acquiring new assets to remain competitive. The systematic allocation of the initial cost of an asset in parts over a time known as its depreciable life is what we mean by *accounting depreciation.* Because accounting depreciation is the standard of the business world, we sometimes refer to it more generally as *asset depreciation.*

The process of depreciating an asset requires that we make several preliminary determinations:

1. *What can be depreciable?* Depreciable property includes buildings, machinery, equipment, and vehicles. Inventories are not depreciable property because they are held primarily for sale to customers in the ordinary course of business. If an asset has no definite service life, the asset cannot be depreciated. For example, *you can never depreciate land.*
2. *What cost base should be used in asset depreciation?* The *cost base* of an asset represents the total cost that is claimed as an expense over an asset's life, that is, the sum of the annual depreciation expenses. The cost base generally includes the actual cost of the asset and all the other incidental expenses, such as freight, site preparation, and installation. This total cost, rather than the cost of the asset only, must be the depreciation base charged as an expense over the asset's life.
3. *What is the asset's value at the end of its useful life?* The salvage value is an asset's value at the end of its life; it is the amount eventually recovered through sale, trade-in, or salvage. The eventual salvage value of an asset must be estimated when the depreciation schedule for the asset is

established. If this estimate subsequently proves to be inaccurate, then an adjustment must be made.

4. *What is the depreciable life of the asset?* Historically, depreciation accounting included choosing a depreciable life that was based on the service life of an asset. Determining the service life of an asset, however, was often very difficult, and the uncertainty of these estimates often led to disputes between taxpayers and the IRS. To alleviate the problems, the IRS published guidelines on lives for categories of assets known as *Asset Depreciation Ranges*, or ADRs. These guidelines specified a range of lives for classes of assets based on historical data, and taxpayers were free to choose a depreciable life within the specified range for a given asset.
5. *What method of depreciation do we choose?* Companies generally calculate depreciation one way when figuring taxes and another way when reporting income (profit) to investors: (1) they use the straight-line method (or declining balance or sum-of-years' digits) for investors and (2) they use the fastest rate permitted by law (known as "modified accelerated cost recovery system [MACRS]") for tax purposes. Under the straight-line method, for an asset with a 5-year life which costs \$10,000 and has a \$1000 salvage value, the annual depreciation charge is (\$10,000 – \$1000)/5 = \$1800. For tax purposes, Congress created several classes of assets, each with a more or less arbitrarily prescribed life called a *recovery period* or *class life*. The depreciable base is not adjusted for salvage value, which is the estimated market value of the asset at the end of its useful life. Table 17.4.1 describes what types of property fit into the different class life groups and the allowed depreciation percentages. Congress developed these recovery allowance percentages based on the declining balance method, with a switch to straight-line depreciation at some point in the asset's life. The MACRS recovery percentages as shown in Table 17.4.1 also employ the half-year convention — that is, they assume that all assets are put into service at midyear and, hence, generate a half-year's depreciation.

Corporate Income Taxes

Corporate taxable income is defined as follows:

$$\begin{aligned}\text{taxable income} &= \text{gross income (revenues)}\\ &\qquad -(\text{cost of goods sold } + \text{ depreciation } + \text{ operating expenses})\end{aligned}$$

Once taxable income is calculated, income taxes are determined by

$$\text{income taxes} = (\text{tax rate}) \times (\text{taxable income})$$

The corporate tax rate structure for 1996 is relatively simple. There are four basic rate brackets (ranging from 15 to 35%) plus two surtax rates (5 and 3%) based on taxable incomes, and businesses with lower taxable incomes continue to be taxed at lower rates than those with higher taxable incomes.

Tax Treatment of Gains or Losses for Depreciable Assets

When a depreciable asset used in business is sold for an amount different from its book value, this gain or loss has an important effect on income taxes. An asset's book value at any given time is determined by

$$\text{book value} = \text{cost base} - \text{total amount of depreciation}$$

The gain or loss is found by

$$\text{gains (losses)} = \text{salvage value} - \text{book value}$$

TABLE 17.4.1 MACRS Depreciation Schedules for Personal Properties with Half-Year Convention

		Personal Property					
	Class	3	5	7	10	15	20
	Depreciation	200%	200%	200%	200%	150%	150%
Year	Rate	DB	DB	DB	DB	DB	DB
1		33.33	20.00	14.29	10.00	5.00	3.750
2		44.45	32.00	24.49	18.00	9.50	7.219
3		14.81*	19.20	17.49	14.40	8.55	6.677
4		7.41	11.52*	12.49	11.52	7.70	6.177
5			11.52	8.93*	9.22	6.93	5.713
6			5.76	8.92	7.37	6.23	5.285
7				8.93	6.55*	5.90*	4.888
8				4.46	6.55	5.90	4.522
9					6.56	5.91	4.462*
10					6.55	5.90	4.461
11					3.28	5.91	4.462
12						5.90	4.461
13						5.91	4.462
14						5.90	4.461
15						5.91	4.462
16						2.95	4.461
17							4.462
18							4.461
19							4.462
20							4.461
21							2.231

Note: "*" denotes year to switch from declining balance to straight line.

Property Class	Applicable Property
3-year	Machine tools
5-year	Automobiles, light trucks, high-tech equipment
7-year	Manufacturing equipment, office furniture
10-year	Vessels, barges, tugs, railroad cars
15-year	Utility property (water, telephone)
20-year	Municipal sewers, electrical power plant

where the salvage value represents the proceeds from the sale less any selling expense or removal cost.

These gains, commonly known as *depreciation recapture*, are taxed as ordinary income. In the unlikely event that if an asset is sold for an amount greater than its initial cost, the gains (salvage value – book value) are divided into two parts (ordinary gains and capital gains) for tax purposes:

$$\begin{aligned} \text{gains} &= \text{salvage value} - \text{book value} \\ &= \underbrace{(\text{salvage value} - \text{cost base})}_{\text{capital gains}} + \underbrace{(\text{cost base} - \text{book value})}_{\text{ordinary gains}} \end{aligned}$$

Capital gains are normally taxed at a different rate from that of ordinary gains.

After-Tax Cash Flow Analysis

In developing an after-tax flow, we are concerned only with those cash flows that result directly from the project. These cash flows, called *incremental cash flows*, represent the change in the firm's total cash flows that occurs as a direct result of undertaking the project. There are several elements that contribute toward the project cash flows. In preparing the cash flow statement which shows sources and uses of cash in project undertaking, we may group them into three areas: (1) cash flow elements associated with operations, (2) cash flow elements associated with investment activities (capital expenditures), and (3) cash flow elements associated with project financing (such as borrowing). The main purpose of this grouping is to provide information about the operating, investing, and financing activities of a project.

- *Operating Activities:* In general, cash flows from operations include current sales revenue, cost of goods sold, operating expense, and income taxes. Cash flows from operations should generally reflect the cash effects of transactions entering into the determination of net income. The interest portion of a loan repayment is a deductible expense when determining net income, and it is included in the operating activities. Since we will usually look only at yearly flows, it is logical to express all cash flows on a yearly basis. We can determine the net cash flow from operations either (1) based on net income or (2) based on cash flow by computing income taxes directly. When we use net income as the starting point for cash flow determination, we should add any noncash expenses (mainly depreciation) back to net income to compute the net cash flow. Thus,

$$\text{net operating cash flow} = \text{net income} + \text{noncash expenses}$$
$$\left(\text{depreciation}\right)$$

Approach 1	Approach 2
Cash revenues (savings)	Cash revenues (savings)
–Cost of goods sold	–Cost of goods sold
–Depreciation	
–Operating expense	–Operating expense
–Interest expense	–Interest expense
Taxable income	
–Income taxes	–Income taxes
Net income + depreciation	Operating cash flow

  In business practice, accountants usually prepare the cash flow statements based on the net income, namely, using Approach 1, whereas Approach 2 is commonly used in many traditional engineering economic texts. If you learn only Approach 2, it is more than likely that you need to be retrained to learn Approach 1 to communicate with the financing and accounting professionals within your organization. Therefore, we will use the income statement approach (Approach 1) whenever possible throughout this section.

- *Investing Activities:* Three types of investment flows are associated with buying a piece of equipment: the original investment, salvage value at the end of its useful life, and working capital investment* or recovery.** We will assume that our outflow for both capital investment and working capital investment is as if they take place in year 0. It is quite possible that both investments will not occur instantaneously, but rather over a few months as the project gets into gear; we could then use year 1 as an investment year. (Capital expenditures may occur over several years before a large investment project becomes fully operational. In this case, we should enter all expenditures

---

* Normally, additional inventories are required to support a new operation and increased accounts receivable. These increases in current assets must be financed. On the other hand, accounts payable will also increase as a result of business expansion and this will reduce the net cash needed to finance inventories and accounts receivable. The difference is known as *net change in working capital.* If this difference is positive, an investment in working must be made.

** As the project approaches termination, inventories are sold off and not replaced, and account receivables are eventually collected. As this change occurs, the firm experiences an end-of-project cash flow (known as *working capital recovery*) that is equal to the net working capital investments that were made when the project was begun.

as they occur.) For a small project, either method of timing these flows is satisfactory, because the numerical differences are likely to be insignificant.

- *Financing Activities:* Cash flows classified as financing activities include (1) the amount of borrowing and (2) repayment of principal. Recall that interest payments are tax deductible expenses so that they are usually classified as operating, not financing, activities.

Then, net cash flow for a given year is simply the sum of the net cash flows from these three activities.

Example 17.4.1 — Developing a Cash Flow Statement

A computerized machining center has been proposed for a small tool manufacturing company. If the new system costing $125,000 is installed, it will generate annual revenues of $100,000 and require $20,000 in annual labor, $12,000 in annual material expenses, and another $8000 in annual overhead (power and utility) expenses. The automation facility would be classified as a 7-year MACRS property. The company expects to phase out the facility at the end of 5 years, at which time it will be sold for $50,000. The machining center will require an investment of $23,331 in working capital (mainly spare parts inventory), which will be recovered in full amount at the end of the project life. Assume that $62,500 of the $125,000 paid for the investment is obtained through a bank loan which is to be repaid in equal annual installments at 10% interest over 5 years. The remaining $62,500 will be provided by equity (for example, from retained earnings). Find the year-by-year after-tax net cash flow for the project at a 40% marginal tax rate based on the net income (Approach 1), and determine the after-tax net present worth of the project at the company's MARR of 15%.

Discussion

We will use the business convention that no signs (positive or negative) are used in preparing the income statement, except in the situation where we have a negative taxable income or tax savings. In this situation we will use (   ). However, in preparing the cash flow statement, we will observe explicitly the sign convention: a positive sign indicating cash inflow, a negative sign or (   ) indicating cash outflow.

Solution

Before presenting the cash flow table, we need some preliminary calculations. The following notes explain the essential items in Table 17.4.2.

- *Depreciation Calculation*:

1. If it is held for all 7 years, we depreciate a 7-year property in respective percentages of 14.29, 24.49, 17.49, 12.49, 8.93, 8.92, 8.93, and 4.46% (see Table 17.4.1).
2. If the asset is sold at the end of the fifth tax year (during the recovery period), the applicable depreciation amounts would be $17,863, $30,613, $21,863, $15,613, and $5581. Since the asset is disposed of in the fifth tax year, the last year's depreciation, which would ordinarily be $11,163, is halved due to the half-year convention.

- *Salvage Value and Gain Taxes*: In year 5, we must deal with two aspects of the asset's disposal — salvage value and gains (both ordinary as well as capital). We list the estimated salvage value as a positive cash flow. Taxable gains are calculated as follows:

1. The total depreciation in years 1 to 5 is $17,863 + $30,613 + $21,863 + $15,613 + $5581 = $91,533.
2. The book value at the end of period 5 is the cost base minus the total depreciation, or $125,000 – $91,533 = $33,467.
3. The gains on the sale are the salvage value minus the book value, or $50,000 – $33,467 = $16,533. (The salvage value is less than the cost base, so all the gain is ordinary.)
4. The tax on the ordinary gains is $16,633 × 40% = $6,613. This is the amount that is placed in the table under "gains tax".

- *Interest and principal repayment*: We first need to compute the size of the annual installments:

$$\$62,500(A/P,10\%,5) = \$16,487$$

TABLE 17.4.2 Cash Flow Statement for the Automated Machining Center Project with Debt Financing (Example 17.4.1)

	0	1	2	3	4	5
Income Statement						
Revenues		$100,000	$100,000	$100,000	$100,000	$100,000
Labor		20,000	20,000	20,000	20,000	20,000
Material		12,000	12,000	12,000	12,000	12,000
Overhead		8,000	8,000	8,000	8,000	8,000
Depreciation		17,863	30,613	21,863	15,613	5,581
Debt interest		6,250	5,226	4,100	2,861	1,499
Taxable income		$35,887	$24,161	$34,037	$41,526	$52,920
Income taxes (40%)		14,355	9,664	13,615	16,610	21,168
Net income		$21,532	$14,497	$20,433	$24,916	$31,752
Cash Flow Statement						
Operating activities						
Net income		21,532	14,497	20,422	24,916	31,752
Depreciation		17,863	30,613	21,863	15,613	5,581
Investment activities						
Investment	(125,000)					
Salvage						50,000
Gains tax						(6,613)
Working capital	(23,331)					23,331
Financing activities						
Borrowed funds	62,500					
Principal repayment		(10,237)	(11,261)	(12,387)	(13,626)	(14,988)
Net cash flow	$(85,831)	$29,158	$33,849	$29,898	$26,903	$89,063

Next, we determine the repayment schedule of the loan by itemizing both the interest and the principal represented in each annual repayment as follows:

Year	Beginning Balance	Interest Payment	Principal Payment	Ending Balance
1	$62,500	$6,250	$10,237	$52,263
2	52,263	5,226	11,261	41,002
3	41,002	4,100	12,387	28,615
4	28,615	2,861	13,626	14,989
5	14,989	1,499	14,988	0

The interest payments are listed under the income statement and the principal payments are listed under the cash flow statement as shown in Table 17.4.2.

- *Investment Analysis:* Once we obtain the project's after-tax net cash flows, we can determine their equivalent present worth at the firm's interest rate of 15%. The present value equivalent of the after-tax cash flow series is

$$PW(15\%) = -\$85{,}351 + \$29{,}158(P/F,15\%,1) + \ldots + \$89{,}063(P/F,15\%,5)$$
$$= \$44{,}439$$

This means that investing $125,000 in this automated facility would bring in enough revenue to recover the initial investment and the cost of funds with a surplus of $44,439.

Effects of Inflation on Project Cash Flows

We now introduce inflation into estimating project cash flows. We are especially interested in two elements of project cash flows — depreciation expenses and interest expenses — that are essentially immune to the effects of inflation. We also consider the complication of how to proceed when multiple price indexes have been used in generating various project cash flows.

Because depreciation expenses (as well as loan repayment) are calculated on some base-year purchase amount, they do not increase over time to keep pace with inflation. Thus, they lose some of their value to defer taxes as inflation drives up the general price level and hence taxable income. Similarly, salvage values of depreciable assets can increase with the general inflation rate and, because any gains on salvage values are taxable, they can result in increased taxes.

Example 17.4.2 — After-Tax Cash Flows under Inflation

A construction firm is offered a fixed-price contract for a 5-year period. The firm will be paid $23,500 (actual dollars) per year for the contract period. In order to accept the contract, the firm must purchase equipment costing $15,000 and requiring $13,000 (constant dollars) per year to operate. The equipment qualifies for 5-year MACRS depreciation and is expected to have a salvage value of $1000 at the end of 5 years. Use a tax rate of 40% and an inflation-free interest rate of 20%. If the general inflation rate $(\bar{f})$ is expected to average 5% over the next 5 years, salvage value at the annual rate of 5%, and operating expenses at 8% per year for the project duration, should the contractor accept the contract?

Solution

The analysis of this situation should explicitly consider inflation, since the contractor is being offered a fixed-price contract and cannot increase the fee to compensate for increased costs. In this problem, as is common practice, we assume that all estimated costs are expressed in today's dollars, and actual costs will be increased due to inflation.

The Excel spreadsheet analysis is shown in Table 17.4.3, where the first five rows are designated as the input fields. Then column C in both the income statement and the cash flow statement is reserved for entering the specific inflation rate for the item listed in that row. Since the O&M costs are responsive to inflation, we can automate the cell entries by using the following cell formulas:

$$\text{cell E12} = \$D\$2^{*}(1 + \$C\$12)$$

$$\text{cell F12} = \text{E12}^{*}(1 + \$C\$12)$$

$$\vdots \qquad \vdots$$

$$\text{cell I12} = \text{H12}^{*}(1 + \$C\$12)$$

Note that the salvage value in cell I27 has been increased at 5%. (When no inflation rate is given for a specific cost category, it is normally assumed that the general inflation rate holds.) Gains taxes on disposal are based on the difference between book value and salvage value, in this case, $1276 – $1728 = ($452) or loss of $452. This results in a tax savings of ($452) (0.40) = $181, as shown in cell I28.

In row 12, operating expenses have been increased at 8%. As explained in the section "Loss of Purchasing Power," actual-dollar cash flows are converted to constant-dollar flows by "deflating" at the general inflation rate. The IRR is calculated at 22.03%, based on the constant-dollar cash flows. This is compared to the MARR of 20%, the inflation-free interest rate, indicating that this is an acceptable contract as long as the 5 and 8% escalation rates are correct.

Since no one can predict inflation rates in any precise manner, it is always wise to investigate the effects of changes in these rates. This is very easy to do with a spreadsheet. For example, we can easily determine the value of the general inflation rate at which this project exactly earns 20%. The value of $\bar{f}$ was adjusted manually until the IRR was exactly 20%. This would not be a good project if $\bar{f}$ were greater than 6.77%

TABLE 17.4.3 Excel's Spreadsheet Application to "What If" Questions — What General Inflation Rate Does the Project Break Even? (Example 17.15)

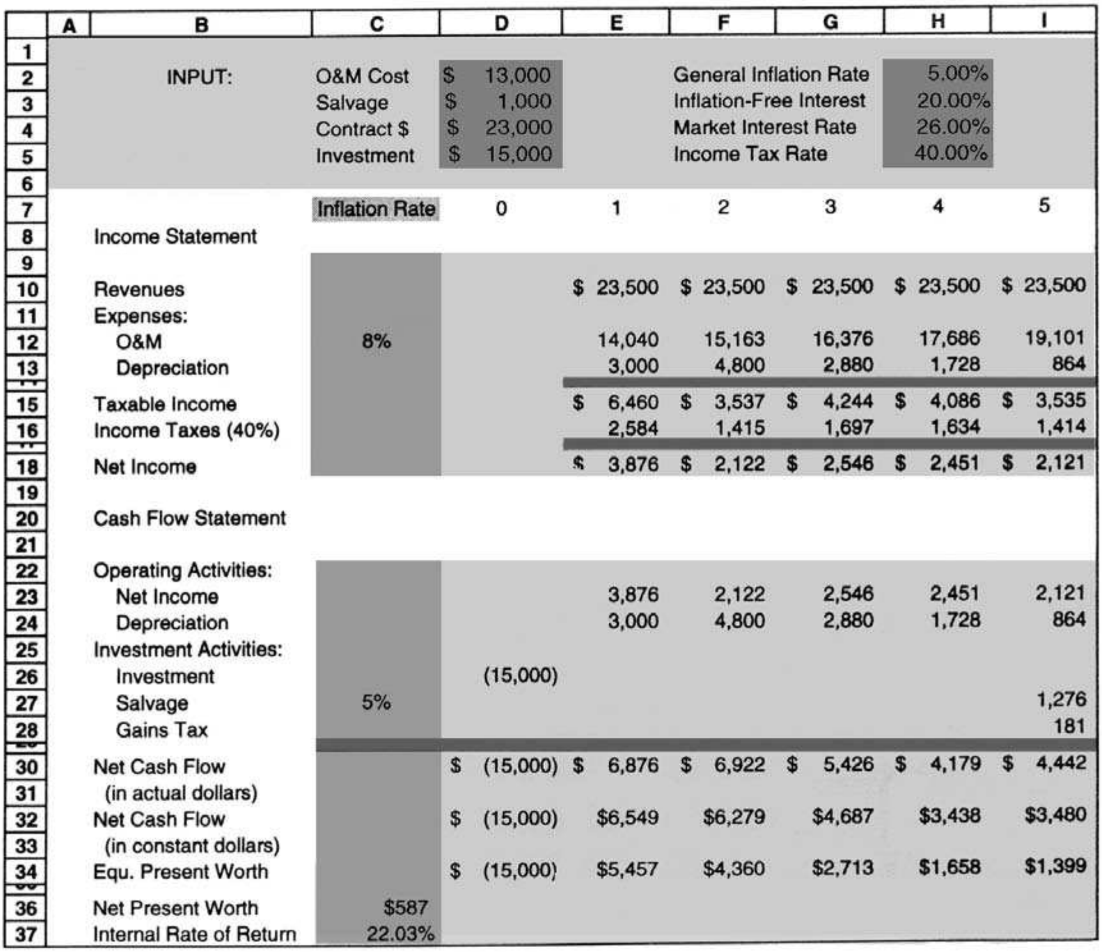

	A	B	C	D	E	F	G	H	I
1									
2		INPUT:	O&M Cost	$ 13,000		General Inflation Rate		5.00%	
3			Salvage	$ 1,000		Inflation-Free Interest		20.00%	
4			Contract $	$ 23,000		Market Interest Rate		26.00%	
5			Investment	$ 15,000		Income Tax Rate		40.00%	
6									
7			Inflation Rate	0	1	2	3	4	5
8		Income Statement							
9									
10		Revenues			$ 23,500	$ 23,500	$ 23,500	$ 23,500	$ 23,500
11		Expenses:							
12		O&M	8%		14,040	15,163	16,376	17,686	19,101
13		Depreciation			3,000	4,800	2,880	1,728	864
15		Taxable Income			$ 6,460	$ 3,537	$ 4,244	$ 4,086	$ 3,535
16		Income Taxes (40%)			2,584	1,415	1,697	1,634	1,414
18		Net Income			$ 3,876	$ 2,122	$ 2,546	$ 2,451	$ 2,121
19									
20		Cash Flow Statement							
21									
22		Operating Activities:							
23		Net Income			3,876	2,122	2,546	2,451	2,121
24		Depreciation			3,000	4,800	2,880	1,728	864
25		Investment Activities:							
26		Investment		(15,000)					
27		Salvage	5%						1,276
28		Gains Tax							181
30		Net Cash Flow		$ (15,000)	$ 6,876	$ 6,922	$ 5,426	$ 4,179	$ 4,442
31		(in actual dollars)							
32		Net Cash Flow		$ (15,000)	$6,549	$6,279	$4,687	$3,438	$3,480
33		(in constant dollars)							
34		Equ. Present Worth		$ (15,000)	$5,457	$4,360	$2,713	$1,658	$1,399
36		Net Present Worth	$587						
37		Internal Rate of Return	22.03%						

(cell H2). (Note that at the exact value of $\bar{f}$ (6.771%), the NPW in cell C36 will be zero or its rate of return would be 20%.) Similarly, you can vary the O&M cost and salvage value to see how the project's profitability changes.

17.5 Sensitivity and Risk Analysis

In previous sections, the cash flows from projects were assumed to be known with complete certainty, and our analysis was concerned with measuring the economic worth of projects and selecting the best investment projects. Although these results can provide reasonable decision bases for many investment situations, we should certainly consider the more usual situation where forecasts of cash flows are subject to some degree of uncertainty. In this situation, management rarely has precise expectations regarding the future cash flows to be derived from a particular project. In fact, the best that the firm can reasonably expect to do is to estimate the range of possible future costs and benefits and the relative chances of achieving a certain return on the investment. We can use the term risk in describing an investment project whose cash flow is not known in advance with absolute certainty, but for which an array of alternative outcomes and their probabilities (odds) are known. We will also use the term project risk to refer to the variability in a project's NPW. A greater project risk means that there is a greater variability in the project's NPW, or simply saying that *risk is the potential for loss*. We may begin analyzing project risk by first determining the uncertainty inherent in a project's cash flows. We can consider risk in a number of ways ranging from making informal judgments to calculating complex economic and statistical analyses. In this section, we will introduce three methods of describing project risk: (1) sensitivity analysis, (2) scenario analysis, and (3) risk analysis. We shall explain each method with a single example (Boston Metal Company).

Project Risk

The decision to make a major capital investment such as the introduction of a new product requires cash flow information over the life of the project. The profitability estimate of the investment depends on cash flow estimations, which are generally uncertain. Many cash flow elements (such as demand) are subject to substantial uncertainty. The common approach is to make single-number "best estimates" for each of the uncertain factors and then to calculate measures of profitability such as NPW or rate of return for the project. This approach has two drawbacks:

1. There is no guarantee that the "best estimates" will ever match actual values.
2. There is no way to measure the risk associated with the investment or the project risk. In particular, the manager has no way of determining either the probability that the project will lose money or the probability that it will generate very large profits.

Because cash flows can be so difficult to estimate accurately, project managers frequently consider a range of possible values for cash flow elements. If there is a range of possible values for individual cash flows, it follows that there is a range of possible values for the NPW of a given project. Clearly, the analyst will want to try to gauge the probability and reliability of individual cash flows occurring and, consequently, the level of certainty about achieving the overall project worth.

Sensitivity Analysis

One way to glean a sense of the possible outcomes of an investment is to perform a sensitivity analysis. This analysis determines the effect on NPW of variations in the input variables (such as revenues, operating cost, and salvage value) used to estimate after-tax cash flows. A *sensitivity analysis* reveals how much the NPW will change in response to a given change in an input variable. In a calculation of cash flows, some items have a greater influence on the final result than others. In some problems, we may easily identify the most significant item. For example, the estimate of sales volume is often a major factor in a problem in which the quantity sold varies among the alternatives. In other problems, we may want to locate the items that have an important influence on the final results so that they can be subjected to special scrutiny.

Sensitivity analysis is sometimes called "what-if" analysis because it answers questions such as: What if incremental sales are only 1000 units, rather than 2000 units? Then what will the NPW be? Sensitivity analysis begins with a base-case situation, which is developed using the most-likely values for each input. Then we change the specific variable of interest by several specific percentages above and below the most-likely value, holding other variables constant. Next, we calculate a new NPW for each of these values. A convenient and useful way to present the results of a sensitivity analysis is to plot *sensitivity graphs*. The slopes of the lines show how sensitive the NPW is to changes in each of the inputs: the steeper the slope, the more sensitive the NPW is to a change in the particular variable. It identifies the crucial variables that affect the final outcome most. We will use Example 17.5.1 to illustrate the concept of sensitivity analysis.

Example 17.5.1 — Sensitivity Analysis

Boston Metal Company (BMC), a small manufacturer of fabricated metal parts, must decide whether to enter the competition to be the supplier of transmission housings for Gulf Electric. Gulf Electric has its own in-house manufacturing facility to produce transmission housings, but it has almost reached its maximum production capacity. Therefore, Gulf is looking for an outside supplier. To compete, the firm must design a new fixture for the production process and purchase a new forge. The new forge would cost $125,000, including tooling costs for the transmission housings. If BMC gets the order, it may be able to sell as many as 2000 units per year to Gulf Electric for $50 each, and the variable production costs,* such as direct labor and direct material costs, will be $15 per unit. The increase in fixed costs** other than depreciation will amount to $10,000 per year. The firm expects that the proposed transmission-housings project would have about a 5-year product life. The firm also estimates that the amount ordered by Gulf Electric for the first year will be ordered in each of the subsequent 4 years. (Due to the nature of contracted production, the annual demand and unit price would remain the same over the project after the contract is signed.) The initial investment can be depreciated on a MACRS basis over the 7-year period, and the marginal income tax rate is expected to remain at 40%. At the end of 5 years, the forge machine is expected to retain a market value of about 35% of the original investment. Based on this information, the engineering and marketing staffs have prepared the cash flow forecasts shown in Table 17.5.1. Since NPW is positive ($40,169) at the 15% opportunity cost of capital (MARR), the project appears to be worth undertaking.

However, BMC's managers are uneasy about this project because there are too many uncertain elements that have not been considered in the analysis. If decided, BMC must make the investment in the forging machine to provide some samples with Gulf Electric as a part of the bidding process. If Gulf Electric does not like BMC's sample, BMC stands to lose the entire investment in the forging machine. On the other hand, if Gulf likes BMC's sample but it is overpriced, BMC would be under pressure to bring the price in line with competing firms. There is even a possibility that BMC would get a smaller order as Gulf may utilize their overtime capacity to produce some extra units. They also are not certain about the variable and fixed cost figures. Recognizing these uncertainties, the managers want to assess the various potential future outcomes before making a final decision. (a) Perform a sensitivity analysis to each variable and (b) develop a sensitivity graph.

Discussion

Table 17.5.1 shows BMC's expected cash flows — but there is no guarantee that they will indeed materialize. BMC is not particularly confident in is revenue forecasts. The managers think that if competing firms enter the market, BMC will lose a substantial portion of the projected revenues. Before undertaking the project described, the company wants to identify the key variables that determine whether the project will succeed or fail. The marketing department has estimated revenue as follows:

$$\begin{aligned}\text{annual revenue} &= (\text{product demand})(\text{unit price})\\ &= (2000)(\$50) = \$100{,}000\end{aligned}$$

The engineering department has estimated variable costs such as labor and material per unit at $15. Since the projected sales volume is 2000 units per years, the total variable cost is $30,000.

Having defined the unit sales, unit price, unit variable cost, and fixed cost, we conduct a sensitivity analysis with respect to these key input variables. This is done by varying each of the estimates by a given percentage and determining what effect the variation in that item has on the final results. If the effect is large, the result is sensitive to that item. Our objective is to locate the most sensitive item(s).

---

* Expenses that change in direct proportion to the change in volume of sales or production.

** Expenses that do not vary as the volume of sales or production changes. For example, property taxes, insurance, depreciation, and rent are usually fixed expenses.

TABLE 17.5.1 A Typical Excel Worksheet Design to Perform Sensitivity Analyses (Example 17.5.1)

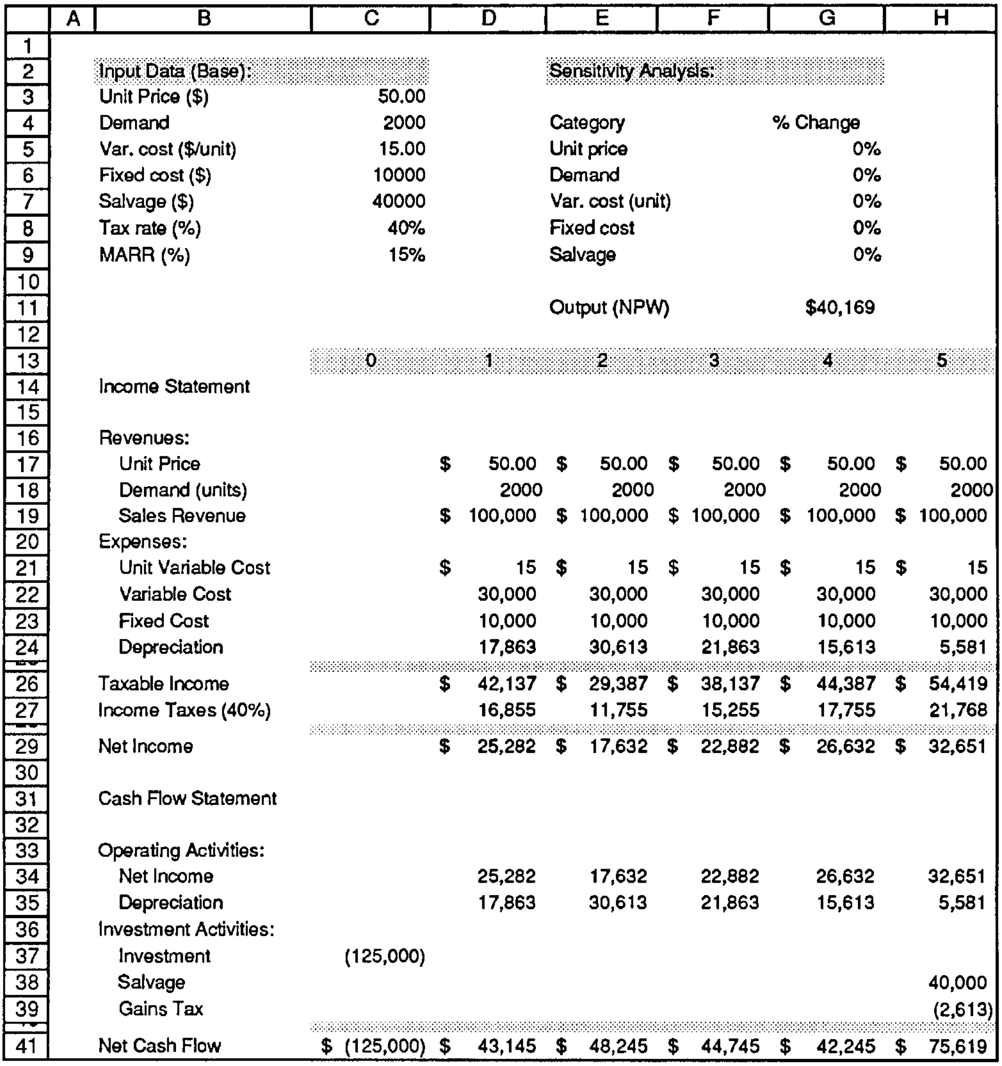

	A	B	C	D	E	F	G	H
1								
2		Input Data (Base):			Sensitivity Analysis:			
3		Unit Price ($)	50.00					
4		Demand	2000		Category		% Change	
5		Var. cost ($/unit)	15.00		Unit price		0%	
6		Fixed cost ($)	10000		Demand		0%	
7		Salvage ($)	40000		Var. cost (unit)		0%	
8		Tax rate (%)	40%		Fixed cost		0%	
9		MARR (%)	15%		Salvage		0%	
10								
11					Output (NPW)		$40,169	
12								
13			0	1	2	3	4	5
14		Income Statement						
15								
16		Revenues:						
17		Unit Price		$ 50.00	$ 50.00	$ 50.00	$ 50.00	$ 50.00
18		Demand (units)		2000	2000	2000	2000	2000
19		Sales Revenue		$ 100,000	$ 100,000	$ 100,000	$ 100,000	$ 100,000
20		Expenses:						
21		Unit Variable Cost		$ 15	$ 15	$ 15	$ 15	$ 15
22		Variable Cost		30,000	30,000	30,000	30,000	30,000
23		Fixed Cost		10,000	10,000	10,000	10,000	10,000
24		Depreciation		17,863	30,613	21,863	15,613	5,581
26		Taxable Income		$ 42,137	$ 29,387	$ 38,137	$ 44,387	$ 54,419
27		Income Taxes (40%)		16,855	11,755	15,255	17,755	21,768
29		Net Income		$ 25,282	$ 17,632	$ 22,882	$ 26,632	$ 32,651
30								
31		Cash Flow Statement						
32								
33		Operating Activities:						
34		Net Income		25,282	17,632	22,882	26,632	32,651
35		Depreciation		17,863	30,613	21,863	15,613	5,581
36		Investment Activities:						
37		Investment	(125,000)					
38		Salvage						40,000
39		Gains Tax						(2,613)
41		Net Cash Flow	$ (125,000)	$ 43,145	$ 48,245	$ 44,745	$ 42,245	$ 75,619

Solution

(a) *Sensitivity analysis:* We begin the sensitivity analysis with a "base-case" situation, which reflects the best estimate (expected value) for each input variable. In developing Table 17.5.2, we changed a given variable by 20% in 5% increments, above and below the base-case value, and calculated new NPWs, holding other variables constant. The values for both sales and operating costs were the expected, or base-case, values, and the resulting $40,169 is called the base-case NPW. Now we ask a series of "what-if" questions: What if sales are 20% below the expected level? What if operating costs rise? What if the unit price drops from $50 to $45? Table 17.5.2 summarizes the results of varying the values of the key input variables.

(b) *Sensitivity graph:* Figure 17.5.1 shows the transmission project's sensitivity graphs for six of the key input variables. The base-case NPW is plotted on the ordinate of the graph at the value 1.0 on the abscissa. Next, the value of product demand is reduced to 0.95 of its base-case value, and

TABLE 17.5.2 Sensitivity Analysis for Six Key Input Variables (Example 17.5.1)

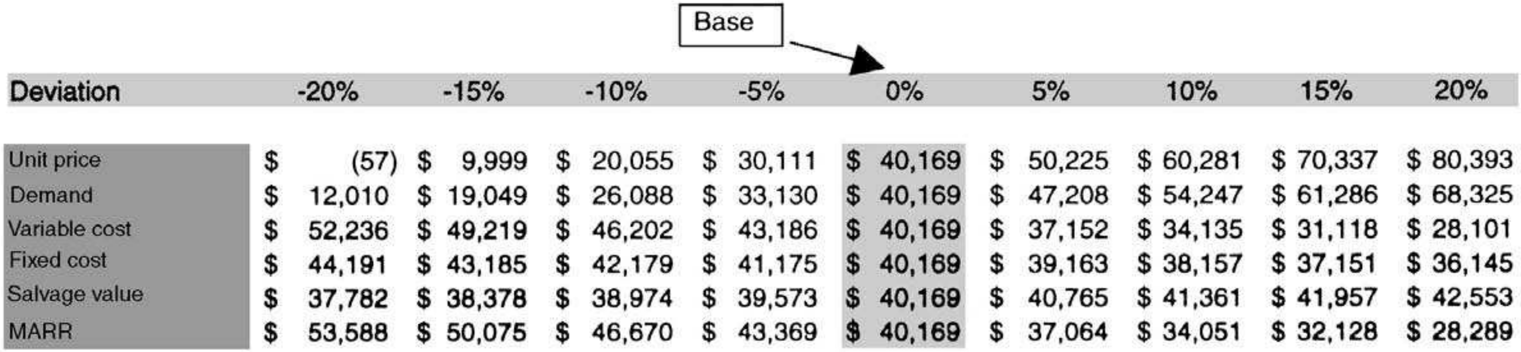

Deviation	-20%	-15%	-10%	-5%	0%	5%	10%	15%	20%
Unit price	$ (57)	$ 9,999	$ 20,055	$ 30,111	$ 40,169	$ 50,225	$ 60,281	$ 70,337	$ 80,393
Demand	$ 12,010	$ 19,049	$ 26,088	$ 33,130	$ 40,169	$ 47,208	$ 54,247	$ 61,286	$ 68,325
Variable cost	$ 52,236	$ 49,219	$ 46,202	$ 43,186	$ 40,169	$ 37,152	$ 34,135	$ 31,118	$ 28,101
Fixed cost	$ 44,191	$ 43,185	$ 42,179	$ 41,175	$ 40,169	$ 39,163	$ 38,157	$ 37,151	$ 36,145
Salvage value	$ 37,782	$ 38,378	$ 38,974	$ 39,573	$ 40,169	$ 40,765	$ 41,361	$ 41,957	$ 42,553
MARR	$ 53,588	$ 50,075	$ 46,670	$ 43,369	$ 40,169	$ 37,064	$ 34,051	$ 32,128	$ 28,289

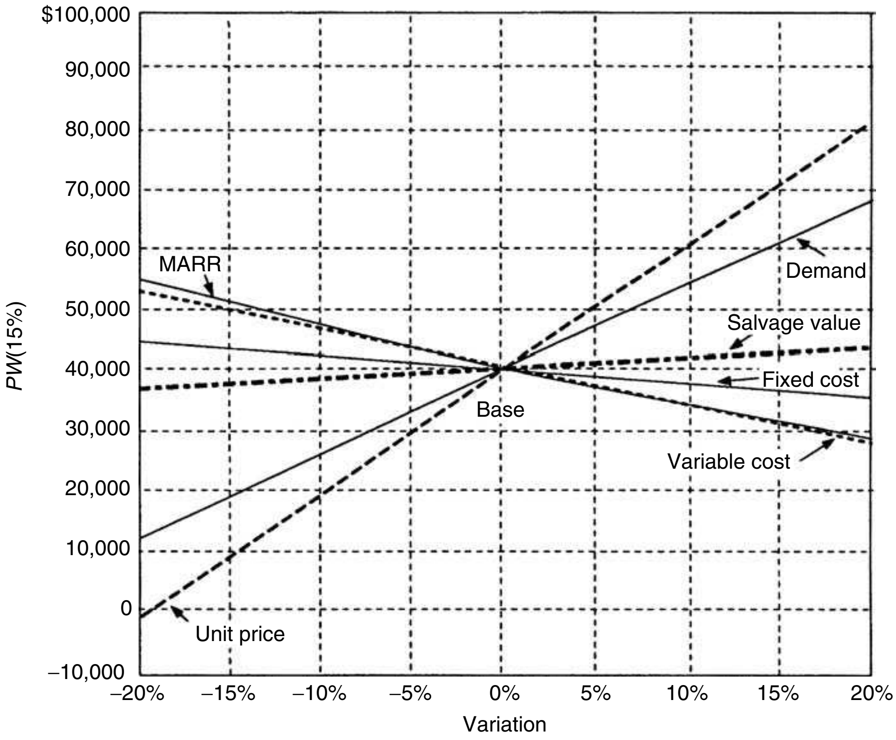

FIGURE 17.5.1 Sensitivity graph — BMC's transmission-housings project (Example 17.5.1).

the NPW is recomputed with all other variables held at their base-case value. We repeat the process by either decreasing or increasing the relative deviation from the base case. The lines for the variable unit price, variable unit cost, fixed costs, and salvage value are obtained in the same manner. In Figure 17.5.1, we see that the project's NPW is very sensitive to changes in product demand and unit price, is fairly sensitive to changes in the variable costs, and is relatively insensitive to changes in the fixed cost and the salvage value.

Graphic displays such as those in Figure 17.5.1 provide a useful means to communicate the relative sensitivities of the different variables on the corresponding NPW value. However, the sensitivity graph does not explain any variable interactions among the variables or the likelihood of realizing any specific deviation from the base case. Certainly, it is conceivable that an answer might not be very sensitive to changes in either of the two items, but very sensitive to combined changes in them.

Scenario Analysis

Although sensitivity analysis is useful, it does have limitations. It is often difficult to specify precisely the relationship between a particular variable and the NPW. The relationship is further complicated by interdependencies among the variables. Holding operating costs constant while varying unit sales may ease the analysis, but in reality, operating costs do not behave in that manner. Yet it may complicate the analysis too much to permit movement in more than one variable at a time. A scenario analysis is a technique that does consider the sensitivity of NPW both to changes in key variables and to the range of likely variable values. For example, the decision-maker may consider two extreme cases, a "worst-case" scenario (low unit sales, low unit price, high variable cost per unit, high fixed cost, and so on) and a "best-case" scenario. The NPWs under the worst and best conditions are then calculated and compared to the expected, or base-case, NPW. Example 17.5.2 will illustrate a plausible scenario analysis for the BMC's transmission-housings project.

TABLE 17.5.3 Scenario Analysis for BMC (Example 17.5.2)

Variable Considered	Worst-Case Scenario	Most-Likely-Case Scenario	Best-Case Scenario
Unit demand	1,600	2,000	2,400
Unit price ($)	48	50	53
Variable cost ($)	17	15	12
Fixed cost ($)	11,000	10,000	8,000
Salvage value ($)	30,000	40,000	50,000
PW (15%)	–$5,856	$40,169	$104,295

Example 17.5.2 — Scenario Analysis

Consider again BMC's transmission-housing project in Example 17.5.2. Assume that the company's managers are fairly confident of their estimates of all the projects's cash flow variables except that for unit sales. Further, assume that they regard a decline in unit sales to below 1600 or a rise above 2400 as extremely unlikely. Thus, decremental annual sales of 400 units define the lower bound, or the worst-case scenario, whereas incremental annual sales of 400 units define the upper bound, or the best-case scenario. (Remember that the most-likely value was 2000 in annual unit sales.) Discuss the worst- and best-case scenarios, assuming that the unit sales for all 5 years would be equal.

Discussion

To carry out the scenario analysis, we ask the marketing and engineering staffs to give optimistic (best-case) and pessimistic (worst-case) estimates for the key variables. Then we use the worst-case variable values to obtain the worst-case NPW and the best-case variable values to obtain the best-case NPW. Table 17.5.3 summarizes the results of our analysis. We see that the base case produces a positive NPW, the worst case produces a negative NPW, and the best case produces a large positive NPW.

By just looking at the results in Table 17.5.3, it is not easy to interpret scenario analysis or to make a decision based on it. For example, we can say that there is a chance of losing money on the project, but we do not yet have a specific probability for this possibility. Clearly, we need estimates of the probabilities of occurrence of the worst case, the best case, the base case (most likely), and all the other possibilities. This need leads us directly to the next step, developing a probability distribution. If we can predict the effects on the NPW of variations in the parameters, why should we not assign a probability distribution to the possible outcomes of each parameter and combine these distributions in some way to produce a probability distribution for the possible outcomes of the NPW? We shall consider this issue in the next section.

Risk Analysis

Quantitative statements about risk are given as numerical probabilities, or as values for likelihoods (odds) of occurrence. Probabilities are given as decimal fractions in the interval 0.0 to 1.0. An event or outcome that is certain to occur has a probability of 1.0. As the probability of an event approaches 0, the event becomes increasingly less likely to occur. The assignment of probabilities to the various outcomes of an investment project is generally called *risk analysis*. In this section, we shall assume that the analyst has available the probabilities (likelihoods) of future events from either previous experience in a similar project or a market survey. The use of probability information can provide management with a range of possible outcomes and the likelihood of achieving different goals under each investment alternative.

Procedure for Developing an NPW Distribution

To develop the NPW distribution, we may follow these steps:

1. Identify all cash flows elements that are random variables. (A *random variable*) is a variable that can have more than one possible value.)
2. Express the NPW (or cash flow series) as a function of random variables.

3. Determine the probability distribution for each random variable.
4. Determine the joint events and their probabilities.
5. Evaluate the NPW equation at these joint events.
6. Order the NPW values in increasing order of NPW.

These steps can best be illustrated by Example 17.5.3.

Example 17.5.3 — Developing an NPW Probability Distribution

Consider the BMC's transmission-housing project. If the unit sales (X) and unit price (Y) were to vary with the following probabilities, determine the NPW probability distribution. Here we assume the situation where both random variables are independent. In other words, observing a typical outcome for random variable X does not have any influence on predicting the outcome for random variable Y.

Demand (X)	Probability	Unit Price (Y)	Probability
1600	0.20	$48	0.30
2000	0.60	$50	0.50
2400	0.20	$53	0.20

Discussion

If the product demand X and the unit price Y are independent random variables, the PW (15%) will also be a random variable. To determine the NPW distribution, we need to consider all the combinations of possible outcomes. The first possibility is the event where x = 1600 and y = $48. With these values as input in Table 17.5.1, we compute the resulting NPW outcome to be $5574. Since X and Y are considered to be independent random variables, the probability of this joint event is

$$\begin{aligned} P(x=1600, y=\$48) &= P(x=1600)\,P(y=\$48) \\ &= (0.20)(0.30) \\ &= 0.06 \end{aligned}$$

There are eight other possible joint outcomes. Substituting these pairs of values in Table 17.5.1, we obtain the NPWs and their joint probabilities in Table 17.5.4 and its NPW distribution as depicted in Figure 17.5.2.

Solution

The NPW probability distribution in Table 17.5.4 indicates that the project's NPW varies between $5574 and $82,808, but that there is no loss under any of the circumstances examined. From the cumulative distribution, we further observe that there is a 0.38 probability that the project would realize an NPW

TABLE 17.5.4 The NPW Probability Distribution with Independent Random Variables (Example 17.5.3)

Event No.	x	y	P(x,y)	Cumulative Joint Probability	NPW
1	1600	$48.00	0.06	0.06	$5,574
2	1600	$50.00	0.10	0.16	$12,010
3	1600	$53.00	0.04	0.20	$21,664
4	2000	$48.00	0.18	0.38	$32,123
5	2000	$50.00	0.30	0.68	$40,168
6	2000	$53.00	0.12	0.80	$52,236
7	2400	$48.00	0.06	0.86	$58,672
8	2400	$50.00	0.10	0.96	$68,326
9	2400	$53.00	0.04	1.00	$82,808

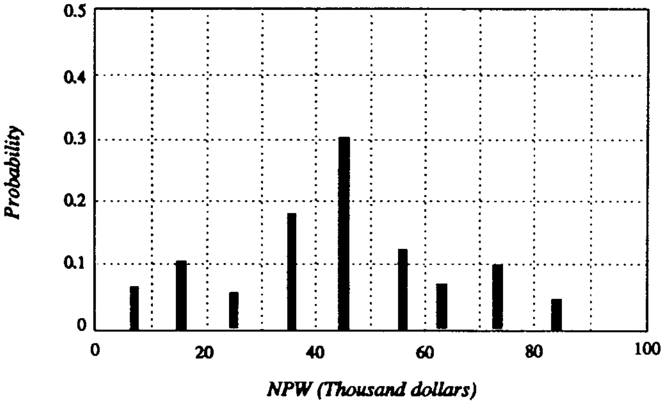

FIGURE 17.5.2 NPW probability distributions: when X and Y are independent (Example 17.5.3).

less than that forecast for the base-case situation ($40,168). On the other hand, there is a 0.32 probability that the NPW will be greater than this value. Certainly, the probability distribution provides much more information on the likelihood of each possible event, as compared with the scenario analysis presented in Table 17.5.3.

Expected Value and Variance

We have developed a probability distribution for the NPW by considering the random cash flows. As we have observed, the probability distribution helps us to see what the data imply in terms of the risk of the project. With the NPW distribution defined, we can further summarize the probabilistic information — the mean and the variance.

The expected value (also called the *mean*) is a weighted average value of the random variable (μ) where the weighting factors are the probabilities of occurrence. (See Table 17.5.5.) The expected value of a distribution tells us important information about the "average" or expected value of a random variable such as the NPW, but it does not tell us anything about the variability on either side of the expected value. Will the range of possible values of the random variable be very small, with all the values located at or near the expected value?

Another measure that we need in analyzing probabilistic situations is a measure of the risk due to the variability of the outcomes. There are several measures of the variation of a set of numbers that are used in statistical analysis — the range and the variance (or standard deviation), among others. The variance and the standard deviation are used most commonly in the analysis of risk situations. We will use Var[X] or σ_x^2 to denote the variance, and σ_x to denote the standard deviation of random variable X. (If there is only one random variable in an analysis, we normally omit the subscript.) The variance tells us the degree of spread, or dispersion, of the distribution on either side of the mean value. As the variance increases, the spread of the distribution increases; the smaller the variance, the narrower the spread about the expected value.

To determine the variance, we first calculate the deviation of each possible outcome x_j from the expected value ($x_j - \mu$), then raise the result to the second power and multiply it by the probability of x_j occurring (that is, p_j). The summation of all these products serves as a measure of the distribution's variability. To be most useful, any measure of risk should have a definite value (unit). One such measure is the standard deviation. To calculate the standard deviation, we take the positive square root of Var[X], which is measured in the same units as is X. The standard deviation is a probability-weighted deviation (more precisely, square root of sum of squared deviations) from the expected value. Thus, it gives us an idea of how far above or below the expected value the actual value is likely to be. For most probability distributions, the actual value will be observed within the $\pm 3\sigma$ range. In our BMC project, we obtain the variance of the NPW distribution, assuming independence between X and Y, as shown in Table 17.5.5.

TABLE 17.5.5 Calculation of the Mean and Variance of NPW Distribution (Example 17.5.3)

Event No.	x	y	P(x,y)	Cumulative Joint Probability	NPW	Weighted NPW
1	1600	$48.00	0.06	0.06	$5,574	$334
2	1600	$50.00	0.10	0.16	$12,010	$1,201
3	1600	$53.00	0.04	0.20	$21,664	$867
4	2000	$48.00	0.18	0.38	$32,123	$5,782
5	2000	$50.00	0.30	0.68	$40,168	$12,050
6	2000	$53.00	0.12	0.80	$52,236	$6,268
7	2400	$48.00	0.06	0.86	$58,672	$3,520
8	2400	$50.00	0.10	0.96	$68,326	$6,833
9	2400	$53.00	0.04	1.00	$82,808	$3,312
						E(NPW) = $40,168

Event No.	x	y	P(x,y)	NPW	(NPW – E[NPW])^2	Weighted (NPW – E[NPW])^2
1	1600	$48.00	0.06	$5,574	1,196,769,744	71,806,185
2	1600	$50.00	0.10	$12,010	792,884,227	79,288,423
3	1600	$53.00	0.04	$21,664	342,396,536	13,695,861
4	2000	$48.00	0.18	$32,123	64,725,243	11,650,544
5	2000	$50.00	0.30	$40,168	0	0
6	2000	$53.00	0.12	$52,236	145,631,797	17,475,816
7	2400	$48.00	0.06	$58,672	342,396,536	20,543,792
8	2400	$50.00	0.10	$68,326	792,884,227	79,288,423
9	2400	$53.00	0.04	$82,808	1,818,132,077	72,725,283
						Var[PW(15%)] = 366,474,326
						Standard Deviation = $19,144

Decision Rule

Once the expected value has been located from the NPW distribution, it can be used to make an accept-reject decision, in much the same way that a single NPW is used when a single possible outcome is considered for an investment project. The decision rule is called the *expected value criterion*, and using it we may accept a single project if its expected NPW value is positive. In the case of mutually exclusive alternatives, we select the one with the highest expected NPW. The use of expected NPW has an advantage over the use of a point estimate, such as the likely value, because it includes all the possible cash flow events and their probabilities.

The justification for the use of the expected value criterion is based on the *law of large numbers,* which states that if many repetitions of an experiment are performed, the average outcome will tend toward the expected value. This justification may seem to negate the usefulness of the expected value criterion in economic analysis, since most often in project evaluation we are concerned with a single, nonrepeatable "experiment" — that is, investment alternative. However, if a firm adopts the expected value criterion as a standard decision rule for *all* its investment alternatives, over the long term the law of large numbers predicts that accepted projects will tend to meet their expected values. Individual projects may succeed or fail, but the average project result will tend to meet the firm's standard for economic success.

The expected-value criterion is simple and straightforward to use, but it fails to reflect the variability of investment outcome. Certainly, we can enrich our decision by incorporating the variability information along with the expected value. Since the variance represents the dispersion of the distribution, it is desirable to minimize it. In other words, the smaller the variance, the less the variability (the potential for loss) associated with the NPW. Therefore, when we compare the mutually exclusive projects, we may select the alternative with the smaller variance if its expected value is the same as, or larger than, those of other alternatives. In cases where there are no clear-cut preferences, the ultimate choice will depend on the decision-maker's trade-offs — how much he or she is willing to take the variability to achieve a higher expected value. In other words, the challenge is to decide what level of risk you are willing to accept and then, having decided on your risk tolerance, to understand the implications of that choice.

17.6 Design Economics

Engineers frequently have to come up with a minimum-cost solution when they have two or more cost components that are affected differently by the same design element. That is, for a single design variable, some costs increase while others decrease. Another valuable extension of the AE analysis in the section on "Annual Equivalent Method," is that these cost components be expressed in equivalent annual form so that we can identify which cost component we need to control to obtain the minimum cost solution to various engineering design problems.

Capital Costs vs. Operating Costs

The AE method is sometimes called the annual equivalent cost method when only costs are involved. In this case, there are two kinds of costs that revenues must cover: *operating costs* and *capital costs*. Operating costs are incurred by the operation of physical plant or equipment to provide service; they include such items as labor and raw materials. Capital costs are incurred by purchasing the assets used in production and service. Normally, capital costs are nonrecurring (that is, one-time costs), whereas operating costs recur as long as the asset is owned.

Because operating costs recur over the life of a project, they tend to be estimated on an annual basis anyway, so for the purposes of an annual equivalent cost analysis, they require no special calculation on our part. However, because capital costs tend to be one-time costs in conducting an annual equivalent cost analysis, we must translate this one-time cost into its annual equivalent over the life of the project. The annual equivalent of a capital cost is given a special name: *capital recovery cost*, designated CR(i).

There are two general monetary transactions associated with the purchase and eventual retirement of a capital asset, its initial cost (I) and its salvage value (S). Taking into account these sums, we calculate the capital recovery cost as

$$CR(i) = I(A/P,i,N) - S(A/F,i,N) \tag{17.6.1}$$

Recalling the algebraic relationships between factors in Table 17.1.1, notice that the (A/P,*i*,N) factor can be expressed as

$$(A/P,i,N) = (A/F,i,N) + i$$

Then, we may rewrite the CR(*i*) as

$$\begin{aligned} CR(i) &= I(A/P,i,N) - S[(A/P,i,N) - i] \\ &= (I - S)(A/P,i,N) + iS \end{aligned} \tag{17.6.2}$$

Minimum-Cost Function

When the equivalent annual total cost of a design variable is a function of increasing (O&M costs) and decreasing cost components (capital costs), we usually can find the optimal value that will minimize its cost.

$$AE(i) = a + bx + \frac{c}{x} \tag{17.6.3}$$

where x is a common design variable, and a, b, and c are constants.

To find the value of the common design variable that minimizes the AE(*i*), we need to take the first derivative, equate the result to zero, and solve for x.

$$\frac{dAE(i)}{dx} = b - \frac{c}{x^2} \tag{17.6.4}$$

$$= 0$$

$$x^* = \sqrt{\frac{c}{b}}$$

The value x^* is the minimum cost point for the design alternative. To illustrate the optimization concept, we will consider selecting an optimal pipe size.

Example 17.6.1 — Economical Pipe Size

As a result of the conflict in the Persian Gulf, Kuwait is studying the feasibility of running a steel pipeline across the Arabian Peninsula to the Red Sea. The pipeline will be designed to handle 3 million barrels of crude oil per day at optimum conditions. The length of the line will be 600 miles. Calculate the optimum pipeline diameter that will be used for 20 years for the following data at $i = 10\%$:

- Pumping power = $1.333Q\Delta P/1{,}980{,}000$ horsepower
- Q = volume flow rate, cubic ft/hr
- $\Delta P = 128Q\mu L/g\pi D^4$, pressure drop lb/sq ft
- L = pipe length, ft
- D = inside pipe diameter, ft
- t = 0.01 D, pipeline wall thickness, ft
- $\mu = 8500$ lb/hr ft, oil viscosity
- $g = 32.2 \times 12{,}960{,}000$ ft/hr^2
- Power cost, \$0.015 per horsepower hour
- Oil cost, \$18 per barrel
- Pipeline cost, \$1.00 per pound of steel
- Pump and motor costs, \$195 per horsepower

The salvage value of the steel after 20 years is assumed to be zero considering the cost of removal. (See Figure 17.6.1 for relationship between D and t.)

Discussion

In general, when progressively larger-size pipe is used to carry a given fluid at a given volume flow rate, the energy required to move the fluid will progressively decrease. However, as we increase the pipe size, the cost to construct the pipe will increase. In practice, to obtain the best pipe size for a particular situation, you may choose a reasonable, but small, starting size. Compute the energy cost of pumping fluid through this size and the total construction cost. Compare the difference in energy cost with the difference in construction cost. When the savings in energy cost exceed the added construction cost, you may repeat the process with progressively larger pipe sizes until the added construction cost exceeds the savings in energy cost. As soon as this happens the best pipe size to use in the particular application is identified. However, we can simplify this search process by using the minimum cost concept as explained through Equation (17.6.3) and Equation (17.6.4).

Solution

We will solve the pipe sizing problem in 8 steps:

1. Since the pipe size will be measured in inches, we will assume the following basic conversion units:
    - 1 mile = 5280 ft
    - 600 miles = $600 \times 5280 = 3{,}168{,}000$ ft
    - 1 barrel = 42 U.S. gal
    - 1 barrel = $42 \text{ gal} \times 231 \text{ in.}^3/\text{gal} = 9702 \text{ in.}^3$
    - 1 barrel = $9702 \text{ in.}^3/12^3 = 5.6146 \text{ ft}^3$
    - Density of steel = 490.75 lb/ft^3

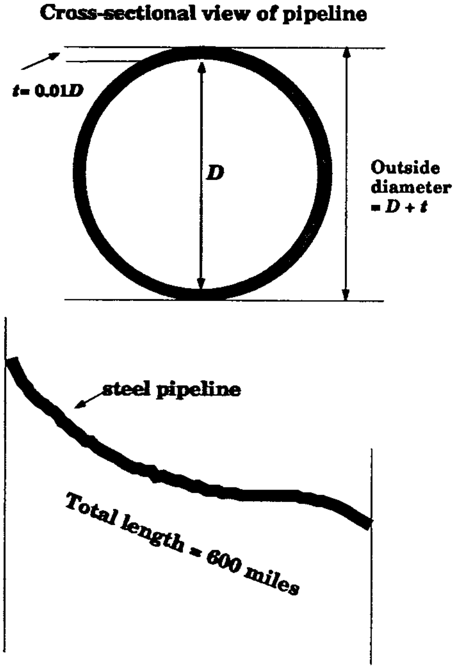

FIGURE 17.6.1 Designing economical pipe size to handle 3 million barrels of crude oil per day (Example 17.6.1).

2. To determine the operating cost in pumping oil, we first need to determine power (electricity) required to pump oil:
   - Volume flow rate per hour:

$$Q = 3{,}000{,}000 \text{ barrels/day} \times 5.6146 \text{ ft}^3/\text{barrel}$$

$$= 16{,}843{,}800 \text{ ft}^3/\text{day}$$

$$= 701{,}825 \text{ ft}^3/\text{hr}$$

   - Pressure drop:

$$\Delta P = \frac{128 Q \mu L}{g \pi D^4}$$

$$= \frac{128 \times 701{,}825 \times 8500 \times 3{,}168{,}000}{32.2 \times 12{,}960{,}000 \times 3.14159 D^4}$$

$$= \frac{1{,}845{,}153{,}595}{D^4} \text{ lb/ft}^2$$

   - Pumping power required to boost the pressure drop:

$$\text{power} = \frac{1.333 Q \Delta P}{1{,}980{,}000}$$

$$= \frac{1.333 \times 701{,}825 \times \dfrac{1{,}845{,}153{,}595}{D^4}}{1{,}980{,}000}$$

$$= \frac{871{,}818{,}975}{D^4} \text{ hp}$$

- Power cost to pump oil:

$$\text{power cost} = \frac{871{,}818{,}975}{D^4}\,\text{hp} \times \$0.015/\text{hp.hr} \times 24\ \text{hr/day} \times 365\ \text{days/year}$$

$$= \frac{\$114{,}557{,}013{,}315}{D^4}\Big/\text{year}$$

3. Pump and motor cost calculation

$$\text{pump and motor cost} = \frac{871{,}818{,}975}{D^4} \times \$195/\text{hp}$$

$$= \frac{\$170{,}004{,}700{,}125}{D^4}$$

4. Required amount and cost of steel

$$\begin{aligned}
\text{cross-sectional area} &= \frac{3.14159\left[(0.51D)^2 - (0.50D)^2\right]}{4} \\
&= 0.032D^2\ \text{ft}^2 \\
\text{total volume of pipe} &= 0.032D^2\ \text{ft}^2 \times 3{,}168{,}000\ \text{ft} \\
&= 101{,}376D^2\ \text{ft}^3 \\
\text{total weight of steel} &= 101{,}376D^2\ \text{ft}^3 \times 490.75\ \text{lb/ft}^3 \\
&= 49{,}750{,}272D^2\ \text{lb} \\
\text{total pipeline cost} &= \$1.00/\text{lb} \times 49{,}750{,}272D^2\ \text{lb} \\
&= \$49{,}750{,}272D^2
\end{aligned}$$

5. Annual equivalent cost calculation

$$\text{capital cost} = \left(\$49{,}750{,}272D^2 + \frac{\$170{,}004{,}700{,}125}{D^4}\right)(A/P,10\%,20)$$

$$= 5{,}843{,}648D^2 + \frac{19{,}968{,}752{,}076}{D^4}$$

$$\text{annual power cost} = \frac{\$114{,}557{,}013{,}315}{D^4}$$

6. Economical pipe size

$$AE(10\%) = 5{,}843{,}648D^2 + \frac{19{,}968{,}752{,}076}{D^4} + \frac{\$114{,}557{,}013{,}315}{D^4}$$

To find the optimal pipe size (D) that results in the minimum annual equivalent cost, we take the first derivative of AE(10%) with respect to D, equate the result to zero, and solve for D.

$$\frac{dAE(10\%)}{dD} = 11{,}687{,}297D - \frac{538{,}103{,}061{,}567}{D^5}$$

$$= 0$$

$$11{,}687{,}297D^6 = 538{,}103{,}061{,}567$$

$$D^6 = 46{,}041.70$$

$$D^* = \mathbf{5.9868\ ft}$$

Note that velocity in a pipe should be ideally no more than around 10 ft/sec due to friction wearing in the pipe. To check to see if the answer is reasonable, we may compute

$$Q = \text{velocity} \times \text{pipe inner area}$$

$$701{,}825\ \text{ft}^3/\text{hr} \times \frac{1}{3{,}600}\ \text{hr/sec} = V\frac{3.14159(5.9868)^2}{4}$$

$$V = 6.93\ \text{ft/sec}$$

which is less than 10 ft/sec. Therefore, the optimal answer as calculated can be practical.

7. Equivalent annual cost at optimal pipe size
   - Capital cost:

$$\text{capital cost} = \left[\$49{,}750{,}272(5.9868)^2 + \frac{170{,}004{,}700{,}125}{5.9868^4}\right](A/P, 10\%, 20)$$

$$= 5{,}843{,}648(5.9868)^2 + \frac{19{,}968{,}752{,}076}{5.9868^4}$$

$$= \mathbf{\$224{,}991{,}039}$$

   - Annual power cost:

$$\text{annual power cost} = \frac{114{,}557{,}013{,}315}{5.9868^4}$$

$$= \mathbf{\$89{,}174{,}911}$$

   - Total annual equivalent cost:

$$\text{total annual cost} = \$224{,}991{,}039 + \$89{,}174{,}911$$

$$= \mathbf{\$314{,}165{,}950}$$

8. Total annual oil revenue

$$\text{annual oil revenue} = \$18/\text{bbl} \times 3{,}000{,}000\ \text{bbls/day} \times 365\ \text{days/year}$$

$$= \$19{,}710{,}000{,}000/\text{year}$$

There are enough revenues to offset the capital as well as operating cost.

Comments

A variety of other criteria exists for choosing pipe size for a particular fluid transfer application. For example, low velocity may be required where there are erosion or corrosion concerns. Alternatively, higher velocities may be desirable for slurries where setting is a concern. Constructional ease will also weight significantly in the choice of pipe size. A small pipe size may not accommodate the head and flow requirements efficiently, whereas space limitations may prohibit selecting large pipe size.

17.7 Project Management

Donald D. Tippett

Engineers, Projects, and Project Management

For a majority of engineers, project work is a way of life throughout their professional careers. Projects build bridges, put humans in space, design and install computer-integrated manufacturing systems, perform research and development (R&D) on state-of-the-art materials, and pursue a thousand other objectives in organizations large and small across the world.

A project has a specific set of objectives and a definite schedule, budget, and set of performance requirements. It has a finite life span and is usually a team effort led by a recognized project manager.

Project management is planning, organizing, leading, and controlling organizational resources to successfully complete the project objectives.

Project Planning

It could be argued that the two most important facets of project management are planning and team building (to be discussed in the section on team building).

What Is Project Planning?

Planning is determining what needs to be done, by whom, and by when.
Planning is decision making based on futurity.
Planning is selecting enterprise objectives, and establishing policies/procedures/programs necessary for achieving them.
Planning is an iterative process and must be performed throughout the life of the project (Kerzner).

Each of these statements adds to an understanding of what project planning is, but why plan? There are a number of reasons:

The planning process serves as a simulation of the project in the planners' minds before significant resources are expended. Thus false starts are avoided and problems are identified and resolved when solutions are the easiest.
The planning process serves as a means of communication, informing all people on the project what will be expected of them.
Plans identify inconsistency and risk.
Plans provide the basis for action.

Plans must be flexible, and provisions should be provided to update them as needed throughout the project. They should include reasonable contingencies and usually require several iterations before they are acceptable.

Whenever possible, the people who will do the work should plan the work. This develops a sense of ownership of the tasks among those who will actually execute them. Also, having the people most familiar with the work do the planning will usually result in a higher-quality, more realistic plan (Rosenau).

Senior managers tend to apply pressure on the project manager to cut the planning process prematurely short. However, cutting short the planning process is usually false economy. As much as 50% of direct labor hours and dollars can be spent before project execution begins, and companies that spend significantly less usually find quality problems during execution (Kerzner).

Project Planning Steps

The steps in sound project planning are as follows:

Issue project charter.
Develop objectives.
Establish statement of work.
Prepare detailed specifications.
Establish project milestones.
Create the work breakdown structure.
Establish detailed schedules.
Establish detailed budgets.
Define responsibilities.
Replan as required.

Project Charter. The first step in a sound planning process is the issuance of a project charter. A project charter is a formal establishing of the project by the upper management chartering authority (a project is not really a project unless it has management's sanction). As a minimum, the charter should (1) designate the purpose of the project, (2) establish the general organizational format for the project, (3) appoint a project manager, and (4) state management's support for the project.

All projects should be formally launched with some sort of charter. For small in-house projects, it may be only a brief memo. Larger projects will have much more extensive charters. A charter puts the organization on notice that the project is being launched and that it has management's acknowledgment and commitment. The charter is the project manager's action authority to perform the project.

Objectives. Project objectives are the basis for all project planning. Objectives must be clearly stated, specific, measurable, and achievable. They should also be realistic and agreed upon by all parties concerned. Objectives should be consistent with the resources available, and with other organizational plans and projects.

Statement of Work/Specifications. The statement of work (SOW) specifically states what the project will do for the customer. For large projects it will be a formal part of the contract. For projects within the organization it might be a memorandum. The SOW specifies the reason for establishing the project, the desired end results, and the performance, budget, and schedule goals. It may also include specific acceptance criteria, as well as a management section that discusses client relationships, management philosophies, project organization and personnel reporting, contingencies, and communications. The establishment of a satisfactory statement of work may require several iterations. However, it is critical that all parties have a detailed understanding of what is to be done before work proceeds.

Depending on the size of the project, detailed specifications may be listed separately, or included as part of the SOW. They define the standards that must be met with respect to materials, labor, prices, equipment, support, and so forth. It is important to firmly establish detailed specifications up front, as small changes in specifications can have major effects on budgets and schedules.

Project Milestones — Project milestones establish the start and end dates of the project (if known), as well as all the significant subsets. Milestones are designated points in time by which certain specific project tasks/accomplishments are to be completed. The set of milestones forms a group of waypoints that provide a basis for status assessment, management reviews, and replanning the project. Because they are simple to understand, they are an important tool for gauging progress.

Work Breakdown Structure — The work breakdown structure (WBS) is a systematic way of defining the component parts of the project. The WBS breaks down the work to be accomplished into a logical hierarchy of sets, subsets, and so forth so that it is put into "bite-sized" chunks that can be easily understood by planners, schedulers, workers, and managers. More specifically, breaking the project's work into manageable pieces

Facilitates the planning process by describing the total job in terms of discrete tasks.
Allows assignment of these tasks to specific groups and individuals.
Forms the framework on which the budget and schedule are built, since each WBS task can easily be estimated in terms of labor, duration, and other required resources.
Facilitates the chore of scheduling, supervision, and project control and information systems by defining exactly who is responsible for each task and establishing a target completion time.
Simplifies purchasing, scheduling, and staging of required materials.

When creating a WBS, keep the following principles in mind:

Routine or repetitive work should not be excessively subdivided.
Subdivide each block of work to a level that is useful to project management; all blocks do not have to have the same number of subdivisions.
Each task should be easily understood and should have an identifiable schedule.
The cost of the smallest subtask should be significant.

It is essential that a work breakdown structure be created. The WBS forms the skeleton on which the plan, schedule, budget, and control system are built. In addition, a completed WBS is the basis for entering project information into any of the myriad of computerized planning and scheduling systems now being used by virtually all project managers.

Scheduling/Budgeting/Responsibilities/Replanning. The remaining components of project planning — developing a schedule and budget, and assigning responsibilities — naturally follow the creation of the WBS. Once the project's work has been separated into a set of manageable subtasks, it is a straightforward process to set about estimating the time and resources required to complete each one (see the section "Estimating and Contracting"). These estimates are then compiled into a project budget. Similarly, responsibility for each WBS component can be assigned to individuals and groups as appropriate and compatible with available resources. While the scheduling process involves a few more intermediate steps (see the next section), it too is a logical extension of the work breakdown structure. Much of the project plan depends on the WBS. Therefore, project managers should pay close attention to it.

Since plans relate to future events but are based on current knowledge, it follows that plans will need to change during the course of the project. As the project team learns lessons along the way, and as events unfold in the dynamic project environment, project plans will need to be adjusted accordingly. Vehicles for accomplishing this process should be established at the outset. Plans must be kept current. Out-of-date plans hurt project credibility. Besides, the project team needs an accurate roadmap if it is to arrive successfully at its desired destination.

Project Scheduling

Creating a viable schedule and adjusting it as necessary throughout the life of the project is an important part of the project manager's responsibilities.

The scheduling cycle (see Figure 17.7.1) begins with the work breakdown structuring process that subdivides the project's work into a set of manageable and easily understood tasks. The next step is to estimate the time, labor hours, and other resources required to complete each task. Then, the relationships between tasks must be documented. Many tasks can be performed in parallel, whereas some must necessarily come before others. In any case, each task's interdependence with every other task must be determined. The project manager is now ready to create the actual schedule, using one of the methods

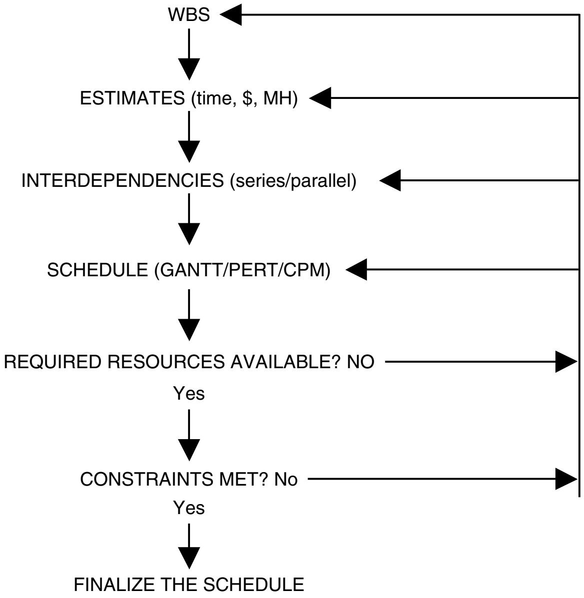

FIGURE 17.7.1 Project scheduling and estimating cycle.

discussed in the next section. Once the schedule is formulated, it must be checked against available resources for feasibility. If the schedule contains periods of time during the project when more resources are called for than will be available, the scheduler must iterate back to an earlier part of the scheduling cycle and make adjustments so that the eventual schedule will prove feasible. Once this is accomplished, the project manager should make a final check to ensure that the proposed schedule will in fact satisfy the project constraints (budget, time, and performance criteria). If constraints are met, the schedule can be finalized.

Scheduling is a continuous process during the life of a project. In the dynamic project environment, changes are always occurring that necessitate replanning and rescheduling. Mechanisms that keep the project plan and schedule valid and current should be put in place at the outset of the project.

Scheduling Methods. The Gantt chart, or bar chart (see Figure 17.7.2), was one of the first techniques used by project managers to schedule and control projects, and it is still widely used. It is simple, graphic, easy to construct and change, and convenient for displaying progress. Project task times are usually shown as horizontal bars that begin and end at the scheduled activity start and end times, respectively. However, Gantt charts do not do a good job of displaying task dependencies and interrelationships. Furthermore, the critical path, the set of sequential activities that define the ultimate length of the project, is not obvious (Rosenau). So, while the Gantt chart is a useful tool for quick overviews and broad statusing of projects, it needs to be augmented by a more comprehensive scheduling tool in all but the most elementary project management situations.

The Critical Path Method (CPM) and Program Evaluation and Review Technique (PERT) are two critical path systems developed to address the shortcomings of the Gantt chart, and enable project managers to do a better job of scheduling complex projects. They both show project task durations, and indicate the earliest task start times as the Gantt chart does, but they also show the *precedence* between activities. This allows the project manager to determine the most critical activities, and more easily modify and determine the status of the schedule.

CPM assumes activity durations are known with a reasonable degree of certainty, and is thus useful in industries like construction that have a long history of performing the various tasks to draw from in formulating accurate project activity estimates (e.g., dig basement, pour footer, etc.) On the other hand,

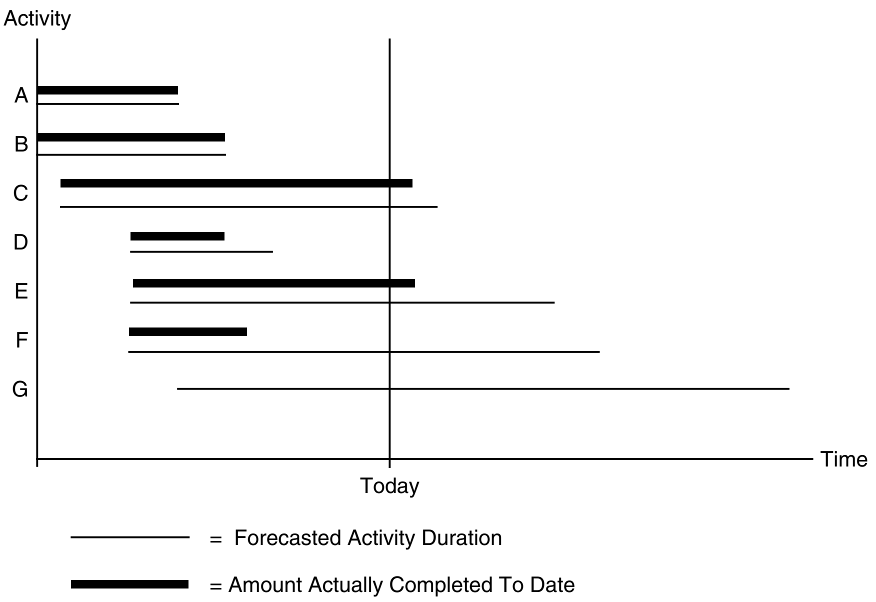

FIGURE 17.7.2 Gantt chart example.

PERT is designed to be used in applications like R&D and aerospace where many activities are being performed for the first time and there is no history to draw on in formulating activity duration estimates. PERT employs statistical techniques to assist the scheduler to devise reasonable activity duration estimates and an estimate for the overall project duration.

Figure 17.7.3 depicts a simple CPM network drawn in the Activity on Node (AON) format. The nodes or circles denote activity. The connecting arrows show precedence between activities. There are various possible routes through the network. The longest route defines the predicted total project duration. The activities on this longest route, or critical path, are called critical activities. Any delay in the execution of these critical activities translates into a delay in overall project completion. Other noncritical activities have a certain amount of leeway (or slack) associated with them that allows the project manager some flexibility in scheduling resources. Thus the project manager should pay special attention to critical activities in making trade-off decisions, as these are the ones that can potentially extend the project duration. However, it should be noted that noncritical activities can potentially become critical if they experience delays greater than their original slack, so the project manager cannot become complacent about noncritical activities either.

In solving the network, forward and backward passes are made according to the formulas given in Figure 17.7.3. Together these two passes determine the earliest and latest starts and finishes for each activity. Also determined are the project's duration, and the critical path (path that contains activities without slack), which represents the predicted project duration. In the example, activities A, C, D, and F have no slack and are thus critical. The path ACDF is the critical path and defines the project duration, 26 days. Once created, the network can be continually updated and used during the life of the project to assist the project manager to understand current project status and make informed trade-off decisions.

It is not feasible to solve any but the simplest PERT/CPM networks by hand. Fortunately, software is widely available for personal computers that is capable of constructing and solving these networks for small and medium-size projects. Very large project networks require the power of larger computers. The Dreger and Suhanic texts (see references) present comprehensive information about using computers in project management. A more detailed exposition of PERT/CPM techniques can be found in the Moder, Phillips, Davis text (see references).

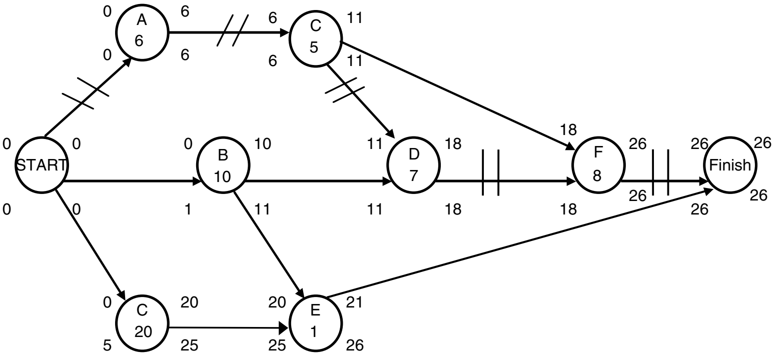

KEY

ES **EF**

RF **LF**

ID = Activity ID

t = Activity Duration

LEGEND

ES = Earliest Activity Start

EF = Earliest Activity Finish

LS = Latest Allowable Activity Start

LF = Latest Allowable Activity Finish

Forward Pass

ES = Max(preceding EF's)

EF = ES + (activity duration)

Backward Pass

LF = Min(succeeding LS's)

LF = LF – (activity duration)

Non-critical Activity Slack = LF – EF = LS – ES

CRITICAL PATH = ACDF = 26 DAYS PROJECT DURATION – ⫽

NON-CRITICAL ACTIVITIES: B (slack = 1 day)

C (slack = 5 days)

E (slack = 5 days)

FIGURE 17.7.3 Example of an AON CPM network.

Staffing and Organizing

In staffing and organizing a project, management must bring together a diverse group of people, equipment, information, and other resources that, when properly integrated, is capable of achieving the project objectives. Each element of the resulting system is critical to overall project success.

Selecting the Project Manager. The project manager is the most critical selection. A person should be selected who:

Serves full time on the project. With few exceptions, appointing a part-time project manager is not practical for projects of any significance. Naming a part-time project manager signals the organization that the project is a low priority. This practice is not fair to the individual or to the project, and usually produces less-than-optimum results.

Has a proven track record. Most project situations are poor training grounds for project managers with little or no experience or training. A project manager's credibility with the organization is vital.

Functions as a manager, not a doer. If the project manager spends all of his or her time performing technical tasks, then, in effect, there is no project manager. With no one in the driver's seat, budgets, schedules, customer relations, and other critical project management components are left unattended.

Possesses good interpersonal skills. A project manager may be called upon at any time to be a communicator, mediator, negotiator, motivator, coach, counselor, and leader.

Project Team Staffing. The project manager may have little or no control over the composition of the project team, as the functional managers of the contributing departments are often the ones who decide which individuals serve on the project. Hence, project managers must be able to mold a potentially broad mix of talents, functional backgrounds, and professional experience into an integrated team. This is one reason why team-building skills are vitally important. (See the section "Team Building.") Given a choice, the project manager would opt for project team members who are assigned full-time to the project, experienced in project work and their discipline, and team players, and who relate well with customer representatives when direct interchange is required.

Organizing for Project Management. Projects are conducted under an infinite variety of organizational structures. Project managers usually have little input in this area and must learn to make the best of the organizational structure in which they find their project operating. However, project managers should bear in mind that, while organizational structures may serve either to facilitate or impede project progress, they are usually not a principal factor in determining overall project success or failure. Other factors, like thorough planning and building a cohesive, motivated project team, are more predictive of project success. Besides, as Kerzner so aptly points out, any organizational form will work if the people want it to.

Nevertheless, project managers should be cognizant of the strengths and weaknesses of the organizational structure under which they are operating so they can make the best of their situation. Table 17.7.1

TABLE 17.7.1 Advantages and Disadvantages of the Three Main Organizational Forms from a Project Management Perspective

Organizational Structure	Advantages	Disadvantages
Functional/Hierarchical/ Classical	• Close control of budget and people • Well-defined authority and communications channels • Well-understood career paths • Best for mass production • Nurtures functional areas; assures up-to-date technology. • Provides security for individuals (in functional groups)	• No one person truly in charge of the entire project • Long lead times, ineffective integration, very slow internal communications • Ineffective communications with the customer • Difficult to know status of projects • Very slow to respond to change • Strongest functional group tends to dominate decision making • Poor conflict resolution, great reliance on hierarchical referral • Tendency to suboptimize
Pure Project/product/ Divisional	• One individual in authority to speak for the project • Quick response to changing environment • Personnel allocated completely to the project • Good communications • Less need for hierarchical referral to resolve conflict • Most likely to complete the project on time	• Less efficient use of resources • Does not nurture functional disciplines • Best when company is project-oriented • Uncertainty for personnel when project ends (where do they go?)
Matrix	• More efficient: project can share personnel and more easily accommodate changing requirements • Good communications • Personnel security (people have homes to go to after project is finished) • Technical disciplines are supported/nurtured • Quick to respond to change • One person speaks for the project	• High potential for conflict • Project personnel must work for two bosses • Heavy penalty in communications requirements and other administrative overhead costs • Best for project-oriented organization • Competition for best resources • Upper management may see matrix as requiring them to give up some authority

TABLE 17.7.2 Six Key Team Building Elements

1. **In all actions, demonstrate respect and consideration for all employees as valued members of the team.** Are employees encouraged by example and admonition to respect each other? Do they know enough about each other's job to appreciate the contributions others are making? Does a general atmosphere of consideration exist?
2. **Identify individual job responsibilities and performance standards and see that they are known.** Are individual discussions held to ensure that each employee knows his or her job's standards and responsibilities? Does each team member understand how his or her portion of the project is important to overall project success?
3. **Work to secure good communications with employees as individuals and as a team.** Do team members feel their inputs and suggestions are valued? Do they receive regular feedback on how they are doing? Is advance warning of changes conveyed whenever possible along with reasons why changes are necessary? Are regular exchange meetings held? Are team members included in decision making?
4. **Establish individual and group goals, preferably in coordination with those concerned.** Are individual goals established for each team member? Is consideration given to each individual's opportunities for professional development? Are group goals established and communicated to the team? Is a goal established that encourages growth in team development factors like team planning, conflict resolution, and problem solving?
5. **Reward teamwork and team building efforts.** Who issues rewards? Project managers? Functional managers? Are rewards mostly based on extrinsic job factors like pay, bonuses, and working conditions, or are they based on intrinsic job factors like accomplishment, recognition, responsibility, and growth? Does management recognize the difference between rewarding an individual as a member of a team, and rewarding an individual as an individual? Are individuals singled out and rewarded for their performance on the project team? Do team members have input into what and how rewards are given and to whom?
6. **Practice and encourage loyalty to the team.** Does the project manager defend team members against unfair criticism? Is there a climate of trust on the project team? Do project managers practice effective leadership?

gives some of the advantages and disadvantages of the three principal organizational structures and their many variants, from a project management perspective.

Regardless of the organizational form used, it is a good idea to create a steering team to oversee and guide important projects. A steering team of senior managers demonstrates management support of the project, helps with integration and hard problems, provides oversight and guidance, makes major dollar decisions, and acts as an interface with upper management.

Team Building

Today's projects characteristically require the efforts of many people from multiple disciplines whose efforts must be effectively integrated to meet project objectives. Further, project managers must cope with dynamic environments, high degrees of organizational complexity, and ever-increasing competitive pressures. Experienced project managers know that the only way to effectively deal with these challenges is to mold their project personnel into true project *teams,* or groups of people with complementary skills who are committed to a common purpose, set of performance goals, and approach for which they hold themselves mutually accountable (Katzenbach and Smith). Teams feature enhanced efficiency, increased motivation, self-regulation, synergistic output, flexibility, and heightened confidence (Raudsepp), all of which are vital to project success in the present competitive environment. Thus, team building is an essential project management skill.

Robert P. Hagen has advanced six key elements of most successful team-building plans which, if implemented by project managers, would greatly enhance the state of team building on project teams (Table 17.7.2).

Project Control

Planning puts the team in a position to launch a project. However, rarely does everything go according to plan. As soon as the project begins, deviations start to occur. Thus, once the project is launched, controlling to the plan becomes a principal function of project management.

It is up to the project control system to keep the project manager apprised of how all components of the project are progressing, and highlight significant problems and deviations from plan so that corrective action can be taken. Without a control system, the project manager has little influence over the project, and it will meander to completion in some form or fashion.

An effective project control system combines a cost accounting function and a cost control function with appropriate mechanisms for monitoring progress against schedule and technical performance targets. The cost accounting function accumulates actual costs, ensures costs are properly allocated, and verifies work is carried out and billed correctly. The cost control function provides the information to support cost analysis, prediction, and reporting. Costs are maintained within budget by taking corrective action wherever predicted costs exceed the budget.

Among the most critical requirements of a project control system is providing a capability to compare budgeted costs to actual costs and then conducting variance analyses that lead to corrective action. The earned value approach to variance analysis is widely used. It compares the budgeted cost of work performed (BCWP), or earned value, with the actual cost of work performed (ACWP) to determine the cost variance (CV). It compares the BCWP with the budgeted cost of work scheduled (BCWS), or planned earned value, to determine the schedule variance (SV).

ACWP and BCWS are fairly straightforward to obtain. On the other hand, it may be difficult to obtain an accurate representation of BCWP. One approach is to use standard dollar expenditures for the project so that x% of the costs are booked for x% of the time. Another is the 50/50 rule, in which half the budget is recorded when an activity is scheduled to begin and the other half when the activity is scheduled to complete. Other alternative approaches may depend on percentage of labor hours expended, parts installed, programs written/tested, and other factors. There are many other possible approaches; however, the object is to somehow measure the percentage complete for project activities (or *earned value*). On some projects the time, trouble, and expense to obtain an accurate BCWP may not be cost effective.

Figure 17.7.4 gives a graphical presentation of the earned value approach and summarizes some quantitative indices useful to project managers conducting variance analysis. Once identified, each critical variance must be investigated to determine the cause and the appropriate corrective action.

Such an investigation should begin at the lowest organizational level by the supervisor involved. It then progresses upward to the project manager who reviews variance causes and approves corrective actions. Normally the project manager will review these results with upper-level management prior to preparing the contractually required reports to the customer.

Estimating and Contracting

Project Estimating. Estimating time and resource requirements on projects is frustrating because the project manager knows in advance that the probability of being exactly correct is slim. The key, then, is to not be afraid to be wrong, but rather simply strive to be as accurate as possible, given what is known at the time.

A simple three-step approach will serve as a starting point for estimating:

1. Top-Down Estimate — Make an initial estimate at an overview level…an order of magnitude estimate using the broad, big picture view.
2. Detailed Bottom-Up Estimate — Follow the top-down estimate with a detailed estimate built from the bottom up. Start with the lowest tasks in the work breakdown structure and work up by task, by department, and so on, arriving at a total figure.
3. Comparison — Compare the two estimates.

In effect, each estimate provides a reality check for the other. If the two are in relative agreement, it is likely that a good estimate has been developed. However, if the two figures are very different, more analysis is indicated. Go back and examine the individual work packages to discover where costs may differ, and to what extent there have been incorrect assumptions made as to the scope and content of work called for. Once the areas of principal differences between the two estimates have been determined, decisions can be taken as to which is correct.

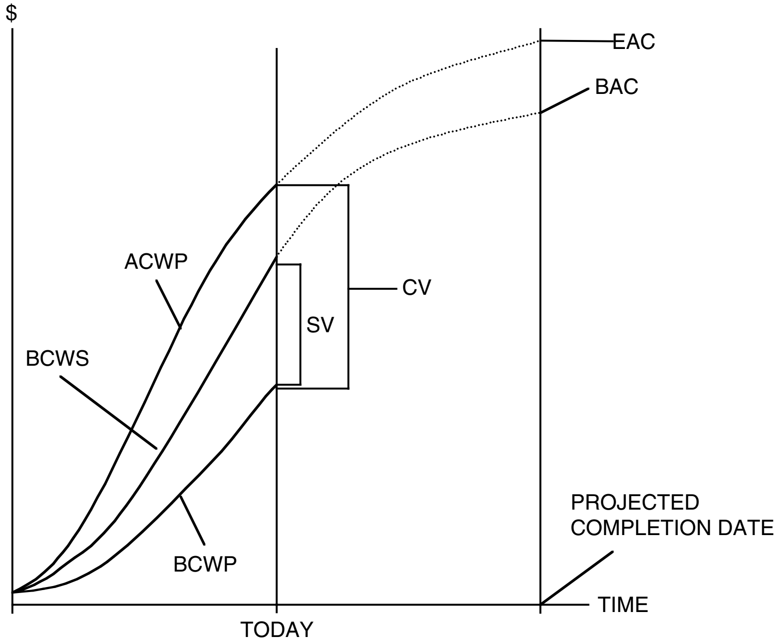

BCWP = BUDGETED COST OF WORK PERFORMED = EARNED VALUE
BCWS = BUDGETED COST OF WORK SCHEDULED = PLANNED EARNED VALUE
ACWP = ACTUAL COST OF WORK PERFORMED
CV = COST VARIANCE = BCWP – ACWP
SV = SCHEDULE VARIANCE = BCWP – BCWS
CV% = COST VARIANCE PERCENTAGE = CV/BCWP
SV% = SCHEDULE VARIANCE PERCENTAGE = SV/BCWS
EAC = ESTIMATE AT COMPLETION = (ACWP/BCWP) = (TOTAL BUDGET)
(NEGATIVE IS UNFAVORABLE)

FIGURE 17.7.4 Graphical earned value presentation.

Contingency planning is an important part of estimating. It is usually not appropriate to place a blanket contingency figure (e.g., 10%) across all tasks. Rather, contingency budgets should be set deliberately, considering each activity individually and being careful not to build contingency on top of contingency.

In developing detailed estimates, time and dollars to cope with the following issues should not be overlooked (Rosenau):

Interfacing with customers, upper management, and other departments
Obtaining customer furnished items
Getting approvals
Working at remote/difficult locations
Training people
Making mistakes
Obtaining security clearances
Placing major subcontracts and purchase orders
Replacing sick and vacationing people

Contracts. There are many types of contractual agreements used on projects. However, most can be categorized as variations on two basic types of contracts: fixed-price and cost-reimbursable. Under a fixed-price contract the customer agrees to pay a specific amount upon satisfactory completion of the project. A cost-reimbursable contract is one in which the customer agrees to reimburse the contractor organization for costs actually incurred in performing the project.

The fixed-price contract presents the lowest financial risk to the customer because the maximum financial liability is specified. This form presents the highest risk to the contractor organization, although it also opens the door for increased profits if the contracted costs can be underrun. On the other hand, under a cost-reimbursable contract, the customer is obligated to reimburse the contractor for all costs incurred, and thus bears considerable risk. The usual arrangement under cost-reimbursable contracts is to add a fixed fee or an incentive fee to the costs to arrive at the total compensation figure due the contractor. Cost-reimbursable contracts are traditionally used when the nature of the project dictates that accurate pricing cannot be determined.

Market conditions also influence the type of contract used. When work is scarce, customer organizations often insist upon fixed price contracts. Conversely, when business is good, customers are not able to insist upon fixed-price contracts, and more cost-reimbursable type contracts are used.

Summary

Project management is among the most challenging undertakings in the field of management today. Project managers routinely face formidable performance requirements, firm budget constraints, and tight schedules. They must organize people from diverse technical backgrounds into a cohesive, motivated team, and then lead that team as it plans and executes its complex tasks in an ever-changing environment.

While the most successful technical people are often promoted to project management, it takes more than a solid technical background to make an effective project manager. To qualify an individual for project management, sound training in the fundamentals is essential, along with on-the-job experience as a project team member and/or assistant project manager or project engineer.

Those characteristics constitute but the tip of the iceberg in terms of required knowledge for project managers, but will perhaps give the uninitiated a starting point. The excellent references we have listed will serve to fill in many of the gaps for the interested reader.

Defining Terms

Activity on Node (AON): A scheduling network in which the circles (or nodes) represent activities, while the connecting lines denote the sequence the activities must follow (see Figure 17.7.3).

Actual cost of work performed (ACWP): Actual dollars expended on a given project activity.

Budgeted cost of work performed (BCWP): Earned value of completed work.

Budgeted cost of work scheduled (BCWS): Planned earned value.

Gantt chart: The Gantt chart, named after Henry L. Gantt, is a bar chart useful in project management to depict planned and actual progress of project activities on a horizontal time scale (see Figure 17.7.2).

Network: A combination of arcs and nodes linked together to represent project activity durations and precedences. Used in conjunction with a solution technique like CPM or PERT, estimates of project completion times, critical activities, and resource requirements can be determined.

PERT/CPM: PERT stands for Program Evaluation and Review Technique, while CPM stands for Critical Path Method. Both are methods for solving a project activity network. CPM is used on projects where activity time estimates are well established, like on construction jobs. PERT is used on projects where times to complete activities are not known with a great deal of certainty, such as in aerospace and R&D applications. Almost always used in conjunction with computer software, these techniques yield estimates of overall project completion times, listings of the most critical activities, and resource requirements by time frame.

Statement of work (SOW): Formal statement delineating specifically what the project will do for the customer. As a minimum it should contain performance, budget, and schedule objectives.

Work breakdown structure (WBS): A logical division of the work involved in the project into a hierarchy of component parts. It forms the basis for subsequent project budgeting, scheduling, and controlling.

References

Dreger, J.B. 1992. *Project Management: Effective Scheduling*, Van Nostrand Reinhold, New York.

Hagen, R.P. 1985. Team building, *Manage*, First Quarter.

Katzenbach, J.R., and Smith, D. K. 1993. *The Wisdom of Teams,* HarperBusiness, New York.

Kerzner, H. 2001. *Project Management: A Systems Approach to Planning, Scheduling, and Controlling*, 7th ed., Van Nostrand Reinhold, New York.

Meredith, J.R. and Mantel S.M. Jr. 1995. *Project Management, A Managerial Approach*, 3rd ed., John Wiley & Sons, New York.

Moder, J.J.; Phillips, C.R., and Davis, E.W. 1983. *Project Management with CPM, PERT, and Precedence Diagramming*, 3rd ed., Van Nostrand Reinhold, New York.

Raudsepp, E. 1984. Effective teamwork, *Manage*, April.

Rosenau, M.D. Jr. 1992. *Successful Project Management*, 2nd ed., Van Nostrand Reinhold, New York.

Shtub, A., Bard, J., and Globerson, S. 1994. *Project Management: Engineering, Technology, Implementation*, Prentice-Hall, Englewood Cliffs, NJ.

Suhanic, G. 2001. *Computer-Aided Project Management,* Oxford University Press, Oxford.

18

Nanotechnology[*]

Sergey Edward Lyshevski
Rochester Institute of Technology

This chapter emphasizes the far-reaching problems in synthesis, design, analysis, modeling, simulation, and simulation of nanomachines. Rotational and translational nanomachines, controlled by nanoscale integrated circuits, can be widely used as nanoscale actuators and sensors. Although this is still a vision that may not materialize in near future, say within 20 to 30 years, fundamental and applied research should be performed. The implications of nanotechnology to motion nanodevices have received meticulous consideration as technologies to fabricate these nanomachines have been studied and developed. Furthermore, basic fundamentals and applied researched have been performed. Organic and inorganic micromachines (fabricated using micromachining technologies) serve as nanomachine prototypes and proof-of-concept paradigm. These micromachines have been tested and characterized. One must address and solve a spectrum of problems in synthesis, analysis, modeling, optimization, biomimicking, and prototyping of nanomachines. These nanomachines and motion nanodevices must be synthesized (devised) before attempts to analyze, optimize, and fabricate them, because basic physical features, energy conversion, operating principles, and other issues significantly contribute to sequential tasks in analysis, control, optimization, and design. This is of particular significance for electromagnetic and chemo-electromagnetic motion nanomachines. This chapter reports and successfully applies distinct concepts

---

[*] Parts of this chapter were published in Lyshevski, S.E., 2002. *NEMS and NEMS: Systems, Devices, and Structures,* CRC Press, Boca Raton, FL and Lyshevski, S.E. 1999, 2004. *Nano- and Micro-Electromechanical Systems: Fundamentals of Micro- and Nano-Engineering,* 1st and 2nd editions, CRC Press, Boca Raton, FL.

and methods. In particular, the field of engineering biomimetics is applied to prototype nanomachines, and the synthesis and classification solver that allows one to synthesize novel nanomachines, as well as classify and refine various motion nanodevices, is discussed. The fundamental, applied, and experimental results are documented in order to accomplish the analysis and design illustrating their significance, validity, and effectiveness.

18.1 Introduction

The benchmarking problems in the synthesis of nanomachines have challenged scientists for a long period of time. All synthesized nano- and microscale machines and motion devices benefit from mimicking of biomachines. Due to nanobiomachines complexity, it is yet unknown how these motion nanobiodevices operate. The basic physics of different electromagnetic-based nanomachines must be examined because nanobiomachines operate based on chemo-electromagnetic phenomena. Distinct feasible electromagnetic nanomachines are reported in this chapter.

Nanomachines and motion nanodevices should be modeled, simulated, and analyzed. We examine the questions of viability of the devised nanomachines studying *Escherichia coli* (*E. coli*) nanobiomotor, magnetotactic bacteria, and so forth. The goal is to further expand nanotechnology and nanosystems horizon by devising new nanomachines and motion nanodevices solving sequential synthesis, modeling, simulation, analysis, and optimization problems. To attain the highest degree of integrity, high-fidelity models are developed and examined. A wide spectrum of interactive software tools, algorithms, and programs have been developed to solve these long-standing problems in heterogeneous simulation and data-intensive analysis. The optimization and control problems should be solved to guarantee the superior overall performance of nanomachines. Using the developed mathematical models, the simulation results illustrate the efficiency of the modeling, analysis, and optimization methods.

18.2 Applications of Engineering Biomimetics in Nanomachines Prototyping

One of the most challenging problems in nanomachine synthesis and prototyping involves the basic physics understanding, analysis, synthesis, and optimization. The synergetic attempts to prototype and design nanomachines have been pursued through analysis of complex patterns and paradigms of evolutionary developed nanobiomachines, for example, *Escherichia coli*, *Salmonella typhimurium*, and others.[1–4] Although promising results have been reported, the basic physics of nanobiomachines is barely comprehended and virtually unknown.[2] At the same time, distinct nanomachines have been devised postulating different electromagnetic fundamentals.[3,4] For example, it is possible that the physics of some nanomachines is based on magnetic media, variable reluctance, or induction electromagnetics. The analysis of the *E. coli* and *Salmonella typhimurium* rotor structures indicates that nanobiowindings can exist. The voltages supplied to these nanowindings can be controlled (regulated) by the nanobiocircuits formed by the proteins that may form nanobioprocessors. As a result, we study different electromagnetic-based nanomachines.

Consider the nanobiomotor of *E. coli* bacteria. The flagella (rotated by nanobiomotors) are used for propulsion. The bacterium is propelled with a maximum speed of 20 μm/sec by flagellar filaments. This filament is driven by a 45 nm rotor of the nanobiomotor embedded in the cell wall. The cytoplasmic membrane forms a stator. This nanobiomotor integrates more than 20 proteins and operates as a result of to the axial *protonomotive* force resulting due to the proton flux. The rated nanobiomotor parameters were found to be as follows:[2]

- Angular velocity is 20 rad/sec.
- Torque is 1×10^{-16} N-m.
- Efficiency is 50% (estimated).

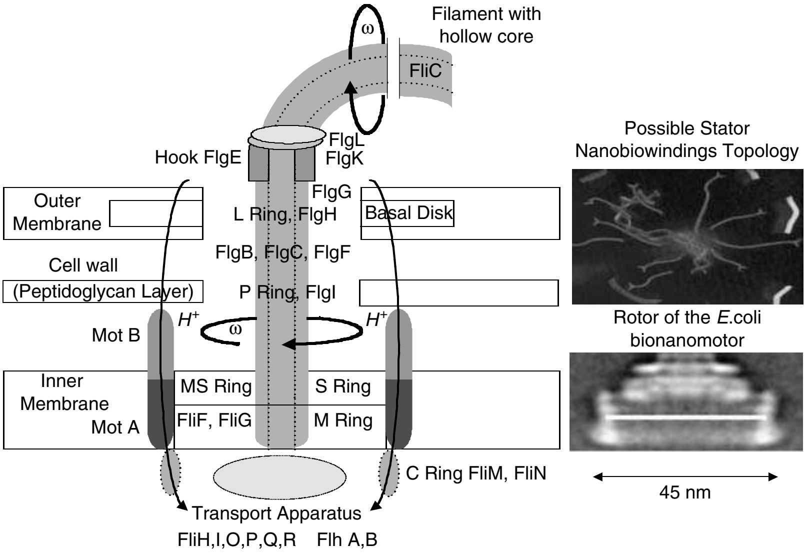

FIGURE 18.2.1 *E. coli* nanobiomotor: integrated nanobiomotor-coupling-flagella complex with different proteins and rings, rotor image, and possible protein-based bionanocircuitry geometry.

It was commonly reported that the *E. coli* nanobiomotor has three *switch* proteins (FliG, FliM, and FliN) that control the torque, angular velocity, and direction of rotation, respectively.[2] These proteins are involved in the flagellar assembly. The flagellum, flexible joint, and nanobiomotor are shown in Figure 18.2.1.[2-4] The nanobiomotor has two major parts: a *stator* (connected to the cell wall) and a *rotor* (connected to the flagellar filament through a flexible joint).

Consider nanobiomotor assembly using common terminology. The stator is built using the so-called MotA and MotB complexes, while the rotor is built by FliF, FliG, FliM, and FliN proteins forming the so-called MS and C rings. The shaft is made from the proteins FlgB, FlgC, FlgF, and FlgG, whereas the bearing is built from the proteins FlgH and FlgI forming the so-called L and P rings. The MS, P, and L rings each contain many copies of FliF, FlgI, and FlgH proteins, respectively. Reference 2 reports that there are eight stator elements (MotA and MotB complexes), each of which exerts the same force. The torque is developed due to axial flux of protons (in marine bacteria and bacteria that live at high pH, the sodium ions establish the axial flux). The source of energy is a transmembrane electrical potential and/or pH gradient. Thus, the *E. coli* nanobiomotor is a chemo-electromagnetic nanobiomachine.

MotA and MotB complexes form a transmembrane channel. According to reference 2, proton translocation may cause the cytoplasmic part of MotA to move or change the geometry, producing the force on FliG. The motor rotates clockwise and counterclockwise, changing the direction as a result of the command signals. When the nanobiomotor rotates clockwise, the flagellar filaments work independently, and the cell body moves erratically with little net displacement (bacterium tumbles). When the nanobiomotor rotates counterclockwise, the filaments rotate in parallel in a bundle that propels the cell body forward (bacterium runs). Although the direction of rotation and some nanobiomotor data can be evaluated, the basic physics of nanobiomachines and their components (proteins) is virtually unknown.[2]

Some bacteria have organic and inorganic magnetic media. In 1962 Professor Lowenstam discovered magnetite (Fe_3O_4) biomineralization in the teeth of chitons, demonstrating that living organisms were able to precipitate the mineral magnetite. In 1975 Richard Blakemore discovered the magnetotactic bacteria. It was found that distinct magnetotactic bacteria contain magnetosomes (magnetic mineral particles) enclosed in the protein-based membranes. In most cases the magnetosomes are arranged in a chain or chains fixed within the cell. In many magnetotactic bacteria, the magnetosome mineral particles are ether 30 to 100 nm magnetite (Fe_3O_4) or, in marine and sulfidic environments, greigite (Fe_3S_4). These

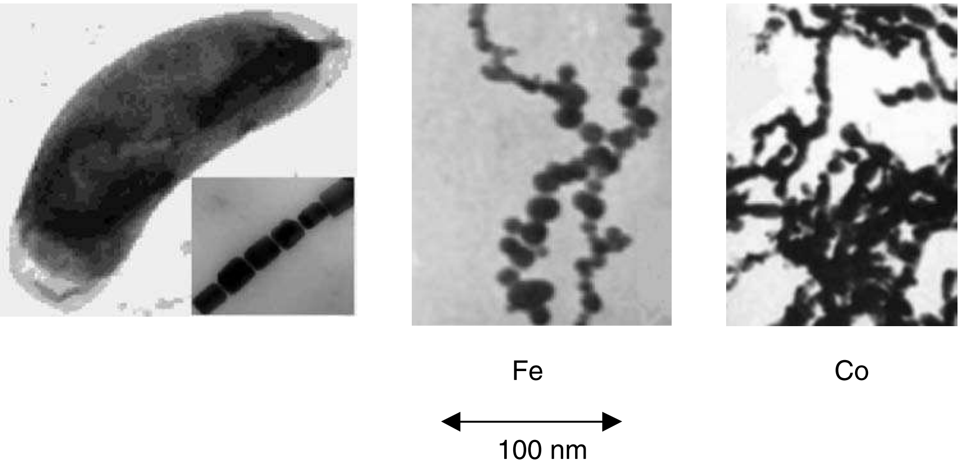

FIGURE 18.2.2 Magnetotactic bacterium and image of a chain of 60–100 nm diameter cylindrical magnetosome mineral magnetic particles. Nanobabricated Fe and Co nanoparticles and their nanoassemblies.

nanoscale permanent magnets sense the magnetic field, and bacteria swim (migrate) along the magnetic field lines. Whether the magnetic mineral particles are magnetite or greigite, the chain of magnetosome particles constitutes a permanent magnetic dipole fixed within the bacterium. Correspondingly, magnetotactic bacteria have two magnetic poles depending on the orientation of the magnetic dipole within the cell. The poles can remagnetized by a magnetic pulse that is greater than the coercive force of the chain of particles. The magnetosome particles that are almost perfectly uniformly magnetized form permanent magnetic domains. All particles are arranged along the chain axis such that the crystallographic magnetic easy axes are also aligned. The size specificity and crystallographic orientation of the chain assembly is optimally designed for magnetotaxis in the geomagnetic field. Magnetosome particles occur in at least three different crystal forms. In *M. magnetotacticum*, cubo-octahedral forms (cubic crystal symmetry of magnetite) is observed. A second type, found in coccoid and vibrioid strains, is an elongated hexagonal prism with the axis of elongation parallel to the 111 crystal direction. A third type, observed in some uncultured cells, is an elongated cubo-octahedral form producing cylindrical, bullet-shaped, teardrop and arrowhead particles, as Figure 18.2.2 shows.

Examining nanomachines and motion nanodevices that can be fabricated using nanotechnology, it is important that these magnetic materials and magnetic nanoassemblies can be created in a straightforward manner. The iron oxide (Fe_3O_4) can be affordably fabricated with 99% purity, and the size of particles is from 15 to 30 nm (the morphology is spherical and the density is 5 g/cm^3). High-energy density nanomagnets can be made. Figure 18.2.2 illustrates the nanotechnology-based fabricated Fe (99% purity, 25 nm size, and 8 g/cm^3 density) and Co (99.8% purity, 27 nm size, and 9 g/cm^3 density) nanoparticles and their assemblies that can be used in electromagnetic (and electrostatic) nanomachines and motion nanodevices. These Fe and Co nanoparticles can be magnetized, making the nanomagnet arrays for nanomachines.

18.3 Nanomachines Synthesis and Classification

The field of engineering biomimetics addresses fundamental design issues that are common to all nanomachines and provides valuable insight in prototyping, synthesis, and design of nanomachines and motion devices. Using recently developed basic results and performing fundamental research,[3,4] researchers have shown that nanobiomachines can operate due to the reluctance difference in the *closed protonomotive* system, interaction of magnetic fields established by nanowindings and magnetic media, induction electromagnetics, and so forth. Nanomachine performance depends on nanomachine operating principle,

TABLE 18.3.1 Nanomachines Synthesis and Classifier

G M		Geometry					
		Plate, P	Spherical, S	Torroidal, T	Conical, N	Cylindrical, C	Asymmetrical, A
Electromagnetic System	*Endless* (Closed), E			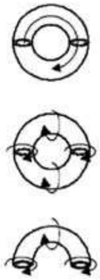	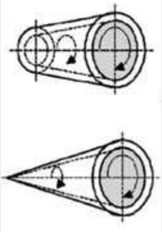	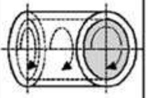	Σ
	Open Ended (Open), O	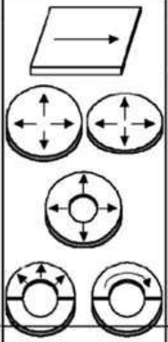	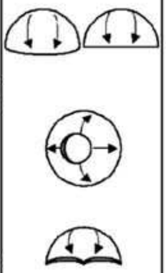	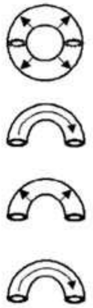	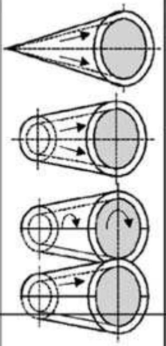	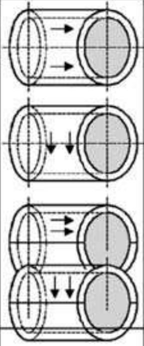	Σ
	Integrated, I	Σ	Σ	Σ	Σ	Σ	Σ

topology, materials, and other factors. Novel nanomachines should be synthesized, and cornerstone synthesis paradigms must be derived. It is evident that electromagnetic systems and geometry can be applied as the basic variables of particular importance. Different synthesis and classification paradigms were developed in References 3–5.

A *nanomachine synthesis and classification solver* is described and demonstrated in Table 18.3.1.[3,4] This solver, which allows one to synthesize and classify electromagnetic-based motion nanodevices, is partitioned into 3 horizontal and 6 vertical strips, and contains 18 sections, each identified by ordered pairs of characters, for example, (*E*, *P*) or (*O*, *C*). Hence, the electromagnetic system–geometric set is given as

$$M \times G = \{(E,F),(E,S),(E,T),\cdots,(I,N),(I,C),(I,A)\},$$

and, in general, we have $M \times G = \{(m,g): m \in M \text{ and } g \in G\}$.

The electromagnetic *synthesis and classification* solver represents nanomachines and nanodevices as

$$M \times G = \{(m,g): m \in M \text{ and } g \in G\},\quad M \times G = \{(E,F),(E,S),(E,T),\cdots,(I,N),(I,C),(I,A)\}$$

Here, the first entry is a letter chosen from the bounded electromagnetic system set, where *E*, *O*, and *I* are the *endless*, *open-ended*, and *integrated* electromagnetic systems, respectively; hence, *M* = {*E*, *O*, *I*}.

The second entry is a letter from the geometric set, where the geometries are denoted as plate (P), spherical (S), torroidal (T), conical (N), cylindrical (C), and asymmetrical (A) geometry, that is, $G = \{P, S, T, N, C, A\}$.

It must be emphasized that the synthesis and classification solver allows one to attain the topological synthesis. For example, radial and axial topology nanomachines result. Using the possible geometry and electromagnetic (chemo-electromagnetic or opto-electromagnetic) systems (*endless*, *open-ended*, and *integrated*), novel organic, inorganic, and hybrid nanoactuators can be synthesized. Different distinct features (induction and synchronous electromagnetics, magnets and ferromagnetic core geometry, magnetization characteristics, *emf* distribution, power, torque, size, packaging, etc.) result. Then, performing modeling, simulation, and analysis, the designer optimizes nanomachine performance. One of the most critical problems is to develop accurate mathematical models that allow the designer to perform data-intensive analysis and heterogeneous simulations in order to guarantee accurate performance predictions.

The analysis of nanobiomachines is far from complete, and there is a significant lack of reliable data.[1–4] There are some possible torque production and energy conversion mechanisms that lead to the corresponding operation of electromagnetic-based nanomachines and motion nanodevices:

1. Synchronous electromagnetics: The torque results due to the interaction of a time-varying magnetic field established by the stator (rotor) windings and a stationary magnetic field established by the rotor (stator) permanent nanomagnets or nanomagnet arrays.
2. Induction electromagnetics: The rotor currents are induced in the rotor windings due to the time-varying stator magnetic field and motion of the rotor with respect to the stator; the torque results due to the interaction of time-varying electromagnetic fields.
3. Variable reluctance electromagnetics (synchronous nanomachine): The torque is produced to minimize the reluctance of the electromagnetic system; for example, the torque is developed by the magnetic system in an attempt to align the minimum-reluctance path of the rotor with the time-varying rotating air gap *mmf*.

18.4 Synthesis, Design and Analysis of Nanomachines

Different nano- and microscale machines and motion devices have been devised and studied in References 3 and 4. In general, the rotational and translational nanomachines can be classified as synchronous and induction. A step-by-step procedure in the nanomachine synthesis and design is as follows:

1. Devise (synthesis, prototyping and classification tasks) nanomachine researching operational principles, topologies, configurations, geometry, electromagnetic systems, and other features.
2. Study electro-chemo-mechanical energy conversion and sensing-feedback-control mechanisms (phenomena).
3. Define application and environmental requirements with performance specifications.
4. Perform electromagnetic, energy conversion, mechanical, vibroacoustic, and sizing/dimension (stator, rotor, nanomagnets, air gap, winding, etc.) estimates.
5. Define (affordable and high-yield) technologies, processes, and materials to fabricate structures (stator, rotor, bearing, post, shaft, etc.) and assembly of nanomachines.
6. Perform coherent electromagnetic, mechanical, vibroacoustic, and thermodynamic design with performance analysis synergetically assessing synthesis, design, and optimization.
7. Modify, refine, and optimize the design.

Thus, in addition to devising nanomachines and motion nanodevices, they should be coherently examined. It is important to accurately model, simulate, and analyze very complex electromagnetic, electromechanical, and vibroacoustic phenomena in motion nanodevices in order to optimize the design. For example, the ultimate goals can be

- Increase efficiency, reliability, robustness, ruggedness, and survivability.
- Maximize the power, torque, and force densities.
- Minimize and attenuate vibrations and noise.
- Minimize losses and torque ripple.

In this way, affordable high-yield fabrication can be achieved. The nanomachine topologies significantly influence nanodevice performance and fabrication. Many of the problems listed have not been addressed and solved yet. To meet our objectives, one must study complex phenomena and perform optimization with ultimate objectives to guarantee superior *achievable* performance (efficiency, robustness, power density, etc.). To attain the desired nanomachines integrity, we must depart from the conventional concepts. We introduce entirely new paradigms that are based on

1. Engineering biomimetics (to prototype nanomachines)
2. The synthesis and classification solver (to synthesize and classify nanomachines)
3. Electromagnetic-mechanical optimal design (to maximize efficiency, robustness, power density, etc.)

To attain our objectives, mathematical models are developed as nanomachines are synthesized. In order to ensure superior *achievable* performance, these nanomachines must be designed for high electromagnetic loads, electromagnetic field and flux (current) densities integrating saturation, hysteresis, and high-frequency harmonics effects. Therefore, the electromagnetic and electromechanical mechanisms must be examined. Hence, the major emphases should be focused on the development and validation of robust and affordable concepts that guarantee significant advantages, for example, increase of efficiency, robustness, reliability, torque density, and expanded operating envelope.

18.5 Synchronous Reluctance Nanomachines

Prototyping and Synthesis of Synchronous Reluctance Nanomachines

The protein folding changes the permeability of the media. This can result in the variable reluctance of the *E. coli* rotor (the MS ring that consists of FliF and FliG proteins) as rotor rotates. At the same time, the *E. coli* nanobiomotor can operate as a synchronous reluctance nanomachine, as shown in Figure 18.5.1.

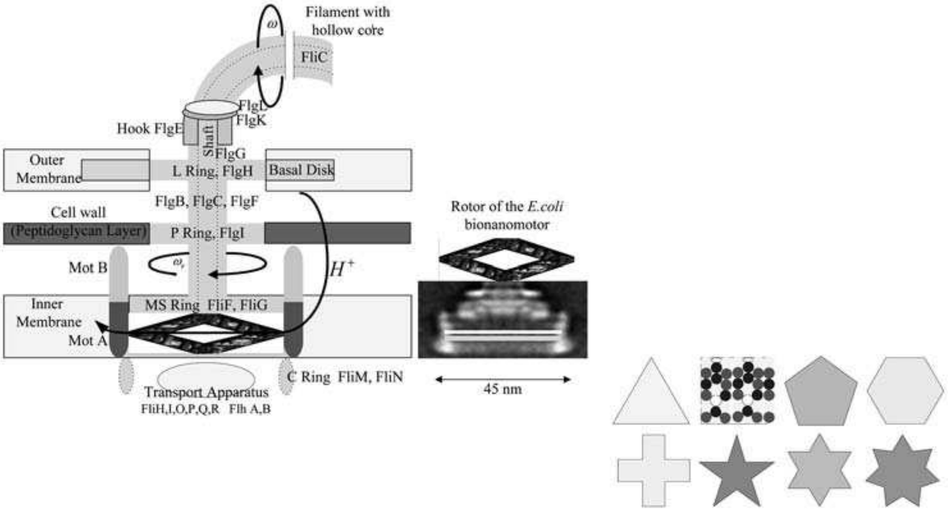

FIGURE 18.5.1 *E. coli* nanobiomotor with a possible rotor protein assembly.

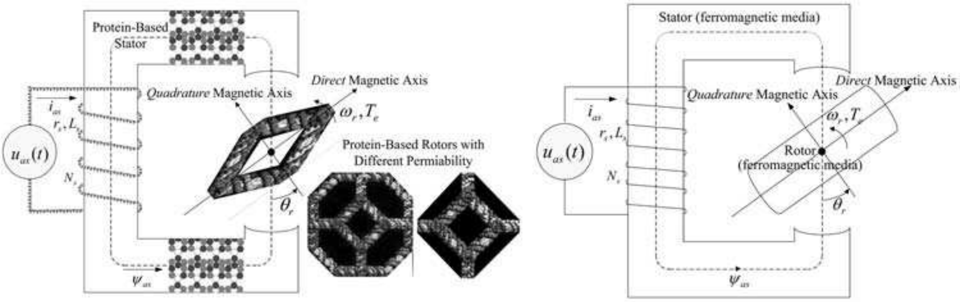

FIGURE 18.5.2 Single-phase reluctance nanomachine and the proposed nanomotor with variable reluctance rotor.

One can hypothesize that there is a possible reluctance difference in the *closed protonomotive* system in the *E. coli* nanobiomotor. Correspondingly, the torque is developed due to change of reluctances as rotor rotates. To illustrate the concept, consider the nanoactuator prototype synthesized using three-dimensional molecular assemblies. For example, the engineered[6] triangle, square, pentagon, heptagon, truncated octahedron, cross, star $N_{5,6,7,\ldots}$, and other geometry of protein assemblies shown in Figure 18.5.1 results in different reluctances due to the distinct length of the protonomotive flux through the media (protein) as rotor rotates. Hence, the reluctance of the magnetic path varies as the rotor rotates as a function of the rotor angular displacement θ_r. This leads one to synthesis of the synchronous reluctance nanomachines. In particular, instead of in the *closed protonomotive* system in the *E. coli* nanobiomotor, we design a nanomachine with the *endless* (*closed*) electromagnetic system that has a different reluctances as the rotor rotates. To illustrate the paradigm, a single-phase reluctance nanoactuator is documented in Figure 18.5.2. This nanomachine can be fabricated as a nanoactuator, shown in Figure 18.5.2.

Modeling, Analysis, and Design of Synchronous Reluctance Nanomachines

Having performed synthesis (and classification) of synchronous reluctance nanomachines, we must now model, simulate, analyze, and optimize those nanomachines. To fulfill our objectives, the augmented mathematical model for the studied single-phase nanomotor is developed as[3]

1. circuitry equation (Kirchhoff's law) is $u_{as} = r_s i_{as} + \dfrac{d\psi_{as}}{dt}$.
2. *tensional-mechanical* equation (Newton's law) is $T_e - B_m\omega_r - T_L = J\dfrac{d^2\theta_r}{dt^2}$.

Here, the nanomachine variables are the phase voltage, current and flux linkages denoted as u_{as}, i_{as} and ψ_{as}; the angular velocity and angular displacement denoted as ω_r and θ_r; and the electromagnetic and load torques denoted as T_e and T_L.

The synchronous reluctance nanomachine parameters are the armature resistance r_s, the moment of inertia J, and the friction coefficient B_m.

As illustrated in Figure 18.5.2, the *quadrature* and *direct* magnetic axes are fixed with the rotor. The rotor rotates with angular velocity ω_r. The magnetizing reluctance $\Re_m$ is a function of the rotor angular displacement θ_r. Using the number of turns N_s, the magnetizing inductance is found to be $L_m(\theta_r) = N_s^2\Re_m^{-1}(\theta_r)$. This magnetizing inductance varies twice per one revolution of the rotor and has minimum and maximum values. In particular, one has $L_{m\min} = N_s^2\Re_{m\max}^{-1}(\theta_r)\Big|_{\theta_r=0,\pi,2\pi,\ldots}$ and $L_{m\max} = N_s^2\Re_{m\min}^{-1}(\theta_r)\Big|_{\theta_r=\frac{1}{2}\pi,\frac{3}{2}\pi,\frac{5}{2}\pi,\ldots}$ The inductance changes as a sinusoidal function of the rotor angular displacement as reported in Figure 18.5.3. Hence, one has $L_m(\theta_r) = \bar{L}_m - L_{\Delta m}f(\theta_r)$, where $\bar{L}_m$ is the average value of the magnetizing inductance; $L_{\Delta m}$ is the half of amplitude of the sinusoidal variation of the magnetizing inductance.

The analytic expression for the $L_m(\theta_r)$ is needed. In general, this can be performed using the finite-element analysis with available high-performance software, for example, MATLAB, ANSYS, or MATHEMATICA. One can approximate these variations of $L_m(\theta_r)$ as $L_m\left(\theta_r\right) = \bar{L}_m - L_{\Delta m}\cos^n 2\theta_r$, $n = 1, 3, 5, \ldots$

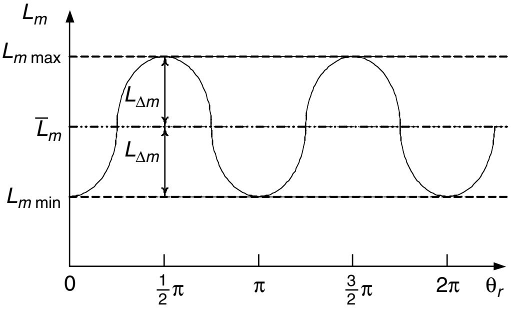

FIGURE 18.5.3 Magnetizing inductance $L_m(\theta_r) = \bar{L}_m - L_{\Delta m} f(\theta_r)$.

The electromagnetic torque, developed by single-phase reluctance nanomotors, is found using the expression for the co-energy as given by $W_c(i_{as},\theta_r) = \frac{1}{2} L_m(\theta_r) i_{as}^2$. Letting $L_m(\theta_r) = \bar{L}_m - L_{\Delta m}\cos 2\theta_r$, one finds

$$W_c(i_{as},\theta_r) = \tfrac{1}{2}\left(L_{ls} + \bar{L}_m - L_{\Delta m}\cos 2\theta_r\right) i_{as}^2$$

Thus, the synchronous reluctance nanomotor electromagnetic torque is given as

$$T_e = \frac{\partial W_c(i_{as},\theta_r)}{\partial \theta_r} = \frac{\partial\left(\frac{1}{2} i_{as}^2 \left(L_{ls} + \bar{L}_m - L_{\Delta m}\cos 2\theta_r\right)\right)}{\partial \theta_r} = L_{\Delta m} i_{as}^2 \sin 2\theta_r$$

The average value of T_e is not equal to zero if the current (magnetic field) is a function of the rotor angular displacement θ_r. As an illustration, let the following current be fed to the motor nanowinding $i_{as} = i_M \operatorname{Re}\left(\sqrt{\sin 2\theta_r}\right)$. Then, the electromagnetic torque is

$$T_e = L_{\Delta m} i_{as}^2 \sin 2\theta_r = L_{\Delta m} i_M^2 \left(\operatorname{Re}\sqrt{\sin 2\theta_r}\right)^2 \sin 2\theta_r \neq 0 \quad \text{and} \quad T_{eav} = \frac{1}{\pi}\int_0^{\pi} L_{\Delta m} i_{as}^2 \sin 2\theta_r d\theta_r = \tfrac{1}{4} L_{\Delta m} i_M^2$$

Making use of Kirchhoff's and Newton's second laws

$$u_{as} = r_s i_{as} + \frac{d\psi_{as}}{dt}, \quad T_e - B_m \omega_r - T_L = J\frac{d^2\theta_r}{dt^2}$$

and taking note of the flux linkage equation $\psi_{as} = \left(L_{ls} + \bar{L}_m - L_{\Delta m}\cos 2\theta_r\right) i_{as}$, one obtains a set of three nonlinear differential equations that models single-phase synchronous reluctance nanomotors as

$$\frac{di_{as}}{dt} = -\frac{r_s}{L_{ls} + \bar{L}_m - L_{\Delta m}\cos 2\theta_r} i_{as} - \frac{2L_{\Delta m}}{L_{ls} + \bar{L}_m - L_{\Delta m}\cos 2\theta_r} i_{as}\omega_r \sin 2\theta_r + \frac{1}{L_{ls} + \bar{L}_m - L_{\Delta m}\cos 2\theta_r} u_{as},$$

$$\frac{d\omega_r}{dt} = \frac{1}{J}\left(L_{\Delta m} i_{as}^2 \sin 2\theta_r - B_m \omega_r - T_L\right)$$

$$\frac{d\theta_r}{dt} = \omega_r$$

The lamped-parameters mathematical model developed is verified through nonlinear simulations. In particular, the 100 nm (length) × 100 nm (height) × 25 nm (width) synchronous nanomotor with 65 nm

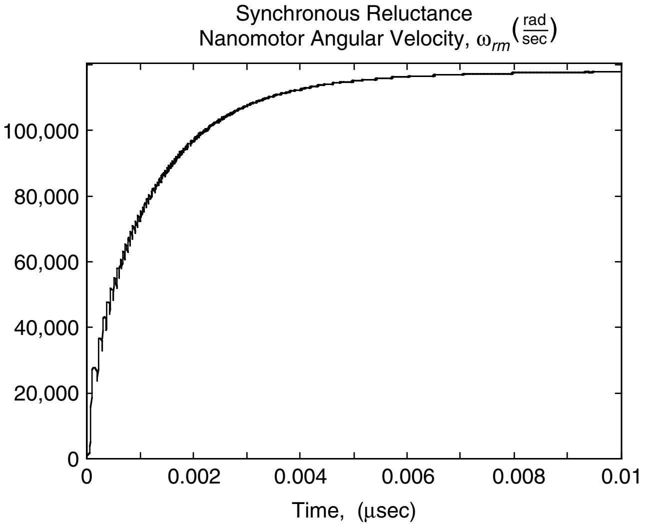

FIGURE 18.5.4 Acceleration of a synchronous reluctance nanomotor.

(length) × 25 nm (width) rotor is examined (see Figure 18.5.2). This nanomotor can be fabricated and nanowindings can be deposited using available nanotechnologies. The relative permeability of the ferromagnetic material was assumed to be $30000\mu_0$, and the friction was neglected. The ratio L_{md}/L_{mq} was assigned to be 4. This ratio significantly influences the electromagnetic torque developed. However, high L_{md}/L_{mq} ratio (to attain higher torque) results in torque ripple and vibrations. The simulation results are represented in Figure 18.5.4.

Maxwell's equations are used to attain high-fidelity modeling of nanomachines.[3] For example, the application of the magnetic potential as the variable gives the following equation to model the dynamics of synchronous reluctance nanomachines:

$$\sigma\frac{\partial \mathbf{A}_z}{\partial t}=\frac{\nabla^2\mathbf{A}_z}{\mu}-\sigma\mathbf{v}\left(\nabla\mathbf{A}_z\right)+\mathbf{J}$$

where $\mathbf{A}_z$ is the z-component of the magnetic potential; $\mathbf{v}$ is the velocity vector; $\mathbf{J}$ is the current density; and σ and μ are the conductivity and permeability.

In general, three-dimensional Maxwell's equations must be applied using conductivity and permeability tensors. These three-dimensional Maxwell's equations, integrated with the relationships for electromagnetic torque, *torsional-mechanical* dynamics, and virboacoustic transient behavior, must be used to model synchronous reluctance nanomachines. Utilizing this high-fidelity modeling concept, high electromagnetic loads and flux densities, saturation, hysteresis, high-frequency harmonics effects, eddy current losses, and other phenomena can be integrated and examined. Although this leads to formidable analytical and numerical difficulties, they can be resolved using high-performance software such as MATLAB.

The synchronous reluctance motors, though quite simple from the fabrication viewpoints, cannot guarantee high performance. As a result, other nanomachines are considered.

18.6 Permanent-Magnet Synchronous Nanomachines

Prototyping and Synthesis of Permanent-Magnet Synchronous Nanomachines

Despite the limited research, availability, and inconsistency, efficient permanent-magnet synchronous nanomachines can be synthesized utilizing the axial topology and endless electromagnetic system. In fact, high-performance axial topology micromachines have been synthesized, designed, tested and characterized.[3]

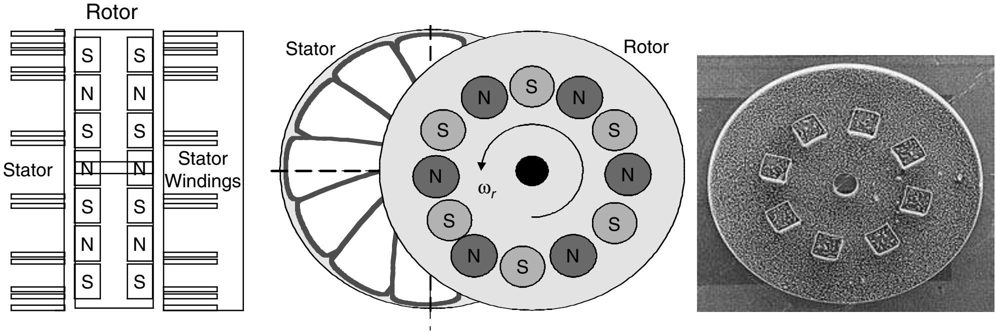

FIGURE 18.6.1 Axial permanent-magnet synchronous nanomachine.

Although these nanomachines are different compared with the *E. coli* nanobiomotor, which may not have permanent magnets, a similar topology is utilized. Furthermore, we progressed to the same well-defined and well-understood inorganic motion nanodevices that can be fabricated utilizing nanotechnology. The advantages of axial topology nanomachines are efficiency and reliability. Fabrication simplicity, affordability, and high-yield result because

1. Nanomagnets are flat (planar) without strict requirements on the surface roughness and uniformity.
2. There are no strict shape and magnetic properties requirements imposed on nanomagnets.
3. Rotor back ferromagnetic material is not required.
4. It is easy to deposit planar nanowires on the flat stator forming nanowindings.

Utilizing the axial topology and endless electromagnetic system, we synthesize permanent-magnet synchronous nanomachines. The synthesized nanomachine is reported in Figure 18.6.1. This nanomachine has well-defined topological analogy compared with the *E. coli* nanobiomotor. It must be emphasized that the documented motion nanodevice can be fabricated, and a prototype of the micromachine with 40 μm rotor was tested and characterized. The planar segmented nanomagnet array, as evident from Figure 18.6.1, can be deposited as thin films nanomagnets.

Modeling of Permanent-Magnet Synchronous Nanomachines

The prototyping and synthesis tasks have been reported and performed. As nanomachines are devised, the sequential analysis and design problems must be researched. In this section we develop an integrated electromagnetic-mechanical-vibroacoustic modeling, analysis, and optimization paradigm to comprehensively *assess and control* electromagnetic, electromechanical, and vibroacoustic phenomena in nanomachines. Our goal is to perform high-fidelity modeling to achieve the highest degree of confidence in simulation, guaranteeing accuracy. In particular, the problems to be researched are modeling (deviations of equations of motion to model complex phenomena and effects in the time domain), heterogeneous simulation, data-intensive analysis, and robust design.

The nanomachine electromagnetics, electromagnetic torque production, and energy conversion are examined. In nanomachines, vibration and noise result due to complex electromagnetic-electromechanical-vibroacoustic phenomena that are studied. Electromagnetic fields modeling is performed applying Maxwell's equations.[3] The following partial differential equations describe time-varying electromagnetic fields in motion nanodevices that are not based on quantum effects:

$$\nabla\times\mathbf{E}=-\mu\frac{\partial\mathbf{H}}{\partial t},\quad \nabla\times\mathbf{H}=\sigma\mathbf{E}+\mathbf{J},\quad \nabla\cdot\mathbf{E}=\frac{\rho_v}{\varepsilon},\quad \nabla\cdot\mathbf{H}=0$$

where **E** and **H** are the electric and magnetic field intensities; **J** is the current density; ε, μ, and σ are the permittivity, permeability, and conductivity tensors, respectively; and ρ_v is the volume charge density.

The Lorenz force, which relates the electromagnetic and mechanical phenomena, is given as

$$\mathbf{F}=\rho_v(\mathbf{E}+\mathbf{v}\times\mathbf{B})=\rho_v\mathbf{E}+\mathbf{J}\times\mathbf{B}$$

The electromagnetic force is found by applying the Maxwell stress tensor. This concept employs a volume integral to obtain the stored energy, and

$$\mathbf{F}=\int_v(\rho_v\mathbf{E}+\mathbf{J}\times\mathbf{B})dv=\frac{1}{\mu}\oint_s \overleftrightarrow{T}_s\cdot d\mathbf{s}$$

where the electromagnetic stress energy tensor is

$$T_s=T_s^E+T_s^M=\begin{bmatrix} E_1D_1-\frac{1}{2}E_jD_j & E_1D_2 & E_1D_3\\ E_2D_1 & E_2D_2-\frac{1}{2}E_jD_j & E_2D_3\\ E_3D_1 & E_3D_2 & E_3D_3-\frac{1}{2}E_jD_j\end{bmatrix}$$

$$+\begin{bmatrix} B_1H_1-\frac{1}{2}B_jH_j & B_1H_2 & B_1H_3\\ B_2H_1 & B_2H_2-\frac{1}{2}B_jH_j & B_2H_3\\ B_3H_1 & B_3H_2 & B_3H_3-\frac{1}{2}B_jH_j\end{bmatrix}.$$

For two regions (air gap *ag* and permanent magnets *pm*), we have the air gap and permanent magnet flux densities as

$$\mathbf{B}_{ag}=\mu_0\mathbf{H}_{ag}\quad\text{and}\quad\mathbf{B}_{pm}=\mu_0\mathbf{H}_{pm}+\mathbf{J}=\mu_0(\mu_r\mathbf{H}_{pm}+\mathbf{M})$$

where **M** is the residual magnetization vector, $M = B_r/\mu_0\mu_r$; B_r is the remanence; and μ_r is the relative recoil permeability.

The negative gradient of the scalar magnetic potential V gives the magnetic field intensity, for example,

$$\mathbf{H}=-\nabla V$$

The scalar magnetic potential satisfies the Laplace equation in free and homogeneous media (with zero current density and $\mathbf{J} = 0$). For axial topology nanomachines, the cylindrical coordinate system is used. We have the equation

$$\nabla\cdot\mathbf{M}=\frac{1}{r}\frac{\partial(rM_r)}{\partial r}+\frac{1}{r}\frac{\partial M_\phi}{\partial r}+\frac{\partial M_z}{\partial z}$$

Solving the partial differential equation[3,7]

$$\frac{1+\chi_t}{r}\frac{\partial}{\partial r}\left(r\frac{\partial V}{\partial r}\right)+\frac{1+\chi_t}{r^2}\frac{\partial^2 V}{\partial\phi^2}+(1+\chi)\frac{\partial^2 V_{ag}}{\partial z^2}=\nabla\cdot\mathbf{M},$$

the three-dimensional air-gap flux density is found as

$$B_{ag\,z}(r,\phi,z)=\frac{\mu_0M_0}{1+\chi}\sum_{i=1}^{\infty}a_i\frac{\sinh\dfrac{v_i\varepsilon h_r}{r}}{\sinh\dfrac{v_i\varepsilon(h_r+g_{ag})}{r}}\cosh\frac{v_i\varepsilon z}{r}\sin v_i\phi$$

where χ and χ_t are the reversible susceptibility along the easy and transverse magnetization axes; a_i is the harmonic amplitude coefficient, and for the trapezoidal-wave magnetization,

$$a_i = \frac{4\sin(2i-1)}{\pi(2i-1)^2};$$

$h_r \le z \le g_{ag} + h_r$, h_r is the rotor thickness.

One-dimensional air-gap flux density is found to be

$$B_{ag\,z}(\phi) = \frac{\mu_0 M_0 h_r}{(1+\chi)(h_r + g_{ag})} \sum_{i=1}^{\infty} a_i \sin v_i \phi \; .$$

Thus, the maximum flux density in the air gap is

$$B_{\max z} = \frac{\mu_0 M_0 h_r}{(1+\chi)(h_r + g_{ag})} \sum_{i=1}^{\infty} a_i (-1)^{i+1} \; .$$

Using the derived equations for the air-gap flux and *emf*

$$emf = \oint \mathbf{E} d\mathbf{l} = -\int_s \frac{\partial \mathbf{B}}{\partial t} \cdot d\mathbf{s}$$

one finds three-dimensional electromagnetic model for nanomachines dynamics, torque production, and vibration. It should be emphasized that the electromagnetic torque is given as

$$\mathbf{T} = \mathbf{m} \times \mathbf{B}$$

The radiated pressure $p(r, \theta, \phi, t)$ is found using the Green function G. We have

$$p(r,\theta,\phi,t) = \rho \int_0^{2\pi} \int_{-R}^{+R} \ddot{\omega}(\phi,z,t) G(r,\theta,\phi) d\phi dz$$

the developed equations of motion model electromagnetic-mechanical-vibroacoustic behavior of synchronous electromagnetic nanomachines.

Optimization of Permanent-Magnet Synchronous Nanomachines

One must attain optimal electromagnetic, mechanical, and vibroacoustic behavior of all nanomachines, including permanent-magnet synchronous motion nanodevices. The electromagnetic and mechanical design is based on the application of Maxwell's equations and tensor calculus in order to optimize the complex electromechanical behavior in nanomachines. For example, the nanomachine electromagnetic system, components (magnets, windings, air gap, etc.) and geometry can be optimized to maximize efficiency (η) and robustness, maximizing the electromagnetic torque (T_e), as well as minimize torque ripple ($\boldsymbol{T}_{er}$), undesirable torque components (T_x and T_y), vibroacoustic signature (p), losses, and so forth. In addition to the *passive optimization*, the *active optimization control* problem can formulated and examined to ensure optimal *achievable* performance. It should be emphasized that although the designer may want to attain the ideal characteristics and performance, usually they cannot be achieved simply due to the physical limits imposed (power and torque densities, current density, angular velocity, etc.).

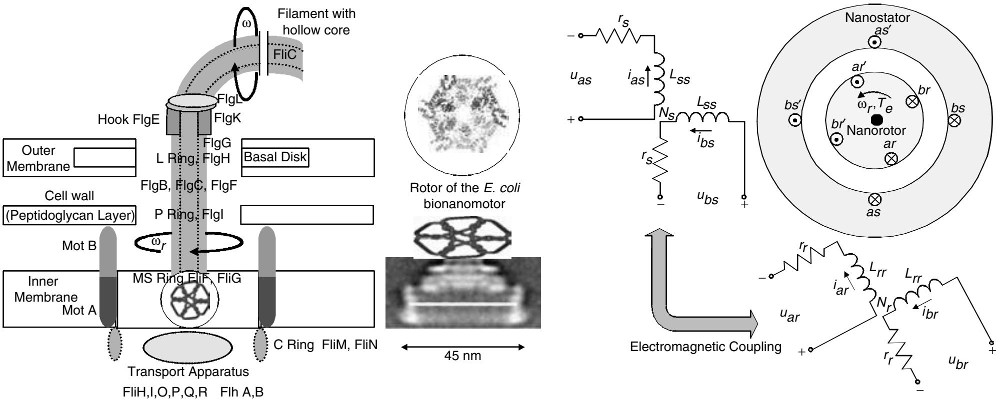

FIGURE 18.7.1 *E. coli* nanobiomotor with assumed short-circuited rotor nanobiowindings and two-phase induction nanomachine.

The mathematical formulation of the active optimization control problem is given as the mini-max nonlinear optimization formulation, for example,

$$\max_{\mathbf{u}\in U} \min\left[\eta, T_e, \mathbf{T}_{er}, T_x, T_y, p(t,r,\theta,\phi)\right]$$

where **u** is the control vector.

Different control variables can be used. For axial and radial topology synchronous nanomachines, the electro-magnetic field is controlled by varying applied phase voltages.

18.7 Induction Nanomachines

Prototyping and Synthesis of Induction Nanomachines

Complex three-dimensional organic complexes and assemblies in *E. coli* and *Salmonella typhimurium* bacteria were studied in this chapter. For example, the 45 nm *E. coli* nanorotor is built as the so-called MS ring that consists of FliF and FliG proteins. These proteins' geometry and folding are unknown. One can assume that short-circuited nanowindings can be formed by these proteins. It should be emphasized that complex three-dimensional organic circuits (windings) can be engineered.[6] As another example, consider the AAA (ATPases Associated with various cellular Activities) interacting protein superfamily. This AAA protein superfamily is characterized by a highly conserved module of more than 230 amino acid residues, including an ATP binding consensus, present in one or two copies in the AAA proteins. The AAA proteins are found in all organisms and are essential for their functionality. The specific attention should be focused on the geometry and folding of different protein complexes and assemblies. In addition, the *E. coli* nanobiomotor and synthesized nanomachines can operate as induction nanomachines; see Figure 18.7.1.

Modeling of Induction Nanomachines

By making use the documented results, the studied two-phase induction nanomachine is illustrated in Figure 18.7.1. The control variables are the phase voltages u_{as} and u_{bs}. To develop lumped-parameter mathematical models of induction nanomachines, we model the stator and rotor circuitry dynamics. As the variables, the voltages applied to the stator and rotor windings (*as*, *bs* and *ar*, *br*, respectively) as well as the stator and rotor currents and flux linkages are used. Using Kirchhoff's voltage law, four differential equations are found to be

- Stator circuitry $u_{as}=r_s i_{as}+\frac{d\psi_{as}}{dt}$ and $u_{bs}=r_s i_{bs}+\frac{d\psi_{bs}}{dt}$
- Rotor circuitry $u_{ar}=r_r i_{ar}+\frac{d\psi_{ar}}{dt}$ and $u_{br}=r_r i_{br}+\frac{d\psi_{br}}{dt}$

Here, the nanomachine variables are the phase voltage, current, and flux linkages u_{as}, u_{bs}, u_{ar}, u_{br}, i_{as}, i_{bs}, i_{ar}, i_{br}, ψ_{as}, ψ_{bs}, ψ_{ar} and ψ_{br}.

The nanomachine parameters are the resistances of the stator and rotor windings r_s and r_r.

The flux linkages are expressed using the phase currents and inductances that are functions of rotor angular displacement. We have

$$\begin{bmatrix}\psi_{as}\\ \psi_{bs}\\ \psi'_{ar}\\ \psi'_{br}\end{bmatrix}=\begin{bmatrix}L_{ss} & 0 & L_{ms}\cos\theta_r & -L_{ms}\sin\theta_r\\ 0 & L_{ss} & L_{ms}\sin\theta_r & L_{ms}\cos\theta_r\\ L_{ms}\cos\theta_r & L_{ms}\sin\theta_r & L'_{rr} & 0\\ -L_{ms}\sin\theta_r & L_{ms}\cos\theta_r & 0 & L'_{rr}\end{bmatrix}\begin{bmatrix}i_{as}\\ i_{bs}\\ i'_{ar}\\ i'_{br}\end{bmatrix}$$

where θ_r is the angular displacement; L_{ss} and L_{rr} are the self-inductances of the stator and rotor windings; L_{ms} is the stator magnetizing inductance; and L_{ls} and L_{lr} are the stator and rotor leakage inductances.

The number of turns in the stator and rotor windings are used. We have the expressions

$$i'_{ar}=\frac{N_r}{N_s}i_{ar},\, i'_{br}=\frac{N_r}{N_s}i_{br}\;,\quad u'_{ar}=\frac{N_r}{N_s}u_{ar},\, u'_{br}=\frac{N_r}{N_s}u_{br}\;,\quad \psi'_{ar}=\frac{N_r}{N_s}\psi_{ar},\, \psi'_{br}=\frac{N_r}{N_s}\psi_{br}$$

Taking note of the turn ratio, we have the following expressions for inductances and rotor resistance:

$$L'_{mr}=L_{ms}=\frac{N_s}{N_r}L_{sr},\, L'_{rr}=L'_{lr}+L_{ms}\quad\text{and}\quad r'_r=\frac{N_s^2}{N_r^2}r_r$$

One obtains the following set of nonlinear differential equations in Cauchy's form to model the stator-rotor circuitry dynamics of induction nanomachines:

$$\begin{aligned}\frac{di_{as}}{dt}=&-\frac{L'_{rr}r_s}{L_{ss}L'_{rr}-L_{ms}^2}i_{as}+\frac{L_{ms}^2}{L_{ss}L'_{rr}-L_{ms}^2}i_{bs}\omega_r+\frac{L_{ms}L'_{rr}}{L_{ss}L'_{rr}-L_{ms}^2}i'_{ar}\left(\omega_r\sin\theta_r+\frac{r'_r}{L'_{rr}}\cos\theta_r\right)\\&+\frac{L_{ms}L'_{rr}}{L_{ss}L'_{rr}-L_{ms}^2}i'_{br}\left(\omega_r\cos\theta_r-\frac{r'_r}{L'_{rr}}\sin\theta_r\right)+\frac{L'_{rr}}{L_{ss}L'_{rr}-L_{ms}^2}u_{as}-\frac{L_{ms}}{L_{ss}L'_{rr}-L_{ms}^2}\cos\theta_r u'_{ar}\\&+\frac{L_{ms}}{L_{ss}L'_{rr}-L_{ms}^2}\sin\theta_r u'_{br},\end{aligned}$$

$$\begin{aligned}\frac{di_{bs}}{dt}=&-\frac{L'_{rr}r_s}{L_{ss}L'_{rr}-L_{ms}^2}i_{bs}-\frac{L_{ms}^2}{L_{ss}L'_{rr}-L_{ms}^2}i_{as}\omega_r-\frac{L_{ms}L'_{rr}}{L_{ss}L'_{rr}-L_{ms}^2}i'_{ar}\left(\omega_r\cos\theta_r-\frac{r'_r}{L'_{rr}}\sin\theta_r\right)\\&+\frac{L_{ms}L'_{rr}}{L_{ss}L'_{rr}-L_{ms}^2}i'_{br}\left(\omega_r\sin\theta_r+\frac{r'_r}{L'_{rr}}\cos\theta_r\right)+\frac{L'_{rr}}{L_{ss}L'_{rr}-L_{ms}^2}u_{bs}-\frac{L_{ms}}{L_{ss}L'_{rr}-L_{ms}^2}\sin\theta_r u'_{ar}\\&-\frac{L_{ms}}{L_{ss}L'_{rr}-L_{ms}^2}\cos\theta_r u'_{br},\end{aligned}$$

$$\frac{di'_{ar}}{dt} = -\frac{L_{ss}r'_r}{L_{ss}L'_{rr}-L_{ms}^2} i'_{ar} + \frac{L_{ms}L_{ss}}{L_{ss}L'_{rr}-L_{ms}^2} i_{as}\left(\omega_r \sin\theta_r + \frac{r_s}{L_{ss}}\cos\theta_r\right) - \frac{L_{ms}L_{ss}}{L_{ss}L'_{rr}-L_{ms}^2} i_{bs}\left(\omega_r \cos\theta_r - \frac{r_s}{L_{ss}}\sin\theta_r\right)$$
$$-\frac{L_{ms}^2}{L_{ss}L'_{rr}-L_{ms}^2} i'_{br}\omega_r - \frac{L_{ms}}{L_{ss}L'_{rr}-L_{ms}^2}\cos\theta_r u_{as} - \frac{L_{ms}}{L_{ss}L'_{rr}-L_{ms}^2}\sin\theta_r u_{bs} + \frac{L_{ss}}{L_{ss}L'_{rr}-L_{ms}^2} u'_{ar},$$

$$\frac{di'_{br}}{dt} = -\frac{L_{ss}r'_r}{L_{ss}L'_{rr}-L_{ms}^2} i'_{br} + \frac{L_{ms}L_{ss}}{L_{ss}L'_{rr}-L_{ms}^2} i_{as}\left(\omega_r \cos\theta_r - \frac{r_s}{L_{ss}}\sin\theta_r\right) + \frac{L_{ms}L_{ss}}{L_{ss}L'_{rr}-L_{ms}^2} i_{bs}\left(\omega_r \sin\theta_r + \frac{r_s}{L_{ss}}\cos\theta_r\right)$$
$$+\frac{L_{ms}^2}{L_{ss}L'_{rr}-L_{ms}^2} i'_{ar}\omega_r + \frac{L_{ms}}{L_{ss}L'_{rr}-L_{ms}^2}\sin\theta_r u_{as} - \frac{L_{ms}}{L_{ss}L'_{rr}-L_{ms}^2}\cos\theta_r u_{bs} + \frac{L_{ss}}{L_{ss}L'_{rr}-L_{ms}^2} u'_{br}.$$

In these differential equations, the angular velocity ω_r and displacement θ_r are used as the state variables. Therefore, the *torsional-mechanical* equation of motion must be incorporated to describe the evolution of induction nanomachines in the time domain. From Newton's second law for rotational motion, we have the following differential equations:

$$\frac{d\omega_r}{dt} = \frac{1}{J}\left(T_e - B_m\omega_r - T_L\right)$$
$$\frac{d\theta_r}{dt} = \omega_r$$

The electromagnetic torque developed by induction nanomotors must be found. Using the co-energy W_c,[3] one has the following relationship for the electromagnetic torque:

$$T_e = \frac{P}{2}\frac{\partial W_c\left(\mathbf{i}_{abs}, \mathbf{i}'_{abr}, \theta_r\right)}{\partial\theta_r} = \frac{P}{2}\mathbf{i}_{abs}^T\frac{\partial \mathbf{L}'_{sr}(\theta_r)}{\partial\theta_r}\mathbf{i}'_{abr} = \frac{P}{2}L_{ms}\begin{bmatrix} i_{as} & i_{bs}\end{bmatrix}\begin{bmatrix} -\sin\theta_r & -\cos\theta_r \\ \cos\theta_r & -\sin\theta_r\end{bmatrix}\begin{bmatrix} i'_{ar} \\ i'_{br}\end{bmatrix}$$
$$= -\frac{P}{2}L_{ms}\left[\left(i_{as}i'_{ar} + i_{bs}i'_{br}\right)\sin\theta_r + \left(i_{as}i'_{br} - i_{bs}i'_{ar}\right)\cos\theta_r\right],$$

where P is the number of poles.

Thus, the *torsional-mechanical* equations of motion are found to be

$$\frac{d\omega_r}{dt} = -\frac{P^2}{4J}L_{ms}\left[\left(i_{as}i'_{ar} + i_{bs}i'_{br}\right)\sin\theta_r + \left(i_{as}i'_{br} - i_{bs}i'_{ar}\right)\cos\theta_r\right] - \frac{B_m}{J}\omega_r - \frac{P}{2J}T_L,$$
$$\frac{d\theta_r}{dt} = \omega_r$$

It should be emphasized that the angular velocity of nanobiomotors is low whereas the output torque is high. In particular, the angular velocity of the *E. coli* nanobiomotor is 20 rad/sec. This suggests that the number of poles may be high. In fact, the output angular velocity of nanomachine is $\omega_{rm} = \frac{2}{P}\omega_r$, and the output torque is given as $T_{em} = \frac{P}{2}T_e$.

Two *torsional-mechanical* differential equations are integrated with the circuitry dynamics to derive a set of nonlinear differential equations to model two-phase induction nanomotors.

Simulation of Induction Nanomachines

The mathematical model developed is verified performing analysis and examining the transient dynamics and steady-state operation. We study an induction nanomotor with 100 nm stator outer diameter. The

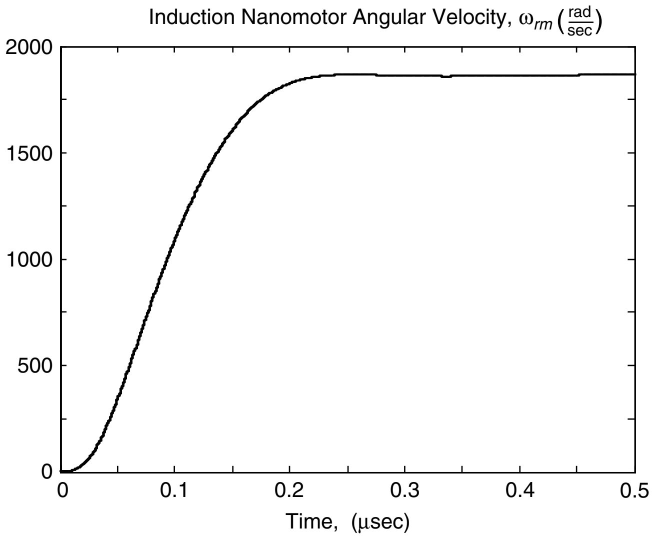

FIGURE 18.7.2 Acceleration of a 100 nm induction nanomotor.

nanomotor parameters are obtained using the dimension estimates, as well as technologies, processes, and materials that can be potentially used to fabricate this nanomachine. In particular, the stator and rotor resistances are found to be $r_s = 3125$ ohm and $r_r = 1890$ ohm. The stator magnetizing inductance is $L_{ms} = 0.000035$ H, whereas the stator and rotor leakage inductances are estimated to be $L_{ls} = L_{lr} = 3 \times 10^{-6}$ H. The friction is neglected ($B_m = 0$), and $P = 2$. The rated phase voltages and currents are estimated to be 3×10^{-3} V and 1 μA, respectively.

The corresponding files to simulate and analyze this induction nanomachine are developed in MATLAB. The angular velocity response (transient dynamics) is illustrated in Figure 18.7.2. It must be emphasized that the angular velocity is controlled by changing the frequency of the phase voltages. The simulations are performed for an open-loop induction nanomotor without a controller, and the limits on the variables are integrated. The peak phase currents are 3 μA. The simulation results illustrate that the induction nanomotor reaches the rated angular velocity within 0.22 μsec. Although, in general additional nonlinear effects should be integrated in the modeling and analysis of nanomachines (nonlinear magnetization, hysteresis, vibration, friction, etc.), the realistic results are obtained.

18.8 Conclusions

This chapter researches benchmarking engineering problems in synthesis, design, and analysis of electromagnetic-based nanomachines and motion nanodevices. This complements the nanotechnology in many ways. In particular, high-performance motion nano- and microdevices have been challenged the society for 50 years, and very limited progress has been achieved to date. Different nanomachines that have analogies and equivalence in nanobiomotors were proposed, prototyped, classified, and examined. The synthesis and classification solver can be applied to devise, refine (modify), and classify novel nanomachines. Accurate assessment of nanomachine performance depends on mathematical models used in design and analysis. Therefore, high-fidelity mathematical models of nanomachines were developed. These electromechanical models were found in the form of nonlinear differential equations. The derived equations of motion allow the designer to study the dynamic and steady-state behavior of nanomachines. This chapter performs fundamental and applied research in response to long-standing unsolved basic problems, engineering enterprise, and emerging evolutionary demands in synthesis of high-performance affordable nanomachines and motion nanodevices. It is important that the reported nanomachines can be fabricated achieving affordable high-yield fabrications due to simplicity, feasibility, and viability of the motion nanodevices documented.

References

1. Drexler, E.K. 2002. *Nanosystems: Molecular Machinery, Manufacturing, and Computations*, Wiley Interscience, New York.
2. Berg, H. C., The rotary motor of bacterial flagella. *J. Annual Rev. Biochemistry*, 72, 19–54, 2003.
3. Lyshevski, S.E., 2002. *MEMS and NEMS: Systems, Devices, and Structures*, CRC Press, Boca Raton, FL.
4. Lyshevski, S.E. 1999, 2004. *Nano- and Microelectromechanical Systems: Fundamentals of Nano- and Microengineering*, 1st and 2nd editions, CRC Press, Boca Raton, FL.
5. Seeman, N.C., DNA engineering and its application to nanotechnology. *Nanotechnology*, 17, 437–443, 1999.
6. Sinkarenko, V., Multiobjective classification of electromechanical energy conversion devices. *Electrodynamics*, 1, 31–35, 1994.
7. Zilichev, Y.N., Numerically-analytical 3D model for calculations of disk type permanent magnet micromotors. *Proc. Conf. Power Electronics and Motion Control*, Warsaw, Poland, 1994.

19

Mathematics

William F. Ames
Georgia Institute of Technology

George Cain
Georgia Institute of Technology

Y. L. Tong
Georgia Institute of Technology

W. G. Steele
Mississippi State University

H. W. Coleman
University of Alabama

R. L. Kautz
National Institute of Standards and Technology

Dan M. Frangopol
University of Colorado

19.1 Tables

Greek Alphabet

Greek Letter	Greek Name	English Equivalent	Greek Letter	Greek Name	English Equivalent
Α α	Alpha	a	Ν ν	Nu	n
Β β	Beta	b	Ξ ξ	Xi	x
Γ γ	Gamma	g	Ο ο	Omicron	o
Δ δ	Delta	d	Π π	Pi	p
Ε ε	Epsilon	e	Ρ ρ	Rho	r
Ζ ζ	Zeta	z	Σ σ ς	Sigma	s
Η η	Eta	e	Τ τ	Tau	t
Θ θ ϑ	Theta	th	Υ υ	Upsilon	u
Ι ι	Iota	i	Φ ϕ φ	Phi	ph
Κ κ	Kappa	k	Χ χ	Chi	ch
Λ λ	Lambda	l	Ψ ψ	Psi	ps
Μ μ	Mu	m	Ω ω	Omega	o

International System of Units (SI)

The International System of units (SI) was adopted by the 11th General Conference on Weights and Measures (CGPM) in 1960. It is a coherent system of units built from seven *SI base units,* one for each of the seven dimensionally independent base quantities: the meter, kilogram, second, ampere, kelvin, mole, and candela, for the dimensions length, mass, time, electric current, thermodynamic temperature, amount of substance, and luminous intensity, respectively. The definitions of the SI base units are given below. The *SI derived units* are expressed as products of powers of the base units, analogous to the corresponding relations between physical quantities but with numerical factors equal to unity.

In the International System there is only one SI unit for each physical quantity. This is either the appropriate SI base unit itself or the appropriate SI derived unit. However, any of the approved decimal prefixes, called *SI prefixes,* may be used to construct decimal multiples or submultiples of SI units.

It is recommended that only SI units be used in science and technology (with SI prefixes where appropriate). Where there are special reasons for making an exception to this rule, it is recommended always to define the units used in terms of SI units. This section is based on information supplied by IUPAC.

Definitions of SI Base Units

Meter: The meter is the length of path traveled by light in vacuum during a time interval of 1/299 792 458 of a second (17th CGPM, 1983).

Kilogram: The kilogram is the unit of mass; it is equal to the mass of the international prototype of the kilogram (3rd CGPM, 1901).

Second: The second is the duration of 9 192 631 770 periods of the radiation corresponding to the transition between the two hyperfine levels of the ground state of the cesium-133 atom (13th CGPM, 1967).

Ampere: The ampere is that constant current which, if maintained in two straight parallel conductors of infinite length, of negligible circular cross section, and placed 1 meter apart in vacuum, would produce between these conductors a force equal to 2×10^{-7} newton per meter of length (9th CGPM, 1958).

Kelvin: The kelvin, unit of thermodynamic temperature, is the fraction 1/273.16 of the thermodynamic temperature of the triple point of water (13th CGPM, 1967).

Mole: The mole is the amount of substance of a system which contains as many elementary entities as there are atoms in 0.012 kilogram of carbon-12. When the mole is used, the elementary entities must be specified and may be atoms, molecules, ions, electrons, or other particles, or specified groups of such particles (14th CGPM, 1971). Examples of the use of the mole:

- 1 mol of H_2 contains about 6.022×10^{23} H_2 molecules, or 12.044×10^{23} H atoms.
- 1 mol of HgCl has a mass of 236.04 g.
- 1 mol of Hg_2Cl_2 has a mass of 472.08 g.
- 1 mol of Hg_2^{2+} has a mass of 401.18 g and a charge of 192.97 kC.
- 1 mol of $Fe_{0.91}$ S has a mass of 82.88 g.
- 1 mol of e^- has a mass of 548.60 μg and a charge of –96.49 kC.
- 1 mol of photons whose frequency is 10^{14} Hz has energy of about 39.90 kJ.

Candela: The candela is the luminous intensity, in a given direction, of a source that emits monochromatic radiation of frequency 540×10^{12} Hz and that has a radiant intensity in that direction of (1/683) watt per steradian (16th CGPM, 1979).

Names and Symbols for the SI Base Units

Physical Quantity	Name of SI Unit	Symbol for SI Unit
Length	meter	m
Mass	kilogram	kg
Time	second	s
Electric current	ampere	A
Thermodynamic temperature	kelvin	K
Amount of substance	mole	mol
Luminous intensity	candela	cd

SI Derived Units with Special Names and Symbols

Physical Quantity	Name of SI Unit	Symbol for SI Unit	Expression in Terms of SI Base Units
Frequency[a]	hertz	Hz	s^{-1}
Force	newton	N	$m \cdot kg \cdot s^{-2}$
Pressure, stress	pascal	Pa	$N \cdot m^{-2} = m^{-1} \cdot kg \cdot s^{-2}$
Energy, work, heat	joule	J	$N \cdot m = m^2 \cdot kg \cdot s^{-2}$
Power, radiant flux	watt	W	$J \cdot s^{-1} = m^2 \cdot kg \cdot s^{-3}$
Electric charge	coulomb	C	$A \cdot s$

Physical Quantity	Name of SI Unit	Symbol for SI Unit	Expression in Terms of SI Base Units
Electric potential, electromotive force	volt	V	$\mathrm{J \cdot C^{-1} = m^2 \cdot kg \cdot s^{-3} \cdot A^{-1}}$
Electric resistance	ohm	Ω	$\mathrm{V \cdot A^{-1} = m^2 \cdot kg \cdot s^{-3} \cdot A^{-2}}$
Electric conductance	siemens	S	$\mathrm{\Omega^{-1} = m^{-2} \cdot kg^{-1} \cdot s^4 \cdot A^2}$
Electric capacitance	farad	F	$\mathrm{C \cdot V^{-1} = m^{-2} \cdot kg^{-1} \cdot s^4 \cdot A^2}$
Magnetic flux density	tesla	T	$\mathrm{V \cdot s \cdot m^{-2} = kg \cdot s^{-2} \cdot A^{-1}}$
Magnetic flux	weber	Wb	$\mathrm{V \cdot s = m^2 \cdot kg \cdot s^{-2} \cdot A^{-1}}$
Inductance	henry	H	$\mathrm{V \cdot A^{-1} \cdot s = m^2 \cdot kg \cdot s^{-2} \cdot A^{-2}}$
Celsius temperature[b]	degree Celsius	°C	K
Luminous flux	lumen	lm	$\mathrm{cd \cdot sr}$
Illuminance	lux	lx	$\mathrm{cd \cdot sr \cdot m^{-2}}$
Activity (radioactive)	becquerel	Bq	$\mathrm{s^{-1}}$
Absorbed dose (or radiation)	gray	Gy	$\mathrm{J \cdot kg^{-1} = m^2 \cdot s^{-2}}$
Dose equivalent (dose equivalent index)	sievert	Sv	$\mathrm{J \cdot kg^{-1} = m^2 \cdot s^{-2}}$
Plane angle	radian	rad	$\mathrm{1 = m \cdot m^{-1}}$
Solid angle	steradian	sr	$\mathrm{1 = m^2 \cdot m^{-2}}$

[a] For radial (circular) frequency and for angular velocity the unit rad $\mathrm{s^{-1}}$, or simply $\mathrm{s^{-1}}$, should be used, and this may not be simplified to Hz. The unit Hz should be used only for frequency in the sense of cycles per second.

[b] The Celsius temperature θ is defined by the equation

$$q/{}^\circ\mathrm{C} = T/\mathrm{K} = 237.15$$

The SI unit of Celsius temperature interval is the degree Celsius, °C, which is equal to the kelvin, K. °C should be treated as a single symbol, with no space between the ° sign and the letter C. (The symbol °K, and the symbol °, should no longer be used.)

Units in Use Together with the SI

These units are not part of the SI, but it is recognized that they will continue to be used in appropriate contexts. SI prefixes may be attached to some of these units, such as milliliter, ml; millibar, mbar; megaelectronvolt, MeV; and kilotonne, kt.

Physical Quantity	Name of Unit	Symbol for Unit	Value in SI Units
Time	minute	min	60 s
Time	hour	h	3600 s
Time	day	d	86 400 s
Plane angle	degree	°	(π/180) rad
Plane angle	minute	′	(π/10 800) rad
Plane angle	second	″	(π/648 000) rad
Length	angstrom[a]	Å	10^{-10} m
Area	barn	b	10^{-28} m^2
Volume	liter	l, L	$\mathrm{dm^3 = 10^{-3}\ m^3}$
Mass	tonne	t	$\mathrm{Mg = 10^3\ kg}$
Pressure	bar[a]	bar	$\mathrm{10^5\ Pa = 10^5\ N \cdot m^{-2}}$
Energy	electronvolt[b]	eV (= $e \times$ V)	$\approx 1.60218 \times 10^{-19}$ J
Mass	unified atomic mass unit[b,c]	u (= m_a(12C)/12)	$\approx 1.66054 \times 10^{-27}$ kg

[a] The angstrom and the bar are approved by CIPM for "temporary use with SI units," until CIPM makes a further recommendation. However, they should not be introduced where they are not used at present.

[b] The values of these units in terms of the corresponding SI units are not exact, since they depend on the values of the physical constants e (for the electronvolt) and N_A (for the unified atomic mass unit), which are determined by experiment.

[c] The unified atomic mass unit is also sometimes called the dalton, with symbol Da, although the name and symbol have not been approved by CGPM.

Conversion Constants and Multipliers

Recommended Decimal Multiples and Submultiples

Multiple or Submultiple	Prefix	Symbol	Multiple or Submultiple	Prefix	Symbol
10^{18}	exa	E	10^{-1}	deci	d
10^{15}	peta	P	10^{-2}	centi	c
10^{12}	tera	T	10^{-3}	milli	m
10^{9}	giga	G	10^{-6}	micro	μ (Greek mu)
10^{6}	mega	M	10^{-9}	nano	n
10^{3}	kilo	k	10^{-12}	pico	p
10^{2}	hecto	h	10^{-15}	femto	f
10	deca	da	10^{-18}	atto	a

Conversion Factors — Metric to English

To Obtain	Multiply	By
Inches	Centimeters	0.393 700 787 4
Feet	Meters	3.280 839 895
Yards	Meters	1.093 613 298
Miles	Kilometers	0.621 371 192 2
Ounces	Grams	$3.527\ 396\ 195 \times 10^{-2}$
Pounds	Kilograms	2.204 622 622
Gallons (U.S. liquid)	Liters	0.264 172 052 4
Fluid ounces	Milliliters (cc)	$3.381\ 402\ 270 \times 10^{-2}$
Square inches	Square centimeters	0.155 000 310 0
Square feet	Square meters	10.763 910 42
Square yards	Square meters	1.195 990 046
Cubic inches	Milliliters (cc)	$6.102\ 374\ 409 \times 10^{-2}$
Cubic feet	Cubic meters	35.314 666 72
Cubic yards	Cubic meters	1.307 950 619

Conversion Factors — English to Metric

To Obtain	Multiply	By[a]
Microns	Mils	25.4
Centimeters	Inches	2.54
Meters	Feet	0.3048
Meters	Yards	0.9144
Kilometers	Miles	1.609 344
Grams	Ounces	28.349 523 13
Kilograms	Pounds	0.453 592 37
Liters	Gallons (U.S. liquid)	3.785 411 784
Millimeters (cc)	Fluid ounces	29.573 529 56
Square centimeters	Square inches	6.451 6
Square meters	Square feet	0.092 903 04
Square meters	Square yards	0.836 127 36
Milliliters (cc)	Cubic inches	16.387 064
Cubic meters	Cubic feet	$2.831\ 684\ 659 \times 10^{-2}$
Cubic meters	Cubic yards	0.764 554 858

[a] Boldface numbers are exact; others are given to ten significant figures where so indicated by the multiplier factor.

Conversion Factors — General

To Obtain	Multiply	By[a]
Atmospheres	Feet of water @ 4°C	2.950×10^{-2}
Atmospheres	Inches of mercury @ 0°C	3.342×10^{-2}
Atmospheres	Pounds per square inch	6.804×10^{-2}
Btu	Foot-pounds	1.285×10^{-3}
Btu	Joules	9.480×10^{-4}
Cubic feet	Cords	**128**
Degree (angle)	Radians	57.2958
Ergs	Foot-pounds	1.356×10^{-7}
Feet	Miles	**5280**
Feet of water @ 4°C	Atmospheres	33.90
Foot-pounds	Horsepower-hours	1.98×10^{6}
Foot-pounds	Kilowatt-hours	2.655×10^{6}
Foot-pounds per minute	Horsepower	3.3×10^{4}
Horsepower	Foot-pounds per second	1.818×10^{-3}
Inches of mercury @ 0°C	Pounds per square inch	2.036
Joules	Btu	1054.8
Joules	Foot-pounds	1.355 82
Kilowatts	Btu per minute	1.758×10^{-2}
Kilowatts	Foot-pounds per minute	2.26×10^{-5}
Kilowatts	Horsepower	0.745712
Knots	Miles per hour	0.868 976 24
Miles	Feet	1.894×10^{-4}
Nautical miles	Miles	0.868 976 24
Radians	Degrees	1.745×10^{-2}
Square feet	Acres	**43 560**
Watts	Btu per minute	17.5796

[a] Boldface numbers are exact; others are given to ten significant figures where so indicated by the multiplier factor.

Temperature Factors

$$°\mathrm{F} = 9/5(°\mathrm{C}) + 32$$

$$\text{Fahrenheit temperature} = 1.8(\text{temperature in kelvins}) - 459.67$$

$$°\mathrm{C} = 5/9\left[(°\mathrm{F}) - 32\right]$$

$$\text{Celsius temperature} = \text{temperature in kelvins} - 273.15$$

$$\text{Fahrenheit temperature} = 1.8(\text{Celsius temperature}) + 32$$

Conversion of Temperatures

From	To		From	To	
Fahrenheit	Celcius	$t_C = \frac{t_F - 32}{1.8}$	Celsius	Fahrenheit	$t_F = (t_c \times 1.8) + 32$
				Kelvin	$T_K = t_c + 273.15$
				Rankine	$T_R = (t_c + 273.15) \times 18$
	Kelvin	$T_k = \frac{t_F - 32}{1.8} + 273.15$	Kelvin	Celsius	$t_c = T_K - 273.15$
				Rankine	$T_R = T_k \times 1.8$
	Rankine	$T_R = t_F + 459.67$	Rankine	Fahrenheit	$t_F = T_R - 459.67$
				Kelvin	$T_K = \frac{T_R}{1.8}$

Physical Constants

General

Equatorial radius of the earth = 6378.388 km = 3963.34 miles (statute)
Polar radius of the earth = 6356.912 km = 3949.99 miles (statute)
1 degree of latitude at 40° = 69 miles
1 international nautical mile = 1.150 78 miles (statute) = 1852 m = 6076.115 ft
Mean density of the earth = 5.522 g/cm^3 = 344.7 lb/ft^3
Constant of gravitation $(6.673 \pm 0.003) \times 10^{-8} \cdot \text{cm}^3 \cdot \text{g}^{-1} \cdot \text{s}^{-2}$
Acceleration due to gravity at sea level, latitude 45° = 980.6194 cm/s^2 = 32.1726 ft/s^2
Length of seconds pendulum at sea level, latitude 45° = 99.3575 cm = 39.1171 in.
1 knot (international) = 101.269 ft/min = 1.6878 ft/s = 1.1508 miles (statute)/h
1 micron = 10^{-4} cm
1 angstrom = 10^{-8} cm
Mass of hydrogen atom = $(1.673\,39 \pm 0.0031) \times 10^{-24}$ g
Density of mercury at 0°C = 13.5955 g/mL
Density of water at 3.98°C = 1.000 000 g/mL
Density, maximum, of water, at 3.98°C = 0.999 973 g/cm^3
Density of dry air at 0°C, 760 mm = 1.2929 g/L
Velocity of sound in dry air at 0°C = 331.36 m/s – 1087.1 ft/s
Velocity of light in vacuum = $(2.997\,925 \pm 0.000\,002) \times 10^{10}$ cm/s
Heat of fusion of water, 0°C = 79.71 cal/g
Heat of vaporization of water, 100°C = 539.55 cal/g
Electrochemical equivalent of silver 0.001 118 g/s international amp
Absolute wavelength of red cadmium light in air at 15°C, 760 mm pressure = 6438.4696 Å
Wavelength of orange-red line of krypton 86 = 6057.802 Å

π Constants

$$\pi = 3.14159\ 26535\ 89793\ 23846\ 26433\ 83279\ 50288\ 41971\ 69399\ 37511$$
$$1/\pi = 0.31830\ 98861\ 83790\ 67153\ 77675\ 26745\ 02872\ 40689\ 19291\ 48091$$
$$\pi^2 = 9.8690\ 44010\ 89358\ 61883\ 44909\ 99876\ 15113\ 53136\ 99407\ 24079$$
$$\log_e \pi = 1.14472\ 98858\ 49400\ 17414\ 34273\ 51353\ 05871\ 16472\ 94812\ 91531$$
$$\log_{10} \pi = 0.49714\ 98726\ 94133\ 85435\ 12682\ 88290\ 89887\ 36516\ 78324\ 38044$$
$$\log_{10} \sqrt{2\pi} = 0.39908\ 99341\ 79057\ 52478\ 25035\ 91507\ 69595\ 02099\ 34102\ 92128$$

Constants Involving *e*

$$e = 2.71828\ 18284\ 59045\ 23536\ 02874\ 71352\ 66249\ 77572\ 47093\ 69996$$
$$1/e = 0.36787\ 94411\ 71442\ 32159\ 55237\ 70161\ 46086\ 74458\ 11131\ 03177$$
$$e^2 = 7.38905\ 60989\ 30650\ 22723\ 04274\ 60575\ 00781\ 31803\ 15570\ 55185$$
$$M = \log_{10} e = 0.43429\ 44819\ 03251\ 82765\ 11289\ 18916\ 60508\ 22943\ 97005\ 80367$$
$$1/M = \log_e 10 = 2.30258\ 50929\ 94045\ 68401\ 79914\ 54684\ 36420\ 76011\ 01488\ 62877$$
$$\log_{10} M = 9.63778\ 43113\ 00536\ 78912\ 29674\ 98645 - 10$$

Numerical Constants

$\sqrt{2}$ = 1.41421 35623 73095 04880 16887 24209 69807 85696 71875 37695
$\sqrt[3]{2}$ = 1.25992 10498 94873 16476 72106 07278 22835 05702 51464 70151
$\log_e 2$ = 0.69314 71805 59945 30941 72321 21458 17656 80755 00134 36026
$\log_{10} 2$ = 0.30102 99956 63981 19521 37388 94724 49302 67881 89881 46211
$\sqrt{3}$ = 1.73205 08075 68877 29352 74463 41505 87236 69428 05253 81039
$\sqrt[3]{3}$ = 1.44224 95703 07408 38232 16383 10780 10958 83918 69253 49935
$\log_e 3$ = 1.09861 22886 68109 69139 52452 36922 52570 46474 90557 82275
$\log_{10} 3$ = 0.47712 12547 19662 43729 50279 03255 11530 92001 28864 19070

Symbols and Terminology for Physical and Chemical Quantities

Name	Symbol	Definition	SI Unit
	Classical Mechanics		
Mass	m		kg
Reduced mass	μ	$\mu = m_1 m_2/(m_1 + m_2)$	kg
Density, mass density	ρ	$\rho = m/V$	$\mathrm{kg \cdot m^{-3}}$
Relative density	d	$d = \rho/\rho^\theta$	1
Surface density	ρ_A, ρ_S	$\rho_a = m/A$	$\mathrm{kg \cdot m^{-2}}$
Specific volume	ν	$\nu = V/m = 1/\rho$	$\mathrm{m^3 \cdot kg^{-1}}$
Momentum	p	$\mathrm{p} = mv$	$\mathrm{kg \cdot m \cdot s^{-1}}$
Angular momentum, action	L	$\mathrm{L} = r \times p$	$\mathrm{J \cdot s}$
Moment of inertia	I, J	$I = \Sigma\, m_i\, r_i^2$	$\mathrm{kg \cdot m^2}$
Force	F	$\mathrm{F} = d\,\mathrm{p}/d\,t = m\,\mathrm{a}$	N
Torque, moment of a force	T, (M)	$\mathrm{T} = r \times F$	$\mathrm{N \cdot m}$
Energy	E		J
Potential energy	E_p, V, Φ	$E_p = \int \mathrm{F} \cdot ds$	J
Kinetic energy	E_k, T, K	$E_k = (1/2)\, mv^2$	J
Work	W, w	$W = \int \mathrm{F} \cdot ds$	J
Hamilton function	H	$H(q,p) = T(q,p) + V(q)$	J
Lagrange function	L	$L(q,\dot{q}) = T(q,\dot{q}) - V(q)$	J
Pressure	p, P	$p = F/A$	Pa, $\mathrm{N \cdot m^{-2}}$
Surface tension	γ, σ	$\gamma = dW/dA$	$\mathrm{N \cdot m^{-1}, J \cdot m^{-1}}$
Weight	$G\ (W, P)$	$G = mg$	N
Gravitational constant	G	$F = Gm_1 m_2/r^2$	$\mathrm{N \cdot m^2 \cdot kg^{-2}}$
Normal stress	σ	$\sigma = F/A$	Pa
Shear stress	τ	$\tau = F/A$	Pa
Linear strain, relative elongation	ε, e	$\varepsilon = \Delta l/1$	1
Modulus of elasticity, Young's modulus	E	$E = \sigma/\varepsilon$	Pa
Shear strain	γ	$\gamma = \Delta x/d$	1
Shear modulus	G	$\mathrm{G} = \tau/\gamma$	Pa
Volume strain, bulk strain	θ	$\theta = \Delta V/V_0$	1
Bulk modulus, compression modulus	K	$K = V_0(dp/dV)$	Pa
Viscosity, dynamic viscosity	η, μ	$\tau_{x,z} = \eta(dv_x/dz)$	$\mathrm{Pa \cdot s}$
Fluidity	ϕ	$\phi = \mathrm{l}/\eta$	$\mathrm{m \cdot kg^{-1} \cdot s}$
Kinematic viscosity	ν	$\nu = \eta/\rho$	$\mathrm{m^2 \cdot s^{-1}}$
Friction coefficient	$\mu, (f)$	$F_{\mathrm{frict}} = \mu F_{\mathrm{norm}}$	1
Power	P	$P = dW/dt$	W
Sound energy flux	P, P_a	$P = dE/dt$	W
Acoustic factors			
Reflection factor	ρ	$\rho = P_r/P_0$	1
Acoustic absorption factor	$\alpha_a, (\alpha)$	$\alpha_a = 1 - \rho$	1
Transmission factor	τ	$\tau = P_u/P_0$	1
Dissipation factor	δ	$\delta = \alpha_a - \tau$	1

Name	Symbol	Definition	SI Unit
		Classical Mechanics	
		Electricity and Magnetism	
Quantity of electricity, electric range	Q		C
Charge density	ρ	$\rho = Q/V$	$C \cdot m^{-3}$
Surface charge density	σ	$\sigma = Q/A$	$C \cdot m^{-2}$
Electric potential	V, ϕ	$V = dW/dQ$	$V, J \cdot C^{-1}$
Electric potential difference	$U, \Delta V, \Delta\phi$	$U = V_2 - V_1$	V
Electromotive force	E	$E = \int(F/Q) \cdot ds$	V
Electric field strength	E	$E = F/Q = -\text{grad } V$	$V \cdot m^{-1}$
Electric flux	ψ	$\psi = \int D \cdot dA$	C
Electric displacement	D	$D = \varepsilon E$	$C \cdot m^{-2}$
Capacitance	C	$C = Q/U$	$F, C \cdot V^{-1}$
Permittivity	ε	$D = \varepsilon E$	$F \cdot m^{-1}$
Permittivity of vacuum	ε_0	$\varepsilon_0 = \mu_0^{-1} c_0^{-2}$	$F \cdot m^{-1}$
Relative permittivity	ε_r	$\varepsilon_r = \varepsilon/\varepsilon_0$	1
Dielectric polarization (dipole moment per volume)	P	$P = D - \varepsilon_0 E$	$C \cdot m^{-2}$
Electric susceptibility	χ_e	$\chi_e = \varepsilon_\tau - 1$	1
Electric dipole moment	p, μ	$P = Qr$	$C \cdot m$
Electric current	I	$I = dQ/dt$	A
Electric current density	j, J	$I = \int j \cdot dA$	$A \cdot m^{-2}$
Magnetic flux density, magnetic induction	B	$F = Qv \times B$	T
Magnetic flux	Φ	$\Phi = \int B \cdot dA$	Wb
Magnetic field strength	H	$B = \mu H$	$A \cdot M^{-1}$
Permeability	μ	$B = \mu H$	$N \cdot A^{-2}, H \cdot m^{-1}$
Permeability of vacuum	μ_0		$H \cdot m^{-1}$
Relative permeability	μ_t	$\mu_\tau = \mu/\mu_0$	1
Magnetization (magnetic dipole moment per volume)	M	$M = B/\mu_0 - H$	$A \cdot m^{-1}$
Magnetic susceptibility	$\chi, \kappa, (\chi_m)$	$\chi = \mu_\tau - 1$	1
Molar magnetic susceptibility	χ_m	$\chi_m = V_m \chi$	$m^3 \cdot mol^{-1}$
Magnetic dipole moment	m, μ	$E_p = -m \cdot B$	$A \cdot m^2, J \cdot T^{-1}$
Electrical resistance	R	$R = U/I$	Ω
Conductance	G	$G = 1/R$	S
Loss angle	δ	$\delta = (\pi/2) + \phi_I - \phi_U$	1, rad
Reactance	X	$X = (U/I) \sin \delta$	Ω
Impedance (complex impedance)	Z	$Z = R + iX$	Ω
Admittance (complex admittance)	Y	$Y = 1/Z$	S
Susceptance	B	$Y = G + iB$	S
Resistivity	ρ	$\rho = E/j$	$\Omega \cdot m$
Conductivity	κ, γ, σ	$\kappa = 1/\rho$	$S \cdot m^{-1}$
Self-inductance	L	$E = -L(dI/dt)$	H
Mutual inductance	M, L_{12}	$E_1 = L_{12}(dI_2/dt)$	H
Magnetic vector potential	A	$B = \nabla \times A$	$Wb \cdot m^{-1}$
Poynting vector	S	$S = E \times H$	$W \cdot m^{-2}$
		Electromagnetic Radiation	
Wavelength	λ		m
Speed of light			
In vacuum	c_0		$m \cdot s^{-1}$
In a medium	c	$c = c_0/n$	$m \cdot s^{-1}$
Wavenumber in vacuum	$\tilde{\nu}$	$\tilde{\nu} = \nu/c_0 = 1/n\lambda$	m^{-1}
Wavenumber (in a medium)	σ	$\sigma = 1/\lambda$	m^{-1}
Frequency	ν	$\nu = c/\lambda$	Hz
Circular frequency, pulsatance	ω	$\omega = 2\pi\nu$	$s^{-1}, rad \cdot s^{-1}$

Name	Symbol	Definition	SI Unit
Classical Mechanics			
Refractive index	n	$n = c_0/c$	1
Planck constant	h		J · s
Planck constant/2π	$\hbar$	$\hbar = h/2\pi$	J · s
Radiant energy	Q, W		J
Radiant energy density	ρ, w	$\rho = Q/V$	$J \cdot m^{-3}$
Spectral radiant energy density			
In terms of frequency	ρ_ν, w_ν	$\rho_\nu = d\rho/d\nu$	$J \cdot m^{-3} \cdot Hz^{-1}$
In terms of wavenumber	$\rho_{\tilde{v}} w_{\tilde{v}}$	$\rho_\nu = d\rho / d\tilde{v}$	$J \cdot m^{-2}$
In terms of wavelength	ρ_λ, w_λ	$\rho_\lambda = d\rho/d\lambda$	$J \cdot m^{-4}$
Einstein transition probabilities			
Spontaneous emission	A_{nm}	$dN_n/dt = -A_{nm}N_n$	s^{-2}
Stimulated emission	B_{nm}	$dN_n/dt = -\rho_\nu(\tilde{v}_{nm}) \times B_{nm}N_n$	$s \cdot kg^{-1}$
Stimulated absorption	B_{nm}	$dN_n/dt = \rho_{\tilde{v}}(\tilde{v}_{nm}) B_{nm}N_n$	$s \cdot kg^{-1}$
Radiant power, radiant energy per time	Φ, P	$\Phi = dQ/dt$	W
Radiant intensity	I	$I = d\Phi/d\Omega$	$W \cdot sr^{-1}$
Radiant excitance (emitted radiant flux)	M	$M = d\Phi/dA_{\mathrm{source}}$	$W \cdot m^{-2}$
Irradiance (radiant flux received)	$E, (I)$	$E = d\Phi/dA$	$W \cdot m^{-2}$
Emittance	ε	$\varepsilon = M/M_{\mathrm{bb}}$	1
Stefan-Boltzmann constant	σ	$M_{\mathrm{bb}} = \sigma T^4$	$W \cdot m^{-2} \cdot K^{-4}$
First radiation constant	c_1	$c_1 = 2\pi h c_0^2$	$W \cdot m^{-2}$
Second radiation constant	c_2	$c_2 = hc_0/k$	K · m
Transmittance, transmission factor	τ, T	$\tau = \Phi_{\mathrm{tr}}/\Phi_0$	1
Absorptance, absorption factor	α	$\alpha = \Phi_{\mathrm{abs}}/\Phi_0$	1
Reflectance, reflection factor	ρ	$\rho = \Phi_{\mathrm{refl}}/\Phi_0$	1
(Decadic) absorbance	A	$A = \lg(1 - \alpha_i)$	1
Napierian absorbance	B	$B = \ln(1 - \alpha_i)$	1
Absorption coefficient			
(Linear) decadic	a, K	$a = A/l$	m^{-1}
(Linear) napierian	α	$\alpha = B/l$	m^{-1}
Molar (decadic)	ε	$\varepsilon = a/c = A/cl$	$m^2 \cdot mol^{-1}$
Molar napierian	κ	$\kappa = a/c = B/cl$	$m^2 \cdot mol^{-1}$
Absorption index	k	$k = \alpha/4\pi \tilde{v}$	1
Complex refractive index	$\hat{n}$	$\hat{n} = n + ik$	1
Molar refraction	R, R_m	$R = \frac{(n^2 - 1)}{(n^2 + 2)} V_m$	$m^3 \cdot mol^{-1}$
Angle of optical rotation	α		1, rad
Solid State			
Lattice vector	R, R_0		m
Fundamental translation vectors for the crystal lattice	$a_1; a_2; a_3, a; b; c$	$R = n_1 a_1 + n_2 a_2 + n_3 a_3$	m
(Circular) reciprocal lattice vector	G	$G \cdot R = 2\pi m$	m^{-1}
(Circular) fundamental translation vectors for the reciprocal lattice	$b_1; b_2; b_3, a^*; b^*; c^*$	$a_1 \cdot b_k = 2\pi\delta_{ik}$	m^{-1}
Lattice plane spacing	d		m
Bragg angle	θ	$n\lambda = 2d \sin\theta$	1, rad
Order of reflection	n		1
Order parameters			
Short range	σ		1
Long range	s		1
Burgers vector	b		m
Particle position vectort	r, R_j		m
Equilibrium position vector of an ion	R_0		m
Displacement vector of an ion	u	$u = R - R_0$	m
Debye-Waller factor	B, D		1

Name	Symbol	Definition	SI Unit
		Classical Mechanics	
Debye circular wavenumber	q_D		m^{-1}
Debye circular frequency	ω_D		s^{-1}
Grüneisen parameter	γ, Γ	$\gamma = aV/\kappa C_v$	1
Madelung constant	α, M	$E_{\text{coul}} = \dfrac{\alpha N_A z + z - e^2}{4\pi\varepsilon_0 R_0}$	1
Density of states	N_E	$N_E = dN(E)/dE$	$J^{-1} \cdot m^{-3}$
(Spectral) density of vibrational modes	N_ω, g	$N_\omega = dN(\omega)/d\omega$	$s \cdot m^{-3}$
Resistivity tensor	ρ_{ik}	$E = \rho \cdot j$	$\Omega \cdot m$
Conductivity tensor	σ_{ik}	$\sigma = \rho^{-1}$	$S \cdot m^{-1}$
Thermal conductivity tensor	λ_{ik}	$J_q = -\lambda \cdot \text{grad}\ T$	$W \cdot m^{-1} \cdot K^{-1}$
Residual resistivity	ρ_R		$\Omega \cdot m$
Relaxation time	τ	$\tau = l/v_F$	s
Lorenz coefficient	L	$L = \lambda/\sigma T$	$V^2 \cdot K^{-2}$
Hall coefficient	A_H, R_H	$E = \rho \cdot j + R_H(B \times j)$	$m^3 \cdot C^{-1}$
Thermoelectric force	E		V
Peltier coefficient	Π		V
Thomson coefficient	μ, (τ)		$V \cdot K^{-1}$
Work function	Φ	$\Phi = E_\infty - E_F$	J
Number density, number concentration	n, (p)		m^{-3}
Gap energy	E_g		J
Donor ionization energy	E_d		J
Acceptor ionization energy	E_a		J
Fermi energy	E_F, ε_F		J
Circular wave vector, propagation vector	k, q	$k = 2\pi/\lambda$	m^{-1}
Bloch function	$u_k(r)$	$\psi(r) = u_k(r) \exp(ik \cdot r)$	$m^{-3/2}$
Charge density of electrons	ρ	$\rho(r) = -e\psi^*(r)\psi(r)$	$C \cdot m^{-3}$
Effective mass	m^*		kg
Mobility	m	$\mu = v_{\text{drift}}/E$	$m^2 \cdot V^{-1} \cdot s^{-1}$
Mobility ratio	b	$b = \mu_n/\mu_p$	1
Diffusion coefficient	D	$dN/dt = -DA(dn/dx)$	$m^2 \cdot s^{-1}$
Diffusion length	L	$L = \sqrt{D\tau}$	m
Characteristic (Weiss) temperature	ϕ, ϕ_w		K
Curie temperature	T_c		K
Neel temperature	T_N		K

Elementary Algebra and Geometry

Fundamental Properties (Real Numbers)

$a + b = b + a$	Commutative law for addition
$(a + b) + c = a + (b + c)$	Associative law for addition
$a + 0 = 0 + a$	Identity law for addition
$a + (-a) = (-a) + a = 0$	Inverse law for addition
$a(bc) = (ab)c$	Associative law for multiplication
$a\left(\frac{1}{a}\right) = \left(\frac{1}{a}\right)a = 1, a \neq 0$	Inverse law for multiplication
$(a)(1) = (1)(a) = a$	Identity law for multiplication
$ab = ba$	Commutative law for multiplication
$a(b + c) = ab + ac$	Distributive law

Division by zero is not defined.

Exponents

For integers m and n,

$$a^n a^m = a^{n+m}$$

$$a^n / a^m = a^{n-m}$$

$$\left(a^n\right)^m = a^{nm}$$

$$(ab)^m = a^m b^m$$

$$(a/b)^m = a^m / b^m$$

Fractional Exponents

$$a^{p/q} = \left(a^{1/q}\right)^p$$

where $a^{1/q}$ is the positive qth root of a if $a > 0$ and the negative qth root of a if a is negative and q is odd. Accordingly, the five rules of exponents given above (for integers) are also valid if m and n are fractions, provided a and b are positive.

Irrational Exponents

If an exponent is irrational (e.g., $\sqrt{2}$), the quantity, such as $a^{\sqrt{2}}$, is the limit of the sequence $a^{1.4}$, $a^{1.41}$, $a^{1.414}$,…

Operations with Zero

$$0^m = 0 \qquad a^0 = 1$$

Logarithms

If x, y, and b are positive $b \neq 1$,

$$\log_b(xy) = \log_b x + \log_b y$$

$$\log_b(x/y) = \log_b x - \log_b y$$

$$\log_b x^p = p \log_b x$$

$$\log_b(1/x) = -\log_b x$$

$$\log_b b = 1$$

$$\log_b 1 = 0 \qquad \textit{Note}: b^{\log_b x} = x$$

Change of Base ($a \neq 1$)

$$\log_b x = \log_a x \log_b a$$

Factorials

The factorial of a positive integer n is the product of all the positive integers less than or equal to the integer n and is denoted $n!$. Thus,

$$n! = 1 \cdot 2 \cdot 3 \cdot \cdots \cdot n$$

Factorial 0 is defined: $0! = 1$.

Stirling's Approximation

$$\lim_{n\to\infty}\left(n/e^n\right)^n \sqrt{2\pi n} = n!$$

Binomial Theorem

For positive integer n

$$\left(x+y\right)^n = x^n + nx^{n-1}y + \frac{n(n-1)}{2!}x^{n-2}y^2 + \frac{n(n-1)(n-2)}{3!}x^{n-3}y^3 + \cdots + nxy^{n-1} + y^n$$

Factors and Expansion

$$(a+b)^2 = a^2 + 2ab + b^2$$

$$(a-b)^2 = a^2 - 2ab + b^2$$

$$(a+b)^3 = a^3 + 3a^2b + 3ab^2 + b^3$$

$$(a-b)^3 = a^3 - 3a^2b + 3ab^2 - b^3$$

$$\left(a^2 - b^2\right) = (a-b)(a+b)$$

$$\left(a^3 - b^3\right) = (a-b)\left(a^2 + ab + b^2\right)$$

$$\left(a^3 + b^3\right) = (a+b)\left(a^2 - ab + b^2\right)$$

Progression

An *arithmetic progression* is a sequence in which the difference between any term and the preceding term is a constant (d):

$$a, a+d, a+2d, \ldots, a+(n-1)d$$

If the last term is denoted l [$= a + (n-1)d$], then the sum is

$$s = \frac{n}{2}(a+l)$$

A *geometric progression* is a sequence in which the ratio of any term to the preceding term is a constant r. Thus, for n terms,

$$a, ar, ar^2, \ldots, ar^{n-1}$$

The sum is

$$S = \frac{a - ar^n}{1 - r}$$

Complex Numbers

A complex number is an ordered pair of real numbers (a, b).

Equality: $(a,b) = (c,d)$ if and only if $a = c$ and $b = d$

Addition: $(a,b) + (c,d) = (a+c, b+d)$

Multiplication: $(a,b)(c,d) = (ac - bd, ad + bc)$

The first element (a, b) is called the *real* part, the second the *imaginary* part. An alternative notation for (a, b) is $a + bi$, where $i^2 = (-1, 0)$, and $i = (0, 1)$ or $0 + 1i$ is written for this complex number as a convenience. With this understanding, i behaves as a number, that is, $(2 - 3i)(4 + i) = 8 + 2i - 12i - 3i^2 = 11 - 10i$. The conjugate of a $a + bi$ is $a - bi$, and the product of a complex number and its conjugate is $a^2 + b^2$. Thus, *quotients* are computed by multiplying numerator and denominator by the conjugate of the denominator, as illustrated below:

$$\frac{2+3i}{4+2i} = \frac{(4-2i)(2+3i)}{(4-2i)(4+2i)} = \frac{14+8i}{20} = \frac{7+4i}{10}$$

Polar Form

The complex number $x + iy$ may be represented by a plane vector with components x and y:

$$x + iy = r(\cos\theta + i\sin\theta)$$

(See Figure 19.1.1.). Then, given two complex numbers $z_1 = \tau_1(\cos\theta_1 + i\sin\theta_1)$ and $z_2 = \tau_2(\cos\theta_2 + i\sin\theta_2)$, the product and quotient are:

Product: $z_1 z_2 = r_1 r_2\left[\cos(\theta_1 + \theta_2) + i\sin(\theta_1 + \theta_2)\right]$

Quotient: $z_1/z_2 = (r_1/r_2)\left[\cos(\theta_1 - \theta_2) + i\sin(\theta_1 - \theta_2)\right]$

Powers: $z^n = \left[r(\cos\theta + i\sin\theta)\right]^n = r^n[\cos n\theta + i\sin n\theta]$

Roots:
$$z^{1/n} = \left[r(\cos\theta + i\sin\theta)\right]^{1/n} = r^{1/n}\left[\cos\frac{\theta + k\cdot 360}{n} + i\sin\frac{\theta + k\cdot 360}{n}\right]$$

$$k = 0, 1, 2, \ldots, n-1$$

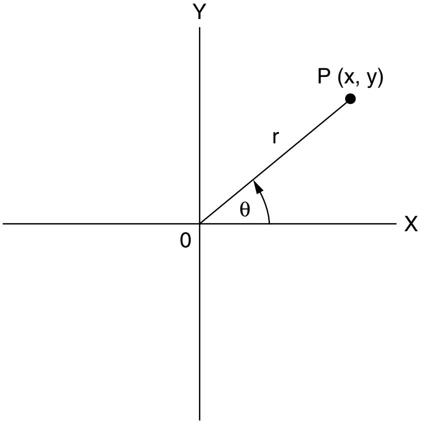

FIGURE 19.1.1 Polar form of complex number.

Permutations

A permutation is an ordered arrangement (sequence) of all or part of a set of objects. The number of permutations of n objects taken r at a time is

$$\begin{aligned} p(n,r) &= n(n-1)(n-2)\cdots(n-r+1) \\ &= \frac{n!}{(n-r)!} \end{aligned}$$

A permutation of positive integers is "even" or "odd" if the total number of inversions is an even integer or an odd integer, respectively. Inversions are counted relative to each integer j in the permutation by counting the number of integers that follow j and are less than j. These are summed to give the total number of inversions. For example, the permutation 4132 has four inversions: three relative to 4 and one relative to 3. This permutation is therefore even.

Combinations

A combination is a selection of one or more objects from among a set of objects regardless of order. The number of combinations of n different objects taken r at a time is

$$C(n,r) = \frac{P(n,r)}{r!} = \frac{n!}{r!(n-r)!}$$

Algebraic Equations

Quadratic

If $ax^2 + bx + c = 0$, and $a \neq 0$, then roots are

$$x = \frac{-b \pm \sqrt{b^2 - 4ac}}{2a}$$

Cubic

To solve $\mathbf{x}^2 + bx^2 + cx + d = 0$, let $x = y - b/3$. Then the *reduced cubic* is obtained:

$$y^3 + py + q = 0$$

where $p = c - (1/3)b^2$ and $q = d - (1/3)bc + (2/27)b^3$. Solutions of the original cubic are then in terms of the reduced curbic roots y_1, y_2, y_3:

$$x_1 = y_1 - (1/3)b \qquad x_2 = y_2 - (1/3)b \qquad x_3 = y_3 - (1/3)b$$

The three roots of the reduced cubic are

$$y_1 = (A)^{1/3} + (B)^{1/3}$$

$$y_2 = W(A)^{1/3} + W^2(B)^{1/3}$$

$$y_3 = W^2(A)^{1/3} + W(B)^{1/3}$$

where

$$A = -\tfrac{1}{2}q + \sqrt{(1/27)p^3 + \tfrac{1}{4}q^2}$$

$$B = -\tfrac{1}{2}q - \sqrt{(1\ 27)p^3 + \tfrac{1}{4}q^2}$$

$$W = \frac{-1 + i\sqrt{3}}{2}, \qquad W^2 = \frac{-1 - i\sqrt{3}}{2}$$

When $(1/27)p^3 + (1/4)q^2$ is negative, A is complex; in this case A should be expressed in trigonometric form: $A = r(\cos\theta + i\sin\theta)$ where θ is a first or second quadrant angle, as q is negative or positive. The three roots of the reduced cubic are

$$y_1 = 2(r)^{1/3}\cos(\theta/3)$$

$$y_2 = 2(r)^{1/3}\cos\left(\frac{\theta}{3} + 120°\right)$$

$$y_3 = 2(r)^{1/3}\cos\left(\frac{\theta}{3} + 240°\right)$$

Geometry

Figure 19.1.2 to Figure 19.1.12 are a collection of common geometric figures. Area (A), volume (V), and other measurable features are indicated.

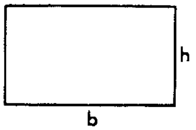

FIGURE 19.1.2 Rectangle. $A = bh$.

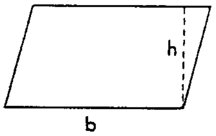

FIGURE 19.1.3 Parallelogram. $A = bh$.

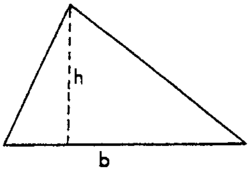

FIGURE 19.1.4 Triangle. $A = 1/2\ bh$.

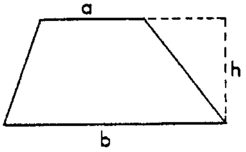

FIGURE 19.1.5 Trapezoid. $A = 1/2\ (a + b)h$.

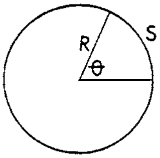

FIGURE 19.1.6 Circle. $A = \pi R^2$; circumference = $2\pi R$, arc length $S = R\ \theta$ (θ in radians).

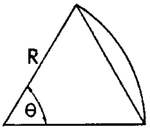

FIGURE 19.1.7 Sector of circle. $A_{\text{sector}} = 1/2R^2\theta$; $A_{\text{segment}} = 1/2R^2\ (\theta - \sin\theta)$.

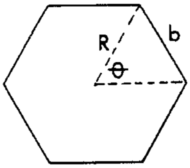

FIGURE 19.1.8 Regular polygon of n sides. $A = (n/4)b^2\ \mathrm{ctn}(\pi/n)$; $R = (b/2)\ \csc(\pi/n)$.

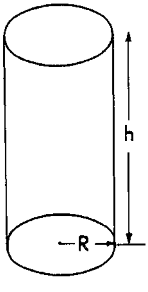

FIGURE 19.1.9 Right circular cylinder. $V = \pi R^2 h$; lateral surface area = $2\pi Rh$.

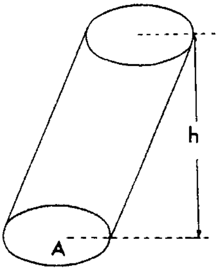

FIGURE 19.1.10 Cylinder (or prism) with parallel bases. $V = Ah$.

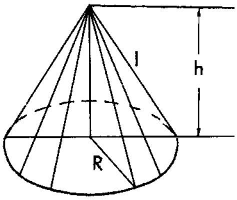

FIGURE 19.1.11 Right circular cone. $V = 1/3\ \pi R^2 h$; lateral surface area $= \pi R l = \pi R\sqrt{R^2 + h^2}$.

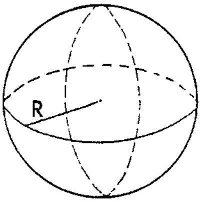

FIGURE 19.1.12 Sphere $V = 4/3\ \pi R^3$; surface area $= 4\pi R^2$.

Table of Derivatives

In the following table, *a* and *n* are constants, *e* is the base of the natural logarithms, and *u* and *v* denote functions of *x*.

Additional Relations with Derivatives

$$\frac{d}{dt}\int_a^t f(x)\,dx = f(t) \qquad \frac{d}{dt}\int_t^a f(x)\,dx = -f(t)$$

If $x = f(y)$, then $\dfrac{dy}{dx} = \dfrac{1}{dx/dy}$

If $y = f(u)$ and $u = g(x)$, then $\dfrac{dy}{dx} = \dfrac{dy}{du}\cdot\dfrac{du}{dx}$ (chain rule)

If $x = f(t)$ and $y = g(t)$, then $\dfrac{dy}{dx} = \dfrac{g'(t)}{f'(t)}$, and $\dfrac{d^2y}{dx^2} = \dfrac{f'(t)g''(t) - g'(t)f''(t)}{\left[f'(t)\right]^3}$

(Note: Exponent in denominator is 3.)

1. $\dfrac{d}{dx}(a) = 0$

2. $\dfrac{d}{dx}(x) = 1$

3. $\dfrac{d}{dx}(au) = a\dfrac{du}{dx}$

4. $\dfrac{d}{dx}(u+v) = \dfrac{du}{dx} + \dfrac{dv}{dx}$

5. $\dfrac{d}{dx}(uv) = u\dfrac{dv}{dx} + v\dfrac{du}{dx}$

6. $\dfrac{d}{dx}(u/v) = \dfrac{v\dfrac{du}{dx} - u\dfrac{dv}{dx}}{v^2}$

7. $\dfrac{d}{dx}\left(u^n\right) = nu^{n-1}\dfrac{du}{dx}$

8. $\dfrac{d}{dx}e^u = e^u\dfrac{du}{dx}$

9. $\dfrac{d}{dx}a^u = \left(\log_e a\right)a^u\dfrac{du}{dx}$

10. $\dfrac{d}{dx}\log_e u = (1/u)\dfrac{du}{dx}$

11. $\dfrac{d}{dx}\log_a u = \left(\log_a e\right)(1/u)\dfrac{du}{dx}$

12. $\dfrac{d}{dx}u^v = vu^{v-1}\dfrac{du}{dx} + u^v\left(\log_e u\right)\dfrac{dv}{dx}$

13. $\dfrac{d}{dx}\sin u = \cos u\dfrac{du}{dx}$

14. $\dfrac{d}{dx}\cos u = -\sin u\dfrac{du}{dx}$

15. $\dfrac{d}{dx}\tan u = \sec^2 u\dfrac{du}{dx}$

16. $\dfrac{d}{dx}\operatorname{ctn} u = -\csc^2 u\dfrac{du}{dx}$

17. $\dfrac{d}{dx}\sec u = \sec u\tan u\dfrac{du}{dx}$

18. $\dfrac{d}{dx}\csc u = -\csc u\operatorname{ctn} u\dfrac{du}{dx}$

19. $\dfrac{d}{dx}\sin^{-1} u = \dfrac{1}{\sqrt{1-u^2}}\dfrac{du}{dx}, \quad \left(-\tfrac{1}{2}\pi \le \sin^{-1} u \le \tfrac{1}{2}\pi\right)$

20. $\dfrac{d}{dx}\cos^{-1} u = \dfrac{-1}{\sqrt{1-u^2}}\dfrac{du}{dx}, \quad \left(0 \le \cos^{-1} u \le \pi\right)$

21. $\dfrac{d}{dx}\tan^{-1} u = \dfrac{1}{1+u^2}\dfrac{du}{dx}$

22. $\dfrac{d}{dx}\operatorname{ctn}^{-1} u = \dfrac{-1}{1+u^2}\dfrac{du}{dx}$

23. $\dfrac{d}{dx}\sec^{-1} u = \dfrac{1}{u\sqrt{u^2-1}}\dfrac{du}{dx},$

$\left(-\pi \le \sec^{-1} u < -\tfrac{1}{2}\pi;\quad 0 \le \sec^{-1} u \le \tfrac{1}{2}\pi\right)$

24. $\dfrac{d}{dx}\csc^{-1} u = \dfrac{-1}{u\sqrt{u^2-1}}\dfrac{du}{dx},$

$\left(-\pi < \csc^{-1} u \le -\tfrac{1}{2}\pi;\quad 0 < \csc^{-1} u \le \tfrac{1}{2}\pi\right)$

25. $\dfrac{d}{dx}\sinh u = \cosh u\dfrac{du}{dx}$

26. $\dfrac{d}{dx}\cosh u = \sinh u\dfrac{du}{dx}$

27. $\dfrac{d}{dx}\tanh u = \operatorname{sech}^2 u\dfrac{du}{dx}$

28. $\dfrac{d}{dx}\operatorname{ctnh} u = -\operatorname{csch}^2 u\dfrac{du}{dx}$

29. $\dfrac{d}{dx}\operatorname{sech} u = -\operatorname{sech} u\tanh u\dfrac{du}{dx}$

30. $\dfrac{d}{dx}\operatorname{csch} u = -\operatorname{csch} u\operatorname{ctnh} u\dfrac{du}{dx}$

31. $\dfrac{d}{dx}\sin^{-1} u = \dfrac{1}{\sqrt{u^2+1}}\dfrac{du}{dx}$

32. $\dfrac{d}{dx}\cosh^{-1} u = \dfrac{1}{\sqrt{u^2-1}}\dfrac{du}{dx}$

33. $\dfrac{d}{dx}\tanh^{-1} u = \dfrac{1}{1-u^2}\dfrac{du}{dx}$

34. $\dfrac{d}{dx}\operatorname{ctnh}^{-1} u = \dfrac{-1}{u^2-1}\dfrac{du}{dx}$

35. $\dfrac{d}{dx}\operatorname{sech}^{-1} u = \dfrac{-1}{u\sqrt{1-u^2}}\dfrac{du}{dx}$

36. $\dfrac{d}{dx}\operatorname{csch}^{-1} u = \dfrac{-1}{u\sqrt{u^2+1}}\dfrac{du}{dx}$

Integrals

Elementary Forms (Add an arbitrary constant to each integral)

1. $\int a\,dx = ax$

2. $\int a \cdot f(x)\,dx = a\int f(x)\,dx$

3. $\int \phi(y)\,dx = \int \frac{\phi(y)}{y'}\,dy, \quad \text{where } y' = \frac{dy}{dx}$

4. $\int (u+v)\,dx = \int u\,dx + \int v\,dx, \quad \text{where } u \text{ and } v \text{ are any functions of } x$

5. $\int u\,dv = u\int dv - \int v\,du = uv - \int v\,du$

6. $\int u\frac{dv}{dx}\,dx = uv - \int v\frac{du}{dx}\,dx$

7. $\int x^n\,dx = \frac{x^{n+1}}{n+1}, \quad \text{except } n = -1$

8. $\int \frac{f'(x)\,dx}{f(x)} = \log f(x), \quad [df(x) = f'(x)\,dx]$

9. $\int \frac{dx}{x} = \log x$

10. $\int \frac{f'(x)\,dx}{2\sqrt{f(x)}} = \sqrt{f(x)}, \quad [df(x) = f'(x)\,dx]$

11. $\int e^x\,dx = e^x$

12. $\int e^{ax}\,dx = e^{ax}/a$

13. $\int b^{ax}\,dx = \frac{b^{ax}}{a\log b}, \quad (b > 0)$

14. $\int \log x\,dx = x\log x - x$

15. $\int a^x \log a\,dx = a^x, \quad (a > 0)$

16. $\int \frac{dx}{a^2+x^2} = \frac{1}{a}\tan^{-1}\frac{x}{a}$

17. $$\int \frac{dx}{a^2-x^2} = \begin{cases} \frac{1}{a}\tan^{-1}\frac{x}{a} \\ \quad\text{or} \\ \frac{1}{2a}\log\frac{a+x}{a-x}, \quad (a^2 > x^2) \end{cases}$$

18. $$\int \frac{dx}{x^2-a^2} = \begin{cases} -\frac{1}{a}\operatorname{ctnh}^{-1}\frac{x}{a} \\ \quad\text{or} \\ \frac{1}{2a}\log\frac{x-a}{x+a}, \quad (x^2 > a^2) \end{cases}$$

19. $$\int \frac{dx}{\sqrt{a^2 - x^2}} = \begin{cases} \sin^{-1} \dfrac{x}{|a|} \\ \qquad \text{or} \\ -\cos^{-1} \dfrac{x}{|a|}, \quad \left(a^2 > x^2\right) \end{cases}$$

20. $$\int \frac{dx}{\sqrt{x^2 \pm a^2}} = \log\left(x + \sqrt{x^2 \pm a^2}\right)$$

21. $$\int \frac{dx}{x\sqrt{x^2 - a^2}} = \frac{1}{|a|} \sec^{-1} \frac{x}{|a|}$$

22. $$\int \frac{dx}{x\sqrt{a^2 \pm x^2}} = -\frac{1}{a} \log\left(\frac{a + \sqrt{a^2 \pm x^2}}{x}\right)$$

Forms Containing $(a + bx)$

For forms containing $a + bx$, but not listed in the table, the substitution $u = (a + bx)\, x$ may prove helpful.

23. $$\int (a + bx)^n \, dx = \frac{(a + bx)^{n+1}}{(n+1)b}, \quad (n \neq -1)$$

24. $$\int x(a + bx)^n \, dx = \frac{1}{b^2(n+2)}(a + bx)^{n+2} - \frac{a}{b^2(n+1)}(a + bx)^{n+1}, \quad (n \neq -1, -2)$$

25. $$\int x^2(a + bx)^n \, dx = \frac{1}{b^3}\left[\frac{(a + bx)^{n+3}}{n+3} - 2a\frac{(a + bx)^{n+2}}{n+2} + a^2\,\frac{(a + bx)^{n+1}}{n+1}\right]$$

26. $$\int x^m (a + bx)^n \, dx = \begin{cases} \dfrac{x^{m+1}(a + bx)^n}{m+n+1} + \dfrac{an}{m+n+1}\displaystyle\int x^m (a + bx)^{n-1} \, dx \\ \qquad\qquad \text{or} \\ \dfrac{1}{a(n+1)}\left[-x^{m+1}(a + bx)^{n+1} + (m+n+2)\displaystyle\int x^m (a + bx)^{n+1} \, dx\right] \\ \qquad\qquad \text{or} \\ \dfrac{1}{b(m+n+1)}\left[x^m (a + bx)^{n+1} - ma\displaystyle\int x^{m-1}(a + bx)^n \, dx\right] \end{cases}$$

27. $$\int \frac{dx}{a + bx} = \frac{1}{b}\log(a + bx)$$

28. $$\int \frac{dx}{(a + bx)^2} = -\frac{1}{b(a + bx)}$$

29. $$\int \frac{dx}{(a + bx)^3} = -\frac{1}{2b(a + bx)^2}$$

30. $$\int \frac{x\,dx}{a + bx} = \begin{cases} \dfrac{1}{b^2}\left[a + bx - a\log(a + bx)\right] \\ \qquad \text{or} \\ \dfrac{x}{b} - \dfrac{a}{b^2}\log(a + bx) \end{cases}$$

31. $$\int \frac{x\,dx}{(a + bx)^2} = \frac{1}{b^2}\left[\log(a + bx) + \frac{a}{a + bx}\right]$$

32. $\int \frac{x\,dx}{(a+bx)^n} = \frac{1}{b^2}\left[\frac{-1}{(n-2)(a+bx)^{n-2}} + \frac{a}{(n-1)(a+bx)^{n-1}}\right], \quad n \neq 1, 2$

33. $\int \frac{x^2\,dx}{a+bx} = \frac{1}{b^3}\left[\frac{1}{2}(a+bx)^2 - 2a(a+bx) + a^2 \log(a+bx)\right]$

34. $\int \frac{x^2\,dx}{(a+bx)^2} = \frac{1}{b^3}\left[a+bx - 2a\log(a+bx) - \frac{a^2}{a+bx}\right]$

35. $\int \frac{x^2\,dx}{(a+bx)^3} = \frac{1}{b^3}\left[\log(a+bx) + \frac{2a}{a+bx} - \frac{a^2}{2(a+bx)^2}\right]$

36. $\int \frac{x^2\,dx}{(a+bx)^n} = \frac{1}{b^3}\left[\frac{-1}{(n-3)(a+bx)^{n-3}} + \frac{2a}{(n-2)(a+bx)^{n-2}} - \frac{a}{(n-1)(a+bx)^{n-1}}\right], \quad n \neq 1, 2, 3$

37. $\int \frac{dx}{x(a+bx)} = -\frac{1}{a}\log\frac{a+bx}{x}$

38. $\int \frac{dx}{x(a+bx)^2} = \frac{1}{a(a+bx)} - \frac{1}{a^2}\log\frac{a+bx}{x}$

39. $\int \frac{dx}{x(a+bx)^3} = \frac{1}{a^3}\left[\frac{1}{2}\left(\frac{2a+bx}{a+bx}\right)^2 + \log\frac{x}{a+bx}\right]$

40. $\int \frac{dx}{x^2(a+bx)} = -\frac{1}{ax} + \frac{b}{a^2}\log\frac{a+bx}{x}$

41. $\int \frac{dx}{x^3(a+bx)} = \frac{2bx-a}{2a^2x^2} + \frac{b^2}{a^3}\log\frac{x}{a+bx}$

42. $\int \frac{dx}{x^2(a+bx)^2} = -\frac{a+2bx}{a^2x(a+bx)} + \frac{2b^2}{a^3}\log\frac{a+bx}{x}$

The Fourier Transforms

For a piecewise continuous function $F(x)$ over a finite interval $0 \le x \le \pi$, the *finite Fourier cosine transform* of $F(x)$ is

$$f_c(n) = \int_0^{\pi} F(x)\cos nx\,dx \quad (n = 0,\ 1,\ 2,\ \ldots) \tag{19.1.1}$$

If x ranges over the interval $0 \le x \le L$, the substitution $x' = \pi x/L$ allows the use of this definition also. The inverse transform is written

$$\bar{F}(x) = \frac{1}{\pi} f_c(0) + \frac{2}{\pi}\sum_{n=1}^{\infty} f_c(n)\cos nx \quad (0 < x < \pi) \tag{19.1.2}$$

where $\bar{F}(x) = [F(x+0) + F(x-0)]/2$. We observe that $\bar{F}(x) = F(x)$ at points of continuity. The formula

$$\begin{aligned} f_c^{(2)}(n) &= \int_0^{\pi} F''(x)\cos nx\,dx \\ &= -n^2 f_c(n) - F'(0) + (-1)^n F'(\pi) \end{aligned} \tag{19.1.3}$$

makes the finite Fourier cosine transform useful in certain boundary value problems.

Analogously, the *finite Fourier sine transform* of $F(x)$ is

$$f_s(n) = \int_0^\pi F(x)\sin nx\, dx \quad (n = 1,\ 2,\ 3,\ \ldots) \tag{19.1.4}$$

and

$$\bar{F}(x) = \frac{2}{\pi}\sum_{n=1}^{\infty} f_s(n)\sin nx \quad (0 < x < \pi) \tag{19.1.5}$$

Corresponding to Equation (19.1.6), we have

$$\begin{aligned} f_s^{(2)}(n) &= \int_0^\pi F''(x)\sin nx\, dx \\ &= -n^2 f_s(n) - nF(0) - n(-1)^n F(\pi) \end{aligned} \tag{19.1.6}$$

Fourier Transforms

If $F(x)$ is defined for $x \geq 0$ and is piecewise continuous over any finite interval, and if

$$\int_0^\infty F(x)\, dx$$

is absolutely convergent, then

$$f_c(\alpha) = \sqrt{\frac{2}{\pi}}\int_0^\infty F(x)\cos(\alpha x)\, dx \tag{19.1.7}$$

is the *Fourier cosine transform* of $F(x)$. Furthermore,

$$\bar{F}(x) = \sqrt{\frac{2}{\pi}}\int_0^\infty f_c(\alpha)\cos(\alpha x)\, d\alpha \tag{19.1.8}$$

If $\lim_{x\to\infty} d^nF/dx^n = 0$, an important property of the Fourier cosine transform,

$$\begin{aligned} f_c^{(2r)}(\alpha) &= \sqrt{\frac{2}{\pi}}\int_0^\infty \left(\frac{d^{2r}F}{dx^{2r}}\right)\cos(\alpha x)\, dx \\ &= -\sqrt{\frac{2}{\pi}}\sum_{n=0}^{r-1}(-1)^n a_{2r-2n-1}\alpha^{2n} + (-1)^r \alpha^{2r} f_c(\alpha) \end{aligned} \tag{19.1.9}$$

where $\lim_{x\to 0} d^rF/dx^r = a_r$, makes it useful in the solution of many problems.

Under the same conditions,

$$f_s(\alpha) = \sqrt{\frac{2}{\pi}}\int_0^\infty F(x)\sin(\alpha x)\, dx \tag{19.1.10}$$

defines the *Fourier sine transform* of *F(x)*, and

$$\bar{F}(x) = \sqrt{\frac{2}{\pi}} \int_0^\infty f_s(\alpha) \sin(\alpha x)\, d\alpha \tag{19.1.11}$$

Corresponding to Equation (19.1.9) we have

$$\begin{aligned} f_s^{(2r)}(\alpha) &= \sqrt{\frac{2}{\pi}} \int_0^\infty \frac{d^{2r}F}{dx^{2r}} \sin(\alpha x)\, dx \\ &= -\sqrt{\frac{2}{\pi}} \sum_{n=1}^{r} (-1)^n \alpha^{2n-1} a_{2r-2n} + (-1)^{r-1} \alpha^{2r} f_s(\alpha) \end{aligned} \tag{19.1.12}$$

Similarly, if *F(x)* is defined for $-\infty < x < \infty$, and if $\int_{-\infty}^{\infty} F(x)\, dx$ is absolutely convergent, then

$$f(x) = \frac{1}{\sqrt{2\pi}} \int_{-\infty}^{\infty} F(x) e^{i\alpha x}\, dx \tag{19.1.13}$$

is the *Fourier transform* of *F(x)*, and

$$\bar{F}(x) = \frac{1}{\sqrt{2\pi}} \int_{-\infty}^{\infty} f(\alpha) e^{-i\alpha x}\, d\alpha \tag{19.1.14}$$

Also, if

$$\lim_{|x|\to\infty} \left| \frac{d^n F}{dx^n} \right| = 0 \quad (n = 1,\ 2,\ \ldots,\ r-1)$$

then

$$f^{(r)}(\alpha) = \frac{1}{\sqrt{2\pi}} \int_{-\infty}^{\infty} F^{(r)}(x) e^{i\alpha x}\, dx = (-i\alpha)^r f(\alpha) \tag{19.1.15}$$

Finite Sine Transforms

	$f_s(n)$	$F(x)$
1.	$f_s(n)=\int_0^\pi F(x)\sin nx\,dx \quad (n=1,\ 2,\ \ldots)$	$F(x)$
2.	$(-1)^{n+1} f_s(n)$	$F(\pi-x)$
3.	$\frac{1}{n}$	$\frac{\pi-x}{\pi}$
4.	$\frac{(-1)^{n+1}}{n}$	$\frac{x}{\pi}$
5.	$\frac{1-(-1)^n}{n}$	1
6.	$\frac{2}{n^2}\sin\frac{n\pi}{2}$	$\begin{cases} x & \text{when } 0<x<\pi/2 \\ \pi-x & \text{when } \pi/2<x<\pi \end{cases}$
7.	$\frac{(-1)^{n+1}}{n^3}$	$\frac{x(\pi^2-x^2)}{6\pi}$
8.	$\frac{1-(-1)^n}{n^3}$	$\frac{x(\pi-x)}{2}$
9.	$\frac{\pi^2(-1)^{n-1}}{n}-\frac{2[1-(-1)^n]}{n^3}$	x^2
10.	$\pi(-1)^n\left(\frac{6}{n^3}-\frac{\pi^2}{n}\right)$	x^3
11.	$\frac{n}{n^2+c^2}\left[1-(-1)^n e^{c\pi}\right]$	e^{cx}
12.	$\frac{n}{n^2+c^2}$	$\frac{\sinh c(\pi-x)}{\sinh c\pi}$
13.	$\frac{n}{n^2-k^2} \quad (k\neq 0,\ 1,\ 2,\ \ldots)$	$\frac{\sinh k(\pi-x)}{\sinh k\pi}$
14.	$\begin{cases} \frac{\pi}{2} & \text{when } n=m \\ 0 & \text{when } n\neq m \end{cases} \quad (m=1,\ 2,\ \ldots)$	$\sin mx$
15.	$\frac{n}{n^2-k^2}\left[1-(-1)^n\cos k\pi\right] \quad (k\neq 1,\ 2,\ \ldots)$	$\cos kx$
16.	$\begin{cases} \frac{n}{n^2-m^2}\left[1-(-1)^{n+m}\right] & \text{when } n\neq m=1,\ 2,\ \ldots \\ 0 & \text{when } n=m \end{cases}$	$\cos mx$
17.	$\frac{n}{(n^2-k^2)^2} \quad (k\neq 0,\ 1,\ 2,\ \ldots)$	$\frac{\pi\sin kx}{2k\sin^2 kx}-\frac{x\cos k(\pi-x)}{2k\sin k\pi}$
18.	$\frac{b^n}{n} \quad (\lvert b\rvert\leq 1)$	$\frac{2}{\pi}\arctan\frac{b\sin x}{1-b\cos x}$
19.	$\frac{1-(-1)^n}{n}b^n \quad (\lvert b\rvert\leq 1)$	$\frac{2}{\pi}\arctan\frac{2b\sin x}{1-b^2}$

Finite Cosine Transforms

$f_c(n)$	$F(x)$
1. $f_c(n) = \int_0^\pi F(x) \cos nx \, dx \quad (n = 0, 1, 2, \ldots)$	$F(x)$
2. $(-1)^n f_c(n)$	$F(\pi - x)$
3. 0 when $n = 1, 2, \ldots; \quad f_c(0) = \pi$	1
4. $\frac{2}{n} \sin \frac{n\pi}{2}; \quad f_c(0) = 0$	$\begin{cases} 1 & \text{when } 0 < x < \pi/2 \\ -1 & \text{when } \pi/2 < x < \pi \end{cases}$
5. $-\frac{1-(-1)^n}{n^2}; \quad f_c(0) = \frac{\pi^2}{2}$	x
6. $\frac{(-1)^n}{n^2}; \quad f_c(0) = \frac{\pi^2}{6}$	$\frac{x^2}{2\pi}$
7. $\frac{1}{n^2}; \quad f_c(0) = 0$	$\frac{(\pi - x)^2}{2\pi} - \frac{\pi}{6}$
8. $3\pi^2 \frac{(-1)^n}{n^2} - 6 \frac{1-(-1)^n}{n^4}; \quad f_c(0) = \frac{\pi^4}{4}$	x^3
9. $\frac{(-1)^n e^c \pi - 1}{n^2 + c^2}$	$\frac{1}{c} e^{cx}$
10. $\frac{1}{n^2 + c^2}$	$\frac{\cosh c(\pi - x)}{c \sinh c\pi}$
11. $\frac{k}{n^2 - k^2}\left[(-1)^n \cos \pi k - 1\right] \quad (k \neq 0, 1, 2, \ldots)$	$\sin kx$
12. $\frac{(-1)^{n+m} - 1}{n^2 - m^2}; \quad f_c(m) = 0 \quad (m = 1, 2, \ldots)$	$\frac{1}{m} \sin mx$
13. $\frac{1}{n^2 - k^2} \quad (k \neq 0, 1, 2, \ldots)$	$-\frac{\cos k(\pi - x)}{k \sin k\pi}$
14. 0 when $n = 1, 2, \ldots; \quad f_c(m) = \frac{\pi}{2} \quad (m = 1, 2, \ldots)$	$\cos mx$

Fourier Sine Transforms

F(x)	$f_s(\alpha)$
1. $\begin{cases} 1 & (0 < x < a) \\ 0 & (x > a) \end{cases}$	$\sqrt{\frac{2}{\pi}} \left[\frac{1 - \cos \alpha}{\alpha}\right]$
2. $x^{p-1} \quad (0 < p < 1)$	$\sqrt{\frac{2}{\pi}} \frac{\Gamma(p)}{\alpha^p} \sin \frac{p\pi}{2}$
3. $\begin{cases} \sin x & (0 < x < a) \\ 0 & (x > a) \end{cases}$	$\frac{1}{\sqrt{2\pi}} \left[\frac{\sin[a(1-\alpha)]}{1-\alpha} - \frac{\sin[a(1+\alpha)]}{1+\alpha}\right]$
4. e^{-x}	$\sqrt{\frac{2}{\pi}} \left[\frac{\alpha}{1+\alpha^2}\right]$
5. $xe^{-x^2/2}$	$\alpha e^{-\alpha^2/2}$

F(**x**)	$f_s(\alpha)$
6. $\cos\frac{x^2}{2}$	$\sqrt{2}\left[\sin\frac{\alpha^2}{2}C\left(\frac{\alpha^2}{2}\right)-\cos\frac{\alpha^2}{2}S\left(\frac{\alpha^2}{2}\right)\right]^*$
7. $\sin\frac{x^2}{2}$	$\sqrt{2}\left[\cos\frac{\alpha^2}{2}C\left(\frac{\alpha^2}{2}\right)+\sin\frac{\alpha^2}{2}S\left(\frac{\alpha^2}{2}\right)\right]^*$

* $C(y)$ and $S(y)$ are the Fresnel integrals

$$C(y)=\frac{1}{\sqrt{2\pi}}\int_0^y\frac{1}{\sqrt{t}}\cos t\,dt$$

$$S(y)=\frac{1}{\sqrt{2\pi}}\int_0^y\frac{1}{\sqrt{t}}\sin t\,dt$$

Fourier Cosine Transforms

$F(x)$	$f_c(\alpha)$
1. $\begin{cases}1 & (0<x<a)\\0 & (x>a)\end{cases}$	$\sqrt{\frac{2}{\pi}}\frac{\sin a\alpha}{\alpha}$
2. $x^{p-1}\quad(0<p<1)$	$\sqrt{\frac{2}{\pi}}\frac{\Gamma(p)}{\alpha^p}\cos\frac{p\pi}{2}$
3. $\begin{cases}\cos x & (0<x<a)\\0 & (x>a)\end{cases}$	$\frac{1}{\sqrt{2\pi}}\left[\frac{\sin[a(1-\alpha)]}{1-\alpha}+\frac{\sin[a(1+\alpha)]}{1+\alpha}\right]$
4. e^{-x}	$\sqrt{\frac{2}{\pi}}\left(\frac{1}{1+\alpha^2}\right)$
5. $e^{-x^2/2}$	$e^{-\alpha^2/2}$
6. $\cos\frac{x^2}{2}$	$\cos\left(\frac{\alpha^2}{2}-\frac{\pi}{4}\right)$
7. $\sin\frac{x^2}{2}$	$\cos\left(\frac{\alpha^2}{2}-\frac{\pi}{4}\right)$

Fourier Transforms

	$F(x)$	$f(\alpha)$
1.	$\dfrac{\sin ax}{x}$	$\begin{cases} \sqrt{\dfrac{\pi}{2}} & \lvert\alpha\rvert < a \\ 0 & \lvert\alpha\rvert > a \end{cases}$
2.	$\begin{cases} e^{iwx} & (p < x < q) \\ 0 & (x < p, x > q) \end{cases}$	$\dfrac{i}{\sqrt{2\pi}} \dfrac{e^{ip(w+\alpha)} - e^{iq(w+\alpha)}}{(w+\alpha)}$
3.	$\begin{cases} e^{-cx+iwx} & (x > 0) \\ 0 & (x < 0) \end{cases} \quad (c > 0)$	$\dfrac{i}{\sqrt{2\pi}(w+\alpha+ic)}$
4.	$e^{-px^2} \quad R(p) > 0$	$\dfrac{1}{\sqrt{2p}} e^{-\alpha^2/4p}$
5.	$\cos px^2$	$\dfrac{1}{\sqrt{2p}} \cos\left[\dfrac{\alpha^2}{4p} - \dfrac{\pi}{4}\right]$
6.	$\sin px^2$	$\dfrac{1}{\sqrt{2p}} \cos\left[\dfrac{\alpha^2}{4p} + \dfrac{\pi}{4}\right]$
7.	$\lvert x\rvert^{-p} \quad (0 < p < 1)$	$\sqrt{\dfrac{2}{\pi}} \dfrac{\Gamma(1-p)\sin\dfrac{p\pi}{2}}{\lvert\alpha\rvert^{(1-p)}}$
8.	$\dfrac{e^{-a\lvert x\rvert}}{\sqrt{\lvert x\rvert}}$	$\dfrac{\sqrt{\sqrt{(a^2+\alpha^2)}+a}}{\sqrt{a^2+\alpha^2}}$
9.	$\dfrac{\cosh ax}{\cosh \pi x} \quad (-\pi < a < \pi)$	$\sqrt{\dfrac{2}{\pi}} \dfrac{\cos\dfrac{a}{2}\cosh\dfrac{\alpha}{2}}{\cosh\alpha + \cos a}$
10.	$\dfrac{\sinh ax}{\sinh \pi x} \quad (-\pi < a < \pi)$	$\dfrac{1}{\sqrt{2\pi}} \dfrac{\sin a}{\cosh\alpha + \cos a}$
11.	$\begin{array}{ll} \dfrac{1}{\sqrt{a^2-x^2}} & (\lvert x\rvert < a) \\ 0 & (\lvert x\rvert > a) \end{array}$	$\sqrt{\dfrac{\pi}{2}} J_0(a\alpha)$
12.	$\dfrac{\sin\left[b\sqrt{a^2+x^2}\right]}{\sqrt{a^2+x^2}}$	$\begin{cases} 0 & (\lvert\alpha\rvert > b) \\ \sqrt{\dfrac{\pi}{2}} J_0\left(\sqrt{b^2-\alpha^2}\right) & (\lvert\alpha\rvert < b) \end{cases}$
13.	$\begin{cases} P_n(x) & (\lvert x\rvert < 1) \\ 0 & (\lvert x\rvert > 1) \end{cases}$	$\dfrac{i^n}{\sqrt{\alpha}} j_{n+1/2}(\alpha)$
14.	$\begin{cases} \dfrac{\cos\left[b\sqrt{a^2-x^2}\right]}{\sqrt{a^2-x^2}} & (\lvert x\rvert < a) \\ 0 & (\lvert x\rvert > a) \end{cases}$	$\sqrt{\dfrac{\pi}{2}} J_0\left(a\sqrt{a^2+b^2}\right)$
15.	$\begin{cases} \dfrac{\cosh\left[b\sqrt{a^2-x^2}\right]}{\sqrt{a^2-x^2}} & (\lvert x\rvert < a) \\ 0 & (\lvert x\rvert > a) \end{cases}$	$\sqrt{\dfrac{\pi}{2}} J_0\left(a\sqrt{a^2-b^2}\right)$

The following functions appear among the entries of the tables on transforms.

Function	Definition	Name
$\mathrm{Ei}(x)$	$\int_{-\infty}^{x} \frac{e^{v}}{v}\,dv$; or sometimes defined as $-\mathrm{Ei}(-x) = \int_{x}^{\infty} \frac{e^{-v}}{v}\,dv$	Exponential integral function
$\mathrm{Si}(x)$	$\int_{0}^{x} \frac{\sin v}{v}\,dv$	Sine integral function
$\mathrm{Ci}(x)$	$\int_{\infty}^{x} \frac{\cos v}{v}\,dv$; or sometimes defined as negative of this integral	Cosine integral function
$\mathrm{erf}(x)$	$\frac{2}{\sqrt{\pi}} \int_{0}^{x} e^{-v^2}\,dv$	Error function
$\mathrm{erfc}(x)$	$1 - erf(x) = \frac{2}{\sqrt{\pi}} \int_{x}^{\infty} e^{-v^2}\,dv$	Complementary function to error function
$L_n(x)$	$\frac{e^x}{n!} \frac{d^n}{dx^n}\left(x^n e^{-x}\right), \quad n = 0,\ 1,\ \ldots$	Laguerre polynomial of degree n

Bessel Functions

Bessel Functions of the First Kind, J_n(x) (Also Called Simply *Bessel Functions*) (Figure 19.1.13)

Domain: $[x > 0]$
Recurrence relation:

$$J_{n+1}(x) = \frac{2n}{x} J_n(x) - J_{n-1}(x), \quad n = 0,\ 1,\ 2,\ \ldots$$

Symmetry: $J_{-n}(x) = (-1)^n J_n(x)$

0. $J_0(20x)$
1. $J_1(20x)$
2. $J_2(20x)$
3. $J_3(20x)$
4. $J_4(20x)$
5. $J_5(20x)$

Bessel Functions of the Second Kind, Y_n(x) (Also Called *Neumann Functions* or *Weber Functions*) (Figure 19.1.14)

Domain: $[x > 0]$
Recurrence relation:

$$Y_{n+1}(x) = \frac{2n}{x} Y_n(x) - Y_{n-1}(x), \quad n = 0,\ 1,\ 2,\ \ldots$$

Symmetry: $Y_{-n}(x) = (-1)^n Y_n(x)$

0. $Y_0(20x)$
1. $Y_1(20x)$
2. $Y_2(20x)$
3. $Y_3(20x)$
4. $Y_4(20x)$
5. $Y_5(20x)$

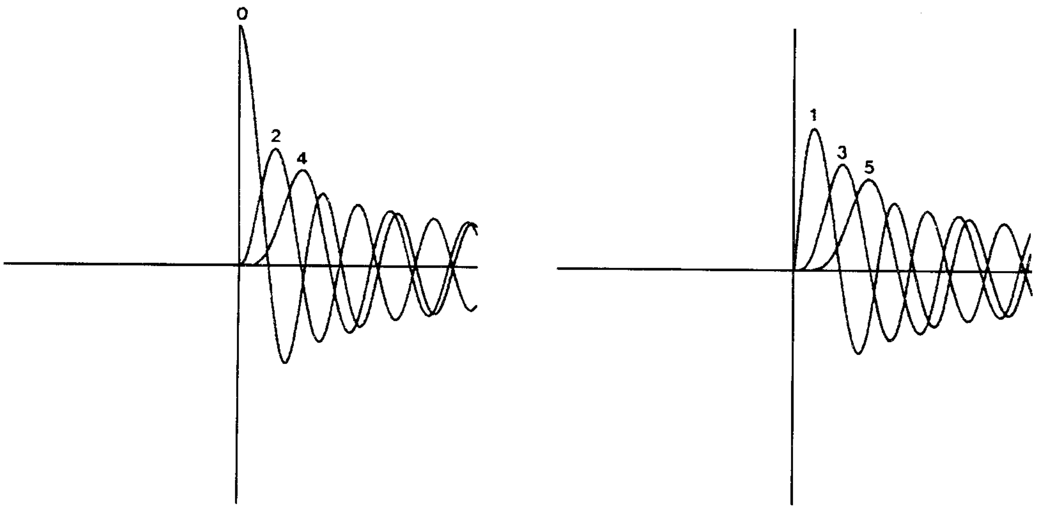

FIGURE 19.1.13 Bessel functions of the first kind.

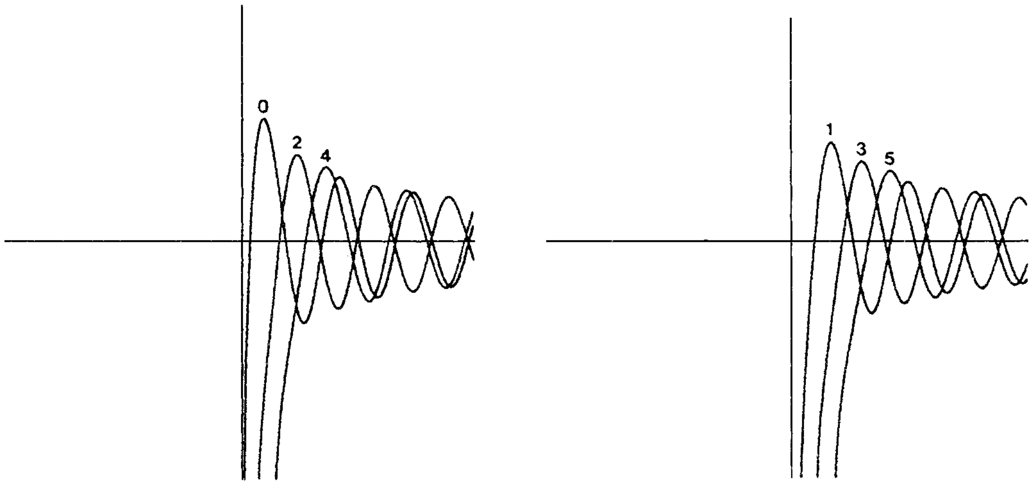

FIGURE 19.1.14 Bessel functions of the second kind.

Legendre Functions

Associated Legendre Functions of the First Kind, $P_n^m(x)$ (Figure 19.1.15)

Domain: $[-1 < x < 1]$

Recurrence relations:

$$P_{n+1}^m(x) = \frac{(2n+1)xP_n^m - (n+m)P_{n-1}^m(x)}{n-m+1}, \quad n = 1, 2, 3, \dots$$

$$P_n^{m+1}(x) = \left(x^2-1\right)^{-1/2}\left[(n-m)xP_n^m(x) - (n+m)P_{n-1}^m(x)\right], \quad m = 0, 1, 2, \dots$$

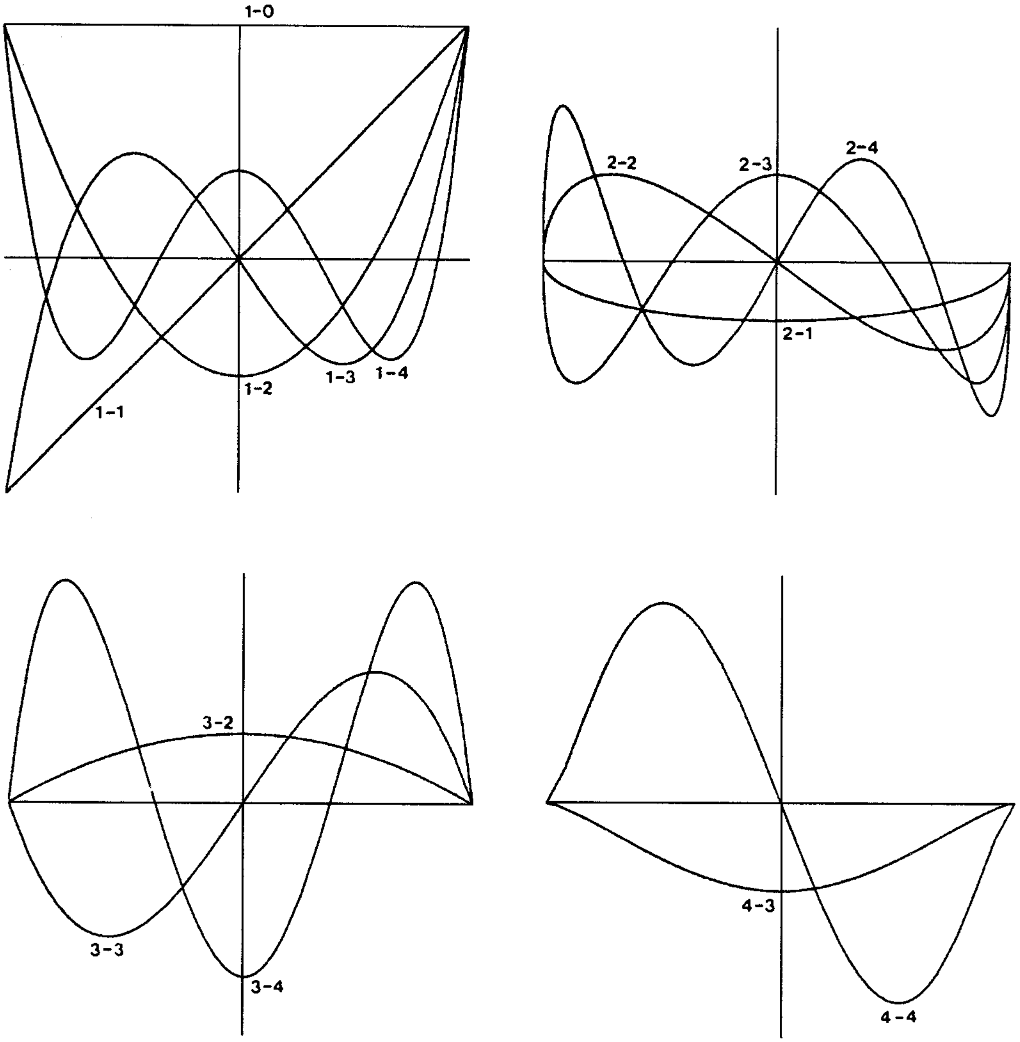

FIGURE 19.1.15 Legendre functions of the first kind.

with

$$P_0^0 = 1 \qquad P_1^0 = x$$

Special case: P_n^0 = Legendre polynomials

1-0. $P_0^0(x)$

1-1. $P_1^0(x)$ 2-1. 0.25 $P_1^1(x)$

1-2. $P_2^0(x)$ 2-2. 0.25 $P_2^1(x)$ 3-2. 0.10 $P_2^2(x)$

1-3. $P_3^0(x)$ 2-3. 0.25 $P_3^1(x)$ 3-3. 0.10 $P_3^2(x)$ 4-3. 0.025 $P_3^3(x)$

1-4. $P_4^0(x)$ 2-4. 0.25 $P_4^1(x)$ 3-4. 0.10 $P_4^2(x)$ 4-4. 0.025 $P_4^3(x)$

Table of Differential Equations

	Equation	Solution
1.	$y' = \frac{dy}{dx} = f(x)$	$y = \int f(x)\,dx + c$
2.	$y' + p(x)y = q(x)$	$y = \exp[-\int p(x)\,dx]\{c + \int \exp[\int p(x)\,dx]q(x)dx\}$
3.	$y' + p(x)y = q(x)y^{\alpha}$ $\alpha \neq 0, \alpha \neq 1$	Set $z = y^{1-\alpha} \rightarrow z' + (1-\alpha)p(x)z = (1-\alpha)q(x)$ and use 2
4.	$y' = f(x)g(y)$	Integrate $\frac{dy}{g(y)} = f(x)\,dx$ (separable)
5.	$\frac{dy}{dx} = f(x/y)$	Set $y = xu \rightarrow u + x\frac{du}{dx} = f(u)$ $\int \frac{1}{f(u)-u}\,du = \ln\lvert x\rvert + c$
6.	$y' = f\left(\frac{a_1x + b_1y + c_1}{a_2x + b_2y + c_2}\right)$	Set $x = X + \alpha, y = Y + \beta$ Choose $\begin{cases} a_1\alpha + b_1\beta = -c_2 \\ a_2\alpha + b_2\beta = -c_2 \end{cases} \rightarrow Y' = f\left(\frac{a_1X + b_1Y}{a_2X + b_2Y}\right)$ If $a_1b_2 - a_2b_1 \neq 0$, set $Y = Xu \rightarrow$ separable form $u + Xu' = f\left(\frac{a_1 + b_1u}{a_2 + b_2u}\right)$ If $a_1b_2 - a_2b_1 = 0$, set $u = a_1x + b_1y \rightarrow$ $\frac{du}{dx} = a_1 + b_1f\left(\frac{u + c_1}{ku + c_2}\right)$ since $a_2x + b_2y = k(a,x + a_2y)$
7.	$y'' + a^2y = 0$	$y = c_1 \cos ax + c_2 \sin ax$
8.	$y'' - a^2y = 0$	$y = c_1e^{ax} + c_2e^{-ax}$
9.	$y'' + ay' + by = 0$	Set $y = e^{-(a/2)x}u \rightarrow u'' + \left(b - \frac{a^2}{4}\right)u = 0$
10.	$y'' + a(x)y' + b(x)y = 0$	Set $y = e^{-(1/2)\int a(x)\,dx} \rightarrow u'' + \left[b(x) - \frac{a^2}{4} - \frac{a'}{2}\right]u = 0$
11.	$x^2y'' + xy' + (x^2 - a^2)\,y = 0$ $a \geq 0$ (Bessel)	i. If a is not an integer $y = c_1J_a(x) + c_2J_{-a}(x)$ (Bessel functions of first kind) ii. If a is an integer (say, n) $y = c_1J_n(x) + c_2Y_n(x)$ (Y_n is Bessel function of second kind)
12.	$(1 - x^2)y'' - 2xy' + a(a+1)y = 0$ a is real (Legendre)	$y(x) = c_1p_a(x) + c_1q_a(x)$ (Legendre functions)
13.	$y' + ay^2 = bx^n$ (integrable Riccati) a, b, n real	Set $u' = ayu \rightarrow u'' - abx^nu = 0$ and use 14
14.	$y'' - ax^{-1}y' + b^2x^{\mu}y = 0$	$y = x^p[c_1J_{\nu}(kx^q) + c_2J_{-\nu}(kx^q)$ where $p = (a+1)/2, \nu = (a+1)/(\mu+2)$, $k = 2b/(\mu+2), q = (\mu+2)/2$
15.	Item 13 shows that the Riccati equation is linearized by raising the order of the equation. The *Riccati chain,* which is linearizable by raising the order, is $u' = uy, \quad u'' = u[y^1 + y^2], \quad u''' = u[y'' + 3yy' + y^3],$ $u^{(iv)} = u[y''' + 4yy'' + 6y^2y' + 3(y')^2 + y^4],\ldots$ To use this consider the second-order equation $y'' + 3yy' + y^3 = f(x)$. The Riccati transformation $u' = yu$ transforms this equation to the linear for $u''' = uf(x)$!	

References

Kanke, E. 1956. *Differentialgleichungen Lösungsmethoden und Lösungen,* Vol. I. Akad. Verlagsges., Leipzig.
Murphy, G. M. 1960. *Ordinary Differential Equations and Their Solutions,* Van Nostrand, New York.
Zwillger, D. 1992. *Handbook of Differential Equations,* 2nd ed. Academic Press, San Diego.

19.2 Linear Algebra and Matrices

George Cain

Basic Definitions

A *Matrix* **A** is a rectangular array of numbers (real or complex)

$$\mathbf{A} = \begin{bmatrix} a_{11} & a_{12} & \cdots & a_{1m} \\ a_{21} & a_{22} & \cdots & a_{2m} \\ \vdots & & & \\ a_{n1} & a_{n2} & \cdots & a_{nm} \end{bmatrix}$$

The *size* of the matrix is said to be $n \times m$. The $1 \times m$ matrices $[a_{i1} \cdots a_{im}]$ are called rows of A, and the $n \times 1$ matrices

$$\begin{bmatrix} a_{1j} \\ a_{2j} \\ \vdots \\ a_{nj} \end{bmatrix}$$

are called *columns* of **A**. An $n \times m$ matrix thus consists of n rows and m columns; a_{ij} denotes the *element,* or *entry,* of **A** in the ith row and jth column. A matrix consisting of just one row is called a *row vector*, whereas a matrix of just one column is called a *column vector.* The elements of a vector are frequently called *components* of the vector. When the size of the matrix is clear from the context, we sometimes write $\mathbf{A} = (a_{ij})$.

A matrix with the same number of rows as columns is a *square* matrix, and the number of rows and columns is the *order* of the matrix. The diagonal of an $n \times n$ square matrix **A** from a_{11} to a_{nn} is called the *main,* or *principal, diagonal.* The word *diagonal* with no modifier usually means the main diagonal. The *transpose* of a matrix **A** is the matrix that results from interchanging the rows and columns of **A**. It is usually denoted by $\mathbf{A}^{\mathrm{T}}$. A matrix **A** such that $\mathbf{A} = \mathbf{A}^{\mathrm{T}}$ is said to be *symmetric.* The *conjugate transpose* of **A** is the matrix that results from replacing each element of $\mathbf{A}^{\mathrm{T}}$ by its complex conjugate, and is usually denoted by $\mathbf{A}^{\mathrm{H}}$. A matrix such that $\mathbf{A} = \mathbf{A}^{\mathrm{H}}$ is said to be *Hermitian.*

A square matrix $\mathbf{A} = (a_{ij})$ is *lower triangular* if $a_{ij} = 0$ for $j > i$ and is *upper triangular* if $a_{ij} = 0$ for $j < i$. A matrix that is both upper and lower triangular is a *diagonal* matrix. The *$n \times n$ identity matrix* is the $n \times n$ diagonal matrix in which each element of the main diagonal is 1. It is traditionally denoted $\mathbf{I}_n$, or simply **I** when the order is clear from the context.

Algebra of Matrices

The sum and difference of two matrices **A** and **B** are defined whenever **A** and **B** have the same size. In that case $\mathbf{C} = \mathbf{A} \pm \mathbf{B}$ is defined by $\mathbf{C} = (c_{ij}) = (a_{ij} \pm b_{ij})$. The product $t\mathbf{A}$ of a scalar t (real or complex number) and a matrix **A** is defined by $t\mathbf{A} = (ta_{ij})$. If **A** is an $n \times m$ matrix and **B** is an $m \times p$ matrix, the product $\mathbf{C} = \mathbf{AB}$ is defined to be the $n \times p$ matrix $\mathbf{C} = (c_{ij})$ given by $c_{ij} = \Sigma_{k=1}^{m} a_{ik}b_{kj}$. Note that the product of an $n \times m$ matrix and an $m \times p$ matrix is an $n \times p$ matrix, and the product is defined only when the number of columns of the first factor is the same as the number of rows of the second factor. Matrix multiplication is, in general, associative: $\mathbf{A}(\mathbf{BC}) = (\mathbf{AB})\mathbf{C}$. It also distributes over addition (and subtraction):

$$\mathbf{A}(\mathbf{B}+\mathbf{C}) = \mathbf{AB}+\mathbf{AC} \quad \text{and} \quad (\mathbf{A}+\mathbf{B})\mathbf{C} = \mathbf{AC}+\mathbf{BC}$$

It is, however, not in general true that $\mathbf{AB} = \mathbf{BA}$, even in case both products are defined. It is clear that $(\mathbf{A} + \mathbf{B})^T = \mathbf{A}^T + \mathbf{B}^T$ and $(\mathbf{A} + \mathbf{B})^H = \mathbf{A}^H + \mathbf{B}^H$. It is also true, but not so obvious perhaps, that $(\mathbf{AB})^T = \mathbf{B}^T\mathbf{A}^T$ and $(\mathbf{AB})^H = \mathbf{B}^H\mathbf{A}^H$.

The $n \times n$ identity matrix $\mathbf{I}$ has the property that $\mathbf{IA} = \mathbf{AI} = \mathbf{A}$ for every $n \times n$ matrix $\mathbf{A}$. If $\mathbf{A}$ is square, and if there is a matrix $\mathbf{B}$ such at $\mathbf{AB} = \mathbf{BA} = \mathbf{I}$, then $\mathbf{B}$ is called the *inverse* of $\mathbf{A}$ and is denoted $\mathbf{A}^{-1}$. This terminology and notation are justified by the fact that a matrix can have at most one inverse. A matrix having an inverse is said to be *invertible,* or *nonsingular,* while a matrix not having an inverse is said to be *noninvertible*, or *singular.* The product of two invertible matrices is invertible and, in fact, $(\mathbf{AB})^{-1} = \mathbf{B}^{-1}\mathbf{A}^{-1}$. The sum of two invertible matrices is, obviously, not necessarily invertible.

Systems of Equations

The system of n linear equations in m unknowns

$$\begin{aligned}
a_{11}x_1 + a_{12}x_2 + a_{13}x_3 + \ldots + a_{1m}x_m &= b_1 \\
a_{21}x_1 + a_{22}x_2 + a_{23}x_3 + \ldots + a_{2m}x_m &= b_2 \\
&\vdots \\
a_{n1}x_1 + a_{n2}x_2 + a_{n3}x_3 + \ldots + a_{nm}x_m &= b_n
\end{aligned}$$

may be written $\mathbf{Ax} = \mathbf{b}$, where $\mathbf{A} = (a_{ij})$, $\mathrm{x} = [\mathrm{x}_1\ \mathrm{x}_2 \cdots \mathrm{x}_m]^T$, and $\mathrm{b} = [\mathrm{b}_1\ \mathrm{b}_2 \cdots \mathrm{b}_n]^T$. Thus A is an $n \times m$ matrix, and x and b are column vectors of the appropriate sizes.

The matrix $\mathbf{A}$ is called the *coefficient matrix* of the system. Let us first suppose the coefficient matrix is square; that is, there are an equal number of equations and unknowns. If $\mathbf{A}$ is upper triangular, it is quite easy to find all solutions of the system. The ith equation will contain only the unknowns $x_i, x_{i+1}, \ldots, x_n$, and one simply solves the equations in reverse order: the last equation is solved for x_n; the result is substituted into the $(n-1)$st equation, which is then solved for x_{n-1}; these values of x_n and x_{n-1} are substituted in the $(n-2)$th equation, which is solved for x_{n-2}, and so on. This procedure is known as *back substitution.*

The strategy for solving an arbitrary system is to find an upper-triangular system equivalent with it and solve this upper-triangular system using back substitution. First suppose the element $a_{11} \neq 0$. We may rearrange the equations to ensure this, unless, of course the first column of $\mathbf{A}$ is all 0s. In this case proceed to the next step, to be described later. For each $i \geq 2$ let $m_{i1} = a_{i1}/a_{11}$. Now replace the ith equation by the result of multiplying the first equation by m_{i1} and subtracting the new equation from the ith equation. Thus,

$$a_{i1}x_1 + a_{i2}x_2 + a_{i3}x_3 + \ldots + a_{im}x_m = b_i$$

is replaced by

$$0 \cdot x_1 + \left(a_{i2} + m_{i1}a_{12}\right)x_2 + \left(a_{i3} + m_{i1}a_{13}\right)x_3 + \ldots + \left(a_{im} + m_{i1}a_{1m}\right)x_m = b_i + m_{i1}b_1$$

After this is done for all $i = 2, 3, \ldots, n$, there results the equivalent system

$$
\begin{aligned}
a_{11}x_1 + a_{12}x_2 + a_{13}x_3 + \ldots + a_{1n}x_n &= b_1 \\
0 \cdot x_1 + a'_{22}x_2 + a'_{23}x_3 + \ldots + a'_{2n}x_n &= b'_2 \\
0 \cdot x_1 + a'_{32}x_2 + a'_{33}x_3 + \ldots + a'_{3n}x_n &= b'_3 \\
&\vdots \\
0 \cdot x_1 + a'_{n2}x_2 + a'_{n3}x_3 + \ldots + a'_{nn}x_n &= b'_n
\end{aligned}
$$

in which all entries in the first column below a_{11} are 0. (Note that if all entries in the first column were 0 to begin with, then $a_{11} = 0$ also.) This procedure is now repeated for the $(n - 1) \times (n - 1)$ system

$$
\begin{aligned}
a'_{22}x_2 + a'_{23}x_3 + \ldots + a'_{2n}x_n &= b'_2 \\
a'_{32}x_2 + a'_{33}x_3 + \ldots + a'_{3n}x_n &= b'_3 \\
&\vdots \\
a'_{n2}x_2 + a'_{n3}x_3 + \ldots + a'_{nn}x_n &= b'_n
\end{aligned}
$$

to obtain an equivalent system in which all entries of the coefficient matrix below a'_{22} are 0. Continuing, we obtain an upper-triangular system Ux = c equivalent with the original system. This procedure is known as *Gaussian elimination*. The number m_{ij} are known as the *multipliers*.

Essentially the same procedure may be used in case the coefficient matrix is not square. If the coefficient matrix is not square, we may make it square by appending either rows or columns of 0s as needed. Appending rows of 0s and appending 0s to make b have the appropriate size equivalent to appending equations 0 = 0 to the system. Clearly the new system has precisely the same solutions as the original system. Appending columns of 0s and adjusting the size of x appropriately yields a new system with additional unknowns, each appearing only with coefficient 0, thus not affecting the solutions of the original system. In either case we may assume the coefficient matrix is square, and apply the Gauss elimination procedure.

Suppose the matrix **A** is invertible. Then if there were no row interchanges in carrying out the above Gauss elimination procedure, we have the *LU factorization* of the matrix **A**:

$$\mathbf{A} = \mathbf{LU}$$

where U is the upper-triangular matrix produced by elimination and L is the lower-triangular matrix given by

$$
\mathbf{L} = \begin{bmatrix} 1 & 0 & \ldots & \ldots & 0 \\ m_{21} & 1 & 0 & \ldots & 0 \\ \vdots & & \ddots & & \\ m_{n1} & m_{n2} & \ldots & & 1 \end{bmatrix}
$$

A *permutation* P_{ij} matrix is an $n \times n$ matrix such that P_{ij} A is the matrix that results from exchanging row *i* and *j* of the matrix A. The matrix P_{ij} is the matrix that results from exchanging rows *i* and *j* of the identity matrix. A product P of such matrices P_{ij} is called a *permutation* matrix. If row interchanges are required in the Gauss elimination procedure, then we have the factorization

$$\mathbf{PA} = \mathbf{LU}$$

where P is the permutation matrix giving the required row exchanges.

Vector Spaces

The collection of all column vectors with n real components is *Euclidean n-space*, and is denoted R^n. The collection of column vectors with n complex components is denoted C^n. We shall use *vector space* to mean either R^n or C^n. In discussing the space R^n, the word *scalar* will mean a real number, and in discussing the space C^n, it will mean a complex number. A subset S of a vector space is a *subspace* such that if $\mathbf{u}$ and $\mathbf{v}$ are vectors in S, and if c is any scalar, then $\mathbf{u} + \mathbf{v}$ and $c\mathbf{u}$ are in S. We shall sometimes use the word *space* to mean a subspace. If $B = \{v_1, v_2, \ldots, v_k\}$ is a collection of vectors in a vector space, then the set S consisting of all vectors $c_1v_1 + c_2v_2 + \cdots + c_mv_m$ for all scalars $c_1, c_2, \ldots, c_m$ is a subspace, called the *span* of B. A collection $\{v_1, v_2, \ldots, v_m\}$ of vectors $c_1v_1 + c_2v_2 + \cdots + c_mv_m$ is a *linear combination* of B. If S is a subspace and $B = \{v_1, v_2, \ldots, v_m\}$ is a subset of S such that S is the span of B, then B is said to *span* S.

A collection $\{v_1, v_2, \ldots, v_m\}$ of n-vectors is *linearly dependent* if there exist scalars $c_1, c_2, \ldots, c_m$, not all zero, such that $c_1v_1 + c_2v_2 + \cdots + c_mv_m = 0$. A collection of vectors that is not linearly dependent is said to be *linearly independent*. The modifier *linearly* is frequently omitted, and we speak simply of dependent and independent collections. A linearly independent collection of vectors in a space S that spans S is a *basis* of S. Every basis of a space S contains the same number of vectors; this number is the *dimension* of S. The dimension of the space consisting of only the zero vector is 0. The collection $B = \{e_1, e_2, \ldots, e_n\}$, where $e_1 = [1,0,0,\ldots, 0]^T$, $e_2 = [0,1,0,\ldots, 0]^T$, and so forth ($e_i$ has 1 as its ith component and zero for all other components) is a basis for the spaces R^n and C^n. This is the *standard basis* for these spaces. The dimension of these spaces is thus n. In a space S of dimension n, no collection of fewer than n vectors can span S, and no collection of more than n vectors in S can be independent.

Rank and Nullity

The *column space* of an $n \times m$ matrix $\mathbf{A}$ is the subspace of R^n or C^n spanned by the columns of $\mathbf{A}$. The *row space* is the subspace of R^m or C^m spanned by the rows or $\mathbf{A}$. Note that for any vector $x = [x_1\ x_2, \cdots x_m]^T$,

$$\mathbf{Ax} = x_1 \begin{bmatrix} a_{11} \\ a_{21} \\ \vdots \\ a_{n1} \end{bmatrix} + x_2 \begin{bmatrix} a_{12} \\ a_{22} \\ \vdots \\ a_{n2} \end{bmatrix} + \ldots + x_m \begin{bmatrix} a_{1m} \\ a_{2m} \\ \vdots \\ a_{nm} \end{bmatrix}$$

so that the column space is the collection of all vectors, $\mathbf{Ax}$, and thus the system $\mathbf{Ax} = \mathbf{b}$ has a solution if and only *if* $\mathbf{b}$ is a member of the column space of $\mathbf{A}$.

The dimension of the column space is the *rank* of $\mathbf{A}$. The row space has the same dimension as the column space. The set of all solutions of the system $\mathbf{Ax} = 0$ is a subspace called the *null space* of $\mathbf{A}$, and the dimension of this null space is the *nullity* of $\mathbf{A}$. A fundamental result in matrix theory is the fact that, for an $n \times m$ matrix $\mathbf{A}$.

$$\text{rank } \mathbf{A} + \text{nullity } \mathbf{A} = m$$

The difference of any two solutions of the linear system $\mathbf{Ax} = \mathbf{b}$ is a member of the null space of $\mathbf{A}$. Thus this system has at most one solution if and only if the nullity of $\mathbf{A}$ is zero. If the system is square (that is, if $\mathbf{A}$ is $n \times n$), then there will be a solution for every right-hand side $\mathbf{b}$ if and only if the collection of columns of $\mathbf{A}$ is linearly independent, which is the same as saying the rank of $\mathbf{A}$ is n. In this case the nullity must be zero. Thus, for any $\mathbf{b}$, the square system $\mathbf{Ax} = \mathbf{b}$ has exactly one solution if and only if rank $\mathbf{A} = n$. In other words the $n \times n$ matrix $\mathbf{A}$ is invertible if and only if rank $\mathbf{A} = n$.

Orthogonality and Length

The *inner product* of two vectors x and y is the scalar x^Hy. The *length*, or *norm*, $\|x\|$, of the vector $\mathbf{x}$ is given by $\|x\| = \sqrt{\mathbf{x}^H\mathbf{x}}$. A *unit vector* is a vector of norm 1. Two vectors x and y are *orthogonal* if $x^Hy = 0$.

A collection of vectors $\{v_1, v_2, \ldots, v_m\}$ in a space S is said to be an *orthonormal* collection if $\mathbf{v}_i^H \mathbf{v}_j = 0$ for $i \neq j$ and $\mathbf{v}_i^H \mathbf{v}_i = 1$. An orthonormal collection is necessarily linearly independent. If S is a subspace (of R^n or C^n) spanned by the orthonormal collection $\{v_1, v_2, \ldots, v_m\}$, then the *projection* of a vector x onto S is the vector

$$\text{proj}(\mathbf{x}; \mathbf{S}) = (\mathbf{x}^H \mathbf{v}_1)\mathbf{v}_1 + (\mathbf{x}^H \mathbf{v}_2)\mathbf{v}_2 + \ldots + (\mathbf{x}^H \mathbf{v}_m)\mathbf{v}_m$$

The projection of x onto S minimizes the function $f(y) = \|x - y\|^2$ for $y \in S$. In other words the projection of x onto S is the vector in S that is "closest" to x.

If **b** is a vector and **A** is an $n \times m$ matrix, then a vector x minimizes $\|b - Ax\|^2$ if only if it is a solution of $A^H Ax = A^H b$. This system of equations is called the *system of normal equations* for the least-squares problem of minimizing $\|b - Ax\|^2$.

If **A** is an $n \times m$ matrix, and rank $\mathbf{A} = k$, then there is a $n \times k$ matrix Q whose columns form an orthonormal basis for the column space of **A** and a $k \times m$ upper-triangular matrix **R** of rank k such that

$$\mathbf{A} = \mathbf{QR}$$

This is called the *QR factorization* of **A**. It now follows that x minimizes $\|b - Ax\|^2$ if and only if it is a solution of the upper-triangular system $Rx = Q^H b$.

If $\{w_1, w_2, \ldots, w_m\}$ is a basis for a space S, the following procedure produces an orthonormal basis $\{v_1, v_2, \ldots, v_m\}$ for S.

Set $\mathbf{v}_1 = \mathbf{w}_1 / \|\mathbf{w}_1\|$.
Let $\tilde{\mathbf{v}}_2 = \mathbf{w}_2 - \text{proj}(\mathbf{w}_2; \mathbf{S}_1)$, where $\mathbf{S}_1$ is the span of $\{\mathbf{v}_1\}$; set $\mathbf{v}_2 = \tilde{\mathbf{v}}_2 / \|\tilde{\mathbf{v}}_2\|$.
Next, let $\tilde{\mathbf{v}}_3 = \mathbf{w}_3 - \text{proj}(\mathbf{w}_3; \mathbf{S}_2)$, where $\mathbf{S}_2$ is the span of $\{\mathbf{v}_1, v_2\}$; set $\mathbf{v}_3 = \tilde{\mathbf{v}}_3 / \|\tilde{\mathbf{v}}_3\|$.

And, so on: $\tilde{\mathbf{v}}_i = w_i - \text{proj}(w_i; S_{i-1})$, where S_{i-1} is the span of $\{v_1, v_2, \ldots, v_{i-1}\}$; set $v_i = \tilde{\mathbf{v}}_i / \|\tilde{\mathbf{v}}_i\|$. This the *Gram-Schmidt procedure.*

If the collection of columns of a square matrix is an orthonormal collection, the matrix is called a *unitary matrix*. In case the matrix is a real matrix, it is usually called an *orthogonal matrix*. A unitary matrix U is invertible, and $\mathbf{U}^{-1} = \mathbf{U}^H$. (In the real case an orthogonal matrix **Q** is invertible, and $\mathbf{Q}^{-1} = \mathbf{Q}^T$.)

Determinants

The *determinant* of a square matrix is defined inductively. First, suppose the determinant det **A** has been defined for all square matrices of order $< n$. Then

$$\det \mathbf{A} = a_{11}\mathbf{C}_{11} + a_{12}\mathbf{C}_{12} + \ldots + a_{1n}\mathbf{C}_{1n}$$

where the numbers C_{ij} are *cofactors* of the matrix **A**:

$$\mathbf{C}_{ij} = (-1)^{i+j} \det \mathbf{M}_{ij}$$

where M_{ij} is the $(n - 1) \times (n - 1)$ matrix obtained by deleting the ith row and jth column of **A**. Now det**A** is defined to be the only entry of a matrix of order 1. Thus, for a matrix of order 2, we have

$$\det \begin{bmatrix} a & b \\ c & d \end{bmatrix} = ad - bc$$

There are many interesting but not obvious properties of determinants. It is true that

$$\det\mathbf{A} = a_{i1}\mathbf{C}_{i1} + a_{i2}\mathbf{C}_{i2} + \ldots + a_{in}\mathbf{C}_{in}$$

for any $1 \le i \le n$. It is also true that det**A** = det$\mathbf{A}^T$, so that we have

$$\det\mathbf{A} = a_{1j}\mathbf{C}_{1j} + a_{2j}\mathbf{C}_{2j} + \ldots + a_{nj}\mathbf{C}_{nj}$$

for any $1 \le j \le n$.

If **A** and **B** are matrices of the same order, then det**AB** = (det**A**)(det**B**), and the determinant of any identity matrix is 1. Perhaps the most important property of the determinant is the fact that a matrix in invertible if and only if its determinant is not zero.

Eigenvalues and Eigenvectors

If **A** is a square matrix, and **Av** = λv for a scalar λ and a nonzero v, then λ is an *eigenvalue* of **A** and v is an *eigenvector* of **A** that *corresponds* to λ. Any nonzero linear combination of eigenvectors corresponding to the same eigenvalue λ is also an eigenvector corresponding to λ. The collection of all eigenvectors corresponding to a given eigenvalue λ is thus a subspace, called an *eigenspace* of **A**. A collection of eigenvectors corresponding to different eigenvalues is necessarily linear-independent. It follows that a matrix of order n can have at most n distinct eigenvectors. In fact, the eigenvalues of **A** are the roots of the nth degree polynomial equation

$$\det(\mathbf{A} - \lambda\mathbf{I}) = 0$$

called the *characteristic equation* of **A**. (Eigenvalues and eigenvectors are frequently called *characteristic values* and *characteristic vectors.*)

If the nth order matrix **A** has an independent collection of n eigenvectors, then **A** is said to have a *full set* of eigenvectors. In this case there is a set of eigenvectors of **A** that is a basis for R^n or, in the complex case, C^n. In case there are n distinct eigenvalues of **A**, then, of course, **A** has a full set of eigenvectors. If there are fewer than n distinct eigenvalues, then **A** may or may not have a full set of eigenvectors. If there is a full set of eigenvectors, then

$$\mathbf{D} = \mathbf{S}^{-1}\mathbf{A}\mathbf{S} \quad \text{or} \quad \mathbf{A} = \mathbf{S}\mathbf{D}\mathbf{S}^{-1}$$

where **D** is a diagonal matrix with the eigenvalues of **A** on the diagonal, and **S** is a matrix whose columns are the full set of eigenvectors. If **A** is symmetric, there are n real distinct eigenvalues of **A** and the corresponding eigenvectors are orthogonal. There is thus an orthonormal collection of eigenvectors that span R^n, and we have

$$\mathbf{A} = \mathbf{Q}\mathbf{D}\mathbf{Q}^T \quad \text{and} \quad \mathbf{D} = \mathbf{Q}^T\mathbf{A}\mathbf{Q}$$

where **Q** is a real orthogonal matrix and **D** is diagonal. For the complex case, if **A** is Hermitian, we have

$$\mathbf{A} = \mathbf{U}\mathbf{D}\mathbf{U}^H \quad \text{and} \quad \mathbf{D} = \mathbf{U}^H\mathbf{A}\mathbf{U}$$

where **U** is a unitary matrix and **D** is a *real* diagonal matrix. (A Hermitian matrix also has n distinct real eigenvalues.)

References

Daniel, J. W. and Nobel, B. 1988. *Applied Linear Algebra.* Prentice Hall, Englewood Cliffs, NJ.
Strang, G. 1993. *Introduction to Linear Algebra.* Wellesley-Cambridge Press, Wellesley, MA.

19.3 Vector Algebra and Calculus

George Cain

Basic Definitions

A vector is a directed line segment, with two vectors being equal if they have the same length and the same direction. More precisely, a *vector* is an equivalence class of directed line segments, where two directed segments are equivalent if they have the same length and the same direction. The *length* of a vector is the common length of its directed segments, and the *angle between* vectors is the angle between any of their segments. The length of a vector u is denoted $|\mathbf{u}|$. There is defined a distinguished vector having zero length, which is usually denoted **0**. It is frequently useful to visualize a directed segment as an arrow; we then speak of the nose and the tail of the segment. The *sum* $\mathbf{u} + \mathbf{v}$ of two vectors **u** and **v** is defined by taking directed segments from **u** and **v** and placing the tail of the segment representing **v** at the nose of the segment representing **u** and defining $\mathbf{u} + \mathbf{v}$ to be the vector determined by the segment from the tail of the **u** representative to the nose of the **v** representative. It is easy to see that $\mathbf{u} + \mathbf{v}$ is well defined and that $\mathbf{u} + \mathbf{v} = \mathbf{v} + \mathbf{u}$. Subtraction is the inverse operation of addition. Thus the *difference* $\mathbf{u} - \mathbf{v}$ of two vectors is defined to be the vector that when added to **v** gives **u**. In other words, if we take a segment from **u** and a segment from **v** and place their tails together, the difference is the segment from the nose of v to the nose of **u**. The zero vector behaves as one might expect; $\mathbf{u} + \mathbf{0} = \mathbf{u}$, and $\mathbf{u} - \mathbf{u} = \mathbf{0}$. Addition is associative: $\mathbf{u} + (\mathbf{v} + \mathbf{w}) = (\mathbf{u} + \mathbf{v}) + \mathbf{w}$.

To distinguish them from vectors, the real numbers are called *scalars*. The product $t\mathbf{u}$ of a scalar t and a vector **u** is defined to be the vector having length $|t|\ |\mathbf{u}|$ and direction the same as **u** if $t > 0$, the opposite direction if $t < 0$, If $t = 0$, then $t\mathbf{u}$ is defined to be the zero vector. Note that $t(\mathbf{u} + \mathbf{v}) = t\mathbf{u} + t\mathbf{v}$, and $(t + s)\mathbf{u} = t\mathbf{u} + s\mathbf{u}$. From this it follows that $\mathbf{u} - \mathbf{v} = \mathbf{u} + (-1)\mathbf{v}$.

The *scalar product* $\mathbf{u} \cdot \mathbf{v}$ of two vectors is $|\mathbf{u}||\mathbf{v}| \cos \boldsymbol{\theta}$, where θ is the angle between **u** and **v**. The scalar product is frequently called the *dot product.* The scalar product distributes over addition:

$$\mathbf{u} \cdot (\mathbf{v} + \mathbf{w}) = \mathbf{u} \cdot \mathbf{v} + \mathbf{u} \cdot \mathbf{w}$$

and it is clear that $(t\mathbf{u}) \cdot \mathbf{v} = t(\mathbf{u} \cdot \mathbf{v})$. The *vector product* $\mathbf{u} \times \mathbf{v}$ of two vectors is defined to be the vector perpendicular to both **u** and **v** and having length $\mathbf{u}||\mathbf{v}| \sin \theta$, where θ is the angle between **u** and **v**. The direction of $\mathbf{u} \times \mathbf{v}$ is the direction a right-hand threaded bolt advances if the vector **u** is rotated to **v**. The vector is frequently called the *cross product.* The vector product is both associative and distributive, but not commutative: $\mathbf{u} \times \mathbf{v} = -\mathbf{v} \times \mathbf{u}$.

Coordinate Systems

Suppose we have a right-handed Cartesian coordinate system in space. For each vector, **u**, we associate a point in space by placing the tail of a representative of **u** at the origin and associating with **u** the point at the nose of the segment. Conversely, associated with each point in space is the vector determined by the directed segment from the origin to that point. There is thus a one-to-one correspondence between the points in space and all vectors. The origin corresponds to the zero vector. The coordinates of the point associated with a vector **u** are called *coordinates* of **u**. One frequently refers to the vector **u** and writes $\mathbf{u} = (x, y, z)$, which is, strictly speaking, incorrect, because the left side of this equation is a vector and the right side gives the coordinates of a point in space. What is meant is that (x, y, z) are the coordinates of the point associated with **u** under the correspondence described. In terms of coordinates, for $\mathbf{u} = (u_1, u_2, u_3)$ and $\mathbf{v} = (v_1, v_2, v_3)$, we have

$$\mathbf{u} + \mathbf{v} = (u_1 + v_1, u_2 + v_2, u_3 + v_3)$$

$$t\mathbf{u} = (tu_1, tu_2, tu_3)$$

$$\mathbf{u}\cdot\mathbf{v} = u_1v_1 + u_2v_2 + u_3v_3$$

$$\mathbf{u}\times\mathbf{v} = \left(u_2v_3 - v_2u_3,\ u_3v_1 - v_3u_1,\ u_1v_2 - v_1u_2\right)$$

The *coordinate vectors* **i**, **j**, and **k** are the unit vectors i = (1, 0, 0), j = (0, 1, 0), and k = (0, 0, 1). Any vector **u** = (u_1, u_2, u_3) is thus a linear combination of these coordinate vectors: u = u_1i + u_2j + u_3k. A convenient form for the vector product is the formal determinant

$$\mathbf{u}\times\mathbf{v} = \det\begin{bmatrix} \mathbf{i} & \mathbf{j} & \mathbf{k} \\ u_1 & u_2 & u_3 \\ v_1 & v_2 & v_2 \end{bmatrix}$$

Vector Functions

A *vector function* **F** *of one variable* is a rule that associates a vector **F**(t) with each real number t in some set, called the *domain* of **F**. The expression $\lim_{t\to t_0} \mathbf{F}(t) = \mathbf{a}$ means that for any $\varepsilon > 0$, there is a $\delta > 0$ such that $|\mathbf{F}(t) - \mathbf{a}| < \varepsilon$ whenever $0 < |t - t_0| < \delta$. If $\mathbf{F}(t) = [x(t), y(t), z(t)]$ and $\mathbf{a} = (a_1, a_2, a_3)$, then $\lim_{t\to t_0} \mathbf{F}(t) = \mathbf{a}$ if and only if

$$\lim_{t\to t_0} x(t) = a_1$$

$$\lim_{t\to t_0} y(t) = a_2$$

$$\lim_{t\to t_0} z(t) = a_3$$

A vector function **F** is *continuous* at t_0 if $\lim_{t\to t_0} \mathbf{F}(t) = \mathbf{F}(t_0)$. The vector function **F** is continuous at t_0 if and only if each of the coordinates $x(t)$, $y(t)$, and $z(t)$ is continuous at t_0.

The function **F** is *differentiable* at t_0 if the limit

$$\lim_{h\to 0}\frac{1}{h}\left[\mathbf{F}(t+h) - \mathbf{F}(t)\right]$$

exists. This limit is called the *derivative* of **F** at t_0 and is usually written $\mathbf{F}'(t_0)$, or $(d\mathbf{F}/dt)(t_0)$. The vector function **F** is differentiable at t_0 if and only if each of its coordinate functions is differentiable at t_0. Moreover, $(d\mathbf{F}/dt)(t_0) = [(dx/dt)(t_0), (dy/dt)(t_0), (dz/dt)(t_0)]$. The usual rules for derivatives of real valued functions all hold for vector functions. Thus if **F** and **G** are vector functions and s is a scalar function, then

$$\frac{d}{dt}(\mathbf{F}+\mathbf{G}) = \frac{d\mathbf{F}}{dt} + \frac{d\mathbf{G}}{dt}$$

$$\frac{d}{dt}(s\mathbf{F}) = s\frac{d\mathbf{F}}{dt} + \frac{ds}{dt}\mathbf{F}$$

$$\frac{d}{dt}(\mathbf{F}\cdot\mathbf{G}) = \mathbf{F}\cdot\frac{d\mathbf{G}}{dt} + \frac{d\mathbf{F}}{dt}\cdot\mathbf{G}$$

$$\frac{d}{dt}(\mathbf{F}\times\mathbf{G}) = \mathbf{F}\times\frac{d\mathbf{G}}{dt} + \frac{d\mathbf{F}}{dt}\times\mathbf{G}$$

If **R** is a vector function defined for t in some interval, then, as t varies, with the tail of **R** at the origin, the nose traces out some object C in space. For nice functions **R**, the object C is a *curve*. If $\mathbf{R}(t) = [x(t), y(t), z(t)]$, then the equations

$$x = x(t)$$

$$y = y(t)$$

$$z = z(t)$$

are called *parametric equations* of C. At points where **R** is differentiable, the derivative $d\mathbf{R}/dt$ is a vector *tangent* to the curve. The unit vector $\mathbf{T} = (d\mathbf{R}/dt)/|d\mathbf{R}/dt|$ is called the *unit tangent vector*. If **R** is differentiable and if the length of the arc of curve described by **R** between $\mathbf{R}(a)$ and $\mathbf{R}(t)$ is given by $s(t)$, then

$$\frac{ds}{dt} = \left|\frac{d\mathbf{R}}{dt}\right|$$

Thus the length L of the arc from $\mathbf{R}(t_0)$ to $\mathbf{R}(t_1)$ is

$$L = \int_{t_0}^{t_1} \frac{ds}{dt}\,dt = \int_{t_0}^{t_1} \left|\frac{d\mathbf{R}}{dt}\right| dt$$

The vector $d\mathbf{T}/ds = (d\mathbf{T}/dt)/(ds/dt)$ is perpendicular to the unit tangent **T**, and the number $\kappa = |d\mathbf{T}/ds|$ is the *curvature* of C. The unit vector $\mathbf{N} = (1/\kappa)(d\mathbf{T}/ds)$ is the *principal normal*. The vector $\mathbf{B} = \mathbf{T} \times \mathbf{N}$ is the *binormal*, and $d\mathbf{B}/ds = -\tau N$. The number τ is the *torsion*. Note that C is a plane curve if and only if τ is zero for all t.

A *vector function* **F** *of two variables* is a rule that assigns a vector $\mathbf{F}(s, t)$ in some subset of the plane, called the *domain* of **F**. If $\mathbf{R}(s, t)$ is defined for all (s, t) in some region D of the plane, then as the point (s, t) varies over D, with its rail at the origin, the nose of $\mathbf{R}(s, t)$ traces out an object in space. For a nice function **R**, this object is a *surface*, S. The partial derivatives $(\partial\mathbf{R}/\partial s)(s, t)$ and $(\partial\mathbf{R}/\partial t)(s, t)$ are tangent to the surface at $\mathbf{R}(s, t)$, and the vector $(\partial\mathbf{R}/\partial s) \times (\partial\mathbf{R}/\partial t)$ is thus *normal* to the surface. Of course, $(\partial\mathbf{R}/\partial t) \times (\partial\mathbf{R}/\partial s) = -(\partial\mathbf{R}/\partial s) \times (\partial\mathbf{R}/\partial t)$ is also normal to the surface and points in the direction opposite that of $(\partial\mathbf{R}/\partial s) \times (\partial\mathbf{R}/\partial t)$. By electing one of these normal, we are choosing an *orientation* of the surface. A surface can be oriented only if it has two sides, and the process of orientation consists of choosing which side is "positive" and which is "negative."

Gradient, Curl, and Divergence

If $f(x, y, z)$ is a scalar field defined in some region D, the *gradient* of **f** is the vector function

$$\operatorname{grad} f = \frac{\partial f}{\partial x}\mathbf{i} + \frac{\partial f}{\partial y}\mathbf{j} + \frac{\partial f}{\partial z}\mathbf{k}$$

If $\mathbf{F}(x, y, z) = F_1(x, y, z)\mathbf{i} + F_2(x, y, z)\mathbf{j} + F_3(x, y, z)\mathbf{k}$ is a vector field defined in some region D, then the *divergence* of **F** is the scalar function

$$\operatorname{div} \mathbf{F} = \frac{\partial F_1}{\partial x} + \frac{\partial F_2}{\partial y} + \frac{\partial F_3}{\partial z}$$

The curl is the vector function

$$\operatorname{curl}\mathbf{F} = \left(\frac{\partial F_3}{\partial y} - \frac{\partial F_2}{\partial z}\right)\mathbf{i} + \left(\frac{\partial F_1}{\partial z} - \frac{\partial F_3}{\partial x}\right)\mathbf{j} + \left(\frac{\partial F_2}{\partial x} - \frac{\partial F_1}{\partial y}\right)\mathbf{k}$$

In terms of the vector operator *del*, $\nabla = \mathbf{i}(\partial/\partial x) + \mathbf{j}(\partial/\partial y) + \mathbf{k}(\partial/\partial z)$, we can write

$$\operatorname{grad} f = \nabla f$$

$$\operatorname{div}\mathbf{F} = \nabla \cdot \mathbf{F}$$

$$\operatorname{curl}\mathbf{F} = \nabla \times \mathbf{F}$$

The *Laplacian operator* is div (grad) $= \nabla \cdot \nabla = \nabla^2 = (\partial^2/\partial x^2) + (\partial^2/\partial y^2) + (\partial^2/\partial z^2)$.

Integration

Suppose C is a curve from the point (x_0, y_0, z_0) to the point (x_1, y_1, z_1) and is described by the vector function $\mathbf{R}(t)$ for $t_0 \le t \le t_1$. If f f is a scalar function (sometimes called a *scalar field*) defined on C, then the integral of f over C is

$$\int_C f(x,y,z)\, ds = \int_{t_0}^{t_1} f[\mathbf{R}(t)] \left|\frac{d\mathbf{R}}{dt}\right| dt$$

If $\mathbf{F}$ is a vector function (sometimes called a *vector field*) defined on C, then the integral of $\mathbf{F}$ over C is

$$\int_C \mathbf{F}(x,y,z) \cdot d\mathbf{R} = \int_{t_0}^{t_1} \mathbf{F}[\mathbf{R}(t)] \frac{d\mathbf{R}}{dt}\, dt$$

These integrals are called *line integrals.*

In case there is a scalar function f such that $\mathbf{F} = \operatorname{grad} f$, then the line integral

$$\int_C \mathbf{F}(x,y,z) \cdot d\mathbf{R} = f[\mathbf{R}(t_1)] - f[\mathbf{R}(t_0)]$$

The value of the integral thus depends only on the end points of the curve C and not on the curve C itself. The integral is said to be *path-independent.* The function f is called a *potential function* for the vector field $\mathbf{F}$, and $\mathbf{F}$ is said to be a *conservative field.* A vector field $\mathbf{F}$ with domain D is conservative if and only if the integral of $\mathbf{F}$ around every closed curve in D is zero. If the domain D is simply connected (that is, every closed curve in D can be continuously deformed in D to a point), then $\mathbf{F}$ is conservative if and only if curl $\mathbf{F} = 0$ in D.

Suppose S is a surface described by $\mathbf{R}(s, t)$ for (s, t) in a region D of the plane. If f is a scalar function defined on D, then the integral of f over S is given by

$$\int\!\!\int_S f(x,y,z)\, dS = \int\!\!\int_D f[\mathbf{R}(s,t)] \left|\frac{\partial \mathbf{R}}{\partial s} \times \frac{\partial \mathbf{R}}{\partial t}\right| ds\, dt$$

If $\mathbf{F}$ is a vector function defined on S, and if an orientation for S is chosen, then the integral $\mathbf{F}$ over S, sometimes called the flux of $\mathbf{F}$ through S, is

$$\int\!\!\int_S \mathbf{F}(x,y,z) \cdot d\mathbf{S} = \int\!\!\int_D \mathbf{F}[\mathbf{R}(s,t)] \left|\frac{\partial \mathbf{R}}{\partial s} \times \frac{\partial \mathbf{R}}{\partial t}\right| ds\, dt$$

Integral Theorems

Suppose **F** is a vector field with a closed domain D bounded by the surface S oriented so that the normal points out from D. Then the *divergence theorem* states that

$$\iiint_D \operatorname{div} \mathbf{F}\, dV = \iint_S \mathbf{F} \cdot \mathbf{dS}$$

If S is an orientable surface bounded by a closed curve C, the orientation of the closed curve C is chosen to be consistent with the orientation of the surface S. Then we have *Stoke's theorem:*

$$\iint_S (\text{curl } \mathbf{F}) \cdot d\mathbf{S} = \oint_C \mathbf{F} \cdot \mathbf{ds}$$

References

Davis, H. F. and Snider, A. D. 1991. *Introduction to Vector Analysis,* 6th ed., Wm. C. Brown, Dubuque, IA.

Wylie, C. R. 1975. *Advanced Engineering Mathematics,* 4th ed., McGraw-Hill, New York.

Further Information

More advanced topics leading into the theory and applications of tensors may be found in J. G. Simmonds, *A Brief on Tensor Analysis* (1982, Springer-Verlag, New York).

19.4 Difference Equations

William F. Ames

Difference equations are equations involving *discrete variables.* They appear as natural descriptions of natural phenomena and in the study of discretization methods for differential equations, which have continuous variables.

Let $y_n = y(nh)$, where n is an integer and h is a real number. (One can think of measurements taken at equal intervals, h, $2h$, $3h$, …, and y_n describes these). A typical equation is that describing the famous Fibonacci sequence — $y_{n+2} - y_{n+1} - y_n = 0$. Another example is the equation $y_{n+2} - 2zy_{n+1} + y_n = 0$, $z \in C$, which describes the Chebyshev polynomials.

First-Order Equations

The general first-order equation $y_{n+1} = f(y_n)$, $y_0 = y(0)$ is easily solved, for as many terms as are needed, by *iteration.* Then $y_1 = f(y_0)$; $y_2 = f(y_1)$,…. An example is the logistic equation $y_{n+1} = ay_n(1 - y_n) = f(y_n)$. The logistic equation has two fixed (critical or equilibrium) points where $y_{n+1} = y_n$. They are 0 and $\bar{y} = (a - 1)/a$. This has physical meaning only for $a > 1$. For $1 < a < 3$ the equilibrium $\bar{y}$ is asymptotically stable, and for $a > 3$ there are two points y_1 and y_2, called a *cycle of period two*, in which $y_2 = f(y_1)$ and $y_1 = f(y_2)$. This study leads into chaos, which is outside our interest. By iteration, with $y_0 = {}^1\!/_2$, we have $y_1 = (a/2)(1/2) = a/2^2$, $y_2 = a(a/2^2)(1 - a/2^2) = (a^2/2^2)(1 - a/2^2)$, ….

With a constant, the equation $y_{n+1} = ay_n$ is solved by making the assumption $y_n = A\lambda^n$ and finding λ so that the equation holds. Thus $A\lambda^{n+1} = aA\lambda^n$, and hence $\lambda = 0$ or $\lambda = a$ and A is arbitrary. Discarding the trivial solution 0 we find $y_n = Aa^{n+1}$ is the desired solution. By using a method called the *variation of constants,* the equation $y_{n+1} - ay_n = g_n$ has the solution $y_n = y_0a^n + \Sigma_{j=0}^{n-1} g_j a^{n-j-1}$, with y_0 arbitrary.

In various applications we find the first-order equation of *Riccati type* $y_ny_{n-1} + ay_n + by_{n-1} + c = 0$ where a, b, and c are real constants. This equation can be transformed to a linear second-order equation by setting $y_n = z_n/z_{n-1} - a$ to obtain $z_{n+1} + (b + a)z_n + (c - ab)z_{n-1} = 0$, which is solvable as described in the next section.

Second-Order Equations

The second-order linear equation with constant coefficients $y_{n+2} + ay_{n+1} + by_n = f_n$ is solved by first solving the homogeneous equation (with right-hand side zero) and adding to that solution any solution of the inhomogeneous equation. The *homogeneous equation* $y_{n+2} + ay_{n+1}\ by_n = 0$ is solved by assuming $y_n = \lambda^n$, whereupon $\lambda^{n+2} + a\lambda^{n+1} + b\lambda^n = 0$ or $\lambda = 0$ (rejected) or $\lambda^2 + a\lambda + b = 0$. The roots of this quadratic are $\lambda_1 = {}^1/_2\,(-a + \sqrt{a^2 - 4b})$, $\lambda_2 = -{}^1/_2\,(a + \sqrt{a^2 - 4b})$ and the solution of the homogeneous equation is $y_n = c_1\lambda_1^n + c_2\lambda_2^n$. As an example consider the Fibonacci equation $y_{n+2} - y_{n+1} - y_n = 0$. The roots of $\lambda^2 - \lambda - 1 = 0$ are $\lambda_1 = {}^1/_2\,(1 + \sqrt{5})$, $\lambda_2 = {}^1/_2\,(1 - \sqrt{5})$, and the solution $y_n = c_1[(1 + \sqrt{5})/2]^n + c_2[(1 - \sqrt{5})/2]^n$ is known as the *Fibonacci sequence.*

Many of the orthogonal polynomials of differential equations and numerical analysis satisfy a second-order difference equation (recurrence relation) involving a discrete variable, say n, and a continuous variable, say z. One such is the *Chebshev equation* $y_{n+2} - 2zy_{n+1} + y_n = 0$ with the initial conditions $y_0 = 1$, $y_1 = z$ (*first-kind* Chebyshev polynomials) and $y_{n-1} = 0$, $y_0 = 1$ (second-kind Chebyshev polynomials). They are denoted $T_n(z)$ and $V_n(z)$, respectively. By iteration we find

$$T_0(z) = 1, \quad T_1(z) = z, \quad T_2(z) = 2z^2 - 1,$$

$$T_3(z) = 4z^3 - 3z, \quad T_4(z) = 8z^4 - 8z^2 + 1$$

$$V_0(z) = 0, \quad V_1(z) = 1, \quad V_2(z) = 2z,$$

$$V_3(z) = 4z^2 - 1, \quad V_4(z) = 8z^3 - 4z$$

and the general solution is $y_n(z) = c_1T_n(z) + c_2V_{n-1}(z)$,

Linear Equations with Constant Coefficients

The genral kth-order linear equation with constant coefficients is $\Sigma_{i=0}^{k} p_i y_{n+k-i} = g_n$, $p_0 = 1$. The solution to the corresponding homogeneous equation (obtained by setting $g_n = 0$) is as follows. (a) $y_n = \Sigma_{i=1}^{k} c_i\lambda_i^n$ if the λ_i are the distinct roots of the characteristic polynomial $p(\lambda) = \Sigma_{i=0}^{k} p_i\lambda^{k-i} = 0$. (b) if m_s is the multiplicity of the root λ_s, then the functions $y_{n,s} = u_s(n)\lambda_s^n$, where $u_s(n)$ are polynomials in n whose degree does not exceed $m_s - 1$, are solutions of the equation. Then the general solution of the homogeneous equation is $y_n = \Sigma_{i=1}^{d} a_i u_i(n)\lambda_i^n = \Sigma_{i=1}^{d} a_i \Sigma_{j=0}^{m_i-1} c_j n^j \lambda_i^n$. To this solution one adds any particular solution to obtain the general solution of the general equation.

Example 19.4.1. A model equation for the price p_n of a product, at the nth time, is $p_n + b/a(1 + \rho)p_{n-1} - (b/a)\rho p_{n-2} + (s_0 - d_0)/a = 0$. The equilibrium price is obtained by setting $p_n = p_{n-1} = p_{n-2} = p_e$, and one finds $p_e = (d_0 - s_0)/(a + b)$. The homogeneous equation has the characteristic polynomial $\lambda^2 + (b/a)(1 + \rho)\lambda - (b/a)\rho = 0$. With λ_1 and λ_2 as the roots the general solution of the full equation is $p_n = c_1\lambda_1^n + c_2\lambda_2^n + p_e$, since p_e is a solution of the full equation. This is one method for finding the solution of the nonhomogeneous equation.

Generating Function (z Transform)

An elegant way of solving linear difference equations with constant coefficients, among other applications, is by use of *generating functions* or, as an alternative, the z transform. The generating function of a sequence $\{y_n\}$, $n = 0, 1, 2, \ldots$, is the function $f(x)$ given by the formal series $f(x) = \Sigma_{n=0}^{\infty} y_n x^n$. The z transform of the same sequence is $z(x) = \Sigma_{n=0}^{\infty} y_n x^{-n}$. Clearly, $z(x) = f(1/x)$. A table of some important sequences is given in Table 19.4.1.

TABLE 19.4.1 Important Sequences

y_n	$f(x)$	Convergence Domain
1	$(1-x)^{-1}$	$\lvert x\rvert < 1$
n	$x(1-x)^{-2}$	$\lvert x\rvert < 1$
n^m	$xp_m(x)(1-x)^{-n-1*}$	$\lvert x\rvert < 1$
k^n	$(1-kx)^{-1}$	$\lvert x\rvert < k^{-1}$
e^{an}	$(1-e^a x)^{-1}$	$\lvert x\rvert < e^{-a}$
$k^n \cos an$	$\dfrac{1-kx\cos a}{1-2kx\cos a+k^2x^2}$	$\lvert x\rvert < k^{-1}$
$k^n \sin an$	$\dfrac{kx\sin a}{1-2kx\cos a+k^2x^2}$	$\lvert x\rvert < k^{-1}$
$\binom{n}{m}$	$x^m(1-x)^{-m-1}$	$\lvert x\rvert < 1$
$\binom{k}{n}$	$(1+x)^k$	$\lvert x\rvert < 1$

* The term $p_m(z)$ is a polynomial of degree m satisfying $p_{m+1}(z) = (mz+1)\cdot p_m(z) + z(1-z)\,p'_m(x)$, $p_1 = 1$.

To solve the linear difference equation $\Sigma_{i=0}^{k} p_i y_{n+k-i} = 0$, $p_0 = 1$ we associate with it the two formal series $P = p_0 + p_1x + \cdots + p_kx^k$ and $Y = y_0 + y_1x + y_2x^{2} + \cdots$. If $p(x)$ is the characteristic polynomial then $P(x) = x^kp(1/x) = \bar{p}(x)$. The *product* of the two series is $Q = YP = q_0 + q_1x + \cdots + q_{k-1}x^{k-1} + q_kx^k + \cdots$ where $q_n = \Sigma_{i=0}^{n} p_i y_{n-i}$. Because $p_{k+1} = p_{k+2} = \cdots = 0$, it is obvious that $q_{k+1} = q_{k+2} = \cdots = 0$ — that is, Q is a polynomial (formal series with finite number of terms). Then $Y = P^{-1}Q = q(x)/\bar{p}(x) = q(x)/x^kp(1/x)$, where p is the characteristic polynomial and $q(x) = \Sigma_{i=0}^{k} q_ix^i$. The roots of $\bar{p}(x)$ are x_i^{-1} where the x_i are the roots of $p(x)$.

Theorem 1. If the roots of $p(x)$ are less than one in absolute value, then $Y(x)$ converges for $\lvert x\rvert < 1$.

Theorem 2. If $p(x)$ has no roots greater than one in absolute value and those on the unit circle are simple roots, then the coefficients y_n of Y are bounded. Now $q_k = g_0$, $q_{n+k} = g_n$, and $Q(x) = Q_1(x) + x^kQ_2(x)$. Hence $\Sigma_{i=1}^{\infty} y_ix^i = [Q_1(x) + x^kQ_2(x)]/[\bar{p}(x)]$.

Example 19.4.2. Consider the equation $y_{n+1} + y_n = -(n+1)$, $y_0 = 1$. Here $Q_1 = 1$, $Q_2 = -\Sigma_{n=0}^{\infty}(n+1)x^n = -1/(1-x)^2$.

$$G(x) = \frac{1 - x/(1-x)^2}{1+x} = \frac{5}{4}\frac{1}{1+x} - \frac{1}{4}\frac{1}{1-x} - \frac{1}{2}\frac{x}{(1-x)^2}$$

Using the table term by term, we find $\Sigma_{n=0}^{\infty} y_nx^n = \Sigma_{n=0}^{\infty}[{}^5/_4(-1)^n - {}^1/_4 - {}^1/_2\, n]x^n$, so $y_n = {}^5/_4(-1)^n - {}^1/_4 - {}^1/_2\, n$.

References

Fort, T. 1948. *Finite Differences and Difference Equations in the Real Domain.* Oxford University Press, London.

Jordan, C. 1950. *Calculus of Finite Differences,* Chelsea, New York.

Jury, E. I. 1964. *Theory and Applications of the Z Transform Method.* John Wiley & Sons, New York.

Lakshmikantham, V. and Trigrante, D. 1988. *Theory of Difference Equations.* Academic Press, Boston, MA.

Levy, H. and Lessman, F. 1961. *Finite Difference Equations.* Macmillan, New York.

Miller, K. S. 1968. *Linear Difference Equations,* Benjamin, New York.

Wilf, W. S. 1994. *Generating Functionology,* 2nd ed. Academic Press, Boston, MA.

19.5 Differential Equations

William F. Ames

Any equation involving derivatives is called a *differential equation*. If there is only one independent variable the equation is termed a *total differential equation* or an *ordinary differential equation*. If there is more than one independent variable the equation is called a *partial differential equation*. If the highest-order derivative is the nth then the equation is said to be nth order. If there is no function of the dependent variable and its derivatives other than the linear one, the equation is said to be *linear*. Otherwise, it is *nonlinear*. Thus $(d^3y/dx^3) + a(dy/dx) + by = 0$ is a *linear* third-order ordinary (total) differential equation. If we replace by with by^3, the equation becomes nonlinear. An example of a second-order linear partial differential equation is the famous wave equation $(\partial^2u/\partial x^2) - a^2(\partial^2u/\partial t^2) = f(x)$. There are two independent variables x and t and $a^2 > 0$ (of course). If we replace $f(x)$ by $f(u)$ (say u^3 or $\sin u$) the equation is nonlinear. Another example of a nonlinear third-order partial differential equation is $u_t + uu_x = au_{xxx}$. This chapter uses the common subscript notation to indicate the partial derivatives.

Now we briefly indicate some methods of solution and the solution of some commonly occurring equations.

Ordinary Differential Equations

First-Order Equations

The *general* first-order equation is $f(x, y, y') = 0$. Equation capable of being written in either of the forms $y' = f(x)g(y)$ or $f(x)g(y)y' + F(x)G(y) = 0$ are *separable* equations. Their solution is obtained by using $y' = dy/dx$ and writing the equations in differential form as $dy/g(y) = f(x)dx$ or $g(y)[dy/G(y)] = -F(x)[dx/f(x)]$ and integrating. An example is the famous *logistic* equation of inhibited growth $(dy/dt) = ay(1 - y)$. The integral of $dy/y(1 - y) = adt$ is $y = 1/[1 + (y_0^{-1} - 1)e^{-at}]$ for $t \geq 0$ and $y(0) = y_0$ (the initial state called the *initial condition*).

Equations may not have unique solutions. An example is $y' = 2y^{1/2}$ with the initial condition $y(0) = 0$. One solution by separation is $y = x^2$. But there are an *infinity* of others — namely, $y_a(x) = 0$ for $-\infty < x \leq a$, and $(x - a)^2$ for $a \leq x < \infty$.

If the equation $P(x, y)dy + Q(x, y)dy = 0$ is reducible to

$$\frac{dy}{dx} = f\left(\frac{y}{x}\right) \quad \text{or} \quad \frac{dy}{dx} = f\left(\frac{a_1x + b_1y + c_1}{a_2x + b_2y + c_2}\right)$$

the equation is called *homogenous* (nearly homogeneous). The first form reduces to the separable equation $u + x(du/dx) = f(u)$ with the substitution $y/x = u$. The nearly homogeneous equation is handled by setting $x = X + a$, $y = Y + \beta$, and choosing α and β so that $a_1\alpha + b_1\beta + c_1 = 0$ and $a_2\alpha + b_2\beta + c_2 = 0$. If $\begin{vmatrix} a_1 & b_1 \\ a_2 & b_2 \end{vmatrix} \neq 0$ this is always possible; the equation becomes $dY/dX = [a_1 + b_1(Y/X)]/[a_2 + b_2(Y/X)]$ and the substitution $Y = Xu$ gives a separable equation. If $\begin{vmatrix} a_1 & b_1 \\ a_2 & b_2 \end{vmatrix} = 0$ then $a_2x + b_2y = k(a_1x + b_1y)$ and the equation becomes $du/dx = a_1 + b_1(u + c_1)/(ku + c_2)$, with $u = a_1x + b_1y$. Lastly, any equation of the form $dy/dx = f(ax + by + c)$ transforms into the separable equation $du/dx = a + bf(u)$ using the change of variable $u = ax + by + c$.

The general first-order linear equation is expressible in the form $y' + f(x)y = g(x)$. It has the *general solution* (a solution with an arbitrary constant c)

$$y(x) = \exp\left[-\int f(x)\,dx\right]\left\{c + \int \exp[f(x)]g(x)\,dx\right\}$$

Two noteworthy examples of first-order equations are as follows:

1. An often-occurring nonlinear equation is the *Bernoulli equation,* $y' + p(x)y = g(x)y^{\alpha}$, with α real, $\alpha \neq 0$, $\alpha \neq 1$. The transformation $z = y^{1-\alpha}$ converts the equation to the linear first-order equation $z' + (1 - \alpha)p(x)z = (1 - \alpha)q(x)$.
2. The famous *Riccati equation,* $y' = p(x)y^2 + q(x)y + r(x)$, cannot in general be solved by integration. But some useful transformations are helpful. The substitution $y = y_1 + u$ leads to the equation $u' - (2py_1 + q)u = pu^2$, which is a Bernoulli equation for u. The substitution $y = y_1 + v^{-1}$ leads to the equation $v' + (2py_1 + q)v + p = 0$, which is a linear first-order equation for v. Once either of these equations has been solved, the general solution of the Riccati equation is $y = y_1 + u$ or $y = y_1 + v^{-1}$.

Second-Order Equations

The simplest of the second-order equations is $y'' + ay' + by = 0$ (a, b real), with the initial conditions $y(x_0) = y_0$, $y'(x_0) = y_0'$ or the boundary conditions $y(x_0) = y_0$, $y(x_1) = y_1$. The general solution of the equation is given as follows.

1. $a^2 - 4b > 0$, $\lambda_1 = {}^1/_2\,(-a + \sqrt{a^2 - 4b})$, $\lambda_2 = {}^1/_2\,(-a - \sqrt{a^2 - 4b})$
   $y = c_1 \exp(\lambda_1 x) + c_2 \exp(\lambda_2 x)$
2. $a^2 - 4b = 0$, $\lambda_1 = \lambda_2 = -\frac{a}{2}$, $y = (c_1 + c_2 x)\exp(\lambda_1 x)$
3. $a^2 - 4b < 0$, $\lambda_1 = {}^1/_2\,(-a + i\sqrt{4b - a^2})$, $\lambda_2 = {}^1/_2\,(-a - i\sqrt{4b - a^2})$,
   $i^2 = -1$

   With $p = -a/2$ and $q = {}^1/_2\sqrt{4b - a^2}$,

   $$y = c_1 \exp[(p + iq)x] + c_2 \exp[(p - iq)x] = \exp(px)[A\sin qx + B\cos qx]$$

   The initial conditions or boundary conditions are used to evaluate the arbitrary constants c_1 and c_2 (or A and B).

   Note that a linear problem with specified data may not have a solution. This is especially serious if numerical methods are employed without serious thought.

For example, consider $y'' + y = 0$ with the boundary condition $y(0) = 1$ and $y(\pi) = 1$. The general solution is $y = c_1 \sin x + c_2 \cos x$. The first condition $y(0) = 1$ gives $c_2 = 1$, and the second condition requires $y(\pi) = c_1 \sin \pi + \cos \pi$ or "$1 = -1$," which is a *contradiction.*

Example 19.5.1 — The Euler Strut. When a strut of uniform construction is subject to a compressive load P it exhibits no transverse displacement until P exceeds some critical value P_1. When this load is exceeded, buckling occurs and large deflections are produced as a result of small load changes. Let the rod of length ℓ be placed as shown in Figure 19.5.1.

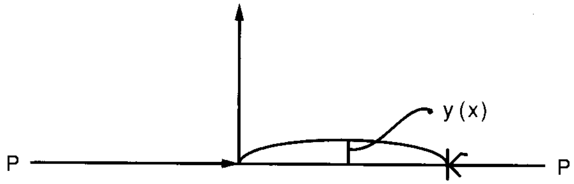

FIGURE 19.5.1

From the linear theory of elasticity (Timoshenko), the transverse displacement $y(x)$ satisfies the linear second-order equation $y'' + (Py/EI) = 0$, where E is the modulus of elasticity and I is the moment of inertia of the strut. The boundary conditions are $y(0) = 0$ and $y(a) = 0$. With $k^2 = P/EI$ the general solution is $y = c_1 \sin kx + c_2 \cos kx$. The condition $y(0) = 0$ gives $c_2 = 0$. The second condition gives $c_1 \sin ka = 0$. Since $c_1 = 0$ gives the trival solution $y = 0$ we must have $\sin ka = 0$. This occurs for $ka = n\pi$, $n = 0, 1, 2, \ldots$ (these are called *eigenvalues*). The first nontrivial solution occurs for $n = 1$ — that is, $k = \pi/a$ — whereupon $y_1 = c_1 \sin(\pi/a)$, with arbitrary c_1. Since $P = EIk^2$ the critical compressive load is $P_1 = EI\,\pi^2/a^2$. This is the buckling load. The weakness of the linear theory is its failure to model the situation when buckling occurs.

Example 19.5.2 — Some Solvable Nonlinear Equations. Many physical phenomena are modeled using nonlinear second-order equations. Some general cases are given here.

1. $y'' = f(y)$, *first integral* $(y')^2 = 2\int f(y)\,dy + c$.
2. $f(x, y', y'') = 0$. Set $p = y'$ and obtain a first-order equation $f(x, p, dp/dx) = 0$. Use first-order methods.
3. $f(y, y', y'') = 0$. Set $p = y'$ and then $y'' = p(dp/dy)$ so that a first-order equation $f\,[y, p, p(dp/dy) = 0$ for p as a function of y is obtained.
4. The *Riccati transformation* $du/dx = yu$ leads to the Riccati chain of equations, which linearize by raising the order. Thus,

Equation in y	Equation in u
1. $y' + y^2 = f(x)$	$u'' = f(x)u$
2. $y'' + 3yy' + y^3 = f(x)$	$u''' = f(x)u$
3. $y''' + 6y^2y' + 3(y')^2 + 4yy'' = f(x)$	$u^{(iv)} = f(x)u$

This method can be generalized to $u' = a(x)yu$ or $u' = a(x)f(u)y$.

Second-Order Inhomogeneous Equations

The general solution of $a_0(x)y'' + a_1(x)y' + a_2(x)y = f(x)$ is $y = y_H(x) + y_p(x)$ where $y_H(x)$ is the general solution of the homogeneous equation (with the right-hand side zero) and y_p is the particular integral of the equation. Construction of particular integrals can sometimes be done by the *method of undetermined coefficients*. See Table 19.5.1. This applies only to the linear constant coefficient case in which the function $f(x)$ is a linear combination of a polynomial, exponentials, sines and cosines, and some products of these functions. This method has as its base the observation that repeated differentiation of such functions gives rise to similar functions.

TABLE 19.5.1 Method of Undetermined Coefficients — Equation $L(y) = f(x)$ (Constant Coefficients)

Terms in $f(x)$	Terms To Be Included in $y_p(x)$
1. Polynomial of degree n	(i) If $L(y)$ contains y, try $y_p = a_0x^n + a_1x^{n-1} + \cdots + a_n$, (ii) If $L(y)$ does not contain y and lowest-order derivative is $y^{(r)}$, try $y_p = a_0x^{n+r} + \cdots + a_nx^r$.
2. $\sin qx$, $\cos qx$	(i) $\sin qx$ and/or $\cos qx$ are not in y_H; $y_p = B \sin qx + C \cos qx$. (ii) y_H contains terms of form $x^r \sin qx$ and/or $x^r \cos qx$ for $r = 0, 1, \ldots, m$; include in y_p terms of the form $a_0x^{m+1} \sin qx + a_1x^{m+1} \cos qx$.
3. e^{ax}	(i) y_H does not contain e^{ax}; include Ae^{ax} in y_p. (ii) y_H contains $e^{ax}, xe^{ax}, \ldots, x^ne^{ax}$; include in y_p terms of the form $Ax^{n+1}e^{ax}$,
4. $e^{px} \sin qx$, $e^{px} \cos qx$	(i) y_H does not contain these terms; in y_p include $Ae^{px} \sin qx + Be^{px} \cos qx$. (ii) y_H contains $x^r e^{px} \sin qx$ and/or $x^r e^{px} \cos qx$; $r = 0,1, \ldots, m$ include in y_p. $Ax^{m+1}e^{px} \sin qx + Bx^{m+1} e^{px} \cos qx$.

Example 19.5.3. Consider the equation $y'' + 3y' + 2y = \sin 2x$. The characteristic equation of the homogeneous equation $\lambda^2 + 3\lambda + 2 = 0$ has the two roots $\lambda_1 = -1$ and $\lambda_2 = -2$. Consequently, $y_H = c_1e^{-x} + c_2e^{-2x}$. Since $\sin 2x$ is not linearly dependent on the exponentials and since $\sin 2x$ repeats after two differentiations, we assume a particular solution with undetermined coefficients of the form $y_p(x) = B \sin 2x + C \cos 2x$. Substituting into the original equation gives $-(2B + 6C) \sin 2x + (6B - 2C) \cos 2x = \sin 2x$. Consequently, $-(2B + 6C) = 1$ and $6B - 2C = 0$ to satisfy the equation. These two equations in two unknowns have the solution $B = -1/20$ and $C = -3/20$. Hence $y_p = -1/20 (\sin 2x + 3 \cos 2x)$ and $y = c_1e^{-x} + c_2e^{-2x} - 1/20 (\sin 2x + 3 \cos 2x)$.

A general method for finding $y_p(x)$ called *variation of parameters* uses as its starting point $y_H(x)$. This method applies to *all* linear differential equations irrespective of whether they have constant coefficients. But it assumes $y_H(x)$ is known. We illustrate the idea for $a(x)y'' + b(x)y' + c(x)y = f(x)$. If the solution of the homogeneous equation is $y_H(x) = c_1\phi_1(x) + c_2\phi_2(x)$, then vary the parameters c_1 and c_2 to seek $y_p(x)$ as $y_p(x) = u_1(x)\phi_1(x) + u_2(x)\phi_2(x)$. Then $y_P' = u_1 \phi_1' + u_2 \phi_2' + u_1' \phi_1 + u_2' \phi_2$ and choose $u_1' \phi_1 + u_2' \phi_2 = 0$. Calculating y_P'' and setting in the original equation gives $a(x)\, u_1'\phi_1' + a(x)\, u_2'\phi_2' = f$. Solving the last two equations for u_1' and u_2' gives $u_1' = -\phi_2 f/wa$, $u_2' = \phi_1 f/wa$, where $w = \phi_1 \phi_2' - \phi_1' \phi_2 \neq 0$. Integrating the general solution gives $y = c_1\phi_1(x) + c_2\phi_2(x) - \{\int[\phi_2 f(x)]/wa\}\phi_1(x) + [\int(\phi_1 f/wa)dx]\phi_2(x)$.

Example 19.5.4. Consider the equations $y'' - 4y = \sin x/(1 + x^2)$ and $y_H = c_1e^{-2x} + c_2e^{-2x}$. With $\phi_1 = e^{2x}$, and $\phi_2 = e^{-2x}$, $w = 4$, so the general solution is

$$y = c_1e^{2x} + c_2e^{-2x} - \frac{e^{-2x}}{4}\int \frac{e^{2x}\sin x}{1+x^2}\,dx + \frac{e^{2x}}{4}\int \frac{e^{-2x}\sin x}{1+x^2}\,dx$$

The method of variation of parameters can be generalized as described in the references.

Higher-order systems of linear equations with constant coefficients are treated in a similar manner. Details can be found in the references.

Series Solution

The solution of differential equations can only be obtained in closed form in special cases. For all others, series or approximate or numerical solutions are necessary. In the simplest case, for an initial value problem, the solution can be developed as a Taylor series expansion about the point where the initial data are specified. The method fails in the *singular case* — that is, a point where the coefficient of the highest-order derivative is zero. The general method of approach is called the *Frobenius method.*

To understand the nonsingular case consider the equation $y'' + xy = x^2$ with $y(2) = 1$ and $y'(2) = 2$ (an initial value problem). We seek a series solution of the form $y(x) = a_0 + a_1(x - 2) + a_2(x - 2)^2 + \cdots$. To proceed, set $1 = y(2) = a_0$, which evaluates a_0. Next $y'(x) = a_1 + 2a_2(x - 2) + \cdots$, so $2 = y'(2) = a_1$ or $a_1 = 2$. Next $y''(x) = 2a_2 + 6a_3(x - 2) + \cdots$. and from the equation, $y'' = x^2 - xy$, so $y''(2) = 4 - 2y(2) = 4 - 2 = 2$. Hence $2 = 2a_2$ or $a_2 = 1$. Thus, to third-order $y(x) = 1 + 2(x - 2) + (x - 2)^2 + R_2(x)$, where the remainder $R_2(x)$ $[(x-2)^3/3]y'''(\xi)$, where $2 < \xi < x$ can be bounded for each x by finding the maximum of $y'''(x) = 2x - y - xy'$. The third term of the series follows by evaluating $y'''(2) = 4 - 1 - 2 \cdot 2 = -1$, so $6a_3 = -1$ or $a_3 = -1/6$.

By now the nonsingular process should be familiar. The algorithm for constructing a series solution about a nonsingular (ordinary) point x_0 of the equation $P(x)y'' + Q(x)y' + R(x)y = f(x)$ (note that $P(x_0) \neq 0$) is as follows:

1. Substitute into the differential equation the expressions

$$y(x) = \sum_{n=0}^{\infty} a_n\left(x - x_0\right)^n, \qquad y'(x) = \sum_{n=1}^{\infty} na_n\left(x - x_0\right)^{n-1}, \qquad y''(x) = \sum_{n=2}^{\infty} n(n-1)a_n\left(x - x_0\right)^{n-2}$$

2. Expand $P(x)$, $Q(x)$, $R(x)$, and $f(x)$ about the point x_0 in a power series in $(x - x_0)$ and substitute these series into the equation.
3. Gather all terms involving the same power of $(x - x_0)$ to arrive at an identity of the form $\Sigma_{n=0}^{\infty} A_n(x - x_0)^n \equiv 0$.
4. Equate to zero each coefficient A_n of step 3.
5. Use the expressions of step 4 to determine a_2, a_3, … in terms of a_0, a_1 (we need two arbitrary constants) to arrive at the general solution.
6. With the given initial conditions, determine a_0 and a_1.

If the equation has a regular singular point — that is, a point x_0 at which $P(x)$ vanishes and a series expansion is sought about that point — a solution is sought of the form $y(x) = (x - x_0)^r \Sigma_{n=0}^{\infty} a_n(x - x_0)^n$, $a_0 \neq 0$ and the index r and coefficients a_n must be determined from the equation by an algorithm analogous to that already described. The description of this Frobenius method is left for the references.

Partial Differential Equations

The study of partial differential equations is of continuing interest in applications. It is a vast subject, so the focus in this chapter will be on the most commonly occurring equations in the engineering literature — the second-order equations in two variables. Most of these are of the three basic types: elliptic, hyperbolic, and parabolic.

Elliptic equations are often called *potential equations* since they occur in potential problems where the potential may be temperature, voltage, and so forth. They also give rise to the steady solutions of parabolic equations. They require boundary conditions for the complete determination of their solution.

Hyperbolic equations are often called *wave equations* since they arise in the propagation of waves. For the development of their solutions, initial and boundary conditions are required. In principle they are solvable by the method of characteristics.

Parabolic equations are usually called *diffusion equations* because they occur in the transfer (diffusion) of heat and chemicals. These equations require initial conditions (for example, the initial temperature) and boundary conditions for the determination of their solutions.

Partial differential equations (PDEs) of the second order in two independent variables (x, y) are of the form $a(x, y)u_{xx} + b(x, y)u_{xy} + c(x, y)u_{yy} = E(x, y, u, u_x, u_y)$. If $E = E(x, y)$ the equation is linear; if E depends also on u, u_x, and u_y, it is said to be *quasilinear,* and if E depends only on x, y, and u, it is *semilinear.* Such equations are classified as follows: If $b^2 - 4ac$ is less than, equal to, or greater than zero at some point (x, y), then the equation is elliptic, parabolic, or hyperbolic, respectively, at that point. A PDE of this form can be transformed into canonical (standard) forms by use of new variables. These standard forms are most useful in analysis and numerical computations.

For hyperbolic equations the standard form is $u_{\xi\eta} = \phi(u, u_\eta, u_\xi, \eta, \xi)$, where $\xi_x/\xi_y = (-b + \sqrt{b^2 - 4ac})/2a$, and $\eta_x/\eta_y = (-b - \sqrt{b^2 - 4ac})/2a$. The right-hand sides of these equations determine the so-called characteristics $(dy/dx)|_+ = (-b + \sqrt{b^2 - 4ac})/2a$, $(dy/dx)|_- = (-b - \sqrt{b^2 - 4ac})/2a$.

Example 19.5.5. Consider the equation $y^2u_{xx} - x^2u_{yy} = 0$, $\xi_x/\xi_y = -x/y$, $\eta_x/\eta_y = x/y$, so $\xi = y^2 - x^2$ and $\eta = y^2 + x^2$. In these new variables the equation becomes $u_{\xi\eta} = (\xi u_\eta - \eta u_\xi)/2(\xi^2 - \eta^2)$.

For parabolic equations the standard form is $u_{\xi\xi} = \phi(u, u_\eta, u_\xi, \eta, \xi)$ or $u_{\eta\eta} = \phi(u, u_\eta, u_\xi, \xi, \eta)$, depending upon how the variables are defined. In this case $\xi_x/\xi_y = -b/2a$ if $a \neq 0$, and $\xi_x/\xi_y = -b/2c$ if $c \neq 0$. Only ξ must be determined (there is only one characteristic) and η can be chosen as any function that is linearly independent of ξ.

Example 19.5.6. Consider the equation $y^2u_{xx} - 2xyu_{xy} + x^2u_{yy} + u_y = 0$. Clearly, $b^2 - 4ac = 0$. Neither a nor c is zero so either path can be chosen. With $\xi_x/\xi_y = -b/2a = x/y$, there results $\xi = x^2 + y^2$. With $\eta = x$, the equation becomes $u_{\eta\eta} = [2(\xi + \eta)u_\xi + u_\eta]/(\xi - \eta^2)$.

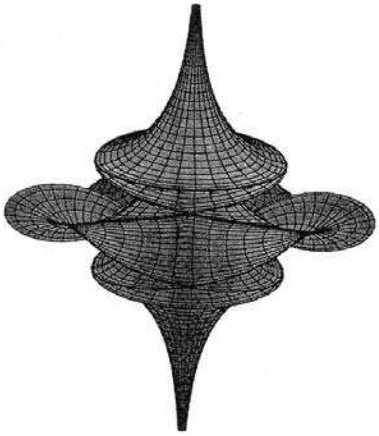

Figure 19.5.2

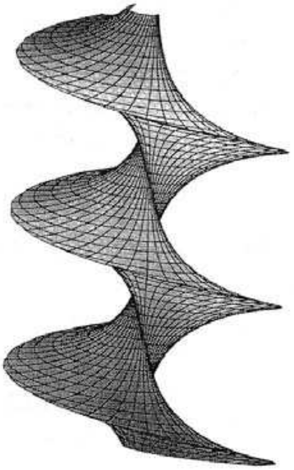

Figure 19.5.3

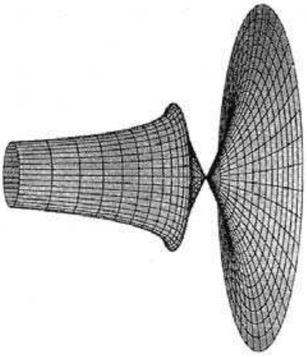

Figure 19.5.4

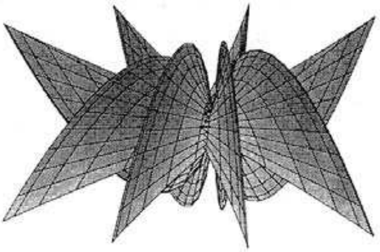

Figure 19.5.5

FIGURE 19.5.2 to 19.5.5 The mathematical equations used to generate these three-dimensional figures are worth a thousand words. The figures shown illustrate some of the nonlinear ideas of engineering, applied physics, and chemistry. Figure 19.5.2 represents a breather soliton surface for the sine-Gordon equation $w_{uv} = \sin w$ generated by a Backlund transformation. A single-soliton surface for the sine-Gordon equation $w_{uv} = \sin w$ is illustrated in Figure 19.5.3. Figure 19.5.4 represents a single-soliton surface for the Tzitzecia-Dodd-Bullough equation associated with an integrable anisentropic gas dynamics system. Figure 19.5.5 represents a single-soliton Bianchi surface.
The solutions to the equations were developed by W. K. Schief and C. Rogers at the Center for Dynamical Systems and Nonlinear Studies at the Georgia Institute of Technology and the University of New South Wales in Sydney, Australia. All of these three-dimensional projections were generated using the MAPLE software package. (Figures courtesy of Schief and Rogers).

For *elliptic equations* the standard form is $u_{\alpha\alpha} + u_{\beta\beta} = \phi(u, u_\alpha, u_\beta, \alpha, \beta)$, where ξ and η are determined by solving the ξ and η equations of the hyperbolic system (they are complex) and taking $\alpha = (\eta + \xi)/2$, $\beta = (\eta - \xi)/2i(i^2 = -1)$. Since ξ and η are complex conjugates, both α and β are real.

Example 19.5.7. Consider the equation $y^2u_{xx} + x^2u_{yy} = 0$. Clearly, $b^2 - 4ac < 0$, so the equation is elliptic. Then $\xi_x/\xi_y = -ix/y$, $\eta_x/\eta_y = ix/y$, so $\alpha = (\eta + \xi)/2 = y^2$ and $\beta = (\eta - \xi)/2i = x^2$. The standard form is $u_{\alpha\alpha} + u_{\beta\beta} = -(u_\alpha/2\alpha + u_\beta/2\beta)$.

Methods of Solution

Separation of Variables. Perhaps the most elementary method for solving linear PDEs with homogeneous boundary conditions is the method of *separation of variables.* To illustrate, consider $u_t - u_{xx} = 0$,

$u(x, 0) = f(x)$ (the initial condition) and $u(0, t) = u(1, t) = 0$ for $t > 0$ (the boundary conditions). A solution is assumed in "separated form" $u(x, t) = X(x)T(t)$. Upon substituting into the equation we find $\dot{T}/T = X''/X$ (where $\dot{T} = dT/dt$ and $X'' = d^2X/dx^2$). Since $T = T(t)$ and $X = X(x)$, the ratio must be constant, and for finiteness in t the constant must be negative, say $-\lambda^2$. The solutions of the separated equations $X'' + \lambda^2 X = 0$ with the boundary conditions $X(0) = 0$, $X(1) = 0$, and $\dot{T} = -\lambda^2 T$ are $X = A \sin \lambda x + B \cos \lambda x$ and $T = Ce^{-\lambda^2 t}$, where A, B, and C are arbitrary constants. To satisfy the boundary condition $X(0) = 0$, $B = 0$. An infinite number of values of λ (eigenvalues), say $\lambda_n = n\pi (n = 1, 2, 3, \ldots)$, permit all the eigenfunctions $X_n = b_n \sin \lambda_n x$ to satisfy the other boundary condition $X(1) = 0$. The solution of the equation and boundary conditions (not the initial condition) is, by superposition, $u(x, t) = \Sigma_{n=1}^{\infty} b_n e^{-n^2\pi^2 t} \cdot \sin n\pi x$ (a Fourier sine series), where the b_n are arbitrary. These values are obtained from the initial condition using the orthogonality properties of the trigonometric function (e.g., $\int_{-\pi}^{\pi} \sin mx \sin n\, x\, d\, x$ is 0 for $m \neq n$ and is π for $m = n \neq 0$) to be $b_n = 2 \int_0^1 f(r) \sin n\, \pi\, r\, d\, r$. Then the solution of the problem is $u(x, t) = \Sigma_{n=1}^{\infty} [2 \int_0^1 f(r) \sin n\, \pi\, r\, d\, r]\, e^{-n^2\pi^2 t} \sin n\, \pi\, x$, which is a Fourier sine series.

If $f(x)$ is a piecewise smooth or a piecewise continuous function defined for $a \le x \le b$, then its Fourier series within $a \le x \le b$ as its fundamental interval (it is extended periodically ouside that interval) is

$$f(x) \sim \tfrac{1}{2} a_0 + \sum_{n=1}^{\infty} a_n \cos\left[2n\pi x/(b-a)\right] + b_n \sin\left[2n\pi x/(b-a)\right]$$

where

$$a_n = \left[\frac{2}{(b-a)}\right] \int_a^b f(x) \cos\left[2n\pi x/(b-a)\right] dx, \quad n = 0,\ 1,\ \ldots$$

$$b_n = \left[\frac{2}{(b-a)}\right] \int_a^b f(x) \sin\left[2n\pi x/(b-a)\right] dx, \quad n = 1,\ 2,\ \ldots$$

The Fourier sine series has $a_n \equiv 0$, and the Fourier cosine series has $b_n \equiv 0$. The symbol ~ means that the series converges to $f(x)$ at points of continuity, and at the (allowable) points of finite discontinuity the series converges to the *average value* of the discontinuous values.

Caution: This method *only* applies to linear equations with homogeneous boundary conditions. Linear equations with variable coefficients use other orthogonal functions, such as the Besel functions, Laguerre functions, Chebyshev functions, and so forth.

Some inhomogeneous boundary value problems can be transformed into homogeneous ones. Consider the problem $u_t - u_{xx} = 0$, $0 \le x \le 1$, $0 \le t < \infty$ with initial condition $u(x, 0) = f(x)$, and boundary conditions $u(0, t) = g(t)$, $u(1, t) = h(t)$. To homogenize the boundary conditions set $u(x, t) = w(x, t) + x[h(t) - g(t)] + g(t)$ and then solve $w_t - w_x = [\dot{g}(t) - \dot{h}(t)]x - \dot{g}(t)$ with the initial condition $w(x, 0) = f(x) - x[h(0) - g(0)] + g(0)$ and $w(0, t) = w(1, t) = 0$.

Operational Methods. A number of integral transforms are useful for solving a variety of linear problems. To apply the Laplace transform to the problem $u_t - u_{xx} = \delta(x)\, \delta(t)$, $-\infty < x < \infty$, $0 \le t$ with the initial condition $u(x, 0^-) = 0$, where δ is the Dirac delta function, we multiply by e^{-st} and integrate with respect to t from 0 to ∞. With the Laplace transform of $u(x, t)$ denoted by $U(x, s)$ — that is, $U(x, s) = \int_0^{\infty} e^{-st} u(x, t)\, dt$ — we have $sU - U_{xx} = \delta(x)$, which has the solution

$$U(x,s) = A(s)e^{-x\sqrt{s}} + B(s)e^{x\sqrt{s}} \qquad \text{for } x > 0$$

$$U(x,s) = C(s)e^{-x\sqrt{s}} + D(s)e^{x\sqrt{s}} \qquad \text{for } x < 0$$

Clearly, $B(s) = C(s) = 0$ for bounded solutions as $|x| \to \infty$. Then, from the boundary condition, $U(0^+, s) - U(0^-, s) = 0$ and integration of $sU - U_{xx} = \delta(x)$ from 0^- to 0^+ gives $U_x(0^+, s) - U(0^-, s) = -1$, so $A = D =$

$1/2\sqrt{s}$. Hence, $U(x, s) = (1/2\sqrt{s})e^{-\sqrt{s}|x|}$ and the inverse is $u(x, t) = (1/2\,\pi i)\int_\Gamma e^{st}U(x, s)\,ds$, where Γ is a Bromwich path, a vertical line taken to the right of all singularities of U on the sphere.

Similarity (Invariance). This very useful approach is related to dimensional analysis; both have their foundations in group theory. The three important transformations that play a basic role in Newtonian mechanics are translation, scaling, and rotations. Using two independent variables x and t and one dependent variable $u = u(x, t)$, the *translation group* is $\bar{x} = x + \alpha a$, $\bar{t} = t + \beta a$, $\bar{u} = u + \gamma a$; the *scaling group* is $\bar{x} = a^\alpha x$, $\bar{t} = a^\beta t$, and $\bar{u} = a^\gamma u$; the *rotation group* is $\bar{x} = x\cos a + t\sin a$, $\bar{t} = t\cos a - x\sin a$, $\bar{u} = u$, with a nonnegative real number a. Important in which follows are the *invariants* of these groups. For the translation group there are two $\eta = x - \lambda t$, $\lambda = \alpha/\beta$, $f(\eta) = u - \varepsilon t$, $\varepsilon = \gamma/\beta$ or $f(\eta) = u - \theta x$, $\theta = \gamma/\alpha$; for the scaling group the invariants are $\eta = x/t^{\alpha/\beta}$ (or $t/x^{\beta/\alpha}$) and $f(\eta) = u/t^{\gamma/\beta}$ (or $u/x^{\gamma/\alpha}$); for the rotation group the invariants are $\eta = x^2 + t^2$ and $u = f(\eta) = f(x^2 + t^2)$.

If a PDE and its data (initial and boundary conditions) are left invariant by a transformation group, then similar (invariant) solutions are sought using the invariants. For example, if an equation is left invariant under scaling, then solutions are sought of the form $u(x, t) = t^{\gamma/\beta} f(\eta)$, $\eta = xt^{-\alpha/\beta}$ or $u(x, t) = x^{\gamma/\alpha} f(tx^{-\beta/\alpha})$; invariance under translation gives solutions of the form $u(x, t) = f(x - \lambda t)$; and invariance under rotation gives rise to solutions of the form $u(x, t) = f(x^2 + t^2)$.

Examples of invariance include the following:

1. The equation $u_{xx} + u_{yy} = 0$ is invariant under rotation, so we search for solutions of the form $u = f(x^2 + y^2)$. Substitution gives the ODE $f' + \eta f'' = 0$ or $(\eta f')' = 0$. The solution is $u(x, t) = c\ln\eta = c\ln(x^2 + t^2)$, which is the (so-called) fundamental solution of Laplace's equation.
2. The nonlinear diffusion equation $u_t = (u^n u_x)_x$ $(n > 0)$, $0 \le x$, $0 \le t$, $u(0, t) = ct^n$ is invariant under scaling with the similar form $u(x, t) = t^n f(\eta)$, $\eta = xt^{-(n+1)/2}$. Substituting into the PDE gives the equation $(f^n f')' + ((n + 1)/2)\eta f' - nf = 0$, with $f(0) = c$ and $f(\infty) = 0$. Note that the equation is an ODE.
3. The wave equation $u_{xx} - u_{tt} = 0$ is invariant under translation. Hence, solutions exist of the form $u = f(x - \lambda t)$. Substitution gives $f''(1 - \lambda^2) = 0$. Hence, $\lambda = \pm 1$ or f is linear. Rejecting the trivial linear solution we see that $u = f(x - t) + g(x + t)$, which is the general (d'Alembert) solution of the wave equation; the quantities $x - t = \alpha$, $x + t = \beta$ are the characteristics of the next section.

The construction of all transformations that leave a PDE invariant is a solved problem left for the references.

The study of "solitons" (solitary traveling waves with special properties) has benefited from symmetry considerations. For example, the nonlinear third-order (Korteweg-de Vries) equation $u_t + uu_x - au_{xxx} = 0$ is invariant under translation. Solutions are sought of the form $u = f(x - \lambda t)$, and f satisfies the ODE, in $\eta = x - \lambda t$, $-\lambda f' + ff' - af''' = 0$.

Characteristics. Using the characteristics the solution of the hyperbolic problem $u_{tt} - u_{xx} = p(x, t)$, $-\infty < x < \infty$, $0 \le t$, $u(x, 0) = f(x)$, $u_t(x, 0) = h(x)$ is

$$u(x,t) = \tfrac{1}{2}\int_0^t d\tau \int_{x-(t-\tau)}^{x+(t-\tau)} p(\xi,\tau)\,d\xi + \tfrac{1}{2}\int_{x-t}^{x+t} h(\xi)\,d\xi + \tfrac{1}{2}\left[f(x+t) + f(x-t)\right]$$

The solution of $u_{tt} - u_{xx} = 0$, $0 \le x < \infty$, $0 \le t < \infty$, $u(x, 0) = 0$, $u_t(x, 0) = h(x)$, $u(0, t) = 0$, $t > 0$ is $u(x, t) = {}^1/_2 \int_{-x+t}^{x+t} h(\xi)\,d\xi$.

The solution of $u_{tt} - u_{xx} = 0$, $0 \le x < \infty$, $0 \le t < \infty$, $u(x, 0) = 0$, $u_t(x, 0) = 0$, $u(0, t) = g(t)$, $t > 0$ is

$$u(x,t) = \begin{cases} 0 & \text{if } t < x \\ g(t-x) & \text{if } t > x \end{cases}$$

From time to time, lower-order derivatives appear in the PDE in use. To remove these from the equation $u_{tt} - u_{xx} + au_x + bu_t + cu = 0$, where a, b, and c are constants, set $\xi = x + t$, $\mu = t - x$, whereupon $u(x, t) = u[(\xi - \mu)/2, (\xi + \mu)/2] = U(\xi, \mu)$, where $U_{\xi\mu} + [(b + a)/4]\, U_\xi + [(b - a)/4]\, U_\mu + (c/4)U = 0$. The transformation $U(\xi, \mu) = W(\xi, \mu) \exp[-(b - a)\xi/4 - (b + a)\mu/4]$ reduces to satisfying $W_{\xi\mu} + \lambda W = 0$, where $\lambda = (a^2 - b^2 + 4c)/16$. If $\lambda \neq 0$, we lose the simple d'Alembert solution. But the equation for W is still easier to handle.

In linear problems discontinuities propagate along characteristics. In nonlinear problems the situation is usually different. The characteristics are often used as new coordinates in the numerical method of characteristics.

Green's Function. Consider the diffusion problem $u_t - u_{xx} = \delta(t)\delta(x - \xi)$, $0 \le x < \infty$, $\xi > 0$, $u(0, t) = 0$, $u(x, 0) = 0$ $[u(\infty, t) = u(\infty, 0) = 0]$, a problem that results from a unit source somewhere in the domain subject to a homogeneous (zero) boundary condition. The solution is called a *Green's function of the first kind.* For this problem there is $G_1(x, \xi, t) = F(x - \xi, t) - F(x + \xi, t)$, where $F(x, t) = e^{-x^2/4t}/\sqrt{4\pi t}$ is the *fundamental* (invariant) *solution.* More generally, the solution of $u_t - u_{xx} = \delta(x - \xi)\,\delta(t - \tau)$, $\xi > 0$, $\tau > 0$, with the same conditions as before, is the Green's function of the first kind.

$$G_1(x, \xi, t - \tau) = \frac{1}{\sqrt{4\pi(t - \tau)}}\left[e^{-(x-\xi)^2/4(t-\tau)} - e^{-(x+\xi)^2/4(t-\tau)}\right]$$

for the semi-infinite interval.

The solution of $u_t - u_{xx} = p(x, t)$, $0 \le x < \infty$, $0 \le t < \infty$, with $u(x, 0) = 0$, $u(0, t) = 0$, $t > 0$ is $u(x, t) = \int_0^t d\tau \int_0^\infty p(\xi, \tau)G_1(x, \xi, t - \tau)]\, d\,\xi$, which is a superposition. Note that the Green's function and the desired solution must both satisfy a zero boundary condition at the origin for this solution to make sense.

The solution of $u_t - u_{xx} = 0$, $0 \le x < \infty$, $0 \le t < \infty$, $u(x, 0) = f(x)$, $u(0, t) = 0$, $t > 0$ is $u(x, t) = \int_0^\infty f(\xi)G_1(x, \xi, t)\, d\,\xi$.

The solution of $u_t - u_{xx} = 0$, $0 \le x < \infty$, $0 \le t < \infty$, $u(x, 0) = 0$, $u(0, t) = g(t)$, $t > 0$ (nonhomogeneous) is obtained by transforming to a new problem that has a homogeneous boundary condition. Thus, with $w(x, t) = u(x, t) - g(t)$ the equation for w becomes $w_t - w_{xx} = -\dot{g}(t) - g(0)\,\delta(t)$ and $w(x, 0) = 0$, $w(0, t) = 0$. Using G_1 above, we finally obtain $u(x, t) = (x/\sqrt{4\pi})\int_0^t g(t - \tau)e^{-x^2/4t}/\tau^{3/2}\, d\tau$.

The Green's function approach can also be employed for elliptic and hyperbolic problems.

Equations in Other Spatial Variables. The sperically symmetric wave equation $u_{rr} + 2u_r/r - u_{tt} = 0$ has the general solution $u(\tau, t) = [f(t - r) + g(t + r)]/r$.

The Poisson-Euler-Darboux equation, arising in gas dynamics,

$$u_{rs} + N(u_r + u_s)/(r + s) = 0$$

where N is a positive integer ≥ 1, has the general solution

$$u(r,s) = k + \frac{\partial^{N-1}}{\partial r^{N-1}}\left[\frac{f(r)}{(r+s)^N}\right] + \frac{\partial^{N-1}}{\partial s^{N-1}}\left[\frac{g(s)}{(r+s)^N}\right]$$

Here, k is an arbitrary constant and f and g are arbitrary functions whose form is determined from the problem initial and boundary conditions.

Conversion to Other Orthogonal Coordinate Systems. Let (x^1, x^2, x^3) be rectangular (Cartesian) coordinates and (u^1, u^2, u^3) be any orthogonal coordinate system related to the rectangular coordinates by $x^i = x^i(u^1, u^2, u^3)$, $i = 1, 2, 3$. With $(ds)^2 = (dx^1)^2 + (dx^2)^2 + (dx^3)^2 = g_{11}(du^1)^2 + g_{22}(du^2)^2 + g_{33}(du^3)^2$, where

$g_{ii} = (\partial x^1/\partial u^i)^2 + (\partial x^2/\partial u^i)^2 + (\partial x^3/\partial u^i)^2$. In terms of these "metric" coefficients the basic operations of applied mathematics are expressible. Thus (with $g = g_{11}g_{22}g_{33}$)

$$dA = \left(g_{11}g_{22}\right)^{1/2}\, du^1\, du^2; \qquad dV = \left(g_{11}g_{22}g_{33}\right)^{1/2}\, du^1\, du^2\, du^3$$

$$\operatorname{grad}\phi = \frac{\vec{a}_1}{\left(g_{11}\right)^{1/2}}\frac{\partial\phi}{\partial u^1} + \frac{\vec{a}_2}{\left(g_{22}\right)^{1/2}}\frac{\partial\phi}{\partial u^2} + \frac{\vec{a}_3}{\left(g_{33}\right)^{1/2}}\frac{\partial\phi}{\partial u^3}$$

($\vec{a}_i$ are unit vectors in direction i);

$$\operatorname{div}\vec{E} = g^{-1/2}\left\{\frac{\partial}{\partial u^1}\left[\left(g_{22}g_{33}\right)^{1/2}E_1\right] + \frac{\partial}{\partial u^2}\left[\left(g_{11}g_{33}\right)^{1/2}E_2\right] + \frac{\partial}{\partial u^3}\left[\left(g_{11}g_{22}\right)^{1/2}E_3\right]\right\}$$

[here $\vec{E} = (E_1, E_2, E_3)$];

$$\begin{aligned}\operatorname{curl}\vec{E} = g^{-1/2}\Bigg\{&\vec{a}_1\left(g_{11}\right)^{1/2}\left(\frac{\partial}{\partial u^2}\left[\left(g_{33}\right)^{1/2}E_3\right] - \frac{\partial}{\partial u^3}\left[\left(g_{22}\right)^{1/2}E_2\right]\right)\\ &+ \vec{a}_2\left(g_{22}\right)^{1/2}\left(\frac{\partial}{\partial u^3}\left[\left(g_{11}\right)^{1/2}E_1\right] - \frac{\partial}{\partial u^1}\left[\left(g_{33}\right)^{1/2}E_3\right]\right)\\ &+ \vec{a}_3\left(g_{33}\right)^{1/2}\left(\frac{\partial}{\partial u^1}\left[\left(g_{22}\right)^{1/2}E_2\right] - \frac{\partial}{\partial u^2}\left[\left(g_{11}\right)^{1/2}E_1\right]\right)\Bigg\}\end{aligned}$$

$$\operatorname{div}\operatorname{grad}\psi = \nabla^2\psi = \text{Laplacian of } \psi = g^{-1/2}\sum_{i=1}^{3}\frac{\partial}{\partial u^i}\left[\frac{g^{1/2}}{g_{ii}}\frac{\partial\psi}{\partial u^i}\right]$$

Table 19.5.2 shows some coordinate systems.

TABLE 19.5.2 Some Coordinate Systems

Coordinate System	Metric Coefficients	
	Circular Cylindrical	
$x = r\cos\theta$	$u^1 = r$	$g_{11} = 1$
$y = r\sin\theta$	$u^2 = \theta$	$g_{22} = r^2$
$z = z$	$u^3 = z$	$g_{33} = 1$
	Spherical	
$x = r\sin\psi\cos\theta$	$u^1 = r$	$g_{11} = 1$
$y = r\sin\psi\sin\theta$	$u^2 = \psi$	$g_{22} = r^2$
$z = r\cos\psi$	$u^3 = \theta$	$g_{33} = r^2\sin^2\psi$
	Parabolic Coordinates	
$x = \mu\nu\cos\theta$	$u^1 = \mu$	$g_{11} = \mu^2 + \nu^2$
$y = \mu\nu\sin\theta$	$u^2 = \nu$	$g_{22} = \mu^2 + \nu^2$
$z = 1/2\,(\mu^2 - \nu^2)$	$u^3 = \theta$	$g_{33} = \mu^2\nu^2$

Other metric coefficients and so forth can be found in Moon and Spencer [1961].

References

Ames, W. F. 1965. *Nonlinear Partial Differential Equations in Science and Engineering, Volume 1.* Academic Press, Boston, MA.

Ames, W. F. 1972. *Nonlinear Partial Differential Equations in Science and Engineering, Volume 2.* Academic Press, Boston, MA.

Brauer, F. and Nohel, J. A. 1986. *Introduction to Differential Equations with Applications,* Harper & Row, New York.

Jeffrey, A. 1990. *Linear Algebra and Ordinary Differential Equations,* Blackwell Scientific, Boston, MA.

Kevorkian, J. 1990. *Partial Differential Equations.* Wadsworth and Brooks/Cole, Belmont, CA.

Moon, P. and Spencer, D. E. 1961. *Field Theory Handbook,* Springer, Berlin.

Rogers, C. and Ames, W. F. 1989. *Nonlinear Boundary Value Problems in Science and Engineering.* Academic Press, Boston, MA.

Whitham, G. B. 1974. *Linear and Nonlinear Waves.* John Wiley & Sons, New York.

Zauderer, E. 1983. *Partial Differential Equations of Applied Mathematics.* John Wiley & Sons, New York.

Zwillinger, D. 1992. *Handbook of Differential Equations.* Academic Press, Boston, MA.

Further Information

A collection of solutions for linear and nonlinear problems is found in E. Kamke, *Differential-gleichungen-Lösungsmethoden und Lösungen,* Akad. Verlagsges, Leipzig, 1956. Also see G. M. Murphy, *Ordinary Differential Equations and Their Solutions,* Van Nostrand, Princeton, NJ, 1960 and D. Zwillinger, *Handbook of Differential Equations,* Academic Press, Boston, MA, 1992. For nonlinear problems see

Ames, W. F. 1968. *Ordinary Differential Equations in Transport Phenomena.* Academic Press, Boston, MA.

Cunningham, W. J. 1958. *Introduction to Nonlinear Analysis.* McGraw-Hill, New York.

Jordan, D. N. and Smith, P. 1977. *Nonlinear Ordinary Differential Equations.* Clarendon Press, Oxford, UK.

McLachlan, N. W. 1955. *Ordinary Non-Linear Differential Equations in Engineering and Physical Sciences,* 2nd ed. Oxford University Press, London.

Zwillinger, D. 1992.

19.6 Integral Equations

William F. Ames

Classification and Notation

Any equation in which the unknown function $u(x)$ appears under the integral sign is called an *integral equation.* If $f(x)$, $K(x, t)$, a, and b are known then the integral equation for u, $\int_a^b K(x, t), u(t)\, dt = f(x)$ is called a *linear integral equation of the first kind of Fredholm type.* $K(x, t)$ is called the *kernel function* of the equation. If b is replaced by x (the independent variable) the equation is an equation of *Volterra type of the first kind.*

An equation of the form $u(x) = f(x) + \lambda \int_a^b K(x, t)u(t)\, dt$ is said to be a linear integral equation of *Fredholm type of the second kind.* If b is replaced by x it is of *Volterra type.* If $f(x)$ is not present the equation is homogeneous.

The equation $\phi(x)\, u(x) = f(x) + \lambda \int_a^{b \text{ or } x} K(x, t)u(t)\, dt$ is the *third kind equation* of Fredholm or Volterra type. If the unknown function u appears in the equation in any way other than to the first power then the integral equation is said to be *nonlinear.* Thus, $u(x) = f(x) + \int_a^b K(x, t) \sin u(t)\, dt$ is nonlinear. An integral equation is said to be *singular* when either or both of the limits of integration are infinite or if $K(x, t)$ becomes infinite at one or more points of the integration interval.

Example 19.6.1. Consider the singular equations $u(x) = x + \int_0^\infty \sin(x\, t)\, u(t)\, dt$ and $f(x) = \int_0^x [u(t)/(x - t)^2]\, dt$.

Relation to Differential Equations

The *Leibnitz rule* $(d/dx)\ \int_{a(x)}^{b(x)} F(x, t)\, dt\ \ \int_{a(x)}^{b(x)} (\partial F/\partial x)\, dt + F[x, b(x)](db/dx) - F[x, a(x)] \times (da/dx)$ is useful for differentiation of an integral involving a parameter (x in this case). With this, one can establish the relation

$$I_n(x) = \int_a^x (x-t)^{n-1} f(t)\, dt = (n-1)! \underbrace{\int_a^x \dots \int_a^x}_{n \text{ times}} f(x)\, \underbrace{dx \dots dx}_{n \text{ times}}$$

This result will be used to establish the relation of the second-order initial value problem to a Volterra integral equation.

The second-order differential equation $y''(x) + A(x)y'(x) + B(x)y = f(x)$, $y(a) = y_0$, $y'(a) = y_0'$ is equivalent to the integral equations

$$y(x) = -\int_a^x \{A(t) + (x-t)[B(t) - A'(t)]\} y(t)\, dt + \int_a^x (x-t) f(t)\, dt + [A(a) y_0 + y_0'](x-a) + y_0$$

which is of the type $(x)y = \int_a^x K(x, t)y(t)\, dt + F(x)$ where $K(x, t) = (t - x)[B(t) - A'(t)] - A(t)$ and $F(x)$ includes the rest of the terms. Thus, this initial value problem is equivalent to a Volterra integral equation of the second kind.

Example 19.6.2. Consider the equation $y'' + x^2y' + xy = x$, $y(0) = 1$, $y'(0) = 0$. Here $A(x) = x^2$, $B(x) = x$, $f(x) = x$, $a = 0$, $y_0 = 1$, $y_0' = 0$. The integral equation is $y(x) = \int_0^x t(x - 2t)y(t)\, dt + (x^3/6) + 1$.

The expression for $I_n(x)$ can also be useful in converting boundary value problems to integral equations. For example, the problem $y''(x) + \lambda y = 0$, $y(0) = 0$, $y(a) = 0$ is equivalent to the Fredholm equation $y(x) = \lambda \int_0^a K(x, t)y(t)\, dt$, where $K(x, t) = (t/a)(a - x)$ when $t < x$ and $K(x, t) = (x/a)(a - t)$ when $t > x$.

In both cases the differential equation can be recovered from the integral equation by using the Leibnitz rule.

Nonlinear differential equations can also be transformed into integral equations. In fact this is one method used to establish properties of the equation and to develop approximate and numerical solutions. For example, the "forced pendulum" equation $y''(x) + a^2 \sin y(x) = f(x)$, $y(0) = y(1) = 0$ transforms into the nonlinear Fredholm equation.

$$y(x) = \int_0^1 K(x,t)\left[a^2 \sin y(t) - f(t)\right] dt$$

with $K(x, t) = x(1 - t)$ for $0 < x < t$ and $K(x, t) = t(1 - x)$ for $t < x < 1$.

Methods of Solution

Only the simplest integral equations can be solved exactly. Usually approximate or numerical methods are employed. The advantage here is that integration is a "smoothing operation," whereas differentiation is a "roughening operation." A few exact and approximate methods are given in the following sections. The numerical methods are found under 19.12.

Convolution Equations

The special convolution equation $y(x) = f(x) + \lambda \int_0^x K(x - t)y(t)\, dt$ is a special case of the Volterra equation of the second kind. $K(x - t)$ is said to be a *convolution kernel.* The integral part is the convolution integral discussed under 19.8. The solution can be accomplished by transforming with the Laplace transform: $L[y(x)] = L[f(x)] + \lambda L[y(x)]L[K(x)]$ or $y(x) = L^{-1}\{L[f(x)]/(1 - \lambda L[K(x)])\}$.

Abel Equation

The Volterra equation $f(x) = \int_0^x y(t)/(x-t)^{\alpha}\, dt$, $0 < \alpha < 1$ is the (singular) Abel equation. Its solution is $y(x) = (\sin \alpha\pi/\pi)(d/dx) \int_0^x F(t)/(x-t)^{1-\alpha} dt$.

Approximate Method (Picard's Method)

This method is one of successive approximations that is described for the equation $y(x) = f(x) + \lambda \int_a^x K(x, t)y(t)\, dt$. Beginning with an initial guess $y_0(t)$ (often the value at the initial point a) generate the next approximation with $y_1(x) = f(x) + \int_a^x K(x, t)y_0(t)\, dt$ and continue with the general iteration

$$y_n(x) = f(x) + \lambda \int_a^x K(x,t) y_{n-1}(t)\, dt$$

Then, by iterating, one studies the convergence of this process, as is described in the literature.

Example 19.6.3. Let $y(x) = 1 + \int_0^x xt[y(t)]^2\, dt$, $y(0) = 1$, With $y_0(t) = 1$ we find $y_1(x) = 1 + \int_0^x xt\, dt = 1 + (x^3/2)$ and $y_2(x) = 1 + \int_0^x xt[1 + (t^3/2)^2 dt$, and so forth.

References

Jerri, A. J. 1985. *Introduction to Integral Equations with Applications,* Marcel Dekker, New York.
Tricomi, F. G. 1958. *Integral Equations.* Wiley-Interscience, New York.
Yosida, K. 1960. *Lectures on Differential and Integral Equations.* Wiley-Interscience, New York.

19.7 Approximation Methods

William F. Ames

The term *approximation methods* usually refers to an analytical process that generates a symbolic approximation rather than a numerical one. Thus, $1 + x + x^2/2$ is an approximation of e^x for small x. This chapter introduces some techniques for approximating the solution of various operator equations.

Perturbation

Regular Perturbation

This procedure is applicable to *some* equations in which a small parameter, ε, appears. Use this procedure with care; the procedure involves expansion of the dependent variables and data in a power series in the small parameter. The following example illustrates the procedure.

Example 19.7.1. Consider the equation $y'' + \varepsilon y' + y = 0$, $y(0) = 1$, $y'(0) = 0$. Write $y(x; \varepsilon) = y_0(x) + \varepsilon y_1(x) + \varepsilon^2 y_2(x) + \cdots$, and the initial conditions (data) become

$$y_0(0) + \varepsilon y_1(0) + \varepsilon^2 y_2(0) + \cdots = 1$$

$$y_0'(0) + \varepsilon y_1'(0) + \varepsilon^2 y_2'(0) + \cdots = 0$$

Equating like powers of ε in all three equations yields the sequence of equations

$$\begin{aligned} &O(\varepsilon^0): y_0'' + y_0 = 0, \qquad && y_0(0) = 1, \qquad && y_0'(0) = 0 \\ &O(\varepsilon^1): y_1'' + y_1 = -y_0', \qquad && y_1(0) = 0, \qquad && y_1'(0) = 0 \\ &\quad\vdots \end{aligned}$$

The solution for y_0 is $y_0 = \cos x$ and using this for y_1 we find $y_1(x) = 1/2\ (\sin x - x\cos x)$. So $y(x;\varepsilon) = \cos x + \varepsilon(\sin\ x - x\cos x)/2 + O(\varepsilon^2)$. Appearance of the term $x\cos x$ indicates a *secular term* that becomes arbitrarily large as $x \to \infty$. Hence, this approximation is valid only for $x \ll 1/\varepsilon$ and for small ε. If an approximation is desired over a larger range of x then the method of multiple scales is required.

Singular Perturbation

The *method of multiple scales* is a singular method that is *sometimes* useful if the regular perturbation method fails. In this case the assumption is made that the solution depends on *two* (or more) different length (or time) scales. By trying various possibilities, one can determine those scales. The scales are treated as dependent variables when transforming the given ordinary differential equation into a partial differential equation, but then the scales are treated as independent variables when solving the equations.

Example 19.7.2. Consider the equation $\varepsilon y'' + y' = 2$, $y(0) = 0$, $y(1) = 1$. This is singular since (with $\varepsilon = 0$) the resulting first-order equation cannot satisfy both boundary conditions. For the problem the proper length scales are $u = x$ and $v = x/\varepsilon$. The second scale can be ascertained by substituting $\varepsilon^n x$ for x and requiring $\varepsilon y''$ and y' to be of the same order in the transformed equation. Then

$$\frac{d}{dx} = \frac{\partial}{\partial u}\frac{du}{dx} + \frac{\partial}{\partial v}\frac{dv}{dx} = \frac{\partial}{\partial u} + \frac{1}{\varepsilon}\frac{\partial}{\partial v}$$

and the equation becomes

$$\varepsilon\left(\frac{\partial}{\partial u} + \frac{1}{\varepsilon}\frac{\partial}{\partial v}\right)^2 y + \left(\frac{\partial}{\partial u} + \frac{1}{\varepsilon}\frac{\partial}{\partial v}\right)y = 2$$

With $y(x;\varepsilon) = y_0(u,v) + \varepsilon y_1(u,v) + \varepsilon^2 y_2(u,v) + \cdots$ we have terms

$$O\left(\varepsilon^{-1}\right): \frac{\partial^2 y_0}{\partial v^2} + \frac{\partial y_0}{\partial v} = 0 \qquad \text{(actually ODEs with parameter } u\text{)}$$

$$O\left(\varepsilon^{0}\right): \frac{\partial^2 y_1}{\partial v^2} + \frac{\partial y_1}{\partial v} = 2 - 2\frac{\partial^2 y_0}{\partial u\partial v} - \frac{\partial y_0}{\partial u}$$

$$O\left(\varepsilon^{1}\right): \frac{\partial^2 y_2}{\partial v^2} + \frac{\partial y_2}{\partial v} = -2\frac{\partial^2 y_1}{\partial u\partial v} - \frac{\partial y_1}{\partial u} - \frac{\partial^2 y_0}{\partial u^2}$$

$$\vdots$$

Then $y_0(u,v) = A(u) + B(u)e^{-v}$ and so the second equation becomes $\partial^2 y_1/\partial v^2 + \partial y_1/\partial v = 2 - A'(u) + B'(u)e^{-v}$, with the solution $y_1(u,v) = [2 - A'(u)]v + vB'(u)e^{-v} + D(u) + E(u)e^{-v}$. Here A, B, D and E are still arbitrary. Now the solvability condition — "higher order terms must vanish no slower (as $\varepsilon \to 0$) than the previous term" (Kevorkian and Cole, 1981) — is used. For y_1 to vanish no slower than y_0 we must have $2 - A'(u) = 0$ and $B'(u) = 0$. If this were not true the terms in y_1 would be larger than those in y_0 ($v \gg 1$). Thus $y_0(u,v) = (2u + A_0) + B_0 e^{-v}$, or in the original variables $y(x;\varepsilon) \approx (2x + A_0) + B_0 e^{-x/\varepsilon}$ and matching to both boundary conditions gives $y(x;\varepsilon) \approx 2x - (1 - e^{-x/\varepsilon})$.

Boundary Layer Method

The boundary layer method is applicable to regions in which the solution is *rapidly varying*. See the references at the end of the chapter for detailed discussion.

Iterative Methods

Taylor Series

If it is known that the solution of a differential equation has a power series in the independent variable (t), then we may proceed from the initial data (the easiest problem) to compute the Taylor series by differentiation.

Example 19.7.3. Consider the equation $(d^2x/dt) = -x - x^2$, $x(0) = 1$, $x'(0) = 1$. From the differential equation, $x''(0) = -2$, and, since $x''' = -x' - 2xx'$, $x'''(0) = -1 - 2 = -3$, so the four term approximation for $x(t) \approx 1 + t - (2t^2/2!) - (3t^3/3!) = 1 + \mathrm{t} - t^2 - t^3/2$. An estimate for the error at $t = t_1$, (see a discussion of series methods in any calculus text) is not greater than $|d^4x/dt^4|_{\max}[(t_1)^4/4!]$, $0 \le t \le t_1$.

Picard's Method

If the vector differential equation $x' = f(t, x)$, $x(0)$ given, is to be approximated by Picard iteration, we begin with an initial guess $\mathrm{x}_0 = \mathrm{x}(0)$ and calculate iteratively $x_i' = f(t, x_{i-1})$.

Example 19.7.4. Consider the equation $x' = x + y^2$, $y' = y - x^3$, $x(0) = 1$, $y(0) = 2$. With $x_0 = 1$, $y_0 = 2$, $x_1' = 5$, $y_1' = 1$, so $x_1 = 5t + 1$, $y_1 = t + 2$, since $x_i(0) = 1$, $y_i(0) = 2$ for $i \ge 0$. To continue, use $x_{i+1}' = x_i + y_i^2$, $y_{i+1}' = y_i - x_i^3$. A modification is the utilization of the first calculated term immediately in the second equation. Thus, the calculated value of $x_1 = 5t + 1$, when used in the second equation, gives $y_1' = y_0 - (5t + 1)^3 = 2 - (125t^3 + 75t^2 + 15t + 1)$, so $y_1 = 2t - (125t^4/4) - 25t^3 - (15t^2/2) - t + 2$. Continue with the iteration $x_{i+1}' = x_i + y_i^3$, $y_{i+1}' = y_i - (x_{i+1})^3$.

Another variation would be $x_{i+1}' = x_{i+1} + (y_i)^3$, $y_{i+1}' = y_{i+1} - (x_{i+1})^3$.

References

Ames, W. F. 1965. *Nonlinear Partial Differential Equations in Science and Engineering, Volume I.* Academic Press, Boston, MA.

Ames, W. F. 1968. *Nonlinear Ordinary Differential Equations in Transport Processes.* Academic Press, Boston, MA.

Ames, W. F. 1972. *Nonlinear Partial Differential Equations in Science and Engineering, Volume II.* Academic Press, Boston, MA.

Kevorkian, J. and Cole, J. D. 1981. *Perturbation Methods in Applied Mathematics,* Springer, New York.

Miklin, S. G. and Smolitskiy, K. L. 1967. *Approximate Methods for Solutions of Differential and Integral Equations.* Elsevier, New York.

Nayfeh, A. H. 1973. *Perturbation Methods.* John Wiley & Sons, New York.

Zwillinger, D. 1992. *Handbook of Differential Equations,* 2nd ed. Academic Press, Boston, MA.

19.8 Integral Transforms

William F. Ames

All of the integral transforms are special cases of the equation $g(s) = \int_a^b K(s, t) f(t)\, d\, t$, in which $g(s)$ is said to be the *transform* of $f(t)$, and $K(s, t)$ is called the *kernel* of the transform. Table 19.8.1 shows the more important kernels and the corresponding intervals (a, b).

Details for the first three transforms listed in Table 19.8.1 are given here. The details for the other are found in the literature.

Laplace Transform

The Laplace transform of $f(t)$ is $g(s) = \int_0^\infty e^{-st} f(t)\, dt$. It may be thought of as transforming one class of functions into another. The advantage in the operation is that under certain circumstances it replaces complicated functions by simpler ones. The notation $L[f(t)] = g(s)$ is called the *direct transform* and

$L^{-1}[g(s)] = f(t)$ is called the *inverse transform*. Both the direct and inverse transforms are tabulated for many often-occurring functions. In general $L^{-1}[g(s)] = (1/2\pi i)\int_{\alpha-i\infty}^{\alpha+i\infty} e^{st}g(s)\,ds$, and to evaluate this integral requires a knowledge of complex variables, the theory of residues, and contour integration.

Properties of the Laplace Transform

Let $L[f(t)] = g(s)$, $L^{-1}[g(s)] = f(t)$.

1. The Laplace transform may be applied to a function $f(t)$ if $f(t)$ is continuous or piecewise continuous; if $t^n|f(t)|$ is finite for all t, $t \to 0$, $n < 1$; and if $e^{-at}|f(t)|$ is finite as $t \to \infty$ for some value of a, $a > 0$.
2. L and L^{-1} are unique.
3. $L[af(t) + bh(t)] = aL[f(t)] + bL[h(t)]$ (linearity).
4. $L[e^{at}f(t)] = g(s - a)$ (shift theorem).
5. $L[(-t)^k f(t)] = d^k g/ds^k$; k a positive integer.

TABLE 19.8.1 Kernels and Intervals of Various Integral Transforms

Name of Transform	(a, b)	$K(s, t)$
Laplace	$(0, \infty)$	e^{-st}
Fourier	$(-\infty, \infty)$	$\frac{1}{\sqrt{2\pi}}e^{-ist}$
Fourier cosine	$(0, \infty)$	$\sqrt{\frac{2}{\pi}}\cos st$
Fourier sine	$(0, \infty)$	$\sqrt{\frac{2}{\pi}}\sin st$
Mellin	$(0, \infty)$	t^{s-1}
Hankel	$(0, \infty)$	$tJ_\nu(st)$, $\nu \geq -\frac{1}{2}$

Example 19.8.1. $L[\sin a\, t] = \int_0^\infty e^{-st}\sin a\, t\, d\, t = a/(s^2 + a^2)$, $s > 0$. By property 5,

$$\int_0^\infty e^{-st}t\sin at\, dt = L[t\sin at] = \frac{2as}{s^2 + a^2}$$

6.
$$\begin{aligned} L[f'(t)] &= sL[f(t)] - f(0) \\ L[f''(t)] &= s^2L[f(t)] - sf(0) - f'(0) \\ &\vdots \\ L\left[f^{(n)}(t)\right] &= s^nL[f(t)] - s^{n-1}f(0) - \cdots - sf^{(n-2)}(0) - f^{(n-1)}(0) \end{aligned}$$

In this property it is apparent that the initial data are automatically brought into the computation.

Example 19.8.2. Solve $y'' + y = e^t$, $y(0) = 1$, $y'(0) = 1$. Now $L[y''] = s^2L[y] - sy(0) - y'(0) = s^2L[y] - s - 1$. Thus, using the linear property of the transform (property 3), $s^2L[y] + L[y] - s - 1 = L[e^t] = 1/(s - 1)$. Therefore, $L[y] = s^2/[(s - 1)(s^2 + 1)]$.

With the notations $\Gamma(n + 1) = \int_0^\infty x^n e^{-x}\,dx$ (gamma function) and $J_n(t)$ the Bessel function of the first kind of order n, a short table of Laplace transforms is given in Table 19.8.2.

7. $L\left[\int_a^t f(t)\,dt\right] = \frac{1}{s}L[f(t)] + \frac{1}{s}\int_a^0 f(t)\,dt.$

TABLE 19.8.2 Some Laplace Transforms

$f(t)$	$g(s)$	$f(t)$	$g(s)$
1	$\frac{1}{s}$	$e^{-at}(1-a\,t)$	$\frac{s}{(s+a)^2}$
t^n, n is a + integer	$\frac{n!}{s^{n+1}}$	$\frac{t\sin at}{2a}$	$\frac{s}{\left(s^2+a^2\right)^2}$
t^n, $n \neq$ a + integer	$\frac{\Gamma(n+1)}{s^{n+1}}$	$\frac{1}{2a^2}\sin at\sinh at$	$\frac{s}{s^4+4a^4}$
$\cos a\,t$	$\frac{s}{s^2+a^2}$	$\cos a\,t\cosh a\,t$	$\frac{s^3}{s^4+4a^4}$
$\sin a\,t$	$\frac{a}{s^2+a^2}$	$\frac{1}{2a}(\sinh at+\sin at)$	$\frac{s^2}{s^4-a^4}$
$\cosh a\,t$	$\frac{s}{s^2-a^2}$	$\frac{1}{2}(\cosh at+\cos at)$	$\frac{s^3}{s^4-a^4}$
$\sinh a\,t$	$\frac{a}{s^2-a^2}$	$\frac{\sin at}{t}$	$\tan^{-1}\frac{a}{s}$
e^{-at}	$\frac{1}{s+a}$	$J_0(a\,t)$	$\frac{1}{\sqrt{s^2+a^2}}$
$e^{-bt}\cos a\,t$	$\frac{s+b}{(s+b)^2+a^2}$	$\frac{n}{a^n}\frac{J_n(at)}{t}$	$\frac{1}{\left(\sqrt{s^2+a^2}+s\right)^n}$
$e^{-bt}\sin a\,t$	$\frac{a}{(s+b)^2+a^2}$	$J_0\left(2\sqrt{at}\right)$	$\frac{1}{s}e^{-a/s}$

Example 19.8.3. Find $f(t)$ if $L[f(t)] = (1/s^2)[1/(s^2-a^2)]$. $L[1/a \sinh a\,t] = 1/(s^2-a^2)$. Therefore, $f(t) = \int_0^t\left[\int_0^t \frac{1}{a}\sinh a\,t\,d\,t\right]d\,t = 1/a^2[(\sinh a\,t)/a - t]$.

$$L\left[\frac{f(t)}{t}\right]=\int_s^\infty g(s)\,ds; \qquad L\left[\frac{f(t)}{t^k}\right]=\underbrace{\int_s^\infty\cdots\int_s^\infty}_{k\text{ integrals}} g(s)(ds)^k$$

Example 19.8.4. $L[(\sin a\,t)/t] = \int_s^\infty L[\sin a\,t)d\,s = \int_s^\infty [a\,d\,s/(s^2+a^2)] = \cot^{-1}(s/a)$.

9. The *unit step function* $u(t-a) = 0$ for $t < a$ and 1 for $t > a$. $L[u(t-a) = e^{-as}/s$.
10. The *unit impulse function* is $\delta(a) = u'(t-a) = 1$ at $t = a$ and 0 elsewhere. $L[u'(t-a) = e^{-as}$.
11. $L^{-1}[e^{-as}g(s)] = f(t-a)u(t-a)$ (second shift theorem).
12. If $f(t)$ is *periodic* of period b — that is, $f(t+b) = f(t)$ — then $L[f(t)] = [1/(1-e^{-bs})] \times \int_0^b e^{-st}f(t)\,dt$.

Example 19.8.5. The equation $\partial^2 y/(\partial t\partial x) + \partial y/\partial t + \partial y/\partial x = 0$ with $(\partial y/\partial x)(0,x) = y(0,x) = 0$ and $y(t,0) + (\partial y/\partial t)(t,0) = \delta(0)$ (see property 10) is solved by using the Laplace transform of y with respect to t. With $g(s,x) = \int_0^\infty e^{-st}y(t,x)\,dt$, the transformed equation becomes

$$s\frac{\partial g}{\partial x}-\frac{\partial y}{\partial x}(0,x)+sg-y(0,x)+\frac{\partial g}{\partial x}=0$$

or

$$(s+1)\frac{\partial g}{\partial x}+sg=\frac{\partial y}{\partial x}(0,x)+y(0,x)=0$$

The second (boundary) condition gives $g(s, 0) + sg(s, 0) - y(0, 0) = 1$ or $g(s, 0) = 1/(1 + s)$. A solution of the preceding ordinary differential equation consistent with this condition is $g(s, x) = [1/(s+1)]e^{-sx/(s+1)}$. Inversion of this transform gives $y(t, x) = e^{-(t+x)}I_0\,(2/\sqrt{tx})$, where I_0 is the zero-order Bessel function of an imaginary argument.

Convolution Integral

The *convolution integral* (*faltung*) of two functions $f(t)$, $r(t)$ is $x(t) = f(t)*r(t) = \int_0^t f(\tau)r(t-\tau)\,d\tau$.

Example 19.8.6. $t * \sin t = \int_0^t \tau \sin(t-\tau)\,d\tau = t - \sin t$.

13. $L[f(t)]L[h(t)] = L[f(t) * h(t)]$.

Fourier Transform

The *Fourier transform* is given by $F[f(t)] = (1/\sqrt{2\pi})\int_{-\infty}^{\infty} f(t)e^{-ist}\,d\,t = g(s)$ and its *inverse* by $F^{-1}[g(s)] = (1/\sqrt{2\pi})\int_{-\infty}^{\infty} g(s)e^{ist}\,d\,t = f(t)$. In brief, the condition for the Fourier transform to exist is that $\int_{-\infty}^{\infty} |f(t)|\,d\,t < \infty$, although certain functions may have a Fourier transform even if this is violated.

Example 19.8.7. The function $f(t) = 1$ for $-a \le t \le a$ and $= 0$ elsewhere has

$$F[f(t)] = \int_{-a}^{a} e^{-ist}\,dt = \int_0^a e^{ist}\,dt + \int_0^a e^{-ist}\,dt = 2\int_0^a \cos st\,dt = \frac{2\sin sa}{s}$$

Properties of the Fourier Transform

Let $F[f(t)] = g(s)$; $F^{-1}[g(s)] = f(t)$.

1. $F[f^{(n)}(t)] = (i\,s)^n\,F[f(t)]$
2. $F[af(t) + bh(t)] = aF[f(t)] + bF[h(t)]$
3. $F[f(-t)] = g(-s)$
4. $F[f(at)] = 1/a\;g(s/a), \quad a > 0$
5. $F[e^{-iwt}f(t)] = g(s + w)$
6. $F[f(t + t_1)] = e^{ist_1}g(s)$
7. $F[f(t)] = G(i\,s) + G(-i\,s)$ if $f(t) = f(-t)(f(t)$ even)
   $F[f(t)] = G(i\,s) - G(-i\,s)$ if $f(t) = -f(-t)(f$ odd)

where $G(s) = L[f(t)]$. This result allows the use of the Laplace transform tables to obtain the Fourier transforms.

Example 19.8.8. Find $F[e^{-a|t|}]$ by property 7. The term $e^{-a|t|}$ is even. So $L[e^{-at}] = 1/(s + a)$. Therefore, $F[e^{-a|t|}] = 1/(i\,s + a) + 1/(-i\,s + a) = 2a/(s^2 + a^2)$.

Fourier Cosine Transform

The *Fourier cosine transform* is given by $F_c[f(t)] = g(s) = \sqrt{(2/\pi)}\int_0^{\infty} f(t)\cos s\,t\,d\,t$ and its *inverse* by $F_c^{-1}[g(s)] = f(t) = \sqrt{(2/\pi)}\int_0^{\infty} g(s)\cos s\,t\,d\,s$. The *Fourier sine transform* F_s is obtainable by replacing the cosine by the sine in the above integrals.

Example 19.8.9. $F_c[f(t)]$, $f(t) = 1$ for $0 < t < a$ and 0 for $a < t < \infty$. $F_c\,[f(t)] = \sqrt{(2/\pi)}\int_0^a \cos s\,t\,d\,t = \sqrt{(2/\pi)}\,(\sin a\,s)/s$.

Properties of the Fourier Cosine Transform

$F_c[f(t)] = g(s)$.

1. $F_c[af(t) + bh(t)] = aF_c[f(t)] + bF_c[h(t)]$
2. $F_c[f(at)] = (1/a)\, g\,(s/a)$
3. $F_c[f(at) \cos bt] = 1/2a\, [g\,((s + b)/a) + g((s - b)/a)],\ a, b > 0$
4. $F_c[t^{2n}f(t)] = (-1)^n(d^{2n}g)/(d\, s^{2n})$
5. $F_c[t^{2n+1}f(t)] = (-1)^n(d^{2n+1})/(d\, s^{2n+1})\ F_s[f(t)]$

Table 19.8.3 presents some Fourier cosine transforms.

TABLE 19.8.3 Fourier Cosine Transforms

$f(t)$	$\dfrac{g(s)}{\sqrt{2/\pi}}$
$\left.\begin{array}{ll} t & 0<t<1 \\ 2-t & 1<t<2 \\ 0 & 2<t<\infty \end{array}\right\}$	$\frac{1}{s^2}[2\cos s - 1 - \cos 2s]$
$t^{-1/2}$	$\pi^{1/2}(s)^{-1/2}$
$\left.\begin{array}{ll} 0 & 0<t<a \\ (t-a)^{-1/2} & a<t<\infty \end{array}\right\}$	$\pi^{1/2}(s)^{-1/2}\ [\cos a\, s - \sin a\, s]$
$(t^2 + a^2)^{-1}$	$\frac{1}{2}\pi a^{-1}e^{-as}$
$e^{-at},\quad a > 0$	$\dfrac{a}{s^2 + a^2}$
$e^{-at^2},\quad a > 0$	$\frac{1}{2}\pi^{1/2}a^{-1/2}e^{-s^2/4a}$
$\dfrac{\sin at}{t}\quad a > 0$	$\begin{cases} \pi/2 & s<a \\ \pi/4 & s=a \\ 0 & s>a \end{cases}$

Example 19.8.10. The temperature θ in the semiinfinite rod $0 \le x < \infty$ is determined by the differential equation $\partial\theta/\partial t = k(\partial^2\theta/\partial x^2)$ and the condition $\theta = 0$ when $t = 0, x \ge 0$; $\partial\theta/\partial x = -\mu$ = constant when $x = 0, t > 0$. By using the Fourier cosine transform, a solution may be found as $\theta(x, t) = (2\mu/\pi) \int_0^\infty (\cos px/p)\,(1 - e^{-kp2t})\ d\,p$.

References

Churchill, R. V. 1958. *Operational Mathematics.* McGraw-Hill, New York.

Ditkin, B. A. and Proodnikav, A. P. 1965. *Handbook of Operational Mathematics* (in Russian). Nauka, Moscow.

Doetsch, G. 1950–1956. *Handbuch der Laplace Transformation,* vols. I-IV (in German). Birkhauser, Basel.

Nixon, F. E. 1960. *Handbook of Laplace Transforms.* Prentice-Hall, Englewood Cliffs, NJ.

Sneddon, I. 1951. *Fourier Transforms.* McGraw-Hill, New York.

Widder, D. 1946. *The Laplace Transform,* Princeton University Press, Princeton, NJ.

Further Information

The references citing G. Doetsch, *Handbuch der Laplace Transformation,* vols. I-IV, Birkhauser, Basel, 1950–1956 (in German) *and* B. A. Ditkin and A. P. Prodnikav, *Handbook of Operational Mathematics,* Moscow, 1965 (in Russian) are the most extensive tables known. The latter reference is 485 pages.

19.9 Calculus of Variations

William F. Ames

The basic problem in the *calculus of variations* is to determine a function such that a certain *functional*, often an integral involving that function and certain of its derivatives, takes on *maximum or minimum values.* As an example, find the function $y(x)$ such that $y(x_1) = y_1$, $y(x_2) = y_2$ and the integral (functional) $I = 2\pi \int_{x_1}^{x_2} y[1 + y')^2]^{1/2}\, d\, x$ is a minimum. A second example concerns the transverse deformation $u(x, t)$ of a beam. The energy functional $I = \int_{t_1}^{t_2} \int_0^L [1/2\ \rho\ (\partial u/\partial t)^2 - 1/2\ EI\ (\partial^2 u/\partial x^2)^2 + fu]\ d\ x\ d\ t$ is to be minimized.

The Euler Equation

The elementary part of the theory is concerned with a *necessary* condition (generally in the form of a differential equation with boundary conditions) that the required function must satisfy. To show mathematically that the function obtained actually maximizes (or minimizes) the integral is much more difficult than the corresponding problems of the differential calculus.

The *simplest case* is to determine a function $y(x)$ that makes the integral $I = \int_{x_1}^{x_2} F(x, y, y')\, dx$ stationary and that satisfies the prescribed end conditions $y(x_1) = y_1$ and $y(x_2) = y_2$. Here we suppose F has continuous second partial derivatives with respect to x, y, and $y' = dy/dx$. If $y(x)$ is such a function, then it must satisfy the *Euler equation* $(d/dx)(\partial F/\partial y') - (\partial F/\partial y) = 0$, which is the required necessary condition. The indicated partial derivatives have been formed by treating x, y, and y' as independent variables. Expanding the equation, the equivalent form $F_{y'y'}y'' + F_{y'y}y' + (F_{y'x} - F_y) = 0$ is found. This is second order in y unless $F_{y'y'} = (\partial^2 F)/[(\partial y')^2] = 0$. An alternative form $1/y'[d/dx(F - (\partial F/\partial y')(dy/dx)) - (\partial F/\partial x)] = 0$ is useful. Clearly, if F does not involve x explicitly $[(\partial F/\partial x) = 0]$ a first integral of Euler's equation is $F - y'(\partial F/\partial y') = c$. If F does not involve y explicitly $[(\partial F/\partial y) = 0]$ a first integral is $(\partial F/\partial y') = c$.

The Euler equation for $I = 2\pi \int_{x_1}^{x_2} y[1 + (y')^2]^{1/2}\, dx$, $y(x_1) = y_1$, $y(x_2) = y_2$ is $(d/dx)[yy'/[1 + (y')^2]^{1/2}] - [1 + (y')^2]^{1/2} = 0$ or after reduction $yy'' - (y')^2 - 1 = 0$. The solution is $y = c_1 \cosh(x/c_1 + c_2)$, where c_1 and c_2 are integration constants. Thus the required minimal surface, if it exists, must be obtained by revolving a catenary. Can c_1 and c_2 be chosen so that the solution passes through the assigned points? The answer is found in the solution of a transcendental equation that has two, one, or no solutions, depending on the prescribed values of y_1 and y_2.

The Variation

If $F = F(x, y, y')$, with x independent and $y = y(x)$, then the *first variation* δF of F is defined to be $\delta F = (\partial F/\partial x)\ \delta y + (\partial F/\partial y)\ \delta y'$ and $\delta y' = \delta\ (dy/dx) = (d/dx)\ (\delta y)$ — that is, they commute. Note that the first variation, δF, of a functional is a first-order change from curve to curve, whereas the differential of a function is a first-order approximation to the change in that function along a *particular curve.* The laws of δ are as follows: $\delta(c_1 F + c_2 G) = c_1 \delta F + c_2 \delta G$; $\delta(FG) = F\delta G + G\delta F$; $\delta(F/G) = (G\delta F - F\delta G)/G^2$; if x is an independent variable, $\delta x = 0$; if $u = u(x, y)$; $(\partial/\partial x)(\delta u) = \delta(\partial u/\partial x)$, $(\partial/\partial y)\ (\delta u) = \delta(\partial u/\partial y)$.

A necessary condition that the integral $I = \int_{x_1}^{x_2} F(x, y, y')\, dx$ be stationary is that its (first) variation vanish — that is, $\delta I = \delta \int_{x_1}^{x_2} F(x, y, y')\, dx = 0$. Carrying out the variation and integrating by parts yields of $\delta I = \int_{x_1}^{x_2} [(\partial F/\partial y) - (d/dx)(\partial F/\partial y')]\ \delta y\, dx + [(\partial F/\partial y')\ \partial y]_{x_1}^{x_2} = 0$. The arbitrary nature of δy means the square bracket must vanish and the last term constitutes the *natural boundary conditions.*

Example. The *Euler equation* of $\int_{x_1}^{x_2} F(x, y, y', y'')\, dx$ is $(d^2/dx^2)(\partial F/\partial y'') - (d/dx)(\partial F/\partial y') + (\partial F/\partial y) = 0$, with natural boundary conditions $\{[(d/dx)(\partial F/\partial y'') - (\partial F/\partial y')]\ \delta y\}_{x_1}^{x_2} = 0$ and $(\partial F/\partial y'')\ \delta y'|_{x_1}^{x_2} = 0$. The Euler equation of $\int_{x_1}^{x_2} \int_{y_1}^{y_2} F(x, y, u, u_x, u_y, u_{xx}, u_{xy}, u_{yy})\, dx\, dy$ is $(\partial^2/\partial x^2)(\partial F/\partial u_{xx}) + (\partial^2/\partial x \partial y)(\partial F/u_{xy}) + (\partial^2/\partial y^2)(\partial F/\partial u_{yy}) - (\partial/\partial x)(\partial F/\partial u_x) - (\partial/\partial y)(\partial F/\partial u_y) + (\partial F/\partial u)$, and the natural boundary conditions are

$$\left[\left(\frac{\partial}{\partial x}\left(\frac{\partial F}{\partial u_{xx}}\right)+\frac{\partial}{\partial y}\left(\frac{\partial F}{\partial u_{xy}}\right)-\frac{\partial F}{\partial u_x}\right)\delta u\right]_{x_1}^{x_2}=0, \qquad \left[\left(\frac{\partial F}{\partial u_{xx}}\right)\delta u_x\right]_{x_1}^{x_2}=0$$

$$\left[\left(\frac{\partial}{\partial y}\left(\frac{\partial F}{\partial u_{yy}}\right)+\frac{\partial}{\partial x}\left(\frac{\partial F}{\partial u_{xy}}\right)-\frac{\partial F}{\partial u_y}\right)\delta u\right]_{y_1}^{y_2}=0, \qquad \left[\left(\frac{\partial F}{\partial u_{yy}}\right)\delta u_y\right]_{y_1}^{y_2}=0$$

In the more general case of $I = \iint_R F(x, y, u, v, u_x, u_y, v_x, v_y)\, dx\, dy$, the condition $\delta I = 0$ gives rise to the two Euler equations $(\partial/\partial x)(\partial F/\partial u_x) + (\partial/\partial y)(\partial F/\partial u_y) - (\partial F/\partial u) = 0$ and $(\partial/\partial x)(\partial F/\partial v_x) + (\partial/\partial y)(\partial F/\partial v_y) - (\partial F/\partial v) = 0$. These are two PDEs in u and v that are linear or quasi-linear in u and v. The Euler equation for $I = \iiint_R (u_x^2 + u_y^2 + u_z^2)\, dx\, dy\, dz$, from $\delta I = 0$, is Laplace's equation $u_{xx} + u_{yy} + u_{zz} = 0$.

Variational problems are easily derived from the differential equation and associated boundary conditions by multiplying by the variation and integrating the appropriate number of times. To illustrate, let $F(x)$, $\rho(x)$, $p(x)$, and w be the tension, the linear mass density, the natural load, and (constant) angular velocity of a rotating string of length L. The equation of motion is $(d/dx)[F\,(dy/dx)] + \rho w^2 y + p = 0$. To formulate a corresponding variational problem, multiply all terms by a variation δy and integrate over $(0, L)$ to obtain

$$\int_0^L \frac{d}{dx}\left(F\frac{dy}{dx}\right)\delta y\, dx + \int_0^L \rho w^2 y \delta y\, dx + \int_0^L p\delta y\, dx = 0$$

The second and third integrals are the variations of 1/2 $\rho w^2 y^2$ and py, respectively. To treat the first integral, integrate by parts to obtain

$$\left[F\frac{dy}{dx}\delta y\right]_0^L - \int_0^L F\frac{dy}{dx}\delta\frac{dy}{dx}\, dx = \left[F\frac{dy}{dx}\delta y\right]_0^L - \int_0^L \frac{1}{2}F\delta\left(\frac{dy}{dx}\right)^2 dx = 0$$

So the variation formulation is

$$\delta\int_0^L\left[\frac{1}{2}\rho w^2 y^2 + py - \frac{1}{2}F\left(\frac{dy}{dx}\right)^2\right]dx + \left[F\frac{dy}{dx}\delta y\right]_0^L = 0$$

The last term represents the *natural boundary conditions*. The term 1/2 $\rho w^2 y^2$ is the kinetic energy per unit length, the term $-py$ is the potential energy per unit length due to the radial force $p(x)$, and the term 1/2 $F(dy/dx)^2$ is a first approximation to the potential energy per unit length due to the tension $F(x)$ in the string. Thus the integral is often called the *energy integral*.

Constraints

The variations in some cases cannot be arbitrarily assigned because of one or more auxiliary conditions that are usually called *constraints*. A typical case is the functional $\int_{x_1}^{x_2} F(x, u, v, u_x, v_x)\, dx$ with a constraint $\phi(u, v) = 0$ relating u and v. If the variations of u and v (δu and δv) vanish at the end points, then the variation of the integral becomes

$$\int_{x_1}^{x_2}\left\{\left[\frac{\partial F}{\partial u} - \frac{d}{dx}\left(\frac{\partial F}{\partial u_x}\right)\right]\delta u + \left[\frac{\partial F}{\partial v} - \frac{d}{dx}\left(\frac{\partial F}{\partial v_x}\right)\right]\delta v\right\}dx = 0$$

The variation of the constraint $\phi(u, v) = 0$, $\phi_u\delta u + \phi_v\delta v = 0$ means that the variations cannot both be assigned arbitrarily inside (x_1, x_2), so their coefficients need not vanish separately. Multiply $\phi_u\delta u + \phi_v\delta v = 0$ by a Lagrange multiplier λ (may be a function of x) and integrate to find $\int_{x_1}^{x_2} (\lambda\phi_u\delta u + \lambda\phi_v\delta v)\, dx = 0$. Adding this to the previous result yields

$$\int_{x_1}^{x_2} \left\{ \left[\frac{\partial F}{\partial u} - \frac{d}{dx}\left(\frac{\partial F}{\partial u_x} \right) + \lambda\phi_u \right] \delta u + \left[\frac{\partial F}{\partial v} - \frac{d}{dx}\left(\frac{\partial F}{\partial v_x} \right) + \lambda\phi_v \right] \delta v \right\} dx = 0$$

which must hold for any λ. Assign λ so the first square bracket vanishes. Then δv can be assigned to vanish inside (x_1, x_2) so the two systems

$$\frac{d}{dx}\left[\frac{\partial F}{\partial u_x} \right] - \frac{\partial F}{\partial u} - \lambda\phi_u = 0, \qquad \frac{d}{dx}\left[\frac{\partial F}{\partial v_x} \right] - \frac{\partial F}{\partial v} - \lambda\phi_v = 0$$

plus the constraint $\phi(u, v) = 0$ are three equations for u, v and λ.

References

Gelfand, I. M. and Fomin, S. V. 1963. *Calculus of Variations*. Prentice Hall, Englewood Cliffs, NJ.

Lanczos, C. 1949. *The Variational Principles of Mechanics.* Univ. of Toronto Press, Toronto.

Schechter, R. S. 1967. *The Variational Method in Engineering,* McGraw-Hill, New York.

Vujanovic, B. D. and Jones, S. E. 1989. *Variational Methods in Nonconservative Phenomena.* Academic Press, New York.

Weinstock, R. 1952. *Calculus of Variations, with Applications to Physics and Engineering.* McGraw-Hill, New York.

19.10 Optimization Methods

George Cain

Linear Programming

Let **A** be an $m \times n$ matrix, **b** a column vector with m components, and **c** a column vector with n components. Suppose $m < n$, and assume the rank of **A** is m. The standard linear programming problem is to find, among all nonnegative solutions of **Ax** = **b**, one that minimizes

$$\mathbf{c}^{\mathrm{T}}\mathbf{x} = c_1 x_1 + c_2 x_2 + \cdots + c_n x_n$$

This problem is called a *linear* program. Each solution of the system **Ax** = **b** is called a *feasible* solution, and the *feasible set* is the collection of all *feasible solutions.* The function $\mathbf{c}^{\mathrm{T}}\mathbf{x} = c_1x_1 + c_2x_2 + \cdots + c_nx_n$ is the cost function, or the objective function. A solution to the linear program is called an *optimal feasible solution.*

Let **B** be an $m \times n$ submatrix of **A** made up of m linearly independent columns of **A**, and let **C** be the $m \times (n - m)$ matrix made up of the remaining columns of **A**. Let $\mathbf{x_B}$ be the vector consisting of the components of **x** corresponding to the columns of **A** that make up **B**, and let $\mathbf{x_C}$ be the vector of the remaining components of **x**, that is, the components of **x** that correspond to the columns of **C**. Then the equation **Ax** = **b** may be written $\mathbf{Bx_B} + \mathbf{Cx_C} = \mathbf{b}$. A solution of $\mathbf{Bx_B} = \mathbf{b}$ together with $\mathbf{x_C} = \mathbf{0}$ gives a solution **x** of the system **Ax** = **b**. Such a solution is called a *basic solution,* and if it is, in addition, nonnegative, it is a *basic feasible solution*. If it is also optimal, it is an *optimal basic feasible solution*. The components of a basic solution are called *basic variables*.

The Fundamental Theorem of Linear Programming says that if there is a feasible solution, there is a basic feasible solution, and if there is an optimal feasible solution, there is an optimal basic feasible solution. The linear programming problem is thus reduced to searching among the set of basic solutions for an optimal solution. This set is, of course, finite, containing as many as $n!/[m!(n - m)!]$ points. In practice, this will be a very large number, making it imperative that one use some efficient search procedure in seeking an optimal solution. The most important of such procedures is the *simplex method*, details of which may be found in the references.

The problem of finding a solution of $\mathbf{Ax} \le \mathbf{b}$ that minimizes $\mathbf{c}^T\mathbf{x}$ can be reduced to the standard problem by appending to the vector $\mathbf{x}$ an additional m nonnegative components, called *slack variables*. The vector $\mathbf{x}$ is replaced by $\mathbf{z}$, where $\mathbf{z}^T = [x_1, x_2 \ldots x_n \; s_1, s_2 \ldots x_m]$, and the matrix $\mathbf{A}$ is replaced by $\mathbf{B} = [\mathbf{A}\ \mathbf{I}]$, where $\mathbf{I}$ is the $m \times m$ identity matrix. The equation $\mathbf{Ax} = \mathbf{b}$ is thus replaced by $\mathbf{Bz} = \mathbf{Ax} + s = \mathbf{b}$, where $s^T = [s_1, s_2, \ldots, s_m]$. Similarly, if inequalities are reversed so that we have $\mathbf{Ax} \le \mathbf{b}$, we simply append $-s$ to the vector x. In this case, the additional variables are called *surplus variables*.

Associated with every linear programming problem is a corresponding dual problem. If the *primal* problem is to minimize $\mathbf{c}^T\mathbf{x}$ subject to $\mathbf{Ax} \ge \mathbf{b}$, and $\mathbf{x} \ge 0$, the corresponding *dual* problem is to maximize $\mathbf{y}^T\mathbf{b}$ subject to $\mathbf{t}^T\mathbf{A} \le \mathbf{c}^T$. If either the primal problem or the dual problem has an optimal solution, so also does the other. Moreover, if $\mathbf{x_p}$ is an optimal solution for the primal problem and $\mathbf{y_d}$ is an optimal solution for the corresponding dual problem $\mathbf{c}^T\mathbf{x_p} = \mathbf{y_d^T b}$.

Unconstrained Nonlinear Programming

The problem of minimizing or maximizing a sufficiently smooth nonlinear function $f(x)$ of n variables, $\mathbf{x}^T = [x_1, x_2 \ldots x_n]$, with no restrictions on x is essentially an ordinary problem in calculus. At a minimizer or maximizer x^*, it must be true that the gradient of f vanishes:

$$\nabla f\left(\mathbf{x}^*\right) = 0$$

Thus x^* will be in the set of all solutions of this system of n generally nonlinear equations. The solution of the system can be, of course, a nontrivial undertaking. There are many recipes for solving systems of nonlinear equations. A method specifically designed for minimizing f is the *method of steepest descent*. It is an old and honorable algorithm, and the one on which most other more complicated algorithms for unconstrained optimization are based. The method is based on the fact that at any point x, the direction of maximum decrease of f is in the direction of $-\nabla f(x)$. The algorithm searches in this direction for a minimum, recomputes $\nabla f(x)$ at this point, and continues iteratively. Explicitly:

1. Choose an initial point x_0.
2. Assume x_k has been computed; then compute $y_k = \nabla f(x_k)$, and let $t_k \ge 0$ be a local minimum of $g(t) = f(x_k - ty_k)$. Then $x_{k+1} = x_k - t_k y_k$.
3. Replace k by $k + 1$, and repeat step 2 until t_k is small enough.

Under reasonably general conditions, the sequence (x_k) converges to a minimum of f.

Constrained Nonlinear Programming

The problem of finding the maximum or minimum of a function $f(x)$ of n variables, subject to the constraints

$$\mathbf{a}(\mathbf{x}) = \begin{bmatrix} a_1(x_1, x_2, \ldots, x_n) \\ a_2(x_1, x_2, \ldots, x_n) \\ \vdots \\ a_m(x_1, x_2, \ldots, x_n) \end{bmatrix} = \begin{bmatrix} b_1 \\ b \\ \vdots \\ b_m \end{bmatrix} = \mathbf{b}$$

is made into an unconstrained problem by introducing the new function $L(x)$:

$$L(\mathbf{x}) = f(\mathbf{x}) + \mathbf{z}^{\mathrm{T}}\mathbf{a}(\mathbf{x})$$

where $\mathbf{z}^{\mathrm{T}} = [\lambda_1, \lambda_2, \ldots, \lambda_m]$ is the vector of *Lagrange multipliers.* Now the requirement that $\nabla L(x) = 0$, together with the constraints $\mathrm{a}(\mathrm{x}) = \mathbf{b}$, give a system of $n + m$ equations

$$\nabla f(\mathbf{x}) + \mathbf{z}^{\mathrm{T}}\nabla\mathbf{a}(\mathbf{x}) = 0$$

$$\mathbf{a}(\mathbf{x}) = \mathbf{b}$$

for the $n + m$ unknowns $x_1, x_2 \ldots, x_n, \lambda_1\lambda_2 \ldots, \lambda_m$ that must be satisfied by the minimizer (or maximizer) x.

The problem of inequality constraints is significantly more complicated in the nonlinear case than in the linear case. Consider the problem of minimizing $f(x)$ subject to m equality constraints $\mathbf{a}(\mathbf{x}) = \mathbf{b}$, and p inequality constraints $\mathrm{c}(\mathrm{x}) \le \mathbf{d}$ [thus $\mathbf{a}(\mathbf{x})$ and $\mathbf{b}$ are vectors of m components, and $\mathrm{c}(\mathrm{x})$ and $\mathbf{d}$ are vectors of p components.] A point x^* that satisfies the constraints is a *regular point* if the collection

$$\left\{\nabla a_1(\mathbf{x}^*), \nabla a_2(\mathbf{x}^*), \ldots, \nabla a_m(\mathbf{x}^*)\right\} \cup \left\{\nabla c_j(\mathbf{x}^*) : j \in J\right\}$$

where

$$J = \left\{j : c_j(\mathbf{x}^*) = d_j\right\}$$

is linearly independent. If x^* is a local minimum for the constrained problem and if it is a regular point, there is a vector $\boldsymbol{z}$ with m components and a vector $\mathbf{w} \ge \mathbf{0}$ with p components such that

$$\nabla f(\mathbf{x}^*) + \mathbf{z}^{\mathrm{T}}\nabla\mathbf{a}(\mathbf{x}^*) + \mathbf{w}^{\mathrm{T}}\nabla\mathbf{c}(\mathbf{x}^*) = 0$$

$$\mathbf{w}^{\mathrm{T}}\left(\mathbf{c}(\mathbf{x}^*) - \mathbf{d}\right) = 0$$

These are the *Kuhn-Tucker conditions.* Note that in order to solve these equations, one needs to know for which j it is true that $c_j(\mathrm{x}^*) = 0$. (Such a constraint is said to be *active.*)

References

Luenberger, D. C. 1984. *Linear and Nonlinear Programming,* 2nd ed. Addison-Wesley, Reading, MA.

Peressini, A. L. Sullivan, F. E., and Uhl, J. J., Jr. 1988. *The Mathematics of Nonlinear Programming.* Springer-Verlag, New York.

19.11 Engineering Statistics

Y. L. Tong

Introduction

In most engineering experiments, the outcomes (and hence the observed data) appear in a random and on deterministic fashion. For example, the operating time of a system before failure, the tensile strength of a certain type of material, and the number of defective items in a batch of items produced are all subject to random variations from one experiment to another. In engineering statistics, we apply the theory and methods of statistics to develop procedures for summarizing the data and making statistical inferences, thus obtaining useful information with the presence of randomness and uncertainty.

Elementary Probability

Random Variables and Probability Distributions

Intuitively speaking, a random variable (denoted by X, Y, Z, etc.) takes a numerical value that depends on the outcome of the experiment. Since the outcome of an experiment is subject to random variation, the resulting numerical value is also random. In order to provide a stochastic model for describing the probability distribution of a random variable X, we generally classify random variables into two groups: the discrete type and the continuous type. The discrete random variables are those which, technically speaking, take a finite number or a countably infinite number of possible numerical values. (In most engineering applications they take nonnegative integer values.) Continuous random variables involve outcome variables such as time, length or distance, area, and volume. We specify a function $f(x)$, called the probability density function (p.d.f.) of a random variable X, such that the random variable X takes a value in a set A (or real numbers) as given by

$$P[X \in A] = \begin{cases} \sum_{x \in A} f(x) & \text{for all sets } A \text{ if } X \text{ is discrete} \\ \int_A f(x)\,dx & \text{for all intervals } A \text{ if } X \text{ is continuous} \end{cases} \tag{9.11.1}$$

By letting A be the set of all values that are less than or equal to a fixed number t, i.e., $A = (-\infty, t)$, the probability function $P[X \le t]$, denoted by $F(t)$, is called the distribution function of X. We note that, by calculus, if X is a continuous random variable and if $F(x)$ is differentiable, then $f(x) = \frac{d}{dx} F(x)$.

Expectations

In many applications the "payoff" or "reward" of an experiment with a numerical outcome X is a specific function of X ($u(X)$, say). Since X is a random variable, $u(X)$ is also a random variable. We define the expected value of $u(X)$ by

$$Eu(X) = \begin{cases} \sum_x u(x) f(x) & \text{if } X \text{ is discrete} \\ \int_{-\infty}^{\infty} u(x) f(x)\,dx & \text{if } X \text{ is continuous} \end{cases} \tag{9.11.12}$$

provided of course, that, the sum or the integral exists. In particular, if $u(x) = x$, the $EX \equiv \mu$ is called the mean of X (of the distribution) and $E(X - \mu)^2 \equiv \sigma^2$ is called the variance of X (of the distribution). The mean is a measurement of the central tendency, and the variance is a measurement of the dispersion of the distribution.

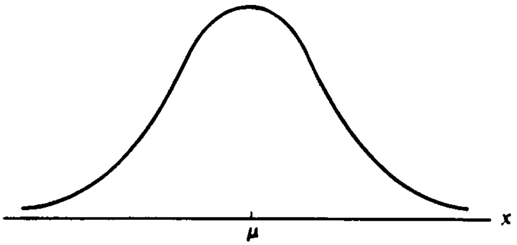

FIGURE 19.11.1 The normal curve with mean μ and variance σ^2.

Some Commonly Used Distributions

Many well-known distributions are useful in engineering statistics. Among the discrete distributions, the hypergeometric and binomial distributions have applications in acceptance sampling problems and quality control, and the Poisson distribution is useful for studying queuing theory and other related problems. Among the continuous distributions, the uniform distribution concerns random numbers and can be applied in simulation studies, the exponential and gamma distributions are closely related to the Poisson distribution, and they, together with the Weibull distribution, have important applications in life testing and reliability studies. All of these distributions involve some unknown parameter(s), hence their means and variances also depend on the parameter(s). The reader is referred to textbooks in this area for details. For example, Hahn and Shapiro (1967, pp. 163–169 and pp. 120–134) contains a comprehensive listing of these and other distributions on their p.d.f.'s and the graphs, parameter(s), means, variances, with discussions and examples of their applications.

The Normal Distribution

Perhaps *the* most important distribution in statistics and probability is the normal distribution (also known as the Gaussian distribution). This distribution involves two parameters: μ and σ^2, and its p.d.f. is given by

$$f(x) = f\left(x;\mu,\sigma^2\right) = \frac{1}{\sqrt{2\pi}\sigma} e^{-\frac{1}{2\sigma^2}(x-\mu)^2} \qquad (9.11.3)$$

for $-\infty < \mu < \infty$, $\sigma^2 > 0$, and $-\infty < \chi < \infty$. It can be shown analytically that, for a p.d.f. of this form, the values of μ and σ^2 are, respectively, that of the mean and the variance of the distribution. Further, the quantity, $\sigma = \sqrt{\sigma^2}$ is called the standard deviation of the distribution. We shall use the symbol $X \sim N(\mu, \sigma^2)$ to denote that X has a normal distribution with mean μ and variance σ^2. When plottting the p.d.f. $f(x; \mu, \sigma^2)$ given in Equation (19.11.3) we see that the resulting graph represents a bell-shaped curve symmetric about μ, as shown in Figure 19.11.1.

If a random variable Z has an $N(0,1)$ distribution, then the p.d.f. of Z is given by (from Equation (19.11.3))

$$\phi(z) = \frac{1}{\sqrt{2\pi}} e^{-\frac{1}{2}x^2} \qquad -\infty < z < \infty \qquad (9.11.4)$$

The distribution function of Z,

$$\Phi(z) = \int_{-\infty}^{x} \phi(u)\, du \qquad -\infty < z < \infty \qquad (9.11.5)$$

cannot be given in a closed form, hence it has been tabulated. The table of $\Phi(z)$ can be found in most textbooks in statistics and probability, including those listed in the references at the end of this section. (We note in passing that, by the symmetry property, $\Phi(z) + \Phi(-z) = 1$ holds for all z.)

Random Sample and Sampling Distributions

Random Sample and Related Statistics

As noted in Box et al. (1978), the design and analysis of engineering experiments usually involves the following steps:

1. The choice of a suitable stochastic model by assuming that the observations follow a certain distribution. The functional form of the distribution (or the p.d.f.) is assumed to be known, except the value(s) of the parameters(s).
2. Design of experiments and collection of data.
3. Summarization of data and computation of certain statistics.
4. Statistical inference (including the estimation of the parameters of the underlying distribution and the hypothesis-testing problems).

In order to make statistical inference concerning the parameter(s) of a distribution, it is essential to first study the sampling distributions. We say that $X_1, X_2, \ldots, X_n$ represent a random sample of size n if they are independent random variables and each of them has the same p.d.f., $f(x)$. (Due to space limitations, the notion of independence will not be carefully discussed here. Nevertheless, we say that $X_1, X_2, \ldots, X_n$ are independent if

$$P\left[X_1 \in A_1, X_2 \in A_2, \ldots, X_n \in A_n\right] = \prod_{i=1}^{n} P\left[X_i \in A_i\right] \tag{19.11.6}$$

holds for all sets $A_1, A_2, \ldots, A_n$.) Since the parameter(s) of the population is (are) unknown, the population mean μ and the population variance σ^2 are unknown. In most commonly used distributions μ and σ^2 can be estimated by the sample mean $\bar{X}$ and the sample variance S^2, respectively, which are given by

$$\bar{X} = \frac{1}{n}\sum_{i=1}^{n} X_i, \qquad S^2 = \frac{1}{n-1}\sum_{i=1}^{n}\left(X_i - \bar{X}\right)^2 = \frac{1}{n-1}\left[\sum_{i=1}^{n} X_i^2 - n\bar{X}^2\right] \tag{19.11.7}$$

(The second equality in the formula for S^2 can be verified algebraically.) Now, since $X_1, X_2, \ldots, X_n$ are random variables $\bar{X}$ and S^2 are also random variables. Each of them is called a statistic and has a probability distribution which also involves the unknown parameter(s). In probability theory there are two fundamental results concerning their distributional properties.

Theorem 1. (Weak Law of Large Numbers). As the sample size n becomes large, $\bar{X}$ converges to μ in probability and S^2 converges to σ^2 in probability. More precisely, for every fixed positive number $\varepsilon > 0$ we have

$$P\left[\left|\bar{X} - \mu\right| \le \varepsilon\right] \to 1, \qquad P\left[\left|S^2 - \sigma^2\right| \le \varepsilon\right] \to 1 \tag{19.11.8}$$

as $n \to \infty$.

Theorem 2. (Central Limit Theorem). As n becomes large, the distribution of the random variable

$$Z = \frac{\bar{X} - \mu}{\sigma \sqrt{n}} = \frac{\sqrt{n}\left(\bar{X} - \mu\right)}{\sigma} \tag{19.11.9}$$

has approximately an $N(0,1)$ distribution. More precisely,

$$P[Z \le z] \to \Phi(z) \text{ for every fixed } z \text{ as } n \to \infty \tag{19.11.10}$$

Normal Distribution-Related Sampling Distributions

One-Sample Case

Additional results exist when the observations come from a normal population. If $X_1, X_2, \ldots, X_n$ represent a random sample of size n from an $N(\mu,\sigma^2)$ population, then the following sample distributions are useful:

Fact 3. For every fixed n the distribution of Z given in Equation (19.11.9) has *exactly* an N(0,1) distribution.

Fact 4. The distribution of the statistic $T = \sqrt{n}(\overline{X} - \mu)/S$, where $S = \sqrt{S^2}$ is the sample standard deviation, is called a Student's t distribution with $\nu = n - 1$ degrees of freedom, in symbols, $t(n - 1)$.

This distribution is useful for making inference on μ when σ^2 is unknown; a table of the percentiles can be found in most statistics textbooks.

Fact 5. The distribution of the statistic $W = (n - 1)S^2/\sigma^2$ is called a chi-squared distribution with $\nu = n - 1$ degrees of freedom, in symbols $\chi^2(\nu)$.

Such a distribution is useful in making inference on σ^2; a table of the percentiles can also be found in most statistics books.

Two-Sample Case

In certain applications we may be interested in the comparisons of two different treatments. Suppose that independent samples from treatments T_1 and T_2 are to be observed as shown in Table 19.11.1.

TABLE 19.11.1 Summarization of Data for a Two-Sample Problem

Treatment	Observations	Distribution	Sample Size	Sample Mean	Sample Variance
T_1	$X_{11}, X_{12}, \ldots, X_{1n_1}$	$\mathcal{N}(\mu_1,\sigma_1^2)$	n_1	$\overline{X}_1$	S_1^2
T_2	$X_{21}, X_{22}, \ldots, X_{2n_2}$	$\mathcal{N}(\mu_2,\sigma_2^2)$	n_2	$\overline{X}_2$	S_2^2

The difference of the population means $(\mu_1 - \mu_2)$ and the ratio of the population variances can be estimated, respectively, by $(\overline{X}_1 - \overline{X}_2)$ and S_1^2/S_2^2. The following facts summarize the distributions of these statistics:

Fact 6. Under the assumption of normality, $(\overline{X}_1 - \overline{X}_2)$ has an $N(\mu_1 - \mu_2, (\sigma_1^2/n_1) + (\sigma_2^2/n_2))$ distribution; or equivalently, for all n_1, n_2 the statistic

$$Z = \left[\left(\overline{X}_1 - \overline{X}_2\right) - \left(\mu_1 - \mu_2\right)\right] \Big/ \left(\sigma_1^2/n_1 + \sigma_2^2/n_2\right)^{1/2} \qquad (19.11.11)$$

has an $N(0,1)$ distribution.

Fact 7. When $\sigma_1^2 = \sigma_2^2 \equiv \sigma^2$, the common population variance is estimated by

$$S_p^2 = \left(n_1 + n_2 - 2\right)^{-1}\left[\left(n_1 - 1\right)S_1^2 + \left(n_2 - 1\right)S_2^2\right] \qquad (19.11.12)$$

and $(n_1 + n_2 - 2)S_p^2/\sigma^2$ has a $\chi^2(n_1 + n_2 - 2)$ distribution.

Fact 8. When $\sigma_1^2 = \sigma_2^2$, the statistic

$$T = \left[\left(\overline{X}_1 - \overline{X}_2\right) - \left(\mu_1 - \mu_2\right)\right] \Big/ S_p\left(1/n_1 + 1/n_2\right)^{1/2} \qquad (19.11.13)$$

has a $t(n_1 + n_2 - 2)$ distribution, where $S_p = \sqrt{S_p^2}$.

Fact 9. The distribution of $F = (S_1^2/\sigma_1^2)/(S_2^2/\sigma_2^2)$ is called an F distribution with degrees of freedom $(n_1 - 1, n_2 - 1)$, in symbols, $F(n_1 - 1, n_2 - 1)$,

The percentiles of this distribution have also been tabulated and can be found in statistics books.

In the following two examples we illustrate numerically how to find probabilities and percentiles using the existing tables for the normal, Student's *t*, chi-squared, and *F* distributions.

Example 10. Suppose that in an experiment four observations are taken, and that the population is assumed to have a normal distribution with mean μ and variance σ^2. Let $\bar{X}$ and S^2 be the sample mean and sample variance as given in Equation (19.11.7).

(a) If, based on certain similar experiments conducted in the past, we know that $\sigma^2 = 1.8^2 \times 10^{-6}$ ($\sigma = 1.8 \times 10^{-3}$), then from $\Phi(-1.645) = 0.05$ and $\Phi(1.96) = 0.975$ we have

$$P\left[-1.645 \le \frac{\bar{X} - \mu}{1.8 \times 10^{-3}\ \ \sqrt{4}} \le 1.96\right] = 0.975 - 0.05 = 0.925$$

or equivalently,

$$P\left[-1.645 \times 0.9 \times 10^{-3} \le \bar{X} - \mu \le 1.96 \times 0.9 \times 10^{-3}\right] = 0.925$$

(b) The statistic $T = 2(\bar{X} - \mu)/S$ has a Student's *t* distribution with 3 degrees of freedom (in symbols, $t(3)$). From the *t* table we have

$$P\left[-3.182 \le 2\left(\bar{X} - \mu\right)\big/S \le 3.182\right] = 0.95$$

which yields

$$P\left[-3.182 \times \frac{S}{2} \le \bar{X} - \mu \le 3.182 \times \frac{S}{2}\right] = 0.95$$

or equivalently,

$$P\left[\bar{X} - 3.182 \times \frac{S}{2} \le \mu \le \bar{X} + 3.182 \times \frac{S}{2}\right] = 0.95$$

This is, in fact, the basis for obtaining the confidence interval for μ given in Equation (19.11.17) when σ^2 is unknown.

(c) The statistic $3S^2/\sigma^2$ has a chi-squared distribution with 3 degrees of freedom (in symbols, $\chi^2(3)$). Thus from the chi-squared table we have $P[0.216 \le 3S^2/\sigma^2 \le 9.348] = 0.95$, which yields

$$P\left[\frac{3S^2}{9.348} \le \sigma^2 \le \frac{3S^2}{0.216}\right] = 0.95$$

and it forms the basis for obtaining a confidence interval for σ^2 as given in Equation (19.11.18).

Example 11. Suppose that in Table 19.11.1 (with two treatments) we have $n_1 = 4$ and $n_2 = 5$, and we let $\bar{X}_1, \bar{X}_2$ and S_1^2, S_2^2 denote the corresponding sample means and sample variances, respectively.

(a) Assume that $\sigma_1^2 = \sigma_2^2$ where the common variance is unknown and is estimated by S_ρ^2 given in Equation (19.11.12). Then the statistic

$$T = \left[\left(\bar{X}_1 - \bar{X}_2\right) - \left(\mu_1 - \mu_2\right)\right]\Big/ S_p\left({}^1\!/_4 + {}^1\!/_5\right)^{1/2}$$

has a $t(7)$ distribution. Thus from the t table we have

$$P = \left[-2.998 \le \left[\left(\bar{X}_1 - \bar{X}_2\right) - \left(\mu_1 - \mu_2\right)\right] \Big/ S_p\left({}^1/_4 + {}^1/_5\right)^{1/2} \le 2.998\right] = 0.98$$

which is equivalent to saying that

$$P\left[-2.998 S_p\left({}^1/_4 + {}^1/_5\right)^{1/2} \le \mu_1 - \mu_2 \le \left(\bar{X}_1 - \bar{X}_2\right) + 2.998 S_p\left({}^1/_4 + {}^1/_5\right)^{1/2}\right] = 0.98$$

(b) The statistic $F = (S_1^2/\sigma_1^2)/(S_2^2/\sigma_2^2)$ has an $F(3,4)$ distribution. Thus from the F-table we have

$$P\left[\left(\frac{\sigma_2^2}{\sigma_1^2}\right)\left(\frac{S_1^2}{S_2^2}\right) \le 6.59\right] = 0.95$$

or equivalently,

$$P\left[\frac{\sigma_2^2}{\sigma_1^2} \le 6.59\frac{S_2^2}{S_1^2}\right] = 0.95$$

The distributions listed above (normal, Student's t, chi-squared, and F) form an integral part of the classical statistical inference theory, and they are developed under the assumption that the observations follow a normal distribution. When the distribution of the population is not normal and inference on the populations means is to be made, we conclude that (1) if the sample sizes n_1, n_2 are large, then the statistic Z in Equation (19.11.11) has an approximate $N(0,1)$ distribution and (2) in the small-sample case, the exact distribution of $\bar{X}$ (of $(\bar{X}_1 - \bar{X}_2)$)) depends on the population p.d.f. There are several analytical methods for obtaining it, and those methods can be found in statistics textbooks.

Confidence Intervals

A method for estimating the population parameters based on the sample mean(s) and sample variance(s) involves the confidence intervals for the parameters.

One-Sample Case

1. Confidence Interval for μ When σ^2 is Known. Consider the situation in which a random sample of size n is taken from an $N(\mu,\sigma^2)$ population and σ^2 is known. An interval, I_1, of the form $I_1 = (\bar{X} - d, \bar{X} + d)$ (with width $2d$) is to be constructed as a "confidence interval or μ." If we make the assertion that μ is in this interval (i.e., μ is bounded below by $\bar{X} - d$ and bounded above by $\bar{X} + d$), then sometimes this assertion is correct and sometimes it is wrong, depending on the value of $\bar{X}$ in a given experiment. If for a fixed α value we would like to have a confidence probability (called confidence coefficient) such that

$$P\left[\mu \in I_1\right] = P\left[\bar{X} - d < \mu < \bar{X} + d\right] = 1 - \alpha \tag{19.11.14}$$

then we need to choose the value of d to satisfy $d = z_{\alpha/2}\dfrac{\sigma}{\sqrt{n}}$, i.e.,

$$I_1 = \left(\bar{X} - z_{\alpha/2}\frac{\sigma}{\sqrt{n}}, \bar{X} + z_{\alpha/2}\frac{\sigma}{\sqrt{n}}\right) \tag{19.11.15}$$

where $z_{\alpha/2}$ is the $(1 - \alpha/2)$th percentile of the $N(0,1)$ distribution such that $\Phi(z_{\alpha/2}) = 1 - \alpha/2$. To see this, we note that from the sampling distribution of $\bar{X}$ (Fact 3) we have

$$P\left[\bar{X} - z_{\alpha/2}\frac{\sigma}{\sqrt{n}} < \mu < \bar{X} + z_{\alpha/2}\frac{\sigma}{\sqrt{n}}\right] = P\left[\frac{\left|\bar{X} - \mu\right|}{\sigma\ \sqrt{n}} \le z_{\alpha/2}\right] \tag{19.11.16}$$

$$= \Phi\left(z_{\alpha/2}\right) - \Phi\left(-z_{\alpha/2}\right) = 1 - \alpha$$

We further note that, even when the original population is not normal, by Theorem 2 the confidence probability is approximately (1 – α) when the sample size is reasonably large.

2. Confidence Interval for μ *When* σ^2 *is Unknown.* Assume that the observations are from an $N(\mu,\sigma^2)$ population. When σ^2 is unknown, by Fact 4 and a similar argument we see that

$$I_2 = \left(\bar{X} - t_{\alpha/2}(n-1)\frac{S}{\sqrt{n}},\ \bar{X} + t_{\alpha/2}(n-1)\frac{S}{\sqrt{n}}\right) \tag{19.11.17}$$

is a confidence interval for μ with confidence probability 1 – α, where $t_{\alpha/2}(n-1)$ is the (1 – α/2)th percentile of the $t(n-1)$ distribution.

3. Confidence Interval for σ^2*.* If, under the same assumption of normality, a confidence interval for σ^2 is needed when μ is unknown, then

$$I_3 = \left((n-1)S^2 \big/ \chi^2_{1-\alpha/2}(n-1),\ (n-1)S^2 \big/ \chi^2_{\alpha/2}(n-1)\right) \tag{19.11.18}$$

has a confidence probability 1 – α, when $\chi^2_{1-\alpha/2}\,(n-1)$ and $\chi^2_{\alpha/2}\,(n-1)$ are the (α/2)th and (1 – α/2)th percentiles, respectively, of the $\chi^2(n-1)$ distribution.

Two-Sample Case

1. Confidence Intervals for $\mu_1 - \mu_2$ *When* $\sigma_1^2 = \sigma_2^2$ *are Known.* Consider an experiment that involves the comparison of two treatments, T_1 and T_2, as indicated in Table 19.11.1. If a confidence interval for $\delta = \mu_1 - \mu_2$ is needed when σ_1^2 and σ_2^2 are unknown, then by Fact 6 and a similar argument, the confidence interval

$$I_4 = \left(\left(\bar{X}_1 - \bar{X}_2\right) - z_{\alpha/2}\sqrt{\sigma_1^2/n_1 + \sigma_2^2/n_2},\ \left(\bar{X}_1 - \bar{X}_2\right) + z_{\alpha/2}\sqrt{\sigma_1^2/n_1 + \sigma_2^2/n_2}\right) \tag{19.11.19}$$

has a confidence probability 1 – α.

2. Confidence Interval for $\mu_1 - \mu_2$ *when* σ_1^2, σ_2^2 *are Unknown but Equal.* Under the additional assumption that $\sigma_1^2 = \sigma_2^2$, but the common variance is unknown, then by Fact 8 the confidence interval

$$I_5 = \left(\left(\bar{X}_1 - \bar{X}_2\right) - d,\ \left(\bar{X}_1 - \bar{X}_2\right) + d\right) \tag{19.11.20}$$

has a confidence probability 1 – α, where

$$d = t_{\alpha/2}\left(n_1 + n_2 - 2\right) S_p \left(1/n_1 + 1/n_2\right)^{1/2} \tag{19.11.21}$$

3. Confidence Interval for σ_2^2/σ_1^2*.* A confidence interval for the ratio of the variances σ_2^2/σ_1^2 can be obtained from the F distribution (see Fact 9), and the confidence interval

$$I_6 = \left(F_{1-\alpha/2}\left(n_1 - 1, n2_1 - 1\right)\frac{S_2^2}{S_1^2}, F_{\alpha/2}\left(n_1 - 1, n2_1 - 1\right)\frac{S_2^2}{S_1^2} \right) \tag{19.11.22}$$

has a confidence probability $1 - \alpha$, where $F_{1-\alpha/2}(n_1 - 1, n_2 - 1)$ and $F_{\alpha/2}(n_1 - 1, n_2 - 1)$ are, respectively, the $(\alpha/2)$th and $(1 - \alpha/2)$th percentiles of the $F(n_1 - 1, n_2 - 1)$ distribution.

Testing Statistical Hypotheses

A statistical hypothesis concerns a statement or assertion about the true value of the parameter in a given distribution. In the two-hypothesis problems, we deal with a null hypothesis and an alternative hypothesis, denoted by H_0 and H_1, respectively. A decision is to be made, based on the data of the experiment, to either accept H_0 (hence reject H_1) or reject H_0 (hence accept H_1). In such a two-action problem, we may commit two types of errors: the type I error is to reject H_0 when it is true, and the type II error is to accept H_0 when it is false. As a standard practice, we do not reject H_0 unless there is significant evidence indicating that it may be false. (In doing so, the burden of proof that H_0 is false is on the experimenter.) Thus we usually choose a small fixed number, α (such as 0.05 or 0.01), such that the probability of committing a type I error is at most (or equal to) α. With such a given α, we can then determine the region in the data space for the rejection of H_0 (called the critical region).

One-Sample Case

Suppose that $X_1, X_2, \ldots, X_n$ represent a random sample of size n from an $N(\mu,\sigma^2)$ population, and $\overline{X}$ and S^2 are, respectively, the sample mean and sample variance.

1. Test for Mean. In testing

$$H_0 : \mu = \mu_0 \text{ vs. } H_1 : \mu = \mu_1\left(\mu_1 > \mu_0\right) \text{ or } H_1 : \mu > \mu_0$$

when σ^2 is known, we reject H_0 when $\overline{X}$ is large. To determine the cut-off point, we note (by Fact 3) that the statistic $Z_0 = (\overline{X} - \mu_0)/(\sigma/\sqrt{n})$ has an $N(0,1)$ distribution under H_0. Thus, if we decide to reject H_0 when $Z_0 > z_\alpha$, then the probability of committing a type I error is α. As a consequence, we apply the decision rule

$$d_1 : \text{reject } H_0 \text{ if and only if } \overline{X} > \mu_0 + z_\alpha \frac{\sigma}{\sqrt{n}}$$

Similarly, from the distribution of Z_0 under H_0 we can obtain the critical region for the other types of hypotheses. When σ^2 is unknown, then by Fact 4 $T_0 = \sqrt{n}(\overline{X} - \mu_0)/S$ has a $t(n-1)$ distribution under H_0. Thus the corresponding tests can be obtained by substituting $t_\alpha(n - 1)$ for z_α and S for σ. The tests for the various one-sided and two-sided hypotheses are summarized in Table 19.11.2 below. For each set of hypotheses, the critical region given on the first line is for the case when σ^2 is known, and that given on the second line is for the case when σ^2 is unknown. Furthermore, t_α and $t_{\alpha/2}$ stand for $t_\alpha(n - 1)$ and $t_{\alpha/2}(n - 1)$, respectively.

2. Test for Variance. In testing hypotheses concerning the variance σ^2 of a normal distribution, use Fact 5 to assert that, under H_0: $\sigma^2 = \sigma_0^2$, the distribution of $w_0 = (n-1)\, S^2/\sigma_0^2$ is $\chi^2(n-1)$. The corresponding tests and critical regions are summarized in the following table (χ_α^2 and $\chi_{\alpha/2}^2$ stand for $\chi_\alpha^2\,(n - 1)$ and $\chi_{\alpha/2}^2\,(n - 1)$, respectively):

Two-Sample Case

In comparing the means and variances of two normal populations, we once again refer to Table 19.11.1 for notation and assumptions.

TABLE 19.11.2 One-Sample Tests for Mean

Null Hypothesis H_0	Alternative Hypothesis H_1	Critical Region
$\mu = \mu_0$ or $\mu \le \mu_0$	$\mu = \mu_1 > \mu_0$ or $\mu > \mu_0$	$\bar{X} > \mu_0 + z_\alpha \frac{\sigma}{\sqrt{n}}$
		$\bar{X} > \mu_0 + t_\alpha \frac{S}{\sqrt{n}}$
$\mu = \mu_0$ or $\mu \ge \mu_0$	$\mu = \mu_1 < \mu_0$ or $\mu < \mu_0$	$\bar{X} < \mu_0 - z_\alpha \frac{\sigma}{\sqrt{n}}$
		$\bar{X} < \mu_0 - t_\alpha \frac{S}{\sqrt{n}}$
$\mu = \mu_0$	$\mu \ne \mu_0$	$\lvert \bar{X} - \mu_0 \rvert > z_{\alpha/2} \frac{\sigma}{\sqrt{n}}$
		$\lvert \bar{X} - \mu_0 \rvert > t_{\alpha/2} \frac{S}{\sqrt{n}}$

TABLE 19.11.3 One-Sample Tests for Variance

Null Hypothesis H_0	Alternative Hypothesis H_1	Critical Region
$\sigma^2 = \sigma_0^2$ or $\sigma^2 \le \sigma_0^2$	$\sigma^2 = \sigma_1^2 > \sigma_0^2$ or $\sigma^2 > \sigma_0^2$	$\left(S^2/\sigma_0^2\right) > \frac{1}{n-1}\chi_\alpha^2$
$\sigma^2 = \sigma_0^2$ or $\sigma^2 \ge \sigma_0^2$	$\sigma^2 = \sigma_1^2 < \sigma_0^2$ or $\sigma^2 < \sigma_0^2$	$\left(S^2/\sigma_0^2\right) < \frac{1}{n-1}\chi_{1-\alpha}^2$
$\sigma^2 = \sigma_0^2$	$\sigma^2 \ne \sigma_0^2$	$\left(S^2/\sigma_0^2\right) > \frac{1}{n-1}\chi_{\alpha/2}^2$
		or $\left(S^2/\sigma_0^2\right) < \frac{1}{n-1}\chi_{1-\alpha/2}^2$

1. Test for Difference of Two Means. Let $\delta = \mu_1 - \mu_2$ be the difference of the two population means. In testing H_0: $\delta = \delta_0$ vs. a one-sided or two-sided alternative hypothesis, we note that, for

$$\tau = \left(\sigma_1^2/n_1 + \sigma_2^2/n_2\right)^{1/2} \tag{19.11.23}$$

and

$$\nu = S_p\left(1/n_1 + 1/n_2\right)^{1/2} \tag{19.11.24}$$

$Z_0 = [\,(\bar{X}_1 - \bar{X}_2) - \delta_0]/\tau$ has an $N(0,1)$ distribution under H_0 and $T_0 = [\,(\bar{X}_1 - \bar{X}_2) - \delta_0]/\nu$ has a $t(n_1 + n_2 - 2)$ distribution under H_0 when $\sigma_1^2 = \sigma_2^2$. Using these results, the corresponding critical regions for one-sided and two-sided tests can be obtained, and they are listed below. Note that, as in the one-sample case, the critical region given on the first line for each set of hypotheses is for the case of known variances, and that given on the second line is for the case in which the variances are equal but unknown. Further, t_α and $t_{\alpha/2}$ stand for $t_\alpha(n_1 + n_2 - 2)$ and $t_{\alpha/2}(n_1 + n_2 - 2)$, respectively.

A Numerical Example

In the following we provide a numerical example for illustrating the construction of confidence intervals and hypothesis-testing procedures. The example is given along the line of applications in Wadsworth (1990, p. 4.21) with artificial data.

TABLE 19.11.4 Two-Sample Tests for Difference of Two Means

Null Hypothesis H_0	Alternative Hypothesis H_1	Critical Region
$\delta = \delta$ or $\delta \le \delta_0$	$\delta = \delta_1 > \delta_0$ or $\delta > \delta_0$	$\left(\bar{X}_1 - \bar{X}_2\right) > \delta_0 + z_\alpha \tau$
		$\left(\bar{X}_1 - \bar{X}_2\right) > \delta_0 + t_\alpha \nu$
$\delta = \delta_0$ or $\delta \ge \delta_0$	$\delta = \delta_1 < \delta_0$ or $\delta < \delta_0$	$\left(\bar{X}_1 - \bar{X}_2\right) < \delta_0 - z_\alpha \tau$
		$\left(\bar{X}_1 - \bar{X}_2\right) < \delta_0 - t_\alpha \nu$
$\delta = \delta_0$	$\delta \ne \delta_0$	$\left\lvert\left(\bar{X}_1 - \bar{X}_2\right) - \delta_0\right\rvert > z_{\alpha/2}\tau$
		$\left\lvert\left(\bar{X}_1 - \bar{X}_2\right) - \delta_0\right\rvert > t_{\alpha/2}\nu$

Suppose that two processes (T_1 and T_2) manufacturing steel pins are in operation, and that a random sample of 4 pins (or 5 pins) was taken from the process T_1 (the process T_2) with the following results (in units of inches):

$$T_1 : 0.7608, 0.7596, 0.7622, 0.7638$$

$$T_2 : 0.7546, 0.7561, 0.7526, 0.7572, 0.7565$$

Simple calculation shows that the observed values of sample means sample variances, and sample standard deviations are:

$$\bar{X}_1 = 0.7616, \quad S_1^2 = 3.280 \times 10^{-6}, \quad S_1 = 1.811 \times 10^{-3}$$

$$\bar{X}_2 = 0.7554, \quad S_2^2 = 3.355 \times 10^{-6}, \quad S_2 = 1.832 \times 10^{-3}$$

One-Sample Case

Let us first consider confidence intervals for the parameters of the first process, T_1, only.

1. Assume that, based on previous knowledge of processes of this type, the variance is known to be $\sigma_1^2 = 1.80^2 \times 10^{-6}$ ($\sigma_1 = 0.0018$). Then from the normal table (see, e.g., Ross (1987, p. 482) we have $z_{0.025} = 1.96$. Thus a 95% confidence interval for μ_1 is

$$\left(0.7616 - 1.96 \times 0.0018/\sqrt{4}, 0.7616 + 1.96 \times 0.0018/\sqrt{4}\right)$$

   or (0.7598, 0.7634) (after rounding off to the 4th decimal place).

2. If σ_1^2 is unknown and a 95% confidence interval for μ_1 is needed then, for $t_{0.023}(3) = 3.182$ (see, e.g., Ross, 1987, p. 484) the confidence interval is

$$\left(0.7616 - 3.182 \times 0.001811/\sqrt{4}, 0.7616 + 3.182 \times 0.001811/\sqrt{4}\right)$$

   or (0.7587, 0.7645)

3. From the chi-squared table with 4 – 1 = 3 degrees of freedom, we have (see, e.g., Ross, 1987, p. 483) $\chi^2_{0.975} = 0.216$, $\chi^2_{0.025} = 9.348$. Thus a 95% confidence interval for σ_1^2 is ($3 \times 3.280 \times 10^{-6}/9.348$, $3 \times 3.280 \times 10^{-6}/0.216$), or ($1.0526 \times 10^{-6}$, $45,5556 \times 10^{-6}$).

4. In testing the hypotheses

$$H_0 : \mu_1 = 0.76 \text{ vs. } H_1 : \mu_1 > 0.76$$

with a = 0.01 when σ_1^2 is unknown, the critical region is $\bar{x}_1 > 0.76 + 4.541 \times 0.001811/\sqrt{4} = 0.7641$. Since the observed value $\bar{x}_1$ is 0.7616, H_0 is accepted. That is, we assert that there is no significant evidence to call for the rejection of H_0.

Two-Sample Case

If we assume that the two populations have a common unknown variance, we can use the Student's *t* distribution (with degree of freedom $\nu = 4 + 5 - 2 = 7$) to obtain confidence intervals and to test hypotheses for $\mu_1 - \mu_2$. We first note that the data given above yield

$$S_p^2 = \frac{1}{7}(3 \times 3.280 + 4 \times 3.355) \times 10^{-6}$$

$$= 3.3229 \times 10^{-6}$$

$$S_p = 1.8229 \times 10^{-3} \qquad \nu = S_p\sqrt{1/4 + 1/5} = 1.2228 \times 10^{-3}$$

and $\bar{X}_1 - \bar{X}_2 = 0.0062$.

1. A 98% confidence interval for $\mu_1 - \mu_2$ is $(0.0062 - 2.998\nu, 0.0062 + 2.998\nu)$ or (0.0025, 0.0099).
2. In testing the hypotheses H_0: $\mu_1 = \mu_2$ (i.e., $\mu_1 - \mu_2 = 0$) vs. H_1: $\mu_1 > \mu_2$ with $\alpha = 0.05$, the critical region is $(\bar{X}_1 - \bar{X}_2) > 1.895\nu = 2.3172 \times 10^{-3}$. Thus H_0 is rejected; i.e., we conclude that there is significant evidence to indicate that $\mu_1 > \mu_2$ may be true.
3. In testing the hypotheses H_0: $\mu_1 = \mu_2$ vs. $\mu_1 \neq \mu_2$ with $\alpha = 0.02$, the critical region is $|\bar{X}_1 - \bar{X}_2| > 2.998\nu = 3.6660 \times 10^{-3}$. Thus H_0 is rejected. We note that the conclusion here is consistent with the result that, with confidence probability $1 - \alpha = 0.98$, the confidence interval for $(\mu_1 - \mu_2)$ does not contain the origin.

Concluding Remarks

The history of probability and statistics goes back to the days of the celebrated mathematicians K. F. Gauss and P. S. Laplace. (The normal distribution, in fact, is also called the Gaussian distribution.) The theory and methods of classical statistical analysis began its developments in the late 1800s and early 1900s when F. Galton and R.A. Fisher applied statistics to their research in genetics, when Karl Pearson developed the chi-square goodness-of-fit method for stochastic modeling, and when E.S. Pearson and J. Neyman developed the theory of hypotheses testing. Today statistical methods have been found useful in analyzing experimental data in biological science and medicine, engineering, social sciences, and many other fields. A non-technical review on some of the applications is Hacking (1984).

Applications of statistics in engineering include many topics. In addition to those treated in this section, other important ones include sampling inspection and quality (process) control, reliability, regression analysis and prediction, design of engineering experiments, and analysis of variance. Due to space limitations, these topics are not treated here. The reader is referred to textbooks in this area for further information. There are many well-written books that cover most of these topics, the following short list consists of a small sample of them.

References

Box, G.E.P., Hunter, W.G., and Hunter, J.S. 1978. *Statistics for Experimenters.* John Wiley & Sons, New York.

Bowker, A.H. and Lieberman, G.J. 1972. *Engineering Statistics,* 2nd ed. Prentice-Hall, Englewood Cliffs, NJ.

Hacking, I. 1984. Trial by number, *Science,* 84(5), 69–70.
Hahn, G.J. and Shapiro, S.S. 1967. *Statistical Models in Engineering.* John Wiley & Sons, New York.
Hines, W.W. and Montgomery, D.G. 1980. *Probability and Statistics in Engineering and Management Science.* John Wiley & Sons, New York.
Hogg, R.V. and Ledolter, J. 1992. *Engineering Statistics.* Macmillan, New York.
Ross, S.M. 1987. *Introduction to Probability and Statistics for Engineers and Scientists.* John Wiley & Sons, New York.
Wadsworth, H.M., Ed. 1990. *Handbook of Statistical Methods for Engineers and Scientists.* John Wiley & Sons, New York.

19.12 Numerical Methods

William F. Ames

Introduction

Since many mathematical models of physical phenomena are not solvable by available mathematical methods one must often resort to approximate or numerical methods. These procedures do not yield exact results in the mathematical sense. This inexact nature of numerical results means we must pay attention to the errors. The two errors that concern us here are *round-off errors* and *truncation errors.*

Round-off errors arise as a consequence of using a number specified by m correct digits to approximate a number which requires more than m digits for its exact specification. For example, using 3.14159 to approximate the irrational number π. Such errors may be especially serious in matrix inversion or in any area where a very large number of numerical operations are required. Some attempts at handling these errors are called *enclosure methods.* (Adams and Kulisch, 1993).

Truncation errors arise from the substitution of a finite number of steps for an infinite sequence of steps (usually an iteration) which would yield the exact result. For example, the iteration $y_n(x) = 1 + \int_0^x xty_{n-1}(t)dt$, $y(0) = 1$ is only carried out for a *few steps*, but it converges in *infinitely* many steps.

The study of some errors in a computation is related to the theory of probability. In what follows, a relation for the error will be given in certain instances.

Linear Algebra Equations

A problem often met is the determination of the solution vector $u = (u_1, u_2, \ldots, u_n)^T$ for the set of linear equations $Au = v$ where A is the $n \times n$ square matrix with coefficients, a_{ij} $(i, j = 1, \ldots, n)$, $v = (v_1, \ldots, v_n)^T$ and i denotes the row index and j the column index.

There are many numerical methods for finding the solution, u, of $Au = v$. The direct inversion of A is usually too expensive and is not often carried out unless it is needed elsewhere. We shall only list a few methods. One can check the literature for the many methods and computer software available. Some of the software is listed in the References section at the end of this chapter. The methods are usually subdivided into *direct* (once through) or *iterative* (repeated) procedures.

In what follows, it will often be convenient to partition the matrix A into the form $A = U + D + L$, where U, D, and L are matrices having the same elements as A, respectively, above the main diagonal, on the main diagonal, and below the main diagonal, and zeros elsewhere. Thus,

$$U = \begin{bmatrix} 0 & a_{12} & & \cdots & a_{1n} \\ 0 & 0 & a_{23} & \cdots & a_{2n} \\ \vdots & \cdots & & \cdots & \\ 0 & 0 & \cdots & \cdots & 0 \end{bmatrix}$$

We also assume the u_js are not all zero and det $A \neq 0$ so the solution is unique.

Direct Methods

Gauss Reduction. This classical method has spawned many variations. It consists of dividing the first equation by a_{11} (if $a_{11} = 0$, reorder the equations to find an $a_{11} \neq 0$) and using the result to eliminate the terms in u_1 from each of the succeeding equations. Next, the modified second equation is divided by a'_{22} (if $a'_{22} = 0$, a reordering of the modified equations may be necessary) and the resulting equation is used to eliminate all terms in u_2 in the succeeding modified equations. This elimination is done n times resulting in a triangular system:

$$\begin{aligned}
u_1 + a'_{12}u_2 + \cdots + a'_{1n}u_n &= v'_1 \\
0 + u_2 + \cdots + a'_{2n}u_n &= v'_2 \\
&\cdots \\
0 + \cdots + u_{n-1} + a'_{n-1,n}u_n &= v'_{n-1} \\
u_n &= v'_n
\end{aligned}$$

where a'_{ij} and v'_j represent the specific numerical values obtained by this process. The solution is obtained by working backward from the last equation. Various modifications, such as the Gauss-Jordan reduction, the Gauss-Doolittle reduction, and the Crout reduction, are described in the classical reference authored by Bodewig (1956). Direct methods prove very useful for sparse matrices and banded matrices that often arise in numerical calculation for differential equations. Many of these are available in computer packages such as IMSL, Maple, Matlab, and Mathematica.

The Tridiagonal Algorithm. When the linear equations are tridiagonal, the system

$$\begin{aligned}
b_1u_1 + c_1u_2 &= d_1 \\
a_iu_{i-1} + b_iu_i + c_iu_{i+1} &= d_i \\
a_nu_{n-1} + b_nu_n \qquad &= d_n, \quad i = 2, 3, \ldots, n-1
\end{aligned}$$

can be solved explicitly for the unknown, thereby eliminating any matrix operations.

The Gaussian elimination process transforms the system into a simpler one of *upper bidiagonal* form. We designate the coefficients of this new system by a'_i, b'_i c'_i and d'_i, and we note that

$$\begin{aligned}
a'_i &= 0, \quad i = 2, 3, \ldots, n \\
b'_i &= 1, \quad i = 1, 2, \ldots, n
\end{aligned}$$

The coefficients c'_i and d'_i are calculated successively from the relations

$$\begin{aligned}
c'_1 &= \frac{c_1}{b_1} \qquad d'_1 = \frac{d_1}{b_1} \\
c'_{i+1} &= \frac{c_{i+1}}{b_{i+1} - a_{i+1}c'_i} \\
d'_{i+1} &= \frac{d_{i+1} - a_{i+1}d'_i}{b_{i+1} - a_{i+1}c'_i}, \quad i = 1, 2, \ldots, n-1
\end{aligned}$$

and, of course, $c_n = 0$.

Having completed the elimination we examine the new system and see that the nth equation is now

$$u_n = d'_n$$

Substituting this value into the $(n-1)$st equation,

$$u_{n-1} + c'_{n-1}u_n = d'_{n-1}$$

we have

$$u_{n-1} = d'_{n-1} - c'_{n-1}u_n$$

Thus, starting with u_n, we have successively the solution for u_i as

$$u_i = d'_i - c'_i u_{i+1}, \quad i = n-1,\ n-2,\ \ldots,\ 1$$

Algorithm for Pentadiagonal Matrix. The equations to be solved are

$$a_i u_{i-2} + b_i u_{i-1} + c_i u_i + d_i u_{i+1} + e_i u_{i+2} = f_i$$

for $1 \le i \le R$ with $a_1 = b_1 = a_2 = e_{R-1} = d_R = e_R = 0$.

The algorithm is as follows. First, compute

$$\delta_1 = d_1/c_1$$
$$\lambda_1 = e_1/c_1$$
$$\gamma_1 = f_1/c_1$$

and

$$\mu_2 = c_2 - b_2\delta_1$$
$$\delta_2 = (d_2 - b_2\lambda_1)/\mu_2$$
$$\lambda_2 = e_2/\mu_2$$
$$\gamma_2 = (f - b_2\gamma_1)/\mu_2$$

Then, for $3 \le i \le R-2$, compute

$$\beta_i = b_i - a_i\delta_{i-2}$$
$$\mu_i = c_i - \beta_i\delta_{i-1} - a_i\lambda_{i-2}$$
$$\delta_i = (d_i - \beta_i\lambda_{i-1})/\mu_i$$
$$\lambda_i = e_i/\mu_i$$
$$\gamma_i = (f_i - \beta_i\gamma_{i-1} - a_i\gamma_{i-2})/\mu_i$$

Next, compute

$$\beta_{R-1} = b_{R-1} - a_{R-1}\delta_{R-3}$$

$$\mu_{R-1} = c_{R-1} - \beta_{R-1}\delta_{R-2} - a_{R-1}\lambda_{R-3}$$

$$\delta_{R-1} = \left(d_{R-1} - \beta_{R-1}\lambda_{R-2}\right)/\mu_{R-1}$$

$$\gamma_{R-1} = \left(f_{R-1} - \beta_{R-1}\gamma_{R-2} - a_{R-1}\gamma_{R-3}\right)/\mu_{R-1}$$

and

$$\beta_R = b_R - a_R\delta_{R-2}$$

$$\mu_R = c_R - \beta_R\delta_{R-1} - a_R\lambda_{R-2}$$

$$\gamma_R = \left(f_R - \beta_R\gamma_{R-1} - a_R\gamma_{R-2}\right)/\mu_R$$

The β_i and μ_i are used only to compute δ_i, λ_i, and γ_i, and need not be stored after they are computed. The δ_i, λ_i, and γ_i, must be stored, as they are used in the back solution. This is

$$u_R = \gamma_R$$

$$u_{R-1} = \gamma_{R-1} - \delta_{R-1}u_R$$

and

$$u_i = \gamma_i - \delta_i u_{i+1} - \lambda_i u_{i+2}$$

for $R - 2 \geq i \geq 1$.

General Band Algorithm. The equations are of the form

$$A_j^{(M)}X_{j-M} + A_j^{(M-1)}X_{j-M+1} + \cdots + A_j^{(2)}X_{j-2} + A_j^{(1)}X_{j-1} + B_jX_j$$

$$+ C_j^{(1)}X_{j+1} + C_j^{(2)}X_{j+2} + \cdots + C_j^{(M-1)}X_{j+M-1} + C_j^{(M)}X_{j+M} = D_j$$

for $1 \leq j \leq N$, $N \geq M$. The algorithm used is as follows:

$$\alpha_j^{(k)} = A_j^{(k)} = 0, \quad \text{for } k \geq j$$

$$C_j^{(k)} = 0, \quad \text{for } k \geq N + 1 - j$$

The forward solution ($j = 1, \ldots, N$) is

$$\alpha_j^{(k)} = A_j^{(k)} - \sum_{p=k+1}^{p=M} \alpha_j^{(p)} W_{j-p}^{(p-k)}, \quad k = M, \ldots, 1$$

$$\beta_j = B_j - \sum_{p=1}^{M} \alpha_j^{(p)} W_{j-p}^{(p)}$$

$$W_j^{(k)} = \left(C_j^{(k)} - \sum_{p=k+1}^{p=M} \alpha_j^{(p-k)} W_{j-(p-k)}^{(p)} \right) \Bigg/ \beta_j, \quad k = 1, \ldots, M$$

$$\gamma_j = \left(D_j - \sum_{p=1}^{M} \alpha_j^{(p)} \gamma_{j-p} \right) \Big/ \beta_j$$

The back solution ($j = N, \ldots, 1$) is

$$X_j = \gamma_j - \sum_{p=1}^{M} W_j^{(p)} X_{j+p}$$

Cholesky Decomposition. When the matrix A is a symmetric and positive definite, as it is for many discretizations of self-adjoint positive definite boundary value problems, one can improve considerably on the band procedures by using the Cholesky decomposition. For the system $Au = v$, the Matrix A can be written in the form

$$A = (I + L)D(I + U)$$

where L is lower triangular, U is upper triangular, and D is diagonal. If $A = A'$ (A' represents the transpose of A), then

$$A = A' = (I + U)' D(I + L)'$$

Hence, because of the uniqueness of the decomposition.

$$I + L = (I + U)' = I + U'$$

and therefore,

$$A = (I + U)' D(I + U)$$

that is,

$$A = B'B, \text{ where } B = \sqrt{D}(I + U)$$

The system $Au = v$ is then solved by solving the two triangular system

$$B'w = v$$

followed by

$$Bu = w$$

To carry out the decomposition $A = B'B$, all elements of the first row of A, and of the derived system, are divided by the square root of the (positive) leading coefficient. This yields smaller rounding errors than the banded methods because the relative error of $\sqrt{a}$ is only half as large as that of a itself. Also, taking the square root brings numbers nearer to each other (i.e., the new coefficients do not differ as widely as the original ones do). The actual computation of $B = (b_{ij})$, $j > i$, is given in the following:

$$
\begin{aligned}
&b_{11} = \left(a_{11}\right)^{1/2}, && b_{1j} = a_{ij}/b_{11}, \quad j \ge 2\\
&b_{22} = \left(a_{22} - b_{12}^2\right)^{1/2}, && b_{2j} = \left(a_{2j} - b_{12}b_{1j}\right)/b_{22}\\
&b_{33} = \left(a_{33} - b_{13}^2 - b_{23}^2\right)^{1/2}, && b_{3j} = \left(a_{3j} - b_{13}b_{1j} - b_{23}b_{2j}\right)/b_{33}\\
&\quad\vdots\\
&b_{ii} = \left(a_{ii} - \sum_{k=1}^{i-1} b_{ki}^2\right)^{1/2}, && b_{ij} = \left(a_{ij} - \sum_{k=1}^{i-1} b_{ki}b_{kj}\right)\Bigg/b_{ii}, \qquad i \ge 2,\ j \ge 2
\end{aligned}
$$

Iterative Methods

Iterative methods consist of repeated application of an often simple algorithm. They yield the exact answer only as the limit of a sequence. They can be programmed to take care of zeros in A and are self-correcting. Their structure permits the use of convergence accelerators, such as overrelaxation, Aitkins acceleration, or Chebyshev acceleration.

Let $a_{ii} > 0$ for all i and $\det A \neq 0$. With $A = U + D + L$ as previously described, several iteration methods are described for $(U + D + L)u = v$.

Jacobi Method (Iteration by total steps). Since $u = -D^{-1}[U + L]u + D^{-1}v$, the iteration $u^{(k)}$ is $u^{(k)} = -D^{-1}[U + L]u^{(k-1)} + D^{-1}v$. This procedure has a slow convergent rate designated by R, $0 < R \ll 1$.

Gauss-Seidel Method (Iteration by single steps). $u^{(k)} = -(L + D)^{-1}Uu^{(k-1)} + (L + D)^{-1}v$. Convergence rate is $2R$, twice as fast as that of the Jacobi method.

Gauss-Seidel with Successive Overrelaxation (SOR). Let $\bar{u}_i^{(k)}$ be the ith components of the Gauss-Seidel iteration. The SOR technique is defined by

$$u_i^{(k)} = (1-\omega)u_i^{(k-1)} + \omega\bar{u}_i^{(k)}$$

where $1 < \omega < 2$ is the overrelaxation parameter. The full iteration is $u^{(k)} = (D + \omega L)^{-1}\{[(1 - \omega)D - \omega U]u^{(k-1)} + \omega v\}$. Optimal values of ω can be computed and depend upon the properties of A (Ames, 1993). With optimal values of ω, the convergence rate of this method is $2R\sqrt{2}$ which is much larger than that for Gauss-Seidel (R is usually much less than one).

For other acceleration techniques, see the literature (Ames, 1993).

Nonlinear Equations in One Variable

Special Methods for Polynomials

The polynomial $P(x) = a_0x^n + a_1x^{n-1} + \cdots + a_{n-1}x + a_n = 0$, with real coefficients a_j, $j = 0, \ldots, n$, has exactly n roots which may be real or complex.

If all the coefficients of $P(x)$ are integers, then any rational roots, say r/s (r and s are integers with no common factors), of $P(x) = 0$ must be such that r is an integral divisor of a_n and s is an integral division of a_0. Any polynomial with rational coefficients may be converted into one with integral coefficients by multiplying the polynomial by the lowest common multiple of the denominators of the coefficients.

Example. $x^4 - 5x^2/3 + x/5 + 3 = 0$. The lowest common multiple of the denominators is 15. Multiplying by 15, which does not change the roots, gives $15x^4 - 25x^2 + 3x + 45 = 0$. The only possible rational roots r/s are such that r may have the value ±45, ±15, ±5, ±3, and ±1, while s may have the values ±15, ±5, ±3, and ±1. All possible rational roots, with no common factors, are formed using all possible quotients.

If $a_0 > 0$, the first negative coefficient is preceded by k coefficients which are positive or zero, and G is the largest of the absolute values of the negative coefficients, then each real root is less than $1 + \sqrt[k]{G/a_0}$ (upper bound on the real roots). For a lower bound to the real roots, apply the criterion to $P(-x) = 0$.

Example. $P(x) = x^5 + 3x^4 - 2x^3 - 12x + 2 = 0$. Here $a_0 = 1$, $G = 12$, and $k = 2$. Thus, the upper bound for the real roots is $1 + \sqrt[2]{12} \approx 4.464$. For the lower bound, $P(-x) = -x^5 + 3x^4 + 2x^3 + 12x + 2 = 0$, which is equivalent to $x^5 - 3x^4 - 2x^3 - 12x - 2 = 0$. Here $k = 1$, $G = 12$, and $a_0 = 1$. A lower bound is $-(1 + 12) = 13$. Hence all real roots lie in $-13 < x < 1 + \sqrt[2]{12}$.

A useful *Descartes rule of signs* for the number of positive or negative real roots is available by observation for polynomials with real coefficients. The number of positive real roots is either equal to the number of sign changes, n, or is less than n by a positive *even* integer. The number of negative real roots is either equal to the number of sign changes, n, of $P(-x)$, or is less than n by a positive even integer.

Example. $P(x) = x^5 - 3x^3 - 2x^2 + x - 1 = 0$. There are three sign changes, so $P(x)$ has either three or one positive roots. Since $P(-x) = -x^5 + 3x^3 - 2x^2 - 1 = 0$, there are either two or zero negative roots.

The Graeffe Root-Squaring Technique

This is an iterative method for finding the roots of the algebraic equation

$$f(x) = a_0x^p + a_1x^{p-1} + \cdots + a_{p-1}x + a_p = 0$$

If the roots are $r_1, r_2, r_3, \ldots$, then one can write

$$S_p = r_1^p\left(1 + \frac{r_2^p}{r_1^p} + \frac{r_3^p}{r_1^p} + \cdots\right)$$

and if one root is larger than all the others, say r_1, then for large enough p all terms (other than 1) would become negligible. Thus,

$$S_p \approx r_1^p$$

or

$$\lim_{p\to\infty} S_p^{1/p} = r_1$$

The Graeffe procedure provides an efficient way for computing S_p via a sequence of equations such that the roots of each equation are the squares of the roots of the preceding equations in the sequence. This serves the purpose of ultimately obtaining an equation whose roots are so widely separated in magnitude that they may be read approximately from the equation by inspection. The basic procedure is illustrated for a polynomial of degree 4:

$$f(x) = a_0x^4 + a_1x^3 + a_2x^2 + a_3x + a_4 = 0$$

Rewrite this as

$$a_0x^4 + a_2x^2 + a_4 = -a_1x^3 - a_3x$$

and square both sides so that upon grouping

$$a_0^2x^8 + \left(2a_0a_2 - a_1^2\right)x^6 + \left(2a_0a_4 - 2a_1a_3 + a_2^2\right)x^4 + \left(2a_2a_4 - a_3^2\right)x^2 + a_4^2 = 0$$

Because this involves only even powers of x, we may set $y = x^2$ and rewrite it as

$$a_0^2 y^4 + \left(2a_0 a_2 - a_1^2\right) y^3 + \left(2a_0 a_4 - 2a_1 a_3 + a_2^2\right) y^2 + \left(2a_2 a_4 - a_3^2\right) y + a_4^2 = 0$$

whose roots are the squares of the original equation. If we repeat this process again, the new equation has roots which are the fourth power, and so on. After p such operations, the roots are 2^p (original roots). If at any stage we write the coefficients of the unknown in sequence

$$a_0^{(p)} \quad a_1^{(p)} \quad a_2^{(p)} \quad a_3^{(p)} \quad a_4^{(p)}$$

then, to get the new sequence $a_i^{(p+1)}$, write $a_i^{(p+1)} = 2a_0^{(p)}$ (times the symmetric coefficient) with respect to $a_i^{(p)} - 2a_1^{(p)}$ (times the symmetric coefficient) $- \cdots (-1)^{\mathrm{i}}\, a_i^{(p)2}$. Now if the roots are r_1, r_2, r_3, and r_4, then $\mathrm{a}_1/\mathrm{a}_0 = -\Sigma_{i-1}^4 r_i$, $a_i^{(1)}/a_0^{(1)} = -\Sigma r_i^2, \ldots, a_i^{(p)}/a_0^{(p)} = -\Sigma r_i^{2p}$. If the roots are all distinct and r_1 is the largest in magnitude, then eventually

$$r_1^{2p} \approx -\frac{a_1^{(p)}}{a_0^{(p)}}$$

And if r_2 is the next largest in magnitude, then

$$r_2^{2p} \approx -\frac{a_2^{(p)}}{a_1^{(p)}}$$

And, in general $a_n^{(p)}/a_{n-1}^{(p)} \approx -r_n^{2p}$. This procedure is easily generalized to polynomials of arbitrary degree and specialized to the case of multiple and complex roots.

Other methods include Bernoulli iteration, Bairstow iteration, and Lin iteration. These may be found in the cited literature. In addition, the methods given below may be used for the numerical solution of polynomials.

General Methods for Nonlinear Equations in One Variable

Successive Substitutions

Let $f(x) = 0$ be the nonlinear equation to be solved. If this is rewritten as $x = F(x)$, then an iterative scheme can be set up in the form $x_{k+1} = F(x_k)$. To start the iteration, an initial guess must be obtained graphically or otherwise. The convergence or divergence of the procedure depends upon the method of writing $x = F(x)$, of which there will usually be several forms. A general rule to ensure convergence cannot be given. However, if a is a root of $f(x) = 0$, a necessary condition for convergence is that $|F'(x)| < 1$ in that interval about a in which the iteration proceeds (this means the iteration cannot converge unless $|F'(x)| < 1$, but it does not ensure convergence). This process is called *first order* because the error in x_{k+1} is proportional to the first power of the error in x_k.

Example. $f(x) = x^3 - x - 1 = 0$. A rough plot shows a real root of approximately 1.3. The equation can be written in the form $x = F(x)$ in several ways, such as $x = x^3 - 1$, $x = 1/(x^2 - 1)$, and $x = (1 + x)^{1/3}$. In the first case, $F'(x) = 3x^2 = 5.07$ at $x = 1.3$; in the second, $F'(1.3) = 5.46$; only in the third case is $F'(1.3) < 1$. Hence, only the third iterative process has a chance to converge. This is illustrated in the iteration table below.

Step k	$x = \dfrac{1}{x^2 - 1}$	$x = x^3 - 1$	$x = (1 + x)^{1/3}$
0	1.3	1.3	1.3
1	1.4493	1.197	1.32
2	0.9087	0.7150	1.3238
3	–5.737	–0.6345	1.3247
4	⋯	⋯	1.3247

Numerical Solution of Simultaneous Nonlinear Equations

The techniques illustrated here will be demonstrated for two simultaneous equations — $f(x, y) = 0$ and $g(x, y) = 0$. They immediately generalize to more than two simultaneous equations.

The Method of Successive Substitutions

The two simultaneous equations can be written in various ways in equivalent forms

$$x = F(x, y)$$

$$y = G(x, y)$$

and the method of successive substitutions can be based on

$$x_{k+1} = F(x_k, y_k)$$

$$y_{k+1} = G(x_k, y_k)$$

Again, the procedure is of the first order and a necessary condition for convergence is

$$\left|\frac{\partial F}{\partial x}\right| + \left|\frac{\partial F}{\partial y}\right| < 1 \qquad \left|\frac{\partial G}{\partial x}\right| + \left|\frac{\partial G}{\partial y}\right| < 1$$

in the iteration neighborhood of the true solution.

The Newton-Raphson Procedure

Using the two simultaneous equation, start from an approximate, say (x_0, y_0), obtained graphically or from a two-way table. Then, solve successively the linear equations

$$\Delta x_k \frac{\partial f}{\partial x}(x_k, y_k) + \Delta y_k \frac{\partial f}{\partial y}(x_k, y_k) = -f(x_k, y_k)$$

$$\Delta x_k \frac{\partial g}{\partial x}(x_k, y_k) + \Delta y_k \frac{\partial g}{\partial y}(x_k, y_k) = -g(x_k, y_k)$$

for Δx_k and Δy_k. Then, the $k + 1$ approximation is given from $x_{k+1} = x_k + \Delta x_k, y_{k+1} = y_k + \Delta y_k$. A modification consists in solving the equations with (x_k, y_k) replaced by (x_0, y_0) (or another suitable pair later on in the iteration) in the derivatives. This means the derivatives (and therefore the coefficients of Δx_k, Δy_k) are independent of k. Hence, the results become

$$\Delta x_k = \frac{-f(x_k,y_k)(\partial g/\partial y)(x_0,y_0) + g(x_k,y_k)(\partial f/\partial y)(x_0,y_0)}{(\partial f/\partial x)(x_0,y_0)(\partial g/\partial y)(x_0,y_0) - (\partial f/\partial y)(x_0,y_0)(\partial g/\partial x)(x_0,y_0)}$$

$$\Delta y_k = \frac{-g(x_k,y_k)(\partial f/\partial x)(x_0,y_0) + f(x_k,y_k)(\partial g/\partial x)(x_0,y_0)}{(\partial f/\partial x)(x_0,y_0)(\partial g/\partial y)(x_0,y_0) - (\partial f/\partial y)(x_0,y_0)(\partial g/\partial x)(x_0,y_0)}$$

and $x_{k+1} = \Delta x_k + x_k$, $y_{k+1} = \Delta y_k + y_k$. Such an alteration of the basic technique reduces the rapidity of convergence.

Example

$$f(x,y) = 4x^2 + 6x - 4xy + 2y^2 - 3$$

$$g(x,y) = 2x^2 - 4xy + y^2$$

By plotting, one of the approximate roots is found to be $x_0 = 0.4$, $y_0 = 0.3$. At this point, there results $\partial f/\partial x = 8$, $\partial f/\partial y = -0.4$, $\partial g/\partial x = 0.4$, and $\partial g/\partial y = -1$. Hence,

$$x_{k+1} = x_k + \Delta x_k = x_k + \frac{-f(x_k,y_k) - 0.4g(x_k,y_k)}{8(-1)-(-0.4)(0.4)}$$

$$= x_k - 0.127\,55 f(x_k,y_k) - 0.051\,02 g(x_k,y_k)$$

and

$$y_{k+1} = y_k - 0.051\,02 f(x_k,y_k) + 1.020\,41 g(x_k,y_k)$$

The first few iteration steps are shown in the following table.

Step k	x_k	y_k	$f(x_k, y_k)$	$g(x_k, y_k)$
0	0.4	0.3	–0.26	0.07
1	0.43673	0.24184	0.078	0.0175
2	0.42672	0.25573	–0.0170	–0.007
3	0.42925	0.24943	0.0077	0.0010

Methods of Perturbation

Let $f(x) = 0$ be the equation. In general, the iterative relation is

$$x_{k+1} = x_k - \frac{f(x_k)}{\alpha_k}$$

where the iteration begins with x_0 as an initial approximation and α_k is some functional.

The Newton-Raphson Procedure. This variant chooses $\alpha_k = f'(x_k)$ where $f' = df/dx$ and geometrically consists of replacing the graph of $f(x)$ by the tangent line at $x = x_k$ in each successive step. If $f'(x)$ and $f''(x)$ have the same sign throughout an interval $a \le x \le b$ containing the solution, with $f(a)$ and $f(b)$ of opposite signs, then the process converges starting from any x_0 in the interval $a \le x \le b$. The process is second order.

Example

$$f(x) = x - 1 + \frac{(0.5)^x - 0.5}{0.3}$$

$$f'(x) = 1 - 2.3105[0.5]^x$$

An approximate root (obtained graphically) is 2.

Step k	x_k	$f(x_k)$	$f'(x_k)$
0	2	0.1667	0.4224
1	1.605	–0.002	0.2655
2	1.6125	–0.0005	⋯

The Method of False Position. This variant is commenced by finding x_0 and x_1 such that $f(x_0)$ and $f(x_1)$ are of opposite signs. Then, α_1 = slope of secant line joining $[x_0, f(x_0)]$ and $[x_1, f(x_1)]$ so that

$$x_2 = x_1 - \frac{x_1 - x_0}{f(x_1) - f(x_0)} f(x_1)$$

In each following step, α_k is the slope of the line joining $[x_k, f(x_k)]$ to the most recently determined point where $f(x_j)$ has the opposite sign from that of $f(x_k)$. This method is of first order.

The Method of Wegstein

This is a variant of the method of successive substitutions which forces or accelerates convergence. The iterative procedure $x_{k+1} = F(x_k)$ is revised by setting $\hat{x}_{k+1} = F(x_k)$ and then taking $x_{k+1} = qx_k + (1 - q)\,\hat{x}_{k+1}$. Wegstein found that suitably chosen qs are related to the basic process as follows:

Behavior of Successive Substitution Process	Range of Optimum q
Oscillatory convergence	$0 < q < 1/2$
Oscillatory divergence	$1/2 < q < 1$
Monotonic convergence	$q < 0$
Monotonic divergence	$1 < q$

At each step, q may be calculated to give a locally optimum value by setting

$$q = \frac{x_{k+1} - x_k}{x_{k+1} - 2x_k + x_{k-1}}$$

The Method of Continuity

In the case of n equations in n unknowns, when n is large, determining the approximate solution may involve considerable effort. In such a case, the method of continuity is admirably suited for use on either digital or analog computers. It consists basically of the introduction of an extra variable into the n equations

$$f_i(x_1, x_2, \ldots, x_n) = 0, \qquad i = 1, \ldots, n$$

and replacing them by

$$f_i(x_1, x_2, \ldots, x_n, \lambda) = 0, \qquad i = 1, \ldots, n$$

where λ is introduced in such a way that the functions depend in a simple way upon λ and reduce to an easily solvable system for $\lambda = 0$ and to the original equations for $\lambda = 1$. A system of ordinary differential equations, with independent variable λ, is then constructed by differentiating with respect to λ. There results

$$\sum_{j=1}^{n} \frac{\partial f_i}{\partial x_j} \frac{dx_j}{d\lambda} + \frac{\partial f_i}{\partial \lambda} = 0$$

where $x_1, \ldots, x_n$ are considered as functions of λ. The equations are integrated, with initial conditions obtained with $\lambda = 0$, from $\lambda = 0$ to $\lambda = 1$. If the solution can be continued to $\lambda = 1$, the values of $x_1, \ldots, x_n$ for $\lambda = 1$ will be a solution of the original equations. If the integration becomes infinite, the parameter λ must be introduced in a different fashion. Integration of the differential equations (which are usually nonlinear in λ) may be accomplished on an analog computer or by digital means using techniques described in a later section entitled "Numerical Solution of Ordinary Differential Equations."

Example

$$f(x, y) = 2 + x + y - x^2 + 8xy + y^3 = 0$$

$$g(x, y) = 1 + 2x + 3y + x^2 + xy - ye^x = 0$$

Introduce λ as

$$f(x, y, \lambda) = (2 + x + y) + \lambda(-x^2 + 8xy + y^3) = 0$$

$$g(x, y, \lambda) = (1 + 2x - 3y) + \lambda(x^2 + xy - ye^x) = 0$$

For $\lambda = 1$, these reduce to the original equations, but, for $\lambda = 0$, they are the linear systems

$$x + y = -2$$

$$2x - 3y = -1$$

which has the unique solution $x = -1.4$, $y = -0.6$. The differential equations in this case become

$$\frac{\partial f}{\partial x} \frac{dx}{d\lambda} + \frac{\partial f}{\partial y} \frac{dy}{d\lambda} = -\frac{\partial f}{\partial \lambda}$$

$$\frac{\partial g}{\partial x} \frac{dx}{d\lambda} + \frac{\partial g}{\partial y} \frac{dy}{d\lambda} = -\frac{\partial g}{\partial \lambda}$$

or

$$\frac{dx}{d\lambda} = \frac{\dfrac{\partial f}{\partial y}\dfrac{\partial g}{\partial \lambda} - \dfrac{\partial f}{\partial \lambda}\dfrac{\partial g}{\partial x}}{\dfrac{\partial f}{\partial x}\dfrac{\partial g}{\partial y} - \dfrac{\partial f}{\partial y}\dfrac{\partial g}{\partial x}}$$

$$\frac{dy}{d\lambda} = \frac{\dfrac{\partial f}{\partial \lambda}\dfrac{\partial g}{\partial x} - \dfrac{\partial f}{\partial x}\dfrac{\partial g}{\partial \lambda}}{\dfrac{\partial f}{\partial x}\dfrac{\partial g}{\partial y} - \dfrac{\partial f}{\partial y}\dfrac{\partial g}{\partial x}}$$

Integrating in λ, with initial values $x = -1.4$ and $y = -0.6$ at $\lambda = 0$, from $\lambda = 0$ to $\lambda = 1$ gives the solution.

Interpolation and Finite Differences

The practicing engineer constantly finds it necessary to refer to tables as sources of information. Consequently, interpolation, or that procedure of "reading between the lines of the table," is a necessary topic in numerical analysis.

Linear Interpolation

If a function $f(x)$ is approximately linear in a certain range, then the ratio $[f(x_1) - f(x_0)]/(x_1 - x_0) = f[x_0, x_1]$ is approximately independent of x_0 and x_1 in the range. The linear approximation to the function $f(x)$, $x_0 < x < x_1$, then leads to the interpolation formula

$$f(x) \approx f(x_0) + (x - x_0) f[x_0, x_1] \approx f(x_0) + \frac{x - x_0}{x_1 - x_0}\left[f(x_1) - f(x_0)\right]$$

$$\approx \frac{1}{x_1 - x_0}\left[(x_1 - x) f(x_0) - (x_0 - x) f(x_1)\right]$$

Divided Differences of Higher Order and Higher-Order Interpolation

The first-order divided difference $f[x_0, x_1]$ was defined above. Divided differences of second and higher order are defined iteratively by

$$f[x_0, x_1, x_2] = \frac{f[x_1, x_2] - f[x_0, x_1]}{x_2 - x_0}$$

$$\vdots$$

$$f[x_0, x_1, \ldots, x_k] = \frac{f[x_1, \ldots, x_k] - f[x_0, x_1, \ldots, x_{k-1}]}{x_k - x_0}$$

and a convenient form for computational purposes is

$$f[x_0, x_1, \ldots, x_k] = \sum_{j=0}^{k}{}' \frac{f(x_j)}{(x_j - x_0)(x_j - x_1)\cdots(x_j - x_k)}$$

for any $k \geq 0$, where the $'$ means the term $(x_j - x_j)$ is omitted in the denominator. For example,

$$f\left[x_0,x_1,x_2\right]=\frac{f\left(x_0\right)}{\left(x_0-x_1\right)\left(x_0-x_2\right)}+\frac{f\left(x_1\right)}{\left(x_1-x_0\right)\left(x_1-x_2\right)}+\frac{f\left(x_2\right)}{\left(x_2-x_0\right)\left(x_2-x_1\right)}$$

If the accuracy afforded by a linear approximation is inadequate, a generally more accurate result may be based upon the assumption that $f(x)$ may be approximated by a polynomial of degree 2 or higher over certain ranges. This assumptions leads to *Newton's fundamental interpolation formula* with divided differences:

$$\begin{aligned}f(x)\approx f\left(x_0\right)+\left(x-x_0\right)f\left[x_0,x_1\right]+\left(x-x_0\right)\left(x-x_1\right)f\left[x_0,x_1,x_2\right]\\+\left(x-x_0\right)\left(x-x_1\right)\cdots\left(x-x_{n-1}\right)f\left[x_0,x_1,\ldots,x_n\right]+E_n(x)\end{aligned}$$

where $E_n(x)$ = error = $[1/(n+1)!]f^{(n-1)}(\varepsilon)\pi(x)$ where $\min(x_0, \ldots, x) < \varepsilon < \max(x_0, x_1,\ldots, x_n, x)$ and $\pi(x) = (x - x_0)(x - x_1)\ldots(x - x_n)$. In order to use this most effectively, one may first form a divided-difference table. For example, for third-order interpolation, the difference table is

$$\begin{array}{c|cccc}
x_0 & f\left(x_0\right) & & & \\
 & & f\left[x_0,x_1\right] & & \\
x_1 & f\left(x_1\right) & & f\left[x_0,x_1,x_2\right] & \\
 & & f\left[x_1,x_2\right] & & f\left[x_0,x_1,x_2,x_3\right] \\
x_2 & f\left(x_2\right) & & f\left[x_1,x_2,x_3\right] & \\
 & & f\left[x_2,x_3\right] & & \\
x_3 & f\left(x_3\right) & & &
\end{array}$$

where each entry is given by taking the difference between diagonally adjacent entries to the left, divided by the abscissas corresponding to the ordinates intercepted by the diagonals passing through the calculated entry.

Example. Calculate by third-order interpolation the value of cosh 0.83 given cosh 0.60, cosh 0.80, cosh 0.90, and cosh 1.10.

$$\begin{array}{l|llll}
x_0=0.60 & 1.185\ 47 & & & \\
 & & 0.7598 & & \\
x_1=0.80 & 1.337\ 43 & & 0.6560 & \\
 & & 0.9566 & & 0.1586 \\
x_2=0.90 & 1.433\ 09 & & 0.7353 & \\
 & & 1.1772 & & \\
x_3=1.10 & 1.668\ 52 & & &
\end{array}$$

With $n = 3$, we have

$$\begin{aligned}\cosh 0.83\approx 1.185\ 47+(0.23)(0.7598)+(0.23)(0.03)(0.6560)\\+(0.23)(0.03)(-0.07)(0.1586)=1.364\ 64\end{aligned}$$

which varies from the true value by 0.000 04.

Lagrange Interpolation Formulas

The Newton formulas are expressed in terms of divided differences. It is often useful to have interpolation formulas expressed explicitly in terms of the ordinates involved. This is accomplished by the Lagrange interpolation polynomial of degree n:

$$y(x)=\sum_{j=0}^{n}\frac{\pi(x)}{\left(x-x_j\right)\pi'\left(x_j\right)}f\left(x_j\right)$$

where

$$\pi(x) = (x - x_0)(x - x_1)\cdots(x - x_n)$$

$$\pi'(x_j) = (x_j - x_0)(x_j - x_1)\cdots(x_j - x_n)$$

where $(x_j - x_j)$ is the omitted factor. Thus,

$$f(x) = y(x) + E_n(x)$$

$$E_n(x) = \frac{1}{(n+1)!}\pi(x) f^{(n+1)}(\varepsilon)$$

Example. The interpolation polynomial of degree 3 is

$$y(x) = \frac{(x - x_1)(x - x_2)(x - x_3)}{(x_0 - x_1)(x_0 - x_2)(x_0 - x_3)} f(x_0) + \frac{(x - x_0)(x - x_2)(x - x_3)}{(x_1 - x_0)(x_1 - x_2)(x_1 - x_3)} f(x_1)$$

$$+ \frac{(x - x_0)(x - x_1)(x - x_3)}{(x_2 - x_0)(x_2 - x_1)(x_2 - x_3)} f(x_2) + \frac{(x - x_0)(x - x_1)(x - x_2)}{(x_3 - x_0)(x_3 - x_1)(x_3 - x_2)} f(x_3)$$

Thus, directly from the data

x	0	1	3	4
$f(x)$	1	1	–1	2

we have as an interpolation polynomial $y(x)$ for (x):

$$y(x) = 1 \cdot \frac{(x-1)(x-3)(x-4)}{(0-1)(0-3)(0-4)} + 1 \cdot \frac{x(x-3)(x-4)}{(1-0)(1-3)(1-4)}$$

$$-1 \cdot \frac{x(x-1)(x-4)}{(3-0)(3-1)(3-4)} + 2 \cdot \frac{(x-0)(x-1)(x-3)}{(4-0)(4-1)(4-3)}$$

Other Difference Methods (Equally Spaced Ordinates)

Backward Differences. The backward differences denoted by

$$\nabla f(x) = f(x) - f(x-h)$$

$$\nabla^2 f(x) = \nabla f(x) - \nabla f(x-h)$$

$$\dots$$

$$\nabla f^n(x) = \nabla^{n-1} f(x) - \nabla^{n-1} f(x-h)$$

are useful for calculation near the end of tabulated data.

Central Differences. The central differences denoted by

$$\delta f(x) = f\left(x + \frac{h}{2}\right) - f\left(x - \frac{h}{2}\right)$$

$$\delta^n f(x) = \delta^{n-1} f\left(x + \frac{h}{2}\right) - \delta^{n-1} f\left(x - \frac{h}{2}\right)$$

are useful for calculating at the interior points of tabulated data.

Also to be found in the literature are Gaussian, Stirling, Bessel, Everett, Comrie differences, and so forth.

Inverse Interpolation

This is the process of finding the value of the independent variable or abscissa corresponding to a given value of the function when the latter is between two tabulated values of the abscissa. One method of accomplishing this is to use Lagrange's interpolation formula in the form

$$x = \psi(y) = \sum_{j=0}^{n} \frac{\pi(y)}{\left(y - y_j\right)\pi'\left(y_j\right)} x_j$$

where x is expressed as a function of y. Other methods revolve about methods of iteration.

Numerical Differentiation

Numerical differentiation should be avoided wherever possible, particularly when data are empirical and subject to appreciable observation errors. Errors in data can affect numerical derivatives quite strongly (i.e., differentiation is a roughening process). When such a calculation must be made, it is usually desirable first to *smooth* the data to a certain extent.

The Use of Interpolation Formulas

If the data are given over equidistant values of the independent variable x, an interpolation formula, such as the Newton formula, may be used, and the resulting formula differentiated analytically. If the independent variable is not at equidistant values, then Lagrange's formulas must be used. By differentiating three- and five-point Lagrange interpolation formulas, the following differentiation formulas result for equally spaced tabular points.

Three-point Formulas. Let x_0, x_1, and x_2 be the three points

$$f'\left(x_0\right) = \frac{1}{2h}\left[-3f\left(x_0\right) + 4f\left(x_1\right) - f\left(x_2\right)\right] + \frac{h^2}{3} f'''(\varepsilon)$$

$$f'\left(x_1\right) = \frac{1}{2h}\left[-f\left(x_0\right) + f\left(x_2\right)\right] + \frac{h^2}{6} f'''(\varepsilon)$$

$$f'\left(x_2\right) = \frac{1}{2h}\left[f\left(x_0\right) - 4f\left(x_1\right) + 3f\left(x_2\right)\right] + \frac{h^2}{3} f'''(\varepsilon)$$

where the last term is an error term and $\min_j x_j < \varepsilon < \max_j x_j$.

Five-point Formulas. Let x_0, x_1, x_2, x_3, and x_4 be the five values of the equally spaced independent variable and $f_j = f(x_j)$.

$$f'\left(x_0\right) = \frac{1}{12h}\left[-25f_0 + 48f_1 - 36f_2 + 16f_3 - 3f_4\right] + \frac{h^4}{5} f^{(v)}(\varepsilon)$$

$$f'(x_1) = \frac{1}{12h}\left[-3f_0 - 10f_1 + 18f_2 - 6f_3 + f_4\right] - \frac{h^4}{20} f^{(v)}(\varepsilon)$$

$$f'(x_2) = \frac{1}{12h}\left[f_0 - 8f_1 + 8f_3 - f_4\right] + \frac{h^4}{30} f^{(v)}(\varepsilon)$$

$$f'(x_3) = \frac{1}{12h}\left[-f_0 + 6f_1 - 18f_2 + 10f_3 + 3f_4\right] - \frac{h^4}{20} f^{(v)}(\varepsilon)$$

$$f'(x_4) = \frac{1}{12h}\left[3f_0 - 16f_1 + 36f_2 - 48f_3 + 25f_4\right] + \frac{h^4}{5} f^{(v)}(\varepsilon)$$

and the last term is again an error term.

Smoothing Techniques

These techniques involve the approximation of the tabular data by a least squares fit of the data using some known functional form, usually a polynomial. In place of approximating $f(x)$ by a single least squares polynomial of degree n over the entire range of the tabulation, it is often desirable to replace each tabulated value by the value taken on by a last squares polynomial of degree n relevant to a subrange of $2M + 1$ points centered, where possible, at the point for which the entry is to be modified. Thus, each smoothed value replaces a tabulated value. Let $f_i = f(x_i)$ be the tabular points and y_j = smoothed values. A first-degree least squares with three points would be

$$y_0 = \tfrac{1}{6}\left[5f_0 + 2f_1 - f_2\right]$$

$$y_1 = \tfrac{1}{3}\left[f_0 + f_1 + f_2\right]$$

$$y_2 = \tfrac{1}{6}\left[-f_0 + 2f_1 + 5f_2\right]$$

A first-degree least squares with five points would be

$$y_0 = \tfrac{1}{5}\left[3f_0 + 2f_1 + f_2 - f_4\right]$$

$$y_1 = \tfrac{1}{10}\left[4f_0 + 3f_1 + 2f_2 + f_3\right]$$

$$y_2 = \tfrac{1}{5}\left[f_0 + f_1 + f_2 + f_3 + f_4\right]$$

$$y_3 = \tfrac{1}{10}\left[f_0 + 2f_1 + 3f_2 + 4f_3\right]$$

$$y_4 = \tfrac{1}{5}\left[-f_0 + f_2 + 2f_3 + 3f_4\right]$$

Thus, for example, if first-degree, five-point least squares are used, the central formula is used for all values except the first two and the last two, where the off-center formulas are used. A third-degree least squares with seven points would be

$$y_0 = \tfrac{1}{42}\left[39f_0 + 8f_1 - 4f_2 - 4f_3 + f_4 + 4f_5 - 2f_6\right]$$

$$y_1 = \tfrac{1}{42}\left[8f_0 + 19f_1 + 16f_2 + 6f_3 - 4f_4 - 7f_5 + 4f_6\right]$$

$$y_2 = \tfrac{1}{42}\left[-4f_0 + 16f_1 + 19f_2 + 12f_3 + 2f_4 - 4f_5 + f_6\right]$$

$$y_3 = \tfrac{1}{21}\left[-2f_0 + 3f_1 + 6f_2 + 7f_3 + 6f_4 + 3f_5 - 2f_6\right]$$

$$y_4 = \tfrac{1}{42}\left[f_0 - 4f_1 + 2f_2 + 12f_3 + 19f_4 + 16f_5 - 4f_6\right]$$

$$y_5 = \tfrac{1}{42}\left[4f_0 - 7f_1 - 4f_2 + 6f_3 + 16f_4 + 19f_5 + 8f_6\right]$$

$$y_6 = \tfrac{1}{42}\left[-2f_0 + 4f_1 + f_2 - 4f_3 - 4f_4 + 8f_5 + 39f_6\right]$$

Additional smoothing formulas may be found in the references. After the data are smoothed, any of the interpolation polynomials, or an appropriate least squares polynomial, may be fitted and the results used to obtain the derivative.

Least Squares Method

Parabolic. For five evenly spaced neighboring abscissas labeled x_{-2}, x_{-1}, x_0, x_1, and x_2, and their ordinates f_{-2}, f_{-1}, f_0, f_1, and f_2, assume a parabola is fit by least squares. There results for all interior points, except the first and last two points of the data, the formula for the numerical derivative:

$$f_0' = \frac{1}{10h}\left[-2f_{-2} - f_{-1} + f_1 + 2f_2\right]$$

For the first two data points designated by 0 and h:

$$f'(0) = \frac{1}{20h}\left[-21f(0) + 13f(h) + 17f(2h) - 9f(3h)\right]$$

$$f'(h) = \frac{1}{20h}\left[-11f(0) + 3f(h) + 7f(2h) + f(3h)\right]$$

and for the last two given by $\alpha - h$ and α:

$$f'(\alpha - h) = \frac{1}{20h}\left[-11f(\alpha) + 3f(\alpha - h) + 7f(\alpha - 2h) + f(\alpha - 3h)\right]$$

$$f'(\alpha) = \frac{1}{20h}\left[-21f(\alpha) + 13f(\alpha - h) + 17f(\alpha - 2h) - 9(\alpha - 3h)\right]$$

Quartic (Douglas-Avakian). A fourth-degree polynomial $y = a + bx + cx^2 + dx^3 + ex^4$ is fitted to seven adjacent equidistant points (spacing h) after a translation of coordinates has been made so that $x = 0$ corresponds to the central point of the seven. Thus, these may be called $-3h$, $-2h$, $-h$, 0, h, $2h$, and $3h$. Let k = coefficient h for the seven points. This is, in $-3h$, $k = -3$. Then, the coefficients for the polynomial are

$$a = \frac{524\sum f(kh) - 245\sum k^2 f(kh) + 21\sum k^4 f(kh)}{924}$$

$$b = \frac{397\sum kf(kh)}{1512h} - \frac{7\sum k^3 f(kh)}{216h}$$

$$c = \frac{-840\sum f(kh) + 679\sum k^2 f(kh) - 67\sum k^4 f(kh)}{3168h^2}$$

$$d = \frac{-7\sum kf(kh) + \sum k^3 f(kh)}{216h^3}$$

$$e = \frac{72\sum f(kh) - 67\sum k^2 f(kh) + 7\sum k^4 f(kh)}{3168h^4}$$

where all summations run from $k = -3$ to $k = +3$ and $f(kh)$ = tabular value at kh. The slope of the polynomial at $x = 0$ is $dy/dx = b$.

Numerical Integration

Numerical evaluation of the finite integral $\int_a^b f(x)\,dx$ is carried out by a variety of methods. A few are given here.

Newton-Cotes Formulas (Equally Spaced Ordinates)

Trapezoidal Rule. This formula consists of subdividing the interval $a \le x \le b$ into n subintervals a to $a + h$, $a + h$ to $a + 2h$, …, and replacing the graph of $f(x)$ by the result of joining the ends of adjacent ordinates by line segments. If $f_j = f(x_j) = f(a + jh)$, $f_0 = f(a)$, and $f_n = f(b)$, the integration formula is

$$\int_a^b f(x)\,dx = \frac{h}{2}\left[f_0 + 2f_1 + 2f_2 + \cdots + 2f_{n-1} + f_n\right] + E_n$$

where $|E_n| = (nh^3/12)|f''(\varepsilon)| = [(b-a)^3/12n^2]|f''(\varepsilon)|$, $a < \varepsilon < b$. This procedure is not of high accuracy. However, if $f''(x)$ is continuous in $a < x < b$, the error goes to zero as $1/n^2$, $n \to \infty$.

Parabolic Rule (Simpson's Rule). This procedure consists of subdividing the interval $a < x < b$ into $n/2$ subintervals, each of length $2h$, where n is an even integer. Using the notation as above the integration formula is

$$\int_a^b f(x)\,dx = \frac{h}{3}\left[f_0 + 4f_1 + 2f_2 + 4f_3 + \cdots + 4f_{n-3} + 2f_{n-2} + 4f_{n-1} + f_n\right] + E_n$$

where

$$|E_n| = \frac{nh^5}{180}\left|f^{(iv)}(\varepsilon)\right| = \frac{(b-a)^3}{180n^4}\left|f^{(iv)}(\varepsilon)\right| \qquad a < \varepsilon < b$$

This method approximates $f(x)$ by a parabola on each subinterval. This rule is generally more accurate than the trapezoidal rule. It is the most widely used integration formula.

Weddle's Rule. This procedure consists of subdividing the integral $a < x < b$ into $n/6$ subintervals, each of length $6h$, where n is a multiple of 6. Using the notation from the trapezoidal rule, there results

$$\int_a^b f(x)\,dx = \frac{3h}{10}\left[f_0 + 5f_1 + f_2 + 6f_3 + f_4 + 5f_5 + 2f_6 + 5f_7 + f_8 + \cdots + 6f_{n-3} + f_{n-2} + 5f_{n-1} + f_n\right] + E_n$$

Note that the coefficients of f_j follow the rule 1, 5, 1, 6, 1, 5, 2, 5, 1, 6, 1, 5, 2, 5, etc.… This procedure consists of approximately $f(x)$ by a polynomial of degree 6 on each subinterval. Here,

$$E_n = \frac{nh^7}{1400}\left[10f^{(6)}(\varepsilon_1) + 9h^2 f^{(8)}(\varepsilon_2)\right]$$

Gaussian Integration Formulas (Unequally Spaced Abscissas)

These formulas are capable of yielding comparable accuracy with fewer ordinates than the equally spaced formulas. The ordinates are obtained by optimizing the distribution of the abscissas rather than by arbitrary choice. For the details of these formulas, Hildebrand (1956) is an excellent reference.

Two-Dimensional Formula

Formulas for two-way integration over a rectangle, circle, ellipse, and so forth, may be developed by a double application of one-dimensional integration formulas. The two-dimensional generalization of the parabolic rule is given here. Consider the iterated integral $\int_a^b \int_c^d f(x, y)\,dx\,dy$. Subdivide $c < x < d$ into m (even) subintervals of length $h = (d - c)/m$, and $a < y < b$ into n (even) subintervals of length $k = (b - a)/n$. This gives a subdivision of the rectangle $a \le y \le b$ and $c \le x \le d$ into subrectangles. Let $x_j = c + jh$, $y_j = a + jk$, and $f_{i,j} = f(x_i, y_j)$. Then,

$$\int_a^b \int_c^d f(x,y)\,dx\,dy = \frac{hk}{9}\Big[\left(f_{0,0} + 4f_{1,0} + 2f_{2,0} + \cdots + f_{m,0}\right) + 4\left(f_{0,1} + 4f_{1,1} + 2f_{2,1} + \cdots + f_{m,1}\right)$$

$$+ 2\left(f_{0,2} + 4f_{1,2} + 2f_{2,2} + \cdots + f_{m,2}\right) + \cdots + \left(f_{0,n} + 4f_{1,n} + 2f_{2,n} + \cdots + f_{m,n}\right)\Big] + E_{m,n}$$

where

$$E_{m,n} = -\frac{hk}{90}\left[mh^4 \frac{\partial^4 f(\varepsilon_1, \eta_1)}{\partial x^4} + nk^4 \frac{\partial^4 f(\varepsilon_2, \eta_2)}{\partial y^4}\right]$$

where ε_1 and ε_2 lie in $c < x < d$, and η_1 and η_2 lie in $a < y < b$.

Numerical Solution of Ordinary Differential Equations

A number of methods have been devised to solve ordinary differential equations numerically. The general references contain some information. A numerical solution of a differential equation means a table of values of the function y and its derivatives over only a limited part of the range of the independent variable. Every differential equation of order n can be rewritten as n first-order differential equations. Therefore, the methods given below will be for first-order equations, and the generalization to simultaneous systems will be developed later.

The Modified Euler Method

This method is simple and yields modest accuracy. If extreme accuracy is desired, a more sophisticated method should be selected. Let the first-order differential equation be $dy/dx = f(x, y)$ with the initial condition (x_0, y_0) (i.e., $y = y_0$ when $x = x_0$). The procedure is as follows.

Step 1. From the given initial conditions (x_0, y_0) compute $y_0' = f(x_0, y_0)$ and $y_0'' = [\partial f(x_0, y_0)/\partial x] + [\partial f(x_0, y_0)/\partial y]\; y_0'$. Then, determine $y_1 = y_0 + h\; y_0' + (h^2/2)\; y_0''$, where h = subdivision of the independent variable.

Step 2. Determine $y_1' = f(x_1, y_1)$ where $x_1 = x_0 + h$. These prepare us for the following.

Predictor Steps.

Step 3. For $n \geq 1$, calculate $(y_{n+1})_1 = y_{n-1} + 2h\, y_n'$.

Step 4. Calculate $(y_{n+1}')_1 = f[x_{n+1}, (y_{n+1})_1]$.

Corrector Steps.

Step 5. Calculate $(y_{n+1})_2 = y_n + (h/2)\,[(y_{n+1}')_1 + y_n']$, where y_n and y_n' without the subscripts are the previous values obtained by this process (or by steps 1 and 2).

Step 6. $(y_{n+1}')_2 = f[x_{n+1}, (y_{n+1})_2]$.

Step 7. Repeat the corrector steps 5 and 6 if necessary until the desired accuracy is produced in y_{n+1}, y_{n+1}'.

Example. Consider the equation $y' = 2y^2 + x$ with the initial conditions $y_0 = 1$ when $x_0 = 0$. Let $h = 0.1$. A few steps of the computation are illustrated.

Step	
1	$y_0' = 2y_0^2 + x_0 = 2$
	$y_0'' = 1 + 4y_0 y_0' = 1 + 8 = 9$
	$y_1 = 1 + (0.1)(2) + \left[(0.1)^2/2\right]9 = 1.245$
2	$y_1' = 2y_1^2 + x_1 = 3.100 + 0.1 = 3.200$
3	$(y_2)_1 = y_0 + 2hy_1' = 1 + 2(0.1)3.200 = 1.640$
4	$(y_2')_1 = 2(y_2)_1^2 + x_2 = 5.592$
5	$(y_2)_2 = y_1 + (0.1/2)\left[(y_2')_1 + y_1'\right] = 1.685$
6	$(y_2')_2 = 2(y_2)_2^2 + x_2 = 5.878$
5 (repeat)	$(y_2)_3 = y_1 + (0.05)\left[(y_2')_2 + y_1'\right] = 1.699$
6 (repeat)	$(y_2')_3 = 2(y_2)_3^2 + x_2 = 5.974$

and so forth. This procedure. may be programmed for a computer. A discussion of the truncation error of this process may be found in Milne (1953).

Modified Adam's Method

The procedure given here was developed retaining third differences. It can then be considered as a more exact predictor-corrector method than the Euler method. The procedure is as follows for $dy/dx = f(x, y)$ and h = interval size.

Steps 1 and 2 are the same as in Euler method.

Predictor Steps.

Step 3. $(y_{n+1})_1 = y_n + (h/24)\,[55y_n' - 59y_{n-1}' + 37y_{n-2}' - 9y_{n-3}']$, where y_n', y_{n-1}', etc…, are calculated in step 1.

Step 4. $(y_{n+1}')_1 = f[x_{n+1}, (y_{n+1})_1]$.

Corrector Steps.

Step 5. $(y_{n+1})_2 = y_n + (h/24)\,[9(y'_{n+1})_1 + 19y'_n - 5y'_{n-1} + y'_{n-2}]$.
Step 6. $(y'_{n+1})_2 = f[x_{n+1}, (y_{n+1})_2]$.
Step 7. Iterate steps 5 and 6 if necessary.

Runge-Kutta Methods

These methods are self-starting and are inherently stable. Kopal (1955) is a good reference for their derivation and discussion. Third- and fourth-order procedures are given below for $dy/dx = f(x, y)$ and h = interval size.

For third-order (error ≈ h^4).

$$k_0 = hf(x_n, y_n)$$

$$k_1 = hf(x_n + \tfrac{1}{2}h, y_n + \tfrac{1}{2}k_0)$$

$$k_2 = hf(x_n + h, y_n + 2k_1 - k_0)$$

and

$$y_{n+1} = y_n + \tfrac{1}{6}(k_0 + 4k_1 + k_2)$$

for all $n \geq 0$, with initial condition (x_0, y_0).

For fourth-order (error ≈ h^5),

$$k_0 = hf(x_n, y_n)$$

$$k_1 = hf(x_n + \tfrac{1}{2}h, y_n + \tfrac{1}{2}k_0)$$

$$k_2 = hf(x_n + \tfrac{1}{2}h, y_n + \tfrac{1}{2}k_1)$$

$$k_3 = hf(x_n + h, y_n + k_2)$$

and

$$y_{n+1} = y_n + \tfrac{1}{6}(k_0 + 2k_1 + 2k_2 + k_3)$$

Example. (Third-order) Let $dy/dx = x - 2y$, with initial condition $y_0 = 1$ when $x_0 = 0$, and let $h = 0.1$. Clearly, $x_n = nh$. To calculate y_1, proceed as follows:

$$k_0 = 0.1[x_0 - 2y_0] = -0.2$$

$$k_1 = 0.1[0.05 - 2(1 - 0.1)] = -0.175$$

$$k_2 = 0.1[0.1 - 2(1 - 0.35 + 0.2)] = -0.16$$

$$y_1 = 1 + \tfrac{1}{6}(-0.2 - 0.7 - 0.16) = 0.8234$$

Equations of Higher Order and Simultaneous Differential Equations

Any differential equation of second- or higher order can be reduced to a simultaneous system of first-order equations by the introduction of auxiliary variables. Consider the following equations:

$$\frac{d^2x}{dt^2} + xy\frac{dx}{dt} + z = e^x$$

$$\frac{d^2y}{dt^2} + xy\frac{dy}{dt} = 7 + t^2$$

$$\frac{d^2z}{dt^2} + xz\frac{dz}{dt} + x = e^x$$

In the new variables $x_1 = x$, $x_2 = y$, $x_3 = z$, $x_4 = dx_1/dt$, $x_5 = dx_2/dt$, and $x_6 = dx_3/dt$, the equations become

$$\frac{dx_1}{dt} = x_4$$

$$\frac{dx_2}{dt} = x_5$$

$$\frac{dx_3}{dt} = x_6$$

$$\frac{dx_4}{dt} = -x_1x_2x_4 - x_3 + e^{x_3}$$

$$\frac{dx_5}{dt} = -x_3x_2x_5 + 7 + t^2$$

$$\frac{dx_6}{dt} = -x_1x_3x_6 - x_1 + e^{x_1}$$

which is a system of the general form

$$\frac{dx_i}{dt} = f_i\left(t, x_1, x_2, x_3, \ldots, x_n\right)$$

where $i = 1, 2, \ldots, n$. Such systems may be solved by simultaneous application of any of the above numerical techniques. A Runge-Kutta method for

$$\frac{dx}{dt} = f\left(t, x, y\right)$$

$$\frac{dy}{dt} = g\left(t, x, y\right)$$

is given below. The fourth-order procedure is shown.

Starting at the initial conditions x_0, y_0, and t_0, the next values x_1 and y_1 are computed via the equations below (where $\Delta t = h$, $t_j = h + t_{j-1}$):

$$k_0 = hf(t_0, x_0, y_0) \qquad l_0 = hg(t_0, x_0, y_0)$$

$$k_1 = hf\left(t_0 + \frac{h}{2}, x_0 + \frac{k_0}{2}, y_0 + \frac{l_0}{2}\right) \qquad l_1 = hg\left(t_0 + \frac{h}{2}, x_0 + \frac{k_0}{2}, y_0 + \frac{l_0}{2}\right)$$

$$k_2 = hf\left(t_0 + \frac{h}{2}, x_0 + \frac{k_1}{2}, y_0 + \frac{l_1}{2}\right) \qquad l_2 = hg\left(t_0 + \frac{h}{2}, x_0 + \frac{k_1}{2}, y_0 + \frac{l_1}{2}\right)$$

$$k_3 = hf(t_0 + h, x_0 + k_2, y_0 + l_2) \qquad l_3 = hg(t_0 + h, x_0 + k_2, y_0 + l_2)$$

and

$$x_1 = x_0 + \tfrac{1}{6}(k_0 + 2k_1 + 2k_2 + k_3)$$

$$y_1 = y_0 + \tfrac{1}{6}(l_0 + 2l_1 + 2l_2 + l_3)$$

To continue the computation, replace t_0, x_0, and y_0 in the above formulas by $t_1 = t_0 + h$, x_1, and y_1 just calculated. Extension of this method to more than two equations follows precisely this same pattern.

Numerical Solution of Integral Equations

This section considers a method of numerically solving the Fredholm integral equation of the second kind:

$$u(x) = f(x) + \lambda \int_a^b k(x,t)u(t)\,dt \qquad \text{for } u(x)$$

The method discussed arises because a definite integral can be closely approximated by any of several numerical integration formulas (each of which arises by approximating the function by some polynomial over an interval). Thus, the definite integral can be replaced by an integration formula which becomes

$$u(x) = f(x) + \lambda(b-a)\left[\sum_{i=1}^{n} c_i k(x, t_i) u(t_i)\right]$$

where $t_1, \ldots, t_n$ are points of subdivision of the t axis, $a \le t \le b$, and the *cs* are coefficients whose values depend upon the type of numerical integration formula used. Now, this must hold for all values of x, where $a \le x \le b$; so it must hold for $x = t_1$, $x = t_2, \ldots, x = t_n$. Substituting for x successively $t_1, t_2, \ldots, t_n$, and setting $u(t_i) = u_i$ and $f(t_i) = f_i$, we get n linear algebraic equations for the n unknowns $u_1, \ldots, u_n$. That is,

$$u_i = f_i + (b-a)\left[c_1 k(t_i, t_1) u_1 + c_2 k(t_i, t_2) u_2 + \cdots + c_n k(t_i, t_n) u_n\right], \qquad i = 1, 2, \ldots, n$$

These u_j may be solved for by the methods under the section entitled “Numerical Solution of Linear Equations.”

Numerical Methods for Partial Differential Equations

The ultimate goal of numerical (discrete) methods for partial differential equations (PDEs) is the reduction of continuous systems (projections) to discrete systems that are suitable for high-speed computer solutions. The user must be cautioned that the seeming elementary nature of the techniques holds pitfalls that can be seriously misleading. These approximations often lead to difficult mathematical questions of adequacy, accuracy, convergence, stability, and consistency. Convergence is concerned with the approach of the approximate numerical solution to the exact solution as the number of mesh units increase indefinitely in some sense. Unless the numerical method can be shown to converge to the exact solution, the chosen method is unsatisfactory.

Stability deals in general with error growth in the calculation. As stated before, any numerical method involves truncation and round-off errors. These errors are not serious unless they grow as the computation proceeds (i.e., the method is unstable).

Finite Difference Methods

In these methods, the derivatives are replaced by various finite differences. The methods will be illustrated for problems in two space dimensions (x, y) or (x, t) where t is timelike. Using subdivisions $\Delta x = h$ and $\Delta y = k$ with $u(i\,h, jk) = u_{i,j}$, approximate $u_x|_{i,j} = [(u_{i+1,j} - u_{i,j})/h] + O(h)$ (forward difference), a first-order $[O(h)]$ method, or $u_x|_{i,j} = [(u_{i+1,j} - u_{i-1,j})/2h] + O(h^2)$ (central difference), a second-order method. The second derivative is usually approximated with the second-order method $[u_{xx}|_{i,j} = [(u_{i+1,j} - 2u_{i,j} + u_{i-1,j})/h^2] + O(h^2)]$.

Example. Using second-order differences for u_{xx} and u_{yy}, the five-point difference equation (with $h = k$) for Laplace's equation $u_{xx} + u_{yy} = 0$ is $u_{i,j} = 1/4[u_{i+1,j} + u_{i-1,j} + u_{i,j+1} + u_{i,j-1}]$. The accuracy is $O(h^2)$. This model is called *implicit* because one must solve for the total number of unknowns at the unknown grid points (i, j) in terms of the given boundary data. In this case, the system of equations is a linear system.

Example. Using a forward-difference approximation for u_t and a second-order approximation for u_{xx}, the diffusion equation $u_t = u_{xx}$ is approximated by the *explicit* formula $u_{i,j+1} = ru_{i-1,j} + (1 - 2r)u_{i,j} + ru_{i+1,j}$. This classic result permits step-by-step advancement in the t direction beginning with the initial data at $t = 0$ $(j = 0)$ and guided by the boundary data. Here, the term $r = \Delta t/(\Delta x)^2 = k/h^2$ is restricted to be less than or equal to 1/2 for stability and the truncation error is $O(k^2 + kh^2)$.

The Crank-Nicolson implicit formula which approximates the diffusion equation $u_t = u_{xx}$ is

$$-r\lambda u_{i-1,j+1} + (1 + 2r\lambda)u_{i,j+1} - r\lambda u_{i+1,j+1} = r(1-\lambda)u_{i-1,j} + [1 - 2r(1-\lambda)]u_{i,j} + r(1-\lambda)u_{i+1,j}$$

The stability of this numerical method was analyzed by Crandall (Ames, 1993) where the λ, r stability diagram is given.

Approximation of the time derivative in $u_t = u_{xx}$ by a central difference leads to an always unstable approximation — the useless approximation

$$u_{i,j+1} = u_{i,j-1} + 2r(u_{i+1,j} - 2u_{i,j} + u_{i-1,j})$$

which is a warning to be careful.

The foregoing method is *symmetric* with respect to the point (i, j), where the method is centered. Asymmetric methods have some computational advantages, so the Saul'yev method is described (Ames, 1993). The algorithms $(r = k/h^2)$

$$(1 + r)u_{i,j+1} = u_{i,j} + r(u_{i-1,j+1} - u_{i,j} + u_{i+1,j}) \qquad \text{(Saul' yev A)}$$

$$(1 + r)u_{i,j+1} = u_{i,j} + r(u_{i+1,j+1} - u_{i,j} + u_{i-1,j}) \qquad \text{(Saul' yev B)}$$

are used as in any one of the following options:

1. Use Saul'yev A only and proceed line-by-line in the $t(j)$ direction, but *always* from the left boundary on a line.
2. Use Saul'yev B only and proceed line-by-line in the $t(j)$ direction, but *always* from the right boundary to the left on a line.

3. Alternate from line to line by first using Saul'yev A and then B, or the reverse. This is related to *alternating direction methods.*
4. Use Saul'yev A and Saul'yev B on the same line and average the results for the final answer (A first, and then B). This is equivalent to introducing the dummy variables $P_{i,j}$ and $Q_{i,j}$ such that

$$(1+r)P_{i,j+1} = U_{i,j} + r\left(P_{i-1,j+1} - U_{i,j} + U_{i+1,j}\right)$$

$$(1+r)Q_{i,j+1} = U_{i,j} + r\left(Q_{i+1,j+1} - U_{i,j} + U_{i-1,j}\right)$$

and

$$U_{i,j+1} = \tfrac{1}{2}\left(P_{i,j+1} + Q_{i,j+1}\right)$$

This averaging method has some computational advantage because of the possibility of truncation error cancellation. As an alternative, one can retain the $P_{i,j}$ and $Q_{i,j}$ from the previous step and replace $U_{i,j}$ and $U_{i+1,j}$ by $P_{i,j}$ and $P_{i+1,j}$, respectively, and $U_{i,j}$ and $U_{i-1,j}$ by $Q_{i,j}$ and $Q_{i-1,j}$, respectively.

Weighted Residual Methods (WRMs)

To set the stage for the method of finite elements, we briefly describe the WRMs, which have several variations — the interior, boundary, and mixed methods. Suppose the equation is $Lu = f$, where L is the partial differential operator and f is a known function, of say x and y. The first step in WRM is to select a class of known basis functions b_i (e.g., trigonometric, Bessel, Legendre) to approximate $u(x, y)$ as ~ $\Sigma\, a_i\, b_i\,(x, y) = U(x, y, a)$. Often, the b_i are selected so that $U(x, y, a)$ satisfy the boundary conditions. This is essentially the *interior method.* If the b_i, in $U(x, y, a)$ are selected to satisfy the differential equations, but not the boundary conditions, the variant is called the *boundary method.* When neither the equation nor the boundary conditions are satisfied, the method is said to be *mixed.* The least ingenuity is required here. The usual method of choice is the interior method.

The second step is to select an optimal set of constants a_i, $i = 1,2, \ldots, n$, by using the residual $R_I(U) = LU - f$. This is done here for the interior method. In the boundary method, there are a set of boundary residual R_B, and, in the mixed method. Both R_I and R_B. Using the spatial average $(w, v) = \int_v wv dV$, the criterion for selecting the values of a_i is the requirement that the n spatial averages

$$\left(b_i, R_E(U)\right) = 0, \qquad i = 1,2,\ldots,n$$

These represent n equations (linear if the operator L is linear and nonlinear otherwise) for the a_i.

Particular WRMs differ because of the choice of the b_js. The most common follow.

1. *Subdomain* The domain V is divided into n smaller, not necessarily disjoint, subdomains V_j with $w_j(x, y) = 1$ if (x, y) is in V_j, and 0 if (x, y) is not in V_j.
2. *Collocation* Select n points $P_j = (x_j, y_j)$ in V with $w_j(P_j) = \delta(P - P_j)$, where $\int_v \phi(P)\delta(P - P_j)dP = \phi(P_j)$ for all test functions $\phi(P)$ which vanish outside the compact set V. Thus, $(w_j, R_E) = \int_v \delta(P - P_j)R_E dV = R_E[U(P_j) \equiv 0$ (i.e., the residual is set equal to zero at the n points P_j).
3. *Least squares* Here, the functional $I(a) = \int_V R_E^2\, dV$, where $a = (a_1, \ldots, a_n)$, is to be made stationary with respect to the a_j. Thus, $0 = \partial I/\partial a_j = 2\int_v R_E(\partial R_E/\partial a_j)dV$, with $j = 1, 2, \ldots, n$. The w_j in this case are $\partial R_E/\partial a_j$.
4. *Bubnov-Galerkin* Choose $w_j(P) = b_j(P)$. This is perhaps the best-known method.
5. *Stationary Functional (Variational) Method* With ϕ a variational integral (or other functional), set $\partial\phi[U]/\partial a_j = 0$, where $j = 1, \ldots, n$, to generate the n algebraic equations.

Example. $u_{xx} + u_{yy} = -2$, with $u = 0$ on the boundaries of the square $x = \pm 1$, $y = \pm 1$. Select an interior method with $U = a_1(1 - x^2)(1 - y^2) + a_2 x^2 y^2 (1 - x^2)(1 - y^2)$, whereupon the residual $R_E(U) = 2a_1(2 - x^2 - y^2) + 2a_2[(1 - 6x^2)y^2(1 - y^2) + (1 - 6y^2) - (1 - x^2)] + 2$. Collocating at (1/3, 1/3) and (2/3, 2/3) gives the two linear equations $-32a_1/9 + 32a_2/243x^2 + 2 = 0$ and $-20a_1/9 - 400a_2/243 + 2 = 0$ for a_1 and a_2.

WRM methods can obviously be used as approximate methods. We have now set the stage for *finite elements.*

Finite Elements

The WRM methods are more general than the *finite elements* (FE) methods. FE methods require, in addition, that the basis functions be finite elements (i.e., functions that are zero except on a small part of the domain under consideration). A typical example of an often used basis is that of triangular elements. For a triangular element with Cartesian coordinates (x_1, y_1), (x_2, y_2), and (x_3, y_3), define natural coordinates L_1, L_2, and L_3 (L_i, $\leftrightarrow (x_i, y_i)$) so that $L_i = A_i/A$ where

$$A = \tfrac{1}{2}\det\begin{bmatrix} 1 & x_1 & y_1 \\ 1 & x_2 & y_2 \\ 1 & x_3 & y_3 \end{bmatrix}$$

is the area of the triangle and

$$A_1 = \tfrac{1}{2}\det\begin{bmatrix} 1 & x & y \\ 1 & x_2 & y_2 \\ 1 & x_3 & y_3 \end{bmatrix}$$

$$A_2 = \tfrac{1}{2}\det\begin{bmatrix} 1 & x_1 & y_1 \\ 1 & x & y \\ 1 & x_3 & y_3 \end{bmatrix}$$

$$A_3 = \tfrac{1}{2}\det\begin{bmatrix} 1 & x_1 & y_1 \\ 1 & x_2 & y_2 \\ 1 & x & y \end{bmatrix}$$

Clearly $L_1 + L_2 + L_3 = 1$, and the L_i are one at node i and zero at the other nodes. In terms of the Cartesian coordinates,

$$\begin{bmatrix} L_1 \\ L_2 \\ L_3 \end{bmatrix} = \frac{1}{2A}\begin{bmatrix} x_2 y_3 - x_3 y_2, & y_2 - y_3, & x_3 - x_2 \\ x_3 y_1 - x_1 y_3, & y_3 - y_1, & x_1 - x_3 \\ x_1 y_2 - x_2 y_1, & y_1 - y_2, & x_2 - x_1 \end{bmatrix}\begin{bmatrix} 1 \\ x \\ y \end{bmatrix}$$

is the linear triangular element relation.

Tables of linear, quadratic, and cubic basis functions are given in the literature. Notice that while the linear basis needs three nodes, the quadratic requires six and the cubic basis ten. Various modifications, such as the Hermite basis, are described in the literature. Triangular elements are useful in approximating irregular domains.

For rectangular elements, the *chapeau* functions are often used. Let us illustrate with an example. Let $u_{xx} + u_{yy} = Q$, $0 < x < 2$, $0 < y < 2$, $u(x, 2) = 1$, $u(0, y) = 1$, $u_y(x, 0) = 0$, $u_x(2, y) = 0$, and $Q(x, y) = Qw\delta(x - 1)\delta(y - 1)$,

$$\delta(x) = \begin{cases} 0 & x \neq 0 \\ 1 & x = 0 \end{cases}$$

Using four equal rectangular elements, map the element I with vertices at (0, 0) (0, 1), (1, 1), and (1, 0) into the local (canonical) coordinates (ξ, η), $-1 \le \xi \le 1$, $-1 \le \eta \le 1$, by means of $x = 1/2(\xi + 1)$, $y = 1/2(\eta + 1)$. This mapping permits one to develop software that standardizes the treatment of all elements. Converting to (ξ, η) coordinates, our problem becomes $u_{\xi\xi} + u_{\eta\eta} = 1/4Q$, $-1 \le \xi \le 1$, $-1 \le \eta \le 1$, $Q = Qw\delta(\xi - 1)\delta(\eta - 1)$.

First, a trial function $\bar{u}\ (\xi, \eta)$ is defined as $u(\xi, \eta) \approx \bar{\mu}\ (\xi, \eta) = \Sigma_{j=1}^{4} A_j\phi_j(\xi, \eta)$ (in element I) where the ϕ_j are the two-dimensional chapeau functions

$$\phi_1 = \left[\tfrac{1}{2}(1-\xi)\tfrac{1}{2}(1-\eta)\right] \qquad \phi_2 = \left[\tfrac{1}{2}(1+\xi)\tfrac{1}{2}(1-\eta)\right]$$

$$\phi_3 = \left[\tfrac{1}{2}(1+\xi)\tfrac{1}{2}(1+\eta)\right] \qquad \phi_4 = \left[\tfrac{1}{2}(1-\xi)\tfrac{1}{2}(1+\eta)\right]$$

Clearly ϕ_i take the value one at node i, provide a bilinear approximation, and are nonzero only over elements adjacent to node i.

Second, the equation residual $R_E = \nabla^2 \bar{u} - 1/4Q$ is formed and a WRM procedure is selected to formulate the algebraic equations for the A_i. This is indicated using the Galerkin method. Thus, for element I, we have

$$\iint_{D_I} \left(\bar{u}_{\xi\xi} + \bar{u}_{\eta\eta} - Q\right)\phi_i(\xi,\eta)\, d\xi\, d\eta = 0, \qquad i = 1,\ldots,4$$

Applying Green's theorem, this result becomes

$$\iint_{D_I} \left[\bar{u}_\xi(\phi_i)_\xi + \bar{u}_\eta(\phi_i)_\eta + \tfrac{1}{4}Q\phi_i\right] d\xi\, d\eta - \int_{\partial D_I} \left(\bar{u}_\xi c_\xi + \bar{u}_\eta c_\eta\right)\phi_i\, ds = 0, \qquad i = 1,2,\ldots,4$$

Using the same procedure in all four elements and recalling the property that the ϕ_i in each element are nonzero only over elements adjacent to node i gives the following nine equations:

$$\sum_{e=1}^{4}\left\{\iint_{D_e}\sum_{j=1}^{9} A_j\left[(\phi_j)_\xi(\phi_i)_\xi + (\phi_j)_\eta(\phi_i)_\eta\right] + \tfrac{1}{4}Q\phi_i\right\} d\xi\, d\eta$$

$$-\sum_{e=1}^{4}\int_{\partial D_e}\left(\bar{u}_\xi c_\xi + \bar{u}_\eta c_\eta\right)\phi\, ds = 0, \quad n = 1,2,\ldots,9$$

where the c_ξ and c_η are the direction cosines of the appropriate element (e) boundary.

Method of Lines

The *method of lines,* when used on PDEs in two dimensions, reduces the PDE to a system of ordinary differential equations (ODEs), usually by finite difference or finite element techniques. If the original problem is an initial value (boundary value) problem, then the resulting ODEs form an initial value (boundary value) problem. These ODEs are solved by ODE numerical methods.

Example. $u_t = u_{xx} + u^2$, $0 < x < 1$, $0 < t$, with the initial value $u(x, 0) = x$, and boundary data $u(0, t) = 0$, $u(1, t) = \sin t$. A discretization of the space variable (x) is introduced and the time variable is left continuous. The approximation is $\dot{u}_i = (u_{i+1} - 2u_i + u_{i-1})/h^2 + u_i^2$. With $h = 1/5$, the equations become

$$\begin{aligned}
u_0(t) &= 0 \\
\dot{u}_1 &= \tfrac{1}{25}\left[u_2 - 2u_1\right] + u_1^2 \\
\dot{u}_2 &= \tfrac{1}{25}\left[u_3 - 2u_2 + u_1\right] + u_2^2 \\
\dot{u}_3 &= \tfrac{1}{25}\left[u_4 - 2u_3 + u_2\right] + u_3^2 \\
\dot{u}_4 &= \tfrac{1}{25}\left[\sin t - 2u_4 + u_3\right] + u_4^2 \\
u_5 &= \sin t
\end{aligned}$$

and $u_1(0) = 0.2$, $u_2(0) = 0.4$, $u_3(0) = 0.6$, and $u_4(0) = 0.8$.

Discrete and Fast Fourier Transforms

Let $x(n)$ be a sequence that is nonzero only for a finite number of samples in the interval $0 \le n \le N - 1$. The quantity

$$X(k) = \sum_{n=0}^{N-1} x(n) e^{-i(2\pi/N)nk}, \quad k = 0, 1, \ldots, N - 1$$

is called the *discrete Fourier transform* (DFT) of the sequence $x(n)$. Its inverse (IDFT) is given by

$$x(n) = \frac{1}{N} \sum_{k=0}^{N-1} X(k) e^{i(2\pi/N)nk}, \quad n = 0, 1, \ldots, N - 1 \quad \left(i^2 = -1\right)$$

Clearly, DFT and IDFT are finite sums and there are N frequency values. Also, $X(k)$ is periodic in k with period N.

Example. $x(0) = 1$, $x(1) = 2$, $x(2) = 3$, $x(3) = 4$

$$X(k) = \sum_{n=0}^{3} x(n) e^{-i(2\pi/4)nk}, \quad k = 0,\ 1,\ 2,\ 3,\ 4$$

Thus,

$$X(0) = \sum_{n=0}^{3} x(n) = 10$$

and $X(1) = x(0) + x(1)e^{-i\pi/2} + x(2)e^{-i\pi} + x(3)e^{-i3\pi/2} = 1 - 2i - 3 + 4i = -2 + 2i$; $X(2) = -2$; $X(3) = -2 - 2i$.

DFT Properties

1. Linearity: If $x_3(n) = ax_1(n) + bx_2(n)$, then $X_3(k) = aX_1(k) + bX_2(k)$.
2. Symmetry: For $x(n)$ real, $\mathrm{Re}[X(k)] = \mathrm{Re}[X(N - k)]$, $\mathrm{Im}[(k)] = -\mathrm{Im}[X(N - k)]$.

3. Circular shift: By a circular shift of a sequence defined in the interval $0 \le n \le N-1$, we mean that, as values *fall off* from one end of the sequence, they are appended to the other end. Denoting this by $x(n \oplus m)$, we see that positive m means shift left and negative m means shift right. Thus, $x_2(n) = x_1(n \oplus m) \Leftrightarrow X_2(k) = X_1(k)e^{i(2\pi/N)km}$.
4. Duality: $x(n) \Leftrightarrow X(k)$ implies $(1/N)X(n) \Leftrightarrow x(-k)$.
5. Z-transform relation: $X(k) = X(z)\big|_{z=e^{i(2\pi k/N)}}$, $k = 0, 1, \ldots, N-1$.
6. Circular convolution: $x_3(n) = \Sigma_{m=0}^{N-1} x_1(m)x_2(n \ominus m) = \Sigma_{\ell=0}^{N-1} x_1(n \ominus \ell)x_2(\ell)$ where $x_2(n \ominus m)$ corresponds to a circular shift to the right for positive m.

One fast algorithm for calculating DFTs is the radix-2 *fast Fourier transform* developed by J. W. Cooley and J. W. Tucker. Consider the two-point DFT $X(k) = \Sigma_{n=0}^{1} x(n)e^{-i(2\pi/2)nk}$, $k = 0, 1$. Clearly, $X(k) = x(0) + x(1)e^{-i\pi k}$. So, $X(0) = x(0) + x(1)$ and $X(1) = x(0) - x(1)$. This process can be extended to DFTs of length $N = 2^r$, where r is a positive integer. For $N = 2^r$, decompose the N-point DFT into *two* $N/2$-point DFTs. Then, decompose each $N/2$-point DFT into *two* $N/4$-point DFTs, and so on until eventually we have $N/2$ *two*-point DFTs. Computing these as indicated above, we combine them into $N/4$ four-point DFTs and then $N/8$ eight-point DFTs, and so on, until the DFT is computed. The total number of DFT operations (for large N) is $O(N^2)$, and that of the FFT is $O(N \log_2 N)$, quite a saving for large N.

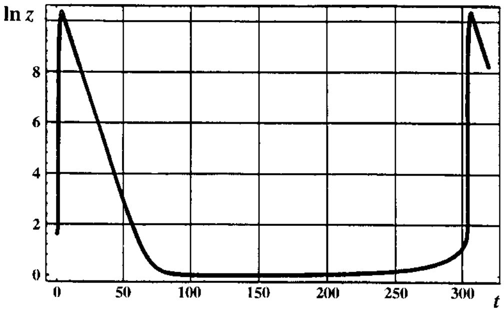

Figure 19.12.1

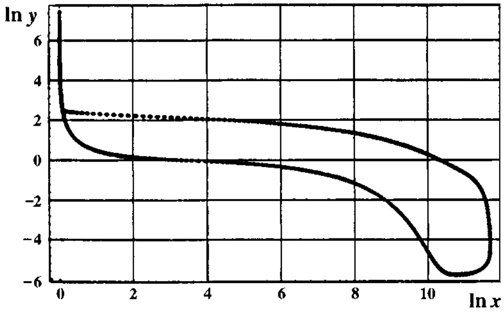

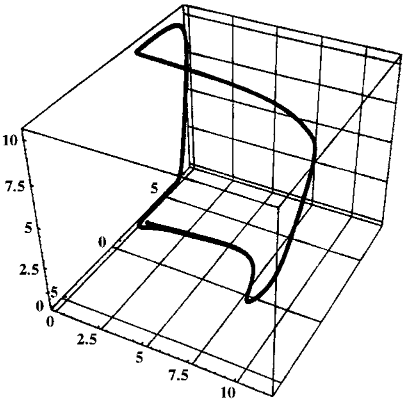

Figure 19.12.2

Figure 19.12.3

FIGURES 19.12.1 to 19.12.3 The "Oregonator" is a periodic chemical reaction describable by three nonlinear first-order differential equations. The results (Figure 19.12.1) illustrate the periodic nature of the major chemical vs. time. Figure 19.12.2 shows the phase diagram of two of the reactants, and Figure 19.12.3 is the three-dimensional phase diagram of all reactants. The numerical computation was done using a fourth-order Runge-Kuta method on Mathematica by Waltraud Rufeger at the Georgia Institute of Technology.

Software

Some available software is listed here.

General Packages

General software packages include Maple, Mathematica, and Matlab. All contain algorithms for handling a large variety of both numerical and symbolic computations.

Special Packages for Linear Systems

In the IMSL Library, there are three complementary linear system packages of note.

LINPACK is a collection of programs concerned with *direct* methods for general (or full) symmetric, symmetric positive definite, triangular, and tridiagonal matrices. There are also programs for least squares problems, along with the QR algorithm for eigensystems and the singular value decompositions of rectangular matrices. The programs are intended to be completely machine independent, fully portable, and run with good efficiency in most computing environments. The LINPACK User's Guide by Dongarra *et al.* is the basic reference.

ITPACK is a modular set of programs for iterative methods. The package is oriented toward the sparse matrices that arise in the solution of PDEs and other applications. While the programs apply to full matrices, that is rarely profitable. Four basic iteration methods and two convergence acceleration methods are in the package. There is a Jacobi, SOR (with optimum relaxation parameter estimated), symmetric SOR, and reduced system (red-black ordering) iteration, each with semi-iteration and conjugate gradient acceleration. All parameters for these iterations are automatically estimated. The practical and theoretical background for ITPACK is found in Hagemen and Young (1981).

YALEPACK is a substantial collection of programs for sparse matrix computations.

Ordinary Differential Equations Packages

Also in IMSL, one finds such sophisticated software as DVERK, DGEAR, or DREBS for initial value problems. For two-point boundary value problems, one finds DTPTB (use of DVERK and multiple shooting) or DVCPR.

Partial Differential Equations Packages

DISPL was developed and written at Argonne National Laboratory. DISPL is designed for nonlinear second-order PDEs (parabolic, elliptic, hyperbolic (some cases), and parabolic-elliptic). Boundary conditions of a general nature and material interfaces are allowed. The spatial dimension can be either one or two and in Cartesian, cylindrical, or spherical (one dimension only) geometry. The PDEs are reduced to ordinary DEs by Galerkin discretization of the spatial variables. The resulting ordinary DEs in the timelike variable are then solved by an ODE software package (such as GEAR). Software features include graphics capabilities, printed output, dump/restart/facilities, and free format input. DISPL is intended to be an engineering and scientific tool and is not a finely tuned production code for a small set of problems. DISPL makes no effort to control the spatial discretization errors. It has been used to successfully solve a variety of problems in chemical transport, heat and mass transfer, pipe flow, etc.

PDELIB was developed and written at Los Alamos Scientific Laboratory. PDELIB is a library of subroutines to support the numerical solution of evolution equations with a timelike variable and one or two space variables. The routines are grouped into a dozen independent modules according to their function (i.e., accepting initial data, approximating spatial derivatives, advancing the solution in time). Each task is isolated in a distinct module. Within a module, the basic task is further refined into general-purpose flexible lower-level routines. PDELIB can be understood and used at different levels. Within a small period of time, a large class of problems can be solved by a novice. Moreover, it can provide a wide variety of outputs.

DSS/2 is a differential systems simulator developed at Lehigh University as a transportable numerical method of lines (NMOL) code. See also LEANS.

FORSIM is designed for the automated solution of sets of implicitly coupled PDEs of the form

$$\frac{\partial u_i}{\partial t} = \phi_i\left(x, t, u_i, u_j, \ldots, \left(u_i\right)_x, \ldots, \left(u_i\right)_{xx}, \left(u_j\right)_{xx}, \ldots\right), \quad \text{for } i = 1, \ldots, N$$

The user specifies the ϕ_i in a simple FORTRAN subroutine. Finite difference formulas of any order may be selected for the spatial discretization and the spatial grid need not be equidistant. The resulting system of time-dependent ODEs is solved by the method of lines.

SLDGL is a program package for the self-adaptive solution of nonlinear systems of elliptic and parabolic PDEs in up to three space dimensions. Variable step size and variable order are permitted. The discretization error is estimated and used for the determination of the optimum grid and optimum orders. This is the most general of the codes described here (not for hyperbolic systems, of course). This package has seen extensive use in Europe.

FIDISOL (finite difference solver) is a program package for nonlinear systems of two-or three-dimensional elliptic and parabolic systems in rectangular domains or in domains that can be transformed analytically to rectangular domains. This package is actually a redesign of parts of SLDGL, primarily for the solution of large problems on vector computers. It has been tested on the CYBER 205, CRAY-IM, CRAY X-MP/22, and VP 200. The program vectorizes very well and uses the vector arithmetic efficiently. In addition to the numerical solution, a reliable error estimate is computed.

CAVE is a program package for conduction analysis via eigenvalues for three-dimensional geometries using the method of lines. In many problems, much time is saved because only a few terms suffice.

Many industrial and university computing services subscribe to the IMSL Software Library. Announcements of new software appear in *Directions*, a publication of IMSL. A brief description of some IMSL packages applicable to PDEs and associated problems is now given. In addition to those packages just described, two additional software packages bear mention. The first of these, the ELLPACK system, solves elliptic problems in two dimensions with general domains and in three dimensions with box-shaped domains. The system contains over 30 numerical methods modules, thereby providing a means of evaluating and comparing different methods for solving elliptic problems. ELLPACK has a special high-level language making it easy to use. New algorithms can be added or deleted from the system with ease.

Second, TWODEPEP is IMSL's general finite element system for two-dimensional elliptic, parabolic, and eigenvalue problems. The Galerkin finite elements available are triangles with quadratic, cubic, or quartic basic functions, with one edge curved when adjacent to a curved boundary, according to the isoparametric method. Nonlinear equatons are solved by Newton's method, with the resulting linear system solved directly by Gauss elimination. PDE/PROTRAN is also available. It uses triangular elements with piecewise polynomials of degree 2, 3, or 4 to solve quite general steady state, time-dependent, and eigenvalue problems in general two-dimensional regions. There is a simple user input. Additional information may be obtained from IMSL. NASTRAN and STRUDL are two advanced finite element computer systems available from a variety of sources. Another, UNAFEM, has been extensively used.

References

General

Adams, E. and Kulisch, U. (Eds.) 1993. *Scientific Computing with Automatic Result Verification,* Academic Press, Boton, MA.

Gerald, C. F. and Wheatley, P. O. 1984. *Applied Numerical Analysis,* Addison-Wesley, Reading, MA.

Hamming, R. W. 1962. *Numerical Methods for Scientists and Engineers,* McGraw-Hill, New York.

Hildebrand, F. B. 1956. *Introduction to Numerical Analysis,* McGraw-Hill, New York.

Isaacson, E. and Keller, H. B. 1966. *Analysis of Numerical Methods,* John Wiley & Sons, New York.

Kopal, Z. 1955. *Numerical Analysis,* John Wiley & Sons, New York.

Rice, J. R. 1993. *Numerical Methods, Software and Analysis,* 2nd ed. Academic Press, Boston, MA.

Stoer, J. and Bulirsch, R. 1976. *Introduction to Numerical Analysis,* Springer, New York.

Linear Equations

Bodewig, E. 1956. *Matrix Calculus*, Wiley (Interscience), New York.

Hageman, L. A. and Young, D. M. 1981. *Applied Iterative Methods,* Academic Press, Boston, MA.

Varga, R. S. 1962. *Matrix Iterative Numerical Analysis,* John Wiley & Sons, New York.

Young, D. M. 1971. *Iterative Solution of Large-Linear Systems,* Academic Press, Boston, MA.

Ordinary Differential Equations

Aiken, R. C. 1985. *Stiff Computation,* Oxford Unitersity Press, New York.

Gear, C. W. 1971. *Numerical Initial Value Problems in Ordinary Differential Equations,* Prentice Hall, Englewood Cliffs, NJ.

Keller, H. B. 1976. *Numerical Solutions of Two Point Boundary Value Problems,* SIAM, Philadelphia, PA.

Lambert, J. D. 1973. *Computational Methods in Ordinary Differential Equations,* Cambridge University Press, New York.

Milne, W.E. 1953. *Numerical Solution of Differential Equations,* John Wiley & Sons, New York.

Rickey, K. C., Evans, H. R., Griffiths, D. W., and Nethercot, D. A. 1983. *The Finite Element Method — A Basic Introduction for Engineers,* 2nd ed. Halstead Press, New York.

Shampine, L. and Gear, C. W. 1979. A User's View of Solving Stiff Ordinary Differential Equatons, *SIAM Rev.* 21:1–17.

Partial Differential Equations

Ames, W. F. 1993. *Numerical Methods for Partial Differential Equations,* 3d ed. Academic Press, Boston, MA.

Brebbia, C. A. 1984. *Boundary Element Techniques in Computer Aided Engineering,* Martinus Nijhoff, Boston, MA.

Burnett, D. S. 1987. *Finite Element Analysis,* Addison-Wesley, Reading, MA.

Lapidus, L. and Pinder, G. F. 1982. *Numerical Solution of Partial Differential Equations in Science and Engineering,* John Wiley & Sons, New York.

Roache, P. 1972. *Computational Fluid Dynamics,* Hermosa, Albuquerque, NM.

19.13 Experimental Uncertainty Analysis

W.G. Steele and H.W. Coleman

Introduction

The goal of an experiment is to answer a question by measuring a specific variable, X_i, or by determining a result, r, from a functional relationship among J measured variables

$$r = r\left(X_1, X_2, \ldots, X_i, \ldots, X_J\right) \tag{19.13.1}$$

In all experiments there is some error that prevents the measurement of the true value of each variable, and therefore, prevents the determination of r_{true}.

Uncertainty analysis is a technique that is used to estimate the interval about a measured variable or a determined result within which the true value is thought to lie with a certain degree of confidence. As discussed in detail by Coleman and Steele (1999), uncertainty analysis is an extremely useful tool for all phases of an experimental program, from initial planning (general uncertainty analysis) to detailed design, debugging, test operation, and data analysis (detailed uncertainty analysis).

Uncertainty analysis is also beginning to be applied in the design process and in the broad area of modeling and simulation. The outcome of a design process is influenced by uncertainties inherent in input information and in the chosen process itself. The degree of accuracy of a simulation (of a flow field around an airplane, for example) is investigated by comparing the simulation output with experimental data in a process called "verification and validation." Such a comparison is obviously influenced by uncertainties in experimental data, in the numerical solution of the equations, and due to the modeling as discussed by Coleman (2003).

The international standard for uncertainty analysis is the International Organization for Standardization (ISO) *Guide to the Expression of Uncertainty in Measurement* (1995). Engineering standards that are consistent with the ISO *Guide* are available from the American Society of Mechanical Engineers (ANSI/ASME PTC 19.1-1998, 1998), the American Institute of Aeronautics and Astronautics (AIAA Standard S-071A-1999, 1999), and the Society of Automotive Engineers (SAE AIR 1678 Rev. A, 2000). These documents present and discuss the assumptions necessary for a "large sample" methodology that is consistent with the ISO *Guide*, but less complex, and that is applicable to the vast majority of engineering testing, including most single-sample tests. This methodology uses the traditional engineering concepts of systematic and random uncertainties. The range of validity of this large-sample approximation has been presented by Steele et al. (1994) and by Coleman and Steele (1995), with illustrations of its use in all aspects of engineering experimentation given by Coleman and Steele (1999).

In the following, the uncertainties of individual measured variables and of determined results are discussed. We conclude this section with an overview of the use of uncertainty analysis in all phases of an experimental program.

Uncertainty of a Measured Variable

For a measured variable X, the total error is caused by both random (precision, or varying) and systematic (bias, or fixed) errors. This relationship is shown in Figure 19.13.1. The possible measurement values of the variable are scattered in a distribution (here assumed Gaussian) around the parent population mean, μ. The parent population mean differs from X_{true} by an amount called the systematic (or bias) error, β. The quantity β is the total fixed error that remains in the measurements after all calibration corrections have been made. In general, there will be several sources of systematic error, such as errors from the calibration standard and calibration process itself, errors due to interactions of the transducer with its environment, and errors from imperfect installation of the transducer. There is usually no direct way to measure these errors, so they must be estimated.

The ISO *Guide* uncertainty model uses the standard deviation of the assumed error distribution for each error source to calculate the uncertainty in the measured variable. This standard deviation quantity is called the *standard uncertainty*. The uncertainty of the measurement of a variable is obtained from the square root of the sum of the squares of the standard uncertainties for all error sources. As described later, for those error sources that are random, or varying, the standard uncertainty can be calculated from multiple measurements of the variable, but for those sources that are systematic, or that remain fixed, the standard uncertainty must be estimated by some other means.

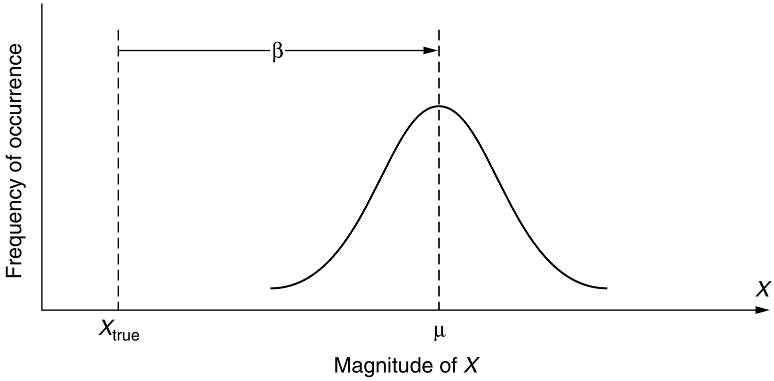

FIGURE 19.13.1 Errors in the measurement of variable X.

For each systematic error source, β_k, the experimenter must estimate a systematic standard uncertainty b_k. Systematic standard uncertainties are usually estimated from previous experience, calibration data, analytical models, and the application of sound engineering judgment.

As discussed in Coleman and Steele (1999), a useful approach for estimating a systematic uncertainty is to assume that the error for a given case is a single realization drawn from some statistical parent distribution of possible systematic errors. For example, suppose a thermistor manufacturer specifies that 95% of samples of a given model are within ±1.0°C of a reference resistance-temperature (R-T) calibration curve supplied with the thermistors. One might assume that the systematic errors (the differences between the reference curve and the actual, but unknown, R-T curves of the various thermistors) result from random processes and therefore belong to a Gaussian parent distribution with a standard deviation, or standard uncertainty, b = 0.5°C. Then the 95% confidence limits defined by ±2b = ±1.0°C would include about 95% of the possible systematic errors that could be realized from the parent distribution. For any single thermistor, this error will appear as fixed since it does not result in variation of the temperature readings when this thermistor is used to repeatedly measure a steady temperature source; however, since the magnitude of the error is unknown, a correction cannot be applied to the temperature readings, so b is used as an estimate of the systematic standard uncertainty resulting from this error.

The choice of a 95% confidence level in the previous example was made based on the thermistor manufacturer's degree of certainty in the specification of the possible interval for the fixed error in a temperature measurement. The quantity needed is the systematic standard uncertainty, b, but sometimes it is difficult to estimate the limits of the fixed error at the standard deviation level, and it is always impossible to estimate these limits at a 100% confidence level. Usually, in engineering practice, the estimate of the limits of the fixed error is made at a reasonably high confidence level, a level in the mid-90% range, or approximately 95%.

The choice of a Gaussian distribution for the possible systematic errors in the example given is generally made since most fixed errors result from some random process that is fixed for a particular experiment. Also, the well-known central-limit theorem states that errors resulting from a combination of a large number of independent sources that are equally likely to be positive or negative have distributions approaching the Gaussian distribution. Since this is usually the case for experiments, almost all experimental uncertainty analyses assume Gaussian distributions. An exception is when no information on the nature of the errors is known or assumed, and all possible error values within a range are taken to be equally probable. In this case a rectangular distribution is used. Obtaining the systematic standard uncertainty from the 95% estimate is simply a matter of dividing the estimate by the appropriate distribution factor (i.e., 2.0 for Gaussian, 1.65 for rectangular ($\sqrt{3} \times 0.95$)).

For each variable, X_i, in the data reduction equation (Equation 19.13.1), there will be a set, K_i, of elemental systematic standard uncertainties b_{i_k} for the significant fixed-error sources. The systematic standard uncertainty for variable X_i is then determined from the systematic standard uncertainty estimates for the K_i elemental error sources for that variable as

$$b_i^2 = \sum_{k=1}^{K_i} b_{i_k}^2 \tag{19.13.2}$$

An estimate of the range of random errors for measurements of a variable is the sample standard deviation, also called the random standard uncertainty. Unlike the systematic error, the random error varies from measurement to measurement. As the number of measurements, N, of a particular variable tends to infinity, the distribution of these measurements becomes Gaussian.

To reflect the entire range of possible measured values of a variable, the measurements used to calculate the random standard uncertainty must be taken over the time frame and conditions that cover the variations in the variable. For example, taking multiple samples of data as a function of time while holding all other conditions constant will identify the random variation associated with the measurement system and the unsteadiness of the test condition. If the random standard uncertainty of the variable being measured is also expected to be representative of other possible variations in the measurement (repeatability of test conditions for example), then these additional error sources will have to be varied while the multiple data samples are taken to determine the standard uncertainty.

When the value of a variable is determined as the mean, $\overline{X}$, of N readings, then the random standard uncertainty is

$$s_{\overline{X}} = \frac{1}{\sqrt{N}}\left[\frac{1}{(N-1)}\sum_{k=1}^{N}\left(X_k - \overline{X}\right)^2\right]^{\frac{1}{2}} \tag{19.13.3}$$

where

$$\overline{X} = \frac{\sum_{k=1}^{N} X_k}{N} \tag{19.13.4}$$

It must be stressed that these N measurements have to be taken over the appropriate range of variations for X as described earlier.

When only a single measurement of a variable is available in the current test so that the value used for the variable is X, then N_P previous readings, X_{P_k}, must be used to find the random standard uncertainty for the variable as

$$s_X = \left[\frac{1}{\left(N_P - 1\right)}\sum_{k=1}^{N_P}\left(X_{P_k} - \overline{X}_P\right)^2\right]^{\frac{1}{2}} \tag{19.13.5}$$

where

$$\overline{X}_P = \frac{1}{N_P}\sum_{k=1}^{N_P} X_{P_k} \tag{19.13.6}$$

If previous information is available that has an effective random standard uncertainty that is representative of what could have been observed if multiple measurements had been made, then this random standard uncertainty as determined from Equation 19.13.5 is the best estimate of the uncertainty associated with the potential variability for the single measurement.

Another situation where previous measurements of a variable are useful is when a small current sample size, N, is used to calculate the mean value, $\overline{X}$, of a variable. If a much larger set of previous measurements for the same test condition is available, then that set can be used to calculate a more appropriate random standard uncertainty for the variable (Steele et al. 1993) as

$$s_{\overline{X}} = \frac{s_X}{\sqrt{N}} \tag{19.13.7}$$

where N is the number of current measurements averaged to determine $\overline{X}$, and s_X is computed from N_P previous measurements using Equation 19.13.5. Typically, these larger data sets are taken in the early "shake-down" or "debugging" phases of an experimental program.

For many engineering applications, the large-sample approximation applies, and the 95% confidence estimate of the uncertainty for variable i (X_i or $\overline{X}_i$) is

$$U_i = 2\sqrt{b_i^2 + s_i^2} \tag{19.13.8}$$

where s_i is found from the applicable Equation 19.13.3, Equation 19.13.5, or Equation 19.13.7. The factor 2 expands the combined systematic and random standard uncertainties to obtain the 95% confidence limits for the uncertainty U_i. The interval $X_i \pm U_i$ or $\overline{X}_i \pm U_i$, as appropriate, should contain $X_{i_{\text{true}}}$ 95 times out of 100.

Uncertainty of a Result

Consider an experimental result that is determined from J measured variables as

$$r = r\left(X_1, X_2, \ldots, X_i, \ldots, X_J\right) \tag{19.13.9}$$

where some variables may be single measured values and others may be mean values. A typical mechanical engineering experiment would be the determination of the heat transfer in a heat exchanger as

$$q = \dot{m} c_p \left(T_o - T_i\right) \tag{19.13.10}$$

where q is the heat rate, $\dot{m}$ is the flow rate, c_p is the fluid specific heat, and T_o and T_i are the heated fluid outlet and inlet temperatures, respectively. For the large-sample approximation, U_r is found as

$$U_r = 2\sqrt{b_r^2 + s_r^2} \tag{19.13.11}$$

where b_r is the systematic standard uncertainty of the result

$$b_r^2 = \sum_{i=1}^{J} (\theta_i b_i)^2 + 2 \sum_{i=1}^{J-1} \sum_{k=i+1}^{J} \theta_i \theta_k b_{ik} \tag{19.13.12}$$

with

$$\theta_i = \frac{\partial r}{\partial X_i} \tag{19.13.13}$$

and s_r is the random standard uncertainty of the result

$$s_r^2 = \sum_{i=1}^{J} \left(\theta_i s_i\right)^2 \tag{19.13.14}$$

The term b_{ik} in Equation 19.13.12 is the covariance of the systematic standard uncertainties. When the elemental systematic standard uncertainties for two separately measured variables are related, for instance when the transducers used to measure different variables are each calibrated against the same standard, the systematic standard uncertainties are said to be correlated and the covariance of the systematic errors is nonzero. The significance of correlated systematic standard uncertainties is that they can have the effect of either decreasing or increasing the uncertainty in the result. The covariance term, b_{ik}, is determined by summing the products of the elemental systematic standard uncertainties for variables i and k that arise from the same source and are therefore perfectly correlated (Brown et al. 1996) as

$$b_{ik} = \sum_{\alpha=1}^{L} b_{i_\alpha} b_{k_\alpha} \tag{19.13.15}$$

where L is the number of elemental systematic error sources that are common for measurements X_i and X_k.

If, for example,

$$r = r\left(X_1, X_2\right) \tag{19.13.16}$$

and it is possible for portions of the systematic standard uncertainties b_1 and b_2 to arise from the same source(s), then Equation 19.13.12 gives

$$b_r^2 = \theta_1^2 b_1^2 + \theta_2^2 b_2^2 + 2\theta_1 \theta_2 b_{12} \tag{19.13.17}$$

For a case in which the measurements of X_1 and X_2 are each influenced by four elemental systematic error sources and sources 2 and 3 are the same for both X_1 and X_2, Equation 19.13.2 gives

$$b_1^2 = b_{1_1}^2 + b_{1_2}^2 + b_{1_3}^2 + b_{1_4}^2 \tag{19.13.18}$$

and

$$b_2^2 = b_{2_1}^2 + b_{2_2}^2 + b_{2_3}^2 + b_{2_4}^2 \tag{19.13.19}$$

while Equation 19.13.15 gives

$$b_{12} = b_{1_2} b_{2_2} + b_{1_3} b_{2_3} \tag{19.13.20}$$

In the general case, there would be additional terms in the expression for the random standard uncertainty of the result, s_r, (Equation 19.13.14) to take into account the possibility of random errors in different variables being correlated. These terms have traditionally been neglected, although random errors in different variables caused by the same uncontrolled factor(s) are certainly possible and can have a substantial impact on the value of s_r (Hudson et al. 1996). In such cases, one would need to acquire sufficient data to allow a valid estimate of the random covariance terms using standard statistical techniques (ISO, 1995). Note, however, that if multiple test results over an appropriate time period are available, these can be used (as described earlier) to directly determine s_r. This value of the random standard uncertainty of the result implicitly includes the correlated error effect.

If a test is performed so that M multiple sets of measurements (X_{1_k}, X_{2_k}, …, X_{J_k}) at the same test condition are obtained, then M results can be determined using Equation 19.13.1 and the mean result, $\bar{r}$, can be determined using

$$\bar{r} = \frac{1}{M} \sum_{k=1}^{M} r_k \tag{19.13.21}$$

The random standard uncertainty of the sample of M results, s_r, is calculated as

$$s_r = \left[\frac{1}{\left(M-1\right)} \sum_{k=1}^{M} \left(r_k - \bar{r}\right)^2 \right]^{\frac{1}{2}} \tag{19.13.22}$$

The uncertainty associated with the mean result, $\bar{r}$, for the "large sample" approximation is then

$$U_{\bar{r}} = 2\sqrt{b_r^2 + s_{\bar{r}}^2} \tag{19.13.23}$$

where

$$s_{\bar{r}} = \frac{s_r}{\sqrt{M}} \tag{19.13.24}$$

and where b_r is given by Equation 19.13.12.

The large sample approximation for the uncertainty of a determined result (Equation 19.13.11 or Equation 19.13.23) applies for most engineering applications even when some of the variables have small numbers of samples. A detailed discussion of the applicability of this approximation is given in Steele et al. (1994) and Coleman and Steele (1995).

The determination of U_r from s_r (or $s_{\bar{r}}$) and b_r using the large-sample approximation is called detailed uncertainty analysis (Coleman and Steele, 1999). The interval $r \pm U_r$ (or $\bar{r} \pm U_{\bar{r}}$) should contain r_{true} 95 times out of 100. As discussed in the next section, detailed uncertainty analysis is an extremely useful tool in an experimental program. However, in the early stages of the program, it is useful to simply estimate the overall uncertainty for each variable, U_i. The overall uncertainty of the result is then determined as

$$U_r^2 = \sum_{i=1}^{J} \left(\theta_i U_i\right)^2 \tag{19.13.25}$$

This determination of U_r is called general uncertainty analysis.

Using Uncertainty Analysis in Experimentation

The first item that should be considered in any experimental program is "What question are we trying to answer?" Another key item is how accurately do we need to know the answer, or what "degree of goodness" is required? With these two items specified, general uncertainty analysis can be used in the planning phase of an experiment to evaluate the possible uncertainties from the various approaches that might be used to answer the question being addressed. Critical measurements that will contribute most to the uncertainty of the result can also be identified.

Once past the planning, or preliminary design, phase of the experiment, the effects of systematic errors and random errors are considered separately using the techniques of detailed uncertainty analysis. In the design phase of the experiment, estimates are made of the systematic and random standard uncertainties, b_r and s_r, and the uncertainty, U_r, expected in the experimental result. These detailed design considerations guide the decisions made during the construction phase of the experiment.

After the test is constructed, a debugging phase is required before production tests are begun. In the debugging phase, multiple tests are run and the random standard uncertainty determined from them is compared with the s_r value estimated in the design phase. Also, a check is made to see if the test results plus and minus U_r compare favorably with known results for certain ranges of operation. If these checks are not successful, then further test design, construction, and debugging is required.

Once the test operation is fully understood, then the execution phase can begin. In this phase, balance checks can be used to monitor the operation of the test apparatus. In a balance check, a quantity, such as flow rate, is determined by different means and the difference in the two determinations, z, is compared to the ideal value of zero. For the balance check to be satisfied, the quantity z must be less than or equal to U_z.

Uncertainty analysis will of course play a key role in the data analysis and reporting phases of an experiment. When an experimental result is reported, the uncertainty should be given along with the associated confidence level, usually 95%. Also, the values and details of the determination of the systematic standard uncertainty, b_r, and the random standard uncertainty, s_r, should be included. When a range of test results is presented as a regression equation, then a statement must be made of the uncertainty of the values obtained from the equation. This topic is discussed in detail in Brown et al. (1998) and in Coleman and Steele (1999).

References

AIAA Standard S-071A-1999. 1999. *Assessment of Wind Tunnel Data Uncertainty.* AIAA, Washington, DC.

ANSI/ASME PTC 19.1-1998. 1998. *Test Uncertainty.* ASME, New York.

Brown, K.K., Coleman, H.W., Steele, W.G., and Taylor, R.P. 1996. Evaluation of correlated bias approximations in experimental uncertainty analysis. *AIAA Journal.* 34(5):1013–1018.

Brown, K.K., Coleman, H.W., and Steele, W.G. 1998. A methodology for determining experimental uncertainty in regressions. *J. of Fluids Eng.* 120:445–456.

Coleman, H.W. 2003. Some observations on uncertainties and the verification and validation of a simulation. *J. of Fluids Eng.* 125:733–735.

Coleman, H.W. and Steele, W.G. 1995. Engineering application of experimental uncertainty analysis. *AIAA Journal.* 33(10):1888–1896.

Coleman, H.W. and Steele, W.G. 1999. *Experimentation and Uncertainty Analysis for Engineers.* 2nd ed. John Wiley & Sons, New York.

Hudson, S.T., Bordelon, W.J. Jr., and Coleman, H.W. 1996. Effect of correlated precision errors on the uncertainty of a subsonic venturi calibration. *AIAA Journal.* 34(9):1862–1867.

ISO. 1995. *Guide to the Expression of Uncertainty in Measurement.* ISO, Geneva, Switzerland.

SAE AIR 1678 Rev. A. 2000. *Uncertainty of In-Flight Thrust Measurements.* SAE, Warrendale, PA.

Steele, W.G., Taylor, R.P., Burrell, R.E., and Coleman, H.W. 1993. Use of previous experience to estimate precision uncertainty of small sample experiments. *AIAA Journal.* 31(10):1891–1896.

Steele, W.G., Ferguson, R.A., Taylor, R.P., and Coleman, H.W. 1994. Comparison of ANSI/ASME and ISO models for calculation of uncertainty. *ISA Transactions.* 33:339–352.

19.14 Chaos

R. L. Kautz

Introduction

Since the time of Newton, the science of dynamics has provided quantitative descriptions of regular motion, from a pendulum's swing to a planet's orbit, expressed in terms of differential equations. However, the role of Newtonian mechanics has recently expanded with the realization that it can also describe chaotic motion. In elementary terms, **chaos** can be defined as **pseudorandom** behavior observed in the steady-state dynamics of a deterministic **nonlinear system**. How can motion be pseudorandom, or random according to statistical tests, and yet be entirely predictable? This is just one of the paradoxes of chaotic motion, which is globally stable but locally unstable, predictable in principle but not in practice, and geometrically complex but derived from simple equations.

The strange nature of chaotic motion was first understood by Henri Poincaré, who established the mathematical foundations of chaos in a treatise published in 1890 [Holmes, 1990]. However, the practical importance of chaos began to be widely appreciated only in the 1960's, beginning with the work of Edward Lorenz [1963], a meteorologist who discovered chaos in a simple model for fluid convection. Today, chaos is understood to explain a wide variety of apparently random natural phenomena, ranging from dripping faucets [Martien, 1985] to the flutter of a falling leaf [Tanabe, 1994] to the irregular rotation of a moon of Saturn [Wisdom, 1984].

Although chaos is used purposely to provide an element of unpredictability in some toys and carnival rides [Kautz, 1994], it is important from an engineering point of view primarily as a phenomenon to be avoided. Perhaps the simplest scenario arises when a nonlinear mechanism is used to achieve a desired effect, such as the synchronization of two oscillators. In many such cases, the degree of nonlinearity must be chosen carefully: strong enough to ensure the desired effect but not so strong that chaos results. In another scenario, an engineer might be required to deal with an intrinsically chaotic system. In this case, if the system can be modeled mathematically, then a small feedback signal can often be applied to eliminate the chaos [Ott, 1990]. For example, low-energy feedback has been used to suppress chaotic behavior in a thermal convection loop [Singer, 1991]. As such considerations suggest, chaos is rapidly becoming an important topic for engineers.

Flows, Attractors, and Liapunov Exponents

Dynamical systems can generally be described mathematically in terms of a set of differential equations of the form

$$d\mathbf{x}(t)/dt = \mathbf{F}\left[\mathbf{x}(t)\right], \tag{19.14.1}$$

where $\mathbf{x} = (x_1, \ldots, x_N)$ is an N-dimensional vector called the **state vector** and the vector function $\mathbf{F} = (F_1(\mathbf{x}), \ldots, F_N(\mathbf{x}))$ defines how the state vector changes with time. In mechanics, the state variables x_i are typically the positions and velocities associated with the potential and kinetic energies of the system. Because the state vector at times $t > 0$ depends only on the initial state vector $\mathbf{x}(0)$, the system defined by Equation (19.14.1) is deterministic, and its motion is in principle exactly predictable.

The properties of a dynamical system are often visualized most readily in terms of trajectories $\mathbf{x}(t)$ plotted in **state space**, where points are defined by the coordinates $(x_1, \ldots, x_N)$. As an example, consider the motion of a damped pendulum defined by the normalized equation

$$d^2\theta/dt^2 = -\sin\theta - \rho d\theta/dt, \tag{19.14.2}$$

which expresses the angular acceleration $d^2\theta/dt^2$ in terms of the gravitational torque $-\sin\theta$ and a damping torque $-\rho d\theta/dt$ proportional to the angular velocity $v = d\theta/dt$. If we define the state vector as $\mathbf{x} = (x_1, x_2) = (\theta, v)$, then Equation (19.14.2) can be written in the form of Equation (19.14.1) with $\mathbf{F} = (x_2, -\sin x_1 - \rho x_2)$. In this case, the state space is two dimensional, and a typical trajectory is a spiral, as shown in Figure 19.14.1 for the initial condition $\mathbf{x}(0) = (0, 1)$. If additional trajectories, corresponding to other initial conditions, were plotted in Figure 19.14.1, we would obtain a set of interleaved spirals, all converging on the point $\mathbf{x} = (0, 0)$. Because the direction of a trajectory passing through a given point is uniquely defined by Equation (19.14.1), state-space trajectories can never cross, and, by analogy with the motion of a fluid, the set of all of trajectories is called a flow.

The tendency of a flow to converge toward a single point or other restricted subset of state space is characteristic of dissipative systems like the damped pendulum. Such an asymptotic set, called an attracting set or **attractor**, can be a fixed point (for which $\mathbf{F}(\mathbf{x}) = 0$) as in Figure 19.14.1, but might also be a periodic or chaotic trajectory. The convergence of neighboring trajectories is suggested in Figure 19.14.1 by a series of ellipses spaced at time intervals $\Delta t = 1.5$ that track the flow of all trajectories originating within the circle specified at $t = 0$. In general, the contraction of an infinitesimal state-space volume V as it moves with the flow is given by

$$V^{-1}\partial V/\partial t = \nabla \cdot \mathbf{F}, \tag{19.14.2}$$

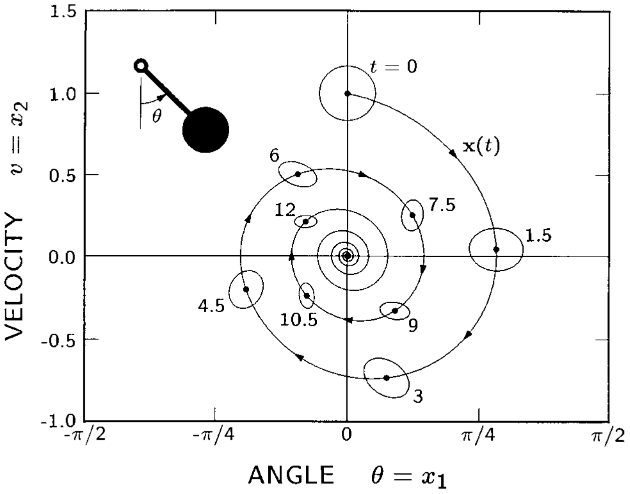

FIGURE 19.14.1 The state-space trajectory $\mathbf{x}(t)$ for a pendulum with a damping coefficient $\rho = 0.2$ for the initial condition $\mathbf{x}(0) = (0, 1)$. The evolution of trajectories initialized in a small circle surrounding $\mathbf{x} = (0, 1)$ is indicated by the ellipses plotted at time intervals of $\Delta t = 1.5$.

where $\nabla \cdot \mathbf{F} = \sum_{i=1}^{N} \partial F_i/\partial x_i$ is the divergence of **F**. For the damped pendulum, $\nabla \cdot \mathbf{F} = -\rho$, so the area of the ellipse shown in Figure 19.14.1 shrinks exponentially as $V(t) = V(0)\exp(-\rho t)$. The contraction of state-space volumes explains the existence of attractors in dissipative systems, but, in conservative systems such as the pendulum with $\rho = 0$, state-space volumes are preserved, and trajectories are instead confined to constant-energy surfaces.

While the existence of chaotic behavior is generally difficult to predict, two essential conditions are easily stated. First, the complex topology of a chaotic trajectory can exist only in a state space of dimension $N \geq 3$. Thus, the pendulum defined by Equation (19.14.2) cannot be chaotic because $N = 2$ for this system. Second, a system must be nonlinear to exhibit chaotic behavior. Linear systems, for which any linear combination $c_1\mathbf{x}_a(t) + c_2\mathbf{x}_b(t)$ of two solutions $\mathbf{x}_a(t)$ and $\mathbf{x}_b(t)$ is also a solution, are mathematically simple and amenable to analysis. In contrast, nonlinear systems are noted for their intractability. Thus, chaotic behavior is of necessity explored more frequently by numerical simulation than mathematical analysis, a fact that helps explain why the prevalence of chaos was discovered only after the advent of efficient computation.

A useful criterion for the existence of chaos can be developed from an analysis of a trajectory's local stability. As sketched in Figure 19.14.2, the local stability of a trajectory $\mathbf{x}(t)$ is determined by considering

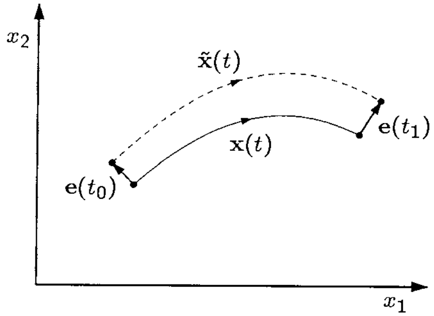

FIGURE 19.14.2 A trajectory $\mathbf{x}(t)$ and a neighboring trajectory $\tilde{\mathbf{x}}(t)$ plotted in state space from time t_0 to t_1. The vectors $\mathbf{e}(t_0)$ and $\mathbf{e}(t_1)$ indicate the deviation of $\tilde{\mathbf{x}}(t)$ from $\mathbf{x}(t)$ at times t_0 and t_1.

a neighboring trajectory $\tilde{\mathbf{x}}(t)$ initiated by an infinitesimal deviation $\mathbf{e}(t_0)$ from $\mathbf{x}(t)$ at time t_0. The deviation vector $\mathbf{e}(t)=\tilde{\mathbf{x}}(t)-\mathbf{x}(t)$ at times $t_1 > t_0$ can be expressed in terms of the Jacobian matrix

$$J_{ij}(t_1,t_0)=\partial x_i(t_1)/\partial x_j(t_0), \tag{19.14.3}$$

which measures the change in state variable x_i at time t_1 due to a change in x_j at time t_0. From the Jacobian's definition, we have $\mathbf{e}(t_1)=\mathbf{J}(t_1,t_0)\mathbf{e}(t_0)$. Although the local stability of $\mathbf{x}(t)$ is determined simply by whether deviations grow or decay in time, the analysis is complicated by the fact that deviation vectors can also rotate, as suggested in Figure 19.14.2. Fortunately, an arbitrary deviation can be written in terms of the eigenvectors $\mathbf{e}^{(i)}$ of the Jacobian, defined by

$$\mathbf{J}\left(t_1,t_0\right)\mathbf{e}^{(i)}=\mu_i\left(t_1,t_0\right)\mathbf{e}^{(i)}, \tag{19.14.4}$$

which are simply scaled by the eigenvalues $\mu_i(t_1,t_0)$ without rotation. Thus, the N eigenvalues of the Jacobian matrix provide complete information about the growth of deviations. Anticipating that the asymptotic growth will be exponential in time, we define the **Liapunov exponents**,

$$\lambda_i=\lim_{t_1\to\infty}\frac{\ln\left|\mu_i\left(t_1,t_0\right)\right|}{t_1-t_0}. \tag{19.14.5}$$

Because any deviation can be broken into components that grow or decay asymptotically as $\exp(\lambda_i t)$, the N exponents associated with a trajectory determine its local stability.

In dissipative systems, chaos can be defined as motion on an attractor for which one or more Liapunov exponents are positive. Chaotic motion thus combines global stability with local instability in that motion is confined to the attractor, generally a bounded region of state space, but small deviations grow exponentially in time. This mixture of stability and instability in chaotic motion is evident in the behavior of an infinitesimal deviation ellipsoid similar to the finite ellipse shown in Figure 19.14.1. Because some λ_i are positive, an ellipsoid centered on a chaotic trajectory will expand exponentially in some directions. On the other hand, because state-space volumes always contract in dissipative systems and the asymptotic volume of the ellipsoid scales as $\exp(\Lambda t)$, where $\Lambda=\sum_{i=1}^{N}\lambda_i$, the sum of the negative exponents must be greater in magnitude than the sum of the positive exponents. Thus, a deviation ellipsoid tracking a chaotic trajectory expands in some directions while contracting in others. However, because an arbitrary deviation almost always includes a component in a direction of expansion, nearly all trajectories neighboring a chaotic trajectory diverge exponentially.

According to our definition of chaos, neighboring trajectories must diverge exponentially and yet remain on the attractor. How is this possible? Given that the attractor is confined to a bounded region of state space, perpetual divergence can occur only for trajectories that differ infinitesimally. Finite deviations grow exponentially at first but are limited by the bounds of the chaotic attractor and eventually shrink again. The full picture can be understood by following the evolution of a small state-space volume selected in the neighborhood of the chaotic attractor. Initially, the volume expands in some directions and contracts in others. When the expansion becomes too great, however, the volume begins to fold back on itself so that trajectories initially separated by the expansion are brought close together again. As time passes, this stretching and folding is repeated over and over in a process that is often likened to kneading bread or pulling taffy.

Because all neighboring volumes approach the attractor, the stretching and folding process leads to an attracting set that is an infinitely complex filigree of interleaved surfaces. Thus, while the differential equation that defines chaotic motion can be very simple, the resulting attractor is highly complex. Chaotic attractors fall into a class of geometric objects called **fractals**, which are characterized by the presence of structure at arbitrarily small scales and by a dimension that is generally fractional. While the existence

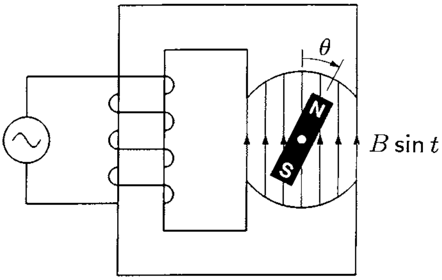

FIGURE 19.14.3 A synchronous motor, consisting of a permanent magnet free to rotate in a uniform magnetic field $B\sin t$ with an amplitude that varies sinusoidally in time.

of objects with dimensions falling between those of a point and a line, a line and a surface, or a surface and a volume may seem mysterious, fractional dimensions result when dimension is defined by how much of an object is apparent at various scales of resolution. For the dynamical systems encompassed by Equation (19.14.1), the fractal dimension D of a chaotic attractor falls in the range $2 < D < N$ where N is the dimension of the state space. Thus, the dimension of a chaotic attractor is large enough that trajectories can continually explore new territory within a bounded region of state space but small enough that the attractor occupies no volume of the space.

Synchronous Motor

As an example of a system that exhibits chaos, we consider a simple model for a synchronous motor that might be used in a clock. As shown in Figure 19.14.3, the motor consists of a permanent-magnet rotor subjected to a uniform oscillatory magnetic field $B\sin t$ provided by the stator. In dimensionless notation, its equation of motion is

$$d^2\theta/dt^2 = -f\sin t \sin\theta - \rho d\theta/dt, \tag{19.14.6}$$

where $d^2\theta/dt^2$ is the angular acceleration of the rotor, $-f\sin t\sin\theta$ is the torque due to the interaction of the rotor's magnetic moment with the stator field, and $-\rho d\theta/dt$ is a viscous damping torque. Although Equation (19.14.7) is explicitly time dependent, it can be cast in the form of Equation (19.14.1) by defining the state vector as $\mathbf{x} = (x_1, x_2, x_3) = (\theta, v, t)$, where $v = d\theta/dt$ is the angular velocity, and by defining the flow as $\mathbf{F} = (x_2, -f\sin x_3 \sin x_1 - \rho x_2, 1)$. The state space is thus three dimensional and large enough to allow chaotic motion. Equation (19.14.7) is also nonlinear due to the term $-f\sin t\sin\theta$, since $\sin(\theta_a + \theta_b)$ is not generally equal to $\sin\theta_a + \sin\theta_b$. Chaos in this system has been investigated by several authors [Ballico, 1990].

By intent, the motor uses nonlinearity to synchronize the motion of the rotor with the oscillatory stator field, so it revolves exactly once during each field oscillation. Although synchronization can occur over a range of system parameters, proper operation requires that the drive amplitude f, which measures the strength of the nonlinearity, be chosen large enough to produce the desired rotation but not so large that chaos results. Calculating the motor's dynamics for $\rho = 0.2$, we find that the rotor oscillates without rotating for f less than 0.40 and that the intended rotation is obtained for $0.40 < \rho < 1.87$. The periodic attractor corresponding to synchronized rotation is shown for $f = 1$ in Figure 19.14.4(a). Here the three-dimensional state-space trajectory is projected onto the (x_1, x_2) or (θ, v) plane, and a dot marks the point in the rotation cycle at which $t = 0$ modulo 2π. As Figure 19.14.4(a) indicates, the rotor advances by exactly 2π during each drive cycle.

The utility of the motor hinges on the stability of the synchronous rotation pattern shown in Figure 19.14.4(a). This periodic pattern is the steady-state motion that develops after initial transients decay and represents the final asymptotic trajectory resulting for initial conditions chosen from a wide area of

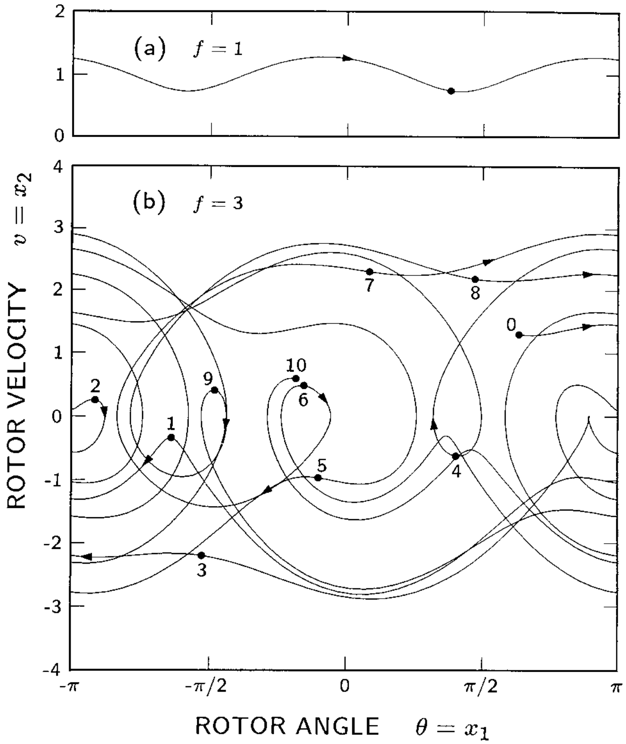

FIGURE 19.14.4 State-space trajectories projected onto the (x_1, x_2) or (θ, v) plane, showing attractors of the synchronous motor for $\rho = 0.2$ and two drive amplitudes, $f = 1$ and 3. Dots mark the state of the system at the beginning of each drive cycle ($t = 0$ modulo 2π). The angles $\theta = \pi$ and $-\pi$ are equivalent.

state space. Because the flow approaches this attracting set from all neighboring points, the effect of a perturbation that displaces the system from the attractor is short lived. This stability is reflected in the Liapunov exponents of the attractor: $\lambda_1 = 0$ and $\lambda_2 = \lambda_3 = -0.100$. The zero exponent is associated with deviations coincident with the direction of the trajectory and is a feature common to all bounded attractors other than fixed points. The zero exponent results because the system is neutrally stable with respect to offsets in the time coordinate. The exponents of -0.100 are associated with deviations transverse to the trajectory and indicate that these deviations decay exponentially with a characteristic time of 1.6 drive cycles. The negative exponents imply that the synchrony between the rotor and the field is maintained in spite of noise or small variations in system parameters, as required of a clock motor.

For drive amplitudes greater than $f = 1.87$, the rotor generally does not advance by precisely 2π during every drive cycle, and its motion is commonly chaotic. An example of chaotic behavior is illustrated for $f = 3$ by the trajectory plotted in Figure 19.14.4(b) over an interval of 10 drive cycles. In this figure, sequentially numbered dots mark the beginning of each drive cycle. When considered cycle by cycle, the trajectory proves to be a haphazard sequence of oscillations, forward rotations, and reverse rotations. Although we might suppose that this motion is just an initial transient, it is instead characteristic of the steady-state behavior of the motor. If extended, the trajectory continues with an apparently random mixture of oscillation and rotation, without approaching a repetitive cycle. The motion is aptly described as chaotic.

The geometry of the chaotic attractor sampled in Figure 19.14.4(b) is revealed more fully in Figure 19.14.5. Here we plot points (θ, v) recording the instantaneous angle and velocity of the rotor at the beginning of each drive cycle for 100,000 successive cycles. Called a **Poincaré section**, Figure 19.14.5 displays the three-dimensional attractor as its intersection with the planes $t = x_3 = 0$ modulo 2π, corresponding to equivalent times in the drive cycle. For the periodic attractor of Figure 19.14.4(a), the rotor

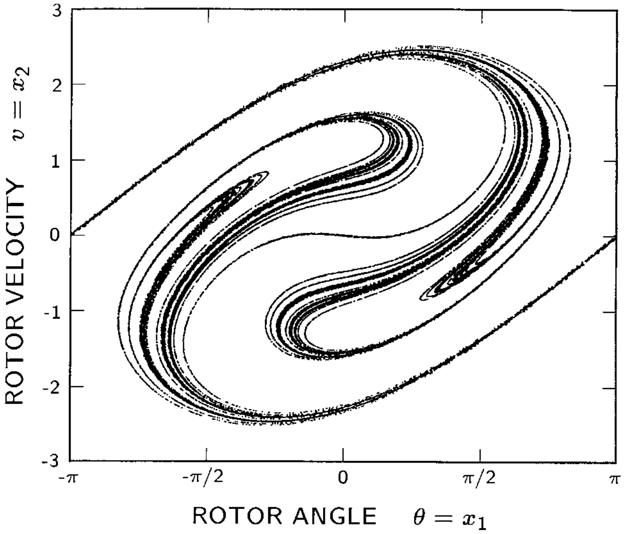

FIGURE 19.14.5 Poincaré section of a chaotic attractor of the synchronous motor with $\rho = 0.2$ and $f = 3$, obtained by plotting points $(x_1,x_2) = (\theta,v)$ corresponding to the position and velocity of the rotor at the beginning of 100,000 successive drive cycles.

returns to the same position and velocity at the beginning of each drive cycle, so its Poincaré section is a single point, the dot in this figure. For chaotic motion, in contrast, we obtain the complex swirl of points shown in Figure 19.14.5. If the system is initialized at a point far from the swirl, the motion quickly converges to this attracting set. On succeeding drive cycles, the state of the system jumps from one part of the swirl to another in an apparently random fashion that continues indefinitely. As the number of plotted points approaches infinity, the swirl becomes a cross section of the chaotic attractor. Thus, Figure 19.14.5 approximates a slice through the infinite filigree of interleaved surfaces that compose the attracting set. In this case, the fractal dimension of the attractor is 2.52 and that of its Poincaré section is 1.52.

The computed Liapunov exponents of the chaotic solution at $\rho = 0.2$ and $f = 3$ are $\lambda_1 = 0$, $\lambda_2 = 0.213$, and $\lambda_3 = -0.413$. As for the periodic solution, the zero exponent implies neutral stability associated with deviations directed along a given trajectory. The positive exponent, which signifies the presence of chaos, is associated with deviations transverse to the given trajectory but tangent to the surface of the attracting set in which it is embedded. The positive exponent implies that such deviations grow exponentially in time and that neighboring trajectories on the chaotic attractor diverge exponentially, a property characteristic of chaotic motion. The negative exponent is associated with deviations transverse to the surface of the attractor and assures the exponential decay of displacements from the attracting set. Thus, the Liapunov exponents reflect both the stability of the chaotic attractor and the instability of a given chaotic trajectory with respect to neighboring trajectories.

One consequence of a positive Liapunov exponent is a practical limitation on our ability to predict the future state of a chaotic system. This limitation is illustrated in Figure 19.14.6, where we plot a given chaotic trajectory (solid line) and three perturbed trajectories (dashed lines) that result by offsetting the initial phase of the given solution by various deviations $e_1(0)$. When the initial angular offset is $e_1(0)=10^{-3}$ radian, the perturbed trajectory (short dash) closely tracks the given trajectory for about 7 drive cycles before the deviation become significant. After 7 drive cycles, the perturbed trajectory is virtually independent of the given trajectory, even though it is confined to the same attractor. Similarly, initial offsets of 10^{-6} and 10^{-9} radian lead to perturbed trajectories (medium and long dash) that track the given trajectory for about 12 and 17 drive cycles, respectively, before deviations become significant. These results reflect the fact that small deviations grow exponentially and, in the present case, increase on average by a factor of 10 every 1.7 drive cycles. If the position of the rotor is to be predicted with an

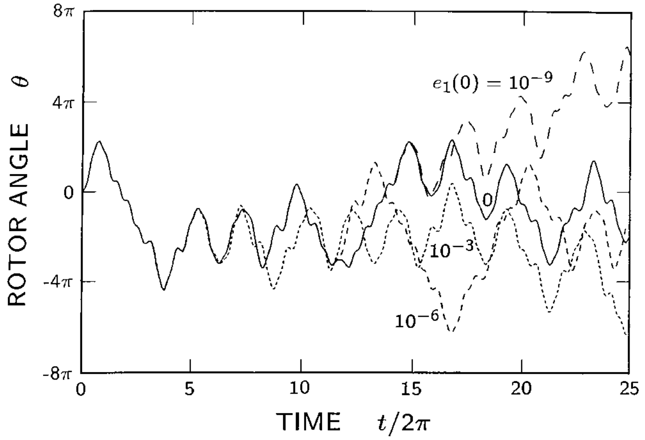

FIGURE 19.14.6 Rotor angle as a function of time for chaotic trajectories of the synchronous motor with ρ = 0.2 and $f = 3$. Solid line shows a given trajectory and dashed lines show perturbed trajectories resulting from initial angular deviations of $e_1(0)=10^{-3}$ (short dash), 10^{-6} (medium dash), and 10^{-9} (long dash).

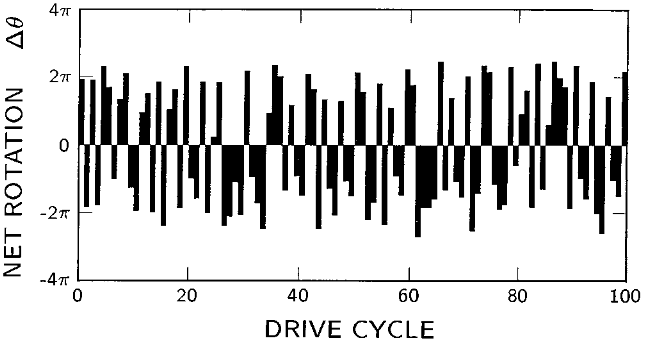

FIGURE 19.14.7 Net rotation of a synchronous motor during each of 100 successive drive cycles, illustrating chaotic motion for ρ = 0.2 and $f = 3$. By definition, $\Delta\theta = \theta(2\pi n) - \theta(2\pi(n-1))$ on the nth drive cycle.

accuracy of 10^{-1} radian after 20 drive cycles, its initial angle must be known to better than 10^{-13} radian and the calculation must be carried out with at least 14 significant digits. If a similar prediction is to be made over 40 drive cycles, then 25 significant digits are required. Thus, even though chaotic motion is predictable in principle, the state of a chaotic system can be accurately predicted in practice for only a short time into the future. According to Lorenz [1993], this effect explains why weather forecasts are of limited significance beyond a few days.

The pseudorandom nature of chaotic motion is illustrated in Figure 19.14.7 for the synchronous motor by a plot of the net rotation during each of 100 successive drive cycles. Although this sequence of rotations results from solving a deterministic equation, it is apparently random, jumping erratically between forward and reverse rotations of various magnitudes up to about 1.3 revolutions. The situation is similar to that of a digital random number generator, in which a deterministic algorithm is used to produce a sequence of pseudorandom numbers. In fact, the similarity is not coincidental since chaotic processes often underlie such algorithms [Li, 1978]. For the synchronous motor, statistical analysis reveals almost no correlation between rotations separated by more than a few drive cycles. This statistical independence is a result of the motor's positive Liapunov exponent. Because neighboring trajectories diverge exponentially, a small region of the attractor can quickly expand to cover the entire attractor, and a small range of rotations on one drive cycle can lead to almost any possible rotation a few cycles later. Thus, there is little correlation between rotations separated by a few drive cycles, and on this time scale the motor appears to select randomly between the possible rotations.

From an engineering point of view, the problem of chaotic behavior in the synchronous motor can be solved simply by selecting a drive amplitude in the range $0.40 < f < 1.87$. Within this range, the strength of the nonlinearity is large enough to produce synchronization but not so large as to produce chaos. As this example suggests, it is important to recognize that erratic, apparently random motion can be an intrinsic property of a dynamical system and is not necessarily a product of external noise. Searching a real motor for a source of noise to explain the behavior shown in Figure 19.14.7 would be wasted effort since the cause is hidden in a noise-free differential equation. Clearly, chaotic motion is a possibility that every engineer should understand.

Defining Terms

Attractor: A set of points in state space to which neighboring trajectories converge in the limit of large time.

Chaos: Pseudorandom behavior observed in the steady-state dynamics of a deterministic nonlinear system.

Fractal: A geometric object characterized by the presence of structure at arbitrarily small scales and by a dimension that is generally fractional.

Liapunov exponent: One of N constants λ_i that characterize the asymptotic exponential growth of infinitesimal deviations from a trajectory in an N-dimensional state space. Various components of a deviation grow or decay on average in proportion to $\exp(\lambda_i t)$.

Nonlinear system: A system of equations for which a linear combination of two solutions is not generally a solution.

Poincaré section: A cross section of a state-space trajectory formed by the intersection of the trajectory with a plane defined by a specified value of one state variable.

Pseudorandom: Random according to statistical tests but derived from a deterministic process.

State space: The space spanned by state vectors.

State vector: A vector $\mathbf{x}$ whose components are the variables, generally positions and velocities, that define the time evolution of a dynamical system through an equation of the form $d\mathbf{x}/dt = \mathbf{F}(\mathbf{x})$, where $\mathbf{F}$ is a vector function.

References

Ballico, M.J. Sawley, M.L., and Skiff, F. 1990. The bipolar motor: A simple demonstration of deterministic chaos. *Am. J. Phys.* 58:58–61.

Holmes, P. 1990. Poincaré, celestial mechanics, dynamical-systems theory and "chaos." *Phys. Reports.* 193:137–163.

Kautz, R.L. and Huggard, B.M. 1994. Chaos at the amusement park: Dynamics of the Tilt-A-Whirl. *Am. J. Phys.* 62:59–66.

Li, T.Y. and Yorke, J.A. 1978. Ergodic maps on [0,1] and nonlinear pseudo-random number generators. *Nonlinear Anal. Theory Methods Appl.* 2:473–481.

Lorenz, E.N. 1963. Deterministic nonperiodic flow. *J. Atmos. Sci.* 20:130–141.

Lorenz, E.N. 1993. *The Essence of Chaos*, University of Washington Press, Seattle, WA.

Martien, P., Pope, S.C., Scott, P.L., and Shaw, R.S. 1985. The chaotic behavior of a dripping faucet. *Phys. Lett. A.* 110:399–404.

Ott, E., Grebogi, C., and Yorke, J.A. 1990. Controlling chaos. *Phys. Rev. Lett.* 64:1196–1199.

Singer, J., Wang, Y.Z., and Bau, H.H. 1991. Controlling a chaotic system. *Phys. Rev. Lett.* 66:1123–1125.

Tanabe, Y. and Kaneko, K. 1994. Behavior of falling paper. *Phys. Rev. Lett.* 73:1372–1375.

Wisdom, J., Peale, S.J., and Mignard, F. 1984. The chaotic rotation of Hyperion. *Icarus.* 58:137–152.

Further Information

A practical introduction to deterministic chaos for undergraduates is provided by *Chaotic and Fractal Dynamics: An Introduction for Applied Scientists and Engineers* by Francis C. Moon. This book emphasizes an experimental point of view, presenting numerous examples drawn from mechanical and electrical engineering.

While written at an undergraduate level, *Chaos: An Introduction to Dynamical Systems* by Kathleen T. Alligood, Tim D. Sauer, and James A. York probes deeply into the mathematical foundations of chaos.

Chaos in Dynamical Systems by Edward Ott gives a rigorous introduction to chaotic dynamics at the graduate level.

Practical methods for experimental analysis and control of chaotic systems are presented in *Coping with Chaos: Analysis of Chaotic Data and the Exploitation of Chaotic Systems*, a reprint volume edited by Edward Ott, Tim Sauer, and James A. York.

19.15 Fuzzy Sets and Fuzzy Logic

Dan M. Frangopol

Introduction

In the sixties, Zaheh (1965) introduced the concept of fuzzy sets. Since its inception more than 30 years ago, the theory and methods of fuzzy sets have developed considerably. The demands for treating situations in engineering, social sciences, and medicine, among other applications that are complex and not crisp have been strong driving forces behind these developments.

The concept of the fuzzy set is a generalization of the concept of the ordinary (or crisp) set. It introduces vagueness by eliminating the clear boundary, defined by the ordinary set theory, between full nonmembers (i.e., grade of membership equals zero) and full members (i.e., grade of membership equals one). According to Zaheh (1965) a fuzzy set A, defined as a collection of elements (also called objects) $x \in X$, where X denotes the universal set (also called universe of discourse) and the symbol $\in$ denotes that the element x is a member of X, is characterized by a membership (also called characteristic) function $\mu_A(x)$ which associates each point in X a real member in the unit interval [0,1]. The value of $\mu_A(x)$ at x represents the grade of membership of x in A. Larger values of $\mu_A(x)$ denote higher grades of membership of x in A. For example, a fuzzy set representing the concept of control might assign a degree of membership of 0.0 for no control, 0.1 for weak control, 0.5 for moderate control, 0.9 for strong control, and 1.0 for full control. From this example, it is clear that the two-valued crisp set [i.e., no control (grade of membership 0.0) and full control (grade of membership 1.0)] is a particular case of the general multivalued fuzzy set A in which $\mu_A(x)$ takes its values in the interval [0,1].

Problems in engineering could be very complex and involve various concepts of uncertainty. The use of fuzzy sets in engineering has been quite extensive during this decade. The area of fuzzy control is one of the most developed applications of fuzzy set theory in engineering (Klir and Folger, 1988). Fuzzy controllers have been created for the control of robots, aircraft autopilots, and industrial processes, among others. In Japan, for example, so-called "fuzzy electric appliances," have gained great success from both technological and commercial points of view (Furuta, 1995). Efforts are underway to develop and introduce fuzzy sets as a technical basis for solving various real-world engineering problems in which the underlying information is complex and imprecise. In order to achieve this, a mathematical background in the theory of fuzzy sets is necessary. A brief summary of the fundamental mathematical aspects of the theory of fuzzy sets is presented herein.

Fundamental Notions

A fuzzy set A is represented by all its elements x_i and associated grades of membership $\mu_A(x_i)$ (Klir and Folger, 1988).

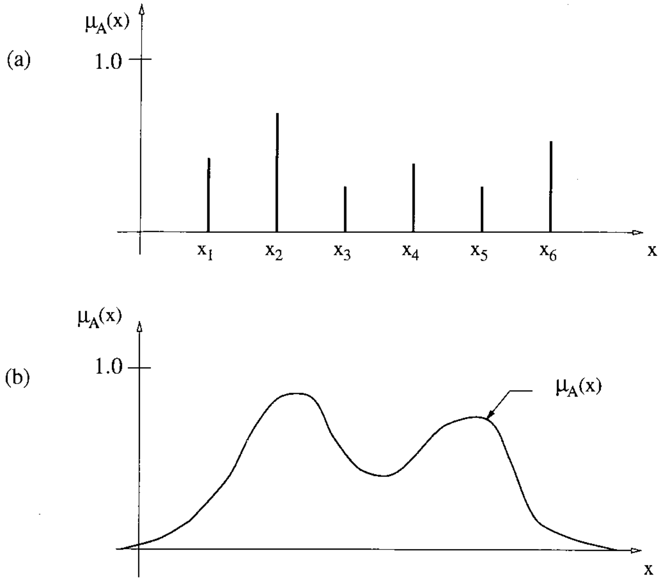

FIGURE 19.15.1 (a) Discrete and (b) continuous fuzzy set.

$$A = \{\mu_A(x_1)|x_1, \mu_A(x_2)|x_2, \ldots, \mu_A(x_n)|x_n\} \qquad (19.15.1)$$

where x_i is an element of the fuzzy set, $\mu_A(x_i)$ is its grade of membership in A, and the vertical bar is employed to link the element with their grades of membership in A. Equation (19.15.1) shows a discrete form of a fuzzy set. For a continuous fuzzy set, the membership function $\mu_A(x)$ is a continuous function of x.

Figure 19.15.1 illustrates a discrete and a continuous fuzzy set. The larger membership grade *max* $(\mu_A(x_i))$ represents the height of a fuzzy set.

If at least one element of the fuzzy set has a membership grade of 1.0, the fuzzy set is called normalized. Figure 19.15.2 illustrates both a nonnormalized and a normalized fuzzy set.

The following properties of fuzzy sets, which are obvious extensions of the corresponding definitions for ordinary (crisp) sets, are defined herein according to Zaheh (1965) and Klir and Folger (1988).

Two fuzzy sets A and B are equal, A = B, if and only if $\mu_A(x) = \mu_B(x)$ for every element x in X (see Figure 19.15.3).

The complement of a fuzzy set A is a fuzzy set $\overline{A}$ defined as

$$\mu_{\overline{A}}(x) = 1 - \mu_A(x) \qquad (19.15.2)$$

Figure 19.15.4 shows both discrete and continuous fuzzy sets and their complements.

If the membership grade of each element of the universal set X in fuzzy set B is less than or equal to its membership grade in fuzzy set A, then B is called a subset of A. This is denoted $B \subseteq A$. Figure 19.15.5 illustrates this situation.

The union of two fuzzy sets A and B with membership functions $\mu_A(x)$ and $\mu_B(x)$ is a fuzzy set $C = A \cup B$ such that

$$\mu_C(x) = \max[\mu_A(x), \mu_B(x)] \qquad (19.15.3)$$

for all x in X.

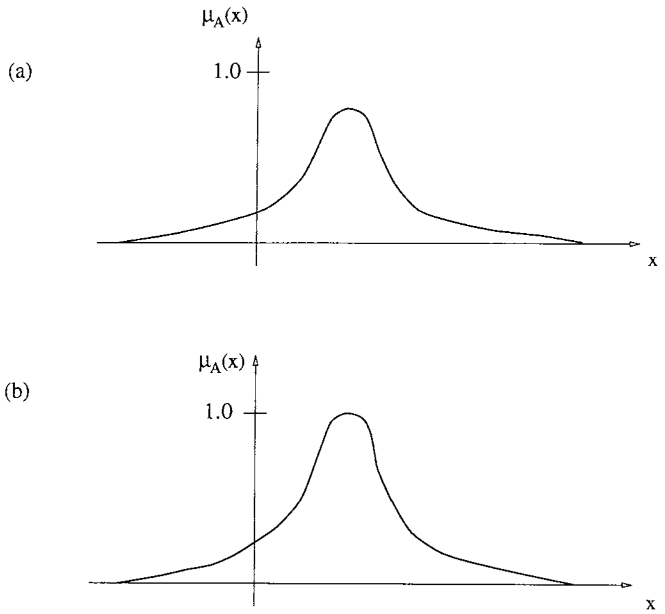

FIGURE 19.15.2 (a) Nonnormalized and (b) normalized fuzzy set.

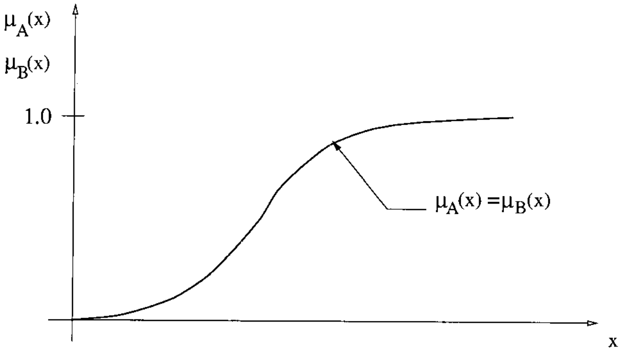

FIGURE 19.15.3 Two equal fuzzy sets, A = B.

Conversely, the intersection of two fuzzy sets A and B with membership functions $\mu_A(x)$ and $\mu_B(x)$, respectively, is a fuzzy set $C = A \cap B$ such that

$$\mu_C(x) = \min\left[\mu_A(x), \mu_B(x)\right] \tag{19.15.4}$$

for all x in X.

Figure 19.15.6 illustrates two fuzzy sets A and B, the union set $A \cup B$ and the intersection set $A \cap B$.

An empty fuzzy set A is a fuzzy set with a membership function $\mu_A(x) = 0$ for all elements x in X (see Figure 19.15.7).

Two fuzzy sets A and B with respective membership function $\mu_A(x)$ and $\mu_B(x)$ are disjoint if their intersection is empty (see Figure 19.15.8).

An α-cut of a fuzzy set A is an ordinary (crisp) set A_α containing all elements that have a membership grade in A greater or equal to α. Therefore,

$$A_\alpha = \left\{x \middle| \mu_A(x) \geq \alpha\right\} \tag{19.15.5}$$

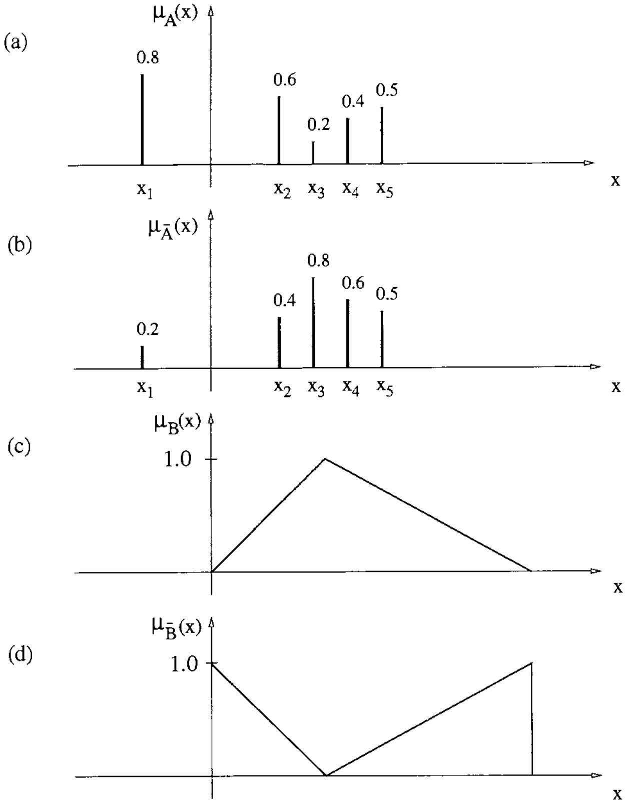

FIGURE 19.15.4 (a) Discrete fuzzy set A, (b) complement $\overline{A}$ of fuzzy set A, (c) continuous fuzzy set B, and (d) complement $\overline{B}$ of fuzzy set B.

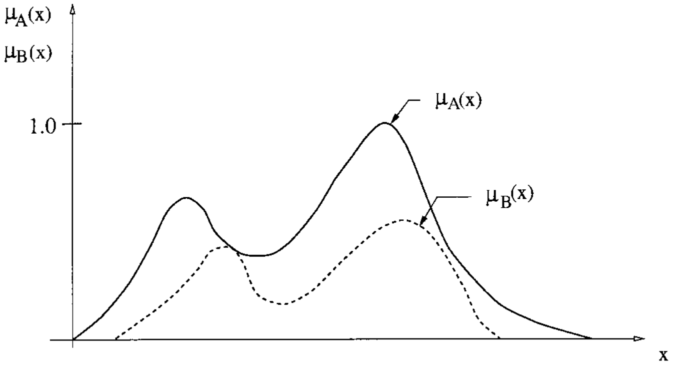

FIGURE 19.15.5 Fuzzy set A and its subset B.

From Figure 19.15.9, it is clear that $\alpha = 0.5$, the α-cut of the fuzzy set A is the crisp set $A_{0.5} = \{x_5, x_6, x_7, x_8\}$ and for $\alpha = 0.8$, the α-cut of the fuzzy set A is the crisp set $A_{0.8} = \{x_7, x_8\}$.

A fuzzy set is convex if and only if all of its α-cuts are convex for all α in the interval [0,1]. Figure 19.15.10 shows both a convex and a nonconvex fuzzy set.

A fuzzy number $\tilde{N}$ is a normalized and convex fuzzy set of the real line whose membership function is piecewise continuous and for which it exists exactly one element with $\mu_{\tilde{N}}(x_0) = 1$. As an example, the real numbers close to 50 are shown by four membership functions in Figure 19.15.11.

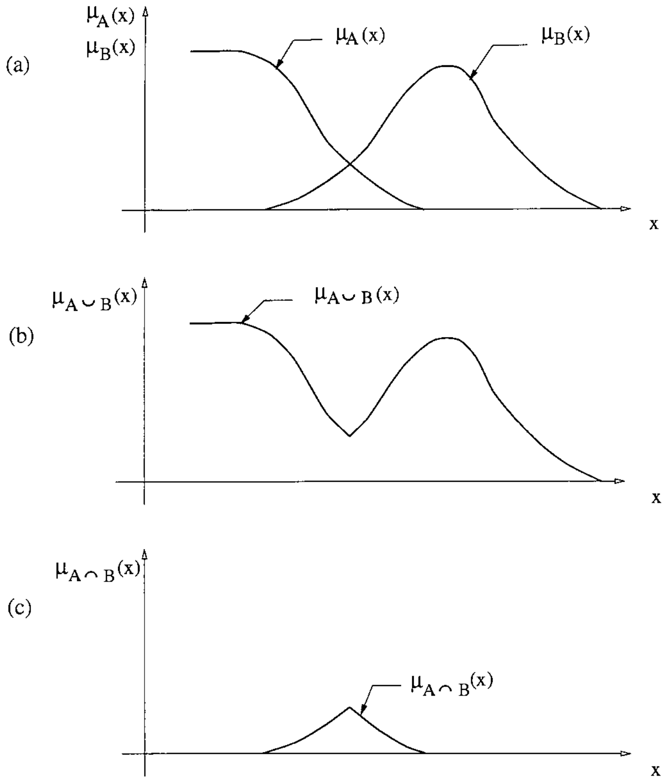

FIGURE 19.15.6 (a) Two fuzzy sets, (b) union of fuzzy sets A ∪ B, and (c) intersection of fuzzy sets A ∩ B.

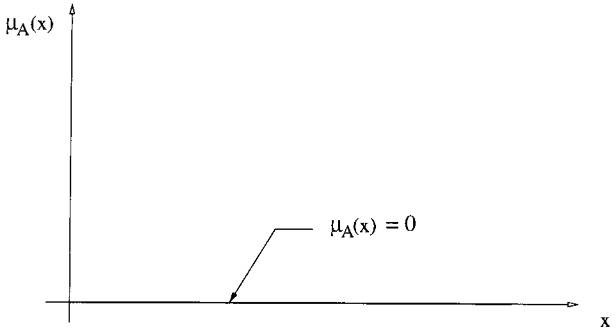

FIGURE 19.15.7 Empty fuzzy set.

The scalar cardinality of a fuzzy set A is the summation of membership grades of all elements of X in A. Therefore,

$$|A| = \sum_{x} \mu_A(x) \tag{19.15.6}$$

For example, the scalar cardinality of the fuzzy set A in Figure 19.15.4(a) is 2.5. Obviously, an empty fuzzy set has a scalar cardinality equal to zero. Also, the scalar cardinality of the fuzzy complement set is equal to scalar cardinality of the original set. Therefore,

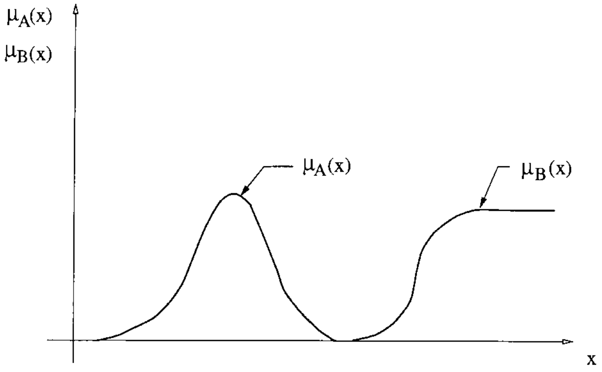

FIGURE 19.15.8 Disjoint fuzzy sets.

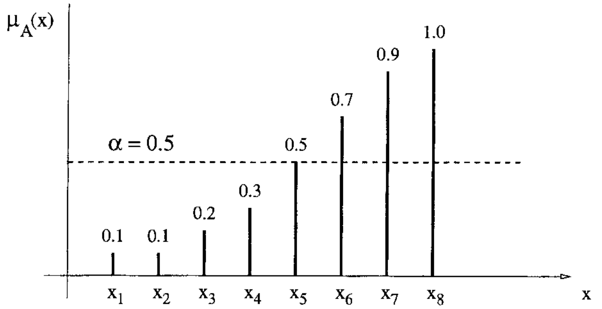

FIGURE 19.15.9 α-cut of a fuzzy set.

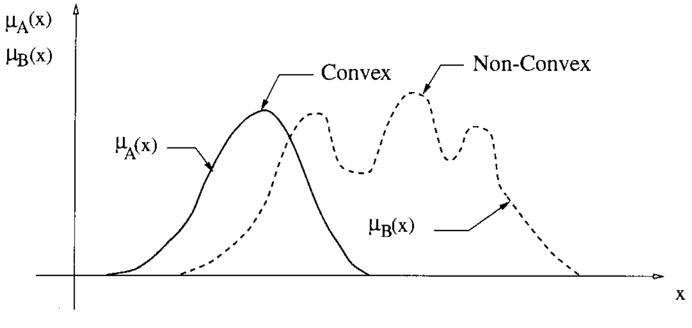

FIGURE 19.15.10 Convex and non-convex fuzzy set.

$$|A| = |\overline{A}| \tag{19.15.7}$$

One of the basic concepts of fuzzy set theory is the extension principle. According to this principle (Dubois and Prade, 1980), given (a) a function f mapping points in the ordinary set X to points in the ordinary set Y, and (b) any fuzzy set A defined on X,

$$A = \{\mu_A(x_1)|x_1, \mu_A(x_2)|x_2, \ldots, \mu_A(x_n)|x_n\}$$

then the fuzzy set B = f(A) is given as

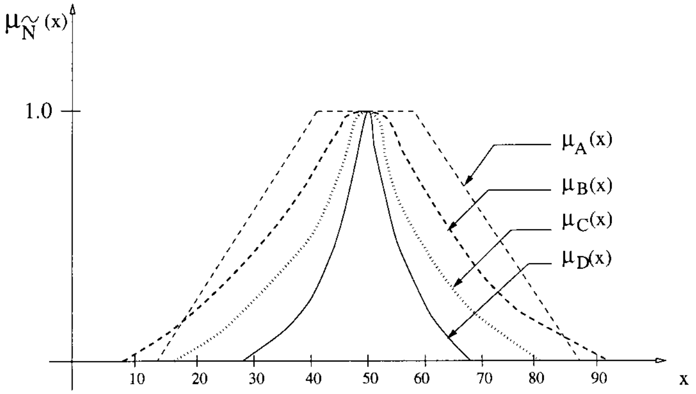

FIGURE 19.15.11 Membership functions of fuzzy sets of real numbers close to 50.

$$B = f(A) = \{\mu_A(x_1)|f(x_1), \mu_A(x_2)|f(x_2), \ldots, \mu_A(x_n)|f(x_n)\} \tag{19.15.8}$$

If more than one element of the ordinary set X is mapped by *f* to the same element y in Y, then the maximum of the membership grades in the fuzzy set A is considered as the membership grade of y in f(A).

As an example, consider the fuzzy set in Figure 19.15.4(a), where $x_1 = -2$, $x_2 = 2$, $x_3 = 3$, $x_4 = 4$, and $x_5 = 5$. Therefore, A = {0.8|–2, 0.6|2, 0.2|3, 0.4|4, 0.5|5} and $f(x) = x^4$. By using the extension principle, we obtain

$$\begin{aligned} f(A) &= \{\max(0.8, 0.6)|2^4, 0.2|3^4, 0.4|4^4, 0.5|5^4\} \\ &= \{0.8|16, 0.2|81, 0.4|256, 0.5|625\} \end{aligned}$$

As shown by Klir and Folger (1988), degrees of association can be represented by membership grades in a fuzzy relation. Such a relation can be considered a general case for a crisp relation.

Let P be a binary fuzzy relation between the two crisp sets X = {4, 8, 11} and Y = {4, 7} that represents the relational concept "very close." This relation can be expressed as:

$$P(X, Y) = \{1|(4,4), 0.7|(4,7), 0.6|(8,4), 0.9|(8,7), 0.3|(11,4), 0.6|(11,7)\}$$

or it can be represented by the two dimensional membership matrix

$$\begin{array}{cc} & \begin{array}{cc} y_1 & y_2 \end{array} \\ \begin{array}{c} x_1 \\ x_2 \\ x_3 \end{array} & \begin{bmatrix} 1.0 & 0.7 \\ 0.6 & 0.9 \\ 0.3 & 0.6 \end{bmatrix} \end{array}$$

Fuzzy relations, especially binary relations, are important for many engineering applications.

The concepts of domain, range, and the inverse of a binary fuzzy relation are clearly defined in Zadeh (1971), and Klir and Folger (1988).

The max-min composition operation for fuzzy relations is as follows (Zadeh, 1991; Klir and Folger, 1988):

$$\mu_{P \circ Q}(x, z) = \max_{y \in Y} \min[\mu_P(x, y), \mu_Q(y, z)] \tag{19.15.9}$$

for all x in X, y in Y, and z in Z, where the composition of the two binary relations P(X,Y) and Q(Y,Z) is defined as follows:

$$R(X,Z) = P(X,Y) \circ Q(Y,Z) \tag{19.15.10}$$

As an example, consider the two binary relations

$$P(X,Y) = \{1.0|(4,4),\ 0.7|(4,7),\ 0.6|(8,4),\ 0.9|(8,7),\ 0.3|(11,4),\ 0.6|(11,7)\}$$

$$Q(Y,Z) = \{0.8|(4,6),\ 0.5|(4,9),\ 0.2|(4,12),\ 0.0|(4,15),\ 0.9|(7,6),\ 0.8|(7,9),\ 0.5|(7,12),\ 0.2|(7,15)\}$$

The following matrix equations illustrate the max-min composition for these binary relations

$$\begin{bmatrix} 1.0 & 0.7 \\ 0.6 & 0.9 \\ 0.3 & 0.6 \end{bmatrix} \circ \begin{bmatrix} 0.8 & 0.5 & 0.2 & 0.0 \\ 0.9 & 0.8 & 0.5 & 0.2 \end{bmatrix} = \begin{bmatrix} 0.8 & 0.7 & 0.5 & 0.2 \\ 0.9 & 0.8 & 0.5 & 0.2 \\ 0.6 & 0.6 & 0.5 & 0.2 \end{bmatrix}$$

Zadeh (1971) and Klir and Folger (1988), define also an alternative form of operation on fuzzy relations, called max-product composition. It is denoted as P(X,Y) ⊗ Q(Y,Z) and is defined by

$$\mu_{P\otimes Q}(x,z) = \max_{y\in Y}\left[\mu_P(x,y),\ \mu_Q(y,z)\right] \tag{19.15.11}$$

for all x in X, y in Y, and z in Z. The matrix equation

$$\begin{bmatrix} 1.0 & 0.7 \\ 0.6 & 0.9 \\ 0.3 & 0.6 \end{bmatrix} \times \begin{bmatrix} 0.8 & 0.5 & 0.2 & 0.0 \\ 0.9 & 0.8 & 0.5 & 0.2 \end{bmatrix} = \begin{bmatrix} 0.8 & 0.7 & 0.5 & 0.2 \\ 0.9 & 0.8 & 0.5 & 0.2 \\ 0.6 & 0.6 & 0.5 & 0.2 \end{bmatrix}$$

illustrates the max product composition for the pair of binary relations P(X,Y) and Q(Y,Z) previously considered.

A crisp binary relation among the elements of a single set can be denoted by R(X,X). If this relation is reflexive, symmetric, and transistive, it is called an equivalence relation (Klir and Folger, 1988).

A fuzzy binary relation S that is reflexive

$$\mu_S(x,x) = 1 \tag{19.15.12}$$

symmetric

$$\mu_S(x,y) = \mu_S(y,x) \tag{19.15.13}$$

and transitive

$$\mu_S(x,z) = \max_{y} \min\left[\mu_S(x,y),\ \mu_S(y,z)\right] \tag{19.15.14}$$

is called a similarity relation (Zadeh, 1971). Equation (19.15.12), Equation (19.15.13), and Equation (19.15.14) are valid for all x,y,z in the domain of S. A similarity relation is a generalization of the notion of equivalence relation.

Fuzzy orderings play a very important role in decision-making in a fuzzy environment. Zadeh (1971) defines fuzzy ordering as a fuzzy relation which is transitive. Fuzzy partial ordering, fuzzy linear ordering, fuzzy preordering, and fuzzy weak ordering are also mathematically defined by Zaheh (1971) and Zimmermann (1991).

The notion of fuzzy relation equation, proposed by Sanchez (1976), is an important notion with various applications. In the context of the max-min composition of two binary relations P(X,Y) and Q(Y,Z), the fuzzy relation equation is as follows

$$\mathbf{P} \circ \mathbf{Q} = \mathbf{R} \tag{19.15.15}$$

where **P** and **Q** are matrices of membership functions $\mu_P(x,y)$ and $\mu_Q(y,z)$, respectively, and **R** is a matrix whose elements are determined from Equation (19.15.9). The solution in this case in unique. However, when **R** and one of the matrices **P**, **Q** are given, the solution is neither guaranteed to exit nor to be unique (Klir and Folger, 1988).

Another important notion is the notion of fuzzy measure. It was introduced by Sugeno (1977). A fuzzy measure is defined by a function which assigns to each crisp subset of X a number in the unit interval [0,1]. This member represents the ambiguity associated with our belief that the crisp subset of X belongs to the subset A. For instance, suppose we are trying to diagnose a mechanical system with a failed component. In other terms, we are trying to assess whether this system belongs to the set of systems with, say, safety problems with regard to failure, serviceability problems with respect to deflections, and serviceability problems with respect to vibrations. Therefore, we might assign a low value, say 0.2 to failure problems, 0.3 to deflection problems, and 0.8 to vibration problems. The collection of these values constitutes a fuzzy measure of the state of the system.

Other measures including plausibility, belief, probability, and possibility measures are also used for defining the ambiguity associated with several crisp defined alternatives. For an excellent treatment of these measures and of the relationship among classes of fuzzy measures see Klir and Folger (1988).

Measures of fuzziness are used to indicate the degree of fuzziness of a fuzzy set (Zimmermann, 1991). One of the most used measures of fuzziness is the entropy. This measure is defined (Zimmermann, 1991) as

$$d(A) = h \sum_{i=1}^{n} S\left(\mu_A\left(x_i\right)\right) \tag{19.15.16}$$

where h is a positive constant and $S(\alpha)$ is the Shannon function defined as $S(\alpha) = -\alpha \ln\alpha - (1 - \alpha) \ln(1 - \alpha)$ for rational α. For the fuzzy set in Figure 19.15.4(a), defined as

$$A = \{0.8|-2,\ 0.6|2,\ 0.2|3,\ 0.4|4,\ 0.5|5\}$$

the entropy is

$$\begin{aligned} d(A) &= h(0.5004 + 0.6730 + 0.5004 + 0.6730 + 0.6931) \\ &= 3.0399\ h \end{aligned}$$

Therefore, for h = 1, the entropy of the fuzzy set A is 3.0399.

The notion of linguistic variable, introduced by Zadeh (1973), is a fundamental notion in the development of fuzzy logic and approximate reasoning. According to Zadeh (1973), linguistic variables are "variables whose values are not members but words or sentences in a natural or artificial language. The motivation for the use of words or sentences rather than numbers is that linguistic characterizations are, in general, less specific than numerical ones." The main differences between fuzzy logic and classical two-valued (e.g., true or false) or multivalued (e.g., true, false, and indeterminate) logic are that (a) fuzzy logic can deal with fuzzy quantities (e.g., most, few, quite a few, many, almost all) which are in general represented by fuzzy numbers (see Figure 19.15.11), fuzzy predicates (e.g., expensive, rare), and fuzzy modifiers (e.g., extremely, unlikely), and (b) the notions of truth and false are both allowed to be fuzzy using fuzzy true/false values (e.g., very true, mostly false). As Klir and Folger (1988) stated, the ultimate goal of fuzzy logic is to provide foundations for approximate reasoning. For a general background on fuzzy logic and approximate reasoning and their applications to expert systems, the reader is referred to Zadeh (1973, 1987), Kaufmann (1975), Negoita (1985), and Zimmermann (1991), among others.

Decision making in a fuzzy environment is an area of continuous growth in engineering and other fields such as economics and medicine. Bellman and Zadeh (1970) define this process as a "decision process in which the goals and/or the constraints, but not necessarily the system under control, are fuzzy in nature."

According to Bellman and Zadeh (1970), a fuzzy goal G associated with a given set of alternatives X = {x} is identified with a given fuzzy set G in X. For example, the goal associated with the statement "x should be in the vicinity of 50" might be represented by a fuzzy set whose membership function is equal to one of the four membership functions shown in Figure 19.15.11. Similarly, a fuzzy constraint C in X is also a fuzzy set in X, such as "x should be substantially larger than 20."

Bellman and Zadeh (1970) define a fuzzy decision D as the confluence of goals and constraints, assuming, of course, that the goals and constraints conflict with one another. Situations in which the goals and constraints are fuzzy sets in different spaces, multistage decision processes, stochastic systems with implicitly defined termination time, and their associated optimal policies are also studied in Bellman and Zadeh (1970).

References

Bellman, R.E. and Zadeh, L.A. 1970. Decision-making in a fuzzy environment. *Management Science*, 17(4), 141–164.

Dubois, D. and Prade, H. 1980. *Fuzzy Sets and Systems: Theory and Applications.* Academic Press, New York.

Furuta, H. 1995. Fuzzy logic and its contribution to reliability analysis. In *Reliability and Optimization of Structural Systems,* R. Rackwitz, G. Augusti, and A. Borri, Eds., Chapman & Hall, London, pp. 61–76.

Kaufmann, A. 1975. *Introduction to the Theory of Fuzzy Subsets,* Vol. 1, Academic Press, New York.

Klir, G.J. and Folger, T.A. 1988. *Fuzzy Sets, Uncertainty, and Information,* Prentice Hall, Englewood Cliffs, New Jersey.

Negoita, C.V. 1985. *Expert Systems and Fuzzy Systems,* Benjamin/Cummings, Menlo Park, California.

Sanchez, E. 1976. Resolution of composite fuzzy relation equations. *Information and Control,* 30, 38–48.

Sugeno, M. 1977. Fuzzy measures and fuzzy integrals — a survey, in *Fuzzy Automata and Decision Processes,* M.M. Gupta, R.K. Ragade, and R.R. Yager, Eds., North Holland, New York, pp. 89–102.

Zadeh, L.A. 1965. Fuzzy sets. *Information and Control*, 8, 338–353.

Zadeh, L.A. 1971. Similarity relations and fuzzy orderings. *Information Sciences.* 3, 177–200.

Zadeh, L.A. 1973. The concept of a linguistic variable and its applications to approximate reasoning. Memorandum ERL-M 411, Berkeley, California.

Zadeh, L.A. 1987. *Fuzzy Sets and Applications: Selected Papers by L.A. Zadeh,* R.R. Yager, S. Ovchinnikov, R.M. Tong, and H.T. Nguyen, Eds., John Wiley & Sons, New York.

Zimmerman, H.-J. 1991. *Fuzzy Set Theory – and Its Applications,* 2nd ed., Kluwer Academic Publishers, Boston.

Further Information

The more than 5000 publications that exist in the field of fuzzy sets are widely scattered in many books, journals, and conference proceedings. For newcomers, good introductions to the theory and applications of fuzzy sets are presented in (a) *Introduction to the Theory of Fuzzy Sets,* Volume I, Academic Press, New York, 1975, by Arnold Kaufmann; (b) *Fuzzy Sets and Systems: Theory and Applications*, Academic Press, New York, 1980, by Didier Dubois and Henri Prade; (c) *Fuzzy Sets, Uncertainty and Information,* Prentice Hall, Englewood Cliffs, NJ, 1988, by George Klir and Tina Folger, and (d) *Fuzzy Set Theory and Its Applications,*, 2nd ed., Kluwer Academic Publishers, Boston, 1991, by H.-J. Zimmerman, among others.

The eighteen selected papers by Lotfi A. Zadeh grouped in *Fuzzy Sets and Applications,* John Wiley & Sons, New York, 1987, edited by R. Yager, S. Ovchinnikov, R.M. Tong, and H.T. Nguyen are particularly helpful for understanding the developments of issues in fuzzy set and possibility theory. Also, the interview with Professor Zadeh published in this book illustrates the basic philosophy of the founder of fuzzy set theory.

20

Patent Law and Miscellaneous Topics

Thomas H. Young
Merchant & Gould, P.C.

George A. Peters
Peters & Peters

B. Johan Ivarsson
University of Virginia

Jeff R. Crandall
University of Virginia

Gregory W. Hall
University of Virginia

Walter D. Pilkey
University of Virginia

Michael Merker
American Society of Mechanical Engineers

Roland Winston
University of California

Walter T. Welford (Deceased)
Imperial College of London

Noam Lior
University of Pennsylvania

Malcolm J. Crocker
Auburn University

Barbara Atkinson
Lawrence Berkeley National Laboratory

Andrea Denver
Lawrence Berkeley National Laboratory

Robert Clear
Lawrence Berkeley National Laboratory

James E. McMahon
Lawrence Berkeley National Laboratory

20.1 Patents and Other Intellectual Property

Thomas H. Young*

The purpose of this section is to provide some very general information about intellectual property protection (especially patents) to nonlawyers.** It is also intended to provide some suggestions for "self-help" to engineers that will enable them to improve the possibility of obtaining and securing appropriate protection for their ideas and developments even before they consult a lawyer. One of the questions an intellectual property attorney frequently hears is "I have a great idea. How do I protect it?" This section should provide at least a starting point for answering that question.

In the case of patents, this section is designed to assist engineers and/or inventors in understanding what is expected of them and how to assist their patent lawyers or agents in the process of protecting their inventions in the United States. Be forewarned, however; the process of obtaining patent, trade secret, and/or copyright protection on such a development is not necessarily a linear one and is often neither short nor easy.

Patents***

What is a patent? The authorization for a patent system stems from the U.S. Constitution, which provides:

> The Congress shall have power… to promote the progress of science and useful arts, by securing for limited times to authors and inventors the exclusive right to their respective writings and discoveries. (U.S. Const. Art. I, § 8)

Although the concept of a patent system did not originate in the U.S., the drafters of the Constitution thought patents and copyrights significant enough to provide for them in the fundamental predicates on which our government is founded. Indeed, Thomas Jefferson, as Secretary of State, was one of the first patent "examiners."

The premise of the constitutional provision is to encourage the disclosure of inventions in the interest of promoting future innovation. Specifically, if inventors were not provided with patent protection for their innovations, they would seek to exploit them in secret. Thus, no one else would be able to benefit from and expand on his or her inventions, so technology would not move as rapidly as it would with full disclosure. Following enactment of the Constitution, Congress promptly adopted and has continuously maintained and updated laws implementing a patent system.

---

* Mr. Young has practiced intellectual property law for more than 25 years, is a partner in the Denver office of the intellectual property law firm of Merchant & Gould headquartered in Minneapolis, Minnesota, and has been an adjunct professor of patent and trademark law at the University of Colorado and University of Denver law schools. The author acknowledges with appreciation the assistance of Mr. George C. Lewis, P.E., an associate at Merchant & Gould, in updating this article.

** This section is in no way intended to provide the reader with all of the information he or she may need to evaluate or obtain intellectual property protection in particular situations on their own. Additional information is available from the Patent and Trademark Office and the Copyright Office in Washington, D.C. and other published references on these subjects. For information on patents and trademarks, the reader may contact the U.S. Patent and Trademark Office, USPTO Contact Center, Crystal Plaza 3, Room 2C02, P.O. Box 1450, Alexandria, VA 22313-1450, call (703) 308-4357, or visit the Patent and Trademark Office website at www.uspto.gov. For information regarding copyrights, contact the U.S. Copyright Office, 101 Independence Ave. S.E., Washington, D.C. 20559-6000, call (202) 707-3000, or visit the Copyright Office website at www.copyright.gov. When applying the legal requirements to a specific issue, the reader is encouraged to consult with a knowledgeable lawyer.

*** The patent laws are codified in 35 United States Code (i.e., "U.S.C.") § 100 *et seq.* Regulations implementing these patent laws, particularly as they relate to the operation of the Patent Office, are found in volume 37 of the Code of Federal Regulations (i.e., "C.F.R."). The internal rules of the Patent Office relating to the examination of patents are contained in the Patent Office "Manual of Patent Examining Procedure" or "M.PE.P" For more information on patents, the following treatises may be helpful: *Chisum on Patents*, Donald S. Chisum, Matthew Bender & Co., New York, 2004; *Patent Law Fundamentals,* Peter D. Rosenberg, 2nd ed., Clark Boardman Callaghan, Rochester, NY, 1995.

Strictly speaking, patents are not contracts; however, because of the premise behind the constitutional provision, patents have sometimes been analogized to contracts between inventors and the U.S. government. The government agrees to allow the inventor exclusive rights to his or her invention for a period of time. In exchange, the inventor agrees to disclose his or her invention, thereby allowing other inventors the benefit of the patentee's work and enabling others to practice the invention after the patent has expired.

What rights does a patent confer? After a patent issues, the patentee has the right to exclude others from making, using, or selling the subject matter claimed in the patent. Currently, the term of a U.S. patent is 20 years from the date the patent application was filed. The patentee is not required to license others to use the invention.

Nevertheless, a patent does not confer the right to do anything. In fact, it is frequently the case that an inventor will receive a patent but will be unable to use the patented invention because it infringes on another's patent. For example, if A obtained the first patent on a laser and B later obtains a patent on the use of a laser in surgery, B cannot make or use the laser in surgery, because it would infringe on A's patent. By the same token, however, A cannot use his laser in surgery, because it would infringe on B's patent. In addition, patent rights are territorially limited, and the use of the same invention in different countries may have different ramifications. Finally, regardless of patent rights, the use of certain technologies (e.g., pharmaceuticals) may be limited by other government regulations and practical considerations.

A significant advantage of a patent over other forms of intellectual property protection, such as copyright or trade secret, is that a patent can be enforced against anyone who utilizes the claimed technology regardless of whether that person copied or misappropriated the technology. Independent development of an infringing device is not a defense.

Who can obtain a patent? Anyone who is the first to invent something that falls into a category of subject matter that is deemed to be patentable may obtain a U.S. patent. A single patent can have several inventors if the subject matter of one or more claims in the patent was jointly conceived or reduced to practice. In that case, each inventor, in essence, obtains his or her own rights to the patent and, in the absence of an agreement, may exploit those rights independently of the other inventor(s). The patent must be obtained by the true inventors or it may be invalid. Thus, persons who did not contribute to an invention should not be named as inventors regardless of the desirability of recognizing their moral or economic support to the process of inventing.

What subject matter is patentable? U.S. patent law provides that

> Whoever invents or discovers any new and useful *process, machine, manufacture, or composition of matter*, or any new and useful *improvement* thereof, may obtain a patent therefore, subject to the conditions and requirements of this title. (35 USC § 101 [emphasis added])

Although the categories of patentable items seem archaic, Congress acknowledged that it intended this language to "include anything under the sun that is made by man."

The development of significant new technologies, such as computers and biotechnology, has challenged the limits of proper patentable subject matter. Nevertheless, with some diversions along the way, courts have continued to expand those boundaries so that they now include computer software, engineered lifeforms and even "methods of doing business" when embodied in properly drafted patent claims. In general, however, laws of nature, scientific truths, and mathematical algorithms are not patentable subject matter in and of themselves. New and useful applications of those concepts, however, may be patented.

What are the standards for patentability? In order to merit a patent, an invention must be new, useful, and nonobvious. The "new" and "useful" standards are defined precisely as one might expect. One may not obtain a patent on an invention that has been invented before and, therefore, is not novel or on one that has no practical utility.

The "nonobvious" standard is a more difficult one. Even if an invention has not been created before, in order to be patentable, it must not have been obvious to one of ordinary skill in the technical field of the invention at the time the invention was made. In other words, a valid patent cannot be obtained on an invention that merely embodies a routine design or the application of principles within the ordinary skill of the art. Whether an invention meets the standard for nonobviousness involves a factual inquiry into the state of the art, the level of ordinary skill in the art, and the differences between what was known in the art and the invention at the time it was made. In addition, both the Patent Office and courts will look at objective evidence of nonobviousness, including the context in which the invention was made (e.g., whether or not there was a long-standing problem that had not been solved by others), recognition of the invention, and its success in the marketplace. Nevertheless, the determination of nonobviousness is not precise. Indeed, the "beauty" of many of the most significant inventions is embodied in their simplicity. As such, they are temptingly "obvious" after the fact, even though courts are theoretically constrained from utilizing hindsight in determining nonobviousness.

How is a U.S. patent obtained? The process of obtaining a patent starts with the invention. "Invention," under U.S. patent law, has two parts. First, there is the "conception" of the invention, which literally refers to the date when the inventor first thought of the novel aspect of his or her invention. Second, there is the "reduction to practice" of the invention, which can refer to a variety of activities. In the case of a mechanical invention, for example, reduction to practice occurs when a working version of the machine is built embodying the invention. However, there is also a legal concept called "constructive" reduction to practice, which occurs when the inventor files a patent application with the Patent Office.

The date of invention is very important in the U.S. Unlike every other country in the world, the U.S. awards patents to the first person to invent it, rather than the first person to file a patent application. Importantly, the date of conception serves as the date of invention in the U.S. so long as the inventor was "diligent" in reducing the invention to practice. If the inventor is not continuously "diligent" (and there is some question as to what that word means, exactly), then the date of invention is considered the date from which the inventor was continuously diligent until the invention was reduced to practice.

The date of invention can be critical to obtaining a patent in the U.S. In foreign countries, however, the only date that matters is the date on which the inventor first filed the patent application. Filing a patent application in the U.S. will normally preserve the inventor's rights abroad if the appropriate foreign patent applications are filed within one year of the U.S. filing date and the other requirements of the Patent Cooperation Treaty are met. Ideally, an inventor should file a patent application directly after the conception of the invention in order to achieve the earliest effective date in both the U.S. and abroad.

Before filing a patent application, an inventor should have a "prior art search" performed. *Prior art* is a term that refers, in part, to materials published before the inventor files the application that are relevant to the issues of novelty and nonobviousness. Having a search done for prior art is a good way to ensure that the invention for which the application is written is patentable and may also provide some insight into whether practice of the invention would infringe on the rights of others. The prior art search enables a preliminary determination of the patentability of the invention and, if it appears patentable, the identification of the patentable features to be focused upon in drafting the application. Nevertheless, there is always some prior art that will not be accessible using economically viable means at the time of application, so an inventor can never be completely sure about the novelty of his invention at the time of filing.

An inventor can apply for a patent from the Patent Office either *pro se* (i.e., on his own) or through a registered patent agent or attorney. The process of obtaining a patent is a complex one, and the inventor's chances of obtaining a valid patent of the broadest possible scope are greatly increased by the use of a qualified agent or attorney. Lists of registered patent attorneys and agents are available from the Patent Office. Patent attorneys may also be located through the *Martindale-Hubbell Law Directory,* state and local bar associations, and other publications, directories, and professional organizations.

This is not to say that inventors, themselves, have not successfully obtained patents from the Patent Office. Nevertheless, busy patent examiners are easily frustrated by *pro se* applicants' lack of familiarity with patent application requirements and Patent Office rules, and those frustrations are evidenced, consciously or unconsciously, in Patent Office "rejections." Familiarity with the stated requirements of the Patent Office and knowledge of its informal workings greatly increase the chances of successfully obtaining a valid patent with the broadest possible scope.

A patent application contains a number of parts, all of which generally fall into two main categories. The first group, known as the "specification," contains a detailed written description of the invention, including relevant drawings or graphs and any examples. The purpose of the specification is to "enable" one of ordinary skill in the art to make and use the invention. In addition, the applicant must disclose the "best mode" of practicing the invention. The "enablement" and "best mode" requirements are intended to fulfill the constitutional purpose of full disclosure of the invention. Thus, a patent that was otherwise properly granted by the Patent Office may nevertheless be invalidated if it is later determined that the inventor failed to teach others how to utilize the invention or tried to maintain the best mode of practicing the invention as a secret.

The second major part of the patent application is the "claims," which are the separately numbered paragraphs appearing at the end of a patent. The claims define the scope of protection that the patent will confer, and they must be clear, definite, and unambiguous. The goal of the applicant in prosecuting a patent is to obtain claims that cover the invention as broadly as possible without including subject matter that is obvious or not novel. For example, if A invented the two-wheeled bicycle, he might claim a vehicle utilizing two round rotating objects for conveyance. Such a claim might prove to be invalid, for example, if carts were previously known. In such a situation, it would be better to claim the bicycle more narrowly as a vehicle with two wheels in tandem.

Once the application is drafted and submitted to the Patent Office, the Patent Office classifies the invention and sends it to an appropriate "art unit." The Patent Office is divided into separate art units that employ examiners who are knowledgeable about, or at least familiar with, particular fields of technology. Eventually, an examiner will read the application, focusing mainly on the claims since they define the legal parameters of the invention. After performing his own patentability search and reviewing the application for other technical defects, the examiner may either "allow" the application to become a patent or reject the application on the grounds that it lacks substantive merit and/or fails to comply with the formalities of a proper patent application. If the examiner rejects some of the claims, he will explain why the claims are not patentable in light of the specific prior art references. This will start a series of communications (in writing, by telephone, or in person) between the examiner and the applicant (or the registered attorney of record). During that process, the claims of the patent will be amended as becomes necessary in an attempt to define patentable subject matter.

If the application is eventually allowed, then a patent will be printed and "issued" several months after payment of the "issuance fee." If the application is not allowed by the examiner and is finally rejected, the inventor can (1) abandon the application and the effort to obtain a patent, (2) file a "continuation" application and start the process over, or (3) appeal the rejection to the Board of Patent Appeals and Interferences and eventually to other courts. It is not uncommon for the process, from filing of the application until allowance, to take several years.

After the application is submitted, it is appropriate to advise the public that a patent is "pending." This remains true until the application has been abandoned or has been issued as a patent. Generally, neither the contents of the application nor even the fact that an application has been filed are publicly available from the Patent Office absent the consent of the applicant. However, the application will be published by the Patent Office approximately 18 months after filing, if the applicant pursues foreign patent protection. Although such publication will result in the loss of any trade secret protection for the technology disclosed in the application, publication does advance the date from which the applicant may obtain compensation for infringement if a patent is granted. After a patent issues, the patent number should be marked on products embodying the patent. This notice serves to start the period running for the collection of damages for patent infringement. Absent such notice, damages do not begin to run until the infringer receives actual notice of the patent.

Several aspects of this process bear particular note. First, once an application has been filed, the Patent Office does not permit the introduction of "new matter" into the application. Although typographical and other simple errors in the application may be corrected, an applicant may not insert additional written material or drawings (e.g., an additional embodiment or further improvement). The reason for this is simple — because the date of invention and the date of filing are both important for U.S. and foreign priority purposes, the Patent Office could not operate efficiently if the subject matter of the application were constantly amended. There would be numerous continuing disputes as to the effective date to be afforded the subject matter of an amended application. Instead, if it is necessary to amend the application substantively, a new "continuation-in-part" application must be filed. If it is filed while the original or "parent" application is still pending, the subject matter common to both applications will retain the original filing date, while the new material will only be afforded the filing date of the later continuation-in-part application. The prohibition on adding "new matter," therefore, places a premium on filing an original application that completely and accurately describes the invention.

Second, the patent application process frequently is not linear. Seldom does an invention constitute a static concept or a single finished embodiment. The concept may change as its full ramifications are slowly revealed through practical experience, and its embodiment in physical articles, compositions, or processes may change after the patent application is filed. Thus, as the invention evolves, it may be necessary to file further continuation-in-part applications to cover the developments that appear during this evolutionary process. To achieve the ultimate objective of obtaining patent protection on commercially viable aspects of the invention, it may be necessary for the inventor and legal counsel to reevaluate the merits of the original application and to take appropriate corrective action in the patent prosecution process.

How can the inventor help? There are a variety of ways in which the inventor can and, in fact, should aid in the process of obtaining a patent.

First, and perhaps foremost, an inventor should keep detailed notes on his research and development throughout the inventive process. All research and/or discoveries should be documented, dated, and witnessed by a noninventor because they may become important later for purposes of determining who was the first to invent. The date of invention may also be useful in convincing the Patent Office or a court that certain prior art dated before the filing of the patent application should, nevertheless, not be applied. In preparing this documentation, it is important to realize that the testimony of the inventor himself or documents authenticated only by the inventor are generally not sufficient to prove priority. There are many reasons for this. Suffice it to say that there is a premium on having the records witnessed contemporaneously by at least one noninventor. Getting a noninventor to witness pages of a lab notebook is one way to accomplish this. Alternatively, the Patent Office will, for a nominal fee, accept and retain for two years "disclosure" documents evidencing the date of conception. An inventor may also file a "provisional" patent application with the Patent Office documenting the date of invention and providing an early filing date for subject matter disclosed in that application and claimed in a full U.S. application filed during the following year. These Patent Office filings are probably the most unquestionable evidence of a date of conception.

An inventor can also assist by performing an informal prior art search of his own before contacting a patent attorney. Filing a patent application is expensive. An inventor should be as confident as possible that he has created something novel before spending the money to draft an application. Typically, a patent attorney will urge that a formal search be performed to ensure that the prior art that the Patent Office examiner is likely to access has been considered. Due to the proliferation of electronic databases for scientific and industry literature, however, there may be additional prior art that is more readily accessible to the inventor. A search of this material can be helpful to the patent attorney in isolating the patentable features of the invention and improving the chances of obtaining a valid patent.

All prior art located by or known to the inventor should be disclosed to the patent attorney so that it can be evaluated and disclosed to the Patent Office, if necessary. In that regard, both an applicant and his attorney are under an affirmative duty to disclose relevant prior art to the Patent Office, and failure to do so can lead to invalidation of the patent.

Once a prior art search has been performed, an inventor should file an application as early as practically possible. As noted previously, this will protect the inventor's rights in foreign countries as well as provide constructive reduction to practice of the invention if it has not already been embodied in a working prototype. Nevertheless, some delay in filing may be desirable in order to permit further testing and corroboration. This is permissible, and in many instances desirable, bearing in mind that under U.S. patent law an application *must* be filed within one year of the first public use, disclosure, sale, or offer of sale of the invention. This deadline cannot be extended and, if violated, will automatically result in the invalidation of the patent. Many other countries do not have a one-year "grace" period; a patent application is immediately barred once there has been a public disclosure in that country or elsewhere. Although there is an "experimental use" exception in the U.S., it is limited to technical experiments (as opposed to test marketing) that are appropriately documented. To be safe, the inventor should contact a patent attorney before publicly disclosing or using an invention or offering it for sale. If any of those events have already occurred, they should be immediately called to the patent attorney's attention.

The inventor is also instrumental in drafting the patent application. The inventor must make sure that the specification is accurate, enables one skilled in the art to practice the invention, and discloses the best way to make and use the invention. Although the art of claim drafting is somewhat of an acquired skill, the inventor should also be involved in that process to make sure that the claims cover the invention and are not easily designed around. Sometimes a patent attorney will draft claims that do not expressly state a physical element or process step, but utilize "means-plus-function" language. In that case, it is highly desirable to describe as many means as possible for fulfilling that element in the application itself, and the inventor is the best source of that type of information. In other words, the inventor should continuously be asking questions of his attorney about whether certain variations of his invention will be adequately protected by the claims as drafted. Finally, the inventor can and should be instrumental in helping the attorney identify the technical/practical differences between the invention and prior art. In short, the prosecution of a patent application should be a team effort between inventor and attorney at each step in the process.

Trade Secrets*

In some instances it may be desirable to protect new technology as a trade secret rather than by patent. For example, an invention may not be patentable; it may be one of numerous small items or know-how that improves one's business. Such items are typically protected as trade secrets. While there is no formal method of acquiring trade secret protection as there is for patents and copyrights, attention must still be paid to their identification and protection. Also, unlike patents and copyrights, trade secrets are protected under state, rather than federal, laws. Therefore, the nuances of trade secret protection may vary depending on which state's laws apply. There are, however, some general principles of trade secrets that are common to most jurisdictions.

What is a trade secret? A "trade secret" may include anything that gives a person an advantage over his competitors and is not generally known to them. It includes compilations of information such as customer lists, compositions, process techniques and parameters, and software. In determining whether something is a protectable trade secret, courts look at the following factors: (1) the extent to which the information is known outside of the trade secret owner's business, (2) the extent to which it is known by employees or others involved in the trade secret owner's business, (3) the extent of measures taken by the trade secret owner to guard the secrecy of the information, (4) the value of the information to the trade secret owner and to his competitors, (5) the amount of effort or money expended by the trade secret owner in developing the information, and (6) the ease or difficulty with which the information could be properly acquired or duplicated by others.

What protection does a trade secret provide? A trade secret protects the owner from improper appropriation of the secret through use or disclosure by a person having an obligation not to do so. The major

---

*See, generally, the Uniform Trade Secrets Act § 1(4), 14 U.L.A. 537 (1980) and *Milgrim on Trade Secrets*, Roger M. Milgrim, Matthew Bender & Co., New York, 2004.

advantage of a trade secret is that it may last indefinitely; the major defect is that if it is lost, it generally cannot be reclaimed. Unlike with patent infringement, a person accused of stealing a trade secret can successfully defend such an accusation by showing that he independently developed the subject matter of the secret. Trade secret protection, therefore, is only as good as the inability of competitors to "reverse-engineer" or to independently develop it.

How can one obtain a trade secret? Whether or not one has a trade secret is ultimately determined judicially in an action for enforcement. The court will look at all of the factors previously noted. At that time it is usually too late to take the actions necessary to establish trade secret protection. Thus, there is a premium for the periodic review and implementation of a program for trade secret protection. Steps that can be taken to protect trade secrets include (1) identifying the types of materials that are deemed to be trade secrets by an organization and notifying employees of the organization's policy to treat this information as trade secrets, (2) restricting access to the trade secrets to only those individuals who have a need to know and who are obligated by contract or otherwise not to use or disclose them, and (3) taking physical precautions to limit access to trade secrets, such as using locked file cabinets or vaults. These are the most fundamental steps that can be taken.

Although legal counsel is frequently consulted in establishing a plan for protecting trade secrets, including the drafting of appropriate confidentiality agreements, the physical steps required should be put in place by the trade secret owner prior to legal consultation.

Copyrights*

Copyright protection is usually associated with writings, songs, paintings, sculpture, and other artistic endeavors. However, it also extends to certain technology, particularly software, databases, and certain architectural plans.

What protection does a copyright provide? Copyright protection is a matter of federal law. Under the federal Copyright Act, protection is available for "original" works of appropriate subject matter, such as those mentioned in the previous paragraph. A copyright provides the exclusive right to reproduce, publicly distribute, publicly perform, publicly display, and make derivative works from an original work of authorship. However, it protects only against "copying" of the protected work and does not provide protection where a work has been independently developed by another. Copying can be presumed where the third party had access to the copyrighted work and there is "substantial similarity" between the third party's work and the original. Further, in certain limited instances, a small portion of a work may be reproduced without liability as a "fair use." The parameters of the "fair use" doctrine are complicated, however, and they are beyond the subject of this section.

Only a modicum of creativity is needed to satisfy the requirement of "originality." On the other hand, protection is limited. It has frequently been stated that a copyright only protects the manner in which something is expressed, rather than the idea or content, which can be an extremely difficult distinction to make. For example, there is significant debate as to the appropriate scope of copyright protection, for both software and databases. Nevertheless, an advantage of a copyright is that it may last for a relatively long period of time. At a minimum, copyright in works created at this time last for the life of the author plus 70 years (or 120 years if the author is a corporate entity).

How is a copyright obtained? Theoretically, in order to obtain a copyright an author need only show that a work is original to him (i.e., that he is in fact the author). Federal protection for copyright attaches as soon as a writing is fixed in a tangible medium (i.e., as soon as it is put on paper, or in memory on a

---

* The federal laws on copyright are codified in the Lanham Act, § 1 *et seq.* For further information on copyrights, the following treatise may be helpful: *Nimmer on Copyright,* Melville B. & David Nimmer, Matthew Bender, New York, 2004.

computer, or anywhere else that it can be "perceived"). Nevertheless, there are two important steps that should be taken to realize the full scope of that protection.

First, it is highly advisable to affix a copyright notice to the work. "Notice" is provided by affixing to the work: (1) the word "Copyright" or the © symbol, (2) the date of first publication, and (3) the name of the copyright owner. Notice should be affixed to the work in an obvious position (such as one of the first pages of a book, an entry screen of a computer program, etc.). A copyright notice should be placed on all drafts of material that may be subject to protection under copyright law. If an author fails to put the notice on his work, copyright protection is not lost; however, an infringer may then use the defense that he innocently thought that the work was within the public domain. Adequate notice precludes the "innocent" infringer defense, and, because it does not cost anything, notice is always a good idea.

In addition, registration of the copyright with the Register of Copyrights at the Library of Congress is also highly recommended. This procedure is relatively simple and inexpensive. It consists of filling out a government form and submitting it with the appropriate filing fee and a sample of the work sought to be copyrighted. If the application *is* acceptable, the Copyright Office returns a copy of the application stamped with the copyright registration number.

In the case of software and databases, there has been concern that an unscrupulous competitor might attempt to purloin valuable information from the sample submitted with the application. In recognition of this problem, the Copyright Office has promulgated rules allowing the submission of only a limited portion of the software or database adequate to identify the copyrighted work.

Although federal registration is not necessary to perfect a copyright, it does have some significant advantages. First, it is necessary to obtain a registration in order to bring suit against an infringer. While it is possible to register the work on an expedited basis immediately prior to commencing the lawsuit, it is not advisable. Early registration (i.e., within 3 months of the first publication of the work) allows an author to elect to sue for "statutory" damages, which can be considerably easier to prove and, possibly, more munificent than "actual" damages. In addition, an author may be able to recover attorneys' fees from a defendant in some cases, but only if the work in question was registered before or soon after publication. In sum, if an author believes that a work is important and might be copied, he should promptly register the work.

Trademarks*

Although trademark protection does not encompass technology per se, any summary of intellectual property protection would be incomplete without a few comments on the scope and availability of trademark rights.

What is a trademark? A trademark is anything that serves to identify the source of a product or service. Trademark protection can be obtained on a wide variety of items, such as words, symbols, logos, slogans, shapes (if they are not functional), tones (such as NBC's three-note tone), and even colors. A trademark owner may assert his rights against a third party that is engaged in conduct that is likely to cause consumers to believe that his goods or services emanate from, are associated or affiliated with, or are sponsored by the trademark owner.

The purpose of trademark protection is twofold: (1) to ensure the public that goods or services offered under a trademark have the quality associated with the trademark owner, and (2) to preserve the valuable goodwill that the trademark owner has established by promoting the mark. Trademark rights may last indefinitely.

How are trademark rights established? Trademarks are protected under both federal and state law. There are two ways to obtain rights in a trademark: use or federal registration. Rights in a mark can be acquired

---

* The federal trademark laws are codified at 17 U.S.C. § 1 *et seq.* For further information on trademarks, the following treatise may be helpful: *McCarthy on Trademarks and Unfair Competition*, J. Thomas McCarthy, Thomson/West, Eagan, MN, 4th ed., 2003.

simply by using the mark in connection with the goods and services. If the mark is a distinctive one (i.e., coined or "made-up" like "Polaroid"), rights are established immediately. On the other hand, if the mark is descriptive, the use must be so prominent and lengthy that the mark has acquired a "secondary meaning" (i.e., the public has come to recognize the term as identifying the source of the goods and services rather than as a reference to the product or service itself). In either case, to establish rights through use, it is desirable to use the designation ™ in connection with the mark, thereby indicating that the owner of the mark asserts that it is a trademark under common law.

In contrast, the process of obtaining a federal trademark registration involves the filing of an application with the U.S. Patent and Trademark Office. The application identifies the mark, the goods and services with which it is used, and, if it is already in use, the date of first use and the date of first use in interstate commerce. A filing fee is also required but is relatively minimal. A trademark examiner will check the application substantively, including the review of previously issued trademarks, to see if there is any conflict. If the examiner allows the application, the mark is published in the *Official Gazette,* which is a weekly publication of the Patent Office. If no one opposes the registration within 30 days after publication, then a registration will be issued. If there is an objection, then an opposition proceeding is initiated, and the applicant and the opposer essentially litigate to determine whether the applicant can obtain a trademark registration. Provided that certain documents are subsequently filed with the Patent Office to affirm and renew the registration, the registration may last indefinitely. The existence of a federally registered trademark is designated by the symbol ®, which is frequently seen on the shoulder of the mark.

A federal trademark registration is a powerful tool in protecting a trademark. By law it serves as "constructive" (i.e., assumed) notice of the registrant's claim of rights throughout the U.S. In essence, the registration acts like a recorded deed to real estate, and anyone who subsequently purchases that property without checking the recorded information does so subject to the interests of record. In contrast, the rights of one who attempts to acquire a trademark only through use are generally limited to the geographic area in which the mark is actually used. Others who subsequently use the mark in other areas of the country may also establish rights. Thus, the first step in selecting a trademark is to search the records of the Patent Office to determine whether a confusingly similar mark has previously been registered. Typically, a trademark search performed by a professional search organization will also reveal state registrations and other common law uses that might cause conflicts with the mark under consideration.

One other advantage to federal registration is that the registrant may begin to acquire protection on a mark prior to actual use. This is accomplished by filing an "intent-to-use" application on a mark that the applicant has made a *bona fide* decision to use. The application is examined as described previously. Although the mark must actually be placed in use before the registration is issued, the registration will provide rights from the date of its filing. Thus, the public is on notice of the applicant's potential rights as soon as the application is filed. The examination process will also give the applicant significant comfort that the mark is available for use before investing a great deal of money in its promotion.

Final Observations

Selecting an appropriate method of acquiring intellectual property protection for a new development may involve several forms of protection. Software, for example, may be protected by patent, trade secret, and copyright protection and may be sold using a registered trademark. In addition, other legal means may be used to protect the software, including appropriate contractual provisions limiting and restricting the rights of a user acquired by license. Those contractual commitments may survive, even if the intellectual property protection is lost.

It is hoped that this section has provided at least a general overview by which the nonlawyer can begin to understand how to protect intellectual property. There are almost never any easy answers to the question of how to protect products, ideas, and services, and it is always advisable to consult a qualified attorney with specific questions. A knowledgeable client, however, can make a significant difference in achieving the strongest protection available.

20.2 Product Liability and Safety

George A. Peters

Introduction

Almost all engineers, at some time in their career, can expect some direct contact or indirect involvement with the legal system. The contact may be in the form of having to answer written interrogatories on technical issues for a company defendant or plaintiff, being personally deposed and having to respond to oral questions under oath, appearing for a company during trial, assisting lawyers in a lawsuit, or personally being a defendant in a lawsuit. Most important is having the ability to translate legal requirements into engineering specifications to assure compliance with the law.

The old maxim "ignorance of the law is no excuse" should be supplemented by an understanding that ignorance of the law may result in unnecessary mistakes (illegal acts) and personal fear when first confronted by an unknown aspect of the legal process. It is essential that the engineer have sufficient understanding to avoid gross errors and omissions, to react appropriately to legal proceedings, and to want to build a basic foundation of knowledge that can be quickly enhanced when needed. This section is only a brief overview that might be illustrative and helpful in both understanding potential legal liability and how to avoid, prevent, or proactively minimize any such legal exposure. If product liability is legal fault for an unsafe design, the question then becomes how to achieve an appropriate level of safety.

Legal Concepts

Fundamental to determining who might be legally "at fault" is the concept of *negligence* which is utilized worldwide in the apportionment of damages (legal redress). Negligence is the failure to exercise ordinary or reasonable care, which persons of ordinary prudence would use to avoid injury to themselves or others. The exact definition is given to jurors, usually in the form of approved jury instructions (the actual operative law), who then apply the law given to them to the facts and circumstances of the case before them. The defenses to allegations of negligence (absence of due care) are, usually, *contributory negligence* (fault) on the part of the plaintiff or *assumption of the risk* on the part of the plaintiff (that risk that is specific and voluntarily assumed, not general or coerced). If there is a violation of a statute or regulation there may be a rebuttable presumption of negligence. Compliance with a technical standard may be some evidence of the exercise of due care. Concepts of *strict liability* involve the presence of a defect that legally caused personal injury or property damage. There are many definitions of a *defect*, such as a failure to perform as safely as an ordinary consumer would expect when used in an intended or reasonably foreseeable manner or "excessive preventable risks."

Foreseeability means that the personal injury, property damage, or environmental harm must have been predictable or knowable at the time of design, manufacture, or sale of the product. Generally, the law requires only *reasonable efforts* to prevent defects, deficiencies, or unsafe conditions. In other words, there should be efforts to predict possible harm and reasonably practical risk reduction efforts to minimize the harm.

The term *engineering malpractice* includes conduct that has personal legal consequences (professional liability) for the individual engineer, conduct that has adverse legal consequences for his or her employer (such as product liability or toxic torts), and conduct having moral or ethical consequences even though it may be legally protected (Peters, 1996a).

There are many other supplemental legal concepts and each state or jurisdiction has summaries of the law (Witkin, 1987–1990), approved jury instructions (Breckinridge, 1994), statutes enacted by the legislature, compendiums of case law decisions by the courts, and regulations issued by executive agencies (all of which are constantly being revised and expanded). Thus, the engineer should always consult with an attorney-at-law before making an interpretation or taking any action that might be within the province of a licensed professional.

There are thousands of technical standards issued by professional associations, trade groups, standards formulation organizations, and government agencies. Compliance with such standards is the first line of liability prevention, but such standards should be exceeded by a confortable margin to accommodate design, material, fabrication, and in-use process variance (Council, 1989). However, there are other important liability prevention measures that should be undertaken during the design process and described in a product liability prevention plan.

Risk Assessment

A central theme in liability prevention is “risk assessment”. The first step in such an assessment is to identify all probable *hazards* (those faults, failures, or conditions that could cause harm), then determine the quantitative *risk* for each (the frequency and severity of harm), and, finally, render a subjective judgment as to *danger* (the presence of excessive preventable danger). It is important to determine what kind of risk assessment is being made and to identify its objective as follows:

1. *Compliance*. The exact method of conducting a risk assessment may be specified by procurement specifications, industry standards, or government regulations. The design objective may be only compliance with the assessment requirement. However, in the process of performing a written risk assessment and classifying the risk into some severity level, it may result in a beneficial safety audit of the product. Where there is “residual risk,” the design of specific warnings and instructions may be required.
2. *Major Compliance Tasks*. Where safe performance is very important, a detailed engineering analysis may be required by contract or regulation. This might involve listing all probable hazards for each component, part, and subsystem, then attempting to quantify the risk estimate for each hazard at the 10^{-6} level of attempted precision. Since this requires a major effort, the primary design and management objective should be product improvements and informed product assurance.
3. *Comparative Analysis*. Some risk assessments involve only an overall risk estimate which is then compared with other similar products or a wide range of products. The objective or use may be for marketing purposes or liability defense. Since the results are gross or macroscopic, such risk assessments generally do not result in product improvement.
4. *Risk Ratings*. Some trade associations may provide generic risk ratings for materials or products. The objective may be for an “informed choice” of procedures and field equipment in order to satisfy a legal “duty of care” or to help determine the “best practical means” of job performance.
5. *System Effectiveness*. Some risk assessments are performed early in the design process, perhaps as part of a reliability analysis, for the purpose of predicting final system effectiveness. The objective may be to check design efforts, reallocate available funds, or refocus management audits to achieve a desired level of system effectiveness. The process may be used to assure that desired system-of-systems performance is achievable.

From the societal viewpoint, some level of risk can be tolerable, acceptable, required, and specified. What is desired at a given locality or time period can be made known by the local common law, government regulations, trade standards, practices, customs, and expectations. From the engineering viewpoint, *risk levels are controllable, adjustable, manageable, and a consequence of the application of appropriate engineering techniques, skills, and information resources.*

Engineering Analysis

Rather than rely only upon an engineer’s subjective and often biased judgment as to what constitutes a safe design, it is advisable to perform specific objective engineering analyses for design safety. This usually includes some systematic approach to identifying failure modes and field hazards, their risk consequences, and alternative design options that might improve the safety performance. This should be supplemented by formal design review sessions that consider information from or about customers and learned intermediaries in the fabrication, packaging, shipping, distribution, and marketing system. Written hazard analyses should include consideration of legal duties (Peters, 1991a,b), liability prevention techniques (Peters, 1996b), and cultural attributes and technical information resources in the worldwide marketplace (Murakami, 1987, 1992). There should be a systems perspective, a cradle-to-ultimate-disposal philosophy, a true understanding of customer needs and characteristics, and appropriate application of specific design safety techniques.

Testing is required to *verify* the engineering analyses, to *prove* the inherent safety of the product or process system, and to *discover* all potential problems before they become manifest postsale. As part of a *product liability mitigation plan*, procedures and costs should be determined for possible accident investigations, product recalls, retrofits, and injury reparations. A continuing (postsale) *product surveillance plan* should cover all foreseeable users, servicing, maintenance, repair, modification, transport, disposal, and recycling of the product and its components. This permits early discovery and resolution of safety problems. It should also include a means for updating a knowledge bank of scientific, engineering, legal, insurance, patent, and foreign standards information useful for future design efforts as well as postsale obligations.

Human Error

Human error is a major source of undesirable variance in human–machine interfaces. Unfortunately, many engineers neglect or virtually ignore the human factors aspects of product and system design. There should be some effort to control human performance and prevent human failure by designing for a wide range of human dimensions, characteristics, and predictable responses (Peters, 1996a). If possible, the physical attributes, kinetics, and creative perceptual abilities of human operators, maintenance and repair personnel, and bystanders should be utilized in design. Human factors should be part of any early engineering analysis, with appropriate testing and safeguarding for human error that cannot otherwise be eliminated. This includes mechanical guards, tamper-resistant features, safe-stop and limited movement switches, proximity sensors with directional control, built-in time for protective behavioral reactions, and the prevention of inadvertent activation and operation. One of the most important sources of helpful information on human error comes from incident and accident reconstruction, but the scope and bias of the inquiry may severely limit the design usefulness of the data obtained; for example,

1. The *fatalistic approach* where human error is considered as being inevitable in an imperfect world. If there is "no fault" other than by the person committing an error or omission, there is little incentive to investigate in detail to determine other factors for purposes of corrective action. This fosters the continuance of tolerable human error, persistent undesirable human error, and a lack of true recognition of causation and preventive actions.
2. The *behavioral approach* which has a focus on individual behavior in an attempt to develop "safer people," safer attitudes, and to develop motivation to "act responsibly." This may result in closer supervision and additional training, with some short-term benefits, but it does not permanently alter the error-inducing situation.
3. The *situational approach* to human error is to blame the situation, the work environment, group interactions, sociotechnical factors, and the overall circumstances of the situation. There is some benefit from a broader perspective to human error since it provides a better understanding of causation.
4. The *product design approach* has an emphasis on the interaction between the user and the engineered product to provide information useful to the design engineer.
5. The *multifactorial approach* is based on the assumption that there is multiple causation for each injury, damage, loss, harm, or error. If special attention is given to each substantial factor or cause, valuable design-oriented information can result. This multifaceted perspective of accident reconstruction has the greatest benefit and is compatible with concepts of pure comparative negligence and the allocation of damages in proportion to the degree of fault.

During any accident investigation or accident reconstruction, care should be exercised to prevent any "spoliation" or distruction of evidence. This requires trained specialists, since even slight changes to the product may obliterate information that becomes critical in later product evaluations.

Warnings and Instructions

As a last resort, for residual risk, appropriate use of warnings and instructions is essential for product liability prevention and the safe use of products (Peters, 1993). Such communications require a specific design engineering effort, plus relevant testing, if they are to be effective. They include warning devices, warnings on labels and packaging, material safety data sheets, instructions for training, insertions in owner's or operator's manuals, and postsale advertisements and letters to all owners. Some regulations require that they be in two languages and in nonlanguage pictorials. Such hazard communications and procedural directions should not be the result of a cursory afterthought, but an ongoing integral part of the design process. There may be neuropsychological considerations in the presentation of information by visual or auditory displays, machine condition and status indicators, and computer-generated information that requires specialized knowledge and testing. The basic premise is to design a referent about a specific hazard so the target individual is adequately informed as to risk and has a reasonable choice as to avoidance behavior. Warnings that fail to communicate their intended message are functionally useless. There is considerable scientific and engineering information regarding the design of warnings and instructions, and the failure to heed such information may result in legal allegations about a failure to warn, instruct, test, or appropriately market a product. The issue becomes what proof exists about whether or not warnings, instructions, or representations would have significantly influenced user behavior, purchaser choices (as, for example, in available options), and use of protective equipment. Warnings are an important liability prevention and design safety objective.

Liability Prevention

Some corporate enterprises elect to have no formal, organized product safety or liability prevention programs. They rely upon common sense, what is quickly deemed necessary, past practices and procedures, and efforts to motivate or convince all employees that everyone is responsible. This offers great future uncertainty in a growing dynamic and changing marketplace. Other companies may offer the illusion of a meaningful program by virtue of provisions in company policy statements, operating manuals, and designated individuals at high levels. The implementation often fails to provide sufficient early design safety assurance to management, timely opportunities to make design improvements that emerge from focused analytic and test efforts, and interactive contact with the user or customer base. Many companies have developed effective programs that are customized to their needs, customs, value systems, and product mix. In some instances, a liability mitigation effort may shift toward liability prevention, product or system safety marketing advantages, or expand to include health effects and environmental considerations.

An important information resource is trade standards that can be used for design guidance. Generally, these are minimum consensus requirements formulated by a select group of interested individuals. Since they are minimum, and are dated, they should be used as checklists in a standards-plus manner. Some are directly applicable standards, but there are also a myriad of peripheral standards that may be of utility in design review, subcontractor purchasing, and general liability avoidance. These are voluntary, but there are other standards that may be more mandatory. Government standards, recommendations, and laws may be local, state or provincial, or national. Awareness of progress in internationally harmonized standards is important because of the potential global reach of marketing and prediction of legal requirements over the life of a product. There are also design specifications, operative legal concepts, and other design requirements. The question is how to efficiently consolidate and make available such requirements.

The design process should be objectively auditable, with design alternatives presented in a system context for management review and decisions. The audit process could include responsible supervision sign-offs, periodic interdepartmental design reviews, independent system safety analysis, and progressive testing. Postproduction changes should be subject to appropriate administrative controls and to evaluations on a system and actual usage basis.

Special means should be provided for the control of variance on all safety critical functions and derivative parameters. Some of the factors that should be considered are costs associated with various actions, internal and outsourcing manufacturing capability and reliability, and likely perturbations during the operating life of the product, installation, its disposal, repair, rebuilding, servicing, disposal, and possible recycling. Also for potential modifications, buyback, and recalls. In other words, an overview as to how product consistency, durability, and product performance can be assured and what the acceptable limits may be in terms of customer expectation and satisfaction. Of particular importance are the actual effects of outsourcing, multiple factory production, and variance control in different geographical, cultural, and technological areas.

In assessing the costs and benefits of various design alternatives, subjectivity should be replaced where possible with objective estimates. Crude categories may be uninformative or misleading and should be avoided. The failure effects to be considered might include property damage, mission or business interruption, repair or replacement costs, company reputation damage, and personal injury. The injuries should be explored and described with some particularity since the details may be relevant both as to severity and possible remedies. This will also permit a realistic set-aside or monetary reserve for contingencies associated with product misadventure or failure. This permits a more intelligent approach to insurance deductibles, insurance limits, self-insurance and excess insurance or monetary reserve probabilities.

Communication is an important attribute of a product liability prevention program. It is not unusual for the responsible design engineers to be unaware or poorly informed of prior failures, malfunctions, problems, complaints, or adverse verdicts. Entry level engineers may repeat mistakes made earlier and subsequently corrected. There may be regular cycles of relearning from the duplication of design issues and their resolution by design studies. In essence, is there an effective method of experience retention and timely recovery? How is such information effectively communicated to *all* engineers involved in relevant design decisions? How is it translated, if necessary, for communication to suppliers, customers, or users? Are local languages, customs, and practices important determinants in communicating avoidance behavior, or constructive actions? Many engineers attempt to avoid or limit their activities relative to written, inferential, or symbolic communications, so special persons may need to be assigned to such tasks or to review the possible effect of the communications.

Determining the causation of problems, complaints, incidents, and accidents provides a valuable source of information for design corrective and preventive action. To yield useful information, a causation analysis must be performed to some detailed level in accordance with established procedures. Simple conclusions as to causation or subjective cursory opinions are usually nonproductive. It takes a depth of understanding to determine all the causal factors that could have design and management interest. Since each incident investigator or accident reconstructionist is biased to some degree and perceives the facts according to their own personal interests, it is wise to have a representative of design engineering present in at least a fair sample of incidents and accidents. If a design safety focused engineer perceives and integrates the facts of an accident, that specialist is more likely to derive helpful design safety implications and findings before there are repeat accidents. Typical cross-departments barriers or limitations to the flow of information may be relieved by utilizing independent or staff engineers for accident reconstruction and external problem resolution. Eithics should trump information management when the company and customer interest should prevail.

Therefore, liability prevention is premised on specifications and standards (design goals), design and development audits (management awareness and choice), variance control (consistency and predictability), communication (knowledge utilization), causation (problem correction), and life cycle costs (reasonable reduction). Each of these considerations can be further elaborated or implemented in a specific fashion depending on the size of the enterprise, its contractual commitments, and the sophistication of its design, production, and distribution procedures. It is well to remember that history has shown that some companies have suffered financial distress or gone bankrupt because of product safety problems while equivalent or similar companies have avoided such problems and have propsered.

Despite beliefs to the contrary, the legal liability system in each country is based on fault. The law provides an economic incentive to try to avoid complaints of fault. It motivates efforts to achieve a reasonable and practical level of safety. Appreciable risk may be assumed by the excessive permissible use of critieria such as tolerable risk and acceptable risk, because these concepts are ambiguous, can be improperly defined, and may vary in meaning in various jurisdictions and countries. Design safety is the true antidote to legal liability. Sufficient safety can be achieved by an effective liability prevention program.

References

Breckenridge, P.G., Ed. 1994. *California Jury Instructions*. 2 vols., West Publishing, St. Paul, MN.

Council Directive of 14 June 1989 on the approximation of the laws of the Member States relating to machinery (89/392/EEC), as amended 20 June 1991 (91/368/EEC) and 14 June 1993 (93/44/EEC). *Note*: the Council is the Council of the European Communities. Conformity is indicated by the CE mark on machinery and safety components which must be accompanied by an EC declaration of conformity (93/465/EEC).

Murakami, Y., Ed. 1987, 1992. *Stress Intensity Factors Handbook*, Vols. 1 and 2 (1987), Vol. 3 (1992), The Society of Material Science (Japan), and Pergamon Press, Elmsford, NY.

Peters, G.A. 1991a. The globalization of product liability law, *Prod. Liability Law J.*, Butterworth Legal Publishers, 2(3), 133–145.

Peters, G.A. 1991b. Legal duty and presumptions that are compatible with current technology and future world trade, *Prod. Liability Law J.*, Butterworth Legal Publishers, 2(4), 217–222.

Peters, G.A. 1993. Warnings and alarms, Chap. 4 in Vol. 5 of *Automotive Engineering and Litigation*, Peters, G.A. and Peters B.J., Eds., John Wiley & Sons, New York, 93–120.

Peters, G.A. 1996a. Engineering malpractice and remedies: advanced techniques in engineering liability, *Technol. Law Insurance*, 1, 3–9.

Peters, G.A. 1996a. Human error prevention, Chap. 8 in *Asbestos Health Risks*, Vol. 12 of the *Sourcebook on Asbestos Diseases*, G.A. Peters and B.J. Peters, Eds., Michie, Charlottesville, VA, 207–234.

Peters, G.A. 1996b. Liability prevention techniques, in *Proceedings of the JSME International Symposium on Product Liability and Failure Prevention*, Fukuoka, Japan, 167–184.

Witkin, B.E. 1987–1990. *Summary of California Law*, 9th ed., 13 vols., Bancroft-Whitney, San Francisco.

Further Information

For more detailed information, on product liability and safety, read:

Peters, G.A. and Peters B.J., Eds. *Sourcebook on Asbestos Diseases: Medical, Legal, and Engineering Aspects,* 14 vols. Michie, Charlottesville, VA, 1980–1997.

Peters, G.A. and Peters B.J., Eds. *Automotive Engineering and Litigation,* 6 vols. John Wiley & Sons, New York, 1984–1993.

Peters, G.A. and Peters, B.J. *Warnings, Instructions, and Technical Communications.* Lawyers & Judges Publishing Co., Inc., Tucson, Arizona, 1999.

Peters, G.A. and Peters, B.J. *Automotive Vehicle Safety.* Taylor & Francis, London, England, 2002.

20.3 Biomechanics

B. Johan Ivarsson, Jeff R. Crandall, Gregory W. Hall, and Walter D. Pilkey

The field of biomechanics applies the theories and methods of classical mechanics to biological systems. More precisely, it is concerned with the forces that act on and within a biological structure and with the

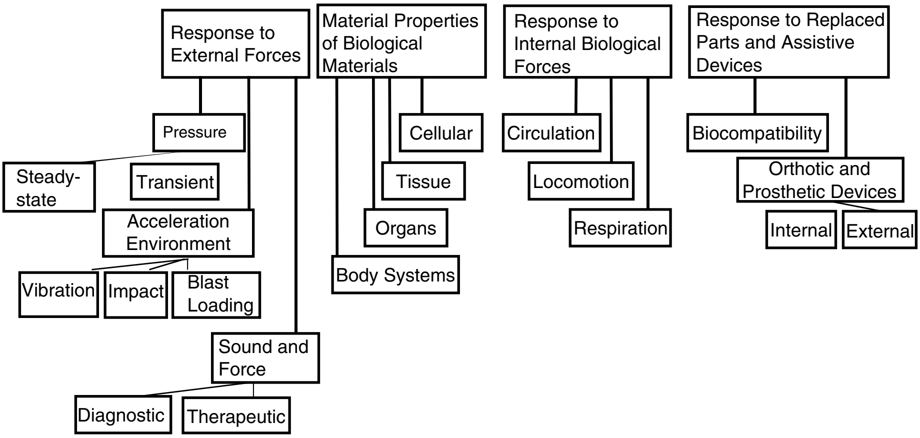

FIGURE 20.3.1 Topics of biomechanics.

TABLE 20.3.1 Physical and Material Properties of Human Cortical and Cancellous Bone

Bone Type	Density (kg/m³)	Elastic Modulus (GPa)	Tensile Strength (MPa)	Compressive Strength (MPa)	Ultimate Elongation (%)	Ultimate Contraction (%)	References
Cortical	1700–2000	5–35[a]	55–200[a]	106–224[a]	0.5–4.9[a]	1.7–2.7[a]	18,22,31,38,46,53
Cancellous	100–1000	0.001–9.8	0.9–5.4	0.1–310	0.9–3.5	1.1–13.4	18,21,26,48

[a] In the direction of the long bone axis.

effects that these forces produce. An overview of topics within the field of biomechanics is provided in Figure 20.3.1. Due to the vast breadth of the field, the authors of this section have not attempted to provide an exhaustive overview of the field of biomechanics. Instead, the section aims to provide a review of material properties of human tissues and factors affecting those properties, as well as brief introductions to the branches of biomechanics known as human body vibrations, impact biomechanics, and computational biomechanics.

Material Properties of Human Tissues

Bone Tissue Mechanics

The term *bone* refers to two types of hard tissue structure: cortical and cancellous bone. Cortical bone is the dense, structured compact bone that comprises the shaft of long bones such as the femur and tibia. Cancellous or trabecular bone is found within the ends of the long bones and the body of the irregularly shaped bones. The mechanical and structural properties of the two types of bone can vary substantially, depending on testing methods as well as such factors as age, gender, and anatomical location. In addition, bone is capable of **remodeling** in response to its environment. Table 20.3.1 summarizes general physical and material properties for the two bone types.

Like most biological materials, bone behaves as an anisotropic, nonhomogeneous, viscoelastic material. Therefore, the values in Table 20.3.1 exhibit a wide range of scatter and variability due to the simplified model of bone as a linearly elastic isotropic material. It is generally adequate, however, to model bone as a linearly elastic anisotropic material at the strain rates found in most experiments. To address the anisotropy, bone is generally considered to exhibit either transverse isotropic or orthotropic behavior. The constitutive equation for a linearly elastic material can be written using a single-index notation for stress and strain as

$$\sigma_i = c_{ij}\varepsilon_j \tag{20.3.1}$$

TABLE 20.3.2 Transverse Isotropic Material Constants for Cortical Bone from the Human Femur[a]

Model	E_1 (GPa)	E_2 (GPa)	E_3 (GPa)	G_{12} (GPa)	G_{13} (GPa)	G_{23} (GPa)	ν_{12}	ν_{13}	ν_{23}	ν_{21}	ν_{31}	ν_{32}
TI	11.5	11.5	17.0	3.6	3.3	3.3	0.58	0.31[b]	0.31[b]	0.58	0.46	0.46

[a] Direction 3 coincides with the long bone axis; the 1 and 2 directions are radial and circumferential, respectively.

[b] Not measured (determined from the relationship: $\nu_{13} = \nu_{23} = (E_1 \times \nu_{31})/E_3$).

Source: Reilly and Burstein (1975)

where the standard summation convention is used with the indices possessing a range of 6. The stress-strain relationship can be similarly expressed in terms of the compliance matrix S_{ij} such that

$$\varepsilon_i = S_{ij}\sigma_j \tag{20.3.2}$$

Equation 20.3.3 represents the compliance matrix of an orthotropic material in terms of the Young's moduli (E_i), the Poisson's ratio (ν_{ij}), and the shear moduli (G_{ij}).

$$\mathbf{S}_{ij} = \begin{bmatrix} 1/E_1 & -\nu_{21}/E_2 & -\nu_{31}/E_3 & 0 & 0 & 0 \\ -\nu_{12}/E_1 & 1/E_2 & -\nu_{32}/E_3 & 0 & 0 & 0 \\ -\nu_{13}/E_1 & -\nu_{23}/E_2 & 1/E_3 & 0 & 0 & 0 \\ 0 & 0 & 0 & 1/G_{23} & 0 & 0 \\ 0 & 0 & 0 & 0 & 1/G_{31} & 0 \\ 0 & 0 & 0 & 0 & 0 & 1/G_{12} \end{bmatrix} \tag{20.3.3}$$

For an orthotropic material, the compliance matrix can be expressed in terms of 12 components, 9 of which are independent. The additional symmetry of the transverse isotropic model results in a further simplification with

$$E_1 = E_2,\ \nu_{12} = \nu_{21},\ \nu_{13} = \nu_{31},\ G_{23} = G_{31},\ E_1 = 2G_{12}\,(1 + \nu_{12}) \tag{20.3.4}$$

The anisotropy of bone requires that it is tested in several directions in order to determine all of the independent elastic coefficients. Table 20.3.2 provides experimentally obtained transverse isotropic material constants for cortical bone from the human femur (Reilly and Burstein 1975).

Soft Tissue Mechanics

The biomechanical properties of soft tissues depend on both the chemical composition and the structure of the tissue. Most soft tissue structures within the body demonstrate aspects of nonhomogeneous, anisotropic, nonlinear viscoelastic behavior. Given the complexity of the constitutive equations and testing *in-vivo*, the material properties are difficult to measure. To simplify the test procedures, homogeneity and linearity are frequently assumed.

The simplest representation of viscoelastic material behavior uses combinations of discrete models consisting of linear springs and dashpots: the Maxwell model and the Kelvin (or Voigt) model. While these models are generally linear approximations of the nonlinear behavior of biological materials, they can often describe material behavior with reasonable accuracy and can help to visualize tissue behavior.

For improved characterization of the soft tissue response, Fung (1993) developed an approximate theory that was based on the theory of linear viscoelasticity but incorporated nonlinear stress-strain characteristics. More complex nonlinear viscoelastic models can provide additional improvements in describing tissue response but require extensive experimental testing to determine the model coefficients.

TABLE 20.3.3 Physical and Biomechanical Properties of Human Articular Cartilage

Density (kg/m^3)	Ultimate Tensile Strength (MPa)	Ultimate Elongation (%)	Tensile Modulus (MPa)	Indentation Stiffness (MPa)	Poisson's Ratio	References
1300	2–40[a]	60–120[b]	3–224[a, c]	4.8–8.4[d]	0–0.4[e]	20,24,29,50,56

[a] Specimens from the superficial and mid-depth cartilage layers of the human femoral head and talus loaded in the direction of the predominant alignment of the collagen fibers in the superficial layer.

[b] Bovine articular cartilage specimens from the superficial, mid-depth, and deep zone layers loaded in the directions of 0, 45, and 90° from the axis of split-line patterns.

[c] Calculated as the slope of the stress-strain curve at Lagrangian stresses of 1 and 10 MPa.

[d] From in-vivo indentation testing on arthroscopy patients.

[e] Applies to the solid matrix of articular cartilage.

Cartilage

In most joints of the body, the ends of the articulating bones are covered with a dense connective tissue known as hyaline articular cartilage. The cartilage is composed of a composite organic solid matrix that is swollen by water (75% by volume). The cartilage serves to distribute load in the joints and to allow relative movement of the joint surfaces with minimal friction and wear. The coefficient of friction for articular cartilage in human synovial joints has been reported to be in the range 0.005 to 0.04 (Mow and Soslowsky 1991).

Some physical and biomechanical properties of articular cartilage are summarized in Table 20.3.3. The experiment of preference for the testing of articular cartilage has historically been the indentation test. Analysis of the test results has used elastic contact theory, the correspondence principle, and the assumption of material incompressibility ($\nu = 0.5$). This analysis ignores the nonhomogeneous and directional properties of articular cartilage and does not take into account considerable finite deformational effects or the flow of the interstitial fluid relative to its porous permeable solid matrix. More recent models of cartilage have used bi-phasic (an elastic solid and a fluid phase) or tri-phasic approach to describe more accurately the mechanical response of cartilage.

Muscle

Three types of muscle comprise the muscular system: cardiac muscle, smooth or involuntary muscle, and skeletal or voluntary muscle. The focus of this section will be on the skeletal muscle used to maintain the body's posture and to provide movement of the body's segments. The response of skeletal muscle is determined by a combination of active and passive components. The force exerted by a muscle is dependent on the length at which it is stimulated, on the velocity of contraction, on the duration of contraction, and on such factors as fatigue, temperature, and prestretching. A general estimate of the strength of the muscle assumes that its strength is proportional to the physiologic cross-sectional area, defined as the muscle volume divided by its true fiber length. The average unit force per cross-sectional area that is exerted by a muscle ranges from 20 to 80 N/cm^2. For more precise calculations, the relationship between the maximum force of muscle and instantaneous rate of change of its length must be considered. Hill's equation is an empirical relationship expressing the rate of muscle shortening as a function of the isotonic force

$$V = \frac{b\left(F_0 - F\right)}{F + a} \quad \text{or} \quad F = \frac{F_0 b - av}{b + v} \qquad (20.3.5)$$

where V is the velocity of shortening, F_0 is the force at zero velocity (isometric condition), and F is the instantaneous force. The constants a and b have units of force and velocity, respectively, and are determined empirically using relationship 20.3.6.

TABLE 20.3.4 Biomechanical Properties of Human Ligaments and Tendons[a]

Tissue	Ultimate Tensile Strength (MPa)	Ultimate Elongation (%)	Tensile Modulus (MPa)	References
Ligament	7.4–52.7	5–44	65.3–1060	5,15,25,27,30,36,37,39,42–45,52
Tendon, patellar	17–78	14–31	239–660	3–5,14,23,40

[a] All values obtained in tests in which the ligament and tendon specimens were loaded in the longitudinal direction (the direction of the predominant alignment of the collagen fibers)

$$K = \frac{a}{F_0} = \frac{b}{V_{\max}} \tag{20.3.6}$$

where $V_{\max} = bF_0/a$, the shortening velocity against no load. For most muscles, the range of the muscle constant is $0.15 < K < 0.25$ (McMahon 1987).

Tendons and Ligaments

Tendons and ligaments are connective tissues composed primarily of collagen fibers and are normally loaded in tension. Tendons transmit forces from muscles to bone in order to

- Execute joint motion
- Store energy

Ligaments attach articulating bones across a joint in order to

- Guide joint movement
- Limit the joint range of motion
- Maintain joint congruency
- Assist in providing joint stability

The biomechanical properties of ligaments and tendons are summarized in Table 20.3.4.

The general stress-strain behavior of connective soft tissue can be represented by four distinct loading regions (Figure 20.3.2). Region I is commonly referred to as the “toe region” and is associated with the straightening or alignment of the randomly ordered structural fibers. Most physiologic loading occurs in this region where there is a small increase in stress for a given increase in strain. Region II characterizes the linear region where the straightened fibers are more uniformly loaded. The tangent to the stress-strain response curve in this linear region is frequently referred to as the elastic stiffness or tensile modulus

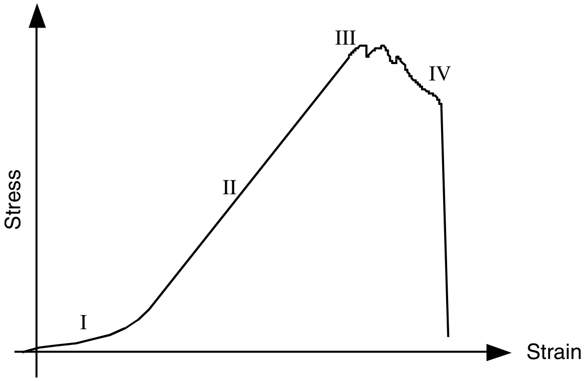

FIGURE 20.3.2 General stress–strain behavior of connective soft tissue.

rather than the elastic modulus in order to emphasize that the soft tissue is not truly behaving as a perfectly elastic material. At the initiation of Region III, small fluctuations in the stress can be observed resulting from microfailures in the soft tissue. The final loading profile, shown in Region IV, exhibits catastrophic failure of the soft tissue.

Factors Affecting Biomechanical Properties

Due to the nature of biological testing, a great deal of variability in the material properties of tissue is evident in the published literature. Unlike traditional engineering materials, there are no standard protocols or procedures for the testing of biological materials. Although some variability can be attributed to differences in the experimental approaches undertaken by the researchers, mechanical behavior of biological materials can also be affected by

- Geometric characteristics
- Loading mode (i.e., tension, compression, torsion)
- Rate and frequency of loading
- Specimen preparation (i.e., temperature, preservation method, hydration)
- Age or health of specimen donor
- Gender
- Temperature
- Anatomical location of load and specimen
- Species

Rate of Loading. All biological materials show, to some extent, viscoelastic material properties, which means that they demonstrate increased stiffness and strength with increased loading rate. Several experimental studies have reported that the stiffness and strength of human cortical and cancellous bone are approximately proportional to the strain rate raised to the power of 0.05 to 0.07 and 0 to 0.07, respectively (McElhaney 1966; Carter and Hayes 1976, 1977; Carter and Caler 1983; Linde et al. 1991; Ouyang et al. 1997). In addition to influencing the material properties, the rate of loading can also affect the patterns of failure of biological materials.

Loading Mode. The stress-strain behavior of biological materials is highly dependent on the orientation of the tissue structure with respect to the direction of loading (Table 20.3.5). Many tissues, such as cortical bone, tendon, and muscles, have organized structures that result in anisotropy of the physical properties. In some cases, the anisotropy exists but due to the complexity and increased variability of the data, it is not incorporated in the constitutive model or experiments.

Anatomic Location. Although homogeneity is often assumed, biological tissues typically exhibit significant differences in material properties depending on the anatomic location. Table 20.3.6 illustrates the variability of material properties with anatomic location using the human meniscus.

TABLE 20.3.5 Material Properties Variation in Human Femoral Cortical Bone Due to Specimen Orientation and Loading Mode

Orientation	Loading Mode	Elastic Modulus (GPa)	Ultimate Strength (MPa)	Ultimate Strain (%)
Longitudinal	Tension	17.4	133	3.1
	Compression	18.2	193	1.9
	Shear	3.3	68	0.33[a]
Transversal	Tension	12.7	51	0.7
	Compression	11.7	133	5.8

[a] Value is in radians and is according to Cowin et al. (1987).
Source: Reilly and Burstein (1975)

TABLE 20.3.6 The Variability of the Tensile Modulus (E) of Human Meniscus with Anatomical Location

Anatomic Location	Medial Anterior	Medial Central	Medial Posterior	Lateral Anterior	Lateral Central	Lateral Posterior
E (MPa)	159.6	93.2	110.2	159.1	228.8	294.1

Source: Mow et al. (1991)

TABLE 20.3.7 Ratio of Age Changes for Ultimate Tensile Strength of Various Human Tissues

Tissue	10–19 years	20–29 years	30–39 years	40–49 years	50–59 years	60–69 years	70–79 years
Femoral cortical bone	0.93	1.00	0.98	0.91	0.76	0.70	0.70
Costal cartilage	1.02	1.00	0.93	0.80	0.56	0.33	0.29
Muscle tissue (Rectus Abdominis)	1.27	1.00	0.87	0.73	0.67	0.60	0.60
Calcaneal tendinous tissue	1.00	1.00	1.00	1.00	1.00	0.95	0.78
Skin	1.00	1.00	1.54	1.54	1.40	1.27	1.07

Source: Yamada (1970)

Age. The material properties of biological materials can vary depending on whether the specimens are obtained from immature, mature, or aging tissue. In general, the ultimate strength of tissues decreases with increasing age. Bone, cartilage, muscle, tendon, and ligaments all show decreases in the ultimate strength and elastic moduli after maturity with increasing age (Table 20.3.7). Several tissues, such as skin and teeth, are exceptions to this general rule and can exhibit increases in some material properties with age.

Storage/Preservation. The increasing complexity of biomechanical testing requires a considerable period of time for each individual test and necessitates tissue storage and preservation. It is essential to ensure that the storage and preservation of biological materials are controlled so that the material property measurements in the laboratory accurately reflect the properties of the tissue in the living state. Biological materials are preserved using one of three methods depending on the required storage interval:

- Refrigeration for short-term storage
- Freezing for long-term storage
- Embalming for long-term storage

Refrigeration and freezing have virtually no effect on the properties of bone tissue. The effects of refrigeration on soft tissue properties, however, are tissue dependent. Freezing of soft tissue can cause ice cavities that disrupt the tissue architecture and result in property changes. The effects of embalming on soft and bone tissue structures exhibit conflicting results depending on the embalming technique, concentrations, duration, and tissue type.

Because many biological materials are composed primarily of water, humidity strongly influences the stress-strain relationships (Table 20.3.8). Therefore, care must be taken to keep biological specimens moist prior to and during testing. The control of the moisture level of specimens is most important when

TABLE 20.3.8 Comparison of Material Properties Between Wet and Dry Tibial Cortical Bone from Humans 20–39 Years of Age

Test Condition	Ultimate Tensile Strength (MPa)	Ultimate Elongation (%)	Elastic Modulus (GPa)
Wet	140.3 ± 1.2	1.50	18.1
Dry	170.7 ± 1.2	1.29	20.6

Source: Yamada (1970)

TABLE 20.3.9 Comparison of Physical and Biomechanical Properties of Bone Specimens Obtained from Different Species

Tissue	Tissue Source	Volumetric Bone Mineral Density (mg/cm^3)	Ultimate Compressive Strength (MPa)	Young's Modulus (GPa)	Calcium Content (mgCa/g dry bone)
Vertebral cancellous bone	Human	178	1.21		
	Dog	340	6.12		
	Pig	373	2.40		
	Cow	449	5.67		
	Sheep	437	13.22		
Femoral and/or tibial cortical bone	Alligator			12.0 ± 2.4	252.9 ± 13.2
	Cow			18.5 ± 2.8	296.8 ± 14.7
	Fallow deer			26.8 ± 3.7	274.1 ± 8.3
	Horse			21.2 ± 1.9	267.8 ± 8.8
	Wallaby			18.7 ± 2.7	274.1 ± 6.0

Sources: Aerssens et al. (1998) and Currey (1988).

analyzing the elastic properties of surface tissues such as skin and hair. Young's modulus of skin at 25% to 30% relative humidity may be 1000-fold greater than that at 100% humidity (Duck 1990).

Species. Animal tissues have been used extensively in biomechanical testing due to their availability. When extrapolating results to humans, care must be taken since significant differences can exist in the structure and material properties between humans and animals due to physiologic and anatomic differences. Table 20.3.9 shows a comparison of some physical and biomechanical properties of bone specimens obtained from human and different animals.

Human Body Vibrations

The human body treated as a viscoelastic mechanical system possesses natural frequencies and accompanying resonant responses. Standards (primarily ISO) are available for determining whole body vibrations and for measuring and predicting the health effects of these vibrations (Griffen 1998). Typically the vibration characteristics of the whole human body are obtained with a person on a shake table (Wei and Griffen 1998). Numerous models, mostly lumped mass models, have been developed to represent the dynamics of humans (Smith 2000). Normally, a shake table is used for studying whole body vibrations, whereas analytical models often are employed to study body part dynamics. The human resonant frequencies found in the literature vary widely, largely because of the variability of human subjects, the difficultly of identifying biofidelic models, and the inaccessibility of many body parts. Some natural frequency ranges for the human body are provided in Table 20.3.10. The values in this table should be treated as being approximate, since the dynamics of internal organs is complex and the results depend on many factors, including the orientation of the person subjected to the excitation (von Gierke and Brammer, 1998).

The interaction of the human and a structure is of major concern since activating a resonant vibration in the human can have adverse effects (Table 20.3.11). For example, both the performance of a machine and the health of its operator depend on the proper control of the dynamic characteristics of the system. A vibration isolator needs to account for the biomechanical properties of the human as well as the dynamic properties of the structure, perhaps over a wide frequency range (Frolov and Furman, 1990 and Balandin et al. 2001).

Impact Biomechanics

The prevention of injury through the development of countermeasures is most effectively achieved through biomechanical testing and analysis. The prevalence of injuries resulting from motor vehicle

TABLE 20.3.10 Resonant Frequencies of the Human Body

Organ	Resonant Frequencies
Whole Body	
Vertical	
Sitting	4–6 Hz
Standing	6–15 Hz
Horizontal on rigid slab	
Longitudinal	1–3.5 Hz
Head	8–40 Hz
Eyes	12–17 Hz
Face and Jaws	4–27 Hz
Throat	6–27 Hz
Chest	2–12 Hz
Lumbar portion of spinal column	4–14 Hz
Shoulders	4–8 Hz
Lungs	4–8 Hz
Abdomen	4–12 Hz
Hands, feet	2–8 Hz
Arms with hands	20–70 Hz

Sources: Frolov and Furman (1990), Sachse et al. (2003), Duarte et al. (2003), von Gierke and Brammer (1998)

TABLE 20.3.11 Vibration Frequency Effects on Humans

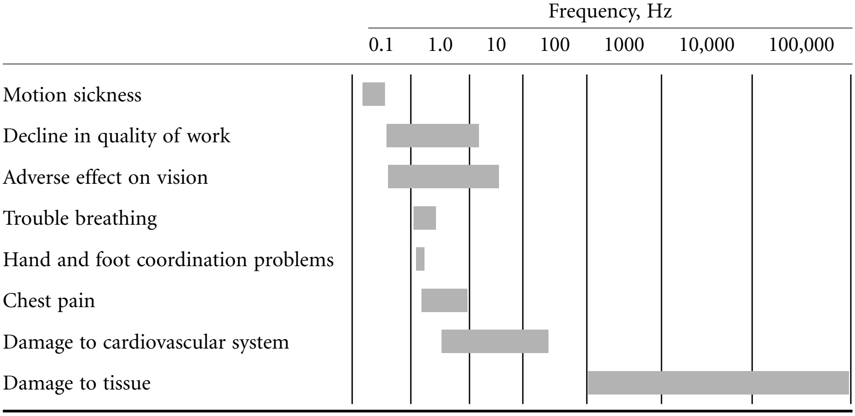

Sources: Frolov and Furman (1990), von Gierke and Brammer (1998)

crashes, sporting activities, and industrial accidents has led to the development of a branch of biomechanics referred to as *impact biomechanics*. In order to achieve the principal aims of prevention of injury through environmental modification, this branch of biomechanics must develop an improved understanding of the mechanisms of injury, descriptions of the mechanical response of the biological materials involved, and information on the human tolerance to impact. Injury criteria for the human body as interpreted by the 50th percentile adult male Hybrid III anthropometric crash test dummy are provided in Table 20.3.12. The injury criteria are provided in terms of engineering parameters of resultant acceleration $a(t)$, displacement $s(t)$, force $F(t)$, and moment $M(t)$.

Computational Biomechanics

Computational mechanics provides a versatile means of analyzing biomechanical systems. Modeling uses either rigid body models composed of rigid masses, springs, joints, and contact surfaces or flexible body models with finite or boundary elements (Table 20.3.13). Software is now available that incorporates the

TABLE 20.3.12 Injury Criteria for the Automotive Impact Environment as Specified for the 50th Percentile Adult Male Crash Test Dummy Hybrid III in Federal Motor Vehicle Safety Standard No. 208

Body Region	Injury Criterion	Formulation	Threshold
Head	Head Injury Criterion (HIC)[a]	$\mathrm{HIC} = (t_2 - t_1)\left[\frac{1}{(t_2 - t_1)}\int_{t_1}^{t_2} a(t)\,dt\right]^{2.5}$	1000/700
Chest	Resultant thoracic acceleration	$a(t)$	60 g[b]
	Compressive deflection of the sternum relative to the spine	$s(t)$	63 mm[c]
Neck	$\mathrm{N_{ij}}$	$N_{ij}(t) = (F_z(t)/F_{zc}(t)) + (M_y(t)/M_{yc}(t))$[d]	1.0
	Peak tension force	$F_z(t)$	4170 N
	Peak compression force	$F_z(t)$	4000 N

[a] t_1 and t_2 are any two points in time ($t_2 > t_1$) separated by no more than 36 ms (threshold = 1000) or 15 ms (threshold = 700). In the formulation for *HIC*, the acceleration $a(t)$ must be expressed in g.

[b] $a(t)$ may exceed 60 g for intervals whose cumulative duration is not more than 3 ms.

[c] The current version of FMVSS 208 includes the proposed value of 63 mm and the old value of 76 mm.

[d] $F_{zc} = 6806$ N when $F_z > 0$. $F_{zc} = -6160$ N when $F_z < 0$. $M_{yc} = 310$ Nm when $M_y > 0$ (when a flexion moment exists at the occipital condyle). $M_{yc} = -135$ Nm when $M_y < 0$ (when an extension moment exists at the occipital condyle).

TABLE 20.3.13 Comparison of Rigid Body and Finite Element Modeling Methods

Model Characteristics	Multibody Model	Finite Element Method
Complexity	Relatively simple	Relatively complex
Fidelity	Requires engineering intuition	Can achieve high fidelity
Efficiency	Efficient	Computationally expensive
Model elements	Springs, point masses, rigid bodies, ellipsoids, joints, and contact planes	Flexible elements: bricks, beams, plates, shells

two modeling techniques and uses multibody modeling to capture overall kinematics of a biomechanical system and flexible body modeling to provide an in-depth study of those regions of particular interest.

The complexity of biological systems and limited constitutive model data often requires simplifying assumptions be made during the development of models. Therefore, it is necessary to verify the model before conducting parametric and sensitivity studies.

References

1. Aerssens, J., Boonen, S., Lowet, G. and Dequeker, J. 1998. Interspecies differences in bone composition, density, and quality: potential implications for *in vivo* bone research. *Endocrinology* 139(2), 663–670.
2. Balandin, D.V., Bolotnik, N.N., and Pilkey, W.D. 2001. *Optimal Protection from Impact, Shock, and Vibration.* Taylor and Francis, Philadelphia.
3. Blevins, F.T., Hecker, A.T., Bigler, G.T., Boland, A.L., and Hayes, W.C. 1994. The effects of donor age and strain rate on the biomechanical properties of bone-patellar tendon-bone allografts. *American Journal of Sports Medicine* 22(3), 328–333.
4. Butler, D.L., Grood, E.S., Noyes, F.R., Zernicke, R.F., and Brackett,K. 1984. Effects of structure and strain measurement technique on the material properties of young human tendons and fascia. *Journal of Biomechanics* 17(8), 579–596.
5. Butler, D.L., Kay, M.D. and Stouffer, D.C. 1986. Comparison of material properties in fascicle-bone units from human patellar tendon and knee ligaments. *Journal of Biomechanics* 19(6), 425–32.

6. Carter, D.R. and Hayes, W.C. (1976) Bone compressive strength: the influence of density and strain rate. *Science* 194(4270), 1174–1176.
7. Carter, D.R. and Hayes, W.C. 1977. The compressive behavior of bone as a two–phase porous structure. *Journal of Bone and Joint Surgery—American Volume* 59(7), 954–962.
8. Carter, D.R. and Caler, W.E. 1983. Cycle-dependent and time-dependent bone fracture with repeated loading. *Journal of Biomechanical Engineering* 105(2), 166–170.
9. Cowin, S.C., Van Buskirk, W.C., and Ashman, R.B. 1987. Properties of Bone. In *Handbook of Bioengineering*. R. Skalak and S. Chien (eds.). McGraw-Hill, New York, 2.1–2.27.
10. Currey, J.D. 1988. The effect of porosity and mineral content on the Young's modulus of elasticity of compact bone. *Journal of Biomechanics* 21(2), 131–139.
11. Duarte, M.L.M. and Filho, L.E. 2003. Perception Threshold's Experimental Evaluation of a Population Subject to Sinusoidal Vibration. In *Proc. X International Symposium on Dynamic Problems of Mechanics*. P.R.G. Kurka and A.T. Fluery (eds.). Brazilian Society of Engineering and Mechanical Sciences, Ubatuba, SP, Brazil.
12. Duck, F.A. 1990. *Physical Properties of Tissue*. Academic Press, San Diego, CA.
13. Federal Motor Vehicle Safety Standard (FMVSS) No. 208; Occupant crash protection. http://www.access.gpo.gov/nara/cfr/waisidx_00/49cfr571_00.html (accessed: 09/04/03).
14. Flahiff, C.M., Brooks, A.T., Hollis, J.M., Vander Schilden, J.L., and Nicholas, R.W. 1995. Biomechanical analysis of patellar tendon allografts as a function of donor age. *American Journal of Sports Medicine* 23(3), 354–358.
15. Fremerey, R., Bastian, L., and Siebert, W.E. 2000. The coracoacromial ligament: anatomical and biomechanical properties with respect to age and rotator cuff disease. *Knee Surgery, Sports Traumatology, Arthroscopy* 8(5), 309–313.
16. Frolov, K.V. and Furman, F.A. 1990. *Applied Theory of Vibration Isolation Systems*. Hemisphere Publishing Corporation, Washington, DC.
17. Fung, Y.C. 1993. *Biomechanics: Mechanical Properties of Living Tissues*, 2nd ed., Springler–Verlag, New York.
18. Gomez, M.A. and Nahum A.M. 2002. Biomechanics of bone. In *Accidental Injury*: *biomechanics and prevention*. A. M. Nahum and J. W. Melvin (eds.). Springer Verlag, New York, 206–227.
19. Griffen, M.J. 1998. A comparison of standardized methods for predicting the hazards of whole–body vibration and repeated shocks. *Journal of Sound and Vibration* 215(4), 883–914.
20. Hasler, E.M., Herzog, W., Wu, J.Z., Muller, W., and Wyss, U. 1999. Articular cartilage biomechanics: theoretical models, material properties, and biosynthetic response. *Critical Reviews in Biomedical Engineering* **27**(**6**), 415–488.
21. Hayes, W.C. 1991. Biomechanics of cortical and trabecular bone: implications for assessment of fracture risk. In *Basic Orthopaedic Biomechanics*. V.C. Mow and W.C. Hayes (eds.). Raven Press, New York, 93–142.
22. Hirsch, C. and Evans, F.G. 1965. Studies on some physical properties of infant compact bone. *Acta Orthopaedica Scandinavica* 35, 300–313.
23. Johnson, G.A., Tramaglini, D.M., Levine, R.E., Ohno, K., Choi, N.Y., and Woo, S.L. 1994. Tensile and viscoelastic properties of human patellar tendon. *Journal of Orthopaedic Research* 12(6), 796–803.
24. Kempson, G.E. 1991. Age-related changes in the tensile properties of human articular cartilage: a comparative study between the femoral head of the hip joint and the talus of the ankle joint. *Biochimica et Biophysica Acta* 1075(3), 223–230.
25. Kennedy, J.C., Hawkins, R.J., Willis, R.B., and Danylchuck, K.D. 1976. Tension studies of human knee ligaments. Yield point, ultimate failure, and disruption of the cruciate and tibial collateral ligaments. *Journal of Bone and Joint Surgery—American Volume* 58(3), 350–355.
26. Kopperdahl, D.L. and Keaveny, T.M. 1998. Yield strain behavior of trabecular bone. *Journal of Biomechanics* 31(7), 601–608.

27. Lee, T.Q., Dettling, J., Sandusky, M.D., and McMahon, P.J. 1999. Age related biomechanical properties of the glenoid-anterior band of the inferior glenohumeral ligament-humerus complex. *Clinical Biomechanics* 14(7), 471–476.
28. Linde, F., Norgaard, P., Hvid, I., Odgaard, A., and Soballe, K. 1991. Mechanical properties of trabecular bone. Dependency on strain rate. *Journal of Biomechanics* 24(9), 803–809.
29. Lyyra, T., Kiviranta, I., Vaatainen, U., Helminen, H.J., and Jurvelin, J.S. 1999. In vivo characterization of indentation stiffness of articular cartilage in the normal human knee. *Journal of Biomedical Materials Research* 48(4), 482–87.
30. Marinozzi, G., Pappalardo, S., and Steindler, R. 1983. Human knee ligaments: mechanical tests and ultrastructural observations. *Italian Journal of Orthopaedics and Traumatology* 9(2), 231–240.
31. McCalden, R.W., McGeough, J.A., Barker, M.B., and Court-Brown, C.M. 1993. Age-related changes in the tensile properties of cortical bone. The relative importance of changes in porosity, mineralization, and microstructure. *Journal of Bone and Joint Surgery — American Volume* 75(8), 1193–1205.
32. McElhaney, J.H. 1966. Dynamic response of bone and muscle tissue. *Journal of Applied Physiology* 21(4), 1231–1236.
33. McMahon, T. A. 1987. Muscle mechanics. In *Handbook of Bioengineering*. R. Skalak and S. Chien (eds.). McGraw–Hill, New York, 7.1–7.26.
34. Mow, V.C., Wenbo, Z., and Ratcliffe, A. 1991. Structure and function of articular cartilage and meniscus. In *Basic Orthopaedic Biomechanics*. V.C. Mow and W.C. Hayes (eds.). Raven Press, New York, 143–198.
35. Mow, V.C. and Soslowsky, L.J. 1991. Friction, Lubrication, and wear of diarthrodial joints. In *Basic Orthopaedic Biomechanics*. V.C. Mow and W.C. Hayes (eds.). Raven Press, New York, 245–292.
36. Neumann, P., Keller, T.S., Ekström, L., Perry, L., Hansson, T.H., and Spengler, D.M. 1992. Mechanical properties of the human lumbar anterior longitudinal ligament. *Journal of Biomechanics* 27(1), 13–24.
37. Neumann, P., Ekström, L.A., Keller, T.S., Perry, L., and Hansson, T.H. 1994. Aging, vertebral density, and disc degeneration alter the tensile stress-strain characteristics of the human anterior longitudinal ligament. *Journal of Orthopaedic Research* 12(1), 103–112.
38. Nigg, B.M. and Grimston, S.K. 1994. Bone. In *Biomechanics of the Musculo*-skeletal *System*. B. M. Nigg and W. Herzog (eds.). John Wiley and Sons, Chichester, England, 48–78.
39. Noyes, F.R. and Grood, E.S. 1976. The strength of the anterior cruciate ligament in humans and Rhesus monkeys. *Journal of Bone Joint Surgery—American Volume* 58(8), 1074–1082.
40. Noyes, F.R., Butler, D.L., Grood, E.S., Zernicke, R.F. ,and Hefzy, M.S. 1984. Biomechanical analysis of human ligament grafts used in knee–ligament repairs and reconstructions. *Journal of Bone and Joint Surgery—American Volume* 66(3), 344–352.
41. Ouyang, J., Yang, G.T., Wu, W.Z., Zhu, Q.A., and Zhong, S.Z. 1997. Biomechanical characteristics of human trabecular bone. *Clinical Biomechanics* 12(7/8), 522–524.
42. Prietto, M.P., Bain, J.R., Stonebrook, S.N., and Settlage, R. A. 1988. Tensile strength of the human posterior cruciate ligament (PCL). *Transactions of the Orthopaedic Research Society* 13, 195.
43. Quapp, K.M. and Weiss, J.A. 1998. Material characterization of human medial collateral ligament. *Journal of Biomechanical Engineering* 120(6), 757–763.
44. Race, A. and Amis, A.A. 1994. The mechanical properties of the two bundles of the human posterior cruciate ligament. *Journal of Biomechanics* 27(1), 13–24.
45. Rauch, G., Allzeit, B., and Gotzen, L. 1988. Biomechanische Untersuchungen zur Zugfestigkeit des vorderen Kreuzbandes unter besonderer Berücksichtigung der Altersabhängigkeit. *Unfallchirurg* 91(10), 437–443.
46. Reilly, D.T., Burstein, A.H., and Frankel, V.H. 1974. The elastic modulus for bone. *Journal of Biomechanics* 7(3), 271–275.
47. Reilly, D.T. and Burstein, A.H. 1975. The elastic and ultimate properties of compact bone tissue. *Journal of Biomechanics* 8(6), 393–405.

48. Røhl, L., Larsen, E., Linde, F., Odgaard, A., and Jørgensen J. 1991. Tensile and compressive properties of cancellous bone. *Journal of Biomechanics* 24(12), 1143–1149.
49. Sachse, R., Pavic, A., and Reynolds, P. 2003. Human-structure dynamic interaction in civil engineering dynamics: a literature review. *Shock and Vibration Digest* 35(1), 3–18.
50. Shrive, N.G. and Frank, C.B. 1994. Articular cartilage. In *Biomechanics of the Musculo–skeletal System*. B.M. Nigg and W. Herzog (eds.). John Wiley and Sons, Chichester, England, 79–105.
51. Smith, S.D. 2000. Modeling differences in the vibration response characteristics of the human body. *Journal of Biomechanics* 33, 1513–1516.
52. Stabile, K.J., Pfaeffle, H.J., Weiss, J.A., Gabriel, M.T., Tomaino, M.M., and Fischer, K.J. 2001. Longitudinal and transverse mechanical properties of the interosseous ligament of the forearm. In *Proc. ASME Bioengineering Conference*, BED-vol. 50, 363–364.
53. Vinz, H. 1969. Die festigkeitsmechanischen Grundlagen der typischen Frakturformen des Kindesalters. *Zentralblatt für Chirurgie* 94(45), 1509–1515.
54. von Gierke, H.E. and Brammer, A.J. 1998. Chapter 44: Effects of Shock and Vibration on Humans. In *Shock and Vibration Handbook.* 4th ed., McGraw-Hill, New York.
55. Wei, L. and Griffen M. J. 1998. Mathematical models for the apparent mass of the seated human body exposed to vertical vibration. *Journal of Sound and Vibration* 212(5), 855–874.
56. Woo, S. L-Y., Mow, V.C. and Lai, W.M. 1987 Biomechanical properties of articular cartilage. In *Handbook of Bioengineering*. R. Skalak and S. Chien (eds.). McGraw-Hill, New York, 4.1–4.44.
57. Yamada, H. 1970. *Strength of Biological Materials.* F.G. Evans (ed.). Williams & Wilkins Co., Baltimore, MD.

20.4 Mechanical Engineering Codes and Standards

Michael Merker

What Are Codes and Standards?

A **standard** can be defined as a set of technical definitions, requirements, and guidelines for the uniform manufacture of items; safety; and/or interchangeability. A **code** is a standard that is, or is intended to be, adopted by governmental bodies as one means of satisfying legislation or regulation. Simply put, standards can range from a general set of minimum requirements to very specific "how-to" instructions for designers and manufacturers.

Voluntary standards, which can run from a few paragraphs to hundreds of pages, are written by experts who sit on the many committees administered by standards-developing organizations (SDOs), such as ASME International. They are not considered voluntary because they are created by volunteers; rather, they are voluntary because they serve as guidelines but do not of themselves have the force of law. ASME International publishes its standards, accredits users of standards to ensure that they have the capability of manufacturing products that meet those standards, and provides a stamp that accredited manufacturers may place on their products, indicating that they were manufactured according to the standard. ASME International cannot, however, force any manufacturer, inspector, or installer to follow ASME International standards. Their use is voluntary.

Why are voluntary standards effective? Perhaps the American Society for Testing and Materials (ASTM) said it best in its 1991 annual report: "Standards are a vehicle of communication for producers and users. They serve as a common language, defining quality and establishing safety criteria. Costs are lower if procedures are standardized; training is also simplified. And consumers accept products more readily when they can be judged on intrinsic merit."

A dramatic example of the value and impact codes and standards have had on our society is provided by ASME International's Boiler and Pressure Vessel Code. Toward the end of the nineteenth century, boilers of every description, on land and at sea, were exploding with terrifying regularity for want of reliably tested materials, secure fittings, and proper valves. They would continue to do so into the twentieth century. Engineers could take pride in the growing superiority of American technology, but they could not ignore the price of 50,000 dead and 2 million injured by accidents annually.

The mechanical engineers who tackled the problems in 1884 began by seeking reliable methods for testing steam boilers. The need for the establishment of universally accepted construction standards would take many more years and resulted in the first edition of the Boiler and Pressure Vessel Code being published by ASME International in 1915.

Codes and Standards—Related Accreditation, Certification, and Registration Programs

Accreditation

Shortly after the Boiler Code was first published, the need emerged for a recognizable symbol to be affixed to a product constructed in accordance with the standards. ASME International commissioned appropriate seals that are now the internationally acknowledged symbols of the society. The symbol is stamped onto the product.

But how does a manufacturer obtain permission to use one of the symbols? Through the ASME International **accreditation** process, the manufacturer's quality control process is reviewed by an ASME International team. If the quality control system meets the requirements of the applicable ASME International code or standard and the manufacturer successfully demonstrates implementation of the program, the manufacturer is accredited by ASME International. This means that the manufacturer may certify the product as meeting ASME International standards and may apply the stamp to the product.

The stamp consists of a modified cloverleaf (from the shape of the ASME International logo), with letter(s) in the center. The letter(s) indicate the code or section of the code met by the product upon which it is placed. Boiler and pressure vessel stamps issued are

A — Assembly of Power Boilers
E — Electric Boilers
H — Heating Boilers, Steel Plate, or Cast-Iron Sectional
HV — Heating Boiler Safety Valves
HLW — Lined Potable Water Heaters
M — Miniature Boilers
N — Nuclear Components
NPT — Nuclear Component Partial
NA — Nuclear Installation/Assembly
NV — Nuclear Safety and Pressure Relief Valves
PP — Pressure Piping
RP — Fiber-Reinforced Plastic Pressure Vessels
S — Power Boilers
U, U2, U3 — Pressure Vessels
UD — Rupture Disk Devices
UM — Miniature Pressure Vessels
UV, UV3 — Pressure Vessel Safety Valves
V — Boiler Safety Valves

ASME International also has accreditation programs for nuclear materials, authorized inspection agencies, organizations that certify elevator inspectors, and reinforced thermoset plastic corrosion-resistant vessels.

Certification

ASME International has also expanded its scope of activity to cover **certification** of individuals. The first program became available in 1992 and covered the qualification and certification of resource-recovery facilities operators. It has since added programs to cover operators of hazardous waste incinerators, medical waste incinerators, and fossil fuel–fired plants. A program to certify an individual's knowledge and ability in the area of geometric dimensioning and tolerancing has also been added.

Registration

Registration is similar to accreditation; however, it is the term used more frequently in the international arena, particularly when dealing with the International Organization for Standardization (ISO) 9000 program on quality assurance systems. ASME International's ISO 9000 Registration Program has been accredited by the American National Accreditation Program for Registrars of Quality Systems (ANSI-RAB) and the Dutch Council for Certification (RvC) in the following industrial sectors:

Primary metals industries
Fabricated metal products
Industrial and commercial machinery and equipment
Reinforced thermoset plastic tanks and vessels
Engineering services

How Do I Get Codes and Standards?

Role of ASME International in Mechanical Engineering Standards

ASME International is a nonprofit educational and technical organization with more than 125,000 members, most of whom are practicing engineers. About 20,000 are students. ASME International has a wide variety of programs: publishing, technical conferences and exhibits, engineering education, government relations, and public education, as well as the development of codes and standards, all aimed at serving the engineering profession, the public, industry, and government.

The ASME International Board of Governors has delegated the codes and standards activity to a 22-member Council on Codes and Standards, which directs all aspects of the program. Under the Council are ten boards, also made up of ASME International members and other interested persons; supervisory boards in turn oversee committees, each responsible for a specific area of standard development.

Committees in one form or another have dealt with standards since the first test code in 1884. Currently, there are more than 100 main committees dealing with over 600 standards that are under regular review and revision. Once a standard is accepted, it is printed and made available to manufacturers, regulatory agencies, designers — anyone with an interest in that particular subject. Close to 3800 individuals serve on these committees and their subcommittees, subgroups, and working groups.

After a standard has been considered and reconsidered at meetings and through many drafts, it is sent to the main committee, representing all interests, which votes on the standard. But this is not the final step. Before the draft becomes a standard and is published and ready for distribution, it is made available for public comment and must be approved by the appropriate ASME International supervisory board. This process is illustrated graphically in Figure 20.4.1. ASME International has been a consistent supporter of the policy of prior announcement of meetings, open meeting rooms, **balanced committees**, public announcements and reviews, appeal mechanisms, and overall procedural **due process**.

Role of ANSI in These and Other Related Standards

In 1911, ASME International was one of a number of organizations that recommended the establishment of an organization to help eliminate conflict and duplication in the development of voluntary standards in the U.S. Such an organization was formed in 1918 and is currently known as the American National Standards Institute (ANSI). ANSI is the U.S. member of the ISO and the administrator of the U.S. National Committee of the International Electrotechnical Committee (IEC). The intent of obtaining ANSI approval of a standard is to verify that in establishing the standard, the originating organization has followed principles of openness and due process and has achieved a consensus of those directly affected by the standard.

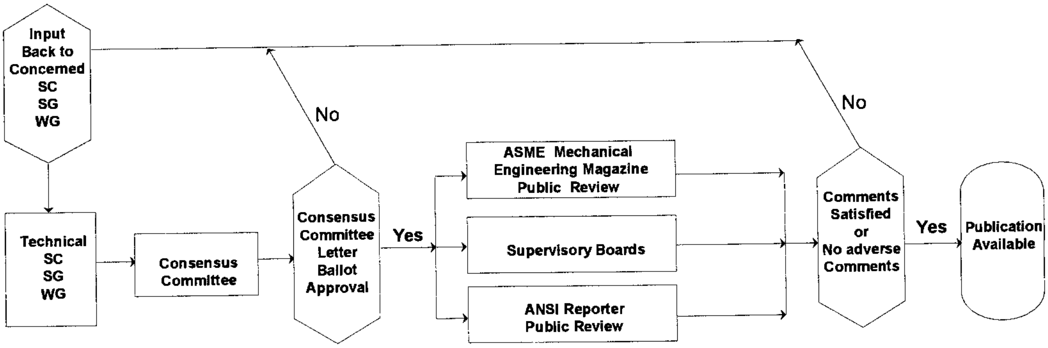

FIGURE 20.4.1 A typical path for standards approval.

What Standards Are Available?

List of Topics Covered by ASME International Standards

The following is a list of topics that are covered by ASME International Standards:

Abbreviations
Accreditation
Air-Cooled Heat Exchangers
Air Cylinders and Adapters
Air Heaters
Atmospheric Water Cooling Equipment
Automatically Fired Boilers
Automotive Lifting Devices
Backwater Valves
Boilers
Bolts
Building Services Piping
Cableways
Cargo Containers
Carriers
Castings and Forgings
Centrifugal Pumps
Chemical Plant and Petroleum Refinery Equipment
Chucks and Chuck Jaws
Cleanouts
Coal Pulverizers
Compressors
Consumable Tools
Conveyors
Coordinate Measuring Machines
Cranes
Deaerators
Density Determination
Derricks
Dial Indicators
Diaphragm Seals
Dies
Diesel and Burner Fuels
Digital Systems
Dimensional Metrology
Dimensioning and Tolerancing
Drafting
Drains
Dumbwaiters
Ejectors
Elevators
Escalators
Exhausters
Fans
Fasteners
Feedwater Heaters
Fittings
Flanges
Floor Drains
Flue Gas Desulfurization
Fluid Flow in Pipes
Fuel Gas Piping
Gage Blanks
Gage Blocks
Gas Flow Measurement
Gas Transmission and Distribution Piping Systems
Gas Turbine Power Plants
Gas Turbines
Gaseous Fuels
Gaskets
Gauges
Graphic Symbols
Hand Tools
High Lift Trucks
Hoists
Hooks

Hydroelectric Equipment
Incinerators
Indicated Power
Industrial Sound
Industrial Trucks and Vehicles
Internal Combustion Engine Generator Units
Ion Exchange Equipment
Jacks
Keys
Keyseats
Knurling
Letter Symbols
Lifts
Limits and Fits
Line Conventions and Lettering
Linear Measurements
Liquid Transportation Systems
Low-Lift Trucks
Machine Guarding
Machine Tools
Manlifts
Material Lifts
Measurement
Mechanical Power Transmission Apparatus
Mechanical Springs
Metric System
Milling Machines
Model Testing
Monorails
Moving Walks
Nuclear Facilities and Technology
Nuts
Oil Systems
Optical Parts
Pallets
Particulate Matter
Performance Test Codes
Pins
Pipe Dimensions
Pipe Threads
Piping
Pliers
Plumbing
Pressure Transducers
Pressure Vessels
Pumps
Quality Assurance
Reamers
Refrigeration Piping
Resource Recovery Facility Operators
Retaining Rings
Risk Assessment
Rivets
Safety and Relief Valves
Screw Threads
Screws
Slings
Slip Sheets
Solid Modeling
Spray Cooling Systems
Stainless Steel Pipe
Stands
Steam-Generating Units
Steel Stacks
Storage/Retrieval Machines
Storage Tanks
Surface Texture
Temperature Measurement
Thermometers
Tools
Transmission Apparatus
Transmission Chains
Turbines
Valves
Washers
Waste Facility Operators
Water Hammer Arresters
Weighing Scales
Welded Aluminum-Alloy Storage Tanks
Wheel Dollies
Wheelchair Lifts
Whirlpool Bathtub Appliances
Wind Turbines
Wrenches

Where Do I Go if the Subject I Want Is Not on This List?

With the constant creation and revision of standards, not to mention the large number of different SDOs, it is impractical to search for standards-related information in anything other than an electronic format. The latest information on ASME International's codes and standards can be found on the World Wide Web (WWW). ASME International's home page is located at http://www.asme.org. It contains a searchable catalog of the various codes and standards available for immediate download in a Portable Document Format (PDF) format and contains information on drafts out for public review and committee meeting schedules, as well as general information about the other areas ASME International is involved with. Another useful Web site is provided by the National Standards System Network (NSSN). This is a project that is still under development, and whose goal is to present a comprehensive listing of all bibliographic information on standards and standards-related material. The NSSN page is located at http://nssn.org. This site is also useful in that it provides links to many of the SDO's Web sites.

Defining Terms

Accreditation: The process by which the ability of an organization to produce a product according to a specific code or standard is evaluated. It is not an actual certification of a specific product, but does provide a third-party evaluation of the manufacturer's competence to certify that individual products are in compliance with the applicable standards.

Balanced committee: A committee in which the consensus body responsible for the development of a standard comprises representatives of all categories of interest that relate to the subject (e.g., manufacturer, user, regulatory, insurance/inspection, employee/union interest). A balanced committee ensures that no one interest group can dominate the actions of the consensus body.

Certification: The process by which an individual's training or abilities to perform a task according to a specific code or standard is evaluated.

Code: A standard that is, or is intended to be, adopted by governmental bodies as one means of satisfying legislation or regulation.

Consensus: This means that substantial agreement has been reached by directly and materially affected interest groups. It signifies the concurrence of more than a simple majority, but not necessarily unanimity. Consensus requires that all views and objections be considered and that an effort be made toward their resolution.

Due process: A procedure by which any individual or organization who believes that an action or inaction of a third party causes unreasonable hardship or potential harm is provided the opportunity to have a fair hearing of their concerns.

Registration: Similar to accreditation, it is the term used more frequently in the international arena, particularly when dealing with the ISO 9000 program on quality assurance systems.

Standard: A set of technical definitions, requirements, and guidelines for the uniform manufacture of items; safety; and/or interchangeability.

Further Information

The Engineering Standard, A Most Useful Tool, by Albert L. Batik, is a comprehensive work covering the impact of standards in marketing and international trade as well as their application to traditional areas such as design, manufacturing, and construction.

The Code: An Authorized History of the ASME Boiler and Pressure Vessel Code, by Wilbur Cross, provides an in-depth look at events that led to need for codes and the pioneers who created the Boiler and Pressure Vessel Code.

20.5 Optics

Roland Winston and Walter T. Welford (Deceased)

Geometrical Optics

Geometrical optics is arguably the most classical and traditional of the branches of physical science. By the time Newton wrote his *Principia*, geometrical optics was already a highly developed discipline. Optical design of instruments and devices has been worked out and improved over the centuries. From the telescopes of Galileo to the contemporary camera lens, progress while impressive has been largely evolutionary with modern design benefiting enormously from the availability of fast, relatively inexpensive digital computers. It is noteworthy that even in the last 20 years progress has been made by extending

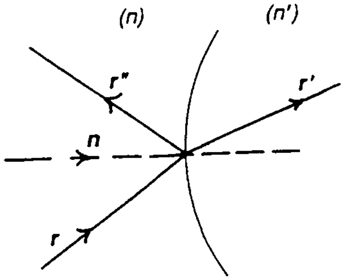

FIGURE 20.5.1

the classical model to problems where image formation is not required, or desired. We shall touch on these developments of "nonimaging optics" later in this section. But first we treat classical geometrical optics. In this model, a "point source" emits rays which are straight lines in a vacuum or in a homogeneous isotropic dielectric medium. Light travels at different speeds in different dielectrics. Its speed is given by c/n, where c is the speed in vacuum (299,792,458 m sec^{-1}) and n, the *refractive index*, depends on the medium and on the frequency of the light.

A ray is refracted at an interface between two media. If **r** and **r′** are unit vectors along the incident and refracted directions, n and n' are the respective refractive indexes, and **n** is the unit normal to the interface, then the ray directions are related by

$$n\mathbf{n} \times \mathbf{r} = n'\mathbf{n} \times \mathbf{r}' \tag{20.5.1}$$

which is the law of refraction, *Snell's law*, in vector form. More conventionally, Snell's law can be written

$$n \sin I = n' \sin I' \tag{20.5.2}$$

where I and I' are the two angles formed where the normal meets the interface, the angles of incidence and refraction. The two rays and the normal must be coplanar. Figure 20.5.1 illustrates these relationships and shows a reflected ray vector $\mathbf{r}''$. Equation (20.5.1) can include this by means of the convention that after a reflection we set n' equal to $-n$ so that, for reflection,

$$\mathbf{n} \times \mathbf{r} = -\mathbf{n} \times \mathbf{r}'' \tag{20.5.3}$$

With a bundle or pencil of rays originating in a point source and traversing several different media, e.g., a system of lenses, we can measure along each ray the distance light would have traveled in a given time t; these points delineate a surface called a *geometrical wavefront*, or simply a *wavefront*. Wavefronts are surfaces orthogonal to rays (the Malus–Dupin theorem). (It must be stressed that wavefronts are a concept of geometrical optics and that they are *not* surfaces of constant phase, phase fronts, of the light waves in the scaler or electromagnetic wave approximations. However, in many situations the geometrical Earth are a very good approximation of phase fronts.) Thus, if successive segments of a ray are of length d_1, d_2, …, a wave front is a locus of constant Σnd or, passing to the limit, $\int n\, dl$. This quantity is called an *optical path length*. (See Figure 20.5.2.)

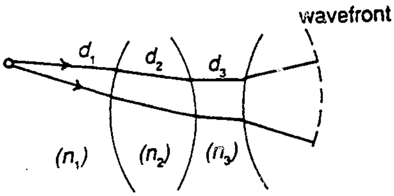

FIGURE 20.5.2

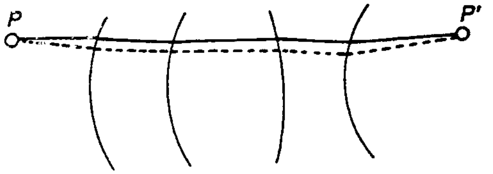

FIGURE 20.5.3

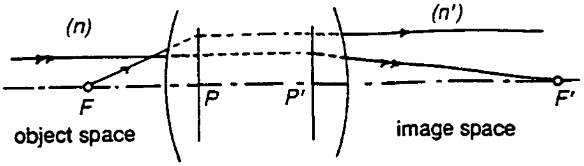

FIGURE 20.5.4

Optical path lengths enter into an alternative to Snell's law as a basis for geometrical optics. Consider any path through a succession of media from, say, P to P'. We can calculate the optical path length W from P to P', and it will depend on the shape of this path, as shown in Figure 20.5.3. Then *Fermat's principle* states that, if we have chosen a physically possible ray path, the optical path length along it will be stationary (in the sense of the calculus of variations) with respect to small changes of the path. (The principle as originally formulated by Fermat proposed a *minimum* time of travel of the light. Stationarity is strictly correct, and it means roughly that, for any small transverse displacement δx of a point on the path, the change in optical path length is of order δx^2.) For our purposes, Fermat's principle and Snell's law are almost equivalent, but in the case of media of continuously varying refractive index it is sometimes necessary to invoke Fermat's principle to establish the ray path. Apart from such cases, either one can be derived from the other.

Either Fermat or Snell can be used to develop the whole edifice of geometrical optics in designing optical systems to form images.

Symmetrical Optical Systems

The axially symmetric optical system, consisting of lenses and/or mirrors with revolution symmetry arranged on a common axis of symmetry, is used to form images. Its global properties are described in terms of *paraxial* or *Gaussian* optics. In this approximation only rays making small angles with the axis of symmetry and at small distances from the axis are considered. In Gaussian optics, we know from symmetry that rays from any point on the axis on one side of the system emerge on the other side and meet at another point on the axis, the *image point*. This leads to the well-known formalism of principal planes and focal planes shown in Figure 20.5.4. A ray entering parallel to the axis passes through F', the second, or image-side, principal focus on emerging from the system, and a ray entering through F, the first principal focus, emerges parallel to the axis. A ray incident on the first, or object-side, principal plane P at any height h emerges from the image-side principal plane P' at the same height h so that the principal planes are *conjugated* planes of unit magnification. Excluding for the moment the special case

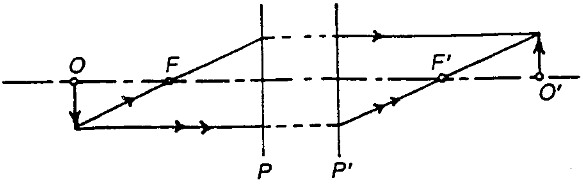

FIGURE 20.5.5

in which a ray entering parallel to the axis also emerges parallel to the axis, these four points yield a useful graphical construction for objects and images, as depicted in Figure 20.5.5.

The two focal lengths f and f' are defined as

$$f = PF, \qquad f' = P'F' \tag{20.5.4}$$

Their signs are taken according to the usual conventions of coordinate geometry, so that in Figure 20.5.4 f is negative and f' is positive. The two focal lengths are related by

$$n'/f' = -n/f \tag{20.5.5}$$

where n and n' are the refractive indexes of the object and image spaces, respectively.

Conjugated distances measured from the principal planes are denoted by l and l', and the conjugate distance equation relating object and image positions is

$$n'/l' - n/l = n'/f' = -n/f \tag{20.5.6}$$

The quantity on the right — that is, the quantity on either side of Equation (20.5.5) — is called the *power* of the system, and is denoted by K.

Another form of the conjugate distance equation relates distances from the respective principal foci, z and z'.

$$zz' = ff' \tag{20.5.7}$$

This equation yields expressions for the transverse magnification:

$$\eta'/\eta = -f/z = -z'/f' \tag{20.5.8}$$

This is useful to indicate paraxial rays from an axial object point O to the corresponding image point O' as in Figure 20.5.6 with convergence angles u and u' positive and negative, respectively, as drawn in the figure. (Paraxial angles are small but diagrams like Figure 20.5.6 can be drawn with an enlarged transverse scale. That is, convergence angles and intersection heights such as h can all be scaled up by the same factor without affecting the validity of paraxial calculations.) Then, if η and η' are corresponding object and image sizes at these conjugates, the following relation exists between them:

$$nu\eta = n'u'\eta' \tag{20.5.9}$$

In fact, for a given paraxial ray starting from O, this quantity is the same at any intermediate space in the optical system. That is, it is an invariant, called the Lagrange invariant. It has the important property that its square is a measure of the light flux collected by the system from an object of size η in a cone of convergence angle u.

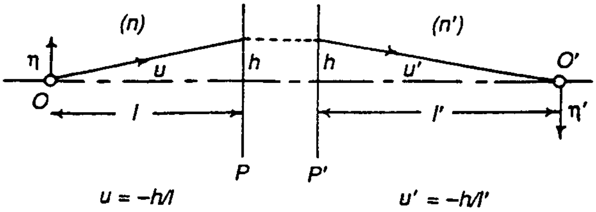

FIGURE 20.5.6

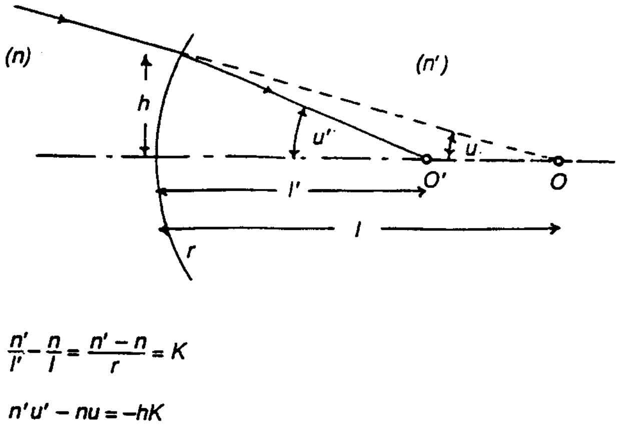

$$\frac{n'}{l'} - \frac{n}{l} = \frac{n' - n}{r} = K$$

$$n'u' - nu = -hK$$

FIGURE 20.5.7

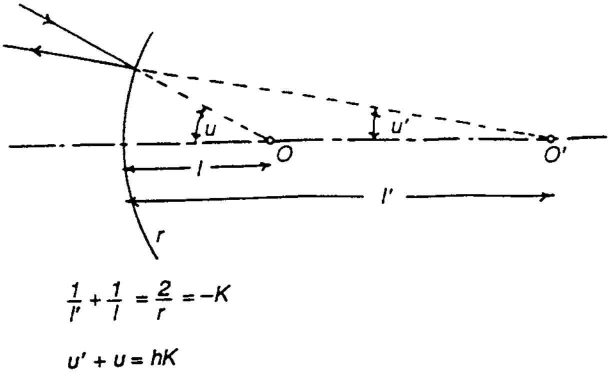

$$\frac{1}{l'} + \frac{1}{l} = \frac{2}{r} = -K$$

$$u' + u = hK$$

FIGURE 20.5.8

The above discussion covers all general Gaussian optic properties of symmetrical optical systems. We next look at particular systems in detail. To do this, we abandon the skeleton representation of the system by its principal planes and foci and consider it as made up of individual refracting or reflecting surfaces.

Figure 20.5.7 and Figure 20.5.8 show the basic properties of a single spherical refracting surface of radius of curvature *r* and of a spherical mirror. In each case *r* as drawn is positive. These diagrams suggest that the properties of more complex systems consisting of more than one surface can be found by tracing paraxial rays rather than by finding the principal planes and foci, and this is what is done in practice. Figure 20.5.9 shows this with an iterative scheme outlined in terms of the convergence angles. The results can then be used to calculate the positions of the principal planes and foci and as the basis of aberration calculations. For details see Welford (1986). The actual convergence angles which can be admitted, as distinguished from notional paraxial angles, are determined either by the rims of individual components or by stops deliberately inserted at places along the axis chosen on the basis of aberration theory. Figure 20.5.10 shows an *aperture stop* in an intermediate space of a system. The components of the system to the left of the stop from an image (generally virtual) which is "seen" from the object position (this image is usually virtual, i.e., it is not physically accessible to be caught on a ground-glass screen like the image in an ordinary looking glass); this image is called the entrance pupil, and it limits the angle of beams that can be taken in from the object. Similarly, on the image side there is an exit pupil, the image of the stop by the components to the right, again usually virtual. This pupil may also determine the angles of beams from off-axis object point *O* and *O*′; the central ray of the beam from *O* passes through the center of the entrance pupil (and therefore through the center of the aperture stop and the center of the exit

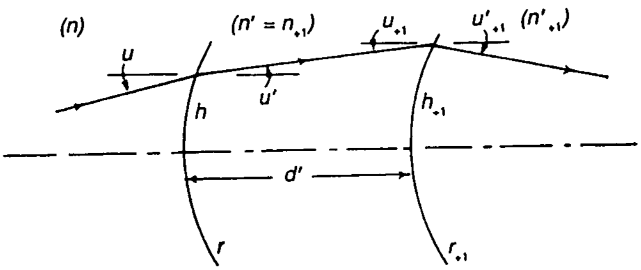

$$n'u' - nu = -hK$$
$$u_{+1} = u'$$
$$h_{+1} = h + d'u'$$
$$n'_{+1}u'_{+1} - n_{+1}u_{+1} = -h_{+1}K_{+1}$$

FIGURE 20.5.9

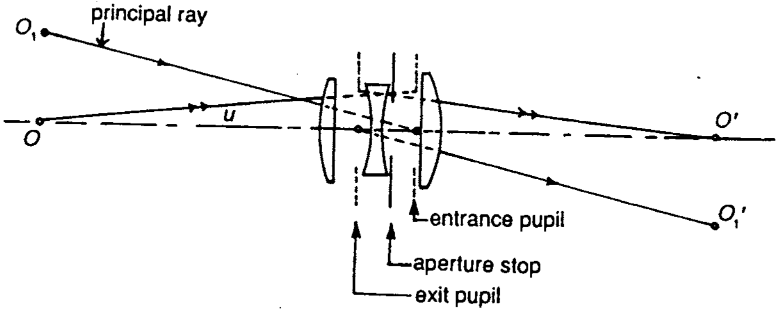

FIGURE 20.5.10

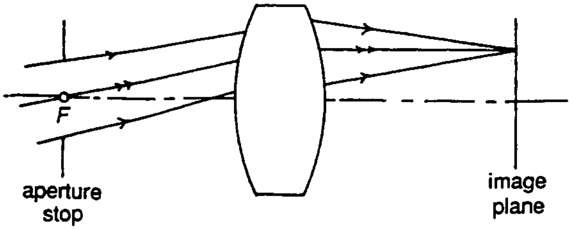

FIGURE 20.5.11

pupil) and it is usually called the *principal*, *chief*, or *reference ray* from this object point. The rest of the beam or pencil from O may be bounded by the rim of the entrance pupil, or it may happen that part of it is *vignetted* by the rim of one of the components.

Although the aperture stop is usually thought of as being inside an optical system, as in a photographic objective, it is sometimes placed outside, and one example is the *telecentric stop* shown in Figure 20.5.11. The stop is at the object-side principal focus, with the result that in the image space all the principal rays emerge parallel to the optical axis. A telecentric stop can be at either the object-side or the image-side principal focus, and the image conjugates can be anywhere along the axis. The effect is that the pupil on the opposite side of the telecentric stop is at infinity, a useful arrangement for many purposes. It may happen that the telecentric stop is between some of the components of the system.

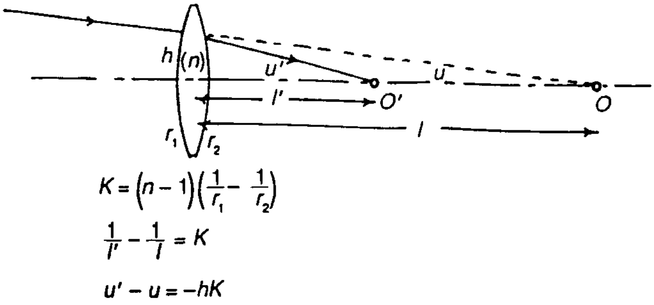

FIGURE 20.5.12

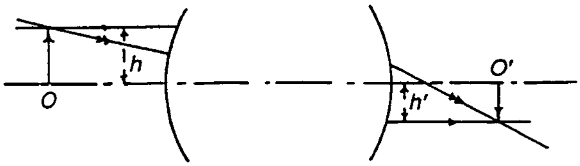

FIGURE 20.5.13

The above information is all that is needed to determine how a given symmetrical optical system behaves in Gaussian approximation for any chosen object plane. Suitable groups of rays can be used to set out the system for mechanical mounting, clearances, etc.; however, it is often easier and adequate in terms of performance to work with the *thin-lens model* of Gaussian optics. This model uses complete lenses of negligible thickness instead of individual surfaces. Figure 20.5.12 shows the properties of a thin lens. A system of thin lenses can be ray traced to find its properties, locate foci and ray clearances, etc., and very often the results will be good enough to use without further refinement. This is particularly true of systems involving unexpanded laser beams, where the beam diameters are quite small.

We omitted from our discussion of Figure 20.5.4 the special case in which a ray incident parallel to the optical axis emerges parallel to the axis, as in Figure 20.5.13. This is an *afocal* or *telescopic* system; it forms an image at infinity of an object at infinity, and the angular magnification is given by the ratio of the ray incidence heights. An afocal system also forms images of objects at finite distances, as indicated by the rays drawn in the figure. The transverse magnification is then constant for all pairs of conjugates.

Plane Mirrors and Prisms

A single-plane mirror used to deflect or rotate an optical axis needs no explanation, but some useful points can be made about combinations of mirrors. Two mirrors at an angle θ turn the beam through 2θ about the line of intersection of the mirror planes, whatever the angle of incidence on the first mirror, as in Figure 20.5.14. The diagram is drawn for a ray in the plane perpendicular to the line of intersection of the mirror planes, but it is equally valid if the ray is not in this plane, i.e., the diagram is a true projection. In particular, if the mirrors are at right angles, as in Figure 20.5.15, the direction of the ray is reversed in the plane of the diagram. Three plane mirrors at right angles to each other, forming a corner of a cube as in Figure 20.5.16, reverse the direction of a ray incident in *any* direction if the ray meets all three mirrors in any order.

These properties are more often used in prisms in the corresponding geometry. Total internal reflection, as in, for example, the right-angle prism (Figure 20.5.17), is a great advantage in using prisms for turning beams. The condition for total internal reflection is

$$\sin I > 1/n \qquad (20.5.10)$$

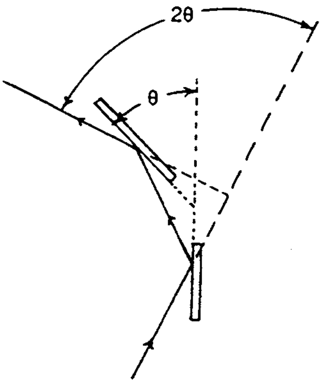

FIGURE 20.5.14

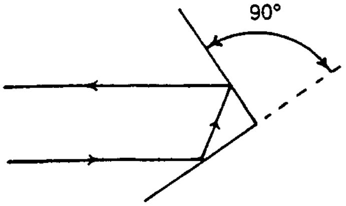

FIGURE 20.5.15

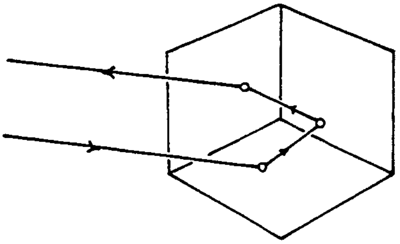

FIGURE 20.5.16

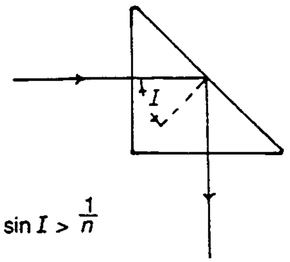

FIGURE 20.5.17

The *critical angle* given by sin$I$ = 1/n is less than 45° for all optical glasses, and probably for all transparent solids in the visible spectrum. Total internal reflection is 100% efficient provided the reflecting surface is clean and free from defects, whereas it is difficult to get a metallized mirror surface that is better than about 92% efficient. Thus, with good anti-reflection coating on the input and output surfaces a prism, such as that shown in Figure 20.5.17, transmits more light than a mirror.

Roof prisms and cube-corner prisms, the analogs of Figure 20.5.15 and 20.5.16, have many uses. The angle tolerances for the right angles can be very tight. For example, roof edges form part of the reversing prism system in some modern binoculars, and an error ε in the right angle causes an image doubling in

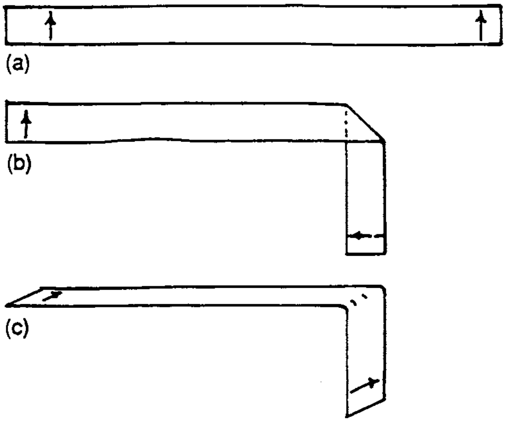

FIGURE 20.5.18

angle of $4n\varepsilon$. The two images are those formed by the portions of the beam incident at either of the two surfaces, which should have been at exactly 90°.

In addition to turning the axis of a system, mirror and prism assemblies sometimes rotate the image in unexpected ways. The effect can be anticipated by tracing, say, three rays from a notional object such as the letter F (i.e., an object with no symmetry). A more direct and graphic method is to use a strip of card and mark arrows on each end as in Figure 20.5.18a. The card is then folded without distorting it as in Figure 20.5.18b to represent, say, reflection at the hypotenuse of the right-angle prism, and the arrows show the image rotation. The process is repeated in the other section, as in Figure 20.5.18c. Provided the folding is done carefully, without distortion, this procedure gives all image rotations accurately for any number of successive reflections.

The Dove prism (Figure 20.5.19) is an example of an image-rotating prism. When the prism is turned through an angle ϕ about the direction of the incident light, the image turns in the same direction through 2ϕ. A more elaborate prism with the same function is shown in Figure 20.5.20. The air gap indicated between the hypotenuses of the two component parts needs to be only about 10 µm or so thick to ensure total internal reflection. Any prism or mirror assembly like this with an odd number of reflections will serve as an image rotator. Figure 20.5.20 illustrates an elegant advantage of prisms over mirrors; the system can be made compact by using the same optical surface both for reflection and for transmission.

Figure 20.5.21 shows a typical beam-splitting (or combining) prism, a component of many diverse optical systems. The beam-splitting surface may be approximately neutral, in which case it would be a thin metal layer, or it may be dichroic (reflecting part of the spectrum and transmitting the rest), or it

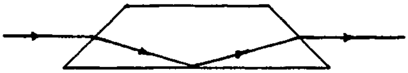

FIGURE 20.5.19

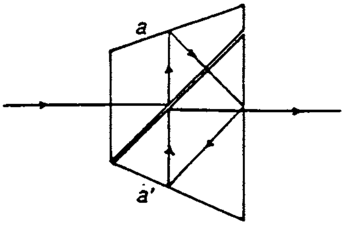

FIGURE 20.5.20

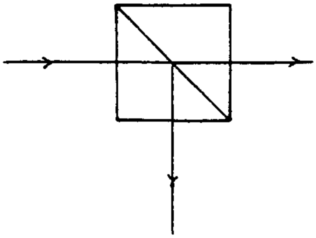

FIGURE 20.5.21

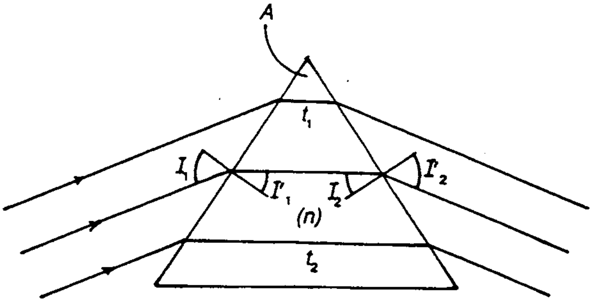

FIGURE 20.5.22

may be polarizing (transmitting the p-polarization and reflecting the s-polarization of a certain wavelength range). In the last two cases the reflecting-transmitting surface is a dielectric multilayer and its performance is fairly sensitive to the angle of incidence.

Prisms as devices for producing a spectrum have been largely replaced by diffraction grating (See Figure 20.5.22). The latter have several advantages for direct spectroscopy, but here are a few specialized areas where prisms are better. Losses in grating through diffraction to unwanted orders are a nuisance in certain astronomical applications where every photon counts. Another example of an area where prisms are preferable is wavelength selection in multiwavelength lasers: a prism inside the laser resonator with adequate angular dispersion ensures that only one wavelength will be produced, and one scans through the available wavelengths by rotating the prisms at and away from the position of minimum deviation. The significance of the minimum deviation position is that the effects of vibrations and placement errors are least. Also, if the shape of the prism is isosceles, the resolving power will be a maximum at minimum deviation. The main formulas relating to dispersing prisms are as follows.

Spectroscopic resolving power:

$$\lambda/\Delta\lambda = (t_1 - t_2)\, dn/d\lambda \tag{20.5.11}$$

where $t_1 - t_2$ is the difference between the path lengths in glass from one side of the beam to the other.

Angular dispersion:

$$dI'_2/d\lambda = \sin A(dn/d\lambda)/(\cos I'_1 \cos I'_2) \tag{20.5.12}$$

$$= 2\sin(A/2)(dn/d\lambda)/\cos I_2 \tag{20.5.13}$$

at minimum deviation.

Spectrum line curvature:

$$1/\text{radius} = \left[(n^2 - 1)/nf\right]\sin A/(\cos I'_1 \cos I'_2) \tag{20.5.14}$$

$$= \left[\left(n^2 - 1\right)/n^2 f\right] 2 \tan I_1 \tag{20.5.15}$$

at minimum deviation, where f is the focal length of the lens which brings the spectrum to a focus.

The spectrum line curvature refers to the observation that the image of the entrance slit of the spectroscope produced by placing a lens after the prism is actually parabolic. The parabola is convex toward the longer wavelengths. The reason the image is curved is that rays out of the principal plane of the prism are deviated more than rays in the plane, a straightforward consequence of the application of Snell's law. For rays with angle out of the plane the extra deviation can be parametrized by an additional contribution to the index of refraction given by

$$dn \approx \varepsilon^2 \left(n^2 - 1\right)(2n) \tag{20.5.16}$$

If the length of the slit image is L, then $\varepsilon \approx L/(2f)$, where f is the focal length of the lens. Moreover, from Equation (20.5.12) we have

$$dI_2'/dn = \sin A / \left(\cos I_1' \cos I_2'\right) \tag{20.5.17}$$

$$= (2/n) \tan I_1 \tag{20.5.18}$$

at minimum deviation. The curvature of the slit image readily follows from these relations.

The typical dispersing prism of constant deviation shown in Figure 20.5.23 has the property that, if it is placed in a collimated beam, the wavelength which emerges at right angles to the incident beam is always at minimum deviation so that the spectrum is scanned by rotating the prism about a suitable axis such as the one indicated.

A prism used a long way from minimum deviation will expand or contract a collimated beam in one dimension. Figure 20.5.24 shows a pair of prisms used in this way to turn a laser beam of elliptical profile (from a diode laser) into a beam of circular profile by expanding it in the plane of the diagram only.

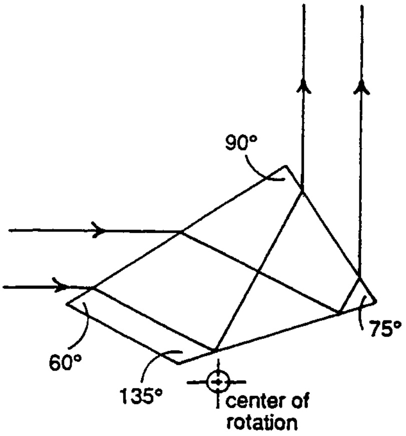

FIGURE 20.5.23

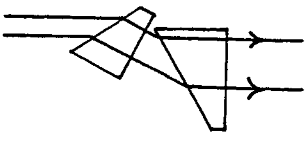

FIGURE 20.5.24

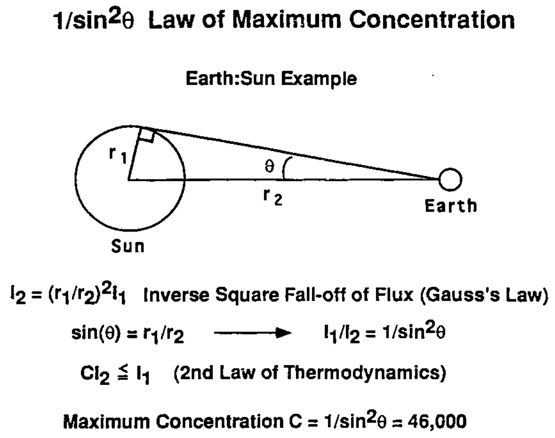

FIGURE 20.5.25

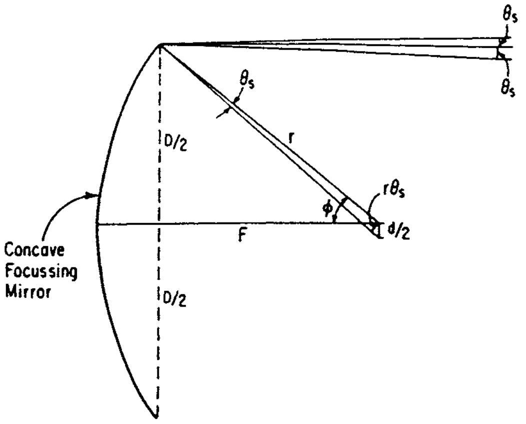

FIGURE 20.5.26

Nonimaging Optics

In one important respect conventional *image-forming* optical design is quite inefficient, that is, in merely concentrating and collecting light. This is well illustrated by an example taken from solar energy concentration (Figure 20.5.25). The flux at the surface of the sun (≈63 W/mm^2) falls off inversely with the square of the distance to a value ≈1.37 mW/mm^2 above the Earth's atmosphere or typically 0.8 to 1 mW/mm^2 on the ground. The second law of thermodynamics permits an optical device (*in principle*) to concentrate the dilute solar flux at Earth so as to attain temperatures up to but not exceeding that of the sun's surface. This places an upper limit on the solar flux density achievable on Earth and correspondingly on the concentration ratio of any optical device. From simple geometry, this limiting concentration ratio is related to the sun's angular size (2θ) by $C_{max} = 1/\sin^2\theta \approx 1/\theta^2$ (small angle approximation). We will call this thermodynamic limit the *sine law of concentration*. Therefore, since $\theta = 0.27°$ or 4.67 mrad, $C_{max} \approx 46{,}000$. When the target is immersed in a medium of refractive index n, this limit is increased by a factor n^2, $C_{max} = n^2/\sin^2\theta$. This means that a concentration of about 100,000 will be the upper limit for ordinary ($n \approx 1.5$) refractive materials. In experiments at the University of Chicago we actually achieved a solar concentration of 84,000 by using a nonimaging design with a refractive medium (sapphire). We would not even have come close using conventional designs, not for any fundamental reason but because imaging optical design is quite inefficient for delivering maximum concentration. For example, consider the paraboloidal mirror of a telescope used to concentrate sunlight at its focus (Figure 20.5.26). We can relate the concentration ratio to the angle 2ϕ subtended by the paraboloid at its focus and the sun's angular size ($2\theta_s$), $C = (\sin\phi\cos\phi/\theta_s)^2 = (^1/_4)\,\sin^2 2\phi/\theta_s^2$, where we have used the small angle approximation for θ_s. Notice that C is maximized at $\phi = \pi/4$, or $C = 1/(4\theta_s^2) = (^1/_4)\,C_{\max}$. In fact, this result does not depend on the detailed shape of the paraboloid and would hold for any focusing mirror. One fares no better (and probably worse) with a lens (a refracting telescope), since the optimum paraboloid in the above example is equivalent in concentrating performance to a lens with focal ratio $f = 1$ which has been corrected for spherical aberration and coma. Such high-aperture lenses are typically complex structures with many components. The thermodynamic limit would require a lens with focal ratio $f = 0.5$ which, as every optical designer knows, is unattainable. The reason for this large shortfall is not hard to find. The paraboloid images perfectly on-axis, but has severe off-axis aberration (coma) which produces substantial image blurring and broadening. Nonimaging optics began in the mid 1960s with the discovery that optical systems could be designed and built that approached the theoretical limit of light collection (the sine law of concentration). The essential point is that requiring an image is unnecessarily restrictive when only concentration is desired. Recognition of this restriction and relaxation of the associated constraints led to the development of nonimaging optics. A nonimaging concentrator is essentially a "funnel" for light. Nonimaging optics departs from the methods of traditional optical design to develop instead techniques for maximizing the collecting power of concentrating elements and systems. Nonimaging designs exceed the concentration attainable with focusing techniques by factors of four or more and approach the theoretical limit (ideal concentrators). The key is simply to dispense with image-forming requirements in applications where no image is required.

Since its inception, the field has undergone three periods of rapid conceptual development. In the 1970s the "string" (see Figure 20.5.27 and Figure 20.5.28) or "edge-ray" method (see Welford and Winston, 1989) was formulated and elaborated for a large variety of geometries. This development was driven by the desire to design wide-angle solar concentrators. It may be succinctly characterized as $\int n\,dl$ = constant along a string. (Notice that replacing "string" by "ray," Fermat's principle, gives all of imaging optics.) In the early 1980s, a second class of algorithms was found, driven by the desire to obtain ideally perfect solutions in three dimensions (3D) (The "string" solutions are ideal only in 2D, and as figures of revolution in 3D are only approximately ideal, though still very useful.) This places reflectors along the lines of flow of a radiation field set up by a radiating lambertian source. In cases of high symmetry such as a sphere or disk, one obtains ideal solutions in *both* 2D and 3D. The third period of rapid development has taken

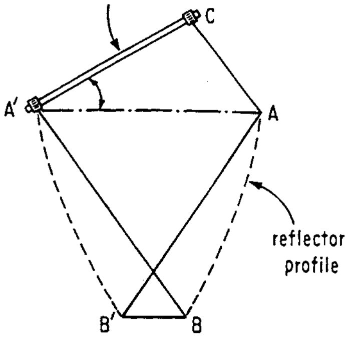

$$\int_W^{B'} n\,dl = \text{Constant.}\ AC + AB' = A'B + BB'$$
$$AC = AA'\sin\theta$$
$$AB' = A'B$$
$$\Rightarrow AA'\sin\theta = BB'$$

FIGURE 20.5.27

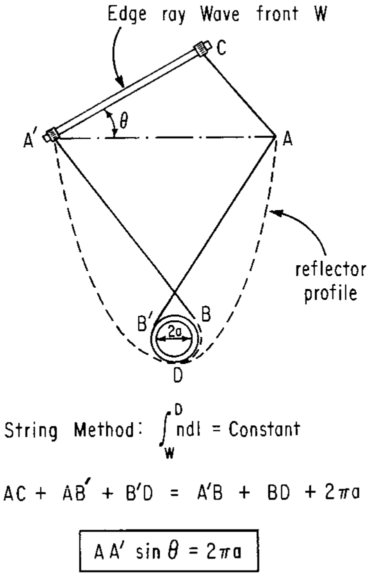

FIGURE 20.5.28

place only in the past several years; its implications and consequences are still in the process of being worked out. This was driven by the desire to address a wider class of problems in illumination that could not be solved by the old methods, for example, uniformly illuminating a plane (e.g., a table or a wall) by a lambertian light source (e.g., a fluorescent light). It is well known that the far-field illuminance from a lambertian source falls off with a power of the cosine of the radiating angle θ. For example, cylindrical radiators (such as a fluorescent lamp) produce a $\cos^2\theta$ illuminance on a distant plane, strip radiators produce a $\cos^3\theta$ illuminance, while circular disk radiators produce a $\cos^4\theta$ illuminance. But suppose one desires a predetermined far-field illuminance pattern, e.g., uniform illuminance? The old designs will not suffice; they simply transform a lambertian source radiating over 2π into a lambertian source radiating over a restricted set of angles. The limitation of the old designs is that they are too static and depend on a few parameters, such as the area of the beam A_1 and the divergence angle θ. One needs to introduce additional degrees of freedom into the nonimaging designs to solve a wider class of problems.

Edge-Ray Optics

One way to design nonimaging concentrators is to reflect the extreme input rays into the extreme output rays. We call this the "edge-ray method." An intuitive realization of this method is to wrap a string about both the light source and the light receiver, then allow the string to unwrap from the source and wrap around the receiver. In introducing the string picture, we follow an insight of Hoyt Hottel (Massachusetts Institute of Technology), who discovered many years ago that the use of strings tremendously simplified the calculation of radiative energy transfer between surfaces in a furnace. Our string is actually a "smart" string; it measures the optical path length (ordinary length times the index of refraction) and refracts in accordance with Snell's law at the interface between different refracting materials. $\int n\,dl$ = constant. The locus traced out turns out to be the correct reflecting surface! Let's see how this works in the simplest kind of problem nonimaging optics addresses: collecting light over an entrance aperture AA' with angular divergence ±θ and concentrating the light onto an exit aperture BB' (Figure 20.5.27). We attach one end of the string to the edge of the exit aperture *B* and the loop at the other end over a line WW' inclined at angle θ to the entrance aperture (this is the same as attaching to a "point at infinity"). We now unwrap the string and trace out the locus of the reflector taking care that string is taut and perpendicular to WW'. Then we trace the locus of the other side of the reflector. We can see with a little algebra that when we are done the condition for maximum concentration has been met. When we start unwrapping the

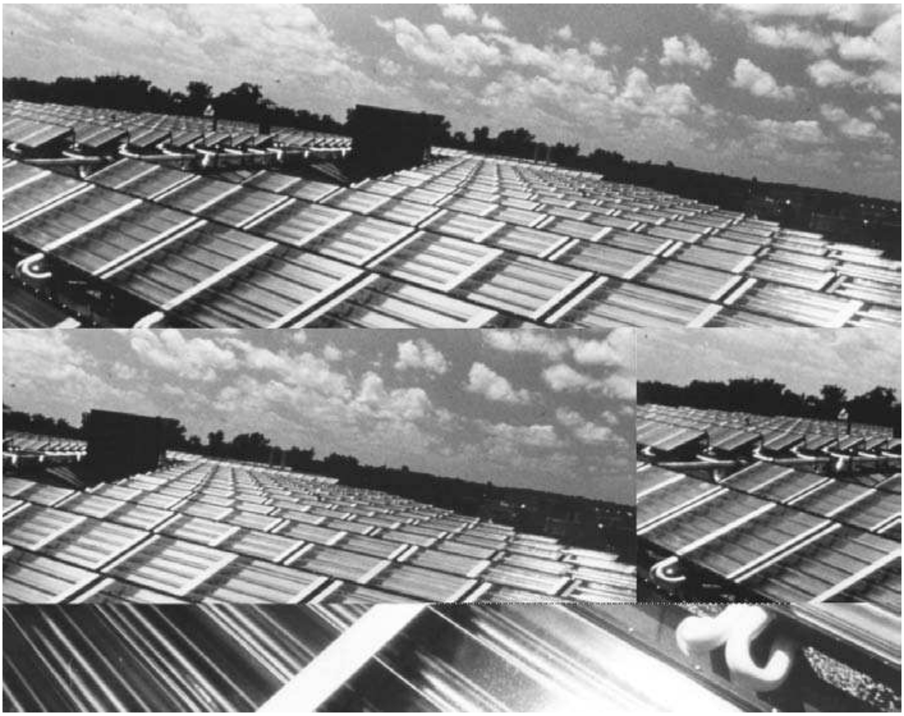

FIGURE 20.5.29

string, the length is $AB' + BB'$; when we finish, the same length is $WA' + A'B$. But $WA' = AA'\sin\theta$, while $AB' = A'B$. So we have achieved $AA'/BB' = 1/\sin\theta$ which is maximum concentration! To see why this works, we notice that the reflector directs all rays at ±θ to the edges BB' so that rays at angles $> \pm\theta$ are reflected out of the system and rejected. Now there is a conservation theorem for light rays called conservation of phase space or "etendue" which implies that if the rays at angles $> \pm\theta$ are rejected, then the rays that have angles $<\theta$ are all collected. Next we can try a more-challenging problem, where the "exit aperture" is a cylinder of radius a (Figure 20.5.28). Now we attach the string to a point on the cylinder and wrap it around the cylinder. When the string is unwrapped, we find that $AA'/2\pi a = 1/\sin\theta$ which is maximum concentration on the surface of the cylinder! Such designs are useful for solar-thermal concentrators since the typical receiver is a tube for carrying fluid. A solar plant for powering air conditioners that uses this design is shown in Figure 20.5.29. As already mentioned, there is an alternative method for designing "ideal" optical systems which bears little resemblance to the "string method" already described. We picture the aggregate of light rays traversing an optical system as a fluid flow in an abstract space called phase space.This is the "space" of ray positions and ray directions multiplied by the index of refraction, so it has twice the number of dimensions of ordinary space. By placing reflectors along the lines of flow of this vector field, nonimaging designs are generated. Flow-line designs are perfect in three dimensions, while the string designs rotated about an axis are not. On the other hand, the number of flow-line designs are much more restricted. For details see Welford and Winston (1989).

Lasers

Lasers are by now a ubiquitous light source with certain properties in addition to coherence and monochromaticity which have to be taken account of in some applications. Aside from many research applications of lasers, the HeNe laser at 632.8 nm wavelength has been available for several decades for alignment, surveying, and the like. But the explosive uses of lasers have come only recently with the advent of the solid-state diode laser. To appreciate the convenience of diode lasers one can draw upon the analogy between transistors and vacuum tubes. Inexpensive diode lasers are in widespread use in compact disk players, optical disk readers, and fiber-optics communications. The list of consumer applications is growing rapidly (e.g., laser pointers). In addition, diode lasers are used in arrays to optically drive (pump) more powerful lasers. The radiation that lasers emit can be highly coherent, and, except for the wavelength, of the same general character as the radiation from a radio frequency oscillator. We can identify four elements common to nearly all lasers (we follow the discussion in Mandel and Wolf, 1995, which should be consulted for details):

1. An optical resonator, generally formed by two or more mirrors;
2. A gain medium in which an inverted atomic population between the laser energy levels is established;
3. An optical pump or energy source to excite the gain medium;
4. A loss mechanism by which energy is dissipated or dispersed.

Figure 20.5.30 shows a typical form of laser, in which the resonator is a Fabry–Perot interferometer, and the amplifier is a gas plasma tube wherein a discharge is maintained. To reduce reflection losses from the plasma tube, its end windows are generally arranged at the Brewster angle for linearly polarized light at the laser frequency. The end mirrors are usually provided with multilayer dielectric coatings to make them highly reflecting. Of course, the output mirror needs to have its reflectivity, R, less than 100%, so that $(1 - R)$ is commonly the main source of the energy loss that has to be compensated by the gain medium. The cavity mirrors play the important role of feeding photons belonging to the laser modes back into the laser cavity. Most of the spontaneously emitted photons traveling in various other directions are lost. However, photons associated with a cavity resonance mode interact repeatedly with the atoms of the gain medium, and their number grows through stimulated emission, as illustrated in Figure 20.5.31. Once one mode is sufficiently populated, the probability for stimulated emission into that mode exceeds the spontaneous emission probability. In general, when the rate at which photons are fed into the optical cavity mode exceeds the rate at which they are lost from the cavity by the loss mechanism, the amplitude of the laser field starts to grow until a steady state is reached. At that point the rate of radiation by the laser equals the net rate at which energy is supplied. It is easy to see that this is achievable by an inverted population between the two atomic laser levels, with more atoms in the upper laser state than in the lower. If N_2, N_1 are the upper state and lower state populations, the rate of absorption of laser photons by the atomic system is proportional to N_1, and the rate of stimulated emission of laser photons by the system is proportional to N_2, with the same constant of proportionality for both. If N_2 exceeds N_1 sufficiently, all the radiation losses can be made good by the atomic system. It can be shown that the condition for laser action (in a single mode) is

$$N_2 - N_1 > 2A(1 - R)/\lambda^2 \tag{20.5.19}$$

where A is the cross-sectional area of the laser and λ is the wavelength.

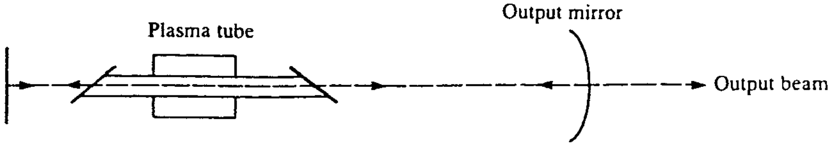

FIGURE 20.5.30 A simple form of laser.

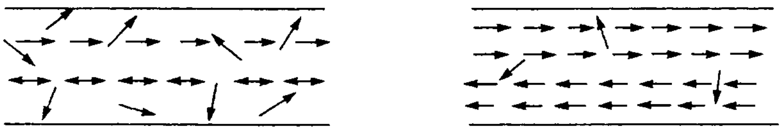

FIGURE 20.5.31 Illustration of the growth of the stimulated emission probability with the intensity of the mode.

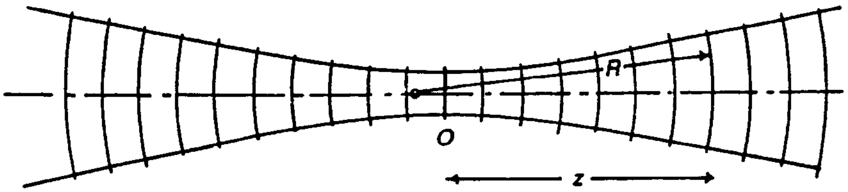

FIGURE 20.5.32

We next summarize how the special properties of laser beams are to be taken into account in optical design. The well-known Gaussian intensity profile of laser beams persists if it is taken through a sequence of lenses along the axis, and at certain points that can be more-or-less predicted by paraxial optics a "focus" is formed. But when, as often happens, the convergence angle in the space in which this occurs is small, say, 1 mrad or less, some departures from the predictions of the paraxial optics occur. We shall examine these effects, since they are of importance in many of the systems already mentioned.

Gaussian Beams

In paraxial approximation the simplest form of a single-mode beam is the TEM_{00} Gaussian beam shown in Figure 20.5.32. Starting from the narrowest part, known as the waist, the beam diverges with spherical phase fronts. The complex amplitude at the waist has the form

$$A = A_0 \exp\left(-r^2/\omega_0^2\right) \tag{20.5.20}$$

where ω_0 is called the beam width and r is a radial coordinate.

At a distance z along the beam in either direction, the complex amplitude is, apart from a phase factor,

$$A = \left(\omega_0/\omega\right) A_0 \exp\left(-r^2/\omega_0^2\right) \tag{20.5.21}$$

where ω is given by

$$\omega(z) = \omega_0\left[1 + \left(\lambda z/\pi\omega_0^2\right)\right]^{1/2} \tag{20.5.22}$$

At a distance z from the waist, the phase fronts have a radius of curvature R given by

$$R(z) = z\left[1 + \left(\pi\omega_0^2/\lambda z\right)^2\right] \tag{20.5.23}$$

The beam contour of constant intensity A_0^2/e^2 is a hyperboloidal surface of (small) asymptotic angle given by

$$\theta = \lambda/\pi\omega_0 \tag{20.5.24}$$

It can be seen that the centers of curvature of the phase fronts are not at the beam waist; in fact the phase front is plane at that point. The geometrical wavefronts are not exactly the same as true phase fronts, and if in this case we postulate that geometrical wavefronts should have their centers of curvature at the beam waist, we have an example of this. However, the difference is small unless the convergence angle is very small or, more precisely, when the Fresnel number of the beam is not much larger than unity:

$$\text{Fresnel number } = \omega^2/\lambda R \tag{20.5.25}$$

There is nothing special about Gaussian beams to cause this discrepancy between phase fronts and geometrical wavefronts; a similar phenomenon occurs with beams which are sharply truncated by the pupil ("hard-edged" beams). But it happens that it is less usual to be concerned with the region near the focus of a hard-edged beam of small Fresnel number, whereas Gaussian beams are frequently used in this way. Thus, Born and Wolf, *Principles of Optics* (1999) show that the phase front at the focus of a hard-edged beam is also plane, but with rapid changes of intensity and phase jumps across the zeros of intensity.

Tracing Gaussian Beams

If the beam is in a space of large convergence angle, say, greater than 10 mrad, it can be traced by ordinary paraxial optics, i.e., using the assumption that for all practical purposes the phase fronts are the same as geometrical wavefronts. In a space of small convergence angle it is necessary to propagate the beam between refracting surfaces by means of the proper Gaussian beam formulas and then use paraxial optics to refract (or reflect) the phase front through each surface in turn. To do this, we need two more formulas to give the position, z, and size of the beam waist starting from the beam size and phase front curvature at an arbitrary position on the axis, i.e., given ω and R. These are

$$z = R\left[1 + \left(\lambda z/\pi\omega^2\right)\right]^{-1} \tag{20.5.26}$$

and

$$\omega_0 = \omega\left[1 + \left(\pi\omega^2/\lambda R\right)^2\right]^{-1/2} \tag{20.5.27}$$

Equation (20.5.22) to Equation (20.5.27) enable a Gaussian beam to be traced through a sequence of refracting surfaces as an iterative process. Thus, starting from a beam waist of given size ω_0 (and angle given by Equation (20.5.24)), we move a distance z to the first refracting surface. At this surface the beam size ω is given by Equation (20.5.22) and the radius of curvature R of the phase front is given by Equation (20.5.23). The radius of curvature R' of the refracted phase front is obtained by paraxial optics using the equation of Figure 20.5.7 and taking R and R' as the conjugate distances l and l'. Then the position and size of the new beam waist are found from Equation (20.5.26) and Equation (20.5.27). These procedures can be carried through all the refracting surfaces of the optical system.

It can be seen from Equation (20.5.26) that z and R are substantially equal when $\lambda R/\pi\omega^2$ is very small. When this is so, there is no need to use these special equations for transferring between surfaces; the iterative equations in Figure 20.5.9 can be used, with the understanding that the paraxial convergence angle u is the equivalent of the asymptotic angle θ in Equation (20.5.24).

There are no simple equations for hard-edged beams corresponding to Equation (20.5.23) to Equation (20.5.27) for use with very small convergence angles. Numerical calculations of the beam patterns near focus have been published for some special cases, and these show, as might be expected, very complex structures near the "focal" region; however, that is defined.

Truncation of Gaussian Beams

The theoretical origin of the Gaussian beam is as a paraxial solution of the Helmholtz equation, i.e., a solution concentrated near one straight line, the axis, but although most of the power is within the region near the axis the solution is nonzero, although very small, at an infinite distance from the axis. Thus, the Gaussian profile is truncated when it passes through any aperture of finite diameter — e.g., a lens mount, an aperture stop, or even the finite-diameter end mirror of a laser resonator — after which it is no longer Gaussian and the above equations are no longer valid! In practice, this need not be a problem, for if the radius of the aperture is 2ω, the complex amplitude is down to 1.8% of its value at the center

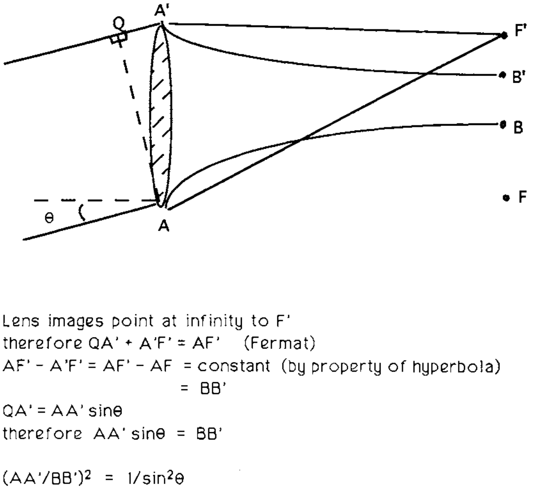

Lens images point at infinity to F'
therefore QA' + A'F' = AF' (Fermat)
AF' − A'F' = AF' − AF = constant (by property of hyperbola)
= BB'
QA' = AA' sinθ
therefore AA' sinθ = BB'

$(AA'/BB')^2 = 1/\sin^2\theta$

FIGURE 20.5.33

and the intensity is 0.03% of its value at the center. Thus, it is often assumed that an aperture of radius 2ω has no significant effect on the Gaussian beam, and this assumption is adequate for many purposes, although not all.

Sometimes it is useful to truncate a Gaussian beam deliberately, i.e., turn it into a hard-edged beam, by using an aperture of radius less than, say, ω. In this way an approximation to the Airy pattern is produced at the focus instead of a Gaussian profile waist, and this pattern may be better for certain purposes, e.g., for printers where the spot must be as small as possible for an optical system of given numerical aperture.

Gaussian Beams and Aberrations

In principle, a Gaussian beam is a paraxial beam, from the nature of the approximations made in solving the Helmholtz equation. However, Gaussian beams can be expanded to large diameters simply by letting them propagate a large distance, and they can acquire aberrations by passing through an aberrating lens or mirror system. The beam is then no longer Gaussian, of course, in the strict sense, but we stress that the conventional optical design idea involving balancing and reduction of aberrations can be applied to systems in which Gaussian beams are to propagate. For example, a *beam expander*, of which one form in shown in Figure 20.5.33, is an afocal system intended to do what its name implies: if it has aberrations as an afocal system, the output beam from a Gaussian input beam will not have truly plane or spherical phase fronts.

Non-Gaussian Beams from Lasers

Not all lasers produce Gaussian beams, even ignoring the inevitable truncation effects of resonator mirrors. Some gas lasers (e.g., helium-neon at any of its lasing wavelengths) produce Gaussian beams when they are in appropriate adjustment, but they can produce off-axis modes with more structure than a Gaussian beam. Other gas lasers (e.g., copper vapor lasers) produce beams with a great many transverse modes covering an angular range of a few milliradians in an output beam perhaps 20 mm across. Some solid-state lasers, e.g., ruby, may produce a very non-Gaussian beam because of optical inhomogeneities in the ruby. Laser diodes, which as already mentioned are becoming increasingly useful as very compact coherent sources, whether cw or pulsed, produce a single strongly divergent transverse mode which is wider across one direction than the other. This mode can be converted into a circular section of approximately Gaussian profile by means of a prism system, as in Figure 20.5.24.

References

Born, M. and Wolf, E. 1999. *Principles of Optics*, Seventh (expanded) edition, Cambridge University Press, Cambridge.

Welford, W.T. 1986. *Aberrations of Optical Systems*, Adam Hilger, Bristol.

Welford, W.T. and Winston, R. 1989. *High Collection Nonimaging Optics,* Academic Press, New York.

Mandel, L. and Wolf, E. 1995. *Optical Coherence and Quantum Optics,* Cambridge University Press., New York.

20.6 Water Desalination

Noam Lior

Introduction and Overview

Water desalination is a process that separates water from a saline water solution. The natural water cycle is the best and most prevalent example of water desalination. Ocean waters evaporate due to solar heating and atmospheric influences; the vapor consisting mostly of fresh water (because of the negligible volatility of the salts at these temperatures) rises buoyantly and condenses into clouds in the cooler atmospheric regions, is transported across the sky by cloud motion, and is eventually deposited back on the earth surface as fresh water rain, snow, and hail. The global freshwater supply from this natural cycle is ample, but many regions on Earth do not receive an adequate share. Population growth, rapidly increasing demand for fresh water, and increasing contamination of the available natural fresh water resources render water desalination increasingly attractive. Water desalinaiton has grown over the last four decades to an output of about 20 million m^3 of fresh water per day, by about 10,000 sizeable land-based water desalination plants.

The salt concentration in the waters being desalted ranges from below 100 ppm wt. (essentially fresh water, when ultrapure water is needed), through several thousand parts per million (brackish waters unsuitable for drinking or agricultural use) and seawater with concentrations between 35,000 and 50,000 ppm. Official salt concentration limits for drinkable water are about 1000 ppm, and characteristic water supplies are restricted to well below 500 ppm, with city water in the United States being typically below 100 ppm. Salinity limits for agricultural irrigation waters depend on the type of plant, cultivation, and soil, but are typically below 2000 ppm.

Many ways are availiable for separating water from a saline water solution. The oldest and still prevalent desalination process is distillation. The evaporation of the solution is effected by the addition of heat or by lowering of its vapor pressure, and condensation of these vapors on a cold surface produces fresh water. The three dominant distillation processes are multistage flash (MSF), multieffect (ME), and vapor compression (VC). Until the early 1980s the MSF process was prevalent for desalination. Now membrane processes, especially reverse osmosis (RO), are economical enough to have taken about one third of the market. In all membrane processes separation occurs due to the selective nature of the permeability of a membrane, which permits, under the influence of an external driving force, the passage of either water or salt ions but not of both. The driving force may be pressure (as in RO), electric potential (as in electrodialysis, ED), or heat (as in membrane distillation, MD). A process used for low-salinity solutions is the well-known ion exchange (IE), in which salt ions are preferentially adsorbed onto a material that has the required selective adsorption property and thus reduce the salinity of the water in the solution.

The cost of desalted water is comprised of the capital cost of the plant, the cost of the energy needed for the process, and the cost of operation and maintenance staff and supplies. In large seawater desalination plants the cost of water is about \$1.4 to \$2/m^3, dropping to less than \$1/m^3 for desalting brackish water. A methodology for assessing the economic viability of desalination in comparison with other water supply methods is described by Kasper and Lior (1979). Desalination plants are relatively simple to operate, and progress toward advanced controls and automation is gradually reducing operation expenses.

The relative effect of the cost of the energy on the cost of the fresh water produced depends on local conditions, and is up to one half of the total.

The boiling point of a salt solution is elevated as the concentration is increased, and the **boiling point elevation** is a measure of the energy needed for separation. Thermodynamically reversible separation defines the minimal energy requirement for that process. The minimal energy of separation $W_{\min}$ in such a process is the change in the Gibbs free energy between the beginning and end of the process, ΔG. The minimal work when the number of moles of the solution changes from n_1 to n_2 is thus

$$W_{\min} = \int_{n_1}^{n_2} (\Delta G)\, dn_W \tag{20.6.1}$$

The minimal energy of separation of water from seawater containing 3.45 wt.% salt, at 25°C, is 2.55 kJ/(kg fresh water) for the case of zero fresh water recovery (infinitesimal concentration change) and 2.91 kJ/(kg fresh water) for the case of 25% freshwater recovery. $W_{\min}$ is, however, severalfold smaller than the energy necessary for water desalination in practice. Improved energy economy can be obtained when desalination plants are integrated with power generation plants (Aschner, 1980). Such dual-purpose plants save energy but also increase the capital cost and complexity of operation.

Two aspects of the basically simple desalination process require special attention. One is the highcorrosivity of seawater, especially pronounced in the higher-temperature destillation processes, which requires the use of corrosion-resistant expensive materials. Typical materials in use are copper–nickel alloys, stainless steel, titanium, and, at lower temperatures, fiber-reinforced polymers (George et al., 1975). Another aspect is scale formation (Glater et al., 1980; Heitman, 1990). Salts in saline water, particularly calcium sulfate, magnesium hydroxide, and calcium carbonate, tend to precipitate when a certain temperature and concentration are exceeded. The precipitate, often mixed with dirt entering with the seawater and with corrosion products, will gradually plug up pipes, and when depositing on heat transfer surfaces reduces heat transfer rates and thus impairs plant performance. While the ambient-temperature operation of membrane processes reduces scaling, membranes are much more susceptible not only to minute amounts of scaling or even dirt, but also to the presence of certain salts and other compounds that reduce their ability to separate salt from water. To reduce corrosion, scaling, and other problems, the water to be desalted is pretreated. The pretreatment consists of filtration, and may inlude removal of air (deaeration), removal of CO_2 (decarbonation), and selective removal of scale-forming salts (softening). It also includes the addition of chemicals that allow operation at higher temperatures without scale deposition, or which retard scale deposition and/or cause the precipitation of scale which does not adhere to solid surfaces, and that prevent foam formation during the desalination process.

Saline waters, including seawater, contain, besides a variety of inorganic salts, also organic materials and various particles. They differ in composition from site to site, and also change with time due to both natural and person-made causes. Design and operation of desalination plants requires good knowledge of the saline water composition and properties (Fabuss, 1980; Heitman, 1991).

The major water desalination processes that are currently in use or in advanced research stages are concisely described below. Information on detailed modeling can be found in the references.

Distillation Processes

Multistage Flash Evaporation (MSF)

Almost all of the large desalination plants use the MSF process shown schematically in Figure 20.6.1. A photo of an operating plant is shown in Figure 20.6.2. The seawater feed is preheated by internal heat recovery from condensing water vapor during passage through a series of stages, and then heated to its top temperature by steam generated by an external heat source. The hot seawater then flows as a horizontal free-surface stream through a series of "stages," created by vertical walls which separate the vapor space of each stage from the others. These walls allow the vapor space of each stage to be maintained at a different pressure, which is gradually decreased along the flow path due to the gradually decreasing

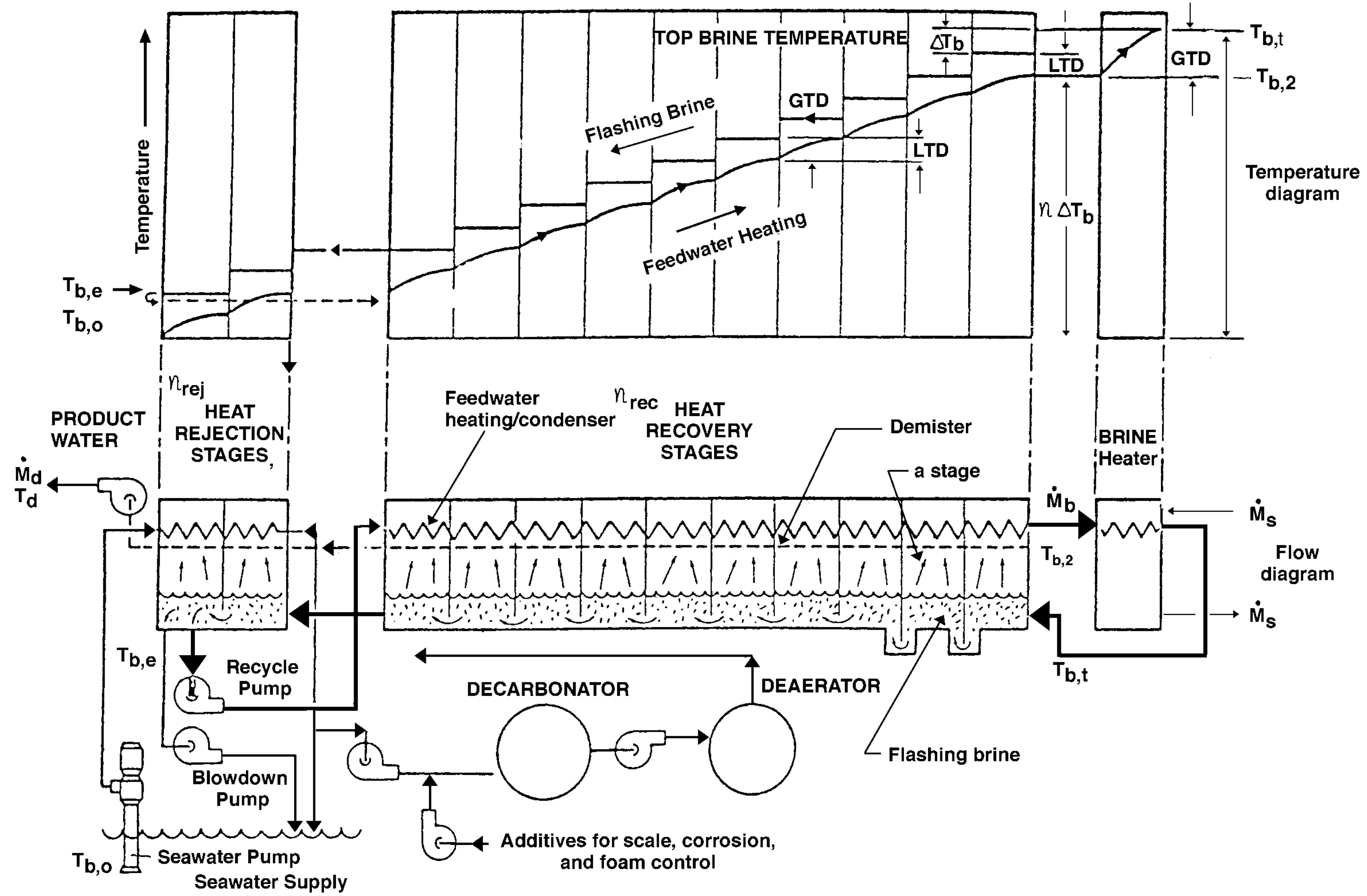

FIGURE 20.6.1 Schematic flow and temperature diagram of the MSF process, for a recirculation type plant.

FIGURE 20.6.2 One of the six units of the 346,000 m^3/day MSF desalination plant Al Taweelah B in Abu Dhabi, United Arab Emirates. (Courtesy of Italimpianti S. p. A.) It is a dual-purpose plant, composed of six identical power and desalination units. Five of the six boilers are seen in the background. The desalination units were in 1996 the largest in the world. They have 17 recovery and 3 reject stages and a performance ratio (PR) of 8.1. The plant also produces 732 MWe of power.

temperature in the condenser/seawater-preheater installed above the free stream. The seawater is superheated by a few degrees celsius relative to the vapor pressure in each stage it enters, and consequently evaporates in each stage along its flow path. The latent heat of the evaporation is supplied by equivalent reduction of the sensible heat of the evaporating water, thus resulting in a gradual lowering of the stream temperature. The evaporation is vigorous, resulting in intensive bubble generation and growth with accompanying stream turbulence, a process known as **flash evaporation** (Lior and Greif, 1980; Miyatake et al., 1992; 1993). One of the primary advantages of the MSF process is the fact that evaporation occurs from the saline water stream and not on heated surfaces (as in other distillation processes such as submerged tube and ME evaporation) where evaporation typically causes scale depostition and thus gradual impairment of heat transfer rates. Also, the fact that the sensible heat of water is much smaller than its latent heat of evaporation, where the specific heat $c_p = 4.182$ kJ/kg/°C change of water temperature and the latent heat is $h_{fg} = 2378$ kJ/kg, and the fact that the top temperature is limited by considerations of scaling and corrosion, dictate the requirement for a very large flow rate of the evaporating stream. For example (in the following, the subscripts *b*, *d*, and *s* refer to brine distillate, and steam, respectively), operating between a typical top temperature $T_{b,t}$ of 90°C at the inlet to the evaporator and an exit temperature $T_{b,e}$ of 40°C corresponding to the ambient conditions, the overall temperature drop of the evaporating stream if 50°C. By using these values, the heat balance between the sensible heat of the water stream, flowing at a mass flow rate $\dot{m}_b$, and the latent heat needed for generating water vapor (distillate) at a mass flow rate $\dot{m}_d$ is

$$\left(\dot{m}_b - \dot{m}_d\right) c_p \left(T_{b,t} - T_{b,e}\right) \approx \dot{m}_d h_{fg} \tag{20.6.2}$$

which yields the brine-to-product mass flow ratio as

$$\frac{\dot{m}_b}{\dot{m}_d} = \frac{h_{fg}}{c_p\left(T_{b,t} - T_{b,e}\right)} + 1 = \frac{2378}{(4.182)(50)} + 1 = 12.37 \tag{20.6.3}$$

Therefore, 12.37 kg of saline water are needed to produce 1 kg of distillate. This high flow rate incurs corresponding pumping equipment and energy expenses, sluggish system dynamics, and, since the stream level depth is limited to about 0.3 to 0.5 m for best evaporation rates, also requires large evaporator vessels with their associated expense.

The generated water vapor rises through a screen ("demister") placed to remove entrained saline water droplets. Rising further, it then condenses on the condenser tube bank, and internal heat recovery is achieved by transferring its heat of condensation to the seawater feed that is thus being preheated. This internal heat recovery is another of the primary advantages of the MSF process. The energy performance of distillation plants is often evaluated by the *performance ratio*, PR, typically defined as

$$\mathrm{PR} \equiv \frac{\dot{m}_d}{\dot{m}_s} \tag{20.6.4}$$

where $\dot{m}_s$ is the mass flow rate of heating steam. Since the latent heat of evaporation is almost the same for the distillate and the heating steam, PR is also the ratio of the heat energy needed for producing one unit mass of product (distillate) to the external heat actually used for that purpose. Most of the heating of the brine stream to the top temperature $T_{b,t}$ is by internal heat recovery, and as seen in Figure 20.6.1, the external heat input is only the amount of heat needed to elevate the temperature of the preheated brine from its exit from the hottest stage at $T_{b,2}$ to $T_{b,t}$. Following the notation in Figure 20.6.1, and using heat balances similar to that in Equation (20.6.3) for the brine heater and flash evaporator, the PR can thus also be defined as

$$\mathrm{PR} = \frac{\dot{m}_b\left(\overline{c_{p,b}}\right)_{e\to t}\left(T_{b,t} - T_{b,e}\right)\Big/h_{fg,b}}{\dot{m}_b\left(\overline{c_{p,b}}\right)_{2\to t}\left(T_{b,t} - T_{b,2}\right)\Big/h_{fg,s}} \approx \frac{T_{b,t} - T_{b,e}}{T_{b,t} - T_{b,2}} \tag{20.6.5}$$

where $(\overline{c_{p,b}})_{e\to t}$ and $(\overline{c_{p,b}})_{2\to t}$ are the specific heats of brine, the first averaged over the temperature range $T_{b,e} \to T_{b,t}$ and the second over $T_{b,2} \to T_{b,t}$. The rightmost expression in Equation (20.6.5) is nearly correct because the specific heat of the brine does not change much with temperature, and the latent heat of evaporation of the brine is nearly equal to the latent heat of condensation of the heating steam. It is obvious from Equation (20.6.5) that PR increases as the top heat recovery temperature $T_{b,2}$ (at the exit from the condenser/brine-preheater) increases. It is also obvious (even from just examining Figure 20.6.1) that increasing the number of stages (matched with a commensurate increase in condenser heat transfer area and assuming no significant change in the overall heat transfer coefficient) for a given $T_{b,t}$, will raise the flash evaporator inlet temperature $T_{b,3}$, which will lead to a rise in $T_{b,2}$ and thus also in the PR.

Assuming that the temperature drop of the flashing brine, ΔT_b, is the same in each stage, the relationship between the number of stages (n) and the performance ratio is

$$\mathrm{PR} = \frac{1}{\dfrac{\mathrm{LTD}}{T_{b,t} - T_{b,e}} + \dfrac{1}{n}} \tag{20.6.6}$$

where LTD is the lowest temperature difference between the flashed vapor and the heated feedwater, in each stage (Figure 20.6.1). Equation (20.6.6) shows that increasing the number of stages increases the PR. This implies that more heat is then recovered internally, which would thus require a larger condenser/brine-preheater heat transfer area. The required heat transfer area, A, *per unit mass of distillate produced* for the entire heat recovery section (composed of n_{rec} stages), and taking average values of the overall vapor-to-feedwater heat transfer coefficient U and LMTD, is thus

$$A = n_{\mathrm{rec}} A_n = n_{\mathrm{rec}} \frac{h_{b,fg}}{U(\mathrm{LMTD})} \tag{20.6.7}$$

LMTD, the log-mean temperature difference between the vapor condensing on the tubes and the heated brine flowing inside the tubes, for an average stage is

$$\text{LMTD} = \frac{\text{GTD} - \text{LTD}}{\ln \dfrac{\text{GTD}}{\text{LTD}}} = \frac{\left(T_{b,t} - T_{b,2}\right) - \text{LTD}}{\ln\left(\dfrac{T_{b,t} - T_{b,2}}{\text{LTD}}\right)} \tag{20.6.8}$$

where GTD is the greatest temperature difference between the flashing brine and the brine heated in the condenser. The size of the heat transfer area per unit mass of distillate is

$$A = \frac{h_{fg,b}}{U} \frac{n_{\text{rec}}}{\left(T_{b,t} - T_{b,e}\right)} \ln\left(\frac{n_{\text{rec}}}{n_{\text{rec}} - PR}\right) \tag{20.6.9}$$

Examination of this equation will show that the required heat transfer area for the heat recovery section per unit mass of distillate produced, A, increases significantly when PR is increased, and decreases slightly as the number of heat recovery stages, n_{rec}, is increased.

The MSF plant shown in Figure 20.6.1 is of the *recirculation* type, where not all of the brine stream emerging from the last evaporation stage is discharged from the plant (as it would have been in a *once-through* type of plant). A fraction of the emerging brine is mixed with pretreated seawater and recirculated into the condenser of the heat recovery section of the plant. Since only a fraction of the entire stream in this configuration is new seawater, which needs to be pretreated (removal of air and CO_2, i.e., deaeration and decarbonation, and the addition of chemicals that reduce scale deposition, corrosion, and foaming), the overall process cost is reduced. The recirculation plant is also easier to control than the once-through type.

While most of the energy exchange in the plant is internal, steady-state operation requires that energy in an amount equal to all external energy input be also discharged from the plant. Consequently, the heat supplied in the brine heater (plus any pumping energy) is discharged in the heat rejection stages section of the plant (Figure 20.6.1). Assuming an equal temperature drop in each stage, and that the pumping energy can be neglected relative to the heat input in the brine heater, indicates that the ratio of the number of the heat-recovery to heat-rejection stages is approximately equal to the performance ratio PR.

Further detail about MSF desalination can be found in Steinbruchel and Rhinesmith, (1980) and Khan (1986). A detailed design of an MSF plant producing 2.5 million gals. of freshwater per day was published by the U.S. government (Burns and Roe, 1969).

Multi-Effect Distillation (ME)

The principle of the ME distillation process is that the latent heat of condensation of the vapor generated in one effect is used to generate vapor in the next effect, thus obtaining internal heat recovery and good energy efficiency. Several ME plant configurations, most prominently the horizontal tube ME (HTME, shown in Figure 20.6.3) and the vertical tube evaporator (VTE, shown schematically in Figure 20.6.4) are in use. In the HTME, vapor is circulated through a horizontal tube bundle, which is subjected to an external spray of somewhat colder saline water. The vapor flowing in these spray-cooled tubes condenses, and the latent heat of condensation is transferred through the tube wall to the saline water spray striking the exterior of the tube, causing it to evaporate. The vapor generated thereby flows into the tubes in the next effect, and the process is repeated from effect to effect.

In the VTE the saline water typically flows downward inside vertical tubes and evaporates as a result of condensation of vapor coming from a higher temperature effect on the tube exterior. While internal heat recovery is a feature common to both MSF and ME processes, there are at least three important differences between them. One is that evaporation in the ME process occurs on the heat transfer surfaces (tubes), while in the MSF process it takes place in the free stream. This makes the ME process much

FIGURE 20.6.3 Two HTME desalination units, each producing 5000 m^3/day, in St. Croix, U.S. Virgin Islands. (Courtesy of I.D.E. Technologies Ltd.)

more susceptible to scale formation. At the same time, the heat transfer coefficient between the vapor and the preheated brine is lower in the MSF process because the heated brine does not boil. In the ME process it does boil, and it is well known that boiling heat transfer coefficients are significantly higher than those where the heating does not result in boiling. In using direct transfer of latent heat of condensation to latent heat of evaporation, instead of sensible heat reduction to latent heat of evaporation as in MSF, the ME process requires a much smaller brine flow than the MSF. Limiting brine concentration in the last effect to about three times that of the entering seawater, for example, requires a brine flow of only about 1.5 times that of the distillate produced. At the same time, a pump (although much smaller than the two pumps needed in MSF) is needed for each effect.

The PR of ME plants is just sightly lower than the number of effects, which is determined as an optimized compromise between energy efficiency and capital cost. Six effects are typical, although plants with as many as 18 effects have been built.

Further detail about ME desalination can be found in Steinbruchel and Rhinesmith (1980) and Standiford, (1986a).

Vapor Compression Distillation (VC)

As stated earlier, the vapor pressure of saline water is lower than that of pure water at the same temperature, with the pressure difference proportional to the boiling point elevation of the saline water. Desalination is attained here by evaporating the saline water and condensing the vapor on the pure water. Therefore, the pressure of the saline water vapor must be raised by the magnitude of that pressure difference, plus some additional amount to compensate for various losses. This is the principle of the vapor compression desalination method. Furthermore, as shown in Figure 20.6.5, the heat of condensation of the compressed vapor is recovered internally by using it to evaporate the saline water. Additional heat recovery is obtained by transferring heat from the concentrated brine effluent and the produced freshwater (which need to be cooled down to as close to ambient conditions as possible anyway) to the feed saline water which is thus preheated. The schematic flow diagram in Figure 20.5.5 shows a design in which the preheated seawater is sprayed onto a bank of horizontal tubes carrying condensing compressed vapor at a temperature higher than that of the seawater. The spray thus evaporates on contact with the exterior of the tube and provides the cooling needed for the internal condensation. Considering

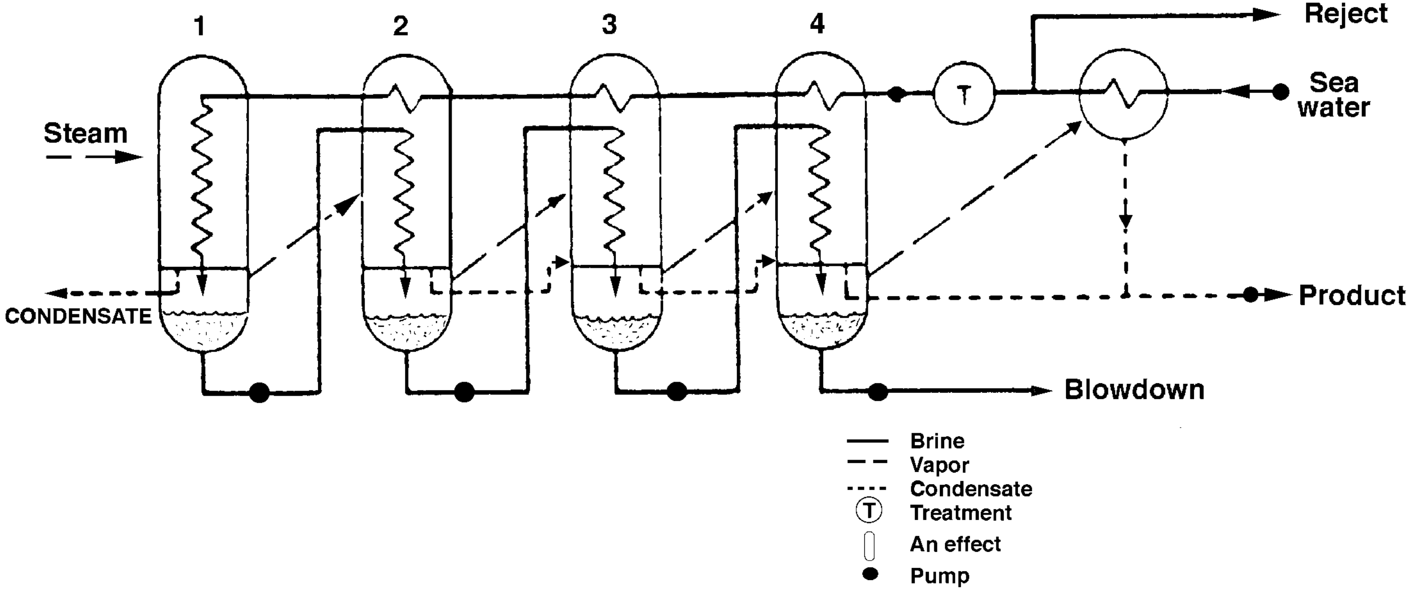

FIGURE 20.6.4 Simplified schematic flow diagram of a typical four-effect VTE desalination plant.

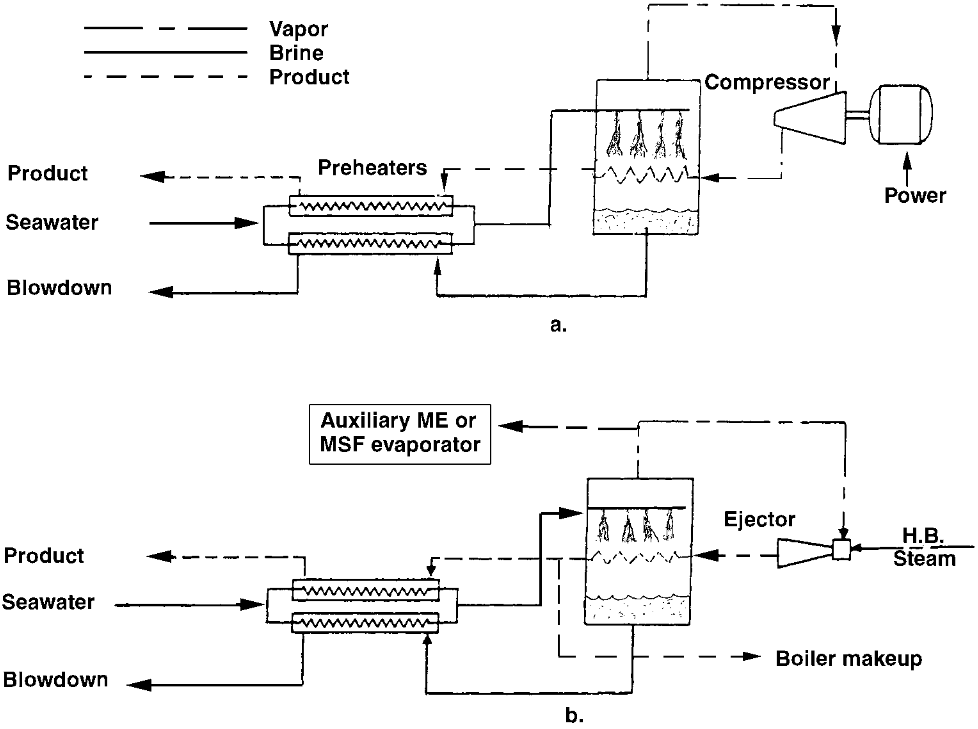

FIGURE 20.6.5 Schematic flow diagram of a basic horizontal-tube VC desalination plant (a) with mechanical, motor-driven compressor; (b) with a thermo-compressor, using an ejector.

the fact that the energy required for vapor compression over a typical overall temperature difference of 4°C and a vapor compressor efficiency of 0.8 is 34 kJ/kg (easily calculated from an enthalpy balance), and that the latent heat of condensation is about 2400 kJ/kg, one can see that a small amount of compression energy enables a large amount of heat to be used internally for desalination. One can thus envisage the VC plant as a large flywheel, wheeling a large amount of energy around at the expense of a small amount needed for sustaining its motion.

The compressor can be driven by electric motors, gas or steam turbines, or internal combustion (usually diesel) engines. The compressor can also be a steam-driven ejector (Figure 20.6.5b), which improves plant reliability because of its simplicity and absence of moving parts, but also reduces its efficiency because an ejector is less efficient than a mechanical compressor. In all of the mentioned thermally driven devices, turbines, engines, and the ejector, the exhaust heat can be used for process efficiency improvement, or for desalination by an additional distillation plant.

Figure 20.6.6 shows a multi-effect VC plant. Using more than a single effect reduces the vapor volume that needs to be compressed. Furthermore, the overall required heat transfer area is also decreased because much of the single-phase heat transfer process in the preheater of the single-effect plant is replaced by the high-heat-transfer condensation–evaporation processes in the effects. Although the ME feature also increases the required compression ratio, the cost of produced water is reduced overall.

Further detail about VC desalination can be found in Steinbruchel and Rhinesmith (1980), Khan (1986), and Standiford, (1986b).

Solar Distillation

The benefits of using the nonpolluting and practically inexhaustible energy of the sun for water desalination are obvious. Furthermore, many water-poor regions also have a relatively high solar flux over a

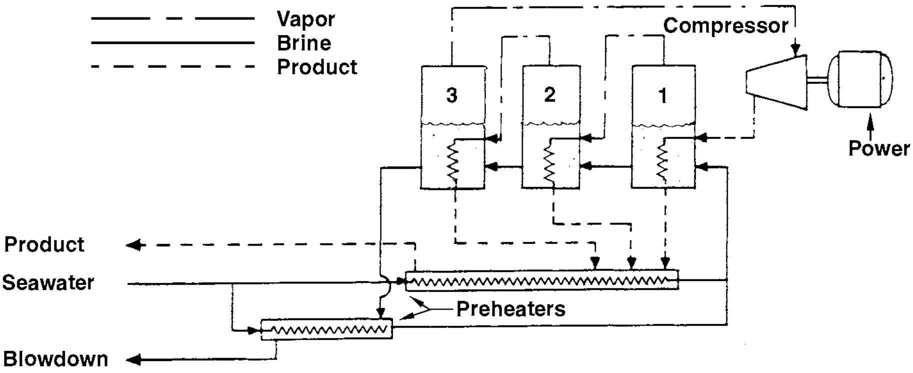

FIGURE 20.6.6 Schematic flow diagram of a ME vapor compression submerged-tube desalinaton plant with three effects.

large fraction of the time. The major impediment in the use of solar energy is economical: the diffuse nature of solar energy dictates the need for constructing a large solar energy collection area. For example, assuming a single-effect solar still efficiency of 50% (which is the upper practical limit for conventional designs), the still would produce at most about 3.5 to 4.8 kg fresh water per m^2 per day, or a 208 to 286 m^2 solar still would be required to produce 1 m^3 of fresh water per day. More realistic still efficiencies increase the area requirement about twofold.

Shown in Figure 20.6.7, a typical solar still consists of a saline water container in which the water is exposed to the sun and heated by it. The temperature rise to above ambient causes net evaporation of the saline water, thus separating pure water vapor from the solution. The vapor condenses on the colder cover, and this destilled water flows to collection troughs.

Solar stills of the type depicted in Figure 20.6.7, in many sizes and constructional variants, have been built and used successfully in many countries in the world. They are simple, easy to construct, reliable, and require very little maintenance although in some regions the covers must be cleaned frequently from accumulated dust or sand.

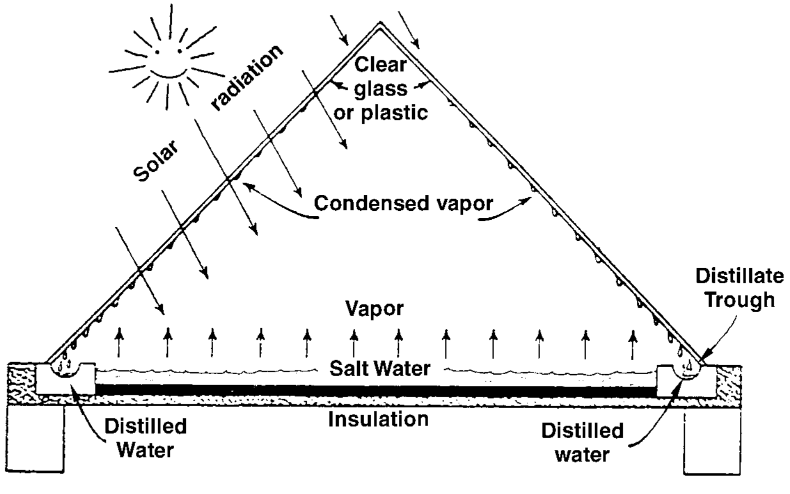

FIGURE 20.6.7 A typical basin-type solar still.

Since the heat of condensation in single-effect stills of the type shown in Figure 20.6.7 is lost to the ambient, more-energy-efficient operation can obviously be achieved in a multi-effect design, where the heat of condensation is used to evaporate additional saline water. A number of such stills were built and tested successfully, but are not commercially competitive yet.

Solar stills integrate the desalination and solar energy collection processes. Another approach to solar desalination is to use separately a conventional desalination process and a suitable solar energy supply system for it. Any compatible desalination and solar energy collection processes could be used. Distillation, such as MSF or ME, can be used with heat input from solar collectors, concentrators, or solar ponds (Hoffman, 1992; Glueckstern, 1995). Net average solar energy conversion efficiencies of solar collectors (Rabl, 1985; Lior, 1991) are about 25% and of solar ponds (Lior, 1993) about 18%, similar to the efficiencies of solar stills, but the MSF or ME plants can operate at preformance ratios of 10 or more, thus basically increasing the freshwater production rate by at least tenfold, or reducing the required solar collection area by at least tenfold for the same production rate.

Solar or wind energy can also be used for desalination processes that are driven by mechanical or electrical power, such as VC, RO, and ED. The solar energy can be used to generate the required power by a variety of means, or photovoltaic cells can be used to convert solar energy to electricity directly.

Freeze Desalination

It is rather well known that freezing of saline water solutions is an effetive separation process in that it generates ice crystals that are essentially salt-free water, surrounded by saline water of higher concentration. This process requires much less energy than distillation, and the problems of corrosion and scaling are markedly reduced due to the much lower operating temperatures. Several pilot plants were constructed and have proven concept viability. Nevertheless, the process has not yet reached commercial introduction for several reasons, such as the difficulty in developing efficient and economical compressors for vapor with the extremely high specific volume at the low process pressure, and difficulties in maintaining the vacuum system leak free and in effecting reliable washing of the ice crystals. A review of freeze desalination processes is given by Tleimat (1980).

Membrane Separation Processes

Reverse Osmosis (RO)

Separation of particulate matter from a liquid by applying pressure to the liquid and passing it through a porous membrane, whereby particles larger than the pore size remain on the upstream side of the membrane and the liquid flows to its downstream side, is well known as *filtration*. Semipermeable very dense membranes that actually separate salt molecules (ions) from the water, by similarly keeping the salt on the upstream side and allowing the pressurized pure water to flow through the membrane, were developed in the 1950s. The reverse of this process, **osmosis**, is well known: for example, if a membrane is placed to separate water from an aqueous salt solution, and the membrane is semipermeable (here meaning that it permits transfer of water only, not the salt components in the aqueous solution), the water will tend naturally to migrate through this membrane into the salt solution. Osmosis is, for example, the major mass transport phenomenon across living cells. The driving force for this water flux is proportional to the concentration difference between the two sides of the membrane, and is exhibited as the so-called **osmotic pressure**, which is higher by 2.51 MPa on the water side of the membrane for typical seawater at 25°C. If a pressure higher than the osmotic pressure is applied on the saline solution side of the membrane, the water flux can be reversed to move pure water across the membrane from the saline solution side to the pure water one. This process is called *reverse osmosis* (and sometimes *hyperfiltration*), and is the basic principle of RO desalination

Unlike filtration of particulates, the selective "filtration" of the water in RO is not due to the relationship of the membrane pore size to the relative sizes of the salt and water molecules. Rather, one way to explain

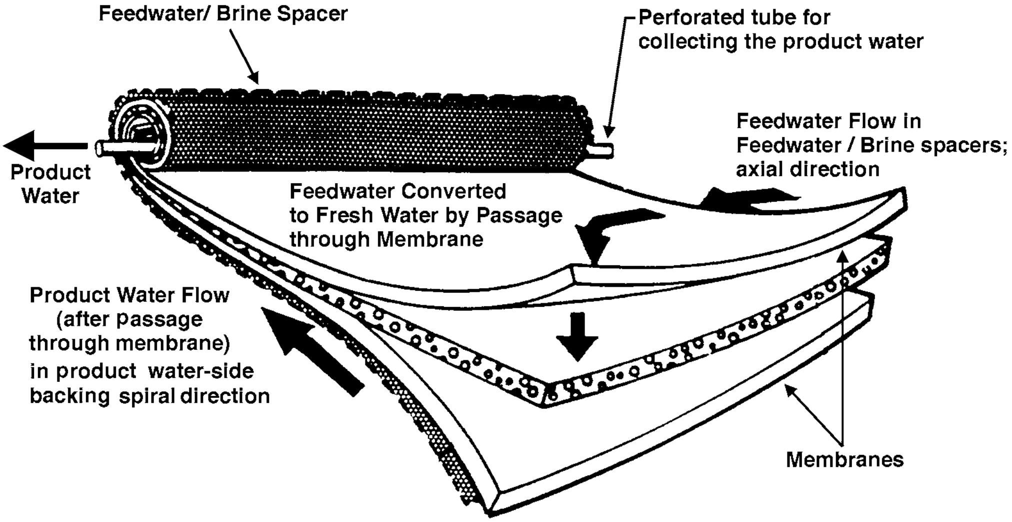

FIGURE 20.6.8 A spiral-wound RO membrane element.

the process is that the very thin active surface layer of the membrane forms hydrogen bonds with water molecules and thus makes them unavailable for dissolving salt. Salt thus cannnot penetrate through that layer. Water molecules approaching that layer are, however, transported through it by forming such hydrogen bonds with it and in that process displacing water molecules that were previously hydrogen bonded at these sites. The displaced water molecules then move by capillary action through the pores of the remainder of the membrane, emerging at its other side.

The most prevalent membrane configurations used in RO plants are of the spiral-wound or hollow-fiber types. The basic spiral-wound-type module (Figure 20.6.8) is made of two sheets placed upon each other and rolled together in an increasing diameter spiral around a cylindrical perforated tube. One of the sheets is in the form of a sandwich typically composed of five layers bonded together along three edges. The two outer layers are the semipermeable membranes. Each of them is backed by a porous material layer for mechanical strength, and the very central layer is a thicker porous material layer that takes up the produced fresh water. The second sheet is a porous mesh through which the high-pressure saline water feed is passed in an axial direction. Product water separates from the saline solution and permeates through the two adjacent semipermeable membranes into the central product water–carrying layer, which conducts it spirally to the unbonded edge of the "sandwich" and to the inner perforated tube. The semipermeable membranes are typically made from cellulose acetate, and more recently from composites of several polymers.

Hollow fiber modules have a configuration similar to a shell-and-tube heat exchanger, with the fibers taking the place of the tubes. A very large number of typicallly 25 to 250 μm outside-diameter semipermeable hollow fibers (wall thickness typically 5 to 50 μm) are bundled together and placed in a saline water pressure vessel. The hollow core of each fiber is sealed on one end. The pressurized saline water is brought into the module (through a central porous feed tube, Figure 20.6.9) to circulate on the exterior surface of the fibers, and water permeates through the fiber wall into its hollow core, through which it flows to a permeate collection manifold at the open end of the fiber bundle. The increasingly concentrated saline water flows radially and is discharged at the exterior shell of the bundle. The hollow fibers are typically made of polyamide or cellulose triacetate, and offer about 20 fold more surface (separation) area per unit volume than the spiral-wound configuration.

The basic approximate equation for the separation process gives the water flux $\dot{m}''_w$ (kg/m^{2}sec) across an RO membrane, in the absence of fouling, as

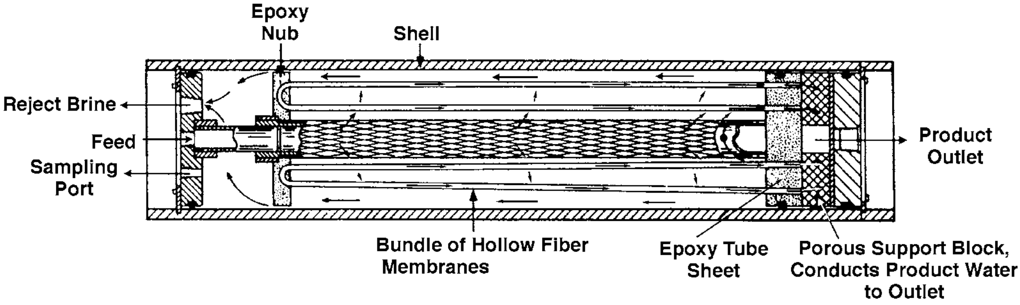

FIGURE 20.6.9 A hollow-fiber RO membrane module. (Du Pont Permasep™.)

$$\dot{m}_w'' = K_{pe} K_{cf}\left[\left(P_f - P_p\right) - \left(\pi_f - \pi_p\right)\right] \tag{20.6.10}$$

where

K_{pe} *water permeability constant* of the membrane (in kg/m²sec Pa), typically increasing strongly as the temperature rises: a plant designed to operate at 20°C may produce up to 24% more water if the water temperature is 28°C,

K_{cf} *compaction correction factor* (dimensionless) which corrects for the fact that the flux is reduced due to densification of the barrier layer (a phenomenon similar to creep) of the membrane, and which increases with the operating pressure and temperature. It is often calculated by the relationship

$$K_{cf} = BC(T)C(P)C(t) \tag{20.6.11}$$

where B is a constant,

$C(T)$ represents the temperature dependence of the Compaction Correction Factor for the particular membrane of interest,

$C(P)$ represents its pressure dependence: while a higher pressure difference across the membrane is shown in Equation (20.6.10) to increase the water flux, higher feed pressure (P_f) also tends to compact the membrane and thus reduce its water flux, typically according to

$$C(P) = P_f^n \tag{20.6.12}$$

where n is a negative number,

and where the time dependence $C(t)$ is represented by

$$C(t) = t^m \tag{20.6.13}$$

where t is the operating time (say, in days) and m is a negative number depending on the membrane.

P water or saline solution pressure (Pa),

π osmotic pressure (Pa),

and the subscripts f and p pertain to the saline feed water and to the desalted product water, respectively.

The required membrane area A can be estimated by

$$A = \frac{\dot{m}_p}{\dot{m}_p'' f} \tag{20.6.14}$$

where $\dot{m}_p$ is the freshwater mass production rate of the plant (kg/sec), and f ($0 < f \leq 1.0$) is the *area utilization factor* that corrects for the fact that the membrane surface is incompletely in contact with the saline water feed stream due to the porous mesh and other devices, such as turbulence promoters, placed in the feed stream path; in a good design $f > 0.9$.

Examination of Equation (20.6.10) shows that water separation rate increases with the water permeability constant K_{pe}. Unfortunately, so does the salt flux across the membrane, resulting in a saltier product. An approximation for this salt flow is

$$\dot{m}_s = KK_s\left(C_{fm} - C_p\right) \tag{20.6.15}$$

where

$\dot{m}_s$ = salt mass transfer rate across the membrane, kg/sec,
K = a proportionality constant, dimensionless,
K_s = *salt permeation constant,* kg/sec, which increases with pressure and temperature.

The salinity of the product water (C_p) can be estimated by the formula

$$C_p = K_{cp}(1 - \eta)\overline{C} \tag{20.6.16}$$

where

K_{cp} = *concentration polarization coefficient,* $\equiv C_{fm} / \overline{C}$ is a measure of the increase of the feedwater salinity at the membrane wall beyond that of the bulk solution,
C_{fm} = salt concentration at the membrane wall,
$\overline{C}$ = bulk salinity of the saline water feed, $\approx (C_f + C_r)/2$,
C_r = salt concentration of the reject brine,
η = *salt rejection factor,* $\equiv$(amount of salts rejected by the membrane)/(amount of salts in the brine feed).

The pressure to be used for RO depends on the salinity of the feed water, the type of membrane, and the desired product purity. It ranges form about 1.5 MPa for low feed concentrations or high-flux membranes, through 2.5 to 4 MPa for brackish waters, and to 6 to 8.4 MPa for seawater desalination. In desalination of brackish water, typical product water fluxes through spiral-wound membranes are about 600 to 800 kg/(m^2day) at a recovery ratio (RR) of 15% and an average salt rejection of 99.5%, where

$$\mathrm{RR} = \frac{\dot{m}_p}{\dot{m}_f} \cong 1 - \frac{C_f}{C_r} \tag{20.6.17}$$

The fluxes in hollow-fiber membranes used in seawater desalination are 20- to 30-fold smaller, but the overall RO system size does not increase, because the hollow-fiber membranes have a much larger surface area per unit volume. The RR and salt rejection ratio are similar to those of spiral-wound membranes.

Since the concentrated reject brine is still at high pressure, it is possible to recover energy by passing this brine through hydraulic turbines, and thus reduce the overall energy consumption by up to 20%. The energy requirements of seawater RO desalination plants with energy recovery are about 5 to 9 kWh, or 18 to 33 MJ, of mechanical or electric power per m^3 fresh water produced. In comparison, the MSF desalination process requires about 120 to 280 MJ of heat and about 15 MJ of mechanical/electric power (for pumping and auxiliaries) per m^3. The energy requirement of the RO process is thus smaller than that of the MSF process even if the RO energy requirement is multiplied by the thermal-to-mechanical (or electrical) power conversion factor of 3 to 4. The specific *exergy* consumption of the MSF process using 120°C steam is about 2- to 3-fold higher than that of the RO process, but becomes comparable in magnitude if the steam temperature is lowered to 80°C.

The life of membranes is affected by gradual chemical decomposition or change. For example, cellulose acetate membranes **hydrolyze** with time. The rate of hydrolysis has a steep minimum at a solution pH of 4.5 to 5.0, and increases drastically with temperature.

Membranes are susceptible to plugging by dirt and to deterioration in their selectivity caused by various species present in the saline water. Careful pretreatment of the feed water is therefore necessary. It typically consists of clarification, filtration, chlorination for destroying organic matter and microorganisms, removal of excess chlorine to prevent membrane oxidation, and dosing with additives to prevent calcium sulfate scaling and foam formation. Periodical chemical or mechanical cleaning is also necessary. Pretreatment and cleaning are significant and increasing fractions of the RO plant capital and operating costs.

Further detail about RO desalination can be found in Sourirajan and Matsuura (1985) and Amjad (1993).

Electrodialysis (ED)

In ED, the saline solution is placed between two membranes, one permeable to cations only and the other to anions only. A direct electrical current is passed across this system by means of two electrodes, cathode and anode, exposed to the solution (Figure 20.6.10). It causes the cations in the saline solution to move toward the cathode, and the anions to the anode. As shown in Figure 20.6.10, the anions can leave the compartment in their travel to the anode because the membrane separating them from the anode is permeable to them. Cations would similarly leave the compartment toward the cathode. The exit of these ions from the compartment reduces the salt concentration in it, and increases the salt concentration in the adjacent compartments. Tens to hundreds of such compartments are stacked together in practical ED

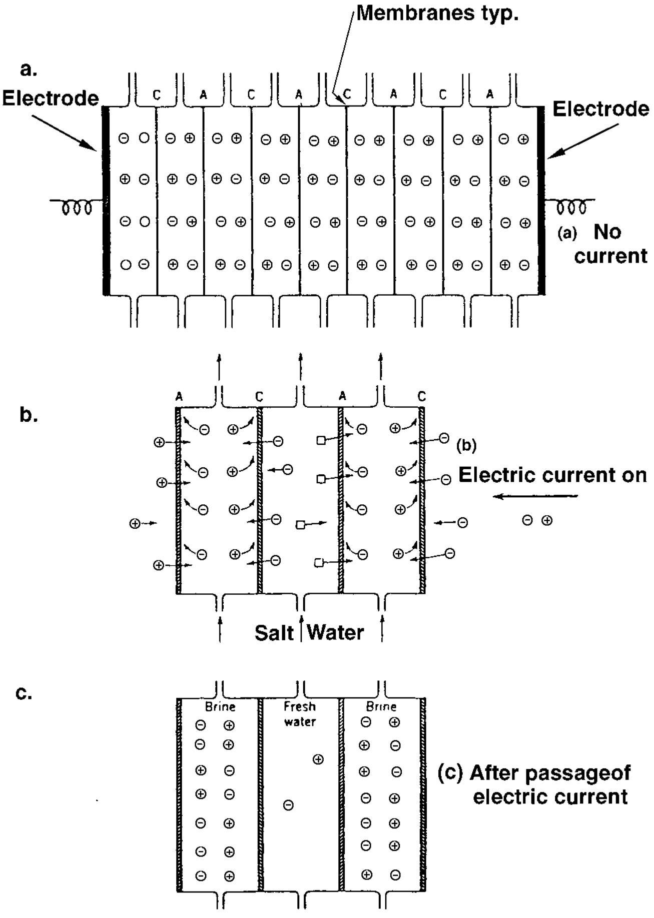

FIGURE 20.6.10 The ED process. *C* and *A* are cation- and anion-permeable membranes, respectively. Application of electric current causes ion transport in a way that salt is depleted in alternate compartments, and enriched in the remaining ones.

plants, leading to the creation of alternating compartments of fresh and salt-concentrated water. ED is a continuous-flow process, where saline feed is continuously fed into all compartments and the product water and concentrated brine flow out of alternate compartments. The flow along the membranes also improves the mass transport there, and the separators between the membranes are constructed to provide good flow distribution and mixing on the membrane surfaces. Membrane sizes are roughly 0.5 × 1 m, spaced about 1 mm apart. Many typed of polymers are used to manufacture these ion-exchange selective membranes, which are often reinforced by strong fabrics made from other polymers or glass fibers.

Careful and thorough feed water pretreatment similar to that described in the section on RO is required. Pretreatment needs and operational problems of scaling are diminished in the electrodialysis reversal (EDR) process, in which the electric current flow direction is periodically reversed (say, three to four times per hour), with simultaneous switching of the water flow connections. This also reverses the salt concentration buildup at the membrane and electrode surfaces, and prevents concentrations that cause the precipitation of salts and scale deposition.

The voltage used for ED is about 1 V per membrane pair, and the current flux is of the order of 100 A/m^2 of membrane surface. The total power requirement increases with the feed water salt concentration, amounting to about 10 MW/m^3 product water per 1000 ppm reduction in salinity. About half this power is required for separation and half for pumping. Many plant flow arrangements exist, and their description can be found, along with other details about the process, in Shaffer and Mintz (1980) and Heitman (1991).

Defining Terms

Boiling point elevation: The number of degrees by which the boiling point temperature of a solution is higher than that of the pure solute at the same pressure.

Flash evaporation: An evaporation process that occurs when a liquid with a free surface is exposed to its vapor, where the vapor is below the saturation pressure corresponding to the temperature of the liquid. The process is typically vigorous, accompanied by rapid growth of bubbles and associated turbulence in the liquid.

Hydrolysis: Decompostion in which a compound is split into other compounds by taking up the elements of water.

Osmosis: The diffusion process of a component of a solution (or mixture) across a semipermeable membrane, driven by the concentration difference (or gradient) of that component across the membrane.

Osmotic pressure: The minimal pressure that has to be applied to the solution (mixture) on the lower concentration side of a membrane permeable to one solution component, for stopping the osmosis of that component through the membrane.

References

Amjad, Z., Ed. 1993. *Reverse Osmosis: Membrane Technology, Water Chemistry and Industrial Applications*. Van Nostrand Reinhold, New York.

Aschner, F.S. 1980. Dual purpose plants, in *Principles of Desalination*, 2nd ed., Part A, K.S. Spiegler and A.D.K. Laird, Eds., Academic Press, New York, chap. 5, 193–256.

Burns and Roe, Inc, 1969. *Universal Design—Report and User's Manual on Design of 2.5 Million Gallon per Day Universal Desalting Plant*, Vols. I–V, U.S. Department of the Interior, O.S.W. Contract No. 14-01-0001-955, Washington, D.C.

Fabuss, B.M. 1980. Properties of seawater, in *Principles of Desalination*, 2nd ed., Part B, K. S. Spiegler and A.D.K. Laird, Eds., Academic Press, New York, Appendix 2, 765–799.

George P.F., Manning, J.A., and Schrieber, C.F. 1975. *Desalinatin Materials Manual*. U.S. Department of the Interior, Office of Saline Water, Washington, D. C.

Glater, J., York, J.L., and Campbell, K.S. 1980. Scale formation and prevention, in *Principles of Desalination*, 2nd ed., Part B, K.S. Spiegler and A.D.K. Laird, Eds., Academic Press, New York, chap. 10, 627–678.

Glueckstern, P. 1995, Potential uses of solar energy for seawater desalination, *Desalination*, 101, 11–20.

Heitman, H.-G. 1990. *Saline Water Processing*, VCH Publications, New York.

Hoffman, D. 1992. The application of solar energy for large scale sea water desalination, *Desalination*, 89, 115–184.

Kasper, S.P. and Lior, N. 1979. A methodology for comparing water desalination to competitive freshwater transportation and treatment, *Desalination*, 30, 541–552.

Khan, A.S. 1986. *Desalination Processes and Multistage Flash Distillation Practice*, Elsevier, Amsterdam.

Lior, N., Ed. 1986. *Measurements and Control in Water Desalinaion*, Elsevier, Amsterdam.

Lior, N. 1991. Thermal theory and modeling of solar collectors, in *Solar Collectors, Energy Storage, and Materials*, F. de Winter, Ed., MIT Press, Cambridge, MA, chap. 4, 99–182.

Lior, N. 1993. Research and new concepts, in *Active Solar Systems*, G.O.G. Löf, Ed., MIT Press, Cambridge, MA, chap. 17, 615–674.

Lior, N. and Greif, R, 1980. Some basic observations on heat transfer and evaporation in the horizontal flash evaporator, *Desalination*, 33, 269–286.

Miyatake, O., Hashimoto, T., and Lior, N. 1992. The liquid flow in multi-stage flash evaporators, *Int. J. Heat Mass Transfer*, 35, 3245–3257.

Miyatake, O., Hashimoto, T., and Lior, N. 1993. The relationship between flow pattern and thermal non-equilibrium in the multi-stage flash evaporation process, *Desalination*, 91, 51–64.

M.W. Kellogg Co. 1975. *Saline Water Data Conversion Engineering Data Book*, 3rd ed., U.S. Department of the Interior, Office of Saline Water Contract No. 14-30-2639, Washington, D.C.

Rabl, A. 1985. *Active Solar Collectors and Their Applications*, Oxford University Press, New York.

Shaffer, L.H. and Mintz, M.S. 1980. Electrodialysis, in *Principles of Desalination*, 2nd ed., Part A, K.S. Spiegler and A.D.K. Laird, Eds., Academic Press, New York, chap. 6, 257–357.

Sourirajan, S. and Matsuura, T., Eds. 1985. *Reverse Osmosis and Ultrafiltration*, ACS Symposium Series 281, American Chemical Society, Washington, D.C.

Spiegler, K.S. and El-Sayed, Y.M. 1994. *A Desalination Primer.* Balaban Desalination Publications, Mario Negri Sud Research Institute, 66030 Santa Maria Imbaro (Ch), Italy.

Spiegler, K.S. and Laird, A.D.K., Eds. 1980. *Principles of Desalination*, 2nd ed., Academic Press, New York.

Standiford, F.C. 1986a. Control in multiple effect desalination plants, in *Measurements and Control in Water Desalination*, N. Lior, Ed., Elsevier, Amsterdam, chap. 2.2, 263–292.

Standiford, F.C. 1986b. Control in vapor compression evaporators, in *Measurements and Control in Water Desalination*, N. Lior, Ed., Elsevier, Amsterdam, chap. 2.3, 293–306.

Steinbruchel, A.B. and Rhinesmith, R.D. 1980. Design of distilling plants, in *Principles of Desalination*, 2nd ed., Part A, K.S. Spiegler and A.D.K. Laird, Eds., Academic Press, New York, chap. 3, 111–165.

Tleimat, B.W. 1980. Freezing methods, in *Principles of Desalination*, 2nd ed., Part B, K.S. Spiegler and A.D.K. Laird, Eds., Academic Press, New York, chap. 7, 359–400.

Further Information

The major texts on water desalination written since the 1980s are Spiegler and Laird (1980), Khan, (1986) (contains many practical design aspects), Lior (1986) (on the measurements and control aspects), Heitman (1990) (on pretreatment and chemistry aspects), and Spiegler and El-Sayed (1994) (an overiew primer). Extensive data sources are provided in George et al. (1975) and M. W. Kellog (1975).

The two major professional journals in this field are *Desalination, The International Journal on the Science and Technology of Desalting and Water Purification* and *Membrane Science*, which often addresses membrane-based desalination processes, both published by Elsevier, Amsterdam.

The major professional society in the field is the International Desalination Association (IDA) headquartered at P.O. Box 387, Topsfield, MA 01983. IDA regularly organizes international conferences, promotes water desalinaton and reuse technology, and is now publishing a trade magazine T*he International Desalination & Water Reuse Quarterly.*

The *Desalination Directory* by M. Balaban Desalination Publications, Mario Negri Sud Research Institute, 66030 Santa Maria Imbaro (Ch), Italy, lists more than 5000 individuals and 2000 companies and institutions in the world of desalinaiton and water reuse.

Two useful (though by now somewhat dated) books on desalination are by Howe, E. D. 1974. *Fundamentals of Water Desalination*, Marcel Dekker, New York, and by Porteous, A. 1975. *Saline Water Distillation Processes*, Longman, London.

Much information on oceans and seawater properties is avaiable in the book by Riley, J. P. and Skinner, Eds. 1975. *Chemical Oceanography*, Academic Press, New York.

20.7 Noise Control

Malcolm J. Crocker

Introduction

Noise is usually defined as unwanted sound. Noise in industry experienced over an extended period can cause hearing loss. Noise in other environments — in buildings, vehicles, and communities from a variety of sources causes speech interference, sleep disturbance, annoyance, and other effects (Crocker, 1997b,d). Noise propagates as sound waves in the atmosphere and as vibration in buildings, machinery, vehicles, and other structures. Noise can be controlled at the *source*, in the *path*, or at the *receiver*. The ear is more sensitive to noise in the mid- to high-frequency range, but fortunately high-frequency is easier to control than low-frequency noise. Several passive methods of noise and vibration control are described. An example of successful noise control is the considerable reduction in passenger jet aircraft noise in the last several years which has made them considerably quieter.

Sound Propagation

Sound waves propagate rather like ripples on a lake when a stone is thrown in (Crocker, 1997c). The ripples spread out from the source of the disturbance as circular waves until they reach a solid body or boundary (such as the lake edge) where reflections occur. The water does not flow from the source, but the disturbance propagates in the form of momentum and energy which is eventually dissipated. Sound waves in air cannot be seen but behave in a similar manner. Sound waves propagating in three dimensions from a source of sound are spherical rather than circular like the two-dimensional water wave propagation. Sound waves propagate at the wave speed (or *sound speed* c) which is dependent only on the absolute temperature T. It is 343 m/sec (1120 ft/sec) at a normal atmospheric temperature of 20°C. The *wavelength* λ of sound is inversely proportional to the *frequency* f in cycles/sec (known as hertz or Hz) and is given by $\lambda = c/f$ Hz. The sound waves result in fluctuations in the air pressure as they propagate. The air pressure difference from the mean atmospheric pressure is defined as the *sound pressure*. A logarithmic measure, the sound pressure level SPL or L_p, is usually used with sound and noise and the units are *decibels* (dB). The sound pressure level is $L_p = 10 \log_{10} (p^2 / p_{\text{ref}}^2)$, where p is the rms sound pressure and p_{ref} is the reference sound pressure 20 μPa (or 20×10^{-6} N/m^2). See Figure 20.7.1 (Crocker, 1997c).

Human Hearing

The human ear has a wide frequency response from about 15 or 20 Hz to about 16,000 Hz (Crocker, 1975; Greenberg, 1997). The ear also has a large dynamic range; the ratio of the loudest sound pressure we can tolerate to the quietest sound that we can hear is about ten million (10^7). This is equivalent to 140 dB. The ear can be divided into three main parts: the outer, middle, and inner ear. The outer ear, consisting of the fleshy pinna and ear canal, conducts the sound waves onto the ear drum. The middle ear converts the sound pressure at the ear drum into the mechanical motion of three small bones (named auditory ossicles: malleus, incus, and stapes) which in turn convert the mechanical motion into waves in the inner ear. Hair cells in the inner ear respond to the excitation and send neural impulses along the auditory nerves to the brain (Figure 20.7.2).

The higher the sound pressure level of a sound, the louder it normally sounds, although the frequency content of the sound is important too. The ear is most sensitive to sound in the mid-frequency range and

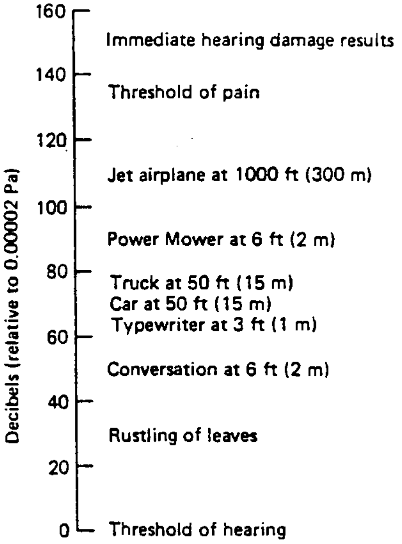

FIGURE 20.7.1 Some typical sound pressure levels.

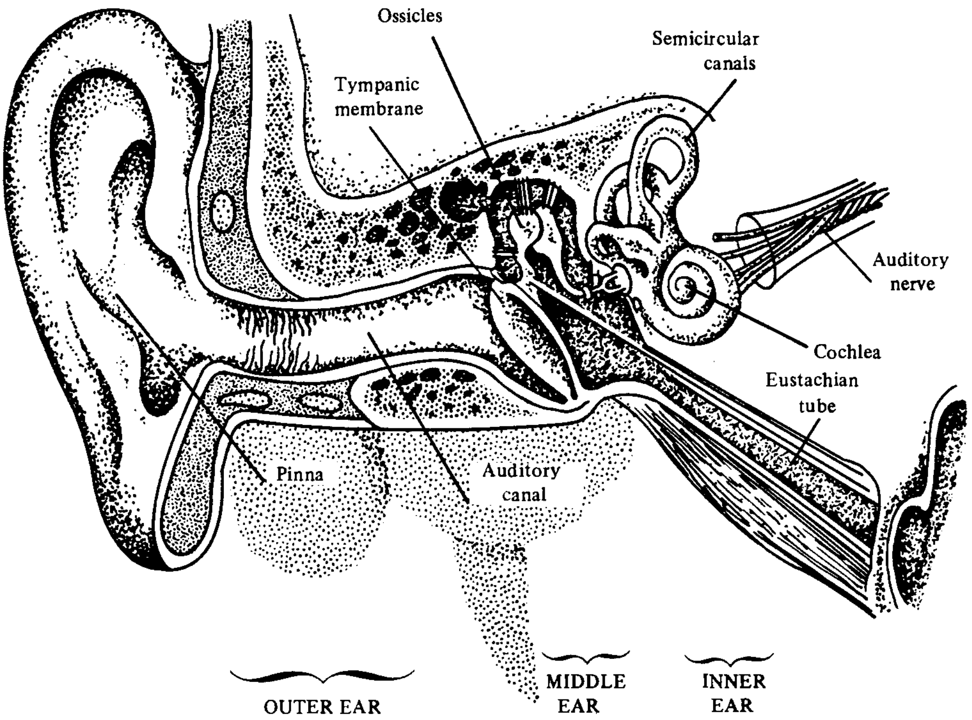

FIGURE 20.7.2 Cross section of the human ear showing the three main parts: outer, middle, and inner ear.

hears sound only poorly at lower frequencies (below 200 or 300 Hz). Most people have a maximum sensitivity to sound at about 4000 Hz (corresponding to a quarter wave resonance in the ear canal, with a pressure maximum at the eardrum). Electrical filters have been produced corresponding approximately to the frequency response of the ear. The A-weighting filter is the one most used and it filters off a considerable amount of the sound energy at low frequencies. The sound pressure level measured with an A-weighting filter is normally known as the A-weighted sound level (or the sound level for short). The anatomy and functioning of the ear are described more completely in several books (Crocker, 1997; Greenberg, 1997).

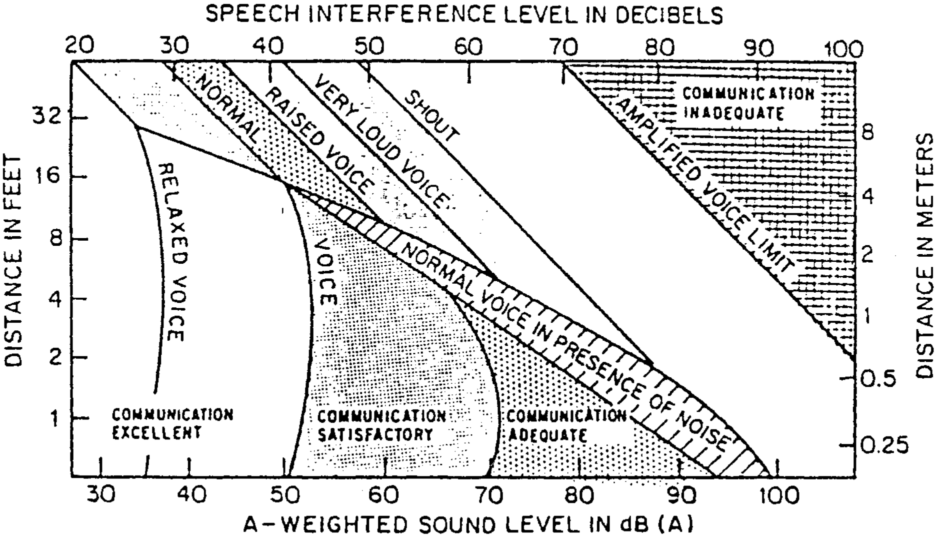

FIGURE 20.7.3 Recommended distances between speaker and listener for various voice levels for just reliable speech communication. (From C.M. Harris *Handbook of Noise Control,* McGraw-Hill, New York, 1979. With permission.)

Noise Measures

There are several rating measures and descriptors used to determine human response to noise. Only a few of the most important can be discussed here. The reader will find more such measures discussed in the literature. [1] Criteria derived from such measures can be used to produce regulations or legislation.

The speech interference level (SIL) is a measure used to evaluate the effect of background noise on speech communication. The SIL is the arithmetic average of the sound pressure levels of the interfering background noise in the four octave bands with center frequencies of 500, 1000, 2000 and 4000 Hz.[1,6]

The speech interference level of the background noise is calculated; then this may be used in conjunction with Figure 20.7.3 to determine if communication is possible at various distances for different voice levels. This figure is for male voices. Since the average female voice is normally quieter, for female voices the horizontal scale should be moved to the right by 5 dB. Use of the results obtained with Figure 20.7.3 and criteria for various spaces in buildings enable decisions to be made whether they are suitable for their desired uses.

The equivalent sound level L_{eq} is the A-weighted sound pressure level averaged over a suitable time period T. The averaging time T can be chosen to be a number of minutes, hours or days, as desired.

$$L_{\mathrm{eq}} = 10\log_{10}\left[(1/T)\int p_A^2\, dt/p_{\mathrm{ref}}^2\right] dB$$

where p_{A} is the instantaneous sound pressure measured using an A-weighting frequency filter. The L_{eq} is also sometimes known as the *average sound level* L_{AT}.

The *day-night equivalent sound level* (DNL) or L_{dn} is a measure that accounts for the different human response to sound at night. It is defined (Crocker, 1997d) as:

$$L_{\mathrm{dn}} = 10\log_{10}\left\{(1/24)\left[15\left(10^{L_d/10}\right) + 9\left(10^{(L_n+10)/10}\right)\right]\right\} dB$$

where L_d is the 15-hr daytime A-weighted equivalent sound level (from 0700 to 2200 hr) and L_n is the 9-hr nighttime equivalent sound level (from 2200 to 0700 hr). The nighttime level is subjected to a 10-dB penalty because noise at night is known to be more disturbing than noise during the day.

There is some evidence that noise that fluctuates markedly in level is more annoying than noise which is steady in level. Several noise measures have been proposed to try to account for the annoying effect of these fluctuations. The percentile levels are used in some measures. The *percentile level* L_n is defined to be the level exceeded n% of the time (Crocker, 1997d). The A-weighted sound level is normally used in Ln.

Response of People to Noise and Noise Criteria and Regulations

In industry, noise is often intense enough to interfere with speech and to create noise conditions that are hazardous to hearing. By using Figure 20.7.3 it is seen that if the SIL is above 50 dB, then the noise will interfere with normal speech communication between male voices at 4 m. If it is above 60 dB, then speech communication even when shouting is barely possible at the same distance. For women the comparable values of SIL are 45 and 55 dB at the same distance. If the SIL is 90 dB, then communication between male voices is only possible at distances less than 0.25 m, even when shouting. A-weighted sound levels are sometimes used instead of SIL values but with somewhat less confidence. It is seen that if one has difficulty in communicating in an industrial situation, then the A-weighted sound level is likely to be above 90 dB. In the United States, OSHA regulations start at this level for an 8-hr period. There is a halving in the allowable exposure time for every 5-dB increase in sound level. See Table 20.7.1. In almost all other countries the allowable exposure time is halved for every 3-dB increase in sound level (Ward, 1997).

Noise in communities is caused by many different sources. In most countries, the maximum equivalent A-weighted sound level L_{eq} is recommended for evaluating different types of noise source (Gottlob, 1995). In some countries there are regulations which use L_{eq} for road traffic noise and railroad noise, although some countries use L_{10} (e.g., the U.K.) or L_{50} (e.g., Japan) for planning permission in which road traffic noise is of concern (Crocker, 1997d; Gottlob, 1995). In the United States the L_{dn} has been used for community noise situations involving aircraft noise at airports and road traffic noise. Table 20.7.2 presents levels of noise given by the U.S. EPA and several other bodies to protect public health. Social surveys in several countries have been used to relate the percentage of respondents highly annoyed by noise to the day-night equivalent sound level, L_{dn} (Crocker, 1997d; Gottlob, 1995). See Figure 20.7.4. (Finegold et al., 1994). It is seen that many studies have shown that aircraft noise appears to be more annoying than other sources, perhaps because of the larger fluctuation in levels with time compared with the other sources. However, some other studies suggest that railroad noise is less annoying than traffic noise and this is borne out by the lower levels used for railroad noise than traffic noise regulations in several European countries (Gottlob, 1995).

Various investigations have shown that noise disturbs sleep (Crocker, 1997d). It is well known that there are several stages of sleep and that people progress through these stages as they sleep. Noise can change the progress through these stages and if sufficiently intense can awaken the sleeper. Recently, sleep disturbance data from several analyses have been reanalyzed and the preliminary sleep disturbance curve

TABLE 20.7.1 Maximum A-Weighted Sound Levels Allowed by the U.S. Occupational Safety and Health Administration (OSHA) for Work Periods Shown during a Workday

Duration per Day (hr)	Sound Level in dB(A)
8	90
6	92
4	95
3	97
2	100
1.5	102
1	105
0.5	110
0.25 or less	115

TABLE 20.7.2 Guidelines from the U.S. Environmental Protection Agency (EPA), World Health Organization (WHO), Federal Interagency on Community Noise (FICON), and Various European Agencies for Acceptable Noise Levels

Authority	Specified Sound Levels	Criterion
EPA Levels Document	$L_{dn} \leq 55$ dB (outdoors) $L_{dn} \leq 45$ dB (indoors)	Protection of public health and welfare with adequate margin of safety
WHO Document (1995)	$L_{eq} \leq 50/55$ dB (outdoors: day) $L_{eq} \leq 45$ dB (outdoors: night) $L_{eq} \leq 30$ dB (bedroom) $L_{max} \leq 45$ dB (bedroom)	Recommended guideline values (Task Force consensus)
U.S. Interagency Committee (FICON)	$L_{dn} \leq 65$ dB	Considered generally compatible with residential development
	$65 \leq L_{dn} \leq 70$ dB	Residential use discouraged
Various European road traffic regulations	$L_{eq} \geq 65$ or 70 dB (day)	Remedial measures required

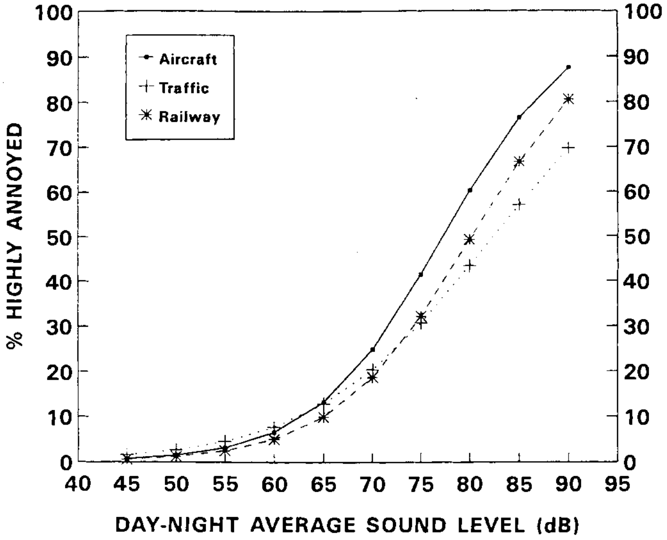

FIGURE 20.7.4 Percentage of survey respondents highly annoyed vs. day-night equivalent sound level for aircraft, road traffic, and railway noise.

given in Figure 20.7.5 has been proposed. A regression fit to these sleep disturbance data (Finegold et al., 1994) gave the following expression (which is also shown graphically in Figure 20.7.5) (Crocker, 1997d; Finegold et al., 1994):

$$\% \text{ Awakenings} = 7.1 \times 10^{-6} L_{AE}^{3.5}$$

where L_{AE} is the indoor A-weighted sound exposure level ASEL.

Noise Control Approaches

The main noise control approaches include use of sound absorption, enclosures, barriers, and vibration isolation and damping (Crocker, 1997c). Most porous materials absorb sound and those materials

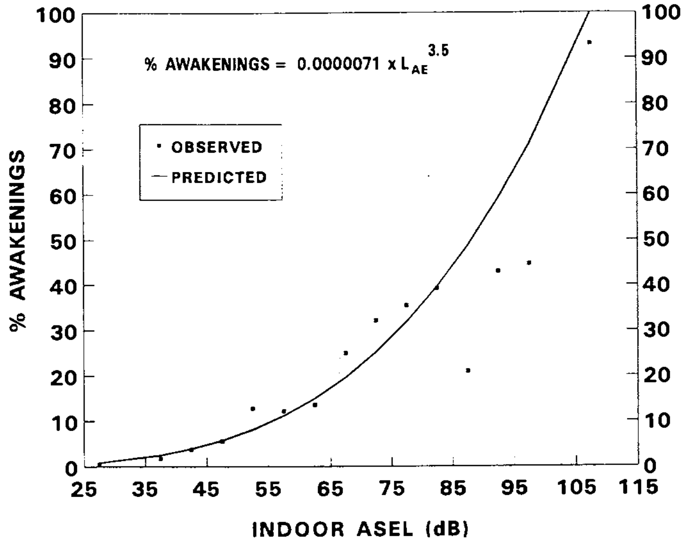

FIGURE 20.7.5 Proposed sleep disturbance curve: percentage of subjects awakened as a function of indoor sound exposure level.

specially made for this purpose include materials such as porous foams and fiberglass. However, ordinary materials such as carpets and drapes are also effective and can be used in building spaces to reduce reverberant sound buildup and noise. Although all these materials are rather ineffective at low frequency, at frequencies above 500 to 1000 Hz they can absorb almost all of the sound energy incident on them and in this case are said to have an absorption coefficient α of one. In industry they are used inside machine enclosures or placed on the walls and inside ceilings of manufacturing buildings to reduce the reverberant noise buildup (Crocker, 1997c).

Enclosures can be used to partially or completely enclose machines (machine enclosures) or to enclose operators of machines (personnel enclosures). The first approach may be regarded as *path* control and the second as *receiver* control. The improvement in noise reduction that these enclosures can achieve is related not only to the so-called transmission loss TL of the enclosure material used, $TL = 10 \log mf - 34$ dB, where m is the mass/unit area of the enclosure walls in kg/m^2 and f is the frequency in Hz, but also to the absorption coefficient α by $10 \log(1/\alpha)$. Thus, enclosures that have massive walls and absorbing material inside are the most effective at reducing noise both as machine enclosures or personnel enclosures. The enclosures should be well sealed to prevent sound being transmitted through leaks. If it is necessary to have a vent or hole in the enclosure for ventilation or for access, then the vent should be lined with sound-absorbing material and be bent or constructed like a labyrinth to try to reduce the direct transmission of noise through the vent or hole. As the relationship for TL indicates, enclosures are generally more effective at high frequency (Crocker, 1997c).

Barriers are used to shield personnel from sound sources. The effectiveness of a barrier depends not only on the effective height of the barrier in wavelengths, but also how far the receiver point is into the sound shadow. Barriers are thus most effective when they are taller (in wavelengths) and thus best for high-frequency noise and also best when placed close to the source or close to the receiver, since such placement increases the shadowing effect. Barriers are used in industry where it is desired to shield personnel from machinery noise sources. It is important in such cases to put sound-absorbing material on the ceiling of the building just above the barrier or on walls just behind a barrier where these surfaces could allow the reflection of sound to bypass the barrier and thus severely reduce its effectiveness (Crocker, 1997c).

The vibration isolation of machine sources from their supports can be particularly useful in reducing the noise produced especially if the machine is small compared with a large flexible support or enclosure that can act as a sounding board and radiate the sound. Soft metal springs or elastomeric isolators are often used as isolators. They should be designed so that the natural frequency of the machine mass on its isolators is much less than the forcing frequency, if possible. Care should be taken that such a design condition does not produce excessive static deflection of the system that could interfere with the proper machine operation. Vibrating pipes and ducts can also be vibration-isolated from walls of buildings using pipe hangers or soft rubber isolators. Vibration breaks made of rubber or similar soft material can be built into elements such as walls in buildings or structural elements in vehicles or machine enclosures to prevent vibration being propagated throughout the building or other structure and being reradiated as noise (Crocker, 1997c).

Damping materials can also be effective at reducing noise when applied properly to structures if their vibration is resonant in nature. Damping materials that are viscous, applied with thicknesses two or three times that of the vibrating metal panel, are particularly effective. Constrained damping layers can be very effective even when the damping layer is relatively thin (Crocker, 1997c).

Figure 20.7.6 shows the reduction in the A-weighted sound level that can be expected using these passive noise control approaches discussed above. Often it is insufficient to use one approach, and greater, more-economic noise reduction can be achieved by using two or more approaches in conjunction.

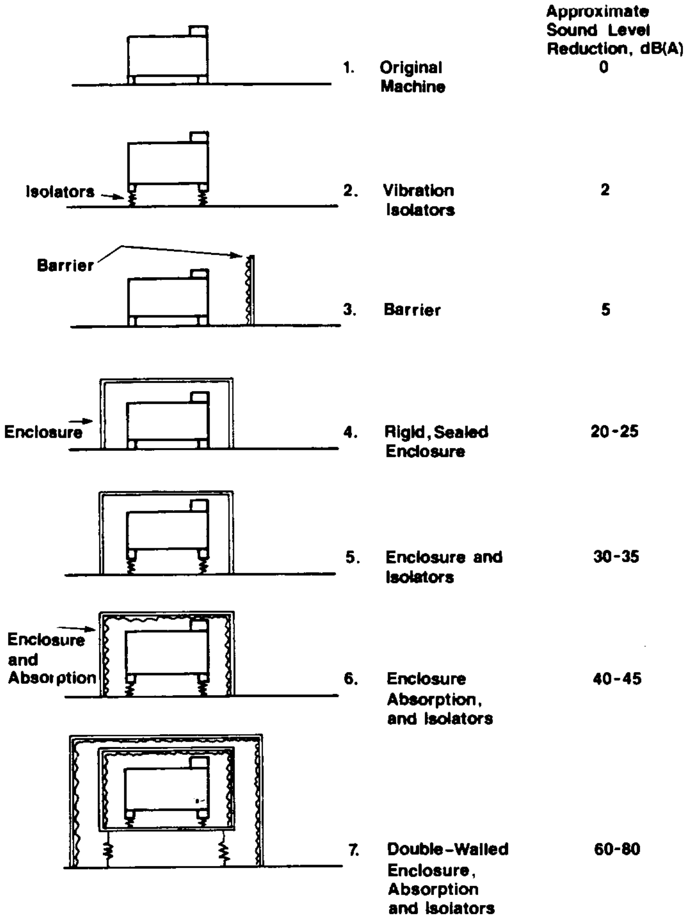

FIGURE 20.7.6 Approximate A-weighted sound level reductions expected from different noise control approaches.

References

Beranek, L.L. and Ver, I.L. 1992. *Noise and Vibration Control Engineering*, John Wiley & Sons, New York.

Crocker, M.J. 1975. in *Noise and Noise Control*, CRC Press, Cleveland, OH, chap. 2.

Crocker, M.J. 1997a. Introduction to linear acoustics, in *Encyclopedia of Acoustics*, M.J. Crocker, Ed., John Wiley & Sons, New York, chap. 1.

Crocker, M.J. 1997b. Noise, in *Handbook of Human Factors and Ergonomics*, 2nd ed., G. Salvendy, Ed., John Wiley & Sons, New York, chap. 24.

Crocker, M.J. 1977c. Noise generation in machinery, its control and source identification, in *Encyclopedia of Acoustics*, M.J. Crocker, Ed., John Wiley & Sons, New York, chap. 83.

Crocker, M.J. 1997d. Rating measures, criteria, and procedures for determining human response to noise, in *Encyclopedia of Acoustics*, M.J. Crocker, Ed., John Wiley & Sons, New York, chap. 80.

Finegold, L.S., Harris, C.S., and von Gierke, H.E. 1994. Community annoyance and sleep disturbance: updated criteria for assessment of the impacts of general transportation noise on people, *Noise Control Eng. J.*, 42(1), 25–30.

Gottlob, D. 1995. Regulations for community noise, *Noise/News Int.*, 3(4), 223–236.

Greenberg, S. 1997. Auditory function, chap. 104; Shaw, E.A.G. Acoustical characteristics of the outer ear, chap. 105; Peake, W.T. Acoustical properties of the middle ear, chap. 106; and Slepecky, N.B. Anatomy of the cochlea and auditory nerve, in *Encyclopedia of Acoustics*, M.J. Crocker, Ed., John Wiley & Sons, New York.

Ward, W.D. 1997. Effects of high-intensity sound, in *Encyclopedia of Acoustics*, M.J. Crocker, Ed., John Wiley & Sons, New York, chap. 119.

20.8 Lighting Technology

Barbara Atkinson, Andrea Denver, Robert Clear, and James E. McMahon

In this section, we describe the technical and operating characteristics of the general categories of lamps, ballasts, and fixtures in use today.*

Because the purpose of a lamp is to produce light, and not just radiated power, there is no direct measure of lamp efficiency. Instead, a lamp is rated in terms of its **efficacy**,** which is the ratio of the amount of light emitted (lumens) to the power (watts) drawn by the lamp. The metric used to express lamp efficacy is lumens per watt (LPW). The theoretical limit of efficacy is 683 LPW and would be produced by an ideal light source emitting monochromatic radiation with a wavelength of 555 nm. The most efficient white light source in the laboratory provides 275–310 LPW. Of lamps currently on the market, the most efficient white light source, the T5 fluorescent lamp with electronic ballast, produces about 100 LPW. High-pressure sodium (not a white light source) can produce as high as 130 LPW.

The efficacies of various light sources are depicted in Figure 20.8.1. Lamps also differ in terms of their size, color, lifetime, optical controllability, dimmability, **lumen maintenance**,*** reliability, convenience in use, maintenance requirements, disposal, environmental impacts (mercury, lead), and electromagnetic and other emissions (e.g., radio interference, ultraviolet [UV] light, and noise).

---

*Much of the contents of this section have been abstracted and updated from Chapter 12B (Energy Efficient Lighting Technologies and Their Applications in the Commercial and Residential Sectors by Barbara Atkinson, Andrea Denver, James E. McMahon, Leslie Shown, and Robert Clear) published in the CRC *Handbook of Energy Efficiency*, Frank Kreith and Ronald E. West, Eds., 1997.

**The efficacies of fluorescent lamp/ballast combinations reported in this section are based on data from the Advanced Lighting Guidelines 2003, and from the Lawrence Berkeley National Laboratory's Lighting Systems Research Group, 2003.

***Over time, most lamps continue to draw the same amount of power but produce fewer lumens. The lumen depreciation of a lamp refers to the extent to which the lamp sustains its lumen output, and therefore efficacy, over time

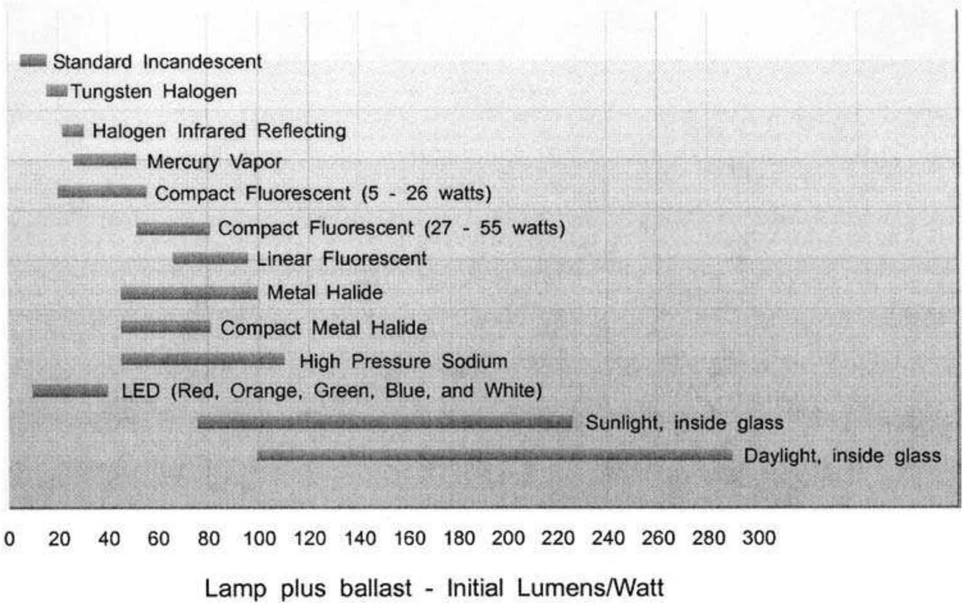

FIGURE 20.8.1 Efficacy comparison of light sources for general lighting. Lamp plus ballast—initial lumens/watts. Ballast watts are included for discharge lamp systems. Sunlight and daylight ranges are calculated inside of single pane clear glass and high performance glass. Source: Advanced Lighting Guidelines, 2003, New Buildings Institute.

The color properties of a lamp are described by its color temperature and its color rendering index. **Color temperature**, expressed in degrees Kelvin (K), is a measure of the color appearance of the light of a lamp. The concept of color temperature is based on the fact that the emitted radiation spectrum of a blackbody radiator depends on temperature alone. The color temperature of a lamp is the temperature at which an ideal blackbody radiator would emit light that is closest in color to the light of the lamp. Lamps with low color temperatures (3000 K and below) emit warm white light that appears yellowish or reddish in color. Incandescent and warm-white fluorescent lamps have a low color temperature. Lamps with high color temperatures (3500 K and above) emit cool white light that appears bluish in color. Cool-white fluorescent lamps have a high color temperature.

The **color rendering index (CRI)** of a lamp is a measure of how surface colors appear when illuminated by the lamp compared to how they appear when illuminated by a reference source of the same color temperature. For color temperatures above 5000 K, the reference source is a standard daylight condition of the same color temperature; below 5000 K, the reference source is a blackbody radiator. The CRI of a lamp indicates the difference in the perceived color of objects viewed under the lamp and under the reference source. There are 14 differently colored test samples, 8 of which are used in the calculation of the general CRI index. The CRI is measured on a scale that has a maximum value of 100 and is an average of the results for the 8 colors observed. A CRI of 100 indicates that there is no difference in perceived color for any of the test objects; a lower value indicates that there are differences. CRIs of 70 and above are generally considered to be good, while CRIs of 20 and below are considered to be poor. Most incandescent lamps have CRIs equal to or approaching 100. Low-pressure sodium lamps have the lowest CRI of any common lighting source; their light is essentially monochromatic.

The **optical controllability** of a lamp describes the extent to which a user can direct the light of the lamp to the area where it is desired. Optical controllability depends on the size of the light-emitting area, which determines the beam spread of the light emitted. Incandescent lamps emit light from a small filament area; they are almost point sources of light and their optical controllability is excellent. In contrast, fluorescent lamps emit light from their entire phosphored area; their light is extremely diffuse and their controllability is poor. In addition, controllability depends on the fixture in which the lamp is used.

Because of their many different characteristics and the variety of applications, no one light source dominates the lighting market. The types of lamps that are commonly available include incandescent, fluorescent, and high-intensity discharge (HID). Induction lighting systems have begun to come into use as well.

Lamps

The *incandescent lamp* was invented independently by Thomas Edison in the U.S. and Joseph Swan in England in the late 1800s. An incandescent lamp produces light when electricity heats the lamp filament to the point of incandescence. In modern lamps the filament is made of tungsten. Because 90% or more of an incandescent lamp's emissions are in the infrared (thermal) rather than the visible range of the electromagnetic spectrum, these lamps are less efficacious than other types of lamps.

The two primary types of standard incandescent lamps are general service and reflector lamps. General service lamps (also known as A-lamps) are the pear-shaped, common household lamps. Reflector lamps, such as flood or spotlights, are generally used to illuminate outdoor areas or highlight indoor retail displays and artwork. They are also commonly used to improve the optical efficiency of downlights (discussed later). Downlights are used where controlling glare or hiding the light source is important. In spite of the fact that they are the least efficacious lamps on the market today, standard incandescent general service lamps are used for almost all residential lighting in the U.S. and are also common in the commercial sector. They have excellent CRIs and a warm color; they are easily dimmed, inexpensive, small, and lightweight, and can be used with inexpensive fixtures. In a properly designed fixture, they permit excellent optical control. In addition, incandescent lamps make no annoying noises, provide no electromagnetic interference, and contain essentially no toxic chemicals. They are simple to install, maintain, and dispose of.

Halogen and *halogen infrared-reflecting (HIR) lamps* are more efficient versions of the incandescent lamp. Halogen lamps produce bright white light and have color temperatures and CRIs that are similar to, or slightly higher than, those of standard incandescent lamps. In addition, they have longer rated lives (2000 or more hours vs. 1000 hours or less), can be much more compact, are slightly more efficacious, and have better lumen maintenance than standard incandescent lamps. Halogen general service lamps are available but are still relatively rare; they offer longer life as well as slightly higher lumen output or lower wattage than standard incandescent lmaps. Halogen technology is also used in small reflector lamps operated on low-voltage transformers. These lamps, also known as dichroics, are used for accent lighting and sparkle in a variety of applications. Reflector lamps using halogen technology have gained market share because they meet the U.S. reflector lamp standards (see below). The HIR technology, which is more efficient than standard halogen, is available in reflector lamps. In general, HIR lamps have a small market share due to their high cost, even though HIR lamps last about 50% longer than regular halogen lamps.

The U.S. Energy Policy Act of 1992 (EPAct) set standards for incandescent reflector lamps that in essence can be met by halogen technology, while standard incandescent reflector lamps do not comply. However, exempted lamps such as bulged reflector (BR) and elliptical reflector (ER) lamps have gained in market share since the standards took effect in 1995. BR and ER lamps employ variations on reflector geometry to more efficiently focus light, but their efficacies are not as high as those of reflector lamps using halogen technology.

Fluorescent lamps came into general use in the 1950s. In a fluorescent lamp, gaseous mercury atoms within a phosphor-coated lamp tube are excited by an electric discharge between two electrodes (cathode and anode). As the mercury atoms return to their ground state, ultraviolet radiation is emitted. This UV radiation excites the phosphor coating on the lamp tube and causes it to flouresce, thus producing visible light (see Figure 20.8.2).

Early fluorescent tubes, and current compact fluorescent lamps as well as some shorter fluorescent tubes, use "preheat start" with an automatic or manual starting switch. "Instant start" lamps use a high voltage to strike the arc of the lamp. Electronic ballasts (discussed later) are available that can instant-start most types of fluorescent lamps. "Rapid start" circuits use low-voltage windings for preheating the

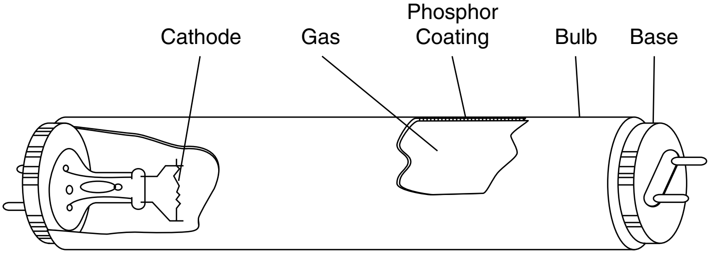

FIGURE 20.8.2 Typical full-size fluorescent lamp. (From Atkinson, B. et al. *Analysis of Federal Policy Options for Improving U.S. Lighting Energy Efficiency: Commercial and Residential Buildings*, Lawrence Berkeley National Laboratory, Berkeley, CA, 1992. With permission.)

electrodes and initiating the arc to start the lamps. "Programmed rapid start" technology further refines the starting circuit.

Fluorescent lamps are far more efficacious than incandescent lamps. The efficacy of a fluorescent lamp system depends on the lamp length and diameter, the type of phosphor used to coat the lamp, the type of ballast used to drive the lamp, the number of lamps per ballast, the temperature of the lamp (which depends on the fixture and its environment), and a number of lesser factors.

The majority of lighting used in the commercial sector is fluorescent. Fluorescent lighting is also common in the industrial sector. The small amount of full-size fluorescent lighting in the residential sector is primarily found in kitchens, bathrooms, garages, and workshops.

EPAct set efficacy standards for 4-ft and 8-ft fluorescent lamps that can be met using reduced wattage, or "energy saver," lamps. These lamps became popular in the 1970s to retrofit full-wattage lamps. The reduced wattage lamp is similar to its full-wattage predecessor, with kypton added to the gas fill and a conductive coating to lower starting voltage. The lumen output is generally reduced proportionate to the wattage reduction.

Fluorescent lamps have long lives and fairly good lumen maintenance. Of the full-size fluorescent lamps available today, *rare-earth phosphor lamps* are the most efficacious. In these lamps, rare-earth phosphor compounds are used to coat the inside of the fluorescent lamp tube. Rare-earth phosphor lamps are also called tri-phosphor lamps because they are made with a mixture of three rare-earth phosphors that produce visible light of the wavelengths to which the red, green, and blue retinal sensors of the human eye are most sensitive. These lamps have improved color rendition as well as efficacy. Fluorescent T8 lamps and those with smaller diameters use rare-earth phosphors almost exclusively. While the reduced wattage halophosphor (cool-white and warm-white) lamps have CRIs of 50 to 60, rare-earth phosphor lamps have CRIs in the 70s and 80s. Standard fluorescent lamps last 12,000 (8-ft) to 20,000 (4-ft) hours.

The most common fluorescent lamps are tubular and 4 feet (1.2 m) in length. Four-foot lamps are also available in U-tube shapes that fit into fixtures with 2-ft dimensions. Lamp tubes with a diameter of 1.5 inches (38 mm) are called T12s, tubes that are 1 inch (26 mm) in diameter are called T8s, and those that are 5/8 inch (16 mm) are called T5s. The 12, 8, and 5 refer to the number of eights of an inch in the diameter of the lamp tube. Lamp tubes are available in other diameters as well. Each type of fluorescent lamp requires a specific ballast, depending on the wattage, length, and current (milliamps) of the lamp.

Four-foot T12 lamps have been available in 34-watt (W) and 40-W versions, with 25-W lamps introduced more recently. The 40-W lamps with halophosphors do not meet EPAct lamp standards, but 40-W lamps are available with rare-earth phosphor technology and higher efficacy that do meet the standards.

T8 lamps, using rare-earth phosphors giving them higher CRIs, were introduced several years ago and have come into wide usage. T5 lamps are an even more recent addition, and have become popular for their better optical control, fit into fixtures, and aesthetics. The maximum efficacy of a T5 lamp is slightly

TABLE 20.8.1 Characteristics and Applications of Typical 4-ft Fluorescent T8 Lamps

Lamp wattage	32W
Efficacy	For two 32W T8s and a single electronic ballast, ~90LPW
Rated lifetime	15,000–20,000 hours
Color Rendering Index	75–86
Color temperature	2700–5000 K
Lumen maintenance	Very good (light output typically declines by 10% to 12% over rated lamp life)
Optical controllability	Poor (very diffuse light)
Technologies for which these lamps are energy-efficient alternatives	These systems are most often replacements for less-efficient fluorescents (T12s with magnetic ballasts).

higher than that of a T8 lamp, and is achieved in ambient conditions that are about 10°C warmer than those optimal for T8 or T12 lamps. T8 and T5 high output (HO) lamps are also available for higher ceiling applications, but this application must be designed to prevent overheating the ballast. Eight-foot lamps have long been available in high output and very-high output (VHO) versions.

The specified or nominal wattage of a lamp refers to the power draw of the lamp alone. The ballast typically adds another 10% to 20% to the power draw, thus reducing system efficacy.

The most common efficient fluorescent lamp-ballast systems available today are T8 lamps operating with electronic ballasts. The characteristics and applications of 4-ft T8 lamps are summarized in Table 20.8.1. High performance T8 lamps are available with higher lumen output, longer rated lifetime, and higher lumen maintenance.

In spite of their much greater efficiency, fluorescent lamps have several disadvantages when compared to incandescent lamps. Standard fluorescent lamps can be dimmed, but require special dimming ballasts that cost more than the dimming controls used for incandescent lamps. Standard fluorescent lamps are larger than incandescent lamps of equivalent output and are harder to control optically. Fluorescent lamps (particularly instant start lamps) are not as economical in situations where they are switched on and off very frequently, as this shortens their life. Fluorescent lamps contain trace amounts of mercury, a toxic metal, and users of large quantities are required to either recycle them or dispose of them at designated facilities. However, mercury is also emitted in the production of electricity, and the net total emission of mercury, including the power plant emissions, is lower for fluorescent lamps than for the incandescent lamps that they replace. Fluorescent lamps also emit more UV light than incandescent lamps. UV light can cause colors to fade, and fabrics to age, and therefore has to be blocked near sensitive materials such as museum displays. Magnetic ballasts and more rarely electronic ballasts, are sometimes noisy and may emit radio interference. Electronic ballasts may interfere with security equipment, such as that used in libraries, and with specialized hospital devices.

Circular fluorescent lamps in 20- to 40-W sizes have been available for many years, but have had a fairly small market. Essentially, a circular lamp is a standard fluorescent lamp tube (as described earlier) that has been bent into a circle. Although they have a more compact geometry than a straight tube, circular lamps are still moderately large (16.5 to 41 cm [6.5 to 16.1 in.] in diameter). Circular lamps are available in several sizes with magnetic or electronic ballasts.

Compact fluorescent lamps (CFLs), which are substantially smaller than standard fluorescent lamps, were introduced to the U.S. market in the early 1980s. In a CFL, the lamp tube is smaller in diameter and is bent into sections. CFLs have much higher power densities per phosphor area than standard fluorescents, and their design was therefore dependent on the development of rare-earth phosphors, which could hold up much better than standard phosphors at high power loadings. CFLs (except for very low-wattage CFLs) are much more efficacious than the incandescent lamps they replace, typically drawing 1/3 to 1/4 of the wattage for similar light output. CFLs sold in the U.S. are also rated to last 9000–10,000 hours, with some newer products having even longer rated livetimes.

CFLs are available as both screw-in replacements for incandescent lamps and as pin-base lamps for hard-wired fixtures. Common CFLs range from 11 to 26 watts, and both higher and lower wattage lamps are available. They may be operated with separate ballasts or purchased as integral lamp/ballast units; integral units with electronic ballasts are the most commonly sold. The electronic ballast provides higher efficacy, eliminates the starting flicker, and has a lighter weight. CFLs have a much higher retail cost than the incandescent lamps they replace, and so consumers have been reluctant to purchase them without discounts or incentives; as they became more popular, their prices have decreased. CFL users in the residential sector encountered some limitations such as inability to dim, difficult fit in fixtures, starting in outdoor use, and overheating in enclosed fixtures. Manufacturers have developed lamps with smaller, more compatible shapes, and lamps that start at low outdoor temperatures; dimmable CFLs became available in the late 1990s. CFL reflector lamps are also available. In the commercial sector, dedicated fixtures with built-in ballasts are often used in downlights, to ensure that incandescents do not replace the CFLs.

Induction lamps are electrodeless fluorescent lamps that produce light by exciting phosphors coating the lamp. The radio frequency (RF) power supply sends an electric current to an induction coil, generating an electromagnetic field. This field excites the mercury in the gas fill, causing the mercury to emit ultraviolet (UV) energy. The UV energy strikes and excites the phosphor coating on the inside of the glass bulb, producing light. Electrodeless lamps have efficacies similar to those of CFLs or metal halide lamps of comparable light output. Electrodeless lamps use rare-earth phosphors, giving them color properties similar to those of higher-end fluorescent lamps. Because the lamp has no electrodes that usually cause lamp failure, the life of this system is determined by the induction coil. Induction lamps are rated at 100,000 hours of life. Because of this long life, and the good color rendition, induction technology has come into use for areas where maintenance to change the lamp is expensive, such as high ceilings in commercial and industrial buildings, atria, tunnels, and roadway sign lighting.

Induction lamps are electronic devices, and like all electronic devices they may generate electromagnetic interference (EMI) if unwanted electromagnetic signals, which can travel through wiring or radiate through the air, interfere with desirable signals from other devices. Shielding of the system to protect people and equipment from these emissions is important. Manufacturers must comply with Federal Communications Commission (FCC) regulations on EMI to sell products in the U.S.

High-intensity discharge (HD) lamps produce light by discharging an electrical arc through a mixture of gases. In contrast to fluorescent lamps, HID lamps use a compact arc tube in which both temperature and pressure are very high. In contrast to a fluorescent lamp, the arc tube in an HID lamp is small enough to permit compact reflector designs with good light control. There are currently three common types of HID lamps available: mercury vapor (MV), metal halide (MH), and high-pressure sodium (HPS). Additionally, low-pressure sodium (LPS) lamps, while not technically HID lamps, are used in some of the same applications as HPS lamps.

Because of their higher light output levels, HID lamps are most often used for exterior applications such as street and roadway lighting, outdoor area pedestrian and parking lot lighting, commercial, industrial, and residential floodlighting and security lighting, and sports lighting. They are also used in large, high-ceilinged, interior spaces such as industrial facilities and warehouses, where good color rendering is not typically a priority. HID lamps are sometimes used for indirect lighting in commercial offices, retail stores, and lobbies. Interior residential applications are rare because of high cost, lower CRI, and high light level. Also, HID lamps take several minutes to warm up to full light output, and if they are turned off or there is a momentary power outage, the lamps must cool down before they will restrike. Some HID lamps are now available with dual arc tubes or parallel filaments. Dual arc tubes eliminate the restrike problem and a parallel filament gives instantaneous light output both initially and on restrike, but at a cost of a high initial power draw and higher lamp cost.

The *mercury vapor (MV) lamp* was the first HID lamp developed. Including ballast losses, the efficacies of MV lamps range from approximately 25 to 50 LPW. Uncoated lamps have a bluish tint and very poor color rendering (CRI ~ 15). Phosphor-coated lamps emit more red but are still bluish, and have a CRI of about 50. Because of their poor color rendition, these lamps are used only where good color is not a priority. MV lamps generally have rated lifetimes in excess of 24,000 hours. Both metal halide (MH) and high-pressure sodium (HPS) HID lamps have higher efficacies than MV lamps and have consequently replaced them in most markets. MV lamps and ballasts are cheaper than the other HID sources and are still often sold as residential security lights. They also persist in some street lighting applications, landscape lighting, and in some other older systems.

Including ballast losses, *metal halide lamps* range in efficacy from 45 to 100 LPW. They produce white light and have CRIs ranging from 65 to almost 90. Lamp lifetimes generally range from only 5,000 to 20,000 hours, depending on the type of MH lamp. Lower-wattage MH lamps (particularly 50-W, 70-W, and 100-W) are now available with CRIs of about 65 to 75 and color temperatures of 2900 to 4200 K. Reasonably good lumen maintenance, longer life, and reduced maintenance costs, along with the fact that they blend more naturally with fluorescent sources, have made MH lamps a very good replacement in the commercial sector for 300-W and 500-W PAR lamps. New fixtures utilizing these lamps, particularly 1-ft by 1-ft recessed lensed troffers (downlights), are becoming common in lobbies, shopping malls, and retail stores. Improvements in color stability have made MH systems cost-effective substitutions for high-wattage incandescent lighting in commercial applications.

Including ballast losses, *high-pressure sodium lamps* have efficacies ranging from 45 LPW for the smallest lamps to 130 LPW for the largest lamps. Standard high-pressure sodium (HPS) lamps emit a yellow-orange light and have poor color rendition in the 20s; high-color rendering versions can have CRIs up to 70 and higher. Like MV lamps, HPS lamps are used only where good color is not a priority. HPS lamps have come to dominate street and roadway lighting because of their high efficacy and long life. The rated lifetimes of HPS lamps rival those of MV lamps and typically exceed 24,000 hours.

Metal halide technology is also becoming increasing popular for outdoor lighting, especially in areas where color rendering is important, and because of people's preference for "white light." Pulse-start technology is improving MH lamp performance in almost every aspect. In MH pulse start lamps, a high-voltage pulse (typically 3 kV minimum) applied directly across the main electrodes initiates the arc. Ignitors are used to provide these starting pulses. The average lifetime of pulse-start MH lamps now approaches that of HPS and MV lamps. With the higher efficacy this technology provides, approaching that of HPS lamps, pulse-start MH lamps now compete with HPS lamps in many outdoor applications. Ceramic arc tube MH lamps, with CRIs as high as 90 and better color consistency, now compete with incandescent sources. MH lamps may fail "non-passively," so users should always follow the manufacturers recommended practices for safe operation of the lamps.

At low light levels, such as those found in many outdoor areas at night, the eye's peripheral vision becomes more sensitive to light that is bluish. Although MH lamps are less efficacious than HPS lamps at high, or "photopic" light levels found during daylight hours, they can actually provide higher visual quality and therefore allow lower light levels, making them more efficacious, at least for peripheral vision, than HPS lamps at low or "scotopic" levels. This has led to increased interest in their use for street lighting.

Low-pressure sodium (LPS) lamps are discharge lamps that operate at lower arc tube loading pressure than do HID lamps. LPS lamps are monochromatic in the yellow spectral band and have CRIs of 0. They have been used for street and tunnel lighting, especially in cities near astronomical observatories, because the LPS color spectrum can easily be filtered out so as not to interfere with telescopes. (In more current efforts to limit "sky glow" as well as glare from outdoor lighting, the emphasis has shifted from lamp types to luminaire light control, with various levels of "cut-off" luminaires directing light downward and not upward, or using shielding to the same effect. For street lighting, calculations suggest that the match of the luminaire light distribution to the street, rather than the cut-off classification, is the most critical factor in limiting sky glow.) The LPS lamp has limitations for many applications where color rendering is important for safety and for identification.

Light-emitting diodes (LEDs) have had recent design advances in color and efficacy and are used in a number of specialty applications. Their advantages are small size, high directional intensities, long life (10,000 to 100,000 hours), and high reliability and durability. The major disadvantages of LEDs at this time are their limited output in lumens per device, their high cost per lumen, their relatively poor color rendering when used as a "white" source, and their relatively low efficacy (15–20 LPW for white light, 15–40 LPW for colors). However, the technology for LEDs is changing rapidly. Efficacies as high as 100 LPW have reported in the laboratory. Light output per device of 10 lumens is attainable now and target values of 100 lumens are projected for the next few years (a standard 60-W incandescent lamp produces about 900 lumens). Research on using organic materials to produce light (OLEDs) is also under way. LEDs have become widely used for traffic lights, exit signs and emergency lights, bicycle warning lights, and in applications where optical control is critical.

Ballasts

Because both fluorescent and HID lamps (discharge lamps) have a low resistance to the flow of electric current once the discharge arc is struck, they require a device to limit current flow. A lamp ballast is an electrical device used to control the current provided to the lamp. In most discharge lamps, a ballast also provides the high voltage necessary to start the lamp. Older preheat fluorescent lamps require a separate starter, but these lamps are becoming increasingly uncommon. In many HID ballasts, the ignitor used for starting the lamp is a replaceable module.

The most common types of fluorescent ballasts are magnetic core-coil and electronic high-frequency ballasts. A *magnetic core-coil ballast* uses a transformer with a magnetic core coiled in copper or aluminum wire to control the current provided to a lamp. Magnetic ballasts operate in the U.S. at the standard AC input frequency of 60 Hz and operate lamps at the same 60 Hz. An *electronic high-frequency ballast* uses electronic circuitry rather than magnetic components to control current. Electronic ballasts use standard 60 Hz power but operate lamps at a much higher frequency (20,000 to 60,000 Hz). Both magnetic and electronic ballasts are available for most fluorescent lamp types.

The *cathode cut-out (hybrid) ballast* is a modified fluorescent magnetic ballast. It uses an electronic circuit to remove the filament power after the discharge has been initiated for rapid-start lamps. Cathode cutout ballasts use approximately 5% to 10% less energy than magnetic ballasts.

Of the ballasts that are currently available for fluorescent lamps, the most efficient option is the electronic ballast. Because an electronic ballast is more efficient than a standard core-coil magnetic ballast in transforming the input power to lamp requirements, and because fluorescent lamps are more efficient when operated at frequencies of 20,000 Hz or more, a lamp/ballast system using an electronic rather than magnetic ballast is more efficacious. T8 lamps can be operated on conventional magnetic ballasts although they are most commonly used with high-frequency electronic ballasts. Operation with electronic ballasts increases the lamp efficacy by about 9% over operation with magnetic ballasts. TS lamps operate exclusively with electronic ballasts.

In addition, electronic ballasts eliminate flicker, weigh less than magnetic ballasts, and operate more quietly. Since electronic ballasts are packaged in cans that are the same size as magnetic ballasts, they can be placed in the same fixtures designed to be used with magnetic ballasts. Fluorescent electronic ballasts are available for standard commercial-sector applications. They have become increasingly popular, particularly in new luminaires as well as in energy-efficiency retrofits. Advances in dimming fluorescent ballasts allow further energy savings through automatic controls.

The upcoming U.S. fluorescent ballast standards essentially require all ballasts driving T12 fluorescent lamps sold in luminaires to be electronic by 2006 and T12 ballasts sold separately (replacement ballasts) to be electronic beginning in 2010.

Most cathode cutout ballasts will not meet the new ballast standards. End users who cannot use electronic fluorescent ballasts for technical reasons (primarily electronic interference with specialized equipment) may use T8 lamps with magnetic ballasts.

The most commonly used ballasts for HID lamps are magnetic, and a number of different types are available. The various types differ primarily in how well they tolerate voltage swings and, in the case of HPS lamps, the increased voltage required to operate the lamp as it ages. Electronic ballasts are also available, although the energy savings are less than for fluorescent systems. As with fluorescent systems, HID electronic ballasts provide flicker-free lighting and regulate lamp power, which increases lamp life and maintains constant color.

Lighting Fixtures

A lighting fixture is a housing for securing lamp(s) and ballast(s) and for controlling light distribution to a specific area. The function of the fixture is to distribute light to the desired area without causing glare or discomfort. The distribution of light is determined by the geometric design of the fixture as well as the material of which the reflector and/or lens is made. The more efficient a fixture is, the more light it emits from the lamp(s) within it. Although the term *luminaire* is sometimes used interchangeably with *fixture, luminaire* refers to a complete lighting system, including the lamps and fixture (which includes the ballast/s).

Types of fluorescent lighting fixtures that are commonly used in the non-residential sectors include recessed troffers, pendant-mounted indirect and indirect/direct fixtures, and surface-mounted fixtures such as wraparound, strip, and industrial fixtures.

Until recently, most offices have been equipped with *recessed troffers*, which are direct (light emitted downward) fixtures and emphasize horizontal surfaces. Many forms of optical control are possible with recessed luminaires. In the past, prismatic lenses were the preferred optical control because they offer high luminaire efficiency and uniform illuminance in the work space.

Offices with electronic equipment have become increasingly common, however, and until fairly recently there was a trend away from the traditional direct lighting fixtures designed for typing and other horizontal tasks because they tend to cause reflections on video display terminal (VDT) screens. No lighting system reduces glare entirely, but some fixtures and/or components can reduce the amount of glare significantly. *Parabolic louvered fixtures* have come into use in office spaces. These fixtures have reflectors in the form of louvers, often aluminized, with parabolic geometry that directs light downward. Because the glossy, vertical VDT screen can potentially reflect bright spots on the ceiling, and because VDT work is usually done with the head up, existing fixtures are also sometimes replaced with indirect or direct/indirect fixtures, which produce light that is considered more visually comfortable. Most indirect lighting systems are suspended from the ceiling. They direct light toward the ceiling, where the light is then reflected downward to provide a calm, diffuse light. Some people describe the indirect lighting as similar to the light on an overcast day, with no shadows or highlights. Generally, indirect lighting does not cause bright reflections on VDT screens. A *direct/indirect fixture* is suspended from the ceiling and provides direct light as well as indirect. These fixtures combine the high efficiency of direct lighting systems with the uniformity of light and lack of glare produced by indirect lighting systems. New, flat-panel liquid crystal display monitors are much less sensitive to reflections than the older cathode-ray tube VDTs, and this may affect the types of fixtures used in offices in the future.

A *wraparound fixture* has a prismatic lens that wraps around the bottom and sides of the lamp, and is always surface mounted rather than recessed. Wraparound fixtures are less expensive than other commercial fixtures and are typically used in areas where lighting control and distribution are not a priority. *Strip* and *industrial fixtures* are even less expensive and are typically used in places where light distribution is less important, such as large open areas (grocery stores, for example) and hallways. These are open fixtures in which the lamp is not hidden from view.

The most common incandescent fixture in the nonresidential sector is the *downlight*, also known as a recessed can fixture. Fixtures designed for CFLs are available to replace incandescent downlight fixtures in areas where lighting control is less critical.

Interior HID fixtures include high-bay and low-bay fixtures (aisle lighters and parking garages, etc.), downlights, and accent lighting. Exterior HID fixtures include street and roadway fixtures (cobrahead, post-top, architectural), floods of all sizes and types (from sports to landscape), wall-mounted, and security fixtures.

Luminaire efficacy rating (LER) is a single metric that expresses *luminaire efficacy*, the luminaire's light output divided by the input power. The formula for fluorescent luminaires is

$$\mathrm{LER} = \frac{\mathrm{LuminaireEfficiency(EFF)}^{*}\mathrm{TotalRatedLampLumens(TLL)}^{*}\mathrm{BallastFactor(BF)}}{\mathrm{LuminaireWattsInput}}$$

Note that the effects of all components of the luminaire system (lamp, ballast, and fixture) are included in the LER. The National Electrical Manufacturers Association (NEMA) Standards Publication No. LE5, "Procedure for Determining Luminaire Efficacy Ratings for Fluorescent Luminaires," specifies the major fluorescent luminaire categories covered and the standard industry test procedures. NEMA's LE5A and LE5B give the procedures for commercial downlight luminaires and HID industrial luminaires.

Increasing Lighting Efficiency

Many existing lighting systems are equipped with relatively inefficient lamps and ballasts. Depending on the age and condition of the fixture, it may be cost-effective to either replace the luminaire or replace the existing lamps and ballasts (retrofit) with more efficient equipment. Care should always be taken to ensure that any changes to a lighting system will improve the quality of lighting as well as the economics. State-of-the-art lighting equipment is now synonymous with energy efficiency and lighting quality.

For more information on retrofitting existing lighting systems with more efficient equipment, refer the Illuminating Engineering Society of North America's LEM-3-04, "IESNA Guidelines for Retrofitting Lighting Systems in Commercial and Institutional Spaces" (see References).

Defining Terms

Ballast: An electrical device used to control the current provided to the lamp. In most discharge lamps, a ballast also provides the high voltage necessary to start the lamp.

Ballast factor: The fractional (luminous) flux of a fluorescent lamp operated on a ballast compared to the flux when operated on the standard (reference) ballast specified for rating lamp lumens.

Color Rendering Index (CRI): A measure of how surface colors appear when illuminated by a lamp compared to how they appear when illuminated by a reference source of the same color temperature. For color temperature above 5000 K, the reference source is a standard daylight condition of the same color temperature; below 5000 K, the reference source is a blackbody radiator.

Color temperature: The color of a lamp's light is described by its color temperature, expressed in degrees Kelvin (K). The concept of color temperature is based on the fact that the emitted radiation spectrum of a blackbody radiator depends on temperature alone. The color temperature of a lamp is the temperature at which an ideal blackbody radiator would emit light that is the same color as the light of the lamp.

Efficacy: The ratio of the amount of light emitted (lumens) to the power (watts) drawn by a lighting system. The unit used to express efficacy is lumens per watt (LPW). Efficacy may be expressed as *lamp efficacy*, using the nominal wattage of the lamp, or as *system efficacy*, using the system watts that include the ballast losses.

Lumen maintenance: The extent to which a lamp sustains its lumen output (and therefore efficacy) over time.

References

Atkinson, B., McMahon, J., Mills, E., et al. 1992. *Analysis of Federal Policy Options for Improving U.S. Lighting Energy Efficiency: Commercial and Residential Buildings*. Lawrence Berkeley National Laboratory, Berkeley, CA. LBL-31469.

Illuminating Engineering Society of North Amercia. 2000. *Lighting Handbook*, 9th ed., Illuminating Engineering Society of North America, New York.

Illuminating Engineering Society of North America. 2004. LEM-3-04, IESNA Guidelines for Retrofitting Lighting Systems in Commercial and Institutional Spaces. Illuminating Engineering Society of North America, New York.

Leslie, R. and Conway, K. 1993. *The Lighting Pattern Book for Homes*, Lighting Research Center, Rensselaer Polytechnic Institute, Troy, NY.

National Electrical Manufacturers Association (NEMA). 2001. Standards Publication LE 5-2001, Procedure for Determining Luminaire Efficacy Ratings for Fluorescent Luminaires. Washington, D.C.

National Electrical Manufacturers Association (NEMA). 1999. Standards Publication LE 5A-1999, Procedure for Determining Luminaire Efficacy Ratings for Commercial, Non-Residential Downlight Luminaires. Washington, D.C.

National Electrical Manufacturers Association (NEMA). 1998. Standards Publication LE 5B-1998, Procedure for Determining Luminaire Efficacy Ratings for High-Intensity Discharge Industrial Luminaires. Washington, D.C.

New Buildings Institute. 2003. *Advanced Lighting Guidelines, 2003.* New Buildings Institute, White Salmon, WA.

U.S. Department of Energy, Technical Support Document Energy Efficiency Standards for Consumer Products: Fluorescent Lamp Ballast, Proposed Rule. Washington, D.C. 2000. (I. Turiel et al.) Federal Register Notice: 65 FR 56740 (Sept. 19, 2000); Docket Number EE-RM-97-500. www.eere.energy.gov/buildings/appliance_standards/residential/gs_fluorescent_lamps.html.

Vorsatz, D., Shown, L., Koomey, J., Moezzi, M., Denver, A., and Atkinson, B. 1997. *Lighting Market Sourcebook for the U.S.*, Lawrence Berkeley National Laboratory, Berkeley, CA.

Further Information

For additional information on performance characteristics of lamps, ballasts, lighting fixtures, and controls, the reader is referred to the CRC Handbook of Energy Efficiency, from which this section has been extracted. Further technical information is available in the Advanced Lighting Guidelines, 2003, published by New Buildings Institute and available through its Web site at http://www.newbuildings.org. The Illuminating Engineering Society of North America (IESNA) has a number of technical publications, which may be ordered through its Website at http://www.iesna.org. National Electrical Manufacturers Association (NEMA) standards are available at http://www.nema.org.

Appendices

Paul Norton
National Renewable Energy Laboratory

Appendix A. Properties of Gases and Vapors

TABLE A.1 Properties of Dry Air at Atmospheric Pressure

Symbols and Units:

K = absolute temperature, degrees Kelvin
deg C = temperature, degrees Celsius
deg F = temperature, degrees Fahrenheit
ρ = density, kg/m^3
c_p = specific heat capacity, kJ/kg·K
c_p/c_v = specific heat capacity ratio, dimensionless
μ = viscosity, N·s/m^2 × 10^6 (For N·s/m^2 (= kg/m·s) multiply tabulated values by 10^{-6})
k = thermal conductivity, W/m·k × 10^3 (For W/m·K multiply tabulated values by 10^{-3})
Pr = Prandtl number, dimensionless
h = enthalpy, kJ/kg
V_s = sound velocity, m/s

Temperature			*Properties*							
K	*deg C*	*deg F*	ρ	c_p	c_p/c_v	μ	k	Pr	h	V_s
100	−173.15	−280	3.598	1.028		6.929	9.248	.770	98.42	198.4
110	−163.15	−262	3.256	1.022	1.420 2	7.633	10.15	.768	108.7	208.7
120	−153.15	−244	2.975	1.017	1.416 6	8.319	11.05	.766	118.8	218.4
130	−143.15	−226	2.740	1.014	1.413 9	8.990	11.94	.763	129.0	227.6
140	−133.15	−208	2.540	1.012	1.411 9	9.646	12.84	.761	139.1	236.4
150	−123.15	−190	2.367	1.010	1.410 2	10.28	13.73	.758	149.2	245.0
160	−113.15	−172	2.217	1.009	1.408 9	10.91	14.61	.754	159.4	253.2
170	−103.15	−154	2.085	1.008	1.407 9	11.52	15.49	.750	169.4	261.0
180	−93.15	−136	1.968	1.007	1.407 1	12.12	16.37	.746	179.5	268.7
190	−83.15	−118	1.863	1.007	1.406 4	12.71	17.23	.743	189.6	276.2
200	−73.15	−100	1.769	1.006	1.405 7	13.28	18.09	.739	199.7	283.4
205	−68.15	−91	1.726	1.006	1.405 5	13.56	18.52	.738	204.7	286.9
210	−63.15	−82	1.684	1.006	1.405 3	13.85	18.94	.736	209.7	290.5
215	−58.15	−73	1.646	1.006	1.405 0	14.12	19.36	.734	214.8	293.9
220	−53.15	−64	1.607	1.006	1.404 8	14.40	19.78	.732	219.8	297.4
225	−48.15	−55	1.572	1.006	1.404 6	14.67	20.20	.731	224.8	300.8
230	−43.15	−46	1.537	1.006	1.404 4	14.94	20.62	.729	229.8	304.1
235	−38.15	−37	1.505	1.006	1.404 2	15.20	21.04	.727	234.9	307.4
240	−33.15	−28	1.473	1.005	1.404 0	15.47	21.45	.725	239.9	310.6
245	−28.15	−19	1.443	1.005	1.403 8	15.73	21.86	.724	244.9	313.8
250	−23.15	−10	1.413	1.005	1.403 6	15.99	22.27	.722	250.0	317.1
255	−18.15	−1	1.386	1.005	1.403 4	16.25	22.68	.721	255.0	320.2
260	−13.15	8	1.359	1.005	1.403 2	16.50	23.08	.719	260.0	323.4
265	−8.15	17	1.333	1.005	1.403 0	16.75	23.48	.717	265.0	326.5
270	−3.15	26	1.308	1.006	1.402 9	17.00	23.88	.716	270.1	329.6
275	+1.85	35	1.285	1.006	1.402 6	17.26	24.28	.715	275.1	332.6
280	6.85	44	1.261	1.006	1.402 4	17.50	24.67	.713	280.1	335.6
285	11.85	53	1.240	1.006	1.402 2	17.74	25.06	.711	285.1	338.5
290	16.85	62	1.218	1.006	1.402 0	17.98	25.47	.710	290.2	341.5
295	21.85	71	1.197	1.006	1.401 8	18.22	25.85	.709	295.2	344.4
300	26.85	80	1.177	1.006	1.401 7	18.46	26.24	.708	300.2	347.3
305	31.85	89	1.158	1.006	1.401 5	18.70	26.63	.707	305.3	350.2
310	36.85	98	1.139	1.007	1.401 3	18.93	27.01	.705	310.3	353.1
315	41.85	107	1.121	1.007	1.401 0	19.15	27.40	.704	315.3	355.8
320	46.85	116	1.103	1.007	1.400 8	19.39	27.78	.703	320.4	358.7

*Condensed and computed from: "Tables of Thermal Properties of Gases", National Bureau of Standards Circular 564, U.S. Government Printing Office, November 1955.

TABLE A.1 (continued) Properties of Dry Air at Atmospheric Pressure

Temperature			*Properties*							
K	*deg C*	*deg F*	ρ	c_p	c_p/c_v	μ	k	*Pr*	*h*	V_s
325	51.85	125	1.086	1.008	1.400 6	19.63	28.15	.702	325.4	361.4
330	56.85	134	1.070	1.008	1.400 4	19.85	28.53	.701	330.4	364.2
335	61.85	143	1.054	1.008	1.400 1	20.08	28.90	.700	335.5	366.9
340	66.85	152	1.038	1.008	1.399 9	20.30	29.28	.699	340.5	369.6
345	71.85	161	1.023	1.009	1.399 6	20.52	29.64	.698	345.6	372.3
350	76.85	170	1.008	1.009	1.399 3	20.75	30.03	.697	350.6	375.0
355	81.85	179	0.994 5	1.010	1.399 0	20.97	30.39	.696	355.7	377.6
360	86.85	188	0.980 5	1.010	1.398 7	21.18	30.78	.695	360.7	380.2
365	91.85	197	0.967 2	1.010	1.398 4	21.38	31.14	.694	365.8	382.8
370	96.85	206	0.953 9	1.011	1.398 1	21.60	31.50	.693	370.8	385.4
375	101.85	215	0.941 3	1.011	1.397 8	21.81	31.86	.692	375.9	388.0
380	106.85	224	0.928 8	1.012	1.397 5	22.02	32.23	.691	380.9	390.5
385	111.85	233	0.916 9	1.012	1.397 1	22.24	32.59	.690	386.0	393.0
390	116.85	242	0.905 0	1.013	1.396 8	22.44	32.95	.690	391.0	395.5
395	121.85	251	0.893 6	1.014	1.396 4	22.65	33.31	.689	396.1	398.0
400	126.85	260	0.882 2	1.014	1.396 1	22.86	33.65	.689	401.2	400.4
410	136.85	278	0.860 8	1.015	1.395 3	23.27	34.35	.688	411.3	405.3
420	146.85	296	0.840 2	1.017	1.394 6	23.66	35.05	.687	421.5	410.2
430	156.85	314	0.820 7	1.018	1.393 8	24.06	35.75	.686	431.7	414.9
440	166.85	332	0.802 1	1.020	1.392 9	24.45	36.43	.684	441.9	419.6
450	176.85	350	0.784 2	1.021	1.392 0	24.85	37.10	.684	452.1	424.2
460	186.85	368	0.767 7	1.023	1.391 1	25.22	37.78	.683	462.3	428.7
470	196.85	386	0.750 9	1.024	1.390 1	25.58	38.46	.682	472.5	433.2
480	206.85	404	0.735 1	1.026	1.389 2	25.96	39.11	.681	482.8	437.6
490	216.85	422	0.720 1	1.028	1.388 1	26.32	39.76	.680	493.0	442.0
500	226.85	440	0.705 7	1.030	1.387 1	26.70	40.41	.680	503.3	446.4
510	236.85	458	0.691 9	1.032	1.386 1	27.06	41.06	.680	513.6	450.6
520	246.85	476	0.678 6	1.034	1.385 1	27.42	41.69	.680	524.0	454.9
530	256.85	494	0.665 8	1.036	1.384 0	27.78	42.32	.680	534.3	459.0
540	266.85	512	0.653 5	1.038	1.382 9	28.14	42.94	.680	544.7	463.2
550	276.85	530	0.641 6	1.040	1.381 8	28.48	43.57	.680	555.1	467.3
560	286.85	548	0.630 1	1.042	1.380 6	28.83	44.20	.680	565.5	471.3
570	296.85	566	0.619 0	1.044	1.379 5	29.17	44.80	.680	575.9	475.3
580	306.85	584	0.608 4	1.047	1.378 3	29.52	45.41	.680	586.4	479.2
590	316.85	602	0.598 0	1.049	1.377 2	29.84	46.01	.680	596.9	483.2
600	326.85	620	0.588 1	1.051	1.376 0	30.17	46.61	.680	607.4	486.9
620	346.85	656	0.569 1	1.056	1.373 7	30.82	47.80	.681	628.4	494.5
640	366.85	692	0.551 4	1.061	1.371 4	31.47	48.96	.682	649.6	502.1
660	386.85	728	0.534 7	1.065	1.369 1	32.09	50.12	.682	670.9	509.4
680	406.85	764	0.518 9	1.070	1.366 8	32.71	51.25	.683	692.2	516.7
700	426.85	800	0.504 0	1.075	1.364 6	33.32	52.36	.684	713.7	523.7
720	446.85	836	0.490 1	1.080	1.362 3	33.92	53.45	.685	735.2	531.0
740	466.85	872	0.476 9	1.085	1.360 1	34.52	54.53	.686	756.9	537.6
760	486.85	908	0.464 3	1.089	1.358 0	35.11	55.62	.687	778.6	544.6
780	506.85	944	0.452 4	1.094	1.355 9	35.69	56.68	.688	800.5	551.2
800	526.85	980	0.441 0	1.099	1.354	36.24	57.74	.689	822.4	557.8
850	576.85	1 070	0.415 2	1.110	1.349	37.63	60.30	.693	877.5	574.1
900	626.85	1 160	0.392 0	1.121	1.345	38.97	62.76	.696	933.4	589.6
950	676.85	1 250	0.371 4	1.132	1.340	40.26	65.20	.699	989.7	604.9
1 000	726.85	1 340	0.352 9	1.142	1.336	41.53	67.54	.702	1 046	619.5
1 100	826.85	1 520	0.320 8	1.161	1.329	43.96			1 162	648.0
1 200	926.85	1 700	0.294 1	1.179	1.322	46.26			1 279	675.2
1 300	1 026.85	1 880	0.271 4	1.197	1.316	48.46			1 398	701.0
1 400	1 126.85	2 060	0.252 1	1.214	1.310	50.57			1 518	725.9
1 500	1 220.85	2 240	0.235 3	1.231	1.304	52.61			1 640	749.4
1 600	1 326.85	2 420	0.220 6	1.249	1.299	54.57			1 764	772.6
1 800	1 526.85	2 780	0.196 0	1.288	1.288	58.29			2 018	815.7
2 000	1 726.85	3 140	0.176 4	1.338	1.274				2 280	855.5
2 400	2 126.85	3 860	0.146 7	1.574	1.238				2 853	924.4
2 800	2 526.85	4 580	0.124 5	2.259	1.196				3 599	983.1

TABLE A.2 Ideal Gas Properties of Nitrogen, Oxygen, and Carbon Dioxide

Symbols and Units:

T = absolute temperature, degrees Kelvin
$\bar{h}$ = enthalpy, kJ/kmol
$\bar{u}$ = internal energy, kJ/kmol
$\bar{s}^\circ$ = absolute entropy at standard reference pressure, kJ/kmol K
[$\bar{h}$ = enthalpy of formation per mole at standard state = 0 kJ/kmol]

Part a. Ideal Gas Properties of Nitrogen, N_2

T	$\bar{h}$	$\bar{u}$	$\bar{s}^\circ$	T	$\bar{h}$	$\bar{u}$	$\bar{s}^\circ$
0	0	0	0	600	17,563	12,574	212.066
220	6,391	4,562	182.639	610	17,864	12,792	212.564
230	6,683	4,770	183.938	620	18,166	13,011	213.055
240	6,975	4,979	185.180	630	18,468	13,230	213.541
250	7,266	5,188	186.370	640	18,772	13,450	214.018
260	7,558	5,396	187.514	650	19,075	13,671	214.489
270	7,849	5,604	188.614	660	19,380	13,892	214.954
280	8,141	5,813	189.673	670	19,685	14,114	215.413
290	8,432	6,021	190.695	680	19,991	14,337	215.866
298	8,669	6,190	191.502	690	20,297	14,560	216.314
300	8,723	6,229	191.682	700	20,604	14,784	216.756
310	9,014	6,437	192.638	710	20,912	15,008	217.192
320	9,306	6,645	193.562	720	21,220	15,234	217.624
330	9,597	6,853	194.459	730	21,529	15,460	218.059
340	9,888	7,061	195.328	740	21,839	15,686	218.472
350	10,180	7,270	196.173	750	22,149	15,913	218.889
360	10,471	7,478	196.995	760	22,460	16,141	219.301
370	10,763	7,687	197.794	770	22,772	16,370	219.709
380	11,055	7,895	198.572	780	23,085	16,599	220.113
390	11,347	8,104	199.331	790	23,398	16,830	220.512
400	11,640	8,314	200.071	800	23,714	17,061	220.907
410	11,932	8,523	200.794	810	24,027	17,292	221.298
420	12,225	8,733	201.499	820	24,342	17,524	221.684
430	12,518	8,943	202.189	830	24,658	17,757	222.067
440	12,811	9,153	202.863	840	24,974	17,990	222.447
450	13,105	9,363	203.523	850	25,292	18,224	222.822
460	13,399	9,574	204.170	860	25,610	18,459	223.194
470	13,693	9,786	204.803	870	25,928	18,695	223.562
480	13,988	9,997	205.424	880	26,248	18,931	223.927
490	14,285	10,210	206.033	890	26,568	19,168	224.288
500	14,581	10,423	206.630	900	26,890	19,407	224.647
510	14,876	10,635	207.216	910	27,210	19,644	225.002
520	15,172	10,848	207.792	920	27,532	19,883	225.353
530	15,469	11,062	208.358	930	27,854	20,122	225.701
540	15,766	11,277	208.914	940	28,178	20,362	226.047
550	16,064	11,492	209.461	950	28,501	20,603	226.389
560	16,363	11,707	209.999	960	28,826	20,844	226.728
570	16,662	11,923	210.528	970	29,151	21,086	227.064
580	16,962	12,139	211.049	980	29,476	21,328	227.398
590	17,26[illegible]	12,356	211.562	990	29,803	21,571	227.728

Source: Adapted from M.J. Moran and H.N. Shapiro, *Fundamentals of Engineering Thermodynamics*, 3rd. ed., Wiley, New York, 1995, as presented in K. Wark. *Thermodynamics*, 4th ed., McGraw-Hill, New York, 1983, based on the *JANAF Thermochemical Tables*, NSRDS-NBS-37, 1971.

TABLE A.2 (continued) Ideal Gas Properties of Nitrogen, Oxygen, and Carbon Dioxide

T	$\bar{h}$	$\bar{u}$	$\bar{s}^\circ$	T	$\bar{h}$	$\bar{u}$	$\bar{s}^\circ$
1000	30,129	21,815	228.057	1760	56,227	41.594	247.396
1020	30,784	22,304	228.706	1780	56,938	42,139	247.798
1040	31,442	22,795	229.344	1800	57,651	42,685	248.195
1060	32,101	23,288	229.973	1820	58,363	43,231	248.589
1080	32,762	23,782	230.591	1840	59,075	43,777	248.979
1100	33,426	24,280	231.199	1860	59,790	44,324	249.365
1120	34,092	24,780	231.799	1880	60,504	44,873	249.748
1140	34,760	25,282	232.391	1900	61,220	45,423	250.128
1160	35,430	25,786	232.973	1920	61,936	45,973	250.502
1180	36,104	26,291	233.549	1940	62,654	46,524	250.874
1200	36,777	26,799	234.115	1960	63,381	47,075	251.242
1220	37,452	27,308	234.673	1980	64,090	47,627	251.607
1240	38,129	27,819	235.223	2000	64,810	48,181	251.969
1260	38,807	28,331	235.766	2050	66,612	49,567	252.858
1280	39,488	28,845	236.302	2100	68,417	50,957	253.726
1300	40,170	29,361	236.831	2150	70,226	52,351	254.578
1320	40,853	29,878	237.353	2200	72,040	53,749	255.412
1340	41,539	30,398	237.867	2250	73,856	55,149	256.227
1360	42,227	30,919	238.376	2300	75,676	56,553	257.027
1380	42,915	31,441	238.878	2350	77,496	57,958	257.810
1400	43,605	31,964	239.375	2400	79,320	59,366	258.580
1420	44,295	32,489	239.865	2450	81,149	60,779	259.332
1440	44,988	33,014	240.350	2500	82,981	62,195	260.073
1460	45,682	33,543	240.827	2550	84,814	63,613	260.799
1480	46,377	34,071	241.301	2600	86,650	65,033	261.512
1500	47,073	34,601	241.768	2650	88,488	66,455	262.213
1520	47,771	35,133	242.228	2700	90,328	67,880	262.902
1540	48,470	35,665	242.685	2750	92,171	69,306	263.577
1560	49,168	36,197	243.137	2800	94,014	70,734	264.241
1580	49,869	36,732	243.585	2850	95,859	72,163	264.895
1600	50,571	37,268	244.028	2900	97,705	73,593	265.538
1620	51,275	37,806	244.464	2950	99,556	75,028	266.170
1640	51,980	38,344	244.896	3000	101,407	76,464	266.793
1660	52,686	38,884	245.324	3050	103,260	77,902	267.404
1680	53,393	39,424	245.747	3100	105,115	79,341	268.007
1700	54,099	39,965	246.166	3150	106,972	80,782	268.601
1720	54,807	40,507	246.580	3200	108,830	82,224	269.186
1740	55,516	41,049	246.990	3250	110,690	83,668	269.763

TABLE A.2 (continued) Ideal Gas Properties of Nitrogen, Oxygen, and Carbon Dioxide

Part b. Ideal Gas Properties of Oxygen, O_2

T	$\bar{h}$	$\bar{u}$	$\bar{s}^\circ$	T	$\bar{h}$	$\bar{u}$	$\bar{s}^\circ$
0	0	0	0	600	17,929	12,940	226.346
220	6,404	4,575	196.171	610	18,250	13,178	226.877
230	6,694	4,782	197.461	620	18,572	13,417	227.400
240	6,984	4,989	198.696	630	18,895	13,657	227.918
250	7,275	5,197	199.885	640	19,219	13,898	228.429
260	7,566	5,405	201.027	650	19,544	14,140	228.932
270	7,858	5,613	202.128	660	19,870	14,383	229.430
280	8,150	5,822	203.191	670	20,197	14,626	229.920
290	8,443	6,032	204.218	680	20,524	14,871	230.405
298	8,682	6,203	205.033	690	20,854	15,116	230.885
300	8,736	6,242	205.213	700	21,184	15,364	231.358
310	9,030	6,453	206.177	710	21,514	15,611	231.827
320	9,325	6,664	207.112	720	21,845	15,859	232.291
330	9,620	6,877	208.020	730	22,177	16,107	232.748
340	9,916	7,090	208.904	740	22,510	16,357	233.201
350	10,213	7,303	209.765	750	22,844	16,607	233.649
360	10,511	7,518	210.604	760	23,178	16,859	234.091
370	10,809	7,733	211.423	770	23,513	17,111	234.528
380	11,109	7,949	212.222	780	23,850	17,364	234.960
390	11,409	8,166	213.002	790	24,186	17,618	235.387
400	11,711	8,384	213.765	800	24,523	17,872	235.810
410	12,012	8,603	214.510	810	24,861	18,126	236.230
420	12,314	8,822	215.241	820	25,199	18,382	236.644
430	12,618	9,043	215.955	830	25,537	18,637	237.055
440	12,923	9,264	216.656	840	25,877	18,893	237.462
450	13,228	9,487	217.342	850	26,218	19,150	237.864
460	13,535	9,710	218.016	860	26,559	19,408	238.264
470	13,842	9,935	218.676	870	26,899	19,666	238.660
480	14,151	10,160	219.326	880	27,242	19,925	239.051
490	14,460	10,386	219.963	890	27,584	20,185	239.439
500	14,770	10,614	220.589	900	27,928	20,445	239.823
510	15,082	10,842	221.206	910	28,272	20,706	240.203
520	15,395	11,071	221.812	920	28,616	20,967	240.580
530	15,708	11,301	222.409	930	28,960	21,228	240.953
540	16,022	11,533	222.997	940	29,306	21,491	241.323
550	16,338	11,765	223.576	950	29,652	21,754	241.689
560	16,654	11,998	224.146	960	29,999	22,017	242.052
570	16,971	12,232	224.708	970	30,345	22,280	242.411
580	17,290	12,467	225.262	980	30,692	22,544	242.768
590	17,609	12,703	225.808	990	31,041	22,809	243.120

TABLE A.2 (continued) Ideal Gas Properties of Nitrogen, Oxygen, and Carbon Dioxide

T	$\bar{h}$	$\bar{u}$	$\bar{s}^\circ$	T	$\bar{h}$	$\bar{u}$	$\bar{s}^\circ$
1000	31,389	23,075	243.471	1760	58,880	44,247	263.861
1020	32,088	23,607	244.164	1780	59,624	44,825	264.283
1040	32,789	24,142	244.844	1800	60,371	45,405	264.701
1060	33,490	24,677	245.513	1820	61,118	45,986	265.113
1080	34,194	25,214	246.171	1840	61,866	46,568	265.521
1100	34,899	25,753	246.818	1860	62,616	47,151	265.925
1120	35,606	26,294	247.454	1880	63,365	47,734	266.326
1140	36,314	26,836	248.081	1900	64,116	48,319	266.722
1160	37,023	27,379	248.698	1920	64,868	48,904	267.115
1180	37,734	27,923	249.307	1940	65,620	49,490	267.505
1200	38,447	28,469	249.906	1960	66,374	50,078	267.891
1220	39,162	29,018	250.497	1980	67,127	50,665	268.275
1240	39,877	29,568	251.079	2000	67,881	51,253	268.655
1260	40,594	30,118	251.653	2050	69,772	52,727	269.588
1280	41,312	30,670	252.219	2100	71,668	54,208	270.504
1300	42,033	31,224	252.776	2150	73,573	55,697	271.399
1320	42,753	31,778	253.325	2200	75,484	57,192	272.278
1340	43,475	32,334	253.868	2250	77,397	58,690	273.136
1360	44,198	32,891	254.404	2300	79,316	60,193	273.981
1380	44,923	33,449	254.932	2350	81,243	61,704	274.809
1400	45,648	34,008	255.454	2400	83,174	63,219	275.625
1420	46,374	34,567	255.968	2450	85,112	64,742	276.424
1440	47,102	35,129	256.475	2500	87,057	66,271	277.207
1460	47,831	35,692	256.978	2550	89,004	67,802	277.979
1480	48,561	36,256	257.474	2600	90,956	69,339	278.738
1500	49,292	36,821	257.965	2650	92,916	70,883	279.485
1520	50,024	37,387	258.450	2700	94,881	72,433	280.219
1540	50,756	37,952	258.928	2750	96,852	73,987	280.942
1560	51,490	38,520	259.402	2800	98,826	75,546	281.654
1580	52,224	39,088	259.870	2850	100,808	77,112	282.357
1600	52,961	39,658	260.333	2900	102,793	78,682	283.048
1620	53,696	40,227	260.791	2950	104,785	80,258	283.728
1640	54,434	40,799	261.242	3000	106,780	81,837	284.399
1660	55,172	41,370	261.690	3050	108,778	83,419	285.060
1680	55,912	41,944	262.132	3100	110,784	85,009	285.713
1700	56,652	42,517	262.571	3150	112,795	86,601	286.355
1720	57,394	43,093	263.005	3200	114,809	88,203	286.989
1740	58,136	43,669	263.435	3250	116,827	89,804	287.614

TABLE A.2 (continued) Ideal Gas Properties of Nitrogen, Oxygen, and Carbon Dioxide

Part c. Ideal Gas Properties of Carbon Dioxide, CO_2

T	$\bar{h}$	$\bar{u}$	$\bar{s}^\circ$	T	$\bar{h}$	$\bar{u}$	$\bar{s}^\circ$
0	0	0	0	600	22,280	17,291	243.199
220	6,601	4,772	202.966	610	22,754	17,683	243.983
230	6,938	5,026	204.464	620	23,231	18,076	244.758
240	7,280	5,285	205.920	630	23,709	18,471	245.524
250	7,627	5,548	207.337	640	24,190	18,869	246.282
260	7,979	5,817	208.717	650	24,674	19,270	247.032
270	8,335	6,091	210.062	660	25,160	19,672	247.773
280	8,697	6,369	211.376	670	25,648	20,078	248.507
290	9,063	6,651	212.660	680	26,138	20,484	249.233
298	9,364	6,885	213.685	690	26,631	20,894	249.952
300	9,431	6,939	213.915	700	27,125	21,305	250.663
310	9,807	7,230	215.146	710	27,622	21,719	251.368
320	10,186	7,526	216.351	720	28,121	22,134	252.065
330	10,570	7,826	217.534	730	28,622	22,552	252.755
340	10,959	8,131	218.694	740	29,124	22,972	253.439
350	11,351	8,439	219.831	750	29,629	23,393	254.117
360	11,748	8,752	220.948	760	30,135	23,817	254.787
370	12,148	9,068	222.044	770	30,644	24,242	255.452
380	12,552	9,392	223.122	780	31,154	24,669	256.110
390	12,960	9,718	224.182	790	31,665	25,097	256.762
400	13,372	10,046	225.225	800	32,179	25,527	257.408
410	13,787	10,378	226.250	810	32,694	25,959	258.048
420	14,206	10,714	227.258	820	33,212	26,394	258.682
430	14,628	11,053	228.252	830	33,730	26,829	259.311
440	15,054	11,393	229.230	840	34,251	27,267	259.934
450	15,483	11,742	230.194	850	34,773	27,706	260.551
460	15,916	12,091	231.144	860	35,296	28,125	261.164
470	16,351	12,444	232.080	870	35,821	28,588	261.770
480	16,791	12,800	233.004	880	36,347	29,031	262.371
490	17,232	13,158	233.916	890	36,876	29,476	262.968
500	17,678	13,521	234.814	900	37,405	29,922	263.559
510	18,126	13,885	235.700	910	37,935	30,369	264.146
520	18,576	14,253	236.575	920	38,467	30,818	264.728
530	19,029	14,622	237.439	930	39,000	31,268	265.304
540	19,485	14,996	238.292	940	39,535	31,719	265.877
550	19,945	15,372	239.135	950	40,070	32,171	266.444
560	20,407	15,751	239.962	960	40,607	32,625	267.007
570	20,870	16,131	240.789	970	41,145	33,081	267.566
580	21,337	16,515	241.602	980	41,685	33,537	268.119
590	21,807	16,902	242.405	990	42,226	33,995	268.670

TABLE A.2 (continued) Ideal Gas Properties of Nitrogen, Oxygen, and Carbon Dioxide

T	$\bar{h}$	$\bar{u}$	$\bar{s}^\circ$	T	$\bar{h}$	$\bar{u}$	$\bar{s}^\circ$
1000	42,769	34,455	269.215	1760	86,420	71,787	301.543
1020	43,859	35,378	270.293	1780	87,612	72,812	302.271
1040	44,953	36,306	271.354	1800	88,806	73,840	302.884
1060	46,051	37,238	272.400	1820	90,000	74,868	303.544
1080	47,153	38,174	273.430	1840	91,196	75,897	304.198
1100	48,258	39,112	274.445	1860	92,394	76,929	304.845
1120	49,369	40,057	275.444	1880	93,593	77,962	305.487
1140	50,484	41,006	276.430	1900	94,793	78,996	306.122
1160	51,602	41,957	277.403	1920	95,995	80,031	306.751
1180	52,724	42,913	278.362	1940	97,197	81,067	307.374
1200	53,848	43,871	279.307	1960	98,401	82,105	307.992
1220	54,977	44,834	280.238	1980	99,606	83,144	308.604
1240	56,108	45,799	281.158	2000	100,804	84,185	309.210
1260	57,244	46,768	282.066	2050	103,835	86,791	310.701
1280	58,381	47,739	282.962	2100	106,864	89,404	312.160
1300	59,522	48,713	283.847	2150	109,898	92,023	313.589
1320	60,666	49,691	284.722	2200	112,939	94,648	314.988
1340	61,813	50,672	285.586	2250	115,984	97,277	316.356
1360	62,963	51,656	286.439	2300	119,035	99,912	317.695
1380	64,116	52,643	287.283	2350	122,091	102,552	319.011
1400	65,271	53,631	288.106	2400	125,152	105,197	320.302
1420	66,427	54,621	288.934	2450	128,219	107,849	321.566
1440	67,586	55,614	289.743	2500	131,290	110,504	322.808
1460	68,748	56,609	290.542	2550	134,368	113,166	324.026
1480	69,911	57,606	291.333	2600	137,449	115,832	325.222
1500	71,078	58,606	292.114	2650	140,533	118,500	326.396
1520	72,246	59,609	292.888	2700	143,620	121,172	327.549
1540	73,417	60,613	292.654	2750	146,713	123,849	328.684
1560	74,590	61,620	294.411	2800	149,808	126,528	329.800
1580	76,767	62,630	295.161	2850	152,908	129,212	330.896
1600	76,944	63,741	295.901	2900	156,009	131,898	331.975
1620	78,123	64,653	296.632	2950	159,117	134,589	333.037
1640	79,303	65,668	297.356	3000	162,226	137,283	334.084
1660	80,486	66,592	298.072	3050	165,341	139,982	335.114
1680	81,670	67,702	298.781	3100	168,456	142,681	336.126
1700	82,856	68,721	299.482	3150	171,576	145,385	337.124
1720	84,043	69,742	300.177	3200	174,695	148,089	338.109
1740	85,231	70,764	300.863	3250	177,822	150,801	339.069

TABLE A.3 Psychrometric Table: Properties of Moist Air at 101 325 N/m^2

Symbols and Units:

P_s = pressure of water vapor at saturation, N/m^2
W_s = humidity ratio at saturation, mass of water vapor associated with unit mass of dry air
V_a = specific volume of dry air, m^3/kg
V_s = specific volume of saturated mixture, m^3/kg dry air

h_a^a = specific enthalpy of dry air, kJ/kg
h_s = specific enthalpy of saturated mixture, kJ/kg dry air
s_s = specific entropy of saturated mixture, J/K·kg dry air

Temperature			*Properties*						
C	*K*	*F*	P_s	W_s	V_a	V_s	h_a	h_s	s_s
−40	233.15	−40	12.838	0.000 079 25	0.659 61	0.659 68	−22.35	−22.16	−90.659
−30	243.15	−22	37.992	0.000 234 4	0.688 08	0.688 33	−12.29	−11.72	−46.732
−25	248.15	−13	63.248	0.000 390 3	0.702 32	0.702 75	−7.265	−6.306	−24.706
−20	253.15	−4	103.19	0.000 637 1	0.716 49	0.717 24	−2.236	−0.6653	−2.2194
−15	258.15	+5	165.18	0.001 020	0.730 72	0.731 91	+2.794	5.318	21.189
−10	263.15	14	259.72	0.001 606	0.744 95	0.746 83	7.823	11.81	46.104
−5	268.15	23	401.49	0.002 485	0.759 12	0.762 18	12.85	19.04	73.365
0	273.15	32	610.80	0.003 788	0.773 36	0.778 04	17.88	27.35	104.14
5	278.15	41	871.93	0.005 421	0.787 59	0.794 40	22.91	36.52	137.39
10	283.15	50	1 227.2	0.007 658	0.801 76	0.811 63	27.94	47.23	175.54
15	288.15	59	1 704.4	0.010 69	0.816 00	0.829 98	32.97	59.97	220.22
20	293.15	68	2 337.2	0.014 75	0.830 17	0.849 83	38.00	75.42	273.32
25	298.15	77	3 167.0	0.020 16	0.844 34	0.871 62	43.03	94.38	337.39
30	303.15	86	4 242.8	0.027 31	0.858 51	0.896 09	48.07	117.8	415.65
35	308.15	95	5 623.4	0.036 73	0.872 74	0.924 06	53.10	147.3	512.17
40	313.15	104	7 377.6	0.049 11	0.886 92	0.956 65	58.14	184.5	532.31
45	318.15	113	9 584.8	0.065 36	0.901 15	0.995 35	63.17	232.0	783.06
50	323.15	122	12 339	0.086 78	0.915 32	1.042 3	68.21	293.1	975.27
55	328.15	131	15 745	0.115 2	0.929 49	1.100 7	73.25	372.9	1 221.5
60	333.15	140	19 925	0.153 4	0.943 72	1.174 8	78.29	478.5	1 543.5
65	338.15	149	25 014	0.205 5	0.957 90	1.272 1	83.33	621.4	1 973.6
70	343.15	158	31 167	0.278 8	0.972 07	1.404 2	88.38	820.5	2 564.8
75	348.15	167	38 554	0.385 8	0.986 30	1.592 4	93.42	1 110	3 412.8
80	353.15	176	47 365	0.551 9	1.000 5	1.879 1	98.47	1 557	4 710.9
85	358.15	185	57 809	0.836 3	1.014 6	2.363 2	103.5	2 321	6 892.6
90	363.15	194	70 112	1.416	1.028 8	3.340 9	108.6	3 876	11 281

Note: The P_s column in this table gives the vapor pressure of pure water at temperature intervals of five degrees Celsius. For the latest data on vapor pressures at intervals of 0.1 deg C, from 0–100 deg C, see "Vapor Pressure Equation for Water", A. Wexler and L. Greenspan, *J. Res. Nat. Bur. Stand.*, 75A(3):213–229, May–June 1971.

[a] For very low barometric pressures and high wet-bulb temperatures, the values of h_a in this table are somewhat low; for corrections see "ASHRAE Handbook of Fundamentals".

* Computed from: Psychrometric Tables, in "ASHRAE Handbook of Fundamentals", American Society of Heating, Refrigerating and Air-Conditioning Engineers, 1972.

TABLE A.4 Water Vapor at Low Pressures: Perfect Gas Behavior pv/T = R = 0.461 51 kJ/kg·K

Symbols and Units:

t = thermodynamic temperature, deg C
T = thermodynamic temperature, K
pv = RT, kJ/kg
u_o = specific internal energy at zero pressure, kJ/kg
h_o = specific enthalpy at zero pressure, kJ/kg
s_l = specific entropy of semiperfect vapor at 0.1 MN/m^2, kJ/kg·K
ψ_l = specific Helmholtz free energy of semiperfect vapor at 0.1 MN/m^2, kJ/kg
ψ_l = specific Helmholtz free energy of semiperfect vapor at 0.1 MN/m^2, kJ/kg
ζ_l = specific Gibbs free energy of semiperfect vapor at 0.1 MN/m^2, kJ/kg
p_r = relative pressure, pressure of semiperfect vapor at zero entropy, TN/m^2
v_r = relative specific volume, specific volume of semiperfect vapor at zero entropy, mm^3/kg
c_{po} = specific heat capacity at constant pressure for zero pressure, kJ/kg·K
c_{vo} = specific heat capacity at constant volume for zero pressure, kJ/kg·K
$k = c_{po}/c_{vo}$ = isentropic exponent, $-(\partial \log p/\partial \log v)_s$

t	T	pv	u_o	h_o	s_l	ψ_l	ζ_l	p_r	v_r	c_{po}	c_{vo}	k
0	273.15	126.06	2 375.5	2 501.5	6.804 2	516.9	643.0	.252 9	498.4	1.858 4	1.396 9	1.330 4
10	283.15	130.68	2 389.4	2 520.1	6.871 1	443.9	574.6	.292 3	447.0	1.860 1	1.398 6	1.330 0
20	293.15	135.29	2 403.4	2 538.7	6.935 7	370.2	505.5	.336 3	402.4	1.862 2	1.400 7	1.329 5
30	303.15	139.91	2 417.5	2 557.4	6.998 2	296.0	435.9	.385 0	363.4	1.864 7	1.403 1	1.328 9
40	313.15	144.52	2 431.5	2 576.0	7.058 7	221.1	365.6	.439 0	329.2	1.867 4	1.405 9	1.328 3
50	323.15	149.14	2 445.6	2 594.7	7.117 5	145.6	294.7	.498 6	299.1	1.870 5	1.409 0	1.327 5
60	333.15	153.75	2 459.7	2 613.4	7.174 5	69.5	223.2	.564 2	272.5	1.873 8	1.412 3	1.326 8
70	343.15	158.37	2 473.8	2 632.2	7.230 0	−7.2	151.2	.636 3	248.9	1.877 4	1.415 9	1.325 9
80	353.15	162.98	2 488.0	2 651.0	7.284 0	−84.3	78.6	.715 2	227.9	1.881 2	1.419 7	1.325 1
90	363.15	167.60	2 502.2	2 669.8	7.336 6	−162.1	5.5	.801 5	209.1	1.885 2	1.423 7	1.324 2
100	373.15	172.21	2 516.5	2 688.7	7.387 8	−240.3	−68.1	.895 7	192.26	1.889 4	1.427 9	1.323 2
120	393.15	181.44	2 545.1	2 726.6	7.486 7	−398.3	−216.8	1.109 7	163.50	1.898 3	1.436 7	1.321 2
140	413.15	190.67	2 573.9	2 764.6	7.581 1	−558.2	−367.5	1.361 7	140.03	1.907 7	1.446 2	1.319 1
160	433.15	199.90	2 603.0	2 802.9	7.671 5	−720.0	−520.1	1.656 4	120.69	1.917 7	1.456 2	1.316 9
180	453.15	209.13	2 632.2	2 841.3	7.758 3	−883.5	−674.4	1.999 1	104.61	1.928 1	1.466 6	1.314 7
200	473.15	218.4	2 661.6	2 880.0	7.841 8	−1 048.7	−830.4	2.396	91.15	1.938 9	1.477 4	1.312 4
300	573.15	264.5	2 812.3	3 076.8	8.218 9	−1 898.4	−1 633.9	5.423	48.77	1.997 5	1.536 0	1.300 5
400	673.15	310.7	2 969.0	3 279.7	8.545 1	−2 783.1	−2 472.5	10.996	28.25	2.061 4	1.599 9	1.288 5
500	773.15	356.8	3 132.4	3 489.2	8.835 2	−3 699	−3 342	20.61	17.310	2.128 7	1.667 2	1.276 8
600	873.15	403.0	3 302.5	3 705.5	9.098 2	−4 642	−4 239	36.45	11.056	2.198 0	1.736 5	1.265 8
700	973.15	449.1	3 479.7	3 928.8	9.340 3	−5 610	−5 161	61.58	7.293	2.268 3	1.806 8	1.255 4
800	1 073.15	495.3	3 663.9	4 159.2	9.565 5	−6 601	−6 106	100.34	4.936	2.338 7	1.877 1	1.245 9
900	1 173.15	541.4	3 855.1	4 396.5	9.776 9	−7 615	−7 073	158.63	3.413	2.407 8	1.946 2	1.237 1
1 000	1 273.15	587.6	4 053.1	4 640.6	9.976 6	−8 649	−8 061	244.5	2.403	2.474 4	2.012 8	1.299 3
1 100	1 373.15	633.7	4 257.5	4 891.2	10.166 1	−9 702	−9 068	368.6	1.719	2.536 9	2.075 4	1.222 4
1 200	1 473.15	679.9	4 467.9	5 147.8	10.346 4	−10 774	−10 094	544.9	1.248	2.593 8	2.132 3	1.216 4
1 300	1 573.15	726.0	4 683.7	5 409.7	10.518 4	−11 863	−11 137	791.0	.918	2.643 1	2.181 6	1.211 5

---

*Adapted from: "Steam Tables", J.H. Keenan, F.G. Keyes, P.G. Hill, and J.G. Moore, John Wiley & Sons, Inc., 1969 (International Edition—Metric Units).

REFERENCE

For other steam tables in metric units, see "Steam Tables in SI Units", Ministry of Technology, London, 1970.

TABLE A.5 Properties of Saturated Water and Steam

Part a. Temperature Table

		Specific Volume m³/kg		Internal Energy kJ/kg		Enthalpy kJ/kg			Entropy kJ/kg · K		
Temp. °C	Press. bars	Sat. Liquid $v_f \times 10^3$	Sat. Vapor v_g	Sat. Liquid u_f	Sat. Vapor u_g	Sat. Liquid h_f	Evap. h_{fg}	Sat. Vapor h_g	Sat. Liquid s_f	Sat. Vapor s_g	Temp. °C
.01	0.00611	1.0002	206.136	0.00	2375.3	0.01	2501.3	2501.4	0.0000	9.1562	.01
4	0.00813	1.0001	157.232	16.77	2380.9	16.78	2491.9	2508.7	0.0610	9.0514	4
5	0.00872	1.0001	147.120	20.97	2382.3	20.98	2489.6	2510.6	0.0761	9.0257	5
6	0.00935	1.0001	137.734	25.19	2383.6	25.20	2487.2	2512.4	0.0912	9.0003	6
8	0.01072	1.0002	120.917	33.59	2386.4	33.60	2482.5	2516.1	0.1212	8.9501	8
10	0.01228	1.0004	106.379	42.00	2389.2	42.01	2477.7	2519.8	0.1510	8.9008	10
11	0.01312	1.0004	99.857	46.20	2390.5	46.20	2475.4	2521.6	0.1658	8.8765	11
12	0.01402	1.0005	93.784	50.41	2391.9	50.41	2473.0	2523.4	0.1806	8.8524	12
13	0.01497	1.0007	88.124	54.60	2393.3	54.60	2470.7	2525.3	0.1953	8.8285	13
14	0.01598	1.0008	82.848	58.79	2394.7	58.80	2468.3	2527.1	0.2099	8.8048	14
15	0.01705	1.0009	77.926	62.99	2396.1	62.99	2465.9	2528.9	0.2245	8.7814	15
16	0.01818	1.0011	73.333	67.18	2397.4	67.19	2463.6	2530.8	0.2390	8.7582	16
17	0.01938	1.0012	69.044	71.38	2398.8	71.38	2461.2	2532.6	0.2535	8.7351	17
18	0.02064	1.0014	65.038	75.57	2400.2	75.58	2458.8	2534.4	0.2679	8.7123	18
19	0.02198	1.0016	61.293	79.76	2401.6	79.77	2456.5	2536.2	0.2823	8.6897	19
20	0.02339	1.0018	57.791	83.95	2402.9	83.96	2454.1	2538.1	0.2966	8.6672	20
21	0.02487	1.0020	54.514	88.14	2404.3	88.14	2451.8	2539.9	0.3109	8.6450	21
22	0.02645	1.0022	51.447	92.32	2405.7	92.33	2449.4	2541.7	0.3251	8.6229	22
23	0.02810	1.0024	48.574	96.51	2407.0	96.52	2447.0	2543.5	0.3393	8.6011	23
24	0.02985	1.0027	45.883	100.70	2408.4	100.70	2444.7	2545.4	0.3534	8.5794	24
25	0.03169	1.0029	43.360	104.88	2409.8	104.89	2442.3	2547.2	0.3674	8.5580	25
26	0.03363	1.0032	40.994	109.06	2411.1	109.07	2439.9	2549.0	0.3814	8.5367	26
27	0.03567	1.0035	38.774	113.25	2412.5	113.25	2437.6	2550.8	0.3954	8.5156	27
28	0.03782	1.0037	36.690	117.42	2413.9	117.43	2435.2	2552.6	0.4093	8.4946	28
29	0.04008	1.0040	34.733	121.60	2415.2	121.61	2432.8	2554.5	0.4231	8.4739	29
30	0.04246	1.0043	32.894	125.78	2416.6	125.79	2430.5	2556.3	0.4369	8.4533	30
31	0.04496	1.0046	31.165	129.96	2418.0	129.97	2428.1	2558.1	0.4507	8.4329	31
32	0.04759	1.0050	29.540	134.14	2419.3	134.15	2425.7	2559.9	0.4644	8.4127	32
33	0.05034	1.0053	28.011	138.32	2420.7	138.33	2423.4	2561.7	0.4781	8.3927	33
34	0.05324	1.0056	26.571	142.50	2422.0	142.50	2421.0	2563.5	0.4917	8.3728	34
35	0.05628	1.0060	25.216	146.67	2423.4	146.68	2418.6	2565.3	0.5053	8.3531	35
36	0.05947	1.0063	23.940	150.85	2424.7	150.86	2416.2	2567.1	0.5188	8.3336	36
38	0.06632	1.0071	21.602	159.20	2427.4	159.21	2411.5	2570.7	0.5458	8.2950	38
40	0.07384	1.0078	19.523	167.56	2430.1	167.57	2406.7	2574.3	0.5725	8.2570	40
45	0.09593	1.0099	15.258	188.44	2436.8	188.45	2394.8	2583.2	0.6387	8.1648	45

TABLE A.5 (continued) Properties of Saturated Water and Steam

		Specific Volume m³/kg		Internal Energy kJ/kg		Enthalpy kJ/kg			Entropy kJ/kg · K		
Temp. °C	Press. bars	Sat. Liquid $v_f \times 10^3$	Sat. Vapor v_g	Sat. Liquid u_f	Sat. Vapor u_g	Sat. Liquid h_f	Evap. h_{fg}	Sat. Vapor h_g	Sat. Liquid s_f	Sat. Vapor s_g	Temp. °C
50	.1235	1.0121	12.032	209.32	2443.5	209.33	2382.7	2592.1	.7038	8.0763	50
55	.1576	1.0146	9.568	230.21	2450.1	230.23	2370.7	2600.9	.7679	7.9913	55
60	.1994	1.0172	7.671	251.11	2456.6	251.13	2358.5	2609.6	.8312	7.9096	60
65	.2503	1.0199	6.197	272.02	2463.1	272.06	2346.2	2618.3	.8935	7.8310	65
70	.3119	1.0228	5.042	292.95	2469.6	292.98	2333.8	2626.8	.9549	7.7553	70
75	.3858	1.0259	4.131	313.90	2475.9	313.93	2321.4	2635.3	1.0155	7.6824	75
80	.4739	1.0291	3.407	334.86	2482.2	334.91	2308.8	2643.7	1.0753	7.6122	80
85	.5783	1.0325	2.828	355.84	2488.4	355.90	2296.0	2651.9	1.1343	7.5445	85
90	.7014	1.0360	2.361	376.85	2494.5	376.92	2283.2	2660.1	1.1925	7.4791	90
95	.8455	1.0397	1.982	397.88	2500.6	397.96	2270.2	2668.1	1.2500	7.4159	95
100	1.014	1.0435	1.673	418.94	2506.5	419.04	2257.0	2676.1	1.3069	7.3549	100
110	1.433	1.0516	1.210	461.14	2518.1	461.30	2230.2	2691.5	1.4185	7.2387	110
120	1.985	1.0603	0.8919	503.50	2529.3	503.71	2202.6	2706.3	1.5276	7.1296	120
130	2.701	1.0697	0.6685	546.02	2539.9	546.31	2174.2	2720.5	1.6344	7.0269	130
140	3.613	1.0797	0.5089	588.74	2550.0	589.13	2144.7	2733.9	1.7391	6.9299	140
150	4.758	1.0905	0.3928	631.68	2559.5	632.20	2114.3	2746.5	1.8418	6.8379	150
160	6.178	1.1020	0.3071	674.86	2568.4	675.55	2082.6	2758.1	1.9427	6.7502	160
170	7.917	1.1143	0.2428	718.33	2576.5	719.21	2049.5	2768.7	2.0419	6.6663	170
180	10.02	1.1274	0.1941	762.09	2583.7	763.22	2015.0	2778.2	2.1396	6.5857	180
190	12.54	1.1414	0.1565	806.19	2590.0	807.62	1978.8	2786.4	2.2359	6.5079	190
200	15.54	1.1565	0.1274	850.65	2595.3	852.45	1940.7	2793.2	2.3309	6.4323	200
210	19.06	1.1726	0.1044	895.53	2599.5	897.76	1900.7	2798.5	2.4248	6.3585	210
220	23.18	1.1900	0.08619	940.87	2602.4	943.62	1858.5	2802.1	2.5178	6.2861	220
230	27.95	1.2088	0.07158	986.74	2603.9	990.12	1813.8	2804.0	2.6099	6.2146	230
240	33.44	1.2291	0.05976	1033.2	2604.0	1037.3	1766.5	2803.8	2.7015	6.1437	240
250	39.73	1.2512	0.05013	1080.4	2602.4	1085.4	1716.2	2801.5	2.7927	6.0730	250
260	46.88	1.2755	0.04221	1128.4	2599.0	1134.4	1662.5	2796.6	2.8838	6.0019	260
270	54.99	1.3023	0.03564	1177.4	2593.7	1184.5	1605.2	2789.7	2.9751	5.9301	270
280	64.12	1.3321	0.03017	1227.5	2586.1	1236.0	1543.6	2779.6	3.0668	5.8571	280
290	74.36	1.3656	0.02557	1278.9	2576.0	1289.1	1477.1	2766.2	3.1594	5.7821	290
300	85.81	1.4036	0.02167	1332.0	2563.0	1344.0	1404.9	2749.0	3.2534	5.7045	300
320	112.7	1.4988	0.01549	1444.6	2525.5	1461.5	1238.6	2700.1	3.4480	5.5362	320
340	145.9	1.6379	0.01080	1570.3	2464.6	1594.2	1027.9	2622.0	3.6594	5.3357	340
360	186.5	1.8925	0.006945	1725.2	2351.5	1760.5	720.5	2481.0	3.9147	5.0526	360
374.14	220.9	3.155	0.003155	2029.6	2029.6	2099.3	0	2099.3	4.4298	4.4298	374.14

TABLE A.5 (continued) Properties of Saturated Water and Steam

Part b. Pressure Table

Press. bars	Temp. °C	Specific Volume m³/kg		Internal Energy kJ/kg		Enthalpy kJ/kg			Entropy kJ/kg · K		Press. bars
		Sat. Liquid $v_f \times 10^3$	Sat. Vapor v_g	Sat. Liquid u_f	Sat. Vapor u_g	Sat. Liquid h_f	Evap. h_{fg}	Sat. Vapor h_g	Sat. Liquid s_f	Sat. Vapor s_g	
0.04	28.96	1.0040	34.800	121.45	2415.2	121.46	2432.9	2554.4	0.4226	8.4746	0.04
0.06	36.16	1.0064	23.739	151.53	2425.0	151.53	2415.9	2567.4	0.5210	8.3304	0.06
0.08	41.51	1.0084	18.103	173.87	2432.2	173.88	2403.1	2577.0	0.5926	8.2287	0.08
0.10	45.81	1.0102	14.674	191.82	2437.9	191.83	2392.8	2584.7	0.6493	8.1502	0.10
0.20	60.06	1.0172	7.649	251.38	2456.7	251.40	2358.3	2609.7	0.8320	7.9085	0.20
0.30	69.10	1.0223	5.229	289.20	2468.4	289.23	2336.1	2625.3	0.9439	7.7686	0.30
0.40	75.87	1.0265	3.993	317.53	2477.0	317.58	2319.2	2636.8	1.0259	7.6700	0.40
0.50	81.33	1.0300	3.240	340.44	2483.9	340.49	2305.4	2645.9	1.0910	7.5939	0.50
0.60	85.94	1.0331	2.732	359.79	2489.6	359.86	2293.6	2653.5	1.1453	7.5320	0.60
0.70	89.95	1.0360	2.365	376.63	2494.5	376.70	2283.3	2660.0	1.1919	7.4797	0.70
0.80	93.50	1.0380	2.087	391.58	2498.8	391.66	2274.1	2665.8	1.2329	7.4346	0.80
0.90	96.71	1.0410	1.869	405.06	2502.6	405.15	2265.7	2670.9	1.2695	7.3949	0.90
1.00	99.63	1.0432	1.694	417.36	2506.1	417.46	2258.0	2675.5	1.3026	7.3594	1.00
1.50	111.4	1.0528	1.159	466.94	2519.7	467.11	2226.5	2693.6	1.4336	7.2233	1.50
2.00	120.2	1.0605	0.8857	504.49	2529.5	504.70	2201.9	2706.7	1.5301	7.1271	2.00
2.50	127.4	1.0672	0.7187	535.10	2537.2	535.37	2181.5	2716.9	1.6072	7.0527	2.50
3.00	133.6	1.0732	0.6058	561.15	2543.6	561.47	2163.8	2725.3	1.6718	6.9919	3.00
3.50	138.9	1.0786	0.5243	583.95	2546.9	584.33	2148.1	2732.4	1.7275	6.9405	3.50
4.00	143.6	1.0836	0.4625	604.31	2553.6	604.74	2133.8	2738.6	1.7766	6.8959	4.00
4.50	147.9	1.0882	0.4140	622.25	2557.6	623.25	2120.7	2743.9	1.8207	6.8565	4.50
5.00	151.9	1.0926	0.3749	639.68	2561.2	640.23	2108.5	2748.7	1.8607	6.8212	5.00
6.00	158.9	1.1006	0.3157	669.90	2567.4	670.56	2086.3	2756.8	1.9312	6.7600	6.00
7.00	165.0	1.1080	0.2729	696.44	2572.5	697.22	2066.3	2763.5	1.9922	6.7080	7.00
8.00	170.4	1.1148	0.2404	720.22	2576.8	721.11	2048.0	2769.1	2.0462	6.6628	8.00
9.00	175.4	1.1212	0.2150	741.83	2580.5	742.83	2031.1	2773.9	2.0946	6.6226	9.00
10.0	179.9	1.1273	0.1944	761.68	2583.6	762.81	2015.3	2778.1	2.1387	6.5863	10.0
15.0	198.3	1.1539	0.1318	843.16	2594.5	844.84	1947.3	2792.2	2.3150	6.4448	15.0
20.0	212.4	1.1767	0.09963	906.44	2600.3	908.79	1890.7	2799.5	2.4474	6.3409	20.0
25.0	224.0	1.1973	0.07998	959.11	2603.1	962.11	1841.0	2803.1	2.5547	6.2575	25.0
30.0	233.9	1.2165	0.06668	1004.8	2604.1	1008.4	1795.7	2804.2	2.6457	6.1869	30.0
35.0	242.6	1.2347	0.05707	1045.4	2603.7	1049.8	1753.7	2803.4	2.7253	6.1253	35.0
40.0	250.4	1.2522	0.04978	1082.3	2602.3	1087.3	1714.1	2801.4	2.7964	6.0701	40.0
45.0	257.5	1.2692	0.04406	1116.2	2600.1	1121.9	1676.4	2798.3	2.8610	6.0199	45.0
50.0	264.0	1.2859	0.03944	1147.8	2597.1	1154.2	1640.1	2794.3	2.9202	5.9734	50.0
60.0	275.6	1.3187	0.03244	1205.4	2589.7	1213.4	1571.0	2784.3	3.0267	5.8892	60.0
70.0	285.9	1.3513	0.02737	1257.6	2580.5	1267.0	1505.1	2772.1	3.1211	5.8133	70.0
80.0	295.1	1.3842	0.02352	1305.6	2569.8	1316.6	1441.3	2758.0	3.2068	5.7432	80.0
90.0	303.4	1.4178	0.02048	1350.5	2557.8	1363.3	1378.9	2742.1	3.2858	5.6772	90.0
100.	311.1	1.4524	0.01803	1393.0	2544.4	1407.6	1317.1	2724.7	3.3596	5.6141	100.
110.	318.2	1.4886	0.01599	1433.7	2529.8	1450.1	1255.5	2705.6	3.4295	5.5527	110.
120.	324.8	1.5267	0.01426	1473.0	2513.7	1491.3	1193.6	2684.9	3.4962	5.4924	120.
130.	330.9	1.5671	0.01278	1511.1	2496.1	1531.5	1130.7	2662.2	3.5606	5.4323	130.
140.	336.8	1.6107	0.01149	1548.6	2476.8	1571.1	1066.5	2637.6	3.6232	5.3717	140.
150.	342.2	1.6581	0.01034	1585.6	2455.5	1610.5	1000.0	2610.5	3.6848	5.3098	150.
160.	347.4	1.7107	0.009306	1622.7	2431.7	1650.1	930.6	2580.6	3.7461	5.2455	160.
170.	352.4	1.7702	0.008364	1660.2	2405.0	1690.3	856.9	2547.2	3.8079	5.1777	170.
180.	357.1	1.8397	0.007489	1698.9	2374.3	1732.0	777.1	2509.1	3.8715	5.1044	180.
190.	361.5	1.9243	0.006657	1739.9	2338.1	1776.5	688.0	2464.5	3.9388	5.0228	190.
200.	365.8	2.036	0.005834	1785.6	2293.0	1826.3	583.4	2409.7	4.0139	4.9269	200.
220.9	374.1	3.155	0.003155	2029.6	2029.6	2099.3	0	2099.3	4.4298	4.4298	220.9

Source: Adapted from M.J. Moran and H.N. Shapiro, *Fundamentals of Engineering Thermodynamics*, 3rd. ed., Wiley, New York, 1995, as extracted from J.H. Keenan, F.G. Keyes, P.G. Hill, and J.G. Moore, *Steam Tables*, Wiley, New York, 1969.

TABLE A.6 Properties of Superheated Steam

Symbols and Units:

T = temperature, °C
T_{sat} = Saturation temperature, °C
ν = Specific volume, m^3/kg
u = internal energy, kJ/kg
h = enthalpy, kJ/kg
S = entropy, kJ/kg·K
p = pressure, bar and μPa

T °C	*v* m^3/kg	*u* kJ/kg	*h* kJ/kg	*s* kJ/kg · K	*v* m^3/kg	*u* kJ/kg	*h* kJ/kg	*s* kJ/kg · K
	p = 0.06 bar = 0.006 MPa (T_{sat} = 36.16°C)				**p = 0.35 bar = 0.035 MPa (T_{sat} = 72.69°C)**			
Sat.	23.739	2425.0	2567.4	8.3304	4.526	2473.0	2631.4	7.7158
80	27.132	2487.3	2650.1	8.5804	4.625	2483.7	2645.6	7.7564
120	30.219	2544.7	2726.0	8.7840	5.163	2542.4	2723.1	7.9644
160	33.302	2602.7	2802.5	8.9693	5.696	2601.2	2800.6	8.1519
200	36.383	2661.4	2879.7	9.1398	6.228	2660.4	2878.4	8.3237
240	39.462	2721.0	2957.8	9.2982	6.758	2720.3	2956.8	8.4828
280	42.540	2781.5	3036.8	9.4464	7.287	2780.9	3036.0	8.6314
320	45.618	2843.0	3116.7	9.5859	7.815	2842.5	3116.1	8.7712
360	48.696	2905.5	3197.7	9.7180	8.344	2905.1	3197.1	8.9034
400	51.774	2969.0	3279.6	9.8435	8.872	2968.6	3279.2	9.0291
440	54.851	3033.5	3362.6	9.9633	9.400	3033.2	3362.2	9.1490
500	59.467	3132.3	3489.1	10.1336	10.192	3132.1	3488.8	9.3194
	p = 0.70 bar = 0.07 MPa (T_{sat} = 89.95°C)				**p = 1.0 bar = 0.10 MPa (T_{sat} = 99.63°C)**			
Sat.	2.365	2494.5	2660.0	7.4797	1.694	2506.1	2675.5	7.3594
100	2.434	2509.7	2680.0	7.5341	1.696	2506.7	2676.2	7.3614
120	2.571	2539.7	2719.6	7.6375	1.793	2537.3	2716.6	7.4668
160	2.841	2599.4	2798.2	7.8279	1.984	2597.8	2796.2	7.6597
200	3.108	2659.1	2876.7	8.0012	2.172	2658.1	2875.3	7.8343
240	3.374	2719.3	2955.5	8.1611	2.359	2718.5	2954.5	7.9949
280	3.640	2780.2	3035.0	8.3162	2.546	2779.6	3034.2	8.1445
320	3.905	2842.0	3115.3	8.4504	2.732	2841.5	3114.6	8.2849
360	4.170	2904.6	3196.5	8.5828	2.917	2904.2	3195.9	8.4175
400	4.434	2968.2	3278.6	8.7086	3.103	2967.9	3278.2	8.5435
440	4.698	3032.9	3361.8	8.8286	3.288	3032.6	3361.4	8.6636
500	5.095	3131.8	3488.5	8.9991	3.565	3131.6	3488.1	8.8342
	p = 1.5 bars = 0.15 MPa (T_{sat} = 111.37°C)				**p = 3.0 bars = 0.30 MPa (T_{sat} = 133.55°C)**			
Sat.	1.159	2519.7	2693.6	7.2233	0.606	2543.6	2725.3	6.9919
120	1.188	2533.3	2711.4	7.2693				
160	1.317	2595.2	2792.8	7.4665	0.651	2587.1	2782.3	7.1276
200	1.444	2656.2	2872.9	7.6433	0.716	2650.7	2865.5	7.3115
240	1.570	2717.2	2952.7	7.8052	0.781	2713.1	2947.3	7.4774
280	1.695	2778.6	3032.8	7.9555	0.844	2775.4	3028.6	7.6299
320	1.819	2840.6	3113.5	8.0964	0.907	2838.1	3110.1	7.7722
360	1.943	2903.5	3195.0	8.2293	0.969	2901.4	3192.2	7.9061
400	2.067	2967.3	3277.4	8.3555	1.032	2965.6	3275.0	8.0330
440	2.191	3032.1	3360.7	8.4757	1.094	3030.6	3358.7	8.1538
500	2.376	3131.2	3487.6	8.6466	1.187	3130.0	3486.0	8.3251
600	2.685	3301.7	3704.3	8.9101	1.341	3300.8	3703.2	8.5892

TABLE A.6 (continued) Properties of Superheated Steam

Symbols and Units:

T = temperature, °C
T_{sat} = Saturation temperature, °C
ν = Specific volume, m^3/kg
u = internal energy, kJ/kg
h = enthalpy, kJ/kg
S = entropy, kJ/kg·K
p = pressure, bar and μPa

T °C	v m^3/kg	u kJ/kg	h kJ/kg	s kJ/kg · K	v m^3/kg	u kJ/kg	h kJ/kg	s kJ/kg . k
	p = 5.0 bars = 0.50 MPa (T_{sat} = 151.86°C)				**p = 7.0 bars = 0.70 MPa (T_{sat} = 164.97°C)**			
Sat.	0.3749	2561.2	2748.7	6.8213	0.2729	2572.5	2763.5	6.7080
180	0.4045	2609.7	2812.0	6.9656	0.2847	2599.8	2799.1	6.7880
200	0.4249	2642.9	2855.4	7.0592	0.2999	2634.8	2844.8	6.8865
240	0.4646	2707.6	2939.9	7.2307	0.3292	2701.8	2932.2	7.0641
280	0.5034	2771.2	3022.9	7.3865	0.3574	2766.9	3017.1	7.2233
320	0.5416	2834.7	3105.6	7.5308	0.3852	2831.3	3100.9	7.3697
360	0.5796	2898.7	3188.4	7.6660	0.4126	2895.8	3184.7	7.5063
400	0.6173	2963.2	3271.9	7.7938	0.4397	2960.9	3268.7	7.6350
440	0.6548	3028.6	3356.0	7.9152	0.4667	3026.6	3353.3	7.7571
500	0.7109	3128.4	3483.9	8.0873	0.5070	3126.8	3481.7	7.9299
600	0.8041	3299.6	3701.7	8.3522	0.5738	3298.5	3700.2	8.1956
700	0.8969	3477.5	3925.9	8.5952	0.6403	3476.6	3924.8	8.4391
	p = 10.0 bars = 1.0 MPa (T_{sat} = 179.91°C)				**p = 15.0 bars = 1.5 MPa (T_{sat} = 198.32°C)**			
Sat.	0.1944	2583.6	2778.1	6.5865	0.1318	2594.5	2792.2	6.4448
200	0.2060	2621.9	2827.9	6.6940	0.1325	2598.1	2796.8	6.4546
240	0.2275	2692.9	2920.4	6.8817	0.1483	2676.9	2899.3	6.6628
280	0.2480	2760.2	3008.2	7.0465	0.1627	2748.6	2992.7	6.8381
320	0.2678	2826.1	3093.9	7.1962	0.1765	2817.1	3081.9	6.9938
360	0.2873	2891.6	3178.9	7.3349	0.1899	2884.4	3169.2	7.1363
400	0.3066	2957.3	3263.9	7.4651	0.2030	2951.3	3255.8	7.2690
440	0.3257	3023.6	3349.3	7.5883	0.2160	3018.5	3342.5	7.3940
500	0.3541	3124.4	3478.5	7.7622	0.2352	3120.3	3473.1	7.5698
540	0.3729	3192.6	3565.6	7.8720	0.2478	3189.1	3560.9	7.6805
600	0.4011	3296.8	3697.9	8.0290	0.2668	3293.9	3694.0	7.8385
640	0.4198	3367.4	3787.2	8.1290	0.2793	3364.8	3783.8	7.9391
	p = 20.0 bars = 2.0 MPa (T_{sat} = 212.42°C)				**p = 30.0 bars = 3.0 MPa (T_{sat} = 233.90°C)**			
Sat.	0.0996	2600.3	2799.5	6.3409	0.0667	2604.1	2804.2	6.1869
240	0.1085	2659.6	2876.5	6.4952	0.0682	2619.7	2824.3	6.2265
280	0.1200	2736.4	2976.4	6.6828	0.0771	2709.9	2941.3	6.4462
320	0.1308	2807.9	3069.5	6.8452	0.0850	2788.4	3043.4	6.6245
360	0.1411	2877.0	3159.3	6.9917	0.0923	2861.7	3138.7	6.7801
400	0.1512	2945.2	3247.6	7.1271	0.0994	2932.8	3230.9	6.9212
440	0.1611	3013.4	3335.5	7.2540	0.1062	3002.9	3321.5	7.0520
500	0.1757	3116.2	3467.6	7.4317	0.1162	3108.0	3456.5	7.2338
540	0.1853	3185.6	3556.1	7.5434	0.1227	3178.4	3546.6	7.3474
600	0.1996	3290.9	3690.1	7.7024	0.1324	3285.0	3682.3	7.5085
640	0.2091	3362.2	3780.4	7.8035	0.1388	3357.0	3773.5	7.6106
700	0.2232	3470.9	3917.4	7.9487	0.1484	3466.5	3911.7	7.7571

TABLE A.6 (continued) Properties of Superheated Steam

Symbols and Units:

T = temperature, °C
T_{sat} = Saturation temperature, °C
v = Specific volume, m^3/kg
u = internal energy, kJ/kg
h = enthalpy, kJ/kg
S = entropy, kJ/kg·K
p = pressure, bar and μPa

T °C	v m^3/kg	u kJ/kg	h kJ/kg	s kJ/kg · K	v m^3/kg	u kJ/kg	h kJ/kg	s kJ/kg · K
	p = 40 bars = 4.0 MPa (T_{sat} = 250.4°C)				**p = 60 bars = 6.0 MPa (T_{sat} = 275.64°C)**			
Sat.	0.04978	2602.3	2801.4	6.0701	0.03244	2589.7	2784.3	5.8892
280	0.05546	2680.0	2901.8	6.2568	0.03317	2605.2	2804.2	5.9252
320	0.06199	2767.4	3015.4	6.4553	0.03876	2720.0	2952.6	6.1846
360	0.06788	2845.7	3117.2	6.6215	0.04331	2811.2	3071.1	6.3782
400	0.07341	2919.9	3213.6	6.7690	0.04739	2892.9	3177.2	6.5408
440	0.07872	2992.2	3307.1	6.9041	0.05122	2970.0	3277.3	6.6853
500	0.08643	3099.5	3445.3	7.0901	0.05665	3082.2	3422.2	6.8803
540	0.09145	3171.1	3536.9	7.2056	0.06015	3156.1	3517.0	6.9999
600	0.09885	3279.1	3674.4	7.3688	0.06525	3266.9	3658.4	7.1677
640	0.1037	3351.8	3766.6	7.4720	0.06859	3341.0	3752.6	7.2731
700	0.1110	3462.1	3905.9	7.6198	0.07352	3453.1	3894.1	7.4234
740	0.1157	3536.6	3999.6	7.7141	0.07677	3528.3	3989.2	7.5190
	p = 80 bars = 8.0 MPa (T_{sat} = 295.06°C)				**p = 100 bars = 10.0 MPa (T_{sat} = 311.06°C)**			
Sat.	0.02352	2569.8	2758.0	5.7432	0.01803	2544.4	2724.7	5.6141
320	0.02682	2662.7	2877.2	5.9489	0.01925	2588.8	2781.3	5.7103
360	0.03089	2772.7	3019.8	6.1819	0.02331	2729.1	2962.1	6.0060
400	0.03432	2863.8	3138.3	6.3634	0.02641	2832.4	3096.5	6.2120
440	0.03742	2946.7	3246.1	6.5190	0.02911	2922.1	3213.2	6.3805
480	0.04034	3025.7	3348.4	6.6586	0.03160	3005.4	3321.4	6.5282
520	0.04313	3102.7	3447.7	6.7871	0.03394	3085.6	3425.1	6.6622
560	0.04582	3178.7	3545.3	6.9072	0.03619	3164.1	3526.0	6.7864
600	0.04845	3254.4	3642.0	7.0206	0.03837	3241.7	3625.3	6.9029
640	0.05102	3330.1	3738.3	7.1283	0.04048	3318.9	3723.7	7.0131
700	0.05481	3443.9	3882.4	7.2812	0.04358	3434.7	3870.5	7.1687
740	0.05729	3520.4	3978.7	7.3782	0.04560	3512.1	3968.1	7.2670
	p = 120 bars = 12.0 MPa (T_{sat} = 324.75°C)				**p = 140 bars = 14.0 MPa (T_{sat} = 336.75°C)**			
Sat.	0.01426	2513.7	2684.9	5.4924	0.01149	2476.8	2637.6	5.3717
360	0.01811	2678.4	2895.7	5.8361	0.01422	2617.4	2816.5	5.6602
400	0.02108	2798.3	3051.3	6.0747	0.01722	2760.9	3001.9	5.9448
440	0.02355	2896.1	3178.7	6.2586	0.01954	2868.6	3142.2	6.1474
480	0.02576	2984.4	3293.5	6.4154	0.02157	2962.5	3264.5	6.3143
520	0.02781	3068.0	3401.8	6.5555	0.02343	3049.8	3377.8	6.4610
560	0.02977	3149.0	3506.2	6.6840	0.02517	3133.6	3486.0	6.5941
600	0.03164	3228.7	3608.3	6.8037	0.02683	3215.4	3591.1	6.7172
640	0.03345	3307.5	3709.0	6.9164	0.02843	3296.0	3694.1	6.8326
700	0.03610	3425.2	3858.4	7.0749	0.03075	3415.7	3846.2	6.9939
740	0.03781	3503.7	3957.4	7.1746	0.03225	3495.2	3946.7	7.0952

TABLE A.7 Chemical, Physical, and Thermal Properties of Gases: Gases and Vapors, Including Fuels and Refrigerants, English and Metric Units

Common name(s)	*Acetylene (Ethyne)*	*Air [mixture]*	*Ammonia, anhyd.*	*Argon*
Chemical formula	C_2H_2		NH_3	*Ar*
Refrigerant number	—	*729*	*717*	*740*
CHEMICAL AND PHYSICAL PROPERTIES				
Molecular weight	26.04	28.966	17.02	39.948
Specific gravity, air = 1	0.90	1.00	0.59	1.38
Specific volume, ft³/lb	14.9	13.5	23.0	9.80
Specific volume, m³/kg	0.93	0.842	1.43	0.622
Density of liquid (at atm bp), lb/ft³	43.0	54.6	42.6	87.0
Density of liquid (at atm bp), kg/m³	693.	879.	686.	1 400.
Vapor pressure at 25 deg C, psia			145.4	
Vapor pressure at 25 deg C, MN/m²			1.00	
Viscosity (abs), lbm/ft·sec	6.72×10^{-6}	12.1×10^{-6}	6.72×10^{-6}	13.4×10^{-6}
Viscosity (abs), centipoises[a]	0.01	0.018	0.010	0.02
Sound velocity in gas, m/sec	343	346	415	322
THERMAL AND THERMODYNAMIC PROPERTIES				
Specific heat, c_p, Btu/lb·deg F or cal/g·deg C	0.40	0.240 3	0.52	0.125
Specific heat, c_p, J/kg·K	1 674.	1 005.	2 175.	523.
Specific heat ratio, c_p/c_v	1.25	1.40	1.3	1.67
Gas constant *R*, ft-lb/lb·deg R	59.3	53.3	90.8	38.7
Gas constant *R*, J/kg·deg C	319	286.8	488.	208.
Thermal conductivity, Btu/hr·ft·deg F	0.014	0.015 1	0.015	0.010 2
Thermal conductivity, W/m·deg C	0.024	0.026	0.026	0.017 2
Boiling point (sat 14.7 psia), deg F	−103	−320	−28.	−303.
Boiling point (sat 760 mm), deg C	−75	−195	−33.3	−186
Latent heat of evap (at bp), Btu/lb	264	88.2	589.3	70.
Latent heat of evap (at bp), J/kg	614 000	205 000.	1 373 000	163 000
Freezing (melting) point, deg F (1 atm)	−116	−357.2	−107.9	−308.5
Freezing (melting) point, deg C (1 atm)	−82.2	−216.2	−77.7	−189.2
Latent heat of fusion, Btu/lb	23.	10.0	143.0	
Latent heat of fusion, J/kg	53 500	23 200	332 300	
Critical temperature, deg F	97.1	−220.5	271.4	−187.6
Critical temperature, deg C	36.2	−140.3	132.5	−122
Critical pressure, psia	907.	550.	1 650.	707.
Critical pressure, MN/m²	6.25	3.8	11.4	4.87
Critical volume, ft³/lb		0.050	0.068	0.029 9
Critical volume, m³/kg		0.003	0.004 24	0.001 86
Flammable (yes or no)	Yes	No	No	No
Heat of combustion, Btu/ft³	1 450	—	—	—
Heat of combustion, Btu/lb	21 600	—		
Heat of combustion, kJ/kg	50 200	—	—	—

[a] For N·sec/m² divide by 1 000.

Note: The properties of pure gases are given at 25°C (77°F, 298 K) and atmospheric pressure (except as stated).

TABLE A.7 (continued) Chemical, Physical, and Thermal Properties of Gases: Gases and Vapors, Including Fuels and Refrigerants, English and Metric Units

Common name(s)	*Butadiene*	*n-Butane*	*Isobutane (2-Methyl propane)*	*1-Butene (Butylene)*
Chemical formula	C_4H_6	C_4H_{10}	C_4H_{10}	C_4H_8
Refrigerant number	—	*600*	*600a*	—
CHEMICAL AND PHYSICAL PROPERTIES				
Molecular weight	54.09	58.12	58.12	56.108
Specific gravity, air = 1	1.87	2.07	2.07	1.94
Specific volume, ft^3/lb	7.1	6.5	6.5	6.7
Specific volume, m^3/kg	0.44	0.405	0.418	0.42
Density of liquid (at atm bp), lb/ft^3		37.5	37.2	
Density of liquid (at atm bp), kg/m^3		604.	599.	
Vapor pressure at 25 deg C, psia		35.4	50.4	
Vapor pressure at 25 deg C, MN/m^2		0.024 4	0.347	
Viscosity (abs), lbm/ft·sec		4.8×10^{-6}		
Viscosity (abs), centipoises[a]		0.007		
Sound velocity in gas, m/sec	226	216	216	222
THERMAL AND THERMODYNAMIC PROPERTIES				
Specific heat, c_p, Btu/lb·deg F or cal/g·deg C	0.341	0.39	0.39	0.36
Specific heat, c_p, J/kg·K	1 427.	1 675.	1 630.	1 505.
Specific heat ratio, c_p/c_v	1.12	1.096	1.10	1.112
Gas constant R, ft-lb/lb·deg F	28.55	26.56	26.56	27.52
Gas constant R, J/kg·deg C	154.	143.	143.	148.
Thermal conductivity, Btu/hr·ft·deg F		0.01	0.01	
Thermal conductivity, W/m·deg C		0.017	0.017	
Boiling point (sat 14.7 psia), deg F	24.1	31.2	10.8	20.6
Boiling point (sat 760 mm), deg C	−4.5	−0.4	−11.8	−6.3
Latent heat of evap (at bp), Btu/lb		165.6	157.5	167.9
Latent heat of evap (at bp), J/kg		386 000	366 000	391 000
Freezing (melting) point, deg F (1 atm)	−164.	−217.	−229	−301.6
Freezing (melting) point, deg C (1 atm)	−109.	−138	−145	−185.3
Latent heat of fusion, Btu/lb		19.2		16.4
Latent heat of fusion, J/kg		44 700		38 100
Critical temperature, deg F		306	273.	291.
Critical temperature, deg C	171.	152.	134.	144.
Critical pressure, psia	652.	550.	537.	621.
Critical pressure, MN/m^2		3.8	3.7	4.28
Critical volume, ft^3/lb		0.070		0.068
Critical volume, m^3/kg		0.004 3		0.004 2
Flammable (yes or no)	Yes	Yes	Yes	Yes
Heat of combustion, Btu/ft^3	2 950	3 300	3 300	3 150
Heat of combustion, Btu/lb	20 900	21 400	21 400	21 000
Heat of combustion, kJ/kg	48 600	49 700	49 700	48 800

[a] For $N \cdot sec/m^2$ divide by 1 000.

TABLE A.7 (continued) Chemical, Physical, and Thermal Properties of Gases: Gases and Vapors, Including Fuels and Refrigerants, English and Metric Units

Common name(s)	*cis-2-Butene*	*trans-2-Butene*	*Isobutene*	*Carbon dioxide*
Chemical formula	C_4H_8	C_4H_8	C_4H_8	CO_2
Refrigerant number	-	—	—	*744*
CHEMICAL AND PHYSICAL PROPERTIES				
Molecular weight	56.108	56.108	56.108	44.01
Specific gravity, air = 1	1.94	1.94	1.94	1.52
Specific volume, ft^3/lb	6.7	6.7	6.7	8.8
Specific volume, m^3/kg	0.42	0.42	0.42	0.55
Density of liquid (at atm bp), lb/ft^3				—
Density of liquid (at atm bp), kg/m^3				—
Vapor pressure at 25 deg C, psia				931.
Vapor pressure at 25 deg C, MN/m^2				6.42
Viscosity (abs), lbm/ft·sec				9.4×10^{-6}
Viscosity (abs), centipoises[a]				0.014
Sound velocity in gas, m/sec	223.	221.	221.	270.
THERMAL AND THERMODYNAMIC PROPERTIES				
Specific heat, c_p, Btu/lb·deg F or cal/g·deg C	0.327	0.365	0.37	0.205
Specific heat, c_p, J/kg·K	1 368.	1 527.	1 548.	876.
Specific heat ratio, c_p/c_v	1.121	1.107	1.10	1.30
Gas constant R, ft-lb/lb·deg F				35.1
Gas constant R, J/kg·deg C				189.
Thermal conductivity, Btu/hr·ft·deg F				0.01
Thermal conductivity, W/m·deg C				0.017
Boiling point (sat 14.7 psia), deg F	38.6	33.6	19.2	−109.4[b]
Boiling point (sat 760 mm), deg C	3.7	0.9	−7.1	−78.5
Latent heat of evap (at bp), Btu/lb	178.9	174.4	169.	246.
Latent heat of evap (at bp), J/kg	416 000.	406 000.	393 000.	572 000.
Freezing (melting) point, deg F (1 atm)	−218.	−158.		
Freezing (melting) point, deg C (1 atm)	−138.9	−105.5		
Latent heat of fusion, Btu/lb	31.2	41.6	25.3	—
Latent heat of fusion, J/kg	72 600.	96 800.	58 800.	—
Critical temperature, deg F				88.
Critical temperature, deg C	160.	155.		31.
Critical pressure, psia	595.	610.		1 072.
Critical pressure, MN/m^2	4.10	4.20		7.4
Critical volume, ft^3/lb				
Critical volume, m^3/kg				
Flammable (yes or no)	Yes	Yes	Yes	No
Heat of combustion, Btu/ft^3	3 150.	3 150.	3 150.	—
Heat of combustion, Btu/lb	21 000.	21 000.	21 000.	—
Heat of combustion, kJ/kg	48 800.	48 800.	48 800.	—

[a] For $N \cdot sec/m^2$ divide by 1 000.

[b] Sublimes.

TABLE A.7 (continued) Chemical, Physical, and Thermal Properties of Gases: Gases and Vapors, Including Fuels and Refrigerants, English and Metric Units

Common name(s)	*Carbon monoxide*	*Chlorine*	*Deuterium*	*Ethane*
Chemical formula	CO	Cl_2	D_2	C_2H_6
Refrigerant number	—	—	—	*170*
CHEMICAL AND PHYSICAL PROPERTIES				
Molecular weight	28.011	70.906	2.014	30.070
Specific gravity, air = 1	0.967	2.45	0.070	1.04
Specific volume, ft^3/lb	14.0	5.52	194.5	13.025
Specific volume, m^3/kg	0.874	0.344	12.12	0.815
Density of liquid (at atm bp), lb/ft^3		97.3		28.
Density of liquid (at atm bp), kg/m^3		1 559.		449.
Vapor pressure at 25 deg C, psia			0.756	
Vapor pressure at 25 deg C, MN/m^2			0.005 2	
Viscosity (abs), lbm/ft·sec	12.1×10^{-6}	9.4×10^{-6}	8.75×10^{-6}	$64. \times 10^{-6}$
Viscosity (abs), centipoises[a]	0.018	0.014	0.013	0.095
Sound velocity in gas, m/sec	352.	215.	930.	316.
THERMAL AND THERMODYNAMIC PROPERTIES				
Specific heat, c_p, Btu/lb·deg F or cal/g·deg C	0.25	0.114	1.73	0.41
Specific heat, c_p, J/kg·K	1 046.	477.	7 238.	1 715.
Specific heat ratio, c_p/c_v	1.40	1.35	1.40	1.20
Gas constant R, ft-lb/lb·deg F	55.2	21.8	384.	51.4
Gas constant R, J/kg·deg C	297.	117.	2 066.	276.
Thermal conductivity, Btu/hr·ft·deg F	0.014	0.005	0.081	0.010
Thermal conductivity, W/m·deg C	0.024	0.008 7	0.140	0.017
Boiling point (sat 14.7 psia), deg F	−312.7	−29.2		−127.
Boiling point (sat 760 mm), deg C	−191.5	−34.		−88.3
Latent heat of evap (at bp), Btu/lb	92.8	123.7		210.
Latent heat of evap (at bp), J/kg	216 000.	288 000.		488 000.
Freezing (melting) point, deg F (1 atm)	−337.	−150.		−278.
Freezing (melting) point, deg C (1 atm)	−205.	−101.		−172.2
Latent heat of fusion, Btu/lb	12.8	41.0		41.
Latent heat of fusion, J/kg		95 400.		95 300.
Critical temperature, deg F	−220.	291.	−390.6	90.1
Critical temperature, deg C	−140.	144.	−234.8	32.2
Critical pressure, psia	507.	1 120.	241.	709.
Critical pressure, MN/m^2	3.49	7.72	1.66	4.89
Critical volume, ft^3/lb	0.053	0.028	0.239	0.076
Critical volume, m^3/kg	0.003 3	0.001 75	0.014 9	0.004 7
Flammable (yes or no)	Yes	No		Yes
Heat of combustion, Btu/ft^3	310.	—		
Heat of combustion, Btu/lb	4 340.	—		22 300.
Heat of combustion, kJ/kg	10 100.	—		51 800.

[a] For N·sec/m^2 divide by 1 000.

TABLE A.7 (continued) Chemical, Physical, and Thermal Properties of Gases: Gases and Vapors, Including Fuels and Refrigerants, English and Metric Units

Common name(s)	*Ethyl chloride*	*Ethylene (Ethene)*	*Fluorine*
Chemical formula	C_2H_5Cl	C_2H_4	F_2
Refrigerant number	*160*	*1 150*	
CHEMICAL AND PHYSICAL PROPERTIES			
Molecular weight	64.515	28.054	37.996
Specific gravity, air = 1	2.23	0.969	1.31
Specific volume, ft^3/lb	6.07	13.9	10.31
Specific volume, m^3/kg	0.378	0.87	0.706
Density of liquid (at atm bp), lb/ft^3	56.5	35.5	
Density of liquid (at atm bp), kg/m^3	905.	569.	
Vapor pressure at 25 deg C, psia			
Vapor pressure at 25 deg C, MN/m^2			
Viscosity (abs), lbm/ft·sec		6.72×10^{-6}	16.1×10^{-6}
Viscosity (abs), centipoises[a]		0.010	0.024
Sound velocity in gas, m/sec	204.	331.	290.
THERMAL AND THERMODYNAMIC PROPERTIES			
Specific heat, c_p, Btu/lb·deg F or cal/g·deg C	0.27	0.37	0.198
Specific heat, c_p, J/kg·K	1 130.	1 548.	828.
Specific heat ratio, c_p/c_v	1.13	1.24	1.35
Gas constant R, ft-lb/lb·deg F	24.0	55.1	40.7
Gas constant R, J/kg·deg C	129.	296.	219.
Thermal conductivity, Btu/hr·ft·deg F		0.010	0.016
Thermal conductivity, W/m·deg C		0.017	0.028
Boiling point (sat 14.7 psia), deg F	54.	−155.	−306.4
Boiling point (sat 760 mm), deg C	12.2	−103.8	−188.
Latent heat of evap (at bp), Btu/lb	166.	208.	74.
Latent heat of evap (at bp), J/kg	386 000.	484 000.	172 000.
Freezing (melting) point, deg F (1 atm)	−218.	−272.	−364.
Freezing (melting) point, deg C (1 atm)	−138.9	−169.	−220.
Latent heat of fusion, Btu/lb	29.3	51.5	11.
Latent heat of fusion, J/kg	68 100.	120 000.	25 600.
Critical temperature, deg F	368.6	49.	−200
Critical temperature, deg C	187.	9.5	−129.
Critical pressure, psia	764.	741.	810.
Critical pressure, MN/m^2	5.27	5.11	5.58
Critical volume, ft^3/lb	0.049	0.073	
Critical volume, m^3/kg	0.003 06	0.004 6	
Flammable (yes or no)	No	Yes	
Heat of combustion, Btu/ft^3	—	1 480.	
Heat of combustion, Btu/lb	—	20 600.	
Heat of combustion, kJ/kg	—	47 800.	

[a] For N·sec/m^2 divide by 1 000.

TABLE A.7 (continued) Chemical, Physical, and Thermal Properties of Gases: Gases and Vapors, Including Fuels and Refrigerants, English and Metric Units

Common name(s)	*Fluorocarbons*			
Chemical formula	CCl_3F	CCl_2F_2	$CClF_3$	$CBrF_3$
Refrigerant number	*11*	*12*	*13*	*13B1*
CHEMICAL AND PHYSICAL PROPERTIES				
Molecular weight	137.37	120.91	104.46	148.91
Specific gravity, air = 1	4.74	4.17	3.61	5.14
Specific volume, ft^3/lb	2.74	3.12	3.58	2.50
Specific volume, m^3/kg	0.171	0.195	0.224	0.975
Density of liquid (at atm bp), lb/ft^3	92.1	93.0	95.0	124.4
Density of liquid (at atm bp), kg/m^3	1 475.	1 490.	1 522.	1 993.
Vapor pressure at 25 deg C, psia		94.51	516.	234.8
Vapor pressure at 25 deg C, MN/m^2		0.652	3.56	1.619
Viscosity (abs), lbm/ft·sec	7.39×10^{-6}	8.74×10^{-6}		
Viscosity (abs), centipoises[a]	0.011	0.013		
Sound velocity in gas, m/sec				
THERMAL AND THERMODYNAMIC PROPERTIES				
Specific heat, c_p, Btu/lb·deg F or cal/g·deg C	0.14	0.146	0.154	
Specific heat, c_p, J/kg·K	586.	611.	644.	
Specific heat ratio, c_p/c_v	1.14	1.14	1.145	
Gas constant R, ft-lb/lb·deg F				
Gas constant R, J/kg·deg C				
Thermal conductivity, Btu/hr·ft·deg F	0.005	0.006		
Thermal conductivity, W/m·deg C	0.008 7	0.010 4		
Boiling point (sat 14.7 psia), deg F	74.9	−21.8	−114.6	−72.
Boiling point (sat 760 mm), deg C	23.8	−29.9	−81.4	−57.8
Latent heat of evap (at bp), Btu/lb	77.5	71.1	63.0	51.1
Latent heat of evap (at bp), J/kg	180 000.	165 000.	147 000.	119 000.
Freezing (melting) point, deg F (1 atm)	−168.	−252.	−294.	−270.
Freezing (melting) point, deg C (1 atm)	−111.	−157.8	−181.1	−167.8
Latent heat of fusion, Btu/lb				
Latent heat of fusion, J/kg				
Critical temperature, deg F	388.4	233.	83.9	152.
Critical temperature, deg C	198.	111.7	28.8	66.7
Critical pressure, psia	635.	582.	559.	573.
Critical pressure, MN/m^2	4.38	4.01	3.85	3.95
Critical volume, ft^3/lb	0.028 9	0.287	0.027 7	0.021 5
Critical volume, m^3/kg	0.001 80	0.018	0.001 73	0.001 34
Flammable (yes or no)	No	No	No	No
Heat of combustion, Btu/ft^3	—	—	—	—
Heat of combustion, Btu/lb	—	—	—	—
Heat of combustion, kJ/kg	—	—	—	—

[a] For $N \cdot sec/m^2$ divide by 1 000.

TABLE A.7 (continued) Chemical, Physical, and Thermal Properties of Gases: Gases and Vapors, Including Fuels and Refrigerants, English and Metric Units

Common name(s)	*Fluorocarbons*			
Chemical formula	CF_4	$CHCl_2F$	$CHClF_2$	$C_2Cl_2F_4$
Refrigerant number	*14*	*21*	*22*	*114*
CHEMICAL AND PHYSICAL PROPERTIES				
Molecular weight	88.00	102.92	86.468	170.92
Specific gravity, air = 1	3.04	3.55	2.99	5.90
Specific volume, ft^3/lb	4.34	3.7	4.35	2.6
Specific volume, m^3/kg	0.271	0.231	0.271	0.162
Density of liquid (at atm bp), lb/ft^3	102.0	87.7	88.2	94.8
Density of liquid (at atm bp), kg/m^3	1 634.	1 405.	1 413.	1 519.
Vapor pressure at 25 deg C, psia		26.4	151.4	30.9
Vapor pressure at 25 deg C, MN/m^2		0.182	1.044	0.213
Viscosity (abs), lbm/ft·sec		8.06×10^{-6}	8.74×10^{-6}	8.06×10^{-6}
Viscosity (abs), centipoises[a]		0.012	0.013	0.012
Sound velocity in gas, m/sec				
THERMAL AND THERMODYNAMIC PROPERTIES				
Specific heat, c_p, Btu/lb·deg F or cal/g·deg C		0.139	0.157	0.158
Specific heat, c_p, J/kg·K		582.	657.	661.
Specific heat ratio, c_p/c_v		1.18	1.185	1.09
Gas constant R, ft-lb/lb·deg F				
Gas constant R, J/kg·deg C				
Thermal conductivity, Btu/hr·ft·deg F			0.007	0.006
Thermal conductivity, W/m·deg C			0.012	0.010
Boiling point (sat 14.7 psia), deg F	−198.2	48.1	−41.3	38.4
Boiling point (sat 760 mm), deg C	−127.9	9.0	−40.7	3.55
Latent heat of evap (at bp), Btu/lb	58.5	104.1	100.4	58.4
Latent heat of evap (at bp), J/kg	136 000.	242 000.	234 000.	136 000.
Freezing (melting) point, deg F (1 atm)	−299.	−211.	−256.	−137.
Freezing (melting) point, deg C (1 atm)	−183.8	−135.	−160.	−93.8
Latent heat of fusion, Btu/lb	2.53			
Latent heat of fusion, J/kg	5 880.			
Critical temperature, deg F	−49.9	353.3	204.8	294.
Critical temperature, deg C	−45.5	178.5	96.5	
Critical pressure, psia	610.	750.	715.	475.
Critical pressure, MN/m^2	4.21	5.17	4.93	3.28
Critical volume, ft^3/lb	0.025	0.030 7	0.030 5	0.027 5
Critical volume, m^3/kg	0.001 6	0.001 91	0.001 90	0.001 71
Flammable (yes or no)	No	No	No	No
Heat of combustion, Btu/ft^3	—	—	—	—
Heat of combustion, Btu/lb	—	—	—	—
Heat of combustion, kJ/kg	—	—	—	—

[a] For N·sec/m^2 divide by 1 000.

TABLE A.7 (continued) Chemical, Physical, and Thermal Properties of Gases: Gases and Vapors, Including Fuels and Refrigerants, English and Metric Units

Common name(s)	*Fluorocarbons*			*Helium*
Chemical formula	C_2ClF_5	$C_2H_3ClF_2$	$C_2H_4F_2$	*He*
Refrigerant number	*115*	*142b*	*152a*	*704*
CHEMICAL AND PHYSICAL PROPERTIES				
Molecular weight	154.47	100.50	66.05	4.002 6
Specific gravity, air = 1	5.33	3.47	2.28	0.138
Specific volume, ft^3/lb	2.44	3.7	5.9	97.86
Specific volume, m^3/kg	0.152	0.231	0.368	6.11
Density of liquid (at atm bp), lb/ft^3	96.5	74.6	62.8	7.80
Density of liquid (at atm bp), kg/m^3	1 546.	1 195.	1 006.	125.
Vapor pressure at 25 deg C, psia	132.1	49.1	86.8	
Vapor pressure at 25 deg C, MN/m^2	0.911	0.338 5	0.596	
Viscosity (abs), lbm/ft·sec				13.4×10^{-6}
Viscosity (abs), centipoises[a]				0.02
Sound velocity in gas, m/sec				1 015.
THERMAL AND THERMO-DYNAMIC PROPERTIES				
Specific heat, c_p, Btu/lb·deg F or cal/g·deg C	0.161			1.24
Specific heat, c_p, J/kg·K	674.			5 188.
Specific heat ratio, c_p/c_v	1.091			1.66
Gas constant R, ft-lb/lb·deg F				386.
Gas constant R, J/kg·deg C				2 077.
Thermal conductivity, Btu/hr·ft·deg F				0.086
Thermal conductivity, W/m·deg C				0.149
Boiling point (sat 14.7 psia), deg F	−38.0	14.	−13.	−452.
Boiling point (sat 760 mm), deg C	−38.9	−10.0	−25.0	4.22 K
Latent heat of evap (at bp), Btu/lb	53.4	92.5	137.1	10.0
Latent heat of evap (at bp), J/kg	124 000.	215 000.	319 000.	23 300.
Freezing (melting) point, deg F (1 atm)	−149.			[b]
Freezing (melting) point, deg C (1 atm)	−100.6			—
Latent heat of fusion, Btu/lb				—
Latent heat of fusion, J/kg				—
Critical temperature, deg F	176.		387.	−450.3
Critical temperature, deg C				5.2 K
Critical pressure, psia	457.6			33.22
Critical pressure, MN/m^2	3.155			
Critical volume, ft^3/lb	0.026 1			0.231
Critical volume, m^3/kg	0.001 63			0.014 4
Flammable (yes or no)	No	No	No	No
Heat of combustion, Btu/ft^3	—	—	—	—
Heat of combustion, Btu/lb	—	—	—	—
Heat of combustion, kJ/kg	—	—	—	—

[a] For N·sec/m^2 divide by 1 000.

[b] Helium cannot be solidified at atmospheric pressure.

TABLE A.7 (continued) Chemical, Physical, and Thermal Properties of Gases: Gases and Vapors, Including Fuels and Refrigerants, English and Metric Units

Common name(s)	*Hydrogen*	*Hydrogen chloride*	*Hydrogen sulfide*	*Krypton*
Chemical formula	H_2	HCl	H_2S	Kr
Refrigerant number	702	—	—	—
CHEMICAL AND PHYSICAL PROPERTIES				
Molecular weight	2.016	36.461	34.076	83.80
Specific gravity, air = 1	0.070	1.26	1.18	2.89
Specific volume, ft³/lb	194.	10.74	11.5	4.67
Specific volume, m³/kg	12.1	0.670	0.093 0	0.291
Density of liquid (at atm bp), lb/ft³	4.43	74.4	62.	150.6
Density of liquid (at atm bp), kg/m³	71.0	1 192.	993.	2 413.
Vapor pressure at 25 deg C, psia				
Vapor pressure at 25 deg C, MN/m²				
Viscosity (abs), lbm/ft·sec	6.05×10^{-6}	10.1×10^{-6}	8.74×10^{-6}	$16.8 \times 10^{-}$
Viscosity (abs), centipoises[a]	0.009	0.015	0.013	0.025
Sound velocity in gas, m/sec	1 315.	310.	302.	223.
THERMAL AND THERMODYNAMIC PROPERTIES				
Specific heat, c_p, Btu/lb·deg F or cal/g·deg C	3.42	0.194	0.23	0.059
Specific heat, c_p, J/kg·K	14 310.	812.	962.	247.
Specific heat ratio, c_p/c_v	1.405	1.39	1.33	1.68
Gas constant R, ft-lb/lb·deg F	767.	42.4	45.3	18.4
Gas constant R, J/kg·deg C	4 126.	228.	244.	99.0
Thermal conductivity, Btu/hr·ft·deg F	0.105	0.008	0.008	0.005 4
Thermal conductivity, W/m·deg C	0.018 2	0.014	0.014	0.009 3
Boiling point (sat 14.7 psia), deg F	−423.	−121.	−76.	−244.
Boiling point (sat 760 mm), deg C	20.4 K	−85.	−60.	−153.
Latent heat of evap (at bp), Btu/lb	192.	190.5	234.	46.4
Latent heat of evap (at bp), J/kg	447 000.	443 000.	544 000.	108 000.
Freezing (melting) point, deg F (1 atm)	−434.6	−169.6	−119.2	−272.
Freezing (melting) point, deg C (1 atm)	−259.1	−112.	−84.	−169.
Latent heat of fusion, Btu/lb	25.0	23.4	30.2	4.7
Latent heat of fusion, J/kg	58 000.	54 400.	70 200.	10 900.
Critical temperature, deg F	−399.8	124.	213.	
Critical temperature, deg C	−240.0	51.2	100.4	−63.8
Critical pressure, psia	189.	1 201.	1 309.	800.
Critical pressure, MN/m²	1.30	8.28	9.02	5.52
Critical volume, ft³/lb	0.53	0.038	0.046	0.017 7
Critical volume, m³/kg	0.033	0.002 4	0.002 9	0.001 1
Flammable (yes or no)	Yes	No	Yes	No
Heat of combustion, Btu/ft³	320.	—	700.	—
Heat of combustion, Btu/lb	62 050.	—	8 000.	—
Heat of combustion, kJ/kg	144 000.	—	18 600.	—

[a] For N·sec/m² divide by 1 000.

TABLE A.7 (continued) Chemical, Physical, and Thermal Properties of Gases: Gases and Vapors, Including Fuels and Refrigerants, English and Metric Units

Common name(s)	*Methane*	*Methyl chloride*	*Neon*	*Nitric oxide*
Chemical formula	*CH_4*	*CH_3Cl*	*Ne*	*NO*
Refrigerant number	*50*	*40*	*720*	—
CHEMICAL AND PHYSICAL PROPERTIES				
Molecular weight	16.044	50.488	20.179	30.006
Specific gravity, air = 1	0.554	1.74	0.697	1.04
Specific volume, ft^3/lb	24.2	7.4	19.41	13.05
Specific volume, m^3/kg	1.51	0.462	1.211	0.814
Density of liquid (at atm bp), lb/ft^3	26.3	62.7	75.35	
Density of liquid (at atm bp), kg/m^3	421.	1 004.	1 207.	
Vapor pressure at 25 deg C, psia		82.2		
Vapor pressure at 25 deg C, MN/m^2		0.567		
Viscosity (abs), lbm/ft·sec	7.39×10^{-6}	7.39×10^{-6}	21.5×10^{-6}	12.8×10^{-6}
Viscosity (abs), centipoises[a]	0.011	0.011	0.032	0.019
Sound velocity in gas, m/sec	446.	251.	454.	341.
THERMAL AND THERMO-DYNAMIC PROPERTIES				
Specific heat, c_p, Btu/lb·deg F or cal/g·deg C	0.54	0.20	0.246	0.235
Specific heat, c_p, J/kg·K	2 260.	837.	1 030.	983.
Specific heat ratio, c_p/c_v	1.31	1.28	1.64	1.40
Gas constant R, ft-lb/lb·deg F	96.	30.6	76.6	51.5
Gas constant R, J/kg·deg C	518.	165.	412.	277.
Thermal conductivity, Btu/hr·ft·deg F	0.02	0.006	0.028	0.015
Thermal conductivity, W/m·deg C	0.035	0.010	0.048	0.026
Boiling point (sat 14.7 psia), deg F	−259.	−10.7	−410.9	−240.
Boiling point (sat 760 mm), deg C	−434.2	−23.7	−246.	−151.5
Latent heat of evap (at bp), Btu/lb	219.2	184.1	37.	
Latent heat of evap (at bp), J/kg	510 000.	428 000.	86 100.	
Freezing (melting) point, deg F (1 atm)	−296.6	−144.	−415.6	−258.
Freezing (melting) point, deg C (1 atm)	−182.6	−97.8	−248.7	−161.
Latent heat of fusion, Btu/lb	14.	56.	6.8	32.9
Latent heat of fusion, J/kg	32 600.	130 000.	15 800.	76 500.
Critical temperature, deg F	−116.	289.4	−379.8	−136.
Critical temperature, deg C	−82.3	143.	−228.8	−93.3
Critical pressure, psia	673.	968.	396.	945.
Critical pressure, MN/m^2	4.64	6.67	2.73	6.52
Critical volume, ft^3/lb	0.099	0.043	0.033	0.033 2
Critical volume, m^3/kg	0.006 2	0.002 7	0.002 0	0.002 07
Flammable (yes or no)	Yes	Yes	No	No
Heat of combustion, Btu/ft^3	985.		—	—
Heat of combustion, Btu/lb	2 290.		—	—
Heat of combustion, kJ/kg			—	—

[a] For N·sec/m^2 divide by 1 000.

TABLE A.7 (continued) Chemical, Physical, and Thermal Properties of Gases: Gases and Vapors, Including Fuels and Refrigerants, English and Metric Units

Common name(s)	*Nitrogen*	*Nitrous oxide*	*Oxygen*	*Ozone*
Chemical formula	N_2	N_2O	O_2	O_3
Refrigerant number	*728*	*744A*	*732*	—
CHEMICAL AND PHYSICAL PROPERTIES				
Molecular weight	28.013 4	44.012	31.998 8	47.998
Specific gravity, air = 1	0.967	1.52	1.105	1.66
Specific volume, ft^3/lb	13.98	8.90	12.24	8.16
Specific volume, m^3/kg	0.872	0.555	0.764	0.509
Density of liquid (at atm bp), lb/ft^3	50.46	76.6	71.27	
Density of liquid (at atm bp), kg/m^3	808.4	1 227.	1 142.	
Vapor pressure at 25 deg C, psia				
Vapor pressure at 25 deg C, MN/m^2				
Viscosity (abs), lbm/ft·sec	12.1×10^{-6}	10.1×10^{-6}	13.4×10^{-6}	8.74×10^{-6}
Viscosity (abs), centipoises[a]	0.018	0.015	0.020	0.013
Sound velocity in gas, m/sec	353.	268.	329.	
THERMAL AND THERMODYNAMIC PROPERTIES				
Specific heat, c_p, Btu/lb·deg F or cal/g·deg C	0.249	0.21	0.220	0.196
Specific heat, c_p, J/kg·K	1 040.	879.	920.	820.
Specific heat ratio, c_p/c_v	1.40	1.31	1.40	
Gas constant R, ft-lb/lb·deg F	55.2	35.1	48.3	32.2
Gas constant R, J/kg·deg C	297.	189.	260.	173.
Thermal conductivity, Btu/hr·ft·deg F	0.015	0.010	0.015	0.019
Thermal conductivity, W/m·deg C	0.026	0.017	0.026	0.033
Boiling point (sat 14.7 psia), deg F	−320.4	−127.3	−297.3	−170.
Boiling point (sat 760 mm), deg C	−195.8	−88.5	−182.97	−112.
Latent heat of evap (at bp), Btu/lb	85.5	161.8	91.7	
Latent heat of evap (at bp), J/kg	199 000.	376 000.	213 000.	
Freezing (melting) point, deg F (1 atm)	−346.	−131.5	−361.1	−315.5
Freezing (melting) point, deg C (1 atm)	−210.	−90.8	−218.4	−193.
Latent heat of fusion, Btu/lb	11.1	63.9	5.9	97.2
Latent heat of fusion, J/kg	25 800.	149 000.	13 700.	226 000.
Critical temperature, deg F	−232.6	97.7	−181.5	16.
Critical temperature, deg C	−147.	36.5	−118.6	−9.
Critical pressure, psia	493.	1 052.	726.	800.
Critical pressure, MN/m^2	3.40	7.25	5.01	5.52
Critical volume, ft^3/lb	0.051	0.036	0.040	0.029 8
Critical volume, m^3/kg	0.003 18	0.002 2	0.002 5	0.001 86
Flammable (yes or no)	No	No	No	No
Heat of combustion, Btu/ft^3	—	—	—	—
Heat of combustion, Btu/lb	—	—	—	—
Heat of combustion, kJ/kg	—	—	—	—

[a] For N·sec/m^2 divide by 1 000.

TABLE A.7 (continued) Chemical, Physical, and Thermal Properties of Gases: Gases and Vapors, Including Fuels and Refrigerants, English and Metric Units

Common name(s)	*Propane*	*Propylene (Propene)*	*Sulfur dioxide*	*Xenon*
Chemical formula	C_3H_8	C_3H_6	SO_2	Xe
Refrigerant number	*290*	*1 270*	*764*	—
CHEMICAL AND PHYSICAL PROPERTIES				
Molecular weight	44.097	42.08	64.06	131.30
Specific gravity, air = 1	1.52	1.45	2.21	4.53
Specific volume, ft^3/lb	8.84	9.3	6.11	2.98
Specific volume, m^3/kg	0.552	0.58		
Density of liquid (at atm bp), lb/ft^3	36.2	37.5	42.8	190.8
Density of liquid (at atm bp), kg/m^3	580.	601.	585.	3 060.
Vapor pressure at 25 deg C, psia	135.7	166.4	56.6	
Vapor pressure at 25 deg C, MN/m^2	0.936	1.147	0.390	
Viscosity (abs), lbm/ft·sec	53.8×10^{-6}	57.1×10^{-6}	8.74×10^{-6}	15.5×10^{-6}
Viscosity (abs), centipoises[a]	0.080	0.085	0.013	0.023
Sound velocity in gas, m/sec	253.	261.	220.	177.
THERMAL AND THERMODYNAMIC PROPERTIES				
Specific heat, c_p, Btu/lb·deg F or cal/g·deg C	0.39	0.36	0.11	0.115
Specific heat, c_p, J/kg·K	1 630.	1 506.	460.	481.
Specific heat ratio, c_p/c_v	1.2	1.16	1.29	1.67
Gas constant R, ft-lb/lb·deg F	35.0	36.7	24.1	11.8
Gas constant R, J/kg·deg C	188.	197.	130.	63.5
Thermal conductivity, Btu/hr·ft·deg F	0.010	0.010	0.006	0.003
Thermal conductivity, W/m·deg C	0.017	0.017	0.010	0.005 2
Boiling point (sat 14.7 psia), deg F	−44.	−54.	14.0	−162.5
Boiling point (sat 760 mm), deg C	−42.2	−48.3	−10.	−108.
Latent heat of evap (at bp), Btu/lb	184.	188.2	155.5	41.4
Latent heat of evap (at bp), J/kg	428 000.	438 000.	362 000.	96 000.
Freezing (melting) point, deg F (1 atm)	−309.8	−301.	−104.	−220.
Freezing (melting) point, deg C (1 atm)	−189.9	−185.	−75.5	−140.
Latent heat of fusion, Btu/lb	19.1		58.0	10.
Latent heat of fusion, J/kg	44 400.		135 000.	23 300.
Critical temperature, deg F	205.	197.	315.5	61.9
Critical temperature, deg C	96.	91.7	157.6	16.6
Critical pressure, psia	618.	668.	1 141.	852.
Critical pressure, MN/m^2	4.26	4.61	7.87	5.87
Critical volume, ft^3/lb	0.073	0.069	0.03	0.014 5
Critical volume, m^3/kg	0.004 5	0.004 3	0.001 9	0.000 90
Flammable (yes or no)	Yes	Yes	No	No
Heat of combustion, Btu/ft^3	2 450.	2 310.	—	—
Heat of combustion, Btu/lb	21 660.	21 500.	—	—
Heat of combustion, kJ/kg	50 340.	50 000.	—	—

[a] For $N \cdot sec/m^2$ divide by 1 000.

TABLE A.8 Ideal Gas Properties of Air

Part a. SI Units

T(K), h and u(kJ/kg), s°(kJ/kg·K)

T	h	p_r	u	v_r	s°	T	h	p_r	u	v_r	s°
200	199.97	0.3363	142.56	1707.	1.29559	450	451.80	5.775	322.62	223.6	2.11161
210	209.97	0.3987	149.69	1512.	1.34444	460	462.02	6.245	329.97	211.4	2.13407
220	219.97	0.4690	156.82	1346.	1.39105	470	472.24	6.742	337.32	200.1	2.15604
230	230.02	0.5477	164.00	1205.	1.43557	480	482.49	7.268	344.70	189.5	2.17760
240	240.02	0.6355	171.13	1084.	1.47824	490	492.74	7.824	352.08	179.7	2.19876
250	250.05	0.7329	178.28	979.	1.51917	500	503.02	8.411	359.49	170.6	2.21952
260	260.09	0.8405	185.45	887.8	1.55848	510	513.32	9.031	366.92	162.1	2.23993
270	270.11	0.9590	192.60	808.0	1.59634	520	523.63	9.684	374.36	154.1	2.25997
280	280.13	1.0889	199.75	738.0	1.63279	530	533.98	10.37	381.84	146.7	2.27967
285	285.14	1.1584	203.33	706.1	1.65055	540	544.35	11.10	389.34	139.7	2.29906
290	290.16	1.2311	206.91	676.1	1.66802	550	554.74	11.86	396.86	133.1	2.31809
295	295.17	1.3068	210.49	647.9	1.68515	560	565.17	12.66	404.42	127.0	2.33685
300	300.19	1.3860	214.07	621.2	1.70203	570	575.59	13.50	411.97	121.2	2.35531
305	305.22	1.4686	217.67	596.0	1.71865	580	586.04	14.38	419.55	115.7	2.37348
310	310.24	1.5546	221.25	572.3	1.73498	590	596.52	15.31	427.15	110.6	2.39140
315	315.27	1.6442	224.85	549.8	1.75106	600	607.02	16.28	434.78	105.8	2.40902
320	320.29	1.7375	228.42	528.6	1.76690	610	617.53	17.30	442.42	101.2	2.42644
325	325.31	1.8345	232.02	508.4	1.78249	620	628.07	18.36	450.09	96.92	2.44356
330	330.34	1.9352	235.61	489.4	1.79783	630	638.63	19.84	457.78	92.84	2.46048
340	340.42	2.149	242.82	454.1	1.82790	640	649.22	20.64	465.50	88.99	2.47716
350	350.49	2.379	250.02	422.2	1.85708	650	659.84	21.86	473.25	85.34	2.49364
360	360.58	2.626	257.24	393.4	1.88543	660	670.47	23.13	481.01	81.89	2.50985
370	370.67	2.892	264.46	367.2	1.91313	670	681.14	24.46	488.81	78.61	2.52589
380	380.77	3.176	271.69	343.4	1.94001	680	691.82	25.85	496.62	75.50	2.54175
390	390.88	3.481	278.93	321.5	1.96633	690	702.52	27.29	504.45	72.56	2.55731
400	400.98	3.806	286.16	301.6	1.99194	700	713.27	28.80	512.33	69.76	2.57277
410	411.12	4.153	293.43	283.3	2.01699	710	724.04	30.38	520.23	67.07	2.58810
420	421.26	4.522	300.69	266.6	2.04142	720	734.82	32.02	528.14	64.53	2.60319
430	431.43	4.915	307.99	251.1	2.06533	730	745.62	33.72	536.07	62.13	2.61803
440	441.61	5.332	315.30	236.8	2.08870	740	756.44	35.50	544.02	59.82	2.63280

TABLE A.8 (continued) Ideal Gas Properties of Air

T(K), h and u(kJ/kg), s°(kJ/kg·K)

T	h	p_r	u	v_r	s°
750	767.29	37.35	551.99	57.63	2.64737
760	778.18	39.27	560.01	55.54	2.66176
770	789.11	41.31	568.07	53.39	2.67595
780	800.03	43.35	576.12	51.64	2.69013
790	810.99	45.55	584.21	49.86	2.70400
800	821.95	47.75	592.30	48.08	2.71787
820	843.98	52.59	608.59	44.84	2.74504
840	866.08	57.60	624.95	41.85	2.77170
860	888.27	63.09	641.40	39.12	2.79783
880	910.56	68.98	657.95	36.61	2.82344
900	932.93	75.29	674.58	34.31	2.84856
920	955.38	82.05	691.28	32.18	2.87324
940	977.92	89.28	708.08	30.22	2.89748
960	1000.55	97.00	725.02	28.40	2.92128
980	1023.25	105.2	741.98	26.73	2.94468
1000	1046.04	114.0	758.94	25.17	2.96770
1020	1068.89	123.4	776.10	23.72	2.99034
1040	1091.85	133.3	793.36	22.39	3.01260
1060	1114.86	143.9	810.62	21.14	3.03449
1080	1137.89	155.2	827.88	19.98	3.05608
1100	1161.07	167.1	845.33	18.896	3.07732
1120	1184.28	179.7	862.79	17.886	3.09825
1140	1207.57	193.1	880.35	16.946	3.11883
1160	1230.92	207.2	897.91	16.064	3.13916
1180	1254.34	222.2	915.57	15.241	3.15916
1200	1277.79	238.0	933.33	14.470	3.17888
1220	1301.31	254.7	951.09	13.747	3.19834
1240	1324.93	272.3	968.95	13.069	3.21751
1260	1348.55	290.8	986.90	12.435	3.23638
1280	1372.24	310.4	1004.76	11.835	3.25510
1300	1395.97	330.9	1022.82	11.275	3.27345
1320	1419.76	352.5	1040.88	10.747	3.29160
1340	1443.60	375.3	1058.94	10.247	3.30959
1360	1467.49	399.1	1077.10	9.780	3.32724
1380	1491.44	424.2	1095.26	9.337	3.34474
1400	1515.42	450.5	1113.52	8.919	3.36200
1420	1539.44	478.0	1131.77	8.526	3.37901
1440	1563.51	506.9	1150.13	8.153	3.39586
1460	1587.63	537.1	1168.49	7.801	3.41247
1480	1611.79	568.8	1186.95	7.468	3.42892
1500	1635.97	601.9	1205.41	7.152	3.44516
1520	1660.23	636.5	1223.87	6.854	3.46120
1540	1684.51	672.8	1242.43	6.569	3.47712
1560	1708.82	710.5	1260.99	6.301	3.49276
1580	1733.17	750.0	1279.65	6.046	3.50829
1600	1757.57	791.2	1298.30	5.804	3.52364
1620	1782.00	834.1	1316.96	5.574	3.53879
1640	1806.46	878.9	1335.72	5.355	3.55381
1660	1830.96	925.6	1354.48	5.147	3.56867
1680	1855.50	974.2	1373.24	4.949	3.58335
1700	1880.1	1025	1392.7	4.761	3.5979
1750	1941.6	1161	1439.8	4.328	3.6336
1800	2003.3	1310	1487.2	3.944	3.6684
1850	2065.3	1475	1534.9	3.601	3.7023
1900	2127.4	1655	1582.6	3.295	3.7354
1950	2189.7	1852	1630.6	3.022	3.7677
2000	2252.1	2068	1678.7	2.776	3.7994
2050	2314.6	2303	1726.8	2.555	3.8303
2100	2377.4	2559	1775.3	2.356	3.8605
2150	2440.3	2837	1823.8	2.175	3.8901
2200	2503.2	3138	1872.4	2.012	3.9191
2250	2566.4	3464	1921.3	1.864	3.9474

TABLE A.8 (continued) Ideal Gas Properties of Air

Part b. English Units

T(°R), h and u(Btu/lb), s°(Btu/lb · °R)

T	h	p_r	u	v_r	s°	T	h	p_r	u	v_r	s°
360	85.97	0.3363	61.29	396.6	0.50369	940	226.11	9.834	161.68	35.41	0.73509
380	90.75	0.4061	64.70	346.6	0.51663	960	231.06	10.61	165.26	33.52	0.74030
400	95.53	0.4858	68.11	305.0	0.52890	980	236.02	11.43	168.83	31.76	0.74540
420	100.32	0.5760	71.52	270.1	0.54058	1000	240.98	12.30	172.43	30.12	0.75042
440	105.11	0.6776	74.93	240.6	0.55172	1040	250.95	14.18	179.66	27.17	0.76019
460	109.90	0.7913	78.36	215.33	0.56235	1080	260.97	16.28	186.93	24.58	0.76964
480	114.69	0.9182	81.77	193.65	0.57255	1120	271.03	18.60	194.25	22.30	0.77880
500	119.48	1.0590	85.20	174.90	0.58233	1160	281.14	21.18	201.63	20.29	0.78767
520	124.27	1.2147	88.62	158.58	0.59172	1200	291.30	24.01	209.05	18.51	0.79628
537	128.34	1.3593	91.53	146.34	0.59945	1240	301.52	27.13	216.53	16.93	0.80466
540	129.06	1.3860	92.04	144.32	0.60078	1280	311.79	30.55	224.05	15.52	0.81280
560	133.86	1.5742	95.47	131.78	0.60950	1320	322.11	34.31	231.63	14.25	0.82075
580	138.66	1.7800	98.90	120.70	0.61793	1360	332.48	38.41	239.25	13.12	0.82848
600	143.47	2.005	102.34	110.88	0.62607	1400	342.90	42.88	246.93	12.10	0.83604
620	148.28	2.249	105.78	102.12	0.63395	1440	353.37	47.75	254.66	11.17	0.84341
640	153.09	2.514	109.21	94.30	0.64159	1480	363.89	53.04	262.44	10.34	0.85062
660	157.92	2.801	112.67	87.27	0.64902	1520	374.47	58.78	270.26	9.578	0.85767
680	162.73	3.111	116.12	80.96	0.65621	1560	385.08	65.00	278.13	8.890	0.86456
700	167.56	3.446	119.58	75.25	0.66321	1600	395.74	71.73	286.06	8.263	0.87130
720	172.39	3.806	123.04	70.07	0.67002	1650	409.13	80.89	296.03	7.556	0.87954
740	177.23	4.193	126.51	65.38	0.67665	1700	422.59	90.95	306.06	6.924	0.88758
760	182.08	4.607	129.99	61.10	0.68312	1750	436.12	101.98	316.16	6.357	0.89542
780	186.94	5.051	133.47	57.20	0.68942	1800	449.71	114.0	326.32	5.847	0.90308
800	191.81	5.526	136.97	53.63	0.69558	1850	463.37	127.2	336.55	5.388	0.91056
820	196.69	6.033	140.47	50.35	0.70160	1900	477.09	141.5	346.85	4.974	0.91788
840	201.56	6.573	143.98	47.34	0.70747	1950	490.88	157.1	357.20	4.598	0.92504
860	206.46	7.149	147.50	44.57	0.71323	2000	504.71	174.0	367.61	4.258	0.93205
880	211.35	7.761	151.02	42.01	0.71886	2050	518.61	192.3	378.08	3.949	0.93891
900	216.26	8.411	154.57	39.64	0.72438	2100	532.55	212.1	388.60	3.667	0.94564
920	221.18	9.102	158.12	37.44	0.72979	2150	546.54	233.5	399.17	3.410	0.95222

TABLE A.8 (continued) Ideal Gas Properties of Air

T(°R), h and u(Btu/lb), s°(Btu/lb · °R)

T	h	p_r	u	v_r	s°	T	h	p_r	u	v_r	s°
2200	560.59	256.6	409.78	3.176	0.95868	3700	998.11	2330	744.48	.5882	1.10991
2250	574.69	281.4	420.46	2.961	0.96501	3750	1013.1	2471	756.04	.5621	1.11393
2300	588.82	308.1	431.16	2.765	0.97123	3800	1028.1	2618	767.60	.5376	1.11791
2350	603.00	336.8	441.91	2.585	0.97732	3850	1043.1	2773	779.19	.5143	1.12183
2400	617.22	367.6	452.70	2.419	0.98331	3900	1058.1	2934	790.80	.4923	1.12571
2450	631.48	400.5	463.54	2.266	0.98919	3950	1073.2	3103	802.43	.4715	1.12955
2500	645.78	435.7	474.40	2.125	0.99497	4000	1088.3	3280	814.06	.4518	1.13334
2550	660.12	473.3	485.31	1.996	1.00064	4050	1103.4	3464	825.72	.4331	1.13709
2600	674.49	513.5	496.26	1.876	1.00623	4100	1118.5	3656	837.40	.4154	1.14079
2650	688.90	556.3	507.25	1.765	1.01172	4150	1133.6	3858	849.09	.3985	1.14446
2700	703.35	601.9	518.26	1.662	1.01712	4200	1148.7	4067	860.81	.3826	1.14809
2750	717.83	650.4	529.31	1.566	1.02244	4300	1179.0	4513	884.28	.3529	1.15522
2800	732.33	702.0	540.40	1.478	1.02767	4400	1209.4	4997	907.81	.3262	1.16221
2850	746.88	756.7	551.52	1.395	1.03282	4500	1239.9	5521	931.39	.3019	1.16905
2900	761.45	814.8	562.66	1.318	1.03788	4600	1270.4	6089	955.04	.2799	1.17575
2950	776.05	876.4	573.84	1.247	1.04288	4700	1300.9	6701	978.73	.2598	1.18232
3000	790.68	941.4	585.04	1.180	1.04779	4800	1331.5	7362	1002.5	.2415	1.18876
3050	805.34	1011	596.28	1.118	1.05264	4900	1362.2	8073	1026.3	.2248	1.19508
3100	820.03	1083	607.53	1.060	1.05741	5000	1392.9	8837	1050.1	.2096	1.20129
3150	834.75	1161	618.82	1.006	1.06212	5100	1423.6	9658	1074.0	.1956	1.20738
3200	849.48	1242	630.12	.9546	1.06676	5200	1454.4	10539	1098.0	.1828	1.21336
3250	864.24	1328	641.46	.9069	1.07134	5300	1485.3	11481	1122.0	.1710	1.21923
3300	879.02	1418	652.81	.8621	1.07585						
3350	893.83	1513	664.20	.8202	1.08031						
3400	908.66	1613	675.60	.7807	1.08470						
3450	923.52	1719	687.04	.7436	1.08904						
3500	938.40	1829	698.48	.7087	1.09332						
3550	953.30	1946	709.95	.6759	1.09755						
3600	968.21	2068	721.44	.6449	1.10172						
3650	983.15	2196	732.95	.6157	1.10584						

Source: Adapted from M.J. Moran and H.N. Shapiro, *Fundamentals of Engineering Thermodynamics*, 3rd. ed., Wiley, New York, 1995, as based on J.H. Keenan and J. Kaye, *Gas Tables*, Wiley, New York, 1945.

TABLE A.9 Equations for Gas Properties

Gas	Molar Mass	Gas Constant	Specific Heats at 25°C			Equation Coefficients for $c_p/R = a + bT + cT^2 + dT^3 + eT^4$						Critical State Properties		Redlich–Kwong Constants		Gas
	M kg/kmol	R kJ/kg·K	c_p kJ/kg·K	c_v kJ/kg·K	k	Temperature Range	a	$b \times 10^3$ K^{-1}	$c \times 10^6$ K^{-2}	$d \times 10^{10}$ K^{-3}	$e \times 10^{13}$ K^{-4}	p_c MPa	T_c K	a $\frac{kPa \cdot m^6 \cdot K^{0.5}}{kmol^2}$	b $m^3/kmol$	
Acetylene, C_2H_2	26.04	0.319	1.69	1.37	1.232	300–1000K	0.8021	23.51	–35.95	286.1	–87.64	6.14	308	8030	0.0362	Acetylene, C_2H_2
						1000–3000K	3.825	6.767	–3.014	6.931	–0.6469					
Air	28.97	0.287	1.01	0.718	1.400	300–1000K	3.721	–1.874	4.719	–34.45	8.531	3.77	132	1580	0.0253	Air
						1000–3000K	2.786	1.925	–0.9465	2.321	–0.2229					
Argon, Ar	39.95	0.208	0.520	0.312	1.667		2.50	0	0	0	0	4.90	151	1680	0.0222	Argon, Ar
Butane, C_4H_{10}	58.12	0.143	1.67	1.53	1.094	300–1500K	0.4756	44.65	–22.04	42.07	0	3.80	425	29000	0.0806	Butane, C_4H_{10}
Carbon Dioxide CO_2	44.01	0.189	0.844	0.655	1.289	300–1000K	2.227	9.992	–9.802	53.97	–12.81	7.38	304	6450	0.0297	Carbon Dioxide CO_2
						1000–3000K	3.247	5.847	–3.412	9.469	–1.009					
Carbon Monoxide CO	28.01	0.297	1.04	0.744	1.399	300–1000K	3.776	–2.093	4.880	–32.71	6.984	3.50	133	1720	0.0274	Carbon Monoxide, CO
						1000–3000K	2.654	2.226	–1.146	2.851	–0.2762					
Ethane, C_2H_6	30.07	0.276	1.75	1.48	1.187	300–1500K	0.8293	20.75	-7.704	8.756	0	4.88	306	9860	0.0450	Ethane, C_2H_6
Ethylene, C_2H_4	28.05	0.296	1.53	1.23	1.240	300–1000K	1.575	10.19	11.25	–199.1	81.98	5.03	282	7860	0.0404	Ethylene, C_2H_4
						1000–3000K	0.2530	18.67	–9.978	26.03	–2.668					
Helium, He	4.003	2.08	5.19	3.12	1.667		2.50	0	0	0	0	0.228	5.20	8.00	0.0165	Helium, He
Hydrogen, H_2	2.016	4.12	14.3	10.2	1.405	300–1000K	2.892	3.884	–8.850	86.94	–29.88	1.31	33.2	143	0.0182	Hydrogen, H_2
						1000–3000K	3.717	–0.9220	1.221	–4.328	0.5202					
Hydrogen, H	1.008	8.25	20.6	12.4	1.667	300–1000K	2.496	0.02977	–0.07655	0.8238	–0.3158					Hydrogen, H
						1000–3000K	2.567	–0.1509	0.1219	–0.4184	0.05182					
Hydroxyl, OH	17.01	0.489	1.76	1.27	1.384	300–1000K	3.874	–1.349	1.670	–5.670	0.6189					Hydroxyl, OH
						1000–3000K	3.229	0.2014	0.4357	–2.043	0.2696					
Methane, CH_4	16.04	0.518	2.22	1.70	1.304	300–1000K	4.503	–8.965	37.38	–364.9	122.2	4.60	191	3210	0.0298	Methane, CH_4
						1000–3000K	–0.6992	15.31	–7.695	18.96	–1.849					
Neon, Ne	20.18	0.412	1.03	0.618	1.667		2.50	0	0	0	0	2.65	44.4	146	0.0120	Neon, Ne
Nitric Oxide, N(	30.01	0.277	0.995	0.718	1.386	300–1000K	4.120	–4.225	10.77	–97.64	31.85	6.48	180	1980	0.0200	Nitric Oxide, NO
						1000–3000K	2.730	2.372	–1.338	3.604	–0.3743					
Nitrogen, N_2	28.01	0.297	1.04	0.743	1.400	300–1000K	3.725	–1.562	3.208	–15.54	1.154	3.39	126	1550	0.0267	Nitrogen, N_2
						1000–3000K	2.469	2.467	–1.312	3.401	–0.3454					
Nitrogen, N	14.01	0.594	1.48	0.890	1.667	300–1000K	2.496	0.02977	–0.07655	0.8238	–0.3158					Nitrogen, N
						1000–3000K	2.483	0.03033	–0.01517	0.001879	0.009657					
Oxygen, O_2	32.00	0.260	0.919	0.659	1.395	300–1000K	3.837	–3.420	10.99	–109.6	37.47	5.04	155	1740	0.0221	Oxygen, O_2
						1000–3000K	3.156	1.809	–1.052	3.190	–0.3629					
Oxygen, O	16.00	0.520	1.37	0.850	1.612	300–1000K	3.020	–2.176	3.793	–30.62	9.402					Oxygen, O
						1000–3000K	2.662	–0.3051	0.2250	–0.7447	0.09383					
Propane, C_3H_8	44.10	0.189	1.67	1.48	1.127	300-1500K	-0.4861	36.63	-18.91	38.14	0	4.26	370	18300	0.0626	Propane, C_3H_8
Water, H_2O	18.02	0.462	1.86	1.40	1.329	300–1000K	4.132	–1.559	5.315	–42.09	12.84	22.1	647	14300	0.0211	Water, H_2O
						1000–3000K	2.798	2.693	–0.5392	–0.01783	0.09027					

Source: Adapted from J.B. Jones and R.E. Dugan, *Engineering Thermodynamics*, Prentice-Hall, Englewood Cliffs, NJ 1996 from various sources: *JANAF Thermochemical Tables*, 3rd ed., published by the American Chemical Society and the American Institute of Physics for the National Bureau of Standards, 1986. Data for butane, ethane, and propane from K.A. Kobe and E.G. Long, "Thermochemistry for the Petrochemical Industry, Part II — Paraffinic Hydrocarbons, C_1–C_{16}" *Petroleum Refiner*, Vol. 28, No. 2, 1949, pp. 113–116.

Appendix B. Properties of Liquids

TABLE B.1 Properties of Liquid Water*

Symbols and Units:

ρ = density, lbm/ft^3. For g/cm^3 multiply by 0.016018. For kg/m^3 multiply by 16.018.

c_p = specific heat, Btu/lbm·deg R = cal/g·K. For J/kg·K multiply by 4186.8

μ = viscosity. For lbf·sec/ft^2 = slugs/sec·ft, multiply by 10^{-7}. For lbm·sec·ft multiply by 10^{-7} and by 32.174. For g/sec·cm (poises) multiply by 10^{-7} and by 478.80. For N·sec/m^2 multiply by 10^{-7} and by 478.880.

k = thermal conductivity, Btu/hr·ft·deg R. For W/m·K multiply by 1.7307.

Temp, °F	At 1 atm or 14.7 psia				At 1,000 psia				At 10,000 psia			
	ρ	c_p	μ	k	ρ	c_p	μ	k	ρ	c_p	μ	k†
32	62.42	1.007	366	0.3286	62.62	0.999	365	0.3319	64.5	0.937	357	0.3508
40	62.42	1.004	323	0.334	62.62	0.997	323	0.337	64.5	0.945	315	0.356
50	62.42	1.002	272	0.3392	62.62	0.995	272	0.3425	64.5	0.951	267	0.3610
60	62.38	1.000	235	0.345	62.58	0.994	235	0.348	64.1	0.956	233	0.366
70	62.31	0.999	204	0.350	62.50	0.994	204	0.353	64.1	0.960	203	0.371
80	62.23	0.998	177	0.354	62.42	0.994	177	0.358	64.1	0.962	176	0.376
90	62.11	0.998	160	0.359	62.31	0.994	160	0.362	63.7	0.964	159	0.380
100	62.00	0.998	142	0.3633	62.19	0.994	142	0.3666	63.7	0.965	142	0.3841
110	61.88	0.999	126	0.367	62.03	0.994	126	0.371	63.7	0.966	126	0.388
120	61.73	0.999	114	0.371	61.88	0.995	114	0.374	63.3	0.967	114	0.391
130	61.54	0.999	105	0.374	61.73	0.995	105	0.378	63.3	0.968	105	0.395
140	61.39	0.999	96	0.378	61.58	0.996	96	0.381	63.3	0.969	98	0.398
150	61.20	1.000	89	0.3806	61.39	0.996	89	0.3837	63.0	0.970	91	0.4003
160	61.01	1.001	83	0.383	61.20	0.997	83	0.386	62.9	0.971	85	0.403
170	60.79	1.002	77	0.386	60.98	0.998	77	0.389	62.5	0.972	79	0.405
180	60.57	1.003	72	0.388	60.75	0.999	72	0.391	62.5	0.973	74	0.407
190	60.35	1.004	68	0.390	60.53	1.001	68	0.393	62.1	0.974	70	0.409
200	60.10	1.005	62.5	0.3916	60.31	1.002	62.9	0.3944	62.1	0.975	65.4	0.4106
250	boiling point 212°F				59.03	1.001	47.8	0.3994	60.6	0.981	50.6	0.4158
300					57.54	1.024	38.4	0.3993	59.5	0.988	41.3	0.4164
350					55.83	1.044	32.1	0.3944	58.1	0.999	35.1	0.4132
400					53.91	1.072	27.6	0.3849	56.5	1.011	30.6	0.4064
500					49.11	1.181	21.6	0.3508	52.9	1.051	24.8	0.3836
600					boiling point 544.58°F				48.3	1.118	21.0	0.3493

†At 7,500 psia.

*From: "1967 ASME Steam Tables", American Society of Mechanical Engineers, Tables 9, 10, and 11 and Figures 6, 7, 8, and 9.

The ASME compilation is a 330-page book of tables and charts, including a 2½ × 3½-ft Mollier chart. All values have been computed in accordance with the 1967 specifications of the International Formulation Committee (IFC) and are in conformity with the 1963 International Skeleton Tables. This standardization of tables began in 1921 and was extended through the International Conferences in London (1929), Berlin (1930), Washington (1934), Philadelphia (1954), London (1956), New York (1963) and Glasgow (1966). Based on these world-wide standard data, the 1967 ASME volume represents detailed computer output in both tabular and graphic form. Included are density and volume, enthalpy, entropy, specific heat, viscosity, thermal conductivity, Prandtl number, isentropic exponent, choking velocity, p-v product, etc., over the entire range (to 1500 psia 1500°F). English units are used, but all conversion factors are given.

TABLE B.2 Physical and Thermal Properties of Common Liquids

Part a. SI Units

(At 1.0 Atm Pressure (0.101 325 MN/m^2), 300 K, except as noted.)

Common name	*Density, kg/m^3*	*Specific heat, kJ/kg·K*	*Viscosity, N·s/m^2*	*Thermal conductivity, W/m·K*	*Freezing point, K*	*Latent heat of fusion, kJ/kg*	*Boiling point, K*	*Latent heat of evaporation, kJ/kg*	*Coefficient of cubical expansion per K*
Acetic acid	1 049	2.18	.001 155	0.171	290	181	391	402	0.001 1
Acetone	784.6	2.15	.000 316	0.161	179.0	98.3	329	518	0.001 5
Alcohol, ethyl	785.1	2.44	.001 095	0.171	158.6	108	351.46	846	0.001 1
Alcohol, methyl	786.5	2.54	.000 56	0.202	175.5	98.8	337.8	1 100	0.001 4
Alcohol, propyl	800.0	2.37	.001 92	0.161	146	86.5	371	779	
Ammonia (aqua)	823.5	4.38		0.353					
Benzene	873.8	1.73	.000 601	0.144	278.68	126	353.3	390	0.001 3
Bromine		.473	.000 95		245.84	66.7	331.6	193	0.001 2
Carbon disulfide	1 261	.992	.000 36	0.161	161.2	57.6	319.40	351	0.001 3
Carbon tetrachloride	1 584	.866	.000 91	0.104	250.35	174	349.6	194	0.001 3
Castor oil	956.1	1.97	.650	0.180	263.2				
Chloroform	1 465	1.05	.000 53	0.118	209.6	77.0	334.4	247	0.001 3
Decane	726.3	2.21	.000 859	0.147	243.5	201	447.2	263	
Dodecane	754.6	2.21	.001 374	0.140	247.18	216	489.4	256	
Ether	713.5	2.21	.000 223	0.130	157	96.2	307.7	372	0.001 6
Ethylene glycol	1 097	2.36	.016 2	0.258	260.2	181	470	800	
Fluorine refrigerant R-11	1 476	.870[a]	.000 42	0.093[a]	162		297.0	180[b]	
Fluorine refrigerant R-12	1 311	.971[a]		0.071[a]	115	34.4	243.4	165[b]	
Fluorine refrigerant R-22	1 194	1.26[a]		0.086[a]	113	183	232.4	232[b]	
Glycerine	1 259	2.62	.950	0.287	264.8	200	563.4	974	0.000 54
Heptane	679.5	2.24	.000 376	0.128	182.54	140	371.5	318	
Hexane	654.8	2.26	.000 297	0.124	178.0	152	341.84	365	
Iodine		2.15			386.6	62.2	457.5	164	
Kerosene	820.1	2.09	.001 64	0.145				251	
Linseed oil	929.1	1.84	.033 1		253		560		
Mercury		.139	.001 53		234.3	11.6	630	295	0.000 18
Octane	698.6	2.15	.000 51	0.131	216.4	181	398	298	0.000 72
Phenol	1 072	1.43	.008 0	0.190	316.2	121	455		0.000 90
Propane	493.5	2.41[a]	.000 11		85.5	79.9	231.08	428[b]	
Propylene	514.4	2.85	.000 09		87.9	71.4	225.45	342	
Propylene glycol	965.3	2.50	.042		213		460	914	
Sea water	1 025	3.76–4.10			270.6				
Toluene	862.3	1.72	.000 550	0.133	178	71.8	383.6	363	
Turpentine	868.2	1.78	.001 375	0.121	214		433	293	0.000 99
Water	997.1	4.18	.000 89	0.609	273	333	373	2 260	0.000 20

[a] At 297 K, liquid.
[b] At .101 325 meganewtons, saturation temperature.

TABLE B.2 (continued) Physical and Thermal Properties of Common Liquids

Part b. English Units

(At 1.0 Atm Pressure 77°F (25°C), except as noted.)

For viscosity in N·s/m^2 (=kg m·s), multiply values in centipoises by 0.001. For surface tension in N/m, multiply values in dyne/cm by 0.001.

Common name	*Density, lb/ft^3*	*Specific gravity*	*Viscosity*		*Sound velocity, meters/sec*	*Dielectric constant*	*Refractive index*
			lb$_m$/ft sec × 10^4	*cp*			
Acetic acid	65.493	1.049	7.76	1.155	1584^{50}	6.15	1.37
Acetone	48.98	.787	2.12	0.316	1174	20.7	1.36
Alcohol, ethyl	49.01	.787	7.36	1.095	1144	24.3	1.36
Alcohol, methyl	49.10	.789	3.76	0.56	1103	32.6	1.33
Alcohol, propyl	49.94	.802	12.9	1.92	1205	20.1	1.38
Ammonia (aqua)	51.411	.826	—	—	—	16.9	—
Benzene	54.55	.876	4.04	0.601	1298	2.2	1.50
Bromine	—	—	6.38	0.95	—	3.20	—
Carbon disulfide	78.72	1.265	2.42	0.36	1149	2.64	1.63
Carbon tetrachloride	98.91	1.59	6.11	0.91	924	2.23	1.46
Castor oil	59.69	0.960	—	650	1474	4.7	—
Chloroform	91.44	1.47	3.56	0.53	995	4.8	1.44
Decane	45.34	.728	5.77	0.859	—	2.0	1.41
Dodecane	47.11	—	9.23	1.374	—	—	1.41
Ether	44.54	0.715	1.50	0.223	985	4.3	1.35
Ethylene glycol	68.47	1.100	109	16.2	1644	37.7	1.43
Fluorine refrigerant R-11	92.14	1.480	2.82	0.42	—	2.0	1.37
Fluorine refrigerant R-12	81.84	1.315	—	—	—	2.0	1.29
Fluorine refrigerant R-22	74.53	1.197	—	—	—	2.0	1.26
Glycerine	78.62	1.263	6380	950	1909	40	1.47
Heptane	42.42	.681	2.53	0.376	1138	1.92	1.38
Hexane	40.88	.657	2.00	0.297	1203	—	1.37
Iodine	—	—	—	—	—	11	—
Kerosene	51.2	0.823	11.0	1.64	1320	—	—
Linseed oil	58.0	0.93	222	33.1	—	3.3	—
Mercury	—	13.633	10.3	1.53	1450	—	—
Octane	43.61	.701	3.43	0.51	1171	—	1.40
Phenol	66.94	1.071	54	8.0	1274^{100}	9.8	—
Propane	30.81	.495	0.74	0.11	—	1.27	1.34
Propylene	32.11	.516	0.60	0.09	—	—	1.36
Propylene glycol	60.26	.968	—	42	—	—	1.43
Sea water	64.0	1.03	—	—	1535	—	—
Toluene	53.83	0.865	3.70	0.550	1275^{30}	2.4	1.49
Turpentine	54.2	0.87	9.24	1.375	1240	—	1.47
Water	62.247	1.00	6.0	0.89	1498	78.54[a]	1.33

[a] The dielectric constant of water near the freezing point is 87.8; it decreases with increase in temperature to about 55.6 near the boiling point.

Appendix C. Properties of Solids

TABLE C.1 Properties of Common Solids*

Material	Specific gravity	Specific heat		Thermal conductivity	
		$\frac{Btu}{lbm \cdot deg\ R}$	$\frac{kJ}{kg \cdot K}$	$\frac{Btu}{hr \cdot ft \cdot deg\ F}$	$\frac{W}{m \cdot K}$
Asbestos cement board	1.4	0.2	.837	0.35	0.607
Asbestos millboard	1.0	0.2	.837	0.08	0.14
Asphalt	1.1	0.4	1.67		
Beeswax	0.95	0.82	3.43		
Brick, common	1.75	0.22	.920	0.42	0.71
Brick, hard	2.0	0.24	1.00	0.75	1.3
Chalk	2.0	0.215	.900	0.48	0.84
Charcoal, wood	0.4	0.24	1.00	0.05	0.088
Coal, anthracite	1.5	0.3	1.26		
Coal, bituminous	1.2	0.33	1.38		
Concrete, light	1.4	0.23	.962	0.25	0.42
Concrete, stone	2.2	0.18	.753	1.0	1.7
Corkboard	0.2	0.45	1.88	0.025	0.04
Earth, dry	1.4	0.3	1.26	0.85	1.5
Fiberboard, light	0.24	0.6	2.51	0.035	0.058
Fiber hardboard	1.1	0.5	2.09	0.12	0.2
Firebrick	2.1	0.25	1.05	0.8	1.4
Glass, window	2.5	0.2	.837	0.55	0.96
Gypsum board	0.8	0.26	1.09	0.1	0.17
Hairfelt	0.1	0.5	2.09	0.03	0.050
Ice (32°)	0.9	0.5	2.09	1.25	2.2
Leather, dry	0.9	0.36	1.51	0.09	0.2
Limestone	2.5	0.217	.908	1.1	1.9
Magnesia (85%)	0.25	0.2	.837	0.04	0.071
Marble	2.6	0.21	.879	1.5	2.6
Mica	2.7	0.12	.502	0.4	0.71
Mineral wool blanket	0.1	0.2	.837	0.025	0.04
Paper	0.9	0.33	1.38	0.07	0.1
Paraffin wax	0.9	0.69	2.89	0.15	0.2
Plaster, light	0.7	0.24	1.00	0.15	0.2
Plaster, sand	1.8	0.22	.920	0.42	0.71
Plastics, foamed	0.2	0.3	1.26	0.02	0.03
Plastics, solid	1.2	0.4	1.67	0.11	0.19
Porcelain	2.5	0.22	.920	0.9	1.5
Sandstone	2.3	0.22	.920	1.0	1.7
Sawdust	0.15	0.21	.879	0.05	0.08
Silica aerogel	0.11	0.2	.837	0.015	0.02
Vermiculite	0.13	0.2	.837	0.035	0.058
Wood, balsa	0.16	0.7	2.93	0.03	0.050
Wood, oak	0.7	0.5	2.09	0.10	0.17
Wood, white pine	0.5	0.6	2.51	0.07	0.12
Wool, felt	0.3	0.33	1.38	0.04	0.071
Wool, loose	0.1	0.3	1.26	0.02	0.3

*Compiled from several sources.

TABLE C.2 Density of Various Solids:* Approximate Density of Solids at Ordinary Atmospheric Temperature

Substance	Grams per cu cm	Pounds per cu ft
Agate	2.5–2.7	156–168
Alabaster		
Carbonate	2.69–2.78	168–173
Sulfate	2.26–2.32	141–145
Albite	2.62–2.65	163–165
Amber	1.06–1.11	66–69
Amphiboles	2.9–3.2	180–200
Anorthite	2.74–2.76	171–172
Asbestos	2.0–2.8	125–175
Asbestos slate	1.8	112
Asphalt	1.1–1.5	69–94
Basalt	2.4–3.1	150–190
Beeswax	0.96–0.97	60–61
Beryl	2.69–2.7	168–169
Biotite	2.7–3.1	170–190
Bone	1.7–2.0	106–125
Brick	1.4–2.2	87–137
Butter	0.86–0.87	53–54
Calamine	4.1–4.5	255–280
Calcspar	2.6–2.8	162–175
Camphor	0.99	62
Caoutchouc	0.92–0.99	57–62
Cardboard	0.69	43
Celluloid	1.4	87
Cement, set	2.7–3.0	170–190
Chalk	1.9–2.8	118–175
Charcoal		
Oak	0.57	35
Pine	0.28–0.44	18–28
Cinnabar	8.12	507
Clay	1.8–2.6	112–162
Coal		
Anthracite	1.4–1.8	87–112
Bituminous	1.2–1.5	75–94
Cocoa butter	0.89–0.91	56–57
Coke	1.0–1.7	62–105
Copal	1.04–1.14	65–71
Cork	0.22–0.26	14–16
Cork linoleum	0.54	34
Corundum	3.9–4.0	245–250
Diamond	3.01–3.52	188–220
Dolomite	2.84	177
Ebonite	1.15	72
Emery	4.0	250
Epidote	3.25–3.50	203–218
Feldspar	2.55–2.75	159–172
Flint	2.63	164
Fluorite	3.18	198
Galena	7.3–7.6	460–470
Gamboge	1.2	75
Garnet	3.15–4.3	197–268
Gas carbon	1.88	117
Gelatin	1.27	79
Glass		
Common	2.4–2.8	150–175
Flint	2.9–5.9	180–370
Glue	1.27	79
Granite	2.64–2.76	165–172
Graphite†	2.30–2.72	144–170
Gum arabic	1.3–1.4	81–87
Gypsum	2.31–2.33	144–145
Hematite	4.9–5.3	306–330
Hornblende	3.0	187
Ice	0.917	57.2
Ivory	1.83–1.92	114–120
Leather, dry	0.86	54
Lime, slaked	1.3–1.4	81–87
Limestone	2.68–2.76	167–171
Linoleum	1.18	74
Magnetite	4.9–5.2	306–324
Malachite	3.7–4.1	231–256
Marble	2.6–2.84	160–177
Meerschaum	0.99–1.28	62–80
Mica	2.6–3.2	165–200
Muscovite	2.76–3.00	172–187
Ochre	3.5	218
Opal	2.2	137
Paper	0.7–1.15	44–72
Paraffin	0.87–0.91	54–57
Peat blocks	0.84	52
Pitch	1.07	67
Porcelain	2.3–2.5	143–156
Porphyry	2.6–2.9	162–181
Pressed wood		
pulp board	0.19	12
Pyrite	4.95–5.1	309–318
Quartz	2.65	165
Resin	1.07	67
Rock salt	2.18	136
Rubber, hard	1.19	74
Rubber, soft		
Commercial	1.1	69
Pure gum	0.91–0.93	57–58
Sandstone	2.14–2.36	134–147
Serpentine	2.50–2.65	156–165
Silica		
Fused transparent	2.21	138
Translucent	2.07	129
Slag	2.0–3.9	125–240
Slate	2.6–3.3	162–205
Soapstone	2.6–2.8	162–175
Spermaceti	0.95	59
Starch	1.53	95
Sugar	1.59	99
Talc	2.7–2.8	168–174
Tallow		
Beef	0.94	59
Mutton	0.94	59
Tar	1.02	66
Topaz	3.5–3.6	219–223
Tourmaline	3.0–3.2	190–200
Wax, sealing	1.8	112
Wood (seasoned)		
Alder	0.42–0.68	26–42
Apple	0.66–0.84	41–52
Ash	0.65–0.85	40–53
Balsa	0.11–0.14	7–9
Bamboo	0.31–0.40	19–25
Basswood	0.32–0.59	20–37
Beech	0.70–0.90	32–56
Birch	0.51–0.77	32–48
Blue gum	1.00	62
Box	0.95–1.16	59–72
Butternut	0.38	24
Cedar	0.49–0.57	30–35
Cherry	0.70–0.90	43–56
Dogwood	0.76	47
Ebony	1.11–1.33	69–83
Elm	0.54–0.60	34–37
Hickory	0.60–0.93	37–58
Holly	0.76	47
Juniper	0.56	35
Larch	0.50–0.56	31–35
Lignum vitae	1.17–1.33	73–83
Locust	0.67–0.71	42–44
Logwood	0.91	57
Mahogany		
Honduras	0.66	41
Spanish	0.85	53
Maple	0.62–0.75	39–47
Oak	0.60–0.90	37–56
Pear	0.61–0.73	38–45
Pine		
Pitch	0.83–0.85	52–53
White	0.35–0.50	22–31
Yellow	0.37–0.60	23–37
Plum	0.66–0.78	41–49
Poplar	0.35–0.5	22–31
Satinwood	0.95	59
Spruce	0.48–0.70	30–44
Sycamore	0.40–0.60	24–37
Teak		
Indian	0.66–0.88	41–55
African	0.98	61
Walnut	0.64–0.70	40–43
Water gum	1.00	62
Willow	0.40–0.60	24–37

†Some values reported as low as 1.6

*Based largely on: "Smithsonian Physical Tables", 9th rev. ed., W.E. Forsythe, Ed., The Smithsonian Institution, 1956, p. 292.

Note: In the case of substances with voids, such as paper or leather, the bulk density is indicated rather than the density of the solid portion. For density in kg/m^3, multiply values in g/cm^3 by 1,000.

TABLE C.3 Specific Stiffness of Metals, Alloys, and Certain Non-Metallics*

Specific stiffness is usually expressed as the modulus of elasticity (in tension) per unit weight-density, i.e., E/ρ, in units of pounds and inches. While the stiffness of similar alloys varies considerably, there are definite ranges and groups to be recognized. Since the specific stiffness of steel is about 100 million, the values in the following table are also approximately the percentage stiffness, referred to steel.

Material	*Specific stiffness, millions*
Beryllium	650
Silicon carbide	600
Alumina ceramics	400
Mica	350
Titanium carbide cermet	250
Alumina cermet	200
Molybdenum and alloys; silica glass	130
Titanium and alloys; cobalt superalloys; soda-lime glass	110
Carbon and low-alloy steel; wrought iron	105
Stainless steel; nodular cast iron; magnesium and alloys; aluminum and alloys	100
Nickel and alloys; malleable iron	95
Iron silicon alloys (cast); iridium; vanadium	90
Monel alloys; tungsten	80
Gray cast iron; columbium alloys	70
Aluminum bronze; beryllium copper	65
Nickel silver; cupronickel; zirconium	55
Yellow brass; nickel cast iron; bronze; Muntz metal; antimony	50
Copper; red brass; tantalum	45
Silver and alloys; pewter; platinum and alloys; white gold	30
Tin; thorium	25
Gold	20
Tin-lead alloy	10
Lead	5

*Compiled from several sources.

TABLE C.4 Thermal Properties of Pure Metals—Metric Units

Metal	*AT ATMOSPHERIC PRESSURE*								*LIQUID METAL*			
	Melting point, °C	*Boiling point, °C*	*Latent heat of fusion, cal/g***	*At 100°K*		*At 25°C (77°F)*			*Specific heat (liquid) at 2000°K, cal/g °C***	*Vapor pressure*		
				Thermal conductivity, watts/cm °C	*Specific heat, cal/g °C***	*Specific heat, cal/g °C***	*Coeff. of linear expansion, ($\times 10^6$) $(°C)^{-1}$*	*Thermal conductivity, watts/cm °C*		*10^{-3} atm*	*10^{-6} atm*	*10^{-9} atm*
										Boiling point temperatures, °K		
Aluminum	660.	2441.	95	3.00*	.115	0.215	25	2.37	.26	1,782	1,333	1,063
Antimony	630.	1440.	38.5	—	.040	.050	9	.185	.062	1,007	741	612
Beryllium	1285.	2475.	324.	—	.049	.436	12	2.18	.78	1,793	1,347	1,085
Bismuth	271.4	1660.	12.4	—	.026	.030	13	.084	.036	1,155	851	677
Cadmium	321.	767.	13.2	1.03	.047	.055	30	.93	.063	655	486	388
Chromium	1860.	2670.	79	1.58	.046	.110	6	.91	.224	1,992	1,530	1,247
Cobalt	1495.	2925.	66	—	.057	.10	12	.69	.164	2,167	1,652	1,345
Copper	1084.	2575.	49	4.83*	.061	.092	16.6	3.98	.118	1,862	1,391	1,120
Gold	1063.	2800.	15	3.45*	.026	.031	14.2	3.15	.0355	2,023	1,510	1,211
Iridium	2450.	4390.	33	—	.022	.031	6	1.47	.0434	3,253	2,515	2,062
Iron	1536.	2870.	65	1.32*	.052	.108	12	.803	.197	2,093	1,594	1,297
Lead	327.5	1750.	5.5	0.396	.028	.031	29	.346	.033	1,230	889	698
Magnesium	650.	1090.	88.0	1.69	.016	.243	25	1.59	.32	857	638	509
Manganese	1244.	2060.	64	—	.064	.114	22	—	.20	1,495	1,131	913
Mercury	−38.86	356.55	2.7	—	.029	.033	—	.0839	—	393	287	227
Molybdenum	2620.	4651.	69	1.79	.033	.060	5	1.4	.089	3,344	2,558	2,079
Nickel	1453.	2800.	71	1.58	.055	.106	13	.899	.175	2,156	1,646	1,343
Niobium (Columbium)	2470.	4740.	68	0.552	.045	.064	7	.52	.083	3,523	2,721	2,232
Osmium	3025.	4225.	34	—	—	.031	5	.61	.039	—	—	—
Platinum	1770.	3825.	24	0.79*	.024	.032	9	.73	.043	2,817	2,155	1,757
Plutonium	640.	3230.	3	—	.019	.032	54	.08	.041	2,200	1,596	1,252
Potassium	63.3	760.	14.5	—	.150	.180	83	.99	—	606	430	335
Rhodium	1965.	3700.	50	—	—	.058	8	1.50	.092	—	—	—
Selenium	217.	700.	16	—	—	.077	37	.005	—	—	—	—
Silicon	1411.	3280.	430	—	.062	.17	3	.835	.217	2,340	1,749	1,427
Silver	961.	2212.	26.5	4.50*	.045	.057	19	4.27	.068	1,582	1,179	952
Sodium	97.83	884.	27	—	.234	.293	70	1.34	—	701	504	394
Tantalum	2980.	5365.	41	0.592	.026	.034	6.5	.54	.040	3,959	3,052	2,495
Thorium	1750.	4800.	17	—	.024	.03	12	.41	.047	3,251	2,407	1,919
Tin	232.	2600.	14.1	0.85	.039	.054	20	.64	.058	1,857	1,366	1,080
Titanium	1670.	3290.	100	0.312	.072	.125	8.5	.2	.188	2,405	1,827	1,484
Tungsten	3400.	5550.	46	2.35*	.021	.032	4.5	1.78	.040	4,139	3,228	2,656
Uranium	1132.	4140.	12	—	.022	.028	13.4	.25	.048	2,861	2,128	1,699
Vanadium	1900.	3400.	98	—	.061	.116	8	.60	.207	2,525	1,948	1,591
Zinc	419.5	910.	27	1.32	.063	.093	35	1.15	—	752	559	449

* Temperatures of maximum thermal conductivity (conductivity values in watts/cm °C): Aluminum 13°K, cond. = 71.5; copper 10°K, cond. = 196; gold 10°K, cond. = 28.2; iron 20°K, cond. = 9.97; platinum 8°K, cond. = 12.9; silver 7°K, cond. = 193; tungsten 8°K, cond. = 85.3.

** To convert to SI units note that l cal = 4.186 J.

TABLE C.5 Mechanical Properties of Metals and Alloys:* Typical Composition, Properties, and Uses of Common Materials

For MN/m^2 multiply strength in thousands of psi by 6.895.

FERROUS ALLOYS

Ferrous alloys comprise the largest volume of metal alloys used in engineering. The actual range of mechanical properties in any particular grade of alloy steel depends on the particular history and heat treatment. The steels listed in this table are intended to give some idea of the range of properties readily obtainable. Many hundreds of steels are available. Cost is frequently an important criterion in the choice of material; in general the greater the percentage of alloying elements present in the alloy, the greater will be the cost.

No.	*Material*	*Nominal composition*	*Form and condition*	*Typical mechanical properties*				*Comments*
				Yield strength (0.2% offset), 1000 lb/sq in.	*Tensile strength, 1000 lb/sq in.*	*Elongation, in 2 in., %*	*Hardness, Brinell*	
	IRON							
1	Ingot iron (Included for comparison)	Fe 99.9	Hot-rolled	29	45	26	90	
			Annealed	19	38	45	67	
	PLAIN CARBON STEELS							
2	AISI–SAE 1020	C 0.20 Mn 0.45 Si 0.25 Fe bal.	Hot-rolled	30	55	25	111	Bolts, crankshafts, gears, connecting rods; easily weldable
			Hardened (water-quenched, 1000°F-tempered)	62	90	25	179	
3	AISI 1025	C 0.25 Fe bal. Mn 0.45	Bar stock					
			Hot-rolled	32	58	25	116	
			Cold-drawn	54	64	15	126	
4	AISI–SAE 1035	C 0.35 Mn 0.75	Hot-rolled	39	72	18	143	Medium-strength, engineering steel
			Cold-rolled	67	80	12	163	
5	AISI–SAE 1045	C 0.45 Fe bal. Mn 0.75	Bar stock					
			Annealed	73	80	12	170	
			Hot-rolled	45	82	16	163	
			Cold-drawn	77	91	12	179	
6	AISI–SAE 1078	C 0.78 Fe bal. Mn 0.45	Bar stock					
			Hot-rolled; spheroidized	55	100	12	207	
			Annealed	72	94	10	192	
7	AISI–SAE 1095	C 0.95 Fe bal. Mn 0.40						
8	AISI–SAE 1120	C 0.2 Mn 0.8 S 0.1	Cold-drawn	58	69	—	137	Free-cutting, leaded, resulphurized steel; high-speed, automatic machining
	ALLOY STEELS							
9	ASTM A202/56	C 0.17 Mn 1.2 Cr 0.5 Si 0.75	Stress-relieved	45	75	18	—	Low alloy; boilers, pressure vessels

TABLE C.5 (continued) Mechanical Properties of Metals and Alloys:* Typical Composition, Properties, and Uses of Common Materials

No.	*Material*	*Nominal composition*	*Form and condition*	*Typical mechanical properties*				*Comments*
				Yield strength (0.2% offset), 1000 lb/sq in.	*Tensile strength, 1000 lb/sq in.*	*Elongation, in 2 in., %*	*Hardness, Brinell*	
10	AISI 4140	C 0.40 Si 0.3 Cr 1.0 Mo 0.2 Mn 0.9	Fully-tempered Optimum properties	95 132	108 150	22 18	240 —	High strength; gears, shafts
11	12% Manganese steel	12% Mn C	Tempered 600°F Rolled and heat-treated stock	200 44	220 160	10 40	— 170	Machine tool parts; wear, abrasion-resistant
12	VASCO 300	Ni 18.5 Ti 0.6 Co 9.0 C 0.03 Mo 4.8	Solution treatment 1500°F; aged 900°F	110	150	18	—	Very high strength, maraging, good machining properties in annealed state
13	T1 (AISI)	W 18.0 V 1.0 Cr 4.0 C 0.7	Quenched; tempered				R(c)	High speed tool steel, cutting tools, punches, etc.
14	M2 (AISI)	W 6.5 Mo 5.0 Cr 4.0 C 0.85 V 2.0	Quenched; tempered				65–66	M-grade, cheaper, tougher
15	Stainless steel type 304	Ni 9.0 C 0.08 Cr 19.0 max	Annealed; cold-rolled	35 to 160	85 to 185	60 8	160 to 400	General purpose, weldable; nonmagnetic austenitic steel
16	Stainless steel type 316	Cr 18.0 C 0.10 Ni 11.0 max Mo 2.5 Fe bal.	Annealed	30 to 120	90 to 150	50 8	165 275	For severe corrosive media, under stress; nonmagnetic austenitic steel
17	Stainless steel type 431	Cr 16.0 Si 1.0 Ni 2.0 C 0.20 Mn 1.0 Fe bal.	Annealed Heat-treated	85 150	120 195	25 20	250 400	Heat-treated stainless steel, with good mechanical strength; magnetic
18	Stainless steel 17-4 PH	Cr 17.0 Co 0.35 Ni 4.0 C 0.07 Cu 4.0 Fe bal.	Annealed	110	150	10	363	Precipitation hardening; heat-resisting type; retains strength up to approx. 600°F

TABLE C.5 (continued) Mechanical Properties of Metals and Alloys:* Typical Composition, Properties, and Uses of Common Materials

CAST IRONS AND CAST STEELS

These alloys are used where large and/or intricate-shaped articles are required or where over-all dimensional tolerances are not critical. Thus the article can be produced with the fabrication and machining costs held to a minimum. Except for a few heat-treatable cast steels, this class of alloys does not demonstrate high-strength qualities.

No.	*Material*	*Nominal composition*	*Form and condition*	*Typical mechanical properties*				*Comments*
				Yield strength (0.2% offset), 1000 lb/sq in.	*Tensile strength, 1000 lb/sq in.*	*Elongation, in 2 in., %*	*Hardness, Brinell*	
	CAST IRONS							
19	Cast gray iron ASTM A48-48, Class 25	C 3.4 Si 1.8 Mn 0.5	Cast (as cast)	—	25 min	0.5 max	180	Engine blocks, fly-wheels, gears, machine-tool bases
20	White	C 3.4 Si 0.7 Mn 0.6	Cast	—	25	0	450	
21	Malleable iron ASTM A47	C 2.5 Si 1.0 Mn 0.55 max	Cast (annealed)	33	52	12	130	Automotives, axle bearings, track wheels, crankshafts
22	Ductile or nodular iron (Mg-containing) ASTM A339 ASTM A395	C 3.4 P 0.1 max Mn 0.40 Ni 1% Mg 0.06 Si 2.5 Fe bal.	Cast Cast (as cast) Cast (quenched, tempered)	53 68 108	70 90 135	18 7 5	170 235 310	Heavy-duty machines, gears, cams, crankshafts
23	Ni-hard type 2	C 2.7 Si 0.6 Mn 0.5 Ni 4.5 Cr 2.0 Fe bal.	Sand-cast Chill-cast (tempered)	— —	55 75	— —	550 625	Strength, with heat- and corrosion-resistance
24	Ni-resist type 2	C 3.0 Si 2.0 Mn 1.0 Ni 20.0 Cr 2.5 Fe bal.	Cast (as cast)	—	27	2	140	
	CAST STEELS							
25	ASTM A27-62 (60-30)	C 0.3 Mn 0.6 Si 0.8 Ni 0.5 Cr 0.4 Mo 0.2		30	60	24	—	Low alloy, medium strength, general application
26	ASTM A148-60 (105-85)			85	105	17	—	High strength; structural application

TABLE C.5 (continued) Mechanical Properties of Metals and Alloys:* Typical Composition, Properties, and Uses of Common Materials

No.	*Material*	*Nominal composition*	*Form and condition*	*Typical mechanical properties*				*Comments*
				Yield strength (0.2% offset), 1000 lb/sq in.	*Tensile strength, 1000 lb/sq in.*	*Elongation, in 2 in., %*	*Hardness, Brinell*	
27	Cast 12 Cr alloy (CA-15)	C 0.15 max Si 1.50 max Ni 1.00 max Mn 1.00 max Cr 11.5–14 Fe bal.	Air-cooled from 1800°F; tempered at 600°F	150	200	7	390	Stainless, corrosion-resistant to mildly corrosive alkalis and acids
			Air-cooled from 1800°F; tempered at 1400°F	75	100	30	185	
28	Cast 29-9 alloy (CE-30) ASTM A296 63T	C 0.30 max Si 2.00 max Ni 8–11 Mn 1.50 max Cr 26–30 Fe bal.	As cast	60	95	15	170	Greater corrosion resistance, especially for oxidizing condition
29	Cast 28-7 alloy (HD) ASTM A297-63T	C 0.50 max Si 2.00 max Ni 4–7 Mn 1.50 max Cr 26–30 Fe bal.	As cast	48	85	16	190	Heat-resistant

SUPER ALLOYS

The advent of engineering applications requiring high temperature and high strength, as in jet engines and rocket motors, has lead to the development of a range of alloys collectively called super alloys. These alloys require excellent resistance to oxidation together with strength at high temperatures, typically 1800°F in existing engines. These alloys are continually being modified to develop better specific properties, and therefore entries in this group of alloys should be considered "fluid". Both wrought and casting-type alloys are represented. As the high temperature properties of cast materials improve, these alloys become more attractive, since great dimensional precision is now attainable in investment castings.

No.	*Material*	*Nominal composition*	*Form and condition*	*Yield strength (0.2% offset), 1000 lb/sq in.*	*Tensile strength, 1000 lb/sq in.*	*Elongation, in 2 in., %*	*Hardness, Brinell*	*Comments*
	NICKEL BASE							
30	Hastelloy X	Co 1.5 max Cr 22.0 W 0.6 C 0.20 max (cast) Fe 18.5 Mo 9.0 C 0.15 max (wrought) Ni bal.	Wrought sheet	52	113.2	43	194	
			Mill-annealed	—	67	17	172	
			As investment cast	46.5	—	—	—	
31	Hastelloy C	Cr 16.0 W 4.0 Mo 17.0 Fe 6.0 C 0.15 max Ni bal.	Sand-cast (annealed)	50	78	5	199	
			Rolled (annealed)	71	130	45	204	
			Investment cast	50	80	10	215	

TABLE C.5 (continued) Mechanical Properties of Metals and Alloys:* Typical Composition, Properties, and Uses of Common Materials

No.	*Material*	*Nominal composition*	*Form and condition*	*Typical mechanical properties*				*Comments*
				Yield strength (0.2% offset), 1000 lb/sq in.	*Tensile strength, 1000 lb/sq in.*	*Elongation, in 2 in., %*	*Hardness, Brinell*	
	NICKEL BASE (Cont.)							
32	Inconel 713C	Ni (+Co) bal. Mo 4.5 Al 6.0 Cr 13.0 Cb 2.0 Ti 0.6	Investment cast	102	120	6	—	
33	In 100	C 18.0 Mo 3.0 Al 55.0 V 1.0 Cr 10.0 Ti 4.7 Co 15.0	Cast					
34	Taz 8	C 125.0 Mo 4.0 W 4.0 Ta 8.0 Cr 6.0 Al 6.0 Zr 1.0 V 2.5	Cast					
35	Nimonic 90	Ni (+Co) 57.00 Mn 0.50 S 0.007 Cu 0.05 Al 1.65 Co 16.90 C 0.05 Fe 0.45 Si 0.20 Cr 20.55 Ti 2.60	Annealed; wrought	90	155	—	260	General elevated temperature applications
36	Inconel X	Ni (+Co) 72.85 Mn 0.65 S 0.007 Cu 0.05 Al 0.75 Cb (+Ta) 0.85 C 0.04 Fe 6.80 Si 0.30 Cr 15.0 Ti 2.50	Annealed Annealed; age-hardened	50 115	115 175	50 25	150 300	
37	Waspaloy	C 0.08 Mo 4.3 Co 13.5 Cr 19.5 Ti 3.0	Cold-rolled	270	275	8	Rc 51	
38	Rene 41	C 0.09 Mo 10.0 Al 1.5 Cr 19.0 Ti 3.1 Co 11.0	Wrought	100	145	—	—	

TABLE C.5 (continued) Mechanical Properties of Metals and Alloys:* Typical Composition, Properties, and Uses of Common Materials

No.	Material	Nominal composition	Form and condition	Typical mechanical properties: Yield strength (0.2% offset), 1000 lb/sq in.	Tensile strength, 1000 lb/sq in.	Elongation, in 2 in., %	Hardness, Brinell	Comments
39	Udimet 700	C 0.08 Cr 15.0 Mo 5.0 Ti 3.5 Al 4.3 Co 18.5	Cold-rolled	280	285	6	Rc 53	
40	T.D. Nickel	Ni 97.5 ThO_2 2.4	Extended and cold-worked	85	100	13	—	High temperature; jet engine parts
	COBALT BASE							
41	Haynes Stellite alloy 25 (L605)	C 0.15 max Cr 20.0 W 15.0 Ni 10.0 Co bal. Mn 1.5	Wrought sheet; mill annealed	63	140	60	244	Wrought products
42	Haynes Stellite alloy 21 AMS 5385 (cast)	C 0.25 Mo 5.5 Ni 2.5 Co bal. Cr 28.5	As investment cast	82	103	8	313 max	For castings

ALUMINUM ALLOYS

Although the strength of aluminum alloys is in general less than that attainable in ferrous alloys or copper-base alloys, their major advantage lies in their high strength-to-weight ratio due to the low density of aluminum. Aluminum alloys have good corrosion resistance for most applications except in alkaline solutions.

No.	Material	Nominal composition	Form and condition	Typical mechanical properties: Yield strength (0.2% offset), 1000 lb/sq in.	Tensile strength, 1000 lb/sq in.	Elongation, in 2 in., %	Hardness, Brinell	Comments
43	3003 ASTM B221	Cu 0.12 Al bal. Mn 1.2	Annealed-O Cold-rolled-H14 Cold-rolled-H18	6 21 27	16 22 29	40 16 10	28 40 55	Good formability, weldable, medium strength; chemical equipment
44	2017 ASTM B221	Mn 0.5 Mg 0.5 Cu 4.0 Al bal.	Annealed-O Heat-treated-T4	10 40	26 62	22 22	45 105	High strength; structural parts, aircraft, heavy forgings
45	2024 ASTM B211	Cu 4.5 Mg 1.5 Mn 0.6 Al bal.	Heat-treated-T4	47	68	19	120	
46	5052 ASTM B211	Cr 0.25 Al bal. Mg 2.5	Annealed-O Cold-rolled and stabilized-H34	13 31	28 38	30 14	47 68	Medium strength, good fatigue properties; street-light standards
47	ASTM B209		Cold-rolled and stabilized-H38	37	42	8	77	

TABLE C.5 (continued) Mechanical Properties of Metals and Alloys:* Typical Composition, Properties, and Uses of Common Materials

No.	*Material*	*Nominal composition*	*Form and condition*	*Typical mechanical properties*				*Comments*
				Yield strength (0.2% offset), 1000 lb/sq in.	*Tensile strength, 1000 lb/sq in.*	*Elongation, in 2 in., %*	*Hardness, Brinell*	
48	7075 ASTM B211	Cu 1.6 Mg 2.5 Cr 0.3 Al bal. Zn 5.6	Annealed-O Heat-treated and artificially aged-T6	15 73	33 83	17 11	60 150	High strength, good corrosion resistance
49	380 ASTM SC84B	Si 9.0 Al bal. Cu 3.5	Die-cast	24	48	3	—	General purpose die casting
50	195 ASTM C4A	Si 0.8 Al bal. Cu 4.5	Sand-cast; heat-treated-T4 Sand-cast; heat-treated and artificially aged-T6	16 24	32 36	8.5 5	60 75	Structural elements, aircraft, and machines
51	214 ASTM G4A	Mg 3.8 Al bal.	Sand-cast-F	12	25	9	50	Chemical equipment, marine hardware, architectural
52	220 ASTM G10A	Mg 10.0 Al bal.	Sand-cast; heat-treated-T4	26	48	16	75	Strength with shock resistance; aircraft

COPPER ALLOYS

Because of their corrosion resistance and the fact that copper alloys have been used for many thousands of years, the number of copper alloys available is second only to the ferrous alloys. In general copper alloys do not have the high-strength qualities of the ferrous alloys, while their density is comparable. The cost per strength-weight ratio is high; however, they have the advantage of ease of joining by soldering, which is not shared by other metals that have reasonable corrosion resistance.

No.	*Material*	*Nominal composition*	*Form and condition*	*Yield strength (0.2% offset), 1000 lb/sq in.*	*Tensile strength, 1000 lb/sq in.*	*Elongation, in 2 in., %*	*Hardness, Brinell*	*Comments*
53	Copper ASTM B152 ASTM B124, B133 ASTM B1, B2, B3	Cu 99.9 plus	Annealed Cold-drawn Cold-rolled	10 40 40	32 45 46	45 15 5	42 90 100	Bus-bars, switches, architectural, roofing, screens
54	Gilding metal ASTM B36	Cu 95.0 Zn 5.0	Cold-rolled	50	56	5	114	Coinage, ammunition
55	Cartridge 70–30 brass ASTM B14 ASTM B19 ASTM B36 ASTM B134 ASTM B135	Cu 70.0 Zn 30.0	Cold-rolled	63	76	8	155	Good cold-working properties; radiator covers, hardware, electrical
56	Phosphor bronze 10% ASTM B103 ASTM B139 ASTM B159	Cu 90.0 Sn 10.0 P 0.25	Spring temper	—	122	4	241	Good spring qualities, high-fatigue strength

TABLE C.5 (continued) Mechanical Properties of Metals and Alloys:* Typical Composition, Properties, and Uses of Common Materials

No.	*Material*	*Nominal composition*	*Form and condition*	*Typical mechanical properties*				*Comments*
				Yield strength (0.2% offset), 1000 lb/sq in.	*Tensile strength, 1000 lb/sq in.*	*Elongation, in 2 in., %*	*Hardness, Brinell*	
57	Yellow brass (high brass)	Cu 65.0 Zn 35.0	Annealed	18	48	60	55	Good corrosion resistance; plumbing, architectural
	ASTM B36		Cold-drawn	55	70	15	115	
	ASTM B134		Cold-rolled (HT)	60	74	10	180	
	ASTM B135							
58	Manganese bronze	Cu 58.5 Zn 39.2	Annealed	30	60	30	95	Forgings
	ASTM B138	Fe 1.0 Sn 1.0	Cold-drawn	50	80	20	180	
		Mn 0.3						
59	Naval brass	Cu 60.0 Zn 39.25	Annealed	22	56	40	90	Condensor tubing; high resistance to salt-water corrosion
	ASTM B21	Sn 0.75	Cold-drawn	40	65	35	150	
60	Muntz metal	Cu 60.0 Zn 40.0	Annealed	20	54	45	80	Condensor tubes; valve stress
	ASTM B111							
61	Aluminum bronze	Cu 92.0 Al 8.0	Annealed	25	70	60	80	
	ASTM B169, alloy A		Hard	65	105	7	210	
	ASTM B124							
	ASTM B150							
62	Beryllium copper 25	Be 1.9 Cu bal.	Annealed, solution-treated	32	70	45	B60 (Rockwell)	Bellows, fuse clips, electrical relay parts, valves, pumps
	ASTM B194	Co or Ni 0.25						
	ASTM B197		Cold-rolled	104	110	5	B81	
	ASTM B196		Cold-rolled	70	190	3	C40	
63	Free-cutting brass	Cu 62.0 Zn 35.5	Cold-drawn	44	70	18	B80 (Rockwell)	Screws, nuts, gears, keys
		Pb 2.5						
64	Nickel silver 18%	Cu 65.0 Zn 17.0	Annealed	25	58	40	70	Hardware, optical goods, camera parts
	Alloy A (wrought)	Ni 18.0	Cold-rolled	70	85	4	170	
	ASTM B122, No. 2		Cold-drawn wire	—	105	—	—	
65	Nickel silver 13% (cast)	Ni 12.5 Pb 9.0	Cast	18	35	15	55	Ornamental castings, plumbing; good machining qualities
	10A	Sn 2.0 Cu bal.						
	ASTM B149, No. 10A	Zn 20.0						
66	Cupronickel 10%	Cu 88.35 Ni 10.0	Annealed	22	44	45	—	Condensor, salt-water piping
	ASTM B111	Fe 1.25 Mn 0.4	Cold-drawn tube	57	60	15	—	
	ASTM B171							

TABLE C.5 (continued) Mechanical Properties of Metals and Alloys:* Typical Composition, Properties, and Uses of Common Materials

No.	*Material*	*Nominal composition*	*Form and condition*	*Typical mechanical properties*				*Comments*
				Yield strength (0.2% offset), 1000 lb/sq in.	*Tensile strength, 1000 lb/sq in.*	*Elongation, in 2 in., %*	*Hardness, Brinell*	
67	Cupronickel	Cu 70.0 Ni 30.0	Wrought					Heat-exchanger process equipment, valves
68	Red brass (cast) ASTM B30, No. 4A	Cu 85.0 Zn 5.0 Pb 5.0 Sn 5.0	As-cast	17	35	25	60	
69	Silicon bronze ASTM B30, alloy 12A	Si 4.0 Fe 2.0 Zn 4.0 Al 1.0 Mn 1.0	Castings					Cheaper substitute for tin bronze
70	Tin bronze ASTM B30, alloy 1B	Sn 8% Zn 4.0	Castings					Bearings, high-pressure bushings, pump impellers
71	Navy bronze		Cast					
	TIN AND LEAD-BASE ALLOYS							
	Major uses for these alloys are as "white"-metal bearing alloys, extruded cable sheathing, and solders. Tin forms the basis of pewter used for culinary applications.							
72	Lead-base Babbitt ASTM B23, alloy 19	Pb 85.0 Sn 5.0 Sb 10.0 As 0.6 Cu 0.5	Chill cast	—	10	5	19	Bearings, light loads and low speeds
73	Arsenical-lead Babbitt ASTM B23, alloy 15	Pb 83.0 Sn 1.0 Sb 16.0 As 1.1 Cu 0.6	Chill cast	—	10.3	2	20	Bearings, high loads and speeds, diesel engines, steel mills
74	Chemical lead	Pb 99.9 Cu 0.06 Bi 0.005 max	Rolled 95%	1.9	2.5	50	5	
75	Antimonial lead (hard lead)	Pb 94.0 Sb 6.0	Chill cast Rolled 95%	— —	6.8 4.1	22 47	(500 kg) 9	Good corrosion resistance and strength
76	Calcium lead	Pb 99.9 Ca 0.025 Cu 0.10	Extruded and aged	—	4.5	25	—	Cable sheathing, creep-resistant pipe
77	Tin Babbitt alloy ASTM B23-61, grade 1	Sb 4.5 Sn bal. Cu 4.5	Chill cast	—	9.3	2	17	General bearings and die casting
78	Tin die-casting alloy ASTM B102-52	Sb 13.0 Sn bal. Cu 5.0	Die-cast	—	10	1	29	Die-casting alloy

TABLE C.5 (continued) Mechanical Properties of Metals and Alloys:* Typical Composition, Properties, and Uses of Common Materials

No.	Material	Nominal composition	Form and condition	*Typical mechanical properties*				Comments
				Yield strength (0.2% offset), 1000 lb/sq in.	Tensile strength, 1000 lb/sq in.	Elongation, in 2 in., %	Hardness, Brinell	
79	Pewter	Sn 91.0 Cu 2.0 Sb 7.0	Rolled sheet, annealed	—	8.6	40	9.5	Ornamental and household items
80	Solder 50–50	Sn 50.0 Pb 50.0	Cast	4.8	6.1	60	14	General-purpose solder
81	Solder	Sn 20.0 Pb 80.0	Cast	3.6	5.8	16	11	Coating and joining, filling seams on automobile bodies

MAGNESIUM ALLOYS

Because of their low density these alloys are attractive for use where weight is at a premium. The major drawback to the use of these alloys is their ability to ignite in air (this can be a problem in machining); they are also costly. Magnesium alloys are used in both the wrought and die-cast forms, the latter being the most frequently used form.

No.	Material	Nominal composition	Form and condition	Yield strength (0.2% offset), 1000 lb/sq in.	Tensile strength, 1000 lb/sq in.	Elongation, in 2 in., %	Hardness, Brinell	Comments
82	Magnesium alloy AZ31B	Zn 1.0 Al 3.0 Mn 0.20 min Mg bal.	Rolled-plate (strain-hardened, then partially annealed)	24	37	18	—	Structural applications of medium strength
			Rolled-sheet (strain-hardened, then partially annealed)	32	42	15	73	
			Annealed	22	37	21	56	
			Extruded	28	38	14	—	
83	Magnesium alloy AZ80A	Zn 0.5 Al 8.5 Mn 0.15 min Mg bal.	Extruded	36	49	11	60	General extruded and forged products
			Extruded (age-hardened)	39	53	6	82	
			Forged (age-hardened)	34	50	6	72	
84	Magnesium alloy AZ92A	Zn 2.0 Al 9.0 Mn 0.10 min Mg bal.	Sand-cast (as cast)	14	24	6	50	
			Sand-cast (solution heat-treated)	14	40	12	55	
			Sand-cast (solution heat-treated and aged)	19	40	5	83	
			Sand-cast (age-hardened)	16	30	18	—	
			Sand-cast and tempered	22	40	3	81	Pressure-tight sand and permanent mold castings; high UTS and good yield strength
85	Magnesium alloy ZK60A	Zn 5.7 Zr 0.55 Mg bal.	Extruded	43	52	12	82	

TABLE C.5 (continued) Mechanical Properties of Metals and Alloys:* Typical Composition, Properties, and Uses of Common Materials

No.	*Material*	*Nominal composition*	*Form and condition*	*Typical mechanical properties*				*Comments*
				Yield strength (0.2% offset), 1000 lb/sq in.	*Tensile strength, 1000 lb/sq in.*	*Elongation, in 2 in., %*	*Hardness, Brinell*	
86	Magnesium alloy AZ91A and AZ91B	Zn 0.6 Mn 0.13 Al 9.0 min Mg bal.	Die-cast (as cast)	22	33	3	67	General die-casting applications
				BERYLLIUM				
87	Beryllium			27	33	1–3	—	Windows, X-ray tubes
			Hot-pressed	38	51			
			Cross-rolled	40	60	10–40	—	Moderator- and reflector-cladding nuclear reactors; heat-shield and structural-member missiles
				60	90			

NICKEL ALLOYS

Nickel and its alloys are expensive and used mainly either for their high-corrosion resistance in many environments or for high-temperature and strength applications. (See Super Alloys, above.)

No.	*Material*	*Nominal composition*	*Form and condition*	*Yield strength (0.2% offset), 1000 lb/sq in.*	*Tensile strength, 1000 lb/sq in.*	*Elongation, in 2 in., %*	*Hardness, Brinell*	*Comments*
88	Nickel (cast)	Ni 95.6 Cu 0.5 Fe 0.5 Mn 0.8 Si 1.5 C 0.8	As cast	25	57	22	110	Good corrosion-resistance applications
89	K Monel	Ni (+Co) C 0.15 65.25 Mn 0.60 Fe 1.00 S 0.005 Si 0.15 Cu 29.60 Al 2.75 Ti 0.45	Annealed	45	100	40	155	High strength and corrosion resistance; aircraft parts, valve stems, pumps
			Annealed, age-hardened	100	155	25	270	
			Spring	140	150	5	300	
			Spring, age-hardened	160	185	10	335	
90	A nickel ASTM B160 ASTM B161 ASTM B162	Ni (+Co) C 0.06 99.40 Fe 0.15 Mn 0.25 Si 0.05 S 0.005 Cu 0.05	Annealed	20	70	40	100	Chemical industry for resistance to strong alkalis, plating nickel
			Hot-rolled	25	75	40	110	
			Cold-drawn	70	95	25	170	
			Cold-rolled	95	105	5	210	
91	Duranickel	Ni (+Co) C 0.15 93.90 Fe 0.15 Mn 0.25 Si 0.55 S 0.005 Al 4.50 Cu 0.05 Ti 0.45	Annealed	45	100	40	160	High strength and corrosion resistance; pump rods, shafts, springs
			Annealed, age-hardened	125	170	25	330	
			Spring	—	175	5	320	
			Spring, age-hardened	—	205	10	370	

TABLE C.5 (continued) Mechanical Properties of Metals and Alloys:* Typical Composition, Properties, and Uses of Common Materials

No.	*Material*	*Nominal composition*	*Form and condition*	*Typical mechanical properties*				*Comments*
				Yield strength (0.2% offset), 1000 lb/sq in.	*Tensile strength, 1000 lb/sq in.*	*Elongation, in 2 in., %*	*Hardness, Brinell*	
92	Cupronickel 55–45 (Constantan)	Cu 55.0 Ni 45.0	Annealed Cold-drawn Cold-rolled	30 50 65	60 65 85	45 30 20	— — —	Electrical-resistance wire; low temperature coefficient, high resistivity
93	Nichrome	Ni 80.0 Cr 20.0						Heating elements for furnaces
94	"S" Monel	Ni 60.0 Cu 29.0 Fe 2.50 max Mn 1.5 max Si 4.0 Al 0.5 max	Sand-casting	80–115	110–145	2	270–350	High-strength casting alloy; good bearing properties for valve seats
	TITANIUM ALLOYS							
	The main application for these alloys is in the aerospace industry. Because of the low density and high strength of titanium alloys, they present excellent strength-to-weight ratios.							
95	Commercial titanium ASTM B265–58T	Ti 99.4	Annealed at 1100 to 1350°F (593 to 732°C)	70	80	20	—	Moderate strength, excellent fabricability; chemical industry pipes
96	Titanium alloy ASTM B265–58T-5 Ti-6 Al-4V		Water-quenched from 1750°F (954°C); aged at 1000°F (538°C) for 2 hr	160	170	13	—	High-temperature strength needed in gas-turbine compressor blades
97	Titanium alloy Ti-4 Al-4Mn		Water-quenched from 1450°F (788°C); aged at 900°F (482°C) for 8 hr	170	185	13	—	Aircraft forgings and compressor parts
98	Ti–Mn alloy ASTM B265–58T-7	Fe 0.5 Ti bal. Mn 7.0–8.0	Sheet	140	150	18	—	Good formability, moderate high-temperature strength; aircraft skin
	ZINC ALLOYS							
	A major use for these alloys is for low-cost die-cast products, such as household fixtures, automotive parts, and trim.							
99	Zinc ASTM B69	Cd 0.35 Zn bal. Pb 0.08	Hot-rolled	—	19.5	65	38	Battery cans, grommets, lithographer's sheet

TABLE C.5 (continued) Mechanical Properties of Metals and Alloys:* Typical Composition, Properties, and Uses of Common Materials

No.	*Material*	*Nominal composition*	*Form and condition*	*Typical mechanical properties*				*Comments*
				Yield strength (0.2% offset), 1000 lb/sq in.	*Tensile strength, 1000 lb/sq in.*	*Elongation, in 2 in., %*	*Hardness, Brinell*	
100	Zilloy-15	Cu 1.00 Zn bal. Mg 0.010	Hot-rolled Cold-rolled	— —	29 36	20 25	61 80	Corrugated roofs, articles with maximum stiffness
101	Zilloy-40	Cu 1.00 Zn bal.	Hot-rolled Cold-rolled	— —	24 31	50 40	52 60	Weatherstrip, spun articles
102	Zamac-5 ASTM 25	Zn (99.99% pure remainder) Al 3.5–4.3 Cu 0.75–1.25 Mg 0.03–0.08	Die-cast	—	47.6	7	91	Die casting for automobile parts, padlocks; used also for die material
	ZIRCONIUM ALLOYS These alloys have good corrosion resistance but are easily oxidized at elevated temperatures in air. The major application is for use in nuclear reactors.							
103	Zirconium, commercial	O_2 0.07 C 0.15 Hf 1.90 Zr bal.	Annealed	40	65	27	B80 (Rockwell)	
104	Zircaloy 2	Hf 0.02 Ni 0.05 Fe 0.15 Other 0.25 Sn 1.46 Zr bal.	Annealed	50	75	22	B90 (Rockwell)	Nuclear power-reactor cores at elevated temperatures

*Compiled from various sources.

TABLE C.6 Miscellaneous Properties of Metals and Alloys

Part a. Pure Metals

At Room Temperature

Common name	*PROPERTIES (TYPICAL ONLY)*						
	Thermal conductivity, Btu/hr ft °F	*Specific gravity*	*Coeff. of linear expansion, μ in./in. °F*	*Electrical resistivity, microhm-cm*	*Poisson's ratio*	*Modulus of elasticity, millions of psi*	*Approximate melting point, °F*
Aluminum	137	2.70	14	2.655	0.33	10.0	1220
Antimony	10.7	6.69	5	41.8		11.3	1170
Beryllium	126	1.85	6.7	4.0	0.024–.030	42	2345
Bismuth	4.9	9.75	7.2	115		4.6	521
Cadmium	54	8.65	17	7.4		8	610
Chromium	52	7.2	3.3	13		36	3380
Cobalt	40	8.9	6.7	9		30	2723
Copper	230	8.96	9.2	1.673	0.36	17	1983
Gold	182	19.32	7.9	2.35	0.42	10.8	1945
Iridium	85.0	22.42	3.3	5.3		75	4440
Iron	46.4	7.87	6.7	9.7		28.5	2797
Lead	20.0	11.35	16	20.6	0.40–.45	2.0	621
Magnesium	91.9	1.74	14	4.45	0.35	6.4	1200
Manganese		7.21–7.44	12	185		23	2271
Mercury	4.85	13.546		98.4			−38
Molybdenum	81	10.22	3.0	5.2	0.32	40	4750
Nickel	52.0	8.90	7.4	6.85	0.31	31	2647
Niobium (Columbium)	30	8.57	3.9	13		15	4473
Osmium	35	22.57	2.8	9		80	5477
Platinum	42	21.45	5	10.5	0.39	21.3	3220
Plutonium	4.6	19.84	30	141.4	0.15–.21	14	1180
Potassium	57.8	0.86	46	7.01			146
Rhodium	86.7	12.41	4.4	4.6		42	3569
Selenium	0.3	4.8	21	12.0		8.4	423
Silicon	48.3	2.33	2.8	1×10^5		16	2572
Silver	247	10.50	11	1.59	0.37	10.5	1760
Sodium	77.5	0.97	39	4.2			208
Tantalum	31	16.6	3.6	12.4	0.35	27	5400
Thorium	24	11.7	6.7	18	0.27	8.5	3180
Tin	37	7.31	11	11.0	0.33	6	450
Titanium	12	4.54	4.7	43	0.3	16	3040
Tungsten	103	19.3	2.5	5.65	0.28	50	6150
Uranium	14	18.8	7.4	30	0.21	24	2070
Vanadium	35	6.1	4.4	25		19	3450
Zinc	66.5	7	19	5.92	0.25	12	787

TABLE C.6 Miscellaneous Properties of Metals and Alloys

Part b. Commercial Metals and Alloys

CLASSIFICATION AND DESIGNATION		*PROPERTIES (TYPICAL ONLY)*					
Material No. (from Table 1-57)	*Common name and classification*	*Thermal conductivity, Btu/hr ft °F*	*Specific gravity*	*Coeff. of linear expansion, μ in./in. °F*	*Electrical resistivity, microhm-cm*	*Modulus of elasticity, millions of psi*	*Approximate melting point, °F*
1	Ingot iron (included for comparison)	42.	7.86	6.8	9.	30	2800
2	Plain carbon steel AISI–SAE 1020	30.	7.86	6.7	10.	30	2760
15	Stainless steel type 304	10.	8.02	9.6	72.	28	2600
19	Cast gray iron ASTM A48–48, Class 25	26.	7.2	6.7	67.	13	2150
21	Malleable iron ASTM A47	—	7.32	6.6	30.	25	2250
22	Ductile cast iron ASTM A339, A395	19	7.2	7.5	60.	25	2100
24	Ni-resist cast iron, type 2	23	7.3	9.6	170.	15.6	2250
29	Cast 28–7 alloy (HD) ASTM A297–63T	1.5	7.6	9.2	41.	27	2700
31	Hastelloy C	5	3.94	6.3	139.	30	2350
36	Inconel X, annealed	9	8.25	6.7	122.	31	2550
41	Haynes Stellite alloy 25 (L605)	5.5	9.15	7.61	88.	34	2500
43	Aluminum alloy 3003, rolled ASTM B221	90	2.73	12.9	4.	10	1200
44	Aluminum alloy 2017, annealed ASTM B221	95	2.8	12.7	4.	10.5	1185
49	Aluminum alloy 380 ASTM SC84B	56	2.7	11.6	7.5	10.3	1050
53	Copper ASTM B152, B124, B133, B1, B2, B3	225	8.91	9.3	1.7	17	1980
57	Yellow brass (high brass) ASTM B36, B134, B135	69	8.47	10.5	7.	15	1710
61	Aluminum bronze ASTM B169, alloy A; ASTM B124, B150	41	7.8	9.2	12.	17	1900
62	Beryllium copper 25 ASTM B194	7	8.25	9.3	—	19	1700
64	Nickel silver 18% alloy A (wrought) ASTM B122, No. 2	19	8.8	9.0	29.	18	2030
67	Cupronickel 30%	17	8.95	8.5	35.	22	2240
68	Red brass (cast) ASTM B30, No. 4A	42	8.7	10.	11.	13	1825
74	Chemical lead	20	11.35	16.4	21.	2	621
75	Antimonial lead (hard lead)	17	10.9	15.1	23.	3	554
80	Solder 50–50	26	8.89	13.1	15.	—	420
82	Magnesium alloy AZ31B	45	1.77	14.5	9.	6.5	1160
89	K Monel	11	8.47	7.4	58.	26	2430
90	Nickel ASTM B160, B161, B162	35	8.89	6.6	10.	30	2625
92	Cupronickel 55–45 (Constantan)	13	8.9	8.1	49.	24	2300
95	Commercial titanium	10	5.	4.9	80.	16.5	3300
99	Zinc ASTM B69	62	7.14	18	6.	—	785
103	Zirconium, commercial	10	6.5	2.9	41.	12	3350

*Compiled from several sources.

TABLE C.7 Composition and Melting Points of Binary Eutectic Alloys:* Binary Alloys and Solid Solutions of Metallic Components

This table represents most of the common binary combinations of metals. For many pairs no eutectic exists; for many others the information is uncertain or unavailable. In a fair number of cases, there is complete mutual solubility in all proportions; hence, there is a smooth temperature vs. composition curve, with no point of inflection from the melting point of one constituent to that of the other. For purposes of comparison, all values must be considered approximate in view of the experimental difficulties and the many sources of data.

Those pairs for which the liquidus curve exhibits more than one cusp are designated by a superscript *a*. In a few cases the cusp selected for this table does not represent the lowest possible melting point for the binary mixture.

Constituents		*Composition*		*Melting point*	
A	*B*	*Mol % B*	*Weight % B*	*K*	*deg F*
Ag	Al	57	25	835	1 044
Ag	As	24	18	813	1 004
Ag	Ca^a	37	18	820	1 017
Ag	Ce^a	80	84	798	977
Ag	Cu	40	28	1 050	1 431
Ag	Ge	25	18	924	1 204
Ag	La^a	72	77	791	964
Ag	Li	99	89	418	293
Ag	Mg^a	83	52	745	882
Ag	Pb	95.3	97.5	577	579
Ag	Pd	25.9	25.6	924	1 204
Ag	Sb	41	44	758	905
Ag	Si	10.5	2.96	1 110	1 539
Ag	Sr^a	77	73	709	817
Ag	Te	65	69	623	662
Ag	Th	7.6	15	1 167	1 641
Ag	Zr	97	93	1 100	1 521
Al	Au^a	59.5	90.0	842	1 056
Al	Ca^a	65	73	818	1 013
Al	Cd	81	90	1 650	2 511
Al	Ce	69	92	928	1 211
Al	Cu^a	17.3	33.0	821	1 018
Al	Fe	32	49.34	1 426	2 107
Al	Ge	29	55	700	801
Al	In	5	18	910	1 179
Al	Mg	70	67.0	710	819
Al	Ni^a	76	87	1 658	2 525
Al	Pt^a	57	90	1 533	2 300
Al	Si	13	13	850	1 071
Al	Th	80	97	1 510	2 259
Al	Zn	88.7	95.0	655	720
As	Co	75	70	1 189	1 681
As	Cu^a	81.6	78.0	958	1 265
As	Fe	75	69	1 103	2 017
As	In	13	18	1 004	1 348
As	Mn	57	49	1 143	1 598
As	Ni^a	63	57	1 077	1 479
As	Sb	80	87	878	1 121
As	Sn^a	40	51	852	1 074
As	Zn^a	20	18	996	1 333
Au	Bi	86.8	85	514	466
Au	Cd	70	57.1	773	932
Au	Ce^a	86	81	793	968
Au	Ge	27	12	629	673
Au	La^a	83	78	834	1 042
Au	Mg	93	62	848	1 067
Au	Mn^a	32	12	1 233	1 760
Au	Na	17	2.3	1 149	1 609
Au	Pb	84	85	488	419
Au	Sb	34.8	24.8	633	680
Au	Si	18.6	3.15	636	685
Au	Sn^a	29.3	19.9	551	532
Au	Te	88	83	689	781
Au	Tl	72	73	404	268
Au	U	14	16	1 128	1 571
B	Hf	13	71	2 130	3 375
B	Ni	57	88	1 263	1 814
B	Ti	7	25	1 700	2 601
B	Zr	88	98	1 920	2 997
Ba	Mg	97	87	891	1 144
Be	Ni	33	76	1 468	2 183
Be	Pu	97	99	910	1 179
Be	Si	33	61	1 363	1 994
Be	Ti	75	94	1 300	2 061
Be	Y	61	94	1 390	2 043
Be	Zr	65	95	1 250	1 791
Bi	Ca	88	58.5	1 059	1 447
Bi	Cd	56	40	420	297
Bi	In^a	78	66	340	153
Bi	K	50	16	615	648
Bi	Mg	85	40	820	1 017
Bi	Na	22	3.0	500	441
Bi	Pb	44	44	397	255
Bi	Sn	57	43	415	288
Bi	Te	90	84	686	775
Bi	Tl^a	53	52	465	378
C	Cr	87	96	1 775	2 736
C	Hf	35	88	3 450	5 751
C	Mo	17	45	2 480	4 005
C	Nb	40	84	3 580	5 985

*Compiled from several sources.

TABLE C.7 (continued) Composition and Melting Points of Binary Eutectic Alloys:* Binary Alloys and Solid Solutions of Metallic Components

Constituents		*Composition*		*Melting point*		*Constituents*		*Composition*		*Melting point*	
A	*B*	*Mol % B*	*Weight % B*	*K*	*deg F*	*A*	*B*	*Mol % B*	*Weight % B*	*K*	*deg F*
C	Ti	36	69	3 050	5 031	Gd	Ni[a]	32	15	943	1 238
C	V	84	96	1 900	2 961	Ge	Mg	38	17	953	1 256
C	W	59	96	2 980	4 905	Ge	Mn[a]	48	41	970	1 287
Ca	Cu	51	62	833	1 040	Hf	Ta	24	24	1 300	1 881
Ca	Mg[a]	32	22	718	833	In	Ni	30	17.97	1 143	1 598
Ca	Na	22	14	983	1 310	In	Sb	68	69	780	945
Ca	Ni	16	22	878	1 121	In	Sn	47	48	390	243
Ca	Sn	19	41	1 010	1 359	Ir	Mo	68	52	2 350	3 771
Cd	Cu	52	38	810	999	Ir	Nb	55	23	2 110	3 339
Cd	In	74	74	400	261	Ir	W	22	12	2 590	4 203
Cd	Pb	71	82	540	513	K	Na	32	21.67	260	−8.6
Cd	Pu	40	59	1 170	1 647	K	Rb	70	84	307	93
Cd	Sb	7.4	8	563	554	K	Sb[a]	68	84	680	765
Cd	Sn	68	69	450	351	K	Tl	84	96	440	333
Cd	Tl	73	83	475	396	La	Mg[a]	38	9.7	970	1 287
Cd	Zn	27	18	540	513	La	Pb[a]	11	15	1 049	1 429
Ce	Cu[a]	28	15	688	779	La	Sn[a]	10	9	993	1 328
Ce	Ru	33	26	923	1 202	La	Tl	16	22	913	1 184
Co	Gd	65	83	913	1 184	Mg	Ni	11	22.98	780	945
Co	Mo	27	38	1 610	2 439	Mg	Pr	4.9	23	858	1 085
Co	Nb	15	22	1 500	2 241	Mg	Pu	15	63	815	1 008
Co	Si[a]	71	54	1 486	2 215	Mg	Sb[a]	86	97	855	1 080
Co	Sn	21	35	1 380	2 025	Mg	Si	53	57	1 223	1 742
Co	Ti[a]	22	19	1 430	2 115	Mg	Sr[a]	70	89	699	799
Co	V	41	38	1 521	2 278	Mg	Th	7	42	855	1 080
Cr	Mo	14	23	1 973	3 092	Mg	Zn	30	53	615	648
Cr	Ni	46	47	1 610	2 439	Mn	Ni	40	42	1 300	1 881
Cr	Ta	13	34	1 950	3 051	Mn	Pd	26	41	1 398	2 057
Cr	Ti	86	85	950	1 251	Mn	Sb	82	91	843	1 058
Cr	V	33	32	2 050	3 231	Mn	Ti[a]	9	7.9	1 460	2 169
Cs	K	50	23	235	−36	Mn	U[a]	75	93	988	1 319
Cs	Na	20.9	4.37	241	−26	Mn	Y[a]	65	75	1 163	1 634
Cs	Rb	50	39	282	48	Mo	Nb	66	65	2 570	4 167
Cu	Ge	34	37	913	1 184	Mo	Ni	64	52	1 590	2 403
Cu	Mg[a]	85.5	69.3	758	905	Mo	Os	21	34	2 650	4 311
Cu	Mn	37	34	1 143	1 598	Mo	Pd	54	57	2 020	3 177
Cu	Pb	15	36	1 230	1 755	Mo	Re	48	64	2 780	4 545
Cu	Pr[a]	69	83	745	882	Mo	Ru	41	42	2 200	3 501
Cu	Sb[a]	63	76	800	981	Mo	Si[a]	17	5.7	2 350	3 771
Cu	Si	30	16	1 075	1 476	Na	Rb	82.1	94.5	269	25
Cu	Te	69	82	617	207	Na	Sb	60	89	678	761
Cu	Ti[a]	27	22	1 133	1 580	Na	Sn	37	75	718	833
Cu	Tl	14.5	35.3	1 357	1 983	Na	Te	55	87	592	606
Cu	U	8.2	25	1 213	1 724	Nb	Ni	58	47	1 450	2 151
Cu	Zr	9.4	13	1 253	1 796	Nb	Pt	54	71	1 970	3 087
Fe	Gd	69	86	1 123	1 562	Nb	Rh	45	31	1 770	2 727
Fe	Mo	21	31	1 725	2 646	Nb	Ru[a]	64	49	2 050	3 231
Fe	Nb	12	18.49	1 643	2 498	Nb	Zr	77	77	2 010	3 159
Fe	Sb	88	94.10	1 021	1 378	Ni	Sb	22	36.90	1 375	2 016
Fe	Si[a]	35	21	1 475	2 196	Ni	Sn	19	32.16	1 403	2 066
Fe	Sn	31	49	1 400	2 061	Ni	Th[a]	35	68	1 303	1 886
Fe	Y	65	75	1 173	1 652	Ni	Ti[a]	39	34	1 390	2 043
Fe	Zr[a]	11	17	1 600	2 421	Ni	V	52	48	1 473	2 192
Ga	Mg[a]	80	58	698	797	Ni	W	20.7	45	1 773	2 732
Ga	Ni	70	66	1 477	2 199	Ni	Zn	69	71	1 148	1 607

TABLE C.7 (continued) Composition and Melting Points of Binary Eutectic Alloys:* Binary Alloys and Solid Solutions of Metallic Components

Constituents		*Composition*		*Melting point*	
A	*B*	*Mol %B*	*Weight %B*	*K*	*deg F*
Pb	Pr	40	31	1 315	1 908
Pb	Pt	5.3	5.0	563	554
Pb	Sb	18	11	520	477
Pb	Sn	73	61	460	369
Pb	Te	85	78	680	765
Pb	Ti	92	74	998	1 337
Pd	Sb	89	90	868	1 103
Pt	Sn	40	29	1 345	1 962
Pu	Zn	73	42	1 100	1 521
Re	W	26	26	3 100	5 121
Sb	Tl	70	80	468	383
Sb	Zn	33	21	780	945
Sb	Zr	82	77	1 700	2 601
Se	Sn	39	49	913	1 184
Se	Tl	26	48	424	304
Si	Th[a]	88	98	1 710	2 619
Si	Ti[a]	86	91	1 600	2 421
Si	Zr[a]	9	24	1 570	2 367
Sn	Te	84	85	678	761
Sn	Tl	31	44	440	333
Sn	Zn	16	9.5	465	378
Te	Tl	30	41	483	410
Th	Ti	40	12	1 463	2 174
Th	Zn[a]	49	21	1 220	1 737
Ti	U	17	51	933	1 220
Ti	Y	6.8	12	1 593	2 408
Ti	Zr	50	66	790	963
U	Zr	70	47	879	1 123

REFERENCES

"Selected Values of Thermodynamic Properties of Metals and Alloys", R. Hultgren, R.L. Orr, P.D. Anderson, K.K. Kelley, John Wiley & Sons, Inc., 1963; a supplement to this publication has been issued periodically by the University of California, 1964–1971.

"Constitution of Binary Alloys", 2nd ed., M. Hansen, McGraw-Hill Book Company, 1958.

"Metals Reference Book", 4th ed., C.J. Smithells, Vol. 2, Butterworth & Co., London, 1967.

"Handbook of Binary Metallic Systems", 2 volumes; translated from Russian, Israel Program for Scientific Translations, Jerusalem. Available from Clearinghouse for Federal Scientific and Technical Information, Springfield, Virginia 22151.

See also *Trans. AIME*, *J. Inst. Metals*, and *Z. Metallkunde*, by indexes.

TABLE C.8 Melting Points of Mixtures of Metals**

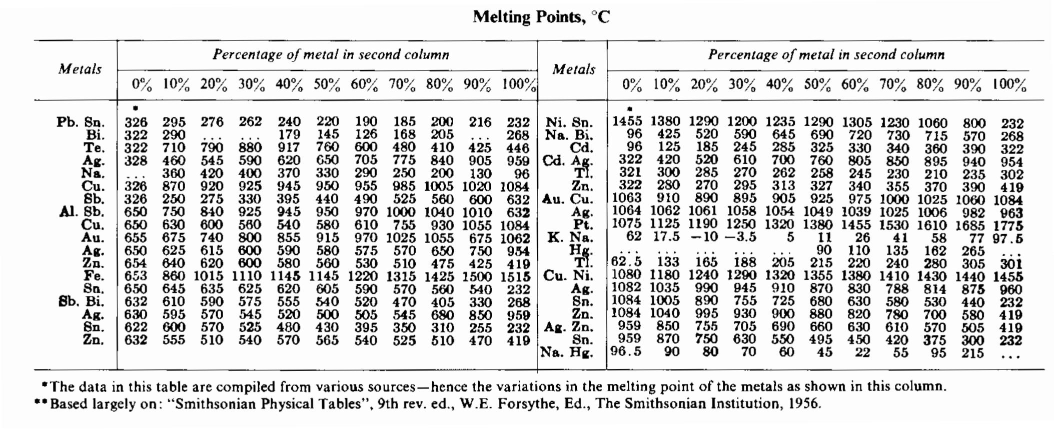

Melting Points, °C

Metals	*Percentage of metal in second column*										
	0% *	10%	20%	30%	40%	50%	60%	70%	80%	90%	100%
Pb. Sn.	326	295	276	262	240	220	190	185	200	216	232
Bi.	322	290	...	...	179	145	126	168	205	...	268
Te.	322	710	790	880	917	760	600	480	410	425	446
Ag.	328	460	545	590	620	650	705	775	840	905	959
Na.	...	360	420	400	370	330	290	250	200	130	96
Cu.	326	870	920	925	945	950	955	985	1005	1020	1084
Sb.	326	250	275	330	395	440	490	525	560	600	632
Al. Sb.	650	750	840	925	945	950	970	1000	1040	1010	632
Cu.	650	630	600	560	540	580	610	755	930	1055	1084
Au.	655	675	740	800	855	915	970	1025	1055	675	1062
Ag.	650	625	615	600	590	580	575	570	650	750	954
Zn.	654	640	620	600	580	560	530	510	475	425	419
Fe.	653	860	1015	1110	1145	1145	1220	1315	1425	1500	1515
Sn.	650	645	635	625	620	605	590	570	560	540	232
Sb. Bi.	632	610	590	575	555	540	520	470	405	330	268
Ag.	630	595	570	545	520	500	505	545	680	850	959
Sn.	622	600	570	525	480	430	395	350	310	255	232
Zn.	632	555	510	540	570	565	540	525	510	470	419
Ni. Sn.	1455	1380	1290	1200	1235	1290	1305	1230	1060	800	232
Na. Bi.	96	425	520	590	645	690	720	730	715	570	268
Cd.	96	125	185	245	285	325	330	340	360	390	322
Cd. Ag.	322	420	520	610	700	760	805	850	895	940	954
Tl.	321	300	285	270	262	258	245	230	210	235	302
Zn.	322	280	270	295	313	327	340	355	370	390	419
Au. Cu.	1063	910	890	895	905	925	975	1000	1025	1060	1084
Ag.	1064	1062	1061	1058	1054	1049	1039	1025	1006	982	963
Pt.	1075	1125	1190	1250	1320	1380	1455	1530	1610	1685	1775
K. Na.	62	17.5	−10	−3.5	5	11	26	41	58	77	97.5
Hg.	...	...	...	...	...	90	110	135	162	265	...
Tl.	62.5	133	165	188	205	215	220	240	280	305	301
Cu. Ni.	1080	1180	1240	1290	1320	1355	1380	1410	1430	1440	1455
Ag.	1082	1035	990	945	910	870	830	788	814	875	960
Sn.	1084	1005	890	755	725	680	630	580	530	440	232
Zn.	1084	1040	995	930	900	880	820	780	700	580	419
Ag. Zn.	959	850	755	705	690	660	630	610	570	505	419
Sn.	959	870	750	630	550	495	450	420	375	300	232
Na. Hg.	96.5	90	80	70	60	45	22	55	95	215	...

*The data in this table are compiled from various sources—hence the variations in the melting point of the metals as shown in this column.

**Based largely on: "Smithsonian Physical Tables", 9th rev. ed., W.E. Forsythe, Ed., The Smithsonian Institution, 1956.

TABLE C.9 Trade Names, Composition, and Manufacturers of Various Plastics

Trade name	*Composition*	*Manufacturer*
Abson	Acrylonitrile-butadiene, ABS polymers	B. F. Goodrich Chemical Co.
Alathon	Polyethylene resins	E. I. du Pont de Nemours & Co., Inc.
Alkor	Furane resin cement	Atlas Minerals & Chemicals Div., The Electric Storage Battery Co.
Amres	Phenolics, urea, and melamine resins	American Marietta Co., Pacific Resins & Chemicals, Inc.
Araldite	Epoxy resins	CIBA Products Co., Div. CIBA Corp.
Atlac	Polyester resins	Atlas Chemical Industries, Inc.
Bakelite	Acrylics, epoxies, phenolics, polyethylenes, copolymers	Union Carbide Corp., Chemicals and Plastics Div.
Bavick-11	Methyl methacrylate and methylstyrene copolymer	J. T. Baker Chemical Co.
Boltaflex	Supported and unsupported flexible vinyl sheeting	The General Tire & Rubber Co.
Boltaron	Rigid polyvinyl chloride sheet	The General Tire & Rubber Co., Chemical & Plastics Div.
Butacite	Polyvinyl butyral resins	E. I. du Pont de Nemours & Co., Inc.
Conolite	Polyester resins and laminates	Shellmar-Betner, Div. Continental Can Co. Woodall Industries, Inc., Conolite Div.
Corvel	Epoxies, vinyls Fusion-bond finishes	The Polymer Corp., Export-Polypenco Div.
Cumar	Paracoumarone-indene resins	Allied Chemical Corp., Plastics Div.
Cycolac	ABS polymers, acrylonitrile-butadiene-styrene copolymers	Marbon Chemical Div., Borg-Warner Corporation
Dacovin	Polyvinyl chlorides	Diamond Shamrock Corp.
Dapon	Diallyl phthalate resins	FMC Corp., Organic Div.
Delrin	Acetal resin and pipe	E. I. du Pont de Nemours & Co., Inc.
Dylan	Polyethylene	Sinclair-Koppers Co.
Dylene	Polystyrene	Sinclair-Koppers Co.
Dylite	Expandable polystyrene	Sinclair-Koppers Co.
Epi-Rez	Epoxy resins	Celanese Coatings Co., Celanese Resin Div.
Epolene	Low molecular-weight polyethylene resins	Eastman Chemical Products, Inc., Sub. Eastman Kodak Company
Epoxical	Epoxy resins	United States Gypsum Co.
Epon	Epoxy resins and curing agents	The Shell Chemical Company, Plastics and Resins Div.
Escon	Polypropylene resins	Enjay Chemical Co., Div. Humble Oil & Refining Company
Estane	Polyurethane materials	B. F. Goodrich Chemical Company
Fluorogreen	Teflon with glass and ceramic fibers, fluorocarbons	John L. Dore Co.
Fluororay	Ceramic-filled fluorocarbons	Raybestos-Manhattan, Inc., Plastic Products Div.
Formica	Melamines	Formica Corp. of American Cyanamid
Forticel	Cellulose propionate sheet films, molding powders	Celanese Plastics Co.
Fortiflex	Polyethylene resins	Celanese Plastics Co.
Fosta-Tuf-Flex	Polystyrene, high-impact	Foster-Grant, Inc.
Furnane	Furanes	Atlas Minerals & Chemicals Div., The Electric Storage Battery Co.
GenEpoxy	Epoxy resins for adhesives, coatings, etc.	General Mills, Inc., Chemical Div.
Genetron	Fluorinated hydrocarbons, monomers, and polymers	Allied Chemical Corp., General Chemical Div.
Geon	Polyvinyl chloride materials	B. F. Goodrich Chemical Co.
Grex	High-density polyethylenes	Allied Chemical Corp., Plastics Div.
Halon	Fluorohalocarbon resins	Allied Chemical Corp.
Hetron	Fire-retardant polyester resin	Hooker Chemical Corp., Durez Plastics Div.
Isothane	Polyurethane foam, ester, and ether	Bernel Foam Products Co., Inc.
Kel-F	Chlorotrifluoroethylene, molding resins, and dispersions	3M Company
Kralac	High-styrene resins, styrene-butadiene copolymers	Uniroyal Chemical, Div. of Uniroyal Inc.
Kralastic	ABS polymers, copolymers	Uniroyal Chemical, Div. of Uniroyal Inc.
Kynar	Polyvinylidene fluoride	Pennsalt Chemical Corp.
Lexan	Polycarbonate resin, film, and sheet	General Electric Company, Plastics Dept.
Lucite	Acrylic resin and syrup	E. I. du Pont de Nemours & Co., Inc.
Lustran	ABS polymers	Monsanto Co.
Lustrex	Styrene molding and extrusion resins	Monsanto Co.
Lytron	Styrene molding and extrusion resins	Monsanto Co.
Madurit	Melamine resins and compounds	Cassella Farbwerke Mainkur, A.G.
Maraglas	Epoxy-casting resin	The Marblette Corporation, Div. of Allied Products
Marlex	Polyethylenes, polypropylenes, copolymers	Phillips Petroleum Co.
Marvinol	Vinyl chloride resins and compounds	Uniroyal Chemical, Div. of Uniroyal Inc.
Merlon	Polycarbonate resins	Mobay Chemical Co.
Micarta	Melamines, phenolics, polyesters	Westinghouse Electric Co., Industrial Micarta Div.
Microthene	Polyethylenes, polyolefins	U.S. Industrial Chemicals Co.
Multrathane	Urethane elastomers	Mobay Chemical Company
Nopcofoam	Polyurethane plastics	Nopco Chemical Co., Plastics Div.
Novodur	Polyacrylonitrile-butadiene-styrene	Farbenfabriken Bayer, A. G.
Opalon	Vinyl chloride resins and compounds	Monsanto Co.
Paraplex	Polyester resins, acrylic-modified polyester resins	Rohm & Haas Company

TABLE C.9 (continued) Trade Names, Composition, and Manufacturers of Various Plastics

Trade name	*Composition*	*Manufacturer*
Permelite	Melamines	Melamine Plastics, Inc., Div. of Fiberlite Corp.
Petrothene	Polyethylene resins, polypropylene resins	U.S. Industrial Chemicals Co.
Piccoflex	Styrene-copolymer resins	Pennsylvania Industrial Chemical Corp.
Piccolastic	Styrene-polymer resins	Pennsylvania Industrial Chemical Corp.
Plaskon	Nylons, melamines, phenolics, polyesters	Allied Chemical Corp.
Pleogen	Alkyds, polyesters, copolymers	Mol-Rez Div., American Petrochemical Corp.
Plexiglas	Acrylics	Rohm & Haas Company
Pliovic	Polyvinyl chlorides	The Goodyear Tire & Rubber Co., Chemical Div.
Plyophen	Phenolic resins	Reichhold Chemicals, Inc.
Poly-Eth	Polyethylene resins	Gulf Oil Corp., U.S. Div. of Gulf Oil Corp.
Polylite	Polyester resins	Reichhold Chemicals, Inc.
Polypenco	Acrylics, chlorinated polyethers, fluorocarbons, nylons, polycarbonates	Polymer Corp.
Resimene	Urea and melamine resins	Monsanto Co.
Resinox	Phenolic resins and compounds	Monsanto Co.
Rhonite	Urea resins	Rohm & Haas Company
Roylar	Polyurethanes	Uniroyal Chemical, Div. of Uniroyal Inc.
Ryertex	Laminated phenolics and rigid polyvinyl chloride extrusions	Joseph T. Ryerson & Son, Inc., Industrial Plastics and Bearings Sales Div.
Super Dylan	Polyethylene	Sinclair-Koppers Co.
Supreme	Polyethylenes	Johns-Manville Company
Sylplast	Urea-formaldehyde compounds	FMC Corp., Organic Chemicals Div.
Teflon	Fluorocarbon resins	E. I. du Pont de Nemours & Co., Inc.
Tenite	Cellulose acetate, cellulose-acetate-polyethylene, polypropylenes, urethane elastomers, copolymers	Eastman Chemical Products, Inc., Sub. Eastman Kodak Co.
Tetran	Fluorocarbons	Pennsalt Chemicals Corp.
Texin	Urethane elastomers	Mobay Chemical Company
Thioment	Polyisoprenes	Atlas Minerals & Chemicals Div., The Electric Storage Battery Co.
Ultrapas	Melamine resins	Dynamit Nobel, A. G.
Ultrathene	Ethylene-vinyl acetates	U.S. Industrial Chemicals Co.
Ultron	Polyvinyl chlorides	Monsanto Co.
Vibrathane	Urethane elastomers	Uniroyal Chemical, Div. of Uniroyal Inc.
Vibrin	Polyester resins	Uniroyal Chemical, Div. of Uniroyal Inc.
Vitel	Polyesters	The Goodyear Tire & Rubber Co., Chemical Div.
Viton	Synthetic rubbers	E. I. du Pont de Nemours & Co., Inc.
Vitroplast	Polyester cements	Atlas Minerals & Chemicals Div., The Electric Storage Battery Co.
Vyron	Polyvinyl chlorides	Industrial Vinyls, Inc.

TABLE C.10 Properties of Commercial Nylon Resins*

Property	*Type 6/6*	*Type 6*	*Type 6/10*	*Type 11*	*Glass-reinforced Type 6/6, 40%*	*MoS_2-filled, $2\frac{1}{2}$%*	*Direct polymerized, castable*
Mechanical							
Tensile strength, psi	11,800	11,800	8200	8500	30,000	10,000 to 14,000	11,000 to 14,000
Elongation, %	60	200	240	120	1.9	5 to 150	10 to 50
Tensile yield stress, psi	11,800	11,800	8500		30,000		
Flexural modulus, psi	410,000	395,000	280,000	151,000	1,800,000	450,000	
Tensile modulus, psi	420,000	380,000	280,000	178,000		450,000 to 600,000	350,000 to 450,000
Hardness, Rockwell	118R	119R	111R	55A	75E–80E	110R–125R	112R–120R
Impact strength, tensile, ft-lb/sq in.	76		160			50–180	80–100
Impact strength, Izod, ft-lb/in. of notch	0.9	1.0	1.2	3.3	3.7**	0.6	0.9
Deformation under load, 2000 psi, 122°F, %	1.4	1.8	4.2	2.02†	0.4§	0.5 to 2.5	0.5 to 1
Thermal							
Heat-deflection temp, °F							
At 66 psi	360	365	300	154	509	400 to 490	400 to 425
At 264 psi	150	152	135	118	502	200 to 470	300 to 425
Coefficient of thermal expansion, per °F	4.5×10^{-5}	4.6×10^{-5}	5×10^{-5}	10×10^{-5}	0.9×10^{-5}	3.5×10^{-5}	5.0×10^{-5}
Coefficient of thermal conductivity, Btu in./hr ft^3 °F	1.7	1.7	1.5				
Specific heat	0.3–0.5	0.4	0.3–0.5	0.58			
Brittleness temp, °F	−112		−166				
Electrical							
Dielectric strength, short time, v/mil	385	420	470	425	480	300 to 400	500 to 600‡
Dielectric constant							
At 60 hz	4.0	3.8	3.9		4.45		3.7
At 10^3 hz	3.9	3.7	3.6	3.3	4.40		3.7
At 10^6 hz	3.6	3.4	3.5		4.10		3.7
Power factor							
At 60 hz	0.014	0.010	0.04	0.03	0.009		0.02
At 10^3 hz	0.02	0.016	0.04	0.03	0.011		0.02
At 10^6 hz	0.04	0.020	0.03	0.02	0.018		0.02
Volume resistivity, ohm-cm	10^{14} to 10^{15}	3×10^{15}	10^{14} to 10^{15}	2×10^{13}	2.6×10^{15}	2.5×10^{13}	
General							
Water absorption, 24 hr, %	1.5	1.6	0.4	0.4	0.6	0.5 to 1.4	0.9
Specific gravity	1.13 to 1.15	1.13	1.07 to 1.09	1.04	1.52	1.14 to 1.18	1.15 to 1.17
Melting point, °F	482 to 500	420 to 435	405 to 430	367	480 to 490	496 ± 9	430 ± 10
Flammability	self ext	self ext	self ext	self ext	self ext	self ext	self ext
Chemical resistance to							
Strong acids	Poor	Poor	Poor	Poor	Poor	Poor	Poor
Strong bases	Good	Good	Good	Fair	Good	Good	Good
Hydrocarbons	Excellent	Excellent	Excellent	Good	Excellent	Excellent	Excellent
Chlorinated hydrocarbons	Good	Good	Good	Fair	Good	Good	Good
Aromatic alcohols	Good	Good	Good	Good	Good	Good	Good
Aliphatic alcohols	Good	Good	Good	Fair	Good	Good	Good

Notes:

Most nylon resins listed in this table are used for injection molding, and test values are determined from standard injection-molded specimens. In these cases a single typical value is listed. Exceptions are MoS_2-filled nylon and direct-polymerized (castable) nylon, which are sold principally in semifinished stock shapes. Ranges of values listed are based on tests on various forms and sizes produced under varying processing conditions.

Because single values apply only to standard molded specimens, and properties vary in finished parts of different sizes and forms produced by various processes, these values should be used for comparison and preliminary design considerations only. For final design purposes the manufacturer should be consulted for test experience with the form being considered. Listed values should not be used for specification purposes.

†2000 psi, 73°F.

‡0.040-in. thick.

**$\frac{1}{2} \times \frac{1}{4}$-in. bar.

§4000 psi, 122°F.

*From: "Nylons", D.D. Carswell, *Machine Design*, 40(29):62, Dec. 12, 1968.

For Conversion factors see Table C.10.

TABLE C.11 Properties of Silicate Glasses*

Most of the commercially produced glass is for windows, bottles, and inexpensive containers; it is a soda-lime-silica glass of fairly uniform composition, similar to glass No. 0080 in the table below and in Table 1-93. The following tables on glasses (Tables 1-92 through 1-103) deal largely with that one-tenth of the glass output for which special properties are required. All data are subject to normal manufacturing variations.

Silica glass is inherently high in viscosity and melting point. These are reduced by fluxes such as Na_2O, K_2O, and B_2O_3. Soda and potash glasses have a high expansion coefficient (column 7), while that of fused silica is very low. Because the borosilicate glasses are intermediate, and their thermal shock resistance is high (e.g., Corning Code 7740 glass), they are widely used for laboratory and kitchen glassware. Aluminosilicate glasses are hard, heat-resisting, and of high chemical durability. Glass hardness (indentation) correlates closely with the elastic modulus (column 14). Lead oxide is also used as flux, with a result of reduced softening point and high refractive index: hence its uses for optical glass and art glass.

Sealing of glass with metal calls for close control of the coefficient of expansion (column 7 and Figure 1-99).

EXPLANATION OF COLUMNS:

Column 5:

B—blown ware
M—multiform
U—panels
P—pressed ware
R—rolled sheet
LC—large castings
S—plate glass
T—tubing and rod

Column 6:

[2] Since weathering is determined primarily by clouding, which changes transmission, a rating for the opal glasses is omitted.

[3] These borosilicate glasses may rate differently if subjected to excessive heat treatment.

Column 8:

Normal service: No breakage from excessive thermal shock is assumed.

Extreme limits: Glass will be very vulnerable to thermal shock. Recommendations in this range are based on mechanical stability considerations only. Tests should be made before adopting final designs. These data are approximate only.

Column 9:

Based on plunging sample into cold water after oven heating. Resistance of 100°C means no breakage if heated to 110°C and plunged into water at 10°C. Tempered samples have over twice the resistance of annealed glass. These data are approximate only.

Column 10:

[4] These data are estimated.

Resistance in °C is the temperature differential between the two surfaces of a tube or a constrained plate that will cause a tensile stress of 1000 psi on the cooler surface.

Column 11:

Viscosity is given in poises. At the strain point the stresses are significantly reduced in a matter of hours, while at the annealing point there is adequate stress reduction in minutes.

Column 12:

Data show relative resistance to sandblasting.

Column 15:

Data at 25°C are extrapolated from high temperature readings and are approximate only.

---

*From: "Properties of Selected Commercial Glasses", Publication B-83, Corning Glass Works.

TABLE C.11 (continued) Properties of Silicate Glasses*

1	2	3	4	5	6			7		8				9		
Glass Code†	Type	Color	Principal Use	Forms Usually Available	Corrosion Resistance			Thermal Expansion 10^{-7}in./in./°C.		Upper Working Temperatures (Mechanical Considerations Only)				Thermal Shock Res. Plates 6″ × 6″		
										Annealed		Tempered		Annealed		
					Weathering	Water	Acid	0-300°C 32-572°F	Room Temp.-Setting Point	Normal Service °C.	Extreme Limit °C.	Normal Service °C.	Extreme Limit °C.	⅛″ Thk. °C.	¼″ Thk. °C.	½″ Thk. °C.
0010	Potash Soda Lead	Clear	Lamp Tubing	T	2	2	2	93	100	110	380			65	50	35
0080	Soda Lime	Clear	Lamp Bulbs	B M T	3	2	2	92	103	110	460	220	250	65	50	35
0120	Potash Soda Lead	Clear	Lamp Tubing	T M	2	2	2	89	98	110	380	—	—	65	50	35
1720	Aluminosilicate	Clear	Ignition Tube	B T	1	1	3	42	52	200	650	400	450	135	115	75
1723	Aluminosilicate	Clear	Electron Tube	B T	1	1	3	46	54	200	650	400	450	125	100	70
1990	Potash Soda Lead	Clear	Iron Sealing	—	3	3	4	124	136	100	310	—	—	45	35	25
2405	Borosilicate	Red	General	B P U			—	43	51	200	480	—	—	135	115	75
2475	Soda Zinc	Red	Neon Signs	T	3	2	2	93	—	110	440	—	—	65	50	35
3320	Borosilicate	Canary	Tungsten Sealing		^{3}1	^{3}1	^{3}2	40	43	200	480	—	—	145	110	80
6720	Soda Zinc	Opal	General	P	^{2}–	1	2	80	92	110	480	220	275	70	60	40
6750	Soda Barium	Opal	Lighting Ware	B P R	^{2}–	2	2	88	—	110	420	220	220	65	50	35
6810	Soda Zinc	Opal	Lighting Ware	B P R	^{2}–	1	2	69	—	120	470	240	270	85	70	45
7040	Borosilicate	Clear	Kovar Sealing	B T	^{3}3	^{3}3	^{3}4	48	54	200	430	—	—	—	—	—
7050	Borosilicate	Clear	Series Sealing	T	^{3}3	^{3}3	^{3}4	46	51	200	440	235	235	125	100	70
7052	Borosilicate	Clear	Kovar Sealing	B M P T	^{3}2	^{3}2	^{3}4	46	53	200	420	210	210	125	100	70
7056	Borosilicate	Clear	Kovar Sealing	B T P	2	2	4	51	57	200	460	—	—	—	—	—
7070	Borosilicate	Clear	Low Loss Electrical	B M P T	^{3}2	^{3}2	^{3}2	32	39	230	430	230	230	180	150	100
7250	Borosilicate	Clear	Seal Beam Lamps	P	^{3}1	^{3}2	^{3}2	36	38	230	460	260	260	160	130	90
7570	High Lead	Clear	Solder Sealing	—	1	1	4	84	92	100	300	—	—	—	—	—
7720	Borosilicate	Clear	Tungsten Sealing	B P T	^{3}2	^{3}2	^{3}2	36	43	230	460	260	260	160	130	90
7740	Borosilicate	Clear	General	B P S T U	^{3}1	^{3}1	^{3}1	33	35	230	490	260	290	180	150	100
7760	Borosilicate	Clear	General	B P	2	2	2	34	37	230	450	250	250	160	130	90
7900'	96% Silica	Clear	High Temp.	B P T U M	1	1	1	8	7	800	1100	—	—	1250	1000	750
7913	96% Silica	Clear	High Temp.	B P R S T	1	1	1	8	7	900	1200	—	—	—	—	—
7940	Fused Silica	Clear	Ultrasonic	U	1	1	1	5.5	7	900	1100	—	—	1250	1000	750
8160	Potash Soda Lead	Clear	Electron Tubes	P T	2	2	3	91	100	110	380		—	65	50	35
8161	Potash Lead	Clear	Electron Tubes	P T	2	1	4	90	97	110	390	—	—	—	—	—
8363	High Lead	Clear	Radiation Shielding	L C	3	1	4	104	112	100	200	—	—	—	—	—
8871	Potash Lead	Clear	Capacitors		2	1	4	102	113	125	300	—	—	55	45	35
9010	Potash Soda Barium	Grey	TV Bulbs	P	2	2	2	89	102	110	380		—		—	—
9700	Borosilicate	Clear	u v Transmission	T U	^{3}1	^{3}1	^{3}2	39	39	220	500	—	—	150	120	80
9741	Borosilicate	Clear	u v Transmission	B U T	^{3}3	^{3}3	^{3}4	39	49	200	390	—		150	120	80

† Corning Glass Works code numbers are used in this table.

TABLE C.11 (continued) Properties of Silicate Glasses*

10	11				12	13	14			15			16			17	18
Thermal Stress Resistance °C.	Viscosity Data†				Impact Abrasion Resistance	Density grams per C.C.	Young's Modulus		Poisson's Ratio	Log$_{10}$ of Volume Resistivity			Dielectric Properties at 1 Mc and 20°C			Refractive Index Sod. D Line (.5893 Microns)	Glass Code
	Strain Point °C.	Annealing Point °C.	Softening Point °C.	Working Point °C.			(10^{6}lb./sq. in)	(10^{6}kg/cm^2)		25°C. 77°F	250°C. 482°F	350°C. 662°F	Power Factor	Dielectric Const.	Loss Factor		
19	395	435	625	985	0.8	2.86	8.9	0.63	.21	17.+	8.9	7.0	.16%	6.7	1.%	1.539	0010
17	470	510	695	1005	1.2	2.47	10.0	0.70	.24	12.4	6.4	5.1	.9	7.2	6.5	1.512	0080
20	395	435	630	980	0.8	3.05	8.6	0.60	.22	17.+	10.1	8.0	.12	6.7	.8	1.560	0120
28	670	715	915	1190	2.0	2.52	12.7	0.89	0.25	—	11.4	9.5	.38	7.2	2.7	1.530	1720
25	670	710	910	1175	2.0	2.64	12.5	0.88	0.25	.	13.5	11.3	.16%	6.3	1.0%	1.547	1723
14	330	360	500	755	—	3.47	8.4	0.59	.25		10.1	7.7	.04	8.3	.33		1990
[4]37	500	530	770	1085	—	2.50	9.9	0.70	0.21	—	—	.	—		—	1.507	2405
[4]17	440	480	690	1040	—	2.59	10.0	0.70	—	—	7.8	6.2		—		1.511	2475
[4]40	500	540	780	1155	—	2.27	9.4	0.66	0.19	—	8.6	7.1	.30	4.9	1.5	1.481	3320
19	510	550	775	1010	—	2.58	10.2	0.72	.21	—	—	—	—	—	—	1.507	6720
[4]18	445	485	670	1040	—	2.59	—	—		—	—	—	—	—		1.513	6750
[4]23	490	530	770	1010	—	2.65	—	—	—	—	—	—	.	—	—	1.508	6810
37	450	490	700	1080	—	2.24	8.6	0.60	.23	—	9.6	7.8	.20	4.8	1.0	1.480	7040
39	460	500	705	1025	—	2.24	8.7	0.61	.22	16.	8.8	7.2	.33	4.9	1.6	1.479	7050
41	435	480	710	1115	—	2.28	8.2	0.58	.22	17.	9.2	7.4	.26	4.9	1.3	1.484	7052
34	470	510	720	1045	—	2.29	9.2	0.65	.21	—	10.2	8.3	.27	5.7	1.5	1.487	7056
66	455	495	—	1070	4.1	2.13	7.4	0.52	.22	17.+	11.2	9.1	.06	4.1	.25	1.469	7070
48	490	540	780	1190	3.2	2.24	9.2	0.65	.20	15.	8.2	6.7	.27	4.7	1.3	1.475	7250
21	340	365	440	560	—	5.42	8.0	0.56	.28	—	10.6	8.7	.22	15.	3.3	—	7570
49	485	525	755	1140	3.2	2.35	9.1	0.64	.20	16.	8.8	7.2	.27	4.7	1.3	1.487	7720
53	515	565	820	1245	3.1	2.23	9.1	0.64	.20	15.	8.1	6.6	.50	4.6	2.6	1.474	7740
52	480	525	780	1210	—	2.23	9.1	0.64	—	17.	9.4	7.7	.18	4.5	.79	1.473	7760
202	820	910	1500	—	3.5	2.18	10.0	0.70	.19	17.	9.7	8.1	.05	3.8	.19	1.458	7900'
211	820	910	1500	—	3.5	2.18	9.6	0.67	.19	—	9.7	8.1	.04	3.8	0.15	1.458	7913
290	990	1050	1580	—	3.6	2.20	10.5	0.74	.16	—	11.8	10.2	.001	3.8	.0038	1.459	7940
[4]18	395	435	630	975	—	2.98	—	—	—	—	10.6	8.4	.09	7.0	.63	1.553	8160
22	400	435	600	860	—	4.00	7.8	0.55	.24	—	12.0	9.9	.06	8.3	0.50	1.659	8161
19	300	315	380	460	—	6.22	7.4	0.52	.27	—	9.2	7.5	.19	17.0	3.2	1.97	8363
17	350	385	525	785	—	3.84	8.4	0.59	.26	—	11.1	8.8	.05	8.4	.42	—	8871
18	405	445	650	1010	—	2.64	9.8	0.69	.21	—	8.9	7.0	.17	6.3	1.1	1.507	9010
45	520	565	805	1200	—	2.26	9.6	0.67	.20	15.	8.0	6.5	—	—	—	1.478	9700
55	410	450	705		—	2.16	7.2	0.51	.23	17.+	9.4	7.6	—	—	—	1.468	9741

†Viscosities at these four temperatures are approximately as follows: $10^{14.5}$ poises at the strain point, 10^{13} poises at the annealing point, $10^{7.8}$ poises at the softening point, at 10^4 poises at the working point.

TABLE C.12 Properties of Window Glass*: Transmittance of Sheet and Plate Glass

Type or tint	*Nominal thickness, in.*	*Weight, lb/ft²*	*Transmittance*	
			Total visible daylight, %	*Direct 90° solar energy, %*
Sheet	$\frac{1}{16}$	0.81	91	89
Sheet	$\frac{5}{64}$	1.00	91	88
Sheet	$\frac{3}{32}$	1.22	90	87
Sheet	$\frac{1}{8}$	1.64	90	86
Sheet	$\frac{3}{16}$	2.47	89	84
Sheet	$\frac{7}{32}$	2.85	89	82
Plate or float	$\frac{1}{8}$	1.64	90	86
Plate or float	$\frac{1}{4}$	3.28	88	79
Plate or float	$\frac{5}{16}$	4.09	88	77
Plate or float	$\frac{3}{8}$	4.91	87	74
Plate or float	$\frac{1}{2}$	6.55	86	70
Plate or float	$\frac{5}{8}$	8.18	85	65
Plate or float	$\frac{3}{4}$	9.83	83	60
Plate or float	$\frac{7}{8}$	11.45	81	55
Plate or float	1	13.13	79	49
Gray[a]	$\frac{1}{4}$	3.28	43	46
Bronze[a]	$\frac{1}{4}$	3.28	49	45
Green[a]	$\frac{1}{4}$	3.28	75	46
Double[b]	$\frac{1}{4}$ each	6.56	78	—

Note: Many types of glass are available, including tempered heat-strengthened glass, laminated shatter-proof glass, conductive-coated glass, reflective-coated glass. Several double-pane combinations are offered.

Direct 90° transmittance of solar ultraviolet radiation through non-tinted window glass is about 85 percent as high as the values for total solar energy transmittance. Ultraviolet transmittance of gray or bronze glass is lower.

Infrared transmittance is considerably lower than visual transmittance. This is significant in view of the large percentage of infrared radiation from most sources.

Visible reflectance of untinted glass is about 8 percent.

Approximate shading coefficients, ASHRAE, $\frac{1}{4}$-in. glass only: clear, 0.93; gray, 0.67; bronze, 0.65; green, 0.67.

Overall heat transfer coefficient of window area (air to air) is usually assumed to be 1.0 Btu/ft² hr, but it is lower if there is no wind.

For other data on shading coefficients, spectral transmittance, coated glass, special glasses, etc., see Tables I-91, 2-19, and 7-19.

[a] Transmittance of tinted glass depends on depth of tint.

[b] Two $\frac{1}{4}$-in. panes with $\frac{1}{2}$-in. air space, sealed.

---

*Tables compiled from several sources.

TABLE C.13 Properties and Uses of American Woods*

Species	*Specific gravity*		*Characteristics*	*Uses*	*Weight*		
	Green	*Dry*			*lb/cu ft, green*	*lb/cu ft, air-dry 12%*	*lb/1000 board ft, air-dry 12%*
Alder, red	0.37	0.41	Low shrinkage; moderate in strength, shock resistance, hardness, and weight†	Furniture; sash; doors; millwork	46	28	2330
Ash, black	0.45	0.49	Light in weight†	Cabinets; veneer; cooperage, containers	52	34	2830
Ash, Oregon	0.50	0.55	Similar to but lighter than white ash†	Similar to white ash	46	38	3160
Ash, white	0.54	0.58	Heavy; hard; stiff; strong; high shock resistance†	Handles; ladder rungs; baseball bats; farm implements; car parts	48	41	3420
Bald cypress (Southern cypress)			Moderate in strength, weight, hardness, and shrinkage**	Building construction; beams; posts; ties; tanks; ships; paneling	51	32	2670
Beech, American	0.56	0.64	Heavy; high strength, shock resistance, and shrinkage; uniform texture†	Flooring; furniture; handles; kitchenwear; ties (treated)	54	45	3750
Birch	0.57	0.63	Heavy; high strength, shock resistance, and shrinkage; uniform texture†	Interior finish; dowels; ties (treated); veneer; musical instruments	57	44	3670
Cottonwood	0.37	0.40	Uniform texture; does not split readily; moderate in weight, strength, hardness, and shrinkage	Crates; trunks; car parts; farm implements	49	28	2330
Douglas fir	0.41	0.44	Moderate in strength, weight, shock resistance, and shrinkage‡	Building and construction; poles; veneer; plywood; ships; furniture; boxes	38	34	2830
Elm	0.57	0.63	Moderate in strength, weight, and hardness; high in shock resistance and shrinkage; good in bending†	Cooperage; baskets; crates; veneer; vehicle parts	54	34	2920
Hemlock, Eastern	0.38	0.40	Moderate in weight, strength, and hardness†	Building and construction; boxes	50	28	2330
Hemlock, Western	0.38	0.42	Moderate in weight, strength, and hardness†	Sash; doors; posts; piles; building and construction	41	29	2420
Hickory, true	0.65	0.73	High toughness, hardness, shock resistance, strength, and shrinkage†	Dowels; spokes; poles; shafts; gymnasium equipment	63	51	4250
Incense cedar	0.35		Uniform texture; easy to season; low shrinkage; shock resistance, weight, and stiffness**	Lumber; fence posts; ties; poles; shingles	45		
Larch, Western	0.48	0.52	Moderate in strength, weight, shock resistance, hardness, and shrinkage‡	Doors; sash; posts; pilings; building and construction	48	36	3000

TABLE C.13 (continued) Properties and Uses of American Woods*

Species	*Specific gravity*		*Characteristics*	*Uses*	*Weight*		
	Green	*Dry*			*lb/cu ft, green*	*lb/cu ft, air-dry 12%*	*lb/1000 board ft, air-dry 12%*
Locust, black	0.66	0.69	High in shock resistance, weight, and hardness; very high strength; moderate shrinkage**	Mine timbers; posts; poles; ties	58	48	4000
Maple	0.44	0.48	High in hardness, weight, strength, shock resistance, and shrinkage; uniform texture†	Flooring; furniture; trim; spools; farm implements	54	40	3330
Oak, red and white	0.57	0.63	High in hardness, weight, strength, shock resistance, and shrinkage; red†, white‡	Trim; ships; flooring; ties; furniture; cooperage; piles	64	44	3670
Pine, jack			Coarse texture; low strength, stiffness, shock resistance, and shrinkage	Box lumber; fuel; mine timber; ties; poles; posts			
Pine, lodgepole	0.38	0.41	Moderate in weight, hardness, strength, shock resistance, and shrinkage; easy to work‡	Poles; mine timber; ties; construction	39	29	2420
Pine			High shrinkage; moderate strength, stiffness, hardness, and shock resistance	General construction; ties; poles; posts			
Pine, Ponderosa	0.38	0.40	Moderate in weight, shock resistance, shrinkage, and hardness; easy to work†	Building; paneling; sash; frames	45	28	2330
Pine, S. yellow	0.47	0.51	Moderate in shock resistance, shrinkage, and hardness; high in strength‡	Building and construction; poles; pilings; boxes	55	41	3420
Pine, sugar	0.35	0.36	Low shock resistance; easy to work; moderate strength†	Sash; counters; blinds; patterns	52	25	2080
Pine, Western white	0.36	0.38	Moderate in strength, shock resistance, shrinkage, and hardness; easy to work†	Building and construction; patterns; boxes	35	27	2250
Red cedar, Eastern and Western	0.44	0.47	High shock resistance; low stiffness and shrinkage; moderate in strength and hardness**	Fence posts; closet liners; chests; flooring	37	37	2750
Redwood	0.38	0.40	Low shrinkage; medium in weight, strength, hardness, and shock resistance**	Posts; doors; interiors; cooling towers	50	28	2330
Spruce, Eastern	0.38	0.40	Moderate in hardness, shock resistance, weight, shrinkage, and strength†	Building; millwork; boxes; ladders	34	28	2330

TABLE C.13 (continued) Properties and Uses of American Woods*

Species	*Specific gravity*		*Characteristics*	*Uses*	*Weight*		
	Green	*Dry*			*lb/cu ft, green*	*lb/cu ft, air-dry 12%*	*lb/1000 board ft, air-dry 12%*
Spruce, Engelmann	0.31	0.33	Generally straight grained; light in weight; low strength as a beam or post; low shock resistance; moderate shrinkage	Mine timber; ties; poles; flooring; studding; paper	39	23	1920
Spruce, Sitka	0.37	0.40	Moderate in weight, hardness, strength, shock resistance, and shrinkage†	Important in boat and plane construction; sash; doors; boxes; siding	33	28	2330
Sycamore	0.46	0.49	High shrinkage; moderate in weight, strength, hardness, and shock resistance†	Boxes; ties; posts; veneer; flooring; butcher blocks	52	34	2830
Tamarack	0.49	0.53	Coarse texture; moderate in strength, hardness, shrinkage, and shock resistance	Ties; mine timber; posts; poles; tanks; scaffolding	47	37	3080
Tupelo			Uniform texture; moderate in strength, hardness, shock resistance; high shrinkage; interlocked grain makes splitting difficult†	Flooring; planking; crates; furniture			
Walnut, black	0.51	0.55	Moderate shrinkage; high weight, strength, hardness, and shock resistance; easily worked and glued**	Gun stocks; cabinets; plywood; furniture; veneer	58	38	3170
White cedar	0.31	0.32	Low shrinkage, weight, shock resistance, and strength; soft; easily worked**	Poles; posts; ties; tanks; ships	24	23	1920
Willow, black			High strength and shock resistance; low beam strength and weight; interlocked grain	Lumber; veneer; charcoal; furniture; sub-flooring; studding			

†Decay resistance low.
‡Decay resistance medium.
**Decay resistance high.
*From: "Materials Data Book", E.R. Parker, McGraw-Hill Book Company, 1967, pp. 252–255.

Note: For weight-density in kg/m^3, multiply value in lb/ft^3 by 16.02.

TABLE C.14 Properties of Natural Fibers*

Because there are great variations within a given fiber class, average properties may be misleading. The following typical values are only a rough comparative guide.

Name	*Specific gravity*	*Tenacity, g/denier*	*Tensile strength, 10^3 psi*	*Elongation at break (dry), %*	*Standard regain, % of dry*[b]	*Fiber diameter, microns*	*Fiber length, in.*	*Fiber shape and kind*	*Resistant to*
ANIMAL ORIGIN									
Wool	1.32	1.0–1.7	17–29	23–35	15–18	17–40	1.5–5	Oval, crimped, scales	Age, weak acids, solvents
Silk	1.25	3.5–5	90	20–25	10	10–13		Flexible, soft, smooth	Heat, solvents, weak acids, wear
Cashmere						15–16	1–4	Round, scales, soft	
Mohair	1.32	1.2–1.5		30	13	24–50	6–12	Round, silky	Wear, age, solvents, weak acids
Camel hair	1.32	1.8		40	13	10–40	1–6	Oval, striated	Age, solvents
VEGETABLE ORIGIN									
Cotton	1.54	2–5	30–120	5–11	7.5–8.5	10–20	0.5–2	Flat, convoluted, ribbon	Age, heat, washing, wear, solvents, alkalies, insects
Jute (bast)	1.5		50	1–1.5	14	15–20		Woody, rough, polygon	
Sisal (leaf)	1.49	2.2	75	2–2.5	13	10–30	Strand 30–40	Stiff, straight	
Flax (bast)	1.52	4–7		2–3	12	15–18	Strand 40–50	Soft, fine	Age, solvents, washing, insects, weak acids, and alkalies
Kenaf (bast)			45			15–30		Polygon or oval	
Hemp (bast)	1.48			2		18–25	Strand 30–70	Polygon or oval, irregular	
Henequen (leaf)			60				Strand 30–60	Finer than sisal	
Abaca (leaf) (Manila)	1.48	2.3–2.9	100	2–3	13		Strand 30–120		
MINERAL ORIGIN									
Asbestos	2.5		40–200			Various	0.5–10	Smooth, straight	Heat to 400 deg C, acids, chemicals, organisms
Glass[a]	2.5	7–12	200–500	3–4.5	0	Various		Circular, smooth	Chemicals, insects
Silicate[a] (Ca, Al, Mg)	2.85				0				Heat to 900 deg C, most chemicals, insects, rot

Note: Wide variations may be expected, especially for different grades of cotton. Wet strength is lower (for rayon, very much lower), but it depends on the duration of soaking. The strength of yarn is only a fraction of the cumulative strength of all individual fibers.

Most fibers exhibit relaxation of stress at constant strain and also increase in elongation at constant load (creep). The stress-strain curve is greatly affected by the rate of extension. When the stress is removed, there is a quick elastic recovery, a delayed recovery, and a permanent set. Hence the elastic behavior of any fiber depends on its stress-strain history. The elastic recoveries of nylon and wool are high; those of cotton, flax, and rayon are much lower.

The heat capacity (specific heat) of most fibers is about one-third that of water.

Other fibers: Fur hair is slightly coarser than silk fibers. Camel and llama hairs are almost as coarse as wool but only about one-third the size of human hair. Horse hair is over 100 microns; hog bristles, over 200 microns. Jute, sisal, and hemp are intermediate between cotton and wool. These are rough average sizes, and many natural fibers range 50% above or below such averages.

[a] Here classified as natural fibers for convenience, although they are man-made by processing.

[b] Expected equilibrium moisture regain of dry fiber, in percent of dry weight, when exposed in air at 70 deg F, 65% relative humidity.

*Compiled from several sources.

TABLE C.15 Properties of Manufactured Fibers[*]

Chemical class; common name (sources)	*Specific gravity*	*Tenacity, g/denier*	*Tensile strength, 10^3 psi*	*Elongation at break, %*	*Regain (standard)*	*Softening point, deg C*	*Melting point, deg C*	*Flammability*	*Brittleness temp, deg C*
CELLULOSE FIBERS (NATURAL)									
Acetate	1.30	1.–1.3	18–25	20–30	6.5	140	230	Melts and burns	
Triacetate	1.32	1.2–1.4	20–28	25–30	3–4.5	225	300	Melts and burns	
Viscose rayon	1.51	2–2.6	30–46	17–25	13.		200[a]	Burns readily	
High-tenacity viscose	1.53	3–5	60–80	10–12	10		200[a]	Burns readily	< −114
Polynosic viscose	1.53	3–5	60–80	8–20	7		200[a]	Burns readily	
Cuprammonium rayon (cupro)	11.52	1.7–2.3	30–45	10–17	12.5		250[a]	Burns readily	
PROTEIN FIBERS (NATURAL)									
Animal: casein (milk)	1.3	1.0	15	60–70	14	100	150	Slow	
Vegetable—seed: soybeans, peanuts, corn	1.3	0.7–0.9	11–14	40–60	11–15	150	250	Slow	
Vegetable—latex: rubber (vulcanized)	1.0	0.4–0.6	4–7	700–900	0	300		Burns	−60
SYNTHETIC FIBERS									
Polyacrylonitrile (acrylic)	1.17	2–5	50–75	25–40	2	190	260	Burns	
Polyamide (nylon)	1.14	4–9	70–120	20–40	4	200	215–250	Slow	< −100
Polyester (PET dacron)	1.38	4–8	70–120	10–50	0.4	225	250–290	Low	
Polyethylene (olefin, low density)	0.92	3–6	40–70	25–40	0.15	90–120	120	Slow	−114
Polyethylene (olefin, high density)	0.95	5–7	60–80	10–20	0.01	120–130	140	Slow	−114
Polypropylene (olefin)	0.91	4.5–8	45–80	15–30	0–0.5	145	160–170	Self-ext. low	−70
Polyurethane (spandex)	1.1	0.5–1.0	7–16	500–700	1.0	190	250	Burns	
Polyvinyl chloride (PVC)	1.38	0.7–2	12–17	100–125	0.1	70	140[a]	No; chars	< −100
Polyvinyl alcohol (PVA)	1.3	3–7	60–90	15–28	5	230	240	Slow	
Polyvinylidene chloride (saran)	1.7	2	40	20–30	0.1	115–135	170	No	
Polytetrafluoroethylene (PTFE)	2.1	1.2–1.4	33	15–30	0	225	300[a]	No	

Note: Mechanical properties are for room temperature and humidity and based on unstressed cross section.

[a] Decomposition; does not melt.

[*] Compiled from several sources.

TABLE C.16 Properties of Rubbers and Elastomers*

Elastomers cannot be classified in any brief and simple manner, nor are they well characterized by the usual mechanical tests. The terms *rubber* and *synthetic rubber* are loosely applied to a great variety of elastic materials, from pure gum natural rubber and pure synthetics to cured, compounded, filled, and even reinforced products.

ASTM designations (D1418) by chemical polymer description are used in the following table; yet within each class the properties can vary widely, depending on the exact composition, heat treatment service temperature, and application. Typical uses, such as rubber springs and cushioning, permit an almost unlimited number of combinations of design variables.

Mechanically, rubbers may be expected to lose strength rapidly with increase in temperature, to show a large hysteresis in stress-strain behavior, to exhibit marked creep and set, and to be greatly affected by rates of load application or frequency of repeated stress. "Heat build-up", i.e., increase in temperature in service, as well as deterioration from environment (sunlight, oils, ozone, etc.) will reduce the valuable properties of many rubbers, both natural and synthetic.

The following data apply to typical samples of commercial elastomers for common uses.

KEY:

A—Acetone
B—Benzene
C—Carbon tetrachloride
D—Carbon disulfide
E—Phenol
F—Sulfur compounds
G—Glycerol or glycol
H—Hexane
I—Acids
J—Alkalies
K—Ketones
L—Alcohols
M—Ammonia
N—Turpentine
O—Coal derivatives; bitumens
P—Petroleum products
R—Aromatics
S—Salts
T—Heat or high temperature
U—Ultraviolet
V—Vegetable oils
W—Weathering
X—Oxidation
Y—Aging
Z—Ozone

Chemical name	*Polyisoprene*	*Butadiene*	*Styrene-butadiene*	*Acrylonitrile butadiene*
Other names	*Natural (or synthetic) rubber NR (IR)*	*BR Cis 4*	*Buna S Styrene SBR, GR-S*	*Nitrile, Buna N Hycar NBR, GR-A*
CHEMICAL AND PHYSICAL				
Specific gravity	0.93	1.0	1.0	1.0
Specific heat	0.40	0.45	0.40	0.47
Thermal conductivity				
W/cm·K	0.001 7	0.002 5	0.002 6	0.002 5
Btu/hr·ft·deg F	0.10	0.14	0.15	0.14
Service temperature, deg C				
min	−25	−40	−20	−20
max	90	90	75	110
Solvents, softeners	D,K,P,V	D,H,N,P	K,P,R,V	C,K,O,R
Resistant to	A,I,J,L	G,I,J,W,Y	G,I,L,S,X	G,I,K,L,P,S, T,V,W
Swelled by	D,P,V	A,P,V	P,V	A,E,N
MECHANICAL AND ELECTRICAL				
Tensile strength				
kg/cm^2 (max)	300.	210.	210.	295.
kpsi (max)	4.3	3.0	3.0	4.2
Elongation at break, %	600.	700.	600.	600.
Vol. resistivity, ohm-cm	10^{15}	10^{15}	10^{14}	10^{10}
Dielectric strength				
kV/cm	235		235	185
V/mil	600.		600.	475.
Dielectric constant	3.0	2.3	2.8	3.0
Power factor (50–100 Hz)	0.003	0.005	0.005	0.007
Rebound	Good	Good	Fair	Good
COMPARATIVE RATINGS—RESISTANCE TO				
Abrasion	Good	Excellent	Good	Excellent
Cold flow (set)	Excellent		Good	Good
Tearing	Good		Poor	Fair
Air permeability	Fair	Good	Fair	Excellent
Oxidation	Fair	Fair	Fair	Fair
Flame	Poor		Poor	Poor

*Compiled from several sources.

TABLE C.16 (continued) Properties of Rubbers and Elastomers*

Chemical name	*Polychloroprene*	*Isobutylene-isoprene*	*Polysulfide*	*Polymethane*
Other names	*Neoprene*[a] *CR, GR-M*	*Butyl* *IIR, GR-I*	*Thiokol*[a] *PS, GR-P*	*Adiprene*[a] *PU*
CHEMICAL AND PHYSICAL				
Specific gravity	1.25	0.95	1.4	1.2
Specific heat	0.5	0.45	0.31	0.45
Thermal conductivity				
W/cm·K	0.002 1	0.001 3	0.003	0.001 3
Btu/hr·ft·deg F	0.12	0.075	0.17	0.075
Service temperature, deg C				
min	−20	−40	−15	−35
max	100	120	90	120
Solvents, softeners	A,B,C,D,I,N,R	D,P	C	
Resistant to	G,L,P,S,T,U,V, W,Y,Z	E,G,J,S,U,V, W,X,Y,Z	L,P,U,Z	P,V,X,Z
Swelled by	C,D,N,R	D,H,P	C,R	B,C,K,R
MECHANICAL AND ELECTRICAL				
Tensile strength				
kg/cm^2 (max)	240.	175.	90.	350.
kpsi (max)	3.5	2.5	1.3	5.0
Elongation at break, %	800.	700.	500.	550.
Vol. resistivity, ohm-cm	10^{11}	10^{17}	10^{8}	10^{11}
Dielectric strength				
kV/cm	195	295	125	195
V/mil	500	750	325	500
Dielectric constant	7.	2.4	8.	7.
Power factor (50–100 Hz)	.04	0.004	0.02	0.04
Rebound	Good	Poor	Poor	
COMPARATIVE RATINGS—RESISTANCE TO				
Abrasion	Excellent	Fair	Poor	Excellent
Cold flow (set)	Excellent	Fair	Poor	Poor
Tearing	Good	Good	Poor	Excellent
Air permeability	Good	Excellent	Good	Excellent
Oxidation	Good	Good	Good	Good
Flame	Excellent	Poor	Poor	Poor

[a] Proprietary.

Appendix D. Gases and Vapors

TABLE D.1 SI Units — Definitions, Abbreviations and Prefixes

BASIC UNITS—MKS

Length	meter	m	Electric current	ampere	A
Mass	kilogram	kg	Thermodynamic temperature	kelvin	K
Time	second	s	Luminous intensity	candela	cd

DERIVED UNITS

Property	*Units*†	*Abbreviations and dimensions*	
Acceleration	meter per second squared	m/s^2	
Activity (of radioactive source)	1 per second	s^{-1}	
Angular acceleration	radian per second squared	rad/s^{-1}	
Angular velocity	radian per second	rad/s	
Area	square meter	m^2	
Density	kilogram per cubic meter	kg/m^3	
Dynamic viscosity	newton-second per sq meter	$N{\cdot}s/m^2$	
Electric capacitance	farad	F	$(A \cdot s/V)$
Electric charge	coulomb	C	$(A \cdot s)$
Electric field strength	volt per meter	V/m	
Electric resistance	ohm		(V/A)
Entropy	joule per kelvin	J/K	
Force	newton	N	$(kg \cdot m/s^2)$
Frequency	hertz	hz	(s^{-1})
Illumination	lux	lx	(lm/m^2)
Inductance	henry	H	$(V \cdot s/A)$
Kinematic viscosity	sq meter per second	m^2/s	
Luminance	candela per sq meter	cd/m^2	
Luminous flux	lumen	lm	$(cd \cdot sr)$
Magnetomotive force	ampere	A	
Magnetic field strength	ampere per meter	A/m	
Magnetic flux	weber	Wb	$(V \cdot s)$
Magnetic flux density	tesla	T	(Wb/m^2)
Power	watt	W	(J/s)
Pressure	newton per square meter	N/m^2	
Radiant intensity	watt per steradian	W/sr	
Specific heat	joule per kilogram kelvin	J/kg K	
Thermal conductivity	watt per meter kelvin	W/m K	
Velocity	meter per second	m/s	
Volume	cubic meter	m^3	
Voltage, potential difference, electromotive force	volt	V	(W/A)
Wave number	1 per meter	m^{-1}	
Work, energy, quantity of heat	joule	J	$(N \cdot m)$

PREFIX NAMES OF MULTIPLES AND SUBMULTIPLES OF UNITS

Decimal equivalent	*Prefix*	*Pronunciation*	*Symbol*	*Exponential expression*
1,000,000,000,000	tera	tĕr′ȧ	T	10^{+12}
1,000,000,000	giga	jĭ′gȧ	G	10^{+9}
1,000,000	mega	mĕg′ȧ	M	10^{+6}
1,000	kilo	kĭl′ō	k	10^{+3}
100	hecto	hĕk′tō	h	10^{+2}
10	deka	dĕk′ȧ	da	10
0.1	deci	dĕs′ĭ	d	10^{-1}
0.01	centi	sĕn′tĭ	c	10^{-2}
0.001	milli	mĭl′ĭ	m	10^{-3}
0.000 001	micro	mī′krō	μ	10^{-6}
0.000 000 001	nano	năn′ō	n	10^{-9}
0.000 000 000 001	pico	pē′kō	p	10^{-12}
0.000 000 000 000 001	femto	fĕm′tō	f	10^{-15}
0.000 000 000 000 000 001	atto	ăt′tō	a	10^{-18}

Appendix E. Miscellaneous

TABLE E.1 Sizes and Allowable Unit Stresses for Softwood Lumber

American Softwood Lumber Standard. A voluntary standard for softwood lumber has been developing since 1922. Five editions of Simplified Practice Recommendation R16 were issued from 1924–53 by the Department of Commerce; the present NBS voluntary Product Standard PS 20-70, "American Softwood Lumber Standard", was issued in 1970. It was supported by the American Lumber Standards Committee, which functions through a widely representative National Grading Rule Committee.

Part a. Nominal and Minimum-Dressed Sizes of Lumber*

Item	*Thicknesses*			*Face widths*		
	Nominal	*Minimum-dressed*		*Nominal*	*Minimum-dressed*	
		Dry,[a] *inches*	*Green, inches*		*Dry,*[a] *inches*	*Green, inches*
Boards[b]				2	$1\frac{1}{2}$	$1\frac{9}{16}$
				3	$2\frac{1}{2}$	$2\frac{9}{16}$
				4	$3\frac{1}{2}$	$3\frac{9}{16}$
				5	$4\frac{1}{2}$	$4\frac{5}{8}$
	1	$\frac{3}{4}$	$\frac{25}{32}$	6	$5\frac{1}{2}$	$5\frac{5}{8}$
				7	$6\frac{1}{2}$	$6\frac{5}{8}$
	$1\frac{1}{4}$	1	$1\frac{1}{32}$	8	$7\frac{1}{4}$	$7\frac{1}{2}$
				9	$8\frac{1}{4}$	$8\frac{1}{2}$
	$1\frac{1}{2}$	$1\frac{1}{4}$	$1\frac{9}{32}$	10	$9\frac{1}{4}$	$9\frac{1}{2}$
				11	$10\frac{1}{4}$	$10\frac{1}{2}$
				12	$11\frac{1}{4}$	$11\frac{1}{2}$
				14	$13\frac{1}{4}$	$13\frac{1}{2}$
				16	$15\frac{1}{4}$	$15\frac{1}{2}$
Dimension				2	$1\frac{1}{2}$	$1\frac{9}{16}$
				3	$2\frac{1}{2}$	$2\frac{9}{16}$
				4	$3\frac{1}{2}$	$3\frac{9}{16}$
	2	$1\frac{1}{2}$	$1\frac{9}{16}$	5	$4\frac{1}{2}$	$4\frac{5}{8}$
	$2\frac{1}{2}$	2	$2\frac{1}{16}$	6	$5\frac{1}{2}$	$5\frac{5}{8}$
	3	$2\frac{1}{2}$	$2\frac{9}{16}$	8	$7\frac{1}{4}$	$7\frac{1}{2}$
	$3\frac{1}{2}$	3	$3\frac{1}{16}$	10	$9\frac{1}{4}$	$9\frac{1}{2}$
				12	$11\frac{1}{4}$	$11\frac{1}{2}$
				14	$13\frac{1}{4}$	$13\frac{1}{2}$
				16	$15\frac{1}{4}$	$15\frac{1}{2}$
Dimension				2	$1\frac{1}{2}$	$1\frac{9}{16}$
				3	$2\frac{1}{2}$	$2\frac{9}{16}$
				4	$3\frac{1}{2}$	$3\frac{9}{16}$
				5	$4\frac{1}{2}$	$4\frac{5}{8}$
	4	$3\frac{1}{2}$	$3\frac{9}{16}$	6	$5\frac{1}{2}$	$5\frac{5}{8}$
	$4\frac{1}{2}$	4	$4\frac{1}{16}$	8	$7\frac{1}{4}$	$7\frac{1}{2}$
				10	$9\frac{1}{4}$	$9\frac{1}{2}$
				12	$11\frac{1}{4}$	$11\frac{1}{2}$
				14		$13\frac{1}{2}$
				16		$15\frac{1}{2}$
Timbers	5 and thicker		$\frac{1}{2}$ off	5 and wider		$\frac{1}{2}$ off

[a] Maximum moisture content of 19% or less.

[b] Boards less than the minimum thickness for 1 in. nominal but $\frac{5}{8}$ in. or greater thickness dry ($\frac{11}{16}$ in. green) may be regarded as American Standard Lumber, but such boards shall be marked to show the size and condition of seasoning at the time of dressing. They shall also be distinguished from 1-in. boards on invoices and certificates.

* Reprinted from: "American Softwood Lumber Standard", NBS PS 20-70, National Bureau of Standards, 1970; available from Superintendent of Documents.

Note: This table applies to boards, dimensional lumber, and timbers. The thicknesses apply to all widths and all widths to all thicknesses.

TABLE E.1 (continued) Sizes and Allowable Unit Stresses for Softwood Lumber

The "American Softwood Lumber Standard", PS 20-70, gives the size and grade provisions for American Standard lumber and describes the organization and procedures for compliance enforcement and review. It lists commercial name classifications and complete definitions of terms and abbreviations.

Eleven softwood species are listed in PS 20-70, viz., cedar, cypress, fir, hemlock, juniper, larch, pine, redwood, spruce, tamarack, and yew. Five dimensional tables show the standard dressed (surface planed) sizes for almost all types of lumber, including matched tongue-and-grooved and shiplapped flooring, decking, siding, etc. Dry or seasoned lumber must have 19% or less moisture content, with an allowance for shrinkage of 0.7–1.0% for each four points of moisture content below the maximum. Green lumber has more than 19% moisture. Table A illustrates the relation between nominal size and dressed or green sizes.

National Design Specification. Part b is condensed from the 1971 edition of "National Design Specification for Stress-Grade Lumber and Its Fastenings," as recommended and published by the National Forest Products Association, Washington, D.C. This specification was first issued by the National Lumber Manufacturers Association in 1944; subsequent editions have been issued as recommended by the Technical Advisory Committee. The 1971 edition is a 65-page bulletin with a 20-page supplement giving "Allowable Unit Stresses, Structural Lumber," from which Part b has been condensed. The data on working stresses in this Supplement have been determined in accordance with the corresponding ASTM Standards, D245-70 and D2555-70.

Part b. Species, Sizes, Allowable Stresses, and Modulus of Elasticity of Lumber

Normal loading conditions: Moisture content not over 19%, No. 1 grade, visual grading. To convert psi to N/m^2, multiply by 6 895.

Species[a]	*Sizes, nominal*	*Typical grading agency, 1971*[b]	*Allowable unit stresses, psi*[d]				*Modulus of elasticity, psi*
			Extreme fiber in bending[c]	*Tension parallel to grain*	*Compression perpendicular*	*Compression parallel*	
CEDAR							
Northern white	2 × 4	NL, NH	1 100	600	205	675	800 000
	2 or 4 × 6+	NL, NH	1 000	575	205	675	800 000
Western	2 × 4	NC	1 450	725	285	975	1 100 000
	2 or 4 × 6+	NC, WW	1 250	725	285	975	1 100 000
FIR							
Balsam	2 × 4	NL, NH	1 300	675	170	825	1 200 000
	2 or 4 × 6+	NL, NH	1 150	650	170	825	1 200 000
Douglas (larch)	2 × 4	WC, NC	2 400	1 200	385	1 250	1 800 000
	2 or 4 × 6+	WC, NC	1 750	1 000	385	1 250	1 800 000
HEMLOCK							
Eastern (tamarack)	2 × 4	NL, NH	1 750	900	365	1 050	1 300 000
	2 or 4 × 6+	NL, NH	1 500	875	365	1 050	1 300 000
Hem-fir	2 × 4	WC, NC	1 600	825	245	1 000	1 500 000
	2 or 4 × 6+	WC, NC	1 400	800	245	1 000	1 500 000
Mountain	2 × 4	WC, WW	1 700	850	370	1 000	1 300 000
	2 or 4 × 6+	WC, WW	1 450	850	370	1 000	1 300 000
PINE							
Idaho white	2 × 4	WW	1 400	725	240	925	1 400 000
	2 or 4 × 6+	WW	1 200	700	240	925	1 400 000
Lodgepole	2 × 4	WW	1 500	750	250	900	1 300 000
	2 or 4 × 6+	WW	1 300	750	250	900	1 300 000

TABLE E.1 (continued) Sizes and Allowable Unit Stresses for Softwood Lumber

Species[a]	*Sizes, nominal*	*Typical grading agency, 1971*[b]	*Allowable unit stresses, psi*[d]				*Modulus of elasticity, psi*
			Extreme fiber in bending[c]	*Tension parallel to grain*	*Compression perpendicular*	*Compression parallel*	
PINE *(continued)*							
Northern	2 × 4	NL, NH	1 600	825	280	975	1 400 000
	2 or 4 × 6+	NL, NH	1 400	800	280	975	1 400 000
Ponderosa (sugar)	2 × 4	WW, NC	1 400	700	250	850	1 200 000
	2 or 4 × 6+	WW, NC	1 200	700	250	850	1 200 000
Red	2 × 4	NC	1 350	700	280	825	1 300 000
	2 or 4 × 6+	NC	1 150	675	280	825	1 300 000
Southern	2 × 4	SP	2 000	1 000	405	1 250	1 800 000
	2 or 4 × 6+	SP	1 750	1 000	405	1 250	1 800 000
REDWOOD							
California	2 or 4 × 2 or 4	RI	1 950	1 000	425	1 250	1 400 000
	2 or 4 × 6 to 12	RI	1 700	1 000	425	1 250	1 400 000
SPRUCE							
Eastern	2 × 4	NL, NH	1 500	750	255	900	1 400 000
	2 or 4 × 6+	NL, NH	1 250	750	255	900	1 400 000
Engelmann	2 × 4	WW	1 300	675	195	725	1 200 000
	2 or 4 × 6+	WW	1 150	650	195	725	1 200 000
Sitka	2 × 4	WC	1 550	775	280	925	1 500 000
	2 or 4 × 6+	WC	1 300	775	280	925	1 500 000

Note: Allowable unit stresses in horizontal shear are in the range of 60–100 psi for No. 1 grade.

[a] Grade designations are not entirely uniform. Values in the table apply approximately to "No. 1." There is seldom more than one better grade than No. 1, and this may be designated as select, select structural, dense, or heavy. In addition to lower grades 2 and 3, there may be other lower grades, designated as construction, standard, stud, and utility. In bending and tension the allowable unit stresses in the lowest recognized grade (utility) are of the order of $\frac{1}{8}$ to $\frac{1}{6}$ of the allowable stresses for grade No. 1. The tabular values for allowable bending stress are for the extreme fiber in "repetitive member uses," and edgewise use. The original tables give correction factors, which are less than unity for moist locations and for short-time loading; they are greater than unity if the moisture content of the wood in service is 15% or less. In general, all data apply to uses within covered structures. From the extensive tables, only the No. 1 grade in nominal 2 × 4 size and 2-in. or 4-in. planks, 6 in., and wider have been selected for illustration.

In a few cases the allowable stresses specified for the Canadian products will vary slightly from those given here for the same species by the U.S. agencies.

[b] Grading agencies represented by letters in this column are as follows:

NC = National Lumber Grades Authority (a Canadian agency)
NH = Northern Hardwood and Pine Manufacturers Association
NL = Northern Lumber Manufacturers Association
RI = Redwood Inspection Service
SP = Southern Pine Inspection Bureau
WC = West Coast Lumber Inspection Bureau
WW = Western Wood Products Association

[c] It is assumed that all members are so framed, anchored, tied, and braced that they have the necessary rigidity.

[d] For short term loads, these values may be increased: add 15% for 2-month snow load; add 33% for wind or earthquake; add 100% for impact load.

REFERENCES

"Wood Handbook", Handbook No. 72, U.S. Department of Agriculture, 1955.

"Timber Construction Manual", American Institute of Timber Construction, John Wiley & Sons, Inc., 1966.

"National Design Specification for Stress-Grade Lumber and Its Fastenings", National Forest Products Association, Washington D.C., 1971.

TABLE E.2 Standard Grades of Bolts

Part a: SAE Grades for Steel Bolts

SAE grade no.	Size range incl.	Proof strength,† kpsi	Tensile strength,† kpsi	Material	Head marking
1	¼–1½			Low- or medium-carbon steel	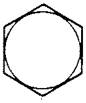
2	¼–¾	55	74		
	⅞–1½	33	60		
5	¼–1	85	120	Medium-carbon steel, Q & T	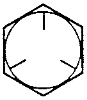
	1⅛–1½	74	105		
5.2	¼–1	85	120	Low-carbon martensite steel, Q & T	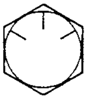
7	¼–1½	105	133	Medium-carbon alloy steel, Q & T‡	
8	¼–1½	120	150	Medium-carbon alloy steel, Q & T	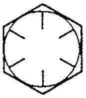
8.2	¼–1	120	150	Low-carbon martensite steel, Q & T	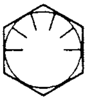

†Minimum values.

‡Roll threaded after heat treatment.

SOURCES: See "Helpful Hints," by Russell, Burdsall & Ward Corp., Mentor, Ohio 44060; and Chap. 23.

Part b: ASTM Grades for Steel Bolts

ASTM designation	Size range incl.	Proof strength,† kpsi	Tensile strength,† kpsi	Material	Head marking
A307	$\frac{1}{4}$ to 4			Low-carbon steel	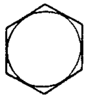
A325 type 1	$\frac{1}{2}$ to 1 $1\frac{1}{8}$ to $1\frac{1}{2}$	85 74	120 105	Medium-carbon steel, Q & T	
A325 type 2	$\frac{1}{2}$ to 1 $1\frac{1}{8}$ to $1\frac{1}{2}$	85 74	120 105	Low-carbon martensite steel, Q & T	
A325 type 3	$\frac{1}{2}$ to 1 $1\frac{1}{8}$ to $1\frac{1}{2}$	85 74	120 105	Weathering steel, Q & T	
A354 grade BC				Alloy steel, Q & T	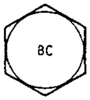
A354 grade BD	$\frac{1}{4}$ to 4	120	150	Alloy steel, Q & T	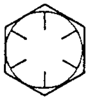
A449	$\frac{1}{4}$ to 1 $1\frac{1}{8}$ to $1\frac{1}{2}$ $1\frac{3}{4}$ to 3	85 74 55	120 105 90	Medium-carbon steel, Q & T	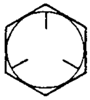
A490type	$\frac{1}{2}$ to $1\frac{1}{2}$	120	150	Alloy steel, Q & T	
A490type 3				Weathering steel, Q & T	

† Minimum value.

Sources: See "Helpful Hints," by Russell,Burdsall&Ward Corp.,Mentor,Ohio 44060; and Chapter 23.

TABLE E.2 (continued) Standard Grades of Bolts

Part c: Metric Mechanical Property Classes for Steel Bolts, Screws, and Studs

Property class	Size range incl.	Proof strength, MPa	Tensile strength, MPa	Material	Head marking
4.6	M5–M36	225	400	Low- or medium-carbon steel	
4.8	M1.6–M16	310	420	Low- or medium-carbon steel	
5.8	M5–M24	380	520	Low- or medium-carbon steel	
8.8	M16–M36	600	830	Medium-carbon steel, Q & T	
9.8	M1.6–M16	650	900	Medium-carbon steel, Q & T	
10.9	M5–M36	830	1040	Low-carbon martensite steel, Q & T	
12.9	M1.6–M36	970	1220	Alloy steel, Q & T	

sources: "Helpful Hints," by Russell, Burdsall & Waard Corp,. Mentor, Ohio 44060; see also Chapter 23 and SAEstandard J1199, and ASTM standard F568.

TABLE E.3 Steel Pipe Sizes

					Areas and Weights				
					Surface Area		*Cross-sectional*		*Weight*
Nominal Pipe Size, in.	*Outside Diameter, in.*	*Schedule Number or Weight*	*Wall Thickness, in.*	*Inside Diameter, in.*	*Outside, ft² /ft*	*Inside, ft² /ft*	*Metal Area, in.²*	*Flow Area, in.²*	*Pipe lb/ft*
¾	1.05	40	0.113	0.824	0.275	0.216	0.333	0.533	1.131
		80	0.154	0.742	0.275	0.194	0.434	0.432	1.474
1	1.315	40	0.133	1.049	0.344	0.275	0.494	0.864	1.679
		80	0.179	0.957	0.344	0.250	0.639	0.719	2.172
1¼	1.660	40	0.140	1.38	0.434	0.361	0.668	1.496	2.273
		80	0.191	1.278	0.434	0.334	0.881	1.283	2.997
1½	1.900	40	0.145	1.61	0.497	0.421	0.799	2.036	2.718
		80	0.200	1.50	0.497	0.393	1.068	1.767	3.632
2	2.375	40	0.154	2.067	0.622	0.541	1.074	3.356	3.653
		80	0.218	1.939	0.622	0.508	1.477	2.953	5.022
2½	2.875	40	0.203	2.469	0.753	0.646	1.704	4.79	5.794
		80	0.276	2.323	0.753	0.608	2.254	4.24	7.662
3	3.5	40	0.216	3.068	0.916	0.803	2.228	7.30	7.58
		80	0.300	2.900	0.916	0.759	3.016	6.60	10.25
3½	4.0	40	0.226	3.548	1.047	0.929	2.680	9.89	9.11
		80	0.318	3.364	1.047	0.881	3.678	8.89	12.51
4	4.5	40	0.237	4.026	1.178	1.054	3.17	12.73	10.79
		80	0.337	3.826	1.178	1.002	4.41	11.50	14.99
5	5.563	10 S	0.134	5.295	1.456	1.386	2.29	22.02	7.77
		40	0.258	5.047	1.456	1.321	4.30	20.01	14.62
		80	0.375	4.813	1.456	1.260	6.11	18.19	20.78
6	6.625	10 S	0.134	6.357	1.734	1.664	2.73	31.7	9.29
		40	0.280	6.065	1.734	1.588	5.58	28.9	18.98
		80	0.432	5.761	1.734	1.508	8.40	26.1	28.58
8	8.625	10 S	0.148	8.329	2.258	2.180	3.94	54.5	13.40
		30	0.277	8.071	2.258	2.113	7.26	51.2	24.7
		80	0.500	7.625	2.258	1.996	12.76	45.7	43.4
10	10.75	10 S	0.165	10.420	2.81	2.73	5.49	85.3	18.7
		30	0.279	10.192	2.81	2.67	9.18	81.6	31.2
		Extra heavy	0.500	9.750	2.81	2.55	16.10	74.7	54.7
12	12.75	10 S	0.180	12.390	3.34	3.24	7.11	120.6	24.2
		30	0.330	12.09	3.34	3.17	12.88	114.8	43.8
		Extra heavy	0.500	11.75	3.34	3.08	19.24	108.4	65.4
14	14.0	10	0.250	13.5	3.67	3.53	10.80	143.1	36.7
		Standard	0.375	13.25	3.67	3.47	16.05	137.9	54.6
		extra heavy	0.500	13.00	3.67	3.40	21.21	132.7	72.1
16	16.0	10	0.250	15.50	4.19	4.06	12.37	188.7	42.1
		Standard	0.375	15.25	4.19	3.99	18.41	182.7	62.6
		extra heavy	0.500	15.00	4.19	3.93	24.35	176.7	82.8
18	18.0	10 S	0.188	17.624	4.71	4.61	10.52	243.9	35.8
		Standard	0.375	17.25	4.71	4.52	20.76	233.7	70.6
		extra heavy	0.500	17.00	4.71	4.45	27.49	227.0	93.5
20	20.0	10 S	0.218	19.564	5.24	5.12	13.55	300.6	46.1
		Standard	0.375	19.25	5.24	5.04	23.12	291	78.6
		extra heavy	0.500	19.00	5.24	4.97	30.6	283.5	104.1
22	22.0	10	0.250	21.50	5.76	5.63	17.1	363	58.1
		Standard	0.375	21.25	5.76	5.56	25.5	355	86.6
		extra heavy	0.500	21.00	5.76	5.50	33.8	346	114.8
24	24.0	10	0.250	23.50	6.28	6.15	18.7	434	63.4
		Standard	0.375	23.25	6.28	6.09	27.8	425	94.6
		extra heavy	0.500	23.00	6.28	6.02	36.9	415	125.5
26	26.0	Standard	0.375	25.25	6.81	6.61	30.2	501	102.6
		extra heavy	0.500	25.00	6.81	6.54	40.1	491	136.2
30	30.0	10	0.312	29.376	7.85	7.69	29.1	678	98.9
		Standard	0.375	29.250	7.85	7.66	34.9	672	118.7
		extra heavy	0.500	29.00	7.85	7.59	46.3	661	157.6
34	34.0	Standard	0.375	33.250	8.90	8.70	39.6	868	134.7
		extra heavy	0.500	33.00	8.90	8.64	52.6	855	178.9
36	36.0	Standard	0.375	35.25	9.42	9.23	42.0	976	142.7
		extra heavy	0.500	35.00	9.42	9.16	55.8	962	189.6
42	42.0	Standard	0.375	41.25	11.0	10.8	49.0	1336	166.7
		extra heavy	0.500	41.00	11.0	10.73	65.2	1320	221.6

*Reprinted with permission, from: “Design Properties of Pipe”, ©1958, Chemetron Corporation.

TABLE E.4 Commercial Copper Tubing*

The following table gives dimensional data and weights of copper tubing used for automotive, plumbing, refrigeration, and heat exchanger services. For additional data see the standards handbooks of the Copper Development Association, Inc., the ASTM standards, and the "SAE Handbook."

Dimensions in this table are actual specified measurements, subject to accepted tolerances. Trade size designations are usually by actual OD, except for water and drainage tube (plumbing), which measures 1/8-in. larger OD. A 1/2-in. plumbing tube, for example, measures 5/8-in. OD, and 2-in. plumbing tube measures 2 1/8-in. OD.

KEY TO GAGE SIZES

Standard-gage wall thicknesses are listed by numerical designation (14 to 21), BWG or Stubs gage. These gage sizes are standard for tubular heat exchangers. The letter *A* designates SAE tubing sizes for automotive service. Letter designations *K* and *L* are the common sizes for plumbing services, soft or hard temper.

OTHER MATERIALS

These same dimensional sizes are also common for much of the commercial tubing available in aluminum, mild steel, brass, bronze, and other alloys. Tube weights in this table are based on copper at 0.323 lb/in^3. For other materials the weights should be multiplied by the following approximate factors:

aluminum	0.30	monel	0.96
mild steel	0.87	stainless steel	0.89
brass	0.95		

Size, OD		*Wall Thickness*			*Flow Area*		*Metal*	*Surface Area*		
in.	*mm*	*in.*	*mm*	*gage*	*in.*^{2}	*mm*^{2}	*Area, in.*^{2}	*Inside, ft*^{2}*/ft*	*Outside, ft*^{2}*/ft*	*Weight, lb/ft*
1/8	3.2	.030	0.76	A	0.003	1.9	0.012	0.017	0.033	0.035
3/16	4.76	.030	0.76	A	0.013	8.4	0.017	0.034	0.049	0.058
1/4	6.4	.030	0.76	A	0.028	18.1	0.021	0.050	0.066	0.080
1/4	6.4	.049	1.24	18	0.018	11.6	0.031	0.038	0.066	0.120
5/16	7.94	.032	0.81	21A	0.048	31.0	0.028	0.065	0.082	0.109
3/8	9.53	.032	0.81	21A	0.076	49.0	0.033	0.081	0.098	0.134
3/8	9.53	.049	1.24	18	0.060	38.7	0.050	0.072	0.098	0.195
1/2	12.7	.032	0.81	21A	0.149	96.1	0.047	0.114	0.131	0.182
1/2	12.7	.035	0.89	20L	0.145	93.6	0.051	0.113	0.131	0.198
1/2	12.7	.049	1.24	18K	0.127	81.9	0.069	0.105	0.131	0.269
1/2	12.7	.065	1.65	16	0.108	69.7	0.089	0.97	0.131	0.344
5/8	15.9	.035	0.89	20A	0.242	156	0.065	0.145	0.164	0.251
5/8	15.9	.040	1.02	L	0.233	150	0.074	0.143	0.164	0.285
5/8	15.9	.049	1.24	18K	0.215	139	0.089	0.138	0.164	0.344
3/4	19.1	.035	0.89	20A	0.363	234	0.079	0.178	0.196	0.305
3/4	19.1	.042	1.07	L	0.348	224	0.103	0.174	0.196	0.362
3/4	19.1	.049	1.24	18K	0.334	215	0.108	0.171	0.196	0.418
3/4	19.1	.065	1.65	16	0.302	195	0.140	0.162	0.196	0.542
3/4	19.1	.083	2.11	14	0.268	173	0.174	0.151	0.196	0.674
7/8	22.2	.045	1.14	L	0.484	312	0.117	0.206	0.229	0.455
7/8	22.2	.065	1.65	16K	0.436	281	0.165	0.195	0.229	0.641
7/8	22.2	.083	2.11	14	0.395	255	0.206	0.186	0.229	0.800
1	25.4	.065	1.65	16	0.594	383	0.181	0.228	0.262	0.740
1	25.4	.083	2.11	14	0.546	352	0.239	0.218	0.262	0.927
1 1/8	28.6	.050	1.27	L	0.825	532	0.176	0.268	0.294	0.655

*Compiled and computed.

TABLE E.4 (continued) Commercial Copper Tubing*

Size, OD		*Wall Thickness*			*Flow Area*		*Metal Area, in.²*	*Surface Area*		*Weight, lb/ft*
in.	*mm*	*in.*	*mm*	*gage*	*in.²*	*mm²*		*Inside, ft²/ft*	*Outside, ft²/ft*	
1 1/8	28.6	.065	1.65	16K	0.778	502	0.216	0.261	0.294	0.839
1 1/4	31.8	.065	1.65	16	0.985	636	0.242	0.293	0.327	0.938
1 1/4	31.8	.083	2.11	14	0.923	596	0.304	0.284	0.327	1.18
1 3/8	34.9	.055	1.40	L	1.257	811	0.228	0.331	0.360	0.884
1 3/8	34.9	.065	1.65	16K	1.217	785	0.267	0.326	0.360	1.04
1 1/2	38.1	.065	1.65	16	1.474	951	0.294	0.359	0.393	1.14
1 1/2	38.1	.083	2.11	14	1.398	902	0.370	0.349	0.393	1.43
1 5/8	41.3	.060	1.52	L	1.779	1148	0.295	0.394	0.425	1.14
1 5/8	41.3	.072	1.83	K	1.722	1111	0.351	0.388	0.425	1.36
2	50.8	.083	2.11	14	2.642	1705	0.500	0.480	0.628	1.94
2	50.8	.109	2.76	12	2.494	1609	0.620	0.466	0.628	2.51
2 1/8	54.0	.070	1.78	L	3.095	1997	0.449	0.520	0.556	1.75
2 1/8	54.0	.083	2.11	14K	3.016	1946	0.529	0.513	0.556	2.06
2 5/8	66.7	.080	2.03	L	4.77	3078	0.645	0.645	0.687	2.48
2 5/8	66.7	.095	2.41	13K	4.66	3007	0.760	0.637	0.687	2.93
3 1/8	79.4	.090	2.29	L	6.81	4394	0.950	0.771	0.818	3.33
3 1/8	79.4	.109	2.77	12K	6.64	4284	1.034	0.761	0.818	4.00
3 5/8	92.1	.100	2.54	L	9.21	5942	1.154	0.897	0.949	4.29
3 5/8	92.1	.120	3.05	11K	9.00	5807	1.341	0.886	0.949	5.12
4 1/8	104.8	.110	2.79	L	11.92	7691	1.387	1.022	1.080	5.38
4 1/8	104.8	.134	3.40	10K	11.61	7491	1.682	1.009	1.080	6.51

TABLE E.5 Standard Gages for Wire, Sheet, and Twist Drills

Gage	(1) Mfrs. steel sheet	(2) USS steel sheet (old)	(3) Birmingham or Stub	(4) W & M or Roebling steel wire	(5) AWG or B & S non-ferrous wire or sheet	Numbered twist drills	Copper wire (AWG)			Sheet steel
							Circular mils	Ohms/1000 ft, 77°F	Lb/1000 ft	Lb/sq ft
0000000		0.500		0.4900						20.00
000000		0.469		0.4615	0.580					18.75
00000		0.438		0.4305	0.516					17.50
0000		0.406	.454	0.3938	0.460		212,000	0.0500	641.0	16.25
000		0.375	.425	0.3625	0.410		168,000	0.0630	508.0	15
00		0.344	.380	0.3310	0.365		133,000	0.0795	403.0	13.75
0		0.313	.340	0.3065	0.325		106,000	0.100	319.0	12.50
1		0.281	.300	0.2830	0.289	0.2280	83,700	0.126	253.0	11.25
2		0.266	.284	0.2625	0.258	0.2210	66,400	0.159	201.0	10.625
3	.2391	0.250	.259	0.2437	0.229	0.2130	52,600	0.201	159.0	10
4	.2242	0.234	.238	0.2253	0.204	0.2090	41,700	0.253	126.0	9.375
5	.2092	0.219	.220	0.2070	0.182	0.2055	33,100	0.319	100.0	8.75
6	.1943	0.203	.203	0.1920	0.162	0.2040	26,300	0.403	79.5	8.125
7	.1793	0.188	.180	0.1770	0.144	0.2010	20,800	0.508	63.0	7.5
8	.1644	0.172	.165	0.1620	0.128	0.1990	16,500	0.641	50.0	6.875
9	.1495	0.156	.148	0.1483	0.114	0.1960	13,100	0.808	39.6	6.25
10	.1345	0.141	.134	0.1350	0.102	0.1935	10,400	1.02	31.4	5.625
11	.1196	0.125	.120	0.1205	0.0907	0.1910	8,230	1.28	24.9	5
12	.1046	0.109	.109	0.1055	0.0808	0.1890	6,530	1.62	19.8	4.375
13	.0897	0.0937	.095	0.0915	0.0720	0.1850	5,180	2.04	15.7	3.75
14	.0747	0.0781	.083	0.0800	0.0641	0.1820	4,110	2.58	12.4	3.125
15	.0673	0.0703	.072	0.0720	0.0571	0.1800	3,260	3.25	9.86	2.813
16	.0598	0.0625	.065	0.0625	0.0508	0.1770	2,580	4.09	7.82	2.5
17	.0538	0.0562	.058	0.0540	0.0453	0.1730	2,050	5.16	6.20	2.25
18	.0478	0.0500	.049	0.0475	0.0403	0.1695	1,620	6.51	4.92	2
19	.0418	0.0437	.042	0.0410	0.0359	0.1660	1,290	8.21	3.90	1.75
20	.0359	0.0375	.035	0.0348	0.0320	0.1610	1,020	10.4	3.09	1.50
21	.0329	0.0344	.032	0.0318	0.0285	0.1590	810	13.1	2.45	1.375
22	.0299	0.0312	.028	0.0286	0.0253	0.1570	642	16.5	1.94	1.25
23	.0269	0.0281	.025	0.0258	0.0226	0.1540	509	20.8	1.54	1.125
24	.0239	0.0250	.022	0.0230	0.0201	0.1520	404	26.2	1.22	1
25	.0209	0.0219	.020	0.0204	0.0179	0.1495	320	33.0	0.970	0.875
26	.0179	0.0187	.018	0.0181	0.0159	0.1470	254	41.6	0.769	0.75
27	.0164	0.0172	.016	0.0173	0.0142	0.1440	202	52.5	0.610	0.6875
28	.0149	0.0156	.014	0.0162	0.0126	0.1405	160	66.2	0.484	0.625
29	.0135	0.0141	.013	0.0150	0.0113	0.1360	127	83.4	0.384	0.5625
30	.0120	0.0125	.012	0.0140	0.0100	0.1285	101	105	0.304	0.5
31	.0105	0.0109	.010	0.0132	0.0089	0.1200	79.7	133	0.241	0.4375
32	.0097	0.0102	.009	0.0128	0.0080	0.1160	63.2	167	0.191	0.4063
33	.0090	0.0094	.008	0.0118	0.0071	0.1130	50.1	211	0.152	0.375
34	.0082	0.0086	.007	0.0104	0.0063	0.1110	39.8	266	0.120	0.3438
35	.0075	0.0078	.005	0.0095	0.0056	0.1100	31.5	335	0.0954	0.3125
36	.0067	0.0070	.004	0.0090	0.0050	0.1065	25.0	423	0.0757	0.2813
37	.0064	0.0066		0.0085	0.0045	0.1040	19.8	533	0.0600	0.2656
38	.0060	0.0062		0.0080	0.0040	0.1015	15.7	673	0.0476	0.25
39				0.0075	0.0035	0.0995	12.5	848	0.0377	
40				0.0070	0.0031	0.0980	9.9	1070	0.0200	
41				0.0066	0.0028	0.0960				
42				0.0062	0.0025	0.0935				
43				0.0060	0.0022	0.0890				
44				0.0058	.0020	0.0860				
45				0.0055	.0018	0.0820				
46				0.0052	.0016	0.0810				
47				0.0050	.0014	0.0785				
48				0.0048	.0012	0.0760				
49				0.0046	.0011	0.0730				
50				0.0044	.0010	0.0700				

Note: The present trend, especially for sheet and strip, is to quote thickness as decimal or fraction of an inch rather than gage number. ANSI Standard preferred thicknesses have been adopted. These preferred sizes for thickness of uncoated sheet, strip, and plate under 0.25 in. are as follows: .224, .220, .180, .160, .140, .125, .112, .100, .090, .080, .071, .063, .056, .050, .045, .040, .036, .032, .028, .025, .022, .020, .018, .016, .014, .012, .011, .010, .009, .008, .007, .006, .005, .004.

KEY: (1) Manufacturer's standard for hot- and cold-rolled uncoated carbon steel sheet and most alloy steel sheet.
(2) U.S. Standard for cold-rolled steel strip and stainless and nickel alloy sheet.
(3) Birmingham or Stub for hot-rolled carbon and alloy steel strip and tubing.
(4) Washburn and Moen, Roebling, or U.S. Steel for steel wire.
(5) American wire gage or Brown and Sharpe for non-ferrous wire, sheet, and strip.

Dimensions in approximate decimals of an inch.

TABLE E.6 Properties of Typical Gaseous and Liquid Commercial Fuels*

Gaseous fuels	*Composition, percent by volume*								*Mol wt of fuel*	*Theor. air/fuel ratio by wt*	*Higher heating value, Btu/lb$_m$*	*Density, lb$_m$/ft^3*
	H_2	*N_2*	*O_2*	*CH_4*	*CO*	*CO_2*	*C_2H_4*	*C_6H_6*				
Blast furnace gas	1.0	60.0	—	—	27.5	11.5	—	—	29.6	0.667	1,170	.075 5[a]
Blue water gas	47.3	8.3	0.7	1.3	37.0	5.4	—	—	16.4	3.759	6,550	.042 2[a]
Carb. water gas	40.5	2.9	0.5	10.2	34.0	3.0	6.1	2.8	18.3	7.299	11,350	.046 6[a]
Coal gas	54.5	4.4	0.2	24.2	10.9	3.0	1.5	1.3	12.1	10.87	16,500	.031 1[a]
Coke-oven gas	46.5	8.1	0.8	32.1	6.3	2.2	3.5	0.5	13.7	17.24	17,000	.032 6[a]
Natural gas (15.8% C_2H_6)	—	0.8	—	83.4	—	—	—	—	18.3	17.24	24,100	.045 1[a]
Producer gas	14.0	50.9	0.6	3.0	27.0	4.5	—	—	24.7	14.29	2,470	.063 6[a]

Liquid commercial fuels	*Vapor*		*Gravity, API, 60°F*	*Distillation*			*Flash point, °F*	*Viscosity, centi-stokes, 100°F*	*Mol wt of fuel*	*Theor. air/fuel ratio by wt*	*Higher heating value, Btu/lb$_m$*	*Density, lb$_m$/ft^3*
	c_p, 60°F	*c_p/c_v, 60°F*		*10%, °F*	*90%, °F*	*End point, °F*						
	(approximately)											
Gasoline	0.4	1.05	63	121	320	397	0	—	113	14.93	20,460	43.8[b]
Gasoline	0.4	1.05	63	118	330	410	0	—	126[c]	14.97	20,260	46.1[b]
Kerosene	0.4	1.05	41.9	370	510	546	130	—	154[c]	14.99	19,750	51.5[b]
Diesel oil (1-D)	0.4	1.05	42	—	550	—	100	1.4–2.5	170	15.02	19,240	54.6[b]
Diesel oil (2-D)	0.4	1.05	36	—	540–576	—	125	2.0–5.8	184	15.06	19,110	57.4[b]
Diesel oil (4-D)	0.4	1.05	—	—	—	—	130	5.8–26.4	198	14.93	18,830	59.9[b]

[a] Based on dry air at 25°C and 760 mm Hg.

[b] Based on H_2O at 60°F, 1 atm ($\rho = 62.367$ lb$_m$/ft^3).

[c] Estimated.

*Abridged from: "Engineering Experimentation", G.L. Tuve and L.C. Domholdt, McGraw-Hill Book Company, 1966; and "The Internal Combustion Engine", 2nd ed., C.F. Taylor and E.S. Taylor, International Textbook Co., 1961.

Note: For heating value in J/kg, multiply the value in Btu/lb$_m$ by 2324. For density in kg/m^3, multiply the value in lb/ft^3 by 16.02.

TABLE E.7 COMBUSTION DATA FOR HYDROCARBONS*

Hydrocarbon	*Formula*	*Higher heating value (vapor),* Btu/lb_m	*Theor. air/fuel ratio, by mass*	*Max flame speed, ft/sec*	*Adiabatic flame temp (in air), °F*	*Ignition temp (in air), °F*	*Flash point, °F*	*Flammability limits (in air), % by volume*	
PARAFFINS OR ALKANES									
Methane	CH_4	23875	17.195	1.1	3484	1301	gas	5.0	15.0
Ethane	C_2H_6	22323	15.899	1.3	3540	968–1166	gas	3.0	12.5
Propane	C_3H_8	21669	15.246	1.3	3573	871	gas	2.1	10.1
n-Butane	C_4H_{10}	21321	14.984	1.2	3583	761	−76	1.86	8.41
iso-Butane	C_4H_{10}	21271	14.984	1.2	3583	864	−117	1.80	8.44
n-Pentane	C_5H_{12}	21095	15.323	1.3	4050	588	< −40	1.40	7.80
iso-Pentane	C_5H_{12}	21047	15.323	1.2	4055	788	< −60	1.32	9.16
Neopentane	C_5H_{12}	20978	15.323	1.1	4060	842	gas	1.38	7.22
n-Hexane	C_6H_{14}	20966	15.238	1.3	4030	478	−7	1.25	7.0
Neohexane	C_6H_{14}	20931	15.238	1.2	4055	797	−54	1.19	7.58
n-Heptane	C_7H_{16}	20854	15.141	1.3	3985	433	25	1.00	6.00
Triptane	C_7H_{16}	20824	15.141	1.2	4035	849	—	1.08	6.69
n-Octane	C_8H_{18}	20796	15.093	—	—	428	56	0.95	3.20
iso-Octane	C_8H_{18}	20770	15.093	1.1	—	837	10	0.79	5.94
OLEFINS OR ALKENES									
Ethylene	C_2H_4	21636	14.807	2.2	4250	914	gas	2.75	28.6
Propylene	C_3H_6	21048	14.807	1.4	4090	856	gas	2.00	11.1
Butylene	C_4H_8	20854	14.807	1.4	4030	829	gas	1.98	9.65
iso-Butene	C_4H_8	20737	14.807	1.2	—	869	gas	1.8	9.0
n-Pentene	C_5H_{10}	20720	14.807	1.4	4165	569	—	1.65	7.70
AROMATICS									
Benzene	C_6H_6	18184	13.297	1.3	4110	1044	12	1.35	6.65
Toluene	C_7H_8	18501	13.503	1.2	4050	997	40	1.27	6.75
p-Xylene	C_8H_{10}	18663	13.663	—	4010	867	63	1.00	6.00
OTHER HYDROCARBONS									
Acetylene	C_2H_2	21502	13.297	4.6	4770	763–824	gas	2.50	81
Naphthalene	$C_{10}H_8$	17303	12.932	—	4100	959	174	0.90	5.9

*Based largely on: "Gas Engineers' Handbook", American Gas Association, Inc., Industrial Press, 1967.

REFERENCES

"American Institute of Physics Handbook", 2nd ed., D.E. Gray, Ed., McGraw-Hill Book Company, 1963.

"Chemical Engineers' Handbook", 4th ed., R.H. Perry, C.H. Chilton, and S.D. Kirkpatrick, Eds., McGraw-Hill Book Company, 1963.

"Handbook of Chemistry and Physics", 53rd ed., R.C. Weast, Ed., The Chemical Rubber Company, 1972; gives the heat of combustion of 500 organic compounds.

"Handbook of Laboratory Safety", 2nd ed., N.V. Steere, Ed., The Chemical Rubber Company, 1971.

"Physical Measurements in Gas Dynamics and Combustion", Princeton University Press, 1954.

Note: For heating value in J/kg, multiply the value in Btu/lb_m by 2324. For flame speed in m/s, multiply the value in ft/s by 0.3048.